JOURNAL OF THE ELECTROCHEMICAL SOCIETY

ELECTROCHEMICAL SCIENCE AND TECHNOLOGY

JANUARY 1977

Titanium-Containing Raney Nickel Catalyst for Hydrogen Electrodes in Alkaline Fuel Cell Systems

K. Mund, G. Richter, and F. von Sturm

Forschungslaboratorien der Siemens AG, 8520 Erlangen, Federal Republic of Germany

ABSTRACT

In alkaline hydrogen-oxygen fuel cells Raney nickel is employed as catalyst for hydrogen electrodes. The rate of anodic hydrogen conversion has been increased significantly by using a titanium-containing Raney nickel. The properties of the catalyst powder, the influence of particle diameter, and the behavior of electrodes under load are described. Impedance measurements have been used to characterize the electrodes. In fuel cell systems the supported electrodes are normally operated at current densities up to 0.4 $A \cdot cm^{-2}$; the overload current density of 1 $A \cdot cm^{-2}$ can be maintained for several hours.

The economic factors of the H_2-O_2 fuel cell are determined essentially by the costs of the catalysts employed in the electrodes. Hence it is rational for commercial applications to avoid the expensive and rare materials such as noble metals. In alkaline electrolyte, the metals nickel and silver are suitable as catalysts for the anode and the cathode, respectively (1, 2). Catalyst powder with large interior surface is used to have a large reactive surface area available. Raney nickel has thus proved useful for the H_2 electrode (2) and it is considered in detail. The active material can be depyrophorized by a slow surface oxidation and the catalytic activity could be increased by annealing at 300°C in hydrogen atmosphere (3). The attainable current density of the electrodes depends strongly on the pretreatment of Raney nickel (2, 4).

A further increment in catalytic activity could be achieved by changing from a binary Raney alloy to a ternary system in which an additional metal such as iron, molybdenum, or titanium has been alloyed to nickel and aluminum (5-7). The objective of the alloy additives is to produce ternary phases in which Ni, Al, and the additive metal are distributed homogeneously. Only such phases yield homogeneous alloy catalysts with highest activity. The additive metals lead to a lower filling of d bands and to lattice defects.

The properties of titanium-containing Raney nickel catalyst are reported here.

Experimental

Preparation of the catalyst.—The Raney alloy has a mass fraction of 50% Al; the rest consists of Ni and Ti in which the titanium content can be varied from 0 to 5%. When the liquid alloy is quenched in a water bath titanium remains dissolved in the two compounds $NiAl_3$ and Ni_2Al_3. A granulate is formed which can be powdered easily in a mill. Powder with a particle diameter of less than 50 μm is employed.

Aluminum is extracted to an extent of 95% in 6M potassium hydroxide at 80°C, titanium remains completely in the catalyst. After washing, the powder is dried in vacuum and subjected to surface oxidation by slow addition of oxygen. This causes the material to lose its pyrophorosity and can be processed readily to electrodes.

Preparation of electrodes.—The alkaline H_2-O_2 cells are constructed according to the principle of supported electrode (Fig. 1) (8, 9). The catalyst layer is supported by a finely porous, asbestos covering layer on the electrolyte side and by a metal screen on the gas

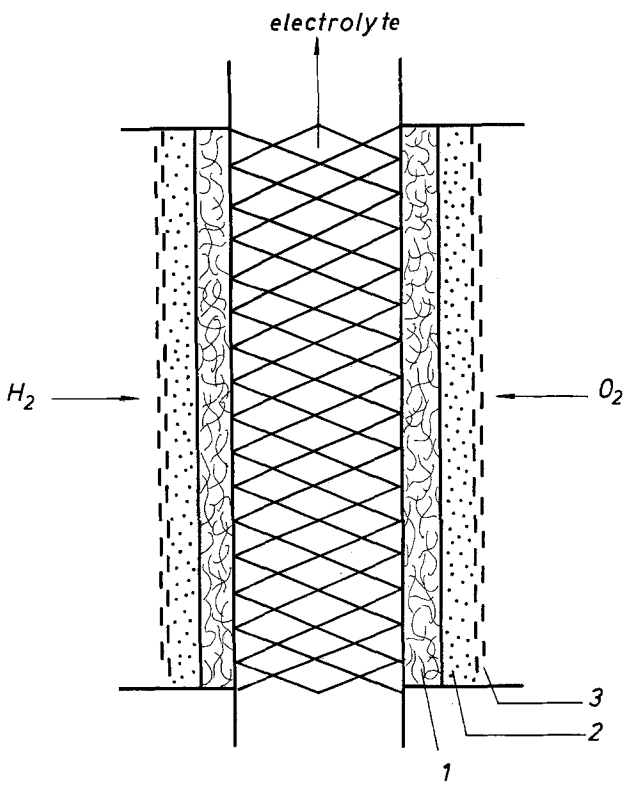


Fig. 1. Principle of a H_2-O_2 fuel cell with supported electrodes: 1, covering layer; 2, catalyst layer; and 3, contacting screen.

Key words: electrocatalyst, fuel cell, hydrogen electrode, Raney nickel, pore model, impedance measurement.

side. The electrolyte flows between both electrodes: the H_2 anode and the O_2 cathode.

Setup for electrode measurements.—If the task involves investigating Raney nickel electrodes only it is practical to use two nickel electrodes and to subject the one to anodic and the other to cathodic current. Only one reaction gas is needed in such a case. This arrangement is also employed for impedance measurements at equilibrium potential and has the advantage that no reference electrode is required (10, 11). The impedance is measured in the frequency range between 10^3 and 10^{-3} c/sec.

Description of the Catalyst Particle and the Reaction Mechanism in Supported Electrodes

The catalyst powder obtained from Raney alloy has a BET surface area of about 70 $m^2 \cdot g^{-1}$ (12). A mean pore radius r_p of $1.6 \cdot 10^{-7}$ cm is found in catalyst particles having a volume porosity p of 34%. Hence it can be estimated that there are about 10^7 pore mouths at the outer surface of a catalyst grain having a radius of $r_k = 10^{-3}$ cm. The catalyst particle is dispersed with long and narrow pores like a sponge.

Various concepts for the reaction in porous electrodes have been developed, each is valid for a special case (13-15). Our conceptions regarding the reaction mechanism in supported Raney nickel electrode can be illustrated by means of Fig. 2. The catalyst particles of the working layer are schematically represented; their micropores are filled with electrolyte. The gas can stream into the active layer via the macropores. Electrolyte bridges are formed between the particles and the particles remain in metallic contact with each other. At the gas/electrolyte interface hydrogen dissolves in the liquid. This reaction is fast and it can be assumed that the saturation concentration is always attained here. Since the outer surface of the catalyst particles is small compared with the internal surface and since the charge-transfer reaction is retarded, the dissolved gas diffuses into the pores and is chemisorbed at the pore wall. After the charge-transfer reaction, the electrons flow across the metallic phase. The electrolyte current seeks its way through the electrolyte to the counterelectrode; during this, a voltage drop at the diaphragm resistance results in the working layer.

The supply of reaction gas to the pores of the catalyst particles is essential for the polarization resistance of supported electrodes; Raney nickel is best utilized if the diffusion paths and correspondingly the pores are not long (16).

Experimental Results and Discussion

Influence of Ti content on the polarization resistance.—The steady-state current-voltage characteristics of supported Raney nickel hydrogen electrodes are linear up to a polarization of 0.1V in 6M KOH as electrolyte; the polarization resistance can therefore be used as a characteristic datum. Figure 3 shows the influence of titanium content in Raney alloy on the polarization

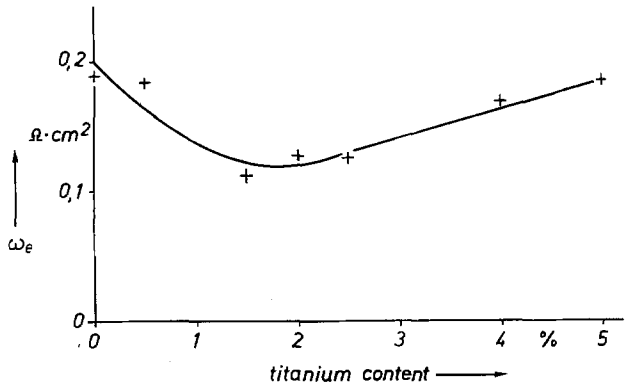


Fig. 3. Effect of Ti content of the Raney alloy on the polarization resistance of supported H_2 electrodes; catalyst loading 100 mg · cm^{-2}, 6M KOH, 80°C, $\Delta p_{H_2} = 1$ bar, *IR* drop eliminated.

resistance when operated on hydrogen. At an electrolyte temperature of 80°C and a catalyst loading of 100 mg · cm^{-2}, a minimum polarization resistance is found at a titanium content of 1.5-2% in the starting alloy. In comparison to the binary Raney alloy 50:50, the polarization resistance is halved at the minimum. The polarization resistance increases at a Ti content of more than 2%; it is assumed in this case that too much oxide covers the catalyst surface.

In all further experiments, a catalyst with a Ti content of 2% in the Raney alloy was used.

Influence of temperature.—The influence of electrolyte temperature on the current-voltage curve of a hydrogen electrode with a catalyst loading of 100 mg · cm^{-2} can be seen in Fig. 4. At 90°C and at a polarization of 60 mV, a current density of 600 mA · cm^{-2} is attained. The electrode can be loaded in steady state with a current density of 1 A · cm^{-2} for several hours. Current densities up to 100 mA · cm^{-2} are possible at room temperature.

Dependence of the polarization resistance on the particle size of catalyst powder.—The large reactive area in the interior of a catalyst particle can be utilized only when the diffusion paths of hydrogen are short. The degree of utilization of the electrocatalyst will reach the ideal value 1 if the diameter of the powder particles is not too large.

The characteristics of supported electrodes consisting of different particle fractions were investigated. Figure 5 shows at the first instance, how the extreme fractions are influenced by the working pressure. The coarse grained material can be loaded even below a pressure of 0.4 bar and the polarization resistance remains constant in spite of further rise in pressure. The polarization resistance is least at a pressure of 1 bar if powder with a diameter < 10 μm is employed.

Current-voltage curves recorded at a working pressure of 1 bar are represented in Fig. 6. They are traced at an electrolyte temperature of 80°C and by choosing

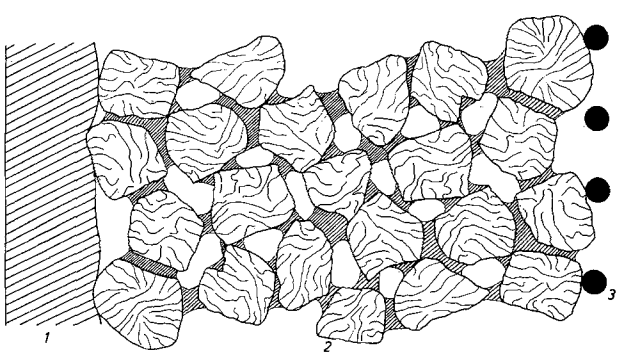


Fig. 2. Schematic representation of the working layer of a supported electrode: 1, covering layer; 2, catalyst layer; and 3, contacting screen.

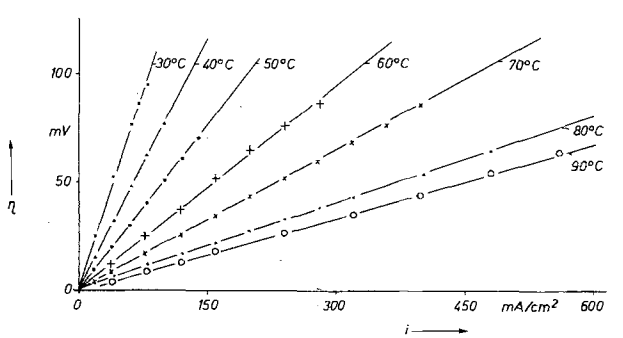


Fig. 4. Influence of electrolyte temperature on the characteristic curves of Raney-Ni-Ti 2 electrodes: catalyst loading 100 mg · cm^{-2}, 6M KOH, $\Delta p_{H_2} = 1$ bar, *IR* drop eliminated.

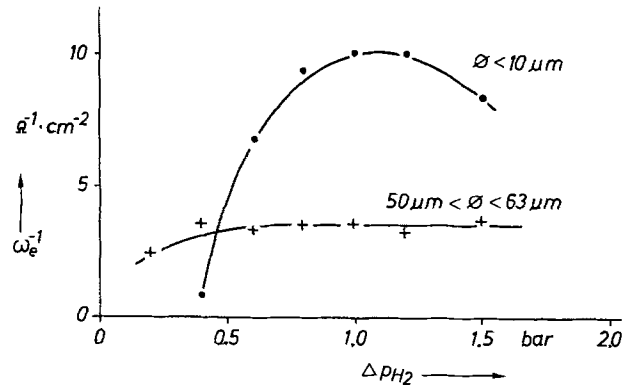


Fig. 5. Reciprocal polarization resistance ω_e^{-1} as a function of the working pressure Δp_{H_2} for two electrodes consisting of catalyst powder with the fractions < 10 µm and 50-63 µm; catalyst loading 100 mg · cm^{-2}, 6M KOH, 80°C.

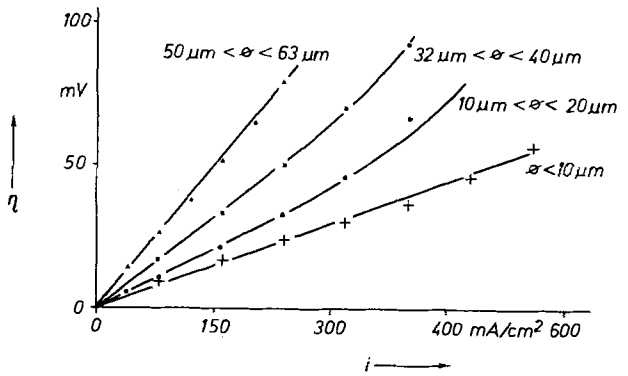


Fig. 6. Characteristic curves of supported Raney-Ni-Ti 2 electrodes with the particle diameter as parameter: catalyst loading 100 mg · cm^{-2}, 6M KOH, $\Delta p_{H_2} = 1$ bar, *IR* drop eliminated, 80°C.

a catalyst loading of 100 mg · cm^{-2}. It can be perceived that the current density of the electrode increases if a catalyst powder with smaller diameter is used.

The reciprocal polarization resistance ω_e^{-1} is plotted against the catalyst loading b at 22° and 80°C in Fig. 7 and 8, respectively. The curves were calculated after matching two parameters with the points of measurement. Considering that the polarization resistance k of the catalyst powder is independent of the potential and that a voltage drop results in the electrolyte inside the working layer of the electrode, the polarization resistance ω_e depending on the thickness d of the electrode can be expressed as (10)

$$\omega_e = \sqrt{\rho \cdot k} \cdot \coth \sqrt{\frac{\rho \cdot d^2}{k}} \qquad [1]$$

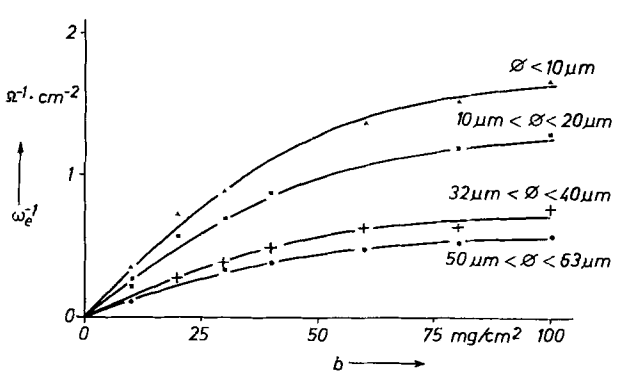


Fig. 7. Reciprocal polarization resistance ω_e^{-1} as a function of the catalyst loading for different particle fractions: 6M KOH, 22°C, $\Delta p_{H_2} = 1$ bar.

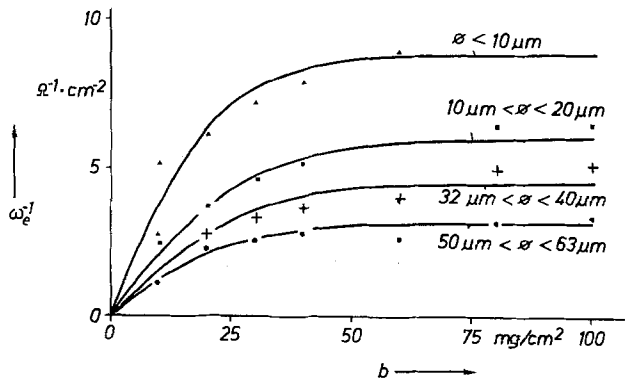


Fig. 8. Reciprocal polarization resistance ω_e^{-1} as a function of the catalyst loading for different particle fractions: 6M KOH, 80°C, $\Delta p_{H_2} = 1$ bar.

where ρ is the electrolyte resistivity inside the working layer; we denote it as diaphragm resistivity. Equation [1] states that at thinner electrodes ($\rho d^2 << k$) the polarization resistance ω_e is determined only by k and d and that for thicker electrodes ($\rho d^2 >> k$) the polarization resistance tends toward a limiting value $\sqrt{\rho k}$.

By matching of the curves with the readings the quantities ρ and k can be determined. In Fig. 9, the diaphragm resistivity ρ is plotted as a function of the mean particle radius r_k of particle fractions; the diaphragm resistance decreases if powder with smaller particle diameter is used.

Polarization resistance k is the second parameter which is recorded as a function of the mean particle radius r_k at temperatures of 22°C in Fig. 10. It is found that with larger radii k increases linearly along with the radius r_k. The traced curves were calculated with the help of a model. The model indicates that there is a limiting value k_o for small radii.

Model for steady-state operation of the hydrogen electrode.—A consideration of the stationary behavior of the electrodes has led to the assumption that with the diffusion in the electrolyte inside the pore, also a surface diffusion of chemisorbed hydrogen along the pore wall is possible (10). An estimation showed that the voltage drop in the electrolyte inside the pore is small compared with the charge-transfer polarization (11). If a single narrow pore of the catalyst particle is regarded and if in addition to the diffusion of hydrogen in pore electrolyte and along the pore wall the charge-transfer mechanism is considered, an expression is obtained for the polarization as a function of the pore current. In the polarization range up to 100 mV, an almost linear relationship between polarization and pore current results. By summing up all pores and by taking into account that the number of pores decreases

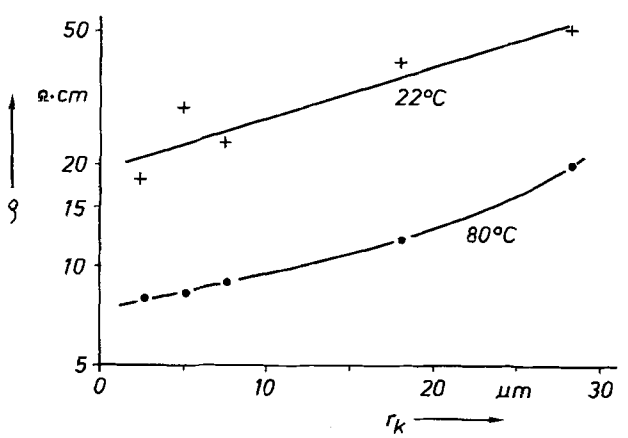


Fig. 9. Diaphragm resistivity ρ as a function of the mean particle radius r_k of the catalyst powder.

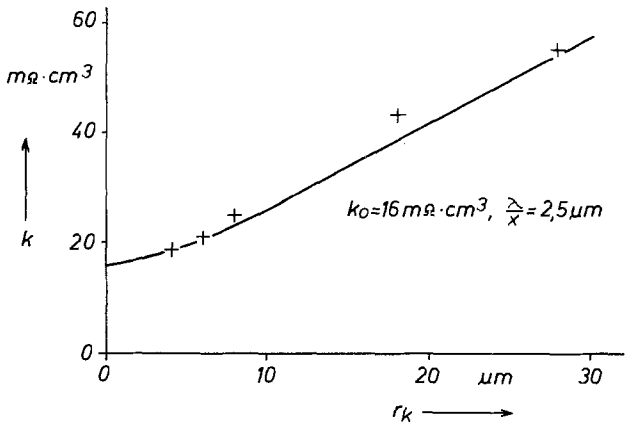


Fig. 10. Polarization resistance k of the catalyst powder as a function of the mean particle radius r_k of the catalyst powder: 6M KOH, 22°C.

from surface to interior of the sphere, an equation is obtained for the polarization resistance k of the catalyst powder (9)

$$k^{-1} = k_o^{-1} \cdot \frac{12\lambda}{r_k^4 \cdot x} \int_0^{r_k} r^2 \cdot \tanh \frac{x(r_k - r)}{r} \cdot dr \quad [2]$$

with

$$k_o = \frac{RT}{0.7\mathbf{F} \cdot \gamma \cdot f \cdot i_o} \quad [3]$$

and

$$\lambda = \sqrt{\frac{n\mathbf{F}}{2i_o} \cdot (r_p \cdot c_{vo} \cdot D_v + 2c_{so} \cdot D_s)} \quad [4]$$

where λ is a depth of penetration and it is dependent on the current density i_o, pore radius r_p, diffusion coefficients D_v and D_s for volume and surface diffusions, and saturation concentration c_{vo} and c_{so} of hydrogen in the electrolyte and at the pore wall. The integral in Eq. [2] contains the radius r inside the sphere, its radius r_k as well as the labyrinth factor x of the pores. The polarization resistance k_o can be evaluated in the case of vanishing radii r_k, it is independent of the parameters of diffusion and is determined by the BET surface area f of the catalyst, the exchange current density i_o, and the density γ of the material in the working layer.

The quotient λ/x and the exchange current density i_o remain as parameters for the calculation of the curve in Fig. 10; all other quantities are known. The value obtained for i_o at 22°C is 2 $\mu A \cdot cm^{-2}$ and at 80°C it is 27 $\mu A \cdot cm^{-2}$. If a labyrinth factor $x = 2$ is assumed, the values found for the depth λ of penetration are 5 and 4 μm, respectively.

Along with Eq. [4], these values of depth of penetration serve to compare the surface and volume diffusion. Values for the saturation concentration c_{vo} and the diffusion coefficient D_v of hydrogen in electrolyte are known ($c_{vo} \cdot D_v = 2 \cdot 10^{-12} \cdot cm^{-1} \cdot sec^{-1} \cdot mol$ at 22°C). It reveals that in the expression for λ (Eq. [4]), the term $2c_{so} \cdot D_s$ should be greater than the term $r_p \cdot c_{vo} \cdot D_v$; this denotes that more hydrogen is transported along the pore wall than in the pore electrolyte. The product $c_{so} \cdot D_s$ amounts to $2.4 \cdot 10^{-18}$ mol $\cdot sec^{-1}$. In order to utilize the catalyst well, a powder with a particle diameter of less than 20 μm should be used.

Impedance measurements for analyzing supported Raney nickel electrodes.—In addition to evaluating the steady-state current-voltage curves it is also possible to analyze the supported Raney nickel electrodes by means of impedance measurements. In order to be able to interpret the locus curves a corresponding model has to be developed.

As in the treatment of steady-state behavior the diffusion of hydrogen and the charge-transfer reaction in a single pore was considered. The pore current has

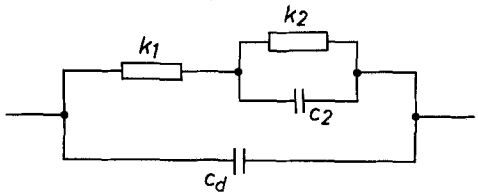


Fig. 11. Equivalent circuit diagram of the catalyst powder determined on the basis of the model.

been calculated for the case of an alternating polarization with smaller amplitudes. Only the double layer capacity remains to be included in the calculation so that the impedance at equilibrium potential can be determined. The equations for the real and imaginary parts of impedance are vague at the first instance. But if the frequency response is considered, the equivalent circuit diagram for the impedance of catalyst powder can be arrived at as represented in Fig. 11. The equivalent circuit diagram consists of two resistances k_1 and k_2 as well as two capacities c_2 and c_d. The following equations are obtained for the resistances (11)

$$k_1 = \frac{RT}{\mathbf{F}} \frac{1}{i_o \cdot f \cdot \gamma} \quad [5]$$

$$k_2 = k_1 \left(-1 + \frac{l}{\lambda} \coth \frac{l}{\lambda} \right) \quad [6]$$

Equation [5] denotes that k_1 is a charge-transfer resistance since it is dependent on the exchange current density i_o and does not contain the diffusion parameters. The pore length l and the depth λ of penetration are concealed in resistance k_2 which is in turn dependent on the exchange current density i_o and the dimensions of diffusion. If the penetration depth is large, k_2 and k_1 tend toward each other. It follows for the capacity c_2

$$c_2 = \frac{n\mathbf{F}(r_p \cdot c_{vo} + 2c_{so})}{2i_o \cdot k_1} \left(1 + \frac{\frac{l}{\lambda} - 3 \sinh \frac{l}{\lambda} \cosh \frac{l}{\lambda}}{2 \frac{l}{\lambda} \cosh^2 \frac{l}{\lambda}} \right) \quad [7]$$

In case of a low penetration depth, Eq. [7] is simplified to

$$c_2 = \frac{n\mathbf{F}}{2} \left(\frac{\mathbf{F}}{RT} \right) (r_p \cdot c_{vo} + 2c_{so}) \gamma \cdot f \quad [8]$$

The capacity c_2 is determined in this limiting case by the concentrations c_{vo} and c_{so} of hydrogen in the pore electrolyte and at the pore wall.

The course of an impedance measurement can be demonstrated by Fig. 12 and 13. At the beginning the electrodes are supplied with hydrogen at low pressure; the electrode is flooded but maintains the reversible potential. Beside the locus curve Im(Re), the imaginary part of the impedance is represented as a function of the angular frequency ω (curves 1 and 2 in Fig. 12). The locus curve traces a quadrant before running almost parallel to the ordinate. In addition to the charge-transfer resistance k_1, the double layer capacity c_d is thus obtained. If the electrode is not supplied with H_2 but with Ar instead and the working pressure Δp is maintained at 1 bar, an impedance diagram is obtained as represented in Fig. 12, curves 3 and 4. In the locus curve the slope of 45° is conspicuous and this could be understood if the complete equivalent circuit diagram of a supported electrode in Fig. 14 is examined. The diaphragm resistivity is denoted as ρ. The impedance Z contains in addition to the impedance k of the cata-

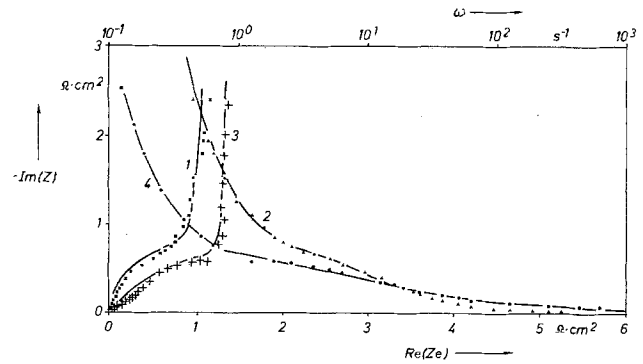


Fig. 12. Impedance measurement of an electrode with H_2 supply at low working pressure (curves 1 and 2) and with Ar supply at $\Delta p_{Ar} = 1$ bar; fraction 50-63 μm, 20 mg · cm^{-2}, 6M KOH, 22°C, $\Delta p_{H_2} = 0.2$ bar, evaluated by matching; $k_1 = 0.6\ \Omega \cdot cm^2$, $\rho d = 1.6\ \Omega \cdot cm^2$.

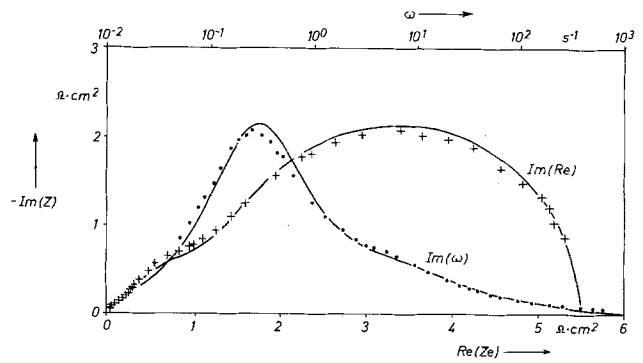


Fig. 13. In comparison to Fig. 12, the electrode is supplied with H_2 at the working pressure $\Delta p_{H_2} = 1$ bar, evaluated by matching: $k_1 = 0.6\ \Omega \cdot cm^2$, $k_2 = 1.6\ \Omega \cdot cm^2$, $c_d = 0.9$ F · cm^{-2}, $c_2 = 1.2$ F · cm^{-2}, $\rho d = 1.6\ \Omega \cdot cm^2$.

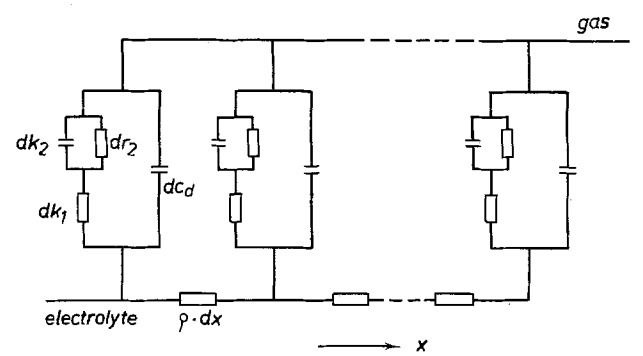


Fig. 14. Equivalent circuit diagram of a supported Raney nickel electrode. In addition to the impedance of catalyst powder, the diaphragm resistance is also considered.

lyst, the diaphragm resistivity ρ and the thickness d of the working layer

$$Z = \sqrt{\rho \cdot k}\coth\sqrt{\frac{\rho \cdot d^2}{k}} \qquad [9]$$

At high frequencies, the impedance k of the catalyst is essentially given by the double layer capacity c_d; Eq. [9] is thus simplified to

$$Z = \sqrt{j \cdot \rho \cdot \omega \cdot c_d} \qquad [10]$$

and it is now realized that the locus curve should have a slope of 45° at high frequencies. If the electrode is supplied with Ar (Fig. 12) it effects the impedance measurement at low frequencies because the capacities c_2 and c_d become dominant in the impedance k of the catalyst; the resistance k_2 is very high. The term coth in Eq. [9] becomes less significant in comparison to Eq. [1] and Eq. [9] is simplified to

$$Z = \frac{k}{d} + \rho\frac{d}{3} \qquad [11]$$

This diaphragm resistivity ρ comes into the real part of the impedance as an additive quantity and can be thus easily evaluated by comparison of locus curves in Fig. 12.

The results of impedance measurement while supplying hydrogen to the electrode under working pressure are represented in Fig. 13. The figure shows that the calculated curves could be matched satisfactorily with the five parameters of the model: k_1, k_2, ρ, c_d, and c_2. In the locus curve, the charge-transfer resistance k_1 acts at high frequencies whereas the resistance k_2 is effective at low frequencies.

From the charge-transfer resistance of 0.6 $\Omega \cdot cm^2$ and from Eq. [5], an exchange current density $i_o = 3$ $\mu A \cdot cm^{-2}$ is obtained. This value can be compared with that of 2 $\mu A \cdot cm^{-2}$ evaluated by steady-state measurements. With pure Raney nickel we found an exchange current density $i_o = 0.4$ $\mu A \cdot cm^{-2}$. From the values of capacity c_2 a surface concentration of hydrogen at the pore wall is obtained as $c_{so} = 2 \cdot 10^{-11}$ mol · cm^{-2}. The calculation of the diffusion coefficient D_s of surface diffusion is quite uncertain because it is strongly influenced by the pore length l which cannot be measured directly and which can only be estimated by the particle radius and a labyrinth factor. The value derived for the diffusion coefficient D_s ranges between $3 \cdot 10^{-8}$ and 10^{-7} cm^2 · sec^{-1}.

The considerations of steady-state and impedance measurements show that the charge-transfer phenomenon and the diffusion of hydrogen are essential for the reaction mechanism in the catalyst; the electrode, as such, is additionally governed by the diaphragm resistance.

Long-term performance and results of a cell.—The long-term performance of the catalyst is essential for the technical exploitation. At an electrolyte temperature of 80°C and at a current density of 300 mA · cm^{-2}, no rise in polarization could be observed over a period of 1000 hr. As the current density was raised to 400 mA · cm^{-2} the polarization increased by 13 $\mu V \cdot hr^{-1}$ (Fig. 15). At 500 mA · cm^{-2} the increase was 24 $\mu V \cdot hr^{-1}$. A fuel cell with an oxygen cathode containing silver as the catalyst yielded a voltage of 0.85V at a current density of 300 mA · cm^{-2} and at an electrolyte temperature of 80°C. This value dropped to 0.7V at a current density of 600 mA · cm^{-2}.

Acknowledgment

This work has been supported by the technological program of the Federal Department of Research and

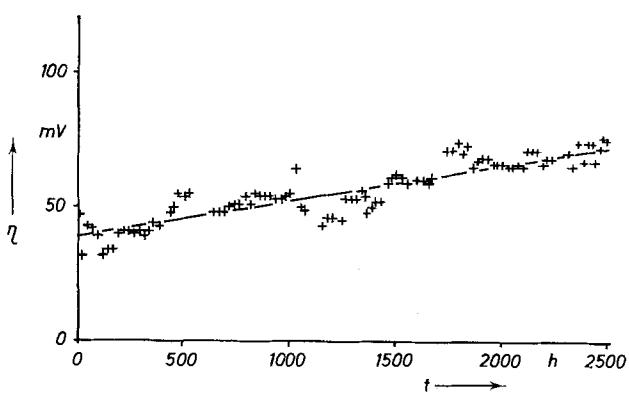


Fig. 15. Galvanostatic long-term performance test with a supported Raney-Ni-Ti 2 electrode: catalyst loading 200 mg · cm^{-2}, 6M KOH, 80°C, $\Delta p_{H_2} = 1$ bar, *IR* drop for the polarization η is eliminated. The polarization rises by 13 $\mu V \cdot hr^{-1}$ at $i = 400$ mA · cm^{-2}.

Technology of the Federal Republic of Germany. The authors alone are responsible for the contents.

Manuscript submitted June 11, 1976; revised manuscript received Aug. 16, 1976. This was Paper 23 presented at the Washington, D.C., Meeting of the Society, May 2-7, 1976.

Any discussion of this paper will appear in a Discussion Section to be published in the December 1977 JOURNAL. All discussions for the December 1977 Discussion Section should be submitted by Aug. 1, 1977.

Publication costs of this article were assisted by Siemens AG.

LIST OF SYMBOLS

b	catalyst loading
c_d	double layer capacity
c_{so}	saturation concentration of H_2 at the pore wall
c_{vo}	saturation concentration of H_2 in the pore electrolyte
c_2	capacity of the impedance
D_s	coefficient of surface diffusion
D_v	coefficient of volume diffusion
d	thickness of the electrode
$\mathbf{F}$	Faraday constant
f	surface area of catalyst powder
i	current density
i_o	exchange current density
$\mathrm{Im}(Z)$	imaginary part of the impedance
j	imaginary unit
k	polarization resistance of catalyst powder
k_o	polarization resistance of catalyst powder, not limited by diffusion
$k_{1,2}$	polarization resistance of the impedance
l	length of a pore
Δp	gas pressure
p	porosity of catalyst grain
r	spherical coordinate
r_k	radius of a catalyst particle
r_p	pore radius
R	universal gas constant
$\mathrm{Re}(Z)$	real part of the impedance
T	temperature
x	labyrinth factor
η	polarization
γ	density of catalyst in the electrode
λ	penetration depth
ρ	diaphragm resistivity
ω	angular frequency
ω_e	polarization resistance of the electrode

REFERENCES

1. F. T. Bacon, in "Fuel Cells," Vol. I, G. J. Young, Editor, Reinhold Publishing Corp., New York (1960).
2. E. Justi and A. Winsel, "Kalte Verbrennung," ("Fuel Cells"), Franz Steiner Verlag, Wiesbaden (1962).
3. F. von Sturm and A. Thieleking, German pat. 1,542,443 (1966).
4. F. von Sturm, H. Cnobloch, H. Nischik, and M. Marchetto, *Abhandl. Sächs. Akad. Wiss. Leipzig*, **5**, 165 (1968).
5. A. G. Pzhenichnikov, R. Kh. Burshtein, D. J. Lainer, N. M. Kagan, G. L. Melikova, and F. Z. Sabirov, UDSSR 147,616 (1961).
6. G. Richter, Third International Symposium of Fuel Cells, Brussels (1969).
7. F. P. Dousek and J. Jansta, *Collect. Czech. Chem. Commun.*, **36**, 2115 (1971).
8. F. v. Sturm, H. Nischik and E. Weidlich, *Ingenieur Digest*, **5**, (1966).
9. F. v. Sturm, "Elektrochemische Stromerzeugung," p. 109, Verlag Chemie, Weinheim (1969).
10. K. Mund, *Siemens Forsch. Entwicklungs-Ber.*, **4**, 1 (1975).
11. K. Mund. *ibid.*, **4**, 68 (1975).
12. H. Ewe, E. Justi, and A. Schmitt, *Electrochim. Acta*, **19**, 799 (1974).
13. S. Srinivasan and H. D. Hurwitz, *J. Chem. Phys.*, **46**, 3108 (1967).
14. J. Giner, *This Journal*, **116**, 1124 (1969).
15. A. Winsel, *Adv. Energy Convers.*, **3**, 677 (1963).
16. K. Mund and F. von Sturm, *Electrochim. Acta*, **20**, 463 (1975).

Activity Coefficients of Dilute Solutions of Lithium in Liquid Aluminum-Tin Alloys: Electromotive Force Measurements and Interpretation

Marie-Louise Saboungi* and Milton Blander

Argonne National Laboratory, Chemical Engineering Division, Argonne, Illinois 60439

ABSTRACT

The activity coefficients of Li solutions dilute in the binary alloy Al-Sn were determined from emf measurements. At $T = 949°K$, dilute solutions of Li in pure liquid Al and in pure liquid Sn follow the Nernst law. The data provide an independent and accurate evaluation of the limiting excess chemical potentials of Li in Al and in Sn, $\mu^{xs}_{Li(Al)} = -2.54$ kcal mol^{-1} (or -10.63 kJ mol^{-1}), and $\mu^{xs}_{Li(Sn)} = -12.22$ kcal mol^{-1} (or -51.14 kJ mol^{-1}), respectively. Variations of the Li activity coefficients with the solvent composition are discussed and various models for the interpretation of dilute solution activity data are reviewed. A refinement of the quasi-lattice theory is suggested where ΔA_i, the specific "bond" free energy corresponding to the changes in interactions in the equilibria (Eq. [16]) for forming the $LiAl_{(Z-i)}Sn_i$ species becomes a function of composition and of i. This new approximation for ΔA_i (Eq. [19]) is shown to give a better representation of the data than previous approximations (*e.g.*, Eq. [18]).

In recent years, there have been an increasing number of experimental investigations of alkali metals and their alloys as a consequence of their potential use in modern technology, *i.e.*, thermonuclear reactors, off-peak energy storage, etc. More specifically, in high temperature batteries, lithium and its alloys appear to be the most attractive candidates for the active

* Electrochemical Society Active Member.

Key words: electromotive forces, lithium alloys, solution theory, activity coefficient, ternary metallic systems.

material in the negative electrode (1, 2). Measurements on such alloys are important not only to broaden the data base but should also prove to be significant from a theoretical point of view. Several theories and models have been developed to provide fundamental insights into the thermodynamic (3-10) and structural (11-16) properties of liquid metals and alloys.

Using the quasi-chemical theory, Alcock and Richardson calculated the activity coefficient of a solute in a binary alloy solvent, assuming equal sizes for the atoms and considering several possibilities for the distribution of the atoms and their preferential surroundings (3, 4). Furthermore, on the basis of the formation of hypothetical molecules in the bulk alloy, Jacob and Alcock (5) carried out more detailed calculations. Wagner has recently worked out significant modifications of the quasi-chemical theory (6). Wagner reaches conclusions equivalent to those derived by Mathieu and co-workers (7, 8) and Lupis and co-workers (9, 10) who used the "surrounded" or "central" atom theory.

A different theoretical approach to this problem deals primarily with the energetics rather than with the form of the thermodynamic functions. The metallic interactions are studied using an effective pair potential, *i.e.*, hard sphere potential (11) coupled with simple or optimized pseudopotentials (12-14). There have been some improvements in these calculations such as the development of optimized electron potentials (15) and of screened potentials (16). However, it seems that more refinements are needed in order to completely describe a system, and to understand both the thermodynamic and the structural data.

In this paper, we report on electromotive force measurements of dilute solutions of Li in molten Al-Sn alloys using the cell

Bi(l) saturated with Li_3Bi(s)/

LiCl-LiF (eutectic mixture)/Li-Al-Sn [1]

Dilute solutions of Li in Al or in Sn are found to behave according to the Nernst law. Furthermore, the limiting excess chemical potentials of Li in pure liquid Al and in pure liquid Sn are close to those obtained by extrapolating earlier data reported in more concentrated solutions by Yatsenko and Saltykova (17) and by Foster, Crouthamel, and Wood (18), respectively. Dilute solutions of Li in the binary solvent, Al-Sn, exhibit negative deviations from ideality for all compositions of the solvent. The variations of the activity coefficients of lithium as a function of the tin atom fraction are discussed on the basis of a generalized quasi-lattice theory developed first for molten salt mixtures by Blander and co-workers (19-21). The equations derived by Blander (19), when rewritten for alloys, are the same as those later derived by Wagner (6). Here, we use a new linear approximation for the energetics of the metallic interactions where the deviations from ideality of the binary solvent are included. In addition, the relative free energies of "bond" formation between Li and Sn are defined and the types of species which might be present in the ternary alloys are discussed.

Experimental

Materials.—The electrolyte was prepared by weighing the appropriate amounts of the salts [70 mol percent (m/o) LiCl, 30 m/o LiF]. Anhydrous purified LiCl was supplied in 200g ampuls by the Anderson Physics Laboratory, Champaign, Illinois. Pure single crystals of LiF (optical grade) from the Harshaw Chemical Company, Cleveland, Ohio, were used without further purification.

Lithium metal (99.97% purity) was purchased from the Foote Mineral Company, Philadelphia, Pennsylvania, in the form of 1 lb ingots sealed in cans under an argon atmosphere. Prior to use, the metal was purified by a method described elsewhere (22, 23). A typical analysis indicated 200 ppm N_2 and 600 ppm O_2.

Aluminum metal (99.9999% purity) was obtained in the form of rods from Materials Research Corporation, Orangeburg, New York. Bismuth metal (99.999% purity) was purchased from United Mineral and Chemical Corporation, New York. Tin metal (99.9% purity) from J. T. Baker Chemical Company, Phillipsburg, New Jersey, was used. Any oxide coating present on the surface of these metals was removed by manual filing; the filing was done slowly to avoid any possible oxidation due to frictional heating of the surface.

Experimental procedure.—The experimental arrangement of the cells and the procedure followed in this investigation are similar to those previously described in Ref. (22). An outer tantalum crucible contained the molten alloy (the positive electrode). A porous high purity beryllia cup suspended in the alloy contained the molten electrolyte, the LiF-LiCl eutectic mixture, in which was immersed the reference electrode. The BeO cup served as a barrier between the two electrode compartments. Presoaking of the cup with the molten electrolyte minimized any possible chemical attack due to penetration into the pores by corrosive elements such as lithium (24). The reference electrode consisted of a premelted (at 1123°K) two-phase binary system with an overall composition of 60.5 atom percent (a/o) Li and 39.5 a/o Bi held in a small tantalum cup which was submerged in the electrolyte. At the temperature of our measurements, $T = 949$°K, this composition provides a Li-Bi solution saturated with the compound Li_3Bi(s). The electromotive force of this two-phase electrode relative to pure Li is well known (25, 26) and has proved to be very stable with respect to small composition changes. In addition, the solubility of metallic Li in the electrolyte is negligible, probably less than 10^{-2} m/o (27, 28), because of its low activity in the reference electrode.

Tantalum leads connected both electrodes to a digital voltmeter (Dana Model 5000, input resistance greater than $10^{10}\Omega$). The temperature was held constant within a couple of degrees and measured with a tantalum-sheathed calibrated (Pt-Pt 10% Rh) thermocouple.

The cells were operated starting with different solvents which were either pure aluminum, pure tin, or an appropriate mixture of Al-Sn. The composition in the bulk alloy was changed by adding successive weighed quantities of Li, Sn, or Al. For each point, the equilibration of the cell with respect to temperature and voltage was rapidly attained [usually less than 2 hr (or 7200 sec) for large additions and 10 min (or 600 sec) for small additions which led to an increment of less than 1 m/o]. The emf's measured were steady and stable within several tenths of a millivolt for periods of observation up to a day. After temperature cycling, the emf's generally returned to the original value, thus demonstrating the reversibility of the cell.

Finally, it should be pointed out that all these operations were completely carried out inside a glove box filled with helium purified according to a method described elsewhere (29). In this inert atmosphere, there were less than 5 ppm water and oxygen was undetected (limit of detection 1 ppm).

Results.—In all that follows, unless specified differently, pure liquid Li is defined as the standard state.

Dilute solutions of Li in Al and in Sn.—Checks of the Nernst law for dilute solutions of Li-M (M ≡ Al or M ≡ Sn) were first carried out at a constant tem-

perature, $T = 949°K$. The emf's, E, of the alloys vary with composition according to the relation

$$E = E°_{Li(M)} - \frac{RT}{F} \ln a_{Li} \quad [2]$$

where R is the gas constant; F, the Faraday constant; a_{Li}, the activity of lithium in the alloys; and $E°_{Li(M)}$, the limiting potential of Li in pure liquid M *vs.* the two-phase reference electrode.

Figure 1 shows the results obtained at 949°K in two separate runs of the cell

Bi(l) saturated with Li_3Bi(s)/
LiCl-LiF(eutectic)/Li-Al [3]

The emf's are plotted as a function of atom fraction of Li in the binary alloy, together with the calculated Nernst slope: $2.3026\ RT/F = 188.30$ mV. A least squares fit of the data leads to a slope of 188.07 ± 0.59 mV which is in excellent agreement with the theoretical value, and to a value of $E°_{Li(Al)} = -536.39 \pm 1.54$ mV. At 949°K, our present value of $E°_{Li(Al)}$ combined with the potential of the reference electrode *vs.* pure lithium, 646.41 mV, as reported previously (25, 26) provides a limiting excess chemical potential of Li in pure liquid Al

$$\mu^{xs}_{Li(Al)} = -2.54 \text{ kcal mol}^{-1} \text{ (or } -10.63 \text{ kJ mol}^{-1})$$

If one extrapolates the data of Yatsenko and Saltykova (17) measured at higher concentrations (≥ 5 m/o Li) and at 1023°K, one obtains an approximate value: $\mu^{xs}_{Li(Al)} \simeq -2.6$ kcal mol^{-1} (or −10.9 kJ mol^{-1}) which is in good agreement with our measurements. The difference of 0.06 kcal mol^{-1} corresponds to an emf discrepancy of 2.5 mV which is remarkably good considering the extrapolation and the difference in temperatures.

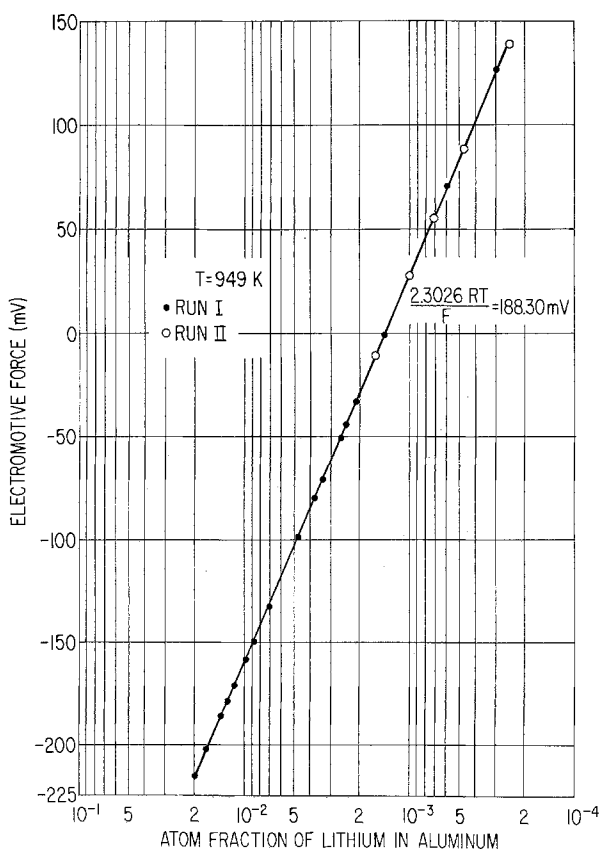


Fig. 1. Electromotive force of the cell
Bi saturated with Li_3Bi(s)/LiF-LiCl(eutectic)/Li-Al at $T = 949°K$ The full and empty circles represent data collected in two different runs. The slope of the line is equal to the calculated Nernst slope, 188.30 mV.

For the dilute solutions of Li in Sn, the data obtained *vs.* the two-phase reference electrode fit well along the Nernst slope of 188.30 mV with a value of $E°_{Li(Sn)} = -116 \pm 1$ mV. The limiting excess chemical potential of Li in pure liquid tin is consequently

$$\mu^{xs}_{Li(Sn)} = -12.22 \text{ kcal mol}^{-1} \text{ (or } -51.14 \text{ kJ mol}^{-1})$$

This value is consistent with the value of −12.36 kcal mol^{-1} (or −51.71 kJ mol^{-1}) obtained by extrapolating the data of Foster *et al.* (18) from higher concentrations of Li (≧10 m/o). Foster *et al.* reported experimental difficulties with their cells, and the standard deviations in the least squares fit of the emf values varied between 1 and 3 mV (18). The difference between these two values of $E°_{Li(Sn)}$ corresponds to about 6 mV.

The fit of the Nernst law equation in the Li atom fraction demonstrates that both dilute solutions of Li-Al and Li-Sn follow Henry's law and therefore the activity coefficient of Li is constant in this concentration range.

Dilute solutions of Li in the Al-Sn alloy.—The potentials of the cell [1] were measured at 949°K for different compositions of the alloy Al-Sn. In all these runs, the atom fraction of Li did not exceed 2.01×10^{-2}, which is within the range of concentration where the Nernst law is obeyed.

Two separate series of measurements were carried out by adding small weighed amounts of Sn to a Li-Al alloy of a given composition ($X_{Li} = 1.63 \times 10^{-3}$ or $X_{Li} = 2.01 \times 10^{-2}$, respectively, with X_i referring to the atom fraction of the ith component in the solution). The experimental values obtained for the electromotive forces, E, at different compositions of the alloy are listed in Table I. By choosing as a standard state the solution of Li at infinite dilution in Al, the activity coefficients of Li, $\gamma_{Li}^{(Al)}$, can be calculated from the following equation

$$\ln \gamma_{Li}^{(Al)} = \ln \frac{\gamma_{Li}}{\gamma_{Li(Al)}} = \frac{-F(E - E°_{Li(Al)})}{RT} - \ln X_{Li} \quad [4]$$

where γ_{Li} represents the activity coefficient of Li referred to pure liquid lithium and $\gamma_{Li(Al)}$, the activity coefficient of lithium at infinite dilution in Al.[1] The values of $\ln \gamma_{Li}^{(Al)}$ are plotted *vs.* X_{Sn} in the inset of Fig. 2.

At higher concentrations of Sn, two separate runs were performed. In the first series of measurements, successive additions of Al were made to a solution

[1] In order to convert these activity coefficients to activity coefficients with pure liquid lithium as standard state, one should add to the right-hand side of Eq. [4] the natural logarithm of $\gamma_{Li(Al)}$ · ($\ln \gamma_{Li(Al)} = -2540$ cal/$RT = -1.347$).

Table I. Emf of cell [1] for dilute solutions of Li and Sn in Al ($T = 949°K$)

I			II		
$10^4 X_{Al}$	$10^2 X_{Li}$	$-E$ (mV)	$10^4 X_{Al}$	$10^3 X_{Li}$	$-E$ (mV)
9799	2.010	217.27	9984	1.630	−12.09
9756	2.003	210.43	9948	1.624	−7.42
9716	1.995	204.19	9892	1.615	1.77
9657	1.982	194.78	9832	1.605	10.25
9603	1.971	187.31	9765	1.594	19.94
9540	1.958	177.37	9718	1.586	26.58
			9674	1.579	32.66
			9610	1.569	41.68
			9549	1.559	49.18
			9450	1.543	62.51

I refers to the set of measurements performed starting with the binary alloy Li-Al at a given composition ($X_{Li} = 0.0201$).
II refers to the set of measurements performed starting with the binary alloy Li-Al at a given composition ($X_{Li} = 0.00163$).
In both cases, weighed amounts of Sn were added to the initial alloy.
X_{Al} and X_{Sn} represent the atom fractions of Al and Sn, respectively, in the Li-Al-Sn alloy.
E represents the emf values obtained in cell [1].

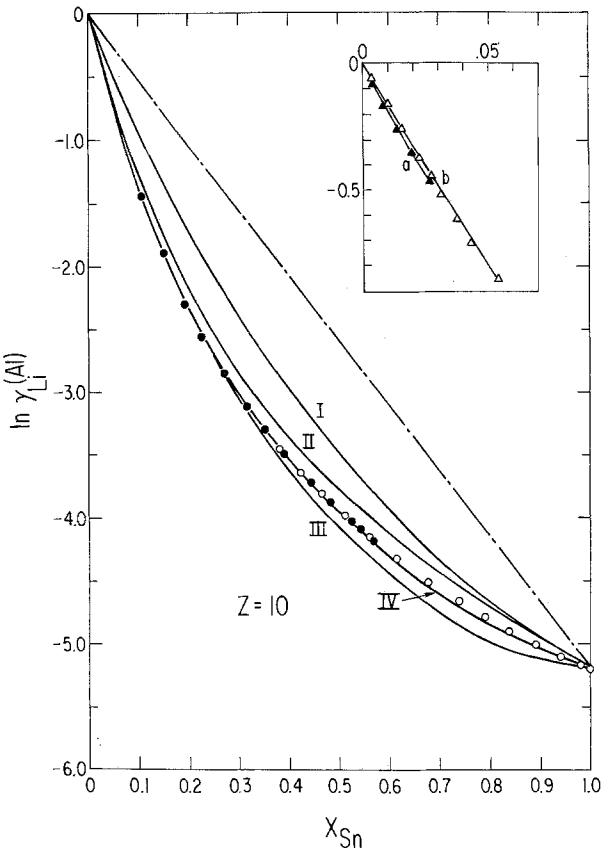


Fig. 2. Variations of $\ln \gamma_{Li}^{(Al)}$ with the composition of the solvent Al-Sn at 949°K, for dilute solutions of Li. ○ refers to the run performed starting with Li-Sn ($X_{Sn} = 0.9850$), ● refers to the run performed starting with Li-Al-Sn ($X_{Li} = 0.0145$ and $X_{Al} = 0.3968$), △ refers to the run performed starting with Li-Al ($X_{Li} = 1.63 \times 10^{-3}$), and ▲ refers to the run performed starting with Li-Al ($X_{Li} = 2.01 \times 10^{-2}$). Curve I is calculated using Eq. [27], curve II is calculated using Eq. [28], curve III is calculated using Eq. [18] for ΔA_i and Eq. [17] for $\gamma_{Li}^{(Al)}$, and curve IV is calculated using Eq. [19] for ΔA_i and Eq. [17] for $\gamma_{Li}^{(Al)}$. Curves a and b give the calculated values of $\ln \gamma_{Li}^{(Al)}$ for the two different runs (initial values of $X_{Li} = 2.01 \times 10^{-2}$ and 1.63×10^{-3}, respectively).

of Li-Sn ($X_{Li} = 0.0150$); in the second series, successive additions of Al were made to a solution of Li-Al-Sn ($X_{Li} = 0.0145$ and $X_{Al} = 0.3968$). By this method, we were able to cover the entire range of Al-Sn concentrations and to double-check the reproducibility of our data. Values of E, X_{Li}, and X_{Sn} are reported in Table II; it should be pointed out that where the compositions overlapped, the emf values in the two runs were remarkably self-consistent (within less than 1 mV). In Fig. 2 values of $\ln \gamma_{Li}^{(Al)}$ calculated from Eq. [4] are plotted *vs.* the mole fraction of tin. The slope of the curve becomes less negative as the atom fraction of Sn increases.

The interpretation of the variations of $\ln \gamma_{Li}^{(Al)}$ are discussed later in terms of the theory presented in the following section.

Theory and Calculations

For the sake of generality, the calculations presented in this section deal with the substitutional ternary system designated as A-B-C. (As the molar volumes of liquid Li, Al, and Sn do not differ greatly, the system under consideration can probably be best considered as a substitutional alloy.)

First, formation of complexes or groupings between A and B are postulated to describe the thermodynamics of dilute solutions of A and B in C. Second, an extension and a modification of the quasi-latttice theory (19-21) are suggested for dilute solutions of

Table II. Emf of cell [1] for different compositions of the binary solvent Al-Sn ($T = 949$°K)

A			B		
$10^4 X_{Al}$	$10^2 X_{Li}$	E (mV)	$10^4 X_{Al}$	$10^2 X_{Li}$	E (mV)
214.8	1.472	227.63	4276	1.374	154.30
452.6	1.436	225.80	4550	1.307	151.75
999.7	1.354	221.81	4776	1.253	149.80
1499	1.279	217.47	5170	1.159	144.95
1983	1.206	213.75	5578	1.061	139.01
2569	1.112	209.15	6137	0.926	128.75
3167	1.028	203.70	6509	0.838	125.26
3780	0.936	197.75	6868	0.751	119.75
4352	0.850	191.35	7386	0.627	110.84
4879	0.770	185.75	7769	0.535	102.70
5370	0.697	179.20	8127	0.449	95.64
5822	0.628	173.38	8584	0.340	85.50
6182	0.574	168.28	8948	0.252	72.25

A refers to the set of measurements performed starting with a binary Li-Sn alloy to which successive weighed amounts of Al were added.
B refers to the set of measurements performed starting with an initial alloy of Li-Al-Sn ($X_{Al} = 0.3968$ and $X_{Li} = 0.0145$) to which successive weighed amounts of Al were added.
X_{Al} and X_{Li} represent the atom fractions of Al and Li, respectively, in the Li-Al-Sn alloy.
E represents the emf values obtained in cell [1].

A in the binary solvent B-C. At all compositions of the solvent, it is assumed that the addition of A leads to changes in the "bonds" between atoms B and C. Finally, the equations obtained for the activity coefficients of A are compared with those derived from other theories.

In all that follows, γ_A (and $\gamma_A^{(C)}$) designate the activity coefficients of A with pure liquid A (and a solution of A at infinite dilution in C) as standard state.

Dilute solutions of A and B in C.—For the two interacting species A and B, the definition of associated species is most precise and meaningful in dilute solutions of A and B in the solvent C.

In this range of concentrations, groupings such as

$$A + B \rightleftharpoons AB \quad K_1 \qquad [5]$$

$$AB + B \rightleftharpoons AB_2 \quad K_2 \qquad [6]$$

$$AB + A \rightleftharpoons A_2B \quad K_{12}, \text{etc.} \qquad [7]$$

may occur in solution. The K_i's are defined as equilibrium constants

$$K_1 = \frac{X'_{AB}}{X'_A X'_B} \qquad [8]$$

$$K_2 = \frac{X'_{AB_2}}{X'_{AB} X'_B} \qquad [9]$$

$$K_{12} = \frac{X'_{A_2B}}{X'_{AB} X'_A}, \text{etc.} \qquad [10]$$

where X'_i refers to the atom fractions of the ith "free species." The atom fractions X_i and X'_i are related by the mass balance relations. The K_i's are true constants in solutions dilute enough so that Henry's law is obeyed. Consequently, deviations from ideality caused only by the formation of these groupings can be calculated using the following definition for the activity coefficients of A: $\gamma_A^{(C)} = X'_A/X_A$. After a series of expansions similar to those used for molten salts (30), one obtains

$$-\ln \gamma_A^{(C)} = K_1 X_B + (K_1 K_2 - \frac{1}{2} K_1^2) X_B^2 + (2K_1 K_{12} - K_1^2) X_A X_B + \ldots \qquad [11]$$

The coefficients in Eq. [11] are similar to the interaction coefficients introduced earlier by Wagner (31). They have thermodynamic significance when calculated as limiting values at infinite dilution of A and B in C.

There are two ways to evaluate the K_i's. One way is graphical; for example, K_1 is the limiting slope of the curve representing the variations of $\ln \gamma_A^{(C)}$ with X_B. The second way consists of a least squares method; values of $\ln \gamma_A^{(C)}$, at fixed values of the number of moles of A, are fitted to the equation

$$-\ln \gamma_A^{(C)} = MX_B + NX_B^2 \quad [12]$$

Details on the advantage of using either procedure and an analysis of the errors related to the coefficients derived are given in a paper by Braunstein, Lindgren, and Blander (30).

In a quasi-lattice formulation (30), a specific bond free energy change, ΔA_i, corresponding to the equilibria [5]-[7] can be defined; ΔA_i is associated with the replacement of an atom C by an atom B in the first coordination shell of an atom A. Statistically, the distribution of the atoms B between the bulk of the solvent B-C and the first coordination shell of A is calculated assuming the nonadditivity of pair bond interactions. (Nonadditivity means that the values of ΔA_i differ for consecutive values of i.) The equations thus derived can be written in our notation

$$K_1 = Z(\beta_1^\circ - 1) \quad [13]$$

$$K_1K_2 = \frac{Z(Z-1)}{2}(\beta_1^\circ\beta_2^\circ - 2\beta_1^\circ + 1) \quad [14]$$

$$K_1K_{12} = \frac{Z(Z-1)}{2}(\beta_1^\circ\beta_{12}^\circ - 2\beta_1^\circ + 1) \quad [15]$$

where $\beta_i^\circ = \exp(-\Delta A_i^\circ/RT)$ and ΔA_i° is the limiting value of ΔA_i at infinite dilution of B in C. These equations combined with Eq. [11] define ΔA_i° for any given value of Z. A negative sign for ΔA_i° indicates a preferential distribution of B atoms around A.

Dilute solutions of A in the solvent B-C.—The thermodynamic properties of A dilute in the binary alloy B-C can readily be described for all compositions of the solvent, in terms of the quasi-lattice theory by properly adapting the expressions obtained for similar situations in molten salt mixtures (19). In this range of concentrations, equilibria [5]-[7] can be written more generally as

$$A[B_{i-1}C_{Z-i+1}] + B[B\,C] \rightleftharpoons A[B_iC_{Z-i}] + C[B\,C] \quad [16]$$

The brackets $[B_{i-1}C_{Z-i+1}]$ and $[B_iC_{Z-i}]$ define the distribution of B and C in the Z positions of the coordination shell of A while [B C] means that the atom preceding the brackets (B or C) is an atom in the bulk alloy and occupies positions which are not near an A atom.

The two regions for the distribution of B and C, that next to an A atom and that in the bulk alloy, are considered in the statistical mechanical calculations. For the activity coefficient of A, one derives the following expression

$$\gamma_A^{(C)} = \left[\sum_{i=0}^{Z} \frac{Z!}{i!(Z-i)!} X_B{}^i(1-X_B)^{Z-i}\beta_o \ldots \beta_i\right]^{-1} \quad [17]$$

where $\beta_o = \exp(\mu^{xs}{}_C(X_B))/RT$ and $\mu^{xs}{}_C(X_B)$ is the excess chemical potential of C in the solvent B-C. The quantity β_o arises from a consideration of the dissolution of A in B-C to form a configuration $A[C_Z]$. β_o represents a correction for the difference between making the configuration $A[C_Z]$ in the binary B-C and in pure C. The quantity β_i ($i = 1, \ldots, Z$) is expressed by $\beta_i = \exp(-\Delta A_i/RT)$.

In principle, one can utilize Eq. [17] to extract values of specific bond free energies for all species by fitting the experimental data for a given value of Z (*e.g.*, $Z = 10$ or $Z = 12$). In practice, there are ambiguities inherent in attempting to fit such a high order polynomial to a curve; in addition, the evaluation of the high order coefficients (*e.g.*, $i > 2$) would be very uncertain. However, as shown in the preceding section, the evaluation of the lower order coefficients, especially that for $i = 1$, K_1 or β_1, is less ambiguous and less uncertain.

A more practical way would be to find an expression allowing one to calculate approximately the relative values of ΔA_i.

Mathieu (7, 8), Lupis (9, 10), and recently Wagner (6), using as a framework for their calculations different models of alloys, suggested a heuristic approximation for ΔA_i which, in our notation, reads

$$\Delta A_i = \Delta A_1^\circ + (i-1)h \quad [18]$$

The quantity h is a constant defined as the free energy difference for consecutive values of i. This particularly convenient approximation is generated from the assumption that the solvation energy of A atoms in the solvent has a parabolic dependence on i.

If one examines Eq. [18], one finds that ΔA_i is assumed to be concentration independent since ΔA_i° is derived at infinite dilution of B in C. Appropriate modifications of Eq. [18] appear to be needed.

The replacement of a C atom by a B atom in the coordination shell of A breaks one bond A-C and creates another bond A-B (reaction [16]). This process also breaks $(1/Z)$ of the contacts between a B atom and the bulk alloy and makes $(1/Z)$ new contacts between a C atom and the bulk alloy. Therefore, a correction to Eq. [18] taking into account deviations from ideality of the solvent is necessary. This correction can be approximated by, $(\mu^{xs}{}_C(X_B) - \mu^{xs}{}_B(X_B))/Z$, where $\mu^{xs}{}_B(X_B)$ is the excess chemical potential of B in the binary solvent B-C. Consequently, a new form for ΔA_i is deduced

$$\Delta A_i = \Delta A_1^\circ + (i-1)h + Z^{-1}[(\mu^{xs}{}_C(X_B) - \mu^{xs}{}_C(X_B = 0)) - (\mu^{xs}{}_B(X_B) - \mu^{xs}{}_B(X_B = 0))] \quad [19]$$

The quantity $(i-1)h$ takes into account the interactions of B and C in the coordination shell around an A atom. The factor Z^{-1} implies that the interactions with the solvent are additive. If such bond additivity is a reasonable approximation for the bulk alloy, then the dependence of ΔA_i on i is expressed independently of its dependence on concentration.

If the quantity $h = 0$, the specific bond free energies are all equal: $\Delta A_1 = \Delta A_i$ ($i = 1, \ldots, Z$). Substituting Eq. [19] in Eq. [17] leads then to the equation derived by Alcock and Richardson (4).

If the solvent B-C behaves as an ideal solution, ΔA_i becomes concentration independent and $\beta_o = 1$. Equations [17] and [19] then become identical to those derived by Mathieu *et al.* (7, 8) and Wagner (6) for interstitial alloys.

If the binary solvent B-C behaves as a regular solution, ΔA_i varies linearly with the composition. The excess Gibbs free energy of mixing of the solvent is then given by

$$\Delta G^{xs}(B\text{-}C) = X_B\mu^{xs}{}_B + (1-X_B)\mu^{xs}{}_C = \frac{1}{2}X_B(1-X_B)\lambda \quad [20]$$

where λ is defined as an interaction coefficient in the alloy B-C. In this case, ΔA_i is expressed by the simple relation

$$\Delta A_i = \Delta A_1^\circ + (i-1)h + \lambda Z^{-1}X_B \quad [21]$$

One may consider some other modifications to Eq. [19]. If the assumption of bond additivity of the

$(Z - 1)$ contacts with the bulk alloy of the atoms surrounding A does not seem appropriate, then one might consider the parameter h to be concentration dependent and/or a function of i. In such cases, at least one more parameter would be necessary to describe the solution properties.

Finally, interstitial alloys can be studied following the same treatment as for reciprocal[2] molten salt mixtures (19). Equations similar to Eq. [17] and [19] should apply. The deviations from ideality of the solvent B-C should be included in the approximate relation for ΔA_i. The factor Z^{-1} preceding the term in brackets in Eq. [19] is replaced by a larger number dependent on the geometry of the sites around A. In addition, the only other changes are due to the differences in the numbers of sites available to an atom; such formal, but not fundamental, differences can always be included by a modification of the concentration scale of the X's in the equilibrium constants, K_i, so that the concentrations are expressed as a fraction of the total sites available to an atom and not necessarily as an atom fraction.

Reconciliation of Theory and Experiment

In this section, our results will be examined in light of the equations we have discussed. A comparison will be made between the experimental results and the calculations for dilute solutions of Li in the binary solvent Al-Sn. We consider that A ≡ Li, B ≡ Sn, and C ≡ Al.

Evaluation of the equilibrium constants.—Values of K_1, K_2, and K_{12} are derived from a least squares fit of the data obtained in dilute solutions of Li and Sn in Al (Table I)

$$K_1 = 17.4 \pm 0.15,\ K_2 = 7.1 \pm 0.3,\ \text{and}\ K_{12} = 10.0 \pm 0.15$$

The uncertainties in these constants are probably about four times larger than the stated precision. The presence of a significant concentration of polynuclear species with more than two Li atoms would increase the uncertainty in K_{12}. In addition, the presence of such species other than Li_2Sn cannot be ascertained with measurements at only two concentrations of Li. For $Z = 10$, for example, we deduce values of the specific bond free energies of $\Delta A_1^\circ = -1.90$ kcal mol^{-1} (or -7.95 kJ mol^{-1}), $\Delta A_2^\circ = -1.83$ kcal mol^{-1} (or -7.66 kJ mol^{-1}) and $\Delta A_{12}^\circ = -2.10$ kcal mol^{-1} (or -8.79 kJ mol^{-1}). The fact that the ΔA_i° are negative indicates that there is a preferential distribution of Sn about Li and of Li about Sn.

At the tin-rich end, one may evaluate the equilibrium constant, K_1', and the specific bond free energy, $\Delta A_1'$, corresponding to

$$Li[Sn_Z] + Al[Sn_Z] \rightleftharpoons Li[Sn_{Z-1}Al] + Sn[Sn_Z] \qquad [22]$$

The quantity, $\Delta A_1'$ is positive since Li is preferentially coordinated by Sn. At $X_{Sn} = 1$, one may write

$$\Delta A_1' = -\Delta A_Z(X_{Sn} = 1) \qquad [23]$$

and

$$\beta_1' = 1/\beta_Z(X_{Sn} = 1) \qquad [24]$$

Consequently, the formal equilibrium constant, K_1', is negative. The reason for this peculiarity has been discussed elsewhere (19). Only if there is an energetic preference for an aluminum in the coordination shell of Li in the Sn-rich solution can K_1' be positive and the limiting slope, $(d \ln \gamma_{Li}^{(Al)}/dX_{Al})_{X_{Li}=X_{Al}=0} = -K_1'$, negative. However, as long as $\Delta A_1'$ is positive, K_1' is negative and the limiting slope is positive.

[2] A reciprocal ionic system contains two different kinds of cations; A^+ and B^+, and two different kinds of anions, X^- and Y^-; it can be schematized by $(A^+,B^+/X^-,Y^-)$. Formally, reciprocal systems are equivalent to interstitial alloys.

A least squares fit of our data leads to $K_1' = -1.72 \pm 0.01$ and $\Delta A_1' = 0.35$ kcal mol^{-1} (or 1.46 kJ mol^{-1}), for $Z = 10$.

The specific bond free energies, ΔA_1° (negative) and $\Delta A_1'$ (positive), usually cannot be determined with the same precision; even if one uses the same method to calculate both of them, the relative uncertainty of $\Delta A_1'$ is generally larger and is especially so when K_1' is close to $-Z$.

Variations of the activity coefficients of Li with the composition of the binary solvent Al-Sn in dilute Li solutions.—Figure 2 gives the variations of $\ln \gamma_{Li}^{(Al)}$ with the tin atom fraction in the ternary alloy Li-Al-Sn dilute in Li. In order to understand these results and to estimate the influence of certain parameters discussed previously, we will calculate $\ln \gamma_{Li}^{(Al)}$ using equations derived from different models.

Using the quasi-chemical theory, Alcock and Richardson (3) derived a simple relation for $\ln \gamma_{Li}$ which in our notation reads

$$\ln \gamma_{Li}^{(Al)} = X_{Sn} \ln \frac{\gamma_{Li(Sn)}}{\gamma_{Li(Al)}} - \frac{\Delta G^{xs}(Al\text{-}Sn)}{RT} \qquad [25]$$

$\Delta G^{xs}(Al\text{-}Sn)$ designates the excess Gibbs free energy of mixing of the binary Al-Sn. It should be pointed out that Darken (32) obtained Eq. [25] without reference to any particular physical model. Later, Alcock and Richardson (4), modifying their assumptions, proposed another equation

$$\gamma_{Li}^{(Al)} = \left[X_{Al}(\gamma_{Al})^{1/Z} + X_{Sn}\left(\frac{\gamma_{Sn}\gamma_{Li(Al)}}{\gamma_{Li(Sn)}}\right)^{1/Z}\right]^{-Z} \qquad [26]$$

where γ_{Al} and γ_{Sn} refer to the activity coefficients of Al and Sn, respectively, in the binary solvent Al-Sn. Substituting the values for $\Delta G^{xs}(Al\text{-}Sn)$, γ_{Al} and γ_{Sn} given in the literature (33, 34) and our experimental values of $\gamma_{Li(Al)}$ and $\gamma_{Li(Sn)}$, Eq. [25] or [26] leads to a poor description of the experimental data. (Note that Eq. [26] can be obtained from Eq. [17] and [19] as a limiting case when $h = 0$.)

One may improve Alcock and Richardson's equations by an empirical modification. To do this, the atom fractions, X, are replaced by volume fractions, $\overline{V}$, defined as follows

$$\overline{V}_{Al} = \frac{X_{Al}V_{Al}}{X_{Al}V_{Al} + X_{Sn}V_{Sn}} \quad \text{and} \quad \overline{V}_{Sn} = 1 - \overline{V}_{Al}$$

where V_{Al} and V_{Sn} represent the molar volumes of Al and Sn, respectively. Equations [25] and [26] can be rewritten as

$$\ln \gamma_{Li}^{(Al)} = \overline{V}_{Sn} \ln\left(\frac{\gamma_{Li(Sn)}}{\gamma_{Li(Al)}}\right) - \frac{\Delta G^{xs}(Al\text{-}Sn)}{RT} \qquad [27]$$

and

$$\gamma_{Li}^{(Al)} = \left[\overline{V}_{Al}(\gamma_{Al})^{1/Z} + \overline{V}_{Sn}\left(\frac{\gamma_{Sn}\gamma_{Li(Al)}}{\gamma_{Li(Sn)}}\right)^{1/Z}\right]^{-Z} \qquad [28]$$

For $Z = 10$, the values obtained for $\ln \gamma_{Li}^{(Al)}$ using Eq. [27] and [28] are plotted in Fig. 2 (curves I and II, respectively). The differences between experiments and curve I are much larger than the combined uncertainties. Curve II gives a much better fit than Eq. [25]-[27]; nevertheless, it does not describe the behavior of these alloys accurately. On the other hand, Eq. [28] is attractive in that there are no adjustable parameters. However, if Z, the coordination number of Li, is used as a parameter, the calculations fit the experiments fairly well for $Z = 7$.

The experimental data may be compared with Eq. [17], using one of the approximations for ΔA_i. The simplest approximation would be Eq. [18] which assumes that ΔA_i is concentration independent. The value of h is obtained from the relation

$$RT \ln \gamma_{Li}^{(Al)}(X_{Sn} = 1) - RT \ln \gamma_{Li}^{(Al)}(X_{Sn} = 0) = \sum_{i=1}^{Z} \Delta A_i(X_{Sn} = 1) = Z\Delta A_1^\circ + \frac{Z(Z-1)}{2} h \quad [29]$$

For $Z = 10$ and $\Delta A_1^\circ = -1.90$ kcal mol^{-1} (or -7.95 kJ mol^{-1}), we derive $h = 0.20$ kcal mol^{-1} (or 0.86 kJ mol^{-1}). The calculated values for $\ln \gamma_{Li}^{(Al)}$ plotted *vs.* X_{Sn} define curve III in Fig. 2. The differences between experimental data and curve III are more important at the tin-rich end than at the aluminum-rich end. This is obviously due to the fact that the calculation uses the limiting slope determined for low values of X_{Sn} which constrains the curve to follow the experimental points initially. The calculations do match the data somewhat better for smaller values of Z ($Z = 8$).

Since the solvent, Al-Sn, exhibits deviations from ideality, the new approximation for ΔA_i (Eq. [19]) should be considered. The quantity h is then evaluated from the following equation similar to Eq. [29]

$$RT \ln \gamma_{Li}^{(Al)}(X_{Sn} = 1) - RT \ln \gamma_{Li}^{(Al)}(X_{Sn} = 0) = Z\Delta A_1^\circ + \frac{Z(Z-1)h}{2} + \mu^{xs}{}_{Sn}(X_{Sn} = 0) \quad [30]$$

For $Z = 10$, we obtain $h = 0.12$ kcal mol^{-1} (or 0.52 kJ mol^{-1}). The curve calculated for $\ln \gamma_{Li}^{(Al)}$ as a function of X_{Sn} is plotted in Fig. 2 and labeled curve IV. The correspondence between the measurements and the calculations is surprisingly good; curve IV exhibits the same asymmetry as the experimental data. This excellent agreement leads us to conclude that, for this case, Eq. [19] gives an accurate approximation for ΔA_i. Finally, calculations were also performed using different values for Z ($Z = 8$ and $Z = 12$); they led to reasonably good agreement with the data.

Within the context of the quasi-lattice theory, the good fit of the measurements with the calculations implies that the distribution of the species can be tentatively estimated. The relative fraction of lithium atoms present in the ith species, $N_i^*(Li)$, can be written as

$$N_i^*(Li) = \frac{Z!}{(Z-i)!i!} X_{Sn}{}^i (1 - X_{Sn})^{Z-i} \gamma_{Li}^{(Al)} \beta_0 \ldots \beta_i \quad [31]$$

where i is an integer varying between 0 and the coordination number, Z. Calculated values of $N_i^*(Li)$ are, of course, model dependent. For $Z = 10$, the relative fractions of Li having 0, 1, 5, 9, and 10 Sn atom(s) as nearest neighbors, are calculated as a function of the atom fraction of Sn. The results are plotted *vs.* X_{Sn} in Fig. 3. As expected, both species 0 and 10 vary monotonically between 0 and 1. However, there is an obvious asymmetry in these curves: the curve for species 0 falls more steeply at $X_{Sn} = 0$ than the curve for species 10 rises at $X_{Sn} = 1$. The curves representing the species 1, 5, and 9 exhibit a maximum and go to zero at both ends $X_{Sn} = 0$ and $X_{Sn} = 1$. It should be noted that the maximum of the curve of the species $i = 1$ is greater than that for the species $i = 9$. In addition, the positions of all the maxima are at values of X_{Sn} less than (i/Z); this arises largely because the values of ΔA_i are always negative and increase monotonically with an increase of i and X_{Sn}. Despite the fact that the plots of Fig. 3 are model dependent, they probably provide a reasonable picture of the distributions of species in the real solution. Similar curves could be obtained for values of Z other than 10.

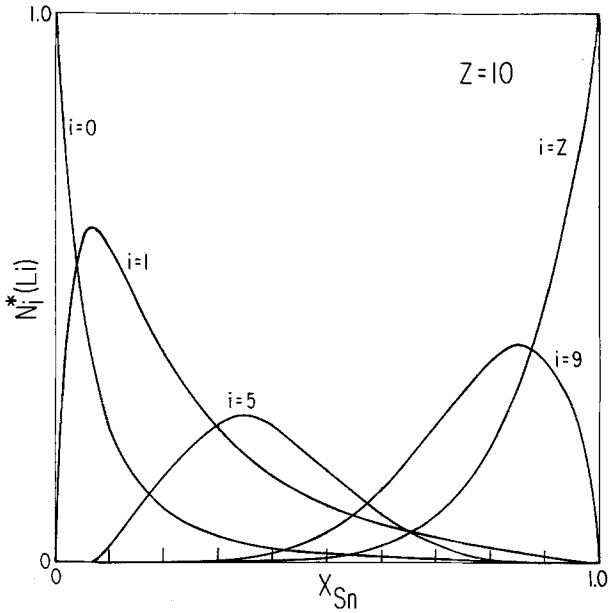


Fig. 3. Variations of the calculated relative fraction of lithium atoms present in the *i*th ($i = 1, \ldots, Z$) species ($LiSn_i$) with the atom fraction X_{Sn} for $Z = 10$.

Concluding Remarks

Accurate measurements of the activity coefficients of dilute solutions of Li in the binary Al-Sn are presented and discussed in the light of several models

The equations derived by Alcock and Richardson (4) from the quasi-chemical theory lead to a fair fit with the data only if an empirical modification is introduced, in which volume fractions are substituted for atom fractions. If, in addition, the coordination number, Z, is considered as an adjustable parameter, the modified equation fits our data fairly well for $Z = 7$.

The equations proposed in this paper are based on the quasi-lattice theory of Blander *et al.* (19-21). The relation obtained for the activity coefficients of lithium is the same as the one derived later using other models (6-10). These equations, with an approximation for the energetics suggested by Wagner (6), Mathieu *et al.* (7, 8), and Lupis *et al.* (9, 10), lead to a satisfactory representation of the data when Z is adjusted to be 8.

Our new approximation for the specific bond free energy, ΔA_i, takes into account the deviations from ideality of the binary solvent. It differs from prior work where ΔA_i is assumed to be concentration independent. Excellent agreement between experiments and calculations is obtained. A more decisive test of this approximation could be made on ternary systems where the solvent exhibits larger deviations from ideality than the present system Al-Sn. In addition, one can use these calculations to estimate the relative proportions of Li in species coordinated with different numbers of Al and Sn atoms.

A theory based on more general principles allowing an exact evaluation of the dependence of ΔA_i on i is obviously needed. Such advances might be realized through analyses of the energetics involved in binary and ternary alloy systems.

Acknowledgments

We gratefully acknowledge fruitful discussions with Professor Carl Wagner. We are indebted to Dr. H. M. Feder for bringing to our attention Eq. [27] and [28] and we thank Mr. R. M. Yonco for purifying the lithium used in these experiments. We appreciate the efforts of Mrs. J. Steinquist for typing this manuscript.

This work was performed under the auspices of the U. S. Energy Research and Development Administration.

Manuscript submitted June 11, 1976; revised manuscript received Aug. 30, 1976. This was Paper 407 presented at the Washington, D.C., Meeting of the Society, May 2-7, 1976.

Any discussion of this paper will appear in a Discussion Section to be published in the December 1977 JOURNAL. All discussions for the December 1977 Discussion Section should be submitted by Aug. 1, 1977.

Publication costs of this article were assisted by Argonne National Laboratory.

REFERENCES

1. E. J. Cairns and R. K. Steunenberg, in "Progress in High Temperature Physics and Chemistry," Vol. 5, C. A. Rouse, Editor, p. 63, Pergamon Press (1973).
2. P. A. Nelson *et al.*, USAEC Report ANL-8109 (1974).
3. C. B. Alcock and F. D. Richardson, *Acta Metall.*, **6**, 385 (1958).
4. C. B. Alcock and F. D. Richardson, *ibid.*, **8**, 882 (1960).
5. K. T. Jacob and C. B. Alcock, *ibid.*, **20**, 221 (1972).
6. C. Wagner, *ibid.*, **21**, 1297 (1973).
7. J. C. Mathieu, F. Durand, and E. Bonnier, *J. Chim. Phys.*, **62**, 1289 (1965).
8. B. Brion, J. C. Mathieu, P. Hicter, and P. Desré, *ibid.*, **67**, 1238 (1970).
9. C. H. P. Lupis and J. F. Elliot, *Acta Metall.*, **15**, 265 (1967).
10. E. Hsin Foo and C. H. P. Lupis, *ibid.*, **21**, 1409 (1973).
11. N. W. Ashcroft and D. C. Langreth, *Phys. Rev.*, **156**, 685 (1967); *ibid.*, **159**, 500 (1967).
12. V. Heine, *Solid State Phys.*, **24**, 38 (1970).
13. V. Heine and D. Wearie, *ibid.*, **24**, 250 (1970).
14. H. R. Leribaux and L. F. Miller, *J. Chem. Phys.*, **61**, 3327 (1974).
15. M. Appapillai and V. Heine, *J. Phys. F.*, **3**, 759 (1973).
16. H. R. Leribaux and M. H. Boon, *Phys. Rev. B*, **11**, 2412 (1975).
17. S. P. Yatsenko and E. A. Saltykova, *Zh. Fiz. Khim.*, **48**, 2366 (1974); *Russ. J. Phys. Chem.*, **48**, 1402 (1974).
18. M. S. Foster, C. E. Crouthamel, and S. E. Wood, *J. Phys. Chem.*, **70**, 3042 (1966).
19. M. Blander, *J. Chem. Phys.*, **34**, 432 (1961).
20. M. Blander and J. Braunstein, *Ann. N.Y. Acad. Sci.*, **79**, 838 (1960).
21. M. Blander and K. Hagemark, *Nucl. Metall.*, **15**, 579 (1969); Conf. 690801 Clearinghouse for Federal Scientific and Technical Information, N.B.S., U.S. Dept. of Commerce, Springfield, Virginia.
22. M. L. Saboungi and M. Blander, *This Journal*, **122**, 1631 (1975).
23. R. M. Yonco, E. Veleckis, and V. A. Maroni, *J. Nucl. Mater.*, **57**, 317 (1975).
24. E. J. Cairns *et al.*, in "Development of High-Energy Batteries for Electric Vehicles," USAEC-ANL-7888 (1971).
25. M. S. Foster, S. E. Wood, and C. E. Crouthamel, *Inorg. Chem.*, **3**, 1428 (1964).
26. E. J. Cairns *et al.*, in "Galvanic Cells with Fused-Salt Electrolyte," USAEC-ANL-7316 (1967).
27. A. S. Dworkin, H. R. Bronstein, and M. A. Bredig, *J. Phys. Chem.*, **66**, 572 (1962).
28. M. V. Smirnov and N. P. Podlesnyak, *Zh. Prikl. Khim.*, **43**, 1463 (1970).
29. M. S. Foster, C. E. Johnson, and C. E. Crouthamel, in "Helium-Purification Unit for High-Purity Inert-Atmosphere Boxes," USAEC-ANL-6652 (1962).
30. J. Braunstein, M. Blander, and R. M. Lindgren, *J. Am. Chem. Soc.*, **84**, 1529 (1962).
31. C. Wagner, "Thermodynamics of Alloys," Addison-Wesley Publishing Co., Inc., Reading, Mass., London (1952).
32. L. S. Darken, *J. Am. Chem. Soc.*, **72**, 2909 (1950).
33. R. Hultgren, P. D. Desai, D. T. Hawkins, M. Gleiser, and K. K. Kelley, "Selected Values of the Thermodynamic Properties of Binary Alloys," American Society for Metals, Metals Park, Ohio (1973).
34. G. Massart, F. Durand, and E. Bonnier, *Bull. Soc. Chim. Fr.*, **15**, 87 (1965).

Electrocatalytic Activity of Metals and Alloys Electrodeposited on Foreign Substrates

II. Oxygen Adsorption on Electrodeposited Palladium on Pyrolytic Graphite

Ikram Morcos*

Hydro-Quebec Institute of Research, Varennes, Quebec, Canada

ABSTRACT

Oxygen coverage was determined as a function of the oxidizing potential in acid and alkaline media on both massive and electrodeposited palladium on pyrolytic graphite electrodes. Oxygen adsorption and oxide formation start at significantly more cathodic potentials in the case of the electrodeposited palladium on graphite as compared to the massive metal. The cathodic shift in the potential and the amount of adsorbed oxygen increase with the increase in the current density applied in depositing the palladium on the graphite substrate. Variation in surface roughness obtained on the basis of differential capacity measurement is too small to account for the increase in electrocatalytic activity. It is concluded that the observed difference in the electrocatalytic activity of both palladium surfaces is most probably due to difference in specific surface energy.

The study of oxygen reduction on electrodes of metal films electrodeposited on pyrolytic graphite (1-3) suggests that the electrocatalytic activity of the deposited metal may be higher than the corresponding activity of the same metal in the massive form. The oxygen reduction is, however, a complex reaction that involves mass transfer, adsorption of reactants and intermediates, as well as charge-transfer reactions of more than one species; and depending on the strength of the metal-oxygen bond, oxygen adsorption may decrease or increase the rate of oxygen reduction at

* Electrochemical Society Active Member.
Key words: palladium, electrodeposited palladium on pyrolytic graphite, oxygen adsorption, scanning electron microscopy, electrocatalytic activity.

the metal surface. Consequently, direct, conclusive, and quantitative information on the intrinsic electrocatalytic properties of the mentioned metal films could not be unambiguously derived from the study of oxygen reduction. But the reverse is true, *i.e.*, the proper understanding of the electrocatalytic properties may be extremely helpful in interpreting the kinetics of such reactions as oxygen reduction.

It is therefore desirable to examine independently the electrocatalytic activity of electrodeposited metal films on pyrolytic graphite toward some single and relatively simple surface processes such as oxygen or hydrogen adsorption. A study of oxygen adsorption on a palladium surface electrodeposited on pyrolytic graphite has been the purpose of the present work.

Experimental

The method of study is one that is well established (4-6) and involves the formation at a fixed potential of an adsorbed layer of oxygen (or oxygen-carrying species), which is then reduced by the application of a cathodic sweep. The amount of charge equivalent to the quantity of oxygen adsorbed is determined by integrating[1] the oxygen reduction peak of the voltammetric curve.

The potential program applied is similar to that used by Rand and Woods (6, 7) and involves the use of a Wenking potentiostat, a Tacussel sweep generator, a Tacussel-type GSTP step function generator, and a Hewlett Packard Type 7004B X-Y recorder. Various oxidizing potentials were used with each electrode and the oxidizing time was always 10 sec. The potential was cathodically swept at a rate of 20 mV/sec.

The study was carried out in both acidic and alkaline media using 1.0*N* H_2SO_4 and 0.1*N* KOH. The first solution was prepared from ultrapure material while the second from AR quality KOH material using in both cases triply distilled water, twice from a permanganate solution.

Palladium on graphite electrodes were prepared by electrodepositing palladium from palladium chloride solution. The substrate was in the form of pyrolytic graphite rods which were mounted on Kel-F exposing only a flat circular area of 0.338 cm^2. The electrodeposition was carried out galvanostatically and different surfaces were prepared by using different current densities and times of deposition. The highest and lowest current densities applied correspond approximately to the maximum and minimum current densities at which a complete adequately adherent palladium layer can be obtained on the graphite. Since pyrolytic graphite is a nonporous material there is no ambiguity in estimating the apparent area of the deposited metal. The electrode was thoroughly washed with triply distilled water after removal from the plating bath. X-ray fluorescence showed that the deposit contained no other metallic impurity. The oxygen adsorption studies were all compared with those obtained on a massive palladium electrode which had an area of 0.478 cm^2 and was in the form of a disk embedded in a Teflon sleeve. The later electrode was, prior to any voltammetric experiment, mechanically polished with alumina, cleaned in conc sulfuric acid and then thoroughly washed in triply distilled water.

A Teflon cell was used which consisted of a large compartment for the working and counterelectrodes and a small one for the reference electrode. The reference electrode was Hg/HgO; 1.0*N* KOH for alkaline medium and Hg/Hg SO_4, saturated K_2SO_4 for acid medium. The solutions were thoroughly saturated with helium before and during each experiment and the electrode was rotated throughout the measurement at 1600 rpm.

The electrodeposited palladium surface was examined by the scanning electron microscope under a magnification of 10,000×. Attempts were also made to estimate the ratio of real surface area of the electrodeposited palladium to that of the massive electrode. For that, the potential dependence of the differential capacitance was measured by an a-c bridge and a d-c polarizing circuit.

[1] The cathodic current following the peak was taken as a base line for the integration to correct for double layer charge.

Results and Discussion

Figure 1 shows the different cathodic sweeps for the reduction of oxygen layer formed on massive palladium at the different oxidizing potentials in He-saturated 1.0*N* H_2SO_4. Figures 2-6 show the corresponding cathodic sweeps obtained under the same experimental conditions as those of Fig. 1, but on different palladium layers which were deposited on pyrolytic graphite at the current densities of 148, 118, 60, 30, 5.1 mA/cm^2 and time of deposition 12 sec, 15 sec, 30 sec, 60 sec and 35 min, respectively. The values of oxidizing potentials are indicated on each figure. The corresponding results obtained in 0.1*N* KOH on massive as well as electrodeposited palladium on graphite electrodes are shown in Fig. 7-12. Tables I and II summarize the dependence of the reduction's peak potential on the oxidizing potential and the type of palladium surface used in each experiment in both acidic and alkaline media, respectively. The dependence of the quantity of adsorbed oxygen obtained by integration from Fig. 1-12 on the oxidizing potential is shown for both media in Fig. 13 and 14, respectively.

The experimental results show significant qualitative and quantitative differences between the characteris-

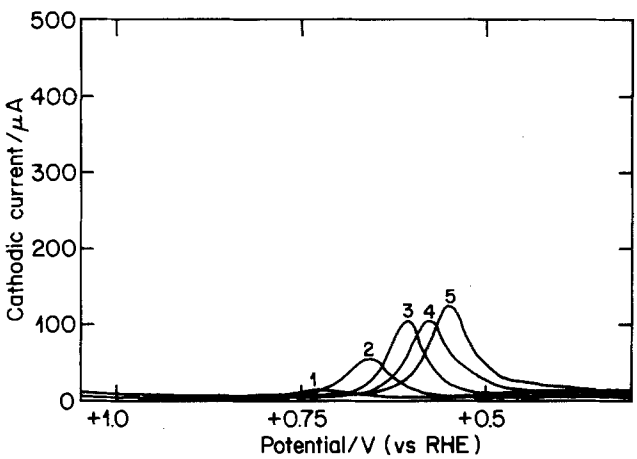


Fig. 1. Oxygen reduction's peak as a function of oxidizing potential on a massive palladium electrode in 1*N* H_2SO_4. Oxidizing potential: curve 1, 1.08V; curve 2, 1.28V; curve 3, 1.48V; curve 4, 1.68V; curve 5, 1.88V.

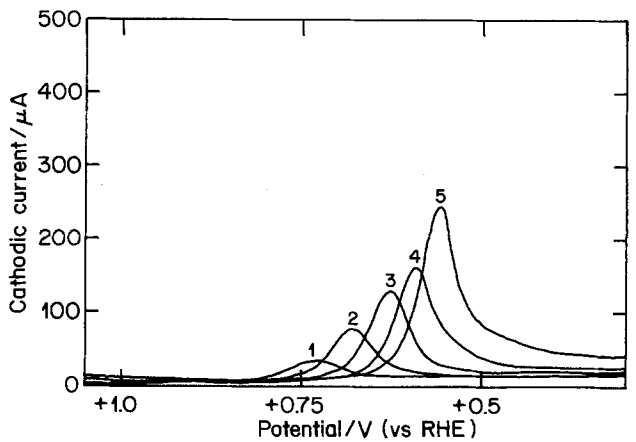


Fig. 2. Oxygen reduction's peak as a function of oxidizing potential in 1*N* H_2SO_4 on a palladium surface electrodeposited on pyrolytic graphite at a current density of 5.1 mA/cm^2. Oxidizing potential: curve 1, 1.08V; curve 2, 1.28V; curve 3, 1.48V; curve 4, 1.68V; curve 5, 1.88V.

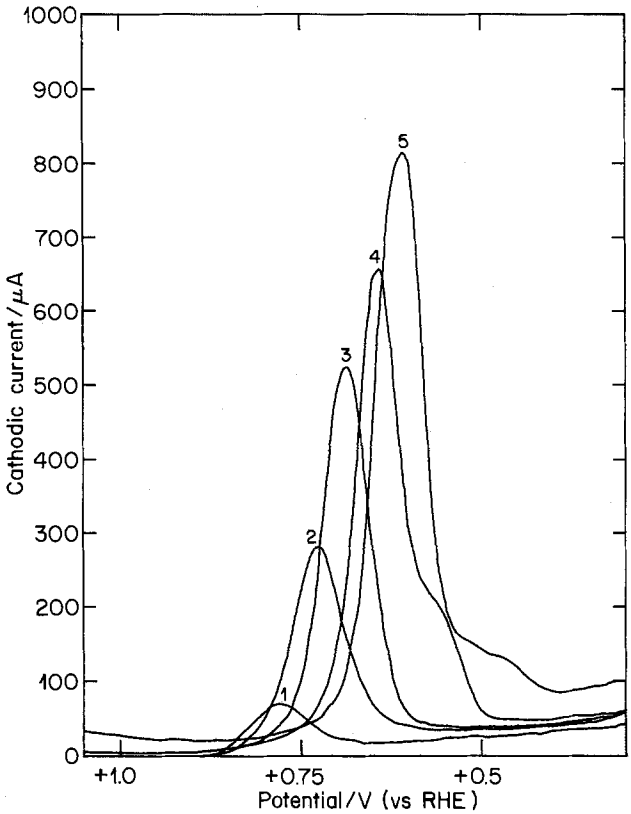


Fig. 3. Oxygen reduction's peak as a function of oxidizing potential in 1N H_2SO_4 on a palladium surface electrodeposited on pyrolytic graphite at a current density of 30 mA/cm^2. Oxidizing potential: curve 1, 1.08V; curve 2, 1.28V; curve 3, 1.48V; curve 4, 1.68V; curve 5, 1.88V.

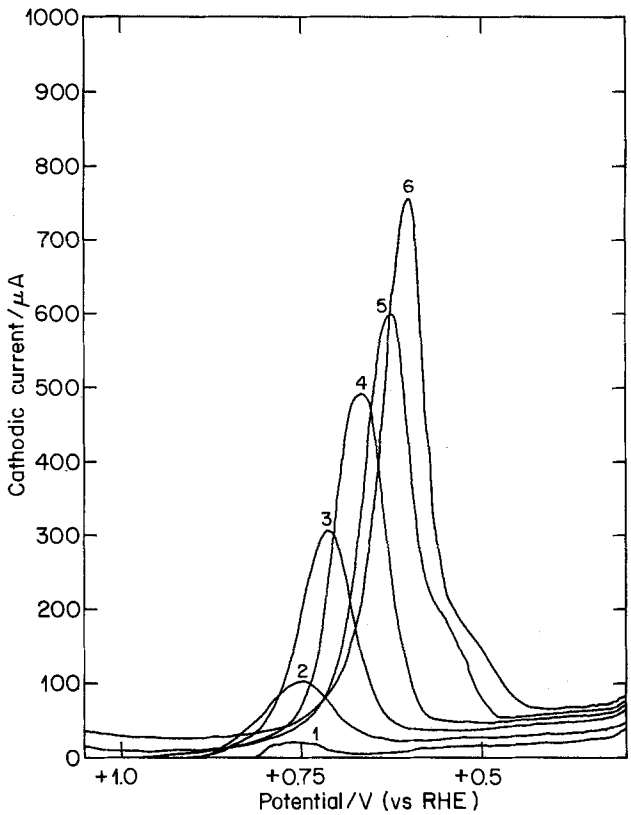


Fig. 4. Oxygen reduction's peak as a function of oxidizing potential in 1N H_2SO_4 on a palladium surface electrodeposited on pyrolytic graphite at a current density of 60 mA/cm^2. Oxidizing potential: curve 1, 0.88V; curve 2, 1.08V; curve 3, 1.28V; curve 4, 1.48V; curve 5, 1.68V; curve 6, 1.88V.

tics of oxygen adsorption on massive and electrodeposited-on graphite palladium. Table I for example shows that the reduction's peak in acid medium is shifted toward more positive potentials in the case of Pd-on graphite as compared to the massive Pd. The magnitude of the shift generally increases with the increase in the current density of the deposition of Pd. A 65-80 mV shift (the exact quantity depends on the oxidizing potential) is observed between the reduction's peak of massive Pd and that of electrodeposited Pd at 148 mA/cm^2. In alkaline medium Table II shows that the corresponding shift in the reduction's peak occurs in the opposite direction and has a smaller magnitude of 20-55 mV. The voltammetry curves for the Pd-on graphite surface are also characterized in alkaline medium by the presence of a small peak at potentials more anodic than those corresponding to the main peak. Figures 13 and 14 show that oxygen adsorption starts at more cathodic potentials in the case of Pd-on graphite as compared with massive Pd, and here again the magnitude of the potential shift increases with the increase in the current density of deposition of Pd. At a surface electrodeposited at 148 mA/cm^2 oxygen adsorption starts in acidic and alkaline media at potentials 300 and 500 mV, respectively, more cathodic than in the case of massive Pd.

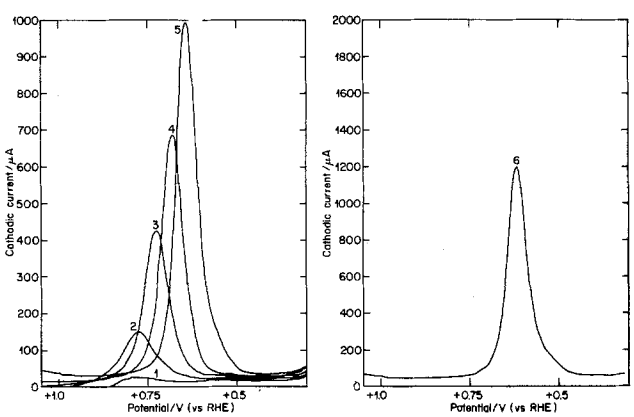


Fig. 5. Oxygen reduction's peak as a function of oxidizing potential in 1N H_2SO_4 on a palladium surface electrodeposited on pyrolytic graphite at a current density of 118 mA/cm^2. Oxidizing potential: curve 1, 0.88V; curve 2, 1.08V; curve 3, 1.28V; curve 4, 1.48V; curve 5, 1.68V; curve 6, 1.88V.

The amount of adsorbed oxygen on a massive electrode reaches a limiting value of 485 and 513 μC/geometric cm^2 in acidic and alkaline media, respectively. If

Table I. Reduction's peak potentials in 1.0N H_2SO_4

Oxidizing potential (RHE)	Massive Pd	Current density of electrodepositing* Pd				
		5.1 mA/cm^2	30 mA/cm^2	60 mA/cm^2	118 mA/cm^2	148 mA/cm^2
1.88	0.555	0.560	0.610	0.600	0.615	0.620
1.68	0.580	0.595	0.645	0.625	0.645	0.645
1.48	0.610	0.625	0.690	0.670	0.680	0.690
1.28	0.660	0.680	0.730	0.710	0.725	0.740
1.080	0.710	0.730	0.780	0.750	0.780	0.790

* Time of deposition in each case is the same as mentioned in the text.

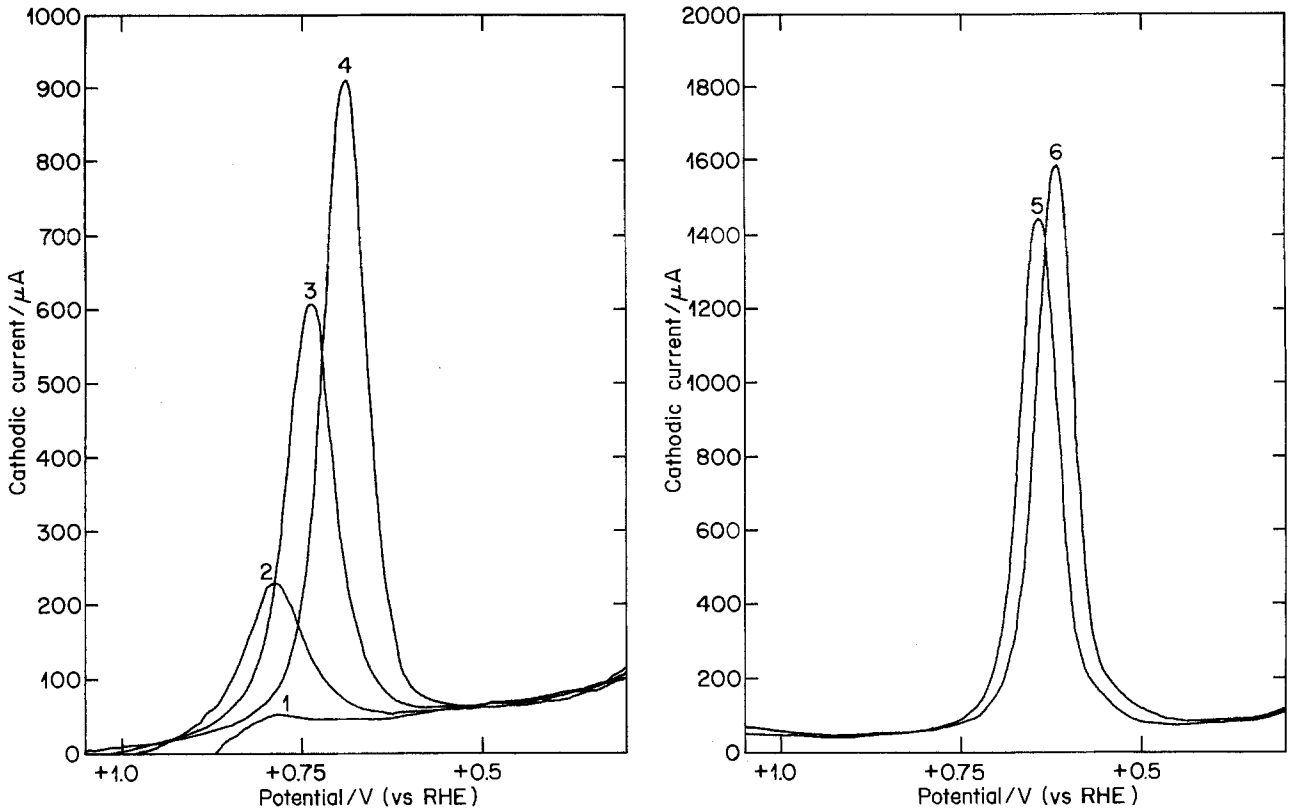


Fig. 6. Oxygen reduction's peak as a function of oxidizing potential in 1*N* H_2SO_4 on a palladium surface electrodeposited on pyrolytic graphite at a current density of. 148 mA/cm². Oxidizing potential: curve 1, 0.88V; curve 2, 1.08V; curve 3, 1.28V; curve 4, 1.48V; curve 5, 1.68V; curve 6, 1.88V.

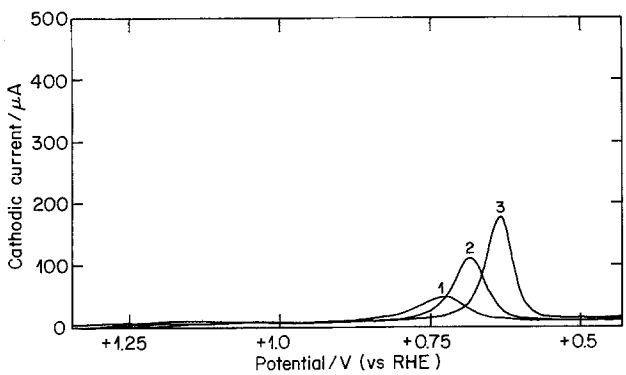


Fig. 7. Oxygen reduction's peak as a function of oxidizing potential in 0.1*N* KOH on a massive palladium electrode. Oxidizing potential: curve 1, 1.325V; curve 2, 1.525V; curve 3, 1.725V.

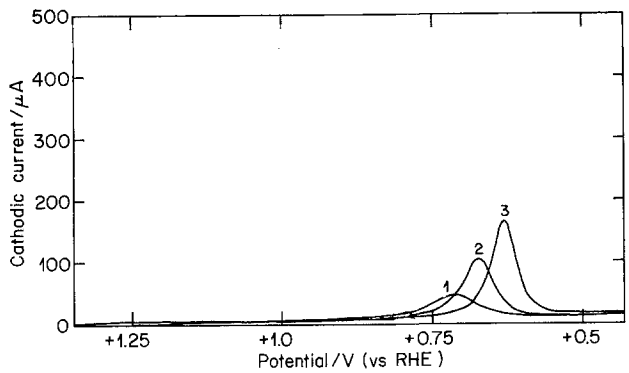


Fig. 8. Oxygen reduction's peak as a function of oxidizing potential in 0.1*N* KOH on a palladium surface electrodeposited on pyrolytic graphite at a current density of 5.1 mA/cm². Oxidizing potential: curve 1, 1.325V; curve 2, 1.525V; curve 3, 1.725V.

the stoichiometry of adsorption is 1 oxygen atom/surface palladium atom and the adsorption of each atom requires the transfer of two electrons, then the charge required for the adsorption of one monolayer of oxygen atoms on a (100) plane would require 424 μC/real cm² (7). The experimentally obtained values in both acid and alkaline media indicate a monolayer adsorption with a surface roughness factor of 1.15-1.2. Rand and Woods (7) reported a similar observation except that the experimental coverage was 690 μC/geometric cm² and consequently they had to assume a surface roughness factor of 1.6.

Pd-on graphite electrodes adsorb significantly larger quantities of oxygen/geometric cm². The plots of Fig. 13 and 14 do not exhibit with such electrodes any limiting adsorption step except in the case of a palladium layer electrodeposited at 5.1 mA/cm² and in alkaline medium. The higher the current density of deposition, the higher is the quantity of adsorbed oxygen. These

Table II. Reduction's peak potentials in 0.1*N* KOH

Oxidizing potential (RHE)	Massive Pd	Current density of electrodepositing* Pd				
		5.1 mA/cm²	30 mA/cm²	60 mA/cm²	118 mA/cm²	148 mA/cm²
1.725	0.637	0.637	0.625	0.620	0.595	0.590
1.525	0.690	0.675	0.6625	0.665	0.640	0.635
1.325	0.725	0.715	0.715	0.7125	0.7125	0.705

* Time of deposition in each case is the same as mentioned in the text.

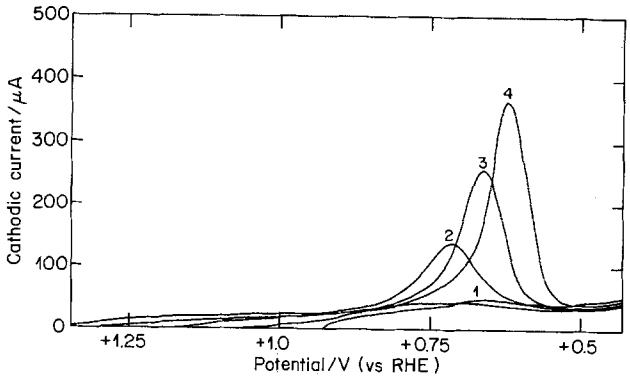


Fig. 9. Oxygen reduction's peak as a function of oxidizing potential in 0.1*N* KOH on a palladium surface electrodeposited on pyrolytic graphite at a current density of 30 mA/cm^2. Oxidizing potential: curve 1, 1.325V; curve 2, 1.525V; curve 3, 1.725V.

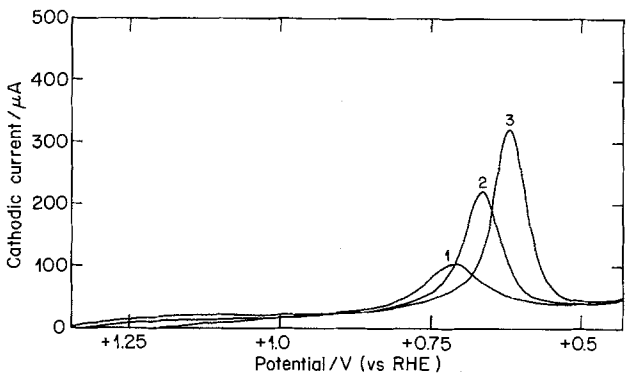


Fig. 10. Oxygen reduction's peak as a function of oxidizing potential in 0.1*N* KOH on a palladium surface electrodeposited on pyrolytic graphite at a current density of 60 mA/cm^2. Oxidizing potential: curve 1, 1.325V; curve 2, 1.525V; curve 3, 1.725V.

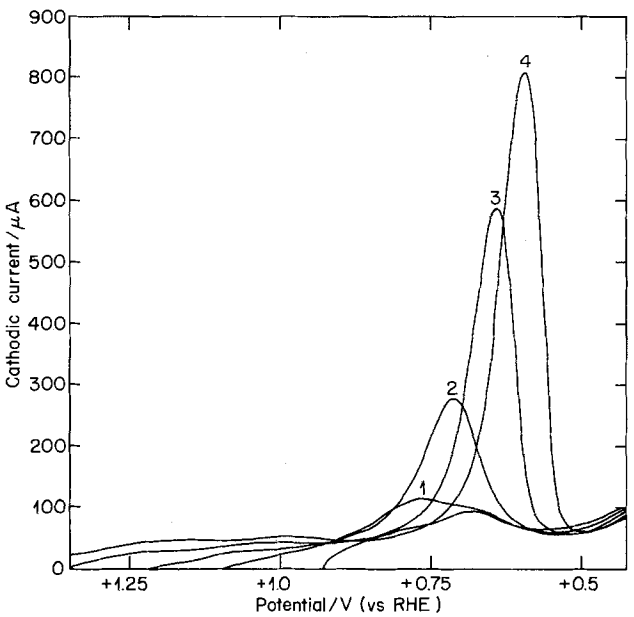


Fig. 11. Oxygen reduction's peak as a function of oxidizing potential in 0.1*N* KOH on a palladium surface electrodeposited on pyrolytic graphite at a current density of 118 mA/cm^2. Oxidizing potential: curve 1, 1.125V; curve 2, 1.325V; curve 3, 1.525V; curve 4, 1.725V.

results mean either a very large surface roughness or a palladium surface which is intrinsically more active (*i.e.*, higher specific surface energy) than a massive palladium electrode, and if the latter assumption is correct one is forced to assume that a phase-oxide layer

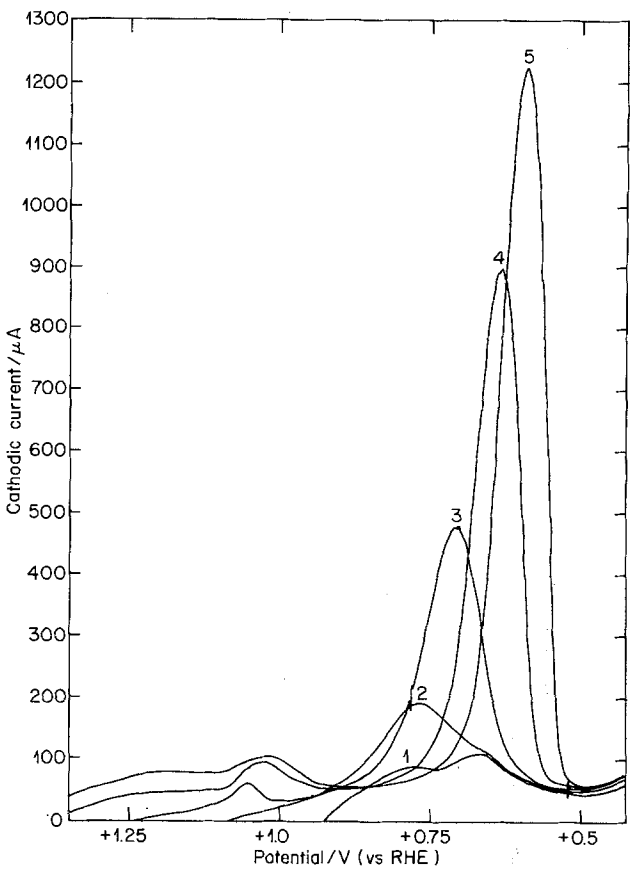


Fig. 12. Oxygen reduction's peak as a function of oxidizing potential in 0.1*N* KOH on a palladium surface electrodeposited on pyrolytic graphite at a current density of 148.0 mA/cm^2. Oxidizing potential: curve 1, 0.925V; curve 2, 1.125V; curve 3, 1.325V; curve 4, 1.525V; curve 5, 1.725V.

is formed at potential more cathodic than in the case of massive palladium. With regard to the latter surface Rand and Woods (7) observed that a palladium-phase oxide does not form at anodizing potentials lower than $\simeq$ 1.8V (RHE) for an oxidizing time of 10 sec.

A qualitative opinion concerning the morphology and surface roughness of the palladium deposits can be obtained from the scanning electron micrographs at 10,000$\times$ magnification, which are shown in Fig. 15. The deposit obtained at 148 mA/cm^2 appears to have more surface roughness than the deposit obtained at 5.1 mA/cm^2, but it is very unlikely that the variation in surface roughness is anything near a ratio of $\simeq$20 which is necessary to account for the observed increase in the amount of adsorbed oxygen.

A conclusive interpretation of the data requires a quantitative evaluation of electrode surface roughness. For the purpose of the present discussion, a knowledge of the relative values of surface roughness is sufficient. This is still a complex problem because hydrogen diffusion into Pd excludes the use of the hydrogen adsorption method (6), which has been successfully used to determine the real surface area of Pt electrodes, and the electrochemical activity toward both hydrogen and oxygen adsorption complicates the use of the capacitance method. At certain potentials however, the latter method can be used to give useful information on the relative surface roughness of the Pd surfaces used in the present work.

Figure 16 shows the cathodically swept capacitance *vs.* potential relationships in 1.0*N* H_2SO_4 for massive Pd and Pd surfaces electrodeposited at 5.1 and 30 mA/geometric cm^2. At a potential of $\simeq$0.4V the capacitances are 32, 32, and 67 μF/cm^2 for the three mentioned surfaces. At this particular potential there should not be any adsorbed hydrogen or oxygen at the surface as indicated on the voltammetry curves of Fig.

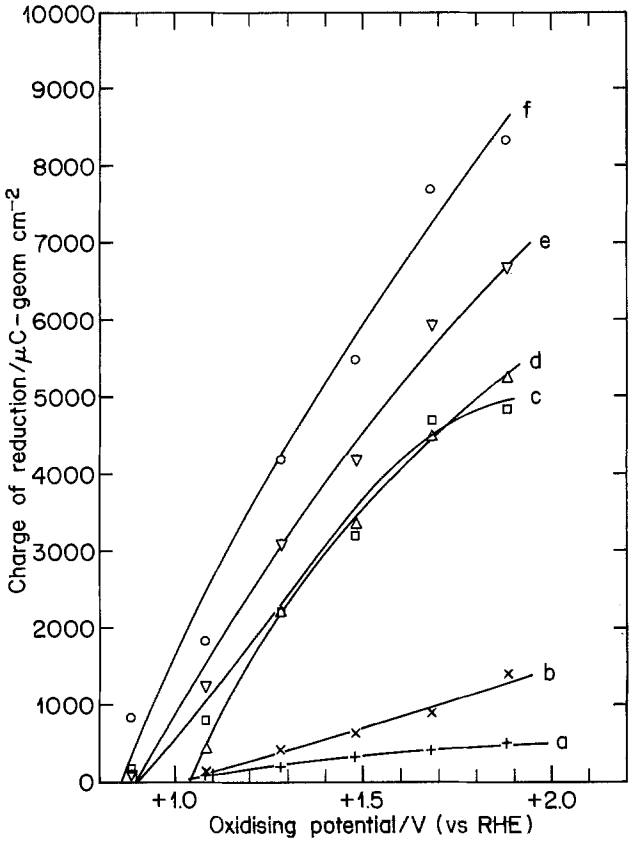


Fig. 13. Quantity of adsorbed oxygen as a function of oxidizing potential in 1.0*N* H_2SO_4 as calculated from Fig. 1-6. a, massive palladium; b, c, d, e, and f, palladium surface electrodeposited on pyrolytic graphite at a current density of 5.1, 30, 60, 118, and 148 mA/cm^2, respectively.

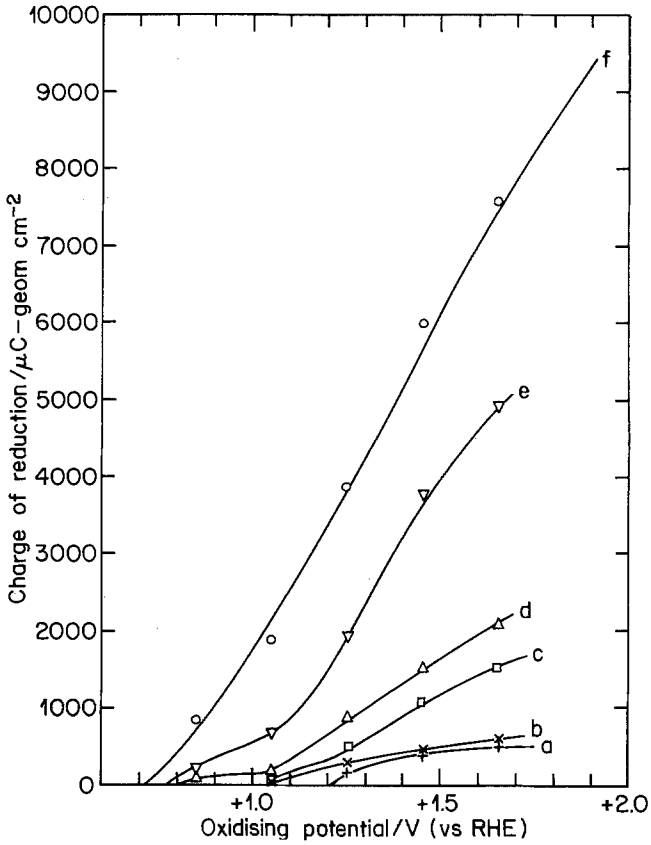


Fig. 14. Quantity of adsorbed oxygen as a function of oxidizing potential in 0.1*N* KOH as calculated from Fig. 7-12. a, massive palladium; b, c, d, e, and f, palladium surface electrodeposited on pyrolytic graphite at 5.1, 30, 60, 118, and 148 mA/cm^2, respectively.

1-3. Consequently these capacitance values should be proportional to the real surface area of the electrodes. These values give relative surface roughness (*i.e.*, surface roughness of electrodeposited Pd/surface roughness of massive Pd) of 1 and 2 for the two Pd electrodeposits, respectively. At potentials more anodic or cathodic the capacitance values of Fig. 16 give approximately the same roughness factors. The capacitance curves obtained in 0.1*N* KOH solution are shown in

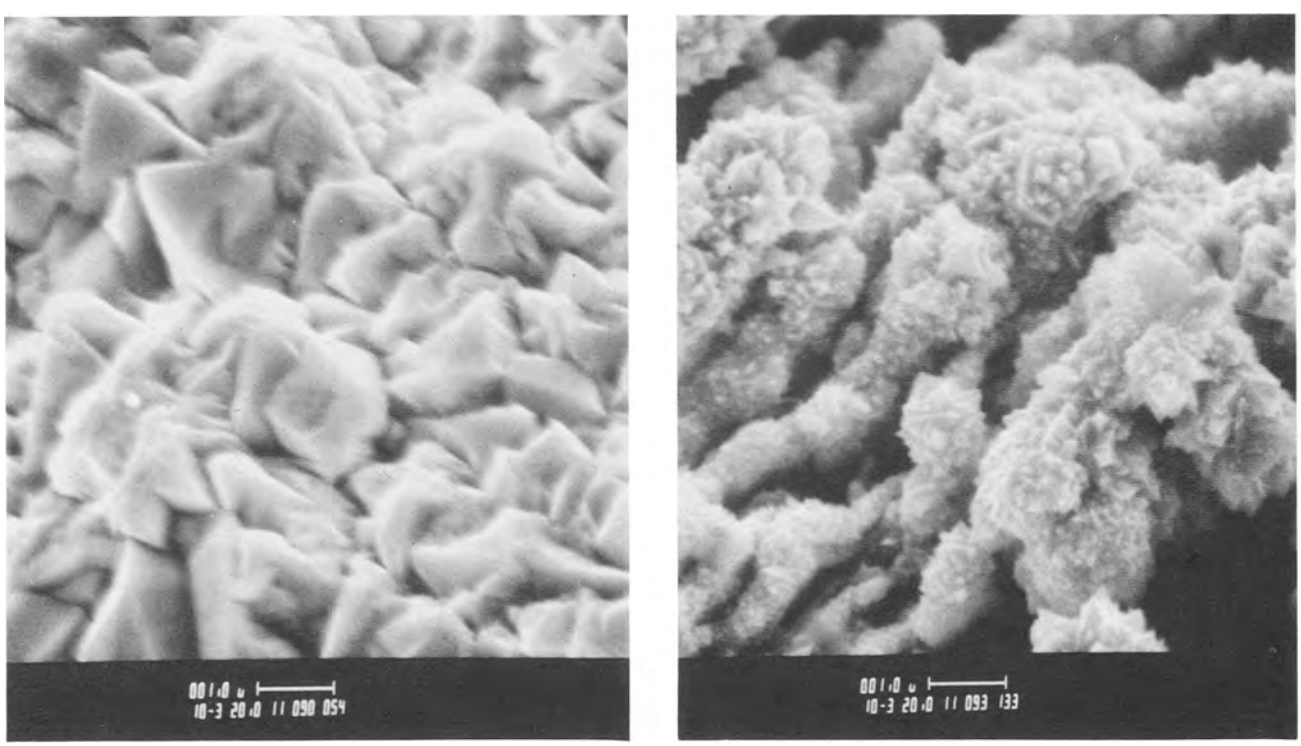


Fig. 15. Scanning electron micrographs for palladium surface electrodeposited on pyrolytic graphite at a 10,000× magnification. Current density of deposition is a (above left), 5.1 mA/cm^2; b, 148 mA/cm^2.

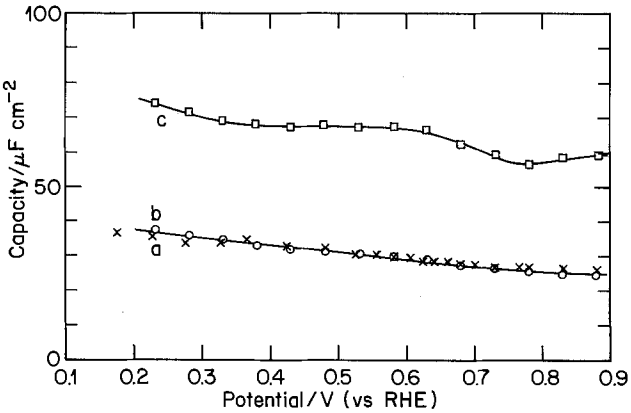


Fig. 16. Differential capacitance vs. potential curves in 1N H_2SO_4 for a, massive palladium; b, c, palladium electrodeposited on pyrolytic graphite at 5.1 and 30 mA/cm², respectively.

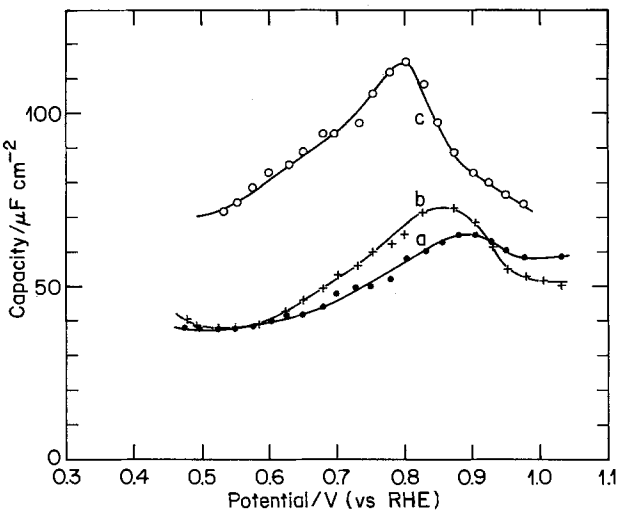


Fig. 17. Differential capacitance vs. potential curves in 0.1N KOH for a, massive palladium; b, c, palladium electrodeposited on pyrolytic graphite at 5.1 and 30 mA/cm², respectively.

Fig. 17. Applying the same argument, it is found that the relative roughness at 0.5V is 1.0 and 2.0 for palladium deposits obtained at 5.1 and 30 mA/cm², respectively. Palladium deposits obtained at the mentioned current densities give sufficiently reproducible capacitance curves. The capacitance can be measured for deposits obtained at higher current densities but the increase in surface roughness is accompanied by an increase in frequency dispersion, and as shown in the present work by an increase in the electrocatalytic activity. Consequently capacitance data obtained with the later deposits may give misleading values of relative surface roughness and will not be used here.

The relative surface roughness values obtained from the capacitance measurement can only account for a very small portion of the observed increase in the electrocatalytic activity of the palladium surface when the latter is electrodeposited on pyrolytic graphite. One must then conclude that the electrodeposited palladium must have a much higher intrinsic activity than the massive surface. The large magnitude of adsorbed oxygen observed in Fig. 13 and 14 must then correspond to the formation of a phase oxide at potentials significantly more cathodic than those at which an oxide forms at massive palladium. This can only occur if the specific surface energy of the electrodeposited palladium is considerably larger than that of the massive surface. A higher specific surface energy will reduce the activation energy necessary to start the formation of the phase oxide. The phenomenon observed here is definitely distinguished from the characteristics of dispersed palladium surfaces studied by Burshtein *et al.* (8). The latter authors reported that the quantity of chemisorbed oxygen on a palladium powder does not exceed a monolayer.

The interpretation of the extraordinary high electrocatalytic activity of Pd-on graphite must have to do with the nature of graphite surface and the effect of such nature on the structural features of the deposited metal. The structure of the resulting deposit must depend on the mechanism of deposition, and in the case of a foreign substrate must also depend on the magnitude of nucleation overpotential at the onset of polarization. The magnitude of nucleation overpotential for the galvanostatic electrodeposition of palladium from palladium chloride solution on both pyrolytic graphite and massive palladium can be determined from the potential-time plots shown in Fig. 18. At a current density of 3 mA/cm² the nucleation overpotential is 100 mV on pyrolytic graphite and is virtually absent on massive palladium. Graphite does not form mixed crystals with electrodeposited metals and that explains the large nucleation overpotential which is indicative of three-dimensional nucleation. It is also noticed that at steady state palladium is electrodeposited with a ≃30 mV higher overpotential as compared to the same on massive palladium. This indicates a variation in the mechanism of palladium deposition in the two cases even after the formation of the first layer of nuclei.

The lack of strong interaction between the electrodeposited metal and the graphite substrate will result in the formation of frozen nonequilibrium structures. The higher the current density of deposition, the higher will be the shift from equilibrium and associated surface energy. That may explain the strong dependence of structure on current density observed in Fig. 15 for the deposition of palladium on pyrolytic graphite. Such dependence is not observed as shown in Fig. 19 when palladium is electrodeposited on massive palladium.[2] In the latter case the variation in current density of deposition causes only a variation in the grain size. In other words, regardless of the rate of the deposition process, a palladium substrate exhibits a strong orienting effect on the deposited palladium. With a graphite substrate this orienting effect is absent and the structure of the deposit becomes almost completely under the influence of the externally controlled conditions of the current density, temperature, bath composition, and

[2] An electrodeposited palladium surface on a massive palladium electrode does not exhibit higher electrocatalytic activity than that of the massive substrate.

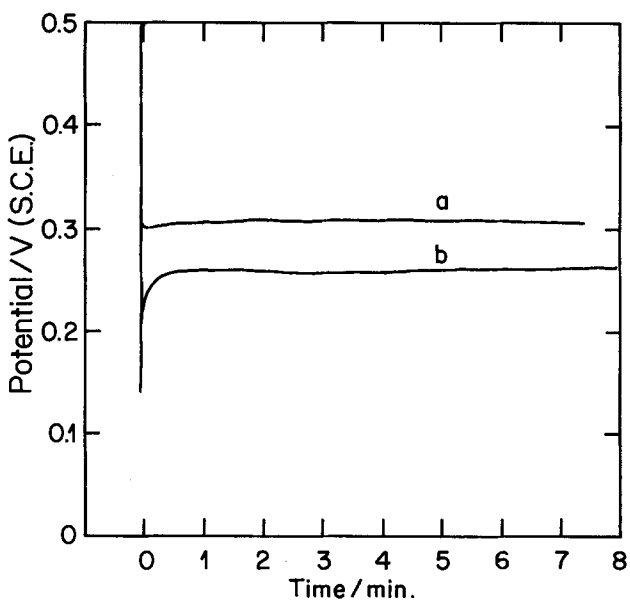


Fig. 18. Potential-time relationships for the deposition of palladium from palladium chloride solution at 3 mA/cm² on a, massive palladium and b, pyrolytic graphite.

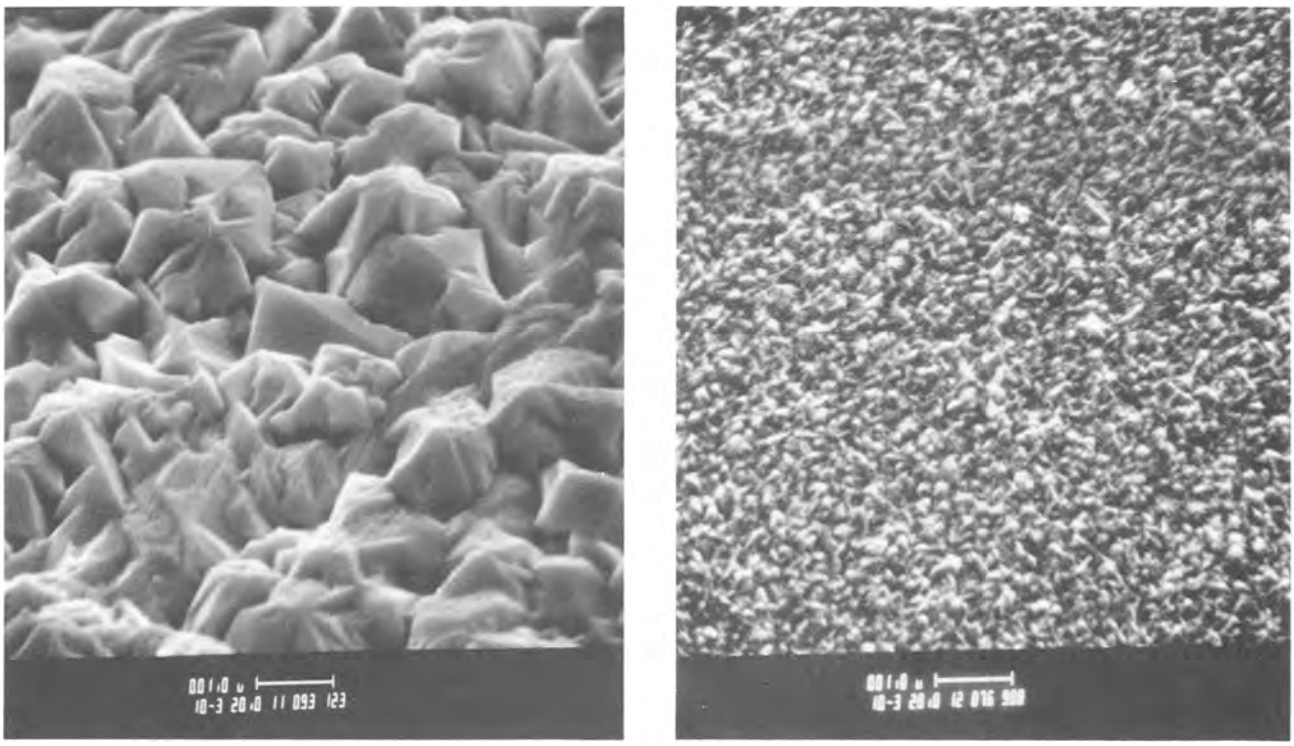


Fig. 19. Scanning electron micrographs for palladium surface electrodeposited on massive palladium at a 10,000× magnification. Current density of deposition is a, (above left), 5.1 mA/cm^2 and b, (above right), 148 mA/cm^2.

solution transport, with the current density playing a major role.

Previous attempts (9-13) to study the effect of structure on the electrocatalytic properties of metal surfaces were all carried out on platinum electrodes. Consequently, it would not be fruitful to discuss previously published work in the light of the present results. Such a discussion will be more meaningful after the approach used in the present paper has been extended to study the electrocatalytic properties of electrodeposited platinum on pyrolytic graphite. The study of the latter properties is presently in progress.

Acknowledgments

The author is indebted to A. Joly for doing the scanning electron microscopy and to A. Gendron for his assistance in obtaining the electrochemical data. For many helpful remarks the author would like to thank Dr. G. Bélanger.

Manuscript submitted June 17, 1976; revised manuscript received Aug. 31, 1976.

Any discussion of this paper will appear in a Discussion Section to be published in the December 1977 JOURNAL. All discussions for the December 1977 Discussion Section should be submitted by Aug. 1, 1977.

Publication costs of this article were assisted by the Hydro-Quebec Institute of Research.

REFERENCES

1. I. Morcos, *This Journal*, **122**, 1008 (1975).
2. I. Morcos, *ibid.*, **122**, 1492 (1975).
3. I. Morcos, U.S. Pat. application 646,994 (1976).
4. S. Gilman, in "Electroanalytical Chemistry," Vol. 8, A. J. Bard, Editor, p. 134, Marcel Dekker, New York (1967).
5. J. P. Hoare, in "Advances in Electrochemistry and Electrochemical Engineering," Vol. 6, P. Delahay, Editor, p. 220, John Wiley & Sons, New York (1967).
6. T. Biegler and R. Woods, *J. Electroanal. Chem.*, **20** 73 (1969).
7. A. J. Rand and R. Woods, *ibid.*, **31**, 29 (1971).
8. R. Kh. Burshtein, M. R. Tarasevich, and V. S. Vilinskaya, *Elektrokhimiya*, **3**, 349 (1967).
9. V. S. Bagotzky, Yu. B. Vassiliev, and I. I. Pyshnograeva, *Electrochim. Acta*, **16**, 2141 (1971).
10. J. T. Lundguist and P. Stonehart, *ibid.*, **18**, 349 (1973).
11. T. Biegler, *Aust. J. Chem.*, **26**, 2571 (1973).
12. L. S. Kanevskii, I. I. Astakhov, V. Sl. Palanker, and V. S. Bagotskii, *Elektrokhimiya*, **7**, 1329 (1971).
13. K. F. Blurton, P. Greenberg, H. G. Oswin, and D. R. Rutt, *This Journal*, **119**, 559 (1972).

Physical Principles Governing Nonideal Behavior of the Zirconia Oxygen Sensor

William J. Fleming*

General Motors Corporation, Research Laboratories, Electronics Department, Warren, Michigan 48090

ABSTRACT

Zirconia galvanic cells of the form

exhaust gas, Pt || stabilized ZrO_2 || Pt, air

are installed in the exhaust pipe of automobile engines to provide a voltage signal indicative of engine air-fuel ratio. To account for deviation of experimental sensor behavior from predicted ideal performance, a physical model of nonideal sensors is derived. Nonideal behavior is accounted for by simultaneous presence of two electrochemical reactions occurring at the anode (exhaust gas) electrode; one reaction involves oxygen and the other involves carbon monoxide. Correlation of calculated sensor characteristics with experimental results shows that nonideal sensor electrodes possess surface adsorption properties and catalytic activities which are many orders of magnitude less than ideal equilibrium values. The present theory indicates that undesired temperature-dependent shifting of sensor voltage curves with respect to engine air-fuel ratio is caused by competition between O_2 and CO gases for triple-point adsorption sites on the anode electrode.

One approach to the problem of reducing exhaust emissions from an automobile engine is to place a catalytic converter into the exhaust gas stream. One such catalyst, called a three-way or equilibrium catalyst, has been reported (1) to convert a high percentage of each of the exhaust gases, HC, CO, and NO, into the gases H_2O, CO_2, and N_2. However, to achieve the three-way conversion, precise metering of the air-fuel (A/F) mixture entering the engine must be maintained throughout the normal operating modes of the engine (1, 2). Closed-loop process control methods are used to regulate the air-fuel ratio of the engine (2-4). The utility of the closed-loop control system depends critically on the availability of a reliable sensor to detect A/F. An electrochemical sensor made of stabilized zirconium dioxide has been demonstrated to serve this purpose (2, 5).

The exhaust gas sensor usually consists of a zirconia tube with porous platinum electrodes formed on both its inner and outer surfaces. One end of the tube is closed so that it can be inserted into the exhaust stream which heats the tube; a schematic illustration of the sensor is shown in Fig. 1. For exhaust temperature in excess of approximately 400°C, the sensor becomes activated due to onset of oxygen ion conduction in the zirconia electrolyte.

To a first approximation the sensor voltage, V, can be calculated from the thermodynamic relationship for reversible transfer of oxygen from cathode to anode. One obtains the equation (6, 7)

$$V = (RT/4\mathbf{F}) \ln [p_{O_2}(\text{air})/p_{O_2}(\text{exh})] \qquad [1]$$

where R is the universal gas constant, T is absolute temperature of the active region of the electrolyte, $\mathbf{F}$ is Faraday's constant, $p_{O_2}(\text{air})$ is the oxygen partial pressure of atmospheric air, and $p_{O_2}(\text{exh})$ is the oxygen partial pressure of the exhaust for the engine A/F ratio and exhaust temperature of interest. It is further assumed that the anode electrode has sufficient catalytic activity to fully equilibrate exhaust gas reactions. Sensor voltage curves calculated by the above procedure are shown in Fig. 2.

Actual sensor behavior deviates from the ideal behavior shown in Fig. 2. The objective of the present work is to derive a physical model of a nonperfect zirconia sensor which will account for nonideal behavior. Particular attention is given to identification of those physical parameters defining the observed performance of experimental sensors.

Experimental

A representative curve of sensor voltage *vs.* engine air-fuel ratio obtained using a computer controlled test facility (8) is shown in Fig. 3. Rate of change of A/F did not exceed 1 A/F ratio unit/min; at this rate transient effects were eliminated and sensor characteristics were measured under essentially steady-state conditions. Further details of the measurement techniques are given elsewhere (5).

Voltage curves like the one in Fig. 3 are usually obtained for at least three exhaust temperatures. Different sensors often exhibit distinguishable characteristics which suggest that sensors can be separated into general groupings. For example, sensors with sharply stepped voltage curves (group A) having better agreement with ideal behavior can be contrasted to sensors with washed-out curves (group B) having poor agreement with ideal behavior. Voltage characteristics for

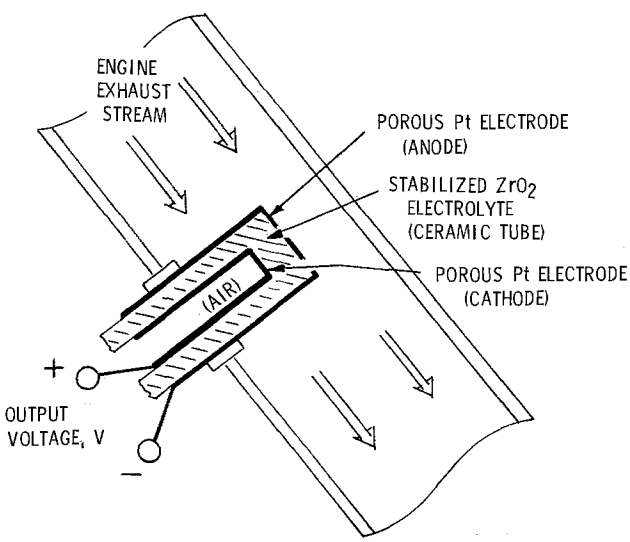


Fig. 1. Schematic illustration of zirconia exhaust sensor (cross-sectional view).

* Electrochemical Society Active Member.
Key words: zirconia, galvanic cells, exhaust gas sensor, solid electrolyte, high temperature.

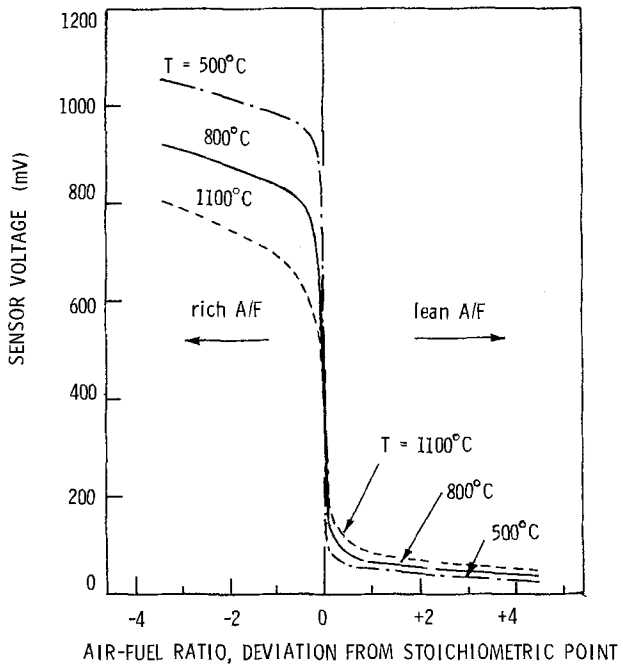


Fig. 2. Ideal sensor voltage curves

a sensor typical of group A are shown in Fig. 4, whereas characteristics typical of group B are shown in Fig. 5.

Departures of sensor behavior shown in Fig. 4 and 5 from the ideal behavior shown in Fig. 2 are summarized as follows: (*i*) transition steplike slopes of the voltage curves of the group B sensor are reduced compared to those of the group A sensor; (*ii*) pronounced drop of voltage level over the entire A/F range with increased exhaust temperature for the group B sensor; (*iii*) shifting of the steplike transitions of the voltage curves of both sensors toward richer A/F for increased exhaust temperature.

Departures of sensor behavior from ideal behavior are detrimental to performance of closed-loop engine control systems. These systems rely on invariance of the steplike voltage transition of the zirconia sensor

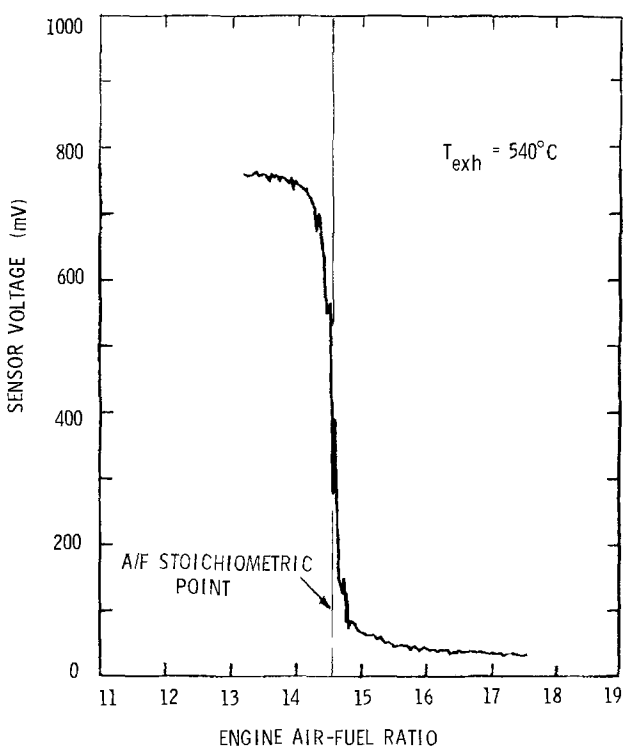


Fig. 3. Experimental sensor voltage curve obtained using computer-controlled test facility (8).

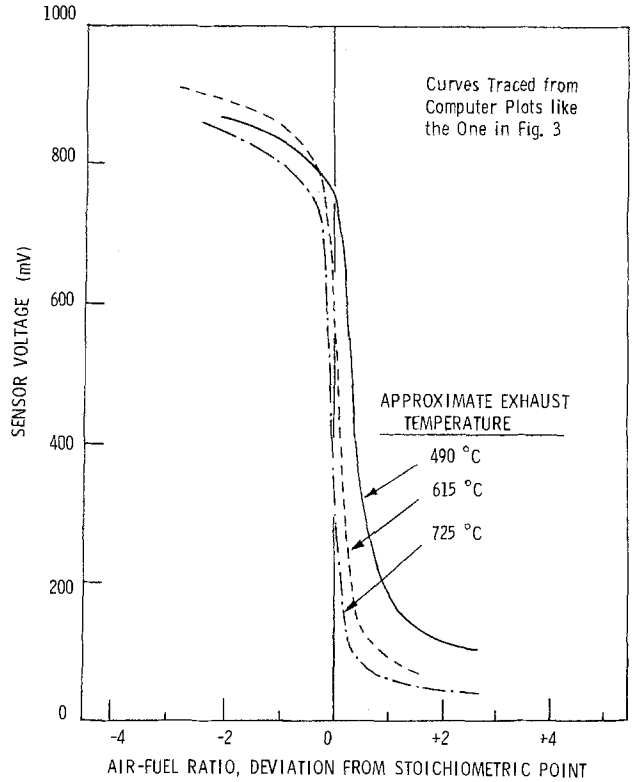


Fig. 4. Experimental voltage curves typical of group A sensors (sharp transition step in good agreement with ideal sensor behavior).

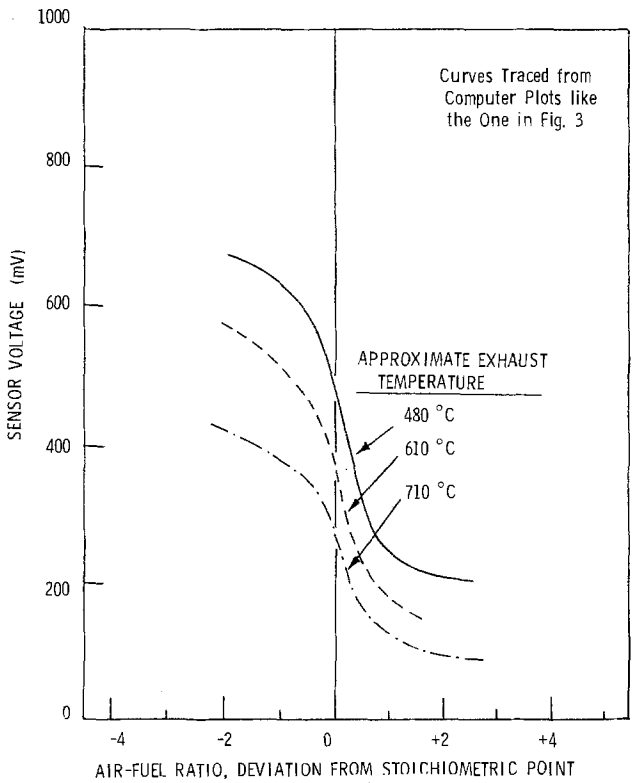


Fig. 5. Experimental voltage curves typical of group B sensors (washed-out transition step in poor agreement with ideal sensor behavior).

for desired accuracy (2-4). In the discussion below, a physical model of nonperfect sensor behavior in automobile exhaust is developed which is intended to provide better understanding of the origins of nonideal sensor characteristics.

Discussion

Derivation of a physical model of the zirconia exhaust gas sensor is difficult because of the complexity of its operating environment. Effort is made here to develop a model which is sufficiently complete to account for the above-described nonideal sensor behavior. One point of emphasis is that in the present application the zirconia galvanic cell simply provides an open-circuit voltage; thus, thermodynamic rather than kinetic considerations are important.

Derivation of physical model.—Simplification is made by assuming homogeneity of the active area of the zirconia cell; active cell area consists of the surface area of the zirconia tube which is exposed to exhaust gas (*cf.* Fig. 1). Effects due to temperature gradients, both lengthwise and transverse to the zirconia tube wall, are ignored. The ionic transport number for oxygen ions in zirconia is assumed equal to unity.

Sensors are represented by an electrochemical cell of the type

$$\text{exhaust gas, Pt} \,||\, \text{stabilized } ZrO_2 \,||\, \text{Pt, air reference} \qquad [2]$$

Since platinum is known to serve as a good cathode material for the air reference electrode (9), electrochemical reactions occurring there are assumed to be well defined. The over-all cathode reaction is

$$O_2 + 4e^- \rightleftarrows 2\,O^= \qquad [3]$$

where $O^=$ denotes an oxygen ion found in the zirconia anion sublattice.

Electrochemical reactions occurring at the anode electrode are not nearly so well defined. It has been suggested that one major cause of the departure of experimental sensor characteristics from ideal behavior is the lack of catalytic activity of the anode electrode (7). Evidence also indicates that the presence of oxidizable gas residuals such as CO, H_2, and hydrocarbons causes pronounced increases in cell voltage even when excess oxygen exists (10, 11). Since automobile exhaust contains a plethora of oxidizable gas residuals including CO, H_2, and up to 200 species of hydrocarbons, the above effects must be considered.

Although CO and H_2 comprise less than a few percent of the total of exhaust gas concentrations, they are nonetheless the major species of oxidizable gases, being at least ten times more abundant than the total of the hydrocarbons. Due to their relatively low concentration, hydrocarbons are assumed to have negligible effect on cell voltage. Effects of H_2 on cell voltage are also neglected for the following reasons. First, studies of gas adsorption show that CO preferentially adsorbs onto Pt when a dilute mixture of CO and H_2 gases is exposed to a Pt surface (12). Second, analytical measurement of gas species evolving during sharp rises in the voltage of a zirconia vacuum gauge indicates that CO is an active gas residual involved in the process of anomalous voltage increase (11). Thus, only the effects of the oxidizable gas, CO, are considered in the present work.

Electrochemical anode reactions.—The presence of CO can affect sensor voltage in either of two ways. First, CO may deplete the local concentration of O_2 at the anode surface by means of the reaction

$$CO' + \tfrac{1}{2}\,O_2' \overset{K_0}{\rightleftarrows} CO_2' \qquad [4]$$

where the anode electrochemical reaction is

$$O_2' + 4e^- \rightleftarrows 2\,O^= \qquad [5]$$

in which case the electrochemical cell is simply an oxygen cell, as shown below

$$p_{O_2'}\text{(anode), Pt} \,||\, \text{stabilized } ZrO_2 \,||\, \text{Pt, } p_{O_2}\text{(air)} \qquad [6]$$

In the above equations O_2', CO', and CO_2' denote gases in the vicinity of the anode electrolyte surface; $p_{O_2'}$ (anode) is the partial pressure of O_2' which exists after completion of reaction [4]; and K_0 is an equilibrium constant for this reaction.

Open-circuit voltage generated by cell [6], subject to electrochemical reactions [3] and [5], is given by

$$V_{O_2} = V_{O_2}^\circ + (RT/4\mathbf{F}) \ln [p_{O_2}\text{(air)}/p_{O_2'}\text{(anode)}] \qquad [7]$$

The standard cell potential, $V_{O_2}^\circ$, in Eq. [7] is determined by the difference of electron electrochemical potentials, $\mu_{e^-}^\circ$, between electrodes (13)

$$V_{O_2}^\circ = [\mu_{e^-}^\circ\text{(anode)} - \mu_{e^-}^\circ\text{(cathode)}]/\mathbf{F} \qquad [8]$$

When all constituent phases (gas, metal electrode, and solid electrolyte) are in thermodynamic equilibrium, electrochemical potentials, $\mu_{e^-}^\circ$, will be the same at both electrodes for cell [6] and $V_{O_2}^\circ$ will equal zero. Exhaust sensors, however, can possess nonequilibrium conditions whereupon the term $V_{O_2}^\circ$ takes on a nonzero value. Nonequilibrium conditions include irreversible reactions, reaction with chemical impurities, and insufficient catalytic activity of the electrodes.

A second way that CO can affect sensor voltage is by direct participation in an electrochemical process by means of the anode reaction

$$CO' + O^= \rightleftarrows CO_2' + 2e^- \qquad [9]$$

in which case the electrochemical cell is the following

$$p_{CO'}\text{(anode), Pt} \,||\, \text{stabilized } ZrO_2 \,||\, \text{Pt, } p_{O_2}\text{(air)} \qquad [10]$$

Open-circuit voltage generated by cell [10], with electrochemical reactions [3] and [9], is given by

$$V_{CO} = V_{CO}^\circ + (RT/2\mathbf{F}) \ln [p_{O_2}{}^{1/2}\text{(air)}\; p_{CO'}\text{(anode)}/p_{CO_2'}\text{(anode)}] \qquad [11]$$

When thermodynamic equilibrium conditions exist, the standard cell potential, V_{CO}°, computed from Eq. [3], [8], and [9] is found equal to

$$V_{CO}^\circ = [\mu_{CO}^\circ\text{(anode)} - \mu_{CO_2}^\circ\text{(anode)} + \tfrac{1}{2}\,\mu_{O_2}^\circ\text{(cathode)}]/2\mathbf{F} \qquad [12]$$

where the electrochemical potentials, μ°, are equal to the Gibbs chemical free energies of the gases CO, CO_2, and O_2 determined at the temperature of interest. For typical exhaust temperatures which range between 450° and 750°C, the equilibrium value of V_{CO}° computed from Eq. [12] decreases from 1140 to 1000 mV as temperature increases. Due to the nonequilibrium conditions cited above, exhaust sensors can possess V_{CO}° values as much as 300 mV lower than the equilibrium values.

Exhaust gas reactions.—For purposes of the present discussion the anode electrode is depicted by the schematic illustration shown in Fig. 6. Exhaust gases of

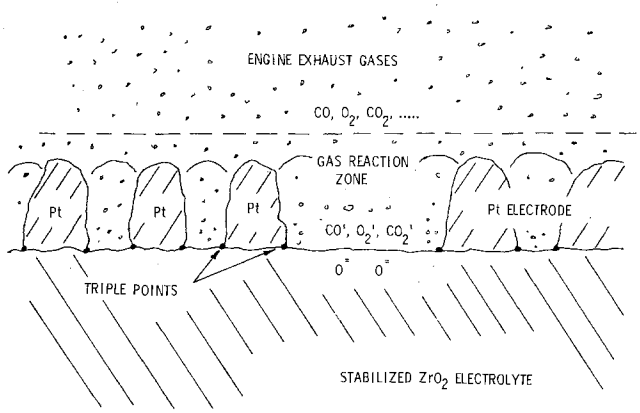


Fig. 6. Schematic representation of physical structure of anode electrode/electrolyte region.

greatest interest here are CO, O_2, and CO_2. Within the electrode pore spaces these gases undergo reaction, thereby giving rise to reacted gases CO′, O_2′, and CO_2′ in the vicinity of the electrode/electrolyte surface.

The method of computing equilibrium partial pressures of engine exhaust gases is well known (14, 15). For simplicity, gas species in the exhaust are herein restricted to the major products of combustion: CO_2, CO, H_2O, H_2, O_2, and N_2. Mole concentrations of these gases are related to engine A/F by chemical balance equations (15). Calculations are made using the assumption that the water gas reaction

$$CO_2' + H_2' \overset{K_w}{\rightleftarrows} CO' + H_2O' \qquad [13]$$

governs the relationship between H_2′ and CO′. Detailed analysis by Barnes *et al.* (14) shows that for exhaust temperatures greater than 480°C, mole concentrations of CO′ and CO_2′, and O_2′ as a function of engine A/F are, to good approximation, determined by standard chemical balance equations combined with the following equilibrium solutions for Eq. [4] and [13]

$$K_o = [CO_2']/[CO'][O_2']^{1/2} \qquad [14]$$

and

$$K_w = [CO'][H_2O']/[H_2'][CO_2'] \qquad [15]$$

Total mixture pressure, p_{mix}, of the exhaust gas is set equal to 1 atm; this value is representative of automobile engines run at low power levels. Solutions for $p_{CO'}$ and $p_{O_2'}$, computed from the expressions $[CO'] \cdot p_{mix}$ and $[O_2'] \cdot p_{mix}$, are shown in Fig. 7 where four cases are computed. [Values of $p_{CO_2'}$ *vs.* A/F have relatively little variation and are not shown here, but can be found elsewhere (14).] Cases 2 through 4 represent various degrees of reaction completion, whereas case 1 is included to show typical levels of CO and O_2 as found in unreacted engine exhaust. Degrees of reaction for cases 2 through 4 are defined by assuming that the constants K_o and K_w of Eq. [14] and [15] could be assigned values which did not correspond to the actual

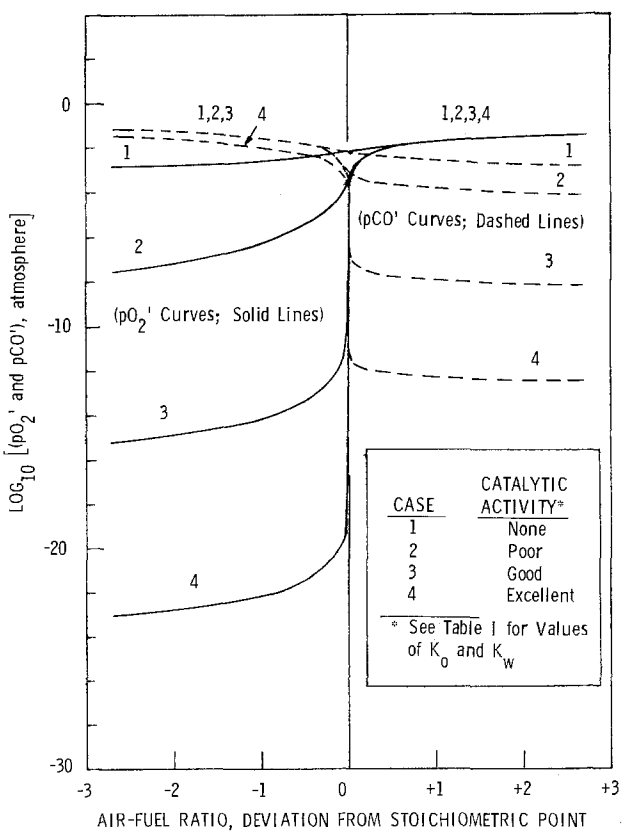


Fig. 7. Partial pressures of reacted gases O_2′ and CO′ in vicinity of anode electrode/electrolyte surface. (Total mixture pressure equals 1 atm.) Table I gives values of constants.

Table I. Values of constants used to calculate $p_{O_2'}$ and $p_{CO'}$ (results plotted in Fig. 7)

CASE	REACTION FREEZING TEMPERATURE	EQUILIBRIUM CONSTANTS* K_o	K_w
1	No Reaction**	--	--
2	1480°C	8.0×10^3	3.80
3	900°C	1.0×10^8	1.38
4	600°C	2.3×10^{12}	0.36

*Defined by Eqs. [14] and [15].

**Typical Engine Exhaust Levels Used Here.

temperature of the exhaust. That is, combustion gas reactions in the engine cylinder were assumed to have stopped at the freezing temperatures given in Table I.

One might think that exhaust flow rate would also affect the degree of completion of gas reactions at the anode electrode. This possibility was investigated by means of a special experiment. Sensor voltage was observed during independent adjustment of engine exhaust flow and temperature (5). Effects of flow on sensor voltage were found to be small compared to those of temperature; for this reason effects of flow are ignored in the present analysis.

Gas adsorption at triple points.—Attention is now given to the electrode/electrolyte interface region of the anode electrode. As depicted in Fig. 6, the anode electrode has a labyrinthine structure with interspersed pores permitting gas/electrolyte contact. Locations where the triple contact electrode/electrolyte/gas exist are shown in Fig. 6. Electrochemical reactions of Eq. [5] and [9] can only occur at or near triple points because these reactions require the simultaneous presence of gases, electrons, and oxygen ions.

Regardless of how fully reacted the exhaust gases, there always exists a joint presence of CO and O_2 in the vicinity of the triple points on the anode electrode; this behavior is shown by the curves of Fig. 7. The problem at hand is as follows. Given the simultaneous presence of CO and O_2, what fraction of the triple points will support electrochemical cell reaction [5] involving O_2, and what fraction will support reaction [9] involving CO? The solution used here is to postulate that CO and O_2 gases compete for adsorption at the triple point sites on the anode electrode. Fuel cell reactions [9] are assumed to occur at sites where CO is adsorbed, whereupon the adsorbed CO state is taken as an intermediate step in the physical mechanism of reaction [9]. In a like manner, triple point sites where CO is not adsorbed are assumed to support the O_2 concentration cell reaction [5]. Existence of adsorbed O_2 and/or absence of adsorbed gas are taken as intermediate steps in the physical mechanism of reaction [5].

The fraction of triple point sites occupied by adsorbed CO is calculated using the Langmuir adsorption isotherm (16). When CO and O_2 molecules occupy single sites in adsorption, the Langmuir expression for the fraction, θ_{CO}, of triple point sites occupied by CO can be written as

$$\theta_{CO} = K_{CO}p_{CO'}/(1 + K_{CO}p_{CO'} + K_{O_2}p_{O_2'}) \qquad [16]$$

where K_{CO} and K_{O_2} are adsorption constants for CO and O_2. For both gas species, CO and O_2, the adsorption constant K is estimated from kinetic gas theory using the following equations (16)

$$K = K^\circ \exp(Q/RT) \qquad [17]$$

and

$$K^\circ = \sigma\Psi^\circ/\nu n_s \quad [18]$$

where Q is the heat of adsorption, σ is the condensation coefficient of sticking probability, Ψ° is the flux of gas molecules at pressure equal to 1 atm colliding with unit area of surface per unit time, ν is the frequency of gas molecule vibration, and n_s is the number of triple point sites at which CO and O_2 compete for adsorption.

As discussed above, the fraction of triple point sites, f_{CO}, supporting CO cell reaction [9] is equated to θ_{CO}

$$f_{CO} = \theta_{CO} \quad [19]$$

where θ_{CO} is given by Eq. [16]. Similarly, the fraction of sites, f_{O_2}, supporting the O_2 cell reaction [5] is given by the fraction of sites where CO is not adsorbed; namely

$$f_{O_2} = 1 - \theta_{CO} \quad [20]$$

Sensor output voltage.—Output voltage of the exhaust sensor due to simultaneous existence of O_2 and CO cell reactions [5] and [9] is determined using the equivalent electrical network model shown in Fig. 8. An independent electrochemical cell is assumed to exist for each triple point site where either reaction [5] or [9] occurs. Of the total number of cells, the fraction f_{O_2} gives rise to voltages V_{O_2} given by Eq. [7], whereas the fraction f_{CO} gives rise to voltages V_{CO} given by Eq. [11]. Furthermore, each cell has internal resistance R_i, assumed identical for all cells. Sensor output voltage, V, is found by application of Norton's theorem to the network shown in Fig. 8; the resulting solution is

$$V = f_{O_2} V_{O_2} + f_{CO} V_{CO} \quad [21]$$

Combination of Eq. [7], [11], and [21] gives the desired final result

$$V = f_{O_2}\{V_{O_2}^\circ + (RT/4\mathbf{F}) \ln [p_{O_2}(\text{air})/p_{O_2}(\text{anode})]\} + f_{CO}\{V_{CO}^\circ + (RT/2\mathbf{F}) \ln [p_{O_2}^{1/2}(\text{air}) \cdot p_{CO}(\text{anode})/p_{CO_2}(\text{anode})]\} \quad [22]$$

where f_{O_2} and f_{CO} are given by Eq. [19] and [20].

Theoretical Results

Effects of the parameters in Eq. [22] on theoretical voltage *vs.* air-fuel ratio (A/F) curves are demonstrated by calculated results. A nominal set of parameter values which describe nonideal sensor behavior is first determined; the parameters then serve as a reference set of values about which a systematic variation of parameter values is made to analyze Eq. [22].

Selection of parameter reference values.—Sensor electrolyte temperature, T, is assumed equal to exhaust temperature which, in turn, is arbitrarily set equal to 600°C. The anode electrode is assumed to possess limited catalytic activity and exhaust gas reactions of Eq. [4] and [13] are assumed to have frozen at 1480°C; the corresponding p_{O_2} and p_{CO} values are shown by case 2 in Fig. 7. Values of p_{CO_2} *vs.* A/F have little variation, ranging between 0.09 and 0.14 atm; appropriate values are used (14). The air reference value, p_{O_2}, is set equal to 0.21 atm. Standard cell potential, $V_{O_2}^\circ$, is assumed negligible and is set equal to zero. Cell potential V_{CO}°

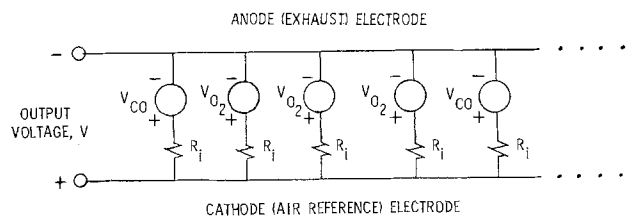


Fig. 8. Representation of sensor by equivalent electrical network of electrochemical cells. The total number of cells consists of the fraction, f_{O_2}, of V_{O_2} cells and the fraction, f_{CO}, of V_{CO} cells.

Table II. Values of parameters used to evaluate adsorption constants

PARAMETERS	SYMBOL	RANGE OF VALUES
Condensation Coefficient*	σ	10^{-4} to 10^{0}, dependent on mobility, transition states, and intermediate complexes involved in gas adsorption process.
Gas flux at pressure of one atmosphere*	Ψ°	3.5×10^{27} to 5.0×10^{27} molecules/m^2-s, dependent on gas molecular weight and gas temperature.
Gas Molecular Vibration Frequency*	ν	1.4×10^{13} to 2.1×10^{13} s^{-1} dependent on gas temperature.
Number of Triple Point Adsorption Sites*	n_s	10^{18} to 10^{16} sites/m^2, dependent on area of electrode/electrolyte interface.**
Universal Gas Constant	R	1.987 cal/g-mole-°K
Exhaust Gas Temperature (Sensor Operating Temperature)	T	720 to 1030°K, dependent on engine operating state.
Heat of Adsorption for CO on Pt	Q_{CO}	10 to 48 kcal/g-mole, dependent on degree and type of coverage, and presence of impurities.***
Heat of Adsorption for O_2 on Pt	Q_{O_2}	10 to 70 kcal/g-mole, dependent on degree and type of coverage, and presence of impurities.***

* Parameter values so denoted apply for both CO and O_2 gases.

** Maximum number of triple point sites is estimated by assuming there exists at most one triple point, i.e., one conducting path for $O^=$ ions per four unit cells of the ZrO_2 lattice; one ZrO_2 unit cell area equals 25 $Å^2$ or 25×10^{-20} m^2. The lower limit of 10^{16} sites/m^2 is arbitrarily chosen equal to 1% of the maximum number.

*** Maximum values of Q_{CO} and Q_{O_2} equal to 48 and 70 kcal/g-mole, respectively, were reported by Heyne and Tompkins (17) for the limited case of near zero coverage on clean Pt films. The lower limit values of 10 kcal/g-mole are arbitrarily chosen to represent cases of high coverage in the presence of impurities.

is assumed to involve nonequilibrium thermodynamic processes and is set equal to 800 mV, which is 270 mV below its equilibrium value at 600°C of 1070 mV.

Adsorption constants K_{O_2} and K_{CO} are more difficult to estimate. Limiting values for the constituent parameters which determine K_{O_2} and K_{CO} are given in Table II; when these values are substituted into Eq. [18], the factors $K_{O_2}^\circ$ and K_{CO}° take on values ranging between 1.7×10^{-8} and 3.6×10^{-2}. Suitable values within the range of values in Table II are chosen on the basis of the following assumptions: (*i*) condensation coefficient equal to 0.5; (*ii*) triple point sites equal to maximum number, 1×10^{18} sites/m^2; (*iii*) heats of adsorption reduced in value due to high coverage and presence of impurities on Pt sites. Resulting values are $K_{O_2}^\circ = K_{CO}^\circ = 1 \times 10^{-4}$ and $Q_{O_2} = Q_{CO} = 25$ kcal/g-mole; these values are used in Eq. [17] to calculate the constants $K_{O_2} = K_{CO} = 1.8 \times 10^2$ for $T = 600$°C.

Calculation of sensor voltage curve.—Systematic variation of parameter values about the above set of reference values is made to study effects on the sensor voltage *vs.* A/F curves calculated from Eq. [22]. Effects due to variation of catalytic activity of the anode electrode are shown in Fig. 9, where curve 2 is calculated for the reference set of parameter values, and curves 1 and 3 correspond to the p_{O_2} and p_{CO} values of cases 1 and 3 shown in Fig. 7. As reaction freezing temperature approaches exhaust temperature, improved catalytic activity of the anode electrode allows exhaust gas reactions to approach equilibrium conditions. The sensor voltage curves of Fig. 9 take on a sharper, more step-like transition at the stoichiometric A/F ratio due to the improved catalytic activity of the electrode.

Effects due to variation of adsorption constants are shown in Fig. 10; here again curve 2 is calculated for

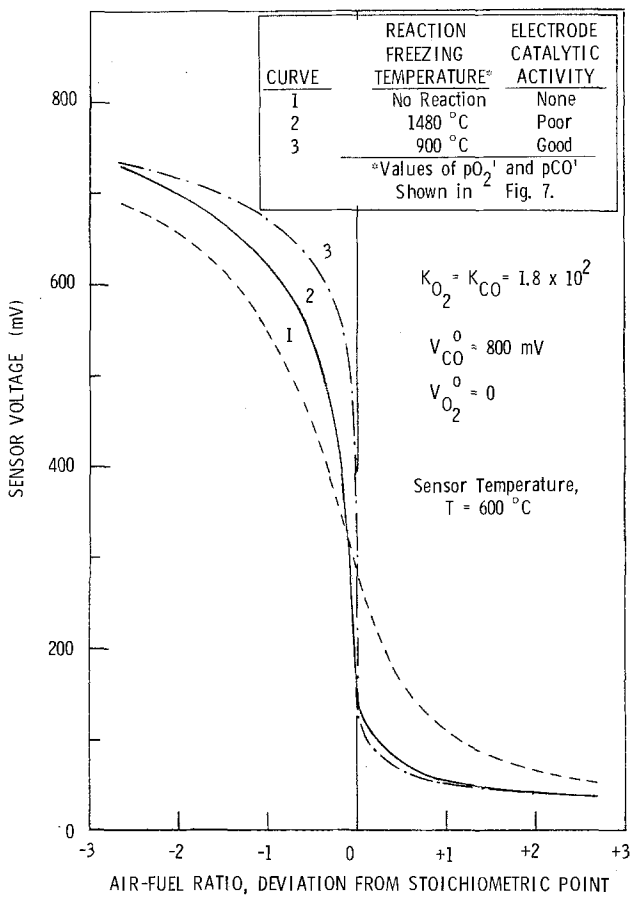


Fig. 9. Effects due to variation of catalytic activity of anode electrode, computed using theoretical model of nonideal sensor.

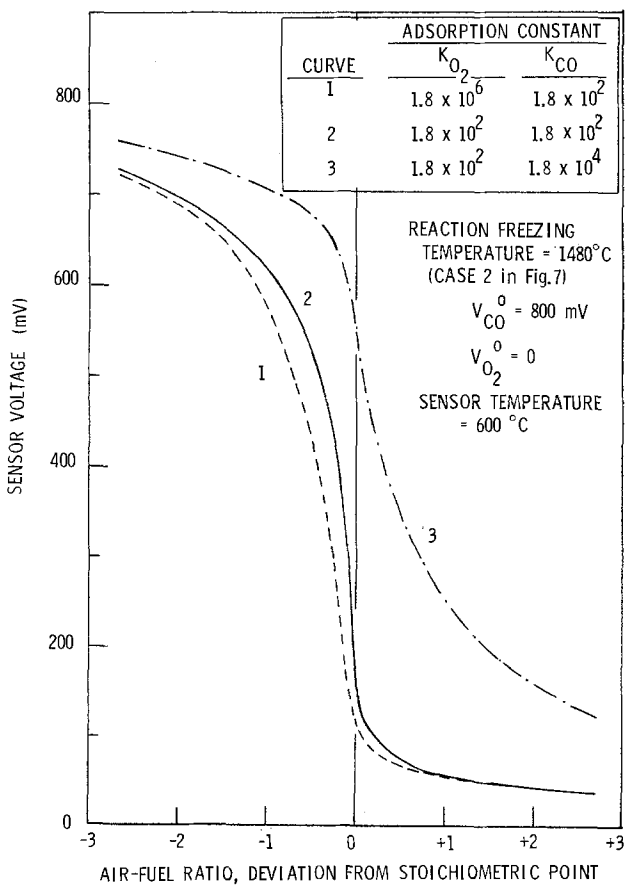


Fig. 10. Effects due to variation of adsorption properties of anode electrode, computed using theoretical model of nonideal sensor.

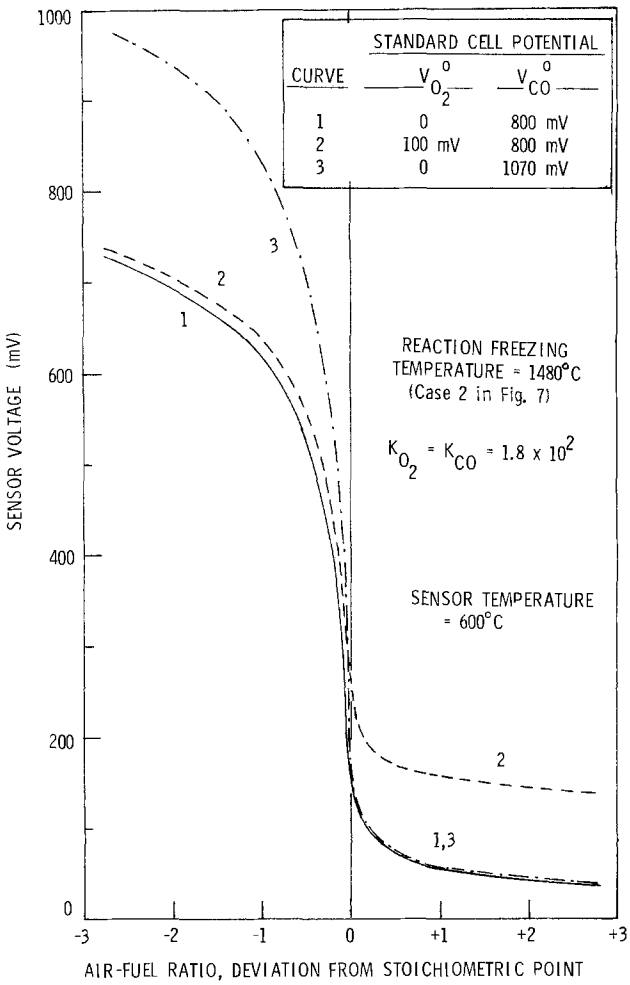


Fig. 11. Effects due to variation of standard cell potentials, computed using theoretical model of nonideal sensor.

the reference set of parameter values. Curves 1 and 3 correspond to varying values of K_{O_2} and K_{CO}. As the magnitude of K_{CO} relative to K_{O_2} decreases, the sensor voltage curves shift toward richer A/F ratios.

Effects due to variation of standard cell potentials are shown in Fig. 11; curve 1 is calculated for the reference set of parameter values, whereas curves 2 and 3 correspond to varying values of $V_{O_2}^\circ$ and V_{CO}°. Voltage levels of the rich and lean A/F tails of the curves are established by the values of the standard cell potentials.

Comparison to experiment.—The characteristics of the sensor curves shown in Fig. 4 and 5 can be related to the theory of Eq. [22] on the basis of the following observations. First, both groups of experimental curves exhibit a shifting of the steplike voltage transitions toward richer A/F for increased exhaust temperature. Second, group A sensor curves of Fig. 4 possess generally sharper voltage transition steps at A/F stoichiometry than do group B sensors of Fig. 5.

Parameter values of Eq. [22] are chosen to reflect the above-described behavior of experimental sensors. All temperature dependence is ascribed to the adsorption constants in order to account for the temperature dependent shifting of the voltage curves toward richer A/F. To obtain this curve shifting trend, the K_{CO} value must exceed the K_{O_2} value at lower temperature, and be smaller than the K_{O_2} value at higher temperature. Parameter values are chosen to give this behavior while being consistent with the range of values given in Table II. The values $K_{O_2}^\circ = 1 \times 10^{-2}$, $K_{CO}^\circ = 1 \times 10^{-7}$, $Q_{O_2} = 20$ kcal/g-mole, and $Q_{CO} = 40$ kcal/g-mole are chosen; K_{O_2} and K_{CO} are each given by Eq. [17] and are evaluated as follows

$$K_{O_2} = 1 \times 10^{-2} \exp(20/RT) \qquad [23]$$

and

$$K_{CO} = 1 \times 10^{-7} \exp(40/RT) \quad [24]$$

Sharper steplike transitions of group A sensors compared to group B sensors are attributed to better catalytic activity of the anode electrode. This behavior is obtained by assigning zero catalytic activity to group B sensor electrodes, whereby the p_{O_2}, and p_{CO}, values of case 1 shown in Fig. 7 are used. A reaction freezing temperature of 1480°C is assigned to group A sensor electrodes, whereby the p_{O_2}, and p_{CO}, values of case 2 shown in Fig. 7 are used. In both cases values for p_{CO_2}, *vs.* A/F have little variation, ranging between 0.09 and 0.14 atm, and appropriate values are used (14). Values of standard cell potentials are chosen to approximate the levels of the rich and lean A/F tails of the experimental sensor curves; the values $V_{CO}^{\circ} = 800$ mV and $V_{O_2}^{\circ} = 0$ are used for the group A sensor and $V_{CO}^{\circ} = 700$ mV and $V_{O_2}^{\circ} = 0$ are used for the group B sensor.

The above parameter values are substituted into Eq. [22] and the computed results are shown in Fig. 12 and 13. Good agreement between the computed curves and the experimental curves shown in Fig. 4 and 5 corroborates the validity of the physical sensor model developed in the preceding section of this paper. Agreement between relative shapes of curves and temperature trends of curves is noteworthy.

One can compare the physical properties of the theoretical models of group A and group B sensors to those of an ideal sensor. Tabulated values of relevant parameters are given in Table III. Note that major differences between ideal sensor parameter values and values for nonideal sensors in Table III are found in catalytic activity and adsorption properties. In particular, group A sensors which have catalytic activity only reduce p_{O_2}, some four orders of magnitude from that of unreacted exhaust, whereas the ideal sensor exhibits twenty orders of magnitude reduction of p_{O_2}, for the same A/F conditions. Moreover, the adsorption constants of both group A and group B sensors are from seven to thirteen orders of magnitude lower than the ideal values. It is beyond the scope of this paper to attempt to identify microscopic properties of electrode materials which give rise to the nonideal values of these parameters. However, future work in this area is suggested as a next step in further understanding of zirconia exhaust gas sensors.

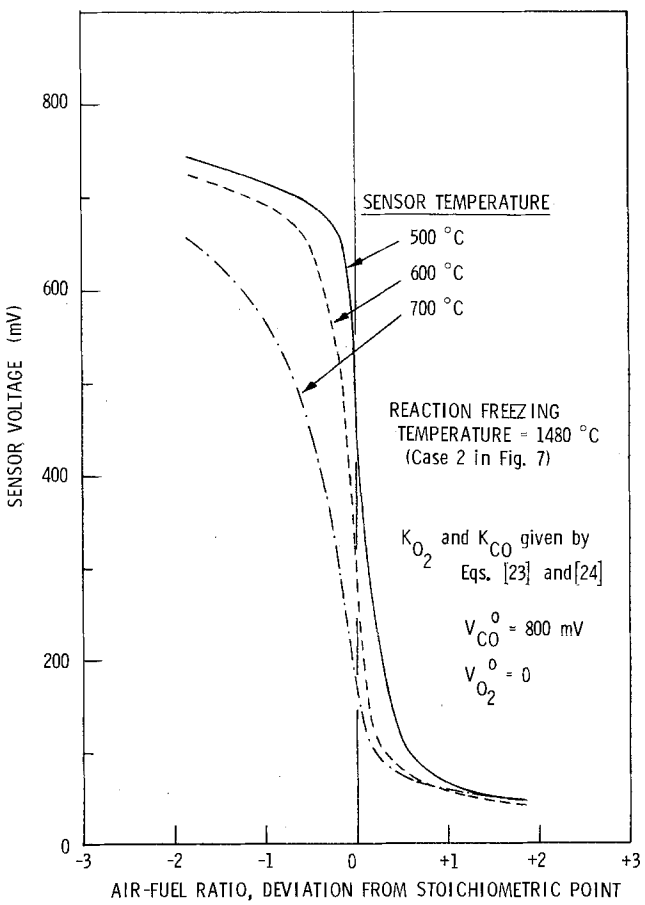


Fig. 12. Theoretical curves exhibiting behavior of group A sensors (*cf.* Fig. 4)

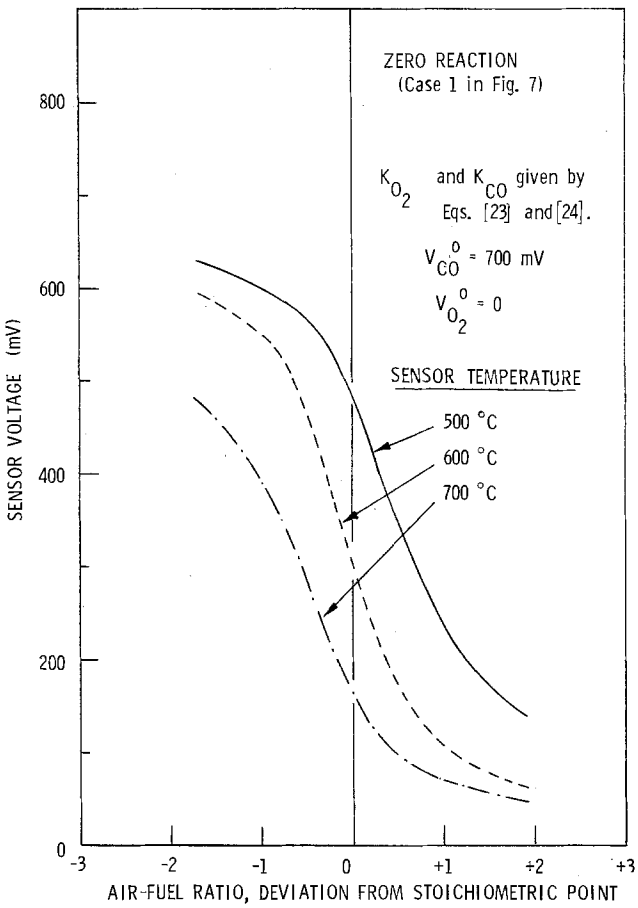


Fig. 13. Theoretical curves exhibiting behavior of group B sensors (*cf.* Fig. 5).

Conclusions

To summarize, there are three physical processes involved in the operation of the zirconia oxygen sensor and each process controls different characteristics of the sensor voltage *vs.* A/F curves. First, the degree of exhaust gas reaction, determined by catalytic activity of the anode electrode, controls the sharpness of the voltage transition step which occurs at the stoichiometric A/F point. Second, relative magnitudes of O_2 and CO gas adsorption properties of the anode electrode determine the A/F ratio at which the steplike voltage transition takes place. Third, standard cell potentials of the O_2 and CO cell reactions establish the voltage

Table III. Comparison of parameter values for theoretical sensor models at exhaust temperature of 600°C

SENSOR TYPE	CATALYTIC ACTIVITY: REACTION FREEZING TEMPERATURE	CATALYTIC ACTIVITY: pO_2 VALUE AT TRIPLE POINTS*	ADSORPTION CONSTANTS: K_{O_2}	ADSORPTION CONSTANTS: K_{CO}	STANDARD CELL POTENTIALS: $V_{O_2}^{\circ}$	STANDARD CELL POTENTIALS: V_{CO}°
Ideal (Fig. 2)	600°C	5.5×10^{-23} atm.	(1×10^{16})†‡	(3×10^{10})†	0	1070 mV
Nonideal Group A (Fig. 12)	1480°C	3.9×10^{-7} atm.	1×10^{3}	1×10^{3}	0	800 mV
Nonideal Group B (Fig. 13)	No Reaction	2.4×10^{-3} atm.	1×10^{3}	1×10^{3}	0	700 mV

* Values of pO_2 are taken from Fig. 7 at a point one air-fuel ratio rich of the stoichiometric point; the ideal value comes from Case 4, the Group A value comes from Case 2, and the Group B value comes from Case 1.

† Maximum values of K_{O_2} and K_{CO} are computed for the ideal sensor using Eqs. [17] and [18] together with the limiting values of Table II.

levels of the rich and lean A/F tails of the sensor curves.

To obtain agreement between experimental sensor characteristics and calculated results, it is found that sensor electrodes must possess surface adsorption properties and catalytic activities which are many orders of magnitude less than ideal equilibrium values. Future efforts to identify microscopic properties of electrode materials which give rise to the nonideal values of these parameters is suggested as a next step in further understanding of zirconia exhaust gas sensors.

Acknowledgments

Experimental results presented here were made possible by assistance provided by W. D. Creps, D. S. Howarth, A. J. Kotwicki, and L. S. Vora of the Automotive Systems Group of the Electronics Department, General Motors Research Laboratories. Special thanks go to fellow members of General Motors Research for helpful discussions on theoretical aspects of this work. These individuals include: J. S. Dunning, J. P. Hoare, and R. A. Sharma of the Electrochemistry Department, G. G. Tibbits of the Physics Department, G. J. Barnes, J. L. Gland, and K. C. Taylor of the Physical Chemistry Department, and D. S. Eddy, D. S. Howarth, and A. J. Kotwicki of the Electronics Department. The author very much appreciates the excellent typing done by J. Fiebelkorn.

Manuscript submitted June 1, 1976; revised manuscript received Sept. 20, 1976. This was Paper 20 presented at the Las Vegas, Nevada, Meeting of the Society, Oct. 17-22, 1976.

Any discussion of this paper will appear in a Discussion Section to be published in the December 1977 JOURNAL. All discussions for the December 1977 Discussion Section should be submitted by Aug. 1, 1977.

Publication costs of this article were assisted by the GM Corporation.

REFERENCES

1. J. B. Pond and T. DePalma, *Automot. Ind.*, **149**, 29 (1973).
2. R. Zechnall, G. Baumann, and H. Eisele, SAE Paper 730566, presented at SAE Automobile Engineering Meeting, Detroit, Michigan, May 14-18, 1973.
3. T. L. Rachel and R. Gunda, Paper 36/3 presented at IEEE Intercon Meeting, New York, New York, March 26-29, 1974.
4. R. A. Spilski and W. D. Creps, SAE Paper 750371 presented at the SAE Automotive Engineering Congress, Detroit, Michigan, February 1975.
5. W. J. Fleming, SAE Papers 760020 and 760379 presented at the SAE Automotive Engineering Congress and Exposition, Detroit, Michigan, February 1976.
6. J. Weissbart and R. Ruka, *This Journal*, **109**, 723 (1962).
7. D. S. Eddy, *IEEE Trans. Veh. Technol.*, **vt-23**, 125 (1974).
8. J. H. Rillings, W. D. Creps, and L. S. Vora, *Proc. IEEE*, **61**, 1622 (1973).
9. C. S. Tedmon, Jr., H. S. Spacil, and S. P. Mitoff, *This Journal*, **116**, 1170 (1969).
10. T. H. Etsell and S. N. Flengas, *ibid.*, **118**, 1890 (1971).
11. C. J. Mogab, *J. Vac. Sci. Technol.*, **10**, 852 (1973).
12. D. W. McKee, *J. Catal.*, **8**, 240 (1967).
13. J. S. Newman, "Electrochemical Systems," chap. 2, Prentice-Hall, Inc., Englewood Cliffs, New Jersey (1973).
14. G. J. Barnes, R. L. Klimisch, and B. B. Krieger, SAE Paper 730200 presented at the SAE International Automotive Engineering Congress, Detroit, Michigan, January 8-12, 1973.
15. B. A. D'Alleva, General Motors Research Laboratories Publication GMR-372, Warren, Michigan, May 15, 1960.
16. D. O. Hayward and B. M. W. Trapnell, "Chemisorption," p. 159, Butterworth and Co., London (1964).
17. H. Heyne and F. C. Tompkins, *Proc. R. Soc. London Ser. A*, **292**, 460 (1966).

The Ionic Conductivity of Beta Lead Fluoride

R. W. Bonne and J. Schoonman*

Solid State Department, State University of Utrecht, Sorbonnelaan 4, Utrecht-De Uithof, The Netherlands

ABSTRACT

The electrical conductivity of nominally pure and doped β-PbF_2 was investigated in the temperature range 300°-700°K. From our measurements, together with literature data, the temperature dependences of the concentration and mobility of the mobile species were calculated. The expression for the anion vacancy mobility is

$$\mu_{V_F} \cdot T = (54 \pm 18) \exp [-(0.23 \pm 0.02)\ \mathrm{eV}/kT]\ \mathrm{cm^2\ V^{-1}\ sec^{-1}\ ^\circ K}$$

and for the mobility of the interstitial anions

$$\mu_{F_i'} T = (5.4 \pm 1.9)\ 10^4 \exp [-(0.60 \pm 0.06)\ \mathrm{eV}/kT]\ \mathrm{cm^2\ V^{-1}\ sec^{-1}\ ^\circ K}$$

The intrinsic concentration of either anion-Frenkel defect was calculated to be

$$[V_F \cdot]_0 = [F_i']_0 = (1.6 \pm 0.5)\ 10^{23} \exp [-(0.44 \pm 0.02)\mathrm{eV}/kT]\ \mathrm{cm^{-3}}$$

The solid electrolyte properties of nominally pure and doped β-PbF_2 have been the subject of recent investigations (1-10). Derrington and O'Keeffe (2) and Benz (8) reported on the unusually high conductivity above about 700°K up to the melting point. The observed behavior cannot be understood from classical ionic motion theories (11, 12). Conductivities below 700°K, however, seem to be governed by the migration of point defects via normal lattice sites and interstitial sites. It is presently well established that these defects are thermally generated in the anion sublattice (3, 7, 13).

Investigations with the Wagner polarization cell have demonstrated that lead fluoride exhibits predominantly ionic conduction (4, 6, 8, 9). Incorporation of monovalent cations on lead ion sites increases the ionic conductivity by increasing the concentration of fluoride ion vacancies (7, 9). The influence of the substitutional incorporation of trivalent cations on the ionic conduc-

* Electrochemical Society Active Member.
Key words: β-lead fluoride, extrinsic conductivity, intrinsic conductivity, ionic conductivity, solid electrolyte.

tivity is still ambiguous. Arkhangel'skaya (14) and Liang and Joshi (7) reported an increased conductivity of lead fluoride upon doping with trivalent impurities. To the contrary, Kennedy and Miles (9) showed the conductivity of β-PbF_2:BiF_3 pellets to decrease as compared to the conductivity of nominally pure material.

In regard to this ambiguity, the nature of applied electrode material has been discussed recently (15, 16). The conductivity of β-PbF_2:BiF_3 pellets exceeds the conductivity of nominally pure samples, when graphite electrodes were used. On the other hand, when Pb electrodes were used the conductivity was lower than that of the nominally pure material. Liang and Joshi (16) proposed the reaction

$$2BiF_3 + 3Pb \rightarrow 2Bi + 3PbF_2 \quad [1]$$

to explain the low conductivity of β-PbF_2:BiF_3 in between Pb electrodes. This reaction, however, will be strictly limited to the electrode surface area, since Bi^{3+} on a lead ion site is expected to be quite immobile, especially in a structure which favors mobile anion Frenkel defects. A recent paper (17) on the novel solid electrolyte $Pb_{1-x}Bi_xF_{2+x}$ ($0 \leqq x \leqq 0.50$) shows that the conductivity increases when x increases to values up to 0.25, whereas for $0.25 < x < 0.50$ the conductivity starts to decrease upon increasing x. The decrease has been accounted for by annihilation of anion vacancies by the excess fluoride ions from BiF_3. Gold electrodes were used in this study (17).

Studies of the frequency dispersion of lead fluoride in between ionically blocking electrodes in order to separate the influence of interfacial polarization phenomena from the bulk electrolyte parameters have attracted much attention as well (3, 5, 10, 17). Several authors observed a strong frequency dependence for frequencies above 1 kHz (3, 5, 9, 17), while others did not observe any dependence in that frequency range (1, 7). It has become evident from the literature data that the type of electrode material is of much importance. The present authors (10) arrive at the conclusion that the frequency-independent values of the conductance are representative for the electrolyte conductivity. The present investigation aims to provide additional data on this electrolyte conductivity of nominally pure and doped β-PbF_2. It is shown that these data, together with the literature data, fit a defect model for β-PbF_2 which adequately describes the reported temperature and concentration dependence of the conductivity of nominally pure and doped β-PbF_2.

Experimental

Materials preparation.—Lead fluoride (Merck, Ultrapure) in the orthorhombic modification (α-PbF_2) was used as starting material. To prepare doped material, LaF_3 (Koch-Light) and AgF (Merck) were used. Before the drying procedure weighted amounts of dopant are added. The materials were dried in graphite crucibles, using the procedure described by Jones (18), and subsequently melted for a few minutes. The melt was then cooled down to room temperature in 5 hr. This procedure yielded transparent crystalline pieces in the case of nominally pure β-PbF_2.

Thin specimens (thickness 0.1-0.2 cm, surface area 0.1-0.5 cm^2) were cut from the crystalline pieces. Surfaces were polished before conductivities were measured.

Liang and Joshi (16) observed that the solubility of YF_3 in β-PbF_2 is less than 0.1 mole percent (m/o). In the present preparations opaque β-PbF_2:LaF_3 was obtained, when 0.5 m/o dopant was added. As is substantiated below, conductivity data reveal that the solubility of LaF_3 in β-PbF_2 amounts to $\sim$ 0.1 m/o. Doping experiments with AgF yielded almost transparent pieces of β-PbF_2:AgF. AgF was added to the β-PbF_2 in a glove box. A small amount of a second phase, presumably AgF, could, however, be observed by an optical microscope in these materials. The interpretation of the conduction data on the doped samples is, therefore, restricted to the observed temperature dependence.

In one experiment a β-PbF_2:AgF crystal was used, which had been kindly made available by Dr. L. Shields of the University of Bradford (U.K.). This material was doped with CaF_2 as well. However, CaF_2 will not be of influence with respect to concentrations of point defects in β-PbF_2.

Conductivity measurements.—The samples were spring loaded between two platinum electrodes in a stainless steel conductivity cell. Electrical contacts between the crystal and the platinum electrodes were established by means of colloidal graphite (Aquadag) or platinum paint (Leitplatin 308A). In the case of doped samples an ambient of purified nitrogen was maintained in the cell, while the nominally pure samples were measured in air, vacuum, and nitrogen (10).

The conductivity of β-PbF_2 in between ionically blocking electrodes is strongly dependent on frequency. Frequency independent conductances represent true bulk properties (10). The admittance parameters of the nominally pure and doped samples were measured in the frequency range 100 Hz-50 kHz with a General Radio Impedance bridge (1608A) with external oscillator (1210C) and an amplifier-null-detector (1232A). For frequencies below 50 Hz admittances were measured in terms of a parallel R-C combination with an a-c bridge in combination with a Wavetek sweep generator (Model 144) and a Tektronix storage scope (Model 504B). To increase the sensitivity a power amplifier (PAR Type 214) was used. The amplitude of the a-c signal was kept below 20 mV peak-to-peak (10).

Results

The temperature dependence of the bulk electrical conductivity as obtained from complex admittance data for β-PbF_2, β-PbF_2:AgF, and β-PbF_2:LaF_3 is shown in Fig. 1. The nominally pure material exhibits two slopes. The conductivity can be represented in these two regions by

$$\sigma T = (1.175 \pm 0.018)\ 10^6 \exp\left[-(0.674 \pm 0.007)\,eV/kT\right]\ \Omega^{-1}\,cm^{-1}\,°K \quad [2]$$

for the low temperature region, and

$$\sigma T = (1.35 \pm 0.06)\ 10^9 \exp\left[-(1.04 \pm 0.06)\ eV/kT\right]\ \Omega^{-1}\,cm^{-1}\,°K \quad [3]$$

for the high temperature region. Conductivities in the high temperature region were corrected for conductivities expressed by Eq. [2], before the calculation was made, which lead to Eq. [3].

The incorporation of the trivalent impurity LaF_3 increases the conductivity. For the extrinsic region the conductivity of β-PbF_2:LaF_3 is represented by (Fig. 1, curve b)

$$\sigma T = (7.59 \pm 0.12)\ 10^4 \exp\left[-(0.496 \pm 0.006)\ eV/kT\right]\Omega^{-1}\,cm^{-1}\,°K \quad [4]$$

At the higher temperatures the conductivity coincides with those represented by Eq. [3]. This points to an intrinsic behavior at the higher temperatures.

The incorporation of the monovalent dopant AgF increases the conductivity as well. The conductivity in the extrinsic region is given by (Fig. 1, curve d)

$$\sigma T = (8.5 \pm 0.5)\ \exp\left[-(0.196 \pm 0.004)\ eV/kT\right]\ \Omega^{-1}\,cm^{-1}\,°K \quad [5]$$

After the first knee the conductivity of these specimens almost coincides with that of the nominally pure material after correction for the low temperature conductivity.

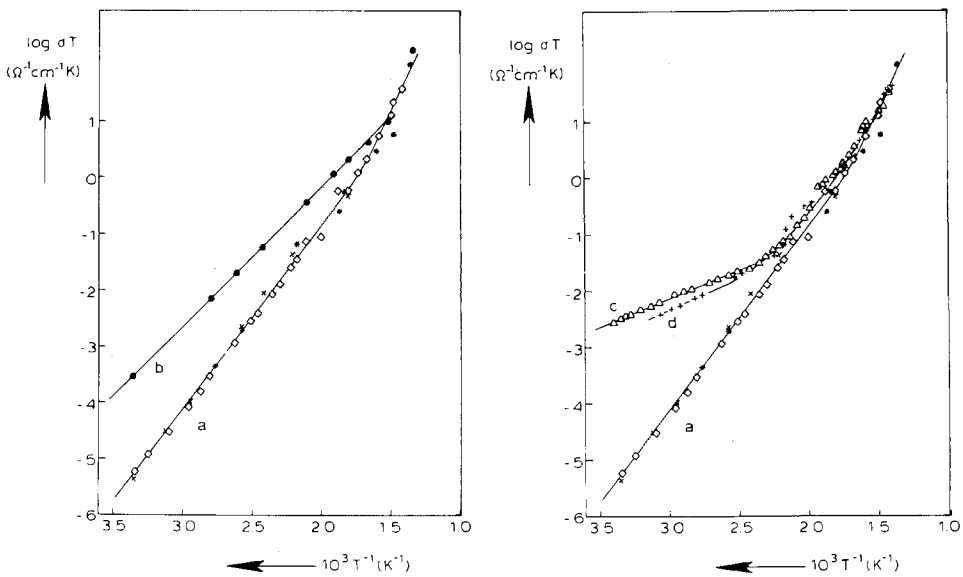


Fig. 1. Temperature dependence of the ionic conductivity of β-PbF_2. Curve a, Nominally pure (10); ×, vacuum; □, N_2; ✻, air. Curve b, LaF_3-dope, N_2. Curve c, AgF-dope, N_2. Curve d, AgF-dope (measurement on a crystal obtained from Dr. L. Shields), N_2.

It should be mentioned that complex admittance plots of the undoped and doped materials pass through the origin over the temperature region involved, indicating negligible electronic conduction in all materials. The present data strongly indicate that the undoped, nominally pure material used in this study exhibits only intrinsic conduction. It is, therefore, possible to determine the migration and formation parameters for fluoride ion vacancies and interstitial fluoride ions. A comparison with the reported data on β-PbF_2 specimens not only supports the model evaluated from the present study, but also provides conclusive evidence as to the nature of the conductivity in these specimens.

Theoretical Aspects of the Ionic Conductivity

In this section we summarize the relevant expressions necessary to give a quantitative description of the electrical conductivity of β-PbF_2. It is generally agreed that β-PbF_2 conducts via point defects in the anion sublattice. The thermal generation of intrinsic point defects is, according to a Frenkel mechanism, given by

$$F_F^{\times} + V_i^{\times} \rightleftarrows V_F^{\cdot} + F_i' \qquad [6]$$

The general relation governing the concentrations of these point defects is

$$K_F = [V_F^{\cdot}][F_i'] = NN' \exp\left(\frac{\Delta S_f}{k}\right) \exp\left(-\frac{\Delta H_f}{kT}\right) \qquad [7]$$

where K_F is the anion Frenkel equilibrium constant, ΔS_f and ΔH_f the formation entropy and formation enthalpy, respectively, N the number of fluoride lattice sites, and N' the number of interstitial sites. The substitutional incorporation of monovalent cations is given by

$$MF \rightarrow M_{Pb}' + V_F^{\cdot} + F_F^{\times} \qquad [8]$$

The incorporation of trivalent cations is represented by

$$MF_3 \rightarrow M_{Pb}^{\cdot} + F_i' + 2F_F^{\times} \qquad [9]$$

Our conductivity data do not indicate the presence of associated defects. In the present evaluation interaction between point defects are therefore not taken into account.

The electrical mobility (μ_i) of point defect i may be expressed by

$$\mu_i = \frac{r_i^2 e}{kT} \nu_i = \frac{r_i^2 e}{kT} \nu_{0,i} \exp\left(\frac{\Delta S_i}{k}\right) \exp\left(-\frac{\Delta H_i}{kT}\right) \qquad [10]$$

where r_i denotes the jump distance, ν_i the jump frequency, ΔS_i and ΔH_i the entropy and enthalpy of motion, respectively, and $\nu_{0,i}$ an attempt frequency of the same order of magnitude as the Debye frequency of particle i. For materials with the fluorite structure r_i will be $(a/2)\sqrt{2}$ for the interstitials, where a is the lattice constant, while for vacancies this jump distance will be $a/2$ (19). If both the anion vacancies and the anion interstitials are mobile, the total intrinsic conductivity can be expressed by (19)

$$\sigma = (K_F)^{1/2} e\mu_{V_F^{\cdot}} + (K_F)^{1/2} e\mu_{F_i'}$$
$$= \frac{a^2e^2}{2kT} (NN')^{1/2} \exp\left(\frac{\Delta S_f}{2k}\right) \exp\left(-\frac{\Delta H_f}{2kT}\right)$$
$$\left\{\frac{\nu_{0,V_F^{\cdot}}}{2} \exp\left(\frac{\Delta S_{V_F^{\cdot}}}{k}\right) \exp\left(-\frac{\Delta H_{V_F^{\cdot}}}{kT}\right)\right.$$
$$\left. + \nu_{0,F_i'} \exp\left(\frac{\Delta S_{F_i'}}{k}\right) \exp\left(-\frac{\Delta H_{F_i'}}{kT}\right)\right\} \qquad [11]$$

For the conductivity in the extrinsic region, one obtains, in the case of a monovalent dopant ($[V_F^{\cdot}]\mu_{V_F^{\cdot}} >> [F_i']\mu_{F_i'}$)

$$\sigma = [V_F^{\cdot}]e\mu_{V_F^{\cdot}} = \frac{a^2e^2}{4kT} [V_F^{\cdot}]\nu_{0,V_F^{\cdot}} \exp$$
$$\left(\frac{\Delta S_{V_F^{\cdot}}}{k}\right) \exp\left(-\frac{\Delta H_{V_F^{\cdot}}}{kT}\right) \qquad [12]$$

and in the case of a trivalent dopant ($[F_i']\mu_{F_i'} >> [V_F^{\cdot}]\mu_{V_F^{\cdot}}$)

$$\sigma = [F_i']e\mu_{F_i'} = \frac{a^2e^2}{2kT} [F_i']\nu_{0,F_i'} \exp$$
$$\left(\frac{\Delta S_{F_i'}}{k}\right) \exp\left(-\frac{\Delta H_{F_i'}}{kT}\right) \qquad [13]$$

These expressions are used in the evaluation of the conductivity data.

The Mobility of the Anion Vacancies

The observed activation enthalpy of ~0.20 eV in the extrinsic conductivity region of the AgF-doped material is well in line with the values reported in the literature (7, 9). Liang and Joshi (7), and also Kennedy and Miles (9), observed an increase in conductivity upon increasing the monovalent dopant concentration, the increased conductivity being concordant with vacancy conduction. Contrary to assumptions of Kennedy (15), the literature provides sufficiently accurate conductivity data for β-PbF_2 doped with KF to obtain a quantitative expression for the temperature dependence of the mobility of the fluoride ion vacancies.

From Eq. [12] it follows that a plot of log $(\sigma T/[V_F^{\cdot}]e)$ $(= \log(\mu_{V_F^{\cdot}} T))$ *vs.* T^{-1} will give a straight

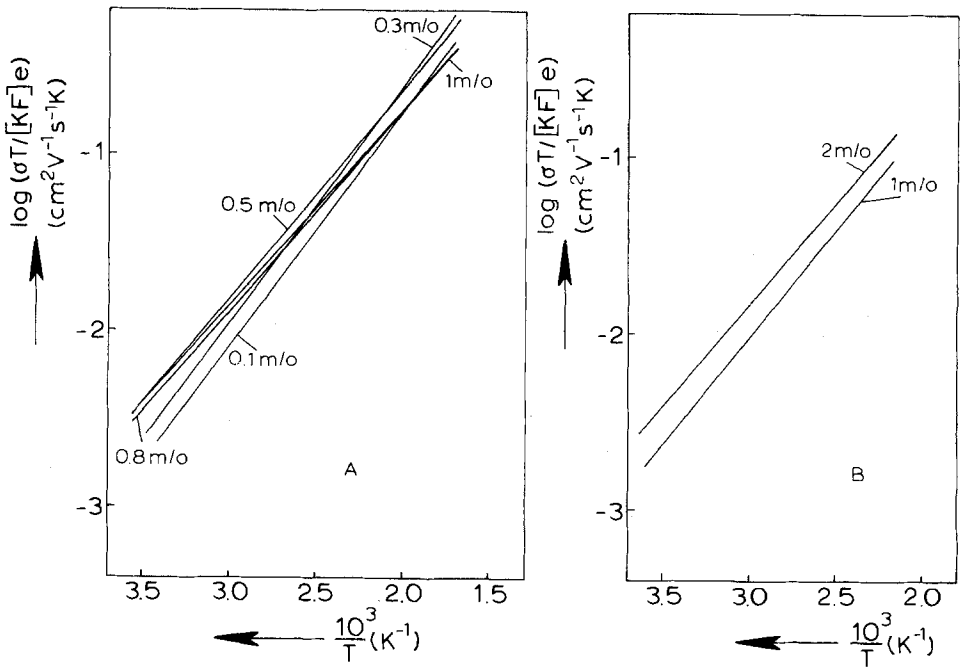


Fig. 2. The logarithm of $\mu_{V_F}\cdot T$, presented as log $(\sigma T/[KF]e)$ vs. T^{-1} for doped crystals. A, Data obtained from Ref. (7). B, Data obtained from Ref. (9).

line, the slope being the enthalpy for vacancy migration. In Fig. 2 the data of Ref. (7) and (9) are plotted as $\log(\sigma T/[KF]e)$ *vs.* T^{-1}, under the assumption $[KF] = [V_F\cdot]$ in accord with reaction [8]. The data for β-PbF_2 doped with 0.1 and 0.5 m/o KF as obtained from Kennedy and Miles (9) were not included in the analysis. It is at present not understood why doping through solid-state diffusion as was done by Kennedy and Miles leads to anomalies for low impurity contents. At higher impurity levels doping by a melt procedure (7) or by solid-state diffusion (9) yields, however, comparable data. From the data of Fig. 2, which exhibit little scatter, we derived for the vacancy mobility,

$$\mu_{V_F}\cdot T = (54 \pm 18)\exp[-(0.23 \pm 0.02)\ eV/kT]\text{cm}^2\,\text{V}^{-1}\,\text{sec}^{-1}\,^\circ\text{K} \quad [14]$$

This expression is to be compared with Eq. [10]. Together with the value 5.927Å (23) for the lattice constant one obtains from the preexponential factor of Eq. [14] for the jump frequency of the fluoride ion vacancies

$$\nu_{V_F}\cdot = (5.3 \pm 1.8)\,10^{12}\exp[-(0.23 \pm 0.02)\,\text{eV}/kT]\text{sec}^{-1} \quad [15]$$

With the approximation (20)

$$\nu_{0,V_F}\cdot = \frac{1}{r_{V_F}\cdot}\left(\frac{\Delta H_{V_F}\cdot}{2m}\right)^{1/2} \quad [16]$$

where m is the mass of the fluoride ion, an estimate for $\nu_{0,V_F}\cdot$ is calculated to be 2.6×10^{12} sec^{-1}. This agrees reasonably with the frequency observed in infrared studies, *viz.*, about 3×10^{12} sec^{-1} (21, 22). With this value, and relation [10], one obtains for the entropy of motion

$$\Delta S_{V_F}\cdot = 0.7k$$

The Frenkel Equilibrium Constant

The scatter in activation enthalpies for conduction of nominally pure β-PbF_2 is considerable at low temperatures (Table I). Speculations as to the nature of the mobile species responsible for activation enthalpies in

Table I. Review of the literature data and present results

Material	ΔH (eV)	T-range (°K)	Proposed by authors*	Present assignment*	Remarks*	Reference
Pure	0.70	300-480	Ex $V_F\cdot$	In $V_F\cdot$	σ, s.c	(1)
	0.94**	480-680	F_i'	In F_i'		
Pure	0.50	300-500	Ex $V_F\cdot$ or ex F_i'	Ex F_i'	σ, p.c.	(3)
	0.60-0.65	300-500	Ex $V_F\cdot$ or ex F_i'	In $V_F\cdot$	σ, s.c	
Pure	0.48	300-470		Ex F_i'	σ, p.c.	(5)
Pure	0.66	300-620	Ex F_i'	In $V_F\cdot$	σ, p.c.	(7)
KF-dopant	0.23	300-540	Ex $V_F\cdot$	Ex $V_F\cdot$	σ, p.c.	
YF_3-dopant	0.66	300-570	Ex F_i'	In $V_F\cdot$	σ, p.c.	
Pure	0.60	300-420		In $V_F\cdot$	σ, s.c	(9)
Pure	0.39-0.50	300-430	Ex $V_F\cdot$ or ex F_i'	Ex $V_F\cdot$ or ex F_i'	σ, p.c.	
	0.66	430-570		In $V_F\cdot$		
KF/NaF-dopant	0.20-0.39	Low T	Ex $V_F\cdot$†	Ex $V_F\cdot$	σ, p.c.	
	0.51	High T	In $V_F\cdot$ or ex F_i'†	In $V_F\cdot$		
BiF_3-dopant	0.53	300-500	Ex $V_F\cdot$	Ex F_i'	σ, p.c.	
Pure	0.66	300-600	Ex F_i'	In $V_F\cdot$	σ, s.c	(10)
	~1.0	600-700	In F_i'	In F_i'		
Pure	0.48	300-500		Ex F_i'	σ, p.c.	(17)
Pure	0.68	300-410	Ex $V_F\cdot$	In $V_F\cdot$	σ, p.c.	(24)
Pure	0.63	230-450	Ex $V_F\cdot$	In $V_F\cdot$	NMR, p.c.	
Pure	0.73	190-620		In $V_F\cdot$	NMR, p.c.	(25)
NaF-dopant	0.32	190-620		Ex $V_F\cdot$	NMR, p.c.	
Pure	0.674	300-580		In $V_F\cdot$	σ, p.c., s.c.	Present results
	1.04	580-700		In F_i'		
AgF-dopant	0.20	300-400		Ex $V_F\cdot$	σ, s.c	
	~0.65	400-560		In $V_F\cdot$		
	~1.0	560-700		In F_i'		
LaF_3-dopant	0.50	300-600		Ex F_i'	σ, s.c	
	~1.0	600-700		In F_i'		

* s.c., single crystal; p.c., polycrystalline sample; ex, extrinsic; in, intrinsic; σ, conductivity.
** A recalculation has shown that the value of 0.94 is correct instead of the reported value of 1.05 eV.
† Kennedy and Miles (9) mention these possibilities. Assuming the vacancy assignment Kennedy and Miles (9) arrive at a value of 0.90 for ΔH_i. According to these authors this low value cast doubt on the extrinsic-intrinsic region hypothesis (see discussion section).

Table II. Model evaluation for intrinsically conducting β-PbF_2

Transition from low to high temperature	$\Delta H_{V_F^\cdot} + \frac{1}{2}\Delta H_f$ (eV)	ΔH_f (eV)	$\Delta H_{F_i'} + \frac{1}{2}\Delta H_f$ (eV)	ΔH_f (eV)
(a) $V_F^\cdot \rightarrow F_i'$	0.674 ± 0.007	0.956 ± 0.016	1.04 ± 0.06	1.09 ± 0.12
(b) $F_i' \rightarrow V_F^\cdot$	1.04 ± 0.06	1.69 ± 0.12	0.674 ± 0.007	0.356 ± 0.018

this temperature region vary from extrinsic conduction via vacancies to extrinsic conduction via interstitials. At first glance it is not evident from the present measurements in which intrinsic region vacancy conduction or interstitial conduction predominates. In Table II the two possibilities are gathered. Possibility (a) assumes that in the low temperature intrinsic region (Eq. [2]) vacancies are the conducting species. Equation [3] then presents the conduction via interstitials. The reversed situation is given by possibility (b). From the values of the experimental conduction activation enthalpies, it is only possible to find a consistent value for the activation enthalpy of the Frenkel equilibrium constant in the case of model (a). In this model intrinsic conduction changes upon increasing temperature from conduction by vacancies to interstitials. From Eq. [11], where in the low temperature (intrinsic) region, $\mu_{V_F^\cdot} > \mu_{F_i'}$, and Eq. [2] and [14] we get for K_F

$$K_F = (2.4 \pm 0.8)10^{46} \exp[-(0.89 \pm 0.04)\,\mathrm{eV}/kT]\,\mathrm{cm}^{-6} \quad [17]$$

In order to arrive at a firm value for ΔH_f we have preferred the use of Eq. [14], since this equation is based on an extended series of doped materials. The value of 0.89 ± 0.04 eV is well in line with the model evaluation presented in Table II.

Equation [17] is to be compared with Eq. [7]. With N, the number of fluoride ion sites, and N', the number of interstitial sites which is equal to $\frac{1}{2}N$, the value of the entropy of formation is calculated to be

$$\Delta S_f = 3.5k$$

The Mobility of the Anion Interstitials

In the previous section we have shown that the high temperature intrinsic region can only be ascribed to conduction via interstitials. It is, therefore, possible to calculate from this region the mobility of the anion interstitials. With Eq. [11], where now $\mu_{F_i'} > \mu_{V_F^\cdot}$, and Eq. [3], and the value of K_F, the mobility of the interstitials is calculated to be

$$\mu_{F_i'}T = (5.4 \pm 1.9)10^4 \exp[-(0.60 \pm 0.06)\,\mathrm{eV}/kT]\,\mathrm{cm}^2\,\mathrm{V}^{-1}\,\mathrm{sec}^{-1}\,^\circ\mathrm{K} \quad [18]$$

The jump frequency of the interstitials can be calculated according to Eq. [15]. This gives

$$\nu_{F_i'} = (2.7 \pm 0.9)10^{15} \exp[-(0.60 \pm 0.06)\,\mathrm{eV}/kT]\,\mathrm{sec}^{-1} \quad [19]$$

The entropy of motion of the interstitials can be calculated in analogy with the calculation of the entropy of motion of the vacancies. With the estimated value of $\nu_{0,F_i'} = 3.0 \times 10^{12}$ sec^{-1}, the entropy is

$$\Delta S_{F_i'} = 6.8k$$

One should bear in mind that the β-PbF_2:LaF_3 crystal exhibited a value of (0.496 ± 0.006) eV for $\Delta H_{F_i'}$. The present calculation also yields the preexponential factor in the equation describing the temperature dependence of the mobility. This preexponential factor cannot be obtained from the low temperature data of the β-PbF_2:LaF_3 sample since LaF_3 was present as a second phase. Figure 3 presents the temperature dependence of the mobilities of the mobile point defects in β-PbF_2.

From the calculated mobility and the observed conductivity in the extrinsic region of β-PbF_2:LaF_3 (Eq. [4]) the concentration of trivalent dopant responsible for the increase in conductivity turns out to be $\sim 2 \times 10^{19}$ cm^{-3}. With the concentration of lead ions, 1.9×10^{22} cm^{-3}, we arrive at a dissolved impurity content of about 0.1 m/o.

Discussion

Kennedy and Miles (9) observe two slopes in the log σT *vs.* T^{-1} curve for nominally pure β-PbF_2 and for β-PbF_2:KF (0.1 m/o). They discuss two possible mechanisms to explain this knee in the conductivity curve. First a transition from extrinsic to intrinsic conduction by $V_F^\cdot$ is considered; this leads to a formation enthalpy of 0.90 eV for anion Frenkel disorder. Their second possibility is a transition from extrinsic conduction $V_F^\cdot$ to extrinsic conduction by F_i'. Kennedy and Miles (9) doubt the first mechanism because of the rather low value of ΔH_f. In addition, they do not rule out the simultaneous presence of Schottky and Frenkel disorder. It should be pointed out that these authors did not observe the third (high temperature) slope as we did for the nominally pure, the β-PbF_2:AgF and the β-PbF_2:LaF_3 samples. In fact, it is this observation which supports the present evaluation and, therefore, the first mechanism of Kennedy and Miles. Their value of 0.90 eV is well in line with the present data.

The present authors (10) have reported the value 0.78 eV for ΔH_f. The conduction activation enthalpy of 0.66 eV (calculated from a log σT *vs.* T^{-1} plot), originally ascribed to the migration enthalpy for interstitials (7), is now interpreted as $(\Delta H_f/2 + \Delta H_m)$ for vacancies. Evaluations of ΔH_f values are very sensitive to extrinsic conduction activation enthalpies. Nevertheless, a rather low value for ΔH_f seems now well established.

Table I summarizes conduction activation enthalpies from reported literature data and the present study on β-PbF_2. If necessary literature data were converted to log σT *vs.* T^{-1} in order to obtain the correct conduction activation enthalpies. The measurements of Derrington and O'Keeffe (2) and Benz (8) are not gathered in this table, since their conductivity plots (log σT *vs.* T^{-1}) show a curvature from low temperature up to temperatures where the conductivity starts

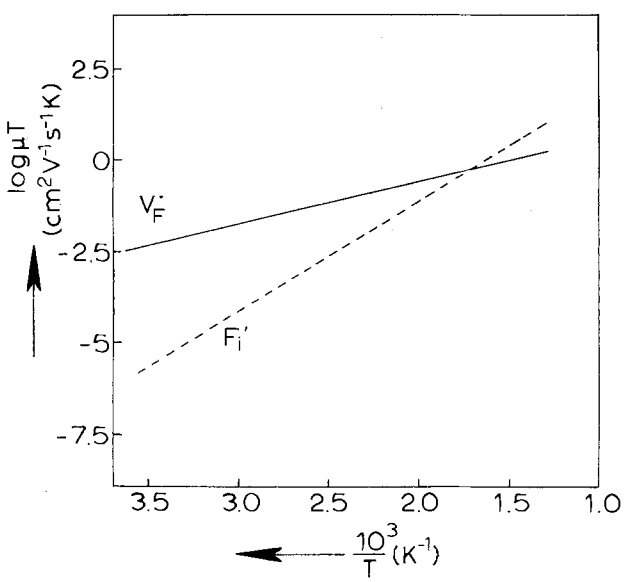


Fig. 3. Mobility of anion vacancies and interstitials as a function of temperature.

to level off. However, both plots clearly show the two regions which we ascribe to intrinsic conduction by V_F' and intrinsic conduction by F_i', while the magnitude of the conductivity in both regions is concordant with the present data. The present model allows in many cases an identification of the mobile species and the nature of the conductivity.

Uncertainties in the calculated values of $\mu_{Fi'}$ and K_F originate mainly from the uncertainty in the mobility of the anion vacancies and Eq. [3]. This mobility was extracted from measurements on samples with different concentrations of KF, and from different literature sources (7, 9). Moreover, different preparation techniques were used in these studies, *e.g.*, melting (7) or solid-state diffusion (9). In neither case, however, is it known to what degree added impurities are actually incorporated into the lattice. Information as to the nature and concentration of remaining impurities in the nominally pure materials is not presented by Liang and Joshi (7), nor by Kennedy and Miles (9). Insight into this parameter could also improve the accuracy of the calculated mobilities. In regard of these considerations the scatter in the log $(\sigma T/[KF]e)$ *vs.* T^{-1} plot is surprisingly low.

From the derived parameters it is possible to calculate the total conductivity as well as the contributions due to the fluoride ion vacancies and to the interstitial fluoride ions in the extrinsic and intrinsic region as a function of temperature. In Fig. 4 the total conductivity is plotted for different monovalent dopant concentrations. In Fig. 5 the total conductivity is plotted for different trivalent-dopant concentrations. Interestingly this plot clearly shows the conductivity to decrease for low dopant concentrations. At high enough dopant levels the conductivity starts to increase. This phenomenon is caused by a change from vacancy conduction to interstitial conduction and originates from the condition $\mu_{Fi'} << \mu_{V_F'}$ at lower temperatures.

In comparison with the commercially available β-PbF_2 crystals (1), which all show intrinsic conductivity, only a few of the undoped crystals prepared for this study exhibited intrinsic conductivity for temperatures above 300°K. The temperature dependence of the conductivity of most of the undoped materials resembled that of the silver-doped β-PbF_2, indicating an effective monovalent impurity content. Our efforts to reproduce experimentally the predicted temperature dependence of crystals with a low trivalent-impurity level as given in Fig. 5, curve b, were, therefore, not successful.

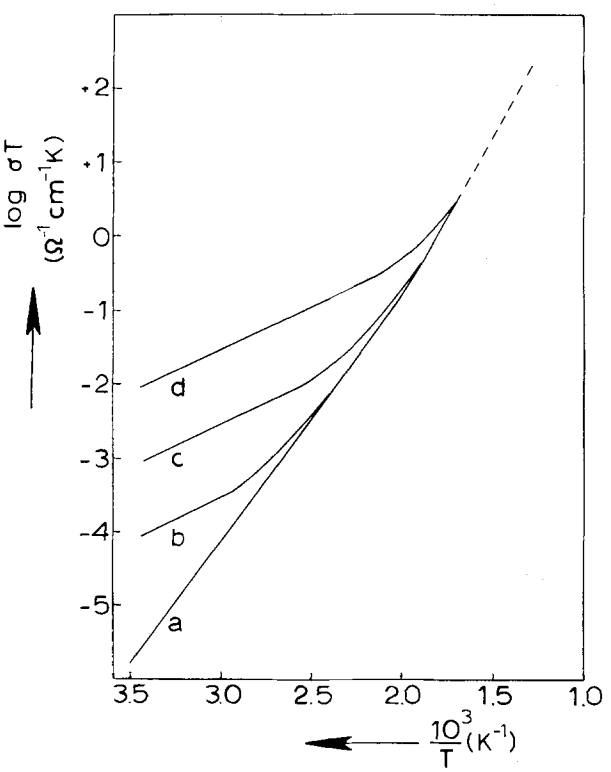


Fig. 4. Calculated intrinsic and extrinsic conductivity of β-PbF_2, doped with monovalent impurities. Curve a, Intrinsic conduction. Curve b, $[10^{17}]$ cm^{-3}. Curve c, $[10^{18}]$ cm^{-3}. Curve d, $[10^{19}]$ cm^{-3}. The dashed line represents conductivity by interstitials, and the solid lines represent conductivity by vacancies.

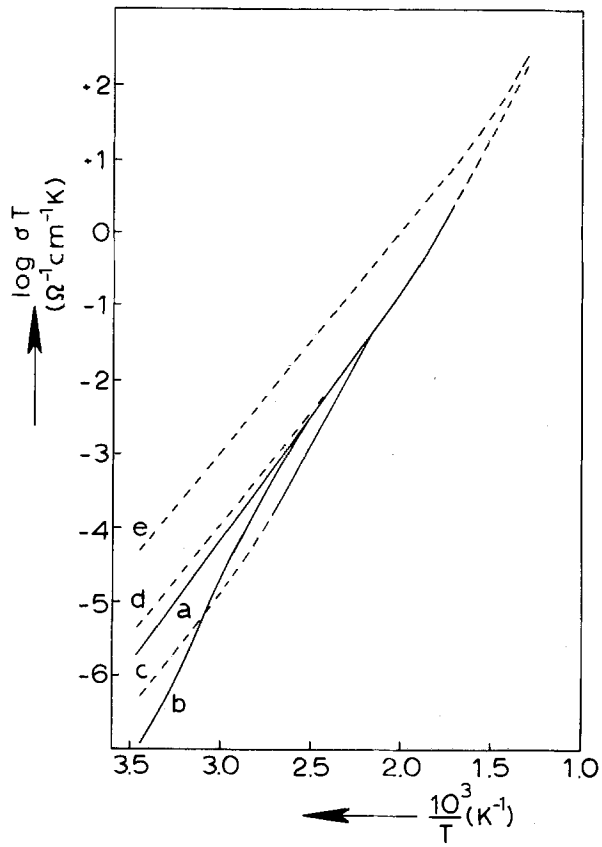


Fig. 5. Calculated intrinsic and extrinsic conductivity of β-PbF_2, doped with trivalent impurity. Curve a, Intrinsic conduction. Curve b, $[10^{17}]$ cm^{-3}. Curve c, $[10^{18}]$ cm^{-3}. Curve d, $[10^{19}]$ cm^{-3}. Curve e, $[10^{20}]$ cm^{-3}. The dashed lines represent conductivity by interstitials, and the solid lines represent conductivity by vacancies.

In Table III the defect parameters for other materials with fluorite structure are gathered. Lead fluoride exhibits, in comparison with these materials, remarkably low enthalpies of formation and migration. In Fig. 6 we have plotted the temperature dependence of the intrinsic point defects in β-PbF_2 and the alkaline earth fluorides. The different behavior of β-PbF_2 probably originates from the large polarizability of the lead ion.

The literature provides several empirical relations between formation enthalpies and melting temperatures. Maycock and Pai Verneker (30) introduced the relation

$$\Delta H_f(\text{eV}) = 3.47 \times 10^{-3}\, T_m(°\text{K}) - 1.08 \qquad [20]$$

Data for a series of alkali halides, silver halides, and polyatomic anion potassium salts, which exhibit either Schottky or Frenkel disorder, were used to derive this relation. The relation (1)

$$\Delta H_f(\text{eV}) = 1.2 \times 10^{-3}\, T_m(°\text{K}) + 0.34 \qquad [21]$$

Table III. Entropy and enthalpy data of materials with fluorite structure.
All ΔH values are in electron volts

	$\Delta H_{F_i'}$	$\Delta S_{F_i'}/k$	$\Delta H_{V_F^\cdot}$	$\Delta S_{V_F^\cdot}/k$	ΔH_f	$\Delta S_f/k$	Reference
CaF_2	0.92	5.6	0.51	1.2	2.45 (2.74)	8.6 (13.4)	(28), (29)
	0.53-1.64		0.52-0.87		2.2-2.8		(26)
SrF_2	0.94	3.1	0.94	2.4	1.74	5.5	(19)
	0.71-1.0		0.94-1.0		1.7-2.3		(26)
BaF_2	0.83	4.2	0.75	2.7	1.60	4.8	(27)
	0.62-0.79		0.56		1.9		(26)
β-PbF_2	0.50		0.23	0.7	0.89	3.5	This work
	0.60*	6.8*					

* Estimated value from high temperature conductivity data.

was derived from data reviewed by Barr and Lidiard (31) for silver halides and anion conductors with Frenkel disorder, among which are the alkaline earth fluorides (1). It should be pointed out that the majority of the compounds used to derive relation [20] exhibit Schottky disorder. Relation [21] seems, therefore, more appropriate for an estimation of the value of ΔH_f for β-PbF_2. These relations lead to ΔH_f values for β-PbF_2 ($T_m = 1095°K$) of 2.72 and 1.66 eV, respectively. Kennedy and Miles (9) used the value 2.72 eV to illustrate that the low ΔH_f value (0.90 eV) for β-PbF_2 casts doubt on the extrinsic-intrinsic region hypothesis. Relation [21] leads, however, to a much lower value. Moreover, it has been well demonstrated (2) that above *ca.* 700°K β-PbF_2 exhibits an almost temperature-independent liquidlike conduction due to a liquidlike disorder in the anion sublattice of β-PbF_2. If this "melting" temperature were to be used, ΔH_f has the value of only 1.2 eV.

CaF_2 and SrF_2 (11) exhibit also a leveling off of the conductivity. However, the differences between the actual melting temperature and the temperature at which liquidlike conduction starts in these fluorides are smaller than for β-PbF_2. A refinement by using the latter temperatures of CaF_2 and SrF_2 will hardly improve relation [21].

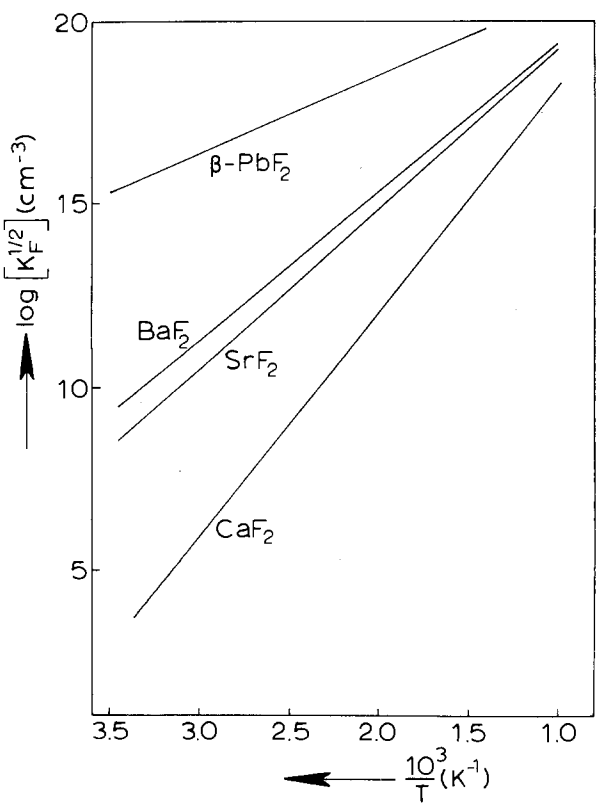


Fig. 6. Concentrations of the anion-Frenkel defects as a function of temperature in CaF_2 (28), SrF_2 (19), BaF_2 (27), and β-PbF_2 (this work).

Acknowledgments

The authors are indebted to Prof. Dr. G. Blasse for encouraging this work and for valuable criticism during the preparation of the manuscript. They gratefully acknowledge the material preparations by Mr. G. J. Dirksen.

Manuscript submitted June 14, 1976; revised manuscript received Aug. 23, 1976.

Any discussion of this paper will appear in a Discussion Section to be published in the December 1977 JOURNAL. All discussions for the December 1977 Discussion Section should be submitted by Aug. 1, 1977.

Publication costs of this article were assisted by the State University of Utrecht.

REFERENCES

1. J. Schoonman, G. J. Dirksen, and G. Blasse, *J. Solid State Chem.*, **7**, 245 (1973).
2. C. E. Derrington and M. O'Keeffe, *Nature (London), Phys. Sci.*, **246**, 44 (1973).
3. J. H. Kennedy, R. C. Miles, and J. Hunter, *This Journal*, **120**, 1441 (1973).
4. J. Schoonman, G. A. Korteweg, and R. W. Bonne, *Solid State Commun.*, **16**, 9 (1975).
5. J. M. Réau, J. Claverie, G. Campet, C. Déportes, D. Ravaine, J. L. Souquet, and A. Hammou, *C.R. Acad. Sci., Ser. C*, **280**, 225 (1975).
6. A. V. Joshi and C. C. Liang, *J. Phys. Chem. Solids*, **36**, 927 (1975).
7. C. C. Liang and A. V. Joshi, *This Journal*, **122**, 466 (1975).
8. R. Benz, *Z. Phys. Chem. N.F.*, **95**, 25 (1975).
9. J. H. Kennedy and R. C. Miles, *This Journal*, **123**, 47 (1976).
10. R. W. Bonne and J. Schoonman, *Solid State Commun.*, **18**, 1005 (1976).
11. C. E. Derrington, A. Lindner, and M. O'Keeffe, *J. Solid State Chem.*, **15**, 17 (1975).
12. C. E. Derrington, A. Navrotsky, and M. O'Keeffe, *Solid State Commun.*, **18**, 47 (1976).
13. C. Tubandt, *Z. Anorg. Allg. Chem.*, **115**, 105 (1921).
14. V. A. Arkhangel'skaya, V. G. Erofeichev, and M. N. Kiseleva, *Soviet Phys. Solid-State*, **14**, 2953 (1973).
15. J. H. Kennedy, *This Journal*, **122**, 1641 (1975).
16. C. C. Liang and A. V. Joshi, *ibid.*, **122**, 1642 (1975).
17. C. Lucat, G. Campet, J. Claverie, J. Portier, J. M. Réau, and P. Hagenmuller, *Mater. Res. Bull.*, **11**, 167 (1976).
18. D. A. Jones, *Proc. Phys. Soc. London, Sect. B*, **65**, 165 (1955).
19. W. Bollmann, P. Görlich, W. Hauk, and H. Mothes, *Phys. Status Solidi A*, **2**, 157 (1970).
20. F. K. Fong, *Prog. Solid State Chem.*, **3**, 135 (1967).
21. J. D. Axe, J. W. Gaglianello, and J. F. Scardefield, *Phys. Rev. A*, **139**, 1211 (1965).
22. R. Srivastava, H. V. Lauer, Jr., L. L. Chase, and W. E. Bron, *Phys. Lett. A.*, **36**, 333 (1971).
23. R. W. G. Wyckoff, "Crystal Structures," Vol. 1, p. 242, Interscience Publishers, New York (1963).
24. J. Schoonman, L. B. Ebert, C. H. Hsieh, and R. A. Huggins, *J. Appl. Phys.*, **46**, 2873 (1975).
25. T. Y. Hwang, M. Engelsberg, and I. J. Lowe, *Chem. Phys. Lett.*, **30**, 303 (1975).

26. W. Hayes, Editor, "Crystals with the Fluorite Structure," p. 101, Clarendon Press, Oxford (1974).
27. W. Bollmann, *Phys. Status Solidi A*, **18**, 313 (1973).
28. W. Bollmann and R. Reimann, *ibid.*, **16**, 187 (1973).
29. W. Bollmann and H. Henniger, *ibid.*, **11**, 367 (1972).
30. J. N. Maycock and V. R. Pai Verneker, *Phys. Status Solidi B*, **44**, 97 (1971).
31. L. W. Barr and A. B. Lidiard, *Phys. Chem.*, **10**, 151 (1970).

Ionic Conductivity of Solid and Liquid $LiAlCl_4$

W. Weppner and R. A. Huggins*

Center for Materials Research, Stanford University, Stanford, California 94305

ABSTRACT

The electrical conductivity of lithium chloroaluminate has been investigated in the temperature range between room temperature and 180°C. It is molten above 145°C. The conduction is practically purely ionic and is attributed to the transport of lithium ions. The experiments show high values for ionic conductivity in the solid state, only exceeded by Li-β-alumina and some LiI-based materials. At 25°C the conductivity was found to be $1 \times 10^{-6}\ \Omega^{-1}\ cm^{-1}$, with an activation enthalpy for σT of 0.47 eV. A-C conductivity measurements were influenced by sample preparation and cell arrangement. The ionic conductivities of this and several other newly found lithium ionic conductors, as well as those previously known, are compared in the temperature range between 20° and 250°C.

In the present efforts to develop new types of high energy and power density storage devices it is of considerable importance to search for better solid lithium ionic conductors. The obvious main advantages of systems based on lithium are its low atomic weight, its relatively rich abundance, the high negative Gibbs free energy of formation of many lithium compounds, and the possibility of using liquid electrodes with fast kinetic properties.

Conduction experiments upon the low melting LiCl-$AlCl_3$ eutectic melt indicated a considerable ionic conductivity even after solidification had occurred. Therefore a detailed investigation of the compound $LiAlCl_4$, one component of the expected eutectoid structure, has been carried out.

The compound lithium chloroaluminate $LiAlCl_4$ was first reported in 1923 by Kendall *et al.* (1). However, there is not yet much information about the properties of this phase. According to the proposed phase diagrams (1-3) (which differ considerably in detail), $LiAlCl_4$ is the only ternary phase that exists in the system LiCl-$AlCl_3$. Especially remarkable is the very low eutectic temperature of about 104°C (1, 2) at the composition of 41 mole percent (m/o) LiCl and 59 m/o $AlCl_3$, and the low melting point of 146°C (1, 2, 4) [132°C (3)] for the compound $LiAlCl_4$.

The crystal structure has not yet been accurately determined. X-ray experiments (3, 4) have indicated that the structure is not isomorphous with the other alkali metal chloroaluminates (4). However, the chlorine ions form tetrahedra about the aluminum ions, and the structure can thus be considered as a quasi-binary compound made up of these isolated tetrahedral $AlCl_4^-$ ions, between which the positively charged alkali metal ions exist. Some evidence has indicated that the tetrahedra may also be distorted (4).

The electrical conductivity of molten LiCl-$AlCl_3$ has been reported in the literature, with values up to 0.35 $\Omega^{-1}cm^{-1}$ at 174°C measured (6). In a few cases this melt has been used as an electrolyte in conventional isothermal (7-9) and thermal batteries (10). More often because of the solubility and dissociation of $LiAlCl_4$ into Li^+ and $AlCl_4^-$ ions in several inorganic and organic nonaqueous solvents, it has been used as a soluble electrolyte in many types of batteries operating in the region of room temperature (11-24).

Experimental Considerations

Lithium chloroaluminate has been prepared by blending and reacting LiCl with $AlCl_3$. LiCl (> 99.3%) from Baker Chemical Company and $AlCl_3$ (puriss. ≥ 99%, iron and water free) from Fluka AG were used. Both materials were pulverized in a mortar and mixed in the appropriate equal molar ratio. The powder was then melted by heating it to 150°-180°C in a Pyrex glass tube in a helium-filled dry box. The initial color of the melt was yellowish brown and a small amount of precipitated LiCl was observed. Water was removed by holding the liquid sample at 180°C overnight. In order to clean the melt from other impurities, small pieces of pure metallic lithium were added gradually. First, the lithium changed both its color and shape rapidly, indicating the reduction of impurities with lower thermodynamic stability than the corresponding lithium compounds. Any aluminum metal that may be formed in this way is not a serious problem, because it can be assumed to be practically insoluble in the molten chloroaluminate (25). The amount of solid LiCl at the bottom of the melt increased slightly during the cleaning procedure. Through this treatment the melt finally became waterlike; colorless, transparent, and with a low viscosity.

Two different experimental arrangements were used to determine the electrical conductivity of solid $LiAlCl_4$ prepared from the melt. In one set of experiments the melt was poured into a test tube containing two parallel molybdenum sheets of about 1 × 5 cm in dimension and with a 0.4 cm spacing, which were kept in position by Teflon holders. The sample was crystallized by cooling the melt *in situ* at a very slow rate. Molybdenum is chemically inert in the presence of lithium (26).

In the second set of experiments the melt was decanted into a Teflon crucible. After quenching, a fine-grained pellet of several millimeters thickness and about 1 cm in diameter resulted. The surfaces were polished with corundum paper in the dry box. Molybdenum sheet electrodes were applied, the system was compressed by springs, and the sample-electrode assembly annealed at 100°C overnight. The cell was then

* Electrochemical Society Active Member.
Key words: solid electrolyte, solid-state ionics, lithium ion conductivity, a-c conductivity, d-c polarization measurements.

placed in an electrically heated glass tube furnace, and flushed with a small flow of carefully dried helium gas. The colors of the samples ranged from translucent to white. At temperatures above 100°C, they became quite soft and ductile.

The electrical conductivity was determined by using a-c bridge techniques in the frequency range between 50 Hz and 100 kHz. The resistances were derived by interpretation (27) of complex impedance plane diagrams of the data, and conductivities were calculated from the measured resistances and the physical dimensions of either the solidified melts or the pellets.

X-ray investigations produced the same diffraction pattern as previously given in the literature (4) for $LiAlCl_4$.

Results and Discussion

Figure 1 is a semilogarithmic plot of the specific conductivity σ, times the absolute temperature T, *vs.* the inverse temperature in the region between 20° and 180°C. As can be seen from Fig. 1, the values for the *in situ* crystallized sample are systematically higher by about 25% than those for the pellets. This is probably due to the less well-defined geometry of the volume of material that contributes to the electrical conductivity in the case of the *in situ* solidified system. Because of the larger dimensions of the sample, the temperature is probably also less uniform,

The activation enthalpy for σT of the solid $LiAlCl_4$ was found to be 0.47 eV (45 kJ/mole). At 25°C the specific conductivity was observed to be about $1 \times 10^{-6}\Omega^{-1}cm^{-1}$. It increases to $1.4 \times 10^{-4}\Omega^{-1}cm^{-1}$ at 140°C, shortly before the compound melts. At the phase transformation the conductivity rapidly increases by a factor of 800. Above the melting point it shows the typically low activation energy and high conductivity of many molten salt electrolytes.

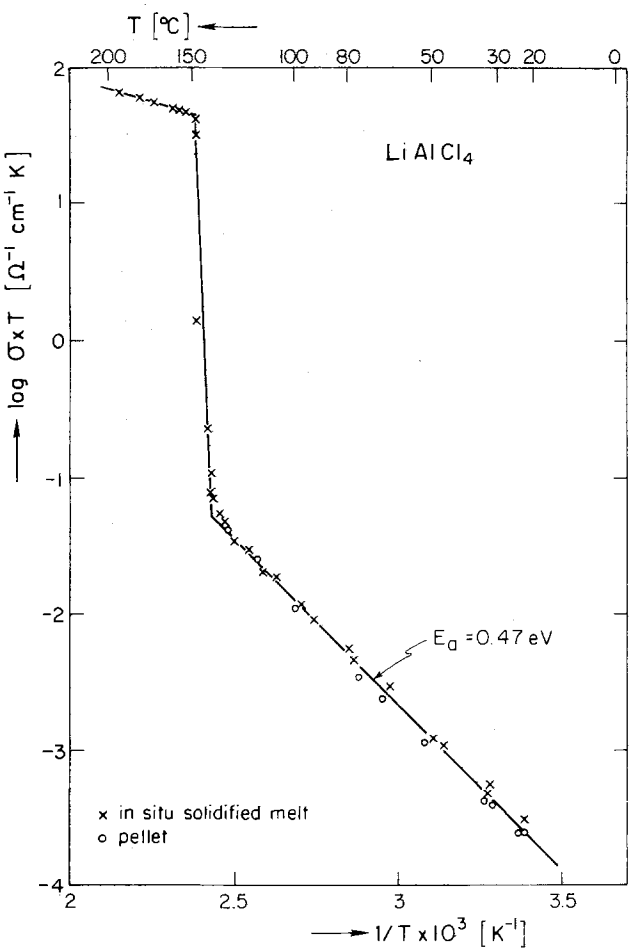


Fig. 1. Semilogarithmic plot of the bulk conductivity of $LiAlCl_4$ times the absolute temperature as a function of the inverse absolute temperature. Results for different experimental situations are indicated as follows: x, *in situ* solidified melt; o, cast pellet.

Significant differences were observed in the complex impedance and admittance plots between the different experimental situations that were investigated. Figure 2 shows the reactance X *vs.* the series resistance R of $LiAlCl_4$, measured under three different circumstances. In one case measurements were made on a cast pellet that was only polished and assembled without further treatment. In the second, the sample as well as the electrodes were annealed at 100°C for 14 hr. A third case involved results obtained on the *in situ* solidified melt. It can be seen from the figure that the heat-treatment of the pellet-electrode system drastically increased the interfacial capacitance by promoting better contact between the electrodes and the electrolyte. This resulted in a better separation of the bulk and interface capacitances, and thus aided the interpretation of the data. The situation is even simpler for the case in which the melt was solidified directly between the electrodes. In this latter case, only a comparatively short straight line with an inclination of about 45° was found over the frequency range between 0.1 and 100 kHz. The difference between the intercepts of the straight lines with the R axis in this figure for the measurements made on the pressed pellet are only due to the somewhat different temperatures at which the two sets of experiments were carried out. As has been shown elsewhere (27, 40), the differences in the observed frequency dependence of the two types of samples cannot be due to internal voids in the electrolyte, but differences in the intergrain contact may make a secondary contribution to the observations. Figure 2 clearly shows that it is very important to examine the frequency dependence of the measured conductivities or resistances in order to properly determine the bulk conductivity. Otherwise, considerable errors may be present in monofrequency measurements in unfavorable experimental setups.

In order to verify the information obtained from the shape of the X-R and B-G plots that the measured conductivities were not determined by transport of electronic species, d-c polarization measurements were made at voltages between 20 and 400 mV.

If the sample is a practically pure electronic semiconductor, the sum of the conductivities of the electrons, σ_e, and the holes, σ_h, calculated from the current

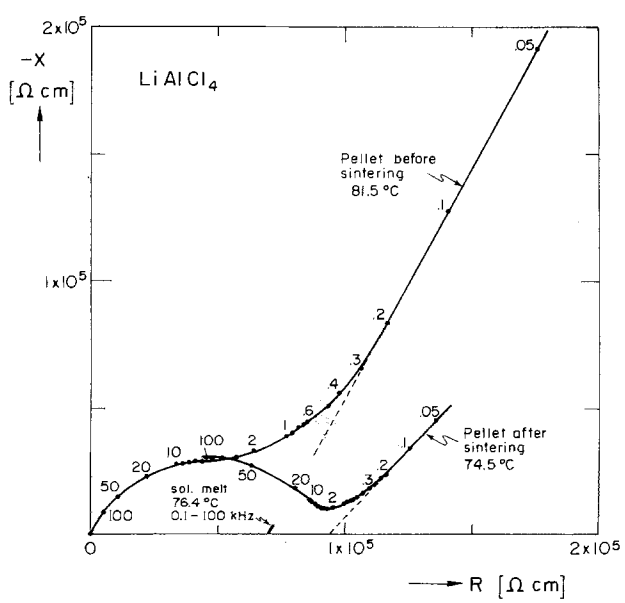


Fig. 2. Complex impedance plane plot for various samples of $LiAlCl_4$. The upper curve resulted from using a cast pellet without further treatment. The intermediate curve shows results from the same pellet, but after annealing the sample and electrodes together at 100°C overnight. The lower line represents the results of the *in situ* solidified melt. The numbers along the curves are the frequencies in kilohertz.

density i and the voltage drop E across a cell of length L

$$\sigma_e + \sigma_h = -\frac{iL}{E} \quad [1]$$

has to have the same magnitude as the conductivity determined by a-c measurements. If the sample is mainly ionic, but also a partially electronic conductor, the situation is similar to that in Hebb-Wagner d-c polarization experiments (28, 29), in which the ionic current is blocked by an inert electrode that is not able to deliver ions. However, in this case the electron and hole conductivities are not fixed at one side. Wagner's d-c polarization current i-voltage E relation (29) may be transformed into

$$i = -\frac{RT}{\mathbf{F}L}\left[1 - \exp\left(-\frac{\mathbf{E}\mathbf{F}}{RT}\right)\right][\sigma_e(O) + \sigma_h(L)] \quad [2]$$

and which becomes under the (often fulfilled) condition $\mathbf{E}\mathbf{F} >> RT$

$$i = -\frac{RT}{\mathbf{F}L}[\sigma_e(O) + \sigma_h(L)] \quad [3]$$

$\sigma_e(O)$ and $\sigma_h(L)$ are the electron conductivity at the left-hand phase boundary and the hole conductivity at the right-hand side of the sample, respectively. The Wagner equation was derived under the limiting assumptions of the validity of the laws of ideal dilute solutions for the concentrations of the electronic species, concentration independent mobilities of electrons and holes, and locally independent chemical potentials of the mobile ions. Therefore, it is identical to Fick's first law and may also be directly derived from it. An inner electric field is not present because of the high ionic conductivity, and the electronic current is only due to diffusion under a concentration gradient.

While the electronic conductivities are essentially locally independent in the case of predominantly electronic conduction, they vary with the position in the sample if we assume a mainly ionic conductor. For the present purpose it is worth noticing that $\sigma_e(O)$ and $\sigma_h(L)$ in Eq. [2] and [3] are both the maximum values of the conductivities of the electrons and holes, respectively, over the entire sample. The measured current density is, therefore, the upper limit of the total electronic and hole conductivities of the sample.

Application of the above analysis of the steady-state d-c polarization results according to Eq. [1], [2], and [3] showed electronic conductivities well below 1% of the total a-c conductivity for the compound $LiAlCl_4$. This indicates essentially pure ionic conductivity in this material. Because of the big, and therefore probably relatively immobile $AlCl_4^-$ ions, the conduction can be regarded as being due to motion of the Li^+ ions exclusively.

In Fig. 3 the conductivity of $LiAlCl_4$ is compared with other well-known and several other newly discovered solid lithium electrolytes. As can be seen from this compilation, $LiAlCl_4$ exceeds all the other materials except Li-β-Al_2O_3 (which is not stable and therefore probably not of importance in many applications) and several lithium iodide-based materials. Also, the activation energy is lower than for most of the other lithium electrolytes, probably because of a structure more favorable to movement of the ions. However, since the detailed structure of $LiAlCl_4$ is not yet known, it is very speculative to discuss the structural reasons for the high ionic conductivity of this material.

In the investigations described here no effort was given to the modification of the $LiAlCl_4$ structure by adding dopants. As observed for closely related materials (30, 31) it seems that it may be possible to improve the ionic conductivity by several orders of magnitude in this manner, and experiments are being undertaken to investigate this possibility.

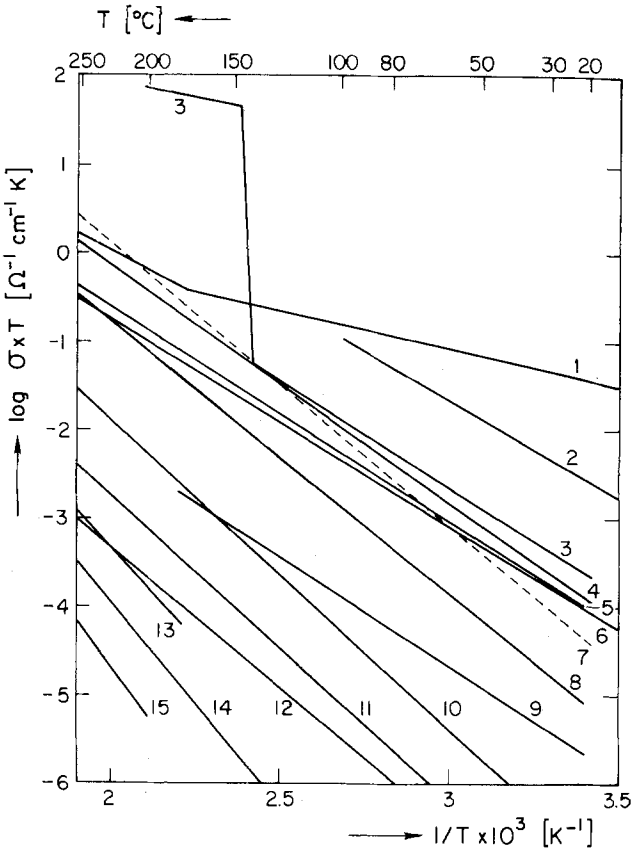


Fig. 3. Comparison of the ionic conductivity of solid and liquid $LiAlCl_4$ with a number of other solid lithium electrolytes in the temperature range 20°-250°C. Materials and literature references are: 1, Li-β-Al_2O_3 (32); 2, LiI + 40 m/o Al_2O_3 (33); 3, $LiAlCl_4$, this investigation; 4, Li_4SiO_4 + 43 m/o Li_3PO_4 (31); 5, $Li_2Ti_3O_7$ (34); 6, LiI (35); 7, Li_3N (96%, impurities not reported) (36); 8, Li_3N (35); 9, Li_2S (Li electrodes) (37); 10, $LiAlSiO_4$ (glass) (38); 11, Li_2S (Mo electrodes) (37); 12, Li_4SiO_4 (31); 13, Li_4GeO_4 (39); 14, $LiAlSiO_4$ (glass ceramic) (38); 15, Li_2GeO_3 (39).

Acknowledgments

This research was supported by the Defense Advanced Research Projects Agency and was monitored by the Office of Naval Research under Contract Number N00014-75-C-1056. One of us (W.W.) also gratefully acknowledges the grant of a NATO scholarship through the German Academic Exchange Service (DAAD).

Manuscript submitted June 25, 1976; revised manuscript received Sept. 1, 1976.

Any discussion of this paper will appear in a Discussion Section to be published in the December 1977 JOURNAL. All discussions for the December 1977 Discussion Section should be submitted by Aug. 1, 1977.

Publication costs of this article were assisted by Stanford University.

REFERENCES

1. J. Kendall, E. D. Crittenden, and H. K. Miller, *J. Am. Chem. Soc.*, **45**, 963 (1923).
2. E. M. Levin, C. R. Robbins, and H. F. McMurdie, "Phase Diagrams for Ceramists," 1969 Supplement, p. 300, The Amer. Ceram. Soc., Inc., Columbus, Ohio (1969).
3. A. I. Morozov, V. G. Kuznetsov, and S. I. Maksimova, *Russ. J. Inorg. Chem.*, **16**, 1773 (1971).
4. K. N. Semenenko, V. N. Surov, and N. S. Kedrova, *ibid.*, **14**, 481 (1969).
5. B. Vandorpe and P. Barbier, *C. R. Acad. Sci., Ser. C*, **266**, 332 (1968).
6. Y. Yamaguti and S. Sisido, *J. Chem. Soc. Jpn.*, **62**, 304 (1941).
7. J. Giner and G. L. Holleck, NASA Report N 70-36944.

8. G. Mamantov, R. Marassi, and J. Q. Chambers, "Proceedings of the Symposium Workshop on Advanced Battery Research and Design," Argonne National Laboratory, p. B-152 (1976).
9. Union Carbide Corp., French Demande 2,198,277 (1974).
10. S. Senderoff, German Offen. 2,241,806 (1974).
11. G. Monnier, *Ann. Chim. (Paris)*, **2**, 14 (1957).
12. A. K. Hoffman, Belgium Pat. 669,396 (1965).
13. M. L. B. Rao and R. W. Holmes, *Electrochem. Technol.*, **6**, 105 (1968).
14. Societé des Accumulateurs Fixes et de Traction, French Pat. 1,556,247 (1969).
15. A. N. Dey and M. L. B. Rao, Brit. Pat. 1,207,739 (1970).
16. J. P. Gabano, French Pat. 2,079,744 (1971).
17. D. L. Maricle and J. P. Mohns, Brit. Pat. 1,258,498 (1971).
18. J. P. Gabano and G. Lehmann, French Pat. 2,082,817 (1972).
19. A. Heller and S. Lieberman, German Offen. 2,263,-115 (1973).
20. G. H. Newman, German Offen. 2,262,660 (1973).
21. G. E. Blomgren and M. L. Kronenberg, German Offen. 2,265,256 (1973).
22. L. Campanella and G. Pistoia, *This Journal*, **120**, 383 (1973).
23. B. K. Makarenko, E. A. Mendzheritskii, R. P. Sobolev, Yu. M. Povarov, and P. A. Sereda, *Elektrokhimiya*, **10**, 355 (1974).
24. J. J. Auborn, U.S. Pat. 3,891,457 (1975).
25. V. N. Storozhenko, *Zh. Fiz. Khim.*, **48**, 1709 (1974).
26. F. A. Shunk, "Constitution of Binary Alloys," Second Supplement, p. 479, McGraw-Hill, New York (1969).
27. I. D. Raistrick and R. A. Huggins, "Proceedings of the Symposium Workshop on Advanced Battery Research and Design," Argonne National Laboratory, p. B-277 (1976).
28. M. Hebb, *J. Chem. Phys.*, **20**, 185 (1958).
29. C. Wagner, "Proc. Int. Comm. Electrochem. Thermodyn. and Kinetics (CITCE)," 7th Meeting, Lindau 1955, p. 361, Butterworth, London (1957).
30. V. A. Plotnikov and P. T. Kalita, *J. Russ. Phys. Chem. Soc.*, **62**, 2195 (1930).
31. Y-W. Hu, I. D. Raistrick, and R. A. Huggins, *Mat. Res. Bull.*, To be published.
32. M. S. Whittingham and R. A. Huggins, in "Solid State Chemistry," R. S. Roth and S. J. Schneider, Editors, NBS Spec. Publ. 364, Washington (1972), p. 139.
33. C. C. Liang, *This Journal*, **120**, 1289 (1973).
34. B. E. Liebert and R. A. Huggins, To be published.
35. C. R. Schlaikjer and C. C. Liang, in "Fast Ion Transport in Solids; Solid State Batteries and Devices," W. van Gool, Editor, p. 685, North Holland Publ. Co., Amsterdam (1973).
36. B. A. Boukamp and R. A. Huggins, To be published.
37. I. D. Raistrick, C. Ho, and R. A. Huggins, *Mat. Res. Bull.* To be published.
38. R. T. Johnson, Jr., B. Morosin, M. L. Knotek, and E. M. Biefeld, *Phys. Lett.*, **54A**, 403 (1975).
39. B. E. Liebert and R. A. Huggins, *Mater. Res. Bull.*, **11**, 533 (1976).
40. R. D. Armstrong, T. Dickinson, and P. M. Willis, *J. Electroanal. Chem.*, **53**, 389 (1974).

Anodic Polarization and Localized Corrosion Behavior of Amorphous $Ni_{35}Fe_{30}Cr_{15}P_{14}B_6$ in Near-Neutral and Acidic Chloride Solutions

T. M. Devine*

General Electric Company, Research and Development Center, Schenectady, New York 12301

ABSTRACT

The anodic polarization and localized corrosion behavior of amorphous $Ni_{35}Fe_{30}Cr_{15}P_{14}B_6$ were obtained in 0.02, 0.2, 0.6, and 2.0M chloride ion solutions of pH 6.6, 4.0, and 1.0. Regardless of the hydrogen ion and chloride ion concentrations of the solution, the alloy remained immune to pitting corrosion. The passive corrosion current density was insensitive to changes in chloride ion concentration. The passive corrosion current density was independent of solution pH between pH 6.6 and 4.0. Decreasing the pH from 4.0 to 1.0 resulted in a threefold increase in passive corrosion current density. The alloy was susceptible to crevice corrosion. Plastic deformation affected neither the passive corrosion current density nor the pitting corrosion resistance. Severe cold-rolling resulted in cracking and crevice corrosion occurred at cracks. The results suggest that the great resistance of amorphous $Ni_{35}Fe_{30}Cr_{15}P_{14}B_6$ to pitting corrosion is due to its resistance to pit nucleation which can be attributed to its high degree of chemical homogeneity and lack of inclusions. The as-received amorphous ribbon is highly chemically inhomogeneous. Auger electron spectroscopy indicates the top surface of the ribbon is greatly enriched with chromium and both surfaces are depleted of phosphorus. Anodic polarization measurements suggest the top surface is covered with a Cr_2O_3 film.

While the electrical, magnetic, and mechanical properties of amorphous alloys have received a great deal of attention, it is only recently that the remarkable corrosion characteristics of some amorphous alloys have been explored (1-4). In particular, we have illustrated the immunity of amorphous $Ni_{35}Fe_{30}Cr_{15}P_{14}B_6$ to pit corrosion in 0.17M NaCl solution (1, 2). By comparison, when the alloy was crystallized by heat-treating in vacuum at 400°C for 2 hr, it became susceptible to pit corrosion in 0.17M NaCl at potentials above +440 mV *vs.* standard hydrogen electrode (SHE). The present work was undertaken to further define the nature and extent of the localized corrosion resistance of amorphous $Ni_{35}Fe_{30}Cr_{15}P_{14}B_6$ and to determine, if possible, whether its corrosion resistance was inherent to its amorphous structure or was related to its chemical composition. The current study presents the anodic polarization, pitting corrosion, and crevice corrosion behavior of amorphous $Ni_{35}Fe_{30}Cr_{15}P_{14}B_6$ in solutions of varying pH and chloride ion activity.

* Electrochemical Society Active Member.
Key words: amorphous alloys, pitting corrosion, anodic polarization.

Experimental Procedure

Amorphous $Ni_{35}Fe_{30}Cr_{15}P_{14}B_6$ was obtained from the Allied Chemical Corporation in the form of ribbon 0.36 cm wide and ~0.007 cm thick. Specimens for potentiodynamic anodic polarization were mechanically polished with silicon carbide paper, finished with 3 μm diamond polishing compound, soldered at one end to an electrical test lead, ultrasonically cleaned in acetone, and rinsed with distilled water. The soldered joint was then masked off from the remainder of the sample with Glyptal® paint. This provided an effective sample size of 4 cm in length by 0.36 cm in width by 0.005 cm in thickness.

The anodic polarization behavior and localized corrosion tendency of amorphous $Ni_{35}Fe_{30}Cr_{15}P_{14}B_6$ were determined at room temperature (22°-25°C) in deoxygenated sodium chloride and hydrochloric acid solutions made from distilled water and chemicals of certified ACS purity. The 1 liter volume test solutions were deoxygenated by bubbling ultrahigh purity nitrogen gas at a flow rate of 0.15 std ft^3/hr for a minimum of 4 hr before testing.

The polarization cell contained the deoxygenated test solution, the test electrode, and two platinum-mesh counterelectrodes. A Luggin-Haber probe and salt bridge filled with the test solution provided a low resistance path between the test specimen and a saturated calomel reference electrode ($E^\circ = 0.244$V) located in a separate beaker filled with the test solution. All measured potentials are reported relative to the standard hydrogen electrode. Polarization tests were conducted by first cathodically polarizing the sample to −1200 mV for ≃30 sec and then, starting at the corrosion potential, cathodically polarizing the sample to a current density of ≃30 μA/cm² before reversing the direction of potential variation and anodically polarizing the specimen. This particular cathodic pretreatment provided highly reproducible corrosion potentials. During polarization the potential difference between the reference electrode and specimen was either continuously varied at a rate of 1 mV/sec with the aid of a Princeton Applied Research Model 173 potentiostat and Model 175 universal programmer, or was incremented in 20 mV steps every 20 sec with the aid of a Wenking potentiostat. Identical polarization results were obtained on similar samples polarized by the two different techniques. Samples were anodically polarized to a maximum potential of 1744 mV. The occurrence of pitting corrosion during polarization was indicated by the presence of hysteresis in the polarization curve on backscanning the potential. Following testing, the surfaces of all samples were examined with an optical microscope at 100× and 500× magnifications.

Results

In an earlier note (2) we indicated the surfaces of as-received $Ni_{35}Fe_{30}Cr_{15}P_{14}B_6$ to be very different chemically from each other and from the bulk composition. In the Appendix the nature and extent of the difference in chemical composition between the two surfaces of the ribbon is further defined and shown to result in different anodic polarization behavior for the two surfaces. Briefly stated, the as-received amorphous ribbon is covered on the top (shiny) surface with a chromium-rich layer. The bottom (dull) surface is relatively rich in iron. Both surfaces are low in nickel and practically devoid of phosphorus. The effect of metallographic polishing is to remove the chemically inhomogeneous surface layers of the amorphous alloy. In order to avoid compositional differences between the two surfaces, all testing was performed on samples metallographically polished to 3 μm diamond.

The effect of chloride ion concentration on the anodic polarization of amorphous $Ni_{35}Fe_{30}Cr_{15}P_{14}B_6$ in solutions of pH 6.6, 4.0, and 1.0 is illustrated in Fig. 1-3. The amorphous alloy was initially active in all solutions and the corrosion potential (as defined by the potential of zero applied current during anodic polarization from the cathodic to the anodic region) decreased with increasing chloride ion content and, for a given chloride ion content, decreased with increasing pH at a rate of ≃55 mV/pH unit. Because of the relatively low critical anodic current densities for passivity and low primary passivation potentials, only a small region of Tafel behavior was observed within the region of active dissolution. As such it is difficult to measure a Tafel slope, β, very accurately. However, β did

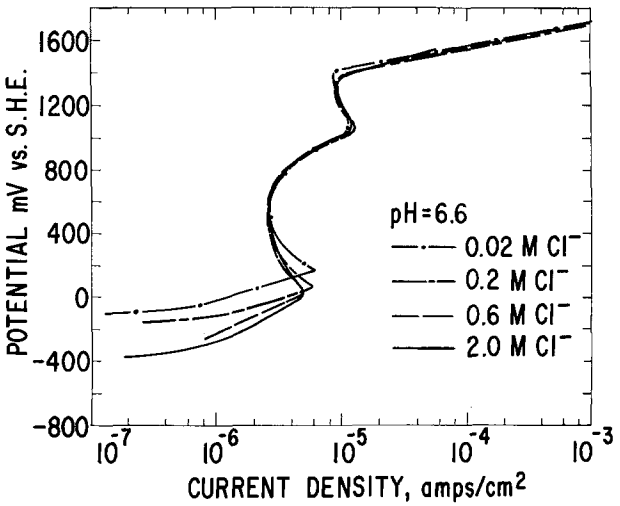


Fig. 1. Anodic polarization of amorphous $Ni_{35}Fe_{30}Cr_{15}P_{14}B_6$ in solutions of pH 6.6 with various chloride ion concentrations.

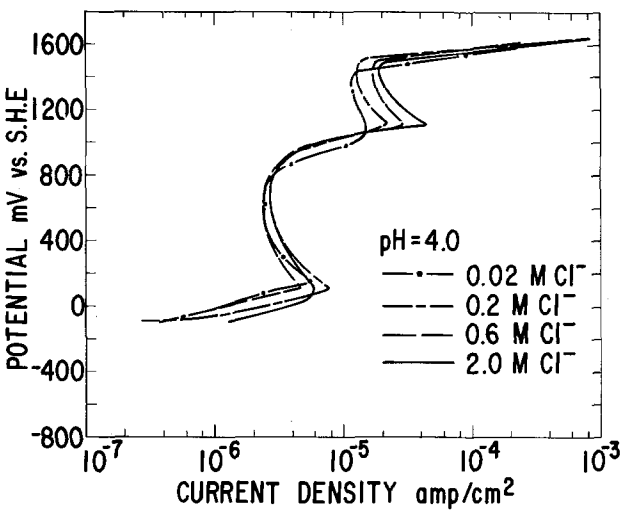


Fig. 2. Anodic polarization of amorphous $Ni_{35}Fe_{30}Cr_{15}P_{14}B_6$ in solutions of pH 4.0 with various chloride ion concentrations.

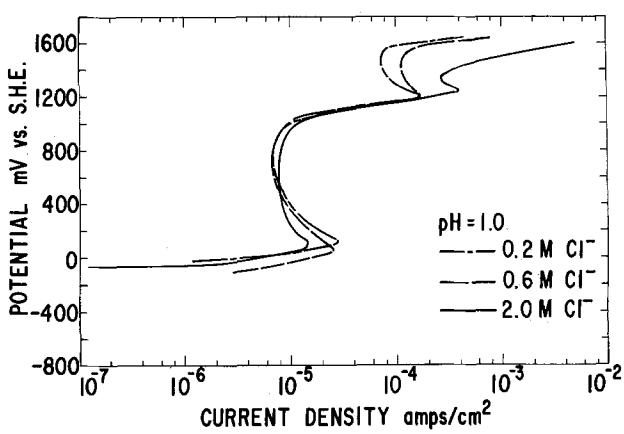


Fig. 3. Anodic polarization of amorphous $Ni_{35}Fe_{30}Cr_{15}P_{14}B_6$ in solutions of pH 1.0 with various chloride ion concentrations.

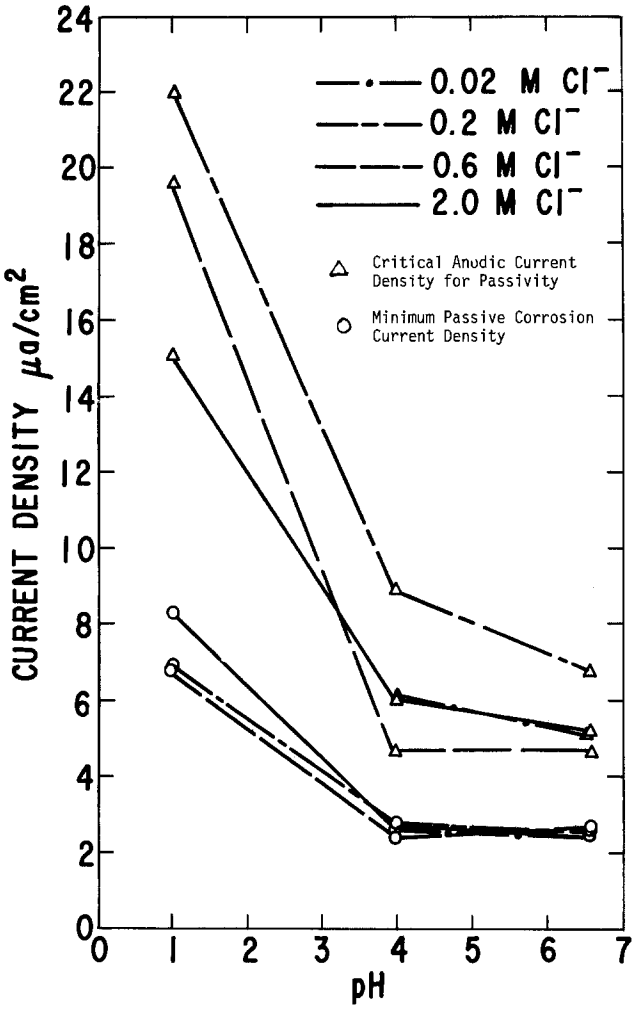


Fig. 4. Critical anodic current density for passivity and minimum passive corrosion current density of amorphous $Ni_{35}Fe_{30}Cr_{15}P_{14}B_6$ as a function of pH and chloride ion concentration.

not vary with chloride ion content in any consistent fashion but an average value of β obtained from solutions of different chloride ion activity progressively decreased with decreasing pH from 0.313 to 0.208 to 0.140V in solutions of pH 6.6, 4.0, and 1.0, respectively. The primary passivation potential decreased as the pH and chloride ion concentration increased. The rate of change of primary passivation potential with pH was $\simeq$24 mV/pH unit. Figure 4 plots the critical anodic current density for passivity in solutions of varying chloride ion content as a function of pH. Each point represents the average value of a minimum of three tests. The maximum deviation from the average value was by a factor of two for the solution of pH 1.0 and a factor of one-half for the solutions of pH 4.0 and 6.6. As indicated, the ease of passivation, when determined by the critical anodic current density, increased with increasing pH. The critical anodic current density for passivity was nearly three times as great in solutions of pH 1.0 as in solutions of pH 4.0 and 6.6. Chloride ion concentration did not have a clear effect except in solutions of pH 1.0 where the critical anodic current density increased with decreasing chloride ion concentration. Figure 4 also plots the minimum passive corrosion current density in solutions of varying chloride ion concentration as a function of pH. Again, each point represents the average value of a minimum of three tests. The maximum deviation from the average value was by a factor of 1.3 for the solutions of pH 1.0 and a factor of 1.08 for the solutions of pH 4.0 and 6.6. The chloride ion concentration clearly had no effect on the minimum passive corrosion current density. The minimum passive corrosion current density was approximately three times as great in solutions of pH 1.0 as in solutions of pH 4.0 and 6.6.

Regardless of chloride ion content, the anodic current density begins to increase at potentials of 540, 640, and 840 mV in solutions of pH 6.6, 4.0, and 1.0, respectively. These potentials were more accurately determined by employing a slower potential sweep rate (6 mV/min) and are plotted in Fig. 5 as a function of solution pH. Also plotted is the potential at which the oxidation reaction rate increases during anodic polarization of the top (shiny) surface of the as-received, unpolished ribbon in 0.17M NaCl (see Fig. 11 and 12 in the Appendix). As indicated, the measured potentials are well below the measured potentials for the evolution of oxygen on platinum. As discussed below, the transpassive potentials probably correspond to the oxidation of Cr_2O_3 in the passive film to $CrO_4^=$.

Regardless of the chloride ion and hydrogen ion concentrations, no pitting corrosion attack occurred in any of the solutions as indicated by microscopic examination of the surface as well as by the lack of hysteresis in the polarization curve on backscanning the potential. Additional anodic polarization tests were conducted in 2.0M HCl and the amorphous alloy was again found immune to pitting corrosion.

In order to further assess the resistance of amorphous $Ni_{35}Fe_{30}Cr_{15}P_{14}B_6$ to localized corrosion in chloride ion media, specimens were potentiostatically polarized in 0.17M NaCl at 844 mV and then scratched with 320 grit silicon carbide paper. In less than 1 sec after the abra-

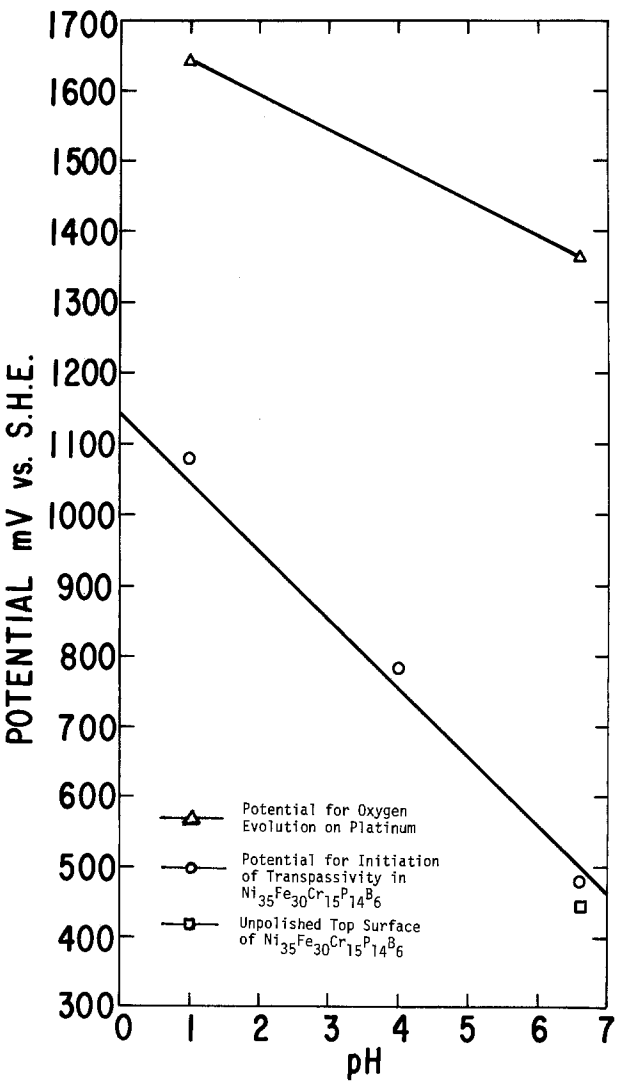


Fig. 5. Potential of initiation of transpassivity of amorphous $Ni_{35}Fe_{30}Cr_{15}P_{14}B_6$ as a function of pH and variation with pH of the potential of oxygen evolution on platinum.

sion stopped, the corrosion rate fell to the same low value as existed prior to the scratching and no localized corrosion was detected.

In spite of the immunity of amorphous $Ni_{35}Fe_{30}Cr_{15}P_{14}B_6$ to pitting corrosion in solutions of low and high hydrogen ion concentration and high chloride ion activity, the material was nevertheless susceptible to crevice corrosion in even dilute NaCl solutions. Figure 6 depicts the anodic polarization behavior in 0.17M NaCl of an amorphous $Ni_{35}Fe_{30}Cr_{15}P_{14}B_6$ specimen in which the Glyptal® paint used to mask the sample test surface was not permitted sufficient time to dry. This produced a crevice at the Glyptal®-metal-solution interface. The appearance of the sample after testing and after the Glyptal® was removed by soaking in acetone is illustrated in Fig. 7. The highly localized nature of the corrosion attack which occurred underneath the Glyptal® at the Glyptal®-specimen-solution interface is evident. The increased corrosion rate at potentials above 800 mV in Fig. 6 is due to the crevice corrosion attack.

Enhanced dissolution is known to accompany the cold-working of crystalline ferrous alloys (5). The anodic polarization behavior of amorphous $Ni_{35}Fe_{30}Cr_{15}P_{14}B_6$ following plastic deformation is illustrated in Fig. 8. The appearance of the sample deformed in pure bending to an outer fiber strain of 3.6% after anodic polarization in 0.17M NaCl to +1645 mV is depicted in Fig. 9. The discrete deformation bands common to amorphous alloys are apparent (6). No enhanced corrosion occurred along these slip steps as has been reported to occur during chemical etching of $Pd_{77.5}Cu_6Si_{16.5}$ (7) and $Ni_{55}Pd_{35}P_{10}$ (8). Plastic deformation to a total strain of 3.6% had no effect on the passive corrosion rate nor on the pitting corrosion resistance of the material. However, as indicated in Fig. 8, cold-rolling the material to 32% reduction in thickness markedly increased the corrosion rate of the alloy. Extensive cracking accompanied the severe cold-work. The appearance of the cold-rolled sample following anodic polarization is depicted in Fig. 10. The sample is severely pitted.

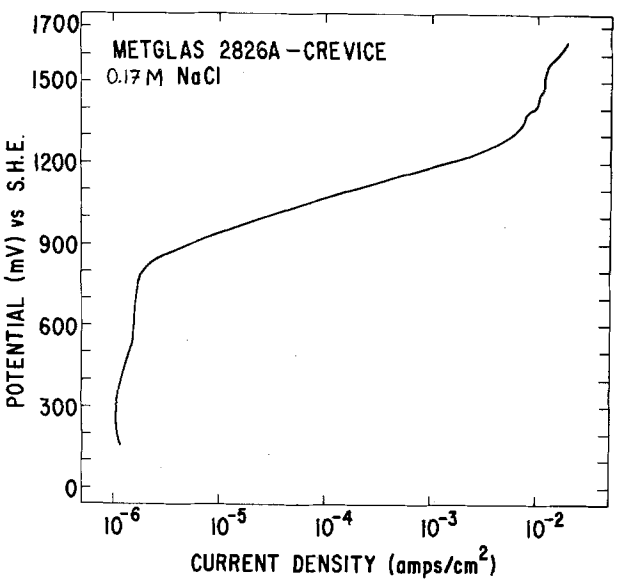


Fig. 6. Anodic polarization of creviced sample of Metglas 2826A in 0.17M NaCl.

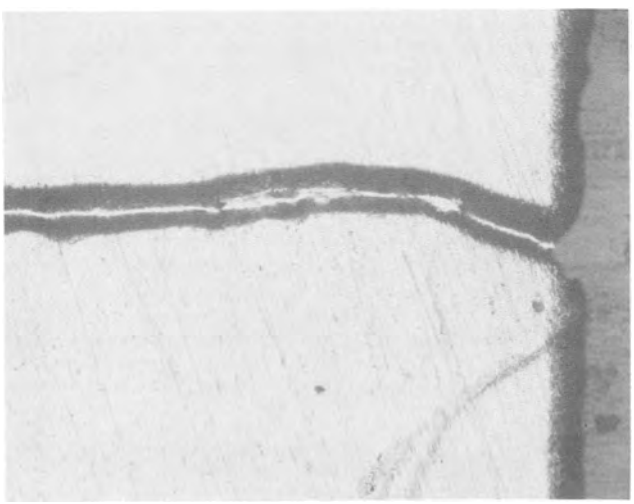


Fig. 7. Appearance of creviced sample of Metglas 2826A after anodic polarization. Glyptal® paint has been removed to reveal the crevice attack. 75×.

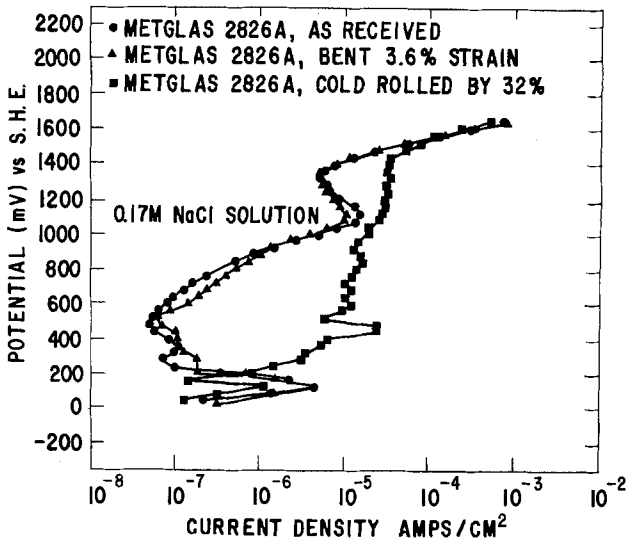


Fig. 8. Effect of cold-work on the anodic polarization of as-received Metglas 2826A in 0.17M NaCl.

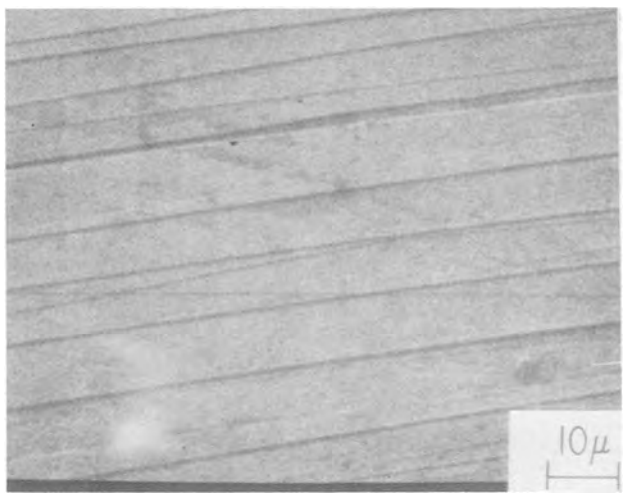


Fig. 9. Appearance of Metglas 2826A plastically bent to a total strain of 3.6% and anodically polarized in 0.17M NaCl.

Discussion

The difference in chemical composition between the two surfaces of amorphous $Ni_{35}Fe_{30}Cr_{15}P_{14}B_6$ ribbon can be attributed to oxidation during processing. As the liquid alloy is ejected from the melt and shot against the substrate, the surface is oxidized. Phosphorus oxide forms rapidly and being volatile leaves the surface entirely. Chromium is also rapidly oxidized to form Cr_2O_3. Iron, nickel, and boron are also oxidized but not nearly as rapidly as chromium. The bottom surface of the ribbon is low in chromium possibly because the chromium oxide film was cracked and removed from the surface when impacted against the cold substrate. The quenched surface was not at tem-

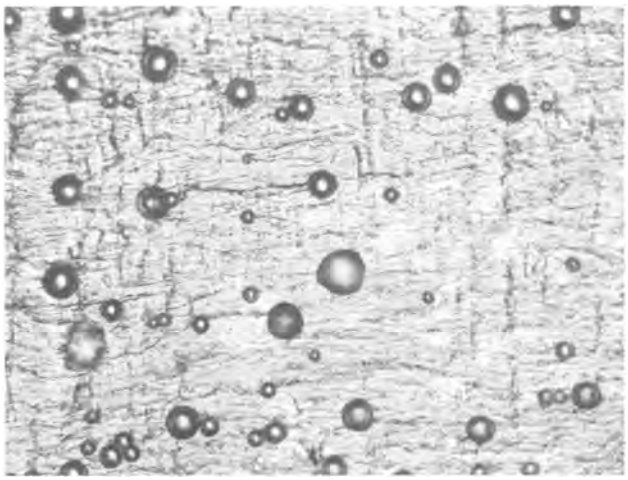


Fig. 10. Photomicrograph of Metglas 2826A cold-rolled to 32% reduction in thickness and anodically polarized in 0.17M NaCl.

perature for sufficient time to permit replenishment with chromium by diffusion from the bulk. The entire top surface was exposed to the atmosphere while still in the liquid state and became covered with a Cr_2O_3 film. This is indirectly supported by the anodic polarization behavior of the top surface in 0.17M NaCl if, as discussed below, we assume the increase in oxidation rate at 445 mV to represent the oxidation of Cr_2O_3 to $CrO_4^=$.

As illustrated in Fig. 5, transpassivity initiated at potentials below the measured potential of oxygen evolution on platinum. The onset of transpassivity probably corresponds to the oxidation of Cr_2O_3 to either $CrO_4^=$ or $Cr_2O_7^=$ according to

$$Cr_2O_3 + 5H_2O \rightarrow 2CrO_4^= + 10\,H^+ + 6e^-$$

$$Cr_2O_3 + 4H_2O \rightarrow Cr_2O_7^= + 8H^+ + 6e^-$$

Although $Cr_2O_7^=$ has a lower standard free energy of formation than $CrO_4^=$, the pH dependence of the transpassive potential is better accounted for by the oxidation of Cr_2O_3 to $CrO_4^=$. Assuming a $CrO_4^=$ activity of $10^{-6.5}$M, the pH dependency of the equilibrium potential for the formation of $CrO_4^=$ from Cr_2O_3 at 25°C is represented in Fig. 5 by the straight line drawn through the data. As can be seen, the measured potentials at which transpassivity initiates agree quite well with the calculated values of the equilibrium potential for the oxidation of Cr_2O_3 to $CrO_4^=$.

Regardless of the chloride ion activity and hydrogen ion concentration of the test solution, pitting did not occur during anodic polarization. Additionally, the passive film formed on amorphous $Ni_{35}Fe_{30}Cr_{15}P_{14}B_6$ repairs itself very well as demonstrated by the ability of the alloy to repassivate after being abraided *in situ* with 320 grit silicon carbide paper while polarized anodically at 844 mV in 0.17M NaCl. In view of the well-known corrosion inhibition properties of phosphate ions, there has been some speculation that phosphorus strongly contributes to the passivity and resistance to pitting of amorphous Fe-Ni-Cr-P alloys (9). This should not be the case based on the early work of Pryor (10) who demonstrated that phosphate ions inhibit the corrosion of iron by increasing the adsorption of oxygen and that inhibition is possible only in solutions of high pH ($pH > 7$) and high dissolved oxygen content. In solutions of low dissolved oxygen content or with $pH < 7$, additions of phosphate ions failed to inhibit corrosion. The inability of chromium-free amorphous alloys $Fe_{80}P_{13}C_7$ (4), $Ni_{40}Fe_{40}P_{14}B_6$, and $Fe_{80}P_{14}B_6$ (11) to passivate during anodic polarization in 1M NaCl demonstrates the inability of phosphorus to passivate the alloys and the necessity of chromium to establish passivity.

Although the amorphous alloy was immune to pitting corrosion in solutions of high hydrogen ion concentration and high chloride ion activity, it was nevertheless susceptible to crevice corrosion in even dilute NaCl solutions. This can be related to the increased corrosion rate of the amorphous alloy in solutions of high hydrogen ion concentrations such as can exist in a crevice. The absence of pitting on the sample strained in tension to 3.6% indicates the film formed on the slip steps to be as resistant to breakdown as the undeformed material. The cracking which resulted from cold-rolling to 32% reduction in thickness has also been observed at the intersection of deformation bands in Ni-Pd-P amorphous alloys following heavy rolling deformation (8). The localized corrosion which occurred during anodic polarization of the cold-rolled sample can be attributed to crevice corrosion at the numerous cracks present.

In view of the susceptibility of amorphous $Ni_{35}Fe_{30}Cr_{15}P_{14}B_6$ to crevice corrosion, the great resistance of the amorphous alloy to pitting corrosion can be attributed to its resistance to pit nucleation. Bond and Lizlovs (12) have demonstrated the immunity of high purity crystalline Fe-Ni-Cr alloys to pitting corrosion in low pH, high chloride ion activity solutions. Such alloys were nevertheless susceptible to crevice corrosion. The immunity of the high purity crystalline alloys to pitting corrosion is lost when impurities such as sulfur are present. Since amorphous $Ni_{35}Fe_{30}Cr_{15}P_{14}B_6$ is quite susceptible to crevice corrosion, one can speculate that if highly soluble inclusions such as sulfides were present in the amorphous alloy, then pits could nucleate at sites of sulfide particle dissolution and pit growth would occur quite readily as in crystalline Fe-Ni-Cr alloys (13). In summary, the ease of passivation and resistance to pitting of amorphous $Ni_{35}Fe_{30}Cr_{15}P_{14}B_6$ can be attributed to its great chemical homogeneity and lack of inclusions. Similarly, the high reproducibility of anodic polarization curves of amorphous $Ni_{35}Fe_{30}Cr_{15}P_{14}B_6$ as compared with the lack of reproducibility (in terms of critical anodic current density for passivity and passive corrosion current density) in crystalline Fe-Ni-Cr alloys can also be attributed to the great chemical homogeneity and lack of inclusions in the amorphous alloy (14).

Acknowledgments

The experimental assistance of Mr. J. R. Ross is gratefully acknowledged. The Auger spectra were obtained by Dr. F. Bacon. The cold-work experiments were performed with Dr. D. Lee. Several very helpful discussions were conducted with Dr. D. A. Vermilyea.

Manuscript submitted May 5, 1975; revised manuscript received Aug. 31, 1976.

Any discussion of this paper will appear in a Discussion Section to be published in the December 1977 JOURNAL. All discussions for the December 1977 Discussion Section should be submitted by Aug. 1, 1977.

Publication costs of this article were assisted by the General Electric Company.

APPENDIX

Surface Composition Inhomogeneity of Amorphous Alloy Ribbon of Metglas 2826A ($Ni_{35}Fe_{30}Cr_{15}P_{14}B_6$)

In an earlier note, we indicated the surfaces of amorphous $Ni_{35}Fe_{30}Cr_{15}P_{14}B_6$ to be highly chemically inhomogeneous (1, 2). The present results further define the nature and extent of this inhomogeneity. Figure 11 compares the anodic polarization characteristics in 0.17M NaCl of as-received Metglas 2826A ($Ni_{35}Fe_{30}Cr_{15}P_{14}B_6$) with specimens of the same material which have been metallographically polished to 3 μm diamond. The as-received amorphous ribbon is initially active, exhibits a maximum active dissolution current of 4.4×10^{-6} A/cm^2 at a potential of 125 mV, and is passive at a potential of 245 mV. It is difficult to estimate the passive corrosion current density of the as-received material because it appears that a second oxi-

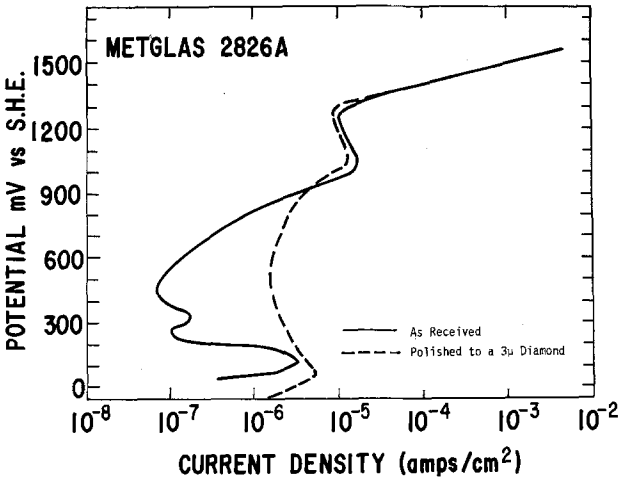


Fig. 11. Anodic polarization of as-received and metallographically polished Metglas 2826A (amorphous $Ni_{35}Fe_{30}Cr_{15}P_{14}B_6$) in 0.17M NaCl.

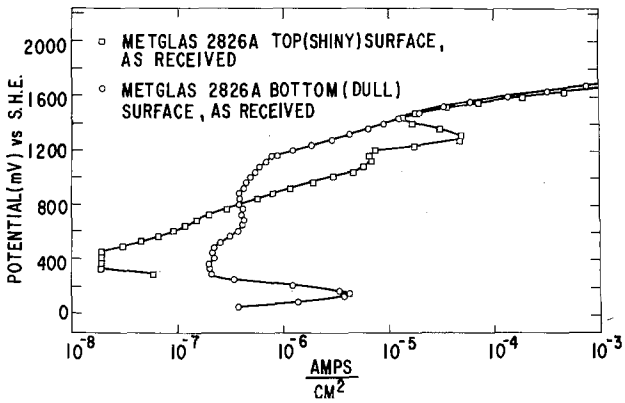


Fig. 12. Anodic polarization of top and bottom surfaces of as-received Metglas 2826A in 0.17M NaCl.

dation reaction occurs at potentials above ~445 mV. The as-received material exhibited secondary passivity between 1125 and 1365 mV. The material was free of pitting as indicated by the absence of hysteresis in the polarization curves on backscanning of the potential. This conclusion was supported by microscopic examination of the specimens after testing with a light microscope at 100× and 500× magnifications. Figure 12 depicts the different anodic polarization characteristics of the two surfaces of the amorphous ribbon sample in 0.17M NaCl. These results were obtained by masking off either the "top" or "bottom" surface of the ribbon with Glyptal® paint and potentiodynamically polarizing the other surface. The bottom surface is dull in appearance; this surface made direct contact with the substrate when the alloy was rapidly cooled from the liquid state by impingement with the cold substrate. This surface is initially active, undergoes an active-to-passive transition during anodic polarization, and does not exhibit secondary passivity. Only a relatively minor increase in oxidation rate was observed at potentials greater than 445 mV during potentiodynamic anodic polarization of the bottom surface. The top surface of the ribbon is shiny in appearance and was the last to solidify. This surface is initially passive and exhibits a very low passive corrosion current density. A marked increase in the oxidation reaction rate occurred at 445 mV. The absence of pitting on both surfaces of the as-received material during anodic polarization was indicated by the absence of hysteresis in the polarization curves on backscanning the potential. This conclusion was confirmed by viewing the sample with a light microscope at 100× and 500× magnifications after anodic polarization.

Chemical analysis of the two surfaces by Auger spectroscopy was performed to determine if compositional differences exist between the two surfaces which would explain their different electrochemical behavior. Figure 13 compares the Auger spectra of the top and bottom surfaces of the ribbon. The top surface is greatly enriched with chromium with only a minor trace of iron present. Both surfaces have little nickel present and no detectable phosphorus. The boron peak-to-peak height is small on both surfaces. The bottom surface has only a small amount of chromium and is chiefly composed of iron. The presence of oxygen and carbon is strongly indicated on both surfaces. The former is probably due to an air-formed film while the presence of the latter is due to contamination. Figure 14 illustrates the change in composition of the top surface following ion milling for 5 min with argon (equivalent to removal of ~700Å). The chromium peak-to-peak height has been reduced by approximately 25% and the iron and nickel peak-to-peak heights have increased by nearly an order of magnitude. The boron peak is approximately unchanged and the phosphorus peak is strongly evident. Similarly, Fig. 15 depicts the changes in composition of the bottom surface following ion milling with argon for 5 min. The chromium peaks are stronger, the iron peak-to-peak heights are reduced by approximately 30% and the nickel peak-to-peak height is increased by a factor of ~8. The phosphorus peak is now strongly apparent. The Auger spectra of the top and bottom surfaces after ion milling for 5 min are practically identical. In order to avoid compositional differences between the two surfaces, all subsequent testing was performed on samples mechanically polished and cleaned as described above.

REFERENCES

1. T. M. Devine and L. Wells, "Anodic Polarization Behavior of an Amorphous Alloy," General Electric Company Report No. 75CRD250 (Nov. 1975).
2. T. M. Devine and L. Wells, *Scr. Metall.*, **10**, 309, (1976).
3. D. Lee and T. M. Devine, Second International Conference on Rapidly Quenched Metals, Massachu-

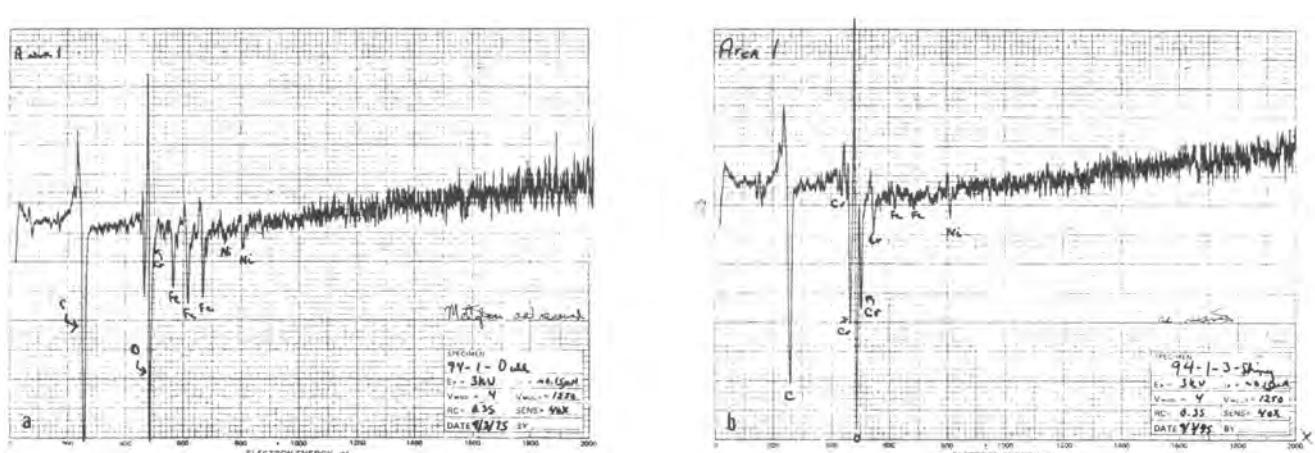


Fig. 13. (a) Auger spectrum of bottom surface of as-received Metglas 2826A, (b) Auger spectrum of top surface of as-received Metglas 2826A.

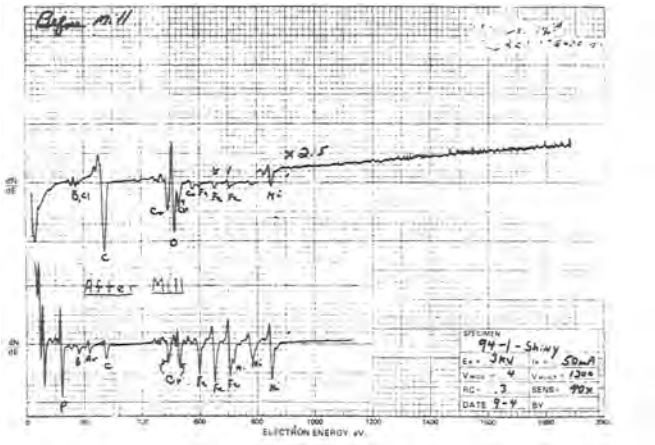


Fig. 14. Effect of ion milling for 5 min on the Auger spectrum of the top surface of as-received Metglas 2826A.

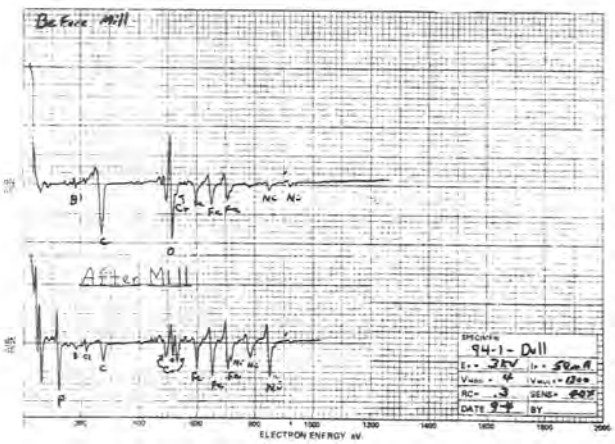


Fig. 15. Effect of ion milling for 5 min on the Auger spectrum of the bottom surface of as-received Metglas 2826A.

setts Institute of Technology, Cambridge, Mass., Nov. 17-19, 1975.
4. K. Hashimoto and T. Masumoto, *ibid.*
5. W. D. France, Fourth International Congress on Metallic Corrosion, Amsterdam, Netherlands, Sept. 7-14, 1969.
6. C. Pampillo, *Scr. Metall.*, **6**, 915 (1972).
7. C. A. Pampillo and H. S. Chen, *Mater. Sci. Eng.*, **13**, 181 (1974).
8. S. Takayama and R. Maddin, *Acta Metall.*, **23**, 943 (1975).
9. M. Naka, K. Hashimoto, and T. Masumoto, *Corrosion*, **32**, 146 (1976).
10. M. J. Pryor and M. Cohen, *This Journal*, **98**, 263 (1951).
11. T. M. Devine, Unpublished results.
12. A. P. Bond and E. A. Lizlovs, *This Journal*, **115**, 1130 (1968).
13. G. S. Eklund, *ibid.*, **121**, 467 (1974).
14. N. D. Greene and R. B. Leonard, *Electrochim. Acta*, **9**, 45 (1964).

Anodic Oxidation of Zirconium: Evidence of Typical Valve Metal Behavior

M. A. Hopper,*[1] J. A. Wright,[2] and D. J. DeSmet*

Department of Physics, University of Alabama, University, Alabama 35486

ABSTRACT

The anodic oxidation of zirconium in dilute sodium carbonate solution was studied by steady-state and transient electrical techniques. An *in situ* ellipsometric method was employed to determine the oxide thickness. The electrical characteristics of the anodization process were found to be similar in most respects to those observed with other valve metals. For growth at constant current, the field in the anodic oxide was found to be independent of oxide thickness, and on suddenly changing the applied current typical voltage transients were observed. The relation between the ionic migration processes involved in the growth of the anodic oxide film and the electrical behavior of the system is discussed.

On anodic oxidation zirconium behaves much like a valve metal but certain features of the anodization process on this metal appear unique. The most marked difference between zirconium and the other valve metals is that growth of the anodic oxide apparently involves the migration of anionic species only, the cationic transport number being essentially zero (1-3). All other valve metals show some detectable cationic transport (1). It might be expected that this unusual ionic migration process would be reflected, in some way, in the electrical behavior of this metal on anodization.

The electrical behavior of zirconium has been examined by a number of workers. Charlesby (4) performed experiments using several electrolytes and estimated the refractive index of the film to be 2.2. He also noted that films formed in sulfuric acid were different in thickness from films formed in other electrolytes under similar conditions. Adams *et al.* (5) studied the electrical behavior of zirconium at potentials below the oxygen evolution potential using aqueous solutions of ammonium borate and sodium carbonate. These authors noted that when the current applied to the zirconium electrode was abruptly raised the potential would overshoot its final value before returning to steady growth conditions. Vermilyea (6), on the other hand, observed only very small electrical transients when the oxidation conditions were abruptly altered above the oxygen evolution potential. This is in contrast to the rather large transients observed with other valve metals when subjected to similar changes. Young (7) noted the absence of voltage transients on zirconium when the formation current density was changed and later reported (8)

* Electrochemical Society Active Member.
[1] Present address: Xerox Research Centre of Canada, 2480 Dunwin Drive, Mississauga, Ontario, Canada.
[2] Present address: Department of Pediatrics, Duke University Medical Center, Durham, North Carolina 27710.
Key words: high field ionic conduction, transients, ellipsometry.

that rapid transient effects could be resolved on switching from constant current to constant potential control. These results suggest that the transient electrical behavior of zirconium on anodization may be related to the nature of the ionic transport process in zirconium oxide.

In his study of the kinetics of anodization of zirconium with electrolytes containing sulfate ions, Young (7) concluded that the electric field in the oxide increased with increasing oxide thickness for a constant applied current. Rogers *et al.* (9) present results that confirm the thickness dependence of the field when anodization is carried out in solutions containing sulfate. They also observed that the field was thickness independent in other electrolytes showing that incorporation of electrolyte species into the zirconium oxide is correlated with the observation of thickness-dependent fields. It should be noted that many other valve metal oxides show measurable electrolyte incorporation but only with zirconium does this appear to result in thickness-dependent fields for constant current growth. For this reason we chose to avoid electrolytes containing sulfate and employed an aqueous solution of sodium carbonate as an electrolyte. It should be noted that the experiments on ionic transport were also performed in electrolytes free of sulfate (1-3).

The present investigation of the anodic oxidation of zirconium was undertaken to determine the extent of the differences in the electrical behavior of the anodization process on this metal from that exhibited by other valve metals. Both steady-state and transient measurements were employed, and an *in situ* ellipsometric technique was used to continuously monitor the thickness of the anodic film. The results obtained are compared with similar measurements on other valve metals and with previous investigations on zirconium. In general the data obtained indicate that the electrical characteristics associated with the anodization of zirconium are similar, in almost all respects, to that of many other valve metals.

Experimental

The samples were prepared from high purity 99.99% zirconium rod (0.6 cm diameter, obtained from Materials Research Corporation) and formed into cylinders approximately 0.6 cm long with a flat ground on the cylindrical surface for use in the optical experiments. The samples were mounted between Teflon washers in a glass sample holder similar to that described previously (10). Removal of the anodic oxide from a zirconium surface is a difficult task and care had to be taken to produce a surface that is "film free" and optically flat. After considerable experimentation the method finally adopted involved careful removal of all visible signs of oxide with fine emery paper, followed by chemical polishing following the procedure described by Cain (11). A bright surface suitable for optical examination is produced using this procedure. The sample area was taken to be the geometrical area of the metal exposed to the solution when the sample was mounted in the holder.

The anodization cell consists of a hollow equilateral glass prism fitted with ground glass joints for mounting the sample holder, reference electrode, and platinum cathode. With this arrangement optical measurements were made at an angle of incidence of 60° with the light passing normally through the cell windows. The solution used for all experiments reported here was 0.1M Na_2CO_3 and reasons for the choice of this particular electrolyte are given below. All measurements were made at room temperature.

The electronic circuitry used was identical to that described previously (10). Potentials and open-circuit transients were recorded on a fast strip chart recorder.

The self-nulling automated ellipsometer used in the investigation was constructed in these laboratories following the general design concepts described by Ord (12). The performance of this instrument has been described elsewhere (13) and is only summarized here. With our zirconium surface the instrument has a nulling time of about 4 sec and provides an angular resolution of 0.01° in both the polarizer and analyzer settings. A quarter-wave plate with its fast axis fixed at −45° is situated between the polarizing prism and the sample. The readings of the polarizer and analyzer angles along with the electrode potential were recorded on a digital printer at the end of every nulling sequence. A He/Ne laser is used as the light source in the instrument and all optical constants reported in this communication are determined at 6328Å.

Results

Optical measurements.—The ellipsometric data obtained during steady-state anodization at 0.5 mA/cm² is shown in Fig. 1. During this experiment the ellipsometer recorded more than 2000 data points only a few of which are plotted in Fig. 1. Starting from point S, corresponding to the nominally bare metal surface, the data trace out the curve in a clockwise direction. The outward spiraling loops shown in this figure are indicative of the growth of a slightly absorbing film on the zirconium substrate. The data can be fit with reasonable precision assuming the oxide has a refractive index of 2.17-0.033i which is independent of oxide thickness. The refractive index of the substrate used in this fit is 2.21-3.04i. The deviation of the data from the theoretical curve for thickness greater than 400 nm may be the result of slight nonuniformities in optical properties of the film or the substrate.

From the optical fit the dependence of the thickness of the film on the potential drop across the oxide was estimated. A linear thickness-potential relationship was observed for the formation of oxide from a solution of 0.1M Na_2CO_3 at constant applied current, the slope giving the field in the oxide as 4.75×10^6 V/cm at a current density of 0.5 mA/cm². The measured field is independent of oxide thickness at this current. The dependence of the electric field in the oxide on the applied current density was estimated from measurement of the voltage-current dependence at 1500 and 3300Å of oxide coverage. The field at

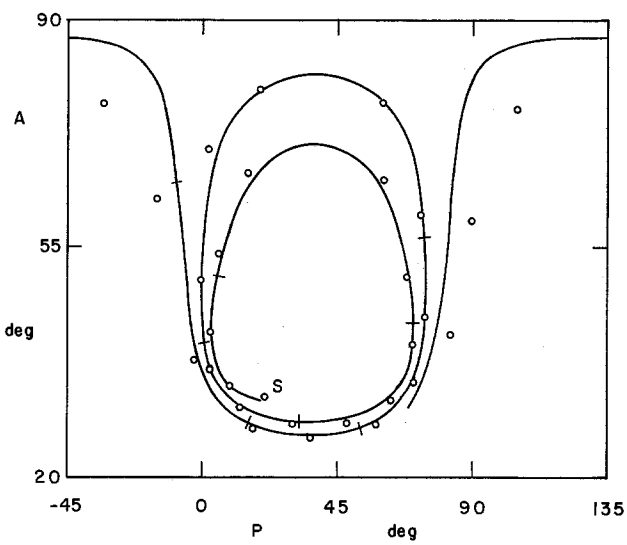


Fig. 1. Ellipsometric data observed on growth of an anodic film on zirconium in 0.1M Na_2CO_3 at 0.5 mA/cm². Data start at point S and trace out loops clockwise. The solid curve represents the best theoretical fit to the data, obtained with a film of refractive index 2.17-0.033i on a substrate of index 2.21-3.04i. Hatch marks indicate thickness increments of 50 nm.

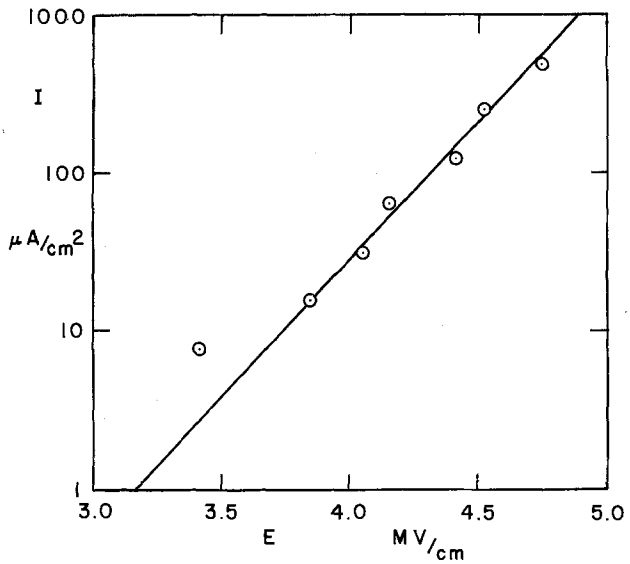


Fig. 2. Current-field dependence for formation of an anodic film on zirconium in 0.1M Na_2CO_3.

any current being equated to the ratio $\Delta V/\Delta D$, where ΔV is the voltage difference between the 1500 and 3300Å data points for the particular applied current, and ΔD is 1800Å. The dependence of the electric field, E, on the applied current density, i, as determined in the above experiment is shown in Fig. 2. This figure exhibits the typical log i *vs.* E dependence found for the formation of valve metal oxides. Writing the dependence of i on E as $i = A \exp(BE)$, the constants A and B have the values 6.9×10^{-12} A/cm² and 3.81×10^{-6} cm/V, respectively, for the data shown in Fig. 2.

An additional observation in the present ellipsometric experiments on zirconium is that changes in the applied current density appear not to affect the optical properties of the anodic film in any detectable way. We observe no optical changes that would indicate the presence of electric field induced birefringence in the layer nor any changes in the refractive index or thickness with changes in the electric field.

Transient electrical measurements.—Studies of the voltage decay following an interruption of the applied current have been used to investigate the oxidation kinetics of tantalum (14), bismuth (10), and vanadium (15). This technique provides an alternative method for obtaining the relation between the applied current density and the electric field strength for a process involving high field ionic conduction. The method has been fully described in the papers quoted above and is only outlined here.

In the present study with zirconium the decay of the electrode potential following an interruption of the current was found to fit a relation of the form

$$V = V_i - V_o \ln(1 + t/\tau) \quad [1]$$

for at least 60% of the total potential change. The fit is performed by varying the single parameter τ to provide a best fit, in the least squares sense, to the measured time dependence of the potential. From this analysis the parameter V_o can be estimated for each separate determination of the open-circuit voltage decay.

Assuming the process occurring after an interruption of the applied current can be modeled by the discharge of the layer capacitance, C, through the anodic film (which only allows passage of an ionic current, i_I), the following differential equation may be applied

$$C dV/dt = -i_I \quad [2]$$

Substitution of V from Eq. [1] gives

$$i_I = CV_o/(\tau + t) \quad [3]$$

This may also be written in the form

$$i_I = i_o \exp(V/V_o) \quad [4]$$

where

$$i_o = \frac{CV_o}{\tau} \exp(-V_i/V_o)$$

The layer capacitance may be estimated using Eq. [3], for $t = 0$ this becomes

$$i = CV_o/\tau \quad \text{or} \quad C = i\tau/V_o \quad [5]$$

In a preliminary investigation of the anodic oxidation of zirconium many different electrolytes were examined. We found that 0.1M Na_2CO_3 gave the most reliable electrical behavior for use with Eq. [1] and the data reported here are confined to experiments with this electrolyte. It is of interest to note that the results of Rogers *et al.* (9) show that, for the low current densities employed in our study, less carbonate is incorporated into anodic zirconium films than are borate or sulfate derived species.

The dependence of V_o on the potential, V_f, appearing across the film prior to interrupting the current was determined for applied current densities of 10, 35, and 100 μA/cm². The results obtained are shown in Fig. 3. V_o increases linearly with V_f at each current density, the slope V/V_o being 10.7, 9.8, and 9.0 at 100, 35, and 10 μA/cm², respectively. The transient analysis also allows the dependence of the reciprocal of the layer capacity, $1/C$, on the formation voltage to be estimated. Experimental $1/C$ *vs.* V_f data are shown in Fig. 4. The $1/C$ data increase linearly with V_f above 30V, below that potential the data appear to lie below that expected on extrapolation of the high voltage linear $1/C$ *vs.* V_f region.

From the experiments described above i_o may be estimated at 10, 35, and 100 μA/cm². The values obtained at these current densities are 1.23, 1.94, and 2.25 nA/cm², respectively. i_o increases with applied current density, and assuming the relation between i_o and i is $i_o = ki^\alpha$ [see Ref. (14)], α may be evaluated. For the limited set of data presented here α is approximately 0.25.

When the anodic applied current density was suddenly switched from one value to another potential transients were consistently observed. Results obtained near a formation potential of 23V on switching from 200 to 40 and then back to 200 μA/cm² are pre-

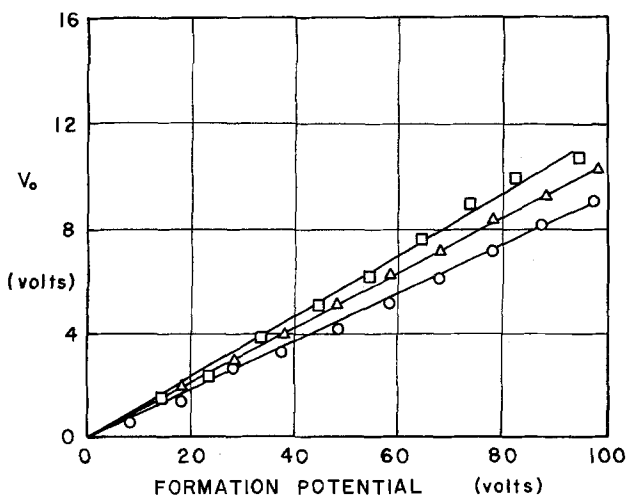


Fig. 3. Measured dependence of V_o on the formation potential, V_f, for applied current densities of 10 μA/cm² (□), 35 μA/cm² (△), and 100 μA/cm² (○).

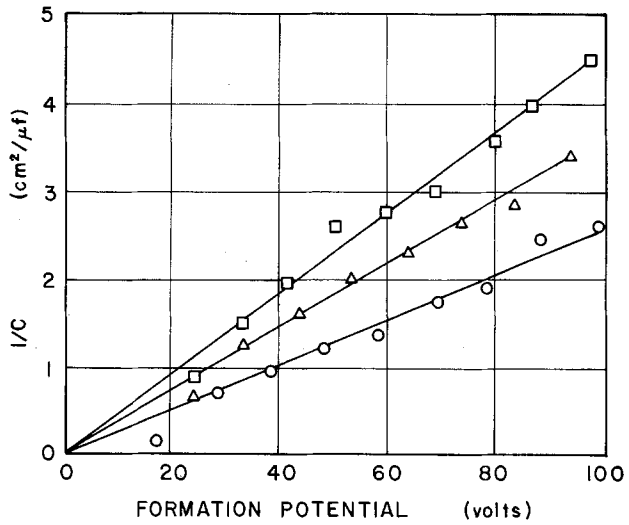


Fig. 4. Variation of reciprocal capacitance with formation potential for applied current densities of 10 μA/cm^2 (□), 35 μA/cm^2 (△), and 100 μA/cm^2 (○).

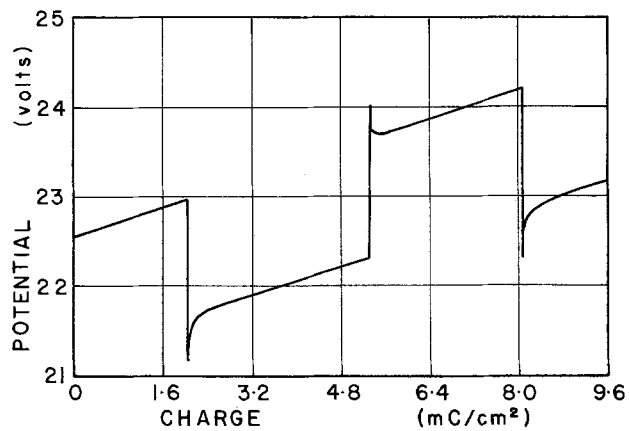


Fig. 5. Potential transients observed on changing the applied current density from 200 to 40 μA/cm^2 and then back to 200 μA/cm^2.

sented in Fig. 5. The changes in potential are shown plotted against the charge passed. The results given in this figure are similar to those found with tantalum (14) and many other metals that form thick insulating anodic oxides (8).

Discussion

The ellipsometric data presented in this communication show that the electric field in the oxide formed on zirconium from a 0.1M sodium carbonate solution is thickness independent at constant applied current. Our measurements were made only up to a current density of 0.5 mA/cm^2 and it is possible that for higher currents other effects occur. These results are in general agreement with the data obtained using a spectrophotometric method of thickness measurement reported by Rogers *et al.* (9). They found that the field in the anodic film on zirconium was independent of thickness for formation at 1 mA/cm^2 but at 10 mA/cm^2 the field increased with increasing thickness. Rogers *et al.* also determined the extent of carbon incorporation into the film and found a correlation between impurity concentration and the thickness-dependent electric field. Other valve metals show considerable electrolyte incorporation on anodization, the system receiving the most attention being tantalum anodized in phosphoric acid electrolytes. With that system, however, no thickness-dependent fields have ever been reported and zirconium thus appears anomalous in this respect. It would appear that the unique ionic migration mechanism is not directly responsible for the thickness-dependent field observed with zirconium, the effect is mainly the result of electrolyte incorporation.

Our optical results indicate that the anodic oxide film formed on zirconium is slightly absorbing at 6328Å. To our knowledge this is the only anodic oxide formed on a valve metal using a wet anodization procedure that exhibits this optical absorption. Masing, Orme, and Young (16) noted a similar absorption effect in reflectivity measurements on zirconium oxide film formed in sulfuric acid solution. They did not determine the optical constants of the film but since their measurements were made at 4358Å no comparison with the present results is possible. Ruiz-Urbeita *et al.* (17) found that sputtered ZrO_2 films show absorption at 6328Å and it would appear reasonable to assume that the optical absorption is an intrinsic property of ZrO_2 and not an artifact associated with electrolyte incorporation.

It is uncertain how film absorption, which almost certainly will vary with wavelength, influences measurement of oxide thickness with a spectrophotometric technique. Estimates of the electric fields based on that method should thus be viewed with caution. Rogers *et al.* (9) fit their spectrophotometric data using a refractive index that is smaller, by about 5% at 6328Å, than our ellipsometric determined index. If this percentage difference applies over the whole optical range, it would lead to an overestimation in the thicknesses measured by Rogers *et al.* by at least 5%. In addition, no correction for film absorption was made and thus the value of the field (4.4×10^6 V/cm) at an applied current of 1 mA/cm^2 given by Rogers *et al.* is not in contradiction with our estimate of 4.9×10^6 V/cm obtained by extrapolation of the data shown in Fig. 2.

The observation that the anodic zirconium oxide film is unaltered by changes in the electric field should be contrasted with the results reported for the anodic oxides on tantalum, niobium, and tungsten (18) and vanadium (19). In addition there is no indication of field induced binefringence in the layer similar to that reported for tantalum (20) or niobium (21) even though the field strength in the zirconium oxide is of similar magnitude. The reason for the absence of field-induced changes in the optical properties of the anodic zirconium oxide film is not known but cannot be ascribed to a lack of experimental sensitivity as we have observed changes in the refractive index with tantalum and niobium oxide films using our ellipsometer.

The dependence of the electric field in the oxide on the applied current density shown in Fig. 2 indicates that the simple relationship $i = A \exp(BE)$ may be applied, as a first-order approximation, to anodization of zirconium in sodium carbonate solution. For the limited range of current used no evidence of a nonlinear ln i *vs.* E dependence was detected. At the lowest current used (approximately 8 μA/cm^2) the experimental field value appears low compared with higher current points. This is probably an indication of some nonionic current becoming important in this region. Generally this behavior is ascribed to "leakage" or some other electronic current. Our experimental values for the parameters A and B in the above equation (viz., 6.9×10^{-12} A/cm^2 and 3.81×10^{-6} cm/V, respectively) are in good agreement with the results of Charlesby (4), who determined $A = 1.6 \times 10^{-11}$ A/cm^2 and $B = 3.4 \times 10^{-6}$ cm/V for anodization of zirconium using a saturated ammonium borate solution, and Adams *et al.* (5) who found $A = 2.9 \times 10^{-11}$ A/cm^2, $B = 4.6 \times 10^{-6}$ cm/V for anodization in ammonium borate and $A = 2 \times 10^{-12}$ A/cm^2, $B = 6 \times 10^{-6}$ cm/V on anodizing in sodium carbonate solution. Even with the sodium carbonate

solution results obtained at currents greater than those used here might lead to complications from electrolyte incorporation. Rogers *et al.* (9) have shown that the impurity content of the anodic film depends strongly on current density above 1 mA/cm^2 and this has a drastic influence on the electrical behavior.

We find that potential transients are readily observable during anodization of zirconium when the applied current is charged abruptly. The transients show all the features of similar effects reported with other valve metal systems. The effects we observe (see Fig. 5) are fairly large: The magnitude of the observed potential overshoot on zirconium is 70% of similar transients observed on tantalum but the relaxation of the potential back to the steady state is more rapid with zirconium. Since marker experiments (1-3) show that growth of the anodic zirconium oxide involves migration of anionic species only the existence of potential translations on changing the anodic current suggests that bipolar ionic transport is not a requirement for potential overshoot.

The form of time dependence of the potential following an interruption of the applied current is similar to that previously reported for similar experiments with Ta (14), V (15), and Bi (10). Analysis of open-circuit potential decay shows that the parameter V_o increases linearly with oxide thickness for constant current growth. The ratio V/V_o is independent of oxide thickness and increases with increasing current. V/V_o is proportional to the electric field in the oxide. The quantity i_o, defined in Eq. [4], was found to increase with applied current in agreement with the results reported for tantalum (14), vanadium (15), and bismuth (10).

Measurements of the potential changes accompanying changes in the applied current density allows a comparison of the steady-state and open-circuit electrical techniques. Using the steady-state relation $i = A \exp(BE)$ an estimate of the change in the steady-state potential, $|\Delta V|_s$, accompanying a change in applied current may be obtained. For the same current change the total change in potential, $|\Delta V|_t$, (measured experimentally at the maximum of the potential overshoot) may be calculated using $i = i_o \exp(V/V_o)$ assuming i_o is constant. For the assumptions outlined above a current change from i_1 to i_2 gives

$$|\Delta V|_t \cdot V/V_o = |\Delta V|_s \cdot BE \qquad [6]$$

Note that if the variation of i_o with i is $i_o = ki^\alpha$ [see Ref. (13)] then the relation between BE and V/V_o is

$$(1 - \alpha)BE = V/V_o \qquad [7]$$

Combination of Eq. [6] and [7] yields

$$(1 - \alpha)|\Delta V|_t = |\Delta V|_s \qquad [8]$$

The present experiments on zirconium oxide gives the field in the oxide at an applied current density of 100 μA/cm^2 as 4.33×10^6 V/cm, and using the experimentally determined value of B, viz., 3.81×10^{-6} cm/V, the value of BE at this current is 16.5. The open-circuit measurements yield a value of 10.7 for V/V_o at 100 μA/cm^2, and using Eq. [7] a value of $\alpha = 0.35$ was determined on substituting the results given above. For transient experiments similar to those shown in Fig. 5 measurements of $|\Delta V|_s$, made by extrapolating the potentials obtained in regions of steady-state growth to the switching point, and $|\Delta V|_t$ gives an estimate of $|\Delta V|_t$: $|\Delta V|_s$ which on substituting in Eq. [8] gives a value for α of 0.3. Our measurement of the current dependence of i_o gives α as 0.25, assuming $i_o = ki^\alpha$. Thus all three separate estimates of this quantity yield a reasonably consistent value, considering the experimental errors involved in each measurement.

Comparison of these transient results with those reported for tantalum (13) shows the similarity in electrical behavior of zirconium and tantalum on anodization. The only significant difference between the metals is that for tantalum $\alpha = 0.63$ which is almost twice the magnitude of the present value, $\simeq$0.3, found with zirconium. It should be noted that only if $\alpha = 0$ would there be no potential overshoot on changing the oxidation current.

In summary the present experiments indicate that the electrical behavior during the formation of an anodic film on zirconium shows most of the characteristics of other valve metals even though oxide growth on this metal occurs via a unique ion transport process. Further, these results should be useful in indicating the wide degree of similarity in electric behavior of metals on anodization under controlled conditions with the eventual goal of obtaining a comprehensive model of the anodization process.

Manuscript submitted Dec. 29, 1975; revised manuscript received July 6, 1976.

Any discussion of this paper will appear in a Discussion Section to be published in the December 1977 JOURNAL. All discussions for the December 1977 Discussion Section should be submitted by Aug. 1, 1977.

REFERENCES

1. J. A. Davies, B. Domeij, J. P. S. Pringle, and F. Brown, *This Journal*, **112**, 675 (1965).
2. J. L. Whitton, *ibid.*, **115**, 58 (1968).
3. C. Ortega and J. Siejka, Paper 86 presented at The Electrochemical Society Meeting, Cleveland, Ohio, Oct. 3-8, 1971.
4. A. Charlesby, *Acta Met.*, **1**, 340 (1953).
5. G. B. Adams, P. van Rysselberghe, and G. C. Willis, *This Journal*, **102**, 502 (1955).
6. D. A. Vermilyea, *ibid.*, **104**, 427 (1957).
7. L. Young, *Trans. Faraday Soc.*, **55**, 632 (1959).
8. L. Young, "Anodic Oxide Films," Academic Press, New York (1961).
9. G. T. Rogers, P. H. G. Draper, and S. S. Wood, *Electrochim. Acta*, **13**, 251 (1968).
10. D. J. DeSmet and M. A. Hopper, *This Journal*, **116**, 1184 (1969).
11. F. M. Cain, in "Zirconium and its Alloys," p. 176, American Society for Metals (1953).
12. J. L. Ord, *Surf. Sci.*, **16**, 155 (1969).
13. M. A. Hopper and D. J. DeSmet, *Bull. Am. Phys. Soc.*, **15**, 1326 (1970).
14. J. L. Ord and D. J. DeSmet, *This Journal*, **116**, 762 (1969).
15. B. H. Ellis, M. A. Hopper, and D. J. DeSmet, *ibid.*, **118**, 868 (1971).
16. L. Masing, J. E. Orme, and L. Young, *ibid.*, **108**, 428 (1961).
17. M. Ruiz-Urbeita, E. M. Sparrow, and E. R. G. Eckert, *J. Opt. Soc. Am.*, **61**, 351 (1971).
18. J. L. Ord, M. A. Hopper, and W. P. Wang, *This Journal*, **119**, 439 (1972).
19. J. C. Clayton, Thesis, University of Alabama (1975).
20. W. D. Cornish and L. Young, *Proc. R. Soc. London, Ser. A*, **335**, 39 (1973).
21. K. K. Yee and L. Young, *Appl. Opt.*, **14** 1316 (1975).

Catalytic Decomposition of Nitric Oxide in the Presence of Alkaline Earth Oxides

Paul Meubus*

Centre du Moyen Nord, Université du Québec à Chicoutimi, Chicoutimi, Quebec, Canada G7H 2B1

ABSTRACT

The alkaline earth oxides of barium, strontium, and calcium have been studied as catalysts for the decomposition of nitric oxide. The low work function characterizing these oxides is liable to favor an electron donor catalytic process which decomposes the nitric oxide molecule. The latter was used diluted in helium and the concentration was varied between 0.5 and 2.5%. Experiments were carried out at, respectively, 650°, 750°, and 850°C. After passage over the catalyst, nitric and nitrous oxides were found in the gaseous phase, as well as nitrogen and oxygen. Within the limits of concentrations used, it was found that the decomposition reaction rates of nitric and nitrous oxides are mutually independent. Reaction rate constants were calculated, showing that constants related to nitric oxide were at least one order of magnitude higher than those related to nitrous oxide this explaining, within the limits of concentrations used, the independent behavior mentioned. The total conversion for nitric oxide was highest for barium oxide, attaining 80% at 850°C, followed by strontium and calcium oxides. Increasing efficiencies coincide with a decrease in work function. Within the limits of nitric oxide used, up to 3% oxygen do not show any inhibitive effect on nitric oxide decomposition. This may be attributed to a large equilibrium constant for oxygen desorption.

Nitric oxide is well known as an air pollutant, the main sources being urban domestic heating during winter and automobile exhaust gases. The role of this oxide in the photochemical processes occurring during urban atmospheric smog conditions has been well described (1) and a large number of studies have been made on the subject of nitric oxide pollution abatement. Some years ago, the decomposition of nitrous oxide (2, 3) was investigated on various metallic oxides, while more recently extensive research was carried out in relationship with the decomposition of nitric oxide in the presence of metallic oxides (4-6), the associated problem of oxygen inhibition also receiving much attention (7, 8). However, most of these oxides, whether considered for the decomposition of nitrous or nitric oxides, do not seem to fulfill the requirements of a suitable catalyst, the main drawback being the slow nitrogen oxides decomposition reaction rate. In this respect, oxygen seems to have a pronounced inhibitive effect in the process of nitrogen oxides catalytic decomposition on metallic oxides. Recently, an interesting method was reported (9), where catalytic decomposition of nitric oxide was performed on zirconia, while the oxygen produced (an inhibitor in this case) was electrolytically removed from the catalyst's surface.

The catalytic decomposition of nitric or nitrous oxides over metallic oxides involves, in most cases, the partial or total rupture of the gas molecule by means of an electron donor type catalytic process. In this respect, metallic oxides with a low work function should deserve some further attention, the alkaline earth oxides being typical examples for this category of oxides (10). Referring to an extensive work related to the subject under consideration, Winter (7) studied the behavior of calcium and strontium oxides among 40 metallic oxides. However, only one initial nitric oxide pressure is used, which is about ten times the maximum nitric oxide pressure experimented in this study. He also predicts an inverse dependence of nitric oxide decomposition rate upon oxygen pressure, but no experimental results are given. Fraser and Daniels (4) include calcium oxide in their study of metallic oxides as possible catalysts for nitric oxide decomposition. Here again, nitric oxide pressure is at least four times higher than in the present study. Also, oxygen effect is not considered. It should be added that the catalysts are prepared by the different authors in a number of ways which preclude any comparison. In the present study, the alkaline earth oxides are obtained by complete decomposition of the corresponding carbonates at 1500°C. In this respect, it is interesting to note that Amirnazmi (8) observes an increased catalytic activity after heating a number of oxides at high temperatures.

In conclusion, only few and scattered results are available in the literature on the subject of nitric oxide decomposition in the presence of alkaline earth oxides. In this respect, the present work describes some further investigation of this type of oxides, using nitric oxide concentrations in helium between 0 and 2.5%. Also, the inhibitive effect of oxygen was experimented with 3% oxygen and 0.5% nitric oxide in helium, the catalyst used being barium oxide. The latter was found the most efficient catalyst among the alkaline earth oxides used, while the nitric oxide and oxygen concentration used were those liable to occur in the case of actual nitric oxide generation in combustion media.

Apparatus and Mode of Operation

The experimental layout is shown on Fig. 1. The reactor was made of a quartz tube 12 cm long and 0.6 cm diameter, surrounded by a graphite mantle which was used as an electrical resistor. The latter took the form of a cylindrical annulus, 8 cm long with outside and inside diameters, respectively, equal to 1.3 and 1.0 cm. Both ends were provided with cooled electrodes and the electrical current was derived from the secondary of a transformer whose primary was controlled with a rheostat. The voltage drop through the graphite heater was of the order of 2V and the current was around 300A. The graphite heater and quartz tube were enclosed in a vessel filled with an inert gas and temperatures inside the quartz tube were recorded with a Chromel-Alumel thermocouple, as a function of the graphite color temperature using a Leeds and Northrup pyrometer (750°-6000°C range). Calibrations were made with various gas flow rates inside the quartz

* Electrochemical Society Active Member.
Key words: nitric oxide decomposition, alkaline earth catalysts, air pollution.

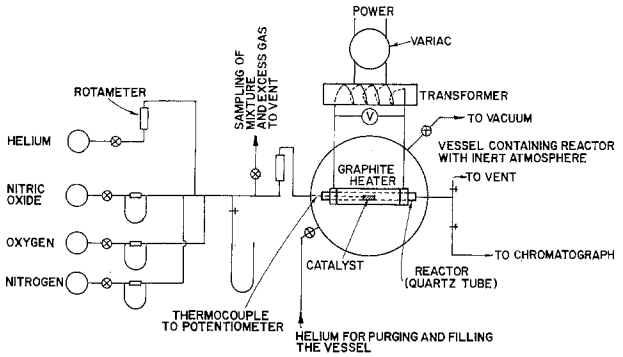


Fig. 1. Experimental layout

tube. Also, a piece of tungsten metal with polished surfaces was positioned in the quartz tube in place of the catalyst sample used for the experiments. Since the geometrical configuration of the quartz tube and metal sample was such that the latter could be considered as a blackbody, surface temperature evaluations were equivalent to those of the catalyst used. Finally, it was found that the gas and solid surface temperatures differed by about 20°C. The temperature (average between bulk gas and catalyst surface) could then be obtained from a measurement of the graphite temperature as mentioned previously. As far as the nitric oxide concentration in the gas bulk and at the catalyst surface was concerned, the diffusion effects were mostly eliminated by using a gas velocity high enough so that the decomposition reaction rates became independent of gas velocity. In this way, pure reaction rates were measured. The helium and nitric oxide used were, respectively, 99.99% (Linde Company) and 99.0% (Canadian Liquid Air). The carbonates used were reagent quality (Baker Company).

The gas mixture was analyzed for nitric and nitrous oxides as well as oxygen and nitrogen, before and after reaction. Also, blank tests were carried out, including all the variables except for the catalyst. A Fisher Hamilton gas partitioner was used, which was provided with a Thermistor detector, 4 ft Porapak Q, and 12 ft Molecular Sieve 5A. The nitric oxide chromatographic detection presents some problems which are summarized in Ref. (8). Referring to these authors, the method adopted in this study was the one described for 3% initial oxygen concentration and less in the mixture nitric oxide-helium used for the experiments. The maximum oxygen concentration generated by the nitric oxide itself was below 1.25% (half the largest nitric oxide concentration used for the tests, say 2.5%), while oxygen inhibition experiments were carried out with 3% oxygen and 0.5% nitric oxide, which could not result in a maximum oxygen concentration higher than 3.25%. This justifies the choice of the method adopted which was not integrally applied, in this respect that the molecular sieve pretreatment with nitric dioxide was omitted. The purpose of this treatment is to avoid nitric oxide disproportionation or oxidation reactions with oxygen. Indeed, it was observed in the present study that the molar $[N_2O/2 + N_2]\%$ was always nearly equal to the molar percent (m/o) oxygen, as recorded at the end of the process, this indicating that no oxygen addition reaction with nitric oxide did occur in the course of reactions.

A helium (carrier gas) velocity of 50 cm³/min was used for the chromatographic analysis of the gas mixtures and the column temperature was kept at 70°C. In this way, adverse effects (nitric oxide oxidation in the gaseous phase) could be obviated in the analysis of the products of reaction. The catalyst was prepared by heating alkaline earth carbonates at 1500°C, in the presence of air, until complete decomposition into oxides and carbon dioxide. In order to determine the conditions required for complete decarbonation, preliminary tests were made and samples were withdrawn at different times from the furnace. Carbon dioxide evolution tests in the presence of acids were performed on these samples. They were also tested in the experimental setup and exposed to a helium-nitric oxide-oxygen mixture with the presence of small amounts of water vapor so as to generate nitric oxide. Resulting gas samples were then checked for the presence of carbon dioxide on the chromatogram. Small alumina vessels were used as containers for the carbonates and resulting oxides. They were 1 cm long and of hemicylindrical shape whose outside diameter fitted with the inside of the quartz tube, thus leaving a free reactor volume of 0.28 cm³ corresponding to the catalytic surface exposed. The latter acquired a glassy and apparently impervious surface after thermal treatment, so that the kinetic calculations could be related to the magnitude of this surface, say 0.60 cm² in all cases, and reaction rates were accordingly expressed in terms of catalyst surface.

Results

Initial nitric oxide concentrations in helium between 0.5 and 2.5% were used for the experiments which were made at atmospheric pressure and catalytic decomposition was carried out at 650°, 750°, and 850°C in the presence of barium, strontium, and calcium oxides, each of these oxides being tested separately. The blank tests did not show any significant variation of the initial nitric oxide concentration. As already mentioned, reaction rate results could have been altered by diffusion processes. Therefore, preliminary tests were made, which showed that velocities of 17 cm³/min were sufficient to make reaction rates independent from diffusion effects. Resulting residence times were of the order of 1 sec and less. Nitric and nitrous oxides, as well as oxygen and nitrogen were found as products of reaction. The rates for nitric and nitrous oxides were calculated from the expressions

$$r = \frac{V}{S}(C_{in} - C_{out}) \qquad [1]$$

or

$$r = \frac{V}{SRT}(p_{in} - p_{out}) \qquad [2]$$

Average pressures were calculated from p_{in} and p_{out} in the case of nitric oxide. In most cases p_{out} did not differ from p_{in} by more than 20%, yielding an average value that could be considered as a constant for the reaction process. Considering the case of nitrous oxide pressure, a balance in nitrogen may be written

$$[NO] + 2[N_2O] + 2[N_2] = [NO]_o \qquad [3]$$

Since [NO] may be considered as an average constant value during the reaction process, one obtains

$$[NO] = \frac{[NO]_o + [NO]_E}{2}$$

and from [3]

$$[N_2O] + [N_2] = \frac{[NO]_o - [NO]_E}{4} \qquad [4]$$

$$[N_2O] + [N_2] = \text{constant} \qquad [5]$$

The rate of formation of nitrous oxide can be written

$$\frac{d[N_2O]}{dt} = \frac{1}{2}\frac{d[NO]}{dt} - \frac{d[N_2]}{dt} \qquad [6]$$

[NO] is a constant and a first-order decomposition reaction rate with respect to nitrous oxide is reported in the literature. As a result, Eq. [6] can be written

$$\frac{d[N_2O]}{dt} = A - B[N_2O] \qquad [7]$$

As discussed later in this study, the reaction rate constant related to A is at least one order of magnitude higher than B. In view of this fact and the form of Eq.

[7], fast accumulation of nitrous oxide should occur at the early stages of the nitric oxide decomposition reaction, so that the initial nitrous oxide pressure can be approximately derived from Eq. [4] where $[N_2] = 0$. This procedure has been adopted in order to determine an average pressure for nitrous oxide

$$p'_{AV} = \frac{4[N_2O]_E + [NO]_o - [NO]_E}{8} \qquad [8]$$

all the terms in the equation being determined either by initial conditions or chromatographic analysis results.

Figures 2, 3, and 4 show the nitric oxide decomposition rate variation when the alkaline earth oxides of, respectively, barium, strontium, and calcium are used. It is observed that, all conditions being equivalent, the decomposition rate is highest for barium oxide, being about two times higher than the corresponding reaction rates for strontium and calcium oxides. Decomposition reaction rates of the nitrous oxide resulting from the decomposition of nitric oxide in the preceding stage are shown in Fig. 5, 6, and 7 for the catalysts already mentioned and in the same order (barium, strontium, calcium oxides). The decomposition rates for nitrous oxide were calculated from Eq. [1] and used for p' and c', while the average pressure for this constituent was determined from Eq. [8]. From these results, it was found that the reciprocal of the decomposition rate for nitric or nitrous oxides was a linear function of the reciprocal of the respective partial pressures. This was true for all the catalysts used, at the various operating temperatures. Results are shown for nitric oxide in Fig. 8, 9, and 10, while those related to nitrous oxide appear in Fig. 11, 12, and 13. It has already been mentioned that gas mixtures made of 0.5% nitric oxide and 3% oxygen in helium were experimented with in order to observe possible oxygen inhibition effects upon the catalyst used. Since 0.5% nitric oxide generates a maximum of 0.25% oxygen, the addition of 3% oxygen should have resulted in a variation of decomposition reaction rate if any inhibition effect had taken place. Barium oxide was experimented with and no inhibition effect was found. It is quite possible that nitric oxide or oxygen concentrations other than those used in this study could lead to different conclusions. However, the

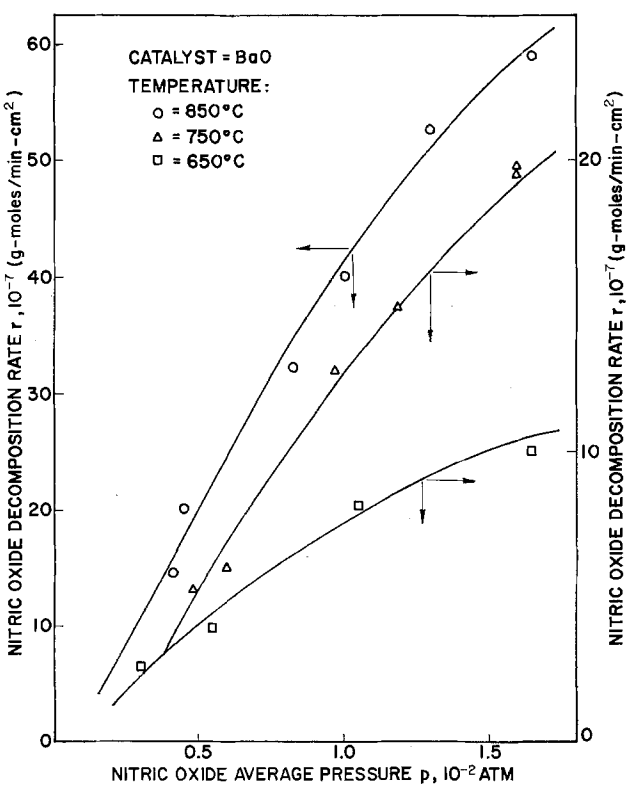


Fig. 2. Decomposition rate of nitric oxide in the presence of barium oxide at various nitric oxide average pressures in helium, different temperatures, and total atmospheric pressure.

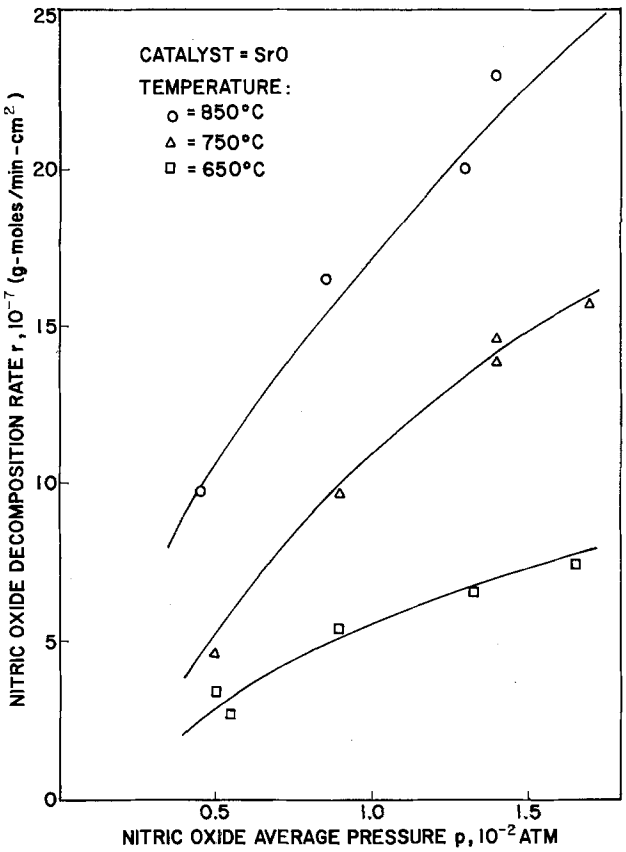


Fig. 3. Decomposition rate of nitric oxide in the presence of strontium oxide at various nitric oxide average pressures in helium, different temperatures, and total atmospheric pressure.

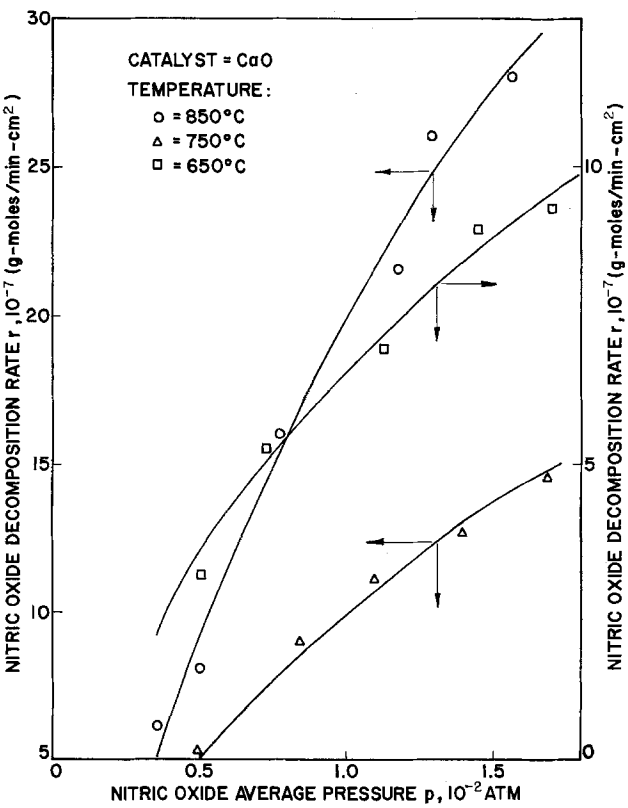


Fig. 4. Decomposition rate of nitric oxide in the presence of calcium oxide at various nitric oxide average pressures in helium, different temperatures, and total atmospheric pressure.

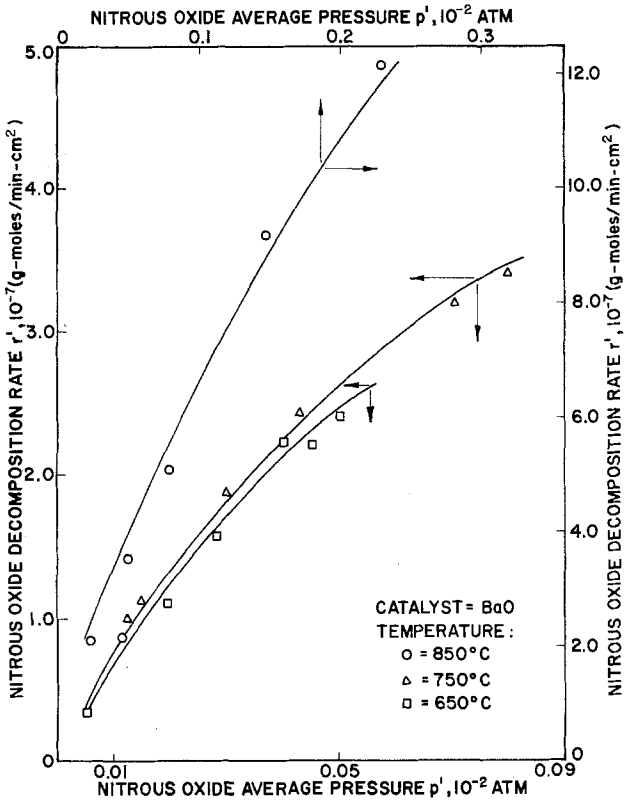


Fig. 5. Decomposition rate of nitrous oxide in the presence of barium oxide at various nitrous oxide average pressures in helium, different temperatures, and total atmospheric pressure.

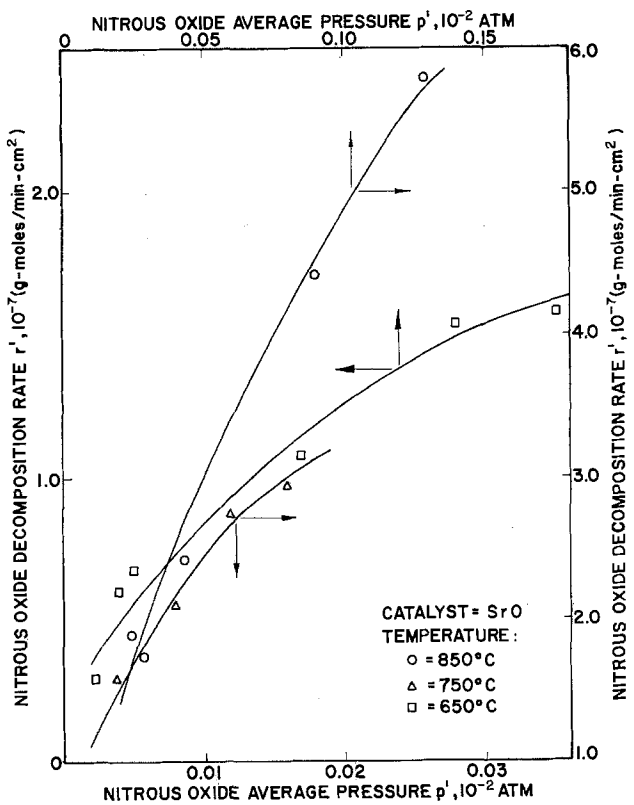


Fig. 6. Decomposition rate of nitrous oxide in the presence of strontium oxide at various nitrous oxide average pressures in helium, different temperatures, and total atmospheric pressure.

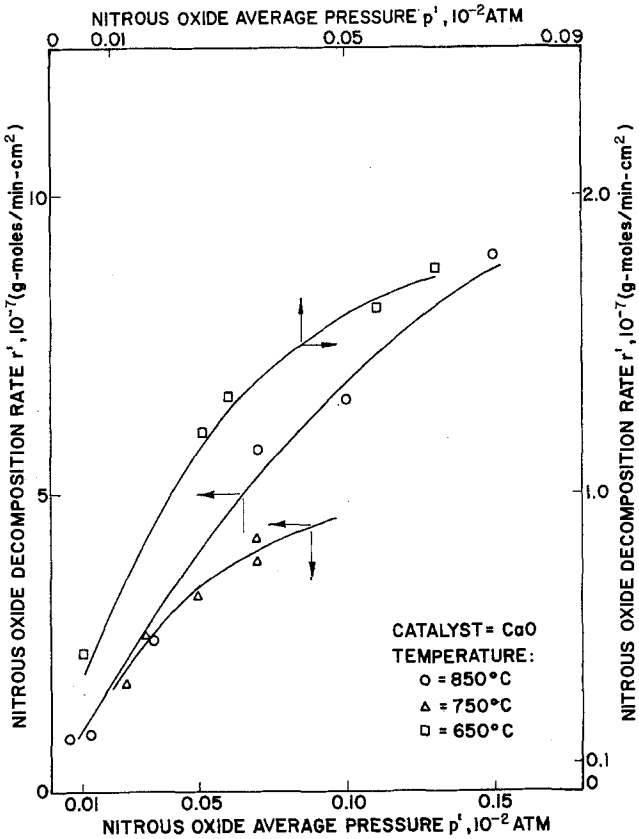


Fig. 7. Decomposition rate of nitrous oxide in the presence of calcium oxide at various nitrous oxide average pressures in helium, different temperatures, and total atmospheric pressure.

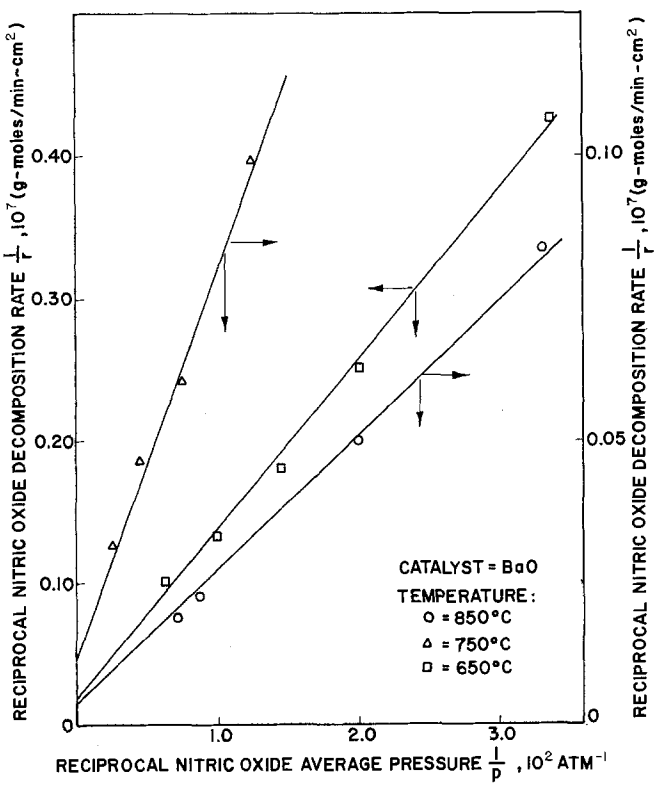


Fig. 8. Linear relationship between nitric oxide reciprocal decomposition rate and reciprocal average pressure, measured at various temperatures and nitric oxide average pressures as well as total atmospheric pressure. Catalyst: barium oxide.

contemplated objective was an evaluation of alkaline earth oxides as nitric oxide decomposition catalysts in the case of combustion media. Therefore, the most efficient catalyst among the three alkaline earth oxides and nitric oxide as well as oxygen concentrations close to combustion exhaust gases were chosen for this kind of investigation. In relationship with the absence of oxygen effect, it should be mentioned that the rate

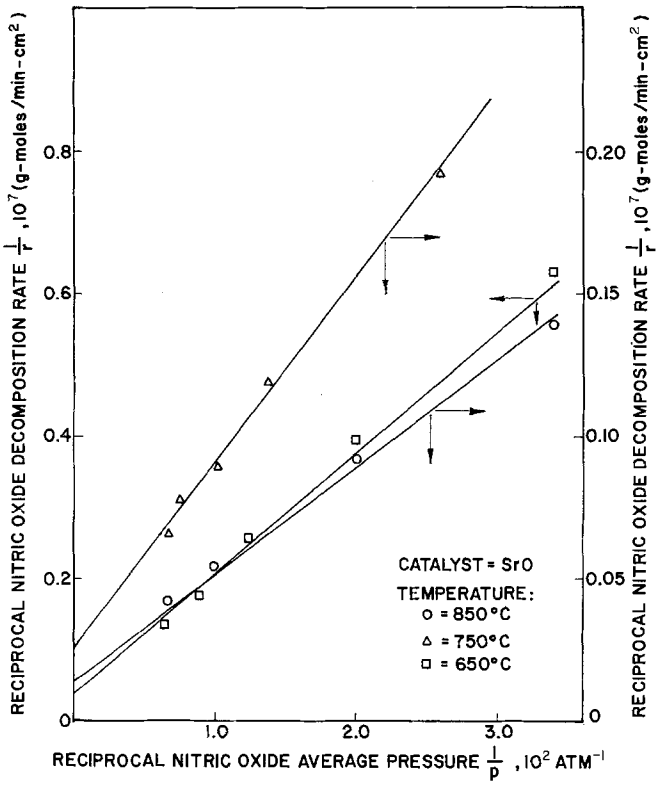


Fig. 9. Linear relationship between nitric oxide reciprocal decomposition rate and reciprocal average pressure, measured at various temperatures and nitric oxide average pressures as well as total atmospheric pressure. Catalyst: strontium oxide.

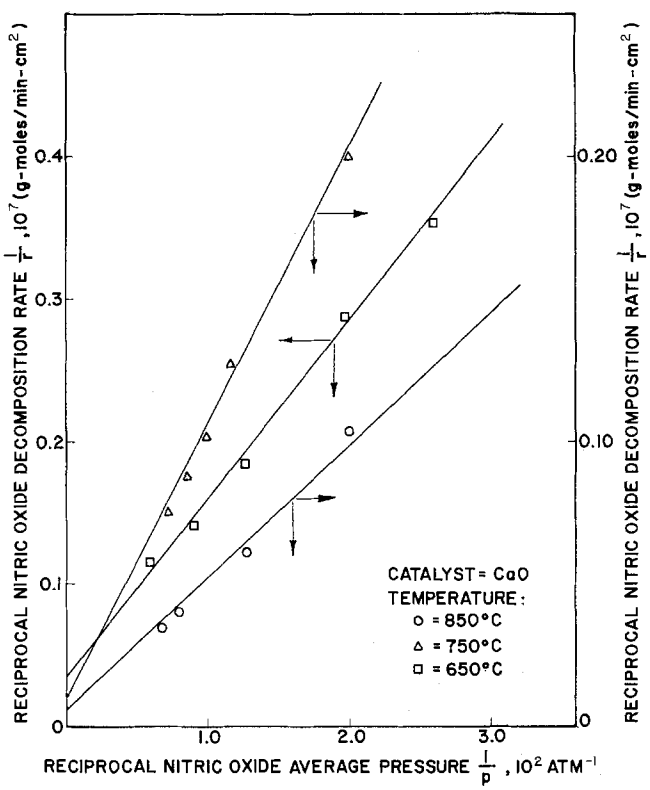


Fig. 10. Linear relationship between nitric oxide reciprocal decomposition rate and reciprocal average pressure, measured at various temperatures and nitric oxide average pressures as well as total atmospheric pressure. Catalyst: calcium oxide.

equations, [22] and [29], found in this work for describing the decomposition reactions of nitric and nitrous oxides imply that the number of adsorption sites of oxygen should be small since the desorption equi-

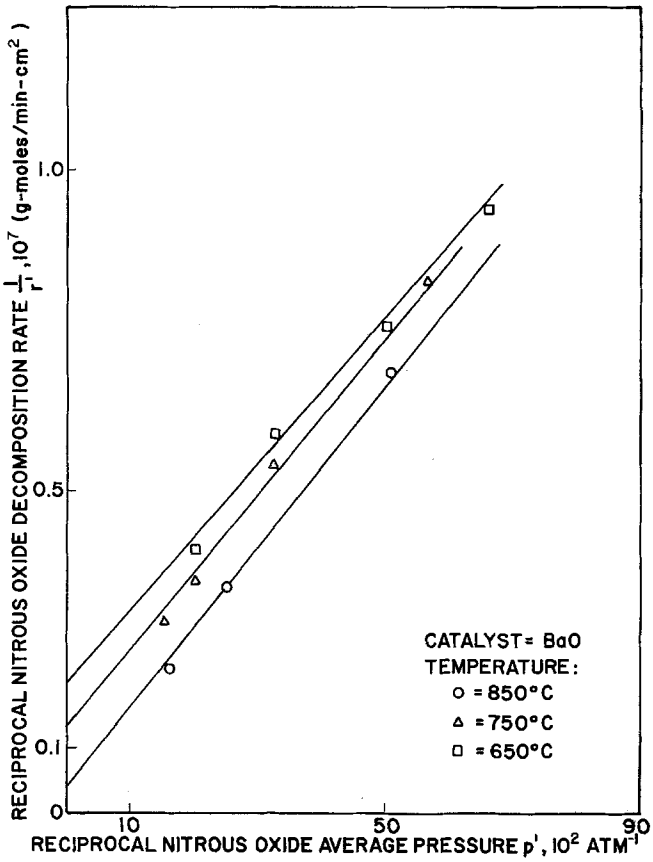


Fig. 11. Linear relationship between nitrous oxide reciprocal decomposition rate and reciprocal average pressure, measured at various temperatures and nitrous average pressures as well as total atmospheric pressure. Catalyst: barium oxide.

librium constants K_3 and K_3' should be high. This could possibly result from the high temperature carbonate treatment and consecutive increase in positive holes associated with the alkaline earth metal formation, which are more liable to accept the electron from O^- in the process of oxygen desorption. However, this is a mere assumption and has not been verified in this study.

Discussion

The nitric oxide molecule may be considered as resonating between the electronic structures (11)

$$: \dot{N} = \ddot{O} : \qquad [9]$$

$$\overset{-}{:} \ddot{N} = \dot{O} \overset{+}{:} \qquad [10]$$

The structure [10] lends itself to an electron donor catalyst mechanism, while equilibrium rupture between [9] and [10] supplies further [10] species at the expense of [9].

Then

$$NO + \overset{\text{from catalyst}}{e} \rightarrow \tfrac{1}{2}N_2O + (\tfrac{1}{2}O)^-_{ADS} \qquad [11]$$

$$(\tfrac{1}{2}O)^-_{ADS} \rightarrow \tfrac{1}{4}O_2 + \overset{\text{to catalyst}}{e} \qquad [12]$$

also, nitrous oxide resonates between the species (12)

$$\overset{-}{:} \ddot{N} = N^+ = \underset{\cdot\cdot}{O} : \qquad [13]$$

$$\overset{-}{:} \underset{\cdot\cdot}{N} = N^+ = \ddot{O} : \qquad [14]$$

$$\overset{-}{:} N \equiv N^+ - \underset{\cdot\cdot}{\ddot{O}} : \qquad [15]$$

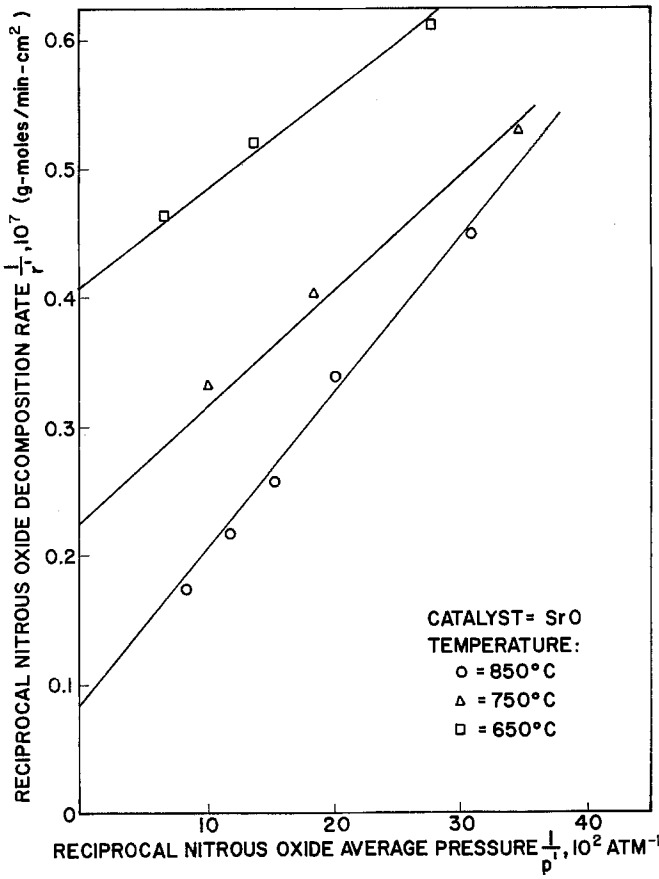


Fig. 12. Linear relationship between nitrous oxide reciprocal decomposition rate and reciprocal nitrous oxide average pressure, measured at various temperatures and nitrous oxide average pressures as well as total atmospheric pressure. Catalyst: strontium oxide.

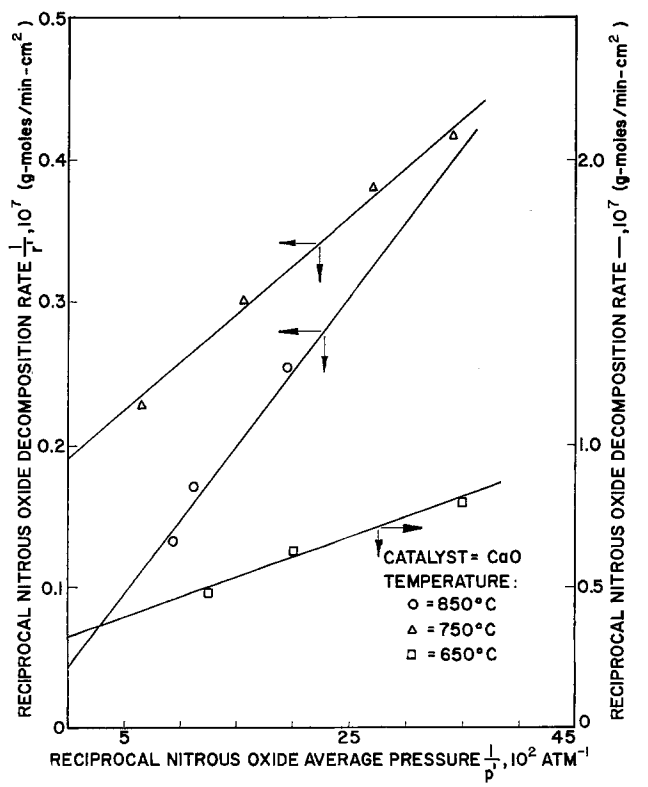


Fig. 13. Linear relationship between nitrous oxide reciprocal decomposition rate and reciprocal average pressure, measured at various temperatures and nitrous oxide average pressures as well as total atmospheric pressure. Catalyst: calcium oxide.

[13] and [14] differing by the nature of some orbitals involved. In the presence of an electron from the catalyst, one nitrogen atom is neutralized, while an excess electron is added to the oxygen atom in [13] and [14], contributing to oxygen attachment to the catalyst. Then

$$N_2O + \overset{\text{from catalyst}}{e} \rightarrow N_2 + (O^-)_{ADS} \quad [16]$$

$$(O^-)_{ADS} \rightarrow \tfrac{1}{2}O_2 \quad [17]$$

These equations suggest that catalysts with low work functions could favor the electronic processes involved. It is well known (10) that alkaline earth oxides behave as n-type semiconductors. The role of impurity levels in the forbidden band seems to be played by metals resulting from dissociated oxides, a reaction which could possibly occur in this case during the carbonate decomposition process carried out at around at least 1500°C. Work functions are as low as 1.2, 1.4, and 1.9 eV for barium, strontium, and calcium oxides, respectively. It is for such reasons that these oxides were tried as catalysts in the present study. The information supplied by Fig. 2-4 on one hand and Fig. 5-7 on the other, shows that the decomposition rates of nitric and nitrous oxides behave independently, implying a fast accumulation of nitrous oxide at the start of the decomposition reaction process, followed by a nitrous oxide pressure variation described by an equation similar to [7]. This aspect has already been discussed in relationship with the nitrous oxide average pressure. Also, the presence of nitrous oxide in the gaseous phase suggests a process of consecutive reactions. The nitric oxide decomposition should proceed through the intermediate desorption of nitrous oxide from sites with adsorption energy Q and subsequent readsorption on sites with adsorption energy Q' and final decomposition into nitrogen and oxygen. The mutual independence of the nitric and nitrous oxides decomposition mechanisms leads to two possible distinct sets of decomposition reaction equations related to these oxides. From Fig. 8-10, $1/r$ and $1/p$ are linearly related and the same holds for $1/r'$ and $1/p'$, this being derived from Fig. 11-13. These features, together with a previous knowledge of general results on the kinetics for solid-gas reaction (13), lead to the conclusions that the sequence of reactions, characterizing the decomposition reaction of nitric and nitrous oxides, should be one site, first-order forward reaction and the surface reaction should be the controlling step. One can now write down the reactions involved and derive some further calculations.

Nitric oxide.—The sequence of steps for a one-site, first-order forward surface reaction with respect to nitric oxide can be written

adsorption

$$NO + X \rightarrow (NOX) \quad [18]$$

surface reaction

$$(NOX) \rightarrow \tfrac{1}{2}N_2O + \tfrac{1}{2}(X - O - X) \quad [19]$$

desorption

$$\tfrac{1}{2}(X - O - X) \rightarrow \tfrac{1}{4}O_2 + X \quad [20]$$

Writing the rate expressions for reactions [18] to [20] with the condition that reaction [19] is the controlling step, one obtains

$$r = \frac{\bar{c}_m k_2 \left(K_1 p - \frac{1}{K_2 K_3} p'^{1/2} p_{O_2}^{1/4} \right)}{1 + k_1 p + \frac{1}{K_3} p_{O_2}^{1/4}} \quad [21]$$

Taking the maximum coverage $\bar{c}_m$ as unity, Eq. [21] meets the requirements of linear relationship between $1/r$ and $1/p$ when

$$r = \frac{k_2 K_1 p}{1 + K_1 p} \quad [22]$$

Table I. Nitric and nitrous oxides decomposition reaction rate and adsorption equilibrium constant for various alkaline earth oxide catalysts

Oxide	Catalyst	k or k', liter/min 650°C	750°C	850°C	K or K', atm^{-1} 650°C	750°C	850°C
NO	BaO	5.0×10^{-6}	8.0×10^{-6}	2.0×10^{-5}	13.0	25.0	40.0
	SrO	2.0×10^{-6}	4.0×10^{-6}	7.0×10^{-6}	25.0	30.0	40.0
	CaO	1.6×10^{-6}	8.0×10^{-6}	1.6×10^{-5}	25.0	13.0	10.0
N_2O	BaO	5.0×10^{-7}	10^{-6}	2.0×10^{-6}	2×10^2	10^3	3×10^3
	SrO	2.0×10^{-7}	5.0×10^{-7}	9.0×10^{-7}	5×10^2	2×10^3	5×10^3
	CaO	2.5×10^{-7}	6.0×10^{-7}	1.6×10^{-6}	3×10^3	5×10^2	2.5×10^2

$$\frac{1}{r} = \frac{1}{k_2}\frac{1}{p} + \frac{1}{k_2 K_1} \qquad [23]$$

Since p is of the order of 10^{-2} atm and p_{O_2} is $p/2$ at most, it may be seen that K_3 in [21] must be large if the equivalence of [21] and [22] is to be obtained. Following Eq. [20], this does mean that the number of sites for oxygen adsorption should be small, also explaining why oxygen does not seem to play an inhibitive role, at least within the limits of concentration used for nitric oxide. This is a possible result of the catalyst preparation at high temperature, as already discussed. Also, a low concentration in oxygen adsorption centers should be associated with a corresponding high nitrous oxide pressure following Eq. [19]. This fact, together with the finding calculated later in this work that the rate constant for nitric oxide decomposition is larger than the corresponding constant for the decomposition of nitrous oxide, confirms the validity of fast initial accumulation for nitrous oxide.

The values for K_1 and k_2 in Eq. [22] were derived from Fig. 8, 9, and 10 which are graphical representations of Eq. [22] for the various oxides studied. As a result, K_1 and k_2 were obtained for barium, calcium, and strontium oxides at temperatures equal to 650°, 750°, and 850°C. Table I summarizes the calculated results. The activation energy could then be obtained from

$$k_2 = k_{O_2}\, e^{-E_2/RT}$$

or

$$\log_{10}K_2 = \log_{10}k_{O_2} - 0.434\frac{E_2}{R}\frac{1}{T} \qquad [24]$$

Figures 14, 15, and 16 show the linear relationship between $\log_{10}k_2$ and $1/T$, from which E_2 was obtained for the various catalysts. Results are contained in Table II. Figures 14, 15, and 16 also show the linear relationship between $\log_{10}K_1$ and $1/T$, following a relationship analog to Eq. [24].

Nitrous oxide.—In view of the linear relationship between $1/r'$ and $1/p'$, the decomposition reaction of nitrous oxide should also be a one-site first-order forward reaction with respect to nitrous oxide. Hence, the following steps may be written, nitrous oxide reacting with new sites X'

adsorption

$$N_2O + X' \rightarrow (N_2OX') \qquad [25]$$

surface reaction

$$(N_2OX') \rightarrow N_2 + (OX') \qquad [26]$$

desorption

$$(OX') \rightarrow \tfrac{1}{2}O_2 + X' \qquad [27]$$

Here again, the surface reaction should be the controlling step and, in a manner similar to that used for nitric oxide, the reaction rate can be written

$$r' = \frac{k_2'\left(K_1' p' - \dfrac{1}{K_2'K_3'} p'_{N_2} p'^{1/2}_{O_2}\right)}{1 + K_1' p' + \dfrac{1}{K_3'} p^{1/2}_{O_2}} \qquad [28]$$

which becomes, for reasons of compatibility with the linear relationship between $1/r'$ and $1/p'$

$$r' = \frac{k_2'K_1' p'}{1 + K_1' p'} \qquad [29]$$

It should be noted here that a model equation, [7], has been used for describing the nitrous oxide pressure variation. The first-order decomposition reaction rate for nitrous oxide used in Eq. [7] is in accordance with the rate equation, [29], experimentally found in this study when p' is small, this being an acceptable approximation in this case. Equation [29] can be written

$$\frac{1}{r'} = \frac{1}{k_2'}\frac{1}{p'} + \frac{1}{k_2'K_1'} \qquad [30]$$

The constants K_1' and k_2' were derived from Fig. 11, 12, and 13, using the relationship expressed by Eq. [23] and their values are found in Table I. The activation energies E_2' were found from Eq. [24] when applied to nitrous oxide, this equation being used in conjunction with Fig. 14, 15, and 16. The calculated values appear in Table II.

Table II. Energy of activation for the decomposition reaction of nitric and nitrous oxides for various alkaline earth oxide catalysts

Catalyst	Energy of activation, kcal/g-mole NO decomposition (E_2)	N_2O decomposition (E_2')
BaO	16.8	15.4
SrO	13.0	14.7
CaO	15.2	23.0

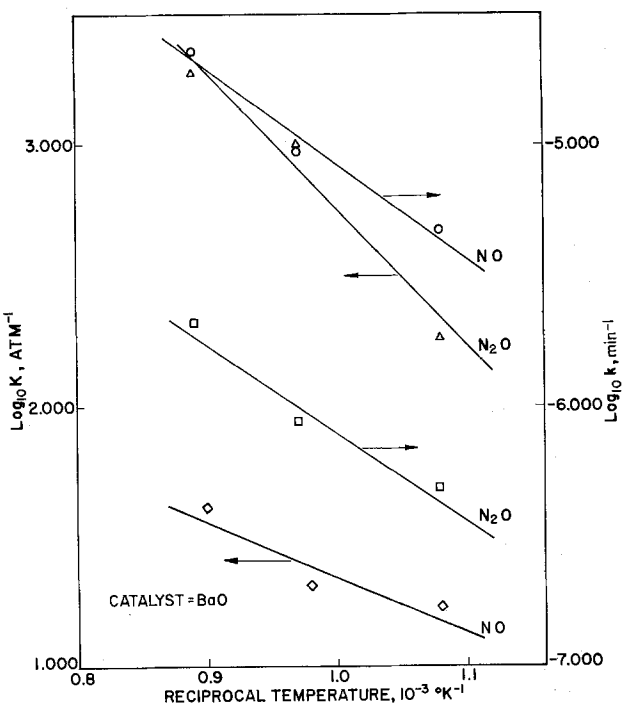


Fig. 14. Linear relationship between $\log_{10}k$ (decomposition rate constant), $\log_{10}K$ (adsorption equilibrum constant), and temperature reciprocal for nitric and nitrous oxides, using barium oxide as catalyst.

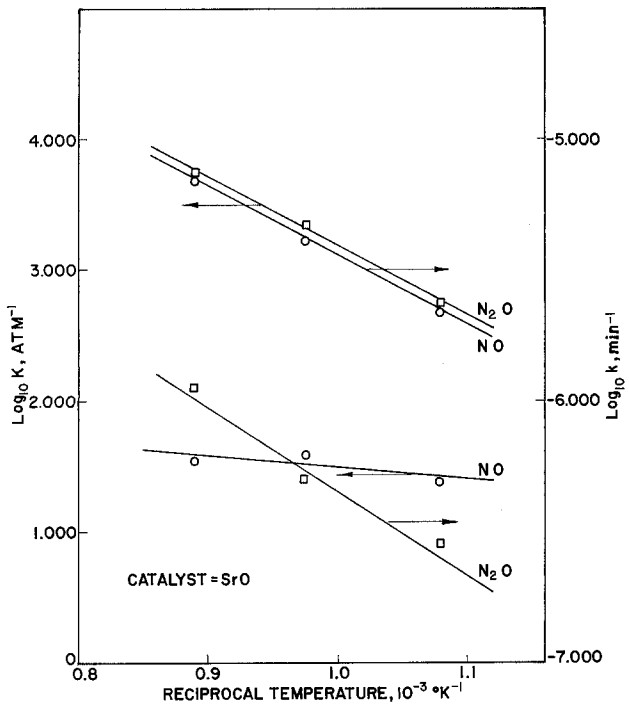


Fig. 15. Linear relationship between $\log_{10}k$ (decomposition rate constant), $\log_{10}K$ (adsorption equilibrium constant), and temperature reciprocal for nitric and nitrous oxides, using strontium oxide as catalyst.

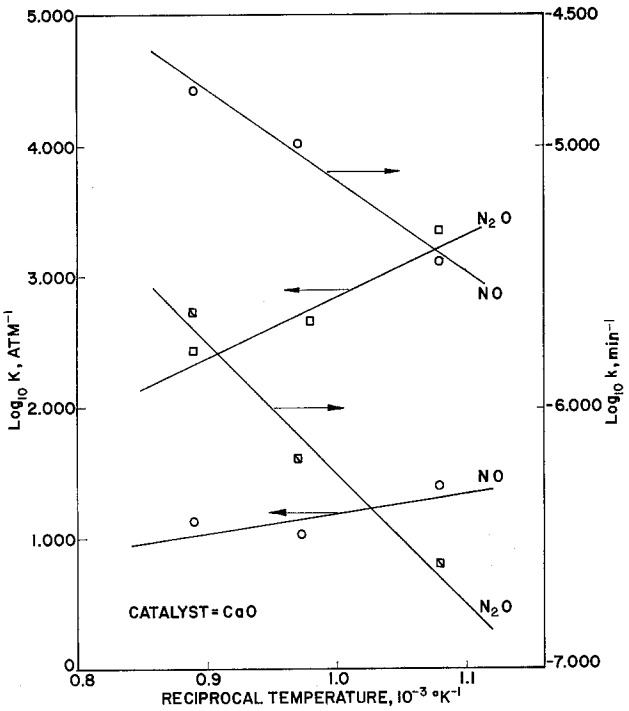


Fig. 16. Linear relationship between $\log_{10}k$ (decomposition rate constant), $\log_{10}K$ (adsorption equilibrium constant), and temperature reciprocal for nitric and nitrous oxides, using calcium oxide as catalyst.

Comparative results between nitric and nitrous oxides decomposition process parameters.—Figure 17 shows the global decomposition of nitric oxide, expressed as percent nitric oxide decomposed, for a 0.5% initial concentration in helium and a residence time of about 1 sec. It is seen that the most efficient catalyst among the alkaline earth oxides used is barium oxide which decomposes up to 60% nitric oxide at 850°C, with extrapolated values at 1000°C showing a decomposition of around 90%. Decomposition efficiencies of

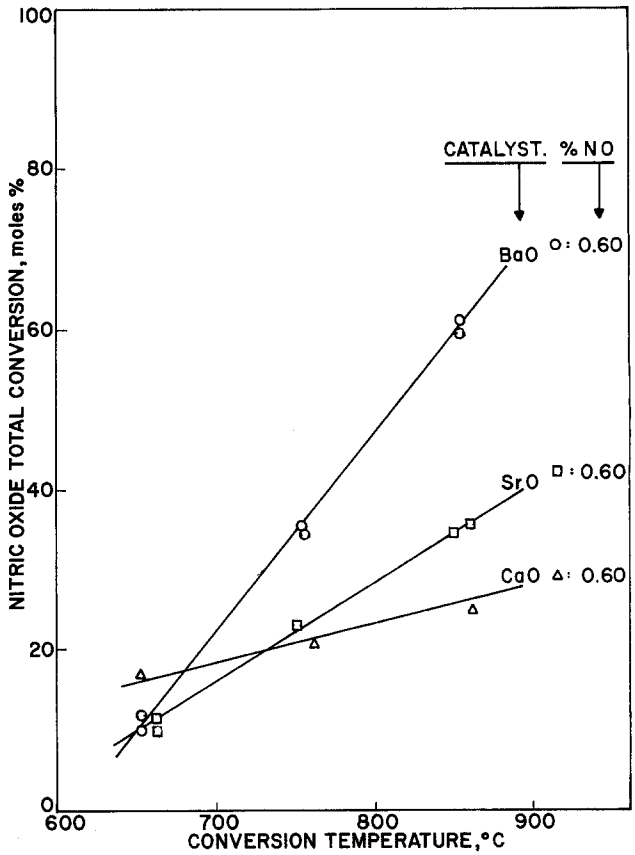


Fig. 17. Nitric oxide total conversion for a 0.6% nitric oxide concentration in helium at atmospheric pressure and a residence time of 1 sec. Catalysts: barium, strontium, and calcium oxides.

around 35 and 45% (extrapolated) are found at 850° and 1000°C, respectively, for strontium oxide, while for the same temperatures, calcium oxide shows efficiencies of 25 and 30%, respectively. At lower temperatures, calcium oxide exhibits higher nitric oxide conversion values than strontium oxide, becoming equivalent to the performance of barium oxide.

Examination of Table I shows calculated rate and equilibrium constants which are in conformity with the observations made on Fig. 17. Indeed, the barium oxide rate constant is more than two times higher than the corresponding constant for strontium oxide for most of the temperatures investigated. However, the nitric oxide adsorption equilibrium constant being higher for strontium oxide at lower temperatures, a combination of reaction rate and equilibrium constants, following Eq. [22] yields results which are in accordance with the trends indicated for barium and strontium oxides on Fig. 17. The same reasoning applies to barium and calcium oxides, for which both effects of rate constant k and equilibrium constant K lead to an explanation of the trends implied by Fig. 17. In this case, it is seen that higher K compensates for lower k at lower temperatures, thus explaining the similar efficiencies of barium and calcium oxides at lower temperatures. On the other hand, at higher temperatures both k and K are higher for barium oxide than for calcium oxide and a considerable difference in efficiency is apparent at 850°C. A comparison of strontium and calcium oxides performance follows in a straightforward way. From these considerations, it is concluded that higher temperatures increase the decomposition efficiency of the alkaline earth oxides; the efficiency being highest for barium oxide followed by strontium and calcium oxides in the order given. Although rate constants increase with temperature in all cases, it should be noted that the adsorption equilibrium constants only increase in the case of barium and strontium oxides, decreasing as far as calcium oxide is concerned. The trends ob-

served for the decomposition of nitrous oxide are quite similar to those reported for nitric oxide, thus corroborating further the results obtained in Fig. 17. Considering the results in Table I, one should note that the decomposition rate constants are generally one order of magnitude higher for nitric oxide when compared to nitrous oxide. This is in accordance with the assumption made for explaining the mutual independency of nitric and nitrous oxides conversion rates, the effect of higher adsorption constant value found for nitrous oxide being compensated by the lower average partial pressure of nitrous oxide prevailing in the gas phase (see Fig. 5-7). Energy of activation values are found in Table II, but do not add much for the interpretation of the results obtained, except for the high relative value of the activation energy related to calcium oxide.

The results obtained seem to confirm the possible relationship between catalyst efficiency and work function, as noted at the start of this study. Indeed, it has been found that the nitric oxide conversion efficiency (global) at 1000°C amounts to 90% for barium oxide, 45% for strontium oxide, and 30% for calcium oxide. Keeping in mind that the respective work functions are 1.1, 1.4, and 1.9 eV, a similar trend is followed by the latter values although other considerations besides the aspect of work function should probably be brought into the picture.

Results of this work vs. literature data.—Since the nitrous oxide decomposition reaction appears to be the controlling step in the present study, the data obtained for this step are compared with the over-all reaction rate data available in the literature for nitric oxide decomposition. The results of this compilation appear on Table III. It can be seen that the activation energy found in this work (14.7 kcal/g-mole) for strontium compares very well with the corresponding value found in Ref. (7). An energy of activation of 23 kcal/g-mole is found in this work for calcium oxide, while exactly the same value is found in Ref. (4) and a somewhat higher one (28 kcal/g-mole) is found in Ref. (7), although this latter value is well within the dispersion that can be found in the literature, discrepancies of 50% being attained for some oxides.

As far as reaction rate constants are concerned, only one value was found in the literature which was related to the present work. Reference (4) gives the nitric oxide over-all decomposition reaction rate constant for calcium oxide at 1033°K or 760°C. These authors obtain a zero order reaction rate constant equal to 5.2×10^{-4} mole liter^{-1} sec^{-1} g^{-1}, the initial nitric oxide concentration in helium being 10%. It can be seen from Eq. [29] that, for such a nitric oxide concentration, the rate constant for calcium oxide found in this work also reduces to a zero order rate constant, since p' should be high enough so that $K'p' >> 1$ (assuming a nitrous oxide concentration of at least 2%). In this case, k_2' can be found from either Fig. 7 for $p' \to \infty$ or Table I, where $k_2' = 6.0 \times 10^{-7}$ g · mole/min · cm^2 for a flow rate of 17 cm^3/min, as indicated above. Since Ref. (4) also supplies the information that 1g CaO presents a surface of 7.9 m^2, one can write

$$k\,[\text{Ref. (4)}] = \frac{5.2 \times 10^{-4}}{7.9 \times 10^4 \times 10^3}\ \text{g mole/cm}^3\ \text{cm}^2\ \text{sec}$$

$$k\,[\text{Ref. (4)}] = 6.6 \times 10^{-12}\ \text{g mole/cm}^3\ \text{cm}^2\ \text{sec}$$

Table III. Compared values for energy of activation and rate constants for nitric oxide decomposition on alkaline earth oxides. The controlling step is the nitrous oxide decomposition rate.

Oxide	Temperature, °C: This work	Ref. (7)	Ref. (4)	Energy of activation, kcal/g-mole: This work	Ref. (7)	Ref. (4)
				Controlling step	Over-all reaction	
SrO	650-850	620-750	—	14.7	15	—
CaO	650-850	580-720	760-1,040	23	28	23

Also

$$k_2'\,[\text{this work}] = \frac{6.0 \times 10^{-7}}{17 \times 60}\ \text{g mole/cm}^3\ \text{cm}^2\ \text{sec}$$

$$k_2'\,[\text{this work}] = 5.4 \times 10^{-10}\ \text{g mole/cm}^3\ \text{cm}^2\ \text{sec}$$

As a result, $k_2'/(k\,[\text{Ref. (4)}] = 80$. Although rather high, this discrepancy still remains within the limits of the variations that can be met in the literature (7) where factors as high as 300 may be found. Finally, if one compares results obtained in this work with the few data found in the literature, it is observed that energy of activation values are very close while reaction rate constants show some discrepancy which is, however, still within the limits of variation found for this kind of thermodynamic parameter.

Conclusions

In the course of this study, it has been found that, among the three alkaline earth oxides experimented with as catalysts for the decomposition of nitric oxide, barium oxide is the most efficient. Using this oxide in conjunction with nitric oxide concentrations between 0 and 2.5% in helium, global decomposition efficiencies of around 60% are attained at 850°C, yielding nitrous oxide, oxygen, and nitrogen. Since nitrous oxide is harmless, this process could be accepted as a possible means for nitric oxide abatement, the noted efficiency being attained for a residence time of around 1 sec. Strontium and calcium oxides have a similar behavior, but to a lesser extent as far as nitric and nitrous oxides decomposition is concerned. For strontium oxide, this global decomposition attains 35% at 850°C and amounts to 25% for calcium oxide at the same temperature.

It was observed that within the limits of nitric oxide concentrations used, the nitric and nitrous oxides decomposition rates are mutually independent, this being true for the three catalysts used. This feature is related to much higher values for decomposition rate constants related to nitric oxide. A combination of the calculated decomposition rate constants and adsorption equilibrium constants for nitric and nitrous oxide values explains the relative conversion efficiencies observed for the catalysts used. The presence of 3% oxygen associated with 0.5% nitric oxide did not seem to have any effect on the performance of barium oxide. Such a behavior is possibly related to a rather low concentration of oxygen adsorption sites. Finally, this catalyst was experimented with for several hours at 850°C without showing any efficiency alteration.

Without definitely qualifying the alkaline earth oxides as catalysts for decomposing nitric oxide at concentrations usually found in pollution problems, the observations made in the present study show interesting features which are worthwhile being investigated further.

Acknowledgments

The author is indebted to the Ministry of Health and Welfare of Canada for grants received during the course of this work. He also thanks Mario Gilbert, research technician, for his valuable cooperation.

Manuscript submitted Dec. 18, 1975; revised manuscript received May 21, 1976. This was Paper 143 presented at the Dallas, Texas, Meeting of the Society, Oct. 5-9, 1976.

Any discussion of this paper will appear in a Discussion Section to be published in the December 1977 JOURNAL. All discussions for the December 1977 Discussion Section should be submitted by Aug. 1, 1977.

Publication costs of this article were assisted by the Université du Québec à Chicoutimi.

LIST OF SYMBOLS

- A decomposition rate constant for nitric oxide in Eq. [7]
- B decomposition rate constant for nitrous oxide in Eq. [7]

C nitric oxide concentration, g · mole/cm³
$\overline{C_m}$ maximum molal adsorption capacity per cm² catalyst, g · mole/cm²
C'_{IN} nitrous oxide concentration as defined in the text from p'
e electron
E_2 activation energy for the nitric oxide decomposition reaction, kcal/g-mole
k decomposition rate constant, arbitrary units
k_2 nitric oxide decomposition rate constant, min^{-1}
k_{O2} k_2 when $T = \infty$ in Eq. [24]
K_1 nitric oxide adsorption equilibrium constant, atm^{-1}
K_2 nitric oxide surface reaction equilibrium constant
K_3 oxygen desorption equilibrium constant in Eq. [20]
K_3' oxygen desorption equilibrium constant in Eq. [27]
$\log_{10}$ logarithm, base 10
[NO], [N_2O], [N_2] concentration in nitric oxide, nitrous oxide, nitrogen, mole fractions; numerically equivalent to atmospheres
p nitric oxide partial pressure, atm
p'_{IN} nitrous oxide partial pressure as defined in the text
r nitric oxide decomposition reaction rate, g-mole/min-cm²
R gas constant
S catalyst surface, cm²
T temperature, °K
V gas flow rate, cm³/min
X active site on catalyst surfaces

Subscripts
ADS adsorbed
AV average
IN pertaining to the inlet of the reactor, except when otherwise defined
E at the end of the reaction
OUT pertaining to the outlet of the reactor
O_2 pertaining to oxygen
o initial

Superscripts
′ pertaining to nitrous oxide

REFERENCES

1. P. A. Leighton, "Photochemistry of Air Pollution," Academic Press, New York (1961).
2. R. M. Dell, F. S. Stone, and P. F. Tiley, *Trans. Faraday Soc.*, **49**, 201 (1953).
3. C. Wagner, *J. Chem. Phys.*, **1**, 69 (1949).
4. J. M. Fraser and F. Daniels, *ibid.*, **62**, 215 (1958).
5. M. Shelef, K. Otto, and H. Gandi, *Atmos. Environ.*, **3**, 107 (1969).
6. T. M. Yur'eva *et al.*, *Kinet. Katal.*, **6**, 941 (1965).
7. E. R. S. Winter, *J. Catal.*, **22**, 158 (1971).
8. A. Amirnazmi, J. E. Benson, and M. Boudart, *ibid.*, **30**, 55 (1973).
9. S. Pancharatnam, R. A. Huggins, and D. M. Mason, *This Journal*, **122**, 869 (1975).
10. J. P. Blewett, *J. Appl. Phys.*, **10**, 668 (1939).
11. L. Pauling, "The Nature of the Chemical Bond," p. 343, Cornell University Press, Ithaca, New York (1960).
12. L. Pauling, *ibid.*, p. 185.
13. J. M. Thomas and W. J. Thomas, "Introduction to the Principles of Heterogeneous Catalysts," p. 459, Academic Press, New York (1967).

Anodic Phenomena in Cryolite-Alumina Melts

II. Chronopotentiometry at Gold and Platinum Anodes

E. W. Dewing*

Aluminum Company of Canada, Limited, Arvida Research Centre, Arvida, Quebec, Canada G7S 4L2

and E. Th. van der Kouwe

South African Atomic Energy Board, Pretoria, South Africa

ABSTRACT

Chronopotentiometric measurements with wire anodes have shown that the transition time is diffusion controlled up to 0.7% Al_2O_3 on gold and up to 1.6% Al_2O_3 on platinum. The diffusion coefficient is $(2.51 \pm 0.12) \times 10^{-5}$ cm² sec^{-1} (std error), at 1020°C. At higher concentrations, formation of oxide films becomes the limiting factor; effectively, the electrodes are being anodized. On an anodized gold electrode fluorine can be discharged. If the current density is high enough (~250 A cm^{-2}), the discharge is diffusion controlled and seems to correspond to "free" (*i.e.*, uncomplexed) fluoride. In pure cryolite, this is estimated to be about 5% of the total fluorine present (corresponding to ~16% dissociation of AlF_6^{3-} to AlF_4^-). It is reduced by addition of Al_2O_3 and also by addition of AlF_3; it is increased by adding NaF.

An instrumental method of determining the alumina content of molten cryolite *in situ* in the electrolytic cells would obviously be of immense interest to the aluminum industry, and this has led to work on chronopotentiometry. Both Richards and Russell (1) and Thonstad (2, 3) have employed graphite anodes, and they seem to have gotten good results. Nonetheless, graphite as an anode material has its problems. The surface is liable to be rough and/or porous, it is subject to air oxidation during introduction into and removal from the cell, and above all, it is difficult to get a small, reproducible surface area. Since alumina concentrations to be measured are high by most electroanalytical standards [2-8 weight percent (w/o)] with a corresponding need for high current densities, this is important.

An obvious way out of the problem is to try metal wire electrodes, which means, in effect, the noble metals since oxygen is going to be liberated. The temperature involved is above the melting point of silver. The work reported here was carried out with platinum and gold.

Initial work in the range 2-8 w/o Al_2O_3 gave most confusing results. At high current densities transitions leading to anode effects were readily observed (*i.e.*,

* Electrochemical Society Active Member.
Key words: cryolite, alumina, chronopotentiometry, gold, platinum, diffusion coefficient, complex ions, dissociation.

the voltage rose to ~50V when the transition occurred, leading to destruction of the wire unless the current was promptly interrupted), but for Pt the transition time was independent of alumina content and with Au it decreased as the Al_2O_3 content went up. Reproducibility with Au was not good enough for the phenomenon to form the basis of an analytical method. In order to sort out the problem the work was extended to alumina concentrations below the range of industrial interest.

Experimental

Several circuits were used in this work, but their principle was the same. Capacitors were charged with a d-c power supply and then discharged through a resistor by triggering a General Electric C30D SCR electronic switch. If the capacitor has capacity C and the total resistance in the circuit is R, then the time constant for the discharge is RC. Provided that $RC >> \tau$, the transition time, then the circuit is effectively constant current for the period of time required. The current itself is given by V/R, where V is the voltage on the capacitor.

Depending on the capacity and voltage rating of the capacitors available and the voltage of the power supply, different circuits can be constructed to suit the current density and transition time ranges desired. Two in particular were used; 6000 μF charged to 40V and 2400 μF charged to 160V. Current densities as high as 360A cm^{-2} were obtained.

It is desirable (and indeed essential when dealing with anode effects where the voltage rises to 50V or more) to have some means of cutting the flow of current when the transition is over. For the high voltage circuit, this was done with a second SCR across the cell. The gate was connected through a Zener diode; as soon as the voltage rose to the level where the diode conducted the second SCR was triggered and the cell was shorted out. For the low voltage circuit, the current was interrupted by an electromechanical relay which opened some 4-10 msec after the current was started. In some of the very high current density work, the electrode was depolarized between pulses with a 4 mA cm^{-2} cathodic current. This did not seem to make any significant difference.

Transition times were read directly from an oscilloscope by eye. Although somewhat subjective, this was not a factor limiting the accuracy of the results. The current was measured by determining the voltage drop across a standardized resistor (either 1 or 0.1 ohm), again with the oscilloscope, the voltage scale of which was calibrated.

Melts were made up by weight from Greenland cryolite and Bayer alumina, and were held in graphite crucibles which served as cathode. The anode wires were immersed 1 cm; their diameters (nominally 0.5 mm), were measured with a traveling microscope.

Results

To give an overview of the problem, Fig. 1 shows values of $i\tau^{1/2}$ (where i is current density and τ is transition time), interpolated for $\tau = 1$ msec, as a function of current density. A diffusion-controlled region does exist at low alumina contents, terminating at about 0.8% Al_2O_3 for gold and 1.7% Al_2O_3 for platinum. Beyond that, it is apparent that some other process has intervened.

The diffusion-controlled region.—Tables I and II show the results obtained in the diffusion-controlled region with gold and platinum wires, respectively, and Fig. 2 shows the transition on platinum. $i\tau^{1/2}$ is effectively independent of current density. If, for the line in Fig. 2, potential is plotted against ln $(\tau^{1/2} - t^{1/2})$, the slope ($= RT/n\mathbf{F}$), corresponds to $n = 2.2$. This treatment is based on the premise that the oxidation product is left on the electrode at constant activity, so that only the concentration of oxide enters the Nernst equation. If on the other hand, one assumes that soluble O^- is

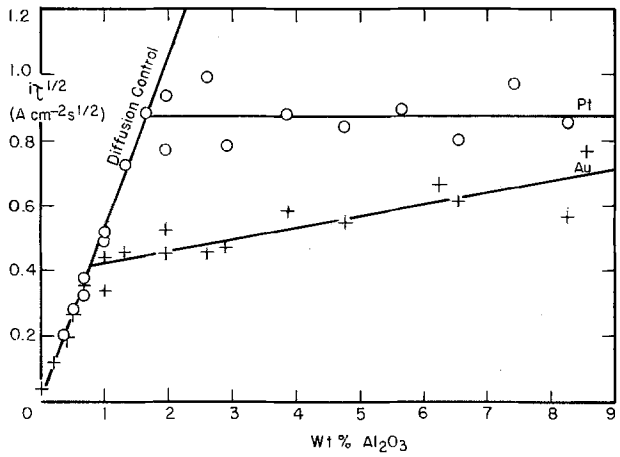


Fig. 1. Plot of $i\tau^{1/2}$ (interpolated for $\tau = 1$ msec), against w/o Al_2O_3. Temperature 1018°-1026°C.

being formed, then the proper function to plot is ln $(\tau^{1/2}/t^{1/2} - 1)$. n, however, is then found to be 3.4, which is completely inconsistent with the hypothesis. It is therefore apparent that a 2-electron oxidation of O^{2-} is occurring.

Figure 3 shows a more detailed plot of the diffusion-controlled region. The line is straight but does not quite pass through the origin, implying that the Greenland cryolite used has a small alumina content itself. The intercept of the line shows this to be 0.027% for this particular batch of cryolite. This may be compared with wet chemical analysis which gave 0.15% Al_2O_3. After displacing the origin to allow for the blank, the line may be represented by

$$\text{w/o } Al_2O_3 = (1.914 \pm 0.046)\ (i\tau^{1/2}) \qquad [1]$$

with a standard deviation of ±0.04% Al_2O_3. The uncertainty of the slope is a standard error.

There is no significant effect of temperature over the 8° range encountered, and there is no significant difference between the results with gold and platinum wires. It is therefore permissible to apply the Sand equation

Table I. Results with gold wires at low alumina contents

Temp (°C)	Alumina added (w/o)	Range of current density (A cm^{-2})	No. of values	$i\tau^{1/2} \times 10^3$ (A cm^{-2} $sec^{1/2}$) Mean ± std error
1018	0	1.1-4.8	5	36.0 ± 0.7
1018	0.20	1.6-9.0	5	121 ± 6
1018	0.40	2.2-20	5	195 ± 18
1018	0.66	4.8-35	4	354 ± 27
1026	0	0.5-2.6	5	31.8 ± 1.0
1026	0.50	4.7-17	5	267 ± 12

Table II. Results with platinum wires at low alumina contents

Temp (°C)	Alumina added (w/o)	Range of current density (A cm^{-2})	No. of values	$i\tau^{1/2} \times 10^3$ (A cm^{-2} $sec^{1/2}$) Mean ± std error	$i\tau$ (μC cm^{-2}) Mean ± std error
1019	0	0.5-2.2	5	27.0 ± 1.3	
1019	0.66	3.5-9.3	4	325 ± 8	
1020	0	0.3-2.8	6	23.9 ± 2.0	
1020	0.33	2.3-9.5	4	201 ± 2	
		1.2-9.5	5		770 ± 43
1020	0.66	5.2-36	4	379 ± 3	
		2.3-9.5	3		880 ± 27
1020	0.99	9.5-36	4	520 ± 4	
		5.2-21	4		821 ± 25
1020	1.00	22.5	1	535	
		10.1	1		760
1020	1.32	21-58	5	728 ± 11	
		12.6	1		680
1020	1.64	21-36	3	884 ± 6	
1026	0	0.5-2.7	4	25.3 ± 2.6	
1026	0.50	4.8-17.3	4	282 ± 7	
		0.5-2.7	4		496 ± 13
1026	0.99	9.5-33	4	497 ± 22	

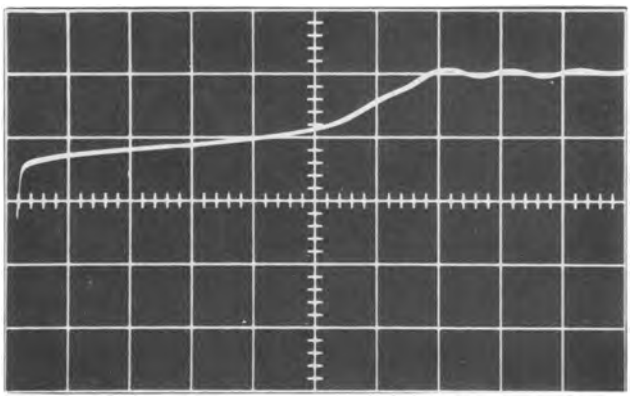


Fig. 2. Diffusion-controlled transition on platinum. 1 w/o Al_2O_3, 22.5 A cm^{-2}, 220 mV/cm vertical, 100 μsec/cm horizontal, τ = 570 μsec. Ripples beyond 700 μsec are believed to be due to platinum being oxidized.

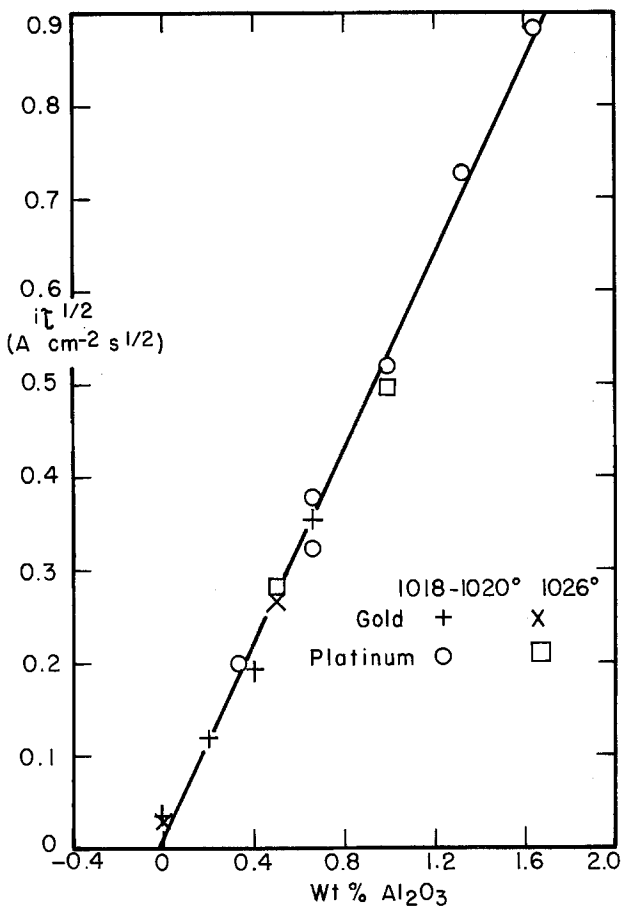


Fig. 3. Diffusion-controlled transition times (τ) as a function of alumina content.

to determine the diffusion coefficient of oxide in the melt

$$\frac{i\tau^{1/2}}{nFC} = \frac{(\pi D)^{1/2}}{2} \qquad [2]$$

where i is the current density (A cm^{-2}), τ is the transition time (sec), n is the number of electrons involved (= 6 for Al_2O_3), **F** is the Faraday (96,487 C/g-equiv.), **C** is the concentration (g mole/ml), and D is the diffusion coefficient (cm^2 sec^{-1}). It should be noted that the product nC is totally independent of any assumptions which may be made about the form in which alumina exists in the melt (*e.g.*, as Al_2O_3, $AlOF_2^-$, etc.). For a solution containing 1 w/o Al_2O_3 at 1020°C, $C = 2.03 \times 10^{-4}$ mole/ml. Hence, with the constant in Eq. [1], $D = (2.51 \pm 0.13) \times 10^{-5}$ cm^2 sec^{-1}. The uncertainty is a standard error. This value may be compared with 2.2×10^{-5} cm^2 sec^{-1} given by Desclaux and Rolin (4) from rotating disk experiments on the rate of solution of alumina, and 1.5×10^{-5} cm^2 sec^{-1} found by Thonstad (2) from chronopotentiometric experiments with graphite anodes. His low value shows that his transition times were short in comparison with the present ones, and suggests that on a graphite electrode not all the surface is working (a maximum of 75%). This is readily understandable if graphite crystallites can only be attacked on the edges and not on the basal plane.

Initial oxide film formation on platinum.—With platinum wires at low alumina contents two separate transitions were observed, as recorded in Table II. One is the diffusion-controlled transition discussed above; the other, coming in general at much shorter times, is illustrated in Fig. 4. Figure 5 shows these other transitions plotted on the basis of log τ *vs.* log i, together with some similar points for higher alumina contents from Table III. The line drawn has a slope of −1, implying that $i\tau$ is constant, rather than $i\tau^{1/2}$ being constant as in the case of diffusion control. $i\tau$ is a quantity of charge, and is

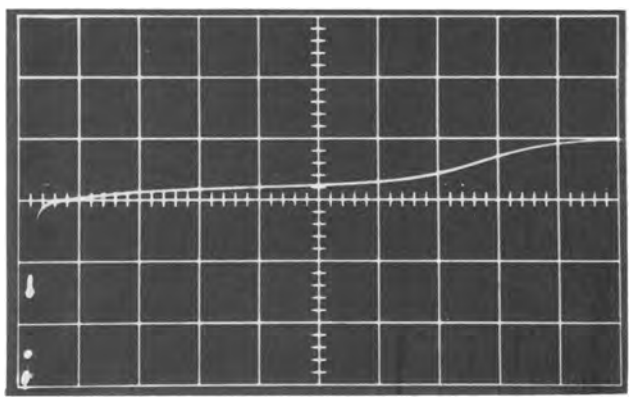


Fig. 4. Initial oxide film formation on platinum. 1 w/o Al_2O_3, i = 10.1 A cm^{-2}, 220 mV/cm vertical, 10 μsec/cm horizontal, τ = 75 μsec. Note the much shorter time scale compared to Fig. 2.

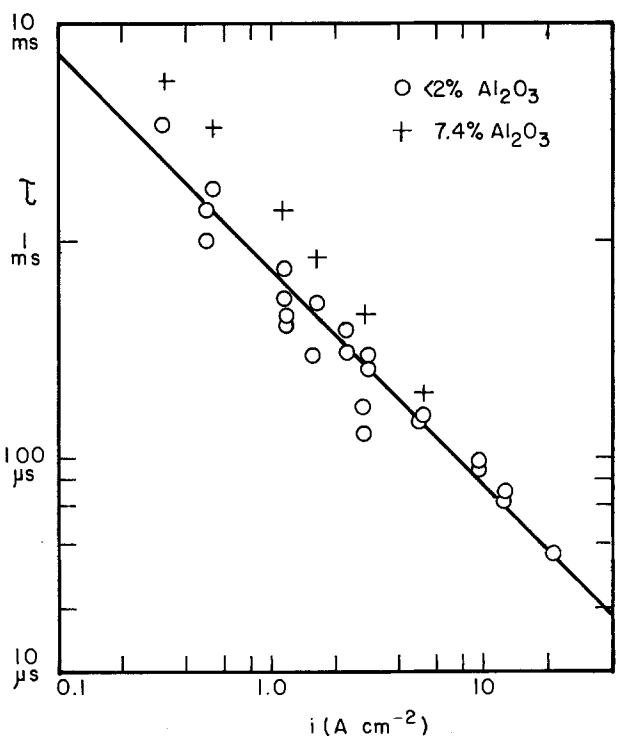


Fig. 5. Initial oxide film formation on platinum. The transition time τ is proportional to $1/i$.

Table III. Results with platinum wires at high alumina contents

Temp (°C)	Alumina added (w/o)	Range of current density (A cm^{-2})	No. of values	$i\tau^{2/3} \times 10^3$ (A cm^{-2} sec$^{2/3}$) Mean ± std error	$i\tau$ (μC cm^{-2}) Mean ± std error
1020	1.96	18-57	5	296 ± 10	
		0.3-5	6		876 ± 53
1020	2.60	18-57	5	315 ± 6	
1020	3.85	21-57	4	279 ± 5	
1020	5.66	21-57	3	284 ± 5	
1020	7.41	28-57	3	308 ± 3	
		0.3-5	6		1485 ± 122
1026	1.96	17-34	3	244 ± 11	
1026	2.91	17-34	3	248 ± 18	
1026	4.76	14-34	4	268 ± 14	
1026	6.54	14-34	4	254 ± 17	
1035	8.25	14-34	4	272 ± 14	
975	8.25	17-34	3	243 ± 7	

$$i\tau = 735\ \mu C/cm^2 \pm 182\ \text{(std deviation)}$$
$$\pm\ 35\ \text{(std error)}$$

This represents formation of a surface film (presumably of platinum oxide), of constant thickness. Similar phenomena have been observed by Mayell and Langer (5) in aqueous solution. They detect several different types of film, but say that 760 μC cm^{-2} corresponds to a monolayer of PtO_2. Although their reasoning regarding the composition is open to question, there seems little doubt that the transitions observed correspond to the completion of the first layer of oxide; the number of oxygen atoms discharged per square centimeter is, however, more than would be expected if the surface is covered with a single close-packed layer of oxygen ions. The radius of an oxygen ion is 0.132 nm, so that in a hexagonal array each ion covers 0.0603 nm^2, and one expects 1.68×10^{15} atoms/cm^2. 735 μC cm^{-2} corresponds to 2.30×10^{15} atoms/cm^2. Either the oxygen ions are forming more than a monolayer, or the surface is rough with a roughness factor of 1.4.

At 7.5% Al_2O_3 the number of coulombs required to form the first layer of oxide seems to have gone up, and at the same time $i\tau$ is not quite constant, ranging from 1040 μC cm^{-2} at 5 A cm^{-2} to 1760 μC cm^{-2} at 0.3 A cm^{-2}. The reason for this effect is not known.

Thicker oxide film formation on platinum.—Table III and Fig. 6 show the results obtained with platinum at high alumina contents. Statistically, temperature and alumina content are not significant, and the slope of the log-log plot is −1.38 with a standard error of ±0.07. A value of −1.5 is thus within the 95% confidence interval (2 std errors), and since this is a value which can be interpreted, it has been adopted. The line drawn in Fig. 6 has a slope of −1.5.

The situation thus is that three separate transitions have been identified. The first, on a log-log plot, has a slope of −1 (*i.e.*, $i\tau$ = constant) and corresponds to the completion of the first layer of oxide. The second has a slope of −2 (*i.e.*, $i\tau^{1/2}$ = constant) and corresponds to diffusion control. The third has a slope of −1.5 (*i.e.*, $i\tau^{2/3}$ = constant); to what is it to be attributed? The situation is shown in Fig. 7, from which all points have been omitted for clarity.

The hypothesis is going to be advanced that the third transition is due to the discharge process being limited by the rate of growth of a relatively thick oxide film (*i.e.*, many atomic layers thick). For such films (which are normally regarded as thin) the growth law when they are forming in the presence of an unrestricted supply of oxidant is often cubic, *i.e.*

$$kt = x^3 \qquad [3]$$

or

$$x \propto t^{1/3} \qquad [4]$$

where x is the thickness of the film and t is time, and k is a constant. At large thickness (above ~100 nm), the exponent changes from 1/3 to 1/2, leading to the normal parabolic law. (For discussion of the implications of these laws see Hauffe (6)). From Eq. [3], which it must be realized represents the maximum rate of film growth

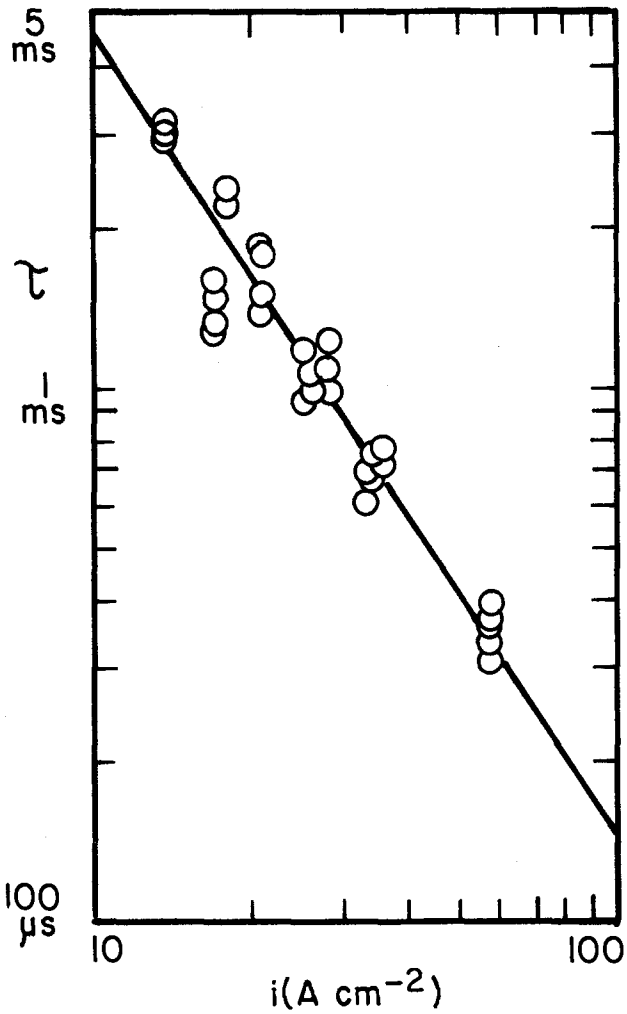


Fig. 6. Transition time as a function of current density for alumina contents above 1.96% (Pt wires). Line drawn has a slope of −1.5.

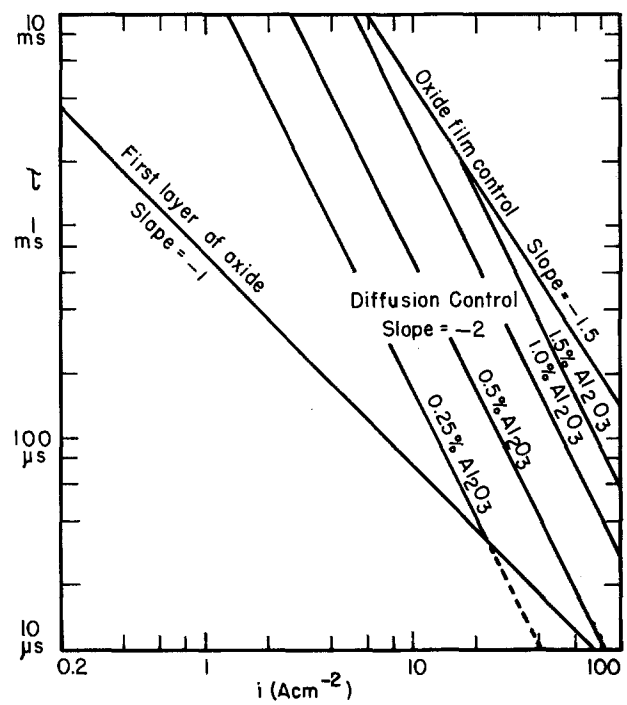


Fig. 7. Transition times as functions of current density (Pt wires-schematic).

Table IV. Results with gold wires at high alumina contents

Temp (°C)	Alumina added (w/o)	Range of current density (A cm^{-2})	No. of values	$i\tau^{2/3} \times 10^3$ (A cm^{-2} sec$^{2/3}$) Mean ± std error
1018	0.99	9-35	6	139 ± 5
1020	1.00	21.9	1	125
1018	1.32	9-35	3	144 ± 8
1018	1.96	9-35	3	166 ± 5
1018	2.60	9-35	3	144 ± 12
1018	3.85	5-35	6	185 ± 5
1018	6.25	5-35	4	210 ± 12
1018	8.54	9-35	3	243 ± 5
1026	0.99	8-32	9	107 ± 5
1026	1.96	9-32	4	143 ± 6
1025	2.91	8-32	3	148 ± 7
1026	4.76	8-32	3	173 ± 8
1026	6.54	9-32	5	194 ± 7
1026	8.25	9-32	4	179 ± 10
975	8.25	9-26	4	184 ± 3

$$dt/dx \propto x^2 \quad [5]$$

and

$$dx/dt \propto x^{-2} \quad [6]$$

This gives an infinite rate at $x = 0$, and the rate decreases as the thickness increases.

In the case of electrolytic oxidation with a constant current density, i, the thickness of the film is proportional to the number of coulombs passed, so that

$$dx/dt \propto i \quad [7]$$

It is assumed that the transition at time τ occurs because the rate of electrolytic oxidation has become equal to the maximum rate, so that

$$dx/dt \propto i \propto x^{-2} \propto (i\tau)^{-2} \quad [8]$$

Hence

$$i^3\tau^2 = \text{constant} \quad [9]$$

or

$$i\tau^{2/3} = \text{constant} \quad [10]$$

which is what is observed.

If this explanation is correct, it implies that the oxygen discharged at the anode is not liberated as gas but goes to form an oxide film. Diffusion control of the transition ceases when the alumina concentration becomes high enough that more oxygen is generated than the oxide film is capable of holding; after that the transition time (for a given current density), becomes independent of the oxide content of the melt.

Initial oxide film formation on gold.—With gold electrodes no reproducible transitions occur analogous to those for the initial oxidation of platinum. Transitions (usually two separate ones) are sometimes but not always seen in the appropriate region.

Thicker oxide film formation on gold.—Figure 8 is a typical example, Table IV shows the results, and some

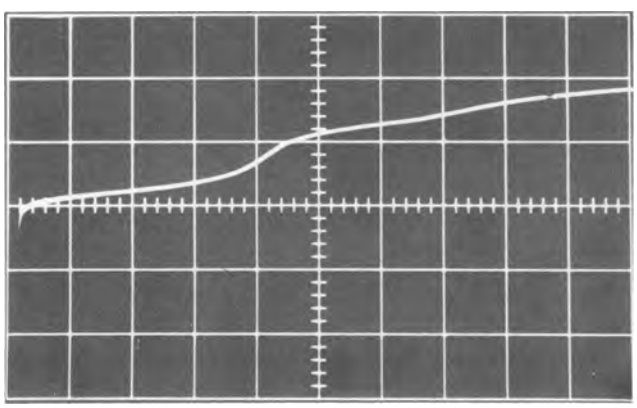


Fig. 8. Oxide film limitation on gold. 1 w/o Al_2O_3, i = 21.9 A cm^{-2}, 220 mV/cm vertical, 100 μsec/cm horizontal, τ = 440 μsec. Note that in contrast to Fig. 2, electrolysis continues smoothly thereafter.

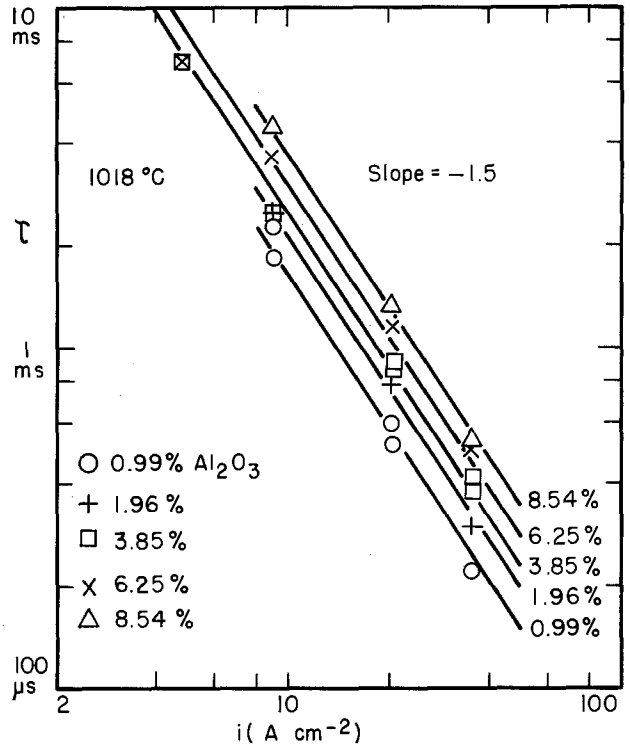


Fig. 9. Transition times as functions of current density for alumina contents above 0.99% (Au wires).

of them are plotted in Fig. 9. Again, a slope of −1.5 is obtained, but this time the values vary somewhat with alumina content. This variation is shown in Fig. 1, where the values interpolated to 1 msec are plotted. The implication is that the inherent rate of oxide film growth is faster in high alumina melts, and this can only be accounted for if the composition of the film is changing. The only change which can be envisaged is that some fluoride ions are being incorporated in the film, the proportion of them varying with alumina content.

Figure 10 shows the results for 8-9% Al_2O_3, including some for very high current densities. The line drawn

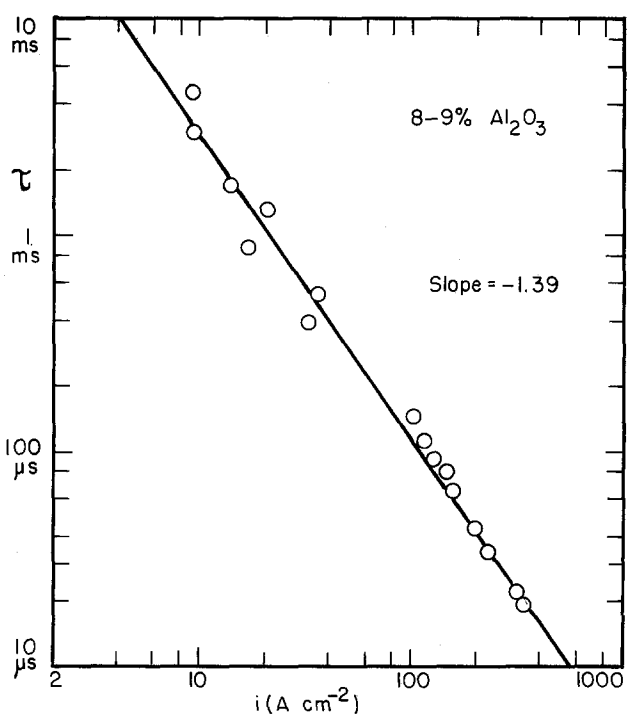


Fig. 10. Transition times as a function of current density for melts containing 8-9% Al_2O_3 (Au wires).

has a slope of -1.39 with a standard error of ± 0.04. This indicates that the film formation mechanism is operative over a very wide range of current densities at this alumina content. At the high current densities the transitions were anode effects.

Discussion of Oxide Film Formation

To postulate that oxide films are forming on platinum and gold at over 1000°C is unorthodox since they are thermodynamically unstable, but it must be borne in mind that the times are less than 5 msec and the current densities are correspondingly high. In 5 msec with $i = 7$ A cm^{-2} (see Fig. 7), a total of 35 mC cm^{-2} are passed, and they will give an oxide film about 14 nm thick. With 200 A cm^{-2} for 44 μsec, a total of 8.8 mC are passed and the calculated thickness is 3.6 nm. These thicknesses are well within the limit of 100 nm, below which the cubic growth law can be expected to hold. The logic for accepting the oxide film hypothesis is as follows:

1. There are only three anodic processes possible; discharge of O^{2-}, discharge of F^-, and dissolution of Au (or Pt).
2. In the diffusion-controlled region, there is no doubt that O^{2-} is being discharged.
3. If it were being discharged as gaseous oxygen, substantial amounts of gas would be formed. For example, with platinum and 1.64% Al_2O_3 a transition time of 1720 μsec was recorded at 21.1 A cm^{-2}. This corresponds to 36 mC cm^{-2} and would generate a gas layer 10^{-2} cm thick. At the same time, the thickness of the diffusion layer ($= \sqrt{2Dt}$) is 3×10^{-4} cm. Generation of this volume of gas would thus inevitably disrupt the diffusion layer and lead to a breakdown of the Sand equation, and yet no such deviation from the Sand equation is observed.
4. If the oxygen is not appearing as gas, it must be present either as an oxide film or in solution in the melt. The latter is inherently unlikely; oxygen is not appreciably soluble in cryolite, and such a mechanism would not account for the difference in results between gold and platinum or for the behavior of the transition outside the diffusion region.
5. There can be no question that when sufficient alumina is present to be beyond the diffusion region the discharge prior to the transition is of oxygen.
6. The law $i\tau^{2/3} =$ constant is, as already shown, consistent with oxide film formation.
7. In melts with no added alumina, chronopotentiometry at high current densities does not lead to anode effects, and the wire dissolves. Similar experiments in melts with 2% or more alumina give anode effects and the wire dissolves very little. This implies that the surface of the electrode is physically changed when operating in the presence of alumina. Some barrier has been formed which prevents gold dissolving.
8. Since gold oxide (Au_2O_3?) and platinum oxide (PtO_2?) are different substances, the difference in behavior of gold and platinum is readily accounted for. Tyurikov *et al.* (7) have also found differences in the discharge of oxygen from molten carbonate on Au and Pt, although they talk in terms of adsorbed oxygen rather than relatively thick layers of oxide.

Fluorine Discharge

Under some circumstances electrolysis on gold continues after the transition due to film growth limitation. It is not possible that oxygen is still the only ion being discharged; if it were the diffusion-controlled transition would be observed subsequently. Presumably oxygen is still discharged as fast as the growing film can absorb it, but the rest of the current must either dissolve gold or discharge fluorine, and little gold dissolution is observed. (If the film formation hypothesis is correct, gold solution would be impossible, as Au ions are presumably already diffusing through the film at the maximum possible rate in order to permit the film to grow.) One therefore concludes that F^- discharge is occurring.

At current densities less than about 100 A cm^{-2} no further transitions were observed, but at very high current densities anode effects occur, as illustrated in Fig. 11. This implies that no subsequent electrochemical process was available to carry the current.

For a melt containing 2% Al_2O_3 the situation is shown in Fig. 12, which gives the observed line for film formation control, where the oxide diffusion control line would be if it were observed, and the experimental results. At very high current densities ($i > 150$ A cm^{-2} or $\tau < 200$ μsec), the line has a slope of -2, showing diffusion control. At lower currents the product $i\tau^{1/2}$ increases rapidly, and below about 100 A cm^{-2} the anode effects are no longer observed at all. Figure 13 shows how the product $i\tau^{1/2}$ varies with alumina content and NaF/AlF_3 ratio; values have been averaged over the range 200-300 A cm^{-2}. It is apparent that transition times become shorter as Al_2O_3 is added and longer as NaF is added.

The most plausible explanation of the results is that fluorine is indeed being discharged, but that not all the fluorine in the melt is available for discharge in times

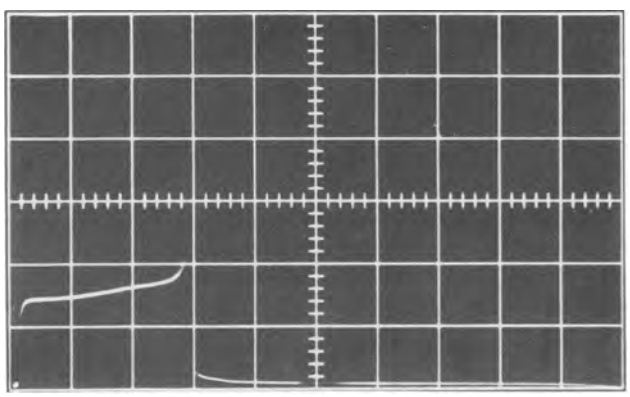


Fig. 11. Anode effect on gold. 6 w/o Al_2O_3, $i = 122$ A cm^{-2}, 11 V/cm vertical, 50 μsec/cm horizontal, $\tau = 145$ μsec. Note that the electronic cutout was set at 53V (4.8 cm on photo); although it has not registered on the film the trace rose to that level in ~5 μsec and then reappeared at the bottom.

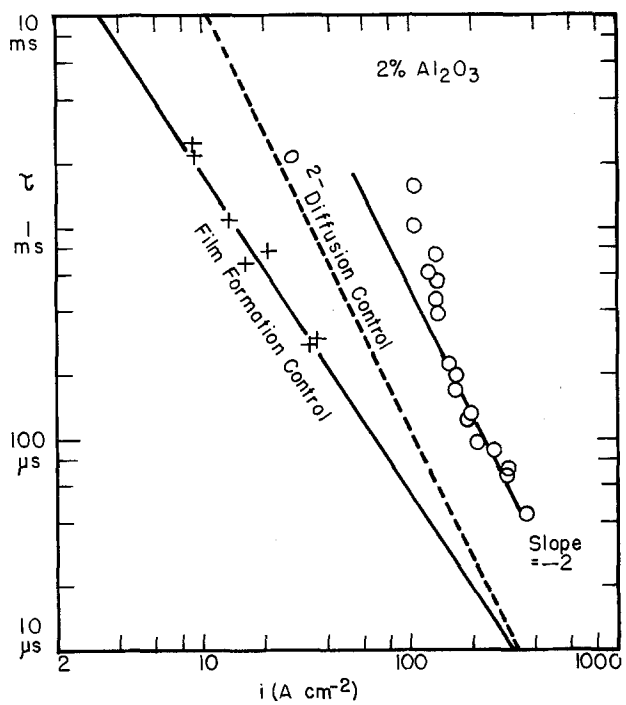


Fig. 12. Transition times as a function of current density for melts containing 2% Al_2O_3 (Au wires).

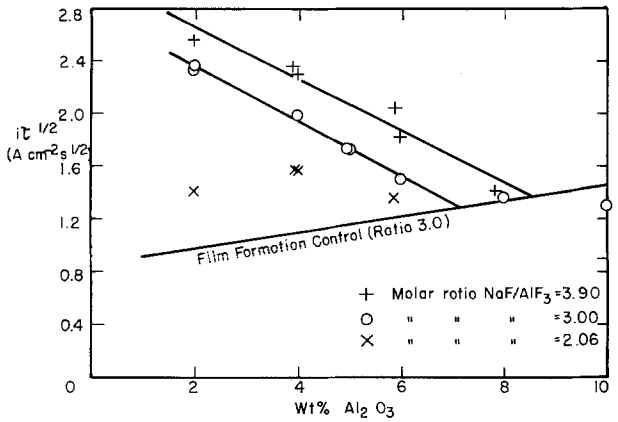


Fig. 13. Transitions at Au anodes at current densities 200-300 A cm^{-2}.

of the order of 100 μsec. For many years models of cryolite melts in terms of partially dissociated AlF_6^{3-} ions (and other complex species), have been invoked to explain the shapes of liquidus curves; the most common equilibrium proposed is

$$AlF_6^{3-} \rightleftharpoons AlF_4^- + 2F^- \qquad [11]$$

Without wishing to tie ourselves to this stoichiometry, we propose that the observed transitions are due to discharge of the "free" fluoride only. On this basis, we can account for the following features:

1. At high current densities the transition is diffusion controlled; at lower currents and longer times the "free" fluoride is replenished by dissociation of complexes (or possibly the diffusion is disrupted by gas bubble formation). According to Paunovic (8), "a decrease in the product $i\tau^{1/2}$ with current density is a diagnostic criterion for the occurrence of a prior chemical reaction, *e.g.*, dissociation of a complex."

2. Addition of NaF increases the supply of free fluoride, addition of Al_2O_3 reduces it, presumably by forming complexes of the type $AlOF_n^{(n-1)-}$. It looks as if the "free" fluoride is being titrated with Al_2O_3, with an end point around 7% Al_2O_3 for an NaF/AlF_3 molar ratio of 3.0, and around 8.5% Al_2O_3 for a ratio of 3.9.

3. Numerical interpretation is reasonable. For a ratio of 3.0, extrapolation to zero alumina (where the transition cannot be observed because of the absence of the protective oxide film) gives $i\tau^{1/2} = 2.8$ A cm^{-2} $sec^{1/2}$. From this must be subtracted a correction for the formation of the oxide film, which is taking all the current initially and some of it subsequently. If the first process of two successive reactions is diffusion controlled the proper procedure (9) is to subtract $i\tau^{1/2}$ for the first transition; in this case this will not be accurate, but the error will not be serious for the present purpose. We therefore subtract 0.9 A cm^{-2} $sec^{1/2}$ to give $i\tau^{1/2} = 1.9$ A cm^{-2} $sec^{1/2}$. Using the Sand equation, [2], and with an estimated value of $D = 5 \times 10^{-5}$ cm^{-2} $sec,^{-1}$ C is found to be 0.0031 moles F^-/ml. The density of cryolite at 1020°C is 2.077 g/ml, so that 1 mole (210g) occupies 101 ml, and the same volume contains 0.32 moles "free" F^-. In terms of equilibrium [11] this represents 16% dissociation of AlF_6^{3-}. A decrease of a factor of 2 in the estimate of D would increase the calculated dissociation to 23%, but it is unlikely that D for "free" F^- is as low as 2.5×10^{-5} cm^2 sec^{-1} since that is the value found for Al_2O_3 which is present as bulky $AlOF_n^{(n-1)-}$ complexes.

Gilbert, Mamantov, and Begun (10) have just published work on the Raman spectrum of molten cryolite from which they deduce that the AlF_6^{3-} ions are about 25% dissociated. In view of the totally different type of experiment and the different assumptions made in working out the results, the agreement is good enough to lend strong support to the view that we are observing transitions due to the discharge of "free" F^-, and that the latter does have a real physical existence.

Although we have not been able to give any quantitative treatment, to explain the departure from the diffusion-controlled line in Fig. 12 requires a lifetime for AlF_6^{3-} ions of the order of a millisecond. The lines in Fig. 13 could form the basis of an analytical method for determining alumina in molten cryolite, but the sensitivity of the calibration to the NaF/AlF_3 ratio (and probably also to CaF_2 content), limits its attraction.

Manuscript submitted July 18, 1975; revised manuscript received May 30, 1976. This was Paper 396 presented at the Washington, D.C., Meeting of the Society, May 2-7, 1976.

Any discussion of this paper will appear in a Discussion Section to be published in the December 1977 JOURNAL. All discussions for the December 1977 Discussion Section should be submitted by Aug. 1, 1977.

Publication costs of this article were assisted by the Aluminum Company of Canada, Limited.

REFERENCES

1. N. E. Richards and E. R. Russell, Paper 192 presented at Electrochemical Society Meeting, New York, New York, May 4-9, 1969.
2. J. Thonstad, *Electrochim. Acta.* **14**, 127 (1969).
3. J. Thonstad, "Light Metals 1974," H. Forberg, Editor, Vol. 1, pp. 137-149. Met. Soc. AIME, New York.
4. P. Desclaux and M. Rolin, *Rev. Int. Hautes Temp. Réfract.*, **8**, 227 (1971).
5. J. S. Mayell and S. H. Langer, *This Journal*, **111**, 438 (1964).
6. K. Hauffe "Oxidation of Metals," Plenum Press, New York (1965).
7. G. S. Tyurikov, N. P. Vasilistov, A. V. Silakov, and Yu. M. Pashkov, *Elektrokhimya*, **5**, 309 (1969).
8. M. Paunovic, *J. Electroanal. Chem.*, **14**, 447 (1967).
9. T. Berzins and P. Delahay, *J. Am. Chem. Soc.*, **75**, 4205 (1953).
10. B. Gilbert, G. Mamantov, and G. M. Begun, *J. Chem. Phys.*, **62**, 950 (1975).

The Effect of Surfactants on the Electro-oxidation of Benzhydrol in Emulsion and Micelle Systems

Thomas C. Franklin* and Lewis Sidarous

Department of Chemistry, Baylor University, Waco, Texas 76703

ABSTRACT

A study was made of the effect of surfactants on the yields of product obtained in the anodic oxidation of aromatic alcohols in water-organic solvent emulsion and micelle systems. It was found that cationic surfactants caused marked increases in the yield while anionic or neutral surfactants caused only small increases in the yield. It was concluded that at least part of the effect was caused by the formation of a film on the surface of the anode which inhibited the competing process, the evolution of oxygen.

As part of the comparison of some electro-oxidations with chemical oxidations a study was initiated into the electro-oxidation of some aromatic alcohols to compare with results obtained in a study using metal oxides as chemical oxidizing agents. This basically is the same problem being investigated in studies of the electrochemical oxidation of organic compounds using nickel peroxide electrodes (1-3). Because of solubility problems it was decided to use emulsion and micelle systems to solubilize the organic compounds while still maintaining the conductivity of an aqueous solution of an electrolyte. Emulsion systems, which have been used for some time in the electrolysis of insoluble liquids suspended in an electrolyte (4, 5), have recently been shown to be especially useful when phase transfer catalysts are used (6, 7). Recently there has been a series of polarographic studies in which the organic compounds were solubilized in the form of micelles (8-12).

Experimental

The model compound chosen for oxidation was benzhydrol and the aqueous phase was 2*N* sodium hydroxide and the organic phase in the emulsion studies was varied but in most experiments it was benzene. The synthesis cell consisted of a 400 ml beaker containing a porous porcelain cup separating the anode and cathode compartments. A saturated calomel reference electrode was connected to the anodic compartment with a Luggin capillary and all voltages listed are referred to the SCE. The counterelectrode was a platinum gauze electrode with a geometrical area of 63.7 cm^2. Similar results were obtained when an H-type cell was used as the reaction vessel with the two compartments separated with a coarse fritted glass disk.

The anode potential was controlled with a Wenking Model 66TA1 potentiostat. In cases where current-voltage curves were recorded, the potential of the potentiostat was varied using a motor-driven potentiometer. The same cell and electrodes were used. The working electrode was a large platinum foil (40.9 cm^2 in area).

All synthesis experiments were performed for 1 hr at room temperature unless otherwise indicated. A variety of stirring conditions was tried including ultrasonic mixing. In the results included in this report the system was mixed and stirred vigorously during the process by using a cone drive stirrer. This was sufficient in these experiments to maintain the emulsion.

After electrolysis, the anolyte mixture was placed in a separatory funnel. In the micelle experiments, the anolyte was extracted with 50 ml of benzene. The organic and aqueous phases were then separated and the analysis was performed using the organic phase. When water miscible solvents were used, the anolyte solution was evaporated to dryness in a flash evaporator; the solid residue was then extracted with benzene, mixed in a separatory funnel with 30 ml of distilled water, and the aqueous layer was discarded.

After washing with water the product, benzophenone, was determined quantitatively either gravimetrically as the 2, 4 dinitrophenylhydrazone derivative or by liquid chromatography. The benzophenone was originally identified by infrared spectrophotometry and by the melting point of 2,4 dinitrophenylhydrazone derivative. It was further confirmed by high pressure liquid chromatography. The benzopinacol was identified and determined using high pressure liquid chromatography.

High pressure liquid chromatography was the primary analytical tool used to identify products and determine yields of the various aldehydes and ketones. The chromatograph used was a Waters ALC202 instrument with a differential refractometer detector. A 2 ft silica gel (Corasil I) column was used with a 50:50 mixture (by volume) of benzene and cyclohexane being used as the solvent. The recorded peaks were integrated with a planimeter. The products were identified by comparing retention times with the retention times of knowns.

The gases evolved at the anode in the benzhydrol reaction were tested using a Model 6500 Basic Carle Gas Chromatograph with parallel silica gel and molecular sieve columns and thermal conductivity detectors.

The following commercial surfactants were used: (*i*) neutral surfactants: Triton X-405 (Rohm and Haas), 70% aqueous solution of octyl phenoxy polyethoxy ethanol, Siponic L-4, L-12, and L-25 (Alcolac, Incorporated), laural alcohol ethoxylate; (*ii*) anionic surfactants: Triton 770 conc (Rohm and Haas), 30% aqueous solution of sodium alkyl aryl polyether sulfate, Triton W-30 conc (Rohm and Haas), sodium alkyl ester sulfonate solution in isopropyl alcohol and water, Spencer Poly-EMII Anionic (Spencer Chemical Company); (*iii*) cationic surfactants: Hyamine 2389 (Rohm and Haas), 50% aqueous solution of 80% methyldodecylbenzyl trimethyl ammonium chloride and 20% methyldodecylxylene bis (trimethyl ammonium chloride), Arquad 2C-50 (Armour Industrial Chemical Company), dicocodimethyl ammonium chloride.

Benzhydrol and benzophenone were recrystallized twice from distilled petroleum ether (60°-110°C). Other solid organic compounds were recrystallized from appropriate distilled solvents. All organic solvents used in this investigation were distilled before

* Electrochemical Society Active Member.
Key words: phase transfer, solubilization.

use. The organic materials were checked for purity by either liquid or gas chromatography.

The other chemicals were the best grade that were conveniently available commercially. The experiments were run on the desk top at room temperature.

The yields reported in the tables are calculated on the basis of the amount of reactant added. Yields calculated on the basis of the amount of reactant consumed would be higher. As expected, as the benzhydrol was consumed the current in a run decayed slowly with time. The decay was, within experimental error, linear. For example, in one run the current varied from 480 to 440 mA and the current at the halfway point was 460 mA; in another run where the current varied from 185 to 160 mA the halfway current was 170 mA. Since this decay was essentially linear, the average current density for a typical run recorded in the tables was obtained by taking the mean of the current density at the beginning and end of the experiment. The current efficiencies were determined by using this mean current and multiplying it by the time to calculate the quantity of electricity passed. The current efficiencies and yields are the averages of several runs.

Results and Discussion

Micelle studies.—Table I shows the yields obtained in a suspension containing 0.005 moles of benzhydrol in 2*N* sodium hydroxide containing 2% (by volume) of commercial preparations of cationic, anionic, and neutral surfactants as solubilizing agents when the potential of the anode was 1.90V. Because of the insolubility of the benzhydrol no yield was obtained in the absence of surfactants. It can be seen that the introduction of a cationic surfactant into the system markedly increased the yield while anionic and neutral surfactants had only small effects. However, the neutral surfactant did increase the yield slightly more than did the anionic surfactants. These results are in agreement with the work of Eberson (6, 7) on the use of phase transfer catalysts to increase the yield of products obtained in anodic cyanations since the cationic detergents are phase transfer catalysts.

In order to obtain a clearer picture of the cause of the effects of the surfactants, current-voltage curves were obtained in the different solutions and suspensions using a voltage scan rate of 3 mV/sec. Figure 1 shows curves obtained in 2*N* sodium hydroxide. It can be seen that the cationic surfactant caused a marked shift in the anodic current voltage curve while the neutral and cationic surfactants caused only slight shifts. It can also be seen that the curve obtained in the presence of the cationic surfactant has a maximum in it. Repeated running of linear voltage sweeps, one after the other, caused this maximum to decrease in height with the number of runs. This type of behavior indicates that something is being oxidized to form a difficultly soluble film on the surface of the platinum. That some substance was being oxidized was further indicated by electrolysis of a solution of the cationic surfactant in sodium hydroxide. Upon extraction of this solution with benzene, a red benzene layer was obtained. Although the color was intense, no peak was obtained with high pressure liquid chromatography so that the product was not identified.

Since quaternary ammonium salts are used as supporting electrolytes in electrolytic oxidations, some question exists as to whether the quaternary salt is the substance being oxidized to form the film. Since the 2*N* sodium hydroxide is expected to slowly degrade the salt to form a tertiary amine, a study was made of the effect of some amines on the yields (Table II). As can be seen, these amines did not cause the increase in yield caused by the quaternary ammonium salts. Also, they did not shift the current-potential curves to an appreciable extent. Although this is indicative that the amines do not cause the observed facts, it does not eliminate the possibility that the tertiary amine formed by the degradation of these long chain surfactants is the cause of the film formation.

Figure 2 shows typical current voltage curves obtained in 2*N* sodium hydroxide containing the cationic surfactant and the same solution containing benzhydrol. These curves were obtained after repeated running of current-voltage curves until the maximum observed in Fig. 1 had disappeared. From these results it was concluded that the hydrophobic film formed on the surface of the platinum excludes water from the electrode surface which increases the potential

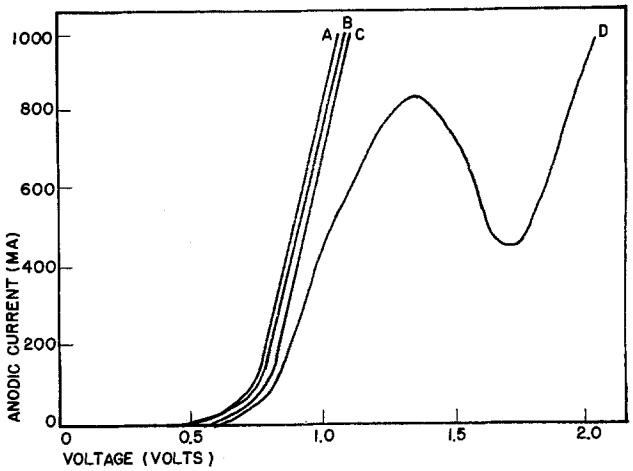


Fig. 1. Effect of different surfactants on the anodic current-potential curves obtained in 2*N* sodium hydroxide: A = no surfactant, B = anionic surfactant, C = neutral surfactant, D = cationic surfactant.

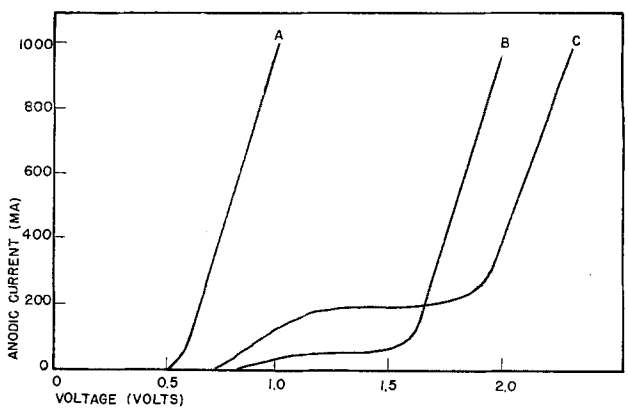


Fig. 2. Current-voltage curves obtained in 2*N* sodium hydroxide containing benzhydrol: A = 2*N* sodium hydroxide, B = 4% solution of Hyamine 2389 in 2*N* sodium hydroxide, C = 0.005M benzhydrol in 4% solution of Hyamine 2389 in 2*N* sodium hydroxide.

Table I. The effect of different types of surfactants on the electro-oxidation of benzhydrol solubilized in micelles

Types of surfactants	% Yield Benzophenone	% Yield Benzopinacol	Typical average current density (mA/cm²)	Average current efficiency
Cationic	29.4	2.9	3.6	64.7%
Anionic	3.5	0.1	2.1	8.3%
Neutral	4.8	0.2	2.1	12.0%

Table II. Effect of amines on the electro-oxidation of benzhydrol in benzene emulsions using platinum electrodes

Amine	Yield of benzophenone
Octylamine	0.0%
sec-butylamine	1.5%
Triethylamine	0.3%

needed to oxidize the water. However, this film is apparently conductive and the organic compound is oxidized on the surface of the film.

The increased yield in the presence of the cationic surfactant then can be attributed, at least in part, to the inhibition of the competing oxidation process, the evolution of oxygen.

Figure 3 shows the effect of different concentrations of surfactants on the yield of benzophenone. It increases with increasing concentration of surfactant until one reaches about 4% then the yield drops off. Correspondingly there is a sharp drop in the current.

Figure 4 shows the variation of percent yield with current efficiency. This data was obtained by increasing the concentration of cationic surfactant. As one increases the concentration of Hyamine 2389, the yield and total current efficiency increase. In fact, the total current efficiency rises above 100%. This led to the conclusion that at least some of the products were produced from a chain mechanism.

$$Ph_2CHOH + OH^- \xrightarrow{-e^-} Ph_2\dot{C}OH + H_2O \quad \text{initiation}$$

$$Ph_2\dot{C}OH \longrightarrow Ph_2C{=}O + H\cdot$$
$$Ph_2\dot{C}HOH + H\cdot \xrightarrow{-e^-} Ph_2\dot{C}OH + H_2 \quad \text{propagation}$$

$$Ph_2\dot{C}OH + H\cdot \longrightarrow Ph_2C{=}O + H_2 \quad \text{termination}$$

Gas chromatographic analysis showed the presence of hydrogen in the gaseous products produced at the anode in agreement with the above mechanism.

Another possible cause of the high current efficiencies would be oxidation of intermediates in the electrolysis in air. This possibility was checked in the benzene emulsion studies by running identical experiments in air, under nitrogen and under oxygen atmospheres. The yield of benzophenone in air was 23.4%, under nitrogen it was 23.6%, and under oxygen it was 23.2%. This lack of change in yield led to the conclusion that autoxidation was not involved. Although this might be different in other solvents it was felt that it was not a likely explanation of the results.

As one increases the temperature one increases both the current and the yield. Table III shows this result using a 4.0% concentration of the cationic surfactant.

Electro-oxidation in Aqueous-Organic Two-Phase Emulsion Systems

Similar studies were made in aqueous-organic emulsions. Benzhydrol could not be oxidized to produce appreciable yields in reasonable times in the benzene emulsions without a surfactant present. Table IV shows that in benzene-2*N* sodium hydroxide emulsions containing 0.4% surfactant, similar to the micelle results, the presence of quaternary ammonium cationic surfactants sharply increased the yield and the current efficiency while anionic and neutral surfactants increased the yield only slightly. Current-voltage curves obtained in these emulsion systems were similar to those obtained in the micelle systems.

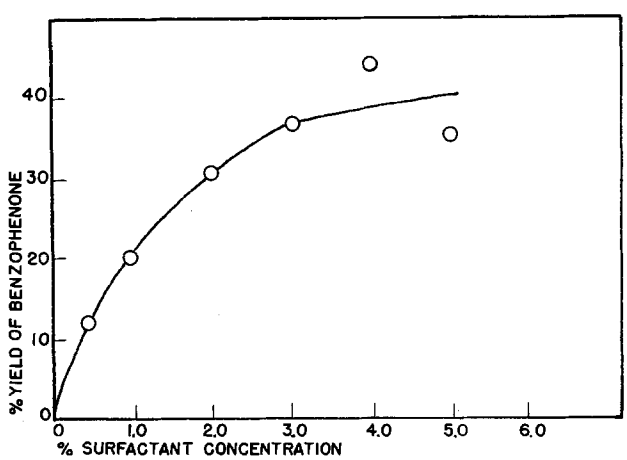


Fig. 3. Effect of cationic surfactant concentrations on the yield of benzophenone obtained from benzhydrol solubilized as micelles in Hyamine 2389.

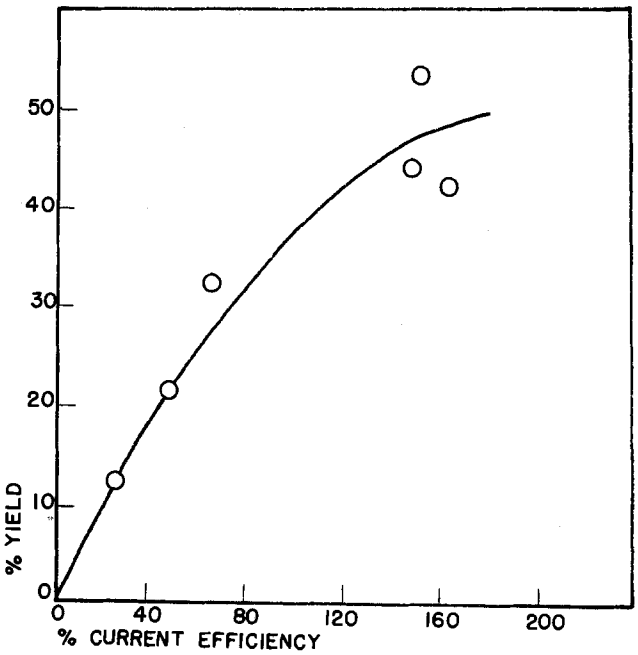


Fig. 4. Relation between the current efficiency and the yield of benzophenone and benzopinacol obtained from the electrolytic oxidation of benzohydrol solubilized in micelles.

Studies were made with different cationic, neutral, and anionic surfactants. In all cases the cationic surfactants increased the yield sharply but the anionic and neutral surfactants changed the yield only by relatively small amounts. Figure 5 shows a comparison of the effect of two different cationic surfactants. It can be seen that with similar surfactants the results are similar.

Although these studies show, in agreement with Eberson, that phase transfer catalysts increase the yield of product it was observed that these long chain cationic surfactants had much more effect than did the more conventional smaller phase transfer catalysts. For example, under conditions similar to Table IV tetraethylammonium bromide produced a yield of only 4.2% and tetraethylammonium chloride produced a yield of 4.1%.

Table III. The effect of temperature on the electro-oxidation of benzhydrol solubilized in micelles

Temperature	% Yield Benzophenone	% Yield Benzopinacol	Typical average current density (mA/cm²)	Average current efficiency
Room temperature	43.4	4.8	2.2	154.6%
60°	86.3	0.2	4.5	128.9%
80°	97.7	0.2	11.7	53.9%

Table IV. Effect of different types of surfactants on the electro-oxidation of benzhydrol in benzene emulsions

Type of surfactant	% Yield Benzophenone	% Yield Benzopinacol	Typical average current density (mA/cm²)	Average current efficiency
None	0.4	0.0	0.3	17%
Anionic (Triton GR-5)	2.8	0.0	3.5	14%
Neutral (Triton X-405)	4.0	0.2	2.7	20%
Cationic (Hyamine 2389)	23.4	1.8	1.9	87%

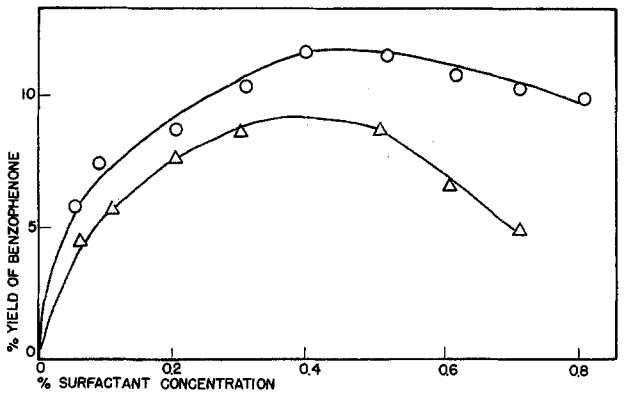


Fig. 5. Effect of different concentrations of cationic surfactant on the yield of benzophenone obtained in benzene emulsions: ○ Hyamine 2389, △ Arquad 2C-50.

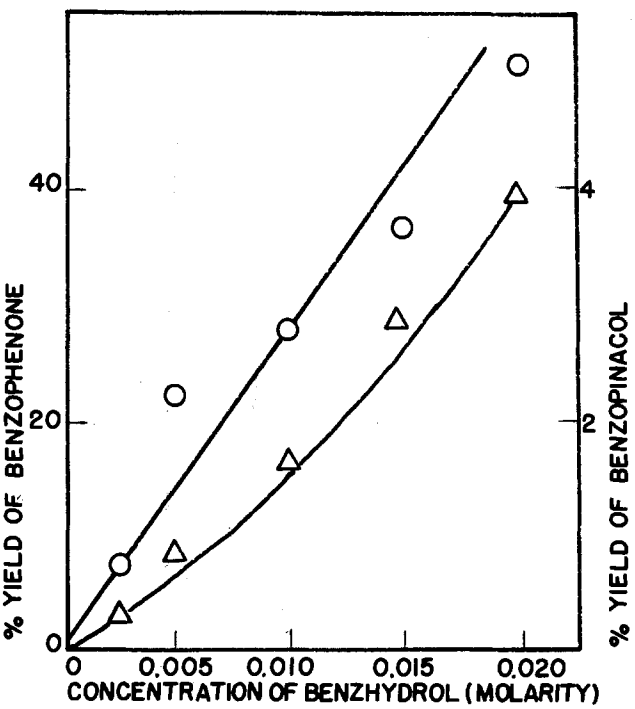


Fig. 6. Relation between the concentration of benzhydrol and the yields of benzophenone and benzopinacol: ○ benzophenone, △ benzopinacol.

As one would expect in a competitive process as the concentration of benzhydrol is increased, the percent yield increases, as can be seen in Fig. 6. There is a small amount of benzopinacol formed in the process and this also can be seen, in Fig. 6, to increase as one increases the concentration of benzhydrol.

Figure 7 shows the effect of potential on the yield of benzophenone and benzopinacol. The curves are similar in shape to the current-voltage curve for oxidation of benzhydrol in the emulsion. The yield increases as the potential rises to about 1.0V. The slight increase in yield between 1.0 and 1.6V follows the slight increase of the current in this region. Above 1.6 the yield rises appreciably. Since this potential region involves the evolution of oxygen, the stirring of the solution probably increases the rate of transport of material to the electrode, thus increasing the yield.

Table V shows the effect of different electrode materials on the yields obtained after electrolysis for 1 hr in benzene emulsions containing 0.4% of Hyamine 2389. It can be seen that best results with the potential held at 1.90V were obtained with platinized and bright platinum.

Table VI shows the effect of different organic solvents on the yield obtained upon addition of 0.4% of

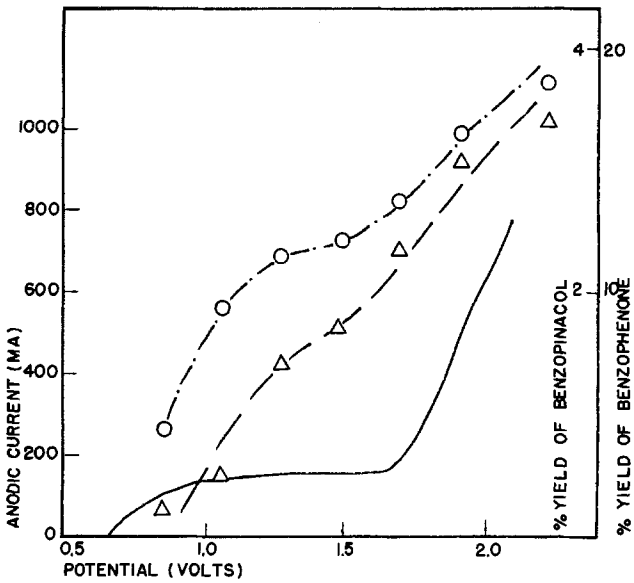


Fig. 7. Effect of potential on yield of products in benzene-sodium hydroxide emulsions: △ benzophenone yield, ○ benzopinacol yield, ——— current-potential curve.

the surfactant (Hyamine 2389) after electrolysis for 1 hr using a bright platinum anode. The decomposition potential of water was essentially shifted to the same potential with all solvents except diethyl ether, dioxane, acrylonitrile, pyridine, acetone, tetrahydrofuran, and methanol. In these solvents there was only a slight shift in the potential and, correspondingly, a low yield. Possibly this means that the electrode film is

Table V. Effect of different anode materials on the yield of benzophenone obtained in benzene emulsions

Anode material	Yield
Platinized platinum	34.8
Bright platinum	23.4
Manganese Dioxide	6.4
Nickel hydroxide	5.4
Cadmium	3.6
Carbon	3.4
Rhodium	3.3
Ruthenium, gold, silver, palladium	0.0

Table VI. Effect of different organic solvents on the yield of benzophenone and benzopinacol obtained in the electro-oxidation of benzhydrol in a mixture of organic solvent and 2M sodium hydroxide

Organic solvent	% Yield benzophenone	Typical average current density (mA/cm²)	Average current efficiency in %
Tetrahydrofuran	4.5	3.0	9.8
Diethyl ether	4.8	2.0	15.4
Methanol	5.0	3.9	8.0
Acetone	5.1	2.8	11.9
Dioxane	6.1	2.6	15
Cyclohexane	6.9	0.6	75.3
Acrylonitrile	7.3	3.0	16
Pyridine	9.3	3.8	16
Propylene carbonate	12.2	4.4	18.1
Propanol	12.9	5.6	12
Methylene chloride	14.3	4.0	23.8
Nitroethane	17.1	2.9	41
Toluene	17.2	3.0	44
Benzene	23.4	1.9	87
Hexamethylphosphoric triamide	23.5	3.1	49.7
O-Dichlorobenzene	24.9	3.8	55
Chlorobenzene	25.4	2.6	64
Iodobenzene	25.8	2.5	67.7
Bromobenzene	26.2	2.5	68.7
Butanol	28.6	2.8	69
Adiponitrile	28.6	4.8	39.1
Isobutyronitrile	34.0	2.4	93
Nitrobenzene	37.7	2.3	107
Phenylacetonitrile	59.8	2.2	178
Acetonitrile	90.0	2.0	286

Table VII. Yield of product obtained in electro-oxidation reactions on platinized platinum anodes in benzene emulsions with a cationic surfactant present (in all cases there was essentially no yield without the surfactant present)

Reactant	Product	% Yield	% Current efficiency
Benzyl alcohol	Benzaldehyde	17.8	56.0
α Methylbenzyl alcohol	Acetophenone	21.3	156.0
p Methylbenzyl alcohol	p Tolualdehyde	29.9	87.0
p Nitrobenzyl alcohol	p Nitrobenzaldehyde	23.3	46.0

soluble in these solvents. Of the other solvents, acetonitrile caused the largest shift and produced the most yield. It is felt that this is caused by the solubility of the acetonitrile in water which increases the solubility of the organic compound in the water (13).

The oxidation of several other aromatic alcohols was studied. In all cases the cationic surfactant caused a major increase in the yield while anionic and neutral surfactants caused only small increases. Table VII shows the results obtained with different alcohols after electrolysis for 1 hr in a solution containing 0.4% Hyamine 2389.

Summary

It has been observed that the introduction of a cationic surfactant markedly increases the yield of product obtained in the electro-oxidation of several aromatic alcohols solubilized in emulsions and micelles, while anionic or neutral surfactants change the yield only slightly. It was concluded from studies using current-voltage curves that this was caused by the formation of a conducting hydrophobic layer on the surface of the electrode. The best results were obtained with the oxidation of benzhydrol to benzophenone.

Acknowledgments

We thank the Robert A. Welch Foundation of Houston, Texas, for financial support of this work.

Manuscript submitted July 6, 1976; revised manuscript received *ca.* Sept. 21, 1976. This was Paper 305 presented at the Washington, D.C., Meeting of the Society, May 2-7, 1976.

Any discussion of this paper will appear in a Discussion Section to be published in the December 1977 JOURNAL. All discussions for the December 1977 Discussion Section should be submitted by Aug. 1, 1977.

Publication costs of this article were assisted by Baylor University.

REFERENCES

1. M. Fleischmann, K. Kovinek, and D. Pletcher, *J. Chem. Soc. Perkin Trans.* **2**, 1396 (1972).
2. M. Fleischmann, K. Kovinek, and D. Pletcher, *Electroanal. Chem.*, **31**, 39 (1971).
3. M. Amjad, M. Fleischmann, D. Pletcher, and C. Smith, Abstract 293, p. 735, The Electrochemical Society Extended Abstracts, Spring Meeting, Washington, D.C., May 2-7, 1976.
4. Fr. Fichter, *Z. Elektrochem.*, **19**, 781 (1913).
5. J. P. Millington and J. Trotman, Abstract 279, p. 700, The Electrochemical Society Extended Abstracts Spring Meeting, Washington, D.C., May 2-7, 1976.
6. L. Eberson and B. Helgee, *B. Chem. Scri.*, **5**, 47 (1974).
7. L. Eberson and B. Helgee, *Acta Chem. Scand.*, **B29**, 451 (1975).
8. S. Hayano and N. Shinozuka, *Bull. Chem. Soc. Jpn.*, **42**, 1469 (1969).
9. S. Hayano and N. Shinozuka, *ibid.*, **43**, 2083 (1970).
10. S. Hayano and N. Shinozuka, *ibid.*, **44**, 1503 (1971).
11. P. G. Westmoreland, R. A. Day, Jr., and A. L. Underwood, *Anal. Chem.*, **44**, 737 (1972).
12. T. Erabi, H. Huira, and M. Tanaka, *Bull. Chem. Soc. Jpn.*, **48**, 1354 (1975).
13. F. W. Steuber and K. Dimroth, *Chem. Ber.*, **99**, 258 (1966).

A General Oscillator Model for Charge Transfer in Polar Media

S. G. Christov

Institute of Physical Chemistry, Bulgarian Academy of Sciences, Sofia 13, Bulgaria

ABSTRACT

The two-frequency oscillator model is used to describe both electron and proton transfer processes in polar solvents. A low frequency is related to the librations of the solvent medium and a high frequency to either the vibrations in the inner coordination shell of an ion or to that of a proton. The general quantum mechanical formulation of reaction rate theory is employed to overcome the restrictions of previous semiclassical treatments of the same model based on perturbation theory. Thus, a complete treatment of the two-frequency oscillator model is proposed which comprise the whole range between adiabatic and nonadiabatic processes and involves nuclear tunneling at arbitrary temperatures as well. The results of earlier theories are derived as particular cases of this more general consideration of the model. A critical discussion of the oscillator model and a comparison with some experimental facts are made.

In a previous paper (1) a quantum theory of electron transfer in solution was proposed, which rests on a recent general formulation of chemical kinetics (2). The role of the polar solvent was taken into account by using the harmonic oscillator model with a single vibration frequency (3, 4). In this way it is possible to treat separately the extreme cases in which either the outer or the inner solvation sheath of the ion changes during the electron transfer. The general method used permits one to avoid the restrictions of the classical theory (3) and the quantum-mechanical perturbation theory previously used (4) in treating electron transfer processes. In this way the whole region between the adiabatic and the nonadiabatic processes was included in a unified treatment, which takes into account nuclear tunneling at any temperature. The main results of earlier theories (3, 4) were obtained as particular cases in the framework of this treatment.

In the present paper we consider a more general oscillator model with two frequencies ν_x and ν_y ($\nu_y > \nu_x$) which can be related to the solvent medium and the inner coordination shell when treating electron transfer between two ions. The same model is also ap-

Key words: potential barrier, adiabatic and nonadiabatic reactions, nuclear tunneling.

plicable to proton transfer processes if the high frequency (ν_y) is attributed to the proton vibration and the low one (ν_x) to the librations of solvent molecules (5). The purpose of this investigation is to apply the general approach used in Ref. (1) to this more general model and to compare the results with those obtained by other authors (5, 6) with the same model but in a different way. A discussion of the approximations introduced in previous treatments and the limitations involved in the oscillator model, in general, are given in the last section of this paper.

The exact expression for the rate constant of any reaction can be written as (1, 2)

$$k_{12} = \kappa \frac{kT}{h} \frac{Z^H}{Z} e^{-E_a/kT}, \quad \kappa = \kappa_t \chi \qquad [1]$$

where E_a is the classical activation energy (at 0°K), Z is the full partition function of reactants (including solvent molecules) and Z^H is a partition function in which the motion along the reaction path is excluded,[1] $\kappa \gtrless 1$ is a quantum correction factor, $\chi \leq 1$ is the "transmission coefficient," and $\kappa_t \geq 1$ is the nuclear "tunneling correction." Both Z^H and Z refer to the initial state[1] for which an equilibrium energy distribution is postulated. The derivation of Eq. [1] implies that a classical "reaction coordinate" x_r can be defined, which is dynamically separable from the other coordinates in the initial state of the system. A hypersurface S_r in the reactants region, normal to x_r, has to be crossed in a direction to the products region for the reaction to occur with a given probability. Equation [1] involves an integration over S_r and summations over all initial and final states of the systems crossing S_r and passing from the reactants to the products region.

From Eq. [1] we obtain the parameters of the Arrhenius equation

$$k_{12} = K_{12}' e^{-E_a'/kT}$$

defined by

$$E_a' \equiv -k \frac{\partial \ln k_{12}}{\partial (1/T)}, \quad K_{12}' \equiv k_{12} e^{E_a'/kT} \qquad [2]$$

as well as the transfer coefficients (1, 2, 7)

$$\beta \equiv -kT \frac{\partial \ln k_{12}}{\partial Q} = \beta_c - kT \frac{\partial \ln \kappa}{\partial Q} \qquad [3a]$$

and

$$\beta' \equiv \frac{\partial E_a'}{\partial Q} = \beta_c + kT^2 \frac{\partial^2 \ln \kappa}{\partial T \, \partial Q} \qquad [3b]$$

where $\beta_c \equiv \partial E_a / \partial Q$ is the classical transfer coefficient and Q is the reaction heat. The corresponding equations for the Arrhenius parameters $E_a' - Q$ and K_{21}' as well as for the transfer coefficients $\alpha = 1 - \beta$ and $\alpha' = 1 - \beta'$, related to the inverse direction of the reaction, can be easily obtained from the above expressions (1, 2, 7).

The Potential Barrier

We consider the two reactants at a fixed distance R and represent the potential energies in the initial and final state in a harmonic approximation by

$$V_1(x,y) = ax^2 + by^2 + Q_1$$
$$V_2(x,y) = a(x - x_o)^2 + b(y - y_o)^2 + Q_2 \qquad [4]$$

where x and y are Cartesian coordinates describing two vibrations with frequencies

$$\nu_x = \frac{1}{2\pi} \sqrt{\frac{2a}{\mu_x}}, \quad \nu_y = \frac{1}{2\pi} \sqrt{\frac{2b}{\mu_y}} \qquad [4a]$$

μ_x and μ_y being the corresponding effective masses.

The equilibrium position of the initial state is chosen to be at the origin ($x = 0$, $y = 0$) of the coordinate system and that of the final state is at the point

[1] The notion of a "transition state" in the sense of Eyring's theory is not introduced in the above formulation (2a,b).

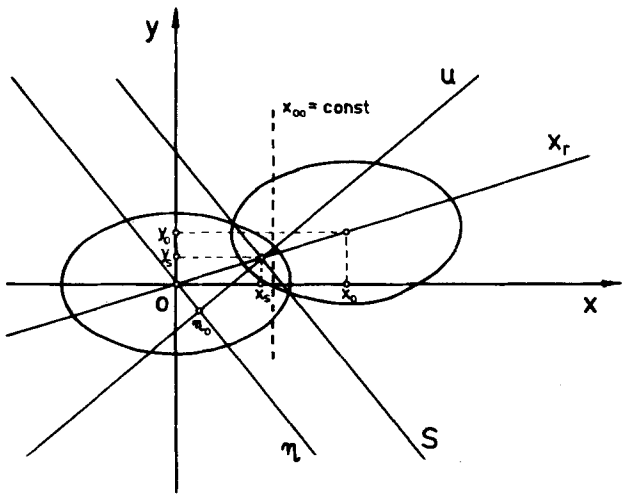


Fig. 1. Projection of the potential surfaces [4] on the plane x,y. The two ellipses correspond to a section $V_1(x,y) = V_2(x,y) =$ const.; $0(x = 0, y = 0)$ initial, x_o,y_o final configuration; S intersection plane of the two paraboloids; x_s,y_s saddle-point; x_r reaction coordinate; u line normal to S, η line parallel to S, η_o crossing point of u and η, x_{oo} = const. line parallel to y ($x_{oo} > x_s$).

($x = x_o$, $y = y_o$). Equation [1] describes two elliptic paraboloids. Their projections on the plane x, y are represented on Fig. 1 by elliptic curves each corresponding to a constant energy value ($V_1 = V_2 =$ const.).

The two paraboloids, Eq. [1], interesect in a plane S and the intersection line has a minimum at a point representing a "saddle-point" with coordinates

$$x_s = \frac{x_o}{2}\left(1 + \frac{Q}{E_r}\right), \quad y_s = \frac{y_o}{2}\left(1 + \frac{Q}{E_r}\right) \qquad [5]$$

where $Q = Q_2 - Q_1$ is the "reaction heat" and

$$E_r = E_r^x + E_r^y = ax_o^2 + by_o^2 \qquad [6]$$

is the sum of the "reorganization energies" of the two oscillators. The height of the "saddle-point," measured from the Q_1 level, is given by

$$E_c' = \frac{(E_r + Q)^2}{4E_r} \qquad [7]$$

Because of the electronic interaction between reactants there is a resonance splitting in the intersection region of the potential surfaces, Eq. [4] so that the height of the saddle-point is lowered by an amount equal to the resonance energy V_{12} at that point. Thus, instead of Eq. [7], we have

$$E_c = E_c' - V_{12} \qquad [8]$$

The line connecting the equilibrium positions (0,0) and (x_o,y_o) is a straight line which goes through the saddle-point (x_s,y_s). It represents the classical "reaction coordinate" x_r, defined by

$$x_r = x\left(1 + \frac{y_o^2}{x_o^2}\right)^{1/2} \qquad [9]$$

The energy profile in a cross cut along x_r (Fig. 2) is obtained by the intersection of two parabolic curves

$$V_1(x_r) = a_r x_r^2 + Q_1$$
$$V_2(x_r) = a_r(x_r - x_r^o)^2 + Q_2 \qquad [10]$$

corresponding to an effective vibration frequency

$$\nu_r = \frac{1}{2\pi} \sqrt{\frac{2a_r}{\mu_r}} = \frac{E_r}{E_r^x/\nu_x + E_r^y/\nu_y} \qquad [11]$$

being the same for the initial and final state. The two curves, Eq. [10], intersect just at the saddle-point

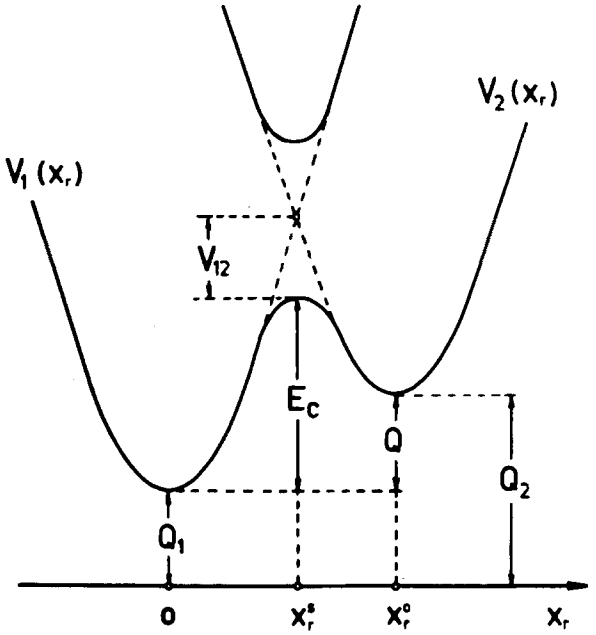


Fig. 2. Energy profile along the reaction coordinate x_r. $V_1(x_r)$ and $V_2(x_r)$ are the potential curves [10] corresponding to the initial and final state; $V_{1,2}$ electronic resonance energy at the crossing point ($x_r = x_r^s$); E_c is the classical activation energy [8] for the endothermic transfer direction ($x_r = 0$ initial, $x_r = x_r^0$ final configuration); $Q = Q_2 - Q_1$ reaction of heat.

(x_s,y_s). Therefore, Eq. [8] represents the classical activation energy for a transition from the initial state (0,0) to the final state (x_o,y_o) along the reaction coordinate x_r.

If the electronic interaction is very weak so that $V_{12} << E_c'$, we have $E_c \simeq E_c'$, hence Eq. [7] is a good approximation for the activation energy. If the interaction is strong (V_{12} large) we can use the expression (1-8)

$$E_c = E_c^\circ + \frac{Q}{2}\left(1 + \frac{\gamma^2 Q}{8E_c^\circ}\right) \qquad [12]$$

where

$$E_c^\circ = \frac{E_c}{4} - V_{12}, \quad \gamma = \frac{2d_o}{x_o} < 1 \qquad [13]$$

and $2d_o$ is the width of a parabolic barrier which approximates the top of the barrier $V(x_r)$ at $Q = 0$. For $V_{12} = 0$, Eq. [12] reduces to Eq. [7] if we set formally $\gamma = 1$.

The classical reaction coordinate, Eq. [9], is a somewhat unusual one since it does not correspond to a minimum of potential energy for motions normal to it except at the points $x_r = 0$, $x_r = x_r^s$, and $x_r = x_r^o$, which determine the initial, the transition, and the final state, respectively. In the initial and final states the reaction coordinate x_r is separable which justifies the use of the rate equation, Eq. [1]. However, in the transition state x_r does not coincide with the coordinate u crossing the saddle-point normal to the intersection plane S of the potential surfaces Eq. [4]. The energy profiles along u are given by the equations

$$V_1(u) = a_u u^2 + \frac{2ax'}{\sqrt{1 + (by_o/ax_o)^2}}u + ax'^2 + Q_1$$

$$V_2(u) = a_u(u - u_o)^2 + \frac{2ax'}{\sqrt{1 + (by_o/ax_o)^2}}(u - u_o) + a(x'' - x_o)^{2+}Q_2 \qquad [14]$$

corresponding to the initial and final state, where

$$\nu_u = \frac{1}{2\pi}\sqrt{\frac{2a_u}{\mu_u}} = \frac{\nu_x^2 E_r^x + \nu_y^2 E_r^y}{\nu_x E_r^x + \nu_y E_r^y} \qquad [15]$$

is the frequency of vibration along u. A comparison with Eq. [11] shows that $\nu_u > \nu_r$. If the resonance splitting is sufficiently large, we can approximate the barrier along u by a parabola with a curvature $|f_u^H| \geq 2a_u$. Therefore, we can define a "characteristic temperature" by (1, 2)

$$T_k = \frac{h\nu_u^H}{\pi k} \geqq \frac{h\nu_u}{\pi k}, \quad \nu_u^H = \frac{1}{2\pi}\sqrt{\frac{f_u^H}{\mu_u^H}} \qquad [16a]$$

where k is the Boltzmann constant, provided $h\nu_u < kT$. If the resonance energy V_{12} is small ($2V_{12} < h\nu_u$) and $h\nu_u > kT$, the characteristic temperature can be estimated by (1)

$$T_k \simeq \frac{h\nu_u}{kK(E_m)}, \quad K(E_m) = \frac{4\pi\sqrt{2\mu_u}}{h}\int_{u_1}^{u_2}\sqrt{V(u) - E_m}du \qquad [16b]$$

where μ_u is the effective mass for motion along u, u_1, and u_2 are the roots of $V(u) - E_m$, and E_m is the highest energy level just below the saddle-point ($E_m < E_c < E_{m+1}$). The derivation of [16a, b] implies an equilibrium energy distribution for motion along u.

We may introduce in a similar way a characteristic temperature T_k^r for the reaction coordinate x_r, hence

$$T_k^r = \frac{h\nu_r^H}{\pi k} \geqq \frac{h\nu_r}{\pi k}, \quad \nu_r^H = \frac{1}{2\pi}\sqrt{\frac{f_r^H}{\mu^H}} \qquad [17a]$$

if the resonance splitting is large and $h\nu_r < kT$, or

$$T_k^r \simeq \frac{h\nu_r}{kK(E_m)}, \quad K(E_m) = \frac{4\pi\sqrt{2\mu_r}}{h}\int_{x_{r,1}}^{x_{r,2}}\sqrt{V(x_r) - E_m}\,dx_r \qquad [17b]$$

if $2V_{12} < h\nu_r$ and $h\nu_r > kT$. Since $\nu_r < \nu_u$, we see that $T_k^r < T_k$, and, therefore, Eq. [16a, b] are to be used as more relevant expressions for the characteristic temperature than Eq. [17a, b].

As shown previously (1, 2) if $T >> T_k$ ($T > 2T_k$) the nuclear tunneling is negligible and if $T << T_k$ ($T < T_k/2$) it plays a dominant role. In the intermediate range ($T_k/2 < T < 2T_k$) the tunneling and the classical transfer mechanism are comparable. In these three temperature ranges we can use different approximations to calculate the rate constant on the basis of expression [1].

The Semiclassical Temperature Range ($T > 2T_k$)

In the high temperature range the most probable path of reaction is the classical reaction coordinate Eq. [9]. Then, the tunneling correction in Eq. [1] is $\kappa_t = 1$ and the transmission coefficient is given by (1, 2)

$$\chi = \int_o^\infty k(\epsilon_r)e^{-\epsilon_r/kT}d\epsilon_r/kT \qquad [18]$$

where $\epsilon_r = E_{x_r} - E_c$, $E_{x_r} = E_o$ being the initial energy for motion along x_r from the initial state ($x_r = 0$) to the final state ($x_r = x_r^o$). The transition probability $k(\epsilon_r)$ can be calculated using the Landau-Zener theory (9) which implies a classical or quasi-classical motion along a separable rectilinear coordinate x_r, *i.e.*, conservation of the energy ϵ_r during the motion along it.[2] Applying the method described in (1) we obtain

$$\chi = \frac{2}{\sqrt{\pi}}\left(\frac{c^2}{kT}\right)^{1/2} << 1 \qquad [19a]$$

$$\chi = 1 - \frac{1}{2}\sqrt{\frac{\pi}{3}}\left(\frac{c^2}{kT}\right)^{1/6}\left\{1 + \mathrm{erf}\left[\sqrt{3}\left(\frac{2c^2}{kT}\right)^{1/6}\right]\right\}e^{-3(c^2/kT)^{1/3}} \qquad [19b]$$

[2] The conditions of validity of the Landau-Zener method have been discussed by Bates (10a) and particularly by Coulson and Zalewski (10b). See also Marcus (3c).

where

$$c = \frac{(2\pi V_{12})^2}{2hF_r}\sqrt{\frac{\mu_r}{2}} = \frac{\pi V_{12}^2}{2h\nu_r\sqrt{E_r}} \quad [20]$$

V_{12} is the resonance integral, μ_r is the effective mass for motion along x_r, $F_r = |\partial(V_1 - V_2)/\partial x_r|_{x=x_r^s}$, x_r^s is the crossing point of the curves, Eq. [10], ν_r is the vibration frequency Eq. [11], and E_r is the total reorganization energy, Eq. [6]. Equation [19a] is valid under the condition $c^2/kT << 1$, *i.e.*, $\chi = 1$ (nonadiabatic reactions) while [19b] applies for the whole range of variation of χ except for $c^2/kT << 1$. If $c^2/kT > 1$, one obtains $\chi \simeq 1$ (adiabatic reactions).

The partition function ratio in Eq. [1] is easily found to be (1)

$$\frac{Z^H}{Z} = \frac{1}{Z_r} = 2\sinh\frac{h\nu_r}{2kT}, \quad \left(\frac{h\nu_r}{kT} < \frac{3}{2}\right) \quad [21]$$

with ν_r given by Eq. [11]. The condition $h\nu_r/kT < 3/2$ follows from Eq. [16a] and [17a].

The classical activation energy is

$$E_a = E_c + Q_1 \quad [22]$$

where for nonadiabatic reactions $E_c \simeq E_c'$ is given by Eq. [7] and for adiabatic reactions $E_c = E_c' - V_{12}$ is to be calculated by Eq. [12].

In this way using Eq. [1] a complete evaluation of the rate constant is possible in the classical temperature range ($T > 2T_k$) for any arbitrary value of c^2/kT and any value of $h\nu_r/kT < 3/2$. In particular, if $h\nu_r/kT << 1$ ($h\nu_r/kT < 0.5$) one gets

$$k_{12} = \frac{V_{12}^2}{h}\left(\frac{\pi}{E_r kT}\right)^{1/2} e^{-Q_1/kT}\, e^{-(E_r+Q)^2/4E_r kT} \quad [23]$$

for nonadiabatic reactions ($\chi << 1$) and

$$k_{12} = \nu_r\, e^{-(Q_1+E_c^0)/kT}\, e^{-\frac{Q}{2kT}\left(1+\frac{\gamma_0^2 Q}{8E_c^0}\right)} \quad [24]$$

for adiabatic reactions ($\chi = 1$), where ν_r is given by Eq. [11], E_r by Eq. [6], and E_c^0 and γ_0 are defined by Eq. [13].

An equation identical with Eq. [23] has been derived by Dogonadze and Kuznetsov (6) in the framework of first-order perturbation theory under the conditions $h\nu_x/kT << 1$ and $h\nu_y/kT << 1$ which are replaced here by the unique conditions $h\nu_r/kT < 0.5$. No equations related to Eq. [24] have been obtained earlier using the oscillator model for charge transfer but similar expressions were derived for arbitrary potentials along the classical reaction path (7, 8). The present treatment covers, however, the whole range between the limiting cases of nonadiabatic and adiabatic reactions for which the formulas [19] for χ apply.

The Intermediate Temperature Range ($2T_k > T > T_k/2$)

Considering the one-dimensional reaction coordinate x_r as a completely separable one, we can calculate the rate constant by Eq. [1] for any temperature ($T \gtrless T_k$) and any vibration frequency ν_r ($h\nu_r/kT \gtrless 1$) using the expressions derived in Ref. (1). Actually, x_r is not separable in the transition region ($x_r \approx x_r^s$) because it does not represent a normal coordinate there. In this intermediate temperature range the nuclear tunneling plays a moderate role and the most probable reaction path is that along the normal coordinate u which crosses the intersection plane S through the saddle-point (Fig. 1). We, therefore, consider a surface S_r which goes through the initial state ($x = y = 0$) along the line η parallel to S. Then, Eq. [1] can be written as

$$k_{12} = \kappa_u \frac{kT}{h}\frac{Z_\eta^H}{Z} e^{-E_a/kT} \quad [25]$$

where

$$\kappa_u = \int_{-E_c}^{\infty} k(\epsilon_u)\, e^{-\epsilon_u/kT}\, d\epsilon_u/kT, \quad Z_\eta^H = \sum_n e^{-E_n^\eta/kT} \quad [26]$$

$\epsilon_u = E_u - E_c$, $E_u = E_u(\eta_0)$ is the initial energy for motion along u, η_0 being the cross-point of η and u, $k(\epsilon_u)$ is the transition probability along u, Z_η^H is the partition function for motion along η.

The transition probability $k(\epsilon_u)$ in Eq. [26], which involves both the electron and nuclear rearrangement, cannot be evaluated exactly in the intermediate temperature range. However, an approximate estimation is possible by independent calculations of the electron transfer probability using the Landau-Zener theory (9) and the nuclear transfer probability by applying stationary state methods (1). This combined treatment is allowed since the Landau-Zener method is valid also for a quasi-classical motion of nuclei (10) involved in a moderate tunneling correction.

The exact transmission coefficient for motion along u is obtained from Eq. [26] if we neglect the nuclear tunneling which gives the expression

$$\chi_u = \int_0^{\infty} k(\epsilon_u)\, e^{-\epsilon_u/kT} d\epsilon_u/kT \quad [27]$$

which is similar to [18] and can be calculated in the same way. Thus, we get again expressions [19a, b] with c replaced by

$$c_u = \frac{(2\pi V_{12})^2}{2hF_u}\sqrt{\frac{\mu_u}{2}} = \frac{\pi V_{12}^2}{2h\nu_u\sqrt{E_r^u}} \quad [28]$$

where ν_u is given by Eq. [15] and the corresponding reorganization energy

$$E_r^u = a_u u_0^2 = \frac{\nu_u}{\nu_y^2}(\nu_x E_r^x + \nu_y E_r^y) \quad [29]$$

is determined by the intersection point u_0 of u with the line $y = y_0$.

If the reaction is adiabatic ($\chi_u = 1$) Eq. [26] gives the nuclear tunneling correction which is found to be (1, 2, 7)

$$\kappa_t = \frac{(\pi/2)(T_k/T)}{\sin[(\pi/2)(T_k/T)]}, \quad (T > T_k/2) \quad [30]$$

where T_k is given by Eq. [16a] if $h\nu_u < kT$. The same expression may be used for approximate estimates of κ_t also for $\chi < 1$, although it may be inaccurate when the exchange integral V_{12} is very small. If the resonance splitting is so small that $2V_{12} < h\nu_u$ and $h\nu_u > kT$, the tunneling correction can be estimated by[3]

$$\kappa_t = 1 + \frac{e^{h\nu_u/kT}}{1 + e^{h\nu_u/kT_k}} \quad [31]$$

where T_k is now defined by [16b]. Thus, the formulas [30] and [31] for κ_t and the expressions [19a, b] for χ with [28] and [29] permit an approximate evaluation of the quantum-correction $\kappa_u \simeq \kappa_t\chi_u$ in [25] in the temperature range $2T_k > T > T_k/2$ (1).

The ratio Z_η^H/Z in [25] is given by

$$\frac{Z_\eta^H}{Z} = \frac{1}{Z_u}\, 2\sinh\frac{h\nu_u}{2kT} \quad [32]$$

which is similar to [21].

[3] Under the above conditions κ_t is given approximately by the formula (1)

$$\kappa_t = 1 + \frac{\sum_n^{0,m} W(E_n^u)\, e^{-E_n^u/kT}}{\sum_n^{m+1,\infty} e^{-E_n^u/kT}}, \quad W(E_n^u) = \frac{1}{1 + e^{K(E_n^u)}}$$

where m is the highest energy level below the barrier peak ($E_m < E_c < E_{m+1}$). In the temperature range $2T_k > T > T_k/2$ the main contributions to the above sums are that from the m level (in the nominator) and the $m + 1$ level (in the denominator) so that using [16b] one gets [31].

Using the above expressions, we can calculate the rate constant in the intermediate temperature range. Especially, we obtain for nonadiabatic reactions the approximate expressions

$$k_{12} = \frac{V_{12}^2}{h}\left(\frac{\pi}{E_r^u kT}\right)^{1/2} \frac{(\pi/2)(T_k/T)}{\sin[(\pi/2)(T_k/T)]} e^{-Q_1/kT} e^{-(E_r^u+Q)^2/4E_r^u kT} \quad [33a]$$

if $h\nu_u/kT < 0.5$ and

$$k_{12} = \frac{V_{12}^2}{h}\left(\frac{\pi}{E_r^u kT}\right)^{1/2}\left(1+\frac{e^{h\nu_u/kT}}{1+e^{h\nu_u/kT_k}}\right) e^{-\left(Q_1-\frac{h\nu_u}{2}\right)\Big/ kT} e^{-(E_r^u+Q)^2/4E_r^u kT} \quad [33b]$$

if $h\nu_u/kT > 2$. For adiabatic reactions one gets

$$k_{12} = \nu_u \frac{(\pi/2)(T_k/T)}{\sin[(\pi/2)(T_k/T)]} e^{-(Q_1+E_c^o)/kT} e^{-\frac{Q}{2kT}\left(1+\frac{\gamma_u^2 Q}{8E_{c,u}^o}\right)} \quad [34a]$$

if $h\nu_u/kT < 0.5$ and

$$k_{12} = \frac{kT}{h}\frac{(\pi/2)(T_k/T)}{\sin[(\pi/2)(T_k/T)]} e^{-\left(Q_1+E_c^o-\frac{h\nu_u}{2}\right)\Big/ kT} e^{-\frac{Q}{2kT}\left(1+\frac{\gamma_u^2 Q}{8E_c^o}\right)} \quad [34b]$$

if $h\nu_u/kT > 2$. The conditions of validity of [33] and [34] are certainly compatible with the limits of the intermediate temperature range $2T_k > T > T_k/2$ ($h\nu_u^H > kT > h\nu_u^H/2\pi$) if $\nu_u^H >> \nu_u$.

The presence of a quantum correction of the form $\kappa = \kappa_t\chi$ in [33a, b] takes into account, although approximately, the compensating effect (1) arising from the electron and the nuclear tunneling, related to χ and κ_t, respectively.

The application of the expression [30] or [31] for κ_t implies that the reaction heat varies in the range (1, 7, 11)

$$-4E_{c,u}^o < Q < 4E_{c,u}^o, \quad E_{c,u}^o = \frac{E_r^u}{4} - V_{12} \quad [35]$$

If, however, $Q \sim \pm 4E_{c,u}^o$, then κ_t depends on Q and can be estimated by (7, 11)

$$\kappa_t = \frac{(\pi/2)(T_k/T)}{\sin[(\pi/2)(T_k/T)]} - \frac{T_k/T}{1-(T_k/T)} e^{(T_k/T-2)\delta_o(E_c^u-Q)}, \quad (T > T_k/2) \quad [36a]$$

$$\kappa_t = 2\delta_o(E_c^u - Q)\left[1+\frac{1}{2}\left(\frac{T_k}{T}-2\right)\delta_o(E_c^u-Q) - \dots\right], \quad (T \simeq T\kappa/2) \quad [36b]$$

if $h\nu_u/kT < 1$. Here $\delta_o = \pi^2 d_u\sqrt{2\mu_u E_{c,u}^o}/hE_{c,u}^o$, $d_u = \gamma_u l_u$ is the half-width of a parabolic barrier which approximates the top region of the real barrier $V(u)$ at $Q = 0$, l_u is the half-width of the barrier, E_c^u is the barrier height which is given by [12] with E_c^o replaced by $E_{c,u}^o$ and γ by $\gamma_u = d_u/l_u < 1$. Therefore

$$E_c^u - Q = E_{c,u}^o - \frac{Q}{2}\left(1-\frac{\gamma_u^2 Q}{8E_{c,u}^o}\right) \quad [37]$$

From the above equations one easily gets the corresponding expressions for the Arrhenius parameters [2] and the transfer coefficients [3a, b]. According to [19] and [30] both χ and κ_t are independent of Q, therefore, from [3a, b], [33], and [34]

$$\beta' = \beta = \beta_c = \frac{1}{2}\left(1+\frac{\gamma_u^2 Q}{4E_{c,u}^o}\right) \quad [38]$$

However, near the boundaries of the range [35], using [36] instead of [30], we get different expressions for β' and β, which give us evidence for nuclear tunneling (1, 2a, 7). We thus find that $\beta' > \beta_c$ and $\beta > \beta_c$. For instance, from [3b] and [36b] ($T \gtrsim T_k/2$)

$$\beta = \beta_c + \frac{kT}{E_c^u - Q} \quad [39a]$$

$$\beta' = \beta_c + \frac{\delta_o kT_k}{4}\left(1-\frac{\gamma_u^2 Q}{4E_{c,u}^o}\right) \quad [39b]$$

where β_c is given by [38], $E_c^u - Q > kT$, $|Q| < 4E_{c,u}^o$ and $\gamma_u < 1$. In particular, from [3b] and [39b] it follows that

$$E_a' = Q, \quad \beta_c = 1 - \frac{\delta_o kT_k}{4}\left(1-\frac{\gamma_u^2 Q}{4E_{c,u}^o}\right) \quad \text{for } \beta' = 1 \quad [40a]$$

$$E_a' = 0, \quad \beta_c = -\frac{\delta_o kT_k}{4}\left(1-\frac{\gamma_u^2 Q}{4E_{c,u}^o}\right) \quad \text{for } \beta' = 0 \quad [40b]$$

Equations [40a, b] refer to the so-called barrierless and activationless processes, respectively. Since $|Q| \lesssim 4E_{c,u}^o$ and $\gamma_u < 1$, we see that in [40a] $\beta_c < 1$ and in [40b] $\beta_c < 0$.

A treatment of the intermediate temperature range using the oscillator model has not been given in previous theories of charge transfer in solution. However, the adiabatic case ($\chi = 1$) was actually considered earlier (7, 8) for more general potentials along the reaction coordinate and the main results of these investigations are related to Eq. [34a, b]. The present paper includes also the whole range between adiabatic and nonadiabatic reactions, the latter being represented by [33a, b]. The barrierless and activationless processes are treated here using [36a, b] which permits inclusion of nuclear tunneling, usually neglected in previous considerations (5, 6). In this respect, it should be emphasized (1, 2a, 7) that the difference between the transfer coefficients β and β', defined by [3a, b] is not taken into account by other authors.

The Low Temperature Range ($T < T_k/2$)

If $\nu_x \sim \nu_y$ and $E_r^x \sim E_r^y$, the most probable reaction path will remain that along the normal coordinate u in the low temperature range ($T < T_k/2$) too. Then, Eq. [25] applies again and $\kappa_u = \chi_u\kappa_t^u$ can be estimated using the procedure developed earlier (1).

We consider now the low temperature range by assuming that in [4] $\nu_y >> \nu_x$ and $y_o << x_o$, so that in [6] $E_r^y < E_r^x$. Then, the nuclear tunneling occurs mainly along lines parallel to the y-axis. The most probable reaction path is that which goes initially from the origin of the coordinate system ($x = y = 0$) along x till some point x_{oo} near to x_s, then crosses the saddle parallel to y till the point $x = x_{oo}$, $y = y_o$ and goes further parallel to x until the final state $x = x_o$, $y = y_o$. We, therefore, consider a surface S_r, representing the initial state, which goes through the origin (0,0) along the y-axis. This surface has to be crossed in direction x. The motion along x is assumed to be a quasi-classical one. Equation [1] can be then written as

$$k_{12} = \kappa_x \frac{kT}{h}\frac{Z_y^H}{Z} e^{-E_a/kT} \quad [41]$$

where (2)

$$\kappa_x = \int_{-E_c}^{\infty} k(\epsilon_x) e^{-\epsilon_x/kT} d\epsilon_x/kT,$$

$$k(\epsilon_x) = \sum_n f(\epsilon_n, T) \sum_{n'} k_{nn'}(\epsilon_x) \quad [42]$$

$$f(\epsilon_n,T) = \frac{e^{-\epsilon_n/kT}}{Z_y^H}, \quad Z_y^H = \sum_n e^{-\epsilon_n/kT} \qquad [43]$$

Here $\epsilon_x = E_x - E_c$, $E_x = E_o$ is the initial energy for motion along x; ϵ_n is the vibration energy along y, Z_y^H is the corresponding partition function; $k_{nn'}$ is the transition probability from the initial state n to the final state n'; $k(\epsilon_x)$ is an average value of the total transition probability $k_n = \sum_{n'} k_{nn'}$ over the initial states n.

The summations over n and n' in [42] must be consistent with the conservation of total energy E, for which using [4] we write the equations

$$E_1 = E_x + \epsilon_n = ax^2 + Q_1 + \epsilon_x + \epsilon_n$$

$$E_2 = E_x' + \epsilon_{n'} = a(x - x_o)^2 + Q_2 + \epsilon_x' + \epsilon_{n'} \qquad [44]$$

corresponding to the initial and final states. Setting $E_1 = E_2$, since $\epsilon_x = \epsilon_x'$, we obtain

$$x_{nn'} = \frac{x_o}{2}\left(1 + \frac{Q - (\epsilon_n - \epsilon_{n'})}{ax_o^2}\right), \quad Q = Q_2 - Q_1 \qquad [45]$$

which determines a set of lines $x = x_{nn'} = \text{const.}$, parallel to y, along which tunneling transitions are possible. The set of points $x_{nn'}$ can be defined as a "transition state" configuration.

Since $\nu_y >> \nu_x$, the motion along x is very slow compared with that along y, so that during the passage of a small interval Δx the system is making many vibrations along y both in the reactants and products potential valley. Traveling slowly from the initial state ($x = 0$, $y = 0$) to the transition state ($x_{nn'}$) in the reactant's valley the system remains in the same quantum state (n). Therefore, there also exists an equilibrium energy distribution in the transition state given by [43]. Passing along any of the lines $x_{nn'} = \text{const.}$ in the product's valley, the system could change its vibrational state ($n = n'$) but afterwards moving slowly parallel to x to the final state ($x = x_o$, $y = y_o$) it remains again in the same quantum state (n'). However, because of the slow motion along x, the probability of a nonadiabatic transition ($n \to n'$) is very small. Therefore, we have reasons to assume that no changes of the quantum number n occur in the transition state too, so that $n = n'$. Then, the transition configuration [45] is reduced to a single point

$$x_{nn} = x_{oo} = \frac{x_o}{2}\left(1 + \frac{Q}{E_r^x}\right), \quad E_r^x = ax_o^2 \qquad [46]$$

Hence, there is a unique line $x_{oo} = \text{const.}$, parallel to y, along which all the transitions from the reactant's to product's valley occur (Fig. 1). It results, at these conditions, that throughout the course of reaction the system remains all the time in the same quantum state n, *i.e.*, the reaction is vibrationally adiabatic. This justifies the use of the notion of an "activated complex" as a stationary state configuration, defined by [46]. It should be noted, however that the line $x_{oo} = \text{const.}$, does not pass through the saddle-point Fig. 1, as seen from a comparison between [5] and [46] ($x_{oo} > x_s$). Only when $E_r^y << E_r^x$ ($E_r \simeq E_r^x$), then, according to [6], $x_{oo} \simeq x_s$ and the system crosses the saddle very near to the saddle-point.

The energy profile along the line $x_{oo} = \text{const.}$ (Fig. 3) represents a symmetric barrier, described by the equations

$$V(x_{oo},y) = \begin{cases} V_1(x_{oo},y) = ax_{oo}^2 + by^2 + Q_1 + u_{12}(y), \\ \qquad\qquad (y < y_o/2) \\ V_2(x_{oo},y) = a(x_{oo} - x_o)^2 + b(y - y_o)^2 \\ \qquad + Q_2 + u_{12}(y), \quad (y > y_o/2) \end{cases} \qquad [47]$$

$u_{12}(y)$ being the electron exchange energy. The barrier height is given by

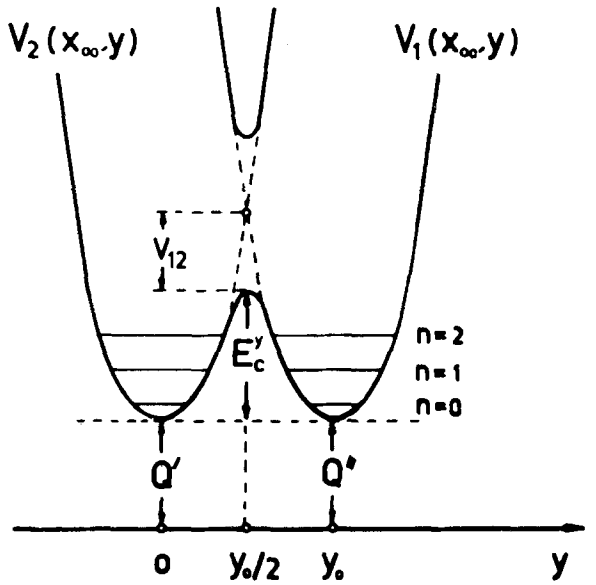


Fig. 3. Energy profile along the line $x_{oo} = \text{const.}$ corresponding to Eq. [47]; $y = 0$ initial and $y = y_o$ final configuration for tunneling parallel to y. $Q' = ax_{oo}^2 + Q_1$ and $Q'' = a(x_{oo} - x_o)^2 + Q_2$ are equal ($Q' = Q''$); V_{12} electronic exchange energy at the intersection point ($y = y_o/2$) of the unperturbed ($u_{12} = 0$) potential curves [47]; E_c^y is the barrier height given by [48].

$$E_c^y = \frac{E_r^y}{4} - V_{12}, \quad E_r^y = by_o^2 \qquad [48]$$

where $V_{12} = u_{12}(y_o/2)$, so that $2V_{12}$ is the resonance splitting at the crossing point ($y = y_o/2$) of the unperturbed parabolic curves [47] ($u_{12} = 0$).

The vibrational adiabatic, involved in the above definition of the activated complex, allows one to assume an identical equilibrium energy distribution in the two symmetrical potential wells on both sides of the barrier [48]. The distribution function is given by [43], hence the partition function Z_y^H, which refers to the initial state, can be related to the transition state as well.

The adiabatic condition $n = n'$ requires that in [42]

$$k_{nn'}(\epsilon_x) = 0 \text{ for } n \neq n';$$

$$k_{nn'}(\epsilon_x) = k_{nn}(\epsilon_x) \neq 0 \text{ for } n = n' \qquad [49]$$

Then [41] can be considered as a generalized expression of activated complex theory which includes a relevant quantum correction κ_x (2b). The adiabatic justification of the usual classical equation ($\kappa_x = 1$) of this theory (12, 13) allows one to describe the slow motion along the reaction coordinate x by a potential function

$$V_n(x) = \begin{cases} V_1(x) + \epsilon_n + u_{nn}(x) = ax^2 + Q_1 \\ \quad + \left(n + \frac{1}{2}\right)h\nu_y + u_{nn}(x), \quad (x < x_{oo}) \\ V_2(x) + \epsilon_n + u_{nn}(x) = a(x - x_o)^2 + Q_2 \\ \quad + \left(n + \frac{1}{2}\right)h\nu_y + u_{nn}(x), \quad (x > x_{oo}) \end{cases} \qquad [50]$$

which involves the electronic energy $V_{12}(x)$ and the energy ϵ_n of the fast vibration along y, including some resonance energy $u_{nn}(x)$, assumed to be large, which is necessary for the adiabatic transition to occur (Fig. 4).

Equation [50] represents a set of potential curves corresponding to the different vibrational states n. These potentials may be used also when considering the quantum effects, *i.e*, the nuclear tunneling along x and the nonadiabatic transitions which can take place only at the "intersection" point x_{oo} of each pair of

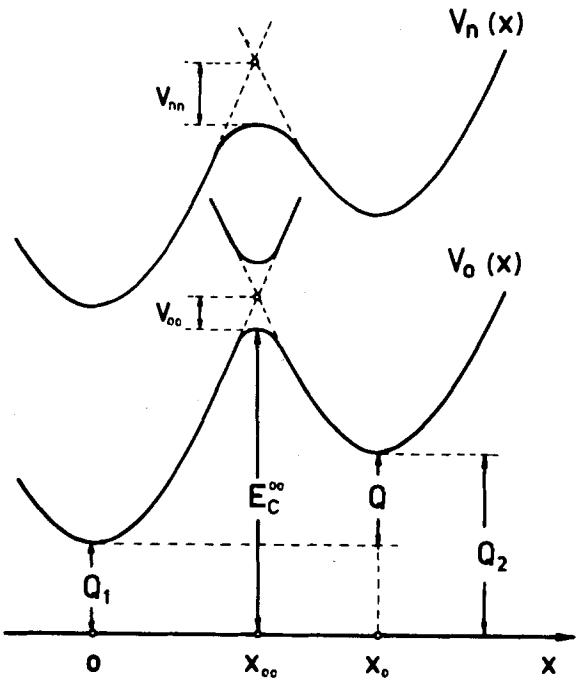


Fig. 4. Adiabatic potential curves corresponding to Eq. [50] ($n = 0$ and $n = n$); $x = 0$ initial and $x = x_0$ final configuration. V_{nn} is the resonance energy [57] at the crossing point ($x = x_{oo}$) of the unperturbed ($u_{nn} = 0$) potential curves [50]. (Note that $V_{nn} > V_{oo}$); E_c^{oo} is the height [53] of the ground state ($n = 0$) potential barrier for the endothermic transfer direction ($0 \rightarrow x_0$); $Q = Q_2 - Q_1$ heat of reaction.

curves [50], corresponding to a given n, if the resonance splitting is not very large.

Using [49] from [41]-[43] we obtain

$$k_{12} = \frac{kT}{hZ} \sum_n \kappa_n e^{-E_c^{nn}/kT} \qquad [51]$$

with

$$\kappa_n = \int_{-E_c^{nn}}^{\infty} k_{nn}(\epsilon_x^n) e^{-\epsilon_x^n/kT} d\epsilon_x^n/kT \qquad [52]$$

$$E_c^{nn} = ax_{oo}^2 + \epsilon_n - V_{nn} + Q_1 \qquad [53]$$

where $\epsilon_x^n = E_x - E_c^{nn}$, E_c^{nn} is the height of any of the potential barriers [50], $2V_{nn} = 2u_{nn}(x_{oo})$ being the resonance splitting at the corresponding crossing point. Setting $\kappa_n = 1$, one gets from [51] a classical rate equation which is related to the Eyring's expression of transition state theory (12b).

To calculate the quantum factors κ_n in [51] we first assume a classical motion along x, *i.e.*

$$k_{nn} = 0 \text{ for } \epsilon_x^n = 0 \quad (E_x < E_c^{nn});$$

$$k_{nn} \neq 0 \text{ for } \epsilon_x^n > 0 \quad (E_x > E_c^{nn}) \qquad [54]$$

so that [52] turns into

$$\chi_n = \int_0^{\infty} k_{nn}(\epsilon_x^n) e^{-\epsilon_x^n/kT} d\epsilon_x^n/kT \qquad [55]$$

which is similar to [18] and [27]. The transition probability k_{nn} involves now the nuclear tunneling only along the line $x_{oo} = \text{const.}$, parallel to y, with a simultaneous rearrangement of the electronic state. This suggests (1, 5) to use again the Landau-Zener theory (9), which leads to the expressions [19] with c replaced by

$$c_{nn} = \frac{(2\pi V_{nn})^2}{2hF_{nn}} \sqrt{\frac{\mu_x}{2}} = \frac{\pi V_{nn}^2}{2h\nu_x \sqrt{E_r^x}} \qquad [56]$$

where

$$V_{nn} = \int \psi_n^{(1)}(y) V_{12} \psi_n^{(2)}(y) dy \qquad [57]$$

is the exchange integral expressed in terms of the wave functions of the y-vibrations in the two potential wells of the "transition state" ($x_{oo} = \text{const.}$) and the electronic resonance energy $V_{12} = u_{12}(y_o/2)$ at the intersection point of the curves [47].

The exchange integral V_{nn} can be used as a matrix element to calculate the transition probability W_{nn} along $x_{oo} = \text{const.}$ in the framework of first-order perturbation theory, which gives (1)

$$W_{nn} = \left(\frac{2\pi V_{nn}}{h\nu_y}\right)^2 << 1 \qquad [58]$$

Alternatively, W_{nn} can be represented as

$$W_{nn} = W_e(\epsilon_n) W(\epsilon_n) \qquad [59]$$

where $W_e(\epsilon_n)$ and $W(\epsilon_n)$ are the probabilities of electron and nuclear rearrangement, respectively. We see from [58] that $W_{nn} << 1$ when either V_{nn} is small or $h\nu_y$ is large and from [59] that $W_{nn} << 1$ when either $W_e(\epsilon_n) << 1$ or $W(\epsilon_n) << 1$. From [58] and [59]

$$V_{nn}^2 = \left(\frac{h\nu_y}{2\pi}\right)^2 W_e(\epsilon_n) W(\epsilon_n) \qquad [60]$$

If $W(\epsilon_n) << 1$ and $0 \lesssim W_e(\epsilon_n) \lesssim 1$, we can use the expressions[4] (14)

$$W_e(\epsilon_n) = \frac{2\pi}{\gamma_n \Gamma^2(\gamma_n)} e^{-2\gamma_n(1 - \ln \gamma_n)},$$

$$\gamma_n = \frac{V_{12}^2}{2\pi h\nu_y} \left[\frac{\pi^2}{E_r^y(E_r^y/4 - \epsilon_n)}\right]^{1/2} \qquad [61]$$

and (1)

$$W(\epsilon_n) = e^{-K(\epsilon_n)},$$

$$K(\epsilon_n) = \frac{4\pi\sqrt{2\mu_y}}{h} \int_{y_1}^{y_2} \sqrt{V(x_{oo}, y) - \epsilon_n}\, dy \qquad [62a]$$

$$W(\epsilon_n) = \frac{h}{4\mu_y \nu_y} \left(\psi_n^{(2)} \frac{d\psi_n^{(1)}}{dy} - \psi_n^{(1)} \frac{d\psi_n^{(2)}}{dy}\right)_{y = y_0/2} \qquad [62b]$$

The quasi-classical formula [62a] has been treated in (1) where $K(\epsilon_n)$ is calculated exactly with the potential [47] at condition that $V_{12} << E_r^y/4$. The more accurate current density expression [62b] is also evaluated exactly, at the same condition, using the harmonic oscillator wave functions (1). The agreement between both formulas is quite good in a large range of variation of the ratio $E_r/h\nu$ (between 10 and 100). The condition $W(\epsilon_n) << 1$ is practically fulfilled if $K(\epsilon_n) > 2$ (14b) which corresponds to $\epsilon_n << E_r^y/4$. This allows one to use [61] with the approximation $\gamma_n \simeq \gamma_o$, *i.e.*

$$W_e(\epsilon_n) \simeq W_e(\epsilon_o), \quad \gamma_n \simeq \gamma_c \simeq \frac{V_{12}^2}{h\nu_y E_r^y} \qquad [61']$$

If $W_e(\epsilon_n) << 1$ and $0 \lesssim W(\epsilon_n) \lesssim 1$ one may use the approximations

$$W_e(\epsilon_n) = 2\pi\gamma_n \qquad [63]$$

$$W(\epsilon_n) = \frac{1}{1 + e^{K(\epsilon_n)}} \qquad [64]$$

[4] Using linear approximation for the potential curves $V_1(y)$ and $V_2(y)$ in their intersection region, the transfer probability is found [14] to be a product $W = W_e W_n$ of two factors, corresponding to electron and nuclear rearrangement, given by [61] and [62a], respectively. The use of these expressions in the low energy range is justified also for the parabolic potentials [47]. One obtains, indeed, for $\gamma_n << 1$, using expressions [63] and [61']

$$W_e(\epsilon_n) \simeq 2\pi\gamma_o = 2\pi V_{12}^2/h\nu_y E_r^y$$

which just coincides with the factor in Eq. [51] in Ref. (4b) related to the harmonic oscillator model. For $\gamma_n >> 1$, $W_e(\epsilon_n) = 1$ and $W(\epsilon_n)$ is again correctly given by [62a]. This suggests that [61] and [62a] may be used for any intermediate value of γ_n ($\gamma_n \gtrless 1$) too.

the first one being obtained from [61] for $\gamma_n << 1$ and the second one is a generalization of [62a] (15, 16).

In this way using [60] to [64] we are able to estimate the exchange integrals [57] for all n consistent with the condition $W_{nn} << 1$. Thus, by means of [56] the transmission coefficients [55] can be evaluated for all values of c_{nn}^2/kT, *i.e.*, for the whole range $0 \leq \chi_n \leq 1$ for which the formulas [19a, b] are applicable.

If $\chi_n = 1$ [*i.e.*, $(c_{nn}^2/kT)^{1/3} > 1$], then κ_n in [51] will represent the nuclear tunneling correction to be calculated by [52] using the potential functions [50]. This has been actually done (1) for arbitrary temperatures both for $h\nu < kT$ and $h\nu > kT$. In particular, if $h\nu_x < kT$, in the region of moderate tunneling along x ($T > T_k/2$) we may use an expression like [30], in which T_k is replaced by

$$T_k^n = \frac{h\nu_{x,n}^H}{\pi k} \qquad [65]$$

$\nu_{x,n}^H$ being determined for any potential $V_n(x)$ by the curvature of the barrier top ($x = x_{oo}$). Expressions for the large tunneling region ($T < T_k^n/2$) are available too (1). The full quantum corrections κ_n in [51] can be estimated approximately by the product[5] $\kappa_n \simeq \kappa_t^n \chi_n$ for any values of χ_n ($0 < \chi_n \leq 1$).

Retaining only the first term ($n = 0$) in [51], by assuming that $h\nu_x/kT < 0.5$ and $h\nu_y/kT > 2$, one gets

$$K_{12} = \nu_x \kappa_o e^{-(E_c^{oo})/kT} \qquad [66]$$

If $T > T_k^o/2$, this expression with [19], [30], [56], [60], [61], [62b], and [65] yields

$$K_{12} = \frac{V_{12}^2}{h}\left(\frac{\pi}{E_r^x kT}\right)^{1/2} e^{-E_r^y/h\nu_y} \frac{(\pi/2)(T_k^o/T)}{\sin[(\pi/2)(T_k/T)]} e^{-Q_1/kT} e^{-(E_r^x+Q)^2/4E_r^x kT} \qquad [67]$$

for nonadiabatic reactions ($\chi_o << 1$) and

$$K_{12} = \nu_x \frac{(\pi/2)(T_k/T)}{\sin(\pi/2)(T_k/T)} e^{-(Q_1+E_{c,x}^o)/kT} e^{-\frac{Q}{2kT}\left(1+\frac{\gamma_x^2 Q}{4E_{c,x}^o}\right)} \qquad [68]$$

for adiabatic reactions ($\chi_o = 1$), where $E_{c,x}^o = E_r^x/4 - V_{oo}$, $\gamma_x = 2d_x/x_o$, $2d_x$ is the width of a parabolic barrier approximating the barrier [50], $V_0(x)$, near its top. Expressions for the intermediate range of χ_o ($0 < \chi_o < 1$) can be easily derived from [66] using [19] and [56].

The parameters [2] of the Arrhenius equation can be calculated from the above rate equations. In the normal range of variation of Q

$$-4E_{c,x}^o < Q < 4E_{c,x}^o, \quad E_{c,x}^o = E_r^x/4 - V_{oo} \qquad [69]$$

we find again that the transfer coefficients [3a, b] are equal ($\beta' = \beta = \beta_c$) and can be expressed by [38] by replacing $E_{c,u}^o$ by $E_{c,x}^o$ and γ_u by γ_x. Near the limits of the range [69], using [36] with T_k^o instead of T_k, one gets equations similar to [39] and [40], which refer to the barrierless and activationless processes in the low temperature range ($T < T_k/2$).

If $T > 2T_k^o$, according to [30] $\kappa_t^o \simeq 1$. Then, the formula [67] turns into an expression which has been first derived by Dogonadze and Kuznetsov (6). The presence of the factor κ_t^o in [67] takes into account for the compensation effect between electron tunneling and nuclear tunneling in nonadiabatic reactions (1). Equations related to [68], which refer to adiabatic reactions have been obtained earlier (7, 8) using arbitrary potentials along the reaction coordinate. In the work of Dogonadze and Kuznetsov (6) the oscillator model is used to derive a classical equation ($\kappa_o = 1$) for adiabatic processes, however, not any explicit relation $E_a(Q)$ between activation energy and heat of reaction is found in that derivation.

[5] See Ref. (1). Note added in proof.

Discussion

The harmonic oscillator model has been first used by Marcus (3a), Levich and Dogonadze (4), to describe the role of the polar solvent in outer sphere electron transfer processes using dielectric continuum theory. Subsequently, the changes of the inner coordination shell have been taken into account by Marcus (3b, c) by making use of the potential energy surfaces. His treatment is essentially based on the classical activated complex theory and is mainly concerned with adiabatic reactions.

The proton transfer processes have been investigated by the present author from point of view of quantum mechanics in a series of papers (7, 8, 10, 15). Initially, use has been made of a rectilinear reaction coordinate, *i.e.*, a one-dimensional potential barrier which involves the interactions of the proton with all surrounding particles (including solvent molecules).[6] Later, a curvilinear reaction coordinate has been considered in the frame of a many dimensional treatment (7a, b, c) which includes all degrees of freedom of the system. On the basis of a recent formulation of reaction rate theory 2) a reconsideration of the previous results of the author's work has been made (7c).

Dogonadze *et al.* (5, 6) have used an oscillator model to treat the proton transfer and, in a similar way, the influence of the inner coordination shell on the electron transfer (6). In that model, an effective low frequency vibration, describing the solvent polarization in terms of continuum theory, is treated classically, while another high frequency (proton) vibration is treated quantum-mechanically. Use is made of first-order perturbation theory and the Franck-Condon approximation, by assuming that the proton transfer takes place at a fixed point of the solvent coordinate. A related modified approach is recently employed by Schmickler (18) in considering redox reactions at electrodes.

The present paper provides a complete treatment, not made in earlier work, of the two-frequency oscillator model for charge transfer. It differs essentially from previous quantum theories (3-6, 18) by using a general method based on a recent formulation of chemical kinetics (2), which overcome the limitations of these theories. In this way, it has been possible to consider the whole range between the limits of adiabatic and nonadiabatic reactions without any restriction concerning nuclear tunneling. Three temperature ranges, corresponding to negligible, moderate, and large tunneling, have been investigated using suitable approximations. The results of the previous treatments of the oscillator model are obtained as special cases as discussed earlier in this paper.

The harmonic approximation for the high frequency vibration does not lead to any limitation of the rate equations obtained. Indeed, the second term in Eq. [4] can be replaced by the expression of a Morse-like potential without changing the following derivations.

The work of Dogonadze *et al.* (5, 6) refers either to the high temperature range ($T > 2T_k$) of nonadiabatic reactions ($\chi << 1$) or to the low temperature range ($T < T_k/2$) of both adiabatic and nonadiabatic reactions ($\chi = 1$ and $\chi << 1$) with the limitation of a classical motion along the solvent coordinate. In that treatment use is made of a harmonic approximation for the proton vibration or, instead, at low temperatures, a "double adiabatic approximation" is used, which consists in including the ground-state energy of the proton into the electronic energy in order to obtain an effective potential governing the motions of the solvent oscillators. Evidently, this is essentially the approach used before by Hirschfelder *et al.* (11) to give a justification of Eyring's transition state theory. However, in addition, account is taken by Dogonadze *et al.* of the nonadiabatic transitions, which are neglected in that justification.

[6] The statement of Dogonadze *et al.* (17) that in the author's work the role of the solvent is entirely ignored is completely misleading. A comment of this point is given elsewhere (18).

Our treatment of the low temperature range, giving expression [51], represents a generalization of the procedure of Hirschfelder *et al.* (12) which permits the inclusion of quantum effects (nuclear tunneling and electronically nonadiabatic transitions) in a vibrationally adiabatic derivation of the equation of activated complex theory. The result of Dogonadze *et al.* (5, 6) is a particular case of formula [51] in which only the first term ($n = 0$) is taken into account and $\kappa_0 \gtrsim 1$ is replaced by $\chi_0 << 1$ to obtain [67] with $\kappa_t^0 = 1$ ($T > T_k^0/2$).

The restriction to the nonadiabatic proton transfer ($\chi_0 << 1$) is, however, not in accordance with the Tafel equation of electrode kinetics which is known to be valid for hydrogen evolution in a very wide range $\Delta\psi$ of electrode potentials ($\Delta\psi \gtrsim 1$V). Equation [67] does not give, indeed, a linear relationship ln k_{12} *vs.* $Q = e_c(\psi - \psi_0)$ (4). In this respect [68], which refers to adiabatic reactions ($\chi_0 = 1$), is certainly to be preferred because of the presence of the factor $\gamma_x < 1$ in the exponent which is shown to be responsible for the practical validity of the Tafel relation (7b, 8).

The restriction to the ground-state proton vibration in [51] is apparently justified as far as $h\nu_y/kT >> 1$.[7] It means that no change of the A-H$^+$ bond length occurs, and consequently, the activation energy in [67] and [68] involves only the reorganization of the solvent. This result disagrees, however, with the well-known experimental fact that the isotope substitutions affect the observed activation energy (20). We, therefore, conclude that either the oscillator model, in general, or at least the above limitation to the ground-state vibration of the proton is not adequate to the real situation in most cases.[7]

The oscillator model is certainly very useful, because of its inherent simplicity, for a quantitative description of the role of the solvent in charge transfer reactions. It appears, however, that it greatly overestimates the part played by the solvent in the activation process. The main imperfection of the model seems to be that it neglects the translation and rotation motions of reactants and solvent molecules (1, 3c). A more complete treatment should take into account, at least for the relative translation of reactants, which would lead to a curvelinear (nonseparable) reaction coordinate, crossing the saddle of the potential surface. Using two dimensional models for gas phase reactions of the type AH + B → A + HB it has been shown (21) that there is a considerable stretching of the A-H bond in the transition region where tunneling mainly occurs. It is plausible that this situation takes place in proton transfer in solution, too. A dynamical description of the process then requires a three-dimensional potential surface but a full quantitative treatment of such a more complicated model seems to be very difficult.

However, it has been shown (7) that in the region of moderate tunneling, rate expressions of the form [33] and [34] can be derived on the basis of [1] for any arbitrary many dimensional system. It should be emphasized that different definitions of the quantum corrections κ_t and χ are valid if instead of [1] a formally similar generalized expression of activated complex theory is used (2b). Only when the reaction coordinate is completely separable both formulations become identical.

These considerations may contribute to a clarification of a much discussed question concerning the role of nonequilibrium solvent polarization in proton transfer processes (4-7, 22, 23). Our treatment of the oscillator model shows that a fluctuation of the solvent would be necessary to make possible the proton transfer only in the low temperature range provided that the transfer distance is relatively small ($y_0 << x_0$), the proton vibration frequency being very high ($\nu_y >> \nu_x$). However, in the intermediate and high temperature ranges the orientation of the solvent molecules keep pace with the proton transfer. Consequently, the irreversible polarization may be important if $T < T_k/2$, while reversible polarization takes place if $T > T_k/2$. These conclusions are likely to be valid for more general barrier models for charge transfer too.

An analysis of the experimental facts concerning isotope effects shows (7) that the tunneling correction to Eyring's rate equation can usually be estimated by the formula [30], which is valid for $T > T_k/2$, T_k being defined by [16a] in terms of the curvature of the barrier along the reaction coordinate just at the saddle-point of the many dimensional potential surface (2, 7). Therefore, the intermediate temperature range is the most important one for proton transfer reactions and probably for redox processes involving high frequency vibrations in the inner coordination shell for which, as discussed above, an equilibrium polarizaton of the solvent medium in the transition state is likely to take place. There are, however, a number of reactions with anomalously large isotope effects (20a) which certainly occur in the low temperature range ($T < T_k/2$). Just for such reactions a more complicated, many dimensional model is needed, which may involve in a large extent nonreversible polarization of the solvent.

The oscillator model considered in this paper is probably adequate to the situation in some solid-state electron and proton transfer processes, where translations and rotations in the medium are strongly restricted. It would be interesting, for instance, to treat on the basis of this model the proton conductance of ice as well as some proton transfer reactions for which extremely large kinetic isotope effects have been observed (20a).

Finally, it should be noted that there is no great difficulty in treating a more general oscillator model, which involves a set of low frequencies and another set of high frequencies, in the same way as the two-frequency model considered in the present paper.

Manuscript received Feb. 25, 1976.

Any discussion of this paper will appear in a Discussion Section to be published in the December 1977 JOURNAL. All discussions for the December 1977 Discussion Section should be submitted by Aug. 1, 1977.

[7] According to [51]-[53] the contribution of each vibrational state n is determined by the product of two factors: the one $\kappa_n \exp V_{nn}/kT$ increases and the other $e^{-\epsilon_n/kT}$ decreases with n. The first factor involves the proton transfer probability [62], which depends very sensitively on the transfer distance y_0. Assuming $y_0 \simeq 0.5$-1A one finds that the term $n = 0$ is the most important in the sum [51]. Replacing the parabolic potentials by Morse-like potentials leads to a more rapid increase of the transfer probability with increasing n, *i.e.*, to a larger contribution of the excited states of the proton.

REFERENCES

1. S. G. Christov, *Ber. Bunsenges. Phys. Chem.*, **79**, 357 (1975).
2. S. G. Christov, (a) *ibid.*, **76**, 507 (1972); (b) *ibid.*, **78**, 537 (1974).
3. R. A. Marcus, (a) *J. Chem. Phys.*, **24**, 966 (1956); (b) *Discuss. Faraday Soc.*, **29**, 21 (1960); (c) *Ann. Rev. Phys. Chem.*, **15**, 155 (1964).
4. V. G. Levich and R. Dogonadze, (a) *Dokl. Akad. Nauk SSSR*, **124**, 123 (1959); **133**, 158 (1960); (b) *Collect. Czech. Chem. Commun.*, **26**, 193 (1961).
5. R. Dogonadze, A. Kuznetsov, and V. G. Levich, *Electrochim. Acta*, **13**, 1025 (1968).
6. R. R. Dogonadze and A. M. Kuznetsov, in "Ithogi nauki i techniki," Vol. 2, Kinetics, Moscow (1973).
7. S. G. Christov, (a) *J. Res. Inst. Catal. Hokkaido Uni.*, **16**, 169 (1968); (b) *Zh. Fiz. Khim.*, **XLII**, 1553 (1968); (c) *Croat. Chem. Acta*, **44**, 67 (1972).
8. S. G. Christov, *Ber. Bunsenges. Phys. Chem.*, **67**, 117 (1963).
9. L. Landau and E. Lifshitz, "Quantum Mechanics," Nauka, Moskva (1974).
10. (a) D. B. Bates, *Proc. R. Soc. London, Ser. A*, **257**, 22 (1960); (b) C. A. Coulson and K. Zalewski, *ibid.*, **268**, 437 (1962).
11. S. G. Christov, (a) *Z. Electrochem.*, **64**, 840 (1960); (b) *Ann. Phys. (Leipzig)*, **15**, 87 (1965).
12. (a) J. O. Hirschfelder and E. Wigner, *J. Chem. Phys.*, **7**, 616 (1939); (b) M. A. Eliason and J. O. Hirschfelder, *ibid.*, **30**, 1426 (1959).

13. L Hofacker, *Z. Naturforsch., Teil A*, **18**, 607 (1963); R. A. Marcus, *J. Chem. Phys.*, **46**, 959 (1967); K. J. Laidler and A. Tweedale, in "Chemical Dynamics," Vol. 21, p. 113, John Wiley & Sons, New York (1971).
14. M. Ovchinnikova, *Dokl. Akad. Nauk SSSR*, **161**, 641 (1965); *Opt. Spektrosk.*, **17**, 821 (1964).
15. S. G. Christov, (a) *Z. Electrochem.*, **62**, 567 (1958); **64**, 840 (1960); (b) *Ann. Phys. (Leipzig)*, **12**, 20 (1963); **15**, 87 (1965); *Phys. Status Solidi*, **42**, 583 (1970).
16. (a) E. Kemble, "Fundamental Principles of Quantum Mechanics," 2nd ed., New York (1958); (b) R. P. Bell, *Trans. Faraday Soc.*, **55**, 1 (1959).
17. R. R. Dogonadze and A. M. Kuznetsov, *J. Res. Inst. Catal. Hokkaido Uni.*, **22**, 93 (1974).
18. S. G. Christov, *ibid*, In press.
19. W. Schmickler, *Ber. Bunsenges. Phys. Chem.*, **77**, 991 (1973).
20. (a) R. P. Bell, *Chem. Soc. Rev.*, **3**, 513 (1974); (b) B. Post and C. F. Hiskey, *J. Am. Chem. Soc.*, **72**, 4203 (1950); **73**, 161 (1951).
21. S. G. Christov and Z. L. Gueorguiev, *ibid.*, **75**, 1748 (1971).
22. R. P. Bell, *Discuss. Faraday Soc.*, **39**, 16 (1965).
23. E. F. Caldin, *Chem. Rev.*, **69**, 135 (1969).

Electrochemical Studies of Mass Transport in High Temperature Electrolytes

C. E. Vallet

Laboratoire de Thermodynamique des Sels Fondus, Universite de Provence, 13397 Marseille, France

and J. Braunstein*

Oak Ridge National Laboratory, Chemistry Division, Oak Ridge, Tennessee 37830

ABSTRACT

Chronopotentiometry with electromigrational depletion (ED) is applied to the evaluation of interdiffusion coefficients in the binary molten salt mixtures 53-47, 65-35, and 70-30 BeF_2-LiF. The effect of composition dependence on the measured values of the diffusion coefficients is discussed for these mixtures and for $AlCl_3$-NaCl mixtures. The method of analysis of the chronopotentiograms is applicable also to the evaluation of mass transfer polarization in high temperature battery electrolytes.

A number of proposed high temperature battery systems employ electrolytes which are complex (1, 2) or polymeric (3, 4), or in which complex or polymeric species are formed. In such systems appreciable changes of mass transport properties occur during charge or discharge. With increasing temperature, electrode kinetics become more rapid, activation polarization decreases, and mass transfer polarization may become a significant factor in the rate of charge and discharge of high temperature batteries. Consequently, reliable values of transport parameters are needed for design and modeling studies. Among needed transport coefficients are the interdiffusion coefficients, which may undergo considerable changes of magnitude with electrolyte composition change, and which are difficult to determine in electrolytes at high temperatures, particularly in viscous melts. The classical methods for determination of diffusion coefficients in liquids, such as the capillary, diaphragm, and NMR spin-echo measurements, are difficult to apply at elevated temperatures and in viscous systems.[1] While pulsed spin-echo measurements may extend the applicability of the NMR method, this method requires nuclei of appropriate spin and, in any case, leads to self-diffusion coefficients rather than interdiffusion coefficients. Electrochemical scanning methods such as polarography, chronopotentiometry, and linear sweep voltammetry have been employed frequently to obtain diffusion coefficients in electrolytes, both at room temperature and at elevated temperatures. With few exceptions, however, these methods are employed with low concentrations of solute ions under conditions such that electrical migration of the electroactive species is suppressed, thus providing only the limiting interdiffusion coefficient at vanishing solute concentration, which is the solute self-diffusion coefficient.

We have shown (5, 6) that electrochemical scanning methods for the measurement of diffusion coefficients need not be restricted to dilute solute ions, and we have employed anodic chronopotentiometry with beryllium electrodes in molten beryllium fluoride-lithium fluoride mixtures containing between 5 and 22 mole percent (m/o) lithium fluoride. Equations have been developed, with the thermodynamics of irreversible processes, to identify the interdiffusion coefficient in this binary system under conditions of simultaneous diffusion and electrical migration. Computations have been developed to obtain mean values of interdiffusion coefficients and to resolve the composition dependent interdiffusion coefficients. The method, with suitable modification for specific systems, should be useful for studying contributions to mass transfer polarization on charge and discharge at electrodes in high temperature battery systems.

We have used the term electromigrational depletion (ED) chronopotentiometry to describe the application of chronopotentiometry to binary melts such as LiF-BeF_2 since the anodic chronopotentiometric transition with an electrode such as beryllium could be attributed to depletion of Li^+ from the anode region via migration, rather than to depletion of an electroactive constituent via the faradaic process, which is responsible for the transition in ordinary chronopotentiometry. We have shown the transference number of Be^{2+} relative to fluoride ions to be zero (and consequently that of Li^+ to be unity) over the composition range between 20 and 80 m/o BeF_2 (7). Our previous measurements have been mainly at higher BeF_2 concentrations, where

* Electrochemical Society Active Member.

Key words: molten fluorides, molten chloroaluminates, mass transfer polarization, interdiffusion, high temperature battery.

[1] Recently reported capillary-tracer measurements of fluoride self-diffusion in molten $LiBeF_3$ lead to unusually high diffusivity and Arrhenius energy (16).

it was presumed that the transference number remained constant and equal to unity. However, it could not be ascertained that the apparent composition dependence of the diffusion coefficients did not include also some concentration dependence of transference numbers. In this paper we present the results of chronopotentiometric measurements in LiF-BeF_2 melts of composition 53, 65, and 70 m/o BeF_2, for which the transference number of Li^+ is known to be constant and equal to unity; these measurements therefore constitute a valid application of ED chronopotentiometry. We show that, although the chronopotentiograms reflect the variation of the interdiffusion coefficient with concentration from the bulk composition to pure BeF_2, analysis of the early portions of the chronopotentiograms, corresponding to melts of compositions close to the bulk composition, yields the interdiffusion coefficient in the bulk melt. In addition to this application of chronopotentiometry to the polymeric melt, BeF_2-LiF, we discuss its application to the complex melt NaCl-$AlCl_3$ and to melts with normal composition-dependent transference numbers, such as $NaNO_3$-$AgNO_3$.

Experimental

The cells, electrodes, purification of materials, and the experimental procedure have been described previously (5). Chronopotentiograms in the 70 m/o BeF_2, 65 m/o BeF_2, and 53 m/o BeF_2 LiF-BeF_2 melts were recorded with a Hewlett-Packard 141A storage oscilloscope and photographed with a Polaroid camera, rather than recorded on a chart recorder. In these mixtures all of the chronopotentiograms were shorter than 10 sec and some were shorter than 1 sec. In order to avoid convection, faster chronopotentiograms were required than in our previous measurements in the more viscous BeF_2-rich melts.

Figure 1 shows a typical chronopotentiogram, obtained in 53 m/o BeF_2 at 380°C. The initial increase of potential is very fast and has been shown (5, 6) to correspond to the *IR* drop for melt of the bulk composition. Because the electrode configuration was not designed to provide a suitable conductance cell, the measurements provide only a relative electrical conductance. However, as shown previously (6), the temperature dependence of the relative conductance, $I/(IR)$, leads to activation energies for conductance consistent with those obtained from directly measured electrical conductance in these melts (8).

The final portion of the chronopotentiogram appears to rise sharply. As will be seen from the discussion to follow, however, the apparent sharpness of the transition may be deceptive. In any case, since the transition corresponds to the composition of nearly pure BeF_2 at the working electrode, and since the diffusion coefficient may be strongly composition dependent, this transition time is not related simply to the diffusion coefficient in the melt of the bulk composition. Rather, the transition time corresponds to a weighted mean diffusion coefficient over the range of compositions varying between the bulk composition and pure beryllium fluoride (6).

At the lowest temperature (380°C), noisy chronopotentiograms such as the one in Fig. 2 were sometimes obtained when low current densities were used. At higher temperatures, even with chronopotentiograms of similar duration (10 sec) to those in the more viscous melts at 380°C, the chronopotentiograms are reproducible and not noisy. Therefore convection probably is not the cause of the noise. The appearance of the noise rather seems related to the slow scanning of composition at low temperature. As the concentration of BeF_2 near the anode increases, the liquidus temperature of the mixture becomes much higher than the temperature of the melt, and solid BeF_2 may precipitate in the vicinity of the working electrode. Similar behavior has been reported by Gilbert *et al.* (9) for anodic chronopotentiometry at an Al electrode in $AlCl_3$-NaCl mixtures. This behavior has not been further investigated, but could prove useful in studies of nucleation and precipitation kinetics.

Analysis of Chronopotentiograms

The analysis of the experimental results must differ from that of ordinary chronopotentiometry. Ordinary chronopotentiometry is applied to very dilute solutions of an electroactive constituent and consequently leads to the self-diffusion coefficient of the dilute constituent. As we have shown previously in ED chronopotentiometry of LiF-BeF_2 mixtures (5, 6) and NaF-BeF_2 mixtures (10), a large range of concentration is spanned and the measurements lead to the mutual diffusion coefficient of Li and Be and of Na and Be. At long times there is a greater difference between the properties of the melt at the indicator electrode and the properties of melt of bulk composition in ED than in ordinary chronopotentiometry. Thus in ED chronopotentiometry of a 50 m/o BeF_2 melt, the composition changes to nearly pure BeF_2 at the indicator electrode. The viscosities (11) change from 0.27 P to 7.63×10^5 P at 600°C and there are comparable differences in electrical conductance. Since the equations have been derived previously, we here give only the essential results.

The potential difference between the reference and working or indicator electrodes may be broken into two parts: a resistive term (*IR*) and the emf of a concentration cell with transference. In a melt MA-$M'A_n$ (such as LiF-BeF_2 or NaCl-$AlCl_3$) where M'^{n+} is the cation produced by the faradaic process at the indicator

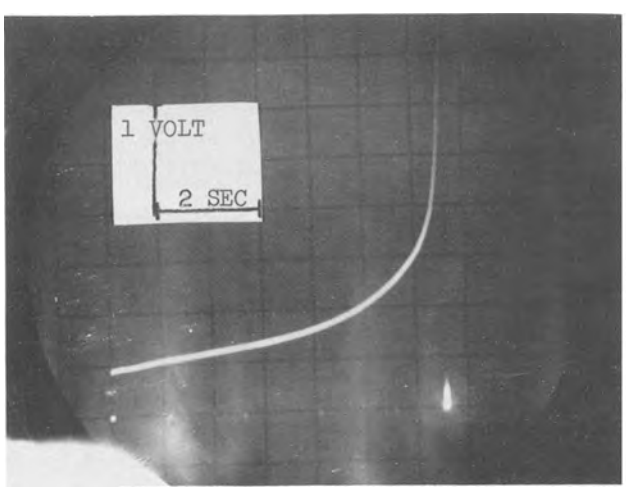


Fig. 1. Typical chronopotentiogram, in 53 m/o BeF_2 melt at 380°C with current density of 1.26 A/cm². EMF at working electrode *vs.* time.

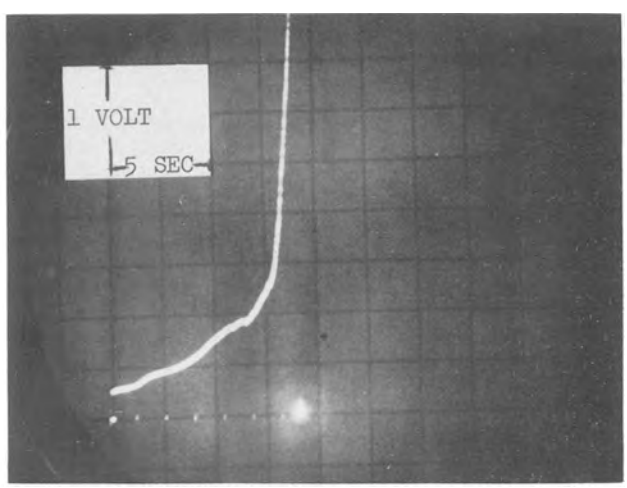


Fig. 2. Noisy chronopotentiogram at slow scan rate in 53 m/o BeF_2 melt at 380°C with current density of 0.72 A/cm².

electrode, the emf of the cell

$$M|MA,M'A_n \;\vdots\; MA,M'A_n|M$$

may be written (5, 6)

$$E = (IR) + \frac{1}{n\mathbf{F}}\int_{y_o}^{y} t_{M^A}\frac{1+(n-1)y}{1-y}\,d\mu_{M'A_n} \quad [1]$$

where y is the mole fraction of $M'A_n$ at the anode surface, $\mu_{M'A_n}$ the chemical potential of $M'A_n$, and t_{M^A} the transference number of M relative to A. The chronopotentiometric transition occurring when MA is depleted at the electrode is a consequence of the thermodynamics of the system as in classical chronopotentiometry, rather than of the buildup of a resistive layer, and should be observed even with measurement of the emf under current interruption conditions.

The flow of cations, M, relative to the common anions taken as frame of reference is (5)

$$J_{M^A} = -D_{M-M'}\frac{\partial C_M}{\partial \xi} + t_{M^A}\,I/\mathbf{F} \quad [2]$$

where $D_{M-M'}$ is the mutual diffusion coefficient of cations, M and M', t_{M^A} is the transference number of cation M relative to anions A, C_M is the concentration of M in equivalents per volume unit[2], and ξ is a distance variable such that equal increments of ξ contain equal numbers of anions A. This transformation accounts for the effects of volume changes with composition on the reference frame for diffusion.

The equation of diffusion may be derived by differentiation of Eq. [2] with respect to the distance variable, leading to

$$\frac{\partial C_M}{\partial t} = \frac{\partial}{\partial \xi}\left(D_{M-M'}\frac{\partial C_M}{\partial \xi}\right) - \frac{\partial}{\partial \xi}\left(t_{M^A}\frac{I}{\mathbf{F}}\right)$$

$$= D_{M-M'}\frac{\partial^2 C_M}{\partial \xi^2} + \frac{dD_{M-M'}}{dC_M}\left(\frac{\partial C_M}{\partial \xi}\right)^2 - I/\mathbf{F}\frac{dt_{M^A}}{dC_M}\left(\frac{\partial C_M}{\partial \xi}\right) \quad [3]$$

Since at the electrode surface the flux of cations M is zero because no M ions cross it, Eq. [2] provides one of the boundary conditions

$$\frac{I}{\mathbf{F}} = \frac{D_{M-M'}}{t_{M^A}}\frac{\partial C_M}{\partial \xi} \qquad \xi = 0, \quad t \geqq 0 \quad [4a]$$

The other boundary condition and the initial condition are the usual ones of chronopotentiometry for semi-infinite diffusion to a plane electrode

$$C_M(t) = C_o \qquad t \geqq 0, \quad \xi \to \infty \quad [4b]$$

$$C_M(\xi) = C_o \qquad t = 0, \quad \xi \geqq 0 \quad [4c]$$

The general second-order nonlinear differential equation (Eq. [3]) is not amenable to analytical solution. With constant diffusion coefficient and unity transference number the diffusion equation and boundary conditions are identical to those of ordinary chronopotentiometry, and the solution is of the same form as the Sand equation, although D is an interdiffusion coefficient rather than a self-diffusion coefficient. However, a useful result can be derived also for the slightly less restrictive assumption of a constant although nonunity transference number. With a constant diffusion coefficient, which could apply over only a small range of composition, Eq [3] and [4a] may be written

[2] In a two-component molten salt mixture (three ion constituents) the faradaic, migrational, and diffusive flows uniquely determine the change of a single composition variable in the system (conveniently taken as the equivalent concentration) irrespective of the number, complexity, and charge of the "species" which may be present.

$$\frac{\partial C_M}{\partial t} = D'_{M-M'}\frac{\partial^2 C_M}{\partial \xi'^2} = (D_{M-M'}/(t_{M^A})^2)\frac{\partial^2 C_M}{\partial (\xi/t_{M^A})^2} \quad [5]$$

$$I/\mathbf{F} = D'_{M-M}\frac{\partial C_M}{\partial \xi'} = (D_{M-M'}/(t_{M^A})^2)\frac{\partial C_M}{\partial (\xi/t_{M^A})} \quad [6]$$

Under these assumptions, the transformations

$$D' = D_{M-M'}/(t_{M^A})^2$$

$$\xi' = \xi/t_{M^A}$$

thus lead to equations of the same form as for ordinary chronopotentiometry for the concentrations at the electrode surface as a function of time

$$C_M(\xi = 0) = C^o - \frac{2I}{\mathbf{F}\sqrt{\pi D_{M-M'}/(t_{M^A})^2}}\sqrt{t} \quad [7]$$

Because the assumption of a constant interdiffusion coefficient is unrealistic, Eq. [7] does not apply rigorously over a wide range of concentration.

In the present work, the three bulk compositions are melts where independent measurements (7) have demonstrated unicationic conduction by lithium ions. As before, by using Eq. [1], including the activity coefficient term, the time dependence of concentration at the electrode surface is calculated from the time dependence of the potential along the experimental chronopotentiograms. Equation [7] is reminiscent of the Cottrell equation for the time dependence of current in chronoamperometry. Setting the concentration of M at the electrode surface equal to zero gives the analog of the Sand equation, but as pointed out earlier, a diffusion coefficient calculated from a transition time may be difficult to interpret. Equation [7] may be put in a useful form for graphical analysis

$$(1 - C_M/C_o)/I = \frac{2}{C_o\mathbf{F}\sqrt{\pi D_{M-M'}/(t_{M^A})^2}}\sqrt{t} \quad [8]$$

In the hypothetical case of diffusion coefficient and transference number independent of composition over the entire composition range, plots of the left-hand side of Eq. [8] *vs.* the square root of time would be linear, with slope inversely proportional to $\sqrt{D_{M-M'}/(t_{M^A})^2}$, up to the transition time, at which $C_M = 0$. The limiting value of the ordinate is then equal to the reciprocal of the current density. Applying such plots to LiF-BeF_2 mixtures in the composition range in which t_{Li^F} is known to be unity (20-80 m/o BeF_2), deviations from linearity result from composition dependence of the diffusion coefficient, providing a useful diagnosis. However, the interdiffusion coefficient in melt of the bulk composition can be obtained from the initial linear portion of plots of the left-hand side of Eq. [8] *vs.* the square root of time, *i.e.*, at short times. The limiting ordinate at long times still should be $1/I$, and the plots at different current densities should be superimposed along the initial linear portions of the curves. This provides a test for consistency of the diffusion coefficients from measurements at different current densities, and is the analog of the constancy of $I\tau^{1/2}$ in classical chronopotentiometry.

Results

ED chronopotentiometric measurements were made in the three bulk compositions of 53, 65, and 70 m/o BeF_2 at several temperatures. At each temperature and composition chronopotentiograms with different current densities were obtained. Figure 3 shows typical plots of Eq. [8] at 570°C in the melt of bulk composition 53 m/o BeF_2. The different symbols refer to different current densities at the working electrode, and the mole fractions of BeF_2 at the indicator electrode are indicated. The three plots are obviously sigmoid in shape, indicating the variation of the interdiffusion coefficients. However a common straight line through the origin of the square root of time plot can be drawn

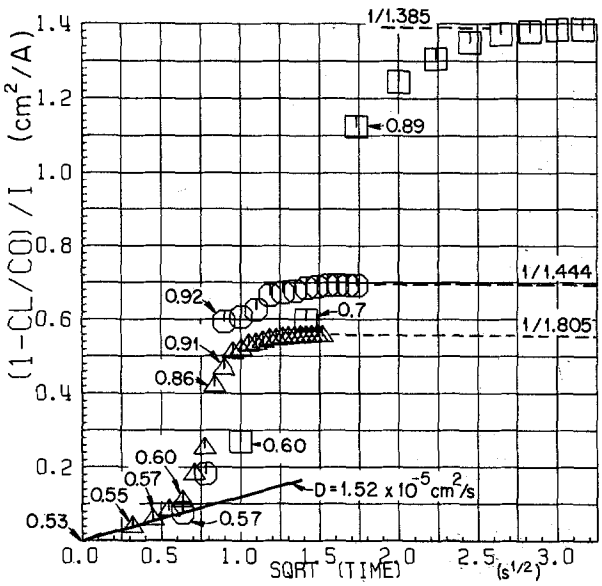


Fig. 3. Dependence of composition at the Be anode on square root of time (Eq. [8]) for the 53 m/o BeF_2 melt at 570°C and with different currents (mA). 500, △; 400, ①; 200, ⊡. Area of the working electrode: 0.277 cm^2. The compositions in mole fraction of BeF_2 are indicated, as is the diffusion coefficient calculated from the initial slope. Horizontal dashed lines are the plateaus calculated as the reciprocal current densities.

through the ordinates calculated from the early parts of chronopotentiograms obtained at differing current densities, as long as the composition change at the electrode surface is sufficiently small. Over the concentration range between 53 and 57 m/o BeF_2, the composition dependence of the interdiffusion coefficient may be neglected in Eq. [7] and [8]. The initial slope of Fig. 3, using Eq. [8] gives the value 1.52×10^{-5} cm^2/sec for the mutual diffusion coefficient of lithium and beryllium in the 53 m/o BeF_2 melt at 570 °C. (The precision is estimated to be about 5%.) As the concentration of BeF_2 increases beyond 60 m/o BeF_2, a sharp departure from proportionality to $\sqrt{t}$ occurs, and as the curves approach their limiting values the plots are no longer exactly superimposable. Since independent measurements (7) show that the transference number is constant up to 80 m/o BeF_2 the curvature in that region arises from the composition dependence of the mutual diffusion coefficient. If mean values of the diffusion coefficient are calculated from Eq. [8], the apparent anomaly of increasing mean values of interdiffusion coefficient with increasing BeF_2 content is found, because of the weighting function. When the concentration of BeF_2 exceeds 80 m/o BeF_2, the transference number of lithium relative to fluoride may decrease; at all three current densities a rapid decrease of slope occurs at about 90 m/o BeF_2. The final parts of plots are plateaus as $(1 - C_L/C_0)/I$ attains slowly its expected value of $1/I$. The corresponding compositions are very close to pure BeF_2 and very likely in this concentration range both interdiffusion coefficient and transference number decrease. In the absence of an analytical solution of the diffusion equation with a concentration-dependent diffusion coefficient, the most reliable results are those from the very early parts of chronopotentiograms where average values of the diffusion coefficient are taken over a small concentration range. However the current densities must be chosen low enough to provide compositions not too far removed from the bulk composition in the early part of the chronopotentiograms. In our previous measurements (5, 6) at higher BeF_2 contents, the initial composition change was too rapid to provide data as close to the bulk composition as in the present work, and the plots probably correspond to the second, or rising portion of the sigmoid curve. However it was possible to resolve the weighted mean diffusion coefficients into composition-dependent values which were mutually consistent when the values calculated for a given composition at the electrode surface in melts of differing initial compositions were compared. In the present work, the composition undergoes too large a change for convenient resolution of the weighted mean. Table I gives values of the mutual diffusion coefficient in melts of three compositions, together with the concentration interval over which the value is averaged. Temperature dependence of the mutual diffusion coefficient in the eutectic melt between 380° and 600°C leads to an activation energy for diffusivity of 9 kcal/mol compared to a value of about 15 kcal/mol for the activation energy for viscous flow (11).

Table I. Mutual diffusion coefficient (cm^2/sec) of lithium and beryllium in LiF-BeF_2 melts

Melt composition, m/o BeF_2	Temperature, °C			
	380	570	600	700
70				1.5×10^{-4} (70-85)
65			4.6×10^{-4} (65-74)	
53	3.4×10^{-6} (53-55)	1.52×10^{-5} (53-55)	1.6×10^{-5} (53-60)	

Discussion

The magnitudes of the interdiffusion coefficients in 53-70 m/o BeF_2 mixtures, shown in Table I, and the activation energy for diffusion, indicate the approach to values expected in ionic liquids with increasing alkali ion concentration and the breakdown of the network structure of BeF_2. Our previous measurements in mixtures containing 78-95 m/o BeF_2 led to estimated interdiffusion coefficients in the range 10^{-6}-10^{-8} cm^2/sec. Solute self-diffusion coefficients of the order of 10^{-6} cm^2/sec have been reported (12) in 30 m/o BeF_2 melts.

In plots such as Fig. 3, the slope of the chord between the origin and a point on the curve corresponds to a mean interdiffusion coefficient for compositions between the bulk or initial composition and the composition at the electrode surface at the corresponding time along the chronopotentiogram. It is clear from the sigmoid shape that these weighted mean values will first decrease with time (increasing chord slope) and then increase with time (decreasing chord slope) as the plateau is approached. In our previous work (6) at higher BeF_2 concentrations, assumption of a weighting function proportional to the alkali ion concentration led to consistency between diffusion coefficients calculated at differing times and concentrations along an individual chronopotentiogram, and diffusion coefficients calculated at the same concentration but different time from chronopotentiograms in melts of differing initial composition. Such a weighting function reflects the fact that in a system in which the diffusion coefficient is decreasing with time, the compositions with higher alkali concentration (and hence higher diffusion coefficient) contribute longer times toward the attainment of a given composition change than do the compositions with low diffusion coefficient.

The sigmoid shape of the approach to the limiting plateau also indicates that the evaluation of a transition time may be rather difficult, and that apparent sharpness of chronopotentiograms may be deceptive. If one applies the Sand equation to a 6 sec, apparently sharp, transition in Fig. 1, the calculated apparent diffusion coefficient is 2×10^{-6} cm^2/sec. The diffusion coefficient calculated from the initial slope in Fig. 3 would require the unrealistic estimate of 9 sec for the transition time if the diffusion coefficient were constant.

ED chronopotentiometric measurements have been reported (9) in NaCl-$AlCl_3$ melts where unicationic

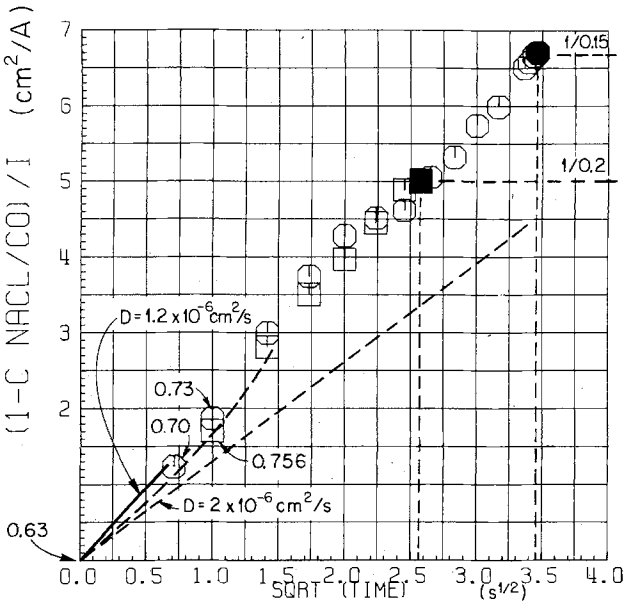


Fig. 4. Dependence of composition at Al anode surface on square root of time in 63 m/o $AlCl_3$-37 m/o NaCl melt from experimental data of Ref. (9) with different currents (mA) at 140°C. 40, ⊡; 30, ⊙. Area of the working electrode: 0.2 cm^2. The filled symbols correspond to the reported graphical transition times (9): 6.6 sec; 12.1 sec. The compositions in mole fraction of $AlCl_3$ at the aluminum anode surface are indicated. The slope of the solid line corresponds to the reported (9) diffusion coefficient, that of the dashed line to the limiting slope of the curve. The plateaus are calculated from the reciprocal current densities.

conductance by sodium ions (relative to chloride) is expected (10) to result from the complexity ($NaAlCl_4$-Al_2Cl_6) of the melts rather than from a network structure as in BeF_2-LiF melts. However, the interdiffusion coefficient of sodium and aluminum probably varies less sharply with composition than that for LiF and BeF_2, since the viscosity does not change as much. Since the diffusion coefficients of Al and Na were calculated from apparently sharp transition times, it seemed of interest to investigate a possible composition dependence by calculations such as those we have presented above.

Figure 4 shows a plot $(1 - C_M/C_0)/I$ derived from the published chronopotentiograms (9) with 0.2 and 0.15 A/cm^2 in the melt 63 m/o $AlCl_3$-37 m/o NaCl at 140°C. The superposition of the two sets of points indicates excellent consistency of the data at the two different current densities. The two filled symbols in Fig. 4 are obtained by taking $C_{Na} = 0$ at transition times of 6.6 and 12.1 sec as graphically determined by the authors in Ref. (9). Although the plateaus are of lesser extent in this chloroaluminate melt than in LiF-BeF_2 mixtures, the assumption of both constant interdiffusion coefficient and transference number probably does not hold over the full composition range spanned during the chronopotentiograms. Because of difficulty in reading the emf at very short times, the initial points probably correspond to compositions already far enough from the bulk composition to belong to the nonlinear intermediate section of the plotted function, and extrapolation through the origin must assume some curvature. This would lead to a lower initial slope and thus a slightly higher value of the diffusion coefficient (perhaps 1.5-1.8 $\times$ 10^{-6} cm^2/sec) than the value 1.2 $\times$ 10^{-6} calculated from the transition time. Since there is little variation of the interdiffusion coefficient in this system, the use of the transition time here does not lead to significant error, as it would in the case of the LiF-BeF_2 system, but it would appear advisable to use all of the potential time data along the chronopotentiogram rather than a single point, the transition time, in the calculation. Similarly, Piron (13) has pointed out the need to test for composition dependence of self-diffusion coefficients obtained from transition times and the Sand equation in anodic dissolution chronopotentiometry of a metal into a supporting electrolyte. In a comparative study of cathodic chronopotentiometry for Ni(II) and of anodic dissolution chronopotentiometry of an Ni electrode in molten LiCl-KCl eutectic, he finds differences of 10-30% between the diffusion coefficients calculated from cathodic and anodic dissolution chronopotentiometry. Moreover, the calculations discussed in this paper should be applicable to mixtures with composition-dependent transference numbers such as LiCl-KCl and other mixtures. We have observed anodic chronopotentiometric transitions at silver electrodes in sodium nitrate-silver nitrate mixtures, for which independent measurements of diffusion coefficients and transference numbers have been made. Preliminary analysis of our measurements is consistent with the reported values of the interdiffusion coefficients (14).

Conclusions

Interdiffusion coefficients may be evaluated from chronopotentiometric measurements over much broader ranges of concentration than in the classical application of this method. Development of the method has passed through three stages. Initially (5) it was applied to a relatively narrow composition range, 95-100 m/o BeF_2, providing mean interdiffusion coefficients approaching the self-diffusion coefficient of Li^+. Next (6) it was applied to melts in which the composition was swept through the range 78-100 m/o BeF_2, and a method was developed for resolving the weighted mean diffusion coefficients into composition-dependent values. Extending the method to mixtures containing 53 m/o BeF_2, in which the composition change is too large to use the weighted mean resolution, we have in this paper presented calculations of interdiffusion coefficients for compositions close to the initial or bulk composition in a region where the transference number is known from independent measurements (7). These estimates of the composition dependence of the interdiffusion coefficients are needed as preliminary values in the development of numerical solution of the flux equations. Although the method has been applied to chronopotentiometry, it should be applicable to other kinds of electrochemical scanning programs, *e.g.*, linear sweep voltammetry and chronoamperometry. In fact, other types of scanning function may prove more useful than chronopotentiometry for resolving diffusion coefficients at compositions near the bulk composition, *i.e.*, at short times. ED chronopotentiometry has been applied to binary polymeric melts and binary complex melts, and should be applicable to the evaluation of transport parameters in electrolytes of wider variety, including proposed battery systems. With suitable modifications it should prove useful in systems where composition-dependent diffusion coefficients may be expected, as in silicates (15) and in the anodic dissolution of metals (13).

Acknowledgment

We are pleased to acknowledge discussion of the manuscript with Dr. S. Cantor. This research was sponsored by the Energy Research and Development Administration under contract with Union Carbide Corporation.

Manuscript submitted May 27, 1976; revised manuscript received Sept. 1, 1976.

Any discussion of this paper will appear in a Discussion Section to be published in the December 1977 JOURNAL. All discussions for the December 1977 Discussion Section should be submitted by Aug. 1, 1977.

Publication costs of this article were assisted by Oak Ridge National Laboratory.

LIST OF SYMBOLS

A	common anion
C_M	concentration of MA (moles/cm^3); (L for LiF, Na for NaCl)
C_o	concentration of alkali halide in the bulk (moles/cm^3)
$D_{M-M'}$	mutual diffusion coefficient of M and M' (cm^2/sec)
D'	transformed mutual diffusion coefficient, $D/(t_M^A)^2$
E	emf between reference and indicator electrodes (V)
F	the faraday (96.487C)
I	current density (A/cm^2)
J_M^A	flow of M relative to A (common anion), equiv./(cm^2/sec)
(IR)	IR drop (V)
M	alkali cation
M'	cation Be or Al
n	charge number of cation
t	time (sec)
t_M^A	transference number of cation M relative to anion A
$\overline{V}_i$	partial equivalent volume of i (i = A or M)
x	distance from electrode surface
y	mole fraction of MA
y_o	mole fraction of MA in the bulk
$\mu_{M'A_n}$	molar chemical potential of $M'A_n$
ξ	distance variable
ξ'	transformed distance variable, ξ/t_M^A

REFERENCES

1. J. Giner and G. L. Holleck, NASA Report No. CR-1541 (1973).
2. S. von Winbush and A. F. Sammells, *This Journal*, **123**, 650 (1976).
3. D. R. Vissers, Z. Tomczuk, and R. K. Steunenberg, *This Journal*, **121**, 665 (1974).
4. Research on electrodes and electrolyte for the Ford Sodium Sulfur Battery semiannual report. National Science Foundation Contract No. NSF-C 805 (AER-73-07199), Ford Motor Co., Dearborn, Mich., (January 1976).
5. C. E. Vallet, H. R. Bronstein, and J. Braunstein, *This Journal*, **121**, 1429 (1974).
6. C. E. Vallet and J. Braunstein, *J. Am. Ceram. Soc.*, **58**, 209 (1975).
7. K. A. Romberger and J. Braunstein, *Inorg. Chem.*, **9**, 1273 (1970).
8. G. D. Robbins and J. Braunstein, in Tech. Report ORNL-4548, pp. 156-159 (August 1970).
9. B. Gilbert, D. L. Brotherton, and G. Mamantov, *This Journal*, **121**, 773 (1974).
10. J. Braunstein, H. R. Bronstein, and J. Truitt, *J. Electroanal. Chem.*, **44**, 463 (1973).
11. S. Cantor, W. T. Ward, and C. T. Moynihan, *J. Chem. Phys.*, **50**, 2874 (1969).
12. G. Mamantov and D. L. Manning, *Anal. Chem.*, **38**, 1494 (1966).
13. D. L. Piron, *Corros. Sci.*, **15**, 383 (1975).
14. J. Richter, *J. Chem. Eng. Data*, **18**, 400 (1973).
15. K. Nagata, M. Kawakami, and K. S. Goto, in "Metal-Slag-Gas Reactions and Processes," Z. A. Foroulis and W. W. Smeltzer, Editors, pp. 183-198, The Electrochemical Society Softbound Symposium Series, Princeton, N.J. (1975).
16. T. Ohmichi, H. Ohno, and K. Furukawa, *J. Phys. Chem.*, **80**, 1628 (1976).

Steady-State Polarization at Porous, Flow-Through Electrodes with Small Pore Diameter

I. Reversible Kinetics

B. G. Ateya* and L. G. Austin

Fuel Science, Department of Material Sciences,
The Pennsylvania State University, University Park, Pennsylvania 16802

ABSTRACT

This paper considers the effect of mass transfer and ohmic limitations on the current-polarization relations for porous flow-through electrodes with fine pores, for reversible one-electron transfer reactions. The model includes mass transfer by both axial forced convection and axial diffusion. A new analytical solution is presented which reduces to a previous solution when axial diffusion is negligible. The effects of axial diffusion and ohmic potential drop in the pore electrolyte on the current and concentration distributions inside the electrode are investigated. Experimental confirmation is presented for some of the predictions and a quantitative comparison between theory and experiment is presented. It is concluded that axial diffusion effects are negligible under many experimental conditions, *e.g.*, normal diffusion coefficient, flow rate, electrode length, etc. The results demonstrate the validity of the one-dimensional model presented here under these conditions.

A porous, flow-through electrode is here defined as a porous inert electrode through which is forced electrolyte containing dissolved reactant, *e.g.*, a redox couple. This type of electrode is of interest because the limiting current density is not controlled by diffusion or natural convection to the interior of the electrode, and very high limiting currents can be obtained even at relatively low electrolyte flow velocities through the electrode. In addition, complete conversion of certain reactants to products can be easily achieved by working at the limiting current. Figure 1 illustrates the system and defines rear supply of reactant to the electrode. Theoretical steady-state treatments of this system have been given by Perskaya and Zaidenman (1), Austin *et al.* (2), Gurevich and Bagotsky (3), and more recently Wroblowa *et al.* (4, 5). A primary assumption in these treatments is that the rate of forced mass flow of reactant through the porous system dominates over axial diffusion so that axial diffusion is not included in the treatments. For this system, there are several theoretical treatments but little experimental work, especially experimental results properly designed to

* Electrochemical Society Active Member.

Key words: flow-through electrodes, polarization, ohmic effect, forced convection, axial diffusion, hydrodynamic dispersion, laminar flow.

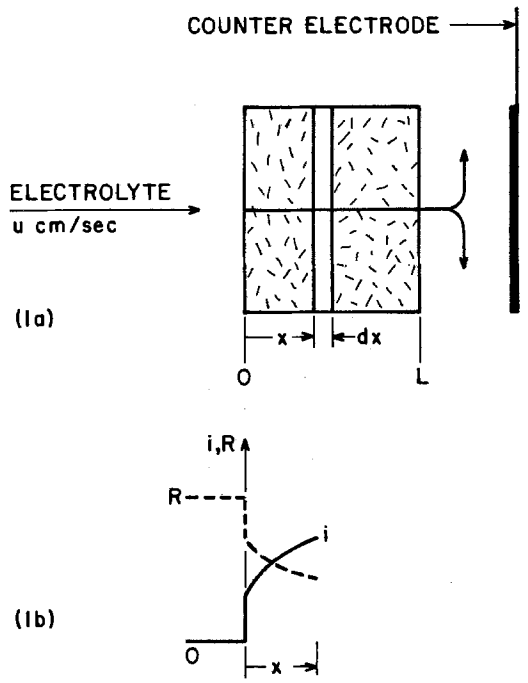


Fig. 1. Model of a flow-through electrode: (a) showing rear reactant supply, (b) illustrating boundary conditions at $x = 0$.

test the validity of a certain model. There are references (5, 6) in the literature in which gross discrepancies between theoretical predictions and experimental findings are left unexplained.

This paper presents some new solutions where axial diffusion is included and gives careful experimental confirmation of some of the solutions. This part gives an analytical solution for one-electron transfer reactions with reversible kinetics, and the corresponding experimental results.

Theoretical Steady-State Treatment

The physical system analyzed consists of a fine pore, isotropic matrix electrode, where the mean pore radius is small (say 1 μm) compared to the electrode thickness, with highly interlinked pores. Under these conditions, the system is treated as one dimensional since radial diffusion will be sufficiently rapid to keep concentration uniform across the pore radius. It is assumed that current density and liquid flow are uniform in the plane of the electrode. Ohmic voltage loss due to electronic conduction in the material of the electrode is assumed negligible, and strongly supported electrolyte is used so that the specific conductance of the electrolyte and the effective diffusion coefficients can be assumed constant, and streaming potential is negligible. It is also implicit in the treatments that flow is fully developed at a short distance into the electrode.

The rear supply case is treated as follows: The Nernst equation for reversible one-electron transfer reaction $R \rightarrow P + e$ can be expressed in the form

$$\eta(x) = \frac{RT}{\mathbf{F}} \ln\left(\frac{P(x)/P_b}{R(x)/R_b}\right) \qquad [1]$$

where R_b is the concentration of reactant in the feed electrolyte, P_b the concentration of product, etc. In the absence of significant diffusion, a mass balance gives $R(x) + P(x) = R_b + P_b$, where $R(x)$ is the reactant concentration at position x in the electrode and $P(x)$ the product concentration. This relation also holds when significant diffusion is present providing the diffusion coefficients of reactant and products are equal. Thus

$$\eta(x) = b \ln\left[\frac{1 + \gamma - \gamma R(x)/R_b}{R(x)/R_b}\right] \qquad [2]$$

where $\gamma = R_b/P_b$ and $b = RT/\mathbf{F}$. Rearranging the above equation and putting it in dimensionless form gives

$$\bar{R}(x) = (1 + \gamma)/[\gamma + \exp\bar{\eta}(x)] \qquad [3]$$

where $\bar{R}(x) = R(x)/R_b$ and $\bar{\eta}(x) = \eta(x)/b$.

Performing a steady-state mass balance on an element of thickness dx at x gives

$$di(x)/dx = n\mathbf{F}[D_{eff}d^2R(x)/dx^2 - udR(x)/dx]$$

Again using dimensionless quantities $\bar{x} = x/L$, $\bar{i}(x) = i(x)/i_L$, and substituting in the above equation gives

$$d\bar{i}(x)/dx = \theta d^2\bar{R}(x)/d\bar{x}^2 - d\bar{R}(x)/d\bar{x} \qquad [4]$$

where θ is the dimensionless group D_{eff}/Lu, and i_L is the maximum current which can be obtained when the reactant is entirely consumed, *i.e.*, $i_L = n\mathbf{F}uR_b$ where u is superficial velocity. For convenience in presentation the bars will be dropped, and it is to be understood that the subsequent equations are in dimensionless form. The rate of mass transfer of reactant in the x direction through a plane at x is the sum of convective and diffusive fluxes $uR(x) - D_{eff}dR(x)dx$, and this must equal the total reactant flux entering the system minus the amount reacted up to x. In dimensionless form this is

$$1 - i(x) = R(x) - \theta dR(x)/dx \qquad [5]$$

which, of course, can also be obtained by integration of Eq. [4].

Ohm's law in dimensionless form is

$$i(x) = (1/\Delta)d\eta(x)/dx \qquad [6]$$

where $\Delta = i_L L\rho_{eff}/b$ is the maximum ohmic potential drop in multiples of b and is obtainable only when the limiting current is supported by reaction over an infinitesimally small element at $x = 0$. Differentiating Eq. [3] and substituting in Eq. [5] using Eq. [6] gives

$$i(x) = \frac{[\exp(\eta(x)) - 1]/[\exp(\eta(x)) + \gamma]}{1 + (1 + \gamma)\Delta\theta \exp\eta(x)/[\exp(\eta(x)) + \gamma]^2} \qquad [7]$$

At $x = 1$, Eq. [7] becomes

$$i = \frac{[\exp(\eta_L) - 1]/[\exp(\eta_L) + \gamma]}{1 + (1 + \gamma)\Delta\theta \exp(\eta_L)/[\exp(\eta_L) + \gamma]^2} \qquad [8]$$

Thus by combining the Nernst equation, the mass-reaction balance and Ohm's law, we have obtained the relation between the exit face polarization and the total current i. Since $\eta_L > 0$, the second term in the denominator of Eq. [8] can be negligible for appropriate values of the product $(1 + \gamma)\Delta\theta$. Equation [8] then becomes

$$\eta_L = 2.3 \log[1 + \gamma i)/(1 - i)] \qquad [9]$$

as previously obtained for the same conditions assuming negligible axial diffusion (2).

The relation between η and x is obtained as follows. Combining Eq. [7] with Eq. [6], separating and integrating from $\eta = \eta_0$ at $x = 0$ to $\eta(x)$ at x gives

$$x\Delta = (1 + \gamma) \ln\left[\frac{\exp(\eta(x)) - 1}{\exp(\eta_0) - 1}\right] + \Delta\theta \ln\frac{[\exp(\eta(x)) - 1][\exp(\eta_0) + \gamma]}{[\exp(\eta_0) - 1][\exp(\eta(x)) + \gamma]} - \gamma[\eta(x) - \eta_0] \qquad [10]$$

Note that η_0 is not zero at $x = 0$ unless η_L and, hence, i are also zero. From Eq. [7], then $i(0)$ is not necessarily zero. This means that to apply the Nernst reversible equation strictly, a finite amount of reac-

tion will occur in an infinitesimal region at $x = 0$ to generate an $i(0)$ which is compatible with Eq. [7] and [8]. The true boundary condition is $i(-0) = 0$ and $i(+0)$ finite. In practice, of course, a finite $i(+0)$ will be supplied by two dimensional reaction in a thin region (as illustrated in Fig. 1b at $x = 0$) including the outside face of the electrode and the pore mouth; the transfer processes become one dimensional at larger values of x. These boundary conditions apply even in the absence of a significant diffusion term in the mass balance.

At $x = 1$, $\eta = \eta_L$; substituting in the above equation and rearranging gives

$$\Delta = \frac{(1+\gamma)\ln\dfrac{\exp(\eta_L)-1}{\exp(\eta_0)-1} - (\eta_L - \eta_0)}{1 - \theta\ln\dfrac{[\exp(\eta_L)-1][\exp(\eta_0)+\gamma]}{[\exp(\eta_L)+\gamma][\exp(\eta_0)-1]}} \quad [11]$$

For a certain η_L (given γ, Δ, and θ as constants) the corresponding value of i is calculated from Eq. [8]. However, for each value of η_L (and, hence, i) there is only one value of η_0 given by Eq. [11], but the form of this equation makes it difficult to separate variables η_0 and η_L. The single correct value of η_0 which corresponds to the specified value of η_L was calculated from Eq. [11] using a simple dichotomous search technique. The value of η_0 thus obtained was used in Eq. [10] to obtain the polarization distribution $\eta(x)$, where $\eta(x)$ was extracted using the same search technique. The value of $\eta(x)$ was then substituted either in Eq. [3] to obtain concentration distribution or in Eq. [7] to obtain current distribution. The use of Eq. [11] with experimental values of η_0, η_L, and i will be given in the results section; if the effect of axial diffusion is negligible, the equation reduces to a simpler form since then the denominator of the right-hand side approaches unity.

Results of Computations

Equations [7] and [10] show that the distribution of reaction through the electrode depends on the parameters Δ and θ. As Δ increases, the location of the reaction is forced toward the exit face. This is illustrated in Fig. 2, which shows the reactant concentration and polarization profiles through the electrode at close to limiting current where nonuniformity of reaction is most pronounced, for a value of γ of 1. For $\Delta = 0$, the current is produced by reaction over an infinitesimally small element at $x = 0$ or, practically, at the external entry surface of the electrode. The total current then crosses the electrode with zero potential drop. This is clearly a hypothetical case. At the other limit of a very large Δ, the current would be supported by reaction in a narrow element at $x = 1$, and $\eta(x) = 0$ for $x < 1$. Generally, η_0 is forced closer to zero as Δ increases, Fig. 2. Considering Eq. [7], [8], and [11], it is seen that the effect of axial diffusion occurs in the terms containing the product $\Delta\theta$. But $\Delta\theta = i_{L\rho_{eff}}D_{eff}/bu = i_L\rho D/bu = n\mathbf{F}\rho DR_b/b = \phi$, where ϕ is similar to the parameter used previously by Austin *et al.* (7-9) to describe the balance between diffusional and ohmic effects in porous flooded-diffusion electrodes

$$\phi = n\mathbf{F}\rho DR_b/b = \Delta\theta \quad [12]$$

Since a large Δ causes less uniform reactant distribution, it also increases the concentration gradient $dR(x)/dx$. Therefore it is the product $\theta\Delta$ and not just θ which is the index of axial diffusion effects. For simple dilute binary electrolyte, the Einstein relation is $D/\mu = RT/\mathbf{F} = b$ and $1/\rho = \mathbf{F}\mu R_b$, where μ is the electrical mobility. Thus $\phi = \mathbf{F}\rho DR_b = 1$, which is the maximum usual value of ϕ for this type of electrolyte, since a supported electrolyte will have a lower value of ρ. In the experiments reported later, reactant concentrations were of the order of 10^{-3}M but the electrolyte was supported by 4*N* HCl, thus giving values of ϕ of 10^{-3} or lower.

For large values of ϕ, the denominator of Eq. [7] becomes significantly greater than one. Figure 3 shows a comparison of the exit face polarization η_L *vs.* current for $\phi = 1$ and 10 and ϕ negligible ($\leq 10^{-2}$). The curve of $\phi = 10$ is obtainable for any combination of Δ and θ values which gives $\phi = \Delta\theta = 10$, *i.e.*, $\theta = 1$, $\Delta = 10$ or $\theta = 10$ and $\Delta = 1$. Significant axial diffusion increases η_L and hence η_0 according to Eq. [11].

Alternatively, for negligible axial diffusion, *i.e.*, $\Delta\theta < 0.01$, the only controlling parameter is Δ, in-

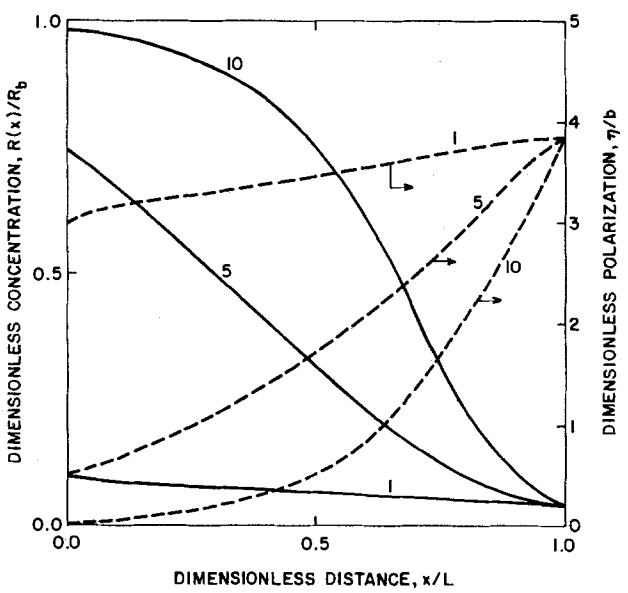


Fig. 2. Effect of ohmic parameter Δ (numbers on the curves) on polarization and concentration profiles in electrode with reversible kinetics; i/i_L — 0.96, negligible diffusion.

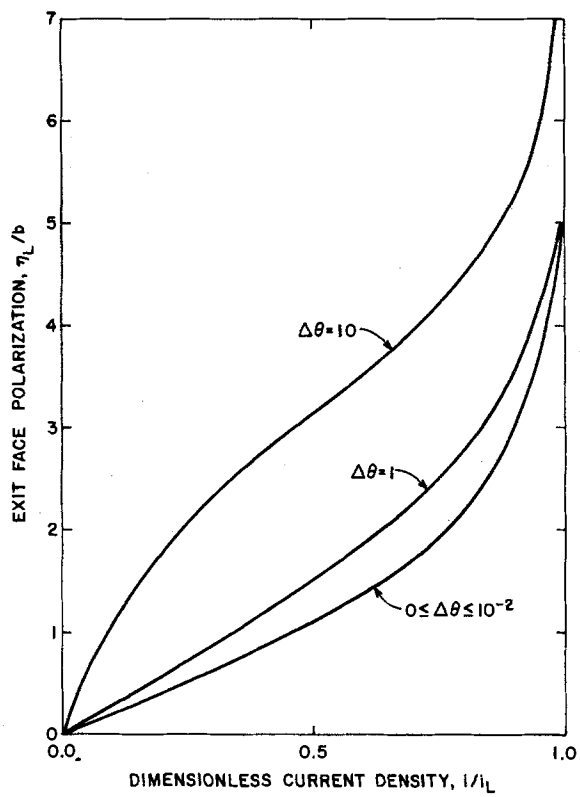


Fig. 3. Effect of axial diffusion on the current *vs.* η_L curves. Values on the curves are for $\phi(= \Delta\theta)$.

crease of which at a constant η_L (Eq. [8]) decreases η_0 according to Eq. [11] (cf. Fig. 7). Under this condition, the current-polarization relation follows the Nernst equation (Eq. [8], and bottom curve in Fig. 3). Note that $\Delta = i_L \rho L/b$ is the product of a convective mass transfer parameter i_L and an ohmic parameter η_L. Hence when Δ is the only controlling parameter, the over-all process is controlled by the rates of both convective mass transfer and ohmic effects. A large Δ value, *i.e.*, high concentration and/or resistivity indicates predominance of ohmic effects, whereas a small Δ value (low concentration and high conductivity) indicates that the process is controlled by convective mass transfer.

Experimental Techniques

To test the equations it was necessary to use redox couples with simple reversible kinetics. The couples chosen were potassium ferro-ferricyanides in 0.5M K_2SO_4 and ferrous-ferric perchlorates in 4*N* HCl. Determination of the diffusion coefficients and kinetics parameters of these couples on basal and edge planes of nonporous pyrolitic graphite are reported elsewhere (10). Porous electrodes were prepared from SP1 graphite (National Carbon Company, New York) which consists of natural graphite flakes of about 20-30 μm diameter and 0.3-0.4 μm thickness, containing a total of less than 6 ppm of impurities.

Nitrogen was purified in a train consisting of a column of anhydrous calcium sulfate, and SP1 graphite trap cooled in a Dry Ice-acetone mixture, a 1 ft long column of copper turnings heated to ~500°C, and finally two different portions of the test electrolyte, through which the gas was bubbled before entering the test solution.

The water used throughout this work was prepared following the procedure recommended by Powers (11). The specific conductivity of the water was about 8×10^{-7} Ω^{-1}-cm^{-1} at 25°C. Hydrochloric acid was prepared by distilling the constant boiling mixture (~6*N*, 108°C) obtained by diluting the concentrated reagent grade material.

Solutions containing the redox couples were prepared by dissolving the calculated weights of Baker reagent grade materials in redistilled water made up to the appropriate concentrations of the respective supporting electrolytes. Some SP1 graphite was added to the solution, and nitrogen bubbled through overnight to deaerate the solution and to stir it with graphite, which removed adsorbable material from the electrolyte. The graphite was then filtered off, and the filtrate kept under nitrogen to retard air oxidation. Dilute solutions were prepared by accurate volumetric dilution of the standard concentrated solutions. Solutions of potassium permanganate, potassium thiosulfate, and iodine were prepared and standardized according to standard analytical procedures (12). The amount of ferric iron present in a ferrous-ferric chloride solution was determined by a simple iodometric technique. The amount of ferrous iron was obtained by titrating against a standard solution of potassium permanganate in the presence of Zimmermann's reagent (13).

Potassium ferrocyanide is known to be a good primary standard substance (13), and potassium ferricyanide was determined by replacing the iron with zinc and then determining the liberated iron iodometrically (14).

The electrode holder for the flow-through tests is illustrated in Fig. 4, and was made from Teflon. The electrode holder was fitted in its place in the cell and a high porosity fritted disk put in the bottom of the holder. A certain weight of SP1 graphite was then introducted evenly in small additions. After every addition the resulting bed was pressed with a pure graphite rod (1/4 in. diameter). When the desired weight of graphite had been added the upper current collector was put on the top of the packed bed and covered with a high porosity filter paper disk. The upper and lower parts of the cell were held together tightly by four bolts, which compressed the bed. The porosity of the resulting packed bed electrode was calculated from a knowledge of its volume and the density of graphite single crystals, 2.266 g/cm^3.

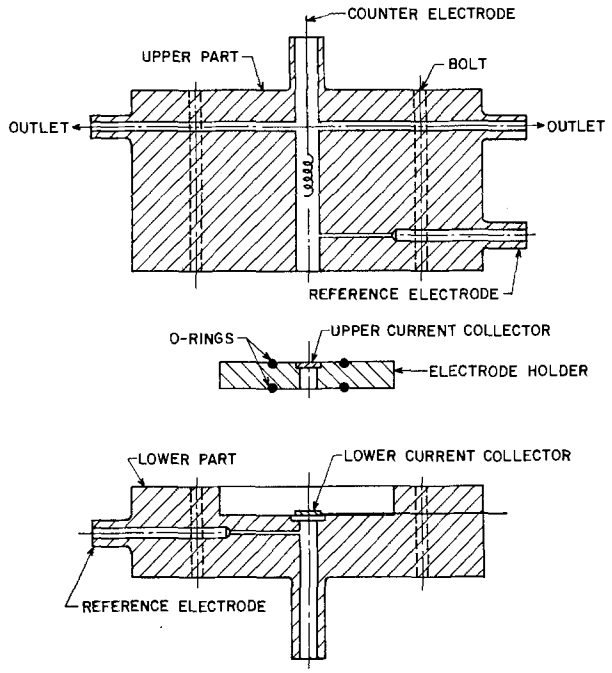


Fig. 4. Schematic of flow-through cell

A longitudinal section of the Lucite flow-through cell used for measuring current-voltage curves on flow-through electrodes, as well as for permeability measurements, is also shown in Fig. 4. It has two current collectors, one on either side of the test electrode in order to enable the electronic conductivity of the test electrode to be measured. A typical specific resistivity value was less than 0.06 Ω-cm. The counter-electrode and current collectors were made of platinum wire and platinum gauze.

A device was constructed (10) to deliver the flowing reactant electrolyte upward through the electrode at constant head. A few minutes were allowed to elapse before measurements were taken. Potentials were measured using a Keithley guarded ground d-c differential digital voltmeter (Type 660). The reference electrode used was a saturated calomel electrode. A steady voltage reading was obtained in less than 1 min and no drift was observed on standing for a few more minutes. The dead space of the cell was about 1.0 cm^3, so at typical flow rates of 0.1 cm/sec, the residence time in the cell was of the order of 30 sec. When the current is increased, the electrolyte leaving the cell is lower in reactant concentration and the possibility exists for back diffusion from previously exited electrolyte. However, because of the low residence time the new steady-state concentrations were soon established.

The *IR* polarization was measured using a fast-switching mercury relay circuit, an oscilloscope, and a C-12 Polaroid camera. While the oscilloscope measured the open-circuit potential, the diaphragm of the camera was opened and a large current was immediately applied to the electrode. The *IR* polarization was given by the blanked-out portion on the voltage-time trace. This was repeated using several faster sweep rates (one to two orders of magnitude faster) to ensure a correct result.

The residual current was measured while the supporting electrolyte flowed through the electrode at

the specified flow rate. The maximum value obtained in the useful potential range was about 0.1 mA/cm² and was thus negligible under all test conditions.

Results and Discussion

Hydrodynamic considerations.—Levich (15) gives the lengths of the entrance regions for laminar flow in a cylindrical tube as $h \sim 0.1\ R\ \mathrm{Re}$ and for the establishment of fully developed diffusion flow, $H \sim uR^2/D$, where R is tube radius and Re the Reynolds number. Typical values for the experimental system we used are $u = 0.1$ cm/sec, $R \approx 1\ \mu$m, kinematic viscosity $\nu \approx 0.01$ cm²/sec, and $D = 5 \times 10^{-6}$ cm²/sec, giving $\mathrm{Re} = 2uR/\nu = 2 \times 10^{-3}$, $h \sim 2 \times 10^{-8}$, and $H \sim 2 \times 10^{-4}$ cm. Thus the regions of developing flow and diffusional regime are negligible compared to any reasonable electrode thickness. Turbulent flow in porous media starts to occur at Reynolds numbers of 1 to 10 (16), so flow in the system considered is well within the laminar region.

Reversibility of the Redox System

By measuring the double layer capacity of both planar (17) and porous (10) graphite electrodes, it was concluded that the surface area of SP1 graphite is approximately 2×10^4 cm²/g. This agrees with the BET area measurement of 2×10^4 cm²/g. The exchange current density of $2 \times 10^{-3}N$ ferro-ferricyanide in 0.5M K_2SO_4 was estimated to be about 10 mA/cm² (10). For an electrode of 0.5 cm thickness and porosity of 0.5 the effective exchange current density i_oSL would be larger than 100 A/cm² of geometric surface area of porous electrode, where S is the specific surface area of the porous electrode in cm²/cm³. This value is much greater than the limiting current for all the flow rates used in the tests. Theoretically, then for negligible axial diffusion the flow-through results with this couple should fit Eq. [9]. Figure 5 shows the results; the slope of 58 mV/decade is the required theoretical result. Kinetic tests (17) showed the exchange current density of the ferrous-ferric couple in $4N$ HCl to be about 0.1 mA/cm² but the high value of effective i_oSL for the porous electrode again predicted a fit to Eq. [9], see Fig. 5.

The limiting currents were calculated from the known velocity and concentration, but it was also easy to determine unambiguously a measured limiting current. Figure 6 shows the excellent correspondence of determined-to-calculated i_L values, where i_L is given by $n\mathbf{F}uR_b$. The data of the Sn^{2+}/Sn^{4+} system were obtained from Ref. (10). It should be noted that it is by no means axiomatic that the measured limiting current should agree with the theoretical value. Both Austin *et al.* (2) and Sioda (18) give experimental results where this is not true. The figure suggests the possible use of flow-through electrodes in coulometric analysis for similar systems.

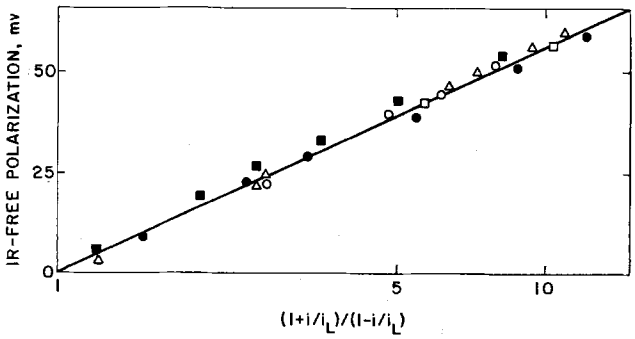


Fig. 5. Results of reversible reactions at a porous flow-through electrode. Oxidation of ferrocyanide ion ▽ = 1.25, ○ = 2, and □ = 2.7 cm/min. Oxidation of ferrous ions ● = 1.5 × 10^{-3}M and ■ = 8 × 10^{-3}M Fe^{2+} at the same flow rate.

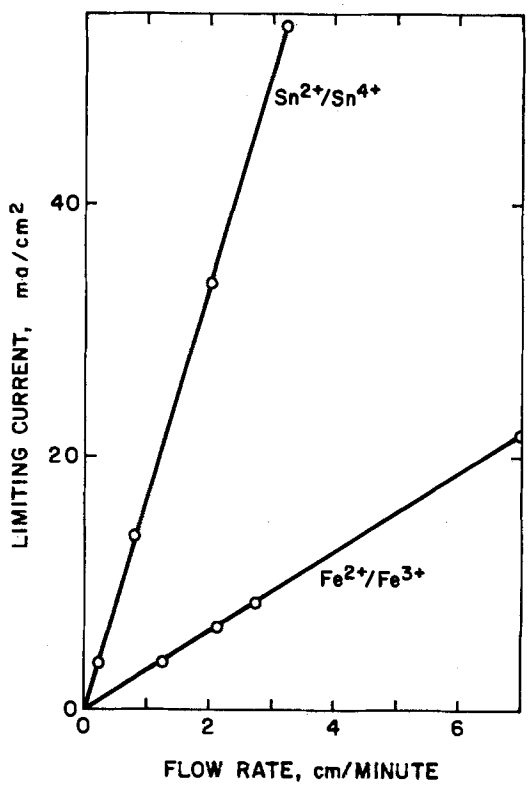


Fig. 6. Comparison of experimental and calculated limiting currents.

Referring again to the theory, it is expected that both of the above sets of experimental results should fit Eq. [11], which is the relation between η_O, η_L, γ, Δ, and θ for reversible conditions. Substituting the measured values of η_O and η_L in Eq. [11] gives values

Table I. Values of Δ calculated from experimental results inserted into Eq. [11]

Test	η_L, mV	η_O, mV	$\log\left(\frac{\exp\frac{2.3(1+\gamma)}{\eta_L}-1}{\exp\frac{\eta_O}{}-1}\right)$	$\gamma(\eta_L-\eta_O)$	$2.3\theta\log\frac{[\exp(\eta_L)-1][\exp(\eta_O)+\gamma]}{[\exp(\eta_O)-1][\exp(\eta_L)+\gamma]}$	Δ
Oxidation of Fe^{2+} in $4N$ HCl	11	1	5.19	0.386	1.35×10^{-4}	4.80
	26	2	6.13	0.926	1.43×10^{-4}	5.20
	32	3	5.97	1.12	1.23×10^{-4}	4.85
	42	3	6.99	1.51	1.38×10^{-4}	5.48
	55	5	7.07	1.93	1.22×10^{-4}	5.14
	69	6	7.86	2.43	1.15×10^{-4}	5.43
	110	13	9.31	3.74	0.79×10^{-4}	5.56
						Mean 5.21
Reduction of Fe^{3+} in $4N$ HCl	11	6	1.41	0.19	3.54×10^{-5}	1.22
	17	10	1.35	0.27	2.86×10^{-5}	1.08
	23	13	1.57	0.38	3.10×10^{-5}	1.18
	38	23	1.69	0.58	2.28×10^{-5}	1.11
	50	30	1.98	0.77	2.04×10^{-5}	1.21
	60	38	2.01	0.85	1.58×10^{-5}	1.16
						Mean 1.16

of Δ shown in Table I for the value of θ of 5.7×10^{-5} calculated from $u = 0.035$ cm/sec, $L = 0.5$ cm, $D_{eff} = 5 \times 10^{-6}$ cm^2/sec (13), porosity = 0.5, and tortuosity = 2.5.

In this connection it may be argued that under conditions of flow of electrolyte through a porous medium there is hydrodynamic dispersion superimposed on molecular diffusion. The over-all longitudinal mass transfer coefficient equals $D_{eff} + E$ where E is the longitudinal dispersion coefficient. Thus axial diffusion effects may be more significant than what we expected on the basis of molecular diffusion alone. Obviously the longitudinal dispersion coefficient depends on the electrolyte flow speed and the properties of the porous medium. This particular area of mass transfer in porous media is not well understood in terms of quantitative relationships (19). For packed sand beds (20), E is given by

$$E = 1.75ud_p, \; 2 < ud_p/D < 50 \qquad [13]$$

where d_p is average particle diameter. Based on an area of 2 m^2/g, the spherical equivalent diameter of the carbon particles of the porous electrode is about 1.5 μm and $E \sim 10^{-5}$. Thus the sum $D + E$ is not of different order than that of D alone, and derived values of θ are still much too small to give significant axial diffusion effects in the current-polarization relations.

It is seen that for both sets of data the axial diffusion term is negligible compared to one. This proves the prediction that under normal conditions (normal diffusion coefficient, flow rate, electrode length, etc.) axial diffusion can be neglected. The values of Δ in Table I enable the tortuosity factor of the electrode to be calculated from the electrode porosity of 0.5. Defining the tortuosity factor q by $\rho_{eff} = q\rho_{true}$/porosity, q is 2.5 from the ferrous-ferric results and 2.1 from the ferro-ferricyanide results. In order to test the effect of Δ on entry and exit face polarizations η_O and η_L, the experimental and theoretical results are compared in Fig. 7. The experimentally measured values of η_L agree very well with the calculated values and are independent of the value of Δ, as predicted by theory. As Δ increases, η_O decreases in quantitative agreement with the theory.

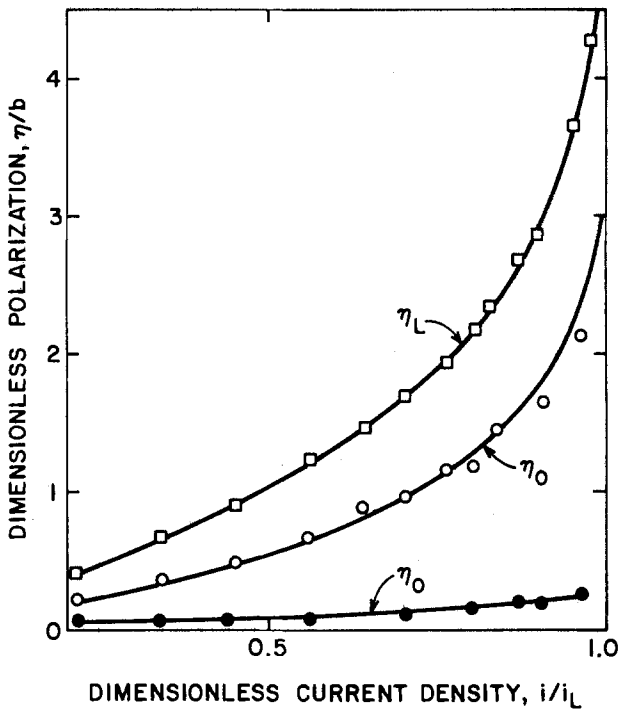


Fig. 7. Effect of the ohmic parameter Δ on the rear face polarization. η_O. ●, Oxidation of ferrous ion in 4N HCl; ○, reduction of ferric ions in 4N HCl; □, front face polarization for both; ———, theoretical curves.

Conclusions

A model is presented for a porous flow-through electrode for one-electron transfer reactions with reversible kinetics. The equations for the system considered include two controlling parameters expressed in dimensionless form. These are (*i*) the ohmic parameter Δ, which is a measure of the ohmic potential drop in the pore electrolyte, which increases with limiting current, pore electrolyte resistivity, and electrode length and (*ii*) the index of diffusion θ, which measures the relative influence of axial diffusion compared to axial convective flow. The effect of axial diffusion is to minimize the concentration gradients caused by the nonuniform distribution of the reaction. Whether the axial diffusion effect is significant or not depends on the product of Δ and θ, which is related to the ϕ criteria by $\Delta\theta = \phi$. For $\phi \leq 10^{-2}$, which is commonly the case under normal experimental conditions, the axial diffusion effect is negligible and the exit face polarization is given by a simple (Nernst) equation and is independent of the value of Δ. As Δ increases, however, the entry face polarization tends to zero. The agreement between theory and experiment is excellent under conditions of negligible axial diffusion which indicates the validity of the proposed model, and the theoretical predictions.

From Fig. 3, it is clear that any meaningful axial diffusion effects should be obtained only for $\Delta\theta \geq 1$. Taking $\Delta = 10$, then $\theta = D/Lu < 0.1$ must be satisfied in order for axial diffusion to be significant. Taking $D = 5 \times 10^{-6}$ cm^2 sec^{-1} and $L = 0.5$ cm, then $u \leq 10^{-4}$ cm sec^{-1} is a necessary condition for detecting axial diffusion effects. Such mass transfer rates are comparable to those obtainable by molecular diffusion and would give residence times of several hours. By operating a porous flow-through electrode at such low flow rates, the main virtue of the system would be eliminated. At low flow rates diffusion of the unconsumed reactant of the exiting electrolyte back into the electrode caused experimental inaccuracy in measurements of the limiting current and could not be readily corrected.

The question of radial diffusion usually arises in treating flow-through electrodes. It has been recently shown (21-23) that the efficiency of reactant conversion is not affected by radial diffusion if $\psi = R^2/2DL \leq 1$. For the present work $\psi \simeq 10^{-4}$, hence radial mass transfer limitations are negligible. The validity of this conclusion was borne out by the good agreement between theoretical and experimental results. For values of $\psi > 1$, a slow radial mass transport process may influence the maximum degree of conversion of a simple redox reaction. This may be accepted for electrodes of large pore diameter, *e.g.*, the 80 mesh folded platinum screen electrode used by Sioda (18, 24), but such electrodes are of limited practical utility because of low reactive area and poor reactant utilization.

Acknowledgment

We gratefully acknowledge the financial support of the National Science Foundation under Contract No. GK-11689.

Manuscript submitted Dec. 12, 1975; revised manuscript received Aug. 20, 1976.

Any discussion of this paper will appear in a Discussion Section to be published in the December 1977 JOURNAL. All discussions for the December 1977 Discussion Section should be submitted by Aug. 1, 1977.

LIST OF SYMBOLS

b	Tafel coefficient, $b = RT/F$
d_p	average particle diameter

D_{free} diffusion coefficient, cm²/sec
D_{eff} effective diffusion coefficient $D_{eff} = D_{free} \times$ porosity/tortuosity
E axial dispersion coefficient given by Eq. [13]
$\mathbf{F}$ Faraday constant, 96,500 C/equiv.
h the distance inside a tubular pore at which laminar flow is fully established $h \approx 0.1R$ Re
H same as above for fully developed diffusional flow $H \approx uR^2/D$
i_L limiting current density, $i_L = n\mathbf{F}uR_b$ A·cm²
i_o exchange current density, A/cm²
i total current produced by the electrode as a fraction of the limiting current
$\bar{i}(x)$ the current flowing at a distance x in the electrode as a fraction of the limiting current
L electrode thickness, cm
$P(x), P_b$ product concentration at position x in the electrode and in feed electrolyte, respectively
q tortuosity factor
$R(x), R_b$ reactant concentration at position x in the electrode and in feed electrolyte, respectively
S specific surface area of the porous electrode, cm²/cm³
T absolute temperature, °K
u superficial flow speed, cm/sec
x distance inside electrode, cm.
α transfer coefficient of reaction
Δ index of ohmic effect, $\Delta = i_L L\rho/b$
θ dimensionless parameter of axial diffusion, $\theta = D_{eff}/Lu$
ϕ dimensionless factor $n\mathbf{F}\rho DR_b/b$
γ ratio of the bulk concentration of the reactant to that of the product in the feed electrolyte
η polarization, V
η dimensionless polarization, η/b
η_0 dimensionless polarization at $x = 0$
η_L dimensionless polarization at $x = L$
μ ionic mobility cm/Vsec
ν kinematic viscosity in Stokes, cm²/sec
ρ specific resistivity of electrolyte, Ω-cm.
ρ_{eff} effective specific resistivity of electrolyte, $\rho_{eff} = \rho q$/porosity

REFERENCES

1. R. M. Perskaya and I. A. Zaidenman, *Proc. Acad. Sci. U.S.S.R., Phys. Chem. Sec.*, **115**, 513 (1957).
2. L. G. Austin, P. Palasi, and R. Klimpel, *Adv. Chem. Ser.* No. 47, p. 35 (1965).
3. I. G. Gurevich and U. S. Bagotsky, *Electrochim. Acta*, 9, 1151 (1964).
4. H. S. Wroblowa, *Electroanal. Chem.*, **42**, 321 (1973).
5. H. S. Wroblowa and A. Saunders, *ibid.*, **42**, 329 (1973).
6. R. Alkire and B. Gracon, *This Journal*, **122**, 1594 (1975).
7. L. G. Austin, in "Handbook of Fuel Cell Technology," C. Berger, Editor, p. 160, Prentice-Hall, Inc., Englewood Cliffs, New Jersey (1968).
8. L. G. Austin, *Trans. Faraday Soc.*, **60**, 1919 (1964).
9. L. G. Austin and E. G. Gagnon, *Trans. AIChE*, **17**, 1057 (1971).
10. B. G. Ateya, Ph.D., Thesis, The Pennsylvania State University (1972).
11. R. W. Powers, *Electrochem. Technol.*, **2**, 163 (1964).
12. A. I. Vogel, "A Text Book of Quantitative Inorganic Analysis," 3rd ed., pp. 282, 354, John Wiley & Son, Inc., New York (1962).
13. I. M. Kolthoff, R. Belcher, V. A. Stenger, and G. Maysuyama, "Volumetric Analysis," Vol. III, p. 53, Interscience Publishers, Inc., New York (1957).
14. I. M. Kolthoff, R. Belcher, V. A. Stenger, and G. Maysuyama, *ibid.*, p. 344.
15. V. G. Levich, "Physiochemical Hydrodynamics," pp. 113, 115, Prentice-Hall, Inc., Englewood Cliffs, New Jersey (1962).
16. M. Muskat, "Physical Principles of Oil Production," 1st ed., p. 126, McGraw-Hill, New York (1949).
17. B. G. Ateya and L. G. Austin, *This Journal*, **120**, 1216 (1973).
18. R. R. Sioda, *Electrochim, Acta*, **17**, 1939 (1972).
19. E. S. Simpson, in "Flow through Porous Media," R.de Wiest, Editor, p. 201, Academic Press, New York (1969).
20. T. K. Perkins and O. C. Johnston, *Soc. Petrol. Eng. J.*, p. 70 (March 1963).
21. H. S. Wroblowa and G. Razumney, *J. Electroanal. Chem.*, **49**, 355 (1974).
22. J. A. Kenkel and A. J. Bard, *ibid.*, **54**, 47 (1974).
23. B. G. Ateya, *ibid.*, In press.
24. R. E. Sioda, *Electrochim. Acta*, **13**, 375 (1968); **15**, 783 (1970).

Technical Notes

Surface Preparation of Epoxy Laminate to Promote Bonding of Electroless Copper

G. V. Elmore*

IBM Corporation, System Products Division, Endicott, New York 13760

The traditional method of obtaining a suitable surface for bonding electroless copper to an epoxy surface is to treat the surface with a solvent swelling agent followed by a chromic-sulfuric acid etch (1). An alternate method of forming a suitable surface is by lamination of the epoxy with a metal foil which has been treated for satisfactory bonding. The metal is then etched away, leaving a replicated surface on the epoxy. Copper foil (2) has been used for this purpose and anodized aluminum (3) also has been used.

* Electrochemical Society Active Member.

Key words: adhesion, aluminum, microroughening.

Experimental

In this investigation a modified zincate treatment for aluminum foil has been developed which creates a micronodular surface coating on the aluminum. This surface, when replicated on epoxy, is suitable for bonding to electroless copper. In this treatment a highly alkaline zincate solution is saturated with CuO (approximately 0.2 g/liter), and the aluminum foil after cleaning is treated in this solution. The simultaneous deposition of copper and zinc creates the micronodular surface on the aluminum. The treatment uses

Table I. Process steps for treatment of aluminum foil

1. 5 min in solution of 20 g/liter of NaOH
2. Spray rinse
3. 1 min in 35% HNO_3
4. Spray rinse
5. 10 min in a solution of 270 g/ilter NaOH, 100 g/liter ZnO, and 0.2 g/liter CuO (saturated)
6. Spray rinse
7. Dry

0.001 in. thick 1145 aluminum of temper H-19. The process steps are given in Table I.

In the laboratory tests, 2 × 3 ft sheets of foil were stretched on plastic frames and were processed 15 sheets at a time in a stainless steel basket. For production, processing a continuous roll would be preferable.

The treated aluminum sheets were laminated with FR-4 epoxy-glass prepreg and the aluminum foil and zinc coating were then removed with HCl. The remaining copper was removed with $CuCl_2$-HCl etchant. The epoxy-glass substrate was then catalytically seeded for electroless copper deposition by treating with a one step solution of $PdCl_2$, $SnCl_2$, and HCl, followed by rinsing. A photoresist was applied, exposed with the desired circuitry, and developed. Copper was deposited by an additive process and the photoresist then stripped away. After stripping, the copper epoxy glass panel was baked for 15 min at 170°C to improve bonding of the copper to epoxy. The bond of the copper to epoxy on four representative panels is shown in Table II.

The peel strength values shown in Table II, 4-6 lb/in., can be compared with other techniques. Anodized aluminum commercially obtained was laminated to FR-4 epoxy, etched, and additively plated with copper. A peel strength of 2.75 lb/in. resulted. Typical solvent swell and etch with chromic-sulfuric acid yielded average values of 4 lb/in. Treated copper foil laminated to FR-4 epoxy glass, etched and additively plated with copper, gave values from 3.5 to 4.25 lb/in.

To test insulation resistance, panels were made with circuitry of parallel lines with 10 mil spacing. Measurements were made after 24 hr and 168 hr while maintaining in a chamber at 32°C and 80% relative humidity. The results are shown in Table III. They show a variation of resistance between 2×10^4 to 2×10^6 megohms, which is quite satisfactory.

Scanning electron microscopy (SEM) was used to obtain the topography of the treated aluminum, the epoxy surface, and the copper surface. These surfaces are shown in Fig. 1, 2, 3, and 4. The micronodular pattern which is capable of forming a mechanical interlocking-type surface is evident. From Fig. 4, it is also evident that the bond fracture was in the epoxy layer since particles of epoxy which pulled off with the copper can be seen.

In later tests with larger volumes of panels, it was found that the bond achieved was sensitive to the number of laminates in a book between press platens. The reason for this is that quality of duplication of the aluminum surface on the epoxy is affected by the flow characteristics of the epoxy during lamination and cure of the epoxy. Thus, in books of 10 laminates, the peel strength varied from 2 to 5.25 lb/in. with an average of 4 lb/in. It was found necessary to restrict the number of laminates between heating platens to two panels for this reason.

Table II. 90° Peel strength of copper from epoxy substrates on treated panels

Panel No. 1 (lb/in.)	Panel No. 2 (lb/in.)	Panel No. 3 (lb/in.)	Panel No. 4 (lb/in.)
5½	5½-5¾	6	5¾
5½	5½	5½	5¼
5½	5	5¼	4½
5½	4½	5-5¼	4
5½	4½	5	4¼
5½-5¾	4½	4¾-5	4
5¼	4¼	4½	4½
5½	4¼	4½	4¼
5½	4½	4¾	4
5½	4½	4½	4¼
5½	4½	4¾	4½
5¾	5½	4¾	4½
5½-5¾	5¼		

Mean 4.94 lb/in.
Std dev. 0.56 lb/in.
3 sigma limits 3.26 to 6.62 lb/in.

Table III. Insulation resistance of four panels at 32°C and 80% relative humidity

Panel No.	24 hr reading, megohm	168 hr reading, megohm
1	6×10^4	2×10^5
	4×10^4	1.2×10^5
	2×10^4	7×10^4
2	1×10^5	1.2×10^5
	2.4×10^4	1×10^5
	2×10^4	7×10^4
3	1×10^5	3×10^5
	1×10^5	3×10^5
4	1.2×10^6	2×10^6
	1.4×10^5	4×10^5
	6×10^4	1.5×10^5

Conclusions

These data show that bonding of electroless copper to epoxy can be achieved with a surface on the epoxy that provides mechanical interlocking of the copper and epoxy. This surface can be obtained by replication of treated aluminum foil on the epoxy to obtain bonds of from 4 to 6 lb/in. between the epoxy and copper.

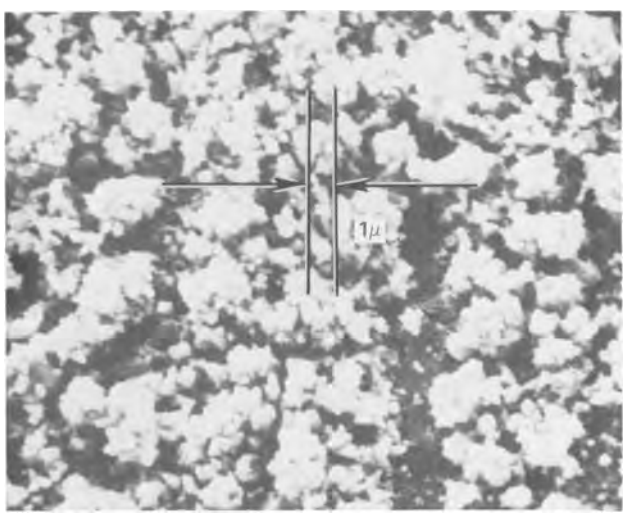


Fig. 1. Surface of treated aluminum

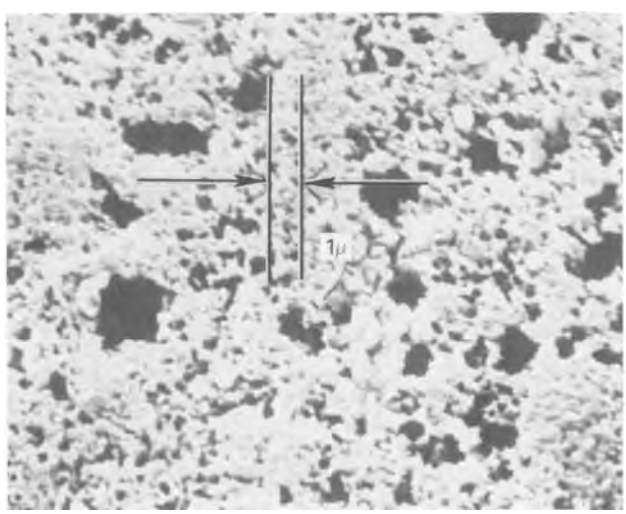


Fig. 2. Surface of treated epoxy

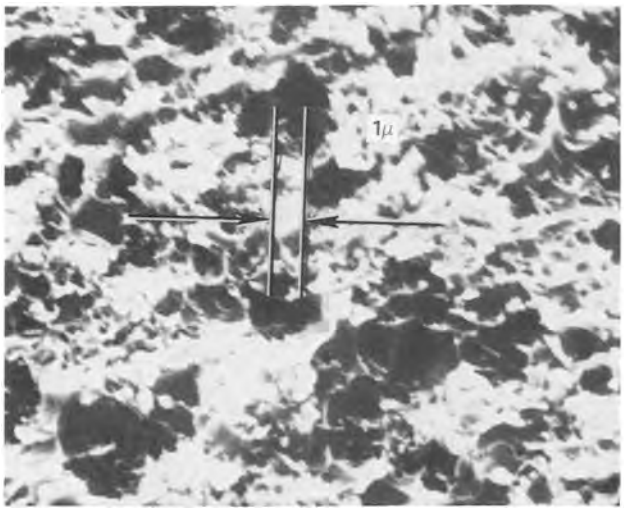


Fig. 3. Epoxy surface after peeling from copper

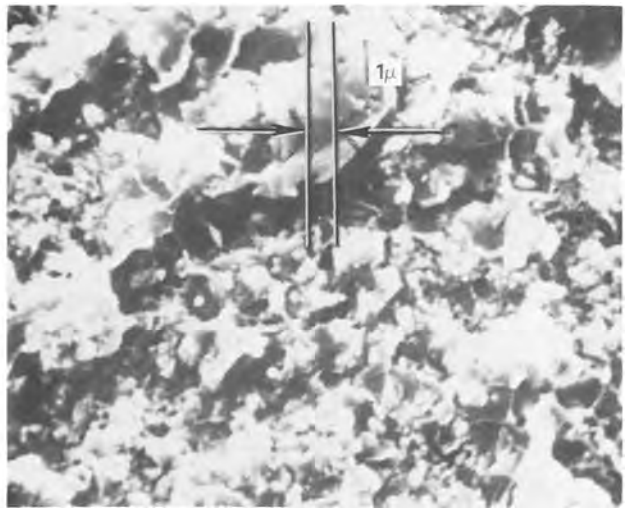


Fig. 4. Copper surface after peeling from epoxy

Acknowledgments

The assistance of Howard Rood and George Hastings in preparing the treated laminates is gratefully acknowledged. Also the contribution of William Merworth in making the SEM photographs is appreciated.

Manuscript submitted May 17, 1976; revised manuscript received Sept. 20, 1976. This was Paper 253 presented at the Las Vegas, Nevada, Meeting of the Society, Oct. 17-22, 1976.

Any discussion of this paper will appear in a Discussion Section to be published in the December 1977 JOURNAL. All discussions for the December 1977 Discussion Section should be submitted by Aug. 1, 1977.

Publication costs of this article were assisted by the IBM Corporation.

REFERENCES

1. M. Mersereau, H. L. Rhodenizer, J. J. Grunwald, and W. P. Innes, U.S. Pat. 3,698,940 (1972).
2. H. L. Rhodenizer, J. J. Grunwald, and W. P. Innes, U.S. Pat. 3,666,549 (1972).
3. J. J. Grunwald, E. D. D'Otlavio, H. L. Rhodenizer, and M. S. Lombardo, U.S. Pat. 3,620,933 (1971).

A Mechanistic Model for the Calculation of Material Balance for a Diaphragm-Type Chlorine Caustic Cell

Z. Nagy[*,1]

Diamond Shamrock Corporation, Divisional Technical Center, Painesville, Ohio 44077

Computer modeling of complex chemical systems, such as an electrochemical cell, can be carried out in two basically different ways. The statistical approach is based on regression equations of the operating variables and on judicious use of adjustable parameters which tailor-fit the model to the experimental data. The mechanistic approach is based on the understanding of the physical-chemical processes taking place in the cell. Often hybrid models are used: the statistical approach is usually based on some prior understanding of the process, and the mechanistic approach is usually forced into the use of adjustable parameters by the lack of reliable physical-chemical constants. The advantage of the mechanistic model is its applicability under a wide range of operating conditions; it is possible to run experiments with the model to predict performance in new situations. The statistical model is applicable only within the range of the original data base of the regression equations. If the model is based on plant data, this range is usually narrow and any extrapolation is questionable.

* Electrochemical Society Active Member.
[1] Present address: Argonne National Laboratory, Chemical Engineering Division, Argonne, Illinois 60439.
Key words: chlorine, caustic, electrolysis, diaphragm, computer.

The only published model for the diaphragm-type chlorine caustic cell is a statistical type by MacMullin (1, 2). A recent accumulation of published physical-chemical constants makes it possible to attempt to mechanistically model this cell. The model can be divided into three parts for convenience of preparation: material balance, energy balance, and diaphragm behavior. These parts are, of course, interrelated and will have to be merged at a later stage. In this communication only the material balance will be discussed. This part of the model uses literature values for most constants and has only one equation with adjustable parameters.

The Mechanistic Base of the Model

The processes occurring in the cell are considered in a somewhat simplified way, not to avoid computational difficulties, but to stay away from areas for which the required physical-chemical constants are not available. These processes, and the simplifying assumptions, will be described briefly before giving the computational details. The over-all assumption is that of steady-state cell operation, and the perfect mixing of the solution by gas evolution both in the anolyte and the catholyte.

That is, all bulk processes are independent of time and space coordinates.

Anode side.—The main electrode reaction, on the titanium-based RuO_2 anode, is the oxidation of chloride ions while the oxidation of water is an efficiency loss

$$2Cl^- \rightarrow Cl_2 + 2e \quad [1]$$

$$2H_2O \rightarrow O_2 + 4H^+ + 4e \quad [2]$$

The portion of the total current lost by water oxidation is expressed as a function of current density, temperature, and the NaCl concentration and *p*H of the anolyte. This is the parametric equation fitted to experimental data.

Some of the chlorine gas produced at the anode will take part in chemical side reactions resulting in unwanted impurities. The chlorine will dissolve in the anolyte and will react to form trichloride ion and hydrolysis products

$$Cl_2(g) \rightleftharpoons Cl_2(aq) \quad [3]$$

$$Cl_2(aq) + Cl^- \rightleftharpoons Cl_3^- \quad [4]$$

$$Cl_2(aq) + H_2O \rightleftharpoons HOCl + H^+ + Cl^- \quad [5]$$

$$HOCl \rightleftharpoons H^+ + OCl^- \quad [6]$$

These reactions are considered to be in equilibrium in the anolyte; all equilibrium constants are known. A reaction too slow to reach equilibrium is the chemical chlorate formation

$$2HOCl + OCl^- \rightarrow ClO_3^- + 2H^+ + 2Cl^- \quad [7]$$

the rate equation of which is also known. These are essentially the same reactions as those considered by de Valera (3) and Kircher *et al.* (4, 5).

Diaphragm.—In the material balance part of the model, the diaphragm is assumed to be a simple, chemically inert and physically stable porous barrier which is preventing the free mixing of the anolyte and catholyte. The solution transfer through the pores is taken to be plug flow. It is assumed that no chemical reactions take place in the diaphragm, neither amongst the dissolved species nor with the diaphragm material. The processes to be considered then are only those of mass transfer from the anode side to the cathode side of the cell. (The hydroxide transfer in the reverse direction is to be calculated by the more complex diaphragm part of the model.) The diffusion in the forward direction can be neglected, as one can estimate that it will be only a few percent of the total mass transport. A flux equation can then be written for each species as

$$J_i = t_i I/z_i F + C_i v \quad [8]$$

The concentration, and through it the transference number, of the species will vary with the distance coordinate in the diaphragm. This complication can be avoided if one divides the diaphragm, in principle, into thin layers so that the concentration variation within a layer will be negligible. Under the conditions of the model (namely the assumptions of steady state and no reaction in the diaphragm), the flux of any species will be the same through all the layers; therefore it is sufficient to carry out the calculations for one arbitrarily selected layer. It is convenient to select the first layer toward the anolyte, in which case one can take the composition of the solution to be the same as that of the anolyte.

Cathode side.—The main cathodic reaction is the reduction of water

$$2H_2O + 2e \rightarrow H_2 + 2\,OH^- \quad [9]$$

Two electrochemical and a chemical side reactions also occur

$$OCl^- + H_2O + 2e \rightarrow Cl^- + 2\,OH^- \quad [10]$$

$$ClO_3^- + 3H_2O + 6e \rightarrow Cl^- + 6\,OH^- \quad [11]$$

$$OCl^- + H_2 \rightarrow Cl^- + H_2O \quad [12]$$

The reduction of hypochlorite in the chlorine cell catholyte has been well documented (4-8), and it is an experimental fact that the catholyte overflow of a normally operating cell does not contain any hypochlorite. There is no basis for dividing the reduction between the electrochemical and the chemical routes, but, as long as the reduction is complete, it is immaterial for the present purposes. The reduction of chlorate has been somewhat controversial (4, 8-10). Our laboratory measurements have confirmed the results of Veselovskaya *et al.* (9), indicating a slow electrochemical reduction of chlorate on the steel cathode.

Computational Details

A flow chart of the program is shown in Fig. 1. The input requirements are summarized in Table I; the parameters in parenthesis are needed as an input for the material balance, but in the full model they will be calculated by the diaphragm and the energy balance sections. The first step is the calculation of the chlorine and caustic production efficiencies from the hydroxide backmigration rate and acid/base content of the feed.

The calculation of the anolyte composition is started with the calculation of the NaCl concentration using Eq. [8] written for sodium ions. An iterative procedure is used since the required parameters depend on the NaCl concentration to be determined. The total flux is known from the feed rate. The transference number has been measured by Mussini and Pagella (11) and their results can be expressed as

$$t_{Na} = 0.3754377 + 4.864677 \times 10^{-4} \times t + (-0.03151785 + 1.455249 \times 10^{-4} \times t) \times m_1 + (0.011552 - 3.588446 \times 10^{-5} \times t) \times m_1^2 + (-1.297191 \times 10^{-3} + 3.044053 \times 10^{-6} \times t) \times m_1^3 \quad [13]$$

The convective flow rate through the anolyte can be obtained by correcting the total feed rate for the materials removed in the anode gas and the material transported by electromigration through the diaphragm. The water vapor pressure over the anolyte is calculated using the equations given by MacMullin (12) neglecting all dissolved components but the NaCl. A correction for water condensation at anode gas temperature is made if needed. The oxygen generation rate is assumed, subject to later iteration. The CO_2 generation rate is calculated from the carbonate content of the feed assuming acidic anolyte and 100% conversion. The gas mixture is treated as ideal gas; the deviation from ideality of the major components is less than 1% at 1 atm pressure and 90°C (13-15). The concentration of the minor anion components of the anolyte is neglected here and the NaCl concentration is set equal to the Na^+ concentration.

The next step is the calculation of the concentration of the minor components based on reactions [3]-[7].

Table I. Summary of input and output

Input	Output
Feed rate	Anolyte composition and flow rate
Feed composition	NaCl, available chlorine (Cl_2(aq), Cl_3^-, HOCl, OCl^-), $NaClO_3$, *p*H
Current	Catholyte composition and flow rate
Geometrical dimensions of cell	NaOH, NaCl, $NaClO_3$
Anolyte level	Anode gas composition and flow rate
(Hydroxide backmigration rate)	Cl_2, O_2, CO_2, H_2O
(Temperature of anolyte, catholyte)	Cathode gas composition and flow rate
(Temperature of anode gas, cathode gas)	H_2, H_2O
	Current efficiencies of Cl_2, NaOH, and H_2 production
	Cl_2 and NaOH loss to O_2, $NaClO_3$, and available chlorine
	Cl_2 or NaOH loss to basic or acid feed
	H_2 loss to ClO_3^- and OCl^- reduction
	Input/output balance for Na, Cl, O, H, and C

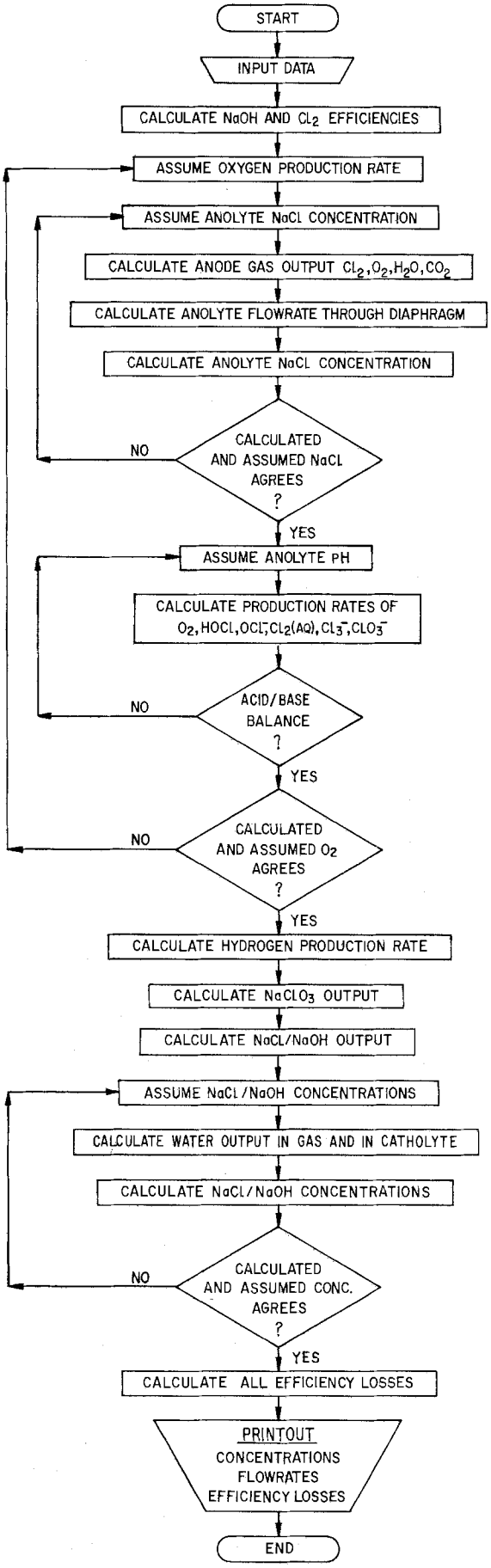


Fig. 1. Flow chart of the program

This is another iterative procedure involving the anolyte *p*H. The chlorine solubility as the sum of $Cl_2(aq) + Cl_3^-$ has been measured by Yokota (16)

$$C_3 = (2.20997 \times 10^{-5} - 2.32597 \times 10^{-6} \times C_1) \times P \times \exp(2302.59/T) \quad [14]$$

The equilibrium constant of reaction [4] is expressed as

$$K = 6.4498 \times 10^{-3} \exp(1030.87/T) \quad [15]$$

based on the data of Cerquetti *et al.* (17, 18). The hypochlorous acid concentration resulting from the chlorine hydrolysis was also measured by Yokota (16) and can be given as

$$C_4 = \exp(-13.8385 - 2.30259 \times 10^{-3} \times t + 5.92106 \times 10^{-2} \times C_1 + 2.30259 \times pH) \quad [16]$$

The dissociation constant of the hypochlorous acid was expressed as

$$K = 3.7508 \times 10^{-6} \exp(-1450.6/T) \quad [17]$$

based on the data of Ref. (19) and other sources identified therein. The activity coefficient of the hydrogen ion was determined from the data of Schwabe (20) giving the *p*H shift resulting from the effect of sodium chloride as

$$\Delta pH = -0.192 \times m_1 \quad [18]$$

The activity coefficients of hypochlorous acid and hypochlorite ions were taken as 2.0 and 0.1, respectively, after Imagawa and Jaksic (21, 22). The production rate of these components is calculated as a product of their concentration and the convective flow rate of the anolyte. That is, for these components the electromigration term is neglected in Eq. [8] as only a negligible portion of them is ionic.

The chlorate production rate is calculated by the kinetic equation of Knibbs and Palfreeman (23) which is in agreement with numerous other determinations (24)

$$\frac{dC_6}{d\tau} = 5.555 \times 10^{-3} \exp(0.6 + 0.056 \times t) \times C_4^2 \times C_5 \quad [19]$$

To obtain the total chlorate production, this is multiplied by the anolyte volume which can be calculated from the anolyte level and cell geometry input data using a 10% correction for bubble filling. The chlorate concentration is calculated with Eq. [8] assuming that the mobility of the chlorate ions is the same as that of the chloride.

The oxygen production rate is calculated with either of the following parametric equations. This is the only equation in the present model which has adjustable parameters; their values were selected to achieve agreement between the calculated and measured oxygen content of the anode gas. (See discussion below.)

$$I_1 = (6.3115 \times 10^{-4} + 1.48291 \times 10^{-6} \times t - 1.61334 \times 10^{-4} \times C_1) \times I^{0.63} \times \exp(1.15129 \times pH) \quad [20]$$

$$I_1 = (1.35066 \times 10^{-3} + 3.17343 \times 10^{-6} \times t - 3.45255 \times 10^{-4} \times C_1) \times I^{0.63} \times \exp(1.15129 \times pH) \quad [21]$$

An acid/base balance is then set up: the acid produced by reactions [2] and [5]-[7] is compared to the hydroxide backmigration corrected for the acid/base in the feed. An equality is required by the steady-state assumption, which allows the iterative determination of the *p*H. Finally, the iteration of oxygen production rate is carried out.

The hydrogen losses are calculated assuming complete reduction of hypochlorite and partial reduction of chlorate (9)

$$I_2 = 3 \times 10^{-3} \times I \times C_6 \quad [22]$$

The final calculation of the catholyte composition is another iterative loop; the vapor pressure equations of MacMullin (12) are used and correction is made for

water condensation in the gas if needed. The cathode gas is treated as an ideal gas mixture. All specific efficiency losses are calculated and the results printed as summarized in Table I.

The algorithms for solution densities were based on International Critical Table (25) values for the NaCl solution and on Ref. (26-29) for the mixed NaCl-NaOH solution.

$$d_1 = 1.0004075 - 7.1687895 \times 10^{-6} \times t - 5.1792075 \times 10^{-6} \times t^2 + 1.054032 \times 10^{-8} \times t^3 + (7.4569085 \times 10^{-3} - 2.960572 \times 10^{-5} \times t + 3.0564225 \times 10^{-7} \times t^2 - 9.3493315 \times 10^{-10} \times t^3) \times w_1 + (1.8372605 \times 10^{-5} + 4.2360185 \times 10^{-7} \times t - 5.1483125 \times 10^{-9} \times t^2 + 1.794537 \times 10^{-11} \times t^3) \times w_1^2 \quad [23]$$

$$d_2 = 1.00686 + 1.147527 \times 10^{-2} \times w_2 - 1.722033 \times 10^{-5} \times w_2^2 - 3.585138 \times 10^{-4} \times t - 2.143812 \times 10^{-6} \times t^2 + 7.550802 \times 10^{-3} \times w_1 \quad [24]$$

Results and Discussion

The model was tested with a series of data sets obtained from two sources. Data were collected from five commercial production cells in the Painesville, Ohio, plant of Diamond Shamrock Corporation; three DS-45 and two DS-85 cells were used. The second set was obtained from four small experimental cells which were built according to the same design principles as the above-mentioned production cells. The results are shown in Table II. The main components were predicted within a few grams per liter and the minor components within a few tenths of a gram per liter. This good fit indicates that the major effects were correctly identified and the neglections and simplifications did not introduce a serious error.

There was, however, an unaccounted effect of the cell hardware design which resulted in the use of two different oxygen equations for the experimental and the production cells (Eq. [20] and [21]). The data of each cell were first individually evaluated for the determination of the oxygen parametric equations. The constants in every equation were somewhat different, but within each group they were close enough for the establishment of the over-all equations. The diaphragm did not introduce any effects as the individual cell equations remained valid after repeated diaphragm changes. While one could indulge in speculations, there is not enough information in the present set of data to allow the identification of the variable responsible for this effect. This, however, introduces only a small variation in the model, the physical-chemical basis of which seems to be well substantiated by the good agreement of the experimental and calculated values.

Acknowledgments

The author is indebted to Mr. E. I. Fogelman for many useful discussions and for supplying the experimental cell data. Thanks are also due to the R&D Management of the Electrochemical Division of Diamond Shamrock Corporation for their encouragement during the course of this work and for their permission to publish it.

Manuscript submitted July 27, 1976; revised manuscript received Sept. 3, 1976. This was Paper 251 presented at the Washington, D.C., Meeting of the Society, May 2-7, 1976.

Any discussion of this paper will appear in a Discussion Section to be published in the December 1977 JOURNAL. All discussions for the December 1977 Discussion Section should be submitted by Aug. 1, 1977.

Publication costs of this article were assisted by Diamond Shamrock Corporation.

Table II. Summary of prediction errors

Variable	Range of observations	Average error
Anolyte NaCl concentration (g/liter)	228-268	−1.3
Anolyte available chlorine (g/liter)	0.6-6.1	−0.42
Anolyte $NaClO_3$ concentration (g/liter)	0.2-6.6	+0.40
Anolyte oxidizing power (as g/liter $NaClO_3$)	0.5-9.1	+0.24
Anolyte pH	3.8-4.8	+0.37
Anode gas O_2 content (%)	0.5-5.9	−0.03
Catholyte NaOH concentration (g/liter)	100-180	−0.5
Catholyte NaCl concentration (g/liter)	123-213	−0.9
Catholyte $NaClO_3$ concentration (g/liter)	0.1-4.2	−0.1

LIST OF SYMBOLS

C_i	concentration of species i (mole/liter)
C_1	concentration of NaCl (mole/liter)
C_2	concentration of NaOH (mole/liter)
C_3	concentration of $Cl_2(aq) + Cl_3^-$ (mole/liter)
C_4	concentration of HOCl (mole/liter)
C_5	concentration of OCl^- (mole/liter)
C_6	concentration of $NaClO_3$ (mole/liter)
d_1	density of NaCl solution (g/cm³)
d_2	density of NaCl-NaOH solution (g/cm³)
$\mathbf{F}$	Faraday number
I	total current density (A/cm²)
I_1	current density producing oxygen (A/cm²)
I_2	current density reducing $NaClO_3$ (A/cm²)
J_i	flux of species i (mole/sec cm²)
m_1	concentration of NaCl (mole/kg H_2O)
P	chlorine pressure (atm)
t	temperature (°C)
t_i	transference number of species i
T	temperature (°K)
τ	time (sec)
v	convective velocity (cm/sec)
w_1	concentration of NaCl (w/o)
w_2	concentration of NaOH (w/o)
z_i	charge of species i

REFERENCES

1. R. B. MacMullin, *Denki Kagaku*, **38**, 570 (1970).
2. R. B. MacMullin, *This Journal*, **120**, 135C (1973).
3. V. de Valera, *Trans. Faraday Soc.*, **52**, 250 (1956).
4. R. L. Murray and M. S. Kircher, *Trans. Electrochem. Soc.*, **86**, 83 (1944).
5. M. S. Kircher, in "Chlorine, Its Manufacture, Properties and Uses," J. S. Sconce, Editor, Reinhold, New York (1962).
6. L. Hammar and G. Wranglen, *Electrochim. Acta*, **9**, 1 (1964).
7. F. Hine and M. Yasuda, *This Journal*, **118**, 170 (1971).
8. V. I. Skripchenko, E. P. Drozdetskaya, and K. G. Ilin, *Zh. Prikl. Khim.*, **48**, 352 (1975).
9. I. E. Veselovskaya, E. M. Kuchinskii, and L. V. Morochko, *ibid.*, **37**, 76 (1964).
10. F. Hine and M. Yasuda, *This Journal*, **118**, 182 (1971).
11. T. Mussini and A. Pagella, *Chim. Ind. (Milan)*, **52**, 1187 (1970).
12. R. B. MacMullin, *This Journal*, **116**, 416 (1969).
13. N. E. Dorsey, "Properties of Ordinary Water Substance," p. 575, Reinhold, New York (1940).
14. A. S. Ross and O. Maass, *Can. J. Res. Sect. B*, **18**, 55 (1940).
15. R. M. Kapoor and J. J. Martin, "Thermodynamic Properties of Chlorine," Engineering Research Institute, University of Michigan, Ann Arbor, Michigan (1957).
16. N. Yokota, *Kagaku Kogaku*, **22**, 476 (1958).
17. A. Cerquetti, P. Longhi, T. Mussini, and G. Natta, *J. Electroanal. Chem.*, **20**, 411 (1969).
18. G. Zimmerman and F. C. Strong, *J. Am. Chem. Soc.*, **79**, 2063 (1957).
19. J. C. Morris, *J. Phys. Chem.*, **70**, 3798 (1966).
20. K. Schwabe, *Electrochim. Acta*, **12**, 67 (1967).
21. H. Imagawa, *Denki Kagaku*, **20**, 571 (1952).
22. M. M. Jaksic, *J. Appl. Electrochem.*, **3**, 307 (1973).
23. N. V. S. Knibbs and H. Palfreeman, *Trans. Faraday Soc.*, **16**, 402 (1920).
24. D. V. Kokoulina and L. I. Krishtalik, *Elektrokhimiya*, **7**, 346 (1971).
25. "International Critical Tables III," pp. 79 and 105,

McGraw-Hill, New York (1928).
26. L. Demolis, *J. Chim. Phys. Phys. Chim. Biol.*, **4**, 528 (1906).
27. A. H. Hooker, *Chem. Metall. Eng.*, **23**, 961 (1920).
28. F. Giordani, *Rend. Accad. Sci. Fis. Mat. Naples*, **30**, 150 (1924).
29. A. Antropoff, *Z. Elektrochem. Angew. Phys. Chem.*, **30**, 457 (1924).

On the Complex Formed by Addition of $TiCl_4$ to Anhydrous Dimethylsulfoxide

C. M. Marschoff,* C. Urribarrí, and P. J. Aragón*,[1]

Departamento de Química, Laboratorio de Electroquímica y Corrosión, Universidad de los Andes, Mérida, Venezuela

In the course of studies on the electrochemical behavior of titanium salts in nonaqueous solvents, it was found that when $TiCl_4$ is added to anhydrous dimethylsulfoxide a very exothermic reaction takes place, and a solid, whose color and texture varies according to the reaction temperature, is formed.

This reaction is only briefly mentioned in the literature (1, 2) and the molecular formula $TiCl_4(DMSO)_2$ is proposed (1). Since no further information on this reaction and the resulting complex was available, and because of the technological importance of titanium, some tests were performed in order to confirm this proposed formula and to study some characteristics of the complex and its solutions that might be of interest for practical purposes.

Experimental

As the reaction showed to be very exothermic and the product reacted both with oxygen and water, the synthesis and analysis of the obtained solid were carried out in an inert atmosphere. DMSO was distilled four times under reduced pressure until it showed no reaction with calcium hydride. Then, it was introduced into the dry box. $TiCl_4$ previously purified by reaction with copper in an inert atmosphere (3) was then added dropwise with continuous stirring.

When the reaction temperature was kept below 40°C, the product was a crystalline, light yellow solid. When the reaction was allowed to proceed at higher temperatures the product was an oily, yellowish orange solid which did not show a definite melting point, suggesting that a mixture of complexes or a polymer had been obtained. The crystalline solid was dried for 3 days at 10^{-4} Torr and then used for the different tests.

Results

Melting point.—The melting point was determined to be 144°-145°C.

Chemical analysis.—Chlorine and sulfur contents were determined gravimetrically. Titanium was also determined by classical gravimetric methods by making the solid react with water and weighing the obtained TiO_2. Carbon was analyzed as CO_2. See Table I.

IR spectrum.—An *IR* spectrum of the solid was scanned using the KBr pellet. The obtained frequencies, together with the results of the elementary analysis, Table II, confirm the molecular formula proposed by previous work (1).

Properties of the solutions.—The solid showed to be insoluble in a wide variety of solvents, including carbon tetrachloride, chloroform, benzene, toluene, ethyl ether, ethyl acetate, carbon disulfide, and acetone. It reacted with water and the lower alcohols giving a white precipitate which, under x-ray analysis, showed to be TiO_2. The complex was found to be soluble only in excess of DMSO, Fig. 1, and was recrystallized from DMSO-benzene mixtures.

Solubility and conductivity measurements were carried out as a function of temperature. The equivalent conductance at infinite dilution, Fig. 2, does not follow a straight line when plotted against temperature and its value between 25° and 45°C is within the range 31-40 Siemens cm^2 $equiv.^{-1}$.

The fact that the Λ° increases with temperature does not correspond, as it should, to a linear relationship (4) and the change in shape of the solubility curve about 40°C suggests that the nature of the solute is modified near this temperature. This is in accordance with the observed change in the reaction product when the reaction temperature reaches 40°C. If the yellow solid is kept at temperatures higher than 40°C a change in color is also observed. According to existing data on the $Cl_4Ti(DMSO)_2$ complex (2, 5) it is concluded that sulfoxide groups are changed into sulfide.

The observed equivalent conductance is sufficiently high that it may be concluded that the complex dissociates into ions. The addition of a few drops of $AgNO_3$ immediately produces precipitation of AgCl. This

Table I. Elementary analysis of the complex, except H and O

Element	Weight, g Expt. 1	Expt .2	Expt. 3	Expt. 4	Expt. 5	Molar ratio
Ti	1.075	0.725	0.833	1.102	0.924	1.00
Cl	3.175	2.140	2.464	3.250	2.727	3.98
S	1.424	0.960	1.100	1.455	1.230	1.98
C	1.048	0.702	0.812	1.085	0.887	3.88

Table II. Observed frequencies and assignments for the addition complex of $TiCl_4$ and DMSO

Frequency, cm^{-1}	Intensity*	Assignment	Reference
3050	ms	C-H stretching of DMSO	(5)
2500-200	w	S-O stretching of DMSO	(5)
1300	ms	C-H deformation of DMSO	(5)
1285	m	C-H deformation of DMSO	(5)
1050-900	s	S-O stretching of DMSO in complexes	(6)
750	s	C-S stretching of DMSO	(5)
420	s	Ti-O stretching	(7)
250	vs	Ti-Cl stretching	(8, 9)

* m, medium; ms, medium strong; s, strong; vs, very strong; w, weak.

* Electrochemical Society Active Member.
[1] Present address: COMINCO Research Center, Toronto, Ontario, Canada.
Key words: titanium, nonaqueous solvents, electrical conductance.

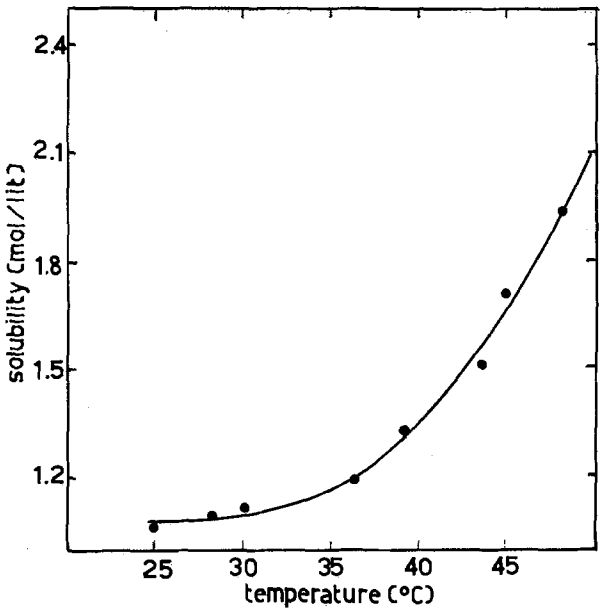


Fig. 1. Solubility curve for $Cl_4Ti(DMSO)_2$ dissolved in DMSO

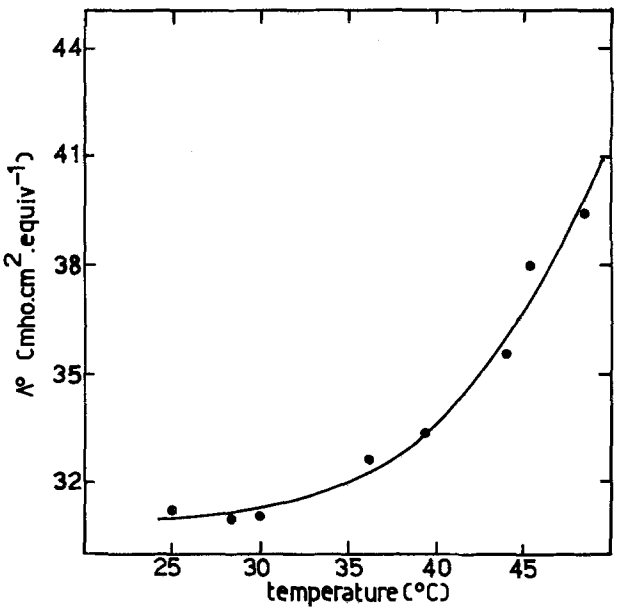


Fig. 2. Equivalent conductance at infinite dilution for DMSO solutions of $Cl_4Ti(DMSO)_2$ as a function of temperature.

shows that Cl^- ions are present in the solution probably through the equilibrium

$$TiCl_4(DMSO)_2 = TiCl_2(DMSO)_2{}^{++} + 2Cl^-$$

Further studies on the dissociation of this complex as well as on the electrolysis of the DMSO solutions are being currently pursued in our laboratory.

Acknowledgment

The authors are indebted to CONICIT for financial support to this work through Grant 31 26 SI 0335.

Manuscript received June 2, 1976.

Any discussion of this paper will appear in a Discussion Section to be published in the December 1977 JOURNAL. All discussions for the December 1977 Discussion Section should be submitted by Aug. 1, 1977.

Publication costs of this article were assisted by the Universidad de los Andes.

REFERENCES

1. H. L. Schläfer and W. Schaffernicht, *Angew. Chem.*, 72, 618 (1960).
2. R. J. H. Clark, "The Chemistry of Titanium and Vanadium," Elsevier Publishing Co., Amsterdam (1968).
3. J. Barksdale, "Titanium," Ronald Press Company, New York (1966).
4. R. A. Robinson and R. H. Stokes, "Electrolyte Solutions," Butterworths, London (1970).
5. A. D. Westland and L. Westland, *Can. J. Chem.*, **43**, 426 (1965).
6. H. H. Szmant, in "Dimethylsulfoxide," S. Jacob, E. Rosenbaum, and D. C. Woods, Editors, Marcel Dekker Inc., New York (1970).
7. F. F. Bentley, L. D. Smithson, and A. L. Rozek, "IR Spectra and Characteristic Frequencies 700-300 cm^{-1}," Interscience Publishers, New York (1968).
8. R. Colton, in "MTP International Review of Science, Inorganic Chemistry," Series One, Vol. 5, D. W. A. Sharp, Editor, Butterworths, London (1972).

Brief Communications

An Interferometric Study of Low Temperature Charging of the Lead-Acid Cell

R. N. O'Brien*

Department of Chemistry, University of Victoria, Victoria, British Columbia, Canada V8W 2Y2

A number of models to explain the relatively low charge acceptance of lead-acid secondary cells at temperatures below −20°C have been proposed. The most recent is that of Valeriote and Gallop (1). Using in part the heterogeneous compositions of the anodic layer postulated by Pavlov and co-workers in a long series of papers which in 1968 (2) gave a correlation of the composition of potentiostatically formed films by x-ray diffraction (and electron microscope) studies with measurements of current, charge, applied potential, and electrode capacitance, they have evolved a relatively satisfactory model. According to Pavlov and Valeriote the method of forming β-PbO_2, the active material, varies with the previous history of

* Electrochemical Society Active Member.
Key words: interferometry, convection, cold-charging, lead acid.

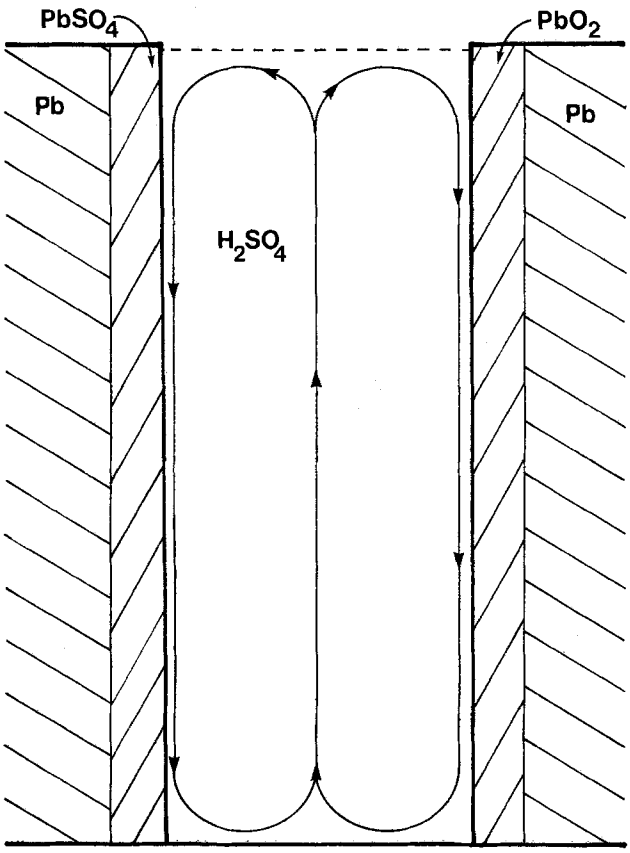


Fig. 1. The natural convection regime expected during the charging cycle.

discharge of the cell and the method of charging. The low temperature resistance to charge acceptance can be explained by one sequence of discharge-charge conditions using Pavlov's mechanism to explain the existence of electrode phases which are chemically unstable in bulk acid solution.

A critical aspect of charge acceptance is the existence of pores in the multicomponent layer between the lead and bulk electrolyte. Valeriote and Gallop suggest several inhibiting mechanisms to charging including pore blockage by precipitation of $PbSO_4$ or PbO_2 or ice formation in the relatively dilute electrolyte in the pores. The present work was begun to investigate solution conditions accompanying low temperature resistance to charge acceptance.

An interferometer containing a micro lead-acid cell of a design previously described (3) was used. The cell was 0.318 cm thick with an electrode area of 0.80 cm^2. Electrodes were made by cycling 99.99% Pb sheet in 4M H_2SO_4 or cut from a standard automotive battery. Interferograms were recorded on videotape and selected ones analyzed. Tapes were viewed and reviewed to assess solution changes at leisure.

If a soluble reducible material were produced at the anode which could diffuse to the cathode and be reduced at temperatures below −20°C, then inability to charge a battery would be explainable but not as simple nonacceptance of charge. A refractive index gradient, caused by higher refractive index for the more oxidized product plus greater concentration of it at the anode, would be expected. No such gradient appeared at any temperature. When the electrolyte in a cell charged at 25° and −30°C was drained, diluted approximately four times, and analyzed by atomic absorption spectrometry, the lead content was the same within the accuracy of the instrument for each sample, but above the predicted solubility. It is considered that suspended lead particles dissolved on sample dilution. In view of these analyses and the absence of a visible concentration gradient, an ionic discharge mechanism of the correct magnitude seems unlikely.

If charging were a simple conversion of $PbSO_4$ to PbO_2 at the anode and $PbSO_4$ to Pb at the cathode with H_2SO_4 evolved at both electrodes, a natural convection pattern as shown in Fig. 1 would result. Because H_2SO_4 is heavier than water, downward convective currents would be generated at both electrodes. Such a pattern was looked for by suspending activated charcoal particles in the electrolyte and recording their movements and also looking for convection-limited diffusion layers. The pattern (Fig. 1) was observed but only on a few of the many runs done.

All possible situations were observed, that is, where there were no concentration gradients and no gas evolution and hence no convection to the most complicated situation where part of each electrode was gassing and other parts showing concentration gradients resulting in erratic convection patterns. Pavlov's model as modified by Valeriote and Gallop predicts such changes in behavior as a function of time when the electrodes are subjected to varying potential regimes in charging and discharging cycles. Figure 2 shows three interferograms taken at 15 sec intervals of charging at 1 mA cm^{-2}, a concentration gradient at the anode (right-hand side PbO_2 formation) with downward convection at that electrode (charcoal particles in suspension were observed) with gas evolution at three points, the bubbles showing as black spheres. The concentration gradient is a maximum at 30 sec and shows convection limitation at 60 sec.

Electrodes cut from an old automotive battery showed the same behavior in general, but the sizes

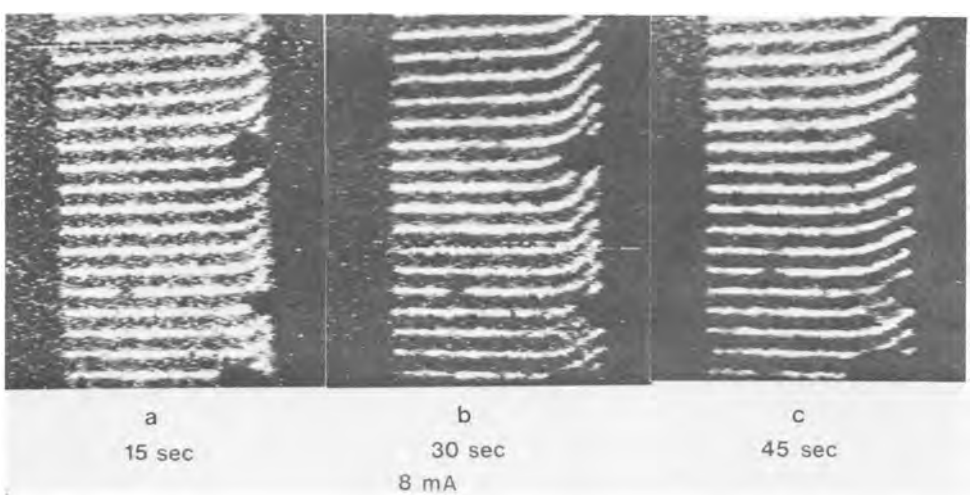


Fig. 2. A series of interferograms taken at 15 sec intervals during a charging cycle at −30°C and 1 mA cm^{-2}.

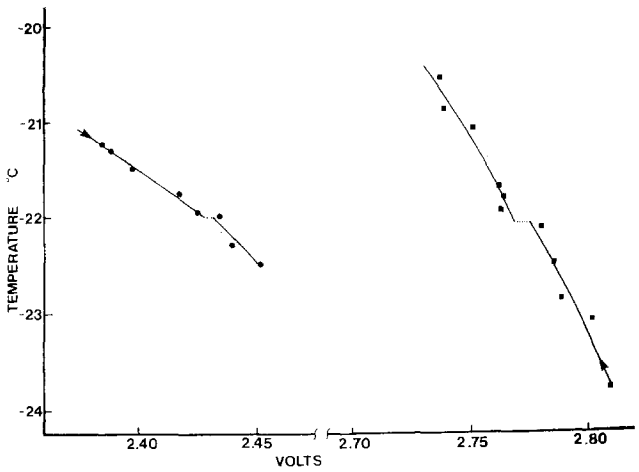


Fig. 3. A plot of the potential required to charge the cell at 10.00 mA cm^{-2} at temperatures between −20° and −24°C.

of electrode surface that tended to behave differently (with and without gas evolution and with and without concentration gradients) were smaller tending to have linear dimensions less than 1 mm.

The electrodes from the automotive battery showed a distinct change in impressed voltage required to charge at a constant current density of 10.00 mA cm^{-2} at −22°C as the temperature was raised or lowered. Figure 3 shows that the slope of the cooling run ($\partial V/\partial T$) is greater than the warming run, but each shows an abrupt change of about 10 mV at −22°C. Valeriote (4) has suggested this is freezing of the liquid in the pores of the heterogeneous $PbSO_4$-PbO_2 layer at the anode.

Acknowledgments

This work was supported by the Defence Research Board of Canada. Most of the experimental work was performed by R. J. Raine.

Manuscript received Aug. 24, 1976.

Any discussion of this paper will appear in a Discussion Section to be published in the December 1977 JOURNAL. All discussions for the December 1977 Discussion Section should be submitted by Aug. 1, 1977.

Publication costs of this article were assisted by the University of Victoria.

REFERENCES

1. E. M. L. Valeriote and L. D. Gallop, *This Journal*, To be published; E. M. L. Valeriote and L. D. Gallop, *ibid.*, To be published.
2. D. Pavlov, *Electrochim. Acta*, **13**, 2051 (1968).
3. R. N. O'Brien, *Rev. Sci. Instr.*, **35**, 803 (1964); R. N. O'Brien, *This Journal*, **113**, 389 (1966).
4. E. M. L. Valeriote, Personal communication.

The Stability of Photoelectrodes

J. O'M. Bockris* and K. Uosaki

School of Physical Sciences, The Flinders University of South Australia, Adelaide, Australia

The stability of a semiconductor electrode under illumination is one of the key points in the prospect for the photoelectrochemical production of hydrogen.

Recently, Harris *et al.* (1) reported that TiO_2 single crystals were not stable and the photocurrents decreased with time in all cases they examined. Similar results were reported by Wrighton *et al.*, although they found no sign of decomposition of TiO_2 (2). Also, Yoneyama *et al.* (3) found that p-GaP was not stable under illumination, although they mentioned that there could be a possibility of obtaining a stable condition by choosing a suitable electrolyte, etc.

The stability of a TiO_2 single crystal cut perpendicularly to the c axis [(001) face] obtained from Nakazumi Crystal Corporation and of a p-type GaP wafer [Zn doped, (111) face] donated by Dr. K. Akita of the Fujitsu Laboratory Limited was examined in 1*N* NaOH solution.

The TiO_2 single crystal was reduced in a hydrogen atmosphere at 800°C for 5 hr (4). An ohmic contact to TiO_2 was obtained by means of indium (5) and a copper wire was soldered onto the indium. The specific resistance of the crystal was 2.0 Ω · cm.

A p-type GaP was etched in HNO_3-HCl (2:1) mixture (6) and an ohmic contact was made by means of Zn-In alloy (3). The specific resistance was 1.3 Ω · cm.

The semiconductor electrodes were mounted in a Teflon electrode holder with an epoxy resin so that only the faces to be examined were exposed to the solution. The electrode area was 0.125 cm^2. A 900W Xe lamp (Canrad-Hanovia 538 C1) was used as a light source and an infrared absorbing filter (Oriel G-776-7100) was placed between the light source and the electrochemical cell. A PAR 173 potentiostat was employed to maintain the electrodes at given potential.

* Electrochemical Society Active Member.

Key words: photoelectrode, titanium dioxide, gallium phosphide, semiconductor electrode.

The results are shown in Fig. 1 for TiO_2 and in Fig. 2 for p-GaP.

Although Harris *et al.* (1) mentioned that the photocurrent of TiO_2 decreased in all cases studied by them and Wrighton *et al.* (2) reported the fall of the photocurrents with time but without details, the photocurrents in our work did not change detectably over 1000 min (Fig. 1).

Also, the photocurrent of p-GaP decreased only slightly with time (Fig. 2). This behavior is different from that reported by Yoneyama *et al.* (3).

These results suggest that the stability of the photocurrent at semiconductors depends upon the preparation, dopant, and pretreatment of the semiconductor

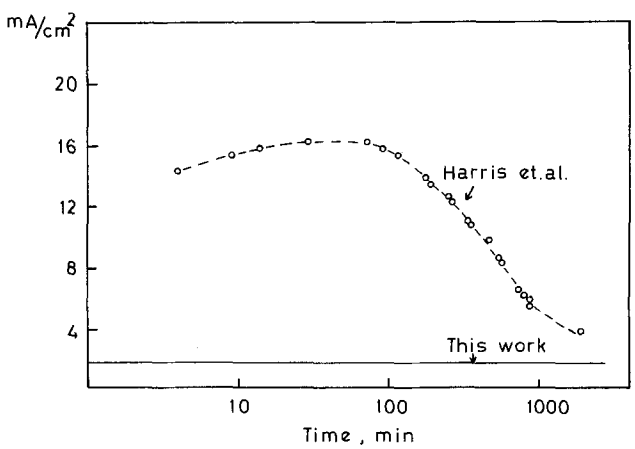


Fig. 1. The photocurrents as a function of time on TiO_2 for the work of Harris *et al.* compared with that of the present work. Potential used by Harris *et al.* at pH = 0 was 2.24V (NHE). Potential used by us at pH = 14 was 1.2V (NHE).

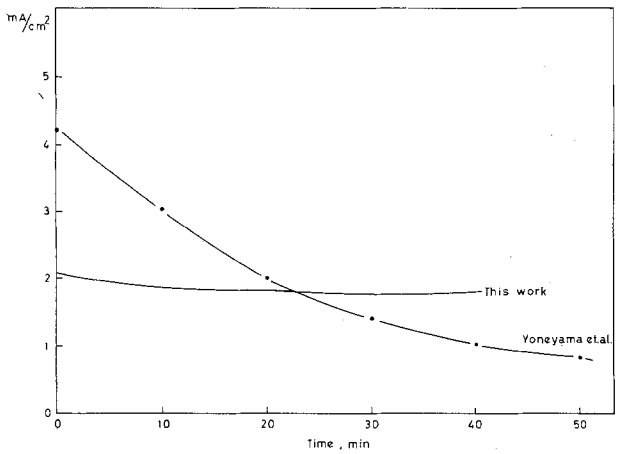


Fig. 2. The photocurrent as a function of time on Zn-doped GaP from the work of Yoneyama *et al.* and that of the present work. Potential used by Yoneyama *et al.* in 1*N* H_2SO_4 was +0.19V (NHE) and the potential used by us in 1*N* NaOH was −0.76V (NHE).

and also solution and illumination conditions. Thus, for the TiO_2 electrode, we carried out a hydrogen atmosphere reduction for 5 hr at 800°C, whereas Harris *et al.* (1) used 15 min at 600°C and Wrighton *et al.* (2) reduced TiO_2 at 700°C for 4 hr.

The main difference both for the TiO_2 and the GaP crystals seems to be the illumination condition. The intensity of light was 0.08 W/cm² in this work, 1.4 W/cm² in the experiment of Harris *et al.* (1), and 8 × 10^{-6} einstein/min (1 mm diam spot) (351, 361 nm doublet emission) which is equivalent to about 5 W/cm² in the work of Wrighton *et al.* (2). Accordingly, the current density of this work was 1.7 mA/cm² and that of Harris *et al.* and Wrighton *et al.* were 16 mA/cm² at maximum and 100 mA/cm², respectively.

The intensity of light was not reported by Yoneyama *et al.* (3) but one may hypothesize that it is stronger than that of this work, because the light of a 500W Hg lamp was focused on to the electrode, while collimated light of a 900W Xe lamp was used in this work.

Manuscript submitted Aug. 17, 1976; revised manuscript received Sept. 20, 1976.

Any discussion of this paper will appear in a Discussion Section to be published in the December 1977 JOURNAL. All discussions for the December 1977 Discussion Section should be submitted by Aug. 1, 1977.

Publication costs of this article were assisted by The Flinders University of South Australia.

REFERENCES

1. L. A. Harris and R. H. Wilson, *This Journal*, **123**, 1010 (1976).
2. M. S. Wrighton, D. S. Ginley, P. T. Wolczanski, A. B. Ellis, D. L. Morse, and A. Linz, *Proc. Nat. Acad. Sci. U.S.A.*, **72**, 1518 (1975).
3. H. Yoneyama, H. Sakamoto, and H. Tamura, *Electrochim. Acta*, **20**, 341 (1975).
4. D. C. Cronemeyer, *Phys. Rev.*, **87**, 876 (1952).
5. D. M. Shub, A. A. Remnev, and V. I. Veselovskii, *Elektrokhimiya*, **9**, 676 (1973).
6. H. C. Gatos and M. C. Lavine, *Prog. Semicond.*, **9**, 1 (1965).

ERRATUM

The following section of the paper, "The Effects of Counterion Size on the Equilibrium Properties of Charged Interfaces," by W. R. Fawcett and T. A. McCarrick, which appeared on pp. 1325-1331 in the September 1976 issue of this JOURNAL was printed incorrectly due to an editorial error.

Counterion effects at other charged interfaces.—Examination of the literature reveals that counterion effects have been observed in studies of the electrical properties of other charged interfaces (27). From a biological point of view, the physical properties of charged monolayers and bilayer lipid membranes (BLM) are often studied in the hope that the experimental results will help elucidate the behavior of membranes in living systems. However, it must be emphasized that counterion effects at artificial membranes do not necessarily correspond to those in living systems. In the following discussion only those effects due to cations as counterions will be considered. In this regard one may distinguish two cation effects at negatively charged monolayers and BLM. The first is the selectivity for cation transport which is often observed in these systems and which depends both on the chemical nature of the film and also on the presence of lipid soluble carriers (28-30). The second effect and that with which this paper is concerned is the nature of the average and local potential profiles at the interfaces of the system and its influence on adsorption of other ions and dipolar molecules and on transport through the film.

Goddard and co-workers (31-34) have studied the effects of counterion nature on the surface pressure and potential at both positively and negatively charged monolayers. For negatively charged head groups, these properties depend both on the nature of the head group and on the nature of the cation in solution. Examination of the literature on cation effects at negatively charged colloids reveals that cation interaction depends very much on the nature of the anionic group and that more than one interaction sequence for alkali metal cations is observed experimentally (35). Cation interaction with BLM does not appear to have been studied in any detail (29, 30) but electrical properties such as BLM capacitance have been found to depend on the nature and concentration of the electrolyte in the surrounding solution (29).

Erlander (35) has shown that cation interaction sequences at negatively charged colloids can be rationalized on the basis of the Frank and Wen model (36) of water structure surrounding the interacting ions with consideration of their effective dielectric constants. Accordingly, ions with high charge to radius ratios are surrounded by A-type water which is strongly bound to the ion by ion-dipole interactions. Most ions are also surrounded by B-type water in which the normal structure is broken and neither ion-dipole nor dipole-dipole interactions predominate. The normal water structure which is determined by dipole-dipole interactions and hydrogen bonding is designated C-type. Thus, Li^+, Mg^{++}, Ca^{++}, Sr^{++}, and Ba^{++} ions are surrounded immediately by A water with a layer of B water beyond the tightly bound dipoles. Cs^+, Rb^+, K^+, Cl^-, Br^-, and I^- do not have any ordering effect and thus are surrounded by a B region only. Na^+ and F^- are considered to have an A region but no B region. Erlander has estimated the effective dielectric constant of the B region surrounding the ions and has argued that ion-ion interaction increases when the effective dielectric constants are similar in magnitude (37). In order to apply these ideas to biological membranes one must know something about the effect of the charged groups at the surface on the structure of the surrounding water molecules. Erlander has argued that the phosphate group in phospholipids which is in close proximity to a base is surrounded by B water with a low effective dielectric constant. Thus, it interacts most strongly with K^+ which has similar characteristics. The interaction sequence ($K^+ > Na^+ > Rb^+ > Li^+ > Cs^+$) then depends on whether the cation has an A region and on the effective dielectric constant of the B region. Similar concepts can be applied to cation interaction with other common negative sites such as carboxylate (35).

In order to develop an electrostatic model for the potential distribution at the membrane/solution interface one must know the relative positions of the charged head group and counterions. At mercury the counterions are normally assumed to be ~5Å from a homogeneous, geometrically smooth metal/solution interface; more precisely, the distance of closest approach of the counterion and thus the potential distribution at the interface depend on the nature of the interaction of both the charged metal surface and the counterion with surrounding water molecules. The surface of the natural membrane is much more heterogeneous in character containing more than one type of phospholipid molecule with interdispensed globules of protein (38); moreover, the phospholipid distribution is often different on the inside and outside walls of the cell membrane (39). Thus, the local potential profile near the interface undoubtedly varies considerably over the surface of the membrane. From the above discussion the interaction of charged head groups at a given site with counterions will be chiefly a function of local water structure. Although one may obtain some impression of this structure by studying artificial membranes with the same charged head groups, it would be preferable to study interfacial structure at the real membrane. Reeves and co-workers (40, 41) have developed an NMR technique for studying the orientation of double layer ions at model membranes based on lyotropic liquid crystals. Application of this technique or another spectroscopic method to real membrane systems could be of considerable help in elucidating the spatial distributions of charged groups and ions at the membrane's surfaces. Levine *et al.* (42) have reviewed the electrostatic models developed to account for the surface potential and surface pressure observed at charged interfaces. They have emphasized the importance of considering the discrete nature of the charge as well as the distribution of counterions with respect of the charged head groups. Undoubtedly, the models developed for charged monolayers could be modified to deal with the potential distribution at each of the charged interfaces of the membrane. An understanding of the electrostatic situation could then be used to elucidate electrostatic factors which play a role in ion transport.

REFERENCES

1. R. Payne. *J. Electroanal. Chem.*, **41**, 277 (1973).
2. D. C. Grahame and R. Parsons, *J. Am. Chem. Soc.*, **83**, 1291 (1961).
3. J. Lawrence, R. Parsons, and R. Payne, *J. Electroanal. Chem.*, **16**, 193 (1968).
4. D. C. Grahame, *J. Am. Chem. Soc.*, **80**, 4201 (1958).
5. R. Payne, *Trans. Faraday Soc.*, **64**, 1638 (1968).
6. A. R. Sears and P. A. Lyons, *J. Electroanal. Chem.*, **42**, 69 (1973).
7. G. J. Hills and R. M. Reeves, *ibid.*, **42**, 355 (1973).
8. E. Dutkiewicz and R. Parsons, *ibid.*, **11**, 100 (1966).
9. D. C. Grahame, *This Journal*, **98**, 343 (1951).
10. S. Levine, G. M. Bell, and D. Calvert, *Can. J. Chem.*, **40**, 518 (1962).
11. G. J. Hills and R. Payne, *Trans. Faraday Soc.*, **61**, 316 (1965).
12. W. R. Fawcett and M. D. Mackey, *J. Chem. Soc. Faraday Trans. I*, **69**, 634 (1973).
13. D. J. G. Ives and G. J. Janz, "Reference Electrodes," p. 198, Academic Press, New York (1961).
14. H. D. Hurwitz, *J. Electroanal. Chem.*, **10**, 35 (1965).
15. S. Lakshmanan and S. K. Rangarajan, *ibid.*, **27**, 127 (1970).

16. S. Lakshmanan and S. K. Rangarajan, *ibid.*, **27**, 170 (1970).
17. R. Payne, *Advan. Electrochem. Electrochem. Eng.*, **7**, 1 (1970).
18. W. R. Fawcett and J. E. Kent, *Can. J. Chem.*, **48**, 47 (1970).
19. C. V. d'Alkaine, E. R. Gonzalez, and R. Parsons, *J. Electroanal. Chem.*, **32**, 57 (1971).
20. J. Kielland, *J. Am. Chem. Soc.*, **59**, 1675 (1937).
21. L. M. Baugh and R. Parsons, *J. Electroanal. Chem.*, **58**, 229 (1975).
22. S. Levine, K. Robinson, and W. R. Fawcett, *ibid.*, **54**, 237 (1974).
23. S. Levine and K. Robinson, *ibid.*, **41**, 159 (1973).
24. W. R. Fawcett, *ibid.*, **22**, 19 (1969).
25. B. G. Chauhan, W. R. Fawcett, and T. A. McCarrick, *ibid.*, **58**, 275 (1975).
26. W. R. Fawcett and M. D. Mackey, *J. Chem. Soc. Faraday Trans. I*, **69**, 140 (1973).
27. H. G. Bungenberg de Jong, in "Colloid Science," Vol. 2, H. R. Kruyt, Editor, Chap. 9, Elsevier, Amsterdam (1949).
28. G. Eisenman, G. Szabo, S. Ciani, S. McLaughlin, and S. Krasne, *Prog. Surface Membrane Sci.*, **6**, 140 (1973).
29. H. Ti Tien, "Bilayer Lipid Membranes, Theory and Practice," Marcel Dekker, New York (1974).
30. D. Papahadjopoulos, "Form and Function of Phospholipids," G. B. Ansell, J. N. Hawthorne, and R. M. C. Dawson, Editors, Chap. 7, Elsevier, Amsterdam (1973).
31. E. D. Goddard, O. Kao, and H. C. Kung, *J. Colloid. Interface Sci.*, **24**, 297 (1967).
32. E. D. Goddard, O. Kao, and H. C. Kung, *ibid.*, **27**, 616 (1968).
33. E. D. Goddard, *Croat. Chem. Acta*, **42**, 143 (1970).
34. E. D. Goddard and H. C. Kung, *J. Colloid. Interface Sci.*, **37**, 585 (1971).
35. S. R. Erlander, *J. Macromol. Sci., Chem.*, **A2**, 1073 (1968).
36. H. S. Frank and W. Y. Wen, *Discussions Faraday Soc.*, **24**, 133 (1957).
37. S. R. Erlander, *J. Macromol. Sci., Chem.*, **A2**, 833 (1968).
38. S. J. Singer and G. L. Nicolson, *Science* **175**, 720 (1972).
39. A. J. Verkleij, R. F. A. Zwaal, B. Roelofsen, P. Comfurius, D. Kastelijn, and L. L. M. Van Deenen, *Biochem. Biophys. Acta*, **323**, 178 (1973).
40. D. M. Chen, L. W. Reeves, A. S. Tracey, and M. M. Tracey, *J. Am. Chem. Soc.*, **96**, 5349 (1974).
41. D. M. Chen, K. Radley, and L. W. Reeves, *ibid.*, **96**, 5251 (1974).
42. S. Levine, J. Mingins, and G. M. Bell, *J. Electroanal. Chem.*, **13**, 280 (1967).

JOURNAL OF THE ELECTROCHEMICAL SOCIETY

SOLID-STATE SCIENCE AND TECHNOLOGY

JANUARY 1977

Semiconductor/Electrolyte Photoelectric Energy Conversion: The Use of a Molydenum Oxide Coating to Avoid Corrosion

S. Gourgaud and D. Elliott

Department of Chemistry, University of Queensland, St. Lucia, Queensland 4067, Australia

ABSTRACT

The electrolytic corrosion of n-type GaAs under illumination is avoided by a coating of hydrated molybdenum oxide (probably MoO_2). This has the properties of a solid redox system and acts as a hole acceptor to the substrate. It is in turn rereduced by some redox species in solution and thus effectively couples hole generation to the oxidation of the electrolyte. The molybdenum oxide can be coated electrolytically to a calculated thickness of at least several hundred angstroms and is capable of storing charge reversibly of many tens of millicoulombs per square centimeter.

Photoelectric energy conversion employing electrolytes rather than solid-state junctions has received some attention in recent years (1-4). A number of experiments have centered on the generation of hydrogen gas in an electrolytic cell containing a suitable semiconductor and counterelectrode [*e.g.*, (5, 6)]. Others have considered the direct conversion to electric power with a similar arrangement.

The general design of a direct conversion device would be according to Fig. 1 for an n-type semiconductor. Light entering the surface of the semiconductor causes electron-hole pair generation if of sufficient energy to cross the bandgap. Electrons promoted to the conduction band drift toward the interior while holes, the minority carriers, drift to the surface. Here they encounter the reduced form, M(red), of the redox couple in solution. This component is oxidized by the holes, transported to the counterelectrode and, there, rereduced. This reduction is driven by the external connection from the semiconductor. The result is a passage of electrons externally in a circuit doing work with no net change in the electrolyte. Analogous arguments may be used for a p-type semiconductor where electrons (the minority carriers) drift to the surface and cause a reduction of some oxidized species in solution.

A photoelectric device based on this design has potential advantages over a conventional solid-state diode in ease of manufacture and scale-up to large sizes. This arises from the following factors: (*i*) use of polycrystalline substrates since no junctions need be grown; (*ii*) optimum light penetration and segregation of optical and electroconductive phenomena; (*iii*) the choice of a wide range of compound semiconductors (*e.g.*, oxides, sulfides, etc.) of which only one carrier type can be made.

In a number of investigations of these types of devices, the principal disadvantages have been the electrolytic corrosion of the semiconductor and the inherent slowness of electrode reactions at such materials. Corrosion occurs for example with holes at an n-type semiconductor because of the preferential oxidation of the substrate compared with that of some ion in solution. Though there are some materials resistant to corrosion, *e.g.*, TiO_2 and SnO_2, their bandgaps are too high for conversion of sunlight. The inherent slowness of electrode reactions involving oxidation or reduction of ions in solution is more fundamental and is related to the relatively small carrier density at the surface of a semiconductor. This slowness is responsible for the preferential oxidation of the electrode and when corrosion can be avoided it then causes unacceptably low currents. Some attempts have been reported where these disadvantages have been obviated by means of a surface coating, *e.g.*, a metal film (7).

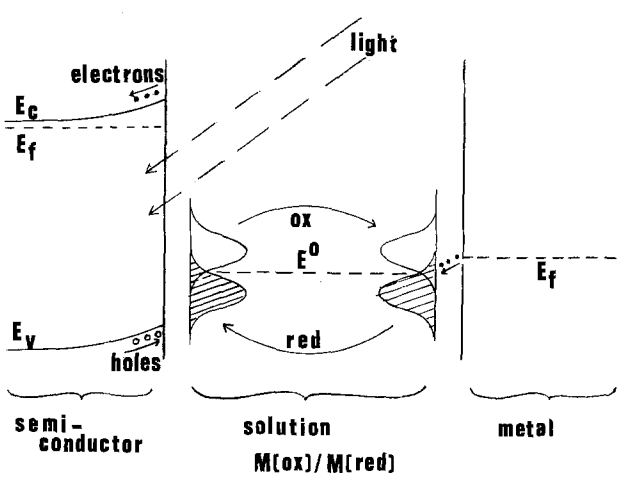


Fig. 1. Diagrammatic representation of photoelectric conversion device: E_c = conduction band; E_v = valence band; E_F = Fermi level; $E°$ = standard potential of M(ox)/M(red).

Key words: photocell, gallium arsenide, semiconductor electrochemistry.

The present investigation had its genesis in the laboratory of Professor P. Handler (University of Illinois). A patent application (Momin and Handler, 1969) described the operation of a $GaAs/H_2SO_4/Pt$ light-sensitive cell with the corrosion problem described above. This paper describes the use of an electrolytically generated surface film consisting of some form of molybdenum oxide ("Mo Ox") which has the properties of a solid redox system. This is able to compete successfully for holes at the surface on an n-type semiconductor, *e.g.*, GaAs, and in turn be rapidly reduced by a soluble redox species, *e.g.*, V^{2+}.

The Electrochemical Generation and Properties of "Mo Ox"

The generation and the oxidation/reduction properties of this material on a solid electrode were observed accidentally as the result of a molybdenum impurity in a sample of KCl (8). It is probably identical with a material described earlier by other authors (9). This was obtained as a dark brown film during the reduction of acidified molybdate on a mercury surface and was identified as a hydrated molybdenum dioxide. For the purpose of investigating its electrochemical properties it has been examined at a hanging mercury drop electrode (HMDE).

Experimental.—The electrode was prepared by catching mercury drops from a polarographic capillary onto a fine platinum wire (0.004 in.). The surface area of the drop was estimated from the mass flow rate through the capillary and the drop time. Potential control was accomplished using a Heath polarograph and measurements were recorded on a Riken-Denshi D72B X-Y recorder. All potential measurements were with respect to the SCE.

Results.—The generation and growth of surface layers were observed under cyclic linear sweep voltammetry (Fig. 2). Starting at −0.1V and scanning negatively in a deaerated but unstirred solution, a peak is observed at about −0.44V due to the reduction of molybdate ion. On scanning positively, a two-step oxidation occurs, with one peak at about −0.37V and another further drawn out at about −0.15V. After resting the electrode (at zero current) and stirring the electrolyte to restore equilibrium, the scan cycle is repeated. The reduction and oxidation peaks are enhanced compared with the initial scan indicating the buildup of some solid material on the electrode surface. Further cycles continue this process. Each negative excursion causes the reduction of molybdate from solution plus the rereduction of the accumulated surface layer which had previously been left in the oxidized form. Each positive excursion causes the oxidation of the accumulated surface layer. The rate of growth slows down as the layer builds up and it eventually reaches a limit (several hours in unstirred solutions). It can conveniently be characterized by the value of stored charge. On a mercury surface this varies with the method of generation and the concentration of Mo in solution. Values of the order of tens of millicoulombs per square centimeter have been observed. 10 mC/cm^2 would correspond to about a 300Å thick layer if the standard density of MoO_2 is assumed (150Å for a two-electron change).

The layer as first produced is initially transparent and shows interference colors. However, it shows a deepening yellow color as it gets thicker and eventually becomes a heavy brown coating. Since the layer is many molecules thick it must be somewhat conductive. The growth is probably limited ultimately by the resistance which causes the potential at the surface to lag behind that of the metal electrode. This also explains the gradual shift of the reduction peaks negatively as the layer grows.

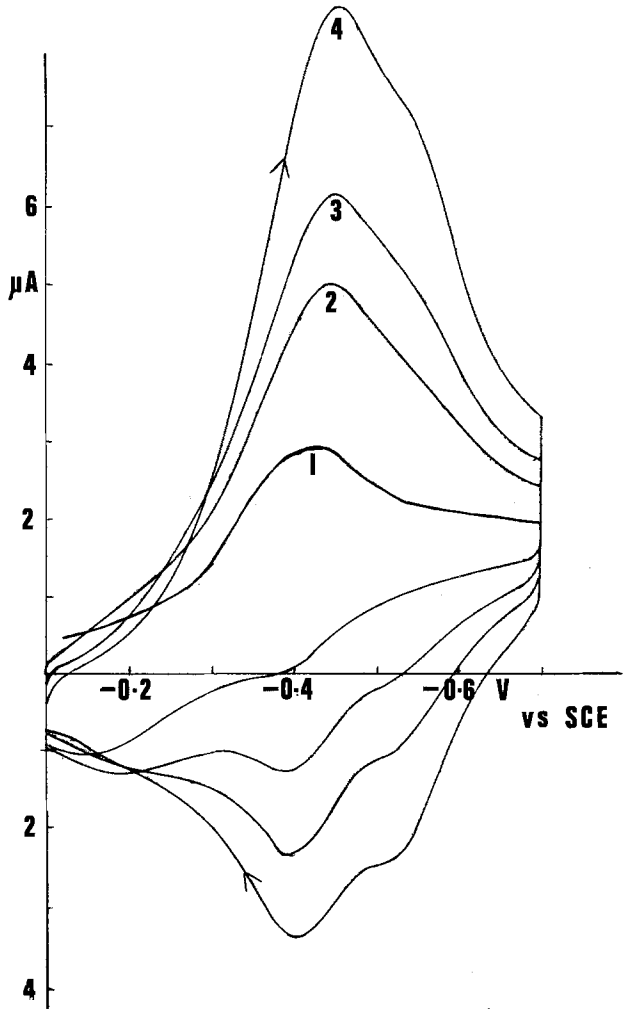


Fig. 2. Current-voltage curve for the reduction of molybdate at the HMDE: sweep rate = 0.5 V/min; area = 0.029 cm^2; solution = 1M NaCl, 0.01M HCl (*p*H 1.8), 7×10^{-4}M Mo (as ammonium molybdate). The numbers on the curves represent successive sweeps.

The reduction/oxidation linear sweep voltamogram is asymmetrical about the current axis; there is much more cathodic current passing than anodic. It is presumed that the hydrogen overvoltage is lowered compared with a mercury surface, so that appreciable hydrogen ion reduction takes place on the layer.

The growth of the layer is sensitive to *p*H, occurring roughly between *p*H 1 and *p*H 4. Figure 3 shows a series of first cyclic scans as a function of *p*H. The first anodic peak is only detectable as a slight inflection in the first scan but the way it subsequently grows can be seen in Fig. 2. Taking the average of the cathodic and first anodic peaks for the second scans as indicating the equilibrium potential of the system, the variation with *p*H is about 0.110 V/*p*H unit, indicating that $2H^+$ ions are involved per electron. A second anodic peak (−0.18V at *p*H 1.8) is prominent at the beginning but ultimately disappears as the layer grows. It also shifts with *p*H (Fig. 3), but at about half the rate compared with the main system. It may represent the reoxidation of some of the layer back to the VIth state (presumably soluble) and is a further explanation for the asymmetry about the current axis; much more Mo(VI) is reduced and reoxidized than subsequently accumulates on the electrode as a stable insoluble layer.

Polarographic measurements have also been made. A two-stage reduction is observed, the first of which is very poorly defined and is approximately half that of the second part. This has been interpreted previously (10-14) as a VI → V step followed by a

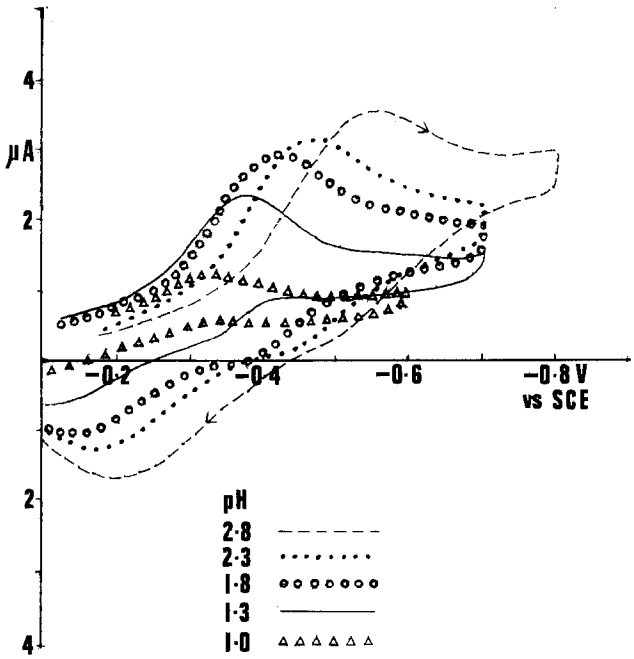


Fig. 3. Reduction of molybdate at the HMDE as a function of pH. First current-voltage cycle. Data as for Fig. 2 except pH varied as shown by addition of HCl.

V → III step. It is therefore suggested that the V and III compounds are solid in this pH range and are responsible for the cyclic linear sweep pattern. The reduction/oxidation can be provisionally represented by the scheme

$$Mo(V)Ox + 4H^+ + 2e \rightleftarrows Mo(III)Ox + 2H_2O$$

Some confirmation of the two-electron transfer may be gained from the shape of the later curves (Fig. 2). As the layer grows a secondary anodic peak emerges, more negative than the main one by about 0.1V. A slight inflection on the cathodic curve in an analogous position seems to represent the same process taking place during reduction. As further growth proceeds, this feature eventually grows to dominate the whole linear sweep pattern. This causes a negative shift to the apparent equilibrium potential (judged from the mean point of the cathodic and anodic peaks). Compared with the graph in Fig. 3, the values for a fully grown layer may be 0.1V or more negative. This factor varies greatly with various parameters, *e.g.*, sweep rate, Mo concentration, etc., which probably influence the physical form of the deposit if not its actual composition.

Physical Properties and Structure of Mo Ox

The material has been examined by a number of techniques. It was prepared in relative bulk for this purpose by electrolytic reduction on a mercury pool ($\approx$ 20 cm^2). A cyclic potential sweep was used, between −0.1 and −0.7V *vs.* SCE at the rate of 2 V/min. 10^{-3}M molybdenum was used (as ammonium molybdate) in a 1M NaCl solution adjusted to pH 1.5 with dilute HCl. The layer was generated for about 3 hr with constant stirring with nitrogen. The Mo Ox film was detached from the mercury by shaking, forming a suspension of small flakes that could be withdrawn from the vessel. The material was collected by centrifuging and was repeatedly washed with 100% alcohol to remove water. It was finally dried under vacuum.

The material appears to be amorphous down to the limit of resolution of the electron microscope. No electron diffraction pattern was detected and no x-ray powder pattern (24 hr Cu-Kα).

Spectroscopic examinations were made in both the infrared and the u.v./visible region. For the former, the material was incorporated into KBr disks and examined on a PE 225 spectrophotometer. The spectra, compared with those for some other molybdenum compounds, showed a large increase in the number of absorption bands (six bands were observed between 1400 and 1000 cm^{-1}, whereas hydrated Mo O_3 has only one and ammonium molybdate has none). This is attributed to a much lower site symmetry in the relatively amorphous compound. Bands appearing at 3595, 3450, 3150, and 1622 cm^{-1} suggest the material is hydrated. However, the direct connection of hydroxyl groups to the metal atom is not indicated from the spectrum. According to Adams (15), evidence for this should occur in the range 500-576 cm^{-1}.

By comparing the spectrum of the film with data given by Mitchell and Trifiro (16), the following assignments have been made:

970 cm^{-1}	stretching	M-O (terminal)
920 cm^{-1}	stretching	M-O (bridging)
735 cm^{-1}	stretching	M-O (bridging)

u.v./visible spectra were determined on a Cary 17 spectrophotometer. The material was ground and in the form of a suspension in absolute alcohol was evaporated onto a quartz plate. No peak was observed in the visible, but a band in the u.v. was observed at 41,500 cm^{-1} (241 nm) which does not correspond to a band in any reported compound.

The tentative conclusion is that the material is a condensed molybdenum oxide molecule of average oxidation state IV involving bridging oxygen linkages and arranged amorphously in the film. This description is similar to that for a colloid and the material has a similar appearance to a gelatinous film when viewed in the visible microscope. It should be noted that in the pH range at which the material is generated condensed polyanions are the stable form for Mo(VI) in solution (*e.g.*, $Mo_6O_{21}^{-6}$).

The Generation and Properties of Mo Ox on n-GaAs

A specimen of n-type GaAs ($\sim 10^{17}$ carriers/cm^3) was cemented with epoxy resin into the end of a glass tube and mounted vertically in a rotating-electrode assembly. The surface of the electrode could be illuminated from underneath using a 100W quartz-iodine projector lamp.

Figure 4 shows the current-voltage behavior for the rotating electrode under cyclic sweep conditions. The reduction peak for molybdenum (IV) is superimposed on the hydrogen evolution reaction and is displaced negatively with respect to the values previously reported for a mercury electrode. This large overvoltage illustrates the slowness of the reduction at the semiconductor surface. On scanning positively, no oxidation of the layer takes place in the absence of light. On illumination, however, the two-stage oxidation occurs, the first peak at about −1.0V, which is close to the flatband potential. The holes responsible for the oxidation are released at the valence band edge about 1.4V more positive than this. The layer grows satisfactorily only when the electrode is scanned in the presence of light between −0.7 and −1.1V. Initial chemical etching is also necessary.[1] If the potential is allowed to go more positive than about −0.6V, the electrode enters a region of anodic dissolution that disrupts the surface Mo Ox layer. Satisfactory growth of the layer does not occur at a surface so eroded and it must be reetched chemically.

[1] 1 part 30% H_2O_2, 1 part H_2O, 3 parts concentrated H_2SO_4.

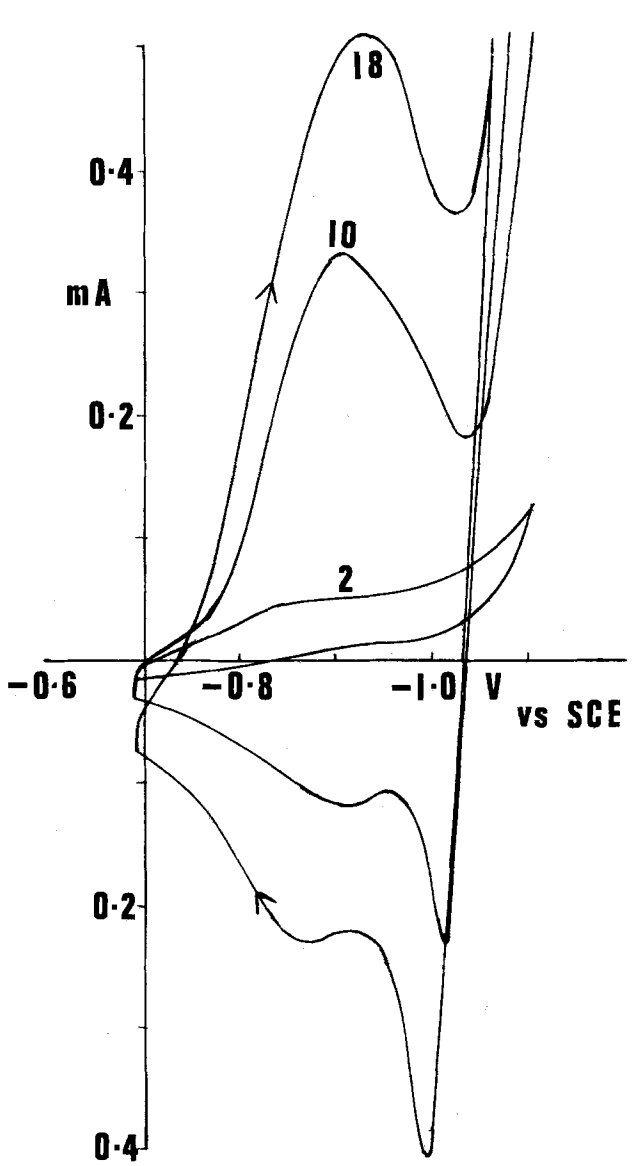


Fig. 4. Current-voltage curves for the reduction of molybdate at a GaAs electrode (under illumination): sweep rate = 2 V/min; area = 0.27 cm^2; rotation = 2000 rpm; solution = 1M NaCl, pH 1.85, 5.6 × 10^{-4} Mo. The numbers on the curves represent particular stages in the sequence of 18 continuous cycles.

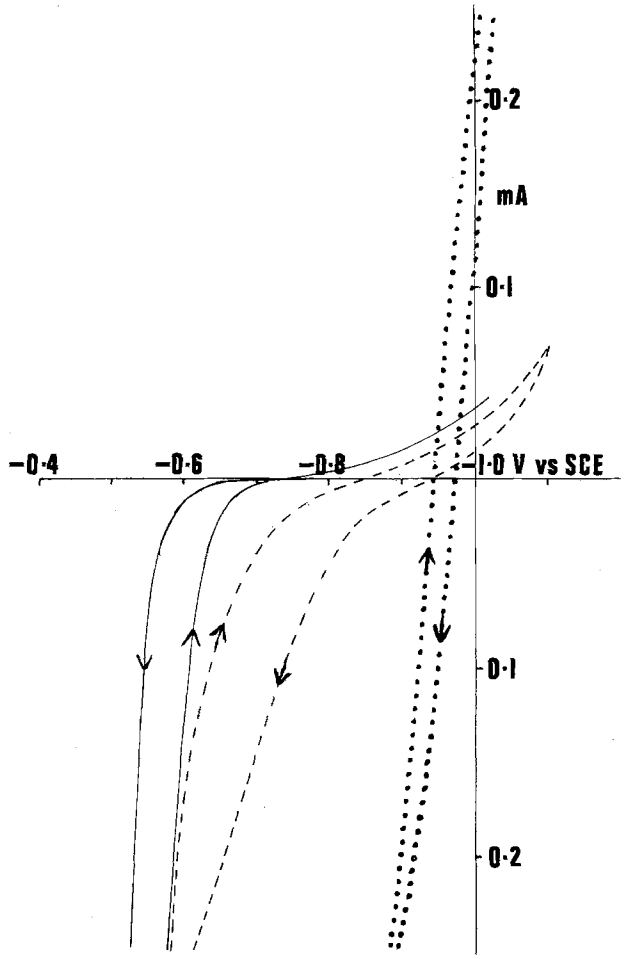


Fig. 5. Oxidation of V^{2+} at a GaAs electrode (under illumination): sweep rate = 0.1 V/min; area = 0.27 cm^2; rotation = 2000 rpm; solution = 1M NaCl, pH 1.35. ——— Oxidation of GaAs alone; – – – – oxidation of V^{2+} at bare GaAs electrode (10^{-1}M V^{2+}); .... oxidation of V^{2+} at Mo Ox-covered GaAs electrode (2×10^{-1}M V^{2+}).

The Oxidation of V^{2+} at a Mo Ox Covered GaAs Surface

The direct oxidation of V^{2+} at an illuminated, bare GaAs surface is sluggish and merges quickly into the anodic dissolution region (Fig. 5). This is a typical result for semiconductors and illustrates the poor coupling between holes accumulating at the surface and any reducing agent in solution. This is in spite of the fact that the holes appear at the valence band edge approximately 0.9V more positive than the V^{2+}/V^{3+} potential. With a surface covering of Mo Ox, however, a large oxidation current for V^{2+} occurs. The V^{2+}/V^{3+} potential is more negative than that for Mo Ox, and presumably the latter is kept in the reduced form. Holes generated in the semiconductor cause the oxidation of the Mo Ox which is then rapidly reduced by the V^{2+} in solution. It is not known at this stage what is the rate-determining step. The net result is the oxidation of V^{2+} in solution at a velocity very much greater than without the Mo Ox layer.

The currents are not very reproducible and are critically dependent on many factors, *e.g.*, the precise composition and performance of the layer, its thickness, the *p*H and composition of the solution, etc. For the particular layer whose growth is shown in Fig. 4 (9.4 mC/cm^2), the currents at constant voltage, after an initial transient, declined very slowly and the following values given in Table I were observed after a few minutes.

The current appears saturated at a potential more positive than about −0.7V suggesting that it is limited by the hole generation process and not by electrode kinetics. The saturation current observed is less than that for a silicon cell with the same light source (11 mA/cm^2). However, since the lamp used was uncorrected and has its peak well in the infrared, the silicon cell (bandgap 1.12 eV, 1.1 μm) would be expected to be more sensitive. Another factor causing lower currents is the absorption of light in the liquid layer between the electrode surface and the glass window. This was not closely controlled for the rotating electrode,

Table I. Solution: 1M NaCl, 0.2M V^{2+}, *p*H 1.5

V (*vs.* SCE)	mA/cm^2
−0.9	0.41
−0.8	1.48
−0.7	2.0
−0.65	2.1

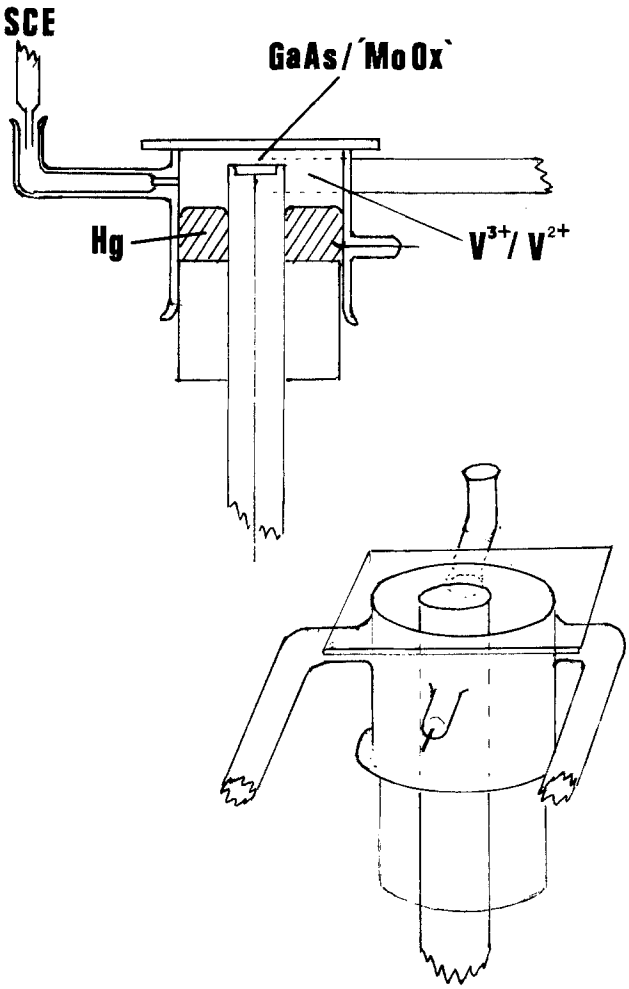


Fig. 6. Diagram of experimental photoelectric conversion cell

but in a working cell could be made very small by making the layer thin enough.

An Experimental Photoelectric Conversion Cell

An experimental cell was constructed as shown in Fig. 6. The GaAs electrode was first plated with the Mo Ox layer before mounting. The counterelectrode was an annular pool of mercury chosen for its high H^+/H_2 overvoltage. The solution containing approximately equal quantities of V^{2+} and V^{3+} was prepared externally by electrolytic reduction and pumped into the cell. Beside the two working electrodes, contact was made to the solution via a SCE. This enabled the potential of the GaAs electrode to be monitored to make sure it did not enter the anodic dissolution region. The open-circuit potential of the cell is the difference between that of the semiconductor (monitored at between -0.95 and -1.0V depending on the precise characteristics of the Mo Ox layer) and the counterelectrode which is determined by the V^{2+}/V^{3+} potential (about -0.52V). A working value of about 0.45V has been obtained. The maximum current is governed by the overvoltage characteristic of each electrode. The properties of the semiconductor/Mo Ox/V^{2+} half of the system have been described above, and the observed currents are not much reduced because of the electrode being stationary, indicating that mass transfer is not a serious limiting effect for these currents.

At the counterelectrode, the intrinsic rate constant of the V^{3+}/V^{2+} system is sufficiently great at a clean Hg surface ($\approx 10^{-3}$ cm/sec) that negligible activation overvoltage should result at *ca.* 20 mA/cm^2. In the actual cell constructed, a significant overvoltage was observed which considerably lowered the operating voltage of the cell. This may be due to surface contamination or concentration polarization, but could be largely eliminated by proper design.

Conclusion

A photoelectric conversion cell based on the preceding concepts seems a practical proposition. However, several factors have to be considered in justifying such a construction over conventional solar cells.

Efficiency.—The intrinsic efficiency of solid-state cells depends on the bandgap of the semiconductor and in sunlight reaches a theoretical maximum for materials with a gap of about 1.4 eV. However, in the present construction the operating voltage depends on electrochemical potentials unrelated to the bandgap, namely the difference between the flatband potential and the redox potential of the electrolyte. The optimum bandgap should be just a little larger than this for maximum conversion. The redox potential should be sufficiently negative to maintain a significant part of the Mo Ox layer in the reduced form, *ca.* < -0.4V. Consequently the only practicable variable is the flatband potential.

This potential at a given carrier concentration and electrolyte composition depends on the chemical nature of the material. With compound semiconductors it becomes more negative with lower molecular weight, *e.g.*, CdS is more negative than CdSe and GaP is more negative than GaAs. This is also the direction of increasing ionic bonding between the elements. Since the bandgap also increases in the same sense (causing lower light absorption and therefore loss of efficiency), there is no advantage in looking for too negative values. There is not enough experimental information available on flatband potentials generally, particularly as a function of electrolyte composition to predict the material of highest efficiency. However, any material with a potential of -1.0V or more negative is worth pursuing experimentally. This includes GaAs, GaP, and probably CdS. An interesting possibility is that the potential may be shifted by surface-active materials in a manner similar to the shift in the ecm (or zero charge potential) of mercury and other metals.

Cost.—The semiconductor/electrolyte construction seems to offer advantages in reducing the cost per watt factor, particularly for large installations. There are, for example, a large range of materials (often one-carrier types, usually n-type) that would lend themselves to large-scale thin film polycrystalline construction. Also, the separation of the optical and electrical regions offers new design possibilities. A major limitation in the unit size of existing solid-state cells arises from the current-carrying capacity of the thin surface layer. If thin enough to allow adequate light penetration, its resistance limits the area to about 10-20 cm^2 for silicon cells (*i.e.*, 0.1-0.2 W/unit for 10% efficiency).

Electrolytes should have a more favorable combination of optical/electrical properties and the layer can be made very thin providing that a cathode of sufficient surface area can be placed nearby. The necessary cathode area is also a flexible design parameter and it could take the form of a transparent conductive film or a metal grid. A grid provided with multiple feed-through contacts passing through holes in the semiconductor would enable the unit to be scaled up to meter sizes.

Stability.—The major problem of semiconductor corrosion is eliminated by operating in a potential range where it does not occur. The Mo Ox layer may also

exert a moderate protective action. The long-term stability of this layer has not been measured in this particular configuration. However, previous results (8) suggest it is very stable. In any case it is renewable by a simple electrolytic process.

The particular electrolyte used, V^{2+}/V^{3+}, is of course prone to oxidation by air and by H^+ (the latter oxidation is dependent on *p*H and the presence of catalytic metal surfaces). Persistence of V^{2+} for several days can be obtained with minimal precautions and it is to be expected that oxidation can be made almost negligible with good design. This electrolyte can also be regenerated electrolytically and since a moderate volume of solution could be used with a large area it could be periodically renewed at negligible energy cost. Even this would be eliminated by the use of more stable redox systems, *e.g.*, Ti^{3+}/TiO^{2+}, in various media. The latter is currently under investigation.

Manuscript submitted April 5, 1976; revised manuscript received Aug. 23, 1976.

Any discussion of this paper will appear in a Discussion Section to be published in the December 1977 JOURNAL. All discussions for the December 1977 Discussion Section should be submitted by Aug. 1, 1977.

REFERENCES

1. H. Gerischer, *J. Electroanal. Chem. Interfacial Sci.*, **58**, 263 (1975).
2. Y. G. Chai and W. W. Anderson, *Appl. Phys. Lett.*, **27**, 183 (1975).
3. H. Gerischer, *Surf. Sci.*, **18**, 97 (1969).
4. H. Gerischer, *This Journal*, **113**, 1174 (1966).
5. A. Fujishima and K. Honda, *Nature*, **238**, 37 (1972).
6. T. Ohnishi, Y. Nakato, and H. Tsubomura, *Ber. Bunsenges. Phys. Chem.*, **79**, 523 (1975).
7. Y. Nakato, T. Ohnishi, and H. Tsubomura, *Chem. Lett.*, 883 (1975).
8. D. Elliott, D. L. Zellmer, and H. A. Laitinen, *This Journal*, **117**, 1343 (1970).
9. P. Lagrange and J. P. Schwing, *C. R. Acad. Sci. (Paris)*, **263**, 848 (1966).
10. D. F. Boltz, T. de Vries, and M. G. Mellon, *Anal. Chem.*, **21**, 563 (1949).
11. E. P. Parry and M. G. Yakuleik, *ibid.*, **26**, 1294 (1954).
12. B. N. Popov and H. A. Laitinen, *This Journal*, **120**, 1346 (1973).
13. L. Capanella and G. Pistoia, *ibid.*, **120**, 383 (1973).
14. G. P. Haight Jr., *Anal. Chem.*, **23**, 1505 (1951).
15. D. M. Adams, "Metal Ligand and Related Vibrations," p. 248, Arnold Limited, London (1967).
16. P. C. H. Mitchell and F. Trifiro, *J. Chem. Soc. A*, **23**, 3183 (1970).

Electro-oxidation of Gallium Arsenide

I. Initial Phase of Film Formation in Tartaric Acid-Water-Propylene Glycol Electrolyte

S. Szpak*

Naval Electronics Laboratory Center, Electronic Material Sciences Division, San Diego, California 92152

ABSTRACT

A standard galvanostatic procedure was used to study the initial phase of anodic oxidation of n-GaAs in a 3 weight percent (w/o) aqueous solution of tartaric acid mixed with propylene glycol. The initial phase is controlled by a two-dimensional growth of oxide from nuclei generated at a rate of about 10^7 cm^{-2} sec^{-1}. The effect of *p*H and illumination was examined in terms of the kinetics of nucleation in a heterogeneous system involving the semiconductor as the solid phase.

Although anodic oxidation of the III-V compound semiconductors in general, and gallium arsenide in particular, has been of considerable interest (1-4), only recent disclosures by Hasegawa, Forward, and Hartnagel (5, 6) and by Hasegawa and Hartnagel (7) have made it attractive for use in the fabrication of electronic devices based on planar configuration. Their approach is of special interest to the semiconductor technologist because of electrolyte stability, reliability of procedure, and excellent reproducibility under normal process control. Glasslike films, approximately 7000Å in thickness, can be obtained in a few minutes.

The electrochemical behavior of this system however, has not been completely investigated. In particular, the initial stages of the film growth need to be explored. It is this aspect of the anodic oxidation that is addressed in this communication.

Experimental

The galvanostatic technique was selected to follow the initial phase of the anodic oxidation because it may

* Electrochemical Society Active Member.
Key words: anodic oxidation, nucleation, growth kinetics, gallium arsenide.

provide clues as to the type of film conductivity and mode of its formation (8). This technique, if combined with an additional observation, *e.g.*, scanning electron microscopy, may yield sufficient information for the determination of the probable mechanism operating during the early stages of anodic oxidation.

Materials and procedure.—All chemicals were of reagent quality and were used without further purification. Triply distilled water was used exclusively throughout this investigation.

A thin slice of the Sn-doped, (111) oriented n-type GaAs (carrier density: 3.8×10^{17} cm^{-3}, mobility: 2200 cm^2 V^{-1} sec^{-1}, and resistivity: 8.5×10^{-3} Ω cm) was mounted on a glass slide using high quality beeswax with the (111)B side contacting the electrolyte. A Ge-Au eutectic alloy ohmic contact was provided on the (111)A side. To assure good reproducibility, the GaAs (111)B surface was anodically oxidized, the oxide stripped in diluted HCl (1:4 by volume), followed by a water rinse and immersion in diluted NH_4OH (1:4 by volume). This procedure was repeated several times.

A current regulator, Model R2 (Leichner Manufacturing Company, Champaign, Illinois), in conjunction with a regulated power supply, Model 3-150B (Dressen-Barnes Corporation, Pasadena, California), served as the constant current source. Electrode potentials were measured against a saturated calomel electrode and were recorded on a Speedomax-G recorder (Leeds and Northrop, North Wales, Pennsylvania). All experiments were carried out in 3 w/o aqueous solution of tartaric acid mixed with propylene glycol in the volume ratio 1:3. Special attention was given to a thorough equilibration of the n-GaAs/electrolyte interphase prior to experimental runs. This was achieved by immersion in an electrolyte until the continuously recorded rest potential attained a steady-state value to within ± 10 mV between samples. The relatively good reproducibility of the rest potential and the reported solubility of the oxide film in the electrolyte employed (7) may well assure the existence of a bare surface prior to the initiation of an anodic process.

Results.—It was concluded, on the basis of published data (7), that two types of observations ought to be helpful in determining the mechanism of film formation, namely (*i*) the effect of electrolyte composition, specifically the OH^- ion concentration and, (*ii*) for the n-type GaAs, the effect of illumination.

A set of potential-time curves for the galvanostatic oxidation of GaAs is shown in Fig. 1. Each curve exhibits characteristics typical of the formation of an ion-conducting layer as indicated by the steep portion of the potential-time curve (8). The increase in the slope with increase of the anodic current is further indication of the ionic conductivity of the anodic film.

Additional information can be extracted from the time needed to achieve full surface coverage, t_{cr} (see discussion below). Qualitatively, as the anodic current is increased, the critical time becomes shorter. It is also of interest to note that no film was formed when the applied anodic current was less than 10.4×10^{-5} A cm^{-2} in an electrolyte with the pH adjusted to 5.1.

The effect of electrolyte pH on the potential-time curves is summarized in Fig. 2. Evidently, their shape is independent of the OH^- ion concentration, within the investigated pH range, but both, the critical time, t_{cr}, and the anodic current density needed for the initiation of film formation, j_{cr}, are strongly affected. The higher the pH, the shorter the critical time, t_{cr}, and the lower the critical anodic current density. This observation refers to the pH of the bulk electrolyte. The pH value in the neighborhood of the surface is affected by the dissolution process to the extent governed by the electrolyte buffer capacity. Here, this change is expected to be rather small in view of relatively flat tartaric acid-NH_4OH neutralization curve for pH < 6.5.

The effect of illumination on the potential-time relationship is shown in Fig. 3. This effect is similar to the one observed on increasing the electrolyte acidity. If the GaAs/electrolyte interphase is illuminated, then both the critical time is longer and the critical anodic current density is larger.

The flat portion of the potential-time curves is associated with the growth of surface coverage with an insulating or badly conducting layer. The relatively small increase in potential with time is, in effect, an increase in the overpotential of the electrochemical process taking place over the continuously decreasing available surface area. A set of scanning electron microscope photographs, shown in Fig. 4, illustrates the time evolution of the surface coverage. In particular, Fig. 4a and 4b show a surface sparingly covered with circular patches. The light patches, indicating an oxide-covered surface, photographed 30 and 60 sec after initiation of the anodic process (points A and B in Fig. 2), are of different sizes indicating different nucleation times and/or different growth rates. With the passage of time, there is an increase in the surface coverage accompanied by a merging of individual

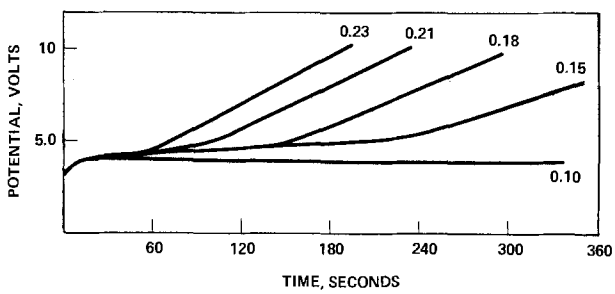


Fig. 1. Galvanostatic potential-time curves as a function of applied anodic current. Electrolyte = pH 5.1; temp = room; current densities (mA cm^{-2}) indicated alongside appropriate curves.

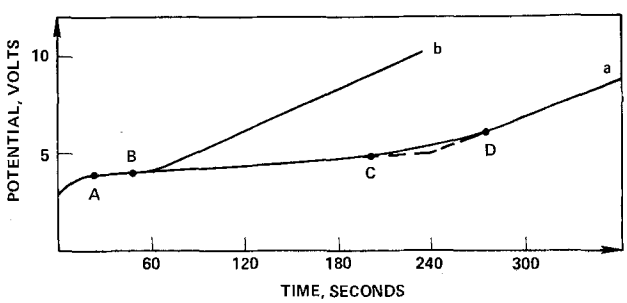


Fig. 2. Effect of pH on V/t curves. Anodic current density, j = 0.156 mA cm^{-2}; curve a = pH 5.1, curve b = pH 6.1. (Points A, B, C, and D indicate times at which SEM examination was undertaken, cf. Fig. 4).

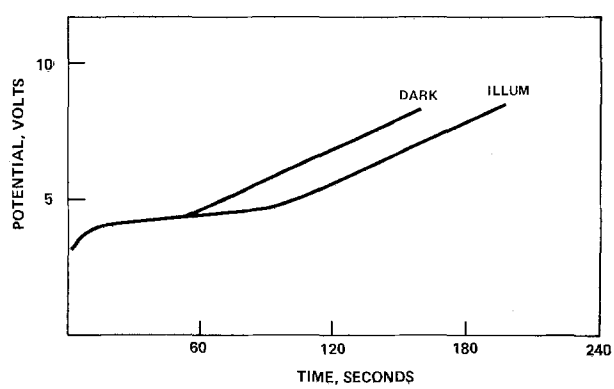


Fig. 3. Effect of illumination on potential-time curves; j = 0.18 mA cm^{-2}, pH = 5.1.

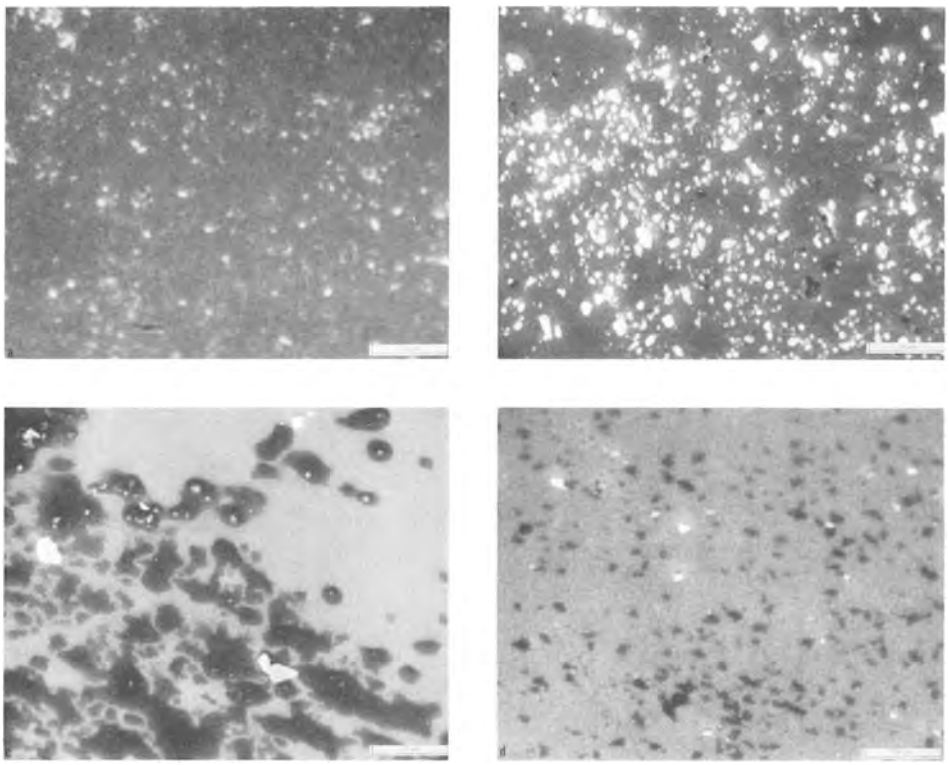


Fig. 4. Scanning electron microscope (SEM) photographs. Electrolyte = pH 5.1; anodic current density, j = 0.156 mA cm^{-2}. SEM photographs taken at (a) 30 sec, (b) 60 sec, (c) 200 sec, and (d) 270 sec after initiation of anodic oxidation.

patches. As the critical time was approached (point C, Fig. 2), the surface was about 80% covered and when the anodization time exceeded the critical time (point D, Fig. 2), the surface was nearly totally covered with a thin layer. An increase in the surface coverage by a growth of individual patches is not an unusual occurrence. This mode of growth may be due to an interaction between various competing processes or it may arise because of preferential dissolution sites induced by an advancing film (9).

Discussion

A cursory examination of Fig. 4 indicates a two-dimensional growth from randomly placed nucleation sites. This observation together with the examination of the effect of illumination on the critical time and critical anodic current density forms a basis for the present analysis.

Kinetics of surface coverage.—An idealized growth of surface coverage is illustrated in Fig. 5. Points P_1, P_2, . . ., are the nucleation sites which grow along the peripheries. Assume for simplicity circular patches having growth rates independent of their radii provided that they grow as separate entities and that the characteristic length of the preceding process, *e.g.*, the diffusion length, is smaller than the patch radius. Assume further that, as the individual patches begin to merge, their growth is by addition of newly formed small patches P_1', P_2', P_3', . . ., rather than by the addition of molecules. The latter assumption is made to emphasize the importance of merging or overlapping of individual patches on the over-all growth of the surface coverage. Under these conditions, a nucleus formed at time, τ, attains at time, t, a radius $r = v(t - \tau)$, where v, cm sec^{-1}, denotes the velocity of radial growth. If the rate of nucleation is Z, cm^{-2} sec^{-1}, then within the time interval, $d\tau$, $Zd\tau$ new nuclei will be generated and the gain in the surface covered, dA, will be given by

$$dA = Z\ (A_o - A)\ v^2\pi(t - \tau)^2 d\tau \qquad [1]$$

or in an equivalent form

$$d\theta = Z\ (1 - \theta)\ v^2\pi(t - \tau)^2 d\tau \qquad [1a]$$

where $\theta = A/A_o$ is the surface coverage. The term $(A_o - A)$ in Eq. [1], or $(1 - \theta)$ in Eq. [1a], was added to indicate that nucleation is excluded from occurring on the surface already covered.

The functional dependence of v on the anodic current density, j, is considered to account for all elementary processes participating in the film formation. The form of this dependence must be consistent with the experimental facts, *e.g.*, with the existence of a critical anodic current density. This requirement suggests a form

$$v = [kj - k_1(x_1, x_2, \ldots, \epsilon)](A_o - A) \qquad [2]$$

Equation [2] consists of two terms multiplied by the available surface area. The first term, kj, denotes the ionization of surface atoms while the second term, $k_1(x_1, x_2, \ldots, \epsilon)$, reflects the effect of electrolyte composition $(x_1, x_2, \ldots)$ as well as the effect of illumination, ϵ, on the formation and growth of the anodic film, that is, it contains also applicable transport information. Adopting Eq. [2] one gets for the critical current

$$j_{cr} = k_1(x_1, x_2, \ldots, \epsilon)/k \qquad [3]$$

Evidently, Eq. [2] is valid for $j > j_{cr}$ and within the time interval $0 < \tau < t_{cr}$.

Substituting Eq. [2] into Eq. [1] and integrating the resulting expression, one obtains

$$\frac{1}{2[kj - k_1]^2}\left[\theta_{cr}^{-2} - 1\right] = \frac{Z\pi}{3} t_{cr}^3 \qquad [4]$$

The integration limits, $\theta = 0$, $\theta = \theta_{cr}$ and $\tau = 0$, $\tau = t_{cr}$ are consistent with the interpretation of the SEM photographs (Fig. 4c and 4d) and the shape of the potential-time curves (*e.g.*, Fig. 2), respectively. They are also consistent with the concepts illustrated in Fig. 5, where the total current, i, in an external circuit, is the sum of currents crossing the GaAs/electrolyte interface, $i_1 = (1 - \theta)A_o j$, and the current crossing the GaAs/oxide interface, $i_2 = \theta A_o j_2$

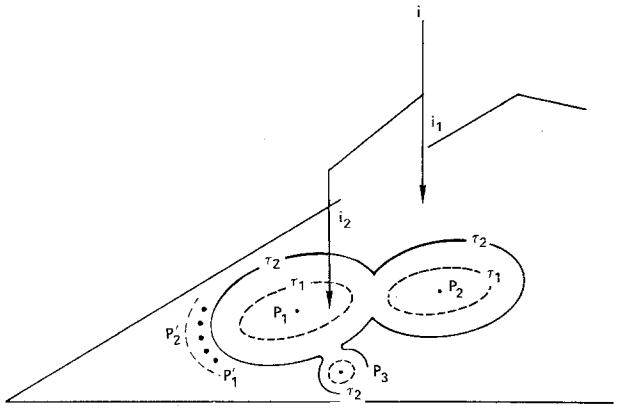


Fig. 5. Representation of model kinetics for surface coverage growth.

$$i/A_o = (1 - \theta)j + \theta j_2 \qquad [5]$$

The magnitude of these currents depends on the resistivity in their paths. Evidently, at $\theta > \theta_{cr}$ or at $\tau > t_{cr}$ the anodic current flows entirely through the GaAs/oxide interface, *i.e.*, $i/A_o = \theta j_2$, and Eq. [1] no longer describes the dominant set of events.

A plot of j *vs.* $t_{cr}^{-3/2}$, shown in Fig. 6, obeys Eq. [4], except at low current densities. A pronounced effect of both OH^- ion concentration and illumination is quite evident.

Kinetics of nucleation.—The rate of formation of critical embryos which can develop into a new phase, *e.g.*, droplet or crystallite, is given by an expression

$$Z = K \exp(-\Delta F/kT) \qquad [6]$$

where K is a constant and ΔF is the free energy of embryo formation (10-12). Since neither the pre-exponential factor nor the free energy of embryo formation are known for this system, the rate of nucleation cannot be assessed. However, with the aid of Eq. [2], [3], and [4] and the examination of Fig. 1 and 4, the nucleation rate can be estimated as follows: The critical surface coverage can be estimated from Fig. 4c and 4d at $\theta_{cr} = 0.9$. The radial velocity, $v = 10^{-6}$ cm sec^{-1}, was found by averaging the patch size measured from the SEM photographs, Fig. 4a and 4b. Over 200 measurements were used for this purpose. The critical current density, $j_{cr} = 10.4 \times 10^{-5}$ A cm^{-2}, was determined by direct observation, *cf.* Fig. 1. Using these values, one gets the rate of nucleation in the electrolyte adjusted to *p*H 5.1 to be approximately 10^7 cm^{-2} sec^{-1}.

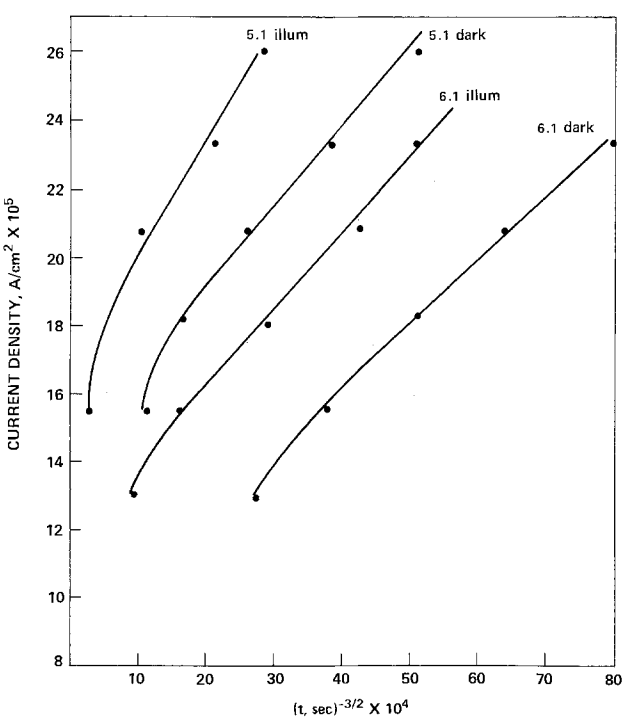


Fig. 6. Plot of j *vs.* $t_{cr}^{-3/2}$

The effect of illumination on the growth of surface coverage can be analyzed in terms of elementary processes. These processes can be divided into two groups: the first group comprises the events that involve the GaAs/electrolyte interface, *e.g.*, adsorption heterogeneous nucleation, etc., while the second group entails the processes which occur in the liquid phase, *e.g.*, homogeneous nucleation, transport phenomena, and the like. It is expected that only the events of the first group will be affected by illumination, especially if the space charge of the extrinsic n-GaAs is in depletion or inversion (13). Conversely, the processes listed in the second group are not likely to be affected by illumination.

In order to follow the effect of illumination on the rate of nucleation, consider Eq. [4] and its graphical representation in Fig. 6. The slope, $s = (C/Z)^{1/2}$, where $C = 3(\theta_{cr}^{-2} - 1)/2k^2\pi$, which was already used in the estimate of the nucleation rate ($Z = 10^7$ cm^{-2} sec^{-1}), can also be used to determine the effect of illumination, with much greater accuracy, however. Better estimates are likely because all quantities entering an expression for C are insensitive to illumination. Thus, when Eq. [4] is combined with Eq. [6], and the ratio taken, then the relationship, Eq. [7]

$$2kT \ln (s_\epsilon/s) = -\Delta F + \Delta F_\epsilon \qquad [7]$$

can be obtained. The subscript ϵ refers to the condition of illumination.

Evidently the condition of illumination is that of a gain in the free energy of the critical embryo formation ($s_\epsilon/s > 1$, *cf.* Fig. 6). In particular, this gain was found to be approximately 0.6 kT per critical embryo for the n-GaAs/electrolyte interphase, when the bulk electrolyte was adjusted to *p*H 5.1.

Additional information concerning the n-GaAs/electrolyte interphase may be obtained by the use of an expression relating ΔF to the surface tension. This relationship for the nucleation on solid surfaces is given by Eq. [8] (10, 14)

$$\Delta F = \frac{1}{3}[\sigma_{12}S_{12} + \sigma_{23}S_{23} - \sigma_{13}S_{13}] \qquad [8]$$

where σ is the surface tension, S the interphase area and subscripts 1, 2, and 3 refer to the solid phase, GaAs, the electrolyte, and the newly formed phase, $Ga_2O_3 \cdot As_2O_3$, respectively. As written, Eq. [8] does not contain an explicit dependence on overpotential. This dependence however, is implied in an expression for σ_{12} and it is likely to be more complex for the semiconductor than for the metal/electrolyte interface.

Substituting Eq. [8] into Eq. [7], and noting that $\sigma_{23}S_{23}$ does not change with illumination, one gets

$$[\sigma_{12}S_{12} - \sigma_{13}S_{13}]_\epsilon - [\sigma_{12}S_{12} - \sigma_{13}S_{13}] = 6\ kT \ln(s_\epsilon/s) \qquad [9]$$

Taking $k = 1.372 \times 10^{-16}$ erg/°K, $s_\epsilon/s = 1.38$ and assuming the radius of the critical embryo, $r_{cr} = 10^{-6}$ cm, one calculates from Eq. [9] an increase in the surface tension due to illumination of approximately 3×10^{-2} erg cm^{-2}. The numerical value of $r_{cr} = 10^{-6}$ cm was selected as a compromise between large critical embryos consisting of 50-250 molecules associated with

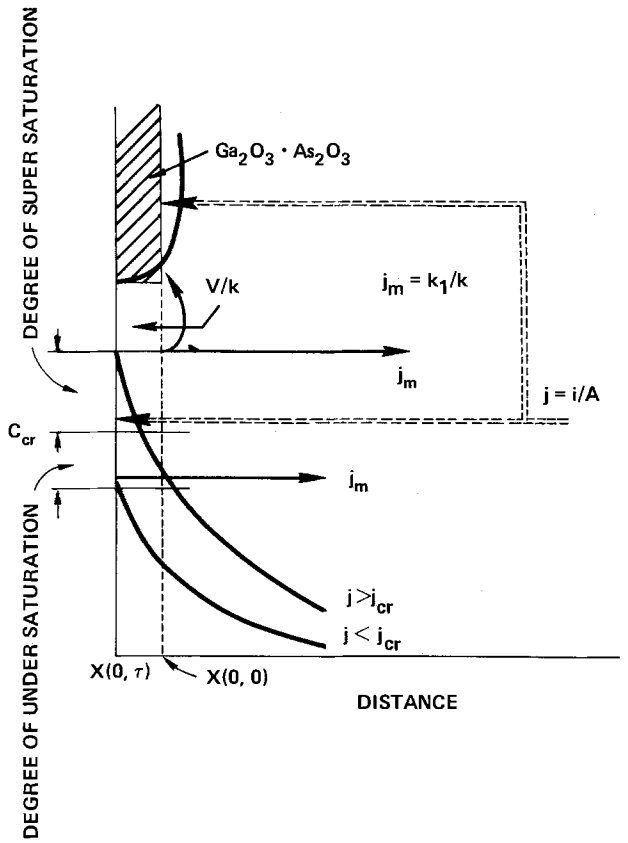


Fig. 7. Representation of elementary processes participating in film growth.

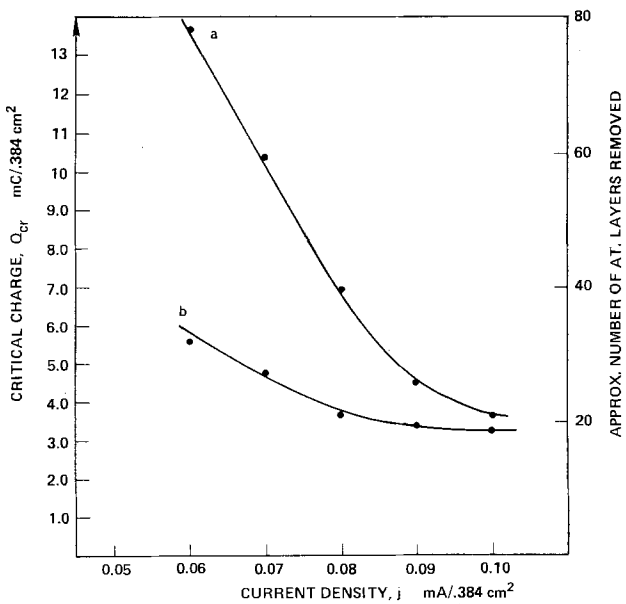


Fig. 8. Critical surface coverage, Q_{cr}, as a function of applied anodic current.

homogeneous nucleation (10) and considerably smaller embryos typical of heterogeneous nucleation, particularly in electrochemical systems (15).

Mechanism of growth.—The set of events leading to the initiation and growth of the surface coverage is summarized in Fig. 7. The anodic current, i, just as in Fig. 5, is split into i_1 and i_2, with the latter being insignificant throughout the considered time interval.

The passage of current across the GaAs/electrolyte interface causes the destruction of the semiconductor surface resulting in ionization of its components and a shift of the interface from $x(0, 0)$ to $x(0, \tau)$. The detailed mechanism of the anodic reaction in this system is not known. For this reason, it will be assumed that the ionized species Ga^{+3} and As^{+3} exist in the same composition as the molecules forming critical embryos immediately after leaving the crystal lattice.

The presence of these species at the interface creates the concentration gradient and initiates mass transport away from the interface, j_m. It is convenient for the present discussion to rewrite Eq. [2] as

$$j = v/k + k_1/k \qquad [10]$$

Here, the first term indicates the part of the equivalent current used up in the formation and the growth of the film and the second term accounts for losses by transport or other causes. The relative magnitude of these terms for the film formation in an electrolyte with the pH adjusted to 5.1 is demonstrated in Fig. 8, where the number of coulombs needed for nearly complete coverage, Q_{cr}, is plotted against the anodic current density. At low current densities, as many as 80 atomic layers were dissolved prior to attainment of full surface coverage, while at higher current densities approximately 9.2 mC cm^{-2}, corresponding to *ca.* 20 atomic layers, were consumed. In the absence of illumination, Fig. 8 curve b, the situation is quite similar except that lower values of Q_{cr} were recorded; the difference due to the applied current density and illumination being attributed to the second term in Eq. [10]. Moreover, the relative magnitudes of these terms vary with time, namely as $\tau \rightarrow t_{cr}$, the first term increases while the second term decreases. In the neighborhood of t_{cr} only the first term needs to be considered.

The spatial distribution of the ionized components of GaAs is shown in Fig. 7. The highest concentration of the relevant species is expected at the GaAs/electrolyte interface extending by diffusion into the bulk. The concentration at the interface should increase monotonically with time at a rate being governed by the diffusional transport and the applied current density. Since the necessary condition for the appearance of a new phase is the existence of supersaturation, it follows that the nucleation should occur preferentially at the GaAs/electrolyte interface. Moreover, because the free energy for the critical embryo formation is less at a solid/liquid interface than in the bulk, the preference for the nucleation at the solid surface is strengthened, thus leading to a two-dimensional film growth.

The effect of illumination is that of an increase in the surface energy of the GaAs/electrolyte interphase. As the free energy for the embryo formation becomes larger, more molecules are required to form the critical embryo. Consequently, the frequency of the appearance of a new phase is less. This results in an enhancement of mass transport for the same anodic current density.

Conclusions

1. The initial stage of film formation is controlled by a two-dimensional growth from nucleation sites generated at a rate of about 10^7 events per cm^2 per second. The initial velocity of radial growth was found to be *ca.* 10^{-6} cm sec^{-1} being substantially higher as the critical time was approached.

2. An expression of the form $j = (C/Z)^{1/2} t_{cr}^{-3/2}$ was derived for this model and experimentally verified for $4.5 < pH < 6.5$ and $0.104 < j < 0.25$ mA cm^{-2}.

3. A reaction path comprising a set of elementary processes for the formation of the anodic film was postulated.

4. The effect of illumination was examined in terms of the kinetics of heterogeneous nucleation on an n-type semiconductor surface and was related to the transport of relevant species.

Acknowledgments

This work was supported by the Naval Electronics Laboratory Center Independent Research Project, Z102.

Manuscript submitted March 22, 1976; revised manuscript received Aug. 10, 1976.

Any discussion of this paper will appear in a Discussion Section to be published in the December 1977 JOURNAL. All discussions for the December 1977 Discussion Section should be submitted by Aug. 1, 1977.

Publication costs of this article were assisted by the Naval Electronics Laboratory Center.

LIST OF SYMBOLS

A	area, cm^2
i	current, A
j	current density, A cm^{-2}
k, k_1	constant defined in Eq. [2]
r	radius, cm
s	slope, see Eq. [4]
S	area (interphase), cm^2
t	time, sec
Z	rate of nucleation, cm^{-2} sec^{-1}
θ	surface coverage
σ	surface tension, erg cm^{-2}
τ	time, sec, see Eq. [1]

Subscripts

cr	refers to critical
e	indicates illuminated

REFERENCES

1. A. G. Revesz and K. H. Zaininger, *J. Am. Ceram. Soc.*, **16**, 606 (1963).
2. C. J. Dell'Occa, G. Yan, and L. Young, *This Journal*, **118**, 89 (1971).
3. W. W. Harvey and J. Kruger, *Electrochim. Acta*, **16**, 2017 (1971).
4. R. A. Logan, B. Schwartz, and W. J. Sundburg, *This Journal* **120**, 1385 (1973).
5. H. Hasegawa, K. Forward, and H. Hartnagel, *Electron. Lett.*, **11**, 53 (1975).
6. H. Hasegawa, K. Forward, and H. Hartnagel, *Appl. Phys. Lett.*, **26**, 567 (1975).
7. H. Hasegawa and H. L. Hartnagel, *This Journal*, **123**, 713 (1976).
8. G. Kortum, "Treatise on Electrochemistry," p. 516, Elsevier Publishing Company, Amsterdam, London, New York (1965).
9. T. Katan, S. Szpak, and D. N. Bennion, *This Journal*, **121**, 757 (1974).
10. R. Defay and I. Prigogine, "Surface Tension and Adsorption," chap. XVIII, Longmans, Green and Company, Ltd., London (1966).
11. J. Frenkel, "Kinetic Theory of Liquids," chap. VII, Dover Publications, Inc., New York (1946).
12. M. Volmer, "Kinetik der Phasenbildung," chap. II, T. Steinkopf Verlag, Dresden (1939).
13. V. A. Myamlin and Yu. V. Pleskov, "Electrochemistry of Semiconductors," Plenum Press, New York (1967).
14. N. H. Fletcher, *J. Chem. Phys.*, **29**, 572 (1958).
15. S. Toschev and I. Markov, *Ber. Bunsenges.*, **73**, 184 (1969).

Surface Morphology and Shape Stability in Silicon Ribbons Grown by the Edge-Defined, Film-Fed Growth Process

T. Surek,* C. B. Hari Rao,* J. C. Swartz, and L. C. Garone

Mobil Tyco Solar Energy Corporation, Waltham, Massachusetts 02154

ABSTRACT

The morphology and shape stability of silicon ribbons grown by the edge-defined, film-fed growth (EFG) technique are described. A theoretical analysis of shape stability is presented for controlled-shape growth (where the ribbon shape is determined by the shape of the meniscus); experimental evidence is introduced to show the inherent stability of the ribbon side and the relative instability of the ribbon edges, in agreement with the theory. The characteristic meniscus angle ϕ_o for constant-dimension growth is shown to depend on the crystallographic orientation of the ribbon surface; the ϕ_o anisotropy is associated with the anisotropy in the crystal-vapor surface free energy in silicon. Growth features which result from faceted growth on peripheral octahedral planes are described, and the competition between faceted growth and controlled-shape growth is analyzed. Various morphological features associated with variations and fluctuations in the EFG process variables are described.

There is considerable interest in applying the edge-defined, film-fed growth (EFG) process to the production of ribbon-shaped crystals of silicon for solar cell applications (1-4). In the EFG method, a capillary die conducts the melt from the crucible to the crystal growth interface just above the top of the die (Fig. 1). The resultant shape of the crystal is determined by the shape of the liquid film (or growth meniscus) which, in turn, is controlled by the perimeter of the die top. In essence, then, crystals of any desired cross-sectional shape can be grown by this technique using an appropriately designed die top. Deviations from controlled-shape crystal growth can occur, however, as a result of the crystallization properties of the material (5).

The fundamental physical problem in controlled-shape crystal growth is the geometric relationship between the meniscus and crystal surface directions at the crystallization front. Recent experiments (6) have shown that the requirement for the constant cross-sectional growth of silicon crystals is that the angle ϕ between the tangent to the meniscus and the growth axis be a constant designated as ϕ_o (for {111} orientation Si crystal surface, $\phi_o = 11°$). Complete analysis of the meniscus shape then shows that the ribbon thickness is related to the die and meniscus geometries by an expression of the form (3, 7)

$$t = f(t_d, s, h_{eff}, \phi_o) \qquad [1]$$

* Electrochemical Society Active Member.

Key words: silicon, shaped crystal growth, crystallization and crystal structure, growth stability, crystal-liquid-vapor interfacial energies.

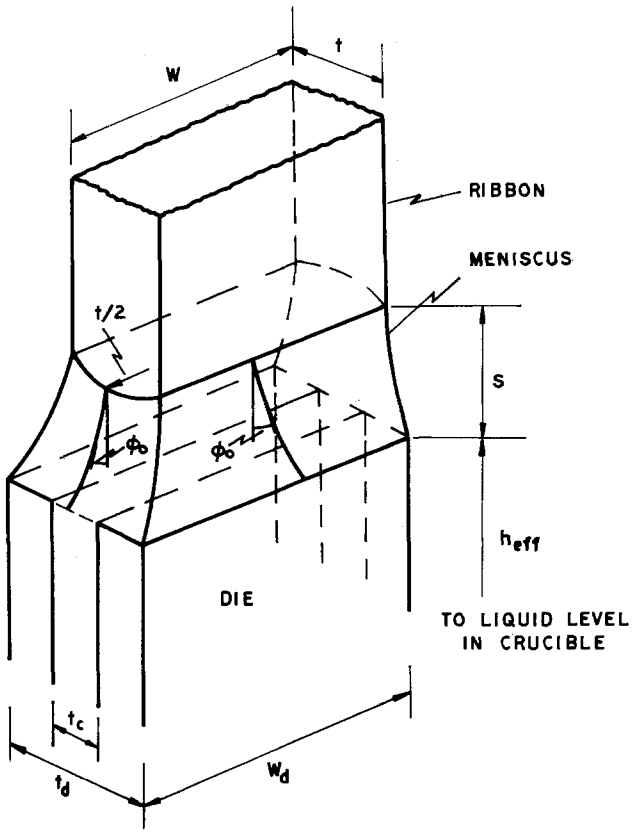


Fig. 1. Schematic illustration of ribbon growth by the EFG process showing the geometrical variables which determine the ribbon shape.

where t_d is the die thickness, s is the height of the meniscus or growth film, and h_{eff} is the effective height of the growth interface above the liquid level in the crucible (see Fig. 1). From the known functional form of f and the experimentally measured values of the other parameters, the ribbon thickness can be readily calculated; good quantitative agreement has been found (7) between the experimental and theoretical values of the ribbon thickness.

The stability of the ribbon dimensions (such as the thickness) in controlled-shape growth will be a function of the process parameters t_d, s, and h_{eff}, and of the material parameter ϕ_o. Variations in the die thickness can, of course, occur during growth as a result of mechanical changes in the edge-defining die dimensions (for example, caused by chemical reaction of the die with liquid silicon). The variable s, in practice, is determined by the details of the heat balance at the crystallization front; for steady-state growth, the rate of heat removal by conduction-radiation through the ribbon must be equal to the sum of the rate of latent heat generation at the interface and the rate at which heat arrives to the interface by conduction through the meniscus film. Perturbations in the parameter h_{eff} can occur as a result of fluctuations in the melt level in the crucible or in the rate of crystal growth (if viscous flow effects in the die capillary are appreciable); in addition, h_{eff} continuously changes during growth as the melt in the crucible is depleted. The angle ϕ_o has been shown previously (6) to depend on the orientation of the crystal surface; the anisotropy of ϕ_o undoubtedly results from the anisotropies of the crystal-vapor and crystal-liquid interfacial free energies of silicon.

In this paper, we examine the theory of ribbon shape stability in EFG as a function of perturbations in the geometrical variables, and present experimental evidence of ϕ_o anisotropy effects on ribbon shape. We then consider the effects of the anisotropic crystallization properties (*i.e.*, faceting) of silicon on controlled-shape growth based on observations in EFG ribbons. Finally, we examine various morphological features frequently observed in EFG silicon ribbons which are primarily associated with variations or fluctuations in the process variables during growth.

Theory of EFG Ribbon Shape Stability

The criterion for the stability of the external shape of a crystal in a meniscus-controlled process such as EFG derives from the finding (6) that the crystal dimension changes when $\phi \neq \phi_o$; the relevant crystal dimension increases when $\phi > \phi_o$ and decreases when $\phi < \phi_o$. Shape stabilization takes place when the resultant change in crystal dimension is such that ϕ approaches ϕ_o again. A condition of shape instability, on the other hand, occurs when ϕ deviates even further from ϕ_o as a result of the shape change. This criterion was recently applied (8) to the various techniques of crystal growth from the melt (Czochralski, floating zone, and EFG of various crystal shapes); here we consider the shape stability of EFG ribbons when the growth is subjected to perturbations in the geometrical variables discussed above. The analysis is divided into separate discussions of the thickness and width dimensions of the ribbon.

Stability of the ribbon thickness.—Figure 2a shows the variation of ribbon thickness with meniscus height for typical values of the experimental variables (*i.e.*, solution of Eq. [1] for $h_{eff} = 2$ cm and $t_d = 0.04$ cm). The curve for $\phi = \phi_o = 11°$ represents all possible pairs of s-t values for growth with a uniform thickness. If a steady-state system (s_A, t_A) in Fig. 2a is perturbed by raising the meniscus height to B, the ribbon thickness should decrease (since $\phi < \phi_o$ at B) to a new steady-state thickness $t_{B'}$. Similarly, a lowering of the meniscus height to C in the figure will lead to a new steady-state thickness $t_{C'}$.

A perturbation in the die thickness t_d is considered in Fig. 2b. When the die thickness increases from t_{d1} to t_{d2}, the initially steady-state system (s_A, t_A) in the figure will fall on the dashed curve $\phi > \phi_o$ for the larger die thickness. It is readily seen that the ribbon thickness should therefore increase to a new steady-state value t_B. Of course, changes in meniscus height may also occur (as a result of changes in the thermal profile accompanying the t_d change), but these can be accommodated in a stable manner (*cf.* Fig. 2a). Localized fluctuations in the die thickness occur frequently in silicon ribbon EFG when graphite dies are used (*e.g.*, as a result of the growth of SiC particles at the die top). A change in the effective die thickness from t_d to the capillary spacing t_c (see Fig. 1) can occur when a critical value of the meniscus height is exceeded; at this height, the angle between the meniscus and the horizontal at the die edge is equal to 30° [the wetting angle of liquid Si on graphite (9)]. For the case examined in Fig. 2a, the critical height is 0.10 cm, thus it is not reached before the ribbon thickness becomes zero. Growth (with a new steady-state thickness) would continue from the inner edges of the die in Fig. 1 if this critical meniscus height were exceeded.

A fluctuation in h_{eff} is examined in Fig. 2c. Here we consider a hypothetically large change in h_{eff} from 4 to 2 cm; the initially steady-state system (s_A, t_A) is again seen to respond to this change by attaining a new steady-state thickness t_B. A similar stabilizing behavior is seen in Fig. 2d when the characteristic value of ϕ_o changes from ϕ_o^1 to $\phi_o^2 < \phi_o^1$ (for example, as a result of a change in the orientation of the ribbon surface caused by twinning).

Stability of the ribbon width.—The treatment of the stability of the width dimension of the ribbon is perforce less satisfying than that of the thickness dimension. The principal difficulty arises in attempting to

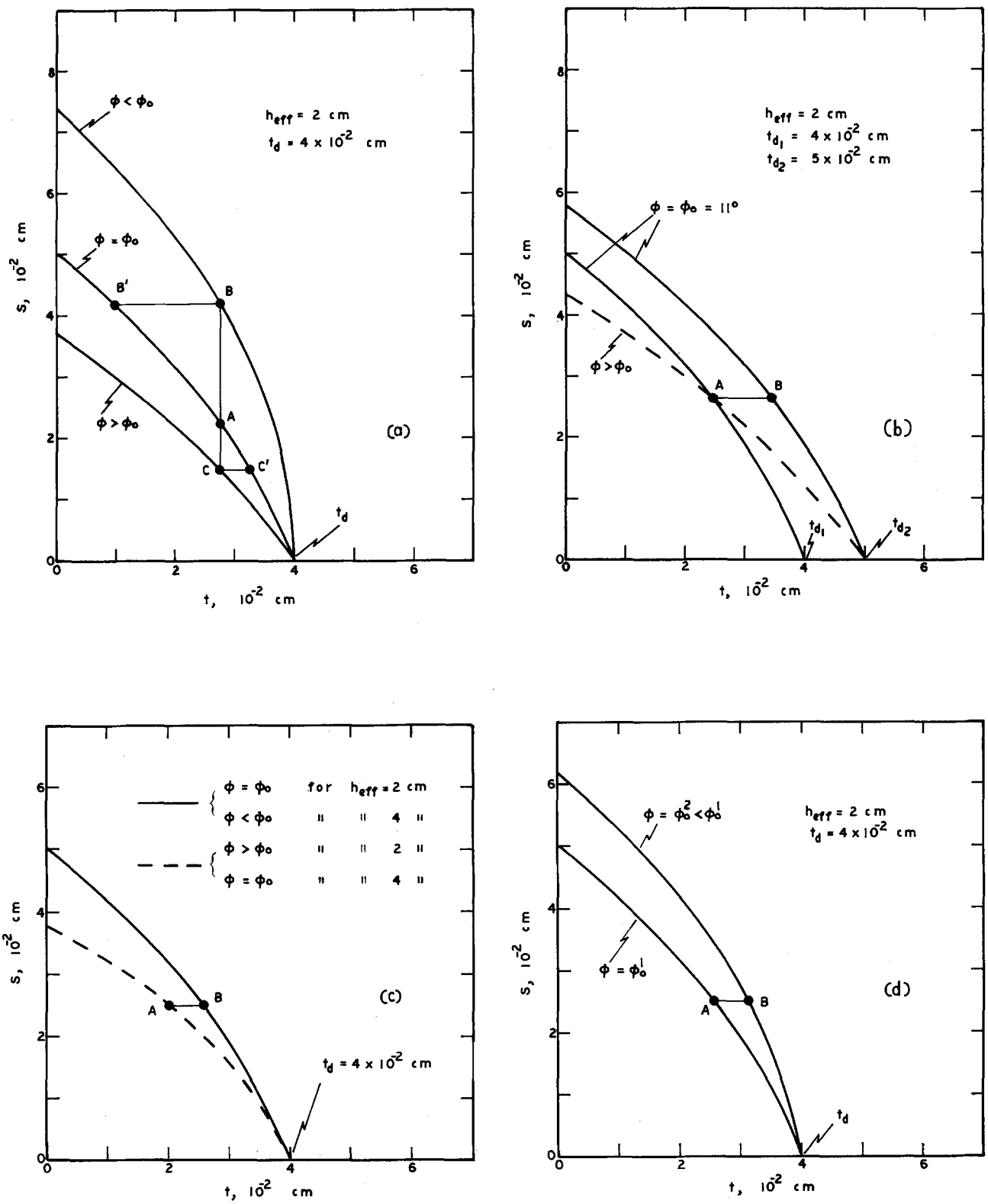


Fig. 2. Meniscus height-ribbon thickness curves in silicon ribbon EFG for various values of die thickness, meniscus angle, and h_{eff}, and analysis of perturbations in the geometrical variables. (a) Perturbation in meniscus height; the steady-state ($\phi = \phi_o$) and non-steady-state ($\phi <$ and $> \phi_o$) curves were calculated for $\phi = 11°$, 0°, and 20°, respectively. (b) Perturbation in die thickness; $\phi = 20°$ for the non-steady-state curve for t_{d_2}. (c) Perturbation in h_{eff}; $\phi_o = 11°$. (d) Perturbation in meniscus angle; $\phi_o^1 = 11°$ and $\phi_o^2 = 5°$.

calculate the meniscus shape near the end of the ribbon where the radius of curvature of the ribbon surface changes continuously from infinity along the side of the ribbon to approximately $t/2$ at the very end of the ribbon (see Fig. 1). An approximation to the ribbon end problem was obtained (8) by considering the shape stability of a rod-shaped crystal of radius $t/2$ growing from a die shaper with a wetted top surface of radius $t_d/2$. Figure 3a shows the variation of $t/2$ with meniscus height for $h_{eff} = 2$ cm and $t_d = 0.04$ cm. The solid line in the figure (where $\phi = \phi_o = 11°$) again represents all possible pairs of s-$t/2$ values for steady-state growth. It can be readily argued in the figure that a steady-state point such as A is stable whereas a point such as D is unstable when the meniscus height is perturbed from the respective steady-state values. In the latter case, for example, an increase in meniscus height to E will result in a de-

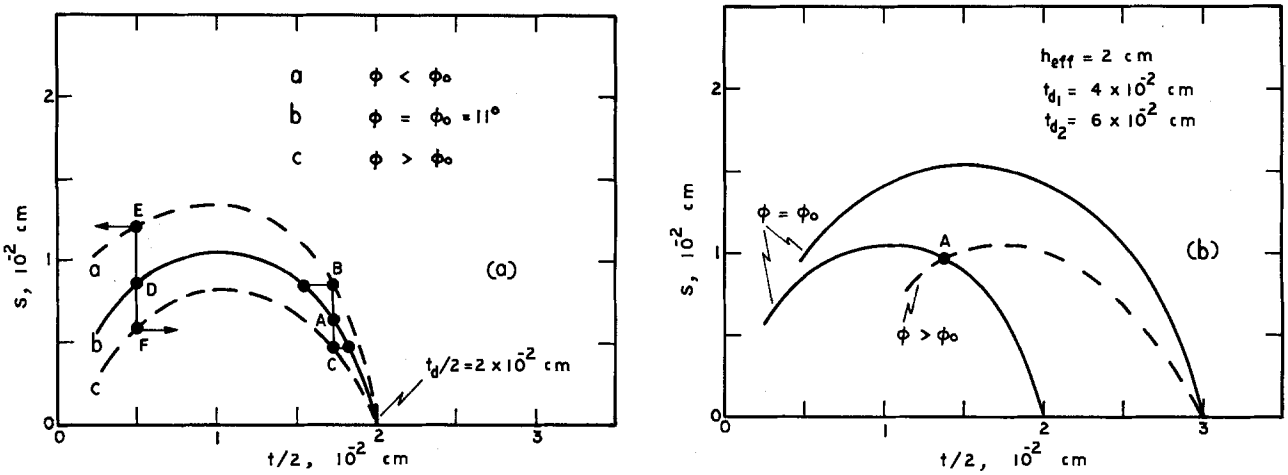


Fig. 3. (a) Variation of t/2 at ribbon end with meniscus height for various values of the meniscus angle and $h_{eff} = 2$ cm. The non-steady-state curves ($\phi \neq \phi_0$) are shown schematically. The steady-state point A is stable, while point D is unstable when the meniscus height is perturbed. (b) Perturbation in the edge-defining die radius ($t_d/2$). The $\phi > \phi_0$ curve for t_{d_2} is shown schematically.

crease in the crystal radius t/2 (since $\phi < \phi_0$); this will lead to a still greater deviation of ϕ from ϕ_0, and thus to an even faster decrease in radius, and so on. It is readily seen in Fig. 3a that the entire portion of the $\phi = \phi_0$ curve where $ds/d\ (t/2) > 0$ is unstable, whereas shape stabilization occurs in the region where $ds/d\ (t/2) < 0$. The detailed analysis (8) of the ribbon end problem shows that the requirement for shape stability is that the edge-defining die radius ($t_d/2$) should not exceed approximately twice the radius of curvature of the ribbon ($t/2$) at the ribbon edge.

The conclusion we reach from the above analysis of the ribbon shape stability is that the side of the ribbon (*i.e.*, the thickness dimension) is inherently stable, whereas the ribbon edge (and, therefore, the width dimension) is only conditionally stable. Perturbations in the geometrical variables at the ribbon edge can readily upset the condition of shape stability, as demonstrated in Fig. 3b. Here we see that an increase in the edge-defining die radius from t_{d_1} to t_{d_2} has resulted in an initially stable system (s_A, $t_A/2$) to fall on a curve with $\phi > \phi_0$ for the new die radius; the system will be unstable with the radius increasing at an ever-increasing rate. In the following sections, we present the results of experimental investigations of the ribbon shape stability, and show frequent examples of the inherent stability of the ribbon side and the comparative instability of the ribbon edge.

Effects of Meniscus Angle Anisotropy on Shape Stability

Previous experience (6) has indicated that the characteristic value of the meniscus angle for the steady-state cross-sectional growth of silicon crystals (*i.e.*, ϕ_0) is a function of the orientation of the crystal surface. This dependence is probably the result of the influence of the surface free energies of the three interfaces on the relative directions of the interfaces at the crystal-liquid-vapor triple junction (10). In this section, we report some morphological observations in EFG ribbons which confirm the existence of a ϕ_0 anisotropy in silicon crystal growth; the observations are extended to obtain a measure of the anisotropy in the crystal-vapor surface free energy in silicon. It should be pointed out here that the $\phi = \phi_0$ requirement is satisfied when the crystal shape is controlled by the shape of the meniscus; when faceted growth occurs on peripheral regions of the solid-liquid interface, this condition is no longer satisfied, as described in the next section.

Crystal defects which have been observed frequently in EFG silicon ribbons are twin boundaries (3, 4). Examples of twin boundary traces on the surface of the ribbon are shown in Fig. 4 for typical low-index seed orientations used in silicon ribbon EFG; the twins extend through the entire thickness of the ribbon. The occurrence of such twinning generally leads to a change in the crystallographic orientation of the ribbon surface and to a change in the growth direction. Since the meniscus height was kept constant in the experiments, the only plausible explanation for the readily visible change in ribbon thickness (see Fig. 4) is that the characteristic value of ϕ_0 has changed upon twinning. In effect, the twinning has resulted in a perturbation in ϕ_0 (*cf.* Fig. 2d); the deviation of the instantaneous meniscus angle from the "new" ϕ_0 during a brief transient period following the twinning then accounts for the change in the ribbon thickness.

Measurements of the thickness change in EFG ribbons were made using a Sloan Dektak surface profile recorder; the results are summarized in Table I. The table lists the average surface elevation change (and root mean square deviation) across the twin boundaries for a number of surface profile traces; the traces were made in both directions across the twin (*e.g.*, {111} to {115} as well as {115} to {111}). The elevation change is typically several microns (the change in ribbon thickness is approximately twice the elevation change), and the transient occurs over a ribbon length of a few tenths of a millimeter (the growth rate was 1-2 cm/min in the experiments and the ribbon thicknesses were in the range of 0.02-0.04 cm).

From the signs of the elevation changes in Table I, we can immediately deduce the relative values of ϕ_0 for the various crystal surface orientations: *viz.*, $\phi_0\{111\} > \phi_0\{115\}$, $\phi_0\{110\} > \phi_0\{114\}$, and $\phi_0\{100\} < \phi_0\{122\}$. From a model (10) which balances the surface tensions at the crystal-liquid-vapor triple junction, one expects that a decrease in ϕ_0 would be associated with an increase in crystal-vapor surface free energy. Indeed, the above variations in ϕ_0 are consistent with the probable order of the surface free energies for these low index faces. A simple calcula-

Table I. Changes in ribbon surface elevation caused by the anisotropy in ϕ_0

Orientation change	No. of tracings	Avg elevation change (μm)	Avg transient distance (mm)
(111)[1$\bar{1}$0] to (511)[$\bar{1}$14] or to (151)[$\bar{1}$14]	22	7.7 ± 3.0	0.2-0.6
(111)[$\bar{2}$11] to (151)[$\bar{2}$17]	7	9.0 ± 2.2	0.3-0.8
(110)[1$\bar{1}$1] to ($\bar{1}$14)[5$\bar{1}$1]	2	1.5 ± 0.7	0.2-0.4
(100)[001] to (122)[2$\bar{2}$1]	3	−1.5 ± 0.4	0.1-0.5
(110)[1$\bar{1}$0] to (110)[$\bar{1}$14]	3	1.8 ± 0.9	0.2-0.5
(110)[1$\bar{1}$1] to (110)[1$\bar{1}$5]	6	3.3 ± 1.2	0.3-0.8

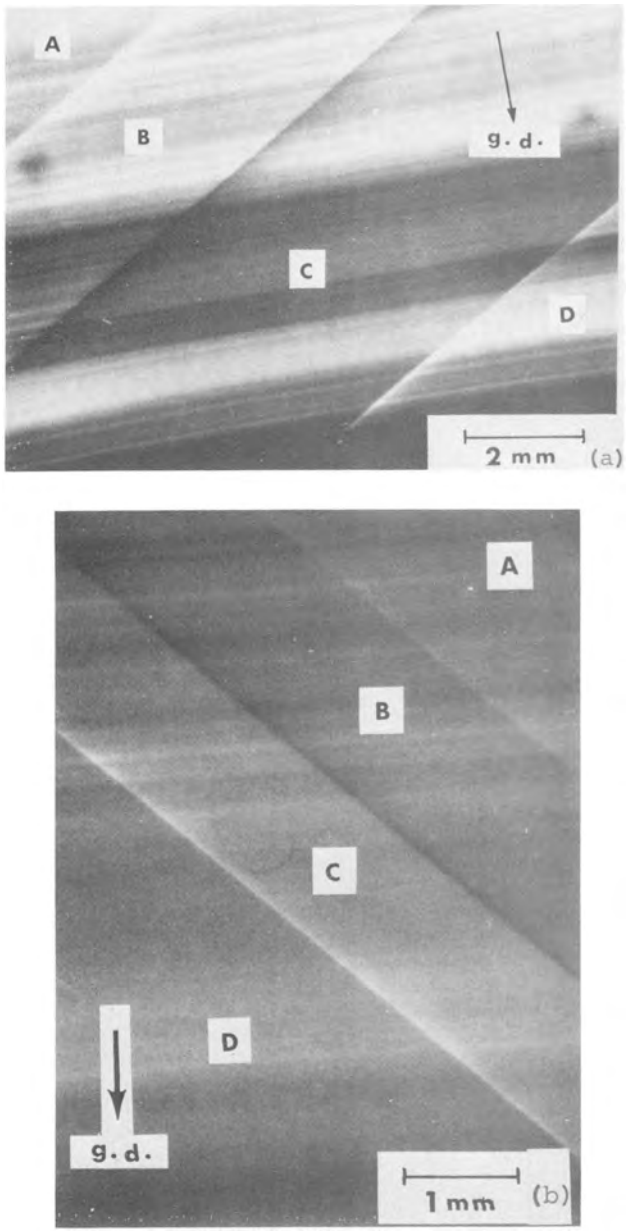


Fig. 4. Examples of twins in EFG silicon ribbon which lead to changes in steady-state ribbon thickness as a result of the ϕ_0 anisotropy. (a) Surface orientation changes from {111} to {115} to {111} to {115} for regions A to D, respectively. (b) Surface orientation changes from {100} to {122} to {100} to {122} for regions A to D, respectively. The arrow denotes the crystal growth direction (g.d.)

tion based on the assumption that the surface energy for each plane varies in proportion to its area resolved in nearest {111} planes gives the ratio of the surface free energies $\gamma\{111\}/\gamma\{122\}/\gamma\{110\}/\gamma\{114\}/\gamma\{115\}/\gamma\{100\}$ as 1.0/1.15/1.22/1.41/1.46/1.73. With the exception of the {122} to {100} transition (where only a small elevation change is observed), the magnitudes of the elevation changes are seen to reflect the change in the surface free energy. The value of ϕ_0 is also expected to depend on the direction and free energy of the solid-liquid interface at the triple junction (10). It is seen in Table I that the crystal growth direction also changes upon twinning; in fact, the last two entries in the table show that a change in the growth direction alone can lead to a change in surface elevation (*i.e.*, a change in ϕ_0). Unfortunately, without the knowledge of the detailed shape of the solid-liquid interface at the triple junction, it is not possible to speculate about the anisotropy in the solid-liquid surface free energy from these results.

Similar transient variations are observed in the width dimension of the ribbon when a twin or other high angle grain boundary emerges at the ribbon edge. Examples of twins initiating from and terminating at the edge of the ribbon are shown in Fig. 5a and 5b, respectively; Fig. 5c shows the change in ribbon width occurring when a high angle grain boundary intersects the surface at the ribbon edge. The changes in ribbon width are seen to be several orders of magnitude greater than the thickness changes in Table I. Of course, it is not practical to describe these variations in ribbon width in terms of a change in crystal surface orientation (which, clearly, is a variable around the ribbon edge). The perturbation now is in the "distribution" of ϕ_0 around the edge of the ribbon which, together with the detailed kinetics of the crystal growth (such as the faceting effects described in the next section), leads to a change in ribbon width. The perturbations at the ribbon edges, as seen in the photographs in Fig. 5, are far more severe than at the ribbon sides, and can frequently lead to large-scale variations in the ribbon width and, on occasion, to an arrest in stable ribbon growth. This would be expected from the shape stability considerations described in the preceding section, where it was shown that the ribbon end stability was a sensitive function of the relative dimensions of the ribbon edge and the die edge.

Figure 6 shows an extreme case of edge instability where many high angle grain boundaries have nucleated in the vicinity of the ribbon edge; the width dimension is seen to be extremely unstable under these conditions. It is not clear at this time, however, whether the polycrystalline structure has resulted from the width being unstable and the growth conditions fluctuating, or the width instability is caused by the polycrystalline growth.

Finally, it should be pointed out that the present examples (Fig. 4 and 5) used to demonstrate the effects of ϕ_0 anisotropy were obtained in the proximity of the seed (*i.e.*, within about 10 cm of ribbon growth) where large single crystal areas are frequently observed. At larger distances from the seed, the seeded orientation is lost as a result of interactions of primary twins, higher order twins, and various other grain boundaries. Recent evidence (11) indicates that, irrespective of the seed orientation, an equilibrium defect structure eventually develops in the ribbon; the orientation is approximately (110) $[\bar{1}12]$ and the ribbon contains a high density of linear boundaries parallel to the growth direction (an example of this structure is shown in a later section). The effects of the ϕ_0 anisotropy are nevertheless observed in all EFG ribbons; the slight changes in surface elevation which result from the ϕ_0 anisotropy, in fact, cause the various boundaries to be readily discernible in the as-grown ribbon.

Effects of Faceting on Ribbon Shape Stability

An important consideration in attempting to achieve controlled-shape growth involves the crystallization properties of the material. Because of the anisotropy in growth rate, silicon often exhibits singular (*i.e.*, faceted) growth on regions of the crystallization front near the {111} orientations. When such faceted growth occurs on peripheral regions of the solid-liquid interface, various ridgelike features result on the crystal surface; such features have been previously observed and analyzed in silicon crystals grown by the Czochralski (12) and floating zone (13) methods and in germanium crystals grown by the Stepanov technique (5). The basic effect of faceted growth on the external shape of the crystal is that the latter is no longer uniquely determined by the shape of the meniscus

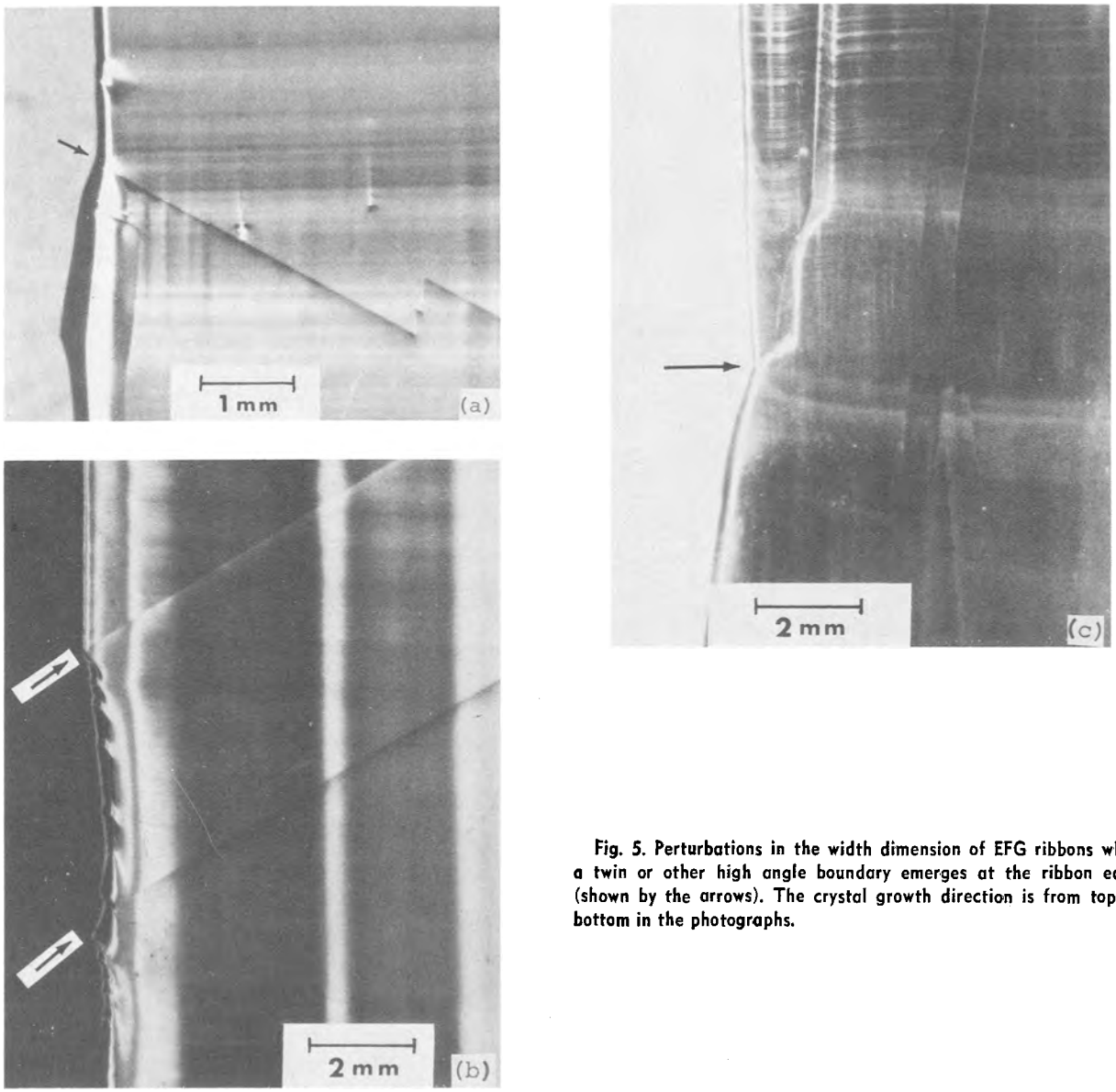


Fig. 5. Perturbations in the width dimension of EFG ribbons when a twin or other high angle boundary emerges at the ribbon edge (shown by the arrows). The crystal growth direction is from top to bottom in the photographs.

at the crystal-liquid-vapor triple junction (*i.e.*, by the $\phi = \phi_0$ requirement), but it is also affected by the detailed kinetics of the layer nucleation and growth on the facets.

All descriptions of faceted growth in silicon consider supercooling as the basis of its origin; for a {111} facet to appear at the solid-liquid interface and for growth to be maintained, a greater supercooling of the melt is required at the faceted region of the crystallization front in order to nucleate the new layer sources. Clearly, then, the shape of the freezing isotherm and its relationship to the close-packed {111} planes affects the faceting tendency and the location of the facets. In general, peripheral faceting is enhanced by a concave (toward the melt) freezing isotherm near the periphery; the tendency to facet is also expected (5, 12, 13) to increase with increasing crystal growth rate, decreasing melt temperature or gradient in the melt at the growth interface, increasing impurity concentration in the melt, and decreasing concentration of crystal dislocations (which can serve as easy nucleation sites for new {111} growth layers). In turn, faceting affects the distribution of dislocations and impurities in the grown crystal. The location of the ridgelike surface features is determined by the anisotropy of growth rate of ledges in various directions on the close-packed (111) surface; the "easy" growth directions (where the ridges appear) correspond to the $[\bar{1}\bar{1}2]$ directions, whereas lateral growth is much slower in the $[11\bar{2}]$ directions (13).

Faceted growth has also been observed frequently, albeit unpredictably, in EFG silicon ribbon growth. The occurrence of faceting is observed during growth by a localized rise (or, on occasion, a fluctuating rise and fall) in the crystallization front; following growth, faceting is evidenced by the various characteristic growth features on the external surface of the ribbon. Below, we describe some typical features observed at the side and edge surfaces of EFG ribbons.

Faceting at the ribbon sides.—The most frequently observed feature of growth faceting is illustrated in Fig. 7. During growth, a sharp, angular rise in the meniscus height is observed about a high angle grain boundary (twin boundary in Fig. 7); the tilt of the growth interface on either side of the boundary depends on the orientation of the {111} planes relative to the growth direction. In the grown ribbon, faceting is evidenced by the breaks in the horizontal surface striae which delineate the instantaneous shape of the solid-liquid interface. (A detailed description of the surface striae is given in a later section.) In the example shown in Fig. 7, the ribbon surface orientation is near (110) and the growth direction is within a few degrees of the $[1\bar{1}2]$ orientation (*i.e.*, approximately $[33\bar{5}]$) on either side of the twin boundary.

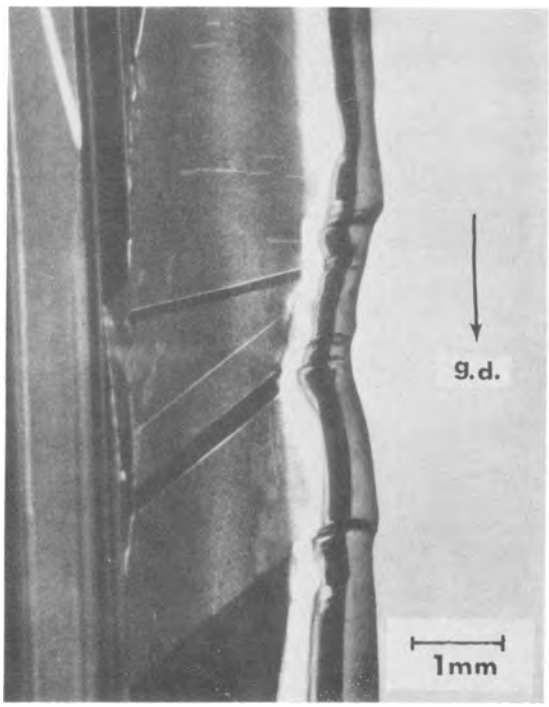


Fig. 6. Fluctuations in ribbon width accompanying the nucleation of many high angle grain boundaries. The arrow denotes the crystal growth direction.

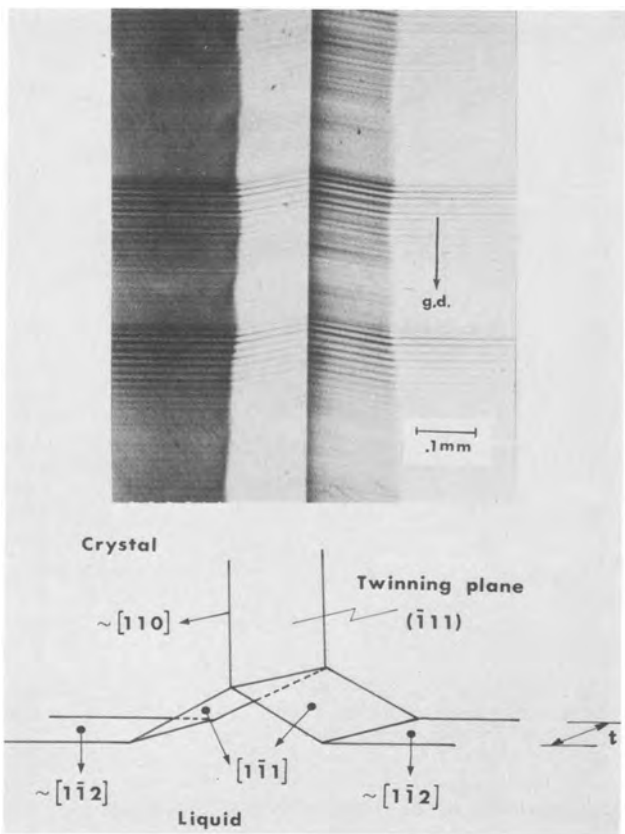


Fig. 7. Growth faceting at a twin boundary in silicon ribbon EFG. The surface striae delineate the shape of the solid-liquid interface (shown in the sketch) during growth.

Faceted growth thus occurs on the $(1\bar{1}1)$ planes, as shown in the sketch in Fig. 7; the angle of ~13° measured from the striae in the figure is close to the value of 14.4° for the angle between the $(1\bar{1}1)$ and $(3\bar{3}5)$ planes.

Growth faceting of the type depicted in Fig. 7 is not restricted to faceting only on peripheral regions of the solid-liquid interface; rather, the entire interface across the thickness of the ribbon can be faceted, as shown in the sketch. Indeed, corresponding breaks in the surface striae can be seen on the reverse side of the ribbon in Fig. 7. Nucleation of new growth layers is likely to occur in these cases along the line of intersection of the two facets where the supercooling is the greatest. For a typical vertical gradient in the liquid of 150°C/cm in EFG ribbon growth, we estimate a maximum supercooling of ~0.4°C from Fig. 7. This undercooling is considerably less than the value of 6°C estimated from studies of faceting in float-zoned silicon crystals (13); the difference is probably the result of the easy nucleation site at the intersection of the facets in this case.

Examples of another type of peripheral faceting are shown in Fig. 8. When the ribbon surface is very close to a {111} orientation, we frequently obtain surface segments which are extremely smooth or mirrorlike. The presence of such "surface facets" is evidenced by a lack of continuity of the horizontal surface striae across these regions, as indicated by the arrows in the figures. Basically, the crystal here exhibits a tendency to extend the low energy {111} external surface, irrespective of the shape which is commanded by the instantaneous meniscus shape (and the $\phi = \phi_0$ requirement). When the ribbon surface plane is slightly misoriented from {111} (which is invariably the case), the tendency to continue the surface facet is counteracted by the meniscus angle effect and the changing thermal conditions as the facet extends into or out of the ribbon plane; faceting thus gets relieved by an appropriate transient in the ribbon thickness. In the example shown in Fig. 8a, the surface facet extends into the ribbon (the angle between the ribbon plane and the facet is ~4° as determined by the Sloan Dektak recorder) and is relieved by an increase in ribbon thickness (where the striae reappear). In Fig. 8b, the surface faceting on the (111) plane (near a (111) $[\bar{2}11]$ ribbon seed) is constricted by growth faceting near the periphery on the oblique $(\bar{1}11)$ plane.

On occasion, complex faceted features are observed on the ribbon surface, as exemplified in Fig. 9. Region A in the figure is primary-twin related to the original ribbon seed orientation, (100) [011]; regions B and C are both first-order twins of region A, hence the boundary between regions B and C is a second-order twin boundary. It is interesting to observe that the faceted features are different on the front (Fig. 9a) and back (Fig. 9b) sides of the ribbon. Of course, this is the result of the octahedral planes on which faceted growth occurs having different inclinations relative to the freezing isotherm near the periphery. The example shows that crystallization (and the formation of the external crystal surface) in one region of the crystal occurs independently of any other region. With the orientation in region A being $(\bar{1}22)$ $[\bar{4}\bar{1}\bar{1}]$, it appears that faceting is more prevalent on the $(\bar{1}11)$ planes at the front of the ribbon than it is on the $(\bar{1}\bar{1}\bar{1})$ planes (which are less inclined to the growth interface) at the back side. A detailed study of the various ridgelike features seen in the figure requires an analysis of the supercooling on the various octahedral planes and of the anisotropic ledge kinetics on these facets. The periodic pattern which is apparent along the second-order twin boundary in Fig. 9a (and extends some 15 cm of growth length) is probably the result of a competition between outward growth on the interface facets in the easy <112> directions and the meniscus angle effect which would tend to contract the ribbon thickness. The changing meniscus angle and shape at the crystal-liquid-vapor

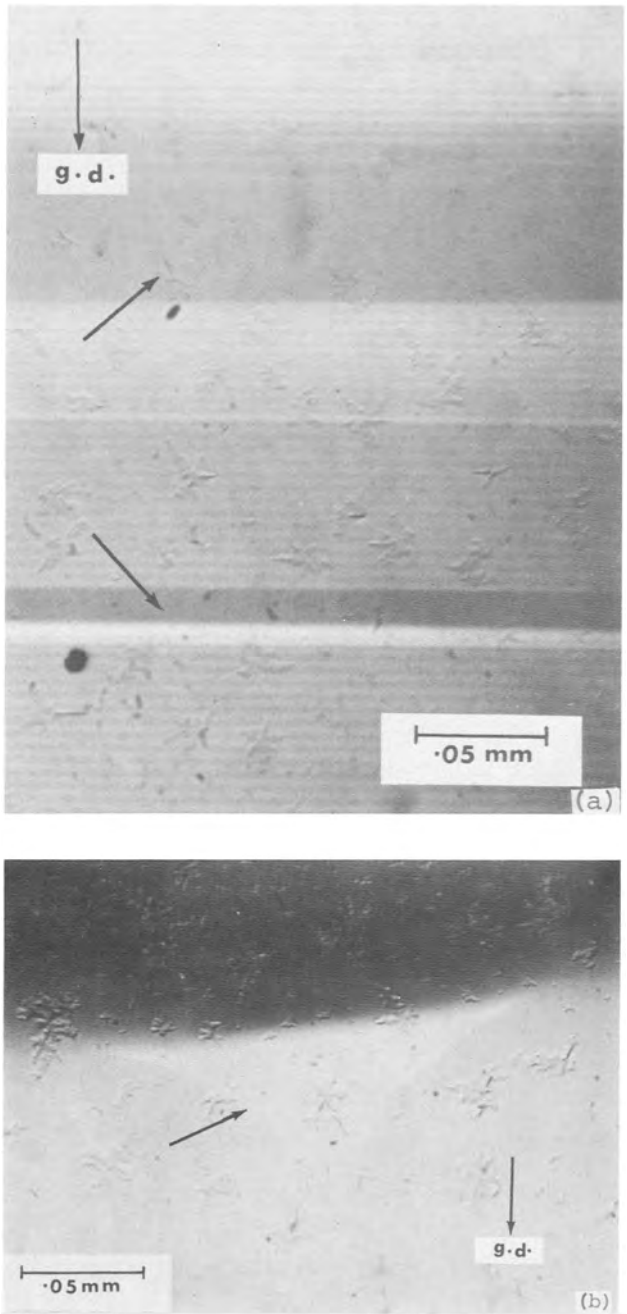


Fig. 8. Surface facets (specular {111} faces) on the side faces of EFG ribbons grown with a nearly {111} surface orientation.

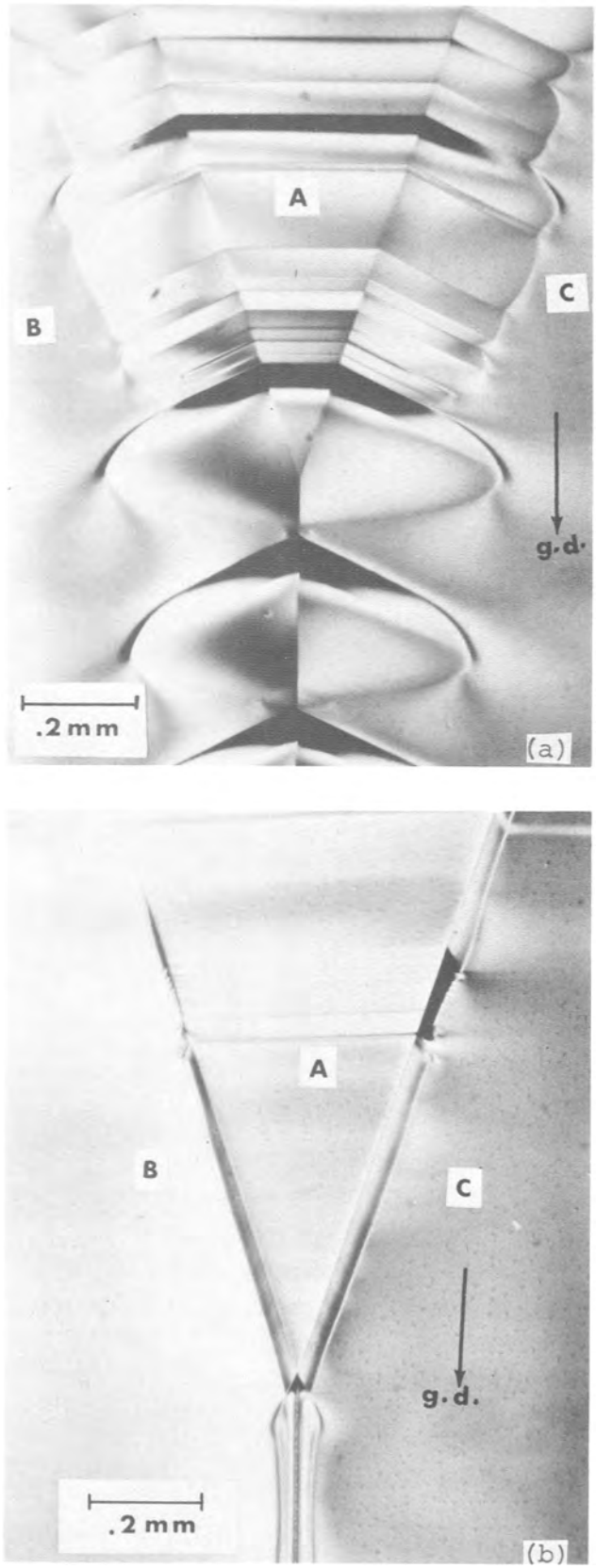


Fig. 9. Complex growth facets observed on the (a) front and (b) back sides of an EFG ribbon seeded in the (100) [011] orientation. The figure demonstrates that crystallization (and the formation of external surface features) occurs in various regions of the ribbon independent of any other region.

triple junction also affect the thermal conditions (*i.e.*, supercooling) at the facet planes.

In general, faceted growth at the ribbon sides has been observed to be very stable; the facets can extend several inches (or, as in the case of the facets in Fig. 7, several feet) along the ribbon length.

Faceting at the ribbon edges.—Examples of faceting at the ribbon edges and its effects on the ribbon width are shown in Fig. 10. Figure 10a is the most frequently observed feature; during growth, it is accompanied by a somewhat periodic fluctuation in the meniscus height at the ribbon edge. These fluctuations can usually persist in a stable manner for a short growth length ($\lesssim$ few centimeters) by which time the growth conditions and crystal orientation (hence the supercooling conditions on the facet planes) may change. As would be expected from the shape stability considerations described above, fluctuations in the shape variables at the ribbon edges are undesirable in that the marginal stability of the ribbon edge (*cf.* Fig. 3) can be readily upset by these fluctuations. Figure 10b shows a case of edge instability associated

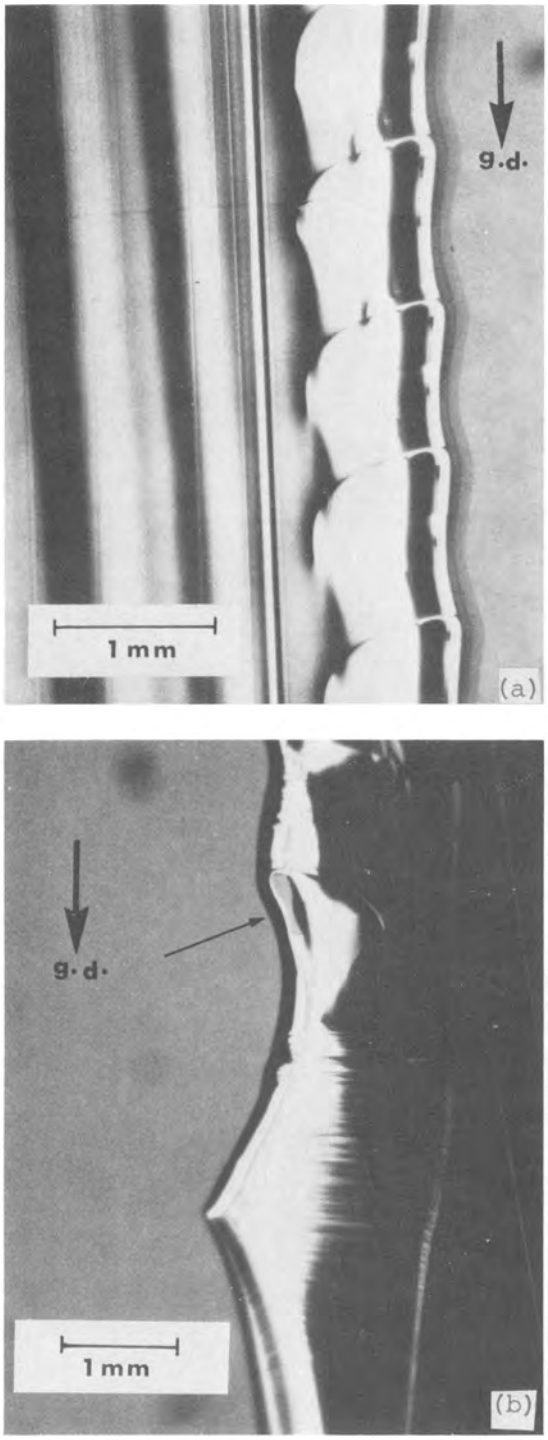


Fig. 10. Growth faceting at the edges of EFG ribbons: (a) faceting accompanied by nearly periodic fluctuations in meniscus height at the ribbon edge (the ribbon orientation is approximately (231) [$\bar{3}$13] near the edge); (b) edge instability caused by rapid lateral growth on peripheral facets. The arrow shows a small, specular surface facet at the ribbon edge.

with faceted growth; extremely rapid lateral growth here has caused the ribbon edge to almost spread past the edge of the die. Faceting at the ribbon edges, and the fluctuating growth conditions which are generally associated with it, often lead to twin nucleation at the ribbon edges (*e.g.*, Fig. 6 and 10b).

Under unusual growth conditions, faceted growth can lead to extremely stable ribbon edges; an example of this is shown in Fig. 11. Here the ribbon surface orientation is (111) and the growth direction is [1$\bar{1}$0]; the ribbon edge has a "lipped" shape (see Fig. 11b)

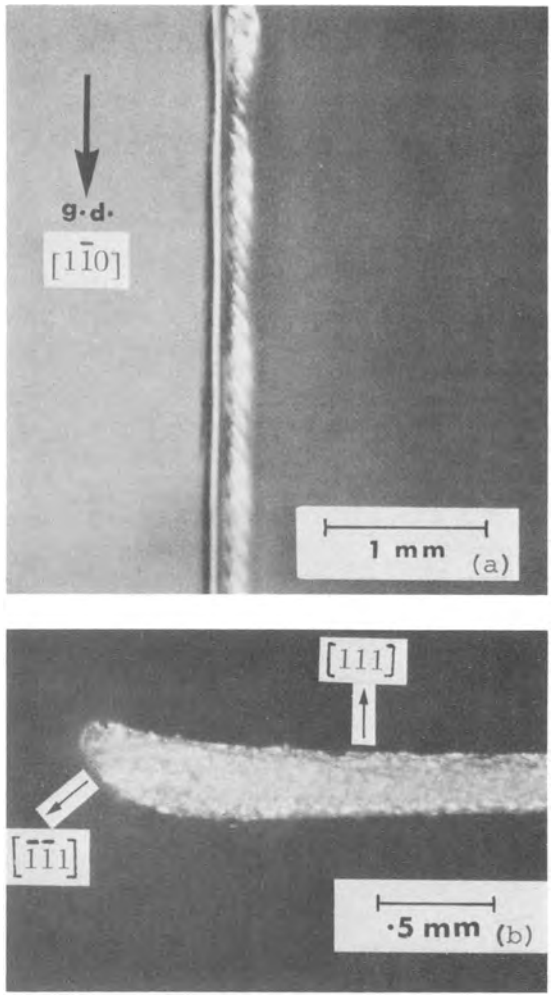


Fig. 11. (a) Side and (b) cross-sectional views of "lipped" ribbon; faceting at the ribbon edges has resulted in extremely stable growth in this case.

with a ($\bar{1}\bar{1}$1) surface facet along the outer edge, as shown in the figure. The lip is curved in the opposite direction at the other edge of the ribbon. The ribbon edge was stable for a few centimeters of growth on one side and nearly 20 cm on the other side; the "stable" growth conditions which were obtained in this growth run could not be consistently reproduced in subsequent trials, however.

In summary, faceted growth is frequently observed in EFG ribbon growth. By far the most important consequence of faceting appears to be that it can override (or, at least, it can compete with) the meniscus angle requirement (*i.e.* $\phi = \phi_0$) for constant cross-sectional growth. The periodic fluctuations of the faceted features are probably the result of such a competition between the two effects. Similar interactions between faceted and controlled-shape growth have been observed in the growth of rod-shaped crystals and ribbons of germanium by the Stepanov process (5). As described above, the tendency for faceted growth is a complex function of the crystal growth conditions such as the growth rate, thermal profiles, impurities, dislocation density, and crystal orientation. Correlations of faceting with the growth conditions in silicon ribbon EFG have not been successful thus far, probably as the result of inhomogeneities in the distribution of dislocations and in the crystallinity of the ribbons. Nevertheless, growth conditions have been achieved where faceting at the ribbon edges (which is, clearly, the primary problem area from the point of view of growth stability) is avoided.

Other Morphological Observations in EFG Ribbons

In this section, we examine some morphological features frequently observed in EFG silicon ribbons which are associated with variations or fluctuations in the process variables during growth.

Variations in the edge-defining die dimensions.—As described above [also in Ref. (4)], mechanical changes in the edge-defining die dimensions occur frequently when graphite dies are used in silicon ribbon EFG (*e.g.*, as a result of SiC particles, die spreading open, mechanical damage, or spill-over at die edges, etc.). Figure 12a shows the typical vertical striae seen on the ribbon surface which result from the meniscus wetting around the SiC particles growing at the die top. Figure 12b illustrates the effect of a spill-over near the edge of the die; the breaks in the striation (denoted by the arrows) were caused by the lateral displacement of the ribbon during growth. In addition to demonstrating the over-all stability of the thickness dimension of the ribbon when subjected to perturbations in the die thickness (*cf.* Fig. 2b), these figures illustrate the effectiveness of the "edge definition" in EFG. In essence, the ribbon surface is a true reproduction of the actual edge-defining die shape. As the meniscus height increases, the resolution of the die features decreases, as would be expected, and the ribbon surface is smoother.

Variations in meniscus height.—The dependence of ribbon thickness on meniscus height for given values of die thickness and h_{eff} (*cf.* $\phi = \phi_0$ line in Fig. 2a) has been quantitatively verified in silicon ribbon growth experiments (7). When the meniscus height was purposely changed in the experiments (by changing the crystal pull rate or the temperature gradient in the meniscus film), the ribbon thickness attained a new steady-state value (as depicted in Fig. 2a) following a brief transient period. The same variations in meniscus height at the ribbon edges were generally observed (7) to lead to an instability (*i.e.*, continued spreading or tapering) of the width dimension of the ribbon.

Localized fluctuations or variations of the meniscus height near faceted regions of the growth interface were described in the preceding section; in these cases, the crystal shape was found to be governed by the detailed kinetics of layer nucleation and growth on the facet planes rather than by a geometrical relationship such as in Eq. [1]. Another type of localized variation in meniscus height frequently occurs at the intersection of high angle grain boundaries (*e.g.*, twin boundaries) with the growth interface at the solid-liquid-vapor triple junction. The effect is probably similar to the grain boundary grooves in solid-liquid interfaces (14); an example of the resulting surface features in EFG ribbon is shown in Fig. 13. The striae delineate the "groove" at the twin boundary; the surface is slightly depressed (*i.e.*, thickness is less) in this region.

Horizontal surface striae.—Many examples of the horizontal striae which are always observed on the surface of EFG ribbons have already been presented, *e.g.*, Fig. 7 and 13. The following observations have been made in relation to these striae: (*i*) the striae are periodic markers of the growth interface; (*ii*) the striae are parallel, except in regions of local acceleration of growth rate (*e.g.*, start of an interface facet); (*iii*) the striae spacing (approximately a few micrometers) is much greater than the amplitude of the striae; (*iv*) striae on either side of a thin ribbon are "in phase," *i.e.*, the ribbon thickness increases on both sides simultaneously; (*v*) the striae never cross (*i.e.*, meltback, if any, is much less than the striae spacing); (*vi*) the striae are not associated with localized variations in impurity or dopant concentration in the ribbon; (*vii*) the striae frequency is independent of the suspended length of the ribbon, of the puller mechanism, and of the frequency of the furnace power supply (60 Hz, 9.6 kHz, and 450 kHz); (*viii*) the striae frequency has been observed to vary from 0 (near the seed where the crystal growth rate is low) to ~150 Hz at the fastest ribbon growth rates achieved thus far (~5 cm/min). There is some evidence that the striae frequency is, in fact, roughly proportional to the growth rate. Further work is in progress to identify the mechanism of the striae formation; it appears to be associated with transient variations of

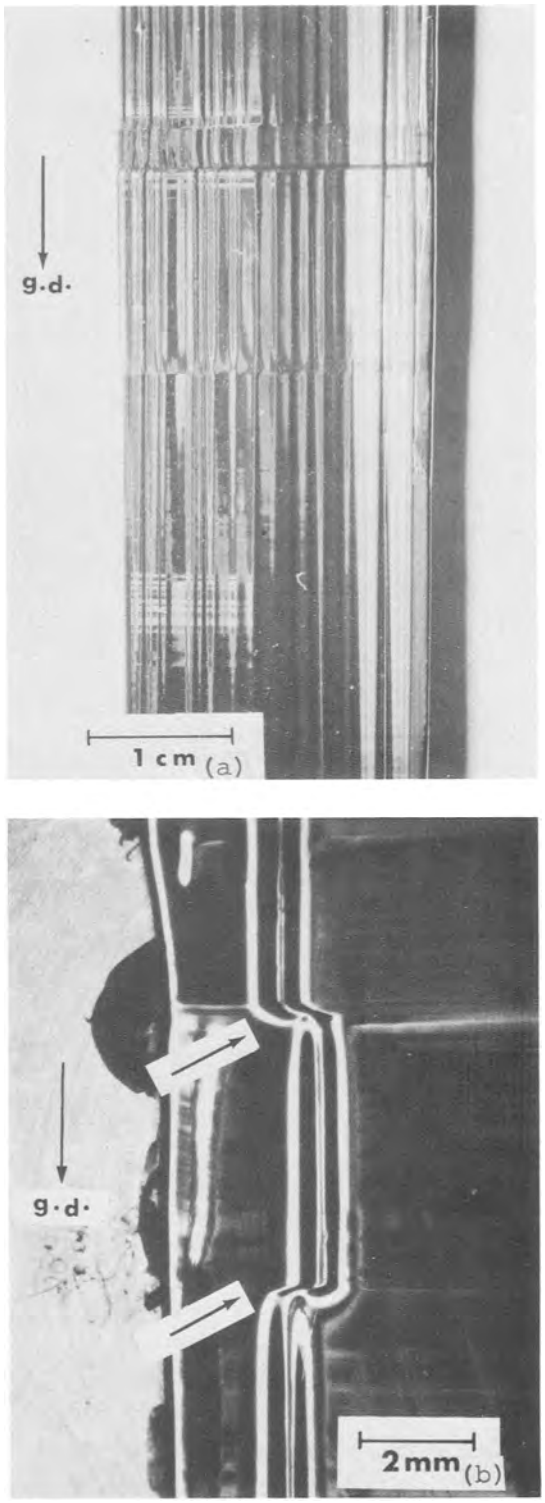


Fig. 12. (a) Vertical striae on EFG silicon ribbon caused by SiC particles which grow at die top. (b) Thick (~1 × 1 mm) striation on ribbon surface caused by spill-over near one edge of die. The ribbon was moved sideways where indicated by the arrows.

the process variables in Eq. [1]. A recent analysis (15) of the time dependence of perturbations in the geometrical variables in the floating zone process showed an oscillatory behavior for that system; the frequency of the oscillations was found to be proportional to the ratio of the growth rate to the length of the molten zone.

Interface breakdown.—In EFG ribbons produced under low gradient, high growth rate conditions (*e.g.*, near the maximum growth rate, which is a function of the thermal environment of the growth setup), we have observed various morphological features which indicate interfacial breakdown phenomena. These features usually take the form of corrugated, dendritic patterns, or wavy surface ridges such as illustrated in Fig. 14. These ridge patterns appear on both sides of the ribbon (nearly simultaneously) and tend to be somewhat symmetrical about the ribbon axis (this is not the case in the example shown in Fig. 14). Analyses have shown that the interfacial breakdown is caused by thermal and/or constitutional supercooling, as described in detail elsewhere (16).

Conclusions

1. Silicon ribbon growth by the EFG process has been shown to occur under one or both of the following conditions: (*i*) controlled-shape growth, where the ribbon shape is determined by the shape of the meniscus at the crystal-liquid-vapor triple junction (*i.e.*, $\phi = \phi_0$ for steady-state cross-sectional growth) and hence by the geometrical process variables (t_d, h_{eff}, and s in Eq. [1]): or (*ii*) faceted growth, where the external shape of the crystal is determined by the detailed kinetics of ledge nucleation and growth on peripheral {111} facets.

2. Theoretical analysis of the ribbon shape stability for controlled-shape growth has shown that the side of the ribbon (*i.e.*, the thickness dimension) is inherently stable, whereas the ribbon edge (*i.e.*, the width dimension) is only conditionally stable when a steady-state growth system is subjected to perturbations in the geometrical variables. The stability of the ribbon edge requires that the edge-defining die radius should not exceed approximately twice the radius of curvature of the ribbon at the ribbon edge. Experimental evidence has been presented to show the inherent stability of the ribbon side and the relative instability of the ribbon edges.

3. The characteristic meniscus angle ϕ_0 for the growth of a constant-dimension crystal in controlled-shape growth has been shown to depend on the crystallographic orientation of the ribbon surface.

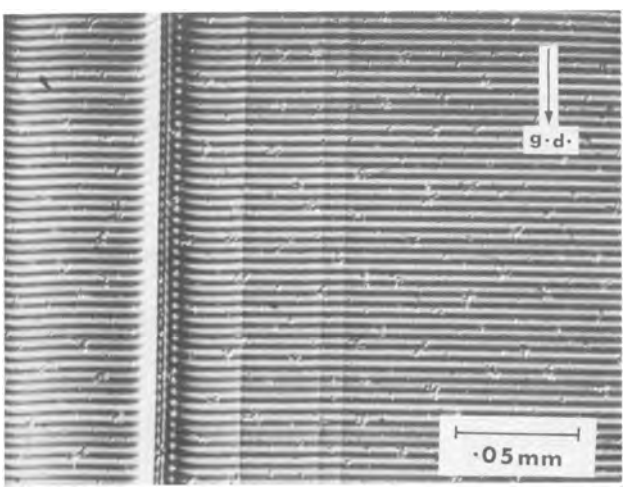


Fig. 13. Groove in growth interface at its intersection with a twin boundary in silicon ribbon EFG showing slight depression in the crystal surface at the groove.

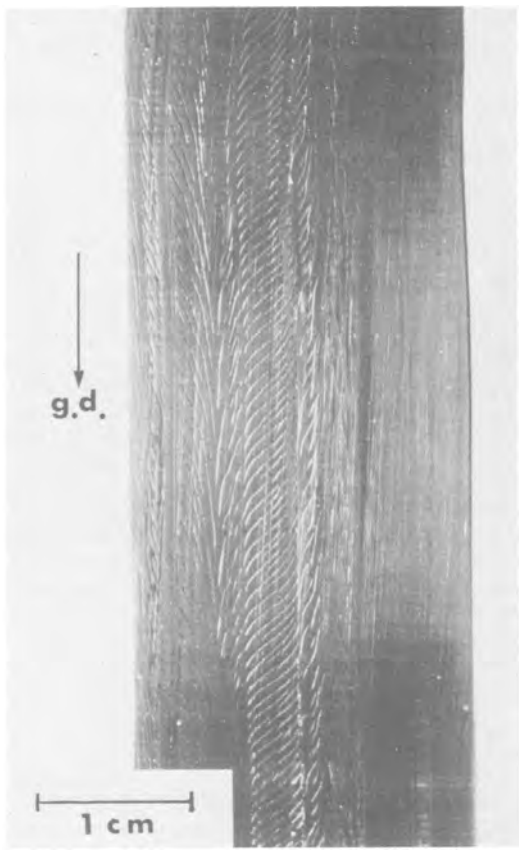


Fig. 14. Wavy surface ridges on EFG ribbon resulting from interfacial breakdown. The growth rate was 5 cm/min.

Observations of ribbon thickness changes which resulted from the ϕ_0 anisotropy were used to obtain a measure of the anisotropy in the crystal-vapor surface free energy in silicon.

4. Faceted growth has been shown to compete with, and, on occasion, completely override controlled-shape growth. If the surface shape in a given region of the ribbon is the result of faceted growth, then the $\phi = \phi_0$ condition does not apply in this region.

5. Faceted growth and ϕ_0 anisotropy did not affect the stability of the ribbon side (*i.e.*, thickness), but were generally observed to lead to instabilities at the ribbon edges (*i.e.*, spreading or tapering of the width dimension).

6. Experiments with various ribbon seed orientations were carried out to obtain the various ϕ_0 anisotropy and faceting features reported in this paper. Irrespective of the seed orientation, an equilibrium defect structure eventually developed in the ribbons; the orientation was approximately (110) [$\bar{1}$12] and the ribbons contained a high density of linear boundaries parallel to the growth direction. An example of this structure is shown in Fig. 15; the edge stability where the linear boundaries extend to very near the ribbon edge (indicated by the oblique arrow) should be noted. Further analysis of this equilibrium defect structure is given in a separate publication (11).

Acknowledgments

The authors are grateful to Professor B. Chalmers, K. V. Ravi, D. N. Jewett, A. D. Morrison, and D. A. Yates for valuable discussions and criticisms and to D. Bliss for technical assistance. We also thank Lincoln Laboratories, Lexington, Massachusetts, for permission to use their Sloan Dektak surface profile recorder. This work was supported in part by a contract from the Jet Propulsion Laboratory, California Institute of Technology, under NASA Contract NAS7-

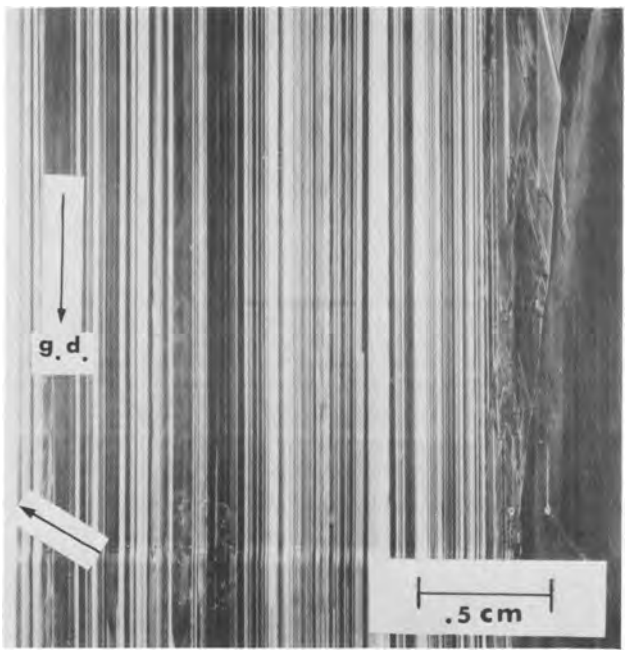


Fig. 15. Etched segment of EFG ribbon showing equilibrium defect structure. The orientation is approximately (110) [$\bar{1}$12]. The oblique arrow denotes one edge of the ribbon.

100 for the U.S. Energy Research and Development Administration, Division of Solar Energy.

Manuscript submitted June 25, 1976; revised manuscript received Sept. 13, 1976.

Any discussion of this paper will appear in a Discussion Section to be published in the December 1977 JOURNAL. All discussions for the December 1977 Discussion Section should be submitted by Aug. 1, 1977.

Publication costs of this article were assisted by the Mobil Tyco Solar Energy Corporation.

REFERENCES

1. H. E. Bates, F. H. Cocks, and A. I. Mlavsky, Proceedings of the Ninth IEEE Photovoltaic Specialists Conference, IEEE, p. 386, New York (1972); H. E. Bates, D. N. Jewett, and V. E. White, Proceedings of the Tenth IEEE Photovoltaic Specialists Conference, IEEE, p. 197, New York (1974).
2. T. F. Ciszek and G. H. Schwuttke, *Phys. Status Solidi A*, **27**, 231 (1975).
3. J. C. Swartz, T. Surek, and B. Chalmers, *J. Electron. Mater.*, **4**, 255 (1975).
4. K. V. Ravi, H. B. Serreze, H. E. Bates, A. D. Morrison, D. N. Jewett, and J. C. T. Ho, Proceedings of the Eleventh IEEE Photovoltaic Specialists Conference, IEEE, p. 280, New York (1975).
5. P. I. Antonov, *J. Cryst. Growth*, **23**, 318 (1974).
6. T. Surek and B. Chalmers, *ibid.*, **29**, 1 (1975).
7. D. A. Yates and T. Surek, Paper 138 presented at The Electrochemical Society Meeting, Washington, D.C., May 2-7, 1976.
8. T. Surek, *J. Appl. Phys.*, **47**, 4384 (1976).
9. J. A. Champion, B. J. Keene, and S. Allen, *J. Mater. Sci.*, **8**, 423 (1973).
10. W. Bardsley, F. C. Frank, G. W. Green, and D. T. J. Hurle, *J. Cryst. Growth*, **23**, 341 (1974).
11. L. C. Garone, C. V. H. Rao, A. D. Morrison, T. Surek, and K. V. Ravi, *Appl. Phys. Lett.*, **29**, 511 (1976).
12. M. G. Milvidskii and A. V. Berkova, *Sov. Phys. Solid State (Engl. Transl.)*, **5**, 374 (1963).
13. T. F. Ciszek, *J. Cryst. Growth*, **10**, 263 (1971).
14. R. J. Schaefer, M. E. Glicksman, and J. D. Ayers, *Philos. Mag.*, **32**, 725 (1975).
15. T. Surek and S. R. Coriell, Paper 140 presented at The Electrochemical Society Meeting, Washington, D.C., May 2-7, 1976.
16. J. C. Swartz, Unpublished research (1976).

Impurity Effects in the Nucleation of Alpha (bcc)-Tantalum or Beta-Tantalum Films

N. Schwartz* and E. D. Feit

Bell Laboratories, Murray Hill, New Jersey 07974

ABSTRACT

Although most studies report β-Ta as the thin film phase deposited during cathodic sputtering, a few reports indicate that α(bcc)-Ta is the initial phase, and β-Ta occurs only because of reaction with oxygen or nitrogen. This study details qualitative evidence that an "X" impurity can exist which at low concentrations prevents the formation of β-Ta and induces the formation of α-Ta, but which may be deactivated by oxygen or nitrogen in a glow discharge. Monolayer films of carbon-containing compounds can act as an X impurity. Organic polymers in particular can be used to nucleate low resistivity α-Ta during deposition over large areas in vacuum stations which previously could only yield β-Ta. Low resistivity α-Ta has applications in thin film capacitors to achieve higher frequency performance.

When β-Ta films were first reported (1), it was stated that it was the form that was obtained by sputtering at the lowest background pressure, while the addition of nitrogen or other gases resulted in the deposition of α-Ta (*i.e.*, bcc) films. Figure 1 is a typical result, showing the phases, resistivity, and temperature coefficient of resistance for 5000Å tantalum films deposited by d-c diode sputtering at various partial pressures of nitrogen in 10-20 mTorr of argon. The persistence of β-Ta down to the lowest background pressures was established in an ultrahigh vacuum station study (2). Since α-Ta films were mechanically unstable (3), β-Ta films became the preferred form for tantalum thin film capacitors (4) in thin film integrated circuits (5). Since that time well over 500,000 ft^2 of thin film tantalum has been deposited in a variety of oil-diffusion-pumped and turbomolecular-pumped batch and in-line d-c diode sputtering systems with the structure being that of β-Ta.

In recent years (6) there have been several very contradictory studies, however, which have indicated that at the lowest background pressure, α-Ta is de-

* Electrochemical Society Active Member.
Key words: sputtering, metastable phases.

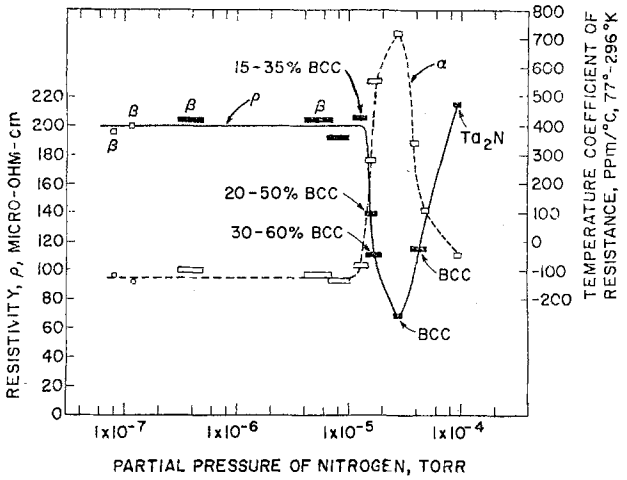


Fig. 1. The resistivity, temperature coefficient of resistance, and phases obtained by sputtering tantalum in argon with various partial pressures of nitrogen (18).

posited, while the addition of oxygen or nitrogen to the argon sputtering gas is a necessary condition for the formation of the β-form. Figure 2 shows several studies of the resistivity and structure of tantalum films sputtered in oxygen-argon mixtures. These studies are significant in that they are the only ones where the oxygen concentrations were determined directly in the films. Figure 3 shows similar studies for the addition of nitrogen and carbon (7), although in all of these studies the analytical techniques are quite different, as are the detailed sputtering conditions. Figure 4 shows another study of the resistivity and structure as a function of nitrogen pressure in the argon gas, and this result has an initial α-phase

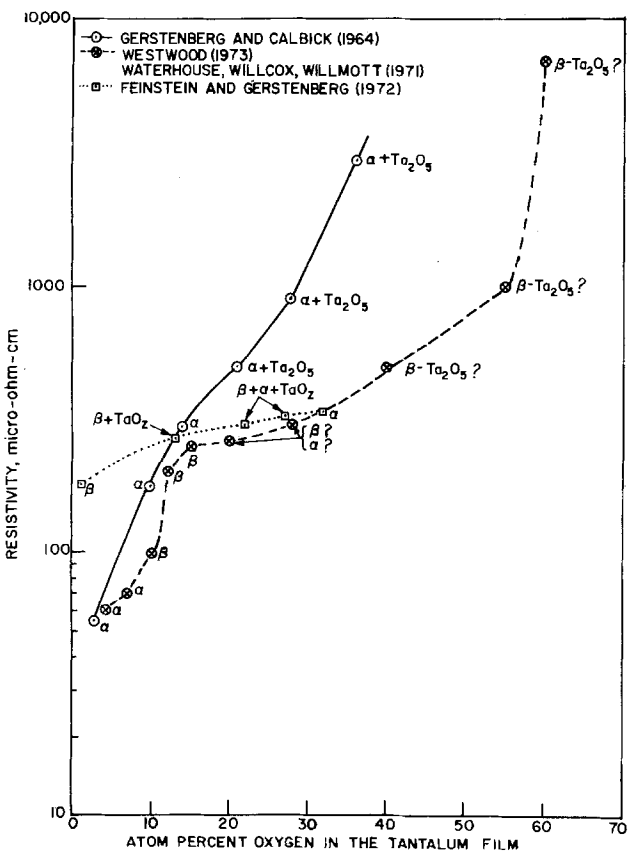


Fig. 2. The resistivity and structure of tantalum films as a function of the oxygen concentration as obtained in three different studies: Gerstenberg and Calbick (8), Feinstein and Gerstenberg (10), Waterhouse *et al.* (11), Westwood (12).

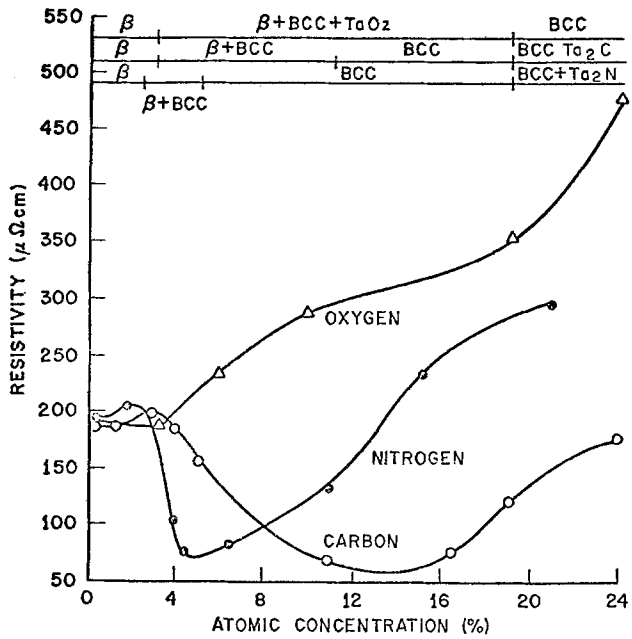


Fig. 3. Resistivity and structure of sputtered tantalum films as a function of the nitrogen, oxygen, and carbon concentration (7).

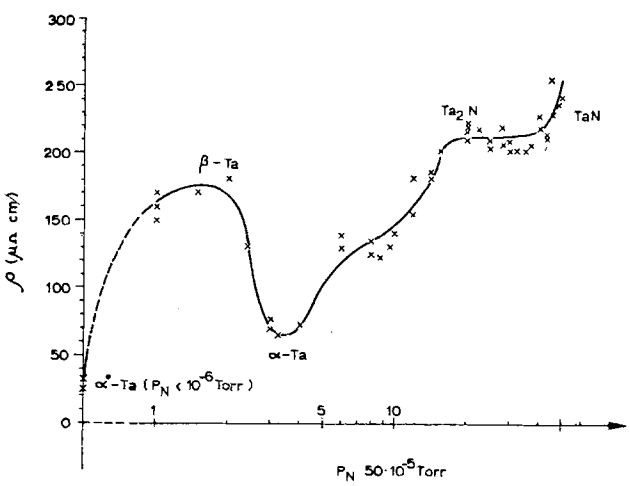


Fig. 4. The resistivity of sputtered tantalum films as a function of the partial pressure of nitrogen in the argon (13).

followed by the β-phase, which then reverts to the α-phase at higher nitrogen pressures and eventually results in the deposition of the tantalum nitride.

In Fig. 2, the results of Gerstenberg and Calbick (8), for films deposited at 500°C, indicated that the initial phase was α-Ta up to about 18 atom percent (a/o) oxygen, and further addition of oxygen results in a cermet of α-Ta plus insulating tantalum oxide,[1] and no β-Ta is formed at these high oxygen concentrations. Feinstein and Gerstenberg (10) repeated those experiments in a later study in a more usual sputtering machine (17) which routinely allowed the deposition of β-Ta; their results indicated the β-phase persisted up to about 10 a/o oxygen, with the subsequent phase being a mixture of α, β, and TaO_z; again after the appearance of the α-phase, the β-phase does not form on the addition of more oxygen. The contradictory studies were those of Waterhouse *et al.* (11) and Westwood (12), who initially observed α-Ta, for films not deliberately heated, while at 10 a/o oxygen the β-phase was formed and persisted up to at least 16 a/o; at 20 a/o the reported x-ray data

[1] This was the only sputtering machine in Bell Laboratories which consistently formed α-films on any clean glass substrate. The α-Ta film formation was not due to deposition on carbon as proposed by Mills (9).

are too indeterminate to decide whether the structure was the α- or β-form. Based on these findings those workers claimed that 10 a/o of oxygen is necessary to form β-Ta. The need for considerable interstitial impurity seems to be confirmed by the results of Schauer *et al.* (13) (Fig. 4), where considerable nitrogen is needed in the gas phase to form the β-phase.

The conclusion that appreciable amounts of oxygen or nitrogen are necessary to form β-Ta has been contradicted by many accurate analyses with a variety of techniques including flash discharge gas analysis (14), electron microprobe (10), Auger analysis (7), and a most sensitive technique, nuclear microanalysis (15). This latter method indicates that β-Ta films can be formed with nitrogen and oxygen concentrations as low as of 0.1-0.2 a/o. However, the evidence by Westwood and Schauer incontrovertibly indicates that under some conditions the addition of oxygen or nitrogen to the argon is necessary to form the β-phase.

A very significant study was performed by Feinstein and Hutteman (16) and confirmed by Axelrod and Marcus (25) (called FHA in this paper) who used a variety of different substrates simultaneously in a standard turbomolecular pumped system (17) and found, under the same vacuum and sputtering conditions, that α-Ta or β-Ta formed depending only upon the substrate type. This indicates that the α- or β-structure is determined at the nucleation stage. They were able to group the substrates (see Table I) into those that yielded α-Ta consistently (Table I, group II) those that formed β-Ta consistently (Table I, group I), or those that formed α-Ta initially but formed β-Ta when the substrate was slightly oxidized or hydrated (Table I, group III). However, even this important result does not have complete generality, since other studies do not always result in the same phase on the same substrate [see the double asterisked items in Table I under "This work" and "Schauer *et al.*"].

In the early phases of a previous study on the resistivity and temperature coefficient of resistance of β-Ta films (18), there were some unreported anomalous and irreproducible results which could be explained by an impurity hypothesis, which also might explain the inconsistencies in the results of the studies described above. The model requires that β-Ta actually is deposited at the very lowest background pressures possible, but that there is a low concentration impurity, to be called "X," either on substrates or in the gas phase, which has an extreme sensitivity for inducing the formation of the α-phase. This hypothesis requires that the addition of oxygen or nitrogen in the gas phase in a glow discharge can remove this low concentration impurity. Moreover, it requires that all studies that report α-Ta as the initial phase have had a variable amount of this X impurity, either in their vacuum station or on their substrates.

This paper reports the qualitative experiments which lead to the X impurity proposal, as well as results which indicate that some model compounds can act as the X impurity, although it is believed that many other species can perform similarly, and perhaps with greater sensitivity.

Table I.

	Substrate	Structure of 5000Å deposited film: Feinstein and Hutteman		This work	Schauer *et al.*
Group I.	Ta_2O_5 (am)	β		β	α**
	Fused SiO_2 (am)	β		β	
	Therm SiO_2 (am)*	β			
	7059 (am)	β		β	
	Al_2O_3 ceram (poly)	β			
	Sapphire, (single cryst)	β		β	
	Si (100), (111), (single cryst)	β		β	
	Cu (poly cryst)*	β			
	Ni (poly cryst)*	β			
	β-Ta (poly cryst)*	β		+	
Group II.	Au (poly cryst)*	α		α	
	Pt (poly cryst)*	α	α	α	
	Pt (poly cryst)			$\alpha + \beta$**	
	Rh*	α			
	Be	α	α	β**	
	W*	α	α	α	
Group III.	α-Ta*	α			
	Mo*	α	β	α	
	Si_3N_4*	α	β		
	Ta_2N*	α	β		
		+	0	+	

* Films on 7059 glass.
** See text.
\+ Freshly cleaned or as deposited.
0 O_2, 250°C, 1.25 hr.

Experimental

Since the controversy summarized above is founded to some extent on the residual gases in the vacuum system, it is imperative that some specification of systems be made in order to eventually compare results. Although many of the other studies have not qualified their stations, it was done with some care in this study. In this paper several quantities will be used: the final pressure with the high vacuum valve completely open after a 4 hr pumpdown, p_F; the pressure before sputtering with the high vacuum valve in the throttling position, p_B; the leak-up rate of the system, L^I, determined by closing the high vacuum valve and measuring the rate of rise of pressure with an ionization gauge; the residual gas spectrum at p_B measured with an EIA 1110A quadrupole residual gas analyzer (QRGA), which has a partial pressure sensitivity of 10^{-14} Torr; and the individual species leak-up rate, L^I_S, measured with the QRGA.

The vacuum station and conditions used were stated previously (18), but briefly, it was a 6 in. CVC DC 704 silicone oil diffusion pumped system, with a liquid nitrogen trap, and a 250 liter glass bell jar. The system was always backfilled with nitrogen and always kept open for a minimum time. Some of those experiments were carried out over a long period of time and the vacuum capability shifted. There were three separate vacuum conditions under which the experiments were performed, and these are given in Table II. Condition A existed when the vacuum station was completely new and had no deposited tantalum on the electrode structure and on the glass bell jar, and no heating was used during the 4 hr pump down period. Condition B existed after many runs, and the deposited tantalum did not adsorb as much gas as glass when the bell jar was opened and also acted as an internal getter when under vacuum; compared to condition A, both p_B and L^I were down by a factor of 2. The last condition, C, was obtained when the station was in condition B but the substrate heater was employed at 550°C (as measured in the heater, 1 cm away from the substrates) for 2 hr during pump down which generally warmed up all parts of the electrode structure and bell jar, and then cooled for 2 hr; after this treatment, p_B was a factor of 10 lower and L^I was a factor of 6 lower than that existing at condition B.

The residual gas spectrum for condition B is given in Fig. 5. For each run, the QRGA was calibrated with nitrogen and the individual peaks are given in terms of equivalent nitrogen pressure. H_2O^+ is the main species, with N_2^+, CO^+, and CO_2^+ being at 2-3% of H_2O, while H_2^+ is about 0.7% of H_2O. There is an appreciable organic background spectrum above mass 44, and the species responsible for mass 78 is present at about 0.4% of that of H_2O^+. Great detail was paid to obtaining these individual unit masses from 1 to

Table II. Vacuum conditions specifications

Condition (see text)	Final pressure, p_F, Torr	Throttled pressure, p_B, Torr	Leak-up rate, (Torr-liter/sec)	Throttled QRGA spectrum	Leak-up rate L^I_S QRGA	Est. substrate surface temp at nucleat. stage, °C	Est. substrate surface temp at end of deposition, °C
A	3×10^{-7}	1×10^{-6}	8.5×10^{-6}	Not avail.	Not avail.	130	220-240
B	1.2×10^{-7}	5×10^{-7}	4.3×10^{-6}	Fig. 5	Not avail.	130	220-240
C	2×10^{-8}	5×10^{-8}	7.5×10^{-7}	Fig. 6	Fig. 7	160-185	200-240

110, since it was suspected that the X impurity might exist at low concentrations.

Figure 6 shows the residual gas spectrum for condition C; the species below mass 44 have decreased in pressure considerably, while the background organic spectrum above mass 44 is essentially similar to condition B. Water is still the main species but is present at 8% of that in condition B. N_2^+, CO^+, and CO_2^+ are now 10% of the H_2O^+ species, H_2^+ is 2.5%, and the species responsible for mass 78 is now 2.7%, primarily because the H_2O peak has decreased by over a factor of 10.

Sputtering systems have to be considered as flow systems, since the gases passing through the space around the electrode structure may consist of the gases desorbing from the walls or entering through small leaks, and leaving by the pumping mechanism of the system. Therefore the leak-up rate of the individual species before the sputtering run and after pumping for 4 hr was determined with the QRGA. When the high vacuum valve is closed there is a large burst of pressure (composed mainly of the species measured in the subsequent leak-up) due to the wiping of the Viton O-ring across the mating flange, and due to the compression of the O-ring. The value of L^I (reported in Table II) was determined during the first 60 sec after this burst of pressure subsides, and then the values of L^R_S were determined. Zero time in Fig. 7 shows the value of the individual species before the valve is closed and $18(H_2O^+)$ is the major peak while $28(N_2^+, CO^+, C_2H_4^+)$ is the second major peak. When the valve is closed, there is the described large burst of pressure, and individual readings start initially for $2(H_2^+)$ at 65 sec. At the end of the run at 700 sec, the major peaks are 28 (identified as N_2^+ because of the identical rate of rise of 14), $2(H_2^+)$, $40(A^+)$, while the initial major species $18(H_2O^+)$ has hardly increased at all. This means that nitrogen is the major incoming species, with a leak-up rate over a factor of 10 higher than that of H_2O, but since it gets pumped faster than H_2O, in a residual gas spectrum it appears lower. This nitrogen is not due to an air leak, since the system was extensively tested with He without finding leaks of this magnitude. Argon is adsorbed in this system because of its use as the sputtering gas, and its leak-up rate is similar to nitrogen. A similar leak-up spectrum is not available for condition B, but initial leak-up rates, determined for the first 100 sec, are compared in Table III. For condition B, the leak-up rate for $18(H_2O)$ is still smaller than that of $28(N_2)$, even though it is the major peak. This phenomenon of inversion of the ratio of mass 18/28 final pressures and leak-up rates has also been found in turbomolecular pump systems. This effect needs further investigation in other systems where the desorbing surfaces can be better defined after exposure to atmosphere.

The substrates used in this work were Corning 7059 glass (an aluminoborosilicate); Ta_2O_5-coated glass formed by complete oxidation of tantalum films sputtered on 7059; unoriented single crystal sapphire; high resistivity (100) silicon; bulk beryllium foil; bulk platinum foil; and evaporated Ti-Pt, Ti-Au, Mo, and W on sapphire. When standard chemical cleaning was used it was the same as used previously (18). Silicon was cleaned sequentially with detergent, etched

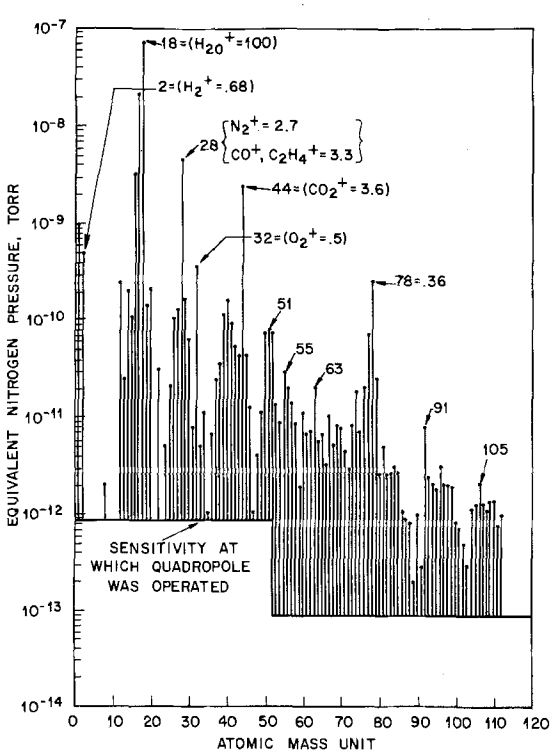


Fig. 5. QRGA spectrum of the vacuum system at the throttled pressure, p_B (vacuum condition B).

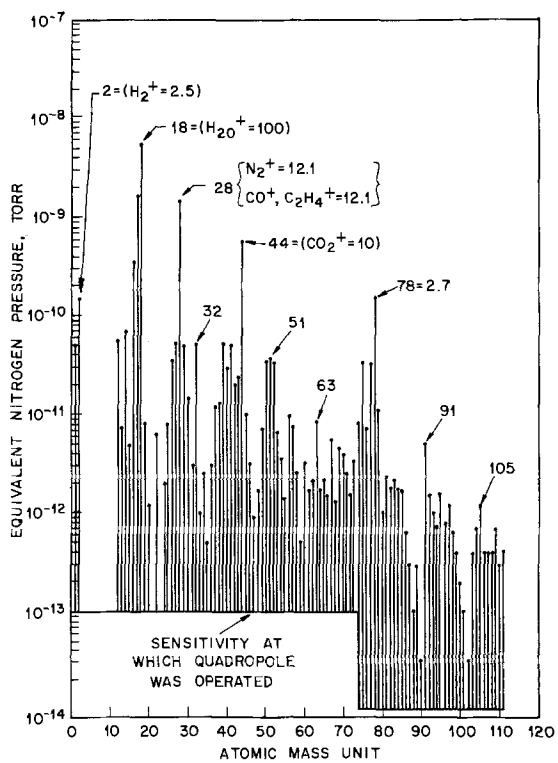


Fig. 6. QRGA spectrum of the vacuum system at the throttled pressure, p_B (vacuum condition C).

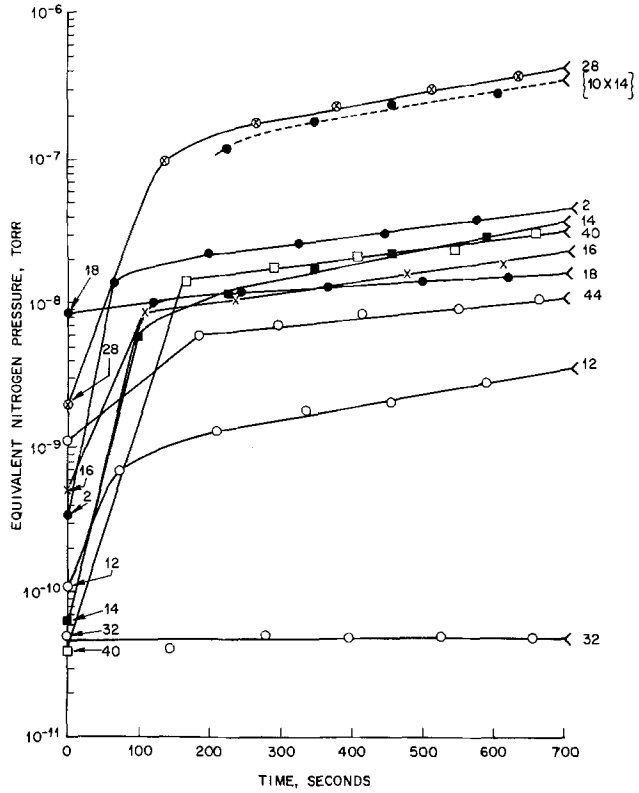


Fig. 7. QRGA leak-up rate spectrum for vacuum condition C

deeply with $HF-HNO_3$, cleaned in $H_2O_2-NH_4OH-H_2O$ at 80°C, followed by a deionized water overflow rinse which gave a hydrophylic surface; in some cases after the H_2O_2 treatment, the surfaces were re-etched slightly with HF, followed by a deionized water overflow rinse to give hydrophobic surfaces. Beryllium foil was degreased and then washed with isopropyl alcohol. The platinum foil was special flow oxygen content foil used for flash discharge analysis, and was cleaned by heating to redness in the oxidizing portion of a Bunsen flame. This technique has been demonstrated earlier to give the lowest oxygen content by flash discharge analysis (14). The metal films were prepared by electron beam evaporation in an ion-pumped system, removed from the system, and stored in a turbomolecular pumped vacuum system at pressure from 1×10^{-7} to 10×10^{-3} Torr. All insulator substrates were given the standard chemical clean, followed by a 550°C air bake.

Since β-Ta converts to the α-form at elevated temperatures, it is necessary to determine the substrate temperatures during deposition. To evaluate this, thin film thermocouples on sapphire were used (19) in the usual substrate position, and the temperature rise determined as a function of presputtering time and sputtering time (*i.e.*, after the shutter was removed). The substrate temperatures at the start and end of the film deposition are given in Table II. Since it will be important later, the shutter temperature was also measured with a bulk thermocouple, and after a 45 min presputtering period at 5 kV and 25 mA, the shutter temperature was 285°C.

The sheet resistance of the films was determined by a four-point probe, while the thickness was determined by weighing a monitor substrate before and after a run, and using the measured area and density of tantalum to calculate the thickness. This weight gain measurement was calibrated against a Talysurf measurement several times. All films deposited in this study were in the 450-500 nm range.

Table III. Individual gas leak-up rates

	B condition	C condition
	(Torr-liters)/sec	
Ionization gauge leak-up rate	2.5×10^{-6}	6.3×10^{-7}
QMS leak-up rate (equivalent nitrogen pressures)		
2(H_2)	2.1×10^{-7}	4×10^{-8}
18(H_2O)	1.7×10^{-7}	6.8×10^{-9}
28(N_2)	4.5×10^{-7}	1.4×10^{-7}
32(H_2O)	2.5×10^{-10}	5.5×10^{-11}
40(A)	1.8×10^{-8}	5.5×10^{-9}
44(CO_2)	1.6×10^{-7}	8.5×10^{-9}

Results

"The new system effect."—The sputtering electrode and ground electrode holders, made of 300 series stainless steel and degreased in trichloroethylene, were installed in the new vacuum station, and sputtering performed under the A condition given in Table I. The resistivities of films deposited in the first consecutive fifty-five days are shown in Fig. 8. The results were highly variable, with the low resistivity films being α-Ta, while the high resistivity films were β-Ta. The dashed lines in Fig. 8 are meant to indicate that the α-Ta films tended to be formed when the system was not used for several days, which seemed to be related to an atmospheric gas effect. After the 44th day (shown by the arrow), the system routinely was opened only for very short periods of time to change substrates only, and from then on, β-Ta films were formed routinely.

Following these series of runs, runs were made which resulted in the data of Fig. 1 under the same vacuum condition A, but deliberate additions of nitrogen were made to the gas phase. In Fig. 1, the α-Ta films were only formed at a flow rate of nitrogen equivalent to a pressure of 2×10^{-5} Torr (the nitrogen flow rate at this pressure is approximately 2.5×10^{-3} Torr-liter/sec). Nitrogen is the gas which has been shown to be the most sensitive addend to the gas phase which causes the formation of α-Ta, yet the α-Ta films formed as shown in Fig. 8, were being deposited at leak-up rates and throttled pressures of 10-100 times less than that of nitrogen. It was at this point that it was realized that an X effect might be possible.

Since atmospheric gases appeared to be implicated a search for possible culprits was made. Baker (20) reported in rf sputtered tantalum films that there was a high variability in the deposit, also obtaining either α- or β-Ta films under nominally the same background pressure and sputtering conditions. In his work, oxygen was not found to form α-Ta preferentially at low partial pressure. Baker supposed that another factor, "such as the absence or presence of water vapor, as suggested by Nakamura *et al.* (21) probably decides which phase is formed." Nakamura states that presputtering for long times leads to the preferential formation of β-tantalum, and by mass

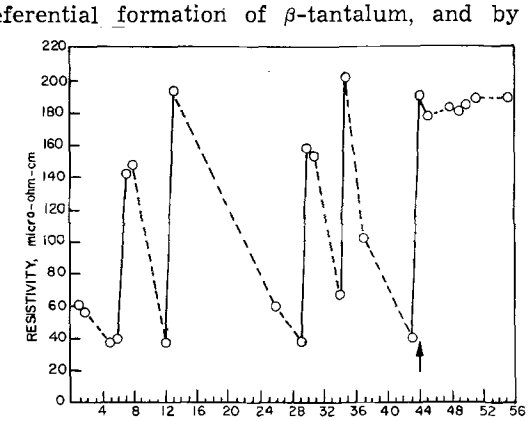


Fig. 8. Resistivity of tantalum films in the first 55 days of use of the new vacuum station.

spectroscopic investigation, this result was correlated with the reduction of water vapor to less than 1×10^{-7} Torr. Slight amounts of added nitrogen also lead to a decrease in water content due to the formation of NO. To confirm whether water vapor could be the X component, deliberate additions of water vapor were made in this system, using the C vacuum conditions, and the results are shown in Fig. 9. In fact, only slight amounts of α-Ta are formed, and only at 1×10^{-4} Torr partial pressure, a factor of 100 times the background pressure during the experiments on the new system effect (Fig. 8).

Silicone oil is the usual charge for diffusion pumps and frequently for turbomolecular pumps when used for oxygen service, and silicon might be considered a possible X candidate. In a later series of experiments in this same vacuum station, under condition C vacuum, tantalum-silicon alloy films were formed by the addition of silane to the argon (22). During the course of those experiments, it was demonstrated that α-Ta films were barely formed, and only at partial pressures of silane slightly above 1×10^{-4} Torr.

A few experiments were made at $1\text{-}5 \times 10^{-6}$ Torr of added CO_2 to the argon and these runs only yielded β-Ta films; this is consistent with the results shown in Fig. 3, which indicates that carbon in the gas phase is less efficient than nitrogen in causing the formation of α-Ta.

These series of experiments appeared to rule out N, H_2O, C, and Si, when introduced in the gas phase, as the X impurity.

The α-Ta dip.—The other evidence for the X impurity hypothesis was in this same system, operating in the B vacuum conditions. This effect is called for convenience, the α-Ta dip and in its most extreme cases is illustrated in Fig. 10. For the first two runs with shutter A, which had been used for a long time in the system, the deposition results consistently in β-Ta. In run 3, a new shutter was put into the system, and left there for the succeeding four runs. In the first run after the new shutter was installed, very low resistivity α-Ta was formed: moreover the effect lasted through the succeeding run, and only after three successive runs with the new shutter was the system again producing high resistivity β-Ta.

The following conditions and treatment of shutters led to the α-Ta dip:

1. Use of a 300 series stainless steel shutter, directly received from the machine shop and stored in air for 3 months, washed with isopropyl alcohol, and air dried before use. Separate experiments indicated that isopropyl alcohol was never responsible for the dip.

2. Taking out either a high purity Ta or stainless steel shutter and etching with $HF\text{-}HNO_3$ to remove

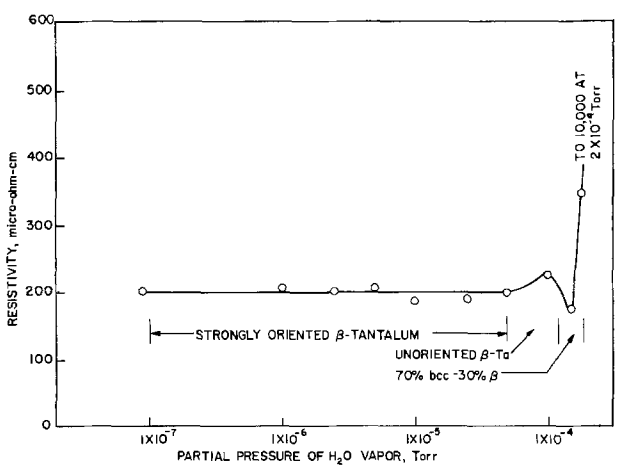


Fig. 9. Resistivity of tantalum films sputtered in argon with various partial pressures of water.

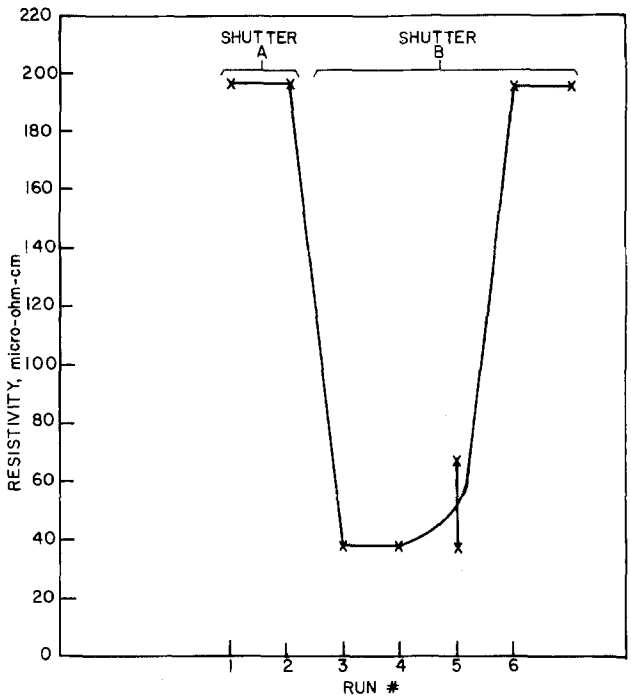


Fig. 10. The α-Ta dip

deposited Ta, washing with either cold or boiling water, isopropyl alcohol and air dried did cause the dip. Drying the shutter at 110°C for 2 days, still caused the dip. Baking a stainless steel shutter at 300°C in air overnight, which caused a brown scale on the surface, prevented the α-Ta dip.

3. Taking out a tantalum shutter and boiling for 2 hr in water, followed by isopropyl alcohol rinse, and air dried, did cause the dip.

4. Taking out a stainless steel shutter, and filing the top and bottom of the shutter to remove the deposited Ta, and putting the shutter directly back, did cause the dip.

Several months later some of these experiments were repeated with the same machine in a new clean laboratory with a copious supply of very high purity deionized water, and the details could not be reproduced exactly. What could be reproduced was that the α-Ta dip was related to an elusive and nonreproducible contaminant in tap water which was used to rinse the shutters in cases 2 and 3 above. Moreover, in the cases discussed above, the substrates were all Corning 7059 glass. In the subsequent experiment, all the normal β-Ta producing substrates were used like Ta_2O_5, 7059, Si, and Al_2O_3. The α-Ta dip was most easily observed with the unoriented single crystal sapphire; with the next most sensitive being 7059 and Ta_2O_5, equally; while the α-Ta dip was never observed with Si(100), even though all of these substrates were simultaneously in the vacuum station whenever a new shutter was installed.

The α-Ta dip could also be observed on the most sensitive substrate, sapphire, when a shutter was taken out of the vacuum station, and stored for about one month completely protected in a glass petri dish, in a Class 100 laminar flow hood in a Class 1000 clean room. Apparently there is an interaction between a tantalum-film coated-stainless steel shutter and air which is capable of acting as an X impurity in a subsequent film deposition on sapphire. If the shutter was stored in air under these conditions for 7 months, then all of the normal β-Ta producing substrates yielded α-Ta.

What these experiments demonstrate is that an impurity, frequently in tap H_2O, and also in air, can be present on the shutter; during the presputter pe-

riod, as the shutter surface warms up to 285°, the impurity is transferred to the substrate surface. However, it is either more strongly adsorbed or is more active on a sapphire surface when compared to a Si(100) surface. Preheat-treatment of the shutter at 110°C does not remove the impurity, but heating in air to 300°C does.

An attempt was made to identify this X impurity using a very sensitive technique, Auger analysis. Two runs were made on 7059 glass: (*i*) The shutter was prepared where it would normally allow the formation of β-Ta on the 7059, and the run proceeded through the presputtering period, but the substrate removed without any Ta deposition; and (*ii*) exactly the same procedure was followed, except the shutter was prepared in such a way that it normally caused the α-Ta dip.

Unfortunately, after the substrates were transferred to the Auger apparatus, no significant differences could be detected between these two 7059 surfaces. In both of these cases, residual gas spectra similar to Fig. 5 differed over the entire spectrum no more than the normal variation.

All of these experiments prove that it is possible to easily contaminate substrates by parts of a sputtering system not in contact with these items. The transfer takes place by very small amounts of an impurity at exceptionally low pressures, and this impurity can prevent the formation of β-Ta. Moreover, it frequently can persist over several runs.

The Feinstein-Hutteman-Axelrod substrate-nucleation effect (FHA).—As indicated, previously detailed studies (16, 25) have concretely shown (Table I) that different substrates in the same vacuum station, under the same deposition conditions, can give either the α- or β-Ta form. Moreover, substrates had been classified as to whether they were α- or β-Ta producing substrates. Verification of this effect in another system was important since it is conceivable that the X impurity was causing the difference in the initial study. This seemed conceivable, since it had already been determined in the present system that foil beryllium and foil platinum had given results in contradiction to FHA (see Table I, This work).

Substrates, used previously by Feinstein-Hutteman, were checked, and were prepared in essence in the same way. Particular substrates were picked either because of their pertinence to thin film technology, or because they had earlier in this work showed some contradiction in their results. Silicon (100) was used with either a hydrophylic surface or hydrophobic surface with identical results. The deposition was performed under the cleanest condition; *i.e.*, Table II-B. The results are summarized in Table I under "This work." All of the substrates used previously by FHA (*i.e.*, 7059, Ta_2O_5, sapphire, W, Mo, Au, Pt) gave the same results as FHA.

FHA classified the substrates into three types: (*i*) oxidized surfaces which always give β-Ta (*i.e.*, Ta_2O_5; 7059; sapphire; and Si, presumed to have an oxide film on surface; (*ii*) essentially oxide-free surfaces which always give α-Ta, and do not oxidize when heat-treated in O_2 or H_2O and continue to give α-Ta (*i.e.*, Pt, Au, W); and (*iii*) essentially oxide-free surfaces which yield α-Ta, but oxidize when heat-treated in O_2 or H_2O and subsequently yield β-Ta (*i.e.*, Ta_2N, Mo). Although the observation of three classifications is essentially correct, the present result on bulk platinum is not compatible with group II, since it should be no different than thin films. One conceivable explanation for FHA is that the X impurity exists in variable amounts in these classes of substrates, and can be removed by heat-treatment in water or oxygen. These possibilities will be considered in the discussion.

Table IV. Resistivity of 5000Å tantalum films deposited on Ta_2O_5 underlay after rubbing with the given material

Material rubbed on Ta_2O_5	Resistivity, μΩ-cm
Dextilose paper*	35
Twill jean cloth*	38
Teflon rod†	36
Scotts laboratory paper wipes*	52
Ta_2O_5*	190

* No transfer of material observed visually.
† Some scattered markings of Teflon observed on surface.

The rubbing effect.—In the course of verifying the FHA, some totally uncleaned 7059 substrates were used simultaneously with all the other cleaned substrates, and this particular 7059 substrate gave α-Ta. The procurement of 7059 has been well specified for Bell System work, and it was surprising that the entire substrate should have the X impurity. The possible major source of impurity is the Dextilose[2] paper which is always interleaved between sheets of 7059 to prevent scratching. To test whether a possible source of X was this paper, cleaned Ta_2O_5 underlay coated substrates were rubbed gently and uniformly with this paper. As controls, various other sources of paper and clean cloth, available in the laboratory, were also used. In order to distinguish the possible mechanical disturbance of the surface from an actual transfer of a chemical constituent, two cleaned Ta_2O_5 underlay surfaces were rubbed against each other. Table IV gives the resistivity of 5000Å tantalum films obtained after rubbing the various specified organic or inorganic materials on the substrates. All the organic materials resulted in low resistivity α-Ta uniformly formed over the 10 cm^2 of the substrate rubbed while the other half of the same substrate resulted in β-Ta. The Ta_2O_5 rubbed substrate resulted in the usual high resistivity β-Ta.

In order to estimate the upper limit of the thickness of the organic layer transferred during rubbing, a 400Å anodic tantalum oxide was rubbed in a similar way with Dextilose paper. According to Vermilyea (23), this thickness of anodic oxide is most sensitive to a visual color match due to change of thicknesses, and has a visual sensitivity equivalent to a change of thickness of 2Å. Since the index of refraction of the film responsible for the thickness change is involved in the color change, and organic polymers have an index of refraction of about 1.4 compared to 2.2 for Ta_2O_5, this thickness sensitivity should be of the order of 3Å. The rubbing experiment caused no change in the color of the anodic oxide, and thickness of the layer of organic material is less than 3Å, or less than a monolayer.

Cast organic films.—In order to achieve α-Ta routinely for potential capacitor applications where its low resistivity would result in better frequency performances (24) hand rubbing did not seem convenient, so a casting technique was applied. Tantalum oxide underlay coated slides were dipped into a very dilute solution of polymer in a highly volatile solvent like acetone. As the substrate is withdrawn from the solution, the acetone evaporates and a uniform, exceptionally thin, layer of polymer can be deposited. The polymer used was Union Carbide VMCA, which is a terpolymer of vinyl chloride, vinyl acetate, and maleic acid. The results of the dipping slides (2.5 × 7.5 cm^2) partially into various decreasing concentrations of this polymer in acetone at room temperature is illustrated in Fig. 11, where the dark colored areas are α-Ta, while the light colored areas are β-Ta. The

[2] Dextilose paper is a purified, lint-free paper, similar to lens paper. R.H. Dexter Company.

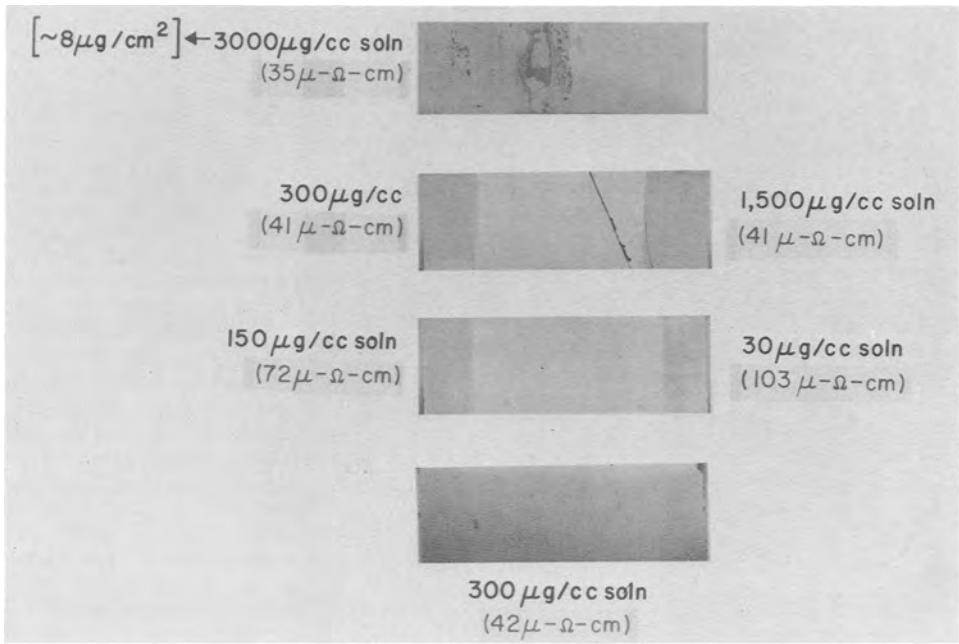


Fig. 11. Nucleation of bcc tantalum on monolayer organic films. α-Ta and β-Ta were formed on the same slide during the same deposition run. The α-Ta was caused by preliminary treatment of the Ta_2O_5 surface with polymer. α-Ta is the dark colored film, while β-Ta is the light colored film. The number in square brackets in the upper left is the weight of VMCA deposited on the surface when the slide was dipped in a solution of 3000 μg VMCA/cm^3 acetone.

demarcation between these areas are the exact position where the slide was dipped into the polymer solution.

In the upper slide (left), 35 $\mu\Omega$-cm α-Ta results when that end was dipped into a solution of 3000 μg VMCA/cm^3 acetone (the amount deposited in the slide was 8 μg/cm^2), while the untreated other end yielded the usual β-Ta in the same deposition. This concentration of polymer was excessive, since some crazing appeared near the interface of α- and β-Ta. The next two[3] slides show the effect of the polymer solution concentration where the concentration was decreased in steps from 1500 to 300 to 150 to 30 μg/cm^3. The resistivity increases slightly to 41 $\mu\Omega$-cm and then rises to 103 $\mu\Omega$-cm. All of these end α-Ta areas have high degree of adherence and are mechanically stable. The lowest slide in this figure was dipped entirely in the same solution as the second-left, to demonstrate that α-Ta can be formed uniformly over a large area. Polypropylene dissolved in toluene is just as effective as VMCA, and the criterion appears to be a carbon-containing compound in small quantities on the surface. The use of polymers, cast out of solution or sprayed on the surface, is an exceptionally convenient and inexpensive technique for preparing surfaces to obtain α-Ta.

Discussion

The verification of the proposal of the possible existence of an X impurity seems amply verified by the new system effect and the α-Ta dip effect. This work has also demonstrated that very low vapor pressure organic compounds are possible candidates for X, while the FHA work suggests other possible candidates like Pt, Au, W, Mo, etc. Finally there may be species which have yet to be investigated, such as that present in tap water or that responsible for the air-shutter interaction.

Of these known species, carbon would have a high probability of clean-up in a sputtering discharge upon the addition of oxygen or nitrogen. Carbon is ubiquitous, and might explain the α-Ta dip when it comes to interactions due to pollutants in tap water and the atmosphere, although other species are still possible. These results should surely indicate that the X impurity can exist, and that it must be taken into account when considering possible mechanisms for the formation of α-Ta. As a direct technological benefit, the cast organic film approach as illustrated in Fig. 11, allows for a simple nonvacuum method to choose whether α-Ta or β-Ta will be formed in the majority of vacuum stations which heretofore have been restricted to producing β-Ta films. Moreover, the α-Ta films so produced have very low resistivity, applicable to specific capacitor applications.

In a glow discharge, the interaction of energetic particles, including secondary electrons, with a monolayer of organic material could be the formation of Ta_2C or TaC. These phases are isomorphous with Ta_2N and TaN, which have already been demonstrated by FHA to yield α-Ta. One possible explanation of the group III type substrates in the FHA is that treatment with hot water or slight oxidation, although actually adding oxygen to the surface, is really destroying the crystallinity of the surface resulting in amorphouslike films which tend to yield β-Ta or is destroying an X impurity like carbon. In this mechanism, the presumed most stable form, α-Ta, needs nucleation by specific surface configurations like Ta_2C particles, while the amorphous surface or unnucleated form results in the presumed metastable phase, β-Ta. Further studies are required to explore the impurity nucleation dominated growth of α-Ta.

Summary

It has been demonstrated that impurities, available in common sources in the laboratory, can prevent the formation of β-Ta.

A polymer casting technique has been developed which allows for nonvacuum preparation of substrates which routinely results in low resistivity α-Ta. This material has benefits for fabricating thin film capacitors with high frequency performance.

This impurity catalyzed formation of α-Ta should be considered as a possible mechanism for those workers who cannot prepare β-Ta.

Manuscript submitted May 17, 1976; revised manuscript received July 15, 1976.

Any discussion of this paper will appear in a Discussion Section to be published in the December 1977 JOURNAL. All discussions for the December 1977 Discussion Section should be submitted by Aug. 1, 1977.

Publication costs of this article were assisted by Bell Laboratories.

[3] The sloping diagonal line, 1/3 from the right of the end of slide 2, is an accidental crack in the slide during mountng.

REFERENCES

1. M. H. Read and C. Altman, *Appl. Phys. Lett.*, **7**, 51 (1965).
2. J. Sosniak, J. Polito, and G. A. Rozgongi, *J. Appl. Phys.*, **38**, 3041 (1967).
3. F. Vratny, B. H. Vromen, and A. J. Harendza-Harmxma, *Electrochem. Technol.*, **5**, 283 (1967).
4. R. W. Berry and D. J. Sloan, *Proc. IRE*, **47**, 1070 (1959).
5. D. A. McLean, *IRE WESCON Convention Record*, **3**, 87 (1959).
6. An extensive review of all of the studies on the sputtering of tantalum is given by P. N. Baker, *Thin Solid Films*, **14**, 3 (1972).
7. R. D. Hutteman, J. M. Morabito, C. A. Steidel, and D. Gerstenberg, *Jpn. J. Appl. Phys., Supplement 2, Part I*, p. 513 (1973).
8. D. Gerstenberg and C. J. Calbick, *J. Appl. Phys.*, **35**, 402 (1974).
9. D. Mills, *J. Can. Ceram. Soc.*, **35**, 48 (1966).
10. L. G. Feinstein and D. Gerstenberg, *Thin Solid Films*, **20**, 103 (1974).
11. N. Waterhouse, P. S. Wilcox, and D. J. Willmott, *J. Appl. Phys.*, **42**, 5649 (1971).
12. W. D. Westwood, *Thin Solid Films*, **15**, 15 (1973).
13. A. Schauer, W. Peters, and W. Juergens, *ibid.*, **8**, R9 (1971); A. Schauer and M. Roschy, *ibid.*, **12**, 313 (1972).
14. W. G. Guldner and R. Brown, in "Measurement Techniques for Thin Films," B. Schwartz and N. Schwartz, Editors, p. 82, The Electrochemical Society Softbound Symposium Series, New York (1967).
15. M. Croset and G. Velasco, *J. Appl. Phys.*, **43**, 1444 (1972).
16. L. G. Feinstein and R. D. Hutteman, *Thin Solid Films*, **16**, 129 (1973).
17. R. W. Berry, P. M. Hall, and M. T. Harris, "Thin Film Technology," p. 236, D. Van Nostrand, Inc., Princeton, N.J. (1968).
18. N. Schwartz, W. A. Reed, P. Polash, and M. H. Read, *Thin Solid Films*, **14**, 333 (1972).
19. M. H. Read and D. H. Hensler, *ibid.*, **10**, 123 (1972).
20. P. N. Baker, *ibid.*, **6**, R57 (1970).
21. N. Nakamura, M. Fujimore, and Y. Nishimura, *Jpn. J. Appl. Phys.*, **9**, 555 (1970).
22. N. Schwartz and F. G. Peters, *Proc. Elec. Comp. Conf.*, **1973**, 251.
23. Quoted by L. Young, "Anodic Oxide Films," p. 77, Academic Press, New York (1961).
24. R. W. Berry, P. M. Hall, and M. T. Harris, "Thin Film Technology," p. 516, D. Van Nostrand, Inc., Princeton, N.J. (1968).
25. N. N. Axelrod and R. B. Marcus, *Thin Solid Films*, **15**, 521 (1973).

Spectroscopic Investigation of Photovoltaic Effects in Doped $LiNbO_3$

E. Krätzig and H. Kurz

Philips GmbH Forschungslaboratorium Hamburg, D 2 Hamburg 54, West Germany

ABSTRACT

Photo-induced currents and voltages determining the photorefractive effect in transition metal doped $LiNbO_3$ crystals have been measured in the spectral region between 1.5 and 4.0 eV. The current density j, the constant κ describing the anisotropic charge transfer, the conductivity σ during illumination, and the saturation field E_s have been investigated. The results yield information on the photorefractive centers and on the optical storage properties of mono- and double-doped $LiNbO_3$.

Light-induced refractive index changes in pyroelectric crystals like $LiNbO_3$ are of considerable interest for the reversible storage of thick phase holograms (1, 2). As shown by Glass *et al.* (3) the index changes result from photovoltaic effects in these crystals induced without externally applied fields; diffusion effects have only small influences under usual experimental conditions. The short-circuited steady-state current density along the crystallographic c axis induced by uniform illumination determines the photorefractive sensitivity, the photo-induced voltages and fields determine the refractive index change and hence the storage capacity. The current density j along the c axis is given by the relation: $j = \kappa \cdot \alpha \cdot J - \sigma \cdot E$, where J is the light intensity, α the absorption coefficient, κ a constant describing the anisotropic charge transport, E the photo-induced field, and $\sigma = \sigma_d + \sigma_l$ the conductivity during illumination containing contributions of dark- and photoconductivity. For $j = 0$ the saturation field E_s is obtained: $E_s = \kappa \cdot \alpha \cdot J/\sigma$.

In this paper we report on spectroscopic investigations of the quantities j, κ, σ, and E_s determining the storage properties of transition metal doped $LiNbO_3$ crystals. We use mono-doped crystals containing various concentrations of Fe, Cu, Mn, and Cr and double-doped crystals containing Fe/Cr, Cu/Cr, Fe/Mn, and Fe/Cu.

Key words: pyroelectrics, photovoltaic effects, photorefractive effects, optical storage.

Experimental

The poled single crystals used in these experiments were grown from congruent melt by A. Räuber, Institut für Angewandte Festkörperphysik, Freiburg, Germany. The crystals have been oxidized and partially reduced by common annealing treatments.

Short-circuited photocurrents in thermal equilibrium have been induced in the spectral range between 1.5 and 4.0 eV by incoherent light of a 1 kW xenon lamp in combination with a grating monochromator. The crystals were uniformly illuminated and edge electrodes of silver paste were used. Because of the influence of light absorption the measured currents are related to a mean light intensity $\bar{J} = J_0 (1 - e^{-\alpha d}) (\alpha \cdot d)^{-1}$, where J_0 is the incident intensity and d the crystal thickness. To reduce the influence of absorption as much as possible very thin crystals (d between 0.1 and 0.2 mm) have been used.

Photo-induced voltages and fields have been measured by applying external fields for compensation. The deviation of j under the influence of an external field has been found to be proportional to the field strength up to values of 10 kV/cm, the largest fields externally applied. For this reason the compensation field can be extrapolated for large values of E_s.

The optical absorption has been measured with a Cary 17 spectrometer *vs.* an undoped reference crystal or *vs.* air. In this case the contribution of reflection

calculated from the refractive index has been subtracted.

Results and Discussion

Mono-doped crystals.—For all dopants investigated the photocurrents in $LiNbO_3$ are directed along the c axis with the +c end negative (4). The photocurrent spectra, however, depend specifically on the dopants. The evaluation of κ from the short-circuited current density j according to the relation $j = \kappa \cdot \alpha \cdot J$ is impeded by different contributions to light absorption. We have always used the entire absorption including transitions, which do not contribute to the photocurrent.

The spectral dependence of κ is shown in Fig. 1 for various Fe-doped crystals partially reduced by common annealing treatments. Because of the small influence of light polarization the results are confined to unpolarized light. For each individual Fe concentration, κ increases with increasing photon energy, reaches a maximum around 3 eV, and decreases at larger photon energies. The κ-values increase with increasing Fe content up to 0.25 weight percent (w/o) Fe_2O_3, the largest Fe concentration used. The dependence of the maximum value κ_{max} on chemical treatments is shown in Fig. 2 for a crystal containing 0.02 w/o Fe_2O_3 and reduced by gradual steps. A measure for the chemical state is the optical absorption band at 2.6 eV, growing by reducing treatments. In the case of oxidized crystals very small κ-values are obtained for all Fe concentrations investigated. However, it should be kept in mind that small inefficient contributions to absorption have large effects on the evaluation of κ in the case of oxidized crystals with very small absorption coefficients. The maximum value of κ grows with increasing absorption, remains constant for a large absorption range, and decreases again in the case of very strongly reduced crystals.

For Cu- and Mn-doped crystals the κ-values are smaller than in the case of Fe dopants, the maximum values are about 1 (pA · cm/mW) for Cu-doped and 0.2 (pA · cm)/mW for Mn-doped crystals. The influence of various concentrations and chemical treatments on κ is smaller than for $LiNbO_3$:Fe.

Glass *et al.* (3) have proposed a model for the photocurrents in $LiNbO_3$:Fe generated without external fields. Electrons are excited directionally from Fe^{2+} to Nb^{5+} ions (intervalence transfer) and are trapped again by Fe^{3+} ions. The directional properties along the c axis result from an asymmetrical lattice site of the Fe^{2+} ions. Dischler and Räuber (5) have suggested that the efficient Fe^{2+} ions are associated with oxygen vacancies.

The maximum of the photocurrent at 3.2 eV differs from the absorption maximum at 2.6 eV corresponding to the intervalence transfer (4). This behavior indicates the increase of the unidirectional transport properties even in the spectral region where the transition probability decreases. Similar results are obtained for Cu-doped crystals, where the photocurrent maximum is observed at 3.7 eV and the maximum of the difference absorption between a reduced and an oxidized crystal at 3.3 eV.

The relatively small influence of chemical treatments on κ indicates that the total directional charge transport is mainly determined by the excitation and not by the recombination process.

A further quantity determining the storage properties is the conductivity $\sigma = \sigma_d + \sigma_l$ during illumination. The dark conductivity σ_d of $LiNbO_3$ crystals is increased by impurities and by reducing treatments. However, for impurity concentrations smaller than 0.1 w/o and moderate reductions the dark conductivity of our samples remains smaller than $2 \cdot 10^{-16}$ $(\Omega\text{-cm})^{-1}$. For very strong reductions σ_d can be increased by several orders of magnitude supporting the interpretation that in this case Nb^{4+} centers have been formed.

The spectral dependence of the photoconductivity σ_l is represented in Fig. 3 for an oxidized and for a partially reduced $LiNbO_3$:Fe crystal. With increasing photon energy σ_l increases for all dopants and chemical treatments investigated. Two different spectral regions for σ_l can be distinguished: In the visible region σ_l increases by reduction, in the near u.v. region σ_l increases by oxidation. This behavior leads to the requirement of two different kinds of centers contributing to photoconductivity.

In the visible region σ_l can be described by the relation $\sigma_l \propto \alpha \cdot J/N$, where the absorption constant α is proportional to the number of Fe^{2+} ions acting as donors and the number of traps N is proportional to the concentration of the Fe^{3+} ions. For this reason we

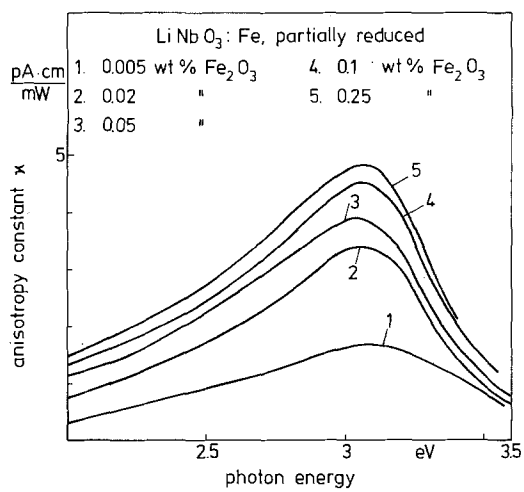


Fig. 1. Spectral dependence of the anisotropy constant κ for various $LiNbO_3$:Fe crystals.

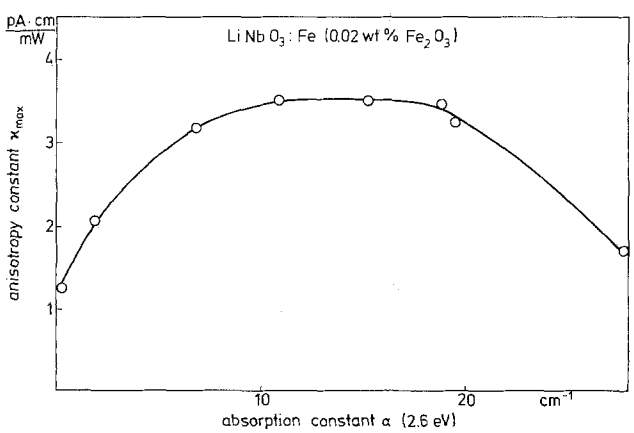


Fig. 2. Dependence of the anisotropy constant κ_{max} on chemical treatments for $LiNbO_3$:Fe.

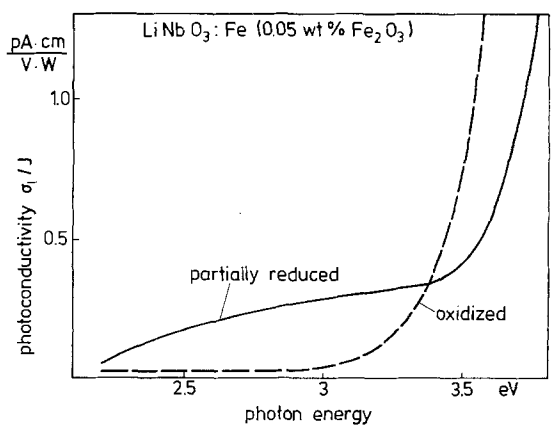


Fig. 3. Spectral dependence of photoconductivity for $LiNbO_3$:Fe

attribute the photoconductivity to field-sensitive electron transfers from Fe^{2+} to Fe^{3+} ions. The above relation is satisfied for Fe concentrations smaller than 0.1 w/o. For crystals with higher concentrations σ_l grows more rapidly than expected indicating additional contributions.

In the near u.v. region the optical absorption is decreased by reducing treatments and is mainly determined by charge transfer processes from oxygen π-orbitals to Fe^{3+} ions. Therefore we attribute the photoconductivity to these excitations and migration of the holes in the valence band. In reduced crystals σ_l decreases rapidly in the region because the holes are trapped by Fe^{2+} ions.

The photo-induced saturation field E_s is independent of light intensity since $E_s = (\kappa \cdot \alpha \cdot J)/\sigma$ and $\sigma \propto J$, if σ_d is small compared to σ_l. In the case of our crystals this is always true for impurity concentrations smaller than 0.1 w/o, for moderate reduction and light intensities of the order of 1 mW/cm². For higher impurity concentrations or stronger reductions the value of E_s for high intensities can be determined by substracting σ_d from σ.

The field E_s grows with increasing photon energy because κ increases, reaches a maximum around 3 eV for Fe, Cu, and Mn dopants and decreases at larger photon energies because σ increases. The spectral dependence of E_s for various Fe concentrations is shown in Fig. 4. The largest E_s values are obtained for concentrations of about 0.1 w/o Fe_2O_3. The dependence of the maximum value $E_{s\,max}$ on chemical treatments is presented in Fig. 5. The smallest E_s values are obtained for oxidized crystals. With an increasing Fe^{2+} concentration, E_s grows rapidly and decreases again due to the increase of σ_l.

A different behavior is observed for Cu-doped crystals: In this case the largest E_s values are observed for oxidized samples.

Double-doped crystals.—In double-doped $LiNbO_3$ crystals two kinds of effects are observed. For certain dopants the optical properties depend on illumination via photochromic effects as discovered by Staebler and Phillips (6). On the other hand the quantities κ and E_s determining the storage properties of Fe- or Cu-doped crystals may be modified by codopants.

For example in Cr-doped $LiNbO_3$ photocurrents and photovoltages are not increased at photon energies smaller than 3.5 eV compared to undoped $LiNbO_3$. In crystals containing Fe/Cr or Cu/Cr, however, the quantities j, κ, σ, and E_s differ from those of Fe- or Cu-doped crystals, respectively. Photochromic effects are of less importance in these double-doped crystals: Fe/Cr-doped samples show very small photochromic effects in the oxidized state vanishing by reducing treatments, Cu/Cr-doped samples show no photochromic effects at all.

For quantitative evaluation we compare a $LiNbO_3$ crystal doped with 0.05 w/o Fe_2O_3 and a crystal doped with 0.05 w/o Fe_2O_3 and 0.05 w/o Cr_2O_3 oxidized and partially reduced by common annealing treatments. In the oxidized state the κ-values of the Fe/Cr-doped sample are a factor of two larger than that of the Fe-doped crystal. In the partially reduced state nearly equal κ-values are obtained for both crystals. However, in the case of the Fe/Cr-doped crystals the absorption contains large contributions from transitions on Cr ions inefficient for the photovoltaic effect as determined from measurements of $LiNbO_3$ crystals doped with Cr only. The subtraction of this inefficient absorption yields also for partially reduced Fe/Cr-doped crystals κ-values which are about a factor of two larger than that of the Fe-doped crystals. Similar results are obtained from measurements of Cu/Cr-doped (0.05 w/o CuO and 0.05 w/o Cr_2O_3) and Cu-doped (0.05 w/o CuO) crystals.

The saturation fields E_s of these crystals indicating the interplay between κ and σ also exhibit considerable differences. In Fig. 6 the fields of Cu/Cr- and Cu-doped samples are compared. In the oxidized and the partially reduced state the fields of the double-doped crystal are considerably larger.

The reason for the increase of κ and E_s in the double-doped crystals is not yet clear. By the additional Cr dopants new centers may be formed or the crystal stoichiometry may be changed. The results on mono-doped samples concerning the impurity concentration and chemical treatments seem to favor the second possibility.

In double-doped $LiNbO_3$ crystals containing Fe/Mn and Fe/Cu photochromic effects are found. A model for the charge transfer during illumination with u.v. or visible light in Fe/Mn-doped samples has been proposed by Staebler and Phillips (6)

$$Mn^{2+} + Fe^{3+} \underset{\text{vis.}}{\overset{\text{u.v.}}{\rightleftharpoons}} Mn^{3+} + Fe^{2+}$$

The analogous process for Fe/Cu-doped samples reads

$$Cu^{+} + Fe^{3+} \underset{\text{vis.}}{\overset{\text{u.v.}}{\rightleftharpoons}} Cu^{2+} + Fe^{2+}$$

Photochromic effects are observed for impurity concentrations smaller than about 0.1 w/o and for oxidized or lightly reduced crystals. In the case of stronger reductions the photochromic effects decrease considerably.

Figure 7 shows the spectra of the photocurrent density and the absorption of a $LiNbO_3$ crystal doped with

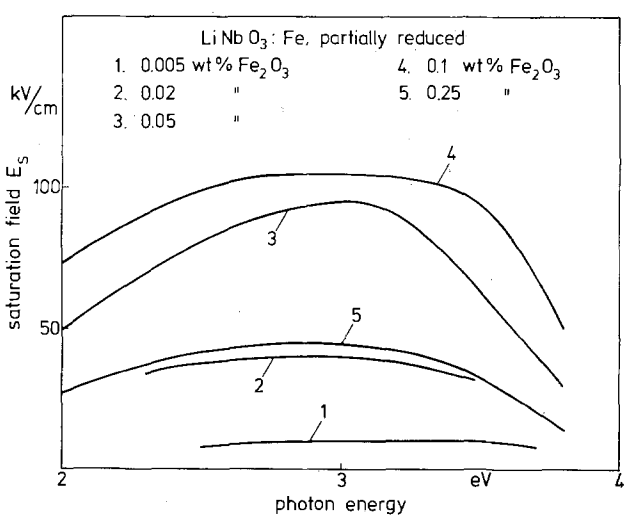


Fig. 4. Spectral dependence of the photo-induced saturation field E_s for various $LiNbO_3$:Fe crystals.

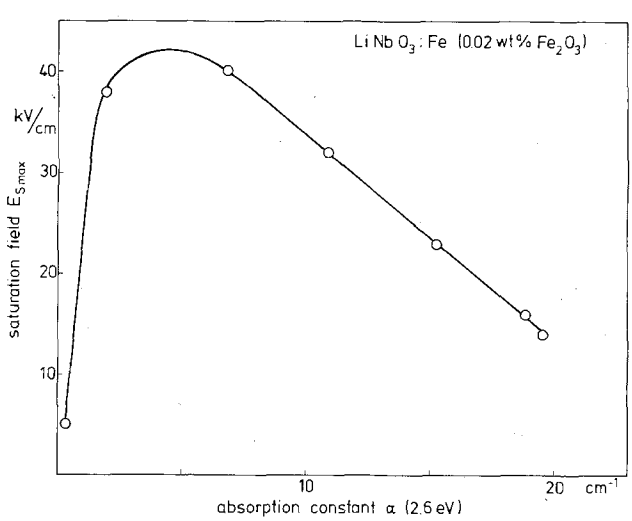


Fig. 5. Dependence of the saturation field $E_{s\,max}$ on chemical treatments for $LiNbO_3$:Fe.

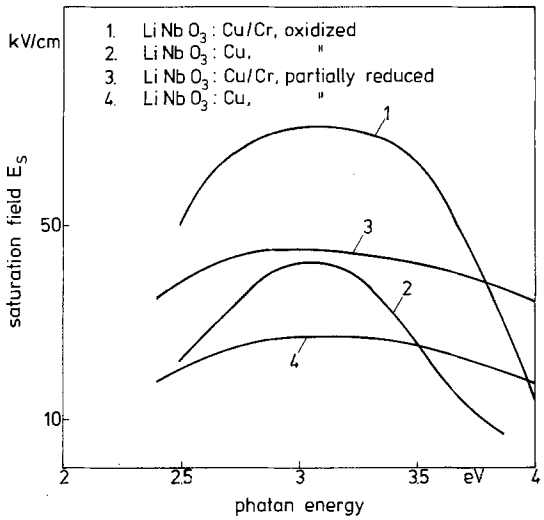


Fig. 6. Comparison of the saturation fields E_S of a Cu (0.05 w/o CuO)- and a Cu/Cr (0.05 w/o CuO, 0.05 w/o Cr_2O_3)-doped $LiNbO_3$ crystal.

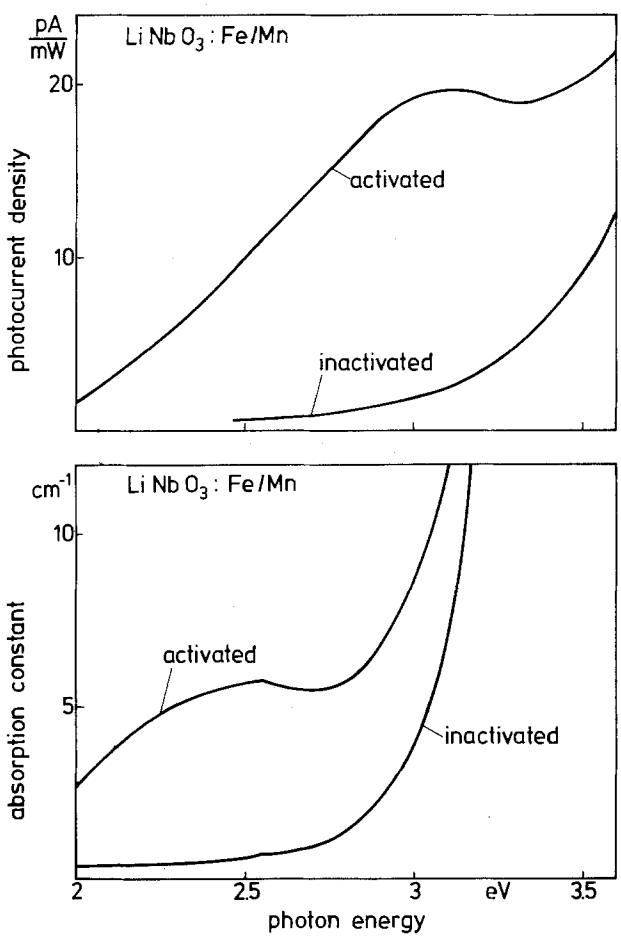


Fig. 7. Photocurrent and absorption spectra of a $LiNbO_3$:Fe/Mn crystal after illumination with u.v. light (activated) and visible light (inactivated).

0.03 w/o Fe_2O_3 and 0.01 w/o $MnCO_3$. The crystal has been activated and inactivated by illumination with u.v. (3.4 eV) and visible (2.5 eV) light, respectively. In the activated state the characteristic photocurrent spectrum of the Fe dopants is observed, in the inactivated state the spectrum of Mn dopants is obtained supporting the above model. Only 5-10% of the Fe dopants are involved in the photochromic switching.

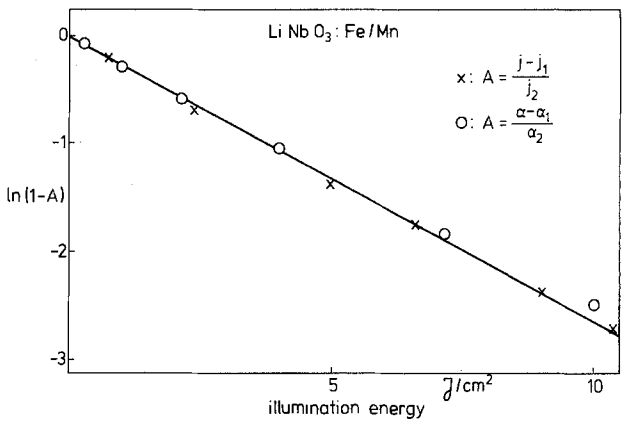


Fig. 8. Simultaneous increase of absorption at 2.6 eV and photocurrent during illumination with u.v. light (3.4 eV) of an inactivated $LiNbO_3$:Fe/Mn crystal.

Measurements of photochromic $LiNbO_3$:Fe/Mn crystals clearly demonstrate the correlation of the absorption band centered at about 2.6 eV and the photocurrent. A crystal has been inactivated by illumination with visible light (2.5 eV). As shown in Fig. 8 the simultaneous increase of the absorption and the photocurrent during u.v. illumination can be described by the relations

$$j(J \cdot t) = j_1 + j_2 (1 - \exp(-k \cdot J \cdot t))$$

and

$$\alpha(J \cdot t) = \alpha_1 + \alpha_2 (1 - \exp(-k \cdot J \cdot t))$$

where j_1, j_2, α_1, α_2, and k are constants. The values of κ and E_S in Fe/Mn- and Fe/Cu-doped samples also depend on optical treatments. In activated crystals κ-values characteristic for Fe dopants are obtained, in inactivated crystals the κ-values correspond to those of Mn or Cu dopants. In these crystals rather large saturation fields have been measured, the values in the activated state exceed 100 kV/cm.

Acknowledgment

We thank B. Dischler and A. Räuber (Institut für Angewandte Festkörperphysik, Freiburg, Germany) for supplying the crystals and helpful discussions. Valuable technical assistance by R. Kobs, J. Reck, M. Rosenkranz, and F. Welz is greatly acknowledged. The work has been partially supported by the German government (Bundesministerium für Forschung und Technologie).

Manuscript submitted July 19, 1976; revised manuscript received Aug. 23, 1976. This was Paper 429 presented at the Washington, D. C., Meeting of the Society, May 2-7, 1976.

Any discussion of this paper will appear in a Discussion Section to be published in the December 1977 JOURNAL. All discussions for the December 1977 Discussion Section should be submitted by Aug. 1, 1977.

Publication costs of this article were assisted by Philips GmbH.

REFERENCES

1. F. S. Chen, J. T. La Macchia, and C. B. Fraser, *Appl. Phys. Lett.*, **13**, 223 (1968).
2. D. L. Staebler, W. J. Burke, W. Phillips, and J. J. Amodei, *ibid.*, **26**, 182 (1975).
3. A. M. Glass, D. van der Linde, and T. J. Negran, *ibid.*, **25**, 4 (1974).
4. E. Krätzig and H. Kurz, *Ferroelectrics*, **10**, 159 (1976).
5. B. Dischler and A. Räuber, *Solid State Commun.*, **17**, 953 (1975).
6. D. L. Staebler and W. Phillips, *Appl. Phys. Lett.*, **24**, 268 (1974).

Influence of the Growth Parameters in GaAs Vapor Phase Epitaxy

L. Hollan, J. M. Durand, and R. Cadoret[1]

Laboratoires d'Electronique et de Physique Appliquee, Limeil-Brévannes, France

ABSTRACT

The vapor growth of gallium arsenide by the arsenic trichloride transport method has been studied by measurement of the growth rate *vs.* several growth parameters varied in broad intervals. Thus the influence of the supersaturation of the source and deposition temperature and of the input arsenic trichloride partial pressure has been studied. Growth has mainly been carried out on (100) crystalline planes, with some experiments on (110). The experimental data allows an estimation of the growth possibilities in unusual conditions, namely at low temperature, low supersaturation, and in a broad range of arsenic trichloride partial pressure. In these latter conditions, pure material is obtained at very high growth rates. All the experimental results can be qualitatively explained by a kinetically controlled growth mechanism involving a surface adsorption layer.

In spite of the very numerous papers dealing with vapor phase epitaxy of GaAs [see for instance review paper of Shaw (1)], the influence of the different growth parameters is not sufficiently known. This is probably due to the fact that the principal motivation is material supply for devices, so that previous authors have not tried to deviate too far from growth conditions giving more rapidly good electrical and morphological results. These conditions then have been generalized in the different laboratories of the world. Furthermore, the few researchers (2) who attempted to vary the growth parameters in much larger intervals came up against experimental difficulties; uncontrolled parasitic nucleation, out-of-equilibrium conditions, etc., made it difficult to obtain significant and reproducible results. Finally, the lack of growth mechanism models did not incite the scientific workers to compile other experimental data than those necessary for the growth of layers orientated toward device production.

Our laboratory having now a long experience of this growth method as well as a suitable growth mechanism model (3), has undertaken a study with very large variations of the growth parameters.

In the "arsenic trichloride" method, the main experimental parameters are the following: (*a*) deposition temperature T_D, (*b*) source temperature T_S, (*c*) input $AsCl_3$ partial pressure p_o, and (*d*) crystallographic orientation of the substrate.

Some authors have already studied the influence of these parameters, but only little mention is made of T_D outside of the 700°-750°C interval (4), 750°C being currently used. Similarly T_S, which determines, for a fixed T_D, the supersaturation and to a lesser extent the Ga/As ratio (5), in most published data is given only indicative values, since, depending on the source geometries, equilibria are only partially reached. The influence of p_o has been studied by Di Lorenzo (6) and also by others (7, 8), because this parameter allows the control of the residual doping through the effect of secondary equilibria on the quartz walls. In our laboratory, a study showing the influence of very large variations of this parameter on the doping and on the growth rate at three deposition temperatures (720°, 750°, and 770°C) has been published (9). Now this study has been extended to a larger temperature range and to the influence of supersaturation. Finally the influence of the crystallographic plane has been studied by several authors (10-13) and a very pronounced anisotropy pointed out. In the present study, besides the common deposition on misoriented 3° off the (001) plane toward the [110], we have also performed some experiments on the less well-known (110) plane which leads to unusual results.

[1] Permanent address: UER de Sciences, Laboratoire de Cristallographie et de Physique des Milieux Condensés, Complexe Scientifique des Cézeaux, B.P. 45, 63170 Aubieres (France).

Key words; crystal growth from vapor, gallium arsenide, crystal structure.

Experimental Results

The experimental growth of GaAs by the $AsCl_3$ method was carried out in equipment similar to that already described elsewhere (14). As we have already mentioned, for an exact knowledge of the growth parameters, it is necessary to reach equilibrium at the source. So, in this study, we have mainly used a boat filled up with GaAs, in which the surface of contact between the polycrystalline material and the $AsCl_3$ and hydrogen mixture is large enough to reach this equilibrium. We have also experimentally checked that the weight loss at the source linearly increased with the arsenic trichloride partial pressure (p_o) even for the highest values of the latter. Another advantage of a GaAs source is to avoid the problems occurring during the saturation (15) so that the supersaturation value and the partial pressures cannot be evaluated. Nevertheless, several experiments have also been carried out with Ga sources, using boats with large Ga surface areas and relatively low gas flow rates in order to reach equilibrium.

The study of the different growth parameters requires a large number of experiments; since it was necessary to limit this number, we have proceeded as follows. In order to avoid any instabilities which could occur during the beginning of the growth, the growth is started with a n^+-doped buffer layer (time t_1). After stabilization, a growth with given conditions (T_S, T_D, p_o) and without doping is carried out during a time t_2 (this time is long enough to grow more than 10 μm); then the dopant is added again and the growth conditions changed (*e.g.*, decrease T_S and T_D by 20°C); after a new period t_3 which is chosen to be much longer than that required for the temperature stabilization, the dopant flow is switched off, and a growth with the new growth conditions is carried out during a time t_4. This procedure can be repeated several times (for practical reasons we have limited it to five) and at the end of the growth the successive layers are revealed on a cleavage plane, and the growth rates are easily evaluated. The doping level of each undoped layer can also be determined by successive etching and $C = f(V)$ measurements. Nevertheless, this procedure is not applicable with Ga sources for any change in the source temperature because of the saturation problems.

Results and Discussion

Influence of the growth temperature.—In any vapor phase growth process, the growth temperature is obviously one of the main parameters and the growth rate τ is usually represented, in previous papers, in the $\log \tau = f(1/T_D)$ diagram, *i.e.*, the logarithm of growth rate *vs.* the inverse of the deposition temperature (5, 16, 17) in order to point out a linear decrease which was roughly interpreted by a kinetic limitation.

Figure 1 shows these types of $\log \tau$ *vs.* $1/T_D$ curves. It must be noticed that contrary to previous studies, the supersaturation was maintained close to a constant value ($T = 80°C$, see definition below), this was necessary to point out the influence of the growth temperature variation only. The curves corresponding to the (100) plane show clearly that with these conditions (namely at constant supersaturation) the generally reported decrease of the growth rate at higher temperatures is not observed. On the other hand, it appears that the previously reported linear decrease, related to an activation energy (5, 16) is not a simple Arrhenius plot. The shape of the curve is in good agreement with the theoretical treatment of Cadoret (3) which explains the nonlinear decrease by an increase of the surface coverage with As-Ga-Cl molecules.

Figure 1 also shows the growth rate variation observed on a (110) plane which is discussed below.

Influence of the source temperature (and supersaturation).—With a given deposition temperature, the supersaturation is mainly determined by the source temperature.

The degree of excess related to the supersaturation by the equation $\beta = \gamma + 1$ can be defined (18) as

$$\beta = \frac{K_{TS} \times d^{1/4}}{K_{TD}} \qquad [1]$$

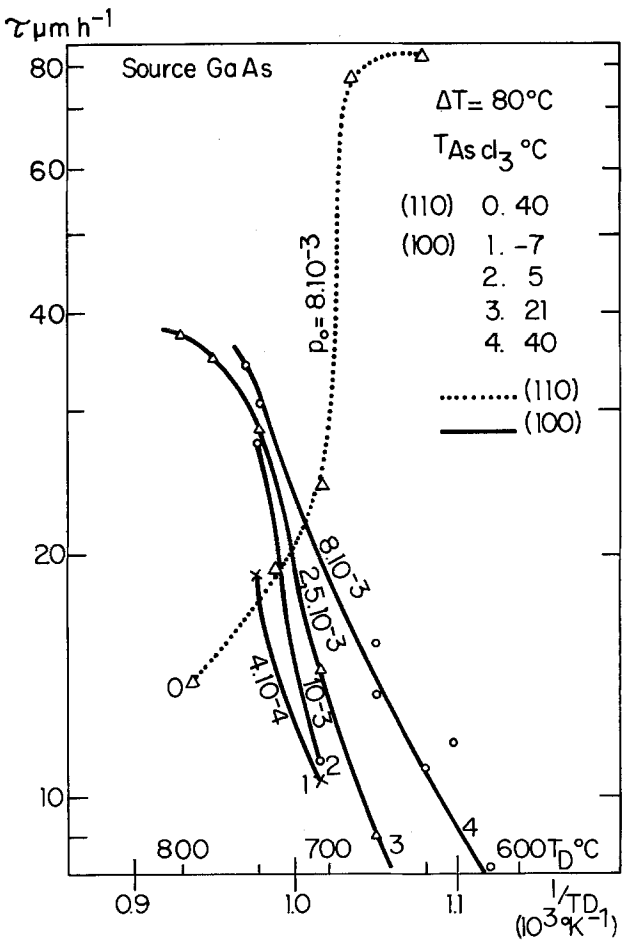


Fig. 1. Effect of substrate temperature on GaAs epitaxial deposition rates for various $AsCl_3$ molecular fraction and for two crystallographic orientations of the substrate.

where d is a dilution factor ($d = 1$ without dilution and $d < 1$ with a hydrogen bypass flow) and K_T are the equilibrium constants corresponding to

$$GaCl + \tfrac{1}{2}H_2 + \tfrac{1}{4}As_4 \rightleftarrows GaAs + HCl$$

at the source and deposition temperatures, respectively. It has been shown experimentally (5) that to a first approximation, and for $T_D > 700°C$, K_T can be represented by Fergusson's thermodynamical data (19)

$$K_T = e^{-\frac{G}{RT}}$$

$$G° \text{ (cal/mole)} = 32170 - 37.2T + 1.07 \ln T + 1.6 \times 10^{-3}T^2 \qquad [2]$$

Experimentally we have measured the growth rate for a given deposition temperature and with increasing source temperatures. These results are first represented in the growth rate *vs.* ΔT diagram (Fig. 2a) in which

$$\Delta T = T_S - T_D \qquad [3]$$

From a theoretical point of view, one of the most interesting parameters is the supersaturation, which can be easily evaluated for each T_D and ΔT using expressions [1], [2], and [3]. Figure 2b gives the representation of the growth rate *vs.* degree of excess.

According to the theoretical treatment of Cadoret (3) the growth rate is given by the relation

$$\tau_{\mu/k} = 1.005 \times 10^{10}\, T_D^{-1/2} \left(\exp -\frac{1.656 \times 10^4}{RT_D} \right) (1 - \theta_{As} - \theta_{AsGaCl}) \cdot p_{HCl} \cdot \gamma \qquad [4]$$

θ_{As} and θ_{AsGaCl} are, respectively, the surface coverages with arsenic atoms and arsenic gallium monochloride molecules, $(1 - \theta_{As} - \theta_{AsGaCl})$ is the surface coverage with the vacant half crystal sites for the arsenic

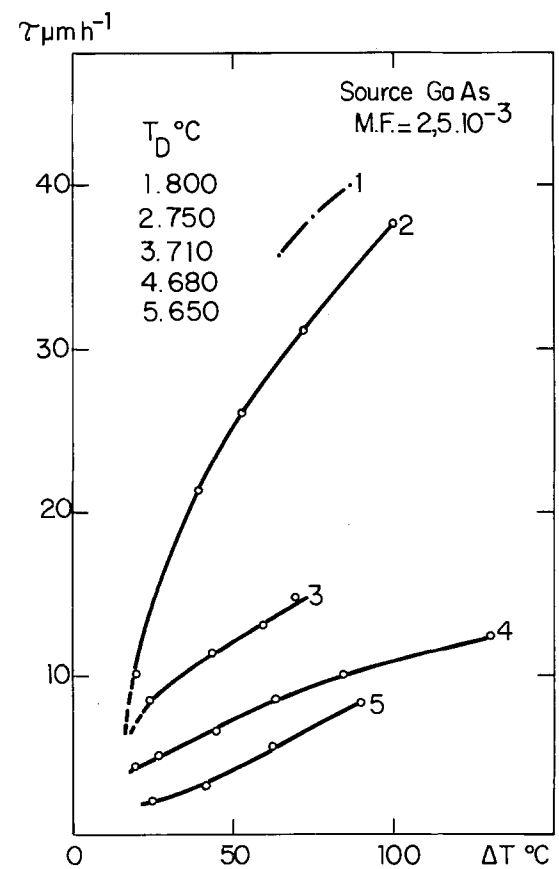


Fig. 2a. Gallium arsenide deposition rates as a function of ΔT ($\Delta T = T_S - T_D$, with T_S = source temperature and T_D = deposition temperature) at several T_D.

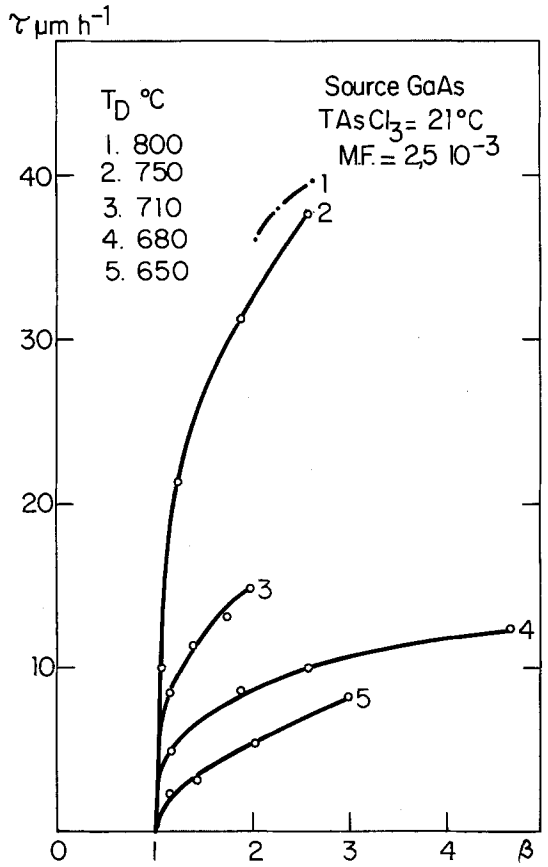


Fig. 2b. Gallium arsenide deposition rates as a function of the degree of excess β related to the supersaturation γ ($\beta = \gamma + 1$) at several T_D.

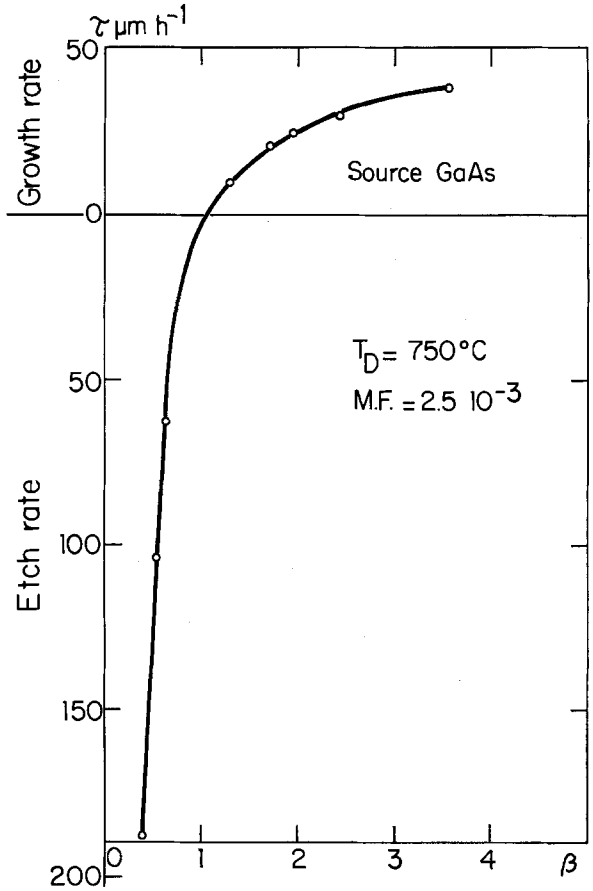


Fig. 3. Effect of the degree of excess β related to the supersaturation on GaAs epitaxial growth or etch rates at $T_D = 750°C$.

deposition, p_{HCl} is the hydrogen chloride partial pressure.

The expression of $(1 - \theta_{As} - \theta_{AsGaCl})$ may be calculated by applying the absolute rate theory to the equilibrium between surfaces and vapor molecules. It increases with the reciprocal partial pressure of gallium monochloride and the substrate temperature

$$(1 - \theta_{As} - \theta_{AsGaCl}) = f(T_D, 1/p_{GaCl}) \qquad [5]$$

Experimentally, an increase of ΔT involves: (*i*) an increase of p_{GaCl} and consequently, according to [5], a decrease of the surface coverage vacant half crystal sites $(1 - \theta_{As} - \theta_{AsGaCl})$, (*ii*) a decrease of p_{HCl}, and (*iii*) an increase of γ [1]. In expression [4] these three variations are in opposition. Since the experimental growth rate increases, the variation of γ appears in this case (increasing ΔT) to be predominant. At the same time, the partial derivative $\partial T/\partial\gamma$ must decrease, which is clearly apparent on Fig. 2a and b.

In order to test the continual increase of $\partial\tau/\partial\gamma$ with decreasing values of the relative supersaturation, we have realized some experiments with negative values of this parameter. The observed etch rates (Fig. 3) give evidence of this behavior which leads to a nonsymmetric but continuous behavior of the etching and growth processes.

Influence of the partial pressures.—In the As-Ga-Cl adsorption controlled growth mechanism, the partial pressures of the chemical species, in equilibrium with the vapor phase, take an important part. It can be shown easily that all these partial pressures are proportional to the input $AsCl_3$ partial pressure. Furthermore, it can also be shown (19) that by varying the $AsCl_3$ molar fraction MF, the supersaturation remains constant.

Consequently, MF appears as a basic parameter in the growth system. The numerical values of MF are deduced from the experimentally determined saturation temperature using the relation $\log p_{o(mm\,Hg)} = 8.7 - (2300/T)$ from Ref. (5) and taking into account a dilution factor d due to the addition of a separate hydrogen carrier flow [see experimental setup in Ref. (20)]. Then $MF = p_o \times d$. In our experiments, $d = 0.4$ with Ga and 0.3 with GaAs source.

Figure 4a and b represent the growth rate variation *vs.* MF at different deposition temperatures, and with two different ΔT values (50° and 80°C). Figure 5 shows the influence of ΔT for a given growth temperature ($T_D = 750°C$). Figures 4a and b clearly show that for deposition temperatures higher than 710°C the growth rate first increases with the $AsCl_3$ molecular fraction and remains constant or slightly decreases in a similar way to that in Ref. (3). This behavior can be explained by Eq. [4].

Nevertheless, the results observed for $T_D > 710°C$ are not always in good agreement with the theoretical anticipations. Such a behavior could be explained either by an adsorption of GaCl molecules in a second layer before filling up the first one, or by a desorption process of two neighboring chlorine atoms by a GaCl molecule according to

$$GaCl + 2(As\text{-}Ga\text{-}Cl) \rightleftarrows 2AsGa + GaCl_3 \qquad [6]$$

Experiments carried out with very high MF values reveal (Fig. 5) a new and unexpected phenomenon: over a critical MF value, the growth rate increases sharply reaching values as high as 50-100 µm/hr. This phenomenon appears more sharply with a Ga source than a GaAs one. In fact, the experimentation at such high MF values becomes difficult: low ΔT values (for instance $\Delta T = 50°C$) must be used to avoid excessive parasitic depositions on the reactor walls. If parasitic depositions occur, obviously the whole phenomenon of growth rate increase is masked. In the case of Fig. 6 a small amount of parasitic nucleation appeared for $MF > 2\text{-}3\ 10^{-2}$. It is therefore possible that in the

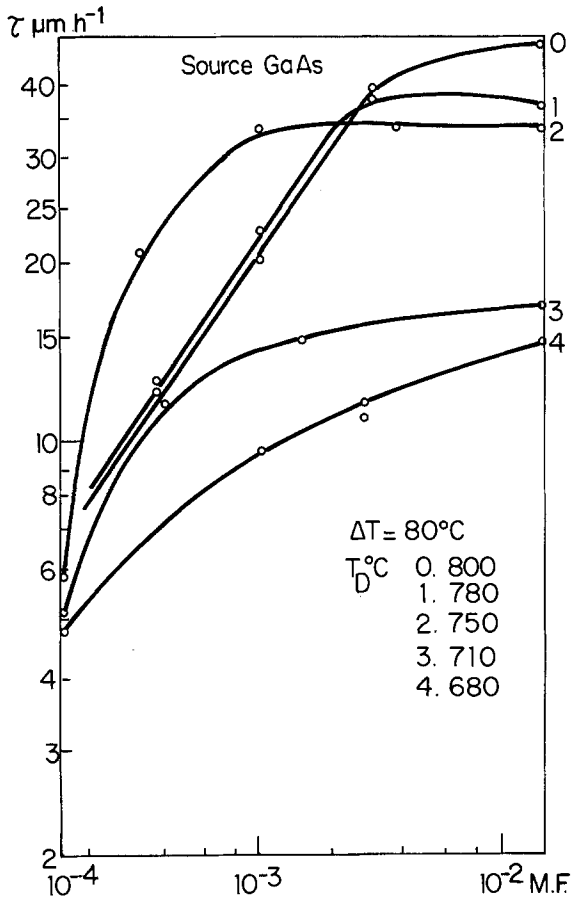


Fig. 4a. Gallium arsenide deposition rates as a function of the $AsCl_3$ molecular fraction at $\Delta T = 80°C$ and for several T_D.

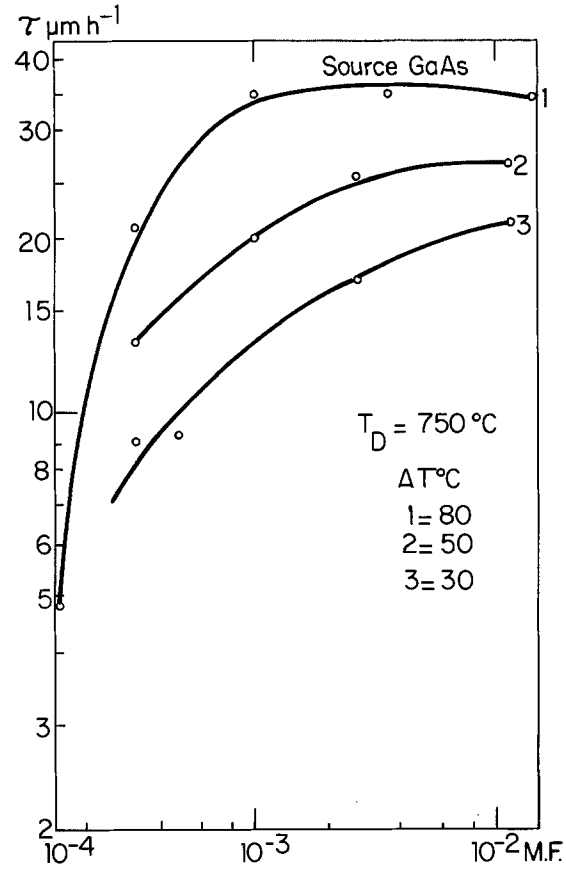


Fig. 5. Gallium arsenide deposition rates as a function of the $AsCl_3$ molecular fraction at $T_D = 750°C$ and for several ΔT.

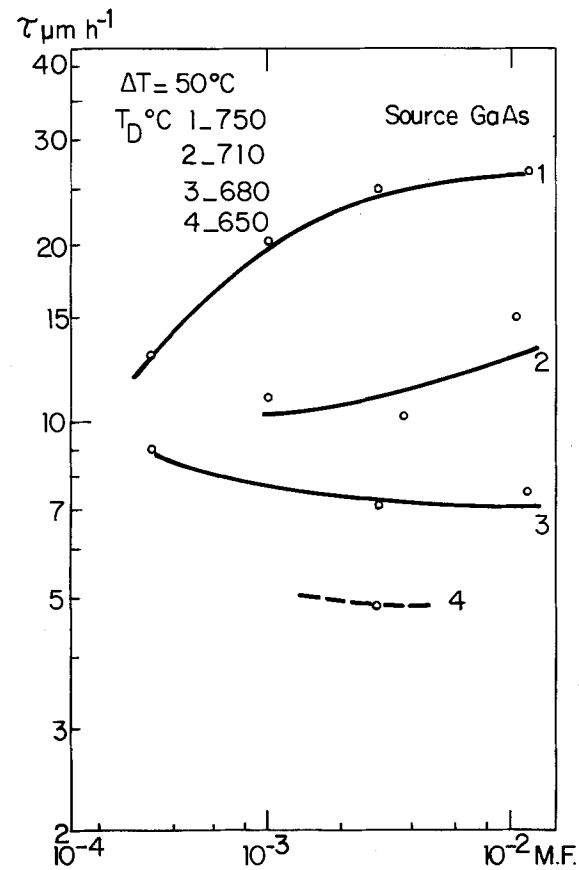


Fig. 4b. Gallium arsenide deposition rates as a function of the $AsCl_3$ molecular fraction at $\Delta T = 50°C$ and for several T_D.

absence of any parasitic deposition, the sharp increase in growth rate would continue (Fig. 6, MF = 10^{-2}).

The two layer model presented by Mutaftschiev (21) and Mutaftschiev and Bonnissen (22) suggests, assuming a two layer GaCl adsorption, that the sharp increase observed might be due to a change in GaCl surface structure, similar to the change in surface roughness of a singular face.

From a practical point of view, this phenomenon could be interesting because of the high growth rate which is accompanied by a low residual dope and high mobility (*e.g.*, with $p_o = 1.8\ 10^{-2}$ atm, $T = 50°C$, $\tau = 55\ \mu m/hr$, $n_{77°K} = 7.7\ 10^{13}$, $\mu_{77°K} = 178{,}000$).

It is pointed out that once more there is an argument in favor of Di Lorenzo's assumption of the p_{HCl} control of the residual doping (6) because in the present case, for a very different growth rate and presumably also quite different growth mechanism, the residual doping is still that given by the extrapolation of the $\log n = f(p_o)$ curve (9).

Growth on the (110) plane.—The (110) faces are characterized by a surface ending through a plane of Ga and As atoms. It is a stepped face and so it may be considered as a face with a great number of half crystal sites like (100). The interaction energy between the As-Ga-Cl molecules adsorbed on such a face having an important effect on the theoretical growth rate, it was particularly interesting to compare the measurements performed on (110) and (100).

In order to obtain reliable experiments in epitaxial growth on a single crystallographic plane, it is necessary to know the influence of the misorientation on the growth rate, the facet growth effects, and also to choose a misorientation (direction and angle) allowing a surface free of macroscopic defects. Analogically to Ref. (23), a study of the growth on (110) centered lens form substrates has been undertaken (24). Thus, for the present experiments, we have chosen a misorienta-

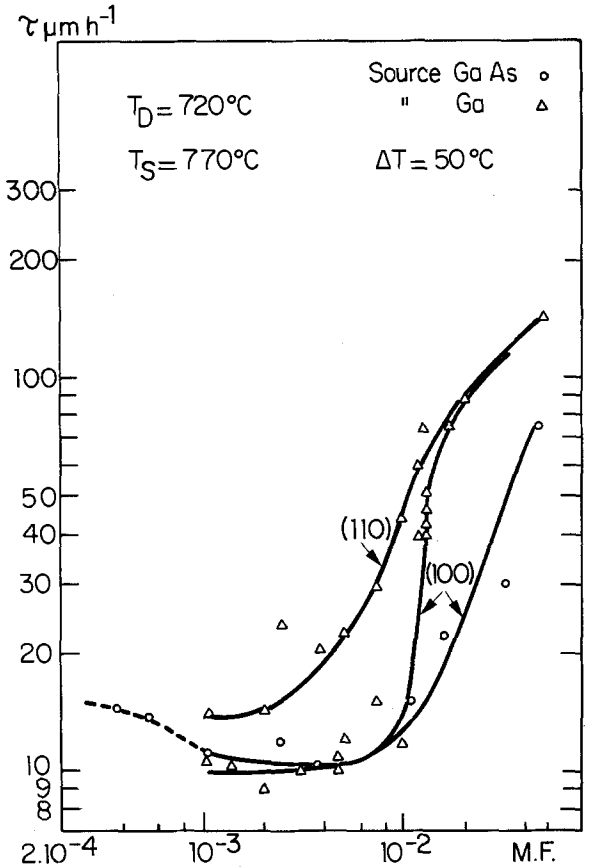


Fig. 6. Effect of the $AsCl_3$ molecular fraction on GaAs epitaxial deposition rates at T_D = 720°C and ΔT = 50°C for two crystallographic orientations of the substrate.

tion of 2° in the 110 direction, which gives perfectly shiny growth surfaces.

In comparison with the usual (100) plane, the (110) presents two anomalous behaviors: The first is the increase of the growth rate with decreasing growth temperature at nearly constant supersaturation values (Fig. 1). In this respect, the (110) plane behaves in a different way than most of the other low index planes: (100), (115), (113)A and B, (112)A and B, (111)A (12, 10) (as far as these experiments realized at increasing supersaturation can be compared). The second is the constant increase of the growth rate with MF in the interval $10^{-3} < MF < 10^{-2}$ (Fig. 6).

The practical consequences of these two effects is that at usual deposition temperature (750°C) and MF (10^{-3} atm), the (110) growth rate value is poor ($\tau \sim 10$ μm/hr), but at low deposition temperature (<720°C) and high MF values, it can be very high. A theoretical explanation may be found in a higher interaction energy between the As-Ga-Cl molecules adsorbed on the (110) surface compared with the (100) one.

Conclusions

As it has been shown throughout this study, the shapes of the growth rate *vs.* growth parameters curves are in good qualitative agreement with a previously described growth model (3) based on a surface adsorption layer of As-Ga-Cl. For instance, the decrease of the $\tau = f(1/T)$ curves appears much more complex than a simple Arrhenius plot. It also appears that at lower temperatures, or on another crystallographic plane, or at very high MF, other desorption processes than this considered in the original paper (3) (*e.g.*, those giving $GaCl_3$ at lower temperature) or other lateral interactions energies [*e.g.*, on (110)] or even double adsorption layers (very high MF) must be considered.

Also, from a practical point of view, some important observations must be emphasized:

With the help of the reported data, the influence of all the main parameters (T_D, ΔT, $AsCl_3$ MF) on the growth rate can be evaluated semiquantitatively by interpolation or extrapolation.

It is possible to grow good surface quality layers at temperatures as low as 600°-650°C (Fig. 1).

It is also possible to use very low partial pressures, for instance values 20 times lower than those usually employed and yet the growth rate remains nearly the same.

At very high MF it is possible to obtain pure material (in the $n = 10^{13}$ at. cm^{-3} range) and this with unusually high growth rates (50-100 μm/hr).

Acknowledgments

The authors would like to thank Mme Mennechez for her collaboration and J. Hallais for helpful discussions.

Manuscript submitted March 23, 1976; revised manuscript received Sept. 2, 1976.

Any discussion of this paper will appear in a Discussion Section to be published in the December 1977 JOURNAL. All discussions for the December 1977 Discussion Section should be submitted by Aug. 1, 1977.

Publication costs of this article were assisted by Laboratoires d'Electronique et de Physique Appliquée.

REFERENCES

1. D. W. Shaw, *J. Cryst. Growth*, **31**, 130 (1975).
2. Private communications.
3. R. Cadoret and M. Cadoret, *J. Cryst. Growth*, **31**, 142 (1975).
4. H. Watanabe and Y. Seki, *ibid.*, **24/25**, 220 (1974).
5. A. Boucher and L. Hollan, *This Journal*, **117**, 932 (1970).
6. J. V. Di Lorenzo and G. E. Moore, Jr., *ibid.*, **118**, 1823 (1971).
7. T. Aoki and Yamaguchi, *Jpn. J. Appl. Phys.*, **10**, 953 (1971).
8. O. Mizuno and H. Watanabe, *J. Cryst. Growth*, **30**, 240 (1975).
9. L. Hollan, 1974 Proc. Vth. Int. Symp. on GaAs, Inst. Phys. Conf., Ser. No. 24, p. 22 (1974).
10. D. W. Shaw, 1968 Proc. 2nd Int. Symp. on GaAs, Inst. Phys. Conf. Ser., p. 50.
11. J. V. Di Lorenzo and A. E. Machale, *This Journal*, **118**, 1516 (1971).
12. L. Hollan and C. Schiller, *J. Cryst. Growth*, **13/14**, 319 (1972).
13. T. Nakanisi and M. Kasiwagi, *Jpn. J. Appl. Phys.*, **13**, 484 (1974).
14. L. Hollan and A. Mircea, 1973 Proc. 4th. Int. Symp. on GaAs, Inst. Phys. Conf. Ser., p. 217.
15. D. W. Shaw, *J. Cryst. Growth*, **8**, 117 (1971).
16. D. W. Shaw, *This Journal*, **117**, 683 (1970).
17. M. Nakagawa and H. Ikoma, *Jpn. J. Appl. Phys.*, **10**, 1345 (1971).
18. J. B. Loyau, A. Oberlin, L. Hollan, and R. Cadoret, *J. Cryst. Growth*, **29**, 176 (1975).
19. R. R. Ferguson and T. Gabor, *This Journal*, **111**, 585 (1964).
20. L. Hollan and A. Mircea, 1972 Int. Symp. on GaAs, Inst. Phys. Conf. Ser., p. 217.
21. B. Mutaftschiev, "Adsorption et Croissance Cristalline," CNRS 231, Paris (1965).
22. B. Mutaftschiev and A. Bonnissen, *Surf. Sci.*, **34**, 649 (1975).
23. L. Hollan and C. Schiller, *J. Cryst. Growth*, **22**, 175 (1974).
24. J. M. Durand and L. Hollan, To be published.
25. J. L. Laporte, Thèse, Université de Clermont-Ferrand, Les Cézeaux, B.P. 45 63170 Aubières (1975).

Chemical Vapor Deposition and Isotope Separation

P. J. Severin

Philips Research Laboratories, Eindhoven, The Netherlands

and H. Lydtin

Philips Forschungslaboratorium Aachen, Aachen, Germany

ABSTRACT

Because chemical vapor deposition (CVD) is based on diffusion, isotope separation should take place if the process is in the diffusion-limited range. The enrichment in a horizontal reactor as used for silicon epitaxy is calculated including thermal diffusion effects. It is found that whereas the deposition rate decreases exponentially along the reactor with characteristic length Λ, the isotope enrichment decreases linearly over the length from maximum to zero at $x = \Lambda$. The maximum value depends in a complex way on the masses and concentrations of the gas to be separated and the second gas, present as a reaction component or carrier gas. The requirements for efficient CVD isotope enrichment, which include fast mixing, a high deposition rate, and high enrichment ratio can be satisfied better by a liquid-source CVD system. An experimental arrangement is described and discussed in terms of heat transfer by film boiling. The absence of an unstable range in the plot of the heat flux against the temperature is ascribed to the effects of the decomposition process which dominates the evaporation. The importance of the increased rate of heat transfer due to the reversible accumulation of energy in chemical reaction products is stressed. The effect of an applied electric field is mentioned. Experiments with carbon deposition from $C_{12}H_{26}$ have shown a $^{12}C/^{13}C$ enrichment ratio up to 0.8%, whereas $\Delta M/2M = 0.3\%$. This effect is attributable to mass and thermal diffusion, selective evaporation, spray fractionation by drops acting as micro-ultracentrifuges, and geometry effects. The possibility of achieving uranium isotope separation with a CVD process has been considered theoretically. Thermodynamically possible reactions are specified by which liquid UF_6 is transformed into solid UF_3, UF_4, and UF_5. In this way uranium should be transported quickly from one condensed phase to another with an increasing lighter isotope concentration in the deposited reaction product. The reactor products can easily be retransformed into UF_6 so that the enrichment cycle can be repeated until the desired isotope ratio is achieved. In principle CVD can also be used as a collector mechanism with laser-induced isotope enrichment.

It is hard to find a field of research more rewarding in terms of direct concern to society than the search for more efficient methods for the generation of electrical energy. Because a fairly large amount of energy must be invested in the nuclear fuel produced by the usual uranium enrichment process, newly formulated proposals are eagerly pursued. The suggested rotating plasma method, the high power laser enrichment method, and the aerodynamic stationary-wall centrifuge technique may become of great importance if the promises of the early research work are realized. The feasibility of each of these methods should in practice be considered not only in terms of the return on the capital invested, but also on the basis of the energy account. A detailed review of proposals and prospects of a number of techniques for isotope separation, particularly of uranium, has been presented recently (1).

Conventional methods of isotope separation are based on gaseous, mass, or thermal diffusion, the method of gaseous diffusion being foremost in the uranium enrichment industry. Because chemical vapor deposition (CVD), as used for the epitaxial growth of silicon, is based on mass and thermal diffusion the deposited product should provide evidence of isotope separation as compared to the starting material. This separation process could even be quite effective, for by the very nature of the CVD process the thermal and partial pressure gradients are high and give rise to a high steady-state mass flow. Upon closer elaboration of this idea it became clear that a number of restricting conditions would have to be imposed to make the CVD process suitable for the purpose of isotope separation. It turned out that a new CVD method (2), though operating under different conditions, satisfied most requirements quite well.

Key words: carbon, chemical vapor deposition, enrichment, film boiling, heat transfer, isotope separation, liquid-source epitaxy, silicon, surface energy.

The purpose of this paper is to draw attention to CVD as a potentially useful method of isotope separation. Therefore, in the next section the principles and constraints of isotope separation by chemical vapor deposition are outlined and some formulas deduced from a simplified model. Thereafter a liquid-source CVD reactor and experimental results and conclusions are discussed. In the last section consideration is given to possible technical applications of this method, especially in the field of uranium isotope enrichment.

Isotope Separation with the CVD Method

Principles of CVD reactor operation.—A number of years ago the epitaxial growth of silicon from SiH_4 diluted in hydrogen in a horizontal water-cooled reactor became the object of a more detailed study. Eversteyn *et al.* (3) concluded from experiments with TiO_2 smoke that the gas flowing over a heated susceptor gave rise to a stagnant layer, whereas the gas in the remaining height of the tube above the susceptor was highly turbulent and thus destroyed all semblance of a temperature gradient. Hence the temperature should drop entirely across the stagnant layer. It was assumed then that the turbulent gas acted as a source of uniform concentration of SiH_4, which diffused across the stagnant layer to be reduced by pyrolysis on the substrate.

A quantitative model was developed which described the flux of SiH_4 by diffusion from the concentration of the flowing source gas to zero concentration at the substrate. The ideal gas law was assumed to be valid in

the stagnant layer with a linear temperature drop. The thickness of the stagnant layer as a function of the gas velocity was determined experimentally and approximated analytically in the theory. The growth rate as a function of the position along the susceptor, as predicted by the theory, was experimentally verified. The angle of tilt of the susceptor needed to minimize the effect of depletion of SiH_4 in the source gas along the reactor was calculated and experimentally confirmed.

It is important to stress that the discussion in this paper is restricted to the CVD process in the diffusion-limited range. With decreasing susceptor temperature the chemical reaction kinetics increasingly control the deposition process. Van den Brekel (4) recently discussed the Nusselt number for mass transfer as the characteristic parameter separating the two regimes in $SiHCl_3$. Mehalso and Diefendorf (5) described in a similar way a system in which the reduction of BCl_3 was limited by HCl desorption.

In the plane geometry shown in Fig. 1 the molecular flux J_y across the stagnant layer follows from the equation of diffusion for a mixture of two gases of widely different concentrations

$$J_y = -\frac{D}{kT}\left(\frac{\partial p}{\partial y} + \alpha\frac{p}{T}\frac{\partial T}{\partial y}\right) \qquad [1]$$

Here the temperature T drops linearly across the stagnant layer of thickness δ from the high value T_s at the susceptor, $y = b$, to the low value T_m at the boundary of the stagnant layer, $y = b - \delta$, according to

$$T(y) = T_s - (T_s - T_m)\frac{b - y}{\delta} \qquad [2]$$

Experimentally the diffusion coefficient has been found to depend on temperature as T^ϵ, where $1.5 \leq \epsilon \leq 2$ corresponds theoretically to various models ranging from elastic spheres to Maxwellian molecules. For mathematical convenience the diffusion coefficient D is here assumed to depend on the temperature as

$$D = D_0\frac{T^2}{T_0^2} \qquad [3]$$

where D_0 is the diffusion coefficient at $T_0 = 300°K$. For the highly diluted SiH_4 the equation of state

$$p = n\,k\,T \qquad [4]$$

would be valid. The thermal diffusion factor α is discussed later. Equation [1] is slightly at variance with the expression used by Eversteyn *et al.* (3), who neglected the thermal gradient. The expression was used correctly by Bloem (6) for a similar problem.

The partial pressure, p, of the diffusing species not only depends on y, as described in Eq. [1], but also varies with the position x along the reactor. Therefore the equation of continuity should be satisfied anywhere in the turbulent layer

$$\frac{\partial J_x}{\partial x} + \frac{\partial J_y(x,y)}{\partial y} = 0 \qquad [5]$$

The above equations can be combined to yield the deposition rate $J_y(x)$, which decreases with x because of depletion due to the deposition reaction

$$J_y(x) = \frac{pD_0T^*}{kT_0^2\delta}\exp -\frac{D_0T^*x}{V_0T_0b\delta} \qquad [6]$$

where p and V_0 are the pressure and velocity of the SiH_4 at the entrance of the reactor and T^* is given by

$$T^* = \frac{\alpha(T_s - T_m)T_m^\alpha}{T_s^\alpha - T_m^\alpha}$$

It can easily be verified that with $\alpha = 1$ the pre-exponential and the exponential factors are smaller by a factor 2 than those found by Eversteyn *et al.* (3), who admitted that the value of D_0 was chosen smaller than suggested elsewhere (7). Effectively, they thus compensated for the neglected thermal gradient.

In principle the velocity, the thermal and the mass boundary layers which all result from horizontal flow in a free convective system as used in CVD, should be effectively describable by dimensionless numbers. This has not yet been done and is beyond the scope of this paper; the above equations will be used only to illustrate the essential requirements to be satisfied in isotope separation and to stress the difference from CVD-reactor optimization for deposition only.

Isotope separation due to diffusion and thermal diffusion.—In the absence of thermal diffusion, the relation of the molecular flux, J, to the partial pressure, p, of the diffusing species can be obtained by integration of Eq. [1], subject to Eq. [2], [3], and [4]

$$J = \frac{pD_0}{kT_0^2\delta}(T_s - T_m)\left(\ln\frac{T_s}{T_m}\right)^{-1} \qquad [6a]$$

In a binary mixture the diffusion coefficient D_{10} depends on the molecular masses M_1 and M_0 of the two components and on the cross-section S as (8)

$$D_{10} \sim \frac{1}{S}\left(\frac{M_0 + M_1}{M_0M_1}\right)^{1/2} \qquad [7]$$

The dependence of D_{10} on M_1 suggested by Shepherd (7) cannot be as $1/\sqrt{M_1}$, but should be due to S which increases with M_1. In agreement with experiments, D_{10} depends on the concentration ratio only to a second approximation in which also the effects of the nature of the intermolecular forces are included. In a mixture of two isotopes of molecular masses M_1 and M_2, diluted in a gas of molecular weight M_0, the two fluxes can be considered independent and therefore the flux of the lighter isotope J_1 exceeds the flux of the heavier isotope J_2 by a factor

$$\frac{J_1}{J_2} = \frac{D_{10}}{D_{20}}\frac{p_1}{p_2} \qquad [8]$$

Writing $\Delta M = M_2 - M_1$ and assuming $\Delta M << M$, where M is M_1 or M_2, the deposited material is enriched over the starting ratio p_1/p_2 by the separation factor γ_D

$$\gamma_D = \frac{D_{10}}{D_{20}} = \left(1 + \frac{\Delta M}{2M}\right)\left(1 - \frac{\Delta M}{2(M + M_0)}\right) \qquad [9]$$

In the determination of the dependence of γ_D on M_0/M, with $\Delta M/M$ as a parameter, it turned out that $\gamma_D^2 - 1$ depended almost linearly on $\Delta M/M$ over the relevant range between 0.1 and 0.01. Thus $(\gamma_D^2 - 1)/(\Delta M/M)$ has been plotted against M_0/M in Fig. 2.

It is evident from Eq. [6a] that always the lighter component is enriched, the effect varying from $\Delta M/2M$ for $M_0 >> M$ down to a very small value for $M_0 << M$. For example, SiH_4 diluted in H_2 with $M_0 = 2$, $M_1 = 32$, $M_2 = 33$, $M_3 = 34$, yields $\gamma_{12} = 1.00089$ and $\gamma_{13} = 1.0017$, whereas SiH_4 diluted in Ar with $M_0 = 40$ yields similarly $\gamma_{12} = 1.0086$ and $\gamma_{13} = 1.0167$. Mass diffusion of a lighter gas in a heavier gas has been described by

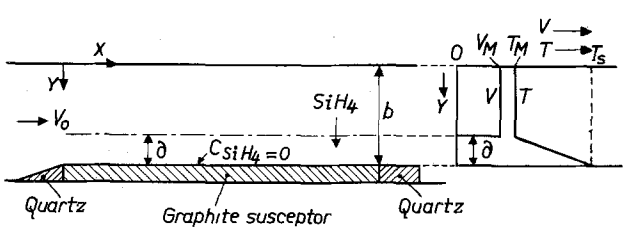


Fig. 1. Stagnant layer of thickness δ and convective layer of thickness b — δ above the horizontal susceptor. The velocity and temperature profiles are shown on the right-hand side.

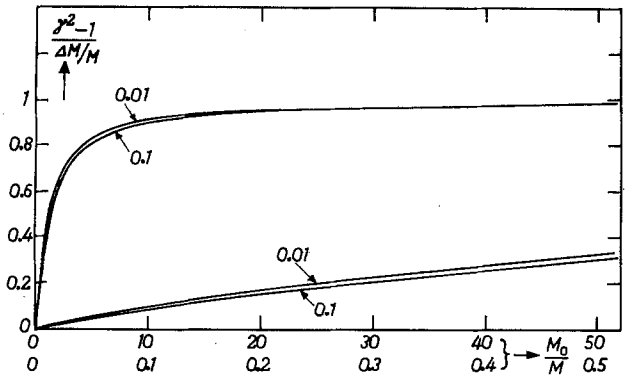


Fig. 2. The dependence of $(\gamma^2 - 1)$ normalized by $\Delta M/M$ as a function of M_0/M for two values of $\Delta M/M$, the lower expanded horizontal scale corresponding to the lower set of curves. Here, γ is γ_D defined in Eq. [2].

Benedict and Boas (9). Technically it is difficult to maintain a pressure difference across the diffusion screen, and though γ_D may be high under the more favorable circumstances of separation of isotopes of a lighter gas diluted in a heavy gas, the amount of separated material deposited decreases as the diffusion coefficient D_{10}, according to Eq. [7].

If thermal diffusion is not neglected, a similar reasoning can be followed with utilization of the result of integration of the full Eq. [1]

$$J = \frac{pD_0}{kT_0^2\delta} T^* \qquad [6b]$$

where T^* is defined in connection with Eq. [6].

The thermal diffusion factor α_{10} of a gas of molecular weight M_1 in a gas of molecular weight M_0 depends in a complex manner on the ratio of the concentrations, masses, and diameters of the molecules and the nature of their interaction (8). Assuming that the molecules are rigid elastic spheres it can be derived that for a diluted gas to a first order of approximation

$$\alpha_{10} = a\left(\frac{M_1}{M_0 + M_1}\right)^{1/2} \qquad [10]$$

where a is a factor of order unity.

Now the ratio of the two fluxes J_1 and J_2 is modified by the combined effects of mass and thermal diffusion to

$$\frac{J_1}{J_2} = \frac{p_1}{p_2} \frac{T^*(\alpha_{10})}{T^*(\alpha_{20})} \gamma_D \qquad [11]$$

Writing $\Delta\alpha = \alpha_{20} + \alpha_{10}$, and assuming $\Delta\alpha << \alpha$, where α is α_{10} or α_{20}, the solid deposited material is enriched over the starting ratio p_1/p_2 in the gas by the separation factor

$$\gamma = \gamma_D \cdot \gamma_T \qquad [12]$$

where γ_T, due to thermal diffusion, can be approximated by

$$\gamma_T = 1 - \Delta\alpha\left[\frac{1}{\alpha} + \frac{1}{1 - \left(\frac{T_m}{T_s}\right)^{\alpha}} \ln\frac{T_m}{T_s}\right] = 1 - c\Delta\alpha \qquad [12a]$$

The difference $\Delta\alpha$ of the thermal diffusion factors can be calculated from Eq. [9] and [10] to be positive and approximately equal to

$$\Delta\alpha = a\left(\frac{M_1}{M_0 + M_1}\right)^{1/2}\left(\frac{D_{10}}{D_{20}} - 1\right) \qquad [12b]$$

so that the deposited material is enriched by the separation factor

$$\gamma = \gamma_D\left[1 - ac\left(\frac{M_1}{M_0 + M_1}\right)^{1/2}(\gamma_D - 1)\right] \qquad [12c]$$

It turns out that, for the usual values of T_m/T_s between 0.3 and 0.5 and of α between 0.1 and 2, the value of c is negative and smaller than unity.

This result is as to be expected on physical grounds: both diffusion and thermal diffusion preferentially transport the lighter isotope to the heated susceptor. The effects of diffusion and thermal diffusion on the growth rate are of about equal importance, and the isotope separation factor turns out to be about equally due to both effects.

The final result Eq. [6] describes the combined effects of diffusion and of thermal diffusion in the reactor. This can be expressed formally, thus defining A and B by

$$J_y = \frac{pDT^*}{A} \exp - \frac{DT^*x}{B} \qquad [6c]$$

With the approximations used, the factor γ can be written as $1 + \Delta\gamma$ with $\Delta\gamma << 1$; hence the relative difference $\Delta J/J$ of the two normalized deposition rates J_1/p_1 and J_2/p_2 can be written as

$$\frac{\Delta J}{J} = \frac{J_1p_2}{J_2p_1} - 1 = \left[\gamma \exp - \frac{DT^*}{B} x\,\Delta\gamma\right] - 1 \qquad [13]$$

Because the exponent is much smaller than unity, this expression can be approximated as

$$\frac{\Delta J}{J} = \Delta\gamma\left(1 - \frac{DT^*}{B} x\right) \qquad [13a]$$

For small values of x the isotope concentration ratio in the deposited material, J_1/J_2, shows the maximum degree of enrichment attainable over the starting ratio p_1/p_2.

Whereas the total deposition rate, $J_1 + J_2$, drops exponentially with decay constant $\Lambda = B/T^*D$ due to depletion, the relative difference $\Delta J/J$ drops linearly, changing sign at a distance Λ. In the actual situation of many deposition processes, *e.g.*, in the case of silicon epitaxy, the characteristic length over which the source gas flux is depleted, is about 0.5m and cannot be varied strongly. Hence with a reactor length of about 1m the enrichment process not only decreases but actually changes sign as the depletion increases, slightly more for the lighter than for the heavier isotope. Only close to the entrance of the reactor is the enrichment process fully operative, over-all the separation process is fully nullified by compensation in the second stage.

The requirements for an ideal CVD reactor for isotope separation.—The strong dependence on position due to depletion substantiates the intuitive feeling that it is at least an order of magnitude easier to maintain a constant flux $J_1 + J_2$ than to maintain a constant isotope ratio J_1/J_2.

In the same way that the isotope separation process is more sensitive to depletion than the deposition process, so any deviation from complete mixing is more harmful to the isotope separation process. Incomplete mixing implies that for the material deposited at position x_0 an extra memory effect exists which originates in the material deposited at positions $x < x_0$. As shown in Eq. [6c] and [13a], this spoils the isotope separation process more than the deposition process. It can also be considered as an effectively smaller value of b, and hence of Λ, with a similar effect.

It is evident from the experimental results on silicon deposition (3) that the mixing due to turbulence is satisfactory to maintain the condition of uniform source gas concentration. If the condition of complete mixing did not hold, so that the lower strata did indeed show a higher depletion of SiH_4 than calculated, this would be manifested by a decrease of the deposition rate and a more pronounced effect of depletion toward the end of the tube. Diffusion of SiH_4 in such a weakly turbulent top layer toward the boundary of the stagnant layer would decrease this effect. The growth rate is

usually chosen to be about 0.6 μm/min, which means about 3 mm of gas is depleted per minute at the interface. The characteristic time for diffusion $\tau \approx b^2/D_0$ is so large that at the usual flow rates the gas has already been replaced several times over the reactor length in such a period. It has been calculated earlier that the mixing time is of the order of about 0.1 sec and probably less. Apparently this is fast enough to maintain the negligible temperature and concentration gradients actually observed. This does not imply that mixing is also intense enough to satisfy the isotope separation requirements.

Let us assume now that complete mixing takes place on a small enough time scale. The main conclusion from the preceding discussion is that the process in which the characteristic length for deposition is slightly shorter than the reactor length, is not ideal for isotope separation. The purpose of the normal CVD process is effective depletion of the source gas with a high growth rate, but the deposited product in isotope separation should comply as nearly as possible with the optimum combination of separation factor and growth rate. The silicon deposition rate can be made almost uniform along the reactor by tilting the susceptor (3). Physically the effect is due to an increase in the gas velocity and a decrease in the boundary layer thickness with increasing x, or a decrease of A and B in Eq. [6c] with increasing x. In the usual range for silicon epitaxy, A turns out to be dominant because $\Lambda \sim B$ is about 0.5m, *i.e.*, about the reactor length. In Eq. [13] the factor A drops out and, due only to B, the effect of tilting on isotope separation is negative. A positive effect could be reached by tilting the susceptor the other way, so that the free space above the susceptor would increase. Although then it would be easier to keep the isotope ratio constant, this effect is counteracted by a decreased over-all deposition rate and efficiency. The effects of tilting are shown schematically in Fig. 3.

In an ideal CVD reactor for isotope enrichment the following properties should be aimed at: (*i*) the mixing time should be short enough to enable the source gas to present a uniform concentration, (*ii*) the growth rate should be small with respect to the amount of source gas available per unit length and presented per unit time, and (*iii*) both the growth rate J and the separation factor γ should be maximized, so that separative power per unit surface area $J(\gamma - 1)^2$ will be maximum.

To sum up this section the proposed CVD system for isotope separation is contrasted to the conventional systems used for isotope separation based on gaseous, mass, or thermal diffusion. The method used for $^{235}UF_6/^{238}UF_6$ isotope separation is based on gaseous diffusion of UF_6 through a thin porous membrane under rarefied gas conditions, corresponding to $M_0 \to \infty$, with $D_{10} \sim 1/\sqrt{M_1}$. With the proposed CVD system the concentration drops over a very small length determined by the thermal boundary layer from a value corresponding to room temperature and about 1 atm to a negligible value, because gaseous material is converted to solid material. The enormous energy losses involved in the diffusion process, due to repeated compression and rarefaction of the gas, should be compared with the nonrecoverable part of the energy accumulated in the reaction products. Mass diffusion has not been widely applied because for the separation factor γ_D to be high, the molecular weight M_1 of the gas to be separated should be low, and the molecular weight of the separating agent M_0 should be high, whereas the concentration gradient and the flux are basically limited by the properties of the diffusing screen. Thermal diffusion has initially been widely used and is still in use for special purposes. Because it is based on the steady-state equilibrium between thermal and concentration gradients, in which only α_{12} is involved, it is an essentially slow process. In the proposed CVD method mass and thermal diffusion cooperate to transport a steady flux of material, slightly more of the lighter than of the heavier component, over very steep concentration and thermal gradients. This should compensate the effects of the modest separation factor which is small due to the properties of mass diffusion mentioned and because for the thermal effect only the difference of the thermal diffusion factors is involved. The separation factor can be enhanced by a higher concentration of the gas to be separated in a gas of higher molecular mass. This system should be analyzed using three dependent equations of diffusion coupling the three species instead of the two independent equations of the type of Eq. [1] used for the two isotopes. Also a more complex expression for α should be used, eventually dependent on y because the concentration ratio depends on y.

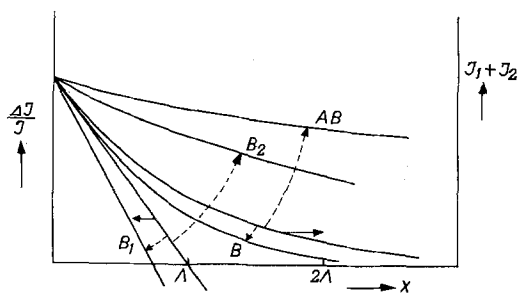


Fig. 3. The x dependence of the total rate of deposition $J_1 + J_2$, on the right-hand side, and of the relative difference $\Delta J/J$, on the left-hand side both schematically indicated. The effects of tilting upward due to the dependence $B(x)$ and due to the dependence of both $A(x)$ and $B(x)$, are shown in the curves labeled B and AB for the total current, and in the curve labeled B_1, for the relative difference, which is unaffected by $A(x)$. In the text it is made clear that downward tilting produces a more uniform relative difference $\Delta J/J$, shown in the curve labeled B_2.

It is shown in the next section that the requirements formulated above for a CVD reactor ideal for isotope separation can be fairly well satisfied if source material from a liquid source is used. Experimental results obtained with silicon in a conventional horizontal reactor have been found and will be reported elsewhere.

Description of the Liquid-Source CVD Process

An experimental reactor for CVD in which both the requirements of intense mixing and small depletion are combined has been described earlier (10), though the requirements for isotope separation were of no relevance then. A tantalum wire was mounted between two arms which also serve as electrical contacts to heat the wire. This assembly as a whole was made to rotate at high speeds (up to 6 m/sec) in an enclosure filled with gas which is pyrolyzed on the heated wire. In this way a carbon layer could be grown from CH_4. Due to the viscosity of the gas it finally rotated as a body with the wire. This undesired effect could be overcome by intense mixing of the gas or by using two arms one above another and rotating in opposite directions.

The experimental work with this arrangement gave rise to the idea (2) of using a liquid instead of a gas as a source material. A similarly heated horizontal wire, 3-5 cm long and 100 μm in diameter, is then surrounded automatically by a cylindrical gas-filled space. This thermal boundary layer plays the role of the stagnant layer in the preceding section. In the theory of heat transfer this phenomenon is known as film boiling (11-14); it is related to the Leidenfrost phenomenon giving rise to the spheroidal state (15).

In general, boiling is considered to be an effective means of heat transfer, the heat flux increasing linearly with the temperature at low temperature. At a critical temperature T_{c1}, however, the nucleate boiling mode changes to the film boiling mode characterized by a much smaller heat transfer coefficient because of the gas film separating the heated solid from the liquid. Between T_{c1} and a higher critical temperature, T_{c2}, the

heat flux density decreases with increasing temperature: the gas film fluctuates and is unstable. Beyond T_{c2} the heat flux increases again with the temperature because the gas film has become continuous and stable.

The dimensions of the layer are determined in a complex way by a number of parameters: a description of heat and mass transport is again beyond the scope of this paper. The pressure in the space is the sum of the partial pressures of evaporated liquid and gaseous reaction products which, of course, in the stationary state is equal to the applied hydrostatic pressure. The gas generated by evaporation at the gas-liquid interface diffuses, as described in the preceding section, to the wire where it is decomposed. The liquid is heated directly by radiation which is emitted by the heated wire and absorbed in a thin layer of liquid and secondly by heat conducted by the gas across the thermal boundary layer. The driving force of the evaporation is the difference between the actual partial pressure of the source gas at the interface and the pressure of the saturated gas at the temperature of the interface. The deposition rate is roughly proportional to the net evaporation rate. Clusters which may be formed in the gaseous layer under some experimental conditions are driven into the liquid by thermal diffusion. As shown in Fig. 4, the liquid is circulated and these particles are filtered out. Noncondensable reaction products leave the gas space as bubbles, of course also transporting part of the source gas. These are separated at the gas-liquid separator.

Film boiling has been the subject of much experimental and theoretical study, because of its crucial importance when the heat flux is the independent variable, as in nuclear reactors (14) and when cooling should be slow at high temperatures, as in actual quenching of metals. In the stationary state the heat flux density at the interface equals the mass of vapor generated per unit time and surface area times the latent heat of evaporation. However, in the film boiling mode as applied to CVD not only the latent heat of evaporation but also the energy of decomposition contribute to the heat transfer rate. Therefore it is much easier to achieve a stable boundary layer with CVD than with conventional film boiling only. In fact in the CVD reactor the unstable region between the two critical temperatures, mentioned above, appears to be absent. Therefore it is reasonable to assume that with increasing temperature the rate of decomposition increases so much that the decrease in heat flux due to the formation of an insulating film by coagulation of an increasing number of gas bubbles is fully compensated. The increased rate of heat transfer due to the accumulation of chemically recoverable energy is an important aspect of liquid-source CVD.

Up to now, carbon, silicon, and silicon carbide have been prepared by the liquid-phase deposition method.

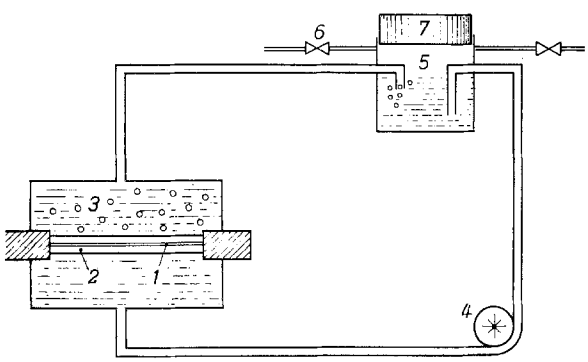


Fig. 4. The liquid-source CVD equipment schematically drawn. The heated wire, 1, is surrounded by a gas-filled cylinder, 2, in the liquid, 3. The liquid is circulated with a pump, 4, the gaseous reaction products and solid reaction products produced in the gas-filled space are separated in the separator, 5. The external pressure of the gas supplied at the inlet, 6, can be controlled with a pressure piston, 7, to influence the reaction rate.

For carbon and silicon carbide deposition, liquid hydrocarbons, such as toluene or dodecane and methylchlorosilanes ($(CH_3)_2SiCl_2$) were used as source materials. For silicon deposition from liquid $SiCl_4$ the reaction mechanism is more complicated, because $SiCl_4$ itself is thermodynamically stable at the temperature of the heated wire and therefore two reaction components, $SiCl_4$ and H_2, should be available at the wire. Gaseous hydrogen was kept under a pressure of as much as 100 atm above the liquid. From the results obtained it is evident that hydrogen transport through the liquid does not limit the growth rate. In all systems deposition rates up to, typically, several millimeters per minute could be obtained, roughly a factor of thousand greater than that of the gas source deposition systems. Increasing the hydrostatic pressure of the system leads in general to an increased deposition rate. With SiC a growth rate of 16 mm/min has been obtained with 100 atm hydrostatic pressure.

In the actual experimental arrangement the growth rate depended on the growth time, because the voltage across the wire was kept constant at about 30V. Hence the current increased due to increasing diameter, and so did the electrical power consumed and the temperature. On the other hand, the temperature tended to decrease because of the increasing area of the radiating surface from about 2900° to 2500°C. Reactions typically last up to 10 sec only. Hitherto no systematic study designed to correlate the various process parameters and physical and chemical properties has been undertaken. Therefore the experiments still show some irreproducibilities in the quantitative results.

In all experiments the energy expenditure turned out to be between 5 and 10 eV per deposited C atom. This energy is partly recoverable when the material is recycled, the total efficiency of the system being of course dependent on the temperatures of decomposition and recomposition. It is interesting to note that because only heating is required, the energy introduced into the system does not need to be electrical. Per carbon atom, the evaporation energy is negligible compared to the decomposition energy.

In sum, the experiments show that CVD from pressurized liquid-source material is a versatile and reliable method to transport rapidly without any loss of material, a certain element from one condensed phase to another. It is also a highly efficient method of transporting heat from a solid, the heat being available partly in the heated vapor, but for the greater part in the high temperature reaction products.

Next, some experimental results of isotope separation with liquid-source CVD and some theoretical considerations are presented.

Some Experimental Results and Their Consequences

Three experiments were set up with the liquid-source equipment described in the preceding section. On a tantalum wire, 100 μm across, carbon was deposited from $C_{12}H_{26}$, known as Shell-Sol T. The layers were grown very fast, at about 1 mm/min, but under not exactly reproducible conditions, as indicated in the preceding section. The three samples as well as the liquid were mass analyzed and the $^{12}C/^{13}C$ ratios were compared.

Because the ratio $^{12}C/^{13}C$ normally amounts to about 98.89/1.11, most of the $C_{12}H_{26}$ molecules will consist of only ^{12}C atoms, 13% will contain only one ^{13}C atom, and the number of those with more ^{13}C atoms can be considered negligible. Therefore, on the assumption that $C_{12}H_{26}$ is the species diffusing in hydrogen, the separation factor γ is a function of the molecular weights $M_0 = 2$, $M_1 = 170$, $M_2 = 171$ and the parameter $\Delta M/2M = 0.003$.

Two samples were deposited in two separate experiments and subsequently mass analyzed by Mook (16). The $^{12}C/^{13}C$ ratios of the starting liquid and of the two samples were determined several times with a reproducibility of $\pm$ 0.05% and the enrichment of ^{12}C in

the deposited material was found to be 0.65% in the first and 0.8% in the second experiment. A third sample deposited in a third experiment and its starting liquid were similarly mass analyzed elsewhere by de Bièvre (17). The enrichment of ^{12}C in the deposited material was found to be $0.33 \pm 0.1\%$.

It is evident that though the experimental conditions prevailing in the thermal boundary layer of the liquid-source equipment are quantitatively different from the experimental conditions in the stagnant layer of a horizontal epitaxial reactor, mainly because of the latent heat of evaporation and the cylindrical geometry, in the transport and deposition processes essentially the same mechanisms are operating.

As it has been remarked before, the description in terms of two independent equations of diffusion and a simple expression for α is not adequate for a system in which the gas cannot be considered as diluted everywhere. A more realistic description could yield a higher separation factor but is beyond the scope of this paper. The experimental results suggest that the proposed isotope separation mechanism may be operative, but also that other mass-dependent processes can be invoked to account for the high separation factor. A number of effects related specifically to this mode of heat transfer are discussed below.

Probably quite important are a number of effects related to evaporation. The evaporation rate below the boiling temperature depends on the mass as $1/\sqrt{M_1}$, and this effect would yield an enrichment of about 0.3%. As stated before, the liquid-to-gas interface across which the evaporation takes place can be far below the boiling temperature. Secondly, the hydrogen released upon pyrolysis leaves the gas-filled space with heavy perturbation of the interface. The processes taking place at a gas-to-liquid interface when gas bubbles are crossing the interface in either direction are spectacular. These phenomena are at present being studied more actively since they are related directly to the environmental effects of the sea (18). A gas bubble on crossing the interface generates a strong deviation from the original surface, which is restored by surface tension. Due to inertial forces the surface generates a jet in which accelerations of up to $10^4 g$ can be reached. Effectively, the bubbles and drops giving rise to accelerated jets may be considered as micro-ultracentrifuges with which fractionation effects can be explained both in seawater and at the heated gas-to-liquid interface. Similar effects are described in Zuber's theory of film boiling (13) where he states that "at high evaporation rates the vapor release appears like small jets." The instability at the gas-to-liquid interface is known as Taylor instability (19), which has been demonstrated experimentally by Lewis (20). The relation to surface tension and viscosity in the development of Taylor instability has been studied by Bellman and Pennington (21).

It is evident that electrical effects must play a role: any excess of lighter ions in conducting liquids should be electrically compensated to reduce the charge of the drop. Drops are known to bear a charge: the splitting off of many fine, negatively charged drops from a big drop of water, which is left positively charged, forms the basis of the theory of the formation of thunderstorms. As demonstrated recently by Kim and Turnbull (22) with drops of freon, also nonconducting liquids can be influenced electrically, surface charge contributing to the conventional surface energy. Not only the formation of drops but also the generation of jets at the gas-to-liquid interface, should be influenced by a d-c field, the basic mechanisms being related (13). A pronounced effect was found indeed in the liquid-source carbon deposition rate when a high d-c field was applied between the heated wire and an electrode outside the CVD reactor, independent of sign of the voltage, as the theory predicts. The authors believe that also the isotope separation factor is affected favorably. From these experiments can be concluded to which extent the isotope enrichment actually found is due to micro-ultracentrifuge effects. It is evident also that with an a-c voltage layers of varying isotope separation can be grown which could have interesting applications. If these effects are studied as a function of frequency the time scales and hence the nature of the processes involved can be analyzed.

Finally the effects of the cylindrical geometry, giving rise to flux crowding near the hot wire, could be of importance.

To sum up, we feel that the enrichment shown in carbon separation may be the result of a number of weighted effects, each of which can give rise to fractionation. The factors discussed are mass diffusion, thermal diffusion, evaporation, spray fractionation, and geometry effects. For a better understanding each of these factors would warrant a more detailed study so that the effect of fractionation in terms of growth rate and separation factor might be optimized.

Possible Applications in the Field of Uranium Isotope Enrichment

In the preceding sections a model for isotope separation with CVD has been elaborated and the equations and ensuing efficiency requirements have been derived. Also some feasible operating arrangements and some experimental results have been discussed. One might, of course, speculate on the possibility of practical application of CVD, perhaps even as an industrial process, to uranium isotope enrichment. Though the well-established technique of diffusion of a rarefied gas through a porous membrane is dominating the scene, with the ultracentrifuge and the gas nozzle techniques as second bests, mass diffusion, thermal diffusion, chemical exchange, distillation, and various other techniques based on physico-chemical transport mechanisms have in the past been studied and used.

The alternative diffusion method based on CVD described in this paper has the advantage of a high partial pressure difference across a short length with a limited source in the gaseous process and a virtually unlimited source in the liquid process, hence a high through-put. Though the process is thought to be based on mass and thermal diffusion, other processes such as evaporation, micro-ultracentrifuge effects, and geometry effects all make integrated contributions by the very nature of the process. The relative importance of these five effects is not known and difficult to assess without much more detailed study.

It is interesting to speculate on the reactions which in this system could be used for uranium enrichment. Uranium hexafluoride is used almost universally because it can be easily volatilized and because fluorine has only one isotope. Therefore it is very well suited to serve as a starting liquid in the CVD process as well.

Thermodynamic calculations, based on data compiled by Barin and Knacke (23), show that UF_6 reacts with hydrogen over a wide temperature range. The reaction products should be solid UF_3, solid or liquid UF_4 (mp 1309°K), solid or liquid UF_5 (mp 621°K), and gaseous HF with the following values of the reaction constant K

$$UF_6 + 3/2\ H_2 \rightarrow \langle UF_3 \rangle_{sol} + 3HF;$$

$$\log K\ (300°\text{-}1000°K) = \frac{8571}{T} + 4.43$$

$$UF_6 + H_2 \rightarrow \langle UF_4 \rangle_{sol} + 2HF;$$

$$\log K\ (300°\text{-}1000°K) = \frac{15644}{T} - 0.146$$

$$UF_6 + \tfrac{1}{2}\ H_2 \rightarrow \langle UF_5 \rangle_{sol} + HF;$$

$$\log K\ (300°\text{-mp°K}) = \frac{10072}{T} - 3.502$$

$$UF_6 + \tfrac{1}{2}\ H_2 \rightarrow \langle UF_5 \rangle_{liq} + HF;$$

$$\log K\ (\text{mp-}900°K) = \frac{7979}{T} - 0.15$$

It is reasonable to assume that these reduction processes are kinetically blocked at low temperatures, as they are in the system WF_6/H_2. The reduction to metallic uranium is thermodynamically impossible in the relevant temperature range

$$UF_6 + 3H_2 \rightarrow \langle U \rangle_{sol} + 6HF;$$

$$\log K\ (300°\text{-}1200°K) = -\frac{26479}{T} - 15.97$$

Deposition of one of the above-mentioned liquid or solid uranium fluorides is thermodynamically possible when a substrate mounted inside liquid UF_6 under a controlled H_2 pressure is heated. If the deposition parameters can be chosen such that the ^{235}U enriched deposited uranium fluoride is in the liquid state, the process can be made to work continuously until the liquid source has reached the critical isotope ratio where further depletion becomes uneconomical. In case the deposition parameters cannot be chosen so favorably as to form a liquid reaction product, the solid deposited reaction product should be removed from the reactor at that critical stage. This removal can be conceived of as a continuous process also. The transformation of UF_3, UF_4, and UF_5 with HF into UF_6 does not present any technical problem and the product is then available for iteration of the enrichment cycle, up to the desired isotope ratio. At this stage, part of the chemically accumulated energy is recovered and used for heating of the substrate. The efficiency of the process depends on the operation temperatures, which should be determined experimentally.

A quite different application of these reactions would be to use CVD as a collector mechanism for selectively laser-excited ^{235}U compounds. In the mechanism, as described vaguely (1), a gas containing molecules of both uranium isotopes is irradiated with laser light of a sufficiently small bandwidth that only ^{235}U containing molecules are excited. These excited molecules are subsequently ionized by incident light of a not so critical wavelength and collected. The ionization should have taken place before the molecule could have lost the excitation energy by collisions and the molecule should be removed sufficiently fast out of the exciting beam to avoid depletion of the gas. It is well known that the chemical reaction velocity can be increased by exciting one of the reaction components. By irradiating the substrate with narrow-band laser light which excites the ^{235}U compound only, the heterogeneous decomposition reaction velocity for this compound is increased above the deposition velocity of the ^{238}U compound. In this way CVD serves as a selective and almost instantaneous collector mechanism for the ^{235}U compound.

Manuscript submitted April 13, 1976; revised manuscript received Aug. 23, 1976.

Any discussion of this paper will appear in a Discussion Section to be published in the December 1977 JOURNAL. All discussions for the December 1977 Discussion Section should be submitted by Aug. 1, 1977.

Publication costs of this article were assisted by Philips Research Laboratories.

REFERENCES

1. Proceedings of the International Conference on Uranium Isotope Separation, London, March 5-7, 1975.
2. B. Lersmacher, H. Lydtin, and R. Wilden, Offenlegungsschrift 2,029,982 (1971).
3. F. C. Eversteyn, P. J. Severin, C. H. van den Brekel, and H. L. Peek, *This Journal*, **117**, 925 (1970); F. C. Eversteyn and H. L. Peek, *Philips Res. Rep.*, **25**, 472 (1970); F. C. Eversteyn, *ibid.*, **29**, 45 (1974).
4. C. H. J. van den Brekel, Abstract 164, p. 431, The Electrochemical Society Extended Abstracts, Fall Meeting, Dallas, Texas, Oct. 5-9, 1975.
5. R. Mehalso and R. J. Diefendorf, in "Chemical Vapor Deposition, Fifth International Conference," J. M. Blocher, Jr., H. E. Hintermann, and L. H. Hall, Editors, p. 84, The Electrochemical Society Softbound Symposium Series, Princeton (1975).
6. J. Bloem, *This Journal*, **117**, 1397 (1970).
7. W. H. Shepherd, *ibid.*, **112**, 988 (1965).
8. S. Chapman and T. G. Cowling, "The Mathematical Theory of Non-Uniform Gases," Cambridge University Press, New York (1970).
9. M. Benedict and A. Boas, *Chem. Eng. Prog.*, **47**, 51, 111 (1951).
10. H. Lydtin, in "Chemical Vapor Deposition, Second International Conference, J. M. Blocher, Jr. and J. C. Withers, Editors, p. 71, The Electrochemical Society Softbound Symposium Series, New York (1970).
11. W. H. McAdams, J. N. Addoms, P. M. Rinaldo, and R. S. Day, *Chem. Eng. Prog.*, **44**, 639 (1948).
12. L. A. Bromley, *ibid.*, **46**, 221 (1950).
13. N. Zuber, *Trans. ASME*, **80**, 711 (1958).
14. "Problems of Heat Transfer and Hydraulics of Two-phase Media, Symposium," S. S. Kutateladze, Editor, Pergamon Press (1969).
15. J. Kistenmaker, *Physica*, **29**, 96 (1963).
16. W. G. Mook, Laboratorium voor Algemene Natuurkunde, Rijksuniversiteit Groningen, Netherlands.
17. P. de Bièvre, Central Bureau for Nuclear Measurements, Geel, Belgium.
18. F. MacIntyre, *Sci. Am.*, (May 1974) 62; M. Komabayasi, *J. Met. Soc. Jpn.*, **42**, 309 (1964).
19. G. Taylor, *Proc. R. Soc. London, Ser. A*, **201**, 192 (1950).
20. D. J. Lewis, *ibid.*, **202**, 81 (1950).
21. R. Bellman and R. H. Pennington, *Quart. Appl. Math.*, **12**, 151 (1954).
22. K. Kim and R. J. Turnbull, *J. Appl. Phys.*, **47**, 1964 (1976).
23. J. Barin and O. Knacke, "Thermodynamic Properties of Inorganic Substances," Springer, Berlin (1973).

The Reduction of Photoresist Stripping Rates in an Oxygen Plasma by By-product Inhibition and Thermal Mass

James F. Battey

International Plasma Corporation, Hayward, California 94544

ABSTRACT

It has been observed that the photoresist stripping rate in an oxygen plasma is slower for a full load of silcon wafers than it is for the center wafer of a three-wafer array. For molecular oxygen flow rates of 500 cm^3/min corresponding to reactor residence times of approximately 5 sec and substrate temperatures from 120° to 200°C, it is shown that 200 cm^3/min of carbon monoxide or 15 cm^3/min of water vapor reduces the atomic oxygen flow from about 33 cm^3/min to about 15 cm^3/min and reduces the stripping rate also by about a factor of two. If water vapor is added to a mixture of molecular oxygen and 200 cm^3/min of carbon monoxide or if carbon monoxide is added to a mixture of molecular oxygen and 15 cm^3/min of water vapor, the atomic oxygen concentration is not appreciably changed. However, the photoresist stripping rates are reduced by a factor of 1.5-2.0. A model is proposed which explains some aspects of the results, and it is shown that the difference in strip times between the full boat and three-wafer array is in most current instances a thermal effect.

The surface chemistry in the planar processing of silicon semiconductor wafers is being done with increasing frequency by gas plasmas excited by rf energy, rather than by liquid reagents. The oldest of the semiconductor plasma applications is the stripping of photoresist from silicon wafers with an oxygen plasma, as reported by Irving (1) and Bersin (2).

It is observed that under otherwise identical conditions an array of 50 2-in. diameter silicon wafers on 3/16-in. spacing will take several times as long to strip as the interior wafer of a three-wafer array spaced 3/16 in. apart. It is known that the reaction rate increases with temperature, and part of the disparity is due to the greater thermal mass of the 50-wafer array.

Another cause for reduced reaction rates is the by-products of the reaction inhibiting the reaction. This work was undertaken to find the conditions under which the most probable by-products of the stripping reaction inhibit the reaction, and the conditions under which stripping is delayed by thermal mass.

Experimental Arrangement

The experimental work was done in an 8-in. diameter cylindrical quartz reactor 13 in. in length. A schematic of the apparatus is shown in Fig. 1. The back of the reactor is a spherical sectioned quartz dome, and the front is a flat quartz door. The gas is introduced into the reactor through a quartz manifold on the bottom of the reactor and parallel to its axis. The gas is exhausted by a forepump from the reactor through a quartz manifold on the top of the reactor and parallel to the reactor axis. The plasma is excited by a rf generator operating at 13.56 Hz and coupled into the plasma through a 50Ω cable, a π impedance-matching network, and two half-cylinder metal electrodes placed around the outside walls of the cylindrical reactor. The top electrode is at electrical ground, and the bottom electrode oscillates between positive and negative voltage with the generator.

Key words: atomic oxygen, catalytic reaction, CO and H_2O by-products.

The exhaust manifold is sufficiently large that the pressure drops in it are negligible, and the pressure in the reactor is measured with a Hastings VT4 vacuum gauge in a quartz tube leading out of the exhaust manifold. A metered flow of molecular oxygen is fed into the reactor from a cylinder of 99.6% minimum-purity oxygen at high pressure through a regulator which reduces the pressure to approximately

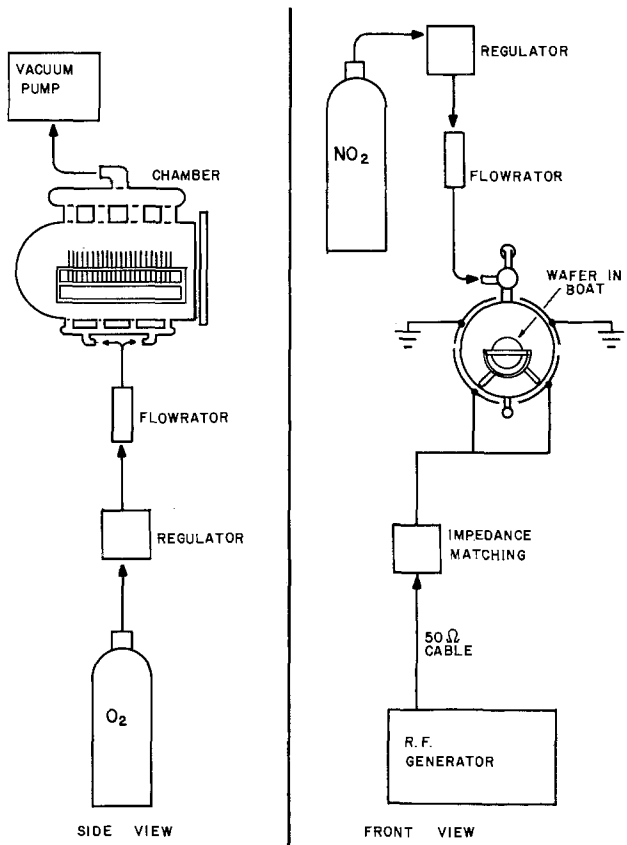


Figure 1.

1 atm, and through a flowmeter, which is connected to the inlet manifold. All gases used were obtained from Matheson. The rf power in the reactor converts some of the molecular oxygen to atomic oxygen (3), and the flow of atomic oxygen in the exhaust can be measured by titrating it (4) with a flow of NO_2 which is introduced into the quartz tube that extends out of the exhaust manifold. The NO_2 was the vapors from 99.5% minimum-purity liquid.

To get reproducible stripping times it was found necessary to put the single wafer on a large aluminum block which had a thermometer inserted in a hole in the block, and to place the block in the same position in the reactor. It was also found necessary to place two thermometers on the external walls of the reactor and require all three thermometers to assume the same temperatures as in a prior experiment.

An additional requirement for reproducibility of strip times is that the internal walls of the quartz reactor, the door, the inlet and exhaust manifolds, the aluminum block and its quartz support structure be "clean." The sole criteria for cleanliness was the ability to reproduce a given minimum stripping time within a few percent under a set of standard conditions. The method of cleaning used was fire polishing with a glassblower's torch and acid etching. Quartz and aluminum oxide presumably have a lower surface recombination rate for atomic oxygen when they are "clean."

The experiments were run with 2-in. diam silicon wafers, covered with 2.0 mg of Waycoat viscosity 40 photoresist spun on with a Headway spinner at 2900 rpm for 20 sec, and then baked for 30 min at 120°C in air.

A Proposed Reaction Rate Model

It has been shown by Abe (5) that photoresist is removed linearly with time from which he concludes that the removal reaction occurs at the surface of the photoresist. Thus, it seems reasonable to treat the photoresist stripping or plasma etching as a three-stage process comprised of the adsorption of an oxygen atom, the reaction of the oxygen with the photoresist to form a simple volatile compound, and the desorption of the compound. Using the notation of catalytic kinetics (6)

$$A_R + X_1 \underset{K_{-1}}{\overset{K_1}{\rightleftarrows}} X_2 \underset{K_{-2}}{\overset{K_2}{\rightleftarrows}} X_3 \underset{K_{-3}}{\overset{K_3}{\rightleftarrows}} A_p + X_1$$

The atomic oxygen, A_R, adsorbs on the site, X_1, to form the adsorbed complex X_2, which reacts to produce the adsorbed product, X_3, which desorbs to give the product, A_p, and regenerates the site to X_1 status. Since photoresist is primarily comprised of CH_2 groups, the principal products might be CO and H_2O. This requires the cooperative action of only a few atoms. If it is assumed that the total number of sites $X_0 = X_1 + X_2 + X_3$ is conserved, and the time rate of change of X_1, X_2, and X_3 is equated to zero in the steady state, an expression for the reaction rate, $R_s = K_2X_2 - K_{-2}X_3$, is obtained. If it is assumed that the reverse reaction rate $K_{-2}X_3$ is small compared to the forward reaction rate, K_2X_2, this reduces to $R_s = K_2X_2$. If it is further assumed that the reaction is the rate-limiting process, and the adsorption and desorption processes are essentially at equilibrium, then $K_1C_RX_1 = K_{-1}X_2$ and $K_3X_3 = K_{-3}C_pX_1$, where C_R is the concentration of reactant and C_p the concentration of the reaction product.

These equalities substituted in the statement of the conservation of site give

$$X_2 = \frac{X_0\left(\frac{K_1}{K_{-1}}\right)C_R}{1+\left(\frac{K_1}{K_{-1}}\right)C_R\left(\frac{K_{-3}}{K_3}\right)C_p} \equiv X_0\left[\frac{K_RC_R}{1+K_RC_R+K_pC_p}\right]$$

and

$$R_S = K_2X_0\left[\frac{K_RC_R}{1+K_RC_R+K_pC_p}\right]^1$$

where K_R and K_p are the equilibrium constants for adsorption of the reactant (atomic oxygen) and product (carbon monoxide and water), respectively. This is the Langmuir-Hinshelwood equation. The K_pC_p term in the denominator of the reaction rate indicates that the products of the reaction can cover the reaction sites and make them unavailable for further reactions. If observations are made in a region of reactant concentrations where the stripping rates are proportional to C_R in the absence of any C_p, then in this region of reactant concentration $K_RC_R << 1$ for any C_p, and the Langmuir-Hinshelwood equation reduces to

$$R_S = K_2X_0\left[\frac{K_RC_R}{1+K_pC_p}\right]$$

If C_p is below some critical values, R_s should be proportional to C_R. Above this value it should be proportional to C_R/C_p.

Strip Rates as a Function of Carbon Monoxide Concentration

Evidence that chemical equilibria exist in a plasma, and that chemical concentrations can be shifted to favor greater or lesser amounts of product formation has been discussed by Blaustein and Fu (7) and by Manes (8). The former authors studied H_2 + CO and H_2 + CO_2 systems with water as a varied additive. Product concentration shifts were found to be consistent with the predictions of Le Chatelier's principle. The latter author showed that statistical mechanics predicted a mass-action law for chemical reactions in a plasma if it is assumed that each degree of freedom of each specie involved in the reaction is in equilibrium. Thus, it was decided to see if the more probable by-products of the reaction would inhibit the reaction.

At constant power and oxygen flow, strip rates were measured on a single wafer as a function of the flow rates of 99.0% minimum-purity CO which was introduced along with the O_2. After the wafer was stripped, the atomic oxygen flow was measured. It is assumed that C_R is proportional to the atomic oxygen flow, and C_p is proportional to the CO flow.

Flow rates are all stated at 1 atm and room temperature. For a flow rate of 500 cm^3/min of molecular oxygen, the light from the titration could not be observed for flow rates of CO in excess of 200 cm^3/min. Hence, the measurements were not made at higher flow rates. Difficulty was experienced in finding a flow rate gauge which would give reproducible measurements of the flow rate of NO_2 over a number of hours' time. Apparently, the NO_2 attacks the gauges. Consequently, gauges were not used for this measurement. Instead, all the gas flows were shut off except the NO_2, which was temporarily suspended with a solenoid valve, while the system was pumped to a low pressure. The NO_2 was then turned back on and the pump was shut off. The time it took the NO_2 flow

[1] It no assumptions are made as to the relative reaction rates, R_s is of the form $X_0\left[\frac{Q_1C_R + Q_2C_p}{1 + Q_3C_R + Q_4C_p}\right]$, where the Q's are complicated algebraic functions of the K's.

rate to raise the pressure in the reactor from 0.2 to 0.7 Torr was then measured with a stopwatch. Since the volume of the reactor is known, the NO_2 flow rate can be calculated.[2] The time required to make the pressure change with a known flow rate was also measured.

After running for the order of an hour with O_2, CO, and NO_2 in a plasma, the time to strip a wafer at 165°C with 100W and 500 cm³/min of O_2 (and no other gases present) became appreciably longer, and traces of a brownish yellow deposit were visible on parts of the reactor and the aluminum block. Combustion analysis showed the presence of hydrogen, carbon, and smaller amounts of nitrogen in the deposit. Presumably oxygen was present also. It was then necessary to acid etch and fire polish the equipment before measurement at standard conditions could be reproduced and data taken.

Strip time and atomic oxygen concentration were measured as a function of carbon monoxide flow in a range from zero to 200 cm³/min in the presence of a background flow of 500 cm³/min of molecular oxygen at five temperatures. Increasing carbon monoxide concentration monotonically decreases strip rates and atomic oxygen concentration; however, plots of strip rate *vs.* atomic oxygen flow rate as shown in Fig. 2 are linear, suggesting that the way in which the carbon monoxide is inhibiting the reaction is by reducing the atomic oxygen concentration. The strip time with no carbon monoxide agrees with other data; however, the slope of strip time *vs.* fill time is about one when the atomic oxygen concentration is varied with molecular oxygen pressure and is about one-half when the atomic oxygen concentration is varied with carbon monoxide. It is as if the presence of the carbon monoxide makes the residual atomic oxygen more effective in stripping. A carbon monoxide plasma itself will strip, but at a rate which is about twenty times slower than an oxygen plasma. Thus, the disparity in slopes is not understood.

The amount of CO required to increase the strip time by a factor of two is larger than the amount of atomic oxygen available with no CO present. The proposed model required two atomic oxygen atoms to be consumed for the creation of each CO molecule when stripping without introducing any CO. Thus, it is improbable that the CO alone created when stripping a boatload of wafers is responsible for the fact that this operation takes several times as long as the stripping of the interior wafer of a three-wafer array. This is particularly clear when consideration is given to the fact that most of the atomic oxygen flows from where it is generated to the exhaust of the reactor without ever diffusing between the wafers and reacting with the photoresist. In the body of the reactor the CO concentration must be considerably smaller than the atomic oxygen concentration.

Stripping time of a single wafer in the presence of CO_2 instead of CO under the same conditions of temperature, power, pressure, and gas flow is not significantly different, within the reproducibility of the data. An explanation for this would be the reaction $CO_2 \rightarrow CO + O$ going essentially to completion, which would give the same concentration of carbon monoxide and atomic oxygen as with the CO plasma, once the atomic oxygen adjusted to steady state. There should be a little less atomic oxygen in the CO_2 plasma, because the amount of atomic oxygen decreases as the pressure of molecular oxygen increases above 1.0 Torr.

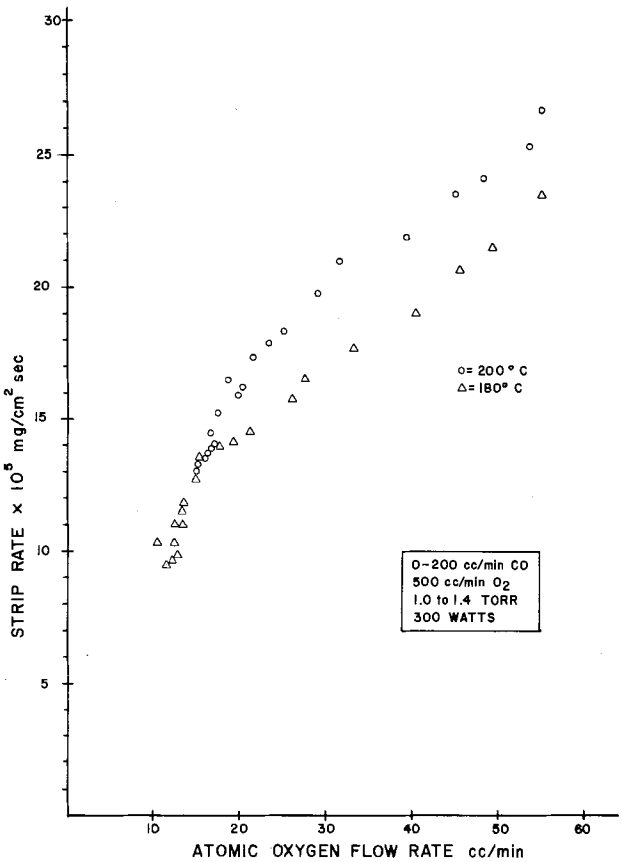


Fig. 2. Strip rate in an oxygen plasma in the presence of carbon monoxide. Increasing carbon monoxide flow rates decreases atomic oxygen flow rates and strip rates.

Strip Rate as a Function of Water Vapor Concentration

The reactor was then fed with two incoming oxygen lines, one of which was drawn through a water bubbler. A total flow rate of 500 cm³/min was maintained, and the water vapor flow rate was varied between zero and about 15 cm³/min by varying the flow of oxygen that went through the bubbler and the flow that did not. The strip times and titration fill times were then measured as a function of H_2O concentration at various temperatures.

Increasing concentrations of water vapor decreased the strip rates and atomic oxygen concentration. Measurements were made at five temperatures. Again, plots of strip rate *vs.* atomic oxygen flow, as shown in Fig. 3, show a linear relationship, suggesting that the way the water vapor inhibits the stripping reaction is by reducing the atomic oxygen concentration. The strip time with no water vapor present agrees with other data, and the slope of strip rate *vs.* atomic oxygen flow is about the same as it is when the atomic oxygen concentration is varied by varying the molecular oxygen pressure. In a number of instances it appears that the initial slope is steeper than the subsequent slope when small amounts of water vapor are being introduced. It is as if the initial amount of water vapor was more effective in slowing the reaction than subsequent amounts. The strip times are essentially doubled at 120°, 140°, and 160°C by the addition of

[2] In mixing the CO and O_2, it was necessary to have a known concentration and consequently pressure of each of the two gases in the reactor. However, if a mass flow rate is first established for one gas, the pressure measured, the first gas turned off, a similar procedure followed for the second gas alone, and then both gases turned on, the resulting total pressure in the reactor is not the sum of the pressures of the two gases taken alone. The mass flow of each gas through the pump must equal the mass flow through the flow rate gauges. Thus, the pressure of each gas at the pump must remain the same, whether they are on individually or together. However, the viscous mass flow through the hose requires that there be a certain difference in the square of the pressure at the ends of the hose. The procedure followed was to set with a flowrator the flow rate of the oxygen coming from the tank to be 500 cm³/min. The flow rate of the CO with no oxygen flowing was then set with a second flowrator to be some desired fraction of the oxygen flow. A large valve between the reactor and the hose was then adjusted so that the total pressure was the sum of the two individual pressures and the flows are in the reported ratios, although the exact values are not known. The effect was only appreciable at the higher CO flow rates.

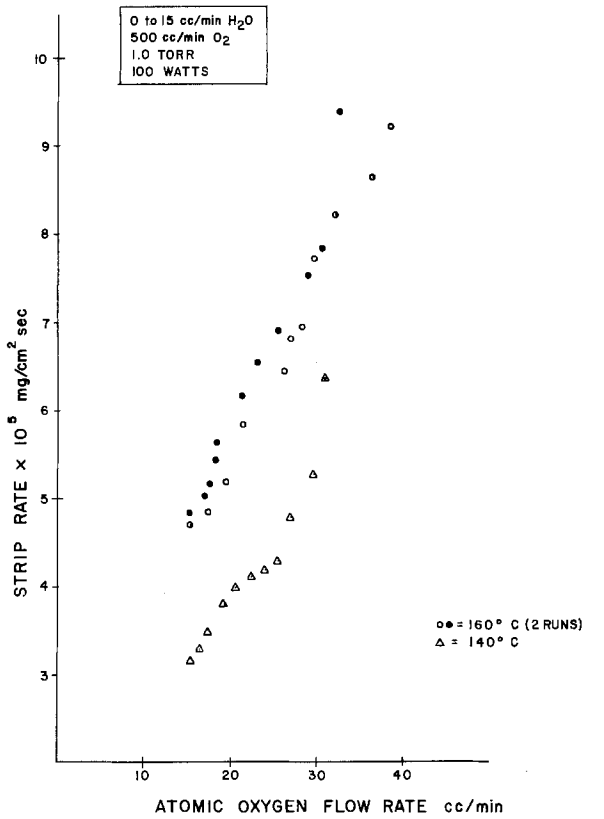


Fig. 3. Strip rate in an oxygen plasma in the presence of water vapor. Increasing water vapor flow rates decreases atomic oxygen flow rates and strip rates.

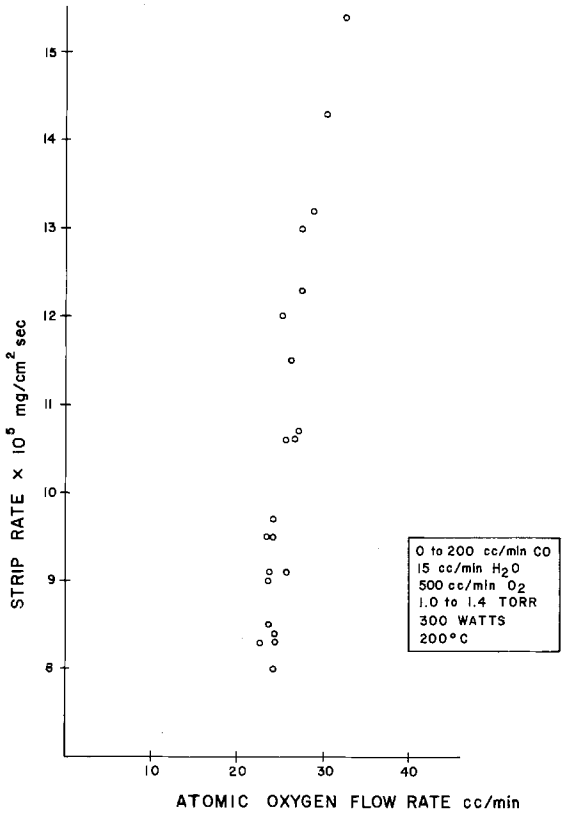


Fig. 4. Strip rate in an oxygen and water vapor plasma in the presence of carbon monoxide. Increasing carbon monoxide flow rates decreases strip rates but has little effect on atomic oxygen flow rates.

15 cm^3/min of water vapor flow. The change seems to be somewhat less at 180° and 200°C.

Extrapolation of the present data suggests that at 1.0 Torr and 300W, the flow of atomic oxygen out the exhaust would be about 75 cm^3/min with no load. It seems unlikely that 15 cm^3/min got converted to H_2O in the stripping reaction, even when it is considered that the atomic oxygen flow in the exhaust where the titration was performed may be smaller than the flow in the chamber due to wall and bulk recombination in the exhaust manifold.

If it is assumed that the principal products of the stripping reaction are CO and H_2O, then these should be generated in more or less equal quantities. Since the inhibiting effect of a given amount of water vapor is much greater than the same amount of carbon monoxide, the water vapor alone would inhibit the stripping first.

A flow of argon in the absence of any CO was added to the molecular oxygen flow in quantities equal to the flow of CO which had been used. The effects are small compared to comparable amounts of CO and can be explained by a reduction in the amount of atomic oxygen, due to the increased pressure.

Strip Rates as a Function of Carbon Monoxide Concentration in the Presence of Water Vapor

All 500 cm^3/min of incoming molecular oxygen was then run through the water bubbler, and CO was introduced in amounts up to 200 cm^3/min. Data were taken at five temperatures. The results were surprising. The CO did not markedly change the flow of NO_2 required to titrate the atomic oxygen. On the other hand, the stripping times were approximately doubled, as can be seen in Fig. 4. The strip time is approximately linear in the flow rate of CO, as shown in Fig. 5. However, the initial slope is steeper, and this effect is more pronounced at 120° and 140° than at 180° and 200°C. The abscissa is plotted as proportional

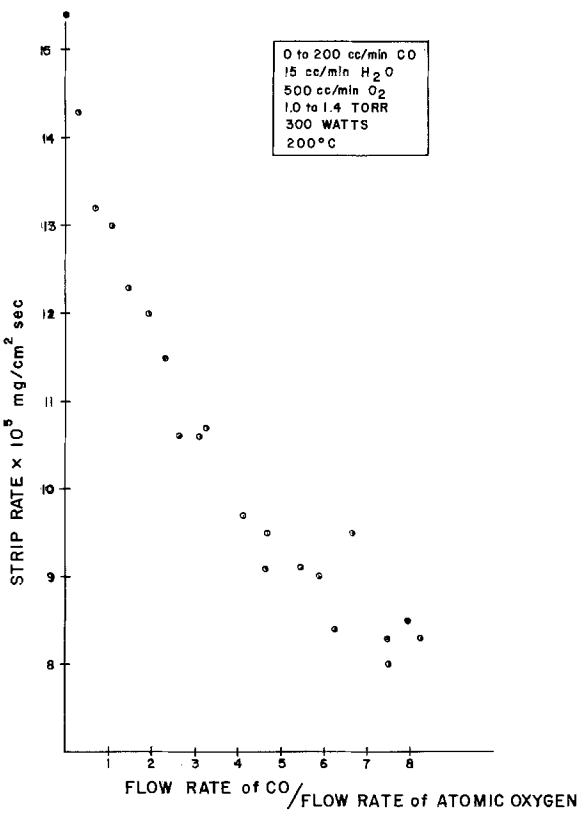


Fig. 5. Strip rate in an oxygen and water vapor plasma as a function of the flow rate of carbon monoxide divided by the flow rate of atomic oxygen.

to the flow rate of CO divided by the flow rate of atomic oxygen under the presumption that strip rate is proportional to the atomic oxygen concentration

divided by the CO concentration. However, since the oxygen concentration is approximately constant for a given temperature, an abscissa that is proportional to the flow rate of CO plots as well.

Increasing the flow of molecular oxygen by 200 cm³/min in the absence of any CO caused no measurable change in either the concentration of atomic oxygen or the strip rate. Titrations were also performed with no CO present and then with CO introduced in the exhaust a few centimeters before the point of titration, with no perceptible change in the amount of NO_2 needed for titration.

Strip Rates as a Function of Water Vapor Concentration in the Presence of Carbon Monoxide

200 cm³/min of CO were then added to the 500 cm³/min of molecular oxygen, and the pressure was allowed to rise from 1.0 to 1.4 Torr. Again, the incoming oxygen was split between a line that went through a water bubbler and one that did not. Measurements were made of strip times and titration fill time at 160°C. Again, within the accuracy of the data, atomic oxygen flow rate and consequently the atomic oxygen concentration was unaffected by the amount of oxygen which had gone through the bubbler, as can be seen in Fig. 6, whereas the strip time approximately doubled between when no oxygen went through the bubbler and when all 500 cm³/min went through the bubbler, as shown in Fig. 7.

Apparently, the role of CO in the presence of about 15 cm³/min of water vapor and of water vapor in the presence of 200 cm³/min of CO is to decrease the stripping rate by covering the reaction sites without substantially changing the concentration of atomic oxygen. Either one of them alone decreases the stripping rate by reducing the atomic oxygen without decreasing the number of reaction sites.

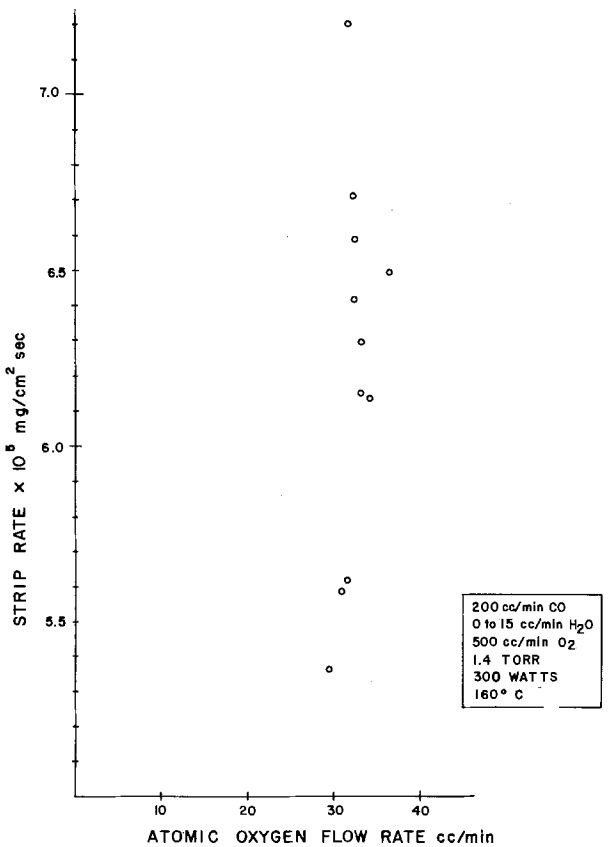


Fig. 6. Strip rate in an oxygen and carbon monoxide plasma in the presence of water vapor. Increasing water vapor flow rates decreases strip rates but has little effect on atomic oxygen flow rates.

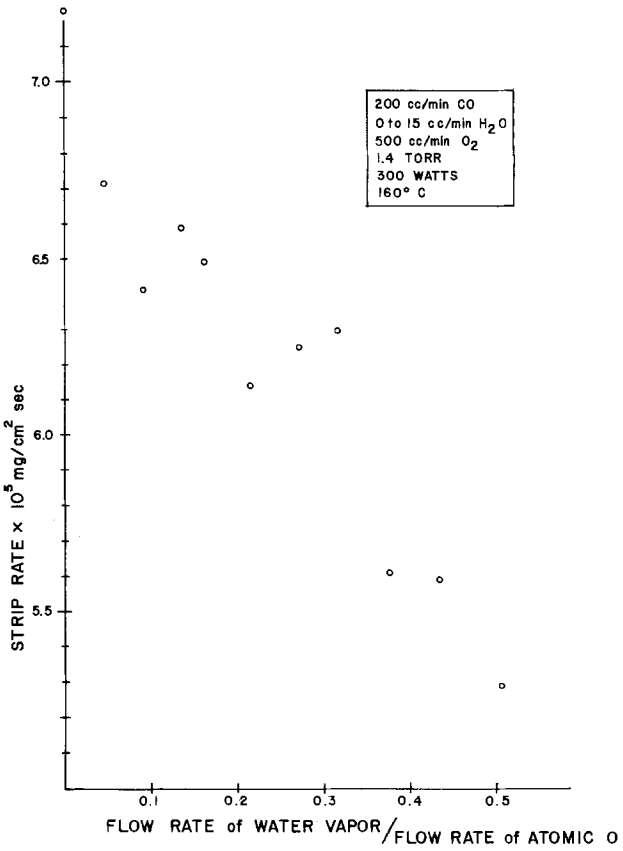


Fig. 7. Strip rate in an oxygen and carbon monoxide plasma as a function of the flow rate of water vapor divided by the flow rate of atomic oxygen.

Strip Time vs. Thermal Load

An experiment was then run in which boatloads of 50 2-in. silicon wafers were stripped with a flow rate of 500 cm³/min at a pressure of 1 Torr with 100W, starting with the reactor at room temperature. A thermometer was thermally coupled to the boat. In the first batch the front, a middle, and a rear wafer were covered with photoresist. The rest of the wafers were bare. The front wafer was stripped clean in 21 min, at which point the power was shut off. The center wafer was completely stripped. The rear wafer had a small spot of photoresist in its center.

A second run was made in which all 50 wafers were covered with photoresist. The front wafer cleared in 18 min and something less than 10 sec. The other wafers were all completely stripped, except for a couple at each end of the boat, which had small spots of photoresist near their centers.

For the same load of wafers variations are to be expected, depending on the thermal contact between the wafers and the boat, and the boat and the reactor. The temperature as a function of time is shown for the two runs, and it will be seen that the boat is heating more slowly in the second run. However, it would seem quite clear that under present operating conditions the principal reason why a load of 50 wafers strips more slowly than the interior wafer of a three-wafer array has to do with the larger thermal mass and slower heating of the 50-wafer system.

Conclusions

The addition of carbon monoxide or water vapor to an oxygen plasma in amounts comparable to the atomic oxygen present reduces the stripping rates of photoresist by approximately a factor of two. The reduction is effected by reducing the atomic oxygen by the same factor. If both carbon monoxide and water vapor are added to an oxygen plasma, the stripping rates are reduced by approximately another

Table I. Temperature as a function of time

Time (min)	Temperature run 1 (°C)	Temperature run 2 (°C)
0	26	26
2	100	72
3	112	84
4	116	89
8	108	108
14	116	120
18	128	127
20	—	130
21	—	130

factor of two without any further reduction in atomic oxygen concentration. Presumably the added gases are covering half of the reaction sites, making them unavailable for further reactions.

Stripping rates are very slow at photoresist temperatures less than 120°C. Thus, greater thermal mass as well as by-product inhibition explains why a full boatload of silicon wafers are slower to strip than a three-wafer array of the same wafer spacing.

Acknowledgments

The author would like to thank Dennis S. Enjaian for taking the experimental measurements and Joseph M. Welty for a major contribution to all aspects of the thinking.

Manuscript submitted June 1, 1976; revised manuscript received July 28, 1976.

Any discussion of this paper will appear in a Discussion Section to be published in the December 1977 JOURNAL. All discussions for the December 1977 Discussion Section should be submitted by Aug. 1, 1977.

Publication costs of this article were assisted by the International Plasma Corporation.

REFERENCES

1. S. M. Irving, Proceedings of the Kodak Photoresist Seminar, Vol. 2 pp. 26-29, Rochester, New York (1968).
2. R. L. Bersin, *Solid State Technol.*, **13**, 39 (June 1970).
3. J. R. Hollahan and A. T. Bell, "Techniques and Applications of Plasma Chemistry," John Wiley & Sons, New York (1974).
4. A. T. Bell and K. Kwong, *AIChE J.*, **18**, 990 (1972).
5. H. Abe, Proceedings of the 6th Conference on Solid State Devices, Tokyo (1974).
6. E. E. Peterson, "Chemical Reaction Analysis," Prentice-Hall, Englewood Cliffs, New Jersey (1965).
7. B. D. Blaustein and Y. C. Fu, in "Chemical Reactions in Electrical Discharges," R. F. Gould, Editor p. 259, American Chemical Society, Washington, D.C. (1969).
8. M. Manes, *ibid.*, p. 133.

Nitrogen Diffusion in Zirconium Nitride

J. G. Desmaison[1] and W. W. Smeltzer*

Department of Metallurgy and Materials Science, McMaster University, Hamilton, Ontario, Canada L8S 4M1

ABSTRACT

Nitrogen diffusion in polycrystalline $ZrN_{0.71-0.79}$ spheres, 60 and 90 μm diameter, was studied by the gas-solid exchange technique using ^{15}N as a tracer at a nitrogen pressure of 220 Torr and at temperatures in the range 1000°-1200°C. These specimens were characterized by chemical analyses, density, lattice parameter, and structural measurements. The tracer diffusion coefficient can be expressed as $D^*(cm^2/sec) = 3.0 \times 10^{-10} \exp(-23{,}000/RT)$. This result, when compared to a previous determination obtained in the same conditions with 254 μm thick plates, confirms that nitrogen transport in this polycrystalline solid at temperatures less than 1200°C is associated with a short-circuit diffusion mechanism.

Using the ^{15}N gas-solid exchange technique we investigated recently (1, 2) the diffusion of nitrogen in 254 μm thick $ZrN_{0.93}$ plates obtained by direct nitridation of 99.995 weight percent (w/o) zirconium sheets at 1150°C. The tracer diffusion coefficient measured at a nitrogen pressure of 220 Torr and at temperatures in the range 1000°-1200°C could be expressed as

$$D^*_N\,(cm^2/sec) = \left(4.1\,^{+88.2}_{-3.9} \times 10^{-6}\right) \exp(36{,}600 \pm 8{,}500)/RT \quad [1]$$

This result when compared to determinations of the chemical diffusion coefficient obtained from Zr nitriding kinetics demonstrated that nitrogen transport in the polycrystalline solid at temperatures less than 1200°C is associated with a short-circuit diffusion mechanism.

The purpose of this investigation was to study the influence of the nitrogen to zirconium ratio in order to gain complementary information on the transport process. Indeed if the role of short-circuiting paths is predominant in the process, the values of the diffusion coefficient should be more dependent on the microstructure of the polycrystalline materials than on the nonstoichiometry, *i.e.*, on the nitrogen vacancy concentration. Accordingly, the reverse situation would prevail for volume nitrogen diffusion in the hypothesis of a vacancy mechanism. In order to obtain substoichiometric nitride samples presenting sufficient homogeneity for diffusion experiments we prepared microspheres in the 45-105 μm range.

Experimental

Preparation and characterization of the spheres.— The spheres were prepared by dropping particles in the 45-75 μm size range through an electric arc, where they melted and spheroidized due to surface tension. The method of preparation and the arc assembly have been described in detail elsewhere (3, 4). The operating characteristics of the arc were 100V and 10-20A in a nitrogen argon atmosphere. Tungsten electrodes and UHP gases (>99.999%), were used. Separation of the spheres from irregularly shaped particles which missed the arc was accomplished by dropping the powder on an inverted watch glass. Only the spheres

* Electrochemical Society Active Member.
[1] Present address: Laboratoire de Chimie Minerale et Cinétique Hétérogène, E.R.A. No. 539 du C.N.R.S., Limoges, France.
Key words: zirconium nitride, nitrogen diffusion, lattice and short-circuit diffusion.

Table I. Analysis of the zirconium nitride used for the preparation of spheres

Element	Content,[1] w/o
N	8.76
Fe	0.07
Cu	0.02
Si	0.06
Ca	0.01
Cr	0.06
Ni	0.04
C	(240 ppm)

[1] After "Ventron Corporation-Alfa Products" [Aldrich Chemical Company (Canada) Limited].

would roll quickly to the bottom. The yield after one pass, ranging between 5-10 w/o was increased to approximatively 25 w/o by recycling the incompletely fused particles through the arc several times.

The starting material was >99% zirconium nitride; the analytical data are shown in Table I. Due to the rather low nitrogen content of this material, the spheres were renitrided for 10 days at 1050°C and subsequently characterized by the techniques (chemical analysis, density, lattice parameter, and structural measurements) presented in our previous work (1, 2).

Determination of the diffusion coefficient.—Nitrogen diffusion was determined by the gas-solid isotopic exchange technique using ^{15}N as a tracer. The details of the apparatus and the procedures have also been described (1, 2). In brief, the nitride sample is heated in a constant and limited volume of ^{15}N enriched nitrogen gas. From the depletion of ^{15}N in the gas, followed by mass spectrometric technique, the diffusion coefficient in the solid can be evaluated by applying the error function equation developed by Carman and Haul (5) with the assumption of an instantaneous phase boundary reaction

$$\frac{C_t - C_s}{C_g - C_s} = \frac{\gamma_1}{\gamma_1 + \gamma_2} e \operatorname{erfc} \frac{3\gamma_1}{\lambda}\sqrt{\tau} + \frac{\gamma_2}{\gamma_1 + \gamma_2} e \operatorname{erfc} \frac{-3\gamma_2}{\lambda}\sqrt{\tau} \quad [2]$$

where $\tau = D^* t/a^2$, $\gamma_1 = \frac{1}{2}\{(1 + 4\lambda/3)^{1/2} + 1\}$ and $\gamma_2 = \gamma_1 - 1$. Here C_t, C_s, and C_g represent the atom fraction of ^{15}N in the atmosphere at time t, in the solid at time zero (taken as the natural abundance 0.0037), and in the atmosphere at time zero, respectively. a is the radius of the spheres, and λ is the ratio of the total mass of nitrogen in the gas phase to that in the solid. The usual criterion for a surface exchange limitation is a curvature of a τ *vs.* t plot, or if the curvature is too small, any offset from the origin of an extrapolated line through the experimental points.

Results

Characteristics of the spheres.—A batch of ~ 6g of golden yellow spheres was obtained and graded using Tyler Sieves. The majority of the spheres were in the diameter ranges 45-75 μm (avg diam = 60 μm) and 75-105 μm (avg diam = 90 μm). Powder photographs and diffractometer traces contained only the characteristic lines of ZrN, proving the single phase structure of the material. X-ray diffraction photographs taken of a few spheres with a precession camera using Zr-filtered Mo radiation demonstrated the polycrystalline nature of the spheres. These spheres consisted of substoichiometric, ZrN_x, with $x = 0.74 \pm 0.01$ for the 60 μm diam and $x = 0.71 \pm 0.01$ for the 90 μm diam. Microscopic examination of the spheres showed that they were not cracked and had a smooth surface with a few irregularites (Fig. 1). Polished cross sections presented a rather rough surface finish resulting partly from a small degree of internal porosity but mainly from surface damage occurring during polishing due to the brittleness of the nitride. Etching revealed a dense network of grain boundaries delimiting grains with average diameter measured to be approximately 10 μm for the 60 μm spheres, and 15 μm for the 90 μm spheres (Fig. 2). The lattice parameter and the experimental density were measured on 60 μm spheres at 23°C. These results are shown in Table II along with the corresponding calculated vacancy concentrations. The sample homogeneity was confirmed by x-ray powder photographs which exhibited sharp splitting of the $K_{\alpha 1}$ and $K_{\alpha 2}$ lines for angles greater than 45°.

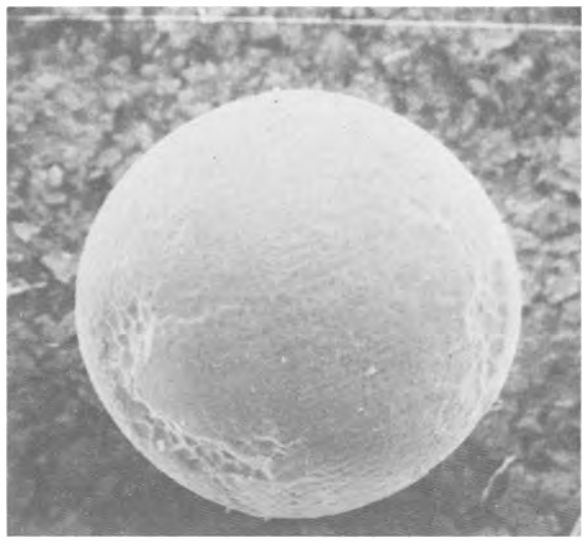


Fig. 1. Scanning electron micrograph of the surface of a sphere (×700).

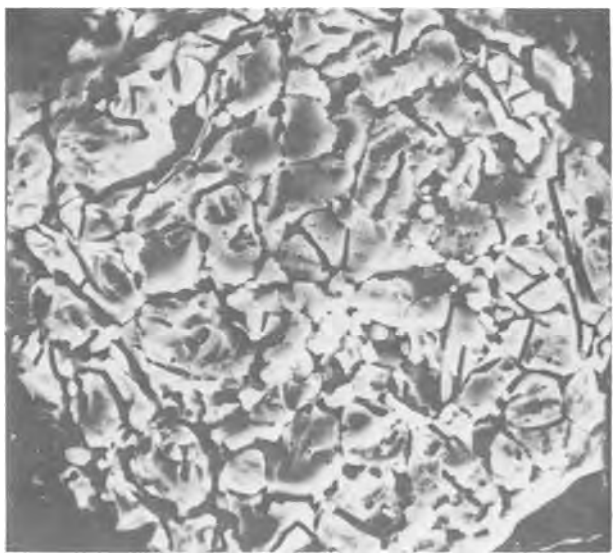


Fig. 2. Etched cross section of a sphere (×1400)

Table II. Vacancy concentration in 60 μm spheres at 23°C

d_p (g/cm³)	a (A)	d_X (g/cm³)	V_{Zr} (%)	V_N (%)
(pycnometer density) 6.80 ± 0.08	(lattice parameter) 4.578 ± 0.002	(x-ray density) 7.03	3.3	28.4

Diffusion.—Runs were performed at 1000°, 1053°, 1101°, 1148°, and 1203°C, and at 220 Torr nitrogen pressure. At the three intermediate temperatures 60 μm spheres were used and 90 μm spheres at the two extreme temperatures. In addition, before the runs at 1101°, 1148°, and 1203°C the samples were annealed for 2 days under the same experimental conditions of temperature and pressure of normal isotopic composition as used for the exchange run. This annealing increased the N/Zr ratio up to 0.79 in the case of 60 μm spheres and 0.78 for 90 μm spheres. For all the runs a sample mass of 500 mg was used, C_g was maintained in the 4.36-7.60% range and λ was kept approximately equal to 1($1.09 < \lambda < 1.21$). With the chosen value of λ the over-all change in C_t for a run ranged from 2.1 to 4.7%.

The dimensionless parameter $D^* t/a^2$ calculated from the experimental data through Eq. [2] *vs.* time is shown in Fig. 3; the corresponding plots can be represented by straight lines passing through the origin which indicate that the surface exchange is not the limiting process. The values of the tracer diffusion coefficient were determined from these plots and an Arrhenius plot of these evaluations is given in Fig. 4. The equation obtained by the least squares method is

$$D^*(\text{cm}^2/\text{sec}) = \left(3.0 \pm \frac{18.8}{2.6}\right) \times 10^{-10} \exp - (23{,}000 \pm 5{,}400)/RT \quad [3]$$

where the limits are at the 95% confidence level.

During the diffusion anneal the samples increased slightly in weight (0.28-0.75%). Also, after exposures higher than 10 hr a few spheres became of brown grayish color and attached to each other, this second effect increasing in intensity with temperature. Microscopic examination and x-ray analysis showed that the change in color and particle agglomeration were due to a slight oxidation of the spheres accompanied with a beginning of sintering of the zirconia formed.

Discussion and Conclusions

Because of the abundance of nitrogen vacancies in substoichiometric zirconium nitride (Table II) nitrogen diffusion in this material ought to be a particularly simple property to interpret. The tracer diffusion coefficient D^* for a vacancy mechanism is proportional to the vacancy concentration. This concentration in the spheres was approximatively 4 times larger than in the $ZrN_{0.93}$ plates consequently, it could be expected to lead to slightly higher values of D^* for spheres. In fact it is the reverse situation which is observed (Fig. 4), the diffusion coefficients for spheres being nearly 100 times smaller. This result is not surprising, as the low values of the preexponential factors and the activation energies, as well as the relatively low temperatures of the diffusion anneals (<0.45 Tm) all suggest that the two sets of measurements represent structure-sensitive diffusion rather than intrinsic volume diffusion.

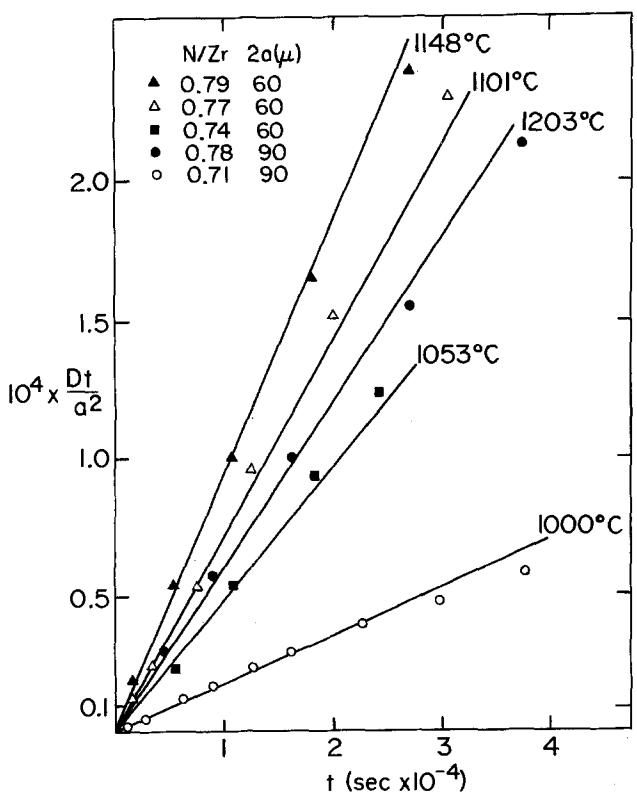


Fig. 3. Experimental results for ^{15}N diffusion in spheres

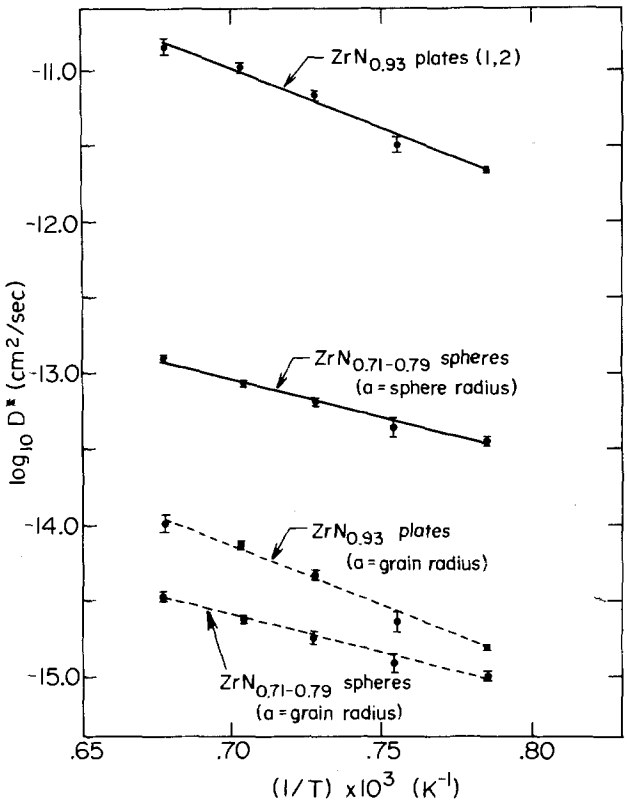


Fig. 4. Arrhenius plot of the nitrogen tracer diffusion coefficients for $ZrN_{0.71\text{-}0.79}$ spheres and $ZrN_{0.93}$ plates. (1,2) text references.

The influence of the microstructure is tested following the procedure by Oishi, Shirasaki *et al.* (6-8) in their investigations of preferential diffusion of oxygen along grain boundaries in polycrystalline MgO and $MgAl_2O_4$. These authors using the ^{18}O gas-solid isotopic exchange technique found that the self-diffusion coefficients in the polycrystalline samples were several orders of magnitude greater than that of single crystals. When they recalculated the diffusion coefficients by taking the grain radius instead of the particle radius, the new values were in good agreement with those for the single crystals. The higher diffusion coefficients for the polycrystalline solid were then interpreted as being due to enhanced oxygen diffusion along the grain boundaries. Thus by applying this computation procedure to the present results it should be possible to gain information on the role played by short-circuit diffusion through grain boundaries. The diffusion coefficients calculated through Eq. [2] by taking the average radii of the grains, *i.e.*, 5 μm for 60 μm spheres, 7.5 μm for 90 μm spheres, and 10 μm for plates can be expressed as

$$D^*(\text{spheres}) = \left(8.0 \begin{matrix} +50.7 \\ -\ 6.9 \end{matrix} \times 10^{-12}\right) \exp - (23{,}000 \pm 5{,}400)/RT \quad [4]$$

$$D^*(\text{plates}) = \left(2.9\ ^{+63.0}_{-\ 2.8} \times 10^{-9}\right) \exp - (36{,}700 \pm 8{,}500)/RT \quad [5]$$

The corresponding Arrhenius plots are shown by dashed lines in Fig. 4. The agreement between the two sets of experiments is greatly improved and can be even considered as good if the uncertainty of the grain size distribution is taken in account. Therefore this result is consistent with the interpretation that preferential diffusion of nitrogen along grain boundaries predominates in the temperature range of interest.

This analysis also demonstrates that other low resistance diffusion paths in the materials play a role, since the activation energies from Eq. [4] and [5] are in poor agreement and both values are much too small for lattice diffusion even though a correction has been made for grain size differences. Such paths can be of structural origin such as ingrown dislocations and microporosity and of excess extrinsic defectiveness in the solid lattice caused by the influence of impurities. The difference between the ZrN density determined by the pycnometer and x-ray techniques (~3 *vs.* 0.7%) and the impurity levels (0.28 *vs.* 0.01%) was higher in the spheres than in plates. The relative effect of these different parameters, however, cannot be distinguished using the presently obtained results. There is also an additional contributing factor to the determination of the lower activation energy for diffusion in the spheres: the spheres increased detectably in weight during a diffusion anneal, and this nitridation which increased with temperature could lower the isotopic exchange, and by extension, the temperature dependence of the diffusion constant.

Acknowledgments

The authors gratefully acknowledge financial support of the National Research Council of Canada.

Manuscript submitted April 26, 1976; revised manuscript received Sept. 13, 1976.

Any discussion of this paper will appear in a Discussion Section to be published in the December 1977 JOURNAL. All discussions for the December 1977 Discussion Section should be submitted by Aug. 1, 1977.

Publication costs of this article were assisted by McMaster University.

REFERENCES

1. J. G. Desmaison and W. W. Smeltzer, *This Journal*, **122**, 354 (1975).
2. J. G. Desmaison and W. W. Smeltzer, Proceedings of the 25th International Meeting, Society Chim. Phys., p. 116 (1975).
3. R. Streiff and W. W. Smeltzer, *J. Nucl. Mater.*, **41**, 109 (1971).
4. A. Madeyski and W. W. Smeltzer, *Mater. Res. Bull.*, **2**, 467 (1967).
5. P. C. Carman and R. A. W. Haul, *Proc. R. Soc., London*, **A222**, 109 (1954).
6. Y. Oishi and K. Ando, *J. Chem. Phys.*, **63**, 376 (1975).
7. S. Shirasaki and Y. Oishi, *Jpn. J. Appl. Phys.*, **10**, 1109 (1971).
8. H. Hashimoto, M. Hama, and S. Shirasaki, *J. Appl. Phys.*, **43**, 4828 (1972).

Technical Note

Auger Characterization of Chemically Etched GaAs Surfaces

I. Shiota, K. Motoya, T. Ohmi, N. Miyamoto, and J. Nishizawa*

Research Institute of Electrical Communication, Tohoku University, Sendai, Japan

Low resistance ohmic contact and high quality Schottky contact on GaAs single crystals are required especially for high frequency devices including IMPATT diodes (1), TUNNET (tunnel injection transit time) diodes (2), and Schottky gate FET (3). However, the surface processing technique of GaAs has not yet been fully established in contrast to that of Si. This is partly ascribed to the deviation from stoichiometry which is characteristic of compound semiconductors such as GaAs (4) and GaP (5), and to the difference in reactivity against a chemical reagent between III and V components. These two factors are closely related to each other and make it very difficult to control precisely the surfaces of III-V compound semiconductors.

The present work was conducted to determine which processing is best suited to the preparation of GaAs surfaces with the minimum oxide film (6, 7). For the purpose of investigation, Auger electron spectroscopy was used in combination with Ar sputter etching which may be most reliable for the analysis of thin film. Auger spectra were taken in a vacuum of 10^{-9} mm Hg at an excitation voltage of 4 kV and a beam current of 1 μA. Simultaneous sputter etching was made at a sputtering voltage of 1 kV and an emission current of 30 mA under a 5×10^{-5} mm Hg Ar atmosphere. In the case of in-depth profiling, the $L_3M_{4,5}M_{4,5}$ Auger peaks for Ga and As and the $KL_{2,3}L_{2,3}$ peaks for oxygen were monitored automatically by a Physical Electronics multiplex control system. Oxide thickness was determined from the sputtering time at which the $OKL_{2,3}L_{2,3}$ Auger peak height attained a minimum value. The sputtering rate of the native Ga oxide produced by chemical etching was assumed to be the same as that of thermally grown Ga oxide on GaAs (8) which was 20 Å/min.

First, we adopted a $H_2SO_4 + H_2O_2 + H_2O$ mixture in the volume ratio of 4:1:1 as a fast etchant of an original GaAs (100) surface which was thoroughly degreased using trichlorethylene and methanol cycles in an ultrasonic bath, followed by a doubly distilled

* Electrochemical Society Active Member.
Key words: slow chemical etching, residual oxide film, low resistance ohmic contact, high quality Schottky contact.

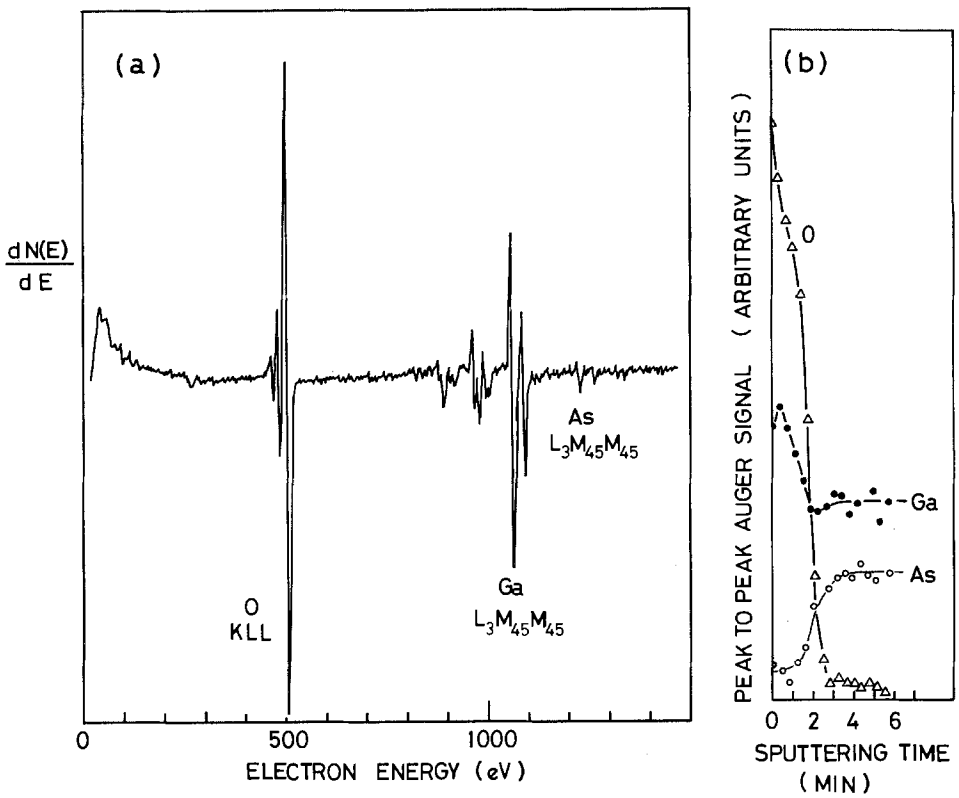


Fig. 1. (a) Auger spectrum of the top surface of a chemically etched GaAs (100) surface by $H_2SO_4 + H_2O_2 + H_2O = 4:1:1$ in volume ratio at 50°C for 3 min (fast etch). (b) Composition profile of the surface of (a).

methanol rinse prior to chemical etching. The Auger spectrum and the composition profile of the surface are shown in Fig. 1 (a) and (b), respectively, after chemical etching at 50°C for 3 min. It is shown that the etched surface is covered with a Ga oxide film, about 50Å thick, containing a small amount of As. Deficiency of As atoms in the oxide is the prominent nature of the thermally grown oxide film on GaAs surfaces at rather high temperatures (8). Such a surface is not appropriate for the formation of low resistance ohmic and Schottky contacts. We found that fast etching produces a thick residual oxide film, while slow etching results in formation of a thin residual oxide film. The thick oxide film remaining after removal of the damaged layer using the fast etch was very slowly dissolved by a slow etchant. Therefore, prior to the application of slow etching, the thick oxide film should first be removed.

Concentrated HF solution was used for removing a considerable thickness of the oxide film by dipping the sample in the solution for 5 min, resulting in a remaining oxide layer thickness of 25 ~ 30Å. Finally, the surface was lightly etched by NaOH (1 mole) + H_2O_2 (0.76 mole) in the volume ratio of 1:1 at 30°C for at least 1 min. The etching rate of this slow etchant was 0.2 μm/min. It is clearly shown in Fig. 2 (a) and (b) that the oxide thickness could be reduced to below 10Å after 1 min of final etching and that the Auger peak heights of Ga and As became smaller in the surface region than in bulk, although the Auger peak ratio of As/Ga was nearly the same as that in bulk. The method described above can also be applied following other etchants with high etching rates such as $CH_3OH + Br_2$ and $NaOH + H_2O_2$. Main results are summarized in Table I where GaAs (100) surfaces are evaluated in terms of residual oxide thick-

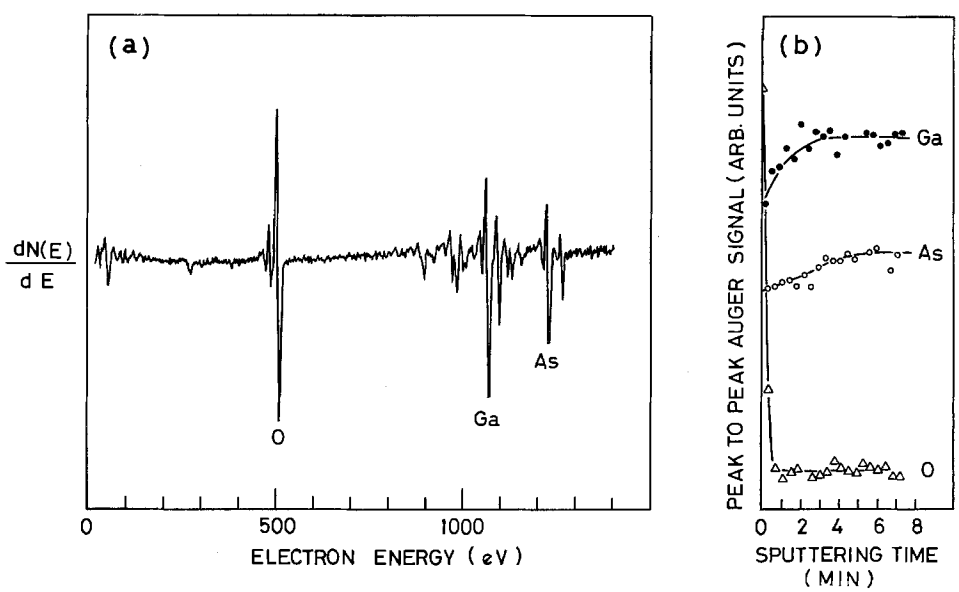


Fig. 2. (a) Auger spectrum from the GaAs (100) surface which was successively processed by conc HF and a slow etching (1 min) following fast etching. (b) Composition profile of the surface of (a).

Table I

	Etching procedure	Residual oxide thickness in Å
I	4:1:1* (50°C, 3 min)	50
	4:1:1 (50°C, 3 min) + conc HF** (5 min)	30
	4:1:1 (50°C, 3 min) + conc HF (5 min) + 1:1*** (30°C, 0.5 min)	10
	4:1:1 (50°C, 3 min) + conc HF (5 min) + 1:1 (30°C, 1 min)	≲10
II	1:1*** (55°C, 10 min)	60
	1:1 (55°C, 10 min) + conc HF	25
	1:1 (55°C, 10 min) + conc HF + 1:1 (30°C, 0.5 min)	15
	1:1 (55°C, 10 min) + conc HF + 1:1 (30°C, 1 min)	10

* 4:1:1 means the volume ratio of H_2SO_4 (98 w/o): H_2O_2 (30 w/o): H_2O. Etching rate is ~3 μm/min at 50°C.
** Conc HF is 49 w/o.
*** 1:1 means the volume ratio is NaOH (1 mole): H_2O_2 (0.76 mole). Etching rate is 0.2 μm/min at 30°C and 1 μm/min at 55°C, respectively.

ness. From the table, it is clear that slow etching for at least 1 min is required to reduce the surface oxide thickness to below 10Å. Not only the aforementioned NaOH + H_2O_2 mixture but also any other etchants with slow etching rates such as 10 H_2SO_4:1 H_2O_2:1 H_2O can serve as slow etchants, regardless of the rate-limiting process of etching kinetics. Table I suggests that the successive processing including HF and slow etching subsequent to fast etching may be a very promising technique for producing a GaAs (100) surface with the least amount of oxide.

By applying this method to the fabrication of ohmic and Schottky contacts, the good contacts were obtained resulting in excellent performance of microwave and millimeter wave GaAs devices. Evaporation and alloy process of Au-Ge is very popular and useful in ohmic contacts to GaAs, however, two main problems exist which give rise to high contact resistance, *i.e.*, the ball-up phenomena and the formation of Au-Ga alloy due to the heat cycle of the alloying process. Thin layer evaporation of Ni following Au-Ge evaporation is usually used in order to suppress the ball-up phenomena with conventionally etched GaAs surfaces, but the ball-up phenomena are not observed if the oxide-free GaAs surface is used. Formation of Au-Ga alloy in the alloying process is suppressed by using the rapid temperature rise alloy process (9) where the temperature of samples is raised within at most 10 sec up to 450°C in the alloying heat cycle (Au-Ga alloy formation occurs at around 300°C). Combination of the oxide-free GaAs surfaces with the rapid temperature rise alloy process leads to excellent ohmic contacts and contact resistance as low as 1×10^{-6} Ω-cm² or less. In addition, a good quality Schottky barrier could be made between Pt and n-GaAs with a very small scatter of 0.93 ± 0.01 eV in barrier height, and the wettability was improved between the GaAs substrate and Ga solvent for multilayer liquid phase epitaxial growth.

For $(\bar{1}\bar{1}\bar{1})$ surfaces, however, the situation is different from that for (100) surfaces; the growth of the native oxide film was limited to a level of 10 ~ 15Å even with fast etchants such as H_2SO_4:H_2O_2:H_2O (3:1:1) and CH_3OH:Br_2 (20:1). The change in composition was observed in the very thin surface layer as in the case of (100) surfaces. The trend that the oxide film is thinner at $(\bar{1}\bar{1}\bar{1})$ surfaces than at (100) surfaces is the same as the trend for oxide films produced by thermal oxidation of GaAs surfaces below 500°C. This result will be presented elsewhere (8).

The present surface processing technique has been found to be useful for the fabrication of various types of contacts and effective as a simple surface preparation method for other purposes.

Acknowledgment

This work was supported in part by a grant from the Ministry of Education, Japan.

Manuscript submitted June 2, 1976; revised manuscript received Sept. 3, 1976.

Any discussion of this paper will appear in a Discussion Section to be published in the December 1977 JOURNAL. All discussions for the December 1977 Discussion Section should be submitted by Aug. 1, 1977.

Publication costs of this article were assisted by Tohoku University.

REFERENCES

1. C. K. Kim *et al.*, *Appl. Phys. Lett.*, **14**, 270 (1969).
2. T. Okabe and J. Nishizawa, 1968 International Electron Device Meeting; J. Nishizawa and T. Ohmi, Proceedings of the 1973 European Microwave Conference, A 10-5.
3. C. A. Mead, *Proc. IEEE*, **54**, 307 (1966).
4. J. Nishizawa, H. Otsuka, S. Yamakoshi, and K. Ishida, *Jpn. J. Appl. Phys.*, **13**, 46 (1974).
5. J. Nishizawa, Y. Okuno, K. Suto, and S. Yamakoshi, *Solid State Commun.*, **14**, 889 (1974).
6. I. Shiota, S. Yamakoshi, N. Miyamoto, and J. Nishizawa, The Second Research Meeting on Surface Electronics, Ministry of Education of Japan, Sendai, Japan (Oct. 1975).
7. T. Ohmi and K. Motoya, *IEE Commun. Jpn.*, Technical Group Meeting, **ed 75-71** (Jan. 1976).
8. I. Shiota *et al.*, To be published.
9. M. Fukuta *et al.*, *IEE Commun. Jpn.*, Technical Group Meeting, **sse 74-82** (Feb. 1975).

Brief Communication

Poly(methyl α-chloracrylate) as a New Positive Electron-Beam Resist

J. N. Helbert, C. F. Cook, Jr., and E. H. Poindexter

U.S. Army Electronics Technology and Devices Laboratory (ECOM), Fort Monmouth, New Jersey 07703

Production of high density integrated circuits by electron-beam lithography relies heavily upon polymer resists for pattern delineation. Although there are many negative resists (1) known, far fewer positive e-beam (1) resists have been found. In this communication, we report positive e-beam resist behavior for poly(methyl α-chloracrylate) homopolymer. Previous radiation experiments (2, 3) with this material indicate that this polymer undergoes radiation degradation at a fairly high rate per unit radiation dose.

Methyl α-chloracrylate monomer was purchased from Polysciences, Incorporated, and was vacuum distilled before use. Poly(methyl α-chloracrylate) (PMCA) polymer was synthesized by conventional azodi-isobutyronitrile free-radial induced polymerization (4). The polymer was fractionally reprecipitated twice from dimethyl formamide using methanol as nonsolvent. The resulting polymer had a number average molecular weight ($\overline{M}_N$) of 125,000 as determined by membrane osmometry, and a polydispersivity of 2.6 as determined by gel permeation chromatography.

Electron-beam exposures were made with an AMR-900 scanning electron microscope operating at 10 kV, which was modified for raster scan pattern control with a flying spot scanner. The beam diameter was 1000Å. The electron dose was measured with a Faraday cup. The electron exposure charge density measurement was checked against the known sensitivity of PMMA using the standard developer (5). The test patterns consisted of sequential groups of lines with varying exposure densities; line widths were typically 1-2 μm with 1-3 μm spacings.

Electron-etched lines in PMCA films dissolved much faster than the unexposed resist when subjected to developer solutions. This occurs because the molecular weight of the irradiated polymer is much smaller (3) than that of the polymer in the unexposed region. The dependence of dissolution rate $\dot{d}$ upon polymer molecular weight has been shown to be (6)

$$\dot{d} = KM^{-A}$$

where M is the molecular weight, and K and A are constants. Although polymer solubility may change with radiation exposure, it is the dissolution rate that is most important for line development in positive resists. Table I lists line exposure charge densities employed for representative line groups in this study. Figure 1 is an SEM photograph of representative developed lines.

The e-beam developer composition is a very important consideration, but its selection is not scientifically clear-cut .Of the many developer solution compositions tried, two were fairly good. The first, a 1:1 $CHCl_3/CCl_4$ mixture, developed the lines, but with line edge blotchiness. The second, 1:1 $CHCl_3$/isopropanol (IPA), was an improvement over the first developer, but some unexposed polymer surface roughness was apparent. Isopropanol is probably a better nonsolvent for PMCA, because its larger molecular size could restrict molecular permeation of nonsolvent.

Key words: electron-beam resists, polymer degradation, acrylate polymers.

Table I. Development charge densities and remaining resist thicknesses for PMCA positive e-beam resist samples

Resist	Exposure development charge density, C/cm²	Remaining resist thickness, Å	Developer	Development time, min
PMCA	5.3×10^{-6}	3400 ± 300*	1:1 $CHCl_3/CCl_4$**	27
PMCA	1.0×10^{-5}	3500 ± 300*	1:1 $CHCl_3/CCl_4$**	17
PMCA	8.4×10^{-6}	2700 ± 300†	1:1 $CHCl_3$/IPA	40
PMCA	6.5×10^{-6}	2600 ± 300†	1:1 $CHCl_3$/IPA	91
PMMA	5×10^{-5}	5400 ± 300‡	1:3 MEK/IPA	1.5

* Original resist thickness 3700 ± 400Å and measured by scanning electron microscope.
** Blotchy and poor line edge development which was improved by replacing CCl_4 nonsolvent with IPA.
† Original resist thickness 3900 ± 300Å and measured by scanning electron microscope.
‡ Original resist thickness 6000 ± 300Å.

Our e-beam development charge densities indicate that PMCA is a significantly more sensitive resist than PMMA (see Table I). These findings are consistent with the higher observed radiation degradation susceptibilities (2, 3) observed for PMCA with respect to PMMA in other types of experiment. Since the only difference between PMMA and PMCA is the substitution of Cl for CH_3 at the α-acrylate group,

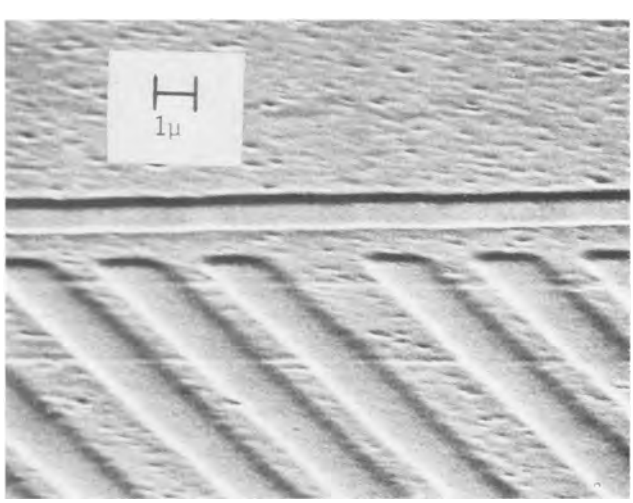


Fig. 1. Developed electron-beam etched lines in PMCA at 3800×. The substrate is a silicon wafer with a 4000Å thick oxide and the exposure dose is 8.4×10^{-6} C/cm². The other sample conditions are found in Table I and text.

the increased sensitivity in PMCA must be attributed to the chlorine substituent. The high electronegativity for chlorine is well known, and it is reasonable to expect a weakening of the main-chain C-C bond by electron polarization toward the halogen substituent (3).

Acknowledgment

The authors would like to thank the Semiconductor Devices & Integrated Electronics Technical Area, for the use of wafer processing equipment and for technical advice.

Manuscript received Aug. 9, 1976.

Any discussion of this paper will appear in a Discussion Section to be published in the December 1977 JOURNAL. All discussions for the December 1977 Discussion Section should be submitted by Aug. 1, 1977.

Publication costs of this article were assisted by the Department of the Army.

REFERENCES

1. L. F. Thompson, *Solid State Technol.*, **17**, 27 (July 1974).
2. J. N. Helbert, B. E. Wagner, P. J. Caplan, and E. H. Poindexter, *J. Appl. Polym. Sci.*, **19**, 1201 (1975).
3. J. N. Helbert, P. J. Caplan, and E. H. Poindexter, *ibid.*, To be published.
4. W. R. Sorenson and T. W. Campbell, "Preparative Methods of Polymer Chemistry," Interscience, New York (1968).
5. M. Hatzakis and A. N. Broers, in "11th Symposium on Electron, Ion, and Laser Beam Technology," R. F. M. Thornled, Editor, p. 337 (1971).
6. K. Ueberreiter, in "Diffusion in Polymers," J. Crank and G. S. Park, Editors, chap. 7, pp. 220-257, Academic Press, New York (1968).

JOURNAL OF THE ELECTROCHEMICAL SOCIETY

ELECTROCHEMICAL SCIENCE AND TECHNOLOGY

FEBRUARY 1977

Discharge Characteristic and Performance of Lithium-Silver Tungstate and Lithium-Silver Molybdate Organic Solvent Batteries

B. Di Pietro and B. Scrosati*

Istituto di Chimica Fisica, University of Rome, Rome, Italy

ABSTRACT

The discharge characteristic and performance of the Li/Ag_2WO_4 and Li/Ag_2MoO_4 couples in $LiAsF_6$-γ-butyrolactone are reported in terms of discharge mechanism, polarization, and cathode efficiency. In both cases the discharge process seems to be characterized by two distinct plateaus. Attention has been mainly focused on the first plateau of the two systems and by means of x-ray and coulometric analyses it has been possible to relate to these plateaus the electrochemical processes consisting of the formation of silver and lithium tungstate, and silver and lithium molybdate, respectively.

Lithium organic solvent batteries are of considerable technological interest since, due to their high specific energy density, they may find important applications as power sources in miniaturized electronic devices such as electric watches, hearing aids, and pacemakers. In recent years several materials have been investigated in order to select the best cathode to couple with lithium in batteries of practical use. Among these materials, silver oxyacid salts have received particular attention because of their insolubility and excellent electrochemical behavior in the most common organic electrolytes. The salts which so far have been most extensively studied are silver chromate (1) and silver phosphate (2). In this work the investigation of the cathodic behavior of the silver oxyacid salts was extended by examining the electrochemical properties of lithium-silver tungstate and lithium-silver molybdate couples in various organic electrolytes. The latter system has been partially examined by Dey and Holmes (3) who reported in a patent the utilization of silver molybdate as a cathode in lithium batteries. Nevertheless, it seemed worthwhile to reconsider the investigation of this system, especially in terms of discharge mechanism and, mainly, to compare the results with those related to the Li/Ag_2WO_4 couple which, to our knowledge, has never been investigated.

Experimental

Silver tungstate was prepared by precipitation adding a solution of silver nitrate to one of sodium tungstate. The precipitate was washed and dried at about 60°C under a purified nitrogen stream. A similar procedure was used to prepare silver molybdate. The purity of the silver salts was controlled by chemical and x-ray analyses. The results of the latter are shown in Fig. 3 and 8 for the tungstate and the molybdate, respectively. Lithium ribbon (Foote Mineral Company) was used as received. Lithium aluminum tetrachloride was prepared by melting equimolar amounts of anhydrous LiCl and $AlCl_3$ at 200°C under nitrogen (4). Lithium hexofluoroarsenate was an Alfa Ventron reagent grade product and was used without further purification.

High purity γ-butyrolactone (BL) was obtained by shaking the commercial product (Merck) in the presence of lithium to remove hydroxylate impurities. Methyl formate (MF) was purified by distillation over molecular sieves (4Å).

The electrolyte solutions, *i.e.*, 1M $LiAlCl_4$-BL, 1.5M $LiAsF_6$-BL, and 2M $LiAsF_6$-MF, prepared following the general procedure described by Campanella and Pistoia (5), were kept in a dry box where the electrochemical cells also were assembled and tested. The latter were of the "button type" and formed by placing into contact a lithium disk, three separator (glass wool) disks soaked with the electrolyte solution, and a pellet of the cathodic material. This pellet was obtained by pressing a thin layer of a mixture of the silver oxosalt and graphite [10 weight percent (w/o) of graphite] on a substrate of inert supporting metal (silver or, in the case of x-ray analyses, copper). The cells, of average total thickness of 0.3 cm and surface area of 1.25 cm^2, were then housed in a plastic container having gold-plated terminals.

The chemical, electrochemical, and x-ray analyses were carried out using standard procedures and equipment.

Results and Discussion

Lithium-silver tungstate system.—The applicability of Ag_2WO_4 as an electrode when coupled with lithium in organic electrolytes was tested by assembling the cell

$$Li/LiAlCl_4\text{-BL}/Ag_2WO_4 \qquad [1]$$

This cell has, at 22°C, an open-circuit voltage (OCV) of 3.0V and a typical polarization curve is reported in Fig. 1. This curve illustrates the ideal behavior of the system in sustaining high current densities before undergoing serious polarization. After examining the discharge capability of the Li/Ag_2WO_4 couple, the influence of the electrolyte on its performance was next considered by using $LiAsF_6$-BL and $LiAsF_6$-MF as

* Electrochemical Society Active Member.

Key words: organic solvent batteries, lithium-silver molybdate and lithium-silver tungstate systems.

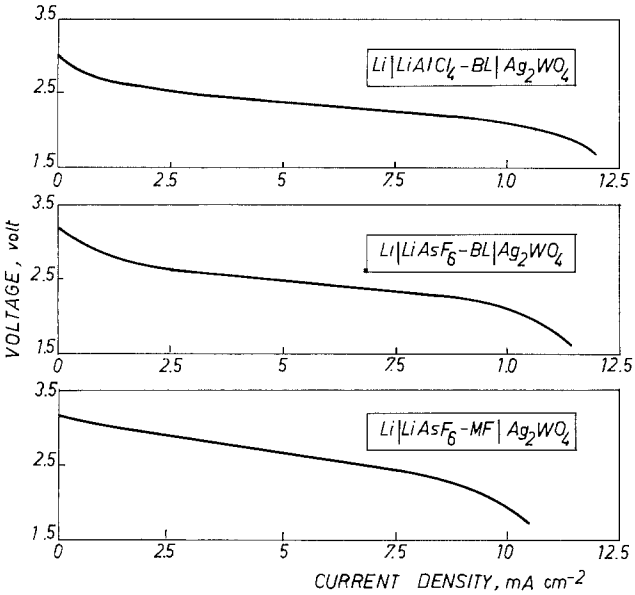


Fig. 1. Typical polarization curves of the Li/Ag_2WO_4 couple in $LiAlCl_4$-BL, $LiAsF_6$-BL, and $LiAsF_6$-MF electrolytes at room temperature.

alternative electrolyte solutions. Their typical polarization curves are also reported in Fig. 1.

The comparison indicates the cell

$$Li/LiAsF_6\text{-}BL/Ag_2WO_4 \qquad [2]$$

as the most effective both in terms of voltage and discharge characteristics. Cell [2] has in fact an OCV of 3.2V at 22°C, and a typical discharge curve (0.5 mA cm^{-2}) is reported in Fig. 2, where are also shown, again for comparison purposes, the typical discharge curves for the other two systems investigated.

It may be noted from Fig. 2 how the discharge process of cell [2] is characterized by two distinct plateaus. In order to determine the number of electrons involved in this process, a coulometric analysis was carried out. Cells containing a known amount of cathodic material (typically around 50 mg) were discharged at low rates (typically 0.25 mA cm^{-2}) and the voltage was followed as a function of time. When the voltage reached zero, the process was considered to be complete and from the coulombs delivered the number of electrons was obtained. This number, as an average of various determinations, was found to be two at the end of the first plateau and close to four at the end of the discharge.

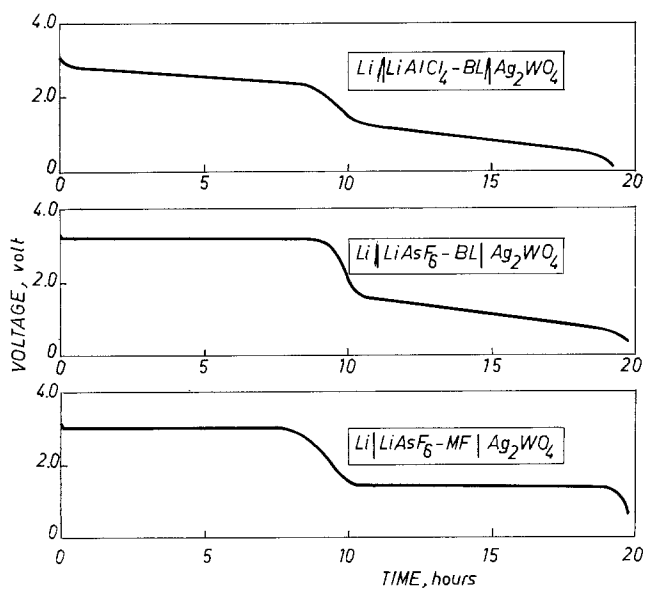


Fig. 2. Typical discharge curves of the Li/Ag_2WO_4 couple in $LiAlCl_4$-BL, $LiAsF_6$-BL, and $LiAsF_6$-MF electrolytes at 0.5 mA cm^{-2} and at room temperature. Average cathodic weight: 40 mg.

In an attempt to characterize further the electrochemical reaction, a low rate discharge of a cell similar to [2], with copper as supporting metal, was interrupted at the end of the first plateau. The cell was disconnected and its cathodic mass was submitted to x-ray analysis. The results of this analysis are schematically reported in Fig. 3 together with the diffraction patterns of the starting material (Ag_2WO_4), of silver and lithium tungstate in its most stable form in air.

It may be first noted from Fig. 3 that the lines of Ag_2WO_4 are absent in the discharge product for the initial reaction. This indicates that this reaction had proceeded to completion after the first plateau and gives further validity to the coulometric analysis. One of the basic assumptions of this analysis was in fact to consider the electrochemical reaction as complete at the end of a slow discharge.

Furthermore, Fig. 3 shows that in the x-ray diffraction pattern for the discharge product, all the lines of silver and the majority of those of lithium tungstate are present. On the basis of this result and of that of the coulometric analysis, one may assume the following

$$2Li + Ag_2WO_4 \rightarrow Li_2WO_4 + 2Ag \qquad [3]$$

as the most probable electrochemical reaction for the initial discharge of cell [2].

The investigation of the electrochemical reaction for the second plateau was carried out with a procedure analogous to that above described. After a complete low rate discharge, the cathodic mass was recovered and submitted to x-ray analysis. The results are compared in Fig. 4 with those for the discharge product

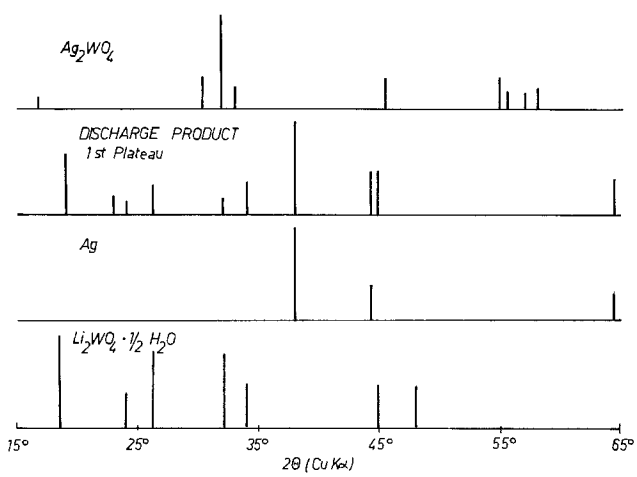


Fig. 3. X-ray diffraction patterns of the starting and discharged cathodic material of the $Li/LiAsF_6$-BL/Ag_2WO_4 cell (first plateau). Data for Ag and $Li_2WO_4 \cdot 1/2\ H_2O$ have been obtained from ASTM card indexes.

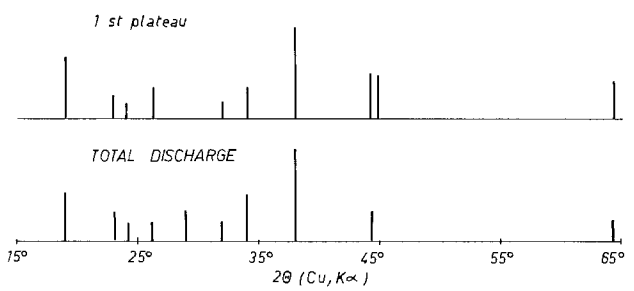


Fig. 4. X-ray diffraction patterns of the cathodic material for the $Li/LiAsF_6$-BL/Ag_2WO_4 cell after the first plateau and after complete discharge.

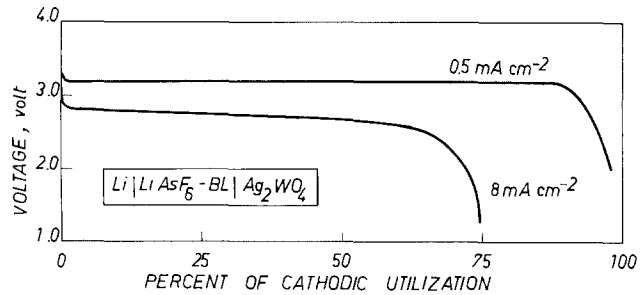


Fig. 5. Typical discharge curves for the Li/LiAsF$_6$-BL/Ag$_2$WO$_4$ cell at low (0.5 mA cm^{-2}) and high (8 mA cm^{-2}) rates and at room temperature (first plateau).

after the first plateau. There are no really substantial differences in the two patterns and therefore the reaction for the second plateau is difficult to interpret. One could tentatively imagine a lithium intercalation process and in an attempt to find evidence for this hypothesis as well as receiving additional information on the over-all cell reaction, open-circuit voltages were determined as a function of discharge depth. On the basis of four electrons change, the OCV was constant at a value of 3.20V for the discharge range from 10 to 40%, corresponding to an equilibrium voltage for reaction [3]. The OCV corresponding to the second plateau decreased monotonically from 2.70 to 1.70V over the discharge range of 60-90%. This seems to support the possibility of an intercalation compound forming as the discharge product in the second reaction. Further work is however necessary to identify this compound.

Further characterization of the Li/Ag$_2$WO$_4$ cell was therefore restricted to the first plateau which remains technologically the most interesting because of its high and constant voltage. Typical discharge curves for various rates are reported in Fig. 5. The excellent behavior of the cell is demonstrated by the fact that, even at discharge current densities of 8 mA cm^{-2}, the discharge voltage and the cathodic efficiency remain as high as 2.7V and 75%, respectively.

Finally, the performance and the energetic characteristic of silver tungstate as cathodic material in type [2] cells are summarized in Table I.

Lithium-silver molybdate system.—The electrochemical behavior of the Li/Ag$_2$MoO$_4$ couple was investigated considering the following cells

$$\text{Li/LiAlCl}_4\text{-BL/Ag}_2\text{MoO}_4 \qquad [4]$$

and

$$\text{Li/LiAsF}_6\text{-BL/Ag}_2\text{MoO}_4 \qquad [5]$$

Cells [4] and [5] showed values of 2.9 and 3.0V at 22°C and the typical polarization and discharge curves (0.5 mA cm^{-2}) are reported in Fig. 6 and 7, respectively.

From Fig. 7, the discharge process of the Li/Ag$_2$MoO$_4$ couple also appears to be characterized by two plateaus, even if not so sharply defined as in the Li/Ag$_2$WO$_4$ case. The electrochemical characterization of the process, based on coulometric analyses, indicated a value

Table I. Performance and energetic characteristic of Ag$_2$WO$_4$ and Ag$_2$MoO$_4$ coupled with lithium in LiAsF$_6$-BL electrolyte at room temperature (first plateau only)

	Ag$_2$WO$_4$		Ag$_2$MoO$_4$	
	Low rate (0.5 mA cm^{-2})	High rate (8 mA cm^{-2})	Low rate (0.5 mA cm^{-2})	High rate (8 mA cm^{-2})
Specific capacity (A-hr/g)	0.115	0.075	0.145	0.070
Mean discharge voltage (V)	3.2	2.7	2.8	2.1
Specific energy density (W-hr/g)	0.370	0.200	0.410	0.150
Efficiency (percent)	98	75	98	50

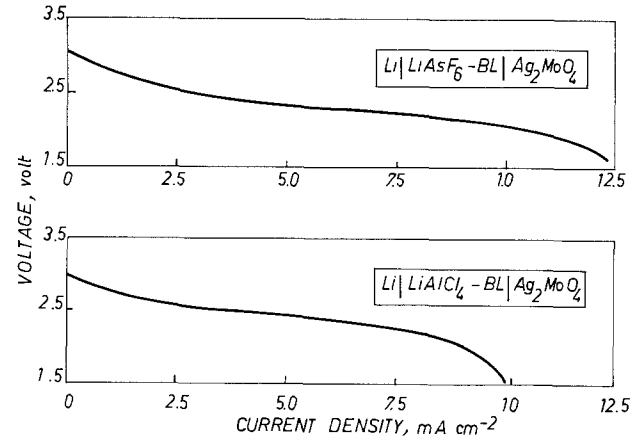


Fig. 6. Typical polarization curves for the Li/Ag$_2$MoO$_4$ couple in LiAsF$_6$-BL and LiAlCl$_4$-BL electrolytes at room temperature.

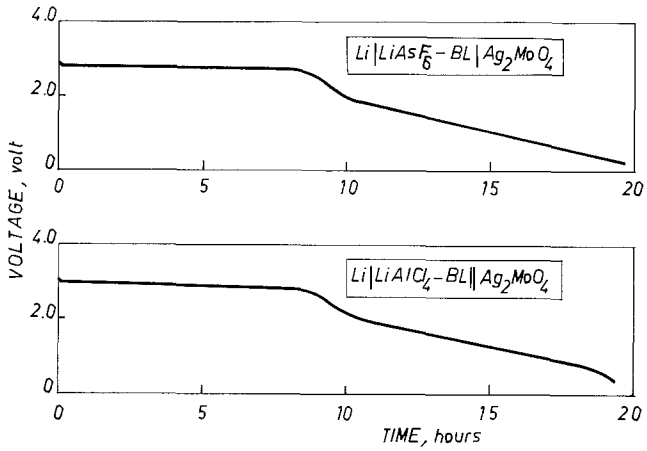


Fig. 7. Typical discharge curves for the Li/Ag$_2$MoO$_4$ couple in LiAsF$_6$-BL and LiAlCl$_4$-BL electrolytes at 0.5 mA cm^{-2} and at room temperature. Average cathodic weight: 40 mg.

of two electrons at the end of the first plateau and of about four at the end of the discharge. The x-ray diffraction patterns of the cathodic mass recovered after the first plateau are reported in Fig. 8, where the diffraction patterns of silver molybdate, silver, and lithium molybdate are also schematically shown. On the basis of the above-reported analyses, one may then assume the following

$$2\text{Li} + \text{Ag}_2\text{MoO}_4 \rightarrow \text{Li}_2\text{MoO}_4 + 2\text{Ag} \qquad [6]$$

as the most probable electrochemical reaction associated to the first plateau of the discharge of cell [5].

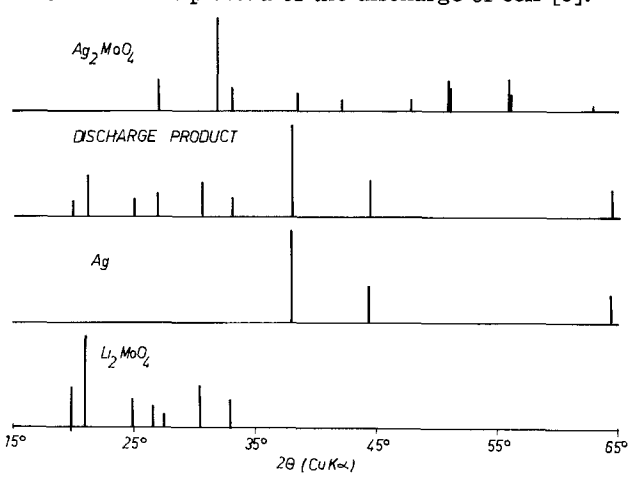


Fig. 8. X-ray diffraction patterns of the starting and discharged cathodic material (first plateau) for the Li/LiAsF$_6$-BL/Ag$_2$MoO$_4$ cell. Data for Ag and Li$_2$MoO$_4$ have been obtained from ASTM card indexes.

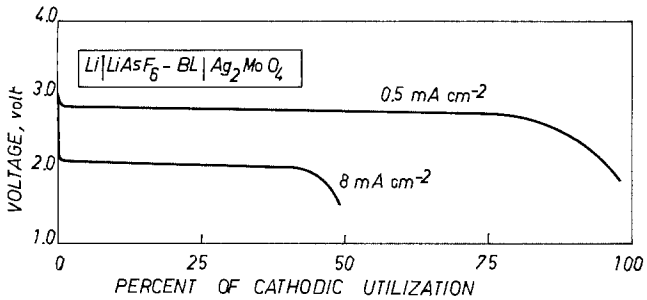


Fig. 9. Typical discharge curves for the $Li/LiAsF_6$-BL/Ag_2MoO_4 cell at low (0.5 mA cm^{-2}) and high (8 mA cm^{-2}) rates and at room temperature (first plateau).

In this case also attention was focused on this plateau due to its high constant voltage, as illustrated by the typical discharge curves of cell [5] at various rates reported in Fig. 9. It may be noted how the voltage of this cell remains always slightly inferior to that of the Li/Ag_2WO_4 cell discharged under comparable conditions (see Fig. 5). In this respect silver tungstate appears to be a more interesting cathode than silver molybdate. On the other hand, the latter shows better energetic characteristics, as indicated by the results in Table I where the performances of the two cathodic materials are compared.

The preference of one of the above-mentioned silver oxosalts would then depend on the type of application. In view of proper technological applications, additional studies may be required for thoroughly defining the stability and the shelf-life of the two systems. These studies are in progress in our laboratory.

Acknowledgments

This work was carried out with a financial support from the Consiglio Nazionale delle Ricerche (C.N.R.).

Manuscript submitted July 21, 1976; revised manuscript received Sept. 27, 1976.

Any discussion of this paper will appear in a Discussion Section to be published in the December 1977 JOURNAL. All discussions for the December 1977 Discussion Section should be submitted by Aug. 1, 1977.

Publication costs of this article were assisted by the University of Rome.

REFERENCES

1. G. Lehmann, T. Rossinoux, G. Gerbier, and J. P. Gabano, "Power Sources 4," D. H. Collins, Editor, p. 299, Oriel Press England (1974).
2. N. Margalit, Abstract 40, p. 103, The Electrochemical Society Extended Abstracts, Fall Meeting, Dallas, Texas, Oct. 5-9, 1975.
3. A. N. Dey and R. W. Holmes, U.S. Pat. 3,822,148 (1974).
4. M. B. Rao, *This Journal*, **114**, 13 (1967).
5. L. Campanella and G. Pistoia, *ibid.*, **118**, 1905 (1971).

Reaction of the Gallium Analog of β''-Alumina with Water

L. M. Foster* and G. V. Arbach

IBM Corporation, Thomas J. Watson Research Center, Yorktown Heights, New York 10598

ABSTRACT

The reaction of the gallium analog of β''-Al_2O_3 with moisture was investigated. This material in finely divided form reacts rapidly with moisture from humid atmospheres to pick up approximately 1 mole of water for each gram-atom of sodium. The water uptake is accompanied by an expansion in the c axis of 11-12%. Monocrystals of the β''-gallate do not show measurable water pickup, and particles of intermediate sizes show intermediate degrees of pickup. The size effect is explained as peripheral attack of water on the crystal, which ceases after a fixed penetration depth. An association of water molecules with the sodium ions to form a complex such as $(NaH_2O)^+$, which increases the coordination of the site, is suggested as the reaction mechanism.

The layered sodium aluminates, β- and β''-alumina, have analogs in the Na_2O-Ga_2O_3 system (1). These gallium-based materials exhibit similar fast ion conduction (2), easy exchange of the alkali ion (3), strongly anisotropic properties, and other characteristics of the alumina prototypes. In particular, they exhibit a sensitivity to moisture similar to some preparations of β- and β''-alumina, but to a greatly enhanced degree.

Moisture take-up by the β-aluminas is a serious technological problem, since it can result in loss of strength and conductivity and eventual deterioration of the formed and sintered bodies that are employed as the conducting separators between the anode and cathode compartments of sodium-sulfur batteries, such as are under development both in the United States and abroad.

There are statements throughout the industry that the β''-form of the sodium aluminate appears to exhibit a greater sensitivity to moisture than the β-form. One must be careful in making this assessment, however, since it is not possible to compare the two materials in identical form. β''-Al_2O_3 transforms to β-Al_2O_3 at about 1500°-1600°C. A sintered ceramic body produced in the β''-phase field will not have the same physical properties, such as grain size, porosity, surface area, etc., as one sintered at a considerably higher temperature in the β-phase field. Moreover, there is usually a change in the Na_2O/Al_2O_3 ratio during this transformation that could result in the formation of a second phase. These extraneous effects could greatly affect moisture sensitivity even though there were no intrinsic differences between the two pure materials. The latest report of the Ford Motor Company effort on the Na-S battery (4) suggests that the sensitivity of β''-Al_2O_3 to moisture is due largely to the presence of the very hygroscopic $NaAlO_2$ at the grain boundaries of the sintered body. This material occurs because of incomplete conversion of the sample to β''-Al_2O_3 at the firing temperature. They found that if the β''-phase is stabilized by the addition of Li_2O so that firing can be carried out at higher temperatures, the conversion to β'' is more complete and the sensitivity to moisture is greatly reduced. Other workers maintain, however, that there is still a

* Electrochemical Society Active Member.

Key words: ionic conductors, sodium gallates, solid electrolytes.

difference in sensitivity between β and β'', irrespective of these complicating factors (5).

The present work is concerned with behavior of the β''-phase of sodium gallate in the presence of moisture. This material was obtainable as pure, large monocrystals, well characterized as to composition, composition uniformity, and the absence of extraneous phases which could complicate interpretation of the results. Information obtained about moisture reaction with this gallium analog will be useful in understanding the moisture problem with the aluminum-based battery separators.

Experimental

Some of the sodium gallate samples that were prepared early in the present study showed a remarkable sensitivity to moisture without parallel in the Na_2O-Al_2O_3 materials. The samples were polycrystalline aggregates obtained by prereacting Na_2CO_3-Ga_2O_3 mixtures, followed by pressing and sintering to form a ceramic body. Some samples of this material would completely deteriorate to powder on standing for a few hours in room air of moderate relative humidity. X-ray powder diffraction examination of the product showed substantial loss of structure, as evidenced by line broadening and a general diffuseness of the pattern. Reaction of alkali oxides with water is in itself not surprising except that in the present cases the moisture was re-evolved and the original highly crystalline character was completely restored by brief heating at 200°-300°C.

The equivalent of the sodium aluminate, $NaAlO_2$, which was held responsible for moisture sensitivity of some β''-Al_2O_3 preparations by the Ford workers, exists in the Na_2O-Ga_2O_3 system as well. This material is also very reactive with water. In the latter system, however, there are two additional phases that are not present in the Na_2O-Al_2O_3 system. These are $3Na_2O \cdot 5Ga_2O_3$ and $Na_2O \cdot 3Ga_2O_3$. $NaGaO_2$ was never encountered in our sintered preparations of β'' sodium gallate that were used in the early studies. If reaction to β'' was incomplete only $3Na_2O \cdot 5Ga_2O_3$ and/or $Na_2O \cdot 3Ga_2O_3$ was found as the second phase. In separate experiments each of these compounds was found to be totally inert to moisture and, if admixed with sintered β''-samples, could not result in spurious behavior with water. Nevertheless, because of the difficulty in fully characterizing those early sintered samples, particularly with regard to the possible presence of small amounts of extraneous phases, emphasis was changed to investigation of single phase, monocrystalline samples. Monocrystalline β''-sodium gallate was prepared by Na_2O vaporization from soda-rich Na_2O-Ga_2O_3 melts. The details of this procedure will be published elsewhere.

Moisture sorption experiments.—Moisture take-up was determined by weight gain of approximately 0.25g samples, as measured with a Cahn recording microbalance. Relative humidity was maintained constant in the balance envelope at 50% with continuously stirred H_2O-H_2SO_4 solutions. Each material was dried at 300°C prior to exposure to moisture. It had been established that this treatment would restore the dry weight of any sample that had taken up moisture during grinding or storage. All sorption experiments were made at room temperature.

Figure 1 shows the weight gain of β''-sodium gallate samples expressed as moles of H_2O per gram-atom of sodium. The various curves are for samples of different particle size. The reason for investigating the behavior of various-size particles will be apparent in the discussion below. The materials were obtained by starting with a monocrystal, which actually showed too little weight gain to appear on the plot (bottom, dashed curve), and then grinding similar monocrystals and screening the material to the sieve fractions indicated on the other curves. The smallest fraction (top curve) was passed through a 325 mesh sieve, with no attempt being made to establish the lower size limit.

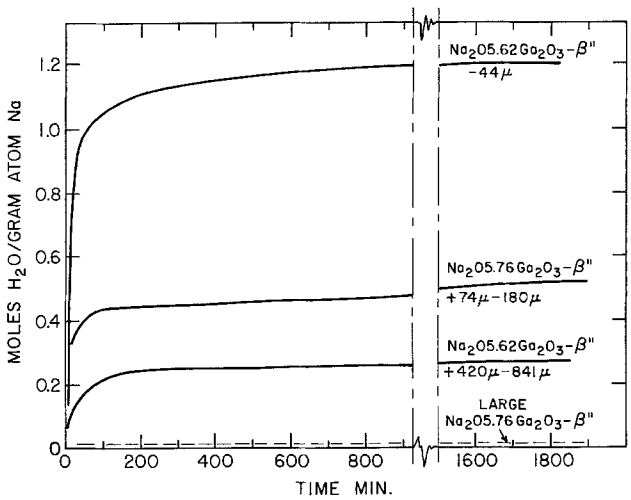


Fig. 1. Moisture take-up as a function of particle size in β''-sodium gallate.

The moisture take-up curves for the β''-gallate do not actually arrive at zero slope in any reasonable time. In one case a sample of the <44 μm material was left in 50% humidity air for 300 hr at which time it had taken up 1.82 moles of H_2O per gram-atom of Na and was still rising extremely slowly.

If a sample that had been carried through a sorption run was heated to 200°-300°C to restore its original weight and then exposed to the humid atmosphere again, the second sorption curve would essentially retrace the first. If there was a difference, it would be as an even sharper knee after the initial very rapid pick-up.

The composition of the crystals was obtained by spectrophotometric determination of sodium compared with that of suitable standards. These gallium materials are completely soluble in hot 50% HCl-H_2O mixtures, and the analysis is straightforward. The two different compositions shown in Fig. 1 are for two different lots of crystals. Their spread (*ca.* ± 1%) is considered to be well within the precision of the determination.

X-ray diffraction analysis.—Crystallographic changes that accompanied the sorption of moisture were observed by x-ray powder diffraction analysis, using nickel-filtered Cu-Kα radiation. The pattern of as-grown β''-$Na_2O \cdot 5.76Ga_2O_3$ is shown in Fig. 2 (top). The structure is rhombohedral with the $R\bar{3}m$ space group. The lattice parameters are $a = 5.84$Å, and $c = 34.53$Å. The pattern of a <44 μm sample that had taken

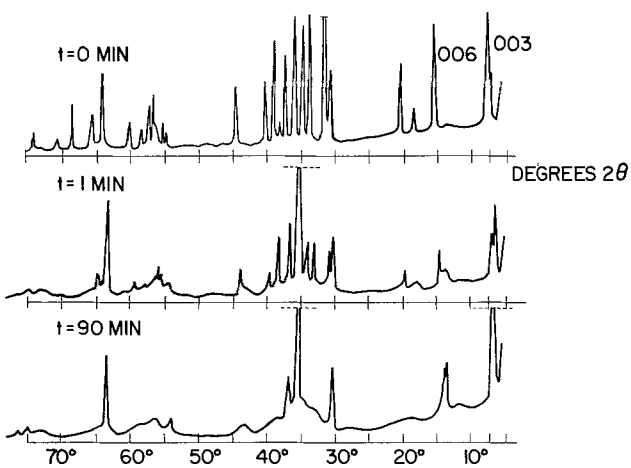


Fig. 2. X-ray diffraction patterns of β''-sodium gallate as a function of time of exposure to 50% humidity air.

up moisture more or less to saturation, and then been redried at 300°C, would be identical. The parameters for the corresponding β''-Al_2O_3 are $a = 5.61$Å, and $c = 35.85$Å (6).

Figure 2 (center) is for a <44 μm sample that had been exposed to humid room air for 1 min. The conspicuous change that has occurred is a general broadening and loss of intensity of the (hkl) reflections with the exception of the (001) which remain narrow but are being replaced by another set corresponding to a new c axis spacing 10-11% larger. Figure 2 (bottom) shows this change complete after 90 min exposure to moisture.

The powder diffraction pattern of the large monocrystal of Fig. 1 after exposure to moisture was identical to Fig. 2 (top), confirming the fact that there had indeed been no water pickup. The patterns for the other two samples of intermediate particle size showed mixtures of "wet" and "dry" phases.

Discussion

The attack of moisture on the β-aluminas that are under development as solid electrolytes for Na-S batteries was early recognized as an important technological problem that had to be overcome. There is still an opinion in the industry that this moisture sensitivity is an intrinsic property of the pure materials (5, 7), and not entirely attributable to extraneous phases, grain boundaries, etc., that reflect the method of preparation of the sample, as has been suggested by others (4). The exceptionally rapid attack of moisture on pure single phase β''-sodium gallate that was observed in the present study shows that this view is unquestionably true, at least in the case of the gallium analog.

The course of the curves of Fig. 1 indicates that water pickup is not determined by a simple diffusion mechanism, for that would allow particles of any size to reach the same level of saturation, given sufficient time. In the short-time regime of the curves, approximately up to the knee, the weight gain very roughly varies directly as the time. After the knee, the water take-up occurs much more slowly. This suggests a surface sorption, although the surface would have to be extremely rough or very deep to account for the amount of water pickup.

The fact that moisture pickup had essentially ceased in the three coarsest samples of Fig. 1, even though large proportions of the samples were still unattacked, as evidenced by the presence of the "dry" phase in their x-ray diffraction patterns, suggests that water diffuses into the surface to some fixed distance, then stops. Assume that the moisture diffuses only along the c planes, and that it penetrates to a depth that is just sufficient to saturate the smallest size fraction, *i.e.*, 44/2 = 22 μm. Then the expected weight gains are calculated as 56, 14, and ≃0% of that of the <44 μm fraction for the >74, <180 μm, >420, <841 μm, and large monocrystal, respectively, in reasonable agreement with the 45, 23, and ≃0% that were calculated from the sorption curves. For these calculations the particle size was taken to be the average for each size fraction.

A very surprising observation was made when a moisture sorption experiment was attempted with particles of a sieve size intermediate between the <44 and >74, <180 μm sizes shown in Fig. 1. Upon exposure to the humid atmosphere, the sample immediately began to lose weight and it was observed that particles were flying out of the sample basket. It was apparent that when particles with a surface-to-volume ratio of some critical value encounter moisture, the strain that sets up around the edges of the highly anisotropic bodies is sufficient to cleave them along the c planes, almost explosively. In smaller particles only small strains can be tolerated before the pieces fall apart and allow access of moisture to all parts; in larger particles the strain is insufficient to cleave them. It was a common observation, however, that even large monocrystals of the β''-gallate frequently cleaved when subjected to small stresses such as encountered during handling and, especially, during sawing. This effect is now understood to be the result of moisture that has penetrated along the c planes to a fixed depth. This places that portion of the crystal under a large compressional stress which, in turn, places the unpenetrated portion under high tensile stress. In this condition, the crystal is very susceptible to cleavage when subjected to additional external stresses.

The mechanism for the entry of water molecules into β''-crystals, and the reason for the penetration ceasing at a fixed depth, is not fully understood at this time and is the subject of continuing study. It is assumed that moisture attack is initially at high energy sites, possibly steps, on the surface. Once the water sites become filled at those locations, no further water can penetrate that volume of the crystal but must diffuse along the misfit dislocation bordering the damaged volume. As these islands of penetrated crystal grow both inwardly and laterally, they eventually coalesce to annihilate the threading dislocations between adjacent islands, thereby preventing further penetration at those points. The final result of such a process would be a crystal which is now impervious to more water, whose edges are under compressional stress due to their water content, and whose center is thereby under tension stress. Similar behavior has been observed in other materials such as MgO monocrystals when exposed to moisture (5).

We will now look at the sites into which water molecules might go. Figure 3 shows three oxygen layers, including the conduction plane, in the β'' precursor structure. If the B plane were filled with oxygens in close-packed arrangement, there would be three more atoms in the positions marked +, and the cubic close-packing sequence of ABC would be maintained through the conducting plane. The three + sites are empty, however, and become the midoxygen (MO) sites between the B plane oxygen (open circle) and similar oxygens in the two adjacent cells.

In the β-Al_2O_3 structure, the two sodium sites, which are in the same positions within a plane as in Fig. 3, are nonequivalent, with the lower energy site, the Beevers-Ross(BR) site, alone being occupied in the

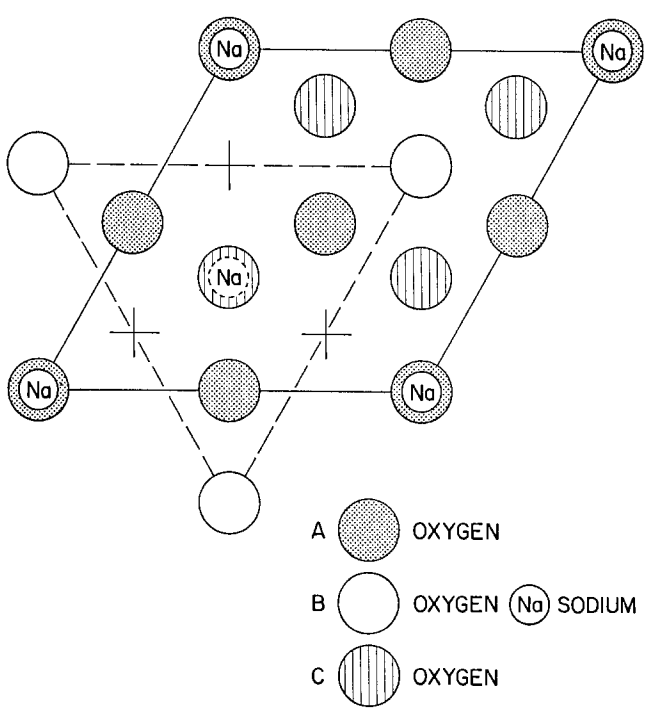


Fig. 3. Three oxygen layers, including the bridging oxygen, of the β''-structure (looking along c axis).

ideal $Na_2O \cdot 11Al_2O_3$ crystal (8). In the actual crystal, which appears to always have excess sodium, the excess goes mostly into the (MO) sites rather than into the second Na site, the anti-Beevers-Ross (ABR) site.

In the β''-structure, because of the different crystal symmetry, the two sodium sites are equivalent, and statistically equal occupancy is expected. The sodiums in both sites are in tetrahedral coordination, with the one shown within the cell in Fig. 3 being immediately below an oxygen of the C plane and above the center of the triangle of oxygens of the A plane, and the corner sodiums being in the reverse situation. The maximum sodium content of the β''-structure is thus twice that of the ideal β-structure, or $Na_2O \cdot 5.5Ga_2O_3$ for the gallium analog. The (MO) positions are also possible sites for sodium in the β''-structure and, in fact, are probably substantially occupied. However, because of repulsion by like charges, it seems highly unlikely that two "normal" Na sites and the (MO) site between them could be occupied simultaneously and, on the average, only two of the three can be occupied at a given time.

As the formula $Na_2O \cdot 5.5Ga_2O_3$ is written, the charge of the additional Na is compensated by oxygen. In the older β-Al_2O_3 literature this was not thought necessarily to be the case, and compensation by aluminum vacancies was proposed as an alternative (6). More recent work of Roth *et al.* (9) has shown, however, that in β-Al_2O_3, at least, compensation of sodium over and above the $Na_2O \cdot 11Al_2O_3$ composition is accomplished by additional oxygen atoms in the conducting plane.

If the mechanism of charge compensation is the same in the β''-structure, ½ oxygen on the average would have to be added per plane in one of the (MO) sites for the formula $Na_2O \cdot 5.5Ga_2O_3$. Roth *et al.* (9) proposed that this was accomplished by M^{+++} ions in the octahedral sites on each side of an (MO) position moving toward the conducting plane and bonding together across the plane through the new oxygen atom. Each new oxygen bridge would thus fill one more close-packed oxygen site in the B layer of Fig. 3. For the β''-formula with the maximum possible sodium, $Na_2O \cdot 5.5Ga_2O_3$, there would thus be $3 - ½ = 2½$ (MO) sites and $2 + ½(2) = 3$ empty octahedral holes (1 on each side of the original oxygen bridge, and ½ on each side of the ½ new oxygen bridge) as possible sites for water molecules.

The actual average analysis of a number of β''-sodium gallate crystals that were used in the present study was $Na_2O \cdot 5.7Ga_2O_3$. This is 1.93 Na atoms per plane, or 0.93 more than in the β-$Na_2O \cdot 11Ga_2O_3$ structure. Thus, there is slightly less sodium than the maximum of 2 atoms per plane that can be accommodated by the structure. This additional 0.93 Na requires 0.465 additional oxygen atoms per plane for charge compensation, which requires that $2 \times 0.465 = 0.93$ Ga atoms (0.465 from each side of the plane) move from their octahedral sites to form the new oxygen bridge. This fills 0.465 (MO) sites to compensate the $¼ \times 4 = 1$ Na atoms that go into the cell corners, and leaves $3 - 0.465 = 2.535$ (MO) sites open per plane.

If these (MO) sites filled with water indiscriminately, there would be a continuous weight gain to 2.535 moles of H_2O per 1.93 gram-atom of Na, or a ratio of 1.31 to 1. The $2 + 0.93 = 2.93$ octahedral holes could accommodate more water to give a total weight gain of $2.535 + 2.93 = 5.465$ moles of H_2O per 1.93 gram-atom of Na, or a ratio of 2.83 to 1.

The above calculations show that there is more than enough space in the conduction plane of the β''-lattice to accommodate a water molecule for each Na atom, and that a discontinuity in the water curve might be expected if such an association occurs. Another break might be expected at 1.31 to 1 when the remainder of the (MO) sites is filled, followed by termination of absorption at 2.83 to 1 when the octahedral sites are full. Only the first was observed in the experimental curve, and it is concluded that the principal interaction of the water is to form a 1 to 1 coordination complex of H_2O with the Na^+ ion. The alkali in the β''-structure is in fourfold coordination as compared to sixfold in the β-structure and eightfold in the (MO) sites. It is a general rule of thumb that a complex will form at a site if by doing so the coordination at the site is increased. Perhaps the action of water is to form a complex analogous to hydronium ion, H_3O^+, *i.e.*, $(NaH_2O)^+$, as had been suggested by Roth and Mitoff (10).

If a hydrate of well-defined composition results when a water molecule bonds to Na, one might expect a sharp x-ray diffraction pattern of this new phase. The fact that this was not observed, as shown in Fig. 2, bottom, indicates that structural changes are occurring in addition to extension of the c parameter. Rotation of spinel-like blocks with respect to each other in a somewhat ill-defined manner could account for the changes.

Filling of the remaining sites in the β''-structure is clearly very difficult and the process is so slow that nothing can be learned from that part of the sorption curve to shed light on the mechanisms involved. In the one experiment where moisture sorption had reached 1.86 moles of H_2O per gram-atom of Na in 300 hr, one could imagine that the curve might be asymptotically approaching 2.83, as required for complete site filling, but it would clearly require several months to demonstrate.

Because of the great similarity between the β''-gallate and β''-Al_2O_3, it is expected that moisture sensitivity of the latter material must also be a property of the pure substance, and that all of the observations of degradation of β''-Al_2O_3 bodies by water cannot be attributed to the presence of impurities and extraneous phases alone.

Manuscript submitted June 15, 1976; revised manuscript received *ca.* Oct. 4, 1976.

Any discussion of this paper will appear in a Discussion Section to be published in the December 1977 JOURNAL. All discussions for the December 1977 Discussion Section should be submitted by Aug. 1, 1977.

Publication costs of this article were assisted by the IBM Corporation.

REFERENCES

1. L. M. Foster and J. E. Scardefield, Abstract 4, p. 14, The Electrochemical Society Extended Abstracts, Spring Meeting, Toronto, Canada, May 11-16, 1975.
2. R. J. Chicotka, Abstract 5, p. 16, *ibid.*
3. R. Title and G. V. Chandrashekhar, Conference on Superionic Conductors, Chemistry, Physics, and Applications, p. 45, Schenectady, N.Y. (May 1976).
4. Ford Motor Company Semiannual Report, Contract No. NSF-C805, RANN, Division of Advanced Energy Research and Technology, Washington, D.C. (Jan. 1976).
5. R. M. Dell, Private communication.
6. M. Bettman and C. R. Peters, *J. Phys. Chem.*, **73**, 1774 (1969).
7. F. G. Will, Abstract 83, p. 221, The Electrochemical Society Extended Abstracts, Spring Meeting, Washington, D.C., May 2-7, 1976.
8. C. A. Beevers and M. A. Ross, *Z. Kristallogr*, **97**, 59 (1937).
9. W. L. Roth, F. Reidinger, and S. J. LaPlaca, Conference on Superionic Conductors, Chemistry, Physics, and Applications, p. 23, Schenectady, N.Y. (May 1976).
10. W. L. Roth and S. P. Mitoff, General Electric Company Technical Information Series, No. 71-C-277 (Sept. 1971).

The Behavior of Lead Alloys as PbO_2 Electrodes

Thomas F. Sharpe*

General Motors Corporation, Research Laboratories, Warren, Michigan 48090

ABSTRACT

An understanding of the corrosion behavior of lead alloys is important because grid corrosion affects the cycle life of the positive plate of the lead-acid battery. Comparisons between pure lead, lead-antimony, and lead-arsenic alloys in various electrochemical studies are discussed in terms of effects of the alloying element on the development and subsequent discharge behavior of PbO_2 in H_2SO_4 electrolyte.

In a previous study (1), low-rate (~0.5 mV/sec) cathodic potential sweeps were carried out on a preanodized antimonial (Pb-4.5%Sb-0.6%Sn) and a nonantimonial (Pb-0.06%Ca-0.6%Sn) alloy to elucidate their behavior near the $PbO_2/PbSO_4$ potential. The cathodic sweep profiles were sensitive to the potential and time of anodic treatment and reflected the buildup of α- and β-PbO_2 in the corrosion film. More importantly, the cathodic sweeps were markedly different for the two alloys for a given anodic pretreatment, which could be ascribed, in part, to an effect of antimony in lowering the rate of forming β-PbO_2 during the anodic pretreatment. That effect was suggested to partially account for the substantial increase in positive plate cycle life when using antimonial grids.

To further elucidate the mechanism by which antimony prolongs positive plate life, these studies were extended to determine the effect of antimony concentration in the alloy, and to compare the effect of antimony and arsenic in the alloy on the behavior of lead as a PbO_2 electrode.

Experimental

Alloys were prepared in ~1 kg master ingots using 99.99+% lead and reagent grade metals. Portions of the ingots were used for the casting of test electrode tabs having a geometric area of 4 cm^2 exposed to the electrolyte.

The full anodic scans extended from the hydrogen evolution region (−1500 mV *vs.* Hg/Hg_2SO_4) to the oxygen evolution region (1600 mV *vs.* Hg/Hg_2SO_4) and were obtained immediately after maintaining the electrodes at −1500 mV *vs.* Hg/Hg_2SO_4 for 0.3 ksec (5 min).

Following the constant potential anodic treatments at values above the $PbO_2/PbSO_4$ reversible potential, the electrodes were discharged either by a cathodic voltage sweep (as previously described) (1) or by an arbitrary constant current of 1.5 mA. The constant current discharge was started within 10 sec after completion of the anodic treatment.

Results

A number of anodic sweeps are shown in Fig. 1. The intensity of the anodic current peak for the Pb → $PbSO_4$ reaction, occurring just above the $Pb/PbSO_4$ reversible potential, was not appreciably affected by either arsenic or antimony at the concentration levels considered in this study. The increase in current above *ca.* 1200 mV is due to PbO_2 formation and oxygen evolution. The anodic peak at −325 mV (Fig. 1-A) is ascribed to the oxidation of antimony in the alloy, with the peak intensity increasing with an increase in antimony concentration. The anodic current peak for oxidation of arsenic in the alloy occurs at −90 mV (Fig. 1-B). That current peak was just discernible at an arsenic concentration of 0.25%.

Cathodic sweeps following 3.6 ksec (1 hr) control at various potentials are shown in Fig. 2, and examples showing the effect of sweep rate following anodic control are given in Fig. 3 and 4. As discussed previously (1), the sweeps are influenced by an anodic reaction occurring at nearly the same potential as the PbO_2 discharge, so that they often exhibit a peculiar oscillatory behavior. In these sweeps, the anodic peaks a are believed to be part of a continuous anodic current profile (as represented schematically by the broken line in Fig. 5) that becomes masked by the buildup of the major cathodic peak b (β-PbO_2 → $PbSO_4$ discharge peak) and the sporadic minor peak c (α-PbO_2 → $PbSO_4$ discharge peak).

At the higher sweep rates and generally following control at high potentials, there is an additional minor cathodic peak (arrow, Fig. 3), at potentials above the β-PbO_2 discharge peak. This peak is believed to be associated with the desorption of excess oxygen reported (2) to exist in these corrosion films.

The effect of antimony additions to pure lead on the shape of current-time (i-t) curves during a constant potential treatment is shown in Fig 6-A. In the case of pure lead, the major process at that potential is oxidation of $PbSO_4$ to β-PbO_2, as indicated by the single current peak in the i-t curve (3). With increased antimony concentration, the current peak has shifted along the time axis and has almost disappeared at the 3.8% Sb concentration level. At 8.2% antimony, the marked

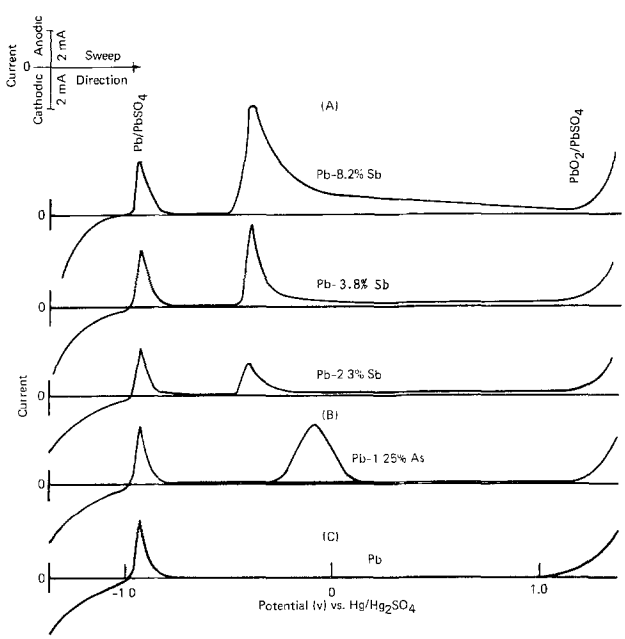


Fig. 1. Anodic potential sweeps for (A) Pb-Sb alloys, (B) Pb-As alloy, and (C) pure Pb in 1.26 sp gr H_2SO_4. Sweep rate = 0.42 mV/sec; electrode area = 4 cm^2.

* Electrochemical Society Active Member.

Key words: lead electrode, lead dioxide electrode, lead corrosion, lead-acid battery, linear sweep voltammetry.

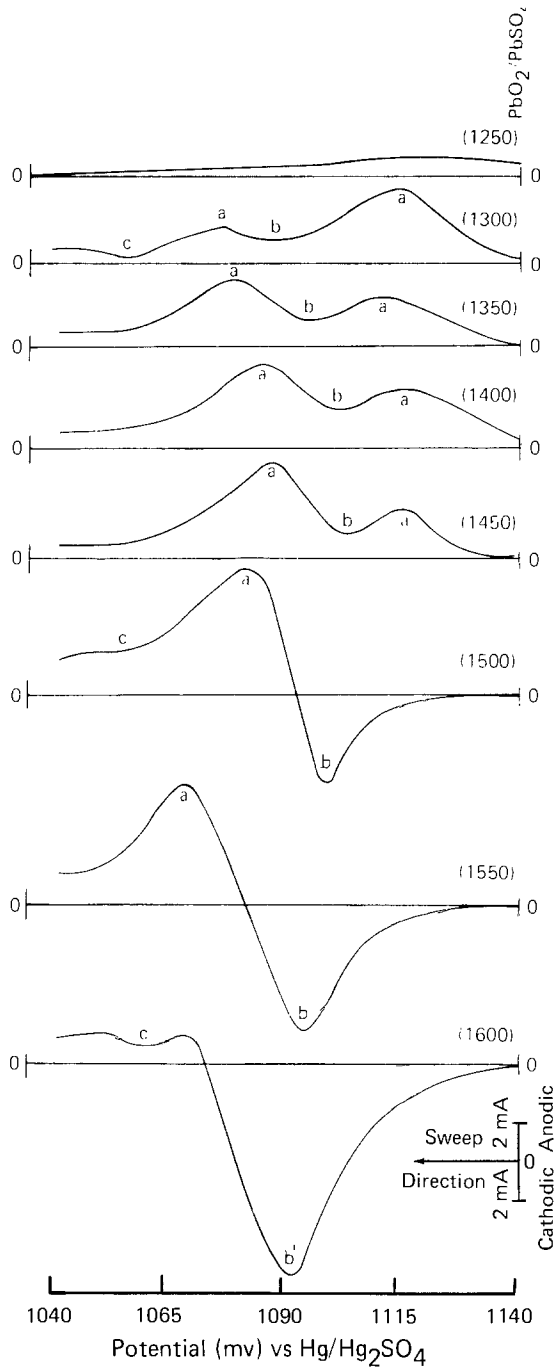


Fig. 2. Cathodic sweeps at 0.42 mV/sec for pure lead following 1 hr anodic control at potentials indicated by numbers on curves. Electrolyte = 1.26 sp gr H_2SO_4; electrode area = 4 cm^2.

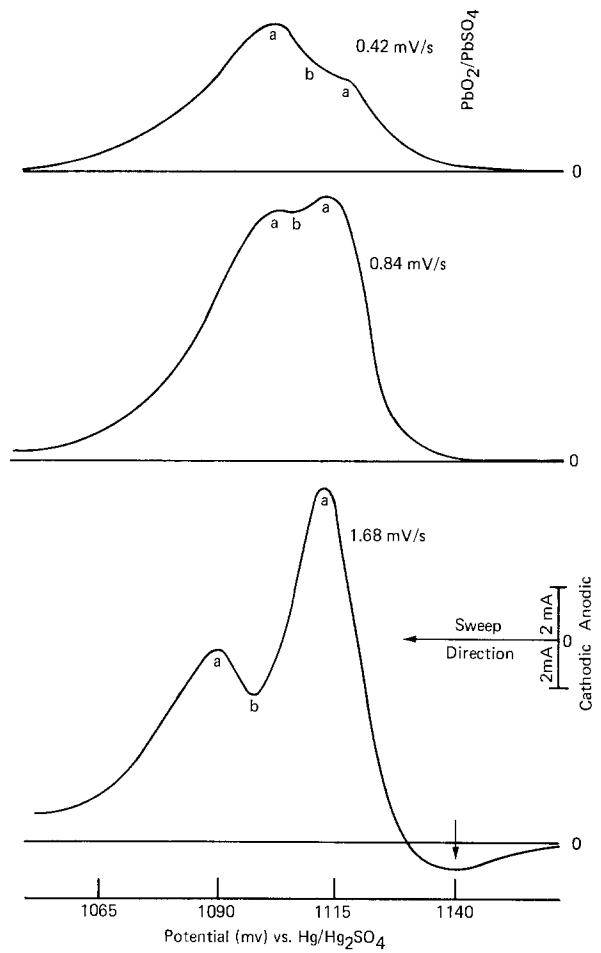


Fig. 3. Effect of cathodic sweep rate on pure lead following anodic control at 1600 mV vs. Hg/Hg_2SO_4 for 3 min. Electrolyte = 1.26 sp gr H_2SO_4; electrode area = 4 cm^2.

increase in current is presumably due to antimony oxidation.

Cathodic potential sweeps obtained after the anodic treatment of Fig. 6-A are shown in Fig. 6-B. These were somewhat sensitive to an antimony concentration at least as low as 2.2%, and displayed a marked reduction in "reactivity" at the 3.8 and 8.2% level. Sweeps following 3.6 ksec (1 hr) control at various potentials for the higher concentrations of antimony are given in Fig. 7, to be compared to those for pure lead in Fig. 2. An interesting result is shown in Fig. 8 for the Pb-3.8% Sb alloy, where the measured current in the sweep (solid line) switches from primarily anodic to primarily cathodic values as the sweep rate is increased. The sweeps in Fig. 8 and in Fig. 3 (for pure lead) were obtained following the minimum time required at the high potential (1600 mV) of anodic pretreatment before significant reactivity was observed (*e.g.*, 0.90 ksec for antimonial lead *vs.* 0.18 ksec for pure lead). For shorter anodic pretreatment, the current in the sweeps was linear and very slightly (<0.5 mA) anodic.

Current-time curves showing the effect of arsenic concentration are exemplified by Fig. 9. The curves are markedly distorted evidently because of background currents due to oxidation of arsenic in the alloy. Examples of cathodic sweeps following anodic treatment, Fig. 10, show that the net current shifts in the anodic direction with increasing arsenic concentration.

In a number of experiments, electrodes were discharged by a constant current following the anodic treatment. These were intended to supplement the cathodic sweeps especially in instances when it was not obvious from the sweeps whether dischargeable PbO_2 had been produced during the anodic pretreatment. The discharges were characterized by two potential plateaus about 30 mV apart (4, 5), occurring just below the $PbO_2/PbSO_4$ reversible potential. For pure lead, the growth of the upper plateau with time of anodic pretreatment was observed to be in proportion to growth of the major cathodic current peak (peak b, Fig. 2) in the cathodic potential sweeps. The lower discharge plateau was always less than 10% of the length of the upper plateau and may be related to the minor cathodic peak (peak c, Fig. 2) in the potential sweeps.

Discharge capacities of the anodically formed PbO_2, calculated from the length of the upper plateau, are given in Table I.

Discussion

An important aspect is the anodic current peaks that appear in the cathodic potential sweeps. A number of sweeps (*e.g.*, Fig. 2-4) suggest that each anodic peak might be treated as an entity, but this leads to difficulty when attempting to explain their buildup and

Table I. PbO_2 discharge capacities in millicoulombs (mC) measured at 1.5 mA. Electrode area = 4 cm^2

Anodic pretreatment	mC						
	Pure Pb	0.8% Sb	2.2% Sb	3.8% Sb	8.2% Sb	0.25% As	0.6% As
1450 mV 3.6 ksec (60 min)	68	72	37	8	8		
1550 mV 3.6 ksec (60 min)	260	180	205	40	38		
1600 mV 0.18 ksec (3 min)	30					3	
0.36 ksec (6 min)	68	27		3		23	
0.90 ksec (16 min)	270	135	108	45	50		46
3.6 ksec (60 min)	380	315	220	118	120	275	158

decay as a function of anodic pretreatment and sweep rate. It is felt that the results can be explained according to the schematic in Fig. 5, where the anodic peaks result from the subtraction of cathodic peaks for the PbO_2 discharge reaction from a continuous background anodic current profile extending throughout the PbO_2 discharge potential region. As greater quantities of dischargeable PbO_2 are formed (Fig. 2), a greater portion of the anodic current profile becomes masked. As the sweep rate is increased (Fig. 3 and 4), both the anodic current profile and the current for β-PbO_2 discharge are enhanced because of diffusion effects, and the β-PbO_2 discharge becomes shifted along the anodic current profile to more negative potentials because of irreversibility.

The anodic current profile would indicate that there is further substrate corrosion during the PbO_2 discharge, since anodic currents are not observed in cathodic potential sweeps for PbO_2 in contact with inert substrates (6). It has been pointed out by Rüetschi (8) that $PbSO_4$ films on lead can act as perm-selective membranes which become impermeable to $SO_4^=$ and HSO_4^- when they have reached a thickness of 1 to several microns. Under that condition, further corrosion of the lead substrate would occur by dissociation of water underneath the $PbSO_4$, precipitation of anodically generated Pb^{2+} in the form of PbO, and the migration of H^+ ions away from the electrode interface. In the present studies, it is postulated that in the cathodic potential sweeps, the $PbSO_4$ forming on the surface of the discharging PbO_2 may possess such perm-selectivity, so that OH^- ions become localized in the interior of the corrosion film and are the species involved in the diffusion process to give the anodic current profile reaction

$$Pb + 2\,OH^- = PbO + H_2O + 2e^-$$

Effect of alloying elements.—In the anodic voltage sweeps (Fig. 1), it is observed that the alloying element reacts at potentials significantly below the PbO_2/$PbSO_4$ reversible potential, so that the element may become depleted from reaction sites before overvoltages for PbO_2 formation are reached. This could account for the observation (7, 9) that when using such an anodic treatment, antimony has no measurable effect on the

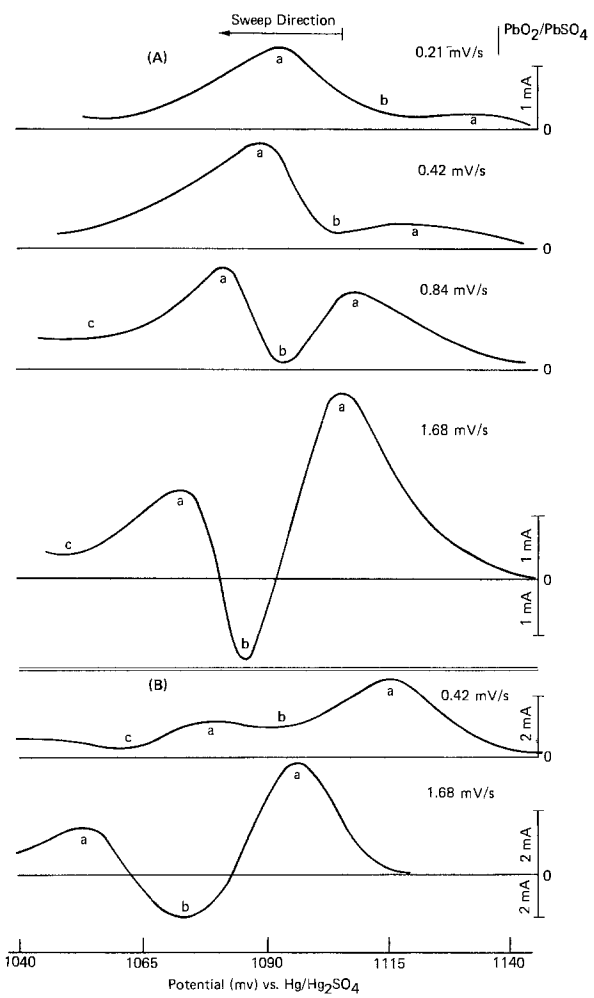


Fig. 4. Effect of cathodic sweep rate on pure lead following anodic control at (A) 1500 mV *vs.* Hg/Hg_2SO_4 for 10 min, (B) 1300 mV *vs.* Hg/Hg_2SO_4 for 1 hr. Electrolyte = 1.26 sp gr H_2SO_4; electrode area = 4 cm^2.

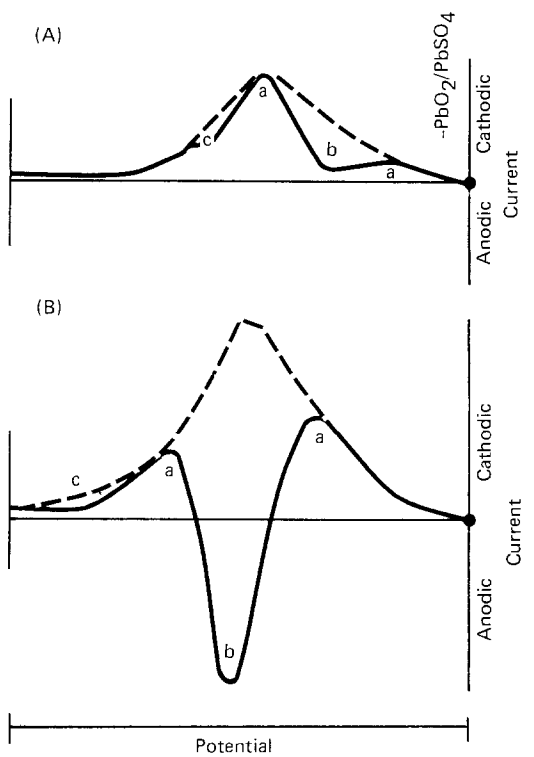


Fig. 5. Schematic for cathodic potential sweep behavior, where B is at a faster sweep rate than A. The solid lines are the current traces and the broken lines represent the anodic current profile.

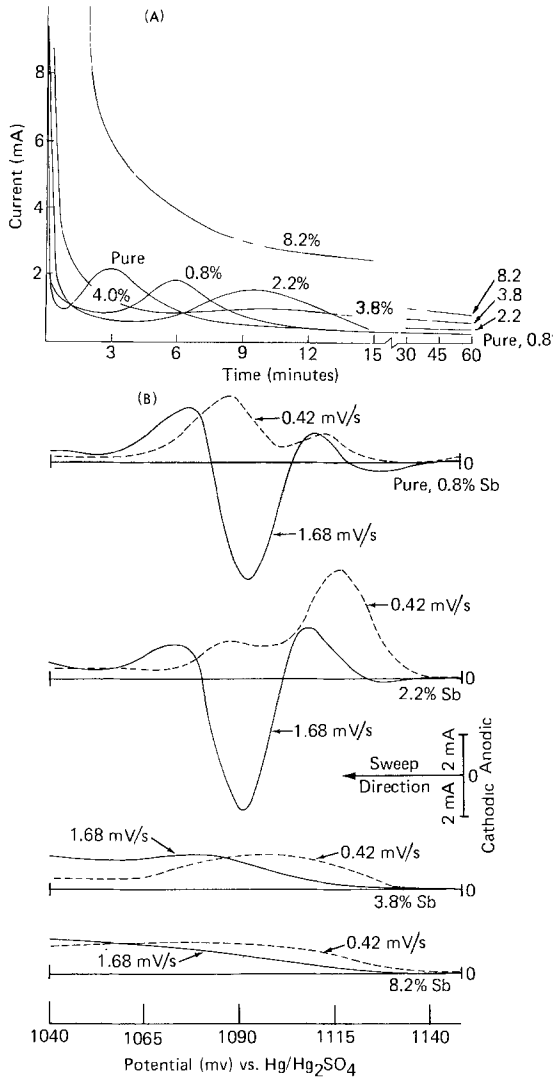


Fig. 6. Current-time curves during 1 hr control at 1450 mV (vs. Hg/Hg_2SO_4) for 1 hr (A) and subsequent cathodic sweeps (B) as a function of antimony concentration. Electrolyte = 1.26 sp gr H_2SO_4; electrode area = 4 cm^2.

development or subsequent discharge behavior of PbO_2. In the present work, however, effects are evident when the alloy is immediately polarized and potentiostated above the $PbO_2/PbSO_4$ reversible potential. That situation would insure reaction of the alloying element in parallel with the development of PbO_2 and is therefore believed to simulate more closely the condition during electrochemical formation of the positive plate.

The effect of increasing antimony concentration on the shape of i-t curves during constant potential treatment above the $PbO_2/PbSO_4$ reversible potential is presumed to be caused by a shift from oxidation of $PbSO_4$ to β-PbO_2 as the major process to oxidation of antimony as the major process. At the potential indicated in Fig. 6-A, the current peak for $PbSO_4$ oxidation has almost disappeared at the 3.8% level, an observation similar to that in earlier work (1) for a 4.5% antimonial alloy.

A treatment of the effect of antimony on the cathodic potential sweeps is complicated by factors such as changes in electrode true surface area and the net currents involved, so that precise determinations of the onset of reactions, current peak areas, etc. is not feasible. In some instances, it appeared that the cathodic current peak for PbO_2 discharge was "buried" in the anodic current profile; an example of this is represented by the uppermost curve in Fig. 8 where one might conclude that there is no PbO_2 discharge (current is a smooth anodic wave). However, the cathodic

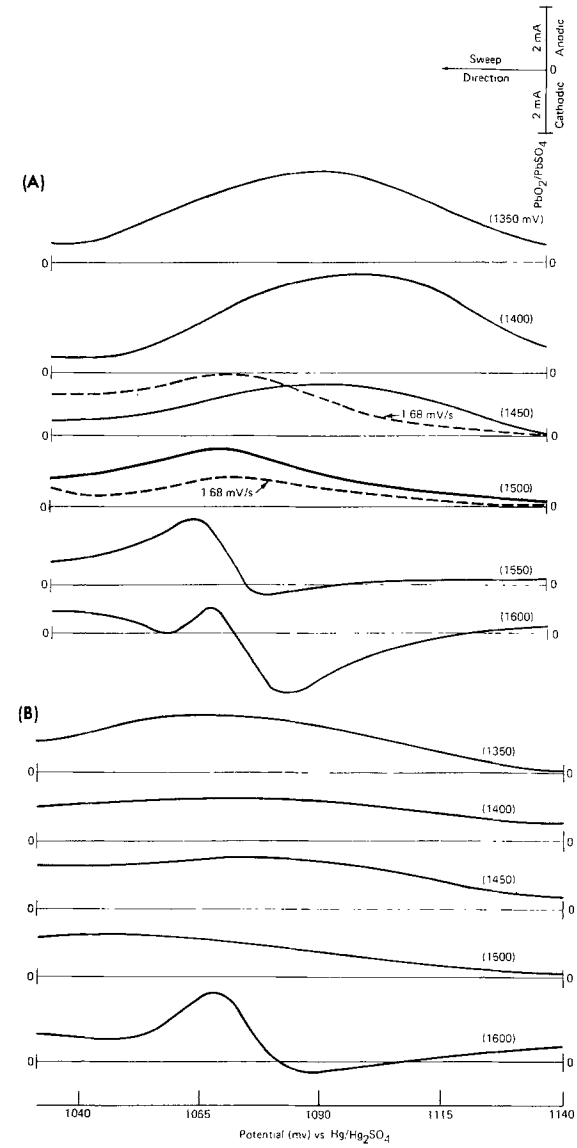


Fig. 7. Cathodic sweeps at 0.42 mV/sec (unless otherwise noted) for Pb-3.8%Sb (A) and 8.2%Sb (B) following 1 hr anodic control at potentials indicated by numbers on curves. Electrolyte = 1.26 sp gr H_2SO_4; electrode area = 4 cm^2.

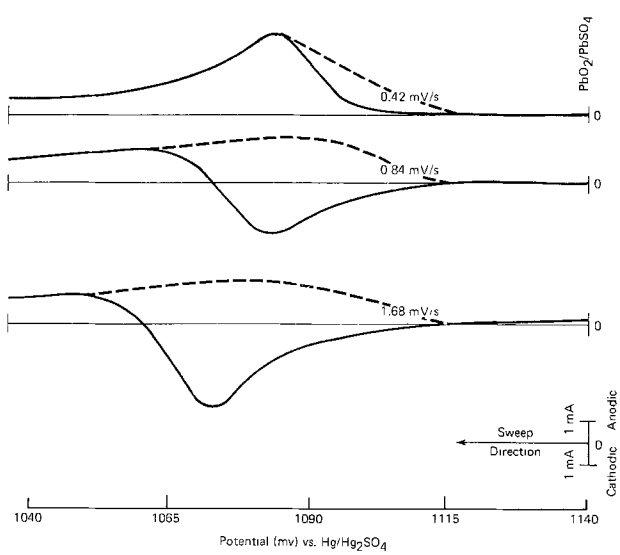


Fig. 8. Effect of cathodic sweep rate on Pb/3.8%Sb following anodic control at 1600 mV vs. Hg/Hg_2SO_4 for 15 min. Electrolyte = 1.26 sp gr H_2SO_4; electrode area = 4 cm^2.

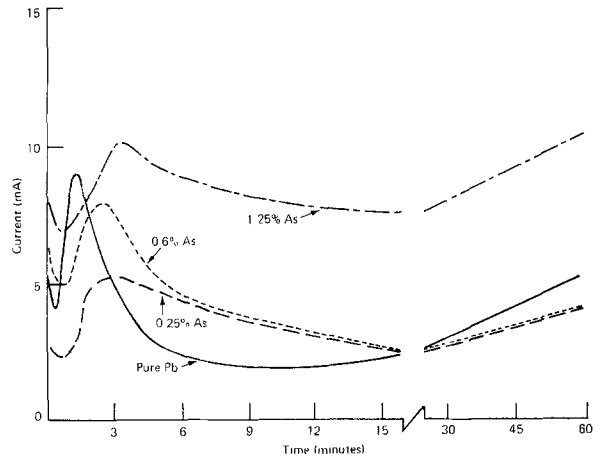


Fig. 9. Current-time curves at 1550 mV *vs.* Hg/Hg_2SO_4 as a function of As concentration. Electrolyte = 1.26 sp gr H_2SO_4; electrode area = 4 cm^2.

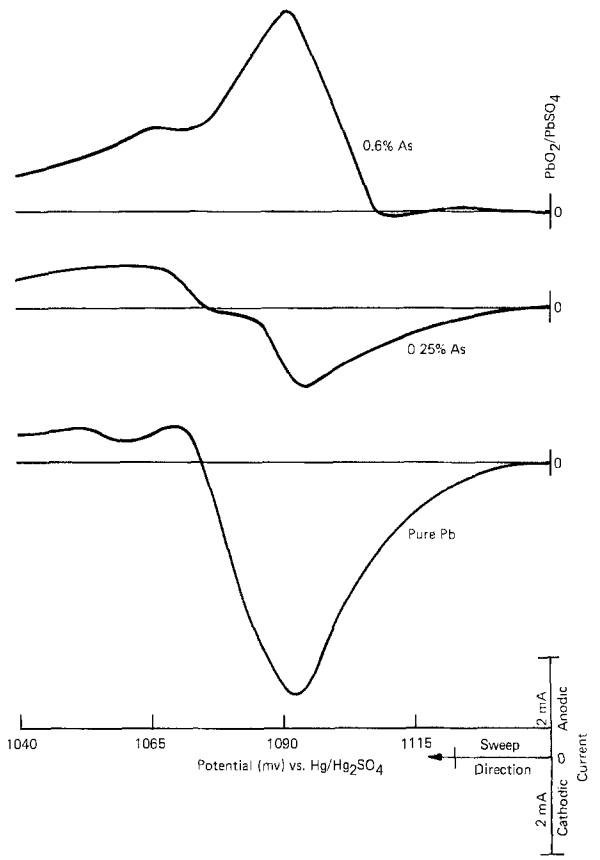


Fig. 10. Effect of arsenic on cathodic sweeps at 0.42 mV/sec following 1 hr anodic control at 1600 mV *vs.* Hg/Hg_2SO_4. Electrolyte = 1.26 sp gr H_2SO_4; electrode area = 4 cm^2.

peak may grow along a profile approximated by the broken lines. This hypothesis is made in context with the curves for the faster sweep rates (which would enhance the cathodic peak) and the observation that on other electrodes, capacity could be obtained in a constant current discharge following the same anodic pretreatment (see Table I).

In view of the complexities, it is yet possible to speculate on the behavior of antimony in accord with the schematic proposed in Fig. 5: At the 2.2% level, there is slightly greater irreversibility in the PbO_2 discharge from that observed on pure lead at a comparable sweep rate, so onset of the major cathodic peak is shifted very slightly along the anodic current profile. At the 3.8 and 8.2% level, the sweeps are consistent with a significant decrease in dischargeable β-PbO_2. The results of Fig. 7, when compared to Fig. 2 for pure lead, confirm an earlier (1) observation that significantly higher anodic pretreatment potentials are required before PbO_2 discharge is indicated in the cathodic sweeps.

At the higher concentrations of antimony, there is also an indication that the nature of the anodic current profile is altered from that for pure lead. This is especially emphasized by comparing the sweeps of Fig. 8 with those of Fig. 3 which were obtained following the incipient formation of PbO_2. For the antimonial alloy, the cathodic peak can be envisioned as a growing along an anodic current profile that is less intense and less dependent on sweep rate than that for pure lead, *i.e.*, the PbO_2 behaves as if it is being discharged from a more inert substrate. Such a condition would be favored if there is less tendency for the proposed Pb → PbO reactions to occur during the cathodic sweeps. Hampson *et al.* (9) obtained electrical impedance measurements on pure lead and lead-antimony binary alloys which could be interpreted in accord with a reduction in thickness and an increase in porosity of the corrosion films with increasing concentrations of antimony. Such a condition may lead to corrosion films having lower perm-selectivity (8) and therefore reduced alkalinity in the film interior.

It is suggested, then, that an alloying element may influence the shape of the cathodic sweeps in a rather complex way by altering both the amount of dischargeable PbO_2 for a given anodic pretreatment, and the anodic current profile intensity, *i.e.*, extent of substrate corrosion during the sweeps. The effect of arsenic on the cathodic sweeps is ascribed, in part, to a decrease in dischargeable PbO_2, since a reduction in capacity was measured in a constant current discharge (Table I) for the same anodic pretreatment indicated in Fig. 10. However, the shift of the net current in the anodic direction occurs in greater proportion than that expected from the decrease in capacity measured by the constant current discharge experiments. Therefore, it is assumed that the sweeps are also influenced because of greater substrate corrosion as the arsenic concentration is increased.

Conclusions

The effect of increasing the antimony concentration in pure lead on the shape of *i-t* curves during potentiostatic control above the $PbO_2/PbSO_4$ reversible potential is attributed to a shift from oxidation of $PbSO_4$ to β-PbO_2 as the major process to oxidation of antimony as the major process.

Cathodic potential sweeps in the region 1140-1040 mV, obtained following the potentiostatic control, can be interpreted in terms of two diffusion-controlled reactions occurring in parallel; PbO_2 discharge and corrosion of the substrate beneath the discharging PbO_2. For the more concentrated antimonial alloys, the sweeps reflect the higher potentials and/or longer times required in the anodic pretreatment to form significant quantities of dischargeable PbO_2, and were also consistent with the view that the PbO_2 behaves as if it is being discharged from a more inert substrate. For an increase in arsenic concentration, the cathodic sweeps were interpreted in terms of a decrease in dischargeable PbO_2 and an increase in substrate corrosion.

Manuscript submitted May 24, 1976; revised manuscript received Sept. 20, 1976. This was Paper 4 presented at the Las Vegas, Nevada, Meeting of the Society, Oct. 17-22, 1976.

Any discussion of this paper will appear in a Discussion Section to be published in the December 1977 JOURNAL. All discussions for the December 1977 Discussion Section should be submitted by Aug. 1, 1977.

Publication costs of this article were assisted by General Motors Corporation.

REFERENCES

1. T. F. Sharpe, *This Journal*, **122**, 845 (1975).
2. P. Rüetschi and B. D. Cahan, *ibid.*, **105**, 369 (1958).

3. P. Rüetschi and R. T. Angstadt, *ibid.* **111**, 1323 (1964).
4. E. Tarter and K. Ekler, *Can. J. Chem.*, **47**, 2191 (1969).
5. P. Rüetschi and B. D. Cahan, *This Journal*, **104**, 406 (1957).
6. J. P. Carr, N. A. Hampson, and R. Taylor, *J. Electroanal. Chem.*, **33**, 109 (1971).
7. H. S. Panesar, "Power Sources 3," D. H. Collins, Editor, p. 79, Oriel Press, Newcastle upon Tyne (1971).
8. P. Rüetschi, *This Journal*, **120**, 331 (1973).
9. M. D. J. Brennan, B. N. Stirrup, and N. A. Hampson, *J. Appl. Electrochem.*, **4**, 49 (1974).

Cost and Size Estimates for a Redox Bulk Energy Storage Concept

Marvin Warshay and Lyle O. Wright

National Aeronautics and Space Administration, Lewis Research Center, Cleveland, Ohio 44135

ABSTRACT

Preliminary capital cost and size estimates were made for an electrochemical bulk energy storage concept. The electrochemical system considered was an electrically rechargeable flow cell with a titanium trichloride|titanium tetrachloride[1]||ferric chloride|ferrous chloride ($TiCl_3|TiCl_4$[1]$||FeCl_3|FeCl_2$) redox couple. The preliminary calculations were made to help determine whether the redox-flow-cell system has an attractive potential as a bulk energy storage system for power load leveling. With the rise in demand for electric power, the problem facing the electric utility industry of meeting peak power demands has been growing more acute. Because present methods of meeting peak power demands are not entirely adequate the electric utility industry has been interested in new methods for meeting peak power demands. On the basis of preliminary capital cost estimates, size estimates, and several other important considerations, the redox-flow-cell system emerges as having great promise as a bulk energy storage system for power load leveling. The size of this system would be less than 2% of that of a comparable pumped hydroelectric plant. The capital cost of a 10 MW, 60 and 85 MW-hr redox system is estimated to be \$190-\$330 per kilowatt. This cost compares well with that of competing systems, especially when one considers that for many sites a saving in transmission costs (up to \$200 per kilowatt) could be realized with the redox system. This saving could be achieved because the redox systems could be built in various sizes and located near the load centers. The other important features of the redox system contributing to its load-leveling application are its low adverse environmental impact, its high efficiency, its apparent absence of electrochemically related cycle life limitations, and its fast response.

The problem of meeting peak power demands is a very important concern of the electric utility industry. The problem is growing more acute as the pressure of rapidly rising demand is being felt.

For future power needs, it would be uneconomical to simply "overdesign" new base-load plants to meet peak power needs. The capital costs of base-load plants are higher than those of most power peaking equipment in use today (2). But the methods of power generating for peak periods used today are not entirely adequate. Most modern peaking is done with internal combustion equipment, gas turbines, and diesel engines, which run on natural gas or petroleum derived fuel. Not only is the efficiency of this equipment lower than that of base-load plants, but also, and more importantly, the fuel cost can be expected to increase greatly and the fuel availability can be expected to continue to decline. Finally, this type of equipment presents potential air pollution problems.

Another method of power peaking which has been attracting increased interest is the pumped hydroelectric system (2). Aside from relatively low cost, it is appealing because of its bulk energy storage capacity. There is an increasing desire to keep base-load plants operating at capacity, even during off-peak hours, and to store the energy for periods of peak demand. In some cases it is because the base-load plants use cheaper fuel (*e.g.*, coal) than the power peaking plants (oil or gas). For a nuclear power plant, maximum economy requires running at full load. Thus, pumped storage offers a means of accomplishing this objective.

However, even the very efficient (on the order of 66%) pumped hydroelectric plants have their disadvantages. Siting and environmental limitations restrict this type of energy storage system. Thus, the growing demands will require development of new energy storage systems to meet the particular requirements of a power plant in the region it serves.

The present report looks into the use of an electrochemical system for bulk energy storage to meet peak power demands. In many ways, electrochemical systems make ideal energy storage and peaking systems. They could be free of siting and environmental problems, provide instant start-up in emergencies, operate at high efficiency, permit minimum distance peak load transmission, and require short construction lead times.

The electrochemical system proposed for consideration is an electrically rechargeable flow cell, which is a new concept for bulk energy storage. The heart of the flow cell is two redox couples (a pair of oxidation-reduction reactions in which the ions of the pair remain soluble in their electrolytes in either their oxidized or reduced states). The two redox couples considered were titanium trichloride|titanium tetrachloride||ferric chloride|ferrous chloride ($TiCl_3|TiCl_4||FeCl_3|FeCl_2$, or $Ti^{+3}|Ti^{+4}||Fe^{+3}|Fe^{+2}$). Preliminary measurements

[1] Current electrochemical evidence (1) suggests that for titanium in acid solution in its +4 valence state, the titanyl ion, TiO^{+2} rather than $TiCl_4$ or Ti^{+4}, is the predominant participant. However, for the purpose of this paper, the reactions will continue to be written and discussed in the simpler form indicating $TiCl_4 \rightarrow TiCl_3 (Ti^{+4} \rightarrow Ti^{+3})$.

Key words: energy storage, redox system, load leveling.

were made with laboratory cells at the NASA Lewis Research Center. [See Ref. (3). In that report, Thaller also discusses several criteria for selection of the redox couples.] In the present report, size and cost calculations are presented for this redox-flow-cell system. The size calculations include electrochemical characteristics and physical size of the power unit and characteristics of the principal auxiliaries. In the cost calculations an estimate is made of the possible cost of a 10 MW, 85 MW-hr plant for load leveling.

The cost estimates for the redox-flow-cell system are quite preliminary. They were made to help determine whether this system has an attractive potential for bulk energy storage in load-leveling applications.

Description of Redox-Flow Cell

The redox-flow cell consists of two compartments containing separate electrolytes and inert carbon electrodes separated by an anion permeable selective ion exchange membrane. On one side an aqueous electrolyte containing a $TiCl_3$-$TiCl_4$ solution (the anolyte) is circulated from its storage tank into the cell and then back to its tank. On the other side an aqueous electrolyte containing an $FeCl_3$-$FeCl_2$ solution (the catholyte) is similarly circulated into the cell and back to its tank (Fig. 1). On discharge, $FeCl_3$ is reduced to $FeCl_2$, while $TiCl_3$ is oxidized to $TiCl_4$. The ion exchange membrane allows the passage of chlorine ions (Cl^-) from one compartment to the other to preserve electroneutrality. Alternatively, a hydrogen ion (H^+) membrane may also be used. (See Fig. 2 for details of electrochemical reactions with either membrane.) The redox-flow cell is electrically rechargeable by simply reversing the direction of flow of current. The redox-flow cell operates at relatively low temperatures, from room temperature to perhaps 80°C.

Size of Redox-Flow-Cell Power Plant

The basis of the size calculation was a 10 MW peak-power-load-leveling plant operating a maximum of 8.5 hr, with an over-all efficiency of 70% and with both electrolytes at 4*M* concentration. The results of this analysis are shown in Table I. The table gives electrochemical characteristics and physical size of the power unit and the characteristics of the principal auxiliaries. Table II contains selected data from a pumped hydroelectric facility [Northfield, Massachusetts, Ref. (4)] which are useful for purposes of comparison. Also see Fig. 3 for a pictorial representation of the 10 MW, 85 MW-hr redox system.

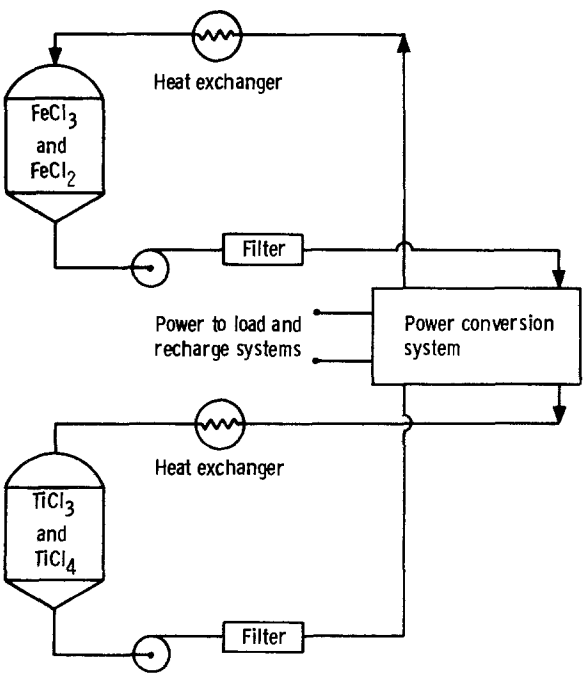


Fig. 1. Electrically rechargeable redox-flow-cell power generation system.

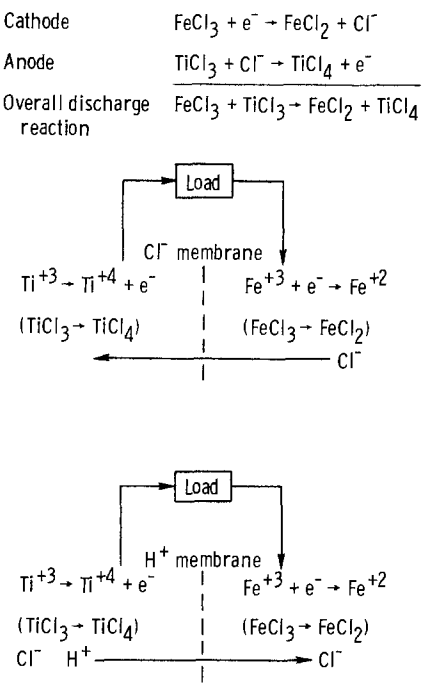


Fig. 2. Electrochemical reactions for redox-flow cell

Cost Estimates for Redox-Flow-Cell Power Plant

A cost estimate was made for a 10 MW, 85 MW-hr power plant. A current density of 108.0 mA/cm² (100 A/ft²), 70% over-all efficiency, [W-hr (a.c.) out/W-hr (d.c.) in], and 4*M* concentrations of electrolytes were assumed.

Pricing.—The capital cost estimates were made during the summer of 1973. The costs of electrochemical materials were obtained from suppliers or from trade publications. The unit costs used in the calculations are shown in Table III. The cost estimates for process equipment were made chiefly with the assistance of process equipment manufacturers.

Table I. Electrochemical and size characteristics of redox-flow-cell power plant [10 MW, 85 MW-hr system; redox flow cell, $TiCl_3|TiCl_4||FeCl_3|FeCl_2$; operating temperature, 80°C;[a] efficiency, 70%]

Electrochemical characteristics	
Current density, mA/cm² (A/ft²)	10.8-108.0 (10-100)
Voltage per cell, V/cell	0.6
Energy density, W-hr/kg reactants + water (W-hr/lb reactants + water)	13.25 (6.0)
Power unit size	
Total electrode area, m² (ft²)	
10.8 mA/cm² (10 A/ft²)	1.55×10^5 (1.67×10^6)
108.0 mA/cm² (100 A/ft²)	1.55×10^4 (1.67×10^5)
Total cell volume, m³ (ft³)	
10.8 mA/cm² (10 A/ft²)	[b] 1.98×10^3 (7×10^4)
108.0 mA/cm² (100 A/ft²)	[b] 1.98×10^2 (7×10^3)
Total power unit volume, m³ (ft³)	
10.8 mA/cm² (10 A/ft²)	6.43×10^3 (2.27×10^5)
108.0 mA/cm² (100 A/ft²)	4.63×10^3 (1.64×10^5)
Characteristics of principal auxiliaries	
Weight of reactants including water, kg (tons)	6.42×10^6 (7.09×10^3)
Shape of reactant tanks	cylindrical with height equal to diameter
Reactant tank volume, m³ (ft³)	
Catholyte tank	[c] 2.225×10^3 (7.86×10^4)
Anolyte tank	[d] 2.225×10^3 (7.86×10^4)

[a] $TiCl_4$ decomposes in hot water to insoluble titanium dioxide (TiO_2) and hydrochloric acid (HCl). Operation in HCl solution would aid solubility and stability. Solubility and stability data lacking to fix operating temperature accurately.
[b] Assumed 1.27 cm (½ in.) spacing between cells.
[c] Based on 14.2m (46.4 ft) height and diameter, 4*M* $FeCl_3$ concentration, and 90% discharge.
[d] Assumed value (solubility data lacking).

Table II. Selected data from Northfield hydroelectric pumped storage facility [1000 MW, 8500 MW-hr (max) system; emergency reserve, 2500 MW-hr]

Upper (man-made reservoir	
Volume of water, m^3 (ft^3)	
Total	2.22×10^7 (7.9×10^8)
Usable portion	1.59×10^7 (5.6×10^8)
Surface area, m^2 (acres)	1.31×10^6 (323)
Maximum water depth, m (ft)	17.1 (56)
Operating head, m (ft)	
Maximum	252 (825)
Minimum	220 (720)
Powerhouse	
Equipment	
Turbine generators (250-MW)	4
Pumps and motors	4
Cavern	
Dimensions, m (ft)	100 × 21.3 × 36.6 (328 × 70 × 120)
Volume, m^3 (ft^3)	7.81×10^4 (2.76×10^6)
Rock excavated, kg (tons)	2.27×10^5 (2.5×10^5)

A good deal of judgment was involved in making these cost estimates. For example, judgment had to be used in selecting the grade of chemical required and also in securing the estimate of electrochemical materials costs. It was obvious that the estimated costs of the electrochemical materials were not necessarily the lowest. The membrane manufacturers, for instance, predicted that future development and increased production savings could halve the present cost of the membrane. Furthermore, one research worker in membrane technology predicted that the membrane cost might even be reduced to less than one-tenth of its present cost. For reasons such as these, two types of electrochemical materials costs were calculated. One was higher or conservative, the other lower or optimistic.

The only pieces of process equipment for which conservative and optimistic costs were calculated were the reactant tanks. If lined, carbon-steel tanks would be suitable for this process, they would be approximately half as costly as stainless steel tanks.

As can be seen in Table III, the differences between the conservative and optimistic capital cost totals are considerable. For the base case power plant (operation at 10 MW for 8.5 hr with 70% efficiency), the difference was over a million dollars; the conservative total cost was $2,867,000, while the optimistic total cost was $1,846,000.

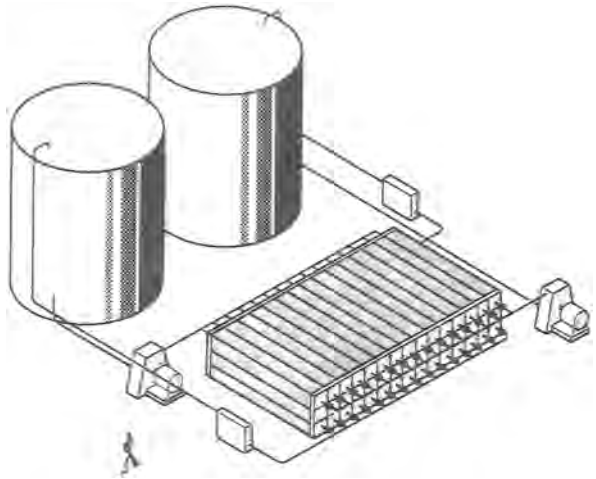


Fig. 3. Pictorial representation of 10 MW, 85 MW-hr redox system.

In addition to this basic cost estimate, conservative and optimistic costs were projected for three other cases. One reflected an assumption of a higher efficiency system, 85% instead of the 70% for the base case. The other two cost projections were for a shorter period of power-load-leveling operation, 6 hr instead of the 8.5 hr for the base case. One of these cost projections was made for 70% efficiency, the other for 85% efficiency.

Design basis.—Some pieces of process equipment, such as pumps, heat exchanger, and filters, were more or less within the standard series of types available. Other pieces of process equipment would have to be

Table III. Cost estimate for redox-flow-cell bulk energy storage system [10 MW, 85 MW-hr system; redox flow cell, $TiCl_3|TiCl_4||FeCl_3|FeCl_2$; Cl^- membrane; efficiency, 70%; 108.0 mA/cm^2 (100 A/ft^2); 4M electrolyte concentration]

(a) Electrochemical materials

Material	Conservative estimate Unit price	Conservative estimate Price of item ($)	Optimistic estimate Unit price	Optimistic estimate Price of item ($)
[a]$TiCl_4$	$0.39/kg	550,000	$0.26/kg	372,000
$FeCl_3$	$0.16/kg	194,500	$0.13/kg	160,000
Cl^- membrane[b]	$43.00/$m^2$	812,000	$21.50/$m^2$	406,000
Electrodes (porous carbon)	$0.88/kg	179,500	$0.59/kg	120,000
		1,736,000		1,058,000

(b) Process equipment

Equipment	Conservative estimate ($)	Optimistic estimate ($)
Reactant tanks[c] (stainless steel wall at $3.0[d]/kg; chlorsulfonated polyethylene lining at $53.80/$m^2$)	490,000	245,000
Redox-cell frames[c] (polypropylene)	150,000	150,000
Filters[c] [0.410 m^3/sec (6500 gal/min)]	70,000	70,000
Heat exchangers (stainless steel tubes at $43.00/$m^2$)	50,000	50,000
Pumps[c] (96.9 kW (130 brake hp); stainless steel tolerant to solids)	48,000	48,000
	808,000	563,000
Instrumentation and installation (40%)	323,200	225,200
	1,131,200	788,200

(c) Totals

Case	Energy (MW-hr)	Efficiency (%)	Conservative estimate Total ($)	Conservative estimate Direct current ($/kW)	Conservative estimate Alternating current ($/kW)[e]	Optimistic estimate[d] Total ($)	Optimistic estimate[d] Direct current ($/kW)	Optimistic estimate[d] Alternating current ($/kW)[e]
Base	85	70	2,867,000	287	327	1,846,000	185	225
[f]Projected case 1	85	85	2,634,000	263	303	1,689,000	169	209
[f]Projected case 2	60	70	2,518,000	252	292	1,625,000	163	203
[f]Projected case 3	60	85	2,338,000	234	274	1,503,000	150	190

[a] Required $TiCl_3$ is not available in bulk quantities, while $TiCl_4$ is. Initially $TiCl_3$ must be electrochemically converted to $TiCl_3$ in redox equipment.
[b] Available membranes not developed for redox-flow cell; opinion of one membrane researcher was that a membrane developed for redox flow might cost as little as $2.69/$m^2$.
[c] Estimated with assistance of manufacturer.
[d] Reactant tanks of carbon steel would cost approximately half as much as stainless steel tanks.
[e] Includes $40/kW cost of transformers, a-c-d-c converters, and switch gear.
[f] Scaled down from base case with following 0.6 power rule: ratio of capacities raised to 0.6 power equals ratio of costs [Ref. (7]. Also see Ref. (8).

custom fabricated, which could make their cost estimates more uncertain. However, storage tanks are normally custom fabricated. In the opinion of a leading tank manufacturer, the requirements of the redox-flow-cell system would present no special difficulties.

Estimating the cost of the redox-cell frames did present a unique problem, since redox-cell frames had never been built. However, the redox battery of cells containing graphite sheet electrodes, a diaphragm, and flowing liquids resembles the filter press to a reasonable extent. Consequently, cost estimates were obtained in cooperation with filter press manufacturers.

Discussion

The redox-flow-cell system has several attractive features. Electrochemically the system is a simple one. Unlike batteries, there are no apparent cycle life limitations due to morphology changes in the active materials of the electrodes. Furthermore, repeated deep discharges should be possible without reducing cycle life. The cell should operate at very high over-all efficiency. Finally, high efficiency does not require high cell temperatures.

The preliminary cost estimates made in this report show that the redox-flow-cell system is also attractive from a cost standpoint for use in bulk energy storage for power peaking. The estimate for the 10 MW plant ranged from \$150 to \$290 per kilowatt, depending upon whether the plant is designed for 6 or 8.5 hr use and whether optimistic or conservative costs are used. In keeping with the paper by Heredy and Parkins (5), a \$40/kW cost was added for a-c—d-c converters, transformers, and switch gear, so that the cost range was brought up to \$190/kW. In the same paper the capital cost of a pumped hydroelectric system in the 10 MW range (2.4-10 hr daily operation) is estimated to range from \$85 to \$200 per kilowatt, while a gas turbine system was estimated to cost \$100-\$200 per kilowatt.

On the basis of these cost estimates plus other reflecting cost of operation, the pumped hydroelectric storage system is potentially the cheapest. [In Ref. (5) the delivered energy cost estimate for the pumped hydroelectric system is the lowest.] However, as mentioned above, geographic or environmental considerations or both may preclude its use. No doubt the high end of the capital cost estimate represents the case where geographic conditions are considerably less than optimum. Also, because of environmental considerations, it may not be possible to create a lake holding 17.1m (56 ft) of water and covering 1.31×10^6 m^2 (323 acres) or to have a site which could provide a 252m (825 ft) head, as was done, for example, for the Northfield hydroelectric project (Table II). On the other hand, a redox bulk energy storage plant of the same output as the Northfield plant would occupy less than one-fiftieth of the volume (Tables I and II). Furthermore, the fact that the redox-flow-cell system can be built in different sizes can be put to good advantage. For example, significant savings in transmission costs can be achieved by dispersing suitably sized redox energy storage devices throughout the system near the load centers rather than using a very large pumped hydroelectric facility at a single site. One report estimates that this transmission cost saving would range between \$60 and \$200 per kilowatt (6). This estimate would hold for a typical utility system where the average transmission length would be about 100 miles and the dispersed energy storage facilities would be sited within urban areas.

Naturally, to advance the redox-flow-cell system toward commercialization will require a great deal of effort. In the research and development area there are numerous performance questions and problem areas which will have to be resolved. Some of these are discussed in this report. In the performance category are the as-yet-unattained 648 W/m^2 (60 W/ft^2) power density and the assumed electrochemical performance at the 4*M* concentrations. In this connection, calculations were made to determine the sensitivity of the capital cost to reduced electrochemical performance, a power density of 324 W/m^2 instead of 648 W/m^2. These are shown in Table IV. In this case the battery stack costs were affected. Also shown in Table IV are the results of calculations made to determine the sensitivity of the capital cost to operation at much lower reactant concentrations, 1*M* instead of 4. In this case the process equipment costs are affected. Comparing these capital costs with the original costs in Table III, it is obvious that the capital costs are quite sensitive to both electrochemical performance (power density) and reactant concentration. The assumed decrease in power density to one-half the original adds between \$63 and \$110 per kilowatt; the assumed decrease in reactant concentration to one-fourth the original adds between \$52 and \$104 per kilowatt. Apparently the capital cost is more sensitive to power density than to reactant concentration. The effects of concentration and power density upon power plant size are shown pictorially in Fig. 4.

Table IV. Sensitivity of cost estimate to power density change and to reactant concentration change

(a) Power density changed from 648 to 324 W/m^2

Case	Energy (MW-hr)	Efficiency (%)	Total capital costs: Conservative estimate Alternating current ($/kW)	Total capital costs: Optimistic estimate Alternating current ($/kW)
Base	85	70	437	288
[a]Projected case 1	85	85	413	272
[a]Projected case 2	60	70	402	266
[a]Projected case 3	60	85	384	253

(b) Reactant concentrations changed from 4 to 1*M*

Case	Energy (MW-hr)	Efficiency (%)	Total capital costs[b]: Conservative estimate Alternating current ($/kW)	Total capital costs[b]: Optimistic estimate Alternating current ($/kW)
Base	85	70	431	290
[a]Projected case 1	85	85	396	267
[a]Projected case 2	60	70	385	261
[a]Projected case 3	60	85	353	242

[a] Scaled down from base case with 0.6 power rule [Ref. (6)].
[b] Used 0.6 power rule [Ref. (6)] and Ref. (7).

Current laboratory work at NASA Lewis Research Center on redox systems is producing some encouraging results. A number of redox couples show promise. The Lewis work on the Ti/Fe system, which has been given the greatest emphasis thus far, indicates

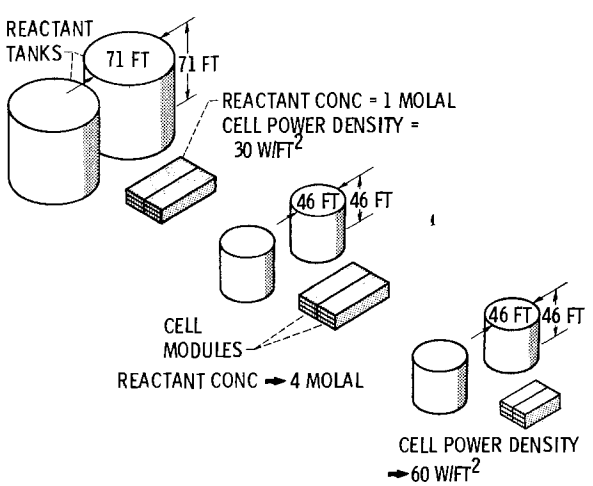


Fig. 4. Pictorial representation of effects of changes in reactant concentration and power density upon size of 10 MW, 85 MW-hr redox system.

that the performance goals cited in this paper are still reasonable. Recently, a power density of 324 W/m^2 has been attained. Part of the Lewis redox program involves work on the membrane, a major technical consideration in this redox concept. Presently, no membrane is available with very low ionic resistance coupled with very good selectivity. In addition, a suitable membrane must be compatible with the reactants, dimensionally stable for long periods, and inexpensive to produce in large sheets. A conclusion of the laboratory work is that membrane life does not appear to be a major problem thus far. While the membranes tested permitted some ion crossover, they exhibited no signs of degradation after several thousand hours of operation. This was evident from the fact that with replacement of the reactant solutions with fresh reactant solutions, the initial performance of the cells was restored.

Another phase of the NASA Lewis Research Center redox work involved the important question of circulating electrical currents between the cells and of the distribution of the reactant flow within the cells. The conclusion of this analytic treatment was that proper design of the cell flow passages is required in order to minimize ionic shunt currents without creating excessive parasitic pumping requirements.

Conclusion

On the basis of capital cost estimates, size estimates, and several other very important considerations, the redox-flow-cell system emerges as having great promise as a bulk energy storage system for power load leveling. The size of this system was estimated to be less than 2% of the size of a comparable pumped hydroelectric storage plant. The capital cost of a 10-MW, 60 and 85 MW/hr redox-flow system was estimated to range from $190 to $330 per kilowatt.

This capital cost range compares well with that for other peaking systems ($85 to $200 per kilowatt), especially when one considers that no transmission credit ($60 to $200 per kilowatt) was included in the redox system capital cost estimates. The transmission savings could be achieved because of the possibility of building redox systems of various sizes and dispersing them throughout the electrical network near the load centers. Coupling these attractive estimates of capital costs and size of the redox-flow system with its low environmental impact, its high efficiency at low temperatures, its apparent absence of electrochemically related cycle life limitations, and its fast response produces a power-load-leveling system of strong potential.

Manuscript submitted May 26, 1976; revised manuscript received Sept. 10, 1976. This was Paper 237 presented at the Dallas, Texas, Meeting of the Society, Oct. 5-9, 1975.

Any discussion of this paper will appear in a Discussion Section to be published in the December 1977 JOURNAL. All discussions for the December 1977 Discussion Section should be submitted by Aug. 1, 1977.

Publication costs of this article were assisted by the National Aeronautics and Space Administration.

REFERENCES

1. L. G. Austin, R. D. Chamberlin, and A. R. Schleicher, "Redox Fuel Cells: The Fuel Regenerator," Pennsylvania State Univ., Contract No. DA49-186-502-ORD-917 (August 1962); Available from NTIS as AD 289559.
2. Arthur D. Little Bulletin Number 503, Arthur D. Little Inc., Cambridge, Massachusetts (Sept.-Oct. 1973).
3. L. H. Thaller, Proceedings of the 9th Intersociety Energy Conversion Engineering Conference, ASME, p. 924, San Francisco, California, Aug. 26-30, 1974.
4. L. H. Thaller, *Eng. News-Rec.*, **186**, 16 (1971).
5. L. A. Heredy and W. E. Parkins, Paper presented at the Winter Power Meeting of IEEE, New York, Jan. 30-Feb. 4, 1972.
6. M. L. Kyle, E. J. Cairns, and D. J. Webster, USAEC Report ANL-7958, Argonne National Laboratory, Argonne, Illinois (1973).
7. R. S. Aries and R. D. Newton, "Chemical Engineering Cost Estimation," McGraw-Hill Book Company, New York (1955).
8. K. M. Guthrie, "Process Plant Estimating, Evaluation, and Control," Craftsman Book Company, Solana Beach, California (1974).

Electrochemical Characterization and Modification of Cadmium Sulfide Composition at 25°C

Jacques Vedel, Michel Soubeyrand, and Egil Castel

Laboratoire d'Electrochimie Analytique et Appliquée, Associé au C.N.R.S., E.N.S.C.P., 75231 Paris Cedex 05, France

ABSTRACT

The feasibility of electrochemical characterization and modification of the composition of a cadmium sulfide sample has been shown. The sample (thickness, 1 μm) was prepared by anodic oxidation of an electrolytic cadmium layer, plated on a platinum electrode, in an aqueous solution of sulfide ions. The sample composition was changed by coulometric oxidation, and the composition variation was observed by the means of the galvanic cell Cd: Cd^{2+} (aq.): Cd_xS. The electrode reaction is thermodynamically reversible in the considered composition range. Two potential-composition diagrams are given, as well as an attempt to interpret some of their parts.

The semiconducting properties of some binary compounds depend on their composition, particularly on their deviation from stoichiometry. The present work describes an electrochemical approach to the characterization of thin layers of cadmium sulfide (the thickness of which varies between 1 and 2 μm) following a technique similar to that proposed by Mathieu and Rickert (1) for the study of copper sulfides.

Key words: cadmium sulfide, stoichiometry, coulometry, potentiometry.

The emf of the galvanic cell

$$\text{Pt} \mid \text{Cd} \;\big|\; \begin{matrix}\text{aqueous solution}\\ \text{of } Cd^{2+} \text{ ions}\end{matrix} \;\big|\; Cd_xS \mid \text{Pt} \qquad [1]$$

is related to the chemical potential of the cadmium in cadmium sulfide, $\mu_{Cd}(Cd_xS)$ by the equation

$$\mu_{Cd}(Cd_xS) - \mu^\circ_{Cd} = -2\mathbf{F}E(x) \qquad [2]$$

where $\mathbf{F}$ is the Faraday constant and μ°_{Cd} the standard

chemical potential of pure cadmium. Thus, $E(x)$ is a measure of cadmium activity in Cd_xS, a thermodynamical quantity that may be related to the activity of a defect, for example, the noncharged interstitial cadmium represented by Cd_i^*. Then, one has

$$\mu_{Cd}(Cd_xS) = \mu^\circ_{Cd_i^*} + RT \ln a(Cd_i^*) \quad [3]$$

By choosing as reference state ($a(Cd_i^*) = 1$) the cadmium-saturated solution (cadmium sulfide in equilibrium with cadmium), for which $E(x) = 0$, one obtains

$$-2\mathbf{F}E(x) = RT \ln a(Cd_i^*) \quad [4]$$

On the other hand, the CdS composition may be modified by the means of an electrochemical reaction: if an emf $E'(x)$ greater than $E(x)$ is applied to cell [1] the flow of a current through the cell is observed. With the aqueous solution acting as a blocking electrode for electrons, the charge transfer reaction must take place at the sulfide-solution interface in order to allow the current flow. This reaction may be schematically represented in the following way

$$Cd_xS - 2(x - x')e \rightarrow Cd_{x'}S + (x - x')Cd^{2+}(aq.) \quad [5]$$

showing a decrease in the cadmium content of the sample.

The composition variation $(x - x')$ is related to the quantity of electricity Q that has flown through the cell by equation

$$x - x' = \frac{Q}{2n_S\mathbf{F}V} \quad [6]$$

where n_S is the number of sulfur atoms per cubic centimeter and V the volume of the sample.

In fact, a constant oxidizing current I was forced to flow through the cell during a time t. Thus, the quantity of electricity was $Q = It$. The cell emf increased during this operation until the value E_{max}. Then the new equilibrium potential value was allowed to establish itself. One must be careful lest the emf E_{max} should ever be less than the emf corresponding to the oxidation of cadmium sulfide into sulfur ($E_{max} \leq 0.7V$). A study of diffusion in thin layers of cuprous sulfide realized in a similar condition (2) has shown us that for polycrystalline layers the transformation was first realized in the joint grains, the equilibration of the small crystal being effected afterwards. In cadmium sulfide, the phenomenon is similar but owing to the low values of diffusion coefficient at room temperature equilibration times varying from 6 to 8 hr were observed for composition changes of 10^{-4} and layers of approximately 1 μm thickness.

Thus, from an analytical point of view, this is a question of coulometric titration with a potentiometry (zero current) as the indicator method.

Experimental

The electrochemical cell (Fig. 1) is the same as that used in a previous study to determine the chemical diffusion coefficient of copper in Cu_xS (2). It allows the two electrochemical operations: coulometric oxidation and potentiometry. To keep equilibration time as short as possible, the working electrode (4) and the auxiliary electrode (7) for the coulometry were disposed perpendicularly in a Pyrex tube ($\phi = 8$ mm) and occupying the entire cross section. Thus, the current lines distribution was uniform, giving a composition variation uniform on the entire sample surface. The reference electrode for potentiometry is a cadmium electrode and is placed in a side compartment (2), connected to the working electrode compartment by a fritted glass disk (3).

The cadmium-rich CdS layers [low values of $E(x)$] are easily oxidized by oxygen. The working electrode compartment and the auxiliary electrode compartment are continuously flushed by a high purity argon flow (1), purified by circulation over a BASF copper activated column. A liquid joint prevents the oxygen retrodiffusion.

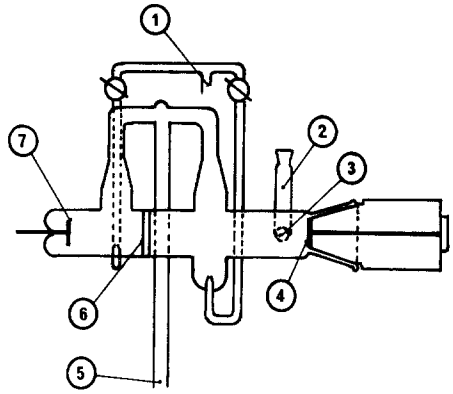


Fig. 1. Schema of the electrochemical cell: 1, argon inlet; 2, reference electrode compartment; 3, fritted glass disk (porosity = 4); 4, cadmium sulfide electrode on platinum support; 5, argon outlet; 6, fritted glass disk separating the two compartments of the electrochemical cell; 7, auxiliary electrode for the coulometry.

The electrochemical cell was maintained in darkness. Electrolyte composition was: Na_2SO_4;0.1 mol liter^{-1}; $CdSO_4$, 0.01 mol liter^{-1}; temperature, 23°C; sample surface area, 33 mm^2; thickness, 1.2 μm. Sample volume was determined by chemical analysis of the layer, following the method indicated by Nechiporenko *et al.* (3).

The CdS layers were prepared by anodic oxidation of an electrolytic cadmium layer, in a solution containing sulfide ions. A cadmium layer (10m) is deposited on a platinum electrode, from a nonstirred solution of 0.1 mole liter^{-1} $CdCl_2$. The platinum electrode was previously submitted to a series of successive electrochemical oxidations and reductions in concentrated nitric acid (current density 1300 Am^{-2}; last operation, oxidation). This allowed a well-adhering sulfide deposit. Afterwards, cadmium was anodically oxidized at controlled potential (— 0.9V *vs.* SCE) in a Na_2S solution (0.5 mole liter^{-1}, pH = 9). The emf $E(x)$ given by one of these layers was equal to zero: thus the formed cadmium sulfide is the so-called cadmium sulfide in equilibrium with cadmium.

Results and Discussion

Verification of the reversibility of the electrochemical reaction.—In order that expression [2] be valid, the electrochemical reaction at the solution-sulfide interface must be thermodynamically reversible. It was assumed that the Cd_xS electrode was reversible toward the activity variations (in the aqueous solution) of Cd^{2+} ions, it was also reversible toward variations of cadmium activity (in the solid). This has been verified using a galvanic cell of the type

Saturated calomel electrode	Aqueous solution of Cd^{2+} ions	Cd_xS or Cd	[7]

The emf of this cell is related to the activity of the aqueous Cd^{2+} ions, $a(Cd^{2+})$, and to the cadmium activity in the sulfide by

$$E = E^\circ + \frac{2.3RT}{2\mathbf{F}} \log \frac{a(Cd^{2+})}{a(Cd)} \quad [8]$$

For constant x values, $a(Cd)$ is also constant and Eq. [8] becomes

$$E = E^{\circ\prime} + \frac{2.3RT}{2\mathbf{F}} \log a(Cd^{2+}) \quad [9]$$

with

$$E^{\circ\prime} = E^\circ - \frac{2.3RT}{2\mathbf{F}} \log a(Cd)$$

Table I. Characteristic parameters of the straight lines $E = f(\log a(Cd^{2+}))$ (Eq. [9])

Electrode	$E^{\circ\prime}$/V potential vs. ENH	Slope/V ±0.001
Cd	-0.408 ± 0.002	0.029
CdS_{x_1}	-0.362 ± 0.002	0.030
CdS_{x_2}	$+0.066 \pm 0.004$	0.030
CdS_{x_3}	0.470 ± 0.003	0.032

The variation of emf E has been determined as a function of the cadmium ion concentration for some unknown values of x. The concentration varied between 10^{-4} and 10^{-1} mole liter^{-1} and the ionic strength remained fixed to the value 0.3, so that the activity coefficient of the Cd^{2+} ions was constant and equal to 0.19. The curves $E = f(\log c(Cd^{2+}))$ were straight lines; the characteristic parameters are reported in Table I. At 23°C, the standard potential of cadmium is equal to −0.403V (4) and the value of the coefficient 2.3 $RT/2F$ is equal to 0.0295V. The observed values of the slopes allow the conclusion of a reversible interface exchange reaction. Thus, the emf of cell [1] is effectively a measure of the cadmium activity in the cadmium sulfide sample. However, one must remark that the standard potential value for the $CdS/S/Cd^{2+}$ system is equal to +0.31V (4). The observed value for the sulfur-saturated sample (composition CdS_{x_3}) is greater (0.47V). This deviation may be attributed to the formation of sulfur in a state different from the standard state of the element. The difference between these two potentials corresponds to a free energy equal to −7500 cal that may be compared with the free energies of some other sulfur species (5): $S_2(g)$, 17,500 cal; $S_6(g)$, −8800 cal; and $S_8(g)$, −5700 cal.

Potential-composition diagrams.—The potential variations as a function of composition are shown on Fig. 2. They were obtained from two different runs, starting from two different electrolytic samples (t = 23°C). Composition variation was obtained by anodic oxidation at constant current. Conversion of experimental It values into x values was obtained using Eq. [6], after determination of the V values by chemical analysis. On one of the curves (solid line) characteristic points are plotted as A, B, C, etc., and on the other one (dashed line), the corresponding points are a, b, c, etc. On these curves the cadmium-rich medium corresponds to points on the left of the diagram, and the cadmium-poor one on the right. The position of the stoichiometric point $x = 1$ is unknown. In order to plot the two curves on the same diagram, it was first observed that both their left parts showed a sigmoidal shape recalling that of

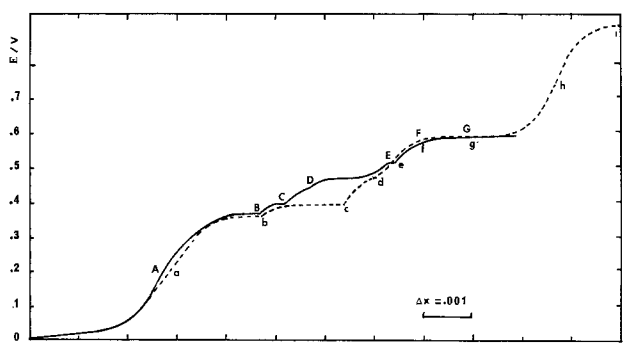


Fig. 2. Potential-composition diagram of cadmium sulfide (t = 23°C). The stoichiometric ratio x is modified by anodic oxidation at constant current, but the stoichiometric point $x = 1$ is unknown. The two curves correspond to two different runs and the correspondence between them was obtained by superposing the two equivalent points A and a.

titration curves. The correspondence has been realized by superimposing both inflection points A and a.

Thus, some similarity may be observed between the two titration curves, with the points A, B, C, ..., as equivalent points. The potentials of the plateaus preceding the points B, C, E, and G are equal to within a few millivolts while their lengths are different. The HI part (corresponding to hi) has not been determined. As for the interpretation of titration curves, the potential variations were studied against the quantity log $|x_J - x|$, where x_J is the value of x at the equivalent point J. For the best defined parts of the curves, that is to say the arcs hi, efg (and EFG), ab (and AB), a0 (and A0), linear variations were observed, the slopes of which are, respectively 0.090, 0.060, 0.120, and 0.180V. They are simply related to the value of the Nernst coefficient at 23°C (0.059V) and the first of them may be explained by making simple assumptions.

Let us first consider the arc hi, which corresponds to cadmium-poor medium. One can suppose that the species causing the deviation to stoichiometry was the doubly ionized cadmium vacancy V_{Cd}'' (6). When the x value is equal to x_H, the vacancy concentration $|V_{Cd}''|$ is very low ($|V_{Cd}''|_{x=x_H} \simeq 0$). When x is modified by anodic oxidation, for example according to the following reaction

$$Cd_{Cd} \rightarrow V_{Cd}'' + 2h^{\cdot} + Cd^{2+}(aq.) + 2e^{-} \qquad [10]$$

the vacancy concentration expressed in site fraction is increased by the quantity

$$|V_{Cd}''|_x - |V_{Cd}''|_{x=x_H} \simeq |V_{Cd}''|_x = x_H - x \qquad [11]$$

where $x_H - x$ is obtained by means of Eq. [6]. (The two electrons appearing in the right-hand side of reaction [10] are brought by the external source of energy to cause the modification of composition; the two electron holes arise from the ionization of the neutral cadmium vacancy: $V_{Cd}^{x} \rightarrow V_{Cd}'' + 2h^{\cdot}$.)

The cadmium vacancies are assumed to be in equilibrium with metallic cadmium, the activity of which is measured by the electrochemical cell. This cadmium activity plays, in fact, the same part as the gaseous cadmium (or sulfur) pressure often used as composition parameter in high temperature studies. The equilibrium is

$$Cd + V_{Cd}'' + 2h^{\cdot} \rightleftharpoons Cd_{Cd} \qquad [12]$$

together with the relation

$$K = a(Cd) \cdot |h^{\cdot}| \cdot f(V_{Cd}'') \cdot |V_{Cd}'')_x \qquad [13]$$

where $|h^{\cdot}|$ is the electron hole concentration, expressed in site fraction, and $f(V_{Cd}'')$ the activity coefficient of ionized vacancies. Considering the electroneutrality condition

$$2|V_{Cd}''|_x = 2|h^{\cdot}|$$

one obtains

$$a(Cd) = \frac{K}{4f(V_{Cd}'')} \cdot \frac{1}{|V_{Cd}''|_x^3} \qquad [14]$$

Combining expressions [4], [11], and [14] gives

$$E = \text{const.} + \frac{3}{2} \cdot \frac{2.3RT}{F} \log (x_H - x) \qquad [15]$$

At 23°C, the value of the coefficient $2.3RT/F$ is equal to 0.059V. Thus, the theoretical slope of the straight line $E = f(\log(x_H - x))$ is equal to 0.0885V, very close to the observed one (0.090V). This result suports the hypothesis of the existence of the defect V_{Cd}''. If the existence of nonionized vacancy is assumed, for example, equilibrium [12] would be replaced by equilibrium [16]

$$Cd + V_{Cd}^{x} = Cd_{Cd} \qquad [16]$$

with

$$K' = a(Cd) \cdot f(V_{Cd}^{x}) \cdot V_{Cd}^{x}$$

and the potential variation would be

$$E = \text{const.} + \frac{1}{2} \cdot \frac{2.3RT}{F} \log (x_H - x)$$

with a calculated slope equal to 0.0295V instead of 0.0885V. Similarly, the defect V_{Cd}' would give a slope equal to 0.059V.

The hypothesis can be made that the plateaus observed in the titration curves are due to impurities introduced in the sample, either during the cadmium electrodeposition or during the formation of the sulfide layer. Particularly, the samples could contain cadmium oxide and/or sodium sulfide. As sulfide and oxide species are similar the presence of dissolved cadmium oxide (*i.e.*, the replacement of a sulfur atom S_S by an oxygen atom O_S) could only slightly modify the cadmium sulfide properties. Sodium sulfide is an ionic compound which dissolves in CdS with more difficulty. It is also possible that the remaining sodium sulfide is transformed into cadmium sulfide during the oxidation of the cadmium in excess. However, as it stands now, it is not possible to state precisely what kind of impurities are involved. But the obtained results show that electrochemical analysis is a possible method of studying cadmium sulfide and, more generally, semiconductors having a possible deviation from stoichiometry.

Manuscript submitted April 26, 1976; revised manuscript received Oct. 4, 1976.

Any discussion of this paper will appear in a Discussion Section to be published in the December 1977 JOURNAL. All discussions for the December 1977 Discussion Section should be submitted by Aug. 1, 1977.

Publication costs of this article were assisted by C.N.R.S.

REFERENCES

1. H. J. Mathieu and H. Rickert, *Z. Phys. Chem., (N.F.)*, **79**, 315 (1972).
2. E. Castel and J. Vedel, *J. Chim. Phys.*, To be published.
3. A. P. Nechiporenko, I. P. Kalinkin, N. G. Ventov, and V. B. Aleskovskii, *Zh. Prikl. Khim. (Leningrad)*, **43**, 2558 (1970).
4. G. Charlot, A. Collumeau, and J. C. Marchon, "Selected Constants, Oxidation-Reduction Potentials of Inorganic Substances in Aqueous Solutions, I.U.P.A.C.," Butterworths, London (1971).
5. W. M. Latimer, "Oxidation Potentials," Prentice-Hall, Englewood Cliffs, N.J. (1938).
6. F. A. Kroger, H. J. Vink, and J. Van Den Boomgard, *Z. Phys. Chem.*, **203**, 1 (1954).

Theoretical and Experimental Study of Flow-Through Porous Electrodes

M. Paulin, D. Hutin, and F. Coeuret*,[1]

Laboratoire des Sciences du Genie Chimique, C.N.R.S., E.N.S.I.C., 54042 Nancy, France

ABSTRACT

The paper deals with the study of flow-through porous electrodes consisting of fixed beds of highly conductive spherical grains. The theoretical treatment is similar to that used to solve chemical engineering problems. It leads to a general expression which allows the calculation of the active volume fraction in an electrode working in industrial operating conditions, and to the subsequent design of such an electrode. The experiments which concern the cathodic deposition of copper from sulfuric $CuSO_4$ solutions allow the determination of effectiveness factors of the electrodes and corresponding effectiveness criterions. For electrodes operated in industrial-like overpotential ranges, the comparison between theory and experiment is satisfactory.

Papers on flow-through porous electrodes are frequently encountered in the literature. This type of electrode is often justified by the fact that it presents a high specific area which makes it suitable for the treatment of dilute solutions that need low current densities. Among its industrial applications, the electrowinning of metals from dilute solutions (liquors from leaching of poor ores, industrial liquid wastes) is frequently considered. Thus the literature of recent years has referred to the fluidized bed electrode (1, 2) for continuous electrowinning and to the fixed bed electrode (3-5) for the concentration of dilute solutions.

The study of the behavior of flow-through electrodes falls within the scope of electrochemical engineering which can be considered as applying to electrochemical processes the principles of analysis and design of the chemical engineering discipline. The analogy between porous electrodes and gas-solid catalytic reactors is not new, at least in the concept of reaction layers which guided the early discussions of porous electrode behavior (6-8). Many other papers on porous electrodes have dealt with the concept of nonuniform reaction rates for different forms of the polarization equation expressing the electrochemical kinetics (9-14). They have been extensively reviewed in a recent paper (15).

In a recent experimental work on flow-through porous electrodes (16), the above-mentioned analogy was confirmed. An effectiveness criterion was defined and studied for the special case of very low overpotentials within the electrodes whereas a generalization was attempted for practical operating conditions. This notion of effectiveness of flow-through porous electrodes is connected with their three-dimensional behavior which would be their main advantage. Such a notion is primordial if it is considered that a very low electrochemically active thickness of the electrode does not bring any further advantage over a classical plate electrode.

The present paper deals with the theoretical and experimental study of flow-through porous electrodes when high local overpotentials exist in the electrodes. The theoretical part examines the behavior of such electrodes by using a mathematical approach similar to that proposed by the chemical engineering discipline for gas-solid catalytic reactors and also for gas-liquid absorption with chemical reaction. The experimental part tests the validity of the theoretical considerations for copper deposition from sulfuric $CuSO_4$ solutions in electrodes consisting of fixed beds of spherical conduct-

* Electrochemical Society Active Member.
[1] Present address: Laboratoire Etudes Aérodynamiques et Thermiques, 86022 Poitiers, France.
Key words: electrochemical engineering, fixed bed electrode, penetration depth, effectiveness criterion, overpotential distribution.

ing grains; it is aimed towards the determination of the effectiveness factors and of the overpotential distributions.

Theoretical

The flow-through porous electrodes selected in the study.—The selected electrode is represented in Fig. 1a. It is considered to be a fixed bed of highly conductive nonporous particles the specific area of which is a_g ($a_g = 6/d_p$ for spherical particles of diameter d_p). Its height is L and its porosity considered as uniform is ϵ. The bottom of the bed is in contact with a current feeder (grid) which acts also as a bed support and through which the electrolyte can flow. The superficial velocity u of the electrolyte entering the bed is assumed uniform in the cross-section area Ω of the containing tube. The electrical conductivity of the electrolyte is γ_0. The counterelectrode is located downstream of the bed with respect to the general flow direction.

The following hypotheses are made:

1. The hydrodynamical and electrochemical operating conditions are steady.
2. The electrical potential and the current density within the electrode depend only on the height x above the current feeder.
3. The continuous phase (electrolyte) in the electrode can be considered as a continuous medium whose electrical conductivity is γ depending on γ_0 and on the tortuosity of the current lines around the particles. For spherical particles γ would be a function of γ_0 and ϵ (17).
4. The velocity u of the electrolyte is sufficiently high to ensure that the concentration change of the electrolyte over the bed height is negligible. This assumes that the equilibrium electrode-solution potential E_{eq} is the same at every point in the electrode. The disposition of Fig. 1a can consequently be seen as simulating the behavior of a horizontal slab of the electrode of Fig. 1b the geometry of which would probably be adopted in industrial uses.
5. The electrical potential ϕ_M of the dispersed phase is considered as constant.
6. The conduction through the continuous phase, whose electrical potential is $\phi_S(x)$, obeys Ohm's law.
7. Double layer and migration effects are negligible.
8. Pore structure and porosity distribution are uniform.
9. The operation is isothermal.

The following theoretical developments consider the absolute values of the electrode potential $E(x) = \phi_M - \phi_S(x)$, of the overpotential $\eta(x) = E(x) - E_{eq}$ and of the current density $i_s(x)$ relative to Ω in the pores of the bed. Consequently they could be applied for cathodic or anodic operation of the flow-through porous electrode.

Differential equation giving the overpotential distribution.—For very low values of the electrode overpotential, η, it is well known that the current density is given by the linear expression

$$i = i_0 \frac{zF}{RT} \eta \qquad [1]$$

where i_0 is the exchange current density (Fig. 2a). The overpotential distribution has been previously obtained for flow-through porous electrodes working accordingly to Eq. [1], *i.e.*, near equilibrium (16). However, such a case is only academic because the practical operating conditions in electrolysis use high overpotentials. Unfortunately the kinetic expressions for the ranges of overpotentials far from equilibrium are too complicated to permit an analytical solution of the problem in a manner similar to Ref. (16).

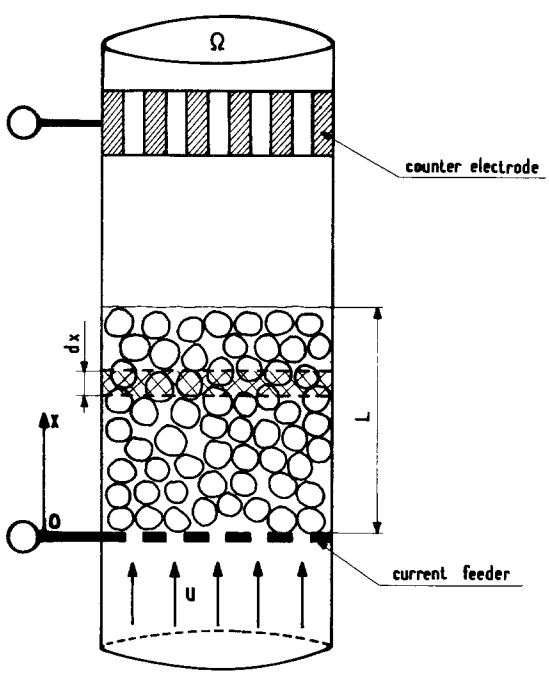
The examination of the present case of practical interest is possible if we recognize that it is always possible to approximate an experimental curve $i = f(\eta)$ to a power function of η

$$i = i_0 \cdot \frac{z \cdot F}{R \cdot T} \cdot \alpha^{1-n} \cdot \eta^n \qquad [2]$$

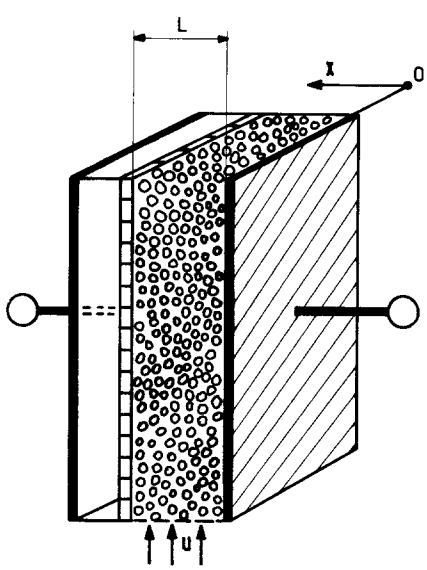
in which n would be a positive exponent lower than one and α a dimensional coefficient (Fig. 2b).

As in previous papers (6, 12, 16), after applying Ohm's law to the electrical conduction through the electrolyte within the bed

$$i_S(x) = -\gamma \cdot \frac{d\phi_S(x)}{dx} = \gamma \cdot \frac{d\eta(x)}{dx} \qquad [3]$$



(a)



(b)

Fig. 1. Schematic view of the cell.

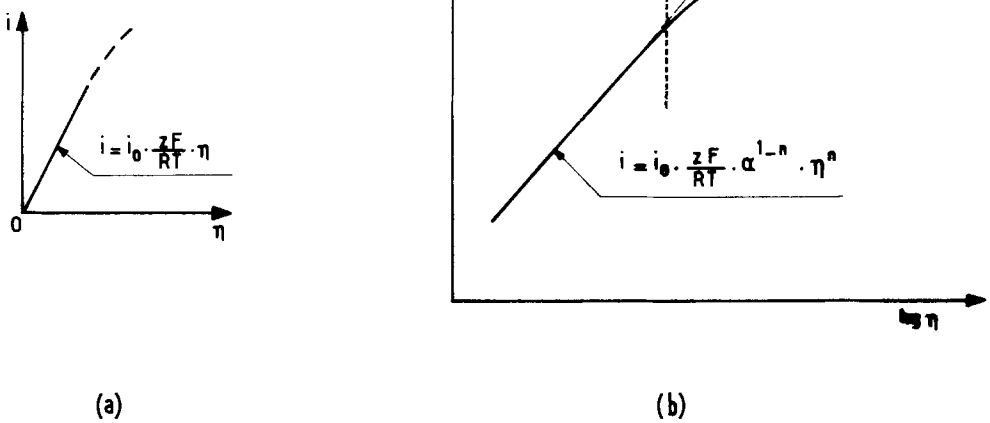


Fig. 2. Kinetic curves for low and high overpotentials.

a balance of the electrical charges in a differential element of thickness dx of the electrode leads to the following equation

$$\frac{d^2\eta(x)}{dx^2} - i_o \cdot \frac{zF}{RT} \cdot \alpha^{1-n} \cdot (1-\epsilon) \cdot a_g \cdot \frac{1}{\gamma} [\eta(x)]^n = 0 \quad [4]$$

the solution of which has to satisfy the boundary conditions

$$\eta(x) = \eta(0) \quad \text{at } x = 0$$

$$\eta(x) = \eta(L) \quad \text{at } x = L$$

It can be seen that for $n = 1$ expressions [2] and [1] are identical and therefore the overpotential distribution $\eta(x)$ obtained by integrating [4] is the distribution previously presented for very low overpotentials (16).

Effectiveness factor and effectiveness criterion.—The effectiveness factor $\mathcal{E}_n$ of the electrode which represents the fraction of the height electrochemically reactive in the electrode is defined by the ratio

$$\mathcal{E}_n = \frac{\text{observed electrolytic current}}{\text{current which would be obtained if } \eta(x) = \eta(L) \text{ at every height } x} = \frac{\gamma \cdot \Omega \cdot \left[\frac{d\eta(x)}{dx}\right]_{x=L}}{i_o \cdot \frac{zF}{RT} \cdot (1-\epsilon) \cdot a_g \cdot \Omega \cdot L \cdot \alpha^{1-n} \cdot [\eta(L)]^n} \quad [5]$$

When $n = 1$ the solution of [4] leads to the following expression of the effectiveness factor

$$\mathcal{E}_1 = \frac{\tanh K_1}{K_1} \quad [6]$$

where K_1 is a dimensionless number which appears as an effectiveness criterion because its value determines the effectiveness factor $\mathcal{E}_1$, *i.e.*, the extent of the three-dimensional character of the electrode (16). The expression for K_1 is

$$K_1 = \left\{ i_o \cdot \frac{zF}{RT} (1-\epsilon) \cdot a_g \cdot \frac{L^2}{\gamma} \right\}^{1/2} \quad [7]$$

Relation [6] has the same mathematical form as that known for the effectiveness of a catalytic reactor with first-order chemical reaction (18). At this point it must be noted that K_1 is not a new parameter. Indeed, expression [7] is the limiting case for a highly conductive dispersed phase of the most general equation [38] of Ref. (15) which expressed a dimensionless exchange current characterizing the penetration depth of the reaction within a porous electrode of uniform electrolyte composition.

This penetration depth, *i.e.*, the distance to which the reaction can penetrate the electrode, is given by

$$\mathcal{E}_1 \cdot L = \frac{\tanh K_1}{K_1} \cdot L \quad [8]$$

The asymptotic expression L/K_1 of [8] is valid only when K_1 is higher than 3 (*i.e.*, when the effectiveness is lower than 0.33) and not for any K_1 value as it can be found in the literature (15).

In the general case, Eq. [4] gives after a first integration

$$\frac{d\eta^+(x)}{dx} = \frac{M}{L} \sqrt{[\eta^+(x)]^{n+1} - [\eta^+(0)]^{n+1}} \quad [9]$$

where $\eta^+(x) = \eta(x)/\eta(L)$ is a reduced overpotential and

$$M = K_1 \cdot \left\{ \frac{2}{n+1} \cdot \left[\frac{\alpha}{\eta(L)} \right]^{1-n} \right\}^{1/2} \quad [10]$$

The value of $\eta^+(0)$ has to satisfy the following equality which is derived from [9]

$$\int_{\eta^+(0)}^{1} \frac{d\eta^+(x)}{\sqrt{[\eta^+(x)]^{n+1} - [\eta^+(0)]^{n+1}}} = \int_0^1 M \cdot d(x/L) = M \quad [11]$$

and the application of definition [5] of the effectiveness would lead to the general expression of $\mathcal{E}_n$

$$\mathcal{E}_n = \frac{1 - [\eta^+(0)]^{n+1}}{K_n} \quad [12]$$

where

$$K_n = \left\{ \frac{n+1}{2} \cdot i_o \cdot \frac{zF}{RT} (1-\epsilon) \cdot a_g \frac{L^2}{\gamma} \left[\frac{\alpha}{n(L)} \right]^{1-n} \right\}^{1/2} \quad [13]$$

The effectiveness, $\mathcal{E}_n$, has been plotted as a function of K_n on bilogarithmic paper for $n = 0$, 0.5, and 1 (Fig.

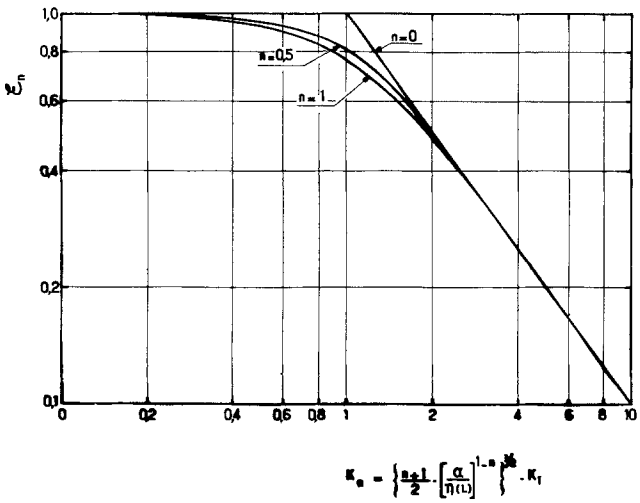


Fig. 3. Representation of expression [12] for $n = 0$, 0.5, and 1

3). Expression [12] for $n = 0.5$ and 0.8 has been calculated from previous numerical determinations of $\eta^+(0)$ using expression [11]; the relative deviation $(\mathcal{E}_n - \mathcal{E}_1)/\mathcal{E}_1$ is represented *vs.* K_n in Fig. 4 for $n = 0.5$ and 0.8. It can be seen that the maximum deviation for $n = 0.5$ is 6.5%, *i.e.*, low compared to the over-all uncertainty in the value of K_n calculated by the user of the diagram in Fig. 3. On the other hand, experience will show later that the practical values of n are higher than 0.5. Therefore it is quite justified to accept the following approximation of [12]

$$\mathcal{E}_n = \frac{\tanh(K_n)}{K_n} \qquad [14]$$

for all practical operating conditions. A similar approximation has been made by Hikita (19) for gas-liquid mass transfer with an irreversible chemical reaction of general order.

Expression [14] allows the calculation of the effectiveness of a flow-through porous electrode with a highly conductive dispersed phase if the effectiveness criterion is known

when $K_n \to 0$, $\mathcal{E}_n \to 1$	(entirely three-dimensional electrode)
when $K_n \to \infty$, $\mathcal{E}_n \to 0$	(two-dimensional electrode, the top of the bed in $x = L$ only being reactive)
when $0 < K_n < \infty$	the electrochemical reaction takes place in a slab whose thickness $\mathcal{E}_n \cdot L$ decreases with increasing values of K_n

Consequently a high effectiveness, *i.e.*, an electrode working throughout almost its whole depth, would be obtained for low K_n values.

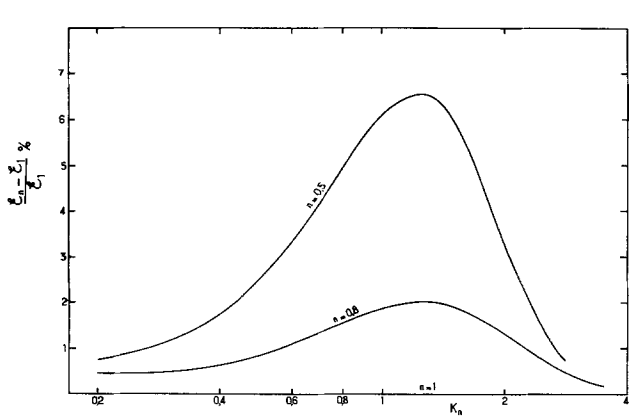


Fig. 4. Relative deviation of $\mathcal{E}_n$ from $\mathcal{E}_1$, for $n = 0.5$ and 0.8

Consequences.—The derivation of the general expression [14] allows the kinetic equation [2] to be approximated in the following manner

$$i = i_0 \cdot \frac{z \cdot F}{R \cdot T} \cdot \alpha^{1-n} \cdot \eta^n \sim \frac{n+1}{2} \cdot i_0 \cdot \frac{z \cdot F}{R \cdot T} \left[\frac{\alpha}{\eta(L)}\right]^{1-n} \cdot \eta \qquad [15]$$

and, as a consequence, the solutions for the overpotential distribution can be transposed from those obtained for the electrode working near equilibrium (16) simply by changing K_1 to K_n. They are

$$\eta(0) = \frac{I \cdot L}{\gamma \cdot \Omega \cdot K_n \cdot \sinh(K_n)} \qquad [16]$$

$$\frac{\eta(L)}{\eta(0)} = \cosh\left(K_n \cdot \frac{x}{L}\right) \qquad [17]$$

$$\frac{\eta(x) - \eta(0)}{\eta(L) - \eta(0)} = \frac{\cosh\left(K_n \cdot \frac{x}{L}\right) - 1}{\cosh(K_n) - 1} \qquad [18]$$

The dimensionless relationship [18] is represented in Fig. 5 for several values of K_n. We can see how the value of K_n influences the form of the distribution and, particularly, that the "penetration depth" of the overpotential profile in the bed decreases with increasing K_n.

Experimental

The cells and their uses.—Two cells have been employed:

Cell I (Fig. 6).—Figure 6a shows a circular column made of altuglass (ID 4 cm) and containing a fixed bed of spherical highly conductive particles (copper or copper-plated graphite). The cathodic current feeder to the bed is a copper grid which also acts as the bed support; the anode is a perforated copper disk. The electrolyte is flowing upward with a uniform superficial velocity u and is successively recirculated through a tank, a centrifugal pump, a valve, and a rotameter. The local electrochemical electrode potential $E(x)$ within the bed is measured by means of the composite probe indicated in Fig. 6a, the bottom of which is detailed in Fig. 6b. This probe was already used and described in Ref. (16). The velocity u is sufficiently high

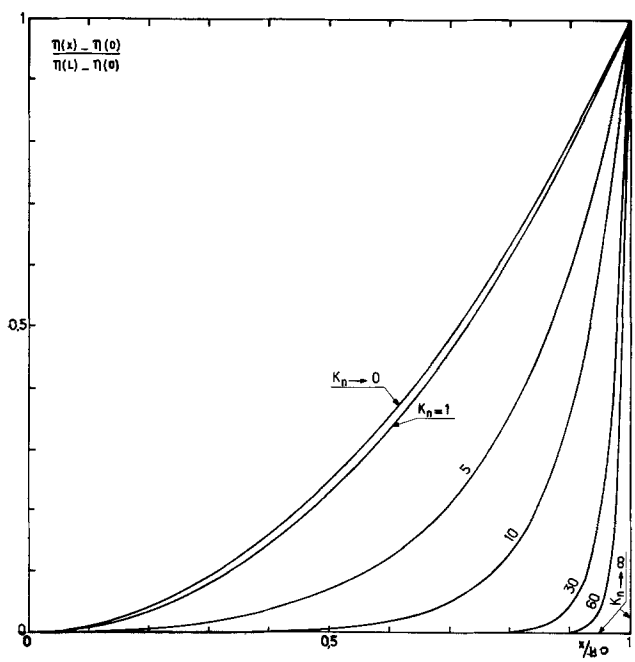


Fig. 5. Influence of K_n on the overpotential distribution

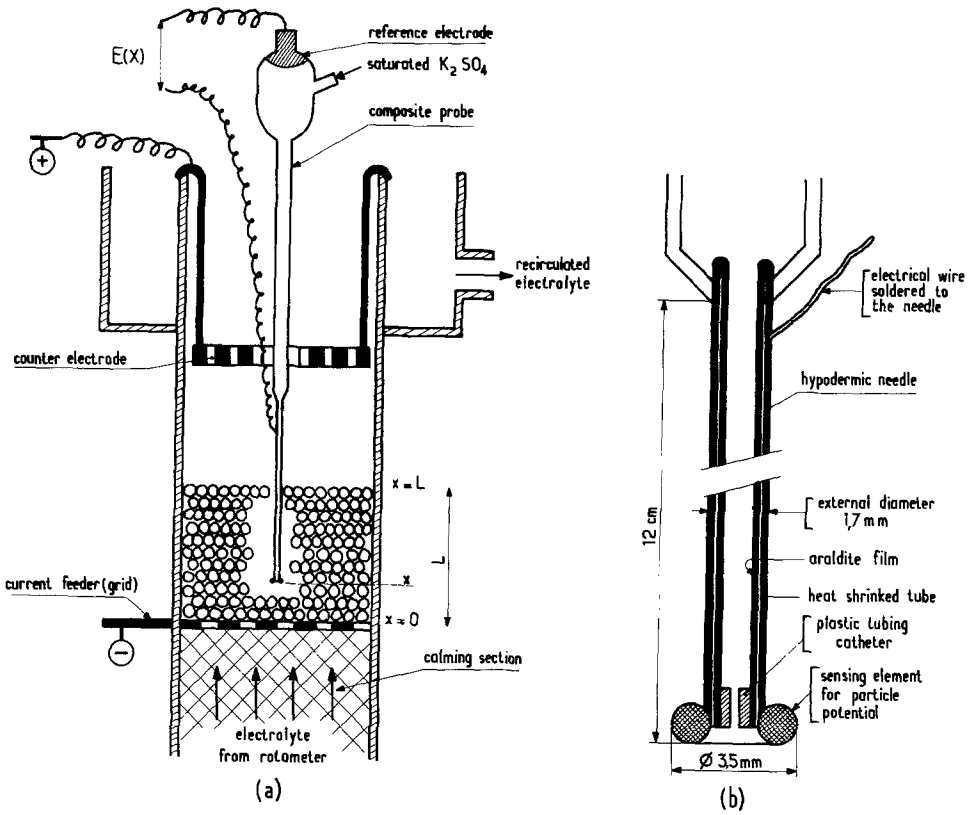


Fig. 6. Schematic view of cell I and of the probe.

so that the copper concentration change is negligible along the bed height L. Therefore the local equilibrium potential E_{eq} may be considered as constant in the bed and the local overpotential $\eta(x)$ can be calculated directly from the indication of the probe. The position x of the sensing element (copper) of the probe is precisely measured within 1/10 mm. The cell is operated at a constant intensity using a potentiostat Tacussel PRT 20-2; the electrode potentials $E(x)$ and the current flowing through the cell are measured with two digital instruments. In all the experimental beds the dispersed phase was equipotential as controlled by measuring the potential drop between the current feeder and the sensing element of the composite probe when this element is located just at the top of the bed. Also, the condition of hypothesis 5 was controlled for the higher beds by finding the metal potential distributions along the bed height. The potential distribution $E(x)$ was always determined a few minutes after applying the current to the cell so that the electrochemical conditions in the bed were steady (at any point, the indication of the probe was constant).

Cell II (Fig. 7).—The cell schematically represented in Fig. 7a obeys the principle of the cell Bennion and

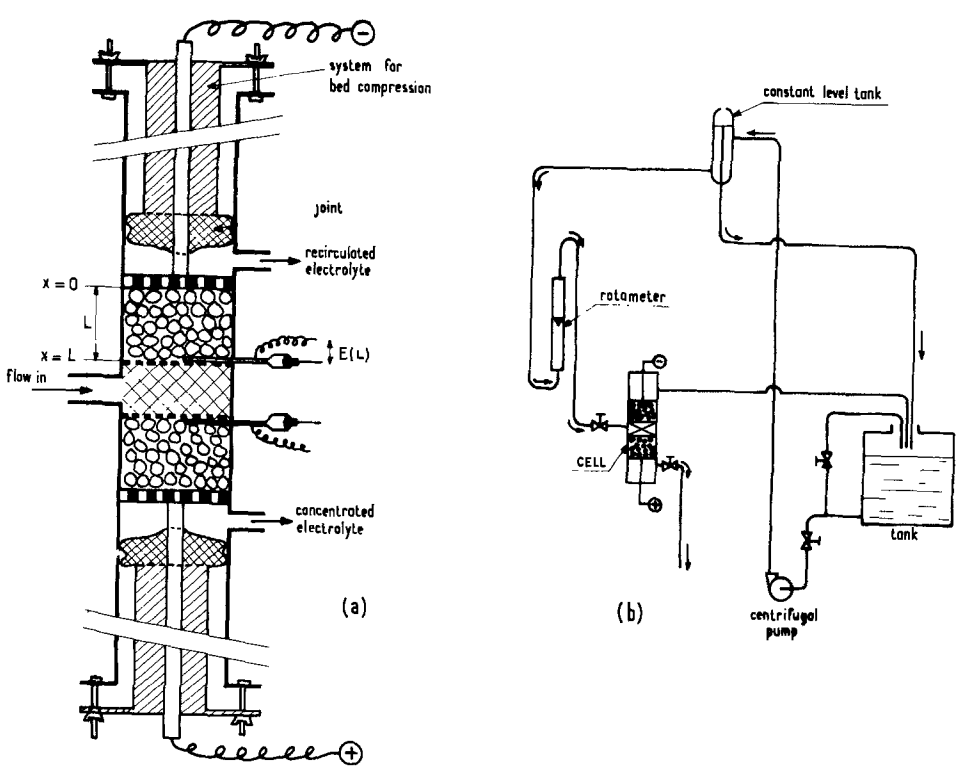


Fig. 7. Schematic view of cell II and of the hydraulic circuit.

Newman proposed (3) for the concentration of dilute solutions of heavy metals; it is incorporated in the hydraulic circuit of Fig. 7b. The cell itself is constructed with two 2.6 cm ID medical syringes made of transparent polyethylene. They have been truncated and assembled on both sides of a calming section of glass beads in which the electrolyte to be treated is distributed.

The upper compartment (cathodic) is supported by a perforated altuglass disk and the bed itself is maintained strongly compressed between that disk and a perforated copper disk which is the current feeder. A hypodermic needle is placed adjacent to the upper face of the altuglass disk. It acts as a composite probe which allows the electrode potential $E(L)$ at $x = L$ to be measured. This probe is realized as that of Fig. 1b except that its external surface is not insulated and is always in contact with the grains of the first layer. Its extremity has no sensing element since this role is played by the external surface of the needle itself. Its internal canal is connected to a saturated K_2SO_4 reference electrode. The lower compartment (anodic) of the cell is realized similarly to the other. The electrolyte flowing out of the cathodic bed is recirculated whereas the concentrated anolyte which is flowing down very slowly is eliminated.

Initially, the cathodic compartment is packed with spherical graphite or lead grains whereas the anodic compartment is packed with previously coppered spherical graphite grains. The compression strength of each bed is such that every dispersed phase is equipotential as can be controlled by measuring the potential drop between the current feeder and the external surface of the corresponding composite probe. From the color change of the grains packed in the cathodic compartment, the bed fraction coppered, *i.e.*, the effectiveness factor, can be determined directly through the wall of the cell after a time sufficiently long (90 min) but not too long to modify the bed texture.

The cell is fed by a Tacussel PRT 20-2 potentiostat, the potential $E(L)$ being imposed in the electrochemical operation. Owing to the negligible variation of the copper electrolyte concentration through the cathodic bed, the equilibrium potential is constant, thus the imposed value $E(L)$ determines the overpotential $\eta(L)$.

Physical and electrochemical data.—Grains and electrolytes.—The spherical grains indicated as A to H in Table I are of various natures and have different diameters d_p. The electrolytes designated as 1 to 6 in the same table are solutions of various $CuSO_4$ concentrations in 1*N* sulfuric acid; their stationary flow rates through the experimented cathodic beds are given in another column of Table I. The bed porosity ϵ in all the experiments was obtained by means of a weight balance on the dispersed phase (known bed weight and particle density, measured bed height) and was found to be between 0.418 and 0.421 for cell I and between 0.384 and 0.395 for the restrained beds of cell II. The uncertainties in such determinations allow for acceptance of ϵ being maintained equal to 0.42 for cell I and to 0.39 for cell II. The electrochemical experiments were carried out at room temperature (20°C).

Exchange current densities.—As in Ref. (16), the exchange current density i_0 for each electrolyte has been determined at 20°C in an adjoining apparatus using the linear expression [1]. The extent $0 \leq \eta \leq 10$ mV of this range has been respected during the determinations. The experimentally obtained values for i_0 are tabulated in Table I.

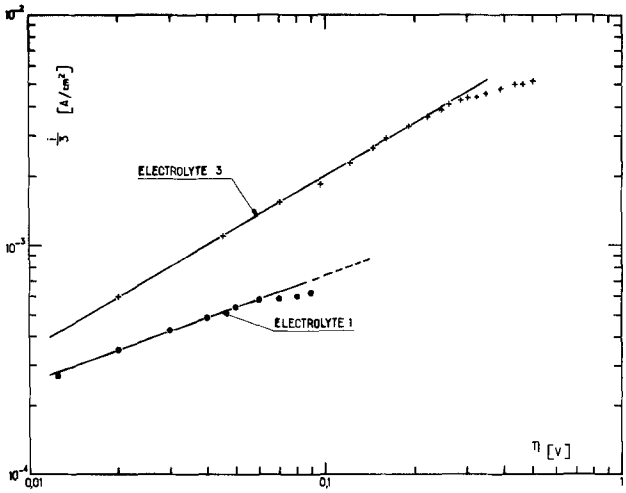


Fig. 8. Examples of experimental kinetic curves

Electrical conductivities.—The electrical conductivity γ_0 of each electrolyte has been measured in the column of Fig 6a itself by determining the solution potential gradients between the anode and the top of the cathodic bed. The method uses only the canal of the composite probe as a Luggin capillary. The γ_0 values are given in Table I.

The apparent electrical conductivity γ of the electrolyte in the pores of the bed was introduced in the model of the flow-through porous electrode. In our study, it can be calculated for each electrolyte by using the following expression

$$\frac{\gamma}{\gamma_0} = \frac{2 \cdot \epsilon}{3 - \epsilon}$$

which satisfactorily gives the relative conductivity of fixed beds of spherical particles and filled with a solution of conductivity γ_0 (20).

Kinetic equations.—For overpotentials far from the equilibrium overpotential, expression [2] is proposed to approximate the kinetic equation. Such an approximation was verified for all the electrolytes using cell I. In order to do it, the sensing element of the composite probe of Fig. 6b is replaced by a coppered graphite grain of diameter 0.3 cm. Such a modified probe is immersed within a fixed bed of glass beads of the same diameter as the sensing element. The flow rate of each electrolyte is set equal to the corresponding flow rate used in the experiments with flow-through electrodes.

The polarization curve $i = f(\eta)$ of the sensing element has been obtained experimentally and reported on double log paper as in Fig. 8 which shows two examples of results. The experimental points are aligned over an extended range of overpotentials allowing the variation of i as given in [2] to be accepted. The values of n and α corresponding to the straight lines and assuming the previously measured values of i_0 are tabu-

Table I. Characteristics of electrolytes and conducting grains

	Electrolytes and $CuSo_4$ concentrations	Flow rate (cm^3/sec)	i_0 (A/cm^2)	γ_0 ($ohm^{-1} \cdot cm^{-1}$)	n	α (V)	Spherical grains		
1	0.005M	4.7	7.02×10^{-5}	0.21	0.50	1.87	Copper	$d_p = 0.4$ cm	A
2	0.01M	4.7	9×10^{-5}	0.20	0.70	1.37	Copper	$d_p = 0.1$ cm	B
3	0.065M	4.7	1.06×10^{-5}	0.20	0.76	395	Coppered graphite	$d_p = 0.3$ cm	C
4	0.01M	19.4	9×10^{-5}	0.20	0.79	2626	Graphite	$d_p = 0.3$ cm	D
5	0.065M	11.2	1.07×10^{-5}	0.20	0.82	2.01	Graphite	$d_p = 0.15$ cm	E
6	0.065M	19.4	1.07×10^{-5}	0.20	0.82	7.29	Graphite	$d_p = 0.1$ cm	F
7	0.138M	19.4	2.6×10^{-4}	0.19	0.79	8135	Graphite	$d_p = 0.06$ cm	G
8	0.138M	19.4	2.6×10^{-4}	0.19	0.79	211,860	Lead	$d_p = 0.12$ cm	H

lated in Table I. It can be seen that in the present study n is always higher than 0.5.

Results and Discussion

Comparison between theory and experiments.—The steady overpotential distributions along the bed height, as measured in cell I, have been plotted according to the reduced form of [18] and give curves like those represented in Fig. 9 and 10 which show the influence of the grain diameter d_p and of the bed height L, respectively. It is seen that the "penetration depth" of the overpotential profile increases with increasing d_p or decreasing L, *i.e.*, with decreasing K_n.

When $\eta(0)$ is almost zero (current feeder at equilibrium) and the product $K_n\ x/L$ large enough, expression [18] takes the simplified form

$$\frac{\eta(x)}{\eta(L)} \approx \exp\left[K_n \cdot \left(\frac{x}{L} - 1\right)\right] \qquad [19]$$

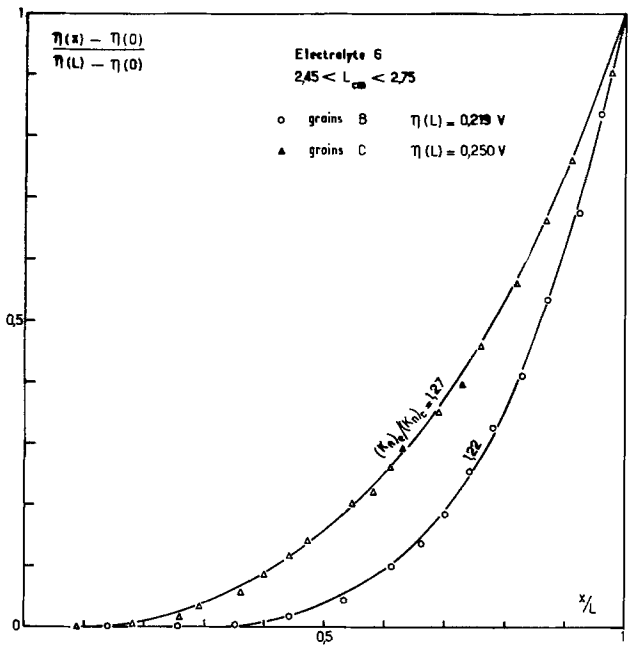


Fig. 9. Experimental dimensionless overpotential distributions showing the influence of d_p.

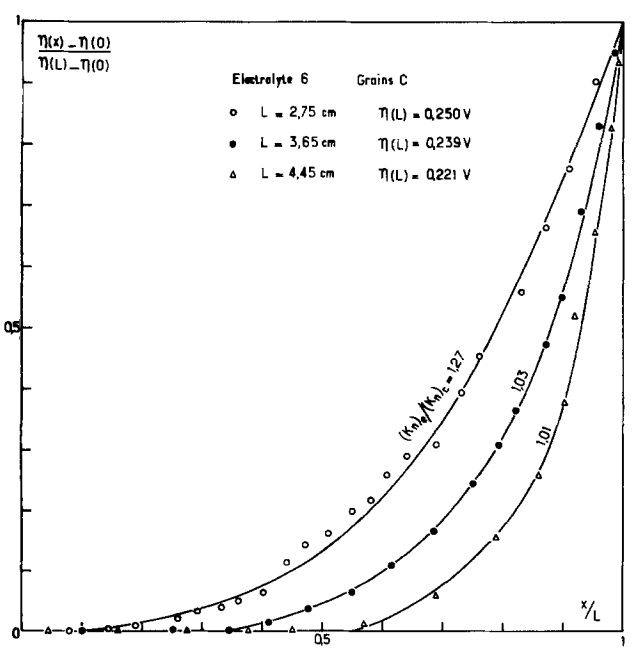


Fig. 10. Experimental dimensionless overpotential distributions showing the influence of L.

which can be used to deduce the experimental values of K_n, $(K_n)_e$, from the overpotential distributions by using semilog paper. Figure 11 gives three examples of such a use of the experimental data.

In order to compare the experimental criterion $(K_n)_e$ with the corresponding theoretical criterion $(K_n)_c$ obtained from [13], the value of the ratio $(K_n)_e/(K_n)_c$ is also indicated for each curve in Fig. 9 and 10. It can be seen that this value is close to unity.

The intercept with the horizontal axis of the lines of Fig. 11 yields the penetration depth of the overpotential profile within the electrode, therefore the value of the experimental effectiveness $(\mathcal{E}_n)_e$, which is equal to the ratio of that depth to the bed height. On the other hand, the calculated value $(\mathcal{E}_n)_c$ of $\mathcal{E}_n$ is given by [14] by introducing the corresponding criterion $(K_n)_c$. The superior part of Table II resumes the values of L, $(\mathcal{E}_n)_e$, $(\mathcal{E}_n)_c$, and of the ratio $(\mathcal{E}_n)_e/(\mathcal{E}_n)_c$ for all the experiments in cell I.

For cell II, and as previously stated, the effectiveness $(\mathcal{E}_n)_e$ of the electrode is obtained directly from the measurement of the height fraction covered with copper since the color transition between graphite and coppered graphite is very sharp. For each experiment, $(\mathcal{E}_n)_c$ is calculated in the same manner as for cell I. The value of L, $(\mathcal{E}_n)_e$, $(\mathcal{E}_n)_c$, and of $(\mathcal{E}_n)_e/(\mathcal{E}_n)_c$ are reported in the inferior part of Table II.

The values of $(\mathcal{E}_n)_e/(\mathcal{E}_n)_c$ in Table II are between 1.01 and 2.04 which indicates that the calculated effectiveness is always underestimated relative to the effectiveness really observed. This is still more evident in Fig. 12 where all the values of $(\mathcal{E}_n)_e$ are reported in function of the corresponding $(K_n)_c$. Comparison of the experimental dotted curve with the continuous theoretical curve obeying Eq. [13] shows that the deviation between these two curves increases with decreasing $(K_n)_c$ and is of the order of 50% for $(K_n)_c = 3$, 25% for $(K_n)_c = 4$, and 17.5% for $(K_n)_c = 15$.

Also, deviations have been previously reported with flow-through porous electrodes operating near equilibrium (16). They were attributed to the fact that the two phases of the electrode were considered as two continuous media from the electrical point of view. Such an explanation still seems reasonable here because the agreement between theory and experiment is better when K_n is high, *i.e.*, all the other parameters being unchanged, when d_p is small or L is high. The smaller d_p or the higher L is, the less local electrical conductivity of the electrolyte in the pores of the bed deviates from the over-all apparent electrical conductivity.

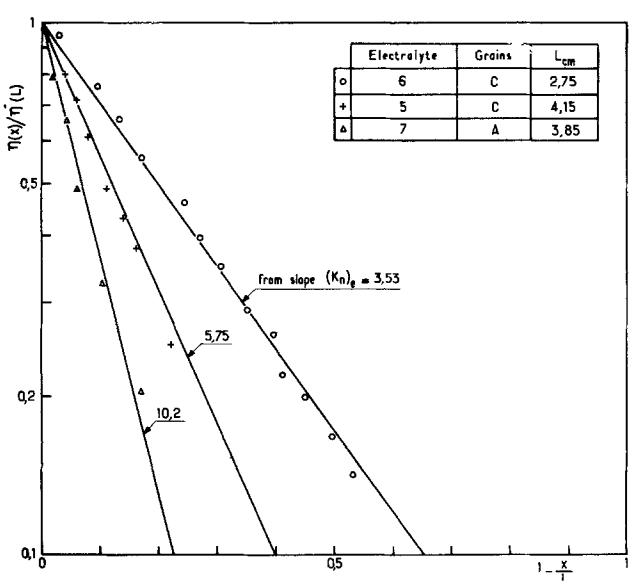


Fig. 11. Examples of determination of $(K_n)_e$ and $(\mathcal{E}_n)_e$

Table II. Calculated and experimental values of the effectiveness factor

Cell	Electrolytes	Grains	L_{cm}	$(\mathcal{E}_n)_e$	$(\mathcal{E}_n)_c$	$\frac{(\mathcal{E}_n)_e}{(\mathcal{E}_n)_c}$	L_{cm}	$(\mathcal{E}_n)_e$	$(\mathcal{E}_n)_c$	$\frac{(\mathcal{E}_n)_e}{(\mathcal{E}_n)_c}$	L_{cm}	$(\mathcal{E}_n)_e$	$(\mathcal{E}_n)_c$	$\frac{(\mathcal{E}_n)_e}{(\mathcal{E}_n)_c}$
I	4	A	3.3	0.189	0.147	1.28								
I	4	B	1.85	0.137	0.07	1.95	4.2	0.067	0.049	1.35				
I	5	C	4.15	0.167	0.165	1.01								
I	6	C	2.75	0.291	0.229	1.27	3.65	0.178	0.172	1.03	4.45	0.160	0.158	1.01
I	6	B	2.45	0.180	0.148	1.22								
I	7	A	3.11	0.085	0.07	1.21	3.85	0.097	0.063	1.62	2.2	0.126	0.100	1.26
I	7	A	2.62	0.109	0.084	1.28	3.85	0.136	0.064	2.14				
I	8	A	3.85	0.080	0.064	1.97	3.91	0.076	0.062	1.75				
II	1	D	3.3	0.420	0.234	1.83	2.6	0.425	0.285	1.48				
II	1	E	2.6	0.342	0.213	1.62	2.17	0.26	0.20	1.30				
II	1	H	2.8	0.231	0.172	1.32								
II	2	D	3	0.433	0.244	1.77	4.8	0.187	0.153	1.22	2.3	0.565	0.320	1.76
II	2	F	3.8	0.158	0.128	1.23								
II	2	G	3	0.133	0.109	1.22	7.0	0.058	0.066	1.12	4.5	0.108	0.090	1.18
II	2	C	1.85	0.620	0.40	1.55								
II	3	D	2.2	0.180	0.164	1.10	4.6	0.086	0.078	1.11				

Validity of the model.—Approximation [15] assumes that $[\eta(x)]^n$ is identical to $(n+1)/2 \cdot \eta \cdot [\eta(L)]^{n-1}$ at every point in the electrode. In order to test such an approximation, the experimental overpotential distributions for different values of $\eta(L)$ in a given electrode have to be compared. Figure 13 gives five experimental dimensionless distributions obtained during the treatment of an electrolyte in a given bed. In this figure two curves have been drawn from [18] by using, respectively, the lowest $\eta(L)$ value (curve 1) and the highest $\eta(L)$ value (curve 2). It can be seen that these two curves deviate only slightly from each other and enclose satisfactorily the experimental points which justifies approximation [15] for all $\eta(L)$.

Equation [2] also supposes that n is constant over all the local electrode overpotential range, thus may be inaccurate when $\eta(x)$ reaches very low values (electrode working in some parts near equilibrium). The theory could be improved by replacing the single equation [2] by a sequence of several kinetic equations, each valid in a specified variation range of η and characterized by a given pair of n and α values. Such a complication would probably bring nothing more to the user of the model. Indeed, the contribution of the bed fraction with very low overpotentials is usually negligible in comparison with the contribution of the rest of the bed.

If the experimental difficulties and the complexity of the system studied are taken into account, the agreement between theory and experiment is satisfactory. Furthermore the fact that the theory gives an underestimated electrode effectiveness makes it very useful for practical calculations.

As was recently outlined (15), many experimental investigations have dealt with current distributions within porous electrodes but only a small number of experimental studies concern the electrochemically active surface area. The present paper gives new information in this last area for electrodes working well below the limiting current, *i.e.*, in conditions where diffusional effects are absent.

Obviously the hypothesis of uniform electrolyte concentration within the electrode restricts the applicability of the analytical approach to systems in which the electrolyte velocity is not low. Also, a restriction follows from the hypothesis of a highly conductive dispersed phase. It is thought that the approach presented here could be used for systems such as low expanded fluidized bed electrodes and more generally for moving beds in which the dispersed phase behaves as highly conductive. For such systems, it is essential that the different parameters which determine the value of K_n are conveniently chosen in order to insure a good effec-

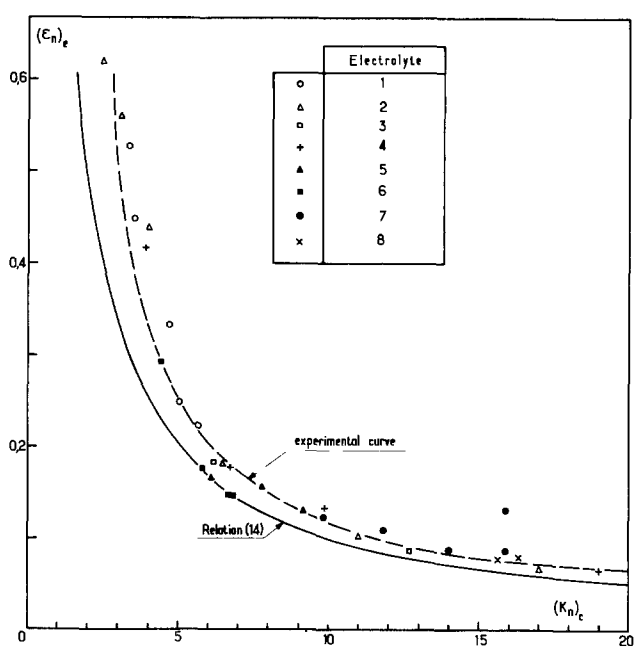


Fig. 12. Variations of $(\mathcal{E}_n)_e$ with $(K_n)_c$ and comparison with the theory.

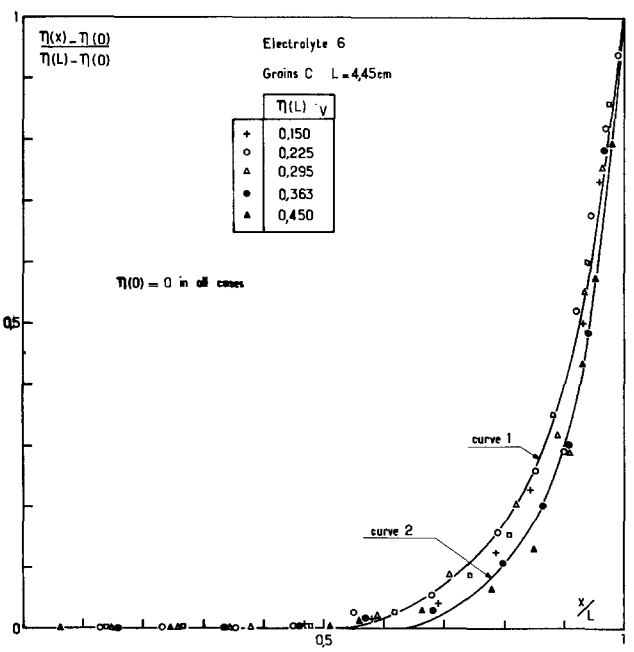


Fig. 13. Experimental dimensionless overpotential distributions in a given electrode for several imposed $\eta(L)$ values.

tiveness which would be an important factor of the investment cost for a given electrochemical reaction.

Expression [13] shows how the parameters can be chosen for guaranteeing a good effectiveness. K_n is small if: (*i*) the exchange current density has a low value (dilute solutions, bad electrocatalytic properties of the constituent material of the particles); (*ii*) the porosity ϵ of the bed is high (loose highly conductive packing); (*iii*) the specific area of the particles is small (not small particle diameters); (*iv*) the dimension L of the bed in the direction of the current lines is small; (*v*) the electrical conductivity γ is high (high values of γ_0 and particles such that the tortuosity of the current lines around them is reduced); (*vi*) the overpotential $\eta(L)$ at the electrode boundary opposite the counterelectrode has a high value.

Conclusion

Flow-through porous electrodes with highly conductive dispersed phases have been studied in a similar manner to solved chemical engineering problems in which mass transfer between two phases results from a competition between diffusion and chemical reaction (gas-solid catalysis, gas-liquid absorption). The analogy between the porous electrode seen as an heterogeneous electrochemical reactor and the gas-solid catalytic reactor is realistic; in the former the electrochemical overpotential plays the same role as the gaseous reactant concentration in the latter.

The general notions of effectiveness criterion K_n and effectiveness factor $\mathcal{E}_n$ which have been introduced are very important for the design of flow-through porous electrodes because the applications of these electrodes are mainly considered with regard to their high specific electrode area and their ability to act as three-dimensional electrodes. The criterion K_n is calculable *a priori* if the electrode, the electrolyte, and the operating conditions are fixed. Conversely, if an effectiveness $\mathcal{E}_n$ is chosen, it is possible to calculate K_n and to find the values of the different parameters of a flow-through porous electrode having the effectiveness $\mathcal{E}_n$. In addition, the approximated theory of these electrodes underestimates the performance which is advantageous from a practical point of view.

It has been shown that the behavior of the electrodes can be studied without using complex kinetic equations. In fact, it is sufficient for the designer to reason as in the chemical engineering discipline by finding a rational approximation. It is hoped that such an approach, which is very convenient for the electrochemical engineer, will be used more and more frequently.

LIST OF SYMBOLS

a_g specific surface area of the particles, cm^{-1}
d_p grain diameter, cm
E_{eq} equilibrium electrode potential, V
$E(x)$ electrode potential at x, V
$\mathcal{E}_n$ effectiveness, dimensionless
$(\mathcal{E}_n)_c$ calculated effectiveness, dimensionless
$(\mathcal{E}_n)_e$ experimental effectiveness, dimensionless
$\mathbf{F}$ Faraday number, 96,500 C/g-equiv.
i absolute current density, A/cm^2
i_0 exchange current density, A/cm^2
$i_s(x)$ current density relative to Ω in the pores of the bed, A/cm^2
I electrolytic current in the cell, A
K_n effectiveness criterion, dimensionless
$(K_n)_c$ calculated effectiveness criterion, dimensionless
$(K_n)_e$ experimental effectiveness criterion, dimensionless
L electrode height, cm
n exponent in [2], dimensionless
R gas constant, 8.31 J/g-mole · °K
T temperature, °K
u superficial electrolyte velocity, cm/sec
x spatial variable along the bed, cm
z number of electrons taking part in electrode reaction, g-equiv./g-mole

Greek characters

α coefficient in [2], V
γ_0 electrolyte conductivity, $\Omega^{-1} \cdot cm^{-1}$
γ apparent electrolyte conductivity in the pores of the bed, $\Omega^{-1} \cdot cm^{-1}$
η overpotential, V
$\eta(x)$ overpotential at x, V
$\eta^+(x) = \eta(x)/\eta(L)$ reduced overpotential, dimensionless
ϵ bed porosity, dimensionless
ϕ_S potential in the solution, V
ϕ_M potential in the dispersed phase, V
Ω cross-section area of the cell, cm^2

Manuscript submitted June 3, 1976; revised manuscript received Sept. 15, 1976. This was Paper 246 presented at the Washington, D.C., Meeting of the Society, May 2-7, 1976.

Any discussion of this paper will appear in a Discussion Section to be published in the December 1977 JOURNAL. All discussions for the December 1977 Discussion Section should be submitted by Aug. 1, 1977.

Publication costs of this article were assisted by C.N.R.S.

REFERENCES

1. J. A. E. Wilkinson and K. P. Haines, *Inst. Min. Metall. Trans. Sect. C*, **81**, 157 (1972).
2. A. J. Monhemius and P. L. N. Costa, *Hydrometall.*, **1**, 183 (1975).
3. D. N. Bennion and J. Newman, *J. Appl. Electrochem.*, **2**, 113 (1972).
4. A. K. P. Chu, M. Fleischmann, and G. J. Hills, *ibid.*, **4**, 323 (1974).
5. A. K. P. Chu and G. J. Hills, *ibid.*, **4**, 331 (1974).
6. J. Euler and W. Nonnenmacher, *Electrochim. Acta*, **2**, 268 (1960).
7. A. Winsel, *Z. Elektrochem.*, **66**, 287 (1962).
8. O. S. Ksenzhek, *Russ. J. Phys. Chem.* (*Engl. Transl.*), **36**, 121 (1962).
9. V. S. Daniel-Bek, *Zh. Fiz. Khim.*, **22**, 697 (1948).
10. A. N. Frumkin, *ibid.*, **23**, 1477 (1949).
11. R. de Levie, in "Advances in Electrochemistry and Electrochemical Engineering," Vol. 6, P. Delahay, Editor, Interscience Publishers, New York (1966).
12. J. S. Newman and C. W. Tobias, *This Journal*, **109**, 1183 (1962).
13. D. Simonsson, *ibid.*, **120**, 151 (1973).
14. S. Szpak and T. Katan, *ibid.*, **122**, 1063 (1975).
15. J. Newman and W. Tiedemann, *AIChE J.*, **21**, 25 (1975).
16. F. Coeuret, D. Hutin, and A. Gaunand, *J. Appl. Electrochem.*, **6**, 417 (1976).
17. F. Coeuret, *Electrochim. Acta*, **21**, 203 (1976).
18. E. E. Petersen, "Chemical Reaction Analysis," Prentice-Hall, Englewood Cliffs, New Jersey (1965).
19. H. Hikita and S. Asai, *Int. Chem. Eng.*, **4**, 332 (1964).
20. G. H. Neale and W. K. Nader, *AIChE J.*, **19**, 112 (1973).

Rotating Ring-Disk Electrodes

V. Isomerization and Reductive Coupling of Dialkyl Maleates

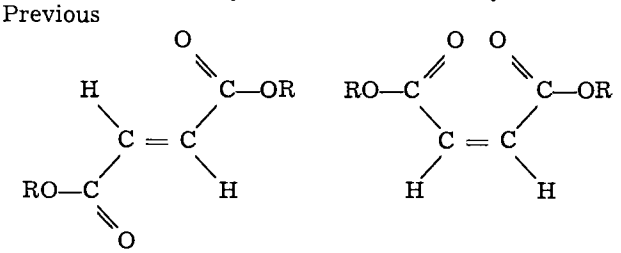
Lun-Shu R. Yeh* and Allen J. Bard**

Department of Chemistry, The University of Texas at Austin, Austin, Texas 78712

ABSTRACT

The rates of isomerization and coupling of the radical anions produced on electroreduction of several dialkyl maleates [methyl (DMM), ethyl (DEM), n-butyl (DBM)] in N,N-dimethylformamide solutions were investigated at the rotating ring-disk electrode (RRDE). Digital simulation methods were employed to obtain appropriate working curves and techniques were established to obtain both the first order isomerization constant (k_1) and the second order dimerization constant (k_2) from collection efficiency measurements. The measured k_1 values; DMM, 2.2; DEM, 6.0; and DBM, 6.7 (sec^{-1}) show an increasing isomerization rate with increasing size of alkyl substituent (R). The coupling rates decrease with increasing R; the k_2 values are: DMM, 1.9×10^5; DEM, 9.1×10^4; and DBM, 6.9×10^4 (M^{-1} sec^{-1}). Comparison of these results to previous measurements of the coupling rates of the corresponding trans-species (*i.e.*, fumarates) indicate that the *cis*-radical anions couple about two thousand times faster than do the *trans*.

The rotating ring-disk electrode has been useful in the investigation of the kinetics of electrode reactions, even for rather complicated mechanisms involving parallel reaction paths and higher order reactions [see (1-6) and references therein]. A particularly interesting electrochemical reaction scheme involves the difference in behavior upon reduction of the *cis*- and *trans*-isomeric dialkyl fumarates and dialkyl maleates. Previous



trans-isomer (or F) *cis*-isomer (or M)

R = CH_3 dimethyl fumarate (DMeF)	R = CH_3 dimethyl maleate (DMM)
R = C_2H_5 diethyl fumarate (DEF)	R = C_2H_5 diethyl maleate (DEM)
R = n-C_4H_9 di-n-butyl fumarate (DBF)	R = n-C_4H_9 di-n-butyl (DBM)

studies (7-10) have shown that in aprotic media the fumarates on reduction form the *trans*-radical anion ($F^{-\cdot}$) which undergoes a relatively slow coupling reaction to a dimeric dianion (D^{2-}) which ultimately produces hydrodimer, while the

$$F + e \rightarrow F^{-\cdot} \qquad [1]$$

$$2F^{-\cdot} \rightarrow D^{2-} \qquad [2]$$

maleates form the *cis*-radical anion ($M^{-\cdot}$) which isomerizes to $F^{-\cdot}$ and also couples much more rapidly to produce the dimeric dianion

$$M + e \rightarrow M^{-\cdot} \qquad [3]$$

$$2M^{-\cdot} \xrightarrow{k_2} D^{2-} \qquad [4]$$

$$M^{-\cdot} \xrightarrow{k_1} F^{-\cdot} \qquad [5]$$

While the qualitative nature of the reaction scheme for DEF and DEM was described, the rate constants for the various processes and the effect of alkyl substituent on the rates of isomerization and coupling were not given. The over-all reaction sequence for the reduction of a dialkyl maleate is quite complex and involves, in addition to reactions [2]-[5], the possibility of cross-coupling ([6]) and electron transfer ([7])

$$M^{-\cdot} + F^{-\cdot} \xrightarrow{k_2} D^{2-} \qquad [6]$$

$$M^{-\cdot} + F \xrightarrow{k_2''} F^{-\cdot} + M \qquad [7]$$

We describe here a digital simulation treatment (2-4, 6) of this reaction scheme at the RRDE and a strategy for determination of the rate constants from the experimental data. The values of these constants for the isomerization and coupling rates for several dialkyl fumarates and maleates are reported and discussed.

Experimental

Apparatus.—The general apparatus and procedures have been previously described (5, 8). A Tacussel Electronique Bipotentiostat, Model Bipad 2, was used for all RRDE experiments. A Wavetek function generator provided a linear d-c potential ramp to drive the Bipotentiostat. A simple operational amplifier adder circuit was used to adjust the starting potential of the scan. In all of the experiments, either the disk or ring was held at a constant potential while the other was scanned. The voltammograms were recorded using a Moseley Model 7100B dual pen strip chart recorder. A Moseley Model 2D-2 Autograf X-Y recorder and Model 7005A X-Y recorder were also used to record the disk and the ring currents simultaneously. A Digitec digital voltmeter Model 204 and a Hewlett-Packard digital voltmeter Model IM-102 were used to measure the potentials of the disk and the ring electrodes. These voltmeters were also used to record the steady-state disk and ring currents simultaneously as well as to calibrate the recorder responses. The RRDE, comprising platinum ring and disk electrodes separated by Teflon, was constructed by Pine Instrument Company, Grove City, Pennsylvania, and had the following dimensions: $r_1 = 0.187$ cm, $r_2 = 0.200$ cm, and $r_3 = 0.332$ cm. The theoretical collection efficiency, *i.e.*, the collection efficiency for a stable intermediate generated at the disk electrode, N, for this RRDE is 0.555. The reference electrode was a silver wire, and the counterelec-

* Electrochemical Society Student Member.
** Electrochemical Society Active Member.
Key words: digital simulation, isomerization, dimerization, cyclic voltammetry, reductive coupling.

trode was platinum foil contained in different compartments separated from the main working electrode (RRDE) compartment by medium porosity sintered-glass frits.

Reagents.—N,N-dimethylformamide (DMF) obtained from Matheson, Coleman, and Bell Chemicals, was treated with molecular sieves and anhydrous cupric sulfate and then by vacuum distillation (11). The purified DMF was subjected to at least three freeze-pump-thaw cycles and was then stored in the dry box (Vacuum Atmospheres Corporation, Hawthorne, California). Tetra-n-butylammonium iodide (TBAI), polarographic grade, obtained from Southwestern Analytical Chemicals, Incorporated, was dried under vacuum and stored in the dry box. Diethyl fumarate (DEF), puriss, purchased from Aldrich Chemical Company was used without further purification. Diethyl maleate (DEM) (Matheson, Coleman, and Bell) containing about 5% diethyl fumarate impurity, was stored in a refrigerator. The DEF in the DEM was removed by preparative gas chromatography using a 6 meter chromatographic column filled with 30% SE 30 on 60/80 Chromosorb P and a column temperature of 175°C. Di-n-butyl fumarate (DBF) and di-n-butyl maleate (DBM) were purchased from Aldrich Chemical Company and used as received. Dimethyl maleate (DMM) was prepared by esterification of maleic anhydride with sulfuric acid and methanol purified by vacuum distillation yielding polarographically pure DMM. The maleic anhydride was purchased from Aldrich Chemical Company. The dimethyl fumarate (DMeF), also from Aldrich Chemical Company, was used after sublimation.

Digital simulation.—The RRDE voltammogram for a solution of DEM (2.55 mm) containing a small amount of DEF in 0.1*M* TBAI-DMF is shown in Fig. 1. The disk voltammogram (curve a) which shows the disk current i_d *vs.* disk potential, E_d, is characterized by the reduction of DEF to the radical anion, at −0.75V, (zone II) followed by the reduction of DEM to its radical anion in zone III. Thus for curve a the following reactions occur at the different potentials at the disk electrode surface and in the bulk solution near the electrode:

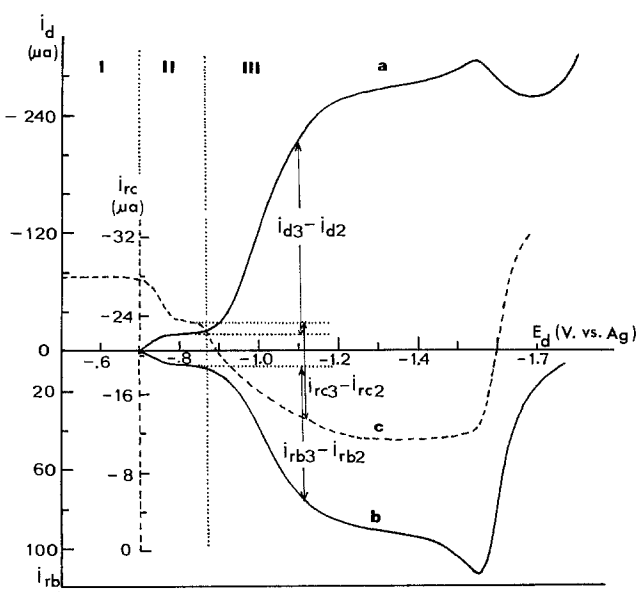


Fig. 1. RRDE voltammograms of diethyl maleate (2.55 mM) with diethyl fumarate impurity in TBAI (0.11M) DMF at a rotation speed of 201 radians/sec. a. Disk current b. Ring current at E_r = 0.0V. c. Ring current at E_r = −0.83V *vs.* Ag R.E.

A. Zone I: no reaction

Zone II: $F + e \rightarrow F^{\cdot -}$ $\quad i_{d2}$

$2F^{\cdot -} \rightarrow D^{2-}$

Zone III: The above reactions and

$M + e \rightarrow M^{\cdot -}$ $\quad (i_{d3} - i_{d2})$

$M^{\cdot -} \rightarrow F^{\cdot -}$ (rotational isomerization)

$2M^{\cdot -} \rightarrow D^{2-}$

$M^{\cdot -} + F^{\cdot -} \rightarrow D^{2-}$

$M^{\cdot -} + F \rightarrow F^{\cdot -} + M$ (charge transfer isomerization)

For the ring electrode held at a ring potential, E_r, of 0.0V any DEF or DEM radical anion formed at the disk which reaches the ring will be oxidized. Thus a scan of the ring current, i_r, *vs.* E_d (curve b) shows waves for the following reactions at the ring in the different zones:

B. Zone I: no reaction

Zone II: $F^{\cdot -} \rightarrow F + e$ $\quad (i_{rb2})$

Zone III: $F^{\cdot -} \rightarrow F + e$ (for $F^{\cdot -}$ generated from F at disk) (i_{rb2})

$F^{\cdot -} \rightarrow F + e$ (for $F^{\cdot -}$ resulting from isomerization) $\}$ $(i_{rb3} - i_{rb2})$

$M^{\cdot -} \rightarrow M + e$

For the ring electrode held at E_r = −0.83V (on the reduction plateau for DEF), a plot of i_r *vs.* E_d (curve c) shows waves for the following reactions:

C. Zone I: $F + e \rightarrow F^{\cdot -}$ (reduction of F transported to ring from disk, gap, and directly) (i_{rc1})

Zone II: $F + e \rightarrow F^{\cdot -}$ (shielded reduction of F transported to ring from gap and directly) (i_{rc2})

Zone III: The above reaction and

$M^{\cdot -} \rightarrow M + e$ $\quad (i_{rc3} - i_{rc2})$

The rate constants for the coupling of $F^{\cdot -}$ can be obtained, as previously described, by studies in the absence of maleate. The goal then is to find the rate constants for the isomerization (k_1) and coupling (k_2) of $M^{\cdot -}$ (Eq. [4] and [5]) from the available data. Let us assume first a negligible contribution from the reactions in [6] and [7]. The collection of $M^{\cdot -}$ left after all possible following reactions at the ring is represented by the current $i_{rc3} - i_{rc2}$. Thus the collection efficiency for $M^{\cdot -}$, N_k, is given by

$$N_k = |(i_{rc3} - i_{rc2})/(i_{d3} - i_{d2})| \qquad [8]$$

The ring current which represents the amount of $F^{\cdot -}$

produced by the isomerization of $M^{\cdot -}$ that reaches the ring, I_R, is

$$I_R = (i_{rb3} - i_{rb2}) - (i_{rc3} - i_{rc2}) \quad [9]$$

The total i_r which would be observed for $M^{\cdot -}$ in the absence of any chemical reactions would be $N(i_{d3} - i_{d2})$, where N is the collection efficiency of the electrode. Thus $N(i_{d3} - i_{d2}) - I_R$ is a measure of the extent of the isomerization reaction, and the isomerization collection efficiency parameter, n_k, defined in [10] can be

$$n_k = N - I_R/(i_{d3} - i_{d2}) \quad [10]$$

used to determine k_1. As in earlier work (5-8), a convenient variable is one related to the flux of reduced species from the disk, *i.e.*, $i_{d3} - i_{d2}$, divided by its limiting value (at *ca.* −1.3V), $(i_{d3,l} - i_{d2,l})$ called *CONI*

$$CONI = \frac{i_{d3} - i_{d2}}{i_{d3,l} - i_{d2,l}}$$

The digital simulations were carried out using the programs and methods previously described (2-6), modified for this reaction mechanism. A listing and description is available (12). The following dimensionless parameters were used to represent the rate constants; (notation follows previous practice and the diffusion coefficients of all species were assumed to be equal)

$$XKT = (0.51)^{-2/3}(\nu/D)^{1/3}\omega^{-1}k_1 \quad [11]$$

$$XKTC = (0.51)^{-2/3}(\nu/D)^{1/3}\omega^{-1}Ck_2 \quad [12]$$

Since the isomerization of $M^{\cdot -}$ to $F^{\cdot -}$ is a first order reaction and the half-life of $M^{\cdot -}$ is independent of the original concentration, a straight line parallel to the $1 - CONI$ axis results in the n_k *vs.* $1 - CONI$ plot for $k_1 >> k_2$. On the other hand when $k_2 >> k_1$ the N_k *vs.* $1 - CONI$ plot will show the upward curvature previously reported (6). Because the isomerization does not depend upon concentration or *CONI* when both isomerization and dimerization are significant, the N_k *vs.* $1 - CONI$ curve will generally show the second order dimerization trend, and the effect of isomerization moves the whole curve up or down, depending upon the relative magnitude of the isomerization effect. Simulation results are shown for keeping *XKT* constant and varying *XKTC* (Fig. 2), and keeping *XKTC* constant and varying *XKT* (Fig. 3). Note that when *XKT* predominates, the N_k *vs.* $1 - CONI$ curve straightens out, when *XKTC* does, it is curved. At high *XKT* and low *XKTC* values the line is almost independent of $1 - CONI$. A rough estimate of n_k can be obtained by extrapolating the N_k *vs.* $1 - CONI$ curve to $1 - CONI \rightarrow 1$, where $i_d \rightarrow 0$, and dimerization is negligible compared to isomerization.

The existence of species $F^{\cdot -}$ (either from the presence of more easily reduced F originally in solution or from isomerization of $M^{\cdot -}$) makes consideration of an additional reaction, the cross coupling to form D^{2-}, reaction [6], necessary. Simulations including this possibility were also carried out, with the dimensionless parameter *XKTD* representing the rate of this reaction, where *XKTD* is exactly the same as *XKTC*, except k_2 is replaced by k_2'. These simulations assume that the coupling of two $F^{\cdot -}$'s is slow compared to the $M^{\cdot -}$ reactions, and need not be considered. Typical results are shown in Fig. 4. The results here depend upon the relative amounts of F and M in the bulk solution (taken as 4:1 in the results of Fig. 4) and this provides a method for ascertaining the importance of cross coupling. Increasing the bulk concentration of F decreases the slope of the N_k *vs.* $1 - CONI$ curve.

Similar behavior results from inclusion of the electron transfer cross reaction [7], with *XKTCC* representing the appropriate dimensionless parameter, containing k_2''. The occurrence of this reaction alone, along with isomerization, causes a negative slope in the N_k *vs.* $1 - CONI$ curves (A and B in Fig. 5), as expected from the similar behavior found for the $R + R^{\cdot -}$ reaction in

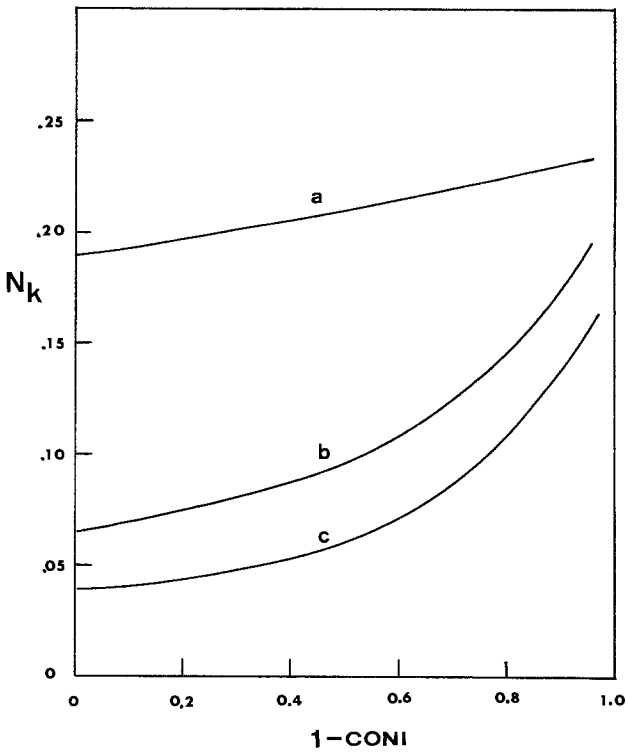


Fig. 2. Simulated collection efficiency for simultaneous reactions: first order parameter *XKT* = 0.77 and second order parameter *XKTC* of a, 0.5; b, 7.0; and c, 15.0.

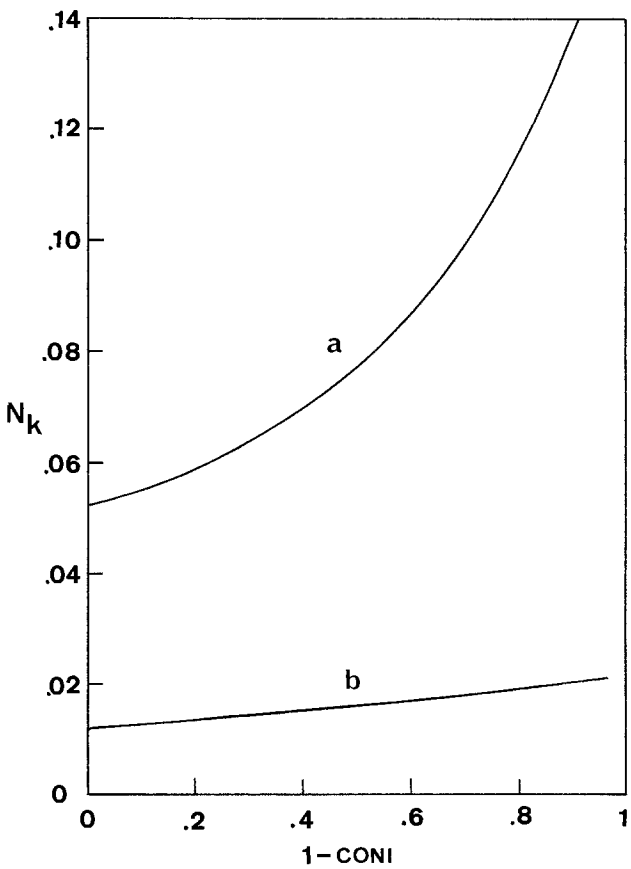


Fig. 3. Simulated collection efficiency for simultaneous reactions: second order parameter *XKTC* = 10, and first order parameter of a, 0.85 and b, 4.0.

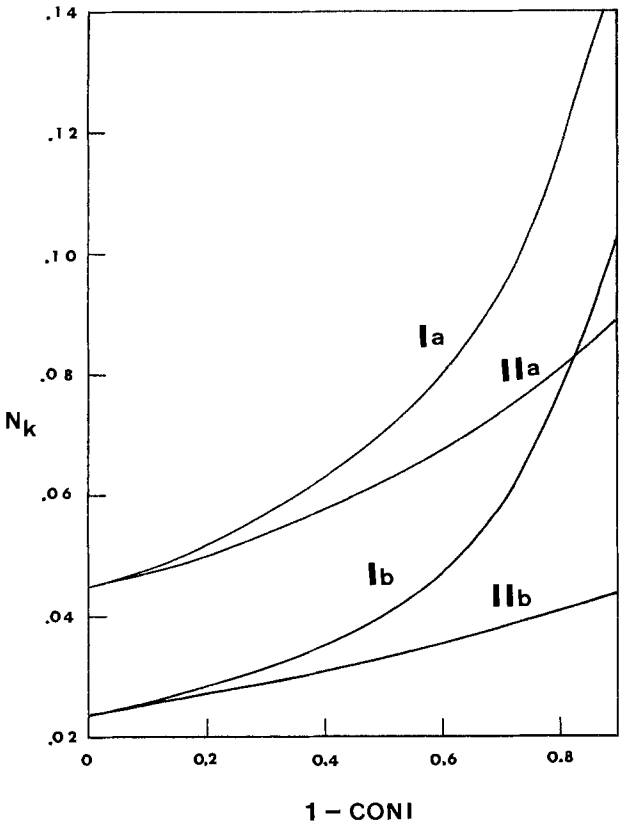


Fig. 4. Collection efficiency for isomerization (*XKT*) and dimerization (*XKTC*) in the presence of cross-coupling dimerization (*XKTD*), [F] = 0.25 [M]). Ia: *XKT* = 0.77, *XKTC* = 13.0; IIa: *XKT* = 0.77, *XKTC* = 7.0, *XKTD* = 7.0; Ib: *XKT* = 0.77, *XKTC* = 30.0; IIb: *XKT* = 0.77, *XKTC* = 15.0, *XKTD* = 15.0.

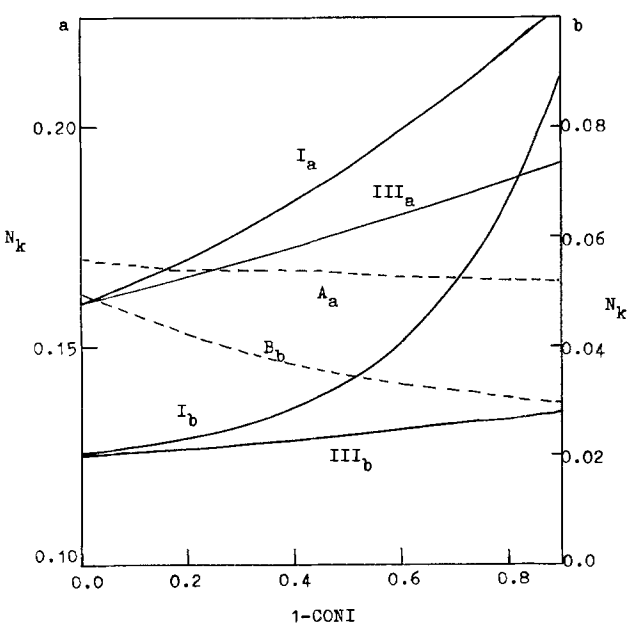


Fig. 5. Collection efficiency for isomerization and dimerization in the presence of $M^{\cdot-}/F$ electron transfer (*XKTCC*). [F] = 0.25 [M]. The subscripts a and b designate the use of a and b scales, respectively. I_a: *XKT* = 0.77, *XKTC* = 0.95; III_a: *XKT* = 0.77, *XKTC* = 0.5, *XKTCC* = 0.25; I_b: *XKT* = 0.77, *XKTC* = 40.0; III_b: *XKT* = 0.77, *XKTC* = 7.0, *XKTCC* = 3.5; A_a: *XKT* = 0.77, *XKTCC* = 0.5; B_b: *XKT* = 0.77, *XKTCC* = 3.5.

hydrodimerizations (6). The inclusion of [7] along with [4] and [5] thus results in decreasing slopes of the working curves (Fig. 5).

Results

Diethyl maleate.—The experimental RRDE voltammogram for DEM containing a small amount of DEF is shown in Fig. 1 and typical experimental results at several values of ω and C are given in Table I. The experimental data were fitted by first obtaining an *XKT* value by simulating the calculated n_k from Eq. [10]. The *XKT* value can also be estimated from the extrapolated N_k value at *CONI* → 0. This value is then used with different trial values of *XKTC*, and the best fit parameters are obtained by a trial and error procedure. The resulting simulated curves based on these two parameters fit the experimental data quite well (Fig. 6). The calculated values of k_1 and k_2 are shown in Table II, based on results with solutions where the DEF concentration was less than 5% that of the DEM. To establish the importance of the cross-coupling reaction [6], experiments where DEF was added to the DEM solutions, were carried out. Typical results of such an experiment, where the concentration of DEF was 24% that of DEM are shown in Fig. 7.

These data could be fitted with a $k_1 = 5.7$ sec^{-1} and $k_2 = 9.6 \times 10^4$ M^{-1} sec^{-1}, which are very close to the values obtained in the absence of excess DEF. This suggests that the $F^{\cdot-}/M^{\cdot-}$ reaction is slow compared to $M^{\cdot-}/M^{\cdot-}$ dimerization. Previous results using double potential step techniques and electron spin resonance spectroscopy (13-15) have fixed the rate constant for the $F^{\cdot-}/F^{\cdot-}$ reaction, [2], under similar conditions at about 44M^{-1} sec^{-1}, so that the *cis*-radical anion dimerizes about 2000 times faster than the *trans*-form.

Dimethyl maleate.—The general behavior of DMM is similar to that of DEM. Freshly prepared DMM, however, does not show a reduction wave for the fumarate during RDE voltammetry, in contrast to the behavior of DEM, where even a sample freshly separated by preparative gas chromatography showed a small DEF wave. A cyclic voltammogram of DMM in the absence of DMeF (Fig. 8) shows an unusual "cross-over" behavior on reversal. On the first reduction scan only the single DMM reduction peak is observed. On the

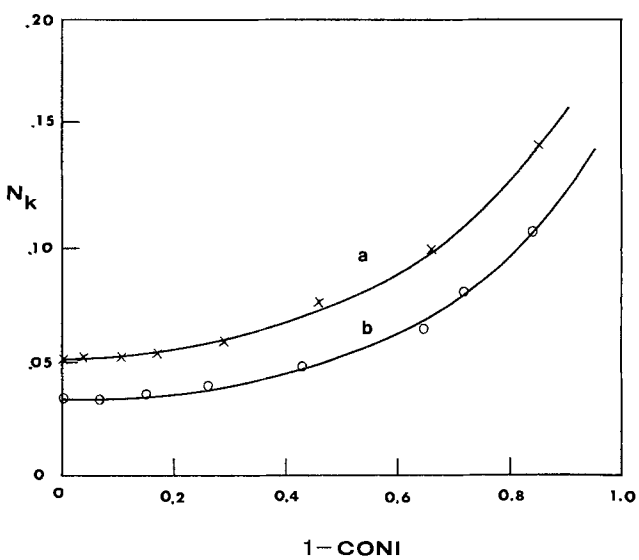


Fig. 6. Collection efficiency of the radical anion of diethyl maleate, 2.65 mM, in 0.1M TBAI-DMF solution, rotation rate at (×) 223 and (○) 164 radians/sec. Solid lines are simulation curves at a, *XKT* = 0.42, *XKTC* = 14.5 (corresponding to k_1 = 6.3 sec^{-1} and $k_2 = 8.25 \times 10^4$ liters/mole-sec); b, *XKT* = 0.53, *XKTC* = 24.0 (corresponding to $k_1 = 5.9$ sec^{-1} and $k_2 = 10.0 \times 10^4$ liters/mole-sec).

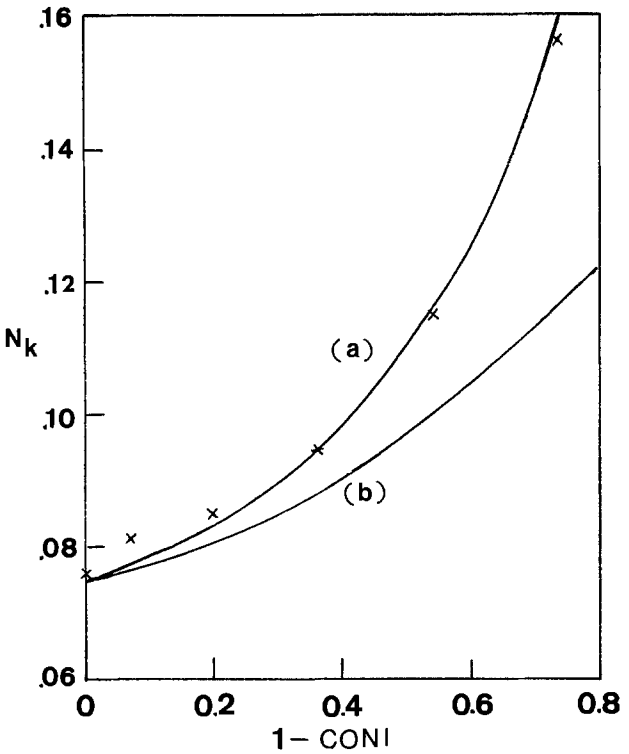


Fig. 7. Collection efficiency of the radical anion of diethyl maleate, 0.95 mM, in the presence of diethyl fumarate, 0.23 mM, in 0.1M TBAI-DMF solution. Experimental results (x) were obtained at rotation rate of 164 radians/sec. Solid lines are simulation curves at (a), $XKT = 0.51$, $XKTC = 7.0$ (corresponding to $k_1 = 5.7$ sec^{-1} and $k_2 = 9.6 \times 10^4$ liters/mole-sec); (b), $XKT = 0.51$, $XKTC = 4.5$, $XKTD = 4.5$.

reverse scan (oxidation of $M^{\cdot-}$ and $F^{\cdot-}$) the curve crosses over the reduction scan curve. This effect implies that a greater amount of reduction in this region (at *ca.* −0.9V) is occurring on the reverse scan than on the forward one. This can be attributed to the $M^{\cdot-}$ catalyzed isomerization of M to F (7) via the reaction sequence [3], [5], and [7], so that the amount of F at the electrode surface on reversal is larger than that present during the first forward scan. Note that this behavior does not occur with subsequent scans or for solutions originally containing DMeF. Similar cyclic voltammograms have been noted by Saveant (16). Notice also that the M reduction wave decreases strongly on repeated scans because of the loss of M via the dimerization, while the $F/F^{\cdot-}$ couple establishes a steady-state wave pair. RRDE studies of DMM exactly parallel those of DEM; typical data are in Table I and the resulting values of k_1 and k_2 are listed in Table II. Experiments in which DMeF was added in amounts up to 25% that of DMM were carried out and again the cross-coupling reaction did not appear to affect the results to a significant extent. Previous measurements of the dimerization rate of DMeF radical anion (5, 14) yield a rate constant of *ca.* $110M^{-1}$ sec^{-1} again about 2000 times smaller than that of the *cis*-radical anion.

Di-n-butyl maleate.—The behavior of DBM is very similar to that of DEM; both show the presence of the fumarate even in highly purified samples. The RRDE experiments parallel those of DEM; typical data and results are given in Tables I and II. The rate constant for DBF radical anion dimerization has been reported as $25M^{-1}$ sec^{-1} (14).

Discussion

The effect of substituent (methyl, ethyl, n-butyl) for the maleates is opposite for the isomerization (k_1) and dimerization (k_2) rate constants. For the dimerization, as the size of the substituent is increased, k_2 decreases; a similar trend is observed for the fumarates (14). Thus the bulky groups hinder the coupling of the radical anions, as expected. For the isomerization, increasing the substituent size causes k_1 to increase. The radical anions isomerize much more rapidly than the parent compounds probably because (*i*) the addition of an electron to the antibonding molecular orbital causes a decrease in the bond order of the central ethylenic bond and (*ii*), the negative charge on the molecule resides to a large extent on the oxygens, causing a coulombic repulsion of the carbonyl groups. Increasing the size of the substituents provides an added steric repulsion and thus increases k_1. Finally, for all compounds the *cis*-radical anions dimerize about 2000 times as rapidly as the *trans*. This can be explained by a larger electron density residing on the ethylenic carbons because of the coulombic repulsion of charge from the *cis*-carbonyls or because of partial twisting around the central bond. Not only is the coupling reaction larger, but these *cis*-radical anions react more rapidly with

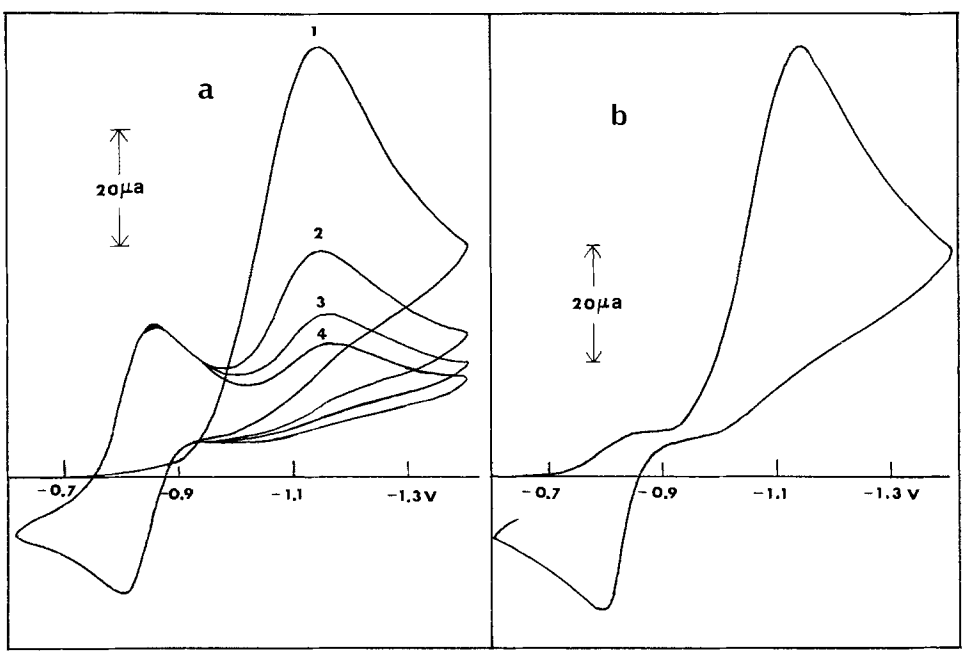


Fig. 8. Cyclic voltammograms of 2.0 mM dimethyl maleate in 0.1M TBAI-DMF solution, voltage scan rate was at 200 mV/sec; a, polarographically pure dimethyl maleate with continuous scans; and b, in the presence of dimethyl fumarate as impurity.

Table I. RRDE results for dialkyl maleates in 0.1M TBAI-DMF solution

ω (sec^{-1})	$i_{d3}-i_{d2}$ ($-\mu$a) (A)	$i_{rb3}-i_{rb2}$ (μa) (B)	$i_{rc3}-i_{rc2}$ (μa) (C)	$N_K=\frac{(C)}{(A)}$	$N-\frac{n_k=(B)-(C)}{(A)}$	CONI
			A. Diethyl maleate			
			(a) 1.85 mM			
164	13.5	5.35	2.09	0.155	0.314	0.108
	27.5	10.06	3.44	0.125	0.313	0.220
	46.5	15.35	4.25	0.0914	0.316	0.372
	59.0	18.60	4.75	0.0805	0.320	0.472
	72.0	22.20	5.15	0.0715	0.317	0.576
	92.0	27.90	5.80	0.0630	0.315	0.736
	112.0	33.30	6.30	0.0562	0.314	0.892
	125.0	36.80	6.60	0.0528	0.313	1.000
223	27.5	10.25	4.54	0.165	0.347	0.187
	45.5	15.6	5.92	0.130	0.341	0.310
	67.0	21.6	7.25	0.108	0.340	0.456
	87.0	26.2	7.70	0.0885	0.342	0 592
	110	31.6	8.70	0.079	0.347	0.748
	131	36.4	9.55	0.073	0.350	0.891
	147	40.4	9.85	0.067	0.347	1.000
			(b) 2.65 mM			
164	34.7	12.2	3.7	0.107	0.310	0.164
	59.7	19.6	4.78	0.080	0.306	0.283
	77.0	23.8	5.0	0.065	0.311	0.365
	120.0	35.5	5.8	0.048	0.307	0.569
	155	45.5	6.05	0.039	0.301	0.734
	180	52 2	6.4	0.0355	0.301	0.853
	195	55.6	6.8	0.035	0.305	0.924
	211	59.8	7.2	0.034	0.306	1.000
223	36.5	13.3	5.3	0.145	0.336	0.150
	82.0	25.7	8.05	0.098	0.339	0.337
	131	37.9	10.0	0.076	0.341	0.539
	172	46.4	10.3	0.060	0.345	0.708
	201	53.6	10.8	0.054	0.342	0.827
	221	59.0	11.6	0.052	0.340	0.909
	234	62.5	12.2	0.052	0.339	0.963
	243	64.9	12.6	0.052	0.340	1.000
			B. Dimethyl maleate			
			(a) 0.52 mM			
106	8.9	2.46	0.99	0.111	0.390	0.299
	13.6	3.55	1.20	0.088	0.382	0.456
	18.5	4.53	1.38	0.075	0.385	0.621
	24.5	5.60	1.49	0.061	0.388	0.822
	28.2	6.45	1.60	0.057	0.383	0.946
	29.8	6.92	1.70	0.057	0.380	1.00
164	13.2	3.47	1.75	0.132	0.425	0.353
	18.8	4.53	2.03	0.108	0.422	0.503
	26.7	5.55	2 21	0.083	0.430	0.714
	31.5	6.46	2.40	0.076	0.426	0.842
	37.4	7.57	2.67	0.071	0.424	1.00
			(b) 1.05 mM			
106	10.8	2.98	1.30	0.120	0.399	0.174
	21.4	4.72	1.50	0.070	0.405	0.346
	30.3	6.27	1.82	0.060	0.408	0.489
	39.4	7.76	1.96	0.050	0.408	0.636
	49.5	9.50	2.19	0.044	0.407	0.800
	55.5	10.56	2.36	0.042	0.407	0.897
	61.9	11.90	2.56	0.041	0.404	1.00
164	24.4	5.62	2.58	0.106	0.430	0.323
	34.8	7.10	2.85	0.082	0.435	0.461
	45.2	8.72	3.21	0.071	0.433	0.600
	58.0	10.22	3.55	0.061	0.440	0.768
	65.5	12.00	3.76	0.057	0.429	0.867
	75.5	13.90	4 29	0.057	0.428	1.00
			C. Di-n-butyl maleate			
			1.30 mM			
180	12.8	5.5	2.24	0.175	0.300	0.144
	22.5	9.0	3.37	0.150	0.305	0.253
	38.1	14.0	4.38	0.115	0.302	0.428
	53.7	18.4	5.13	0.096	0.309	0.604
	67.5	22.0	5.26	0.078	0.307	0.870
	83.5	27.2	6.26	0.075	0.304	0.940
	89.0	28.7	6.38	0.072	0.304	1.000
230	17.1	7.4	3.6	0.210	0.333	0.143
	25.0	10.1	4.5	0.180	0.330	0.242
	42.4	15.7	6.3	0.148	0.333	0.410
	60.6	21.4	7.5	0.124	0.327	0.590
	76.9	25.6	8.1	0.105	0.328	0.745
	96.2	30.6	9.1	0.094	0.331	0.933
	103.0	32.5	9.5	0.092	0.331	1.000

added electrophiles such as acrylonitrile (7) or CO_2 (12, 17).

We conclude by referring to some related studies of isomerization of radical anions. Hayon and Simic (18) used a pulse radiolysis technique to study the formation and reactions of DMM and DMeF radical anions in aqueous solutions. They found no appreciable isomerization of DMM^- within the time window of their experiment ($\sim$ 0.1 μsec), which is consistent with the k_1 value reported here. Moreover strong hydrogen bonding in water may stabilize the *cis*-configuration. Ion pairing can also stabilize the radical anion and decrease the isomerization rate. Thus Szwarc and co-workers (19, 20) found that in THF solutions in the presence of alkali metal ions, stilbene radical anion isomerized slowly and the over-all isomerization reaction proceeded via the ion paired dianion. In HMPA, however, where the ion pairs were dissociated, isomerization of *cis*-stilbenide was reported. A study of the effect of ion pairing on the isomerizaton of maleate radical anions in DMF would be of interest but would probably be difficult, because the dimerization rates would be expected to become very rapid under these conditions (14).

Table II. Calculated isomerization rate constant (k_1) and dimerization rate constant (k_2) of dialkyl maleate radical anions from RRDE results in 0.1M TBAI-DMF solutions

Conc (mM)	ω (sec^{-1})	XKT	k_1 (sec^{-1})	XKTC	k_2 (M^{-1} sec^{-1})
			A. Diethyl maleate		
1.85	164	0.5	5.6	13.0	9.12×10^4
	223	0.41	6.2	9.5	9.06
2.65	164	0.53	5.9	24.0	10.0
	223	0.42	6.3	14.5	8.25
			Avg.: 6.0		9.1×10^4
			B. Dimethyl maleate		
0.52	106	0.30	2.15	13.0	1.75×10^5
	164	0.22	2.44	10.5	2.24
1.05	106	0.26	1.86	25.5	1.74
	164	0.21	2.33	16.5	1.75
			Avg.: 2.20		1.9×10^5
			C. Di-n-butyl maleate		
1.30	180	0.53	6.4	7.7	7.20×10^4
	230	0.45	7.0	5.5	6.57
			Avg.: 6.7		6.9×10^4

Acknowledgment

The support of this research by the Robert A. Welch Foundation and the National Science Foundation (CHE 71-03344) is gratefully acknowledged.

Manuscript submitted July 7, 1976; revised manuscript received Sept. 24, 1976.

Any discussion of this paper will appear in a Discussion Section to be published in the December 1977 JOURNAL. All discussions for the December 1977 Discussion Section should be submitted by Aug. 1, 1977.

Publication costs of this article were assisted by The University of Texas.

REFERENCES

1. W. J. Albery and M. L. Hitchman, "Ring-Disc Electrodes," Oxford University Press, London (1971).
2. K. B. Prater and A. J. Bard, *This Journal*, **117**, 207 (1970).
3. *Ibid.*,335 (1970).
4. *Ibid.*, 1517 (1970).
5. V. J. Puglisi and A. J. Bard, *ibid.*, **119**, 829 (1972).
6. *Ibid.*, **119**, 833 (1972).
7. A. J. Bard, V. J. Puglisi, J. V. Kenkel, and A. Lomax, *Faraday Discuss. Chem. Soc.*, **56**, 353 (1973).
8. V. J. Puglisi and A. J. Bard, *This Journal*, **120**, 748 (1973).
9. A. V. Il'yasov, Yu. M. Kargin, and V. Z. Kondranina, *Izv. Akad. Nauk. SSR, Ser Khim.*, **5**, 927 (1971).
10. A. V. Il'yasov, Yu. M. Kargin, N. N. Sotnikova, V. Z. Kondranina, B. V. Mel'nikov, and A. A. Vafina, *ibid.*, **5**, 932 (1971).
11. L. R. Faulkner and A. J. Bard, *J. Am. Chem. Soc.*, **90**, 6284 (1968).
12. L. S. R. Yeh, Ph.D. Dissertation, The University of Texas at Austin, Austin, Texas (1976).
13. W. V. Childs, J. T. Maloy, C. P. Keszthelyi, and A. J. Bard, *This Journal*, **118**, 874 (1971).
14. M. J. Hazelrigg and A. J. Bard, *ibid.*, **122**, 211 (1975).
15. I. B. Goldberg, D. Boyd, R. Hirasawa, and A. J. Bard, *J. Phys. Chem.*, **78**, 295 (1974).
16. J. M. Saveant, Private communication (1976).

17. L. S. R. Yeh and A. J. Bard, *This Journal*, To be published.
18. E. Hayon and M. Simic, *J. Am. Chem. Soc.*, **95**, 2433 (1973).
19. G. Levin, T. A. Ward, and M. Szwarc, *ibid.*, **96**, 270 (1974).
20. T. A. Ward, G. Levin, and M. Szwarc, *ibid.*, **97**, 258 (1975).

Electrochemical Studies of Antitumor Antibiotics

I. Cyclic Voltammetric Study of Mitomycin B

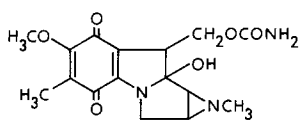
Gopalakrishna M. Rao,* J. William Lown, and James A. Plambeck*

Department of Chemistry, University of Alberta, Edmonton, Alberta, Canada

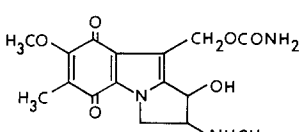
ABSTRACT

Mitomycin B, a mitosane quinone-containing antibiotic, was investigated by HMDE cyclic voltammetry in aqueous media at 37.5°C. The observations are consistent with a mechanism in which mitomycin B is reversibly reduced, at −0.200V *vs.* SCE, to the hydroquinone, following which the aziridine ring opens rapidly. The significance of the mechanism is discussed in relation to the antineoplastic activity of certain antibiotics of the mitosane class.

Mitomycin B, **1**, is a member of the mitosane class of agents and is produced by *Streptomyces caespitosus* together with mitomycin C, an antitumor antibiotic of clinical significance (1, 2). This class of agents is part of the larger group of aminoquinone-containing antibiotics which act as inhibitors of DNA synthesis, such as streptonigrin (3), porfiromycin (1), the actinomycins (4), and aziridinoquinones (5), many of which exhibit significant antineoplastic activity. It is currently considered (6) that the mitosanes *in vivo* undergo an initial reduction by a cellular reductase, mediated by NADPH, to form the hydroquinones. The latter rapidly lose methanol or water to form an activated species which can induce covalent cross-links between complementary strands of DNA. These cross-links prevent strand separation during the semiconservative replication process (2)



1



2

MITOMYCIN B

Mitomycin C and related quinone-containing derivatives have been observed to cause extensive degradation of DNA in addition to cross-linking (7, 8). Hitherto this has been attributed to the stimulation of the production of intracellular deoxyribonucleases in the cell repair cycle (9, 10). Recently, however, we demonstrated (11) that when mitomycin C and streptonigrin are reduced in the presence of oxygen they generate superoxide and hydroxyl radicals which degrade DNA by single strand scission analogous to radiation damage.

For these reasons a detailed study of the redox behavior of the mitosanes is of interest; it is our purpose to investigate the initial reduction process *in vitro*, together with such related chemical processes as are accessible to electroanalytical investigation.

Experimental

The Princeton Applied Research (PAR) Model 9300-9301 polarographic cell was employed in a three-electrode configuration which included a conventional aqueous saturated calomel reference electrode, to which all potentials in this paper are relative unless otherwise specified, a platinum counterelectrode, and a PAR Model 9323 hanging mercury drop working electrode. The cell temperature was maintained at physiological temperature of 37.5° ± 0.02°C by circulation of thermostated water. Cyclic voltammetry was done using the PAR Model 173-175-176 configuration. The resulting curves were recorded on an X-Y recorder or photographed on an oscilloscope as required by the scan rate, ν, which was varied from 20 mV/sec to 500 V/sec. The pH of each solution was measured both before and after each run using an Accumet Model 520 pH meter and a combination glass-SCE electrode.

Samples of mitomycin B were kindly supplied by American Cyanamid Company Lederle Laboratories, Pearl River, New York, and by Kyowa Hakko Chemical Company, Japan, and were used as received. A derivative of this compound, **2**, in which the aziridine ring was opened was prepared by mild acid hydrolysis according to the procedure of Stevens *et al.* (12). The crude hydrolysate was then recrystallized from the mixture of ether and pentane as a yellow-orange solid. This derivative **2**, which we do not believe to have been prepared previously, is a yellow solid, mp 70°-72°C, soluble in water, chloroform, and ether; it can be precipitated from ether by addition of pentane. Its spectral characteristic absorbances (nanometers) and log of molar absorptivity are: 236, 4.16; 286, 4.06; 355, 3.26; 442, 2.89. Its infrared spectrum in $CHCl_3$ has the following absorbances (nanometers): 2960, 2920 (CH_3 sym. str.); 2860; 1715 (carbamate C=O); 1660, 1645 (quinone C=O); 1595; 1450; 1395; 1250 (=C—O—C antisym. str.); 1085; 1000 (=C—O—C sym. str.). All other chemicals were reagent grade and were used without further purification.

Fresh stock solutions of $1.3 \times 10^{-3}M$ mitomycin B were prepared daily and protected from light. Sample solutions were prepared in a cell itself as $3.3 \times 10^{-4}M$ mitomycin B, 0.1*M* phosphate buffer, and 0.1*M* KCl supporting electrolyte. The derivative **2** was treated in a similar manner. All solutions were deaerated with purified nitrogen for 10 min prior to a run and blanketed with it during a run.

Results

Typical results for the cyclic voltammetry of **1** at pH 6.58 are shown in Fig. 1, which shows a pair of well-defined peaks (cathodic IC and anodic IA) and a second pair of small peaks (cathodic IIC and anodic IIA). No other peaks were observed even when the potential scan was extended up to supporting electrolyte discharge at −1.6V.

* Electrochemical Society Active Member.
Key words: cyclic voltammetry, antibiotic mitosane, quinone, DNA, antineoplastic, antitumor.

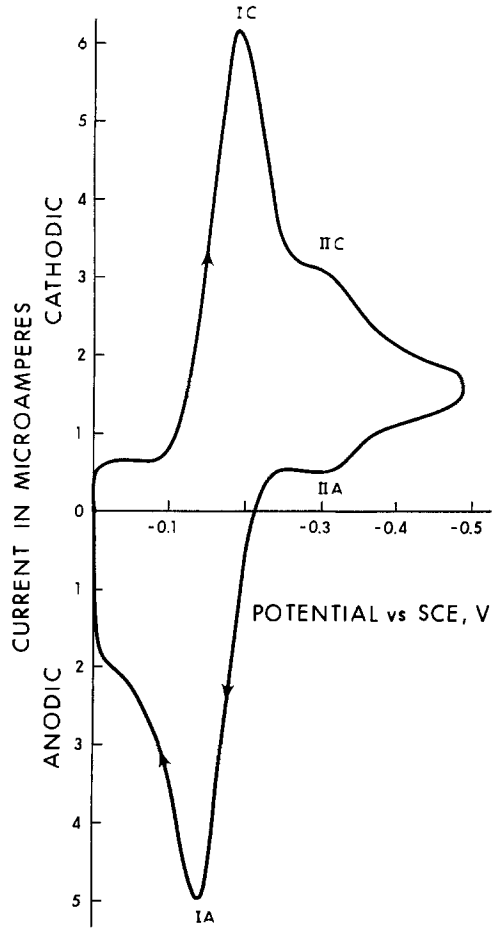


Fig. 1. Cyclic voltammogram of 1, pH 6.58 ± 0.02 in phosphate buffer, 37.5°C, ν = 500 mV/sec.

The pH dependence, over the range of 6-8.5, of E_p of IC corresponds to the theoretical slope of 61.7 mV/pH unit as expected for a two-electron, two-proton process at 37.5°C. The ratio of $I_p(IA)/I_p(IC)$ was unity throughout this pH range. The peak potentials of IC and IA at pH 7 are

$$E_p(IC) = -0.215 \pm 0.005V$$

and

$$E_p(IA) = -0.180 \pm 0.005V$$

These peak potentials are independent of ν up to at least 50 V/sec. At higher ν, to 500 V/sec, $E_p(IC)$ shifts more cathodic by about 30-50 mV/tenfold increase in ν and $E_p(IA)$ shifts less cathodic by 15-50 mV/tenfold increase in ν. The ratio of $I_p(IC)/\nu^{1/2}$ remains virtually constant with scan rate up to 5 V/sec, and thereafter increases slightly with further increase in ν. All the above-mentioned facts and the separation of $E_p(IC)$ and $E_p(IA)$ by *ca.* 30 mV suggest that the electrode process is a reversible two-electron transfer at $\nu \leq 10$ V/sec. This is supported by the fact that the difference between the peak potential E_p and the half-peak potential $E_{p/2}$ for IC is 30 ± 2 mV. The value of the reversible formal potential (equivalent to a polarographic half-wave potential) calculated from these peak potentials is −0.200 ± 0.005V.

Multicycle runs at 500 mV/sec of **1** (Fig. 2) show IC and IA; IIC and IIA appear as barely visible shoulders to IC and IA during the first cycle. The peak potentials of both IC and IA do not change over the first ten cycles. Further cycling shifts IC more cathodic and IA less cathodic. Both peak heights decrease as expected with cycling and the peaks are no longer distinguishable beyond twenty cycles. The peak potentials of IIC and IIA shift little if at all with continued cycling. For the first three cycles, $I_p(IIC)$ decreases with cycling while $I_p(IIA)$ increases. Thereafter, both $I_p(IIC)$ and

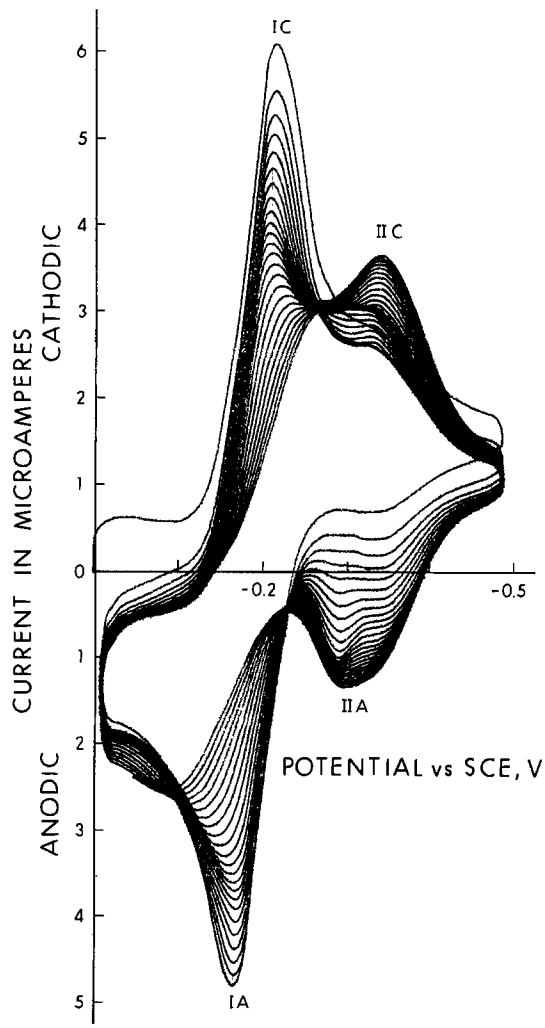


Fig. 2. Multicycle voltammogram of 1, pH 6.95 ± 0.02 in phosphate buffer, 37.5°C, ν = 500 mV/sec.

$I_p(IIA)$ increase with cycling. With continued cycling, a shoulder and a peak appear on IIA and finally are seen to merge with it into one single peak (−0.305V). After the first three cycles, IIC starts to grow and finally gives a well-developed peak at −0.340V. Multicycle runs at 50 mV/sec (Fig. 3) are similar to those at 500 mV/sec except that only four to five cycles are needed to reach steady state while twenty cycles are needed at 500 mV/sec.

The multicycle runs of **1** described above indicate that both of the second peaks, II, grow at the expense of the first peaks, I. It was suspected that the species giving rise to peaks II was mitomycin B in which the aziridine ring had opened. This latter compound can be formed by acid hydrolysis of **1**. Therefore, a solution of **1** at pH 6.6 was treated with a few drops of hydrochloric acid to obtain a solution of pH 2; the acid hydrolysis was allowed to continue for 20 min. The cyclic voltammetry (ν = 500 mV/sec) of this new solution, **1′**, gave three cathodic peaks (IIC, IVC, and VC) and an anodic peak (IIA). [When the pH of solution **1** of pH 6.6 was made highly acidic, *i.e.*, 2, the positive shift of IC and IA was so great they could no longer be observed. The peaks of IIC and IIA were still within the observable potential range.] The peaks IIC and IIA were fully developed and their heights are comparable with IC and IA of **1**.

A few drops of concentrated KOH were added to solution **1′** to restore its pH to about 6. Let this solution be **1″**. A typical cyclic voltammogram of **1″** at ν = 500 mV/sec (Fig. 5) shows two cathodic peaks (IIC and IIIC), an anodic peak (IIA), and the absence

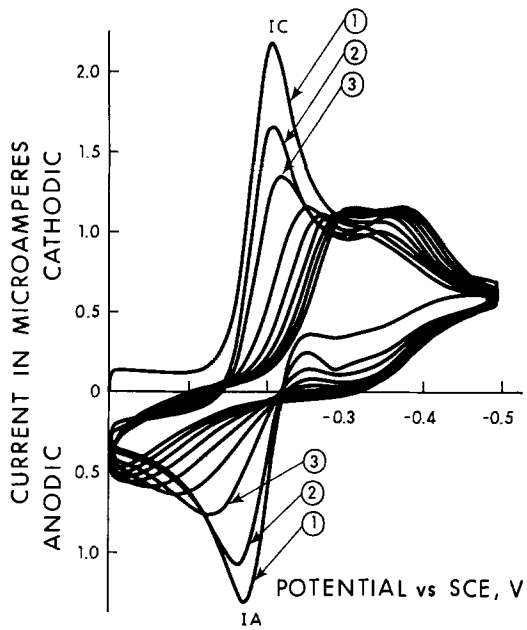


Fig. 3. Multicycle voltammogram of 1, pH 6.95 ± 0.02 in phosphate buffer, 37.5°C, ν = 50 mV/sec.

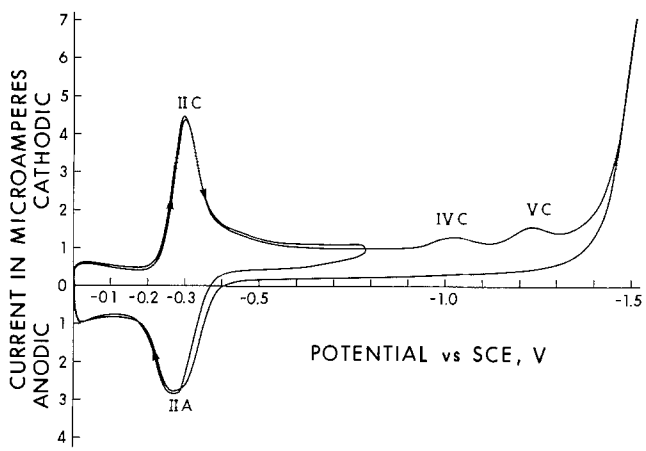


Fig. 4. Cyclic voltammogram of 2, pH 6.38 ± 0.02 in phosphate buffer, 37.5°C, ν = 500 mV/sec.

of peaks IC and IA. Cyclic voltammetry of **1"** over the larger potential range of 0 to −1.6V showed, in addition to IIC, IIIC, and IIA, and the absence of IC and IA, two cathodic peaks IVC and VC and a barely visible anodic peak at IIIA. These are discussed below since the same peaks are observed with the solution of ring-opened derivative 2. The peak height of IIA is visibly less when the 0 to −1.6V cycle is used than when the 0 to −0.6V cycle is used.

The pH dependence of E_p(IIC) of **1"** over the pH range 6-8.5 corresponds to the theoretical slope of 61.7 mV/pH unit as expected for a two-electron, two-proton process at 37.5°C. The ratio of I_p(IIA)/I_p(IIC) was slightly less than unity in this pH range. The peak potential of IIC and IIA at pH 7 are

$$E_p(\text{IIC}) = -0.335 \pm 0.005\text{V}$$

and

$$E_p(\text{IIA}) = -0.305 \pm 0.005\text{V}$$

The peaks IIC and IIA of **1"** behave similarly to the peaks IC and IA of **1** with scan rate. However, I_p(IIC)/$\nu^{1/2}$ increases with ν at higher ν to a greater extent than does IC. The separation of E_p(IIC) and E_p(IIA) by *ca.* 30 mV suggests that the electrode process is a reversible two-electron transfer process at $\nu \leq 10$ V/sec. This

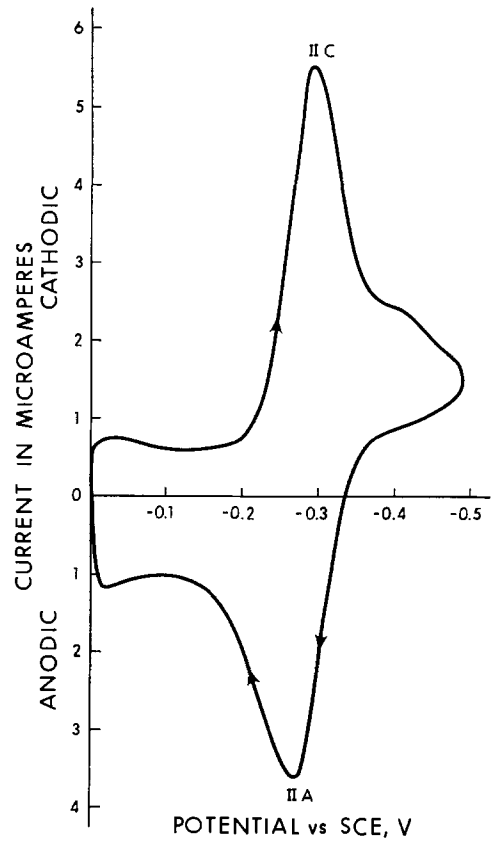


Fig. 5. Cyclic voltammogram of 1", pH 6.3 ± 0.02 in phosphate buffer, 37.5°C, ν = 500 mV/sec.

is supported by the fact that E_p(IIC) − $E_{p/2}$(IIC) is 30 ± 2 mV. The value of reversible formal potential (equivalent to a polarographic $E_{1/2}$) calculated from E_p of the second process is −0.320 ± 0.005V.

Both the IIIC and IIIA peaks are poorly defined, the definition of IIIC being slightly better than that of IIIA. These peaks are observed primarily in the biological pH region (pH 6-7.5). The pH dependence of E_p(IIIC) corresponds to 62 mV/decade and E_p at pH 7 is 0.450 ± 0.01V. The disappearance of IIIC and IIIA above pH 7.5 does not mean that the species responsible for this process are destroyed because these peaks reappear after restoration of pH to 6.0.

The appearance of IVC and VC and the absence of the corresponding anodic peaks show that these processes are not reversible. The peaks IVC and VC appear around −1.05 and −1.25V, respectively. Disappearance of IIIC results in slight increase in the peak height of IVC.

Cyclic voltammetric analysis of solutions of the ring-opened derivative, 2, gave peaks IIC, IIA, IVC, and VC (Fig. 4). The peaks IVC and VC are irreversible and appear at similar potentials as those for **1'** (and **1"**). The peaks IIC and IIA are identical in potential [E_p(IIC) = −0.325 ± 0.005V and E_p(IIA) = −0.300 ± 0.005V at pH 7] and behavior with scan rate and pH to the peaks of IIC and IIA of **1"**.

Multicycle runs of solutions of 2 at 500 and 50 mV/sec are identical. There is very little to no change in IIA with cycling. After the first cycle, E_p of IIC shifted by *ca.* 20 mV cathodic and its I_p decreased sharply by perhaps ¼ of its original value. On continued cycling, E_p of IIC shifted very slightly toward negative values and its I_p increased very slightly. The final peak potentials are: E_p(IIC) = −0.370 ± 0.005V and E_p(IIA) = −0.300 ± 0.005V.

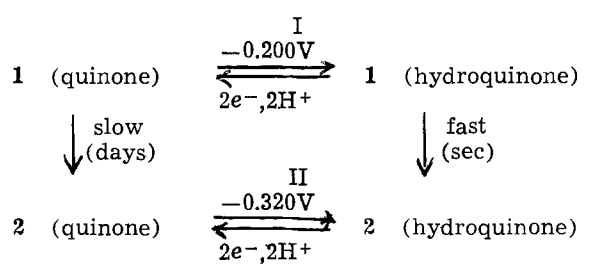
Discussion

On the basis of the above results we may conclude that under these conditions the initial reduction of

mitomycin B is a reversible two-electron, two-proton reduction of the quinone structure to the hydroquinone. This process is responsible for the peaks designated I and has a reversible formal potential of -0.200 ± 0.005V. The aziridine ring of mitomycin B can be opened by acid hydrolysis and the resulting compound, **2**, can also undergo a reversible two-electron, two-proton reduction of the quinone structure. This process is responsible for the peaks designated II and has a reversible formal potential of -0.320 ± 0.005V. The remaining processes, which are the possibly reversible III and the irreversible cathodic IV and V, cannot be unambiguously defined other than as due to further reaction products of the reduced form of **2**. Loss of the carbamate moiety can occur, but soluble carbamates (urethane, n-butylcarbamate, and phenylcarbamate) were not found to be electrochemically active over the region 0 to -1.6V. Increases of ν to even 500 V/sec showed no evidence of additional peaks or of peak splitting such as would be expected if a semiquinone intermediate of lifetime greater than *ca.* 1 msec were present in the reduction of **1**. This observation does not exclude the formation of semiquinones of **1** or **2** as intermediates *in vivo* or in oxygenated solutions by subsequent air oxidation of the hydroquinones. Indeed, semiquinones are obligatory intermediates in the production of superoxide and hydroxyl radicals which degrade DNA (11). Semiquinone EPR signals were obtained (13) on reduction of mitomycin B in dimethylformamide, a solvent in which, however, the stability of the semiquinone would be much greater than in the present aqueous work.

The observations of increases in the IIC-IIA peaks, and decrease in the IC-IA system as this occurs, with multiple cycles demonstrates that the opening of the aziridine ring of mitomycin B is very slow, in that solutions are stable for several days in the absence of light at physiological pH, but that ring opening of the reduced form is very much more rapid, of the order of at most a few seconds. This quantitative demonstration is in agreement with previous postulates concerning the reductive activation of the mitosanes (2). Specifically, reduction to the hydroquinone releases the pyrrolizidine ring nitrogen lone pair for conjugative assistance in the opening of the aziridine ring.

The magnitude of the difference in potential between the reversible reductions of the quinones of **1** and of **2**, 120 mV, also indicates a close relationship between the redox power of the quinone system and the opening of the aziridine ring. The reduction of mitomycin B is so much easier than reduction of the ring-opened form **2** that, for both thermodynamic and kinetic reasons, the activation process *in vivo* probably begins with the reduction of mitomycin B itself to the hydroquinone



This explanation is consistent with the available *in vivo* evidence. Iyer and Szybalski (14) studied the cross-linking of native DNA by the mitomycins in the presence of cell lysates. Activation of the mitomycins was observed when a cell lysate of *bacillus subtilis, sarcina lutea, or cytophaga johnsonii* was added to a reaction mixture containing mitomycin and DNA, either that of the above-mentioned bacteria or of other species including human cells. Heating, aging, or aeration destroyed the ability of the cell lysate to activate the mitomycin; however, this ability of the dialyzed lysate could be restored by the addition of NADPH or of a system capable of generating NADPH, whereas [in contrast to streptonigrin (15)] NADPH is ineffective as a mitomycin-activating agent in the absence of the lysate.

Further, enzymatic reduction of mitomycin C and its metabolic inactivation by liver homogenates was reported by Schwartz, Sodergren, and Philips (16), who also postulated that reduction is associated with the metabolic activation of mitomycin. Their results indicate that the activation process of mitomycin action is related to NADPH-dependent enzymatic reduction of mitomycin to its hydroquinone derivative by a quinone reductase within the cell (17).

The redox behavior of mitomycin examined herein is therefore directly relevant to the *in vivo* situation. Also, the subsequent reoxidation of the hydroquinone form of the antibiotic is necessary to produce the superoxide radical anion shown to be involved in the degradation of cellular DNA (11). Since the oxidative machinery of the cell is integrated into or associated with its membrane, it seems likely that a similar ECE reaction may occur *in vivo* with the antibiotic at this site.

Acknowledgment

We are grateful to Mr. G. L. Weir of this Department for preparation of **2** and to the National Research Council of Canada for support of this research through Operating Grants to J.W.L. and J.A.P.

Manuscript submitted March 15, 1976; revised manuscript received Sept. 30, 1976.

Any discussion of this paper will appear in a Discussion Section to be published in the December 1977 JOURNAL. All discussions for the December 1977 Discussion Section should be submitted by Aug. 1, 1977.

Publication costs of the article were assisted by the University of Alberta.

REFERENCES

1. J. S. Webb, D. B. Cosulich, J. H. Mowat, J. B. Patrick, R. W. Broschard, W. E. Meyer, R. P. Williams, C. F. Wolf, W. Fulmor, C. Pidacks, and J. E. Lancaster, *J. Am. Chem. Soc.*, **84**, 3185 (1962).
2. W. Szybalski and V. N. Iyer, in "Antibiotics I—Mechanism of Action," D. Gottleib and P. D. Shaw, Editors, pp. 221-245, Springer-Verlag, New York (1967).
3. K. V. Rao, K. Beimann, and R. B. Woodward, *J. Am. Chem. Soc.*, **85**, 2532 (1963); Streptonigrin NSC 45383 clinical brochure, National Cancer Institute, U.S.N.I.H., March 1968, pp. 1-20.
4. H. Brockmann, *Fortschr. Chem. Org. Naturst.*, **18**, 1 (1960).
5. J. A. Montgomery, T. P. Johnston, and Y. F. Shealy, in "Medicinal Chemistry", Part I, A. Burger, Editor, p. 695, Wiley-Interscience, New York (1970).
6. S. Kinoshita, K. Uzu, K. Nakano, M. Shimizu, T. Takahashi, and M. Matsui, *J. Med. Chem.*, **14**, 103 (1971).
7. E. Reich, A. J. Shatkin, and E. L. Tatum, *Biochem. Biophys. Acta*, **45**, 608 (1960).
8. S. Wakaki, *Cancer Chemother. Rep.*, **13**, 79 (1961).
9. W. Kersten, *Biochem. Biophys. Acta*, **55**, 558 (1962).
10. Y. Nakato, K. Nakato, and Y. Sakamoto, *Biochem. Biophys. Res. Commun.*, **6**, 339 (1961).
11. J. W. Lown, A. Begleiter, D. Johnson, and A. R. Morgan, *Can. J. Biochem.*, **54**, 110 (1976).
12. G. L. Stevens, K. G. Taylor, M. E. Munk, W. S. Marshall, K. Noll, G. D. Shah, and K. Uzu, *J. Med. Chem*, **8**, 1 (1964).
13. J. B. Patrick, R. P. Williams, W. E. Meyer, W. Fulmor, D. B. Cosulich, R. W. Broschard, and J. S. Webb, *J. Am. Chem. Soc.*, **86**, 1889 (1964).
14. V. N. Iyer and W. Szybalski, *Proc. Natl. Acad. Sci.*, **50**, 355 (1963); V. N. Iyer and W. Szybalski, *Science*, **145**, 55 (1964).
15. R. Cone, A. R. Morgan, J. W. Lown, and S. K. Hasan, *Can. J. Biochem.*, **54**, 219 (1976).
16. H. S. Schwartz, J. E. Sodergren, and F. S. Philips, *Science*, **142**, 1181 (1963).
17. C. Martins, in "Enzymes," Vol. I, P. D. Boyer, H. Lardy, and K. Myrback, Editors, p. 517, Academic Press, New York (1963).

Electrochemical Studies of Antitumor Antibiotics

II. Polarographic and Cyclic Voltammetric Studies of Mitomycin C

Gopalakrishna M. Rao,* Asher Begleiter, J. William Lown, and James A. Plambeck*

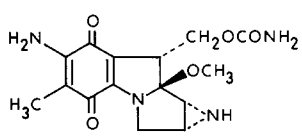
Department of Chemistry, University of Alberta, Edmonton, Alberta, Canada

ABSTRACT

Mitomycin C, a quinone-containing antibiotic, was investigated by polarography and cyclic voltammetry in aqueous media at 37.5°C. The observations are consistent with a mechanism in which mitomycin C is reversibly reduced, at −0.368V vs. SCE, to the hydroquinone, following which the aziridine ring opens rapidly. The significance of the mechanism is discussed in relation to the antineoplastic activity of mitomycin C.

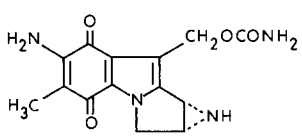
Mitomycin C, **1**, a member of the mitosane class of agents (1, 2), is an antitumor antibiotic used, for example, in the treatment of stomach cancer in Japan. Like mitomycin B, the subject of our previous paper (3), it is produced by *Streptomyces caespitosus* and acts as an inhibitor of DNA synthesis. It is currently considered (3, 4) that mitosanes *in vivo* undergo an initial reduction by a cellular reductase, mediated by NADPH, to form the hydroquinones. The hydroquinones rapidly lose water or methanol to form an activated species which can induce covalent cross-links between complementary strands of DNA. These cross-links prevent strand separation during the semiconservative replication process (1). Degradation of DNA by mitomycin C and related compounds has also been observed (5-7) which we (7) have shown can be attributed to the formation of superoxide and hydroxyl radicals by reaction of oxygen with the reduced forms of mitomycin C and other mitosanes.

It is therefore the purpose of the present paper to investigate the initial reduction process of mitomycin C *in vitro*, together with such related processes as are amenable to electroanalytical investigation. To this end we have employed polarography and cyclic voltammetry to study mitomycin C itself, **1**, mitomycin C which has undergone demethoxylation, **2**, and mitomycin C which has undergone both demethoxylation and opening of the aziridine ring, **3**

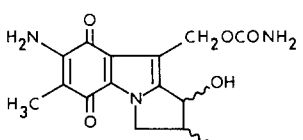


1

Mitomycin C



2



3

Experimental

Polarographic glass and Teflon cells of conventional design were employed in three-electrode assembly. The current-sampled d-c polarographic studies were made with a Model 174A polarographic analyzer (Princeton Applied Research) equipped with Model 174/70 drop timer. Polarograms were recorded on a Sargent model recorder. Cyclic voltammetric measurements and the other experimental conditions were as described previously (3).

* Electrochemical Society Active Member.

Key words: polarography, cyclic voltammetry, antibiotic, mitomycin C, quinone, DNA, antineoplastic, antitumor.

Mitomycin C was obtained from Calbiochem and Kyowa Hakko Kogyo Chemical Company, Japan, and was used as received. Demethoxylated mitomycin C, **2**, and ring-opened mitomycin C, **3**, were prepared as follows.

Demethoxylated mitomycin C, **2**: Mitomycin C (33 mg, 0.1 mmole) was hydrogenated over 5% palladium on charcoal in 10 ml of ethyl acetate. After one equivalent of hydrogen was absorbed, the solution was filtered and the filtrate exposed to air oxidation. Removal of the solvent *in vacuo* gave 8 mg of **2** as a purple solid which was purified by recrystallization from ethyl acetate: petroleum ether. The absorption spectrum in H_2O was: (λ_{max} in nanometers, log of molar absorptivity ϵ): 248, 3.90; 318, 3.60; 364, 3.79; 547, 2.52 in the ultraviolet/visible. The infrared peaks observed had ν_{max} (KBr disk) of: 3320 (Br), 1713 (CO of $OCONH_2$), 1650 (quinone C=O), 1600, 1548, 1325, 1210 cm^{-1}. This preparation follows the general procedure of Ref. (8).

Aziridine ring-opened mitomycin C, **3**: Hydrolysis of mitomycin C was carried out according to the procedure of Ref. (8) using hydrochloric acid. The crude hydrolysate was recrystallized from dimethylformamide:water and isolated in 17% yield. The absorption spectrum in CH_3OH was: (λ_{max} in nanometers, log of molar absorptivity ϵ): 248, 3.95; 309, 3.78; 343, 3.32; 562, 2.73 in the ultraviolet/visible. The infrared peaks observed had ν_{max} (KBr disk): 3390 (Br), 1695 (CO of $OCONH_2$); 1650 (quinone C=O), 1594 and 1376 cm^{-1}.

In addition to phosphate buffer ($5.9 < pH < 8.1$), acetate ($pH < 5.9$), and tris ($pH > 8.1$) buffers were also used in polarographic measurements. The polarographic drop time was controlled at 1.0 sec and the mercury flow rate was 0.93 mg/sec. The reversibility of the polarographic electrode reaction was determined from conventional log $((i_d - i)/i)$ plots.

Results

Polarographic analysis of aqueous **1** solutions yielded graphs containing the cathodic waves IC-IVC, of which IVC is observable only at $pH > 6.5$. The IC wave ($E_{1/2} = -0.368 \pm 0.003$V at pH 7) log plot gave a reversible two-electron slope. The pH dependence of $E_{1/2}$ corresponds to the theoretical slope of 61.7 mV/pH unit expected for a two-electron, two-proton process at 37.5°C at $pH > 5.4$ (Fig. 1) and the wave height remains approximately constant at 0.57 μA over the range $5.4 < pH < 8.5$. At $pH < 5.4$, the height of the wave decreased markedly and the $E_{1/2}$ *vs.* pH plot had a slope of over 90 mV/pH unit. The material responsible for this wave is irrecoverably destroyed immediately at $pH < 4$, so that the decrease cannot be due to a reversible protonation equilibrium. The second wave IIC ($E_{1/2} = -0.486 \pm 0.005$V at pH 7) is drawn out in shape (and shown by a log analysis not to be reversible); its height decreased from 0.53 μA from pH 4-6, then rose again to regain its original height at pH

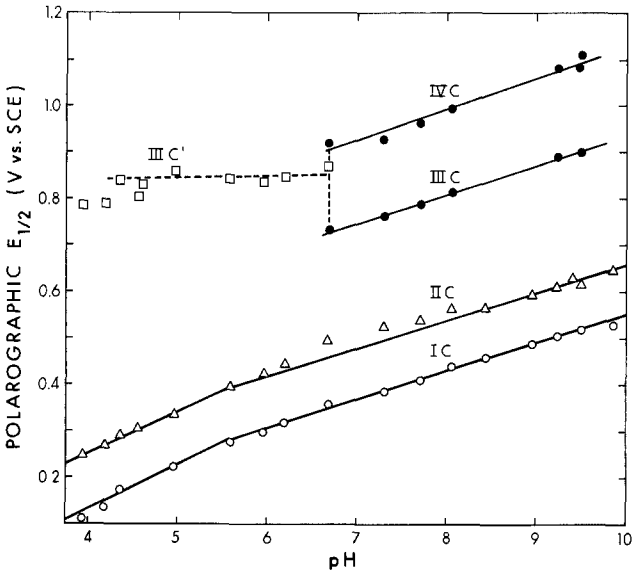


Fig. 1. pH dependence of half-wave potentials of aqueous 1. 3.4 × 10^{-4}M solutions in solutions of buffer, acetate (pH < 5.9), phosphate (5.9 < pH < 8.1), trizma (pH > 8.1); ○, first wave; △, second wave; □, third wave with no splitting; ●, third wave with splitting.

> 8.5. The value of $E_{1/2}$ varied with pH by 90 mV/pH unit at pH < 5.8 and 61 mV/pH unit at pH > 5.8 (Fig. 1). This wave is not affected by making the solution acidic (pH < 4) for a short period of time. A third wave IIIC', irreversible, appears to split into two smaller waves, IIIC and IVC (total height of IIIC + IVC observed in the basic range is less than or equal to the height of the single wave IIIC' observed in the acidic range), neither reversible, at pH > 6.5 (Fig. 1). The slope of $E_{1/2}$ *vs.* pH is approximately the theoretical slope of 61.7 mV/pH unit for both of the split waves; the value of $E_{1/2}$ for IIIC' in the acidic region changes less, if at all, with pH. At pH 7.0, we have $E_{1/2}$ values of −0.745 ± 0.005V for IIIC and −0.925 ± 0.005V for IVC. The variation in the height of IIIC' (or total height of IIIC + IVC) with pH follows the trend of IIC, that is, greater at both acidic and basic ends, and lesser in the intermediate pH range. This variation suggests that the species reduced at the potentials corresponding to IIIC and IVC may be the product or products of the reduction which occurs at the potential corresponding to IIC.

Figure 2 is a typical cyclic voltammogram of **1** at 200 mV/sec. It shows four cathodic peaks (IC-IVC) and one anodic peak (IIA; IA is absent). The appearance of IIIC and IVC, and the absence of the corresponding anodic peaks IIIA and IVA, show that these processes are not reversible, in agreement with our polarographic findings. These peak potentials E_p are more negative than E_p values calculated from corresponding $E_{1/2}$ values, as is expected for irreversibility. Most of the cyclic voltammetric studies were restricted to the potential range 0 to −0.85V to avoid complications arising from these processes. With the range thus restricted, only IC and IIC are observed at ν < 100 mV/sec. At ν = 100 mV/sec, IA and IIA become visible; at ν = 200 mV/sec. IIC splits into two peaks. With increasing ν, the increase in the height of IC and IA is much greater than the corresponding increase in height of IIC and IIA. At very fast scan rates, 2 V/sec ≤ ν ≤ 10 V/sec, IC and IA are very well defined and separated by 35 ± 5 mV (Fig. 3). The peak potential E_p of IC shifts toward more cathodic potential by *ca.* 10 mV for each tenfold increase in scan rate, which is consistent (9) with the mechanism proposed below. Correspondingly, E_p of IA shifts toward more negative potential by *ca.* 20 mV for each tenfold increase in scan rate. The $I_{p,cath}/\nu^{1/2}$ ratio increases slightly with the increase in scan rate. For IC, the difference between the peak potential E_p and the half-peak potential $E_{p/2}$ is 28 ± 2 mV and the measured polarographic $E_{1/2}$ of −0.368 coincides with the calculated $E_{1/2}$ of −0.369V obtained from E_p of −0.383V as expected (9) for a two-electron reversible process. For IIC, E_p remains constant at −0.506 ± 0.005V over the range 500 mV/sec ≤ ν ≤ 10 V/sec. However, IIC appears to split into two peaks at ν = 200 mV/sec with E_p of −0.470 and −0.510V, the latter value being the same as that for IIC at ν > 200 mV/sec. Nevertheless, at ν < 200 mV/sec there appears only one broad peak, whose peak potential shifts toward more cathodic potential from −0.470V by about 60 ± 5 mV for every tenfold decrease in scan rate. The corresponding broad anodic peak IIA, which does not split, is not present if the switching potential is −0.85V *vs.* SCE and ν < 100 mV/sec. On further increase in scan rate, IIA appears and E_p shifts toward more cathodic potential by about 60 ± 10 mV up to ν = 2 V/sec; it remains constant at −0.509 ± 0.003V at faster scan rates. The ratio I_p of IIA/I_p of IIC was found to be approximately constant at 0.75. The ratio $I_p/\nu^{1/2}$ for IIC is also nearly constant. The separation of peak potentials between IIC and IIA is 60 ± 10 mV, at 200 mV/sec ≤ ν ≤ 1 V/sec.

Polarographic analysis of a solution of the slightly soluble ring-opened derivative **3** gives curves in which IC is barely observable. Cyclic voltammetry of **3** shows very small peaks for IC and IA identical in potential and behavior with those of **1**, such as would arise from

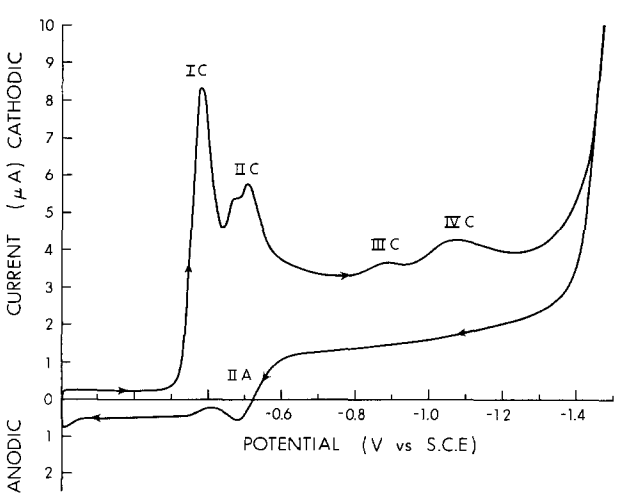


Fig. 2. Cyclic voltammogram of 1 (3.4 × 10^{-4}M), pH 6.98 ± 0.02 in phosphate buffer, 37.5°C, ν = 200 mV/sec.

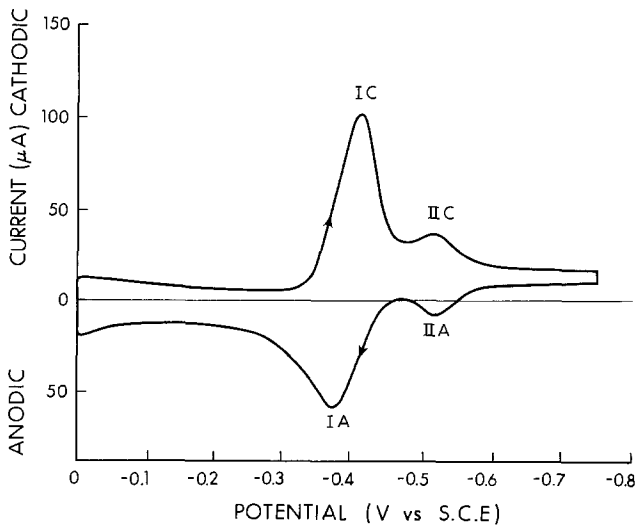


Fig. 3. Cyclic voltammogram of 1 (3.4 × 10^{-4}M), pH 6.98 ± 0.02 in phosphate buffer, 37.5°C, ν = 10 V/sec.

< 5% of unreacted **1** remaining in the preparation of **3** as could reasonably be the case since the preparation was carried out on only a few milligrams. The irreversible waves IIIC and IVC of solutions of **3** are identical to those of **1**.

The polarographic wave for IIC is present in distorted form. It cannot be resolved even using differential pulse mode, in which two barely distinguishable peaks appear at $pH > 9$ while the second is a small shoulder upon the first at $pH < 9$. The combination has a value of $E_{1/2}$ identical to that of IIC for **1** and $dE_{1/2}/dpH$ is 60 mV/pH unit. The irreversible waves IIIC and IVC observed with **3** behave identically to those observed with **1**. The cyclic voltammetric peak IIC behaves similarly to peak IIC of **1** for 200 mV/sec $< \nu <$ 50 V/sec. However, IIC splits into two peaks at scan rates 200 and 100 mV/sec. The height of the leading peak is slightly greater at 200 mV/sec. At $\nu < 100$ mV/sec, only one broad peak IIC can be distinguished. Its potential shifts slightly more negative from −0.475V by *ca.* 15 mV for every tenfold decrease in ν. The corresponding anodic peak IIA is visible at all scan rates and becomes sharper at faster scan rates; E_p remains constant at −0.470 ± 0.005V at all scan rates. The ratio $I_pC/\nu^{1/2}$ for IIC is almost constant up to scan rate 200 mV/sec and then increases with further increase in scan rate. The difference $(E_p - E_{p/2})$ is 40-50 mV for IIC, and E_p for IIA and IIC are separated by *ca.* 35 mV.

Polarographic analysis of a solution of the slightly soluble demethoxylated derivative **2** gave waves identical to those of **1**; the $E_{1/2}$ of IC for **2** differed by less than 5 mV from that of IC for **1**. The distortion of IIC, though of the same form as that observed for **3**, was barely noticeable. The cyclic voltammogram of **2** was similar to that of **1**. At 10 mV/sec $< \nu <$ 1000 mV/sec, the E_p of IC and IA and their dependence with scan rate are identical to those of **1**. At $\nu > 1000$ mV/sec, however, both IC and IA of **2** become severely distorted. The ratio $I_p/\nu^{1/2}$ for IC is nearly constant up to $\nu = 1000$ mV/sec and then increases with ν. The difference $(E_p - E_{p/2})$ for IC is 35 mV. The potentials E_p of IA and IC are separated by *ca.* 60 mV for 200 mV/sec $< \nu <$ 1000 mV/sec. The splitting and values of E_p for IIC and IIA of **2** at scan rates up to 2 V/sec are identical to those of **3**. At scan rates faster than 2 V/sec, E_p for IIC and IIA of **2** shift toward more anodic potentials. The ratio $I_p/\nu^{1/2}$ for IIC remains constant up to $\nu = 1000$ mV/sec, and then appears to increase with further increase in ν.

A typical example of a multicycle sweep is shown in Fig. 4 for **2**; similar waves are observed for **1** and **3**, except that for **3** the IC peak is extremely small. All compounds show a IC, a split IIC, and a IIA peak during the first cycle; **1** also shows a small IA peak. In the second cycle, we can see IC only as a shoulder, IIC (the split peak appearing at more negative potential than during the first cycle), and IIA. Only IIC and IIA appear after the second cycle. Although both **2** and **3** reach steady state in five cycles, **1** reached steady state only after sixteen cycles. The cathodic peak height decreases and E_p shifts toward more negative potential as the number of cycles increases, while the anodic peak height increases and E_p shifts toward more negative potential (for **2** and **3**, the shift in E_p with the number of cycles is negligible). At steady state, the cathodic and the anodic peak potentials are separated by *ca.* 65 ± 5 mV and the absolute ratio of I_p of IIA to I_p of IIC is 0.60 ± 0.05; the procedure of Nicholson (10) gives a value for this ratio of approximately unity as expected for a reversible process.

Multicycle runs at 20 mV/sec are similar to those at 200 mV/sec for **1** and **3** but not for **2**, which then takes considerably more cycles to reach the steady state.

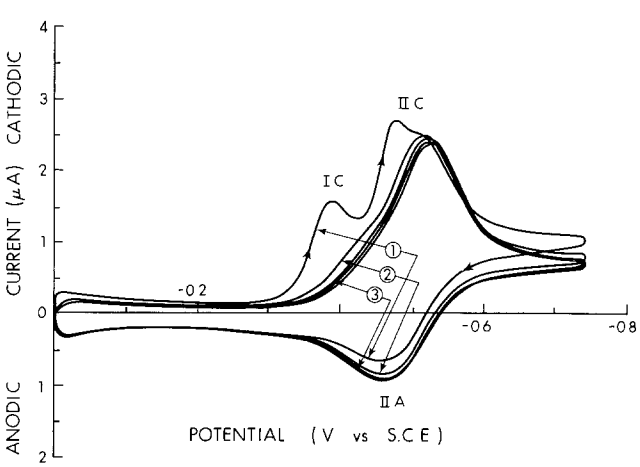


Fig. 4. Multicycle voltammogram of 2 (3.4×10^{-4}M), pH 6.98 ± 0.02 in phosphate buffer, 37.5°C, $\nu = 200$ mV/sec.

Discussion

On the basis of the above results, the mechanism of the reduction of mitomycin C at pH 7 is considered as belonging to the ECE (electrochemical-chemical-electrochemical) class, where C represents one or more steps. The electrochemical steps are considered to be R-R (reversible-reversible) (11) and the chemical steps are considered irreversible. The initial electrochemical step responsible for the waves and peaks designated I has a reversible formal potential of −0.368 ± 0.003V at pH 7 and is a reversible two-electron, two-proton reduction of the quinone structure to the hydroquinone. At $pH < 5.4$, the polarographic current is lower due to the irreversible opening of the aziridine ring. This view is reinforced by the cyclic voltammetry which shows peak IA at, and only at, very high scan speeds.

Polarography is not capable of providing information on the chemical step which follows reduction of **1** but this step can be characterized using the cyclic voltammetric data. This reaction must be both rapid and irreversible to explain the single-scan voltammetric curves, and the absence of IC and IA from the later scans of the multicycle voltammetry provides additional proof.

From our cyclic voltammetric measurements of mitomycin B, we have recently shown that the ring opening of the reduced form is very rapid, of the order of seconds (3), compared to the ring opening of the oxidized form. Thus the chemical reaction of mitomycin probably is demethoxylation and aziridine opening following the reduction to the hydroquinone. The differences in the behavior of wave I between **1** and **2**, though slight, are real at high scan rates indicating that the demethoxylation following reduction proceeds at an extremely high but finite rate. The observation that wave I is absent from the electrochemical reduction of the aziridine ring-opened **3** and the close similarity to the behavior of **2** shows that the kinetic chemical process following reduction is, at least in part, due to the aziridine ring-opening reaction. The process responsible for the waves and peaks designated II has a reversible formal potential −0.486 ± 0.005V at pH 7 and is clearly the two-electron, two-proton reduction of the ring-opened and demethoxylated **3** to corresponding hydroquinone. This process is almost certainly electrochemically reversible as shown by the cyclic voltammetry of **3** but does not appear so in voltammetry of **1** due to the irreversible chemical steps preceding it.

The rate of the chemical reaction K_f that follows the initial reduction of **1** can be estimated from the cyclic voltammetry. Use of the ratio I_p for IA to I_p for IC in the voltammetric curves in which IA is measurable (9, 10) does not give a satisfactory value of K_f, probably due to the interference of process II; however, estimated K_f values are close to 10 sec^{-1}. The half-life for the hydroquinone of **1** is estimated as 0.07 sec. This is consistent with a mechanism in which at the reduction

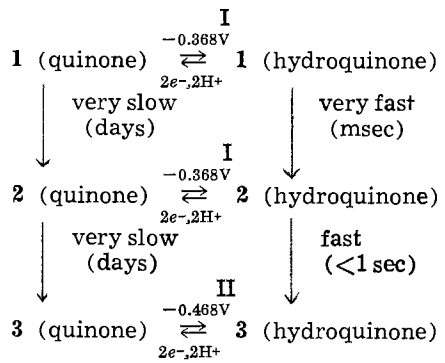
potential of **1** there is an initial reduction of **1** to its hydroquinone, which rapidly converts to the hydroquinone of **2** and, slightly less rapidly, to the hydroquinone of **3**. At this potential, the hydroquinone of **3** is immediately oxidized to the quinone **3**, which is then present and available for reduction in process II at a more negative potential later in the scan. As scan speeds increase, the time available for the chemical steps is decreased and hence the height of IIC decreases, relative to that of IC, with ν as can be seen by comparison of Fig. 2 and 3.

Mild acid hydrolysis of **1** affords regiospecifically a mixture of the stereoisomeric ring opened compounds *cis* and *trans* in a ratio of 86:14 (8, 12). Therefore, the two split peaks at $\nu = 100$ mV/sec separated by 40 mV may be due to the *cis* and *trans* isomers of ring opened mitomycin C. The remaining processes corresponding to the irreversible cathodic IIIC and IVC are probably due to the further reaction products of the reduced form of **3**; a similar explanation was given for IIIC, IVC, and VC of mitomycin B (3).

Our experimental findings do not demonstrate the presence of semiquinone intermediates of mitomycin C derivatives, which are obligatory intermediates in the production of superoxide and hydroxyl radicals which degrade DNA (7). Our observations, however, do not preclude the formation of semiquinones of mitomycin C derivatives as intermediates *in vivo*, under alkaline conditions, or in oxygenated solution by subsequent air oxidation of the hydroquinones. Moreover, *in vivo* the semiquinone may be produced within the DNA helix from the free hydroquinone by interaction with cytosine as postulated by Murakami (13) to explain the promoting effect of deoxycytidilic acid observed by Iyer and Szybalski (14). Recent sulfite oxidation evidence may indicate mitomycin C semiquinone formation in a liver microsomal system open to oxygen (17).

In general, semiquinone EPR signals are obtained under alkaline conditions (15) because the stability of semiquinones increases with increasing *p*H. The existence of the semiquinone of mitomycin C with a 10 sec lifetime under the highly alkaline conditions of sodium borohydride reduction as shown by Nagata *et al.* (16) therefore does not contradict our results, which were carried out in the physiological *p*H region.

Compounds **1** and **2** are closely similar if not identical in reduction potential whereas **3** is markedly more difficult to reduce. The magnitude of the difference in potential between the reversible reduction of the quinones of **1** and of **3**, 120 mV, is the same value observed for the difference in reversible formal potential of mitomycin B and its ring-opened derivative (3). This reinforces our earlier statement that there exists a close relationship between the redox power of the quinone system and the opening of the aziridine ring. The reduction of mitomycin C, like that of mitomycin B, is so much easier than reduction of the ring-opened form **3** that, for both thermodynamic and kinetic reasons, the activation process *in vivo* (3) probably begins with the reduction of mitomycin C itself to its hydroquinone



Manuscript submitted April 19, 1976; revised manuscript received Sept. 30, 1976.

Any discussion of this paper will appear in a Discussion Section to be published in the December 1977 JOURNAL. All discussions for the December 1977 Discussion Section should be submitted by Aug. 1, 1977.

Publication costs of this article were assisted by the University of Alberta.

REFERENCES

1. W. Szybalski and V. N. Iyer, in "Antibiotics I—Mechanism of Action," D. Gottleib and P. D. Shaw, Editors, pp. 221-245, Springer-Verlag, New York (1967).
2. J. S. Webb, D. B. Cosulich, J. H. Mowat, J. B. Patrik, R. W. Broschard, W. E. Meyer, R. P. Williams, C. F. Wolf, W. Fulmor, C. Pidacks and J. E. Lancaster, *J. Am. Chem. Soc.*, **84**, 3185 (1962).
3. G. M. Rao, J. W. Lown, and J. A. Plambeck, *This Journal*, **124**, 195 (1977).
4. S. Kinoshita, K. Uzu, K. Nakano, M. Shimizu, T. Takahashi, and M. Matsui, *J. Med. Chem.*, **14**, 103 (1971).
5. E. Reich, A. J. Shatkin, and E. L. Tatum, *Biochem. Biophys. Acta*, **45**, 608 (1960).
6. S. Wakaki, *Cancer Chemother. Rep.*, **13**, 79 (1961).
7. J. W. Lown, A. Begleiter, D. Johnson, and A. R. Morgan, *Can. J. Biochem.*, **54**, 110 (1976).
8. G. L. Stevens, K. G. Taylor, M. E. Munk, W. S. Marshall, K. Noll, G. D. Shah, and K. Uzu, *J. Med. Chem.*, **8**, 1 (1964).
9. R. S. Nicholson and I. Shain, *Anal. Chem.*, **36**, 706 (1964).
10. R. S. Nicholson, *ibid.*, **38**, 1406 (1966).
11. R. S. Nicholson and I. Shain, *ibid.*, **37**, 178 (1965).
12. W. G. Taylor and W. A. Remers, *J. Med. Chem.*, **18**, 307 (1975).
13. H. Murakami, *J. Theor. Biol.*, **10**, 236 (1966).
14. V. N. Iyer and W. Szybalski, *Science (N.Y.)*, **145**, 55 (1964).
15. B. Venkataraman and G. K. Fraenkel, *J. Am. Chem. Soc.*, **77**, 2707 (1955).
16. C. Nagata and A. Matsuyama, Progr. Antimicrob. Anticancer Chemother., Proc. 6th Int. Congr. Chemother., **2**, 423 (1969).
17. K. Handa and S. Sato, *Gann*, **66**, 43 (1975).

The Oxidation of Alcohols at a Nickel Anode in Alkaline t-Butanol/Water Mixtures

Mohammed Amjad, Derek Pletcher, and Carmen Smith

Department of Chemistry, The University, Southampton S09 5NH, England

ABSTRACT

The oxidation of a range of phenylethanols, benzyl alcohols, and allyl alcohols at a nickel electrode in a series of t-butanol/water mixtures has been investigated. The alcohols give well-formed but kinetically controlled oxidation waves at the potential of the Ni^{II}/Ni^{III} surface change, and the limiting current densities are low. The phenylethanols and allyl alcohols give only carboxylic acids in good yields; the benzyl alcohols give a mixture of aldehyde and carboxylic acid although in a good combined yield. The ratio of aldehyde/carboxylic acid can be changed substantially by variation of the hydroxide ion concentration and in some cases the product may be all acid or all aldehyde depending on the electrolysis conditions.

In an earlier paper (1) it was reported that at a nickel anode in aqueous potassium hydroxide, simple n-alcohols were oxidized to carboxylic acids in current and organic yields in excess of 90%. It was suggested that the rate-determining step in this oxidation was a chemical reaction, hydrogen abstraction from the α-carbon of the alcohol by a nickel oxide [closely related to the chemical reagent, nickel peroxide (2)] formed anodically on the surface of the nickel, *i.e.*

$$Ni \xrightarrow{\text{aqu.KOH}} Ni(OH)_2 \overset{-e}{\rightleftarrows} NiO(OH) + H^+ \qquad [1]$$

$$NiO(OH) + RCH_2OH \xrightarrow{\text{r.d.s.}} Ni(OH)_2 + \dot{R}CHOH \qquad [2]$$

$$\dot{R}CHOH \xrightarrow[\text{further steps}]{} \text{products} \qquad [3]$$

Although these oxidations are not synthetically significant, nickel peroxide has been reported to be a useful reagent for the oxidation of a range of benzyl and allyl alcohols (2, 3). Hence it was considered of interest to attempt the oxidation of larger alcohols at a nickel electrode in alkaline media.

In order to carry out such electrolyses simply it is necessary to find a solvent where such alcohols are soluble but the electrochemistry of the nickel electrode is essentially the same as in aqueous solution. Hence in this paper we discuss the electrochemistry of nickel and the oxidation of benzyl alcohols and phenylethanols in a series of tertiary butanol/water mixtures. It should also be noted that the solvent medium is important in determining the products from the chemical oxidations with nickel peroxide; in aqueous alkali the products were carboxylic acids but in an organic solvent the main products were aldehydes (3). Thus it is possible that the products from the anodic oxidations could be controlled by suitable choice of the solvent medium.

Experimental

Steady-state and cyclic voltammetric experiments were carried out in a two-compartment cell. The working electrode was constructed from Koch Light, Limited nickel rod (purity > 99.998%) and was in the form of a disk electrode with a PTFE sheath. Prior to the electrochemical measurements the nickel electrode was polished with fine alumina powder and washed with distilled water; its potential was then cycled in the electrolysis medium at 0.1v sec^{-1} between 0.0 and 0.7V until the charge associated with the Ni^{II}/Ni^{III} transition became constant [approximately 5-8 cycles]. The auxiliary electrode was a Pt loop in the same compartment as the nickel anode but the saturated calomel reference electrode (Radiometer Type K401) was in a different compartment separated by a tap and Luggin capillary mounted on a glass syringe, so that the position of the tip with respect to the nickel disk could readily be adjusted. Preparative electrolyses were carried out employing a constant current (0.3 mA cm^{-2} unless otherwise stated) and a one-compartment cell, volume 250 cm^3. The working electrode was a 300 cm^2 nickel gauze (purity > 95%) in the form of a cylinder, and the stainless steel rod cathode was placed at the axis of the cylinder; during electrolyses the solution was stirred by a slow stream of nitrogen. All electrochemical experiments were carried out using a Chemical Electronics valve or transistorized potentiostats; where necessary a Chemical Electronics pulse generator, Type R.B.1 and a Hewlett-Packard 7035 X-Y recorder were also employed. An electronic integrator was employed for coulometry.

Solutions were prepared from triply distilled water, GPR grade tertiary butanol (Hopkin and Williams, Limited), and AR grade potassium hydroxide (B.D.H., Limited), sodium hydroxide (B.D.H., Limited), and sodium perchlorate (Koch-Light, Limited). The organic substrates were obtained from B.D.H., Limited, May and Baker, Limited, Koch Light, Limited, Aldrich Chemical Company, Limited, or Chemical Procurement, Limited, and where necessary the purity of the compounds was checked using glc. (a Pye 104 chromatograph and an OV-17 silicon oil column at 140°C).

Preparative electrolyses were generally carried out using a constant current of 0.3 mA cm^{-2} and 0.04 moles of the alcohol dissolved in 200 cm^3 of the solvent/electrolyte. The electrolyses were terminated after the passage of 2**F**/mole of substrate. Alcohol and aldehyde products were extracted from the electrolysis medium with ether, and carboxylic acids were extracted similarly after the solution had been acidified. Following evaporation of the ether and any t-butanol the products were examined by IR, NMR and mass spectroscopy using a Unicam SP 200, a Perkin Elmer R12 at 60 MHz, and a AEI MS12 mass spectrometer, respectively. The yields of the carboxylic acids were based on the weight of isolated pure product, and the amount of alcohol and aldehyde in the alkaline extracts was estimated from the NMR spectra and by glc. Where aldehydes were major products, their yields were checked by preparing the 2,4-dinitrophenylhydrazone derivatives and weighing. In most cases retention times and spectra were compared with those for authentic samples.

Results

The electrochemistry of nickel in alkaline t-butanol/water mixtures.—Curve (a) of Fig. 1 shows a cyclic

Key words: nickel oxide, electrosynthesis, aldehydes, dehydrogenation.

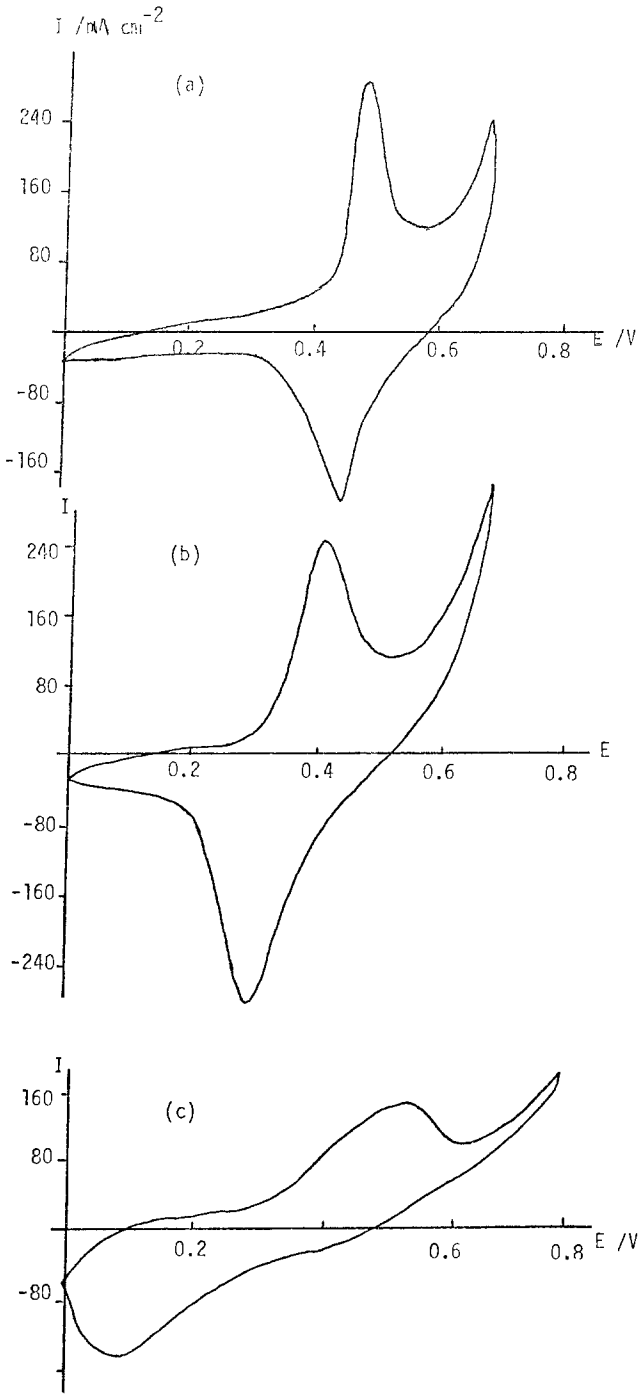


Fig. 1. Cyclic voltammograms for a nickel electrode in various t-butanol/water mixtures containing 0.1M KOH. Potential scan rate 0.03 V sec^{-1}. Potentials vs. SCE (a) 0% t-C_4H_9OH; (b) 67% t-C_4H_9OH; (c) 80% t-C_4H_9OH.

voltammogram run between 0.0 and 0.65V *vs.* SCE for a nickel electrode in purely aqueous 0.1M potassium hydroxide; the major features are an oxidation peak at + 0.46V and a reduction peak at + 0.41V on the reverse sweep. No steady-state current is observed in this potential range although oxygen evolution occurs at slightly more positive potentials, and hence the peaks on the cyclic voltammograms must be due to surface changes. This is confirmed by the shape of the peaks and the observation that the charges under the oxidation and reduction peaks are equal and approximately independent of potential scan rate. Several earlier papers (4-7) have discussed the nature of this surface oxidation/reduction process which is generally written

$$Ni(OH)_2 \rightleftarrows NiO(OH) + H^+ + e$$

The charge under the peaks ($\simeq$700 μC cm^{-2}) indicates that with a polished nickel electrode at most a few monolayers of the surface are oxidized. Moreover most of the features of the voltammograms indicate that the electron transfer is rapid although if this is the case the observation of a peak separation remains unexplained.

When the cyclic voltammetry is repeated in a series of t-butanol/water mixtures each containing 0.1M potassium hydroxide, it can be seen that with increasing t-butanol content the peaks become less sharp and the peak separation increases. Up to 70% t-butanol, however, the cyclic voltammograms continue to show well-formed surface oxidation and reduction peaks and the charges associated with each process remain the same; curve (b) of Fig. 1 shows the cyclic voltammogram for 67% t-butanol/33% water, and it can be seen that at 0.03 V sec^{-1} the oxidation process occurs at E_p = 0.40V and the peak separation is 125 mV (in contrast to the purely aqueous solutions these parameters depend slightly on scan rate). Above 70% t-butanol the quality of the peak shape deteriorates rapidly [see curve (c) in Fig. 1]. This change is not associated with uncompensated solution resistance and hence these experiments suggest that above 70% butanol the electrochemistry of nickel changes, the electron transfer rates decreasing markedly. Below 70% t-butanol, however, the electrochemistry of nickel is apparently essentially similar to that in completely aqueous alkaline media.

Variation of the temperature between 0° and 70°C did not produce marked changes in the cyclic voltammetry at any solvent composition.

Kinetic experiments with 2-phenylethanol.—The *I-E* curve from a slow linear potential sweep experiment for a solution of 2-phenylethanol (0.1M) in 67% t-butanol/33% water containing 0.1M potassium hydroxide at a nickel electrode is shown in Fig. 2. It can be seen that there is a well-formed oxidation wave $E_{1/2}$ = 0.37V but the current in the plateau region (0.15 mA cm^{-2}) is much less than that expected for a diffusion-controlled oxidation of 2-phenylethanol. The kinetic nature of the wave is confirmed by experiments with a rotating nickel electrode; the current in the plateau region is independent of rotation rate. The plateau current is also independent of hydroxide ion concentration.

Steady-state *I-E* data obtained by a point by point technique showed that the Tafel slope was (60 mV)$^{-1}$ and that over the whole oxidation wave the current is proportional to the concentration of 2-phenylethanol (0.01—0.25M). *I-E* curves were also measured at a series of temperatures for a solution 0.1M in 2-phenylethanol in the 67% t-butanol/33% water + 0.1M potassium hydroxide. As expected for a kinetically controlled wave, the limiting current increases substantially with increasing temperature (see Table I); with increasing temperature, the oxygen evolution current also commenced at less positive potentials and hence the plateau region became more restricted.

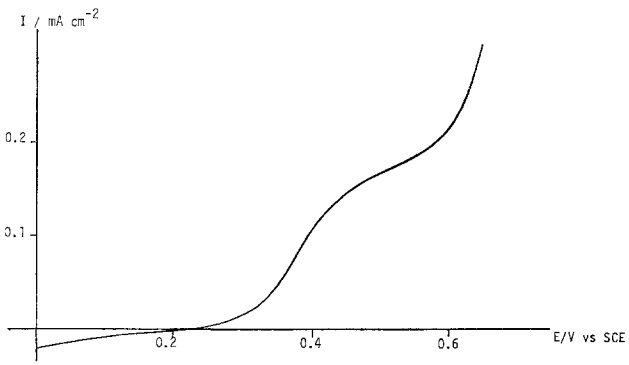


Fig. 2. *I-E* curve recorded by a slow linear potential sweep technique for a solution of 0.1M 2-phenylethanol in 67% t-butanol/33% water + 0.1M KOH at a nickel electrode.

Table I. Limiting currents for the oxidation of 0.1M 2-phenylethanol at a Ni electrode in 67% t-C_4H_9OH/33% H_2O + 0.1M KOH at a series of temperatures

T(°C)	I_L(mA cm^{-2})
15	0.11
25	0.16
35	0.21
45	0.30
55	0.44
80	0.90

Finally the *I-E* curves were investigated as a function of solvent composition and the limiting current varied substantially with the ratio of t-butanol/water; in water, the limiting current was 0.34 mA cm^{-2} but in 67% t-butanol the value was much lower, 0.15 mA cm^{-2}.

No variation in the product of the oxidation (2-phenylacetic acid, see later) was observed with changes in these reaction conditions.

Kinetic experiments with other alcohols.—*I-E* curves were recorded for 0.1M solutions of a range of primary alcohols in 67% t-butanol/33% water containing 0.1M potassium hydroxide. Each gave a well-formed oxidation wave at the potential for the oxidation of the nickel but although all the waves are clearly kinetically controlled, the magnitude of the limiting currents varied substantially; values of the limiting currents are reported in Table II. In all cases the Tafel slopes were (65 ± 5 mV)$^{-1}$ and the current was proportional to the substrate concentration (0.01-0.2M) over the whole oxidation wave.

I-E curves were similarly recorded for 0.1M solutions of a number of aldehydes; uniformly the limiting currents were much lower than for the corresponding alcohol.

Preparative electrolyses.—It is clear from the experiments above that a range of 2-phenylethanols, benzyl alcohols, and allyl alcohols may be oxidized at a nickel anode in alkaline t-butanol/water. The maximum current densities at which the oxidations may be performed are low, however, and the formation of several grams of product on a reasonable timescale requires the use of a large area anode. On the other hand it is possible to carry out the electrolysis at constant current and in an undivided cell.

In Table III the products and yields from a series of electrolyses carried out at room temperature in 67% t-butanol/33% water containing 0.1M potassium hydroxide are reported. The yields of major products are based on the weight of the isolated product (or derivative) and are characterized spectroscopically. Minor products were estimated by glc and NMR spectroscopy. No radical coupling products could be identified. The product of the cathode reaction was generally hydrogen and in some electrolyses slow oxygen evolution from the anode was also observed. In such cases the current yields could presumably be improved by use of a lower current density. The kinetic experiments would indicate that the rate of product

Table II. Limiting currents for the oxidation of 0.1M alcohols at a Ni anode in 0.1M KOH 67% t-C_4H_9OH/33% H_2O at 25°C. I_L in mA cm^{-2}

X-⟨⟩-CH_2OH		X-⟨⟩-CH_2CH_2OH		ROH	
X	I_L	X	I_L	R	I_L
H	0.26	H	0.15	C_2H_5	0.44
NO_2	0.38	Cl	0.04	$C_6H_5CH=CH-CH_2$	0.16
CH_3	0.23	OCH_3	0.07	$C_6H_5CH_2CH_2CH_2$	0.04
OCH_3	0.20			CH_2	0.05
OH	0.07				

Table III. Products and yields from the constant current (0.3 mA cm^{-2}) oxidation of primary alcohols in 67% t-C_4H_9OH/33% H_2O + 0.1M KOH. The electrolyses were carried out on 0.04 mole substrate in 200 cm^3 of solvent and were terminated after passage of 2F/mole. Yields are based on weight of products isolated

Alcohol	Current yields		Organic yields	
	Aldehyde	Carboxylic acid	Aldehyde	Carboxylic acid
a) X-⟨⟩-CH_2OH				
X = H	36	32	45*	21
X = NO_2	trace	86	trace	91
X = CH_3	56	32	66	23
X = OCH_3	67	18	83	9
X = OH	20	—	67	—
b) X-⟨⟩-CH_2CH_2OH				
X = H	—	57	—	60
X = OCH_3	—	50	—	90
X = Cl	—	34	—	71
c) Others				
$C_6H_5CH=CHCH_2OH$	40	34	60	40
	—	26	—	71
$C_6H_5CH_2CH_2CH_2OH$	—	59	—	70

* Approximately one half of this product was reduced at the cathode to benzpinacol.

formation could be increased by use of a higher temperature and where solubility considerations permit, the use of a solvent with less t-butanol. A few experiments with 2-phenylethanol and benzyl alcohol would suggest that this is the case; yields were not much affected by such changes in the electrolysis conditions.

Table IV reports the yields of products from the oxidation of benzyl alcohol at different *p*H. It can be seen that the ratio of aldehyde to acid changes dramatically, the aldehyde being favored in the less alkaline solutions. The current yields do decrease, however, presumably as oxygen evolution becomes more important. In the "neutral" 0.1M sodium perchlorate medium a cyclic voltammogram does not show the characteristic oxidation peak prior to oxygen evolution which is observed in alkaline media. On extending the sweep into oxygen evolution, however, a poorly formed reduction peak is observed on the reverse sweep.

In no electrolyses was corrosion of the cathode observed. A small amount of nickel corrosion was occasionally seen; this was not reproducible, it contributed negligibly to the current, and seemed to occur at random patches on the gauze. It also appeared that corrosion of the anode was minimized by use of a high purity nickel.

Discussion

Alkaline t-butanol/water mixtures have been shown to be a convenient medium for the oxidation of alcohols at a nickel anode despite the low current densities at

Table IV. Products and yields from the anodic oxidation of benzyl alcohol in various electrolytes. Other conditions as Table III

Electrolyte	Current yield		Organic yield	
	Aldehyde	Acid	Aldehyde	Acid
1M Et_4NOH	24	64	28	57
0.1M NaOH	36	32	45	21
0.01M NaOH + 0.1M $NaClO_4$	42	5	79	3
0.1M $NaClO_4$	30	—	91	—

which the oxidations must be carried out. A range of primary alcohols have been studied and in all cases the total organic yield of aldehyde and carboxylic acid is high (see Table III). The 2-phenylethanols, 3-phenylpropanol, and the simple allylic alcohols give only the carboxylic acid, while the alcohols with a conjugated unsaturated system α to the site of primary oxidation, *i.e.*, the benzyl alcohols and cinnamyl alcohol, give a mixture of aldehyde and carboxylic acid. The fraction of aldehyde is increased by an electron donating group in the phenyl ring.

The aldehydes are synthetically the more interesting products and a number of experiments with the object of maximizing the fraction of this product were carried out. The most useful experimental parameter proved to be the pH of the electrolysis medium. The results of a series of oxidations of benzyl alcohols are reported in Table IV; in 1.0M hydroxide the major product is benzoic acid but in 0.01M hydroxide the amount of aldehyde exceeds that of the acid by a factor of twenty-six and in the "neutral" medium no benzoic acid was isolated.

In earlier papers (1, 4) it was shown that the mechanism of the oxidation of simple aliphatic alcohols (and amines) at a nickel anode in aqueous alkaline solutions is

$$Ni(OH)_2 \rightleftarrows NiOOH + H^+ + e$$

$$NiOOH + RCH_2OH \xrightarrow{\text{slow step}} Ni(OH)_2 + \dot{R}CHOH$$

$$\dot{R}CHOH \xrightarrow{\text{further steps}} \text{products}$$

In addition, an equation relating the rate constant for the slow chemical step to the limiting current density was formulated (4). Although this derivation requires certain assumptions which were later criticized (8), there is little doubt that the limiting currents for a series of related compounds is a useful guide to the relative rates of the reaction between the compounds and the higher nickel oxide. The electroanalytical experiments with the phenylethanols and benzyl alcohols in the t-butanol/water mixtures would suggest that the mechanisms of these oxidations are similar.

Curve (a) in Fig. 3 shows a plot of log I_L *vs.* σ, the Hammebb substituent constant for the series of p-substituted benzyl alcohols; these substitution constants reflect the electron withdrawing/donating ability of the p-substituent. In view of the variation in the products isolated and the dependence of the limiting current density on n, the over-all number of electrons transferred as well as the rate constant for the chemical step, however, it is more correct to plot log I_L/n_{avg} *vs.* σ where n_{avg} is the average number of electrons transferred calculated from the product distribution. Curve (b) of Fig. 3 is such a plot. It can be seen that I_L/n_{avg} and hence the rate constant is independent of the electron donating ability of the para-substituent; this is further evidence that the transition state for the chemical reaction is uncharged, and hence this data is compatible with the chemical step being hydrogen abstraction.

Some limited conclusions are also possible concerning the nature of the reactions following the rate-determining step. Clearly it is unlikely that the aldehydes are intermediates in the formation of the carboxylic acids since (*i*) it has been shown that in this system aldehydes oxidize much less rapidly than the corresponding alcohols and (*ii*) in the case of the benzyl alcohols, the ratio of acid/aldehyde products does not reflect the predicted relative ease of oxidation of the

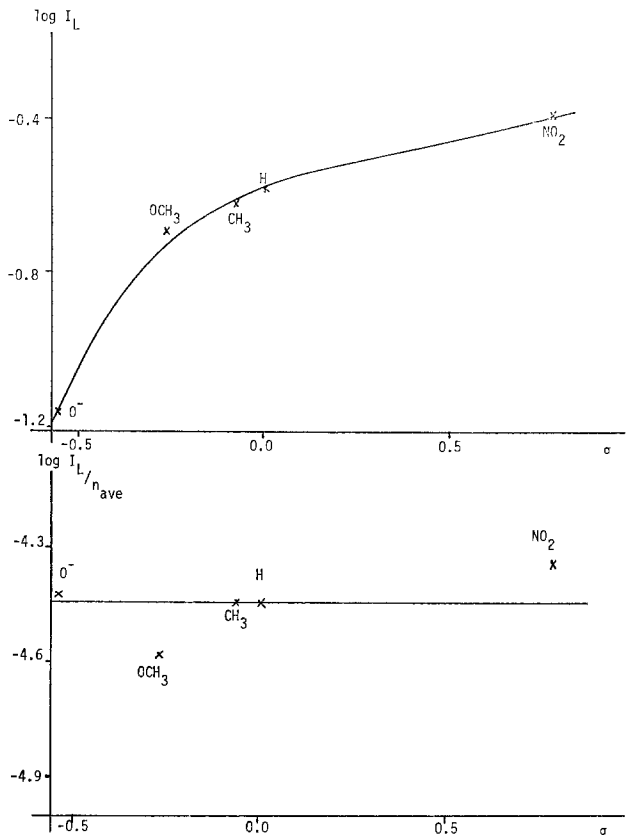


Fig. 3. Variation of the rate of oxidation with substituent for a series of p-substituted benzyl alcohols. (a) log I_L *vs.* σ; (b) log I_L/n_{avg} *vs.* σ.

aldehydes, *i.e.*, contrary to the experimental data it would be expected that an electron donating group would make oxidation easier and reduce any tendency to stabilize the aldehyde by hydration. Hence it must be concluded that the oxidation of these alcohols occurs on the surface of the nickel oxide electrode and that the formation of aldehyde or acid depends on the stability to desorption of a surface species with an intermediate degree of oxidation. The variation of the products with hydroxide ion concentration must then be attributed to a change in the nickel oxide surface with pH.

Manuscript submitted April 30, 1976; revised manuscript received Aug. 23, 1976.

Any discussion of this paper will appear in a Discussion Section to be published in the December 1977 JOURNAL. All discussions for the December 1977 Discussion Section should be submitted by Aug. 1, 1977.

REFERENCES

1. M. Fleischmann, K. Korinek, and D. Pletcher, *J. Chem. Soc., Perkins Trans. 2*, **1972**, 1396.
2. M. V. George and K. S. Balachandran, *Chem. Rev.*, **75**, 491 (1975).
3. K. Nakagawa, R. Konaka, and T. Nakata, *J. Org. Chem.*, **27**, 1597 (1962).
4. M. Fleischmann, K. Korinek, and D. Pletcher, *J. Electroanal. Chem.*, **31**, 39 (1971).
5. M. A. Sattar and B. E. Conway, *Electrochim. Acta*, **14**, 695 (1969).
6. B. E. Conway and M. A. Sattar, *J. Electroanal. Chem.*, **19**, 351 (1968).
7. D. M. MacArthur, *This Journal*, **117**, 422, 729 (1970).
8. G. Vértes and G. Horanyi, *J. Electroanal. Chem.*, **52**, 47 (1974).

Single Electrode Heat Effects

I. Peltier Entropies of Gas Electrodes in Carbonate Paste Electrolytes

T. Jacobsen

Fysisk-Kemisk Institut, The Technical University of Denmark, DTH 2800 Lyngby, Denmark

and G. H. J. Broers

Inorganic Chemistry Department, State University at Utrecht, Utrecht, The Netherlands

ABSTRACT

Standard Peltier entropies for the reactions

$$\tfrac{1}{2}\,O_2 + CO_2 + 2e^- \rightarrow CO_3^{--}$$

$$2CO_2 + 2e^- \rightarrow CO + CO_3^{--}$$

in molten carbonate paste electrolytes at 1000°K have been determined from thermogalvanic measurements. The results are −217 and −118 J/mole°K, respectively. No dependence on electrolyte composition is observed. The reversible part of the Peltier entropy for the oxygen electrode reaction is estimated from thermodynamic data and reasonable agreement with the experimental results is found. It is concluded that the main contribution to the Peltier entropy arises from the transition from gaseous to liquid state, whereas the transfer entropies of the ionic species are of minor importance.

In power-producing electrochemical cells, heat is liberated from the electrode reactions and the irreversible losses. In most cells working on solid- or liquid-state reactants, the entropy of reaction will in practice be of minor importance compared to the contributions from ohmic resistance and electrode polarization. However, if the electrode reactions have a net consumption or production of gaseous components, the entropy change will be considerable, due to the transition of state, and has to be taken into account. On the basis of the over-all heat evolved in a single cell during load, the temperature distribution in fuel cell batteries has been treated (1-3), but so far little attention has been paid to the single electrode heat balance and temperature gradients inside single cells caused by nonsymmetrical heat evolution at cathode and anode.

The heat evolved at a reversible electrode is determined by the Peltier entropy of the electrode reaction, which may be found from thermogalvanic measurements. Previously, the Peltier entropies of high temperature gas electrodes in ionic conducting oxides like ZrO_2 (4) and ThO_2 (5) have been investigated, and we have reported some preliminary results for carbonate electrolytes (6), which still left some uncertainty about the dependence on temperature and carbonate composition.

In this paper, the Peltier entropies of the $O_2 + CO_2$ and the $CO + CO_2$ electrode are determined. In part II of this paper, the heat evolved at the electrode during the irreversible passage of current is related to the Peltier entropies and some effects of the temperature gradients created are discussed.

Theory

For the thermogalvanic cell involving a mixture of molten carbonates

$$Pt(T)\,|O_2 + CO_2|Me_2CO_3|O_2 + CO_2|Pt(T + \Delta T) \qquad [A]$$

with the electrode reaction

$$1/2\,O_2 + CO_2 + 2e^- \rightarrow CO_3^{--} \qquad [1]$$

the Peltier entropy $\Delta S_P(O_2, CO_2)$ may be determined from the thermogalvanic force ΔTGF by the equation (7)

$$2\mathbf{F}\frac{\Delta TGF}{\Delta T} = \Delta S_P(O_2, CO_2) = \Delta S_P^{\circ}(O_2, CO_2) + R \ln p(O_2)\,\tfrac{1}{2}p(CO_2) \qquad [2]$$

where the standard Peltier entropy is given by

$$\Delta S_P^{\circ}(O_2, CO_2) = [S^{\circ}(CO_3^{--}) - 1/2S^{\circ}(O_2) - S^{\circ}(CO_2) - 2S^{\circ}(e^-)] + \Delta\hat{S} \qquad [3]$$

The first term in Eq. [3] is the reversible entropy of reaction, whereas $\Delta\hat{S}$[1] is the entropy of transfer corresponding to the homogeneous part of the thermogalvanic force, *i.e.*, the thermal diffusion potential in the electrolyte and the electrode leads.[2] $\Delta\hat{S}$ is composed of the transfer entropies of the species carrying the current according to

$$\Delta\hat{S} = t(CO_3^{--})\hat{S}(CO_3^{--}) - 2t(Me^+)\hat{S}(Me^+) - 2\hat{S}(e^-) \qquad [4]$$

These excess entropies of transfer arise from the fact that transported particles are not average particles but a selected ensemble, thus carrying an excess entropy, the transfer entropy (8). Compared to the equilibrium term in Eq. [3], involving a transition from gaseous to liquid state, the transfer term [4] is expected to be of secondary importance.

For the cell

$$Pt(T)\,|CO + CO_2|Me_2CO_3|CO + CO_2|Pt(T + \Delta T) \qquad [B]$$

having the electrode reaction

$$2CO_2 + 2e^- \rightarrow CO + CO_3^{--} \qquad [5]$$

we obtain the expressions

[1] The entropy of transfer $\hat{S}$ is related to the transported entropy S^* used in Ref. (7) by the equation $\hat{S} = S^* - S$.

[2] It is noted that since the single electrode potential is not a measurable quantity, the numerical separation of the thermal emf into contributions from the homogeneous and heterogeneous transfer processes can only be performed on the basis of a convention.

Key words: thermocell, Peltier entropy, molten carbonate, gas electrodes.

$$2\mathbf{F}\frac{\Delta TGF}{\Delta T} = \Delta S_P(CO, CO_2) = \Delta S_P^\circ(CO, CO_2) + R\ln\frac{p^2(CO_2)}{p(CO)} \quad [6]$$

$$\Delta S_P^\circ(CO, CO_2) = [S^\circ(CO_3^{--}) + S^\circ(CO) - 2S^\circ(CO_2) - 2S^\circ(e^-)] + \Delta\hat{S} \quad [7]$$

where $\Delta\hat{S}$ is also determined by Eq. [4].

Subtracting [7] from [3] yields

$$\Delta S_P^\circ(O_2, CO_2) - \Delta S_P^\circ(CO, CO_2) = S^\circ(CO_2) - 1/2S^\circ(O_2) - S^\circ(CO) \quad [8]$$

which shows that Peltier entropies of different electrodes in the same media are related by well-known thermodynamic magnitudes, not involving single ion or transport properties.

When a cell similar to [B] contains an equilibrated mixture of "C-H-O gases" (such as reformed hydrocarbons), the only species of importance above the carbon deposition temperature are the gases H_2, CO, CH_4, H_2O, and CO_2 (9). Their equilibrium partial pressures are given by the reactions

$$H_2 + CO_2 \rightleftarrows H_2O + CO \quad [9]$$

$$K_s = \frac{p(H_2O)p(CO)}{p(H_2)p(CO_2)} \quad [10]$$

$$4H_2 + CO_2 \rightleftarrows CH_4 + 2H_2O \quad [11]$$

$$K_m = \frac{p(CH_4)p(H_2O)^2}{p(H_2)^4p(CO_2)} \quad [12]$$

The Peltier entropy of this cell can be found from simple thermodynamic equilibrium considerations for the isothermal cell

$$(a)\,Pt(T)|C\text{-}H\text{-}O|Me_2CO_3|O_2 + CO_2|Pt(T)\,(c) \quad [C]$$

The "C-H-O" electrode reaction is a superposition of CO, H_2, and CH_4 oxidation reactions. In the case of an equilibrated gas mixture, these reactions will be linear combinations of the CO equilibrium [5] and the gas phase equilibria [9] and [11]. The Peltier entropy for the mixed "C-H-O" electrode reaction can, therefore, be calculated from the temperature dependence of the emf on the basis of the CO electrode reaction [5] when the change in gas phase composition is taken into account.

$$\Delta S = 2\mathbf{F}\frac{dE}{dT} = \Delta S_P(O_2, CO_2) - \Delta S_P(C\text{-}H\text{-}O)$$

$$\Delta S = -\tfrac{1}{2}S^\circ(O_2) - S^\circ(CO) + S^\circ(CO_2) + R\ln[p(O_2)^{1/2}p(CO_2)]_c + R\frac{d}{dT}\left[T\ln\frac{p(CO)}{p(CO_2)^2}\right]_a \quad [13]$$

This yields in combination with [2] and [8]

$$\Delta S_P(C\text{-}H\text{-}O) = \Delta S_P^\circ(CO, CO_2) - R\ln\frac{p(CO)}{p(CO_2)^2} - RT\frac{d}{dT}\ln\frac{p(CO)}{p(CO_2)^2} \quad [14]$$

Equation [14] reduces to [6] for the pure CO, CO_2 cell [B]. The last two terms in [14] can be calculated from the equilibrium constants K_s and K_m and the corresponding standard reaction enthalpies ΔH_s° and ΔH_m° when C/H/O atomic ratios of the fuel gas are given. An example is given in part II of this paper.

Experimental

Figure 1 shows the experimental arrangements. The electrolyte, a rather stiff paste of 45 weight percent (w/o) Me_2CO_3 and 55 w/o MgO prepared by careful mixing of the dry powders, heating overnight at 750°C in an Al_2O_3 crucible, and subsequent grinding in an alumina ball mill, is pressed into an alumina tube at a temperature just above the melting point.

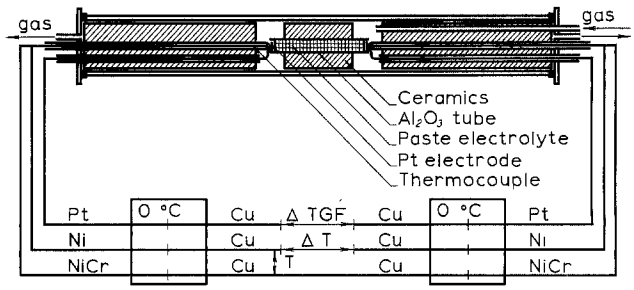


Fig. 1. Experimental setup for the determination of thermogalvanic forces in paste electrolyte.

The platinum electrodes are fixed at the end of the thermocouple protection tubes. During the initial heating of the oven, when the temperature had just passed the melting point of the electrolyte, the thermocouples were pressed against the electrolyte in order to ensure a proper electrode-electrolyte contact.

The gas mixtures were fed to the center of the oven and removed from both ends in order to avoid disturbance from CO disproportionation with associated carbon deposition in the colder parts when reducing atmosphere was applied. Furthermore, the gas volume and space time were reduced by ceramic plugs also serving as heat insulation between the two electrode compartments.

The oven is equipped with two separate bifilar heating coils supplied from voltage-stabilized transformers. The thermocouples are Ni/NiCr. The thermogalvanic force and the thermocouple voltage difference, ΔTEF, are recorded on a Servogor two-channel recorder connected to the outputs of the two Hewlett-Packard 3420 differential voltmeters. Utilizing the zero suppression feature of these instruments, full scale deflections of 100 μV for TGF and 10 μV for TEF are obtained on the recorder.

The experimental procedure is as follows: 45 min after a change of heating coil voltage, ΔTGF and ΔTEF are recorded for 15 min. Before and after the recording the temperature is read. The recordings are made in order to eliminate the effect of minor instabilities and drift due to voltage fluctuations in the mains. The voltage of the colder heating coil is then increased, thus creating a reverse temperature difference of approximately 15°C and a higher average temperature. After a 45 min equilibration period, the next set of readings is made. When the upper temperature limit of 900°C is reached, the measurements are repeated for decreasing temperature levels till the point of solidification, or in case of CO-CO_2 mixtures to the carbon deposition temperature of about 760°C (9).

Because of the thermocouple-electrode distance and the rather high thermal conductivity of the alumina tubes, the measured temperature differences are about 10% larger than the actual electrode temperature differences. To correct for this systematical error, the electrolyte is substituted by a Pt 10% Rh wire embedded in MgO and contacting the Pt electrodes. The thermoelectric force of this differential thermocouple is then determined using the procedure described above. A correction function is calculated from literature data.

Computation Procedure

The experimental procedure where only one set of ΔTGF, ΔTEF, and TEF readings is obtained at each temperature makes the calculation of the Seebeck

coefficient more complex than with the usual technique, where the Seebeck coefficient is calculated from the slope of a ΔTGF *vs.* ΔTEF plot at a fixed temperature. On the other hand, the method yields more information from the experimental effort, especially with respect to the temperature dependence.

The relation between the thermogalvanic force and the thermoelectric force of the thermocouples may be written as

$$\Delta TGF = \frac{\epsilon_E}{\epsilon_T'} [\Delta TEF + A(T)] \quad [15]$$

where ϵ_E and ϵ_T' are the Seebeck coefficients of the electrode and the apparent Seebeck coefficient of the thermocouples containing the systematical temperature error mentioned above. $A(T)$ is the temperature dependent offset error of the thermocouples.

If $\epsilon_E(T)$ and $A(T)$ are expanded in power series with respect to temperature

$$\epsilon_E = \sum_{i=0} e_i (T - T_0)^i \quad [16]$$

$$A = \sum_{j=0} a_j (T - T_0)^j \quad [17]$$

Eq. [15] may be rewritten as

$$\Delta TGF = \frac{1}{\epsilon_T'} \left[\Delta TEF \sum_{i=0} e_i (T - T_0)^i + \sum_{i=0} e_i \sum_{j=0} a_j (T - T_0)^{i+j} \right] \quad [18]$$

This equation shows how $\epsilon_E(T)$ may be determined from a multiple regression analysis with respect to $\Delta TEF\ (T - T_0)^i$, i = 0, 1, 2, . . . and $(T - T_0)^l$, l = 0, 1, 2, . . . when $\epsilon_T'(T)$ is known.

$\epsilon_T'(T)$ may be obtained from the calibration experiments, where the thermogalvanic cell is substituted by a differential Pt/Pt 10% Rh thermocouple. In this case the Seebeck coefficient of Pt/Pt 10% Rh relative to ϵ_T' may be determined from Eq. [18]. Comparing this power series with literature data (10), also expanded in a power series, yields an analytical expression for ϵ_T' and allows the calculation of the Seebeck coefficients for the electrodes on the basis of Eq. [18].

Results and Discussion

In all cases, the colder electrode constituted the positive pole of the cell. Tables I and II give the experimental Seebeck coefficients and the standard Peltier entropies for the $O_2 + CO_2$ and the $CO + CO_2$ electrode. No temperature dependence is observed in any case. It is noted that the deviations between values obtained for identical electrolytes are larger than expected from the standard deviations calculated in the regression analysis. This indicates that the main error source is the reproduction from one experiment to another of electrode and thermocouple position inside the oven. Thus no significant dependence of the Peltier entropy on carbonate composition is found. This very small dependence of the Peltier entropy on the melt composition is expected, since the main entropy contribution originates from the transition from gaseous to liquid state, whereas the change with composition is in the order of mixing entropies.

Table I. Peltier entropy for the reaction $1/2\ O_2 + CO_2 + 2e^- \rightarrow CO_3^{--}$ in the temperature range 800°-1150°K

Electrolyte equimolar	mV/°K	Std dev, mV/°K	p_{CO_2}, atm	p_{O_2}, atm	ΔS_P^o, J/mole °K
$(Li,Na)_2CO_3$	−1.18	0.02	0.62	0.38	−220
$(Li,Na)_2CO_3$	−1.17	0.07	0.65	0.35	−218
$(Li,K)_2CO_3$	−1.14	0.01	0.65	0.35	−213
$(Li,Na,K)_2CO_3$	−1.14	0.02	0.67	0.33	−212
$(Li,Na,K)_2CO_3$	−1.20	0.02	0.65	0.35	−223
Average					−217

Table II. Peltier entropy for the reaction $2CO_2 + 2e^- \rightarrow CO + CO_3^{--}$ in the temperature range 1050°-1150°K

Electrolyte equimolar	mV/°K	Std dev, mV/°K	p_{CO_2}, atm	p_{CO}, atm	ΔS_P^o, J/mole °K
$(Li,Na)_2CO_3$	−0.66	0.02	0.50	0.50	−122
$(Li,K)_2CO_3$	−0.64	0.02	0.55	0.45	−120
$(Li,Na,K)_2CO_3$	−0.63	0.01	0.50	0.50	−116
$(Li,Na,K)_2CO_3$	−0.63	0.03	0.50	0.50	−116
Average					−118

As a check on the experimental values, the difference between the Peltier entropies for the two electrodes may, according to Eq. [8], be calculated and compared to literature data. Using the mean values in Tables I and II we obtain

$$S^o(CO_2) - \tfrac{1}{2}S^o(O_2) - S^o(CO) = \Delta S_P^o(O_2, CO_2) - \Delta S_P^o(CO, CO_2) = -217 + 118 = -99\ \text{J/mole°K}$$

compared to the value of −87.4 J/mole°K at 1000°K given in (11). This discrepancy is somewhat larger than expected from the standard deviations. The $CO + CO_2$ electrode is, in contrast to the $O_2 + CO_2$ electrode, very sensitive to minor changes in gas phase composition, which may be caused by convective mixing at the electrodes with partly decomposed gas from colder parts of the oven. Thus, the Peltier entropy determined for the $CO + CO_2$ electrode is less reliable and may be responsible for the deviation.

The reversible part of the Peltier entropy can be estimated on the basis of thermodynamic data. However, in order to obtain the entropy of the carbonate ion, it is necessary to know the contributions from vibration and rotation of the polyatomic ion. This difficulty may be avoided if, for example, the oxygen electrode reaction [1] is separated into the reactions

$$\tfrac{1}{2}\ O_2 + 2e^- \rightarrow O^{--} \quad [19]$$

$$O^{--} + CO_2 \rightarrow CO_3^{--} \quad \text{(solvation of } O^{--}) \quad [20]$$

From literature data the entropies of alkali oxides in the liquid state have been estimated as a function of temperature (12). Distributing the entropy equally among the ions and neglecting the mixing entropy, we obtain for an equimolar mixture of Li_2O and Na_2O at 1000°K the value

$$S^o(O^{--}) = (152 + 204)/6 = 59\ \text{J/mole°K}$$

For the combination of O^{--} and CO_2, Andersen (12, 13) has determined the free energy and entropy change in different carbonate melts. Using the value for $(Li, Na)_2CO_3$ gives

$$\Delta S^o(2\,O) = -126\ \text{J/mole°K}$$

which yields the estimate on the entropy of the carbonate ion in the liquid state

$$S^o(CO_3^{--}) = \Delta S^o(2\,O) + S^o(CO_2) + S^o(O^{--}) = -126 + 269 + 59 = 202\ \text{J/mole°K}$$

The transported entropy, $S^*(e^-)$, of the electron is calculated from the absolute thermoelectric force of Pt at 1000°K (10)

$$S^*(e^-) = S^o(e^-) + \hat{S}(e^-) = 17.1\ 10^{-6}\ 96{,}500 = 1.65\ \text{J/mole°K}$$

The reversible part of the Peltier entropy is now calculated as

$$\Delta S_{P,rev}^{\circ}(O_2, CO_2) = S^{\circ}(CO_3^{--}) - \tfrac{1}{2} S^{\circ}(O_2) - S^{\circ}(CO_2) - 2S^{\circ}(e^-) \simeq 191 \text{ J/mole°K}$$

which is rather close to the experimental Peltier entropy of −217 J/mole°K. The uncertainties introduced by the assumptions made above may readily account for the discrepancy. Thus, as expected the entropies of transfer only constitute a minor part of the Peltier entropies of gas electrodes in molten carbonates.

Acknowledgments

The authors are indebted to F. Haslev and L. Christiansen for their participation in the experimental work. The many valuable discussions with B. K. Andersen and other colleagues are greatly appreciated. This work has been supported by Statens Teknisk Vidneskabelige Fond.

Manuscript submitted May 27, 1976; revised manuscript received Aug. 1, 1976. This was Paper 171 presented at the New York, New York, Meeting of the Society, May 4-9, 1969.

Any discussion of this paper will appear in a Discussion Section to be published in the December 1977 JOURNAL. All discussions for the December 1977 Discussion Section should be submitted by Aug. 1, 1977.

LIST OF SYMBOLS

E	electromotive force (V)
$\mathbf{F}$	Faraday constant (C/mole)
ΔH	enthalpy of reaction (J/mole)
p	partial pressure (atm)
t	transport number
T	temperature (°K)
TEF	thermoelectric force (V)
TGF	thermogalvanic force (V)
S	entropy (J/mole°K)
ΔS_P	Peltier entropy (J/mole°K)
S^*	entropy of transported species (J/mole°K)
$\hat{S}$	excess entropy of transported species (J/mole°K)
ϵ	Seebeck coefficient (V/°K)
K	equilibrium constant

REFERENCES

1. D. Gidaspow and B. S. Baker, *AIChE J.*, **11**, 825 (1965).
2. D. Gidaspow, B. S. Baker, B. C. Jee, and F. Oliva, *Chem. Eng. Prog. Symp. Ser.*, **63**, 63 (1967).
3. B. S. Baker, D. Gidaspow, and D. Wasan, in "Advances in Electrochemistry and Electrochemical Engineering," Vol. 8, C. W. Tobias, Editor, Interscience, New York (1971).
4. R. J. Ruka, J. E. Bauerle, and L. Dykstra, *This Journal*, **115**, 497 (1968).
5. N. M. Tallan, *ibid.*, **118**, 345 (1971).
6. T. Jacobsen, Abstract 171, p. 427, The Electrochemical Society Extended Abstracts, Spring Meeting, New York, New York, May 4-9, 1969.
7. H. Holtan, P. Mazur, and S. R. de Groot, *Physica*, **19**, 1109 (1953).
8. J. N. Agar, in "Advances in Electrochemistry and Electrochemical Engineering," Vol. 3, P. Delahay, Editor, Interscience, New York (1963).
9. G. H. J. Broers and B. W. Treijtel, *Adv. Energy Conver.*, **5**, 365 (1965).
10. Landolt-Börnstein, 6. Aufl. II Band 6. Teil, Springer Verlag, Berlin (1959).
11. Landolt-Börnstein, 6. Aufl. II Band 4. Teil, Springer Verlag, Berlin (1961).
12. B. K. Andersen, Thesis, The Technical University of Denmark (1975).
13. B. K. Andersen, Troisiemes Journées d'Etude de Piles a Combustible, Bruxelles, 1969.

Single Electrode Heat Effects

II. Single Electrode Heat Evolution

T. Jacobsen

Fysisk-Kemisk Institut, The Technical University of Denmark, DTH 2800 Lyngby, Denmark

and G. H. J. Broers

Inorganic Chemistry Department, State University at Utrecht, Utrecht, The Netherlands

ABSTRACT

The heat evolution at a single irreversibly working electrode is treated on the basis of the Brønsted heat principle. The resulting equation

$$\frac{dQ}{dt} = \left(T\frac{\Delta S_P}{n\mathbf{F}} + \eta \right) i$$

is analogous to the expression for the total heat evolution in a galvanic cell with the exception that $-\Delta S$ is substituted by the Peltier entropy, ΔS_P, of the electrode reaction. η is the overvoltage at the electrode. This equation is applied to a high temperature carbonate fuel cell. It is shown that the Peltier entropy term by far exceeds the heat production due to the irreversible losses, and that the main part of heat evolved at the cathode is reabsorbed at the anode. Finally, effects like thermal corrosion, caused by internal temperature gradients, are discussed.

Most treatments of heat effects in galvanic cells are based on the over-all heat evolution calculated from the reversible heat evolution, $-T\Delta S$, and the polarization losses. So far, little attention has been paid to the single electrode heat evolution. In galvanic cells working on solid- or liquid-state reactants and products, the main heat evolution is caused by the polarization losses, whereas in most fuel cells involving a net consumption of gaseous components, the single electrode reactions contribute considerably to the heat evolution at moderate loads. They may give rise to rather large temperature gradients inside the cell. In porous gas diffusion electrodes, temperature gradients may cause convection in the electrolyte film through gradients in

Key words: heat evolution, molten carbonate fuel cells, Peltier entropy, thermal corrosion.

surface tension (1), thus reducing the effective diffusion layer thickness. Furthermore, in high temperature cells where the equilibrium concentration of electrode metal in the electrolyte is not extremely low, temperature gradients along the electrode surface may cause thermal corrosion, ruining the electrode structure by removing active parts of the electrode. This phenomenon has been observed in practice (2) when a leakage of anode gas into the cathode compartment caused a local temperature rise, which removed the electrode area surrounding the leak. Finally, the so-called self-regulation mechanism of porous high temperature cathodes preventing sintering of the porous structure (3) may possibly be explained in terms of a dissolution redeposition reaction caused by temperature gradients in the electrode.

The aim of this paper is a thermodynamic treatment of the single electrode heat evolution in a galvanic cell under load. These heats are calculated for high temperature carbonate fuel cells on the basis of the Peltier entropies determined in part I of this paper (8). An experimental verification of the heat effect is also presented. Finally, some of the effects caused by temperature gradients are briefly discussed.

Single Electrode Heat Balance

Considering the molten carbonate fuel cell anode reaction

$$CO + CO_3^{--} \rightarrow 2CO_2 + 2e^- \qquad [1]$$

the mass fluxes will be as outlined in Fig. 1.

It is noted that a bulk flow of electrolyte is introduced in Fig. 1 in order to obtain the apparent transport numbers of zero for Me^+ and unity for CO_3^{--} with the electrode as reference frame. The transport numbers t_+ and t_- describe the movement of ions relative to the liquid structure and might be determined by the diaphragm method (4). In contrast to the transport numbers with reference to the electrode, these transport numbers do not depend on the nature of the electrode, *i.e.*, whether anion or cation electrodes are used. This distinction between transport numbers relative to the electrodes and to the liquid structure is, in principle, important, since the movement of ions through the liquid structure involves an excess entropy of transport (5). In practice, it is of minor importance for gas electrode reactions, where the main heat effect is caused by the transition from gaseous to condensed state.

In order to determine the heat flow into the electrode compartment during steady-state conditions, we apply the Brønsted heat principle (6)

$$T\delta S'' = -\Sigma\, \Delta P_i \delta K_i \qquad [2]$$

The heat principle states that in an infinitesimal process transferring the quantity δK_i from the potential P_i to $P_i + \Delta P_i$ the loss of work $-\Delta P_i \delta K_i$ is equivalent to the irreversible heat production $T\delta S''$. In the case of reversibility, the thermodynamic equilibrium conditions may be derived from [2] on the basis of the conditions $\delta S'' = 0$ (7).

Performing an entropy balance on the electrode compartment in the steady state yields

$$\delta S = \delta S' + \delta S'' = 0 \qquad [3]$$

where $\delta S'$ is the entropy flow from the surroundings,

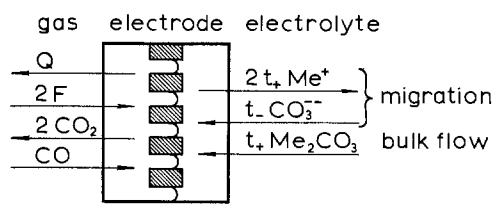


Fig. 1. Mass and heat fluxes into the anode compartment. Electrode reaction: $CO + CO_3^{--} \rightarrow 2CO_2 + 2e^-$.

in the form of heat and reactants. If the heat principle [2] is applied to the process in Fig. 1, we obtain for the transfer of an electric charge δq

$$T\delta S'' = -\left[(2\mu(CO_2) + 2\mu(e^-) - \mu(CO) - \bar{\mu}(CO_3^{--})\right]\frac{\delta q}{2F} \qquad [4]$$

which may be rewritten as

$$T\delta S'' = \left[\left(-\frac{\bar{\mu}(e^-)}{F} - \phi\right) - \{2\mu(CO_2) - \mu(CO) - \mu(CO_3^{--})\}\frac{1}{2F}\right]\delta q \qquad [5]$$

where the term $(-\bar{\mu}(e^-)/F - \phi)$ is the single electrode potential. In Eq. [5] the chemical potentials refer to the system boundary and since this is chosen to enclose all irreversible processes like diffusion and reaction at the electrode, except for the electric conduction in electrode leads and electrolyte, they do not depend on the degree of irreversibility. As $\delta S'' = 0$ holds for equilibrium conditions, we obtain the relation for the entropy production

$$T\delta S'' = \left[\left(-\frac{\bar{\mu}(e^-)}{F} - \phi\right] - \left(-\frac{\bar{\mu}(e^-)}{F} - \phi\right)\right]_{eq}\delta q = \eta\delta q \qquad [6]$$

where η is the overvoltage.

Taking into consideration that species transported by a migration mechanism carry an entropy, S^*, differing from the partial molar entropy (5), the entropy flux into the electrode compartment is, according to Fig. 1, written as

$$\delta S' = -\frac{\delta Q}{T} + [-2S^*(e^-) - 2S(CO_2) + S(CO) - 2t(Me^+)S^*(Me^+) + t(CO_3^{--})S^*(CO_3^{--}) + t(Me^+)S(Me_2CO_3)]\frac{\delta q}{2F} \qquad [7]$$

Introducing the excess entropy of transported species, $\hat{S} = S^* - S$, we obtain

$$\delta S' = -\frac{\delta Q}{T} + [-2S(e^-) - 2S(CO_2) + S(CO) + S(CO_3^{--}) + \Delta\hat{S}]\frac{\delta q}{2F}$$

where

$$\Delta\hat{S} = t(CO_3^{--})\hat{S}(CO_3^{--}) - 2t(Me^+)\hat{S}(Me^+) - 2\hat{S}(e^-) \qquad [8]$$

Comparing the entropy terms in Eq. [8] with Eq. [4]-[7] in part I of this paper (8), they are identified as the Peltier entropy ΔS_P of the CO electrode reaction. Thus, combining Eq. [3], [6], and [8], we obtain the final expression for the heat evolution due to the partly irreversible n electron single electrode reaction[1]

$$\frac{dQ}{dt} = \left(T\frac{\Delta S_P}{nF} + \eta\right)i \qquad [9]$$

where the sign convention of a positive anodic current is adopted. Since the term ηi, is always positive, whereas

[1] Although Eq. [9], to simplify the notation, has been derived on the basis of the CO,CO_2 electrode reaction, the result holds for the "general" reaction Red + $CO_3^{--} \rightarrow$ Ox + CO_2 + 2e$^-$ where (Ox,Red) is ($\frac{1}{2}O_2$,), (CO_2,CO), (H_2O,H_2), or ($2H_2O$ + CO_2,CH_4)/4. This is easily seen by substituting $2\mu_{CO}$, $2S_{CO}$, μ_{CO_2}, and S_{CO_2} with μ_{Red}, S_{Red}, $\mu_{Ox} + \mu_{CO_2}$, and $S_{Ox} + S_{CO_2}$ in the derivation.

the sign of $i\Delta S_P$ changes with the current direction, Eq. [9] holds for both anodic and cathodic reactions.

Peltier Entropy of a Mixed Electrode Reaction

As practical fuel cell applications will often involve mixed electrode reactions, like the oxidation of reformed hydrocarbons, we shall go into detail somewhat on the calculation of the Peltier entropy for the C-H-O fuel electrode.

For gaseous mixture of H_2 (h), CO (c), CH_4 (m), H_2O (w), and CO_2 (d) in thermal equilibrium, the Peltier entropy per mole CO_3^{--} has been derived previously (Ref. (8), Eq. [14]). Denoting the partial pressures of the different species by the above-mentioned symbols h, c, etc., we have

$$\Delta S_P(\text{fuel}) = \Delta S_P^\circ(CO,CO_2) - R \ln \frac{c}{d^2} - RT \frac{\partial}{\partial T}\left(\ln \frac{c}{d^2} \right) \quad [10]$$

It is noted that the Peltier entropy of the mixed electrode reaction does not depend on the kinetically controlled relative contributions from the different electrode reactions. This is due to the assumption of a gas in thermal equilibrium, which implies that the gas phase composition at a total pressure P and a given C/H/O ratio is fixed by the equilibrium conditions

$$H_2 + CO_2 \rightarrow H_2O + CO, \text{ with } K_s = cw/hd \quad [11]$$

$$\frac{1}{4}[4H_2 + CO_2 \rightarrow CH_4 + 2H_2O], \text{ with } K_m^{1/4} = \frac{m^{1/4}w^{1/2}}{hd^{1/4}} \quad [12]$$

$$h + c + m + w + d = P \quad [13]$$

A method to calculate the various partial pressures at given P and T from tabulated values of K_s and K_m has been given earlier (9).

The value of the last term in [10] can be calculated on the basis of a mass balance applied to Eq. [11] and [12], using the relations involving the reaction enthalpies: $\partial \ln K_s/\partial T = \Delta H_s^\circ/RT^2$ and $\partial \ln K_m^{1/4}/\partial T = \Delta H_m^\circ/4RT^2$. The result can be written as

$$-RT \frac{\partial}{\partial T}\left(\ln \frac{c}{d^2} \right) = -\left(\frac{1}{c} + \frac{2}{d} \right) \frac{P}{T} \frac{\alpha_{22}\Delta H_s^\circ - \alpha_{12}\Delta H_m^\circ/4}{\alpha_{11}\alpha_{22} - \alpha_{12}^2} + \left(\frac{1}{2d} - \frac{1}{2P} \right) \frac{P}{T} \frac{\alpha_{12}\Delta H_s^\circ - \alpha_{11}\Delta H_m^\circ/4}{\alpha_{11}\alpha_{22} - \alpha_{12}^2} \quad [14]$$

where

$$\alpha_{11} = P(1/h + 1/c + 1/w + 1/d) \quad [15]$$

$$\alpha_{12} = P(1/h + \tfrac{1}{2}w + \tfrac{1}{4}d) \quad [16]$$

$$\alpha_{22} = P(1/h + 1/16m + 1/4w + 1/16d - 1/4P) \quad [17]$$

For fuels containing negligible amounts of CH_4 (high temperatures, low hydrogen contents), $\alpha_{22} \rightarrow \infty$, and [14] reduces to

$$-RT \frac{\partial}{\partial T}\left(\ln \frac{c}{d^2} \right) = -\frac{\Delta H_s^\circ}{T}\left(\frac{1}{c} + \frac{2}{d} \right) \Big/ \left(\frac{1}{h} + \frac{1}{d} + \frac{1}{w} + \frac{1}{d} \right) \quad [14a]$$

From the basic data given in Tables I and II, typical heat evolutions at the electrodes of a working molten carbonate cell have been calculated in Table III. It is observed that the heat evolution due to the Peltier effect exceeds the irreversible losses by more than an order of magnitude and equals the amount of heat produced by an overvoltage in the order of 1V. Furthermore, it is noted that about two-thirds of the heat evolved at the cathode is reabsorbed at the anode. Thus, the internal heat fluxes in the working cell are by far larger than would be estimated from a heat balance on the entire cell and rather large temperature gradients will be present in the electrolyte.

Table I. Equilibrium composition of fuel gas at 1 atm and 1000°K. Nominal composition 0.5 atm H_2 + 0.5 atm CO_2.

	H_2 (h)	CO (c)	CH_4 (m)	H_2O (w)	CO_2 (d)
Partial pressure (atm)	0.269	0.229	7.5×10^{-4}	0.230	0.271

The calculation is based on the thermodynamic data (9): K_S = 0.723; ΔH_S° = 34.8 kJ/mole; Eq. [11] and K_m = 0.404 atm$^{-1/2}$; $\Delta H_m^\circ/4$ = −47.7 kJ/mole; Eq. [12].

Table II. Peltier entropies at 1 atm and 1000°K

$\Delta S_P(O_2,CO_2)$	= −236 J/mole °K	Calculated from Eq. [2] in Ref. (8)
$\Delta S_P^\circ(CO,CO_2)$	= −129.5 J/mole °K	Calculated from Eq. [8] in Ref. (8)
ΔS_P(fuel)	= −167 J/mole °K	Calculated from Eq. [10]-[14]

The calculated values are based on $\Delta S_P^\circ(O_2,CO_2)$ = −217 J/mole °K (8).
Cathode gas = 0.14 atm O_2 + 0.28 atm CO + 0.58 atm N_2.
Anode gas = composition given in Table I.

Table III. Heat evolution in a working molten carbonate fuel cell at 100 mA/cm²

		Anode	Cathode	Electrolyte
$iT\Delta S_P/2F$	mW/cm²	−86.5	122.3	
$i\eta$	mW/cm²	5.0	5.0	5.0
dQ/dt	mW/cm²	−81.5	127.3	5.0

The values calculated are based on the data given in Tables I and II and the assumption of a polarization at cathode, anode, and electrolyte corresponding to 0.5 Ω · cm² each.

Verification of the Heat Effect

The heat effect predicted by Eq. [9] has been experimentally determined in the high temperature cell shown in Fig. 2. Details in the construction of the cell

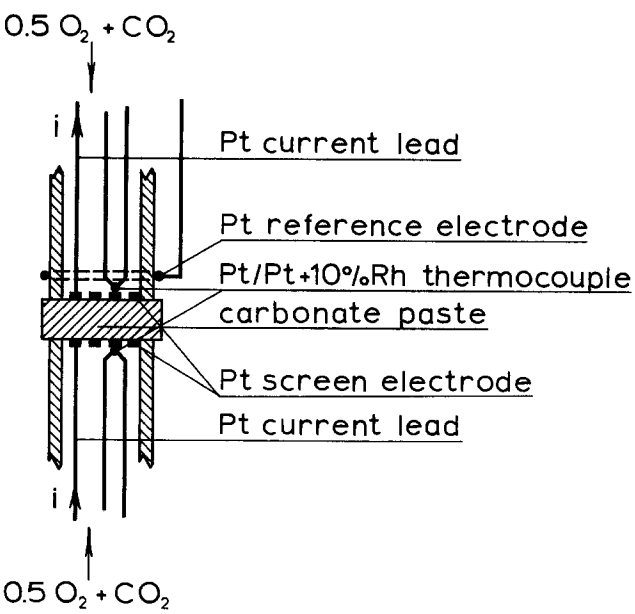


Fig. 2. Cell used for the investigation of heat effect

and the preparation of the carbonate paste electrolyte are given elsewhere (10). The Pt screen electrodes were contacted by Pt/Pt + 10% Rh thermocouples and the temperature rise, ΔT, at each electrode was determined as a function of the current. For practical reasons a mixture of 0.5 vol O_2 + 1 vol CO_2 was applied to both electrodes giving the electrode reactions

$$\tfrac{1}{2}\,O_2 + CO_2 + 2e^- \underset{\text{anode}}{\overset{\text{cathode}}{\rightleftharpoons}} CO_3^{--} \qquad [18]$$

For not-too-large current densities, the steady-state overvoltage may be expressed in terms of an electrode resistance, and the temperature rise, being proportional to the heat evolution, can, according to Eq. [9], be written as

$$\Delta T = k\frac{dQ}{dt} = k\left[\, T\frac{\Delta S_P}{n\mathbf{F}} + i(Z_o + R) \,\right] i \qquad [19]$$

where k (cm^2 °K/W) is a constant inversely proportional to the local heat conduction, Z_o is the d-c impedance due to the electrode reaction (diffusion, charge transfer etc.), and R is the electrolyte resistance. For symmetry reasons the joule heating will be distributed almost equally between the electrodes and R is thus expected to be approximately half the total anode-cathode electrolyte resistance.

Figures 3 and 4 show the experimental results plotted as $\Delta T/i$ *vs.* i and, as predicted by Eq. [19], a linear relationship is obtained. It is noted that whereas the cathode reaction causes a temperature rise, the entropy absorption in the anodic direction cools the electrode. From the standard Peltier entropy, ΔS_P^o, given in part I of this paper, we obtain

$$\Delta S_P(O_2,CO_2) = \Delta S_P^o(O_2,CO_2) + R \ln p_{O_2}^{1/2} p_{CO_2} = -225 \text{ J/mole°K}$$

The polarization resistances were determined from steady-state current-voltage curves measured against the reference electrode and corrected for IR drops. The total electrolyte resistance was measured by a.c. at 10 kHz. The results were

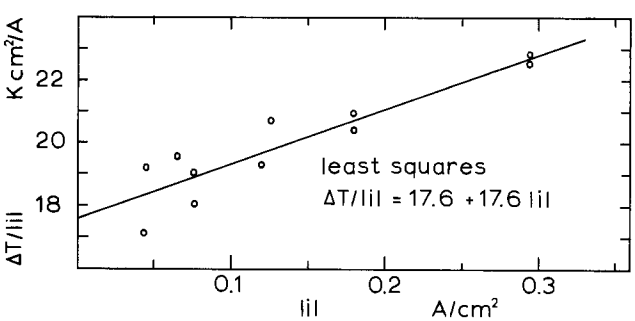


Fig. 3. $\Delta T/|i|$ *vs.* $|i|$ for the cathodic reaction 1/2 O_2 + CO_2 + $2e^- \rightarrow CO_3^{--}$.

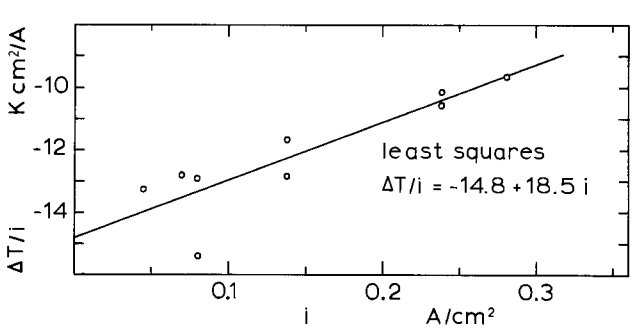


Fig. 4. $\Delta T/i$ *vs.* i for the anodic reaction $CO_3^{--} \rightarrow$ 1/2 O_2 + CO_2 + $2e^-$.

cathode	$Z_o = 0.50\ \Omega \cdot cm^2$
anode	$Z_o = 0.55\ \Omega \cdot cm^2$
electrolyte	$2R = 1.60\ \Omega \cdot cm^2$

Inserting these values and $T = 1006$°K in Eq. [19], we obtain the theoretical temperature rise

$$\text{cathode} \quad \Delta T = ik(-1.17 + 1.30i);\ i < 0$$

$$\text{anode} \quad \Delta T = ik(-1.17 + 1.35i);\ i > 0$$

Comparing these expressions with the experimental equations in Fig. 3 and 4, good agreement is obtained with the values $k = 15$°K cm^2/W and 13°K cm^2/W for cathode and anode, respectively. The somewhat differing k values obtained are probably due to the vertical position of the cell, involving some asymmetry in heat conduction.

It should be noted that the large temperature effect of 35°K cm^2/A observed here holds for a small cell with 0.8 cm^2 electrode area and 0.4 cm electrolyte thickness. As this cell has severe heat losses through the electrode leads and thermocouples, a larger effect should be expected for practical cells.

Thermal Corrosion

In gas diffusion electrodes, the electrode structure is obviously one of the most important properties. It is known that high temperature fuel cell electrodes, after a certain period of time, obtain a porosity which is essentially determined by the operating conditions and does not depend on the initial electrode structure (3, 10). This very feature of high temperature systems reflects the fact that in the time scale relevant for practical applications, months or even years, the solubility and thus the mobility of electrode material is not negligible. The structural regenerating process, counteracting electrode sintering, has been illustrated by an Ag wire immersion experiment in liquid carbonate (3). It was observed that Ag was removed from the wire below the electrolyte level and redeposited in a porous form at the meniscus. As is shown below, this process, can be explained in terms of thermal corrosion, rather than by gradients in oxygen partial pressure as originally suggested.

The equilibrium

$$2Ag + \tfrac{1}{2}\,O_2 + CO_2 \rightarrow Ag_2CO_3 \text{ (in } Me_2CO_3) \qquad [20]$$

has been studied as a function of temperature for a series of carbonate melts (3). In most cases, the solubility of Ag was found to decrease with increasing temperature. Thus, a thermal process where Ag is dissolved at low temperature and redeposited at higher temperature might be expected to proceed spontaneously. This will indeed be the case as long as there is no electronic contact between the metal at the two temperatures. However, in the immersed wire experiment the contact is established and the redistribution process may be the electrochemical reaction

$$Ag \rightarrow Ag^+ + e^- \qquad [21]$$

The temperature dependence of [21] can be determined from the Peltier entropy which may be estimated as

$$\Delta S_P(Ag^+) = S_{Ag} - S_{Ag^+}{}^* - S_{e^-}{}^* \simeq \tfrac{1}{2}(\Delta S_{Ag_2CO_3} - \Delta S_P(O_2,CO_2)) \qquad [22]$$

where $\Delta S_P(O_2,CO_2)$ is the Peltier entropy of the oxygen electrode given by Eq. [3] in part I of this paper (8). $\Delta S_{Ag_2CO_3}$ (*cf.* [20]) is estimated from the temperature dependence of the solubility equilibrium and we obtain a value in the order of 100 J/mole°K for the Peltier entropy of reaction [21] in equilibrium with $p_{O_2} = p_{CO_2} = 1$ atm. As this entropy difference is positive, in contrast to the entropy difference for the chemical dissolution of Ag [20], a transport of Ag from

high to low temperature through the electrochemical mechanism involves a simultaneous transfer of entropy from high to low temperature and the process is spontaneous. Thus, the effect of the electronic contact is a reversing of the thermal corrosion process. Aten *et al.* (11) observed and interpreted similar phenomena for silver and copper in 1925 and in aqueous solutions also this kind of process has been observed for Ag electrodes and explained in terms of a thermal emf (12), which is equivalent to the entropy argument

In the immersion wire experiment as well as in single laboratory fuel cells, the electrode leads will act as heat sinks and create a temperature gradient at the electrolyte surface. Thus, the thermal process will remove electrode material dipping into the electrolyte and deposit material at the gas side of the electrode. This continuous renewal of the electrode surface may be, at least partially, responsible for the stability of high temperature porous electrodes (3, 10). In a fuel cell battery the effect of the thermal redistribution is difficult to predict since the temperature gradients depend on the position inside the battery. However, the existence of this process means that temperature gradients should be taken into account in the construction of high temperature systems in order to ensure long-term stability. Temperature gradients along the electrodes should be reduced as far as possible. Since Peltier entropies are dependent on the various partial pressures, large fuel and oxygen conversions per single pass may entail these gradients and thus active parts of the electrodes may be removed completely and redeposited elsewhere. An extreme case has been observed by Trachtenberg (2). Furthermore, cathodes should be kept under constant load in order to reduce the equilibrium concentration of ions from the electrodes in the electrolyte.

Finally, it should be mentioned that temperature gradients may contribute to the formation of the electrolyte films in porous gas electrodes through the Marangoni effect, *i.e.*, flow due to gradients in surface tension. Lightfoot (1) has treated this effect quantitatively and concludes that temperature gradients as low as a few tenths of a degree per centimeter may produce a 1 μm film, which is the order of magnitude observed in practice (13, 14).

Acknowledgments

The authors are indebted to Mr. H. J. J. van Ballegoy who carried out the experimental verification of the heat effect. The many valuable discussions with B. K. Andersen and other colleagues are greatly appreciated. This work has been supported by Statens Teknisk Videnskabelige Fond.

Manuscript submitted May 27, 1976; revised manuscript received Oct. 8, 1976. This was Paper 171 presented at the New York, New York, Meeting of the Society, May 4-9, 1969.

Any discussion of this paper will appear in a Discussion Section to be published in the December 1977 JOURNAL. All discussions for the December 1977 Discussion Section should be submitted by Aug. 1, 1977.

LIST OF SYMBOLS

$\mathbf{F}$	Faraday constant (C/mole)
H	enthalpy (J/mole)
i	current (A)
K	equilibrium constant
n	number of electrons
P	pressure
p	partial pressure (atm)
q	electric charge (C)
Q	heat (J)
S	entropy (J/mole °K)
ΔS_P	Peltier entropy (J/mole °K)
S'	entropy flow (J/mole °K)
S''	irreversible entropy production (J/mole °K)
S^*	entropy of transported species (J/mole °K)
$\hat{S}$	excess entropy of transported species (J/mole °K)
t	time (sec)
t_i	transport number
T	temperature (°K)
η	overvoltage (V)
ϕ	electric potential (V)
$\underline{\mu}$	chemical potential (J/mole)
μ	electrochemical potential (J/mole)

REFERENCES

1. E. N. Lightfoot and V. Ludvikson, *This Journal* **113**, 1325 (1966).
2. I. Trachtenberg, in "Hydrocarbon Fuel Cell Technology," B. S. Baker, Editor, Academic Press, New York (1965).
3. M. Schenke and G. H. J. Broers, "Power Sources Symposium, Brighton, 1966," D. H. Collins, Editor, Pergamon Press, Oxford (1967).
4. A. Klemm, in "Molten Salt Chemistry," M. Blander, Editor, Interscience, New York (1964).
5. J. N. Agar, in "Advances in Electrochemistry and Electrochemical Engineering," Vol. 3, P. Delahay, Editor, Interscience, New York (1963).
6. J. N. Brønsted, *Phil. Mag. Ser. 7*, **29**, 449 (1940).
7. J. N. Brønsted, *J. Phys. Chem.*, **44**, 699 (1940).
8. T. Jacobsen and G. H. J. Broers, *This Journal*, **124**, 207 (1977).
9. G. H. J. Broers and B. W. Treijtel, *Adv. Energy Conver.*, **5**, 365 (1965).
10. G. H. J. Broers and M. Schenke, in "Hydrocarbon Fuel Cell Technology," B. S. Baker, Editor, Academic Press, New York (1965).
11. A. H. W. Aten, H. J. Hertog, and L. Westenberg, *Trans. Electrochem. Soc.*, **47**, 265 (1925).
12. R. J. Roethlein, *This Journal*, **119**, 1427 (1972).
13. R. H. Muller, *ibid.*, **113**, 943 (1966).
14. G. H. J. Broers, Proceedings of the International Symposium on Fuel Cells, Dresden, DDR (1967).

Semiconductor Electrodes

X. Photoelectrochemical Behavior of Several Polycrystalline Metal Oxide Electrodes in Aqueous Solutions

Kenneth L. Hardee* and Allen J. Bard**

Department of Chemistry, The University of Texas at Austin, Austin, Texas 78712

ABSTRACT

An investigation was made of the photoelectrochemical properties of several polycrystalline metal oxide electrodes prepared by chemical vapor deposition, direct oxidation of the metal, or heating of suitable metal salt solutions. Further data are given on the behavior of the previously discussed TiO_2 and Fe_2O_3 electrodes including tunneling effects and the operation of the Fe_2O_3 in a solar cell. Other n-type materials studied were V_2O_5, WO_3, and PbO. WO_3 and PbO showed good anodic photocurrents but only WO_3 appeared stable. Bi_2O_3 showed both n- and p-type photocurrents, but had a poor stability. CuO produced a good cathodic photocurrent (indicating p-type behavior) with a photoresponse at wavelengths of 700 nm and below. Two other oxides, Cr_2O_3 and CoO, exhibited small p-type photoeffects.

Recent research on photosensitized reactions at semiconductor electrodes, aimed toward the photodecomposition of water and the construction of photogalvanic cells for use in solar energy conversion devices, has prompted investigations of new electrode materials. Suitable electrodes should be easily prepared and inexpensive, show stable behavior in use over long time periods of operation, and have a small bandgap (E_g) to allow efficient utilization of the solar energy spectrum. Most investigations to date have centered upon the more familiar semiconductor compounds, *e.g.*, Si, GaAs, GaP, ZnO, CdS, and TiO_2, usually in the form of single crystals. Stable electrodes, such as TiO_2, are large bandgap materials ($E_g \geq 3$ eV), while materials with smaller gaps, *e.g.*, Si and CdS, tend to be unstable. Moreover, the high cost and difficulty of obtaining single crystals of other compounds have limited investigations of other materials. Recently, polycrystalline semiconductors, prepared, for example, by chemical vapor deposition, have been shown to be suitable electrode materials and to behave similarly to single crystal electrodes (1, 2). The use of polycrystalline materials allows investigation of a wider range of compounds and is also of interest in any practical utilization of semiconductor electrodes. We describe here the photoelectrochemical behavior of a number of semiconducting oxides prepared in polycrystalline form. Further details are given on the nature and behavior of polycrystalline TiO_2 and Fe_2O_3, which we discussed previously (1, 2). Other oxides that show photoelectrochemical effects are Bi_2O_3, WO_3, PbO_2, V_2O_5, and CuO. Several other polycrystalline oxides, *i.e.*, CdO, MnO_2, and SrO exhibited little or no photoeffects.

Experimental

Several different methods of preparation of the polycrystalline electrodes were employed (Table I). The chemical vapor deposition (CVD) (TiO_2, Fe_2O_3, V_2O_5, WO_3, CdO, Cr_2O_3, MnO_2) followed the procedure outlined previously (1, 2). The corresponding acetylacetonate served as the vapor source, except for W and Ti where WCl_6 and $Ti(O_2C_3H_7)_4$ were used. Pt-foil substrates were employed for all electrodes. Oxides could also be prepared by direct oxidation of the metal. Thus Bi_2O_3 and lead oxide electrodes were prepared by melting the metal and allowing a surface film to form by air oxidation, at *ca.* 450°C. Finally, oxide films were formed by painting a suitable salt solution on Pt foil and then heating in a flame. Electrodes of WO_3, CuO, manganese oxide, CdO, Cr_2O_3, and SrO were produced in this manner. All Pt substrate electrodes had a copper wire attached to the back of the Pt foil with indium solder and were then sealed in a glass tube with Apiezon wax or silicone rubber (Dow Corning).

The single crystal V_2O_5 was generously donated by Professor A. B. Scott of Oregon State University. A 0.3 cm^2 piece was used with two Ag paint (Ernest Fullam, Incorporated, Schenectady, New York) contacts and was mounted in silicone rubber. The current-voltage response between the two contacts indicated ohmic behavior. The hematite was obtained from David New-Minerals (Stevensville, Montana). Contact was made to an approximately 0.5-1 cm thick sample with Ag paint.

X-ray diffraction was done on a General Electric XRD-6 diffractometer. A Joel, Incorporated (Tokyo, Japan) scanning electron microscope was used for examining the electrode surfaces. All electrochemical measurements were performed with buffered Na_2SO_4

Table I. Preparation and properties of materials used in this study

Substance	Preparation*	Type	E_g**	V_{fb}***	Photocurrent†
TiO_2	CVD	n	3.0	0 5 (*i*)	Good, stable
Fe_2O_3	CVD	n	2 2	−0.1 (*ii*)	Good, stable
	SE	n	2 2	−0.1 (*ii*)	
V_2O_5	CVD	n	2.75	+0.54 (*i*)	Poor, unstable
	XTAL	n	2.75	+ 0 80 (*i*)	
WO_3	CVD	n	2.6	−0.4 (*ii*)	Good, stable
	SE	n	2.6	−0.2 (*ii*)	Good, stable
	DOM	n	2.6	−0.25 (*ii*)	Good, unstable
Bi_2O_3	DOM	n	2.8	−0.08 (*ii*)	Good, unstable
		p	2.8		Fair, unstable
PbO	DOM	n	2.8	−0.3 (*ii*)	Good, unstable
CuO	SE	p	1.7	+0.3 (*i*)	Good, unstable
Cr_2O_3	CVD	p	unknown	—	Poor, unstable
	SE				
CoO	CVD	p	unknown	—	Poor, unstable
	SE				
CdO	CVD	—	—	—	None
	SE				
MnO_2	CVD	—	—	—	None
	SE				
SrO	SE	—	—	—	None

* CVD = chemical vapor deposition, SE = evaporation of solution on substrate, DOM = direct oxidation of metal.

** E_g is estimated from the wavelength of the onset of the photocurrent.

*** (*i*) pH of 7, value estimated from potential of onset of photocurrent; (*ii*) pH of 9 (V *vs.* SCE).

† Good, fair, and poor refer to relative magnitude of photocurrent.

* Electrochemical Society Student Member.

** Electrochemical Society Active Member.

Key words: photoelectrochemistry, solar cells, photovoltaic cells, semiconductors.

solutions. A simple H-cell with separate auxiliary and working compartments and with a Pyrex window was used. A saturated calomel (SCE) was the reference electrode. Electrochemical equipment consisted of a Princeton Applied Research (PAR) Model 173 potentiostat, a PAR Model 175 universal programmer, and a Houston Instruments (Austin, Texas) Model 2000 omnigraphic X-Y recorder. Illumination was done with either the full output of a 450-W xenon lamp (Oriel Corporation, Stamford, Connecticut) or the output of a Model 7240 grating monochromator (Oriel Corporation). Absolute light intensity measurements were made using an EG&G Model 550 Radiometer (EG&G, Incorporated, Salem, Massachusetts). The current *vs.* wavelength curves were corrected for intensity variations by normalizing the spectral output of the lamp-monochromator system to 470 nm and using the resulting values to correct the measured photocurrent curves, shown by dotted i-λ curves.

Results and Discussion

Titanium dioxide.—As reported earlier (1), the current (i) *vs.* potential (E) curves for a CVD TiO_2 electrode are quite similar to those of single crystal rutile. Typical i-E and i *vs.* wavelength (λ) curves for a CVD TiO_2 electrode are shown in Fig. 1. Examination of the CVD electrode surface with a scanning electron microscope (SEM) reveals a uniform, smooth surface of polycrystalline material (Fig. 2). There are no grain boundaries visible, but there are numerous cracks across the surface which range up to 1000Å wide. These cracks probably form during the high temperature treatment the electrode is subjected to during preparation. An edge view of the surface, accomplished by cutting the electrode and polishing the edge, reveals layers of oxide corresponding roughly to the different deposition (3-5 layers). The cracks are visible along the surface but none appear to penetrate directly to the substrate. From this edge view, the total thickness of the oxide layer was measured as about 40 μm.

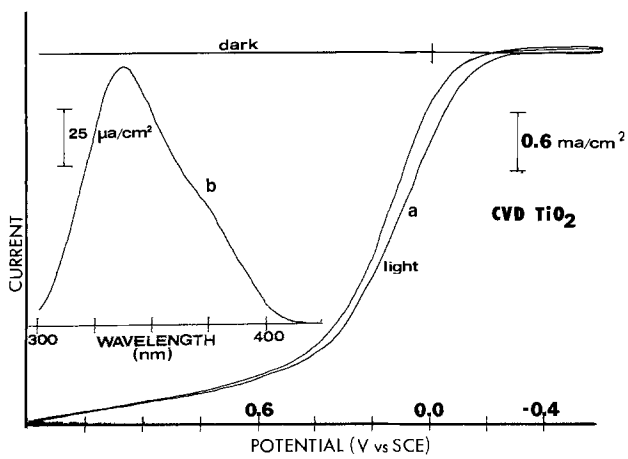


Fig. 1. (a) Current *vs.* potential curve for CVD TiO_2, 0.5M KCl, in dark and illuminated with Xe lamp. (b) Current *vs.* wavelength curve under same conditions, $E = +0.800$V *vs.* SCE.

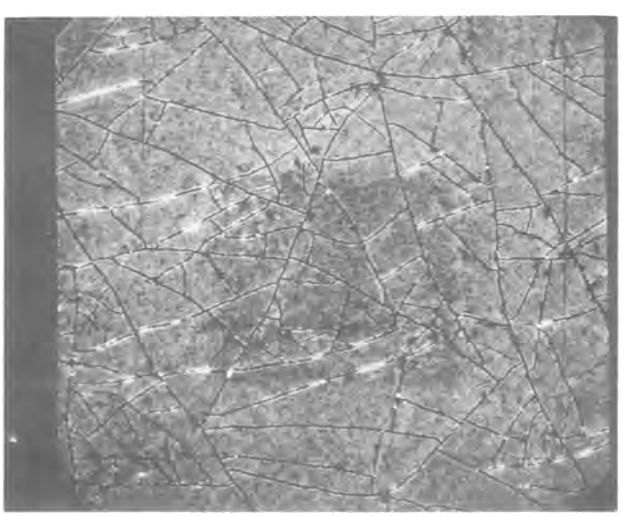


Fig. 2. Scanning electron micrograph of surface of CVD TiO_2. Magnification is 600×.

X-ray diffraction patterns of the CVD TiO_2 electrode were typical powder patterns indicating polycrystalline material primarily in the rutile form of TiO_2. A small percentage ($\leq$ 10%) of anatase was also present. X-ray diffraction of an electrode that only had one coat of oxide deposited at about 150°C, but which was not heated further, revealed a pattern that was totally anatase. This electrode showed only a very low photocurrent. Thus the high temperature treatment is necessary not only to prevent flaking between coats and allow thicker coats to be deposited, but also to convert the film into the photoresponsive rutile form of TiO_2.

The thickness of the film on the electrodes affects the shape and magnitude of the photocurrent *vs.* potential curve. In Fig. 3 are given curves for several CVD TiO_2 electrodes prepared with increasing relative thicknesses (by depositing successive coats). As the film becomes thicker, the shape of the curve becomes more typical of a single crystal n-type semiconductor, exhibiting a sharper current rise and a more well-defined plateau. The effect of thickness on curve shape might be explained by the increasing absorbance of light in the space charge region (3). Alternately, the extent of recombination of electrons and holes might decrease with thickness as a more homogeneous film forms. The current *vs.* wavelength curves were similar for all of the electrodes.

The quantum efficiency of the CVD TiO_2 electrode is quite high in the plateau region. Typically, the quantum efficiency is $\geq$ 60% at the wavelength of maximum response (*ca.* 335 nm). Variations in the quantum efficiency from one electrode to another can be ascribed to variations in the thickness, as described above, and in the percentage of rutile actually present in the electrode.

As reported previously (1), at potentials of about 2.0V *vs.* SCE in neutral solutions (and at more nega-

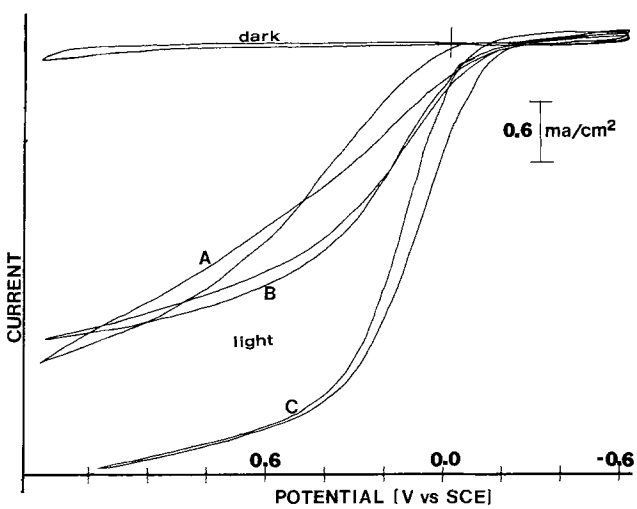


Fig. 3. Current *vs.* potential curves for CVD TiO_2 with varying relative thickness of film: (a) one 1 min coat, (b) two 2 min coats, (c) four 2 min coats.

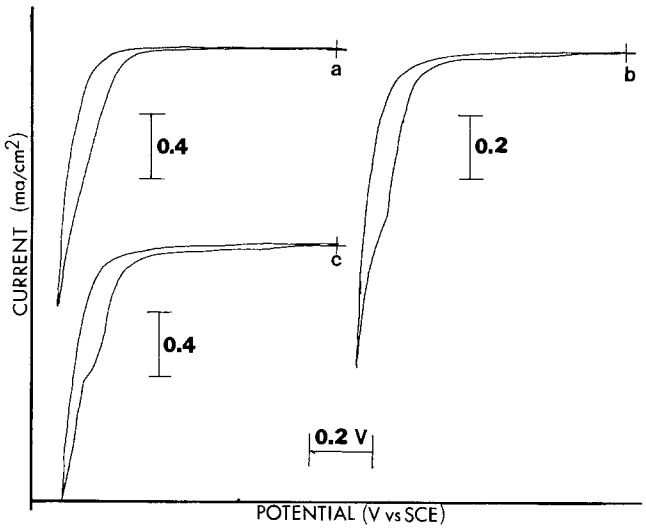


Fig. 4. Current *vs.* potential curves for CVD TiO_2 with addition of I^-: (a) 0.5M Na_2SO_4 (b) 0.5M Na_2SO_4 + 3.8 mM NaI, (c) 0.5M Na_2SO_4 + 7.5 mM NaI.

tive potentials at higher pH values), a large anodic current rise is observed in the dark for the CVD TiO_2 electrodes (Fig. 4a). Vigorous gas evolution is observed on the electrode surface. This current is attributed to tunneling of electrons from solution through the space charge region and into the conduction band. The narrow space charge region which is necessary for this tunneling is the result of the high doping level in the CVD TiO_2 electrode. For a single crystal electrode, appreciable anodic currents are usually not observed until potentials > 3V *vs.* SCE (16), depending, again, upon the doping level. The higher doping level in the CVD TiO_2 is the result of the more homogeneous reduction possible with thin films. The influence of a titanium substrate on the doping is apparently minimal, since similar effects are obtained with Pt substrates.

Addition of I^- to the solution produces a shoulder on the dark anodic current rise (Fig. 4b and c) with a height proportional to the concentration of I^-. The current is due to the oxidation of the I^-, and is similar to that observed on highly doped ZnO (6). The redox level of I^- lies nearer the flatband potential than the H_2O/O_2 level does. Thus the I^- is located where a narrower part of the space charge exists and electrons will tunnel at lower potentials, producing the observed curve. Addition of Br^- to the solution instead of I^- produced no noticeable addition to the tunneling current, since its level is near that of the H_2O/O_2 potential.

The behavior of CVD TiO_2 is fairly typical of an n-type semiconductor, with low anodic dark currents and well-defined anodic photocurrent plateaus. Because of the ease of doping of the thin films, they exhibit tunneling effects usually seen only at highly doped single crystal electrodes. With these properties, as well as its stability, CVD TiO_2 is useful as a comparison electrode in examining the behavior of the other oxide electrodes investigated in this study.

Iron oxide.—We have previously shown that iron oxide shows a good photoelectrochemical response at longer wavelengths in the visible region than that of TiO_2 (2). In that study we assumed, from the wavelength for the onset of the photocurrent, that the bandgap was about 2.2 eV, and from the procedure used in fabrication, that the oxide was Fe_2O_3. We have now examined the material with x-ray diffraction and a SEM. The results show that the film is primarily α-Fe_2O_3 (hematite), with a small amount of γ-Fe_2O_3

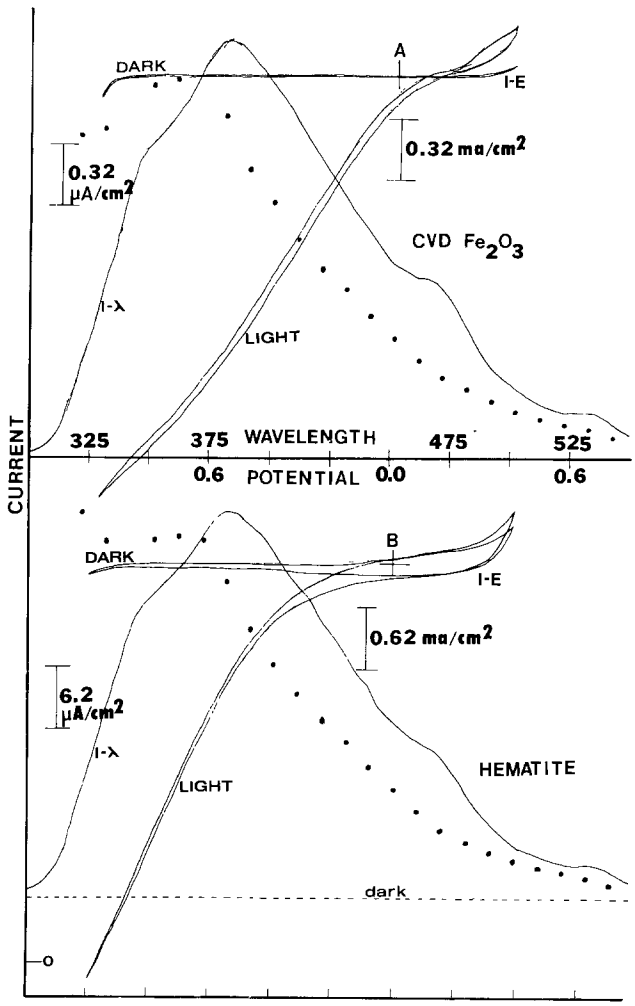


Fig. 5. Current *vs.* potential and current *vs.* wavelength curves for (a) CVD Fe_2O_3 in 0.25M Na_2SO_4, pH 9, (b) natural hematite in 0.5M Na_2SO_4. E = 0.600V *vs.* SCE for i-λ curves. Current scale for corrected i-λ curve is 2× uncorrected scale shown.

(*ca.* 20%) and γ-Fe_2O_3 (*ca.* 10%). The surface was very smooth with no visible cracks seen with the SEM for magnifications of 20,000×.

The i-E and i-λ curves for a CVD Fe_2O_3 electrode and a piece of natural hematite are shown in Fig. 5. The two i-λ curves are almost identical in shape, suggesting that the α-Fe_2O_3 form of the oxide is indeed the photoresponsive one.

Attempts made to deposit Fe_2O_3 on iron were unsuccessful, because the film flaked off during the high heat-treatment. Films on Pt which were not heated showed a very poor photoresponse, so the treatment is necessary to convert the film to α-Fe_2O_3 and make it n-type (7). Attempts at heating Fe_2O_3 on Fe in vacuum were also not successful, since the apparatus could not apparently achieve the required high temperatures (*ca.* 1200°-1400°C). Simply heating Fe plates until an oxide coating formed produced a slight photoresponse, but it was not nearly as large as that of CVD Fe_2O_3 on Pt, since, again, the formation of the required structure and doping levels could not be achieved without the oxide flaking off. CVD of the Fe_2O_3 was not necessary for good photoresponse, however. Electrodes made by heating a mineral oil slurry of the acetylacetonate or a solution of $FeCl_3$ in a flame on a Pt substrate showed good response. CVD does, however, allow better control of the reaction and thus more uniformity in the film, making it more useful for producing large area electrodes.

As with CVD TiO_2, the thickness of the film affects the shape and magnitude of the photocurrent *vs.* po-

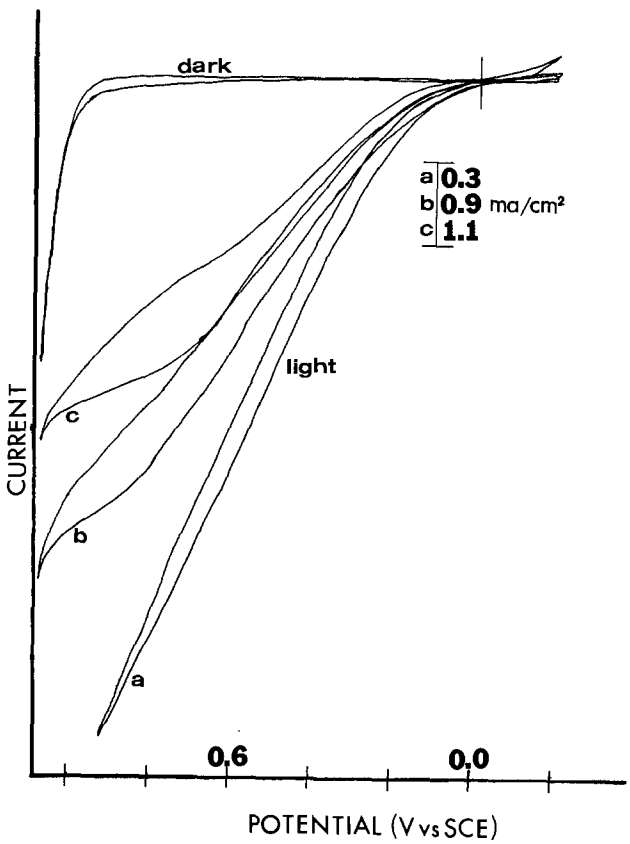


Fig. 6. Current vs. potential curves for CVD Fe_2O_3 of varying thicknesses in 0.25M Na_2SO_4 pH 9.2 solution: (a) 0.6 μm thick, (b) 1.7 μm thick, (c) 6.8 μm thick.

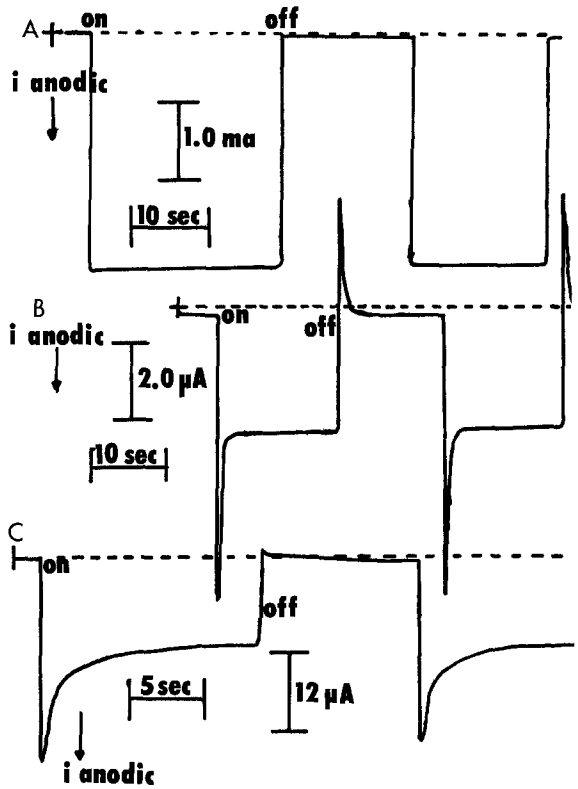


Fig. 7. Transient (*i-t*) curves in 0.25M Na_2SO_4 pH 9 for (a) CVD Fe_2O_3, white light, $E = 0.600$V; (b) CVD Fe_2O_3, monochromatic light, $\lambda = 375$ nm; (c) CVD TiO_2, $E = -0.300$V, $\lambda = 375$ nm.

tential curve (Fig. 6). The much lower anodic current observed on the return sweep is due to adherence of gas bubbles to the electrode surface. Tapping the electrode dislodges the bubbles and increases the current. Thicknesses were estimated by weighing the samples before and after deposition and assuming a density of 5.2 g/cm^3 for Fe_2O_3. For the thickest film twelve coats of Fe_2O_3 were chemically vapor deposited. (One coat equals approximately the amount required to cause no further changes in the interference color, *i.e.*, color becomes steady blue gray). As the film becomes thicker, a plateau region appears, but it never becomes as sharp as that for TiO_2. This indicates a greater recombination effect or lower absorptivity for the Fe_2O_3. Similar *i-E* curves were observed by depositing successive coats on the same electrode and making photocurrent measurements between coats.

The efficiency for the CVD Fe_2O_3 electrode depends, as does that for TiO_2, on the potential and wavelength. Photocurrent densities of the order of 6 mA/cm^2 have been obtained with Xe white light, which is comparable to that for TiO_2 with the same lamp. However, since Fe_2O_3 responds over a wider wavelength region, higher current densities would be expected. Thus the over-all quantum efficiency for Fe_2O_3 is somewhat lower than that of TiO_2. The transient photocurrent-time behavior found with Fe_2O_3 depends upon the light intensity and E and differs from that seen with CVD TiO_2 (Fig. 7). Under high illumination intensities (full Xe lamp output) no transient peaks are observed (curve a). When the intensity was decreased to about 1% of its level with a neutral density filter, a small anodic transient peak appears. At the very low light intensities of monochromatic light (curve b), sharp anodic transients were observed, with the steady photocurrent at these intensities being less than half of the peak value. When the light was turned off, a cathodic peak transient appeared. Similar behavior occurred at all wavelengths where Fe_2O_3 is responsive at similar light intensities (less than 1 mW/cm^2). Vigorous stirring of the solution had only a small effect on the steady current. Memming (8) observed a similar transient response at TiO_2. We have also observed this effect at CVD TiO_2; however, it occurs only on the rising portion of the *i-E* curve (Fig. 7c). On the plateau the transient for TiO_2 is like that for Fe_2O_3 in white light, with both intense white and weak monochromatic light. Notice that in the TiO_2 transient the cathodic peak occurring when the light is turned off is much smaller than the very small anodic one, while with Fe_2O_3 (Fig. 7b) the cathodic transient is of the order of one-half of the anodic one. As the potential is increased for TiO_2, the anodic transient remains well defined, disappearing on the plateau region.

This transient can be explained in terms of surface recombination or backreaction of the photogenerated species. Thus the oxygen (or hydroxyl radicals) which is produced by the photogenerated holes is thermodynamically reducible at potentials on the rising portion of the *i-E* curve. A backreaction between these and any electrons at the surface produces a backreaction [which is equivalent to a surface electron-hole recombination (3)] and a cathodic current component. This component decreases as the potential is made more positive, as expected. The effect of light intensity suggests that the extent of the backreaction is rather constant and independent of the intensity level, *e.g.*, reaching its maximum level when the surface is saturated with oxidized species. Thus, at high light intensities these transients are not observed. The results also suggest that this backreaction is more important for Fe_2O_3 than for TiO_2. The existence of this backreaction cathodic current can also be demonstrated by the following experiment. If the initial potential of a Fe_2O_3 electrode in the dark is set at $+0.80$V and scanned in a negative direction, a small cathodic current is observed at high sensitivity. Illuminating the electrode briefly and then scanning shows an increase

in this cathodic current due to the oxygen produced. Thus the quantum efficiency for photo-oxidation depends upon the light intensity, being smaller at lower intensities and giving anomalously low results for the monochromatic light. The effect of the backreaction is negligible, however, at the higher white (Xe) light intensities, since the transients are not observed under these conditions.

As with CVD TiO_2, Fe_2O_3 shows a large anodic current rise and gas evolution in the dark at potentials greater than about +1.2V. This probably represents tunneling of electrons into the conduction band. However, addition of I^- and $Fe(CN)_6^{4-}$ produced markedly different results at Fe_2O_3 than at TiO_2. The cyclic voltammetric curves for Fe_2O_3 and Pt electrodes of similar area with these species are shown in Fig. 8. For iodide oxidation E_{pa} at Fe_2O_3 is 0.417V, with a peak separation of 0.142V (compared to E_{pa} = 0.417V and ΔE_p of 0.118V at Pt). From simple area considerations, this anodic current for I^- oxidation at Fe_2O_3 cannot be due to exposed Pt under the Fe_2O_3. Neither does the SEM picture show cracks in the film. The curve for $Fe(CN)_6^{-4}$ is markedly different between Pt and Fe_2O_3. These results can be explained by a combination of conduction band and tunneling mechanisms. From the photocurrent *vs.* potential curves, the onset of photocurrent gives an estimate of the flatband potential. For Fe_2O_3 the flatband potential lies about 0.5V positive of that of TiO_2. This implies that the conduction band of Fe_2O_3 is 0.5 eV lower than that of TiO_2. Since the $E^{o'}$s for I^-/I_2 and $Fe(CN)_6^{-4}/Fe(CN)_6^{-3}$ are +0.54 and +0.35V *vs.* NHE, respectively, the redox levels of these couples must lie in the vicinity of the conduction band of Fe_2O_3. The near reversible behavior of the I^-/I_2 couple indicates that the overlap with the conduction band is quite good. The anodic current could be either tunneling or normal electron transfer at the conduction band edge. The $Fe(CN)_6^{-4}/Fe(CN)_6^{-3}$ curve appears irreversible with the anodic wave being almost a plateau. The cathodic wave is shifted in a negative direction but has a more diffusion-controlled shape. If the distribution functions of the $Fe(CN)_6^{-4}/Fe(CN)_6^{-3}$ couple are widely separated, such that $Fe(CN)_6^{-4}$ does not overlap well with the conduction band of Fe_2O_3, then the oxidation would proceed by tunneling and the reduction by a normal conduction band mechanism. The anodic wave is similar to that seen by Pettinger, Schoppel, and Gerischer (6) for Fe^{+2} at highly doped ZnO, which was interpreted as due to tunneling currents. Thus the Fe_2O_3 electrode must be highly doped, since it shows large anodic current rise in the dark, accompanied by gas evolution. The difference in behavior between Fe_2O_3 and TiO_2 can be ascribed to the higher lying conduction band in TiO_2, resulting in a poorer overlap with both the I^-/I_2 and $Fe(CN)_6^{-3}/Fe(CN)_6^{-4}$ distribution functions.

Fe_2O_3 solar cell.—A large (*ca.* 10 cm^2 area) Fe_2O_3 electrode was fabricated and operated in a solar cell arrangement with a fuel cell-air cathode similar to that of Laser and Bard for TiO_2 (4). In such a cell, oxygen is photogenerated at the Fe_2O_3 and is reduced at the fuel cell cathode, so that the net effect is conversion of light to electrical energy. Figure 9a gives the response curves (current, voltage, and power) for a typical cell with 1*M* NaOH electrolyte and irradiation with the Xe lamp. The potentiostatic *i-E* curves for this cell in the dark and under illumination are shown in Fig. 10. Maximum response of the electrode was achieved by focusing the light onto about 4 cm^2 of the electrode. The corresponding curves for operation in direct, unfocused sunlight are given in Fig. 11. If the sunlight was focused onto 1 cm^2 with a 10.5 cm diameter lens, currents of at least 8 mA could be achieved through a 1Ω load resistor. Vigorous gas evolution was observed from the illuminated spot. This Fe_2O_3 solar cell operated for more than 6 hr in unfocused sunlight and over 2 hr with the Xe lamp with no deterioration in response. Because the flatband potential of the Fe_2O_3 is rather positive, the output voltage and power of this cell are rather low. The current capabilities in the sunlight are quite good and suggest that it would be useful for solar decomposition of water in conjunction with a suitable p-type cathode.

The Fe_2O_3 solar cell was also operated using the I^-/I_2 reaction at a *p*H of about 9 with Xe lamp illumination (Fig. 9b). Initially no I_2 was present in the solution. After operation for a short time through a 1Ω load, the solution became yellow, indicating the production of I_2. The Fe_2O_3 electrode was very near

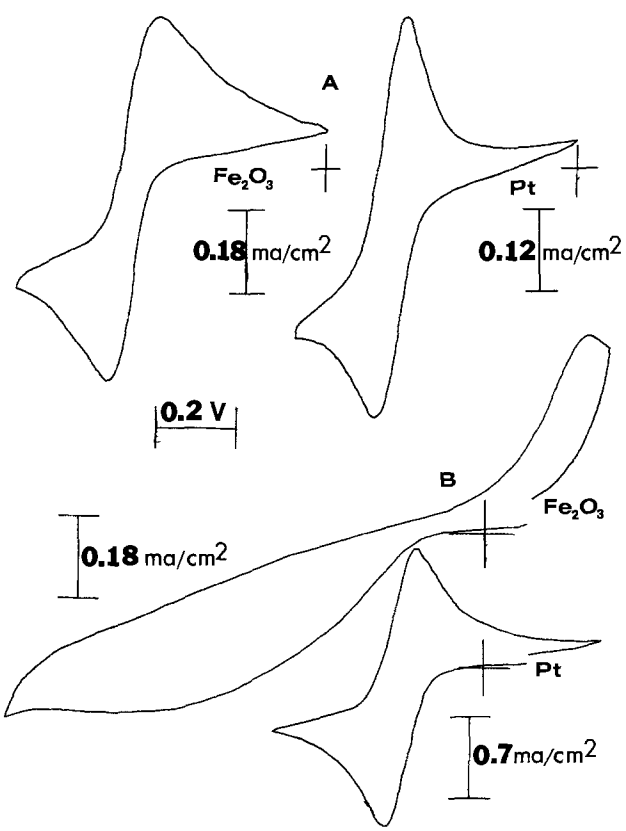


Fig. 8. (a) Cyclic voltammogram for CVD Fe_2O_3 and Pt in 0.5M Na_2SO_4 with 3.8 mM NaI. (b) Cyclic voltammogram for CVD Fe_2O_3 and Pt in 0.5M Na_2SO_4 with 7.5 mM $K_4Fe(CN)_6$.

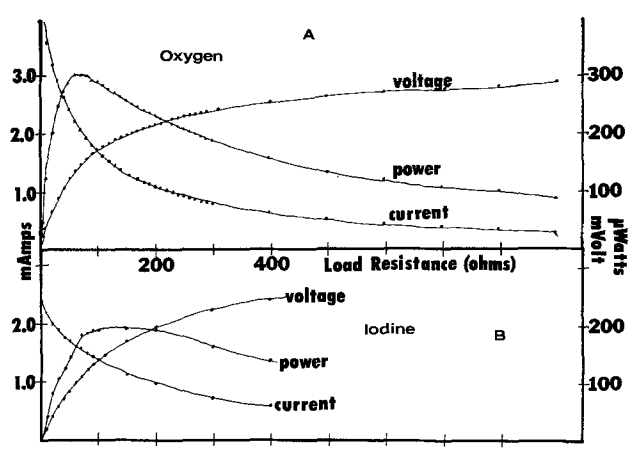


Fig. 9. Current, power, and voltage vs. load resistance for Fe_2O_3 solar cell. Xe lamp. (a) 1M NaOH, oxygen saturated; (b) 0.25M Na_2SO_4, *p*H 9, 33 mM NaI.

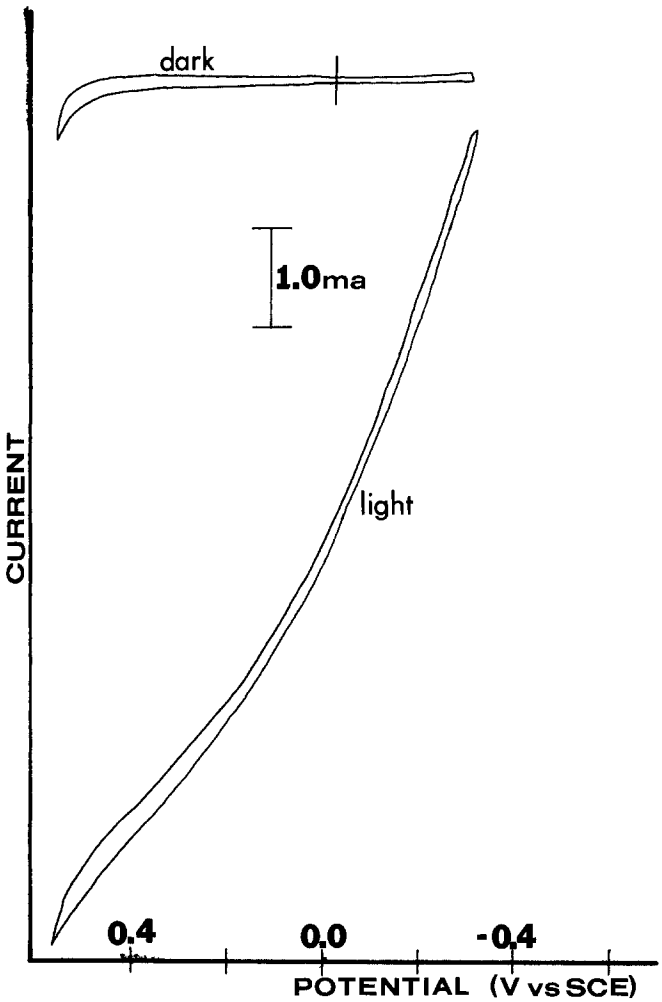


Fig. 10. Current *vs.* potential for Fe_2O_3 solar cell electrode in 1M NaOH.

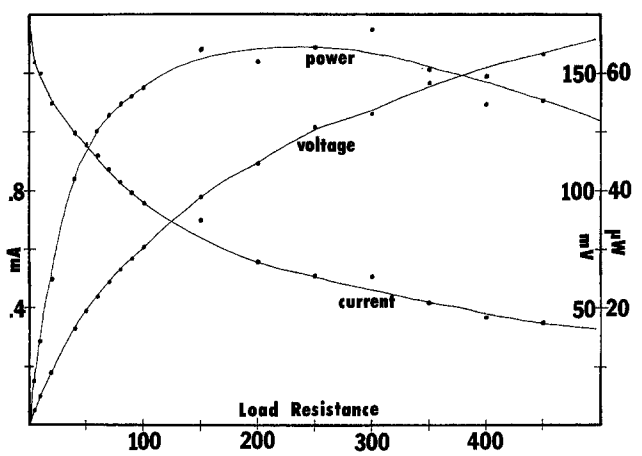


Fig. 11. Current, power, and voltage *vs.* load resistance for Fe_2O_3 solar cell, in 1M NaOH, oxygen saturated, direct sunlight.

the window, so the absorption of light by the I_2 was minimal. Prolonged bubbling of N_2 gas through the cell produced only a small decrease in the current. In contrast, during the operation of the cell without the I^-/I_2 couple, N_2 caused the current to decay ten times as fast, with the current finally approaching zero. The current was restored by bubbling O_2. Thus, the over-all solar cell reaction involves I^- oxidation at the Fe_2O_3 and I_2 reduction at the cathode. The rapid production of I_2 and the over-all effect on cell operation with I^- present indicate that the efficiency for photocatalytic generation of I_2 is relatively high, as it also is at TiO_2 (5). Thus Fe_2O_3 should work well and offer the advantage of longer wavelengths when used as an electrode for photoelectrosynthesis (5).

Bismuth oxide.—Photocurrents with anodic gas evolution were also observed at bismuth oxide electrodes prepared by heating bismuth metal; attempts at producing the oxide by CVD using $BiCl_3$ were unsuccessful. Typical *i-E* and *i-λ* curves in *p*H 8, Na_2SO_4 solution, with and without illumination, are shown in Fig. 12. There is a very low anodic and cathodic dark current (<0.1 $\mu A/cm^2$), although on the initial scan with a new electrode some anodic current was observed (dotted line), probably representing further oxidation of the surface. This current disappeared on subsequent scans. Scanning first in the dark to −0.4V *vs.* SCE did not result in any increase in the anodic dark current. With illumination both anodic and cathodic photocurrents are observed. The anodic photocurrent begins at approximately the same potentials as with Fe_2O_3 and exhibits a similar shape. Because of the method of preparation, the oxide film thickness could not be controlled easily, so that the effect of thickness on the *i-E* curve shape was not determined. Heating the sample longer (45 min *vs.* 2 min) produced lower photocurrents, but similar shapes. When the potential was held at +0.60V, gas evolution was observed during illumination. The photocurrent slowly decayed with time, unlike the behavior at TiO_2 or Fe_2O_3. After 1 hr of illumination, the photocurrent had decayed to about 0.4 its original value.

The maximum anodic photocurrent densities [*ca.* 1.6 mA/cm^2 with white (Xe) light] were obtained for Bi_2O_3 electrodes heated only a few minutes. Thus the over-all efficiency for photo-oxidation appears much less than that for TiO_2 or Fe_2O_3. After illumination, the electrode surface color had changed from an initial gray to yellow. The resistance of the electrode (measured with an ohmmeter between the surface and the contact) remained of the order of a few ohms. Dark currents before and after illumination also remained low.

Examination of the electrode surface by x-ray diffraction reveals the presence of two forms of Bi_2O_3, and α- and γ-forms. The relative amount of the two forms was dependent on the length of time the Bi sample was heated. After heating 3-5 min the $\alpha:\gamma$

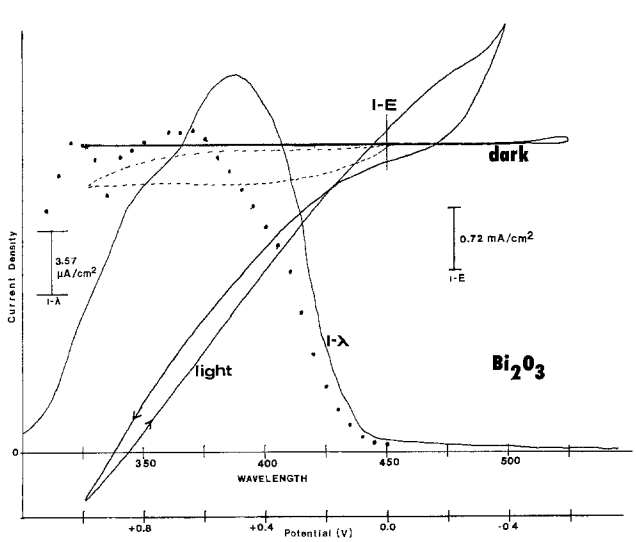


Fig. 12. Current *vs.* potential and current *vs.* wavelength curves for Bi_2O_3 in 0.25M Na_2SO_4 *p*H 8. $E = 0.80$V for *i-λ* curve. Current scale for corrected *i-λ* curve (···) is 2× value shown for uncorrected curve.

ratio was 60:40; after 45 min, the α:γ ratio was 90:10. Since these latter samples had less γ-Bi_2O_3 and showed lower photocurrents, the anodic photocurrent is probably attributable to the γ-Bi_2O_3.

X-ray examination of the electrode after the 1 hr illumination with subsequent decay in photocurrent and appearance of a yellow surface revealed no new forms of bismuth oxide. The x-ray data were not accurate enough to conclude whether or not the γ was converted to α-form, causing the photocurrent decay, or whether the yellow coating which could be a thin film of α-Bi_2O_3, was blocking the surface to further anodic photocurrents.

Unlike the other semiconductors, Bi_2O_3 exhibited both anodic and cathodic photocurrents. Bi_2O_3 has been reported to be an amphoteric semiconductor with n- and p-type behavior (12). It is not known how the presence of both the α- and γ-Bi_2O_3 affects the type of conductivity of the material. Figure 13 shows a cathodic i-E scan from 0.00V. The light was manually chopped during the course of the scan revealing the current to be a cathodic photocurrent, and not the result of the reduction of an anodically produced species (*e.g.*, O_2). The cathodic current is increased after an anodic scan with light, but the primary increase is a photosensitive one. The current becomes cathodic at about +0.2V and also responds to the chopping of the light. This cathodic photocurrent is probably due to the reduction of absorbed oxygen, while at more negative potentials reduction of the Bi_2O_3 also seems to occur. If the potential is held at −0.48V under illumination, a larger anodic dark current is seen similar to the dotted line in Fig. 12 upon a subsequent scan to positive potentials.

When the potential is scanned to −1.4V (Fig. 14), a large reduction peak at −1.05V *vs.* SCE is observed. Illumination shifts the peak to more positive potentials by about 0.1V and alters its shape slightly. The anodic dark current increased as a result of this scan and did not return to the low values initially present. The yellow color formed anodically under illumination disappeared after scanning over the reduction peak. It only reappeared with anodic scans and illumination, or in scans to large positive potentials, where oxygen evolution occurs, in the dark. The exact nature of this coating is, again, unknown as no x-ray peaks assignable to any other form of bismuth oxide were distinguishable.

The photocurrent *vs.* wavelength curves are given for both the anodic (Fig. 12b) and cathodic photocurrents (Fig. 13b). The onset of the photocurrent

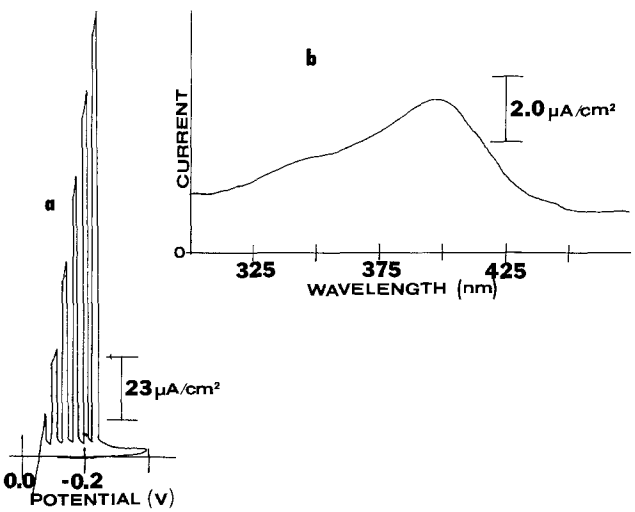


Fig. 13. (a) Current *vs.* potential curve for Bi_2O_3, chopped white light, in 0.25M Na_2SO_4, pH 9. (b) Current *vs.* wavelength for cathodic photocurrent; E = −0.475V *vs.* SCE.

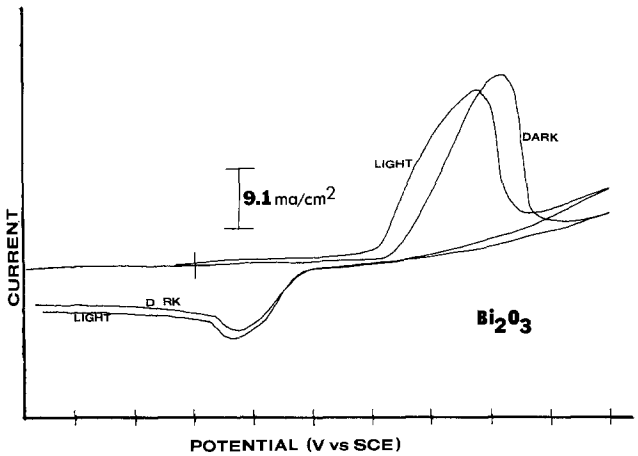


Fig. 14. Current *vs.* potential curve for Bi_2O_3 in 0.25M Na_2SO_4, pH 9.

occurs at about 450 nm (corresponding to an E_g of 2.8 eV) for both curves. The shape of the cathodic curve is not accurate because of the instability in the cathodic currents, and reduction of the oxide. The curve shape is similar to the anodic photocurrent curve, however. Note that the observed photoeffects cannot be ascribed to changes in photoconductivity of the Bi_2O_3 film, since the measured film resistance is low (a few ohms) and was not affected appreciably by illumination. The differences in semiconductor behavior between α- and γ-Bi_2O_3 are not known. The corrected anodic photocurrent *vs.* potential curve shows a steeper rise than those for Fe_2O_3 on TiO_2, possibly indicating a difference in transitions. Although Bi_2O_3 is not stable and has a bandgap only slightly smaller than that of TiO_2, it offers the interesting property of both n- and p-type behavior.

Tungsten oxide.—Hodes, Cahen, and Manassen (9) have observed photosensitized generation of oxygen at polycrystalline WO_3 electrodes prepared by oxidation of the metal or by decomposition of ammonium tungstate on glass. We have observed similar behavior at WO_3 electrodes made by heating W foil, thermally decomposing WCl_6 on Pt, and CVD of WO_3 on Pt. The i-E curves for all of these electrodes show quite similar behavior (Fig. 15). Unlike Hodes *et al.*, we found the anodic photocurrent at a W-foil electrode changed upon repetitive anodic scans with light. The photocurrent increased on each subsequent scan and two anodic peaks appeared at 0.2 and 0.4V *vs.* SCE. After these scans, the dark i-E scan showed a much higher anodic current (about one-half of the photocurrent) which showed the same peaks. This behavior could represent some further oxidation of the W foil or the oxide which, although nominally WO_3 by x-ray diffraction, is probably a nonstoichiometric form. This same behavior occurred for several different W-foil electrodes. The electrode surface was a deep blue before and after illumination. This behavior (appearance of peaks) was not observed for either of the WO_3-Pt electrodes. The photocurrent *vs.* time curves at E = 0.60V *vs.* SCE were quite stable for 10-20 min, with gas evolution observed. The photocurrent then gradually decayed. Examination of the surface revealed that parts of the electrode were bare Pt. Apparently the film had poor adhesion to the Pt. X-ray diffraction revealed the material on the Pt to be WO_3, but did not distinguish slight alterations in composition.

The differences in the oxide composition between the three types of electrodes are evident from the photocurrent *vs.* wavelengths curves (Fig. 15). All show an absorbency beginning at wavelengths corresponding to about 2.6 eV *vs.* the 2.8 eV reported as

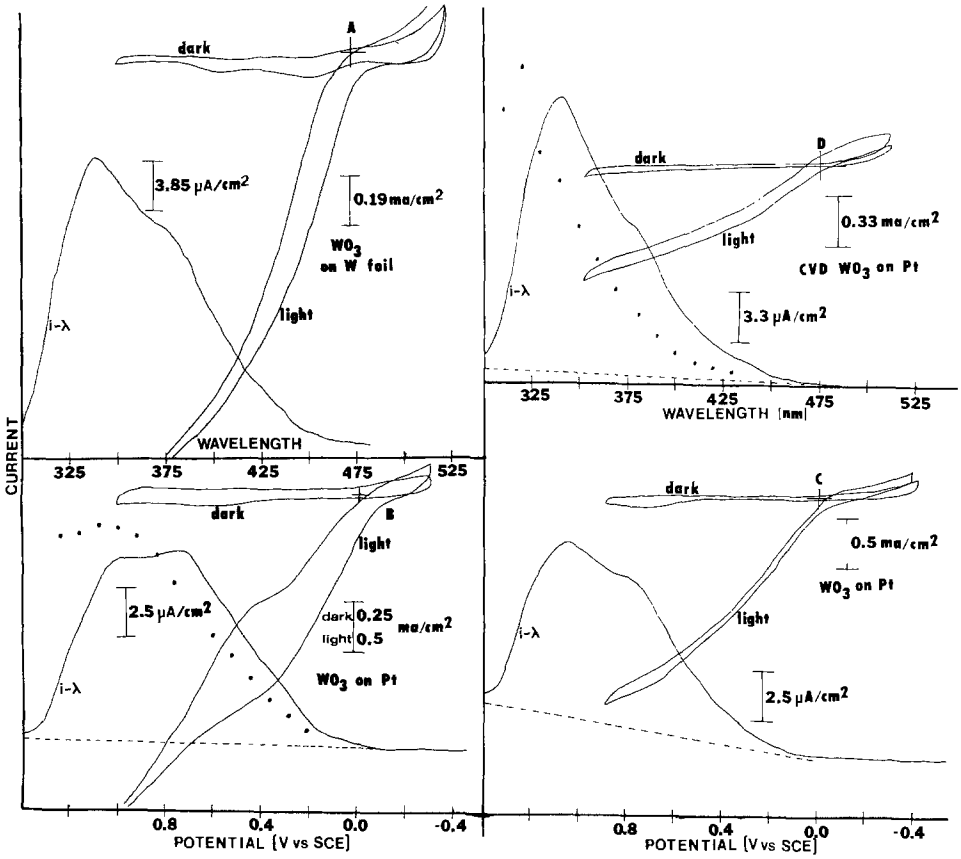


Fig. 15. Current vs. potential and current vs. wavelength curves for (a) WO_3 on W foil, 0.25M Na_2SO_4, pH 8; (b-c) WO_3 on Pt (formed from heating WCl_6 in EtOH solution), 0.25M Na_2SO_4, pH 9; (d) CVD WO_3 on Pt, 0.25M Na_2SO_4, pH 9. All i-λ curves at E = 0.600V vs. SCE. Corrected current scale is 2× uncorrected scale.

the bandgap of WO_3 (10). The shift in the peak location, similar to that observed by Hodes *et al.* (9), must represent structural or composition differences between the polycrystalline and single crystal materials.

Lead oxide.—Another metal oxide that has been found to exhibit photoelectrochemical effects is lead oxide; an i-E curve with a pH 9 0.25*M* Na_2SO_4 solution is shown in Fig. 16. The anodic dark current was usually low, although on some electrodes it was quite high initially but decreased to values shown in Fig. 16a or lower after illumination. With light a somewhat larger photocurrent was observed on the initial scan of a new electrode. The current then remained approximately constant on subsequent scans. The surface changed from an initial blue gray to a bronze brown color; this, coupled with the decrease in dark currents observed after illumination, indicates that at least part of the photocurrent contributes to further oxidation of the surface.

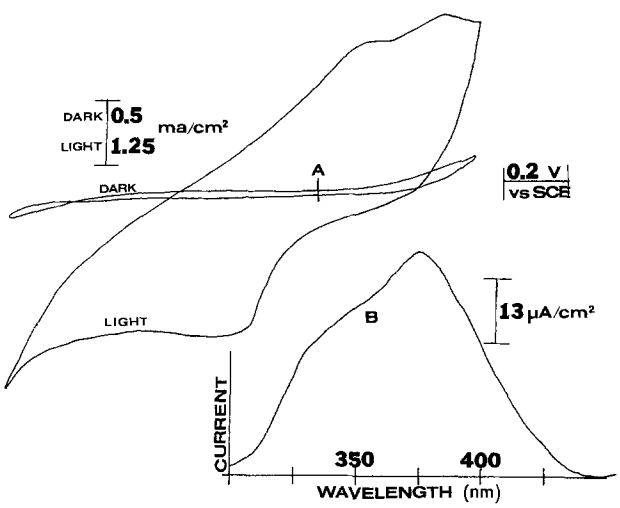


Fig. 16. Current vs. potential and current vs. wavelength curves for lead oxide in 0.25M Na_2SO_4, pH 9. E = 0.600V vs. SCE for i-λ curve.

After an anodic scan with light, the subsequent cathodic current was much higher, sometimes exceeding the anodic photocurrents. The cathodic current gradually decayed in the dark over several scans. It decayed rapidly when the potential was held at −0.2 to −0.4V. However, anodic scans under illumination again increased the subsequent cathodic current. A few gas bubbles were visible on the electrode surface under illumination, but the quantity was much less than that observed at TiO_2 or Fe_2O_3 at similar currents. Moreover, the magnitude of the cathodic current was too large to be accounted for by reduction of adsorbed oxygen. Both an anodic and cathodic transient response similar to those observed with Fe_2O_3 but present even under white light illumination were also found with lead oxide. This again is an indication of a reductive current causing an over-all loss in efficiency in the electrode.

Thus the anodic photocurrent is probably primarily that due to further oxidation of the electrode surface, while the cathodic current is the reduction of the newly formed oxide. X-ray diffraction examination performed on an electrode surface after prolonged illumination indicated the presence of Pb, PbO (litharge), PbO_2 (platernite), and Pb_3O_4 (minium). The bandgaps of these oxides are approximately 2.8, 2.0, and 2.1 eV, respectively (10). From the photocurrent *vs.* wavelength curve, Fig. 16b, a value of about 2.8 eV is obtained, suggesting that PbO is probably responsible for the photocurrent. PbO has been studied as a photoconductor in the solid state (13-15). According to Tennant (13), PbO is a photosensitizer with an absorption spectrum similar to what we observed at the PbO electrode (Fig. 16b). Thus the properties of the electrode are consistent with PbO and the other oxides are, then, the products of the photo-oxidation. The existence of other stable oxides offers a competing path for photo-oxidation of water at PbO

electrodes, compared to TiO_2 and Fe_2O_3 which have no such stable higher oxides. These preliminary experiments showing the reversible behavior of the lead oxide electrode, *i.e.*, photo-oxidation and dark reduction

$$PbO + 2\,OH^- \underset{\text{dark } (+2e)}{\overset{\text{light } (+2h^+)}{\rightleftharpoons}} PbO_2 + H_2O$$

suggest the interesting possibility of using a lead oxide electrode in a "photochargeable" battery. Moreover, PbO_2 has been used often as an electrode for the oxidation of organic compounds (17), so the PbO electrode might also be useful in photoelectrosynthesis. These possibilities are under investigation.

Copper oxide.—A typical *i-E* curve for a copper oxide electrode formed by the oxidation of $CuNO_3$ on Pt is shown in Fig. 17. For comparison, the *i-E* curve for a Pt foil of similar area in the same solution (0.25*M* Na_2SO_4, pH 6.7) is also given. X-ray diffraction of the oxide coating reveals it to be all CuO, which, as shown by the cathodic photoeffect, exhibits a p-type behavior. The onset of the photocurrent occurs at about 0.28V (*vs.* SCE), giving a potential shift of about 0.5V from the dark current rise at the same electrode. Both curves showed negative shifts in potential with increasing *p*H. The shapes of the dark and light curves are significantly different, suggesting that the photocurrent processes are not the same as those occurring during passage of the dark current. The dark current rise showed a hysteresis loop which usually indicates a change in the electrode surface. No loop is seen in the photocurrent curve, which is quite similar in shape to the *i-E* curve seen with the Pt electrode, where the cathodic current rise represents H^+ reduction and the resultant anodic peak on reversal is hydrogen oxidation.

No gas bubbles were seen at the CuO electrode under illumination. However, this could be the result of the relatively low currents and to the instability of the photocurrent. Over a 10 min period, the photocurrent decayed to approximately a quarter of its original value. The surface color changed from an initial black to a black interspersed with gold. Anodic dark scans after prolonged illumination revealed a larger anodic current similar to that in Fig. 17a. An x-ray diffraction pattern of the electrode after formation of the gold areas still revealed only CuO present, but some Pt was also found (~1%) where it had been absent before, indicating removal of some of the CuO.

The photocurrent *vs.* wavelength curve given in Fig. 18 shows a very wide spectral range for CuO, extending to about 700 nm corresponding to a bandgap of 1.7 eV. No literature value of the bandgap was found for comparison. The monochromatic photocurrent depended upon the stirring rate, indicating some diffusional nature to the photocurrent consistent with at least some H^+ reduction. The cathodic current in the dark probably represents reduction of the oxide, since it shows the hysteresis loop and occurs about 0.5V before the H^+ reduction on Pt. The cathodic photocurrent probably represents both H^+ and oxide reduction. The wide spectral range of CuO and its p-type behavior offer interesting possibilities in conjunction with an n-type electrode (*e.g.*, Fe_2O_3) for solar energy use, provided the apparent instability can be overcome.

Vanadium oxide.—Although V_2O_5 dissolves in aqueous solutions (acidic or alkaline), it was of interest to see if it also exhibited any photoeffect. Electrodes of single crystal and CVD material were used. The *i-E* and *i-λ* curves for both electrodes are given in Fig. 19. Onset of the photocurrent occurs at about 0.58V for CVD material and at about 0.8V for the single crystal. The crystal had a higher resistance (about 12 kohm) than the CVD electrode. Both *i-λ* curves are similar, although the CVD curve is broader in the shorter wavelength region. Both give an absorption edge of 450 nm corresponding to a bandgap of 2.75 eV, which is about the bandgap listed for V_2O_5 (10). The CVD electrode dissolved during use which probably affected the magnitude of the photocurrent, and thus the shape of the *i-λ* curve. The single crystal electrode, which was initially smooth, had striations in the surface after use. Because of its instability and the relatively low photocurrents observed, the processes giving rise to the photocurrent were not investigated further.

Other oxides.—Oxides of Cd, Co, Cr, Mn, and Sr were formed by CVD and by thermal decomposition of suitable solutions onto Pt substrates. No noticeable (at least a 10 μA difference between dark and light) photoeffects were observed for the oxides of Mn, Cd, or Sr. Oxide electrodes of Cr and Co exhibited low cathodic photocurrents superimposed on the dark currents. Both Cr_2O_3 and CoO have been reported to be p-type semiconductors (11). For Cr_2O_3 in *p*H 9, 0.25*M* Na_2SO_4, an approximately constant cathodic photocurrent of 45 μA/cm² (observed by manually chopping the light) was superimposed on a dark current of 0-150 μA/cm² (potential range, 0.0 to −0.80V).

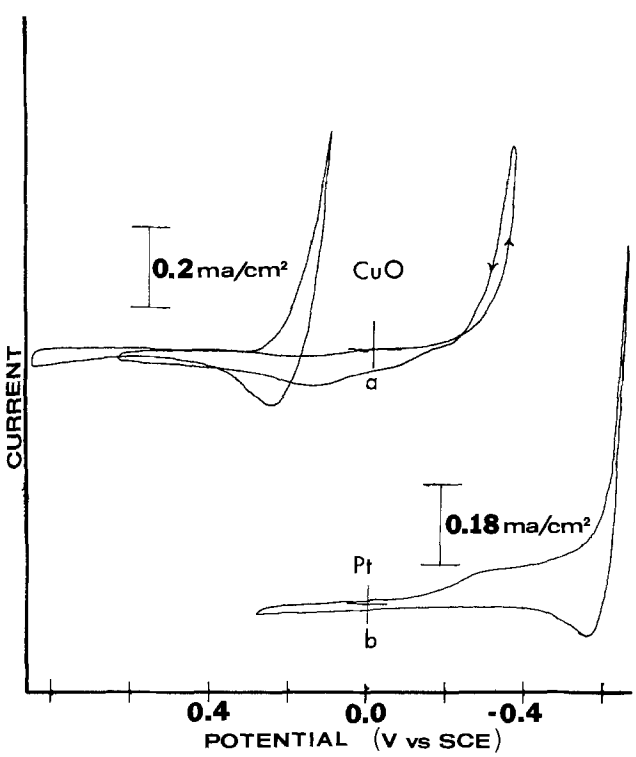


Fig. 17. Current *vs.* potential curve for (a) CuO and (b) Pt in 0.25M Na_2SO_4, *p*H 6.72.

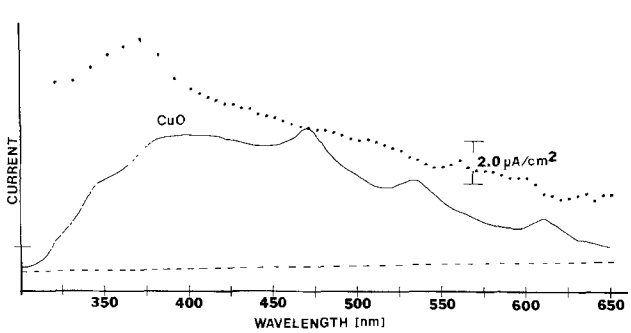


Fig. 18. Current *vs.* wavelength curve for CuO. $E = 0.00V$ *vs.* SCE, 0.25M Na_2SO_4, *p*H 6.72.

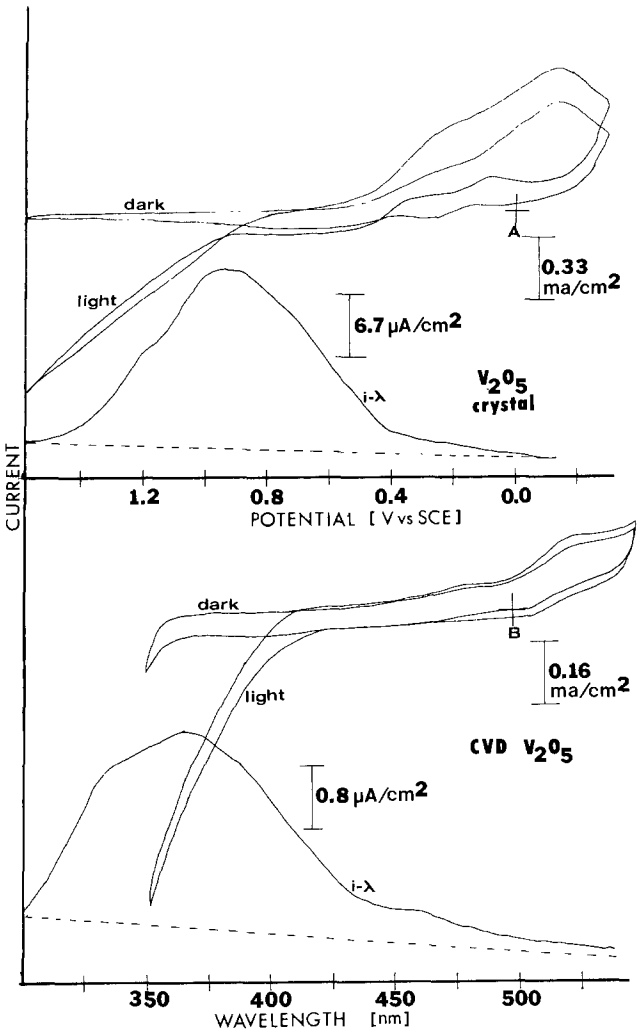


Fig. 19. Current vs. potential and current vs. wavelength curves in 0.5M Na_2SO_4 for (a) V_2O_5 single crystal, $E = 1.50V$ vs. SCE for i-λ curve; (b) CVD V_2O_5, $E = 1.00V$ vs. SCE for i-λ curve.

For CoO the photocurrent increased with potential. An instantaneous photocurrent of 0.2 mA/cm^2 at −0.90V was observed, superimposed on a dark current of 0.3 mA/cm^2. The current for these electrodes (in both dark and light) was not sufficiently stable with time to obtain good i-λ curves.

Conclusion

The results given here demonstrate that a number of metal oxides can be used as semiconductor electrodes which show photosensitized electrode reactions. Moreover, polycrystalline materials are useful for surveying promising semiconductor materials. Several methods (CVD, thermal decomposition of solutions, direct oxidation of metals, anodization, and sintering) can be employed with similar results. Thus, while single crystals are still valuable for detailed studies of the effect of structure on the photoeffect and fundamental studies of efficiency, information on the nature of the photocurrent and material stability can be easily gained from polycrystalline materials. For use in practical devices, good stability is required, including small tendency to dissolve directly or under illumination, stability against photo-oxidation (for n-type materials), and stability against photoreduction (for p-type materials). This stability depends upon the location of the valence band, but also upon the existence of higher or lower oxidation states.

Of the oxides examined only TiO_2, Fe_2O_3, and possibly WO_3 appeared to be stable enough for water oxidation. Only Fe_2O_3 offers stability and the relatively low bandgap needed for solar energy uses. None of the oxides examined seemed to have as negative a flatband potential as TiO_2. However, the shapes of most of the i-E curves did not exhibit the well-defined shape of that for TiO_2, making estimates of the actual flatband potential from the onset of the photocurrent difficult. Fe_2O_3, WO_3, Bi_2O_3, and PbO all showed an onset of photocurrent at approximately the same potential, indicating that the conduction band locations are about the same. One approach to finding useful materials may involve modification of the structure or composition of TiO_2, Fe_2O_3, and WO_3 by introduction of impurity bands or the formation of ternary compounds involving these.

Acknowledgments

The support of this research by the National Science Foundation (MPS74-23210) is gratefully acknowledged. We are indebted to Professor A. B. Scott for the sample of single crystal V_2O_5 and to Kay Poteet for assistance with x-ray and SEM analysis.

Manuscript submitted July 7, 1976; revised manuscript received Aug. 27, 1976.

Any discussion of this paper will appear in a Discussion Section to be published in the December 1977 JOURNAL. All discussions for the December 1977 Discussion Section should be submitted by Aug. 1, 1977.

Publication costs of this article were assisted by The University of Texas at Austin.

REFERENCES

1. K. L. Hardee and A. J. Bard, *This Journal*, **122**, 739 (1975).
2. K. L. Hardee and A. J. Bard, *ibid.*, **123**, 1024 (1976).
3. D. L. Laser and A. J. Bard, *ibid.*, **123**, 1837 (1976).
4. D. L. Laser and A. J. Bard, *ibid.*, **123**, 1027 (1976).
5. S. N. Frank and A. J. Bard, Submitted for publication.
6. B. Pettinger, H. R. Schoppel, and H. Gerischer, *Ber. Bunsenges. Phys. Chem.*, **78**, 450 (1974); *ibid.*, **78**, 1024 (1974).
7. R. F. G. Gardner, F. Sweett, and D. W. Tanner, *J. Phys. Chem. Solids*, **24**, 1175 (1963); *ibid.*, **24**, 1183 (1963).
8. F. Mollers, H. J. Tolle, and R. Memming, *This Journal*, **121**, 1160 (1974).
9. G. Hodes, D. Cahen, and J. Manassen, *Nature*, **260**, 312 (1976).
10. W. H. Strehlow and E. L. Cook, *J. Phys. Chem. Ref. Data*, **2**, 163 (1973).
11. "Transition Metal Oxides," NBS Report NSRDS 49.
12. H. Gobrecht, S. Seeck, H. E. Bergt, A. Martens, and K. Kossman, *Phys. Status Solidi*, **34**, 569 (1969).
13. W. C. Tennant, *J. Phys. Chem.*, **72**, 1078 (1968).
14. M. J. Shea and W. C. Michels, *J. Chem. Phys.*, **59**, 2764 (1973).
15. R. C. Keezer, D. L. Bowman, and J. H. Becker *J. Appl. Phys.*, **39**, 2062 (1968).
16. P. J. Boddy, *This Journal*, **115**, 199 (1968).
17. N. Sato, T. Sekine, and K. Sugino, *ibid.*, **115**, 242 (1968) and references therein.

Semiconductor Electrodes

XI. Behavior of n- and p-Type Single Crystal Semconductors Covered with Thin n-TiO_2 Films

Paul A. Kohl,* Steven N. Frank, and Allen J. Bard****

Department of Chemistry, The University of Texas at Austin, Austin, Texas 78712

ABSTRACT

Single crystal semiconductors (n-Si, p-Si, n-GaAs, p-GaAs, n-GaP, n-InP, and n-CdS) were coated with n-type TiO_2 by a chemical vapor deposition technique, and the electron and hole transfer properties across the heterojunction so produced were investigated. The quality of the deposited TiO_2 film depended upon several factors including temperature and substrate material. When high quality crack-free TiO_2 coats were obtained on n-type substrates, the substrate was stabilized with no dissolution during the photo-oxidation of water. However, the oxidation was due only to the photoexcitation of the TiO_2, and any holes produced in the substrate were not transferred through the TiO_2 to the solution. The use of p-type substrates coated with TiO_2 as photocathodes was limited by band-bending requirements at the p-n heterojunction and the TiO_2-solution interface.

The utilization of small bandgap (E_g) semiconductor electrodes, *i.e.*, $E_g < 2.5$ eV, such as CdS, Si, and GaAs, for the efficient conversion of solar energy to electrical or chemical energy in electrochemical cells is limited by the dissolution or decomposition of the semiconductor itself (1). Photoeffects and the electrochemical behavior of semiconductor electrodes have been described elsewhere [see, *e.g.*, (2-4) and references therein]. Various attempts have been made to stabilize the surface of small bandgap semiconductors without changing their electrochemical properties for hole or electron transfer through the electrode-solution interface. For example, thin metal films have been deposited on the surface of the semiconductor (5) or different redox couples (*e.g.*, Na_2S/S with CdS) have been added to the solution to allow a preferential electrode reaction rather than the dissolution of the semiconductor (6-9). N-type TiO_2, SnO_2, and $SrTiO_3$ show sufficient stability so as not to decompose during the photo-oxidation of water (10-12). However, these have bandgaps $\geq$ 3.0 eV so that they utilize only a very small percentage of the solar spectrum.

There has recently been some interest in using chemically vapor deposited coatings on semiconductor electrodes. For example, CVD TiO_2 coats on n-CdS have been reported (13) to increase its efficiency as a photoanode and decrease the dissolution of the CdS. Other work in this area (14) indicates that n-GaP with TiO_2 coatings stabilize the GaP against photodissolution at potentials positive of the flatband. The heterojunction produced at the interface of the two dissimilar semiconductors creates an energy barrier to the transfer of carriers across the junctions with a magnitude determined by the relative position of the conduction and valence bands, as shown in the discussion following. This barrier would be expected to hinder the flow of photogenerated carriers from the substrate through the protective coating. However, energy levels and surface states may exist in the bandgap region and be utilized for electron transfer reactions, *e.g.*, an intermediate level has been proposed for TiO_2 (6). If these levels extend into the semiconductor and can be considered "bandlike," the possibility exists for the transfer of electrons and holes through the coating via these intermediate levels.

In this work, various small bandgap semiconductors (n-Si, p-Si, n-CdS, n-GaAs, p-GaAs, n-GaP, and n-InP) were coated with polycrystalline TiO_2 by chemical vapor deposition (CVD) to examine the resulting electrical properties both with and without a solution interface. The position of the valence and conductions bands *vs.* vacuum for the various semiconductors is shown in Fig. 1 (15, 16). The procedure for obtaining a good TiO_2 film on small bandgap single crystal semiconductors, a modification of the one previously described (17), the electrode properties, and the conditions by which photoexcited electrons or holes are transferred from the substrate to the solution via the large bandgap TiO_2 film on the surface are reported.

Experimental

The low resistivity single crystal semiconductors used as substrates for chemical vapor deposition of polycrystalline TiO_2 were about 1 mm thick and were polished with 0.5 μm alumina. The CVD, with the apparatus described previously (17), was done at various substrate temperatures (100°-600°C) to find the optimum temperature for a good quality TiO_2 film. The annealing process was performed either on a hot plate

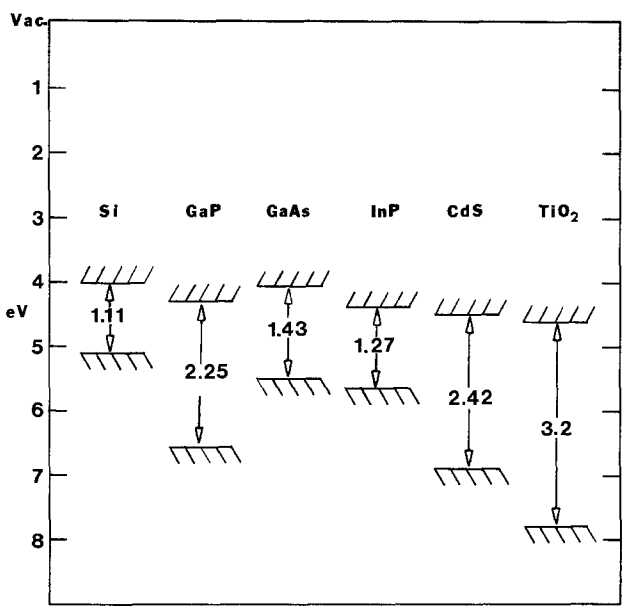


Fig. 1. Relative position of the valence and conduction bands vs. vacuum of the various semiconductors used.

* Electrochemical Society Student Member.
** Electrochemical Society Active Member.
Key words: photoelectrochemistry, heterojunctions, semiconductors, photovoltaic cells.

at 600°C or under high vacuum at 700°C; the flame method used previously was not employed here because of the easy oxidation of most semiconductor materials at flame temperatures in the presence of oxygen. The n-type TiO_2 was reduced to increase its conductivity by passing hydrogen gas over the heated sample or by heating in a high vacuum.

The n-GaP, n-GaAs, and p-GaAs were obtained from Atomergic Chemicals (Long Island, New York). The n-Si and p-Si crystals were donated through the courtesy of Texas Instruments (Dallas, Texas), and the n-CdS and n-InP were originally obtained from National Lead and donated by Dr. D. I. Tchernev (Lincoln Laboratories, Massachusetts Institute of Technology). Ohmic contacts were made to the n-CdS, n-InP, and n-GaP by electroplating indium on the back side of the crystals using a 0.1*M* $InCl_3$ solution. The n-GaP contact was heated in a hydrogen atmosphere at about 400°C for several hours to make it ohmic. Ohmic contacts were obtained with p-GaAs and p-Si (3) by electroplating gold from a 0.1*M* $Au(CN)_2^-$ solution on the rear side. Contact to n-Si (3) was made by electroplating nickel from a 0.1*M* $Ni(NO_3)_2$ solution and to n-GaAs (18) by first plating indium, then gold, and alloying at 400°C in a hydrogen atmosphere. To confirm that the contacts were ohmic, a second contact was made to the rear side; in all cases of good contacts the resistance between the contacts was small and the current was directly proportional to the applied potential independent of polarity. A wire was connected to the ohmic contact with conducting silver epoxy (Allied Products Corporation, New Haven, Connecticut). The back and sides of the crystal were then sealed with nonconducting 5 min epoxy (Devcon Corporation, Danvers, Massachusetts). The crystals were then mounted on a small glass disk connected to a glass tube with silicone adhesive (Dow Corning, Midland, Michigan) which allowed a path for the wire. When an ohmic contact was made on the front side of the crystal on the TiO_2, it was accomplished with silver epoxy and the contacts insulated as described above. Duplicate semiconductor electrodes were prepared in an identical manner except without the TiO_2 film for comparison with the filmed electrodes.

All chemicals were reagent grade and all solutions were prepared with triply distilled water, with the first distillation from alkaline potassium permanganate.

A three-compartment cell, similar to previous designs (6), was used for all electrochemical measurements. The reference compartment made electrical contact with the main compartment via a porous Vycor glass junction. The counterelectrode was a platinum wire and the reference electrode was a silver wire in 0.1*M* $AgNO_3$. However, all values are reported *vs.* a saturated calomel electrode (SCE). The main compartment had an optically flat Pyrex window.

A PAR 173 potentiostat and PAR 175 universal programmer (Princeton Applied Research Corporation, Princeton, New Jersey) were used. Data were recorded on a Houston Instruments Model 2000 X-Y recorder. For photoexcitation experiments, a 450W xenon lamp and grating monochromator (Oriel Corporation, Stamford, Connecticut) were used. The electron micrographs were taken with a scanning electron microscope (SEM) JSM-2 (Japan Electron Optical Laboratory Company, Limited) with an x-ray fluorescence spectroscopy attachment (Canberra Industries) for elemental analysis of the surfaces.

The concentrations of Cd^{+2} and Ga^{+3} in solution from dissolution of the electrodes were determined polarographically at a dropping mercury electrode using a PAR 170 electrochemical system. Standard solutions were prepared from cadmium chloride and gallium metal dissolved in sulfuric acid. The solutions were degassed with prepurified nitrogen gas and the gallium was diluted and buffered with a 1*M* NH_3/1*M* NH_4Cl solution.

Results

The polycrystalline TiO_2 coats obtained were all hard and durable. The number of cracks and holes which formed in these coatings depended upon several factors, including the nature of the substrate material, the substrate temperature during deposition, the rate of heating and cooling of the substrate, the thickness of the TiO_2 coats, the number of TiO_2 coats applied, and the method of doping the TiO_2.

N-type substrate/n-TiO_2/solution.—Durable, crack- and hole-free coats of TiO_2 were obtained on n-Si and n-InP (Fig. 2a) by performing the CVD at a substrate temperature of 500°-600°C. At this temperature the coats annealed without additional heating and cooling (17). The substrate was held at this temperature for several hours to give at least a partial conversion from the anatase to ruile structure, and hydrogen gas was then passed over the surface to reduce it. The sample was then allowed to cool slowly over a 24 hr period.

The current *vs.* potential (i-E) curve for the n-InP/TiO_2 electrode with the TiO_2 exposed to solution (Fig. 3a) showed a cathodic dark current characteristic of an n-type semiconductor and an anodic photocurrent due to the oxidation of water, with bubbles being given off at the electrode surface and approximately a 60 mV/*p*H change in the onset of photocurrent. The current *vs.* wavelength (i-λ) plot (Fig. 3b) showed that the photocurrent absorption spectrum for the n-InP/TiO_2 electrode was identical to that of TiO_2. After several hours of illumination at +0.5V, there was no change in the amount of photocurrent or in the i-λ plot. There was also no visual decomposition of the TiO_2 film or apparent dissolution of the InP. In Fig. 3, the results of an uncoated n-InP electrode are shown for comparison. Similar results were observed with the n-Si/TiO_2 electrode. The TiO_2 was crack- and hole-free with anodic photoeffects observed and bubbles evolved at the surface only for $\lambda < 400$ nm (3.1 eV).

Crack-free TiO_2 coats were never obtained on n-CdS, even after repeated attempts using different conditions, as discussed above. The best coats were obtained by CVD at 600°C as before, but with reduction in high vacuum at 600°C. The electron micrographs are shown in Fig. 2b. With fast heating and cooling processes, there were at least ten times as many cracks. The i-λ curve, Fig. 4a, showed a large peak at about 480 nm due to the absorption of CdS with the current increasing with subsequent scans. The small current at about 350 nm, due to the excitation of TiO_2, decreased with time as the TiO_2 film deteriorated, as shown in Fig. 2c. The current *vs.* time curve, Fig. 4b, showed that the anodic photocurrent of pure CdS decreased, probably because of the formation of sulfur on the surface. With a TiO_2 film, the current increased with time, corresponding to the breakup of the TiO_2 film; the final current was limited by the sulfur buildup. Even for the portions of the TiO_2 that do not flake off, a sulfur layer can be seen to underlie the remaining and still durable TiO_2 film. Analysis of the solution, after passage of an anodic photocurrent for a given time, showed about 1% less Cd^{+2} from the dissolution of CdS with TiO_2 on the surface as compared to CdS without TiO_2. Bubbles were not seen on the surface because of the small amounts of current going to the oxidation of water.

Crack- and hole-free coats were also not obtained on n-GaAs and n-GaP. Similar i-λ plots to those of n-CdS/TiO_2 were obtained with an absorption peak at about 350 nm, and a photocurrent which decreased with time. However, the substrate absorption peak currents increased with time because of the soluble products of dissolution. Bubbles were evolved at the electrode surface until a visible deterioration of the TiO_2 film was evident and solution analysis confirmed the presence of gallium.

P-type substrate/n-TiO_2/solution.—To examine further the band structure and possibilities for electron

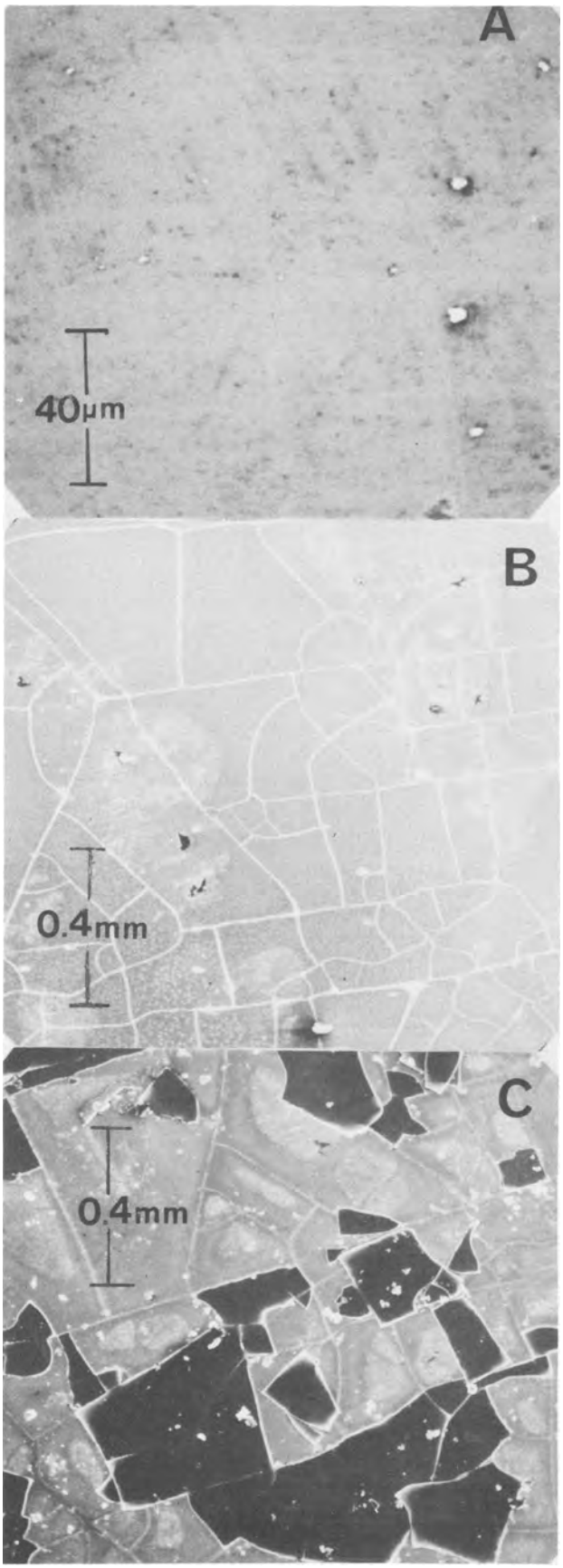


Fig. 2. (a) High contrast electron micrograph of n-Si with TiO_2 on the surface. The white spots are mounds of TiO_2 and the dark spots are shadows. (b) Electron micrograph of the n-CdS/TiO_2 electrode before use. The surface is covered with TiO_2 and the cracks are less than 10,000Å wide. (c) Electron micrograph of n-CdS/TiO_2 in (b) after the passage of current and dissolution of CdS. The dark areas are TiO_2 and light areas are CdS with sulfur in the cracks.

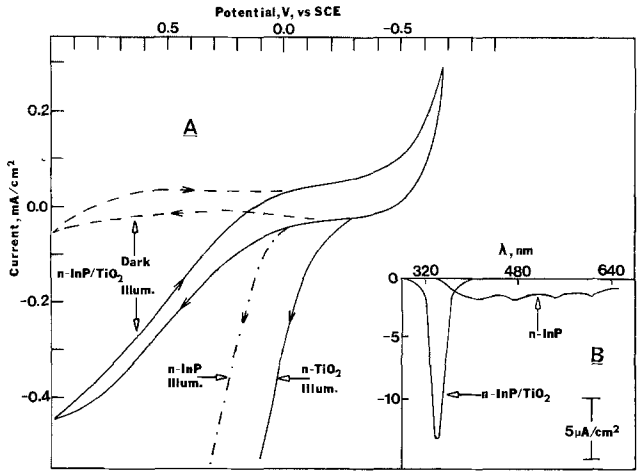


Fig. 3. (a) Current *vs.* potential for the n-InP/TiO_2 electrode in 0.5*M* Na_2SO_4, both in the dark and illuminated. The photocurrents of n-InP and n-TiO_2 are shown for comparison. (b) Current *vs.* wavelength for n-InP/TiO_2 and n-InP at +0.5V *vs.* SCE in 0.5*M* Na_2SO_4 (uncorrected for lamp intensity-monochromator spectral variations).

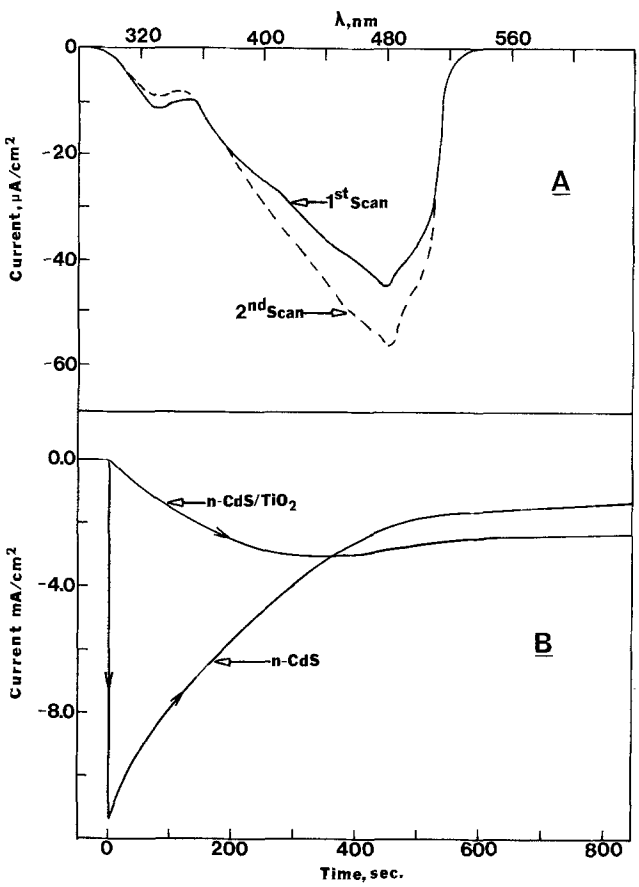


Fig. 4. (a) Current *vs.* wavelength for n-CdS/TiO_2 in 0.5*M* Na_2SO_4 at +0.5V (uncorrected for lamp intensity-monochromator spectral variations); (b) current *vs.* time for n-CdS/TiO_2 and n-CdS illuminated with white light in 0.5*M* Na_2SO_4 at +0.5V *vs.* SCE.

and hole transfer through the TiO_2, p-type materials were used as the substrates. This, in effect, gives holes in the substrate which are available for possible electron transfer to the solution without illumination.

Crack-free and stable coats of TiO_2 were obtained on p-Si and p-GaAs by the same procedure as described for n-Si and n-InP. The *i-E* curve of p-Si/TiO_2 (Fig. 5a) can be divided into three regions as indicated.

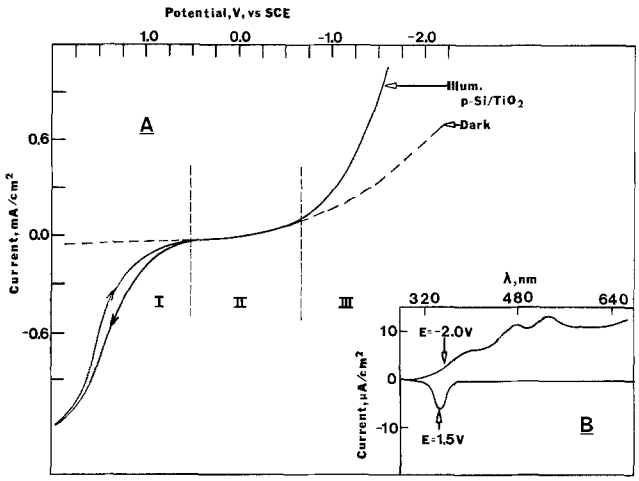


Fig. 5. (a) Current *vs.* potential for p-Si/TiO_2 in the dark and illuminated in 0.5*M* Na_2SO_4; (b) current *vs.* wavelength for p-Si/TiO_2 in 0.5*M* Na_2SO_4 at +1.5V and −2.0V *vs.* SCE (uncorrected for lamp intensity-monochromator spectral variations).

Significant photocurrents occurred in regions I and III. The anodic photocurrent in region I (Fig. 5b) is due to electron/hole pair formation in the TiO_2 resulting in the oxidation of water with bubbles evolved at the electrode surface. The potential for the onset of anodic photocurrent was *p*H dependent (*i.e.*, 60 mV/*p*H). In region III, the cathodic photocurrent can be attributed to the reduction of H^+ by photoexcitation of the p-silicon with again approximately a 60 mV/*p*H change in the onset of cathodic photocurrent. After several hours of illumination, there was no change in the cathodic or anodic photocurrents, nor was there a change in the i-λ curves. The same characteristic three regions were obtained on p-GaAs/TiO_2, but with the onset of significant anodic photocurrent at about +0.2V and significant cathodic photocurrent at about −0.7V in 0.5*M* Na_2SO_4.

i-V curves.—To investigate the TiO_2-substrate heterojunction, the current-voltage (i-V) curves on the solid-state junctions alone were taken by applying the indicated voltage to the front TiO_2 contact with respect to the rear substrate contact (Fig. 6a). Similar results were obtained for the various other substrate materials used. These results are discussed in the next section.

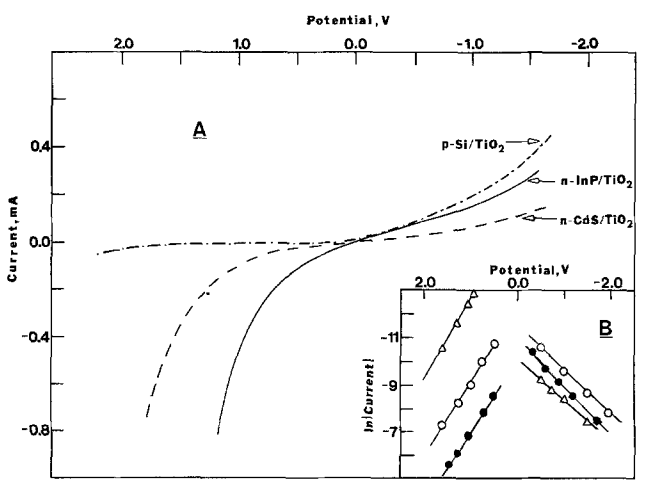


Fig. 6. (a) Current *vs.* voltage across the heterojunctions: p-Si/TiO_2, n-InP/TiO_2, n-CdS/TiO_2. (b) Natural log of current *vs.* voltage: △ = p-Si/TiO_2, ○ = n-CdS/TiO_2, ● = n-InP/TiO_2.

Discussion

The results for n-InP and n-Si with TiO_2 on the surface show the photo-oxidation of water can only be accomplished by the excitation of an electron-hole pair in the TiO_2. The creation of a hole in the n-type substrate has no mechanism for transfer through the TiO_2 to the solution. The observed 60 mV/*p*H shift in the onset of photocurrent at the TiO_2-covered substrates reflects the shift in the surface hydroxide equilibrium brought about by *p*H changes, as discussed by Honda and co-workers (19) for TiO_2 single crystals. The small bandgap substrates are stabilized with completely reproducible results from day to day and with no passivation or change in behavior.

Although the results are inconclusive, it appears that a similar lack of hole transfer through the film occurs in the other n-type semiconductors used in this study. The dissolution processes which occur at n-GaP, n-CdS, and n-GaAs appear to be taking place through the cracks in the TiO_2 (Fig. 2b and 2c). The increase in anodic photocurrent with time correlates with the removal of TiO_2 from the surface, just as the decrease in current at $\lambda = 350$ nm and the decrease in evolution of bubbles correlates with the removal of TiO_2.

The results for p-GaAs and p-Si with TiO_2 on the surface (Fig. 5) also show that the anodic photo-oxidation of water, region I, is due only to the excitation of an electron-hole pair in the TiO_2. The small dark current, even at +2.0V, shows that holes are not transferred through the TiO_2 to the solution. The cathodic photocurrent, region III of Fig. 5, is due to the reduction of hydrogen ion by photoexcited electrons in the conduction band of the substrate material that transfer through the TiO_2 to the solution. The potential at which this takes place is even more negative than that required for the reduction of hydrogen ion at a platinum electrode in the same solution. Region II of Fig. 5 lies between these two extreme regions with very small anodic photocurrents due to the excitation of TiO_2 and very small cathodic photocurrents from the excitation of the substrate. The substrates were again stable with no change in behavior with time.

The nature of the heterojunction produced between the small bandgap substrate and TiO_2 can be represented to a first approximation by simple band structures, shown in Fig. 7 (20). This neglects such things as the change in work function of TiO_2 with interaction with the water (21) or air pressure (16). This also does not consider the possibility of intermediate compounds being formed at the junction creating additional barriers, or the presence of surface states. The potential barrier at the n-n heterojunction arises from the mismatch of the conduction bands and Fermi levels. If the energies of the conduction bands and Fermi levels of the n-substrate and TiO_2 were equal with an ideal junction, there would be no barrier to the majority carriers (22). This model is qualitatively confirmed by the results in Fig. 6a, where the current varies with the exponential of the barrier potential, which changes in proportion to the applied potential. This is demonstrated in Fig. 6b by the linearity of the ln i *vs.* V plot. Therefore, because of the higher barrier for an electron to go from the TiO_2 to the n-type substrate, the conduction band of the substrate is higher than that of the TiO_2. The valence band of the TiO_2 must then lie far below that of the substrate. Therefore, a hole in the valence band of the substrate cannot travel downhill to the TiO_2 valence band without extreme band bending even if the nonidealities in the heterojunction, as mentioned above, are considered. It might be possible for hole transfer to occur through an intermediate level located in the bandgap region of the TiO_2 (6). However, no evidence for this type of transfer was found in these studies.

When the electrodes are used in solution, there are two junctions to be considered: the substrate/TiO_2 heterojunction and the TiO_2/solution interface. At equi-

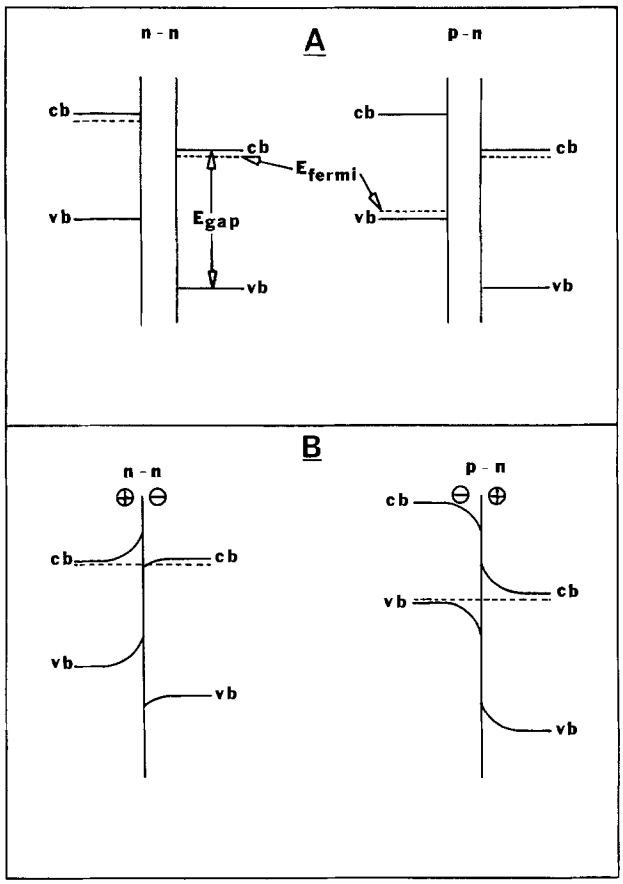


Fig. 7. Example of a n-n heterojunction and a p-n heterojunction (a) before contact, (b) after contact with the resulting band bending and charge separation.

librium, all Fermi levels must be equal. When a potential, ΔE, is applied to the electrode with respect to the solution and current flows, the position of the TiO_2 Fermi level is determined by the relative barriers at the two junctions (22). Assuming that the rate-determining step of the reaction at the TiO_2/solution interface is first order in concentration of holes or electrons at the surface, the current will depend not only upon the band bending of the TiO_2 at the solution interface but also upon the band bending of the substrate and TiO_2 at the heterojunction. A given current corresponds to a unique band-bending situation at both junctions. If a change in pH affects the potential drop between the electrode surface and solution, then the applied potential must be changed an equal amount to obtain the same band-bending situation and current. This explains the observed 60 mV/pH shift in onset of photocurrent.

Conclusion

Protective films of TiO_2 can be obtained by CVD on some semiconductor substrates without cracks. However, when cracks are present, dissolution of the substrate material can occur, with photocurrents caused by substrate dissolution at absorption wavelengths of the substrate. There does not appear to be any advantage in depositing TiO_2 on the n-type substrates used in this work, compared to the photo-oxidation of water over a CVD TiO_2 electrode itself, because of the inability to transfer holes from the substrate through the TiO_2. The use of p-type substrates coated with n-TiO_2 as photocathodes is limited by the band-bending requirements at the junctions and the barrier potential which must be overcome at the heterojunction, so that the required "negative overpotentials" for useful conversion of light energy do not occur.

Acknowledgments

We gratefully acknowledge the National Science Foundation (MPS74-23210) and the Robert A. Welch Foundation (F-079) for the support of this research. Some preliminary experiments in this field were carried out in this laboratory by Dr. Daniel Laser. We are indebted to Kaye Poteet for obtaining the SEM micrographs.

Manuscript submitted June 16, 1976; revised manuscript received Sept. 1, 1976.

Any discussion of this paper will appear in a Discussion Section to be published in the December 1977 JOURNAL. All discussions for the December 1977 Discussion Section should be submitted by Aug. 1, 1977.

Publication costs of this article were assisted by The University of Texas at Austin.

REFERENCES

1. H. Gerischer and W. Mindt, *Electrochim. Acta*, **13**, 1329 (1968).
2. H. Gerischer, in "Physical Chemistry: An Advanced Treatise," Vol. 9A, H. Eyring, D. Henderson, and W. Jost, Editors, Academic Press, New York (1970).
3. D. Laser and A. J. Bard, *J. Phys. Chem.*, **80**, 459 (1976).
4. V. A. Myamlin and Y. U. Pleskov, "Electrochemistry of Semiconductors," Plenum Press, New York (1967).
5. Y. Nakato, T. Ohnishi, and H. Tsubomura, *Chem. Lett.*, **1975**, 883.
6. S. N. Frank and A. J. Bard, *J. Am. Chem. Soc.*, **97**, 7427 (1975).
7. A. B. Ellis, S. W. Kaiser, and M. S. Wrighton, *ibid.*, **98**, 1635 (1976).
8. S. R. Morrison, *Surf. Sci.*, **15**, 363 (1969).
9. K. H. Beckmann and R. Memming, *This Journal*, **116**, 368 (1969).
10. T. Watanabe, A. Fujishima, and K. Honda, *Bull. Chem. Soc. Jpn.*, **49**, 355 (1976).
11. M. S. Wrighton, D. S. Ginley, P. T. Wolczanski, A. B. Ellis, D. L. Morse, and A. Linz, *Proc. Nat. Acad. Sci. U.S.A.*, **72**, 1518 (1975).
12. F. Möllers and R. Memming, *Ber. Bunsenges. Phys. Chem.*, **76**, 469 (1972).
13. J. O'M. Bockris and K. Uosaki, Paper 14 (Inorganic Section) presented at the American Chemical Society Meeting, New York, New York, April 1976.
14. D. Laser, Unpublished results, 1975.
15. A. L. Milnes and D. L. Feucht, "Heterojunctions and Metal-Semiconductor Junctions," Academic Press, New York (1972).
16. T. Iida and H. Nozaki, *Bull. Chem. Soc. Jpn.*, **42**, 243 (1969).
17. K. Hardee and A. J. Bard, *This Journal*, **122**, 739 (1975).
18. R. K. Willardson and A. C. Beer, Editors, "Semiconductors and Semimetals," Vol. 7A, p. 65, Academic Press, New York (1971).
19. T. Watanabe, A. Fujishima, and K. Honda, *Chem. Lett.*, **1974**, 897.
20. T. L. Tansley, in "Semiconductors and Semimetals," Vol. 7A, R. K. Willardson and A. C. Beer, Editors, Academic Press, New York (1971).
21. E. N. Figurouskaya, *Kinet. Katal.*, **10**, 453 (1969).
22. R. M. Walzer, Private communication.

The Transient Response of the Sulfur/Polysulfide Electrode Based on a Varying Concentration Model

Yuen-Koh Kao[1] and Peter C. Wayner, Jr.

Department of Chemical and Environmental Engineering, Rensselaer Polytechnic Institute, Troy, New York 12181

ABSTRACT

A computer simulation of the transient behavior of the sulfur electrode of a Na/S battery operating in the single phase region was obtained. The results show the relative, effect of concentration and conductivity on the cell performance. The predominant effect is due to the variation of the chemical potential of sulfur with concentration which causes the cell to operate uniformly. This advantage is partially offset by high current densities, large cell dimensions, and unmatched melt and felt conductivities. Capacity loss, which has been experimentally observed, is theoretically demonstrated.

The application of the sodium/sulfur system as a secondary battery has attracted considerable attention. It has the potential to fulfill the need for an efficient and inexpensive energy storage device. The transport processes associated with this battery are somewhat unique in that the "electrolyte" is a ceramic, β-alumina, which is permeable to only the sodium ion. The β-alumina separates one of the reactants, liquid sodium, from the other, polysulfide (sulfur when fully charged) which is usually contained within a graphite felt electronic conductor matrix (1). The operating characteristics are further complicated by the sulfur/Na_2S_x phase diagram which, depending on the composition, shows both immiscible and solid phases (2).

Most of the previous work concerning the battery concentrated on the material properties of the system and the experimental operation of the battery, *e.g.*, (3-5). Except for Ref. (5, 6), very little research addressed the problem of modeling the complicated sulfur electrode. Gibson (6) using the continuum modeling approach of Newman and Tobias (7) evaluated the effect of melt and felt conductivity on the reaction rate distribution. However, he neglected the more significant effect of concentration. The results of the study showed a large spatial variation in the reaction rate which would lead to incorrect conclusions concerning the operation of the battery. In a later work by the present authors (8), a sulfur electrode model was developed that included the effect of a hypothetical concentration distribution. The results of the study demonstrated that the dominant effect on cell operation was due to concentration gradients.

The present study concerns the transient behavior of the sulfur electrode using the more realistic uniform concentration of $Na_2S_{5.25}$ as the starting point. These results demonstrate how the selective effects of conductivity and the transient change in the concentration affect the operation of the sulfur electrode. The predominant effect is due to the variation of the chemical potential of sulfur with concentration which causes the cell to operate uniformly. The annoying phenomenon of capacity loss, which has been observed in many experimental studies, (3-5), is also present in the results of these studies.

Formulation

The annular shaped sulfur electrode studies herein is bounded on the inside by the outer wall of the ceramic tube ($r = R_o$) which contains the sodium and which is an ionic conductor of sodium ions. It is bounded on the outside ($r = R_1$) by an electronic conducting container. The annular space contains graphite felt impregnated with sodium polysulfide and/or molten sulfur. During discharge, the sodium ions, after giving up an electron to the external circuit, migrate through the solid β-alumina electrolyte to form various polysulfides in the sulfur electrode when sulfur atoms receive two electrons from the external circuit. The basic approach followed is the continuous model of Newman and Tobias (7). Some of the following equations [1]-[4] were developed in an earlier paper (8). The following assumptions were used in deriving the equations:

1. The sulfur electrode can be modeled by the superposition of two continua.

2. There is no capacitance effect in the melt/felt interface; the conservation of charge gives the following equation

$$(i_1 + i_2)\, r = I_{R_o} R_o$$

where i_1 and i_2 are the current densities in the melt and felt phases, and I_{R_o} is the current of the melt phase at the β-alumina and sodium polysulfide interface.

3. The electrode kinetics can be modeled using a diffusion model. The electrode reaction is assumed to be $S + 2e^- \rightleftarrows S^=$. The limiting species are assumed to be S and $S^=$ in the anodic and cathodic direction, respectively. Further simplification is achieved by assuming that the respective limiting current densities are the same in either direction (8)

$$i_s = -i_l \tanh(\alpha\eta)$$

where

$$\alpha = \mathbf{F}/RT,\ \eta = \phi_2 - \phi_1 - \Delta\phi_e;\ \Delta\phi_e = (\phi_2 - \phi_1)_{i_s=0}$$

4. The current equation for the melt which includes the effect of concentration gradients is (8)

$$i_1 = -k_1 \nabla\phi_1 + \frac{k_1}{2\mathbf{F}}(1 - 2W_s)\nabla\mu_1{}^2$$

where $k_1 = 1.5376 - 1.9264\, w_s$ [this interpolation equation, in which w_s is the weight fraction of atomic sulfur, is based on experimental results (9)], W_s is the "Washburn number" which is defined as the number of moles of sulfur that passes through a reference plane in the same direction as a Faraday of charges passes through that plane. The plane is chosen such that no sodium ion passes through it. Cheaver and Davies (10) indicated that sulfur atom moves only with the sulfur ion and hence $W_s = -c_1/2c_3$. The chemical potential of atomic sulfur which is also based on the same work is interpolated and gives the following equation

$$\frac{\mu_1}{2\mathbf{F}} = \frac{\mu_1{}^*}{2\mathbf{F}} + (-690.9970 + 384.9642x - 74.8151x^2 + 5.05331x^3),$$

[1] Present address: Department of Chemical and Nuclear Engineering, University of Cincinnati, Cincinnati, Ohio 45221.

Key words: single-phase, discharge, molten salt, capacity loss.

[2] This equation can also be obtained according to Eq. [34] of Newman and Tiedman's work (15).

in mV for $x \leq 5.25$ at 350°C. The formulation is completed by including following conservation of changes equations for each phase

$$\frac{\partial i_1}{\partial r} = \frac{1}{r} i_1 - a i_s$$

$$\frac{\partial i_2}{\partial r} = \frac{1}{r} i_2 + a i_s$$

Eliminating ϕ_1, ϕ_2, i_2 from the above equations and after defining appropriate dimensionless variable leads to the following dimensionless current equation (8)

$$\frac{\partial^2 j}{\partial y^2} = C_t \frac{\partial j}{\partial y} + C_t{}^2 j + \left[1 - \beta^2 \left(\frac{\partial j}{\partial y} + C_t j \right)^2 \right] \quad [1]$$

$$\left[\gamma \left\{ j - \frac{k_1}{k_1 + k_2} \left(\frac{R_o}{R_o - y\Delta R} \right) \right\} - \frac{x}{\beta} (b' + 2c'x + 3d'x^2) \frac{\partial x}{\partial y} \right]$$

where $j = i_1/I_{R_o}$, x is the "x" in Na_xS_x,

$$y = (r - R_o)/(R_1 - R_o)$$

$$C_t = \frac{\Delta R}{y\Delta R + R_o}$$

$$\beta = \frac{I_{R_o}}{a i_1 \Delta R}$$

$$\gamma = a i_1 \Delta R^2 \left(\frac{1}{k_1} + \frac{1}{k_2} \right)$$

The molar flux equations for atoms sulfur, sodium ions, and sulfide ions are obtained from the multicomponent diffusion equations. Introducing the chemical potential of sodium sulfide μ and the current density of the melt i_1, and by choosing v_2, the velocity of sodium ions, as the reference velocity, after the elimination of v_1 and v_3 resulted in the following flux equations

$$N_1 = \frac{K_{31} c_1}{(K_{21} + K_{31}) c_3 Z_3} \frac{i_1}{\mathbf{F}} + \frac{c_1}{K_{12} + K_{13}} c \nabla \mu + c_1 v_2$$

$$N_2 = c_2 v_2$$

$$N_3 = \frac{i_1}{Z_3 \mathbf{F}} + c_3 v_2$$

According to Cleaver and Davies (10), sulfur atoms move with sulfide ions, that is $K_{13} = \infty$, therefore the flux equation now becomes

$$N_1 = W_s \frac{i_1}{\mathbf{F}} + c_1 v_2 \quad [2]$$

$$N_2 = c_2 v_2 \quad [3]$$

$$N_3 = \frac{i_1}{2\mathbf{F}} + c_3 v_2 \quad [4]$$

Notice that N_1 and N_3 are redundant and only one of them is needed to describe the system. The equations of continuity for the species in cylindrical coordinates are

$$\frac{\partial c_i}{\partial t} = -\frac{1}{r} \frac{\partial}{\partial r} \left[r \frac{\partial N_i}{\partial r} \right] + R_i \quad [5]$$

where R_i is the rate of production of species i in molar units, with $R_2 = 0$ and

$$R_3 = -R_1 = -\frac{1}{2\mathbf{F}r} \frac{\partial}{\partial r} (r\, i_1) \quad [6]$$

The determination of the reference velocity, v_2, follows the approach proposed by Kirkwood *et al.* (11). The flux relative to the cell is related to the flux relative to v_2 by the following equation

$$(rN_i)_C = (rN_i)_R + c_i v_2 r \quad [7]$$

where c_i is the molar concentration of species i and subscript C and R denote quantities relative to the cell and relative frames.

After differentiating the above equation with respect to r, taking the sum over all i and multiplying both sides by their respective partial molar volumes, the following equation is obtained

$$\sum_{i=1}^{3} V_i \frac{\partial}{\partial r} (rN_i)_C = \sum_{i=1}^{3} V_i \frac{\partial}{\partial r} (rN_i)_R + \frac{\partial}{\partial r} (v_2 r) \sum_{i-1}^{3} c_i V_i + \sum_{i=1}^{3} \left(\frac{\partial c_i}{\partial r} V_i \right) v_2 r \quad [8]$$

Since $\sum c_i V_i = 1$ and $\sum V_i \frac{\partial c_i}{\partial r} = 0$ by the Gibbs-Duhem equation the above equation becomes

$$\sum_{i=1}^{3} V_i \frac{\partial}{\partial r} (rN_i)_C = \sum_{i=1}^{3} V_i \frac{\partial}{\partial r} (rN_i)_R + \frac{\partial}{\partial r} (v_2 r) \quad [9]$$

Then summing the equations of continuity of all species after multiplying both sides by their respective partial molar volumes and using the Gibbs-Duhem equation, the following equation is obtained

$$\sum_{i=1}^{3} V_i \frac{\partial c_i}{\partial t} = 0 = \sum_{i=1}^{3} \left[-\frac{1}{r} \frac{\partial}{\partial r} (rN_i)_C \right] V_i + \sum_{i=1}^{3} R_i V_i \quad [10]$$

Combining Eq. [9] and [10], the following equation for the reference velocity, v_2, is obtained

$$\frac{\partial}{\partial r} (rv_2) = V_1 \frac{\partial}{\partial r} \left[r(1 - 2W_s) \frac{i}{2\mathbf{F}} \right] \quad [11]$$

For simplicity the following equations are used to relate the concentration to the value of x in Na_2S_x

$$c_1 = (x - 1)/(19 + 18.4x)$$

$$c_2 = 2/(19 + 18.4x)$$

$$c_3 = (19 + 18.4x)^{-1}$$

The partial molar volumes are: $V_1 = 18.4$, $V_2 = V_3 = 37.4/3$ cm³/mole.

In arriving at these values, it was assumed that the partial molar volumes of Na^+ and $S^=$ ions, V_2 and V_3, were the same. As was stated in a paper by Newman and Chapman (12), this assumption is adopted for convenience only and should not be attached to any physical interpretation. Since only one equation is needed because of electroneutrality, we use the equation for atomic sulfur, which is

$$\frac{\partial c_1}{\partial t} = -\frac{1}{r} \frac{\partial}{\partial r} \left\{ r \left[(1 - 2W_s) \frac{i}{2\mathbf{F}} + c_1 v_2 \right] \right\} \quad [12]$$

After using $W_s = -c_1/2c_3$ and Eq. [11], the above equation becomes

$$\frac{\partial c_1}{\partial t} = \frac{1}{r} \frac{\partial}{\partial r} \left[\left(\frac{1}{V_1} - c_1 \right) v_2 r \right] \quad [13]$$

In terms of x in Na_2S_x, Eq. [13] becomes

$$\frac{\partial x}{\partial t} = \frac{(18.4x + 19)^2}{18.4r} \frac{\partial}{\partial r} \left(\frac{v_2 r}{18.4x + 19} \right) \quad [14]$$

After introducing the dimensionless current density and space coordinate, j and y, into Eq. [11] and [14] we obtain

$$\frac{\partial}{\partial y}\left(\frac{v_2}{C_t}\right) = \frac{V_1 I_{R_0}}{2F}\frac{\partial}{\partial y}\left(\frac{jx}{C_t}\right) \quad [15]$$

$$\frac{\partial x}{\partial t} = \frac{(19+18.4x)^2 C_t}{18.4\,\Delta R}\frac{\partial}{\partial y}\left[\frac{v_2}{C_t(19+18.4x)}\right] \quad [16]$$

Equations [1], [15], and [16] form the set of equations that describe the transient response of the sulfur electrode, or more precisely, the polysulfide phase of the sulfur electrode. Since sulfur is nonconductive, no electrochemical reaction takes place in the sulfur zone of the electrode.

The boundary conditions for the current equation on discharge are defined so that all the current is in the melt at $y = 0$, the ceramic/melt interface, and in the felt at $y = 1$, the sulfur/polysulfide interface

$$j(0,t) = 1; \quad j(1,t) = 0 \quad [17]$$

The boundary condition for v_2 can only be defined consistently for the case when the cell operates in the single phase region. This difficulty arises from the use of the Washburn number, W_s, which implies that atomic sulfur moves only with the sulfide ion. Therefore, no mechanism is available in this model for transporting the reactant, sulfur, across the sulfur/polysulfide interface. Hence, the following numerical simulation is limited to the single phase region where the over-all sulfur content is less than the saturation value. For the cases studied below the maximum value of x

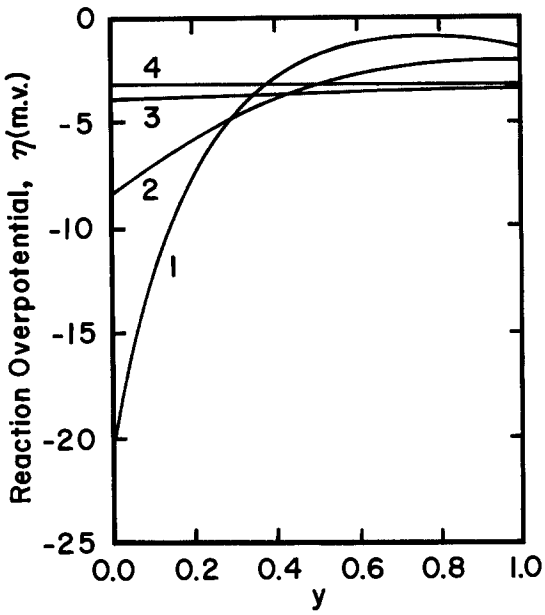


Fig. 2. Overpotential distributions for conditions listed in the caption of Fig. 1.

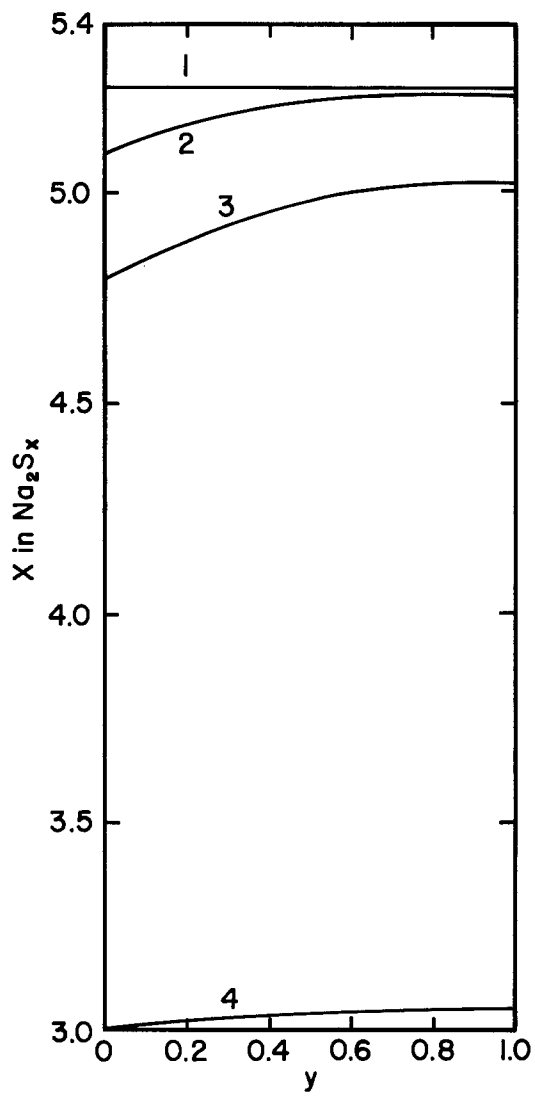


Fig. 1. Concentration profiles of polysulfide electrode after curve 1, 0 sec; curve 2, 45 sec; curve 3, 285 sec; curve 4, 3660 sec; with initial thickness $\Delta R = 0.2587$ cm, $k_2 = 3$ ohm^{-1}cm^{-1}, $a = 100$ cm^{-1}, $i_1 = 0.05$ A/cm^2, $I_{R_0} = 0.12345$ A/cm^2.

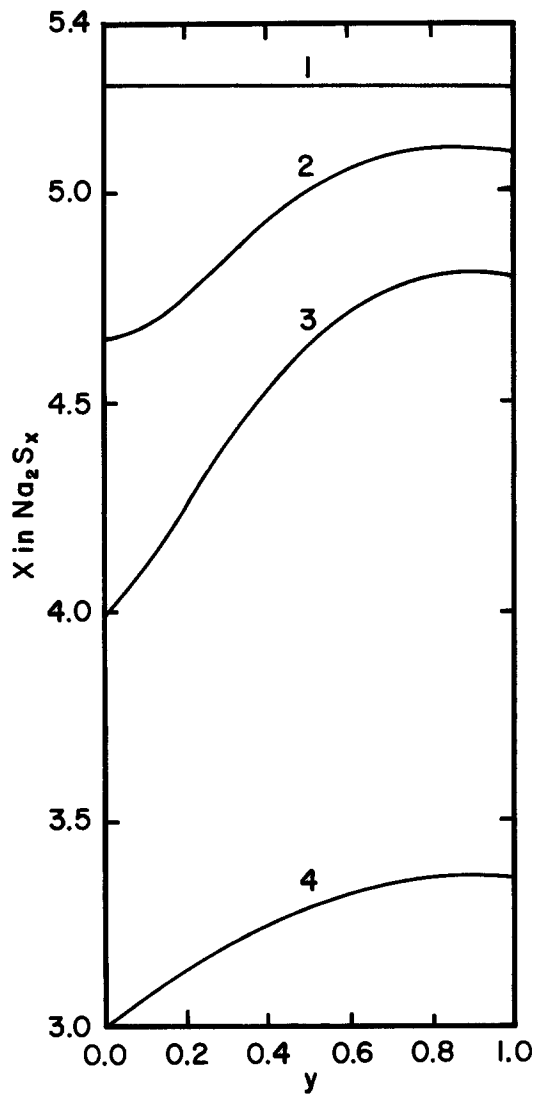


Fig. 3. Concentration profiles of polysulfide electrode after curve 1, 0 sec; curve 2, 42.75 sec; curve 3, 110.25 sec; curve 4, 450 sec; discharges at $I_{R_0} = 0.823$ A/cm^2; other conditions are the same as those listed in the caption of Fig. 1.

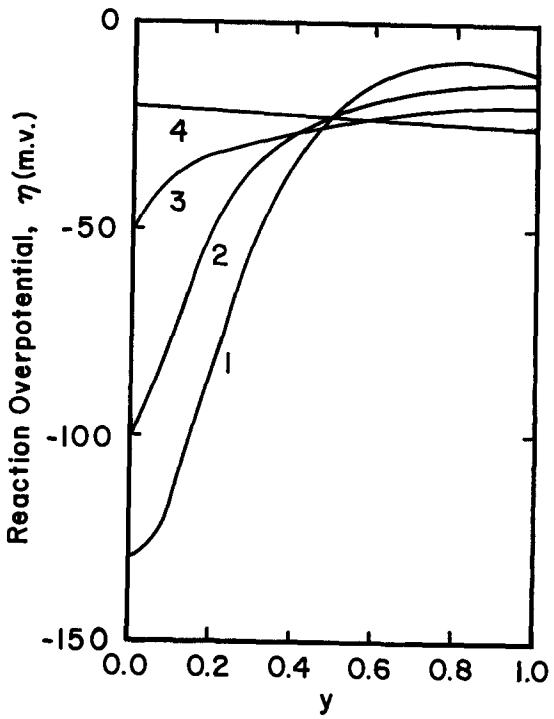


Fig. 4. Overpotential distributions for conditions listed in the caption of Fig. 3.

in Na_2S_x is 5.25, which corresponds to a cell temperature of 350C.

The slight volume change resulting from the change in sulfur concentration was included as a slight variation in the thickness of the electrode. In this case, v_2 at the backing plate is given by

$$v_2(R_1, t) = \frac{dR_1}{dt} = \frac{I_{R_0}R_0}{2\mathbf{F}}(2V_2 + V_3 - V_1) = 19\frac{I_{R_0}R_0}{2\mathbf{F}R_1} \quad [18]$$

For the following results based on the simulation of the sulfur electrode using Eq. [1], [15], and [16] the initial concentration profile was assumed to be uniform, $x(y, 0) = 5.25$.

Numerical Results and Discussion

The orthogonal collocation method (13) with ten interior collocation points was used to obtain the solution to the coupled nonlinear partial differential equations [1], [15], and [16] with boundary conditions [17]. The results show several interesting features. In general, the initial nonuniform reaction rate distribution tends to become more uniform as the discharge proceeds and the initial uniform concentration distribution becomes less uniform. For some cases, the computed potential loss is less than that obtained using a uniform concentration model. Due to the resulting nonuniform concentration profile, there is a capacity loss which depends on the current density. Therefore, a closely monitored operation is necessary to prevent the accumulation of capacity losses from cycle to cycle.

In Fig. 1 and 2, the transient values of concentration and reaction overpotential are presented for the following cell: $R_0 = 0.3$ cm, $\Delta R = 0.2587$ cm, $I_{R_0} = 0.12345$ A/cm^2 based on the outer surface area of the ceramic tube, uniform initial concentration of $Na_2S_{5.25}$, $i_l = 50$ mA/cm^2, $a = 100$ cm^{-1}, $k_2 = 3$ ohm^{-1} cm^{-1}. In Fig. 3 and 4, the results for the same cell with $I_{R_0} = 0.823$ A/cm^2 are presented. The simulation was continued until the value of x in Na_2S_x dropped below 3.0 at some point in the cell. At this point, the precipitation of solid, nonconductive sodium disulfide was presumed to occur. Comparison of Fig. 1 with Fig. 3 demonstrates that the nonuniformity of concentration increases with current

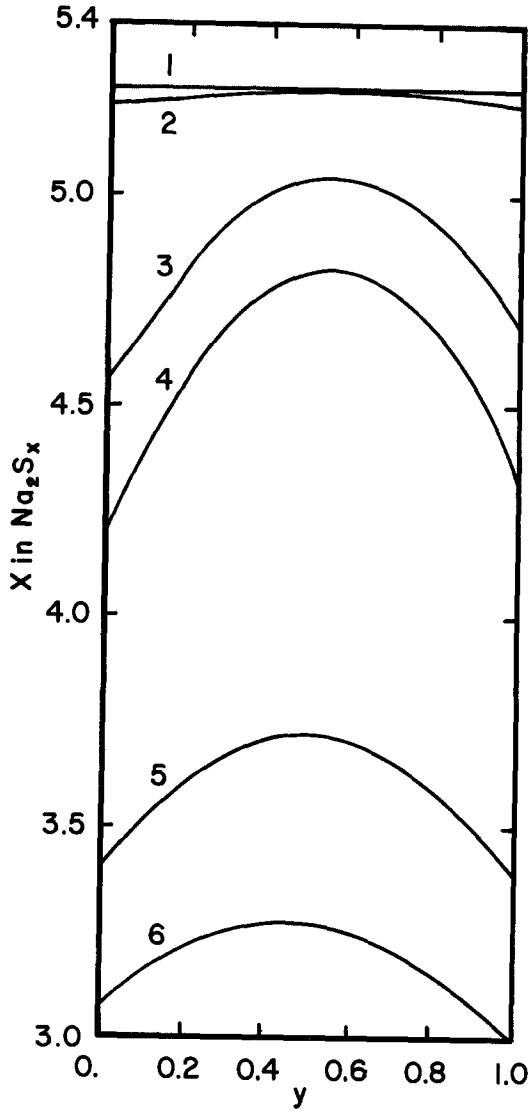


Fig. 5. Concentration profiles of polysulfide electrode after curve 1, 0 sec; curve 2, 2.25 sec; curve 3, 54 sec; curve 4, 99 sec; curve 5, 346.5 sec; curve 6, 492.8 sec; $k_2 = 0.3$ ohm^{-1}cm^{-1}; all other conditions are the same as those listed in the caption of Fig. 1.

load. Therefore, the unusable capacity (represented by the area under curve 4) increases with current load. The concentration and reaction rate profiles at earlier stages of discharge at the lower current load are different from those at the higher current load. This is an inherent feature of the diffusional kinetics used herein. This feature disappears with the use of a linear kinetics model.

The numerical results for a lower felt conductivity ($k_2 = 0.3$ ohm^{-1}cm^{-1}) and a higher current load ($I_{R_0} = 0.823$ A/cm^2) are presented in Fig. 5 and 6. All other parametric values are the same as those used above. In contrast to the higher felt conductivity case shown in Fig. 3, the sulfur rich zone is now located in the midsection of the electrode. The initial reaction rate distribution is very nonuniform but tends to become more uniform as the concentration distribution becomes nonuniform. The initial reaction rate distribution is similar to that calculated by Gibson (6) for the uniform concentration case with equal melt and felt conductivities. However, in contrast to the uniform concentration results, as this cell discharges the nonuniform concentration of sulfur causes the reaction distribution to become more uniform. The capacity loss for this cell is represented by the area under curve 6. It can also be concluded that the sulfur rich zone will form in the region where less reaction is predicted by the simpler uniform concentration model. However, the transient

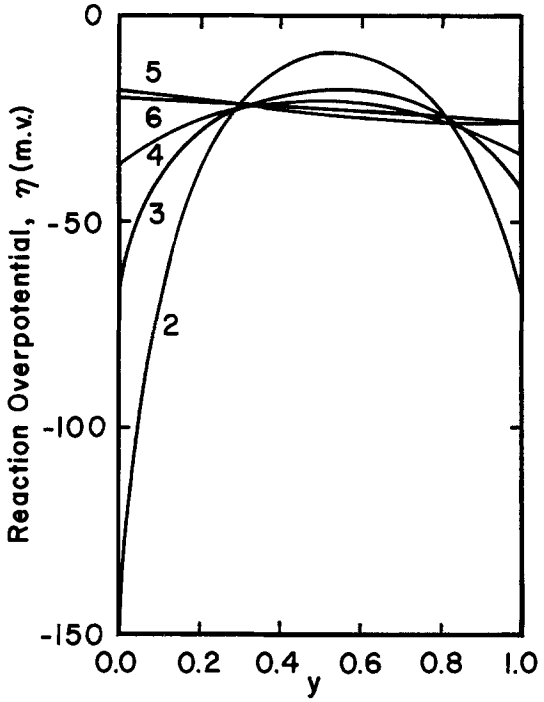


Fig. 6. Overpotential distributions for conditions listed in the caption of Fig. 5.

magnitude of the concentration distribution cannot be predicted by the simpler model.

Comparison of Fig. 7 and 8 with Fig. 1 and 2 shows the effect of electrode thickness. The initial thickness of the electrode for the case presented in Fig. 7 and 8 is 1 cm. In the other cases this thickness is 0.2587 cm. The results demonstrate that a larger variation in the concentration develops in the thicker electrodes. According to Eq. [1], a larger concentration distribution is needed to offset the increased ohmic effect resulting from the thicker electrode.

In Fig. 9 the computed cell voltage history for the following three operating conditions is presented: (*i*) $I_{R_0} = 0.12345$ A/cm^2; (*ii*) $I_{R_0} = 0.37035$ A/cm^2; and (*iii*) $I_{R_0} = 0.823$ A/cm^2. In these calculations the ceramic was assumed to have a thickness of 0.2 cm with a resistivity of 5 Ω-cm and the contact resistance between the graphite felt and backing plate was assumed to be 0.1 Ω-cm^2. It is interesting to note that there is an increase in the cell voltage at the earlier stages of discharge in the single phase region for the case of a discharge rate equal to 0.823 A/cm^2. This phenomenon has also been observed experimentally (14). The initial reduction in cell resistance results from the development of the concentration profile which reduces the effective resistance of melt. A higher OCV is also available in the nonuniform concentration case compared to the uniform concentration case because the concentration of sulfur in part of the cell is above the average value. The discharge curves in Fig. 9 are terminated at the instant when x in Na_2S_x is less than 3.0 in some region of the cell. At this point the precipitation of solid, nonconductive sodium disulfide is presumed to occur. The results demonstrate that, for a cell of the same expected capacity, the capacity loss increases with current load. The percent of theoretical capacity available for use is plotted as a function of load in Fig. 10. For a cell operating at 0.823 A/cm^2, the capacity loss is 20% based on a cell operating in the single phase region only or approximately 6% based on an initial charge of pure sulfur.

These results can be applied qualitatively to a cell with a two-dimensional concentration profile by assuming that the model applies to small regions of the electrode. In this case, the concentration effect enhances

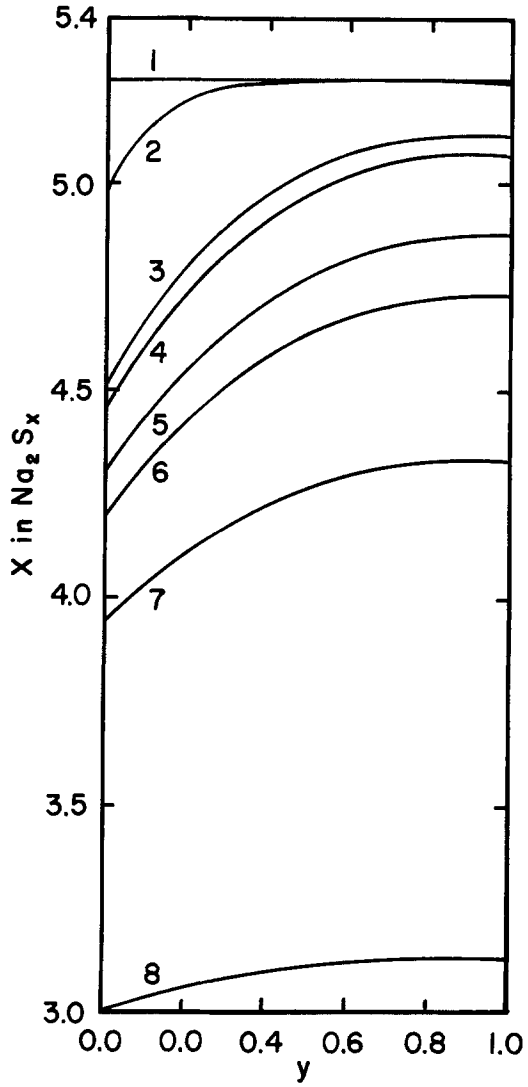


Fig. 7. Concentration profiles of a thicker polysulfide electrode, after curve 1, 0 sec; curve 2, 720 sec; curve 3, 1650 sec; curve 4, 2070 sec; curve 5, 3630 sec; curve 6, 4800 sec; curve 7, 8310 sec; curve 8, 24,660 sec; with initial thickness $\Delta R = 1.0$ cm, $I_{R_0} = 0.12345$ A/cm^2, all other conditions are the same as those listed in the caption of Fig. 1.

the local reaction distribution until nonconductive sodium disulfide precipitates. Then this region becomes inoperative, and the total cell slowly loses capacity. This effect can become accumulative unless these regions are recharged or the precipitation avoided on discharge. The design of a reliable high capacity battery depends on minimizing the capacity losses described by the above transient model.

Conclusions

The predominant effect on cell performance is due to the variation of the chemical potential of sulfur with concentration which causes the cell to operate uniformly. This advantage is partly offset by high current densities, large cell dimensions, and unmatched melt and felt conductivities. Further, a nonuniform concentration distribution results in the loss of cell capacity due to the premature precipitation of sodium disulfide, which can be cumulative. Therefore, a battery should be designed so that the nonuniform concentration effect is used to enhance the operation of the cell but is restricted to small regions so that the accompanying capacity loss is minimized.

Acknowledgment

Support for this study was provided by the National Science Foundation under the RANN program (NSF-C805) through the Ford Motor Company.

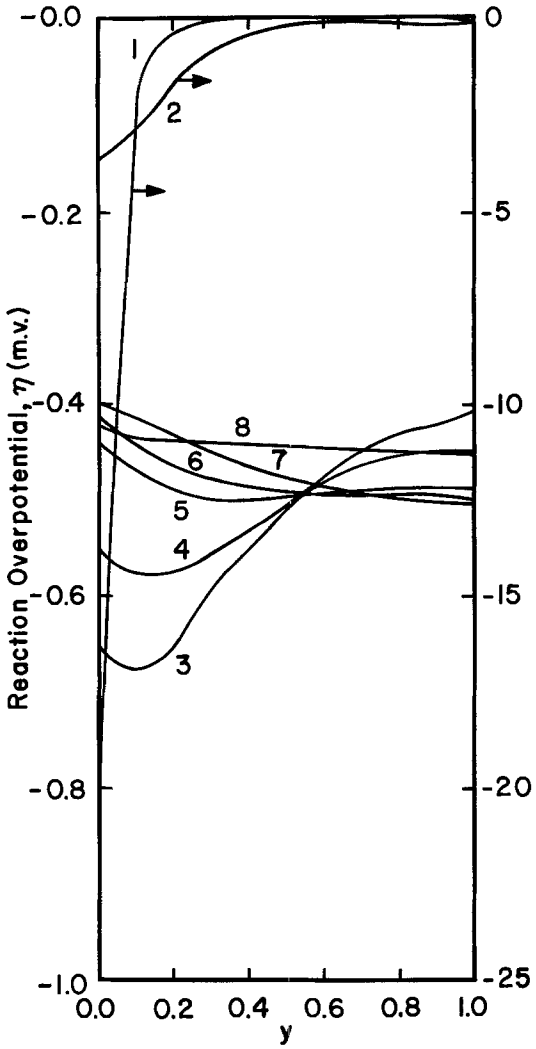


Fig. 8. Overpotential distributions for conditions listed in the caption of Fig. 7.

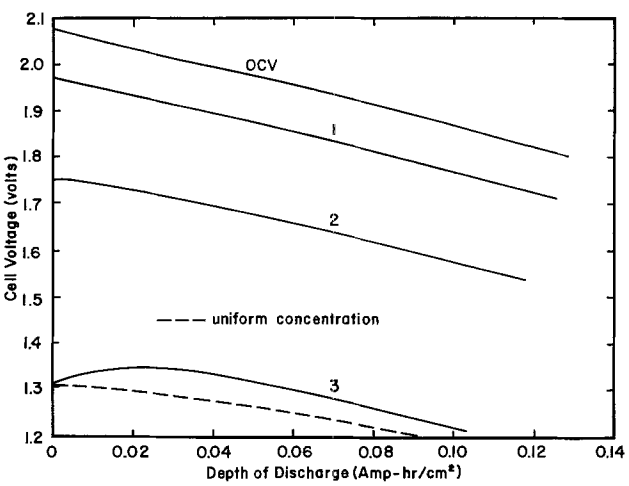


Fig. 9. Computed cell voltage history for cell discharges at curve 1, $I_{R_0} = 0.12345$ A/cm^2; curve 2, $I_{R_0} = 0.37035$ A/cm^2; and curve 3, $I_{R_0} = 0.823$ A/cm; all other conditions are the same as those listed in the caption of Fig. 1.

Manuscript submitted Feb. 25, 1976; revised manuscript received Oct. 1, 1976.

Any discussion of this paper will appear in a Discussion Section to be published in the December 1977 JOURNAL. All discussions for the December 1977 Discussion Section should be submitted by Aug. 1, 1977.

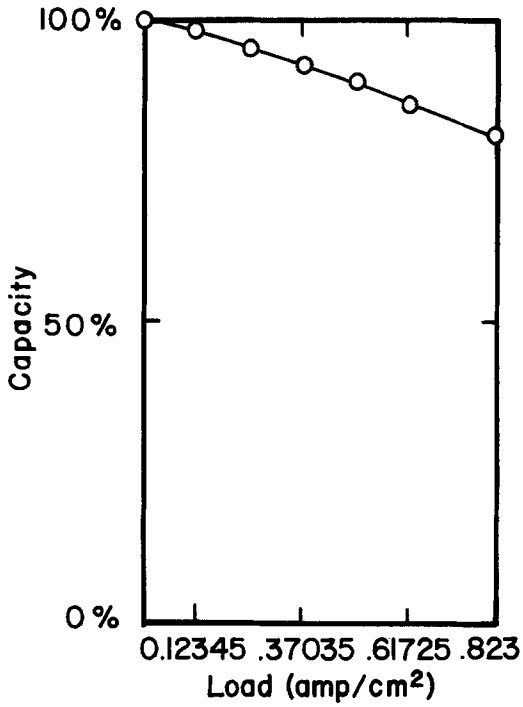


Fig. 10. Estimated capacity loss for a cell with initial thickness, $\Delta R = 0.2587$ cm.

LIST OF SYMBOLS

a	activity; surface area per unit volume
b'	$bn\mathbf{F}/RT$, $b = 384.9642$ mV
c	molar concentration
c'	$cn\mathbf{F}/RT$, $c = 74.8151$ mV
C_t	$\Delta R/(y\Delta R + R_0)$
d'	$dn\mathbf{F}/RT$, $d = 5.0553$ mV
$\mathbf{F}$	Faraday
i	current density
I_{R_0}	current density at $r = R_0$
j	i_1/I_{R_0}
k	conductivity
K	drag coefficient
N	molar flux
r	radial position
R	gas constant
R_0	radius of ceramic outer surface
R_1	radius of outer surface of active electrode
T	temperature
V	molar volume
v	velocity
W_s	Washburn number
w_s	weight fraction of sulfur
x	x in Na_2S_x
y	dimensionless radius position, $= (r - R_0)\ (R_1 - R_0)$
α	$\mathbf{F}/RT$
β	$I_{R_0}/a\ i_1\Delta R$
γ	$ai_1(\Delta R)^2\ \alpha(1/k_1 + 1/k_2)$
δ	$1/\beta$
ΔR	active electrode thickness
η	overpotential
μ	electrochemical potential
ϕ	potential

Subscripts

1	melt, sulfur
2	felt, sodium ion
3	sulfide ion
l	limiting current

REFERENCES

1. J. T. Kummer and N. Weber, "A Sodium-Sulfur Secondary Battery," Auto. Eng. Cong., Detroit, Michigan S.A.E. 670179, (1967).
2. N. K. Gupta and R. P. Tischer, *This Journal*, **119**, 1033 (1972).
3. "Sodium-Sulfur Battery Development," Final Report, EPRI project RP 128, July 1974.
4. "Development for Solid Electrolyte Batteries," Final Report, EPRI project RP 127, Oct. 1974.
5. "Research on Electrode and Electrolyte for the Ford Sodium-Sulfur Battery," Annual Reports,

NSF—RANN Contract C-805, July 1974 and July 1975.
6. J. G. Gibson, *J. Appl. Electrochem.*, **4**, 125 (1974).
7. J. Newman and C. W. Tobias, *This Journal*, **109**, 1183 (1962).
8. Y. K. Kao and P. C. Wayner, Jr., *ibid.*, **123**, 632 (1976).
9. B. Cleaver *et al.*, *Electrochim. Acta*, **18**, 719 (1973).
10. B. Cleaver and A. J. Davies, *ibid.*, **18**, 733 (1973).
11. J. G. Kirkwood *et al.*, *J. Chem. Phys.*, **33**, 1505 (1960).
12. J. Newman and T. W. Chapman, *AIChE J.*, **19**, 343 (1973).
13. J. N. Villadsen, "Selected Approximation Method for Chemical Engineering Problems," Institut fur Kemiteknik, Numerisk Instut Denmarks Techniske Hojskole, Copenhagen, Denmark (1970).
14. R. Minck, Private communication (1973).
15. J. Newman and W. Tiedmann, *AIChE J.*, **21**, 25 (1975).

Brief Communication

Investigation into the Immobilization of the Sodium Electrode in the Sodium-Sulfur Battery

Reinhard Knödler, Werner Baukal, and Wolfgang Kuhn

Battelle-Institut e.V., Frankfurt am Main, West Germany

The negative electrode in the sodium-sulfur battery consists of liquid sodium at a temperature of 300°-400°C. Investigations were carried out in order to find out whether liquid sodium can be immobilized without influencing the electrical performance of the electrode. In the case of the lithium-sulfur battery this has been successful (1).

Experimental

The electrochemical behavior of an immobilized sodium electrode was investigated in cells of the type

Na (immobilized)/β-Al_2O_3/Na (freely mobile)

Immobilization has been achieved using stainless steel felts (Brunswick Corporation, Skokie, Illinois, and Württembergische Metallwarenfabrik, Geislingen, West Germany). The felts investigated had porosities between 80 and 90% and pore sizes between about 40 and 120 μm. β-Al_2O_3 was used in the form of closed-end tubes[1,2] (9 mm ID, 50 mm length) or of disks[3] onto which an α-Al_2O_3 cylinder was sealed with a special glass, thus giving "cups" (18 mm ID). In either configuration the outside contained freely mobile sodium and the inside the sodium immobilized by the felt.

The experiments were carried out in an argon atmosphere at 350°C. Double-distilled sodium was filled into the outer compartment and was transferred to the inner one by electrolysis through the β-Al_2O_3. In the tube configuration the sodium in both compartments was at the same level. For operation of the cell, a current was applied and its bias was reversed after equal time intervals so that the sodium level at both sides remained almost unchanged. The current densities applied ranged from 10 up to 400 mA/cm^2. From the voltage measured and the dimension of the cup/tube, it was possible to calculate a specific resistance. Its value does, in general, not represent the resistivity of the ceramic, but is rather a convenient standardized figure. For example, if part of the ceramic surface is not covered with sodium because of wetting problems, the standardized cell resistance increases, though the ceramic itself remains unchanged.

Results

The β-Al_2O_3 cups showed essentially the same behavior as the tubes. It was possible to extract sodium electrically and again fill it into the felt. Figure 1 shows a plot of the standardized resistance for a typical experiment using a β-Al_2O_3 tube. The resistance during charge (*i.e.*, filling the felt from outside) remained almost unchanged, whereas during discharge (removing the sodium from the felt) the resistance started to rise toward the end of the process.

This resistance increase can be employed to set a limit to the amount of sodium which can usefully be discharged from the felt. Choosing arbitrarily an increase by a factor of 2 as the limit, 70-80% of the sod-

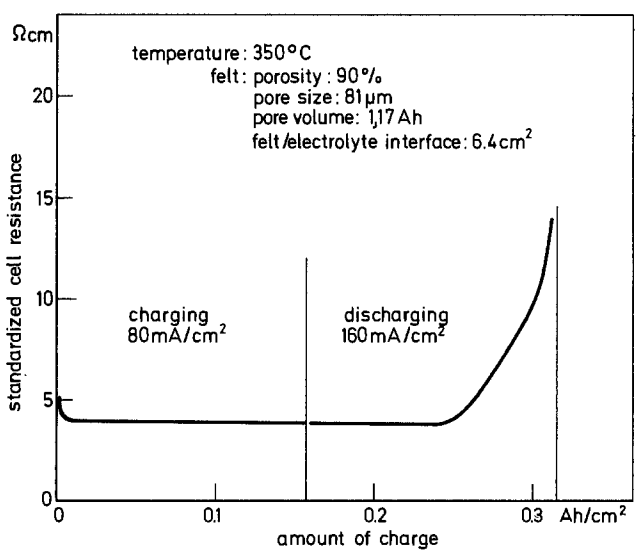


Fig. 1. Cycling behavior of a cell of the type Na (immobilized)/β-Al_2O_3/Na (freely mobile). The amount of sodium in the felt at the beginning of the cycle corresponded to 0.16 A-hr equivalent to 14% of the pore volume.

[1] Tubes: 9.3 weight percent (w/o) Na_2O, 3.0 w/o MgO, balance Al_2O_3.
[2] The tubes were kindly supplied by Brown, Boveri & Cie., AG, Heidelberg, West Germany.
[3] Disks: 8.7 w/o Na_2O, 0.7 w/o Li_2O, balance Al_2O_3.

Key words: sodium-sulfur battery, sodium immobilization, battery design, safety.

ium content in the felt may be utilized under optimized conditions. This optimization concerns the felt and the contact between felt and ceramic and will be discussed later. A total amount of at least 95% of the sodium can be discharged if higher resistances are taken into account.

In the region where the resistance increased, the cell showed nonohmic behavior, *i.e.*, the resistance depended on the current density. In addition, the resistance rise started at a higher discharge depth if a lower current density was applied. In the region of constant resistance, however, the current-voltage relationship was linear within several orders of magnitude of current density. In this ohmic region, the standardized resistance of the cell had the same value as the resistivity of the ceramic which had been determined by independent a-c measurements using graphite electrodes (2).

Contrary to the behavior described above, the removal of nonimmobilized sodium from the inner part of the tube resulted in a linear increase in resistance.

From a series of measurements using various felts the optimum pore size turned out to be about 80 μm at an optimum porosity of about 90%.

Further experiments with β-Al_2O_3 tubes showed that it is important to achieve a close contact between the electrolyte and the felt in order to utilize the highest possible amount of the immobilized sodium in discharging the cell. A good fit and, consequently, a good contact at the interface have been achieved by forming the felt by spark erosion. In some cases this good fit could also be obtained by using a smaller inner metal felt core without exact fit and a layer of steel wool wrapped around this core.

Immobilization of the sodium in the felt has been confirmed by an experiment in the cup configuration, in which the felt was kept at a distance of about 3 mm from the electrolyte surface. After the cup had been filled in the usual way, only the freely mobile sodium below the felt could be discharged. The sodium in the felt remained there even against the effect of gravity. Thus, the contact between the felt and the β-Al_2O_3 ceramic is essential for draining the sodium off the felt by a cathodic current.

Some experiments were discontinued in the course of a charge or a discharge half-cycle when, according to the charge balance over all previous cycles, the moiety of the pore volume of the felt was filled. After cross-sectioning and polishing under moisture-free conditions, microscopic inspection revealed that the sodium was distributed uniformly over the whole volume of the felt.

This has led to a new design concept for the battery: the sulfur electrode is kept inside the beta-alumina tubes, thus minimizing corrosion problems, and the sodium electrode, immobilized in metal felt, can be placed outside. Since the resistance of the metal felt is much lower than that of graphite felt, a multicell arrangement in parallel connection with a common sodium electrode can be conceived.

Experiments over several charge/discharge cycles showed that there was no change in the behavior of the metal felt with respect to its immobilizing properties and that the presence of the felt had no influence on the degradation of the ceramic.

Discussion

The outstanding feature of the interface between the sodium-filled metal felt and the β-Al_2O_3 ceramic is the resistance rise and the simultaneous transition from ohmic to nonohmic behavior when the felt is being depleted of sodium. The onset and magnitude of this phenomenon depends on the pore size of the felt, on the electric current applied, and on the quality of the contact between felt and ceramic.

In the ohmic part, the agreement between the standardized resistance of the cell and the resistivity of the ceramic shows that the whole interface felt/ceramic is covered with a continuous sodium film. A sodium film should also be present at the individual fibers of the felt. Delivery of sodium from the volume of the felt to the interface is then accomplished over those fibers which touch the ceramic surface.

On prolonged depletion of the felt, the nonohmic region is entered: the counteraction between the retaining capillary force exerted by the felt pores and the drain exerted by the cathodically polarized ceramic is shifted toward the retention side. Only part of the felt fibers touching the ceramic surface are still covered with a sodium film and are able to deliver sodium to the electrolyte. The sodium reaching the interface is drained off immediately and cannot spread over the whole ceramic surface. Thus, the standardized cell resistance increases.

Conclusion

The results of the investigation show that a sodium-sulfur battery with no freely mobile sodium is feasible. In particular, immobilization of the sodium can be achieved without major influence on the performance of the sodium electrode and, hence, the battery.

Acknowledgments

This work was supported by the Bundesministerium für Forschung und Technologie (within the Energy Research Program directed by Kernforschungsanlage Jülich), by Brown, Boveri & Cie., AG, Heidelberg, by Gesellschaft für elektrischen Strassenverkehr, Düsseldorf, and by STEAG AG, Essen.

Manuscript received March 26, 1976.

Any discussion of this paper will appear in a Discussion Section to be published in the December 1977 JOURNAL. All discussions for the December 1977 Discussion Section should be submitted by Aug. 1, 1977.

Publication costs of this article were assisted by Battelle-Institut e.V.

REFERENCES

1. H. Shimotake, M. L. Kyle, V. A. Maroni, and E. J. Cairns, Proceedings of the First International Electric Vehicle Symposium, p. 392, Phoenix, Arizona (Nov. 1969).
2. W. Baukal and R. Knödler, *J. Appl. Electrochem.*, **5**, 105 (1975).

JOURNAL OF THE ELECTROCHEMICAL SOCIETY

SOLID-STATE SCIENCE AND TECHNOLOGY

FEBRUARY 1977

On the Mechanism of GaAs Anodization

D. J. Coleman, Jr., D. W. Shaw, and R. D. Dobrott

Texas Instruments Incorporated, Central Research Laboratories, Dallas, Texas 75222

ABSTRACT

The oxygen distribution in anodic oxides on GaAs grown from electrolytes prepared with H_2O^{16} and H_2O^{18} has been analyzed with an ion microprobe mass analyzer. The data show that as the oxide grows, additional oxygen is incorporated into the film at the oxide-electrolyte interface. The implications to the mechanism of oxide growth are discussed.

Anodic oxide films grown on GaAs have been reported by many authors (1-4) using various electrolytes. Because of the potential technological significance of these oxides, the details of their growth mechanism is of primary importance. Basic to this understanding is the identification of the nature of the mobile species within the growing oxide film during anodization. Consider, for example, interstitial ion transport. If oxygen were the only mobile species, then the oxide would grow by formation of new layers at the oxide/semiconductor interface. On the other hand, if the ions from the semiconductor were the mobile species, then the oxide would thicken by addition of layers at the oxide/electrolyte interface. Presumably if both ions were mobile new oxide would be produced at both interfaces or even within the bulk of the existing oxide.

Pursuant to such arguments, several techniques have been utilized to identify the mobile species in metal and semiconductor anodization. A simple technique places an inert marker layer in the oxide and the subsequent location of its position (5) or its effect on the substrate (6) infers the mobile ionic species. α- and β-spectroscopy have been useful by implanting radioisotopes (7, 8) into the surface to be oxidized and tracking their depth at various stages of oxidation by observation of the emitted lineshape characteristic of the implanted isotope. Amsel and Samuel (9) grew sequential oxides from aqueous electrolytes prepared with H_2O^{18} and H_2O^{16} on aluminum and then determined the location of the O^{18} isotope by means of the O^{18} (p, α) N^{15} reaction.

In spite of its increasing significance to GaAs technology, the GaAs anodization process has not been investigated with respect to the nature of the mobile species. Accordingly, we have examined ionic mobility in GaAs anodization from an aqueous electrolyte. The GaAs anodic oxides were prepared in a manner similar to that of Ansel and Samuel in that sequential anodic oxides were grown from H_2O^{18} and H_2O^{16} electrolytes. However, for analysis of the isotopic distribution of the oxygen atoms in resulting oxides, an ARL ion microprobe mass analyzer (IMMA) was employed. This instrument sputters small areas of the oxides with a relatively high energy ion beam and mass analyzes the sputtered ions by double focusing techniques. IMMA is ideally suited for this type of study in that depth distributions are easily obtained by collecting the signal in a number of equal time increments each of which corresponds to a thin depth section of the sputtered oxide.

Key words: anodic films, anodic oxides, ion transport.

The anodizations were performed in small (about 1 cm^3) Pyrex containers that could be stoppered when not in use to prevent loss by evaporation. A 0.02M $NH_4H_2PO_4$ electrolyte was used with a Pt cathode. Two electrolyte baths were prepared, one from deionized water with natural abundance (99.8%) of O^{16} and the other from O^{18} enriched water received from Mound Laboratory certified as 96.6% O^{18}. Initial oxidations performed in the enriched water electrolyte exhibited runaway current-time behavior and surface pitting typical of electrolyte contamination (10). After a single distillation in a Pyrex apparatus, the enriched water electrolyte exhibited the usual current-time behavior.

The anodizations were carried out on {001} surfaces of n-type (2×10^{17} cm^{-3}) GaAs wafers. The wafers were 200 μm thick and chemical-mechanically polished on both sides. Residual damage after polishing was removed by a 10 min etch in an H_2SO_4:H_2O_2:H_2O, 8:1:1 etchant. Just prior to oxide growth each specimen was cleaned with an initial anodization with subsequent stripping of the resulting oxide in dilute HCl. Sample dimensions of approximately 5×15 mm were utilized with cleaved edges. Each sample was held in Au plated tweezers for anode contact and immersed approximately 10 mm into the electrolyte. A constant 30V anodic potential was applied to grow the first oxide. The initial current was about 30 mA for all samples in both electrolyte baths and fell rapidly decreasing to about 0.5 mA after 1 min. After growth of the first oxide layer each sample was removed from the electrolyte, rinsed, and blown dry. The initial oxides were uniformly gold colored and approximately 300Å thick. A second anodization was performed by immersing the lower 5 mm of each sample in the opposite electrolyte bath from that used to form the first oxide and applying a constant 60V potential. For this second oxidation, the initial currents were typically 15 mA and fell rapidly again to near 0.5 mA after 1 min. The oxide on the lower half of each sample was, thereby, increased in thickness to nearly 800Å and appeared royal blue in color.

A total of four samples including two controls were prepared according to Table I to form a complete complement of combinations of the natural and enriched water electrolyte baths for the two oxidations.

Table I. Electrolyte combinations used for sample preparation

Sample designation	Initial 30V oxidation	Sequential 60V oxidation
HL	H_2O^{18}	H_2O^{16}
LH	H_2O^{16}	H_2O^{18}
HH	H_2O^{18}	H_2O^{18}
LL	H_2O^{16}	H_2O^{16}

After oxidation each sample was depth profiled in the IMMA using a 10 kV N_2^+ primary sputter beam which was focused to a diameter of approximately 25 μm. The beam was rastered to cut a crater of 400 × 320 μm which gave an effective sputter rate of about 0.4 Å/sec. Both mass 16 and 18 positive ion data were obtained from the same sputter crater by electrostatic isotope switching the mass analyzed beam and synchronous gating of two identical 200 MHz scalers every 100 msec with a 10 msec scintillator decay period between each isotope period. To avoid the effects of the crater wall at the extrema of the raster, the scalers were gated on only when the primary beam was sputtering the central 1/9 of the crater bottom. The primary beam was rastered at 30 frames/sec and 50 lines/frame to assure that the crater wall rejection gating and the isotope gating were asynchronous. The depth collection time increment was 22 sec which corresponds to an apparent depth resolution of approximately 8Å ignoring ion plasma intermixing of the atoms in the solid.

Figures 1 through 4 show the distribution of O^{18} and O^{16} obtained from the IMMA analysis of the four samples. The data clearly show that the oxygen isotope

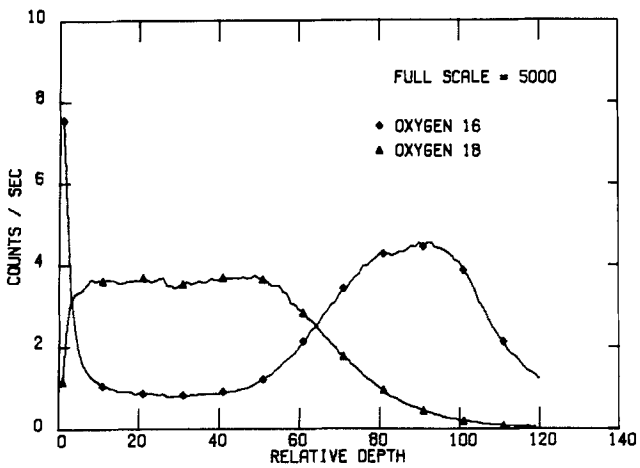


Fig. 1. Isotopic oxygen distribution for sample LH oxidized first in H_2O^{16} and then in H_2O^{18}.

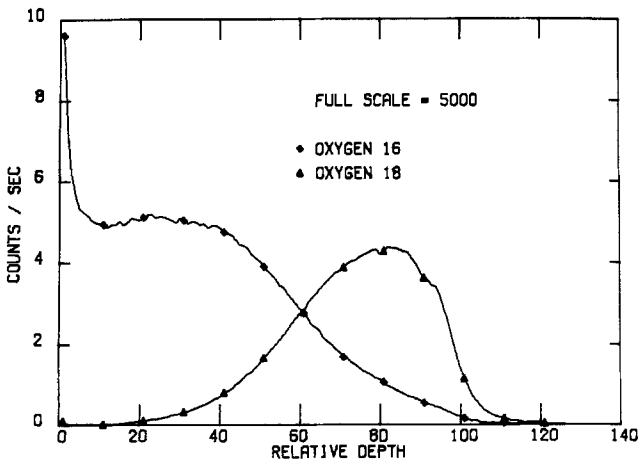


Fig. 2. Isotopic oxygen distribution for sample HL oxidized first in H_2O^{18} and then in H_2O^{16}.

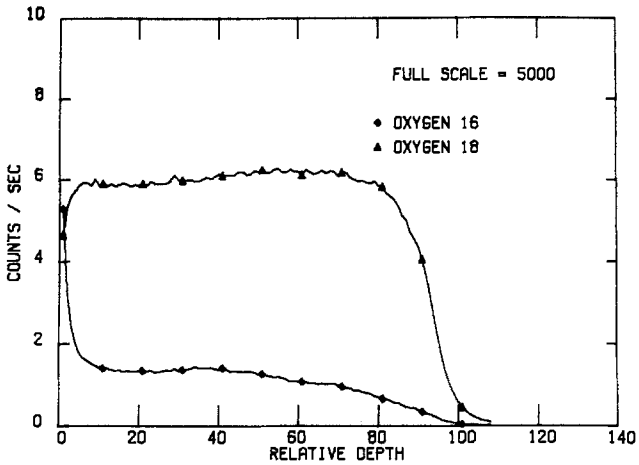


Fig. 3. Isotopic oxygen distribution in control sample HH oxidized in H_2O^{18}.

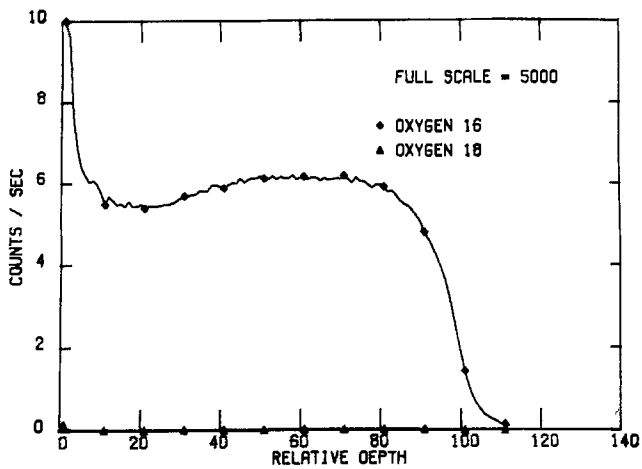


Fig. 4. Isotopic oxygen distribution in control sample LL oxidized in H_2O^{16}.

near the surface of each anodized specimen is incorporated from the last electrolyte from which the oxide was grown. The oxygen signal from the first 10 relative depth units should be ignored in the depth profiles since the oxygen ionization probability does not reach equilibrium until the sputtered depth reaches the initial implant depth of the primary ions (~100Å). The O^{16} content of the oxides grown in the enriched water electrolytes was higher than expected. However, this does not affect the interpretation, since control samples, HH and LL, were used to establish the reference isotopic abundances. The intersection of the O^{16}-O^{18} profiles are at about the half-maximum of each profile and appear symmetrical around this point. This suggests the actual interface is rather sharp and the width is entirely due to the analysis technique. This broadening is inherent in the sputtering process where the high energy sputter ions can penetrate the solid to a significant depth (100-200Å) and, by a collision process, these ions redistribute atoms in both backward and forward directions.

In summary, we have demonstrated that in GaAs anodization, oxygen is incorporated into the growing oxide at the oxide-electrolyte interface as opposed to the oxide-semiconductor interface. This fact and the simple hypothesis that mass transport occurs through the interstices of the growing oxide leads one to conclude that Ga and As are mobile in the oxide. An alternate hypothesis is substitutional migration. As shown by Amsel and Samuel substitutional propagation of either oxygen or metal ions can result in an oxygen distribution similar to that observed. However, the results of the experiments reported here eliminate interstitial

oxygen migration as the predominate transport process during GaAs anodization.

Acknowledgments

The authors wish to express their appreciation to Dr. R. J. Jasinski for several helpful discussions and suggestions. They further wish to acknowledge the experimental assistance of H. H. Marberry and D. E. Littlefield.

Manuscript submitted March 29, 1976; revised manuscript received Aug. 16, 1976.

Any discussion of this paper will appear in a Discussion Section to be published in the December 1977 JOURNAL. All discussions for the December 1977 Discussion Section should be submitted by Aug. 1, 1977.

Publication costs of this article were assisted by Texas Instruments Incorporated.

REFERENCES

1. S. M. Spitzer, B. Schwartz, and G. D. Weigle, *This Journal*, **122**, 397 (1975).
2. B. J. Sealy and P. L. F. Hemment, *Thin Solid Films*, **22**, S39 (1974).
3. H. Hasegawa, K. E. Forward, and H. L. Hartnagel, *Appl. Phys. Lett.*, **26**, 567 (1975).
4. H. Muller, F. H. Eisen, and J. W. Mayer, *This Journal*, **122**, 651 (1975).
5. D. A. Vermilyea, *Acta Met.*, **2**, 482 (1954).
6. E. A. Benjamini, E. F. Duffek, C. A. Mylroie, and F. Schulenburg, *This Journal*, **110**, 266C (1963).
7. J. A. Davies and B. Domeij, *ibid.*, **110**, 849 (1963).
8. R. L. Graham, F. Brown, J. A. Davies, and J. P. S. Pringle, *Can. J. Phys.*, **41**, 1686 (1963).
9. G. Amsel and D. Samuel, *J. Phys. Chem. Solids*, **23**, 1707 (1962).
10. R. A. Logan, B. Schwartz, and W. J. Sundburg, *This Journal*, **120**, 1385 (1973).

Photoluminescence Due to Al, Ga, and B Acceptors in 4H-, 6H-, and 3C-SiC Grown from a Si Melt

A. Suzuki,* H. Matsunami, and T. Tanaka

Department of Electronics, Kyoto University, Kyoto 606, Japan

ABSTRACT

Single crystals of 4H-, 6H-, and 3C-SiC have been grown from a silicon melt in a graphite crucible. Visible photoluminescences due to Al, Ga, and B acceptors in these crystals are studied in the temperature range from 2° to 450°K. The luminescence color varies from violet to near-infrared depending on the energy level of the acceptor and the energy gap of the polytype. All the luminescences at low temperatures are thought to be due to pair recombination between the N donor introduced unintentionally and the Al, Ga, or B acceptor. Each spectrum consists of a zero-phonon peak and its phonon replicas. At higher temperatures, another emission appears owing to the recombination of free electrons with bound holes at the acceptors. From the luminescence spectra and the thermal quenching of the emission intensity, the ionization energy of Ga is found to be a little larger than that of Al, while B has much larger ionization energy. The values obtained for 4H-SiC are 168 meV + E_x, 249 meV + E_x, and 628 meV + E_x for Al, Ga, and B, respectively, where E_x is the exciton binding energy of the order of 10 meV. Owing to the deep level of the B acceptor, the luminescence has a different spectrum from those due to Al and Ga, and is intense even at room temperature.

Silicon carbide (SiC) has a large number of different crystal structures referred to as "polytypes." Since each polytype has a different energy gap (2.3-3.3 eV), SiC will be a useful semiconductor for various visible light emitting devices by a combination of polytypes and luminescent centers. A number of SiC light emitting diodes have been fabricated up to date, but their luminescent efficiencies have been low (1). One of the main causes is a high temperature process (above 2000°C) usually used for the crystal growth and the impurity doping, which makes it difficult to obtain good crystals and control impurity doping.

Brander *et al.* (2) and the authors (3) have fabricated 6H-SiC blue light emitting diodes by liquid phase epitaxial growth from a silicon (Si) melt. The blue luminescence has shown relatively high quantum efficiency. Since this method has the advantage of low growth temperature (about 1600°C), it will be suitable for the fabrication of light emitting devices. But there have been very few reports on visible-luminescence centers in SiC crystals grown from a Si melt. In this paper, visible photoluminescences due to Al, Ga, and B acceptors in 4H-, 6H-, and 3C-SiC crystals grown from a Si melt are investigated. The ionization energies of the three acceptors are presented and the recombination processes are discussed.

* Electrochemical Society Student Member.
Key words: visible-luminescence centers, donor-acceptor pair recombination, solution growth, polytypes.

Crystal Growth

The method of solution growth from a Si melt in a graphite crucible has been used for the preparation of 3C-SiC crystals by several researchers (4, 5). But the authors have found that single crystals of 4H- and 6H-SiC in addition to 3C-SiC were obtained without any seed crystal when the following two conditions were satisfied: (*i*) the temperature of the Si melt is higher (about 1800°C) than usually used for the growth of 3C-SiC; (*ii*) the temperature gradient of the melt is kept as small as possible (less than 5°C/cm). The arrangement for the crystal growth is shown in Fig. 1. In order to realize condition *ii*, the temperature of the bottom of the crucible was set slightly higher than that of the upper part, because the bottom was apt to be cooled by thermal conduction through the graphite support.

The crucible was made of dense and high purity graphite (apparent density 1.60 g/cm^3, ash content 0.02%). Its size was 40 mm in depth and 25 mm in

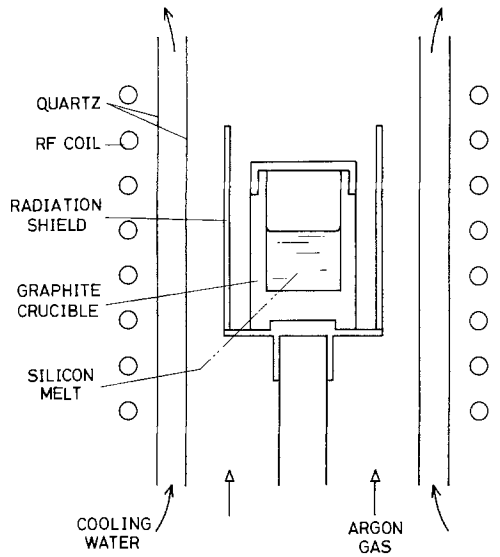


Fig. 1. Arrangement for solution growth of SiC single crystals

inner diameter. A graphite lid was used to avoid evaporation of silicon. The crucible was baked at about 1850°C for 2-3 hr under the flow of pure argon gas before the growth. After the crucible was filled with a 26g charge of pure polycrystalline silicon, it was kept at a growth temperature of 1800°C for 8 hr. The gas ambient during the growth was pure argon flowing at about 200 cm^3/min. After the growth, the silicon was removed with a 1:1 mixture of HF and HNO_3.

A large number of SiC single crystals grew on the inner wall of the crucible. The typical crystal size was 0.8 × 0.8 × 0.2 mm^3. The inner wall near the bottom was dissolved away slightly. The polytypes of the crystals in the crucible were identified as 4H, 6H, and 3C by x-ray oscillation photographs about their <0001> axes. Some examples of the photograph are shown in Fig. 2. The quality of 6H-SiC crystals seemed to be poorer than those of 4H- and 3C-SiC, because every spot in the photograph of 6H-SiC was somewhat diffused.

Nine kinds of samples were prepared for the photoluminescence measurements, that is, 4H-, 6H-, and 3C-SiC doped with Al, Ga, and B. Al-doped and Ga-doped crystals were grown from the Si melt with 0.01-0.1 atomic percent (a/o) Al metal and 1 a/o Ga metal in excess, respectively. B-doped crystals were obtained using B-doped (2×10^{-3} a/o) silicon as a source material. The impurities of Al, Ga, and B act as acceptors in SiC, but all the crystals were n-type containing unknown donors of the order of 10^{19} cm^{-3}. The donors were probably nitrogen introduced unintentionally from the residual air in the crucible material and in the ambient, because nitrogen is very apt to be introduced into SiC and acts as a donor (3).

Photoluminescence

Using a 250W high pressure mercury lamp as an excitation source, photoluminescence was measured at various temperatures between 2° and 450°K. The suitably filtered u.v. light of 365 nm from the lamp was focused on the sample. Luminescence from the sample was detected by a grating spectrometer and a photomultiplier.

At low temperatures, all the samples emitted intense photoluminescences of various visible colors from violet for 4H-SiC:Al to red for 3C-SiC:Ga. Only 3C-SiC:B emitted near-infrared luminescence. The color of each luminescence and the wavelength of its maximum emission peak at 77°K are shown in Table I. The luminescences of the Al-doped and the

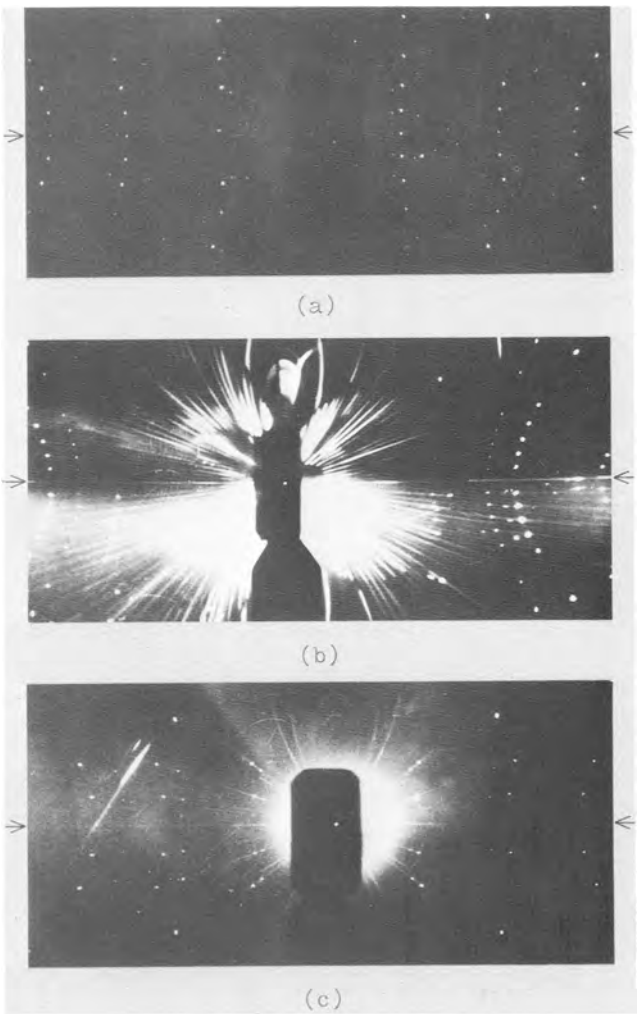


Fig. 2. X-ray oscillation photographs about the <0001> axes of SiC crystals, (a) 4H, (b) 6H, and (c) 3C polytypes. (The arrows indicate the center lines.)

Ga-doped samples were quenched below room temperature. But the B-doped samples showed intense luminescence even at room temperature, and the colors were much the same as at low temperatures.

Figure 3 shows luminescence spectra due to the different luminescent centers in 4H-SiC at 77°K. Spectra due to the same kind of centers in the different polytypes are shown in Fig. 4, 5, and 6. These spectra had the following five features. (*i*) The spectra due to Ga and B were on the lower energy side than the spectrum due to Al by 50-100 meV and 500-700 meV, respectively, for the three polytypes. (*ii*) The spectra of 6H-SiC and 3C-SiC due to the same kind of centers were on the lower energy side than 4H-SiC by 250-300 meV and 850-950 meV, respectively. (*iii*) All the spectra due to Al and Ga were similar in shape. Each spectrum had several peaks, among which the highest energy one (B_0) was rela-

Table I. Colors of photoluminescences from SiC of three polytypes. Each value is the wavelength of the maximum peak at 77°K (unit = nm).

Poly-type	Luminescence center		
	Al	Ga	B
4H	Violet 419	Blue 431	Green yellow 542
6H	Blue 465	Green 488	Yellow orange 621
3C	Orange 612	Red 646	Infrared 870

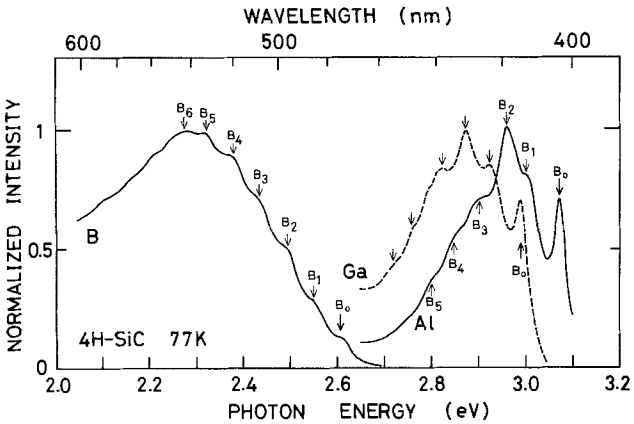


Fig. 3. Luminescence spectra of the Al-doped, Ga-doped, and B-doped 4H-SiC crystals at 77°K.

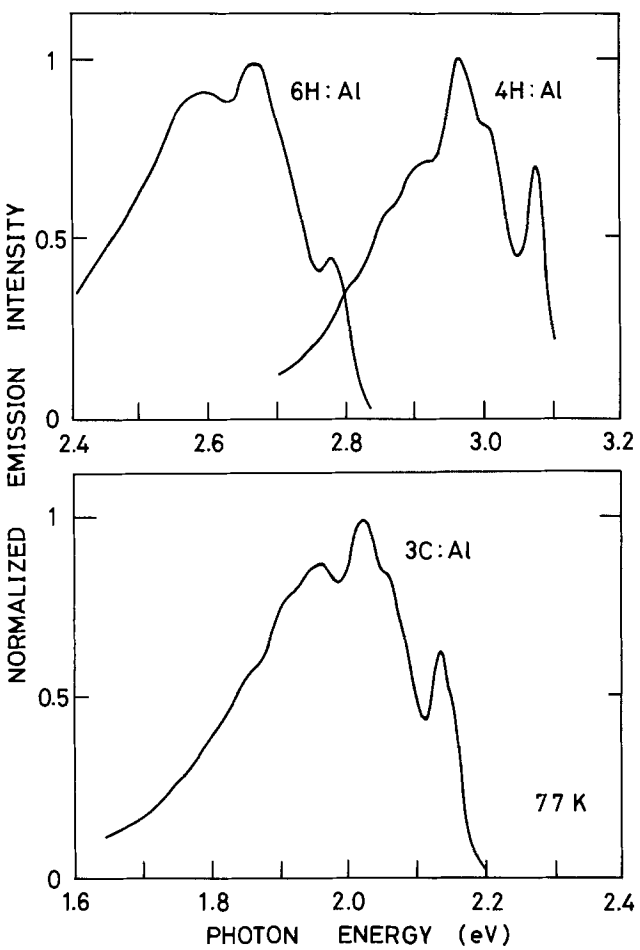


Fig. 4. Luminescence spectra of the Al-doped 4H-, 6H-, and 3C-SiC crystals at 77°K.

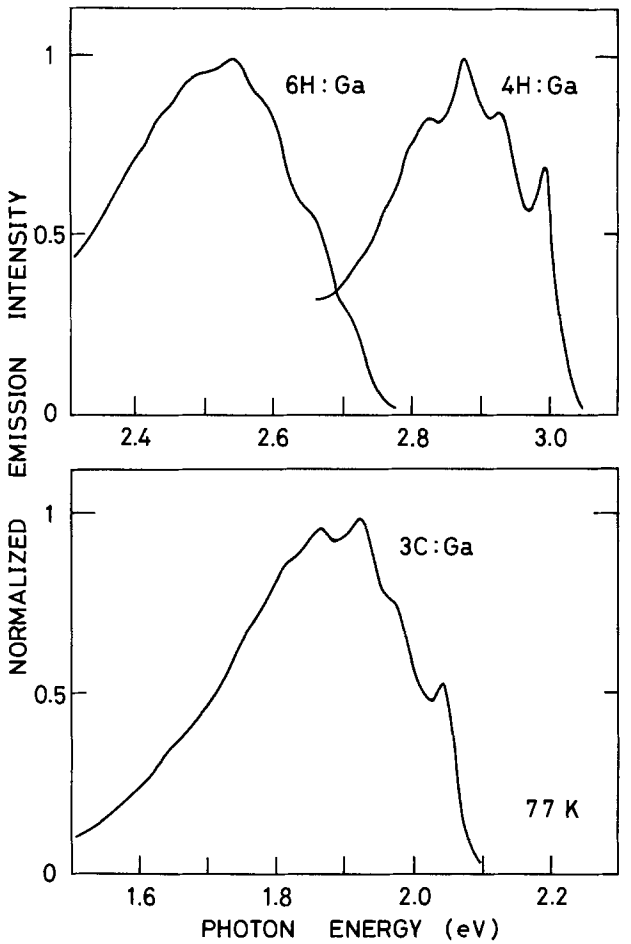


Fig. 5. Luminescence spectra of the Ga-doped 4H-, 6H-, and 3C-SiC crystals at 77°K.

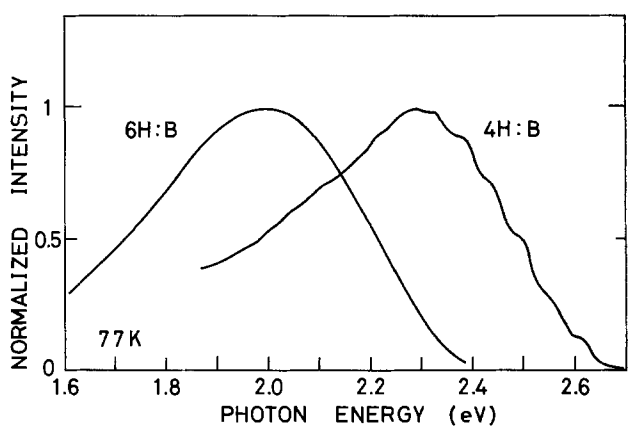


Fig. 6. Luminescence spectra of the B-doped 4H- and 6H-SiC crystals at 77°K.

tively sharp. (*iv*) The spectra due to B were "bell-shaped" ones with a very broad spectral width. (*v*) Each peak in the spectra of 6H-SiC was a little broader than that of 4H- and 3C-SiC.

Luminescence spectra at 2°K were much the same as at 77°K, but each peak was a little sharper. The energy of the highest energy peak or hump (B_0) of each spectrum, and the energy differences between B_0 and the other peaks on the lower energy side (B_1-B_6) are given in Table II from the data at 2°K. [For 3C-SiC:B, the data reported by Yamada *et al.* (6) were adopted. Their crystals were prepared by a similar method to ours.] The spectrum of 6H-SiC:B showed two humps on the higher energy side at 2°K like the spectrum of 4H-SiC:B at 77°K shown in Fig. 6.

Above 77°K, another peak (A_0) appeared on the higher energy side of the B_0 peak and became dominant with increasing temperature as shown in Fig. 7 for 3C-SiC:Al as an example. The energies of the A_0 peaks obtained for several samples are given in Table III.

The temperature dependence of the luminescence intensity of 4H-SiC is shown in Fig. 8 as a function of reciprocal temperature. The luminescences due to Al, Ga, and B decreased exponentially above 150°, 175°, and 350°K, with activation energies of 160 ± 20, 240 ± 20, and 520 ± 20 meV, respectively. The luminescences of 6H- and 3C-SiC also showed similar temperature dependences. The emission intensity due to B considerably increased with increasing tempera-

Table II. Photon energy of the zero-phonon peak B_0, and energy differences between B_0 and its phonon replicas B_i ($i = 1, 2, \ldots, 6$) at 2°K

Peak	Al			Ga			B			Contributing phonon
	4H	6H	3C	4H	6H	3C	4H	6H	3C	
B_0	3.067 (eV)	2.774	2.133	2.990	2.725	2.040	2.610	2.334	1.635**	
B_1	71 (meV)	64	72	66	61	68	60	59	69**	LA
B_2	112*	117*	114*	118*	125	120*	115	116	116**	LO
B_3	162		179	167	187*	185	177			LA + LO
B_4	223	208	217	229	239	234	231			2LO
B_5	268	270		273	299	292	286			LA + 2LO
B_6					339	346	335*	354*		3LO

* Maximum peak.
** Yamada *et al.* [Ref. (6)].

ture before the thermal quenching occurred, which will be discussed elsewhere (7).

Discussion

Comparisons of the spectra.—The authors have investigated the luminescences of the Al-doped and the Ga-doped 4H-SiC in detail (8). The luminescences were found to be due to donor-acceptor pair recombination at low temperatures and due to free-to-acceptor recombination at higher temperatures. The five features of the spectra described in the preceding section offer some properties of the three acceptors in the three polytypes. Considering feature *iii*, all the luminescences due to Al and Ga may be pair emissions between the N donor and the Al or Ga acceptor. Each relatively sharp peak (B_0) at the highest energy is a zero-phonon peak and the others (B_1-B_6) are its phonon replicas. Since the spectra due to B of the three polytypes resembled that of 3C-SiC:N,B reported by Yamada and Kuwabara (6,9), they also may be due to pair recombination between the N donor and the B acceptor. The first hump (B_0) at the highest energy can be regarded as a zero-phonon peak. All the A_0 peaks which were observed on the higher energy side of the B_0 peaks at higher temperatures are thought to be due to the recombination of free electrons with bound holes.

Table III. Photon energy of the A_0 peak

Sample	Photon energy (eV)	Temperature (°K)
4H-SiC:Al	3.101	129
4H-SiC:Ga	3.025	148
4H-SiC:B	2.644	126
6H-SiC:Al	2.801	132
3C-SiC:Al	2.150	120

The energy differences among the spectra of the three polytypes (feature *ii*, Fig. 4, 5, and 6) are ac-

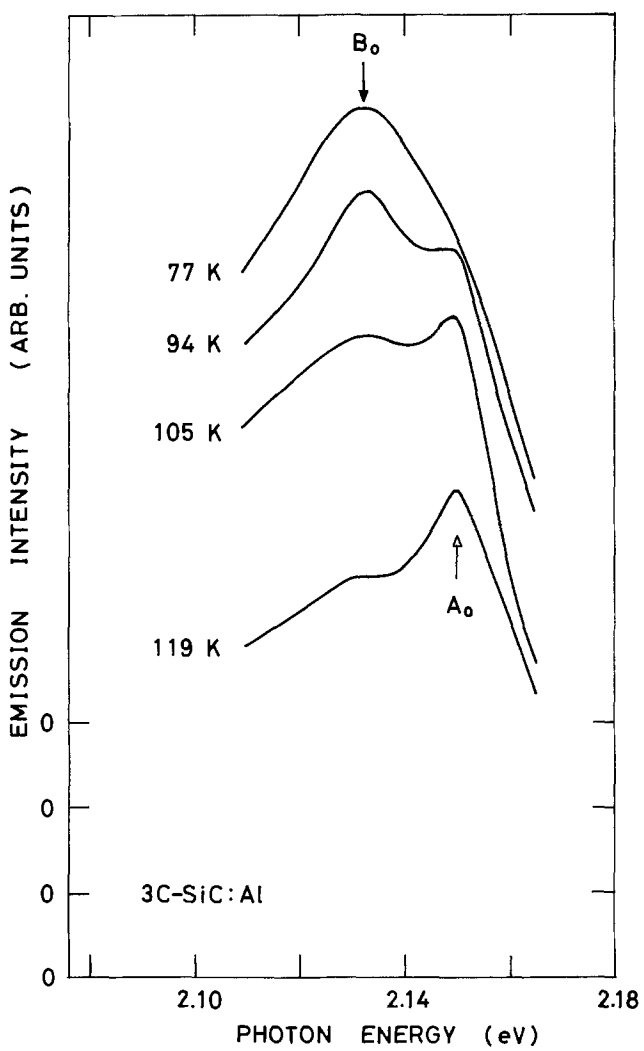


Fig. 7. Spectral change of the A_0 and the B_0 peaks of the Al-doped 3C-SiC crystal with increasing temperature.

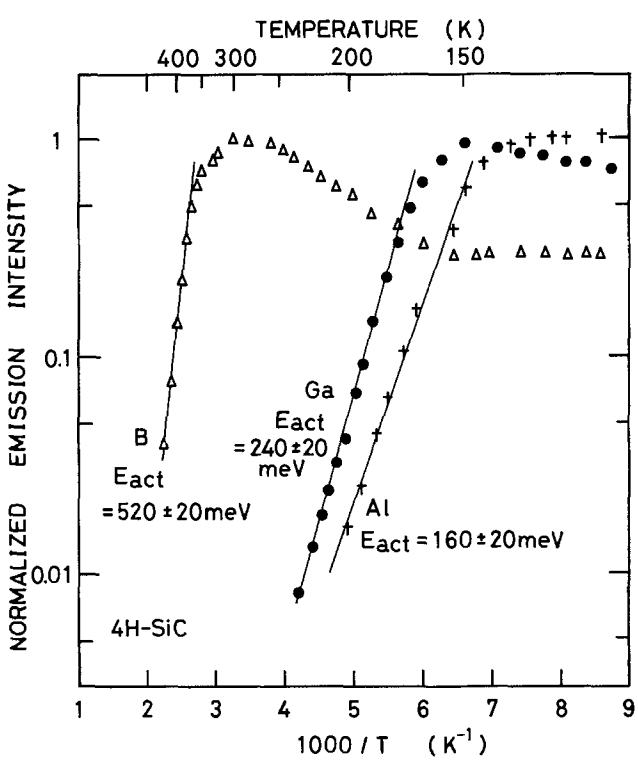


Fig. 8. Temperature dependence of the emission intensities of the Al-doped, Ga-doped, and B-doped 4H-SiC crystals.

counted for by the difference of the energy gap, because the energy gaps at 2°K are 2.390 eV + E_x, 3.023 eV + E_x, and 3.265 eV + E_x for 3C-, 6H- and 4H-SiC, respectively (10), where E_x is the exciton binding energy of the order of 10 meV (11).

The energy differences among the spectra due to the three acceptors (feature *i*, Fig. 3) may be attributed to the different energy levels of the acceptors. Therefore, the ionization energy of the Ga acceptor is a little larger than that of the Al acceptor, while that of the B acceptor is much larger.

Each peak of 6H-SiC was somewhat broader than that of 4H- and 3C-SiC (feature *v*). This might be related to the relatively poor quality of 6H-SiC crystals as shown in Fig. 2.

Spectra due to the B acceptors.—The bell-shaped spectra with a very broad spectral width of the B-doped samples (feature *iv*, Fig. 6) are presumably caused by the deep energy level of the B acceptor. Generally, the luminescence spectrum due to a deep center is composed of a weak zero-phonon peak and intense phonon replicas with simultaneous emissions of multiple phonons owing to the strong lattice-impurity interaction (12, 13). It is due to this strong interaction that the B_6 peaks were the maximum peaks for the B-doped samples, while the B_2 or B_3 peaks for the Al-doped and the Ga-doped samples as in Table II.

SiC has two kinds of lattice sites, namely, Si sites and C sites. Previous luminescence studies have shown that N and B substitute the same kind of sites, while Al the other one (6, 14). According to the relative atomic sizes, N and B probably occupy the C sites, while Al and Ga the Si sites. This may be related to the result that the B acceptor has much larger ionization energy than the Al and the Ga acceptors.

Phonon replicas.—Much the same dispersion curves have been reported for the same mode of phonons of every polytype (15, 16). In Table II, the same B_i peak of every sample is separated from each zero-phonon peak B_0 by an almost constant value independent of polytypes and acceptors. This may indicate that the same mode of phonon contributes to the same B_i peak of every sample. From the values in Table II and the phonon energies, the B_1 and the B_2 peaks are found to be LA and LO phonon replicas, respectively. The other replicas may be due to combinations of these two modes as given in Table II. The phonon energies of the B_1 replicas are a little smaller than the value of LA phonon at the zone boundary (75-80 meV), while those of the B_2 replicas are near the value of LO phonon at the zone center (119-121 meV) rather than at the zone boundary (102-105 meV) (15, 16).

Ionization energies.—From the photon energy $h\nu_A$ of the zero-phonon peak A_0 due to the recombination of free electrons with bound holes, the ionization energy E_a of the acceptor can be obtained by the following relation (17)

$$E_a = E_{gx} + E_x + kT - h\nu_A \qquad [1]$$

where E_{gx}, E_x, and kT are the exciton energy gap, the exciton binding energy, and the thermal energy of the free electron, respectively. The sum of E_{gx} and E_x is the energy gap.

The photon energy $h\nu_B$ of the zero-phonon peak B_0 of pair emission is expressed by

$$h\nu_B = E_{gx} + E_x - (E_d + E_a) + E_c \qquad [2]$$

where E_d is the ionization energy of the donor and E_c is the coulomb energy term (18). From Eq. [1] and [2], one gets

$$E_d = h\nu_A - h\nu_B - kT + E_c \qquad [3]$$

Using the values of $h\nu_B$ and $h\nu_A$ in Tables II and III, and E_{gx} given in Ref. (10), one obtains E_a and E_d by Eq. [1] and [3]. The results thus obtained are shown in Table IV. [The values of E_a and E_d for 4H-SiC:Al and 4H-SiC:Ga were obtained by more detailed investigations by the authors (8).]

Table IV. Ionization energies of Al, Ga, and B acceptors and N donor (unit = meV)

	4H Al	4H Ga	4H B	4H Al	6H Al	3C Al
E_a	168 + E_x	249 + E_x	628 + E_x	168 + E_x	231 + E_x	248 + E_x
E_d	59	51	23 + E_c	59	16 + E_c	7 + E_c

E_a, E_d = the ionization energies of the acceptor and the donor, respectively.
E_x = the exciton binding energy.
E_c = the coulomb energy term.

Since the value of E_x is 13.5 meV for 3C-SiC (11), the ionization energy of Al in 3C-SiC is obtained as 262 meV, which is in good agreement with 260 ± 15 meV by Long *et al.* (19). (Their crystals were prepared by vapor phase growth.) The value of 168 meV + E_x for Al in 4H-SiC may be compared with 150 meV + E_x by Hagen *et al.* (20) and 180 meV + E_x by Gorban' *et al.* (21). (Their crystals were also prepared by vapor phase growth.) When E_x is assumed to be of the same order in the three polytypes, the ionization energy of Al in 4H-SiC is 60-80 meV smaller than those in 6H- and 3C-SiC. The value of E_x possibly differs among the three polytypes. But since E_x does not probably exceed E_d [55 ± 7 meV (8)], the difference of 60-80 meV cannot be accounted for only by the difference in E_x. The Ga and the B acceptors in 4H-SiC also seemed to show somewhat smaller ionization energies than those in 6H- and 3C-SiC.

The ionization energy of the Ga acceptor in SiC was obtained by the authors for the first time. The ionization energy of the B acceptor has been found to be 390 meV for 6H-SiC by Hall-effect measurements (22). Kuwabara *et al.* have recently reported much larger ionization energy of 735 meV for B in 3C-SiC by luminescence studies (9). The present investigation has also given a large ionization energy of 628 meV + E_x for B in 4H-SiC.

The coulomb energy term E_c obtained for 4H-SiC:Al and 4H-SiC:Ga was 29 and 25 meV, respectively (8). If these values are used as E_c in Table IV, 48-52 meV is obtained as E_d for 4H-SiC:B. This value is in agreement with 59 and 51 meV for 4H-SiC:Al and 4H-SiC:Ga, respectively, obtained by another method in Ref. (8). Therefore, one kind of donor, namely nitrogen, participates in the pair recombination of the three kinds of 4H-SiC samples with the different acceptors. Similarly, 41-45 meV for 6H-SiC:Al and 32-36 meV for 3C-SiC:Al are obtained as E_d. These are a little smaller than the value for 4H-SiC. Since 6H- and 3C-SiC have larger absorption coefficients for the exciting light owing to their smaller energy gaps, the excitation is probably done in a smaller volume near the sample surface. This may produce the same effect that is brought about by the increase of excitation intensity. Then, the pair separation making the most contribution to the B_0 peak becomes small and the coulomb energy term E_c becomes large (18). Therefore, E_d for 6H- and 3C-SiC will be able to approach the value for 4H-SiC.

Thermal quenching.—The thermal quenching shown in Fig. 8 was probably brought about by thermal release of bound holes at the acceptors into the valence band, because the luminescences due to the three acceptors began to be quenched at different temperatures with different activation energies. The probability of thermal ionization of bound holes may be expressed as $s \cdot \exp(-E_a/kT)$, where s is a constant and E_a is the ionization energy of the acceptor. Then,

the quenching activation energy can be regarded as E_a, and the quenching begins at higher temperature for larger E_a (23). The activation energies of 160 ± 20, 240 ± 20, and 520 ± 20 meV obtained for the luminescences due to Al, Ga, and B in 4H-SiC (Fig. 8) almost agree with the ionization energies of the respective acceptors determined above (Table IV).

Summary

In 4H-, 6H-, and 3C-SiC grown from a Si melt, Al, Ga, and B acceptors were found to act as visible-luminescence centers at low temperatures. The luminescence color varied from violet to near-infrared depending on the energy level of the acceptor and the energy gap of the polytype. The luminescences at low temperatures were due to pair recombination between the N donor introduced unintentionally and the Al, Ga, or B acceptor. Each spectrum consisted of a zero-phonon peak and its phonon replicas. The contributing phonons were LA, LO phonons and their combinations. At higher temperatures, another emission appeared owing to the recombination of free electrons with bound holes.

From the luminescence spectra and the temperature dependence of the emission intensity, the ionization energy of Ga was found to be a little larger than that of Al in the three polytypes, while B had much larger ionization energy. The ionization energies of Al, Ga, and B in 4H-SiC were 168 meV + E_x, 249 meV + E_x, and 628 meV + E_x, respectively, where E_x is the exciton binding energy of the order of 10 meV. The ionization energy of the N donor was 55 ± 7 meV.

Owing to the deep level of the B acceptor, the spectra were different from those due to Al and Ga, and phonon replicas with simultaneous emissions of multiple phonons were dominant. The luminescence due to B was intense even at room temperature.

The ionization energies of the Al acceptor in 6H- and 3C-SiC were 231 meV + E_x and 248 meV + E_x, respectively. Even if the difference in E_x among the polytypes is taken into consideration, the value for 4H-SiC was smaller than those for 6H- and 3C-SiC.

Acknowledgment

The authors would like to thank Dr. K. Kuroiwa for his valuable advice about the crystal growth.

Manuscript submitted Aug. 10, 1976; revised manuscript received Oct. 1, 1976.

Any discussion of this paper will appear in a Discussion Section to be published in the December 1977 JOURNAL. All discussions for the December 1977 Discussion Section should be submitted by Aug. 1, 1977.

REFERENCES

1. R. B. Campbell and H.-C. Chang, in "Semiconductors and Semimetals," Vol. 7, R. K. Willardson and A. C. Beer, Editors, p. 625, Academic Press, New York (1971).
2. R. W. Brander and R. P. Sutton, *J. Phys. D*, **2**, 309 (1969).
3. A. Suzuki, M. Ikeda, N. Nagao, H. Matsunami, and T. Tanaka, *J. Appl. Phys.*, To be published.
4. F. A. Halden, in "Silicon Carbide—A High Temperature Semiconductor," J. R. O'Connor and J. Smiltens, Editors, p. 115, Pergamon Press, Oxford (1960).
5. W. E. Nelson, F. A. Halden, and A. Rosengreen, *J. Appl. Phys.*, **37**, 333 (1966).
6. S. Yamada and H. Kuwabara, in "Silicon Carbide—1973," R. C. Marshall, J. W. Faust, Jr., and C. E. Ryan, Editors, p. 305, University of South Carolina Press, Columbia (1974).
7. A. Suzuki, H. Matsunami, and T. Tanaka, *Phys. Status Solidi A*, To be published.
8. A. Suzuki, H. Matsunami, and T. Tanaka, Submitted to *J. Phys. Chem. Solids*.
9. H. Kuwabara and S. Yamada, *Phys. Status Solidi A*, **30**, 739 (1975).
10. W. J. Choyke, in "Silicon Carbide—1968," H. K. Henisch and R. Roy, Editors, p. 141, Pergamon Press, New York (1969).
11. D. S. Nedzvetskii, B. V. Novikov, N. K. Prokof'eva, and M. B. Reifman, *Sov. Phys. Semicond. (Engl. Transl.)*, **2**, 914 (1969).
12. T. H. Keil, *Phys. Rev.*, **140**, A601 (1965).
13. M. Tajima and M. Aoki, *Jpn. J. Appl. Phys.*, **13**, 812 (1974).
14. W. J. Choyke and L. Patrick, *Phys. Rev. B*, **2**, 4959 (1970).
15. W. J. Choyke, D. R. Hamilton, and L. Patrick, *ibid.*, **133**, A1163 (1964).
16. D. W. Feldman, J. H. Parker, Jr., W. J. Choyke, and L. Patrick, *ibid.*, **173**, 787 (1968).
17. K. Colbow, *ibid.*, **141**, 742 (1966).
18. D. G. Thomas, J. J. Hopfield, and W. M. Augustyniak, *ibid.*, **140**, A202 (1965).
19. N. N. Long, D. S. Nedzvetskii, N. K. Prokofeva, and M. B. Reifman, *Opt. Spektrosk.*, **29**, 388 (1970).
20. S. H. Hagen, A. W. C. van Kemenade, and J. A. W. van der Does de Bye, *J. Lumin*, **8**, 18 (1973).
21. I. S. Gorban', V. A. Gubanov, and V. M. Efimov, *Sov. Phys. Solid State (Engl. Transl.)*, **14**, 2010 (1973).
22. G. A. Lomakina, *ibid.*, **7**, 475 (1965).
23. M. Tajima and M. Aoki, *Jpn. J. Appl. Phys.*, **13**, 819 (1974).

Fluorescence of Eu^{3+} in Lithium Zinc Tantalate, $Li_{14}ZnTa_4O_{18}$

A. Wachtel* and T. J. Isaacs

Westinghouse Electric Corporation, Research and Development Center, Pittsburgh, Pennsylvania 15235

ABSTRACT

A new compound, $Li_{14}ZnTa_4O_{18}$, was found and its Eu-activated fluorescence as well as its crystal symmetry was studied. It is face-centered cubic, with $a_o = 4.212$Å. The emission spectrum shows considerable line broadening and the fluorescence as a function of Eu concentration suggests the presence of two emitting sites, both of which tend to dissociate into nonluminescent defects at high firing temperatures. Replacement of Zn by Mg or of Ta by Nb leads to isomorphic compounds with similar fluorescence; replacement of Zn by Ca produced a multiphase material containing a moderate amount of the same cubic phase.

There has been considerable interest in Eu^{3+} activated phosphors for over a decade because of their technical usefulness as red emitters. Thus far, only four compounds, Y_2O_3, Gd_2O_3, Y_2O_2S, and YVO_4, have met the spectral, quantum efficiency, physical, and cost requirements for successful phosphor hosts, although YVO_4 degrades somewhat under 254 nm excitation.

Calcium oxide (CaO) (1), when activated with Eu^{3+}, has excellent spectral energy distribution and quantum efficiency, but it is hygroscopic, and therefore presents certain difficulties in lamp applications. This compound has the rock salt structure, with the Eu^{3+} probably in a defect associated center. We decided to look into other materials with this type of lattice.

Four compounds initially were studied. These are Li_3TaO_4, Li_3NbO_4, Li_3SbO_4, and "$Li_2Zn_{0.5}Ta_{0.5}O_3$" (2).[1] Both Li_3TaO_4 and Li_3SbO_4 were reported to be tetragonal; Li_3NbO_4 and $Li_2Zn_{0.5}Ta_{0.5}O_3$ were thought to be cubic. All are supposed to have orderings of the halite structure. Of these four compounds, when activated with Eu^{3+}, only $Li_8Zn_2Ta_2O_{11}$ and Li_3SbO_4 displayed significant fluorescence in the 610 nm region; the latter, however, accompanied by a broad band in the blue region. The others emitted only weakly under 254 nm excitation. Further work in attempting to optimize $Li_8Zn_2Ta_2O_{11}$:Eu^{3+} led to the discovery of $Li_{14}ZnTa_4O_{18}$.

Experimental

Samples were prepared by solid-state reaction of the component oxides or carbonates (reagent or luminescent grade purity) in covered 99.9% alumina crucibles in air at temperatures of 800°-1400°C. Weight losses due to volatilization of Li_2CO_3 were compensated for by appropriate additions between firings in order to obtain stoichiometric compositions. Some of the products were subsequently fired in sealed platinum capsules at 1500°C.

The materials thus prepared were examined by x-ray powder diffraction using either the Debye-Scherrer method or diffractometer. Some samples also were studied under the polarizing microscope to detect extraneous phases.

Fluorescence intensity of Eu^{3+} under 254 nm excitation was measured with a spectra brightness spot meter using filters to favor the region of $^7F_2$ emission near 613 nm. Data are reported as percent of Y_2O_3:Eu^{3+}.

Emission spectra were taken with a resolution of 0.3 nm over the range of 500-720 nm, using 300 nm excitation. The scanning system was corrected for response *vs.* wavelength.

The excitation spectrum was run with a 500W xenon arc passed through two tandem quarter-meter Jarrell-Ash monochrometers. The resolution was again 0.3 nm. The correction for quantum output *vs.* wavelength was made relative to 2,2'-dihydroxy-1, 1'-naphtaldiazine (3).

Results

Our x-ray diffraction powder patterns of $Li_8Zn_2Ta_2O_{11}$ indicated the presence of more than one phase in significant amounts. We obtained the same results at firing temperatures up to the fusion point of the material, and concluded that there was not a true compound of this composition.

Because of the interesting fluorescence spectrum, however, we searched for the emitting compound by examining various compositions in the system Li_2O-ZnO-Ta_2O_5. Among these, only the compound having the ratio $7Li_2O \cdot ZnO \cdot 2Ta_2O_5$ produced the same spectrum and with much higher intensity, when activated with Eu^{3+}. In order to synthesize it, relatively high firing temperatures (≧1300°C) were required. Our analysis of the x-ray powder diffraction pattern (Table I) indicated that this compound has face-centered cubic symmetry (the possible space groups being F23, Fm3, F432, F$\bar{4}$3m, and Fm3m) with lattice parameter $a_o = 4.212$Å. This cell size is in good agreement with the value of 4.214Å given for $Li_2Zn_{0.5}Ta_{0.5}O_3$ (2), and comparison of the powder patterns of these two materials shows that $Li_{14}ZnTa_4O_{18}$ is a major constituent in our composition corresponding to $Li_8Zn_2Ta_2O_{11}$. We did not ascertain the other phases present in this composition.

Compositions of the type $(7 \pm 1)Li_2O \cdot (1 \pm 0.5\ ZnO) \cdot (2 \pm 0.5\ Ta_2O_5)$ contained additional phases and displayed weaker fluorescence if activated by Eu^{3+}. This was particularly pronounced on reducing Li_2O or ZnO or increasing Ta_2O_5.

Introduction of Eu in $Li_{14}ZnTa_4O_{18}$ gives rise to red fluorescence which is well excited by 254 nm, and

Table I. X-ray diffraction powder data for $7Li_2O \cdot ZnO \cdot 2Ta_2O_5$

hkl	*d*	I/I_o
111	2.4175	49
200	2.0941	100
220	1.4847	62
311	1.2683	25
222	1.2137	15
400	1.0526	8
331	0.9665	4
420	0.9419	12
422	0.8598	7
511	0.8107	5

$a_o = 4.212 \pm 0.003$A.

* Electrochemical Society Active Member.

[1] According to the proportion $4Li_2O \cdot 2ZnO \cdot Ta_2O_5$ which was employed in the present study, the formula should read $Li_8Zn_2Ta_2O_{11}$.

Key words: lithium zinc tantalate, lithium magnesium tantalate, europium, fluorescence, cubic, x-ray diffraction.

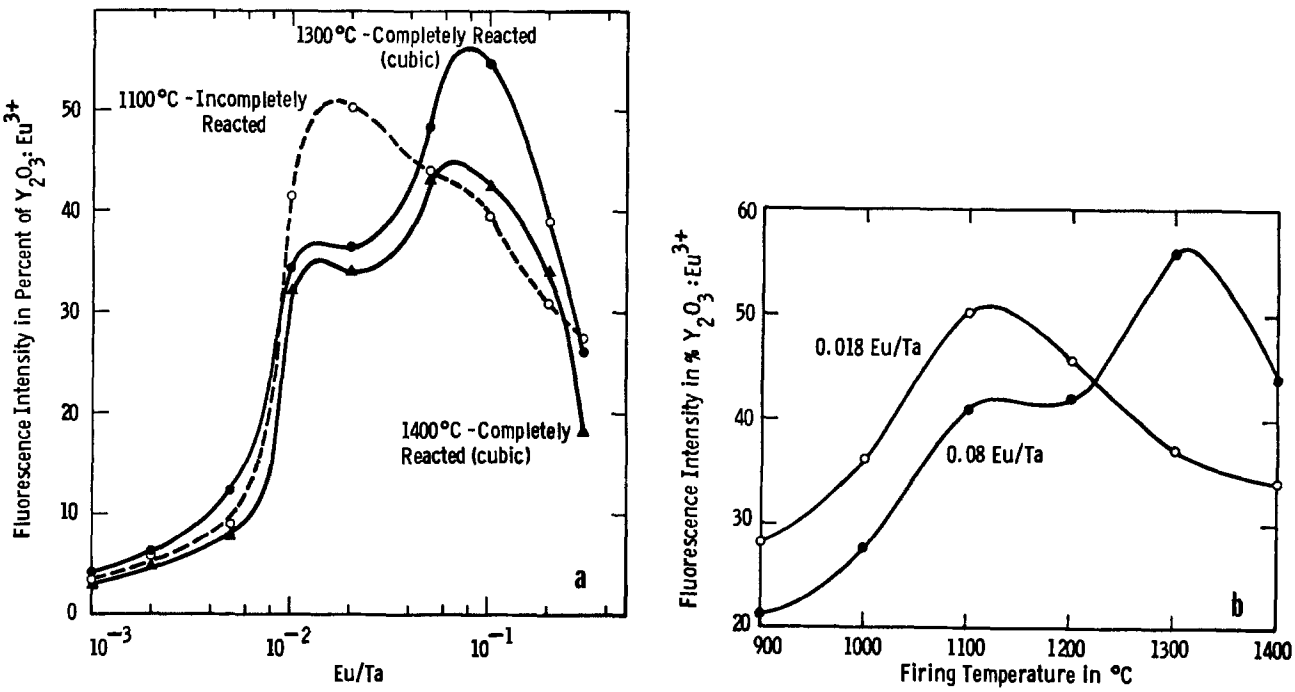


Fig. 1. (a) 254 nm-excited fluorescence intensity of $Li_{14}ZnTa_4O_{18}$ prepared at three firing temperatures as a function of Eu concentration. (b) 254 nm-excited fluorescence intensity of $Li_{14}ZnTa_4O_{18}$:0.036 Eu_2O_3 and of $Li_{14}ZnTa_4O_{18}$:0.16 Eu_2O_3 as a function of firing temperature.

whose intensity bears an interesting relationship to Eu concentration and firing temperature. This is illustrated in Fig. 1. In Fig. 1a, we note that there are two maxima with respect to Eu concentration, the relative intensities of which are a function of firing temperature. In Fig. 1b, the same data are replotted for the two presumably optimum Eu concentrations, and we again note the occurrence of two maxima which are now in terms of firing temperature and whose relative intensities are a function of Eu concentration. Some samples with 0.0035 and 0.05 Eu/Ta were fused at 1500°C in sealed Pt tubes and displayed still weaker fluorescence although the x-ray powder diffraction patterns remained the same. Introduction of 0.1 Eu/Ta resulted in complete solubility and near-maximum fluorescence; introduction of 0.2 Eu/Ta resulted in the appearance of faint lines of a second phase in the x-ray powder diffraction pattern. The doping by Eu_2O_3 also causes a slight lattice expansion (a_o = 4.222Å for 0.05 Eu/Ta). Attempts at charge compensation were generally unrewarding; compositions prepared according to $Li^+ + Zn^{2+} = Eu^{3+}$, $Zn^{2+} + Eu^{3+} = Ta^{5+}$, or $Zn^{2+} + Ta^{5+} = Eu^{3+} + Zr^{4+}$ remained cubic but displayed slightly reduced fluorescence, while compositions corresponding to $Li^+ + Eu^{3+} = 2Zn^{2+}$ also gave rise to extraneous phases at higher doping levels in addition to lowered fluorescence intensity.

Figure 2 shows the emission spectra of $Li_{14}ZnTa_4O_{18}$: 0.007 Eu_2O_3 fired at 1100°C (dashed curve) and fused at 1500°C (solid curve). It can be seen that in spite of the relatively low doping level (0.0035 Eu/Ta), there is considerable line broadening, particularly in the high temperature fired (single phase cubic) material. Because of the width of the $^7F_2$ manifold, its relative intensity, compared to total emission, is appreciably higher than $Y_2O_3:Eu^{3+}$. The emission spectrum of preparations fired at 1100°C shows better resolution of the satellite lines but is otherwise quite similar.

In contrast to the emission, the excitation spectrum for 612.5 nm emission is highly structured. This is seen in Fig. 3 for $Li_{14}ZnTa_4O_{18}$:0.2 Eu_2O_3 fired at 1300°C, *i.e.*, despite a relatively high doping level (0.1 Eu/Ta). The primary excitation occurs in a broad band centered near 245 nm; excitation into the Eu levels near 400 nm ($^7F_0$-$^5D_3$) and 470 nm ($^7F_0$-$^5D_2$) is weak due to low absorption strength.

Replacement of Zn by Mg resulted in the same cubic powder pattern (a_o = 4.202Å), as well as similar emission and excitation spectra. The primary $^5D_0$-$^7F_2$ emission line as well as most of the excitation lines of $Li_{14}MgTa_4O_{18}:Eu^{3+}$ are displaced 0.5-1 nm to shorter wavelength as compared to the Zn compound, and the 254 nm excited emission intensity is slightly lower than that of similarly prepared $Li_{14}ZnTa_4O_{18}:Eu^{3+}$. Somewhat weaker fluorescence is also observed in the analogous composition containing Ca instead of Zn. This, however, is a multiphase system containing unidentified lines in the powder pattern along with the group of lines belonging to the cubic structure seen in the Zn and Mg compounds. It was not investigated further. Replacement of Zn by other divalent ions led to different structures and weak fluorescence. $Li_{14}ZnNb_4O_{18}:Eu^{3+}$ displays the same structure (a_o = 4.220Å with 0.1 Eu_2O_3) as the tantalate after formation

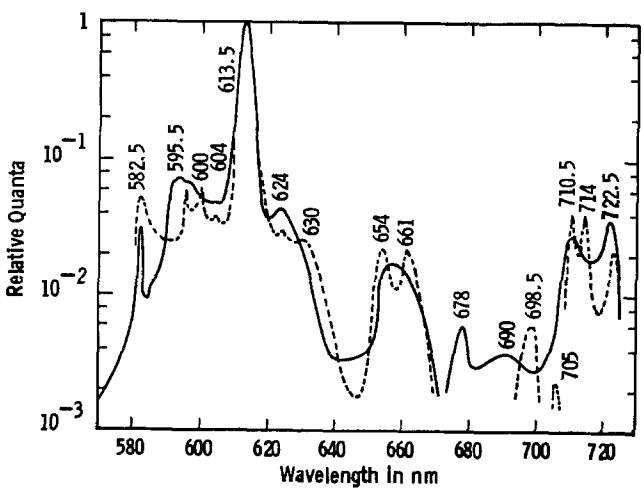


Fig. 2. Emission spectra of $Li_{14}ZnTa_4O_{18}$:0.007 Eu_2O_3 prepared at two firing temperatures: dashed curve = 1100°C; solid curve = 1500°C.

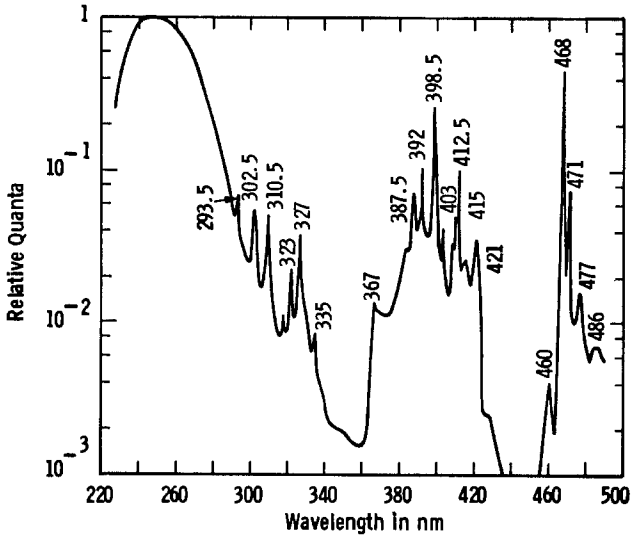


Fig. 3. Excitation spectrum for 612.5 nm emission of $Li_{14}ZnTa_4O_{18}$:0.2 Eu_2O_3.

at only 1100°C (sintering) but its fluorescence is only about one-third as intense. The analogous vanadate is noncubic and nonfluorescent.

Figure 4 shows that an appreciable difference between the Eu-activated Zn and Mg compounds is seen only in the diffuse reflectance spectra in the 290-390 nm region. Otherwise, both compounds clearly show a fundamental absorption edge near 230 nm which is not very different for the Zn or Mg species, and a broad absorption of $Li_{14}MgTa_4O_{18}$:0.2 Eu_2O_8 which is in good agreement with its excitation spectrum. The additional absorption of the doped Zn compound between 290 and 390 nm is apparently not related to excitation. On the other hand, weak absorption at the two conspicuous Eu-excitation lines could be detected.

A search for Eu^{3+} emission in known compounds in the Li_2O-ZnO-Ta_2O_5 system revealed very weak intensities throughout except for Li_7TaO_6:0.05 Eu (4), which emits a broad line centered at 610.5 nm with about 20% of the intensity of $Y_{1.9}Eu_{0.1}O_3$. Moreover, all

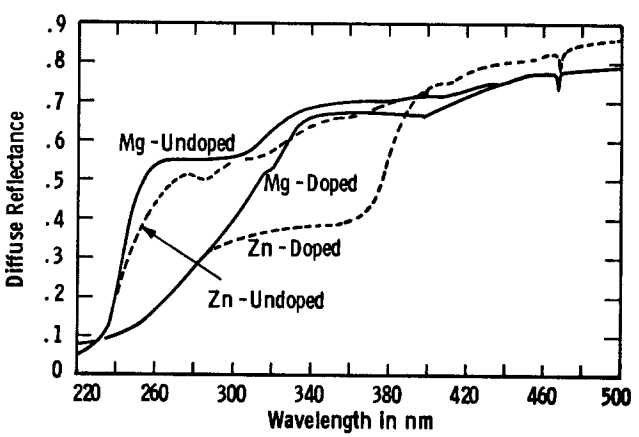


Fig. 4. Diffuse reflectance spectra of cubic $Li_{14}ZnTa_4O_{18}$ and $Li_{14}MgTa_4O_{18}$ with and without 0.2 Eu_2O_3 per mole.

compounds except for the multiphase composition $Li_8Zn_2Ta_2O_{11}$ displayed emission spectra which are different from that of $Li_{14}ZnTa_4O_{18}$:Eu^{3+}.

We found that the compound $Li_{14}ZnTa_4O_{18}$ hydrolyzes fairly readily in water.

Discussion

The presence of two maxima of fluorescence intensity as a function of Eu concentration (Fig. 1) suggests that the one which predominates in incompletely reacted mixtures (low Eu) is due to some other compound which forms in the course of the solid-state reaction which leads to $Li_{14}ZnTa_4O_{18}$ at higher firing temperatures. We have observed, however, that at least none of the known Li- or Zn-tantalates or the known ternary compound $LiZnTa_3O_9$ (5) can be responsible for this. Moreover the emission spectrum of the multiphase composition corresponding to $Li_8Zn_2Ta_2O_{11}$:Eu, obtained at high temperatures, is identical to that of $Li_{14}ZnTa_2O_{18}$:Eu (Fig. 2), although the fluorescence intensity is appreciably lower. We conclude, therefore, that intermediary phases formed during the solid-state reaction are essentially nonfluorescent and that two emitting Eu^{3+} sites in $Li_{14}ZnTa_2O_{18}$ are formed, one of which obtains early in the reaction ($\leq$1100°C) and is metastable. At temperatures sufficient to complete the reaction (~1300°C), another Eu^{3+} center predominates at higher Eu concentrations and could be due to association of two or more Eu sites. This concept is also supported by the widths of the Eu^{3+} emission lines in the compound (Fig. 2). At still higher firing temperatures (1400°, 1500°C) the emission of both centers decreases; thus, it seems that even the second center which forms at high temperature is unstable and tends to decompose into isolated impurities and defects. The mechanism for the phenomenon was not determined. It is unlikely, however, that it occurs via interaction with vacancies which seem to be the only source of charge compensation in this system.

Acknowledgments

We wish to express appreciation to Dr. F. M. Ryan for emission and excitation spectra, to W. Gaida for x-ray diffraction powder patterns, and to E. Metz for help in preparing the materials.

Manuscript submitted July 19, 1976; revised manuscript received Oct. 7, 1976.

Any discussion of this paper will appear in a Discussion Section to be published in the December 1977 JOURNAL. All discussions for the December 1977 Discussion Section should be submitted by Aug. 1, 1977.

Publication costs of this article were assisted by the Westinghouse Electric Corporation.

REFERENCES

1. W. Lehmann, *J. Lumin.*, **6**, 455 (1973).
2. L. H. Brixner, *J. Inorg. Nucl. Chem.*, **16**, 162 (1960).
3. A. Bril and A. W. de Jager-Veenis, Abstract 204, p. 479, The Electrochemical Society Extended Abstracts, Spring Meeting, Toronto, Canada, May 11-16, 1975.
4. R. Scholder and H. Glaser, *Z. Anorg. Allg. Chem.*, **327**, 15 (1964).
5. S. P. Kutolin, T. V. Revzina, and N. I. Kaslina, *Dokl. Akad. Nauk SSSR*, **175**, 407 (1967).

Generation and Propagation of Defects in Indium Antimonide

H. U. Walter[1]

Department of Physics, University of Alabama, Huntsville, Alabama 35807

ABSTRACT

Density of volume defects due to foreign particle inclusions in Czochralski-grown InSb crystals is 10^2-10^3/cm^3 as detected by x-ray topography. The larger ones of these inclusions are frequently sources of dislocations. Dislocations in Czochralski-grown crystals are randomly oriented and curvilinear. InSb crystals prepared in space by partial remelting of Czochralski-grown seeds and regrowth after a 1 hr thermal soak period are markedly different. The density of inclusions is greatly reduced since foreign particles are accumulated during soak at the remelt boundary and at the melt surface. Dislocations originating from particles at the seed boundary are the cause of a sudden increase of dislocation density in the first portion of regrown material. Rectilinear dislocations (pure edge and 60° type) are observed rather exclusively in the bulk of space-grown crystals. Since larger inclusions are absent, few defects are generated, and the density of dislocations decreases along the axis of the samples due to outgrowing of rectilinear dislocations that are inclined to the growth axis. Increasing radial thermal gradients causes an increase of dislocation density in the crystal section solidified last. Generation and multiplication of dislocations due to radial thermal gradients become appreciable at gradients of about 10°-15°C/cm.

The catalogue of possible defects in the zinc blende (sphalerite) structure, in which indium antimonide crystallizes, has been derived by Holt (1) on the basis of Hornstra's theoretical analysis of possible structures of dislocations in the diamond lattice (2). Experimentally, dislocations in indium antimonide were overwhelmingly studied by chemical etching techniques, *e.g.*, (3-10); x-ray topography was not employed extensively (11-17).

It is well known that mechanisms by which dislocations are generated are not intrinsic to the growth process, but rather due to insufficient control of growth conditions. The following mechanisms have been identified: propagation of dislocations into the growing crystal from the seed, poor epitaxy during seeding, incorporation of foreign particles, shear strains arising from thermal strains or external mechanical constraints, shear strains due to compositional variations accompanied by lattice parameter changes, misorientation due to dendritic growth, and the mechanism of collapsing vacancy disks, which is especially important in metal crystals.

Because of the variety of causes of dislocations and the complexity of solidification processes, cause and effect relationships are difficult to analyze. Lack of control of solidification is largely due to transient fluid flow that is inherent with some of the crystal growth techniques, and, more importantly, transient flow due to gravity-driven convection. These random convective disturbances affect the solidification rate and solid-liquid interface morphology, which results in degradation of structural perfection and in chemical inhomogeneities of crystals grown from the melt.

One approach to virtually eliminate gravity-driven convection is to experiment in orbiting laboratories. With quiescent melts that could presumably be obtained in a low gravity environment, programmable and stable temperature fields could be applied, and solid-liquid interface shape would reflect isotherm shape not only on a macroscale, but on a microscale as well. Solidification rates could be programmed and constitutional supercooling could be avoided by applying sufficiently steep thermal gradients without introducing turbulent gravity-driven convection. In addition, novel containerless processing techniques could be employed in low gravity environment, thus not only eliminating contamination from crucible material, but also eliminating mechanical stress and spurious nucleation at crucible walls. Space experimentation should, therefore, be of particular interest for studying highly doped semiconductors, high melters, and highly reactive materials, structural perfection of melt-grown crystals in general should be improved.

This paper describes the defect properties of InSb single crystals prepared by a containerless technique on board of Skylab. Defect properties of space-grown crystals are compared with Czochralski-grown crystals that were used as seeds. This comparison is of interest since it should aid in understanding the influence of disturbances due to convective fluid flow on crystal perfection.

Experimental

Crystal growth.—Crystals used as seeds were grown by the Czochralski method from ingot compounded from 6*N* elemental material under the following conditions: crucible, high purity (6*N*) carbon; growth atmosphere, 1 atm high purity (6*N*) hydrogen; pulling rate, 5-25 μm sec; crucible rotation, 30 rpm; seed rotation, 0 rpm; growth direction, [$\bar{1}\bar{1}\bar{1}$] for undoped material (5 samples) and approximately [110] seed crystal orientation for heavily selenium-doped ($n \approx 10^{19}$/cm^3) material (1 sample). Crystal growth in space was performed as follows: Czochralski-grown crystals (8 mm diameter) were partially backmelted (18 mm) in a gradient furnace so that large drops ($\approx$ 15 mm diameter) of uncontained melt were formed at the end of the seed crystals. These drops were directionally solidified during controlled cool-down (0.6°C/min) of the furnace after a 1 hr soak period. Thermal equilibration and melt homogenization was achieved during soak. Additional parameters were as follows: gradient in the melt, 15°-35°C/cm; growth rate, 3-7 μm/sec; gravity levels during growth, 10^{-4}-10^{-7}G; growth atmosphere, 6*N* hydrogen; size of samples obtained, $\approx$ 18 mm long, $\approx$ 10 mm diameter, bottle-shaped. Crystal growth procedure and crystal

[1] Present address: Deutsche Forschungs- und Versuchsanstalt für Luft- und Raumfahrt, Institut fur Werkstoff-Forschung, 5000 Köln 90, Linder Höhe, Germany.

Key words: indium antimonide, dislocations, inclusions, space processing.

morphology have been described in detail elsewhere (18).

Etching.—Density and distribution of defects in seed crystals and sections regrown in space were first determined by chemical etching. Crystals grown along [$\bar{1}\bar{1}\bar{1}$] were cut in 1.5 mm thick wafers perpendicular to the axis of growth. Cutting was done with a wire saw (wire thickness 0.25 mm) carrying a slurry of 10-20 μm SiC in glycerine and water. After mechanical polish with 0.03 μm alumina, the wafer surfaces were chemically polished and etched in a modified CP-4 etchant (2 conc HNO_3 + 1 conc HF + 1 glacial CH_3COOH). After counting of etch pits, the wafers were again etched in an etchant consisting of 1 part 30% H_2O_2, 1 part 48% HF, 8 parts H_2O, 0.4% n-butylthiobutane. Modified CP-4 reveals In dislocations (α-dislocations) on {111} faces, the etchant with butylthiobutane as inhibitor reveals Sb dislocations (β-dislocations) (8, 19) on both {111} and {$\bar{1}\bar{1}\bar{1}$} surfaces. Both types of etch pits are generally associated with 60° dislocations as has been shown by successive grinding and etching (3, 5, 19). Since pits due to Sb dislocations could not always be identified unambiguously, some wafers were also etched in 0.2*N* Fe^{+++} in 6*N* HCl at 95°C (5). Material grown along [110] was etched in the same fashion, {111} cuts parallel and inclined to the growth direction were studied.

X-ray topography.—Seed material and space-grown crystals were investigated by means of scanning reflection topography (20), transmission Lang topography (21), and anomalous transmission topography (22-24). CuKα and AgKα radiation were used; beam divergence was kept such that recorded images were due to Kα_1 radiation only. Geometrical (vertical) resolution was typically 2-4 μm; topographs were recorded on Ilford nuclear plates, emulsion L-4, 25 μm thick; plates were developed at 0°C.

Linear mass absorption coefficient μ for InSb is about 1500/cm for CuKα and 90/cm for AgKα radiation. Required sample thickness t for $\mu t \leqq 1$ (Lang topographs) is $t \leqq 0.1$ mm for AgKα, and for $\mu t \geqq 10$ (Borrmann topographs) thickness is $\geqq 1$ mm for AgKα and $\geqq 0.07$ mm for CuKα radiation. Samples were prepared by lapping with 0.03 μm alumina followed by chemical polishing one side at a time in $5HNO_3$:$3CH_3COOH$:2HF at 0°C. Preparation of sufficiently thin, large and undamaged crystal wafers with constant thickness is difficult; InSb is very brittle and cleaves well along {110}, chemical polishing results frequently in terracing of the surfaces. Larger, sufficiently thin wafers tend to bend elastically under their own weight; smaller sections were, therefore, investigated.

Results

Undoped crystals grown in [$\bar{1}\bar{1}\bar{1}$] direction.—Over-all morphology of a typical crystal grown along [$\bar{1}\bar{1}\bar{1}$] is shown in Fig. 1. The boundary between Czochralski-grown seed and space-grown section is clearly delineated. Scanning reflection topographs obtained from as-grown surfaces are shown in Fig. 2. Figures 2a and b are symmetrical reflections from {110} surface facet areas with <220> diffraction vector; Fig. 2c shows a reflection from a ($\bar{1}\bar{1}1$) surface facet, diffraction vector is [$\bar{1}\bar{1}1$]. Single Bragg reflexes indicate over-all single crystallinity; structure due to imperfections is only observed in the seed areas and the very first and last portions of space-grown crystals. The flat ($\bar{1}\bar{1}1$) surface facet region is clearly visible in Fig. 2c; otherwise, reflexes from the center of the space-grown crystals are remarkably homogeneous.

Figure 3 gives In-dislocation profiles obtained by etching of wafers cut perpendicular to the axis of growth (sample E1 and D2). A sudden increase in

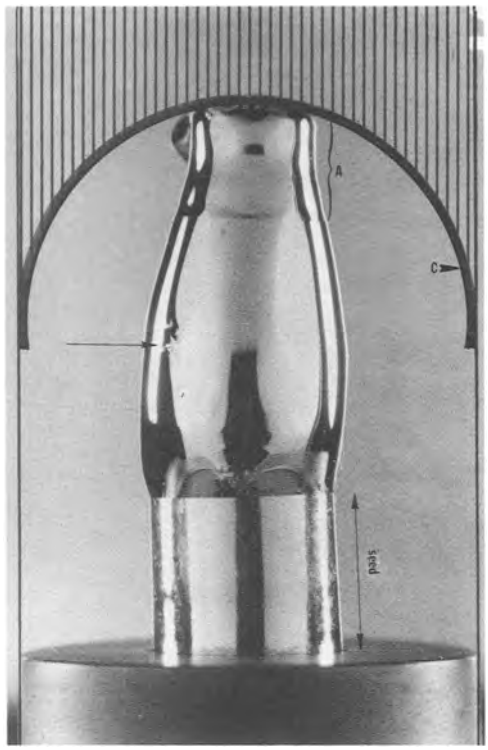


Fig. 1. InSb crystal grown by a containerless method during Skylab mission SL-3. Czochralski-grown, [$\bar{1}\bar{1}\bar{1}$] oriented, 8 mm diameter cylindrical seed is mounted in graphite support at bottom. Boundary between seed and space-grown crystal is clearly delineated. The morphology of the section indicated by A was affected by interference of the melt with the graphite heating cavity C. Arrow indicates an accumulation of oxide particles on surface of space-grown crystal.

etch pit density in the first few millimeters of space-grown material is followed by a steep, rather linear decrease over the major portion of the crystals. Minima are reached at $\approx$ 70/cm^2 (D2) and $\approx$ 40/cm^2 (E1). Dislocation density increases sharply to 10^4/cm^2 in both crystals within the last few millimeters.

Dislocation clusters shown in Fig. 4a and pseudo-hexagonal arrays of etch pits ("stars") shown in Fig. 4b could only be observed in Czochralski-grown seed material and at the meltback interface between seeds and space-grown crystals. Density of clusters and stars was 1-10/cm^2; this type of defects has to be attributed to foreign particle inclusions as is discussed later. β-dislocations were by a factor of 2 to 10 less frequent than α-dislocations; axial distribution of β-pits was similar as for α-pits.

Scanning reflection topographs of {110} and {211} longitudinal sections of crystals grown along [$\bar{1}\bar{1}\bar{1}$] were rather featureless. An example is shown in Fig. 5. The only structure resolved is due to surface roughness resulting from chemical polishing. Dislocations and inclusions in seed material as revealed by Borrmann anomalous transmission topography are shown in Fig. 6; no particular directionality of dislocation lines is observed. Lang topographs of the interface between seed and space-grown crystal (meltback interface) and of various sections of space-grown material are shown in Fig. 7-10. Dark dots decorate the meltback interface (Fig. 7); the diffraction contrast was independent of reflections employed, which indicates that these features are due to strain fields around inclusions of foreign material. Interface curvature radius for the initial meltback interface determined from these topographs is 20-25 mm. At the very end of solidification when the melt is in contact with the graphite heating cavity, the interface radius ultimately

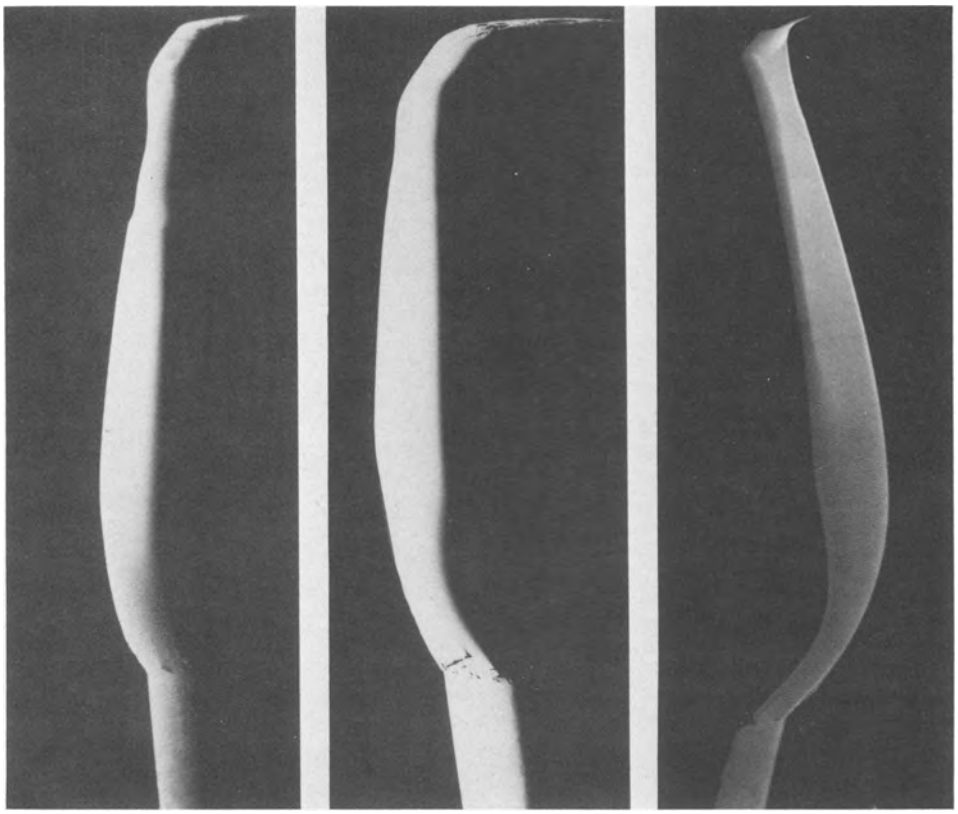


Fig. 2. Scanning reflection topographs of as-grown samples. Seed at bottom, image contrast reversed, CuKα_1 radiation. (a, left) [$2\bar{2}0$] reflection from ($1\bar{1}0$) facet region, (b, center) [$2\bar{2}0$] reflection from ($1\bar{1}0$) facet region, (c, right) [$\bar{1}\bar{1}\bar{1}$] reflection from ($\bar{1}\bar{1}\bar{1}$) facet region. Structure next to the meltback interface is due to surface irregularities that were caused by accumulations of solid particles.

assumes the radius of the cavity, which is 8 mm. Dislocations in the bulk of space-grown crystals are exclusively rectilinear (Fig. 8, 9). Increasingly dense and irregular networks of dislocations as well as strain fields appear toward the heating cavity end of the crystals (Fig. 10). Axes of rectilinear dislocations in the bulk are [$1\bar{1}0$], [$\bar{1}0\bar{1}$], and [$0\bar{1}\bar{1}$], inclined (35°, 26°) to the [$\bar{1}\bar{1}\bar{1}$] growth direction. Departure from strict orientation along <110> directions amounts to a few degrees. Directions of Burger's vectors were determined in the usual manner by determining diffraction vectors for which maximum significant differences in diffraction contrast of dislocation images is obtained. Burger's vectors are along <110> and 60° inclined to the axes of rectilinear dislocations. Dislocations in the bulk of crystals grown in space along [$\bar{1}\bar{1}\bar{1}$] are, therefore, 60° dislocations with {111} slip planes oblique to the growth direction. [$1\bar{1}0$] dislocations (Fig. 8) appear as long streaks since they are (within accuracy of wafer orientation) parallel to the surface of the ($1\bar{1}0$) wafer investigated. [$\bar{1}0\bar{1}$] and [$0\bar{1}\bar{1}$] oriented dislocations are inclined to the wafer surface at an angle of 30°. They are, therefore, much shorter in the topographs (Fig. 9), approximately 0.2 mm according to a wafer thickness of about 100 μm. No discrimination could be made between α- and β-dislocations in the topographs since this would require determination of the sense of Burger's vectors. Dislocations at the heating cavity end of crystals (Fig. 10) are also of the 60° type, whereas, segments consisting of pure screw and pure edge dislocations with axes along <211> directions could be observed in seed material.

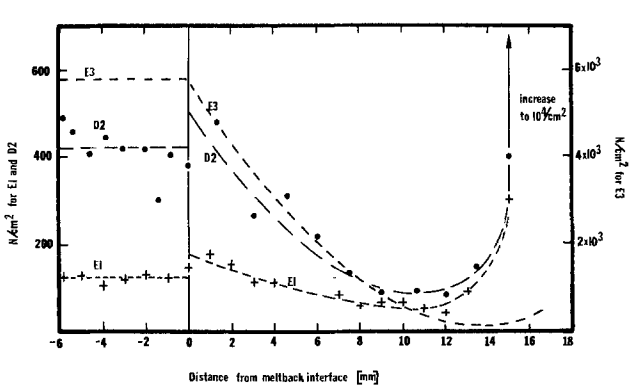


Fig. 3. Variation of density of In dislocations along axes of specimens. E1, D2 are undoped samples grown along [$\bar{1}\bar{1}\bar{1}$]; E3 is selenium doped, seed orientation approximately [110].

Selenium-doped crystal grown in [$\bar{1}32$] direction.— Aside from dopant striations in the initial and terminal transient of solidification, which could be explained by a basic mechanism not associated with fluid flow (25), defect characteristics of material grown perpendicular to [$\bar{1}\bar{1}\bar{1}$], the usual growth direction for InSb, were significantly different.

A scanning reflection topograph of a central, longitudinal (111) section of the crystal is shown in Fig. 11. The topograph was taken using AgKα radiation with 2θ setting at the slope of the Kα_1 peak, and not as usually with 2θ setting coinciding with the Kα_1 intensity maximum. Contrast due to lattice parameter variations is exaggerated by this technique. A schematic of this topograph is given in Fig. 12. Dopant striations perpendicular to the growth axis in the first third, visible only in the original emulsion, and wavelike striations in the section solidified last (region G in Fig. 12) could be attributed to changes of liquidus temperature and growth kinetics (25). In this context, they are of interest only insofar as they contribute to the defect properties of the sample. Delineation of the meltback interface (H in Fig. 12) is due to an abrupt change in selenium concentration ($k_{eff} \approx 0.2$). Curvature radius is $\approx$ 20 mm. Most distinct are traces of ($\bar{1}11$) slip planes (A in Fig. 12) that were originally present in the seed and two dark streaks (B in Fig. 12) that are due to shadows cast by distinct grooves in the surface resulting from chem-

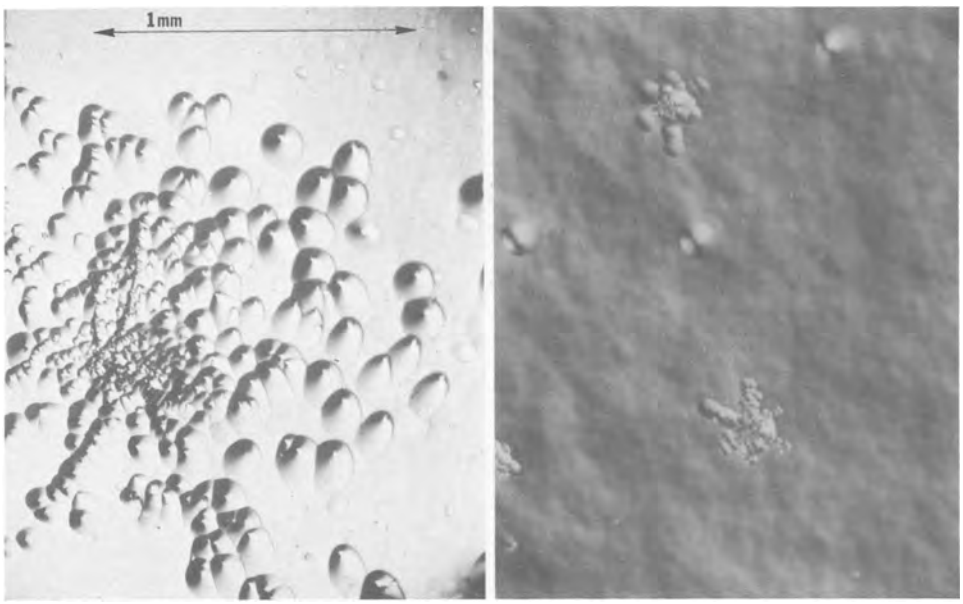


Fig. 4. (a, left) Cluster of dislocations in seed, (b, right) pseudohexagonal array of etch pits on (111) surface

ical etching of rectilinear dislocations lying directly at the wafer surface. Arrow-shaped features (C) are due to dislocations close to the surface within reach of the probing beam (4-6 μm).

A striking feature is the over-all intensity variation along the axis of the topograph, highest x-ray intensity is reflected from the seed region (D in Fig. 12). This effect is not caused by shifts of the Bragg angle due to selenium concentration variation but reflects crystalline perfection instead. Diffracted intensity is greater for imperfect regions since a larger wavelength spread and larger beam divergence contribute to the diffracted intensity. Of an incident beam, that has, for example, 4 min divergence, a typical value required for separation of $K\alpha_1$ and $K\alpha_2$, perfect crystals will diffract only within a divergence of a few seconds of arc. This spread increases with increasing crystal imperfection. Similar considerations apply for wavelength spread. The decrease of diffracted intensity along the axis as shown in a transmittance curve (intensity values reversed) in Fig. 13 is, therefore, indication of gradually improving crystal perfection. This interpretation is confirmed by density profiles of dislocation etch pits (Fig. 3 and 14), and also by the geometry and density of defects revealed in x-ray topographs (Fig. 15). Again, dislocations are rectilinear in the space-grown section, they lie rather ex-

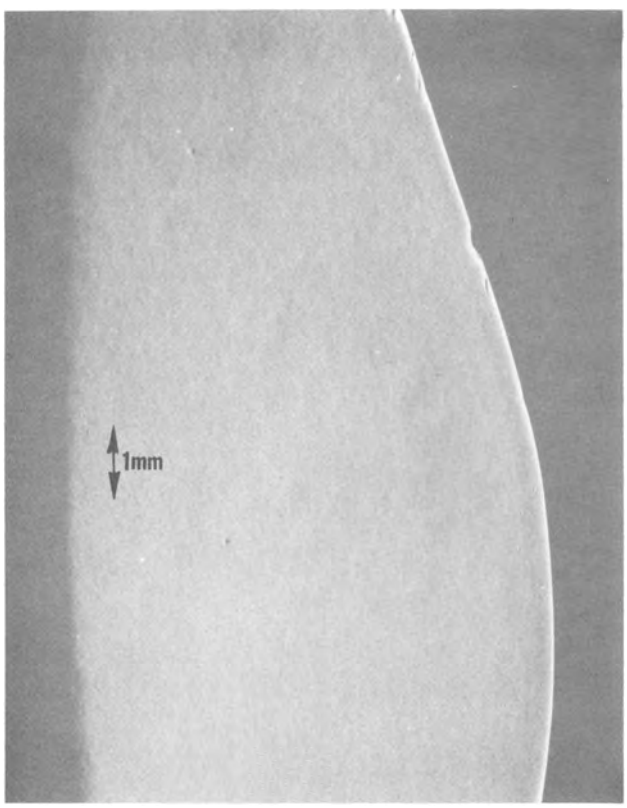


Fig. 5. [$2\bar{2}0$] scanning reflection topograph of ($1\bar{1}0$) longitudinal section of crystal grown in [$\bar{1}\bar{1}\bar{1}$] direction; center of space-grown section. Features are due to surface roughness. CuKα radiation. Image contrast reversed.



Fig. 6. Typical example of seed material grown by Czochralski technique. ($1\bar{1}0$)-[$\bar{2}\bar{2}0$] anomalous transmission topograph. Scale mark 100 μm.

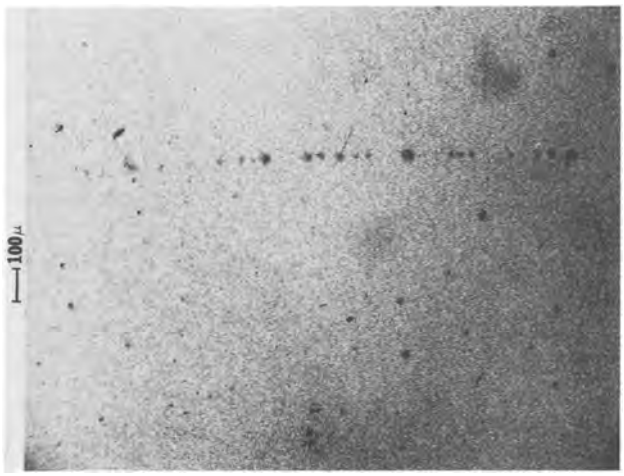


Fig. 7. Lang transmission topograph of $(1\bar{1}0)$ wafer, diffraction vector $[00\bar{4}]$. Remelt interface decorated with oxide inclusions. Scale mark 100 μm. Sample thickness 70-100μ, AgKα radiation.



Fig. 8. Lang transmission topograph of center section of space-grown crystal. Wafer surface $(1\bar{1}0)$, $[\bar{2}\bar{2}2]$ reflection. Pendellösung fringes toward slightly beveled edge of sample, Axes of dislocations in $[\bar{1}\bar{1}0]$ direction. Scale mark 100 μm.

clusively in the (111) plane parallel to the axis of growth. 60° dislocations with $[0\bar{1}1]$ dislocation axis (Fig. 15a) and pure edge dislocations with $[1\bar{2}1]$ axis (Fig. 15b) are inclined 10.9° and 19.1°, respectively, to the $[1\bar{3}2]$ growth axis. Consequently, these dislocations terminate on the crystal surface as seen in the topographs. The last section (G in Fig. 12) is virtually free of dislocations (Fig. 15); intensity variations are due to wavelike dopant striations that were also observed by differential etching in the terminal region of solidification.

Discussion

The simplest complete dislocations in the sphalerite structure with slip plane {111} are 60° dislocations (α and β) with axis $\vec{a}$ and Burger's vector $\vec{b}$ along <110> directions, edge dislocations (α and β) with $\vec{a}$ <112> and $\vec{b}$ <110>, 30° dislocations (α and β) with $\vec{a}$ <112> and $\vec{b}$ <110>, and screw dislocations along <110> (1). All of these types have been observed in as-grown and in plastically deformed InSb (9, 12, 15-17). Single crystals virtually free of dislocations have been reported; typical values given by Shesta-

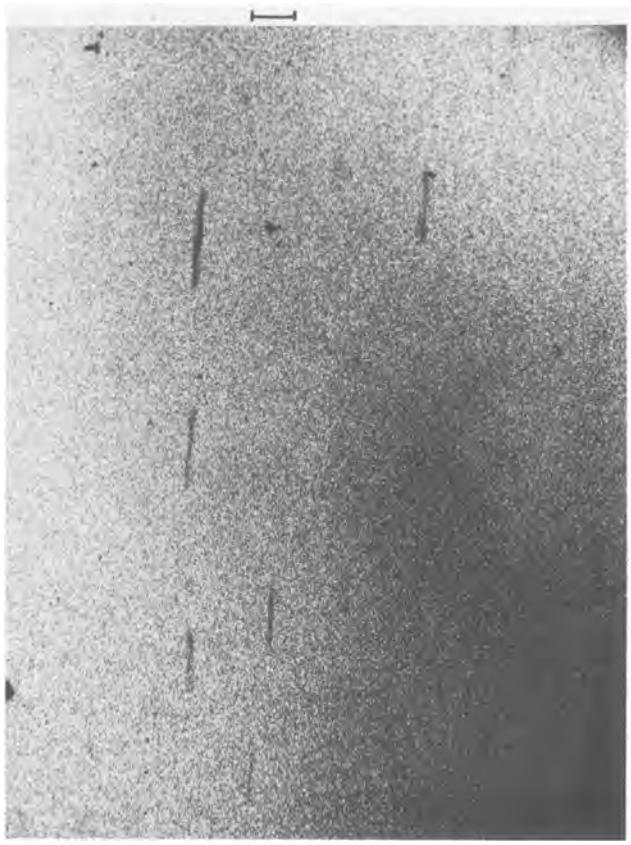


Fig. 9. Lang topograph of center of space-grown section. Wafer surface $(1\bar{1}0)$, $[\bar{2}\bar{2}2]$ reflection. Dislocation axis $[\bar{1}0\bar{1}]$. Scale mark 100 μm.

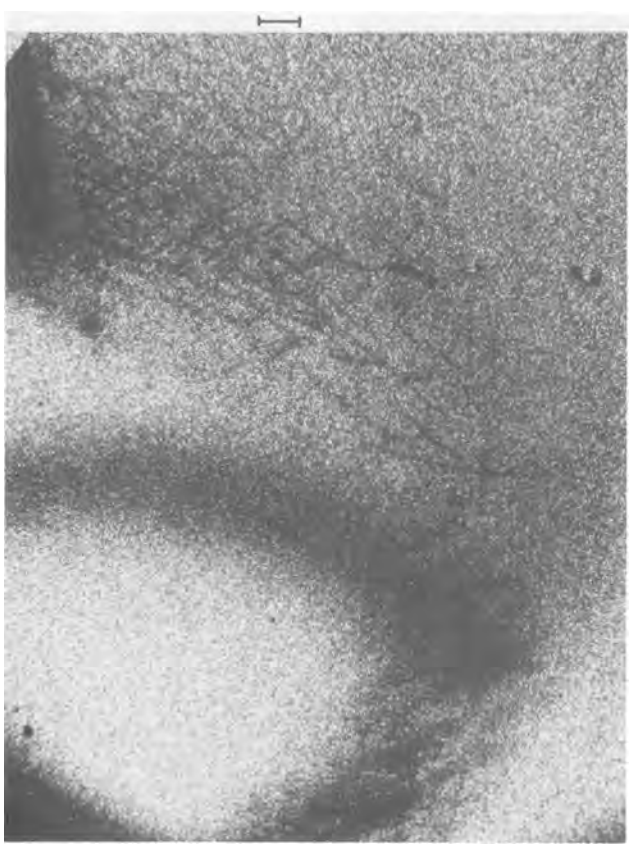


Fig. 10. $(1\bar{1}0)$-$[\bar{2}\bar{2}2]$ Lang topograph of heating cavity end of sample. Scale mark 100 μm.

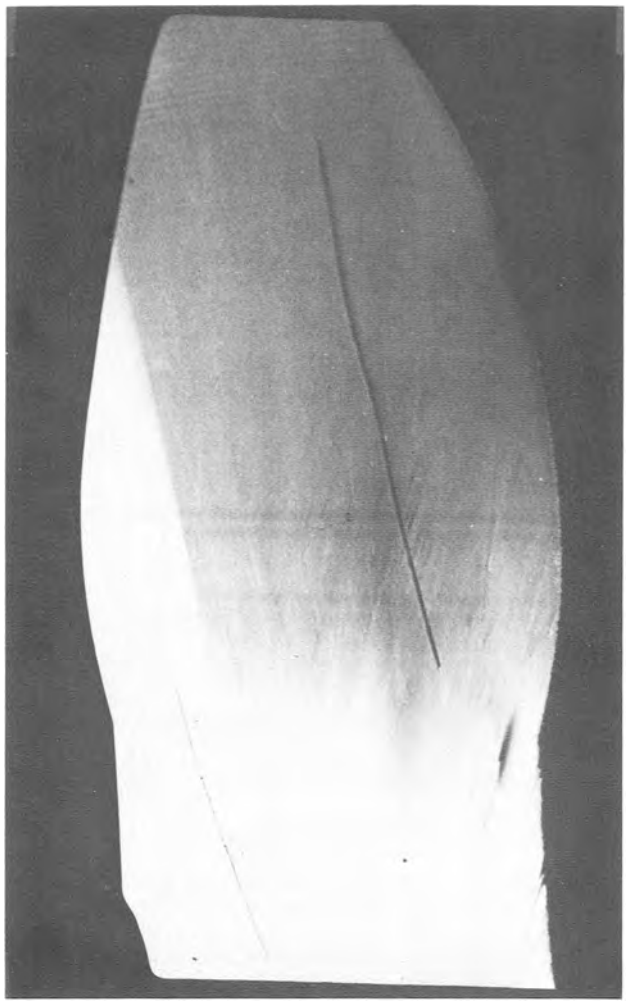


Fig. 11. Scanning reflection topograph of longitudinal (111) section of space-grown InSb(Se) crystal with seed. Growth direction [$1\bar{3}2$], seed diameter 8 mm. AgKα radiation. Contrast reversed. See Fig. 12.

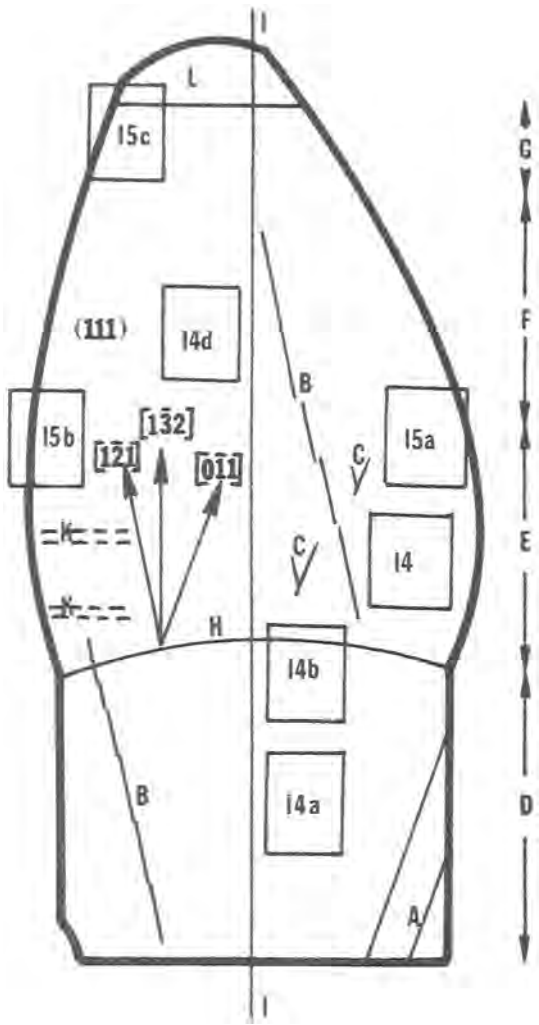


Fig. 12. Schematic of topograph shown in Fig. 11, image areas of Fig. 13-15. Crystallographic directions are indicated. A, Traces of ($\bar{1}$11) slip planes in seed; B, shadows due to grooves in the wafer surface resulting from etching of rectilinear dislocations lying directly at the wafer surface; C, images of dislocations close to surface; D, Czochralski-grown seed; E, striated section; F, homogeneously doped region; G, striated section; H, remelt line; I, location of photometric scan shown in Fig. 13; K, artifacts due to scanning; L, cavity end cut off for electrical characterization.

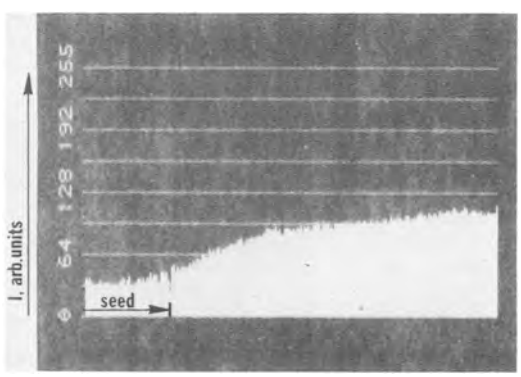


Fig. 13. Photometric scan along axis of topograph shown in Fig. 11 as indicated in Fig. 12.

kova *et al.* (26) are 2-11 $\times$ 10^2/cm^2 for Czochralski-grown and 10^4-10^6/cm^2 for zone-refined crystals.

Regarding the dislocation profiles for samples E1 and D2 (Fig. 3), it is evident that there are mechanisms leading to a sudden increase in density of dislocations in the regrown material directly adjacent to the seed, another mechanism by which the density gradually decreases along the axis, and finally a mechanism due to which the density increases sharply toward the heating cavity end.

The increase at the seed boundary is caused by inclusions of foreign material accumulated at the meltback interface. Imperfections caused by poor epitaxy as well as multiplication of dislocations by thermal shock when bringing an insufficiently preheated seed in contact with melt are ruled out due to the approach of backmelting of a larger seed to provide the molten material.

Oxide particles are always observed on InSb melt surfaces unless double crucible or bottom pouring techniques are used. As a result of crucible rotation and since crucible and crystal axis do not usually coincide during Czochralski growth, the particles are constantly swept to the solid-liquid interface and are consequently grown in.

Inclusions of foreign species have been observed in a variety of materials, *e.g.*, Si (27), GaAs (28, 29), and also InSb (12, 13, 14, 16). Size of inclusions in InSb is usually 10-20 μm (12, 13, 16); density may be as high as 10^3/cm^3 (13). Excess Al, Si, and O could be detected by electron microprobe analysis at these sites (13, 16). Depending on the difference of the thermal expansion coefficients between crystal matrix and inclusions, strain fields that develop around larger inclusions (>20-40 μm with InSb) can cause plastic deformation (Fig. 4).

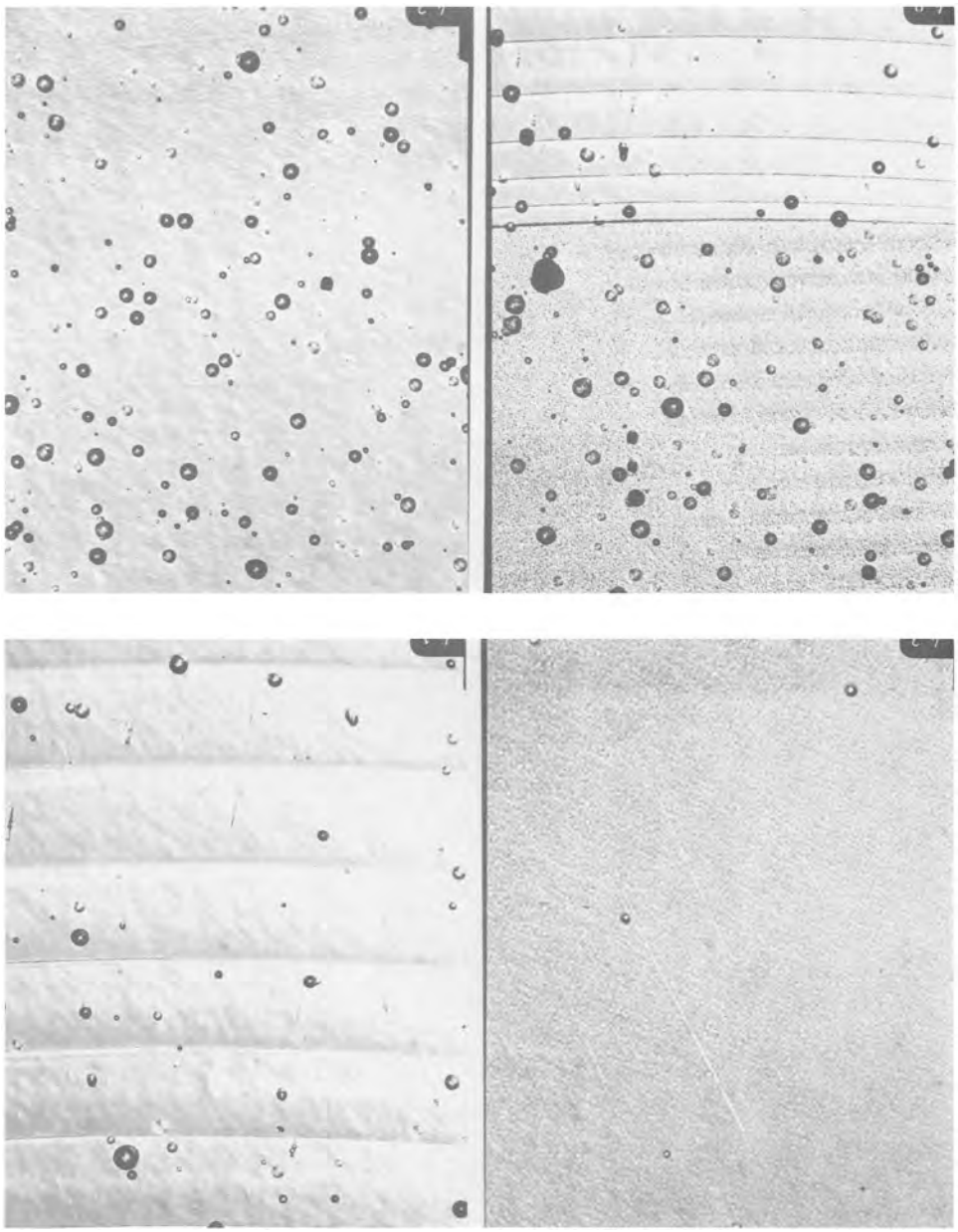


Fig. 14. Etch pit density variation along axis of selenium-doped sample; areas as indicated in Fig. 12. (a, upper left) Seed crystal, pit density $6 \cdot 10^3/cm^2$. 56×. (b, upper right) Seed crystal at bottom with dim rotational striations, space-grown portion at top with distinct non-rotational striations in the initial transient region of solidification. Over-all pit density $5 \cdot 10^3/cm^2$. 56×. (c, lower left) Striated region toward periphery of space-grown crystal. Pit density $2 \cdot 10^3/cm^2$. 56×. (d, lower right) Homogeneously doped center section, virtually without dislocation etch pits. 56×.

As mentioned, molten material for space solidification was provided by partial remelting of a larger seed. During melting and 1 hr soak, particles in the melt could drift to the melt surface and to the seed interface. For reasons of free energy balance, these interfaces acted as sinks. Particle accumulations could be found on the surfaces of all crystals (arrow in Fig. 1); size of inclusions visible at the remelt boundary (Fig. 7) is 5-25 μm, concentration is of the order of 1000/cm² interface. Only one line defect seems to originate from one of the inclusions in Fig. 7. However, to produce an increase of dislocation density in the space-grown material adjacent to the seed of the order of 100/cm² as in E1 and D2 (Fig. 3), only one dislocation needs to originate from one out of 10 inclusions at the interface. Curve E3 in Fig. 3 shows no such maximum, the reason is that the seed had a 10 times higher dislocation count to start with; an increase of the order of 100/cm² is, therefore, not noticeable.

Heterogeneous nucleation experiments indicate that there are 10^6-10^8 foreign particles per cubic centimeter in most molten materials. Their removal from the bulk of the melt due to adsorption at the remelt interface and accumulation at the melt surface resulted in a melt that had exceptionally low concentration of foreign particles. This was especially so since the melt was not in contact with a container and there were no sources of renewed contamination. Aside from serving as nucleation sites for grains and twins (30) and acting as dislocation sources, inclusions may serve as pinning sites for dislocations, a prerequisite for Frank-Read sources. Strain fields surrounding the great number of submicroscopic inclusions may also be one of the reasons for the striking difference between the geometry of line defects in seed (irregular) and space-grown material (rectilinear). Without local strain centers dislocations are more likely to be arranged in minimum free energy configurations. The energy per unit length of a dislocation is proportional to the square of the Burger's vector, minimum free energy may, therefore, be achieved by configurations where the total length of dislocation lines per unit volume is minimum (rectilinear). It is generally observed that dislocations tend to become increasingly unidirectional with lower dislocation density and improved crystal perfection.

The fact that dislocations follow basic crystallographic directions as straight lines may also be understood as an indication of a solidification process that was undisturbed by random fluid flow. Convective flow results in transient growth rate and interface

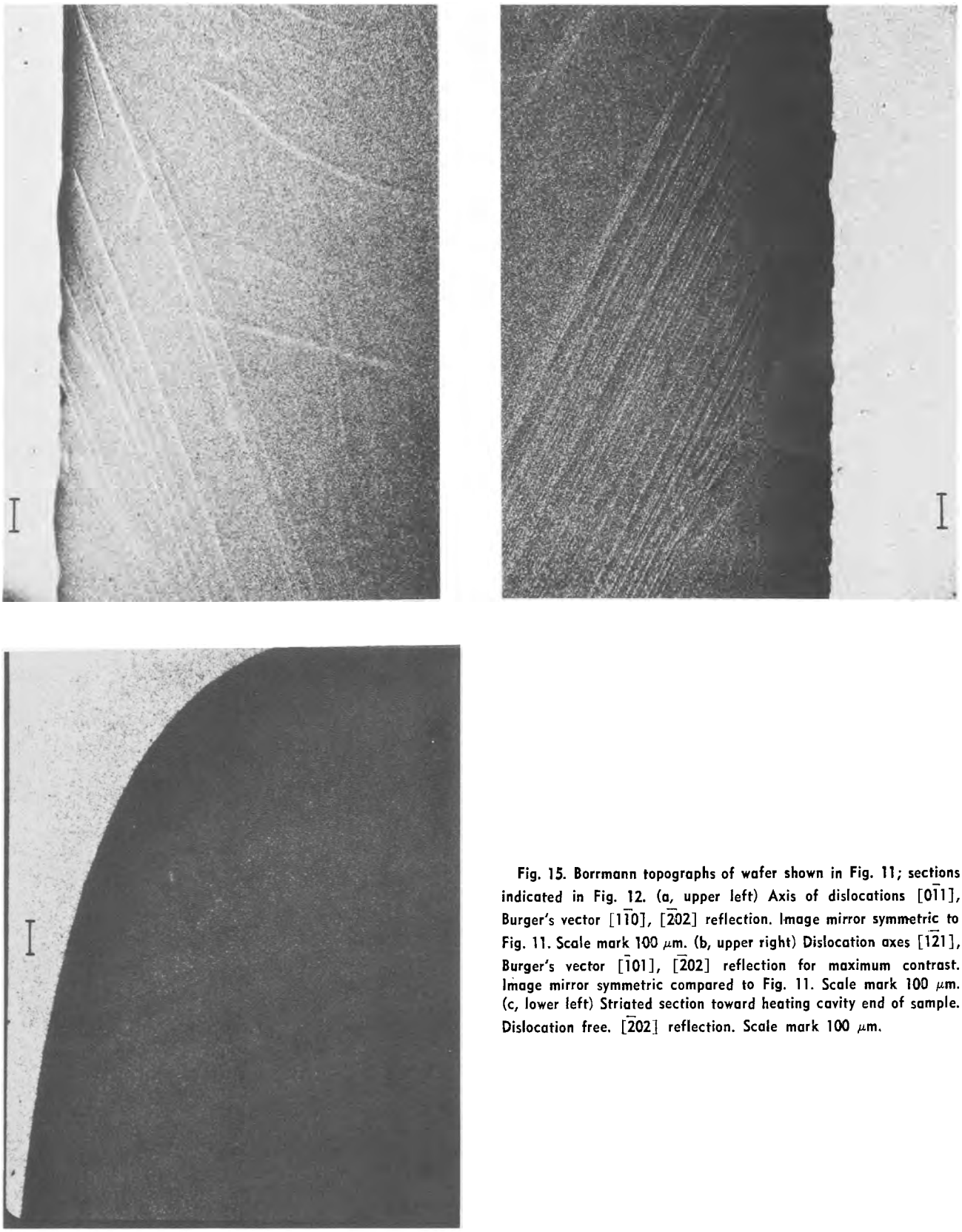


Fig. 15. Borrmann topographs of wafer shown in Fig. 11; sections indicated in Fig. 12. (a, upper left) Axis of dislocations $[0\bar{1}1]$, Burger's vector $[1\bar{1}0]$, $[\bar{2}02]$ reflection. Image mirror symmetric to Fig. 11. Scale mark 100 μm. (b, upper right) Dislocation axes $[\bar{1}21]$, Burger's vector $[\bar{1}01]$, $[\bar{2}02]$ reflection for maximum contrast. Image mirror symmetric compared to Fig. 11. Scale mark 100 μm. (c, lower left) Striated section toward heating cavity end of sample. Dislocation free. $[\bar{2}02]$ reflection. Scale mark 100 μm.

morphology perturbations, resulting local radial thermal gradients may become sufficiently large so that new dislocations are generated due to thermal stress. However, the overwhelming number of smaller local strain fields may only affect the directionality of already present defects.

Rectilinear dislocations with axes inclined to the growth direction terminate on the crystal surface after a characteristic growth distance. With the dislocation systems observed ({111} slip planes), outgrowing of dislocations is most favored if the angle between growth axis and {111} slip planes is large; most preferable is <100> seed orientation, and increasingly less favorable are <111>, <211>, <321>, <110> orientations. Since there is no evidence of sources of dislocations in the main volume of space-grown crystals, the continuous decrease of dislocation density is simply a result of outgrowing of disloca-

tions that were originally projected from the seed and from the meltback interface. Outgrowing is also reflected in radial dislocation density profiles, they are rather flat near the meltback interface and become increasingly U-shaped toward the end with minimum in the center of crystals (*e.g.*, Fig. 11).

The steep increase in dislocation density to $\approx 10^4$/cm^2 in material solidified when in contact with the graphite heating cavity (Fig. 3) is readily explained in terms of increasing thermal stress. Interface curvature radius for samples D2 and E1 was 20-25 mm at the beginning of solidification (see Fig. 7) and assumed the radius of the furnace cavity of 8 mm when in contact with it at the end. For E3 the radius was approximately 25 mm at the beginning of solidification in space (see Fig. 11 and 14), 18 mm after 14 mm of growth and 14 mm at the end since this crystal did not extend to the bottom of the heating cavity. Axial thermal gradients in the solid determined experimentally and by computation were 65° ± 5°C/cm. Radial thermal gradients from center to periphery of samples are about 7°C/cm at 25 mm radius, 9°C/cm at 20 mm, 11°C/cm at 18 mm, 14°C/cm at 14 mm, and 25°C/cm at 8 mm interface curvature radius. Dislocation density increases at coordinates that correspond to radial gradients of about 20°C/cm (D2 and E1, Fig. 3) and 14°C/cm (E3). InSb becomes plastic above 200°C, which is equivalent to about 2/3 T_m [°K] (31). The density of dislocations N produced by radial gradients and plastic flow can be estimated from the equation (32)

$$N = \frac{\alpha}{b}\frac{dT}{dr}$$

α is the linear expansion coefficient ($\approx 5 \cdot 10^{-6}$/°C), b is the Burger's vector ($4.58 \cdot 10^{-8}$ cm for <1/2 1/2 0> in InSb), dT/dr is the radial thermal gradient. At radial gradients of 14°-20°C/cm N is calculated as $1.5 \cdot 10^3$/cm^2 to $2.2 \cdot 10^3$/cm^2. These values are in good agreement with the observed densities

Generation of dislocations due to compositional stress in selenium-doped material could not be observed, even though striae in the initial transient region of solidification mark abrupt changes in dopant concentration as determined by differential etching and spreading resistance measurements.

Acknowledgment

This work was supported by NASA contract.

Manuscript submitted June 7, 1976; revised manuscript received Sept. 16, 1976.

Any discussion of this paper will appear in a Discussion Section to be published in the December 1977 JOURNAL. All discussions for the December 1977 Discussion Section should be submitted by Aug. 1, 1977.

Publication costs of this article were assisted by the University of Alabama.

REFERENCES

1. D. B. Holt, *J. Phys. Chem. Solids*, **23**, 1353 (1962).
2. J. Hornstra, *ibid.*, **5**, 129 (1958).
3. J. D. Venables and R. M. Broudy, *J. Appl. Phys.*, **29**, 1025 (1958).
4. J. W. Faust and A. Sagar, *ibid.*, **31**, 331 (1960).
5. H. C. Gatos and M. C. Lavine, *J. Phys. Chem. Solids*, **14**, 169 (1960).
6. H. C. Gatos and M. C. Lavine, *This Journal*, **107**, 433 (1960).
7. H. C. Gatos and M. C. Lavine, *ibid.*, **107**, 427 (1960).
8. M. C. Lavine, H. C. Gatos, and M. C. Finn, *ibid.*, **108**, 974 (1961).
9. S. A. Erofeeva and Yu. A. Osipyan, *Sov. Phys. Solid State (Engl. Transl.)*, **16**, 2076 (1975).
10. H. Steinhardt and S. Schäfer, *Acta Met.*, **19**, 65 (1971).
11. M. Ya. Skorokhod, L. I. Datsenko, and A. D. Tkalenko, *Sov. Phys. Solid State (Engl. Transl.)*, **8**, 593 (1966).
12. T. I. Olkhovikova and I. L. Shulpina, *ibid.*, **10**, 1678 (1969).
13. T. I. Olkhovikova, I. L. Shulpina, V. S. Ivleva, V. I. Selyanina, and V. G. Fomin, *ibid.*, **13**, 497 (1971).
14. V. S. Ivleva, T. I. Olkhovikova, V. I. Selyanina, V. G. Fomin, and I. L. Shulpina, *Soviet Phys. Crystallogr. (Engl. Transl.)*, **17**, 168 (1972).
15. I. L. Shulpina, N. D. Polchkova, and T. I. Olkhovikova, *Izv. Akad. Nauk SSSR, Ser. Fiz.*, **37**, 2340 (1973).
16. T. I. Olkhovikova, I. L. Shulpina, V. S. Ivleva, V. I. Selyanina, and V. G. Fomin, *Bull. Acad. Sci. USSR, Phys. Ser.*, **35**, 447 (1971).
17. K. Sumino, H. Shimizu, and R. Wagatsuma, *J. Phys. Soc. Jpn.*, **34**, 1697 (1973).
18. H. U. Walter, American Institute of Aeronautics and Astronautics, Paper No. 74-1241 (1974).
19. H. C. Gatos, M. C. Finn, and M. C. Lavine, *J. Appl. Phys.*, **32**, 1174 (1961).
20. J. K. Howard and R. D. Dobrott, *Appl. Phys. Lett.*, **7**, 101 (1965).
21. A. R. Lang, *J. Appl. Phys.*, **29**, 597 (1958).
22. G. Borrmann, W. Hartwig, and H. Imler, *Z. Naturforsch. Teil A*, **13**, 423 (1958).
23. H. Barth and R. Hosemann, *ibid.*, **13**, 792 (1958).
24. G. H. Schwuttke, *J. Appl. Phys.*, **33**, 2760 (1962).
25. H. U. Walter, *This Journal*, **123**, 1098 (1976).
26. N. A. Shestakova, M. A. Gurevich, and V. S. Ivleva, *Sov. Phys. Crystallogr. (Engl. Transl.)*, **9**, 635 (1965).
27. E. D. Jungbluth, *J. Appl. Phys.*, **36**, 3112 (1965).
28. E. D. Jungbluth, *This Journal*, **112**, 580 (1965).
29. T. Iizuka, *Jpn. J. Appl. Phys.*, **7**, 485 (1968).
30. W. C. Dash, *J. Appl. Phys.*, **30**, 459 (1959).
31. J. W. Allen, *Phil. Mag.*, **2**, 1475 (1957).
32. E. Billig, *Proc. R. Soc. London, Ser. A*, **235**, 39 (1956).

Molecular Beam Epitaxial Growth of InP

J. H. McFee* and B. I. Miller*

Bell Laboratories, Holmdel, New Jersey 07733

and K. J. Bachmann*

Bell Laboratories, Murray Hill, New Jersey 07974

ABSTRACT

Epitaxial layers of InP have been grown on the $(\bar{1}\bar{1}\bar{1})$ face (P face) of InP substrates by molecular beam epitaxy. The layers were grown at substrate temperatures ranging from 220° to 510°C, using separate In and P sources. Unintentionally doped layers grown above ~350°C appear to be single crystal with $n = 2\text{-}5 \times 10^{16}$ cm^{-3} and $\mu = 2000\text{-}3500$ cm^2/Vsec. Layers grown at substrate temperatures below ~350°C appear to be composed of well-oriented crystallites, and have poor electrical and photoluminescent properties. Orientation-dependent faceting is a prominent feature of layers grown on $(\bar{1}\bar{1}\bar{1})$ substrates at temperatures >350°C. Epitaxial InP layers have also been grown on the (111) face (In face) and the (100) face of InP substrates. Orientation-dependent faceting is much less prominent for growth on the (100) face, and it is possible to obtain smooth, featureless (100) epitaxial layers.

Molecular beam epitaxy (MBE) is now an established technique for growing epitaxial semiconductor layers. MBE has been applied to GaAs (1-7), AlGaAs (1, 2), GaP (8), GaAsP (8), InP (9-11), and to the II-VI semiconducting compounds (12). The significant characteristics of MBE are: (*i*) kinetic (as opposed to equilibrium) growth conditions, (*ii*) relatively slow growth rates (a few monolayers per second), and (*iii*) simplicity of flux control (*e.g.*, by opening and closing shutters in front of the beam sources). Therefore, as compared to LPE or VPE growth techniques, a different set of conditions determines the composition and dopant incorporation in MBE. Also MBE permits abrupt changes, almost on an atomic scale, in the composition and doping profiles of the growing layer. Because of this precise flux control, MBE has been successfully used to grow "superlattice" structures (13-15) in GaAs, having periodicities as small as ~50Å. In addition, MBE has been successfully applied to the fabrication of GaAs and GaAs/AlGaAs semiconductor devices such as injection lasers, varactor and IMPATT diodes, FET's, etc., where precise tailoring of the composition and/or doping profile is a critical requirement. [See Ref. (1) for a comprehensive list of references dealing with MBE device fabrication.]

In this paper, we present our results on the MBE growth of InP from elemental In and P sources. This study was initiated primarily because of the recent interest in the InP/CdS heterojunction solar cell (16). The objective was to fabricate a thin film version of such a cell. In addition, InP shows promise for making low noise microwave devices such as transferred electron amplifiers (17) and oscillators. MBE grown InP layers would be especially advantageous in this application, because here again the doping profile is a crucial parameter.

Farrow (9-11) has recently reported growing InP on (100) and $(\bar{1}\bar{1}\bar{1})$ InP substrates by MBE using In and InP as sources. At growth temperatures in excess of 400°C, he reports smooth epitaxial growth on the (100) face. His unintentionally doped layers were typically n-type with $N_D\text{-}N_A \sim 10^{17}$ cm^{-3}, and with 300°K mobilities in the range 1000-2000 cm^2/Vsec. Growth from elemental sources (P and In) affords independent control of the P_4/In ratio as well as the possibility of lower unintentional doping due to the higher purities (99.9999+% pure) of the elements as compared to InP (generally less than 99.999% pure). In addition, because of the requirement to lattice match InP to CdS in the InP/CdS solar cell, our growth efforts have been concentrated on the InP $(\bar{1}\bar{1}\bar{1})$ growth face which lattice matches to CdS and which can be polished to a damage-free condition. We also report some preliminary results of growth on the (111) and (100) faces. A further objective of our study has been to establish the limits on the substrate temperature for epitaxy. For CdS and many other substrates a low growth temperature is desirable to prevent decomposition.

* Electrochemical Society Active Member.

Key words: molecular beam epitaxy, indium phosphide, semiconductor films, epitaxy.

Experimental

MBE Growth System

The MBE growth system used here is similar to that used by Cho (1) and others to grow epitaxial semiconductor films. It consists of an 18 in. diameter bakeable ultrahigh vacuum system capable of pumping down to the 10^{-10} Torr range. The horizontal cross section of the system is shown in Fig. 1. Installed on the vacuum system are evaporating ovens, a 3 keV electron diffraction system (RED), a 10 keV Auger system with a 3 keV sputter gun, a quadrupole mass analyzer, a precision sample manipulator, and a scattered laser light detector.

Ovens.—The main ovens are cylindrical in shape (5 cm long × 1 cm diam) consisting essentially of a helical-wound Ta heating element which encloses a pyrolytic BN (99.999% pure) crucible. Several layers of 0.0005 in. Ta foil are wound on the outside of each oven as a heat shield. Heater and support construction is entirely of Ta or Mo. Each oven has its own shutter and all five main ovens are enclosed by a liquid nitrogen (LN_2) shroud. A gold-plated copper nose cone (see shaded parts in Fig. 1) is attached to the LN_2 shroud to limit beam spread from the main ovens. The main ovens are used for high temperature evaporants, *i.e.*, In or Ga, and dopants like Sn, Be, Mg, etc. The cylindrical BN crucibles are reentrant on the bottom and open at top. The reentrant tube allows the thermocouple to be inserted toward the center of the crucible providing a better thermal contact between it and the charge.

For the high vapor pressure phosphorus, we use a large capacity (20 cm^3) auxiliary oven similar to that suggested by Ilegems (18) for As in GaAs MBE. This oven has an Al body with embedded heaters and a separately heated ceramic "snout" aimed at the substrate.

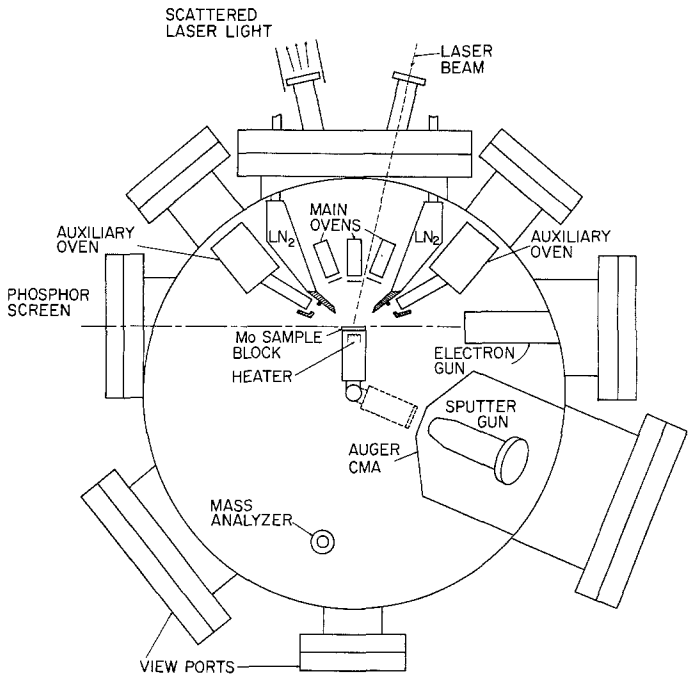


Fig. 1. Horizontal cross section of 18 in. diameter ultrahigh vacuum system. Section taken through growth plane of stainless steel bell jar.

Generally, the auxiliary ovens are run at temperatures less than 400°C and for that reason Al was found to be a convenient construction material. Subsequent use of these ovens in MBE growth has shown no attack on the Al by the phosphorus and no apparent contamination problems. In fact, layers grown using one of the main ovens (BN crucible) as the phosphorus source exhibited the same electrical and photoluminescent properties as those layers grown using the Al auxiliary oven as the phosphorus source. In order to limit the phosphorus beam spread from the snout, a gold-plated copper "ear" is attached to the nose cone of the LN_2 shroud. Generally, with the auxiliary ovens ten growth runs can be made before reloading.

Reflection electron diffraction (RED).—A RED system similar to one described by Cho (1) and others is used to monitor the surface crystal structure before and during growth. It consists of a 3 keV electron gun which produces a 1 mm diameter beam at glancing incidence to the sample. The RED pattern is observed on a 4 in. diameter phosphor screen (Fig. 1).

Auger cylindrical mirror analyzer (CMA).—In order to determine the surface stoichiometry as well as impurities on the surface a 10 keV CMA made by Varian Associates was used. With care, surface impurities as small as 0.1% could be detected. In addition, a 3 keV sputter gun is mounted 15° from the vertical so that the sample can be sputtered while an Auger spectrum is being taken. Generally sputtering is done at 3 keV with 2 $\mu A/cm^2$ Ar^+ current density. A useful feature of the Auger system is a scanning mode, similar to that found on a scanning electron microscope, which allows precise visual determination of the area being analyzed or sputtered.

Quadrupole mass analyzer.—A precision quadrupole mass analyzer (U.T.I. Model 100C, 1-300 amu) is used to monitor the partial pressures in the system before and during a growth run. In addition, the mass analyzer is located so that it has an unobstructed view of the main ovens allowing the beam fluxes to be monitored continuously during a run. Furthermore, the axis of the analyzer is perpendicular (approximately) to the incoming beams so that the quadrupole elements will not become coated during the course of several evaporations, causing the analyzer to change calibration. To enhance the sensitivity of the mass analyzer, a beam chopper is placed in the system ahead of the analyzer so that phase sensitive techniques can be used. Typically growth proceeds at In fluxes of 3×10^{14} cm^{-2} sec^{-1} corresponding to a growth rate of 0.5 μm/hr. Using the chopper, dopant fluxes in many instances as low as a few parts per million of In can be detected.

Precision sample manipulator.—The sample holder is a Varian precision sample manipulator modified to allow heating of the substrates to 800°C. All parts of the sample holder subject to heating were replaced by Mo and Ta. The substrates are mounted on a Mo sample block 2.5 cm × 2.5 cm × 3 mm thick. A thermocouple is inserted into a hole drilled in the sample block. As shown in Fig. 1, the sample can be rotated to face the main ovens (growth position) or to face the CMA for sputter cleaning and/or surface composition analysis.

Scattered laser light system.—In order to observe the smoothness of the epitaxial layer during growth, a laser beam is incident on the layer and the scattered (nonspecular) light is monitored as shown in Fig. 1 (19). The incident beam is provided by a 6328Å He-Ne laser and is chopped at 90 Hz. The scattered light is detected by a photomultiplier and lock-in amplifier. It is found that the scattered light signal is extremely sensitive to any change in surface smoothness. This technique has proved to be our most useful real-time monitor of layer quality.

Determination of Growth Parameters

From earlier MBE experiments on III-V semiconductors, it is clear that the substrate temperature and the ratio of excess P_4 to In fluxes will be critical parameters for the growth of high quality epitaxial layers of InP. As in the case of GaAs, the congruent temperature (*i.e.*, the temperature above which the substrate no longer evaporates stoichiometrically) is a safe upper limit on substrate temperature during epitaxial growth. Farrow finds that for the (100) face of InP, the congruent temperature is 365° ± 10°C (9) and for the $(\bar{1}\bar{1}\bar{1})$ he finds it to be 325° ± 10°C (11). We have roughly determined the upper limit of the congruent temperature for the $(\bar{1}\bar{1}\bar{1})$ face of InP and get a value of about 415°C. Farrow (9), for example, grew at 300°C and obtained stoichiometric growth of InP on a (100) InP substrate, however a large percentage of his samples were polycrystalline. The question therefore arises: Is it possible to grow above the congruent temperature? From these studies Farrow concluded that the maximum congruent evaporation rate from the (100) InP surface is only 10^{-5} monolayers/sec. It appears, therefore, that even above the congruent temperature it may be possible to grow epitaxial layers if enough P_4 (or P_2) is present in the beam to compensate for the loss of phosphorus from the surface. In fact, Farrow (10) was able to stabilize an InP (100) surface with a P_4 beam at temperatures in excess of 450°C. More recently (11) he has reported the growth of epitaxial films of InP at temperatures greater than the congruent temperature. Using this approach, we have grown epitaxial layers at substrate temperatures up to 510°C with a suitably high P_4 flux. For example, to grow at a rate of 0.5 μm/hr at 450°C, the P_4 and In fluxes at the sample are 3×10^{15} and 3×10^{14} cm^{-2} sec^{-1}, respectively. We find, at 450°C, that when the P_4:In ratio falls below about 10:1 nonstoichiometric growth occurs as evidenced by the buildup of In droplets on the surface.

Sample and Sample Preparation

The InP substrates used in these studies were grown by the liquid encapsulated Czochralski (LEC) method, details of which have been described earlier (20, 21). The InP crystals were pulled along the (100) axis and had a dislocation density which ranged from 10^3 to 10^5 cm^{-2}. For morphology studies, Sn-doped substrate material ($n = 5 \times 10^{17}$) was used and for electrical tests

Cr-doped substrate material ($\rho = 5000$ Ω-cm) was used at first; subsequently, semi-insulating Fe-doped (22) substrate material ($\rho > 10^8$) was used.

The InP substrates were mounted on Mo blocks using In solder. In the case of the (100) and ($\bar{1}\bar{1}\bar{1}$) (phosphorus) faces, the samples were lapped to a mirror finish on dextalose paper saturated with a 5% Br:95% CH_3OH solution. In order to gauge the perfection of the lapped surface, the sample was subjected to illumination by He-Ne laser light while being viewed under a microscope (19). Again, as in the scattered laser light probe on the MBE system, any surface imperfections will scatter the laser light into the objective of the microscope where they appear as points of light. Typically, the samples are polished so that there are less than 2-4 points appearing per square millimeter.

In the case of the (111) (In) face of InP, we were unable to find a purely chemical technique, so Syton HT-30 chemo-mechanical polish was used. Now, under incident laser light several hundred points of light per square millimeter were visible in addition to many scratches and other imperfections.

Run Procedure

The InP was grown from elemental sources of In and red P, both of which were 99.9999+% pure. In the case of In, the major impurity was Sn at 0.7 ppm, while for the P the major impurity was Mg at 0.3 ppm.

After the sample is prepared as described above, it is immediately loaded into the vacuum system which is flushed with dry N_2 during the loading operation. When a vacuum of 10^{-6} Torr is obtained, the sample is heated to 365°C and the In oven to 440°C overnight. In addition, during the same period the vacuum chamber walls are baked at about 150°C. Under these bakeout conditions, the partial pressure of phosphorus coming from the auxiliary oven remains negligible. The following morning, after the walls have cooled, the LN_2 traps are filled and the Ti sublimitation pump turned on. A short time later the total pressure in the system is 10^{-9} Torr or less. A typical partial pressure spectrum of the residual gas under these conditions is shown in Fig. 2. It can be seen from Fig. 2 that the above procedure has resulted in a minimal H_2O vapor content. Omission of the bakeout may result in a H_2O vapor content an order of magnitude larger. The largest components of residual gas prior to growth appear to be H_2, Ar, Ne, and P. Smaller amounts of CO_2, He, and N_2 (or CO) are also present. Under growth conditions, when the In and P_4 sources are at operating temperatures, the predominant background gas is P_4 at 2×10^{-6} Torr. The only significant changes observed in the background spectrum under growth conditions are an increase of an order of magnitude in the $M = 28$ amu peak (N_2 or CO) and a decrease in H_2O vapor by a factor of two.

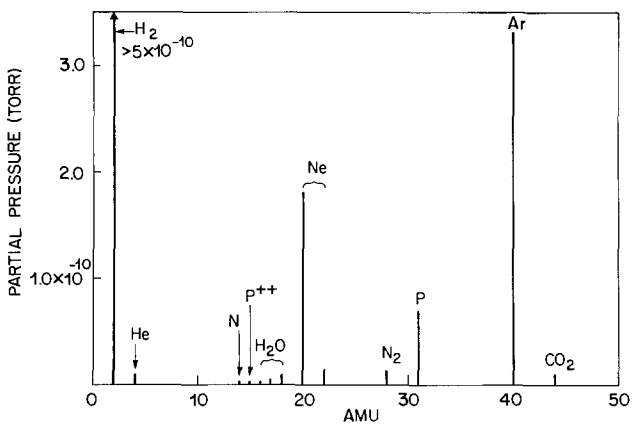


Fig. 2. Partial pressure spectrum of residual gases in bell jar after pump down and bakeout. Total pressure approximately 10^{-9} Torr. Substrate at 365°C, In oven at 440°C, and P oven at room temperature.

Once the base pressure of $\leq 10^{-9}$ Torr has been reached, the source ovens are heated to their operating temperatures. For ~0.5 μ/hr growth rate the In source temperature is at 690°C while the P_4 source temperature is at 345°C. These numbers are appropriate for an In source to sample distance of 6.5 cm.

Before commencing growth, it is essential that the substrate surface be free of contamination. In order to insure this condition, the surface is routinely sputtered in a 5×10^{-5} Torr Ar atmosphere at 3 kV with a current of 1.5 μA/cm² for 10 min. The beam from the sputter gun is scanned over the substrate to obtain uniform removal of contaminants. Following sputtering an Auger spectrum is taken to determine the cleanliness of the surface. An illustration of the effectiveness of this procedure is shown in Fig. 3. Figure 3a shows

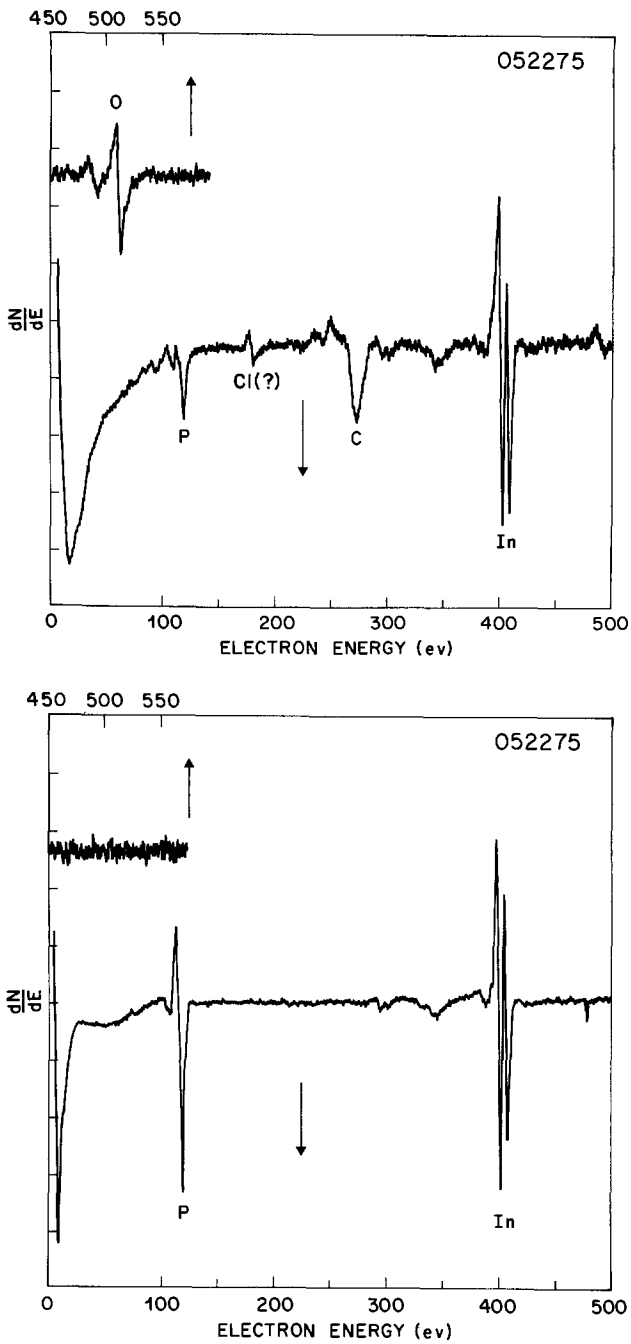


Fig. 3. (a, top) Auger spectrum of an unsputtered InP substrate which has not been outgassed overnight at 365°C in the usual manner. (b, bottom) Auger spectrum after sputtering of same InP substrate referred to in (a). Sputtering conditions: 3 keV Ar^+, 1.5 μA/cm², 10 min duration.

the Auger spectrum of an unsputtered InP substrate which had not been baked out overnight. It can be seen that the surface is rather heavily contaminated with O and C and has a trace of Cl. Also, there is considerable disparity between the amplitudes of the P and In peaks. Figure 3b shows the spectrum obtained after sputtering. All traces of C, O, and Cl have disappeared and the In and P peaks are more nearly equal in size. It should be noted that the P peak shape and height is very sensitive to the presence of surface contaminants and thus is a very useful gauge of surface contamination.

It is possible to obtain a relatively clean sample exhibiting a spectrum similar to that shown in Fig. 3b without sputtering, by heating the sample overnight as described above. However, this result is strongly dependent on the sample preparation technique and in order to insure reproducibility from run to run, sputtering is routinely done. The substrate is normally annealed at 365°C for 1 hr after sputtering.

After the substrate surface has been sputtered clean and annealed, it is rotated into growth position (see Fig. 1) where the RED pattern can be observed on the phosphor screen before, during, and after a growth run. For example, by following the sample preparation and sputter cleaning procedure described earlier, a RED pattern like that shown in Fig. 4 is obtained in the case of a $(\bar{1}\bar{1}\bar{1})$ substrate face. This pattern exhibits streaks whose spacing corresponds to the InP (111)-2 surface structure. In other words, the streaked nature of Fig. 4 is indicative of an undamaged, reconstructed two-dimensional crystal surface. Further evidence of the essentially undamaged nature of the substrate surface are the diagonal bright bands (Kikuchi lines) seen in Fig. 4 which would not be observed if an appreciable amount of point defects or elastic strain was present (23). Depending on the temperature and orientation of the substrate, various changes may occur in the RED pattern when growth is started. These details are discussed below.

Another technique which is very useful for monitoring the smoothness of the substrate and epitaxial layer is the use of scattered (nonspecular) laser light. As in the case of RED, the scattered light can be observed before and during a growth run. A properly lapped substrate will scatter very little light, as described earlier. Upon initiation of growth, a change occurs in the scattered light level. Growth of a very smooth epitaxial layer such as on the (100) surface causes a gradual decrease in the scattered light level during the course of a run. In contrast, when growing on the $(\bar{1}\bar{1}\bar{1})$ surface, the scattered light will increase gradually as the layer grows due to faceting. An abrupt increase in the scattered light level upon initiation of growth indicates either a polycrystalline or a nonstoichiometric (*i.e.*, In droplets on the surface) layer.

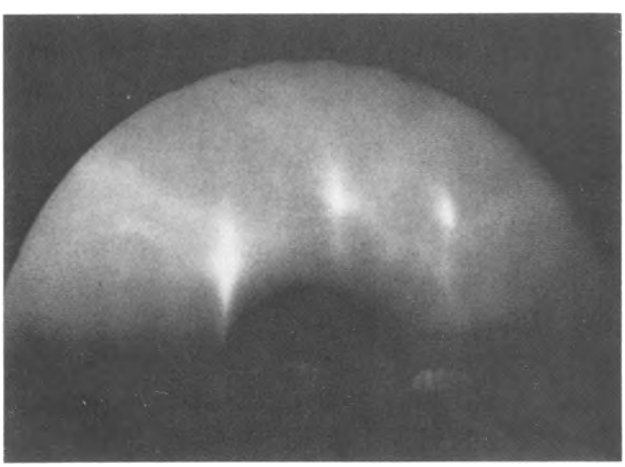


Fig. 4. 3 keV RED pattern obtained from $(\bar{1}\bar{1}\bar{1})$ InP substrate after overnight outgassing at 365°C and sputter cleaning (110 azimuth). Half-order streaks indicate a $(\bar{1}\bar{1}\bar{1})$-2 surface structure.

Results

$(\bar{1}\bar{1}\bar{1})$ Orientation

InP layers have been grown at substrate temperatures ranging from 220° to 510°C. These layers were undoped and typically were 2 μm thick. At a growth rate of 0.5 μm/hr, we find that single crystal epitaxial growth occurs at substrate temperatures above 325°-350°C. Above these temperatures the surface morphology of the epitaxial layer exhibits a faceted structure with threefold symmetry characteristic of the $(\bar{1}\bar{1}\bar{1})$ growth axis. Also, these epitaxial layers are n-type ($n \sim 3 \times 10^{16}$) and have Hall mobilities which are comparable to that of bulk InP of this same carrier concentration. The photoluminescent efficiency of these epitaxial layers is also comparable to that of bulk InP; layers grown at 450°C have a maximum photoluminescent efficiency.

Below 325°-350°C, the epitaxial layers exhibit a gradual loss of crystalline properties as a function of decreasing growth temperatures. The deterioration of crystalline properties is evidenced by the gradual disappearance of the threefold faceted morphology of the epitaxial surface and changes in the RED and x-ray diffraction patterns. Scanning electron microscope (SEM) photographs of these epitaxial surfaces indicate that the layers are polycrystalline. Furthermore, the layers grown below 325°-350°C have very low mobilities and high carrier concentrations ($n \sim 10^{18}$) and exhibit very poor photoluminescent efficiencies.

In order to study the nature of the threefold morphology of the epitaxial layers grown at high temperature, we selected a growth temperature of 450°C. This temperature is well above the lower limit of substrate temperatures necessary for single crystal epitaxial growth.

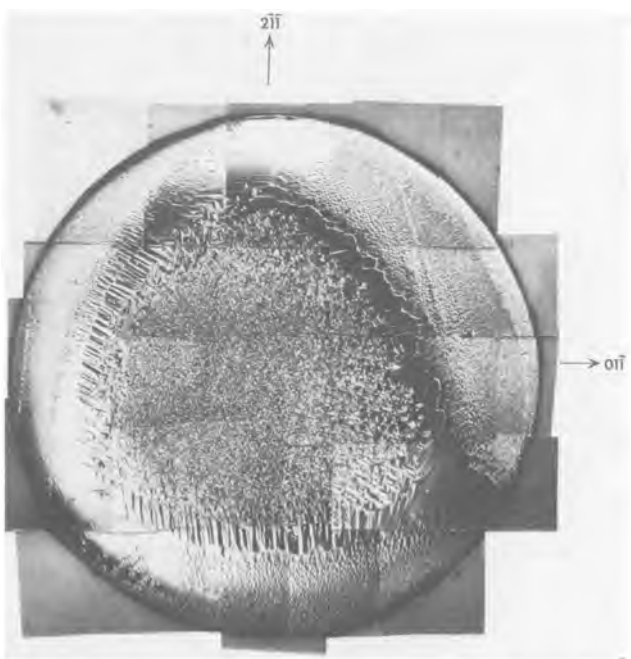


Fig. 5. Nomarski interference-contrast photograph of an InP epitaxial layer grown at 450°C on a disk-shaped $(\bar{1}\bar{1}\bar{1})$ substrate. Chemical polishing of the substrate produces a lens-shaped convex surface whose central area is aligned parallel to $(\bar{1}\bar{1}\bar{1})$ within $\pm$10 min and whose perimeter is tilted off $(\bar{1}\bar{1}\bar{1})$ by $\sim$1°. Arrows indicate azimuthal directions in the plane of the substrate.

Growth at 450°C.—Initially it was observed that epitaxial layers grown on the $(\bar{1}\bar{1}\bar{1})$ face showed prominent nonuniform morphological features such as pyramids, smooth bands, and "shingles." At first, these features were suspected to be caused by surface defects related to sample preparation or by nonuniform growth condition, *i.e.*, spatial variation of the In or P_4 beams. As more layers were grown, it became obvious that there was a strong correlation between these morphological features and substrate orientation. This dependence of the morphology of epitaxial layers on orientation and not on defects has been observed by Shimbo *et al.* (24) in VPE silicon. In the VPE growth of GaAs, DiLorenzo (25) has reported a dramatic decrease of pyramidal growth for small misorientations of the substrate from (100). Rode (26) has developed a theory of surface energy as a function of misorientation from a singular surface such as the (100) and (111) surfaces of diamond-type and zinc blende crystal structures. He finds that morphological features such as low angle terraces, hillocks, and pyramids are probable for surface orientations within a few degrees of (100) and (111). An essential result of Rode's theory when applied to epitaxial growth is the critical dependence of surface morphology on the precise orientation of the substrate.

In order to elucidate the morphological features of the InP epitaxial layers grown on the $(\bar{1}\bar{1}\bar{1})$ face at 450°C, a series of growth runs were made on disk-shaped substrates. The disk-shaped substrates were x-ray oriented to within 10 min of the $(\bar{1}\bar{1}\bar{1})$. During lapping and polishing, the surface of the disk-shaped sample becomes lens shaped (convex) with the local normal at the perimeter tilted off the $(\bar{1}\bar{1}\bar{1})$ by ~1°. Figure 5 shows an epitaxial layer grown at 450°C on such a disk-shaped substrate (5 mm diameter), taken by Nomarski interference contrast to enhance the surface features. As can be seen, the morphology clearly exhibits the threefold nature of the [111] growth axis. This threefold pattern always appears for layers grown on accurately oriented $(\bar{1}\bar{1}\bar{1})$ disk-samples grown under identical conditions. On this basis we conclude that the morphological features seen on this face are solely dependent on the local substrate normal. Three distinct areas can be seen in Fig. 5:

1. The central region, which is within ±10 min of the $(\bar{1}\bar{1}\bar{1})$, shows a pyramidal growth the details of which are shown in Fig. 6a. It should be emphasized that the features in Fig. 5 and 6 are greatly exaggerated by the Nomarski interference contrast. For example, the pyramids of Fig. 6a are extremely shallow, having heights of only 2000-5000Å and faces inclined to the $(\bar{1}\bar{1}\bar{1})$ by ~0.9°.

2. The three equivalent smooth bands occurring at the 12, 4, and 8 o'clock positions in Fig. 5 appear mirror

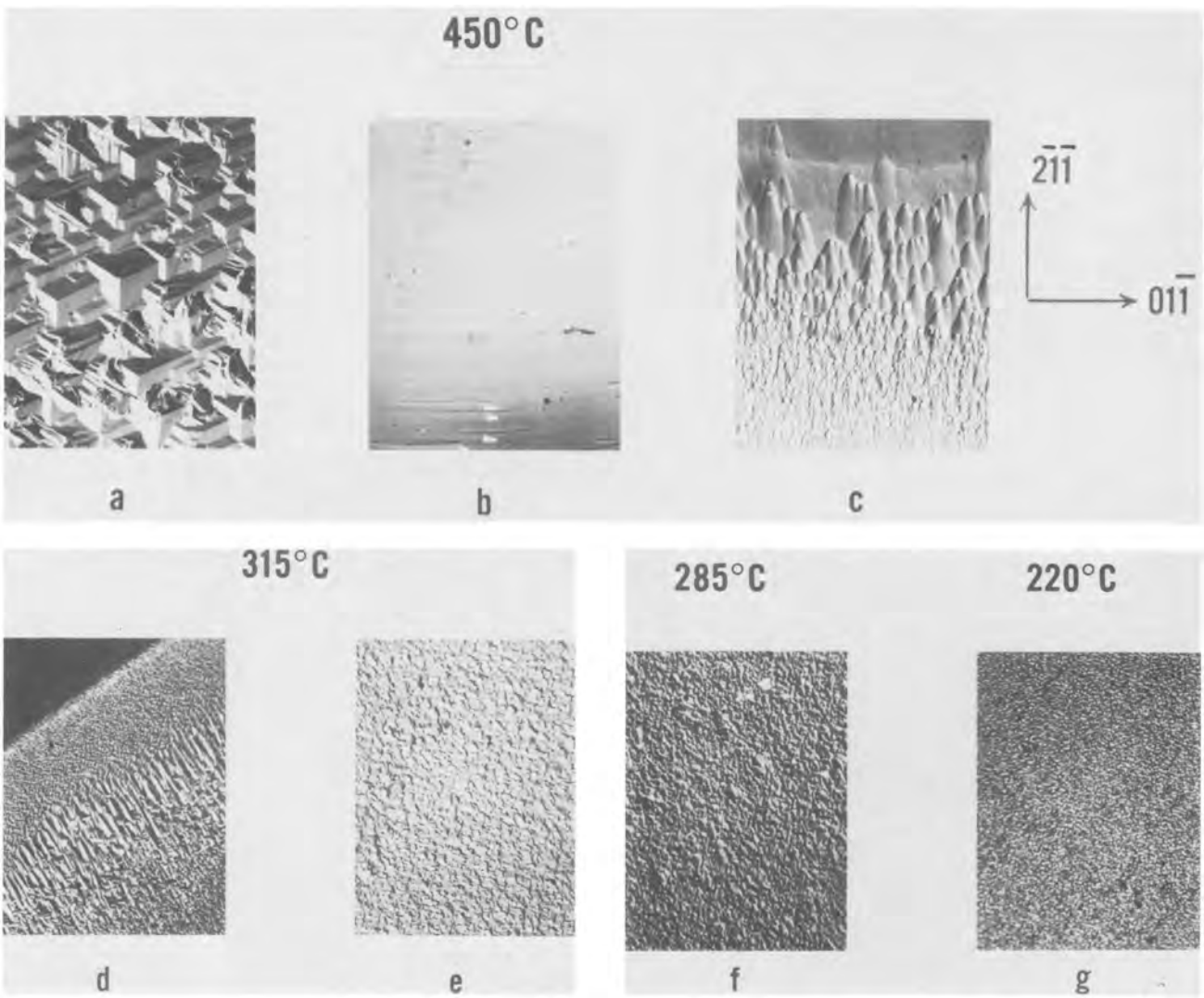


Fig. 6. Nomarski interference-contrast photographs showing details of surface morphology of InP epitaxial layers grown on $(\bar{1}\bar{1}\bar{1})$ face at various substrate temperatures, T_S. (a) Center region of layer shown in Fig. 5 (T_S = 450°C), 128×. (b) "Smooth" region near top edge in Fig. 5, 128×. (c) "Roof-shingle" region near bottom edge in Fig. 5, 200×. (d) Near edge of layer grown at T_S = 315°C, 256×. (e) Central region of layer in (d), 1000×. (f) T_S = 285°C, 1000×. (g) T_S = 220°C, 1000×.

smooth to the eye. Under interference contrast they are devoid of any features except parallel smooth steps which are observable only at maximum contrast. This region is shown under higher magnification in Fig 6b. The step height is estimated to be no greater than several hundred angstroms. The band at the top of Fig. 5 (12 o'clock position) is tilted off the $(\bar{1}\bar{1}\bar{1})$ by $\gtrsim 1°$ toward $2\bar{1}\bar{1}$ azimuth. Based on these results, a 1 $\times$ 1 cm square substrate was intentionally tilted off the $(\bar{1}\bar{1}\bar{1})$ by $\sim 2°$ toward the 211 azimuth and an epitaxial layer grown on it at 450°C. Figure 7 shows the central part of the resulting epitaxial layer. Now the smooth band extends almost the full 1 cm length of the sample in the $2\bar{1}\bar{1}$ direction but is only about 1.5 mm wide in the $01\bar{1}$ direction. Along the $2\bar{1}\bar{1}$ direction the tilt of the smooth band surface with respect to the (111) direction varies from 2° to 4°. However, along the $01\bar{1}$ direction the component of the tilt of the smooth band is from $-0.1°$ to $+0.1°$ with respect to the $(\bar{1}\bar{1}\bar{1})$. The limited extent of the smooth band in the $01\bar{1}$ direction is mainly due to the dependence of the morphology on azimuth, as seen in Fig. 5 (disk sample). Figure 7 illustrates the difficulty in growing large featureless layers on $(\bar{1}\bar{1}\bar{1})$ substrates.

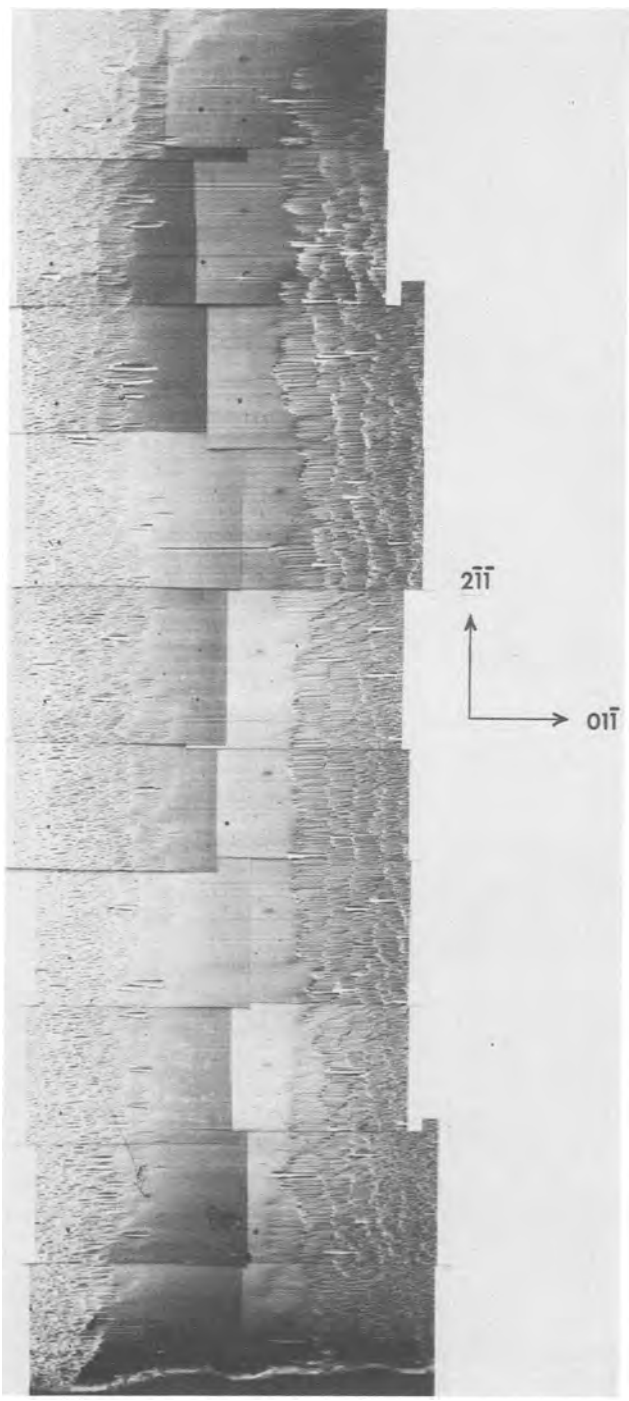


Fig. 7. Nomarski interference-contrast photograph of InP epitaxial layer grown at 450°C on 1 $\times$ 1 cm square InP substrate tilted off $[\bar{1}\bar{1}\bar{1}]$ by $\sim 2°$ toward $2\bar{1}\bar{1}$ azimuth. "Smooth" region extends nearly across whole width of sample.

3. Lying between the three smooth bands are three "shingled" regions separated from the central pyramidal area by a transition belt. Figure 6c shows the shingled area and the transition area in more detail. The distinguishing feature of the shingled region is its twofold nature, as differentiated from the threefold pyramids and one-dimensional steps in the smooth bands.

The morphological features of Fig. 5 can be taken as evidence of the single crystal nature of the epitaxial layer since they show the growth habit of the $(\bar{1}\bar{1}\bar{1})$ face. Furthermore, evidence based on RED, x-ray diffraction, and scanning electron microscopy also shows that the layers grown at 450°C are single crystal. Figure 8a shows the RED pattern of a $(\bar{1}\bar{1}\bar{1})$ epitaxial layer grown at 450°C. The streaked nature of the RED is indicative of relatively smooth single crystal growth. The spacing of the streaks corresponds to the periodicity of the unreconstructed $(\bar{1}\bar{1}\bar{1})$ InP surface for the (110) azimuth. There appears to be no clear evidence of twinning in Fig. 8a. Cho (2, 4) finds that when growing on the $(\bar{1}\bar{1}\bar{1})$ surface of GaAs a $(\bar{1}\bar{1}\bar{1})$-$(19)^{1/2}$ structure appears in the RED pattern for a (110) azimuth and not the unreconstructed $(\bar{1}\bar{1}\bar{1})$ as seen here. In other respects, the InP surface shows the same type of reconstruction as observed in GaAs by Cho. For example, results on epitaxial layers grown on (100) InP show the (100)-C(2$\times$8) surface reconstruction as reported by Cho (12) on the (100) GaAs face. In general, the RED patterns observed from epitaxially grown (100) InP films are sharper and more detailed than those observed from (111) films because of the more smooth and nearly featureless growth obtained for the (100) layers. Details of the RED patterns obtained from (100) epitaxial layers will be the subject of a future publication.

The crystalline nature of the InP epitaxial layers was also studied by x-ray analysis. A cylindrical camera was used in which the primary beam is perpendicular to the cylinder axis. The primary beam was incident on the epitaxial layers $\sim 7°$ from grazing so as to maximize the path length of the x-ray beam through the epitaxial layer. In this way, x-ray scattering from the single crystal substrate was reduced. Nickel-filtered Cu radiation at 25 kV was used. Thus there was a strong CuKα component in the primary beam which would produce Debye-Scherrer rings if randomly oriented crystallites were present in the layers. In addition to the CuKα line, the primary x-ray beam contained a continuous spectrum which would give rise to a Laue diffraction pattern from a single crystal layer. Figure 8b shows the x-ray diffraction pattern obtained from the same sample referred to in Fig. 8a. The notable features in Fig. 8b are the lack of Debye-Scherrer rings and a Laue pattern which is identical to that obtained from a single crystal InP substrate. When this technique was applied to polycrystalline InP films grown on glass substrates, Debye-Scherrer rings and no Laue pattern were observed, indicating completely random orientation of the crystallites. Polycrystalline InP films (grown on single crystal CdS substrates) having some degree of orientation were also examined and showed Debye-Scherrer rings having intensity variations around their circumferences. The absence

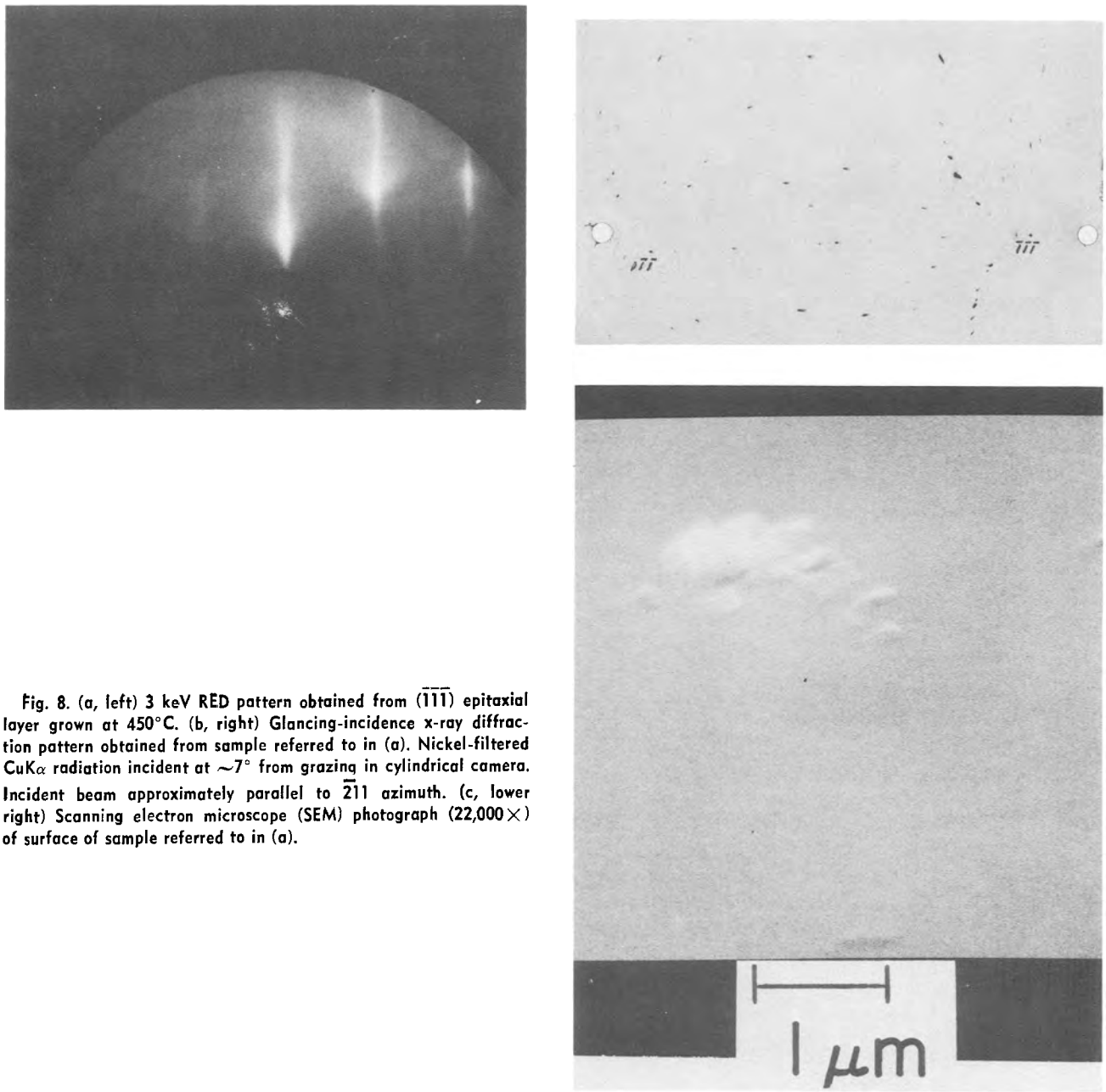


Fig. 8. (a, left) 3 keV RED pattern obtained from $(\bar{1}\bar{1}\bar{1})$ epitaxial layer grown at 450°C. (b, right) Glancing-incidence x-ray diffraction pattern obtained from sample referred to in (a). Nickel-filtered CuKα radiation incident at ~7° from grazing in cylindrical camera. Incident beam approximately parallel to $\bar{2}11$ azimuth. (c, lower right) Scanning electron microscope (SEM) photograph (22,000×) of surface of sample referred to in (a).

of these features in Fig. 8b indicates the single crystalline nature of this epitaxial layer.

Figure 8c is a 22,000× SEM photograph of the surface of the epitaxial layer grown at 450°C. At this magnification, the surface is essentially featureless and shows no grain boundaries and few surface defects. The large white object at the upper left is a conveniently located dust particle which aided in focusing.

Some additional evidence bearing on the quality of the epitaxial samples grown at 450°C is their electrical and photoluminescent properties which are discussed in the following section.

Properties of epitaxial layers as a function of growth temperatures.—Crystalline properties.—Epitaxial layers were grown at substrate temperatures ranging from 220° to 510°C at a growth rate of 0.5 μm/hr. As the growth temperature is reduced below 325°-350°C, the faceted nature of the surface morphology (as seen in Fig. 5) gradually disappears. Figure 6 contrasts the surface features of epitaxial layers grown at 450°, 315°, 285°, and 220°C on disk-shaped substrates. Figures 6d and 6e show a region near the edge and near the center, respectively, of the epitaxial layer grown at 315°C. In Fig. 6d, only a vestige of the shingle structure seen in Fig. 6c remains. Figure 6e shows a granular surface with only a vestige of the 450°C pyramidal structure (Fig. 6a) remaining. At even lower growth temperatures, the entire surface of the disk becomes completely granular. Comparison of Fig. 6e, 6f, and 6g shows that the grain size decreases as the growth temperature is lowered. Using the SEM, the layers shown in Fig. 6e, 6f, and 6g were examined under higher magnification (20,000×) as seen in Fig. 9. The surface appears to divide into regions which range from several microns in size at 315°C growth temperature to a fraction of a micron at a growth temperature of 220°C. The resemblance of Fig. 9a-c to electron micrographs of polycrystalline films (48) and the tendency of grain size to decrease with decreasing growth temperature (48) lead us to believe that the InP layers grown below 325°-350°C are polycrystalline. It is interesting to compare these surfaces grown at less than 325°C to that shown in Fig. 8c, which was grown at 450°C.

Although it appears that films grown below 325°-350°C are polycrystalline, the RED patterns corresponding to 315° and 285°C (Fig. 10a and 10b) indicate that the crystallites are still well aligned, i.e., they are still in orientational registry with the substrate. The RED patterns are still streaked and the spacing of the streaks corresponds to the substrate periodicity. How-

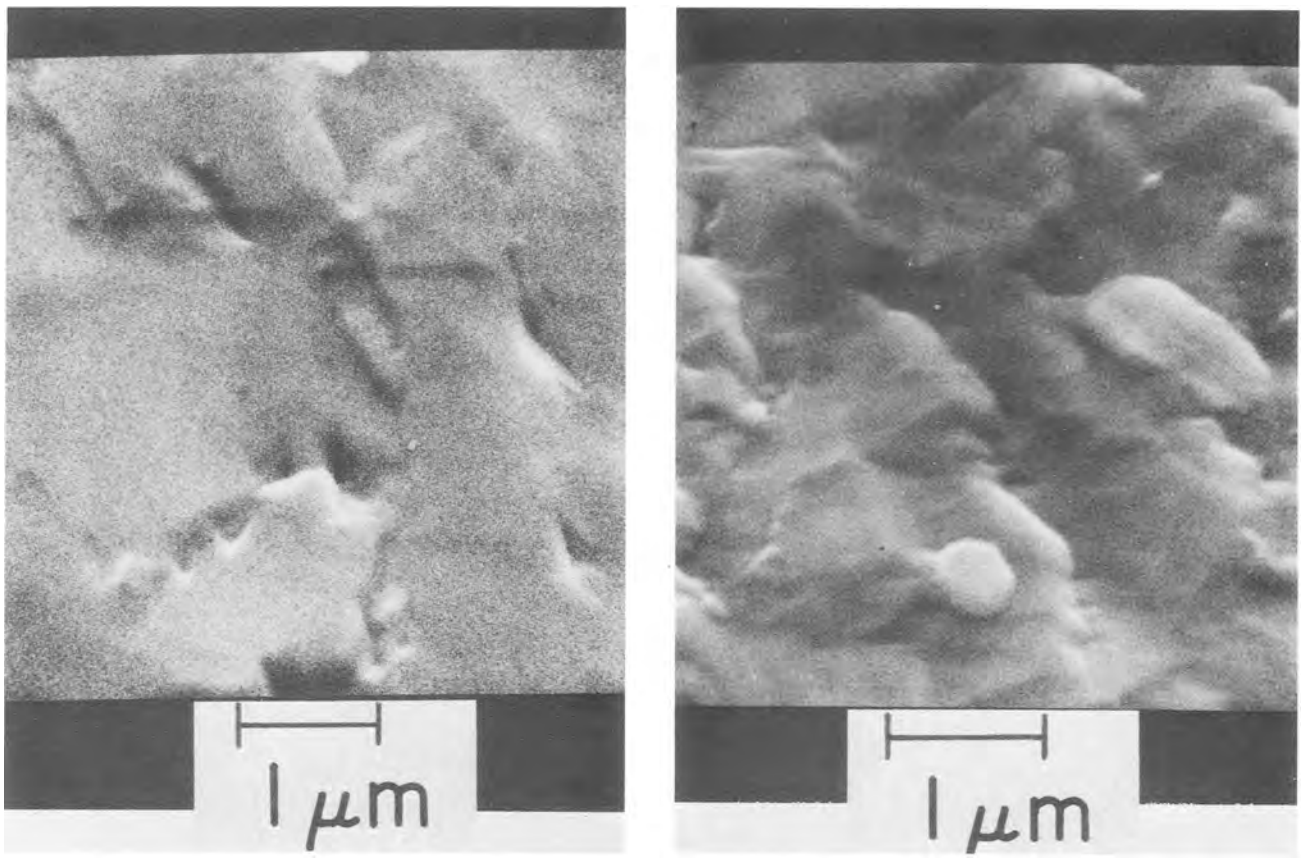


Fig. 9. (a, left) SEM photograph (~20,000×) of surface of epilayer grown at $T_S = 315°C$ (See Fig. 6e). (b, right) SEM photograph (~20,000×) of surface of epilayer grown at $T_S = 285°C$ (see Fig. 6f). (c, lower right) SEM photograph (~20,000×) of surface of epilayer grown at $T_S = 220°C$ (See Fig. 6g).

ever, with decreasing temperature the intensity of the electron diffraction diminishes and the streaked nature tends to disappear; compare Fig. 10a (growth temperature of 315°C) with Fig. 10b (growth temperature of 285°C). In fact, no structure at all could be observed in the RED from the sample grown at 220°C, and for that reason no diffraction pattern corresponding to that temperature is shown here.

The samples grown below 325°-350°C were also examined using the x-ray technique described earlier. Figure 11 shows an x-ray diffraction pattern obtained from an InP layer grown at 220°C. Except for several

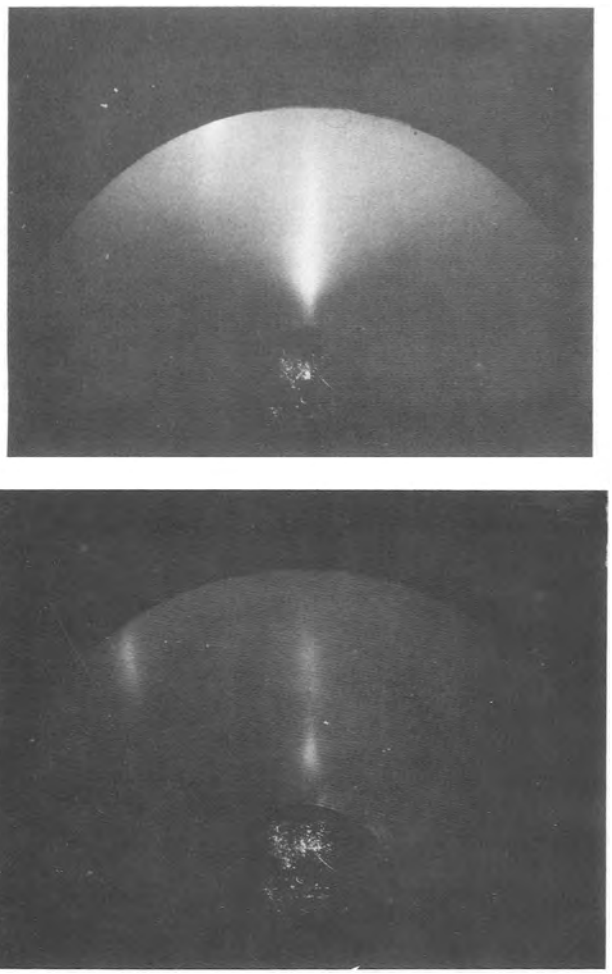


Fig. 10. (a, top) 3 keV RED pattern obtained from epilayer grown at $T_S = 315°C$ (see Fig. 6e). Azimuth: [110]. (b, bottom) 3 keV RED pattern obtained from epilayer grown at $T_S = 285°C$ (See Fig. 6f). Azimuth: [112].

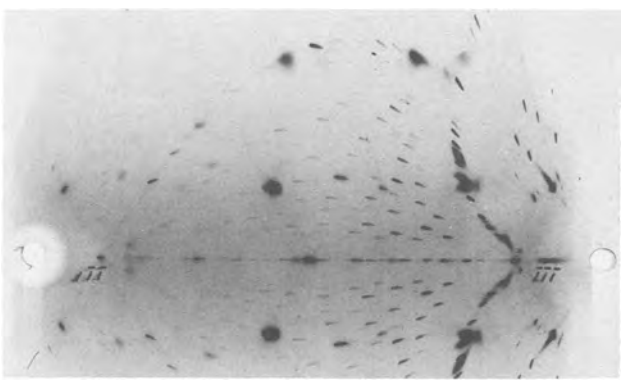


Fig. 11. Glancing-incidence x-ray diffraction pattern obtained from epilayer grown at $T_S = 220°C$ (see Fig. 6g). Incident beam in $\bar{2}11$ azimuth.

very faint Debye-Scherrer rings, this x-ray diffraction pattern is essentially a Laue spot pattern similar to that obtained from the layer grown at 450°C (see Fig. 8b). However, a number of large diffuse Laue spots in addition to the sharper Laue spots are seen in Fig. 11. As the growth temperature is lowered below 325°-350°C, the number of large diffuse spots in the x-ray diffraction patterns tends to increase. On the basis of these x-ray diffraction patterns, it appears that even at a 220°C growth temperature, the polycrystalline InP epitaxial layer consists of well-oriented grains. However, the large diffuse spots in the x-ray pattern indicate some lack of crystalline perfection.

It is possible to grow InP epitaxially in excess of 450°C if the P_4/In ratio is increased in an appropriate fashion (10), analogous to the case of GaAs (2). The only obstacle to growth at higher substrate temperatures is the need for higher P_4 pressure in the vacuum station. At a substrate temperature of 450°C, the P_4 pressure is 1-2 $\times$ 10^{-6} Torr and any sizable increase of P_4 pressure above this level is impractical. Therefore the maximum substrate temperature used to date has been 510°C. Epitaxial layers grown at 510°C are almost identical in all respects (SEM, RED, and x-ray) to those grown at 450°C except for somewhat more pronounced faceting of the surface.

Electrical and optical properties.—Mobilities and carrier concentrations were measured on epitaxial layers approximately 2 μm thick grown on semi-insulating InP using the van der Pauw technique. These epitaxial layers are sufficiently thick (>1 μm) that their electrical properties at 300°K should be characteristic of bulk material (40). Contacts were made by spark-welding Au-2%Sn wires (0.002 in. diam) to the epitaxial layers, affording good ohmic contacts. The room-temperature carrier concentration (n) and mobility (μ) of these unintentionally doped layers is shown in Fig. 12 as a function of growth temperature. One very prominent feature of Fig. 12 is the sudden rise in n below 350°C and sudden drop in μ below 320°C.

Above 350°C, n appears to be nearly independent of growth temperature with a possible slight downward trend with decreasing temperature. Similarly, the mobility above 320°C is nearly constant at a level near that of bulk n-type InP. Typical of this growth temperature region are the electrical properties at 450°C where n (300°K) $\simeq$ 3 $\times$ 10^{16} cm^{-3} and μ (300°K) $\simeq$ 3000 cm^2/Vsec. Hall effect and resistivity measurements were also made at 77°K on a few of the InP epitaxial layers which showed the highest room-temperature mobility. The carrier concentration was observed to decrease by a factor of two at 77°K as compared to

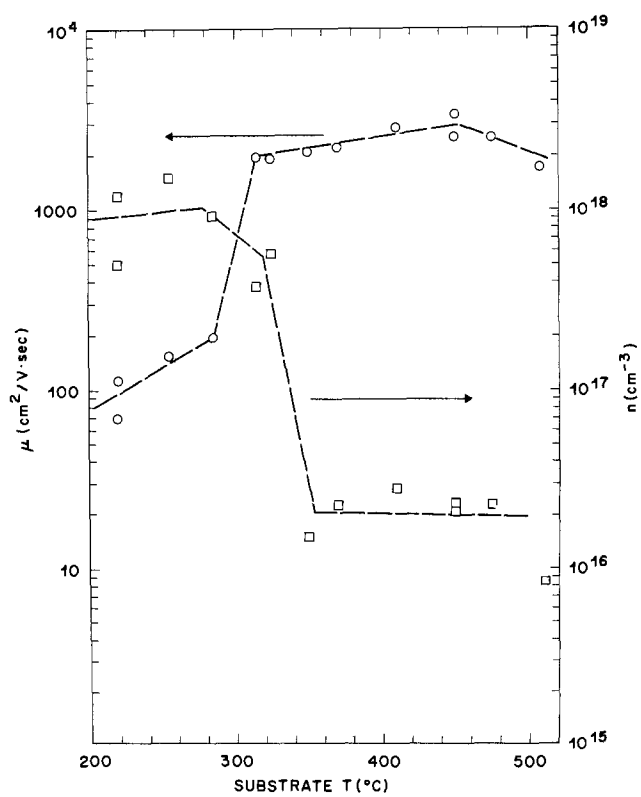


Fig. 12. 300°K carrier concentration ($n \equiv N_D - N_A$) (squares) and Hall mobility (μ) (circles) of ($\bar{1}\bar{1}\bar{1}$) InP epitaxial layers as a function of growth temperature.

300°K, and the mobilities at 77°K were two to four times higher than at 300°K. When compared to Rode's theoretical n *vs.* μ relationship for InP (49), the 77°K data indicate a compensation ratio $(N^+ + N^-)/n \simeq 4$. Also the observed carrier freeze-out indicates the presence of deep levels in these films which, as will be seen below, are not evident in the photoluminescent results.

Below 325°-350°C growth temperature, the 300°K mobility drops abruptly and then continues to decline gradually with decreasing growth temperature, while n is nearly constant at a high level of 10^{18} cm^{-3}. It is obvious from Fig. 12 that the electrical properties of the films deteriorate at the same growth temperatures (325°-350°C) at which the epitaxial layers undergo a transition from single crystal to polycrystal. This suggests that these two phenomena are related.

Photoluminescence measurements on InP epitaxial films offer a nondestructive means of determining their properties and quality. In addition to being able to determine impurity energy levels for the photoluminescence spectra, Joyce and Williams (27) have established the relationship between the half-width of the band-to-band photoluminescent peak at 1.410 eV (77°K) and the carrier concentration. For n-InP, they find a monotonic increase in the half-width as a function of carrier concentration for the range $10^{16} \leq n \leq 2 \times 10^{18}$. Photoluminescence measurements were performed on our epitaxial layers at 300° and 77°K. For this purpose, we used a 4880Å line from an Ar ion laser and a ½m single pass spectrometer whose resolution was 16Å. The power level of the 4880Å beam was accurately monitored in order to properly compare the photoluminescent peak heights from different samples. Figure 13 shows the photoluminescent spectra of the InP epitaxial layers grown from 450° to 285°C. The peak height of each spectrum in arbitrary units is indicated to the right of each peak and has been normalized to 1 mW input power. Each spectrum is plotted on a linear intensity scale, but for clarity of presentation they are displaced vertically by an arbitrary amount.

The spectrum of the layer grown at 450°C shown in Fig. 13a, appears to be very similar to Joyce and Williams' (27) undoped VPE sample where $\mu = 44{,}000$ cm^2 V^{-1} sec^{-1} at 77°K. As in Joyce and Williams' case, the half-width of the 1.410 eV peak is very narrow, characteristic of a carrier concentration $\leq 10^{16}$ cm^{-3}; also there is no evidence of any peaks below 1.410 eV, thus indicating the absence of any compensating acceptors. In their same high mobility sample, Joyce and Williams observed a hint of an exciton peak in the 80°K spectrum at slightly above 1.410 eV, which they attributed to the high quality of their sample. This exciton peak is not observed in Fig. 13a, suggesting that these MBE grown InP layers are not equal in quality to the best VPE material.

For layers grown at temperatures above 450°C, almost no change occurred in the spectrum as compared to Fig. 13a other than a slight narrowing in the half-width of the 1.410 eV peak. In contrast, those samples grown at lower temperatures (Fig. 13b-13e) show an increasing half-width for the 1.410 eV peak as the growth temperature is lowered. In Fig. 14 the half-width $\Delta E/E$ of the 1.410 eV band-to-band photoluminescent peak is plotted as a function of growth temperature. As in Fig. 12, a transition temperature is evident at about 350°C where the half-width increases abruptly with decreasing temperature. In view of the relation between $\Delta E/E$ and carrier concentration, it can be seen from Fig. 12 that the abrupt increase in $\Delta E/E$ is due to the sudden increase of carrier concentration below 350°C. Above 350°C, Fig. 14 indicates a gradual decrease in $\Delta E/E$ with increasing growth temperature, which is clearer evidence of the downward trend of the carrier concentration with increasing temperature as seen in Fig. 12.

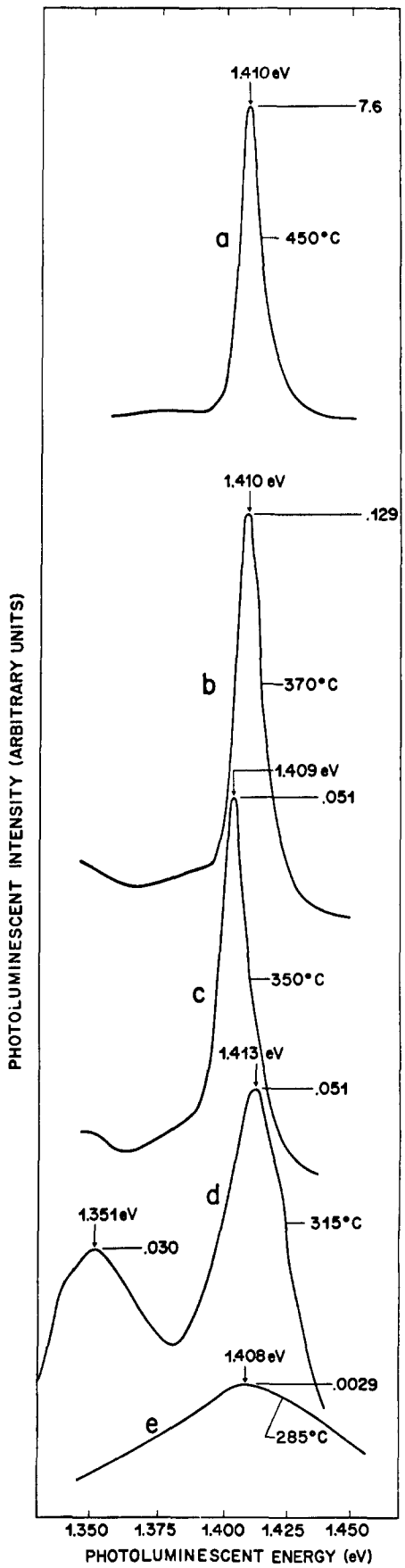


Fig. 13. Photoluminescent intensity spectrum at 77°K of $(\bar{1}\bar{1}\bar{1})$ InP epitaxial layers grown at various temperatures indicated on curves. Intensity scale is linear, but curves are displaced vertically for clarity so they do not overlap. Peak heights are indicated on curves. Argon ion laser line at 4880Å used for excitation.

Referring back to Fig. 13c and 13d, a lower energy peak (at 1.351 eV) appears in the spectrum corre-

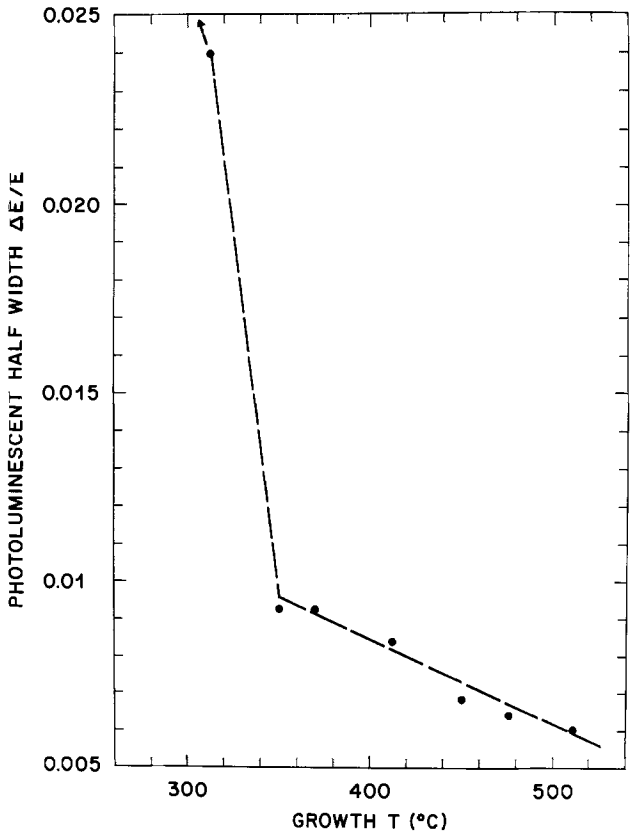


Fig. 14. Photoluminescent half-width ($\Delta E/E$) of InP epitaxial layers as a function of growth temperature. Data taken from Fig. 13.

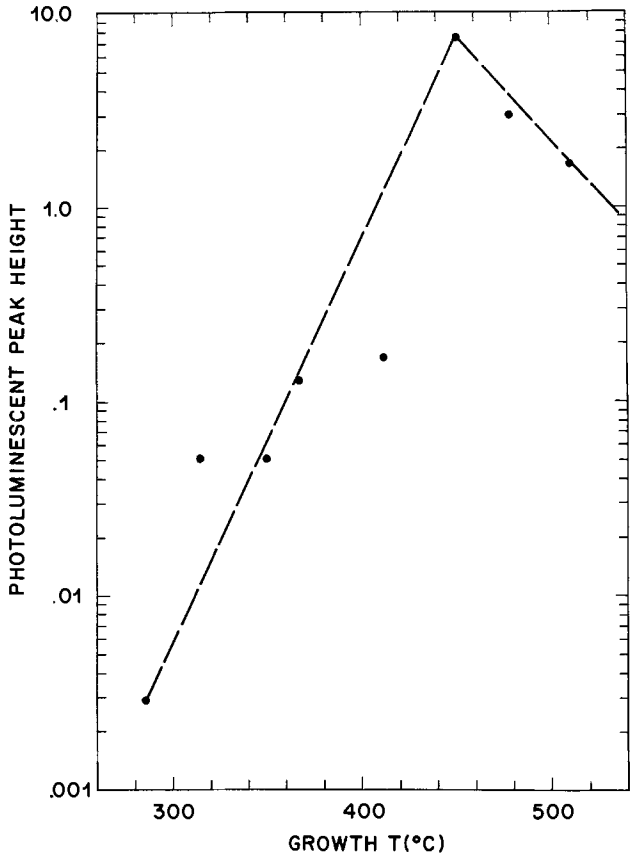


Fig. 15. Photoluminescent peak height (arbitrary units) of InP epitaxial layers as a function of growth temperature. Data taken from Fig. 13.

sponding to a growth temperature of 350°C and becomes pronounced at growth temperature of 315°C. This 1.351 eV peak is quite distinct from the 1.37 eV peak usually reported in the photoluminescence at 77°K for unintentionally doped InP (27-30). Furthermore, this 1.351 eV peak does not correspond to any known impurity level (28) in InP, nor has it been reported in the literature. Therefore, it appears that this 1.351 eV peak may be inherent to the MBE growth process at low substrate temperatures, and can be associated with the presence of defects. Peaks corresponding to defect structures have been seen in the photoluminescence spectrum of GaAs (31). The fact that the 1.351 eV peak is not evident in Fig. 13e (growth temperature of 285°C) may be ascribed to the very low photoluminescent efficiency of this sample and the consequent poor signal-to-noise ratio.

Figure 15 illustrates the dependence of the photoluminescence peak height on growth temperature. Because these results correspond to a constant pump power, Fig. 15 is also a plot of the photoluminescent efficiency *vs.* growth temperature. Although there is considerable scatter in the data due to different surface conditions from one sample to the next, the figure clearly shows a decrease of four orders of magnitude as the growth temperature is reduced from 450° to 285°C. No photoluminescent signal could be detected under any conditions from those samples grown below 285°C. The highest photoluminescent efficiency corresponds to a growth temperature near 450°C.

(111) and (100) Orientations—Preliminary Results

MBE growth of InP on the (111) In face of InP substrates was also studied. As mentioned earlier, a Syton chemo-mechanical polish was necessary in this case in order to prepare the substrate. The epitaxial layer was grown at 450°C at a growth rate of 0.5 μm/hr. An epitaxial layer was also grown on a $(\bar{1}\bar{1}\bar{1})$ semi-insulating substrate at the same time as a control. Tests on the control layer showed it to be typical of a 450°C run, as

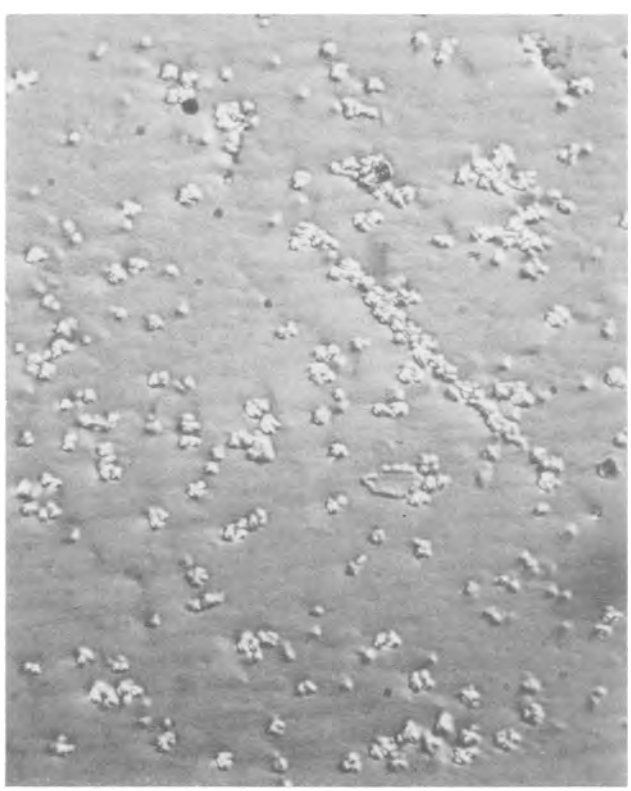


Fig. 16. Nomarski interference-contrast photograph of surface of InP epitaxial layer grown on (111) InP substrate (indium face) at 450°C (500×).

described earlier. Figure 16 is a Nomarski interference contrast photograph (500×) of the surface of the epi-

taxial layer grown on the (111) face. The distinguishing feature of the surface morphology, in this case, is the rather uniform distribution of small point imperfections. Probably these imperfections are associated with substrate damage produced by the chemomechanical surface preparation (32). The underlying surface structure as seen in Fig. 16 is relatively smooth and free of facets as compared to ($\bar{1}\bar{1}\bar{1}$) epitaxial layers (Fig. 6a-6c). It appears, therefore that relatively smooth and uniform epitaxial layers could be grown on the (111) face if a suitable chemical etch (comparable to Br:methanol for the $\bar{1}\bar{1}\bar{1}$ face) were found.

Epitaxial growth on (100) substrates is found to be markedly different than growth on the ($\bar{1}\bar{1}\bar{1}$) face. Orientation-dependent faceting is still observed, but on a much reduced scale. For some choices of substrate orientations near the (100) essentially smooth featureless films are obtained over the entire sample area (0.5 × 0.5 cm) at reduced growth rate.

Discussion

Growth and Morphology

From these results it appears that single crystal epitaxial layers grown on the ($\bar{1}\bar{1}\bar{1}$), (111), and (100) substrates exhibit entirely different morphologies. Highly faceted, orientation-dependent morphology is obtained for ($\bar{1}\bar{1}\bar{1}$) layers, while the (111) layers appear to have a less faceted nature and the (100) layers are relatively featureless. The implication of these facts for device application is that MBE growth on the ($\bar{1}\bar{1}\bar{1}$) face is least promising of the three orientations. The extreme sensitivity of the surface morphology to substrate orientation has been shown in Fig. 5 and 7. On the basis of this we conclude that smooth uniform layers can grow only if the substrate orientation is held within ±5 min over the entire surface. Needless to say, unless smooth layers can be grown, they cannot be used as waveguides, and it is also possible that the surface roughness will have a detrimental effect on their electrical properties. Although the results of MBE growth on the (111) and (100) faces are only preliminary, it appears that they are to be preferred for device applications.

In the case of the ($\bar{1}\bar{1}\bar{1}$) orientation, we have shown the importance of substrate temperature as a parameter in epitaxial growth of InP. All these results refer to a standard flux level corresponding to a growth rate of 0.5 μm/hr. It is well known, however, that the flux level plays an important role in epitaxial growth (33). For this reason, a few layers were grown on ($\bar{1}\bar{1}\bar{1}$) substrates at higher and lower flux levels. At 450°C substrate temperature, the flux level was lowered by a factor of ten with no apparent effect on the epitaxial growth. The flux level was also increased by a factor of four over the 0.5 μm/hr growth rate and a layer grown at a substrate temperature of 400°C. For this run, the P_4:In ratio was maintained at the normal level of ≥10:1 in order to obtain stoichiometric growth. The substrate temperature was chosen to be 400°C to further insure against the buildup of In droplets on the surface. In this case, the morphology of the resulting layer resembled that of the polycrystalline layer shown in Fig. 6d and 6e. However, the layer shown in Fig. 6d and 6e was grown under standard flux conditions (0.5 μm/hr) at 315°C. The 300°K electrical measurements made on this high flux sample give $\mu = 400$ cm^2 V^{-1} sec^{-1} and $n = 6 \times 10^{17}$ cm^{-3}, which corresponds to the electrical properties of a layer grown at about 300°C (see Fig. 12) at the standard flux rate. It appears, therefore, that the effect of growing at a higher flux is to shift the polycrystalline-crystalline transition to higher temperatures. This observed behavior is reasonable on theoretical grounds. Moazed (34) has applied nucleation theory to epitaxial growth and finds that decreasing flux should produce a decrease in the epitaxial temperature, *i.e.*, the temperature corresponding to the transition between epitaxial and randomly oriented growth (polycrystalline growth). In particular, he concludes that at low supersaturation (corresponding to low flux rates) only preferred epitaxial sites will act as nucleation sites, whereas at high supersaturation, random nucleation is more likely. In addition, he concludes that a decrease in substrate temperature lowers the ratio of epitaxial nucleation to random nucleation and therefore epitaxy is not favored at low substrate temperatures. This latter result is also in agreement with our observation. Experimentally, the increase of epitaxial temperature with increased growth rate has also been observed by Cho (35) in the MBE growth of GaP on (111) CaF_2, and by Krikorian and Sneed (36) for the growth of Ge films by evaporation onto (111) Ge and (111) CaF_2 substrates at a background pressure of 10^{-8} Torr.

It is interesting to compare the morphology obtained for epitaxial growth on ($\bar{1}\bar{1}\bar{1}$) InP and ($\bar{1}\bar{1}\bar{1}$) GaAs. In earlier work in the same MBE system, we were able to grow essentially smooth, featureless epitaxial layers of GaAs on ($\bar{1}\bar{1}\bar{1}$) GaAs substrates at 600°C. In other words, no faceting as seen in Fig. 5 for ($\bar{1}\bar{1}\bar{1}$) InP was seen for ($\bar{1}\bar{1}\bar{1}$) GaAs. Smooth, featureless epitaxial ($\bar{1}\bar{1}\bar{1}$) GaAs layers have also been reported by Cho (2, 4) and Gonda *et al.* (5). It is interesting to observe that on (100) GaAs, Gonda *et al.* report pyramidal epitaxial growth at substrate temperatures in excess of 600°C, smooth featureless growth at substrate temperatures of 480°C, and polycrystalline growth at a substrate temperature of 430°C. This suggests that in GaAs there may exist a range of substrate temperatures corresponding to smooth featureless growth lying somewhere between the polycrystalline and faceting temperature regions. If such a region exists for InP, we have been unable to find it in exploring the substrate temperature range from 220° to 510°C in 30° increments. It appears that the mechanism responsible for faceting in InP is markedly different than for GaAs and may be an interesting subject for further study.

Structure of Epitaxial Layers

RED results.—Our RED results on ($\bar{1}\bar{1}\bar{1}$) InP differ in two important ways from those reported by Cho on ($\bar{1}\bar{1}\bar{1}$) GaAs (2, 4). Firstly, Cho's RED pattern obtained from the heated substrate before growth is a spot pattern with prominent Kikuchi lines. In contrast to this, we see the streaked pattern shown in Fig. 4. As noted above, our substrates are routinely sputtered to insure a contamination-free surface prior to growth. According to Cho (46), the substrate RED patterns shown in Ref. (2) and (4) correspond to unsputtered surfaces. Moreover, in agreement with our observations, Cho finds that sputtered substrate surfaces tend to yield streaked RED patterns. A possible explanation of these results is that thermal etching of the substrate prior to sputtering roughens the surface and gives it a three-dimensional aspect. Subsequent sputtering may tend to smooth the surface so that a two-dimensional streaked RED pattern results. A second difference between Cho's GaAs RED results and our RED on InP is that after many monolayers of GaAs are grown on the ($\bar{1}\bar{1}\bar{1}$) GaAs face, a diffraction pattern corresponding to ($\bar{1}\bar{1}\bar{1}$)-$\sqrt{19}$ surface reconstruction is seen by Cho (4), while under similar circumstances for InP we only see the diffraction pattern of the unreconstructed surface (Fig. 8a). The failure to observe the ($\bar{1}\bar{1}\bar{1}$)-$\sqrt{19}$ structure in InP is not understood; however, the difference in surface forces of GaAs *vs.* InP, as well as different impurity reactions, may affect the surface reconstruction differently in these two cases. For example, it is known (47) that the silicon ($\bar{1}\bar{1}\bar{1}$)-$\sqrt{19}$ structure is seen when Ni is present as a contami-

nant, while Cho (4) finds the $(\bar{1}\bar{1}\bar{1})$-$\sqrt{19}$ structure on apparently contamination-free GaAs.

X-ray results.—The x-ray diffraction patterns proved to be very useful in determining the structure of the polycrystalline InP layers grown below 325°-350°C. Referring back to the diffraction pattern of the layer grown at 220°C (Fig. 11), it is seen that the pattern shows a number of large, diffuse Laue spots in addition to sharper Laue spots (37). Analysis shows that the most prominent diffuse spots in Fig. 11 are produced by the intense CuKα component of the primary x-ray beam. These large, intense diffuse spots are not seen in the x-ray diffraction pattern of the single crystal layer grown at 450°C (Fig. 8b). Their presence in Fig. 11 is perhaps due to a slight spread in the orientations of the crystallites in the 220°C InP layer, which allows the Bragg condition to be satisfied in these several directions for the CuKα line. Examination of this same InP layer with white tungsten x-radiation produced a Laue diffraction pattern which was free of the intense diffuse spots. In addition to sharp Laue spots, the tungsten pattern contained a symmetric array of less intense diffuse spots (some of which are evident in Fig. 11). Analysis of the tungsten pattern disclosed that these diffuse spots corresponded to twinning on the $[\bar{1}\bar{1}\bar{1}]$ axis. Furthermore, the angular size of the spots (~2°) indicates a characteristic size of ~60Å for the twinned regions. Such a "microtwin" is a well-known type of stacking fault (38). Examples of various kinds of stacking faults on (111) planes of the fcc lattice are given by Barrett (39). From this point of view, the 60Å characteristic size would correspond to the repeat distance in the stacking fault plane. A general conclusion which may be drawn from the x-ray diffraction data taken on those layers grown below 325°-350°C is that the layers are composed of well-aligned crystallites which have increasing stacking fault density as the growth temperature is lowered. The tendency for stacking fault density to increase with decreasing growth temperature has been observed in VPE Si films (40) and Ge films vapor deposited on CaF_2 under UHV (10^{-9}- 4×10^{-7} Torr) conditions (41).

Electrical and Optical

The most striking feature of the electrical properties of our epitaxial layers (Fig. 12) is the sharp transition which occurs in the mobility and carrier concentration in the 325°-350°C growth temperature range. It is known that the grain size in polycrystalline films can have a strong influence on their mobilities, but the effect does not become pronounced until the grain size falls below 1 μm (40). In Fig. 12, the mobility drops abruptly by an order of magnitude in the temperature range from 315° to 285°C, while the grain size decreases from ~3 to ~1 μm, respectively. For this range of grain size, the largest change in mobility that could be expected from Ref. (40) is a factor of 2 or 3. Furthermore, the large change in carrier concentration which accompanies the mobility transition cannot be ascribed to grain size. One possible cause of the abrupt decrease in carrier concentration for growth temperatures from 300° to 350°C in Fig. 12 may be a decrease of the sticking coefficient with increasing temperature of an unintentional n-type dopant coming from the source materials (In or P), the oven structures, or heated surroundings. However, we recall that the growth run at a substrate temperature of 400°C at four times normal growth rate (2 μm/hr) resulted in a layer where $n = 6 \times 10^{17}$ cm^{-3} and $\mu = 400$ cm^2 V^{-1} sec^{-1}. This result rules out any sticking coefficient explanation because a smaller rather than larger carrier concentration would be predicted for growth at 400°C. The most reasonable explanation of the transition in the electrical properties shown in Fig. 12, as well as the high flux results stated above, involves the appearance of defect structures (42) such as stacking faults with decreasing substrate temperatures. We have already presented x-ray evidence for the presence of stacking faults in those layers grown below 325°-350°C and there is experimental evidence that stacking faults will lead to the kind of electrical behavior shown in Fig. 12. For example, Sloope and Tiller (43) observe an almost identical transition in the electrical properties of (111) Ge (p-type) films grown on CaF_2 as a function of growth temperature. They correlate their results with the presence of defects such as stacking faults or dislocations. According to Sloope and Tiller, the defects may give rise to several acceptor states (singly or doubly ionized) which increase the carrier concentration and act as scattering sites. In our case, the photoluminescent data (Fig. 13) show a peak at 1.351 eV which first appears at a growth temperature of 350°C and is very prominent at 315°C. This occurs just at the transition between crystalline and polycrystalline layer growth and hence it appears that this peak also arises from crystal defects such as stacking faults, etc. In analogy with Sloope and Tiller's proposal, it is suggested that the defects in those InP layers grown below 350°C produce multiple energy levels in the bandgap. In addition to the level (probably an acceptor) at ~60 meV (corresponding to the 1.351 eV peak), there must be a majority of shallow donor levels to account for the increase of n-type conductivity observed in these samples. It should be pointed out that the ~60 meV level we observe in those InP layers grown below 350°C does not correspond to any reported donor or acceptor level in InP (16, 27, 30, 44, 45). The closest acceptor level is Cd at 50 meV, which is highly unlikely in MBE grown layers due to its low sticking coefficient.

Conclusion

We have demonstrated that from elemental molecular beam sources single crystal InP epitaxial layers can be grown on the $(\bar{1}\bar{1}\bar{1})$ face of InP substrates in a temperature range from 350° to 510°C. On the $(\bar{1}\bar{1}\bar{1})$ face, faceting occurs depending on the exact misorientation from the $(\bar{1}\bar{1}\bar{1})$ axis. The quality of the films as determined from the mobility and photoluminescence compares favorably with that of bulk InP. Below 350°C the epitaxial layers become aligned polycrystals with an increasing density of defects, *i.e.*, stacking faults, with lowered growth temperature. Also at these low growth temperatures the carrier concentration becomes very high and the mobility drops due to the increase in the number of crystal defects. The photoluminescence data show a 60 meV level coming in below growth temperatures of 350°C associated with the increase of defects. The observed structural and electrical properties of our layers as a function of growth temperature are in general agreement with the results reported by others for epitaxial deposition of Si, Ge, and GaAs films. Single crystal InP epitaxial layers have also been grown on the (111) and (100) faces of InP and exhibit very little faceting. Relatively smooth and featureless growth has been observed in the (100) face, suggesting that this face may be the most promising for device application. The electrical properties and doping of the layers grown on the (100) face are presently being studied.

Acknowledgments

We would like to thank W. Wiegmann, M. Ilegems, A. Cho, A. Gossard, E. E. Chaban, and J. Robinson, Jr. for help and advice in planning the MBE system. We want to acknowledge the valuable help of E. Buehler in growing the single crystal InP substrates. We also wish to express our appreciation to D. L. Rode for helpful discussions on surface morphology and for measurement of pyramid height and slope on our $(\bar{1}\bar{1}\bar{1})$ epitaxial layers. We would like to especially thank Mrs. A. A. Pritchard for technical assistance.

Manuscript submitted Aug. 2, 1976; revised manuscript received Oct. 13, 1976.

Any discussion of this paper will appear in a Discussion Section to be published in the December 1977 JOURNAL. All discussions for the December 1977 Discussion Section should be submitted by Aug. 1, 1977.

Publication costs of this article were assisted by Bell Laboratories.

REFERENCES

1. A. Y. Cho and J. R. Arthur, in "Progress in Solid State Chemistry," Vol. 10, G. Somerjai and J. McCaldin, Editors, Pergamon Press, New York (1975). This review article contains 147 references.
2. A. Y. Cho, M. B. Panish, and I. Hayashi, Proceedings of the 3rd International Symposium on GaAs and Related Compounds, Institute of Physics, p. 18, London (1970).
3. A. Y. Cho, *J. Appl. Phys.*, **42**, 2074 (1971).
4. A. Y. Cho, *ibid.*, **41**, 2780 (1970).
5. S. Gonda, Y. Matsushima, Y. Makita, and S. Mukai, *Jpn. J. Appl. Phys.*, **14**, 935 (1975).
6. A. Y. Cho, *J. Vac. Sci. Technol.*, **8**, S31 (1971).
7. A. Y. Cho and I. Hayashi, *Solid-State Electron.*, **14**, 125 (1971).
8. M. Naganuma and K. Takashashi, *Phys. Status Solidi*, **31**, 187 (1975).
9. R. F. C. Farrow, *J. Phys. D*, **7**, L121 (1974).
10. R. F. C. Farrow, *ibid.*, **8**, L87 (1975).
11. R. F. C. Farrow, Abstract 214, p. 547, The Electrochemical Society Extended Abstracts, Fall Meeting, Dallas, Texas, Oct. 5-9, 1975. Also R. F. C. Farrow, Private communication.
12. D. L. Smith and V. Y. Pickhardt, *J. Appl. Phys.*, **46**, 2366 (1975).
13. L. L. Chang, L. Esaki, W. E. Howard, and R. Ludeke, *J. Vac. Sci. Technol.*, **10**, 11 (1973).
14. A. Y. Cho, *Appl. Phys. Lett.*, **19**, 467 (1971).
15. R. Dingle, W. Wiegmann, and C. H. Henry, *Phys. Rev. Lett.*, **33**, 827 (1974).
16. S. Wagner, J. L. Shay, K. J. Bachmann, and E. Buehler, *Appl. Phys. Lett.*, **26**, 229 (1975).
17. R. Corlett, I. Griffith, and J. J. Purcell, Proceedings of the 5th International Symposium on GaAs and Related Compounds, Institute of Physics, p. 89 (1975).
18. M. Ilegems, Private communication. Also see M. Ilegems and R. Dingle, Proceedings of the 5th International Symposium on GaAs and Related Compounds, Institute of Physics, p. 1 (1975).
19. W. Wiegmann, Private communication.
20. K. J. Bachmann, E. Buehler, J. L. Shay, and A. R. Strnad, *J. Electron. Mater.*, **4**, 389 (1975).
21. K. J. Bachmann, E. Buehler, J. L. Shay, and D. L. Malm, Proceedings of the 5th International Symposium on GaAs and Related Compounds, Institute of Physics, p. 121 (1975).
22. O. Mizuno and H. Watanabe, *Electron. Lett.*, **11**, 118 (1975).
23. E. Bauer, in "Techniques of Metals Research," Vol. II, Part 2, R. F. Bunshah, Editor, chap. 15, Interscience, New York (1969).
24. M. Shimbo, J. Nishizawa, and T. Terasaki, *J. Cryst. Growth*, **23**, 267 (1974).
25. J. V. DiLorenzo, *ibid.*, **17**, 189 (1972).
26. D. L. Rode, *Phys. Status Solidi A*, **32**, 425 (1975).
27. B. D. Joyce and E. W. Williams, Proceedings of the 3rd International Symposium on GaAs and Related Compounds, Institute of Physics, p. 57 (1970).
28. E. W. Williams, W. Elder, M. G. Astles, M. Webb, J. B. Mullin, B. Straughan, and B. Tufton, *This Journal*, **120**, 1741 (1973).
29. R. C. C. Leite, *Phys. Rev.*, **157**, 672 (1967).
30. J. U. Fischbach, G. Benz, N. Stath, and M. H. Pilkuhn, *Solid State Commun.*, **11**, 725 (1972).
31. C. M. H. Driscoll, A. F. W. Willoughby, and E. W. Williams, *J. Mater. Sci.*, **9**, 1615 (1974).
32. A. Cho also reports poor growth on syton-polished substrates of GaAs. See Ref. (4).
33. Much work has been done on the flux dependence of epitaxial growth by VPE and sputtering as well as MBE. See for example I. H. Khan, in "Handbook of Thin Film Technology," L. I. Maissel and R. Glang, Editors, chap. 10, McGraw-Hill, New York (1970).
34. K. L. Moazed, in "The Use of Thin Films in Physical Investigations," J. C. Anderson, Editor, p. 203, Academic Press, Inc., New York (1966).
35. A. Y. Cho, *J. Appl. Phys.*, **41**, 782 (1970).
36. E. Krikorian and R. J. Sneed, *ibid.*, **37**, 3665 (1966).
37. As mentioned previously, the primary x-ray beam was near grazing incidence on the epilayer surface in order to minimize scattering from the substrate. However, the spots to the right in Fig. 11 are forward scattered and therefore correspond to relatively small Bragg angles. Thus many of these spots are produced by short wavelength, highly penetrating components of the primary beam. For this reason many of the sharp spots in the right one-third of Fig. 11 are characteristics of the single crystal substrate. In contrast, the spots to the left in Fig. 11 corresponded generally to strongly absorbed, longer wavelength x-rays, and are characteristic of the grown layer.
38. M. L. Hammond and D. J. Rowcliffe, in "Techniques of Metals Research," Vol. II, Part 2, R. F. Bunshah, Editor, chap. 18, p. 801, John Wiley, New York (1969).
39. C. S. Barrett, "Structure of Metals," 3rd ed., pp. 451-453, McGraw-Hill, New York (1966).
40. L. I. Maissel and M. H. Francombe, in "An Introduction to Thin Films," chap. 7, Gordon and Breach Science Publishers, New York (1973).
41. B. W. Sloope and C. O. Tiller, *J. Appl. Phys.*, **37**, 887 (1966).
42. M. Naganuma and K. Takahashi [Ref. (8)] observed a sharp decrease in resistivity of MBE GaAs films associated with the transition from single crystal to polycrystalline growth as a function of substrate temperature. They attribute the observed decrease in resistivity to "carrier generating dislocations."
43. B. W. Sloope and C. O. Tiller, *J. Appl. Phys.*, **38**, 140 (1967).
44. A. M. White, P. J. Dean, K. M. Fairhurst, W. Bardsley, E. W. Williams, and B. Day, *Solid State Commun.*, **11**, 1099 (1972).
45. U. Heim, O. Roder, H. J. Queisser, and M. Pilkuhn, *J. Lumin.*, **3**, 542 (1970).
46. A. Y. Cho, Private communication.
47. A. J. Van Bommel and F. Meyer, *Surf. Sci.*, **8**, 467 (1967).
48. C. A. Neugebauer, in "Handbook of Thin Film Technology," L. I. Maissel and R. Glang, Editors, chap. 8, McGraw-Hill, New York (1970).
49. D. L. Rode, *Phys. Rev. B*, **3**, 3287 (1971).

Damage Effects in Boron and BF_2 Ion-Implanted p^+-n Junctions in Silicon

B. A. MacIver and E. Greenstein*

General Motors Corporation, Research Laboratories, Warren, Michigan 48090

ABSTRACT

Boron- and BF_2-implanted p^+-n junctions are compared. At 50V reverse bias BF_2-implanted diodes, fabricated in <100> silicon and annealed in a wet O_2 atmosphere, typically exhibited two orders of magnitude lower leakage than B-implanted diodes on the same wafer. The improved reverse I-V characteristics of the BF_2-implanted junctions are related to the BF_2 implant damage. Excessive leakage current in B-implanted diodes is correlated with oxidation-induced defects using scanning electron microscopy. Argon damage implant experiments indicate that an amorphous surface region caused by the BF_2 implant prevents the propagation of defects into the junction region during anneal in a wet oxygen atmosphere.

The annealing behavior of BF_2 implants into silicon has been studied by Müller *et al.* (1). Prussin (2) has related the leakage currents of n^+-p^+ diodes prepared on B- and BF_2-implanted silicon surfaces to oxidation-induced dislocations which he refers to as ternary defects. He has also shown that certain combinations of implant and anneal treatment can minimize ternary defect generation and n^+-p^+ junction leakage. The present work concerns the effects of BF_2 implants on the electrical properties of p^+-n junctions in silicon when BF_2 is substituted for boron to implant the p^+ region.

This paper presents experimental results relating implant damage, annealing atmosphere, and crystal orientation to junction leakage. We found that the leakage current is substantially reduced when large fluences (*i.e.*, $\geq 10^{15}/cm^2$) of BF_2 ions are substituted for B ions for implants into <100> n-type silicon annealed in wet oxygen. Sirtl etching was combined with scanning electron microscopy to correlate residual damage and junction leakage.

Experimental Procedure

Arrays of 1.14×10^{-3} cm^2 circular diodes were fabricated in <100> and <111> oriented, 1-2 Ω-cm, n-type, polished silicon. A 7000Å thick thermal oxide was grown and patterned as a mask for the subsequent implants. One-half of each wafer was implanted with $2 \times 10^{15}/cm^2$ of 50 keV B. The other half was implanted with either 144 keV BF_2 or 50 keV B plus a damage implant of F, Ne, or Ar. The damaging species were implanted with energies of 100, 100, and 144 keV, respectively. The wafers were positioned at 7° from the normal to the beam axis to minimize channeling.

When all implants were completed the wafers were annealed at 1100°C in dry O_2, dry N_2, or sequential dry-wet-dry O_2 for 100 min to activate and redistribute the boron. The sequential anneal consisted of 30 min in dry O_2, then 60 min in wet O_2 followed by 10 min in dry O_2, and is referred to herein as a wet oxidation. The diodes were completed using conventional processing. Aluminum contacts were applied within the diode perimeter and sintered at 500°C for 10 min in forming gas. Diode samples were next probed with 80V reverse bias applied ($V_{BD} \approx 120V$) and the leakage current was measured. Sections of each wafer region were then chemically etched to remove the metal and the oxide. These sections were Sirtl etched for 30 sec and scanning electron micrographs were made of the silicon surface in the junction region.

Results and Discussion

B- and BF_2-implanted diodes.—Fig. 1 shows typical reverse I-V characteristics of B- and BF_2-implanted diodes in <100> silicon that were annealed using the wet oxidation process. The BF_2-implanted diode I-V curve has near ideal slope (≈ 0.6) out to avalanche at just over 100V. The B-implanted diode from the same wafer has a rather soft I-V curve above 10V and at 50V the leakage current is almost two orders of magnitude higher than that of the BF_2-implanted diode.

Scanning electron micrographs of the Sirtl-etched surfaces of diodes of Fig. 1 are shown in Fig. 2. The B-implanted diode (Fig. 2a) has a high density of deep damage dislocation clusters. The BF_2-implanted diode (Fig. 2b) is completely free of gross damage defects although a fine matrix of smaller overlapping defects is evident. Figures 1 and 2 show a correlation between leakage current and dislocation clusters. This is in agreement with earlier reports (3, 4) that precipitates or strain in oxidation-induced defects give rise to excessive leakage in p-n junctions.

Anneal atmosphere and orientation effects.—Diodes prepared by implanting B into <100> silicon and an-

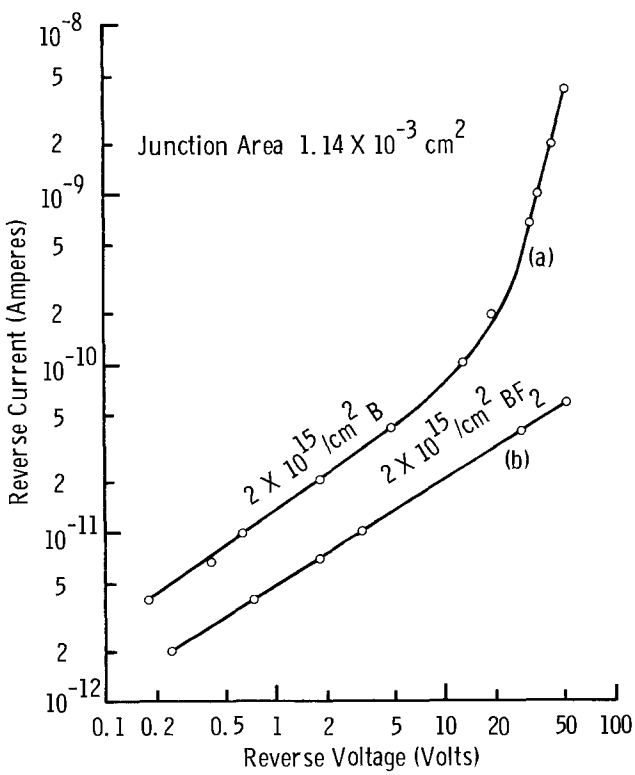


Fig. 1. Reverse I-V characteristics for B- and BF_2-implanted diodes in <100> silicon. Anneal conditions; 1100°C, 30 min dry O_2, 60 min wet O_2, 10 min dry O_2.

* Electrochemical Society Active Member.
Key words: oxidation defects, amorphous, leakage current.

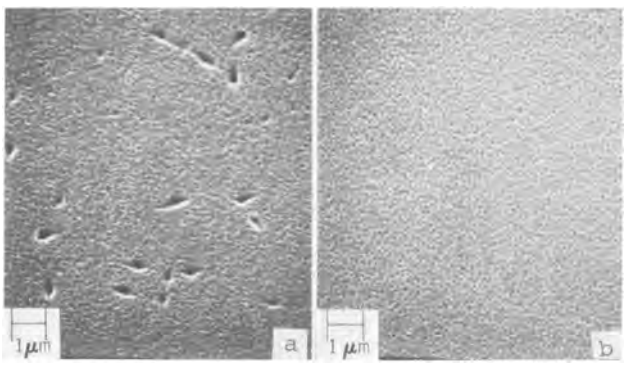


Fig. 2. Scanning electron micrographs of Sirtl-etched surfaces of diodes for which reverse I-V curves are given in Fig. 1. (a) Implanted with 2 × 10^{15}/cm^2 B at 50 keV and (b) implanted with 2 × 10^{15}/cm^2 BF_2 at 144 keV. The diodes were annealed at 1100°C; 30 min dry O_2, 60 min wet O_2, 10 min dry O_2.

nealing at 1100°C for 100 min in dry O_2 or in dry N_2 had low leakage characteristics resembling that of Fig. 1, curve (b). Likewise diodes prepared by implanting B into <111> silicon and subjected to a wet oxidation anneal also exhibited low leakage. Scanning electron micrographs of these Sirtl-etched diode surfaces are shown in Fig. 3.

The dry O_2 and N_2 annealed samples (Fig. 3a and 3b) show none of the damage dislocation clusters that appear in wet O_2-annealed, B-implanted, <100> surfaces (*e.g.*, Fig. 2a). Prussin (5) has shown that wet oxidation enhances defect expansion and Prussin and Fern (6) have shown that a dry N_2 anneal reduces structural defects and n^+-p^+ junction leakage in bipolar transistors with implanted bases. These results suggest that a wet oxidizing anneal atmosphere stimulates the growth of defects that contribute to our p^+-n junction leakage.

The <111> oriented sample annealed using the wet oxidation process (Fig. 3c) shows a large defect density although leakage currents for these diodes were as low as those of BF_2-implanted diodes. Seidel *et al.* (7) have reported less gain degradation due to oxidation-induced defects in bipolar transistors fabricated on <111> silicon than in those fabricated on <100> silicon. They suggest that the differences are associated with either the orientation differences of oxidation-induced defects or their depth distribution. It appears from Fig. 3c, that the low leakages we observe in our B-implanted junctions on <111> silicon may be due to the fact that the defects lie mainly in the <111> plane and do not penetrate the junction.

Damage effects.—To clarify the role of BF_2 in reducing dislocation clusters and leakage current, diodes were prepared by implanting 2 × 10^{15}/cm^2 of 50 keV B together with various fluences or fluorine, neon, or

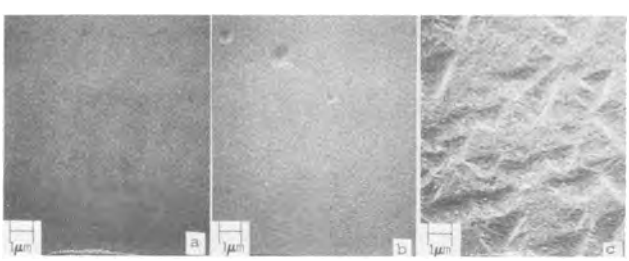


Fig. 3. Scanning electron micrographs of Sirtl-etched boron-implanted diode surface. (a) <100> Silicon, dry O_2 annealed at 1100°C for 100 min, (b) <100> silicon, dry N_2 annealed at 1100°C for 100 min, and (c) <111> silicon, 1100°C anneal, 30 min dry O_2, 60 min wet O_2, 10 min dry O_2.

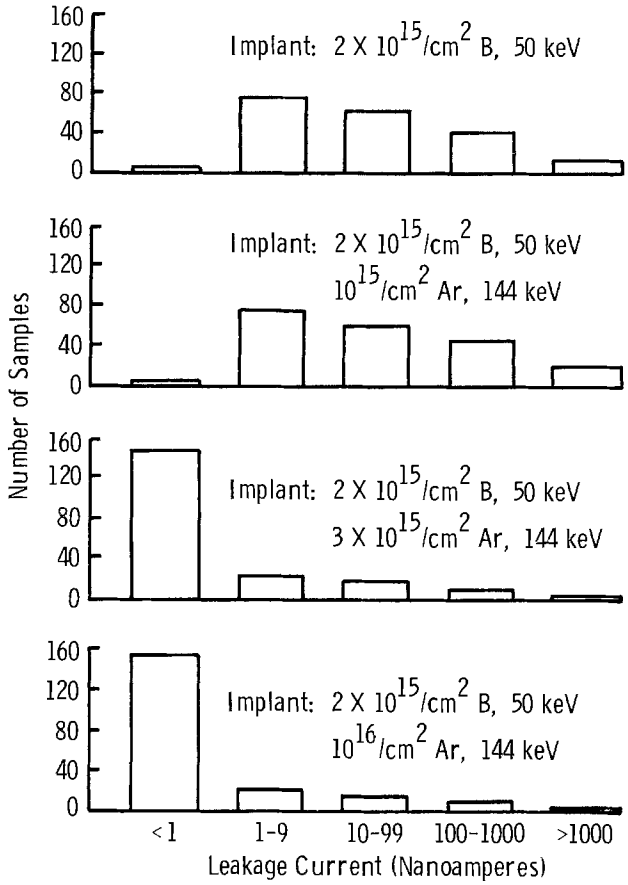


Fig. 4. Histograms of leakage currents at −80V of B-implanted diodes in <100> silicon showing the effect of additional argon damage. The implants were annealed at 1100°C; 30 min in dry O_2, 60 min in wet O_2, 10 min in dry O_2.

argon and annealed using the wet oxidation process. Only the results for 144 keV Ar are discussed here but they apply equally well to 100 keV F and to 100 keV Ne. For leakage current evaluation the diodes were measured at 80V reverse bias.

Histograms of diode leakage current of B-implanted diodes and for B-implanted diodes with selected fluences of implanted Ar are plotted in Fig. 4. These histograms are significant for two reasons:

1. They show that an additional Ar fluence also reduces diode leakage so the reduced leakage observed with BF_2 implants can be assumed to be due to the damage provided by the heavier BF_2 ion.

2. The reduction in leakage current is achieved only when the damage fluence is 3 × 10^{15}/cm^2 or larger. This is close to the 100 keV Si fluence (*i.e.*, 5 × 10^{15}/cm^2) Bauer (8) found necessary to obtain an amorphous layer in silicon implanted with 10^{15}/cm^2 B. These results suggest then, that in order to eliminate dislocation clusters and the attendant excess diode leakage the implant damage must be sufficient to drive the surface amorphous.

Further evidence for the amorphous argument is seen in the scanning electron micrographs of Fig. 5. These are Sirtl-etched surfaces of B-implanted diodes with three different Ar damage fluences. At the 10^{14}/cm^2 Ar fluence level there is little difference from an undamaged diode (see Fig. 2a). At the 10^{15}/cm^2 fluence level dislocation clusters are still clearly evident though not as pronounced. However, at the 10^{16}/cm^2 fluence level dislocation clusters have completely disappeared. Nelson (9) has reported that when a B-implanted silicon surface is driven amorphous and then annealed it is relatively free of crystalline defects.

It should also be noted that the fluence required to drive a silicon surface amorphous has been shown (10) to decrease with increasing flux. In a cursory experi-

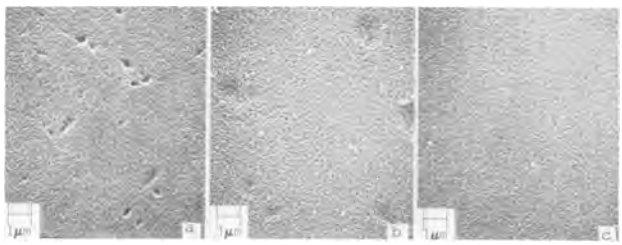


Fig. 5 Scanning electron micrographs of Sirtl-etched boron-implanted diodes with various fluences of argon added. (a) 1×10^{14}/cm^2 144 keV Ar, (b) 1×10^{15}/cm^2 144 keV Ar, and (c) 1×10^{16}/cm^2 144 keV Ar. The diodes were annealed at 1100°C; 30 min dry O_2, 60 min wet O_2, 10 min dry O_2.

ment we found that diodes implanted with 2×10^{15}/cm^2 of BF_2 at a flux of 3 μA/cm^2 had significantly lower leakage than diodes implanted with the same fluence of BF_2 at a flux of 1 μA/cm^2. For all other work reported here B was implanted at 0.2 μA/cm^2 and BF_2 and Ar were implanted at 2 μA/cm^2.

Based on the progressive decrease in dislocation clusters as the Ar damage fluence is increased (Fig. 5) one might expect a continuous decrease in leakage current with increasing damage fluence. The leakage current data of Fig. 4 do not show such a trend. A possible explanation is provided by the work of Ravi *et al.*, who show that diode leakage characteristics depend on the voltage thresholds of individual defects and that these are independent of the size and, to some extent, the density of defects.

Summary and Conclusions

Residual surface damage in B-implanted p^+-n junctions in silicon nucleates dislocation clusters which expand during a subsequent 1100°C anneal in a wet oxidizing atmosphere. If the junction is in <100> silicon the dislocation clusters give rise to excess leakage when the junction is reverse biased. The excess leakage is probably due to strain introduced during the oxidation process or to metal or SiO_2 precipitates on the oxidation-induced defects.

However, when sufficient damage is provided through the implantation of BF_2 or B plus another damaging ion, the silicon surface becomes amorphous. The presence of the amorphous surface layer during subsequent anneal in a wet oxidizing atmosphere inhibits the growth of defects which contribute to the junction leakage current.

Acknowledgments

The authors wish to acknowledge the contributions of others. Mr. T. Schreiber provided scanning electron micrographs. Ms. B. J. Vannoy assisted in device processing. Dr. M. C. Steele supported the work and participated in helpful discussions.

Manuscript submitted June 14, 1976; revised manuscript received Sept. 14, 1976.

Any discussion of this paper will appear in a Discussion Section to be published in the December 1977 JOURNAL. All discussions for the December 1977 Discussion Section should be submitted by Aug. 1, 1977.

Publication costs of this article were assisted by General Motors Corporation.

REFERENCES

1. H. Müller, H. Ryssel, and I. Ruge, in "Second International Conference on Ion Implantation in Semiconductors," I. Ruge and J. Graul, Editors, p. 85, Springer-Verlag, Berlin (1971).
2. S. Prussin, in "Proceedings of 4th International Conference on Ion Implantation," S. Namba, Editor, Plenum Press, New York (1975).
3. A. W. Fisher and J. A. Amick, *This Journal*, **113**, 1054 (1966).
4. K. V. Ravi, C. J. Varker, and C. E. Volk, *ibid.*, **120**, 533 (1973).
5. S. Prussin, *J. Appl. Phys.*, **45**, 1635 (1974).
6. S. Prussin and A. M. Fern, *This Journal*, **122**, 830 (1975).
7. T. E. Seidel, R. S. Payne, R. A. Moline, W. R. Costello, J. C. C. Tsai, and K. R. Gardner, IEEE International Electron Devices Meeting, p. 581, Washington D.C. (1975).
8. L. O. Bauer, in "Proceedings of 2nd International Conference on Ion Implantation," I. Ruge and J. Graul, Editors, pp. 70-79, Springer-Verlag, Berlin (1971).
9. R. S. Nelson, "Proceedings of the European Conference on Ion Implantation," September 1970, Peter Perigrinus, pp. 212-218.
10. F. H. Eisen and B. Welch, "Ion Implantation," pp. 459-464, Gordon and Breach, London (1970).

The Diffusion of Implanted Boron in Silicon

Robert P. Ricco

Western Electric Company, Incorporated, Reading, Pennsylvania 19603

Joseph I. Goldstein

Department of Metallurgy and Materials Science, Lehigh University, Bethlehem, Pennsylvania 18015

and J. Gordon McCallum

Western Electric Company, Incorporated, Engineering Research Center, Princeton, New Jersey 08540

ABSTRACT

The diffusion of randomly implanted boron in silicon during high temperature processing was studied using a $10^{15}/cm^2$ dose of 300 keV boron ions. An anodization-etch sheet-resistance method was used for measuring the diffusion profiles. A computer simulation, utilizing the Crank-Nicolson finite-difference analog, was used to model the diffusions and to aid in interpreting the data. Effects of SiO_2 capping and various ambients (N_2, H_2, and N_2-1% O_2) on boron out-diffusion were investigated. The experiments showed that out-diffusion at 1000°C in N_2 is negligible, but out-diffusion at 1200°C in H_2 is quite significant. A self-capping effect that prevents out-diffusion was observed in the N_2 and N_2-1% O_2 atmospheres at 1200°C.

The use of ion implantation in semiconductor device manufacture is an attractive alternative to conventional diffusion. One advantage of ion implantation is the accurate control of the total number of implanted ions. The implant serves as a predeposition which is then followed by a drive-in diffusion to achieve the desired impurity distribution. The implant concentration profiles of common dopants in silicon are fairly well known (1, 2). When the implant is subjected to heat-treatment, however, the effects of the furnace ambient (3) and the capping material on the impurity distribution (4, 5) obtained in the drive-in step are not as well understood.

The implanted ion dose and the implant profile can be greatly affected if significant out-diffusion occurs at the surface of the silicon during heat-treatment. The amount of out-diffusion depends on the evaporation coefficient, h, which relates the flux in the solid at the surface to the surface concentration (6). In principle, h can vary from zero, implying no evaporation at the surface, to infinity, implying that all the dopant reaching the surface will evaporate. The actual values of h depend upon such factors as temperature and ambient gases. Langer and Goldstein (7) found experimentally that over the temperature range from 1190° to 1380°C the evaporation coefficient of boron from silicon in a hydrogen ambient is given by

$$h = 27.96 \exp(-2.481/kT)\,\text{cm/sec} \qquad [1]$$

The purpose of the present study was to investigate experimentally and theoretically the distribution of implanted boron in silicon after the drive-in diffusion step. The effects of oxide capping and of various ambient atmospheres (N_2, H_2, N_2-1% O_2) upon out-diffusion were studied. Although the impurity profile produced by implantation is often approximated by a Gaussian distribution, in agreement with published data (8) we found that the Gaussian is not an accurate representation of the implanted profile. Therefore, a computer model, using finite-difference solutions to the diffusion equation, was employed to calculate the redistribution of the implanted ions during the drive-in step.

Computer Simulation

The diffusion of boron in silicon can be described by Fick's second law

$$\frac{\partial c}{\partial t} = \frac{\partial}{\partial x}\left(D\frac{\partial c}{\partial x}\right) \qquad [2]$$

where $c(x, t)$ is the concentration of boron and D is the diffusion coefficient. If D is not a function of concentration, Eq. [2] reduces to

$$\frac{\partial c}{\partial t} = D\frac{\partial^2 c}{\partial x^2} \qquad [3]$$

This equation has been solved analytically for certain well-behaved initial profiles, but for the case of an implanted profile such a solution is not available. The most useful of the methods for solving differential equations such as the diffusion equation utilize finite-difference techniques. One of these, the Crank-Nicolson finite-difference analog, as described by von Rosenberg (9), is second-order correct with respect to both independent variables and, in addition, stable over a wide range of increments of the variables. We used the Crank-Nicolson method for computer simulation of the diffusion process. Two types of boundary conditions were considered. The first specified an out-diffusion flux at the surface given by

$$hC = -D\frac{\partial c}{\partial x}\bigg|_{x=0} \qquad [4]$$

where C is the surface concentration and $\frac{\partial c}{\partial x}\Big|_{x=0}$ is the concentration gradient at the surface. The second boundary condition specified no out-diffusion, corresponding to $\frac{\partial c}{\partial x}\Big|_{x=0} = 0$.

Experimental Procedure

The experiments were performed on 1¼ in. diam wafers of n-type, (111) silicon with a background phosphorus concentration of approximately 10^{15} atoms/cm^3. Each wafer was implanted with a boron dose of 10^{15} atoms/cm^2 at 300 keV. A random implant was achieved by tilting the sample 7° off the <111> direction about an axis 10° to the [110] flat.

To obtain boron concentration profiles, each sample was anodized and etched (10) to strip away thin layers of silicon and allow the use of differential sheet-resistance measurements. Anodization was performed in a water-cooled bath, at 21°C, which contained an elec-

Key words: implantation, capping, redistribution, annealing, impurities.

trolyte of 1.1g of potassium nitrite in 100 ml of tetrahydrofurfuryl alcohol. A platinum-foil cathode was used and a copper-plated clip held the wafer in the electrolyte. The thickness of the oxide produced was measured by ellipsometry to be 925 ± 50Å. After the oxide film was stripped and the sample rinsed and dried, the sheet resistance was measured in darkness with a linear four-point probe placed at the center of the wafer. No size correction was used since the probe spacing was only 0.040 in. The total concentration profile was measured by removing approximately 400Å of silicon in each of 40 anodization-etch steps.

The data obtained by the profiling were in the form of sheet resistances at known distances from the original surface. The data reduction was performed with a computer program (11) that derives the values of resistivity, $\rho(x)$, from sheet resistance, $\rho_s(x)$, by using the expression (12)

$$\rho(x)^{-1} = \frac{1}{0.4343\,\rho_s(x)} \frac{d}{dx} [\log_{10} \rho_s(x)] \qquad [5]$$

The resistivity profiles were converted to concentration profiles by using a fifth-order approximation to Irvin's data for hole mobility in silicon (13).

The diffusion times and temperatures to be used were calculated with the computer simulation program using a Gaussian distribution as the initial condition. To obtain initial profiles, two of the implanted wafers were annealed to remove the initial damaged regions in 2 liter/min dry nitrogen for 30 min at 950°C in a tube whose cross-sectional area was 24 cm². According to the above calculation, no measurable diffusion of boron should occur during this time period. For profiles at 1000°C, two wafers were diffused in 1 liter/min dry nitrogen for 2 hr 11 min and 14 hr 45 min. Two other wafers were capped with 5000Å of vapor-deposited SiO_2 to prevent out-diffusion. In order to prevent diffusion during capping, the oxide deposition was performed at a low temperature, 420°C, using the following reaction of silane and oxygen

$$SiH_4 + 2\,O_2 \rightarrow SiO_2\ (\text{solid}) + 2H_2O$$

These wafers were then diffused in a 2 liter/min ambient of 99% nitrogen-1% oxygen at 1200°C, one for 30 min and the other for 60 min. As controls, two uncapped implanted wafers were diffused under the same conditions. Three other uncapped samples were diffused at 1200°C for 60 min in the following ambient atmospheres: pure H_2 at 20 liter/min, 99% nitrogen-1% oxygen at 2 liter/min, and pure N_2 at 4 liter/min.

Computer calculations of boron concentration profiles were performed for the same times and temperatures as the experimental runs. A comparison of calculated and measured profiles was then made. The values used for the diffusion coefficient of boron in silicon were calculated from the expression given by Kendall and DeVries (14) with $D_o = 1.4$ cm²/sec and $Q = 3.5$ eV, which yields $D_{1000°C} = 1.83 \times 10^{-14}$ cm²/sec and $D_{1200°C} = 1.40 \times 10^{-12}$ cm²/sec.

Results and Discussion

The initial profile for boron, measured after the sample was annealed at 950°C for 30 min in a 2 liter/min dry N_2 ambient to activate the boron acceptors, is shown in Fig. 1. The curve is Gaussian but it does exhibit a high surface concentration. This effect was observed for both the initial profile samples. Because of some inconsistencies in the sheet-resistance data within the first quarter micrometer, the concentration data were smoothed in this region. The smoothing led to an error under 50% in the surface concentration and had no effect on the final computed profiles. A high surface concentration has been reported by Davies (17), who used junction depth measurements for measuring implanted boron profiles. Values of the range, R, and straggle, σ, were 7000 and 1000Å, respectively, and compare favorably within experimental limits to the LSS

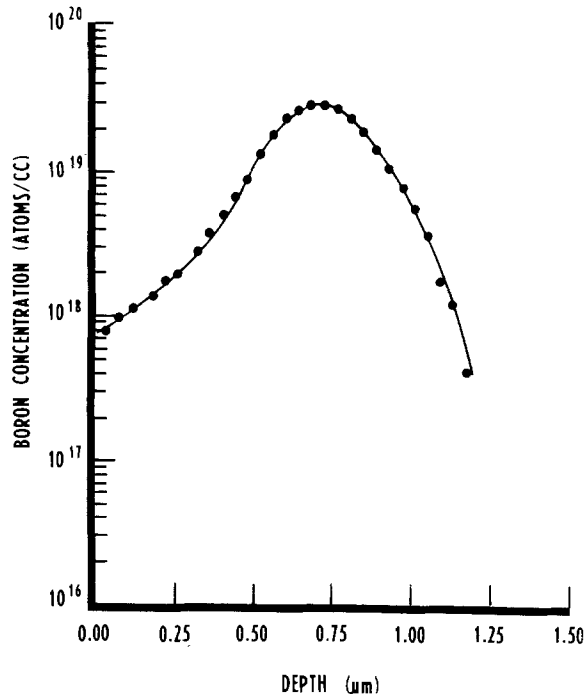


Fig. 1. Initial boron profile obtained after 950°C anneal for 30 min. Solid line is computer fit to experimental points.

(15) values, calculated using Eisen's corrections (2), of 6800 and 1000Å, respectively.

The profiles measured after annealing at 1000°C in N_2 for 2 hr 11 min and for 14 hr 45 min are shown in Fig. 2 and 3, respectively. Computer simulations using h values of 0 cm/sec and 10^{-9} cm/sec are also plotted. It is impossible within the resolution limits of the experiment to determine the value of h for best fit from the 2 hr 11 min curves. It is, however, evident from the 14 hr 45 min curves that the value of h is much smaller than 10^{-9} cm/sec. A good fit is obtained with $h = 0$ and is indistinguishable from that obtained for $h \leq 10^{-10}$ cm/sec, indicating that for these conditions no out-diffusion occurs. No oxide or nitride was observed on the sample surfaces after diffusion.

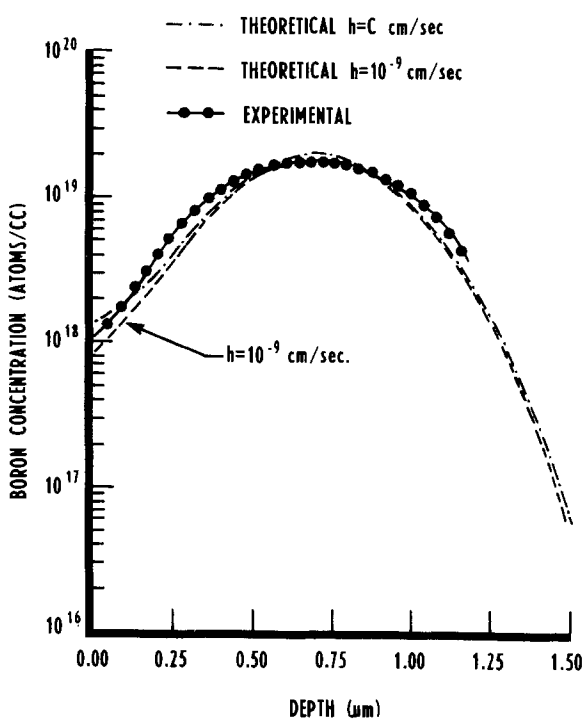


Fig. 2. Boron profile after diffusion at 1000°C for 2 hr 11 min in N_2. The parameter h is the evaporation coefficient.

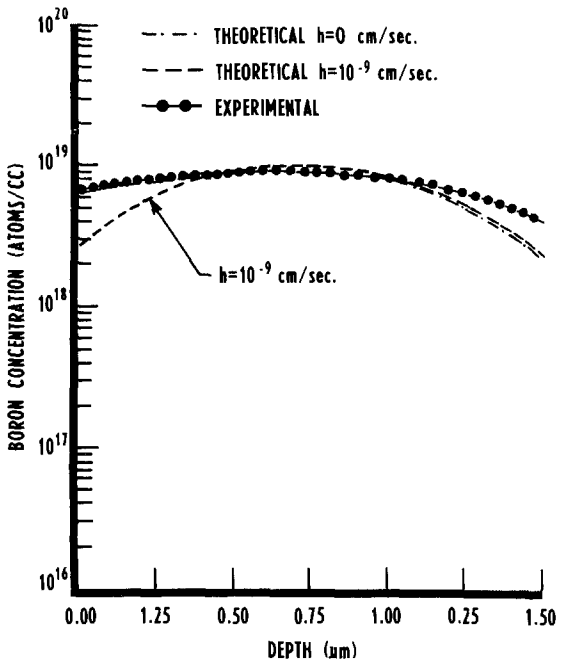


Fig. 3. Boron profile after diffusion at 1000°C for 14 hr 45 min in N_2.

The curves in Fig. 4 show the profiles obtained for the diffusions at 1200°C in a 2 liter/min N_2-1% O_2 ambient. The experimental points for 30 and 60 min diffusion times for the uncapped samples and for the samples capped with 5000Å SiO_2 are shown along with the theoretical simulation curves for $h = 0$ cm/sec. The agreement between the calculated and experimental results for the capped samples is within the experimental accuracy. The close correspondence with the theoretical curves for $h = 0$ in the case of the uncapped samples indicates that no out-diffusion took place in the samples in spite of the lack of an applied capping material. Although these results suggest that an oxide forms on the silicon surface during diffusion in N_2-1% O_2 at 1200°C, no oxide layer was visible on the samples after diffusion. However, a layer of SiO_2 less than 800Å in thickness is not generally visible to the eye. Therefore, to check the possibility of oxide growth an additional sample was diffused at 1200°C for 60 min in 2 liter/min of N_2-1% O_2. An oxide layer about 700Å thick was detected and measured using the fact that a buffered HF solution will etch SiO_2 at a constant rate until the wafer finally becomes hydrophobic. A similar diffusion was done in 4 liter/min N_2 to check for silicon nitride formation at 1200°C. In this case, a layer could be seen on the surface but it was not an oxide since it did not etch in buffered HF. Possibly the layer may have been silicon nitride. The differences between the measured and calculated profiles for the 60 min diffusions at 1200°C in N_2-1% O_2, while within the estimated limits of experimental error, are significantly greater than those for the other diffusions in N_2-1% O_2 and N_2. The reason for this is not understood. The process of boron transfer from silicon to the SiO_2 surface layer (5) is not expected to play a significant role in the redistribution of boron in these experiments since the amount of SiO_2 thermally grown was small. In the case of the capped samples, the effect was assumed to be negligible since no thermal oxide was grown on the samples.

The calculated boron profiles after diffusion lie below the measured ones at the larger distances from the surface. A larger value of D would give a better fit but no attempt was made to adjust D since this would not have contributed significantly to a better understanding of the behavior of boron at the ambient-wafer interface.

Figure 5 shows the profile obtained after diffusion in 20 liter/min of pure H_2 for 60 min at 1200°C. Curves for the computer simulation using Langer and Goldstein's (7) experimental value of $h = 9.1 \times 10^{-8}$ cm/sec and a value of $h = 10^{-8}$ cm/sec are shown for comparison. Values of $h > 10^{-7}$ cm/sec give curves that have a greater drop near the surface and lie generally below the measured values. Values of $h < 10^{-9}$ cm/sec result in curves which closely approximate $h = 0$. A considerable amount of out-diffusion took place in the hydrogen sample, in marked contrast to the negligible amount noted for the N_2-1% O_2

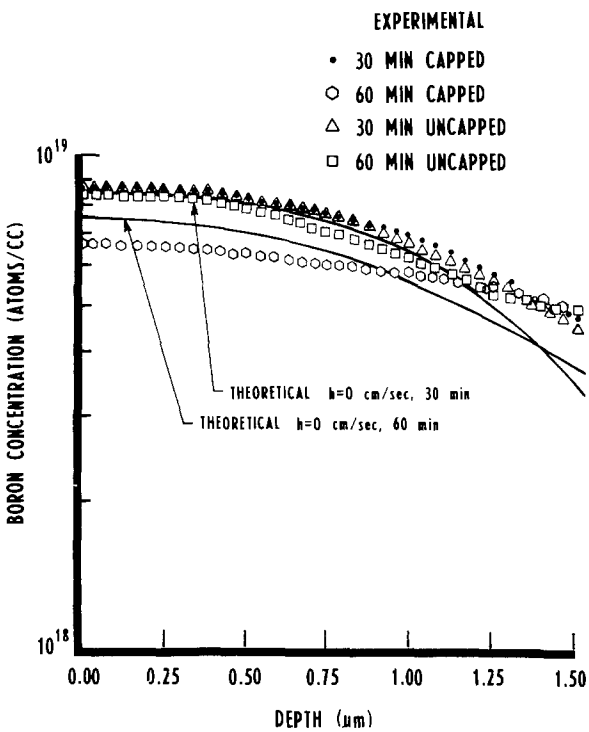


Fig. 4. Boron profiles after copped and uncapped diffusions at 1200°C in 99% N_2-1% O_2.

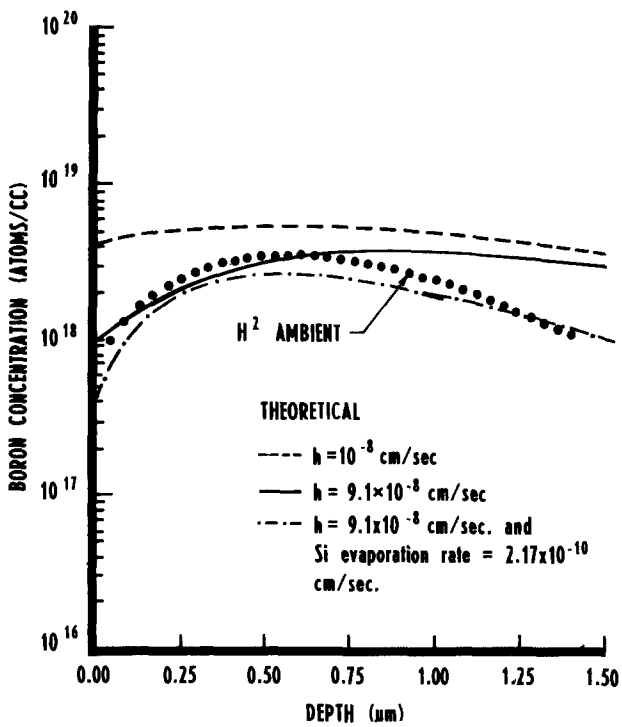


Fig. 5. Boron profile after diffusion at 1200°C for 60 min in H_2

samples (Fig. 4). In one computer calculation allowance was made for the silicon evaporation that occurs at 1200°C in hydrogen according to Tung (16). The rate of evaporation used in this moving boundary simulation was 2.17×10^{-10} cm/sec, as determined experimentally by Langer and Goldstein (7). The profile for the hydrogen diffusion is well approximated by this theoretical curve, as expected, because the hydrogen allowed no oxide or nitride growth. The effect of this out-diffusion is considerable, resulting in nearly twice the value of sheet resistance measured for the capped samples.

The results reported here are subject to the following experimental errors. The anodization step could result in an error of ±2% max in the oxide thickness. This is insignificant for any one step but could become sizable after a large number of steps. The sheet resistance measurement by four-point probe was found to yield a ±5% variation for multiple readings on the same spot. The data reduction technique, being primarily analytical in nature, has only those errors normally introduced by computer calculations associated with it. An error can be associated with the use of Irvin's mobility data, particularly in high concentration regions ($>10^{18}$ atoms/cm^3) (3). Due to the use of an electrical measurement technique, a loss of resolution occurred in two areas. For those samples which had low surface concentrations, the resistivity method of measurement introduces data scatter because of a lack of impurities at the surface. Near the interior p-n junction a large degree of inaccuracy can occur since the sheet resistance approaches the junction asymptotically. A direct measurement of the impurity concentrations would allow more accurate profiles to be taken. This is particularly true for the as-implanted profile, which cannot be found by electrical measurements because annealing is required to activate the impurities.

Acknowledgments

The authors wish to thank Paul Langer, Bell Laboratories, Allentown, for his assistance with the hydrogen diffusion and the data reduction. They would also like to thank C. M. Drum, Bell Laboratories, Allentown, for the implants and C. A. Adams, Western Electric Engineering Research Center, Princeton, for the anodization apparatus. This paper was submitted by Robert P. Ricco as a partial requirement for the M. S. degree Lehigh University (May 1973).

Manuscript submitted Sept. 4, 1974; revised manuscript received Sept. 22, 1976.

Any discussion of this paper will appear in a Discussion Section to be published in the December 1977 JOURNAL. All discussions for the December 1977 Discussion Section should be submitted by Aug. 1, 1977.

Publication costs of this article were assisted by the Western Electric Company, Incorporated.

REFERENCES

1. B. L. Crowder, Editor, "Ion Implantation in Semiconductors and Other Materials," Plenum Press, New York (1973).
2. J. W. Mayer, L. Eriksson, and J. A. Davies, "Ion Implantation in Semiconductors," Academic Press, New York (1970).
3. S. Wagner, *This Journal*, **119**, 1570 (1972).
4. R. H. Krambeck, *ibid.*, **121**, 588 (1974).
5. J. L. Prince and F. N. Schwettmann, *ibid.*, **121**, 705 (1974).
6. A. S. Grove, "Physics and Technology of Semiconductor Devices," p. 67, John Wiley & Sons, Inc., New York (1967).
7. P. H. Langer and J. I. Goldstein, Abstract 65, p. 168, The Electrochemical Society Extended Abstracts, Spring Meeting, San Francisco, California, May 12-17, 1974.
8. D. E. Davies, *Appl. Phys. Lett.*, **13**, 243 (1968).
9. D. U. von Rosenberg, "Methods for the Numerical Solution of Partial Differential Equations," Americal Elsevier Publishing Co., Inc., New York (1969).
10. R. P. Donovan, in "Fundamentals of Silicon Integrated Device Technology," Vol. I, R. M. Burger and R. P. Donovan, Editors, p. 56, Prentice-Hall, Inc., Englewood Cliffs, N.J. (1967).
11. P. H. Langer, Private communication.
12. R. P. Donovan and R. A. Evans, in "Silicon Device Processing," C. P. Marsden, Editor, p. 123, NBS Special Publication No. 337, U.S. Gov't. Printing Office, Washington, D.C. (1970).
13. T. P. Lee, *IEEE Trans. Electron Devices*, **ed-13**, 881 (1966).
14. D. L. Kendall and D. B. DeVries, in "Semiconductor Silicon," R. R. Haberecht and E. L. Kern, Editors, p. 358, The Electrochemical Society Softbound Symposium Series, New York (1969).
15. J. Lindhard, M. Scharff, and H. E. Schiott, in "Matematiskfysiske Meddeleser udgivet af Det Kongelige Danske Videnskabernes Silskab," Vol. 33, No. 14 (1963).
16. S. K. Tung, in "Metallurgy of Semiconductor Materials," J. B. Schroeder, Editor, p. 95, Interscience, New York (1962).
17. D. E. Davies, *Solid-State Electron.*, **13**, 229 (1970).

Ionic Conductivity of Doped Cerium Trifluoride

Takehiko Takahashi,* Hiroyasu Iwahara, and Toyomi Ishikawa

Department of Applied Chemistry, Faculty of Engineering, Nagoya University, Nagoya 464, Japan

ABSTRACT

The electrical conductivities of the tysonite-type fluorides based on CeF_3 in the sintered state were measured for various aliovalent cation dopants. Doping of difluoride such as CaF_2, SrF_2, or BaF_2 up to 5 mole percent made the conductivity increase while the doping of tetrafluoride such as ThF_4 led it to decrease. These facts together with the experimental results of electrolysis indicated that the specimens were fluoride ion conductors resulting from the easy movement of fluoride ion vacancies. The activation energies for conduction at the high temperature range above 250°C were, in general, about 0.25 eV irrespective of divalent dopant species, while those at lower temperatures were 0.28 ~ 0.50 eV depending on the dopant species. Their conductivities are, in general, higher than those of the LaF_3-based electrolytes which are also the tysonite-type fluorides. $(CeF_3)_{0.95}(CaF_2)_{0.05}$ had the highest conductivity among the tysonite-type fluorides ever examined.

Some of the solid fluorides with large cations have been known to be fluoride ion conductors. They hold considerable promise for use as solid electrolytes; for example, LaF_3 has been used in fluoride ion selective electrodes (1), and CaF_2 as the electrolyte in galvanic cells used in the thermodynamic study of fluorides, carbides, and oxides at high temperatures (2). Besides, Baukal has recently called attention to the potentiality of high power batteries using solid fluoride electrolytes (3). It is, in general, desirable for the electrolyte to have the highest conductivity possible for practical use. The solid electrolytes discovered currently, however, do not always satisfy this demand.

The fluoride electrolytes can be classified into two categories by their crystal structures: The first is the fluorite-type which covers many difluorides of Group II in the Periodic Table and the second is the tysonite-type which includes trifluorides of rare earth metals. While there are a number of studies on the conductivity of the former group, the conductivity studies of the latter group are few and have been almost entirely limited to those on LaF_3 (4-9) because of the rare occurrence of these materials.

Recently, Nagel and O'Keeffe (10) measured the conductivities of tysonite-type CeF_3 as well as of LaF_3, and found that conductivities of the former were one order of magnitude higher than those of the latter over a wide range of temperature. They also measured the conductivities of $La_{0.95}Sr_{0.05}F_{2.95}$, a derivative of tysonite-type LaF_3, and observed that the conductivites were more than ten times higher than those of pure LaF_3. These results suggest that fluoride ion conduction in tysonite-type compounds may be concerned with fluoride ion vacancies, and that, if such defects can be formed in CeF_3 in an appreciable amount by adding some aliovalent fluoride, higher conductivities than that of $La_{0.95}Sr_{0.05}F_{2.95}$ can be expected.

To examine these, we prepared some solid solutions based on CeF_3 and measured their conductivities as well as their electrolytic properties. CaF_2, SrF_2, BaF_2, and ThF_4 were examined as aliovalent dopants. Because of the difficulties of obtaining single crystals with the desired composition and size, all of the specimens examined were polycrystalline sinters.

Experimental

Preparation of the sintered specimens.—In order to eliminate the ammonium fluoride included in the reagent, the cerium trifluoride (purity above 99%) obtained from Katayama Kagaku Company Limited was subjected to preliminary heating at 400°C in an argon stream which was dried with phosphorus pentoxide. The resultant powdery fluoride was mixed with calcium, strontium, barium, or thorium fluoride at a designated ratio and hand-pressed into pellets. The pellets were calcined at 750°C for 4 hr. Then, they were crushed into powder and ground finely in an agate mortar. The powder was pressure-molded hydrostatically under 3 ton/cm^2 into cylindrical shapes (diameter 4 ~ 5 mm, length 5 ~ 7 mm) or disks (diameter 10 mm, thickness 1 ~ 1.5 mm), and sintered at 870° ~ 900°C for 4 hr. The calcining and sintering were performed in argon which had been passed through heated spongy titanium metal and phosphorus pentoxide to eliminate oxygen and water, respectively.

X-ray diffraction and density measurements.—The sintered fluorides thus obtained were subjected to x-ray diffraction analysis to make sure of the formation of solid solutions and to determine the lattice parameters. A Rigaku-Denki x-ray diffractometer with CuKα irradiation source was used for the determination of the lattice parameter at a scanning rate of 0.25 deg/min adopting CaF_2 as an internal standard.

The theoretical densities of the specimens were calculated from the lattice parameters thus obtained and compared with powder densities measured with the normal pycnometric method using n-butanol at 25°C.

Conductivity measurements.—The cylindrical-shaped specimens were used for conductivity measurements. Graphite was smeared on both ends of the specimen rod for electrodes, and it was inserted between graphite disk current collectors in the furnace. The furnace was gastight and argon gas dried with phosphorus pentoxide was flowed through it. The conductivity was measured by an a-c bridge (Ando Denki LCR-6) with a capacity compensator. A measuring frequency of 10 kHz was adopted, in the vicinity of which the dependence of conductivity on the frequency was fairly small. Other electrode materials such as silver paste and graphite paste were also tried, but they were not as stable and independent of frequency as the smeared graphite electrode.

In order to clarify the charge carrier in the specimen, electrolysis by Tubandt's method was performed by contacting three disk-shaped specimens face to face and by adopting the smeared graphite electrodes on both end faces of the pile. The electrolysis products were identified by x-ray diffraction with each surface of the anolyte and the catholyte.

Results

The sinters.—The sintered specimens thus prepared were hard and dense; the porosities calculated from

* Electrochemical Society Active Member.

Key words: cerium trifluoride, fluoride ion conductivity, tysonite-type fluoride.

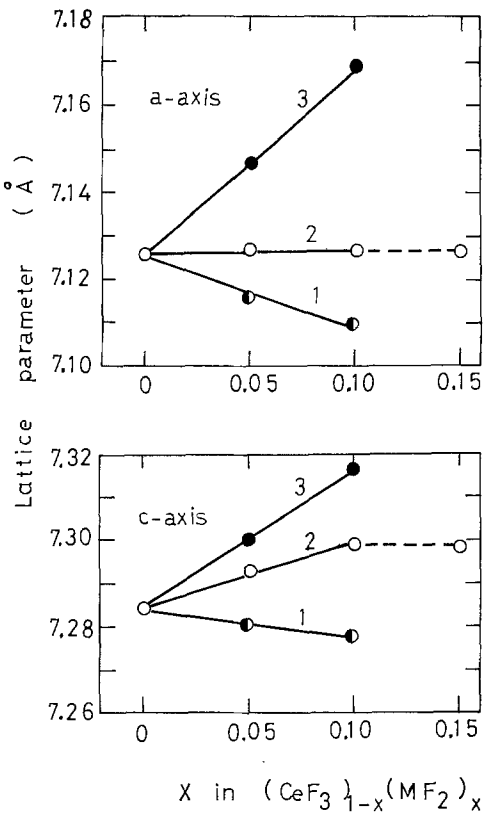


Fig. 1. Lattice parameters of tysonite-type solid solutions based on CeF_3. 1, M = Ca; 2, M = Sr; 3, M = Ba.

powder density and apparent density of the sintered block were less than 5%.

X-ray diffraction patterns of the difluoride-doped specimens $(CeF_3)_{1-x}(MF_2)_x$ showed tysonite-type phase only when the dopant concentrations were less than 10 mole percent (m/o) ($x \leq 0.1$). Figure 1 shows the lattice parameters of pure and doped samples. They obeyed Vegard's rule at least up to 10 m/o, and the larger the radius of the doped ion, the larger the lattice parameter became for both the a- and c-axis. These results indicated that the tysonite-type solid solution formation ranged in these systems up to, at least, 10 m/o MF_2. The specimen doped with 15 m/o SrF_2 gave small diffraction lines of SrF_2 indicating that the solubility of SrF_2 was less than 15 m/o.

In Table I the observed powder densities are compared with the theoretical values calculated from lattice parameters assuming that either fluoride ion vacancies or cation interstitials were formed on doping 5 m/o of MF_2 to CeF_3. The observed values were in good agreement with the values calculated based on the former assumption, suggesting that the fluoride ion vacancies were formed by adding MF_2 as a result of charge compensation.

An x-ray diffraction pattern of 5 m/o ThF_4-doped specimen gave additional lines to the original pattern indicating that the solubility was less than 5 m/o. However, diffraction lines of the tysonite phase at high angle were shifted slightly suggesting a little solubility.

Though the fluoride samples were hydrolyzed to form CeO_2 in wet air at high temperatures, they were stable in dry air (dried with P_2O_5) even at 300°C.

Table I. Comparison of observed density with calculated densities assuming that fluoride ion vacancies or cation interstitials are formed on doping MF_2 to CeF_3

Specimen	Calculated density (g/cm³)		Observed density (g/cm³)
	Anion vacancy	Cation interstitials	
CeF_3	6.13		6.16 ± 0.05
$(CeF_3)_{0.95}(CaF_2)_{0.05}$	5.97	6.07	5.95 ± 0.03
$(CeF_3)_{0.95}(SrF_2)_{0.05}$	6.01	6.12	5.98 ± 0.03
$(CeF_3)_{0.95}(BaF_2)_{0.05}$	6.05	6.16	6.00 ± 0.03

Conductivity.—Arrhenius plots of conductivity of $(CeF_3)_{1-x}(CaF_2)_x$ are presented in Fig. 2 for various compositions. The conductivity of pure CeF_3 above 200°C was close to that of the single crystal reported by Nagel *et al.* (broken line) (10). The conductivities increased by adding CaF_2 to CeF_3 and maximum conductivity lay at 5 m/o CaF_2 compositions. The conductivity of this fluoride was about one order of magnitude higher than that of pure CeF_3, and the value at 200°C (1×10^{-2} Ω^{-1}-cm^{-1}) was several times higher than that of $La_{0.95}Sr_{0.05}F_{2.95}$ reported by Nagel *et al.* (10) (see Fig. 8). In this system, each Arrhenius plot consists of two regions, that is, the lower slope at higher temperatures and the higher inclination at lower temperatures. The change in slope takes place at about 200°C.

As shown in Fig. 3, the conductivities of the CeF_3-SrF_2 system also increased with increasing content of SrF_2 up to 5 m/o. At a higher content of SrF_2 than this, the dependence of conductivity on composition became ambiguous. The conductivity of 5 m/o SrF_2-doped sample at the high temperature range was almost the same as that of $(CeF_3)_{0.95}(CaF_2)_{0.05}$. The Arrhenius plots are also divided into two regions in this case.

As shown in Fig. 4, the relation between the conductivity and the composition in the CeF_3-BaF_2 system was not as regular as the previous two systems. The change in slope at about 200°C is not significant. The maximum conductivity, however, was also observed at 5 m/o of dopant content.

In contrast to the case of difluoride doping, the conductivities decreased by adding ThF_4 to CeF_3 as shown in Fig. 5. It should be noticed in this case that the solubility of ThF_4 was lower than 5 m/o. Nevertheless, this result may indicate that even a small amount of doping caused the conductivity to decrease remarkably. Besides this, the slope of Arrhenius plot differed conspicuously from those for MF_2-doped specimens; in

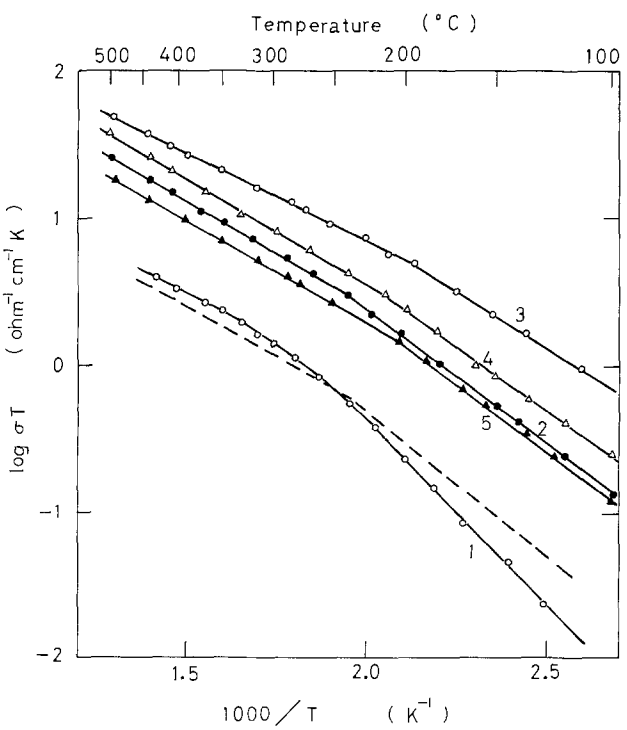


Fig. 2. Arrhenius plots of conductivity for $(CeF_3)_{1-x}(CaF_2)_x$. 1, $x = 0.00$; 2, $x = 0.025$; 3, $x = 0.05$; 4, $x = 0.075$; 5, $x = 0.10$; broken line, CeF_3 single crystal after Ref. (10).

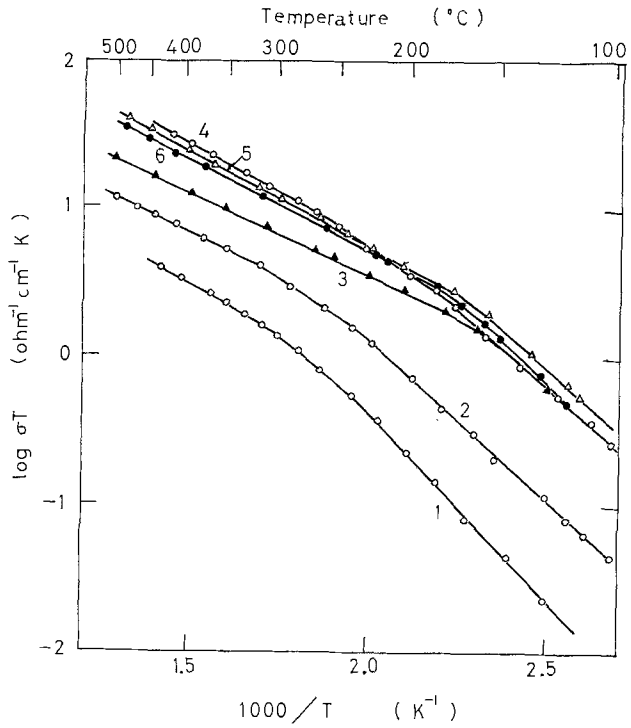


Fig. 3. Arrhenius plots of conductivity for $(CeF_3)_{1-x}(SrF_2)_x$. 1, $x = 0.00$; 2, $x = 0.01$; 3, $x = 0.02$; 4, $x = 0.05$; 5, $x = 0.07$; 6, $x = 0.10$.

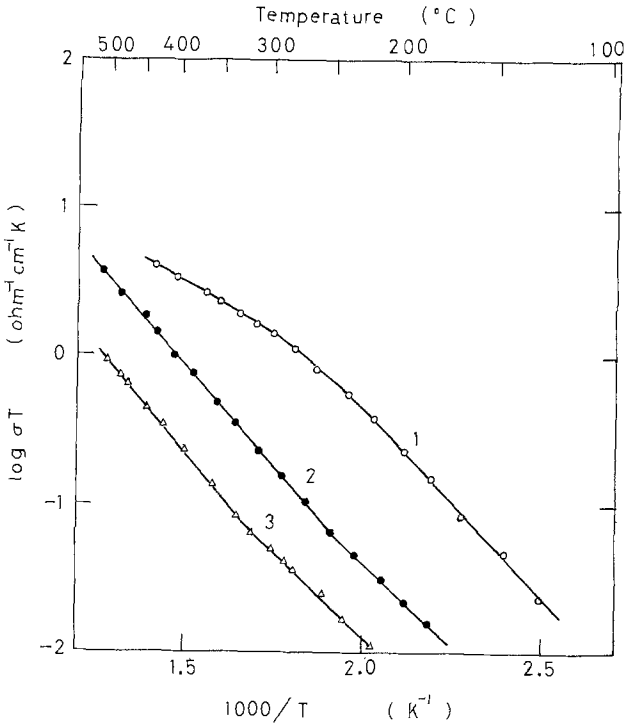


Fig. 5. Arrhenius plots of conductivity for $(CeF_3)_{1-x}(ThF_4)_x$. 1, $x = 0.00$; 2, $x = 0.025$; 3, $x = 0.05$.

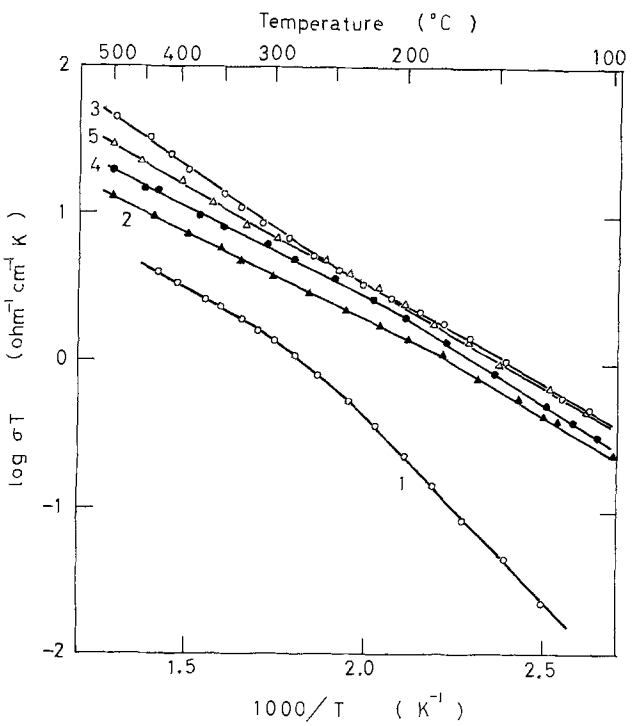


Fig. 4. Arrhenius plots of conductivity for $(CeF_3)_{1-x}(BaF_2)_x$. 1, $x = 0.00$; 2, $x = 0.025$; 3, $x = 0.05$; 4, $x = 0.075$; 5, $x = 0.10$.

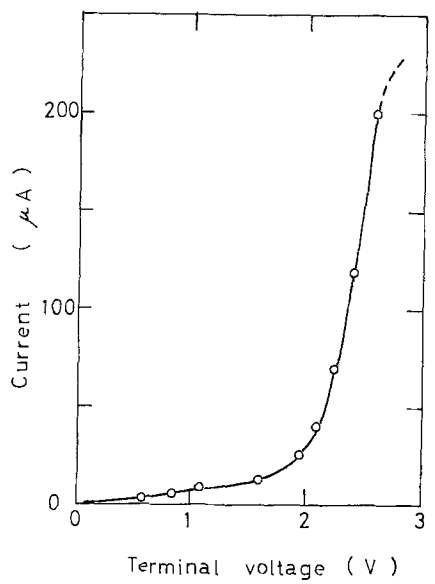


Fig. 6. Electrolysis curve of $(CeF_3)_{0.95}(CaF_2)_{0.05}$ at 300°C in dry air. (The electrodes are smeared graphites. Specimen size, 0.78 $cm^2 \times 0.1$ cm.)

the latter case, the slope at high temperatures is lower than that at low temperatures, whereas in ThF_4-doped specimens, the slope at high temperatures is rather steep compared to that at low temperatures.

Electrolytic properties.—Figure 6 shows the terminal voltage-d-c current curve for $(CeF_3)_{0.95}(CaF_2)_{0.05}$ using smeared graphite electrodes under dry air at 300°C. A decomposition voltage of about 2.0V is considerably lower than that expected from the free enthalpy of formation for the fluoride. When the same measurement was performed in a vacuum, the decomposition current could not be measured clearly at least up to 10V because of the instability of the current with time. X-ray diffraction patterns of the surfaces of the anolyte and catholyte after electrolysis in dry air at 300°C using the smeared graphite electrodes were recorded. The catholyte surface gave the diffraction patterns of CeO_2, while the anolyte surface remained unchanged showing the initial pattern of the tysonite. When the electrolysis was carried out in a vacuum, the resultant x-ray diffraction pattern of the catholyte surface was somewhat broad retaining the initial pattern of the tysonite. However, this catholyte surface was recognized to change to CeO_2 after exposure to air at room temperature for a few days, suggesting that the catholyte surface was reduced to metallic cerium by electrolysis in vacuum.

If oxygen gas is involved electrochemically with the cathode reaction, one of the possible reactions at the cathode may be

$$CeF_3 + O_2 + 3e^- = CeO_2 + 3F^- \quad [1]$$

and the corresponding anode reaction would be

$$3F^- = \frac{3}{2}F_2 + 3e^- \quad [2]$$

thus the over-all reaction may be

$$CeF_3 + O_2 = CeO_2 + \frac{3}{2}F_2 \quad [3]$$

The decomposition voltage estimated from the free energy change of Eq. [3] is 1.8V. Therefore, an observed decomposition voltage of 2.0V in air may be rational considering an additional overvoltage of about 0.2V.

In order to ascertain the charge carrier in the electrolyte, the changes in weight of the anolyte, bulk, and catholyte were measured after electrolysis in dry air at 300°C using smeared graphite electrodes. The results are given in Table II for $(CeF_3)_{0.95}(CaF_2)_{0.05}$. In this table, the calculated weight changes are based on the assumption that the oxides were formed as a result of the cathode reactions such as Eq. [1] or as a result of the reactions of movable cations with oxygen such as

$$Ce^{3+} + O_2 + 3e^- = CeO_2 \quad [4]$$

or

$$Ca^{2+} + \frac{1}{2}O_2 + 2e^- = CaO \quad [5]$$

and that fluorine generated at the anode was caught by smeared graphite or dissolved into the anolyte. The observed changes in weight are in good agreement with the values assumed as fluoride ions being charge carriers

Discussion

The doping of divalent fluoride up to 5 m/o makes the conductivity increase in all cases examined, whereas the addition of tetravalent fluoride makes it decrease. A representative example for this can be seen in Fig. 7, in which the isothermal conductivities were plotted against the dopant content for a CaF_2-doped sample (toward the right-hand side along the abscissa) together with ThF_4-doped one (toward left-hand side along the abscissa). This fact suggests that the ionic current is carried by mobile fluoride ion vacancies, and that the vacancy concentration increases by doping difluoride and decreases by doping tetrafluoride as shown in the following equations

$$CaF_2\ (CeF_3) \rightarrow Ca'_{Ce} + 2F^x_F + V^{\cdot}_F \quad [6]$$

$$ThF_4\ (CeF_3) + V^{\cdot}_F \rightarrow Th^{\cdot}_{Ce} + 4F^x_F \quad [7]$$

The formation of fluoride ion vacancies by doping of the difluoride was also supported by the result of density measurements shown in Table I. However, the effect of doping on conductivity is not as remarkable as in the case of the solid solution based on fluorite-type fluoride such as NaF-doped CaF_2 (11), in which doping

Table II. Change in weight by electrolysis of $(CeF_3)_{0.95}(CaF_2)_{0.05}$

Specimen disk	Change in weight (mg)				
	Observed	Calculated			
		F^-	Ce^{3+}	Ca^{2+}	e^-
Anolyte	+2.2	+2.2	−7.7	−4.6	0.0
Bulk	0.0	0.0	0.0	0.0	0.0
Catholyte	−1.0	−1.0	+6.6	+3.3	0.0

300°C in dry air. Amount of electricity, 11.4C.

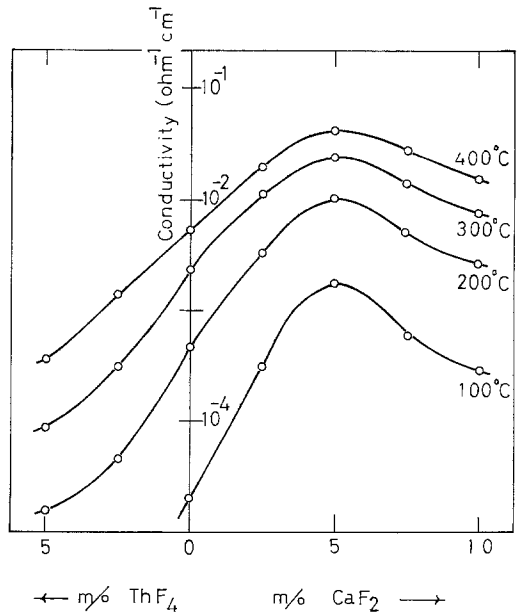


Fig. 7. Isothermal conductivity plots of CaF_2- and ThF_4-doped CeF_3.

of 1 m/o dopant makes the conductivity increase by more than three orders of magnitude. The decrease in conductivity by adding ThF_4 can be explained by a decrease in the concentration of the vacancies which are present in pure CeF_3 as intrinsic defects. The high conductivity of pure CeF_3 compared to pure CaF_2 and its considerable decrease by adding ThF_4 suggest that the concentration of intrinsic vacancies is appreciably high like that in LaF_3, in which the intrinsic defects are reported to be the Schottky type (4).

Arrhenius plots shown in Fig. 2-5 consist, in general, of two regions: the low slope region at high temperatures and the steep slope range at low temperatures. A similar form was also reported by Sher *et al.* in the case of LaF_3 (4). According to them, the activation energy for conduction in LaF_3 crystal was 0.46 eV in the low temperature range (<350°K), whereas in the high temperature range above 400°K, it was only 0.08 eV in spite of the fact that there existed no phase transition between the two regions. The reason for this has not been fully explained. However, according to the NMR study by Lee (12), there exist three kinds of nonequivalent fluoride ion sites in the CeF_3 crystal. At 285°K, fluoride ions in only one of these are mobile whereas at 520°K fluoride ions in all kinds of fluoride ion sites are mobile; the activation energy for motion in this case being 0.13 eV. Table III summarizes the activation energies for conduction calculated from the slope of Arrhenius plot for 2.5 or 2.0 m/o doped specimens. In the high temperature range, the activation energies are low and show almost the same values independent of doped species (except Th^{4+}). This suggests that the conduction mechanism may be the same in this region irrespective of the

Table III. Activation energy for conduction in CeF_3-based fluorides

Dopant	Activation energy (eV)	
	High temperature range, >250°C	Low temperature range, <200°C
Pure	0.26 (>300°C)	0.50
CaF_2	0.25	0.37
SrF_2	0.25	0.42
BaF_2	0.24	0.28
ThF_4	0.54	0.45

At nearly equal dopant content (0.02 ~ 0.025 m/o).

doped species although the value of activation energy (about 0.25 eV) is higher than the 0.13 eV reported from the NMR study at 520°K. The activation energies in the low temperature range are higher than those in the high temperature region, and the values differ somewhat from each other, suggesting that these quantities may be related to defect interaction, for example, to the association of fluoride ion vacancies with dopant cations. In the system CeF_3-ThF_4, the concentration of fluoride ion vacancies is small according as Eq. [7]. The high activation energy for conduction in this system may be ascribed to the intrinsic (thermal) defect conduction and/or to the strong association force between the fluoride ion and the dopant cation Th^{4+} which has larger positive charge than that of the host cation Ce^{3+}. However, quantitative discussions should not be made here, since the specimens examined were not single crystals but sintered polycrystalline samples.

The small electronic conductivity in the specimens was not quantitatively studied in this work. However, estimating from the residual current in the electrolysis curves (*e.g.*, Fig. 6), the electronic conductivities were less than 10^{-3} times smaller than the ionic conductivities in all cases examined. A preliminary experiment using Wagner's polarization method showed that the electronic conductivity of $(CeF_3)_{0.95}(CaF_2)_{0.05}$ was the order of 10^{-7} Ω^{-1}-cm^{-1} at 300°C when using graphite as a blocking electrode and a mixture of graphite and carbon fluoride ($C:CF_{1.00} = 1:1$ in weight) as the counterelectrode. This result, however, had some uncertainty because the slope of the potential *vs.* logarithm of current curve deviated from the theoretical value, the reason for this is still under investigation. Negligibly small electronic conduction was also proved by the fact that the galvanic cell constructed as

$$Pb,PbF_2/(CeF_3)_{0.95}(CaF_2)_{0.05}/Bi,BiF_3$$

gave the theoretical value calculated from the free energy change of the following reaction

$$3PbF_2 + 2Bi = 2BiF_3 + 3Pb$$

The details of this experiment are to be reported elsewhere.

Finally, if attention is focused on the magnitude of the conductivity as a fluoride ion solid electrolyte, CeF_3-based sinters can be said to belong to the highest conductors together with KF-doped β-PbF_2 (13). Their conductivities are higher than those of LaF_3-based solid electrolytes as shown in Fig. 8, which compares conductivities for various fluorides (note that the longitudinal axis does not represent log σT but conductivity itself). $(CeF_3)_{0.95}(CaF_2)_{0.05}$ has the highest conductivity among the tysonite-type fluorides.

Conclusion

It has been shown that the doping of difluoride to the tysonite-type trifluoride CeF_3 makes the conductivity increase up to 5 m/o of dopants, while the doping of tetrafluoride leads it to decrease. These facts together with the experimental result of electrolysis indicate that the specimens are fluoride ion conductors resulting from easy movement of fluoride ion vacancies. Though the CeF_3-based electrolytes are stable in dry air at moderate temperature (up to at least 300°C), they change to oxides at the cathode quantitatively when they are subjected to electrolysis.

As to the fluoride ion conductivity the CeF_3-doped electrolytes are, in general, higher than the LaF_3-based ones which are the same tysonite-type fluoride as

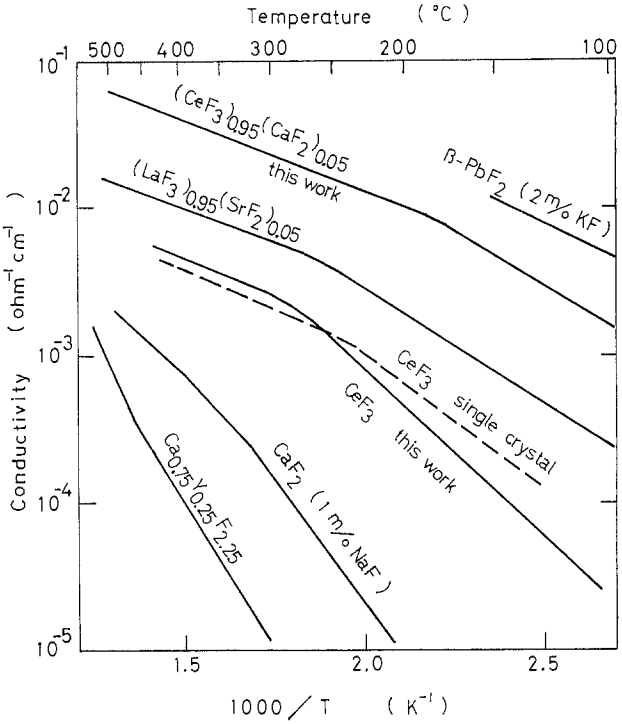


Fig. 8. Comparison of conductivities for various fluoride electrolytes [Ref. (10, 13)].

CeF_3. The highest conductivity was observed in the $(CeF_3)_{0.95}(CaF_2)_{0.05}$ sintered specimen.

Manuscript submitted July 7, 1976; revised manuscript received Oct. 5, 1976.

Any discussion of this paper will appear in a Discussion Section to be published in the December 1977 JOURNAL. All discussions for the December 1977 Discussion Section should be submitted by Aug. 1, 1977.

Publication costs of this article were assisted by Nagoya University.

REFERENCES

1. M. S. Frant and J. W. Ross, *Science*, **154**, 1553 (1966).
2. J. Hladik, Editor, "Physics of Electrolytes," chap. 14, pp. 623-677, Academic Press, New York (1972).
3. W. Baukal, Paper 19 presented at the Electrochemical Society Fall Meeting, Atlantic City, New Jersey, Oct. 4-8, 1970; W. Baukal, *Electrochim. Acta*, **19**, 687 (1974).
4. A. Sher, R. Solomon, K. Lee, and M. W. Muller, *Phys. Rev.*, **144**, 593 (1966).
5. R. Solomon, A. Sher, and M. W. Muller, *J. Appl. Phys.*, **37**, 3427 (1966).
6. W. L. Fielder, NASA Tech. Notes D-5505 (1969).
7. C. O. Tiller, A. C. Lilly, and B. C. LaRoy, *Phys. Rev. B*, **8**, 4787 (1973).
8. A. C. Lilly, B. C. LaRoy, C. O. Tiller, and B. W. Whiting, *This Journal*, **120**, 1673 (1973).
9. M. O'Keeffe, *Science*, **180**, 1276 (1973).
10. L. E. Nagel and M. O'Keeffe, "Fast Ion Transport in Solids," Solid State Batteries and Devices," W. van Gool, Editor, p. 165, North Holland Publishing Co., Amsterdam (1973).
11. R. W. Ure, *J. Chem. Phys.*, **26**, 1363 (1957).
12. K. Lee, *Solid State Commun.*, **7**, 363 (1969).
13. J. H. Kennedy and R. C. Miles, *This Journal*, **123**, 47 (1976).

Formation and Properties of Porous Silicon Film

Yoshinobu Arita and Yoshio Sunohara

Nippon Telegraph and Telephone Public Corporation,
Electrical Communication Laboratories, Musashino-shi, Tokyo, Japan

ABSTRACT

Porous silicon film (PSF) on silicon was formed by anodic reaction in 50 weight percent (w/o) hydrofluoric acid. Effects of parameters on the PSF formation rate, density, crystalline structure, and cross section structure have been studied. Current density and acceptor concentration in p-type silicon PSF formation, as well as current density, illumination light intensity, and donor concentration in n-type silicon PSF formation, were mainly found to play important roles in determining the PSF crystalline and porous structure. The surface crystalline structure in the p-type silicon PSF changes from the clean Kikuchi pattern to a broad pattern when acceptor concentration decreases. In the n-type silicon PSF, the crystalline structure tends to change from single crystal to amorphous as current density becomes smaller, donor concentration decreases, illumination light intensity becomes strong, and reaction time is longer. The cross section, in the p- and the n-type silicon PSF, is virtually dense at a very thin layer close to the surface, becoming more porous at the inner region compared with the surface. The holes injection effect on the PSF formation in n-type silicon has been investigated. It is found that PSF formation without holes injection occurs uniformly at anodic reaction after the order of 0.1 μm thick PSF is formed with holes injection. It is thought that anodic dissolution occurs at the local silicon surface under anodic conditions by which the single crystal PSF is obtained. It was found that the PSF composition consists mainly of silicon and a small amount of hydrogen, oxygen, and fluorine.

PSF was found by Uhlir (1) and Turner (2) when an electropolishing experiment was conducted below about 10% HF concentration. PSF was formed by anodic reaction in the concentrated HF. It has been shown that such films have very chemically active properties, and that the composition of such films consists mainly of silicon, fluorine, and hydrogen (2-4). No detailed investigation made on the PSF composition has been reported in previous literature (2-4).

Models of the PSF formation mechanism have been proposed by Turner (2), and subsequently by Memming and Schwandt (5). Based on these models, anodic dissolution has been suggested as occurring over the entire silicon surface in reaction to the anodic conditions under which the PSF crystalline structure becomes amorphous. Theunissen (6) reported that single crystal PSF was anodically formed in 5% HF.

No studies have been reported so far with respect to the PSF crystalline and cross section structure, the PSF nature, and the effects of anodic reaction parameters on these factors.

Recently, application to isolation of integrated circuits was investigated, using the chemically active nature of the PSF (7).

In this paper, the formation and properties are studied in detail. Initially, the relationship between the electrode potential and the current density varying with p- and n-type silicon resistivity is discussed. Effects of the anodic reaction parameters on the formaton rate, density, crystalline and cross section structure in the p- and the n-type silicon PSF, and the properties are clarified. The holes injection effect is investigated after silicon surface changes into PSF with a certain thickness. A model is proposed based on Turner's investigation (2) to account for the experimental observation that a single crystal PSF is obtained. Finally, the composition of PSF made in this work is determined.

Experimental Procedures

Wafer preparation.—Silicon wafers used for this work consisted of 0.006 Ω-cm, 7 Ω-cm p-type (boron doped), and 0.007 ohm-cm n-type (antimony doped) made by the Czochralski method. Etch pit density was less than 500 per square centimeter. Most of this study with higher specific resistivity was performed by using epitaxial silicon wafers described as follows. In the p-type case, p on p^+ epitaxial silicon was used, whose layer thickness and dopant were 20 μm and boron, respectively. Resistivity was over a wide range (6.2-0.28 Ω-cm). Substrate thickness, dopant, and resistivity were 200 μm, boron, and 0.006 Ω-cm, respectively. On the other hand, in the n-type case, n on n^+ epitaxial silicon was used whose layer thickness and dopant were 20 μm and phosphorus, respectively. Resistivity was over a wide range (5.5-0.09 Ω-cm). Substrate thickness, dopant, and resistivity were 200 μm, antimony, and 0.007 Ω-cm, respectively. Crystal orientation of all types of silicon used was on the (111) plane.

PSF formation.—The electrolytic cell for PSF formation by anodic reaction has been given in a previous paper (8). Anodic reaction was performed by xenon lamp (300 and 500W) illumination to generate holes in the n-type silicon but without illumination for the p-type silicon. Unless otherwise noted, 50 w/o HF was used. The silicon wafer was covered with acid-proof wax (Apiezon wax) to perform anodic reaction selectively in the wafer. The anode and cathode were connected to the silicon wafer and gold wire, respectively. A constant current source was used as electric power.

The ultrasonic oscillator source was used immediately to remove H_2 bubbles that evolve at a porous silicon surface under the anodic reaction. Imperfection in bubble removal under the anodic reaction causes PSF thickness nonuniformity and the PSF surface comes off locally, especially when the PSF becomes thicker.

All experiments were performed without electropolishing.

Electrode potential and current.—The potential of the silicon electrode was controlled with a potentiostat (TOA Electronics Limited PGS-70A) in conjunction with a slow linear potential sweep scanner and an X-Y plotter to record the relationship between current-potential data. The reference electrode was a saturated calomel electrode (SCE). The SCE capillary tip end was dipped in HF and positioned at one corner of the silicon wafer to perform anodic reaction.

Physical and chemical characterization.—A cross

Key words: anodic dissolution, porous silicon film, hydrofluoric acid electrolyte, hole generation center.

section obtained by lapping within a plane inclined from the PSF surface (angle lapping method) shows a clean boundary between the anodic reaction layer and the silicon substrate in the p-type silicon. Therefore, the PSF thickness was determined as that between the PSF surface and the boundary. On the other hand, the angle lapping PSF surface was etched lightly in an etchant (60 HNO_3:1HF or 20 HNO_3:1HF) to determine the PSF thickness in the high resistivity n-type silicon. The PSF density was obtained by measuring the weight difference before and after anodic reaction, and the actual volume of the PSF. The PSF thickness to be etched off in NaOH solution was measured by a Talystep instrument. SiO_2 film was chemically deposited on the PSF surface to be etched off to prevent scratches by Talystep tracing. The PSF crystalline structure was studied by reflection electron diffraction (ED) and by x-ray diffraction. Surface features of the as-grown PSF and the etched PSF surface were examined by the two-stage replication method, using an electron microscope (EM). A cross section by the angle lapping method was etched lightly in HNO_3-HF system reagent and was then examined by a scanning electron microscope (SEM). The PSF composition and atomic bonds were investigated by infrared and sparked mass spectroscopy.

Results and Discussion

Relationship between electrode potential (η) and current density (J), and reaction time (t).—Current-potential curves for two specific resistivities in the p-type silicon are presented in Fig. 1. The Tafel relationship was obtained only over a short range of minus potential (curve 2 in Fig. 1). Curve 1 increases exponentially with increasing η, and curve 2 increases slowly with increasing η in the anodic region. Illumination has no significant effect on PSF formation of the p-type silicon. On the other hand, similar curves for the n-type silicon are shown in Fig. 2 and 3. When resistivity is high in the anodic region, initial J increases with increasing η, and then J saturates with increasing η due to hole diffusion, finally increasing rapidly with increasing η. The J saturation tendency becomes obscure as resistivity decreases from about 5 to about 0.007 Ω-cm. The PSF surface comes off locally at a region where J increases sharply with increasing η. As shown in Fig. 2, this phenomenon occurs at the η indicated by the arrow. Saturation J increases with increasing illumination light intensity (I_p) and with decreasing resistivity. As observed later, PSF structure in the thickness direction changes largely due to the J value in the anodic reaction.

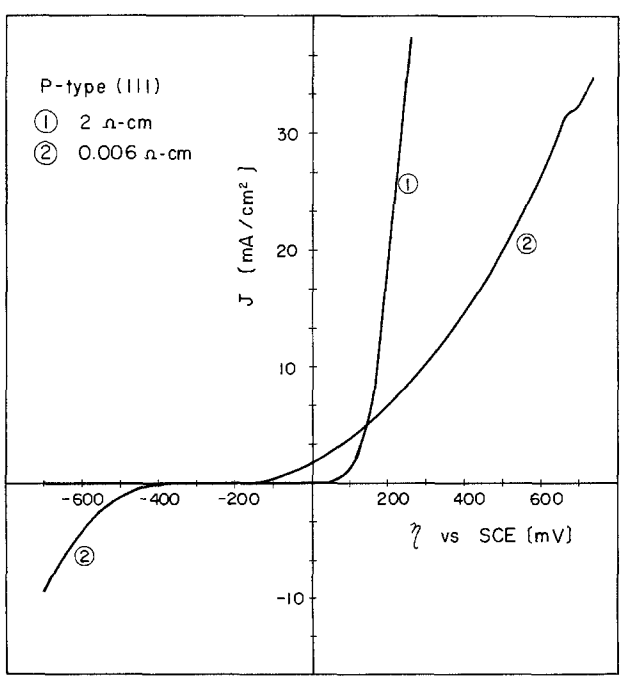


Fig. 1. Potentiostatic current potential curves of p-type silicon anodic reaction.

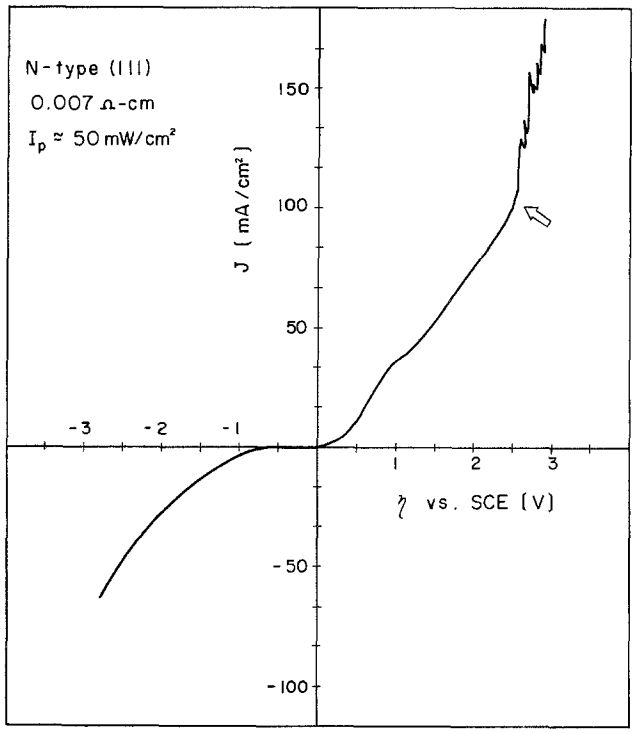


Fig. 2. Potentiostatic current potential curves of n-type silicon anodic reaction.

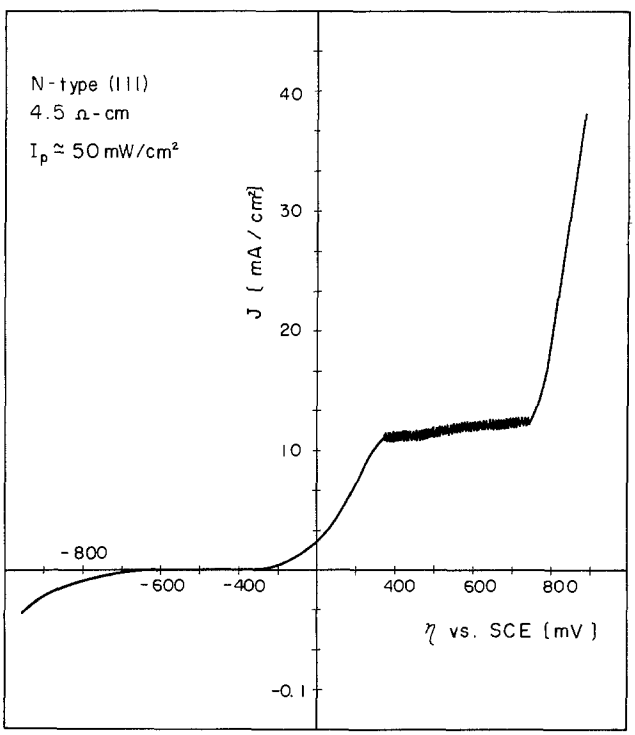


Fig. 3. Potentiostatic current potential curves of n-type silicon anodic reaction. Note that the longitudinal axis plus region scale is ten times that of the minus region scale.

Hysteresis is observed between the ascending and descending curves of η *vs.* J relationships in both the p- and the n-type silicon. It is considered that hysteresis was due to a decrease of the effective dissolution area and to a difference between the state of the silicon surface caused by anodic dissolution and the state of PSF surface at η decrease, because SiF_4, free

Si, and H_2 produced by anodic dissolution remain in the PSF. Consequently, H_2 gas evolution during anodic dissolution is one of the reasons for this phenomenon. J decreases compared with an earlier J to the same η, when cyclic measurement of the η *vs.* J curve is effected. This decrease tendency of J becomes marked with the increasing resistivity of silicon.

The relationship between η and t in anodic reaction of the p-type silicon is shown in Fig. 4. η of silicon is about -0.2V when immersed in HF solution for a long time. At the start of anodic reaction, η increases rapidly and then decreases to a steady-state value.

PSF thickness (T_h)-reaction time (t) relationships and surface color.—T_h (determined from the angle lapping methods) increases with increasing t (see Fig. 5). The slope increases with increasing J. This linear relationship is not established as the t becomes still longer (7) and T_h is proportional to the square root of t at the first approximation. The shift from linear relationship is dependent on the anodic conditions.

Repetitive interference colors can be observed earlier in the PSF formation. The visual surface color of PSF of high resistivity, p-type silicon is a deeper black compared with that of the low resistivity, p-type silicon, and repetitive interference colors cannot be observed when T_h becomes the thickness. On the other hand, the anodic reaction for PSF of high resistivity, n-type silicon remains as a certain interference color, even when T_h becomes more than several microns thick. This result seems to be due to the PSF refraction index difference between a layer near the PSF surface and the inner region. The surface color of the lower resistivity, n-type silicon PSF is found to be similar to that of the p-type silicon PSF.

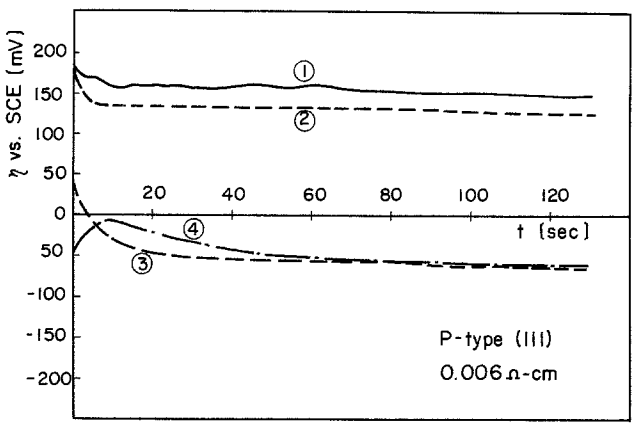


Fig. 4. Electrode potential *vs.* reaction time curves for p-type silicon. ① $J = 10$ mA/cm², ② $J = 5$ mA/cm², ③ $J = 0.4$ mA/cm², ④ $J = 0.04$ mA/cm².

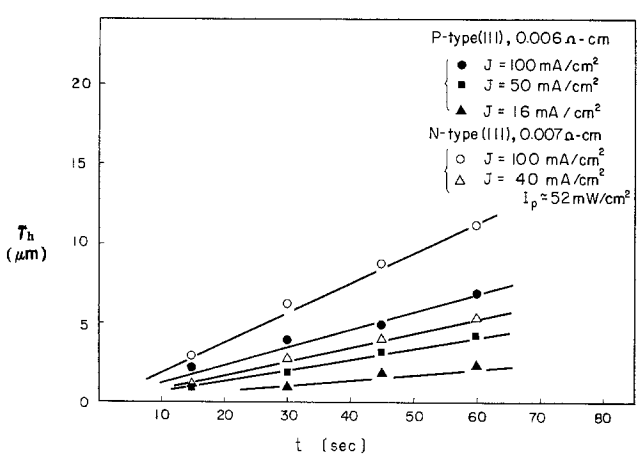


Fig. 5. PSF thickness (T_h) and anodic reaction time (t) relationship.

A convex surface is observed visually, immediately after anodic reaction, when the PSF becomes about 100 μm thick. Radius of the PSF curvature decreases with increasing T_h and with increasing time kept in the air. It is thought that a convex surface is apparently caused by oxidation of the PSF.

Formation rate.—Effects of HF concentration (n_{HF}) and of HF temperature (T) on the formation rate was determined within a range where T_h is proportional to t. It is evident that the formation rate increases linearly with increasing HF concentration. Increasing J on the anodic reaction results in a rapid increase in the formation rate (f_{nHF}) on n_{HF}. When J is small, n_{HF} seems to have little influence on f_{nHF}. A little electropolishing was observed in Fig. 6 when n_{HF} is 15% HF at 100 mA/cm² and 5% HF at 30 mA/cm². In general, the critical current density which electropolishing caused increases with the increasing n_{HF} (see Fig. 6).

The formation rate does not change very greatly with increasing T over a range of from 5° to 65°C (see Fig. 7). The HF temperature seems to have little influence on the formation rate.

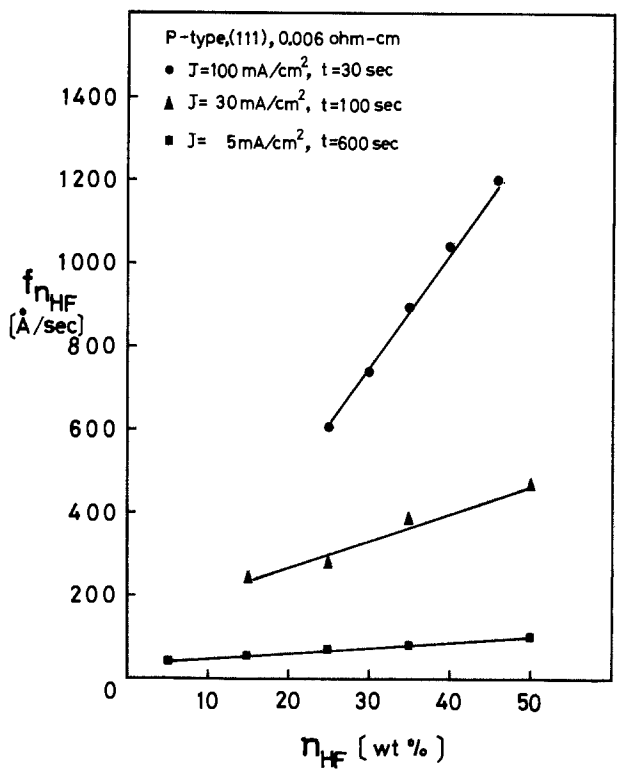


Fig 6. HF concentration (n_{HF}) effect on the PSF formation rate

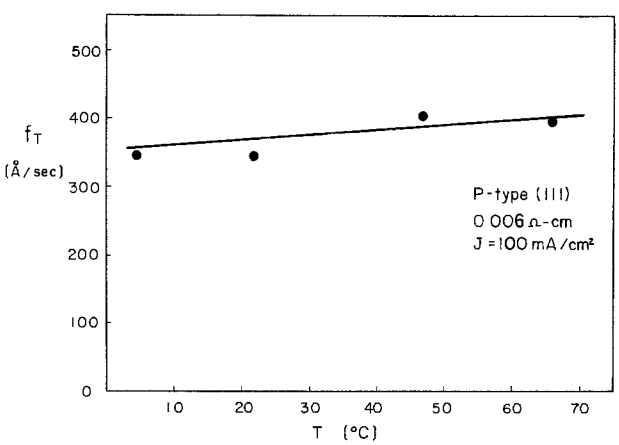


Fig. 7. HF temperature (T) effect on the PSF formation rate

Dependence of the formation rate upon J is shown in Fig. 8 over the 20-100 mA/cm² range for the p- and the n-type silicon PSF. Increasing J results in a linear increase of the rate for the p-type silicon PSF. For the n-type silicon PSF, the rapid initial formation rate is followed by a slower increase with J. The formation rate increases slowly with increasing J, when I_p becomes weaker. It should be noted that the formation rate decreases with increasing I_p below about $J \simeq 40$ mA/cm², and increases with increasing I_p above about $J = 40$ mA/cm². The PSF surface crystalline structure tends to become amorphous below about 40 mA/cm² with increasing I_p. On the other hand, the PSF surface crystalline structure becomes a single crystal structure above about 40 mA/cm² with increasing I_p.

The formation rate as a function of I_p, at 30 and 150 mA/cm², is shown in Fig. 9. The results reveal two characteristics: (*i*) the formation rate decreases slowly with increasing I_p at 30 mA/cm²; (*ii*) on the other hand, the initial formation rate increases rapidly with increasing I_p, and will not increase further even if I_p increases at 150 mA/cm². From the study of relation between η and J, η decreases with the increasing I_p at 30 mA/cm², but a little η decrease occurs when I_p increases at 150 mA/cm²; thus the η decrease corresponds to a decrease of the PSF formation rate. The results shown in Fig. 9 may account for the above-mentioned fact.

Variation in the formation rate with dopant concentration (N_A, N_D) at 30 and 150 mA/cm² is shown in Fig. 10. That of the p-type silicon PSF increases with increasing N_A; *i.e.*, hole concentration. On the other hand, there is a significant difference in the profile of curves for the n-type silicon PSF, whose maximum is between 10^{16} and 10^{17} cm^{-3} in donor concentration, compared with that of the p-type silicon PSF. A sharp curve with the maximum is observed with the increasing J, and a curve with the maximum becomes broad with decreasing J.

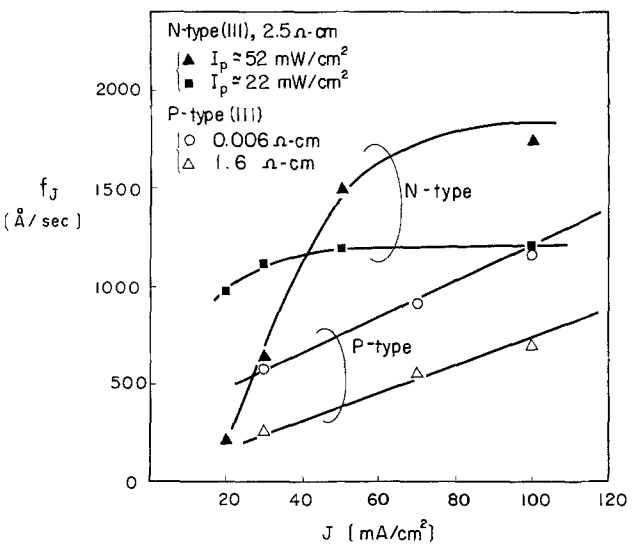


Fig. 8. Current density (J) effect on the PSF formation rate

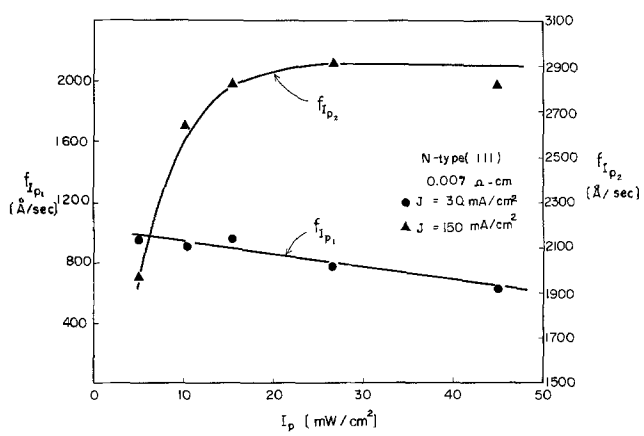


Fig. 9. Illumination light intensity (I_p) effect on the PSF formation rate.

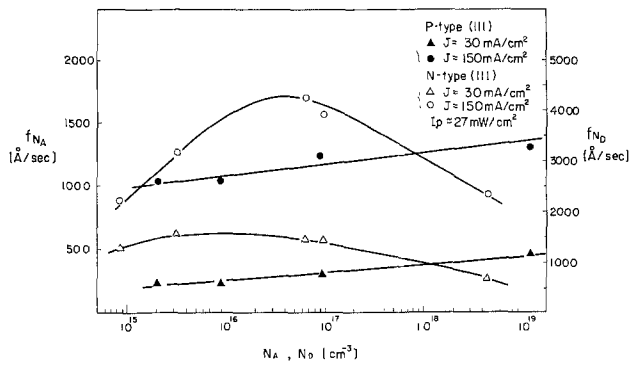


Fig. 10. Acceptor concentration (N_A) and donor concentration (N_D) effects on the PSF formation rate.

Illumination interception effects.—Supplying holes is necessary for PSF formation of the n-type silicon. The illumination interception effect on T_h is shown in Fig. 11. Q is a charge flowing through a cell. When the over-all anodic reaction is performed with illumination, T_h increases linearly with increasing Q. When the first anodic reaction was carried out under the conditions of $J = 100$ mA/cm², $Q = 0.2$ C/cm², $I_p = 50$ mW/cm² and the second anodic reaction was performed under the conditions of $J = 100$ mA/cm², $I_p = 0$, it was found that PSF was formed. This result was observed in spite of n-type silicon resistivity. Theunissen reports that a brownish black, pitted surface was formed in 5% HF for impurity concentrations between 2×10^{18} and 2×10^{16} cm^{-3}, and in the range below about 2×10^{16} cm^{-3} no measurable dissolution occurred and no channels were detected (6). When donor concentration and the depletion layer voltage are 10^{15} cm^{-3} and 10V, respectively, the calculated maximum electric field is lower than the value of the breakdown field. When PSF is formed below 10V in 50% HF for a specimen of donor concentration 10^{15} cm^{-3} without

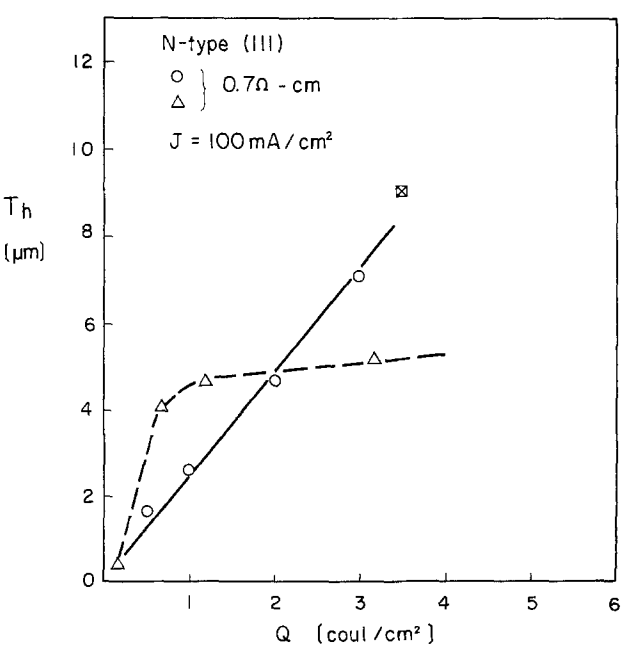


Fig. 11. I_p effect on T_h: ○ illumination during the entire anodic reaction, △ two-step reactions.

illumination, an etch channel is locally formed in the wafer. However, PSF is uniformly formed in the wafer without illumination after the thin silicon surface layer changes to PSF with illumination. From these results, the anodic reaction in high resistivity, n-type silicon is considered as follows. Assuming that hole generation centers are produced at the boundary between the silicon substrate and the PSF formed by first reaction with illumination, second anodic reaction proceeds uniformly and self-catalytically due to hole generation at the boundary without illumination.

Symbol ⊠ in Fig. 11 shows T_h formed by the following process through two step reactions. Initially, anodic reaction is effected at $J = 100$ mA/cm^2, $Q = 0.5$ C/cm^2, $I_p = 50$ mW/cm^2 and secondary at $J = 100$ mA/cm^2, $Q = 3$ C/cm^2 without illumination. These results indicate that T_h increases in the second reaction, compared with a small Q in the first reaction, when Q in the first anodic reaction becomes larger. Figure 12 shows photographs of a cross section of the sample described above. The cross section surface is etched off in 20 HNO_3:1HF for about 2 sec. Figure 12, a and b, indicates samples made by first and second anodic reaction, respectively. It was found that the PSF formation without holes injection occurs after PSF of an order of about 0.1 μm thickness is formed with holes injection, in spite of the n-type silicon resistivity.

Weight loss (ΔW) and PSF density (ρ_{por}).—The amount of silicon dissolution into HF was measured by ΔW before and after anodic reaction. N_A and N_D dependence on ΔW are shown in Fig. 13. Experimental run time is about 10 min. Regarding the p-type silicon, ΔW is nearly constant below about 10^{16} cm^{-3} in N_A and becomes smaller above 10^{16} cm^{-3}. On the other hand, regarding the n-type silicon, ΔW has a minimum at approximately 10^{16} cm^{-3} in N_D. The fact that as-grown PSF had a very active property made it difficult to obtain data that had little scatter. However, it was possible to obtain data that had no scatter by maintaining the process between before ΔW measurement and after PSF formation. The relation between PSF density and dopant concentration is obtained by using the curves in Fig. 13. This result is shown in Fig. 14. ρ_{por} of the p-type silicon with increasing N_A remains constant up to about 10^{16} cm^{-3}; then it increases rapidly. At $J = 150$ mA/cm^2, the relation between ρ_{por} and N_A is nearly the same as that at $J = 30$ mA/cm^2, but only the ρ_{por} value decreases. In the n-type silicon, ρ_{por} up to about 10^{16} cm^{-3} increases with increasing N_D, reaches a maximum, and then decreases. ρ_{por}, at $J = 30$ mA/cm^2, does not decrease markedly below about 10^{16} cm^{-3} in N_D compared with that at $J = 150$ mA/cm^2. ρ_{por} is determined by the amount of the local anodic dissolution point, the amount of dissolution silicon at the same point, and pore distribution in the thickness direction. It was noted that curves of ρ_{por} *vs.* dopant concentration are found to be similar to the formation rate *vs.* dopant concentration curves (see

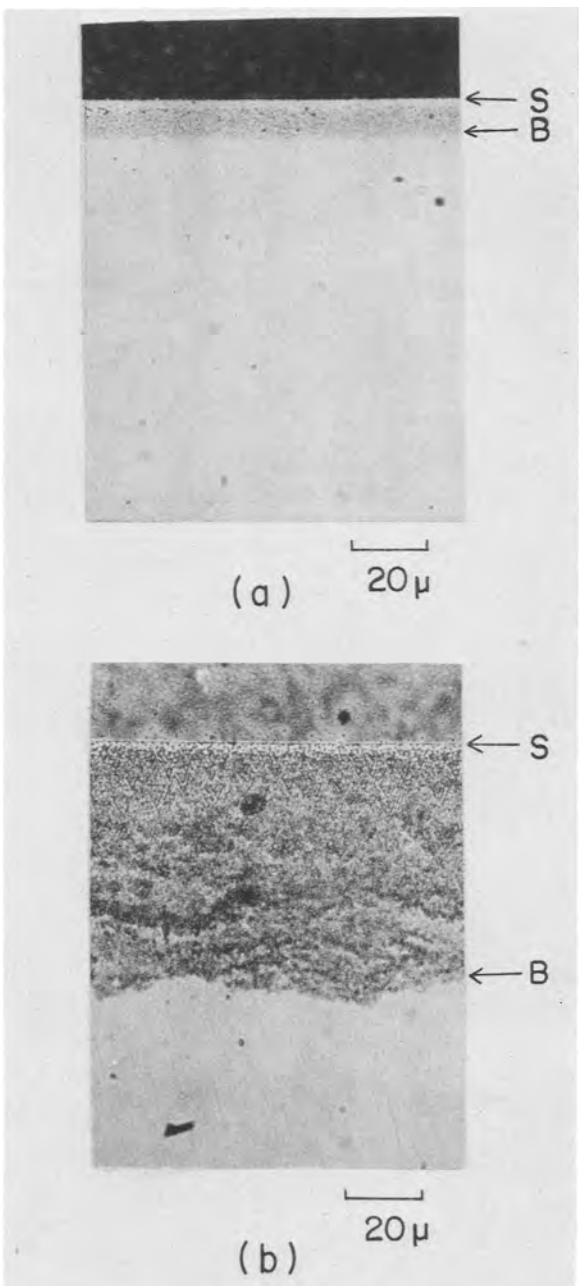


Fig. 12. PSF cross section: S is the PSF surface, B is the boundary between PSF and the silicon substrate.

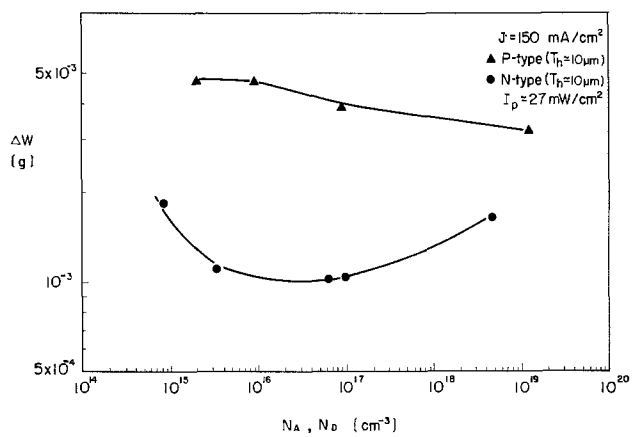


Fig. 13. Relationship of weight loss before and after anodic reaction and dopant concentration. The formation area was 3 cm^2.

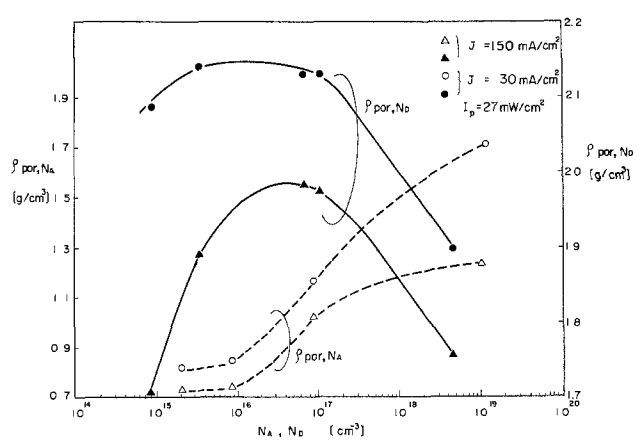


Fig. 14. Dopant concentration effect on the PSF density

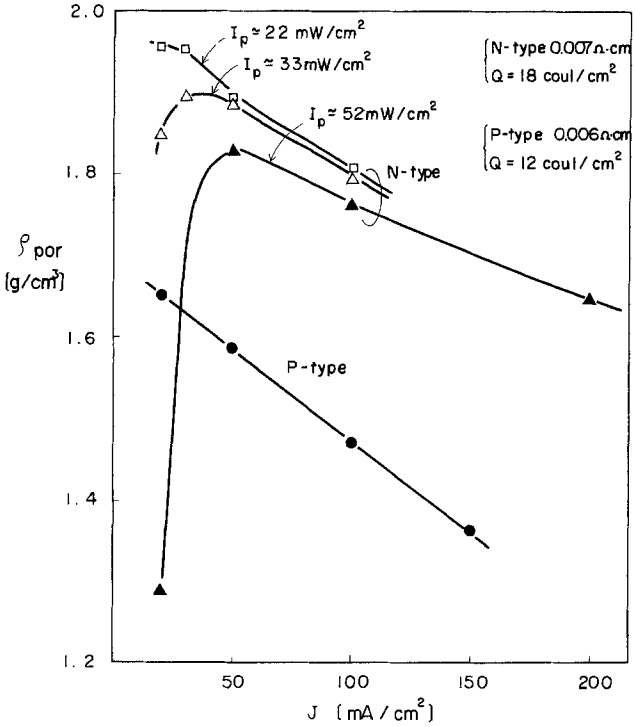


Fig. 15. J effect on the PSF density

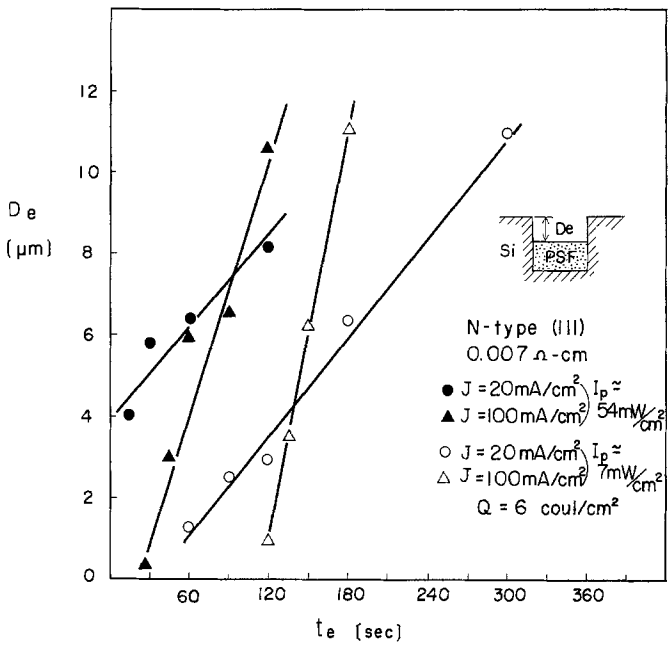


Fig. 16. Relationship of thickness (D_e) to be etched off in 20% NaOH solution (at 22°C) and etching time (t_e).

Fig. 10). It is considered that there is a certain correlation between the formation rate and ρ_{por}. Note that ρ_{por} of the p-type silicon changes markedly with N_A in comparison with that of the n-type silicon with N_D.

ρ_{por} of the p- and the n-type silicon, as a function of J, is shown in Fig. 15. That of the p-type silicon decreases linearly with increasing J. On the other hand, that of the n-type silicon first increases with increasing J against strong I_p, reaches a maximum, and then decreases. At I_p = 52 mW/cm², electropolishing begins to occur below about 20 mA/cm². At weak I_p (22 mW/cm²), the density peak is not reached and ρ_{por} decreases with increasing J. The reason that the ρ_{por} maximum appears seems to be due to the fact that, as will be revealed later from the PSF cross section structure, the average diameter of the void increases with decreasing J and the amount of the effective void increases with increasing J.

PSF structure examination in the thickness direction by chemical etching.—The relation between the PSF thickness (D_e) to be etched off in 20% NaOH solution at 22°C and the etching time (t_e) is shown in Fig. 16. D_e increases abruptly with increasing t_e for PSF formed at a strong I_p and a small J. D_e increases with increasing I_p for the same J and with increasing J for the same I_p. Surface structure of PSF formed at a strong I_p and a small J seems to be rough, while that of PSF formed at a weak I_p and a large J seems to be dense. From these results, it is revealed that variation of the PSF structure in the thickness direction is strongly dependent on I_p and J magnitude. On the other hand, the etching rate of single crystal silicon, for the same etchant as described above, is nearly zero. The reason that the PSF etching rate is very high is considered to be that PSF has a large surface area, weak bonding of silicon at the residual single crystal silicon surface, and various crystal orientations due to the porous structure.

PSF crystalline and cross section structure.—A reflection ED pattern, an EM photograph of as-grown PSF, a SEM photograph of a PSF cross section etched off in 60 HNO_3:1HF for 5 sec, and a PSF cross section photomicrograph are shown in Fig. 17a, b, c, and d, respectively. The p-type silicon resistivity used was 0.006 Ω-cm. Anodic reaction was performed under the conditions of J = 150 mA/cm², t = 60 sec. The ED

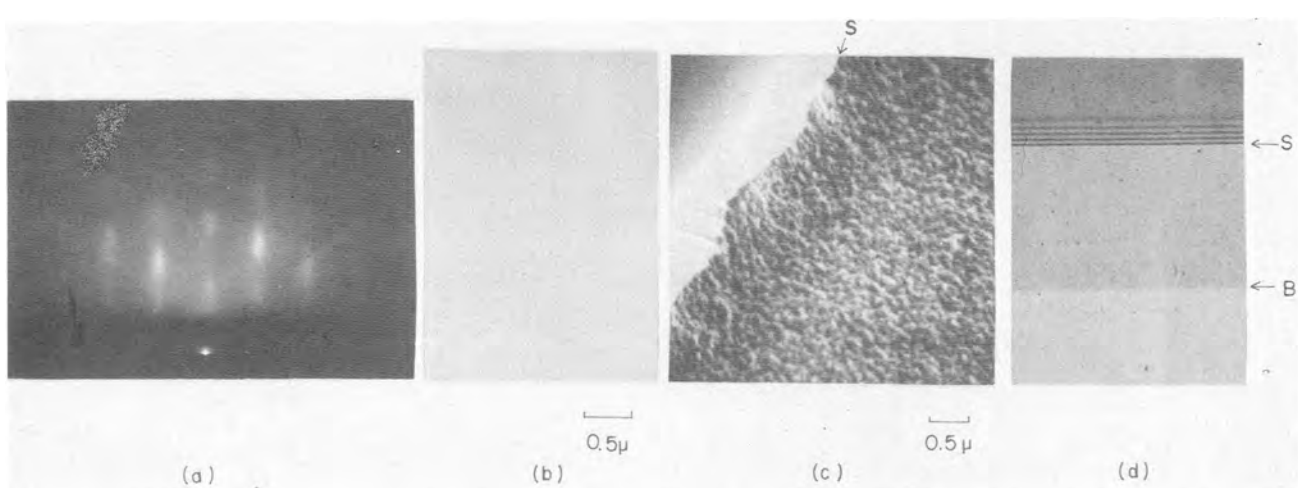


Fig. 17. Crystalline and cross section structure of the low resistivity, p-type silicon PSF: (a) ED pattern, (b) EM photograph, (c) SEM photograph, (d) photomicrograph.

pattern shows a weak halo pattern superimposed on the Kukuchi pattern. This halo pattern becomes stronger with increasing air drying time at room temperature. The surface feature is visually quite smooth and mirror surfaced. A very thin layer close to the PSF surface is dense and the inner region is rough. The boundary between PSF and the silicon substrate is clear.

The crystalline structure and feature in the thickness direction are shown in Fig. 18, A-E. The silicon used is the same as that shown in Fig. 17. Anodic reaction was performed under the conditions of $J = 100$ mA/cm^2, $t = 60$ sec. Figures 18a and b are an ED pattern and an EM photograph, respectively. Figure 18A is rinsed in 50% HF after air drying at room temperature for several hours. Figures 18B, C, D, and E are etched off in 60 HNO_3:1HF for 2, 3, 10, and 60 sec, respectively. In Fig. 18A, the crystalline structure is a single crystal and the surface feature is very smooth, but it is evident that many pits appear. Average diameter of the pits is approximately several hundred angstroms. The amount of pits increases with increasing air-drying time at room temperature. An evolution of many bubbles on the PSF surface was observed during rinsing in 50% HF. The location of bubble evolution seems to coincide with the PSF surface pits. These pits cannot be observed when as-grown PSF is rinsed in 50% HF for several hours after the anodic reaction, and also when they are immersed in H_2O for several days after the anodic reaction. The reason that many bubbles evolved locally at the PSF surface seems to be that amorphous silicon or SiF_2 (which formed locally during the anodic reaction) is oxidized, and finally H_2 gas evolved when the oxide dissolves in the HF. These considerations lead to the following two possible reactions

$$2SiF_2 + O_2 = SiO_2 + SiF_4 \quad [1]$$

or

$$\underset{\text{(amorphous)}}{Si} + O_2 = SiO_2 \quad [2]$$

From Fig. 18B, C, D, and E it is shown that the ED pattern, with increasing etching time, changes from the single crystal pattern to a polycrystal pattern of silicon superimposed on a mosaic pattern. Next, a study was made as to whether the polycrystal silicon ring pattern is due to intrinsic PSF structure or the appearance of an extrinsic effect caused by the chemical etching treatment. As will be seen later herein, PSF crystalline structure in the thickness direction obtained by x-ray diffraction is the single crystal. Thus, it seems that this ring pattern is due to the extrinsic effect. The etched surface pit changes from random distribution to distribution along a grainlike boundary with increased etching time. The PSF crystalline structure formed under the condition of $J = 1$ mA/cm^2 is nearly the same as that of $J = 100$ mA/cm^2.

X-ray diffraction of PSF about 100 μm thick is shown in Fig. 19. It is revealed that PSF has a single crystal structure. Consequently, this result indicates that anodic reaction by Turner's model (2) occurs at local points on an atomic scale, leaving the crystal orientation.

An ED pattern, an EM photograph of the as-grown PSF surface, an SEM photograph of a PSF cross section, and a PSF cross section photomicrograph are shown in Fig. 20a, b, b*, c, c*, and d, respectively. The p-type silicon resistivity used was 1.5 Ω-cm. Anodic reaction was performed under the conditions of $J = 100$ mA/cm^2, $t = 60$ sec for Fig. 20a, b, b*, c, d, and of $J = 30$ mA/cm^2, $t = 360$ sec for Fig. 20c*. b* and c, c* in Fig. 20 were etched off in 5% NaOH solution for 3 sec and in 60 HNO_3:1HF for 5 sec, respectively. The ED pattern becomes broad, compared with that of Fig. 17. Distortion of the PSF surface crystalline structure occurs when the p-type silicon resistivity becomes higher as anodic reaction is performed under the same condition. The PSF crystalline structure, in the inner region, is a mosaic pattern. The surface feature is nearly the same as that of Fig. 17 (see b in Fig. 20). Grainlike boundaries are observed on the PSF surface

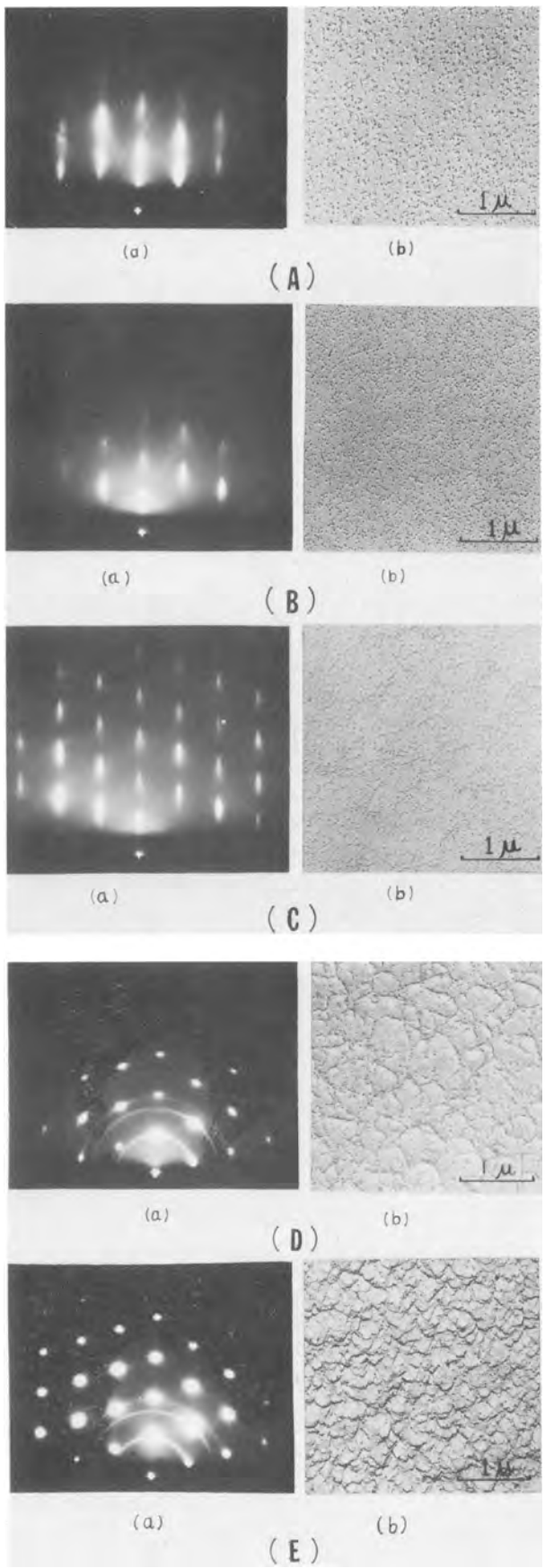


Fig. 18. Variation of crystalline structure and feature in the PSF thickness direction.

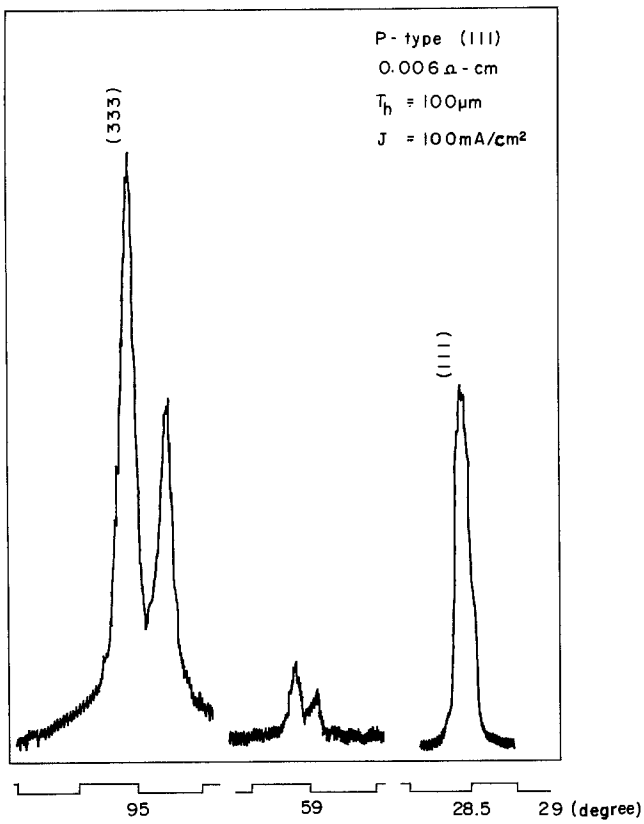
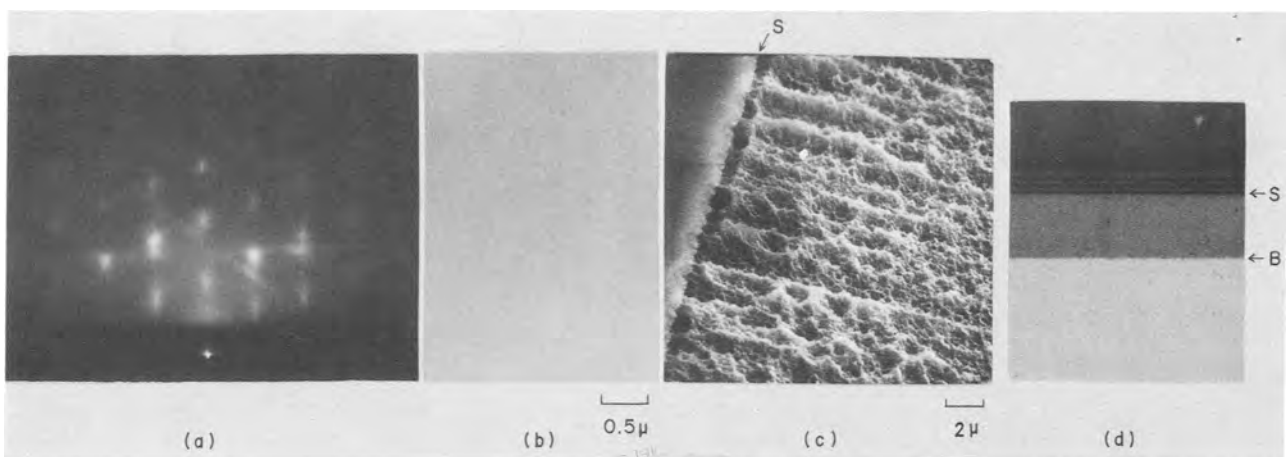


Fig. 19. (111) oriented p-type silicon PSF x-ray diffraction spectrum.

etched off (see b* in Fig. 20). The PSF cross section, except for the PSF surface, becomes rough structured with increasing J, compared with c and c* in Fig 20, and also with decreasing N_A. The PSF surface is virtually dense, as well as that in Fig. 17. As is evident from Fig. 20d, there is a small irregularity of the boundary line between PSF and the silicon substrate compared with that of 0.006 Ω-cm resistivity. It seems that this irregularity correlates with the distribution of acceptor atoms. The visual color of the PSF cross section is a deeper black, the same color as the PSF surface.

An ED pattern, an EM photograph of the as-grown PSF surface, an SEM photograph of the angle lapping surface to be etched off in 60 HNO_3:1HF for 5 sec, and a cross section photomicrograph are shown in Fig. 21a, b, c, and d, respectively. The n-type silicon resistivity used was 0.007 Ω-cm. Anodic reaction was performed under the conditions of $J = 100$ mA/cm², $t =$ 60 sec, $I_p = 54$ mW/cm². The crystalline structure of the as-grown PSF is single crystal, having a mosaic pattern over the inner region, as well as that of Fig. 18 (5). The PSF cross section structure is dense at the surface and rough in the inner region, and is similar to that formed by high N_A silicon.

An ED pattern, an EM photograph of the as-grown PSF surface, an SEM photograph of the angle lapping surface to be etched off in 60 HNO_3:1HF for 5 sec, and a cross section photomicrograph are shown in Fig. 22a, b, c, c*, and d, d*, respectively. Layer resistivity of the n-type epitaxial silicon used was 0.6 Ω-cm. Anodic reaction was performed under the conditions of $J = 100$ mA/cm², $t = 60$ sec, $I = 54$ mW/cm² for Fig. 22a, b, c, d, d*, and of $J = 30$ mA/cm², $t = 50$ sec, $I_p = 27$ mW/cm² for Fig. 22c*. d* in Fig. 22 was etched off in 60 HNO_3:1HF for 5 sec. The ED pattern indicates a weak halo pattern superimposed on the Kikuchi pattern at the PSF surface and the mosaic pattern in the inner region. The feature of the as-grown PSF surface is very smooth, although local pits are evident. The PSF cross section structure is virtually dense at the surface and rough in the inner region. Local voids of large diameter are observed at $J = 30$ mA/cm². No boundary can be observed between PSF and the silicon substrate



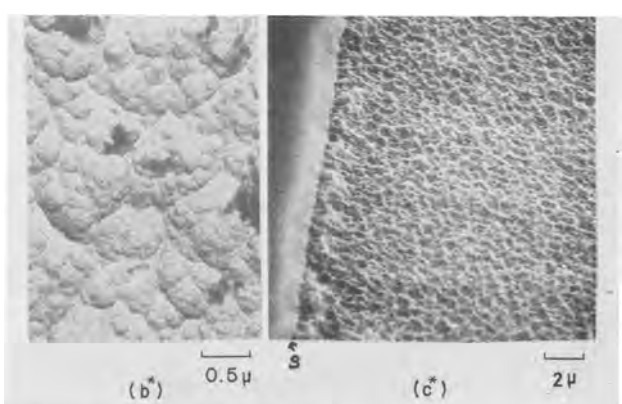


Fig. 20. Crystalline and cross section structure of the high resistivity p-type silicon PSF: (a) ED pattern, (b), (b*) EM photographs, (c), (c*) SEM photographs, (d) photomicrograph.

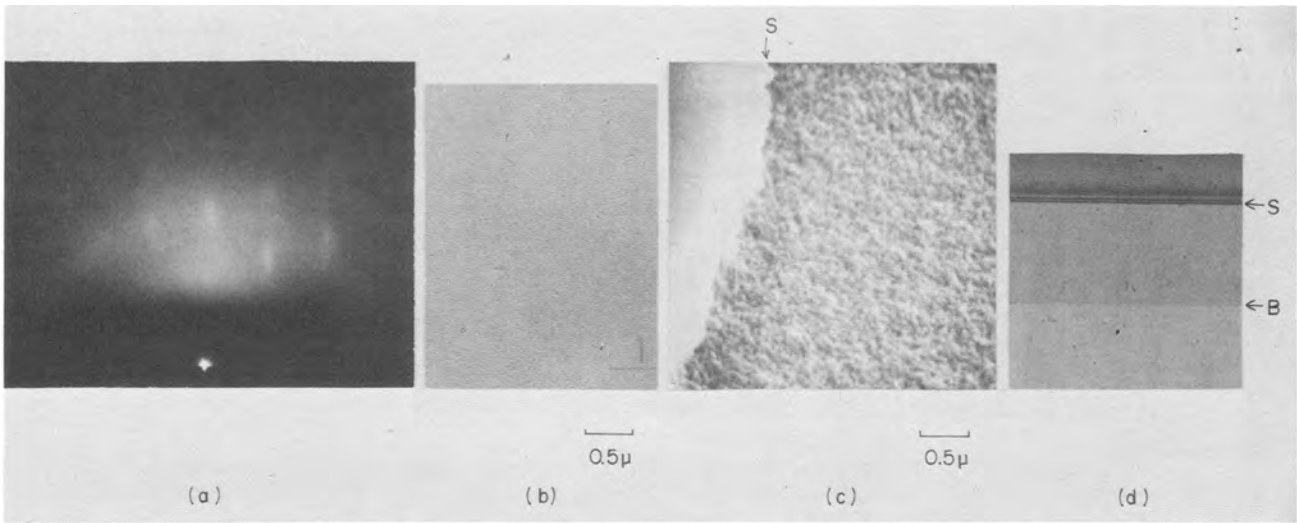


Fig. 21. Crystalline and cross section structure of the low resistivity, n-type silicon PSF: (a) ED pattern, (b) EM photograph, (c) SEM photograph, (d) photomicograph.

(see Fig. 22d). This result is caused by the fact that the PSF density is close to that of the silicon. A porous silicon layer becomes clearly observable by etching the angle lapping surface (see Fig. 22d*).

From the above results, the PSF surface crystalline structure change is investigated, while varying the main anodic reaction parameters (N_D, I_p, J, t). When N_D becomes lower and I_p becomes stronger, and when

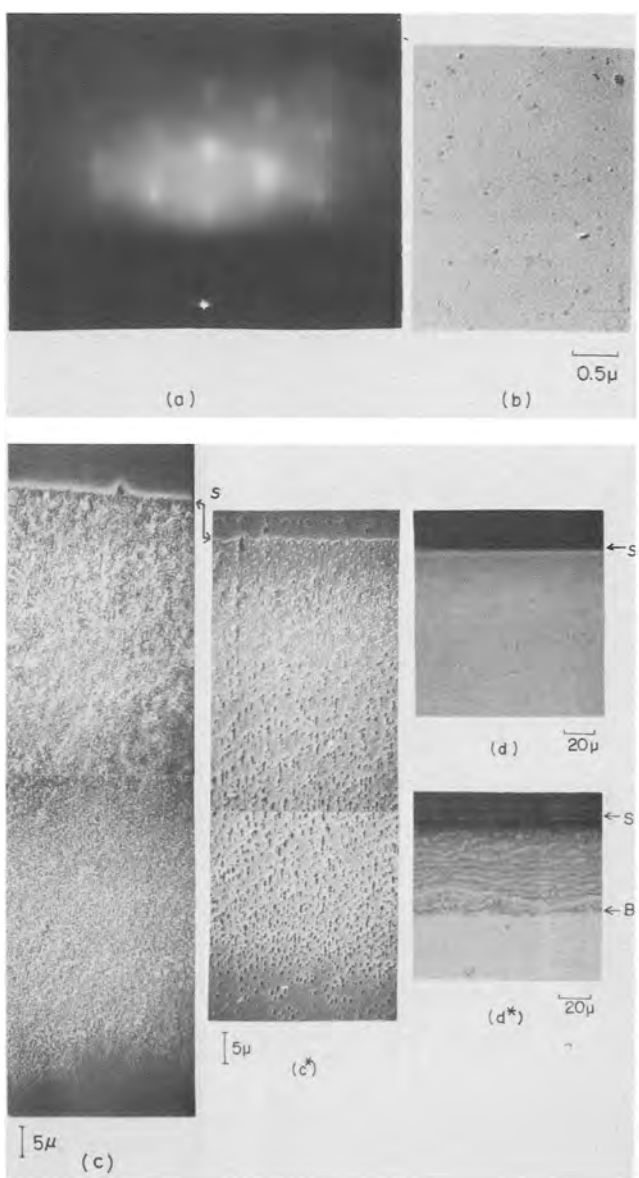


Fig. 22. Crystalline and cross section structure of the high resistivity, n-type silicon PSF: (a) ED pattern, (b) EM photograph, (c), (c*) SEM photographs, (d), (d*) photomicrographs.

J becomes smaller and t becomes longer, the ED pattern of the PSF crystalline structure changes from the Kikuchi pattern to a very weak broad silicon pattern superimposed on a halo pattern, and finally to a halo pattern, and electropolishing begins to appear. This halo pattern seems to be caused by PSF surface oxidation in air drying and amorphous silicon formed under the anodic reaction. The crystalline structure is a mosaic pattern in the PSF inner region, even when it is amorphous at the PSF surface. The relation between the crystalline structure of the PSF surface and the anodic reaction parameters (N_D, I_p, J, t) is qualitatively unified in Fig. 23. The boundary between the single crystal and the amorphous region has a broad line. The amorphous region enlarges when t becomes longer and N_D decreases.

Effects of Ip and J on the PSF cross section structure are shown in Fig. 24. The layer resistivity of the n-type epitaxial silicon used was 2.5 Ω-cm. Figures 24a, b, c, d, and e are photomicrographs of a PSF cross section. Figures 24b* and c* are SEM photographs of cross sections shown in Fig 24b and c, respectively. Anodic

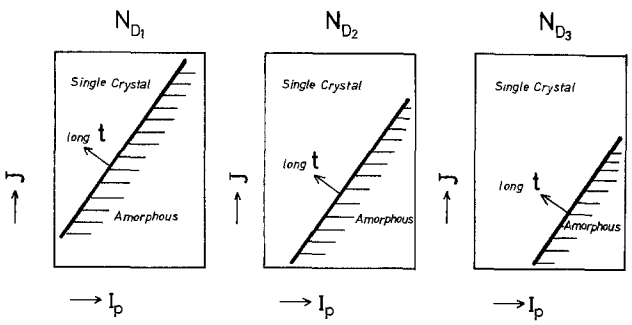


Fig. 23. Illustration of anodic conditions dependence on the n-type silicon PSF surface crystalline structure. Where, $N_{D_1} < N_{D_2} < N_{D_3}$.

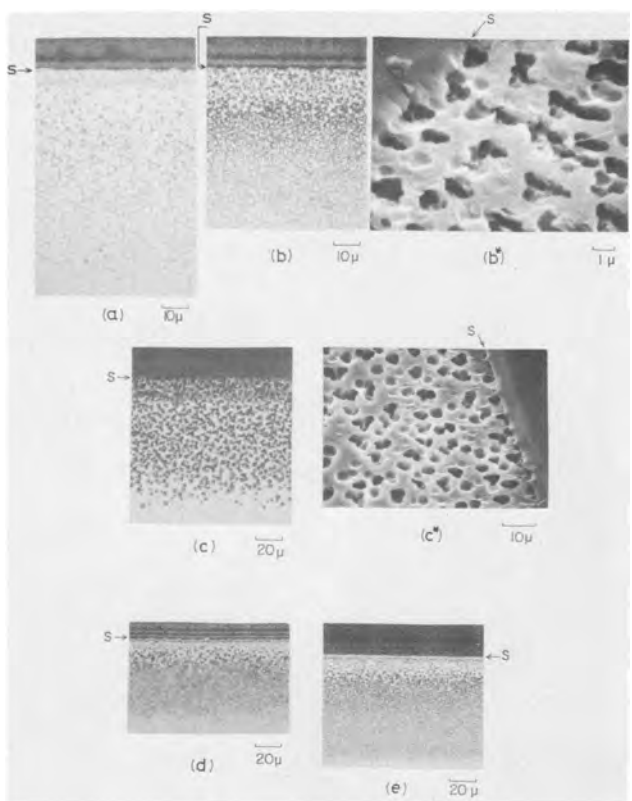


Fig. 24. I_p and J effects on PSF cross section structure with n-type silicon 2.5 Ω-cm resistivity: (a), (b), (c), (d), and (e) are photomicrographs; (b*) and (c*) are SEM photographs.

reaction conditions of Fig. 24a, b, c, d, and e were $J = 30$ mA/cm², $I_p = 7$ mW/cm², $t = 120$ sec; $J = 30$ mA/cm², $I_p = 27$ mW/cm², $t = 120$ sec; $J = 30$ mA/cm², $I_p = 54$ mW/cm², $t = 120$ sec; $J = 150$ mA/cm², $I_p = 7$ mW/cm², $t = 30$ sec; and $J = 150$ mA/cm², $I_p = 27$ mW/cm², $t_p = 30$ sec, respectively. All PSF cross sections were etched in 60 HNO_3:1HF for 5 sec. The cross section feature indicates that the region close to the PSF surface is dense compared with the inner region of PSF. Many voids appear clearly along the (100) direction by etching when the n-type silicon resistivity becomes higher. When I_p increases, the voids in the layer close to the PSF surface tend to increase and the effective diameter of the voids increases. On the other hand, when J increases, the amount of voids in PSF increases.

Anodic dissolution points seem strongly dependent on the dopant atom position. At a lower dopant concentration, it is considered that local dissolution occurs, compared with the anodic dissolution of silicon with a high dopant concentration.

PSF atomic bonds and composition (8).—A typical infrared absorption spectrum from as-grown PSF reveals that the atomic bonds in PSF are Si-H, Si-Si, and Si-O. The characteristic infrared absorption peak of as-grown PSF is unstable Si-Si bonds at approximately 16 μm.

The existence of a few percent of fluorine atoms in as-grown PSF was confirmed by sparked mass spectroscopy, although the existence of those atoms was not confirmed by infrared absorption spectroscopy. The same result was obtained for both the p- and the n-type silicon PSF.

Summary

1. When t is short, T_h is nearly proportional to t. This linearity shifts when t becomes longer.

2. In the p-type silicon with high resistivity, J increases exponentially with increasing η. J, however, increases slowly with increasing η when the resistivity is very low. In the n-type silicon with high resistivity, first J increases with increasing η, saturates, and finally increases rapidly. The PSF structure varies largely in each region. As for the n-type silicon with low resistivity, current saturation becomes obscure.

3. The formation rate is strongly dependent on J, N_A, and η_{HF} in the p-type silicon PSF, and increases with increasing J, N_A, and η_{HF}. In the n-type silicon PSF, the formation rate is strongly dependent on N_D, J, I_p, and η_{HF}. It has a maximum at about 10^{16} cm^{-3} in N_D. The rate initially increases rapidly with increasing J and is then nearly saturated. It increases with increasing I_p at a large J and decreases with increasing I_p at a small J.

4. ρ_{por} of p-type silicon PSF increases with an increasing N_A and decreases linearly with increasing J. ρ_{por} of the n-type silicon PSF has a maximum at about 10^{16} cm^{-3} in N_D. ρ_{por} has a maximum at about 50 mA/cm² in J when I_p becomes stronger. When I_p becomes weaker, no ρ_{por} maximum appears and ρ_{por} decreases with increasing J. ρ_{por} decreases with increasing I_p. The degree of density variation with dopant concentration of the p-type silicon PSF is larger than that of the n-type silicon.

5. Electropolishing under illumination was observed in the n-type silicon PSF when anodic reaction was effected under conditions of a very small J and a strong I_p.

6. When the silicon surface order of 0.1 μm thickness changes to PSF under hole injection, PSF formation continues without hole injection, in spite of resistivity in the n-type silicon.

7. PSF is very rapidly etched by alkali solution etchant at room temperature.

8. Crystalline structure of the p-type silicon PSF surface is single crystal and the PSF inner region has a mosaic pattern. The single crystal pattern is de-

formed when N_A is lower. That of the n-type silicon PSF surface varies from a single crystal pattern to amorphous according to the anodic conditions (N_D, I_p, J, t). The crystalline structure of the PSF inner region indicates a mosaic pattern even when that of the PSF surface is amorphous.

9. The cross section structure of the p-type silicon PSF is nearly uniform, except for a very thin layer close to the surface, and the surface layer is dense compared with an inner region. That of the n-type silicon PSF is strongly dependent on N_D, J, and I_p. The structure difference between the PSF surface layer and an inner region is remarkable when N_D is lower, I_p is strong, and J becomes lower. The PSF surface layer is dense and an inner region is rough.

10. Anodic dissolution occurs at local points of the silicon surface under the anodic condition by which the single crystal PSF is obtained. The PSF formation model proposed by Turner (2) is applicable under the anodic condition by which anodic dissolution occurs at local points.

11. It is revealed that the PSF composition mainly consists of silicon, with a very small amount of fluorine, hydrogen, and oxygen.

Acknowledgments

We thank Dr. H. Toyoda for kindly providing encouragement during the course of this work. We also thank Dr. K. Ono for his helpful suggestions on electron diffraction analysis. We gratefully acknowledge the contribution of S. Hirota, who made observation by electron microscope and by reflection electron diffraction. Further, we appreciate the helpful comments on PSF formation made earlier in this work by Y. Watanabe and Y. Igarashi.

Manuscript received July 7, 1976.

Any discussion of this paper will appear in a Discussion Section to be published in the December 1977 JOURNAL. All discussions for the December 1977 Discussion Section should be submitted by Aug. 1, 1977.

Publication costs of this article were assisted by the Nippon Telegraph and Telephone Public Corporation.

REFERENCES

1. A. Uhlir, *Bell Syst. Tech. J.* **35**, 333 (1956).
2. D. R. Turner, *This Journal*, **105**, 402 (1958).
3. H. C. Gatos, "Surface Chemistry of Metals and Semiconductors," John Wiley & Sons, New York (1960).
4. K. H. Beckmann, *Surf. Sci.*, **3**, 314 (1965).
5. R. Memming and G. Schwandt, *ibid.*, **4**, 109 (1966).
6. M. J. J. Theunissen, *This Journal*, **119**, 351 (1972).
7. Y. Watanabe, Y. Arita, T. Yokoyama, and Y. Igarashi, *ibid.*, **122**, 1351 (1975).
8. Y. Arita, K. Kuranari, and Y. Sunohara, *Jpn. J. Appl. Phys.*, **15**, 1655 (1976).

Preparation of Nitrides by Active Nitrogen[1]

II. Si_3N_4

M. Shiloh and B. Gayer

Soreq Nuclear Research Centre, Yavne, Israel

and F. E. Brinckman

National Bureau of Standards, Washington, D.C. 20234

ABSTRACT

A general method for the preparation of nitrides is described by which active nitrogen, excited in a microwave cavity, is subsequently reacted with SiI_4 vapors formed *in situ* by passing iodine vapors over heated silicon powder. The temperature dependence of the deposition of Si_3N_4 on polished Si wafers was measured and compared with calculated thermodynamic data of similar reactions with nonactive nitrogen. The kinetic measurements were related to the special flow characteristics of the system. The over-all reaction

$$4(N)_g + 3(SiI_4)_g \rightarrow (Si_3N_4)_s + 6(I_2)_g$$

was found to be exothermic. Two regions of different slopes were obtained from the Arrhenius plot

$$\Delta E_{(280°\text{-}450°C)} = -3070 \text{ cal/mole}$$

$$\Delta E_{(450°\text{-}600°C)} = -8600 \text{ cal/mole}$$

The calculated temperature dependence of the enthalpy change of the corresponding reaction with nonactive nitrogen was shown to be almost constant in the range studied. Similar values of negative activation energy were obtained for the assumed second-order rate-determining reaction: $N + SiI_4 \rightarrow SiN + 2I_2$.

Much work has been done on the preparation of amorphous films of Si_3N_4 on single crystal wafers of silicon, because of the importance of such films in the technology of silicon electronic devices (1-11). The method mainly used is the reaction of SiH_4 with NH_3. Though this reaction is favorable thermodynamically at rather low temperatures, it can be carried out only above 700°C for kinetic reasons (2-4). The problem becomes much more difficult kinetically when NH_3 is replaced by the exceptionally stable N_2 molecule as the nitriding agent.

The main method used to overcome the kinetic barrier is the excitation of the reacting gases by an

[1] Part I: M. Shiloh and J. Gutman, *Mater Res. Bull.*, 8, 711 (1973).

Key words: CVD Si_3N_4 films, active nitrogen reactions, activation energy, SiI_4 reactions, flow reactors.

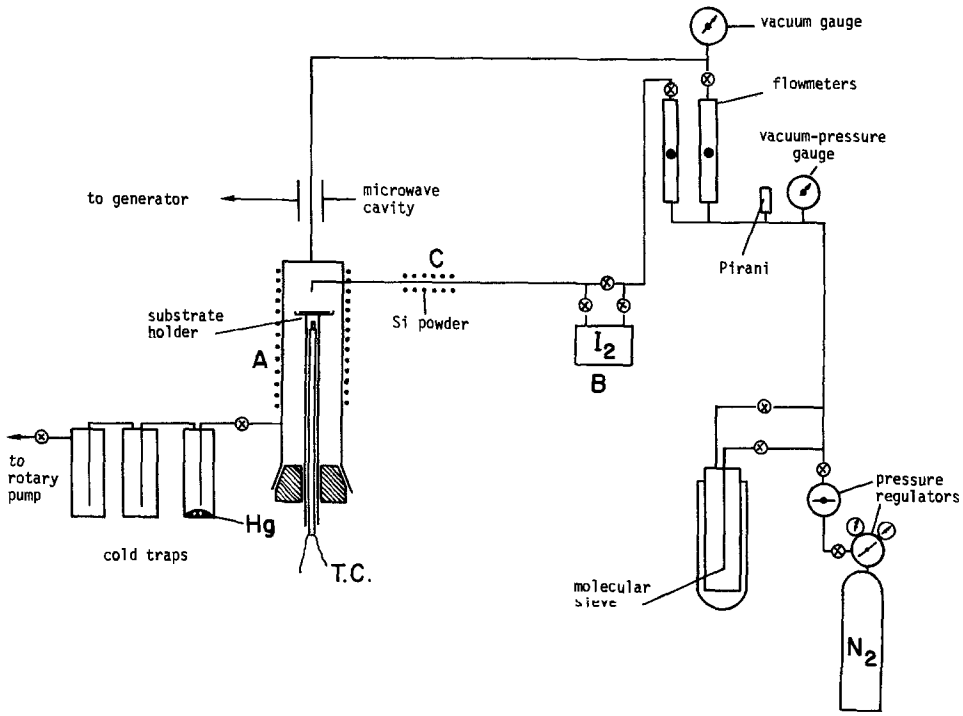


Fig. 1. Schematic diagram of the flow system for preparing nitrides.

electric field produced by d-c or rf power sources. Several works were published on the preparation of Si_3N_4 films by rf or microwave glow discharge excitation, most of them using NH_3 and SiH_4 as the reactants. In all cases both reactants are excited in the vicinity of the substrate (8-14). In a patented method (15) Si_3N_4 films are produced by exciting a mixture of N_2 and $SiBr_4$ vapors by a d-c discharge, forming a plasma in the region of the substrate.

In the present work a general method is described for the preparation of nitrides by microwave excitation of the N_2 reactant alone. The active nitrogen thus produced is then reacted on a substrate with an appropriate volatile compound. The substrate can be maintained at any desired temperature and is not affected by the temperature or other factors in the excitation region. The source of Si is SiI_4 vapor, formed *in situ* by reacting iodine vapor with silicon. Thus, the starting materials for the process are nitrogen, silicon, and iodine which are easier to handle than ammonia, silane, or the silicon halides. Because the substrate and the SiI_4 vapors are not affected by the microwave field in the antenna zone, it is easier to control and analyze the process, especially the temperature dependence of the over-all reaction. The operating pressure used (in the range 5-80 mm Hg) is higher than in previously reported glow discharge methods. This prevents the coating of the reactor walls, which occurs at lower pressures. The reaction that we use is also more favorable thermodynamically at lower temperatures, which is an important advantage in device fabrication. Data on the growth rate of Si_3N_4, produced in this work by the reaction between active nitrogen and SiI_4, are compared with calculated values from available thermodynamic data on reactions with nonactive nitrogen and are related to the flow characteristics of our system.

Experimental

A schematic diagram of the flow system is presented in Fig. 1. The main flow of purified nitrogen is metered to the main reactor (A) after passage through the microwave cavity. A second flow of nitrogen carrier is passed through the iodine reservoir (B) into the SiI_4 reactor (C), which contains silicon powder at 600°-700°C. SiI_4 vapor is formed by reaction with iodine and is carried to the main reactor through a nozzle in the center. The parallel streams of active nitrogen and SiI_4 vapor flow perpendicular to a polished silicon wafer and deposit Si_3N_4 on its surface. The temperature of the tube connecting reactor (C) to the main reactor (A) was about 200°C.

The main reactor is described in Fig. 2. The pressure in the reactor is controlled by the pumping speed of the rotary pump and the setting of the inlet needle-valve of the active nitrogen stream. The upper limit of the pressure is determined by the ability to sustain the discharge in the microwave cavity. In our system we could reach up to about 80 mm Hg. The outlet stream from the reactor, which contains iodine, is passed through mercury and liquid nitrogen cold traps before it enters the rotary pump. The reactor is made of quartz and resistively heated. Teflon valves and Viton O-rings were used in sections which are in contact with iodine vapors.

Matheson oxygen-free nitrogen was used after being further purified by passage through a 5A molecular sieve trap to remove moisture. Iodine and silicon powder were of analytical reagent grade. The polished silicon wafers, after cleaning with T.C.E., HF, and deionized water, were placed on a quartz pedestal equipped with a thermocouple to measure the reaction temperature. The wafers used were 200μ thick, which permitted *IR* transmission measurements. The flow rate of both streams was measured by rotameters at atmospheric pressure. The microwave source was a Raytheon 100W 2540 MHz generator. The entire system was helium leak tested to meet high vacuum requirements. The deposition rate was determined by weighing the Si_3N_4 films formed on the wafers at measured time intervals (usually 30 min). Density of 3.2 g/cm^3 (24) was used to calculate the thickness. Agreement within 5% with Talysurf measurements was found. The refractive index values were in the range 1.9-2.0 measured by reflected light interference) which correspond to the density value used (24) and serve as an indication to the purity of the film. The purity of the Si_3N_4 films was checked by examining the *IR* transmission spectrum. A typical *IR* spectrum is shown in Fig. 3. It shows the same characteristic absorption band of Si-N bonds measured for Si_3N_4 films formed by CVD from SiH_4-NH_3 or sputtering of Si in N_2 (24). Traces of water cause the formation of NH_4I and the appearance of the characteristic absorption peak of NH_4^+ near 1400 cm^{-1}. The flow rates of both the main stream and the iodine carrier were kept constant at 300 and 15 cm^3/min (STP), respectively. The total pressure in the

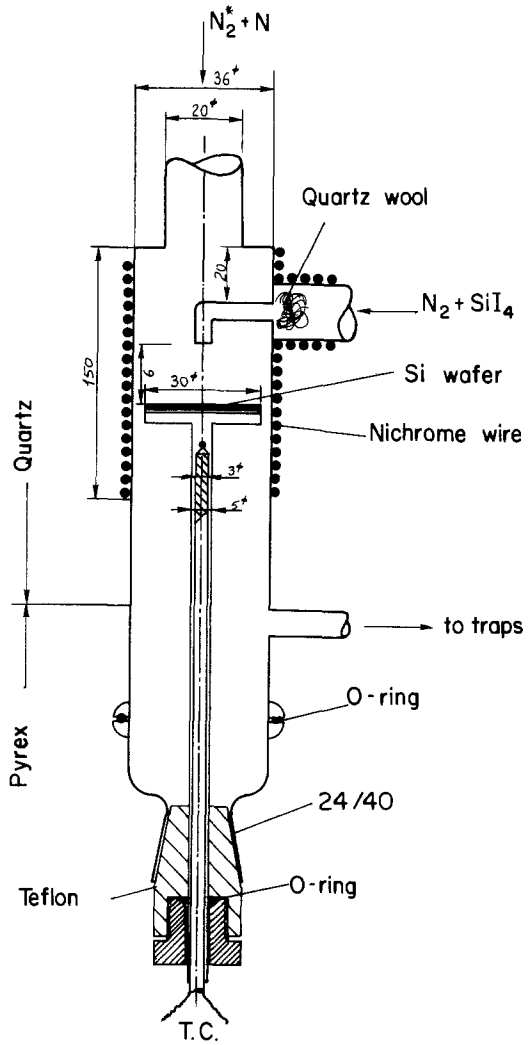


Fig. 2. Schematic diagram of the main reactor

reactor was maintained at 7 mm Hg. The temperature of the iodine reservoir was held at 22°C, corresponding to 0.24 mm Hg of I_2 (17). The low flow rate of the iodine carrier insured sufficient contact time for equilibration in both the iodine reservoir (B) and the silicon iodide generator (C). No free iodine was found in the nonactive nitrogen carrier leaving reactor (C). The amount of iodine carried to the reactor by a stream of nitrogen was measured at known time intervals and was found to correspond to saturation of the carrier stream.

When the carrier stream, containing SiI_4 vapors, meets the yellow afterglow of active nitrogen an intense blue stream of excited iodide vapor is observed. Under the flow conditions of our system the diameter of the blue flame was about the same as that of the nozzle, *i.e.*, 2 mm, with gradual broadening towards the substrate. The reaction between SiI_4 and active nitrogen, under the conditions studied, was heterogeneous and Si_3N_4 was deposited only on the silicon wafer. Because of the large diameter of the wafer (30 mm) compared with the distance to the nozzle (6 mm), all the Si_3N_4 was deposited in a circular area of about 20 mm in diameter. By observing the shape of the blue zone it was possible to adjust the flow rates and the distance from the nozzle in preliminary experiments to insure that deposition occurs only within the wafer area. Interference fringes were observed only at the circumference of the deposition area, within 2 mm of the edge.

Results and Discussion

Thermodynamics of the reaction between SiI_4 *and nitrogen.*—Plot (a) in Fig. 4 shows the temperature

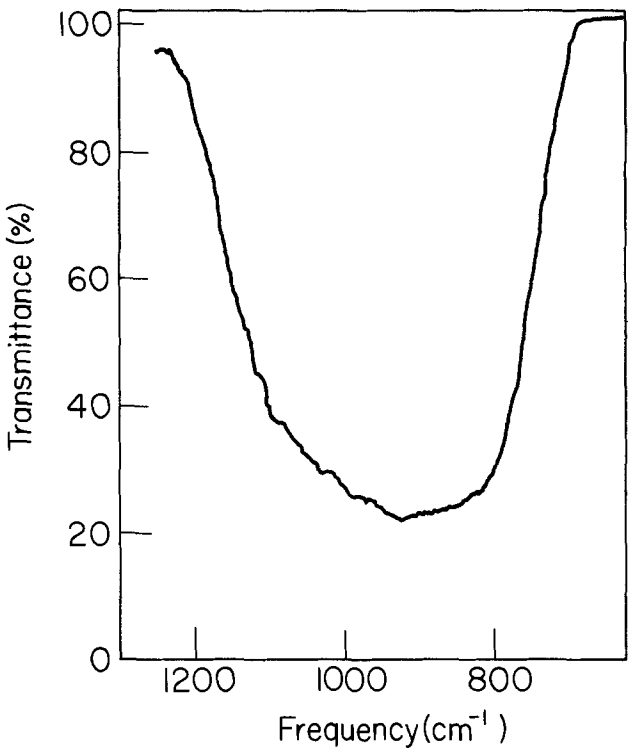


Fig. 3. Typical *IR* spectrum of Si_3N_4

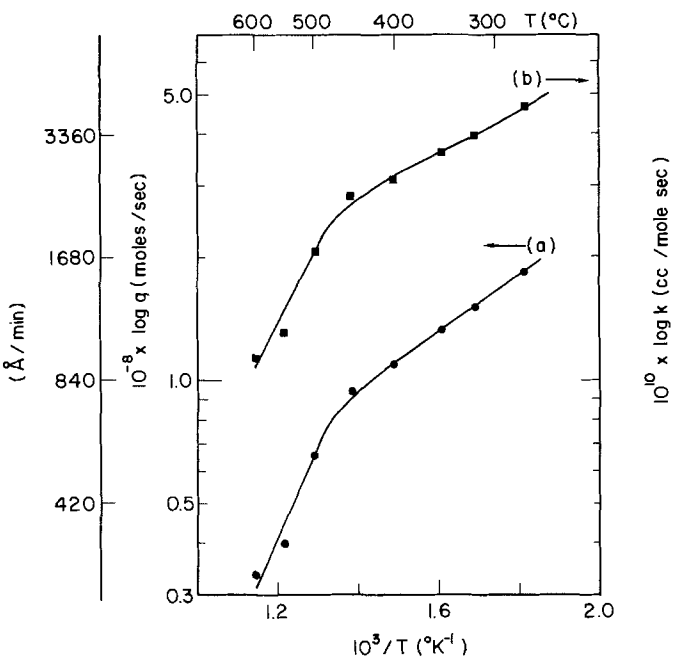


Fig. 4. Temperature dependence of deposition rate of Si_3N_4 by reaction of SiI_4 and active N_2. (a) Measured deposition rate; (b) calculated second-order rate constant, according to Eq. [4].

dependence of the deposition rate of Si_3N_4 from the reaction between SiI_4 and active nitrogen, as obtained in this work. Assuming N atoms to be the main reactant in active nitrogen (23), the deposition may be described by the following over-all reaction

$$3SiI_4 + 4N \rightarrow Si_3N_4 + 6I_2 \qquad [1]$$

Plot (b) in Fig. 4 shows the temperature dependence of the calculated second-order rate constant, assuming the following rate-determining bimolecular reaction

$$SiI_4 + N \xrightarrow{k} SiN + 2I_2 \qquad [2]$$

where k is the constant in the following rate equation

$$\frac{d[\mathrm{SiN}]}{dt} = k[\mathrm{N}][\mathrm{SiI_4}] \qquad [3]$$

It is assumed that breaking Si-I bonds and forming Si-N bonds as in Eq [2] would be much slower than the further reaction of Si-N with N atoms (both are unstable species) to form the stable phase of Si_3N_4. The reaction is assumed to occur mainly on the surface of the substrate, which serves, as a third body, to absorb the excess of energy released by the reaction. The integrated form of Eq. [3] is given by

$$k = 2.3 \log \frac{[\mathrm{SiI_4}]_i[\mathrm{N}]_f}{[\mathrm{SiI_4}]_f[\mathrm{N}]_i} \Big/ \; t([\mathrm{N}]_i - [\mathrm{SiI_4}]_i) \qquad [4]$$

(for $[\mathrm{N}]_i \neq [\mathrm{SiI_4}]_i$). The initial ($i$) and final ($f$) concentrations of the reactants in Eq. [4] after the time interval t (which is the contact time of the flowing reactants with the wafer) are calculated as follows

1. $[\mathrm{SiI_4}]_i = \dfrac{\dot{n}_1}{\Sigma \dot{n}_i} \times \dfrac{P}{RT}$ moles/cm^3

where: $\dot{n}_1$ is the inlet flow rate of SiI_4 in the carrier stream; $\Sigma \dot{n}_i$ is the total flow rate of the carrier stream; P is the total pressure in the reactor

2. $[\mathrm{N}]_i = \dfrac{2X_dP}{RT}$ moles/cm^3

where X_d is the degree of dissociation of N_2.

3. $[\mathrm{SiI_4}]_f = \dfrac{(\dot{n}_1 - 3q)}{\Sigma \dot{n}_1} \dfrac{P}{RT}$ moles/cm^3

where q is the deposition rate of Si_3N_4. The rate of consumption of SiI_4 by reaction [1] is $3q$.

The values of the known parameters in our experiments are: $R = 82$ atm cm^3/°K mole, $P = 0.92 \times 10^{-2}$ atm, $\dot{n}_1 = 1.92 \times 10^{-7}$ moles/sec (corresponding to $P_{SiI_4} = 0.12$ Torr), $X_d = 0.01$ (Ref. 18), $\dot{n}_2 = 44.6 \times 10^{-7}$ moles/sec (flow rate of N atoms corresponding to $X_d = 0.01$), $\Sigma \dot{n}_i = 112 \times 10^{-7}$ moles/sec, $t = 1.2 \times 10^{-2}$ sec (calculated from the linear velocity of the main stream, 124 cm/sec, and the wafer radius, 1.5 cm).

As can be seen $\dot{n}_2 >> \dot{n}_1$ in these experiments. We can therefore assume that the change in concentration of atomic nitrogen after reacting with SiI_4 is very small and therefore, $[\mathrm{N}]_i \approx [\mathrm{N}]_f$. Inserting the above expressions and data in Eq. [4] one obtains

$$k = 5.69 \times 10^8 \times T \times \log \left(\frac{1.92 \times 10^{-7}}{1.92 \times 10^{-7} - 3q} \right) \text{cm}^3/\text{mole sec} \qquad [4a]$$

Equation [4a] relates the second-order rate constant of reaction [2] to the reaction temperature (T) and the deposition rate of Si_3N_4 (q). The Arrhenius plot of k is shown in Fig. 4 as plot (b).

The experimental results as represented in Fig. 4 show that the deposition rate, in the range 280°-600°C, increases with decreasing temperature, which indicates that reaction [1] is exothermic. As the deposition occurred entirely within the wafer area, deposition is assumed to be completed while the reactants are in contact with the substrate. Therefore, it is reasonable to assume that steady-state conditions prevail near the surface.

Two regions of different slopes are seen in the Arrhenius plot (Fig. 4), with that above 450°C having about twice the negative value of the activation energy. Plots (a) and (b) exhibit very similar shapes and slopes. Values of activation energy for the deposition reaction derived from the plots are given in Table I. In order to compare reaction [1] with the corresponding reaction with nonactive nitrogen, the temperature dependence of $\Delta G°$ and $\Delta H°$ for nonactive nitrogen was derived from available data. The corresponding functions for $SiCl_4$ were also compared. [SiH_4 was excluded because it has been reported that no condensable product is formed by reaction with active nitrogen (23).]

Table I. Activation energy for reaction of SiI_4 with active N_2

Temperature range (°C)	ΔE_a (cal/mole)	ΔE_b (cal/mole)
280-450	−3070	−2550
450-600	−8600	−7670

$\Delta G°(T)$ for the formation of $(SiCl_4)_g$ and $(Si_3N_4)_s$ from the elements are given in Ref. (17)

$$(\mathrm{SiCl_4})_g = (\mathrm{Si})_s + 2(\mathrm{Cl_2})_g \qquad [5]$$

$$\Delta G° = 155{,}600 + 3.64T \log T - 43.9T \text{ (cal/mole)} \qquad [5a]$$

$$(\mathrm{Si_3N_4})_s = 3(\mathrm{Si})_s + 2(\mathrm{N_2})_g \qquad [6]$$

$$\Delta G° = 177{,}000 + 5.76T \log T - 96.3T \text{ (cal/mole)} \qquad [6a]$$

$\Delta G°(T)$ for the formation of $(SiI_4)_g$ was derived from $C°_P(T)$ functions for $(Si)_s$, $(I_2)_g$, and $(SiI_4)_g$ from Ref. (19), and $\Delta H°_{298}$ and $S°_{298}$ values from Ref. (17, 20, 21)

$$(\mathrm{SiI_4}) = (\mathrm{Si})_s + 2(\mathrm{I_2})_g$$

$$\Delta H°_{298} = +59.0 \text{ (kcal/mole)}$$

$$\Delta S°_{298} = +21.0 \text{ (cal/mole °K)}$$

$$\Delta C°_p = 1.99 - 0.74 \times 10^{-3}T - 0.06 \times 10^5 T^{-2} \text{(cal/mole °K)} \qquad [7]$$

Inserting these values in the general equation for $\Delta G°$ (17) the following expression is obtained

$$\Delta G° = 59{,}580 + 4.57T \log T - 44.1T \text{ (cal/mole)} \qquad [7a]$$

From [5a], [6a], and [7a] the following relations are obtained

$$3(\mathrm{SiI_4})_g + 2(\mathrm{N_2})_g = (\mathrm{Si_3N_4})_s + 6(\mathrm{I_2})_g \qquad [8]$$

$$\Delta G° = 1800 + 7.97T \log T - 36.1T \text{ (cal/mole)} \qquad [8a]$$

$$3(\mathrm{SiCl_4})_g + 2(\mathrm{N_2})_g = (\mathrm{Si_3N_4})_s + 6(\mathrm{Cl_2})_g \qquad [9]$$

$$\Delta G° = 289{,}000 + 5.16T \log T - 35.4T \text{ (cal/mole)} \qquad [9a]$$

It is seen that reaction [6] is strongly endothermic and reaction [5] is almost independent of temperature (very slightly exothermic). From [8a] one obtains, for reaction [8]

$$\Delta H° = 1800 - 3.47T \text{ (cal/mole)} \qquad [10]$$

which gives, in the temperature range of our experiments 280°-600°C

$$-190 \text{ cal/mole} > \Delta H > -1230 \text{ cal/mole}$$

In Fig. 5 $\log K_p(T)$ is compared for these reactions. It is clear that for a favorable process at low temperatures SiI_4 should be chosen as the reactant. The experimental values of activation energy for reaction [1] given above show that the reaction with active nitrogen is more exothermic than the corresponding reaction with nonactive nitrogen, as expected

Flow characteristics of the process.—The geometry of the main reactor (A) is shown in Fig. 2. Under our experimental conditions the flow of both streams was laminar. The linear velocity of the main stream (containing the active nitrogen) was $v_2 = 124$ cm/sec and that of the SiI_4 carrier at the exit from the nozzle was $v_1 = 2010$ cm/sec

The flow conditions of this process are basically different from those existing in systems with a turbulent flow at atmospheric pressure, on the one hand, and vacuum systems controlled by molecular flow mecha-

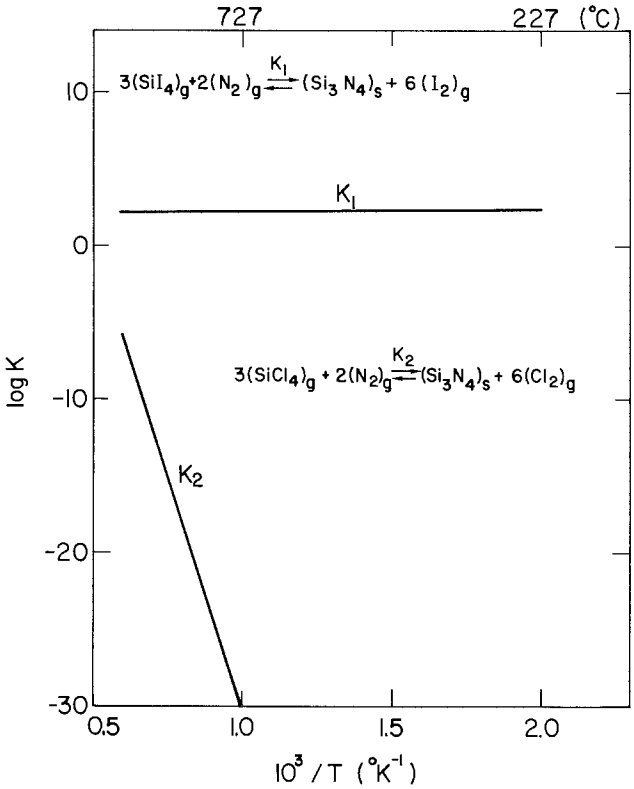


Fig. 5. Temperature dependence of equilibrium constants for the formation of Si_3N_4 from SiI_4 or $SiCl_4$ and nonactive N_2.

nisms on the other. The flow in the present system is not very far from the transition range between the viscous and molecular flow, as defined by the transition pressure P_t (22)

$$P_t = 95.7\sqrt{\frac{T}{M}\frac{\eta}{D}} \qquad [11a]$$

$$P_t = 8.59\sqrt{\frac{T}{M}\frac{\eta}{\lambda_t}} \qquad [11b]$$

where T is temperature, M is molecular weight, η is viscosity, D is reactor diameter, λ_t is mean free path in the transition range. The transition range is defined between $P_u = 10P_t$ as the upper limit and $0.1P_t$ as the lower limit. For our system at 873°K, $P_u = 0.54$ Torr. Accordingly, at 7 Torr, as in our experiments, the pressure is in the viscous flow region. λ_u, from [11b] is 3.23×10^{-2} cm compared with the mean free path of 2.94×10^{-3} cm at 873°K and 7 Torr.

We found experimentally that below 3 Torr, when diffusion becomes the controlling mechanism, the stream of SiI_4 carrier expands and diffuses into the main stream of active nitrogen so that the reactor wall is also coated with Si_3N_4. The observed blue glow results from excitation of SiI_4 by its mutual diffusion with active N_2. At 7 Torr the cross section of the SiI_4 stream is circular. The outward diffusion of SiI_4 causes the broadening of the blue glow towards the substrate, this effect being less pronounced at higher linear velocities of the carrier.

The total inlet flow rate of SiI_4, $\dot{n}_1$, as calculated from the carrier flow rate and known vapor pressure of I_2, was 1.92×10^{-7} moles/sec. The total inlet flow rate of atomic nitrogen, calculated from the main stream flow rate and measured degree of dissociation, $X_d = 0.01$, from Ref. (18) was 44.6×10^{-7} atoms/sec.

Although atomic nitrogen is introduced in excess of SiI_4 only part of it is mixed with SiI_4 by diffusion The linear velocity of the SiI_4 stream is about 16 times that of the main stream, containing atomic nitrogen, so that in the short distance between the nozzle and the wafer the main stream can be considered as a static medium into which the SiI_4 stream is injected. Using the following general equation of diffusion rate (21), the material transport velocities by diffusion and convection of the gas stream can be compared

$$\dot{n}_A = D_o \times \frac{A}{L} \times \frac{\Delta P_A}{P_t} \times T^{0.8} \times 0.5 \times 10^{-7} \text{ moles/sec} \qquad [12]$$

where A is cross section of diffusion path (cm^2), L is length of diffusion path (cm), D_o is diffusion coefficient at STP (cm^2/sec), P_t is total pressure, ΔP_A is partial pressure difference of transported material.

Inserting the data related to the diffusion of SiI_4 from the nozzle to the wafer into a carrier beam with a diameter of $d = 2$ mm gives, at 873°K, $(\dot{n}_1)_D = 6 \times 10^{-10}$ moles/sec compared with 1.92×10^{-7} moles/sec by convection. On the other hand the rate of diffusion of atomic nitrogen into the SiI_4 carrier beam is much more pronounced. Inserting into Eq. [12] the following factor, $A/L = 2\pi dL/d$, where L and d are the length and diameter of the SiI_4 beam, respectively, one obtains

$$(\dot{n}_2)_D = D_o \times 2\pi L \times \frac{\Delta P_2}{P_t} \times T^{0.8} \times 0.5 \times 10^{-7} \text{ moles/sec} \qquad [13]$$

for the rate of diffusion of atomic nitrogen into the carrier beam. ΔP_2 is the partial pressure difference of atomic nitrogen across the diffusion path.

It is seen from Eq. [13] that under steady-state conditions the diffusion rate of atomic nitrogen into the SiI_4 beam does not depend on the diameter of the beam (or of the nozzle) but only on the distance from the nozzle to the wafer. Thus, when the nozzle diameter is changed and the other parameters are kept constant, the rate of mixing of the reactants by diffusion is not affected. On the other hand, the rate of mixing by diffusion increases linearly with the distance (or time interval) between nozzle and wafer. Inserting the data obtained in our experiments ($D_o = 0.1$ cm^2/sec, $P_t = 0.92 \times 10^{-2}$ atm, $\Delta P_2 = 1.84 \times 10^{-4}$ atm, $T_{max} = 873$°K, $L = 0.6$ cm) one obtains

$$(\dot{n}_2)_D = 0.844 \times 10^{-7} \text{ atoms/sec}$$

Thus, at least 33% of the N atoms required for complete reaction with SiI_4, *i.e.*, 2.56×10^{-7} atoms/sec, are mixed with the carrier beam before it reaches the wafer. The SiI_4 stream is spread on the wafer to a thickness of 0.5 mm (assuming that it slows down to the linear velocity of the main stream) so that complete reaction with N atoms on the surface is insured. With the pressure used in our experiments, the barrier of a stagnant film, as in flow systems at atmospheric pressure, is not significant.

Acknowledgment

The research was supported by a grant from the United States-Israel Binational Science Foundation (BSF), Jerusalem, Israel.

Manuscript submitted May 13, 1976; revised manuscript received Aug. 31, 1976.

Any discussion of this paper will appear in a Discussion Section to be published in the December 1977 JOURNAL. All discussions for the December 1977 Discussion Section should be submitted by Aug. 1, 1977.

REFERENCES

1. C. J. Mogab, P. M. Petroff, and T. T. Sheng, *This Journal*, **122**, 815 (1975).
2. P. S. Schaffer and B. Swaroop, *Ceram. Bull.*, **49**, 536 (1970).
3. T. Arizumi, H. Ogawa, and T. Nishinaga, "Proceedings of the International Conference on Physics and Chemistry of Semiconductor Heterojunctions and Layer Structures," p. V-7, Budapest (1970).

4. M. T. Duffy and W. Kern, *RCA Rev.*, **31**, 742 (1970).
5. K. Tanabashi and K. Kobayashi, *Jpn. J. Appl. Phys.*, **12**, 641 (1973).
6. L. V. Gregor, in "Thin Film Dielectrics," Frederick Vratny, Editor, p. 447, The Electrochemical Society Softbound Symposium Series, New York (1969).
7. A. W. Harsley, *Electronics*, **42**, 84 (Jan. 1969).
8. R. Gereth and W. Scherber, *This Journal*, **119**, 1248 (1972).
9. R. C. G. Swann, R. R. Mehta, and T. P. Cauge, *ibid.*, **114**, 713 (1967).
10. R. J. Joyce, H. F. Sterling, and J. H. Alexander, *Thin Solid Films*, **1**, 481 (1967/68).
11. Y. Kuwano, *Jpn. J. Appl. Phys.*, **8**, 876 (1969).
12. Y. Shima, T. Miyazaki, N. Nakamura, E. Adachi, and T. Tokuyama, *ibid.*, **12**, 309 (1973).
13. Y. Kuwano, *ibid.*, **7**, 88 (1968).
14. Y. Kuwano, *ibid.*, **8**, 876 (1969).
15. H. F. Sterling and R. C. G. Swann, *Solid-State Electron.*, **8**, 653 (1965).
16. A. Andrusnuk, W. C. Erdman, and A. A. Bergh, U.S. Pat. 3,424,661 (1969).
17. O. Kubaschewski, E. L. Evans, and C. B. Alcock, "Metallurgical Thermochemistry," Pergamon Press, New York (1967).
18. R. E. W. Jansson and C. A. Middleton, *Br. J. Appl. Phys.*, **18**, 1079 (1967).
19. K. K. Kelly, Bull. 584, U.S. Bureau of Mines (1960).
20. H. Schäfer *et al.*, *Z. Anorg. Allg. Chem.*, **352**, 122 (1967).
21. H. Schäfer, "Chemical Transport Reactions," Academic Press, New York (1964).
22. C. M. Van Atta, "Vacuum Science and Engineering," McGraw-Hill Publishing Co., New York (1965).
23. R. Storr, A. N. Wright, and C. A. Winkler, *Can. J. Chem.*, **40**, 1296 (1962).
24. E. A. Taft, *This Journal*, **118**, 1341 (1971).

Ionic Conductivity in Pure and Cadmium-Doped Cuprous Iodide

Tsuneo Matsui and J. Bruce Wagner, Jr.*

Materials Research Center and Department of Materials Science and Engineering, Northwestern University, Evanston, Illinois 60201

ABSTRACT

The ionic conductivity of CuI has been measured as a function of temperature between 100° and 470°C using the a-c method. The measurements have been made on a pure sample and also on samples doped with CdI_2 in concentrations between 0.02 and 0.50 mole percent (m/o). The results have been analyzed using Koch and Wagner's method (1) as applied by Teltow (2) to obtain the values of the energies of formation and migration, the concentrations and mobilities of the copper interstitial ions ($Cu^{\cdot}_i$) and copper vacancies (V'_{Cu}). The curvature in the temperature dependence of conductivity is discussed. In the low temperature extrinsic region of CuI doped with 0.50 m/o CdI_2, the data yield the migration energy for copper vacancies and also the association energy between cadmium ions and copper vacancies. The two phase transitions of solid CuI have been also studied by conductivity measurements. At both transitions (369° and 407°C), the abrupt jumps in the conductivity curves are discussed in relation to entropy changes.

The predominant lattice defects in ionic crystals can be conveniently investigated by measuring the ionic conductivity of crystals containing known concentrations of aliovalent cations (1-5). These dopants change the concentration of lattice defects, preserving charge neutrality and chemical equilibrium. The values of the energies of formation and migration, the concentrations, and the mobilities of the two species of charge carriers have been obtained from such studies. This technique was originated by Koch and Wagner (1) and has been developed by Teltow (2, 3) and is reviewed by Lidiard (6).

Many measurements have been made on crystals having the NaCl structure [AgCl, AgBr (1-4), alkali halides (4, 7-9)], but not many have been made on copper halides. Unlike AgBr and AgCl which have the NaCl structure, copper halides exhibit two structures, one is the zinc blende structure and the other is the wurtzite structure. Several different investigations (6, 10, 11-13) indicate that the predominant intrinsic defects in copper halides are Frenkel cation pairs (copper interstitials, $Cu^{\cdot}_i$, and copper vacancies, V'_{Cu}).

In this paper we report an investigation of the total conductivity of pure CuI and CuI doped with CdI_2. The experimental results are analyzed to obtain information about the value of the energies of formation and migration, the concentrations, and the mobilities of $Cu^{\cdot}_i$ and V'_{Cu}, respectively, by using Koch and Wagner's method (1).

* Electrochemical Society Active Member.
Key words: mobility, copper interstitials, copper vacancies, defect concentration.

Theory

The formula for the conductivity of a crystal containing a molar fraction, C, of some aliovalent ion is derived by Teltow (2) and by Lidiard (6).

In predominantly ionic conductors such as copper iodide, the ionic conductivity, σ, may be written as

$$\sigma = Nq\ (x_v u_v + x_i u_i) \qquad [1]$$

where N is the number of copper ions per unit volume, u the mobility, q the electronic charge, x the molar fractions of defects, and the subscripts v and i refer to copper vacancies and interstitial copper ions, respectively. The reaction equation and the law of mass action for a Frenkel defect[1] may be written as

$$Cu_{Cu} + V_i = V'_{Cu} + Cu^{\cdot}_i \qquad [2]$$

and

$$x_v \cdot x_i = K^{-1} \equiv x_o^2 \qquad [3]$$

where x_o is the molar fraction of the intrinsic defects. By doping CdI_2 into CuI, copper vacancies are produced as follows

[1] The notation of Kroger and Vink is used (14).

$$CdI_2 = Cd^{\cdot}_{Cu} + V'_{Cu} + 2I_I \quad [4]$$

The electroneutrality condition requires that

$$x_v = C + x_i \quad [5]$$

where C denotes the molar fraction of CdI_2 added and hence the concentration of cadmium ions on copper ion sites according to Eq. [4]. Hence Eq. [3] becomes

$$x_v(x_v - C) = x_o^2 \quad [6]$$

or

$$x_v = \frac{C}{2}\left\{1 + \left(1 + \frac{4x_o^2}{C^2}\right)^{1/2}\right\} \quad [7]$$

Substituting Eq. [3] and [7] into [1], we have

$$\sigma = Nqx_o(u_v + u_i)\left[\sqrt{\left(\frac{C}{2x_o}\right)^2 + 1} - \left(\frac{C}{2x_o}\cdot\frac{\phi - 1}{\phi + 1}\right)\right] \quad [8]$$

where

$$\phi = u_i/u_v \quad [9]$$

For the pure crystal, the intrinsic conductivity is written as

$$\sigma_o = Nqx_o(u_v + u_i) \quad [10]$$

Thus, the conductivity isotherm is expressed by

$$\frac{\sigma}{\sigma_o} = \sqrt{\left(\frac{C}{2x_o}\right)^2 + 1} - \left[\frac{C}{2x_o}\cdot\frac{\phi - 1}{\phi + 1}\right] \quad [11]$$

There is a minimum in the σ/σ_o *vs.* C curve at

$$(C)_{min.} = \frac{x_o(\phi - 1)}{\sqrt{\sigma}} \quad [12]$$

$$(\sigma/\sigma_o)_{min.} = \frac{2\sqrt{\phi}}{1 + \sigma} \quad [13]$$

Experimental

The samples used in this study were sintered pellets of pure CuI and CuI doped with CdI_2. For pure CuI, ultrapure anhydrous CuI powder (99.9998% Alfa Products, Ventron Corporation) was used without further purification. Doped specimens were made by mixing the ultrapure CuI powder with the appropriate amount of CdI_2 powder (99.0% Alfa Products, Ventron Corporation), from which some of the water had previously been removed by heating at about 110°C in a Pyrex glass tube connected to a vacuum pump. The CdI_2 was added in concentrations of 0.02, 0.05, 0.10, 0.20, 0.30, 0.40, and 0.50 mole percent (m/o). Herrmann (15) has reported that CdI_2 is soluble in CuI in all concentrations. These pure and doped powders were pressed at 50,000 psi in a 0.319 in. diameter steel die. The freshly prepared pellets were sintered at 375°C for 16 hr and then at 550°C for 30 hr under a slow flow rate of purified argon gas (about 0.1 cm/sec). The argon gas was purified by passing first over heated copper turnings at about 400°C, and then through a tube of silica gel to remove water vapor. After sintering the size of pellets was about 8 mm in diameter and about 2 mm long, and the density was 92-93% of the theoretical value of pure CuI. The pellets were then polished and washed successively in acetone.

To make the conductivity measurements, the sample was sandwiched between the reversible copper electrodes which were 99.999% pure copper rod obtained from American Smelting and Refining Company, and electrical contact was ensured by applying a slight pressure by means of springs. The sample was annealed at 500°C for 2 hr prior to measurements to ensure a good interface contact. Copper halides, when equilibrated with copper electrodes exhibit virtually 100% ionic conduction (10), like the silver halides equilibrated with silver electrodes (16). A Marshall resistance furnace was used in a horizontal position. The temperatures were controlled to ±1°C by a Leeds and Northrup Electromax controller and the temperature was measured by Doric digital voltmeter using Chromel-Alumel thermocouples. The phase transformations provided a check on the temperature. The electrical conductivity was measured using a General Radio a-c bridge (1650A) at 1000 Hz.

Results and Discussion

Measurements of the total electrical conductivity of a pure CuI sample and seven doped samples containing different concentrations of CdI_2 were carried out in the temperature range of 100°-470°C. The results are shown in Fig. 1 and 2. The previous data on partial electronic hole conductivity of CuI by Wagner and Wagner (10) are also shown in Fig. 1 and 2. Comparing values of the total electrical conductivity and the electronic hole conductivity of CuI, it follows that the electronic conduction makes only a small contribution to the total conductivity of samples equilibrated with copper above 300°C. Thus the total conductivities reported in this study are essentially ionic conductivities above 300°C. On a given sample, the experimental error in the conductivity measurements is about ±3% above 300°C, but is ±6% below 300°C.

Typical curves of the relative conductivity *vs.* molar percentage of cadmium iodide are shown in Fig. 3 for the α-, β-, and γ-phases at 440°, 390°, 325°C, respectively. Table I gives the values of concentration and mobility calculated from the data of Fig. 1, 2, and 3, on the basis of Eq. [10], [12], and [13] for various temperatures. The mobilities of copper vacancies and interstitials, thus obtained, are shown as a function of temperatures in Fig. 4. The temperature dependence of the concentrations of Frenkel defects is also shown

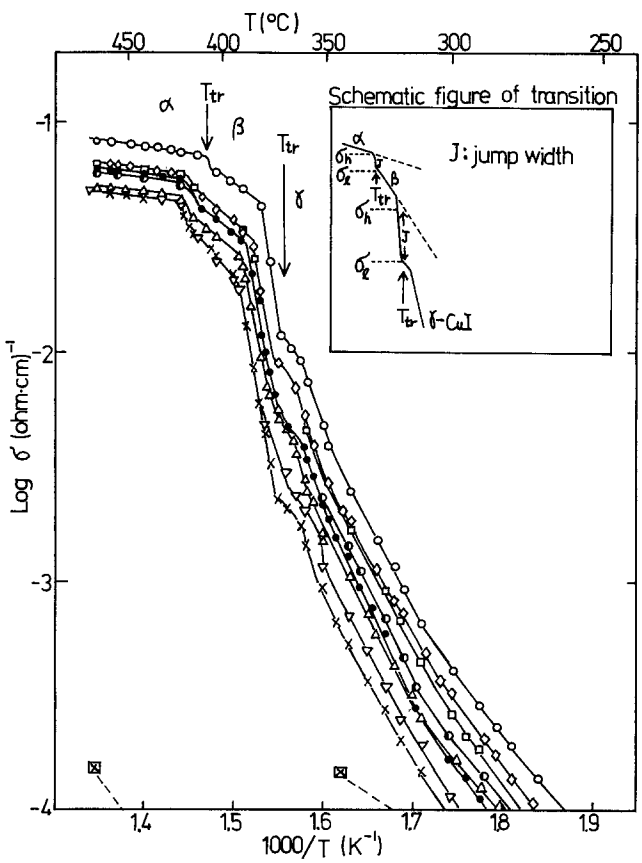


Fig. 1. The temperature dependence of the electrical conductivity of pure CuI and CuI-CdI_2 crystals at high temperature. This study: ○ pure CuI, ◇ 0.02 m/o CdI_2, ● 0.05, △ 0.10, × 0.20, ▽ 0.30, ◐ 0.40, □ 0.50. ⊠ Electronic hole conductivity according to Wagner and Wagner (10).

Table I. Values of concentrations and mobilities at various temperatures for cuprous iodide

Temperature (°C)	$(C)_{min.}$, m/o (±0.005)	$(\sigma/\sigma_0)_{min.}$ (±0.005)	x_0 ($\times 10^{-2}$ m/o)	u_v ($cm^2/V \cdot sec$)	u_i ($cm^2/V \cdot sec$)
γ-CuI 325	0.230	0.205	(2.41 ± 0.10)	(2.02 ± 0.05) × 10^{-5}	(1.89 ± 0.10) × 10^{-3}
340	0.230	0.220	(2.59 ± 0.10)	(4.02 ± 0.05) × 10^{-5}	(3.24 ± 0.10) × 10^{-3}
350	0.230	0.235	(2.78 ± 0.10)	(6.80 ± 0.05) × 10^{-5}	(4.79 ± 0.10) × 10^{-3}
β-CuI 390	0.255	0.325	(4.39 ± 0.10)	(1.10 ± 0.05) × 10^{-3}	(3.94 ± 0.10) × 10^{-2}
395	0.260	0.345	(4.77 ± 0.10)	(1.24 ± 0.05) × 10^{-3}	(3.93 ± 0.10) × 10^{-2}
400	0.265	0.385	(5.54 ± 0.10)	(1.44 ± 0.05) × 10^{-3}	(3.59 ± 0.10) × 10^{-2}
α-CuI 420	0.215	0.600	(8.06 ± 0.10)	(3.13 ± 0.05) × 10^{-3}	(2.82 ± 0.10) × 10^{-2}
440	0.215	0.610	(8.31 ± 0.10)	(3.42 ± 0.05) × 10^{-3}	(2.54 ± 0.10) × 10^{-2}
470	0.215	0.620	(8.48 ± 0.10)	(3.62 ± 0.05) × 10^{-3}	(3.01 ± 0.10) × 10^{-2}

Table II. Values of migration energy and formation energy

Phase (temperature range, °C)	Formation energy for Frenkel defects (kcal/mole)	Migration energy for copper vacancy (kcal/mole)	Migration energy for copper interstitial (kcal/mole)
α-CuI (420-470)	1.91 ± 0.10	4.39 ± 0.50	2.74 ± 0.50
β-CuI (390-400)	34.0 ± 0.50	25.7 ± 0.50	—
γ-CuI (325-350)	9.70 ± 0.50 (apparent)	37.2 ± 0.50 (apparent)	28.8 ± 0.50 (apparent)
(160-200)	—	5.30 ± 0.50	—

in Fig. 5. The migration energies and formation energies calculated from the data of Fig. 4 and 5, respectively, are summarized in Table II. In Table II, the migration energy and formation energy for the γ-phase are "apparent values," because the temperature dependence of the conductivity in the γ-phase cannot be fitted by a single straight line but a curved line, and thus the temperature dependence of the mobility, and concentrations do not yield a straight line. An apparent straight line portion of the curve is exhibited over only a short temperature range. The small values of the formation energy of ionic defects in the α- and γ-phase [the crystal structure of these two phases is the zinc blende structure, on the other hand the β-phase is the wurtzite structure (17)] are due to the saturation of the concentration of defects created by thermal energy at high temperatures. The small values of migration energies for copper interstitials and copper vacancies in the α-phase are due to the random positions of the cations as obtained from time-average structure determinations (17). The large values of the "apparent" migration energies for copper vacancies and copper interstitials in the γ-phase cannot be easily explained, but probably are due to the weakness of lattice structure, as is described briefly later.

In Fig. 2, a small linear slope for the variation of the conductivity with temperature between 160° and 200°C is observed with the highest doped sample containing 0.50 molar percentage of CdI_2. This region is the extrinsic region (18, 19), where the concentration of copper ion vacancies produced by the introduction of CdI_2 (whose reaction is expressed by Eq. [4]) is high compared to the concentration of intrinsic defects (for example even at 325°C, the concentration of the intrinsic defects is 0.024 m/o). By using the extrinsic vacancy region, we can calculate the migration energy and the mobility of copper vacancies, and these data are shown in Table II and Fig. 6, respectively.

At still lower temperatures than those in which the vacancies are presumably not associated, the conductivity data of the doped crystal containing 0.50 m/o

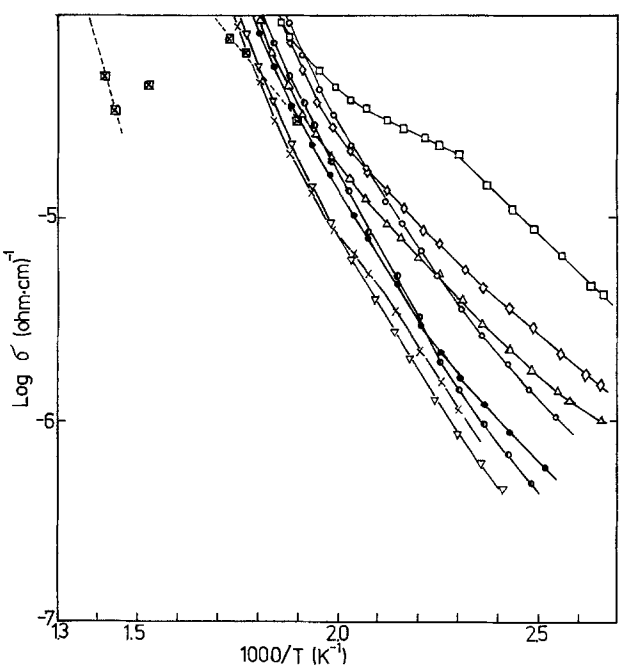


Fig. 2. Low temperature continuation of the temperature dependence of the electrical conductivity shown in Fig. 1.

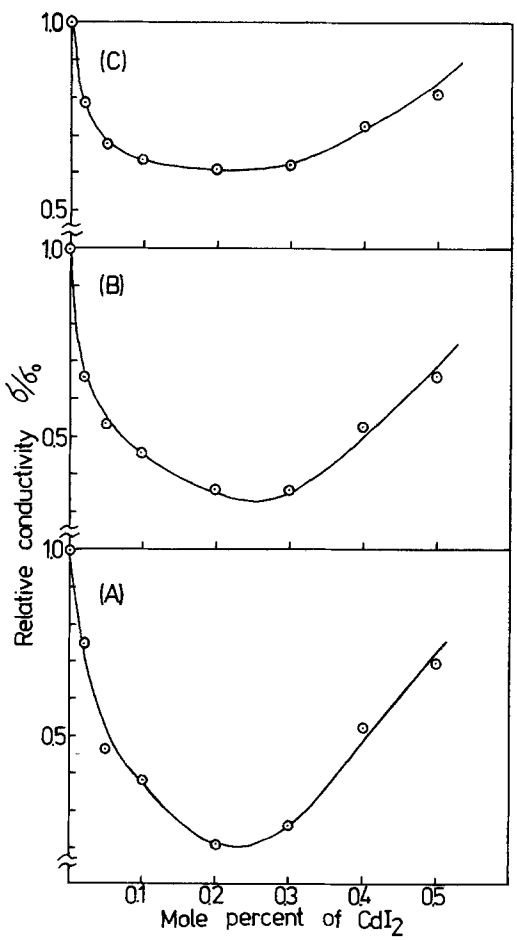


Fig. 3. The relative conductivity of CuI, σ/σ_0, as a function of the CdI_2 content for various temperatures: (A) γ-CuI, 325°C; (B) β-CuI, 390°C; (C) α-CuI, 440°C.

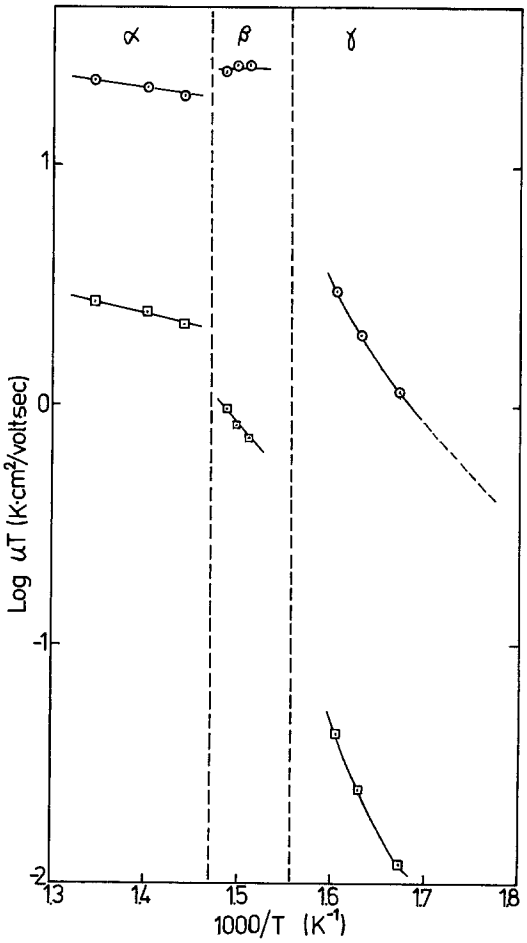


Fig. 4. The temperature dependence of the mobilities for copper vacancies and copper interstitials. ⊙ Mobility of copper interstitials, □ mobility of copper vacancies.

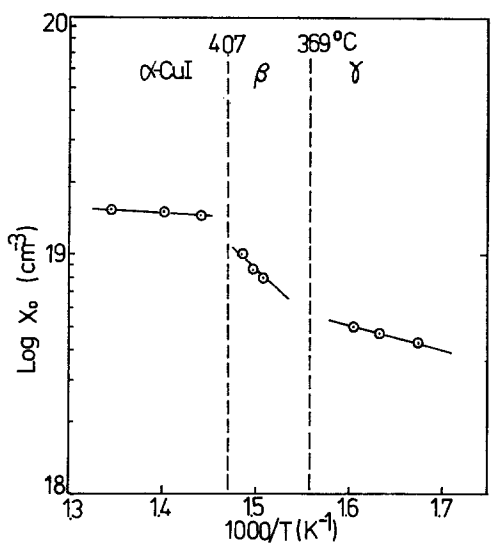


Fig. 5. The temperature dependence of the concentrations of Frenkel defects in CuI.

CdI_2 increase in slope. This region may be taken to be the association region (18, 19). In conjunction with the value of the migration energy of copper vacancies obtained above, this slope yields an energy of association between $(Cd_{Cu}^{\cdot} \cdot V'_{Cu})$ of 8.53 ± 0.46 (kcal/mole). This association energy is similar to the values, 8.76 (kcal/mole) for $(Cd_{Na}^{\cdot} \cdot V'_{Na})$ and 7.38 (kcal/mole) for $(Cd_{K}^{\cdot} \cdot V'_{K})$, calculated by Bassani and Fumi on the basis of the Born-Mayer model (20). In the con-

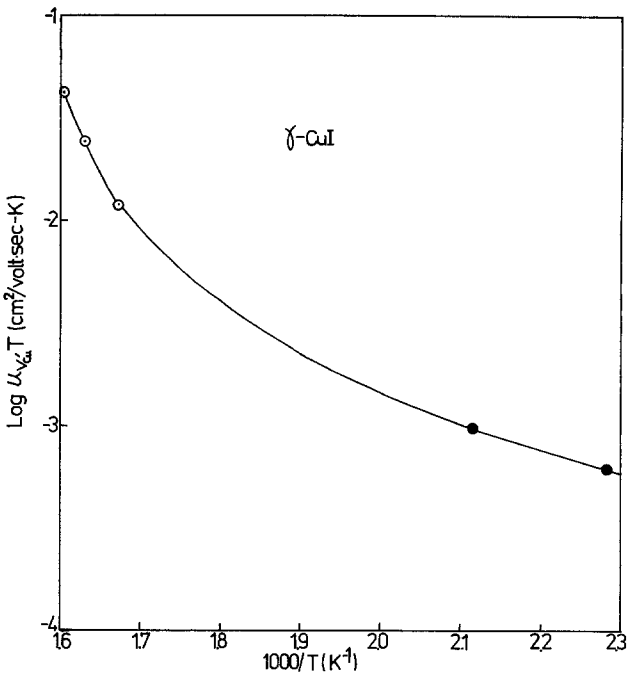


Fig. 6. The temperature dependence of the mobility for copper vacancies in γ-CuI.

ductivity curve of the doped crystals with 0.20, 0.30, and 0.40 m/o CdI_2, a little steeper slope is also seen below about 200°C, but the data are not sufficient for a calculation of the association energy.

Generally in the pure alkali and silver halides a knee in the conductivity curve is exhibited at a low temperature, below which the conductivity is affected by impurities (extrinsic region) which are accidentally present or by grain boundaries (5-9, 18-19). No such well-defined knee is seen in the temperature dependence of the conductivity of our pure CuI down to a temperature as low as 100°C, but a curved line is obtained for all temperatures from 100° to 369°C in the γ-phase. This curvature cannot be explained only by considering the contribution of the copper vacancies in addition to predominant copper interstitials. This behavior is the same as the previous results of Wagner and Wagner (10). Such a concave upward curvature in the high temperature region is also observed for AgBr (1, 2, 4), NaCl (7), and LiF (8).

Various explanations suggested previously for the curvature in AgBr are reviewed by Lawson (21). The curvature may be explained by two contributions: One is the rapidly increasing Schottky defects in addition to the predominant Frenkel defects, and the other is the weakness of lattice structure. The first suggested explanation for the anomalous conductivity at high temperatures has been put forth on the basis of the analysis of the pressure variation of the conductivity by Kurnick (4). The second suggestion is due to Lidiard (6, 22, 23) who rephrased the idea in terms of an effect due to a rapidly increasing dielectric constant on the Debye-Hückel terms in the free energy. The rapid increase in dielectric constant for AgBr has been observed by Everett, Lawson, and Smith (24). The upward bend in the variation of the thermal expansion coefficient for AgBr with temperature has been also observed by Zieten (25).

In the case of CuI, however, there are no such data with the exception of the x-ray diffraction study by Miyake, Hoshino, and Takenaka (17). They have measured the intensity change of diffraction lines with temperature in detail and from which the temperature dependence of the Debye-Waller factors for Cu and I ion have been calculated They found that the crystal structure of the γ-phase begins to change anomalously

at about 130C, and finally transforms to the high temperature structure of the α-phase having a disordered structure (an average structure). The Debye-Waller factor can be related to the mean square displacement of ions, and thus the mean square displacement for copper ions already increases abruptly from about 130°C showing the effect of anharmonicity, although the mean square displacement for iodine ions varies linearly with temperature (17, 26). From these x-ray data, it was inferred that the mobility for copper ions increases abruptly with increasing temperature in the γ-phase. This corresponds to our mobility data shown in Fig. 4 and 6. In summary, the curvature in the conductivity of the γ-phase may be due to the anomalous lattice weakening change with temperature. To clarify the mechanism of this curvature in γ-CuI, other extensive measurements are required.

Miyake, Hoshino, and Takenaka (17) have also studied the phase transitions in CuI by x-ray and calorimetric measurements. According to their data, copper iodide crystal undergoes two phase transitions, one at 369°C from the γ-phase with the zinc blende structure to the β-phase with the wurtzite structure, and the second at 407°C from the β-phase to the α-phase, again with the zinc blende structure. These transitions are of the first order and the transition entropies calculated from the specific heat measurements are 2.64 cal/mol · deg at the γ-β transition and 1.13 cal/mol · deg at the β-α transition.

As shown in Fig. 1, an abrupt jump in the electrical conductivity curve was observed at both the γ-β and the β-α transitions. The jump at the transition may be related to the entropy change at the phase transition (27). This jump width J is written as

$$J = \log \sigma_h(Tr) - \log \sigma_l(Tr) = \log \left[\frac{\sigma_h}{\sigma_l} \right]_{Tr}$$

$$= \log \frac{x_h(u_i + u_v)_h}{x_l(u_i + u_v)_l}$$

$$\simeq \log \frac{x_h u_{i,h}}{x_l u_{i,l}} \qquad [14]$$

because

$$u_i >> u_v \qquad [15]$$

where σ is the electrical conductivity at the transition temperature (Tr), and subscripts h and l are for high and low temperature phases, respectively.

The mobility, u, can be related to the diffusion coefficient D by using the Nernst-Einstein relation as follows (28)

$$u = qD/kT \qquad [16]$$

$$D = \lambda d^2 \nu \exp(-\Delta G/RT) = \lambda d^2 W \qquad [17]$$

where q is the charge of an electron, λ the geometric factor, d the diffusion length, ν the ion jump frequency at $T = \infty$, ΔG the change in Gibbs free energy for ionic migration, and W the probability for ionic migration. From Eq. [14], [16], and [17], the following equations are derived

$$J = \log \left[\frac{x_h \lambda_h d_h^2 \nu_h \exp(-\Delta G_h/RTr)}{x_l \lambda_l d_l^2 \nu_l \exp(-\Delta G_l/RTr)} \right] \qquad [18]$$

$$= \log \left[\frac{x_h \lambda_h d_h^2 W_h}{x_l \lambda_l d_l^2 W_l} \right] \qquad [19]$$

The entropy is related to the probability for ionic migration as follows

$$S = R \ln W = R \ln [\nu \exp(-\Delta G/RT)] \qquad [20]$$

Then we have

$$\Delta S = R \ln \left[\frac{W_h}{W_l} \right] \qquad [21]$$

$$= 2.303R \log \left[\frac{\nu_h \exp(-\Delta G_h/RTr)}{\nu_l \exp(-\Delta G_l/RTr)} \right] \qquad [22]$$

and thus

$$J = \log \left[\frac{x_h \lambda_h d_h^2}{x_l \lambda_l d_l^2} \right] + \frac{\Delta S}{2.303R} \qquad [23]$$

Equation [23] indicates that the difference between the jump width, J, and the entropy change at the phase transition depends on the nature of phase transition, especially the change of crystal structure, since λ and d depend on crystal structure.

The jump widths, J, in the conductivity curve at the γ-β transition and at the β-α transition of CuI are 0.465 and 0.0792, respectively. The difference between jump width and entropy change of the same transition can be calculated from Eq. [23] as follows

$$J - \frac{\Delta S}{2.303R} = \log \left[\frac{x_h \lambda_h d_h^2}{x_l \lambda_l d_l^2} \right]_{\gamma\text{-}\beta} = -0.112$$

so that $[x_h \lambda_h d_h^2 / x_l \lambda_l d_l^2]_{\gamma\text{-}\beta} = 0.77$ for the γ to β transition. For the β to α transition

$$J - \frac{\Delta S}{2.303R} = \log \left[\frac{x_h \lambda_h d_h^2}{x_l \lambda_l d_l^2} \right]_{\beta\text{-}\alpha} = -0.168$$

so that $[x_h \lambda_h d_h^2 / x_l \lambda_l d_l^2]_{\beta\text{-}\alpha} = 0.68$.

The phase transition and the crystal structures of the three modifications in cuprous bromide (CuBr) have also been studied by x-ray and calorimetric measurement (29). Cuprous bromide crystals undergo two phase transitions, one at 385°C from the γ-phase with the zinc blende structure to the β-phase with the wurtzite structure, and the second at 470°C from the β-phase to the α-phase with body-centered structure similar to α-AgI which closely resembles the "average" structure of α-CuI (29). These transitions are also first order and the transition entropies are 2.1 cal/mole deg at the γ-β transition and 0.9 cal/mole deg at the β-α transition. Accordingly it may be expected that CuBr is an analog to CuI.

The electrical conductivity of CuBr has also been measured between 150° and 450°C by Wagner and Wagner (10). From their data, the jump width is 0.346 for the γ-β transition in CuBr. The same calculation for CuBr as for CuI is made as follows

$$J - \frac{\Delta S}{2.303R} = \log \left[\frac{x_h \lambda_h d_h^2}{x_l \lambda_l d_l^2} \right]_{\gamma\text{-}\beta} = -0.113$$

This value is in good agreement with that for the γ-β transition in CuI, indicating the validity of the Eq. [23]. We can estimate the jump width in the electrical conductivity of CuBr at the β-α transition by using Eq. [23] and the value of entropy change at the β-α transition, assuming the same correspondence between the β-α transitions in CuBr and in CuI as the γ-α transition in CuBr and in CuI. The jump width is 0.0286 and the ratio between the electrical conductivity of the α- and β-phase is 1.07.

It is seen from Fig. 5 that the ratios of the concentration of copper interstitials are $[x_h/x_l]_{\gamma\text{-}\beta} \simeq 1.0$ at the γ-β transition and $[x_h/x_l]_{\beta\text{-}\alpha} \simeq 1.3$ at the β-α transition. Using these values, $\lambda_h d_h^2/\lambda_l d_l^2$ can be calculated to be 0.77 for the γ-β transition and 0.52 for the β-α transition, respectively. Assuming the copper interstitial diffusion mechanism in the zinc blende (fcc) structure of the γ-phase, the geometric factor λ and the diffusion length d are 4 and 6.11/2Å[2] (half of the lattice constant), respectively, and also assuming the copper interstitial mechanism only along the a-axis in the hexagonal wurtzite structure of the β-phase, the value of λ and x are 3/2 and 4.32Å[2], respectively. Using these values, we can calculate the ratio $[\lambda_h d_h^2/\lambda_l d_l^2]_{\gamma\text{-}\beta}$ to be 0.75, which is in good agreement with the value 0.77 calculated from J and ΔS.

[2] 6.11 and 4.32A are the lattice constants of the γ- and β-phase at the γ-β phase transition (369°C), respectively (17).

Since the lattice constant of the β-phase at the β-α transition has not been reported, we cannot estimate the value of $[\lambda_h d_h^2/\lambda_l d_l^2]_{\beta\text{-}\alpha}$, but this small value 0.52 may be due to the very small value of d in the α-phase which is the "average" structure of copper ions.

Summary

From the measurements of ionic conductivity on pure CuI and CuI doped with different concentrations of CdI_2, the concentrations of intrinsic defects, mobilities, and the energies of formation and migration of copper vacancies and copper interstitials were calculated on the basis of Koch and Wagner's theory. The association energy between cadmium ions and copper vacancies calculated using the data of CuI doped with 0.50 m/o CdI_2, was 8.53 ± 0.46 (kcal/mole). The difference between jump width in the conductivity curve at the phase transition in the present study and entropy change of CuI (17) was calculated, and was in good agreement with that of CuBr at the same type of transition.

Acknowledgments

This work was supported by the Advanced Research Projects Agency of the Department of Defense and was monitored by the Materials Research Center of Northwestern University under Grant No. DAHC 15 73 G-19.

Manuscript submitted June 28, 1976; revised manuscript received Sept. 28, 1976.

Any discussion of this paper will appear in a Discussion Section to be published in the December 1977 JOURNAL. All discussions for the December 1977 Discussion Section should be submitted by Aug. 1, 1977.

Publication costs of this article were assisted by Northwestern University.

REFERENCES

1. E. Koch and C. Wagner, *Z. Phys. Chem. (B)*, **38**, 295 (1937).
2. J. Teltow, *Ann. Phys. (Leipzig)*, **5**, 63, 71 (1949).
3. I. Ebert and J. Teltow, *ibid.*, **15**, 268 (1955).
4. S. W. Kurnick, *J. Chem. Phys.*, **20**, 218 (1951).
5. H. W. Etzel and R. T. Mauer, *ibid.*, **18**, 1003 (1950).
6. A. B. Lidiard, *Handb. Phys.*, **20**, 246 (1957).
7. D. L. Kirk and P. L. Pratt, *Proc. Br. Ceram. Soc.*, **9**, 215 (1967)
8. T. G. Stoebe and P. L. Pratt, *ibid.*, **9**, 181 (1967).
9. E. Barsis, E. Lilley, and A. Taylor, *ibid.*, **9**, 203 (1967).
10. J. B. Wagner and C. Wagner, *J. Chem. Phys.*, **26**, 1597 (1957).
11. J. E. Mayer and R. B. Levy, *ibid.*, **1**, 647 (1933).
12. Y. W. Hsueh and R. W. Christy, *ibid.*, **39**, 3519 (1963).
13. J. Teltow, *Z. Phys. Chem. (Leipzig)*, **195**, 197 (1950).
14. F. A. Kröger and H. J. Vink, *Solid State Phys.*, **3**, 588 (1956).
15. G. Herrmann, *Z. Anorg. Chem.*, **71**, 296 (1911).
16. B. Ilschner, *J. Chem. Phys.*, **28**, 1109 (1958).
17. S. Miyake, S. Hoshino, and T. Takenaka, *J. Phys. Soc. Jpn.*, **7**, 19 (1952).
18. L. Heyne, *Electrochim. Acta*, **15**, 1251 (1970).
19. F. A. Kröger, "The Chemistry of Imperfect Crystals," North-Holland Published Co., Amsterdam (1964).
20. F. Bassani and F. E. Fumi, *Nuova Cimento*, **11**, 274 (1954).
21. A. W. Lawson, *J. Appl. Phys.*, **33**, 466 (1962).
22. A. B. Lidiard, *Phys. Rev.*, **94**, 29 (1954).
23. A. B. Lidiard, *ibid.*, **112**, 54 (1958).
24. G. Everett, A. W. Lawson, and G. E. Smith, *ibid.*, **123**, 1589 (1961).
25. W. Zeiten, *Z. Phys.*, **145**, 125 (1956).
26. T. Matsubara, *J. Phys. Soc. Jpn.*, **38**, 1076 (1975).
27. H. Inaba, T. Matsui, and K. Naito, *J. Nucl. Mater.*, **58**, 115 (1975).
28. P. G. Shewmon, "Diffusion in Solids," McGraw-Hill Book Co., New York (1963).
29. S. Hoshino, *J. Phys. Soc. Jpn.*, **7**, 560 (1952).

Effect of Metallic Impurities (Ag, Mn) on the Kinetics of the Reaction of Zinc with Gaseous Phosphorus

Yoshinori Sasaki and Shiro Ueda

Department of Synthetic Chemistry, Chiba University, Yayoi-cho, Chiba 280, Japan

ABSTRACT

A study was undertaken on the kinetics and mechanism of the phosphidation of zinc and zinc containing one atomic percent (a/o) of silver or manganese at 390°C in phosphorus vapor of 1 atm. The phosphidation reactions were parabolic and therefore rate limited by a diffusion process. A marker experiment indicated that zinc was the component that diffused. An x-ray and electron microprobe analysis showed that at the phosphide-metal interface the compound Zn_3P_2 was formed, and that at the outer layers solid solutions of phosphorus in the Zn_3P_2 matrix were formed. The rate of phosphidation of Zn-Mn (1 a/o), Zn and Zn-Ag (1 a/o) decreased in that order. It is postulated that silver decreased the cation vacancy concentration in the phosphide layer and manganese increased it because their valences, respectively, are smaller than and larger than that of zinc. Consequently, the mechanism of phosphidation of zinc appears to be controlled by diffusion of zinc ion in the phosphide lattice.

The phosphidation of zinc has been extensively studied by many workers. The two phosphides are known: ZnP_2 and Zn_3P_2. The crystal structures of ZnP_2 (1, 2) and Zn_3P_2 (3) have been studied in detail and their thermodynamic data (4, 5) also given. The polymorphic transition (6, 7) in ZnP_2 at high temperatures and high pressures, and the kinetics (8) of reaction of zinc with phosphorus at high pressures have been investigated.

Key words: zinc phosphide (Zn_3P_2), phosphidation kinetics, mechanism, diffusion, cation vacancy.

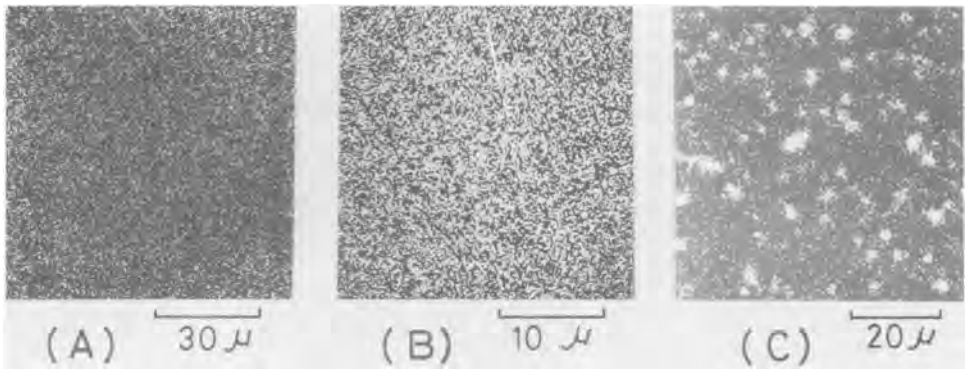


Fig. 1. X-ray images showing distributions of impurities in metallic zinc: (a) AgL_α from Zn-Ag (1 a/o); (b) MnK_α from Zn-Mn (1 a/o); (c) GaL_α from Zn-Ga (1 a/o).

The great majority of work on zinc phosphides has dealt with their preparation (9, 10) and crystal structures. The present study was undertaken to elucidate the mechanism of the reaction between metallic zinc and gaseous phosphorus.

Experimental

A zinc ingot with a purity of 99.999%, made by the Mitsui Mining & Smelting Company Limited, was cut into rectangles of approximately 20 × 5 × 2 mm. According to an analysis by the manufacturer, the impurity level of the zinc was as follows: Pb = 0.3 ppm, Cd, Cu, and Fe = 0.5 ppm. The coupons were abraded with a 0/9 emery paper, then washed with a refined toluene. Their geometric surface areas and weights were measured.

A zinc-silver alloy was prepared by heating the metallic mixture of an atomic ratio Zn/Ag = 99.00 at 960°C for 3.5 hr in an evacuated-sealed silica tube. Silver having a purity over 99.9%, made by the Kojima Kagaku Yakuhin K. K., was used. Quantitative analysis of silver in this alloy by Volhard's method indicated 1.0 a/o. A zinc-manganese alloy also was obtained in the same way with conditions of 1000°C and 8 hr. The manganese had a purity over 99.99% and was made by Johnson Matthey Chemicals Limited. According to colorimetric analysis of MnO_4^{-1} ion obtained by oxidizing the manganese in this alloy, the content of manganese was 1.0 a/o.

In order to examine the homogeneity of the alloys prepared, their x-ray images (Fig. 1) were obtained with a scanning electron microscope (JSM-U3, Japan Electron Optics Laboratory Company Limited).

Since metallic zinc and gallium are mutually insoluble, an example of their heterogeneous alloy is given for reference in the same figure. Figure 1 shows both silver and manganese to be uniformly dispersed respectively in metallic zinc.

Purification of red phosphorus was similar to that described previously (11).

The reaction apparatus consisted of a porcelain tube maintained in two temperature zones, the first zone being used to heat the sample sheet in an evacuated-sealed glass tube, and the second zone, to control the vapor pressure of phosphorus in this glass tube. The apparatus and experimental methods employed in this study are described in detail in a previous paper (11).

Results and Discussion

Kinetic results are shown in Fig. 2 on phosphidation of the sample sheets exposed to phosphorus vapor of 1 atm at 390°C. At this temperature, gaseous phosphorus consists of a P_4 molecule. Because a sealed tube was used to contain the phosphorus vapor, it was not possible to make continuous measurements of weight change. Each point represented here was obtained by phosphidizing an individual specimen. The phosphidation kinetics followed a parabolic rate law under the experimental conditions used; hence, the rate-determining step was apparently a diffusion or a transport process of zinc or phosphorus. It had been confirmed beforehand that metallic silver and manganese also react with phosphorus vapor at 390°C.

Values of the parabolic rate constants were 9.1 ± 1.1, 14.6 ± 1.6, and 19.6 ± 1.2 $mg^2cm^{-4}hr^{-1}$ for Zn-Ag (1 a/o), Zn, and Zn-Mn (1 a/o), respectively.

Figure 3 illustrates the x-ray diffraction patterns of the powder, surface, and reverse side of the phosphide film, employing nickel-filtered copper radiation. These patterns reveal the products to be composed of Zn_3P_2.

The Kirkendall effect relating to the diffusion process was examined for the phosphidation of zinc with use of a glass fiber as a marker. The specimen phosphidized was embedded in a polyester resin, and its cross section was polished with finely divided chromium oxide powder. Figure 4a shows a cross section of the scale and the position of the glass fiber marker. This was confirmed in the SEM by SiK_α radiation as shown in Fig. 4b. Since the marker is situated in the neighborhood of the phosphide-metal interface, the reaction is controlled by diffusion of zinc through the phosphide layer.

The distribution of phosphorus in this scaling film, obtained with the SEM, is given in Fig. 4c, which shows that the content of phosphorus in the scale decreases toward inner scale layers. It must be noted that a plateau having a certain constant content of phosphorus is present in the bulk phosphide. The composition of this plateau should correspond to Zn_3P_2 from the x-ray

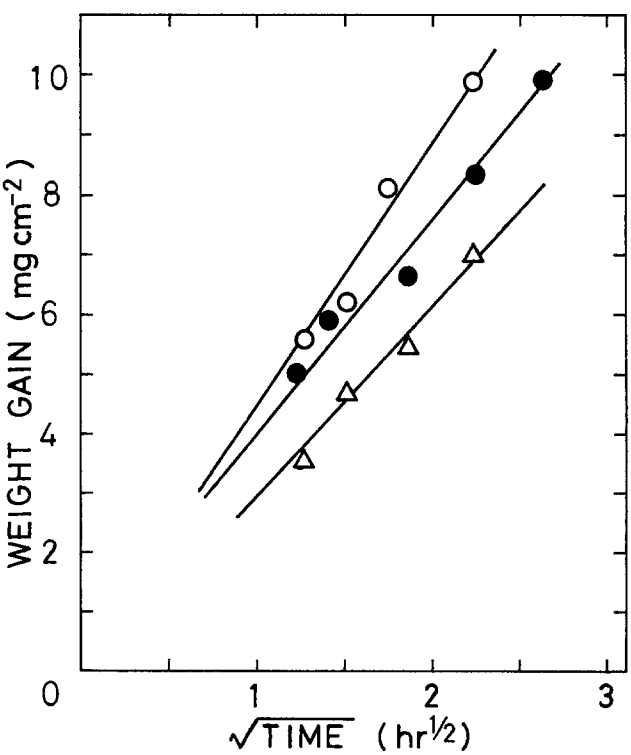


Fig. 2. Phosphidation of pure and impure zinc at 390°C in 1 atm phosphorus: ○ Zn-Mn (1 a/o); ● Zn; △ Zn-Ag (1 a/o).

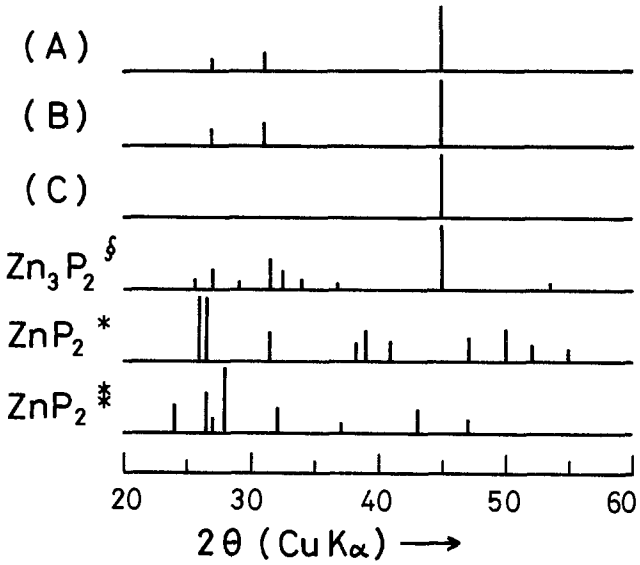


Fig. 3. X-ray diffractograms of zinc phosphides obtained at 390°C in phosphorus vapor of 1 atm: (a) powder; (b) surface; (c) reverse side, compared with literature patterns: § Zn_3P_2 (8), * tetragonal ZnP_2 (8), ⁂ monoclinic ZnP_2 (8).

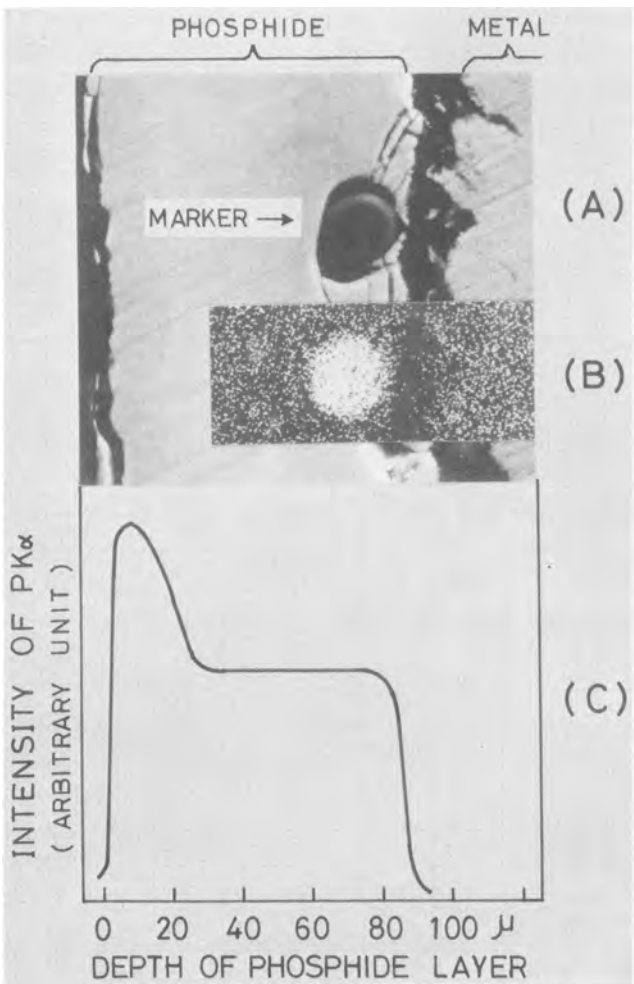


Fig. 4. Transverse cross section of zinc phosphide scale formed at 390°C for 18 hr in 1 atm phosphorus, and distribution of phosphorus in this scale by SEM: (a) cross section; (b) SiK_α image; (c) distribution.

diffraction pattern. Since the x-ray diffraction studies show that ZnP_2 is not formed even at the outer surface of the scale, it is assumed that the observed higher concentration of phosphorus represents a solid solution of phosphorus in the Zn_3P_2 matrix.

The reactivity of Zn-Mn (1 a/o), Zn, and Zn-Ag (1 a/o) with phosphorus decreased in that order, as mentioned above. It is noteworthy that the added small amounts of silver hinder the phosphidation of zinc, whereas the added manganese, on the contrary, promotes it. Because silver has a lower valence than zinc, we presume that the addition of silver causes a decrease in the cation vacancy concentration in the phosphide lattice, and, on the other hand, manganese having an equal or higher valence causes an increase in the concentration of cation vacancies in the scale. Consequently, the following equations might be expected

$$\tfrac{1}{2}P_4 \rightleftharpoons Zn_3P_2 + 3Zn\square'' + 6\oplus$$

$$2Ag_3P + 3Zn\square'' \rightleftharpoons 6Ag\bullet'(Zn) + Zn_3P_2$$

$$2MnP \rightleftharpoons Zn\square'' + 2Mn\bullet\cdot(Zn) + Zn_3P_2$$

where $\oplus$ denotes an electron hole. A black circle was used as the symbol for the substitution of cation into the lattice. A dot and prime denote the excess and deficient positive charge, respectively.

Figures 5 and 6 show the distribution profiles of zinc, phosphorus, silver, and manganese in the scale layers. It is obvious from Fig. 5 that the silver was concentrated in the metal alloy side near the phosphide-alloy interface, while its content in the scale was decreased. This could be explained by assuming that the reactivity of zinc with phosphorus is larger than that of silver with phosphorus. The addition of silver to zinc seems to cause the delay of the phosphidation of zinc, because not only the cation vacancy was decreased but silver hindered the diffusion of zinc on the phosphide-metal interface.

On the other hand, Fig. 6 shows that the manganese added was approximately uniformly dispersed in both

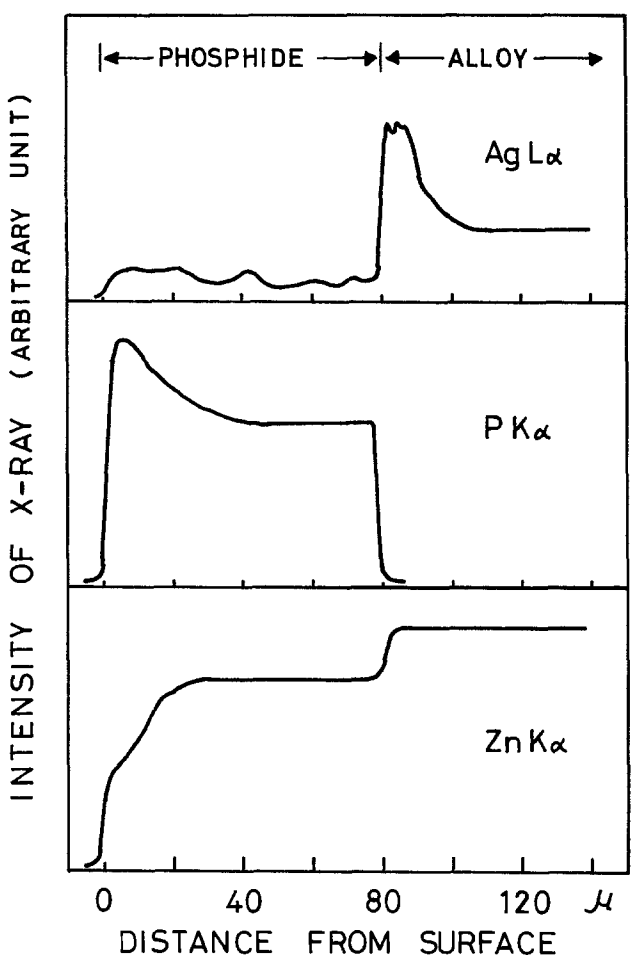


Fig. 5. Distribution profiles of silver, phosphorus, and zinc in the phosphide layer and the alloy phase.

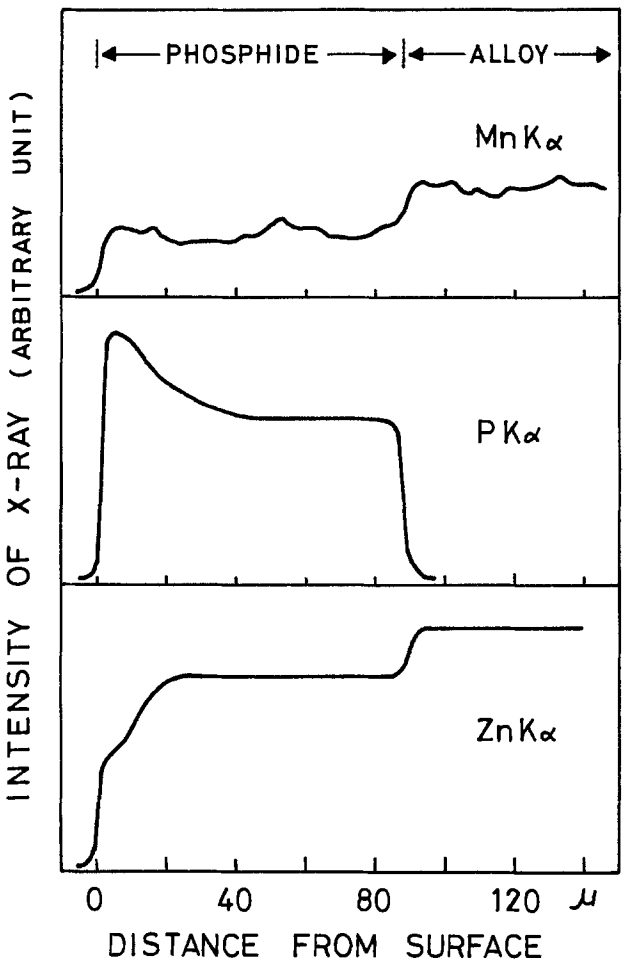


Fig. 6. Distribution profiles of manganese, phosphorus, and zinc in the phosphide layer and the alloy phase.

the phosphide phase and the alloy phase during the phosphidation.

Although it cannot necessarily be concluded that the diffusion process of phosphidation of metals is generally based on such a mechanism, the possibility of lattice diffusion such as the above for the phosphidation mechanism is reasonable.

Acknowledgments

The authors wish to thank Professor E. Kawai for his permission to use the SEM, Mr. K. Oda and Mr. N. Misono for their SEM measurement, and Mr. T. Sato for his assistance in the experimental work.

Manuscript submitted June 29, 1976; revised manuscript received Sept. 25, 1976.

Any discussion of this paper will appear in a Discussion Section to be published in the December 1977 JOURNAL. All discussions for the December 1977 Discussion Section should be submitted by Aug. 1, 1977.

REFERENCES

1. I. J. Hegyi, E. E. Loebner, E. W. Poor, Jr., and J. G. White, *J. Phys. Chem. Solids*, **24**, 333 (1963).
2. J. G. White, *Acta Crystallogr.*, **18**, 217 (1965).
3. M. V. Stackelberg and R. Paulus, *Z. Phys. Chem.*, **B28**, 427 (1935).
4. A. S. Jordan, *This Journal*, **118**, 1362 (1971).
5. R. C. Schoonmaker, A. R. Venkitaraman, and P. K. Lee, *J. Phys. Chem.*, **71**, 2676 (1967).
6. J. Osugi and Y. Tanaka, *J. Chem. Soc. Jpn.*, **90**, 618 (1969).
7. Y. Tanaka, *Rev. Phys. Chem. Jpn.*, **38**, 151 (1968).
8. J. Osugi and Y. Tanaka, *J. Chem. Soc. Jpn.*, **90**, 538 (1969).
9. J. C. Hutter, *Ann. Chim. (Paris)*, **8**, 450 (1953).
10. G. Brauer, "Handbook of Preparative Inorganic Chemistry," Vol. 2, 2nd ed., p. 1081, Academic Press, New York (1963).
11. Y. Sasaki, A. Kato, and S. Ueda, *This Journal*, **118**, 101 (1971).

Energy Transfer Between Rare Earth Ions in a Potassium Feldspar Glass

G. Baran, T. Y. Tien, and W. J. O'Brien

The University of Michigan, Ann Arbor, Michigan 48109

ABSTRACT

Nonradiative energy transfer was observed between rare earth ions in a potassium feldspar glass. Observation was made of the quenching of terbium fluorescence through interactions with dissimilar lanthanide ions. The severity of quenching is dependent on the energy gap between the fluorescing level of terbium and the closest lower lying level of another lanthanide ion and a numerical constant characteristic of the host. The value of this host constant, 2246 cm^{-1}, is indicative of a high probability of phonon-assisted energy transfer. Energy transfer was also observed between dysprosium and samarium when 405 and 425 nm radiation was used for excitation. The site symmetry of Eu^{3+} in potassium feldspar glass was evaluated through analysis of the emission spectrum and appears to be C_s.

The phenomenon of energy transfer between rare earth ions in various hosts has been studied by several investigators. Transfer of energy by radiative means, when emission by one ion is absorbed by another ionic species, has been observed by Nakazawa and Shionoya (1) in glasses containing dysprosium and neodymium. Nonradiative energy transfer between dissimilar ions was investigated by Dexter (2). It was found that energy transfer could occur if the overlap between the emission band of the sensitizer ion and the absorption band of the activator ion was large, *i.e.*, the two levels were in resonance with one another. The dependence of nonradiative transfer on the distance between sensitizer and activator ions was summarized by Blasse and Bril (3). The limiting distance between ions in a host in order for transfer by coulomb interaction to occur was found to be 27Å. Reisfeld (4) observed nonradia-

Key words: fluorescence, rare earths, energy transfer, glass.

tive energy transfer in glasses between thulium and erbium and between terbium and gadolinium. The energy levels participating in the transfer were not strictly in resonance with each other. Therefore, it was proposed that the transfer was made possible by the presence of lattice phonons which served to bridge the energy difference. Resonant energy transfer from terbium and europium in a tungstate host to other rare earth ions was investigated by Van Uitert and Iida (5). They found that the emission of terbium from the $^5D_4$ level was quenched by energy transfer from that level to the closest lower lying level of a dissimilar rare earth ion. The probability of transfer was dependent on the energy difference between the two levels and a constant equal to the vibrational constant of the tungstate group.

The fluorescent spectral character of rare earths is dependent to some degree on the host structure. The effect of nearest neighbor ions may result in a shift of the excited rare earth ion energy levels several hundred cm^{-1}, causing energy transfer paths between dissimilar ions to vary with different hosts. Feldspar glass is of interest as it is a host containing no nonbridging oxygen ions which should favor phonon-assisted energy transfer. Also, this composition is used in porcelains.

The chemical formula for potassium feldspar is $K_2O \cdot Al_2O_3 \cdot 6SiO_2$. Aluminum and silicon oxygen tetrahedra make up the continuous framework structure, with potassium occurring in the interstitial sites with 6-9 nearest neighbor oxygen ions (6). It has been reported that the entropy of fusion of crystalline feldspars is low and that short-range order in the glassy state should be similar to that in the disordered crystalline phase sanidine (7).

The dependence of Eu^{3+} emission spectra on site symmetry was observed by Blasse and Bril (8). The presence of an inversion center at the site caused the transition $^5D_0$-$^7F_2$ to be very weak. Jorgensen and Judd (9) identified that transition as a "pseudoquadrupole" which would only occur if the europium ion was located in certain sites. Reisfeld (4) found that europium sites in phosphate glasses were characterized by C_s symmetry. In order to further characterize the structure of feldspar glass, the emission of Eu^{3+} ions was studied to identify the ionic site symmetry.

Experimental Procedure

The starting materials used for preparation of the glasses were aluminum hydroxide, silicon dioxide, and potassium carbonate hydrate. The rare earth oxides used were Dy_2O_3, Eu_2O_3, Tb_4O_7, Tm_3O_3, and Sm_2O_3. The materials for the glasses were all reagent grade, while the rare earth oxides were luminescent grade. The concentrations of the rare earth ions in the glasses were maintained at 0.1, 0.5 and 1.0 mole percent (m/o). Prior to formulation, weight loss factors were determined for the aluminum hydroxide and the potassium carbonate hydrate and appropriate corrections were made. The charge balance was maintained by substituting the potassium ions with rare earth ions on a 1:3 atomic ratio.

Appropriately weighed quantities of the host materials were ground under acetone and air dried. They were then placed in platinum crucibles, calcined at 800°C for 8 hr and reground. The rare earth ions were added as nitrate solutions to the powder, dried at 90°C, and reground. The dry powder was then fused by an oxygen-natural gas flame with a pure silica rod used to support the molten mass. Due to the high viscosity and melting point of the glass (1540°C), it proved impossible to pour the glass into a standard size and shape. Therefore, specimens were made as large as possible then ground with silicon carbide to assume a suitable shape for spectroscopy.

The instrument used for fluorescent analysis was a spectrophotofluorimeter.[1] The excitation source was a xenon lamp and the detector a photomultiplier tube with S-20 response characteristics. The selection of aperture and slit width yielded resolution within 6 nm. Calibration of the emission monochrometer was done using a mercury lamp, while calibration of the excitation monochrometer was done using a quinine sulfate standard solution.

The spectral data were digitized and treated by a computer program. The main purpose of the program was to correct the intensity values for lamp output variability and photomultiplier tube response characteristics. In this manner direct comparison of relative intensities was possible.

[1] American Instrument Company, Incorporated, Silver Spring, Maryland 20910.

Results and Discussion

Energy transfer.—The quenching of terbium fluorescence due to the $^5D_4$-$^7F_5$ transition at 545 nm (Fig. 1) was studied in samples with 0.5 m/o Tb^{3+} and 0.5 m/o of Tm^{3+} or Dy^{3+} or Pr^{3+}. The $^5D_4$ level of terbium was excited directly with 488 nm radiation in order to avoid energy losses at higher levels. The three coactivating ions have similar ground state spin configurations. The results are presented in Fig. 2, where the intensity value of 1.0 represents the intensity of terbium emission when it alone is the activator and the relative intensity of the peak at 545 nm when coactivating ions are present are plotted against ΔE, the difference in energy between the $^5D_4$ level of Tb^{3+} and lower lying levels of the other ions. The intensity of terbium emission is seen to decrease as the energy difference ΔE decreases. The values for ΔE were taken from crystal spectra documented by Dieke (10). The nearest lower lying levels of the coactivating ions are the $^6F_{1/2}$ level of dysprosium, the $^3F_2$ level of thulium, and the $^1D_2$ level of praeseodymium. The energy difference between the $^5D_4$ level of terbium and the abovementioned levels of the coactivator ions was found to be critical in determining the probability of resonant energy transfer which would lead to quenching of terbium fluorescence.

The quenching of terbium emission by coactivating rare earth ions may be used to draw conclusions regarding the ease with which lattice phonons may bridge energy differences between energy levels of dissimilar ions. The slope of the line in Fig. 2 yields a parameter $\Delta E/2246$ cm^{-1} and the constant 2246 cm^{-1} is interpreted as a host material constant. It happens to be equal to about twice the fundamental vibrational

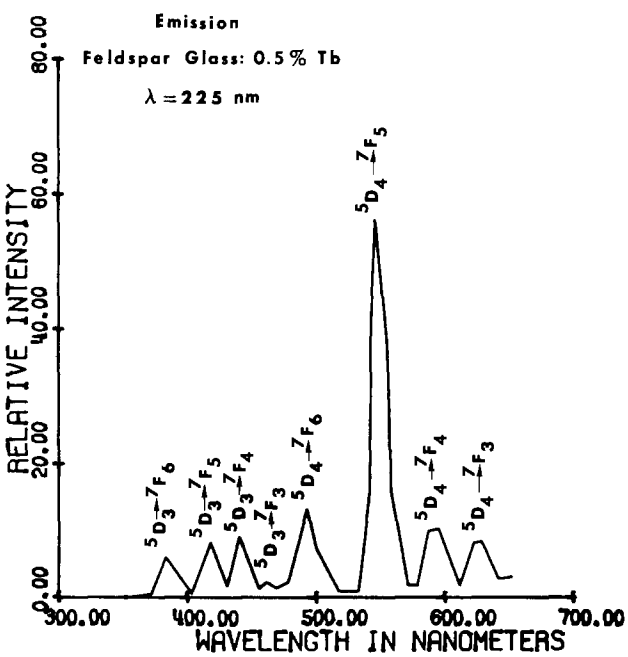


Fig. 1. Emission spectrum of 0.5% Tb^{3+} in potassium feldspar glass with excitation wavelength of 225 nm.

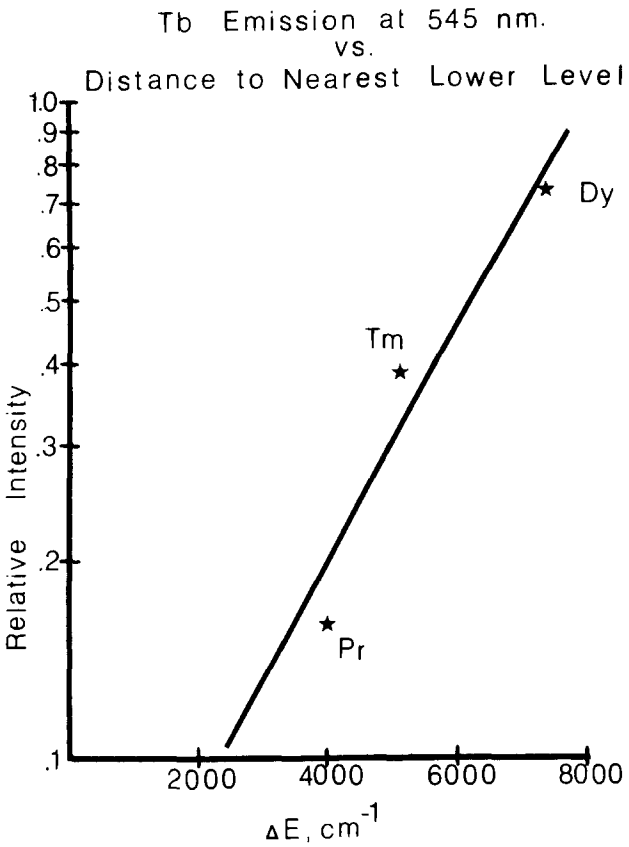


Fig. 2. Quenching of the $^5D_4$-$^7F_5$ transition of Tb^{3+} in potassium feldspar glass by equal concentrations of Tm^{3+}, Dy^{3+}, and Pr^{3+}.

constants of Si-O and Al-O bonds (1000-1130 cm^{-1}). According to Miyakawa and Dexter (11), the probability of phonon-assisted energy transfer "W" may be described by: $W = W(0) \exp(-\beta \Delta E)$, where $W(0)$ is the energy transfer probability when no phonon lines overlap, ΔE the energy gap between the levels of the sensitizer and the activator ions, and β a constant determined by the lattice. The quantity $|1/\beta|$ is therefore comparable to the constant derived in this work which is 2246 cm^{-1} for potassium feldspar glass.

The parameter $\Delta E/2246$ cm^{-1} is indicative of the "number" of phonons needed to bridge the energy gap ΔE between two levels of dissimilar rare earth ions in potassium feldspar glass. The high numerical value of this energy constant, compared to ~850 cm^{-1} in a tungstate host, is an indication of good vibronic coupling between the rare earth ion and the host. This result supports the view of the feldspar structure as being a highly interconnected one with few nonbridging oxygen ions. It is therefore expected that potassium feldspar glass may serve as a good host for observation of resonant, phonon-assisted energy transfer.

The presence of energy transfer was found in the sample containing 0.5% Dy^{3+} and 0.5% Sm^{3+}. With these concentrations, the average distance between Dy^{3+} and Sm^{3+} ions is approximately 26.5Å, a distance low enough so that energy transfer by coulomb interaction may occur. Excitation of this sample by 352 nm radiation to the upper levels of Dy^{3+} caused no energy transfer to occur. Transfer did occur under excitation by 425 and 405 nm radiation. For comparison, typical excitation and emission spectra of Dy^{3+} and Sm^{3+} are shown in Fig. 3-6.

Excitation by 425 nm radiation of the sample containing 0.5% Dy^{3+} and 0.5% Sm^{3+} results in the appearance of new Sm^{3+} peaks at 685, 702, and 730 nm (see Fig. 7). As samarium shows no absorption at 425 nm, the inference is that energy transfer occurs from dysprosium to samarium. The proposed path is from the $^4G_{11/2}$ level of Dy^{3+} to the $^4F_{5/2}$ level of Sm^{3+},

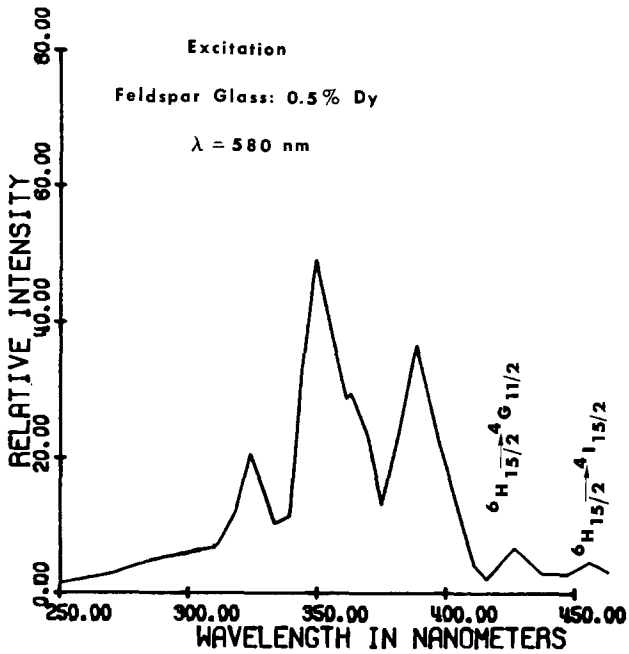


Fig. 3. Excitation spectrum of 0.5% Dy^{3+} in potassium feldspar glass with emission wavelength of 580 nm.

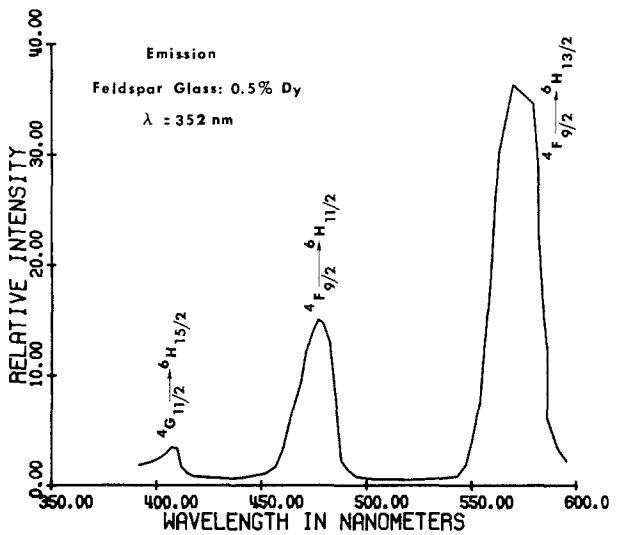


Fig. 4. Emission spectrum of 0.5% Dy^{3+} in potassium feldspar glass with excitation wavelength of 352 nm.

subsequent nonradiative decay of Sm^{3+} to the $^4I_{13/2}$ and $^4G_{5/2,7/2}$ levels and radiative transitions from these levels.

The emission spectrum which results when 405 nm radiation is used for excitation is more difficult to interpret (see Fig. 8). Certainly the peaks at 702 and 730 nm correspond well to samarium transitions. However, the peak at 685 nm may be due to either the $^4I_{15/2}$-$^6H_{9/2}$ transition of Dy^{3+} or the $^4I_{13/2}$-$^6F_{5/2}$ transition of Sm^{3+}. This peak does not occur in the spectrum of either ion alone, so it is evident that some energy transfer must be occurring, else the 702 and 730 nm Sm^{3+} peaks would not occur. Future work will be done in an effort to identify the transition responsible for the peak at 685 nm when 405 nm radiation is used for excitation.

Site symmetry.—The emission spectrum of Eu^{3+} is presented in Fig. 9. The excitation radiation used (393 nm) excited the ion to the $^5L_6$ level at 25,400 cm^{-1}. The site symmetry could be characterized with respect to the presence of an inversion center by examining the spectrum for the appearance of magnetic dipole transi-

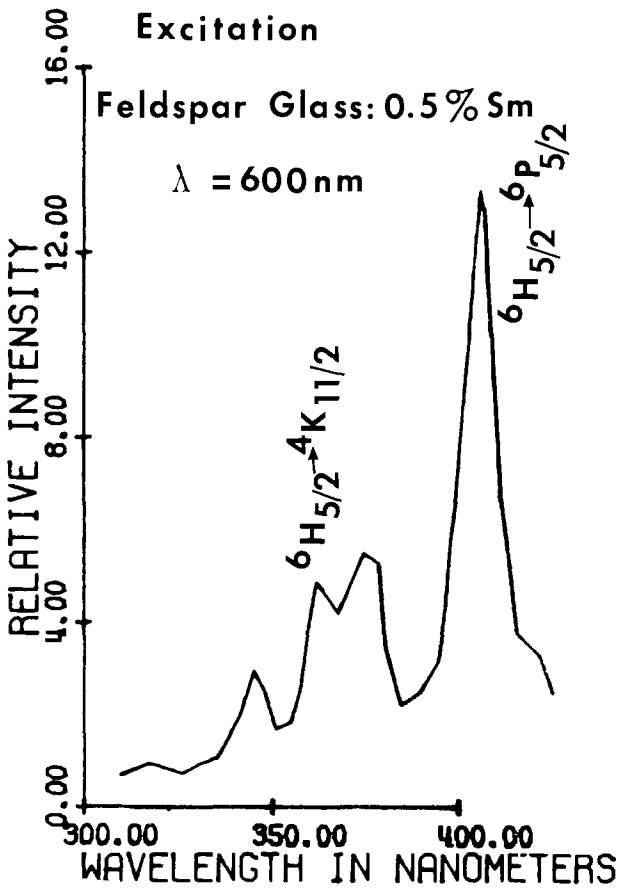


Fig. 5. Excitation spectrum of 0.5% Sm^{3+} in potassium feldspar glass with emission wavelength of 600 nm.

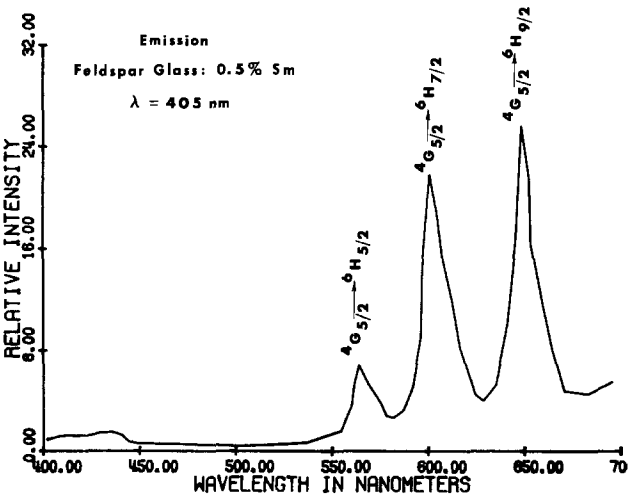


Fig. 6. Emission spectrum of 0.5% Sm^{3+} in potassium feldspar glass with excitation wavelength of 405 nm.

tions. In the case of Eu^{3+}, the $^5D_0$-$^7F_1$ transition is a magnetic dipole transition with $\Delta J = 1$. The $^5D_0$-$^7F_2$ transition is a pseudoquadrupole transition and is hypersensitive to the presence of an inversion center at the Eu^{3+} site. The greater intensity of this transition when compared with the intensity of the magnetic dipole indicates that no center of inversion is present at the eruopium ion site.

The $^5D_0$-$^7F_2$ hypersensitive transition of Eu^{3+} may only occur in a site having one of the following symmetries: C_s, C_1, C_2, C_{2v}, C_{3v}, C_{4v}, and C_6. The highly symmetric groups (the latter four) may be eliminated from consideration due to the low probability of occurrence of such a site in glass. The C_s site for Eu^{3+} in phosphate glass proposed by Reisfeld was formed

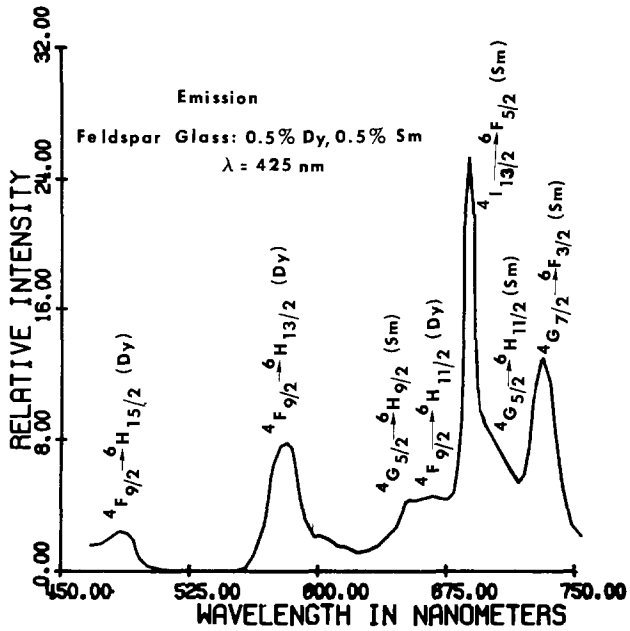


Fig. 7. Emission spectrum of 0.5% Dy^{3+} and 0.5% Sm^{3+} in potassium feldspar glass with excitation wavelength of 425 nm.

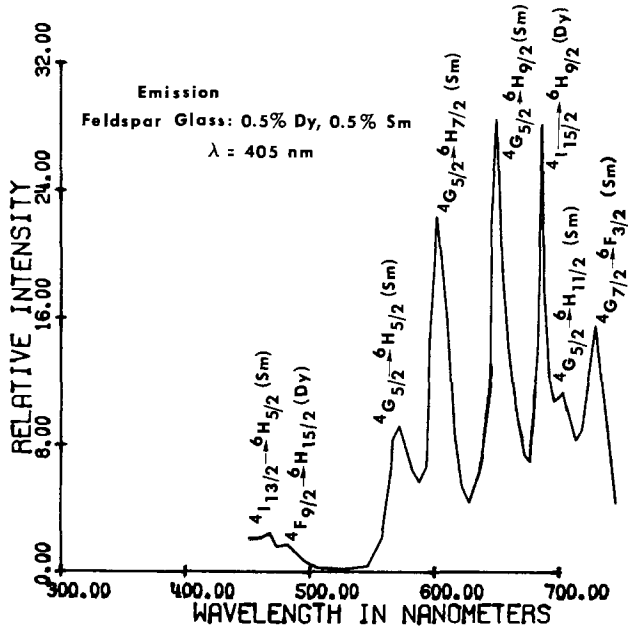


Fig. 8. Emission spectrum of 0.5% Dy^{3+} and 0.5% Sm^{3+} in potassium feldspar glass with excitation wavelength of 405 nm.

with eight oxygen ions located at cube corners with the rare earth ion located at the center of the cube. An eightfold site is possible in potassium feldspar, as the alkali ion in sanidine, a disordered crystalline potassium feldspar, has between 6 and 9 nearest neighbor oxygen ions. The substitution of the rare earth ions for potassium ions in this glass should make it probable that the rare earth ion also has between 6 and 9 nearest neighbor oxygen ions. It is therefore possible that the europium ion is in a site with C_s symmetry in potassium feldspar glass as well. If the rare earth ion is located in a "half" of a sanidine unit cell, which may be composed either of the group 4Al + 4Si or of the group 2Al + 6Si (7), the reflection plane present in C_s symmetry would cut through the cube made up of oxygen ions with aluminum tetrahedra lying directly opposite each other on both sides of the mirror plane. If a totally random distribution of silicon and aluminum tetrahedra surround the rare earth ion, the site symmetry will be C_1. The vibronic coupling between the rare earth ion and the host may then occur through

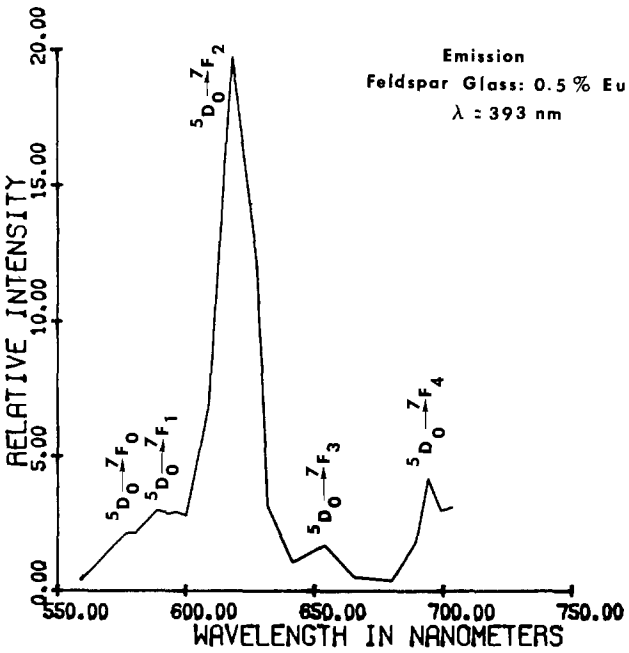


Fig. 9. Emission spectrum of 0.5% Eu^{3+} in potassium feldspar glass with excitation wavelength of 393 nm.

bonded interactions with the excess negative charges which exist due to oxygen ions belonging to aluminum tetrahedra.

Acknowledgments

The authors wish to thank B. J. Evans and E. F. Gibbons for their helpful discussion. This research was supported by U.S.P.H.S. Grant DE 00181 from the National Institutes of Health, Bethesda, Maryland. It represents a portion of a Ph.D. thesis by George Baran submitted to the H. H. Rackham School of Graduate Studies at the University of Michigan.

Manuscript received Aug. 23, 1976.

Any discussion of this paper will appear in a Discussion Section to be published in the December 1977 JOURNAL. All discussions for the December 1977 Discussion Section should be submitted by Aug. 1, 1977.

Publication costs of this article were assisted by the University of Michigan.

REFERENCES

1. I. Nakazawa and S. Shionoya, *Appl. Phys. Lett.*, **6**, 117 (1965).
2. D. L. Dexter, *J. Chem. Phys.*, **21**, 836 (1953).
3. G. Blasse and A. Bril, *Philips Tech. Rev.*, **31**, 304 (1970).
4. R. Reisfeld, *Struct. Bonding*, **13**, 53 (1966).
5. L. G. Van Uitert and S. Iida, *J. Chem. Phys.*, **31**, 186 (1963).
6. Sir L. Bragg, Editor, "The Crystalline State, Vol. IV: Crystal Structure of Minerals," Cornell University Press, Ithaca, N.Y. (1965).
7. T. F. W. Barth, "Feldspars," Wiley Interscience, London (1969).
8. G. Blasse and A. Bril, *J. Chem. Phys.*, **45**, 3327 (1966).
9. C. K. Jorgensen and B. R. Judd, *Mol. Phys.*, **8**, 281 (1964).
10. H. M. Crosswhite and H. Crosswhite, Editors, "Spectra and Energy Levels of Rare Earth Ions in Crystals," Wiley Interscience, New York (1968).
11. T. Miyakawa and D. L. Dexter, *Phys. Rev. B*, **1**, 2961 (1970).

Technical Notes

Rapid Determination of the Distribution of ^{31}P in Neutron-Irradiated Silicon

A. Yusa and Y. Yatsurugi

Komatsu Electronic Metals Company, Limited, Hiratsuka, Japan 254

and T. Takaishi

Institute for Atomic Energy, Rikkyo University, Yokosuka, Japan 240-01

Neutron transmutation doping is a very promising method for the production of high quality n-type silicon for high power devices such as thyristors and diodes (1-5). The homogeneity of the distribution of ^{31}P produced is governed by the irradiating neutron flux distribution. Usually, a silicon rod to be irradiated is inserted into a vertical irradiation port in a reactor core and rotated with some mechanical device. Thus, we can reduce the effect of the inhomogeneity of the flux along the radial direction. In contrast to this, the effect of the inhomogeneity along the axial direction cannot be reduced by rotating. The distribution of ^{31}P along the axis is directly proportional to that of neutron flux, which is lower in the top and bottom regions of the core. Then, we must carefully select a portion of the port appropriate to homogeneous doping. Since the flux distribution depends upon the geometry of the core assembly which changes frequently, a method for the rapid determination of the flux distribution is required. We report in this note upon a suitable method in which β-radiation from ^{31}Si produced by neutron irradiation is measured.

The neutron activation cross section is a function of the neutron energy, and hence the energy spectrum of neutrons affects the amount of neutron transmutation. This effect is remarkable, when a concerned nucleus

Key words: neutron transmutation doping, β-activity of silicon, neutron-flux distribution.

has a resonance absorption peak in the region of the epi-thermal neutron, as is the case with ^{59}Co and ^{197}Au. Hence, a neutron monitor of such a material must be carefully used in the silicon transmutation doping. In some cases, troublesome calibration might be required, but the silicon monitor presented herein can be used without any such trouble.

^{31}Si decays and transforms to ^{31}P with a half-life of 2.62 hr, emitting β-radiation of 1.47 MeV. We measured this β-radiation with a solid-state detector of the catheter type (Type-CASRAD, Toshiba Electric Company) which is designed to detect β-radiation of 1.7 MeV from ^{32}P in biological systems (6). The detector head consisted of a p-n junction of Si with a diameter of 2.3 mm, and was held in a nickel collimeter sheath of 3.2 mm diam. Such a compact geometry as this enabled us to measure a concentration of β-emitters contained in a very narrow region. A reverse bias of *ca.* 40V was supplied to the detector from a dry battery. The counting system used was of a conventional type, consisting of a charge sensitive preamplifier, linear amplifier, single channel pulse height analyzer, and scaler. Selecting an appropriate discrimination level for noise, the background counting rate was reduced to less than 2 cpm. The conditions of the measurements were chosen so that the total counts measured in a pregiven counting time of 24 sec were not less than 20,000 counts. Such a short counting time as this was necessarily required to obtain as many data as possible with a given silicon sample. The total counts of 20,000 are subjected to a statistical error of about 0.7%.

The silicon sample irradiated was etched with mixture of 3 parts conc HNO_3 and 1 part conc HF to remove surface contaminations, washed with water, and then set on a traveling plate of a X-Y stage. In the course of successive measurements, it took 30 sec to position a given point of the sample just beneath the detector head by operating the X-Y stage. Thus, we could obtain experimental data at a rate of one point per minute. If we measure the β-activity of a silicon sample giving an initial counting rate of 40,000 counts per 24 sec until it decreases to 20,000 counts per 24 sec, about 150 experimental points can be obtained. A short irradiation for silicon of about 10 min gives the above activity even in a small reactor with a power of 100 kW. Thus, we can

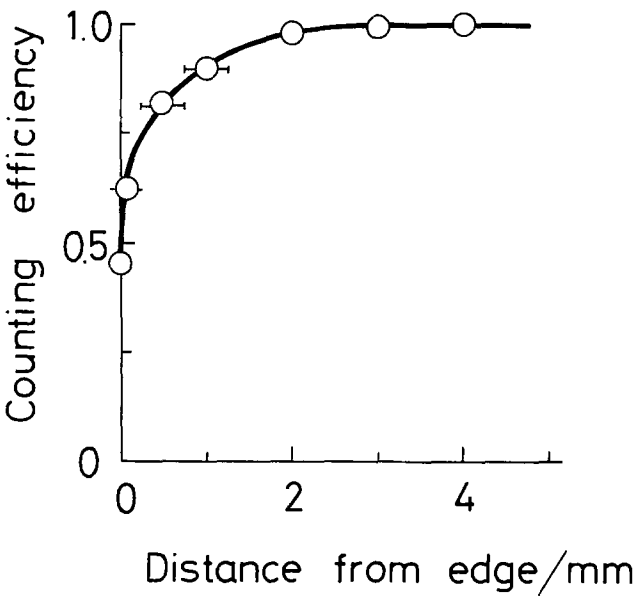


Fig. 1. Effect of the sample edge on the β-radiation counting efficiency of the solid-state detector.

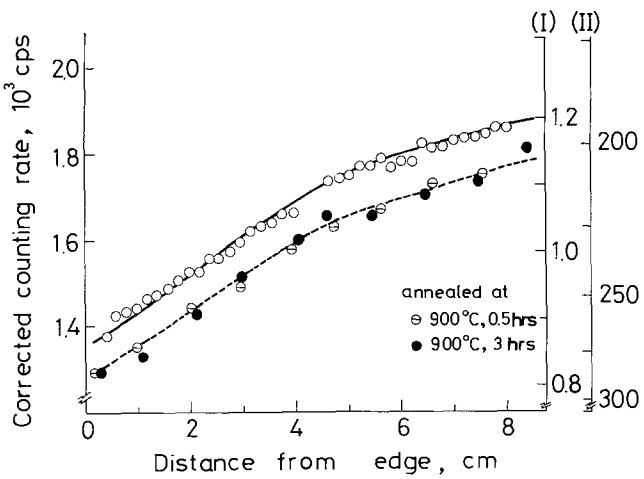


Fig. 2. Profile of the activity of ^{31}Si along the rod axis. The solid curve refers to the counting rate of β-radiation from ^{31}Si; the dotted curve refers to the neutron flux density deduced from the resistivity of the irradiated silicon. Units of right-hand side ordinate: (I), 10^{12} $n \cdot cm^{-2} \cdot sec^{-1}$; (II), Ω cm.

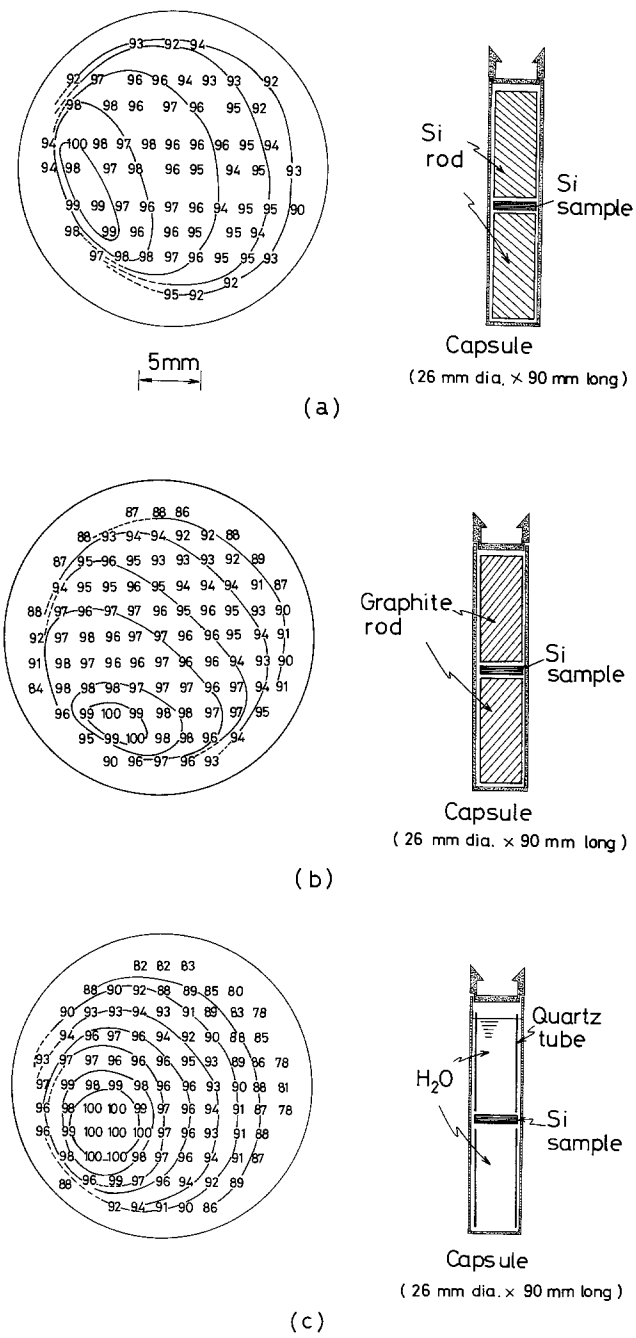


Fig. 3. Some examples of the relative distribution of ^{31}P in the plane of a silicon wafer irradiated under the conditions: (a) perturbed by silicon; (b) perturbed by graphite; (c) perturbed by light (natural)-water.

construct a distribution map of the neutron flux in the irradiation facility, within 3 hr.

The effect of the sample edge on the counting efficiency was investigated by the use of a silicon plate, 1 mm thick, which was homogeneously neutron irradiated. The calibration curve is shown in Fig. 1. No edge effect could be detected at a point located 2 mm inside the edge.

A silicon rod (25 mm diam × 80 mm long) was irradiated in a Triga-Mark II reactor of Rikkyo University. The neutron fluence amounted to about $1.4 \times 10^{17} n \cdot cm^{-2}$. The activity of ^{31}Si contained in the sample was measured along the orientation flat, and is shown in Fig. 2. The ordinate in the left-hand side expresses, in a relative scale, the counting rate which is corrected for the decay of the activity, and that in the right-hand side the neutron flux density deduced by the following procedure.

The concentration of ^{31}P produced, $[^{31}P]$, and the neutron flux density F are mutually related by the simplified equation

$$[^{31}P] = N(^{31}Si) = [^{30}Si]\,\sigma \int_0^\tau F\,dt \qquad [1]$$

where $N(^{31}Si)$ denotes the integrated total amount of ^{31}Si produced by the reaction, $^{30}Si(n, \gamma)\ ^{31}Si$. $[^{30}Si]$ designates the concentration of ^{30}Si ($1.54 \times 10^{21} cm^{-3}$), σ the cross section for the reaction (0.107 barns), and τ the irradiation time. To complete the map of the flux distribution by applying the one-point calibration method, the value for F at some point must be determined. We adopted the value of F determined previously from β-γ coincidence measurements of an irradiated gold foil. On the other hand, one can determine the absolute value of F from measurements of the electric resistivity, ρ, of an irradiated and annealed silicon sample. In this case the irradiation requires a longer time. If the sample is so highly pure that almost all of the carriers are supplied from the ^{31}P produced, the values of $[^{31}P]$ and hence that of F are easily determined from ρ measurements. Silicon wafers (25 mm diam × 1 mm thick) were cut from the irradiated silicon rod and annealed at 900°C for 0.5 and 3 hr in a nitrogen and oxygen stream, respectively. Their resistivities were measured with a four-point probe placed on the center of the wafers and are shown in Fig. 2. The two methods gave somewhat different values, as can be seen in the figure. Let us designate by subscripts c and ρ the values deduced from the first and second method, respectively. Then, we get empirically

$$F_\rho = 0.95 F_c.$$

Uncertainties in our measurements are ±5% for the absolute value of the resistivity, and ±6% for that of the neutron flux determined by the β-γ coincidence measurement method. Hence, the factor 0.95 in the above relation is a reasonable one. By the use of the present method, we can determine easily the distribution of ^{31}P in the plane of a silicon wafer irradiated under various conditions. Some examples are shown in Fig. 3. These samples, of course, were not rotated during irradiation. If the hills in the maps of Fig. 3. were located at the center, the rotation of the silicon rod might not reduce the inhomogeneity in the distribution of ^{31}P. These maps may be used to estimate the effectiveness of the rotation in the homogeneous doping.

Acknowledgment

The present authors would like to thank T. Sugita of Toshiba Electric Company who kindly furnished the solid-state detector.

Manuscript submitted July 15, 1976; revised manuscript received Oct. 7, 1976.

Any discussion of this paper will appear in a Discussion Section to be published in the December 1977 JOURNAL. All discussions for the December 1977 Discussion Section should be submitted by Aug. 1, 1977.

Publication costs of this article were assisted by the Komatsu Electronic Metals Company, Limited.

REFERENCES

1. M. Tannenbaum and A. D. Mills, *This Journal*, **108**, 171 (1961).
2. C. N. Klahr and M. S. Cohen, *Nucleonics*, **22**, 62 (1964).
3. M. Schnöller, *IEEE Trans. Electron Devices*, **ed-21**, 313 (1974).
4. W. E. Hass and M. Schnöller, *J. Electron. Mater.*, **5**, 57 (1976).
5. H. A. Herrmann and H. Herzer, *This Journal*, **122**, 1568 (1975).
6. H. Ueda, Y. Sasaki, M. Iio, S. Kaihara, K. Machida, I. Ito, S. Takayanagi, T. Kobayashi, and T. Sugita, *J. Nucl. Med.*, **10**, 713 (1969).

Origin of the Fixed Charge in Thermally Oxidized Silicon

Herbert Goronkin

Varian Associates, Beverly, Massachusetts 01915

The thermal oxidation of silicon under ultraclean conditions gives rise to a net positive fixed charge, Q_{ss}, which is believed to be located in the oxide near the oxide-silicon interface region. The magnitude of Q_{ss} determines several important electrical parameters such as MOS threshold voltages and junction breakdown voltages. It is important in device fabrication that Q_{ss} be both minimized and reproducible. Therefore, a great deal of attention has been paid to process parameters affecting Q_{ss}.

It is well established that, following thermal oxidation, anneals between 900° and 1200°C in inert gas ambients will result in a reduction in Q_{ss}. The decrease can be as great as an order of magnitude. Recently, there have been reports of Q_{ss} slowly increasing with time following the relatively more rapid initial decrease (1, 2). Figure 1 shows some of the reported behavior. The existence of the positive $Q_{ss}(t)$ slope shows that the anneal cannot proceed for unlimited times to minimize Q_{ss}; there appears to be an optimum time that depends on the anneal temperature and ambient.

Deal *et al.* (3) suggested that excess silicon in thermally grown SiO_2, near the silicon surface, may be ionic and could be the source of Q_{ss}. It has been suggested (1) that the increase in Q_{ss} during inert gas anneal arises from the breaking of Si-Si or Si-O bonds in the strained interface region. The strain in this transition region would have to help ionize Si or SiO_2 at the anneal temperatures and maintain the charged state after return to thermal equilibrium. The breaking of bonds at elevated temperatures can be accompanied by reorientation of molecular clusters in the transition region which can give rise to either a net positive or negative change in oxide charge magnitude. Resulting Q_{ss} would not be monotonic with

Key words: silicon oxide, fixed charge, surface states, silicon diffusion.

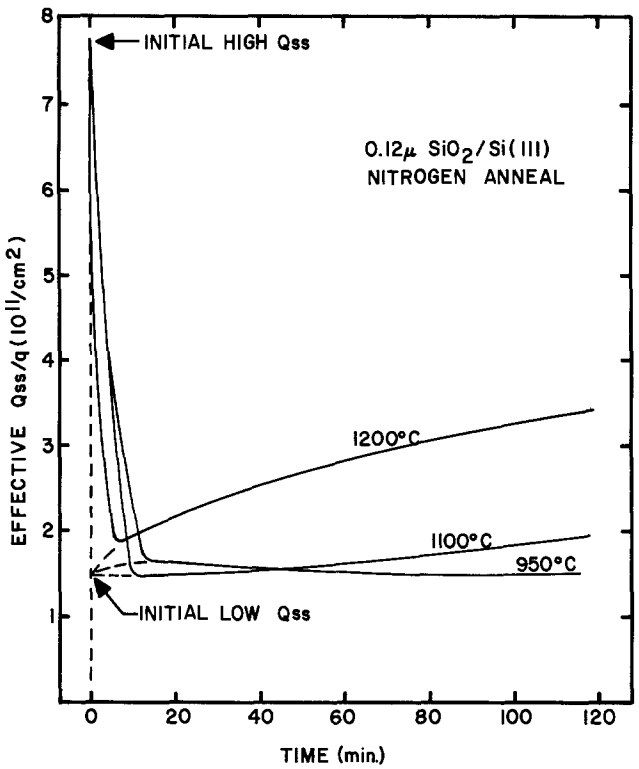


Fig. 1. Dependence of effective Q_{ss}/q on anneal in nitrogen for times of 0-120 min at various temperatures from Ref. (1).

time which is contrary to observations. It seems more probable that there is an introduction of additional charge into the interface region.

We propose that via diffusion of silicon atoms, the diffusion of ionic silicon into the transition region would provide a source of positive charge causing Q_{ss} to increase monotonically with time. It was the purpose of this work to see if the concept of solid-state diffusion could explain the observed variation of $Q_{ss}(t)$.

Theory

We consider SiO_2 grown in dry oxygen and subsequently annealed in an inert ambient. The resulting experimental curve of $Q_{ss}(t)$ is regarded as consisting of two contributions, a term $Q_{ss}^-(t)$ which decreases in magnitude with time and $Q_{ss}^+(t)$ which increases. In the simple theory presented here, excess silicon is the origin of Q_{ss} and each excess silicon atom is singly ionized.

The nature of the two terms are described in the following assumptions.

1. The postoxidation value of the interface region width is x_{io} and the average density of excess silicon ions therein is N_{si}. The initial value of fixed charge is related to N_{si} by

$$Q_{sso} = N_{si}\, x_{io} \qquad [1]$$

The neutral ambient post oxidation anneal reduces $Q_{ss}(t)$ to a minimum value. The corresponding interface region width is x_i and the minimum observed value of Q_{ss} is given by

$$Q_{ssm} = N_{si}\, x_i \qquad [2]$$

The maximum reduction in Q_{ss} arising from neutralization of ionic silicon by excess oxygen in the oxide is given by

$$\Delta Q = N_{ox}\, x_o \qquad [3]$$

where N_{ox} is the solid solubility of oxygen in SiO_2 at the growth temperature and x_o is the oxide thickness.

This assumption is based on the idea that, should oxidation of a silicon surface suddenly cease by either elimination of the source or reduction in temperature, there will be a nearly uniform distribution of oxygen throughout the oxide. Subsequent high temperature annealing in an inert ambient allows diffusion of the unreacted oxygen. That portion diffusing to the interface oxidizes elemental silicon which can no longer contribute to Q_{ss}^-. Since the rate of change of Q_{ss}^- will depend on the amount of charge present, we can write

$$\frac{d\,Q_{ss}^-(t)}{dt} = -\frac{Q_{ss}^-(t)}{\tau} \qquad [4]$$

where τ will depend on temperature and the diffusion constant of oxygen in silicon dioxide. Using Eq. [1], [2], and [3], the solution to Eq. [4] is

$$Q_{ss}^-(t) = (N_o\, x_o + N_{si}\, x_i)\, e^{-t/\tau} = (Q_{sso})\, e^{-t/\tau} \qquad [5]$$

2. Measurements (4) have indicated that the width of the interface region between silicon and thermally grown silicon dioxide is on the order of 25Å. Across this transition region, the concentration of elemental silicon changes is from about 5×10^{22} cm^{-3} to zero. This gives a concentration gradient of about 10^{29} cm^{-4}. There is a difference in bonding energies from the 1.84 eV Si-Si bonds on one side of the transition region to the 2.9 eV Si-O bonds on the other. At elevated temperatures, the strain due to unrelaxed bonds and the difference in chemical potential of silicon on the silicon side of the transition region and silicon on the oxide side combine to produce a driving force for diffusion from the silicon region towards the SiO_2 region. Then $Q_{ss}^+(t)$ can be defined as

$$Q_{ss}^+(t) = \int_0^{x_i} N_s(x)\, dx \qquad [6]$$

where x_i is the width of the interface region. $N_s(x)$ is the density of silicon atoms in the interface region and arises from the diffusion of silicon according to the relation

$$N_s(x) = N_{so}\, \mathrm{erfc}\, \frac{x}{2\sqrt{Dt}} \qquad [7]$$

which is analogous to the redistribution of impurities during epitaxial growth. D is the diffusion constant of silicon in the transition region and t is time. N_{so} is the volume density of silicon in the substrate within a diffusion length of x_i.

Equation [6] is solved, using Eq. [7], to give

$$Q_{ss}^+(t) = N_{so}\{x_i\, \mathrm{erfc}\, (x_i/2\sqrt{Dt}) + 2\sqrt{Dt/\pi}\,(1 - \exp[-(x_i^2/4\,Dt)])\} \qquad [8]$$

$Q_{ss}(t)$ is found by adding the two contributions to give

$$Q_{ss}(t) = Q_{ss}^-(t) + Q_{ss}^+(t) \qquad [9]$$

For $x_i << 2\sqrt{Dt}$, $Q_{ss}^+(t)$ approaches zero. For $x_i >> 2\,Dt$, $Q_{ss}^+(t)$ behaves as $2N_{so}\sqrt{Dt}$.

Experimental

The wafers used in this investigation were 4-6 Ω-cm phosphorus-doped silicon with <111> orientation. They were cleaned with an ammonium fluoride-HF solution, an HF dip, several water rinses, and spun dry. Oxidations were performed at 1000°C using dry oxygen in a fused quartz tube with a high purity liner. After 1300Å of oxide was grown, the wafers were withdrawn (push and pull rates were about 3 min) and annealed in a similar furnace at 1100°C in dry nitrogen for various times up to 140 hr. Aluminum dots were deposited through an evaporation mask on the oxide. Oxide from the back side of the wafer was removed and aluminum deposited thereon. The wafers were sintered at 495°C in N_2 for 30 min.

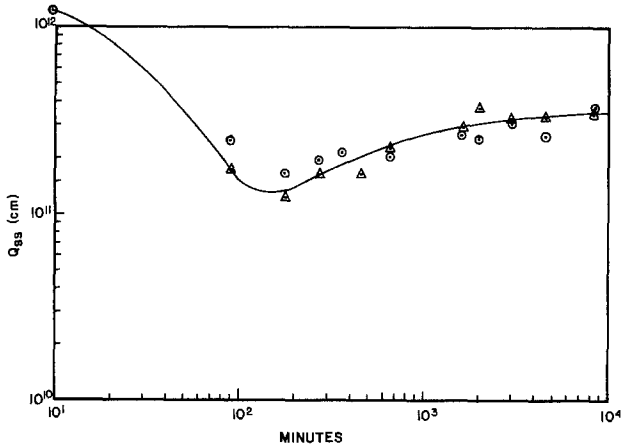


Fig. 2. Variation of Q_{ss} with time in dry N_2 at 1100°C. x_o = 1300Å. Solid curve = theory.

The oxide thickness, x_o, was measured with a Rudolph Routine 100 ellipsometer. The value of Q_{ss} was determined from the relation

$$\frac{Q_{ss}}{q} = \frac{2.13 \times 10^{10}\ (-V_{FB})}{x_o(\mu)}\ \text{charge/cm}^2 \qquad [10]$$

where V_{FB} is the flatband voltage. The mobile ion charge density was determined from the shift in the C-V curves using bias-temperature stress of 300°C, 5 min, +15V to be less than 3×10^{10} cm^{-2}.

Results and Discussion

Figure 2 shows variation of $Q_{ss}(t)$. The circles and triangles are experimental data. The solid curve is theory. Table I gives the values of parameters used in the theoretical curve.

Although the exponential dependence of $Q_{ss}^-(t)$ gives a reasonable fit to the data, there are not enough data points for $t < 90$ min to rule out other functions. Because of the limited number of oxygen molecules available for reaction at the interface, a Gaussian dependence might be more appropriate.

The value of τ was determined from the curve in Fig. 2. Using Eq. [1], [2], and [3], N_{ox} is found to be 7.3×10^{16} molecule/cm^3 which is in good agreement with the published value of 5×10^{16} molecule/cm^3 for the solubility of O_2 in SiO_2 at 1000°C (5). Using Eq. [1] and [2], the data give a value of about 10 for the ratio of initial to final transition layer thickness. Almost 90% of the excess silicon in the transition layer following oxidation was consumed by unreacted oxygen in the first 130 min of inert ambient anneal. At the minimum of $Q_{ss}(t)$, the rate of silicon consumption equals the rate of silicon replenishment via outdiffusion from the substrate.

The results for $Q_{ss}^+(t)$ show that the association of diffused silicon atoms with Q_{ss} predicts the observed behavior. There are only two adjustable parameters in $Q_{ss}^+(t)$. N_{so} is simply a constant of proportionality. It was found by shifting the $Q_{ss}(t)$ curve along the Q axis to obtain the best fit to the data. Its magnitude is considerably less than the bulk density of silicon atoms (5×10^{22} cm^{-3}), and corresponds to the density of silicon atoms within a diffusion length of the transition region that have sufficiently low binding energy to diffuse due to termination of the periodic lattice.

Table I.

Parameter	Value at 1100°C
τ	30 min
D	5×10^{-19} cm^2/sec
x_i	2.5×10^{-7} cm
N_{si}	4×10^{17} cm^{-3}
N_{so}	1.7×10^{18} cm^{-3}

The other parameter is the diffusion constant which, when varied, shifts $Q_{ss}^+(t)$ along the time axis of Fig. 2. A change of half an order of magnitude in D will shift the curve by about the same amount in time. The best fit can be found without knowledge of N_{so}. The value of D at 1100°C is several orders of magnitude less than that for some of the common silicon dopants in SiO_2 and accounts for the small magnitude of the transition region width.

The diffusion constant found here may only be valid for silicon diffusing through the transition region. The small value of x_i and the analytical technique described above show that far larger times are required for measurable concentrations of silicon to diffuse past the transition region and well into the oxide lattice.

The shape of Q_{ss} in the region where $Q_{ss}(t)$ increases is a sensitive function of the value of x_i. For $x_i \geq 160$Å, Q_{ss} increases as the square root of time to 10^4 min. For $x_i = 10$Å, Q_{ss} saturates at about 10^3 min.

The value found for x_i must represent an average value since $Q_{ss}(t)$ continued to increase throughout the anneal. If silicon diffusion is the primary mechanism for increasing $Q_{ss}(t)$, a saturation in Q_{ss} would imply an equilibrium value for x_i.

The data indicate that $Q_{ss}^+(t)$ can be associated with ionic silicon. The presence of elemental silicon diffusing into the interface region and leaving a charged vacancy in the periodic lattice can explain many of the effects that anneal ambients have on Q_{ss}. For example, anneals in oxygen should decrease Q_{ss} by an amount which is approximately the solubility of molecular oxygen in SiO_2 multiplied by the oxide thickness. This agrees with the Q_{ss}-oxygen triangle (3) which relates final Q_{ss} to the final oxidation temperature and ambient. The decreasing Q_{ss} with temperature for the oxygen leg implies an increasing concentration of molecular oxygen with increasing temperature which is in the same direction as the expected increase in solubility with increasing temperature. It follows that in order to decrease Q_{ss}, the concentration of excess oxygen in the oxide should be increased in order to increase the reaction rate with excess silicon.

The value of Q_{ss} obtained from Eq. [10] is ambiguous since it can contain contributions from N_{ss}, the density of fast states which are located at the interface. The two can be separated by measuring the flatband shift in the C-V curve between room and liquid nitrogen temperatures (6). The model described here can be used to explain these properties. The increase in N_{ss} after annealing in inert ambients probably arises from the diffusion of silicon into the silicon side of the transition region. The decrease in N_{ss} with hydrogen anneal is seen as neutralization of Si ions by formation of Si-H molecules.

Summary

The fixed charge and fast states in thermally grown silicon oxides have been associated with silicon which has diffused into the transition region from the surface region of the single crystal substrate. The diffusion follows the complementary error function dependence. A value for the diffusion constant of silicon in the transition region of 5×15^{-19} cm^2/sec at 1100°C was found. The density of silicon atoms that can diffuse is four orders of magnitude less than the bulk density and provides a measure of the thickness of the surface region of the terminated silicon lattice. The magnitude of fixed charge at the end of oxidation or oxygen anneals has been associated primarily with unreacted oxygen and excess silicon in the oxide.

Acknowledgments

Part of this work was performed while the author was with the General Electric Company, Integrated

Circuits Center, Syracuse, New York. I would like to thank Dr. L. Cordes for his encouragement and stimulating conversations about this work.

Manuscript submitted March 8, 1976; revised manuscript received Aug. 27, 1976.

Any discussion of this paper will appear in a Discussion Section to be published in the December 1977 JOURNAL. All discussions for the December 1977 Discussion Section should be submitted by Aug. 1, 1977.

Publication costs of this article were assisted by Varian Associates.

REFERENCES

1. B. E. Deal, *This Journal*, **121**, 198C (1974).
2. D. W. Hess and B. E. Deal, *ibid.*, **122**, 1123 (1975).
3. B. E. Deal, M. Sklar, A. S. Grove, and E. H. Snow, *ibid.*, **114**, 266 (1967).
4. R. A. Clarke, R. L. Tapping, M. A. Hopper, and L. Young, *ibid.*, **122**, 1347 (1975).
5. A. S. Grove, "Physics and Technology of Semiconductor Devices," John Wiley & Sons, New York (1967).
6. D. M. Brown and P. V. Gray, *This Journal*, **115** 760 (1968).

Brief Communications

Contacts to p-Type InP

F. A. Thiel, D. D. Bacon, E. Buehler, and K. J. Bachmann*

Bell Laboratories, Murray Hill, New Jersey 07974

Contacts to p-type InP have recently gained some interest in the context of near-infrared LED's (1) and n-CdS/p-InP solar cells (2). Pure In metal (3) and Au-Zn alloys (4) have been described thus far as suitable materials for making contacts to p-InP. Electroplated Au/Zn/Au contacts sintered into the InP result in excellent ohmic contacts with a resistance $\leq 10^{-3}$ Ω cm² to moderately resistive InP (1-10 Ω cm material) (4). However, in the process of sintering Au-alloy contacts it is difficult to control the depth of penetration into the InP. Also, for large-area InP/CdS solar cells it would be desirable to find an inexpensive contact material that could be applied after the deposition of the InP film without interrupting the production process. In-contacts to thin films of InP on CdS would be a natural choice under fabrication conditions where In metal is reacted with PH_3(5). However, as shown in Fig. 1, pure In does not result in an ohmic contact to moderately resistive p-InP and we evaluate, therefore, In-Zn and In-Cd alloys as possible alternatives for contacting p-InP and compare them with Au-Zn and Au-Cd contacts.

The metal alloys were applied as sputtered films or ball contacts on slabs of p-InP of typical dimensions 0.5 × 2 × 15 mm. The contacts were sintered on a carbon strip heater in forming gas and the contact area was measured by microscopic examination (typically 0.5 mm diameter). Also, we sintered 0.05 mm diameter Au-2% Zn and Au-2% Cd wire contacts to the InP slabs. All contacts were evaluated on polished surfaces since rough surfaces or etched surfaces required considerably higher sintering temperatures leading to inferior contact properties. *I-V* curves were measured between two contacts of the same size. The bulk resistivity of the InP was determined by four-point probe measurements. The optimum sintering temperature was between 400° and 450°C for typically 5 min.

Figure 1 shows *I-V* characteristics obtained for various contact materials. In and In-5% Cd contacts have rectifying characteristics. Approximately linear *I-V* characteristics are observed for AuCd, AuZn, and In-5% Zn contacts, with the lowest contact resistance ($<10^{-2}$ Ω cm²) obtained for the Au-2% Cd contacts.

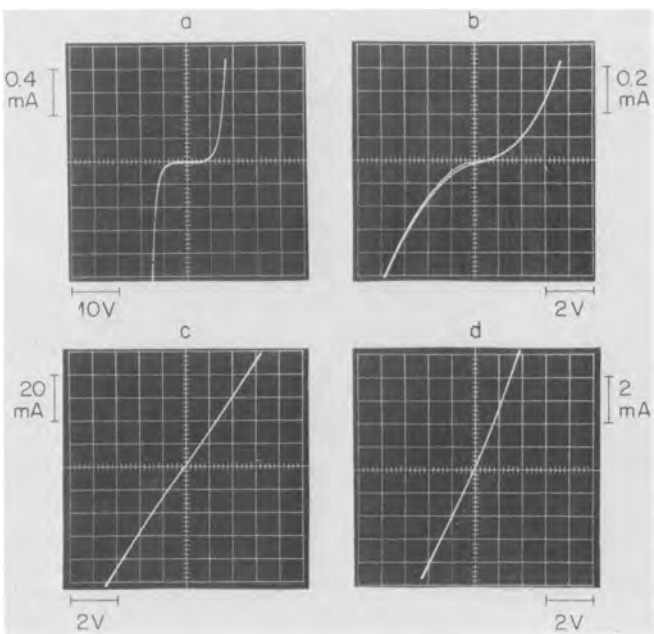


Fig. 1. Two-point *I-V* curves for (a) In, (b) In-5% Cd, (c) In-5% Zn, and (d) Au-2% Zn contracts to p-type InP (N_A-N_D = 5 × 10^{16} cm^{-3}, μ_h = 78 cm²V^{-1}sec^{-1}, ρ = 1.65 Ω cm). Contact area (cm²): (a) 1.7 × 10^{-3}, (b) 2.0 × 10^{-3}, (c) 2.4 × 10^{-3}, (d) ~10^{-4}. Bulk resistance between contacts (Ω): (a) 183, (b) 47, (c) 60, (d) 60. Contact resistance (Ω cm²): (a) ~10^3, (b) 60, (c) 0.02, (d) ~0.01.

Since InZn, but not InCd, results in an ohmic contact and the primary difference in the properties of Zn and Cd acceptor impurities in InP is the considerably faster diffusion of Zn, we believe that diffusion plays an important role in the formation of the contact. The properties of the best InZn contacts are similar to those of our AuZn contacts that have a contact resistance of ~0.01 Ω cm². In view of the results of Ref. (4), electroplating produces evidently a better contact than sputtered or mechanically attached metals sintered

* Electrochemical Society Active Member.
Key words: contacts, solar cells, p-InP.

JOURNAL OF THE ELECTROCHEMICAL SOCIETY

ELECTROCHEMICAL SCIENCE AND TECHNOLOGY

MARCH 1977

Rare Earth Cobaltites as Oxygen Electrode Materials for Alkaline Solution

T. Kudo, H. Obayashi, and M. Yoshida

Hitachi, Limited, Central Research Laboratory, Kokubunji, Tokyo 185, Japan

ABSTRACT

The perovskite-type compounds $Ln_{1-x}M_xM'O_3$ (Ln = lanthanoid element, M = alkaline earth element, M' = transition metal element) are examined as oxygen electrode materials for an alkaline solution. A porous sintered electrode consisting of a compound like $Nd_{1-x}Sr_xCoO_3$ ($x = 0.2$) is satisfactory in both polarization characteristics and stability under working conditions. However, a polytetrafluoroethylene (PTFE) bonded type electrode barely functions as an oxygen electrode even at a current density as low as 10 mA/cm^2. The electrode oxide undergoes reduction instead of acting as a reduction catalyst for gaseous oxygen to hydroxy ions. From a practical point of view, the sinter-type electrodes are promising as metal-air secondary battery cathodes because they are stable to anodic oxidation during charge periods.

The perovskite-type compounds like $La_{1-x}Sr_xCoO_3$ exhibit high electrical conductivity ($\simeq 10^4\ \Omega^{-1}$-cm^{-1}) at room temperature (1, 2). These compounds have been investigated as cathode materials for high temperature fuel cells (3). However, they have become the subject of renewed attention as oxygen electrode materials for alkaline solution working at moderate temperatures, not only due to their large electrical conductivity but also to their electrocatalytic activity which rivals that of platinized platinum (4).

The authors have studied the electrochemical behavior of $Nd_{1-x}Sr_xCoO_3$ in an aqueous alkaline solution (5). The oxygen ion diffusivity in these compounds is extraordinarily large ($D \simeq 10^{-11}$ cm^2/sec for $x = 0.2$ at 25°C) when compared with ordinary oxides. Their electrochemical redox reaction takes place reversibly in an alkaline solution as

$$O^{2-}(\text{lattice}) + 2Co^{4+} + H_2O + 2e \leftrightharpoons V_O^{\cdot\cdot} + 2Co^{3+} + 2\,OH^- \quad [1]$$

where $V_O^{\cdot\cdot}$ is a doubly ionized oxygen ion vacancy. One of the purposes of this study is to further investigate the reduction of oxygen to hydroxy ions on these compounds in connection with the above results. Another is to examine these compounds as possible oxygen electrode materials. From a practical point of view, the oxygen electrodes obtained here are useful in metal-air secondary batteries, not only because their performance is as good as that of platinized platinum electrodes, but also they are resistive to anodic oxidation during metal electrode chargings.

Experimental

PTFE-bonded type electrode.—A powder of the complex oxide compounds was prepared by sintering a homogeneous mixture of the component metal acetates at 800°C in air for 2 hr. The details of sample oxide preparations can be found in a previous paper (2). X-ray analyses showed only the diffraction pattern of the perovskite structure. The BET specific surface area of the powder was about 5 m^2/g. A complex oxide paste was prepared by adding a PTFE suspension (Mitsui Fluoro Chemical Company, 14.5% solid content) to the oxide powder together with deionized water and vigorously stirring. The amount of PTFE suspension was 0.7 ml/g of the oxide powder. To facilitate the separation of the water and the paste, acetone was added after the agitation was stopped. Then, the paste was spread on a nickel screen (60 mesh, 20 × 30 mm) so that its bulk density was about 75 mg/cm^2. The pasted screen was then pressed with a sheet of nonwoven PTFE on one side by applying a 500 kg/cm^2 pressure and was sintered at 250°C for 30 min in air to enhance its water repellency. The final electrode thickness was about 0.07 cm.

Sinter-type electrode.—Methyl cellulose (1% aqueous solution) was added to the oxide powder as a binder and it was pressed in a die (12 mmϕ or 30 × 35 mm rectangular) applying a 100 kg/cm^2 pressure to give a 2 mm thick disk (or plate). This disk was sintered at 900°C in air for 2 hr. The sintered disk showed about 60% porosity. As a current collector, a piece of platinum net was attached on one side of the disk by baking at 700°C with gold paste (Tokuriki Chemicals). Then, the disk was impregnated with a solution of fluorinated polyacryloester (FC-706, 3M Company) and dried at a temperature of approximately 100°C. Fluorinated polymer was used as a hydrophobant because it dissolves thoroughly in hexafluorinated xylene. In this way, the fluorinated polymer easily penetrates into pores of the electrode, in contrast with the very limited penetration of a PTFE suspension. After being dried at room temperature, the disk was mounted with an epoxy resin on an acryl case and oxygen or air was introduced into the gas compartment at the back of the electrode, while the front surface was in contact with a KOH solution.

Key words: air electrode, perovskite-type oxide, metal-air battery, rare earth cobaltite.

Measurements.—The electrode potentials were measured *vs.* a Hg/HgO reference electrode using a potentiometric recorder (QPD54, Hitachi). Constant rate potential sweep measurements were conducted employing a Type NL-101 potentiostat (Nichia Keiki Company). As a constant current d-c source, a Metronix 621 power supply was used. Temperatures of the electrolyte were controlled to 25° ± 1°C. The specific conductivity of the mixed oxides was measured by a d-c four-probe method, the details of which were reported in previous works (2, 6).

Results and Discussion

The results of potential sweep measurements of a PTFE-bonded type $La_{1-x}Sr_xCoO_3$ ($x = 0.1$) oxygen electrode, are shown in Fig. 1. When the potential is swept starting at a more anodic value ($E = 0.65$V *vs.* Hg/HgO) than that for oxygen evolution (point A in Fig. 1) toward the cathodic direction at a constant sweep rate of 50 mV/min, a cathodic current starts at $E = 0.12$V (point B). This current may be considered as resulting from the reduction of oxygen

$$\tfrac{1}{2}\,O_2 + H_2O + 2e = 2\,OH^- \qquad [2]$$

and/or by the reduction of the electrode itself (5) expressed in Eq. [1]. However, if the oxygen ion diffusion rate in the crystal lattice is sufficiently large, oxygen ions consumed by the reaction in Eq. [1] may be supplied without delay by the reaction

$$\tfrac{1}{2}\,O_2 + V_O^{\cdot\cdot} + 2e = O^{2-}\,(\text{lattice}) \qquad [3]$$

at the gas/electrode interface. Thus, the total reaction would be expressed by Eq. [2], even if the reaction of Eq. [1] takes place. This situation should be true when the cathodic current density is small. However, the reaction expressed by Eq. [1] seems to prevail with an increase in the current density as a result of the delay in oxygen diffusion through the oxide. It has been ascertained that the increase in nonstoichiometry of compounds like $La_{1-x}Sr_xCoO_{3-\delta}$ reduces their conductivity (2). In this respect, the current decrease between points C and D in Fig. 1 may be attributed mainly to the resistivity increase resulting from the reduction of the electrode according to Eq. [1]. When the potential reached −1.2V (point E) where hydrogen began to evolve with the decomposition of the oxide, the sweeping direction was reversed. The cathodic current decreased showing a marked hysteresis, with the anodic current beginning at +0.15V (point F). Since this is much more cathodic than the oxygen evolving potential, an electrochemical reoxidation of the electrode oxide has taken place.

Figure 2 shows the polarization characteristics of $Nd_{1-x}Sr_xCoO_3$ air electrodes *vs.* current densities at their early stages. The PTFE-bonded type electrode was not able to give a stationary potential when the current density exceeded 10 mA/cm² (dotted line). On the contrary, the sinter-type electrode (in the case of $x = 0.2$) showed flat I-V characteristics and gave very stable potentials. No increase in the polarization was observed after a 100 hr test at 20 mA/cm².

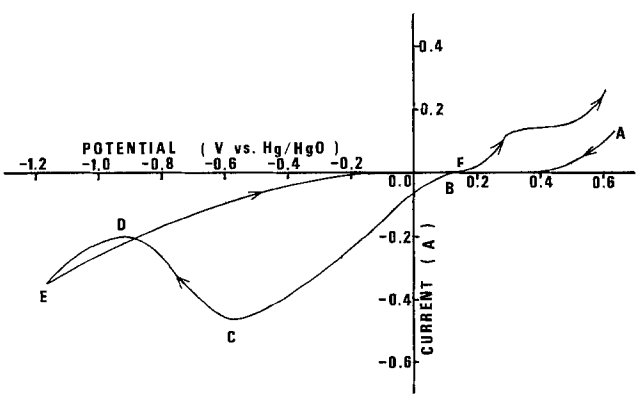


Fig. 1. Potential sweep of a PTFE-bonded $La_{0.9}Sr_{0.1}CoO_3$ in a 30% KOH solution. Sweep rate 50 mV/min.

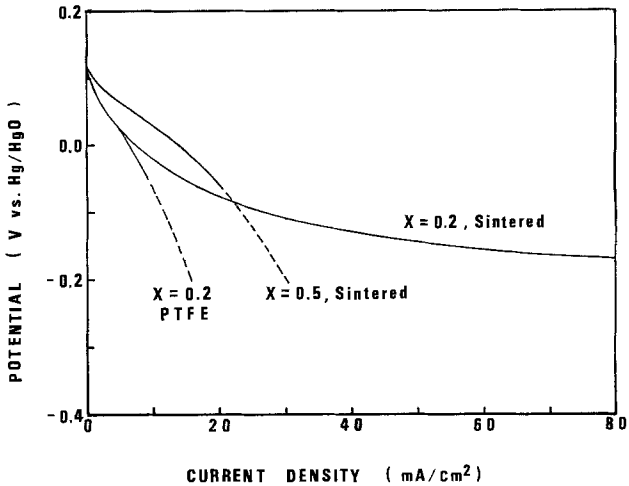


Fig. 2. Comparison of cathode polarization characteristics of various $Nd_{1-x}Sr_xCoO_3$ air electrodes at 25°C.

To explain the difference between the two electrodes, the ohmic polarization in the PTFE-bonded type electrode was measured as a function of discharge time using the current interruption technique. The result shown in Fig. 3 indicates that an increase in polarization can possibly be attributed to the increase in the resistivity in the electrode rather than to other polarizations such as activation. In the PTFE-bonded type electrode, electrical contact is due to the mechanical contact among oxide particles, making its resistivity rather high. Thus, the local current density in the vicinity of the current collector (Ni net) is much higher than the geometrically calculated average value. As a result of this high local current density, the oxide undergoes reduction as shown in Fig. 1 and this results in a drastic increase in electrode resistivity.

In the case of the sintered electrodes, in which particles of the oxides are in closer contact with each other, deterioration of the above kind cannot easily take place. However, a similar decline in the polarization characteristics with time was observed with sintered electrodes of a different Sr content ($x = 0.5$), when the current density exceeded 20 mA/cm² (Fig 2). This is probably due to the delay of oxygen supplied to the electrode/electrolyte interface from the gaseous phase. There may be three possible paths for oxygen to diffuse to the interface, *i.e.*, (*i*) through the electrolyte, (*ii*) over the oxide particle surface, and (*iii*) through the bulk of the oxide particles (as O^{2-} in this case). It is reasonable to assume that diffusion through

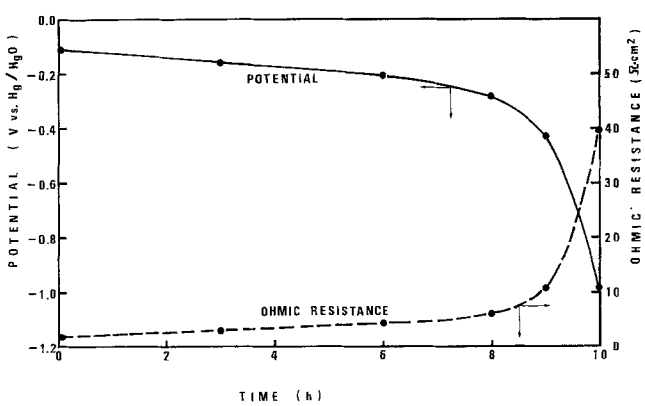


Fig. 3. Correlation of electrode potential and ohmic resistance for a PTFE-bonded $La_{0.9}Sr_{0.1}CoO_3$. Potentials were recorded during a constant current discharge of 15 mA/cm² and resistance was measured by the current interrupter method.

the bulk of the oxide plays the most important role in the case of the relevant oxygen electrodes, because those in which $x = 0.2$ and 0.5 show quite different characteristics in spite of their similarities in pore distributions and surface area. In fact, according to our previous study (5), the oxygen ion diffusion constant for $Nd_{1-x}Sr_xCoO_3$ ($x = 0.5$) is 7.6×10^{-14} cm²/sec at 25°C, which is a hundredth of that for $x = 0.2$. To sum up, the poor characteristics observed in the electrode consisting of $Nd_{1-x}Sr_xCoO_3$ ($x = 0.5$) core is attributed to the relatively small oxygen ion diffusivity.

Figure 4 shows the relationship between the polarization characteristics and x in $Nd_{1-x}Sr_xCoO_3$ for the sintered electrodes. In the range between $x = 0.0$ and 0.2, the polarization characteristics improve with the increase in x, resulting mainly from the decrease in specific resistivity in the x's range (7). The initial characteristics of the electrode in which $x = 0.3$ were almost the same as those in which $x = 0.2$, but the former potential gradually decreased in this case and it became conspicuous after 20 hr testing at 20 mA/cm², while no change in the polarization was observed for more than 100 hr in the case of $x = 0.2$. In the case of $x = 0.4$, however, stationary potentials were not observed at higher current densities. For $x = 0.5$, the stationary potentials were not observed even at a current density as small as 1 mA/cm². Results represented in this figure further support our interpretation that the I-V characteristics are the cumulative effects of the internal resistivity of the electrodes (resistivity of the oxides) and their bulk oxygen ion diffusivity.

In Fig. 5 polarization characteristics of the electrodes consisting of $Ln_{1-x}Sr_xCoO_3$ (Ln stands for La, Pr, Nd, and Sm; $x = 0.2$) are shown. Only these rare earth elements gave a single phase compound when the present preparation method was employed. The order of the polarization characteristics (La > Nd > Pr > Sm) agrees with that of the electrical conductivity data with the exception of Pr, which has a rather stable +4 valence state besides +3, whereas the others have predominantly stable +3 valency. The polarization of all Ln-type electrodes does not change in the first several hundred hours. Although deteriorations in the characteristics after that period resulted not only from the properties of these oxides but also from other factors such as the water repellency treatment, the order of the electrode life was represented as Nd > Pr ≃ Sm > La. The lifetime at 20 mA/cm² was more than 400 hr for Ln = Nd, but it was only about 200 hr for Ln = La.

The electrodes in which the A-site of the perovskite-type crystal lattice has been substituted by other alkaline earth elements than Sr, showed considerably different characteristics as shown in Fig. 6.

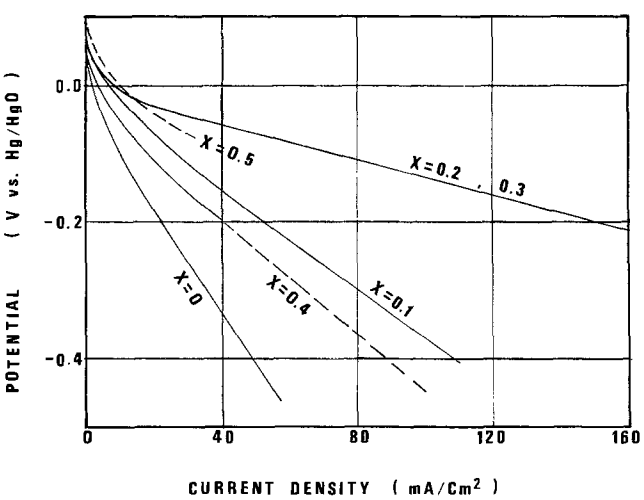


Fig. 4. Electrode potentials of $Nd_{1-x}Sr_xCoO_3$ oxygen electrodes during discharge with different Sr contents at 25°C.

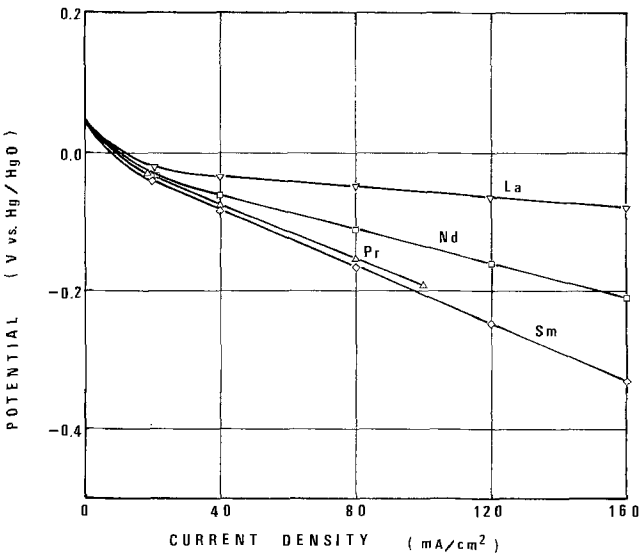


Fig. 5. Electrode potentials of $Ln_{0.8}Sr_{0.2}CoO_3$ oxygen electrodes during discharge at 25°C. Lifetimes of electrodes were in the order of Nd > Pr ≃ Sm > La.

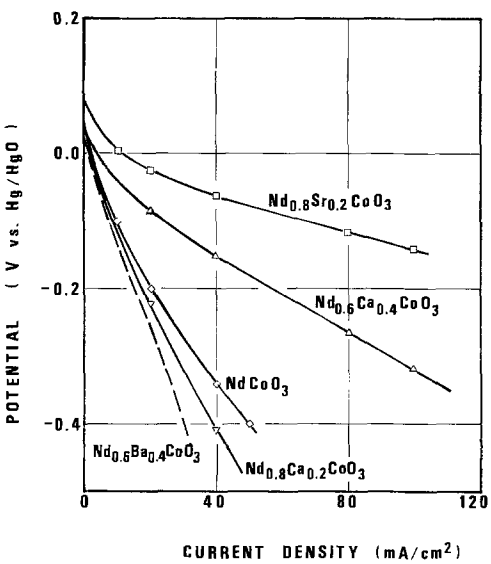


Fig. 6. Electrode potentials of (Nd, M)CoO_3 (M = Ca, Sr, and Ba) showing the effects of A-site substituting alkaline earth elements.

Among the substituting elements tested, potentials were the highest in the case of Sr, Ca, and Ba in that order. Whereas the Sr-substituted compounds showed monotonous increase in potential up to $x = 0.3$, the Ca-substituted compounds showed a decrease in potential when $x = 0.2$ ($Nd_{0.8}Ca_{0.2}CoO_3$), and when $x = 0.4$, its behavior was greatly improved. Thus far, this kind of change in performance is not readily explained. It is noteworthy that in the Ca-substituted electrodes, the polarization increase was not observed for 300 hr even when x was as large as 0.4. This fact is economically important since the use of expensive rare earth elements can be minimized by using these compounds. In the Ba case, the electrode potential was not very much improved and the electrode comprising $Nd_{0.6}Ba_{0.4}CoO_3$ was unable to show a stationary potential.

The effects of substitution of A-sites by these elements are twofold; *i.e.*, to increase the conductivity of the oxides and to modify their crystal structure. Of these, the doping of all three alkaline earth elements has a similar effect on the first point. However, the crystal structure is much affected by different ion dopings and we suspect that the difference in electrode

performance is attributable to some extent to their different crystal structures.

The final approach to improve the electrode characteristics by materials research is to substitute the B-site, *i.e.*, sites for Co^{3+} or Co^{4+} with an element which has an appropriate ionic radius and valence state. The elements Al, V, Cr, Mn, Fe, and Ni were picked as possible ones. Of all these elements, only Mn and Cr form the compounds $Nd_{1-x}Sr_xCo_{1-y}M'_yO_3$ ($x = 0.2$, and M' = Mn and Cr) in the full range of y which lies between 0 and 1, as long as the synthetic method is the one previously described. For other elements, the solubility limit is approximately $y = 0.1$. Representative results for sinter-type oxygen electrodes in which $x = 0.2$ and $y = 0.1$ or 0.2 are shown in Fig. 7. All B-site substituted electrodes exhibited poorer characteristics than nonsubstituted ones. This is mainly due to poorer electronic conductivity values than those of B-site nonsubstituted compounds. Nevertheless, it should be noted in connection with lifetime that Ni-substituted ($y = 0.1$) electrodes do not show any increase in polarization for more than 600 hr.

A life test using air instead of oxygen shows the advantage of Ni-substituted electrodes (see Fig. 8). The lifetimes of the electrodes in this study are more heavily influenced by oxygen partial pressures than ordinary ones because the electrode oxides undergo

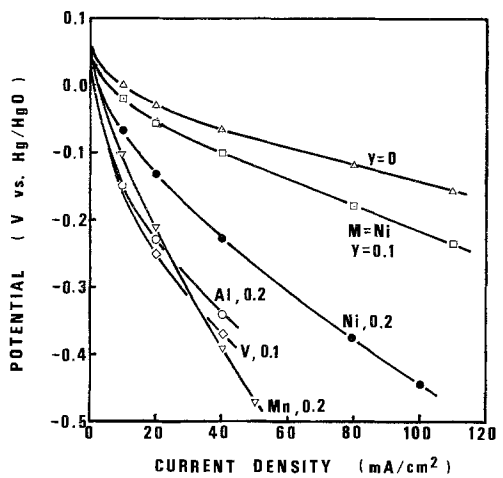


Fig. 7. Electrode potentials of $Nd_{0.8}Sr_{0.2}Co_{1-y}M'_yO_3$ (M' = Al, V, Mn, and Ni) showing the effects of B-site substituting transition metal elements.

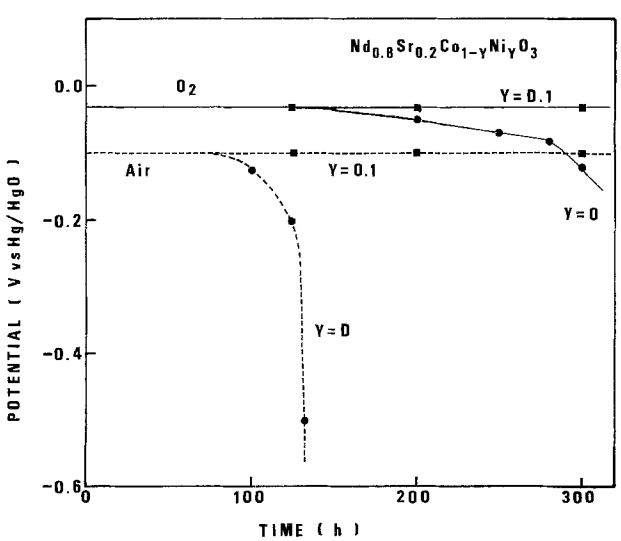


Fig. 8. Comparison of lifetimes of Ni-substituted and nonsubstituted $Nd_{0.8}Sr_{0.2}Co_{1-y}Ni_yO_3$ ($y = 0$ and 0.1) compounds for oxygen and air electrodes. Prolonged life is more clearly shown for Ni-substituted cobalites in air electrode performance.

reduction and decomposition unless sufficient oxygen (or oxygen ion) is supplied to the reaction zone. Although the electrode consisting of $Nd_{1-x}Sr_xCoO_3$ ($x = 0.2$) gives a stable potential for more than 400 hr at 20 mA/cm² if pure oxygen is used as a depolarizer, its lifetime is shortened to 130 hr if air is used. However, the Ni-substituted electrode keeps its initial characteristics for 550 hr even if air is used. It is hard to give a detailed explanation on the effect of doped Ni, but we believe this may be attributed to the enhancement of the oxygen ion diffusivity in the crystal lattice by Ni^{3+}.

Let us now consider the application of these electrodes to secondary batteries like a Zn/air battery. The present study was undertaken in an attempt to obtain an electrode with a resistance to anodic oxidation. Conventional electrodes such as carbon matrix type ones have the disadvantage that they would become corroded by anodic oxidation if they were used as counterelectrodes for charging a metal electrode. Thus, it is necessary to equip a metal/air battery with an auxiliary charging electrode. This has been one of the main drawbacks to the development of these secondary batteries.

As reported previously (5), the oxides used in the present electrodes undergo a reversible redox reaction within the range of $0 \leq \delta \leq x/2$, where δ represents a nonstoichiometric parameter in $Ln_{1-x}Sr_xCoO_{3-\delta}$. When $\delta = 0$ has been established, further passage of anodic current to these compounds only results in the evolution of oxygen from the electrolyte and the oxides themselves remain stable.

A charge-discharge life test has been conducted using a Cd/air cell in which the Cd electrode is charged using the air electrode as a counterelectrode. Figure 9 shows the I-V characteristics of $Nd_{0.9}Sr_{0.1}Co_{0.9}Ni_{0.1}O_3$ air electrodes at several stages during the life cycle tests. In this case, potentials were measured using a reference Zn electrode. The charge and discharge periods were 4 hr, respectively, and the current density employed in each period was 20 mA/cm².

The improvement in the I-V characteristics at earlier stages (between 20th and 80th cycles) may be due to an increase in the electrode/electrolyte interfacial area, resulting from weakening of the water repellency of the electrode. On the other hand, the deterioration observed after the 80th cycle may be considered to be the result of a decrease in the air/electrode interface, resulting also from the decomposition of the hydrophobant. Although the hydrophobant used in this study inevitably undergoes hydrolysis in alkaline solutions, the lifetime of the electrode is not solely controlled by its decomposition rate. The fact that the electrode keeps fairly good characteristics even after

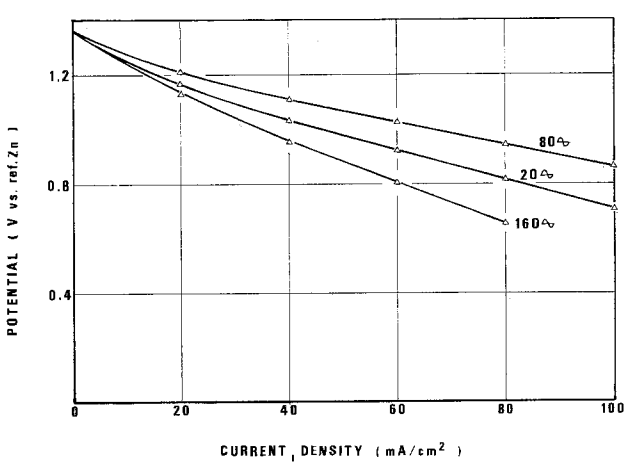


Fig. 9. Electrode potentials of a $Nd_{0.9}Sr_{0.1}Co_{0.9}Ni_{0.1}O_3$ air electrode at several stages of a charge-discharge cycle test. Test conditions are 4 hr/4 hr charge/discharge and 20 mA/cm² constant current density.

1200 hr (corresponding to 160 cycles) in the case of the cycle test while the electrode with the same composition has a lifetime as short as 550 hr in the case of the continuous discharge test seen in Fig. 8 suggests that the deterioration advances very slowly during the charge periods. In fact, it has been revealed by another experiment that an electrode undergoing the continuous charge extending for 500 hr shows almost the same I-V characteristics as the initial ones. These experimental results suggest that the deterioration is advanced by the self-aggravating cycle, namely, (*i*) wetting caused by the decomposition of the hydrophobant, (*ii*) lack of oxygen supply by (*i*), (*iii*) reduction of oxide by (*ii*), (*iv*) increase of resistivity and resulting current concentration by (*iii*), and acceleration of wetting by (*iv*).

Thus to obtain an electrode with a longer lifetime, it is necessary to search for a hydrophobant which is stable in alkaline solutions and has good penetrability into the electrode as well. If a suitable hydrophobant can be found, these types of air electrodes would be promising for metal/air batteries because of their excellent resistivity to anodic oxidation.

Manuscript submitted Dec. 16, 1975; revised manuscript received Nov. 1, 1976.

Any discussion of this paper will appear in a Discussion Section to be published in the December 1977 JOURNAL. All discussions for the December 1977 Discussion Section should be submitted by Aug. 1, 1977.

Publication costs of this article were assisted by Hitachi, Limited.

REFERENCES

1. G. H. Jonker and J. H. van Santen, *Physica*, **19**, 20 (1953).
2. H. Obayashi, T. Kudo, and T. Gejo, *Jpn. J. Appl. Phys.*, **13**, 1 (1974).
3. C. S. Tedmon, Jr., H. S. Spacil, and S. P. Mitoff, *This Journal*, **116**, 1170 (1969).
4. D. B. Meadowcroft, *Nature*, **226**, 847 (1970).
5. T. Kudo, H. Obayashi, and T. Gejo, *This Journal*, **122**, 159 (1975).
6. T. Kudo and H. Obayashi, *ibid.*, **122**, 142 (1975).
7. H. Obayashi and T. Kudo, *Denki Kagaku*, **44**, 503 (1976).

A New Niobium Selenide Cathode for Nonaqueous Lithium Batteries

D. W. Murphy,* F. A. Trumbore,* and J. N. Carides

Bell Laboratories, Murray Hill, New Jersey 07974

ABSTRACT

The γ-"$NbSe_4$" phase, with a single phase composition range $NbSe_{4.0}$ to $NbSe_{4.5}$, is shown to behave as an electrochemically active, reversible cathode material in nonaqueous lithium cells. The cell data, together with the results of n-butyl lithium reaction studies, indicate a topotactic reaction to give an Li_4NbSe_{4+x} (x = 0-0.5) discharge product. Cycle data are presented for nonaqueous lithium cells with cathodes of either $NbSe_4$ containing small amounts of fibrous $NbSe_3$ or hot-pressed composites of $NbSe_{4+x}$ with graphite and polyethylene.

As part of a continuing program on transition metal chalcogenide cathodes in nonaqueous secondary cells, we report here on the use of the γ-"$NbSe_4$" phase first prepared by Selte and co-workers (1, 2), who claimed three different "$NbSe_4$" phases. Meerschaut and Rouxel (3) identified one of these phases (β) as $NbSe_3$ by single crystal x-ray determination. Its use as a reversible cathode material in nonaqueous lithium cells has been described (4-7). The γ-phase was reinvestigated by Guemas *et al.* and found to have the limiting composition $NbSe_{4.5}$ (8, 9). Unit cell parameters were reported, but as yet the full structure has not appeared.

In view of the reversibility of $NbSe_2$ (10-12)[1] and $NbSe_3$ (4-7) in nonaqueous lithium cells, we investigated these limiting compositions of this higher selenide as cathode materials.

Experimental

Materials.—Niobium powder (30 μm, 99.95% purity), selenium shot (5*N* purity), graphite powder (325 mesh), lithium foil (Foote Mineral Company), n-butyl lithium (Alfa Inorganics), and polyethylene powder (Microthene 500 U.S. Industrial Chemicals) were used as received. Propylene carbonate (PC) and tetraglyme were vacuum distilled from lithium while lithium perchlorate (Alfa Inorganics) was vacuum dried at ~ 150°C. Separator bags were made from 1 mil thick polypropylene (Celgard KKX-2, Celanese Plastics Company).

Niobium selenide preparation.—Single phase niobium selenide powder samples in the composition range $NbSe_{4.0}$ to $NbSe_{4.5}$ were prepared by heating the appropriate amounts (~ 6g, total weight) of Nb and Se in sealed, evacuated fused quartz ampuls. The ampuls were heated from 400° to 500°C ($NbSe_{4.0}$) or to 550°C ($NbSe_{4.5}$) at a rate of about 25°/day and then held at the higher temperature for 2-3 days.

When Nb-Se mixtures of nominal composition $NbSe_{4.0}$ were directly heated to 550°C for 3 days, the result was a mixture of predominantly $NbSe_{4+x}$ plus small amounts of $NbSe_3$ fibers as shown by the scanning electron microscope (SEM) photograph in Fig. 1.

Construction of test cells.—With one exception, all of the test cells were constructed by sandwiching the appropriate selenide cathodes between two 15 mil thick Li anodes of the same shape, all three electrodes being contained in polypropylene separator bags wet with tetraglyme. The electrodes were placed in a glass vessel, 1*M* $LiClO_4$ in PC added as the electrolyte and the cell evacuated in the port of a Vacuum Atmospheres dry box. All cells were constructed in this dry box

* Electrochemical Society Active Member.

Key words: chalcogenide cathodes, secondary batteries, topotactic reactions.

[1] In Ref. (10) $NbSe_2$ was reported to be a host material for iodine. The electrochemical activities of the analogous compounds NbS_2 (11) and TiS_2 (12) were demonstrated, probably accounting for the two plateaus (one due to I_2 and one to $NbSe_2$) in the original discharge curves of this reference.

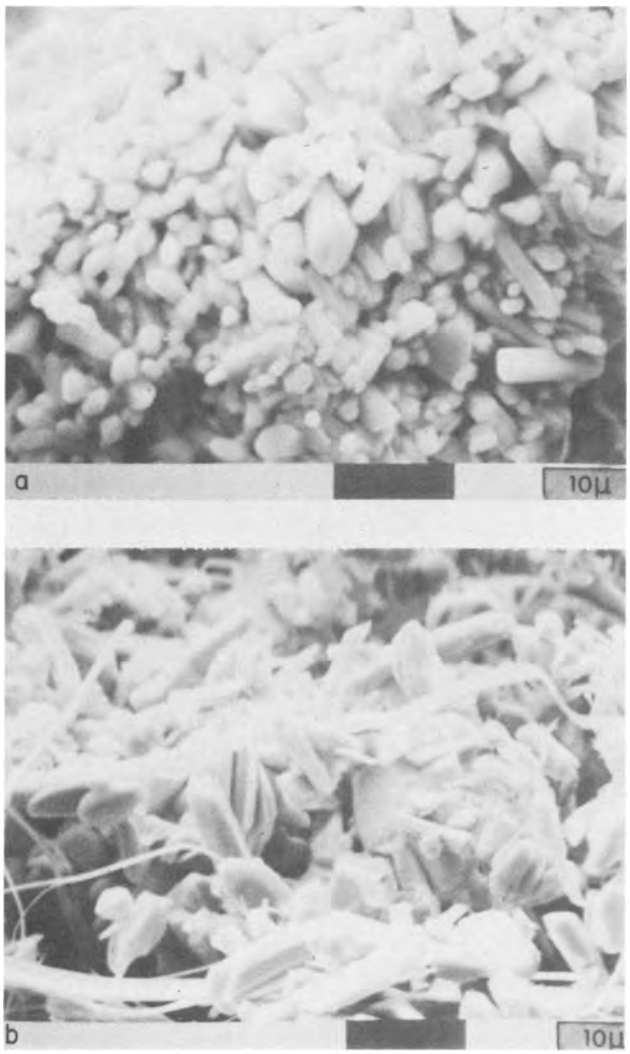


Fig. 1.(a) SEM photograph of single phase $NbSe_{4.5}$. (b) SEM photograph of "nominal" $NbSe_{4.0}$ containing a small amount ($\lesssim$5%) of fibrous $NbSe_3$.

under argon. The cells were placed in Mason jars with electrical feedthroughs and removed from the dry box for charge-discharge cycling.

Single phase $NbSe_{4+x}$ was formed into "composite" cathodes by hot pressing, typically, 65 weight percent (w/o) $NbSe_{4+x}$ powder (150 mesh), 30 w/o graphite, and 5 w/o polyethylene. After rolling this mixture in a ball mill for $\sim$ 16 hr, it was pressed to 6500 psi at 130°C for 3 min onto an expanded nickel screen which serves as a current collector. A typical composite cathode was 3 cm × 3 cm × 0.6 mm weighing 1.6g (exclusive of the nickel screen). A convenient test cell arrangement for the composite cathodes was found to be one in which the anode-cathode-anode sandwich was placed horizontally in a Petri dish containing $\sim$ 8 cm^3 of electrolyte solution. A Teflon block served as a weight on top of the sandwich to promote uniform contact of the electrodes.

A "pocket" cathode of "nominal" $NbSe_{4.0}$ (containing electrically conducting $NbSe_3$ fibers) was prepared by placing slices of the $NbSe_4$ in a nickel pocket (1 × 3 × 0.1 cm), obtained by forming and welding 5 mil perforated nickel sheet. The corresponding "pocket" cell was of a conventional geometry with the electrode sandwich placed vertically in a rectangular glass vessel.

Cycling of cells.—The above cells were tested using essentially two different cycle modes. In the "float" mode the cells were cycled at constant current for selected charge and discharge times, with the charging taking place potentiostatically at 2.7V after the cell reached this upper voltage limit. In the "voltage-limited" cycle mode, the cell was cycled at constant current between 2.8 and 1.0V using a solid-state cycling apparatus which immediately switches from charge to discharge (or vice versa) on reaching the upper (lower) voltage limit.

Results

Unlike the lower selenides of niobium which show metallic conductivity, the $NbSe_{4+x}$ phase was found to be a relatively poor electronic conductor ($\rho \approx 30$ Ω-cm) (13). Hence, composite cathodes, with graphite added to increase conductivity, were used to a large extent. However, a "nominal" composition $NbSe_4$ containing small amounts of $NbSe_3$ (barely detectable by x-ray powder patterns) fibers (see Fig. 1) could be formed (by appropriately varying the growth conditions). This small amount of $NbSe_3$ served to bind the sample together in an open structure much like felt and to impart good conductivity to the entire sample.

A cell[2] consisting simply of a Li anode and a small fiber matte cathode (79 mg) of "nominal" $NbSe_4$ immersed in 1*M* $LiClO_4$ in PC was slowly discharged to determine the capacity of the cathode and the approximate shape of the equilibrium discharge curve (Fig. 2). The capacity corresponded to essentially four (3.8) Li per Nb or one Li per Se. These values compare favorably to those for $NbSe_2$ and $NbSe_3$ which have theoretical capacities of one and three Li per Nb, respectively (14-17). This small $NbSe_4$ cell was over 96% rechargeable.

Pocket cells using the same nominal $NbSe_4$ were prepared from a collection of sliced sections ($\sim$ 50 mil thick) of the fiber matte placed in perforated nickel pockets as described in the experimental section. Cycle data obtained in the voltage-limited mode for a typical pocket cell are shown in Fig. 3. This cell failed after 28 cycles due to Li anode failure. The decrease in capacity on cycling is attributable to at least three factors, namely, (*i*) an inherent decrease in capacity of the cathode after the first cycle or so, (*ii*) higher resistance due to buildup of particulate Li, and (*iii*) smaller charge acceptance in the voltage-limited mode as compared to the float mode. The voltage-limited mode leads

[2] This cell was the only test cell which did not fall into the composite or pocket cell categories described in the experimental section. The loose structure of this matte provided a large surface area exposed to the electrolyte. Pocket cell material was much more densely packed.

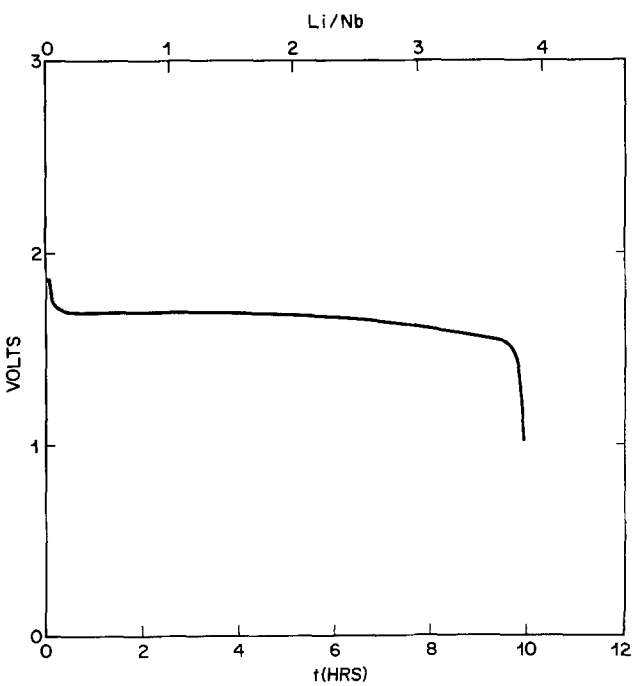


Fig. 2. Semiequilibrium discharge curve for a Li/1M $LiClO_4$ in PC/"nominal" $NbSe_{4.0}$ (79 mg) cell showing the reaction of essentially four equivalents of Li per $NbSe_4$. i_D = 2.0 mA.

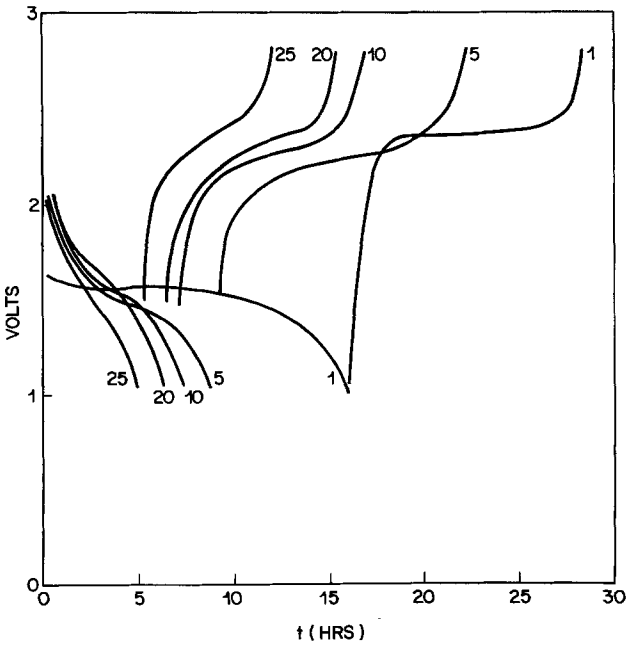


Fig. 3. Cycle behavior of a Li/1M $LiClO_4$ in PC/"nominal" $NbSe_{4.0}$ (314 mg) pocket cell cycled between 2.8 and 1.0V in the voltage-limited mode. $i_D = i_C = 5$ mA (cycles 1-4); $i_D = 5$ mA, $i_C = 3.6$ mA (cycles 5-25); $j_D = 16$ mA/g $NbSe_4 = 1$ mA/cm^2.

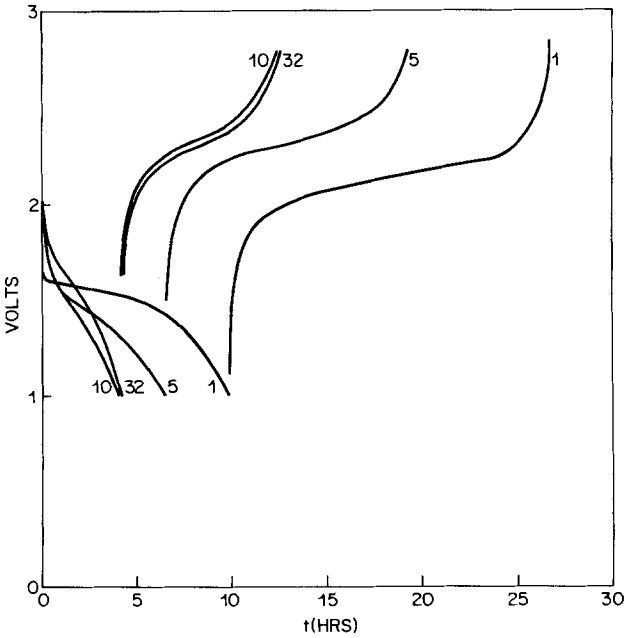


Fig. 5. Cycle behavior of a Li/1M $LiClO_4$ in PC/$NbSe_{4.0}$ (1.01g) composite cathode cell cycled between 2.8 and 1.0V in the voltage-limited mode. $i_D = 10$ mA, $i_C = 5$ mA, $j_D = 9.9$ mA/g $NbSe_{4.0} = 0.55$ mA/cm^2.

to a shallower average depth of discharge (percent of theoretical capacity) of the cathode than does the float mode. At any rate, Fig. 3 demonstrates the reversibility of the nominal $NbSe_4$.

Cycle data for typical cells employing the composite hot pressed cathodes (single phase $NbSe_{4+x}$-graphite-polyethylene) and cycled in the voltage-limited mode are shown in Fig. 4 and 5. It appears from the data presently available that cells employing $NbSe_{4.5}$ cathodes fail sooner than those cells in which $NbSe_{4.0}$ cathodes are used. For the $NbSe_{4.5}$ cells discharged to 1V, failure has occurred by cracking of the composite often leading to complete lift-off from the nickel screen. The increasing steepness and voltage of the charging curves (Fig. 4) is consistent with a higher resistance and nonuniform current distribution associated with cracking and/or lift-off and is indicative of incipient cathode failure, as confirmed by reconstruction with new lithium and electrolyte. Better results are evident for the composite $NbSe_{4.0}$ cell as shown in Fig. 5. Here we see a leveling off of discharge capacity (actually an improvement from the 10th to 32 cycle!) typical of the voltage-limited cycling mode. In addition, the charging curves do not show the pronounced steep slope shown by the $NbSe_{4.5}$ cell in Fig. 4. The $NbSe_{4.0}$ cell failed after $\sim$ 50 cycles due to lithium failure. Reconstruction of this cell with fresh Li returned the capacity to $\sim$ 40 mA-hr at 10 mA discharge current and $>$ 100 mA-hr at 5 mA.

The behavior of $NbSe_{4.5}$ and $NbSe_{4.0}$ composite cells cycled in the float mode to a depth corresponding to only one Li per $NbSe_{4+x}$ is shown in Fig. 6 and 7. Limiting the depth of discharge helped alleviate the

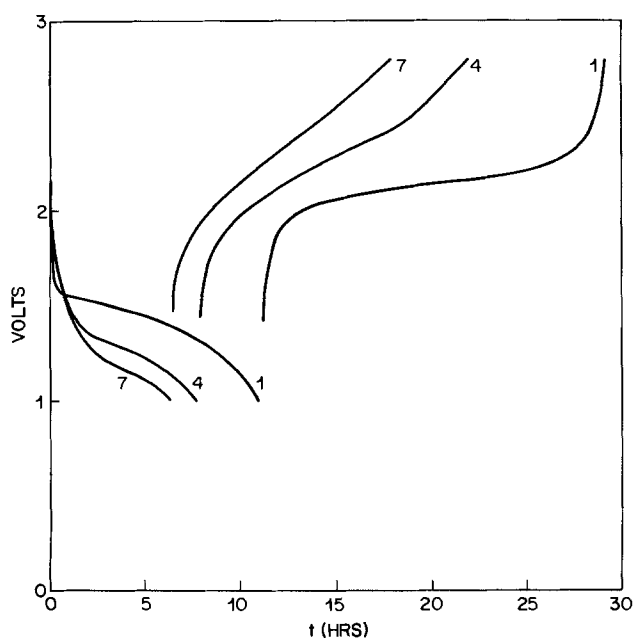


Fig. 4. Cycle behavior of a Li/1M $LiClO_4$ in PC/$NbSe_{4.5}$ (1.05g) composite cathode cell cycled between 2.8 and 1.0V in the voltage-limited mode. $i_D = 10$ mA, $i_C = 5$ mA, $j_D = 9.5$ mA/g $NbSe_{4.5} = 0.55$ mA/cm^2.

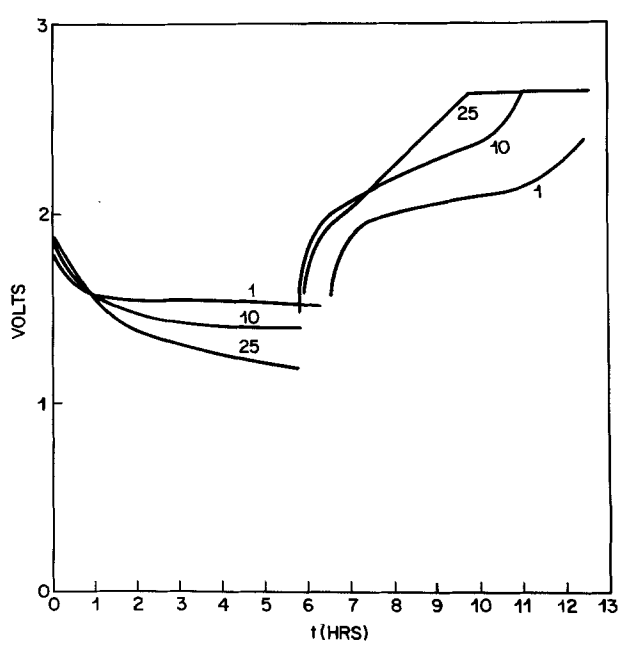


Fig. 6. Cycle behavior of a Li/1M $LiClO_4$ in PC/$NbSe_{4.5}$ (472 mg) composite cathode cell cycled in the float mode at a depth corresponding to one Li per $NbSe_{4.5}$. $i_D = i_C = 5$ mA, $j_D = 10.6$ mA/g $NbSe_{4.5} = 0.4$ mA/cm^2.

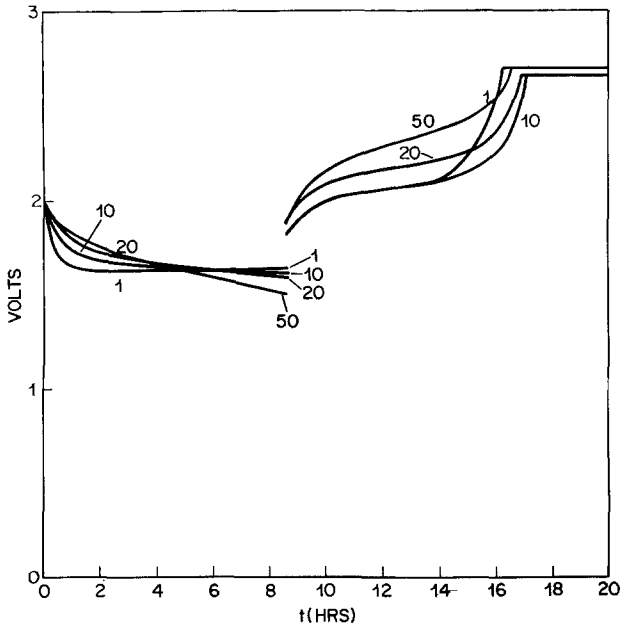


Fig. 7. Cycle behavior of a Li/1M $LiClO_4$ in PC/$NbSe_{4.0}$ (212 mg) composite cathode cell cycled in the float mode at a depth corresponding to one Li per $NbSe_{4.0}$. $i_D = i_C = 1.5$ mA, $j_D = 7.1$ mA/g $NbSe_{4.0} = 0.33$ mA/cm^2.

mechanical breakup of the cathodes. In the case of $NbSe_{4.5}$ composite cells, there was some beneficial effect but the decrease in end-of-discharge voltage and increasing steepness of the charging curve (see Fig. 6) with continued cycling show that the resistance problem remains. Reconstructing the cells with new lithium and new electrolyte did not improve the charge-discharge behavior, confirming that the increased resistance was in the cathode and probably was due to cracks not sufficiently extensive to cause complete failure. On the other hand, consistent with the results of voltage-limited cycling, the $NbSe_{4.0}$ composite cells suffered only slightly on float-mode cycling as shown in Fig. 7. Here, there is only a slight decline in end-of-discharge voltage after 20 cycles while the charge curve, though at a higher voltage, is reasonably flat.

We have used n-butyl lithium to mimic cell discharge (18) on pure samples in order to elucidate the products of cell discharge. With excess n-BuLi, $NbSe_{4.0}$ and $NbSe_{4.5}$ consumed 6.4 and 7.5 moles, respectively. X-ray powder patterns (see Fig. 8) of these products clearly showed the presence of Li_2Se, but no niobium selenide products could be identified. When four equivalents of n-BuLi were used, no Li_2Se was observed and the x-ray powder patterns were very similar to the pure $NbSe_{4+x}$, although weaker. A small amount of Li_2Se appears to be present with 5 moles of n-BuLi. $NbSe_{4+x}$ is triclinic, making a determination of the unit cell in Li_4NbSe_{4+x} impossible from our data.

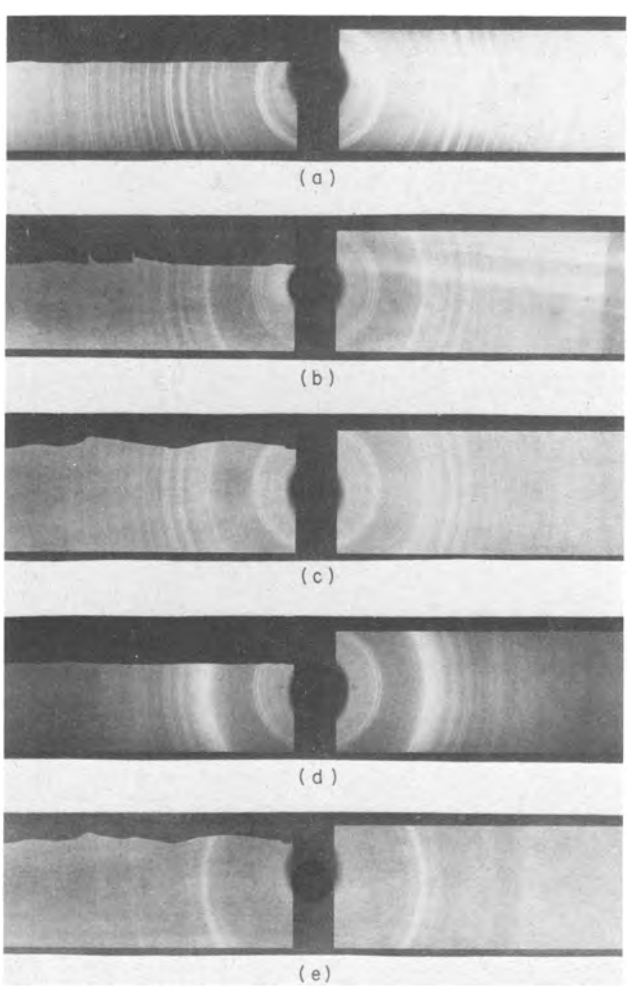


Fig. 8. X-ray powder patterns of $NbSe_{4+x}$ and various compounds with lithium. (a) $NbSe_{4.0}$, (b) Li_4NbSe_4, (c) $Li_4NbSe_{4.5}$, (d) $NbSe_{4.5}$ + 5 n-BuLi, and (e) $NbSe_{4.5}$ + excess (7.4 n-BuLi).

Discussion

The similarity in powder patterns of $NbSe_{4+x}$ and Li_4NbSe_{4+x} suggests that the cell discharge reaction is a topotactic incorporation of Li as found in $NbSe_3$ (17) and several other systems (19). Even though the detailed structure of the $NbSe_{4+x}$ phase is unknown, some reasonable guesses may be made from closely related systems and our results here. $NbSe_3$ may be thought of as $Nb^{4+}Se^{2-}(Se_2)^{2-}$ and replacement of the Se^{2-} by another Se_2^{2-} would give $Nb^{4+}(Se_2^{2-})_2$. Such a structure (see Fig. 9) is found in VS_4 (20), NbS_2Cl_2 (21) (two Cl^- are isoelectronic with an S_2^{2-} unit), and $NbTe_4$ (22). VS_4 and NbS_2Cl_2

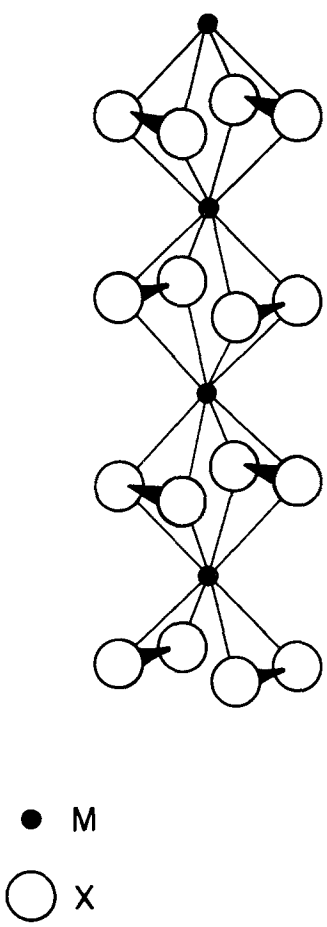


Fig. 9. The chain structure of VS_4

are van der Waals bonded chain compounds, while $NbTe_4$ has substantial Te-Te bonding between chains. We feel that the $NbSe_4$ structure is closely related to this structure type but more complex, as indicated by the triclinic unit cell (VS_4 is monoclinic) and by the ability to incorporate more Se. It is tempting to consider $NbSe_{4.5}$ as $Nb^{5+}(Se_2^{2-})_2Se_{0.5}^{2-}$. Whatever the detailed structure, we feel the essential features $NbSe_4$ will contain are two Se_2^{2-} units and an open structure through which Li may diffuse. We also speculate that the greater tendency of $NbSe_{4.5}$ cathodes to crack may be due to the crowding of 4 Li into the $NbSe_{4.0}$ structure, already containing the additional 0.5 Se, resulting in a greater expansion than for $NbSe_{4.0}$ cathodes.

The flatness of the discharge curve (Fig. 2) for "nominal" $NbSe_4$ suggests either a two-phase system or formation of a ternary phase in which the free energy of formation is nearly constant over the entire range. Although the first is more common, the latter explanation is possible in this case with the energy equivalence owing to the cleavage of Se-Se bonds, the energy of each being nearly independent of the integrity of other Se-Se bonds.

We conclude that the topotactic nature of the cell discharge reaction is responsible for the reversibility of the cell reaction. This type of topotactic reaction has been demonstrated now in a number of secondary lithium cells containing cathodes of certain transition metal dichalcogenides and $NbSe_3$, V_2O_5, and MoO_3 (19). Cell degradation, where not due to Li failure, is believed to be caused by mechanical breakup of the cathodes, rather than any chemical irreversibility.

The main objective of this work was to demonstrate the electrochemical reversibility of the $NbSe_{4+x}$ cathode reaction, rather than to optimize the fabrication of the electrodes themselves. This reversibility has been demonstrated now for the series $NbSe_2$, $NbSe_3$, and $NbSe_{4+x}$.

Acknowledgments

The authors are indebted to J. Broadhead and D. O. Feder for helpful suggestions on the manuscript and to T. M. Putvinski for the design and construction of the voltage-limited mode cycling apparatus.

Manuscript submitted July 16, 1976; revised manuscript received Oct. 26, 1976. This was Paper 70 presented at the Las Vegas, Nevada, Meeting of the Society, Oct. 17-22, 1976.

Any discussion of this paper will appear in a Discussion Section to be published in the December 1977 JOURNAL. All discussions for the December 1977 Discussion Section should be submitted by Aug. 1, 1977.

Publication costs of this article were assisted by Bell Laboratories.

REFERENCES

1. K. Selte and A. Kjekshus, *Acta Chem. Scand.*, **19**, 1002 (1965).
2. K. Selte, E. Bjerkelund, and A. Kjekshus, *J. Less-Common Met.*, **11**, 14 (1966).
3. A. Meerschaut and J. Rouxel, *ibid.*, **39**, 197 (1975).
4. J. Broadhead and F. A. Trumbore, Paper 178 presented at The Electrochemical Society Meeting, Chicago, Illinois, May 13-18, 1973.
5. F. A. Trumbore and J. Broadhead, Paper 179 presented at The Electrochemical Society Meeting, Chicago, Illinois, May 13-18, 1973.
6. F. A. Trumbore, J. Broadhead, and T. M. Putvinski, Paper 61 presented at The Electrochemical Society Meeting, Boston, Massachusetts, Oct. 7-11, 1974.
7. J. Broadhead, F. J. Di Salvo, and F. A. Trumbore, U. S. Pat. 3,864,167 (1975).
8. L. Guemas, A. Meerschaut, and P. Palvadeau, *C. R. Acad. Sci., Series C*, **28**, 297 (1975).
9. J. Rouxel, Private communication.
10. J. Broadhead, in "Power Sources 4," D. H. Collins, Editor, p. 469, Oriole Press, Newcastle upon Tyne, England (1973).
11. G. L. Holleck, F. S. Shuker, and S. B. Brummer, Paper No. 759070, 10th Intersociety Energy Conversion Engineering Conference, IEEE, Newark, Delaware (1975).
12. M. S. Whittingham, *Science*, **192**, 1126 (1976).
13. F. J. Di Salvo, Private communication.
14. D. W. Murphy and F. A. Trumbore, *This Journal*, **123**, 960 (1976).
15. M. B. Dines, *Mater. Res. Bull.*, **10**, 287 (1975).
16. D. W. Murphy, F. J. Di Salvo, G. W. Hull, Jr., and J. V. Waszczak, *Inorg. Chem.*, **15**, 17 (1976).
17. R. R. Chianelli and M. B. Dines, *ibid.*, **14**, 2417 (1975).
18. M. B. Armand, in "Fast Ion Transport in Solids," W. van Gool, Editor, North Holland Press, New York and Amsterdam (1973).
19. M. S. Whittingham, *This Journal*, **123**, 315 (1976).
20. R. Allmann, I. Baumann, A. Kutoglu, H. Rosch, and E. Hellner, *Naturwissenschaften*, **51**, 263 (1964).
21. H. G. V. Schnering and W. Beckmann, *Z. Anorg. Allg. Chem.*, **347**, 231 (1966).
22. K. Selte and A. Kjekshus, *Acta Chem. Scand.*, **18**, 690 (1964).

Ionic Conductivity of Monocrystals of the Gallium Analogs of β- and β''-Alumina

G. V. Chandrashekhar and L. M. Foster*

IBM Thomas J. Watson Research Center, Yorktown Heights, New York 10598

ABSTRACT

A-C and d-c conductivities of monocrystals of the gallium analogs of β- and β''-alumina were measured over the temperature range from room temperature to 350°C, using both reversible and ion-blocking electrodes. Conductivities of the gallates are substantially higher than those of the corresponding aluminates, and Na-β''-gallate has the highest conductivity [$\simeq$ **1** $(\Omega\text{-cm})^{-1}$ at 300°C] that has been reported for any alkali ion conductor. The transport number for electrons in the gallates is less than 10^{-6} at 300°C.

The layered sodium aluminates, β- and β''-alumina, have analogs in the Na_2O-Ga_2O_3 system (1, 2). Since these gallium analogs share many of the properties of the aluminum prototypes and, in particular, exhibit fast ion conduction (3) and easy exchange of the alkali ion (4), it is apparent that they have highly defective structures similar to those of β- and β''-Al_2O_3.

Chicotka (3) and Brinkhoff (5) reported preliminary measurements of the conductivity of incompletely characterized, sintered, and polycrystalline Na-gallate

* Electrochemical Society Active Member.
Key words: solid electrolyte, ionic conductor, gallium oxide.

specimens. We have now prepared monocrystals up to about 1 cm^2 in area of both the β- and β''-phases (6), and in this paper we report the electrical conductivity of these optimized samples, using both reversible and ion-blocking electrodes to separate the ionic and electronic contributions.

Experimental

Monocrystals of the β- and β''-phases were prepared in separate experiments by Na_2O vaporization from soda-rich melts held at the temperatures appropriate for the growth of each product. The crystal growth procedure is reported elsewhere (6). The sodium content of the samples was determined spectrophotometrically by comparison with suitable standards. The gallates dissolve readily in hot HCl and the analysis is straightforward. The compositions were $Na_2O \cdot 6.2Ga_2O_3$ and $Na_2O \cdot 5.7Ga_2O_3$ for the β- and β''-phases, respectively.

The crystals could be cleaved quite easily along c-planes into slabs about 1 mm thick. The conductivity in these sections is parallel to c-faces. These pieces were prepared for conductivity measurements by cutting with a low speed diamond saw into rectangular shapes about 8 × 3 mm, using kerosene as the coolant. They were cleaned with benzene and acetone prior to contacting, and stored in a desiccator. These gallates, like their aluminum analogs, are susceptible to moisture (7), and all of the operations involved in sample preparation must be carried out in a dry environment.

In order to apply ion-blocking electrodes, a specimen was sputter etched in argon at $\simeq 10^{-3}$ Torr, then a thin film of gold was applied by sputtering *in situ* to opposite ends of the bar.

Reversible electrodes consisted of pads of glass fiber filter mat, saturated with molten $NaNO_3$-$NaNO_2$ eutectic. The specimen bar was held by pressure between two such pads held in turn between gold pressure blocks to which gold lead wires were welded.

It was generally not possible to remove one type of contact from a specimen and contact it again with the other type. Therefore, the two contacting procedures were employed with different samples cut from the same crystal or from crystals prepared in duplicate runs.

The contacted specimen was contained in a small furnace and resistance measurements were made as a function of temperature from room temperature to 300°C with the blocking electrodes, and from 225° to 350°C with the reversible electrodes.

The contribution to the measured resistance from the cell itself was investigated by measuring Na-β-Al_2O_3 monocrystalline samples[1] of identical cross section but of different lengths, and extrapolating the resistance to zero length. The cell resistance was found to be only about 1% of the sample resistance for both types of electrodes, and was disregarded.

Resistance measurements were made as a function of temperature at a frequency of 5 × 10^5 Hz. Chicotka (3) had previously shown that the resistance of polycrystalline ceramic sodium gallate samples was insensitive to frequency above 10^5 Hz and, in fact, decreased by less than 5% from 2 × 10^4 to 10^5 Hz. A General Radio Corporation Type 1606-A radio frequency bridge and a Tektronix Type 190-A constant amplitude high frequency signal generator were used. A General Radio Corporation Type 1650-A impedance bridge was used for d-c measurements.

Results and Discussion

The conductivity was measured for several crystals of β- and β''-Na-gallate and β-Al_2O_3. Good agreement was obtained in duplicate measurements with each material. Results for typical cases are shown in Fig. 1. It is seen that the data produce a linear relation between the log of the conductivity-temperature product, σT, and $1/T$ over the entire temperature ranges investigated (generally 225°-350°C, but from 350°C down to room temperature with the samples of β''-gallate and β-aluminate with blocking electrodes). This is consistent with the general relation

$$\sigma = (\sigma_0/T)\exp(-E/kT)$$

and suggests that a single ion migration mechanism predominates over the entire range, though admittedly the range is short. Moreover, the slopes of the plots are sufficiently similar to suggest that the conduction mechanism is the same for all three of the materials studied, although this would be surprising in view of the differences in structure of the conducting plane in the hexagonal β- and rhombohedral β''-phases. It is apparent, at any rate, that the disparity among activation energies for the layered conductors that was reported in the early literature resulted from spurious effects and reflected sample history, contact problems, etc., rather than fundamental differences between materials.

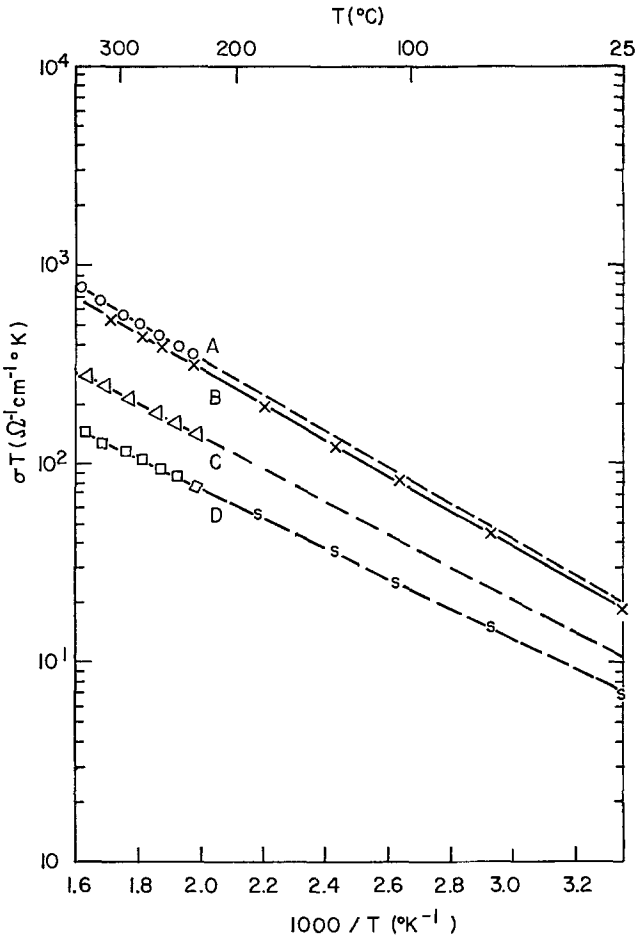


Fig. 1. Log(σT) vs. $1/T$ for aluminum and gallium fast ion conductors. o-o-o β''-Na-gallate (reversible electrodes); x-x-x β''-Na-gallate (blocking electrodes); △-△-△ β-Na-gallate (reversible electrodes); □-□-□ β-Na-aluminate (reversible electrodes); s-s-s β-Na-aluminate (blocking electrodes).

Table I gives the measured values of conductivity at 300°C and the measured and extrapolated values at room temperature for the various samples, as well as the activation energies calculated from the plots of Fig. 1. For comparison, values for monocrystalline Na-β-alumina reported by Fielder *et al.* (8) and by Whittingham and Huggins (9) are included. The sample measured by Fielder *et al.* was from a Czochralski-grown boule that was obtained from the same source as ours and so can probably be considered a duplicate. It is seen that our results agree very well with theirs. The

[1] Obtained from the Crystal Products Division of the Union Carbide Corporaton.

Table I. Conductivity data for sodium gallates and aluminates

Sample	T°C	Electrodes	A-C conductivity at 5×10^5 Hz $(\Omega\text{-cm})^{-1}$	D-C conductivity $(\Omega\text{-cm})^{-1}$	E, eV
Na-β″-gallate	300	$NaNO_3$-$NaNO_2$	1.02	0.99	0.178
	25		0.071[a]		0.178
Na-β″-gallate	300	Sputtered gold	0.95		0.178
	25	Sputtered gold	0.063		
Na-β-gallate	300	$NaNO_3$-$NaNO_2$	0.37		0.16
	25		0.37[a]		
Na-β-Al_2O_3	300	$NaNO_3$-$NaNO_2$	0.215[b]		0.155
	300	Sputtered gold	0.215[b]		0.155
	25	Sputtered gold	0.024[b]		
Na-β-Al_2O_3	300	Molten Na	0.215[c]		0.155
	25		0.024[a]		
Na-β-Al_2O_3	300	Na-W-bronze	0.174[d]		0.164
	25	Na-W-bronze	0.014		
Na-β″-Al_2O_3	300	?	0.4[e]		0.156[f]

[a] Extrapolated to 25°C.
[b] Sample obtained from Crystal Products Division, Union Carbide Corporation.
[c] Data from Fielder, *et al.* [Fig. 2, Ref. (8)].
[d] Data from Whittingham and Huggins (9). 300°C data taken from curve of Fig. 1, Ref. (9).
[e] Highest value reported for sintered, Li_2O-stabilized sample by Ford Motor Company, Ref. (14).
[f] Ford Motor Company contract report, Ref. (15). (Other activation energies reported as high as 0.208 eV, depending on sample history.)

sample measured by Whittingham and Huggins was obtained from the Carborundum Company and had possibly been cleaved from a larger cast mass. Their sodium tungsten bronze electrodes were shown to be reversible to sodium ions from 820° to −150°C, and the single activation energy applied over the entire range. The somewhat lower conductivity for that sample can undoubtedly be attributed in part to the lower sodium content ($Na_2O \cdot 9.5Al_2O_3$).

It is also seen from Table I that the two-probe d-c measurement on Na-β″-gallate, using the molten salt electrodes and small currents to minimize polarization, agrees reasonably well with the a-c measurement at 5×10^5 Hz.

It is obviously important to determine if electronic conductivity contributes to charge transport in the gallate materials. It had previously been shown to be negligible in Ag-β-Al_2O_3 (10), and since this property should not be affected by substitution of single valency ions in the ionic conducting plane, Na-β-Al_2O_3 was also considered to be purely ionically conducting. Because of the greater likelihood of multivalency occurring in gallium than in aluminum, electronic conduction cannot be ruled out *a priori* in the gallates. However, Lorenz *et al.* (11) and Harwig *et al.* (12) showed that Ga_2O_3 crystals grown under oxidizing conditions were insulating ($\rho > 10^6$ Ω-cm). Our crystals were grown in 1 atm of air, which was comparable to their growth environments. For our own investigation of electronic conductivity, a two-probe d-c measurement was made on a Na-β″-gallate sample at 300°C with ion-blocking gold electrodes. After an initial rapidly decaying current transient, the conductivity fell to $<10^{-6}$ of the a-c conductivity for the same sample.

We accept the a-c measurements with molten salt electrodes (curves A, C, and D, Fig. 1) as giving the correct sodium ion conductivity of these materials. However, since the much simpler sputtered gold contacts on sputter-etched surfaces provide sufficiently equivalent results when employed at high frequency, we recommend their use.

Conductivity data for monocrystalline Na-β″-Al_2O_3 are not available and there is some question whether that material can be prepared in the pure form (*i.e.*, without MgO or Li_2O stabilization) (13). The Na-β″-Al_2O_3 data in Table I are for high density, sintered, Li_2O-stabilized bodies reported in recent Ford Motor Company contract reports (14).

It is seen that the sodium gallates are severalfold better ionic conductors than their aluminum counterparts. Severalfold difference in conductivity between two samples of a substance where the conductivity is entirely electronic, such as a semiconductor, is not considered significant, and might be encountered between two independent measurements of the same sample because of nonohmicity of contacts, introduction of low concentrations of trapping centers by heating, etc. In ionic conductors, on the other hand, ion mobility is determined almost entirely by crystal structure and is relatively insensitive to trace impurities and sample history. Severalfold difference in conductivity in this case between two materials implies either a major difference in structure, or a severalfold difference in concentration of the conducting species.

Since in the ionic conductors of the β-alumina type the crystal defects that permit ion migration are "built-in," *i.e.*, not thermally generated, all of the activation energy is presumably involved in determining the ion mobility

$$\mu = (q\nu a^2/kT) \exp(-E/kT)$$

while the number of carriers remains fixed, and the conductivity is

$$\sigma = nq\mu = (nq^2\nu a^2/kT) \exp(-E/kT)$$

Since the activation energies are similar in the three materials of Fig. 1, the differences in specific conductance are principally in the preexponent $\sigma_0 = nq^2\nu a^2/k$.

It is first necessary to see if the differences in conductivity can be explained by differences in sodium concentration, n. Densities were calculated for the three materials from the volumes of their unit cells calculated from the x-ray lattice parameters, assuming that each surplus Na atom beyond one atom per plane is accompanied by a half-oxygen atom for charge compensation. This may be an oversimplification of the real situation, but the error introduced cannot be large. The densities are: β-$Na_2O \cdot 9Al_2O_3$, 3.256 g/cm³; β-$Na_2O \cdot 6.2Ga_2O_3$, 5.335 g/cm³; β″-$Na_2O \cdot 5.7Ga_2O_3$, 5.236 g/cm³. From these densities, and the specific conductances at 300°C from Table I, equivalent conductances were calculated as 32.2, 42.4, and 110.1 (cm²/Ω-equiv.), respectively. This wide spread between the materials shows that the conductivity differences cannot be accounted for to any significant degree by differences in total sodium content and thus, if all of the Na is active in carrying current, must reside largely in the remaining variables in the preexponent: the attempt frequency, ν, and/or the jump distance, a. Taking a as the distance from a Beevers-Ross site to a mid-oxygen position in the two β-phases (1.62Å for β-Al_2O_3; 1.68Å for β-gallate), and from a normal Na site to a mid-oxygen position in the β″-phase (1.68Å for β″-gallate), attempt frequencies of 1.47×10^{12}, 1.98×10^{12}, and 7.30×10^{12} sec^{-1} are calculated at 300°C, and 1.56×10^{12}, 2.07×10^{12}, and 7.47×10^{12} sec^{-1} at room temperature for the β-aluminate, β-gallate, and β″-gallate, respectively. This choice of jump distance assumes that the mid-oxygen position is a possible site for sodium, as was shown to be the case in β-Al_2O_3 (13). Alternatively, a can be taken as the entire distance between the Beevers-Ross and anti-Beevers-Ross sites in the β-phase materials, or between two normal Na sites in the β″-phase, in which case the calculated attempt frequencies becomes one-fourth of the values above.

No physical significance can be claimed for these attempt frequencies until corroborating experiments can be performed, and it is recognized that the calculations are sensitive to the choice of model for the diffusion process as well as to the choice of the jump distance. Their magnitude appears to be reasonable, however. Our choice of the jump distance (being only the distance from the usual sodium site to a mid-oxygen position $a/(4 \cos 30°) = 1.68$Å away) arose from the difficulty in accounting for the high conductivity of β″-Na-gallate if only the two "normal" Na sites per plane are considered. With the composition $Na_2O \cdot 5.7Ga_2O_3$, 1.93 of the two equivalent sites are filled ac-

cording to the view that all of the Na is in the conducting plane (actually two equivalent planes very slightly separated in the β''-structure). A hopping mechanism involving only the 0.07 remaining empty sites would not seem to be very efficient, especially if the charge on the surplus Na^+ is compensated by additional bridging oxygens which would greatly restrict Na^+ movement in some directions. If the mid-oxygen positions are also possible Na^+ sites, a considerably larger fraction of sites are vacant.

An alternative explanation of the high conductivity of β''-Na-gallate would be that part of the sodium is involved in forming oxygen bridges [playing the role of Mg in MgO-stabilized β''-Al_2O_3, (13) for example] and thus is not involved in conduction, but provides more empty Na^+ sites in the conduction plane to assist in the hopping process. Precise location of the sodium in β''-Na-gallate is obviously an important experiment to be performed. This work is underway and will be reported later.

It is instructive to compare the conductivity of the sodium gallate with that of the excellent Ag^+ ion conductor α-AgI. The specific conductance of β''-Na-gallate at 300°C is about one-half that of α-AgI (16). All of the Ag^+ is assumed to be conducting in α-AgI, and its equivalent conductance is $\simeq$78 (cm^2/Ω-equiv.). On a similar basis, the equivalent conductance of β''-Na-gallate is 110 (cm^2/Ω-equiv.), or still greater if only part of the Na^+ is available for conduction. As pointed out by Whittingham and Huggins (9), it is the equivalent conductance, which is proportional to the mobility of the conducting species, that is important when studying the processes that occur in fast ion conductors.

Manuscript submitted Aug. 24, 1976; revised manuscript received Nov. 1, 1976.

Any discussion of this paper will appear in a Discussion Section to be published in the December 1977 JOURNAL. All discussions for the December 1977 Discussion Section should be submitted by Aug. 1, 1977.

Publication costs of this article were assisted by IBM Corporation.

REFERENCES

1. L. M. Foster and H. C. Stumpf, *J. Am. Chem. Soc.*, **73**, 1590 (1951).
2. J. P. Boilot, J. Thery, and R. Collongues, *Mater. Res. Bull.*, **8**, 1144 (1973).
3. R. J. Chicotka, Abstract 4, p. 14, The Electrochemical Society Extended Abstracts, Spring Meeting, Toronto, Canada, May 11-16, 1975.
4. R. S. Title and G. V. Chandrashekhar, Conference on Superionic Conductors, Chemistry, Physics and Applications, p. 45, Schenectady, New York (May 1976).
5. H. C. Brinkhoff, *J. Phys. Chem. Solids*, **35**, 1225 (1974).
6. L. M. Foster and J. E. Scardefield, *This Journal*, **124**, 434 (1977).
7. L. M. Foster and G. V. Arbach, *ibid.*, **124**, 164 (1977).
8. W. L. Fielder, H. E. Kautz, J. S. Fordyce, and J. Singer, *ibid.*, **122**, 528 (1975).
9. M. S. Whittingham and R. A. Huggins, *J. Chem. Phys.*, **54**, 414 (1971).
10. M. S. Whittingham and R. A. Huggins, *This Journal*, **118**, 1 (1971).
11. M. R. Lorenz, J. F. Woods, and R. J. Gambino, *J. Phys. Chem. Solids*, **28**, 403 (1967).
12. T. Harwig, G. J. Wubs, and G. J. Dirksen, *Solid State Commun.*, **18**, 1223 (1976).
13. W. K. Roth, F. Reidinger, and S. J. LaPlaca, Conference on Superionic Conductors, Chemistry, Physics and Applications, p. 23, Schenectady, New York (May 1976).
14. Ford Motor Company Semi-annual Report, Jan. 1976, RANN, Division of Advanced Energy Research and Technology, Washington, D.C. (Contract No. NSF-C805).
15. *Ibid.*, July 1974.
16. L. W. Strock, *Z. Phys. Chem.*, **B25**, 441 (1934).

Why Alkaline Cells Leak

Michael N. Hull* and Herbert I. James[1]

ESB Incorporated, Technology Center, Yardley, Pennsylvania 19067

ABSTRACT

The creepage of alkaline electrolytes along negatively polarized electrodes has been studied experimentally and theoretically. One driving force for this phenomenon is the production of OH^- ions arising from the electrochemical reduction of oxygen and/or the evolution of hydrogen occurring in a thin reaction zone above the observed electrolyte meniscus. Movement of water into this zone causes it to thicken and increase in conductivity with the result that the reaction zone moves along the electrode.

A problem is defined.—Alkaline cell leakage may be divided into (*i*) "nonelectrochemical leakage," and (*ii*) "electrochemically driven creepage." In the former case, leakage arises from physical factors such as an improperly sealed cell, separator fibers or scratches in the seal interface, etc. and can appear at either electrode. We shall address ourselves to the second case, *viz.*, electrochemically driven creepage which manifests itself in the movement of the electrolyte along the negative electronically conducting surface abutting the seal.

Although the cell voltage can be the sole source of the power that causes electrolyte creepage (1), it can be shown that creepage may be driven along a single electrode poised at a sufficiently negative potential. For example, if 1.5V are applied between two nickel electrodes in an alkaline electrolyte, the negatively polarized electrode will exhibit creepage. However, one may produce an equivalent effect by shorting a nickel electrode to an electrode of zinc. In this case, the voltage is zero yet creepage will be observed to occur up both electrodes and, on breaking the connection, will continue only along the zinc. Ergo, electrochemically driven creepage is an electrode potential dependent phenomenon rather than voltage dependent. The questions to be answered are therefore these: Why does an alkaline solution creep along a negatively charged metallic substrate? What factors influence the rate and what steps can be taken to stop the movement?

Electrocapillarity: a partial explanation.—The term "electrocapillary drive" arises frequently as an explanation for creepage, suggesting that the charged surface by being more easily wetted by the electrolyte will

* Electrochemical Society Active Member.
[1] Present address: Xerox Corporation, Webster, New York 14580.
Key words: alkaline leakage, electrochemical creepage, electroosmosis, reaction zone.

draw up the liquid. The magnitude of this effect is comparatively small in that the meniscus height (h) at an uncharged metal surface is approximately 0.1 cm while that at a surface with a large excess positive or negative charge is ~0.3 cm (2-4). Again, the above effect is static in that a change of electrode potential will cause a simultaneous change in the interfacial tension of the system to a new equilibrium value and the system will return to a state of rest. Electrolyte creepage in contrast is dynamic since no equilibrium state appears to be reached and liquid movement continues indefinitely until the whole surface is covered.

Electrocapillarity: a longer look.—As shown in Fig. 1 and described above, the application of a negative potential will cause the meniscus height (h) to readjust to a new value. Further, the system within a matter of minutes will return to a state of rest. However, if observation of the strip is continued over a period of several hours, it becomes apparent (especially in the presence of oxygen or air) that a thin liquid film (Δ) is growing up the strip above the meniscus. The film thickens slowly with time and after several days it has grown to a length of several centimeters compared to the initial meniscus change which was of the order of 2-3 mm. Some driving force in addition to that of simple electrocapillary action is clearly operative and the problem is reduced to determining the source of power for this process.

> The awful shadow of some unseen Power
> Floats, tho' unseen, amongst us.
>
> *Shelley, Hymn to Intellectual Beauty*

Experimental Arrangement—The Cell and Circuitry

The experimental arrangement shown in Fig. 2 incorporated the following features. (*i*) A sealed glass cell with provision for controlling the atmosphere above the KOH electrolyte. (*ii*) A partially immersed test strip the surface of which could be viewed through a traveling microscope mounted externally to the cell. The test strip was lowered into the solution so that the bottom of the strip just touched the surface of the liquid and permitted the meniscus to form. This particular positioning of the strip insured that the total current flow to or from the strip would be the result of electrochemical reactions that occurred in the metal-liquid meniscus layers and not include a current component arising from electrochemical reactions proceeding at a part of the metal surface immersed in the bulk electrolyte. (*iii*) An electrical arrangement consisting of a potentiostat A, d-c voltage source, Hg-HgO reference electrode, and platinum counterelectrode whereby the electrode potential of the metal strip could be continuously controlled at specifically desired

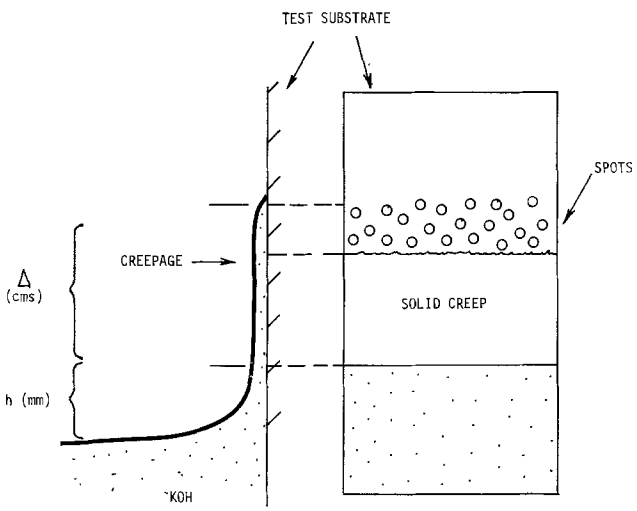


Fig. 1. Side view of the growing liquid film above the meniscus of a partially immersed metal plate and visual appearance of electrolyte creepage.

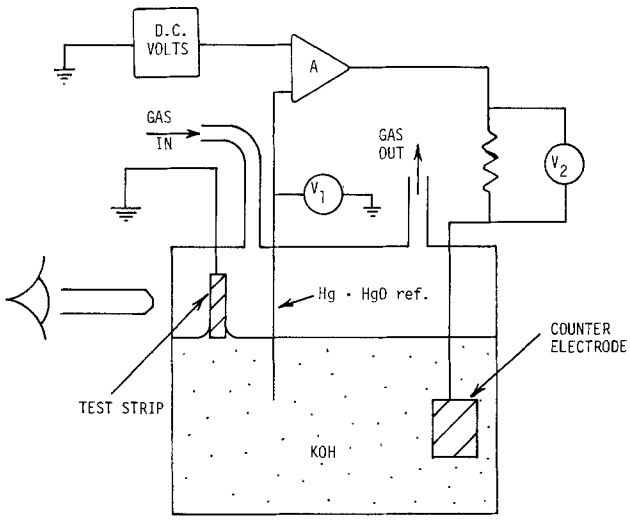


Fig. 2. Diagrammatic illustration of the cell and circuitry configuration.

values. The electrode potential and current flow to the strip were monitored by means of voltmeters V_1 and V_2, respectively, and the length of the creep above the meniscus (Δ) was concurrently recorded by means of the calibrated microscope.

In Fig. 1, the visual appearance of creepage is also illustrated. The observed sequence of events was: spots would begin to form above the meniscus; as these spots enlarged in volume, they would coalesce into a solid film of creepage and new spots would begin to form ahead of the solid front. Measurements of the position of both the solid and the spot fronts were recorded.

Experimental Results

The influence of potential and oxygen.—When a nickel strip is placed in 1M KOH in the presence of oxygen at an applied electrode potential of −0.9V *vs.* Hg-HgO (this is approximately the potential of a cadmium electrode in alkaline solution), a reduction current is observed to flow. Further, as time progresses, the reduction current is observed to increase proportionately to that of the area of the climbing creepage film as shown in Fig. 3. Removal of the oxygen, by flushing the cell with argon, will cause the current to drop precipitously and the rate of climb of the creepage to decrease markedly. It may be concluded, therefore, that at this particular potential, the electroreduction of oxygen is the reaction which gives rise to the current flow. In view of the electrode placement, it is evident the whole of this current flow is concentrated in the meniscus and creepage layer on the nickel surface. Furthermore, one may deduce that the rate of oxygen reduction is limited only by the available surface area for reaction.

In contrast to the above, electrodes such as silver which are extremely active catalysts for the reduction of oxygen, show a rapid current climb to a very high value and thereafter the current is limited to this value, even though the creepage height is continually increasing (Fig. 3). The source of this current limitation appears to be resistance polarization losses in the creepage film, that is, IR drop. This may be confirmed by variation of the applied electrode potential between the point at which O_2 reduction commences (0.0V) and that for the onset of visible hydrogen evolution (~ −1.3V). As shown in Fig. 4, a linear variation of the current with potential results. Thus in the case of electrodes such as nickel, which exhibit moderate overpotential for the electroreduction of oxygen, the rate of production of hydroxyl ions by the reaction

$$O_2 + 2H_2O + 4e^- \rightarrow 4\,OH^- \qquad [1]$$

is controlled by the area of the electrode covered by a film of electrolyte. Conversely, low overpotential electrodes, such as silver, exhibit such high current

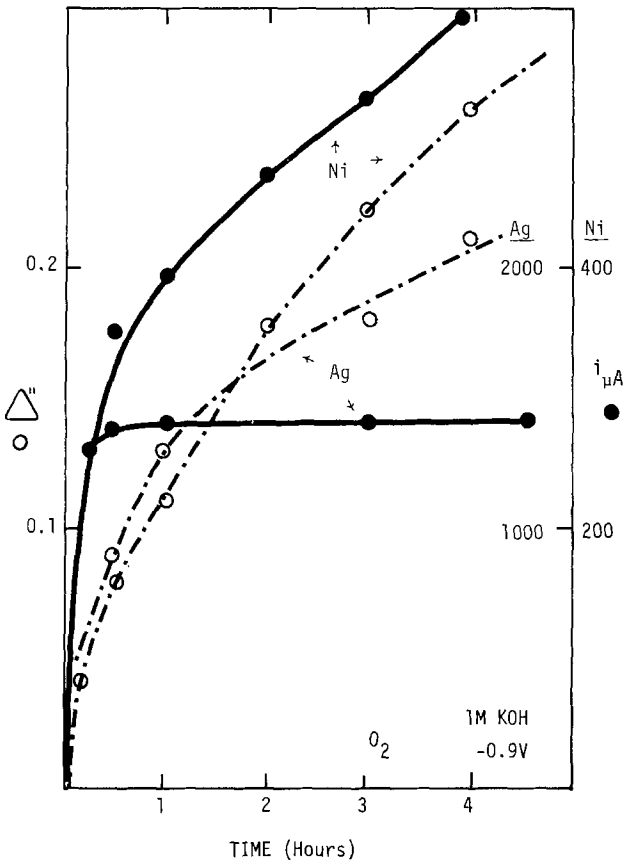


Fig. 3. Reduction current (i) and creepage height (Δ) as a function of time. 0.25 in. wide nickel and silver strips just touching electrolyte surface. 1M KOH, O_2, $E_{App} = -0.9V$ (Hg-HgO).

densities that the electrolyte conductivity in the meniscus and creepage layers becomes the rate-controlling parameter in a short time after reduction is commenced.

The dependence of the rate of creepage on the electrode potential and the gaseous atmosphere surrounding the test strip is detailed in Fig. 5. Oxygen or nitrogen was presaturated with moisture to the relative humidity level present above the test electrolyte and the height of the creepage was measured after 24 hr at a fixed electrode potential. We may divide the figure into two separate potential ranges by a vertical line that indicates the point above which hydroxyl ions can be produced (in addition to those from O_2 reduction) by the evolution of H_2 in the meniscus and creepage layers according to

$$2H_2O + 2e^- \rightarrow 2\,OH^- + H_2 \qquad [2]$$

The figure shows that, for electrode potentials in the range -0.2 to -0.9V, the amount of creepage in the presence of oxygen increases with increasing negative electrode potential. Removal of the oxygen leads to a situation in which practically no creepage will be observed within a 24 hr period. In the potential range more negative than -0.9V, even in the absence of oxygen, a sharply increasing amount of creepage is observed with increase in the potential. This sharp increase corresponds to the onset of hydrogen evolution through reaction [2]. Thus the amount of creepage observed at the cadmium electrode potential (~ -0.9V) is extremely sensitive to the availability of oxygen while that at the zinc electrode potential (~ -1.35V) is somewhat less. In this latter case, particularly if oxygen access to the strip is hindered, creepage will still occur in an amount proportional to the rate at which reaction [2] is occurring in the creepage film.

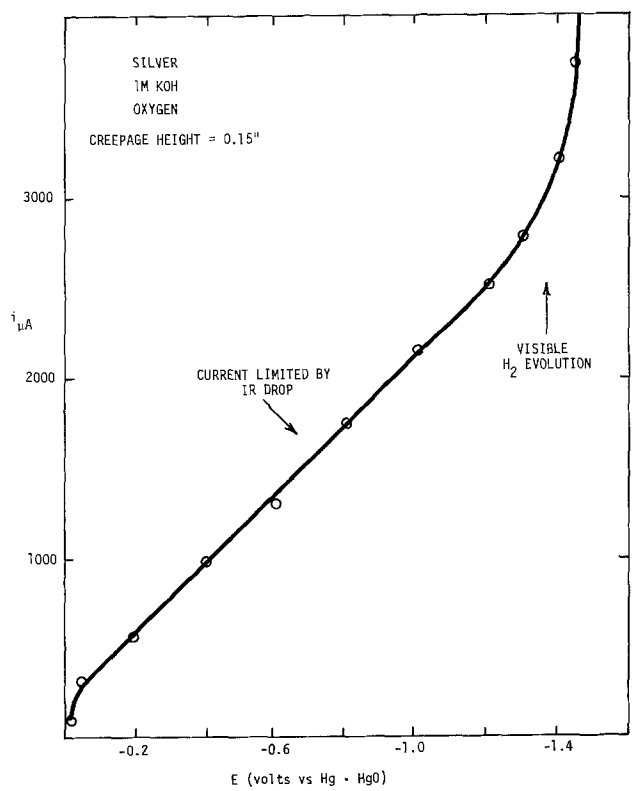


Fig. 4. Current-voltage plot obtained on a silver plate with a creepage layer of 0.15 in. length. All conditions as for Fig. 3.

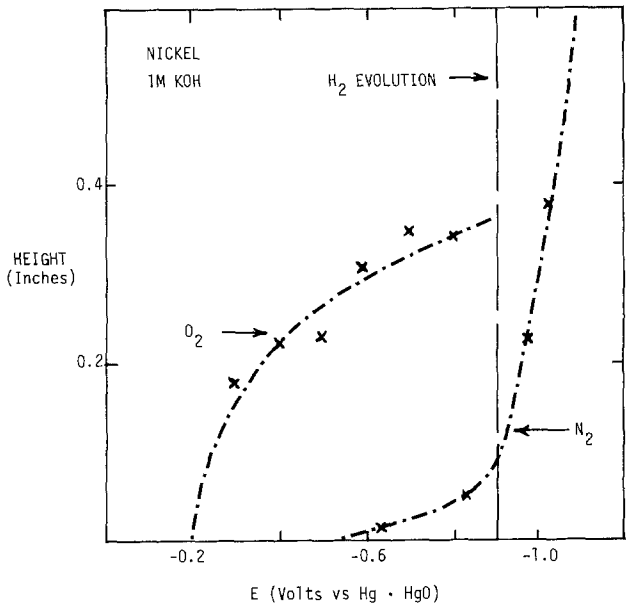


Fig. 5. Height of the solid creepage front for nickel in 1M KOH after 24 hr in O_2 or N_2 as a function of electrode potential.

The influence of electrolyte concentration.—Under all experimental conditions, the creepage rate (and current flow to the strip) declines as the electrolyte concentration is increased. This point is illustrated in Fig. 6 for silver in 5 and 10M KOH. The creepage rate is linearly related to the relative viscosity of the particular KOH electrolyte used as shown in Fig. 7. (The points plotted for 1M NaOH and 1M LiOH will be discussed presently.) As the KOH concentration rises, the viscosity increase becomes much more rapid and, consequently, the rate of creepage is increasingly slowed. Each incremental increase in electrolyte concentration becomes progressively more significant in decreasing the rate of increase of Δ.

The cations: Li^+, Na^+, K^+, and their ionic mobilities.—In the previous section, consideration of sodium and lithium hydroxides was deferred because differences between the relative viscosities of the equimolar concentrations of KOH, NaOH, and LiOH shown in Fig. 7 were evidently too small to explain the large decrease in the creepage rate as the cation was changed from

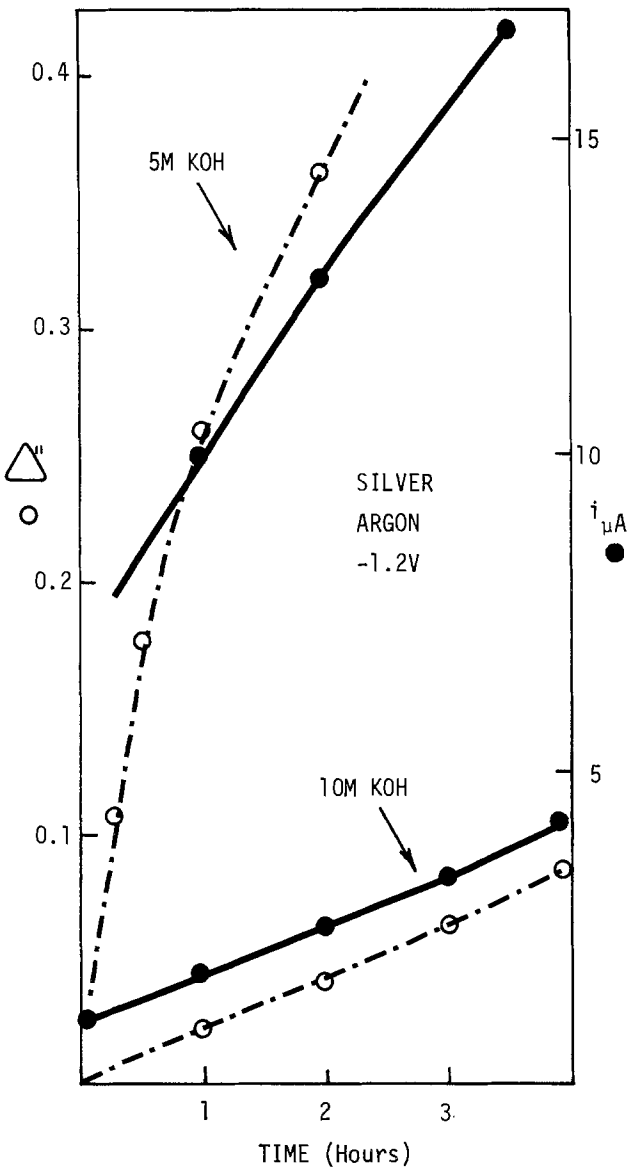


Fig. 6. Reduction current and creepage height as a function of time on a 0.25 in. wide silver plate in 5 and 10M KOH · argon; $E_{App} = -1.2V$.

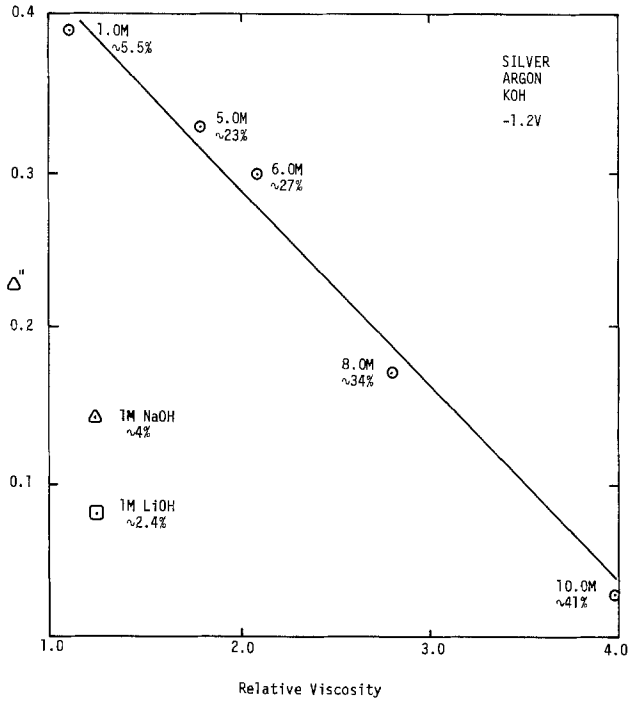


Fig. 7. Variation of the creepage height as a function of the KOH electrolyte relative viscosity Ag, argon, $E_{App} = -1.2V$. Concentration of KOH given in weight percent and moles per liter.

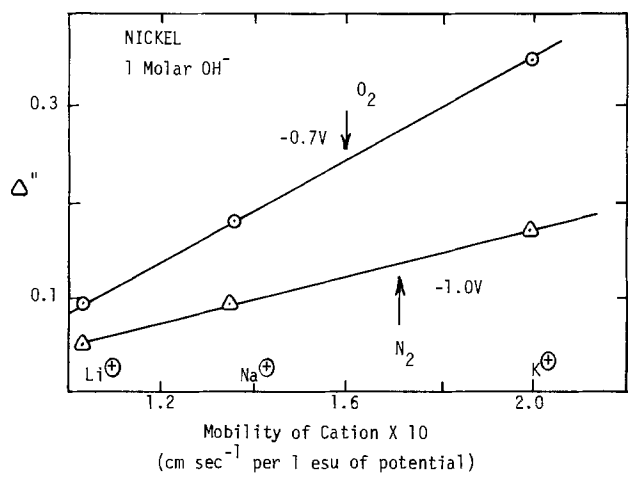


Fig. 8. Variation of Δ in O_2 at $-0.7V$ and N_2 at $-1.0V$ for a nickel strip as a function of the cation ionic mobility.

K^+ to Na^+ to Li^+. The reason for this difference lies partly in the effect of the cation mobility on the creepage rate. The experimental results are that the cation mobility shows a linear relationship to Δ under a variety of conditions (Fig. 8). The decrease in mobility $K^+ > Na^+ > Li^+$ is due to the greater degree of hydration which becomes associated with an ion as the ionic radius is decreased.

The two factors of increase in viscosity of the electrolyte and decrease in the cation mobility lead to a reduction in the rate of alkaline electrolyte creepage. As we have seen from Fig. 7, at a concentration of 1M, the difference in creepage rate between the three electrolytes was solely a question of mobility. At higher concentrations, however, equimolar concentrations of KOH and NaOH and LiOH differ also quite markedly in their relative viscosities. Thus, for example, at a concentration of 8M, a sodium hydroxide solution has nearly three times the relative viscosity of potassium hydroxide. At these high concentrations, both the relative viscosity and relative cation mobility effects play a serendipitous role in lowering the creepage rate of a NaOH or LiOH electrolyte when compared to an equivalent electrolyte of KOH.

The effect of substrate: chemical and physical differences.—A number of metals and alloys were used as substrates in the "as-received" condition and a wide variation in their relative creepage rates was observed as shown in Fig. 9. There are a number of chemical and physical reasons why such differences should appear. On the "chemical" side, one would anticipate that differences in the oxygen reduction overpotential and/or differences in the hydrogen evolution overpotential would lead to different rates in the production of OH^- and, consequently, in the rate of creep. On the "physical" side, the presence of surface scratches or different types of surface oxide layers that wick up electrolyte by capillary action are of utmost importance. This is well demonstrated by the plots presented in the figure for the two strips of Inconel 600 which were tested; one of which had been abrasively cleaned with a detergent while the other had been washed gently in organic solvents. A difference in the rate of creepage was produced between the two samples that was as wide as the whole range of differences of the individual metal and alloy samples tested in the as-received condition, that is, with just a gentle organic solvent wash to remove surface grease.

To clarify the role played by overpotential differences between the different metals and alloys, it would be necessary to polish each of the samples to a common degree of surface roughness and repeat the creepage rate determinations. For materials we tested in the

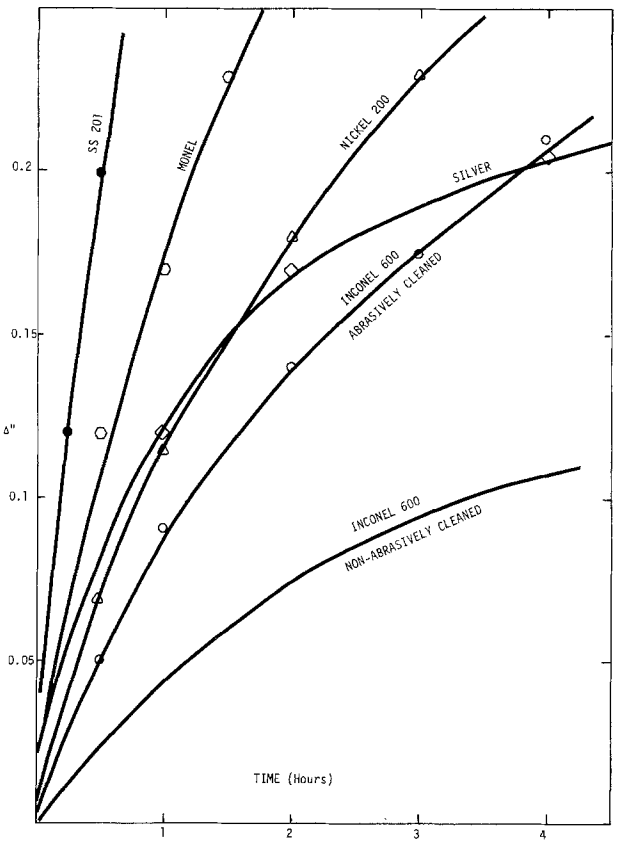


Fig. 9. Variation of Δ with time for a series of metal substrates in 1M KOH and O_2 and an applied potential of −0.9V.

form received, the order from best to worst alkaline electrolyte creepage is:

1. Inconel 600
2. Nickel 200
3. Inconel 601
4. Nickel alloy 440
5. Monel
6. SS 201
7. SS 301

Theoretical Discussion and Experimental Analysis

Two electrochemical reactions that can proceed at a negative electrode in alkaline solution and produce hydroxyl ions are

$$O_2 + 2H_2O + 4e^- \rightarrow 4\,OH^- \qquad [1]$$

if $E > 0.0$V *vs.* Hg-HgO and

$$2H_2O + 2e^- \rightarrow 2\,OH^- + H_2 \qquad [2]$$

if $E > -0.9$V. No corresponding electrochemical reactions can be written for a positive electrode, under otherwise identical electrolyte conditions, supporting the hypothesis that these reactions are responsible for negative electrolyte creep. A further interesting observation is that the reduction current has a tendency to increase with increase in the electrode area covered by the creepage film. This is one of the basic principles utilized in the operation of porous electrodes in fuel cells (in these, the porous electrode maximizes the available wetted electrode surface exposed to the gaseous reactant) and is a phenomenon that has been studied by a large number of people (5-12). Their conclusions may be summarized by examining how a reaction, such as the electroreduction of oxygen, will proceed at an electrode immersed in bulk electrolyte compared to one covered by a thin layer of electrolyte, only microns thick. Figure 10 depicts a metal strip which was completely immersed in KOH through which a stream of pure O_2 is being bubbled. An insulated wire is connected to the strip by means of which

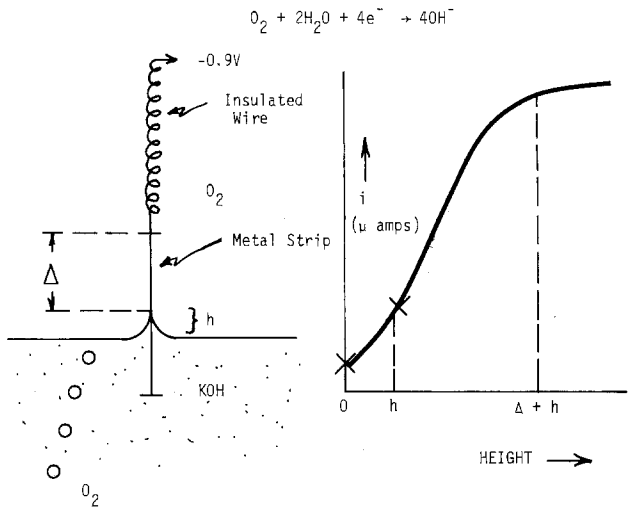


Fig. 10. Diagrammatic representation of the current flow to a metal strip in O_2 saturated KOH at $E_{App} = -0.9$V under various degrees of immersion.

an electrode potential of −0.9V (Hg-HgO) is imposed on the strip. How will the reduction current vary as the metal strip is withdrawn from the electrolyte, that is, as one transposes from a strip covered by bulk electrolyte to one covered only by a thin electrolyte film?

In the totally immersed condition, a steady-state current will be observed whose magnitude is controlled by the rate of diffusion of dissolved oxygen to the electrode surface through the bulk solution. This current is represented by the "X" on the current-height plot corresponding to a height of the strip above the electrolyte surface of zero. When the electrode has been withdrawn to a point which is just sufficient to form the maximum meniscus, (h), a pronounced increase in the reduction current is observed. Diffusion of O_2 present above the electrolyte to the electrode surface in the meniscus region has become quite fast because of the thinning of the liquid layers in the region. Thus, although the electrode surface exposed in the meniscus region is very small compared to that remaining completely immersed in the bulk electrolyte, the current density in the meniscus region undergoes a marked increase. Thus most of the current flowing to the strip arises from the electrochemical reaction proceeding in the meniscus region.

Further withdrawal of the metal strip from the solution leads to a quite unexpected phenomenon. Instead of the current attaining a maximum value at the point (h) where the maximum meniscus height is developed, a limiting value is not reached until the strip is withdrawn to a height of ($\Delta + h$) from the electrolyte. At this point, the greatest fraction of the total current now flowing is concentrated in a zone of width Δ above the visible meniscus. There exists, therefore, an extremely thin electrolyte layer on the electrode above the meniscus across which extremely rapid passage of oxygen occurs.

The idea developed above may now be applied to understanding the magnitude and the spatial relationship of the electrochemical reactions [1] and/or [2] occurring at a partially immersed metal plate. In Fig. 11, a situation is shown in which a metal strip has been partially immersed in a KOH electrolyte and to which a potential of −0.9V is being applied. If the relative humidity above the solution is high, a film of moisture will be present on the electrode surface above the meniscus. Both O_2 reduction and H_2 evolution will tend to yield the highest current density where the diffusive transport of O_2 to the surface or of H_2 away from the surface is kinetically easiest, that is, in the moisture film just above the visible electrolyte meniscus. Accordingly, the current magnitude at each segment of the electrode surface can be spatially depicted by the dotted trace on the left-hand side of

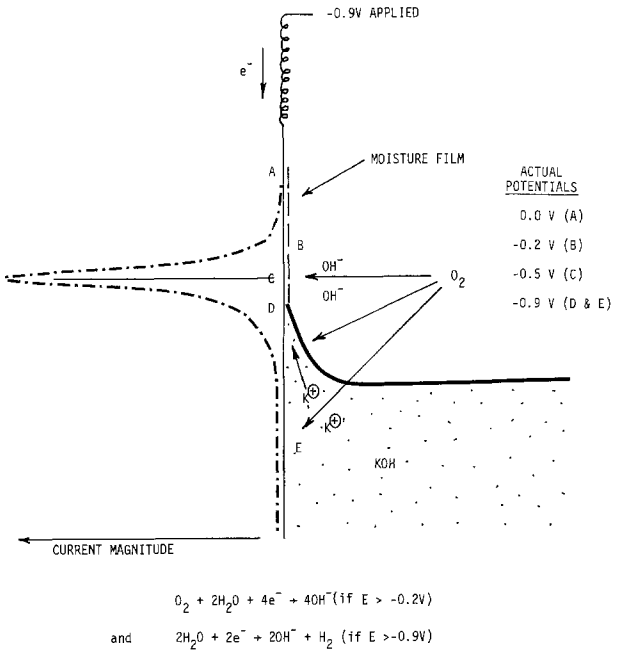


Fig. 11. Spatial distribution of the current density and electrode potential at a partially immersed metal plate in KOH solution and O_2 at −0.9V.

Fig. 11. Hydroxyl ions are being rapidly produced above the meniscus and in order that electroneutrality conditions be preserved, these hydroxyl ions must migrate toward the bulk electrolyte, potassium ions must migrate toward the meniscus top, or some balancing combination of these two migration requirements must concurrently occur. (Under bulk electrolyte conditions, both the hydroxyl and potassium ions are mobile and the potassium hydroxide concentration tends to rise at the site of the reduction reaction.)

The rapid rise in the current magnitude, as one passes from the bulk electrolyte to the meniscus and into the thin electrolyte layer, does not continue indefinitely. Rather, as shown in Fig. 11, a peak value is attained beyond which the current decays back to zero since the tendency for the current to increase, due to the thinness of the electrolyte layer, is opposed by the high electrolyte resistance of this layer to ionic migration. The further up the strip above the meniscus that one measures, the greater becomes the electrolyte resistance and hence the greater the *IR* polarization loss. Due to this *IR* loss, the actual potential driving the electroreduction of oxygen (or evolution of H_2) in the thin film region falls off spatially as shown on the right-hand side of the figure. At the top of the meniscus, the whole of the −0.9V is present to drive the electrode reaction, but the presence of a current flow in the thin layer above the meniscus causes an increasingly greater degree of *IR* drop to be produced in the higher electrode regions until a point is reached (0.0 to −0.2V) above which there is no driving force for O_2 reduction remaining. At this point, the current density has fallen to zero.

There thus exists a "reaction zone" on a partially immersed metal plate which exists from a point within the meniscus region to a point several millimeters above the visible top of the meniscus. In Fig. 11, this reaction zone encompasses that portion of the electrode surface beneath the current peak.

The primary point which has been established is that at the negative electrode of alkaline cells, two electrochemical reactions are possible which lead to the production of hydroxyl ions. Further, it has been established that these reactions take place preferentially in a reaction zone which lies above the visible electrolyte meniscus. In this zone, the hydroxyl ion concentration rises to a value greater than the bulk electrolyte. For this to occur, a counterbalancing movement of positive ions must migrate into the zone and since the ionic mobility of K^+ exceeds that of Na^+, which, in turn, exceeds that of Li^+, this concentration increase occurs at a rate proportional to these mobilities.

This lack of equilibrium between the concentration of KOH in the reaction zone and in the bulk electrolyte must be opposed either by the diffusion of KOH from the high to the low region of concentration or by a movement of water into the reaction zone which will tend to dilute the concentration of alkali there and return it to a state of equilibrium with the bulk electrolyte. The experimental observation is that the reaction zone thickens and moves up the semi-immersed plate. Accordingly, it must now be determined by what mechanism the water is made to move toward the reaction zone.

Of the species involved in reactions [1] and [2], all except the water has a specifically defined source and path to the reaction zone. Taking reaction [1] as an example, it is clear that O_2 arrives from the gaseous phase, the OH^- ions are generated *in situ* and the K^+ ions arrive from the bulk electrolyte by the process of electromigration. The source and path by which water arrives in the reaction zone is, at first glance, not self-evident as both the liquid and the gaseous phases (especially if the relative humidity is high) are potentially capable of providing the required amount. Nor is it certain that each phase does not supply a fraction of the total amount of water. Accordingly, we shall consider two main scenarios which cover the most probable mechanisms for the transport of the water.

The first of these involves electro-osmotic movement of the electrolyte along the negatively charged metal surface. Above the meniscus, the electrode surface is covered with a monolayer of water, especially if the relative humidity conditions are high, *i.e.*, the reaction zone initially consists of a very thin layer of extremely dilute electrolyte. There will thus exist a significant diffuse double layer of positive charge in this region generated by the net negative charge on the metal surface. Should one now apply a potential gradient along such a solution, electro-osmotic movement of the liquid will occur as illustrated in Fig. 12. In this, a negatively charged capillary contains a dilute electrolyte with a positively charged diffuse layer. If now a current is caused to flow through the solution from a zinc electrode undergoing oxidation at one end to a nickel electrode on which oxygen reduction (or hydrogen evolution) is proceeding at the other, there will be a pressure drop produced along the capillary of a magnitude proportional to the driving voltage (and thus the current passing) and the liquid will move toward the cathode. Clearly, the greater the mobility of the positive ion, the faster it will travel from one electrode toward the other and hence the greater will be the resultant pressure "push" and the faster the movement of the bulk liquid. Again, as the viscosity is increased, the resultant pressure push will cause a decreasing volume of electrolyte to flow along the

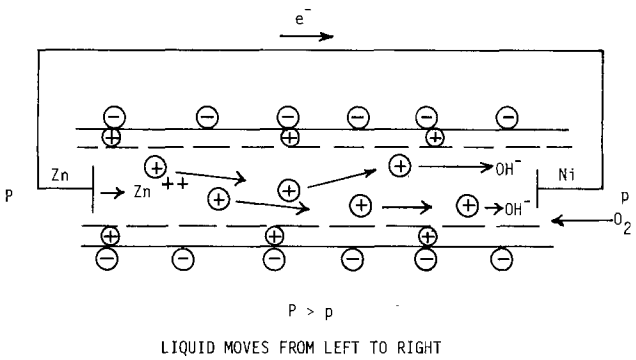


Fig. 12. Electroreduction of O_2 and oxidation of zinc in a dilute electrolyte adjacent to a negatively charged surface.

tube in the stipulated unit of time. (In this example, only the excess charge in the dilute electrolyte is depicted for simplicity.)

Figure 13 summarizes how electro-osmotic movement of the electrolyte thus forces the solution between the negative terminal and the seal. Analogously to the situation described in Fig. 12, the cathodic reduction of oxygen (or evolution of hydrogen) occurring in the reaction zone is driven by dissolution of the negative anode material. The net negative charge present on the terminal substrate in the seal area leads to the establishment of a net positive charge in the reaction zone. Production of hydroxyl ions in the reaction zone leads to electromigration of positive ions into the zone, some of which are part of the net diffuse layer charge. A differential ΔP thus exists between the meniscus and the reaction zone forcing movement of liquid toward the reaction zone and, hence, eventually out of the cell.

A second source of water for the reaction zone is the water vapor present above the surface of the bulk electrolyte. As electroreduction proceeds in the reaction zone and the concentration of the zone increases, the equilibrium relative humidity of the vapor phase above the zone declines to a value lower than that in equilibrium with the bulk electrolyte. As shown in Fig. 14, the relative humidity above a 30% KOH bulk electrolyte is approximately 58%. (The atmosphere introduced into the vicinity of the electrolyte could, of course, have a higher relative humidity than this, but for discussion purposes we will assume equilibrium between the bulk electrolyte and the vapor phase.) If a steady-state concentration of, say, 40% KOH is maintained in the reaction zone by the electroreduction reactions, there will be an equilibrium relative humidity above this zone of only 35%. Thus a transfer of water from the vapor phase to the liquid phase in the reaction zone by the process of condensation will occur. The volume of liquid will thus tend to be expanded both in volume and in surface area coverage of the partially immersed electrode and this process will continue until the electrochemical reactions cease and the reaction zone electrolyte is equilibrated to that of the bulk solution.

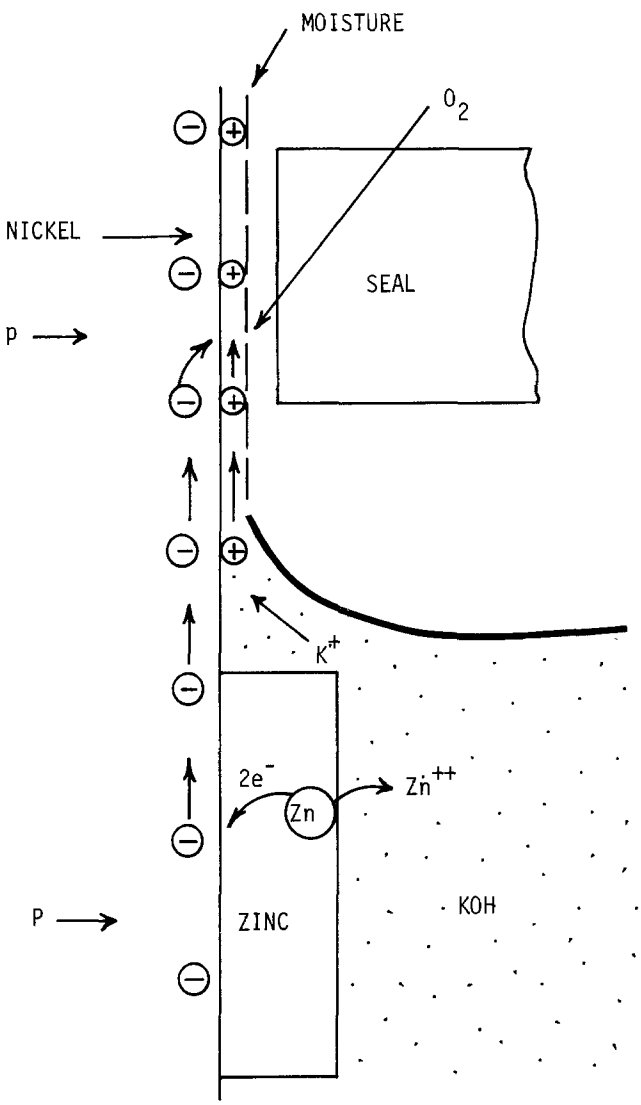


Fig. 13. Spatial separation of the electrochemical reactions proceeding at an idealized metal-seal interface in the presence of zinc, O_2, and KOH.

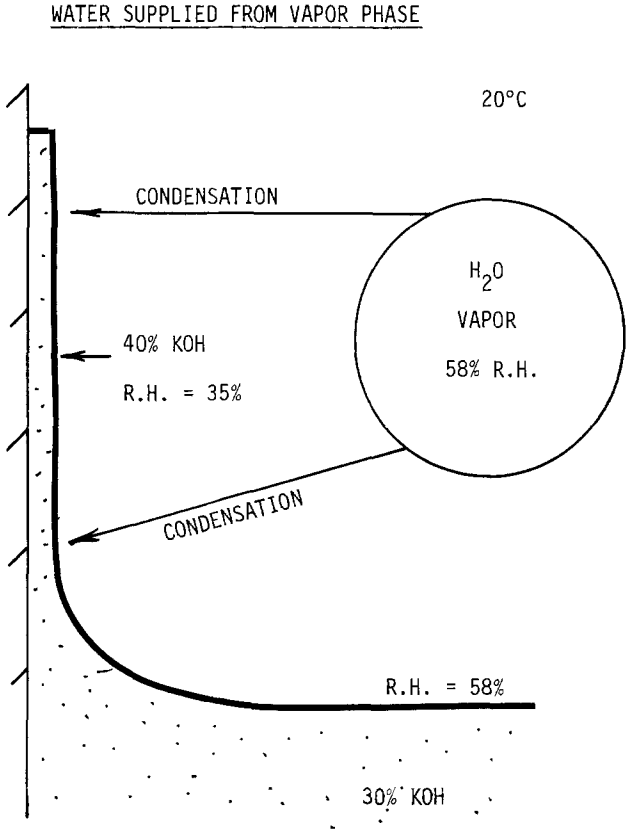


Fig. 14. Equilibrium relative humidities (and direction of water transport) above a bulk electrolyte and in the presence of a partially immersed metal plate exhibiting creepage.

This process of ingress of water to the reaction zone from the vapor phase occurs at a rate that is proportional to the existing relative humidity of the gaseous phase (more correctly, to the RH difference between the reaction zone and the bulk electrolyte but one may assume that the steady-state concentration in the reaction zone reaches a constant value and hence to the equilibrium RH above the zone). Thus, since the bulk electrolyte equilibrium relative humidity decreases as the concentration is increased, the driving force for transfer of water from the bulk electrolyte to the vapor phase and then to the reaction zone where it is observed visually as "creepage" also decreases with concentration.

Two ways by which water can be brought to the reaction zone have now been considered in some detail. The probability is that both mechanisms operate to some degree but that one or the other predominates under the particular ambient conditions present at any particular time. The result is, however, that the reaction zone increases in volume and one must now proceed to a consideration of the effects this volume change will produce on the resistivity of the liquid layer and hence on the spatial distribution of the *IR* polarization losses in the reaction zone.

The result of the increase in the electrolyte concentration of the reaction zone is that the resistance to ionic current flow decreases in the zone and hence the

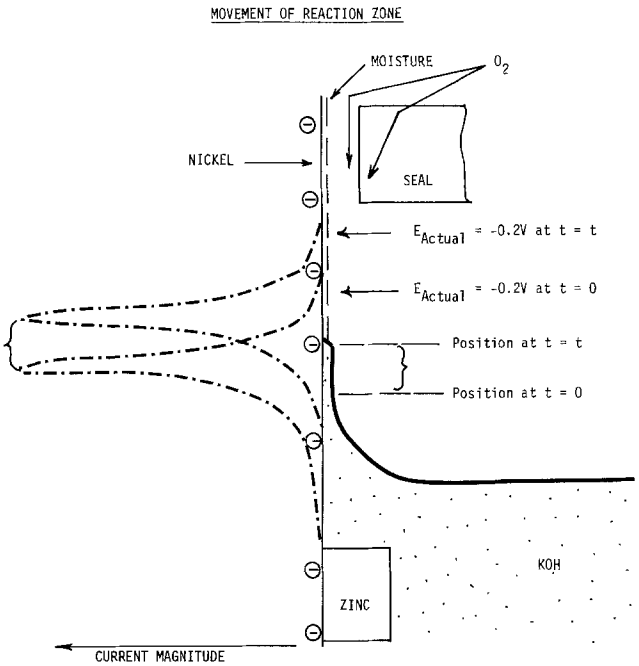


Fig. 15. The spatial distribution of the reaction zone and the concurrent minimum electrode potential for O_2 evolution as a function of time at a partially immersed metal plate exhibiting creepage.

IR polarization begins to fall. Consequently, current flow can commence at a slightly higher part of the partially immersed strip where previously, because of the *IR* polarization, there was an insufficient potential to drive the electroreduction reactions. The reaction zone thus maintains a fairly constant width, but its position moves ahead of the thickening creepage layer at a rate determined by the rate at which the electrolyte layers below it are decreasing in ionic resistance. For example, as shown in Fig. 15 between times $t = 0$ and $t = t$, the position of the creepage front, through electroreduction of O_2 and transport of water into the initial reaction zone, has moved appreciably. The sharp drop in the *IR* polarization loss of the creepage layer between these two positions has permitted the leading edge of the reaction zone to progress up the strip by an equivalent amount. Thus the reaction zone moves inexorably toward the seal and to a limitless supply of O_2 and moisture and cell failure due to electrochemically driven creepage.

Conclusions

Negatively charged electrodes in alkaline electrolytes will tend to reduce oxygen according to

$$O_2 + 2H_2O + 4e^- \rightarrow 4\,OH^- \qquad [1]$$

and if the potential is sufficiently negative to liberate H_2 according to

$$2H_2O + 2e^- \rightarrow 2\,OH^- + H_2 \qquad [2]$$

Both [1] and [2] produce alkalinity at the site of reaction and this "site of reaction" localizes preferentially in a reaction zone above the meniscus since oxygen diffusive transport to the electrode surface and hydrogen transport away occur at their fastest rates on regions of the surface where the electrolyte is thinnest. Concentration of the electrolyte in the reaction zone increases the conductivity of this region and the driving negative potential can then extend to points further along the electrode surface. The preferential reaction zone thus is caused to move along the electrode and electrolyte creepage is the result.

The prevention of electrolyte creepage caused by reaction [1] is easily accomplished if adequate sealing with respect to oxygen access to the reaction zone region is provided. Reaction [2] is more difficult to prevent since most alkaline cells operate at negative electrode potentials that lie outside the stability region of water. Since water itself is the reactant in this case, it is consumed and must be provided to the reaction zone if creepage is to continue. There are several distinct sources for this water supply; an important one is water vapor from the atmosphere. Under conditions of high relative humidity and inadequate sealing of the cell with respect to water vapor transmission through the seal material itself or along the interface between the electrode surface and the seal, an accelerated rate of creepage will result.

Electrolyte creepage by reactions [1] and [2] is the result of cathodic reactions proceeding above the meniscus at a partially immersed electrode driven by a corresponding anodic reaction (*e.g.*, oxidation of zinc to form zinc hydroxide or zincate in the case of alkaline cells with zinc anodes) proceeding on the submerged part of the same electrode. Such cathodic reactions can, however, be driven by an anodic reaction occurring on a spatially separated second electrode provided an electrolyte bridge exists between the two electrodes. Thus, in the presence of high humidity, an electrolyte bridge can form between the anode and cathode terminals of a cell and the cell voltage will then produce hydrogen evolution and O_2 reduction at the negative terminal (with increase in alkalinity) and O_2 evolution or anodic corrosion of the positive terminal. This voltage-dependent mechanism of negative seal failure will be discussed in a subsequent publication.

Manuscript submitted Sept. 15, 1976; revised manuscript received Nov. 15, 1976.

Any discussion of this paper will appear in a Discussion Section to be published in the December 1977 JOURNAL. All discussions for the December 1977 Discussion Section should be submitted by Aug. 1, 1977.

Publication costs of this article were assisted by ESB Incorporated.

REFERENCES

1. J. L. S. Daley, U.S. Pat. 3,068,312.
2. I. Morcos and H. Fischer, *J. Electroanal. Chem.*, **17**, 7 (1968).
3. I. Morcos, *J. Colloid Interface Sci.*, **37**, 410 (1971).
4. I. Morcos, *J. Phys. Chem.*, **76**, 2750 (1972).
5. H. C. Weber, H. P. Meissner, and D. A. Sama, *This Journal*, **109**, 884 (1962).
6. F. G. Will, *ibid.*, **110**, 145 (1963).
7. T. Katan, S. Szpak, and E. A. Grens, *ibid.*, **112**, 1166 (1965).
8. D. N. Bennion and C. W. Tobias, *ibid.*, **113**, 589 (1966).
9. R. H. Muller, *ibid.*, **113**, 943 (1966).
10. Yu. A. Mazitov, K. I. Rozental, and V. I. Veselovskii, *Russ. J. Phys. Chem. (Engl. Transl.)*, **38**, 234 (1964).
11. Yu. A. Mazitov, K. I. Rozental, and V. I. Veselovskii, *ibid.*, **38**, 366 (1964).
12. Yu. A. Mazitov, N. A. Fedotov, and N. A. Aladzhalova, *ibid.*, **39**, 117 (1965).

Adsorption of n-Decylamine on Zinc from Acidic Chloride Solution

H. B. Rudresh and S. M. Mayanna

Department of Chemistry, Central College, Bangalore University, Bangalore 560 001, India

ABSTRACT

The adsorption of n-decylamine on zinc from acidic chloride solution has been studied using the corrosion technique. The corrosion rates of zinc in acidic chloride solution containing n-decylamine are measured as a function of n-decylamine concentration. The degree of surface coverage as calculated from the corrosion rates is used to calculate the free energy of adsorption of n-decylamine. The variation of negative free energy of adsorption with surface coverage is interpreted in terms of change in the mechanism of inhibitor action of n-decylamine with concentration. The synergistic effect of n-decylamine and chloride ions is discussed from the viewpoint of adsorption models.

Despite the extensive use of inhibitors in the corrosion process, little is known of their function because of the complexity of the process. Understanding of the inhibitive action during corrosion requires a knowledge of the adsorption of inhibitor at the electrode-solution interface (1). Adsorption isotherms of the inhibitors for the corrosion process have been discussed (2-4). Adsorption of n-decylamine on several metals from solution has been studied (5). Zinc is an industrially important metal and is corroded by several corrosive agents of which the aqueous acids are the more dangerous. Results on the corrosion of zinc, reported in earlier work, make use of rough and etched surfaces. This investigation examines the adsorption of n-decylamine (n-DA) on an electropolished zinc surface from acidic chloride solution.

Experimental

Solutions were prepared from freshly distilled, preelectrolyzed hydrochloric acid (AR) and recrystallized potassium chloride (AR) using triply distilled water. Zinc (99.999%) was fixed in Tygon tubing and it was mechanically polished on 4/0 emery paper using ethanol as lubricant. The crystal surface was electropolished in a stirred solution of ethanol containing 35% of orthophosphoric acid at a cell potential of 3.5V for 8 min using a stainless steel cathode (6). The chemical and anodic dissolutions were carried out up to 1 hr at 30° ± 0.1°C in a three-necked Pyrex glass cell containing the stirred acidic chloride solution (0.99M KCl + 0.01M HCl) with the desired amount of n-DA (Fluka AG). n-DA in solution up to 10^{-3}M did not alter the pH of the acidic chloride solution. Zinc in solution after chemical dissolution was estimated polarographically and the dissolution rate (milligrams per square centimeter per hour) was evaluated. A 90V battery in series with a variable resistance was used as a constant current source. A saturated calomel electrode and a platinized platinum electrode were used as the reference and auxiliary electrodes, respectively. The corrosion potential and overpotentials were recorded using d-c VTVM with an accuracy of ± 5 mV.

Results

Zinc was dissolved in a stirred acidic chloride solution containing various concentrations (10^{-8}-10^{-3}M) of n-DA at 30°C and the dissolution rates were evaluated. n-DA was found to have a significant effect on the dissolution rate. The dissolution rate decreased gradually with the increase in concentration of n-DA and decreased markedly when the concentration was above 10^{-4}M. At each concentration of n-DA, inhibitor efficiency was calculated using the equation

$$\%p = \left(\frac{\gamma_o - \gamma_i}{\gamma_o}\right) \times 100$$

where p is protection and γ_o is the uninhibited and γ_i the inhibited corrosion rate. The maximum inhibitor efficiency (90%) was observed at 10^{-3}M n-DA. The variation of dissolution rate and inhibitor efficiency, with concentration of inhibitor, is shown in Fig. 1.

The corrosion potential both in the acidic chloride solution and in the presence of n-DA slightly decreased with time to a steady value. However, the steady corrosion potential values were always higher in the presence of n-DA. The anodic overpotential on zinc in the acidic chloride solution was found to be dependent on the n-DA concentration. The anodic overpotential of zinc in the acidic chloride solution at various concentrations of n-DA is shown in Fig. 2. An increase in the concentration of n-DA shifted the polarization curves toward more positive potentials. An anodic Tafel slope of 29 ± 5 mV sec was obtained with and without n-DA.

The surface coverage (θ) of n-DA at different concentrations of n-DA was calculated using the equation (2)

$$(1 - \theta) = \left(\frac{\gamma_i}{\gamma_o}\right)$$

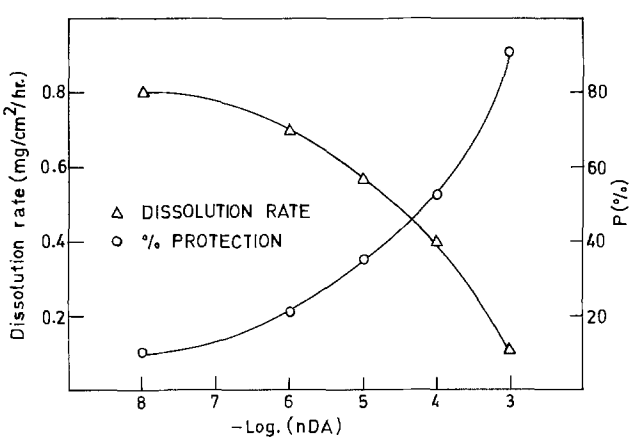


Fig. 1. Variation of dissolution rate and %p with n-DA concentration.

Key words: surface coverage, inhibitor, free energy of adsorption, synergistic effect.

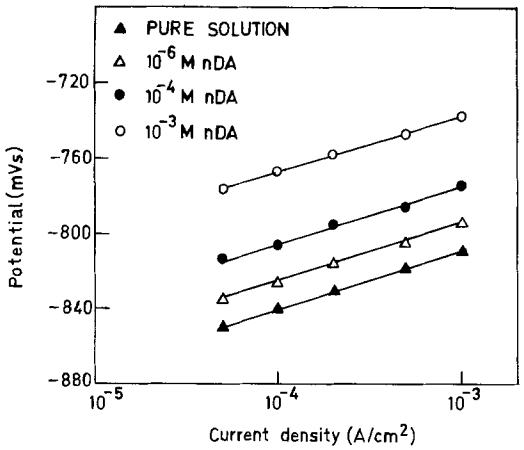


Fig. 2. Effect of n-decylamine on the anodic polarization of zinc in acidic chloride solution.

One could calculate the apparent free energy of adsorption of the inhibitor from θ-values using the equation (5)

$$\Delta G^{o}_{a} = -2.303\,RT \log \left[\frac{55.4\theta}{C_o\,(1-\theta)^n} \cdot \frac{\{\theta + (1-\theta)n\}^{n-1}}{n^n} \right]$$

where C_o is the concentration of inhibitor in the bulk of the solution and n is the size factor. Using the above equation, with $n = 9$ for flat adsorption of n-DA on the surface and $n = 3$ in the perpendicular direction to the surface, the apparent free energies of adsorption (ΔG^{o}_{a}) were calculated. Figure 3 gives the variation of ΔG^{o}_{a} of n-DA with θ. The negative ΔG^{o}_{a} decreased with increase of θ but increased markedly when θ was above 0.6. There is a slight change in the ΔG^{o}_{a} value with change in the n value from 9 to 3. However, the same trend in the variation of ΔG^{o}_{a} with θ is noticed for different n values.

It is shown in Fig. 1 that the effective concentration range of n-DA lies above 10^{-4}M. Hence, the dissolution of zinc in acidic chloride solution with various concentrations of n-DA ($>10^{-4}$M) at different temperatures was also carried out. At each temperature, for a given concentration of n-DA, ΔG^{o}_{a} was calculated. The entropy of adsorption ΔS^{o}_{a} was evaluated from the relation between ΔG^{o}_{a} and T (Fig. 4). From the values of ΔG^{o}_{a} and ΔS^{o}_{a}, the heat of adsorption

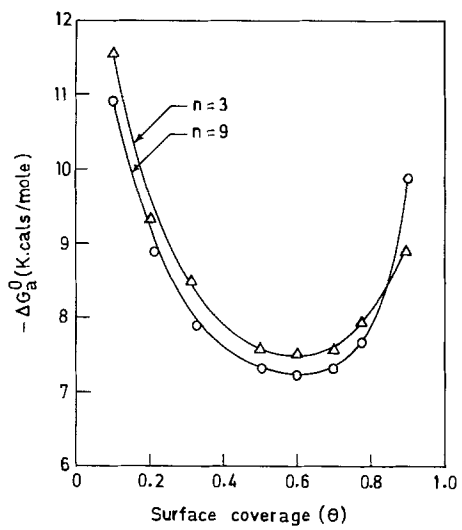


Fig. 3. ΔG_a^{o} for n-decylamine on zinc as a function of surface coverage (θ).

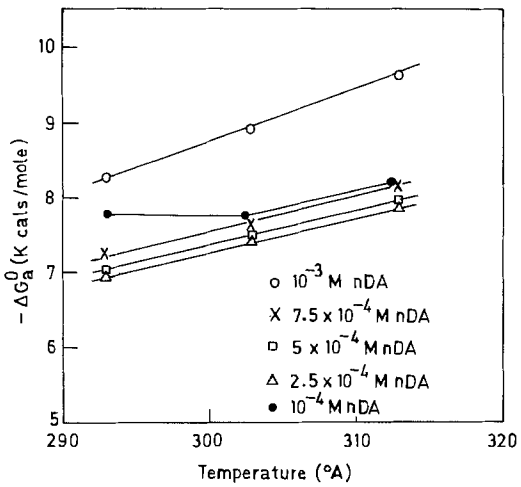


Fig. 4. Relation between ΔG_a^{o} and T at different concentrations of n-DA.

ΔH^{o}_{a} was calculated. Table I gives the values of ΔH^{o}_{a} and ΔS^{o}_{a} at different concentrations of n-DA. The values of ΔH^{o}_{a} and ΔS^{o}_{a} are positive, which increased on increasing the concentration of n-DA.

Discussion

The mechanism of the anodic dissolution reaction of zinc in acidic chloride solution is as follows (7)

$$Zn \longrightarrow Zn^{+} + e$$

$$Zn^{+} \xrightarrow[\text{rds}]{} Zn^{++} + e$$

The results observed (Fig. 2) with and without n-DA indicate the inhibition of the dissolution process without affecting the mechanism. The dissolution reaction initiates on the surface of the metal at the reaction sites (surface defects). Due to adsorption, n-DA perhaps prevents the removal of zinc ions from the reaction sites on the surface. This is usually observed by the increase in the dissolution potential (8), which depends on the concentration of the inhibitor or θ. This is in accordance with the observed results (Fig. 5) that the dissolution potential increases linearly with θ.

Chloride ions are known to adsorb on the metal surface (9). Amines are able to adsorb on the metal surface even at a high concentration of chloride ions (10). Chloride ion has slight effect on the corrosion of zinc in acidic solution (7). The synergistic effect of chloride ions and n-DA in acid corrosion inhibition of steel has been reported (11). The synergistic effect is a complex phenomena and no single mechanism accounts for all observations.

The variation of ΔG^{o}_{a} with θ (Fig. 3) indicates the change in the mechanism of inhibitor action with n-DA concentration. From Fig. 1, it is clear that n-DA is not a film-forming inhibitor on the zinc surface. On the basis of the earlier works (10-12), and observed results, the following models for n-DA adsorption are proposed

Table I. Heat of adsorption (ΔH^{o}_{a}) and entropy of adsorption (ΔS^{o}_{a}) of n-DA at different concentrations

Concentration of n-DA (M)	Heat of adsorption (ΔH^{o}_{a}) (kcal/mole)	Entropy of adsorption (ΔS^{o}_{a}) (cal/deg/mole)
2.5×10^{-4}	9.8	45
5×10^{-4}	10.6	52
7.5×10^{-4}	11.3	65
1×10^{-3}	12.8	75

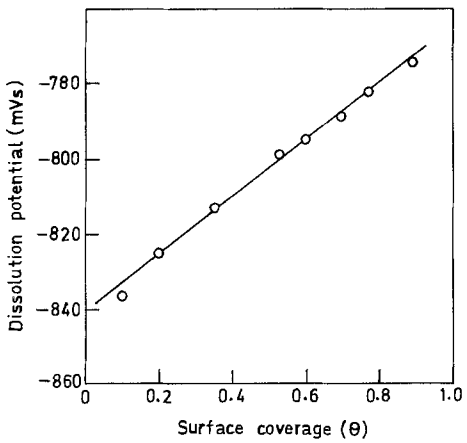


Fig. 5. Variation of dissolution potential with surface coverage (θ) of n-DA at 30°C.

Cl^- R^+	Cl^- R^+	R^+ Cl^-
Cl^- R^+	R^+ Cl^-	R^+ Cl^-
Cl^- R^+	Cl^- R^+	R^+ Cl^-
Cl^- R^+	R^+ Cl^-	R^+ Cl^-
Cl^- R^+	Cl^- R^+	R^+ Cl^-
Model I	Model II	Model III

Adsorption from solution is influenced by several interactions between the metal and the components both on the surface and in the bulk of the solution. At very low concentration (10^{-8}M), n-DA cations (R^+) from solution gather around the chloride ions, previously adsorbed on the zinc surface, and as a result tend to be weakly bound to the chloride ions (model I). In the case of rather weak adsorption of chloride ions, R^+ at high concentration tends to withdraw the chloride ions on the surface into the solution (12). Hence, on increasing the concentration of n-DA from 10^{-8} to 10^{-4}M, coadsorption of cations and chloride ions is possible (model II). The extent of desorption of chloride ions from the surface depends on the extent of adsorption of R^+, which is a function of the concentration of n-DA. When the concentration of n-DA is increased above 10^{-4}M, the chloride ions on the surface provide a better electrostatic condition, which promotes a direct adsorption of cations on the surface through its polar group ($n = 3$). This is probably seen in the nonlinear relation between ΔG°_a and T at 10^{-4}M n-DA (Fig. 4). This is also in accordance with the increase in negative ΔG°_a with θ above 10^{-4}M n-DA, which is the characteristic feature of lateral interaction between adsorbed n-DA molecules on the surface (5). The positive values of ΔH°_a and ΔS°_a can be explained as a result of the occurrence of the replacement process (13, 14) during adsorption of n-DA on the surface.

Acknowledgments

The authors are grateful to Prof. M. Shadaksharaswamy, Principal and Head of the Department of Chemistry, Central College, Bangalore University, for his encouragement. One of us (H.B.R.) wishes to thank CSIR, New Delhi, for financial support.

Manuscript submitted Aug. 16, 1976; revised manuscript received Oct. 20, 1976.

Any discussion of this paper will appear in a Discussion Section to be published in the December 1977 JOURNAL. All discussions for the December 1977 Discussion Section should be submitted by Aug. 1, 1977.

REFERENCES

1. Z. A. Iofa and A. A. Medvedeva, *Dokl. Akad. Nauk SSR*, **69**, 213 (1940)
2. S. M. Mayanna, *This Journal*, **122**, 251 (1975).
3. S. M. Mayanna and T. H. V. Setty, *Corros. Sci.*, **15**, 627 (1975).
4. M. F. Ahmed, S. M. Mayanna, and F. Pushpanaden, in 6th International Congress on Metallic Corrosion, University of Sydney, Australia (1975).
5. J. O'M. Bockris and D. A. Swinkels, *This Journal*, **111**, 736 (1964).
6. P. A. Jacquet, *Met. Rev.*, **1**, 157 (1956).
7. T. Hurlen, *Acta Chem. Scand.*, **16**, 1337, 1346 (1962).
8. B. S. Sheshadri and S. M. Mayanna, *Electrodeposition Surf. Treat.*, **3**, 189 (1975).
9. Ja. M. Kolotyrkin, *This Journal*, **108**, 209 (1961).
10. T. Murakawa, S. Nagura, and N. Hackerman, *Corros. Sci.*, **7**, 79 (1967).
11. N. Hackerman, E. S. Shavely, and J. S. Payne, Jr., *This Journal*, **113**, 677 (1966).
12. T. Murakawa, T. Kato, S. Nagura, and N. Hackerman, *Corros. Sci.*, **8**, 483 (1968).
13. E. Gileadi, Symposium Europe'en sur les Inhibiteurs de Corrosion, Comptes Rendus, p. 543, Ferra, Italy (1965).
14. A. I. Amar and M. W. Khalil, *Electrochim. Acta*, **16**, 939 (1971).

Search for Gold Cyanide Inclusions in Cobalt-Hardened Gold Electrodeposits

R. L. Cohen, K. W. West, and M. Antler[1]

Bell Laboratories, Murray Hill, New Jersey 07974

ABSTRACT

We have studied samples of cobalt-hardened gold electrodeposits via Mössbauer spectroscopy to search for microprecipitates of gold compounds *in situ*. Plated layers were found to contain no detectable AuCN, $KAu(CN)_2$, or $KAu(CN)_4$. The upper limits determined for the presence of these phases exclude the possibility that all the carbon found in this hard gold plate could be incorporated in the deposit in these forms. We have determined the recoil-free fraction for $KAu(CN)_2$ and $KAu(CN)_4$.

Gold electrodeposits containing small amounts of other metals are widely used as contact materials in separable electronic connectors and in relays for low energy switching applications. Cobalt or nickel, from *ca.* 0.3-1.6 atom percent (a/o) [0.1-0.5 weight percent (w/o)], are the most used hardeners and are deposited in the gold from buffered acid solutions of $KAu(CN)_2$. This small metal addition raises the hardness of the plated layer to 140-220 kg/mm^2 and produces surfaces

[1] Bell Laboratories, Columbus, Ohio 43212.

which have low and stable contact resistance and good wear resistance (1). However, a considerable amount of carbon, nitrogen, and hydrogen are also deposited in the plated layer (2-7). The presence of these impurities reduces the observed density of plated layers below that of pure gold, may result in bubbling or cracking of the surface due to gas evolution on heating, and may have deleterious effects on its solderability and ultrasonic bondability (6,8,9).

In 1969, it was reported (8) that some of these impurities could be directly observed by dissolving out the gold (using aqua regia) from the hard gold plate. The carbonaceous material was often found to retain the shape of the original piece of gold plate, and was given the name "polymer." Because of the economic importance of these hard gold plates, many studies have been carried out to determine the quantity and nature of the carbonaceous impurities (2-6). The metallic character of the gold layer makes it effectively impossible to use the standard techniques of optical and infrared spectroscopy or magnetic resonance to study the carbonaceous impurities. As discussed above, some attempts have been made to dissolve out the gold matrix, leaving behind the impurities to be studied. Unfortunately, there is no guarantee that the extracted impurities are unchanged by this processing.

We have used the technique of Mössbauer spectroscopy (10) to study the composition of cobalt-hardened gold in a completely nondestructive way. This paper discusses the search for Au compounds in the plated layer.

Mössbauer spectroscopy is a technique based on γ-ray resonance absorption by nuclear levels. The energy of an excited level of an atomic nucleus is altered slightly ($\sim 10^{-7}$ eV) by the surroundings of the ion. These changes may be detected and measured via Mössbauer spectroscopy. Comparison of the measured spectra with those of known compounds can then be used to determine the composition of the material under study.

For the Au^{197} nucleus used here these perturbations result from (*i*) the electronic density at the nucleus, which leads to the "isomer shift," a change in the energy levels, and (*ii*) the quadrupole coupling, which leads to a splitting of the nuclear energy levels, and thus a symmetric doublet spectrum. The field gradient which produces the quadrupole splitting arises from asymmetric disposition of the ligand ions, and is identically zero in the ideal fcc structure. Any configuration of ligand ions leads to a particular, distinct value of isomer shift and quadrupole splitting of the gold nuclear resonance, and these parameters are observed via the Mössbauer effect. In the research reported on here, we compare the Mössbauer spectra of plated samples with spectra of known gold compounds to search for the presence of particular impurities in the electrodeposits.

In these experiments, only the Au nuclei contribute to the resonance absorption observed.

There are two important advantages to this approach: First, the radiation used here, the 77 keV γ-ray of Au^{197}, will penetrate through $\sim$0.5 mm of gold, so that plated layers can be studied without thinning or special treatment. The total radiation dose received by the sample is at least 1000 times less than that in an x-ray diffraction experiment, so radiation damage should not be significant. Second, the "Mössbauer parameters" characterizing a given compound are determined almost entirely by the first and second nearest neighbor shells around the atom being studied. Thus, microprecipitates containing only a few molecules of a substance exhibit Mössbauer spectra like those of the bulk material.

In view of the relative novelty of the Mössbauer spectroscopy technique for investigations like these, it is worthwhile to discuss some of the previous studies on very fine particles. For gold microcrystals of about 60Å diameter, Schroeer *et al.* (11) found the isomer shift to be less than 0.1 mm/sec different from that of bulk gold. For the same particles, Marshall and Wilenzick (12) found a small increase (about 5%) in the recoil-free fraction (efficiency with which the Mössbauer effect is observed) over that of bulk gold. For granular tin of 45Å mean particle size, Akselrod *et al.* (13) found no changes in the isomer shift or line width from bulk tin values, and a small (less than 2%) decrease in the recoil-free fraction. Akselrod *et al.* also found that for the intergranular SnO phase, with an estimated grain size of 20Å, the isomer shift, quadrupole coupling, and resonance line width were identical with the corresponding values for bulk materials. Cohen *et al.* (14) made measurements on colloidal sols of Pd-Sn alloy which showed that for $\sim$20Å particles, the Mössbauer line was essentially the same as that of the bulk alloys. Mössbauer measurements in iron-containing biological molecules are routinely made using samples in which the individual molecules are isolated in a frozen matrix (*i.e.*, "clusters" consisting of a single molecule are studied) and sharp and well-defined spectra are obtained (15). These experiments, plus many others on "glassy" systems where there is no long range order, demonstrate that the Mössbauer spectra can be used with high reliability to characterize the local environment of the atom (in this case, Au) being studied, even when the particle size is extremely small.

In general, detection of second phases via x-ray diffraction is limited to cases where at least 2-5% of the material is in the second phase (16). The sensitivity is much poorer if the second phase is very finely divided or of poor crystallinity, conditions which we would expect here. In fact, Okinaka and Nakahara (17) have recently reported high concentrations of voids or inclusions in the 20Å size range in cobalt-hardened gold; inclusions of this size would yield such broad x-ray lines as to be almost undetectable.

Experimental Technique

The samples studied were approximately 33 μm (1.3 mil) thick layers of production cobalt-hardened gold plated on copper coupons from an Autronex Cl[2] bath that had been replenished many times with gold and hardener materials. The bath was thus representative of those actually used in manufacturing plants. The current density and temperature during plating were 1 A/dm^2 and 32°C. Analysis of adjacent material showed the cobalt content to be 0.80 a/o, potassium 0.28 a/o, and carbon 3.45 a/o. The copper backing was etched off with ammonium persulfate, and 10 of the hard gold layers were stacked to make a single absorber 330 μm thick to accentuate saturation effects (see below).

Measurements were made in transmission geometry with a drive which has already been described (18), with data collection by up-down multiscaling. The γ-rays were emitted from Au^{197} produced by the decay of Pt^{197}, made by neutron irradiation of Pt^{196} metal. The absorber was maintained at 4°K and the source at about 8°K during the measurements.

Results and Data Analysis

The absorption spectrum of the 10 layer absorber is shown in Fig. 1. The line has approximately the shape and position expected for Au metal (19) or a dilute alloy of cobalt in gold. Figure 1 also shows the line positions reported (20) for three possible Au cyanides. All those compounds have symmetric doublets for their Mössbauer spectra; the spectrum of Au-Co alloy should be a slightly broadened singlet. Although the left-hand line of each of the gold cyanides is close to the main Au line and would not be resolvable, the right-hand lines are reasonably far from the Au peak, and we have looked only for them in the computer analysis of the data. The spectrum of Fig. 1 shows

[2] TM SelRex Company, Division of Oxy-Metal Industries, Nutley, New Jersey.

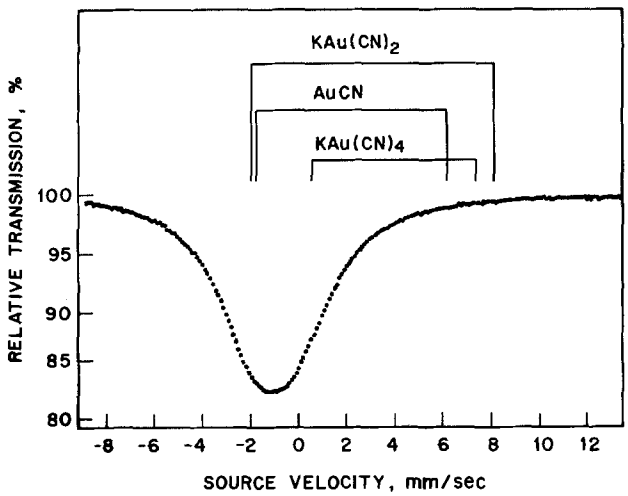


Fig. 1. Mössbauer spectrum of the gold plate sample studied in these experiments, using a source of Pt^{197} in Pt. Known line positions for the doublet spectra of the gold cyanides are shown. Data described as "run 1" in Table I are shown. On this scale, point-to-point variations from counting statistics are invisible. (Five million counts/channel.)

immediately that large quantities of the gold cyanides are not present. Processing of the data by computer least squares fitting is necessary to extract all of the possible information, however.

One possible approach to this problem would be a detailed line shape analysis, starting with the inherent Lorentzian line profile of the Mössbauer resonance, and inserting additional terms for the thickness (saturation) broadening, dispersion (21), and cobalt alloying. Aside from the obvious complications of this approach, the relatively poorly characterized nature of the deposit itself makes it very difficult to accurately describe the alloy. Thus we have chosen the empirical technique of taking the right-hand shoulder of the line (where the distinctive peaks of the cyanides lie) and least squares fitting that with a shoulder of Lorentzian line shape as shown in Fig. 2. For the limited velocity range used, this function represents an adequate fit to the data. The greatly magnified spectrum (Fig. 2A) still shows no obvious peaks where they would be expected for the gold cyanides.

To demonstrate that the technique is in fact sensitive to the small amounts of AuCN which might be present, we have superimposed on the data of Fig. 2 a calculated line showing the spectrum which would be obtained if the sample contained 2 mole percent (m/o) AuCN (see below). The curve has been calculated from the known (20,22,23) width, position, and intensity of the AuCN resonance lines. The data clearly exclude this interpretation.

We have further refined the analysis by constraining the least squares fitting routine to search for Lorentzian lines of width 2.2 mm/sec (this value typical of Au compounds) and positions expected for the gold cyanides in the experimental spectrum. Results of this analysis have been compared with line shapes of a pure solid solution of 0.67 a/o Co in Au, prepared by melting, and then annealing the elements at 800°C in H_2. The results of this analysis for two different sets of measurements on the same absorber are shown in Table I. All of the least squares fits showed χ^2 consistent with there being only statistical deviations between the data and fitted model.

This approach yields the line intensities (in counts) for the anticipated impurities. The following factors must be considered to infer the mole percentage limits of the impurities from the line intensities:

1. Line intensities must be doubled to allow for the other line of the doublet, since the resonance absorption is divided into two lines of equal intensity.

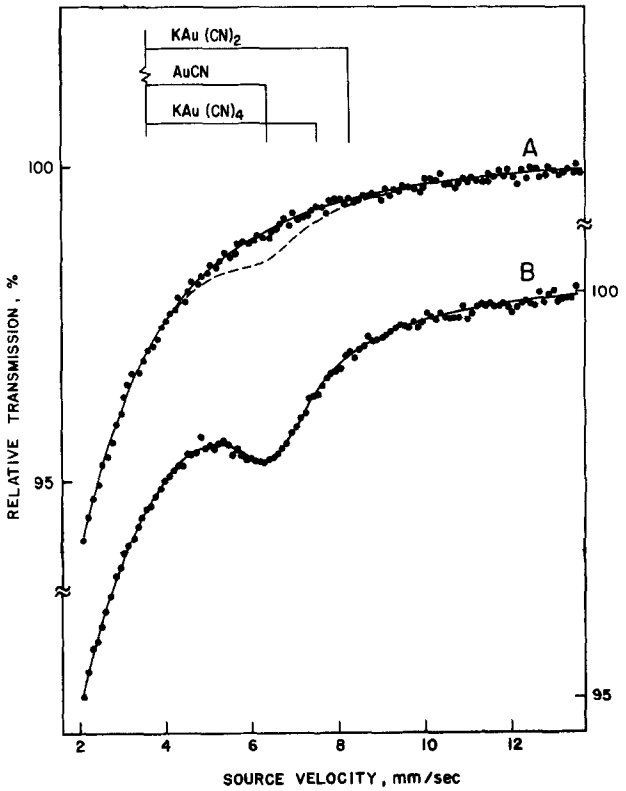


Fig. 2. A. Expanded view of the right-hand shoulder of the line shown in Fig. 1, with a least squares fit line describing a Lorentzian shoulder. The dashed line, determined as described in the text, shows the spectrum that would be obtained if 2% of the Au were in the form of AuCN. Line positions for the right-hand lines of the other gold cyanides are also shown. B. Expanded view of the right-hand shoulder of the Mössbauer resonance obtained with a composite absorber consisting of 627 mg/cm^2 of Au metal and 35 mg/cm^2 of Au as AuCN. The least squares fit line (shoulder of Lorentzian, plus AuCN line at appropriate position) is shown.

2. The relative Debye-Waller factors (recoil-free fraction, or f value) of the cyanides to that of the Au alloy must be considered. From Ref. (23), we find f/f_{Au} for AuCN and $KAu(CN)_2$ to be 0.5 and 0.08, respectively. We have also measured f/f_{Au} for $KAu(CN)_4$[3] and $KAu(CN)_2$ to be 0.31 and 0.08, respectively, with an estimated accuracy of ~15%. These relative f values are listed in Table I and used in the calculations. Using the determination (24) that $f_{Au} = 0.19$ at 4°K, absolute f values at 4°K for AuCN, $KAu(CN)_2$, and $KAu(CN)_4$ are 0.10, 0.015, and 0.06, respectively.

3. The absorber has intentionally been made very "thick" to increase saturation effects, which make the observed size of the resonance absorption increase only slowly for thick absorbers. Since the absorber is "thin" in terms of the gold cyanide, the gold cyanide

[3] We are indebted to Ms. Winifred Heppler, Dr. M. O. Faltens, and Prof. D. A. Shirley for providing us with a sample of this material.

Table I. Least squares fit results for gold cyanide compounds in cobalt-hardened gold

Compound, x	Run	Resonance absorption counts* Au	x	f_x/f_{Au}	x/mole Au*
AuCN	1	868 × 10^3	−159 ± 1447		−0 0001 ± 0.0011
	2	152 × 10^3	662 ± 510	0.5	0 003 ± 0.002
$KAu(CN)_2$	1	868 × 10^3	−818 ± 959		−0.004 ± 0 005
	2	152 × 10^3	60 ± 360	0.081	+0.001 ± 0.006
$KAu(CN)_4$	1	868 × 10^3	−429 ± 1184	0.31	−0.0005 ± 0.0015
	2	152 × 10^3	733 ± 387		0.005 ± 0.003

* Stated error limits are one standard deviation.

lines increase in intensity almost linearly with absorber thickness, while the main gold line increases only slowly. Thus, the use of a thick absorber increases the intensity of the impurity lines relative to the main line. For the value of $t = 10$ we use here, this magnification factor can be estimated from Ref. (22) to be 6.1. Saturation effects also produce broadened lines and are responsible for the excess (over the 2.2 mm/sec mentioned) linewidth observed in Fig. 1.

Although all of these effects are well established theoretically and widely confirmed experimentally, we have also validated the over-all approach and size of the saturation corrections by making a measurement on a compound absorber consisting of 627 mg/cm^2 of Au metal plus 35 mg/cm^2 of Au in the form of AuCN. The spectrum of this composite absorber is shown in Fig. 2B, with the right-hand line of the AuCN clearly visible. Least squares fitting of these data according to the procedures used for the CI samples, using the parameters shown in Table I, gave a value of 31 mg/cm^2 for the amount of gold in the AuCN phase. This confirms the validity of the analysis.

Table II shows the weighted average of the results of Table I for the various gold cyanides. For each material sought, the Mössbauer results are consistent with complete absence of that phase. Also shown are the upper limits for the mole percentage of the potassium gold cyanides obtained from the analysis for potassium.

Discussion

The main conclusion from this research is that the quantity of gold cyanides observed is far too small to account for the amount of carbon in this material. Analysis on other sections of this plated sample showed that 3.5 m/o C was present. Raub *et al.* (2) have reported N/C = 0.5-0.6 for Au-Co samples plated from similar baths under similar conditions. Thus, if we assume that their results describe our samples, and that all the N is present as CN, there would be about 2 m/o CN present.

Table II shows the amounts of the various cyanides that would be found if all of this cyanide were combined with the gold. It can be seen that the Mössbauer results exclude the possibility that a large fraction of the CN could be present as AuCN. Both the Mössbauer results and the potassium analysis show that at most 30% of the CN could be present as $KAu(CN)_2$.

Thus, our main conclusion is that the large amounts of CN observed in hard gold plates are either combined with the (Co) hardener, or occluded in the plate structure without forming well-defined gold cyanides. Forthcoming papers will discuss these possibilities.

Our conclusions are in disagreement with recent suggestions (2), but are based on specific tests sensitive to the microscopic structure of the deposit. There is, of course, always the possibility that sample-to-sample variations play some role in the differing interpretations.

Table II. Limits on presence of gold cyanides

Compound, x	From Mossbauer analysis, m/o	From potassium analysis, m/o	If all CN were in form x, m/o
AuCN	0.06 ± 0.1	—	2
$KAu(CN)_2$	-0.2 ± 0.4	0.28	1
$KAu(CN)_4$	0.1 ± 0.1	0.28	0.5

Acknowledgment

We would like to thank F. B. Koch, R. Sard, and L. N. Schoenberg for helpful discussion, and T. Y. Kometani for the atomic absorption analysis of potassium.

Manuscript submitted April 22, 1976; revised manuscript received Sept. 20, 1976.

Any discussion of this paper will appear in a Discussion Section to be published in the December 1977 JOURNAL. All discussions for the December 1977 Discussion Section should be submitted by Aug. 1, 1977.

Publication costs of this article were assisted by Bell Laboratories.

REFERENCES

1. M. Antler, in "Gold Plating Technology," F. H. Reid and W. Goldie, Editors, chap. 21 and 22, pp. 259-294, Electrochemistry Publications, Ltd., Ayr, Scotland (1974).
2. C. J. Raub, A. Knödler, and J. Lendvay, *Plat. Surf. Finish.*, **63**, 35 (1976).
3. F. H. Reid, Proceedings of the Fifth Plating in the Electronics Industry Symposium, American Electroplaters' Society, p. 67, New York (1975).
4. E. Raub, C. J. Raub, A. Knödler, H. P. Wiehl, *Werkst. Korros.*, **8**, 643 (1972).
5. L. Holt and J. Stanyer, *Trans. Inst. Met. Finishing*, **50**, 24 (1972).
6. M. V. Davis, Proceedings of the Fourth Plating in the Electronics Industry Symposium, American Electroplaters' Society, p. 210, Indianapolis (1973).
7. M. Antler, *Plating*, **60**, 468 (1973).
8. G. B. Munier, *ibid.*, **56**, 1151 (1969).
9. D. J. Huettner and R. C. Sanwald, *ibid.*, **59**, 750 (1972).
10. G. K. Wertheim, "Mössbauer Effect: Principles and Applications," Academic Press, New York (1964).
11. D. Schroeer, R. F. Marzke, D. J. Erickson, S. W. Marshall, and R. M. Wilenzick, *Phys. Rev. B*, **2**, 4414 (1970).
12. S. W. Marshall and R. M. Wilenzick, *Phys. Rev. Lett.*, **16**, 219 (1966).
13. S. Akselrod, M. Pasternack, and S. Bukshpan, *Phys. Rev. B*, **11**, 1040 (1975).
14. R. L. Cohen and K. W. West, *This Journal*, **120**, 502 (1973); R. L. Cohen and R. L. Meek, *J. Colloid Interface Sci.*, **55**, 156 (1976).
15. See, *e.g.*, "Applications of Mössbauer Spectroscopy," Vol. 1, R. L. Cohen, Editor, pp. 129-196, Academic Press, New York (1976).
16. H. P. Klug and L. E. Alexander, Editors, "X-Ray Diffraction Procedures," p. 404, John Wiley & Sons, Inc., New York (1954).
17. Y. Okinaka and S. Nakahara, *This Journal*, **123**, 1284 (1976).
18. R. L. Cohen, *Rev. Sci. Instrum.*, **37**, 957 (1966).
19. R. L. Cohen, in "Mössbauer Isomer Shifts," G. K. Shenoy and F. E. Wagner, Editor, North-Holland, Amsterdam (1976).
20. H. D. Bartunik, W. Potzel, R. L. Mössbauer, and G. Kaindl, *Z. Phys.*, **240**, 1 (1970).
21. D. J. Erickson, J. F. Prince, and L. D. Roberts, *Phys. Rev. C*, **8**, 1916 (1973).
22. S. Margulies and J. R. Ehrman, *Nucl. Instrum. Methods*, **12**, 131 (1961).
23. L. Pfeiffer, R. S. Raghavan, C. P. Lichtenwalner, and K. W. West, *Phys. Rev. Lett.*, **30**, 635 (1973).
24. D. J. Erickson, L. D. Roberts, J. W. Burton, and J. D. Thomson, *Phys. Rev. B*, **3**, 2180 (1971).

Tin (IV) Sensitizer for Photoselective Metal Deposition of Cobalt and Nickel from Alkaline Baths

B. K. W. Baylis, N. E. Hedgecock, and M. Schlesinger*

Department of Physics, University of Windsor, Windsor, Ontario, Canada N9B 3P4

ABSTRACT

Sn(IV) sensitizer can be used to achieve electroless plating in either basic Ni or Co metallizing baths, but only if an additional reducing bath is used between the activation step and the last rinse. Irradiation with ultraviolet light before this reduction step prevents subsequent plating for both Ni and Co. When irradiation follows reduction it inhibits Ni plating. The effects of different reducing agents on the subsequent plating from acidic Ni, basic Ni, Co, and Cu baths are reported. Possible mechanisms for ultraviolet inhibition of metal plating are discussed.

In a previous publication (1) we showed that an aged Sn(IV) chloride solution can serve as a sensitizer for electroless copper plating and for nickel plating from an acidic bath. Ultraviolet irradiation of the substrate after Sn(IV) sensitization and Pd(II) activation was shown to have a marked effect on subsequent metal plating. In a copper bath, plating occurred only on the irradiated surface, producing a clear, sharp negative image, which we call a "stimulated" negative [see Ref. (2)]. In an acidic nickel bath, plating occurred only on the nonirradiated surface, producing a clear, sharp positive image of the photomask.

In the light of these results, the performance of this sensitizing system with other metal plating baths was studied. This paper describes results obtained using alkaline nickel (3) and cobalt (3, 4) baths, both using hypophosphite as reducing agent.

Experimental

All chemicals were of A.C.S. reagent grade, supplied by Fisher or Canlab, and were used without further purification.

Sensitizer.—The preparation of this bath is described in detail in Ref. (2).

Activator, acidic nickel bath, and copper bath.—The preparation of these baths is described in Ref. (1).

Exposure system and procedure.—These were described in Ref. (1) except that rinse times were shortened to 1 min and that an infrared lamp was usually used to dry the samples after activation.

Alkaline nickel and cobalt baths and reducing baths.—The composition of these baths are listed in Table I. Except as noted, all baths were used at room temperatures.

Substrate.—All samples were prepared on Esco precleaned microscope slide glasses. These were wiped with paper tissues before use.

Results

All samples in the present study were dipped in aged Sn(IV) sensitizer, rinsed, dipped in Pd(II) activator, and dried. The designation [Sn(IV) · Pd(II)] refers to the catalytic substance present on the substrate after these steps are completed.

The procedure described in Ref. (1) for obtaining selective deposition of Ni (from acidic solution) and of Cu involves the above steps, followed by the sequence: u.v. irradiation, rinse, metallization.

Plating from basic Ni and Co baths.—Using alkaline Ni and Co baths, no plating is obtained with the above procedure on either the irradiated or nonirradiated surface. However, if the catalytic surface is immersed in an acidic hypophosphite reducing bath before the metallization step, plating does occur in either metallizing bath.[1] [The reduction step is also necessary to give plating from an alkaline Ni-B bath of the type used by Gorbunova (5).] Ultraviolet light inhibits Ni-P plating, whether irradiation precedes or follows the reduction step. Co plating is inhibited only if reduction follows u.v. irradiation.

Various hypophosphite reducing baths were used, based upon the metallizing baths. (For two examples, see Table I). These reducing baths were all successful if the *p*H had been lowered to between 5.3 and 5.9. The reducing agent in the copper bath, formaldehyde in strong base, proved also effective as a reducing bath, but only when fresh and concentrated [undiluted solution "B" used in making Cu plating baths, Ref. (1)] or when the glass slide was hot when immersed in the reducing bath. If u.v. irradiation follows reduction, the results with formaldehyde are substantially the same as those with acidic hypophosphite, although with poor reliability. For instance, the amount of cobalt plating in the irradiated area varied from being the same as that on the nonirradiated section to being much more, giving enhanced negative images of the photomask. If irradiation precedes reduction in hot formaldehyde, however, both Ni and Co plating occur on the irradiated surface.

Heating the reduced catalyst does not noticeably affect subsequent Co plating, but impairs Ni plating. Hence the drying step prior to u.v. irradiation is accomplished by draining at room temperature, indicated by D in Table II.

[1] It was possible to obtain Co plating using Sn(IV) sensitizer without the reduction step if the metallizing bath temperature was raised to 80°C, once the *p*H of the bath had fallen to about 6 due to ammonia evolution. If the sample had been irradiated with u.v. light, the irradiated areas did not plate, giving rise to a positive image of the photomask.

Table I. Composition of baths

(Quantities given for 1 liter of solution)

	Ni	Co	Reducing bath No. 1	Reducing bath No. 2
$CoSO_4 \cdot 7H_2O$		35g		
$NiSO_4 \cdot 6H_2O$	30g			
$NaH_2PO_2 \cdot H_2O$	10.6g	40g	40g	17.5g
Na_3 citrate	100g	35g	35g	
NH_4Cl	53.6g			
$(NH_4)_2SO_4$		70g	70g	
Na_2 succinate				14.5g
Succinic acid				1.0g
*p*H (adjusted with NaOH)	8.3-8.6	8.8-9.0		
*p*H (adjusted with HCl)			5.3-5.9	As made

* Electrochemical Society Active Member.

Key words: electroless, sensitizer, tin (IV), photoselective nickel, cobalt, copper.

Table II. Effect of additional reduction step on photoselective deposition from alkaline plating baths

Sequence*					Metal bath	Irradiation U.V.	Irradiation No u.v.	Image type
S R_1 A IR	UV	R_2	—	—	Co or Ni	No	No	—
	UV	R_2	F	R_3	Co or Ni	Yes	Yes	—
	UV	R_2	P	R_3	Co or Ni	No	Yes	Positive
	F or P	D	UV	R_3	Co	Yes	Yes	—
	F or P	D	UV	R_3	Ni	No	Yes	Positive
	UV	R_2	—	—	Cu	Yes	No	Stim. negative
	UV	R_2	P or F	R_3	Cu	Yes	Yes	—
	F or P	IR or D	UV	R_3	Cu	Yes	Yes	—

* S refers to Sn(IV) sensitizer bath (2 min), R_1 = first rinse (1 min), A = Pd(II) activator bath (2 min), IR = infrared lamp (3-5 min), UV = ultraviolet lamp (6 min), R_2 and R_3 = second and third rinses (usually running distilled water), P = acidic hypophosphite solution (1 min), F = fresh, concentrated, basic formaldehyde bath (1 min), Ni = basic Ni bath (11 to 40 min), D = room temperature drain to dryness (about 20 min), Co = basic cobalt bath (8-30 min), Cu = basic copper bath (about 1 min).

Plating from the acidic electroless Ni bath.— The effects of the additional reducing baths on acidic Ni plating (1) were also studied. The only effect of the additional hypophosphite bath is to somewhat slow the rate of plating. This applies whether the reduction step is carried out before or after the u.v. irradiation.

If basic formaldehyde is used as the reducing bath, a positive image is again obtained whether the reduction step precedes or follows u.v. irradiation. Thus the formaldehyde does not appear to affect subsequent plating in an acidic nickel bath. (Positive images were also obtained using an acidic Ni-B bath. No noticeable effects of a reduction step, using dimethyl amine borane, were found.)

Plating from the electroless copper bath.—The acidic hypophosphite reduction step causes subsequent copper plating to occur both on the irradiated and on the nonirradiated areas (that is, full plating), whether the reduction step precedes or follows the u.v. irradiation. Prereduction with concentrated basic formaldehyde, either before or after u.v. irradiation, results in full plating only if the slide is hot when placed in the formaldehyde solution or when the sample is heated afterward.

All these results are summarized schematically in Table II.

Discussion

In Ref. (1) we suggested that the reason that the tin (IV) sensitizer is effective for Ni plating from the acidic bath, but not for Cu plating, is that the hypophosphite (in the Ni bath) can reduce the attached Pd(II) to Pd(O), but formaldehyde (in the Cu bath) cannot. Our present results strongly suggest that a reduction of the catalyst [Sn(IV) · Pd(II)] does occur prior to Ni and Co plating, and that this reduction can proceed in acidic hypophosphite, but not in neutral or basic hypophosphite.

Remembering that the copper bath is strongly basic, it becomes plausible that it is the change in *p*H rather than the change in reducing agent or metal ion that determines whether reduction of Pd(II) and hence plating occurs onto the catalyst. The effect of raising *p*H on hypophosphite is, however, to increase its reduction potential [for example, see Ref. (6)] so that the above results cannot be explained just on the basis of the change in *p*H on the hypophosphite. Moreover, Pd(II) is much harder to reduce in basic solution than in acid because it forms $Pd(OH)_2$, which has a lower reduction potential than $PdCl_2$. Therefore, one reason that no plating occurs on nonirradiated [Sn(IV) · Pd(II)] in basic plating baths, is that $Pd(OH)_2$ forms which cannot be reduced and cannot catalyze metal plating. However, if the glass slide is hot or the formaldehyde solution used in making the copper bath is very fresh, copper plating does occur on the nonirradiated catalyst. This shows that basic formaldehyde is very nearly capable of reducing nonirradiated [Sn(IV) · Pd(II)], and that concentration, temperature, and freshness are critical.[2]

[2] This fact has been exploited to eliminate background in the stimulated copper negative images by always using for the copper baths formaldehyde solutions that are at least one day old.

Meek (7) has suggested that some time in the metallizing bath is necessary before the material present on the substrate after Sn(II) sensitization and Pd(II) activation is capable of catalyzing Cu plating. This may indicate that even for the [Sn(II) · Pd(II)] system, reduction in the metallizing bath is a necessary step in producing an active catalyst.

In our case, the catalyst is reduced in the reducing bath to a form which we designate [Sn(IV) · Pd(O)] which is capable of catalyzing plating from all four of the metallizing baths studied so far. It is also capable of catalyzing the decomposition of hypophosphite, resulting in hydrogen evolution. Ultraviolet irradiation at this point changes the catalyst in a way which prevents subsequent Ni plating from either bath, but which does not prevent Co or Cu plating. It was observed that simply heating the sample after reduction had a similar but less pronounced effect on the catalyst in that decreased Ni plating was observed, but Co and Cu plating were not affected. These facts suggest that the effect of u.v. light on reduced catalyst, [Sn(IV) · Pd(O)], is to decrease in some way the number of active catalytic sites. Such an interpretation was given by Kelly and Vondeling (8) to their result that longer irradiation times rendered [TiO_2 · Pd(O)] catalytic sites inactive for Ni, but not for Ag or Cu, which plated even on "overexposed" catalyst. They also estimated that the minimum amount of Pd(O) required to initiate Ag deposition is 8-16 × 10^{12} atoms/cm^2, whereas the minimum for Ni plating is nearer 32 × 10^{12} atoms/cm^2. Their results suggest that the threshold amount of Pd(O) necessary to catalyze metallization is similar for Ag and Cu. Our results, if u.v. light is presumed simply to decrease the number of active sites, indicate that the threshold for Cu is lower than that for Ni, and furthermore, that the threshold for Co is intermediate.

The effect of u.v. light on [Sn(IV) · Pd(II)] is not understood at this time. It has been shown here that u.v. renders [Sn(IV) · Pd(II)] capable of catalyzing

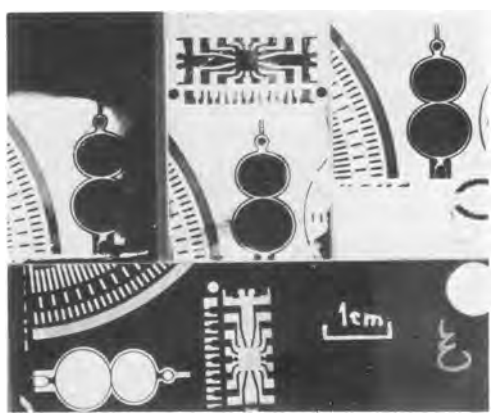


Fig. 1. Contact print of glass slides with imaged deposits obtained from various electroless metallizing baths. Left to right: Co-P (80°C), alkaline Ni-P, acidic Ni-P; below: Cu.

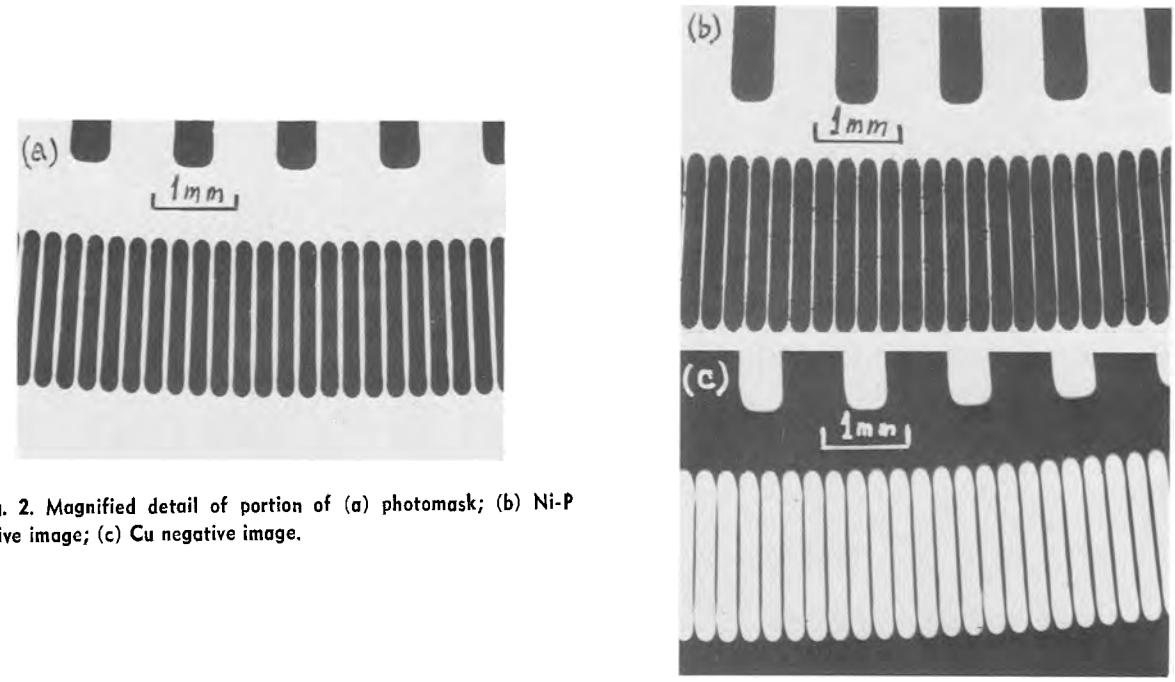


Fig. 2. Magnified detail of portion of (a) photomask; (b) Ni-P positive image; (c) Cu negative image.

Cu plating, but not Ni or Co plating. This could be explained by assuming that the u.v. light initially reduces [Sn(IV) · Pd(II)] to [Sn(IV) · Pd(O)] [as suggested by Kelly and Vondeling (8) for the [TiO_2 · Pd(II)] system] and then decreases the number of active catalytic sites below the threshold necessary for Ni and Co. If this were the case, irradiation times shorter than some minimum should result in more efficient plating for all three metals. No such minimum was found in the present work, however; indeed for copper plating the longer the irradiation time, the faster the plating.

In Table II it is noted that if the irradiated catalyst is reduced with hot formaldehyde, Co and Ni (alkaline) plating will occur. No plating will occur if the reducing agent is hypophosphite, acidic or basic. This result shows that formaldehyde interacts with irradiated [Sn(IV) · Pd(II)] to form a catalyst for basic plating baths, and that hypophosphite does not. This selectivity shows that irradiation of [Sn(IV) ·Pd(II)] results in more than just a decrease in the density of active [Sn(IV) · Pd(O)] sites.

It is possible that one effect of irradiation is to affect the crystallinity of the catalytic material. This was found (9) to be the case with the catalyst based on Sn(II) sensitizer. Attempts to investigate this by electron diffraction have so far been inconclusive.

The catalytic status of the tin-palladium material at various stages of the process can be seen in the following schematic chart:

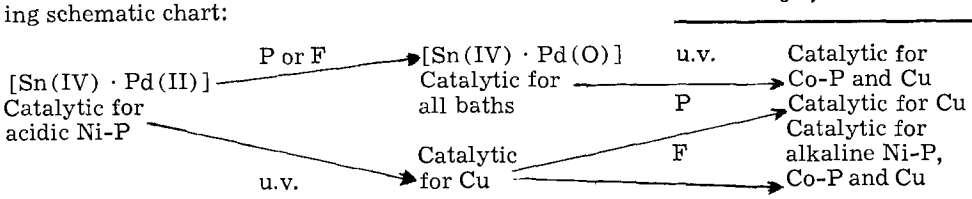


Image quality.—The quality of both the nickel positive and copper negative images is high with respect to both contrast and definition. Figure 1 shows examples of images obtained from the metallizing baths discussed in this paper. The highest quality so far has been obtained using the acidic nickel bath and the copper bath, with which most of our work has been done (1).

In Fig. 2 the finest detail on the photomask and corresponding areas on a nickel positive and copper negative are shown. It should be taken into account that the images are distorted due to the nonparallel light passing through the photomask in our simple optical arrangement.

Conclusion

These results indicate that it should be possible to use Sn(IV) as a sensitizer for quite a range of metallizing baths, and thus take advantage of the sharp images Sn(IV) produces. Basic metallizing baths may require a preliminary acidic reducing bath.

Our best procedure to date for the production of positive images from the basic Ni-P bath is as follows: A clean dry microscope slide is immersed for 2 min in a long-lived Sn(IV) sensitizer bath [see Ref. (2)]. After rinse and activation, the slide is dried under an infrared lamp and then immersed in an acidic hypophosphite bath for 1 min. After the slide is rinsed and allowed to drain to dryness, it is irradiated through an appropriate mask for 6 min with u.v. light. After another rinse the slide is immersed in the alkaline Ni bath described in Table I.

Manuscript submitted June 23, 1976; revised manuscript received Sept. 24, 1976.

Any discussion of this paper will appear in a Discussion Section to be published in the December 1977 JOURNAL. All discussions for the December 1977 Discussion Section should be submitted by Aug. 1, 1977.

Publication costs of this article were assisted by the University of Windsor.

REFERENCES

1. B. K. W. Baylis, A. Busuttil, N. E. Hedgecock, and M. Schlesinger, *This Journal*, **123**, 348 (1976).
2. B. K. W. Baylis, A. Busuttil, N. E. Hedgecock, and M. Schlesinger, *ibid.*, **123**, 1376 (1976).
3. S. L. Chow, N. E. Hedgecock, M. Schlesinger, and J. Rezek, *ibid.*, **119**, 1614 (1972).
4. A. S. Frieze, R. Sard, and R. Weil, *ibid.*, **115**, 586 (1968).
5. K. M. Gorbunova, M. V. Ivanov, and V. P. Moiseev, *ibid.*, **120**, 613 (1973).
6. Handbook of Chemistry and Physics, 51st ed., p. D112, Chemical Rubber Co., Cleveland, Ohio

(1970); W. M. Latimer, "The Oxidation States of the Elements and their Potentials in Aqueous Solutions," Prentice Hall, New York (1952).
7. R. L. Meek, *This Journal*, **122**, 1478 (1975).
8. J. J. Kelly and J. K. Vondeling, *ibid.*, **122**, 1103 (1975). For a description of the mechanism, see F. Möllers, H. J. Tolk, and R. Memming, *ibid.*, **121**, 1160 (1974).
9. S. L. Chow, N. E. Hedgecock, M. Schlesinger, and J. Rezek, *ibid.*, **119**, 1013 (1972).

Ligand Effects in Electroless Copper Deposition

Milan Paunovic*[1]

Kollmorgen Corporation, Photocircuits Division, Research and Development Laboratory, Glen Cove, New York 11542

ABSTRACT

The induction period and cathodic processes in electroless deposition of copper have been studied by galvanostatic, chronopotentiometric, and potential sweep methods. It is shown that the factors which determine the duration of the induction period are the type and concentration of the ligand that is complexing the copper ions. The rate-determining factor is the rate of establishment of the potential of the partial anodic process. Dissociation of a copper complex preceding the charge transfer in the electrochemical and electroless deposition of copper has been studied by chronopotentiometry and potential sweep method. Chronopotentiometric $i\tau^{1/2} = f(i)$ and potential sweep $i/v^{1/2} = f(v)$ functions have been used to estimate the relative rates of dissociation. The properties of the complexes of Cu(II) with ethylenediaminetetraacetic acid (EDTA), N,N,N',N'-tetrakis-2 (2-hydroxypropyl)ethylenediamine (Quadrol), cyclohexane-1, 2-diamine-N,N,N',N'-tetraacetic acid (CDTA), and tartaric acid have been studied. The galvanostatic transient technique has been used for kinetic studies of copper deposition. A definite correlation has been established between the rate of dissociation of the complex and the rate of metal deposition. The rate of deposition of copper and the rate of dissociation of complex as a function of a ligand increase in the order: tartrate, EDTA, Quadrol, CDTA complex.

In a previous paper electroless deposition of metals was interpreted on the basis of the mixed potential theory (1). The mixed potential theory interprets the over-all process of the electroless deposition of metals in terms of electrochemical parameters of the partial electrode processes: reduction of the metal ions and oxidation of the reducing agent (1-4). Upon immersion of a piece of a metal into a solution capable of electrolessly depositing metal, each of these partial reactions strives to establish its own equilibrium potential. The result of this process is establishment of a steady state with the resultant potential, the steady-state mixed potential, E_{MP}. These nonsteady-state processes that lead to the establishment of the steady-state mixed potential represent the initial period in the electroless deposition of metals called the induction period (5). In the steady-state deposition the metal substrate is considered to be statistically divided into cathodic and anodic areas with corresponding processes of oxidation and reduction occurring simultaneously and spatially separated. Since these cathodic and anodic areas are part of the same piece of the metal, they are "short-circuited" and there is a flow of electrons between these areas. Thus, on the basis of the mixed potential theory there are two types of processes in electroless deposition of metals: (*i*) nonsteady-state processes and (*ii*) steady-state processes. Our primary interest here is the induction period and partial cathodic processes under steady-state conditions.

Induction period.—We define the induction period as the time necessary to reach the mixed potential E_{MP} at which the steady-state metal deposition occurs. In the present report we are interested in the basic characteristics of the nonsteady-state processes that lead to the establishment of the steady-state mixed potential, E_{MP}, and the factors that determine the duration of the induction period in the electroless deposition of metals. Induction period phenomena have been detected in the case of electroless deposition of copper and nickel on Pt, Cu, and Ni substrates (5). An interesting case of induction period was reported by Dumesic, Koutsky, and Chapman (6). These authors have recorded the rates of electroless deposition of copper on a silver activated glass substrate and have detected three distinct growth regions: the initial rate region, "the transition point," and the final rate region. In the first region electroless deposition of copper occurs on the silver substrate and in the third region on the copper substrate. The second region corresponds to the induction period for deposition of copper on a copper substrate as discussed in this report. Initial stages of electroless deposition of copper, up to the thickness of 1000Å, have been studied by Sard (7) and it was concluded that development of the copper film proceeds by repeated three dimensional nucleation. The type of deposited copper, its physical and morphological properties, and adhesion to the substrate, depend, in the great extent, upon these first layers deposited at the very beginning of deposition. Knowledge of the mechanism of formation of these first layers is of practical and fundamental interest.

Partial cathodic processes.—The partial cathodic process is the reduction of the complexed copper ions. One of the fundamental problems is electrochemical deposition of metals from complex ions, and also in electroless deposition of metals, is the problem of the electroactive species. The electroactive species can be the complexed or the noncomplexed metal ion. In the first case the kinetic scheme of the process of metal deposition is one of simple charge transfer. In the second case the kinetic scheme is of charge transfer preceded by the dissociation of the complex (8).

The primary purpose of this section of study is the investigation of the mechanism of the cathodic proc-

* Electrochemical Society Active Member.
[1] Present address: Department of Chemistry, Adelphi University, Garden City, Long Island, New York 11530.
Key words: copper, formaldehyde, electroless plating, induction period, mixed potential.

esses, and the role of the dissociation of a copper complex, in the electroless deposition of copper. The significance of these studies is that they introduce additional factors that have to be considered in (*i*) describing parameters and (*ii*) in selecting ligands for electroless deposition of metals.

Dissociation of a complex metal ion prior to the charge transfer has been studied electrochemically by polarography, chronopotentiometry, and potential sweep methods. In our approach we have used both chronopotentiometry and potential sweep methods.

For the single reversible and irreversible electrochemical reaction the $i\tau^{1/2}$ chronopotentiometric function is a constant value for constant concentration and independent of the current density (τ, the transition time). In the case when an electrochemical reaction is preceded by a chemical reaction $i\tau^{1/2}$ is a function of the current density, equilibrium constant, and the rate constants of the preceding chemical reaction (8). The potential sweep current function related to our problem is the $i_p/v^{1/2}$ function where i_p is the peak current and v the rate of potential scan. In the case of the single-step electrochemical reaction $i_p/v^{1/2}$ is a constant value for constant concentration and independent of the potential scan. When an electrochemical reaction is preceded by a chemical reaction, the i_p function and the $i_p/v^{1/2}$ function, depend on K, k_f, and k_b (9).

Partial anodic processes.—The partial anodic process is the oxidation of formaldehyde. The mechanism of the anodic oxidation of formaldehyde was studied by Buck and Griffith (10) and Saito (11). On the basis of these studies the most important characteristics of the kinetic scheme for anodic oxidation of formaldehyde are: (*a*) the electroactive species is the methylene glycolate anion; (*b*) the electrochemical reaction is preceded by dissociative adsorption of the electroactive species, *i.e.*, the surface dehydrogenation reaction; and (*c*) the rate-determining step is the electron transfer involving the adsorbed species. The possibility of the direct oxidation of the methylene glycolate anion without an adsorbed intermediate state is not ruled out.

Experimental

For our studies we have chosen four ligands: tartaric acid, EDTA, Quadrol (BASF Wyandotte Corporation), and CDTA (Fig. 1). We have chosen these ligands because they show significant differences in the rate of electroless deposition of copper and thus are good examples for comparison. We have studied corresponding complexes of copper at concentrations of 0.05M $CuSO_4$, 0.06 and 0.15M ligands at 25°C, pH = 12.50 in an argon atmosphere. For the study of the polyelectrodes, 2.5 g/liter of paraformaldehyde has been added to the solution.

We have used two types of all-glass electrochemical cells: a one-compartment and a three-compartment cell. Electrodes have been prepared as described previously (1).

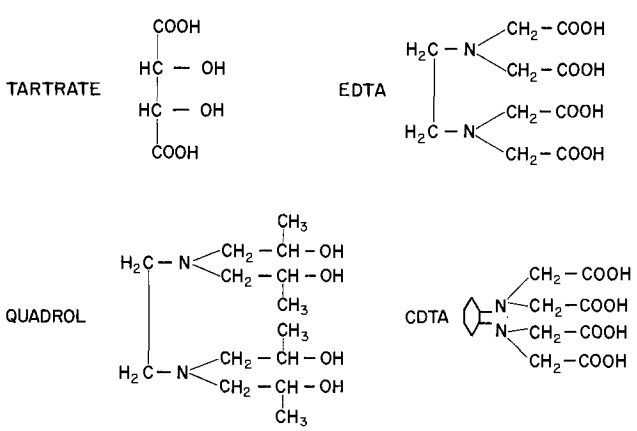


Fig. 1. Structures of the ligands used in this work

A transistorized constant current power supply made in our laboratory has been used as a current source in galvanostatic and chronopotentiometric measurements. A Tacussel (Lyon, France) potentiostat Type PIT 20-2A and function generator Type GSTP 2 have been used in potential sweep and potentiostatic measurements. The current potential or potential time curves have been recorded on (*i*) the Tektronix 564 B storage oscilloscope with plug-in units: Type 3A6 dual-trace amplifier; Type 2B67 time base and Type 2A63 differential amplifier, or (*ii*) Hewlett Packard 7004A recorder with plug-in units: d-c coupler Model 17170A; d-c preamplifier Model 17171A; time base Model 17172A and d-c offset Model 17174A. Oscilloscope traces were photographed with the Polaroid camera C-27.

Results

Induction period.—The over-all process.—The study of the induction period starts with a very simple experiment in which a piece of metal is immersed in a solution for electroless deposition of a metal and the potential of the metal recorded from the time of immersion (or the time of addition of the reducing agent), *i.e.*, the time zero, until the steady-state mixed potential is established. A typical recorded curve for the electroless deposition of copper on copper substrate is shown in Fig. 2. The curve has been recorded for the system in an argon atmosphere. For an air atmosphere, and in the presence of additives in the solution, the duration of the induction period can be considerably longer. For example, for electroless deposition of copper on the copper substrate from the electroless solution that is 0.2M in EDTA and 0.1M in $CuSO_4$ with 0.5 g/liter paraformaldehyde at pH 12.50 and 25°C, the induction period in the argon atmosphere is 140 sec but in the air atmosphere it is 350 sec. For practical plating solutions operated in an air atmosphere and containing additives, induction periods of 30 min to 1 hr are not unusual. This gives rise to another important reason for studying induction period phenomena. For example, in practical operations in the production of printed circuit boards for the electronics industry this induction time represents a loss of production time

Partial processes.—The problem of the induction period for the over-all process can be decomposed into problems of the open-circuit potentials (5) of the oxidation and reduction partial reactions, *i.e.*, individual induction period for each process.

A typical curve representing the change of the open-circuit potential (OCP) with time, for the reducing agent, is given in Fig. 3. The OCP for the Cu/Cu^{+2} system is reached instantaneously, within instrumentation limits. From a comparison of these OCP curves one can conclude that the rate of establishment of the OCP of the reducing agent, CH_2O, is the rate-determining partial reaction in the establishment of the steady-state mixed potential (5).

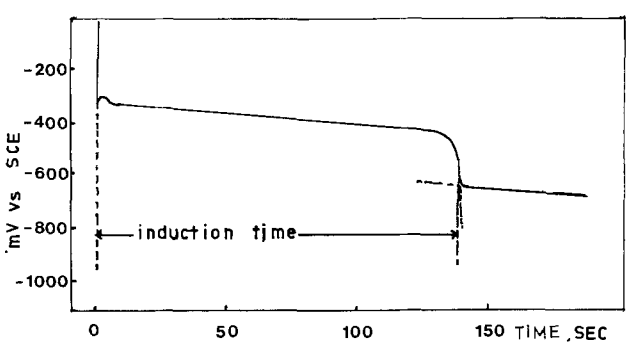


Fig. 2. Induction period for the solution 0.3M EDTA, 0.05M $CuSO_4$, pH 12.50, 2.5 g/liter paraformaldehyde, Cu electrode 2.2 cm^2, 25°C, SCE reference electrode, argon atmosphere.

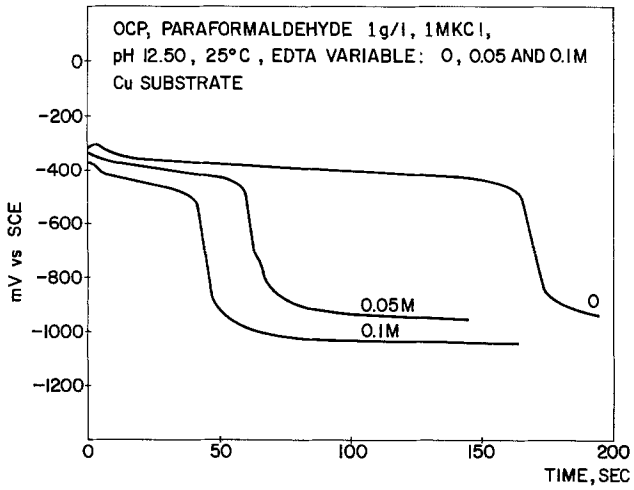


Fig. 3. Open-circuit potential for the solution 1 g/liter paraformaldehyde, pH 12.50. 25°C, Cu electrode, SCE reference electrode.

Major factors that determine the time necessary to reach the rest potential of the reducing agent are type and concentration of the ligand present.

The influence of the type of ligand present can be illustrated with the following example. In a supporting electrolyte that is 1M KCl, pH 12.50, 25°C and with 1 g/liter of paraformaldehyde, the t_{OCP} in the absence of a ligand is 210 sec. Addition of 0.1M tartrate or 0.1M EDTA to the electrolyte gives t_{OCP}'s of 240 and 45 sec, respectively. The influence of concentration of the ligand is illustrated in Fig. 3. For 0.2 and 0.3M EDTA the values are the same as for 0.1M EDTA.

Partial cathodic processes.—Single electrode: reduction of Cu(II) EDTA.—If a triangular wave is applied to the single electrode in the solution of Cu(II)EDTA complex a current potential curve with two peaks is obtained, Fig. 4. These two peaks appear at all compositions of the solution. The first peak we will designate the prewave and the second the main wave. At some ligand/Cu(II) ion ratios and at certain scan rates there is a small third cathodic wave at more positive potentials. Since this wave appears only under specific conditions we will not discuss it here.

Reduction of Cu(II) EDTA complex was studied for the solution that was 0.05M $CuSO_4$, 0.006M EDTA, pH = 12.50 at 25°C, in an argon atmosphere.

Prewave.—Our first analysis of the prewave consists of the analysis of the transition time values at different current densities and of the plot of the $i\tau^{1/2}$ *vs.* current density. The result of one of these plots is shown in Fig. 5. The observed increase of the function $i\tau^{1/2}$ with an increase in the current density [the diagnostic criterion (8)] indicates the adsorption of the electroactive species. The same conclusion is obtained from an analysis of the potential sweep functions as shown

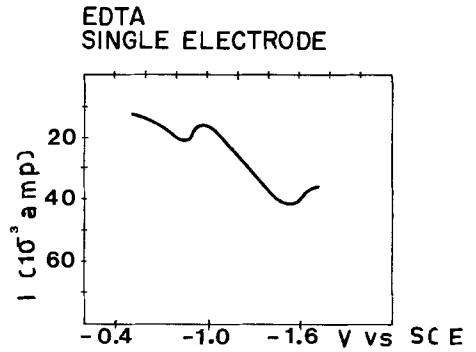


Fig. 4. Current potential curve for the single electrode, $A = 0.680$ cm^2; $v = 2.0$ Vsec^{-1}.

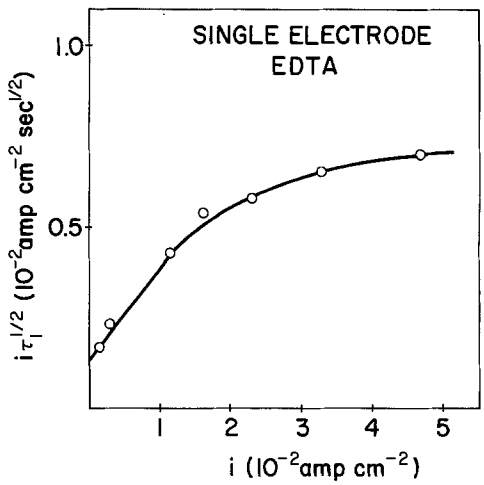


Fig. 5. Chronopotentiometric function for the first transition time

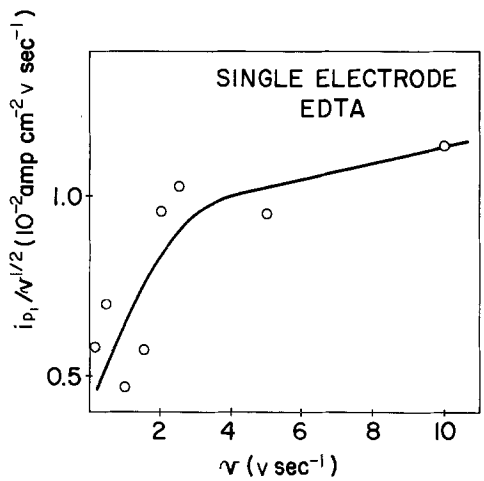


Fig. 6. Potential sweep function for the first wave

in Fig. 6. The function $i_p/v^{1/2}$ *vs.* v shows characteristics of the reduction of the adsorbed electroactive species (9).

Thus, both methods, chronopotentiometric and potential sweep, show that the prewave is due to the reduction of the adsorbed species. In order to identify this wave further we have used the potential sweep method; in one case varying concentration of the supporting electrolyte, and in another case varying concentration of the Cu(II) complex. Results of the analysis are shown in Table I. It is seen from the table that the peak current of the first wave changes with the change of concentration of the supporting electrolyte and that of the second wave does not. Varying the concentration of the Cu(II) complex in the solution does not change the peak current of the first step. On the basis of these results one can conclude that the

Table I. Potential sweep data for the first and second wave for single electrode

ELECTRODEPOSITION OF Cu FROM Cu (II) COMPLEX IOMS

Cu TARTRATE $i_p = f(\phi_2)$

	0.0 KCl	0.1MKCl	1.0MKCl	
i_{p_1}, 10^{-3}amp cm^{-2}	1.32	1.62	2.12	X_2 PLANE
i_{p_2}, 10^{-3}amp cm^{-2}	8.60	8.76	8.60	OUTSIDE X_2 PLANE

Cu EDTA $i_p = f(C^S)$

Cu EDTA	i_{p_1} amp cm^{-2}
5mM	1.03×10^{-3}
50mM	1.04×10^{-3}

first step is due to the reduction of Cu(II) ions in the X_2 plane of the double layer, and in the second step the reduction of ions outside of the X_2 plane (12).

Main wave.—The main wave has been analyzed in the same way as the prewave. Figure 7 shows the change of the $i_p/v^{1/2}$ *vs.* the scan rate. A decrease of $i_p/v^{1/2}$ with the increase of the scan rate is a diagnostic criterion for the kinetic scheme where the charge transfer is preceded by a chemical reaction (9). Chronopotentiometric results shown in Fig. 8 lead to the same conclusions (8).

Thus, both methods show that the reduction of the Cu(II) EDTA complex is preceded by the dissociation of the complex.

Single electrode: reduction of tartrate, Quadrol, and CDTA complexes of Cu(II).—All these complexes have been analyzed in the same way as the Cu(II) EDTA complex. The experimental conditions were: 0.05M $CuSO_4$, 0.06M ligand, pH = 12.50 at 25°C in the argon atmosphere. Results are shown in Fig. 9. One can conclude that in all cases studied the charge transfer is preceded by the dissociation of the complex. It is interesting to observe, however, that the slopes of the linear portions of the curves are considerably different.

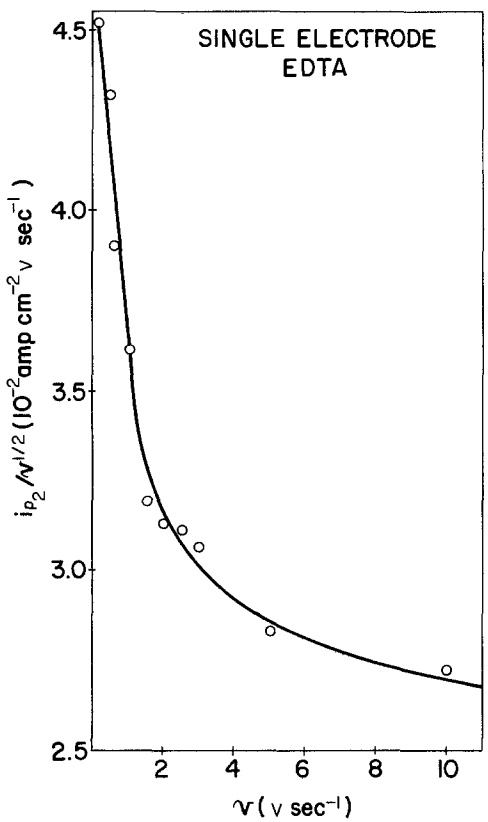


Fig. 7. Potential sweep function for the second wave

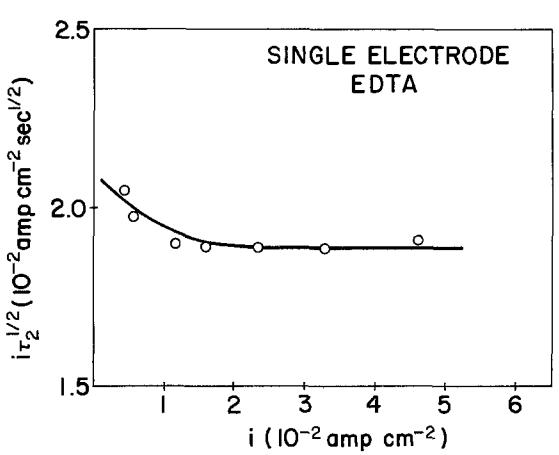


Fig. 8. Chronopotentiometric function for the second transition time

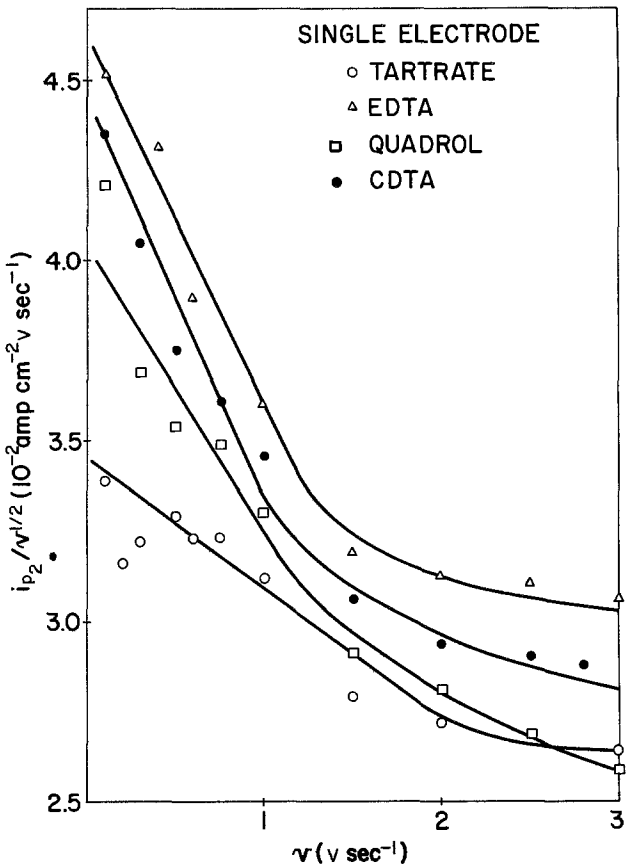


Fig. 9. Potential sweep function for the second wave

Polyelectrode.—Current potential curves for the polyelectrodes show only one peak in the studied potential range. The value of the peak current is of the same order of magnitude as the peak current of the main wave for the single electrode. Chronopotentiometric curves and potential sweep curves are shown in Fig. 10 and 11. It is seen that the same kinetic scheme, complex dissociation, is valid for the polyelectrode as for the main wave of the single electrode.

Rate of electroless deposition and the rate of dissociation of the complex.—The rate of electroless deposition of copper has been determined electrochemically and gravimetrically. The rate expressed electrochemically, *i.e.*, the deposition current, is obtained from the cathodic polarization curve for the polyelectrode. Both methods are in agreement in the limits reported previously. Results are compared in Tables II and III. The first conclusion from these tables is that there is a direct proportionality between the rate of deposition and the rate of dissociation of the complex as indicated by the slope of the curves $i_p/v^{1/2}$ *vs.* v. The plot of the i_{dp} *vs.* the slope is a straight line.

Discussion

Partial cathodic processes.—Kinetic scheme.—From our studies of the single electrode one can conclude that the reduction of the studied metal complexes proceeds simultaneously from the species adsorbed at the

Table II. Deposition current (i_{dp}) and the rate of dissociation of the complex R = ligand/Cu^{2+} = 1.2

Cu(II) complex with the ligand	i_{dp} 10^{-3} A/cm^2	Single electrode $\partial(i_{p2}/v^{1/2})/\partial v$ 10^{-2}
Tartrate	0.15	0.36
Quadrol	0.27	0.79
EDTA	0.38	1.02
CDTA	0.80	1.11

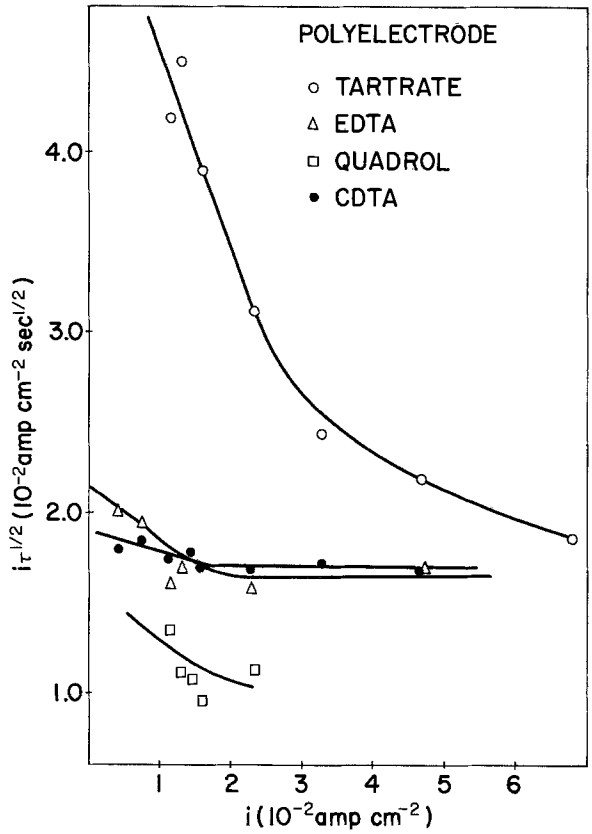


Fig. 10. Chronopotentiometric functions for the polyelectrode

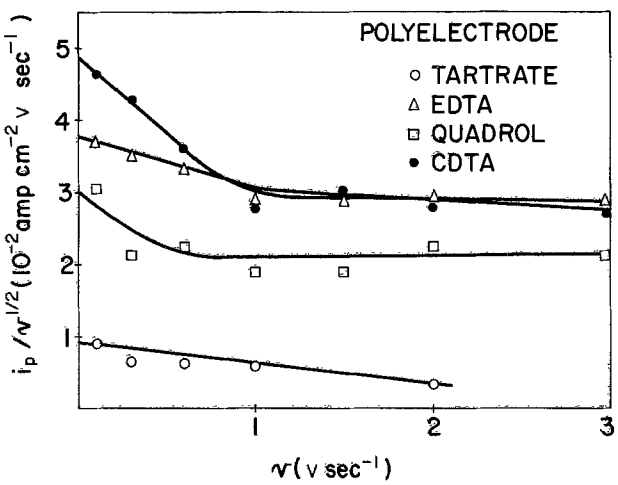


Fig. 11. Potential sweep functions for the polyelectrode

electrode and the species resulting from the dissociation of the complex.

Since the prewave shows characteristics of the process involving reduction of adsorbed species, and since the deposition current increases with the increase of the ligand/copper(II) ratio from 1.2 to 3.0, one can conclude that the mechanism of the first wave is the catalytic mechanism of the type proposed and studied by Mark *et al.* (13). According to this theory the ligand is interposed between the electrode and the metal ion and forms the surface complex. This can be taken at least as a temporary explanation until further studies are available.

Table III. Deposition currrent (i_{dp}) and the rate of dissociation of the complex R = ligand/Cu^{2+} = 3.0

Cu(II) complex with the ligand	E_{MP_2} −mV *vs.* SCE	i_{dp} 10^{-3} A/cm^2	Single electrode $\partial(i_{p2}/v^{1/2})/\partial v$ 10^{-2}
Tartrate	610	0.75	0.54
EDTA	650	1.0	0.71
Quadrol	680	3.6	1.02
CDTA	685	5.4	1.12

The reaction of dissociation of the complex occurs in the reaction layer which can be in the first approximation taken as the outer Helmholtz plane, as compared to the prewave reaction which takes place in the X_2 plane.

Rate of deposition and the rate of dissociation of the metal complex.—We have discussed the relationship between the rate of dissociation of the complex and the deposition current. Another desirable aspect of the discussion of the rate of deposition is one that will include the stability constant of the complex. This aspect cannot be discussed now since there is not enough data on the composition of the solutions used in electroless deposition of copper. To give just one example of the complexity of this problem let us mention that at *p*H higher than 11 there are at least three simultaneously existing complexes in the solution of Cu(II) ions and EDTA: CuEDTA, Cu(OH)EDTA, and $Cu(H_2O)$EDTA. The stability constant of the CuEDTA complex is $10^{18.8}$ and that of Cu(OH)EDTA is 10^2.

We would like to point out some of the factors one has to take into account when trying to compare different complexes with respect to the rate of deposition and the stability constant of the complex. The two most important factors are as follows: (*a*) simultaneous existence of the complex where the metal ion is fully coordinated by the ligand and the complexes where the metal ion is partially coordinated by the ligand, and (*b*) division of functions between different complexes. By this we mean the possibility of the situation when one complex species is controlling the bulk properties and the other species is controlling the electrochemical activity at the electrode.

Since we have established correlation between the rate of electroless deposition of metal and the rate of dissociation of the metal complex it is important to consider dissociation and formation kinetics of metal complexes in order to interpret differences found in the rate of dissociation and in order to find a basis for selection of the ligand which could be used in electroless plating. Additional information, besides the knowledge of a set of elementary steps in the kinetic scheme, is needed in order to understand kinetics and mechanism of deposition at the molecular level.

By comparing rates of dissociation of examined complexes we expect to determine the factors that control the kinetics of reactions. Assuming that the formation and dissociation of the bonds beyond the second are fast in comparison with the two first bonds we can base our discussion on the kinetics of ligands forming two bonds only, *i.e.*, bidentate ligands.

The general dissociative mechanism proposed by Eigen (14) expresses the reaction between hydrated metal ions with the bidentate ligand, *e.g.*, with two nitrogen donor atoms, by the following scheme

$$M(H_2O)_6^{a+} + \begin{matrix} N^{b-} \\ | \\ N \end{matrix} \overset{K_{os}}{\rightleftarrows} M(H_2O)_6^{a+} \cdots \begin{matrix} N^{b-} \\ | \\ N \end{matrix} \qquad [1]$$

$$M(H_2O)_6^{a+} \cdots \begin{matrix} N^{b-} \\ | \\ N \end{matrix} \overset{k_2}{\underset{k_{-2}}{\rightleftarrows}} (H_2O)_5M \begin{matrix} N^{a-b} \\ | \\ N \end{matrix} \qquad [2]$$

$$(H_2O)_5M \begin{matrix} N^{a-b} \\ | \\ N \end{matrix} \overset{k_3}{\underset{k_{-3}}{\rightleftarrows}} (H_2O)_4M \begin{matrix} N^{a-b} \\ | \\ N \end{matrix} \qquad [3]$$

where K_{os} is the equilibrium constant for the formation of an outer sphere complex (the association constant); k_2 and k_{-2} are the rate constants for the first metal-nitrogen bond formation and rupture, respectively; k_3 and k_{-3} are the rate constants for second metal-nitrogen bond formation and rupture, respectively, or closing and opening the ring. The over-all dissociation

rate constant k_d^{ML} (L, ligand) for the above kinetic scheme is given by (15)

$$k_d^{ML} = \frac{k_{-2}k_{-3}}{(k_{-2} + k_3)} \quad [4]$$

and if $k_3 >> k_{-2}$ as is usually the case

$$k_d^{ML} = \frac{k_{-2}k_{-3}}{k_3} \quad [5]$$

Many experimental results can be interpreted by assuming that (15-21) the rate of dissociation of a complex is sterically controlled by the formation step k_3, Eq. [5].

According to Eq. [5] a decrease in the rate constant k_3 produces an increase in the dissociation rate constant k_d^{ML}. Dissociation of tartrate, EDTA, Quadrol, and CDTA complexes of copper can be compared in terms of k_3 rate constants. Since k_3 is the formation rate constant one should briefly consider factors that determine the rate of formation of a complex. According to the general dissociative mechanism the first step is formation of the outer-sphere complex. The second step involves rupture of metal-water bond, formation of the intermediate with the lower coordination number (5 for copper), and insertion of the ligand into the inner coordination sphere. With the polydentate ligand having different donor atoms in the same molecule, in our case N and O, the initial bonding can be to a nitrogen donor (mechanism I) or to an alcoholic oxygen donor atom (mechanism II). Tartrate, EDTA, Quadrol, and CDTA have two alternative mechanisms for formation of the first metal-ligand bond. Both of these mechanisms involve steric hindrance (17, 18). Steric factors in k_2 or k_3 reflect the fact that majority of possible ligand configurations in the outer-sphere (for k_2) or in the single-bonded ligand (k_3) have to have a configuration suitable for bonding or configurational change has to occur. Configurational changes of complexes used in this work involve rotational barriers around a single bond and the barrier for boat-chair configurational change (CDTA). Since the rotational barrier increases with the size of substituent (—CH_2COOH, —$CH_2CH[OH]CH_3$) and since barrier for the boat-chair change is larger than the rotational barrier (22) it follows that the steric hindrance increases in the following order: tartrate, EDTA, Quadrol, CDTA. The rate constants k_3 decrease in the same order. According to Eq. [5] the decrease in k_3 results in an increase of k_d^{ML}. Thus, k_d^{ML} increases in the order: tartrate, EDTA, Quadrol, CDTA. Thus the steric hindrance in the rate constant k_3, with Eq. [5], explains complex dissociation rate results obtained in this work. This discussion in terms of the general dissociative mechanism for the metal complexes can provide basis for selection of ligands in electroless deposition.

Above results point to k_3 steric control in the dissociation of metal complexes. One should also take into account that the internal conjugate base mechanism (ICB) can mask part of the steric effect due to enhancement of the rate of formation (17). Future work in selection of ligands for electroless deposition of metals should consider also steric effects (15) on k_{-2} and k_{-3}.

Acknowledgments

I am pleased to thank Dr. Robert Lippman, Adelphi University, Chemistry Department, for valuable comments during the preparation of the manuscript. Particular thanks are due to Dr. Karl Egerer, the Vice-President, and John McCormack, Director of Research, Photocircuits, for the permission to publish this paper.

Manuscript submitted June 11, 1976; revised manuscript received Oct. 6, 1976.

Any discussion of this paper will appear in a Discussion Section to be published in the December 1977 JOURNAL. All discussions for the December 1977 Discussion Section should be submitted by Aug. 1, 1977.

Publication costs of this article were assisted by the Kollmorgen Corporation.

REFERENCES

1. M. Paunovic, *Plating*, **55**, 1161 (1968).
2. Y. Okinaka, Abstract 144, p. 383, The Electrochemical Society Extended Abstracts, Fall Meeting, Detroit, Michigan, Oct. 5-9, 1969.
3. F. Donahue and F. L. Shippey, *Plating*, **60**, 135 (1973).
4. F. Donahue, *Oberflaeche-Surf.*, **13**, (12), 301 (1972).
5. M. Paunovic, Abstract 143, p. 361, The Electrochemical Society Extended Abstracts, Fall Meeting, Cleveland, Ohio, Oct. 3-8, 1971.
6. J. Dumesic, J. A. Koutsky, and T. W. Chapman, *This Journal*, **121**, 1405 (1974).
7. R. Sard, *ibid.*, **117**, 864 (1970).
8. M. Paunovic, *J. Electroanal. Chem.*, **14**, 447 (1967); M. Paunovic, Paper 146 presented at The Electrochemical Society Meeting, Detroit Michigan, Oct. 5-9, 1969.
9. R. S. Nicholson and I. Shain, *Anal. Chem.*, **36**, 706 (1964).
10. R. S. Buck and L. R. Griffith, *This Journal*, **109**, 1005 (1962).
11. M. Saito, *Metal Surf. Technol. Jpn.*, **17**, 14 (1966).
12. P. Delahay, "Double Layer and Electrode Kinetics," Interscience, New York (1965).
13. H. B. Mark Jr., L. R. McCoy, E. K. Eisner, and H. C. McDonald, Jr., *J. Phys. Chem.*, **72**, 1083 (1968).
14. M. Eigen and R. G. Wilkins, *Adv. Chem.*, **49**, 55 (1965).
15. D. B. Rorabacher, *Inorg. Chem.*, **5**, 1891 (1966).
16. T. S. Turan, *ibid.*, **13**, 1584 (1974).
17. D. B. Rorabacher, T. S. Turan, J. A. Defever, and W. G. Nickels, *ibid.*, **8**, 1498 (1969).
18. D. B. Rorabacher and D. B. Moss, *ibid.*, **9**, 1313 (1970).
19. T. S. Turan and D. B. Rorabacher, *ibid.*, **11**, 288 (1972).
20. J. W. Brubaker, Jr., A. F. Pearlmutter, J. E. Stuehr, and T. V. Vu, *ibid.*, **13**, 559 (1974).
21. D. B. Rorabacher and D. B. Moss, *ibid.*, **9**, 1313 (1970), Margerum discussion.
22. M. S. Newman, "Steric Effects in Organic Chemistry," John Wiley & Sons, Inc., New York (1956).

Electrocarboxylation Reactions

Rotating Ring-Disk Electrode, Voltammetric, and Electron Spin Resonance Studies of Dialkyl Fumarates and Maleates

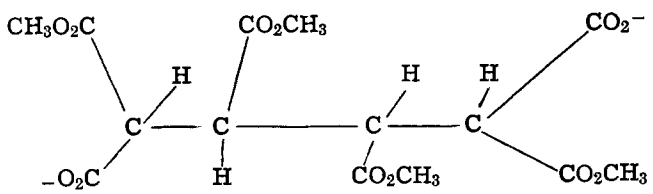
Lun-Shu R. Yeh* and Allen J. Bard**

Department of Chemistry, The University of Texas at Austin, Austin, Texas 78712

ABSTRACT

The reduction of the diactivated olefins dimethyl fumarate (DMeF), diethyl fumarate (DEF), di-n-butyl fumarate (DBF), dimethyl maleate (DMM), diethyl maleate (DEM), and di-n-butyl maleate (DBM), in N,N-dimethylformamide-tetra-n-butylammonium iodide solutions saturated with dissolved carbon dioxide at a platinum electrode has been studied by rotating ring-disk electrode and cyclic voltammetry and *in situ* electron spin resonance spectroscopy. The results indicate that the rate-determining step for each compound is the reaction of the radical anion with CO_2; the radical anions are also involved in the dimerization and (for maleates) isomerization reactions which occur in the absence of CO_2. The coupling of the carboxylated radical to dimeric carboxylate is rapid. The rate constants for the reaction of the radical anions with CO_2 were faster for maleates than for fumarates; pseudo-first order rate constants for a saturated CO_2 solution (*ca.* 0.2*M*) are DMeF, 1.5 sec^{-1}; DEF, 0.47 sec^{-1}; DBF, 0.35 sec^{-1}; DMM, 32.0 sec^{-1}; DEM, 19.4 sec^{-1}; and DBM, 18.0 sec^{-1}.

There have been numerous studies of the reactions of electrogenerated radical anions of diactivated olefins (1-12). Hydrodimers are the major product for reductions in aprotic solvents such as N,N-dimethylformamide (DMF), formed by coupling of radical anions followed by protonation. Thus for dialkyl fumarates (abbreviated throughout as F) the reaction sequence is



1 or $^{-}O_2CDCO_2^{-}$

$$F + e \rightarrow F^{\cdot -} \quad [1]$$

$$2F^{\cdot -} \xrightarrow{k_{2F}} D^{2-} \quad [2]$$

Recent studies (12, 13) show that the *cis*-forms (maleates or M) follow a similar reaction scheme

$$M + e \rightarrow M^{\cdot -} \quad [3]$$

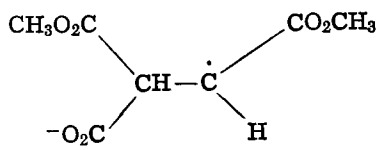
$$2M^{\cdot -} \xrightarrow{k_{2M}} D^{2-} \quad [4]$$

but that the coupling rate for the radical anions derived from the maleates is about 2000 times that of the fumarate anions. Moreover, isomerization of $M^{\cdot -}$ also occurs

$$M^{\cdot -} \xrightarrow{k_1} F^{\cdot -} \quad [5]$$

Cross-coupling between $M^{\cdot -}$ and $F^{\cdot -}$ is also possible, but this rate is apparently slow compared to the reaction of two $M^{\cdot -}$'s (12).

Carbon dioxide has been shown to react with organic anionic intermediates generated electrochemically in aprotic media (14-17). Recently, Tyssee and Baizer (18, 19) studied the reduction of diactivated olefins in the presence of CO_2. For dimethyl maleate (DMM), production of the carboxylated dimer (**1**), 1,2,3,4-tetramethyl-1,1,2,3,4,4-butanehexacarboxylate, was demonstrated. These authors suggested



2 or $MCO_2^{\cdot -}$

two possible reaction paths leading to **1**: dimerization of $M^{\cdot -}$, [4], followed by reaction with CO_2

$$D^{2-} + 2CO_2 \rightarrow {}^{-}O_2CDCO_2^{-} \quad [6]$$

or reaction of $M^{\cdot -}$ with CO_2 to form the carboxylated radical anion (**2**) followed by dimerization

$$M^{\cdot -} + CO_2 \xrightarrow{k_M} MCO_2^{\cdot -} \quad [7]$$

$$2MCO_2^{\cdot -} \rightarrow {}^{-}O_2CDCO_2^{-} \quad [8]$$

An alternate path would involve coupling of $MCO_2^{\cdot -}$ with M followed by reduction and carboxylation, but the independence of yield of **1** with initial concentration of maleate makes this route less likely (19). An additional reaction path involves the ECEC sequence, [3], [7], followed by further reduction of **2**

$$MCO_2^{\cdot -} + e \rightarrow MCO_2^{2-} \quad [9]$$

$$MCO_2^{2-} + CO_2 \rightarrow {}^{-}O_2CMCO_2^{-} \quad [10]$$

3

where **3** is 1,2-dimethyl 1,1,2,2-ethanetetracarboxylate (18). The reduction in [9] occurs at somewhat more negative potentials than that in [3], so that this path is not significant at potentials of the first reduction wave.

In the work described here, the rate constants for the reaction of the radical anions with CO_2 were determined and the reaction paths of the carboxylated intermediates investigated. The reaction scheme for the maleates is quite complicated, since the rather rapid coupling and isomerization reactions [(for DMM, k_{2M}

* Electrochemical Society Student Member.
** Electrochemical Society Active Member.
Key words: reductive coupling, rotating disk electrode, *cis-trans*-isomerization, carboxylation.

$= 1.9 \times 10^5\ M^{-1}\ sec^{-1}$ and $k_1 = 2.2\ sec^{-1}$ (12)] occur in addition to the carboxylation reactions. The fumarates have a slower coupling reaction, and diethyl fumarate (DEF) and di-n-butyl fumarate (DBF) show no appreciable coupling on the RRDE time scale [for DEF and DBF, $k_{2F} = 44\ M^{-1}\ sec^{-1}$ and $25\ M^{-1}\ sec^{-1}$, respectively (5)]. Thus in the absence of CO_2 both DEF and DBF show the theoretical collection efficiency, N, for generation of radical anions at the disk and collection at the ring electrode. Here, changes in the collection efficiency upon addition of CO_2 for different concentrations of DEF and DBF can be used to study the reaction of $F^{\cdot -}$ and CO_2. The study was also extended to the maleates, taking account of their inherent reactions using rate constants determined previously (12), so that a comparison of the reactivity of the radical anions derived from the *cis-* and *trans-* forms of the same species could be made.

Experimental

The reagents, purification schemes, apparatus, and techniques were the same as those previously described (12). The CO_2 was instrument grade 99.99% from Big Three Industries, Incorporated. The RRDE with platinum disk and ring electrodes, constructed by Pine Instrument Company (Grove City, Pennsylvania), had $r_1 = 0.187$ cm, $r_2 = 0.200$ cm, and $r_3 = 0.332$ cm with a collection efficiency of 0.555.

In carboxylation experiments, CO_2 was bubbled through the solution for at least 30 min before the trials, and CO_2 was passed over the solution surface during the experiments. The cell was as used previously (12) with a Pt wire spiral auxiliary electrode in a separate compartment and a silver wire pseudo-reference electrode (Ag RE) also in a separate chamber connected to the RRDE chamber by sintered-glass disks. The electron spin resonance (ESR) measurements, carried out with a Varian Associates (Palo Alto, California) Model E-9 spectrometer at 100 kHz field modulation, followed the usual arrangement for *intra muros* electrochemical methods (20) with a Varian electrolytic cell accessory. The electrolysis current was maintained at a low level so that the working electrode potential was at the foot of the first reduction wave. Nitrogen was continually being bubbled in the solution reservoir before and during the experiments when they were conducted in the absence of CO_2. The flat cell was flushed with nitrogen before oxygen-free solution containing DMF, TBAI, and sample was introduced into it. The same solution in the reservoir was then continually bubbled with CO_2 before and during the experiments involving reactions with CO_2. The flat cell compartment was then flushed with an excess amount of CO_2-saturated solution to rinse it before a new experiment was conducted.

The concentration of dissolved CO_2 in the 0.1*M* TBAI-DMF solution was determined by adding 13 ml of 0.1*M* TBAI-DMF solution to a 25 ml volumetric flask followed by the placement of loosely packed glass fiber in the neck of the flask. CO_2 was slowly bubbled through this solution for 20 min and an increase in weight of 115 mg was observed. This corresponds to 0.2*M* dissolved CO_2 in the solution at room temperature (*ca.* 24°C) (neglecting any loss of DMF); the literature value for pure DMF at 20°C is 0.228*M* (21).

Results and Discussion

Dimethyl fumarate (DMeF), Diethyl fumarate (DEF), and Di-n-butyl fumarate (DBF).—Cyclic voltammograms for 0.1*M* TBAI-DMF solutions of DEF in the absence and presence of CO_2 are given in Fig. 1; the results for DMeF and DBF are very similar. The large decrease in the reversal anodic peak height indicates the consumption of $F^{\cdot -}$ by CO_2. The cathodic peak height does not change upon addition of CO_2, showing that the ECE route leading to **3** is not significant on this time scale (at these potentials). No additional oxidation peaks were observed suggesting that the $FCO_2^{\cdot -}$ formed is rapidly consumed in a following reaction.

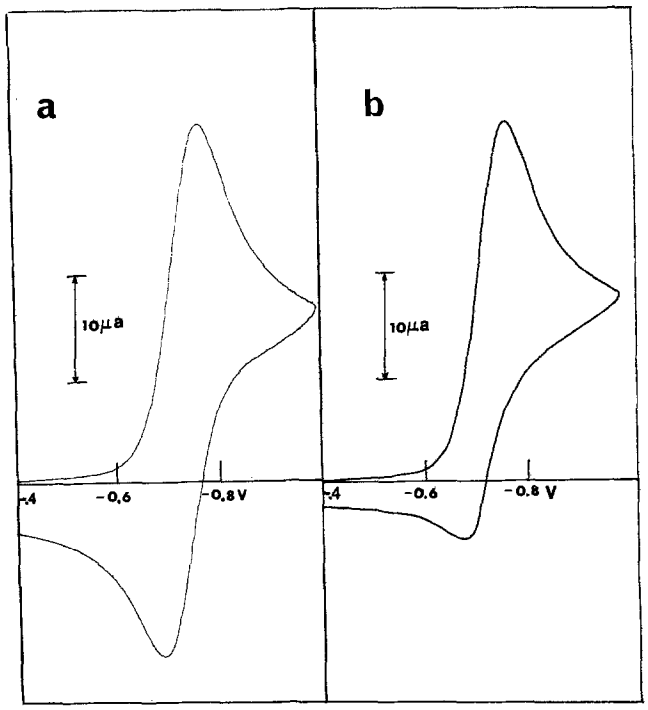


Fig. 1. Cyclic voltammograms (v = 100 mV/sec) of 0.1M TBAI-DMF solutions of 1.22 mM diethyl fumarate (a) without and (b) saturated with CO_2.

Rotating disk electrode (RDE) voltammograms (i_d *vs.* E_d) taken in the absence of CO_2 for millimolar solutions of DMeF and DEF exhibit a reduction wave at $E_{1/2} = -0.75$V *vs.* Ag-RE followed by a dip (at *ca.* −1.60V) in i_d after development of a well-defined plateau (22,23). This dip develops into a second reduction wave on addition of water or acid. In the presence of CO_2, the reduction potential of the first wave of these compounds shifted slightly (10-20 mV) to less negative potentials and the dip disappeared. This disappearance can be attributed to the reaction of F^{2-} with CO_2 thus decreasing the extent of the F^{2-}/F reaction which produces the dip (22). This effect was not investigated further and the discussion here is limited to processes occurring at the first reduction wave. Typical RDE data for the fumarates and values of the Levich constant $i_{d,l}/\omega^{1/2}C$ (where $i_{d,l}$ is the limiting disk current, ω is the angular velocity, and C the concentration) are given in Table I. For DBF this constant is essentially independent of ω and C. For DEF and DMeF a slight decrease in the Levich constant with increasing C is observed, perhaps caused by a small contribution of polymerization reaction consuming parent material. To obtain information about the rate of the $F^{\cdot -}/CO_2$ reaction and the mechanism of the reaction, RRDE experiments were undertaken, and the variation of the kinetic collection efficiency, N_k, expressed as the ratio of the ring current, i_r, to the disk current, i_d

$$N_k = |i_r/i_d| \qquad [11]$$

as a function of the disk current parameter *CONI* (4), where

$$CONI = |i_d/i_{d,l}| \qquad [12]$$

at different values of ω and C was determined. These N_k values were compared to working curves obtained by digital simulation (24) assuming the following reaction

$$F^{\cdot -} + CO_2 \xrightarrow{k_F} FCO_2^{\cdot -} \qquad [13]$$

Table I. Typical rotating disk electrode data for the first reduction waves in DMF-0.1M TBAI solutions in the presence of saturated CO_2

Concentration, C (mM)	Rotational rate ω (sec^{-1})	Limiting disk current $i_{d,1}$ (μA)	$i_{d,1}/\omega^{1/2}C$
	A. Dimethyl fumarate		
1.83	157	169	7.37
	207	194	7.37
	257	218	7.43
2.44	109	183	7.18
	157	222	7.26
	207	258	7.34
	257	288	7.36
3.56	109	256	6.88
	157	313	7.02
	207	360	7.03
	257	398	6.97
5.09	109	345	6.50
	157	418	6.55
	207	474	6.48
	257	528	6.48
	B. Diethyl fumarate		
1.82	109	107	5.63
	157	130	5.70
	207	148	5.65
2.43	109	142	5.60
	157	172	5.65
	207	196	5.60
	257	218	5.60
3.65	109	210	5.51
	157	252	5.51
	207	292	5.56
	257	320	5.47
4.87	109	278	5.47
	157	334	5.47
	207	378	5.39
	257	420	5.38
6.10	109	348	5.46
	157	416	5.44
	207	487	5.55
	257	536	5.48
	C. Di-n-butyl fumarate		
1.54	109	75.6	4.70
	157	92.0	4.77
	207	105	4.74
	257	118	4.78
2.20	109	110	4.79
	157	132	4.79
	207	154	4.86
	257	172	4.88
3.3	109	160	4.64
	157	196	4.74
	207	225	4.74
	257	254	4.80
4.4	109	218	4.75
	157	266	4.82
	207	305	4.82
	257	332	4.71
5.9	109	290	4.71
	157	357	4.83
	207	406	4.78
	257	458	4.84
7.7	109	380	4.73
	157	458	4.75
	207	528	4.77
	257	583	4.72
	D. Dimethyl maleate		
0.52	157	47.7	7.32
	207	54.4	7.27
1.05	157	95.1	7.23
	207	108	7.16
2.10	109	157	7.15
	157	186	7.08
3.15	109	227	6.90
	157	271	6.87
4.20	109	302	6.88
	157	362	6.88
	E. Diethyl maleate		
1.24	157	95	6.10
	207	108	6.06
	257	121	6.09
1.86	157	141	6.05
	207	161	6.02
	257	179	6.02
2.48	157	181	5.82
	207	208	5.82
	257	231	5.80
3.72	157	251	5.40
	207	288	5.39
	F. Di-n-butyl maleate		
1.10	157	72	5.22
	207	82	5.18
	257	92	5.21
1.54	157	99	5.14
	207	114	5.15
	257	126	5.11
2.42	207	178	5.10
	257	193	4.98

was rate determining. This reaction can be considered as a pseudo-first-order one, since the concentration of CO_2 in a saturated solution is 50-100 times that of the $F^{\cdot-}$. As in previous studies (4, 24), the dimensionless kinetic parameters XKT (first-order reactions) and $XKTC$ (second-order reactions), defined as

$$XKT = (0.51)^{-2/3}\nu^{1/3}D^{-1/3}\omega^{-1}k_1 \quad [14]$$

$$XKTC = (0.51)^{-2/3}\nu^{1/3}D^{-1/3}\omega^{-1}Ck_2 \quad [15]$$

were employed.

Typical RRDE results for DMeF, DEF, and DBF are shown in Table II. In the absence of CO_2, $N_k = N$, the theoretical collection efficiency (0.555), for both DEF and DBF. In the presence of CO_2, N_k is appreciably smaller than N for both compounds, showing a significant extent of reaction between the radical anion and dissolved CO_2 on the RRDE time scale. The independence of N_k with concentration and $CONI$ for these two compounds agrees very well with an uncomplicated pseudo-first-order mechanism. Typical results for DMeF are shown in Fig. 2. The slight dependence of N_k on $CONI$, can be attributed to the simultaneous occurrence of the $F^{\cdot-}$ dimerization reaction (12). However, the N_k values are considerably smaller than those under identical conditions but without dissolved CO_2.

The experimental points in Fig. 2 were fit by using the known dimerization parameter, $XKTC$, and adding the pseudo-first-order reaction parameter XKT for k_F. Values of k_{2F} were obtained previously (12); for

Table II. Collection efficiency at the RRDE in CO_2-saturated 0.1M TBAI-DMF solutions

Concentration, C (mM)	Rotation rate (rad/sec)	i_d (μA)	$CONI$ ($i_d/i_{d,1}$)	N_k
		Dimethyl fumarate		
0.83	109	8.6	0.137	0.454
		16.4	0.262	0.455
		27.2	0.434	0.453
		38.5	0.615	0.450
		48.1	0.768	0.449
		57.9	0.925	0.446
0.83	157	10.0	0.132	0.470
		19.4	0.255	0.469
		32.2	0.424	0.466
		45.6	0.600	0.466
		57.2	0.753	0.463
		70.0	0.921	0.462
1.37	109	13.2	0.129	0.426
		40.2	0.394	0.420
		57.5	0.564	0.416
		73.0	0.716	0.416
		85.0	0.833	0.417
		95.8	0.939	0.414
		102.0	1.000	0.412
1.37	157	27.2	0.139	0.445
		44.7	0.360	0.443
		64.9	0.523	0.441
		84.7	0.683	0.438
		109.5	0.883	0.438
		116.0	0.935	0.437
		124.0	1.000	0.435
		Diethyl fumarate		
1.82	157	24.5	0.188	0.522
		57.1	0.439	0.523
		90.1	0.692	0.525
		128	0.983	0.523
3.65	157	44.5	0.176	0.524
		100.3	0.398	0.522
		160	0.635	0.525
		223	0.885	0.524
		252	1.00	0.523
4.87	157	57.5	0.172	0.522
		125.3	0.375	0.524
		199	0.596	0.523
		259	0.775	0.525
		324	0.970	0.522
6.10	157	136	0.328	0.525
		178	0.428	0.522
		260	0.625	0.523
		330	0.793	0.521
		398	0.957	0.522
		Di-n-butyl fumarate		
3.30	157	45.0	0.230	0.531
		99.8	0.510	0.533
		150.5	0.770	0.530
		177.2	0.906	0.529
		195.5	1.00	0.530
1.54	157	34.1	0.372	0.531
		55.2	0.601	0.530
		70.5	0.766	0.533
		92.0	1.000	0.532

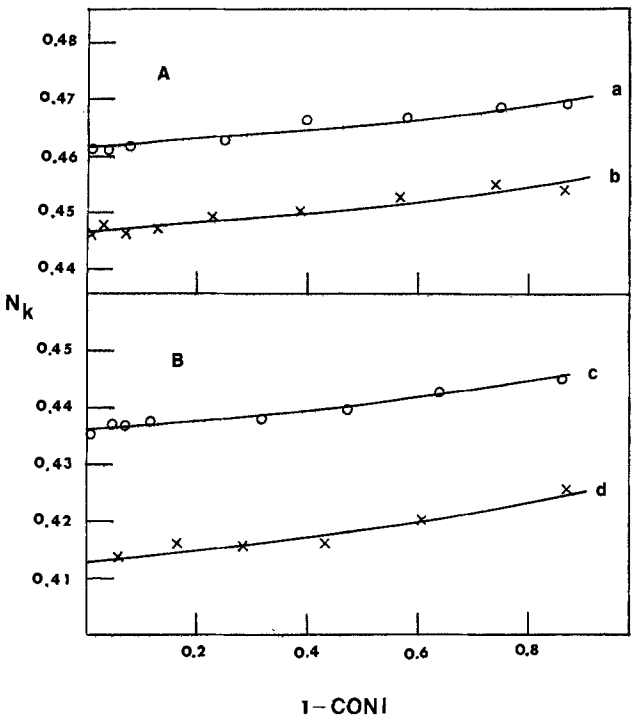


Fig. 2. Collection efficiency (N_k) vs. 1-*CONI* for dimethyl fumarate in presence of CO_2. Experimental points: (x) $\omega = 109$ sec^{-1}, (o) $\omega = 157$ sec^{-1}, (A) 0.83 mM DMeF, (B) 1.37 mM DMeF. Theoretical lines correspond to (a) $XKTC = 0.0086$, $XKT = 0.135$; (b) $XKTC = 0.0127$, $XKT = 0.16$; (c) $XKTC = 0.0144$, $XKT = 0.18$; (d) $XKTC = 0.0208$, $XKT = 0.22$.

DMeF $k_{2F} = 110$ M^{-1} sec^{-1}. *XKTC* values were calculated for the various concentrations and rotation rates used in this work. For example, line a in Fig. 2 was generated by digital simulation using $XKTC = 0.0127$ and $XKT = 0.16$ for $C = 0.83$ m*M*. These lines fit the experimental points quite well. Values of *XKTC* for DEF and DBF were negligible compared to *XKT*. Values of *XKT* and k_F for these three compounds obtained by this method at different *C* and ω values are given in Table III. The average values of k_F are DMeF, 1.5, DEF, 0.47, and DBF, 0.35 (sec^{-1}). The fit of the data to this pseudo-first-order mechanism is persuasive evidence for the reaction sequence [13] and [16] with rapid coupling of the $FCO_2^{\cdot -}$

$$2FCO_2^{\cdot -} \rightarrow {}^-O_2CDCO_2^- \qquad [16]$$

In an attempt to detect $FCO_2^{\cdot -}$, several ESR experiments were undertaken. A 10 m*M* DEF solution was reduced with a constant current of 20 μA in a flat cell inside the cavity of the ESR spectrometer. The steady-state spectrum which resulted after about 1 min of electrolysis was essentially the same as those previously reported (20, 25). The spectrum obtained in a saturated CO_2 solution was the same as that from a CO_2-free system. The ESR spectrum of $FCO_2^{\cdot -}$ would be different than that of $F^{\cdot -}$, since the added CO_2 would change the symmetry and the proton hyperfine coupling constants. Hence the $FCO_2^{\cdot -}$ species must be too short-lived to detect by this method. The reaction of $F^{\cdot -}$ and CO_2 can be seen, however, from the time dependence of the spectra (Fig. 3). After steady-state signals were generated, the constant current responsible for generating the radical anion was turned off and the spectrum was recorded immediately at a

Table III. Calculated rate constants for reactions of fumarate radical anions in the presence of CO_2 from RRDE results[a]

Concentration, *C* (mM)	Rotation rate ω (sec^{-1})	*XKTC*[b]	k_{2F}[b] (M^{-1} sec^{-1})	XKT_F[c]	$(XKT_F)\omega$[c]	k_F (sec^{-1})
			A. Dimethyl fumarate			
0.83	109	0.0127	1.1×10^2	0.16	17.4	1.2
	157	0.0086	1.1×10^2	0.135	21.2	1.4
	207	0.0067	1.1×10^2	0.11	22.8	1.5
1.37	109	0.0208	1.1×10^2	0.22	24.0	1.6
	157	0.0144	1.1×10^2	0.18	28.3	1.9
				Avg	22.7	1.5 ± 0.2
			B. Diethyl fumarate			
1.83	109		44[d]	0.055	5.45	0.41
	157			0.045	7.06	0.47
	207			0.037	7.66	0.51
	257			0.025	6.43	0.43
2.43	109			0.059	6.43	0.43
	157			0.042	6.60	0.44
	207			0.034	7.04	0.47
3.65	109			0.064	6.98	0.46
	157			0.045	7.06	0.47
	207			0.035	7.24	0.48
	257			0.028	7.20	0.48
4.87	109			0.066	7.20	0.48
	157			0.047	7.38	0.49
	207			0.033	6.83	0.46
	257			0.026	6.67	0.45
6.10	109			0.066	7.20	0.48
	157			0.047	7.38	0.49
	207			0.035	7.24	0.48
	257			0.026	6.67	0.45
				Avg	6.93	0.47 ± 0.02
			C. Di-n-butyl fumarate			
1.10	109		26[d]	0.050	5.45	0.36
	157			0.031	4.86	0.32
	207			0.022	4.55	0.30
1.54	109			0.055	6.00	0.40
	157			0.033	5.18	0.35
	207			0.020	4.55	0.28
2.20	109			0.048	5.23	0.35
	157			0.034	5.34	0.36
	207			0.025	5.18	0.35
3.30	109			0.057	6.21	0.41
	157			0.034	5.34	0.36
	207			0.026	5.38	0.36
				Avg	5.27	0.35 ± 0.03

[a] The solutions were all 0.1*M* TBAI in DMF. The RRDE had $r_1 = 0.187$ cm, $r_2 = 0.200$ cm, and $r_3 = 0.332$ cm.
[b] *XKTC* is digital simulation parameter for dimerization of the anion radicals $2F^{\cdot -} \rightarrow D^{2-}$ with reaction rate constant k_{2F} from Ref. (4).
[c] $XKTF = (0.51)^{-2/3} \nu^{1/3} D^{-1/3} \omega^{-1} k_F$, $\nu = 0.00849$ cm^2/sec for the reaction of the radical anion with saturated CO_2, $F^{\cdot -} + CO_2 \xrightarrow{k_F} FCO_2^{\cdot -}$ as a pseudo-first-order reaction.
[d] Negligible dimerization reaction on the RRDE time scale, data from Ref. (5).

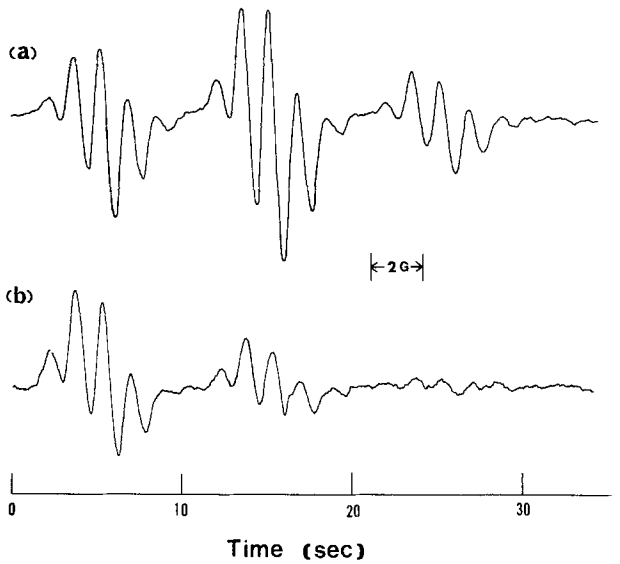


Fig. 3. ESR spectra of 10 mM diethyl fumarate in 0.1M TBAI-DMF electrolyzed at 20 μA in (a) absence and (b) saturated with CO_2. Scan rate 40 G/min.

high scan rate (40 G/min). At this scan rate, good resolution was sacrificed but any differences in signal intensities with time were recorded. In the presence of CO_2 (Fig. 3b) the ESR signals decayed almost to zero 30 sec after the current was turned off. On the other hand, ESR signals still remained reasonably strong in the absence of CO_2 (Fig. 3a) when the generating current was turned off after the same period of time.

Dimethyl maleate (DMM), diethyl maleate (DEM), and di-n-butyl maleate (DBM).—The analysis of the behavior of the maleates parallels that of the fumarates, but is more complicated because of the rapid isomerization and coupling reactions of $M^{\cdot-}$. In the presence of CO_2 the voltammetric reduction waves at the RRDE (at −1.0V *vs.* Ag-RE) are shifted slightly (10-20 mV) toward less negative potentials with essentially no change in the Levich constant (Table I) compared to solutions without CO_2. Variation of N_k with *CONI* [(defined as in (12)] was determined at several values of C and ω; typical results are given in Fig. 4. For determinations of N_k, E_r was adjusted to −0.8V *vs.* Ag-RE, on the plateau of the fumarate reduction wave (where F is reduced to $F^{\cdot-}$ and $M^{\cdot-}$ is oxidized to M). Under these conditions the contribution of $M^{\cdot-}$ oxidation to the ring current can be determined, as discussed previously (12). The N_k values so obtained were used to determine the pseudo-first-order rate constant, k_M (or *XKT*), using the values of k_1 and k_{2M} measured in the absence of CO_2 and digital simulation methods. The solid lines in Fig. 4 are such simulated curves and results for maleates are given in Table IV. Note that carboxylation of $F^{\cdot-}$ (resulting

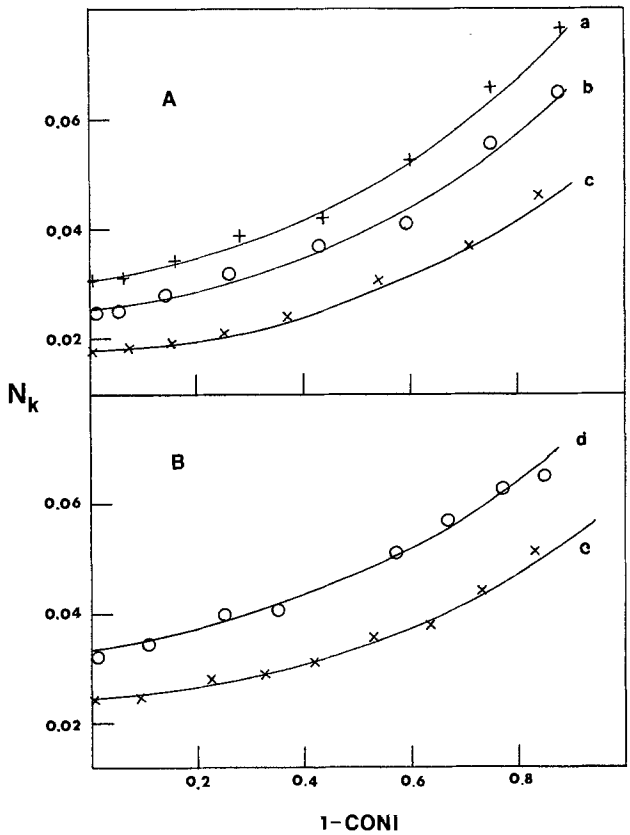


Fig. 4. Collection efficiency (N_k) *vs.* 1-*CONI* for diethyl maleate in presence of CO_2. Experimental points: (x) $\omega = 157$ sec^{-1}, (o) $\omega = 207$ sec^{-1}, (+) $\omega = 257$ sec^{-1}, (A) 2.66 mM DMM, (B) 1.24 mM DMM. Theoretical lines correspond to the following respective values of *XKTC* (dimerization), *XKT* (isomerization), and *XKT* (CO_2 reaction): (a) 12, 0.35, 1.30; (b) 14.9, 0.435, 1.34; (c) 19.7, 0.57, 1.63; (d) 8.16, 0.435, 1.51; (e) 10.8, 0.57, 1.78.

Table IV. Calculated rate constants for reactions of maleate anion radicals in the presence of CO_2 from RRDE results[a]

Concentration, C (mM)	Rotation rate ω (sec^{-1})	$XKTC$[e]	k_{2M}[e] (M^{-1} sec^{-1})	XKT_1[f]	k_1[f] (sec^{-1})	XKT_M[c]	k_M[c] (sec^{-1})
			A. Dimethyl maleate				
0.52	157	9.35	1.88×10^5	0.21	2.2	2.89	30.2
	207	7.1	1.88×10^5	0.16	2.2	2.54	35.0
1.05	157	18.9	1.88×10^5	0.21	2.2	2.79	29.2
	207	14.3	1.88×10^5	0.16	2.2	2.44	33.7
						Avg	32.0 ± 2.8
			B. Diethyl maleate				
1.24	157	10.8	9.1×10^4	0.57	6.0	1.78	18.6
	207	8.16	9.1×10^4	0.435	6.0	1.51	20.8
2.26	157	19.7	9.1×10^4	0.57	6.0	1.63	17.1
	207	14.9	9.1×10^4	0.435	6.0	1.34	18.5
	257	12.0	9.1×10^4	0.35	6.0	1.30	22.2
						Avg	19.4 ± 1.9
			C. Di-n-butyl maleate				
1.97	207	9.90	6.88×10^4	0.48	6.7	1.32	18.2
	257	7.98	6.88×10^4	0.39	6.7	0.96	16.4
2.42	207	12.10	6.88×10^4	0.48	6.7	1.42	19.6
	257	9.75	6.88×10^4	0.39	6.7	1.04	17.7
						Avg	18.0 ± 1.4

[a,c] As defined in the footnote of Table III.
[e] Dimerization of radical anions from Ref. (12).
[f] Isomerization of maleate radical anions to fumarate radical anions from Ref. (12).

from isomerization of $M^{-\cdot}$) does not enter into this calculation, since E_r is such that $F^{-\cdot}$ is not oxidized at the ring, and $FCO_2^{-\cdot}$ is too short-lived to be detected. The values of k_M so calculated are: DMM, 32; DEM, 19; and DBM, 18 (sec^{-1}).

Conclusions

The carboxylation reactions of the *cis-* and *trans-*radical anions in general follow previously reported behavior (12, 13). The reaction rate constants decrease slightly as the alkyl group becomes more bulky, because of steric hindrance. The maleate radical anions are much more reactive toward CO_2 than the corresponding *trans-* species, as has previously been seen for radical ion coupling and for reaction with acrylonitrile. This has been attributed to greater electron density at the central ethylenic carbon atoms because of charge repulsion of the neighboring carbonyl groups.

Acknowledgments

The support of this research by the Robert A. Welch Foundation and the National Science Foundation (CHE 71-03344) is gratefully acknowledged.

Manuscript submitted July 7, 1976; revised manuscript received Sept. 30, 1976.

Any discussion of this paper will appear in a Discussion Section to be published in the December 1977 JOURNAL. All discussions for the December 1977 Discussion Section should be submitted by Aug. 1, 1977.

REFERENCES

1. M. M. Baizer, in "Organic Electrochemistry," M. M. Baizer, Editor, chap. XIX, Marcel Dekker, Inc., New York (1973).
2. J. P. Petrovich, M. M. Baizer, and M. R. Ort, *This Journal*, **116**, 743 (1969).
3. W. V. Childs, J. T. Maloy, C. P. Keszthelyi, and A. J. Bard, *ibid.*, **118**, 874 (1971).
4. V. J. Puglisi and A. J. Bard, *ibid.*, **119**, 829 (1972).
5. M. J. Hazelrigg and A. J. Bard, *ibid.*, **122**, 211 (1975).
6. I. B. Goldberg, D. Boyd, R. Hirasawa, and A. J. Bard, *J. Phys. Chem.*, **78**, 295 (1974).
7. E. Lamy, L. Nadjo, and J. M. Savéant, *J. Electroanal. Chem.*, **42**, 189 (1973).
8. E. Lamy, L. Nadjo, and J. M. Savéant, *ibid.*, **50**, 141 (1974) and numerous references therein.
9. R. D. Grypa and J. T. Maloy, *This Journal*, **122**, 377 (1975).
10. R. D. Grypa and J. T. Maloy, *ibid.*, **122**, 509 (1975).
11. I. Vartires, W. H. Smith, and A. J. Bard, *ibid.*, **122**, 894 (1975).
12. L. S. R. Yeh and A. J. Bard, *ibid.*, **124**, 189 (1977).
13. A. J. Bard, V. J. Puglisi, J. V. Kenkel, and A. Lomax, *Faraday Discuss. Chem. Soc.*, **56**, 353 (1973).
14. S. Wawzonek and A. Gunderson, *This Journal*, **111**, 324 (1964).
15. S. Wawzonek, R. C. Duty, and J. H. Wagenknecht, *ibid.*, **111**, 74 (1964).
16. N. L. Weinberg, A. K. Hoffmann, and T. B. Reddy, *Tetrahedron Lett.*, **1971**, 2271.
17. R. Dietz and M. E. Peover, *Discuss. Faraday Soc.*, **45**, 154 (1968).
18. D. A. Tyssee and M. M. Baizer, *J. Org. Chem.*, **39**, 2819 (1974).
19. D. A. Tyssee and M. M. Baizer, *ibid.*, **39**, 2823 (1974).
20. I. B. Goldberg and A. J. Bard, in "Magnetic Resonance in Chemistry and Biology," J. N. Herak and K. J. Adamic, Editors, p. 297, Marcel Dekker, Inc., New York (1975).
21. H. Stephene and T. Stephene, "Solubility of Inorganic and Organic Compounds," Vol. 1, Part 2, p. 1063, MacMillan Co., New York (1963).
22. J. M. Nigretto and A. J. Bard, *This Journal*, **123**, 1303 (1976).
23. J. P. Petrovich, M. M. Baizer, and M. R. Ort, *ibid.*, **116**, 749 (1969).
24. K. B. Prater and A. J. Bard, *ibid.*, **117**, 1517 (1970) and references therein.
25. S. F. Nelsen and J. P. Gillespie, *J. Org. Chem.*, **40**, 2391 (1975).

The Ag^+-Ag Exchange Reaction in Aqueous Acidic Nitrate Electrolyte

D. Larkin

Department of Chemistry, Towson State University, Towson, Maryland 21204

and N. Hackerman*

Department of Chemistry, Rice University, Houston, Texas 77001

ABSTRACT

The exchange reaction at polycrystalline silver electrodes has been investigated for the system Ag-$AgNO_3$-KNO_3 using a faradaic impedance method. The exchange reaction was determined to be adatom diffusion controlled and the exchange current was found to be dependent on pH. It is suggested that H_3O^+ inhibits the exchange reaction through an adsorption process which blocks the crystal growth sites.

Few investigations have been made of the exchange mechanism for the system

$$Ag^+_{(soln)} + e \rightleftharpoons Ag_{(s)} \qquad [1]$$

in aqueous solutions. This is surprising as silver would not be expected to suffer, to the same degree, from the formation of oxide or hydroxide films on the electrode surface as do many other more extensively studied metals, *i.e.*, the exchange reaction should not be complicated by the possibility of chemical and electrochemical reactions of the type

$$M(H_2O)^{n+}_{y(soln)} \rightleftharpoons M(H_2O)^{n+}_{y(ads)}$$

$$M(H_2O)^{n+}_{y(ads)} \rightleftharpoons M(OH)_n + nH_3O^+ \qquad [2]$$

$$M(OH)_{n(ads)} + ne \rightleftharpoons M_{(solid)} + nOH^-_{(soln)}$$

The absence of a surface oxide or hydroxide film is further indicated by the large polarizable region exhibited by silver (1) [~0.5 to −1.1V (NHE)]. This

* Electrochemical Society Active Member.

suggests that silver would be a suitable solid metal for investigating the electrode exchange reactions. Previous studies which have been made with this system have, however, yielded quite different values for the kinetic parameters.

In a preliminary investigation, Mehl and Bockris (2), using a galvanostatic technique, showed that the rate-determining step for the exchange reaction in the system Ag-$AgClO_4$-$HClO_4$ (aqueous) was dependent on the overpotential (η). For $\eta < 60$ mV [*i.e.*, low i (current)], the reaction was surface diffusion controlled while at larger overpotential (*i.e.*, high i), the charge transfer reaction was rate determining. Using a value of $i_o = 1 \times 10^{-1}$ A · cm^{-2} (for $[AgClO_4] = 2 \times 10^{-1}$M) where i_o = the exchange current for the charge transfer reaction at the equilibrium potential obtained by extrapolation of the η-log$i$ relation at $\eta < 60$ mV, the surface coverage of the electrode by adatoms was calculated to be $\simeq$10%. Despic and Bockris (3), again, using a galvanostatic technique showed that for the system Ag-$AgClO_4$-$HClO_4$ (aqueous) the rate-controlling step was dependent on the overpotential. This investigation is of interest because of the careful techniques used in solution purification and electrode preparation. Values of i_o varying from 0.04 to 1.8 A · cm^{-2} were obtained and appear to be dependent on the electrode used, electrode preparation, and concentration of $AgClO_4$ (concentrations of $AgClO_4$ used were 3.64×10^{-1}, 7.24×10^{-2}, and 1.21×10^{-3}M). The adatom concentration at equilibrium (C^o_{ad}) was calculated and values in the range 3×10^{-11} to 1.6×10^{-9} mole · cm^{-2} were reported which also appear to be dependent on the electrode used and the electrode preparation. In addition, a value of $\sim$76 μF · cm^{-2} for the double layer capacitance of the silver electrodes was given. Gerischer and Tischer (4) using a potentiostatic jump and double impulse methods studied the system Ag-$AgNO_3$-$HClO_4$ and reported exchange currents $i_o = 0.15$ A · cm^{-2} (for $[Ag^+] = 10^{-3}$M) and $i_o = 4.5$ A · cm^{-2} (for $[Ag^+] = 10^{-1}$M) for the charge transfer process from which a "standard exchange current" ${}^oi = 24$ A · cm^{-2} was calculated by normalizing the concentrations to $Ag^+ = 1.0$M using the relationship

$$i_o = {}^oi \left[\frac{[Ag^+]}{[Ag^+]_o} \right]^\alpha$$

where α = transfer coefficient, $[Ag^+]_o = 1.0$M, and $[Ag^+]$ = experimental silver concentration. In addition, they showed that the adatom concentration at the electrode surface was dependent on current density and that the lattice incorporation process was the slow step in the reaction. Gerischer (5), in a further study using a galvanostatic technique, investigated the system Ag-$AgClO_4$-$HClO_4$ and concluded that the adatom layer is an intermediate product of the over-all reaction which covers at least 1% of the surface at 25°C with an enthalpy of formation of $\sim$10.5 kcal · $mole^{-1}$. The bonding of the layer showed 30-40% ionic character. Lorenz (6), using an impedance technique, studied the system Ag-$Ag(NH_3)_2^+$ and reported that the crystalline growth is determined by surface diffusion rates as predicted by theory. Canagaratna and Karunathilaka (7), using a faradaic impedance method, studied the system Ag-$AgNO_3$-KNO_3. Unfortunately, their method of electrode construction and apparent lack of any attempt to purify their solutions makes it likely that their electrodes were "poisoned" by organic surfactants. This is indicated by their impedance plots which, in one of our (D.L.) previous experiments are typical of plots obtained in "impure" solutions. Recently, Cachet *et al.* (8) studied the system Ag-$AgNO_3$-KNO_3 using both polycrystalline and single crystal (100), (110), and (111) silver electrodes. They suggest the possible interaction of the nitrate anions with silver ions to form adsorbed species on the electrode surface of the type $Ag(NO_3)_{ads}$.

Previously, one of us (D.L.) has had some success in studying solid metal systems in ultrapure electrolytes. The present paper represents our results obtained with polycrystalline silver electrodes under similar conditions using the faradaic impedance method.

Experimental

Electrode construction.—Silver wire (supplied by Materials Research Corporation, Marz grade 5*N*) was covered with polyethylene film and sealed into a glass tube. (The polyethylene film was produced by covering the silver electrode with polyethylene powder and gently heating until a thick layer of polyethylene was built up.) This material has been shown previously to be nonsurfactant by observing its effects over a period of time on the double layer capacitance of a sitting mercury drop electrode; no decrease in capacitance was noted. The polyethylene sheath was then cut laterally to expose a cross section of the silver wire. The nominal area of the silver electrode was 4×10^{-3} cm^2.

Electrode preparation.—The silver electrode was first polished on roughened glass using bidistilled water as a lubricant, then etched electrochemically in 10% v/v nitric acid at 100 μA (per electrode area) for 30 sec and then allowed to etch chemically for 30 sec. The electrode was washed immediately with bidistilled water and transferred to the electrolytic cell. After each measurement, the electrode was polished back on roughened glass to expose an essentially new electrode surface. A reoccurring problem with this method of electrode preparation was that after repeated use the etching solution appeared to "age" and produced electrodes which behaved erratically. The reason for this could not be ascertained; use of a new etching solution invariably solved the problem.

Electrolytic cell.—The electrolytic cell consisted of three compartments; one containing a reference electrode (mercurous sulfate/mercury) separated by a potassium nitrate (1.0M) salt bridge from the other two which were connected via a coarse frit and contained, respectively, a platinum gauze counterelectrode (nominal area 100 cm^2) and the test electrode. The electrolyte solution was under an atmosphere of oxygen-free nitrogen and purified by continuous circulation through purified (12) activated charcoal. Silver solutions are well known to be light sensitive and because of the long purification times needed (see below) these cell solutions needed to be shielded from light. The cell was therefore constructed from Pyrex glass and then all outside surfaces of the cell were covered with a dark brown stain which was "fired" into the glass in an annealing oven. The stain penetrated a small distance into the glass but did not diffuse through the glass to the inside surfaces of the cell. This technique was very successful and, once in the cell, no deterioration of the silver solutions was noted even after long periods of time (many weeks).

All solutions were prepared using ACS grade reagents and bidistilled water. The solutions were kept at a constant NO_3^- concentration (1.0M) throughout all the experiments.

Electrical circuit.—All measurements were made using a Schering bridge (frequency range 20 Hz-20 kHz) of essentially the same design as described by Farr and Hampson (9). The analysis of the data was performed by an iterative technique which has been used in a number of previous papers (10, 11) and was first described by Farr and Hampson (9). This method was modified to enable the computer to select the best fit of R_L (the frequency-independent resistive component) and C_L (the frequency-independent capacitive component) of the electrode impedance; previously these were selected by inspection.

Results

Satisfactory impedance behavior was obtained only after exhaustive purification. The criterion adopted was

Table I. Values of R_D at differing $[Ag^+]$ concentrations, pH = 2.40; $[NO_3^-] = 1.0M$

[Ag+] Concentrations	0.52M	0.175M	0.141M	0.098M	0.061M	0.033M
R_D in ohms	4.1	4.1	3.75	4.1	3.8	4.4
	3.6	4.05	3.4	4.25	3.8	3.8
	3.6	3.7	3.4	3.75	3.7	4.0
	4.0	3.6	3.95	3.4	3.8	3.7
	3.8	3.85	3.75	4.0	3.7	3.4
	4.1	4.2	4.0	4.2	3.6	4.2
	3.6	3.65	3.95	4.25	4.0	3.8
	4.2	4.4	3.75	4.2	3.9	3.7
	4.0	3.5	3.5	4.25	3.5	4.0
	4.2	4.05	3.4	4.2	3.5	4.1
	4.0	—	3.3	3.9	4.2	—
	4.1	—	4.0	3.7	3.5	—
	—	—	4.0	4.05	3.75	—
	—	—	3.9	—	3.8	—
	—	—	—	—	4.2	—
Average value of R_D in ohms	3.9 ± 0.2	3.9 ± 0.3	3.7 ± 0.3	4.0 ± 0.3	3.8 ± 0.2	3.9 ± 0.3

that a steady value of R_D (the exchange resistance) was obtained over a period of at least 3 days. Continuous circulation of the solution through activated charcoal for a period of 10 days was generally adequate to achieve this. Initially, even in purified solutions, stable values for R_D were not obtained until 24 hr after etching and placing in the electrolytic cell. Figure 1 shows typical time-dependent behavior of the electrodes. The time to reach a constant value was independent of $[Ag^+]$ concentration and pH. Electrodes reached a stable value of R_D after ~24 hr and this value was constant for many days.[1] Figure 2 shows typical impedance plots of R_R and $1/\omega C_R$ *vs.* $\omega^{-1/2}$ for varying concentrations of $[Ag^+]$ at constant pH. Table I gives values of R_D obtained at different $[Ag^+]$ concentrations. Each value is for an essentially new electrode surface (see electrode preparation above for details). Table II shows typical values of R_D obtained at constant $[Ag^+]$ concentrations and varying pH. The same criteria for each value of R_D in Table II holds as for Table I. Figure 3 shows the variation of R_D and C_L (the frequency-independent capacitive component of the electrode impedance) as a function of pH. There was no variation in R_L (the frequency-independent resistive component of the electrode impedance).

The electrode potential *vs.* mercurous sulfate/mercury reference electrode was measured as a function of $[Ag^+]$ concentrations and showed good nernstian behavior with $n = 1.05$.

Discussion

The Schering bridge was found to operate satisfactorily over a frequency range 20 Hz-20kHz; the lower limit being set by the null detector and the upper limit

[1] Constant values for R_D for periods up to 1 week were recorded.

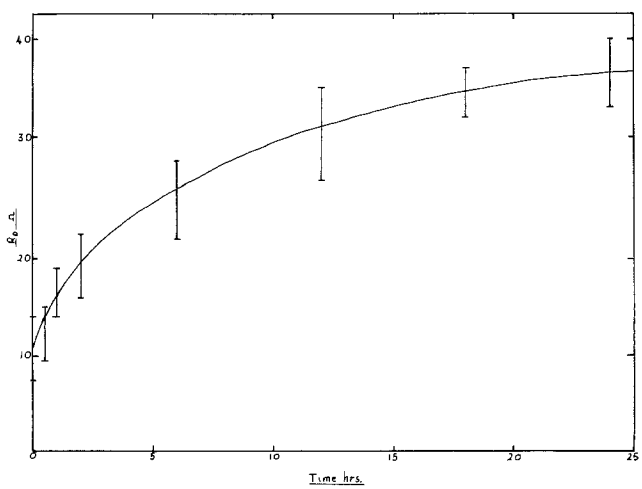


Fig. 1. Plot of R_D vs. time (hr), pH = 2.40, $[Ag^+] = 0.141M$, $[NO_3^-] = 1.0M$.

Table II. Values of R_D at differing pH, $[Ag^+] = 0.033M$, $[NO_3^-] = 1.0M$

pH	1.55	2.40	2.95	3.40
R_D in ohms	3.7	4.4	3.5	2.6
	3.8	3.8	3.5	2.8
	3.5	4.0	4.0	2.7
	4.2	3.7	3.5	2.5
	4.0	3.4	3.1	2.6
	3.9	4.2	2.8	2.8
	—	3.8	3.4	2.9
	—	3.7	2.6	—
	—	4.0	—	—
	—	4.1	—	—
Average value of R_D in ohms	3.9 ± 0.2	3.9 ± 0.3	3.3 ± 0.4	2.7 ± 0.2

by the increasing effect of random phase shifts introduced by the nonideality of the circuit components. However, from Fig. 2, it can be seen that impedance measurements are not reported below a frequency of

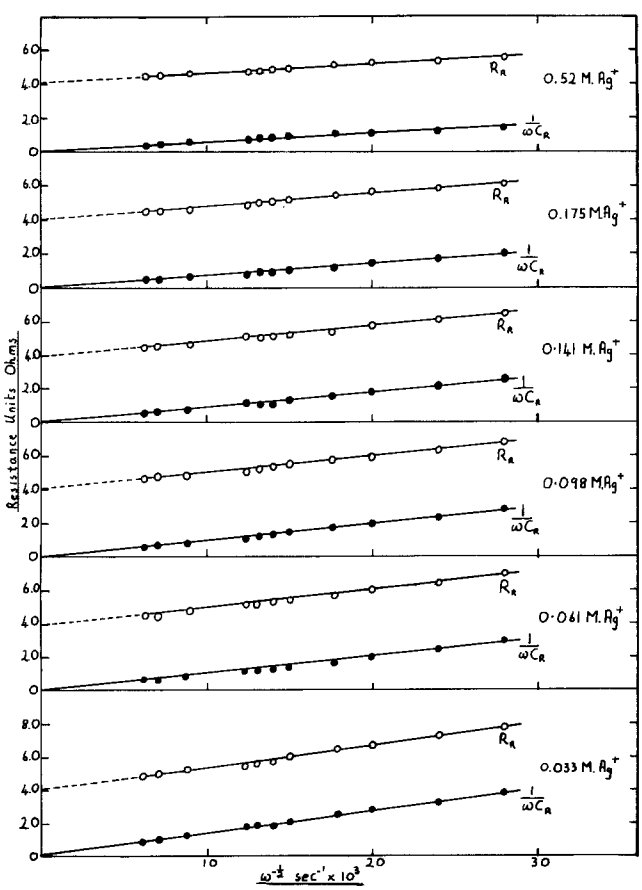


Fig. 2. Plots of R_R and $1/\omega C_R$ vs. $\omega^{-1/2}$ at differing $[Ag^+]$ concentrations, pH = 2.40.

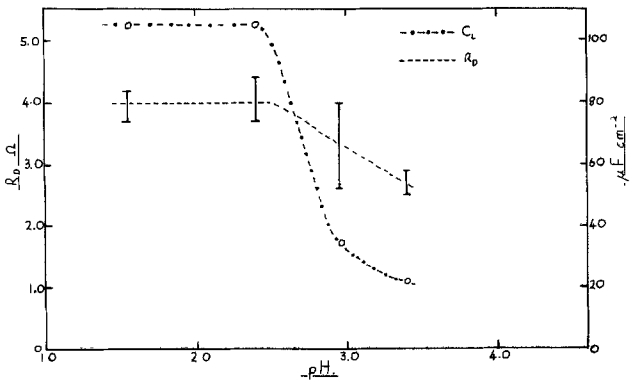
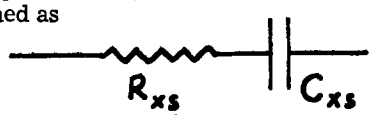


Fig. 3. Plots of R_D and C_L vs. pH, $[Ag^+] = 0.033M$, $[NO_3^-] = 1.0M$.

100 Hz. Experimentally, the total electrode impedance is determined as



where $1/C_{xs} = 1/C_{(ref)} + 1/C_{(test)}$, $C_{(ref)}$ = the capacitance of the platinum auxiliary electrode, and $C_{(test)}$ = the capacitance of the test electrode, as long as $C_{(ref)} >>> C_{(test)}$ then $1/C_{xs} \simeq 1/C_{(test)}$. For experimental systems, where large exchange currents are being measured, $C_{(test)} \simeq C_{(ref)}$ and the above approximation becomes invalid. For the data presented here at frequencies <100 Hz, $C_{(test)} \simeq C_{(ref)}$ which resulted in deviations from linearity for the plots of R_L and $1/\omega C_L$ *vs.* $\omega^{-1/2}$ at frequencies <100 Hz.

The analysis of our impedance data depends on C_L being frequency independent. However, C_L contains as one of its components the double layer capacitance C_{dl} (discussed below) which while theoretically independent of frequency can, in fact, vary with frequency because of frequency dispersion effects. In our present work these frequency dispersion effects do not appear to be significant as they would be expected to cause a deviation from linearity in our impedance plots. It can be seen from Fig. 1 that such effects, due to this process, were not observed and therefore any frequency dispersion effects of C_{dl}, if present, must contribute an error no greater than other experimental errors in our measurements.

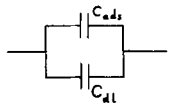
Figure 1 shows typical time dependent behavior of silver electrodes after introduction into the electrolytic cell. The time to reach a steady value of R_D was ~24 hr and was independent of $[Ag^+]$ concentration and pH. This time-dependent behavior has been discussed previously (13, 14) and is considered to be due to an equilibration process between the electrode surface and the solution with which it is in contact. The exchange current i_o calculated from the relationship

$$R_D = \frac{RT}{zFi_o}$$

gave an average value of 3.8 ± 0.2 A · cm^{-2} at pH values of ~2.4 and less while at greater values of pH this rose to a value of 5.5 ± 0.2 A · cm^{-2}. These values are larger than those reported by previous workers (2, 5, 7) which we attribute to the stringent purification technique used in this study. Consequently, the values of i_o reported here are probably more representative of the "true" value of the exchange current for the Ag^+-Ag reaction.

Table II shows that, within experimental error, at pH 2.4, the exchange current is independent of $[Ag^+]$ concentrations. This result is consistent with a rate-controlling step of adatom diffusion across the electrode surface and is in agreement with the results reported in previous studies (2-5).

Figure 3 shows that the value of R_D decreases at pH values larger than ~2.4 and is paralleled by a decrease in the value of C_L, the frequency-independent capacitive component of the electrode impedance. The value of C_L at pH 3.40 is that of the double layer capacitance of a polycrystalline silver electrode at a similar electrode potential (1). At pH values less than ~2.4, C_L can be considered as composed of two capacitances in parallel



C_{dl} = double layer capacitance, C_{ads} = capacitance due to an absorbed species at the electrode surface, where

$$C_L = C_{dl} + C_{ads}$$

It is suggested that the absorbed species is probably the hydronium ion (H_3O^+). At pH values ~2.4 and less, H_3O^+ is absorbed on the surface while at greater values of pH, H_3O^+ desorbs and, consequently, $C_{ads} \rightarrow 0$ and $C_L \rightarrow C_{dl}$. The effect reported here appears small and we suggest, therefore, that the H_3O^+ absorption is weak and that it may compete with other adsorbed species (*e.g.*, NO_3^- which has been suggested by Cachet *et al.* (8) to be absorbed at silver electrodes). The decrease in the value of R_D which accompanies the desorption of H_3O^+ suggests that H_3O^+ is inhibiting the Ag^+-Ag exchange reactions. As reported here and elsewhere (2-5), adatom diffusion is the rate-determining step, thus it appears that H_3O^+ may block the crystal growth sites on the silver metal electrodes, thereby inhibiting the reaction. At larger values of pH, H_3O^+ is desorbed and a corresponding increase in the exchange current is observed.

Acknowledgments

The authors wish to thank the Robert A. Welch Foundation of Houston, Texas, for their support of this work.

Manuscript submitted Aug. 4, 1976; revised manuscript received Oct. 25, 1976.

Any discussion of this paper will appear in a Discussion Section to be published in the December 1977 JOURNAL. All discussions for the December 1977 Discussion Section should be submitted by Aug. 1, 1977.

Publication costs of this article were assisted by Rice University.

REFERENCES

1. N. A. Hampson, D. Larkin, and J. R. Morley, *This Journal*, **114**, 817 (1967).
2. W. Mehl and J. O'M. Bockris, *J. Chem. Phys.*, **27**, 818 (1957).
3. A. R. Despic and J. O'M. Bockris, *ibid.*, **32**, 389 (1960).
4. H. Gerischer and R. P. Tischer, *Z. Elektrochem.*, **61**, 1159 (1957).
5. H. Gerischer, *ibid.*, **62**, 256 (1958).
6. W. Lorenz, *Z. Phys. Chem. (Leipzig)*, **17**, 136 (1958).
7. S. G. Canagaratna and S. A. G. R. Karunathilaka, *J. Electroanal. Chem.*, **60**, 65 (1975).
8. C. Cachet, M. Froment, F. Wenger, and R. Wiart, *ibid.*, **61**, 121 (1975).
9. P. G. Farr and N. A. Hampson, *Trans. Faraday Soc.*, **62**, 3493 (1966).
10. N. A. Hampson and D. Larkin, *ibid.*, **65**, 1600 (1969).
11. N. A. Hampson and D. Larkin, *J. Electroanal. Chem.*, **18**, 401 (1968).
12. G. Barker, in "Modern Electroanalytical Methods," G. Charlot, Editor, p. 122, Elsevier, Amsterdam (1958).
13. N. A. Hampson and D. Larkin, *Electrochim. Acta*, **15**, 581 (1970).
14. D. Larkin, Ph.D. Thesis, Loughborough University of Technology (1968).

Electrochemical Synthesis of Tetrapropyl and Tetrabutyl Derivatives of Lead and Tin Via Alkyl-Zinc Intermediates

Giuliano Mengoli

Laboratorio di Polarografia ed Elettrochimica Preparativa, C.N.R., C.P. 1075, 35100 Padova, Italy

ABSTRACT

A novel electrochemical route, which gives favorable results for the synthesis of tetraethyl compounds of lead and tin, has been successfully applied to the preparation of higher tetraalkyl derivatives of the same metals. This synthesis may be accomplished by electrolyzing an alkyl halide between a zinc cathode and a lead or tin anode in an undivided cell. DMF and DMSO are suitable solvents and an alkaline salt may be used as the supporting electrolyte. The features of the synthetic process are mainly determined by cathodic zinc alkylation, which supplies the zinc alkyl intermediates for the anodic reaction. Thus tetraalkyl compounds of lead and tin are easily synthesized at room temperature when alkyl iodides are utilized, whereas poor yields are obtained when alkyl bromides are used as the alkylating material. However, it was found that by selecting suitable experimental conditions and by adding catalytic amounts of a lower alkyl iodide to the alkyl bromides, these halides too may be satisfactorily employed in the synthetic process.

Although industrial interest in electro-organic syntheses has been claimed repeatedly, few processes have so far found any practical application (1, 2).

However, because of their technological importance, the electro-organic syntheses of organometallic compounds, mainly the alkyl derivatives of lead and tin, exhibit some favorable features.[1] Indeed, the traditional chemical routes to these compounds often suffer from unsatisfactory yields, hazardous manufacturing operations, and can cause considerable pollution problems.

In such processes the electrodes may replace chemical reagents of high energy content, *i.e.*, sodium or potassium alloys and Grignard compounds (3) and because the molecular weights of the products are relatively high, satisfactory amounts of material are produced for each faraday of electricity consumed.

Useful results have been obtained for the syntheses of tetraethyl lead by the electrolysis of aluminum and magnesium ethyl derivatives at a lead anode, or by the reduction of ethyl halides at a sacrificial lead cathode (4-6).

However, the results were less satisfactory for the preparation of tin compounds as passivation of the tin anodes often occurred (5) whereas only for tetramethyl tin could good yields be obtained by the sacrificial reduction of alkyl halides (7-9).

Butyl chloride can be reduced at a tin cathode with the formation of butyl tin derivatives (10); the process although very interesting gives only tin compounds of low degrees of alkylation; the same syntheses fail at lead cathodes.

An alternative electrochemical route to the lower tetraalkyl derivatives of lead and tin has been recently devised in the author's laboratory: this synthesis basically consists in the electrolysis of an alkylating agent, alkyl halide (11, 12) or alkyl sulfate (13), between a zinc cathode and a lead or tin anode in an undivided cell. Good electrochemical solvents as dimethylformamide and dimethylsulfoxide are employed and cheap alkaline supporting electrolytes may be utilized.

The aim of this paper is to test the effectiveness of the method for synthetizing some higher tetralkyl derivatives of lead and tin: The contribution of the cathode and anode reactions to the process are examined and discussed.

[1] The manufacture of tetramethyl lead and tetraethyl lead by electrochemical methods has been run commercially for the past 10-15 years by the Nalco Chemical Company, Freeport, Texas (R. M. Hurd, Private communication).

Experimental

Materials.—The alkyl halides utilized in this work were commercially available reagent grade chemicals and were used as supplied. The supporting electrolytes, $NaClO_4$ and tetrabutylammonium perchlorate (TBAP), were dried at 70°C in a vacuum oven before use. The electrolytic solvents, dimethylformamide (DMF) and dimethylsulfoxide (DMSO), were dried by $CaCO_3$ and CaH_2, respectively, and distilled before use. Zinc, lead, and tin, 99% purity grade, were used for the electrodes. Nitrogen, 99.8% purity, was used for degassing the electrolytic cells.

Apparatus and procedure.—Lead and tin organocompounds were prepared by electrolyzing amperostatically (100 mA) 25 ml of solution placed in the simple undivided cell shown in Fig. 1. This consisted of a glass cylinder, a, equipped with a thermostated jacket, b; the cell was sealed at the top by a Teflon plug, c, bearing two glass tubes, d, for degassing the solution by nitrogen and two copper wires, e, for making the electrical contact with the electrodes. The cathode, f, was a zinc sheet rolled in the form of a cylinder (immersed area $\simeq$18 cm^2). The anode, g, was a lead or tin rod placed at the center of the zinc cylinder (immersed area $\simeq$5 cm^2). The distance between the electrodes was 0.5 cm.

Microscale experiments for elucidating the cathode and anode processes were performed by examining

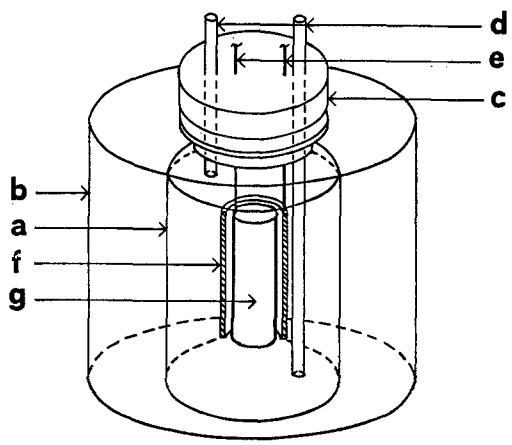


Fig. 1. Electrolytic cell used for the preparation of lead and tin tetraalkyl derivatives.

each electrode reaction separately using a steady-state potentiostatic technique.

Thus the reduction of alkyl halides at zinc was studied in a divided cell equipped with the following electrodes: the working electrode was a zinc disk (area $\simeq 0.2$ cm^2) which was sealed into a Teflon sheath; the secondary electrode was a platinum net which was separated from the cathode compartment by a N2 sinter glass. The reference electrode was an aqueous SCE and was separated from the working electrode by a Luggin capillary and a tap.

The same cell was used for investigating the anode reaction: the zinc electrode was thus substituted by a lead (or tin) microanode (area $\simeq 0.2$ cm^2) and some zinc alkyls were produced *in situ* by heating (or polarizing cathodically) a zinc sheet placed in the same compartment in the presence of suitable concentrations of alkyl halide. The amount of zinc alkyls formed was estimated from the weight loss of the zinc sheet.

The basic electric equipment used for the experiments was a 557 Amel potentiostat.

Analysis.—At the end of each preparative run the weight loss of both electrodes was determined, and the organolead (or organotin) compounds were recovered by extraction with n-hexane from the reaction mixture diluted with water. Their identification was made by gas chromatographic analysis using known standards: tetrapropyl and tetrabutyl derivatives were commercially available whereas the other organocompounds were prepared using published methods (3).

A Perkin Elmer Model 3920 gas chromatograph was used: it was equipped with a 2m column, $\phi = 2$ mm, packed with 8% bis(m-phenoxyphenoxy) berine + 2% Apiezon L on Chromosorb (80-100 mesh). The column temperature ranged from 100° to 160°C; the gas carrier (nitrogen) had a flow rate = 50 ml/min.

The presence of minor amounts of alkyl tin compounds was ascertained in a few instances by submitting the electrolysis products to mass spectrometric analysis, using a Hitachi-Perkin Elmer Model RMU 6 mass spectrometer.

Results

Synthesis of tetrapropyl lead and tetrapropyl tin.—Table I shows the experimental conditions and the results for the synthesis of tetrapropyl lead and tetrapropyl tin.

The runs were performed at 25°C using propyl iodide as the alkylating material and $NaClO_4$ as the supporting electrolyte.

The synthesis was studied in terms of the dependence on the propyl iodide concentration and the quantity of electricity passed. In addition to the variation of these parameters in the runs of Table I the weight loss of the electrodes, the number of faradays passed per gram atom of anode dissolved is reported together with the yield of organoderivative based on both the quantity of electricity passed and the loss in weight of the anode. The current yields were computed by assuming that 4**F** are necessary for producing 1 mole of tetraalkyl derivative.

It is clear that the process is based on the production of zinc alkyl intermediates at the cathode which are converted into organolead or organotin compounds at the anode. The formation of zinc alkyls (deducible from the cathode loss) consequently controls the efficiency of the whole synthetic process. Although a negligible weight loss occurred when using the same conditions as in Table I for unpolarized zinc sheets, the cathode dissolution of the runs (Tables I-II) cannot only be related to current effects but is largely determined by the concentration of propyl iodide in the system.

Additionally, the weight loss of the anode does not follow a constant stoichiometry with the quantity of electricity passed, to a first approximation the number of faradays required for the dissolution of one gram atom decreases from 4 to 2 as the propyl iodide concentration increases. For this reason the yields of tetraalkyl derivative based on the current may exceed 100% and often result in double those based on anode loss.

It has to be noted that the anode metal not converted to tetraalkyl derivative is generally present in solution

Table I. Synthesis of tetrapropyl lead and tetrapropyl tin

Run No.	C_3H_7I (mole/liter)	Anode	Coulombs	Zn loss (g)	Anode loss (g)	Faradays for anode dissolution	$Me(C_3H_7)_4$ currrent yield, %*	$Me(C_3H_7)_4$ yield based anode loss, %*
1	1.02	Pb	360	0.27	0.27	2.82	28.1	19.8
2	1.02	Pb	480	0.25	0.30	3.35	14.1	11.8
3	1.50	Pb	360	0.53	0.39	1.94	111.5	54.0
4	2.05	Pb	360	0.58	0.28	2.75	101.0	69.4
5	2.05	Pb	720	1.51	0.79	1.95	63.6	31.0
6	0.51	Sn	360	0.22	0.11	3.73	40.7	37.9
7	0.51	Sn	500	0.21	0.20	2.97	30.1	22.3
8	1.02	Sn	180	0.31	0.11	1.95	112.9	55.0
9	1.02	Sn	360	0.58	0.23	1.90	135.3	64.2
10	1.02	Sn	480	0.71	0.29	1.98	136.8	67.7
11	1.50	Sn	360	0.35	0.22	1.97	100.5	49.5

* Me = Pb or Sn.

Table II. Synthesis of tetrabutyl lead and tetrabutyl tin

Run No.	C_4H_9I (mole/liter)	Anode	Coulombs	Zn loss (g)	Anode loss (g)	Faradays for anode dissolution	$Me(C_4H_9)_4$ current yield, %*	$Me(C_4H_9)_4$ yield based on anode loss, %*
12	0.87	Pb	360	0.42	0.28	2.73	6.9	4.7
13	0.87	Pb	720	0.38	0.32	4.71	5.1	6.0
14	1.31	Pb	360	0.45	0.24	3.15	17.4	13.7
15	1.31	Pb	720	0.83	0.40	3.86	34.3	33.0
16	1.75	Pb	180	0.72	0.20	1.90	187.6	89.1
17	1.75	Pb	360	0.93	0.39	1.96	154.1	75.5
18	1.75	Pb	618	1.73	0.97	1.36	159.3	54.1
19	0.87	Sn	360	0.31	0.22	1.96	15.6	7.6
20	0.87	Sn	720	0.43	0.35	2.49	14.0	8.7
21	1.31	Sn	180	0.64	0.11	1.96	79.8	39.1
22	1.31	Sn	360	0.88	0.22	1.96	94.0	46.0
23	1.31	Sn	720	1.22	0.44	2.00	72.1	36.0
24	1.75	Sn	360	1.40	0.22	1.96	97.3	47.6

* Me = Pb or Sn.

at some lower degree of alkylation, the mass spectroscopic analysis moreover gave evidence of the presence of higher molecular weight organotin compounds containing the Sn-Sn bond.

Synthesis of tetrabutyl lead and tetrabutyl tin.—Table II reports data which refer to the synthesis of tetrabutyl lead and tetrabutyl tin.

The experimental conditions of the runs were similar to those adopted for the synthesis of tetrapropyl derivatives: the concentration of the alkyl iodide is the main parameter which still affects the sacrificial loss of both the electrodes and the yields of the tetraalkyl derivative. The remarks above are again valid for a preliminary consideration of these data.

Synthesis of tetraisoamyl tin.—The experimental conditions and the results obtained for the synthesis of tetraisoamyl tin by using 1-iodo-3-methylbutane as alkylating material are reported in Table III.

At room temperature the sacrificial dissolution of the zinc caused by cathodic polarization is low when compared with the losses of Tables I and II, and the yield of organotin is very poor. However, an increase of temperature leads to active dissolution of the polarized zinc with a parallel greatly increased formation of tetraisoamyl tin.

The last column of Table III shows the extent of the zinc dissolution for unpolarized sheets (under the same conditions) caused by purely chemical reaction at various temperatures; it can be deduced that during the electrolytic process the spontaneous reaction is negligible below 50°C in comparison with that cathodically promoted: In contrast the zinc alkyl formation appears to mainly follow a chemical route at the highest temperatures.

In some instances (runs No. 35-37) the electrolyses were carried out using high concentrations of 1-iodo-3-methylbutane in the presence of small amounts of ethyl iodide: No substantial increase of yield was obtained in DMF (run No. 36), but the runs performed in DMSO (No. 35, 37) exhibited some ethyl iodide catalytic effect on the formation of tetraisoamyl tin and mixed isoamyl ethyl tin compounds.

Synthesis of tetrapropyl tin and tetrabutyl tin using alkyl bromides as alkylating agents.—When different concentrations of propyl bromide in DMF were electrolyzed between a zinc cathode and a tin anode, low yields of tetrapropyl tin and propyl tin bromides were generally obtained. Better results were accomplished by electrolyzing propyl bromide containing TBAP (2%) but in the absence of any solvent: The related runs are reported in Table IV (No. 38, 39).

Very poor yields of tin butyl derivatives were also obtained in DMF at room temperature for various butyl bromide concentrations, whereas the results improved when the temperature was raised to 110°C.

However, the process could reach its optimum yield when high concentrations of butyl bromide containing small amounts of DMSO and catalytic concentrations of ethyl iodide were electrolyzed between 100° and 110°C (runs 42-46). Under these conditions, when considering the formation of mixed butylethyl tin compounds (not reported in Table IV), more than 80% of the dissolved tin was alkylated.

By adopting a similar procedure (*i.e.*, DMSO solvent, ethyliodide catalyst, and high concentrations of propyl bromide) and selecting an electrolysis temperature in the range 55°-80°C, results comparable to those obtained with propyliodide were reached for the synthesis of tetrapropyl tin too.

For instance, on electrolyzing at 78°C 25 ml of a DMSO solution containing 7.68M propyl bromide and 0.249M ethyl iodide, after 400C the yields (based on

Table IIIa. Synthesis of tetraisoamyl tin

Run No.	t (°C)	$C_5H_{11}I$ (mole/liter)	Coulombs	Zn loss (g)	Sn loss (g)	Faradays for anode dissolution	$Sn(C_5H_{11})_4$ current yield %	$Sn(C_5H_{11})_4$ yield based on anode loss, %	Zn loss without polarization (g)
25	20	1.11	360	0.09	0.11	3.98	3.6	3.5	0.00
26	40	1.86	360	0.19	0.22	1.97	11.6	5.7	0.01
27	50	1.11	360	0.19	0.22	1.95	19.6	9.5	0.04
28	50	1.86	360	0.41	0.22	2.01	32.1	16.1	0.07
29	60	1.11	360	0.40	0.23	1.92	28.0	13.4	—
30	60	1.11	720	0.59	0.44	1.96	18.2	8.9	0.37
31	60	1.86	180	0.44	0.11	1.88	51.1	24.0	—
32	60	1.86	360	0.69	0.23	1.91	59.5	28.4	—
33	80	1.11	360	0.84	0.22	1.95	71.3	34.7	0.95
34	80	1.86	360	1.92	0.22	1.93	95.7	46.1	—

Table IIIb. Synthesis of tetraisoamyl tin in the presence of EtI 0.187M

Run No.	t (°C)	$C_5H_{11}I$ (mole/liter)	Coulombs	Zn loss (g)	Sn loss (g)	$Sn(C_5H_{11})_4$ current yield, %	Mixed SnR_4 current yield, %	$Sn(C_2H_5)_4$ current yield, %	Total current yield, %
35*	40	1.86	360	1.38	0.22	19.9	29.9	3.8	53.6
36	40	1.86	360	0.23	0.22	3.2	7.3	—	10.5
37*	50	1.49	360	1.64	0.22	38.5	38.5	4.7	61.3

* DMSO solvent.

Table IV. Synthesis of tetrapropyl tin and tetrabutyl tin using alkyl bromides as alkylating agents

Run No.	t (°C)	C_3H_7Br, mole/liter	C_4H_9Br, mole/liter	DMSO, %	Coulombs	Zn loss (g)	Sn loss (g)	SnR_4 current yield, %*	$Sn(C_4H_9)_3Br$ current yield, %
38	50	10.25	—	—	360	0.09	0.23	25.2	—
39	50	10.25	—	—	855	0.21	0.49	31.6	—
40	100	—	4.65	50	400	0.34	0.27	4.9	—
41	110	—	7.91	15	400	0.13	0.26	10.3	29.9
42**	100	—	4.65	48	400	0.37	0.27	13.5	20.5
43**	100	—	6.89	24	400	0.30	0.30	17.0	23.9
44**	100	—	7.73	15	400	0.32	0.25	49.5	7.5
45**	110	—	7.73	15	360	0.45	0.25	93.6	17.2
46†	110	—	7.82	15	360	0.26	0.23	48.2	61.9

* | R = C_3H_7 or C_4H_9.
** With | C_2H_5I | = 0.25 mole liter^{-1}.
† With | C_2H_5I | = 0.125 mole liter^{-1}.

the dissolved tin) were: 66.8% for tetrapropyl tin and 21.0% for mixed propyl-ethyl compounds.

Use of butyl chloride as alkylating material.—After electrolyzing butyl chloride (70%), DMSO (28%), ethyl iodide (2%) between a zinc cathode and a tin anode at 100°C, no appreciable amount of tetrabutyl tin was detected by gas chromatography, however some moiety attributable to butyl tin halides was detected by mass spectrometric analysis.

Reduction of alkyl halides at zinc.—Steady-state current-potential curves were obtained for the reduction of different concentrations of propyl iodide, butyl iodide, and 1-iodo-3-methylbutane at zinc in DMF at 25°C, using $NaClO_4$ (2%) as the supporting electrolyte. The typical curves shown in Fig. 2 and 3 were plotted by points, on recording for each potential the stationary current after ≧3 min of potentiostatic electrolysis.

Propyl iodide and butyl iodide (Fig. 2) are reduced very easily at zinc; indeed, for both the halides the reduction potential is very close to that for zinc dissolution (the dotted part of the curves), for similar concentrations the limiting currents are lower for butyl iodide than for propyl iodide.

The potential shift from the zinc dissolution shown in Fig. 3 for the reduction of 1-iodo-3-methylbutane probably indicates some different pathway followed by this reaction: in addition the limiting currents obtained with this halide are substantially lower than for other alkyl iodides.

The steady-state current-potential curves obtained for the reduction of propyl bromide and butyl bromide using TBAP (2%) as the supporting electrolyte are shown in Fig. 4. In contrast with the previous results one can observe the very negative potentials necessary for obtaining appreciable reduction currents.

Oxidation of zinc alkyls at lead and tin.—Figures 5 and 6 show the steady-state current-potential curves referring to the various systems which may oxidize lead and tin during the synthetic process: the curves were obtained in DMF at 25°C using TBAP (2%) as the supporting electrolyte.

The most anodic curve of Fig. 5 refers to the system TBAP/DMF in the absence of any depolarizer: since the macroscale electrolysis gave no practical metal dissolu-

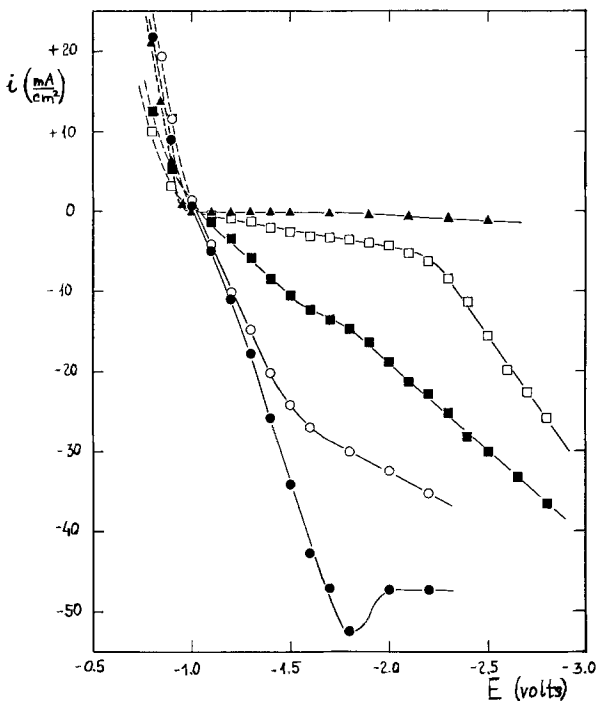


Fig. 2. Steady-state current *(i)*-potential *(E)* curves for propyl and butyl iodides at zinc electrode in DMF at 25°C. The dotted part of the curves is due to zinc oxidation. $[C_3H_7I]$ is equal to: (●) 1.050 mole liter^{-1}; (○) 0.525 mole liter^{-1}. $[C_4H_9I]$ is equal to: (■) 0.437 mole liter^{-1}; (□) 0.218 mole liter^{-1}. (▲) Steady-state curve of the system DMF/$NaClO_4$.

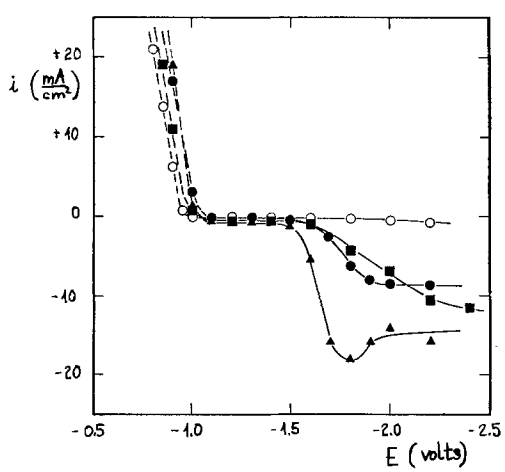


Fig. 3. Steady-state current-potential curves for 1-iodo-3-methylbutane at zinc electrode in DMF at 25°C. $[C_5H_{11}I]$ is equal to: (▲) 0.750 mole liter^{-1}; (■) 0.375 mole liter^{-1}; (●) 0.187 mole liter^{-1}; (○) 0.000 mole liter^{-1}.

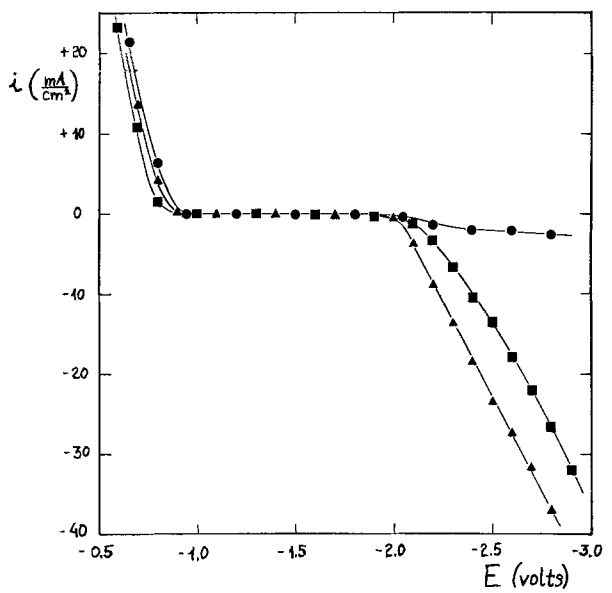


Fig. 4. Steady-state current-potential curves for (▲) $[C_3H_7Br]$ = 0.533 mole liter^{-1}, and (■) $[C_4H_9Br]$ = 0.464 mole liter^{-1}, at zinc in DMF at 25°C. (●) Steady-state curve for the system DMF-TBAP.

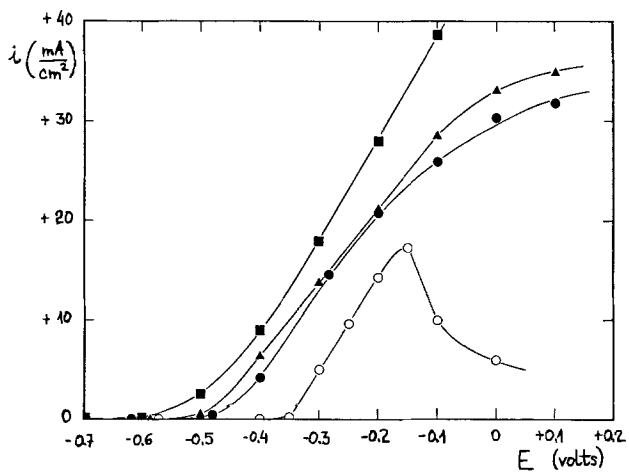


Fig. 5. Oxidation current-potential curves at lead in DMF at 25°C. (○) DMF-TBAP without any depolarizer. (●) $[I^-]$ = 0.315 mole liter^{-1}. (▲) Zinc propyls = 0.086 mole liter^{-1}. (■) Zinc butyls = 0.171 mole liter^{-1}.

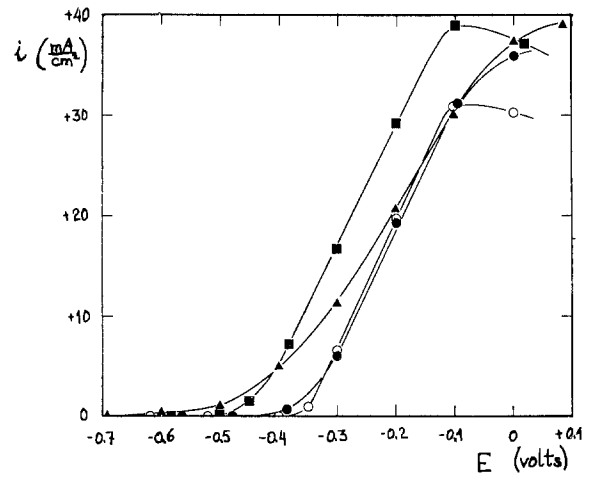


Fig. 6. Oxidation current-potential curves at tin in DMF at 25°C. (○) DMF-TBAP without any depolarizer. (●) $[I^-]$ = 0.315 mole liter^{-1}. (▲) Zinc propyls = 0.457 mole liter^{-1}. (■) Zinc butyls = 0.105 mole liter^{-1}.

tion under these conditions, the process may likely be ascribed to solvent oxidation, products of which are probably responsible for anode passivation at increasing potentials.

The full points of Fig. 5 refer to the anode reaction obtained in the presence of iodide ions (0.315M): the dissolution of the anode with a 2 F/g at. stoichiometry by macroelectrolysis suggests that in this case the lead oxidation is catalyzed by I^- ions.

These results were not appreciably affected when minor amounts of alkyl iodides were added to the systems above.

The subsequent curves of Fig. 5 were recorded in the presence of propyl and butyl zinc derivatives (probably a mixture of mono and dialkyl zinc compounds). For zinc propyls the resulting anodic process (triangles in Fig. 5) practically overlaps with the full points curve, but the direct oxidation of zinc butyls may be deduced from the shift of the electrode process (square in Fig. 5) to more cathodic potential and the substantial current increase.

For similar experimental conditions the oxidation data obtained at tin anode reproduce the behavior described above as can be seen from Fig. 6.

Discussion

The low reactivity at 25°C of unpolarized zinc sheets with propyl and butyl iodides indicates that the possible intervention of either the chemical reaction

$$RI + Zn \rightarrow RZnI \qquad [1]$$

or a spontaneous corrosion process

$$\text{anodic } Zn \rightarrow Zn^{2+} + 2e^-$$

$$\text{cathodic } RI + Zn + e^- \rightarrow RZn^{\cdot} + I^- \qquad [2]$$

which could be important with lower alkyl iodides, is not substantial under the experimental conditions of Tables I-II.

On the other hand, as was previously observed, the cathodic process cannot be explained by a simple electrochemical reaction, since the weight loss of the polarized zinc largely exceeds the provisions of Faraday's law for a sacrificial reduction of the type

$$2RX + 2e^- \xrightarrow{Zn} R_2Zn + 2X^- \qquad [3]$$

where X = I or Br. Consequently, a catalytic process promoted by the electrode potential would appear to be operating; the catalyst is probably a monoalkylate zinc,[2] which once produced at the cathode initiates the formation of zinc alkyls by a chain mechanism similar to that suggested for the reduction of benzyl iodides at mercury (15)

$$RI + e^- \xrightarrow{Zn} RZn^{\cdot} + I^-$$

$$RZn^{\cdot} + RI \rightarrow RZn^+ + I^- + R^{\cdot} \qquad [4]$$

$$R^{\cdot} + Zn \rightarrow RZn^{\cdot}$$

Assuming that this mechanism is valid provides a satisfactory explanation not only for the excessive zinc loss observed in the preparative runs but also for the results of the steady-state experiments. It is apparent that during the reduction of propyl and butyl iodide at zinc, a mixed potential is established mainly as RZn^+ is reduced: under these conditions the reversibility of the reduction curves with the anodic dissolution (see Fig. 2) is readily understood and the decrease in the limiting current when passing from propyl to butyl iodide is explained by a decreased activity of the autocatalytic cycle [4] as the size of the alkyl group is increased.

In the case of 1-iodo-3-methylbutane (Fig. 3), the shift of the reduction to a more cathodic potential (0.5V at 25°C) cannot be due to any great extent to a lower reducibility of the R-I bond for this compound but is probably due to the absence of catalytically produced RZn^+ species. This fact is supported by the loss of polarized zinc at room temperature (Table III, No. 25) which is not far from the provisions of the sacrificial reaction [3].

It is clear that the outline above may be considerably changed when some energy is fed into the system by heating: According to the data of Table III, the catalytic cycle [4] may be activated by a temperature increase, the purely chemical processes of type [1] and [2] become prevailing at 80°C.

The sacrificial route probably occurs during the reduction of alkyl bromides (Fig. 4): In this case the very negative potentials necessary for the cleavage of the R-Br bond decrease the yields of reaction [3] since the free radical intermediates may be further reduced to produce the corresponding hydrocarbons (5). Here the ability of minor amounts of ethyl iodide to cause an excess of butyl bromide to be converted into zinc butyl (Table IV, runs No. 42-46) further underlines the existence of some catalytic process thus emphasizing the occurrence of the radical exchange reactions described by mechanism [4].

It may be noted finally that the reduction of Zn^{2+} ions, either liberated at the anode (discussed at the beginning of this paper) or formed by disproportionation of zinc alkyl iodides (16), may support the cathodic reaction at some stage of the process. When alkyl iodides are used as alkylating agents, this fact does not decrease zinc alkyl formation which only requires the catalytic intervention of the cathode: On the contrary, the reduction of Zn^{2+} ions may conveniently recycle some zinc. On the other hand, when alkyl bromides are used under galvanostatic conditions, as the concentration of Zn^{2+} increases sacrificial reaction [3] may be inhibited, this inconvenience is however eliminated when minor amounts of an easily reduced alkyl iodide are added to the alkyl bromides.

Anodic process.—As was mentioned above, the current yields for the synthesis of lead and tin tetraalkyl derivatives were computed on the basis of the following anodic process

$$4RZnI - 4e^- \xrightarrow{Me} MeR_4 + 4Zn^{2+} + 4I^-$$

$$2R_2Zn - 4e^- \xrightarrow{Me} MeR_4 + 2Zn^{2+} \qquad [5]$$

where Me = Pb or Sn.

This reaction scheme (when substituting Mg for Zn) is usually suggested for Grignard electrosynthesis on the assumption that magnesium alkyls directly oxidize

[2] The peculiarities of lead cathodic alkylation were explained by the catalytic intervention of the monoalkylated species EtPb (14).

to alkyl-free radicals which in turn react with the anode metal (4-6). Indeed, Fleischmann *et al.* found that the oxidation of magnesium ethyl compounds at a lead anode in THF gives current-potential curves with well-formed waves and current plateaus, but the formation of lead-carbon bonds during the electrode process was only inferred from the fact that the oxidation of magnesium ethyls occurs much less readily on an inert electrode (17).

On the other hand, the early observations of Kondyrev (18) show that lead and tin anodes dissolve according to a 2 **F**/g at. stoichiometry in ethereal solutions of Grignard compounds: Furthermore in the Grignard anodic synthesis of tetramethyllead and tetraethyllead the current yields computed on the basis of the above stoichiometry (reactions [5]) often give results close to 200% (6).

The same disconcerting picture is offered here by the steady-state data and from the preparative runs here reported. Thus it seems likely that the formation of lead and tin tetraalkyl derivatives does not follow a single route.

When the potential of the polarization curves of zinc alkyls are a few millivolts less positive than the direct anode oxidation catalyzed by I^- ions (or when the two processes are overlapping as happens for zinc propyls), the anodic reaction in part provides the required oxidized form (Pb^{2+} or Sn^{2+}) of the recipient metal.

Tetraalkyl derivatives are consequently formed by the following reactions

$$Me^{2+} + 2RZnI \rightarrow MeR_2 + 2Zn^{2+} + 2I^-$$

$$2MeR_2 \rightarrow MeR_4 + Me \qquad [6]$$

where Me = Pb or Sn, which may take place homogeneously in the solution. Alkylation of more than 50% of the dissolved anode is accomplished by processes of the type

$$MeR_2 + RI \rightarrow R_3MeI$$

$$R_3MeI + RZnI \rightarrow MeR_4 + Zn^{2+} + 2I^-$$

$$Me + ZnR_2 + 2RI \rightarrow MeR_4 + Zn^{2+} + 2I^- \qquad [7]$$

which most probably occur in the chemical synthesis of lead and tin organoderivatives (3, 19).

On the other hand, when the size and the electron density of the zinc alkyls make their direct oxidation possible at the anode (as for zinc butyls) formation of tetraalkyl derivatives may proceed by reaction [5].

However, the data of the preparative runs suggest that at high zinc alkyl concentration, their direct oxidation again agrees with a two-electron reaction, which would mean that in this case also dialkyl lead (or dialkyl tin) is the main product of the process

$$2RZnI - 2e^- \xrightarrow{Me} MeR_2 + 2Zn^{2+} + 2I^-$$

whereas further alkylation of the unstable MeR_2 species may take place homogeneously by the reactions discussed above.

Acknowledgments

I am indebted to the experimental work of Mr. F. Furlanetto, Mr. B. Facchin, and Mr. G. P. Silvestri of C.N.R.

Manuscript submitted April 27, 1976; revised manuscript received Oct. 20, 1976.

Any discussion of this paper will appear in a Discussion Section to be published in the December 1977 JOURNAL. All discussions for the December 1977 Discussion Section should be submitted by Aug. 1, 1977.

REFERENCES

1. M. Baizer, Editor "Organic Electrochemistry," Marcel Dekker Inc., New York (1973).
2. N. L. Weinberg, "Technique of Electroorganic Synthesis," Vol. I-II, John Wiley & Sons, Inc., New York (1974).
3. G. E. Coates, M. L. H. Green, and K. Wade, "Organometallic Compounds," Vol. I, p. 375, Methuen, London (1967).
4. A. P. Tomilov and I. N. Brago, "Progress in Electrochemistry," p. 261, Plenum Press, London (1971).
5. H. Lehmkuhl in "Organic Electrochemistry," M. Baizer, Editor, p. 261, Marcel Dekker, Inc., New York (1973).
6. G. A. Teodoradze, *J. Organomet. Chem.*, **88**, 1 (1975).
7. H. E. Ulery, *This Journal*, **119**, 1474 (1972).
8. M. Fleischmann, G. Mengoli, and D. Pletcher, *Electrochim. Acta*, **18**, 231 (1973).
9. O. R. Brown, E. R. Gonzales, and A. R. Wright, *ibid.*, **18**, 369 (1973).
10. H. E. Ulery, *This Journal*, **120**, 1493 (1973).
11. G. Mengoli and F. Furlanetto, *J. Electroanal. Chem.*, **73**, 119 (1976).
12. G. Mengoli and S. Daolio, *J. Appl. Electrochem.*, **6**, 521 (1976).
13. G. Mengoli and S. Daolio, *J. Chem. Soc., Chem. Commun.*, **1976**, 97.
14. M. Fleischmann, D. Pletcher, and C. J. Vance, *J. Electroanal. Chem.*, **29**, 325 (1971).
15. N. S. Hush and K. B. Oldham, *ibid.*, **6**, 34 (1963).
16. G. E. Coates, M. L. H. Green, and K. Wade, "Organometallic Compounds," Vol. 1, p. 122, Methuen, London (1967).
17. M. Fleischmann, D. Pletcher, and C. J. Vance, *J. Organomet. Chem.*, **40**, 1 (1972).
18. N. V. Kondyrev, *Ber. Dtsch. Chem. Ges.*, **58**, 459 (1925).
19. V. T. Bychkov and N. S. Vyazankin, *Zh. Obshch. Khim.*, **35**, 687 (1965).

The Kinetics of the Potentiostatic Oxidation of Lead Sulfate Films on Lead in Sulfuric Acid Solution

E. M. L. Valeriote* and L. D. Gallop
Defence Research Establishment Ottawa, Ottawa, Ontario, Canada K1A, 0Z4

ABSTRACT

Models, proposed by Pavlov and Ruetschi to describe the multiphase electrode structure of anodically oxidized lead/sulfuric acid solutions, have been quantitatively tested, modified, and elaborated in accordance with the experimental evidence. The current, during oxidation at constant potential in the region of lead dioxide formation, is shown to be controlled sequentially by at least three diffusion processes, followed by at least two electrocrystallization stages and further intervals of diffusion control. The natures and concentrations of the diffusing species are quantitatively characterized on the basis of kinetic and thermodynamc data. The corresponding values of *p*H in the electrode pores are calculated. A reversal of the *p*H gradient in the pores apparently occurs in close association with the onset of β-PbO_2 production. It is following this stage of the anodic oxidation that the charging kinetics become qualitatively dependent on temperature. At normal temperatures, growth of β-PbO_2 at the expense of lead sulfate occurs. At very low temperatures this process is blocked, resulting in poor subsequent charge acceptance.

Substantial progress has been made during the past ten years (1-12) in characterizing the composition of anodic films on lead in sulfuric acid solutions and in developing theoretical models (5, 7, 9-11) to explain the formation and stability in these films, of divalent lead compounds thermodynamically impossible in an acidic environment. Although the existence and conditions of formation of these compounds are now reasonably well established, only a small amount of semiquantitative work, most notably by the Pavlov school, has been done to study the kinetics of the processes taking place and to determine the relative importance of some of the several mechanisms proposed (5, 6, 9).

In a previous paper (13) the results of a number of electrochemical techniques, applied to the study of anodic oxidation of $PbSO_4$ at temperatures from $-50°$ to 0°C, were discussed. Potentiostatic transient data were found to fit a mathematical model in which current was controlled by two-dimensional nucleation and growth of PbO_2. The quantitative agreement of the data with either a model for progressive nucleation or for instantaneous nucleation was particularly good at low temperature ($\leq -20°C$) over a wide range of overpotentials. Several diffusion-limited processes precede and follow the nucleation and growth period, however, which were discussed (13) without any firm conclusions being reached.

In the present paper a quantitative treatment of potentiostatic current-time transients is presented for all the stages of anodic oxidation of divalent lead in 35% sulfuric acid at normal room temperatures up to the beginning of the formation of β-PbO_2 and oxygen evolution. Data obtained at lower temperatures and by potentiodynamic and other methods will not be discussed in detail except for purposes of comparison, since the thermodynamic data required for their quantitative treatment are not all available.

Experimental

The electrochemical measurements were made using a PAR® Model 170 electrochemistry system (Princeton Applied Research Corporation, Princeton, New Jersey) with auxiliary high impedance recorders and digital meters to facilitate simultaneous determination of current, charge, electrode potential, and other relevant electrochemical parameters.

A rotating disk electrode (RDE) of 0.441 cm^2 area was inserted through a loosely fitting Teflon cap into the main part of the Pyrex three-compartment electrochemical cell. The RDE was rotated only to elaborate certain results obtained when the electrode was stationary. Side compartments, containing counterelectrode (platinized Pt) and reference electrode (Hg/Hg_2SO_4/35% H_2SO_4), were connected to the main cell through 1-2 mm capillary tubing. The connection from the reference compartment entered the main cell at bottom center and narrowed down to a fine capillary tip about 1 mm below the center of the RDE. The lead disk (> 99.995% purity, Cominco, Trail, British Columbia, Canada) was chemically and mechanically polished using standard techniques and electrochemically oxidized to lead sulfate in 35% reagent grade sulfuric acid. Except as otherwise stated, experiments were carried out beginning with a well-cycled electrode maintained at least 1V above the $Pb/PbSO_4$ potential for several days prior to the acquisition of quantitative results. The current was measured as a function of time during a series of potential steps to various constant oxidation potentials. Each charge step was preceded by a constant potential discharge at 0.4V, until the net reduction current had decayed to 3.0 μA.

In order to obtain reproducible current-time transients, care was taken to terminate each charging experiment before the decreasing current, following the nucleation and growth period, had begun to increase substantially once more at the onset of β-PbO_2 formation and oxygen evolution.

Further experimental details have already been reported (13) or are described below where necessary.

Results and Discussion

Theoretical treatment.—For an electrode reaction under potentiostatic control, the current density i, with charge transfer and diffusion rate control, is a function of time according to the relationship (14)

$$i = i(o)\exp(\lambda^2 t)\,\mathrm{erfc}(\lambda\sqrt{t}) \qquad [1]$$

where

$$\lambda = \frac{i_o}{ZF}\left[\frac{1}{C_r D_r^{1/2}}\exp\left(\frac{\alpha ZF}{RT}\eta\right) + \frac{1}{C_o D_o^{1/2}}\exp\left(\frac{-(1-\alpha)ZF}{RT}\eta\right)\right] \qquad [2]$$

and $i(o)$, the current density at $t = 0$ is given by

$$i(o) = i_o \cdot \left[\exp\left(\frac{\alpha ZF}{RT}\eta\right) - \exp\left(\frac{-(1-\alpha)ZF}{RT}\eta\right)\right] \qquad [3]$$

* Electrochemical Society Active Member.
Key words: models, charging, diffusion, basic sulfates, oxides.

Under normal potentiostatic conditions, λ (as defined by Eq. [2]) is a constant which depends on the electron exchange and mass transfer parameters, whereas $i(o)$ is independent of mass transfer.

The current density is thus determined by the time t, the overpotential η, the exchange current density i_o, the transfer coefficient α, the charge transfer valency Z and the equilibrium concentrations C_o, C_r and diffusion coefficients D_o, D_r of the oxidized and reduced species.

In the limit of very small time, the current density is proportional to $\sqrt{t}$ according to

$$i = i(o)\,[1 - 2\lambda t^{1/2}/\pi^{1/2}] \text{ for } \lambda t^{1/2} << 1 \qquad [4]$$

At large values of time the current becomes proportional to $t^{-1/2}$

$$i = i(o)/\lambda\sqrt{\pi}t^{1/2} \text{ for } \lambda t^{1/2} >> 1 \qquad [5]$$

Although λ and $i(o)$ are dependent on i_o and α, the combination $i(o)/\lambda$ is not and is given by

$$\frac{i(o)}{\lambda} = \frac{ZFC_oC_r\sqrt{D_oD_r}\cdot[1 - \exp(-ZF\eta/RT)]}{C_o\sqrt{D_o} + C_r\sqrt{D_r}\exp(-ZF\eta/RT)} \qquad [6]$$

At high positive overpotentials, $i(o)/\lambda = ZFD^{1/2}C$ where $C_r\sqrt{D_r}$ has been replaced by $D^{1/2}C$ for the purposes of this study. Thus, using the slope and intercept of the linear i-$\sqrt{t}$ dependence one obtains from Eq. [4]

$$D^{1/2}C = -2i(o)^2/ZF\sqrt{\pi}(di/dt^{1/2}) \quad \text{for} \quad \lambda t^{1/2} << 1 \qquad [7]$$

and for the linear i-$t^{-1/2}$ dependence from Eq. [5]

$$D^{1/2}C = \frac{\sqrt{\pi}}{ZF}\left(\frac{di}{dt^{-1/2}}\right) \quad \text{for} \quad \lambda t^{1/2} >> 1 \qquad [8]$$

These equations were applied to the analysis of the diffusion-controlled portions of potentiostatic current-time transients obtained at various temperatures from $-50°$ to $+25°$C.

A current-time transient for a selected run at 25°C is given in Fig. 1 to illustrate the general dependencies observed at all temperatures. This particular run was obtained at a potential of 1.1V with respect to the Hg/Hg_2SO_4/35% H_2SO_4 reference electrode, to which all potentials in this paper are referred, and is plotted against two time scales in order to indicate all of the time intervals analyzed. Intervals A to I are labeled on the more sensitive time scale (0-20 sec) and I to J are labeled for longer times.

Pre-nucleation-and-growth diffusion-limited currents.—In interval A, where $t \leq 0.1$ sec, no data were extracted due to the limitations of recorder response time. During this period, double layer charging and the charge transfer reaction would be expected to control the current. Because of the high electrode resistance (13), at $t = 0$ the time constant for double layer charging is appreciable (~ 0.01 sec) but the process is complete well before $t = 0.1$ sec.

For $t \geq 0.1$ sec, the linear relationships between i and $\sqrt{t}$ (interval B) were obtained at potentials from 0.9 to 1.4V (Fig. 2a, inset). Values of $i(o)$ and λ were extracted using Eq. [4] and the region of linearity was found to extend up to values of $\lambda t^{1/2} \leq 0.36$.

Two linear i-$t^{-1/2}$ regions were obtained during intervals C and D (Fig. 2b). The first (C, right-hand side of Fig. 2b) had a slope very nearly twice that of the second segment (D), suggesting a sudden halving of the value of Z or $D^{1/2}C$ (Eq. [8]). The linearity occurred for values of $1 > \lambda\sqrt{t} \geq 0.3$, assuming a value of λ derived from the i-$t^{1/2}$ plots. However, Eq. [8] is only valid for $\lambda\sqrt{t} >> 1$. Values of λ in the range 0.45-0.84 were obtained from the i-$\sqrt{t}$ plots. For these values of λ, t must be greater than 35 sec in order that

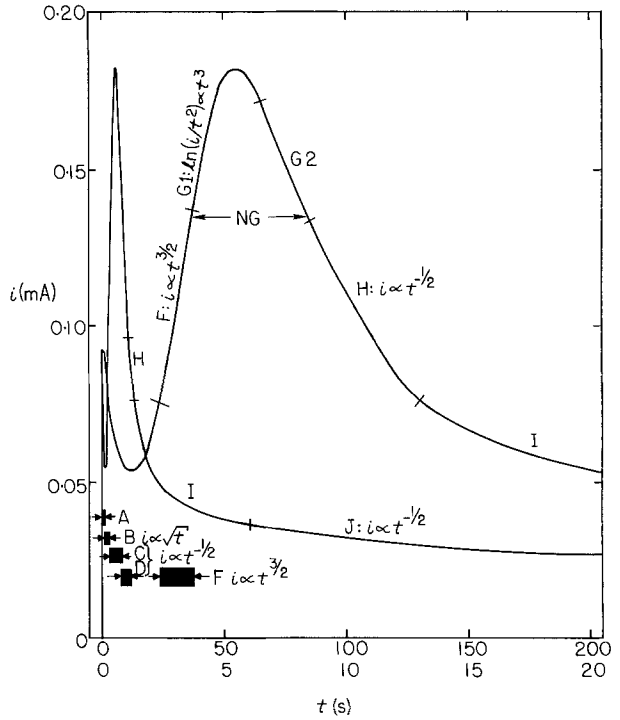


Fig. 1. Potentiostatic anodic transient at 25.0°C, 1.1V (Hg/Hg_2SO_4), for 0.44 cm^2 "lead sulfate" disk electrode in 35% sulfuric acid solution, following a 0.4V discharge to 3.0 μA reduction current. Current-time dependencies were determined as indicated on the curve plotted on the more sensitive (0-20 sec) time scale for intervals B-H. The same transient, showing interval H-J, is also plotted on the 0-200 sec time scale.

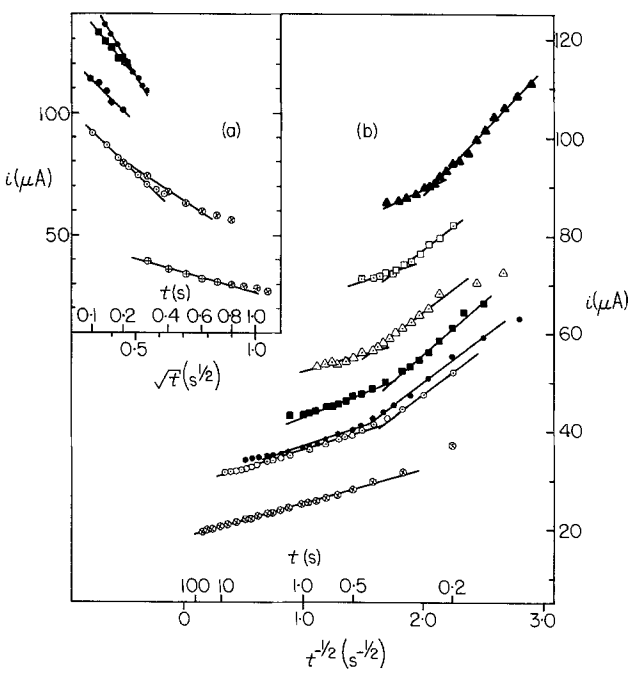


Fig. 2. Current vs. (a) $\sqrt{t}$ (inset) and (b) $t^{-1/2}$ dependencies for intervals B, C, and D of Fig. 1 at various charging potentials: ⊕, 0.9V; ⊗, 1.0V; ⊙, 1.1V; ●, 1.2V; ■, 1.3V; ⧋, 1.4V; □, 1.5V; ▲, 1.6V.

$\lambda\sqrt{t}$ be greater than 5 and therefore the linearities of i *vs.* $t^{-1/2}$ observed at $t < 35$ sec must correspond to diffusion processes involving different species than that responsible for the linearity of i *vs.* $\sqrt{t}$, or to drastically different conditions of concentration or electroactive area. For the i-$t^{-1/2}$ lines, the value of λ must be greater than 12 in order to satisfy $\lambda\sqrt{t} > 5$ for the linear portions of Fig. 2b. From Eq. [2] at a high value

of overpotential, λ is a function of $D^{1/2}C$ and of the electron exchange parameters i_o and α. To what extent are changes in each of these terms responsible for the increase of λ?

If different electron exchange processes are involved for the linearities observed in Fig. 2a and 2b, the values of i_o would be expected to differ. From Eq. [2], at high overpotentials, a plot of ln λ as a function of electrode potential should give a straight line, the slope of which can be used to calculate the anodic transfer coefficient, α. Although a large scatter was observed, the value of $Z\alpha$ determined by such a plot was 0.04 ± 0.01. Such a value is unusually low in comparison to the value of $\alpha = 0.5$ normally assumed for heterogeneous electron exchange and indicates an oxidation step in which, for $Z = 1$, only about 4% of the applied overpotential is effective in determining the rate of the current-limiting process. Further evidence for low values of α are obtained from the data for intervals C and D (Fig. 2b). Equation [5] requires that the i-$t^{-1/2}$ dependencies have a zero current intercept at infinite time, whereas positive intercepts were always observed. This suggests that either there is spherical or other nonlinear diffusion occurring or that a steady-state oxidation process is taking place in parallel with a linear-diffusion-controlled process. In order that Eq. [5] represent the total observed current, rather than only the diffusion-limited current, a second constant term i_∞ should be added which represents the intercept at $t^{-1/2} = 0$. i_∞ was a function of potential and was found to obey a Tafel relationship with a very large Tafel slope, corresponding to $Z\alpha = 0.10 \pm 0.02$ for interval C and $Z\alpha = 0.06 \pm 0.01$ for interval D.

Low values of α (0.05-0.2) have been reported for some other electrode reactions in which the reactant species is a divalent cation in a nonspecifically adsorbed electrolyte (15). The cathodic transfer coefficients reported for the reduction of Cd(II) in nonspecifically adsorbed electrolytes had values ≤ 0.15. For 0.5M K_2SO_4 at pH = 2, the electrolyte most closely resembling sulfuric acid, an approximate value of 0.08 was obtained. Such low values have been attributed to an electron exchange process in which the slow step is a heterogeneous chemical process. In the case of reduction of Ni^{++} in $NaClO_4$ solutions, for example, values of $\alpha \sim 0.05$ have been attributed to rate control by the partial dehydration of the Ni ion at the interface. Such a very low value as 0.04 could also be due to a slow preceding homogeneous dissociation step (15).

It seems reasonable to consider that the sharp increase in λ at the end of the linear i-$\sqrt{t}$ region is at least partially due to an increase in α. However, an increase of $Z\alpha$ from 0.04 to any value greater than 0.2 would also result in a much stronger dependence of λ on potential, and therefore of the time of the beginning of the linearity of the i-$t^{-1/2}$ plots on potential, than was observed (Fig. 2b). Hence the observed increase in λ by a factor of more than 14 must be principally due either to an increase of i_o or to a decrease of $D^{1/2}C$.

Values of $D^{1/2}C$, calculated from the data for intervals B-D are shown in Table I for duplicate sets of experiments with two electrodes. An electrode area equal to the geometrical area of 0.44 cm^2 and the indicated values of Z (to be justified later) were assumed.

Comparison of $D^{1/2}C$ values in the last two columns of Table I with those in the third-to-last column indicates that the values of $D^{1/2}C$ are 10 to 16 times larger during the i-$\sqrt{t}$ linear region (B) compared to the immediately following linear i-$t^{-1/2}$ region (C). This change of $D^{1/2}C$ could account almost completely for the over fourteenfold increase in λ. Since a substantial increase of α is not indicated, the change in i_o must also be relatively unimportant, suggesting that an equally rapid electron exchange reaction is probably occurring for both values of λ but that the rate-controlling step or the electroactive area has changed.

The $D^{1/2}C$ values, given in Table I, differ by orders of magnitude from any corresponding to species in bulk solution. Furthermore, as at low temperatures (13), the inverse dependence of diffusion current on disk rotation rate was in complete contradiction to a model including current limitation by diffusion from the bulk electrolyte. Therefore, in order to proceed further in interpreting these results, a model representing the physically and electrochemically changing states of the interface must be assumed. Before attempting this interpretation one final note of caution should be made.

The values of $D^{1/2}C$ given in Table I have all been based on the assumption that the electrode area is the same as that of the initially smooth lead substrate. If the real electrode area is larger or smaller than this geometric area, the values of $D^{1/2}C$ calculated will be proportionately smaller or larger, respectively. However, the values calculated for λ are unaffected since the area term cancels out in the ratio $i/i(o)$ in Eq. [4] and [5]. Hence, if the area had changed appreciably, a fortuitously compensating change in i_o would also have had to occur in order to explain the similar magnitudes of the fractional changes in λ and $D^{1/2}C$.

Elaboration of the model.—It is now well established that the interior of anodic films formed on lead in aqueous sulfuric acid solutions, over a wide range of potentials, consists of several chemical species, thermodynamically unstable in acid solutions. An excellent review of the literature up to 1969 has been published by Burbank *et al.* (1), in which many of these species and the approximate electrochemical conditions of formation have been schematically illustrated and discussed. In addition to the electrochemical methods, the identification techniques applied have been x-ray and electron diffraction, optical and electron microscopy, and chemical analysis.

Pavlov model.—More recently, further refinement of a model of the anodic film has become possible based on the previous work and on additional experimental and theoretical studies (2-11). Pavlov and co-workers (2-7,

Table I. 25°C, Constant potential charge following a discharge to 3.0 μA reduction current at 0.4V

Charging potential (V)	i-$\sqrt{t}$ (Fig. 2a, electrode 2) No. of runs	λ	$\lambda t^{1/2}$ at end of linear region (B)	$D^{1/2}C$ ($Z = 1$) $\times 10^9$	i-$t^{-1/2}$ (Fig. 2b, electrode 1) $D^{1/2}C \times 10^{10}$ $Z = 2$ 1st linear region (C)	$Z = 1$ 2nd linear region (D)
0.9	1	0.45	0.36	2.78	—	—
1.0	3	0.61 ± 0.06	0.30 ± 0.04	4.62 ± 0.34	—	2.8
1.1	2	0.65 ± 0.03	0.22 ± 0.02	3.96 ± 0.24	3.8	3.4
1.2	2	0.81 ± 0.04	0.18 ± 0.03	5.42 ± 0.76	3.9	3.7
1.3	1	0.61	0.13	6.72	4.3	4.1
1.4	1	0.84	0.15	9.96	4.0	3.1
1.5		—	—	—	3.9	3.5
1.6		—	—	—	5.3	4.9
				Electrode 1 mean	4.2 ± 0.4	3.6 ± 0.5
				Electrode 2 mean	4.6 ± 0.9 (0.9-1.3V)	5.1 ± 0.7 (0.9-1.3V)

10) have correlated the composition of the anodic layer, as determined by x-ray diffraction studies of potentiostatically formed films, with measurements of current, charge, applied potential, and electrode capacitance (2, 4). Earlier ambiguities in the assignment of diagnostic diffraction lines were resolved by correlation with chemical analytical determinations (2). Under galvanostatic conditions of formation, the x-ray diffraction results were correlated as a function of time with electrode potential, capacitance, resistance, and electron microscopic observations (3). Phase compositions were also determined at the surface and over cross sections of positive plates (6) and of negative plates (7) using the electron microprobe and these were related to measurements of the density of the sulfuric acid, x-ray diffraction intensities, porosity, and surface pore size distribution as a function of time. As a result of this work, the potential interval lying between the equilibrium potential of the $Pb/PbSO_4$ electrode (−956 mV with respect to the $Hg/Hg_2SO_4/1N$ H_2SO_4 reference electrode) and the onset of appreciable oxygen evolution (by about +1400 mV) can be divided into three major regions (2, 4, 6):

1. −956 to −400 mV where the anodic film consists of $PbSO_4$ deposited on the lead substrate.

2. −400 to ~ +900 mV where the film consists predominantly of tetragonal PbO together with small amounts of the basic sulfates of lead, of $5PbO \cdot 2H_2O$ or orthorhombic PbO and of α-PbO_2 beneath a layer of $PbSO_4$. The PbO-tet is commensurate in quantity with the $PbSO_4$ which protects the PbO from attack by the acid electrolyte. The composition of the interior of the film as a function of applied potential could be further subdivided, although with some loss of accuracy. Diffraction lines for monobasic lead sulfate, $PbO \cdot PbSO_4$, appeared at potentials more positive than −400 mV (2). This diffraction line (at 2.95Å) was later (6) reassigned to $2PbO \cdot PbSO_4$ on the basis of comparison with other diffraction lines, but no confirmatory evidence for the reassignment has been published. Tetragonal PbO appeared at −300 mV. At −200 mV the amounts of PbO-tet and mono (or di) basic lead sulfates remained small compared to $PbSO_4$ even after 70 hr of oxidation and tribasic sulfate was detected. Diffraction lines due to either $5PbO \cdot 2H_2O$ or to PbO-orth were obtained at potentials $\geq$ 0. At +300 mV PbO-tet and $PbSO_4$ were present in approximately equal amounts following the initial formation of the protective $PbSO_4$ layer. α-PbO_2 was detected above +500 mV but in very small concentrations below +900 mV.

The existence of hydrated lead monoxide and tribasic sulfate within these films may be the reason for the existence of a chemically bonded form of hydrogen present in electrochemically formed PbO_2 film, which is not present in chemically prepared PbO_2. Caulder *et al.* (16), using DSC, found that this hydrogen was associated with the evolution of water at 180°C and showed, using NMR, that the hydrogen-hydrogen separation exceeded 2Å and was therefore not due to the presence of free water molecules. No suggestions for the chemical nature of the species were offered (16, 17), but the disappearance of this form with increased cycling (17) may be due to the disappearance of hydrated divalent lead compounds. Also relevant to this are the observations by Simon *et al.* (18) that positive plates, formed after high temperature curing, contained a high proportion of electrochemically inactive PbO_2 (and by inference, less of the different form of hydrogen) which formed on an unusually large number of tetrabasic lead sulfate crystals. Hydrated lead monoxide as $5PbO \cdot 2H_2O$ is not stable at temperatures above 60°C and tribasic sulfate above 80°C (19), but instead form tetrabasic sulfate or other anhydrous compounds.

3. > 900 mV where the content of divalent lead species decreases with increasing potential and that of α-PbO_2 increases in the interior of the film. The composition depends strongly on oxidation potential and oxidation time. The major component of the anodic layer beneath the $PbSO_4$ is α-PbO_2 at 1000 mV. At potentials $\geq$ 1200 mV, the $PbSO_4$ is oxidized to β-PbO_2 in an acidic environment near the electrode surface following the prior formation of α-PbO_2 in the alkaline interior.

Pavlov-Ruetschi model.—Theoretical models to explain the creation and maintenance of an alkaline interior, which is necessary for the formation of the basic sulfates, lead monoxide, and α-PbO_2, have been developed (5, 7, 9-11). In the model developed by Ruetschi (11), when the lead sulfate layer, formed anodically or by corrosion, becomes sufficiently thick (> 1 μm), macropores (or intercrystalline spaces) become practically closed. Experimental evidence was presented (11) to show that the lead sulfate then becomes essentially impermeable to $SO_4^=$, HSO_4^-, and Pb^{++} but remains permeable to H^+, OH^-, certain other ions, and probably H_2O. Corrosion of Pb beneath the $PbSO_4$ layer, or precipitation of anodically generated Pb^{++}, results in migration of H^+ away from the electrode interface due to the hindered diffusion of other ions. This creates a basic environment in the interior of the electrode, between the lead substrate and the protective lead sulfate, and generates a considerable diffusion potential across the lead sulfate layer.

Values of *p*H equal to that of the bulk solution, pH_s, were assumed (11) in the case of potential-determining sites at the electrode surface, where reactant species enjoy unhindered access to the electrolyte. In this case, no diffusion potential exists across the $PbSO_4$ layer and electrode potentials can be calculated directly from the potential-determining electrochemical couple.

When the electrochemical reaction occurred beneath the $PbSO_4$ layer, in the electrode interior, a value of pH_i was calculated by consideration of equilibria between species known to be present. Two cases were considered: (*i*) the equilibrium conditions for coexistence of $PbSO_4$ and $PbO \cdot PbSO_4$, which yielded a value of $pH_i = 6.35$ and a value of diffusion potential, E_d, of 0.405V for 4.2M H_2SO_4 bulk electrolyte; (*ii*) the equilibrium corresponding to minimum solubility of PbO (20), which results in a value of $pH_i = 9.34$ and $E_d = 0.581$V.

Whether PbO exists in the form PbO-tet, PbO-orth, $Pb(OH)_2$, or $5PbO \cdot H_2O$ has no significant quantitative effect on the calculation of electrode potentials or *p*H. Hence the use here of the general term PbO implies that no distinction is being drawn between these polymorphs.

The potential between the lead substrate and a reference electrode at the electrode/solution interface, E_r, includes the diffusion potential, which must be added to a calculated reversible potential, E, for an assumed electrochemical couple, in order to make a comparison with experimentally observed reversible potentials. Assuming that E was controlled by the equilibria between Pb or PbO_2 and $PbSO_4$, basic sulfates or PbO, Ruetschi (11) calculated $E_r = E + E_d$, and compared these values with experimental arrest potentials, observed during open-circuit discharge of anodic films, formed potentiostatically on lead. Good agreement was reported between the calculated and observed potentials.

There seems to be no fundamental reason for Ruetschi's choice of a value of $pH_i = 9.34$, corresponding to minimum solubility of PbO. Solid PbO may coexist in equilibrium with its saturated solution and basic lead sulfates over a range of *p*H. Although the experimental evidence supports the assumption of case (*i*) above, with $pH_i = 6.35$, it does not necessarily support case (*ii*) with $pH_i = 9.34$. As duly noted (11), the electrochemical reactions of PbO with both Pb and PbO_2 have a potential dependence, E, of 59 mV/*p*H unit, thus

exactly canceling the dependence of E_d on pH_i. Although the choice of pH_i determines the calculated value of E_d, it has no effect on the calculated value of E_r for the reactions involving PbO. Hence the reported agreement with experiment would not have been altered by a choice of values of pH_i based on other meaningful assumptions. It might be more correct to replace assumption (*ii*) above by one based on the conditions for coexistence of equilibria between $PbSO_4$ and $3PbO \cdot PbSO_4 \cdot H_2O$ or PbO with constituents of the pore solution. Hence, in a similar manner as for case (*i*) above, values of pH_i can be calculated, based on equilibrium solubility-pH (19) or potential-pH (12) relationships, for the coexistence of $PbSO_4$ and basic sulfates or PbO, at a sulfate ion activity, corresponding to the solubility product of $PbSO_4$ ($a_{Pb^{++}} = a_{SO_4^{=}} = 10^{-3.9}$ mole liter^{-1}). Such calculated pH_i values, which are thus average values corresponding to mixed potentials, are given in Table II.

The values of pH in Table II were calculated using the equations of Ruetschi and Angstadt (9) and Pavlov (12). The small concentration gradients of hydroxyl and sulfate ions, which must exist in the solution between the phases (except for the first entry), have been neglected. The calculation of $PbOH^+$ concentration is discussed in a later section. It should be noted that the first value of pH 6.7 for the coexistence of $PbSO_4$ and $PbO \cdot PbSO_4$ disagrees with the value of pH 6.35 calculated by Ruetschi (11) because Ruetschi used the equations of Bode and Voss (19) based on somewhat different thermodynamic data. If one uses the thermodynamic data of Ruetschi and Angstadt (9) and a value of $\Delta G^\circ(Pb^{++}) = -5.81$ kcal/mole, corresponding to $E^\circ = -0.126$V (21), to calculate the expressions given in Bode and Voss's Table 3, different constants are obtained for all the equations containing $a_{Pb^{++}}$ [Eq. [2], [4], [6], and [8], Ref. (20)]. However, the remaining equations appear to be consistent. Combinations of the equations of Ruetschi and Angstadt with the equilibrium equation: $Pb^{++} + 2e = Pb$; $E = -0.216 + 0.0296 \log a_{Pb^{++}}$ gives the same revised values of the constants as are obtained from the thermodynamic data. The errors in the Bode and Voss calculations appear to be due to inconsistent thermodynamic data. Accordingly, the more consistent data (9) were used for the calculated values shown in Table II. Values of pH_i, corresponding to coexistence of $PbO \cdot PbSO_4$ and $3PbO \cdot PbSO_4 \cdot H_2O$, in equilibrium with the pore solution were similarly calculated and have also been included in Table II.

Possible supporting evidence for the existence of such pseudoequilibrium pH_i values, lower than the value of 9.34, assumed by Ruetschi, is presented below. However the choice of pH_i value does not qualitatively alter the conclusions of Ruetschi (11), and would have only a minor quantitative effect on the thermodynamical arguments presented in support of a detailed multiphase model of the lead acid electrode structures.

This model is essentially similar to that proposed earlier by Pavlov (12) and others (1, 19) but differs in the assignment (3, 10) of the equilibria determining open-circuit and galvanostatic arrest potentials. Thus Pavlov presented similar thermodynamical arguments (12) for the case of an alkaline interior of pH 7.8-9.2 in 1*N* H_2SO_4, but the diffusion potential across the lead sulfate layer was not considered. The Pavlov school also presented much more detailed analytical evidence and interpretation of the mechanisms of the electrode reactions (5-7) and attempted a finer discrimination between the roles of the basic sulfates of lead.

Since the models are generally compatible, differing principally in the detail of interpretation of experimental results, use of both models will be made as the basis for further interpretation of the present experimental results.

Interpretation.—Prenucleation-and-growth processes in order of appearance.—For the experiments described, the electrode potential had been previously maintained well above the $Pb/PbSO_4$ potential for several days or weeks. It may, therefore, be assumed that the protective lead sulfate layer had essentially attained its maximum thickness. Prior to each potentiostatic oxidation step, the electrode was maintained at 0.4V until the reduction current had decayed to 3.0 μA. At 0.4V, following prior oxidation to PbO_2, the observed net reduction current consists of a current component for PbO_2 reduction, superimposed on a smaller background oxidation current due to anodic corrosion of lead. Eventually except at low temperatures, a net oxidation current may be observed if the potential is held at 0.4V for a long period of time According to Ruetschi's model (11), immediately before application of the potential step the electrode should consist of a thick layer of PbO ($\sim$ 1 μm) on the lead substrate (with possible traces of α-PbO_2) covered by a relatively thin layer of basic sulfates, increasing in $PbSO_4/PbO$ ratio toward the electrolyte surface, and finally a thick ($\sim$ 1 μm) layer of $PbSO_4$. The initial pH of the solution in contact with PbO at the reaction site in the electrode pores will be taken as 8.5, and the $a_{SO_4^{=}}$ as $10^{-3.9}$ (Table II). These activities arise partly as the result of consumption of acid and production of water during the immediately preceding discharge. They are also due to the chemical corrosion and electrochemical background oxidation of the lead substrate under conditions of hindered diffusion of lead and sulfate ions (11, 12) out of and into the $PbSO_4$ pores, respectively. In order to maintain electroneutrality in the pores, some of the corrosion current must be carried by the more mobile H^+ or OH^- ions leading to alkalinization of the pore solution. A zone of crystallization of $PbSO_4$ will be established in the pores at some distance from the metal (10) and a solution supersaturated with respect to $PbSO_4$ will be established in the region where the opposite Pb^{++} and $SO_4^{=}$ ionic flows meet one another. The alkalinization will occur on the metal side of this precipitation zone where $C_{Pb^{++}} > C_{SO_4^{=}}$ (10).

In alkaline solutions, reaction between Pb^{++} and OH^- ions favors the formation of ionic hydroxy complexes such as $Pb(OH)^+$, $Pb(OH)_3^-$, and $HPbO_2^-$ in addition to the solid phases (10) already described. Thermodynamic calculations, based on stability constants (22 a-f) or other thermodynamic data (11, 19), indicate that for pH $\leq$ 9, the concentrations of $HPbO_2^-$ and of $Pb(OH)_3^-$ ($\leq 10^{-5}$M) are insignificant in comparison to that of Pb^{++} or $PbOH^+$ and can reasonably be neglected even at pH 10. Values of stability or hydrolysis constants for $PbOH^+$ at 25°C have been variously reported, with stability constants ranging from $10^{6.1}$ (22b) to $10^{7.8}$ (22a). An intermediate value of $10^{6.9}$, obtained polarographically (22c), was arbitrarily assumed in order to calculate $[PbOH^+]$, already given (Table II). The concentration of $PbOH^+$ exceeds that of Pb^{++} for pH > 7.1, independently of the $a_{SO_4^{=}}$ and, hence, $PbOH^+$ must be considered in interpreting the experimental data.

A value of $C = [Pb(OH)^+] = 3.2 \times 10^{-3}$M at pH = 8.5 (Table II) can be used to determine a value of the diffusion coefficient from the values of $D^{1/2}C$ in Table I corresponding to the linear i-$\sqrt{t}$ region of Fig. 2a, obtained in interval B between 0.1-0.5 sec fol-

Table II

Coexisting phases in aqueous H_2SO_4 solution	log $a_{Pb^{++}}$ = −3.9 mole/liter; log $a_{SO_4^{=}}$ = −3.9 mole/liter: Equilibrium pH_i	[$PbOH^+$] (M)
$PbSO_4/PbO \cdot PbSO_4$	6.7	5.0×10^{-5}
$PbSO_4/3PbO \cdot PbSO_4 \cdot H_2O$	6.9	7.9×10^{-5}
$PbO \cdot PbSO_4/3PbO \cdot PbSO_4 \cdot H_2O$	7.3	2.0×10^{-4}
$PbSO_4/4PbO \cdot PbSO_4$	8.0	1.0×10^{-3}
$PbSO_4/PbO$	8.5	3.2×10^{-3}

lowing application of the potential step. An average value of $D \sim 3 \times 10^{-6}$ cm^2 sec^{-1} was thus obtained. At pH = 8.0, potential-dependent values of $D = 0.8 \times 10^{-5}$ to 9.9×10^{-5} cm^2 sec^{-1} were obtained with an average of 3×10^{-5} cm^2 sec^{-1}, a reasonable value for the diffusion of a monovalent cation in aqueous solution. In view of the uncertainty in the choice of the stability constant used to calculate [Pb(OH)$^+$], the uncertainty in the calculated diffusion coefficient is at least one order of magnitude. Thus it is possible to deduce only an approximate average pH under the experimental conditions for which Eq. [7] is valid. The experimental values of $D^{1/2}C$, however, were determined much more accurately, so that the potential dependence of $D^{1/2}C$ clearly indicates that pH_i differed as a function of the constant applied potential. If one proceeds from the opposite point of view, therefore, and assumes a particular value of D, which is a constant characteristic of the PbOH$^+$ ion, and uses the experimental values of $D^{1/2}C$, a much more accurate estimate of [PbOH$^+$] can be made. From this, pH values can be calculated with a large but constant uncertainty ($\sim$ 0.5 pH units), but the relative variation of pH with potential can be determined with the higher accuracy of the experimental $D^{1/2}C$ values. A value of $D = 2 \times 10^{-5}$ cm^2 sec^{-1} [*cf.* monovalent ions of comparable size (21)] was thus assumed in order to obtain the results given in Table III.

Although there may be a constant correction for each of the values of pH in Table III, the differences will be relatively accurate. There thus appears to be a definite increase in the pH within the pores as a function of electrode potential during this diffusion-limited period. If the pH was initially controlled at pH = 8.5 (Table II) or greater, some decrease of pH may have taken place during the prior double layer charging interval. Since the linear i-$\sqrt{t}$ region begins later and lasts for a longer time at lower overpotentials and since the currents are smaller, a larger decrease of pH can occur as PbO is consumed, and more nearly equilibrium values of pH exist.

Immediately following this process, the two linear i-$t^{-1/2}$ regions (Fig. 2b) which were observed must correspond to different processes, as discussed earlier. During the first of these processes ($t \lesssim 0.4$ sec), the slope observed showed no significant potential dependence. An oxidation state of $Z = 2$ was postulated. Assuming that this species is Pb^{++} at a concentration of $10^{-3.9}$M, a value of $D = 1.1(\pm 0.1) \times 10^{-5}$ cm^2 sec^{-1} was calculated from the values of $D^{1/2}C$ of Table I. This is in good agreement with the published (21) value of 0.98×10^{-5} for Pb^{++} at infinite dilution.

The second linear i-$t^{-1/2}$ region in Fig. 2b, has a slope, again with no significant potential dependence, of one-half that of the first region. A diffusing species with $Z = 1$ and $D = 2 \times 10^{-5}$ cm^2 sec^{-1} was therefore assumed, and a value of $C = 8.1(\pm 1.1) \times 10^{-5}$M was calculated from the $D^{1/2}C$ values of Table I. If this species is again assumed to be PbOH$^+$, a pH of 6.9 can be calculated, as before. Inspection of Table II suggests that during this interval the pH is controlled at a fairly constant value by equilibria involving $PbSO_4$ and $3PbO \cdot PbSO_4 \cdot H_2O$ and/or $PbO \cdot PbSO_4$.

A problem of interpretation arises in attempting to explain why diffusion control should shift from PbOH$^+$ to Pb^{++} and then back again to PbOH$^+$ at potentials greater than 1.0V. According to the processes of formation postulated by Pavlov and Iordanov (4), at 0.4V, before application of the potential step, the spaces beneath the lead sulfate are filled with basic sulfates and PbO. The latter covers the underlying lead (see Fig. 6a). Immediately following application of the potential step, and double layer charging, we may postulate that the current is limited by the rate of dissolution of PbO or $Pb(OH)_2$ at the lead surface. This would explain the very low value of $Z\alpha$, for the electron exchange reaction, as being due to this preceding slow chemical dissolution.

Table III

Charging potential (V)	$D^{1/2}C \times 10^9$ (Table I)	C = [PbOH$^+$] ($D = 2 \times 10^{-5}$ cm^2 sec^{-1}) (M)	pH_i ($a_{Pb^{++}} = 10^{-3.9}$)
0.9	2.78	6.20×10^{-4}	7.8
1.0	4.62	1.03×10^{-3}	8.0
1.1	3.96	8.9×10^{-4}	7.9
1.2	5.42	1.21×10^{-3}	8.1
1.3	6.72	1.50×10^{-3}	8.2
1.4	9.96	2.2×10^{-3}	8.3

Bode and Voss (23) have pointed out the close similarities in the structures of lead, tetragonal PbO, and α-PbO_2. Thus we might expect that the α-PbO_2 formed could easily deposit on either the exposed lead or on the PbO surface. Initially the deposition should begin on the only available electronically conducting phase, the lead. During the linear i-$\sqrt{t}$ region, diffusion of PbOH$^+$ to the lead therefore becomes rate controlling. The amount of charge passed up to the end of interval B corresponds to less than a monolayer of Pb covered by PbO_2. Since PbO_2 is electronically conducting, the electron exchange sites may now shift from the lead to the PbO_2 and the latter can extend itself further into the PbO deposit as isolated growing filaments. This process, as has been shown, is limited at first by diffusion of Pb^{++} ions at potentials $\geqq$1.1V, then by diffusion of PbOH$^+$ ions. The absence of a Pb^{++} intermediate diffusion mechanism at 0.9 and 1.0V may be due to a greater degree of lateral spreading or isolated nucleation of the α-PbO_2 deposit on the Pb surface to which diffusion of Pb^{++} ions from the pores in the lead sulfate is more difficult. During the last diffusion interval (D) before the current minimum, the PbO_2 reaction sites have apparently grown up toward the basic sulfate zone, decreasing the electrode resistance by the formation of α-PbO_2. The capacitance remains unchanged (13) since the latter is determined by the PbO_2 accessible to the electrolyte in the pores, in parallel with the $PbSO_4$ surface, and the area of the former is still insignificantly small.

The end of this linear region corresponds to the first minimum in the potentiostatically controlled current. The current rise following this minimum culminates in a maximum [with coordinates (t_m,i_m)] which may be followed by other extrema at certain potentials at temperatures $\geqq -10$°C. At low temperatures only a single maximum is observed, which previously has been quantitatively shown (13) to be due to a current-limiting process of two-dimensional nucleation and growth of PbO_2. In a previous paper (13), a divergence of the experimental data from the model was noted to occur during the early part of the current rise. This was tentatively attributed to the large and rapid change in electrode resistance which occurs during this stage of the charging process. It appears now, however, that it is more likely due to mixed current control by diffusion and three-dimensional progressive nucleation and growth (see Fig. 6b), as evidenced by the data of Fig. 3.

Such mixed control leads to a linear dependence of current on $t^{3/2}$ (24), as observed in the present work with the thick $PbSO_4$ film and elsewhere (25) during the direct anodic oxidation of polished lead in sulfuric acid solutions. To a first approximation, the slopes of the lines shown in Fig. 3 are proportional to the cube of the diffusing reactant concentration (24) and to $t_m^{3/2}/i_m$. Hence the slopes are very sensitive to reactant concentration. Since the proportionality constant is not known, it can only be said from Fig. 3 that the value of C is approximately 35 times smaller at 0.9V and 6 times smaller at 1.0V than the average values for the higher potentials. The amount of charge passed by the beginning of the linear i-$t^{3/2}$ region was greater at the lower potentials and the height of the two-dimensional nuclei formed later was significantly less at 0.9V (13).

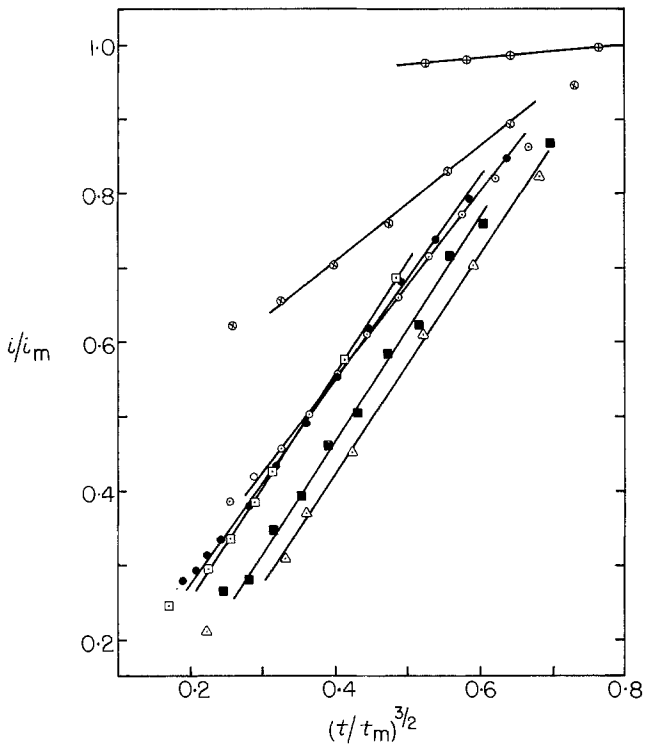


Fig. 3. Current (units of i_m) vs. time$^{3/2}$ (units of $t_m^{3/2}$) for interval F of Fig. 1. Values of (t_m, i_m) are indicated for each potential: ⊕, 0.9V (21.5 sec, 18.5 μA); ⊗, 1.0V (7.4 sec, 70.8 μA); ⊙, 1.1V (5.5 sec, 182 μA); ●, 1.2V (2.57 sec, 481 μA); ■, 1.3V (1.40 sec, 758 μA); △, 1.4V (0.71 sec, 1.460 mA).

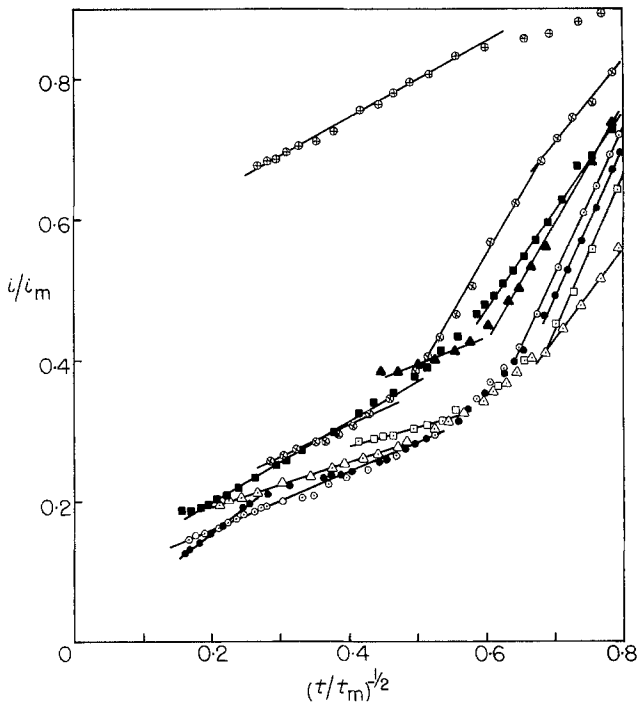


Fig. 4. Current vs. time$^{-1/2}$ (units of i_m, $t_m^{-1/2}$) at various potentials during diffusion-limited intervals H-J (Fig. 1), following nucleation-and-growth interval NG. Values of (t_m, i_m) are indicated for each potential: ⊕, 0.9V (21.5 sec, 18.5 μA); ⊗, 1.0V (7.4 sec, 70.8 μA); ⊙, 1.1V (5.5 sec, 182 μA); ●, 1.2V (1.97 sec, 467 μA); ■, 1.3V (1.72 sec, 583 μA); △, 1.4V (0.71 sec, 1.460 mA); ◙, 1.5V (0.69 sec, 2.07 mA); ▲, 1.6V (0.40 sec, 3.27 mA).

Thus it would appear that a larger number of smaller nuclei are formed near the Pb/PbO interface at 0.9V than at higher potentials and that, as a consequence, the reactant ions, originating further up the pores, have less accessibility to the reaction site. The pores leading to the reaction zone must become smaller since the formation of PbO_2 from Pb or PbO-tet involves an increase in molar volume (26) which would initially tend to restrict the pores.

As the growth of α-PbO_2 proceeds during region F however, mechanical stresses will be set up in the PbO layer (4) due to this volume increase which may physically force crystals apart and create porous intercrystalline spaces. Furthermore, the volume change for the formation of PbO_2 from the basic sulfates is negative (26). These two effects should combine to increase the pore volume and α-PbO_2 network exposed to the pore solution during region F. At −20°C most of the resistance decrease and the initial capacitance increase occurred during this interval (13) and may be attributed to the increase in pore volume and α-PbO_2 surface area.

During the subsequent interval (region NG) the current has been shown (13) to be controlled by two-dimensional nucleation and growth as the α-PbO_2 spreads laterally beneath the lead sulfate causing a strong capacitance increase, and forming a dense anodic layer (see Fig. 6c), and possibly more intercrystalline spaces in the protective lead sulfate layer. Although the fit to the nucleation and growth model was only valid for region G1 for the particular run shown in Fig. 1, the range of validity increased as temperature decreased and typically included all of interval NG at low temperatures and often even a wider range, extending to both sides of NG.

Post-nucleation-and-growth diffusion currents.—Following interval NG, further linearities between i and $t^{-1/2}$, indicating diffusion-limited oxidation steps, were observed (13) during intervals H, I, and J (Fig. 4). The slopes of interval H correspond to values of pH = 8.9-9.5, increasing with potential from 1.1 to 1.6V, if the diffusing species is assumed to be $PbOH^+$, or to values of pH = 2.4-1.8, decreasing with potential over the same potential range, if the diffusing species is assumed to be H^+ at a pH controlled by the sulfate-bisulfate equilibrium (9). However the linearities in interval H, when extrapolated, gave a negative current intercept at infinite time, in contradiction to the zero current intercept required by Eq. [5]. A probable explanation for such negative intercepts is that the diffusion-limiting process did not begin at $t = 0$, as required for the validity of Eq. [5], but at some later time, t_o. Reasonable choices for t_o should lie in the range of t_o = 1.2-1.7 t_m, *i.e.*, near the completion of nucleation-and-growth control. In fact, it was found that zero or positive intercepts were obtained for $t_o \geq 1.3\ t_m$ and that, furthermore, the range of linearity was increased so that a single linear i-$t^{-1/2}$ dependence was obtained for most of an interval combining H and I and, in some cases, part of J. The results of transforming the data from a time scale with $t_o = 0$ (Fig. 4) to $t_o = 1.5\ t_m$ are shown in Fig. 5. The intervals H, I, and J indicated refer only to the data for 1.1V, for comparison with Fig. 1. Larger values of t_o do not appreciably extend the linearity to longer times but result in a reduction of the linear range at short times. It appears from Fig. 5 that a diffusion-controlled process begins at $t_o \simeq 1.5\ t_m$; that a linear i-$t^{-1/2}$ interval begins at $t \simeq 2t_m$, extending for several multiples of t_m and that at very long times (corresponding roughly to interval J of Fig. 1), a second diffusion-limited process begins to control the current. Since the current intercepts are almost all small and positive, some contribution to the total current by a steady-state parallel process, such as a corrosion reaction, is suggested.

The values of $ZD^{1/2}C$ obtained from the linear i-$t^{-1/2}$ intervals (Table IV) are of the same order of magnitude as those for interval B and at least one order of magnitude larger than those for intervals C and D (Table I). As had been the case for the previous diffusion processes, reasonable values for D could not be

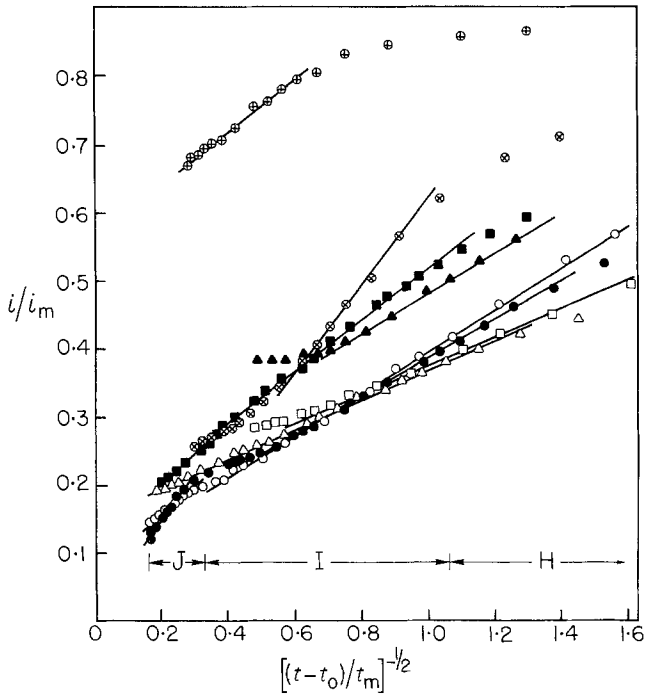


Fig. 5. Current *vs.* time$^{-1/2}$ (units of i_m, $t_m^{-1/2}$) for $t_0 = 1.5\ t_m$. Symbols and data are identical to Fig. 4. Intervals H, I, and J are indicated for the run at 1.1V (Fig. 1).

obtained from $ZD^{1/2}C$ for any values of ZC corresponding to the species present in bulk solution.

It is difficult to predict whether the next stage of oxidation, following interval NG, should involve further oxidation of unconsumed PbO beneath the α-PbO_2 layer (Fig. 6d) or oxidation of $PbSO_4$ above it. Only three plausible diffusion processes could be envisioned which could correspond to values of $ZD^{1/2}C$ within one order of magnitude of those obtained.

1. From the amount of charge passed, it is unlikely that all of the PbO in the electrode interior has been consumed up to this stage of the oxidation. Furthermore, Ruetschi's self-depassivation results (11) and x-ray analyses of the composition of positive plates during formation (6) indicate that PbO continues to be present in positive electrodes after substantial oxidation times. Once the layer of basic sulfates has been oxidized, further oxidation of PbO, which had temporarily been short circuited by α-PbO_2, might occur (Fig. 6d) Values of $[PbOH^+]$ and the thermodynamic values of *p*H corresponding to $[PbOH^+]$ values (assuming $[Pb^{++}] = 10^{-3.9}$M) were calculated as before. The calculated values of *p*H (Table IV) were found to increase with potential but lie within the range of values of PbO stability. Proportionately lower values of *p*H would have been obtained if the $[Pb^{++}]$ was greater than that assumed. Values of $[Pb^{++}]$ calculated assuming that this was the diffusing species are higher than those corresponding to lead sulfate dissolution and would correspond to highly supersaturated solutions. At higher potentials the concentrations of $[PbOH^{++}]$, and thus *p*H, might be expected to be higher, as observed, since the later commencement of diffusion control at lower potentials suggests a greater degree of prior consumption of basic material.

2. If the unconsumed PbO becomes isolated (or permanently short circuited by the α-PbO_2) during the nucleation and growth period, the reaction zone within the pores should begin to advance into the $PbSO_4$ layer. Chemical processes involving the dissolution of unconsumed PbO and basic sulfates may continue with deposition of $PbSO_4$ crystals on the outwardly advancing PbO_2 zone (5, 6). When the available $PbO/PbSO_4$ ratio has become sufficiently small, the *p*H will be expected to decrease quickly, due to the acid production which accompanies oxidation, and formation of β-PbO_2 will begin to take precedence over α-PbO_2 formation. During the transition from an alkaline interior to that of bulk electrolyte, a stable *p*H plateau might be expected near *p*H 2 due to the buffering action of the bisulfate-sulfate equilibrium (9). If one assumes $D = 9.34 \times 10^{-5}$ cm^2 sec^{-1} (21) for the H^+ ion, the values of *p*H shown in the second-to-last pair of columns of Table IV are obtained. These values are substantially less than the *p*H = 1.9 expected for maximum buffering capacity and tend to rule out the hypothesis of such a mechanism for *p*H stability within the pores unless the electroactive surface area is less than 10% of the assumed geometric area.

3. Whether or not the *p*H is arrested near *p*H = 2 by the sulfate-bisulfate equilibrium, it should continue to decrease as oxidation progresses. At lower *p*H, Pb^{4+} (or possibly some other complex tetravalent lead ion) becomes increasingly stable according to the equation (20)

$$\log a_{Pb^{+4}} = -7.10 - 4.00\,pH \qquad [9]$$

Values tabulated in the final two columns of Table IV were derived by assuming $Z = 4$ and $D \simeq 10^{-5}$ for the Pb^{+4} ion and calculating *p*H from the above equation, using the value of $C_{Pb^{+4}}$ obtained from $ZD^{1/2}C$. A more recent equation (27), $\log a_{Pb^{4+}} = -8.26 - 4.00$ *p*H, would result in values of *p*H 0.3 units more negative than those shown in Table IV.

According to these calculations, the *p*H must be of the order of -1 to permit an interpretation based on diffusion limitation by the Pb^{+4} ion. Acid is being continually produced at the reaction site and such a value is not unrealistic since the *p*H of the bulk electrolyte is approximately -0.5 and there are no longer any mechanisms for the consumption of acid in the pores. Thus a steady-state acid concentration in the pores more acidic than that of the bulk electrolyte would not be surprising. The acidity excess would be greater at higher potentials (*i.e.*, higher current densities), as observed (Table IV), since the *p*H would not be controlled thermodynamically but by a steady-state process involving production and diffusion of acid.

Evidence exists to support this reversal of acid diffusion during the formation of both positive (3) and negative (7) plates. For approximately the first one-third of constant current charging, the density of bulk

Table IV. Postnucleation-and-growth diffusion-limited intervals (H-J)

E vs. Hg/Hg_2SO_4	No. of runs	$ZD^{1/2}C \times 10^9$ 1st linear interval	$ZD^{1/2}C \times 10^9$ 2nd linear interval (J)	Calculated *p*H for postulated diffusing species shown: $C = [PbOH^+]$, $D = 2 \times 10^{-5}$, $Z = 1$		$C = [H^+]$, $D = 9.34 \times 10^{-5}$, $Z = 1$		$C = [Pb^{+4}]$, $D = 1 \times 10^{-5}$, $Z = 4$	
				1st	2nd	1st	2nd	1st	2nd
0.9	1	1.34	—	7.5	—	3.9	—	−0.78	—
1.0	1	5.2	2.6	8.1	7.8	3.3	3.6	−0.93	−0.85
1.1	1	5.5	7.9	8.1	8.2	3.3	3.1	−0.93	−0.97
1.2	2	7.2 ± 0.7	18.5	8.2	8.6	3.1	2.7	−0.96	−1.07
1.3	2	11.5 ± 0.6	17.5 ± 1.1	8.4	8.6	2.9	2.7	−1.02	−1.06
1.4	2	11.4 ± 0.1	—	8.4	—	2.9	—	−1.01	—
1.5	2	15.3 ± 0.2	—	8.5	—	2.8	—	−1.05	—
1.6	1	26.0	—	8.8	—	2.6	—	−1.10	—

electrolyte decreases during positive plate formation (5). Thereafter it increases for the duration of the charge. If the changes in electrolyte density are due to diffusion of acid into and out of the plate, the plate interior must be less acidic initially and become more acidic than the bulk electrolyte when about one-third of the plate capacity has been accepted.

Pavlov and Iordanov (4) also concluded that, since the amount of β-PbO_2 formed at potentials above 1.0V was substantially larger than that of oxidized $PbSO_4$ and tet-PbO (as determined by x-ray diffractometry), an ionic current of Pb^{4+} must pass through the anodic layer to form β-PbO_2 at the solution interface prior to oxygen evolution. It is during this final diffusion-limited region that the formation of β-PbO_2 at the surface appears to begin.

Correlation of faradaic and a-c components.—In order to gain further information about the surface state of the electrode, potentiostatic measurements of the components of a superimposed 10 Hz alternating current were made at several temperatures. Although no detailed quantitative correlations between the a-c components and the faradaic current were made at 25°C, such detailed comparisons were made at lower temperatures (13). Except as noted below, the behavior of these parameters, under the conditions of the potential step experiments, were very similar at all temperatures until the end of the final diffusion-limited region. Using the previously published results (13), it is possible to gain some insight into the changes taking place at the electrode/electrolyte interface during this stage of oxidation. At temperatures ≥ -30°C a regular oscillation in current and differential capacity was observed during the final diffusion interval (J). The passage of charge during one period corresponded to the deposition or dissolution of approximately one or two monolayers. Thus it was suggested (13) that no appreciable roughening of the surface had yet occurred. At −20°C and 1.3V, oscillations first appeared in the capacitance at a time $(t/t_m)^{-1/2} = 0.6$ but the oscillations did not become regular in amplitude until $(t/t_m)^{-1/2} = 0.28$, almost precisely at the beginning of the final diffusion region. Prior to the commencement of the oscillations, the differential capacitance showed a pronounced shoulder at $(t/t_m)^{-1/2} = 0.8$, coinciding with the beginning of the diffusion process of interval H. Although the capacitance had been increasing strongly during the prior nucleation and growth region, the rate of increase dropped following the shoulder, by a factor of more than 50.

It would thus appear that a sharp decrease in the rate of PbO_2 surface formation by consumption of the basic sulfate layer (Fig. 6c) at the base of the $PbSO_4$ pores occurs at $(t/t_m)^{-1/2} = 0.8$. Following consumption of further PbO, beneath the newly completed α-PbO_2 layer, controlled by the diffusion of $PbOH^+$, the *p*H decreases rapidly as $(t/t_m)^{-1/2}$ approaches 0.28 (beginning of interval J). The capacitance data suggest only a slow growth of PbO_2 surface during and following this transition. However, it is possible that the site of the electrochemical process changes from the PbO_2 surface to that of $PbSO_4$ forming the pore walls, where Pb^{4+} ions may be generated which can diffuse to the PbO_2 and chemically deposit. In this case the active electrode area may be expected to change. The sign of this change is difficult to predict: although the pore walls probably represent a larger area than that of PbO_2 at the pore base, it is likely that only the $PbSO_4$ near the pore base can become active due to its high resistivity. The charges passed between current and capacitance oscillations suggest that no large change in active area has occurred. If this conclusion is incorrect, however, the rejection of other current-limiting diffusing species, on the basis of the $ZD^{1/2}C$ values, may be invalidated. If the change in the active area is small, the pH need be only slightly different than shown in Table IV to support the postulated diffusion control by Pb^{4+} ions. This point is extremely germane to the problem of poor charge acceptance of the lead acid battery positive plate at very low temperatures. It is during this last interval of diffusion control studied, that significant qualitative differences appear between charging currents at very low and at normal temperatures. Except at very high overpotentials, the current during this period, plotted against $t^{-1/2}$, can be extrapolated to zero at very low temperatures. At normal temperatures it begins instead to markedly increase as β-PbO_2 growth occurs and roughening of the electrode surface takes place.

The oscillations in capacitance and current may be due to the repetitious accumulation of Pb^{4+} ions, to form a saturated or supersaturated solution, followed by surface nucleation of PbO_2 and growth of a new monolayer. The sequence of oxidation steps apparently does not reach this stage at temperatures below −30°C. At −50°C the capacitance continued to increase and no oscillations were observed to the termination of the experimental run at $t > 30\ t_m$, by which time the charge passed was about one-half, but the capacitance less than 10%, of the corresponding values at −20°C (13). [Note, the scale for Q is incorrectly labeled in Fig. 2(a) of Ref. (13). The ordinate scale should be multiplied by 10 to obtain Q in $n\mathbf{F}$.] The temperature dependence will be discussed in more detail in a later paper. The mechanism proposed during this interval consists firstly of electrochemical generation of Pb^{4+} from $PbSO_4$ in close proximity to the PbO_2 at the bottom of the lead sulfate pores. This may also be accompanied by some chemical dissolution of α-PbO_2 to form Pb^{4+}. The Pb^{4+} ions can then diffuse down the pores toward the bulk electrolyte along a gradient of decreasing H^+ concentration. As a consequence of the increasing *p*H, a zone of precipitation of β-PbO_2 onto $PbSO_4$ by chemical reaction of Pb^{4+} with H_2O will be established, advancing toward the mouth of the pore, until reaching the exterior surface in contact with bulk electrolyte. The current and capacitance oscillations observed may be associated with the deposition of monolayers at the electrode/solution interface. Initially, the β-PbO_2 thus chemically formed near the surface may be electronically isolated from the PbO_2 at the base of the pores so that oxygen evolution cannot occur, except on the PbO_2 deep within the pores. At the same time cavities will be developing at the bottom of the $PbSO_4$ layer due to the dissolution and oxidation of $PbSO_4$ and β-PbO_2 may be depositing on the α-PbO_2 base by the oxidation of Pb^{++} ions. Once this deposit grows sufficiently to come into contact with any isolated β-PbO_2 already formed near the surface, or grows to the surface, the mechanisms should change once again. Oxidation of $PbSO_4$ will create a porous network of β-PbO_2, due to the smaller molar volume of the latter, accompanied by increased PbO_2 surface area and a sharply rising current. The kinetics controlling this current increase have already been studied (28) and shown to be three-dimensional nucleation and growth of PbO_2 on $PbSO_4$. The tetravalent lead ion diffusion may be a precursor to the three-dimensional nucleation and growth, in the same way as intervals B to F appeared to create the conditions to initiate two-dimensional growth. An increase of oxygen evolution should then accompany further increase of PbO_2 surface area.

Effect of film age.—As has been noted, most of the potential oxidation steps were carried out beginning with a well-established lead sulfate layer. In order to determine the effect of the lead sulfate history, these experiments were repeated using newly formed, or relatively young, films. Potential step experiments were done on lead sulfate electrodes which had been formed on lead within the previous 48 hr. Some cycling preceded the experimental runs to improve reproducibility. When held at 0.4V following oxidation, the current decayed to an oxidation current of approximately

30 μA, indicating that passivation of the underlying lead was not yet complete. Although the oxidation steps were begun, as before at a potential of 0.4V and when the net reduction current had decayed to 3.0 μA, discharge of the PbO_2 was expected to be less complete than observed for thicker films due to the oxidation component contained in the net reduction current.

At 25°C a very short period of conditioning preceded the series of experimental runs. A newly polished lead electrode was allowed to stand overnight at 0.8V in fresh electrolyte and a few potential step charges and discharges were carried out before the acquisition of quantitative data. Under these conditions, no appreciable diffusion-limited current was observed before the nucleation and growth phase, confirming the expected less complete discharge of PbO_2 in the PbO layer. Following nucleation and growth, $ZD^{1/2}C$ values were obtained, somewhat larger than for the thick films (by a factor of 3 to 15) during the first diffusion-limited period, corresponding to pH values of 8.5-9.6. These remain within the range of PbO stability assuming $PbOH^+$ diffusion, and suggest a higher rate of anodic lead corrosion. In the last diffusion-limited region, $ZD^{1/2}C$ values were almost identical for the thick and the thin films.

At 15°C, a longer preconditioning period was employed (40 hr in the electrolyte and several hours of cycling between 0.6 and 1.8V), although the lead sulfate film was still expected to be less completely developed than for the standard runs. In this case two linear i *vs.* $t^{-1/2}$ regions were observed before nucleation-and-growth control at potentials $\leq$1.3V during some runs but the first was poorly reproducible and had a slope less than twice that of the second. At potentials >1.4V no current minimum occurred before nucleation and growth. From the second, well-defined linear region, values of $D^{1/2}C$ as a function of potential, assuming $Z = 1$, had values very nearly the same as those shown in Table III, corresponding to pH values ranging from 7.8 at 1.0V to 8.2 at 1.3V.

In the post-nucleation-and-growth diffusion regions, values of $ZD^{1/2}C$ were obtained which were intermediate to those for thick and thin films at 25°C for the first linear region, and the same for the final, as expected. At much lower temperatures, experiments were carried out to determine the effect of a longer, deeper prior discharge (but still at 0.4V) on the diffusion characteristics. These results are discussed in another paper (29).

Conclusions

Borrowing from the models of Pavlov and Iordanov (4) and Ruetschi (11), the anodic layer at 0.4V, before application of the potential step, will have a structure such as schematically illustrated in Fig. 6a. Basic lead sulfates fill the macropores, formed from the $PbSO_4$ intercrystalline spaces, and the $PbSO_4$/PbO interface consists of basic lead sulfates with a graduated $PbO/PbSO_4$ ratio. The micropores and the pore electrolyte are not shown.

Upon application of the potential step, PbO is hydrolyzed, or $Pb(OH)_2$ dissociates, to produce $PbOH^+$ and OH^- ions. The $PbOH^+$ diffuses to the lead surface where it is oxidized at a local pH of about 8 to produce α-PbO_2 nuclei and H^+ ions. Since the overlying $PbSO_4$ is impermeable to Pb^{+2} and $SO_4^=$, migration of the H^+ or OH^- ions through the $PbSO_4$ must occur to carry the current. Upon deposition of less than a monolayer, the α-PbO_2 begins to grow as filaments, perhaps of about molecular diameter, at a rate limited by diffusion of Pb^{2+} ions dissolved from the base of the lead sulfate layer and/or formed by anodic corrosion of lead. When these filaments reach the zone of basic lead sulfates where the pH is about 7, the basic sulfates may begin to dissolve to produce $PbOH^+$, OH^-, Pb^{++}, and $SO_4^=$. The latter two diffuse to and precipitate on the lead sulfate and the current-limiting

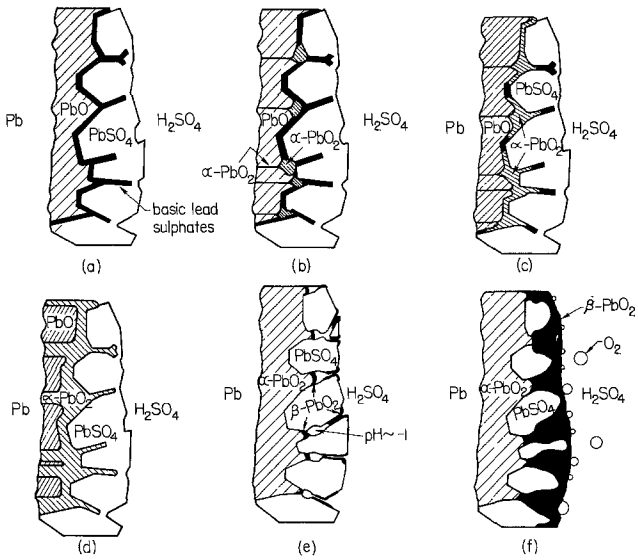


Fig. 6. Models schematically illustrating the progressive growth and composition of an anodic deposit on lead in sulfuric acid solutions following formation of a thick lead sulfate layer (see text).

diffusing species becomes $PbOH^+$ once again. Dissolution of basic sulfates results in the creation of microvoids and pore enlargement around the ends of the PbO_2 filaments due to the large associated decrease in molar volume. These spaces provide "growing room" first during the subsequent three-dimensional growth with slow diffusion (Fig. 6b), then during the two-dimensional lateral growth of α-PbO_2 into the basic sulfate layer (Fig. 6c).

During the first diffusion-limited interval following control by two-dimensional growth, formation of α-PbO_2 proceeds at the expense of underlying PbO (Fig. 6d). Following consumption of the basic reactants, the pH rapidly decreases. At sufficiently low pH, the diffusion of Pb^{4+} ion generated at the α-$PbO_2/PbSO_4$ interface, limits the rate. The diffusing tetravalent lead may react with water and deposit on the α-PbO_2, (or with less likelihood on the $PbSO_4$) at the pore bases. At potentials less than 1.1V, this reaction will cease or may never occur if the pores are sufficiently large to maintain or reduce the internal acidity below or equal that of bulk electrolyte and only the background oxidation of PbO to α-PbO_2 and Pb to PbO will continue. At higher potentials diffusing tetravalent lead may continue to deposit on the β-PbO_2, thus growing toward the electrode surface. If nucleation onto the $PbSO_4$ does not require too great an activation energy, the Pb^{4+} ions might diffuse much further down the pores before reaching a state of supersaturation (as bulk electrolyte pH is approached) and depositing near the electrode surface (Fig. 6e). The observed current and capacitance oscillations are attributed to such a mechanism. Once the two zones of β-PbO_2 join together, $PbSO_4$ is oxidized to form a porous PbO_2 layer at normal temperatures (Fig. 6f), following a three-dimensional nucleation and growth law, and simultaneous oxygen evolution can occur. At very low temperatures, the development of the porous PbO_2 layer is somehow inhibited. This inhibition may be due to preferential persulfate formation (30), pore blockage by $PbSO_4$ and PbO_2 precipitation or ice formation, or some other unknown mechanism. At present it is difficult to state the precise cause with the available data. Further experimental studies at low temperatures will be reported (29) and work, similar to that of the Pavlov school, has been commissioned in order to obtain the necessary additional information to resolve this question.

Acknowledgments

This work was issued as Defence Research Establishment Ottawa Report No. 743.

Manuscript submitted April 13, 1976; revised manuscript received Oct. 1, 1976.

Any discussion of this paper will appear in a Discussion Section to be published in the December 1977 JOURNAL. All discussions for the December 1977 Discussion Section should be submitted by Aug. 1, 1977.

Publication costs of this article were assisted by the Defence Research Establishment Ottawa.

REFERENCES

1. J. Burbank, A. C. Simon, and E. Willihnganz, in "Advances in Electrochemistry and Electrochemical Engineering," Vol. 8, P. Delahay and C. W. Tobias, Editors, pp. 157-251, John Wiley & Sons, New York (1971).
2. D. Pavlov, C. N. Poulieff, E. Klaja, and N. Iordanov, *This Journal*, **116**, 316 (1969).
3. D. Pavlov and R. Papova, *Electrochim. Acta*, **15**, 1483 (1970).
4. D. Pavlov and N. Iordanov, *This Journal*, **117**, 1103 (1970).
5. D. Pavlov, Proceedings of the Symposium on Batteries for Traction and Propulsion, p. 135, Columbus Section of The Electrochemical Society (1972).
6. D. Pavlov, G. Papazov, and V. Iliev, *This Journal*, **119**, 8 (1972).
7. D. Pavlov, V. Iliev, G. Papazov, and E. Bashtavelova, *ibid.*, **121**, 854 (1974).
8. W. O. Butler, C. J. Venuto, and D. V. Wisler, *ibid.*, **117**, 1339 (1970).
9. P. Ruetschi and R. Angstadt, *ibid.*, **111**, 1323 (1964).
10. D. Pavlov, *Electrochim. Acta*, **13**, 2051 (1968).
11. P. Ruetschi, *This Journal*, **120**, 331 (1973).
12. D. Pavlov, *Ber. Bunsenges.*, **71**, 398 (1967).
13. E. M. L. Valeriote and L. D. Gallop, in "Power Sources 5," D. H. Collins, Editor, Academic Press, London (1975); Defence Research Establishment Ottawa, DREO Report No. 717 (May 1975).
14. K. J. Vetter, "Electrochemical Kinetics. Theoretical Aspects," English edition, p. 365, Academic Press, New York (1967).
15. G. C. Barker, in "Transactions of the Symposium on Electrode Processes," E. Yeager, Editor, pp. 325-367, John Wiley & Sons, New York (1967).
16. S. M. Caulder, J. S. Murday, and A. C. Simon, *This Journal*, **120**, 1516 (1973).
17. A. C. Simon, S. M. Caulder, and J. T. Stemmle, *ibid.*, **122**, 461 (1975).
18. A. C. Simon, S. M. Caulder, G. W. Mao, and W. Lannoye, Abstract 43, p. 107, The Electrochemical Society Extended Abstracts, Fall Meeting, New York, New York, Oct. 13-17, 1974.
19. H. Bode and E. Voss, *Electrochim. Acta*, **1**, 318 (1959).
20. P. Delahay, M. Pourbaix, and P. Van Rysselberghe, *This Journal*, **98**, 57 (1951).
21. R. Parsons, "Handbook of Electrochemical Constants," Butterworths, London (1959).
22. L. G. Sillén, "Stability Constants of Metal-Ion Complexes, Section I: Inorganic Ligands," The Chemical Society, London (1964); (a) Å. Olin, *Acta Chem. Scand.*, **14**, 126 (1960); (b) A. B. Garrett, S. Vellenga, and C. M. Fontana, *J. Am. Chem. Soc.*, **61**, 367 (1939); (c) G. W. Goward, Thesis, Princeton University (1954); (d) A. A. Vlček *Coll. Czech. Chem. Comm.*, **20**, 400 (1955); (e) C. J. Nyman, D. K. Roe, and R. A. Plane, *J. Am. Chem. Soc.*, **83**, 323 (1961); (f) J. W. Olver and D. N. Hume, *Anal. Chim. Acta*, **20**, 559 (1959).
23. H. Bode and E. Voss, *Ber. Bunsenges.*, **60**, 1053 (1956).
24. J. A. Harrison and H. R. Thirsk, in "Electroanalytical Chemistry," Vol. V, A. J. Bard, Editor, Marcel Dekker, New York (1971); "A Guide to the Study of Electrode Kinetics," Academic Press, London (1972).
25. J. L. Dawson, Private communication (1974).
26. J. Burbank, *This Journal*, **113**, 10 (1966).
27. M. Pourbaix, "Atlas D'Equilibres Électrochimiques," p. 487, Gauthier-Villars & Cie, Paris (1963).
28. M. Fleischmann and H. R. Thirsk, *Trans. Faraday Soc.*, **51**, 71 (1955).
29. E. M. L. Valeriote and L. D. Gallop, *This Journal*, **124**, 380 (1977).
30. C. Gardner and F. Rocheleau, DREO Technical Note No. 75-1, Dept. of National Defence, Ottawa, Canada (1975).

Low Temperature Oxidation Kinetics of Anodic Films on Lead in Sulfuric Acid Solution

E. M. L. Valeriote* and L. D. Gallop

Defence Research Establishment Ottawa, Ottawa, Ontario, Canada K1A 0Z4

ABSTRACT

A multiphase model of anodic films on lead in sulfuric acid, previously developed to describe the oxidation of lead at room temperature, has been applied to potentiostatic transient data at very low temperatures (0° to −50°C). Freezing of the dilute pore electrolyte is proposed, such that ionic diffusion and equilibria must occur in a thin layer of adsorbed water between the ice and pore walls The experimentally determined activation energies and entropies of diffusion indicate that desorption of water or dehydration of ions plays an important role in the activation process. Except for the effects of the more limited electrolyte volume within the pores upon freezing, the electro-oxidation processes follow a similar sequence above and below the freezing point. However, eventual reactant depletion, due to kinetically hindered equilibria and reduced electrolyte volume in the pores, leads to cessation of charge acceptance at very low temperatures, before appreciable β-PbO_2 formation can occur.

Results of a study of the oxidation of thick divalent lead films, in 35% aqueous sulfuric acid at low temperatures, have previously been discussed (1). The initial potentiostatic oxidation kinetics were found to obey a two-dimensional nucleation-and-growth law particularly well at temperatures below −20°C. As the temperature is increased, the range (in terms of both time and applied potential) of the model's validity decreased. Several diffusion-limited processes preceded and followed the nucleation and growth interval. Rate laws were found, which described very well the sequence of processes governing the oxida-

* Electrochemical Society Active Member.
Key words: diffusion, activation, freezing, pores, charging.

tion, from the time of application of the potential step, until the time at which a qualitative dependence of the rate on temperature became apparent. The results of potentiostatic transient experiments at 25°C were discussed quantitatively (2) in terms of a model based on those developed by Ruetschi and Pavlov *et al.* (3-7). The model was elaborated, describing the formation of α-PbO_2 beneath a protective lead sulfate film. Evidence was presented for current control by the sequential processes of $PbOH^+$ and Pb^{++} diffusion, three-dimensional and two-dimensional electrocrystallization, and $PbOH^+$ ionic diffusion, before the formation of β-PbO_2 begins. A reversal of the pH gradient in the pores apparently occurs in close association with the onset of β-PbO_2 production, which results in a small oxidation current, limited by diffusion of tetravalent lead. Following or during this stage of the anodic oxidation, the charging kinetics become qualitatively dependent on temperature.

In the present paper, the potentiostatic transient data, obtained at lower temperatures (0°C to −50°C), are discussed in terms of the same model in order to elucidate the reasons for poor low temperature charge acceptance of positive electrodes in the lead acid battery.

Experimental

The electrochemical measurements were made using a PAR® Model 170 electrochemistry system (Princeton Applied Research Corporation, Princeton, New Jersey) with auxiliary high impedance recorders and digital meters to facilitate simultaneous determination of current, charge, electrode potential, and other relevant electrochemical parameters.

A rotating disk electrode (RDE) of 0.441 cm^2 area was inserted through a loosely fitting Teflon cap into the main part of the Pyrex three-compartment electrochemical cell. The RDE was rotated only to elaborate certain results obtained when the electrode was stationary. Side compartments, containing counterelectrode (platinized Pt) and reference electrode ($Hg/Hg_2SO_4/35\%$ H_2SO_4), were connected to the main cell through 1-2 mm capillary tubing. The connection from the reference compartment entered the main cell at bottom center and narrowed down to a fine capillary tip about 1 mm below the center of the RDE. The lead disk (>99.995% purity, Cominco, Trail, British Columbia, Canada) was chemically and mechanically polished using standard techniques and electrochemically oxidized to lead sulfate in 35% reagent grade sulfuric acid. Experiments were carried out with a single well-cycled electrode maintained at least 1V above the $Pb/PbSO_4$ potential at all times and temperatures during the acquisition of quantitative results. The current was measured as a function of time during a series of potential steps to various constant oxidation potentials and at 10°C intervals from −50° to 0°C. Each charge step was preceded by a constant potential discharge at 0.4V, until the net reduction current had decayed to 3.0 μA.

In order to obtain reproducible current-time transients, care was taken to terminate each charging experiment before the decreasing current, following the nucleation and growth period, had begun to increase substantially.

Further experimental details have already been reported (1) or will be described below where necessary.

Results

When the experiments were carried out in the standard way, *i.e.*, constant potential charging following discharge to 3.0 μA at 0.4V, three diffusion-controlled currents were observed at 25°C prior to the first current minimum followed by nucleation-and-growth control (2). The slopes of the two linear segments of the i *vs.* $t^{-1/2}$ plots were in the ratio 2:1. It was argued (2) that the currents were limited

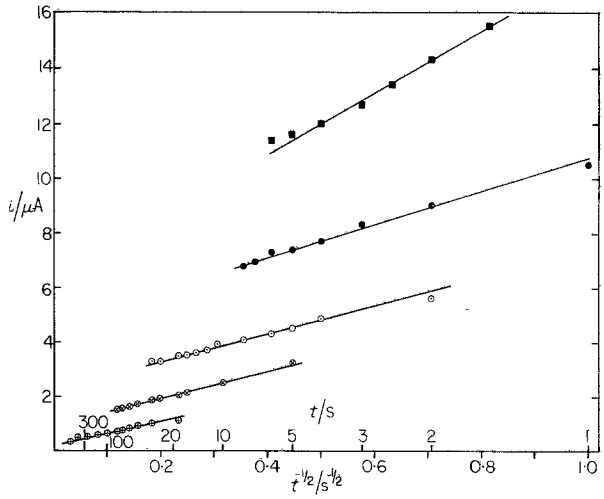


Fig. 1. Current-time characteristics for the early stage of potentiostatic oxidation of an anodic film on lead in 35% sulfuric acid at −40°C. The disk electrode of 0.44 cm^2 area was previously discharged at 0.4V to a reduction current of 3.0 μA. Charging potentials (relative to the Hg/Hg_2SO_4 reference electrode) were: ⊕, 0.9V; ⊗, 1.0V; ⊙, 1.1V; ●, 1.2V; ■, 1.3V.

during these two intervals by the diffusion of Pb^{++} and $PbOH^+$ which were present at approximately equal concentrations in the slightly alkaline pore electrolyte beneath the $PbSO_4$. At temperatures ≤0°C, only one unambiguously diffusion-limited interval was observed. A typical example of the linear i-$t^{-1/2}$ dependence is given in Fig. 1 for data obtained at −40°C and at various applied potentials. During some experimental runs at −50°C there were indications of an earlier diffusion-limited interval at times of less than 1 or 2 sec following application of the potential step. An oscillographic recording method would have been useful to obtain accurate enough data to quantitatively discuss this earlier interval. As an alternative, the electrode was discharged more deeply prior to the charging step. The data obtained following discharge at the same potential (0.4V) as during the standard experiment, but for a longer period of time (until the current decayed to values between 40 and 70 nA), are displayed in Fig. 2. As in the

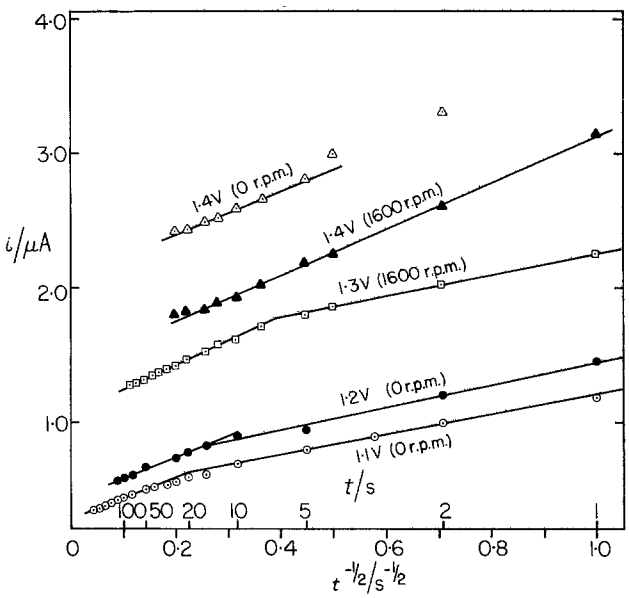


Fig. 2. Current-time characteristics for 35% sulfuric acid at −40°C, as in Fig. 1, but following discharge at 0.4V to reduction currents of 40-70 nA. Potentials and angular speed of electrode are indicated on the graph.

experiments at 25°C under the standard regime, two linear i *vs.* $t^{-1/2}$ dependencies were observed, with slopes in the ratio of 1:2, separated by a very sharp change of slope. However, the order was reversed, *i.e.*, the slope of the earlier linear segment at −40°C, following deep discharge, was smaller than that of the latter by a factor of two at potentials of 1.1-1.3V. No significant dependence of slope on rotation rate of the disk electrode was observed, although the current was higher for a stationary electrode, than for one which was rotating as was also observed during linear scan voltammetry experiments (1).

During the interval following control by nucleation and growth, similar dependencies of potentiostatic current on time were observed at all temperatures. At least two linear i *vs.* $t^{-1/2}$ intervals are observed before the current either approaches zero or reaches a minimum, depending on temperature and potential. The results have already been reported for temperatures of −50°C (1) and 25°C (2).

Discussion

Calculation of diffusion parameters.—From the slopes of the linear i-$t^{-1/2}$ segments, values of $ZD^{1/2}C$ are obtained (2) where Z is the charge on the diffusing species of concentration C. Assuming that the diffusion coefficient D obeys on Arrhenius-type equation and that Z and C are independent of temperature, values of the activation energy of diffusion, $\Delta H^{\neq}$, can be obtained from the slope of log $(ZD^{1/2}C)$ plotted as a function of $1/T$. Values of $\Delta H^{\neq}$ for the post-nucleation-and-growth diffusion-limited intervals of approximately 40 kJ/mole (10 kcal/mole) were previously reported (1).

The assumption of a temperature-independent concentration is of unlikely validity, however. Furthermore, correct values of Z and C must be assigned at each temperature in order to obtain valid estimates of the preexponential factor in the Arrhenius equation and hence of the entropy of activation of the rate-limiting process.

At 25°C values of Z and C and the nature of the diffusing species were inferred from the data, using available kinetic and thermodynamic parameters for a multiphase model of the electrode (2). Values for relevant parameters at low temperatures are generally unavailable however and so have had to be estimated by relying on the following assumptions.

1. The same sequence of processes occurs at all temperatures up to the beginning of the formation of β-PbO_2. This assumption is based on the similarity of the potentiostatic transients at all temperatures studied (2).

2. The equilibrium concentration of the current-limiting diffusing species can be accurately estimated as a function of temperature by assuming a temperature-independent ΔH for the concentration-determining equilibria and that the integrated form of the van't Hoff equation (8) applies, *i.e.*, that

$$\ln\left(\frac{K_2}{K_1}\right)=\frac{-\Delta H}{R}\left(\frac{1}{T_2}-\frac{1}{T_1}\right)$$

where K_2 and K_1 are the equilibrium constants at temperatures T_2 and T_1, respectively.

3. Near-equilibrium conditions prevail during charging so that the equilibrium concentrations thus calculated can be identified with the quantity C in the values of $ZD^{1/2}C$ extracted from the kinetic data. This assumption may be the least tenable at the lowest temperatures and when there is appreciable current flow.

In order to obtain the temperature dependence of D, values of C were calculated for the diffusion-limited charging stages for which values of $ZD^{1/2}C$ had been obtained at most temperatures. It was assumed that the same diffusing species limited the current as at 25°C (2). The bisulfate-sulfate equilibrium was also considered, although previously judged unlikely (2). Accordingly, the van't Hoff equation was applied to the following equilibria

$$PbSO_4 = Pb^{++} + SO_4^{=} \quad \Delta H = 3.0 \text{ kcal/mole} \quad [I]$$

$$Pb^{++} + OH^- = PbOH^+ \quad \Delta H = -7.6 \text{ kcal/mole} \quad [II]$$

$$HSO_4^- = H^+ + SO_4^{=} \quad \Delta H = -5.2 \text{ kcal/mole} \quad [III]$$

In the case of [I], the value of ΔH was estimated from the solubility of $PbSO_4$ in water at 25° and 0°C (9) and from tables of thermodynamic data (10). Values of C as a function of T were thence obtained assuming that $C = [Pb^{++}] = [SO_4^{=}] = \sqrt{K_{sp}}$, *i.e.*, that the concentration of Pb^{++} is controlled by the solubility of $PbSO_4$ in near-neutral pore electrolyte solution (2, 3).

In the case of [II], ΔH was estimated from reported stability constants (11) of $10^{7.51}$ at 25°C (11a) and $10^{6.39}$ at 100°C (11b), determined by similar methods. Values of $C = [PbOH^+]$ could then be calculated as a function of temperature and pH using the value of $[Pb^{++}]$ obtained from [I]. For the bisulfate-sulfate equilibrium [III], ΔH was estimated from tables of thermodynamic data (10) and from values of the equilibrium constant determined over the range 5°-55°C (12).

The values of C thus calculated are given as a function of temperature in Table I. At 25°C the values of $D^{1/2}C$ for Pb^{++} and for $PbOH^+$ at pH = 7 are approximately equal. Thus the observed ratio of slopes $(ZD^{1/2}C)$ of 2:1 at 25°C previously discussed (2) supported the ratio of Z values of 2:1. It was, therefore, inferred that the last diffusing species to limit the current, before the first current minimum, was $PbOH^+$, and further that this stage was immediately preceded by limiting Pb^{++} diffusion. The ratio of slopes of 1:2 at −40°C, following deep discharge (Fig. 2), still supports the same sequence of rate limitation in spite of the apparent reversal in time of the ratio of slopes. This is explained by the much lower value of $[Pb^{++}]$ in comparison to $[PbOH^+]$ at −40°C. Thus, in order to interpret the single diffusion-limited interval observed following the standard discharge at −40°C (Fig. 1) and other low temperatures, the most probable assignment of diffusing species is the $PbOH^+$ ion.

Using the values of $C = [PbOH^+]$ at pH = 7 from Table I, values of D were calculated from the experimental data at each temperature and an Arrhenius plot was constructed (Fig. 3). At potentials below the reversible potential (in 35% sulfuric acid) of 1.087V, *i.e.*, at 0.9 and 1.0V, a linear relationship between log D and $1/T$ was obtained over most of the temperature range investigated. If the diffusion coefficient is given by

$$D = D_0 \exp(-\Delta H^{\neq}/RT)$$

Table I. Values of C (μmole cm^{-3}) calculated from van't Hoff equation

Species	Pb^{++}	$PbOH^+$	$PbOH^+$	H^+
ΔH (kcal/mole)*	3.0	−7.6	−7.6	−5.2
Equation	[I]	[II]	[II]	[III]
T(°C)		pH = 7	pH = 9	
25	0.147	0.117	11.7	12.4
15	0.123	0.153	15.3	16.8
0	0.092	0.24	24	28
−10	0.075	0.33	33	40
−20	0.060	0.46	46	59
−30	0 047	0 68	68	91
−40	0.036	1.02	102	144
−50	0.027	1.59	159	237

* 1 kcal = 4.18 kJ.

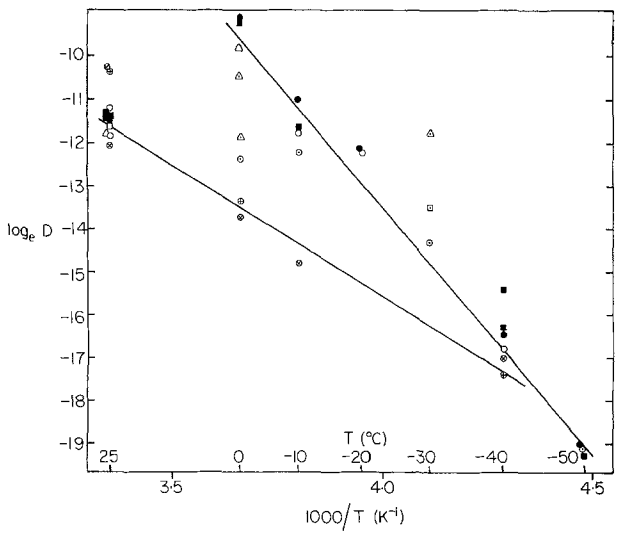


Fig. 3. Arrhenius plot for prenucleation-and-growth-peak diffusion-limited interval, assuming that the diffusing species is $PbOH^+$, pH = 7 (see text). Applied potentials were: ⊕, 0.9V; ⊗, 1.0V; ⊙, 1.1V; ●, 1.2V; ■, 1.3V; △, 1.4V; □, 1.5V.

values of $\Delta H^{\neq} = 11.4 \pm 0.9$ kcal/mole and log $D_o = 3.1 \pm 0.7$ describe the dependence of the diffusion coefficient on temperature. It is of interest to note that the values of D at 25°C and at higher potentials also fall on the same line. However, at higher potentials the linear dependence of log D on $1/T$ was not observed above 0°C. For the range of −50°-0°C, values of $\Delta H^{\neq} = 23.4 \pm 1.6$ kcal/mole and log $D_o = 14.6 \pm 1.5$ were determined for charging potentials of 1.1-1.5V. If it is assumed instead that the diffusing species is Pb^{++}, values of $\Delta H^{\neq} = 9 \pm 1.5$ and log $D_o = 3.5 \pm 1.1$ are obtained for the same range of temperature and potentials, but no unambiguous linear region is found at 0.9 and 1.0V.

Such high values of $\Delta H^{\neq}$ and D_o were also obtained from analysis of the diffusion-limited currents in the intervals following the nucleation and growth peak. Accordingly, the significance of such values will not be discussed until the derived results for the later intervals have been presented.

From the results at 25°C (2), it was concluded that the first diffusion-limited interval following nucleation-and-growth control was due to $PbOH^+$ diffusion at pH values increasing from 8.1 at 1.0V to 8.8 at 1.6V. In order to remain consistent with the semi-infinite linear diffusion model, it was concluded that this diffusion process could not begin until two-dimensional nucleation and growth were virtually complete. If the coordinates of the nucleation and growth peak were (t_m, i_m), this occurred at $t_o \simeq 1.5\ t_m$ for all potentials. If there had been some other explanation for the apparent inconsistency (negative current intercepts at infinite time) with the model and the diffusion processes began instead at $t_o = 0$, the diffusing species could have been either $PbOH^+$ at pH = 9.0 ± 0.5, or H^+ at pH ≃ 2, controlled by the sulfate-bisulfate equilibrium.

The reduced variable plots for the postnucleation-and-growth interval at −20°C are shown in Fig. 4. Similar results have previously been published for data obtained at −50°C (1) and at 25°C (2). As at 25°C, the intercept of the first linear i-$t^{-1/2}$ interval in the range $0.6 < (t/t_m)^{-1/2} < 0.8$ yields a negative current intercept at infinite time. If it is assumed that the diffusion process does not begin at $t_o = 0$, but after completion of the two-dimensional nucleation and growth process at $t_o \gtrsim 1.5\ t_m$, negative current intercepts (although less negative) were still obtained at all temperatures below 0°C, except at

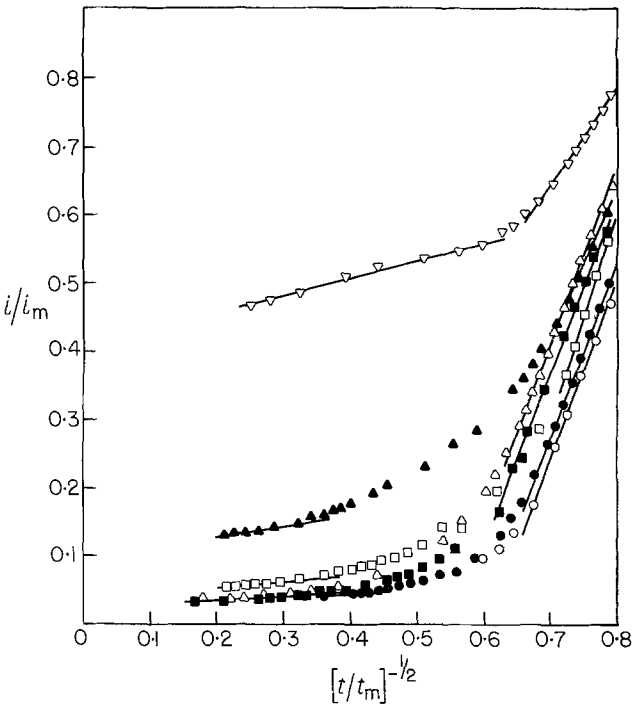


Fig. 4. Reduced variable plot of current vs. $t^{-1/2}$ for potentiostatic transients at various potentials and at −20°C, for postnucleation-and-growth interval. Values of (t_m, i_m) are indicated for each potential: ⊙, 1.1V (250 sec, 36.6 μA); ●, 1.2V (78 sec, 124 μA); ■, 1.3V (31.0 sec, 244 μA); △, 1.4V (14.55 sec, 473 μA); □, 1.5V (13.0 sec, 680 μA); ▲, 1.6V (10.45 sec, 898 μA); ▽, 1.7V (7.9 sec, 1.120 mA).

high potentials (≧ 1.5V for $t_o = 1.5$-$2.0\ t_m$) and at underpotentials (0.9 and 1.0V). This is illustrated for the same −20°C data in Fig. 5 for $t_o = 1.5\ t_m$.

It is apparent that some other or additional explanation is required for the negative intercepts at low temperatures. The shapes of such reduced variable plots are so little dependent on temperature that it is difficult to believe that different mechanisms for oxidation are operative at 25°C from those at temperatures below 0°C. What further effects could cause

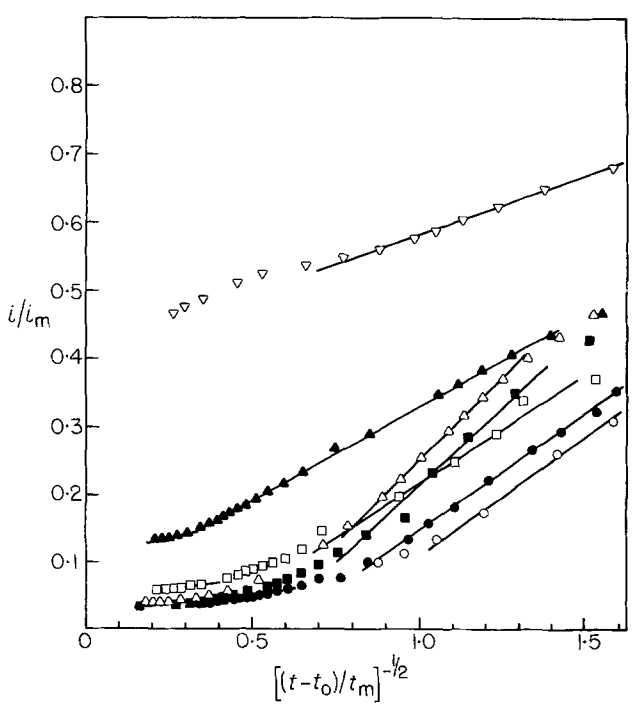


Fig. 5. Current vs. time$^{-1/2}$ (units of i_m, $t_m^{-1/2}$) for $t_o = 1.5\ t_m$. Symbols and data are identical to those of Fig. 4.

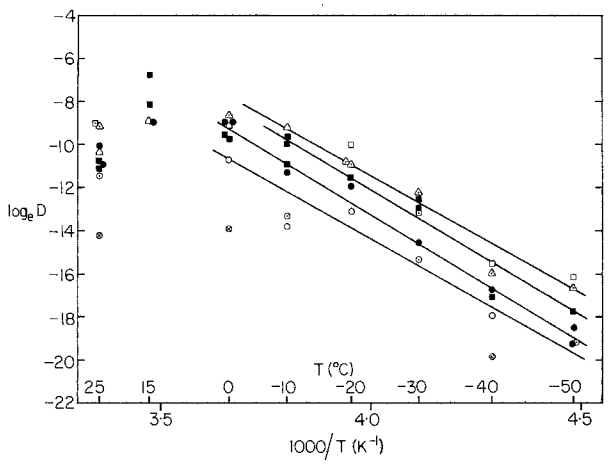


Fig. 6. Arrhenius plot for first diffusion-controlled postnucleation-and-growth-peak interval, assuming that the diffusing species is $PbOH^+$, pH = 9 (see text). Symbols have same significance as in Fig. 3.

the current to decrease more quickly at low temperatures than predicted by the diffusion model? One possibility is that, because of the longer time scales (*i.e.*, larger values of t_m) for oxidation at low temperatures, the diffusion layer begins to approach the dimensions of the film during the postnucleation-and-growth period, except at high overpotentials, where the values of t_m are still relatively small; *e.g.*, at 1.7V, t_m = 4-8 sec with no appreciable temperature dependence from 0° to −50°C [but note (2) that t_m was smaller by more than a factor of 10 at 25°C]. If the diffusion layer exceeds the film dimensions, erroneous application of the model would yield "virtual" concentrations, larger than the true concentrations at the source of the diffusing ions, and therefore high values of $ZD^{1/2}C$, *i.e.*, high i-$t^{-1/2}$ slopes. This explanation, however, fails to account for the more normal diffusionlike dependence of i on $t^{-1/2}$ at very long times. Furthermore, it would not be expected that the linearity of the i-$t^{-1/2}$ plots would be retained because the "virtual" concentration would be increasing with time so that the slope would also be expected to increase with time.

An alternative explanation is that depletion of the reactant species occurs at low temperatures due to partial blockage of the pores (discussed below) so that only a limited quantity of reactant is available for oxidation. As reactant is progressively consumed, the current would have to fall more quickly than predicted by the semi-infinite linear diffusion model. Such an effect might not necessarily predict a linear dependence of i on $t^{-1/2}$, but the deviation from linearity at longer times would be in the direction observed.

From data, such as given in Fig. 4, and the temperature dependence of concentration from Table I, values of diffusion coefficients were calculated as a function of temperature assuming that $C = [PbOH^+]$ at pH = 9. Very similar values were also obtained for $C = [H^+]$. The results are given in Fig. 6, where a linear dependence of ln D on $1/T$ can be observed at potentials of 1.1-1.4V over the temperature range of −50°-0°C. The parameters of the fitted lines are given in Table II for each potential and are of the order of $\Delta H^{\neq} = 23$ kcal/mole and $D_0 = 10^{-14}$. Although a somewhat more rigorous treatment would have been obtained by using the slopes of data plotted in the manner of Fig. 5, the values of the parameters of Fig. 6 would not be appreciably altered.

During the final diffusion-limited interval at 25°C, it was postulated (2) that the current was limited by the diffusion of tetravalent lead ions and that the internal acidity of the electrolyte in the pores of the electrode was greater than that in the bulk electrolyte. Following or during this interval the charging behavior at low temperatures appeared to become qualitatively different than at temperatures ≥ 0°C. Values of $ZD^{1/2}C$ yielded $D \geq 10^{-5}$ cm²/sec for $C \leq 10^{-5}$M. If $C = [Pb^{4+}]$, a pH of the order of −1 was necessary to obtain reasonable values of $D \simeq 10^{-5}$ cm²/sec. This local pH appeared to be determined by kinetic factors, not thermodynamic ones. Therefore, no estimate of the dependence of pH or of $[Pb^{4+}]$ on temperature is possible. Furthermore, the diffusing species may well be different at low temperatures than at 25°C. To obtain the activated diffusion parameters for this interval, a constant value of $C = 10^{-6}$ mole/cm³ was assumed (this corresponds to a temperature-independent local pH of −1.2 if a further assumption is made that Pb^{4+} is the diffusing ion) and the resulting Arrhenius plots are given in Fig. 7. Values of $\Delta H^{\neq}$ of the order of 10 kcal/mole (see Table II) were obtained for potentials ≥ 1.2V. At 1.1V, the slope was substantially smaller, corresponding to $\Delta H^{\neq} = 3.5 \pm 1$ kcal/mole.

Calculation of parameters of the activated state.— The theory of absolute reaction rate predicts that the diffusion coefficient can be described by an equation of the form (13)

$$D = e\lambda^2\left(\frac{kT}{h}\right)\exp(\Delta S^{\neq}/R)\exp(-\Delta H^{\neq}/RT)$$

where e is the base of the natural logarithms and λ, the "jump distance," is the distance between successive

Table II. Experimental activation parameters of diffusion

Diffusion interval ($i \propto t^{-1/2}$)	Potential (Hg,Hg_2SO_4) (V)	$\Delta H^{\neq}$ kcal mol^{-1}	$\log_{10} D_0$	$\Delta S^{\neq}$ (cal mole^{-1} °K^{-1})*	$\Delta H^{\neq}/T_0$ (cal mole^{-1} °K^{-1})*
Pre-nucleation-and-growth					
(a) $C = [PbOH^+]$	0.9-1.0	11.4 ± 0.9	3.1 ± 0.7	23	43
Fig. 3	1.1-1.4	23.4 ± 1.6	14.6 ± 1.5	75	94
(b) $C = [Pb^{++}]$	1.1-1.3	9.0 ± 1.5	3.5 ± 1.2	~25	36
First post-nucleation-and-growth	1.1	21.8	12.8	67	88
(a) $C = [PbOH^+]$					
Fig. 4	1.2	23.4	14.6	75	94
	1.3	22.9	14.7	76	92
	1.4,1.5	21.6	13.9	72	87
(b) $C = [H^+]$	1.1	23.1	13.6	71	93
	1.2	24.2	15.2	78	98
	1.3	23.9	15.4	79	96
	1.4	22.7	14.6	75	92
Last post-nucleation-and-growth	1.1	3.5 ± 1	−1.4	2	14
$ZC = 10^{-6}$ mole cm^{-3}	1.2-1.4	10.1 ± 2	4.3	28	41
Fig. 5	1.5	9.4 ± 2	4.3	28	37
	1.6	10.1 ± 2	5.2	32	40

* 1 cal = 4.184J.

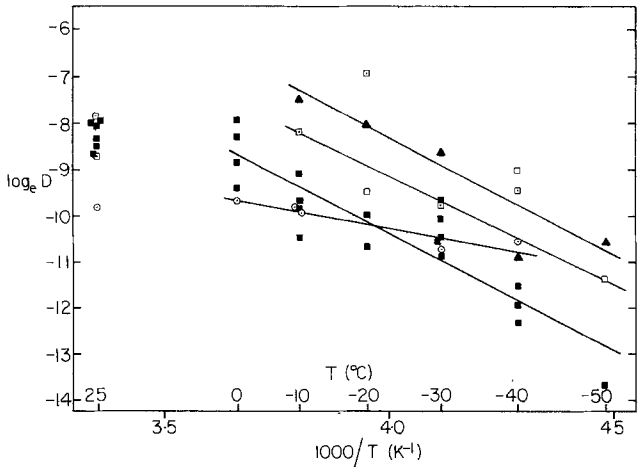


Fig. 7. Arrhenius plot for last diffusion-limited interval, assuming a temperature-independent diffusion-limiting species of concentration C = 10^{-6} mole cm^{-3}. Applied potentials were: ⊙, 1.1V; ■, 1.2-1.4V; ⊡, 1.5V; ▲, 1.6V.

equilibrium positions of the diffusing species. $\Delta S^{\neq}$ and $\Delta H^{\neq}$ are the molar activation entropy and energy, respectively, and the remaining constants have their usual significance.

From the experimental data one obtains a relationship of the form

$$D = D_0 \exp(-\Delta H^{\neq}/RT)$$

Thus, assuming an appropriate value for λ, $\Delta S^{\neq}$ can be obtained from the values of D_0 using the equation

$$\Delta S^{\neq}/R = \ln D_0 - \ln(e\lambda^2 kT/h)$$

For the values of $\Delta S^{\neq}$ given in Table II, it was assumed that $\lambda^2 \simeq 10^{-15}$ cm^2, *i.e.*, that λ was of the order of magnitude of the diameter of one water molecule. T was taken as the temperature at the middle of the linear range. The calculated values of $\Delta S^{\neq}$ are relatively insensitive to the value of the last term of the last equation above, for the large values of D_0 observed. Thus the choices of λ^2 and T do not become very important until log D_0 becomes less than 3 (at which point the error in $\Delta S^{\neq}$ becomes 10% for an error in $\lambda^2 T$ of a factor of 2). Included in Table II, for comparison with $\Delta S^{\neq}$, are values of $\Delta H^{\neq}/T$, calculated using the same average value of T as used for calculating $\Delta S^{\neq}$.

Interpretation.—The experimental results at 25°C were found to fit a multiphase model of the positively polarized lead electrode in sulfuric acid solution (2). The major feature of the model was a slightly alkaline (pH = 7-9) electrolyte in the pores between a protective lead sulfate layer and the lead substrate. The electrode material in this interior part of the electrode consisted of PbO, α-PbO_2, and basic sulfates of lead.

Such a dilute pore solution (as was required to fit the model) would certainly have been frozen if in the bulk state. In the pores a significant fraction of the water might be expected to be adsorbed on the pore walls or to be influenced by the short-range orienting forces of such adsorbed water.

A number of questions need to be answered in order to interpret the data presented. Some such questions are: Does the pore solution freeze at low temperature? If so what effects would such freezing have on the transport properties of the pore electrolyte constituents? Do the same diffusing species control the charging current at temperatures below the freezing point as at 25°C? If freezing does not occur, why not?

The similarity of the potentiostatic transients at all temperatures suggests that freezing does not occur. However, the sharp break in the Arrhenius plots at temperatures of 0° to −10°C suggests that it does. There are other such apparently conflicting phenomena and not only in this particular electrochemical system. In the case of water adsorbed on clays, for example, dielectric relaxation experiments, carried out in the microwave frequency range, indicated that below −10°C all water in excess of about two layers between the clay plates had formed ice (14). When the same experiments were done at radio frequencies, a dispersion in the two-layer-thick films of adsorbed water was observed. The unfrozen film of water decreased in thickness as the temperature was lowered from 0° to −10°C and then decreased no further below −10°C to below −50°C. The unfrozen water film must be strongly bound to the clay surface to resist freezing even at temperatures below −50°C.

Some idea of the type and strength of bonding of water on solids more similar to the lead electrode than clay can be deduced from thermal desorption studies of water on metal oxide surfaces. Studies of the adsorption of water vapor on PuO_2 (15) yielded desorption energies of 68 and 20 kcal/mole for the first and second adsorbed water layers, respectively, corresponding to 58 and 10 kcal/mole, respectively, for desorption to the aqueous phase. These may be compared to values (similarly converted to aqueous phase/solid phase adsorption) of 30 and 5 for ThO_2 (16), 19 and 9 for TiO_2 (17), and 50 and 10 for MgO (18) and W (15). It was proposed (15) that the larger adsorption energy corresponded to a dissociative chemisorption of water on the solid oxide, whereby one water molecule dissociated and reacted with one surface oxygen to produce two hydroxyl groups, each bound to a surface metal atom. The smaller adsorption energy was due to the "quasi chemisorption" of a second water layer onto the hydroxylated surface by hydrogen bonding. Beyond this second layer bulk water characteristics were quickly reached.

Such values, particularly for the case of TiO_2 (17) are similar to the activation energies given in Table II. Values of $\Delta H^{\neq} \gtrsim 13$ kcal mole^{-1} for PbO_2 formation have also been obtained from cyclic voltammetry measurements (19). An exception is the 3.5 kcal mole^{-1} activation energy for the last diffusion interval at 1.1V, which is characteristic of diffusion in bulk electrolyte.

The values of $\Delta H^{\neq}$ are therefore consistent, for the most part, with a model of the electrode in which the electrolyte in the pores is frozen, except for two or three layers of adsorbed water on the pore walls. The concentration-determining chemical equilibria and diffusion processes must therefore take place within an adsorbed film between the ice and pore walls (except for proton conduction which occurs very well in ice). Under such conditions, the dielectric constant of the aqueous film would be reduced, therefore favoring the formation of less highly charged (Z = 0 or 1) species than in bulk solution. Other changes in transport properties (*e.g.*, viscosity, diffusion) and thermodynamic properties (*e.g.*, equilibrium constants, activity coefficients) would also be expected to occur. It may be that such changes invalidate the rather simple-minded estimation of concentrations used here and that species other than those postulated on the basis of the 25°C experiments are the diffusing ions. Furthermore, it may be that the chemical reactions controlling the reactant concentrations are much further from equilibrium at low temperatures than at 25°C. No answers can be given to these objections at the present time except to explore further the consistency between the experimentally derived results and the model.

The values of $\Delta S^{\neq}$ (Table II) calculated from D_0 are unusually large for activated diffusion. Although

the large values of $\Delta H^{\neq}$ (~23 kcal/mole) might be interpreted as due to solid-state diffusion (1), this interpretation becomes less tenable in view of the concomitantly large values of $\Delta S^{\neq}$. The latter suggest the participation of desorption and/or desolvation processes during formation of the activated complex. Furthermore, the similar magnitudes of $\Delta S^{\neq}$ and $\Delta H^{\neq}/T$ suggest the possibility of a phase change such as desorption. Further evidence relevant to the role of desorption (or desolvation) was obtained at 25°C (2) where unusually low values of the transfer coefficient, near the beginning of the potentiostatic charge interval, were obtained. Such low values of α may have been due to rate control by the partial dehydration of the reactant ion or by a slow preceding homogeneous dissociation step.

Calculation of absolute values of the standard ionic entropies of solution (or hydration) is approximate because of the difficulties of determining an acceptable value for the reference ion (20, 21). The most recent, and probably most reliable, compilation (21) estimates values of $-\Delta S^{\neq}$ (hydration) of the order of 30 cal mole^{-1} °K^{-1} for small monovalent cations. For Ba^{++} and Sr^{++}, the ions most similar to Pb^{++} in size and charge, values of $-\Delta S \simeq 60$ cal mole^{-1} °K^{-1} are given (20).

If ionic diffusion occurs through, or within the influence of, layers of adsorbed water, desolvation (at least in part) of the diffusing ion probably is included in the activation process. In order for diffusion to occur to or from a reaction site, desorption of adsorbed water is also likely to be necessary. Values of ΔS for desorption from the charged electrode surface are expected to be of the same order of magnitude as from an ion, *i.e.* $\Delta S > 0$ and several tens of entropy units in magnitude.

Thus the model which emerges, for diffusion at low temperatures, is that of a near-surface diffusion process in the water layer between the pore walls and ice activated by partial ionic desolvation and/or electrode desorption processes. For those processes having values of $\Delta H^{\neq} \simeq 10$ kcal mole^{-1} and $\Delta S^{\neq} \simeq 28$ cal mole^{-1} °K^{-1}, the activation may involve desorption of the second "pseudochemisorbed" water layer from the electrode, or partial desolvation of the diffusing ion. For the values of $\Delta H^{\neq} \simeq 23$ kcal mole and $\Delta S^{\neq} \simeq 75$ cal °K^{-1} mole^{-1}, activation may involve desorption of the chemisorbed (hydroxylated) layer of surface water or both desorption and partial desolvation processes. Some part of the value of $\Delta S^{\neq}$ may be due to irreversibility but since this is impossible to estimate it is difficult to be more specific about the details of the activation process.

One experimental value that was obtained for the final diffusion process at 1.1V does not fall into either of these categories. In this case the values of the activation parameters were typical of diffusion in bulk aqueous solution. However, it is possible that the potentiostatic transients for the experiments at 1.1V were not followed for a long enough period of time and that the results obtained at this potential are characteristic of fortuitous linearities in the intermediate time interval following nucleation and growth previously mentioned (2). Examination of the i/i_m *vs.* $(t/t_m)^{-1/2}$ plots for the data at −40°C suggests that the experiment was terminated too soon, *i.e.*, at too large a value of $(t/t_m)^{-1/2} \simeq 0.45$, and that at least one more linear region might have been expected to occur had the experiment been continued. At −50°C the experiment had definitely been terminated prematurely. Hence the activation parameters calculated for 1.1V applied potential may be spurious.

The values obtained for $\Delta H^{\neq}$ and $\Delta S^{\neq}$ depend on a number of stated but unproven assumptions. The values of D_0 and hence $\Delta S^{\neq}$ will also be sensitive to the electrode roughness factor and to the slope of the Arrhenius plots, *i.e.*, to $\Delta H^{\neq}$. The latter term is independent of electrode area but sensitive to changes of roughness factor or values of ZC with temperature, terms which are used to calculate the temperature dependence of D. Even if these assumptions are seriously wrong, however, the calculated values of $\Delta S^{\neq}$ still would be larger than expected for diffusion in bulk electrolyte, unless the dissociation reactions which determine reactant concentrations have very large and positive values of ΔH, or the concentrations decrease much more strongly with temperature than calculated, for other reasons. Furthermore, very large roughness factors would have to be obtained to seriously alter the interpretation of the large $\Delta S^{\neq}$ values.

In view of the number of assumptions required to interpret the experimental results in a consistent manner, it would be unreasonable to claim that solid-state diffusion has been completely disproven, or that the sequence of rate-limiting diffusion processes proposed is correct in all its details. However, whether or not all of the diffusing species have been correctly identified, it is possible to construct a model of the kinetics of the constant potential charging process consistent with all of the quantitative results presented here and in the previous paper (2). The conclusions, based on such a model, are summarized as follows.

Conclusions

The first stages of the potentiostatic formation of lead dioxide on lead in aqueous sulfuric acid proceeds in a similar manner at 25°C as at lower temperatures (to ≤ −50°C) with one important difference. At 25°C, before application of the charging potential, the electrolyte deep within the pores is relatively dilute and slightly alkaline due to the impermeability of a thick lead sulfate film to certain ions responsible for the creation and maintenance of an alkaline electrode interior. At temperatures much below 0°C, the electrolyte in the pores probably freezes except for a very thin film (a few molecular diameters) of adsorbed water between the pore walls and the frozen electrolyte. At low temperatures, therefore, the diffusion processes must take place through this adsorbed water phase or through a barrier caused by some other mechanism of pore blockage. Furthermore, the chemical reactions, which supply reactants for the electrochemical steps or remove products, must also occur in this interfacial phase, probably with altered equilibrium constants or under conditions further removed from equilibrium.

Rate-limiting diffusion of ions, such as $PbOH^+$ or Pb^{++}, is controlled by an activation process involving partial dehydration of the diffusing ion and/or desorption of interfacial water. Prior to the two-dimensional nucleation and growth interval (when basic sulfates are oxidized in a thin layer beneath the lead sulfate), the current appears to be controlled almost entirely by the diffusion of $PbOH^+$ ions at low temperatures. The interval of control by Pb^{++} ions which appeared at room temperature is almost completely absent at low temperatures due to the relative decrease of $[Pb^{++}]$ with respect to $[PbOH^+]$ as temperature decreases. Following growth of the α-PbO_2 layer separating PbO from $PbSO_4$, further diffusion control occurs. At first, oxidation of PbO beneath the α-PbO_2 layer is apparently limited by $PbOH^+$ diffusion.

The PbO continues to be oxidized at 25°C until consumed, at which time the internal pH decreases to a value less than that of bulk electrolyte and β-PbO_2 production is initiated. At low temperatures, depletion of reactant $PbOH^+$ within the pores results from pore blockage, probably due to ice formation, and to the slowness of reestablishment of the equilibrium controlling its concentration.

The last of the diffusion-controlled processes investigated appeared to involve the diffusion of tetravalent lead at 25°C to product β-PbO_2 nuclei and initiate three-dimensional growth of β-PbO_2 on $PbSO_4$ in contact with bulk electrolyte. At low temperatures, this stage does not appear to be attained and the oscillations of faradaic current and capacitance related to its occurrence (2) are completely absent below −30°C. The current, instead of increasing once more as occurs at higher temperatures, decreases monotonically toward zero. This would be expected if the internal acidity of the electrode remained well below that of the bulk electrolyte and unoxidized PbO remained beneath the $PbSO_4$ and α-PbO_2, near the end of charge acceptance. A steady-state concentration of $PbOH^+$ much lower than its solubility might be attained, limited by the rate of its production within the confinement of the adsorbed water layer or blocked pore spaces, whereas at high temperatures production and diffusion of reactant ions would be much quicker. It is also possible that pores eventually become almost completely closed at low temperatures due to the presence of ice and the positive volume of oxidation of PbO to PbO_2 or due to persulfate production (22) and adsorption.

Still other reasons might be suggested, but first it would be of interest to obtain chemical or physical information to test the model postulated to fit the electrochemical data. Work along these lines has been commissioned and is currently in progress.

Acknowledgments

This work was issued as Defence Research Establishment Ottawa Report No. 742.

Manuscript submitted April 13, 1976; revised manuscript received Oct. 1, 1976.

Any discussion of this paper will appear in a Discussion Section to be published in the December 1977 JOURNAL. All discussions for the December 1977 Discussion Section should be submitted by Aug. 1, 1977.

Publication costs of this article were assisted by the Defense Research Establishment Ottawa.

REFERENCES

1. E. M. Valeriote and L. D. Gallop, in "Power Sources 5," D. H. Collins, Editor, p. 55, Academic Press, London (1975); Def. Res. Est. Ottawa, DREO Report No. 717 (May 1975).
2. E. M. Valeriote and L. D. Gallop, *This Journal*, **124**, 370 (1977).
3. P. Ruetschi, *ibid.*, **120**, 331 (1973).
4. P. Ruetschi and R. Angstadt, *ibid.*, **111**, 1323 (1964).
5. D. Pavlov, Proceedings of the Symposium on Batteries for Traction and Propulsion, p. 135, Columbus Section of The Electrochemical Society (1972).
6. D. Pavlov, G. Papazov, and E. Bashtavelona, *This Journal*, **121**, 854 (1974).
7. D. Pavlov, *Electrochim. Acta*, **13**, 2051 (1968).
8. S. Glasstone, "Testbook of Physical Chemistry," 2nd ed., pp. 828-31, Macmillan, London (1948).
9. G. W. Vinal, "Storage Batteries," 4th ed., p. 183, John Wiley & Sons, New York (1955).
10. "Handbook of Chemistry and Physics," 45th ed., The Chemical Rubber Company, Cleveland, Ohio (1964).
11. L. G. Sillén, "Stability Constants of Metal-Ion Complexes, Section I: Inorganic Ligands," The Chemical Society, London (1964); (a) J. K. Wood, *J. Chem. Soc.*, **97**, 878 (1910); (b) C. Kullgren, *J. Phys. Chem.*, **85**, 466 (1913).
12. R. A. Robinson and R. H. Stokes, "Electrolyte Solutions," 2nd ed., p. 387, Butterworths, London (1959).
13. S. Glasstone, K. J. Laidler, and H. Eyring, "The Theory of Rate Processes," p. 524, McGraw-Hill, New York (1941).
14. P. Hoekstra and W. T. Doyle, *J. Colloid Interface Sci.*, **36**, 513 (1971).
15. J. L. Stakebake, *J. Phys. Chem.*, **77**, 581 (1973).
16. H. F. Holmes, E. L. Fuller, Jr., and C. H. Secoy, *ibid.*, **72**, 2095 (1968).
17. C. M. Hollabaugh and J. J. Chessick, *ibid.*, **65**, 109 (1961).
18. P. J. Anderson, R. F. Horlock, and J. F. Oliver, *Trans. Faraday Soc.*, **61**, 2754 (1965).
19. T. G. Chang, M. M. Wright, and E. M. L. Valeriote, Paper No. 7, Proceedings of the Tenth International Power Sources Symposium, Brighton, England (September 1976); DREO Report No. 753.
20. R. A. Robinson and R. H. Stokes, "Electrolyte Solutions," 2nd ed., pp. 16, 70, Butterworths, London (1959).
21. J. E. Desnoyers and C. Jolicoeur, in "Modern Aspects of Electrochemistry," Vol. 5, J. O'M. Bockris and B. E. Conway, Editors p. 16ff., Plenum Press, New York (1969).
22. C. Gardner and F. Rocheleau, DREO Technical Note No. 75-1, Dept. of National Defence, Ottawa, Canada (1975).

Moving Resistive Wire Electrodes

Richard Alkire* and Richard Varjian*,[1]

Department of Chemical Engineering, University of Illinois, Urbana, Illinois 61801

ABSTRACT

The current and potential distributions have been calculated along the surface of a resistive wire moving with steady speed along the axis of a cylindrical electrolysis cell. The wire movement creates a laminar boundary layer of nonuniform thickness in an otherwise stagnant electrolyte. The mathematical analysis includes consideration of ohmic wire resistance, convective mass transport, ohmic electrolyte resistance, charge-transfer polarization, and cell geometry. Transport equations describing cell operation at all fractions of the limiting current were solved by the method of orthogonal collocation. A comparison between calculations which use a local mass transfer coefficient to describe the mass transfer process, and those which use a complete solution of the convective diffusion equation, gave agreement to within 15% over a wide range of parameter space which includes most practical applications of moving resistive wire electrodes.

The behavior of an electrolysis cell can often depend on factors such as cell geometry electrolyte resistance, electrode polarization, and mass transport. The relative importance of these several factors depends on the level of current passing through the cell. Because the current distribution within a cell is usually not uniform, the relative importance of these factors can vary with position within the cell. Therefore it is helpful to know the current distribution in order to understand which factors control cell behavior.

The present investigation is concerned with a cell having an electrode of significant ohmic resistance. The resistive loss in the metal phase leads thereby to a nonuniform potential distribution in the metal which may adversely affect the current distribution along the surface. For many systems electrodeposits of high quality are obtained only over a narrow range of current density. Therefore a highly nonuniform current distribution can be detrimental to product quality owing to variations in plating thickness, adherence, mechanical properties, composition, and appearance. In light of these practical considerations, the present study has been undertaken to elucidate the behavior of moving resistive electrodes. A mathematical model has been developed (1) which takes simultaneous account of the concentration field and the potential fields in both the electrode and electrolyte phases. The study expands on an earlier analysis of resistive wire electrodes in the absence of concentration overpotential (2).

The development of theoretical models of resistive electrodes was reviewed previously (2) and it was noted that the role of mass transfer was incorporated in only two treatments: with uniform stirring (3) and with unsteady-state diffusion (4). Experimental studies on wire electrodes were also reviewed previously (2); since then, measurements have been reported on the current distribution along resistive wires (5) and the mass transfer rates for various flow configurations (6).

The movement of a continuous wire or sheet through a liquid leads to the formation of a hydrodynamic boundary layer along its surface. The literature on industrial wireplating indicates that for typical wire velocities and tank dimensions, the Reynolds number is 10^7 for tin plating (0.25 m/sec, 4m bath length) and 8×10^4 for alloy plating (0.02 m/sec, 4m bath length). Since the laminar boundary layer is stable up to Reynolds numbers between 1 to 5×10^6 (7, 8), the laminar convective diffusion equation seems to be a reasonable basis for predicting mass transport of reactants to the wire surface in practical cell configurations.

Fundamental studies on laminar heat, mass, and momentum transfer at moving filaments and sheets have been carried out in relation to fiber and sheet processing in the plastic, paper, and film industries. The pioneering hydrodynamic work of Sakiadis (9) employed the von Karman-Pohlhausen integral approximation to integrate the laminar boundary layer equations. The same integral method was used to integrate the heat transfer equation (10) and comparison with experimental data (11) indicated that natural convection effects were important (12). The von Karman-Pohlhausen technique was also used to determine the mass transfer coefficient on a moving cylinder (13), and to evaluate the heat transfer between a cylindrical laminar liquid jet and the surrounding gas phase (14). Sakiadis' tabulated data for the stream function were fit to a power series and substituted into the convective diffusion equation to generate a mass transfer correlation (15). Other integral approximations were also used for the hydrodynamic equations which gave good agreement with drag measurements (16). Numerical methods of integration have also been used for the hydrodynamic boundary layer equations (17-19) and compared with approximate methods (20); non-Newtonian fluids have also received treatment by numerical integration of the hydrodynamic equations (21, 22). An exhaustive theoretical treatment of laminar transport at moving continuous surfaces was provided by Crane (23). The stability of the laminar boundary layer was estimated for wires (7) and sheets (8) to be in the vicinity of Reynolds numbers (based on wire length) of $1\text{-}5 \times 10^6$. Heat transfer to moving surfaces has also been carried out under conditions of turbulent transport (24) and radiative transport (25). Problems involving coupled convection in adjacent liquid phases, as encountered in fiber-spinning operations, have been treated by several methods including similarity transformations (26, 27), numerical methods (28), perturbation methods (29), the method of matched asymptotic expansions (30), and conjugate methods (38).

Comparison of transport rates at moving and stationary surfaces (31) has indicated that the transport coefficients at moving surfaces are higher than at stationary surfaces provided that the Schmidt or Prandtl numbers exceed unity, an observation also noted by Chin (15). Electrochemical limiting current experiments with moving wires in an otherwise stationary electrolyte (7) have confirmed that the limiting current varies with $Sc^{1/2}$ instead of $Sc^{1/3}$ as found at stationary planar solid surfaces. The implications of this observation will be developed more fully in the development of Eq. [4] below.

It is abundantly clear that a great deal of existing fundamental work on laminar and turbulent boundary

* Electrochemical Society Active Member.
[1] Present address: Dow Chemical USA, Central Research Inorganic Laboratory, Midland, Michigan 48640.
Key words: current distribution, mathematical model, mass transfer, laminar flow, resistive wire.

layer phenomena can be used to describe mass transfer aspects of moving wire electrochemical systems. The flow configuration of industrial electrolysis cells may, however, be more complex than could be accounted for by simple boundary layer models. Wire vibrations (32) or the existence of more complex flow fields outside the boundary layer (6) require that the mass transfer coefficient be determined experimentally under limiting current conditions. However, mass transfer correlations determined at the limiting current are not strictly valid for predicting mass transport behavior below the limiting current. Naturally the question arises as to what errors would be encountered when an empirical limiting current correlation is used to account for mass transport during electrodeposition below the limiting current.

In the study reported below, a model is developed for a resistive wire electrode moving with steady speed through an electrolysis cell. Mass transfer through the laminar boundary layer on the wire surface is accounted for by a rigorous method and by an approximate method, and the two methods are compared. The rigorous method consists of solving the convective diffusion equation along with the potential field equations in both electrolyte and electrode phases; this approach is valid at all fractions of the limiting current density. The approximate method consists of using a local mass transfer coefficient as measured, for example, by the limiting current distribution, to account for mass transfer processes below the limiting current.

Mathematical Development

Figure 1 illustrates essential features of the electrolysis cell to be studied. A wire electrode moves along the axis of the cell with velocity V_s, and electrolysis proceeds on the wire surface under steady conditions. A cylindrical counterelectrode extends the length of the cell. Owing to the motion of the wire through the cell a steady fluid motion is established within the cell, one characteristic feature being the presence of a hydrodynamic boundary layer adjacent to the moving wire. The thickness of the hydrodynamic boundary, which varies with position along the wire, is depicted in greatly exaggerated fashion by the dashed line in Fig. 1. Although hydrodynamic end effects, at $z = 0$ and $z = L$, are expected to be complex, the region of complexity is small with respect to the wire length and are disregarded in the following treatment. Owing to the nonuniform boundary layer, the limiting current density varies with position along the wire. Electrical contact to the wire may be made on either or both sides of the cell.

The following analysis of a moving resistive wire electrode incorporates the effects of ohmic resistance of the wire electrode, activation overpotential of the electrochemical reaction, ohmic resistance of the electrolyte, concentration overpotential associated with the mass transfer boundary layer, geometry of the electrolysis cell, and mode of electrical contact. Several characteristics of the electrochemical system have been assumed to exist: (*i*) Electrolysis occurs under steady conditions, and the system is isothermal; (*ii*) the wire electrode is long and thin so that the potential distribution within it is one-dimensional; (*iii*) a single electrochemical reaction occurs with reversible Butler-Volmer kinetics; (*iv*) the wire electrode moves with steady velocity and without vibration and the boundary layer along its surface is laminar; (*v*) supporting electrolyte suppresses migration of reactants, and the Schmidt number is large; and (*vi*) the counterelectrode surface area is sufficiently large that it is unpolarized.

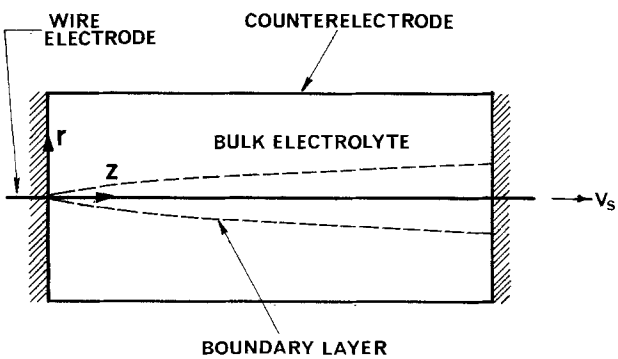


Fig. 1. Cell geometry for moving wire model

Two methods were used for incorporating mass transport effects into the model. The more rigorous method involved integrating the equation of convective diffusion. The second method used an algebraic expression for local variation of the mass transfer coefficient.

As indicated in Fig. 1, the coordinate system is fixed at the left end of the cell, where the wire enters. The z-coordinate is along the wire length, while the r-coordinate extends from the wire surface, r_1, to the tubular counterelectrode surface at r_2.

The electrochemical reaction at the metal surface is

$$s_1 M_1^{z_1} = s_2 M_2^{z_2} + ne^-$$

The local reaction rate depends on the local potential difference between metal and solution phases, and upon the local concentration of reactant at the electrode surface

$$j(z) = i_o \left\{ \left(\frac{c_{s,1}(z)}{c_{b,1}} \right)^{(\gamma+\alpha)} e^{\frac{\alpha nF}{RT}[\phi_m(z) - \phi_s(z)]} - \left(\frac{c_{s,2}(z)}{c_{b,2}} \right)^{(\gamma-\alpha+1)} e^{\frac{(\alpha-1)nF}{RT}[\phi_m(z) - \phi_s(z)]} \right\} \quad [1]$$

The variation of potential in the wire phase is related to the reaction rate distribution along its surface by

$$j(z) = \frac{r_1 \sigma}{2} \frac{d^2\phi_m(z)}{dz^2} \quad [2]$$

The boundary conditions on Eq. [2] depend on the mode of electrical contact. For contact at the left side only

$$\phi_m(0) = \phi_A, \quad \frac{d\phi_m(L)}{dz} = 0$$

for the right side only

$$\frac{d\phi_m(0)}{dz} = 0, \quad \phi_m(L) = \phi_A$$

and for both sides

$$\phi_m(0) = \phi_A, \quad \phi_m(L) = \phi_A$$

Although the variation of potential in the solution phase is generally two-dimensional for the cell configuration under study, our earlier work in the absence of mass transfer effects (2) indicated that a one-dimensional approximation is valid for all cell geometries associated with practical applications. At significant fractions of the limiting current density, the approximation is expected to continue to hold since the ohmic resistance of the electrolyte phase would exert an even smaller influence on the over-all system behavior. The potential in the solution phase at the outer edge of the mass transfer boundary layer is therefore related to the reaction rate distribution by

$$j(z) = \frac{\kappa}{r_1 \ln\left(\frac{r_2}{r_1}\right)} \phi_s(z) \quad [3]$$

In order to obtain a relationship between the reac-

tion rate distribution and the concentration distribution of reactant at the electrode surface, two methods were investigated.

Convective diffusion equation.—When, following our introductory remarks, the Schmidt number is large in a moving wire system, then experiments have shown that the average limiting current varies with the square root of the wire speed. This observation is consistent with the interpretation that the velocity within the mass transfer boundary layer is essentially constant and is equal to the speed of the wire: that is, mass transfer analysis follows the penetration theory formulation (39). The convective diffusion equation is therefore

$$v_s \frac{\partial c_i}{\partial z} = D_i \frac{1}{r} \frac{\partial}{\partial r}\left(r \frac{\partial c_i}{\partial r} \right) \qquad [4]$$

In order to use Eq. [4] to relate the surface concentration to the surface flux, it is necessary first to calculate the limiting current density for which the boundary conditions on Eq. [4] would be

$$c_i = 0 \quad \text{at} \quad r = r_1, \quad z > 0$$
$$c_i = c_{b,i} \quad \text{at} \quad r = \infty, \quad z > 0$$
$$c_i = c_{b,i} \quad \text{at} \quad z = 0$$

The solution of Eq. [4] yields (33) the limiting current distribution

$$\underset{\text{lim}}{j(z)} = \frac{n\mathbf{F}D_i}{s_i} \frac{\partial c_i}{\partial r}\bigg|_{r=r_1} = \frac{4n\mathbf{F}c_{b}D_i}{s_i \pi^2} \int_0^\infty e^{\frac{-D_i u^2 z}{v_s}} \frac{du}{u[J_0^2(ur_1) + Y_0^2(ur_1)]} \qquad [5]$$

For electrolysis cells of typical industrial size, the quantity $D_i z/v_s r_1^2$ is less than unity so that Eq. [5] may be expressed as

$$\underset{\text{lim}}{j(z)} \simeq \frac{n\mathbf{F}c_{b}D_i}{s_i r_1} \left\{ \left(\frac{\pi D_i z}{v_s r_1^2} \right)^{-1/2} + \frac{1}{2} - \frac{1}{4\pi} \left(\frac{\pi D_i z}{v_s r_1^2} \right)^{1/2} + \frac{1}{8\pi} \left(\frac{\pi D_i z}{v_s r_1^2} \right) + \cdots \right\} \qquad [6]$$

By applying Duhamel's theorem to Eq. [6], a relationship is obtained between the surface concentration and the surface flux (reaction rate) which is valid at all fractions of the limiting current density for both reactant and product species

$$j_i(z) = \frac{n\mathbf{F}D_i}{s_i r_1} \int_0^z \frac{dc_i}{dz_0}\bigg|_{r=r_1} \left\{ \left[\frac{\pi D_i (z - z_0)}{v_s r_1^2} \right]^{-1/2} + \tfrac{1}{2} - \tfrac{1}{4}\pi \left[\frac{\pi D_i (z - z_0)}{v_s r_1^2} \right]^{1/2} + \tfrac{1}{8}\pi \left[\frac{\pi D_i (z - z_0)}{v_s r_1^2} \right] + \cdots \right\} dz_0 \qquad [7]$$

Equations [2], [3], and [7] describe the transport of chemicals and energy to the reactive surface where electrolysis occurs by Eq. [1] These four equations may be made dimensionless by defining

$$\zeta = \frac{z}{L} \qquad \rho = \frac{r}{r_1}$$
$$C_{s,i} = \frac{c_{s,i}}{c_{b,i}} \qquad \Phi = \frac{n\mathbf{F}}{RT}\phi$$
$$J = \frac{2Lj}{r_1 i^*} \qquad \beta = \frac{n\mathbf{F}Li^*}{\sigma RT}$$

so that the dimensionless model equations are

$$J(\zeta) = \frac{\xi}{\beta} \left\{ C_{s,1}(\zeta)^{(\gamma+\alpha)} \exp\left[\alpha(\Phi_m(\zeta) - \Phi_s(\zeta)\right] - C_{s,2}(\zeta)^{(\gamma-\alpha+1)} \exp\left[(\alpha - 1)(\Phi_m(\zeta) - \Phi_s(\zeta))\right] \right\} \qquad [8]$$

$$J(\zeta) = \frac{1}{\beta} \frac{d^2\Phi_m(\zeta)}{d\zeta^2} \qquad [9]$$

$$J(\zeta) = \frac{2}{\psi\beta \ln \rho_0} \Phi_s(\zeta) \qquad [10]$$

$$J(\zeta) = \frac{\xi}{s_i \chi_i a \beta} \left\{ \int_0^\zeta \frac{\partial C_{s,i}}{\partial \zeta_0}\bigg|_{\zeta=1} \left[\left(\frac{\pi(\zeta - \zeta_0)}{\mathrm{Re_L Sc_i} a^2} \right)^{-1/2} + \tfrac{1}{2} - \tfrac{1}{4}\pi \left(\frac{\pi(\zeta - \zeta_0)}{\mathrm{Re_L Sc_i} a^2} \right)^{-1/2} + \tfrac{1}{8}\pi \left(\frac{\pi(\zeta - \zeta_0)}{\mathrm{Re_L Sc_i} a^2} \right) + \cdots \right] \right\} d\zeta_0 \qquad [11]$$

The method of electrical contact is used to define the boundary conditions for Eq. [9]. Referring to Fig. 1, the conditions

$$\Phi(0) = \Phi_A, \qquad \Phi'(1) = 0$$

correspond to making electrical contact on the left side (where the wire enters) and not on the right side. The conditions

$$\Phi'(0) = 0, \qquad \Phi(1) = \Phi_A$$

correspond to making electrical contact on the right side only (where the wire leaves the cell). Making electrical contact on both sides of the cell corresponds to the conditions

$$\Phi(0) = \Phi_A, \qquad \Phi(1) = \Phi_A$$

Results will be presented for all three possible contact configurations.

In the model, the potential Φ_A is the independent variable. The current β is computed after the potential distribution is known. Notice that β appears in the model only as the product βJ; the current and the current distributions are therefore evaluated after having the potential distribution in hand by requiring that $\int_0^1 J dZ = 1$.

The parameters which appear in the model equations are

$$\xi = \frac{2n\mathbf{F}L^2 i_0}{\sigma r_1 RT}, \qquad \chi_1 = \frac{i_0 L}{n\mathbf{F}c_{b,i}D_i}$$
$$\psi = \frac{r_1^2 \sigma}{L^2 \kappa}, \qquad \mathrm{Re_L} = \frac{v_s L}{\nu}, \qquad \mathrm{Sc_i} = \frac{\nu}{D_i}$$
$$a = \frac{r_1}{L}, \qquad \rho_0 = \frac{r_2}{r_1} \qquad [12]$$

Equations [8], [9], [10], and [11] were solved by the method of orthogonal collocation (34, 35). The basis of the method lies in proposing a trial solution to the problem in the form of a finite series of orthogonal polynomials. The N coefficients of the finite series are then suitably chosen to force the trial solution to satisfy the actual system equations at N distinct points, where N is a small number. The number of collocation points, N, is carefully chosen to obtain the best estimate of the total current passing through the cell. The collocation points are picked as the zeroes of the Legendre polynomials of degree N shifted to be orthogonal in the closed interval [0, 1]. Integral quantities (for example, the total current) are then evaluated with use of Gauss-Legendre quadrature. Details concerning the present problem, including computer program listings, are available (1).

Mass transfer coefficient equation.—The second method used to account for concentration variations is

to use the local mass transfer coefficient, as defined under limiting current conditions, to describe mass transfer processes at currents beneath the limiting current. In order to be comparbale with the preceding rigorous model, the local mass transfer coefficient used here will be chosen so as to give the same limiting current density as Eq. [4]; for simplicity, however, radial curvature terms have been deleted. By this method, the relation between reaction rate and surface concentration is

$$j(z) = \frac{nF}{s_i}\left(\frac{D_i v_s}{\pi z}\right)^{1/2} [c_{b,i} - c_{s,i}(z)] \qquad [13]$$

or, in dimensionless notation

$$J(\zeta) = \frac{\xi}{s_i \chi_i \beta^-}\left(\frac{\mathrm{Re_L Sc_i}}{\pi\zeta}\right)^{1/2} [1 - C_{s,i}(\zeta)] \qquad [14]$$

By this method, the model consists of Eq. [8], [9], [10], and [14]. For this approximation, in which curvature effects have been neglected, the mass transfer coefficient is assumed to vary with position as though the surface concentration were constant, an assumption which would not conform to actual conditions below the limiting current. However, it is of interest to examine such an approximation since, as mentioned earlier, mass transfer behavior in complex flow fields may only be available in the form of limiting current correlations.

The equations were linearized about trial solutions, placed in finite difference form and solved by matrix inversion (36) with successive correction toward convergence.

Results and Discussion

The dimensionless parameters listed in Eq. [12] can be used to estimate the relative importance of wire resistance, electrode polarization, electrolyte resistance, mass transport, and cell geometry. The parameters ξ, ψ, ρ_0, and a appeared in our earlier treatment (2) and received attention as to their qualitative influence on system behavior in the absence of mass transport effects. The parameter ξ has a large value when a very rapid reaction occurs on an electrode of low conductivity; provided that operation is below the limiting current, the applied potential would be consumed more by the electrode resistance overpotential than by charge-transfer overpotential. Therefore the electrochemical reaction would tend to occur primarily near the electrical contact end of the wire and the current distribution along the wire would be nonuniform. The parameter ψ has a large value when the applied potential is consumed more by ohmic losses in the electrolyte than by ohmic losses in the electrode phase. The geometric parameters ρ_0 and a describe the cell configuration and influence the potential distribution in the electrolyte phase.

The influence of mass transport limitations depends on how close the current is to the limiting current. The average limiting current density for moving wires is determined by integrating Eq. [5] over the length of the wire electrode. Numerical results (37) are given in dimensionless form by the solid line in Fig. 2. The dotted line in Fig. 2 corresponds to the limiting current obtained from the approximation of Eq. [6]; it is this approximate form which appears in Eq. [11] of the model. It may be seen from Fig. 2 that the approximation is accurate to within 4.8% when $1/\mathrm{Re_L Sc_i} a^2 = 1$. For typical industrial cells, the value of $1/\mathrm{Re_L Sc_i} a^2$ rarely exceeds unity so that the approximation of Eq. [6] is adequate. The approximation is used because it is more conveniently manipulated than Eq. [5]. Finally, the dashed line in Fig. 2 corresponds to the neglect of all curvature terms in which case the limiting current is

$$\beta_{\mathrm{lim}} = \frac{2\xi}{s_i \chi_i}\left(\frac{\mathrm{Re_L Sc_i}}{\pi}\right)^{1/2} \qquad [15]$$

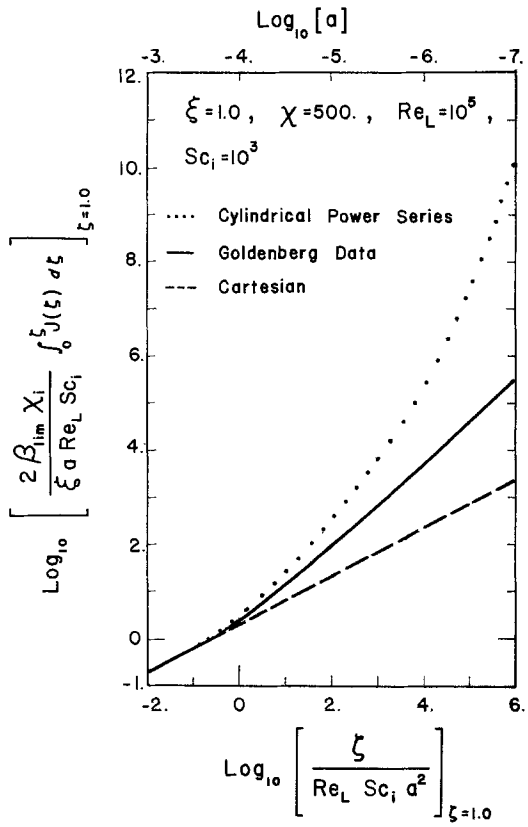


Fig. 2. Average limiting current density for moving wires and sheets

and the limiting current distribution is $J_{\mathrm{lim}} = \frac{1}{2}\sqrt{\zeta}$. As seen from Fig. 2, the neglect of radial curvature terms is appropriate under the condition that $\zeta/\mathrm{Re_L Ss_i} a^2 < 0.1$. In summary, Fig. 2 provides the limiting current density for moving wire electrodes. If the current density flowing in the cell is at an appreciable fraction of the limiting current density then mass transfer processes will influence behavior.

In the following paragraphs the role of mass transfer processes near the limiting current are discussed. Results are given both for the convective diffusion model and for the simpler mass transfer coefficient model. In all cases reported, the potential distribution in the electrolyte phase falls within the region where the one-dimensional approximation of Eq. [3] is accurate as has been described previously (2). The system parameters which were held constant in this study are given in Table I.

Convective diffusion equation model.—Equations [8] through [11] define the convective diffusion equation model. Calculated polarization curves are given in Fig. 3 for three different flow rates and three different electrical contact configurations. At high polarizations, the limiting current plateau is independent of contact configuration since mass tranfer alone controls the system. At currents below the limiting current, the dual contact mode offers the highest current for a given applied potential since the dual contacts offset somewhat the effects of electrode resistance. Above about 25% of limiting current, the left-hand contact provides a higher current than the right-hand mode owing to the variation of mass transfer rates along the wire. When the electrical contact is on the right, much of the applied potential is consumed by IR-drop along the

Table I. Values of system parameters held constant in this study

$\mathrm{Sc_1} = \mathrm{Sc_2} = 10^3$
$\chi_1 = \chi_2 = 5 \times 10^2$
$\gamma = \alpha = 0.5$
$\xi = 1.0$
$\psi = 10^{-2}$
$\rho_0 = 10^3$
$a = 10^{-3}$

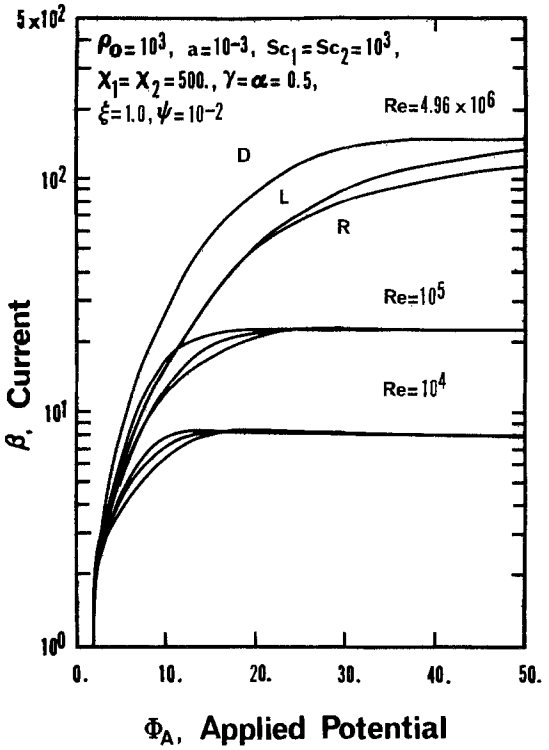


Fig. 3. Effect of wire speed and electrical contact on polarization curve of moving resistive wire electrodes.

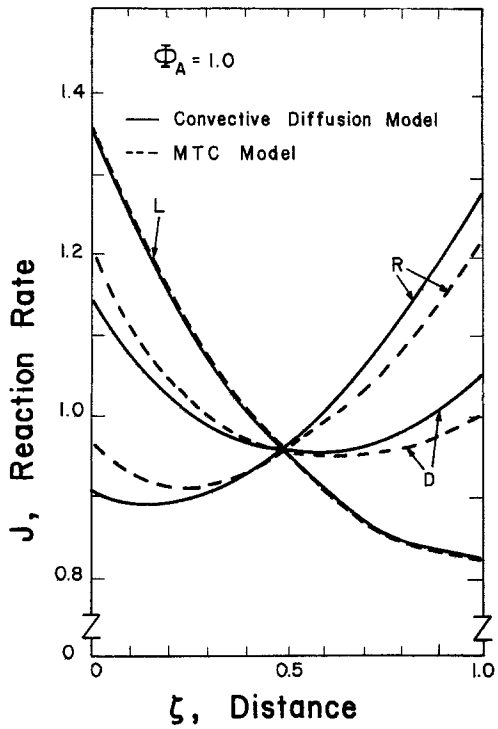


Fig. 4. Current distribution along wire electrode at low applied potential. (———: convective diffusion model; - - - -: MTC model).

wire and by concentration polarization along the downstream regions; when electrical contact is on the left, much more of the applied potential is consumed by charge transfer since the boundary layer thickness is much thinner along the upstream surface. The difference in total current between the dual and single contact modes becomes more significant as the wire speed increases because the ohmic loss along the wire increases as the current increases. The dual contact configuration minimizes ohmic (IR) losses in the wire electrode.

Figure 4 gives current distribution curves for three different contact modes. For Fig. 4, the applied potential is low and the total current is about 3.5% of the limiting current. The solid lines in Fig. 4 correspond to the convective diffusion equation model; the dashed lines will be discussed later. Owing to the electrode resistance, the current distribution is nonuniform and therefore depends on the mode of electrical contact. It is also seen that the dual contact mode is not symmetric, and that the right-hand contact gives a more uniform distribution than the left-hand mode. That is, even at this small fraction of limiting current (3.5%), the mass transport effect on the current distribution is clearly evident.

The solid lines in Fig. 5 give current distribution curves for three different contact modes at a medium polarization. The total current is 56, 51 and 77% of the limiting current for the left- right-, and dual-contact modes. The distributions are similar in shape to those in Fig. 4, but are more nonuniform owing to the higher current which exacerbates the effect of the electrode resistance on the current distributions. It is seen in Fig. 5 that the most uniform current distribution is encountered when electrical contact is made on the right-hand side of the cell.

At an applied potential of 16.0 units, not shown, the current distributions for the left- and dual-contact modes are highly nonuniform and are very close to the limiting current distribution. Under the same conditions, the current distribution for the right-hand contact is extremely uniform, even though at nearly 80% of the limiting current density.

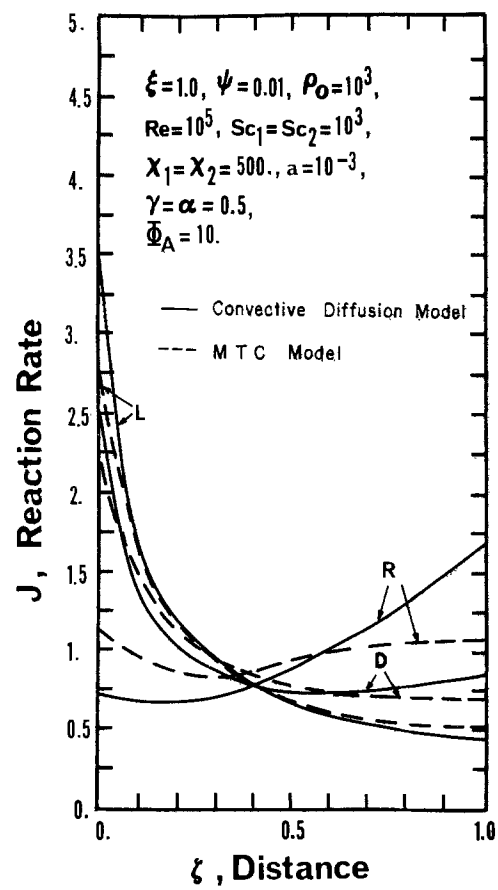


Fig. 5. Current distribution along wire electrode at medium applied potential. (———: convective diffusion model; - - - -: MTC model).

Because the reaction rate distribution is made dimensionless such that $\int_0^1 J d\zeta = 1$, a measure of uniformity of the rate distribution is

$$U = \int_0^1 (|J - 1|) d\zeta$$

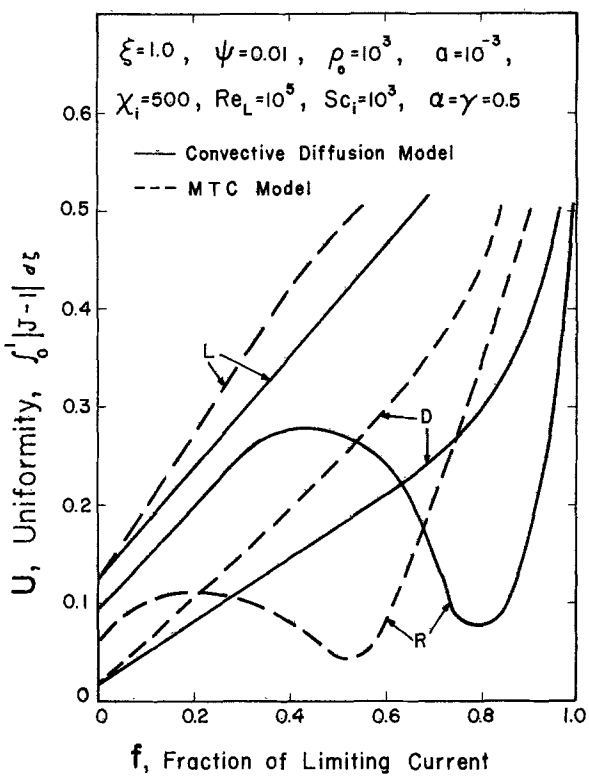


Fig. 6. Uniformity of the current distribution at various fractions of limiting current. (———: convective diffusion model; - - - -: MTC model).

By this definition, U has the value of zero if the current distribution is uniform; the larger the value of U, the more nonuniform the current distribution. Figure 6 illustrates how the reaction uniformity, U, depends on electrical contact mode at various fractions of the limiting current density. The parameter values used in Fig. 6 were chosen so that the electrode resistance would have the greatest effect on system behavior. The solid lines are results calculated with the rigorous convective diffusion equation model. Figure 6 shows the mode of electrical contact which provides the most uniform current distribution depends on the fraction of limiting current at which deposition is carried out. It is seen that above 60% of the limiting current the right-hand contact provides the most uniform current distribution. At low fractions of the limiting curent, near $f = 0$, the uniformity depends upon parameters ξ, ψ, ρ_0, and a, as discussed previously (2). Although the right-hand contact may provide a more uniform current distribution in many cases, the dual contact always consumes the least power since it minimizes the IR-losses associated with electrode resistance.

Calculations have also been made with neglect of curvature terms in the convective diffusion equation. That is, only the first term in the expansion on the right side of Eq. [11] was used. The limiting current for this case is given by Eq. [15] and is shown by the dashed line in Fig. 2. Although the limiting current was affected by neglecting radial terms, it was found that the current distributions were not. That is, the current distributions given by the solid lines in Fig. 4 and 5 (curvature terms included) agree everywhere within 5% of the current calculations obtained upon neglect of curvature terms. Therefore the results presented in Fig. 6 may also be used in the analysis of moving sheets and strips.

Mass transfer coefficient model.—Equations [8], [9], [10], and [14] define the mass transfer coefficient (MTC) model. Results have been calculated for the same system parameters as used for the convective diffusion model in order to ascertain whether the simpler model provides an adequate representation of the system.

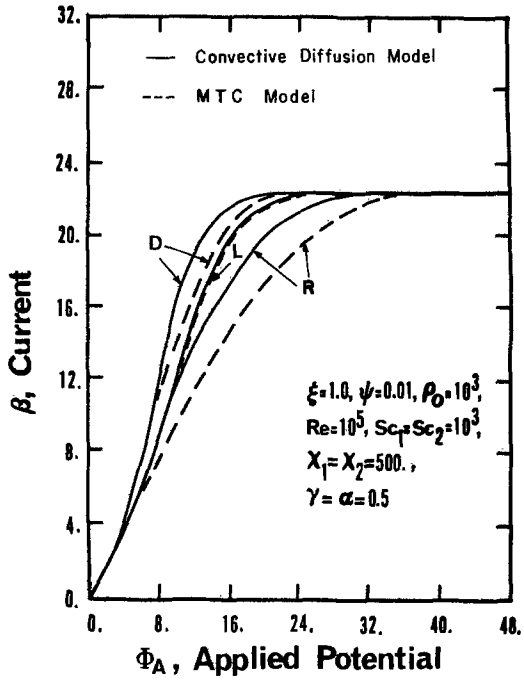


Fig. 7. Comparison of polarization curves predicted by convective diffusion model and MTC model.

Figure 7 gives calculated polarization curves. The dashed lines correspond to the MTC model. Because the simpler model does not include radial curvature terms, it seemed reasonable to make the comparison with the convective diffusion equation model under conditions where curvature terms were not included. Therefore the solid lines in Fig. 7 do not include curvature effects which influence the limiting current plateau. Comparison between the more rigorous model (solid lines) and highly approximate MTC model (dashed lines) shows, for left-hand contact, an excellent agreement over the entire range of potential. For right-hand contact, the approximate MTC model predicts currents which are up to 15% lower than the more rigorous model. The discrepancy is less for dual contact. It is seen that although the simple approximation predicts a greater concentration polarization than may actually occur, the error is relatively small even under the worst of circumstances. That is, for at least some applications, the approximate mass transfer coefficient model can provide results which are within reasonable engineering tolerances.

The dashed lines in Fig. 4 through 6 give results calculated with the mass transfer coefficient model. At low polarizations, Fig. 4 shows that the MTC model shifts the current distribution to the left since it overestimates the concentration polarization along the downstream wire surface. The current distributions agree everywhere within 5%. At medium polarization, Fig. 5 illustrates that the MTC model gives excellent agreement for left- and dual-contact configurations, but that errors up to 60% are encountered for the right-hand case. Depending on the purpose for which current distributions calculations are needed, the simple MTC model may not be suitable for the worst possible case considered here. The reaction uniformity predicted by the MTC model is shown by the dashed lines in Fig. 6. Once again it is seen that the simple MTC model gives an adequate representation of behavior in all but a limited range of operating conditions.

These results illustrate that highly rigorous models are often not necessary for guiding the work-up of engineering applications. For resistive electrodes, it has been shown that appreciable errors with the MTC model are encountered only when the current contact is at the downstream side of the electrode and when operation is between about 30 and 90% of the limiting current density.

Conclusions

A rigorous model has been developed for calculating the current distribution along a moving resistive wire electrode at all fractions of the limiting current. The model includes simultaneous consideration of the potential field in both electrode and electrolyte phases, and the concentration field in the mass transfer boundary layer at the wire surface. The orthogonal collocation method of calculation was found to be highly efficient. The model has illustrated conditions under which advantage of the electrode resistance may be taken to obtain uniform current distributions. The rigorous model does not take into account natural convection effects.

Various approximations to the rigorous model have been investigated. Curvature of the mass transfer boundary layer has been found to influence the limiting current density but not the current density distributions. Therefore the results reported here can be applied to moving sheets or strips as well as to moving wire applications.

A very simple model has been investigated which uses the mass transfer coefficient determined at limiting current conditions in order to calculate the concentration overpotential. The simple model agrees very well with more rigorous calculations except when electrical contact to the resistive electrode is made far from the upstream region where the mass transfer boundary layer is thin. These results indicate that information gained from limiting current measurements can, in most cases, be incorporated in a model to predict behavior below the limiting current.

The models investigated in this study are quite flexible and could be modified to suit special circumstances. For example, other reaction rate expressions could be used instead of the simple reversible case used here. The existence of multiple electrode reactions could be incorporated, as encountered during alloy deposition, gassing, or other situations. Consideration of the counterelectrode could also be incorporated, including charge-transfer, mass transport, and counterelectrode resistance effects. In summary, the modeling procedure reported here provides a rational basis for the study of a wide variety of electrochemical engineering systems.

Acknowledgment

This study constituted partial fulfilment of requirements for a Doctor of Philosophy degree in the Department of Chemical Engineering, University of Illinois, Urbana-Champaign. Financial support was received from the National Science Foundation (Grants GK-36623 and ENG 72-04168).

Manuscript submitted Aug. 2, 1976; revised manuscript received Oct. 15, 1976.

Any discussion of this paper will appear in a Discussion Section to be published in the December 1977 JOURNAL. All discussions for the December 1977 Discussion Section should be submitted by Aug. 1, 1977.

Publication costs of this article were assisted by the University of Illinois.

LIST OF SYMBOLS

English characters

- a aspect ratio of wire electrode, dimensionless
- C_{si} surface concentration of species i, dimensionless
- c_i concentration of species i, mole/cm^3
- c_{bi} bulk concentration of species i, mole/cm^3
- c_{si} concentration of species i adjacent to electrode surface, mole/cm^3
- D_i diffusion coefficient of species i, cm^2/sec
- $\mathbf{F}$ Faraday's constant, 96,500 C/g-equiv.
- i_m current density in metal electrode, A/cm^2
- i_o exchange current density, A/cm^2
- i over-all current density based on wire cross section, A/cm^2
- J local reaction rate along electrode, dimensionless
- j local reaction rate along electrode, A cm^2
- L length of electrolysis cell, cm
- N number of collocation points, dimensionless
- n number of electrons in electrode reaction, g-equiv./g-mole
- R universal gas constant, 8.31 J/g-mole °K
- Re_L Reynolds number based on cell lengths, dimensionless
- r_1 spatial coordinate in radial direction, cm
- r_2 radius of wire electrode, cm
- r radius of counterelectrode, cm
- Sc_i Schmidt number of species i, dimensionless
- s_i stoichiometric coefficient of reacting species i, $s_i > 0$ for anodic reactant, $s_i < 0$ for cathodic reactant, dimensionless
- T temperature, °K
- v_s velocity of moving wire electrode, cm/sec
- y spatial coordinate normal to wire surface, cm
- z spatial variable in axial direction, cm
- z_i charge number of species i, dimensionless

Greek characters

- α transfer coefficient, dimensionless
- β over-all current density based on wire cross section, dimensionless
- γ exponent expressing concentration dependence of exchange current density, dimensionless
- ζ spatial variable in axial direction, dimensionless
- κ electrolyte conductivity, $(\Omega\text{-cm})^{-1}$
- ξ reaction velocity parameter dimensionless
- ρ spatial variable in radial direction, dimensionless
- ρ_o geometric parameter, dimensionless
- σ electrode conductivity, $(\Omega\text{-cm})^{-1}$
- Φ potential in electrolyte, dimensionless
- Φ_A applied potential, dimensionless
- Φ_m potential in metal electrode dimensionless
- Φ_s potential in electrolyte adjacent to electrode surface, dimensionless.
- ϕ potential in electrolyte, V
- ϕ_A applied potential, V
- ϕ_m potential in metal electrode, V
- ϕ_s potential in electrolyte adjacent to electrode surface, V
- χ_i diffusivity parameter of species i, dimensionless
- ψ conductivity parameter, dimensionless

REFERENCES

1. R. D. Varjian, Ph.D. Thesis, University of Illinois, Urbana-Champaign (1976).
2. R. Alkire and R. Varjian, *This Journal*, **121**, 622 (1974).
3. R. Alkire, *ibid.*, **118**, 1935 (1971).
4. R. Alkire and A. Tvarusko, *ibid.*, **119**, 340 (1972).
5. A. Tvarusko, *ibid.*, **121**, 660 (1974).
6. A. Tvarusko, *Plating*, **58**, 983 (1971); *ibid.*, **60**, 345 (1973); *ibid.*, **61**, 139 (1974); *J. Appl. Electrochem.*, **5**, 151 (1975); *Electrochim. Acta*, **20**, 945 (1975); *This Journal*, **119**, 43 (1972); *ibid.*, **120**, 87 (1973); *ibid.*, **123**, 489 (1976).
7. J. W. Rotte and W. J. Beek, *Chem. Eng. Sci.*, **24**, 705 (1969); J. W. Rotte, G. L. J. Tummers, and J. L. Dekker, *ibid.*, **24**, 1009 (1969).
8. F. K. Tsou, E. M. Sparrow, and E. M. Kurtz, *J. Fluid Mech.*, **26**, 145 (1966).
9. B. C. Sakiadis, *AIChE J.*, **7**, 26, 221, 467 (1961).
10. R. M. Griffith, *Ind. Eng. Chem., Fundam.*, **3**, 245 (1964).
11. J. F. Griffin and J. L. Throne, *AIChE J.*, **13**, 1210 (1967).
12. D. E. Bourne and D. G. Elliston, *Int. J. Heat Mass Transfer*, **13**, 583 (1970); D. E. Bourne and H. Dixon, *ibid.*, **14**, 1323 (1971).
13. K. S. Rao and R. S. Sharma, *Indian J. Technol.*, **10**, 166 (1972).
14. R. D. Kaplan and L. H. Shendalman, *Int. J. Heat Mass Transfer*, **16**, 1231 (1973).
15. D. T. Chin, *This Journal*, **122**, 643 (1975).
16. E. A. Koldenhof, *AIChE J.*, **9**, 411 (1963).
17. L. E. Erickson, L. T. Fan, and V. G. Fox, *Ind. Eng. Chem. Fundam.*, **5**, 19 (1966).
18. L. J. Crane, *Z. Angew. Math. Phys.*, **23**, 201 (1972).
19. B. Gampert, *Z. Angew. Math. Mech.*, **54**, T118 (1974).
20. V. G. Fox, L. E. Erickson, and L. T. Fan, *AIChE J.*, **14**, 726 (1968).

21. V. G. Fox, L. E. Erickson, and L. T. Fan, *ibid.*, **15**, 327 (1969).
22. J. L. White, *Can. J. Chem. Eng.*, **46**, 294 (1968).
23. L. J. Crane, *Ing. Arch.*, **43**, 203 (1974).
24. F. K. Tsou, E. M. Sparrow, and R. J. Goldstein, *Int. J. Heat Mass Transfer*, **10**, 219 (1967).
25. C. A. Rhodes and C. C. Chen, *J. Heat Transfer*, **96**, 32 (1974).
26. N. C. Shih and S. Middleman, *Polym. Eng. Sci.*, **10**, 4 (1970); G. Vasudevan and S. Middleman, *AIChE J.*, **16**, 614 (1970).
27. V. G. Fox and F. Hagin, *AIChE J.*, **17**, 1014 (1971).
28. W. W. Lee and R. T. Davis, *Chem. Eng. Sci.*, **27**, 2129 (1972).
29. S. Chen, *J. Eng. Math.*, **5**, 219 (1971).
30. H. E. Eickhoff *AIAA J.*, **12**, 392 (1974).
31. C. A. Rhodes and H. Kaminer, *ibid.*, **10**, 331 (1972).
32. B. G. van der Hegge Zijen, *Appl. Sci. Res.*, **A7**, 205 (1958).
33. H. Carslaw and J. Jaeger, "Conduction of Heat in Solids," pp. 334 ff, Oxford University Press, London, England (1959).
34. J. V. Villadsen and W. E. Stewart, *Chem. Eng. Sci.*, **22**, 1483 (1967); J. P. Sφrensen and W. E. Stewart, *ibid.*, **29**, 811, 827, 833 (1974).
35. R. Cabán and T. W. Chapman, *This Journal*, **123**, 1036 (1976).
36. J. S. Newman, *Ind. Eng. Chem. Fundam.*, **7**, 514 (1968).
37. H. Goldenberg, *Proc. Phys. Soc.*, **69B**, 256 (1956).
38. K. Chida and Y. Katto, *Int. J. Heat Mass Transfer*, **19**, 461 (1976).
39. R. B. Bird, W. E. Stewart, and E. N. Lightfoot, "Transport Phenomena," chap. 17.5, John Wiley & Sons, Inc., New York (1961).

JOURNAL OF THE ELECTROCHEMICAL SOCIETY

SOLID-STATE SCIENCE AND TECHNOLOGY

MARCH 1977

The Identification of the Mobile Ion during the Anodic Oxidation of Silicon

W. D. Mackintosh and H. H. Plattner

Atomic Energy of Canada Limited, Chalk River Nuclear Laboratories, Chalk River, Ontario, Canada

ABSTRACT

The mobile species during anodic oxidation of Si is shown to be largely, if not entirely, the anion. This was accomplished by introducing noble gases as markers into the surface layer of specimens by ion implantation. The positions of the markers before and after oxidation in a variety of electrolytes were determined by Rutherford backscattering analysis.

During anodic oxidation either the cation or the anion or both must migrate across the thickening oxide film. The mobile ion can be identified, or, if both move, the relative mobilities can be deduced by tagging a thin surface layer with a completely immobile marker atom and determining its position after anodizing the specimen. If the marker is found at the surface then oxidation has taken place by inward migration of the anion to form the film beneath the marked layer. If the marker is found at the substrate/oxide interface the opposite process has occurred. An intermediate position indicates both cation and anion have moved and the relative mobilities are proportional to the relative thicknesses of the oxide on either side of the marker atoms. Such experiments have been carried out for Al (1, 2), Hf (1), Nb (1), Ta (1, 3), U (4), W (1), and Zr (1, 5) using markers of inert gas atoms introduced in the surface layers by ion implantation with low energy accelerators.

The inert gas atoms were chosen as markers on the grounds that they are the most likely to remain uncharged within the oxide lattice and hence are not influenced by the application of the electrical field. In addition their large size suggests that they should not diffuse through the lattice at room temperature. Pringle (3), in particular, discusses the question of the immobility of Ar, Kr, and Xe in the anodic oxidation of Ta.

On the other hand, Brown and Mackintosh (2), Whitton (5), and Mackintosh, Brown, and Plattner (6) have shown that a great many other species introduced into the surface layers of Al or Zr move during anodization. The direction of motion appears to depend on the charge of the species and on the original position of the implanted atoms in the surface layers. Many cases were found in which a species behaves differently when introduced into a preformed oxide layer which was subsequently thickened, than it did when introduced into the metal substrate beneath the air-formed oxide. Such species are obviously unsuitable as markers.

Up to this time the identification of the charge carrier in the anodic oxidation of Si has been based on evidence obtained by introducing P and B into oxide layers by anodizing in electrolytes containing phosphate and borate anions (7, 8). In Ref. (7) ^{32}P was incorporated into an oxide film by anodizing in tetrahydrofurfuryl alcohol containing ^{32}P as the phosphate. When this film was subsequently thickened in either a solution of N-dimethylpropionamide or in tetrahydrofurfuryl alcohol containing nonradioactive phosphate, the active ^{32}P was found in the inner layers. It was concluded that the oxide film had thickened by outward movement of the Si. However, from the same observation an equally valid conclusion could have been reached; that during anodization the phosphate moves inward.

In Ref. (8) the B was found at the outer surface leading to the conclusion that the anion was largely the species that migrated. The apparent difference in behavior was attributed to the presence of the borate in the electrolyte rather than the alternative explanation that either P or B, or both, moved during anodization in the way that many species have been shown to move in Al.

Additionally, it has been shown by Pringle (9) that both P atoms introduced by ion implantation and PO_3^{---} ions introduced via the electrolyte are mobile during the oxidation of Ta. Since experience with other systems indicates that the inert gas atoms were good, if not quite perfect, immobile markers while other species were more likely to be mobile, we have investigated the anodic oxidation of silicon using Kr and Xe as markers. We have also investigated the behavior of P when introduced into oxide films by having phosphate ions present in the electrolyte.

In the literature cited above various methods were used to locate the initial and final positions of the marker. In the present work marker locations were determined by Rutherford backscattering analysis. The principles of this technique for measurements of film thickness and the depth of foreign atoms have been described extensively (10-12) and references therein. The essence of the method is that if a He ion of known energy (in this case 2 MeV) is scattered from a surface atom, the resultant energy loss can be calculated from the kinematics of the system. Any additional energy loss observed is due to the fact that the struck atom is not on the surface and therefore the He ion suffers energy loss in both its ingoing and outgoing trajectories. This loss can be interpreted to give the depth of the atom. Similarly, the difference in energy between He ions scattered from the Si atoms of the outer sur-

Key words: anodic oxidation, ion implantation, noble gas markers, Rutherford backscattering, silicon.

face layer of the oxide and the Si atoms of the outer layer of the substrate (substrate/oxide interface) can be interpreted to give the thickness of the oxide.

Detector resolution and to a lesser extent drifts in accelerator energy and amplifier gain set a limit to the precision with which depths and oxide thickness may be measured. The precision obtainable is ~ 2 $\mu g/cm^2$ and is essentially constant over the range of depths involved in this work.

The number of detected He ions backscattered from the implanted ions is dependent on the number of implanted atoms present. It is possible to obtain the absolute amount of implanted atoms (10-12) but for these experiments it was sufficient to compare the total count after normalization to the same integrated beam current (*i.e.*, same number of incident particles) to observe any changes in the amount of implant occurring during anodization.

Experimental

Anodization.—A variety of specimens was used in this work. Some were thin wafers cut very closely parallel to the (111) plane while others were tablets ⅜ in. thick cut some 10° off the (111) plane. Most were p-type boron-doped although one n-type phosphorus-doped specimen was also used. The surfaces of all specimens were prepared by vibratory polishing with 0.3 μm alumina, followed by ultrasonic cleaning to remove the abrasive. They were then degreased in trichlorethylene, etched for 5 min in 0.5M HF and washed thoroughly. Oxidations were carried out in a Teflon cell constructed for this purpose in such a way that only 0.7 cm^2 of the polished surface was exposed to the electrolyte. The electrical connection was made by diffusing gold into a small area on the back of the specimen and firmly contacting this area to a copper plate contained in the body of the cell. All specimens were anodized, then stripped of oxide in 0.5M HF before proceeding further with the experiments.

Experiments were carried out with the following electrolytes: (*a*) 0.1M aqueous solution of H_3BO_3 and $Na_2B_4O_7 \cdot 10H_2O$ (13), (*b*) 0.4M solution of KNO_3 in N-methylacetamide (14), and (c) 0.3M solution of KNO_2 in tetrahydrofurfuryl alcohol (15). For experiments involving the behavior of P, we used an electrolyte of tetrahydrofurfuryl alcohol containing 15 volume percent (v/o) pyrophosphoric acid (prepared by dissolving P_2O_5 in the minimum amount of water possible) (7). All anodizations were carried out at constant current at densities of 15 mA/cm^2 for electrolyte (*a*) and 6 mA/cm^2 for the remainder. The process was terminated at a voltage commensurate with the thickness desired, the necessary thickness *vs.* voltage data being obtained from the literature cited. Although in most cases, oxides exhibiting even coloration across the whole area were obtained, any chance specimens not evenly colored were discarded.

Marker location analysis.—The experimental arrangements for obtaining the Rutherford backscattering spectra of the He ions were identical with that described in Ref. (2). Briefly, they consist of a Van de Graaff accelerator delivering a beam of 2 MeV He ions, a target chamber, and a surface barrier detector (resolution 17 keV FWHM) placed to observe ions scattered through 150°, together with the electronics and pulse height analyzer. A time of irradiation was chosen that resulted in the accumulation of $\sim$ 500 counts in the peak derived from the marker atoms using a beam current of 15 nA. The beam current was integrated during the irradiation so that the counts derived from the implanted atoms from one run could be normalized to that of another.

Ion implantation.—The inert gas atoms Kr or Xe were introduced into the Si surface layers with a low energy mass separator. The amounts implanted were 5×10^{14} atoms/cm^2 for Xe and 1×10^{15} for Kr. These are the minimum amounts conveniently detected by Rutherford backscattering analysis. The energies employed were in the range 25-110 keV.

Procedure.—Specimens with prepared surfaces were anodized to give a film thickness of ~ 16 $\mu g/cm^2$. They were then implanted with the chosen marker at an energy that would insure that the greater part of the implanted material was located within the oxide film. Rutherford backscattering spectra were obtained. The specimens were then further anodized to a chosen voltage and analyzed again. Computer analysis of the data was then carried out to obtain the position of the markers, the thicknesses of the oxide films, and the count of He ions backscattered from the implanted atoms.

Results and Discussion

Figure 1 shows the spectra obtained from a specimen in which Kr was implanted at 45 keV into a preformed oxide layer. The solid line is the spectrum before the oxide was thickened further, the dotted line that obtained afterward.

The continuum to the left is derived from the substrate. It contains a marked step as the density of the Si atoms in the oxide is considerably less than that in the underlying substrate. The dashed vertical line D marks the energy of the He ions backscattered from the outer surface of the preformed oxide while E and F mark the energies at the surface of the substrate, before and after thickening, respectively. These were obtained by computer smoothing of the data and taking the position to be the point at half-height of the step. The difference in energy between these points can be converted to oxide thickness. The energy interval between the vertical lines D and E corresponds to an oxide thickness of 20 $\mu g/cm^2$, while that between D and F corresponds to an oxide thickness of 35.5 $\mu g/cm^2$. In this example, the specimen was anodized in methylacetamide.

The peaks to the right are derived from scattering from the Kr. The vertical dashed line labeled A represents the calculated energy of He ions scattered from Kr atoms hypothetically located exactly at the surface. That labeled B represents the center of the peak before thickening shown by the solid line. This position was obtained by fitting the data to a Gaussian and determining the center point of the full width, half-maximum height. The peak position B is displaced to a position 15 keV lower in energy than the "surface" position A. This difference corresponds to a depth of 8 $\mu g/cm^2$ for He ions backscattered from Kr in SiO_2. This position is the median range of Kr atoms implanted at 40 keV with the low energy mass separator.

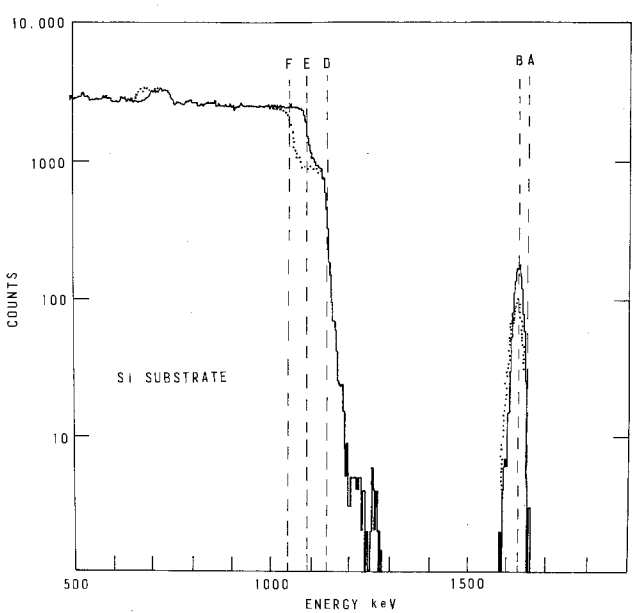


Fig. 1. The solid line shows the spectrum obtained from a specimen in which Kr was implanted at 45 keV into a preformed oxide layer 20 $\mu g/cm^2$ thick. The dotted line is the spectrum after the oxide was thickened to 35.5 $\mu g/cm^2$.

Table I. Marker position for implants in preformed oxides

Sample number	Implant species	Implant energy	Preformed oxide thick., $\mu g/cm^2$	Electrolyte	Additional oxide grown, $\mu g/cm^2$	Position shift, $\mu g/cm^2$	Corrected position, $\mu g/cm^2$
1	Kr	45	8.5	THF	25.5	+2	+4
2	Xe	50	15	THF	19	−3	−2
3	Xe	110	15.5	Acetamide	13	−3	−2
4	Xe	110	13	Acetamide	19	−4	−3
5	Kr	55	15	Acetamide	16	+2	+3
6	Kr	55	15	Acetamide	14.5	+2	+3
7	Kr	45	20	Acetamide	15.5	+2	+3
8	Xe	20	9.5	Borate	41	0	0
9	Xe	30	11	Borate	66	0	0
10	Xe	30	11	Borate	19	0	0
11	Kr	45	8.5	Glycol	19.5	0	+1
12	Kr	45	8.5	Glycol	19.5	+2	+3
13	Kr	50	15	Phosphate in THF	10	+2	+3
14	Kr	50	19	1st phosphate in THF 2nd THF	15	+4	+5
				Average	24		+0.8 ± 0.5

The position of the peak after thickening, shown by the dotted line, is almost coincident with its position before thickening.

All specimens, embracing the use of all electrolytes listed earlier, and the use of Xe as well as Kr, gave much the same result. In Table I we list the details of each and in column 7 give the difference between the original implant position and the position after oxidation. Positive numbers indicate positions deeper in the specimen, negative numbers positions nearer the surface. Those deeper below the surface are within the limits of precision of the analytical method (± 2 $\mu g/cm^2$). However some shifts to positions of higher energy are outside the limits. We attribute this to the known fact that some Si dissolves in the electrolyte during anodization (16). We did not investigate this phenomenon in detail but in Ref. (16) the loss of Si was found to be equivalent to 2 $\mu g/cm^2$ of SiO_2 when anodizing in acetamide for sufficient time to form 30 $\mu g/cm^2$ of oxide. We found evidence that there was a similar loss with other organic electrolytes. Due to the fact that the original implant distribution extends to the surface, loss of Si to the electrolyte results in the loss of some of the implanted atoms. We observed such losses reflected as a diminished peak area in the backscattered spectra. The loss in Fig. 1 is, for example, 25%. Unfortunately the loss of implanted material cannot be directly related to the amounts of Si dissolving in the electrolytes as we have no precise information on the shape of the implant distribution. We can only assume that, because the implant losses were similar from one organic electrolyte to the other, the loss of Si to the electrolyte is much the same as that reported in Ref. (15). We have consequently corrected the values for the implant shift to allow for this loss and list these in the last column. They have been rounded off to the nearest microgram per square centimeter. On the other hand, aqueous borate electrolytes evidently do not dissolve any Si as there was no loss of noble gas. No corrections were made.

In general then, the marked preformed oxide layer was found to be located at, or close to the outer surface after thickening. From this fact and taking into account the precision of the analytical method and the uncertainty in the amount of Si dissolving, we deduced that at least 80% of the new oxide growth had taken place by inward migration of the anion in five (No. 5, 6, 7, 13, 14) of the samples, 85% in two (No. 1 and 12), and 95% in one (No. 11). The remaining six clearly exhibit exclusive migration of the anion. It is also apparent that these results do not show a tendency for any one of the electrolytes used to behave differently from the others in respect to mobile ion migration. Thus, they can reasonably be considered as a group. The average thickness is 24 $\mu g/cm^2$ and the average corrected position is +0.8. The deviation is 0.5. From this it can be said that 95± 5% of the oxide growth was due to inward migration of the oxidizing species.

A similar number of silicon specimens, covered only by the natural air-formed oxide, were implanted with either Kr or Xe. In these the greater fraction of the implanted atoms was located in the substrate beneath the thin surface oxide. On analysis after anodization the implant distribution was found to be broadened and the center displaced to a position of lower energy. Both broadening and displacement were due to the change in mass, density, and stopping power which occur when Si is converted to SiO_2. When suitable corrections were made for these effects, we obtained results that were entirely consistent with those obtained for implants into preformed oxide films. These are shown in Table II.

As these results are in contradiction to those of Ref. (7), clearly, either P or the noble gases are not suitable markers. We therefore carried out a series of experiments to investigate the behavior of P when introduced into oxides by using an electrolyte containing phosphate ions.

In these experiments we formed a film on specimens by anodizing to 150V in an organic electrolyte containing no phosphate. We then anodized a further 20V in the electrolyte containing phosphate. This is illustrated in Fig. 2A. This was again anodized in the first electrolyte for another ~ 80V.

Irrespective of how the film grows the distance from the substrate/oxide interface cannot decrease if the phosphate is immobile (Fig. 2B, C, and D). However, if mobile, we would expect this distance to decrease by the inward movement of the negative ions as did negative ions in aluminum (2). Consequently, the essential test for movement is the distance from the interface to the phosphate-containing layer before and after formation of the third layer.

Measurements of this distance by Rutherford backscattering techniques is not a straightforward matter because the masses of Si and P are so near each other. The peak derived from P on the surface of SiO_2 can be resolved from the Si edge if a beam energy of 2.4 MeV is used, but it cannot be resolved if the P is buried in the oxide. We therefore had to resort to etching techniques so that analysis was always carried out on specimens with the P at or near the surface. The resolution attainable under these circumstances is illustrated in Fig. 3A. The lower data points joined

Table II. Marker positions for substrate implants.

Sample number	Implant species	Implant energy	Electrolyte	Oxide thick., $\mu g/cm^2$	Corrected position, $\mu g/cm^2$
1	Xe	40	Borate	44	+1
2	Xe	40	Borate	35	+3
3	Xe	40	Borate	35	0
4	Xe	40	Borate	59	+3
5	Kr	30	Acetamide	30	+1
6	Kr	30	Acetamide	24	+1
7	Kr	30	THF	30	+1
8	Kr	50	THF	36	−3
9	Kr	40	THF	43	0
10	Kr	40	THF	39	0
11	Kr	50	THF	36	−3
			Average	37	0.3 ± 0.5

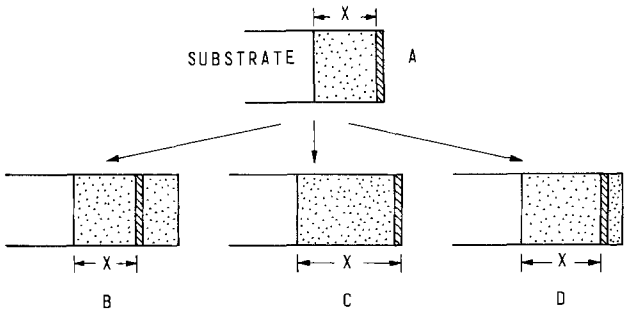


Fig. 2. The positions of a layer of oxide containing P if the phosphate ions are immobile. A, the dotted area represents the oxide which was formed in an electrolyte containing no phosphate and the cross-hatched area that formed with phosphate in the electrolyte. B, illustrates its position if A is further oxidized in phosphate-free electrolyte and if growth takes place solely by outward migration of Si; C, if growth takes place solely by inward migration of the anion, and D, if growth takes place by both outward migration of Si and inward migration of oxidant. In B the distance, x, between the interface and the P layer remains the same as that in A; in C, x increases by the thickness of oxide grown in the final oxidation; in D, x increases by a fraction of the thickness of the oxide grown. In no case should the final value of x be less than its initial value in A.

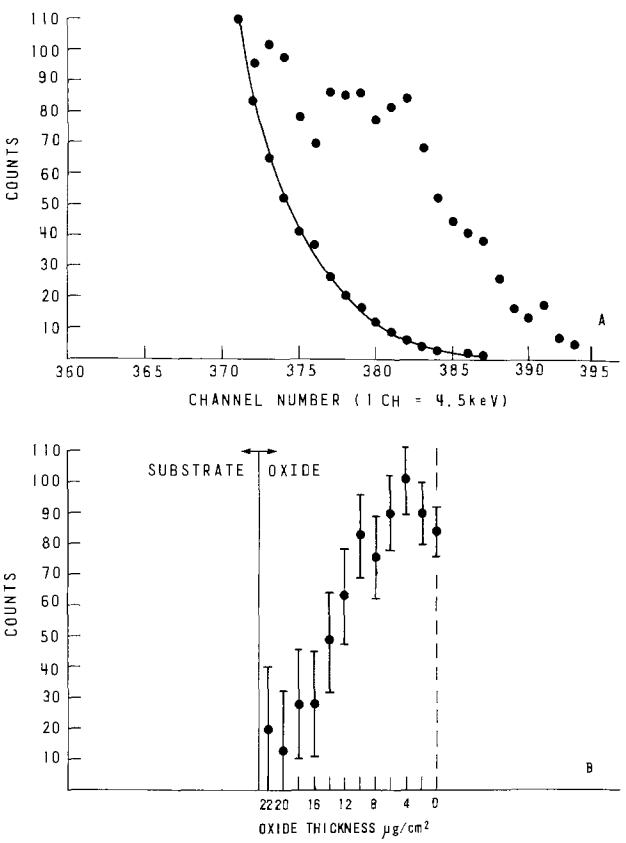


Fig. 3. A. Part of a Rutherford backscattering spectrum derived from Si and P. The lower data points joined by a solid line are derived from Si in a specimen oxidized to 150V in phosphate-free electrolyte. The upper data points are derived from P in the specimen after having been further anodized for 20V in an electrolyte containing phosphate. B. The distribution of P in the oxide deduced from the spectrum. The position of the interface represented by the solid vertical line was obtained from the full spectrum.

by a smoother curve is a part of the spectrum from a specimen anodized in normal electrolyte to 150V. These counts are derived from the Si edge. Superimposed on this are the data points obtained from the specimen after it had been further anodized (20V) in the electrolyte containing phosphate. The counts obtained from the Si have to be subtracted from these data points to give the counts derived from the P itself.

In Fig. 3B this subtraction has been made, the resulting precision indicated by error bars, the channel number (*i.e.*, energy scale) converted to depth scale and the data points folded about the half-height channel which marks the surface position. The line indicating the interface of substrate and oxide was obtained from the oxide step in the full spectrum in the same manner as in the noble gas experiments. Its precision is indicated by the error bar at the top of the line.

Now, it can be clearly seen in Fig. 3B, despite the error introduced by the lack of clean resolution of the P peak from the Si edge, that the distribution of the P is very wide. In the course of this work we had occasion to examine six other similarly prepared specimens. The width of the distribution measured at half-maximum height averaged 10 $\mu g/cm^2$ after correcting for the detector resolution.

If the P were immobile and thus contained entirely within the layer added by anodizing in the phosphate-containing electrolyte, the P distribution should be very close to 2.2 $\mu g/cm^2$ thick (Fig. 2A). This value was obtained in separate experiments. Since oxide thicknesses cannot be determined closer than $\pm$ 2 $\mu g/cm^2$ we could not obtain the thickness of the added layer from the difference in thickness measurements made before and after the layer was formed. Instead we anodized two specimens in normal electrolyte to 150V and two in the phosphate electrolyte to the same voltage, measured the oxide thickness then reanodized to 300V in both cases and again measured. We obtained the same rate of oxide formation for both electrolytes, viz, 0.11 $\mu g/cm^2/V$.

Thus the fact that the P distribution is 10 $\mu g/cm^2$ thick when it should only be 2.2 $\mu g/cm^2$ already provides evidence that the P is penetrating into the original oxide layer, *i.e.*, moving inward.

In the next part of the experiment we prepared a specimen as before (150V no phosphate, 20V phosphate) then anodized in the normal electrolyte for a further 75V. The P peak could not be discerned in its spectrum. This observation confirms that made in Ref. (6), viz., the oxide layer grown in a normal electrolyte on a specimen previously oxidized in an electrolyte containing phosphate, contains no P. In order to locate the P with respect to the interface we had to remove this last formed layer. We therefore determined the etch rate of the normal oxide in 0.2M HF in separate experiments. We used this established rate while removing the third layer to ensure that the correct amount was dissolved. Thus the specimen was again in a state in which the P could be resolved from the Si by our method of analysis.

In Fig. 4A we show the distribution obtained. It is wider and, more importantly, the point of maximum concentration has moved closer to the substrate oxide interface. We were able to reproduce this result in three other specimens within the precision expected of the measurement techniques. All specimens, when etched to thickness less than that of the original normally formed layer, contained amounts of phosphate consistent with the distribution determined by backscattering analysis. One, for example, etched to a thickness of 6 $\mu g/cm$ contained $\sim$ 20% of the original amount of P.

The specimen of Fig. 4A was anodized again in phosphate-free electrolyte and again etched. The result is shown in Fig. 4B. Clearly the point of maximum P distribution is now nearer to the substrate/oxide interface.

All these experiments yield results that indicate inward movement of P during anodic oxidation. It is therefore not a valid marker for the investigation of silicon and oxygen migration.

Conclusions

In our experiments, two different noble gases, Kr and Xe, were introduced into the surface layers of

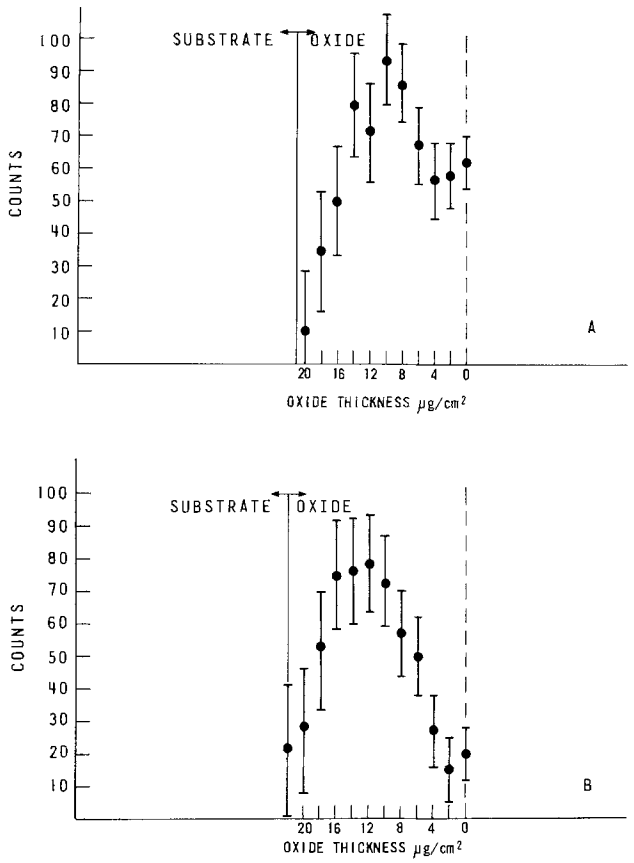


Fig. 4. A. The distribution of P in a specimen anodized to 150V in phosphate-free electrolyte, a further 20V in an electrolyte containing phosphate, and again in the first electrolyte for 75V followed by HF etching to remove the last-formed layer. The data points were derived from the P peak in the spectrum, the interface position from the oxide step in the spectrum, as in Fig. 3. B. The distribution of P in the same specimen as A after reanodizing a further 80V and removing the additional layer formed.

specimens as markers. Some of those specimens were covered only with the natural air-formed oxide, some with a preformed oxide film. Four different electrolytes were used for anodizing. In every case the markers were found to be very close to the outer oxide surface. In view of this consistency of the results we conclude that within the experimental error, the data indicate that inward movement of the anion is responsible for oxide growth when the listed electrolytes and current densities are used. In this respect anodic oxidation resembles thermal oxidation (17). We have also shown that P moves inward somewhat faster than the advancing oxide front, hence accounting for the observation of Ref. (7) that a phosphorus-free layer can be formed over one containing phosphorus even though the oxide grows by anion movement.

Acknowledgments

It is a pleasure to acknowledge the assistance of O. M. Westcott for mass separator operations and J. Lori and D. Lanteigne for Van de Graaff operations.

Manuscript submitted Jan. 27, 1976; revised manuscript received Oct. 1, 1976.

Any discussion of this paper will appear in a Discussion Section to be published in the December 1977 JOURNAL. All discussions for the December 1977 Discussion Section should be submitted by Aug. 1, 1977.

Publication costs of this article were assisted by Atomic Energy of Canada Limited.

REFERENCES

1. J. A. Davies, B. Domeij, J. P. S. Pringle, and F. Brown, *This Journal*, **112**, 675 (1965).
2. F. Brown and W. D. Mackintosh, *ibid.*, **120**, 1096 (1973).
3. J. P. S. Pringle, *ibid.*, **119**, 482 (1972).
4. W. D. Mackintosh and H. H. Plattner, *ibid.*, **123**, 523 (1976).
5. J. L. Whitton, *ibid.*, **115**, 58 (1968).
6. W. D. Mackintosh, F. Brown, and H. H. Plattner, *ibid.*, **121**,1281(1974).
7. P. F. Schmidt and A. E. Owen, *ibid.*, **111**, 682 (1964).
8. J. Kraitchman and J. Oroshink, *ibid.*, **114**, 1105 (1967).
9. J. P. S. Pringle, Abstract 97, p. 214, The Electrochemical Society Extended Abstracts, Spring Meeting, Toronto, Canada, May 11-16, 1975.
10. W. D. Mackintosh and J. A. Davies, *Anal. Chem.*, **41**, 26A (1969).
11. W. D. Mackintosh, in "Characterization of Solid Surfaces," P. F. Khan and G. R. Larrabee, Editors, Plenum Press, New York (1974).
12. W. K. Chu, J. W. Mayer, M.-A. Nicolet, T. M. Buck, G. Amsel, and F. Eisen, in "Ion Beam Surface Layer Analysis," J. W. Mayer and J. F. Ziegler, Editors, Elsevier Sequoia S.A., Lausanne (1974).
13. M. A. Wilkins and G. Dearnaley, U.K. Atomic Energy Authority Report, AERE R-5875.
14. P. F. Schmidt and W. Mickel, *This Journal*, **104**, 230 (1957).
15. P. F. Schmidt, T. W. O'Keeffe, J. Oroshnik, and A. E. Owen, *ibid.*, **112**, 800 (1965).
16. J. A. Davies, G. C. Ball, F. Brown, and B. Domeij, *Can. J. Phys.*, **42**, 1070 (1964).
17. A. S. Grove, "Physics and Technology of Semiconductor Devices," p. 23, John Wiley & Sons, Inc., New York (1967).

The Defect Structure of Phosphorus-Doped CdTe

F. A. Selim*,[1] and F. A. Kröger*

Department of Materials Science, University of Southern California, Los Angeles, California 90007

ABSTRACT

Room temperature Hall effect measurements on P-doped CdTe crystals cooled from equilibrium with atmospheres of well-defined Cd and Te_2 pressures at high temperature have made it possible to arrive at a defect model for P-doped CdTe. Temperature dependence of the Hall effect from 77° to 335°K showed P to give rise to shallow acceptor levels at $E_v + 0.035$ eV. The acceptors are probably P_{Te} and P_i. The number of holes per P atom is close to one at low P contents after annealing at medium Cd pressures. The ratio decreases with increasing P concentration and by annealing at low or high cadmium pressure, indicating self-compensation. At high p_{Cd} the self-compensation involves native defects ($Cd_i^{\cdot\cdot}$). At low p_{Cd} it involved $P_{Cd}^{\cdot\cdot\cdot}$. At high P concentrations neutral associates $(P_{Cd}P_i)^\times$ and $(P_{Cd}2P_i)^\times$ are formed. The same model, with one additional constant, accounts for the solubility of phosphorus in CdTe.

P as a dopant is known to give p-type conductivity in CdTe. While originally acceptor centers formed were thought to give a level at $E_v + 0.38$ eV (1), later investigations showed acceptor levels at $E_v + 0.05$ eV (2-4). Generally, P concentrations $\geqq 10^{18}$ cm^{-3} were used, and the hole concentration was found to be considerably less than that of P, indicating a large degree of self-compensation (3-5). A higher degree of electrical compensation was observed after annealing at low cadmium pressure than at high cadmium pressure (5). An increase in the hole concentration was observed in samples implanted with P if Cd was implanted at the same time (6). Diffusion studies by Hall and Woodbury (5) show a double penetration profile, a fast one and a slow one. The fast diffusion at 900° and 950°C shows a decrease of diffusion rate with increasing p_{Cd} at $p_{Cd} < 0.3$ atm, independence of p_{Cd} occurring for $p_{Cd} > 0.3$ atm; the behavior at low p_{Cd} is uncertain. The same study (5) shows the solubility of P in CdTe at 900° and 950°C in equilibrium with a vapor of variable cadmium pressure but with constant Cd:P weight ratio of 100:1 to be proportional to p_{Cd} at $p_{Cd} > 10^{-1}$ atm, but to be independent of p_{Cd} at $p_{Cd} < 10^{-1}$ atm.

A reference to the defect structure of P-doped CdTe is found in the paper by Arkadeva *et al.* (6) where an increase of the hole concentration in P-doped CdTe after addition of Cd is attributed to an increase of P_{Te}, an acceptor at the cost of P_{Cd}, a donor. In the present paper, new results of Hall effect measurements on P-doped crystals are presented, and a defect model for P-doped CdTe is developed explaining both the new results and Hall and Woodbury's solubility data. Temperature dependence of the Hall effect in quenched crystals at low temperatures is used to determine the position of the acceptor level and the degree of self-compensation.

Experimental

Sample preparation.—Crystal boules of CdTe, doped respectively with 6×10^{16}, 2×10^{17}, 2×10^{18}, and 5×10^{19} P cm^{-3} were grown by unidirectional solidification of the melt by B. V. Dutt and E. Miller of our laboratory. The distribution coefficient $k \approx 0.1$. The P content was determined by spectrographic analysis and by mass spectrographic analysis.[2] The crystals were cut into plates of $10 \times 10 \times 2$ mm, lapped with 3200 mesh abrasive, washed in trichloroethylene, then rinsed in deionized water and etched with a solution of 10 weight percent (w/o) bromine in methanol.

Annealing of samples.—For annealing, crystal samples together with some Cd or Te were enclosed in an evacuated quartz glass tube. The tubes were placed in a two-temperature furnace and then annealed for 2 hr, a time shown to be sufficient to reach equilibrium. Prior to evacuation, the wall of the tube at the end where the crystal is located was thinned down by pulling the quartz when it softened. This procedure, recommended by de Nobel (7), was followed to increase the rate of cooling during quenching after the high temperature anneal. The crystals were annealed under cadmium pressures between the maximum pressure determined by the phase diagram and the minimum pressure region where sublimation occurs. Pressures close to the minimum pressure point where $p_{Cd} \approx 2p_{Te_2}$ were not used to avoid sublimation of the crystal. For pressures between the sublimation region and the tellurium side of the phase diagram, the crystals were annealed under Te_2 pressure. After the anneal, the crystals were quickly cooled to room temperature by shifting the quartz tube out of the furnace followed by quenching with ethylene glycol.

Hall effect and resistivity measurements.—The van der Pauw (8) method was used to measure the Hall effect and resistivity. A cloverleaf-shaped sample made by notching the four sides was used initially, but the notching was abandoned when we learned both from our own experiments and from those by Chwang *et al.* (9) that these notches, which increased the chances of breaking the crystals, do not appreciably increase the accuracy of the measurement. The apparatus used for the measurement of the Hall effect as a function of temperature in the range 77°-335°K was described by Beguwala (10). Carrier concentrations were calculated from the Hall constant R_H by the relation $c_h = 3\pi/8\ 1/R_H q$, where q is the electronic charge. Mobilities (μ_h) were calculated from the conductivity $\sigma_h = c_h q \mu_h$.

Electrical contacts.—Ohmic contacts to the samples, which were almost all p-type were made by electroless gold plating from a $HAuCl_4$ solution on a surface polished chemically with "Mirrolite," a polishing agent (marketed by Materials Development Company, Los Angeles, California). Ag epoxy was alloyed on top of the gold to attach the lead wires. All contacts were tested by a curve tracer to check their ohmicity before the electrical measurements were made.

Results and Discussion

Hole concentrations measured at room temperature on samples of various P concentration annealed at

* Electrochemical Society Active Member.
[1] Present address: Westinghouse Research Laboratories, Pittsburgh, Pennsylvania 15235.
[2] We are indebted to Maynard H. Hunt of the Materials Characterization Branch, Air Force Cambridge Research Laboratories, AFSC, for performing the latter analysis.

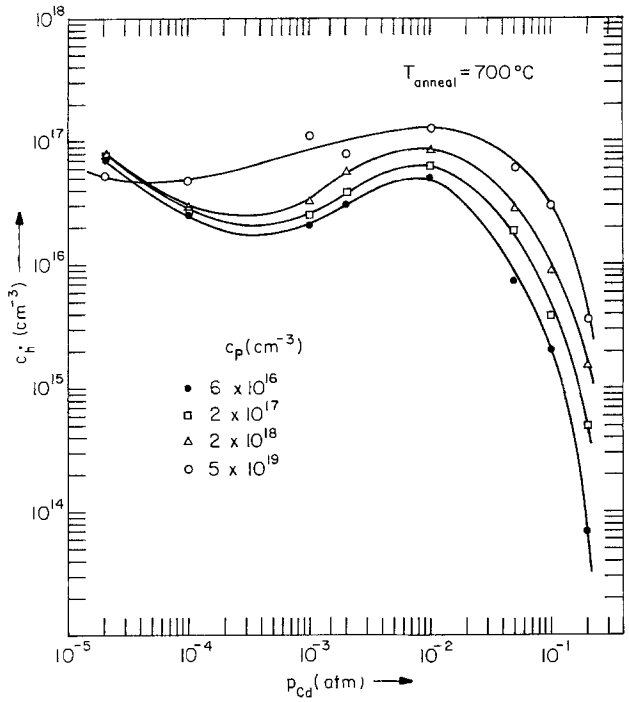


Fig. 1. Hole concentrations in CdTe with various P dopants for crystals cooled after annealing at 700°C under different Cd pressures.

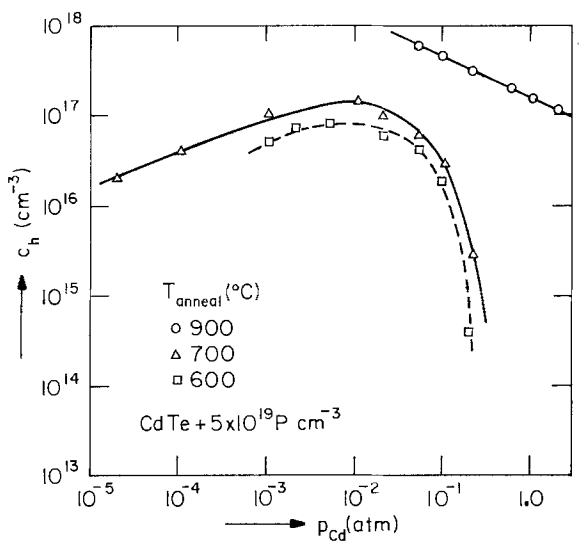


Fig. 2. Hole concentrations in CdTe + 5 × 10^{19} P cm^{-3} quenched after an anneal at high temperature where the crystal is in equilibrium with an atmosphere of different cadmium pressures.

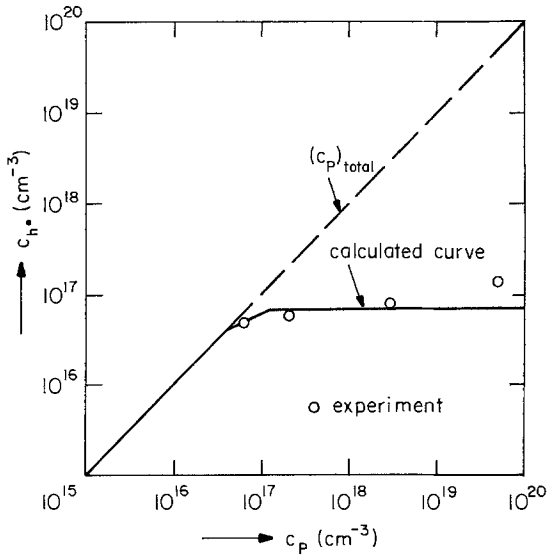


Fig. 3. Hole concentrations for CdTe with various P concentrations cooled after annealing at 700°C at $p_{Cd} = 10^{-2}$ atm.

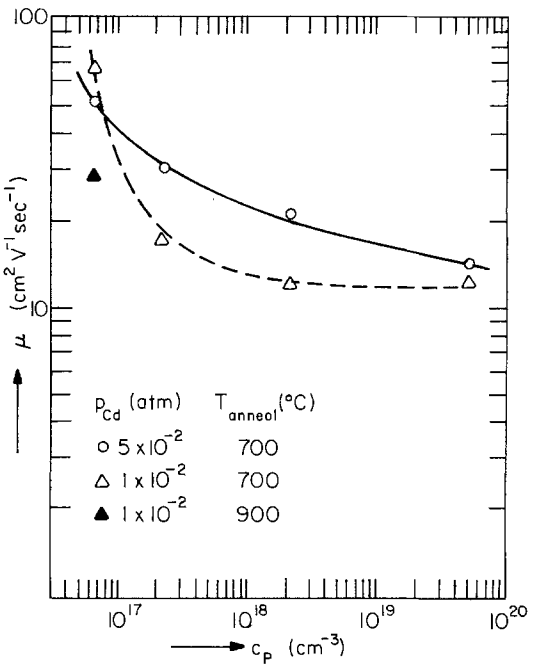


Fig. 4. Hole mobility at 25°C as a function of phosphorus concentration in crystals cooled after annealing under various conditions.

700°C under various cadmium pressures are shown in Fig. 1. Figure 2 shows similar data for CdTe + 5 × 10^{19} P cm^{-3} annealed at 600°, 700°, and 900°C. Samples with 6 × 10^{16} P cm^{-3} cooled after annealing at 900°C at high p_{Cd} have a high resistance. Figure 3 shows the dependence of the hole concentration on P content for samples cooled after annealing at 700°C under $p_{Cd} = 10^{-2}$ atm. Hole mobilities at room temperature in samples of various P content, annealed at 700°C under medium p_{Cd} are shown in Fig. 4. Characteristic features of Fig. 1-4 are:

1. The sharp reduction in c_h at the highest p_{Cd} in all samples annealed at 700°C.

2. Equality of the concentrations of holes and P in the sample with 6 × 10^{16} P cm^{-3} after annealing at $p_{Cd} = 10^{-2}$ atm and the gradual decrease in the ratio c_h/c_P with increasing c_P.

3. Increase of the annealing temperature increases the ratio c_h/c_P.

4. Samples annealed at medium to high p_{Cd} show hole concentration decreasing with increasing p_{Cd}; $c_h \propto p_{Cd}^m c_P^n$, with $m = -1/2$ to $-1/4$ and $n = 1/8$ to $1/2$.

5. Samples annealed at medium to low p_{Cd} show hole concentrations decreasing with decreasing p_{Cd}; $c_h \propto p_{Cd}^m c_P^n$, with $m \approx 1/4$ to $1/3$ and $n \leq 1/6$. This indicates P donor action.

6. At the lowest p_{Cd}, c_h increases with decreasing p_{Cd}, approaching the concentrations expected in undoped CdTe; here native acceptors come to the fore.

7. The hole mobility is largest for the low concentration sample in which $c_h \approx c_P$, it drops at higher c_P where $c_h << c_P$.

Acceptor levels.—In order to obtain information about the ionization energy of the acceptors responsible for the holes observed in the various samples, the Hall effect of a number of samples was measured as a function of temperature between room temperature and 77°K. Results for samples in which P dominates the results are shown in Fig. 5. Two activation

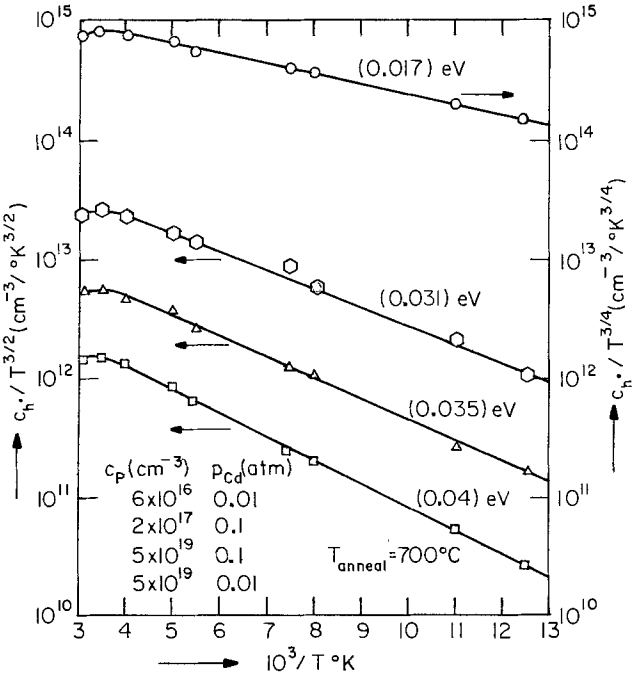


Fig. 5. Plots of $c_h/T^{3/2}$ and $c_h/T^{3/4}$ vs. $10^3/T$ used for determining the acceptor ionization energies in P-doped CdTe.

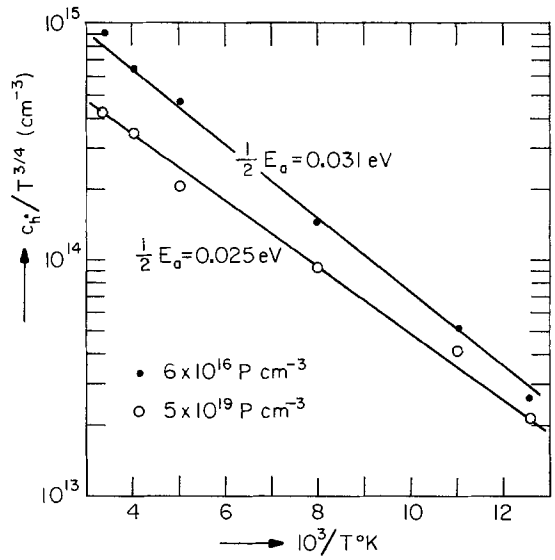


Fig. 6. Plots of $c_h/T^{3/4}$ vs. $10^3/T$ for samples annealed at 700°C and $p_{Cd} = 2 \times 10^{-5}$ atm having V_{Cd}' as the dominant ionized acceptor.

energies, differing by a factor two, are observed. The smaller value, ≈0.017 eV, is found for samples in which $c_h \approx c_P$. All other samples show the larger value. The latter represent the full ionization energy E_{aP} of the P acceptor, either P_i' or P_{Te}'; the small value represents 1/2 E_{aP} to be expected in uncompensated samples. Table I shows our values for E_{aP} together with values reported in the literature. The table also shows mobility values. The highest mobility [neglecting a doubtful value calculated from Ref. (3)] is found in the low concentration sample with $c_h \approx c_P$. The observed value, $\mu_h = 68$ cm^3 V^{-1} sec^{-1}, is almost identical to the value 70 cm^2 V^{-1} sec^{-1} reported for undoped CdTe. Lower values found at higher c_P (see Fig. 4) are the result of increased scattering at impurities expected in the presence of larger concentrations of charged and neutral species. Figure 6 shows the temperature dependence of the hole concentration for samples annealed in a manner to make native acceptors, probably V_{Cd}, dominant. The fact that the acceptors dominant in these samples, which were annealed at low p_{Cd}, are different from those present at a higher p_{Cd} is indicated by the shape of the isotherms of Fig. 1, which show an increase in the hole concentration with decreasing p_{Cd} at low p_{Cd} following a decrease at medium p_{Cd}. These samples show activation energies of 0.025-0.031 eV which, identified with half the ionization energy as expected for $c_h \approx c_{V_{Cd}'}$, gives $E_{V_{Cd}'} - E_V = 0.05 - 0.062$ eV, close to the values reported in the literature (13). For interpretation of the preexponential factors see below.

Defect species expected in CdTe-P.—In principle, P can form three basic defects: P_{Te}, a single acceptor, P_i, a single or multiple acceptor, and P_{Cd}, a triple donor. In addition, complexes of these species, either with ionized native defects or with other P species may occur. In particular, the multiply ionized donor, $P_{Cd}^{\cdots}$ should be expected to associate with negatively charged native defects or with P_i' or P_{Te}', forming species such as $(P_{Cd}V_{Cd})$; $(P_{Cd}P_i)$; $(P_{Cd}P_i)^{\times}$.

The single species will be dominant at low c_P, neutral or charged associates becoming dominant at large c_P. It is this dominance that must be held responsible for the large degree of self-compensation observed at larger c_P.

Local mode studies (14) indicate the presence of two species. One of these is either P_{Te} or P_i. Studies on alloys (Cd,Mg)Te:P and (Cd,Zn)Te:P (15) show that the other is an associate with properties fitting the species $(P_{Cd}P_i)^{\times}$ proposed below to explain the solubility data by Hall and Woodbury (5).

Defect equilibria in the system CdTe-P.—The equilibrium between a binary compound MX such as CdTe and the vapor of one of its constituents can be formulated with the aid of quasichemical defect equations and the corresponding mass action relations (16). Combining mass action relations for various incorporation reactions with the electroneutrality condition and the P balance, one can find expressions for the concentrations of various defects as $f(p_{Cd}, p_{P_2})$ or as

Table I. Hole mobilities and ionization energies of acceptor centers in P-doped CdTe

$c_P = N[P]$, cm^{-3}	$c_h = N[h\cdot]$, cm^{-3} 300°K	μ_h (25°C), cm^2 V^{-1} sec^{-1}	T_{prep}, °C	p_{Cd}, atm	E_{aP}, eV	Ref.
6 × 10^{16}	6 × 10^{16}	68	700	0.01	0.034	†
5 × 10^{19}	1.4 × 10^{17}	15	700	0.01	0.03	†
					0.38	(1)
3 × 10^{19}	2.8 × 10^{17}	20	950	high		(5)
3 × 10^{19}	10^{15}	7.6	950	low		(5)
10^{19}	8 × 10^{16}	132*		low	0.05	(3)
	6.7 × 10^{16}				0.11	(11)
1.2 × 10^{18}	1.2 × 10^{16}	10			0.05	(4)
	5 × 10^{16}	50	450	sat.	0.05	(2)
	6 × 10^{15}			low		(2)
	3.1 × 10^{17}	17.5				(12)

* Calculated from ρ and μ_h as given in the paper.
† This paper.

Table II. Defect formation reactions and the corresponding mass action relations; square brackets indicate concentrations in site fractions

	Reactions	Enthalpy	Mass action relation
1.	$1/2\,P_2(g) + V_i^{\times} \rightleftarrows P_i^{\times}$	$H_{P_i}{}^{\times}$	$K_{P_i}{}^{\times} = [P_i^{\times}]/p_{P_2}{}^{1/2}$
2.	$P_i^{\times} \rightleftarrows P_i' + h^{\cdot}$	E_{aP_i}	$K_{aP_i} = [P_i'][h^{\cdot}]/[P_i^{\times}]$
3.	$1/2\,P_2(g) + V_{Cd}^{\times} \rightleftarrows P_{Cd}^{\times}$	$H_{P_{Cd}}{}^{\times}$	$K_{P_{Cd}}{}^{\times} = [P_{Cd}^{\times}]/[V_{Cd}^{\times}]p_{P_2}{}^{1/2}$
4.	$P_{Cd}^{\times} \rightleftarrows P_{Cd}^{t\cdot} + te'$	$E_{a\,P_{Cd}}{}^{\times}$	$K_{a\,P_{Cd}} = [P_{Cd}^{t\cdot}]\,[e']^t/[P_{Cd}^{\times}]$
5.	$P_2(g) + V_{Cd}^{\times} + V_i^{\times} \rightleftarrows (P_{Cd}P_i)^{\times}$	$H_{P(P_{Cd}P_i)}{}^{\times}$	$K_{P(P_{Cd}P_i)}{}^{\times} = [(P_{Cd}P_i)^{\times}]/[V_{Cd}^{\times}]p_{P_2}$
6.	$3/2\,P_2(g) + V_i^{\times} \rightleftarrows (P_{Cd}2P_i)^{\times}$	$H_{P(P_{Cd}2P_i)}{}^{\times}$	$K_{P(P_{Cd}2P_i)}{}^{\times} = [(P_{Cd}2P_i)^{\times}]/[V_{Cd}^{\times}]p_{P_2}{}^{3/2}$
7.	$1/2\,P_2(g) + Cd(g) \rightarrow P_{Te}^{\times} + Cd_{Cd}^{\times}$	$H_{P_{Te}}$	$K_{P_{Te}} = [P_{Te}^{\times}]/(p_{Cd}p_{P_2}{}^{1/2})$
8.	$P_{Te}^{\times} \rightarrow P_{Te}' + h^{\cdot}$	$E_{aP_{Te}}$	$K_{aP_{Te}} = [P_{Te}'][h^{\cdot}]/[P_{Te}^{\times}]$
9.	$2P_i^{\times} + V_{Cd}^{\times} \rightarrow (P_{Cd}P_i)^{\times} + V_i^{\times}$	$H_{(P_{Cd}P_i)}{}^{\times}$	$K_{(P_{Cd}P_i)}{}^{\times} = [(P_{Cd}P_i)^{\times}]/[P_i^{\times}]^2\,[V_{Cd}^{\times}]$
10.	$3P_i^{\times} + V_{Cd}^{\times} \rightarrow (P_{Cd}2P_i)^{\times} + V_i^{\times}$	$H_{(P_{Cd}2P_i)}{}^{\times}$	$K_{(P_{Cd}2P_i)}{}^{\times} = [(P_{Cd}2P_i)^{\times}]/[P_i^{\times}]^3\,[V_{Cd}^{\times}]$

Neutrality condition: $[h^{\cdot}] + 2[Cd_i^{\cdot\cdot}] = [e'] + [V_{Cd}'] + [P_i'] + [P_{Te}']$

Phosphorus balance: $[P_{Cd}^{t\cdot}] + [P_{Te}'] + [P_i'] + 2[(P_{Cd}P_i)^{\times}] + 3[(P_{Cd}2P_i)^{\times}] = [P_{total}]$

$f(p_{Cd}, [P]_{total})$. Although exact solutions can be obtained, insight into complex changes taking place upon variation of p_{Cd} or [P] is more easily obtained by deriving approximate solutions by a procedure in which the neutrality condition and the P balance are approximated by their dominant terms (17).

When this is done, the concentrations of all defects are obtained as expressions of the form [defect] $\propto p_{Cd}{}^m[P]_{total}{}^n$ or [defect] $\propto p_{Cd}{}^r p_{P_2}{}^s$ with m, n, r, and s real integers or simple fractions. Table II lists defect formation reactions and the corresponding mass action relations for the defect species that were found to be important as a result of this work. Symbols used are those proposed by Kröger and Vink (16).

Table III lists values of the exponents m, n, r, and s in the expressions for the concentrations of holes, P species, and native defects that are valid for various approximations to the neutrality condition and the P balance expression. Comparison of the pressure dependence of carriers with those expected for the various models makes it possible to decide which model fits the data.

Expressions for boundaries between ranges characterized by different approximations to the P balance and the neutrality condition are obtained by equating expressions for the concentration of any one of the species in two adjacent ranges. Expressions for range boundaries obtained in this way for the [P] *vs.* p_{Cd} fields and the p_{P_2} *vs.* p_{Cd} fields are given in Table IV.

Establishment of a defect model.—In establishing the defect structure of P-doped CdTe we have to take into account the results of Hall effect measurements by us and others, local mode studies (14, 15), and Hall and Woodbury's diffusion and solubility measurements (5). Also, the model should be consistent with the defect structure and the corresponding thermodynamic parameters for undoped CdTe (13) in such a way that one of the two species dominating the neutrality condition in undoped CdTe also dominates the neutrality condition in the adjoining range in doped CdTe. Further requirements are that P is present as an acceptor species at high p_{Cd}, but as a donor at low p_{Cd}. Consideration of the transformation reactions

$$P_{Cd}^{\times} + Cd(g) \rightleftarrows Cd_{Cd}^{\times} + P_i^{\times};$$

$$\text{and } P_i^{\times} + Cd(g) \rightleftarrows Cd_{Cd}^{\times} + P_{Te}^{\times}$$

shows that we may expect $P_{Te}^{\times}$ to be most important at high p_{Cd}, $P_{Cd}^{\times}$ at low p_{Cd}, and $P_i^{\times}$ in between. Whereas the choice of $P_{Cd}^{\times}$ as the donor species is clear, there are no compelling reasons for favoring either $P_i^{\times}$ or $P_{Te}^{\times}$ as the acceptor species. Yet, as we shall see, a good description of the solubility data requires the presence of both P_{Te} and P_i. Therefore, we introduce both species.

Figure 7 shows a set of isotherms accounting for the observed hole concentrations in CdTe-6 $\times$ 10^{16} P cm^{-3} after annealing at 700°C. The sharp cutoff of the hole concentration observed at high p_{Cd} (see Fig. 1) occurs at the point where at high temperature $c_e = c_h = K_i{}^{1/2}$. At p_{Cd} below the cutoff, $c_h \propto p_{Cd}{}^{-1/2}$ as required for a defect structure dominated by [P'] $\approx 2[Cd_i^{\cdot\cdot}]$, P' being either P_i' or P_{Te}'. The concentration of holes becomes equal to that of P at medium p_{Cd}. In this range $[P_{Cd}^{t\cdot}]$ rapidly increases with decreasing p_{Cd}, leading to a new range (XIV) governed by $[P_i'] \approx t[P_{Cd}^{t\cdot}]$ with $t = 2$ or 3. In this range $c_h \propto p_{Cd}{}^{1/(t+1)}$. The available information is not sufficient to decide between the two values of t, but $t = 3$ is most likely. While c_h decreases with decreasing p_{Cd}, the concentration of native acceptors A_n' increases, leading to a new range (XVI) governed by $[A_n'] = t[P_{Cd}^{t\cdot}]$. Now $c_h \propto p_{Cd}{}^{-1}$, and rapidly range I is reached where $[A_n'] \approx [h^{\cdot}]$. The phase boundary coincides approximately with the boundary between ranges I and XVI. The theoretical isotherms are valid for 700°C. However, most of the concentrations remain unchanged after cooling so that we can compare the room temperature values of c_h with the calculated isotherms. There is only one complication. According to Ref. (13), at 700°C A_n' consists for 42% of V_{Cd}' and for 58% of Te_i' with only the former having a level close enough to the valence band to leave its holes free upon cooling. As a result, one would expect a sharp drop in c_h in the range where $[Te_i'] > [h^{\cdot}]$. This is not observed. Possible explanations are:

1. Te_i' has an acceptor level in a position similar to that of V_{Cd}'.

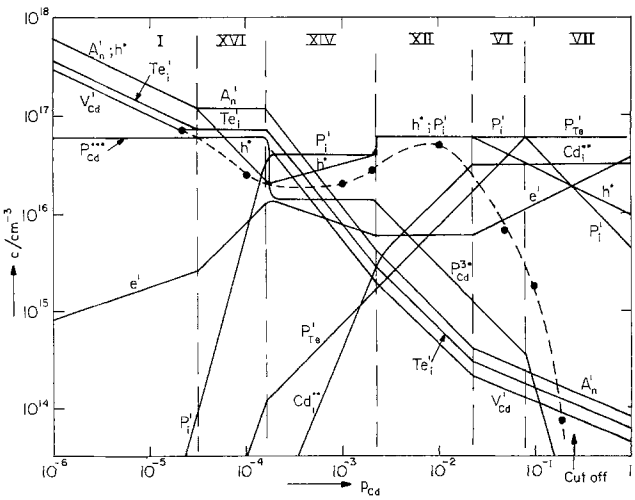


Fig. 7. Defect isotherms in Brouwer approximation for CdTe + 6 $\times$ 10^{16} P cm^{-3} at 700°C.

Table III. Parameters of the phosphorus solubility and the concentrations of other defect species for various simplifications of the neutrality condition and/or P balance

	Types of defects	$[P]_{total}$ = Constant $[\ ] \propto p_{Cd}{}^{r}[P]^{s}$		[P] variable $[\ ] \propto p_{Cd}{}^{m}p_{P_2}{}^{n}$	
		r	s	m	n
I.	$[h\cdot] \approx [V_{Cd}']$	−1/2	0	−1/2	0
	$[P_{Cd}{}^{t\cdot}] \approx [P_{total}]$	0	1	−(t + 2)/2	1/2
	$Cd_i{}^{\cdot\cdot}$	0	0	0	0
	P_i'	(t + 3)/2	1	1/2	1/2
	$(P_{Cd}P_i)^{\times}$	(t + 1)	2	−1	1
II.	$[h\cdot] \approx [V_{Cd}']$	−1/2	0	−1/2	0
	$[P_i'] \approx [P_{total}]$	0	1	1/2	1/2
	$Cd_i{}^{\cdot\cdot}$	0	0	0	0
	$(P_{Cd}P_i)^{\times}$	−2	2	−1	1
	$P_i{}^{\times}$	−1/2	1	0	1/2
	$P_{Cd}{}^{t\cdot}$	−(t + 3)/2	1	−(t + 2)/2	1/2
III.	$[e'] \approx [h\cdot]$	0	0	0	0
	$[P_i'] \approx [P_{total}]$	0	1	0	1/2
	V_{Cd}'	−1	0	−1	0
	$Cd_i{}^{\cdot\cdot}$	1	0	1	0
	$P_i{}^{\times}$	0	1	0	1/2
	$(P_{Cd}P_i)^{\times}$	−1	2	−1	1
IV.	$[e'] \approx 2[Cd_i{}^{\cdot\cdot}]$	1/3	0	1/3	0
	$[P_i'] \approx [P_{total}]$	0	1	1/3	1/2
	V_{Cd}'	−2/3	0	−2/3	0
	$(P_{Cd}P_i)^{\times}$	−5/3	2	−1	1
	$P_i{}^{\times}$	−1/3	1	0	1/2
	$h\cdot$	−1/3	0	−1/3	0
V.	$[e'] = 2[Cd_i{}^{\cdot\cdot}]$	1/3	0	1/3	0
	$[P_{Te}'] = [P]_{total}$	0	1	2/3	1
	$h\cdot$	−1/3	0	−1/3	0
VI.	$[P_i'] \approx 2[Cd_i{}^{\cdot\cdot}] \approx [P_{total}]$	0	1	1/3	1/3
	$h\cdot$	−1/2	1/2	−1/3	1/6
	V_{Cd}'	−1/2	−1/2	−2/3	−1/6
	$P_i{}^{\times}$	−1/2	3/2	0	1/2
	$P_{Cd}{}^{t\cdot}$	−(t + 3)/6	(t + 3)/2	−(t + 3)/3	(t + 3)/6
	$(P_{Cd}P_i)^{\times}$	−2	3	−1	1
	$(P_{Cd}2P_i)^{\times}$	−5/2	9/2	−1	3/2
	P_{Te}'	1	1	4/3	1/3
VII.	$[P_{Te}'] \approx 2[Cd_i{}^{\cdot\cdot}] = [P]_{total}$	0	1	1	1/3
	$h\cdot$	−1/2	1/2	0	1/6
	P_i'	−1	1	0	1/3
	$P_{Cd}{}^{t\cdot}$	−(t + 5)/2	(t + 3)/2	−1	(t + 3)/6
	$(P_{Cd}2P_i)^{\times}$	−7/2	9/2	−1	3/2
	A_n'	−1/2	−1/2	−1	−1/6
VIII.	$[P_i'] \approx 2[Cd_i{}^{\cdot\cdot}]$	5/9	2/9	1/3	1/3
	$3[(P_{Cd}2P_i)^{\times}] \approx [P_{total}]$	0	1	−1	3/2
	$P_i{}^{\times}$	1/3	1/3	0	1/2
	V_{Cd}'	−7/9	−1/9	−2/3	−1/6
	$(P_{Cd}P_i)^{\times}$	−1/3	2/3	−1	1
	$h\cdot$	−2/9	1/9	−1/3	1/6
	$P_{Cd}{}^{t\cdot}$	−(t + 3)/12	(t + 3)/4	−(t + 3)/3	(t + 3)/6
IX.	$[P_{Te}'] \approx 2[Cd_i{}^{\cdot\cdot}]$	11/9	1/9	1	1/3
	$3[(P_{Cd}2P_i)^{\times}] = [P]_{total}$	0	1	−1	3/2
	$h\cdot$	1/9	1/18	0	1/6
X.	$[P_i'] \approx t[P_{Cd}{}^{t\cdot}]$	(t − 2)/3(t + 1)	1/3	−1/(t + 1)	1/2
	$3[(P_{Cd}2P_i)^{\times}] \approx [P_{total}]$	0	1	−1	3/2
	V_{Cd}'	−(t +2)/(t + 1)	0	−(t + 2)/(t + 1)	0
	$Cd_i{}^{\cdot\cdot}$	1 + 1/(t + 1)²	0	1 + 1/(t + 1)²	0
	$(P_{Cd}P_i)^{\times}$	−1/3	2/3	−1	1
	$h\cdot$	1/(t + 1)	0	1/(t + 1)	0
XI.	$[P_i'] \approx t[P_{Cd}{}^{t\cdot}]$	(t − 1)/2(t + 1)	1/2	−1/(t + 1)	1/2
	$2[(P_{Cd}P_i)^{\times}] \approx [P_{total}]$	0	1	−1	1
	V_{Cd}'	−(t + 2)/(t + 1)	0	−(t + 2)/(t + 1)	0
	$Cd_i{}^{\cdot\cdot}$	1 + 1/(t + 1)²	0	1 + 1/(t + 1)²	0
	$h\cdot$	1/(t + 1)	0	1/(t + 1)	0
	$(P_{Cd}2P_i)^{\times}$	1/2	3/2	−1	3/2
XII.	$[h\cdot] \approx [P_i] \approx [P_{total}]$	0	1	0	1/4
	V_{Cd}'	−1	−1	−1	−1/4
	$Cd_i{}^{\cdot\cdot}$	1	2	1	1/2
	$P_i{}^{\times}$	0	2	0	1/2
	P_{Te}'	1	1	1	1/4
	$(P_{Cd}P_i)^{\times}$	−1	4	−1	1
	$(P_{Cd}2P_i)^{\times}$	−1	6	−1	3/2
	$P_{Cd}{}^{t\cdot}$	−1	t + 2	−1	(t + 2)/4
XIII.	$[P_i'] = 2[Cd_i{}^{\cdot\cdot}]$	2/3	1/3	1/3	1/3
	$2[(P_{Cd}P_i)^{\times}] \approx [P_{total}]$	0	1	−1	1
	V_{Cd}'	−5/6	−1/6	−2/3	−1/6
	$h\cdot$	−1/6	1/6	−1/3	1/6
	$(P_{Cd}2P_i)^{\times}$	1/2	3/2	−1	3/2
	$P_{Cd}{}^{t\cdot}$	−(t + 3)/6	(t + 3)/6	−(t + 3)/3	(t + 3)/6
XIV.	$[P_i'] \approx t[P_{Cd}{}^{t\cdot}] = t[P_{total}]$	0	1	−1/(t + 1)	1/2
	$(P_{Cd}P_i]^{\times}$	(1 − t)/(t + 1)	2	−1	1
	$Cd_i{}^{\cdot\cdot}$	1 + 1/(t + 1)²	0	1 + 1/(t + 1)²	0
	V_{Cd}'	−(t + 2)/(t + 1)	0	−(t + 2)/(t + 1)	0
	$h\cdot$	1/(t + 1)	0	1/(t + 1)	0
	P_{Te}'	1	1	t/(t + 1)	1/2
XV.	$[V_{Cd}'] \approx t[P_{Cd}{}^{t\cdot}]$	−(2t + 1)/2(t + 1)	1/2(t +1)	−1	1/2(t + 1)
	$2[(P_{Cd}P_i)^{\times}] = [P_{total}]$	0	1	−1	1
	P_i'	(t + 2)/2(t + 1)	(t + 2)/2(t + 1)	0	(t + 2)/2(t + 1)
	$h\cdot$	−1/2(t + 1)	−1/2(t + 1)	0	−1/2(t + 1)
XVI.	$[V_{Cd}'] \approx t[P_{Cd}{}^{t\cdot}] \approx [P_{total}]$	0	1	−1	1/2(t + 1)
	$(P_{Cd}P_i)^{\times}$	2t + 1	2(t + 1)	−1	1
	P_i'	t + 2	t + 2	0	(t + 2)/2(t + 1)
	$Cd_i{}^{\cdot\cdot}$	−1	2	1	−1/(t + 1)
	$h\cdot$	−1	−1	0	−1/2(t + 1)
	P_{Te}'	t + 3	t + 2	1	(t + 2)/2(t + 1)

Table IV. Range boundary parameters

Regions	$(p_{Cd})_{X,Y}{}^{r}\,[P]_{total}{}^{s}$ = constant		$(p_{Cd})_{X,Y}{}^{m}\,p_{P_2}{}^{n}$ = constant	
X-Y	r	s	m	n
I-II	1	0	1	0
I-XVI	1	2	−(t + 1)	1
II-III	1	0	1	0
II-XII	1	2	2	1
III-IV	1	0	1	0
III-XII	0	1	0	1
IV-V	1	0	1	0
IV-VI	−1	3	0	1
V-VII	−1	3	2	1
VI-VII	1	0	1	0
VI-VIII	−5	7	−8	7
VI-XII	1	1	4	1
VI-XIII	−1	1	−2	1
VI-XIV	−(t + 3)*	(t + 1)	−2(t + 4)	(t + 1)
VII-IX	−1	1	−12	7
VIII-X	−(2t + 11)	(t + 1)	−2(t + 4)	(t + 1)
VIII-XIII	1	1	0	1
VIII-IX	−6	1	1	0
X-XI	1	1	0	1
XI-XIII	−(t + 7)	(t + 1)	−2(t + 4)	(t + 1)
XI-XIV	(1 − t)	(t + 1)	−2t	(t + 1)
XI-XV	3	1	2	1
XII-XIV	−1	(t + 1)	−4	(t + 1)
XIV-XVI	(t + 2)	(t + 1)	2	1
XV-XVI	1	1	1	1

* t = degree of ionization of $P_{Cd}{}^{t\cdot}$.

2. Te_i precipitates during cooling.

3. The ratio between the concentrations of the two species is different from that reported in Ref. (13). It is not possible to decide this question at this point.

If we accept the ranges governing the sample with a low P concentration as given in Fig. 7, we can predict the manner in which the range boundaries vary with the P concentration by using the information of Table IV. New ranges may occur if new species become dominant. A set of regions accounting for almost all the experimental data is shown in Fig. 8. For the characterization of the various regions, see Table II. The figure is constructed in such a way that transitions between regions occur if one of the species dominating the neutrality condition or the P balance in a region is changed. The defect structure of undoped CdTe as proposed in Ref. (13) is represented by regions I-V. It contains an intrinsic region (III) at medium p_{Cd}, regions IV and V dominated by e' and $Cd_i{}^{\cdot\cdot}$ at high p_{Cd} and regions I and II dominated by $h^{\cdot}$ and $V_{Cd}{}'$. The difference between I and II and between IV and V is due to a difference in the major P species present as a minority species. Regions at high P concentration have neutral associates $(P_{Cd}P_i)^{\times}$ and $(P_{Cd}2P_i)^{\times}$ as the dominant phosphorus species. According to the model as presented, in ranges XIV, XI, and X, $c_h \propto p_{Cd}{}^{1/(t+1)}$ but independent of P concentration and thus does not account for a small increase in c_h observed at the highest P concentration (see Fig. 1 and 3). This discrepancy is removed by replacing range XIV by a range governed by $[h^{\cdot}] = [P_i']$, with $[P]_{total} = 2[(P_{Cd}P_i)^{\times}]$, giving $c_h \propto p_{Cd}{}^{1/4}c_P{}^{1/4}$. However, this model requires that measurement of $c_h(T)$ gives $\frac{1}{2}\,E_{aP}$ as the activation energy of carrier liberation, whereas the full value E_{aP} is $\approx$ 0.038 eV is observed (data not shown in Fig. 5). Also, this model does not give the steep rise in c_h with decreasing p_{Cd} observed at the lowest p_{Cd}. Therefore, this change is not justified. Figure 9 shows a region-plot in terms of p_{Cd} and p_{P2}. Figure 10 shows defect concentrations as a function of $(c_P)_{total}$ for samples annealed at 700°C under $p_{Cd} = 10^{-2}$ atm. Values of constant $K_{(PCdPi)}$ of Table II, reaction 9, has been chosen to fit the results shown in Fig. 3. A similar adaptation to results of Fig. 2 lead to values of this constant at 900°C and thus to the constant as $f(T)$

$$K_{(PCdPi)} = 500 \exp + (1.73\ \text{eV}/kT)\ \text{site}\ fr^{-1}$$

The model as presented finds support in the results of a microstructure investigation by Rustomji and Narayanan (18).

Interpretation of solubility data.—According to Hall and Woodbury (5) the solubility of P in crystals equilibrated at 900°C with a vapor of Cd and P_2 with a constant weight ratio of Cd to P of 100:1 corresponding to a partial pressure ratio $p_{P_2}:p_{Cd} = 1.82 \times 10^{-2}$ varies with $p_{Cd}{}^{m}p_{P_2}{}^{n} = 1.82 \times 10^{-2}\,p_{Cd}{}^{m+n}$ with $m + n$

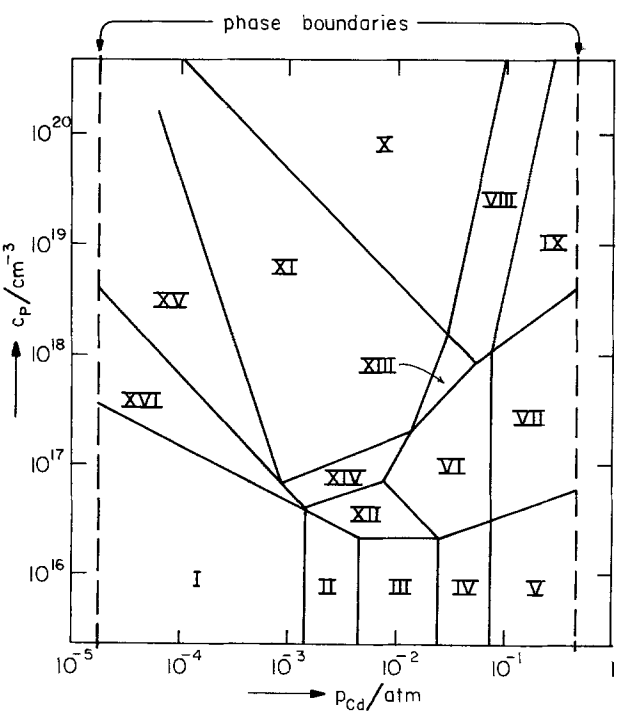


Fig. 8. Range boundary diagram for P-doped CdTe at 700°C in a plot of c_P vs. p_{Cd}.

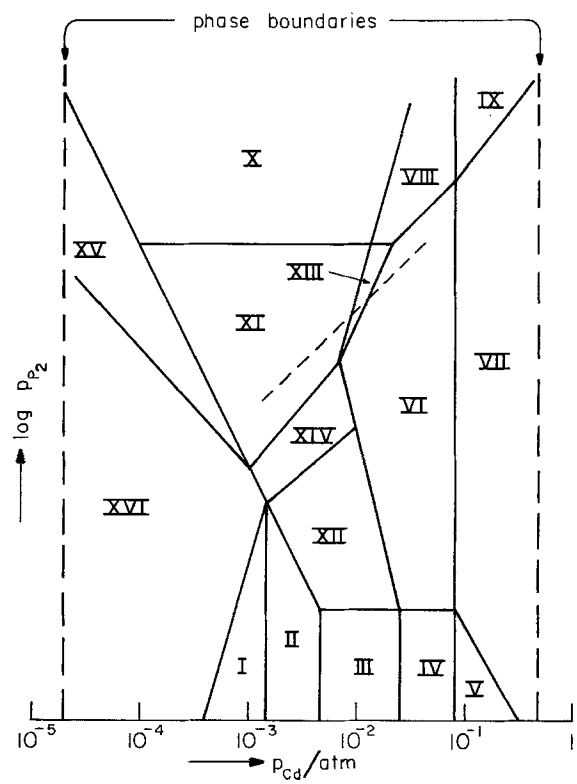


Fig. 9. Range boundary diagram for P-doped CdTe at 700°C in a plot of p_{P_2} vs. p_{Cd}. The dashed line under 45° corresponds to a path with $p_{P_2} \propto p_{Cd}$ as in Hall and Woodbury's solubility experiments.

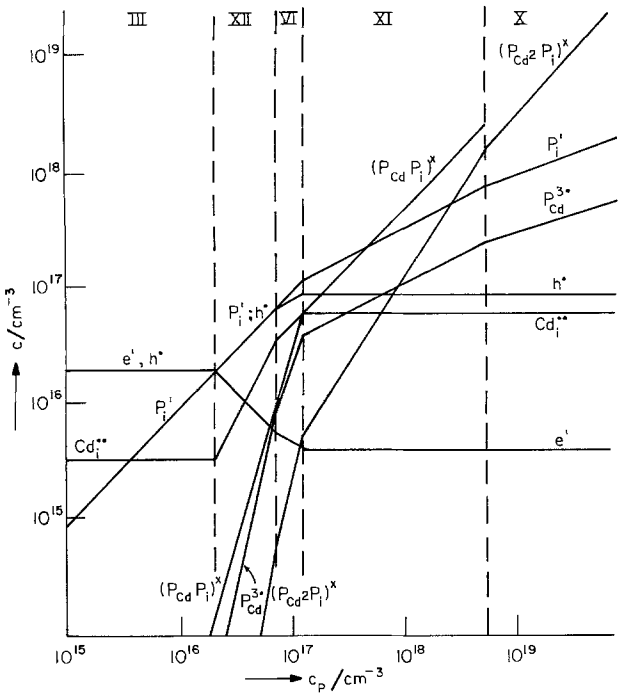


Fig. 10. Defect isotherms as $f(c_P)$ for $p_{Cd} = 10^{-2}$ atm, T = 700°C.

≈ 0 at $p_{Cd} \leq 0.1$ atm and $m + n \approx 0.7$ at $p_{Cd} \geq 0.1$ atm. According to our model, $m + n = 0$ in regions XI and XIII due to the predominance of the species $(P_{Cd}P_i)^\times$. On the other hand, $m + n = 0.67$ in the adjacent region VI, while $m + n = 1.33$ in region VII. Hall and Woodbury's experiments correspond to a line under 45° through a figure such as Fig. 9 (but drawn for 900° rather than 700°C). The experimental results, both as to the absolute value of the concentrations of phosphorus and the variation with p_{Cd} are accounted for by our model if we use for the constants regulating the formation of native defects the parameters given in Ref. (13), and $[(P_{Cd}P_i)^\times] = 3.7 \times 10^{18}$ cm^{-3}, $(K_{P_i\times})_{900°C} = 5 \times 10^{18}$ cm^{-3}, and $(K_{P_{Te}\times})_{900°C} = 10^{19}$ cm^{-3}.

Figure 11 shows the individual contributions to c_P by the various defects

$$[P] = [P_i'] + [P_{Te}'] + [P_{Cd}^{3\cdot}] + 2[(P_{Cd}P_i)^\times] \quad [1]$$

The concentrations of the various charged species are

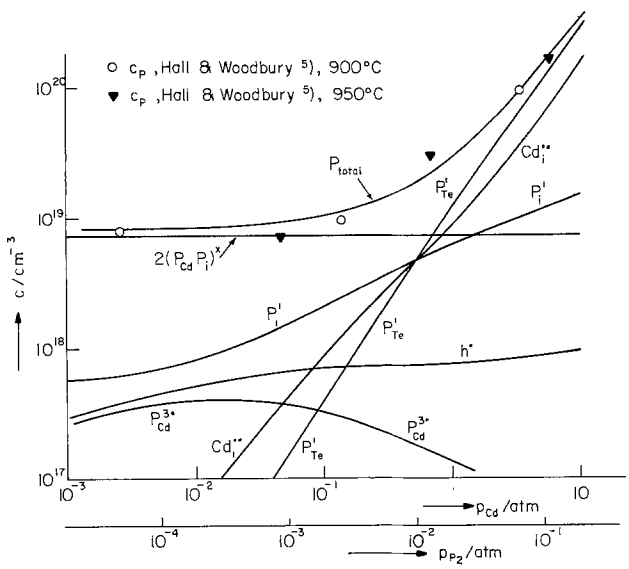


Fig. 11. Contributions to c_P at 900° and 950°C in CdTe equilibrated with a vapor of Cd + P_2 according to Hall and Woodbury (5).

found by expressing in the neutrality condition

$$[e'] + [P_i'] + [P_{Te}'] = 2[Cd_i^{\cdot\cdot}] + [P_{Cd}^{3\cdot}] + [h\cdot] \quad [2]$$

the concentrations of all species in terms of that of $h\cdot$

$$\frac{K_I}{c_h} + \frac{K_{aP_i}K_{P_i}{}^\times f p_{Cd}{}^{1/2}}{c_h} + \frac{K_{aP_{Te}}K_{P_{Te}}{}^\times f p_{Cd}{}^{3/2}}{c_h} = \frac{2K_{CdI}}{K_I{}^2} p_{Cd} c_h{}^2 + f\pi K p_{Cd}{}^{-1/2} c_h{}^3 + c_h \quad [3]$$

with $\pi K = K_{dP_{Cd}} \times K_{P_{Cd}} \times K_i{}^{-3} K_{CdV}{}^{\times -1} = 2.4 \times 10^{-36}$ cm^6, $f = (1.82 \times 10^{-2})^{1/2} = 0.135$, $(K_{AP_i}) \approx (K_{aP_{Te}})_{900°C} = 6.83 \times 10^{18}$ cm^{-3} (see next section). Solving this equation gives $c_h(p_{Cd})$, and the value of each term in the above equation is equal to the concentration of the corresponding defect in the neutrality condition. πK has been chosen to make $P_{Cd}{}^{3\cdot}$ dominant in the neutrality condition as required for range XI; a smaller πK, making holes the dominant positive species, would give an equally good representation of the solubility. On the other hand, dropping of either P_i' or P_{Te}' (with adjustment of the formation constant of the remaining species) leads to loss of accuracy of the representation of the solubility.

Interpretation of the low temperature Hall effect data on the basis of the defect model.—The number of charge carriers as a function of temperature gives information about the degree of compensation of the acceptors and their ionization energy. In the following, the hole concentration as $f(T)$ in p-type samples annealed under conditions corresponding to various regions of the range boundary diagram is discussed on the basis of the defect model.

The concentration of holes is related to the concentrations of neutral and ionized acceptors. For P_i as the major acceptor

$$\frac{[P_i'][h\cdot]}{[P_i{}^\times]} = K_{aP} = \frac{N_v}{gN} \exp(-E_{aP}/kT) \quad [4]$$

where E_{aP} is the acceptor depth measured from the valence band edge, N_v is the density of states in the valence band, equal to $2(2\pi m_h{}^* kT/h^2)^{3/2}$, N is the number of molecules CdTe per cm^3, g is a degeneracy factor equal to g_v (number of valence band maxima) times $g_{P_i\times}/g_{P_i'}$. Square brackets indicate concentrations in site fractions. The general neutrality condition is [2] and the phosphorus balance is [1]. At low P concentrations, medium p_{Cd} of anneal, and $T \geq$ 250°K, $[P]_{total} \approx [P_i'] \approx [h\cdot]$, independent of temperature. At lower temperature, $[P]_{total} \approx [P_i{}^\times]$ but $[P_i'] \approx [h\cdot]$ and

$$\frac{c_h}{T^{3/4}} = \left(\frac{c_{P,total}}{g}\right)^{1/2} \left(\frac{2\pi mk}{h^2}\right)^{3/4} \left(\frac{m_h{}^*}{m}\right)^{3/4} \exp(-E_{aP}/2kT) \quad [5]$$

A plot of log $c_h/T^{3/4}$ *vs.* T^{-1} gives a slope equal to $\frac{1}{2}E_{aP}$. This applies to the sample with 6×10^{16} P cm^{-3} annealed at 700°C at $p_{Cd} = 10^{-2}$ atm (Fig. 5) which yields $E_{aP} = 0.034$ eV. The intercept with the axis at $T^{-1} = 0$ has the value 1.7×10^{15} cm^{-3}/degree$^{3/2}$. Equating this with the preexponential factor of [5] with $m_h{}^* = 0.35$m (19) leads to $c_{P,total}/g = 2.9 \times 10^{15}$ cm^{-3} and thus $g \approx 20$. With $g_v = 4$ this indicates $g_{P_i\times}/g_{P_i'} = 5$.

At larger p_{Cd}, but the P concentration still low

$$[P_i'] \approx 2[Cd_i^{\cdot\cdot}] + [h\cdot] \approx [P]_{total} - [P_i{}^\times] >> [h\cdot]$$

we get

$$\frac{[h\cdot]\{2[Cd_i^{\cdot\cdot}] + [h\cdot]\}}{\{[P]_{total} - 2[Cd_i^{\cdot\cdot}] - [h\cdot]\}} = \frac{N_v}{gN}\exp(-E_{aP}/kT) \quad [6]$$

an expression that is equivalent to the well-known formula for p-type semiconductors in which the acceptors are partially compensated by donors (20). A plot of $[h\cdot]/T^{3/2}$ *vs.* $1/T$ now has the slope E_{aP}. For a sample with 2×10^{17} P cm^{-3} annealed at 700°C with $p_{Cd} = 0.1$ atm (the lower curve of Fig. 5), we find $E_{aP} = 0.04$ eV. The value of the intercept interpreted with $m_h^* = 0.35$m (19), $g \approx g_v = 4$ gives $c_{Cd_i^{\cdot\cdot}} = 1.8 \times 10^{16}$ cm^{-3}, close to the value 2.4×10^{16} cm^{-3} expected from the defect isotherms for this sample under the condition as given. Use of $g = 20$ as indicated by the sample with $[h\cdot] \approx [P_i']$ leads to $c_{Cd_i^{\cdot\cdot}} \approx 9.5 \times 10^{17}$ cm^{-3}, much larger than the expected value.

At higher P concentrations the P balance changes to

$$[P]_{total} = [P_{Te}^{\times}] + [P_{Te}'] + 3[(P_{Cd}2P_i)^{\times}]$$

giving

$$\frac{[h\cdot]\{2[Cd_i^{\cdot\cdot}] + [h\cdot]\}}{\{[P]_{total} - 3[(P_{Cd}2P_i)^{\times}] - 2[Cd_i^{\cdot\cdot}] - [h\cdot]\}} = \frac{N_v}{gN}\exp(-E_{aP}/kT) \quad [7]$$

A plot of $[h\cdot]T^{-3/2}$ *vs.* $1/T$ again has the slope E_{aP}. Samples 3 and 4 of Fig. 5 give $E_{aP} = 0.035$ and 0.031 eV. From the intercepts of the two middle curves of Fig. 6 for $c_{P,total} = 5 \times 10^{19}$ cm^{-3} with $m_h^* = 0.35$m, $g \approx g_v = 4$, and $[Cd_i^{\cdot\cdot}]$ as calculated from the model we compute for the concentration of $(P_{Cd}2P_i)^{\times}$ the values 4.3×10^{18} and 3.3×10^{18} cm^{-3}, close to the value 1.67×10^{19} cm^{-3} calculated from the defect model. Again $g = 20$ gives a worse fit.

We also applied the method of least squares to Eq. [4], [6], and [7], using a programmable calculator HP-65, for the experimental data of $c_h\cdot$ *vs.* $10^3/T$ of Fig. 5 and 6 in order to obtain the values of the unknown parameters of the equations. The results obtained were the same.

Summary

Single crystals of CdTe doped with various amounts of phosphorus were grown from the melt. Samples were annealed at different cadmium pressures at 700°, 800°, and 900°C, and Hall effect measurements were carried out on samples cooled to room temperature after the anneal. Defect isotherms are accounted for on the basis of a model in which phosphorus acts as an acceptor (P_{Te} and/or P_i) at high p_{Cd} and as a donor P_{Cd}, forming ($P_{Cd}P_i$), at low p_{Cd} as well as at high phosphorus concentrations. This model also accounts for the solubility or phosphorus in CdTe under various conditions. The phosphorus acceptor level (of P_{Te}' and/or P_i') is found to be at E_v + 0.035 eV.

Acknowledgment

This work was supported by the Defense Advanced Research Projects Agency under Contract No. F 19628-72-C-0275, Project 2055.

Manuscript submitted May 17, 1976; revised manuscript received Aug. 31, 1976.

Any discussion of this paper will appear in a Discussion Section to be published in the December 1977 JOURNAL. All discussions for the December 1977 Discussion Section should be submitted by Aug. 1, 1977.

REFERENCES

1. D. A. Jenny and R. H. Bube, *Phys. Rev.*, **96**, 1190 (1954).
2. G. A. Kachurin, V. M. Zelevinskaya, and L. W. Smirnov, *Sov. Phys. Semicond. (Engl. Transl.)*, **2**, 1527 (1969).
3. E. R. Morehead and G. Mandel, *Phys. Lett.*, **10**, 5 (1964).
4. E. N. Arkadeva, O. A. Agrinskaya, and Yu. V. Rud, *Sov. Phys. Solid State (Engl. Transl.)*, **8**, 2260 (1967).
5. R. B. Hall and H. H. Woodbury, *J. Appl. Phys.*, **39**, 5361 (1958).
6. E. N. Arkadeva, M. I. Guseva, O. A. Matveev, and V. A. Sladkova, *Sov. Phys. Semicond. (Engl. Transl.)*, **9**, 563 (1975).
7. D. de Nobel, *Philips Res. Rep.*, **14**, 361 (1959).
8. L. J. van der Pauw, *Phillips Tech. Rev.*, **20**, 220 (1959).
9. R. Chwang, B. J. Smith, and C. R. Crowell, *Solid-State Electron.*, **17**, 1217 (1974).
10. M. M. Beguwala, Ph.D. Thesis, University of Southern California (1974).
11. R. Ishikawa and T. Mitsuma, *Jpn. J. Appl. Phys.*, **5**, 1171 (1966).
12. V. Capek, K. Zimmermann, C. Konak, M. Popova, and P. Polivka, *Phys. Status Solidi B*, **59**, 739 (1973).
13. S. S. Chern, H. R. Vydyanath, and F. A. Kröger, *J. Solid State Chem.*, **14**, 33 (1975); *ibid.*, **15**, 369 (1975).
14. B. V. Dutt and W. G. Spitzer, *J. Appl. Phys.*, In press.
15. B. V. Dutt and W. G. Spitzer, *ibid.*, In press.
16. F. A. Kröger and H. J. Vink, in "Solid State Physics," Vol. 3, F. Seitz and D. Turnbull, Editors, p. 307 Academic Press (1956).
17. G. Brouwer, *Philips Res. Rep.*, **9**, 366 (1954).
18. S. Rustomji and G. H. Narayanan, Paper submitted to *Phys. Status Solidi.*
19. D. de Nobel, *Philips Res. Rep.*, **14**, 361, 430 (1959).
20. J. S. Blakemore, "Semiconductor Statistics," p. 139, Pergamon Press, Inc. (1962).

CdF_2:YbF_3:ErF_3—An Efficient Infrared to Visible Upconverting System

Martha Greenblatt

Department of Chemistry, Rutgers University, New Brunswick, New Jersey 08903

and E. Banks*

Department of Chemistry, Polytechnic Institute of New York, Brooklyn, New York 11201

ABSTRACT

Single crystals of CdF_2 doubly doped with YbF_3 and ErF_3 efficiently convert infrared radiation (~0.93 μm) from a Si:GaAs diode to red and green light. By varying the Yb concentration, phosphors have been made which produce a red or green visual response. For the series of crystal samples of CdF_2:1% ErF_3:1-10% YbF_3 studied: at YbF_3 concentrations below 3%, only red Er^{3+} emission peaks were observed (6450-6800Å); at 3% YbF_3, red and green spectra (5300-5700Å) were observed, the green bands being much less intense; the most intense phosphor contained 10 mole percent (m/o) Yb^{3+}, and the green intensity was an order of magnitude higher than the red. Charge compensation by NaF of the rare earth ions in CdF_2:1% ErF_3:10% YbF_3 greatly reduces the intensity of emission bands, as well as the intensity of the absorption band at 976 nm, in agreement with previous studies of the absorption spectra properties of the YbF_3:CdF_2 system (1). Recent results of ^{19}F NMR of single crystals of CdF_2 containing high concentrations of YbF_3 and ErF_3, respectively, indicate that most of the rare earth ions and their associated interstitial fluorides are found in $(M^{3+}\text{-}F^-)_2$ dimers in the crystal (2). The intense absorption band observed at 976 nm in Yb^{3+}-doped CdF_2 can be assigned to this dimer, which is destroyed by the use of Na^+ as a charge compensator in place of interstitial fluoride, the native charge compensating defect. Similarly, as the accepted mechanism of the infrared-to-visible conversion in the Yb^{3+} sensitized Er^{3+} activated systems involves the transfer of two infrared photons from Yb^{3+} to Er^{3+}, phosphor emission by diode excitation will decrease when the $(M^{3+}\text{-}F^-)_2$ complex is destroyed by NaF substitution. The 976 nm strong absorption band was also observed in samples (10% Yb, 1% Er) prepared with 1-50 m/o of CaF_2 substituted for CdF_2 without appreciable decrease in the intensity; however the emission intensities of both green and red bands were significantly enhanced for all of the samples codoped with CaF_2. There appears to be a plateau for the compositions 1.5-3% CaF_2 and a decrease in the 4.5 and 10% CaF_2 samples. Of all the materials investigated to date, YF_3 and $BaYF_5$ codoped with Yb^{3+} and Er^{3+} are reported to be the most efficient upconverting systems with a quantum efficiency between 10^{-4} and 10^{-3} ($\lambda = 0.97$ μm). The quantum efficiency of CdF_2:10% YbF_3:1% ErF_3 is found to be 0.23% and that of CdF_2:10% YbF_3:1% ErF_3:2.5% CaF_2, 0.70%. These values were obtained under intense excitation with a GaAs diode. Lower values might be found at lower excitation densities.

Infrared excited visible fluorescence has attracted considerable attention in recent years (1-5). In combination with GaAs:Si diodes emitting in the near infrared (0.91-1 μm), phosphor materials capable of converting infrared to visible light are potential display or infrared detecting devices.

All the known phosphors of this class use trivalent rare earth ions. The systems which produce the brightest visible light use Yb^{3+} as the sensitizer with Er^{3+}, Ho^{3+}, or Tm^{3+} as the activator. The host crystals in which the most efficient upconversion has been obtained are YF_3, $BaYF_5$, LaF_3, and α-$NaYF_4$, doped with Yb^{3+} and Er^{3+}. The Yb^{3+} ions can absorb the GaAs infrared emission and are able to transfer most of the energy to Er^{3+} ions, both in their ground state and excited state, which then emit the green or red depending on concentration and the host crystal. Similarly, Yb^{3+} in combination with Ho^{3+} upconverts in the green or red and Yb^{3+} with Tm^{3+} in the appropriate host crystals upconverts in the blue.

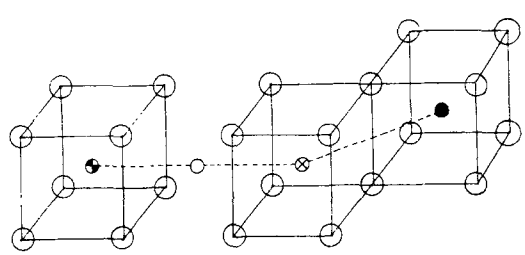
In the first part of this paper a brief review of the spectroscopic properties of CdF_2 doped with small concentrations of YbF_3 is presented. The infrared visible upconverting properties of CdF_2:Yb:Er system are then discussed in detail.

* Electrochemical Society Active Member.

Key words: infrared-visible upconversion, rare earth luminescence, CdF_2:Yb^{3+},Er^{3+}.

CdF_2:YbF_3—The 976 nm Band

CdF_2 has the fluorite structure (Fm3m) of CaF_2 shown in Fig. 1. This may be visualized as a cubic lattice of fluoride ions in which every other body center position is occupied by divalent cadmium. Rare earth



○ F^-

⊗ $R.E.^{3+}$ Ion Substitutionally in a Cd^{2+} Position

○ Nearest Neighbor Interstitial Position (I00 Direction)

● Nearest Neighbor Cd^{2+} Position (II0 Direction)

◔ Next Nearest Neighbor Cd^{2+} Position (I00 Direction)

Fig. 1. The symmetry of sites in the CdF_2 (RE) system

ions can enter the lattice substitutionally at the Cd^{2+} sites. Compensation for the excess charge of the tripositive rare earth ions in CdF_2 has been shown to occur by the incorporation of fluoride ions into the interstitial sites (6). The interstitial fluoride ion is either a nearest neighbor of RE^{3+}, an electrostatically favorable arrangement, in which case the symmetry around the rare earth is reduced to tetragonal, or the interstitial fluorides may be at a distance from the rare earth ion, thus preserving the cubic symmetry of the RE site. Charge compensation can also be attained by the introduction of univalent ions, such as Na^+, for each trivalent ion. The nearest neighbor Cd^{2+} sites are in [110] directions, and if the compensating Na^+ goes into one of these positions the symmetry around the RE is reduced to orthorhombic.

The absorption spectrum of CdF_2:0.1 Yb^{3+} single crystals was found to be unusual (7); the spectrum consists of an intense band at 976 nm and a less intense broad band absorption extending to about 900 nm. As NaF was added to the $CdF_2:Yb^{3+}$ system the intensity of the 976 nm band decreased. A sample containing sufficient sodium for complete charge compensation showed a spectrum which resembled that of Yb^{3+} in other solids, *e.g.*, yttrium gallium garnet, $YbCl_3 \cdot 6H_2O$, or CaF_2. This spectrum consists mainly of a sharp line at 962 nm and a broader absorption at 920 nm (8). In Fig. 2, the energy level diagram of Yb^{3+} in CdF_2 and CaF_2 is shown (9). On the basis of the oscillator strength of the absorption bands as well as the expected crystal field splitting of states in a cubic environment, Abbruscato *et al.* assigned the 962 nm band to the $\Gamma_7 \rightarrow \Gamma_7'$ and the 920 band as due to $\Gamma_7 \rightarrow \Gamma_8'$ transitions. They showed that the 976 nm band cannot be part of a cubic or noncubic spectrum of isolated Yb^{3+} ions in CdF_2. In addition, ESR measurements of $CdF_2:Yb^{3+}$ showed only sites of cubic symmetry, while the ESR of $CdF_2:Yb^{3+}:Na^+$ indicated Yb^{3+} in both cubic and orthorhombic sites. The ESR of $CaF_2:Yb^{3+}$ showed Yb^{3+} in cubic and tetragonal environments in the crystal (9).

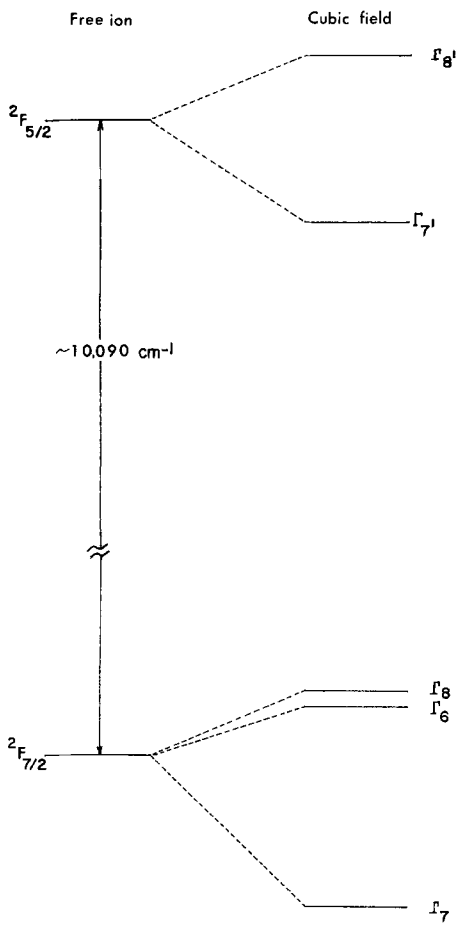


Fig. 2. Energy levels of the Yb^{3+} ion, free and in a cubic crystal field.

The main difference between the optical absorption of Yb^{3+} in CdF_2 and in CaF_2 has been the absence of the intense 976 nm absorption in CaF_2. Weller has shown that as little as 0.1% CaF_2 in the CdF_2:0.1 YbF_3 system decreased the intensity of the 976 nm band drastically and at about 7% CaF_2 content, the 976 nm band disappeared completely (10). Prener and Kingsley have shown that when CdF_2 crystal doped with Yb^{3+} or other RE ion is heated in Cd vapor to 500°C, the insulating transparent crystal becomes semiconducting and colored. Apparently the interstitial fluorides migrate to the surface and oxidize Cd. The liberated electrons do not reduce the rare earth (except Eu) but remain in a diffuse state over the 12 nearest neighbor Cd^{2+} ions. If Ca^{2+} is added the semiconducting property decreases until at 8% CaF_2, it disappears completely (11). On the basis of the above evidence Abbruscato *et al.* postulated that the 976 nm band in $CdF_2:Yb^{3+}$ is not an f-f transition but might be due to some center involving Yb^{3+} and interstitial F^-, Yb^{3+}-Yb^{3+} interactions via interstitial F^- or some similar defect.

^{19}F NMR in $CdF_2:Yb^{3+}$

The ^{19}F NMR measurement of CdF_2 doped with Er^{3+} and Yb^{3+} was undertaken in the hope of finding further evidence for the mechanism responsible for the unusual properties of CdF_2 doped with rare earth ions. In addition to the main resonance from the bulk of the lattice fluorides, weaker anisotropic resonances for two types of fluoride ions were detected (12, 13); one having axial symmetry about the [111] axes and the other one with its symmetry axis along the [100] axis. The [111] resonances were identified as the lattice fluorides adjacent to one rare earth ion. The [100] resonance can only arise from the interstitial fluorides (see Fig. 1) and their intensity indicates that this resonance accounts for nearly all the interstitial fluorides in the crystal. It has been shown that the anisotropy of the [100] ^{19}F resonance can only be explained by assuming each interstitial fluoride must have two rare earth ions at adjacent Cd^{2+} sites in which the RE^{3+}-F^--RE^{3+} angle is 90°. This is most readily explained by assuming that most of the rare earth ions and their associated interstitial fluorides are found in $(Re^{3+}\text{-}F^-)_2$ dimers as shown in Fig. 3. The [100] NMR spectrum could also be explained by zigzag chains of rare earth-interstitial fluoride along the (110) direction.

The ^{19}F NMR results appear to offer an explanation of the above-described ESR and optical spectra of Yb^{3+}-doped CdF_2 which showed only cubic ESR and additional bands not attributable to cubic sites. The additional bands can be assigned to this dimer; the lack of any ESR signal from these dimers can probably be attributed to spin exchange interactions between the two metal ions in the dimer. This would be equally true for the chain model.

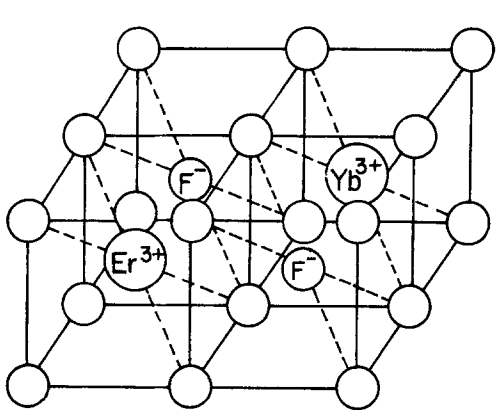


Fig. 3. Orthorhombic cluster site, showing unlike ion pairing

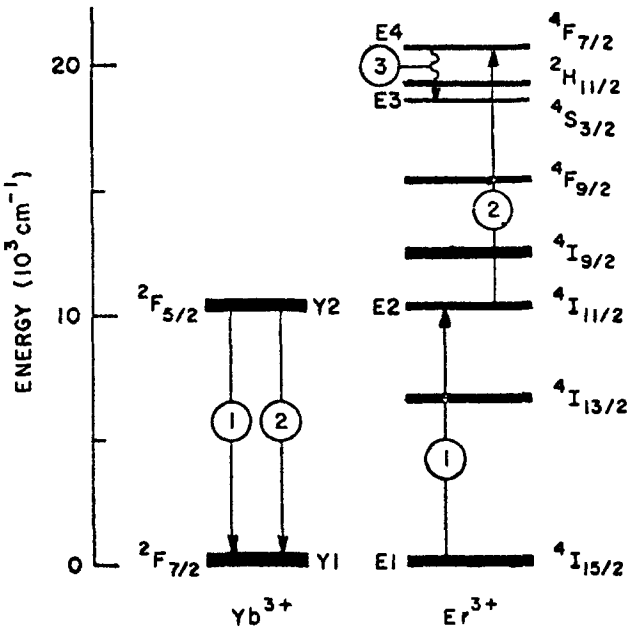


Fig. 4. Energy level diagram for Yb^{3+} and Er^{3+} showing the upconversion process.

CdF_2:Yb^{3+}:Er^{3+}—Infrared Visible Phosphor

The intense absorption band observed in CdF_2:Yb^{3+} at 976 nm suggested that efficient infrared-visible upconversion might be enhanced in CdF_2 crystals doped with Yb^{3+} and Er^{3+} if the primary absorption process is more efficient compared with other systems.

Figure 4 is an energy level diagram of Yb^{3+} and Er^{3+} showing the upconversion process in the green (14). Ytterbium ions absorb infrared radiation in the 0.91-1 μm range; an excited ytterbium ion transfers its energy to an erbium ion which is excited to the $^4I_{11/2}$ manifold; a second transfer of infrared quantum excites the $^4I_{11/2}$ to the $^4F_{7/2}$ level. The erbium then decays nonradiatively to the $^4S_{3/2}$ level, followed by visible fluorescence from $^4S_{3/2}$ in the region of 540 nm. In this process, two quanta of infrared are absorbed for every quantum of visible light emitted, and the intensity of green emission is found to increase as the square of the infrared exciting power (15). The conversion of infrared into red can take place by various routes, by the absorption of two or three quanta. In fluoride hosts, excitation spectra in the 350-500 nm range show that the most important path for red emission in Yb^{3+}-Er^{3+} samples is excitation of Er^{3+} to the $^4I_{11/2}$ level (by the transfer of energy from infrared-excited Yb^{3+}) followed by rapid nonradiative decay to the $^4I_{13/2}$ manifold; a second quantum of energy excites the electron from $^4I_{13/2}$ to $^4F_{9/2}$ from which red fluorescence is observed (16). The three quantum process for red emission has also been observed at high rare earth ion concentrations, with excitation of Er^{3+} by two quanta to ($^4I_{15/2} \rightarrow {}^4I_{11/2} \rightarrow {}^4F_{7/2}$), followed by nonradiative transition to $^4S_{3/2}$; from $^4S_{3/2}$ transition to $^4I_{13/2}$ accompanied by the back transfer of an infrared quantum to Yb^{3+}; a third quantum excites the Er^{3+} from $^4I_{13/2}$ to $^4F_{9/2}$ followed by transition to the ground state and red emission.

The complexity of the mechanism for upconversion implies that many factors affect the efficiency of the process. The purity of the samples is extremely important (17).

Experimental

CdF_2 was prepared from 99.999% pure cadmium metal (American Smelting and Refining Company) by precipitation with hydrofluoric acid. ErF_3, YbF_3, of purity > 99.9% (Lindsay Division of the American Potash and Chemical Corporation), NaF and CaF_2 of 99.99% purity were used. The CdF_2 single crystals doped and codoped with various concentrations of YbF_3, ErF_3, NaF, and CaF_2 were grown by the Bridgman technique; a graphite crucible was slowly lowered through a temperature gradient in the work coil of an rf generator, the crucible being maintained in an argon atmosphere. The weights were measured accurately before and after crystal growth; weight loss was attributed to CdF_2, hence the concentration of dopants reported is the minimum concentration possible. The crystals were cut to a uniform thickness of 1.7 mm and polished. Absorption spectra of samples were recorded on a Cary Model 14 spectrophotometer at room temperature. For the emission measurements, a thin disk (1.7 mm) of a polished single crystal was placed near the dome of a GaAs:Si diode (Texas Instruments Model TIXL 16) operated at 2A. The infrared radiation ($\sim$ 0.93 μm) emitted by the diode is absorbed by the phosphor which then emits visible light. The fluorescent output of the crystal was analyzed with the monochromator of a Spex spectrometer and detected with an (ITT-F-W-130-Products for Research) photomultiplier S20.

Results and Discussion

Figure 5 shows the emission spectrum of CdF_2:10% YbF_3:1% ErF_3 [all percent concentrations represent mole percent (m/o)] the most efficient phosphor in the series CdF_2:1-10% YbF_3:1% ErF_3 studied. A complex spectrum of three stronger bands at 538.3, 543.6, and 552.5 nm and two weaker broad bands at $\sim$ 522 and 530 nm are observed in the green region, and several peaks at 623.3, 652.0, 656.5, and 666.5 nm in the red. The intensity of emission bands in the 550 nm region is an order of magnitude greater than the intensity of the red bands and the crystal displays a bright green visible fluorescence. Samples of CdF_2:1-2% YbF_3:1% ErF_3 showed fluorescence bands only in the red; CdF_2:3% YbF_3:1% ErF_2 emitted in the green and the red, but bands in the green were much weaker than bands in the red. The effect of increasing the concentration of Yb^{3+} on the intensity of several of the emission bands is shown in Fig. 6. The intensity of both green and red emission increases with increasing concentration of Yb^{3+}; apparently the optimum concentration of Yb^{3+} is $\sim$ 20% in the CdF_2:Yb:Er system for green emission.

One of the objects of studying the infrared-to-visible upconverting properties of CdF_2:YbF_3:ErF_3 system was to shed further light on the origin of the 976 nm absorption band. The intensity of the emission bands is greatly reduced when NaF is introduced to replace interstitial F^- charge compensation by substitutional Na^+ which in effect destroys the $(M^{3+}\text{-}F_{int.}^-)_2$ clusters, and reduces the intensity of the 976 nm band. The emission spectrum of CdF_2:3.5% NaF:10% Yb:1% ErF_3 is shown in Fig. 7. The increased structure in

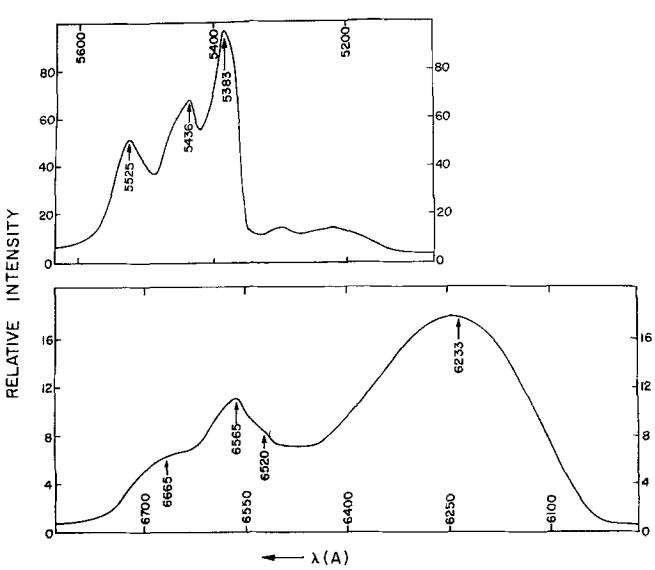


Fig. 5. Emission spectrum of CdF_2:10% YbF_3:1% ErF_3 (room temperature). Excitation by Si:GaAs diode ($\lambda \approx$ 0.93 μm).

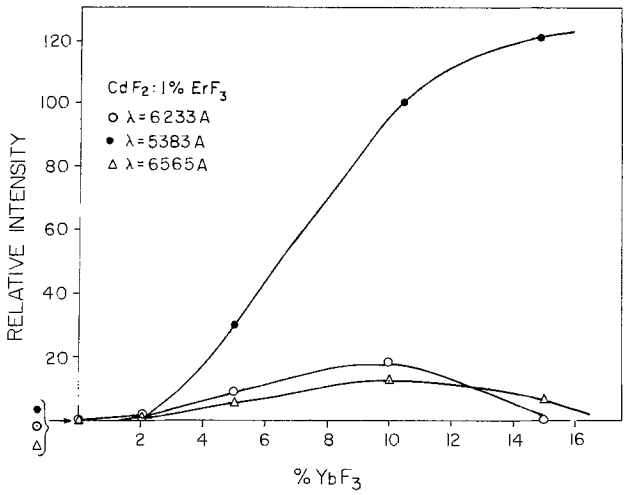


Fig. 6. Variation of relative intensity of various bands *vs.* Yb^{3+} concentration (Er^{3+} constant at 1 m/o).

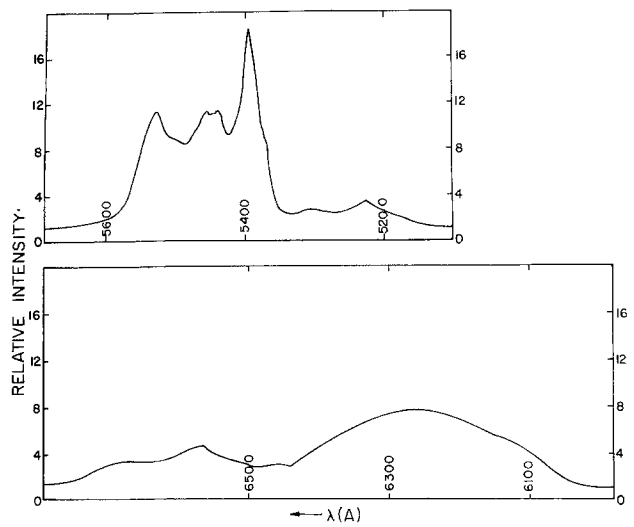


Fig. 7. Emission spectrum of CdF_2:10% YbF_3:1% ErF_3:3.3% NaF (diode excitation).

the emission bands observed is in agreement with the decreased site symmetry of the rare earth ion when Na^+ enters the lattice substitutionally, lifting the degeneracy of the excited states of the rare earth ion giving rise to the emission. The absorption spectra of Yb^{3+}-doped samples charge compensated with NaF show similar decreases in the intensity of the 976 nm band with increasing NaF concentration (7).

The results of CaF_2 substitution into the CdF_2: Yb: Er phosphor were unexpected. In Fig. 8 the variation with

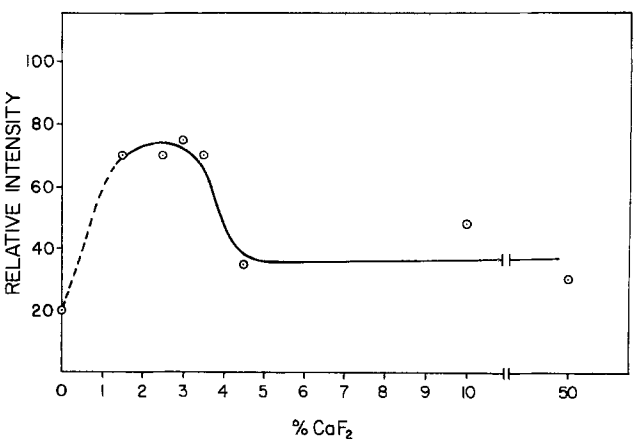


Fig. 8. Variation of relative intensity of 5383Å peak with CaF_2 concentration in $(CdF_2)_{1-x}(CaF_2)_x$:10% YbF_3:1% ErF_3.

CaF_2 concentration of intensity of the strongest green emission band (538.3 nm) is shown. For all the compositions CdF_2: 10% YbF_3: 1% ErF_3: 1.5-10% CaF_2 studied, the intensity of the emission bands is significantly enhanced both in the green and red regions of the spectra; however the increase in intensity is not very sensitive to the CaF_2 concentration. There appears to be a plateau for the composition range 1.5-3.5% CaF_2 and a decrease in intensity of the emission bands for the 4.5 and 10% CaF_2-doped samples. The absorption spectra of CdF_2: 10% YbF_3: 1% ErF_3 doped with 1-10% CaF_2, respectively, show no appreciable diminution in the 976 band intensity, with increasing concentration of CaF_2 at these high Yb^{3+} concentrations. In the light of the results on ^{19}F NMR with the proposed $(M^{3+}\text{-}F^-)_2$ dimers, it is tempting to propose that the effect of CaF_2 may be enhancement of the formation of mixed pair complexes (Er^{3+}-$F_{int.}^-$-Yb^{3+}) over pure complexes (Er^{3+}-$F_{int.}^-$-Er^{3+}) or (Yb^{3+}-$F_{int.}^-$-Yb^{3+}). Such centers would provide the most efficient energy transfer path for upconversion. Previous work has shown that the 976 nm band does not decrease appreciably in intensity when a second rare earth ion is present (8).

Efficiency.—The quantum efficiency of CdF_2: 10% YbF_3: 1% ErF_3 and CdF_2: 10% YbF_3: 1% ErF_3: 2.5% CaF_2 crystals, respectively, was measured as follows: the crystal was placed near the dome of the GaAs: Si diode and the fluorescent output was measured by a Clairex-CL-603 cadmium selenide photocell in conjunction with a Keithley 149 micromillivoltmeter. The voltage reading of the meter with diode alone ($= A =$ total infrared emission), the diode plus phosphor ($= B$ = total infrared transmitted and visible emitted), and the diode + phosphor + filter ($= C =$ visible emitted and transmitted by the filter) was measured, and the quantum efficiency calculated from the formula

$$\eta = \frac{C \times f}{A - B}$$

where f = attenuation factor of the filter (Corning No. 1-57). The formula, although approximate, is valid when $Cf << (A - B)$, which is true in this case. Determined in this way, the quantum efficiency of CdF_2: 10% YbF_3: 1% ErF_3 is 0.23% and that of CdF_2: 10% YbF_3: 1% ErF_2: 2.5% is 0.70%. The efficiency of green emitting GaP diode is about 0.1% (18). The quantum efficiency of the most efficient upconverting systems is between 10^{-2} and 10^{-1}% ($\lambda_{ex} = 0.97$ μm) (19). These values are difficult to compare due to differences in the condition of measurement. Our measurements were on single crystals, and well-known upconverting phosphors are available as powders. Grinding our samples would expose them to the well-known degradation of luminescence efficiency by crystal damage. Since our measurements were made at high excitation densities, the reported high efficiency compared to other materials may be attributable to this, at least in part. On the other hand, preliminary excitation studies on this phosphor system indicate that the quantum efficiency would most likely be improved with 976 nm excitation. These studies show a major excitation peak near 976 nm, corresponding to the "dimer" absorption band. A complete study of the excitation spectra is now in progress.

Conclusion

A new efficient infrared to visible upconverting system CdF_2: YbF_3: ErF_3: CaF_2 in single crystal form has been prepared. At the optimum concentrations of the rare earth ions (10 Yb: 1 Er) and codoped with ~ 3.5% CaF_2, in combination with a GaAs: Si diode emitting at ~ 0.93 μm the phosphor fluoresces a bright green. Quantum efficiency measurements indicate this system to be a highly efficient upconverting phosphor.

The upconverting properties of the system codoped with NaF are in agreement with previously measured spectroscopic properties of the CdF_2: Yb system and

support the existence of $(M^{3+}\text{-}F_{int.}^{-})_2$ dimers, or similar complex centers.

The enhancement of the upconversion upon introducing CaF_2 into the system is contrary to predictions based on previously reported spectral data in the CdF_2:CaF_2:Yb system, which showed quenching of the intense 976 nm absorption band. The quantum efficiency of the most efficient phosphor system CaF_2: 10% YbF_3:1% ErF_3:2.5% CaF_2 studied is 0.70%.

Acknowledgments

The authors thank G. DeLhery of the U.S. Army Signal Research and Development Laboratory for quantum efficiency measurements. This research was supported by Grants DA-ARO-D-31-124-G-1036, DA-ARO-D-31-124-72-G-7, and DAAG-29-75-G-0096 from the Army Research Office, Durham, North Carolina, and contract No. F44620-74-C-0056, Joint Services Electronics Program.

Manuscript submitted Aug. 16, 1976; revised manuscript received Oct. 30, 1976.

Any discussion of this paper will appear in a Discussion Section to be published in the December 1977 JOURNAL. All discussions for the December 1977 Discussion Section should be submitted by Aug. 1, 1977.

REFERENCES

1. N. Bloembergen, *Phys. Rev. Lett.*, **2**, 84 (1959).
2. F. Auzel, *Compt. Rend.*, **262**, 1016 (1966).
3. F. W. Ostermeyer, Jr., *Metall. Trans.*, **2**, 747 (1971).
4. R. A. Logan *et al.*, *Appl. Phys. Lett.*, **13**, 139 (1968).
5. L. G. Van Uitert *et al.*, *Mater. Res. Bull.*, **4**, 777 (1969).
6. M. Rubenstein and E. Banks, *This Journal*, **106**, 104 (1959).
7. E. Banks and P. Wagner, *J. Chem. Phys.*, **44**, 713 (1966).
8. V. Abbruscato, E. Banks, and B. R. McGarvey, *ibid.*, **49**, 903 (1968).
9. M. T. Weber and R. W. Bierig, *Phys. Rev.*, **134**, A1492 (1963).
10. P. Weller, *Inorg. Chem.*, **5**, 736 (1966).
11. J. S. Prener and J. D. Kingsley, *J. Chem. Phys.*, **38**, 667 (1963).
12. E. Banks, M. Greenblatt, and B. R. McGarvey, *ibid.*, **58**, 4787 (1973).
13. Mustafa *et al.*, *ibid.*, **62**, 2700 (1975).
14. G. H. Dieke, "Spectra and Energy Levels of Rare Earth Ions in Crystals," p. 142, Interscience, New York (1968).
15. L. F. Johnson *et al.*, *J. Appl. Phys.*, **43**, 1125 (1972).
16. J. L. Sommerdijk and A. Bril, *Philips Tech. Rev.*, **34**, 24 (1974).
17. Y. Seki and Y. Furukawa, *Jpn. J. Appl. Phys.*, **10**, 891 (1971).
18. L. F. Johnson *et al.*, *Appl. Phys. Lett.*, **15**, 48 (1969).
19. A. Bril *et al.*, *This Journal*, **122**, 660 (1975).

Preparation of Y_2O_2S:Eu Phosphor Particles of Different Sizes by a Flux Method

Luuji Ozawa*

Zenith Radio Corporation, Chicago, Illinois 60639

ABSTRACT

The preparation of Y_2O_2S:Eu phosphor in sodium-sulfide flux was studied as a means of obtaining different particle sizes (3-50 μm). Atmospheric control is absolutely necessary above 1050°C to prevent oxidation of both Y_2O_2S and the flux. It is found that the particle size distribution of the raw material (Y_2O_3) is reproduced in the starting particle of growth Y_2O_2S. The growth rate of small and nonaggregated single crystals of Y_2O_2S:Eu can be expressed by the equation, $d\phi/dt = A \exp(-\Delta E/kT)$.

Y_2O_2S:Eu phosphor is used as the red primary in color TV picture tube screens because of its high brightness (1) and factory reclaimability (2). There are many ways to prepare the powdered Y_2O_2S:Eu (3). Ormand and Banks (4) have reported recently a reproducible procedure of Y_2O_2S preparation by means of firing Y_2O_3 in a controlled gas mixture of N_2, H_2O, and H_2S. They obtain the Y_2O_2S powder of average particle size of 5-20 μm, depending on the firing temperature. The preparation procedure used widely in the phosphor production, however, is the flux method (5): It consists of firing a mixture of Y_2O_3, sodium carbonate, and sulfur. The particle size of Y_2O_2S obtained with this flux method at 1000°C is not a strong function of time and temperature and median particle size is about 4 μm by the sedimentation weight method. Firing above 1050°C in air results in an increase in the amount of Y_2O_3 in the final products.

In this report, we have studied the growth of microcrystals of Y_2O_2S:Eu with sodium sulfide flux under a controlled atmosphere. The growth of the crystals is a strong function of time and temperature. It is suggested that the particles grow from the saturated solution of sodium sulfide by means of a thermal fluctuation caused by dissolution and deposition of Y_2O_2S:Eu.

Experimental Procedure

Y_2O_3 (5-9's) and Eu_2O_3 (3-9's) were used to prepare the Y_2O_2S:Eu. The rare earth oxides were dissolved in hot nitric acid and precipitated with hot oxalic acid. The precipitate was dried and then heated in air at 1000°C for 2 hr to convert it to Y_2O_3:Eu. This oxide plus sulfur and sodium carbonate were mixed in a ball mill. Then the mixture was fired at various temperatures and times, using alumina crucibles mounted in a quartz tube. After firing, the samples were washed with hot deionized water several times to remove the residual sulfur and sodium compounds. The products obtained were analyzed by x-ray diffraction (XRD). The presence of Y_2O_3:Eu in Y_2O_2S:Eu at a concentration less than 5 mole percent (m/o), which is the limit for detection by XRD, can be determined by its luminescence under 254 nm excitation; Y_2O_3:Eu has an isolated luminescence line at 611 nm. The particle size distribution of the

* Electrochemical Society Active Member.
Key words: crystal nucleation, crystal growth, cathodoluminescence.

phosphor was determined by the sedimentation weight method using 3g samples. The median particle size was determined graphically from these sedimentation data on log-normal probability graph paper (6).

Results and Discussion

Y_2O_2S:Eu phosphors were prepared by the flux method by heating a mixture of Y_2O_3:Eu, sodium carbonate and sulfur to various temperatures ranging 1000°-1300°C. The technique of heating oxides with a large amount of sodium carbonate and sulfur is well known as the sulfide fusion method used in analytical chemistry to convert oxides to soluble sulfides. The reaction between sodium carbonate and excess sulfur at high temperature produces Na_2S_x (x = 1-5; mp varies from 200° to 950°C, depending on x). Hence Na_2S_x will be referred to as the flux. The products of sulfide fusion are usually sulfides. In our case, however, XRD analysis showed that the final products prepared under well-controlled conditions were always oxysulfides (Y_2O_2S rather than Y_2S_x or $NaYS_2$); about 0.01 weight percent (w/o) sodium in the Y_2O_2S was detected by flame analysis. With an uncontrolled firing atmosphere of air the products usually contained Y_2O_3 and, sometimes, $Y_2O_2SO_4$.

By firing at 1000°C in air, the temperature (T) and time (t) are not critical to the final results; we usually obtained 90-95% oxysulfide, although the final products sometimes had a light brown body color. The body color of the samples before washing was yellow brown. By firing above 1100°C in air, the yield of oxysulfide was markedly decreased with increasing T and t. The surface layer of the samples fired above 1100°C before washing was increasingly white with increasing T and t. The samples fired at 1250°C for more than 5 hr in air had a completely white color which was confirmed by XRD to be Y_2O_3, $Y_2O_2SO_4$, and Na_2SO_4.

Oxidation of products.—A mixture of sodium carbonate and excess sulfur was heated. The mixture was melted above 500°C. After the solution cooled to room temperature, the products heated below 1000°C were brownish yellow, presumably a mixture of Na_2S_x. The colors of Na_2S_x are light pink (x = 1), light yellow (x = 2), and red (x = 5). Above 1100°C, a colorless Na_2SO_4 as a consequence of oxidation of Na_2S_x was obtained.

In order to understand the stability of Y_2O_2S at high temperature in air, the oxidation of Y_2O_2S between 300° and 1300°C has been studied by differential thermal analysis (DTA) and XRD. Figure 1 shows the DTA curve of Y_2O_2S obtained with the temperature rising at a rate 15°C/min. Table I shows the analytical results by DTA and XRD. The results indicate the stepwise oxidation of Y_2O_2S to Y_2O_3 via $Y_2O_2SO_4$ as an intermediate. Y_2O_2S is stable below 700°C. As the temperature is increased to 750°C, the oxidation of Y_2O_2S to $Y_2O_2SO_4$ begins, and in the region 750°-900°C both Y_2O_2S and $Y_2O_2SO_4$ coexist (the first broad exothermic band in Fig. 1). Above 950°C, the DTA curve shows a slight dip followed by another broad exothermic band, and the third phase, Y_2O_3, appears. This three-phase region extends from 950° to 1050°C. In this temperature region, the amount of Y_2O_2S decreases rather sharply while the Y_2O_3 phase increases. However, $Y_2O_2SO_4$ is the major constituent. At 1075°C the decomposition of Y_2O_2S is complete and a two-phase region ($Y_2O_2SO_4$ and Y_2O_3) is maintained for a narrow temperature range; about 12°C wide. Continued heating beyond 1075°C produces a strong endothermic reaction representing complete decomposition of $Y_2O_2SO_4$. Beyond 1100°C, XRD data indicate a one-component phase, Y_2O_3, is present.

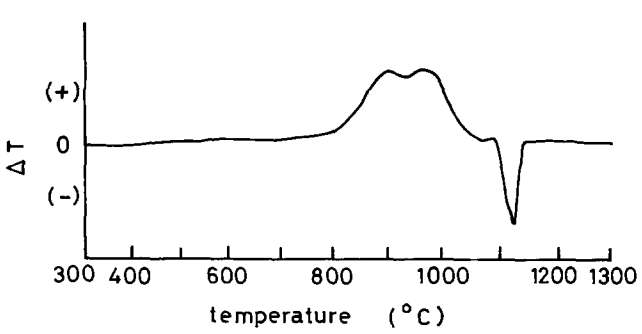


Fig. 1. Differential thermal analysis of Y_2O_2S:Eu in air

Table I. Oxidation of Y_2O_2S between 300° and 1300°C in air

Temperature (°C)	Number of phases	Compounds*
Below 700	1	$\underline{Y_2O_2S}$
750	2	$\underline{Y_2O_2S}$ + $Y_2O_2SO_4$(t)
800-900	2	$\underline{Y_2O_2S}$ + $Y_2O_2SO_4$(s)
950-975	3	$\underline{Y_2O_2S}$(s) + $Y_2O_2SO_4$ + Y_2O_3(s)
1075	2	$Y_2O_2SO_4$(s) + $\underline{Y_2O_3}$
Above 1125	1	$\underline{Y_2O_3}$

* (t) trace, (s) small amount, and underline is major compound.

Thus both Y_2O_2S and Na_2S_x are completely oxidized by heating beyond 1100°C in air.

Control of firing atmosphere.—The above results indicate that atmospheric control is absolutely necessary for the preparation of Y_2O_2S at $T > 1100$°C. Firing in a flow of inert gas such as N_2 resulted in final products containing varying amount of Y_2O_3. The flowing gas probably carried the sulfur out from the crucible. Satisfactory results, even at 1300°C, were obtained with the following procedures: The air in the quartz tube, in which the alumina crucibles were mounted, was first flushed out with wet nitrogen and the tube then put in the furnace. The tube was sealed after the samples reached the given temperature (about 30 min). The pressure in the sealed tube was slightly positive with respect to atmosphere. The amount of sodium carbonate and sulfur was not critical to the particle size and brightness of the final products; however, the best results were obtained with a mixing ratio of Y_2O_3, sodium carbonate, and sulfur of 1:1.5:4 (in mole fraction). Excess sulfur was always required for good reproducible results. With this procedure we obtained Y_2O_2S:Eu phosphors of median particle sizes of 3-50 μm.

The presence of europium in concentration of 10 m/o or less does not affect the crystal growth. When the mixture, fired at temperature above 1050°C more than 2 hr, is properly blended, equal quality phosphor is obtained whether Eu_2O_3 is present initially in solid solution, $(Y_{1-x}Eu_x)_2O_3$, or as a separate phase, Y_2O_3 + Eu_2O_3.

Note that cathodoluminescence intensities of the powder phosphors studied were independent of the particle sizes within the experimental error of ±5%.

Particle size distribution of Y_2O_2S:Eu.—Figure 2 shows a photograph at 260× magnification of particles of Y_2O_2S:Eu prepared at 1300°C for 5 hr. It can be seen that the particles have excellent crystal perfection with uniform faces. Particles of this quality are obtained by firing above 1050°C. If the temperature is below 1000°C, or the firing time less than 2 hr, aggregate particles of low crystal perfection are obtained.

Figure 3 shows the particle size distribution (PSD) of samples prepared at 1250°C for different t (2, 3, 5, and 8 hr) on log-normal probability graph paper. The PSD is determined with 3g samples containing 10^7 particles, so the data in Fig. 3 are statistically

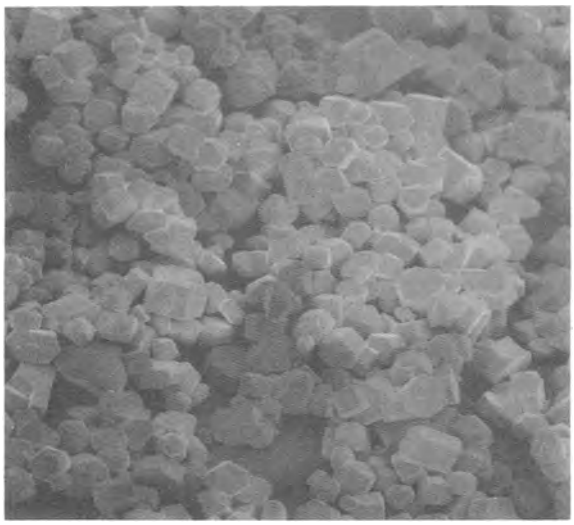


Fig. 2. Scanning electron micrograph of particles of Y_2O_2S:Eu fired at 1300°C for 5 hr under 260× magnification.

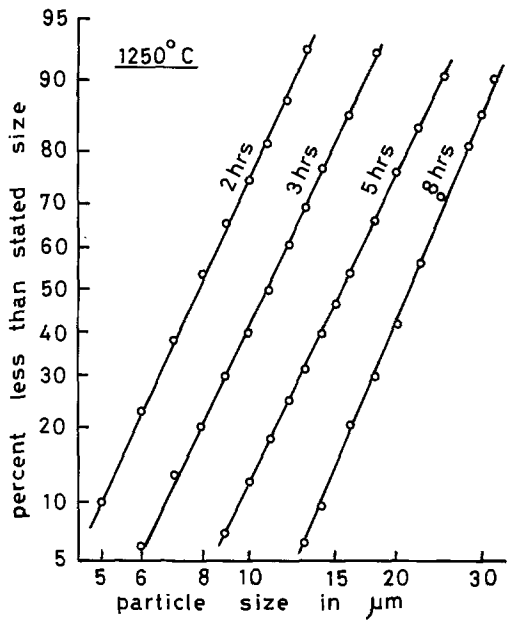


Fig. 3. Particle size distributions of Y_2O_2S:Eu fired at 1250°C for 2, 3, 5, and 8 hr on log-normal probability paper. Particle size was determined by calculation from weight sedimentation method.

representative of the mother PSD of the mother samples. The PSD of all the samples followed a log-normal distribution in which the distribution shifts with t; the standard deviation is $\sigma = 0.44$. Similar results were also obtained for T between 1100° and 1300°C. When the PSD belongs to the same distribution pattern with the same σ, we can use the median particle size ϕ_M in discussion instead of all the parameters of the PSD.

Crystal nucleation and growth.—The growth of Y_2O_2S particles of different sizes is discussed in terms of the formation of crystal nuclei and their growth in the flux. To our knowledge, there is no report regarding this subject, notwithstanding the importance of the preparation of Y_2O_2S:Eu phosphor.

The particles in Fig. 2 appear as smooth, well-formed and nonaggregated single crystals, indicating that they grow from individual seed crystals rather than from aggregates of crystallization nuclei. The result is also indicative that each crystal has its own domain in the flux and the crystals grow from a saturated solution of the domain under a slow cooling rate; however, samples cooled slowly from 1300°C (at 2°C/min) and those cooled quickly (removal of crucible from furnace directly to room temperatures) have the same PSD. Thus the Y_2O_2S particles (crystals) are grown in the furnace at constant temperature. A suggestive observation is the appearance of the fired mixture, which is in the form of a rod standing in the crucible: After 16 hr at 1300°C, the flux solution still remains in the whole of the rod instead of flowing to the crucible bottom, even though the pure flux is liquid at 500°C. This may be explained as follows: Assuming that the solubility and mobility of Y_2O_2S in the flux solution are very small, the dissolution of a particle of Y_2O_3, subsequent crystal nucleation and growth of a Y_2O_2S seed crystal may be restricted to a small volume (domain) of the flux solution just covering one particle. As the temperature increases, all of one Y_2O_3 particle is dissolved suddenly in a small volume V_1 of the flux solution, decreasing the solution temperature locally. The dissolved Y_2O_3 is immediately converted to Y_2O_2S as a result of chemical reaction with the sulfur in the flux. If the solubility of Y_2O_2S in the flux solution is very small (this is proven by the high yield, 95-98%, of Y_2O_2S), the flux solution in V_1 is saturated instantly with Y_2O_2S. A first nucleation of Y_2O_2S then occurs in this saturated solution. The Y_2O_2S dissolved in V_1 deposits on the first crystallization nucleus before several nuclei. If this is true, the size and distribution of the Y_2O_2S seed crystals produced at 1000°C (as described later in this section) should be similar to those of the Y_2O_3 raw material. Figure 4 shows the PSD's of the Y_2O_3 raw material (curve A), the Y_2O_2S prepared at 1000°C for 2 hr firing (curve B), Y_2O_2S prepared at 1100°C for 2 hr firing (curve C), and the primary particles of Y_2O_2S prepared at 1000°C for 2 hr firing (curve D). It can be seen in Fig. 4 curves A and B that the PSD of Y_2O_2S fired at 1000°C ($\phi_M = 3.5$ μm, $\sigma = 0.57$) is in good agreement with the PSD of the Y_2O_3 raw material ($\phi_M = 3.2$ μm, $\sigma = 0.57$). The standard deviations ($\sigma = 0.57$) of both PSD's, however, are larger than that of Y_2O_2S fired above 1100°C for $t > 2$ hr ($\sigma = 0.44$, curve C and Fig. 3). This is because of aggregation of particles of both Y_2O_3 raw material and Y_2O_2S fired at 1000°C. When the Y_2O_2S was prepared from a well ballmilled mixture of the primary (nonaggregated) particles of Y_2O_3 and the fine powder of sodium carbonate and sulfur passed through 200 mesh sieve, the PSD of the resulting Y_2O_2S prepared at 1000°C

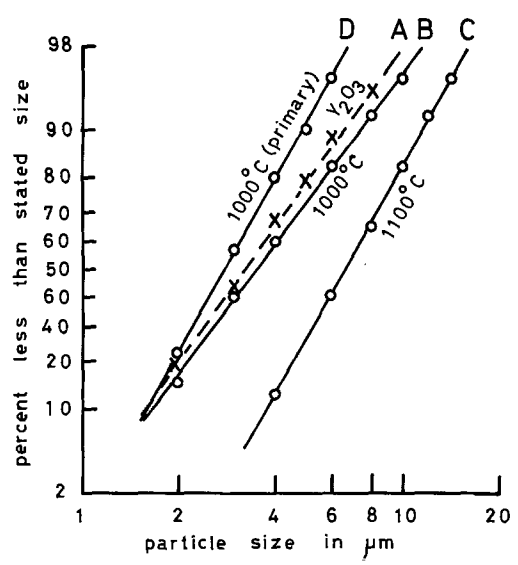


Fig. 4. Particle size distributions of Y_2O_2 raw material (curve A), Y_2O_2S:Eu prepared at 1000°C for 2 hr firing (curve B), Y_2O_2S:Eu prepared at 1100°C for 2 hr firing (curve C), and primary particles of Y_2O_2S:Eu prepared at 1000°C for 2 hr firing (curve D).

was improved: $\phi_M = 2.8$ μm, $\sigma = 0.44$ (curve D). The PSD of Y_2O_2S fired at 1000°C thus corresponds to the PSD of the Y_2O_3 raw material, suggesting that the flux solution surrounds each Y_2O_3 particle, including the aggregated particles, and forms Y_2O_2S particles, thereby reproducing the PSD of the Y_2O_3.

The flux temperature then increases. A few Y_2O_2S particles are dissolved suddenly in the heated flux solution of the volume $V_2 > V_1$, absorbing thermal energy locally. A saturated solution of Y_2O_2S exists in V_2 and Y_2O_2S deposits on the surfaces of one available Y_2O_2S crystal remaining in equilibrium with the solution in V_2. Y_2O_2S particles thus grow by the repetition of the above process (Fig. 5). For such a process of growth, aided by the above-described thermal fluctuation cycle, the rate of the particle growth $d\phi/dt$, as a first approximation, will be given by

$$\frac{d\phi}{dt} = A \exp\left(\frac{-\Delta E}{kT}\right) \quad [1]$$

where A is a constant for a given flux and crystal, k the Boltzmann constant, T the temperature in °K, and ΔE the activation energy which is given by a combination of Gibbs' free energy on the crystal surface and an activation energy of diffusion of Y_2O_2S in the flux. Then we have

$$\phi = At \exp\left(-\frac{\Delta E}{kT}\right) \quad [2]$$

The particle size is thus a function of both firing temperature and time.

Figure 6 shows the curves of particle size as a function of the firing time (hr) plotted on a log-log basis. The parameter is the firing temperature T (°C). All of the data obtained with firing time longer than 2 hr fit the straight lines which converge at 0.5 hr. The particle size at 0.5 hr (the effective seed crystal size) is estimated to be about 3 μm.

Figure 7 shows the curves of the same data used in Fig. 6; here the logarithm of the particle size is plotted against the reciprocal of the temperature (log/°K). The data again fit straight lines in which the slopes depend on the firing times; perhaps the effective diffusion of Y_2O_2S in the flux is increased with the firing times. The lines converge at 1000°C, at which the particle growth is effectively started. The estimated initial seed crystal size at 1000°C is about 3 μm.

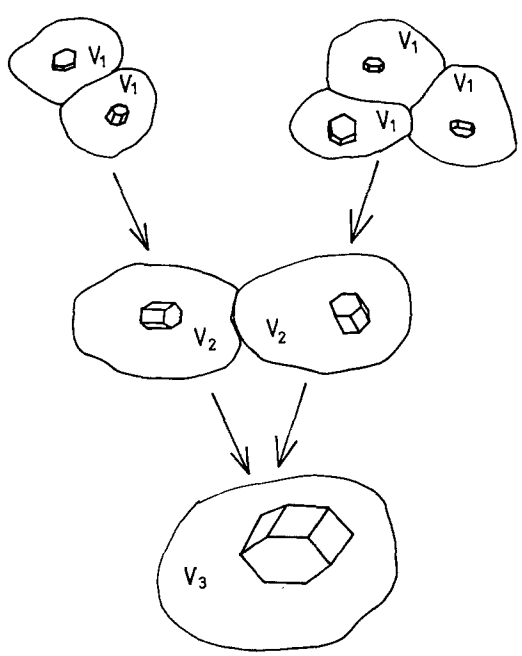


Fig. 5. Particle growth model of Y_2O_2S:Eu with sodium sulfide flux.

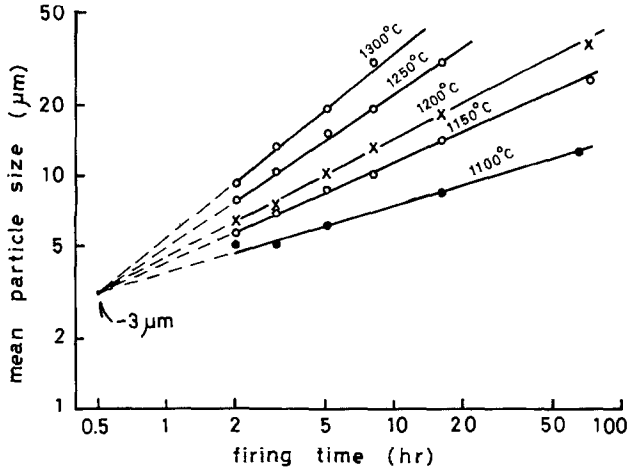


Fig. 6. Relationship between median particle sizes and firing times at various temperatures.

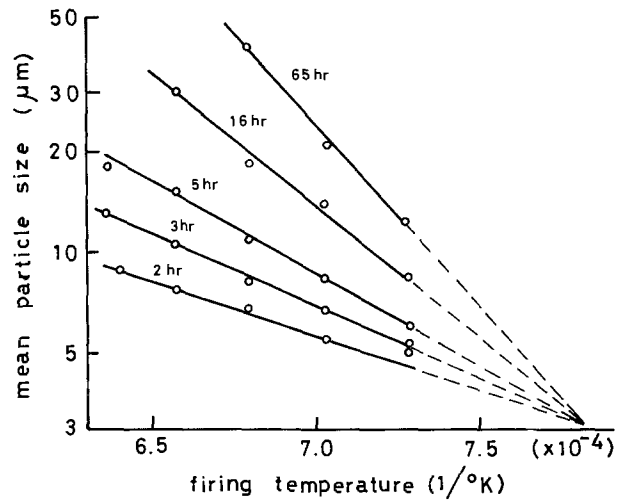


Fig. 7. Median particle sizes as a function of the reciprocal of the firing temperature (°K). Parameter is firing times.

In these experiments we used aggregated particles of Y_2O_3; the PSD of the primary particles was $\phi_M = 2.8$ and $\sigma = 0.44$. Thus the initial (seed) particle size estimated from Fig. 6 and 7 is in good agreement with the primary particle size of the Y_2O_2S fired at 1000°C.

Thus all the experimental data on the growth of Y_2O_2S:Eu crystals (particles) are consistent with Eq. [2].

Summary

We have shown that by using a controlled atmosphere good microcrystalline Y_2O_2S:Eu particles of a wide range of sizes can be grown from a sodium sulfide flux. The particle size distribution (PSD) of Y_2O_3 solid reagent is reproduced in the PSD of the product, Y_2O_2S:Eu. Any aggregated Y_2O_2S particles that are produced from aggregated Y_2O_3 are separated by the flux into primary particles which then grow by deposition on the smooth surfaces of the crystal from the saturated solution in accordance with Eq. [2]. The growth is believed to occur by means of a thermal fluctuation cycle of dissolution and deposition of Y_2O_2S:Eu.

Acknowledgments

The author wishes to thank Drs. H. N. Hersh, H. Forest, G. Arai, and Z. Kun for helpful discussions, and Ms. H. Stanczyk for her assistance in preparation of samples.

Manuscript submitted July 19, 1976; revised manuscript received Oct. 25, 1976.

Any discussion of this paper will appear in a Discussion Section to be published in the December 1977 JOURNAL. All discussions for the December 1977 Discussion Section should be submitted by Aug. 1, 1977.

Publication costs of this article were assisted by Zenith Radio Corporation.

REFERENCES

1. M. R. Royce, U. S. Pat. 3,418,246 (1968); P. N. Yocom, U. S. Pat. 3,418,247 (1968).
2. S. S. Trond, J. S. Martin, J. P. Stanavage, and A. L. Smith, *This Journal*, **116**, 1047 (1969).
3. M. Koskenlinna, M. Leskela, and L. Niinisto, *ibid.*, **123**, 75 (1976), and their references (3) to (11).
4. D. W. Ormond and E. Banks, *ibid.*, **122**, 152 (1975).
5. M. R. Royce, A. L. Smith, S. M. Thomsen, and P. N. Yocom, Abstract 86, p. 201, The Electrochemical Society Extended Abstracts, Spring Meeting, New York, May 4-9, 1969.
6. J. M. Dallavalle, "Micrometrics," Pitman Publishing Corp., New York (1948).

Surface Charge Decay Characteristics of Photoconducting Binder Layers

P. K. C. Pillai, S. K. Aggarwal, and K. K. Roy

Department of Physics, Indian Institute of Technology, Delhi, New Delhi 110029, India

ABSTRACT

Various surface charge characteristics of HgI_2:CdS binder layers in polystyrene are discussed with special reference to their application in electrophotography. The binder layers are made with different compositions of HgI_2 and CdS. From the measurements of such parameters as the charge acceptance, contrast potential, and the spectral sensitivity, it is concluded that the layer containing HgI_2 and CdS in the ratio 60:40 by weight gives the most convincing results for its utilization in charge transfer electrophotography.

The electrophotographic technique consists of (*i*) the charging of a thin layer of photoconducting insulator, (*ii*) discharging the charged surface by a light pattern, and (*iii*) finally, the development with a suitable toner.

The electrophotographic plates consist mostly of an amorphous selenium layer on a metallic substrate or paper coated with zinc oxide in binder (1, 2). A binder-type plate can have significant advantages over Se-coated plates or ZnO-coated paper. It eliminates the costly process of vacuum evaporation of Se on aluminum substrates.

The binder-type plate consists of a mixture of photoconducting powder dispersed uniformly in an insulating resin binder. The resin or binder holds the photoconducting powder together. The binder also plays vital role in the charging and the discharging characteristics (3-6) of the layer. It also protects the layer from the moisture.

A variety of photoconducting material, *e.g.*, ZnO (1), CdS (4), ZnCdS (7-8), etc. have so far been used in binder-type electrophotography. Recently, the authors have developed a photoconductor system with a high value of I_{photo}/I_{dark} (5×10^3) and dark resistivity (10^{13} Ω-cm). The system consists of a uniform mixture of HgI_2 and CdS, in appropriate ratio, dispersed in polystyrene which acts as the binder. The substrate used here is NESA-coated glass plate because HgI_2 reacts chemically with metallic substrates.

The present paper deals with the determination of important electrophotographic characteristics such as contrast potential and spectral sensitivity of the HgI_2:CdS mixed system. The results illustrate that the system containing HgI_2 and CdS in the ratio 60 and 40 by weight has the most optimum characteristics to find its place in transfer electrophotography.

Experimental

Preparation of layers.—Fine powders of HgI_2 (BDH India Limited) and CdS (REACHIM, USSR) were used in the preparation of the layers. The proportion of HgI_2 in the system was varied from 0 to 100%. The powders, taken in appropriate ratio, were mixed and properly ground to get a homogeneous mixture. This mixture was added to polystyrene (60% by weight of the system) dissolved in benzene and the whole was milled to achieve a uniform dispersion of the photoconductor particles in the binder. The mixture was then poured over a conducting glass substrate and was allowed to undergo slow evaporation in benzene atmosphere. By varying the benzene content in the solution, the viscosity and hence the thickness of the layer can be controlled. Residual benzene in the layer was removed by keeping the plate in an air oven at 50°C for 4 hr.

Measurement techniques.—The HgI_2:CdS binder layers backed by the NESA-coated glass was mounted on a platform which could be slided under the corona unit during the charging mode or to the vibrating condenser probe assembly for charge measurements (Fig. 1). The photodischarge of the layers could be achieved by illuminating the layers through the probe by a 100W tungsten lamp. Following studies were made on the layers: (*i*) Surface potential as a function of grid voltage, corona voltage, and the time of charging. (*ii*) Decay of surface potential in dark as well as under different intensities of white light illumination to calculate the maximum contrast potential and optimum exposure to achieve it. The light of different intensities was obtained with the help of Kodak neutral density filters. (*iii*) Photodischarge of the layers at different wavelengths to calculate the spectral sensitivity.

For the determination of the spectral sensitivity, the photodischarge of the layer was noted when irradiated with light of different wavelengths but the same intensity. This was achieved by introducing Kodak narrow bandpass filters against the 100W tungsten lamp whose distance from the photoconductor surface was so adjusted that the radiations of different wavelengths incident on the photoconductor surface have the same intensity. Light intensity mea-

Key words: electrophotography, xerography, binder layer, cadmium sulfide, mercuric iodide.

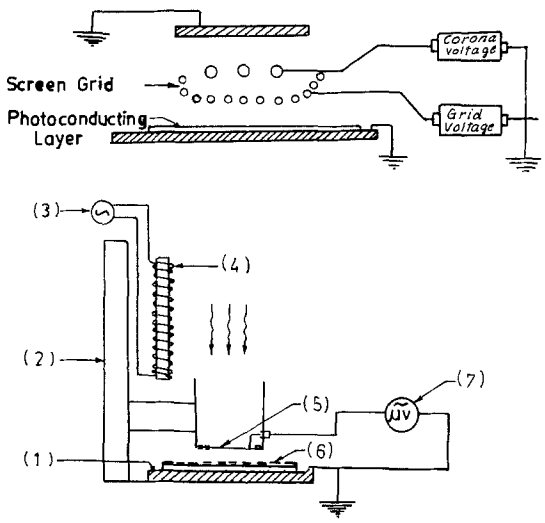


Fig. 1. Experimental setup

surements at the photoconductor surface was made by a standard 686 Mullard photoelectric bulb.

Results and Discussion

Charge acceptance.—One of the important factors in electrophotographic process is the amount of charge that can be applied to and retained on the surface of the photoconducting insulating layer. The surface charges, besides depending on the nature of the photoconductor, also depend on other ambient conditions, viz., corona voltage, grid voltage, and charging time (Fig. 2-4).

Decay characteristics of the surface potential.—The most important use of the apparatus, described in the measurement technique, is in the study of the decay characteristics of the charged layer. The surface potential depends on the electronic properties of the photoconductor, *e.g.*, carrier generation efficiency and mobility. It also depends on the mode of exposure. The surface potential also varies with temperature and relative humidity which were almost constant, of values 30°C and 40%, respectively, during the course of the investigation.

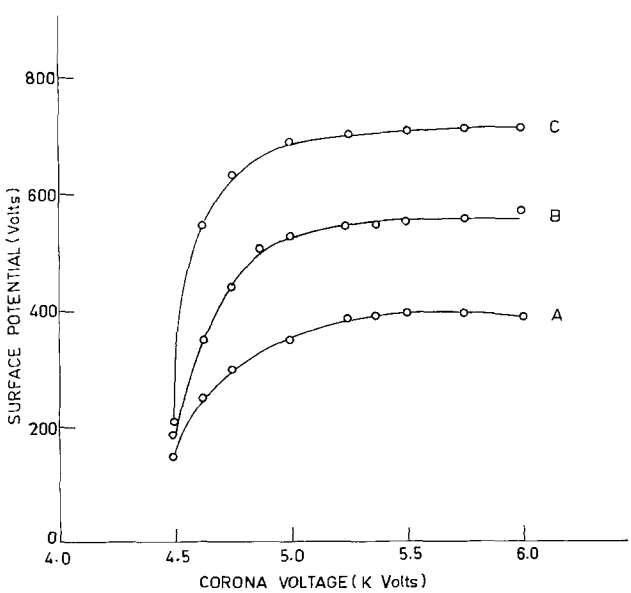


Fig. 2. Surface potential vs. corona voltage for the (60:40) layer for different grid voltages: A = 1500V, B = 1100V, C = 700V.

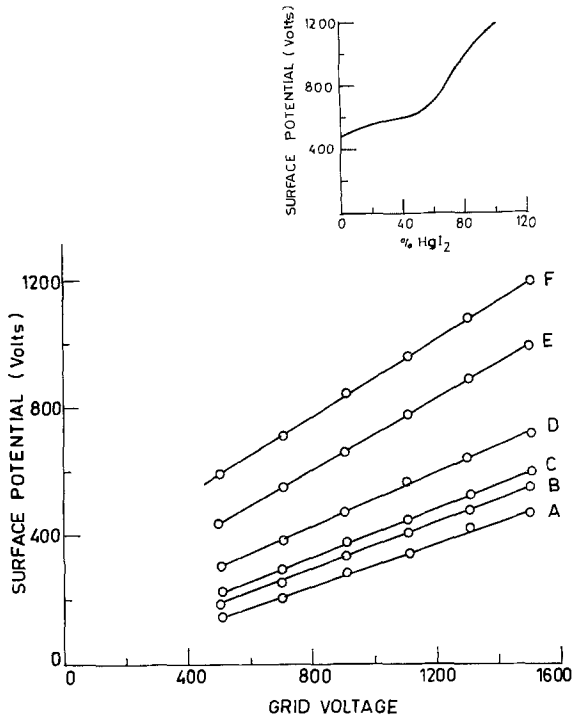


Fig. 3. Surface potential vs. grid voltage for the layer of different HgI_2:CdS compositions. A = 0:100, B = 20:80, C = 40:60, D = 60:40, E = 80:20, F = 100:0. Inset: Surface potential (at 1500 grid voltage) vs. % HgI_2.

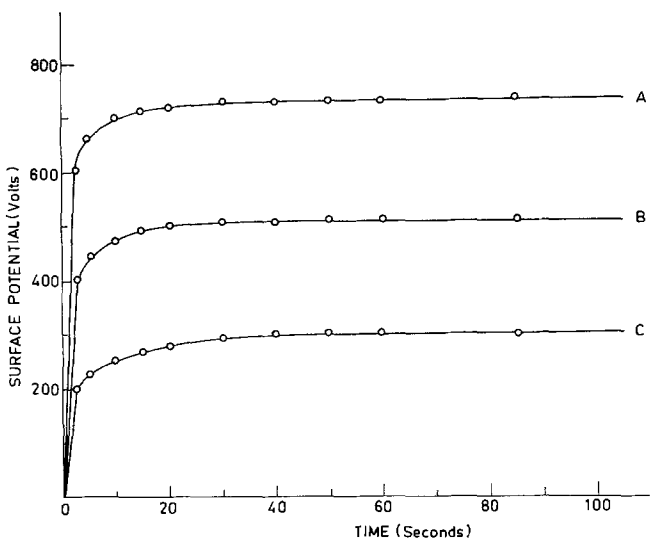


Fig. 4. Surface potential vs. charging time for the (60:40) layer for different grid voltages: A = 1500V, B = 1000V, C = 500V.

Contrast potential.—Contrast potential is one of the most important parameters which determines the applicability of a photoconductor system in electrophotography, since it is this factor which determines the successful toning of the electrostatic image. It is defined as the difference in the surface potential of areas illuminated by different intensities of light for the same duration. In the copying of a black and white document, the light intensities usually differ by an order of magnitude.

Considering two areas of the photoreceptor illuminated with light intensities I and dI, where d is related to the optical density D of the dark subject by $d = 10^{-D}$, the contrast potential V_c could be expressed as

$$V_c(X) = V(dX) - V(X)$$

where X is the exposure ($X = I \cdot t$).

Figure 5 depicts the contrast potential *vs.* exposure curves for layers containing different proportions of HgI_2 and CdS. V_0 indicates the initial potential in the different layers. Maximum contrast potential is found in the layer containing HgI_2 and CdS in the ratio of 60 to 40 by weight. With an initial potential (V_0) of 710V, the maximum contrast potential is almost 430V, *i.e.*, $0.6V_0$ which seems quite satisfactory for electrophotographic purposes.

Spectral sensitivity.—The effective photosensitivity of a particular photoconductive insulating layer is related to the rate of decay of the surface charge when light of a given intensity and wavelength band impinges upon the surface. This rate of decay depends primarily on the quantum efficiency for exciting charge carriers to a state of conduction and the effective mobility of these carriers in moving through the layer. The number of carriers released will depend on the amount (determined by the intensity) and energy (determined by the wavelength) of the incident light.

The photosensitivity of the electrophotographic layer can be expressed in terms of the rate of change of surface charge with exposure

$$S_\lambda = \frac{C\Delta V}{I \cdot t_h}$$

where C = capacitance per unit area, I = light intensity, t_h = half-decay time, and ΔV = reduction in the surface potential to one-half of its initial value.

The above formula is valid only for those systems where dark decay of the surface potential is negligibly small. Since dark decay in HgI_2:CdS binder layers is quite appreciable, the above formula can be modified as

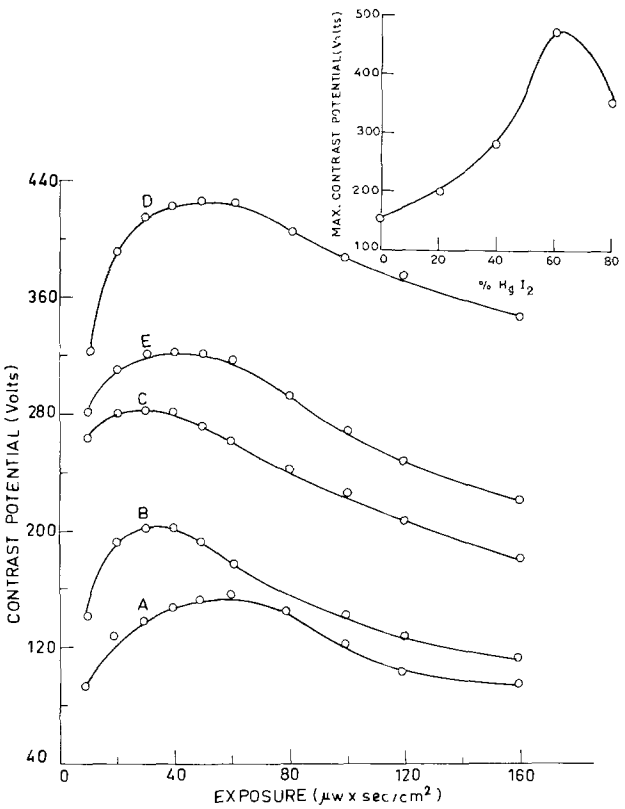


Fig. 5. Contrast potential *vs.* exposure for different HgI_2:CdS compositions at the dark charge level V_0. A = 0:100::HgI_2:CdS, V_0 = 384V; B = 20:80, V_0 = 425V; C = 40:60, V_0 = 446V; D = 60:40, V_0 = 710V; E = 80:20, V_0 = 1097V. Inset: Maximum contrast potential *vs.* % HgI_2.

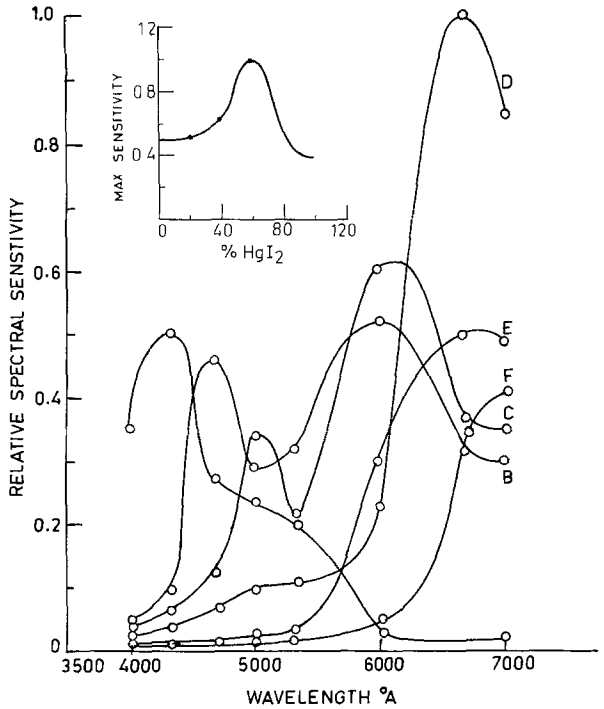


Fig. 6. Relative sensitivity *vs.* wavelengths for different HgI_2: CdS compositions. A = 0:100, B = 20:80, C = 40:60, D = 60:40, E = 80:20, F = 100:0. Inset: Maximum sensitivity *vs.* % HgI_2.

$$S_\lambda = \frac{C\Delta V_f}{I \cdot t_h}$$

where V_f represents the dark potential at the half-decay time and $\Delta V_f = V_f - V/2$.

For the calculation of the photosensitivity, the layers were charged to a fixed initial potential and then their decay was observed under monochromatic radiations of the same intensity.

The plots of spectral sensitivity *vs.* wavelength and maximum sensitivity *vs.* percentage of HgI_2 are given in Fig. 6. From the plot, we get the information that the position of the spectral sensitivity peak gradually shifts toward the long wavelength region as the percentage of HgI_2 is increased. For pure HgI_2 and pure CdS layers, the peak position is at 7000 and 4330Å, respectively. The peaks corresponding to the mixed layer lie between these two values. This implies that the mixing of HgI_2 and CdS has a definite effect on the spectral sensitivity and, together with the shift, the relative magnitude of the sensitivity is also affected as is evident from the inset. It is found that the layer containing 60:40 by weight of HgI_2 and CdS has the maximum sensitivity.

Summary and Conclusion

From the above studies, it is clear that pure HgI_2 and pure CdS layers do not have the desirable electrophotographic characteristics. But the electrophotographic characteristics are considerably improved by mixing the two in the ratio 60:40 by weight. Though the exact phenomenon responsible for this observation is not fully understood, it can be concluded at least that a gradual change in such properties, as the contrast potential and spectral sensitivity, takes place as the percentage of HgI_2 is increased and it is maximum for the 60:40 binder layer. However, the system is not as sensitive as the commercially exploited "Se" and "ZnO," but enough scope exists for further improvement in its characteristics.

Acknowledgments

Two of the authors (S. K. A. and K. K. R.) gratefully acknowledge the financial assistance provided by C.S.I.R. and N.C.E.R.T. (India), respectively.

Manuscript submitted June 14, 1976; revised manuscript received Oct. 1, 1976.

Any discussion of this paper will appear in a Discussion Section to be published in the December 1977 JOURNAL. All discussions for the December 1977 Discussion Section should be submitted by Aug. 1, 1977.

REFERENCES
1. R. M. Schaffert, "Electrophotography," Focal Press, London and New York (1965).
2. C. J. Young and H. C. Greig, *RCA Rev.*, **15**, 469 (1954).
3. O. C. Klein, *TAPPI*, **47**, 145A (September 1964).
4. M. Smith and A. J. Behringer, *J. Appl. Phys.*, **36**, 3475 (1965).
5. D. S. Most, *TAPPI*, **50**, (August 1967).
6. P. K. C. Pillai *et al.*, *Photogr. Sci. Eng.*, Accepted for publication.
7. D. W. Chapman and F. J. Stryker, *ibid.*, **11**, 126 (January 1967).
8. P. K. C. Pillai, S. K. Aggarwal, and P. K. Nair, *ibid.*, **20**, (Nov.-Dec. 1976).
9. R. C. Ahuja, Ph.D. Thesis, Indian Institute of Technology, Delhi (1975).

The Use of an Internal Reference in Cathodoluminescence

Lyuji Ozawa* and H. N. Hersh*

Zenith Radio Corporation, Chicago, Illinois 60639

ABSTRACT

A new method to determine the slopes of the concentration-dependence curves of cathodoluminescence in the concentration region below 10^{-4} mole fraction is described. The method involves the measurement of the relative cathodoluminescence intenstiy of activator with respect to a deliberately added rare earth used as an internal reference, and gives results of significantly greater accuracy and precision which are independent of the sample preparation and measurement geometry. In Y_2O_3, under electron excitation, Sm^{3+}, Eu^{3+}, and Dy^{3+} are excited predominantly via the host, and Pr^{3+}, Tb^{3+}, Ho^{3+}, Er^{3+}, and Tm^{3+} are excited only directly.

It has recently been suggested (1) that the probability, S, of energy transfer from an excited host to an activator can be determined from the slope of the concentration-dependence curve below 10^{-3} mole fraction measured under conditions of continuous excitation. Since S is a fundamental parameter of cathodoluminescence (CL) efficiency (2-6) it is important to have accurate ways of determining it. Although S can in principle be determined using bandgap irradiation of the host crystal the method is not usually accurate and is not generally applicable because of the existence of interfering bands (*e.g.*, charge transfer) in the bandgap region, as indicated in Fig. 1. In general the concentration-dependence (CD) method can yield more accurate values of S since the slope can be measured accurately.

In this report, we describe a method of determining the luminescence intensity of rare earth activators in phosphors as a function of concentration with greater accuracy and precision than heretofore by measuring the ratio of the cathodoluminescence intensity (RCI) of the activator to that of deliberately added rare earth internal reference. In this method, effects due to variation in synthesis procedure, level of contamination, and measurement geometry can be removed from the final results. Consequently the slope of the CD curves of rare earth activated phosphors can be determined with less than 3% error.

Experimental

The phosphors studied were rare earth activated yttrium oxides where the activators were trivalent Pr, Sm, Eu, Tb, Dy, Ho, Er, and Tm. The yttrium oxide and rare earth components were 6*N* and 4*N* pure, respectively. The phosphor preparation method and the procedure for measuring CL intensities under continuous excitation have been described in previous publications (7, 8). The median particle size of Y_2O_3 was about 3 μm and independent of the firing temperature (800°-1400°C) of the rare earth oxalates (if new crucibles were used). A reproducible procedure for obtaining larger particles is to fire in borax flux (1 weight percent) or to fire large particles of Y_2O_2S in air above 1200°C to convert to Y_2O_3; large particles of Y_2O_2S yield large particles of Y_2O_3 up to 20 μm in size. The median particle size of the phosphor powders was determined by a sedimentation weight method using potassium silicate as the dispersant. Excitation spectra were obtained with a Perkin Elmer fluorescence spectrometer MPF-4.

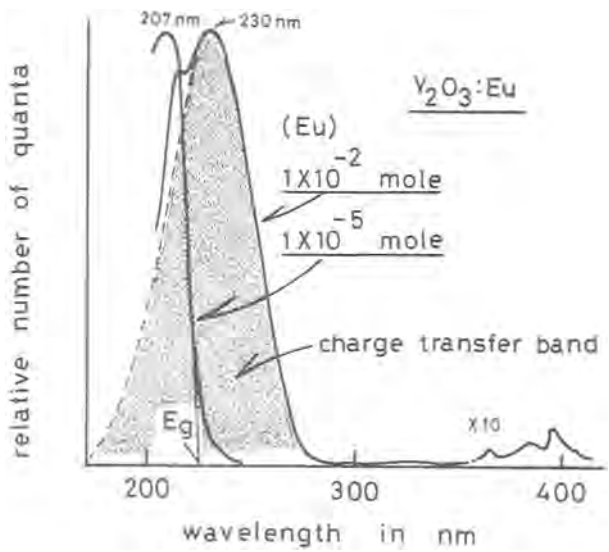


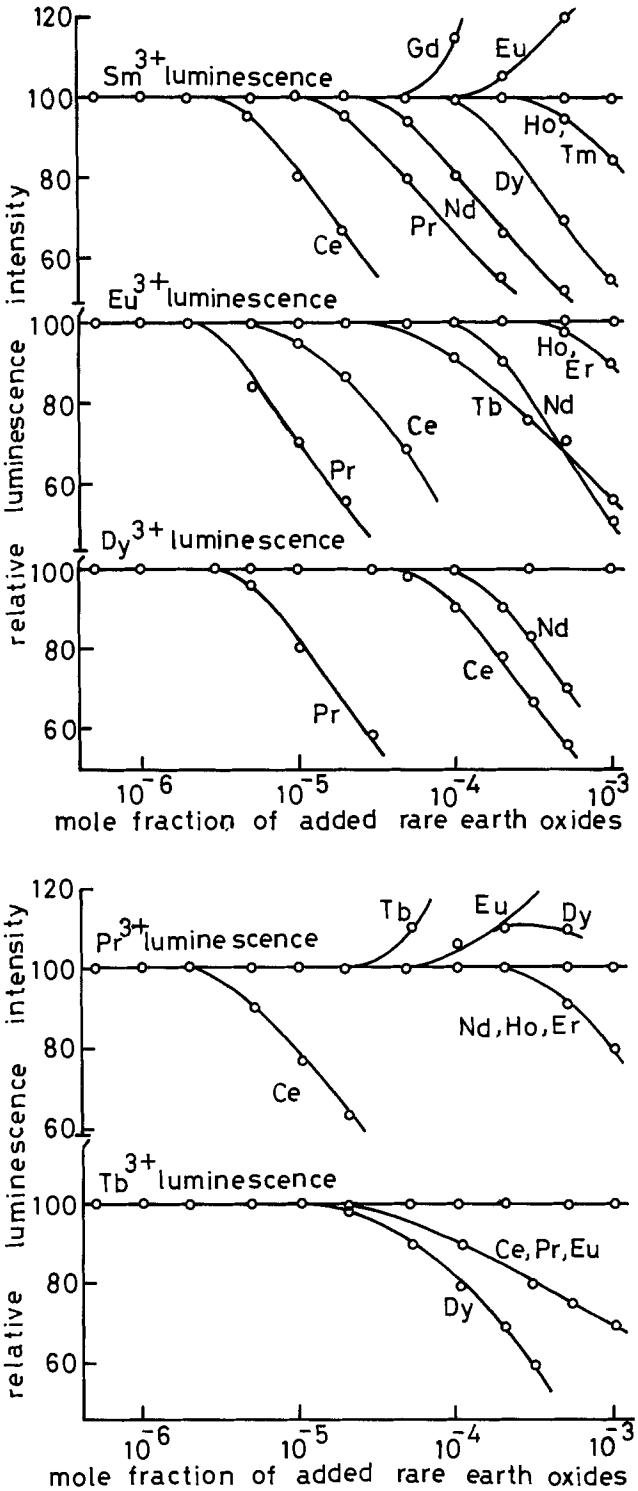
Fig. 1. Excitation spectra of Y_2O_3:Eu for 611 nm luminescence. The europium concentrations are 1×10^{-2} and 1×10^{-5} mole fraction. The shadowed area is the charge transfer band.

Results and Discussion

Internal reference.—The rare earth internal reference must not interfere with the rare earth activator by either quenching or enhancing its luminescence. Figure 2 shows examples of such interferences as the concentration of each possible reference rare earth is increased. It can be seen that Ce and Pr are the strongest interferants except in Tb and Ho phosphors. Inter-

* Electrochemical Society Active Member.

Key words: quantum efficiency, concentration dependence, crystal perfection, excitation mechanism.



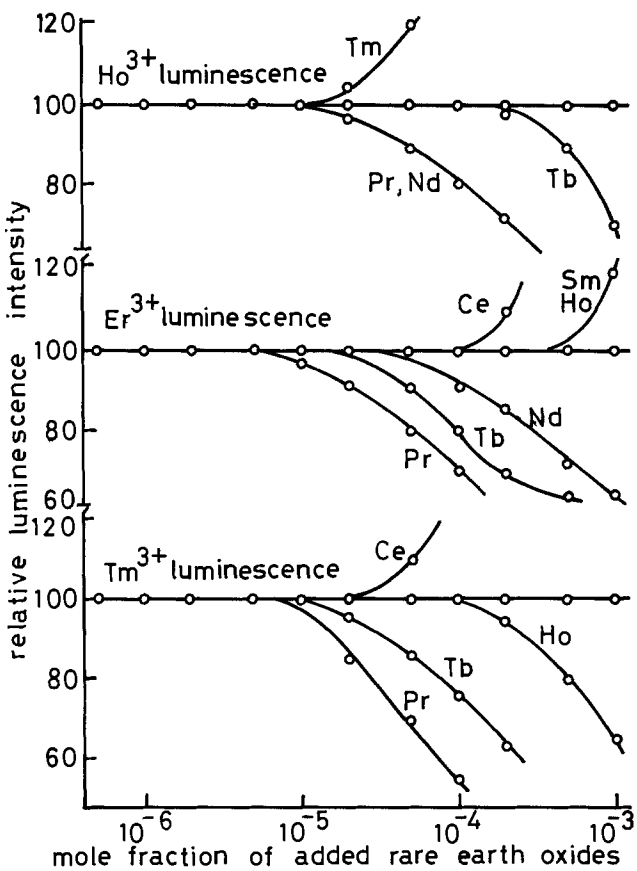


Fig. 2. Interferences in rare earth luminescence as the concentration of foreign rare earth in the phosphor is increased from 10^{-6} to 10^{-3} mole fraction. The activator concentration of each phosphor was 10^{-3} mole fraction.

ferences in the concentration region below 10^{-2} mole fraction are presumably due to the electrostatic multipolar interactions (9). From the point of view of least interference and highest luminescence intensity, terbium (and dysprosium if Ce and Pr are present to less than 1 ppm) is the best internal reference for Y_2O_3 phosphors.

Accuracy and precision.—Figure 3 shows the RCI of Dy at 572 nm *vs.* Tb (10 ppm). It may be seen that the measured absolute intensities of Tb (10 ppm) and Dy show much scatter from sample to sample, but the RCI's of Dy fall smoothly on a straight line of slope 0.80, indicating the high precision of this method. The 0.80 slope of the RCI (Dy/Tb) curve is independent of the Tb reference concentration below 100 ppm even though the values of the RCI (Dy/Tb) are inversely proportional to the reference concentration. Similar results have also been obtained for the combination Eu and Dy; in this case the Eu/Dy RCI's fall on a straight line of slope 1.0.

Figure 4 shows the results for a triply activated Y_2O_3 containing equivalent amounts of Eu, Dy, and Pr as a function of concentration, using Tb (5 ppm) as the internal reference. (The CL of Pr was not determined because of its relatively weak intensity.) The RCI curves extrapolate smoothly to zero on a linear plot, indicating the high accuracy of this method. Pr interferes with Eu above 3 pm, and with Dy above 5 ppm, but Tb causes no interference with Pr below 10 ppm. At 10 ppm Pr, the Eu and Dy CL intensities are quenched 40 and 20%, respectively. These results are in accord with Fig. 2.

In order to demonstrate the superior precision of the RCI method, the CL data of Fig. 3 were taken by deliberately varying the physical arrangement of the samples and detector in the demountable cathode-

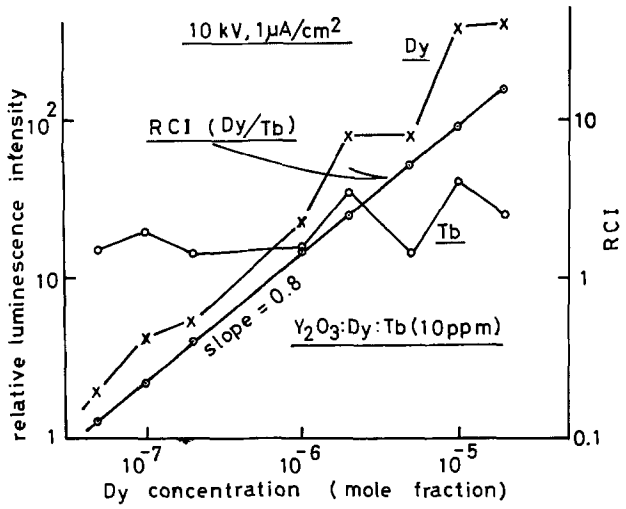


Fig. 3. Cathodoluminescence intensities of Dy^{+3} (572 nm) and Tb^{+3} (543 nm) and RCI (Dy/Tb) of Y_2O_3:Dy:Tb (10 ppm) as a function of dysprosium concentration.

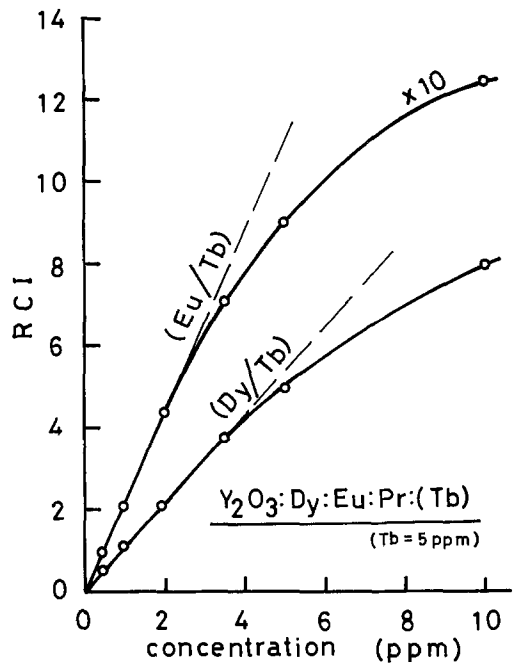


Fig. 4. Relative cathodoluminescence intensities of the combinations of (Eu/Tb) and (Dy/Tb) of Y_2O_3:Dy:Eu:Pr:Tb (5 ppm) containing equivalent amounts of each activator vs. activator concentration.

ray instrument which is very geometry sensitive as can be seen from the scatter in the data for Dy and Tb (broken-line curves). The smooth RCI curve of Fig. 3 shows the RCI method removes all the geometry sensitivity from the final results.

The RCI for Y_2O_3 phosphor is furthermore invariant to the synthesis procedure, the degree of crystallization, the firing temperature, and the level of the contamination by common metals. Figure 5 shows the CL intensity and RCI (Dy/Tb) of Y_2O_3:Dy(20 ppm):Tb(30 ppm) prepared at different temperatures (800°-1400°C) and 3 hr firing time. Although the CL intensities of the activator and reference both increase with firing temperature (Fig. 5A), the RCI is independent of the firing temperature (Fig. 5B). The accuracy and precision of the RCI method is still maintained in the presence of 10 ppm Fe, Ni, Mn, or Pb, even though the CL intensities of Dy and Tb are decreased by about 20% (see Table I). Thus the RCI method is a significantly more reliable way of determining the concentration dependence of luminescence of rare earths in Y_2O_3.

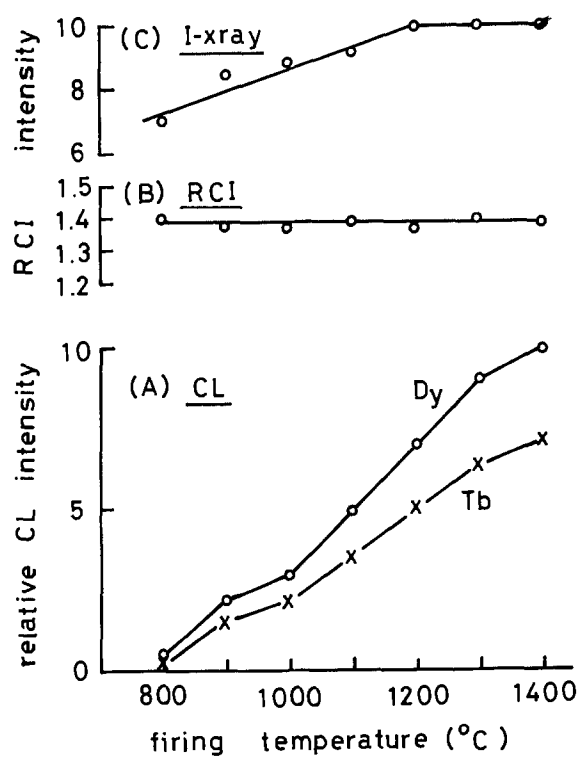


Fig. 5. (A) Cathodoluminescence intensity of Dy and Tb; (B) RCI (Dy/Tb); (C) x-ray reflection intensity from (400) plane. All data for Y_2O_3:Dy (120 ppm):Tb (30 ppm) fired at various temperatures.

Slopes of RCI curves.—There are three types of concentration dependences exhibited when log RCI is plotted *vs.* log activator concentration: the experimental slopes are either numerically equal to unity, or are somewhat greater or less than unity (Fig. 6), depending on the combination of activator and reference. (The slopes are independent of the concentration of the reference although the RCI values are inversely proportional to the reference concentration.) This is related to the fact that some rare earths are excited through the host and others are excited only directly. It has been previously shown for Y_2O_2S (1, 10) that the luminescence intensity of directly excited activators (*e.g.*, Ho) at very low concentrations increases linearly with activator concentration (*i.e.*, $L = kC$) and exhibits no particle size effect whereas the luminescence of host-excited activators (*e.g.*, Eu) increases sublinearly with activator concentration ($L = KCS$, where $0 < S \leq 1$) and exhibits a particle size effect. Table II lists for Y_2O_3 the activators which, under electron excitation, are excited predominantly via the host and those which are excited only directly, as based upon their concentration-dependence curves. If rare earths are classified according to whether they are directly or host excited, there are four possible combinations of

Table I. Interference effect of common metals (10 ppm) on cathodoluminescence intensities of Dy and Tb and on RCI (Dy/Tb)

	Blank	Fe	Ni	Mn	Pb
Dy	37.5	31	30	30	29
Tb	105	88	82	86	80
RCI(Dy/Tb)	0.36	0.35	0.37	0.35	0.36

Table II. Excitation mechanisms of rare earths in Y_2O_3 under cathode-ray excitation, and the slopes of the logarithmic concentration dependence curves

	Cathode-ray excitation	
	Host	Direct
Rare earths	Sm, Eu, Dy	Pr, Tb, Ho, Er, Tm
Slopes	0.80	1.00

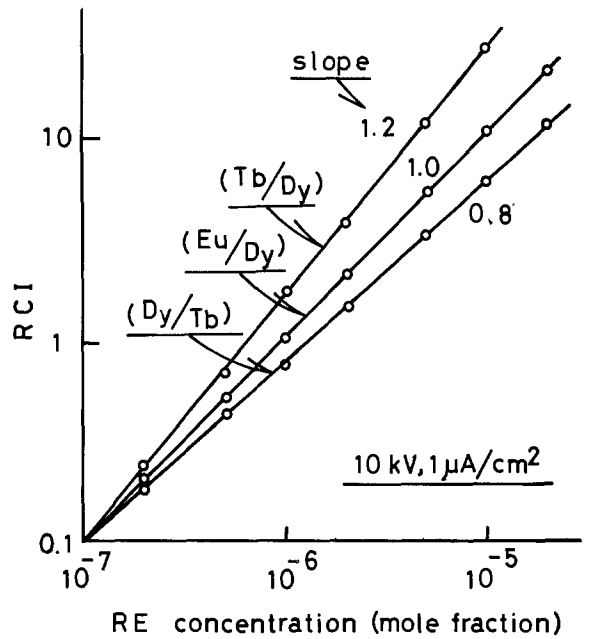


Fig. 6. Normalized RCI curves of the various combinations of excitations of activators by cathode-rays, showing slopes characteristic of the activator/reference combination. The reference concentrations are: 2 ppm (Tb/Dy), 1 ppm (Eu/Dy), and 30 ppm (Dy/Tb).

activator and reference which yield different slopes for the RCI CD curves. The slopes may be calculated from the ratio $L_{activator}/L_{reference}$, as a function of activator concentration, where $L_{reference}$ is a constant at a fixed concentration, *e.g.*, for the host/direct case, the concentration dependence of the RCI is $k'CS$. Thus if we pair a host-excited activator ($S = 0.8$) with a directly excited reference of fixed concentration, the expected RCI slope should be 0.8 (see Table III). Similarly if we pair directly excited activator and a directly excited reference, the RCI slope should be 1.0. This is true for some phosphors but only where the reference is directly excited (Table III). However where the reference is host excited the experimental slope is quantitatively greater than expected and the explanation for this is not clear.

Crystal perfection.—In all the work described above, the median particle size was 3 ± 0.5 μm. In order to determine the role of crystal perfection on the RCI, two types of experiments were performed: in the first, the particle size was maintained constant at 3 μm but the crystal was progressively more thoroughly annealed; in the second, the particle size was increased and the RCI was determined for the two activator concentrations.

Figure 5A shows the increased efficiency of 3 μm particles with increasing firing temperature. The improvement in crystal perfection with increased firing temperature is seen in Fig. 5C by the increased x-ray line intensities (plus decrease in half-widths, not shown). Nonetheless, so long as the particle size remains unchanged, the RCI for the host/direct case (Fig. 5B) does not change with annealing temperature. This is a decided advantage in trace analytical work; in addition this result may be used (see below) to speculate on the role of crystal perfection in luminescence.

Since the x-ray diffraction half-widths decrease with heat-treatment it is clear that the crystal may contain fewer defects and/or the activator may experience a more precisely defined local environment. (Changes in the positions of the ions surrounding an activator result in different crystal field symmetries and electrical field strengths which are known to affect optical transition probabilities.) For the case of a host-excited activator and a directly excited reference, if the increased crystal perfection is due to fewer defects this will result in enhanced energy transfer between the host and activator and the RCI will increase; however, if higher temperatures change the crystal field strength this may equally affect the optical transitions of both the activator and reference, the transitions of interest of both the activators. The reference and the RCI will be relatively invariant to improvement in crystal quality. Since the RCI remains constant (Fig. 5B) it is believed that increased crystal perfection, as developed by a higher annealing temperature, increases the transition probabilities of the emitting ions.

Particle-size effect.—It has been previously shown for cathodoluminescent phosphors that there is a particle size effect superposed on the concentration dependence (1,10), viz., when log CL intensity is plotted *vs.* log concentration, the slope has a break in it at a characteristic concentration (C_D^*) for each particle size. (An explanation for this has been previously given (1, 10).) Thus it is of interest to consider the behavior of the RCI as a function of particle size for the host/direct case (where there is a particle size effect in the phosphor).

The particle size was varied from 3 to 10 μm by growing the Y_2O_3 with two activator concentrations in a borax flux at temperatures between 800° and 1400°C; the median particle sizes for each temperature were: 3 μm, 800°C; 5 μm, 1000°C; 7 μm, 1200°C; and 10 μm, 1400°C. Figure 7 shows the normalized CD curves of Y_2O_3:Dy (3 and 10 μm particle size) under electron and photoexcitation and the corresponding values of C_D^*. It should be noted that the experimental C_D^* value is only approximate because C_D^* depends on the particle size; in the present case there is a log-normal distribution of particle sizes; *i.e.*, the particles are not all of the same size. As expected a particle size effect is present for the two chosen concentrations (Fig. 7). Furthermore, in accordance with theoretical expectation (1, 10) the RCI has two opposite trends, for one concentration, increasing with firing temperature (particle size), and decreasing for the other concentration. The reason for these opposite trends is related to those concentrations, and can be explained qualita-

Table III. RCI concentration dependence for possible combinations of type of excitation and observed slopes of RCI curves

Combinations	Expected slope	Experimental slope
Host/direct	0.8	0.8 ± 0.02*
Direct/direct	1.0	1.00 ± 0.02**
Host/host	0.80	1.00 ± 0.02†
Direct/host	1.0	1.2 ± 0.03‡

* = Dy/Tb, Eu/Tb, Sm/Tb; ** = Tb/Tm, Tb/Er; † = Eu/Dy, Dy/Eu; ‡ = Tb/Dy, Er/Eu.

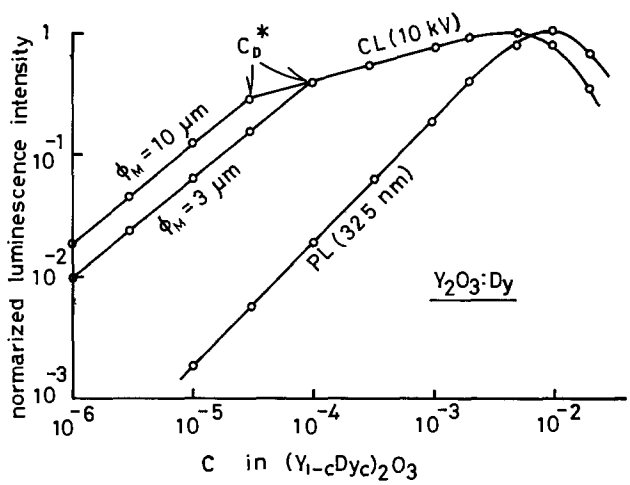


Fig. 7. Concentration-dependence curves of luminescence intensity of Y_2O_3:Dy for two particle sizes, 3 and 10 μm, under electron and direct photoexcitation.

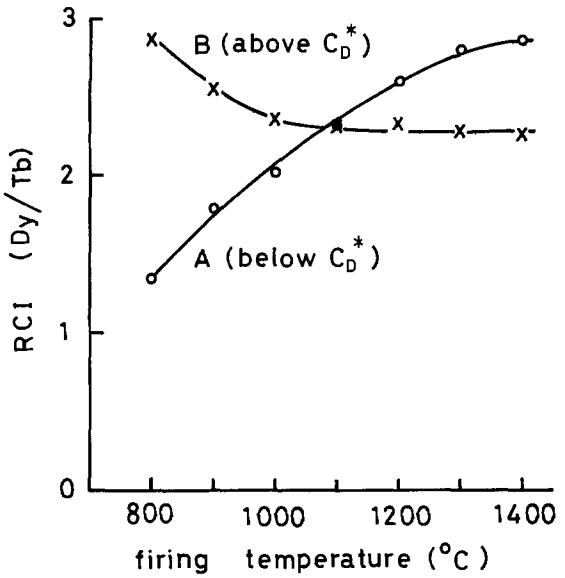


Fig. 8. RCI (Dy/Tb) of Y_2O_3:Dy (20 ppm):Tb (30 ppm), curve A (below C_D^*), and of Y_2O_3:Dy (100 ppm):Tb (50 ppm), curve B (slightly above C_D^*), fired at various temperatures using borax flux.

tively in terms of the active volume V_a involved in the luminescence (1, 10) which is controlled by the concentration in particle volume V_ϕ. The explanation is as follows. In curve A of Fig. 8 the Dy concentration (20 ppm) is somewhat lower than C_D^* for the largest particle size in the series ($C_D^* \sim$ 30 ppm for 10 μm), and the number of Dy activators involved in the excitation is increased as the particle volume V_ϕ gets larger even though the electron penetration depth is constant; consequently the RCI increases as the particle size increases. When $V_a < V_\phi$ (which occurs when the Dy concentration is higher than C_D^* for smallest particle size), V_a is limited by the activator concentration and is constant for a given activator concentration; hence the RCI will not show a particle size effect. Curve B in Fig. 8 shows the RCI of the Y_2O_3:Dy(100 ppm):Tb (50 ppm) prepared at different growth temperatures ($C_D^* \sim$ 100 ppm for 3 μm particle size). The RCI decreases as the particle size increases between 800° and 1000°C, and above 1000°C remains constant. The decrease in RCI between 800° and 1000°C is believed to be caused by the approach of the particle size-limited volume V_ϕ to the concentration-limited volume V_a, *i.e.* the Dy concentration (100 ppm) is effectively slightly higher than the nominal C_D^* value. [Note that without the flux, the particle size was independent of the firing temperature, and the RCI data (using 20 ppm Dy) did not show a particle size effect (Fig. 5B).]

Conclusion

It has been demonstrated that the measurement of the relative cathodoluminescence intensity of activator with respect to a deliberately added rare earth internal reference has certain advantages: (*i*) It yields a more accurate and precise determination of the slopes of concentration-dependence curves for cathodoluminescence (less than 3% error), (*ii*) it can be used to reveal the role of the crystal lattice perfection in cathodoluminescence, (*iii*) it reveals the type of excitation mechanism of the particular activator, and (*iv*) it can be used for quantitative determinations of trace amounts of rare earth impurities.

Acknowledgments

The authors wish to thank H. Stanczyk for her assistance in preparation of the samples, H. Forest for discussion, and G. Arai for x-ray data.

Manuscript submitted June 14, 1976; revised manuscript received Oct. 20, 1976.

Any discussion of this paper will appear in a Discussion Section to be published in the December 1977 JOURNAL. All discussions for the December 1977 Discussion Section should be submitted by Aug. 1, 1977.

Publication costs of this article were assisted by Zenith Radio Corporation.

REFERENCES

1. L. Ozawa and H. N. Hersh, *Phys. Rev. Lett.*, **36**, 683 (1976).
2. J. D. Kingsley and G. W. Ludwig, *This Journal*, **117**, 353 (1970).
3. V. D. Meyer, *J. Appl. Phys.*, **41**, 4059 (1970).
4. W. Lehmann, *This Journal*, **118**, 1164 (1971).
5. R. C. Alig and S. Bloom, *Phys. Rev. Lett.*, **35**, 1522 (1975).
6. J. L. Sommerdijk and A. Bril, *This Journal*, **122**, 952 (1975).
7. L. Ozawa, H. Forest, P. M. Jaffe, and G. Ban, *ibid.*, **118**, 482 (1971).
8. L. Ozawa and H. N. Hersh, *ibid.*, **122**, 1222 (1975).
9. M. Inoguchi and F. Hirayama, *J. Chem. Phys.*, **43**, 1978 (1965).
10. L. Ozawa and H. N. Hersh, *Appl. Phys. Lett.*, **28**, 727 (1976).

Electrical Activity of Epitaxial Stacking Faults

R. B. Marcus, M. Robinson,* T. T. Sheng, S. E. Haszko, and S. P. Murarka*

Bell Laboratories, Murray Hill, New Jersey 07974

and L. E. Katz*

Bell Laboratories, Allentown, Pennsylvania 18103

ABSTRACT

The scanning electron microscope has been used in the electron beam induced current (EBIC) mode to measure the electrical activity of stacking fault polyhedra formed during the epitaxial growth of (111) and (100) silicon from $SiCl_4$. Epitaxial films were grown in three different epi reactor facilities on wafers processed in two different facilities. Schottky barriers were used to collect the electron beam induced current. Defining electrical activity as carrier recombination seen at zero or low reverse bias (well below avalanche), two main observations are made: *i*) The occurrence of electrical activity is related to the facility in which buried layer processing and wafer cleaning were done prior to epi deposition, and is not due to the epi reactor. One facility in which buried layer processing was carried out was found to be contaminated with heavy metal impurities; all epi faults on wafers processed in this facility were found to be active primarily at the corners of the fault polyhedra; faults on samples which received buried layer processing in another facility were found to be electrically inactive. (*ii*) Transmission electron microscope studies of the identical faults examined in EBIC show that the degree of electrical activity is correlated with the mass of precipitate present at the corner of a fault polyhedron, and both vary from corner to corner within the polyhedron.

One class of Si epitaxial stacking faults nucleates at the epi-substrate interface and grows in size as the film thickness increases (1). The surface density of these faults varies from effectively zero to well over $10^3/cm^2$ depending in part on substrate surface treatment. Stacking faults may limit device performance if they are electrically active and if the surface density of the faults is high compared with the active device area. The electrical activity of individual stacking faults can be probed with the scanning electron microscope in the electron beam induced current (EBIC) mode. This mode of examination has been used to image defects in silicon using pn junctions (2-4) or Schottky barriers (5, 6) to collect the EBIC current. It is expected that a defect that appears as a recombination center in EBIC analysis will act as a current generation center when in the space charge region and thus will contribute to leakage in reverse biased pn and Schottky barrier junctions and in storage time devices; alternatively, the same defect will act as a recombination center when outside the space charge region and contribute to leakage in forward-biased junctions.

In this study the electrical activity of epitaxial stacking faults was determined in material grown from $SiCl_4$ in three deposition reactors, on silicon substrates prepared in two separate processing facilities. It is important to note that the EBIC data were collected under conditions of very low or no applied reverse bias, well below avalanche, and "electrical activity" refers to the ability of a site to act as a recombination center to reduce the local current collected by the junction at that site; Ravi *et al.* (4) defined an "electrically active" fault as one which generated EBIC current in excess of current generated in a defect-free region. In addition to data on the nature of electrical activity at epi stacking faults, certain electrically active stacking faults were examined by transmission electron microscopy for more detailed analysis and these results are reported.

* Electrochemical Society Active Member.

Key words: epitaxial silicon, silicon defects, stacking faults, scanning electron microscopy.

Experimental

Samples.—The substrates used in this investigation were (111) and (100) 2 and 3 in. diameter 5-20 Ω-cm p-type 0.015-0.020 in. thick dislocation-free silicon wafers. Most of these wafers went through standard buried layer processing before being inserted in the epi reactor: high temperature steam oxidation, buried layer photolithography, buried layer Sb diffusion or As implant, 1200° or 1250°C drive-in, oxide strip, HCl vapor etch, and epitaxial deposition. Epitaxial silicon was deposited in a horizontal-type reactor from $SiCl_4$, AsH_3, and H_2 at 1120°-1150°C (optical) immediately after an HCl vapor etch at 1150°-1200°C (optical) which removed 0.3-0.5 μm substrate material. The epi films were 0.2 or 3 Ω-cm n-type and were grown over a thickness range 10-15 μm.

Two different facilities were used for buried layer processing; they are called facility A and facility B in this paper. Two different epi reactors were used in facility A and one epi reactor was used in facility B; these are called reactors A-1 and A-2, and reactor B, respectively.

Samples were prepared for transmission electron microscopy by (*i*) lapping the sample to a thickness of ~0.005 in., (*ii*) ultrasonically punching out a 3.0 mm diameter disk, (*iii*) chemically thinning in HF:HOAC:HNO_3 (3:3:5), and (*iv*) ion milling to a final thickness of ~1 μm. The samples were examined in a 200 keV JEOL microscope equipped with a Kevex x-ray microanalyzer.

EBIC analysis.—EBIC analysis was performed in a Cambridge S-4 instrument, which was equipped with an energy dispersive x-ray analysis system. Samples were prepared for EBIC studies by treating with buffered HF for 10 sec to remove residual surface oxide followed by deionized water rinse and spin dry. 60-800Å gold was deposited by W filament evaporation at ~10^{-5} Torr through a 0.005 in. thick Mo shadow mask consisting of holes 1/16 and 1/8 in. diameter. Most studies were performed on the smaller Schottky barriers. An external, continuously variable battery supply provided reverse bias to the Schottky diode circuit.

Table I. Standard EBIC conditions

		Typical value	Typical range
Beam energy		19 keV	Fixed
Beam current at substrate	Faraday cage	7.0×10^{-10}A	Fixed
	Silicon	5.2×10^{-10}A	Independent of Si thickness (0.015-0.020 in.), orientation ((111), (100))
	Au dot	4.3×10^{-10}A	Varies slightly with Au thickness
EBIC current	Silicon	3.30×10^{-6}A*	$2\text{-}4 \times 10^{-6}$A*
	At strong recombination center	2.95×10^{-6}A*	Within ~10% of background EBIC current

* Over buried layer region. EBIC current is lower over nonburied layer regions.

The signal was fed into a Cambridge Instruments specimen current amplifier. Most of the data were obtained over the range 10^{-6}-10^{-8}A. A gold plated 0.002 in. tungsten probe in the specimen chamber could be externally moved over three coordinates with a precision of ~600 μm per control rotation, and was used to contact the Au dots. Most images were recorded at a frame time of 40 sec and a line scan time of 0.040 sec over a magnification range of 20-1000×.

A standard set of conditions was chosen for a number of the EBIC studies in order to be able to describe semiquantitatively the strength of EBIC signals and relate these data to microstructural details of stacking faults. These conditions are given in Table I. Also shown in Table I are typical variations in values of parameters for a fixed beam energy and current. Most of the studies were performed at 19 keV and at zero or very low (<1V) applied reverse bias. We observed no effect of bias on the EBIC signal. Some studies were made at 10-11 keV in order to improve the spatial resolution of defects near the sample surface.

The EBIC images in this report are direct records; white contrast corresponds to larger current.

Optical microscopy.—Low magnification (<200×) interference contrast optical micrographs were taken on samples with and without gold dots. The stacking faults could be clearly seen due to the slight change in elevation of the Si surface across the fault boundary.

X-ray topography.—X-ray transmission topographs were taken at 45 keV and 25 mA beam current using a Rigaku-Denku x-ray source with a rotating anode. Diffraction occurred off one set of {220} planes normal to the (111) surface. The x-ray topograph in Fig. 1 is a print of the original. Black contrast corresponds to enhanced x-ray signal.

Sampling technique.—Immediately prior to insertion in the scanning electron microscope, each wafer was cleaved into a piece ~ 1 × ½ in. which included an edge of the original wafer. The reverse *I-V* characteristics of 3-5 small (1/16 in. diameter) Schottky barriers were measured, and two of the dots nearest the edge of the wafer and with good reverse characteristics were examined by EBIC.

A total of 26 samples were examined using EBIC. In two cases (samples 6 and 11) Schottky barriers far apart on the original 2 in. wafers were measured with identical results. This gives no assurance, of course, that there were no variations in stacking fault properties across a wafer in each of the 24 remaining cases, but such a variation is considered unlikely.

Results

All samples used in this study contained epitaxial stacking faults. In a number of wafers the faults were observed only over the nonburied layer regions. The faults were easily identified by optical microscopy as complete triangles or squares (depending on substrate orientation) or as the corresponding incomplete figure.

Our ability to identify all epitaxial stacking faults by optical microscopy was established by comparing optical micrographs and x-ray topographs of the same area. In addition to being certain that all faults could be detected optically, we needed to be sure that all faultlike features seen optically were indeed faults and not simply regions where faults had been present and subsequently annihilated. An interference contrast micrograph of sample 1 is shown in Fig. 1a, and Fig. 1b

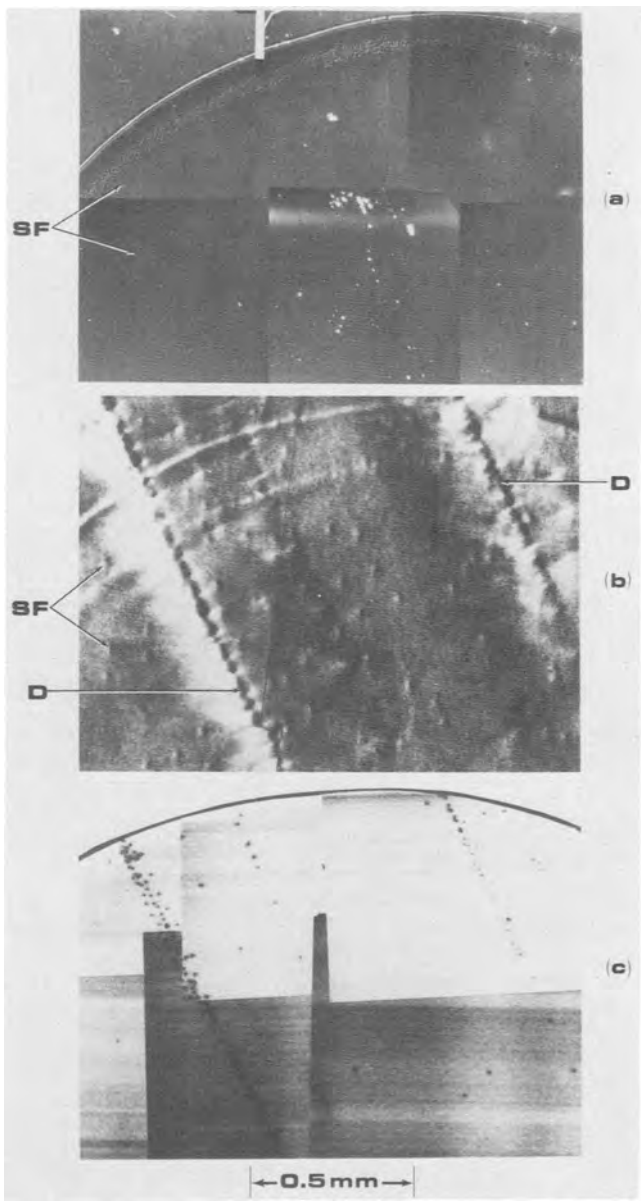


Fig. 1. As-deposited epi sample, no subsequent treatment. Sample 1. (a) Optical interference contrast micrograph of part of one 1/16 in. diameter Schottky barrier dot showing stacking faults (SF). (b) X-ray topograph of same area as (a) showing contrast features due to slip dislocations (D) and stacking faults (SF). (c) Zero-bias EBIC image of same area showing recombination centers which coincide with dislocation sites shown in (b).

Table II. Electrical activity at epitaxial stacking faults

Orientation	Sample	Buried layer facility	Epi reactor	Epi run	EBIC at stacking faults
111	1	A	A-1	1	None
111	2				
111	3				
111	4	A	A-1	2	None
111	5				
111	6	A	A-2	3	None
111	7	A	A-2	4	None
111	8				
111	9				
111	10				
111	11	A	A-2	5	None
111	12				
111	13				
111	14				
111	15				
111	16	B	B	6	At corners
111	17	B			
100	18	—			
100	19	B			
100	20	B	B	8	At corners
100	21	B	B	9	At corners
100	22	B	B	10	At corners
111	23	A	B	11	None
111	24	A, B*	B	11	Simple faults: none Complex faults: at corners
111	25	A	A-1	12	None
100	26	B	A-1	12	At corners

* Sample 24 had buried layer diffusion performed in facility A, drive-in and subsequent processing was performed in facility B.

and 1c show a transmission x-ray topograph and an EBIC image, respectively, of the same area.

Recombination sites appear in the EBIC image as black spots (Fig. 1c) and are correlated with dislocations seen in the x-ray topograph (Fig. 1b). The black-white contrast pairs in Fig. 1b are due to stacking fault strain fields and are correlated with the stacking fault features shown in Fig. 1a. Thus, there is a one-to-one correlation of stacking fault features which appear in the optical micrograph and sites of existing stacking faults, but no recombination is observed at these sites in this particular sample.

Table III. EBIC measurements at stacking fault recombination center, sample 16 (Fig. 2)

Recombination center	$I_{EBIC}(\mu A)$
A	2.95
B	3.05
C	3.10
D	2.95
E	3.20
F	3.00
G	2.95
H	3.05
I	3.05
Away from center	3.30

Results of EBIC analysis of epi films grown in various reactors are summarized in Table II. Recombination, when it occurred, was generally found only at the dislocations at the corners of the stacking fault polyhedra, or at dislocations bounding single planar faults. Figure 2 shows optical and EBIC photographs of epi faults in 13 μm thick 3 Ω-cm (111) and (100) epi. Note that strong recombination occurs at the corners of the stacking fault polyhedra, and that the magnitude of the recombination varies at different sites. A quantitative measure of EBIC current at the corners of stacking fault polyhedra indicates the recombination strength at these corners. Such data are given in Table III for the faults shown in Fig. 2b. Conditions used for these measurements have been given in Table I. A moderate variation in strength of the nine recombination centers is noted with values ranging from 3 to 10% less than the background EBIC current (3.30×10^{-6}A). These are typical observations.

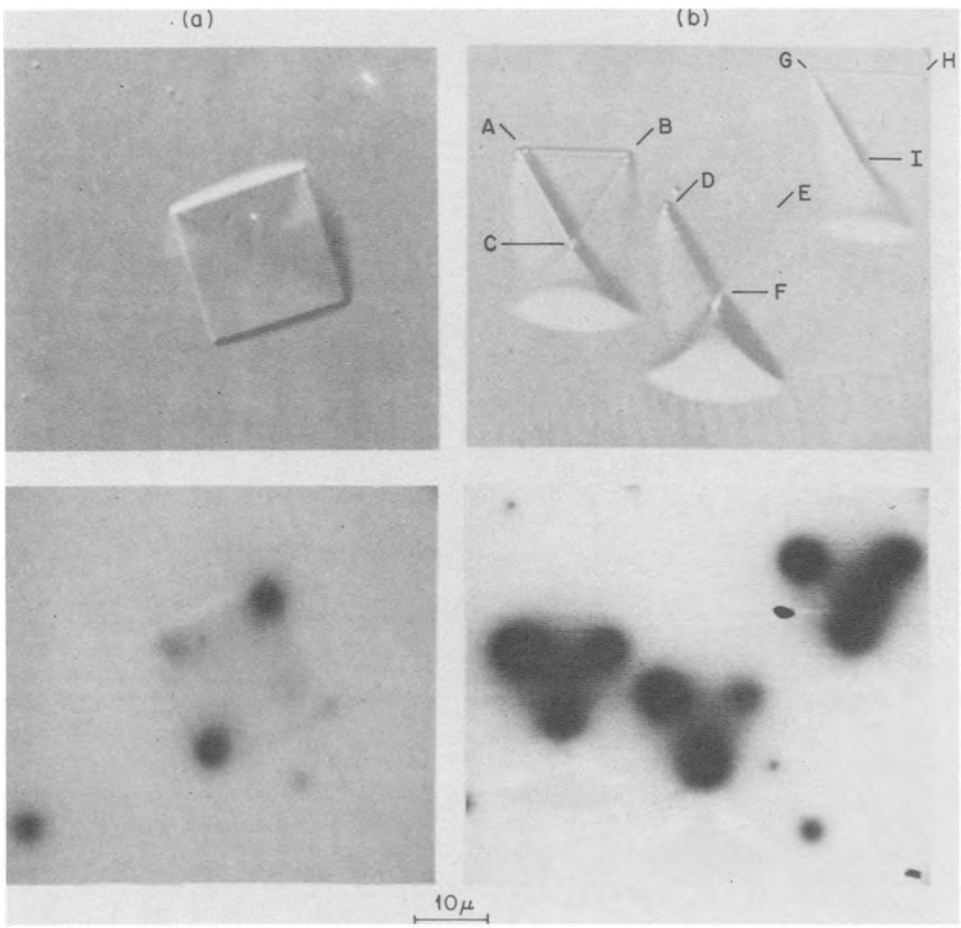


Fig. 2. Interference contrast (upper) and EBIC (lower) photographs of (100) sample 18 (a) and (111) sample 16 (b). Both EBIC conditions were zero volts applied bias; beam energy 15 keV (a) and 19 keV (b).

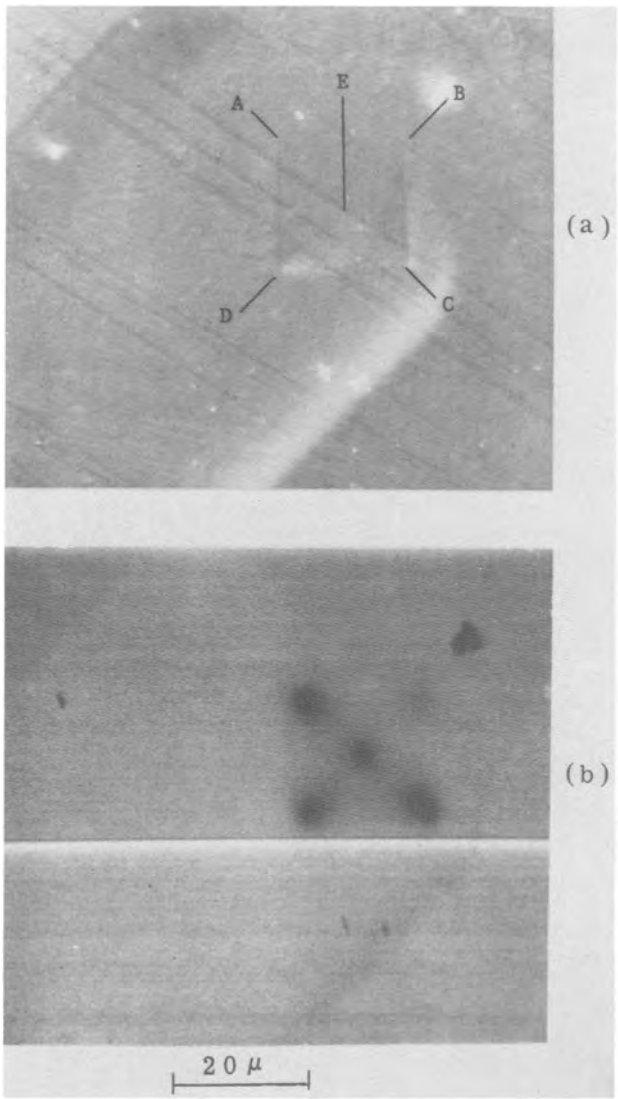


Fig. 3. Interference contrast (a) and EBIC (b) photographs of (100) sample 19. EBIC conditions were zero bias, 13 keV.

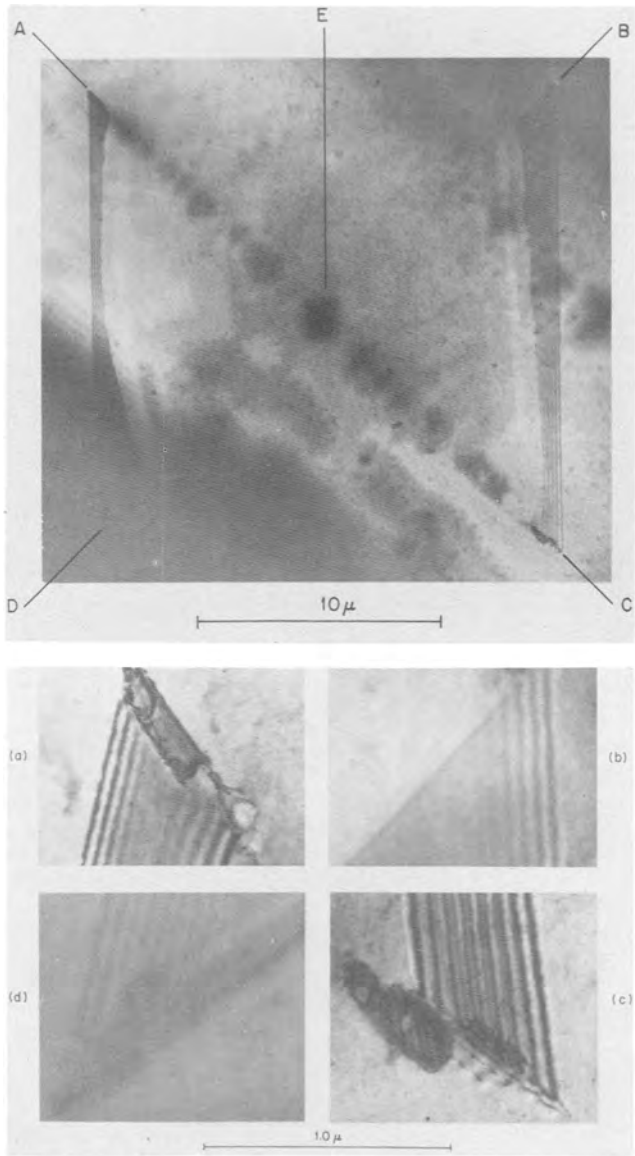


Fig. 4. (a) Transmission electron micrograph of fault defect shown in Fig. 2 and (b) enlargements of micrographs of the ends of the faults. Micrographs are bright field, taken under two-beam conditions.

Figure 3 shows a similar set of photographs of a stacking fault defect in (100) sample 19 with 13 μm thick 3 Ω-cm epi. The large rectangular feature is a buried layer region; corners A, D, C are situated over the buried layer region, while corner B is not. This region was thinned and examined in the transmission electron microscope. A TEM photograph of this fault defect is shown in Fig. 4a and micrographs of the four corners (A, B, C, and D) are shown in Fig. 4b. Dark field examination of corners A, B, and C shows that precipitates are present; large precipitates are present at corners A and C, while a smaller precipitate is present at corner B. This distribution of precipitate correlates with the variations observed in recombination strength. Although corner D could not be examined thoroughly because the sample was quite thick in that region, the bright field photograph of corner D in Fig. 4b indicates that a large precipitate is probably present at this corner too. X-ray analysis of the precipitate at corner A shows the presence of Ni. No diffraction pattern could be obtained from the precipitate and its structure has not been identified.

The dark rectangular feature at the center at E (Fig. 4a) and the chain of dark regions extending from corner A to corner C were examined under various diffraction conditions in the TEM. The conclusion is that these are not precipitates but are rather thick regions of Si, which probably resulted from precipitate shadowing during ion milling. The precipitates have been milled away. The reason for the existence of strong recombination at E is not clear. This point is ~13 μm below the surface as determined from the geometry of the fault. The EBIC images at dislocations which bound faults show that the maximum depth supplying EBIC information is ~5 μm at 20 keV (see Fig. 2 and 3). Therefore it seems unlikely that the point of origin of the two faults is the source of the EBIC recombination signal at E.

Results on samples 1-22 suggest that the electrical activity of faults may be related to the reactor used to grow the epi. Additional experiments (samples 23-26) disproved this idea. Samples 23 and 24 both were cleaned and simultaneously received epi in reactor B; sample 23 received all buried layer processing in facility A while sample 24 had Sb (buried layer) diffusion performed in facility A with the drive-in and all subsequent processing being done in facility B. Epi stacking faults appeared on sample 23, virtually identical in appearance to those shown in Fig. 1. On sample 24 two classes of epi faults appeared, distinguished by their optical appearance as well as by their electrical activity (see Fig. 5). One type appears as a simple polyhedron, typical of epi faults generally found on material grown in facility A and reactors A-1 and A-2 (samples 1-15, Fig. 1). These were electrically inactive. This is the only instance where inactive faults

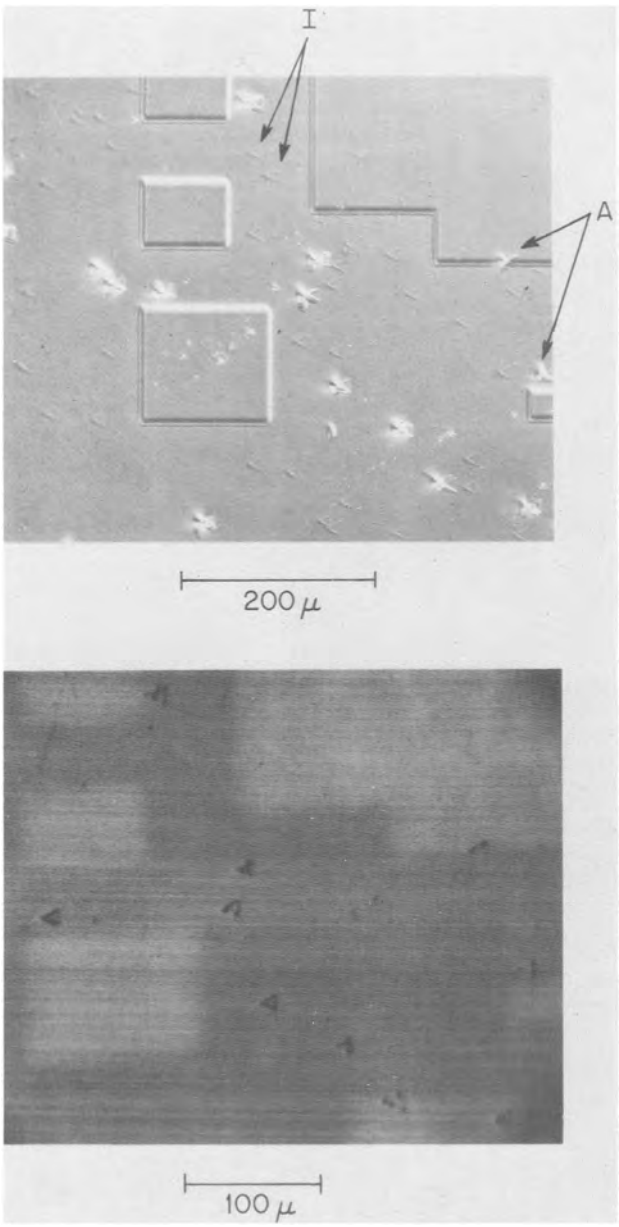


Fig. 5. Interference contrast (a) and EBIC photographs (b) of sample 24. Both inactive (I) and electrically active (A) faults can be seen. EBIC conditions were zero bias, 19 keV.

have been produced in reactor B. A second type appears complex and shows electrical activity at the corners of the polyhedra, typical of epi faults generally found on material grown in facility B (samples 16-22, Fig. 2 and 3). TEM studies of these faults are underway.

Samples 25 and 26 had buried layers processed in facilities A and B, respectively. Epi was deposited simultaneously in reactor A-1. Sample 25 had simple inactive fault polyhedra typical of samples 1-15 and 23 and sample 26 had more complex, electrically active faults typical of samples 16-22. This is the only instance where active faults have been produced in one of the A reactors.

Discussion

The data show that the electrical activity of stacking faults is related to the facility in which buried layer processing was carried out; facility A produces material with inactive faults and facility B produces material with active faults. One exception is sample 18 which received no buried layer processing, yet which had active faults. Active faults are produced in both (111) and (100) material. Neutron activation analysis of the reactor B epi films shows negligible heavy metal contamination, while analysis of wafers receiving standard facility B cleans at the time of these experiments has occasionally shown Au, Br, Cr, Cu, Ni, and Na present on the wafers. The electrical activity of faults in samples that have received all (samples 16-17; 19-22) or part (sample 23) of buried layer processing in facility B, and the activity of faults in sample 18 which received only a clean prior to epi growth in reactor B, is thus attributed to the presence of a contaminant which enters the substrate during buried layer processing or appears on the substrate surface following clean from a contaminant in one of the cleaning solutions. It is noted that in one case (sample 23) a facility B clean did not produce active faults.

The films deposited on facility B substrates contained epi faults which were active only at the partial dislocations which bound a fault.[1] Some similar observations are made by Ravi *et al.* (4), on oxidation-induced stacking faults in silicon. They probed these stacking faults with *I-V* measurements and EBIC analysis using 4 μm deep p^+n junctions formed by B diffusion. Their analysis showed a relationship between stacking fault length and "electrical activity," the latter being defined as the onset of current multiplication (as seen in EBIC) with increasing reverse bias. Their main interpretation of this relationship (one of two they present) is that a stacking fault interferes with the B diffusion process to form precipitates which thereby influence junction properties locally about the defect. The main differences between the experiment of Ravi *et al.* and the one reported here are (*i*) no pn junction was used in these experiments, (*ii*) attention in this work is focused on the magnitude of recombination occurring at very low reverse bias, well below avalanche, and (*iii*) the mechanism of fault formation and the resulting fault properties are quite different. In spite of these essential differences it is quite clear that both studies show that decorated defects (faults and partial dislocations in Ravi's case, dislocations only in our case) have a significant effect on electrical activity compared with undecorated defects.

Kato *et al.* (2) studied epi faults in (111) Si using EBIC on n^+p junctions, and their published micrograph [Fig. 2a, Ref. (2)] shows recombination over the area bounded by the intersection of an epi fault tetrahedron with the surface. Since we have obtained a similar EBIC result [recombination over the entire faulted surfaces of stacking faults forming a tetrahedron in (111) epi Si], only when epi deposition was followed by an oxidation, it is considered likely that Kato's observations are due to the interaction of thermal treatments (P diffusion in Kato's case) with the epi faults.

The only published information to date on EBIC studies of stacking faults using a Schottky barrier instead of a pn junction is an article by Kawado *et al.* (6). They examined oxidation-induced stacking faults in (001) Si and microprecipitates in (111) Si. Their EBIC photograph of oxidation-induced faults is similar to ours in that recombination is visible only at the partial dislocation sites. No analysis had been made of these faults to determine if precipitates were present.

In our case a qualitative correlation has been made between the apparent mass of precipitate and the strength of that site as a recombination center. Quantitative EBIC measurements on other fault polyhedra show a typical attenuation of 3-6 $\times$ 10^{-7}A (3-10%) at a recombination site; presumably this variation is also correlated with precipitate mass.

Conclusion

EBIC analysis has been made of the electrical activity of stacking fault polyhedra formed during epi

[1] An exception is some of the active fault polyhedra in sample 24 where recombination was also found at the intersection of faults with the surface (see Fig. 5b).

growth of Si from $SiCl_4$. Carrier recombination has been observed at the corners of fault polyhedra and at dislocations bounding single planar faults in some samples; no recombination at faults has been found in other samples. The occurrence of electrical activity is related to the facility in which buried layer processing and wafer cleaning was done prior to epi deposition, and is not due to the epi reactor. Au, Br, Cr, Cu, Ni, and other impurities occasionally have been found on wafers cleaned in the facility which produced electrically active faults. TEM analysis of the corners of electrically active polyhedral faults showed precipitates present; with Ni detected in one precipitate. In one polyhedral fault structure the mass of precipitate correlated with the strength of electrical activity as measured by the attenuation of the magnitude of the EBIC signal.

Acknowledgments

The authors acknowledge the help of I. A. Blech and P. Petroff in the transmission electron microscope analysis and L. C. Kimerling and H. J. Leamy for useful discussions on this problem.

Manuscript submitted Aug. 25, 1976; revised manuscript received Oct. 16, 1976.

Any discussion of this paper will appear in a Discussion Section to be published in the December 1977 JOURNAL. All discussions for the December 1977 Discussion Section should be submitted by Aug. 1, 1977.

Publication costs of this article were assisted by Bell Laboratories.

REFERENCES

1. S. Mendelson, *J. Appl. Phys.*, **35**, 1570 (1964).
2. T. Kato, T. Matsukawa, and R. Shimizu, *Appl. Phys. Lett.*, **26**, 415 (1975).
3. J. J. Lander, H. Shreiber, and T. Buck, *ibid.*, **3**, 206 (1963).
4. K. V. Ravi, C. J. Varker, and C. E. Volk, *This Journal*, **120**, 533 (1973).
5. H. J. Leamy, L. C. Kimerling, and S. D. Ferris, 33rd Annual Proceedings of the Electron Microscope Society of America, p. 260 (1975).
6. S. Kawado, Y. Hayaiuji, and T. Adachi, *Jpn. J. Appl. Phys.*, **14**, 407 (1975).

Gallium Arsenide Phosphide Schottky Barrier Field Effect Transistor

R. K. Pancholy[1] and W. W. Grannemann

The University of New Mexico, Albuquerque, New Mexico 87131

ABSTRACT

Fabrication processes have been developed for gallium arsenide phosphide Schottky-barrier field effect transistor (SBFET) on an insulating gallium arsenide substrate. Process techniques as well as results of electrical characterization of the device structure including the GaAsP-GaAs interface are described. Formation of a conductive layer near the GaAsP-GaAs interface is postulated, and an anlaysis of its effects on transistor characteristics is presented.

Interest in gallium arsenide phosphide has been increasing in the past few years due to its potential advantages such as high electron mobility and variable energy bandgap resulting in high frequency, high temperature, and electroluminescence applications including light emitting diodes, lasers, microwave field effect transistors, and infrared detectors. By changing the phosphorus mole fraction x in $GaAs_{1-x}P_x$, the energy bandgap may be changed from 1.43 eV for $x = 0$ (*i.e.*, GaAs, direct bandgap) to 2.25 eV for $x = 1$ (*i.e.*, GaP, indirect bandgap) at room temperature (23°C). Gallium arsenide phosphide on semi-insulating gallium arsenide provides an ideal material for device applications, as device isolation required for circuit applications can be easily achieved by the formation of active GaAsP island regions. For majority carrier devices such as field effect transistors, the conductivity can be modulated by either a metal insulator semiconductor structure, a reverse bias p-n junction, or a Schottky barrier metal-semiconductor junction.

The major difficulty in the development of GaAsP technology has been the dissociation of the semiconductor at high temperature during diffusion and oxidation. This paper reports development of a low temperature (<550°C) process for the fabrication of GaAsP Schottky barrier field effect transistors (SBFET's).

[1] Present address: Electronics Research Division, Rockwell International, 3370 Miraloma Avenue, Anaheim, California 92803.

Key words: gallium arsenide phosphide, gallium arsenide, Schottky barrier FET, GaAsP-GaAs interface, III-V device processing.

Fabrication

The SBFET's were fabricated on a tellurium-doped n-type $GaAs_{1-x}P_x$ epitaxial layer with a phosphorus mole fraction, $x = 0.34$. The epitaxial layer with impurity carrier concentration of 2.2×10^{16} atoms/cm^3 and electron mobility of 1160 cm^2/Vsec, was grown on a semi-insulating GaAs substrate of 10^8 Ω-cm resistivity (1). The initial epitaxial layer thickness was reduced to approximately 1μ by chemical etching in order to permit complete channel pinch-off against the semi-insulating substrate.

The fabrication process is shown in Fig. 1, where after initial cleaning the active regions of the transistors are defined by selective removal of the epitaxial film (2) as shown in Fig. 1(b). Selective etching of the GaAsP film was performed using a 5:1:1 acid etch (5 parts H_2SO_4:1 part 30% H_2O_2:1 part DI water) in conjunction with positive photoresist (AZ-1350). Negative photoresists were experimentally determined to be less suitable, as the photoresist remover (microstrip) reacts with the GaAsP surface.

The etch rate of GaAsP with 5:1:1 etch was defined for a number of samples with varying phosphorus mole fractions x at room temperature. Figure 2 summarizes these experimental results, which indicate that the etch rate for $GaAs_{1-x}P_x$, with $x = 0.5$ is considerably slower than the reported 2μ per min etch rate for GaAs (3). With $x = 1.0$, *i.e.*, GaP, no sig-

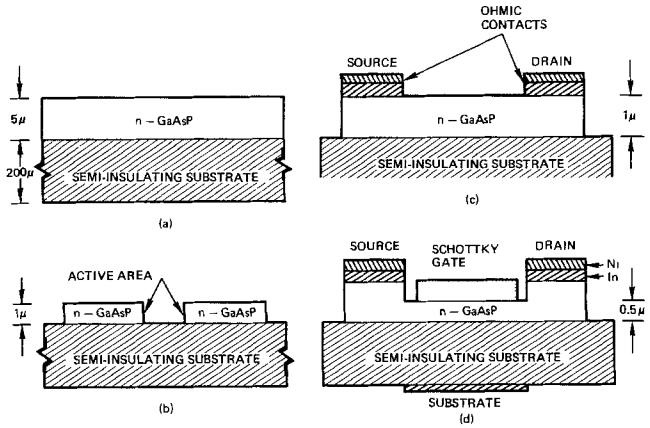


Fig. 1. Fabrication process for GaAsP SBFET. (a) N-type starting material; (b) island etch to define active device regions; (c) formation of ohmic contact for the source and the drain; (d) formation of the Schottky barrier gate.

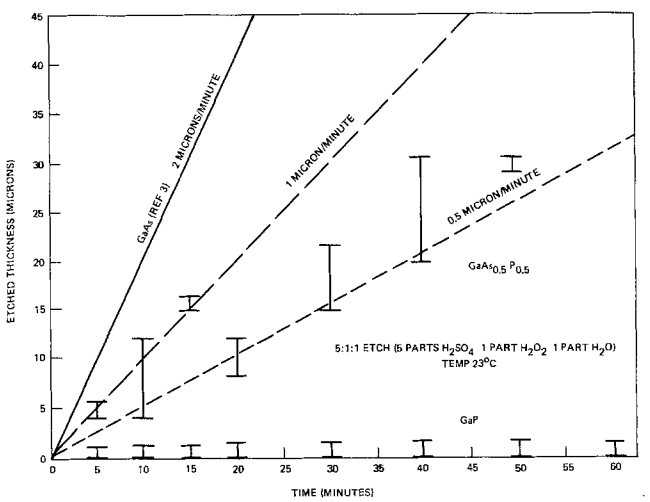


Fig. 2. Thickness of the epitaxial $GaAs_{1-x}P_x$, $x = (0.5, 1.0)$, etched with 5:1:1 etch at room temperature vs. time. The error bars represent data scatter observed in different samples.

nificant reduction in the thickness of the sample could be detected after 1 hr of etching at room temperature. These results indicate that phosphorus content in the epitaxial layer significantly affects the etch rate of these films.

Other acid etchants such as HF, buffered HF, HNO_3, and HCl produced anisotropic etching of $GaAs_{0.5}P_{0.5}$. Under a magnification of 50-100×, a nonuniform grainy surface was observed after the acids reacted with GaAsP for less than 1 min at room temperature.

Both negative photoresist and HCl based acids play important roles in silicon technology. Because of the adverse reaction of reagents with GaAsP, it is apparent that new methods must be developed.

Several metals and metal combinations including Au, Ag, Al, Ge, In, Ni, Cr, and double metallization layers of Au-Ge, Ag-Ge, and In-Ni were evaluated to form ohmic contacts to n-$GaAs_{0.5}P_{0.5}$ (for the source and the drain regions of the SBFET). The contacts were evaluated using a test pattern consisting of 10 mil diam metal dots spaced 25 mils apart on the surface of the $GaAs_{0.5}P_{0.5}$ epitaxial layer. All metal depositions were performed by resistive-heated evaporation at a pressure of less than 1×10^{-6} Torr. The sintering time and temperature were optimized in each case to ensure ohmic contacts. The results of these experiments are summarized in Fig. 3 where contact characteristics of various metal combinations, as functions of sintering time, are shown. Each contact variation was sintered for 15 min in nonoxidizing ambient in temperature increments of 50°C, starting

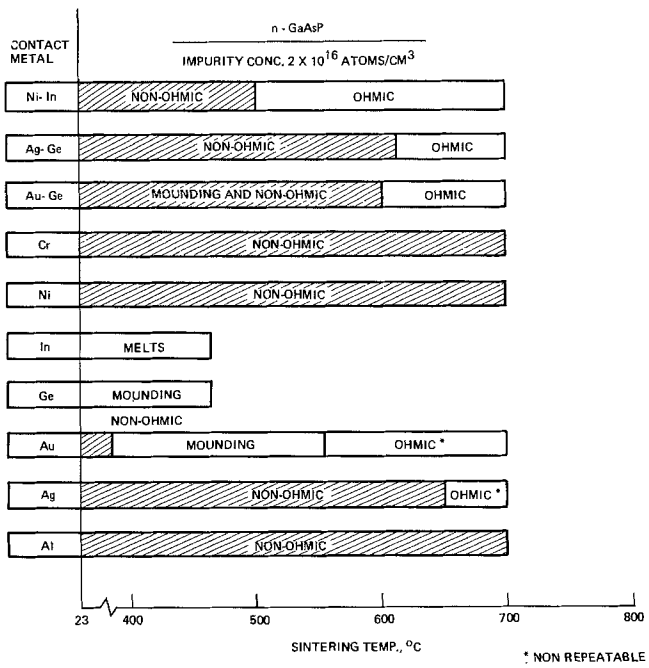


Fig. 3. Contact characteristics vs. sintering temperature

at a temperature of 400°C. The contact characteristics were evaluated at room temperature (23°C) before sintering and after the sample returned to room temperature at the end of each successive sintering cycle. The criterion used to define ohmic quality in Fig. 3 was the appearance of a linear *I-V* characteristic through 0V. The contact sintering cycles were continued until either ohmic characteristics resulted or a temperature limit of 700°C was reached. The upper limit on temperature was established because of possible GaAsP surface damage at temperatures higher than 710°C (4).

The most repeatable low resistance ohmic contacts, at low sintering temperatures, were achieved with a double metallization layer of indium and nickel. Other metal combinations exhibited nonohmic characteristics even after sintering at 600°C. Several metals, *e.g.*, Ge, Au, and Au-Ge double layer, exhibited a "mounding" characteristic due to high surface tension. Gold and silver metal combinations successfully used for ohmic contacts to GaAs (5, 6) produced highly resistive nonrepeatable contacts to n-type $GaAs_{0.5}P_{0.5}$. The presence of phosphorus and a low concentration of Te ($2.2 \times 10^{16}/cm^3$) in the epitaxial layer and a higher percentage of Ge in the Au-Ge double layer are the major experimental differences between the results reported here and those in Ref. (5) and (6). The observed ohmic characteristics of the indium-nickel double layer are probably due to the diffusion of indium into GaAsP during the sintering process, thus providing the higher donor impurity concentration in the epitaxial film under the nickel layer.

The source and the drain regions of the transistor were defined using the double layer of indium-nickel with positive photoresist lifting techniques. The device structure, after source and drain definition, is shown in Fig. 1(c).

The Schottky-barrier gate of the field effect transistor was formed by resistive evaporation of aluminum at a pressure of less than 1×10^{-6} Torr, on a clean GaAsP surface. Before evaporation, the epitaxial GaAsP layer was chemically etched down to approximately 1.0μ thickness in order to pinch off the channel with the gate depletion region. The Schottky-barrier gate was defined by photoresist lifting techniques. The completed device structure is shown in Fig. 1(d), and the device dimensions are shown in Fig. 4.

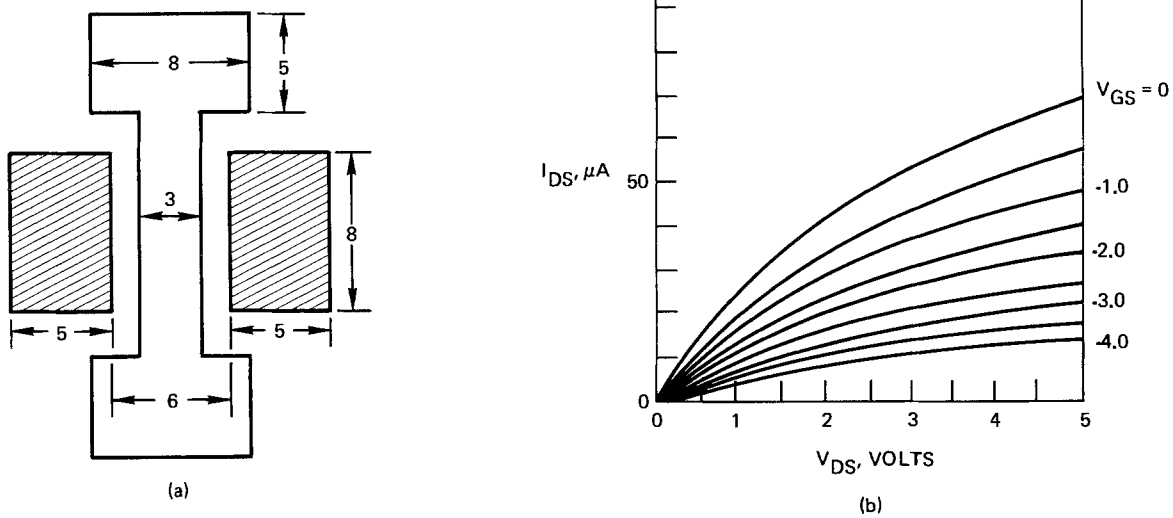


Fig. 4. SBFET structure and characteristics. (a) SBFET structure with dimensions in mils; (b) three-terminal characteristics of SBFET No. 61-3.

Electrical Characteristics of the SBFET

The three-terminal drain characteristics of a typical SBFET fabricated in the manner described above are shown in Fig. 4. The incomplete pinch-off characteristic exhibited by these devices indicates the presence of a current conduction mechanism which is not under the control of the gate. For the SBFET, the pinch-off voltage, V_{PO}, defined as the gate-source voltage required to reduce the channel current to zero, is given by

$$V_{PO} = \frac{qN_D a^2}{2\epsilon_S} \qquad [1]$$

where a, N_D, and ϵ_S are the thickness, impurity concentration, and the dielectric constant of the epitaxial layer, respectively, and q is the electronic charge. The reverse bias depletion region width of the Schottky gate extends from the metal-semiconductor interface to the GaAsP-GaAs interface at this voltage, thus pinching off the channel.

For a GaAsP layer doped to 2.2×10^{16} atoms/cm^3 with a dielectric constant of 11.0, the theoretically calculated pinch-off voltage for 1 μm epitaxial layer thickness is 18V, whereas for a 0.75 μm epitaxial layer it is 10.1V. The pinch-off voltage is experimentally determined by a graphical technique based on the square law transfer characteristics of the SBFET (8-11), where the drain current, I_D, is given by

$$I_D = I_O\left(1 - \frac{V_{GS}}{V_{PO}}\right)^n \qquad [2]$$

where $n \approx 2.0$, V_{GS} is the gate-source voltage, and I_O is the value of I_D at $V_{GS} = 0$, in the saturation region. Therefore, a plot of $\sqrt{I_D}$ *vs.* V_{GS} yields a zero current intercept equal to the pinch-off voltage V_{PO} as shown in Fig. 5.

Assuming a uniform carrier concentration, the observed pinch-off voltage corresponds to an epitaxial layer thickness of 0.82 μm, which is well within the range of thickness established for the epitaxial layer by etching experiments. The maximum transconductance observed for these devices was 1600 μmhos.

The Schottky barrier gate capacitance-voltage characteristics, measured at 1 MHz, are shown in Fig. 6. Two significant effects can be observed in Fig. 6; the decrease in the capacitance at large negative voltage and the hysteresis effect at low negative voltage. The sudden drop in the capacitance at approximately −8V indicates the absence of any charge exchange mechanisms near the edge of the depletion region. This situation can occur when the reverse bias Schottky barrier gate depletion region extends up to the

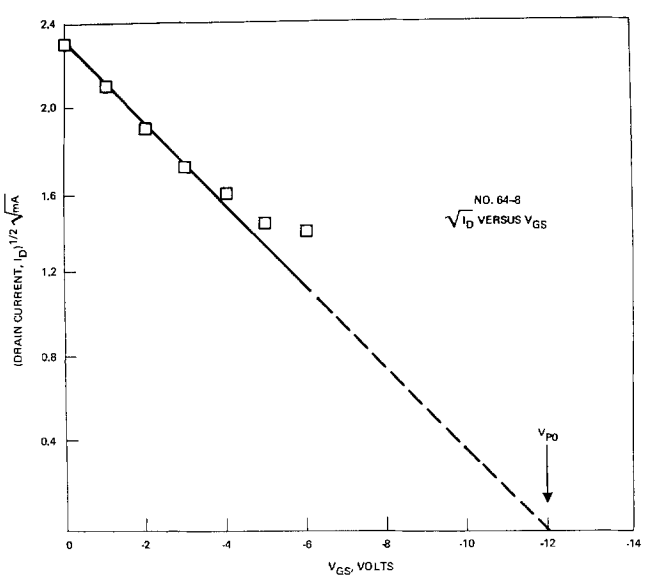


Fig. 5. $\sqrt{I_D}$ *vs.* gate voltage for n-GaAsP SBFET

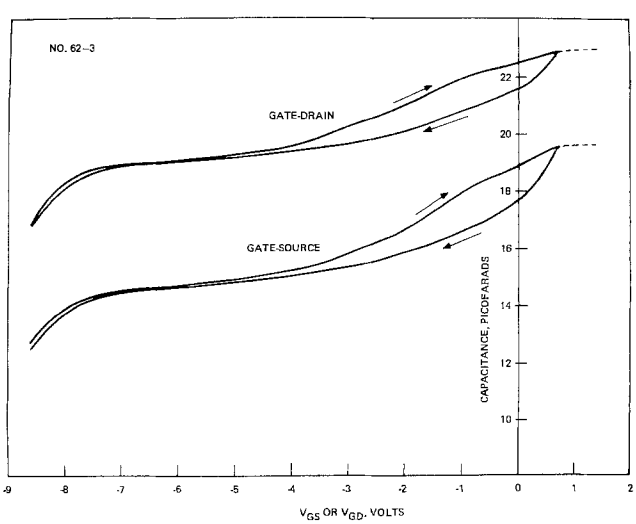


Fig. 6. Schottky gate capacitance-voltage characteristics

GaAsP-GaAs interface and there is a sudden change in the n-type impurity carrier concentration. The observation of a hysteresis effect at low reverse voltages indicates presence of charge trapping and/or ion migration mechanism at the surface of the device. At low gate voltages, the depletion width of the reverse biased Schottky barrier gate does not extend deep into the GaAsP (for the given impurity concentration), thus the hysteresis effect observed here is not related to charge trapping or ion migration at the GaAsP-GaAs interface. Since no surface passivation techniques were used for protection of the device surface, the observed effect could be related to exposure of the device to moisture. A thin layer of oxide (gallium oxide, Ga_2O_3, and gallium phosphate, $GaPO_4$) may form over the exposed surface between the gate and the drain/source region during the fabrication process (4). Hysteresis effects in thermally grown GaAsP oxides have been observed, and similar effects may be responsible for the observed effects here.

Discussion

The *I-V* characteristics of the SBFET's indicate the existence of a current conduction path between the drain and the source which is not modulated by the gate voltage. This current could occur, for example, if the depletion region of the Schottky gate does not extend all the way to the GaAsP-GaAs interface before exceeding the reverse bias breakdown voltage of the Schottky-barrier junction. As the reverse breakdown voltage of the Schottky gate was experimentally determined to be greater than −10V, this possibility can be ruled out. The other mechanisms for current conduction between the drain and source are the formation of a current conduction path near the GaAsP-GaAs interface and possibly edge effects. Edge effects should be partially under the control of the gate voltage. As no control over the drain current is observed beyond low gate voltage, this effect also seems to play an insignificant role.

The observed drain current could be further reduced by application of a reverse bias on the GaAs substrate, indicating that the current flows close to the GaAsP-GaAs interface. For example, at $V_{GS} = 0$, $V_{DS} = 5$V and no substrate bias, the drain current was 1.6 mA for device 63-15. This current was reduced to 0.95 mA at −45V substrate bias. Other device parameters such as channel conductance and transconductance exhibited similar substrate bias modulation characteristics. The *C-V* measurement indicates that the impurity concentration near the interface is very small.

To explain the observed characteristics, formation of a highly disordered conductive layer near the GaAsP-GaAs due to a sudden change in the phosphorus mole fraction is postulated. The inclusion of phosphorus in lattice sites during the growth of $GaAs_{0.5}P_{0.5}$ on a GaAs substrate may result in additional stresses to be present at the interface. The lattice mismatch results in formation of a disordered region near the interface. Similar effects in epitaxial GaAs on a semi-insulating GaAs substrate have been observed (7). These observations suggest formation of a disordered, high resistivity layer near the GaAsP-GaAs interface as shown in Fig. 7. The current conduction through the layer, using this model, is a function of applied drain voltage, but the conduction is independent of gate voltage. The nonsaturation characteristics of the SBFET observed in Fig. 4 can be seen, in part, as a result of the increased conduction through this layer.

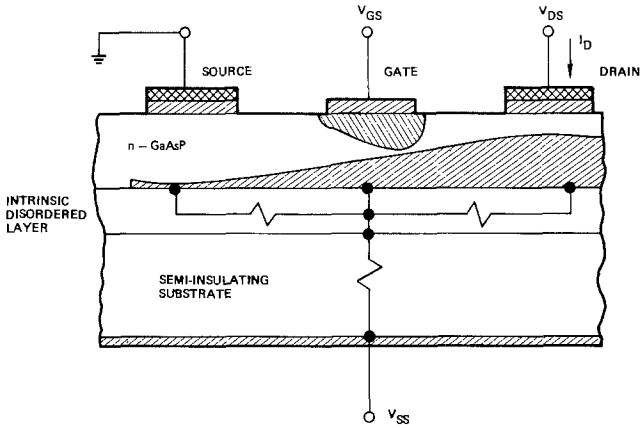


Fig. 7. SBFET with intrinsic layer near the GaAsP-GaAs interface

The GaAsP-GaAs interface thus seems to play an important role in determining the characteristics of the devices. A possible approach to improve the device quality is to grow GaAsP on semi-insulating GaAsP with the same phosphorus mole fraction or to use other techniques such as ion implantation to control the impurity concentration as well as the phosphorus mole fraction x in $GaAs_{1-x}P_x$.

Acknowledgment

This work was supported by the Office of Naval Research and was submitted to the University of New Mexico as partial fulfillment for the requirements of the degree of Ph.D.

Manuscript submitted Oct. 21, 1975; revised manuscript received Oct. 14, 1976. This was Paper 156 presented at the Toronto, Canada, Meeting of the Society, May 11-16, 1975.

Any discussion of this paper will appear in a Discussion Section to be published in the December 1977 JOURNAL. All discussions for the December 1977 Discussion Section should be submitted by Aug. 1, 1977.

Publication costs of this article were assisted by Rockwell International.

REFERENCES

1. Supplied by Monsanto Company, St. Louis, Missouri.
2. R. K. Pancholy, G. J. Kuhlmann, and W. W. Grannemann, Paper presented at 14th Electronic Materials Conference, AIME, Boston, Aug. 1972.
3. G. G. Reeves and R. P. Donovan, "Gallium Arsenide Technology," Vol. II, Technical Report AFAL-TR-72-312, pp. 4-8 (1973).
4. D. H. Phillips, W. W. Grannemann, L. E. Coerver, and G. J. Kuhlmann, *This Journal*, **120**, 1087 (1973).
5. R. H. Cox and H. Strack, *Solid-State Electron.*, **10**, 1213 (1967).
6. J. S. Harris, Y. Nannichi, G. L. Pearson, and G. F. Day, *J. Appl. Phys.*, **40**, 4575 (1969).
7. W. Hooper, B. R. Cairns, *et al.*, Technical Report AFAL-TR-69-30, Air Force Avionics Laboratory, Wright-Patterson Air Force Base, Ohio, Feb. 1969.
8. P. Richman, "Characteristics and Operation of MOS Field Effect Transistors," pp. 142-144, McGraw-Hill Book Co., New York (1967).
9. B. D. Wedlock, *Proc. IEEE*, **57**, 75 (1969).
10. L. J. Sevin, "Field-Effect Transistors," pp. 21-22, McGraw-Hill Book Co., New York (1965).
11. I. Richer and R. D. Middlebrook, *Proc. IEEE*, **51**, 1145 (1965); R. D. Middlebrook, *ibid.*, **51**, 1146 (1963).

Growth of Monocrystals of the Gallium Analog of β''-Al_2O_3 by Na_2O Evaporation

L. M. Foster* and J. E. Scardefield

IBM Thomas J. Watson Research Center, Yorktown Heights, New York 10598

ABSTRACT

A crystal growth practice was developed for producing monocrystals of the gallium analog of β''-Al_2O_3. The method involves evaporation of Na_2O from a molten Na_2O-Ga_2O_3 charge held in a boat that is located in a furnace with a steep temperature gradient so that the product grows from one end. Monocrystals up to about 1 cm in size have been grown. Their composition is $Na_2O \cdot 5.7Ga_2O_3$, which corresponds to 96.5% occupancy of the available Na sites. The space group is $R\bar{3}m$ and the lattice parameters are a = 5.84Å and c = 34.53Å.

There are many parallels in the chemistry of gallium and aluminum. In 1951 Foster and Stumpf (1) showed the isomorphism between the oxides of the two systems and, in particular, prepared the alkali gallates analogous to sodium and potassium β-Al_2O_3. In 1974, Foster and Scardefield (2) prepared monocrystals of the β-form of Na-gallate by flux growth from NaF-Ga_2O_3 solutions.

Boilot *et al.* (3) showed that the rhombohedral variant, β''-Na-gallate, also existed, and proposed a tentative phase diagram locating the β- and β''-phase fields in the Na_2O-Ga_2O_3 system. Chicotka (4) reported ionic conductivity measurements on sintered ceramic Na-gallate samples that were principally the β''-form.

In addition to offering the possibility of new solid electrolytes with potential practical applications, the gallium analogs provide an additional medium in which to study the process of fast ion conduction. In particular, since the binary oxide systems where one component is Ga_2O_3 are lower melting than the corresponding systems with Al_2O_3, the synthesis and growth of research crystals is facilitated The present study concerns the preparation of monocrystals of the rhombohedral β''-Na-gallate.

Experimental

The Na_2O-Ga_2O_3 phase diagram proposed by Boilot *et al.* (3) is shown in Fig. 1. We take exception to certain features of that diagram. Namely, we have established the existence of the compound $Na_2O \cdot 3Ga_2O_3$, which does not appear in Fig. 1; we have not been able to demonstrate congruent melting of the β-form at about 85.8 mole percent (m/o) Ga_2O_3, as indicated; and we find a different composition for the Na_2O-rich boundary of the β''-phase field. We have not investigated other aspects of the system to determine if there are other areas of disagreement. Our own investigation of the Na_2O-Ga_2O_3 diagram was interrupted by the finding that the method that both we and Boilot *et al.* employed to locate the various phase fields, namely, x-ray identification of the phases present in small quenched samples, was not yielding reliable results because of composition changes that occurred on heating. For example, three samples of approximately 0.25g each of a well-mixed, prereacted charge of composition $Na_2O \cdot 6Ga_2O_3$ (prepared by reacting Na_2CO_3-Ga_2O_3 mixtures overnight at 1100°C) were encapsulated in autogenously welded platinum tubes, held at 1375°, 1425°, and 1450°C, respectively, for 5 hr to equilibrate, then water quenched. The entire contents of each capsule was then analyzed for sodium with the following results: 1375°, $Na_2O \cdot 5.95Ga_2O_3$; 1425°, $Na_2O \cdot 8.70Ga_2O_3$; 1450°, $Na_2 \cdot 9.15Ga_2O_3$. Clearly, the Na_2O vapor that should be in equilibrium with the samples at each temperature was being lost by reaction with the platinum so that there could be no assurance that the phases present in a quenched sample truly represented equilibrium phases at the high temperature.

However, several features of the diagram of Fig. 1 appear to be qualitatively correct, and the diagram was a useful guide in setting up preliminary crystal growth experiments. It was confirmed in the present study that growth from soda-rich melts yielded only the hexagonal β-phase if the precipitation temperature exceeded $\simeq$1420°C, and only the β''-phase when the temperature was below $\simeq$1400°C, more or less in agreement with the peritectic transition shown at 1410°C in Fig. 1.

It is clear from Fig. 1 that if the composition of a melt were continuously changed by adding Ga_2O_3 or removing Na_2O so as to move toward the liquid + β'' two-phase field from the left, a crystal of β'' would just begin to precipitate when the liquidus was reached. If the Ga_2O_3/Na_2O ratio were further increased, the crystal would grow while the liquid remained at the liquidus composition. A growth procedure was devised wherein such a composition change was effected by Na_2O evaporation. Boilot *et al.* (3) has previously shown that the β''-gallate phase appears in such a process, but had obtained only small platelets.

Whereas an isothermal experiment would be desirable to ensure that the precipitating solid had a fixed composition, it would lead to nucleation and growth throughout the charge and make recovery of the product difficult. The final procedure, therefore, incorporated a steep temperature gradient to ensure that the product nucleated and grew entirely in one end of the container from which it could be easily recovered.

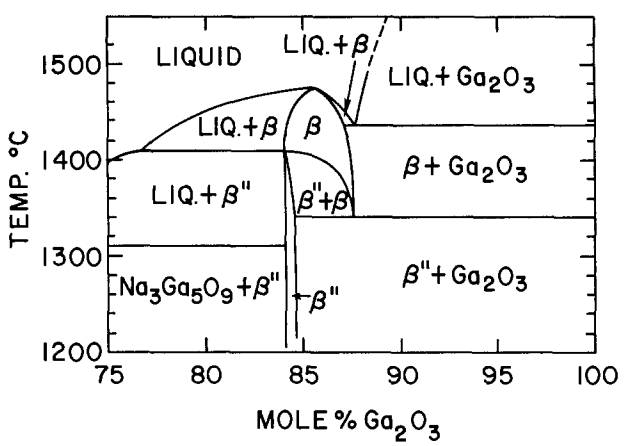


Fig. 1. Na_2O-Ga_2O_3 phase diagram proposed by Boilot *et al.* (3).

* Electrochemical Society Active Member.

Key words: solid electrolytes, Na_2O-Ga_2O_3 system, phase diagrams.

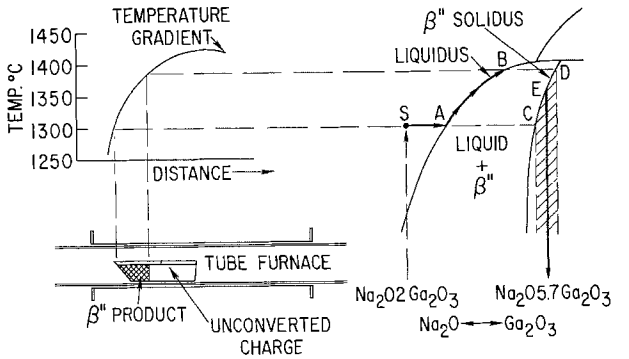


Fig. 2. Procedure for growth of β"-Na-gallate by Na_2O evaporation.

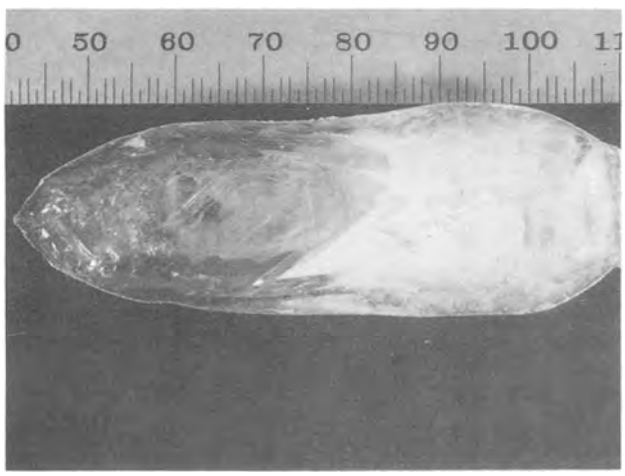


Fig. 3. Na_2O-Ga_2O_3 charge partially converted to β"-Na-gallate (clear crystal in left-hand end).

The growth procedure is described by Fig. 2. A platinum boat with one end drawn out to a point was filled with a charge of composition $Na_2O \cdot 2Ga_2O_3$. This composition was found to be completely liquid at 1300°C. The practice that was generally followed was to melt down a powdered charge, allow this to freeze, add more charge, etc., until the boat was quite full. The boat was placed in the temperature gradient shown, with the cold end at about 1310°C. It was desirable to have the temperature fall off rapidly away from the hot end of the boat as well so that Na_2O vapor would condense there rather than back into the charge in the cold end of the boat. The temperature was very carefully controlled without cycling with a Eurotherm[1] controller.

Referring to Fig. 2, at the start of an experiment the melt in the cold end of the boat is at position S on the right-hand figure, with the composition $Na_2O \cdot 2Ga_2O_3$. As Na_2O evaporates from the boat the composition moves to the right until the liquidus is reached at A. Further Na_2O loss results in precipitation of β"-solid of composition C. As the end of the boat becomes filled with the growing solid, the advancing solid-liquid interface moves up the temperature gradient, the liquidus moves along the heavy curve from A toward B, and the composition of the solid moves from C toward D. The experiment must be stopped at approximately the point shown to avoid converting part of the charge to the β-phase.

In a representative experiment, with a starting charge of 30g in a boat of dimensions ½ × ½ × 2½ in., the condition shown in Fig. 2, with about 30% of the charge converted to β"-solid, was achieved in 2 weeks' time. This resulted from a 6.1% weight loss due to Na_2O evaporation from a charge whose initial composition was $Na_2O \cdot 2Ga_2O_3$. Figure 3 is a photograph showing a top view of the platinum boat with its contents

[1] Eurotherm Corporation, Reston, Virginia.

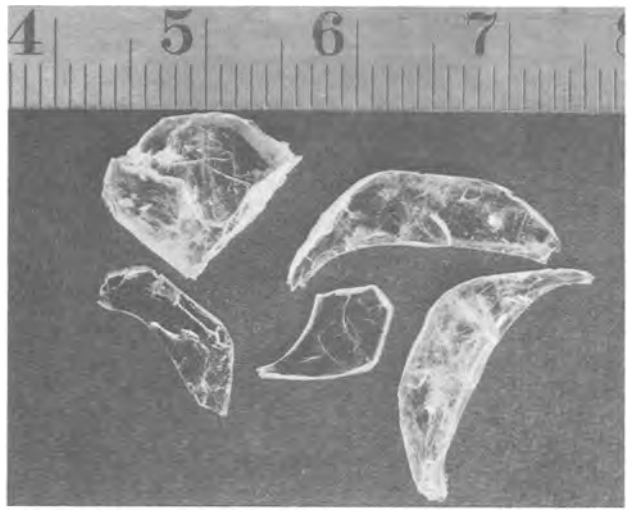


Fig. 4. β"-Na-gallate monocrystals

after a typical run. The entire mass of β"-solid was seldom one crystal, but monocrystals such as shown in Fig. 4 could be easily obtained by cleaving along obvious c planes.

The compositions of the liquidus at 1310°C (point A) was determined as $Na_2O \cdot 2.15Ga_2O_3$ in the following manner. A run was terminated just after β"-solid had begun to form in the cold end of the boat. The entire contents of the boat, excluding the small amount of β"-crystal, was then analyzed to obtain the average composition of the liquid that had been in equilibrium with the solid at the growth temperature.

A melt of $aN_2O \cdot 2.15Ga_2O_3$ composition freezes in the $3Na_2O \cdot 5Ga_2O_3$-$Na_2O \cdot 3Ga_2O_3$ two-phase field. A material balance calculation based on the original charge weight and composition and the Na_2O loss showed the frozen liquid to consist of 49% of $3Na_2O \cdot 5Ga_2O_3$ and 51% of $Na_2O \cdot 3Ga_2O_3$ by weight, in excellent agreement with an x-ray powder diffraction analysis of the ground and mixed residue which showed the two phases present in approximately equal proportions.

In principle, it should also be possible to determine the actual position of the solidus boundary, shown schematically running from C to D in Fig. 2, by analyzing the β"-solid that precipitated at positions in the boat corresponding to known temperatures. This was attempted in one case where the entire β"-solid was one crystal, fortuitously oriented with the c axis normal to the length of the boat so that a flat, clean surface running the entire length of the crystal (≃16 mm) could be exposed by cleaving. The sodium content was determined by electron microprobe analysis, sampling stepwise along the entire length of the crystal. The composition was $Na_2O \cdot 5.76Ga_2O_3$, at all positions with Na determined to ± 5%.

This finding can have two possible interpretations; either the solidus boundary is vertical from C to D, or the solid equilibrated after growth to some average composition indicated by the point E in Fig. 2. It is not possible to choose between these two interpretations. The fact that Na^+ is extremely mobile in an electric field or when it is being exchanged with other ions does not necessarily mean that composition equilibration would also be rapid, since this would be determined by the rate of the slower charge compensation process and not by the rapid Na^+ migration.

The lattice parameters of the β"-crystal are a = 5.84Å and c = 34.53Å. The space group is $R\bar{3}m$.

Discussion

This investigation has yielded large monocrystals of the rhombohedral β"-form of an alkali oxide-sesquioxide fast ion conductor for the first time in pure (*i.e.*, unstabilized) form. Roth *et al.* have presented argu-

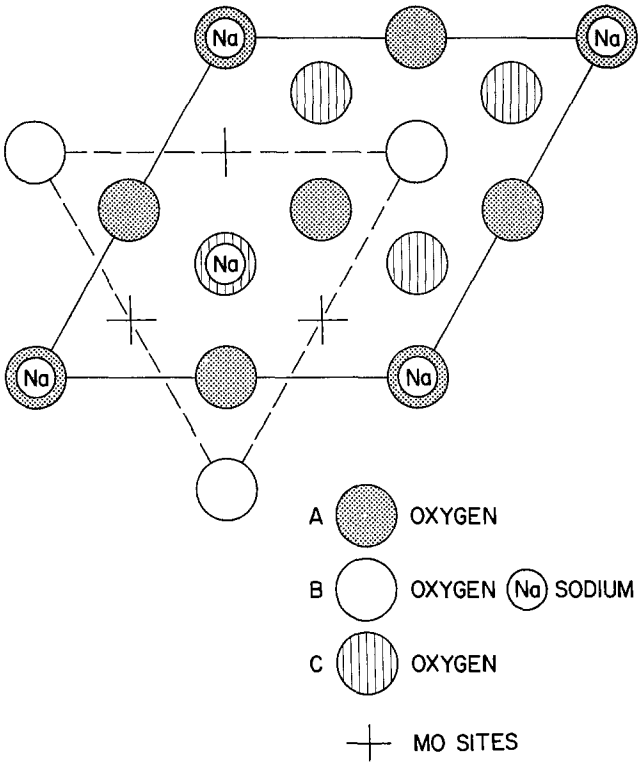


Fig. 5. Three oxygen layers of the β″-structure, including conduction plane. Na sites are shown full, but extra bridging oxygens in + sites required for compensation are not shown.

ments that Mg stabilization is necessary to produce the β″-phase in the aluminum system (5). They suggested that the action of the large Mg^{++} ion is to provide necessary strain relief when substituted for Al^{+++} at a tetrahedral site within the spinel block. In addition, the magnesium increases the concentration of Na^+ available for conduction, since each Mg^{++} that replaces an Al^{+++} is presumably accompanied by a Na^+ for charge compensation. Though Mg stabilization might be required in β″-Al_2O_3, it obviously is not required for the gallium analog. This is additional justification for working in the gallium system, since the basic processes of ionic mobility and conduction can be studied without complications due to the presence of a foreign ion whose role is not completely understood.

Since the β″-gallate that is grown by the present method precipitates at the β″ solidus boundary, its composition is that of the most soda-rich edge of its solid solution phase field. (The composition range of the solid solution has not yet been established and might actually be very narrow.) This material thus has the highest equilibrium Na content possible in the β″-gallate structure. The composition of the product from the illustrative experiment that was described earlier was $Na_2O \cdot 5.76Ga_2O_3$, determined by electron microprobe analysis. In other experiments, the Ga_2O_3/Na_2O ratio ranged from a high of 5.75 to a low of 5.65 to 1, as determined by a more accurate spectrophotometric method. These differ by only about ± 1% in actual Na content, which is well within the precision of the method. A composition of $Na_2O \cdot 5.7Ga_2O_3$ is taken as an average of a considerable number of determinations.

The Na sites that were the Beevers-Ross (BR) and anti-Beevers-Ross (ABR) sites in the hexagonal β-structure (6) are equivalent sites in the rhombohedral β″-structure. They are shown filled in Fig. 5. There are two sites per conduction plane in the unit cell. With the composition $Na_2O \cdot 5.7Ga_2O_3$, there are on the average 1.93 Na atoms per plane; *i.e.*, the sites are 96.5% full. β″-Na-gallate is an excellent Na ion conductor (7), which is perhaps surprising in view of the low density of cation vacancies available, and it suggests that Na^+ migration is principally via the mid-oxygen (MO) spaces shown as + in Fig. 5.

If charge compensation for the additional sodium in the β″-phase over that in the ideal β-composition of $Na_2O \cdot 11Ga_2O_3$ is accomplished by additional bridging oxygens in the (MO) sites, as had been suggested by preliminary results of Kahn *et al.* (8), $0.93 \div 2 = 0.465$ additional sites would thus be occupied, leaving $3 - 0.465$ (MO) sites available to assist in conduction of the sodium.

Manuscript submitted July 6, 1976; revised manuscript received Oct. 27, 1976.

Any discussion of this paper will appear in a Discussion Section to be published in the December 1977 JOURNAL. All discussions for the December 1977 Discussion Section should be submitted by Aug. 1, 1977.

Publication costs of this article were assisted by IBM Corporation.

REFERENCES

1. L. M. Foster and H. C. Stumpf, *J. Am. Chem. Soc.*, **73**, 1590 (1951).
2. L. M. Foster and J. E. Scardefield, *This Journal*, **123**, 141 (1976).
3. J. P. Boilot, J. Thery, and R. Collongues, *Mater. Res. Bull.*, **8**, 1144 (1973).
4. R. J. Chicotka, Abstract 5, p. 16, The Electrochemical Society Extended Abstracts, Spring Meeting, Toronto, Canada, May 11-16, 1975.
5. W. L. Roth, F. Reidinger, and S. J. LaPlaca, Conference on Superionic Conductors, Chemistry, Physics and Applications, Schenectady, New York (May 1976).
6. C. A. Beevers and M. A. Ross, *Z. Kristallogr.*, **97**, 59 (1937).
7. G. V. Chandrashekhar and L. M. Foster, *Bull. Mater. Sci.*, In press.
8. A. Kahn, J. P. Boilot, and J. Thery, *Mater. Res. Bull.*, **11**, 397 (1976).

The Effects of Geometry on Diffusion-Controlled Chemical Reaction Rates in a Plasma

James F. Battey

International Plasma Corporation, Hayward, California 94544

ABSTRACT

The photoresist strip rate at the edge and center of an array of silicon wafers is calculated for an oxygen plasma. The etch rate at the edge is essentially independent of wafer diameter and spacing, whereas the etch rate at the center increases linearly with increasing wafer spacing and is inversely proportional to the square of wafer diameter. Thus, a plasma stripping or etching system has a processing rate which can be specified in silicon area per unit time. The degree of inhomogeneity between edge and center also depends on the probability of reaction when a reactive specie hits the photoresist. Experimental measurements confirm the predicted functional dependence, except with an oxygen plasma the strip rate at the center of the wafer varies inversely as the cube of the wafer diameter rather than as the square. The implication is that two atomic oxygen atoms react simultaneously with the photoresist, perhaps as $CH_2 + 2\,O \rightarrow CO + H_2O$, or more probably as $O + O + \text{wall} \rightarrow O_2 + \text{wall}$.

In most low pressure plasmas created by capacitively coupling rf energy into a cylindrical cross-section reactor, the glow discharge is confined to a region near the walls of the reactor. The effect is analogous to the electrical skin effect in a metal conductor. The electrical current is carried in this region and the active species are created in this region. In an oxygen plasma the active specie is atomic oxygen which has a sufficiently long life to diffuse through the interior of the reactor. If the flow rates are small, the concentration of atomic oxygen is substantially constant, apart from the region immediately adjacent to the walls.

If a boatload of silicon wafers is introduced in an oxygen plasma, the atomic oxygen must diffuse between the wafers in order to strip the photoresist. The strip rate is calculated for the edge of the wafer and the center of the wafer as a function of wafer spacing and diameter, background oxygen concentration, and probability that an oxygen atom reacts when it hits the photoresist. Experimental measurements are made to examine the predicted functional dependence.

The mathematical model is also applicable to calculating the degree of inhomogeneity across the face of a wafer in an etching plasma or in a diffusion operation.

Experimental Arrangement

The experimental work was done in an 8 in. diameter cylindrical quartz reactor 13 in. in length. A schematic of the apparatus is shown in Fig. 1. The back of the reactor is a spherical sectioned quartz dome, and the front is a flat quartz door. The gas is introduced into the reactor through a quartz manifold on the bottom of the reactor and parallel to its axis. The gas is exhausted by a forepump from the reactor through a quartz manifold on the top of the reactor and parallel to the reactor axis. The plasma is excited by a radio frequency generator operating at 13.56 MHz and coupled into the plasma through a 50Ω cable, a pi impedance matching network, and two half-cylinder metal electrodes placed around the outside walls of the cylindrical reactor. The top electrode is at electrical ground, and the bottom electrode oscillates between positive and negative voltage with the generator.

Key words: semiconductors, photoresist stripping, plasma etching.

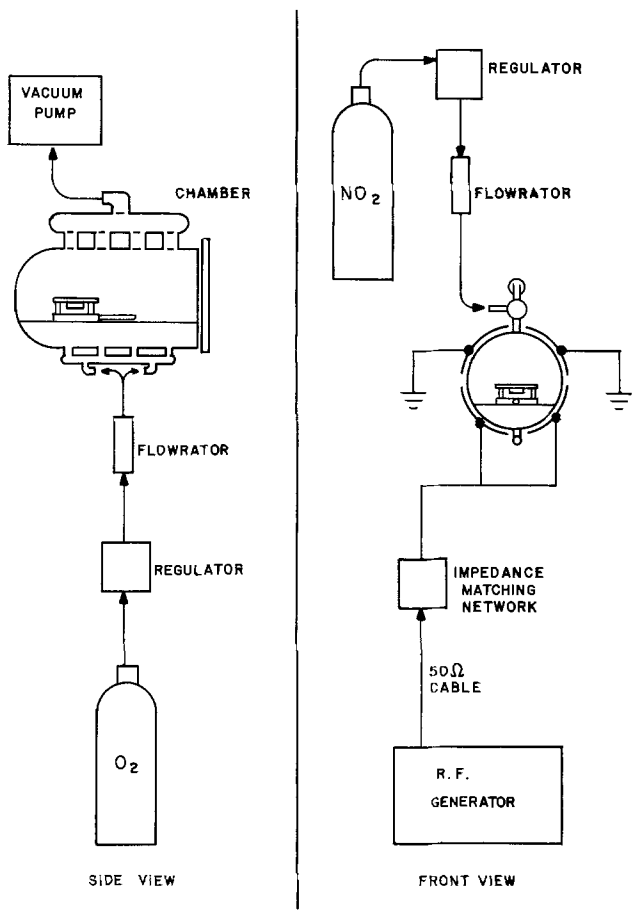


Fig. 1. Diagram of the experimental apparatus

The exhaust manifold is sufficiently large that the pressure drops in it are negligible, and the pressure in the reactor is measured with a Hastings VT4 vacuum gauge in a quartz tube leading out of the exhaust manifold. A metered flow of molecular oxygen is fed into the reactor from a cylinder of 99.6% minimum purity oxygen at high pressure through a regulator which reduces the pressure to approximately 1 atm,

and a flowmeter, which is connected to the inlet manifold. The rf power in the reactor converts some of the molecular oxygen to atomic oxygen, and the flow of atomic oxygen in the exhaust can be measured by titrating it (2) with a flow of NO_2 which is introduced into the quartz tube which extends out of the exhaust manifold.

In order to obtain reproducible stripping times, it was found necessary to put the single wafer on a large aluminum block which had a thermometer inserted in a hole in the block, and to place the block in the same position in the reactor. It was also found necessary to place two thermometers on the external walls of the reactor and require all three thermometers to assume the same temperatures as in a prior experiment.

An additional requirement for reproducibility of strip times is that the internal walls of the quartz reactor, the door, the inlet and exhaust manifolds, the aluminum block and its quartz support structure be cleaned using firepolishing with a glassblower's torch and acid etching. Quartz and aluminum oxide presumably have a lower surface recombination rate for atomic oxygen when they are "clean."

The presence of a second silicon wafer coaxial, parallel, and at a stipulated distance from the first wafer is simulated by a circular glass slide clamped to a heat sink which is thermally coupled to the heat sink on which the silicon wafer rests. The glass slide can be moved with respect to the silicon wafer by means of calibrated set screws.

The experimental procedure was to scrape the photoresist off a small area at the center and the edge of the wafer, measure the photoresist thickness with a Sloan Dektak surface profile measuring system, strip the wafer for a length of time sufficient to remove a significant amount, but not all, of the photoresist from the center and edge of the wafer, and measure the thickness of the residual photoresist.

Analysis

The difference in strip rate between the edge and center of a wafer in a linear array can be calculated, if an assumption is made about the probability that an oxygen atom will chemically react with the photoresist when it hits it.

Assume two 2 in. wafers parallel to one another spaced 3/16 of an inch apart with their surfaces parallel to an axis through their centers, with photoresist covering the facing surfaces. The problem is to calculate the concentration of atomic oxygen as a function of position between the wafers. If it is assumed that the primary method of atomic oxygen removal is by chemical reaction with the photoresist and volume recombination mechanisms can be ignored, and if it is further assumed that the by-products of the reaction are present in concentrations that have a negligible effect on the reaction rate, then the problem becomes mathematically the same as the conduction of heat in a solid cylinder with a radiation boundary condition at the photoresist-covered wafer surfaces and a constant oxygen concentration or temperature at the side of the cylinder formed by drawing lines between the edges of the wafers.

Let ν represent the atomic oxygen concentration, z represent the distance along the axis between the wafers, one of which is at $z = 0$ and the other at $z = \ell$, and r represent the radial distance from the center of the wafers to the edges which are at $r = a$. The radiation boundary condition equates the diffusion current into the wafers, $D \left.\frac{d\nu}{dz}\right|_{z=0}$, where D is the diffusion coefficient of atomic oxygen in molecular oxygen, to the reaction rate at the surface which is assumed (and we have shown experimentally) to be linear in ν. From kinetic theory the number of oxygen atoms striking the wafer surface per unit area and time is $\frac{1}{4}\bar{\nu}\nu$, where $\bar{\nu}$ is the average velocity. If p is the probability of reacting per strike, then the boundary condition can be written

$$D \left.\frac{d\nu}{dz}\right|_{z=0} = \frac{1}{4}\bar{\nu}p\nu(z=0)$$

or

$$\left.\frac{d\nu}{dz}\right|_{z=0} = h\nu(z=0)$$

where $h = \bar{\nu}p/4D$. Kinetic theory also says that $D \approx 1/3\,\bar{\nu}\lambda$ where λ is the mean free path so $h \approx 3p/4\lambda$. At 1 Torr $\lambda \approx 0.01$ cm so $h \approx 130$, and an experimental determination of h will give an approximate value of p.

The boundary condition that $\nu = \nu_0$ at $r = a$ assumes that the photoresist stripping process causes a negligible change in the atomic oxygen concentration outside the region between the wafers.

Since atomic oxygen generation or recombination between the wafers is assumed not to happen, conservation of atomic oxygen requires that ν be a solution to $\nabla^2\nu = 0$. The solution to the equation which conforms to the boundary conditions is (3)

$$\nu = 2\nu_0 \sum_{n=1}^{\infty} \frac{I_0(\alpha_n r)\{\alpha_n \cos \alpha_n z + h \sin \alpha_n z\}}{I_0(\alpha_n a)\{(\alpha_n^2 + h^2)\,\ell + 2h\}} \left\{ \sin \alpha_n \ell + \frac{h}{\alpha_n}(1 - \cos \alpha_n \ell) \right\}$$

where the α_n are the positive roots of

$$\tan \alpha \ell = \frac{2\alpha h}{\alpha^2 - h^2}$$

and

$$I_0(\alpha_n r) = \sum_{m=0}^{\infty} \frac{(\frac{1}{2}\alpha_n r)^2}{(m!)^2}$$

is the zero order solution to the modified Bessel equation. By the ratio test the series is absolutely convergent. Since the convergence is independent of z and r, it is uniformly convergent in any bound region. Thus ν and its derivatives are continuous functions of z and r, and term by term differentiation of its series representation is permissible. The chemical reaction rate at any point on the wafer is equal to the diffusion current at that point into the wafer, or

$$D \left.\frac{d\nu}{dz}\right|_{\substack{z=0 \\ r=a}} = 2D\nu_0 \sum_{n=1}^{\infty} \frac{\alpha_n h \left\{ \sin \alpha_n \ell + \frac{h}{\alpha_n}(1 - \cos \alpha_n \ell) \right\}}{(\alpha^2{}_n + h^2)\,\ell + 2h}$$

and

$$D \left.\frac{d\nu}{dz}\right|_{\substack{z=0 \\ r=0}} = 2D\nu_0 \sum_{n=1}^{\infty} \frac{\alpha_n h \left\{ \sin \alpha_n \ell + \frac{h}{\alpha_n}(1 - \cos \alpha_n \ell) \right\}}{\{(\alpha^2{}_n + h^2)\,\ell + 2h\} I_0(\alpha_n a)}$$

In numerically evaluating I_0 in the interval $r = 0$ to $r = a$, it should be noted that it is a power series, and the remainder value of the terms not calculated is equal to or less than the first term not calculated, evaluated at a.

As $\alpha_n \ell$ gets large

$$\tan \alpha_n \int = \frac{2\alpha_n \int h \int}{(\alpha_n \int)^2 - (h \int)^2}$$

$$\rightarrow (\alpha_n \int)^2 - (n-m)\pi\alpha_n \int - 2h \int \cong 0$$

if $\alpha_n >> h$, and m is the number of the first root to fall in the first quadrant, and

$$\alpha_n \int = \frac{1}{2}(n-m)\pi + \frac{1}{2}[(n-m)^2\pi^2 + 8h \int]^{1/2}$$

$$\cong (n-m)\pi + \frac{2h \int}{(n-m)}\pi$$

if $(n-m)\pi >> 8h \int$. Also

$$\sum_{n-m=r}^{\infty} \frac{\alpha_n h \left\{ \sin \alpha_n \int + \frac{h}{\alpha_n}(1 - \cos \alpha_n \int) \right\}}{(\alpha_n^2 + h^2) \int + 2h}$$

becomes

$$\sum_{n-m=r}^{\infty} \frac{2h^2 \int}{(n-m)^2\pi^2}$$

for even $n-m$, and goes to zero for odd $n-m$. Now

$$\sum_{n-m=2}^{\infty} \frac{1}{(n-m)^2_{\text{even}}} = \frac{\pi^2}{24}$$

so the remainder, Re, for even $n-m$ is

$$\text{Re} \equiv \sum_{n-m=r}^{\infty} \frac{\alpha_n h \left\{ \sin \alpha_n \int + \frac{h}{\alpha_n}(1 - \cos \alpha_n \int) \right\}}{(\alpha_n^2 + h^2) \int + 2h}$$

$$\cong \frac{2h^2 \int}{\pi^2} \left\{ \frac{\pi^2}{24} - \sum_{n-m=2}^{n-m=r-1} \frac{1}{(n-m)^2} \right\}$$

The reaction rates at the edge of the wafer and at the center were calculated for values of h of 25, 2.5, 0.25, 0.025, and 0.0025. The results are shown in Table I. For the reaction rate at the edge of the wafer, 32 terms are calculated for $h = 25$, 5 for $h = 2.5$ and 0.25, 3 for $h = 0.025$, and 2 for $h = 0.0025$ before calculating Re. A single term is adequate for the reaction rate at the center in all instances. The terms corresponding to values of $\alpha_n \int$ lying close to odd $n\pi$'s are quite uncertain since $\sin \alpha_n \int + \frac{h}{\alpha_n}(1 - \cos \alpha_n \int)$ is the difference between two approximately equal numbers. However, since these terms are small, it does not make much difference.

The root equation can be written so that it is a function of $h \int$ and $\alpha \int$. Thus the roots listed here can be used for a different $\int$ spacing by making an appropriate adjustment of the h values. Thus, the $\alpha_n \int$'s calculated here for 3/16 in. spacing can be used for 3/8 in. spacing by associating them with h values smaller by a factor of two than those listed here. Also, by symmetry, the case of one of the facing wafer surfaces coated and a 3/16 in. spacing corresponds to both faces coated at a 3/8 in. spacing.

Similarly

$$\left. \frac{1}{D\nu_0} D \frac{d\nu}{dz} \right|_{\substack{z=0 \\ r=a}}$$

can be written so that it is equal to the product of h and a function that depends only on $h \int$ and $\alpha \int$, *i.e.*

$$h \sum_{n=1}^{\infty} \frac{2\alpha_n \int \left\{ \sin \alpha_n \int + \frac{h \int}{\alpha_n \int}(1 - \cos \alpha_n \int) \right\}}{(\alpha_n \int + h \int)^2}$$

Thus, the value of the function for a different $\int$ can be found by taking the value calculated here for 3/16 in. spacing but at an h value appropriate for the $h \int$ product physically desired. Thus, the functions calculated here for 3/16 in. spacing can be used for 3/8 in. spacing by taking its value for an h that is twice the value physically desired.

In Table I it can be observed that the calculated values of

$$\left. \frac{1}{D\nu_0} D \frac{d\nu}{dz} \right|_{\substack{z=0 \\ r=a}}$$

are equal to h within a few percent for h of 25 or 2.5, and more closely than that for smaller values of h. The implication of this is that the value of the function is substantially equal to one for any physically realizable values of h and values of $\int$ small enough for the assumed boundary conditions to be applicable. $1/D\nu_0 \, d\nu/dz = h$ is the condition for a single plane surface. Thus, the strip rate at the edge of a wafer array is substantially the same as for a single wafer.

If it is assumed that n CH_2 groups are removed for every oxygen atom consumed, the chemical reaction rate for a single wafer is $nhD\nu_0$. It is known that $h \approx 0.158$ cm^{-1} at 160°C from the difference in etch rates at the edge and center in these experiments. ν_0 has been measured by titrating the flow of atomic oxygen with NO_2 and is about 7.4×10^{14} at./cm³. It is not clear what value of D should be used due primarily to the uncertainty in the gas temperature. However, a value of 700 cm/sec² does not seem unreasonable. For the power and pressure associated with ν_0, the strip time is about 94 sec. There are about 4.25×10^{21} CH_2 groups per square centimeter, which leads to a value of n of about 550. Thus, although it has been shown that carbon monoxide and water vapor can inhibit the reaction and thus are probably by-products of the reaction, it seems clear that most of the photoresist must come off in larger atomic groups.

The roots and $D\, d\nu/dz \Big|_{\substack{z=0 \\ r=a}}$ do not depend on a, so the values of these quantities calculated here can be used for different diameter wafers. $D\, d\nu/dz \Big|_{\substack{z=0 \\ r=0}}$ is inversely proportional to $I_0(\alpha_n a)$. However, $I_0(\alpha_n a)$ is proportional to a^2, and the calculated values of $D\, d\nu/dz \Big|_{\substack{z=0 \\ r=0}}$ can be converted to a different diameter wafer by multiplying by the square of the ratio of the old diameter divided by the new diameter. For 4 in. wafers, the calculated values of $D\, d\nu/dz \Big|_{\substack{z=0 \\ r=0}}$ for 2 in. wafers should be divided by four.

If the values of h are small, $2\alpha h/\alpha^2 - h^2 \approx 2h/\alpha$, $\tan \alpha \int \approx \alpha \int \approx 2h/\alpha$, and $\alpha \approx (2h/\int)^{1/2}$. All the terms in the series summation for I_0 contain an α_n^2 and consequently are inversely proportional to $\int$. Thus, the strip rate at the center is proportional to $\int$.

Thus, increasing wafer diameter by a factor, f, leads to greater edge-to-center inhomogeneity in strip rates, which can be corrected by increasing wafer spacing by a factor f^2. Thus, a particular plasma stripping system has a capacity which can be specified in silicon area, independent of wafer diameter.

Table I. Calculated relative strip rates at the edge and center of an array of wafers as a function of the relative probability that an oxygen atom reacts when it strikes the photoresist

h	$\left. \frac{1}{D\nu_0} D \frac{d\nu}{dz} \right\|_{\substack{z=0 \\ r=a}}$	$\left. \frac{1}{D\nu_0} D \frac{d\nu}{dz} \right\|_{\substack{z=0 \\ r=0}}$
25	24.19	1.416×10^{-4}
2.5	2.442	7.712×10^{-3}
0.25	0.2494	0.04813
0.025	0.02500	0.02126
0.0025	0.002500	0.002458

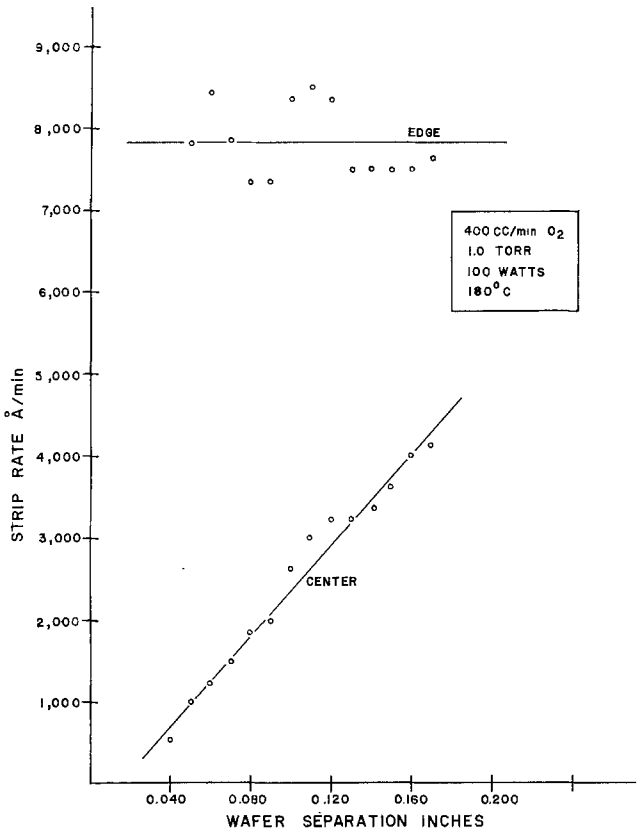


Fig. 2. Strip rate at the wafer edge and center as a function of wafer separation under conditions of constant molecular oxygen flow rate, pressure, and power. The edge strip rate is independent of separation, whereas the center strip rate is linear in separation.

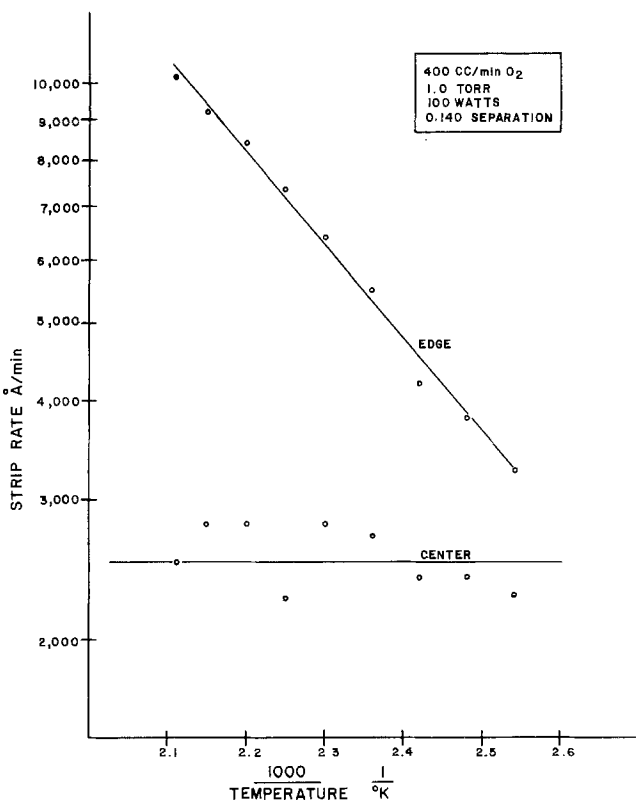


Fig. 3. Strip rate at the wafer edge and center as a function of temperature under conditions of constant molecular oxygen flow rate, pressure, and power. The edge strip rate varies exponentially as $-E/RT$, where E is approximately 6.5 kcal/mole. The center strip rate is approximately independent of temperature.

Experimental Results

The fact that $D\, dv/dz \Big|_{\substack{z=0 \\ r=0}}$ is proportional to $\int$ means that for small wafer spacing the center strip rate should be linear in $\int$ with a slope of 1 and, ignoring thermal effects and loading time, the wafer per hour capacity is independent of $\int$. It is seen in Fig. 2 that the strip rate is linear in $\int$. The reason for this is that larger wafer spacing allows more atomic oxygen between the wafers. If the wafer spacing becomes too large, the boundary condition that $v = v_0$ at $r = a$ becomes a poor approximation, and the analysis fails. Operation in the nonlinear region reduces the capacity of the equipment. The center strip rate experimentally approaches zero more rapidly at small $\int$ because $\int$ is approaching the mean free path which introduces an effect similar to a reduction in the diffusion coefficient.

In Fig. 3 the strip rate at the edge and the strip rate at the center are shown as a function of temperature. The strip rate at the edge varies exponentially as $-E/RT$ where E is about 6.25 kcal/mole. To a first approximation the strip rate at the center is independent of temperature in the range of 120°-200°C. It should be emphasized that this is not true at lower temperatures where the center strip rates are much longer. Also, it will no longer be true once a ring around the edge of the wafer has cleared. Thus, an additional specification on a plasma stripping system is the time to heat a load of wafers from room temperature to 120°C. The approximate temperature in-

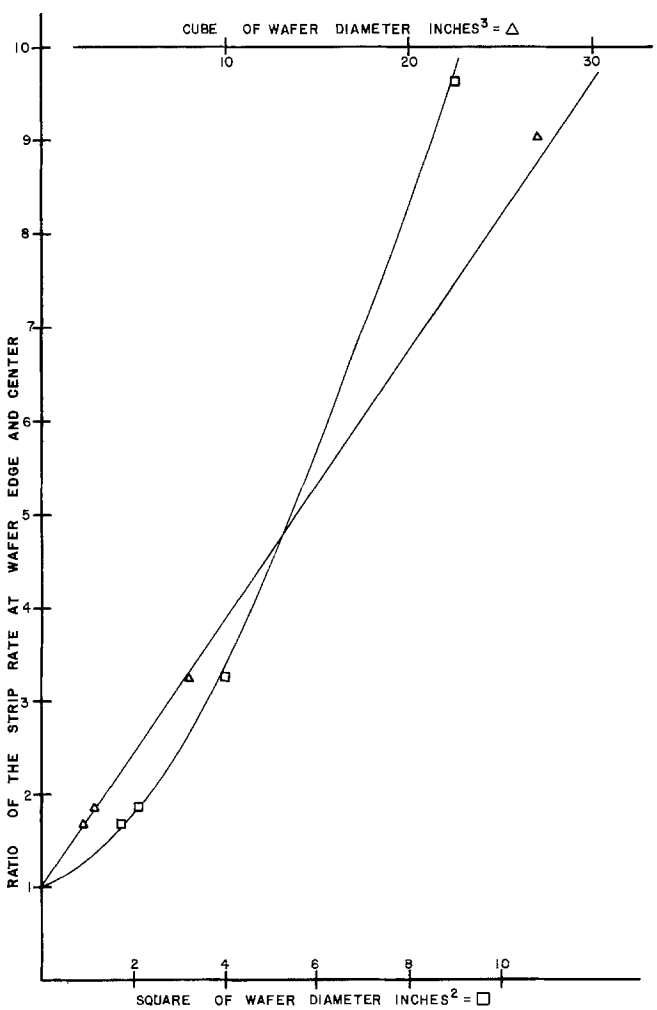


Fig. 4. The ratio of the strip rate at the wafer edge and center as a function of wafer diameter under conditions of constant molecular oxygen flow rate, pressure, and power. The edge strip rate is independent of wafer diameter. The center strip rate is inversely proportional to the cube of the diameter.

dependence of the center strip rate is explained by the fact that the product of the probability of the atomic oxygen atom reacting and the number that reach the center are approximately constant.

In Fig. 4 the ratio of the strip rate at the center of the wafer to the strip rate at the edge is plotted as a function of the square and cube of the diameter of the wafer. The absolute strip rates were not very reproducible, presumably due to varying surface recombination rates at the jigging which held the wafer and the slide. However, the ratios were within a standard deviation of about 10%. Contrary to the predictions of the analysis, it appears that the ratio varies more nearly as the cube of the diameter.

This can be qualitatively understood if it is assumed that two atomic oxygen atoms simultaneously react with a CH_2 group to form CO and H_2O, or an appreciable amount of the atomic oxygen recombines in a three-body reaction involving two oxygen atoms and the wafer. The latter explanation seems more probable since other experiments have shown the strip rate to be linear in oxygen concentration. Three bodies are needed to simultaneously conserve energy and momentum. The correct boundary condition to $\nabla^2 \nu = 0$ would then involve equating the diffusion current of oxygen atoms into the wafer surface to a term proportional to the square of the oxygen atom concentration at the surface.

Wafers of a given diameter have a certain ratio of oxygen concentration and strip rate at the edge and center. A larger wafer may be thought of as a wafer of the smaller diameter surrounded by an additional ring. The ratio of oxygen concentration and strip rate at the smaller diameter and center should be the same for the larger wafers as for the smaller wafers. However, the ratio at the larger diameter to the smaller diameter would be lower for the square law than the linear boundary condition for the larger wafers because the region is one of higher atomic oxygen concentration than the region inside the smaller diameter. If the atomic oxygen concentration and strip rate are presumed to be a fixed quantity at the edge of the wafers, these quantities will be lower at the smaller diameter and center of the larger wafers than the linear boundary condition predicts. Thus, the square law boundary condition has the effect of making the ratio of the strip rate at the center to the edge have a larger than square law dependence on the diameter of the wafers.

Manuscript received Sept. 2, 1976.

Any discussion of this paper will appear in a Discussion Section to be published in the December 1977 JOURNAL. All discussions for the December 1977 Discussion Section should be submitted by Aug. 1, 1977.

Publication costs of this article were assisted by the International Plasma Corporation.

REFERENCES

1. J. F. Battey, *IEEE Trans. Electron Devices*, **ed-24**, 140 (1977).
2. A. T. Bell and K. Kwong, *AIChE J.*, **18**, 990 (1972).
3. H. S. Carslaw and J. C. Jaeger, "Conduction of Heat in Solids," p. 220, Clarendon Press, Oxford (1959).
4. J. F. Battey, *This Journal*, **124**, 147 (1977).

Liquid Phase Epitaxial Growth of Semi-insulating GaAs Crystals

Mutsuyuki Otsubo and Hidejiro Miki

Mitsubishi Electric Corporation, Central Research Laboratories, Itami, Hyogo 664 Japan

ABSTRACT

Semi-insulating GaAs crystals were grown by liquid phase epitaxy from a Ga solution doped with Cr metal. The room temperature resistivity of the layers was $10^{-2} \sim 10^{7}$ Ω · cm, depending on the doping concentration of Cr, the background donor concenetration, arsenic vapor pressure, and the cooling rate. It was found that the grown layers became semi-insulating only when the background donor concentration of the undoped layer is lower than 1.0×10^{15} cm^{-3}. Higher arsenic vapor pressure and the higher cooling rate give layers with higher resistivity. The threshold voltage, at which the *I-V* curve changes from linear to $V^{3\sim4}$ dependence, varies with the square of the thickness with electron injecting contacts. The activation energy obtained from the temperature dependence of resistivity increases as the room temperature resistivity increases. The highest obtained was 0.71 eV.

Semi-insulating GaAs crystals have been widely used as the substrates for microwave devices such as planar-type Gunn diodes, Schottky barrier gate field effect transistors (MESFET's), and integrated circuits.

Semi-insulating GaAs bulk crystals can be grown from melt by O_2 doping (1-3) and Cr doping (4). In O_2-doped semi-insulating GaAs crystals, however, it is difficult to produce a homogeneous crystal over an ingot (3, 5-6) and the resistivity in the crystal is readily changed by heat-treatment (5, 7). From these points of view, bulk semi-insulating crystals are currently produced from melt by Cr doping. Cronin and Haisty (4) showed that the solubility of Cr in GaAs is on the order of 10^{17} cm^{-3} and an effective segregation coefficient is 6.4×10^{-4}. So, more than $10^{19} \sim 10^{20}$ cm^{-3} of Cr should be added to the melt in order to compensate the background donor concentration of $10^{16} \sim 10^{17}$ cm^{-3}. Such a high Cr concentration in the melt suggests the presence of a second phase.

In applications for microwave devices such as planar-type Gunn diodes and MESFET's, the device performances at higher frequency are affected by the semi-insulating substrate properties (8-9). The most successful technique is use of an epitaxial buffer layer between a semi-insulating substrate and an epitaxial layer (10-11). The buffer layer must be high quality with very low net doping and, it is hoped, with lower total impurity content than the substrate materials. So epitaxial growth technology is required for the preparation of semi-insulating GaAs films with higher quality.

The semi-insulating GaAs crystals with room temperature resistivities greater than 10^{8} Ω · cm can be grown from vapor phase by using chromyl chloride

Key words: high resistivity materials, III-V compounds, field effect transistors, chromium metals, planar devices.

(CrO_2Cl_2) as a doping agent (12). On the other hand, semi-insulating GaAs crystals have not yet been obtained from liquid phase by Cr doping because it had been considered that Cr acted as a shallow donor (13). However, we have obtained semi-insulating crystals from liquid phase by Cr doping (14).

This paper describes the preparation and properties of the Cr-doped epitaxial semi-insulating GaAs crystals grown by liquid phase epitaxy.

Experimental

Apparatus.—Liquid phase epitaxial growth was performed by a conventional tipping technique (15) and a sliding technique (16). A glassy carbon boat and a graphite boat, which were baked at 900°C for several hours under a Pd-diffused H_2 gas flow, were used for the tipping and sliding techniques, respectively.

Growth solution.—A Ga solution (99.99999%) is saturated at the tip temperature with the undoped boat-grown GaAs polycrystal and then heated at 900°C for 10 hr under an H_2 gas flow prior to the doping experiment of Cr. A massive Cr metal (99.999%) was added into the Ga solution without any cleaning. The Ga solution was heated at 900°C for 3 hr under an H_2 gas flow for every growth.

Substrate.—Growth was carried out mainly on the semi-insulating, Cr-doped, <100> oriented GaAs substrate. Si-doped n^+-crystal was sometimes used for investigating the current-voltage (I-V) curve of the epitaxial semi-insulating layer. These wafers were sliced within 1° from the (100) plane and then lapped with 4000 mesh Al_2O_3 abrasive. After being degreased and rinsed, they were chemically etched with $3H_2SO_4$-$1H_2O_2$-$1H_2O$ prior to the epitaxial growth.

Liquid phase epitaxial growth.—Epitaxial growth was performed at the tip temperatures ranging from 700° to 850°C with cooling rates of 0.1 ~ 7.0°C/min. The details of the growth procedure were reported previously (17). The background donor concentration, C_B, which is defined by the carrier concentration of the layer grown without any Cr doping, was varied by adding a known amount of Sn into the solution.

Resistivity measurement.—The resistivity of the epitaxial layer was obtained by measuring the resistance of the rectangular shaped samples which were cut down from the epitaxial wafers scraped off the substrate. Ohmic contacts to the end of the sample were made by soldering In dots at 450°C for 90 sec under an H_2 gas flow. In order to determine whether the In contacts were ohmic or not, the resistance of the rectangular shaped semi-insulating bulk crystal was measured by the four-probe method with different intervals. Resistivities of these samples were 4.0 ~ 6.4 × 10^7 Ω · cm. Thus, it seems that In contacts may be used for resistivity measurement. The resistance of the sample was measured in the dark using an electrometer (TR-8651).

Evaluation of the epitaxial layers.—Etch pits on a (100) surface were revealed by etching the epitaxial wafer in molten KOH (18) for 5 min and were then observed by an optical microscope. Inclusions were detected by x-ray microanalysis.

Results and Discussion

Preparation of Epitaxial Semi-insulating GaAs Crystals

Effect of background donor concentration on the resistivity of the epitaxial layers.—Figure 1 shows the relation between the resistivity of the epitaxial layer and the content of Cr added into a Ga solution for various C_B. The epitaxial layers were grown at a tip temperature of 800°C with a cooling rate of 2.5°C/min. Flow rate of an H_2 gas was 0.8 liter/min. The resistivity of the layer was increased by increasing

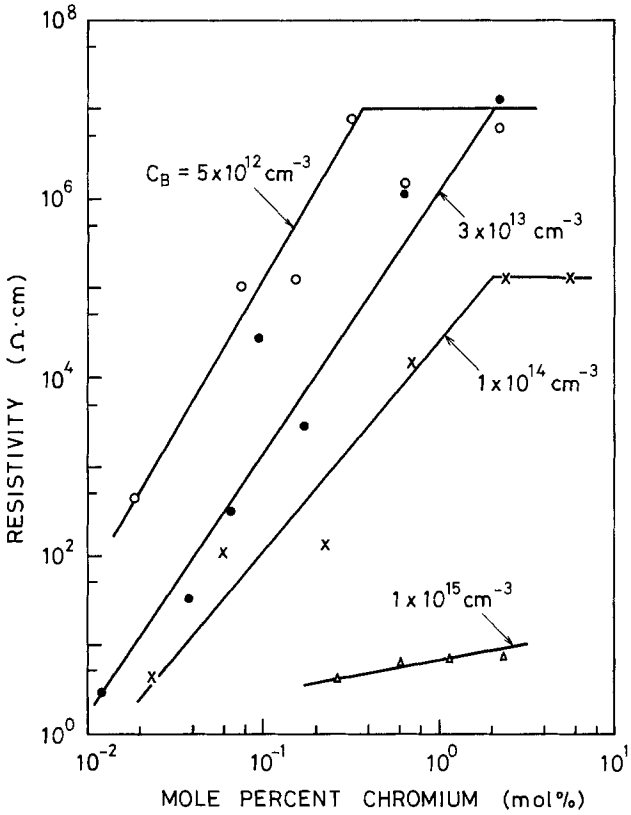


Fig. 1. Relation between the resistivity in the epitaxial layers and the content of Cr to be added to a Ga solution for various background donor concentrations. The epitaxial growth was performed at a tip temperature of 800°C with a cooling rate of 2.5°C/min.

the content of Cr in the solution. The epitaxial semi-insulating layers with room temperature resistivity greater than 10^7 Ω · cm were obtained when C_B was less than 3.0 × 10^{13} cm^{-3}. It was found that the layer becomes semi-insulating only when C_B is lower than 1.0 × 10^{15} cm^{-3} under these growth conditions. It is important to reduce C_B in producing higher quality semi-insulating GaAs layers.

Figure 2 shows the relation between the content of Cr in a solution and the resistivity of the layer grown at a tip temperature of 850°C with a cooling rate of 2.5°C/min. Under these growth conditions, the undoped layers were p-type with the free hole concentrations on the order of 1.0 × 10^{13} cm^{-3}. The resistivity of the layers was almost the same as that of undoped layers even though 3.4 mole percent (m/o) Cr was added to the solution and thus the semi-insulating layers had not been obtained. When 0.02 m/o Sn was added to the solution in addition to the 3.4 m/o Cr, however, semi-insulating layers with room temperature resistivity greater than 10^5 Ω · cm were obtained. This is thought to result from the fact that Cr in GaAs appears to act as an electron trap, reducing the donor concentration. Accordingly, if the grown layer is expected to turn out p-type, then donor impurities should be added to a level in excess of the expected acceptor concentration. The same situation has been observed in producing bulk semi-insulating GaAs crystals from melt by Cr doping.

Effect of cooling rate on the resistivity of the epitaxial layers.—Figure 3 shows the effect of cooling rate on the resistivity of the epitaxial layers. In this experiment, the epitaxial growth was performed under the conditions of a tip temperature of 800°C, Cr content in the solution of 0.8 m/o, and C_B of 1.0 × 10^{13} cm^{-3}. The numbers in Fig. 3 indicate the growth sequence. The resistivity of the epitaxial layers increases exponentially with the cooling rate up to

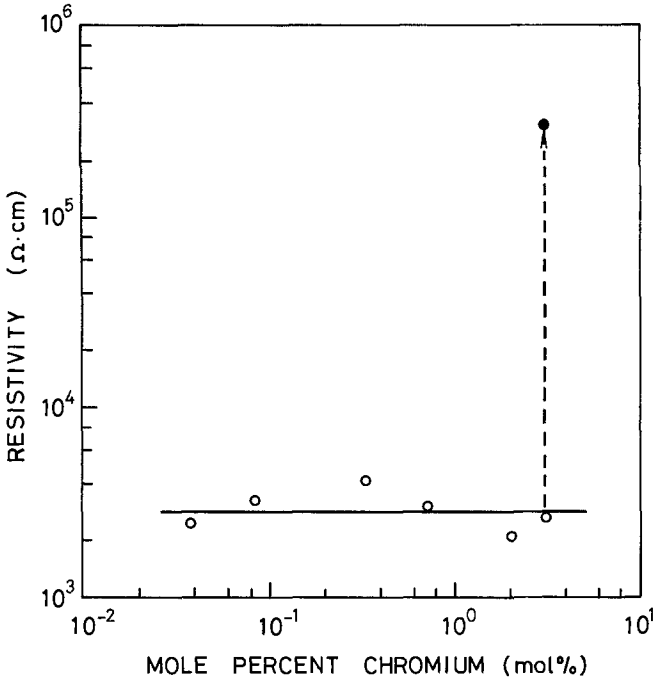


Fig. 2. Relation between the resistivity in the epitaxial layers grown at a tip temperature of 850°C with a cooling rate of 2.5°C/min and the content of Cr for the background hole concentration of 1.0 × 10^{13} cm^{-3}. A closed circle is the resistivity of the layer grown by using a Ga solution containing 0.02 m/o Sn in addition to 3.4 m/o Cr.

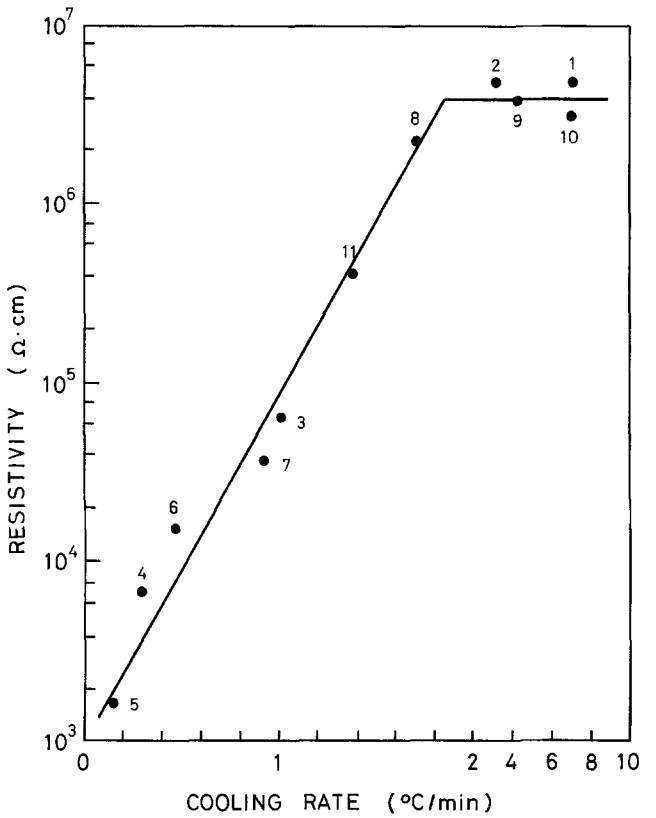


Fig. 3. The effect of cooling rate on the resistivity of the epitaxial layers grown at a tip temperature of 800°C with the doping concentration of Cr of 0.8 m/o and the background donor concentration of 1.0 × 10^{13} cm^{-3}.

1.8°C/min and is then constant, independent of the cooling rate greater than 1.8°C/min. This is supposed to be due to the fact that the rapid cooling rate results in local As supersaturation at the solid-liquid interface and a reduction in As vacancy concentration (19). Also, a change in impurity incorporation associated with cooling rate is expected. This may result in an increase in the effective segregation coefficient of Cr. It is presumed from this experiment that Cr atoms occupy Ga sites and/or complexes associated with Ga vacancies and introduce an electron trap. Fistul *et al.* (20) showed in their investigation of the electron paramagnetic and spin resonance that Fe atoms occupied Ga sites in the Fe-doped semi-insulating GaAs grown from melt. The same situation was observed in the Cr-doped semi-insulating GaP. It is known that Cr atoms replace the Ga atoms in the lattice of GaP (21).

Effect of arsenic vapor pressure on the resistivity of the epitaxial layers.—In order to confirm this hypothesis, the epitaxial growth was performed under a mixed gas atmosphere, a Pd-diffused H_2 gas, and an arsenic vapor. The apparatus used in this experiment is schematically shown in Fig. 4. This is similar to that used by Nelson (15) except that another Ga-GaAs solution (second solution), which supplies an arsenic vapor downstream, is added in addition to a growth Ga-GaAs solution (first solution). An arsenic vapor evaporated from the second solution, which is transported to the region of the first solution, suppresses the evaporation of arsenic from the first solution. It is supposed that this gives higher arsenic concentration at the solid-liquid interface. The details of the growth procedures have been reported previously (22). The epitaxial growth was carried out under the following conditions; a tip temperature of 800°C, a cooling rate of 0.9°C/min, Cr content in the first solution of 0.8 m/o, and GaAs content in the second solution of 2.4 m/o. Results are shown in Fig. 5, in which group a and group b

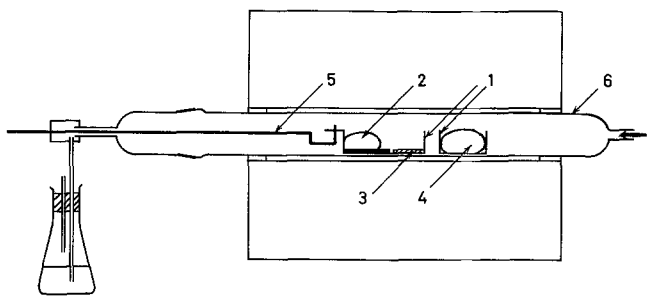


Fig. 4. Schematic diagram of the epitaxial growth apparatus for investigating the effect of adding arsenic vapor into an H_2 gas on the resistivity of the epitaxial layers. 1. Glassy carbon boat, 2. first solution, 3. substrate, 4. second solution, 5. pulling rod, 6. quartz tube.

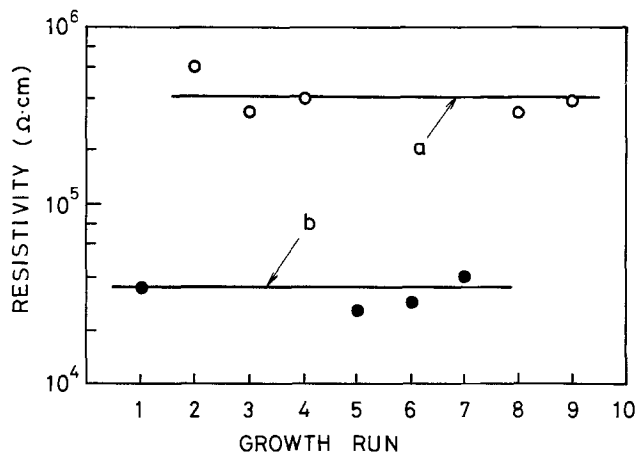


Fig. 5. The effect of the ambient gas on the resistivity of the epitaxial layers. Group a and b were grown under a mixed and an H_2 gas atmosphere, respectively. The layers were grown at a tip temperature of 800°C with a cooling rate of 0.9°C/min with a content of 0.8 m/o Cr.

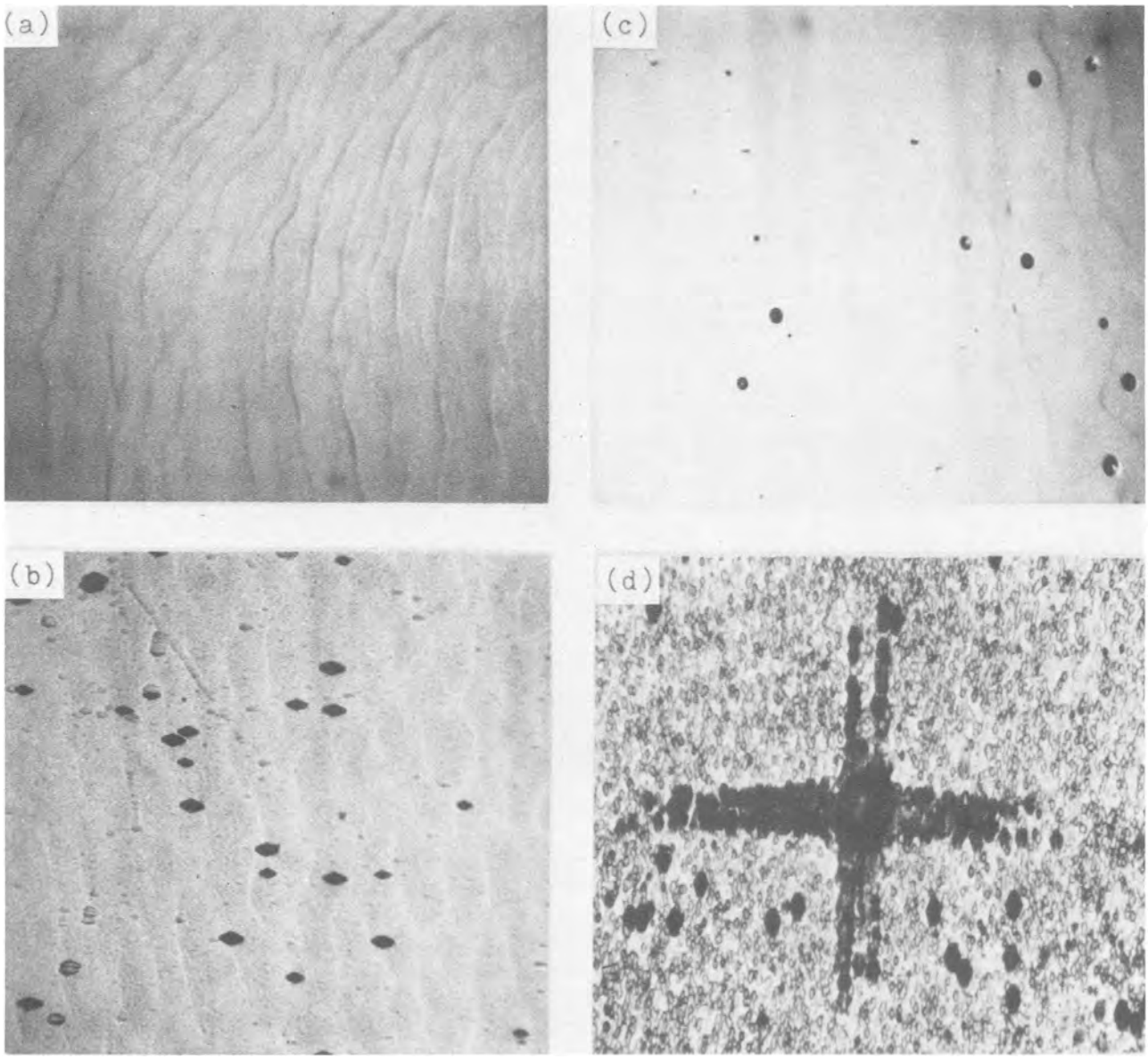


Fig. 6. Microphotographs of as-grown (a, c) and etched (b, d) surfaces in the crystals grown from a Ga solution containing 1.2 m/o Cr (a, b) and 2.2 m/o Cr (c, d). The epitaxial layer surfaces were etched with molten KOH.

show the resistivities in the epitaxial layers grown under a mixed gas and an H_2 gas atmosphere, respectively. The numbers in Fig. 5 stand for growth sequence. The resistivity of the layer grown under a mixed gas atmosphere (a) was one decade higher than that of the layer grown under an H_2 gas atmosphere (b). Growth rate was increased in group a by an amount of 5 $\sim$ 10%. Figure 5 also seems to suggest that Cr atoms occupy Ga sites and/or form complexes associated with Ga vacancies.

Surface morphology of the grown layers.—Figure 6 shows the surface morphology in the epitaxial semi-insulating layers. These layers were grown by a sliding technique at a growth temperature of 800°C. The surface morphology in the layer grown from the solution which contained less than 1.2 m/o Cr was little different from that in the layer without any Cr doping (a, b). However, when more than 2.2 m/o Cr was added in a solution, the grown layer contained inclusions as shown in Fig. 6c and dislocations along with <110> direction originated at inclusions were observed in Fig. 6d. These dislocations are thought to be generated by the difference in the thermal expansion coefficient between GaAs crystal and inclusions.

X-ray microanalysis.—These inclusions were examined by x-ray microanalysis. The Ga and Cr were detected but As was not. Although the composition of these inclusions has not yet been identified, we believe that these are Cr compounds associated with Ga. Gimelfarb *et al.* (23) showed that the inclusion in a Cr-doped bulk semi-insulating GaAs was composed of Cr compound associated with As. It is probable that such a difference is due to the difference in the growth method. From this experiment, Cr content in a solution should be less than 1.0 m/o at 800°C for producing homogeneous semi-insulating layers.

Preparation of n-Type Layers by Cr Doping

As mentioned above, it is thought that Cr atoms act as a shallow donor in the liquid phase epitaxially grown GaAs and that it is not possible to obtain semi-insulating layers from liquid phase by Cr doping (13). This is inconsistent with our experimental findings of the semi-insulating layer from liquid phase by Cr doping (14). So the epitaxial growth conditions for growing n-type layers by Cr doping were investigated.

Epitaxial growth of n-type GaAs layers by Cr doping.—Figure 7 shows the relation between the carrier

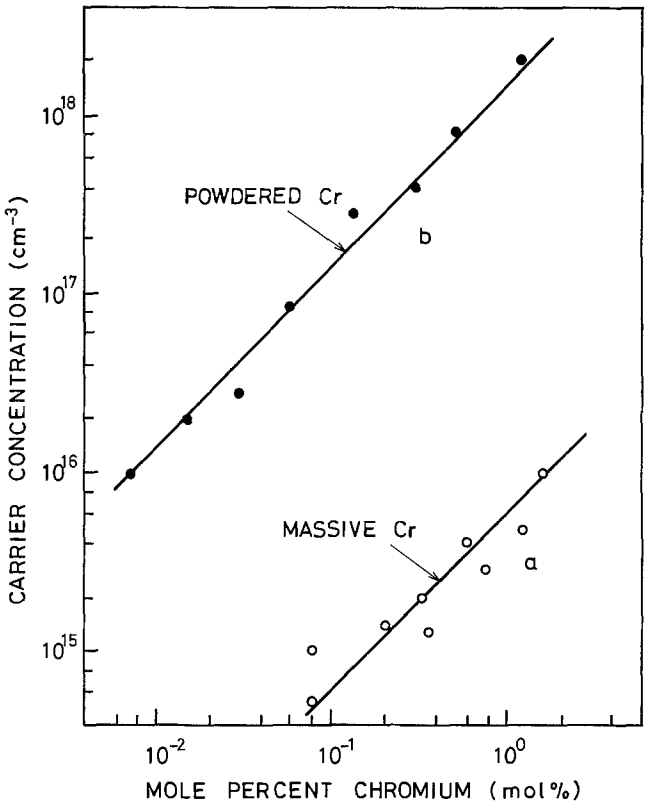


Fig. 7. Relation between carrier concentrations in the layers grown at a tip temperature of 700°C with a cooling rate of 2.5°C/min and the content of Cr in the solution. Groups a and b were grown by using Ga solutions doped with a massive Cr and a 100 mesh powdered Cr, respectively.

concentration of the grown layer and the content of Cr in a Ga solution. In the experiment, growth was performed at a tip temperature of 700°C with a cooling rate of 2.5°C/min. A massive Cr metal (99.999%) and a 100 mesh powdered Cr (99.9% up) were used as the dopants. In both cases, the donor concentration of the grown layer increases with increasing the content of the Cr added to the solution. These results might be taken to show that Cr atoms act as a shallow donor as first indicated by Andre *et al.* (13). However, as the Ga solution containing 1.0 m/o powdered Cr, resulting in the n-type layers with donor concentration of 10^{18} cm^{-3}, was heated at 900°C under a Pd-diffused H_2 gas flow, the resistivity of the grown layer increased with heating times. This is shown in Fig. 8. Figure 8 seems to indicate that the layer with the higher donor concentration is caused by contamination of oxygen in the dopant. It is well known that oxygen acts as a shallow donor in a liquid phase epitaxially grown GaAs (24). It is possible that the epitaxial layer with the higher resistivity was caused by evaporation of oxides due to heating the solution. The difference in the donor concentration in the two layers, one doped with a massive Cr metal and the other doped with a 100 mesh powdered Cr, is supposed to be due to the difference in the content of oxygen in the two dopants.

When the epitaxial growth was performed at a tip temperature of 800°C, the grown layer was still semi-insulating even if a solution doped with a massive Cr metal was used with no heating before epitaxial growth. This is due to the difference in the distribution coefficients of oxygen at 800° and 700°C. The distribution coefficient of oxygen is higher in the lower temperatures (17).

After all, it is possible that the origin of producing n-type layers with higher donor concentration by Cr doping is due to oxidation of Cr. These results indicate that it is necessary to heat the solution containing Cr under a purified H_2 gas flow at the higher temperature for producing the semi-insulating layers.

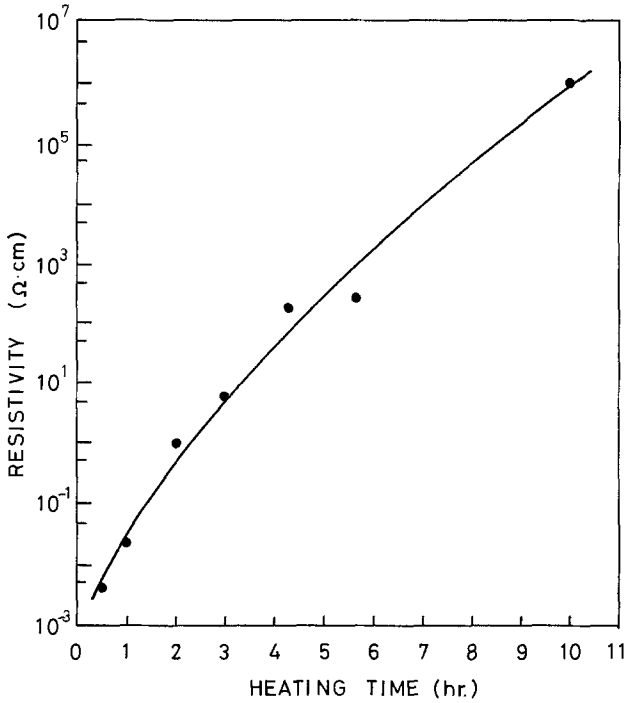


Fig. 8. Heating effect of a Ga solution containing 1.0 m/o powdered Cr. The solution was heated at 900°C under a Pd-diffused H_2 gas flow.

Electrical Properties of Semi-insulating GaAs Crystals

I-V curves.—Figure 9 shows *I-V* curves at room temperature for the epitaxial semi-insulating GaAs with various thicknesses (a-c) and for a bulk semi-insulating GaAs (d). The samples were n^+-i-n^+ shaped in structure. The epitaxial semi-insulating layer (10-40 μm thick) and the n^+ layers (Te doped,

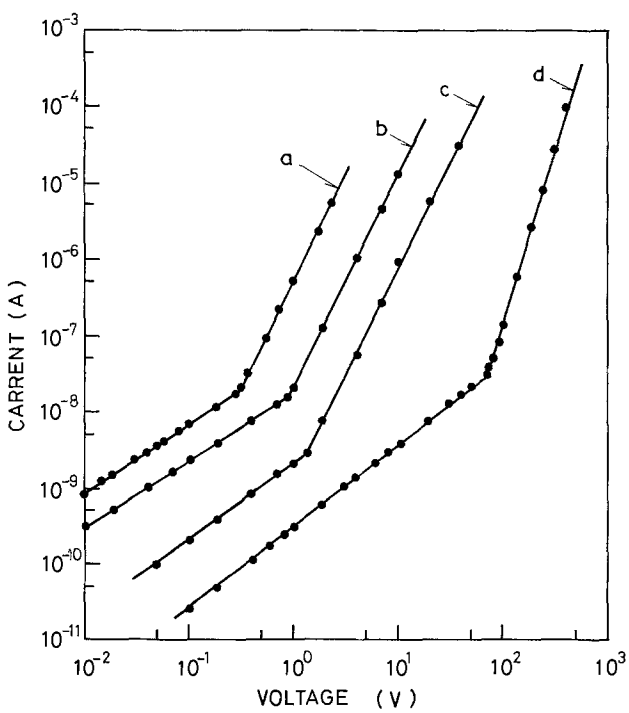


Fig. 9. Current-voltage curves for the epitaxial semi-insulating GaAs crystals with various thicknesses. The samples were n^+-i-n^+ shaped structures. (a-c) and (d) are for the epitaxial and a bulk crystals, respectively. The thicknesses of the samples are 13 μm for (a), 28 μm for (b), 40 μm for (c), and 240 μm for (d).

1-2 μm thick) with donor concentration of 7.0×10^{17} cm^{-3} were successively grown on the Si-doped n^+-substrate ($n \simeq 1.0 \times 10^{18}$ cm^{-3}) by a sliding technique. For a bulk semi-insulating GaAs, the n^+-layers were grown on both faces. Ohmic contacts to the n^+-layers were formed by alloying the evaporated Au-12 weight percent (w/o) Ge eutectic alloy at 450°C for 1 min under a flowing H_2 gas. The mesa-shaped structure was formed by etching with $3H_2SO_4$-$1H_2O_2$-$1H_2O$ through the Au-12 w/o Ge metal.

I-V curves obey Ohm's law at low voltages in all samples. Above a threshold voltage, *I* increases with $V^{3\sim4}$ for the epitaxial semi-insulating layers and with $V^{4\sim5}$ for a bulk semi-insulating GaAs, similar to what has been observed in a Cr-doped semi-insulating GaAs with electron injecting contacts (25). The resistivities of the samples calculated in the ohmic region were $1.0 \sim 9.0 \times 10^8$ $\Omega \cdot$ cm for the epitaxial semi-insulating layers and 1.1×10^9 $\Omega \cdot$ cm for a bulk crystal. The resistivities obtained from *I-V* curves are 1 ~ 2 orders higher than those obtained from the measurement of resistances in rectangular shaped samples. The origin of the difference in resistivity is unclear.

The threshold voltage, at which the *I-V* curve does change from linear dependence to $V^{3\sim4}$ dependence, varies with the square of the sample thickness. This is shown in Fig. 10. This behavior was similar to that observed in the undoped and the oxygen-doped bulk semi-insulating GaAs with electron injecting contacts (25-26) and was identical to the theory predicted by Lampert *et al.* (27, 28).

Heat-treatment.—Figure 11 shows the effect of heat-treatment on the epitaxial semi-insulating GaAs (a, b) grown under the different background donor concentrations, in which it is compared to that on a bulk semi-insulating GaAs (c). Heat-treatment was performed at the desired temperatures for 30 min under a purified H_2 gas flow. Samples a and b were grown under the background donor concentrations of 1.0×10^{13} cm^{-3} and 5.0×10^{14} cm^{-3}, respectively.

Figure 11 indicates that the change in the resistivity in the layer grown under the lower C_B has occurred at a temperature lower than that in the layer grown under the higher C_B. For sample a which was grown under the higher C_B, the resistivity began to decrease at 500°C and finally reduced to the value of the undoped layer followed by a gradual increase above 600°C.

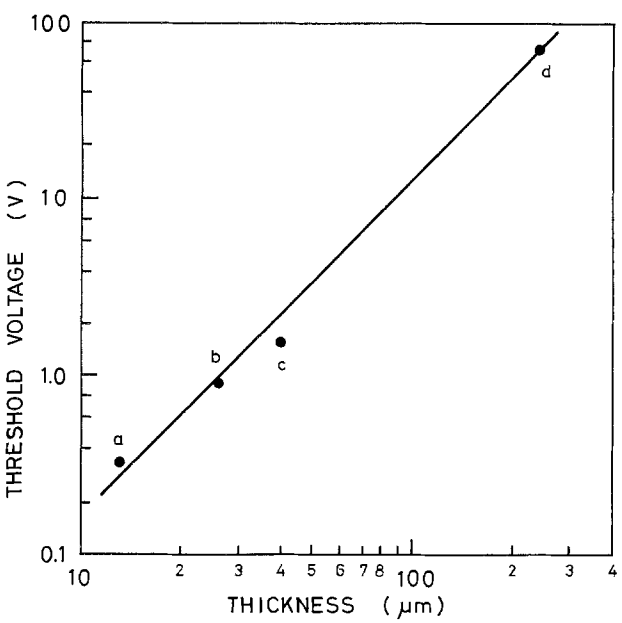


Fig. 10. Threshold voltages *vs.* thickness of the semi-insulating GaAs crystal with electron injecting contacts.

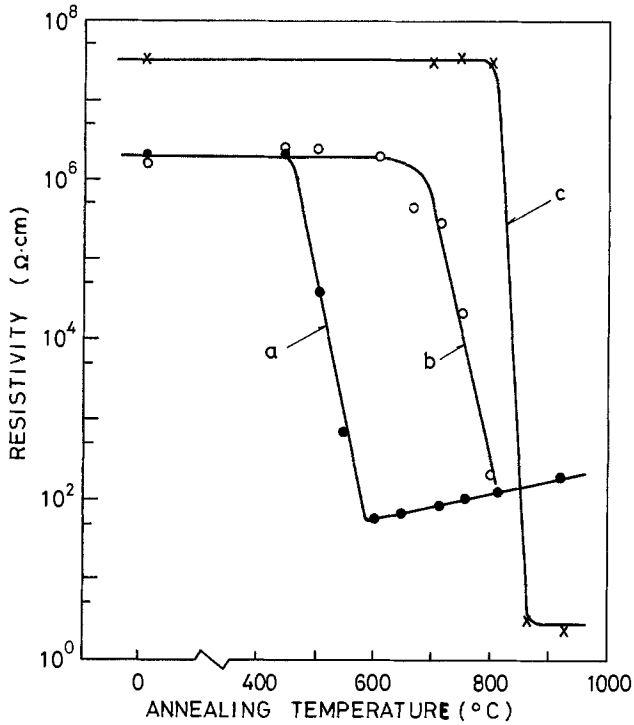


Fig. 11. The effect of heat-treatment on the epitaxial semi-insulating GaAs crystals grown under different background donor concentrations Samples a and b were grown under the background donor concentrations of 1.0×10^{13} cm^{-3} and 5.0×10^{14} cm^{-3}, respectively. Sample c is a bulk semi-insulating crystal. Heat-treatment was performed for 30 min under an H_2 gas flow.

While for sample b the resistivity began to decrease at 650°-700°C, which was higher than that in sample a. On the other hand, in a Cr-doped bulk semi-insulating GaAs (c), no change in the resistivity was observed at less than the heating temperature of 800°C, which was higher than that in the epitaxial semi-insulating samples.

Temperature dependence of the resistivity.—The resistivity in the rectangular shaped epitaxial semi-insulating GaAs was measured at various temperatures and the result is shown in Fig. 12. The resistivity increased exponentially with the reciprocal temperature in all samples with higher room temperature resistivities. The dependence of the activation energy on the room temperature resistivity has already been observed in GaAs (30) and GaP (31) and is well known as Meyer's rule. Although Meyer's rule has not been satisfactorily explained so far, the most likely explanation is thought to be a series of deep levels produced by several impurities (31). The highest activation energy obtained from Fig. 12 is 0.71 eV, which is nearly equal to the activation energy of Cr level of 0.74 eV (32).

Summary and Conclusions

Semi-insulating GaAs layers with room temperature resistivity in the order of 10^7 $\Omega \cdot$ cm have been obtained by liquid phase epitaxy by Cr doping. Preparation and properties of the epitaxial semi-insulating GaAs have been described.

The resistivity of the epitaxial layer increases with increasing the content of Cr added to a solution. Inclusions were present in the layers grown from the solution containing more than 2.0 m/o Cr. The epitaxial semi-insulating layers with higher quality were obtained by reducing the background donor concentration.

Higher cooling rates give layers with higher resistivities, and epitaxial growth under controlled arsenic pressure also gives an epitaxial layer with

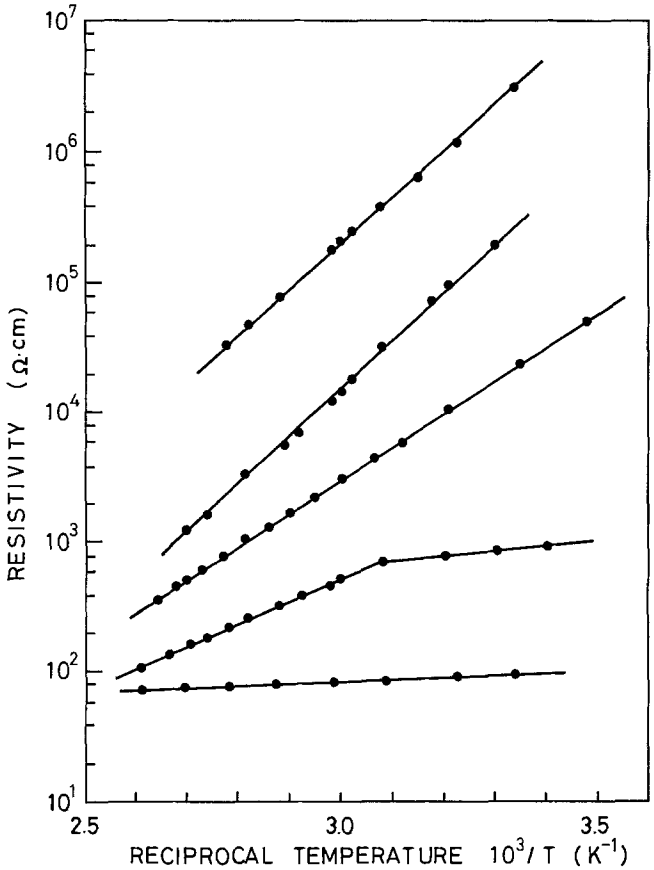


Fig. 12. Temperature dependence of resistivity in the epitaxial semi-insulating GaAs with different room temperature resistivity.

higher resistivity. It is possible that Cr atoms occupy Ga sites and/or form complexes with Ga vacancies.

It is possible that the origin of producing n-type layers with higher donor concentration by Cr doping is due to oxidation of Cr as a dopant.

Current-voltage curves obey Ohm's law at low voltages and above a threshold voltage, current increases in proportion to $V^{3\sim4}$. The threshold voltage varies with the square root of the thickness of the semi-insulating layer.

A decrease in resistivity of the sample due to heat-treatment was observed at lower temperature in the samples grown under lower background donor concentration.

The activation energy obtained from the temperature dependence of the resistivity is higher in the samples with higher room temperature resistivity. The highest one is 0.71 eV.

Acknowledgments

The authors wish to thank Mr. S. Kawazu for his helpful discussion on *I-V* curves and Mr. Y. Ogata and Mr. M. Demizu for measurement of x-ray microanalysis. The authors would like to thank Dr. K. Shirahata for encouragement throughout this work.

Manuscript submitted May 10, 1976; revised manuscript received Oct. 25, 1976.

Any discussion of this paper will appear in a Discussion Section to be published in the December 1977 JOURNAL. All discussions for the December 1977 Discussion Section should be submitted by Aug. 1, 1977.

Publication costs of this article were assisted by the Mitsubishi Electric Corporation.

REFERENCES

1. R. W. Haisty, E. W. Mehal, and R. Stratton, *J. Phys. Chem. Solids*, **23**, 829 (1962).
2. N. G. Ainslie, S. E. Blum, and J. F. Woods, *J. Appl. Phys.*, **33**, 2391 (1962).
3. J. F. Woods and N. G. Ainslie, *ibid.*, **34**, 1469 (1963).
4. G. R. Cronin and R. W. Haisty, *This Journal*, **111**, 874 (1964).
5. J. M. Woodall and J. F. Woods, *Solid State Commun.*, **4**, 33 (1966).
6. J. M. Woodall, *Trans. Metall. Soc. AIME*, **239**, 378 (1967).
7. R. Cox and E. W. Mehal, *ibid.*, **244**, 1809 (1968).
8. L. Cohen, F. Drago, B. Shortt, R. Socci, and M. Urban, Proceedings of the First International Symposium on GaAs, Institute of Physics, Phys. Soc., p. 153 (1969).
9. P. L. Hower, W. W. Hoper, D. A. Tremere, W. Lehrer, and C. A. Bittman, *ibid.*, p. 187.
10. N. A. Slaymaker and J. A. Turner, Proceedings of the European Microwave Conference Third, Brussels (1973).
11. T. Nozaki, M. Ogawa, T. Terao, and H. Watanabe, Proceedings of the Fifth International Symposium on GaAs and Related Compounds, Institute of Physics, p. 46 (1975).
12. O. Mizuno, S. Kikuchi, and Y. Seki, *Jpn. J. Appl. Phys.*, **10**, 208 (1971).
13. E. Andre and J. M. LeDuc, *Mater. Res. Bull.*, **4**, 149 (1969).
14. M. Otsubo and H. Miki, *Jpn. J. Appl. Phys.*, **13**, 1655 (1974).
15. H. Nelson, *RCA Rev.*, **24**, 603 (1963).
16. M. B. Panish, I. Hayashi, and S. Sumski, *J. Quantum Electron.*, **5**, 310 (1969).
17. M. Otsubo and H. Miki, *Jpn. J. Appl. Phys.*, **13**, 797 (1973).
18. J. G. Grabmaier and C. B. Walton, *Phys. Status Solidi*, **32**, K13 (1969).
19. M. Ettenberg and H. Kressel, *Appl. Phys. Lett.*, **26**, 478 (1975).
20. V. I. Fistul, L. Ya. Pernova, E. M. Omelyanovskii, E. P. Rashevskaya, N. N. Solovev, and O. V. Pelevin *Sov. Phys. Semicond. (Engl. Transl.)*, **8**, 311 (1974).
21. S. A. Abagyan, G. A. Ivanov, Yu. N. Kuzunetsov, Yu. A. Okunov, and Yu. E. Shanurin, *ibid.*, **7**, 989 (1974).
22. M. Otsubo and H. Miki, *Jpn. J. Appl. Phys.*, **14**, 621 (1975).
23. F. A. Gimelfarb, B. G. Girieh, M. G. Milvidskii, O. V. Pelevin, and V. I. Fistul, *Sov. Phys. Solid State (Engl. Transl.)*, **11**, 1612 (1970).
24. R. Solomon, Proceedings of the Second International Symposium on GaAs, Institute of Physics, p. 11 (1969).
25. R. W. Haisty and P. L. Hoyt, *Solid-State Electron.*, **10**, 795 (1967).
26. E. W. Mehal, R. W. Haisty, and D. W. Shaw, *Trans. Metall. Soc. AIME*, **233**, 596 (1965).
27. M. A. Lampert, *Phys. Rev.*, **103**, 1648 (1956).
28. M. A. Lampert, A. Rose, and R. W. Smith, *J. Phys. Chem. Solids*, **8**, 464 (1959).
29. Y. Sato, *Jpn. J. Appl. Phys.*, **12**, 242 (1973).
30. S. Akai, R. Shimoda, K. Watanabe, and K. Koe, *Sumitomo Denki*, **10**, 62 (1971).
31. M. L. Young and S. J. Bass, *J. Phys. D*, **4**, 995 (1971).
32. S. M. Sze and J. G. Irvin, *Solid-State Electron.*, **10**, 795 (1967).

Oxygen Ions in Individual Nitrate Melts

K. E. Johnson* and P. S. Zacharias

Department of Chemistry, University of Regina, Regina, Saskatchewan, Canada S4S 0A2

ABSTRACT

Sodium nitrate and potassium nitrate melts were electrolytically reduced using a Ag^+/Ag reference electrode and a platinum working electrode in platinum cells. Cyclic voltammograms recorded for the nitrate melts are presented and discussed. Electrolysis was carried out for the individual melts and the products identified chemically. The experimental data indicate the preferential formation of peroxide in $NaNO_3$ and superoxide in KNO_3 besides the primary reduction product, nitrite. Preliminary results on the colored platinum complex formed in the nitrate melts during electrolysis are also presented.

The electroreduction of nitrate ions in fused alkali nitrates has been the subject of numerous investigations by different workers during the past several years. The primary products of the electroreduction of the nitrate have been correctly identified (1, 2) as nitrite and oxide according to reaction [1] though other processes involving the production of nitrogen

$$NO_3^- + 2e^- \rightarrow NO_2^- + O^{2-} \qquad [1]$$

and different oxides of nitrogen were also thought to be occurring concomitantly (2, 3). The oxide species produced in the nitrate melt was regarded to be nonreactive under the experimental conditions on the basis of a simple Lux-Flood formalism. In contrast to this assumption, recent studies on oxide chemistry in molten $NaNO_3$-KNO_3 eutectic by Zambonin and Jordan (4) indicated that the oxide species is unstable in the melt conditions and is converted into peroxide and superoxide ions. These investigations were carried out using a rotating platinum electrode in platinum cells to avoid any side reactions involving silica and the moisture level was kept below 10^{-6}M. Further studies in pure $NaNO_3$-KNO_3 eutectic using voltammetric techniques (5) showed the following processes to be prevalent in the electrochemical reduction of nitrate at a platinum electrode

$$NO_3^- + 2e^- \rightleftharpoons NO_2^- + O^{2-}$$

followed by

$$O^{2-} + NO_3^- \rightleftharpoons NO_2^- + O_2^{2-} \text{ (fast)} \qquad [2]$$

$$O_2^{2-} + 2NO_3^- \rightleftharpoons 2NO_2^- + 2O_2^- \text{ (slow)} \qquad [3]$$

The presence of superoxide in $NaNO_3$-KNO_3 eutectic has been detected by EPR signals also (6).

The oxygen electrode in molten $NaNO_3$-KNO_3 eutectic at platinum or gold surfaces has been described as a superoxide electrode as in [4]

$$O_2 + e^- \rightleftharpoons O_2^- \qquad [4]$$

assuming greater stability for the superoxide (7). However, Fredericks and co-workers (8) state that the potentiometric results obtained at platinized electrodes are in agreement with reaction [5]

$$\tfrac{1}{2}\, O_2 + 2e^- \rightleftharpoons O^{2-} \qquad [5]$$

This implies a greater stability for the oxide ion in molten nitrates.

Bartlett and Johnson studied the reduction of $NaNO_3$ and KNO_3 individually and reported the formation of differently colored catholytes during electrolysis depending on the cathodes used (3). With a platinum cathode at controlled potential they observed the formation of green catholytes which were thought to be due to a platinum nitrosyl complex. If peroxide and/or superoxide are produced in the electroreduction of the nitrates as observed recently, they may greatly influence the composition of the platinum complex produced.

The $NaNO_3$-KNO_3 mixture, which was the solvent for most of the experiments performed, is a suitable melt for the peroxide and superoxide species produced in the reduction of the nitrate. This is because the sodium will favor the presence of peroxide while potassium favors the superoxide species (9). We have carried out experiments separately in $NaNO_3$ and KNO_3 to find out the major reduction species in these systems. In $NaNO_3$, peroxide should be the major species along with nitrite while in KNO_3 the superoxide should be the predominant species apart from the nitrite if the reactions [1], [2], and [3] are the major reduction processes involved.

In the investigations of Zambonin (4-7), except for the instrumental identification of the reduction products, no chemical analysis on the different species is reported. In the subsequent sections of this paper we discuss the results obtained from cyclic voltammetry, electrolysis, and the chemical analysis of the reduction products of $NaNO_3$ and KNO_3. Results from the preliminary investigations of the colored platinum complexes produced during the massive electrolysis of the nitrate melts are also included.

Experimental

AR grade $NaNO_3$ and KNO_3 were dried initially at 120°C for 24 hr in a vacuum oven and by bubbling pure dry nitrogen through the melts. The removal of moisture was monitored by the characteristic cathodic water wave by cyclic voltammetry (10). Experiments were performed at 335°C for $NaNO_3$ and at 345°C for KNO_3.

A platinum crucible was the container for the nitrate melts. Two Pyrex tubes (fritted disk, fine grade) lined with gold foil were dipped into the molten salt and the melt was allowed to diffuse through the frits. The reference electrode (0.06M Ag^+/Ag) was coulometrically generated in one of the frits from pure silver wire using a Sargent coulometer Model IV. The working electrode for the cyclic voltammetry was a platinum microelectrode of area 2×10^{-3} cm^2 obtained by fusing platinum wire (thickness 0.5 mm) into a Pyrex glass tube. For the electrolysis, the working electrode was a platinum macroelectrode obtained by welding a piece of platinum sheet (thickness 0.1 mm) to platinum wire. This was placed in the second fritted disk. All the voltammetric and electrolysis experiments were done with a Princeton Applied Research electrochemistry system Model 170. A nitrogen atmosphere was maintained throughout the experiments.

The chemical analyses for nitrite, peroxide, and superoxide were done by the following procedure (11). Nitrite was estimated spectrophotometrically: The

* Electrochemical Society Active Member.

Key words: nitrate melts, oxide species, cyclic voltammetry, electrolysis, chemical analysis.

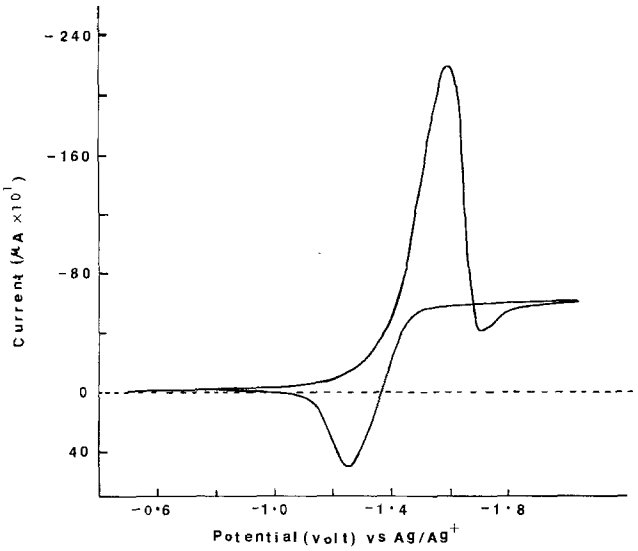


Fig. 1. Cyclic voltammogram of molten $NaNO_3$ at 335°C. Sweep rate 100 mV sec^{-1}.

sample was treated with EDTA, sulfanilic acid, naphthylamine hydrochloride, and sodium acetate buffer to give a reddish purple color in the pH range 2-2.5. By measuring the absorbance of this solution at 520 nm, the amount of nitrite was obtained using a standard curve procedure. The amount of superoxide was determined by measuring the amount of oxygen liberated using a Warburg apparatus (12): a known quantity of the electrolysis product was treated with required quantities of glacial acetic acid and diethyl phthalate solution to convert the superoxide to O_2 and H_2O_2 and from the volume of oxygen measured, the amount of superoxide in the mixture was found. The total amount of peroxide and superoxide was determined by mixing a known amount of the sample with required amounts of concentrated hydrochloric acid, boric acid, and urea at ~ 4°C and titrating with standard $KMnO_4$ solution (13). The oxide content in the melt was determined by dissolving the melt in a known volume of distilled water and titrating with dilute HNO_3 making due allowance for oxide derived from O_2^{2-} and O_2^-.

Results

A cyclic voltammogram of $NaNO_3$ recorded using a platinum microelectrode and Ag^+/Ag reference electrode is presented in Fig. 1. Electrolysis was done in a separate compartment within the melt using platinum foil cathodes. The massive electrolysis produced a dark blue compound. Analytical results of the products are given in Tables I and II.

Figure 2 represents the typical cyclic voltammogram for KNO_3. Massive electrolysis using a platinum foil cathode produced a dark blue product. Analytical results for the electrolysis products are included in Tables I and II.

Discussion

Figure 1 represents the cyclic voltammogram of $NaNO_3$. It consists of a cathodic peak at −1.6V and an anodic peak at −1.26V. The cathodic peak is due to the reduction of the nitrate to nitrite and oxide and the anodic peak to the oxidation of the insoluble oxide formed at the platinum electrode

Table I. Chemical analysis of the products formed in the short-term electrolysis of nitrate melts

	Voltage vs. Ag^+/Ag	$F \times 10^3$	Composition (moles/F) O^{2-}	O_2^{2-}	O_2^-	$O^{2-} + O_2^{2-} + O_2^-$	NO_2^-
$NaNO_3$	−2.0	2.25	0.03	0.37	0.14	0.54	0.60
	−2.0	1.10	0.04	0.44	0.14	0.62	0.66
KNO_3	−2.0	1.15	0.02	0.05	0.53	0.60	0.62
	−2.0	1.25	0.05	0.07	0.54	0.66	0.68

Table II. Chemical analysis of the products formed in the massive electrolysis of nitrate melts with Ag^+/Ag reference electrode and platinum working electrode. Electrolysis times 4-10 hr, faradays passed 8×10^{-3}-2×10^{-2}

Voltage	Percent composition NO_2^-	O_2^{2-}	O_2^-
	$NaNO_3$		
−1.5	34.2	2.4	<<1
−2.0	35.5	2.0	<<1
−2.0	46.0	2.0	—
−2.0*	50.0	1.8	—
	KNO_3		
−1.75	42.2	<<1	2.0
−2.0	48.2	<<1	2.3
−2.0	49.9	—	1.9
−2.0	46.1	—	1.9

* Denotes gold working electrode.

to superoxide (3, 5). In $NaNO_3$-KNO_3 melt the oxide formed is further converted to peroxide and superoxide. Superoxide gives rise to three additional peaks (*vide infra*) in the cyclic voltammogram (5). The absence of any other peak, other than the two peaks already mentioned for $NaNO_3$, excludes the possibility of any immediate superoxide formation in this melt. The formation of peroxide cannot be monitored by the voltammogram since there is no characteristic peak associated with it. Chemical analysis of the electrolysis products (Tables I and II) shows the presence of peroxide while superoxide is practically absent. It is known that of the two species, sodium easily forms the peroxide while superoxide is formed only under more drastic conditions. Hence it is reasonable to assume that in pure $NaNO_3$ melt, under the present experimental conditions, the oxide is converted to peroxide with greater ease and superoxide is not produced in any detectable quantity.

In another set of experiments, known amounts of Na_2O_2 were added to $NaNO_3$ melt while recording the cyclic voltammogram. This added peroxide did not alter the profile of the current-voltage curve.

The cyclic voltammogram of KNO_3 is presented in Fig. 2: The waves are not well defined. It is characterized by anodic peaks at −0.66, −0.95, and −1.55V and cathodic peaks at −0.8 and −1.3V. The cathodic peak at −1.6V and the anodic peak at −1.26V, observed for $NaNO_3$, are absent in this case. It is well established that the reduction of nitrate results in the formation of a cathodic peak only if sodium (or lithium) ions are present; if potassium is the solvent cation the current rises without the formation of a peak (2, 3). This has been explained by postulating a very large difference in solubility (3) between K_2O and Na_2O (or Li_2O) and, more recently, to the fast production of superoxide which is a much more soluble species than oxide

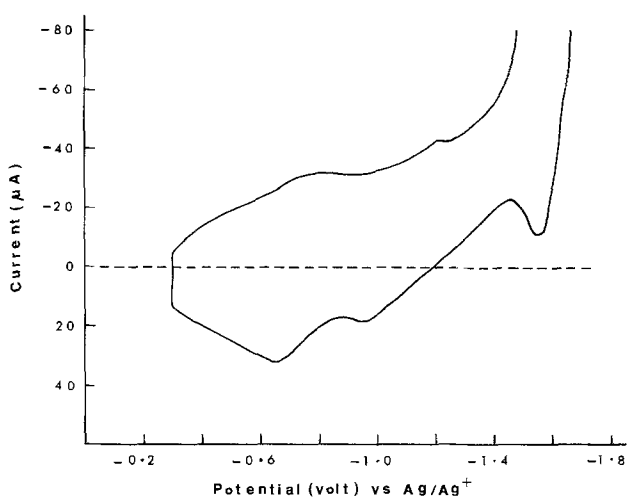


Fig. 2. Cyclic voltammogram of molten KNO_3 at 345°C. Sweep rate 50 mV sec^{-1}.

in nitrate melt (14). The presence of superoxide in $NaNO_3$-KNO_3 mixture is characterized (5) by an anodic peak at −0.69V (oxidation of superoxide to molecular oxygen) and a cathodic peak at −0.8V (regeneration of superoxide). These processes can be represented as in Eq. [6]

$$O_2^- \rightleftharpoons O_2 + e^- \quad [6]$$

Another cathodic peak appears at −1.38V corresponding to the reduction of superoxide to peroxide. By comparing the KNO_3 peaks with those of $NaNO_3$-KNO_3 mixture, it can be said that the anodic peak at −0.66V represents the oxidation of superoxide to oxygen and the subsequent regeneration of superoxide from oxygen is shown by the cathodic peak at −0.8V. The cathodic peak at −1.3V corresponds to the reduction of superoxide to peroxide. Therefore from the current-voltage curve one can infer that superoxide is formed in KNO_3 melt. Massive electrolysis performed in the melt produced a very small quantity of peroxide in addition to superoxide (Tables I and II). Since potassium has a greater tendency to form the superoxide, it is reasonable to assume that in KNO_3 melt, superoxide is the favored species. Addition of known amounts of KO_2 to KNO_3 melt, while recording the cyclic voltammogram, gave a well-defined and stronger cathodic peak at −1.3V as expected. The small peak at −0.95V may arise from the oxidation of soluble K_2O.

The results of the chemical analysis of the products of short term ($\leq$ 1 hr) electrolysis are given in Table I. The major reduction product is nitrite in both $NaNO_3$ and KNO_3. Of the other possible species peroxide forms the major product in $NaNO_3$ while superoxide is the main species in KNO_3. Possible reaction paths for the reduction of $NaNO_3$ and KNO_3 melts are expressed by reactions [1] to [3]. Reaction [1] produces equal amounts of nitrite and oxide, reaction [2] results in equal amounts of nitrite and peroxide, while reaction [3] ends with equal amounts of nitrite and superoxide. However, in the over-all reduction process, oxide is partially consumed in reaction [2] for the production of peroxide which in turn is partially converted to superoxide in reaction [3]. The total sum of the species, oxide, peroxide, and superoxide remaining at the end of the process should equal the amount of nitrite present in the nitrate melts. The experimental results closely follow this pattern. In $NaNO_3$ melt only a small portion of the peroxide is converted to superoxide while in KNO_3 most of the peroxide is converted to superoxide leaving only a small amount of peroxide in this melt. This conversion is controlled by the stability of these species in the two nitrate melts. This observation is in agreement with the results obtained from the cyclic voltammograms (*vide supra*).

Denoting the equilibrium constants of reactions [2] and [3] by K_2 and K_3, thus

$$K_2 = \frac{[O_2^{2-}]\,[NO_2^-]}{[O^{2-}]\,[NO_3^-]}, \quad K_3 = \frac{[O_2^-]^2\,[NO_2^-]^2}{[O_2^{2-}]\,[NO_3^-]^2}$$

we calculate approximate values for the two systems as in Table III. K_3 in the individual melts is much larger than in the $NaNO_3$-KNO_3 eutectic (4) ($\sim 10^{-11}$) as expected.

The results of the chemical analysis of the products of massive electrolysis are given in Table II. In $NaNO_3$ $\sim$ 2% peroxide is formed with no detectable amount of superoxide while in KNO_3 $\sim$ 2% of superoxide is present with very little peroxide. In both these nitrate melts a blue-colored platinum complex is formed during electrolysis. It is reported that both peroxide and superoxide oxidize platinum metal to the +4 oxidation state (15) while they get reduced to oxide. Since in the electrolysis peroxide and superoxide are produced in $NaNO_3$ and KNO_3, respectively, with platinum as the cathode, a substantial amount of these generated species will be lost in the process of oxidizing the platinum electrode, which may very well account for the observed low concentration of these species. The analytical results clearly indicate that in $NaNO_3$ there is a preferential formation of peroxide while in KNO_3 the superoxide predominates. Since both $NaNO_3$ and KNO_3 produced a blue-colored platinum complex, we have carried out some preliminary investigations to identify them. These compounds are unstable and become colorless in air. We could also generate the same colored species by heating a mixture of nitrite, peroxide, or superoxide and platinum metal or a platinum salt. Since peroxide or superoxide is essential for the formation of this species, platinum presumably is oxidized to the +4 oxidation state (*vide supra*). Also the peroxo species are structurally involved in the formation of this blue complex since heating K_2PtCl_6 and nitrite alone could not produce it. Electrolysis of $NaNO_3$ or KNO_3 produces nitrite, peroxide, or superoxide and these products with the platinum electrode produce the blue-colored platinum complex. Based on the preliminary data available we tentatively assign a dimeric structure to the complex with a peroxide or superoxide bridging unit similar to the structure of decammine-μ-peroxo dicobalt cation (16), with platinum in the +4 oxidation state and nitrite groups occupying the coordination sites around platinum. Further work on this is in progress.

Table III. Oxide equilibrium constants in nitrates

	$F \times 10^3$	$100\ K_2$	$10^5\ K_3$ (mole/kg)
$NaNO_3$	1.10	24	9.1
	2.25	50	8.5
KNO_3	1.25	4.9	240
	1.15	10	540

Acknowledgment

This work was supported by the National Research Council of Canada.

Manuscript submitted Sept. 16, 1976; revised manuscript received Nov. 19, 1976.

Any discussion of this paper will appear in a Discussion Section to be published in the December 1977 JOURNAL. All discussions for the December 1977 Discussion Section should be submitted by Aug. 1, 1977.

Publication costs of this article were assisted by the University of Regina.

REFERENCES

1. G. J. Hills and K. E. Johnson, Proceedings of the 2nd International Congress on Polarography, Cambridge, 1959, p. 974, Pergamon Press, London (1961).
2. H. S. Swofford, Jr. and H. A. Laitinen, *This Journal*, **110**, 814 (1963).
3. H. E. Bartlett and K. E. Johnson, *ibid.*, **114**, 64 (1967).
4. P. G. Zambonin and J. Jordan, *J. Am. Chem. Soc.*, **89**, 6365 (1967); *ibid.*, **91**, 2225 (1969).
5. P. G. Zambonin, *J. Electroanal. Chem.*, **24**, 365 (1970).
6. P. G. Zambonin, *J. Phys. Chem.*, **78** 1294 (1974).
7. P. G. Zambonin, *J. Electoanal. Chem.*, **33**, 243 (1971).
8. M. Fredericks, R. B. Temple, and G. W. Thickett, *ibid.*, **38**, A5 (1972).
9. R. B. Heslop and P. L. Robinson, "Inorganic Chemistry," p. 313, Elsevier Publishing Co., New York (1967).
10. M. Peleg, *J. Phys. Chem.*, **71**, 4553 (1967).
11. K. E. Johnson, J. Matthews, and P. S. Zacharias, To be published.
12. E. Seyb, Jr. and J. Kleinberg, *Anal. Chem.*, **23**, 115 (1951).
13. I. M. Kolthoff and E. B. Sandell, "Textbook of Quantitative Inorganic Analysis," p. 604, Macmillan, New York (1950).
14. P. G. Zambonin and A. Cavaggioni, *J. Am. Chem. Soc.*, **93**, 2854 (1971).
15. S. Shibata and M. P. Sumino, *Electrochim. Acta*, **20**, 871 (1975).
16. W. P. Schaefer and R. E. Marsh, *J. Am. Chem. Soc.*, **88**, 1978 (1966).

β Fe_2O_3: Preparation of Thin Films by Chemical Vapor Deposition from Organometallic Chelates and Their Characterization

Lina Ben-Dor and Eli Fischbein

Department of Inorganic and Analytical Chemistry, The Hebrew University of Jerusalem, Jerusalem, Israel

and Israel Felner and Zvi Kalman

Racah Institute of Physics, The Hebrew University of Jerusalem, Jerusalem, Israel

ABSTRACT

Thin films of a new iron oxide phase, β-Fe_2O_3, were prepared by chemical vapor deposition (CVD) from tris(trifluoroacetylacetonato) iron (III) at 300°C in the presence of oxygen onto a variety of substrates. The films were characterized by x-ray diffraction analysis, scanning electron microscopy, and Mössbauer spectroscopy. For the latter measurements the films were prepared from enriched $^{57}Fe_2O_3$. The ultraviolet, visible, and infrared spectra of the films were also recorded. The iron (III) oxide phase prepared was bcc having the bixbyite structure, Ia3 space group and the lattice constant a_o = 9.393Å. There are 16 formula molecules to the unit cell and the two iron atoms occupy two nonequivalent distorted octahedral lattice sites: $\bar{3}$(8b); 2(24d).

During the last ten years great emphasis has been attached to the preparation of electronic and magnetic materials such as III-V and II-VI semiconductors and oxides by chemical vapor deposition (CVD) using organometallic compounds and chelates, such as trimethyl and triethyl metal compounds (1-7), alkoxides (8-12), metal carbonyls (13-14), and β-diketonates. Among the β-diketonates, the most frequently used are acetylacetonates (15-16), trifluoroacetylacetonates (17), and dipivaloylmethane (18).

These compounds are being used owing to the following advantages: relative high vapor pressure, stability in a definite temperature range, resistance to hydrolysis, and availability and/or ease of preparation and handling. Since these compounds decompose in the appropriate atmospheres at relatively low temperatures, the products obtained contain less defects and stresses and afford the possibility of using temperature sensitive substrates, and high density of coverage is obtained.

The study of Fe_2O_3 by CVD undertaken here was the first step (16) in a project concerned with the study of binary and ternary magnetic oxide films. A large amount of interest is centered around high temperature CVD iron oxide films as magnetic material (19, 20) from starting material of iron chlorides. Deposition of iron oxide films from iron pentacarbonyl was carried out by both MacChesney *et al.* (13) and Gallagher *et al.* (14). Their aim was the study of the films for semitransparent masking. The as-grown films were usually amorphous and after annealing the α-Fe_2O_3 phase was obtained. The films also contained some Fe^{2+} (based on Mössbauer data) and CO and CO_2 as impurity (infrared spectrum). Other films prepared by the sputtering technique were studied for photomask applications by a group in Bell Laboratories (21, 22) and a detailed review of the properties of such iron oxide films was presented (23). Low temperature CVD iron oxide has been obtained also by exposing a substrate to an aerosol of the chelate in an organic solvent (24). There is no mention of the phase obtained and the authors encounter difficulties in the adhesion of the film to the substrate, the control of the size of the aerosol droplets, and the thickness of the films. A report of Fe_2O_3 prepared by CVD from the acetylacetonate discusses the optical qualities of the oxide layers without mentioning experimental or structural details (25).

Recently, ferrocene in an oxidizing atmosphere was used by both Gibart *et al.* (26) and by us as a starting material. Thompson (27) used poly(vinylferrocene) both at 200W, 4 MHz of oxygen plasma, or thermally at 380°C to obtain Fe_2O_3 films. The author points out the advantages and disadvantages of the procedure. In the present work films of a new phase of iron (III) oxide were prepared by low temperature CVD using the trifluoroacetylacetonate. The films were characterized by a wide variety of physical methods.

Key words: chemical vapor deposition, β-Fe_2O_3 (β-iron oxide), bixbyite structure, organometallic compounds, thin films.

Experimental

Preparation.—Thin films of iron (III) oxide were prepared from tris(trifluoroacetylacetonato) iron (III)-$Fe(F_3CCOCHCOCH_3)_3$ (Pierce Chemicals) by chemical vapor deposition in presence of both dry and wet oxygen gas. The system (Fig. 1) used is a conventional one composed of the evaporator kept at 180°C and the reactor kept at 300°C. The evaporator is U-shaped and the reactor is an inverted bell jar on a rotating hot plate. This plate was mounted on a laboratory jack for easy loading and unloading of the substrates. The system is made of Pyrex glass, and Tygon tubing is used for connections. Argon gas is used as the carrier gas and both its flow and that of oxygen is monitored by rotameters. In all cases the flow of the oxygen was ten times that of the carrier gas. The interval between the source and the bell jar was heated to 220°C by means of a heating tape. The temperature at various points was monitored via thermocouples by appropriate controllers and a special heavy-duty thermocouple was used on the rotating hot plate. The substrates were arranged concentrically on the hot plate. The following materials were used as substrates: microscope-cover soda glass, fused silica, potassium bromide and calcium fluoride single crystal slices, and polycrystalline and single crystal alumina. The adhesion of film to all the substrates was very good as was proved by the "Scotch-tape

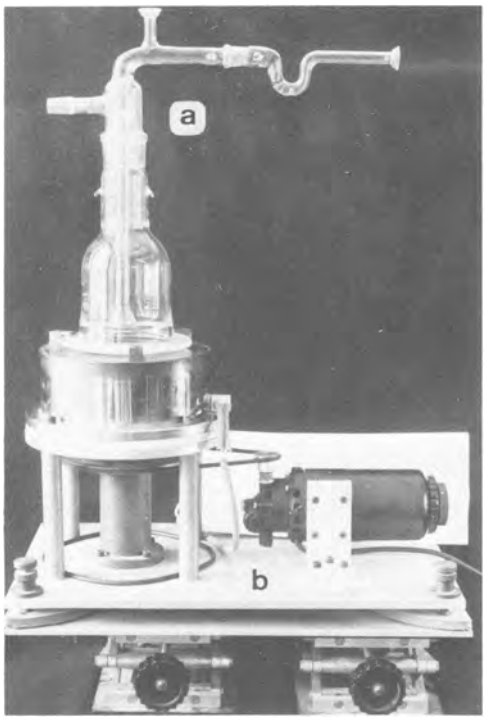


Fig. 1. The CVD system (a) glass bell jar assembly, (b) rotating heating plate on platform with motor.

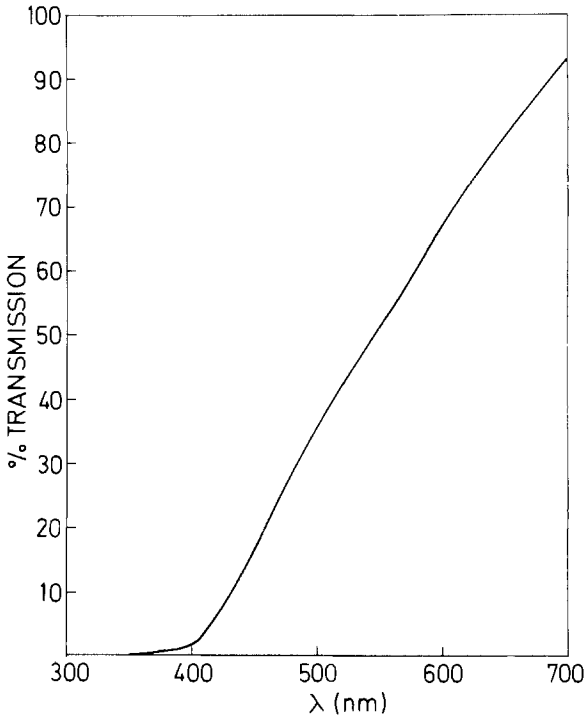


Fig. 2. Transmission of β-Fe_2O_3

test." The thickness of the films was in the range of 0.1 to a few microns. When the deposition rate is comparatively low (low flow of carrier gas) one can see the series of color interference patterns of the film. The color of the thicker films ranges from yellow to brownish red depending on thickness.

The isotopically enriched chelate for Mössbauer measurements is not available commercially and the following procedure was used for preparation, based on Fay and Piper (28):

From A.E.R.E., England, an amount of $^{57}Fe_2O_3$ was purchased, 25 mg of which were dissolved by heating in 30 ml of 6*N* HCl. Solid sodium acetate was added until the *p*H reached 1; then borax was added until *p*H = 3. This mixture of buffers was used in order to prevent formation of the very stable iron acetate; this change thus slightly optimizes the original procedure (28). Dropwise and with stirring an alcoholic 20% solution of the ligand (bidistilled) was introduced into the above buffered iron (III) aqueous solution and the chelate allowed to precipitate overnight. The red precipitate was proven by microanalysis to be tris(trifluoroacetylacetonato) iron (III) and the yield obtained was 85%.

Electronic and vibrational spectra.—The absorption spectra of the films deposited on sapphire or fused silica in the range 700-200 nm show no peaks; however, depending on thickness a broad absorption beginning at ~650 nm and rising steeply into the ultraviolet is observed. This behavior complies with the requirements of "see through" masks (21, 22) which are used in integrated circuit technology, viz.: (*i*) sufficient light absorption below 400 nm, *ca.* 1% transmission; (*ii*) sufficient transmission at the sodium D line (~600 nm) for viewing purposes, a representative film ~2000Å thick has *ca.* 60% transmission; (*iii*) easy and fast etching in 6M HCl due to the actual low temperature existing on the insulating substrate during the growth of the films (cf. Fig. 2 showing percentage transmission of a film).

On annealing the films in air to 500°C the β-phase slowly transforms to the α-phase until complete transformation is achieved, as seen from the distinct and characteristic u.v. and visible spectra and x-ray diffraction. The u.v. spectrum (Fig. 3) shows three charge-transfer bands (L → M) at 320, 260, and 205 nm; the visible spectrum showing d-d transitions, has already been published (16).

The infrared range is clean, showing 90-100% transmission in the range 20,000-400 cm^{-1}. Thus, the films, deposited in this case on KBr or CaF_2 slices, contain neither adsorbed water nor functional "OH" groups and no carbonyl, carbonate, nor residual organic materials.

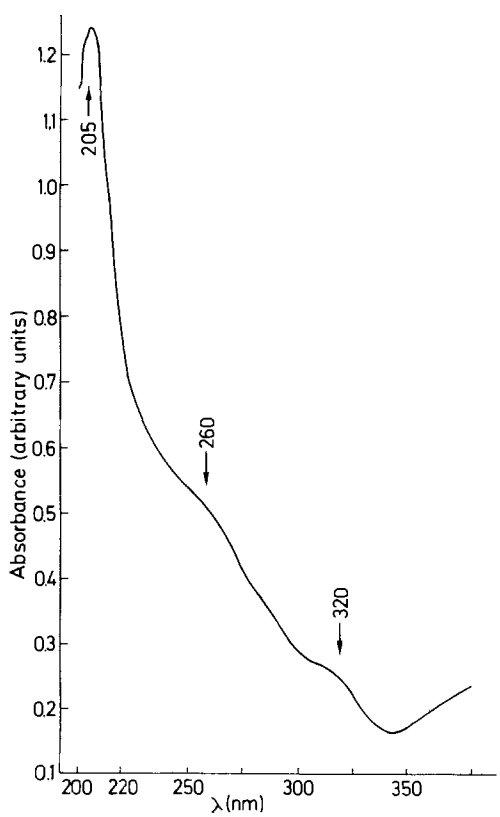


Fig. 3. Spectrum of α-Fe_2O_3 obtained from annealing the β-phase

X-ray diffraction data.—All of the films obtained were well crystallized even though low deposition temperature often gives amorphous films without discernible (x-ray) peaks (14). The line patterns of this iron oxide phase could not be found in the Powder Diffraction File (1975) but reference to an identical cubic phase appeared in Wyckoff's Crystal Structure (29a) and in Structure Reports (29b), Pearson's Handbook of Lattice Spacings (30), and finally in Landolt-Bornstein's Tables (31). This new phase was discovered by Bonnevie-Svendsen (22) who in 1956 had prepared it from the hydrolysis of $FeCl_3 \cdot 6H_2O$, naming it β-Fe_2O_3. This body-centered cubic oxide stemming from CaF_2 structure (Fig. 4) by taking the origin half-way up the edge of the unit cell, belongs to the Ia3 space group ($D5_3$). It is isostructural with α-Mn_2O_3 or bixbyite structure (also referred to as β-Mn_2O_3) and is identical to the C structure of the rare earth oxides (especially the heavier ones).

X-ray powder diffraction diagrams were carried out in three different modes.

Mode I.—Thin films adhering strongly to the substrate were photographed on an oscillation camera (30 mm radius, oscillation range 5°) with Co or Cr radiation, at glancing angles of ~5° to 10°, in order to increase the beam path length of the sample. Photographs so obtained are not sufficient for determination of precise cell dimensions (center of sample inaccurately defined) but can be used for identification of the phases in the sample.

Mode II.—In one case the film could be detached from the substrate by means of adhesive tape. The tape with the adhering film was photographed on a Guinier-De Wolff camera, using Co radiation. The photograph was of sufficiently good quality to give accurate cell dimensions. The sample contained also about 30% α-Fe_2O_3, whose lines were used as internal standard.

Mode III.—One sample (on a polycrystalline alumina substrate) was sufficiently thick to permit the determination of a number of reflected intensities by means of a diffractometer, employing Cr radiation. The patterns obtained showed lines of both the substrate and the film sample. Rather broad slits (1°) were employed as the sample lines were in any case broadened due to small particle size.

Patterns of all samples contained lines (sometimes in addition to those of α-Fe_2O_3) of the cubic body-centered material (32, 33) distinctly different from α-Fe_2O_3.

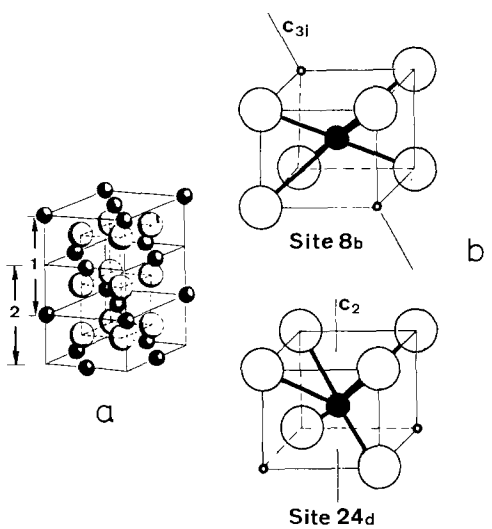


Fig. 4. Bixbyite structure: (a) showing the relation to fluoride; (b) the two nonequivalent octahedral sites.

Table I. Crystallographic data for β-Fe_2O_3

H K L	Guinier d_{obs} (Å)	Guinier I_{obs}	Diffractometer d_{obs} (Å)	Diffractometer I_{obs}	d_{calc} (Å)	I_{calc}
2 1 1	3.827	m	3.82	17	3.834	17
2 2 2	2.710	s	2.72	100	2.711	100
4 0 0	2.347	m	2.35	25	2.348	13
4 1 1	2.210	mw*	2.21	3	2.213	0.5
3 3 2	2.002	mw	2.00	6	2.002	6
4 3 1	1.842	m	1.84	7	1.842	7
5 2 1	1.715	w	**		1.715	1.5
4 4 0	1.660	s	1.66	32	1.660	34
6 1 1 5 3 2	1.523	vw	1.52	2	1.523	1.5
5 4 1 6 2 2	1.415	* m	1.416	24	1.416	24
6 3 1	1.386	vw	**		1.385	5
6 3 3					1.278	0.2
7 2 1			1.275	3	1.278	3.3
5 2 2					1.278	0.1

* Overlap with α-Fe_2O_3 line.
** Overlap with alumina line.

From the Guinier-De Wolff photographs (mode II) the cell edge was determined to be $a_0 = 9.393 \pm 0.03$, Table I, column 2. Visual inspection of intensities showed a close similarity to the pattern published for bixbyite (JCPDS cards 8-10) space group Ia3.

Intensities were obtained from a diffractometer trace (mode III), using CrKα radiation. Measured relative intensities relate to the F values by means of

$$I_{HKL} = K \frac{1 + \cos^2 2\theta}{\sin^2\theta \cos\theta} \cdot \frac{1 - \exp(-2\mu D/\sin\theta)}{2\mu} [F_{HKL}]^2 M_{HKL}$$

where K is a constant for all reflections, D is the sample thickness, μ linear absorption coefficient, and M_{HKL} multiplicity of the plane HKL. The value μD was determined by comparing the intensities of the lines of the substrate (polycrystalline alumina) appearing in the sample pattern, with those of the substrate alone. The value for μD so obtained was 0.08 indicating the sample thickness of ~2 μm. It is to be noted that the β-Fe_2O_3 lines were considerably broader than the alumina lines indicating a mean crystalline particle size of 500Å.

As the material is isostructural with bixbyite the atoms were assumed to be in analogous positions. Structure factors were calculated by the standard equation (neglecting temperature corrections) and best fit with measured intensities was obtained for the following parameter of the space group Ia3

Fe_I in (8b)	¼	¼	¼	
Fe_{II} in (24d)	u	0	¼	$u = -0.026$
O in (48e)	$x = 0.38$	$y = 0.16$	$z = 0.40$	

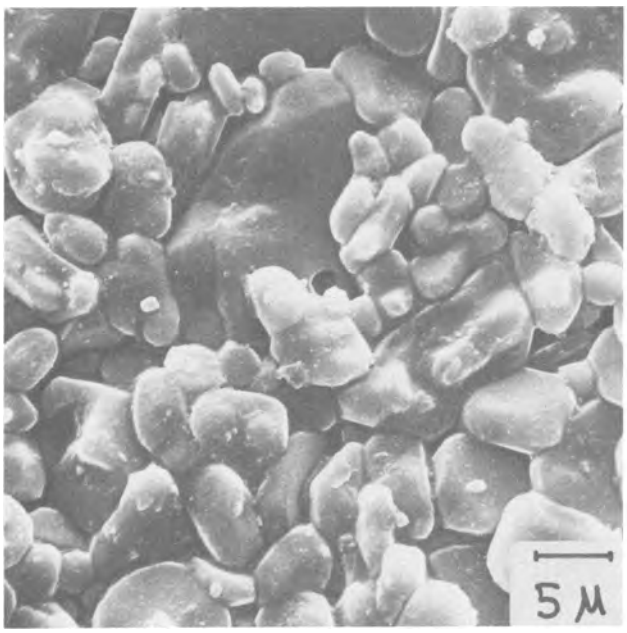
The estimated error for these parameters is 0.02 (for u it is 0.003).

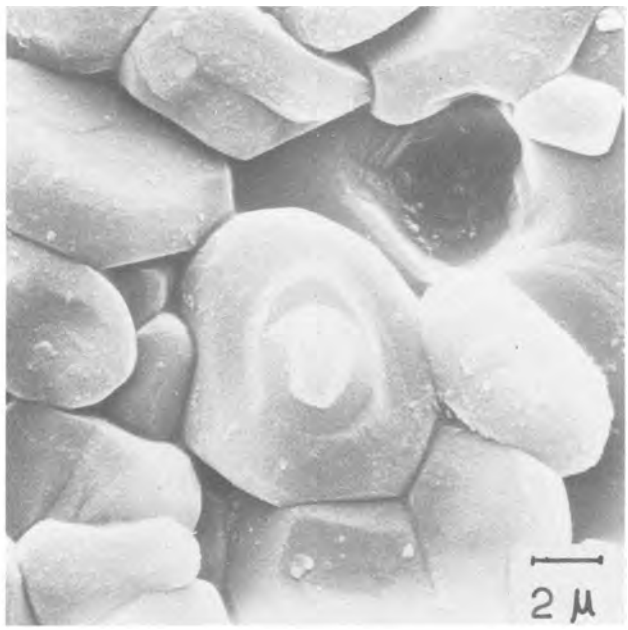
Table I shows the crystallographic data for β-Fe_2O_3. The density calculated from the x-ray data is 5.14 g cm^{-3}. After annealing the films in air to ~500°C, α-Fe_2O_3 is obtained as was proved by x-ray and electron diffraction (26) and absorption spectra.

It should be noted that the films deposited under dry conditions were identical with those deposited in the presence of oxygen saturated with water at 20°C. Water does not change the morphology or structure of the films, although it does accelerate the rate of deposition.

Mössbauer data.—Mössbauer spectra[1] of the films prepared from enriched ^{57}Fe were measured in the tem-

[1] A detailed Mössbauer study will be published elsewhere.





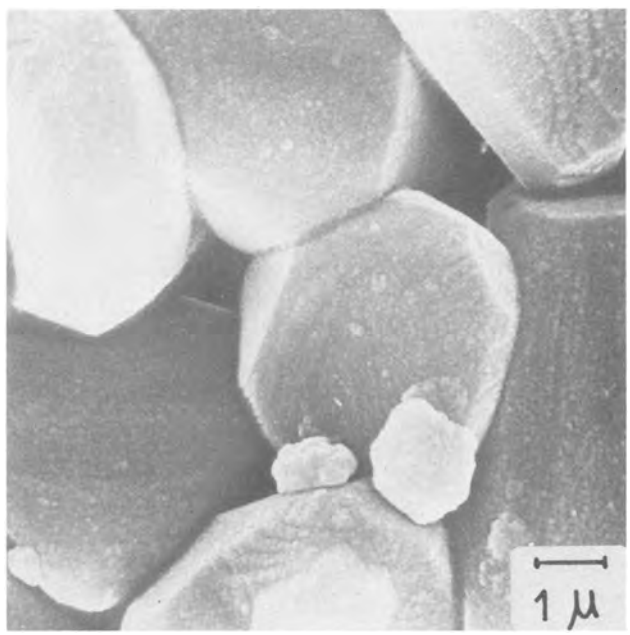
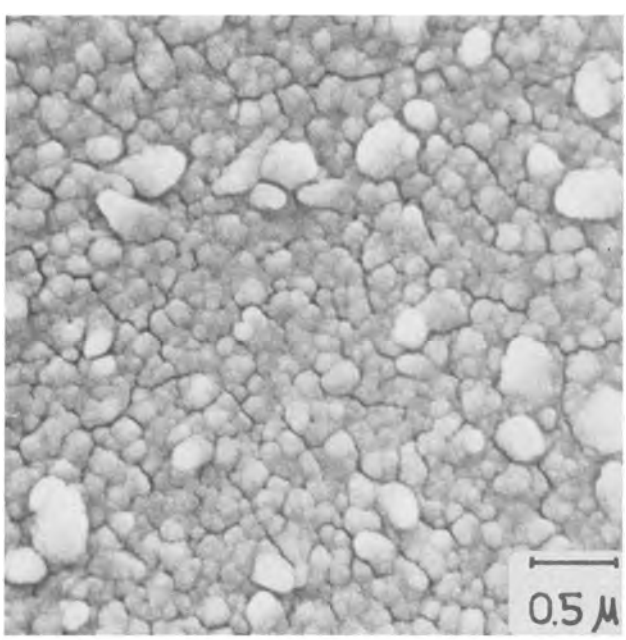


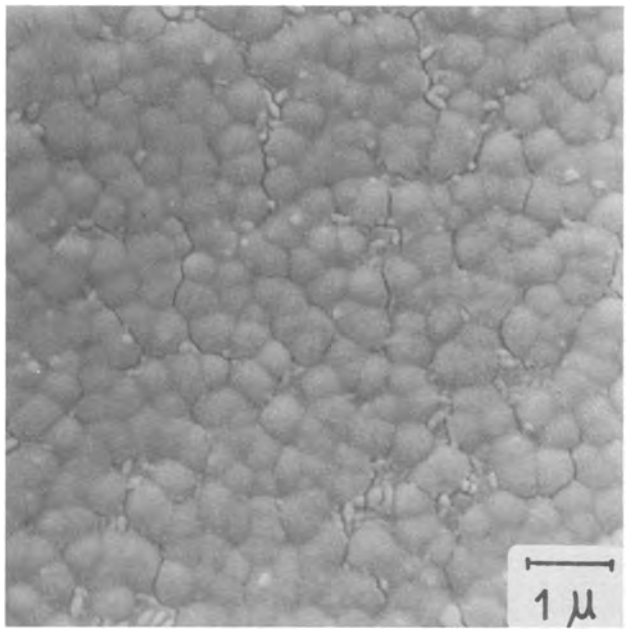
Fig. 5. Surface appearance of iron oxide film (a) as deposited at 300°C; (b) after 500° anneal showing faces of α-Fe_2O_3; (c) after 800° anneal showing well-developed grains.

perature range 4°-500°K, using a ^{57}Co in Cu source. There is no signal belonging to Fe^{2+}, as has been observed by Gallagher *et al.* (14), the isomer shift being typical of trivalent iron. The spectra at temperatures above 106°K are composed of two electric quadrupole hyperfine spectra with relative intensities of 3:1. Below 106°K magnetic hyperfine splittings are observed, which are composed of two subspectra with relative intensities of 3:1. The intense subspectrum corresponds to Fe^{3+} ions in the d sites and the weak subspectrum corresponds to Fe^{3+} in the b sites. This is the only oxide of iron which is not ordered magnetically at room temperature.

Scanning electron microscopy (SEM).—Micrographs were taken on the Stereoscan S4 of Cambridge Instruments, and simultaneously x-ray elemental analysis using an energy dispersive system was used to analyze the films. The only element found within the limits of sensitivity of the instrument was iron (Fe). The films were coated with gold or conducting carbon before introducing the samples into the microscope. Figure 5a shows the film deposited on polycrystalline alumina at 300°C. The size of the average grain is ~5 μm. The hole in the central plate was probably formed by sintering intergrowth with adjacent crystallites. It is to be noted that the grains are irregular in shape, possibly grown from coalescence of several small crystallites. The phase obtained is β-Fe_2O_3. Figure 5b shows the same film after annealing at 500°C in air. The phase shown is mostly α-Fe_2O_3 as seen also from the geometrical crystal faces. Surface diffusion is the predominant transport mechanism for growth as can be seen from the growth of Frank terraces and spirals on top of the crystallites. The size of the cavity is ~3 μm and that of the largest grain is ~8 μm. The same phase further annealed is shown in Fig. 5c, at 800°C. Well-shaped hexagonal grains are seen and terraces on some of their faces, as well.

The β-phase deposited on amorphous fused silica or on single crystal alumina is greatly modified compared to the above-mentioned morphology (Fig. 6a, b). The grains are much smaller (0.4-0.25 μm), very irregular in shape, and densely arranged. We could not explain this difference except perhaps that the





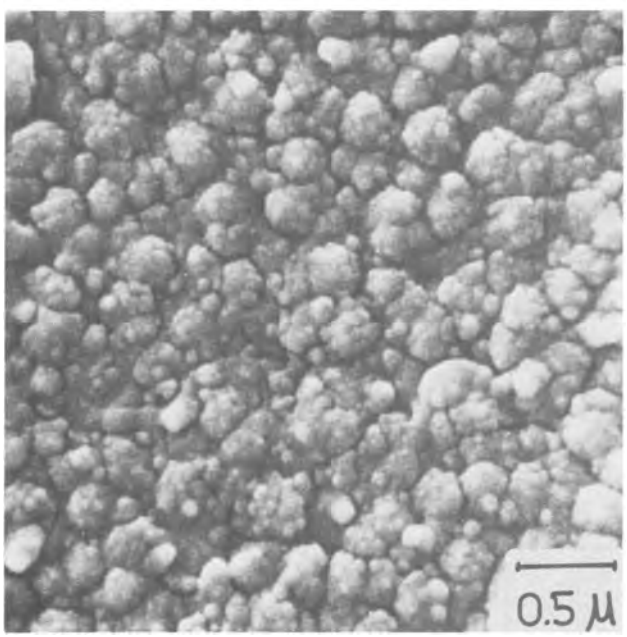


Fig. 6. Surface appearance of iron oxide film as deposited at 300°C: (a) on amorphous silica; (b) on single crystal alumina; (c) on KBr single crystal.

polycrystalline material affords better and more nucleation sites. Other oxide deposits on microscope-cover soda glass, show the same features as those described above. In contrast, sputtered films (22) and those prepared by CVD starting from iron pentacarbonyl (14, 22) have smaller grain size (~500Å). The larger grain size shown in the micrographs here, is probably due to the difference in experimental condition such as starting material and growth temperature, to which the deposits are so sensitive. Figure 6c shows the deposit on KBr; the grains are still small but twice as large as those in Fig. 6a, b. This difference might be due to the rather unsmooth surface of the slice which had not been polished mechanically or chemically before the deposit, contrary to the case in Fig. 6a, b. Figures 7a, b show the effect of 1 mW, red laser irradiation during growth on the morphology of the deposit upon fused silica. Even in the largest magnification obtained no distinct grains could be observed and it is suggested that an epitaxial growth or extremely small grains with preferred orientation were obtained, but further work must be carried out before final decision can be made.

Discussion

The existence of a new cubic stable phase of iron (III) oxide is in fact known since 1958 from Bonnevie-Svendsen's brief study whereby the material was identified as β-Fe_2O_3. For the last 15 years a group headed by Geller of Bell Laboratories has been studying (34-36) various aspects of binary and ternary oxides of the bixbyite structure, those being various systems of sesquioxides with Fe_2O_3. In a study of the solid solution Sc_2O_3-Fe_2O_3 (34) Vegard's law was shown up to the ratio of 1:1 and extrapolated to pure Fe_2O_3. The extrapolated lattice constant obtained was 9.401Å, and the authors declare that if such a material could have existed it would have the bixbyite structure. In a later study (35), solid solutions with Mn_2O_3 were studied (up to 1:1 ratio) and again the possible existence of "β-Fe_2O_3" was predicted despite the former 1958 communication concerning this new phase.

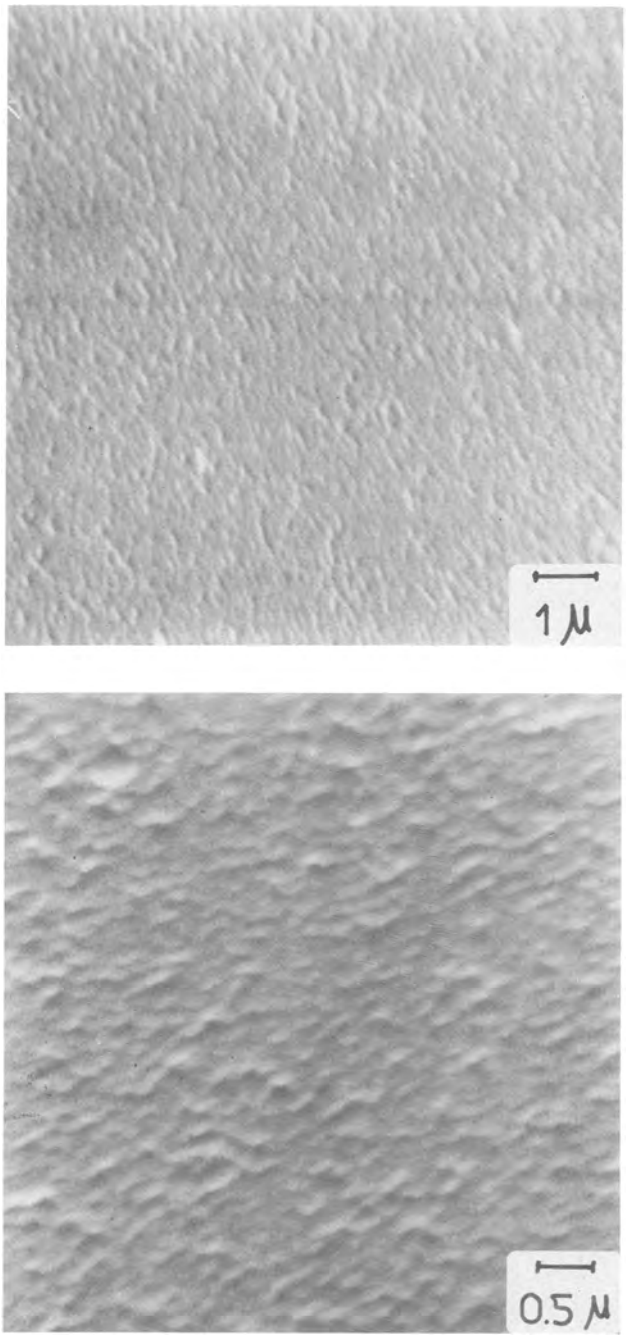


Fig. 7. Micrograph view of iron oxide film laser irradiated during growth: (a) magnification 8000×; (b) magnification 16,000×.

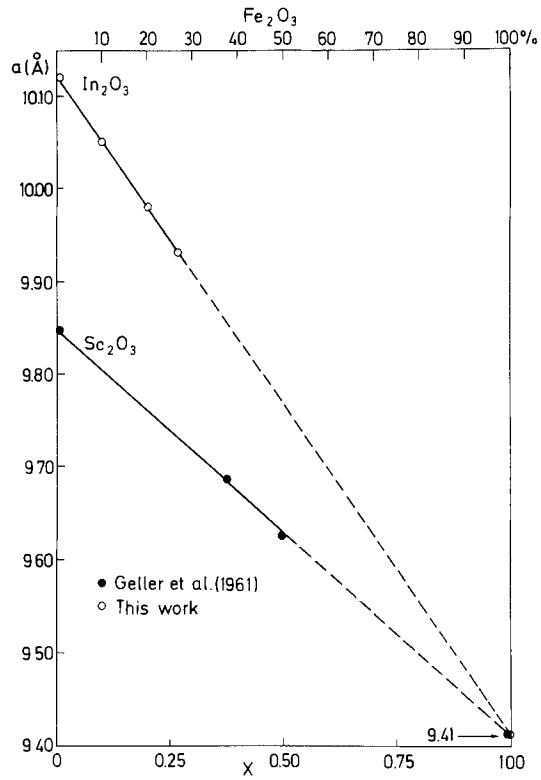


Fig. 8. Vegard's law extrapolation for solid solutions of In_2O_3 and Sc_2O_3 with Fe_2O_3.

Following the above reports, we prepared solid solutions of In_2O_3-Fe_2O_3 (Fig. 8). It can be seen that up to 27% Fe_2O_3 in In_2O_3 one obtains a pure C-structure; above that concentration the pure structure starts to be contaminated with the corundum phase of Fe_2O_3. The linear Vegard's law for both Sc_2O_3 and In_2O_3 with Fe_2O_3 on extrapolation cut at the same lattice constant for 100% Fe_2O_3 thus proving that if this iron phase "could be prepared" it would have a lattice constant identical or very similar to the experimental value 9.41Å. The only mention in the current literature of β-Fe_2O_3 is found in Okamoto's study on β-FeOOH (37) and that only *en passant*. Recently, two reports appeared concerning the preparation of β-FeOOH and "β"-Fe_2O_3 (38, 39). The latter compound was prepared from dehydration of the former, both having a tetragonal structure. The authors claim the use of the letter "β" to their new iron (III) oxide phase having also overlooked the original work of Bonnevie-Svendsen. Clearly, a new letter should be assigned to this tetragonal oxide.

As a result of the fact that the discovery of β-Fe_2O_3 had been overlooked by the scientific community several experimental results in various studies could not be properly understood. Thus, Gallagher *et al.* (14) discussing the preparation of iron oxide films from $Fe(CO)_5$ encounter some strange Mössbauer behavior. We believe that his results could be explained on the basis of formation of β-Fe_2O_3 (probably not well crystallized). Similarly, some other Mössbauer data published by a Russian team (40) could be perhaps due to the formation of β-Fe_2O_3.

The main challenge now is to prepare some bulk material of pure β-Fe_2O_3 in order to study the complete magnetic behavior. Further work is being carried out on various other oxides which are known to have or are predicted to have the bixbyite structure such as Ga_2O_3, Rh_2O_3, etc. and also on ternary systems such as ferrites and garnets.

Conclusions

In this study β-Fe_2O_3 films were deposited and characterized. It is the only known stable oxide of iron (III) which is paramagnetic at room temperature, the ordering temperature being below 106°K. Using the chelate with trifluoroacetylacetone, CVD proved to be a satisfactory and easy method of obtaining films of reproducible qualities. Owing to their structure and magnetic properties, these films might be useful for catalysis in organic synthesis (similarly to Er_2O_3), and based on their absorption qualities they might be useful as photomasks and optical filters.

Acknowledgments

The authors are deeply indebted to Professor B. T. Matthias from San Diego, California, and Professor I. Sunagawa, Sendai, Japan, for fruitful discussions and helpful suggestions. Thanks are due to the immense help invested by Professor S. Ofer and others of the group of Nuclear Physics: to I. Rubinstein for helping with film deposition and, lastly, to the SEM group, all of them, of The Hebrew University.

Manuscript submitted March 10, 1976; revised manuscript received Sept. 15, 1976.

Any discussion of this paper will appear in a Discussion Section to be published in the December 1977 JOURNAL. All discussions for the December 1977 Discussion Section should be submitted by Aug. 1, 1977.

Publication costs of this article were assisted by The Hebrew University of Jersusalem.

REFERENCES

1. H. M. Manasevit and W. I. Simpson, *This Journal*, **116**, 1725 (1969).
2. H. M. Manasevit and W. I. Simpson, *ibid.*, **118**, 644 (1971).
3. H. M. Manasevit, *ibid.*, **118**, 647 (1971).
4. H. M. Manasevit, *J. Crystal Growth*, **13/14**, 306 (1972).
5. M. T. Duffy and W. Kern, *RCA Rev.*, **31**, 754 (1970).
6. P. Andre, J. Hallais, and C. Schiller, *J. Cryst. Growth*, **31**, 147 (1975).
7. J. E. Andrews and M. A. Littlejohn, *This Journal*, **122**, 1273 (1975).
8. J. A. Aboaf, *ibid.*, **114**, 948 (1967).
9. L. A. Ryabova and Ya. S. Savistskaya, *Thin Solid Films*, **2**, 141 (1968).
10. C. C. Wang, K. H. Zaininger, and M. T. Duffy, *RCA Rev.*, **31**, 728 (1970).
11. S. Pakswer and P. Skong, in "Chemical Vapor Deposition, Second International Conference," J. M. Blocher, Jr., and J. C. Withers, Editors, p. 619, The Electrochemical Society Softbound Symposium Series, New York (1970).
12. K. J. Sladek and W. W. Gibert, in "Proceedings of the Third International Conference on Chemical Vapor Deposition," p. 215 (1973).
13. J. B. MacChesney, P. B. O'Connor, and M. V. Sullivan, *This Journal*, **118**, 776 (1971).
14. P. K. Gallagher, W. R. Sinclair, R. A. Fastnacht, and J. P. Luongo, *Thermochim. Acta*, **8**, 141 (1974).
15. L. A. Ryabova, Ya. S. Savitskaya, and R. N. Sheftal, *Zh. Prikl. Khim.*, **38**, 1863 (1965).
16. L. Ben-Dor, R. Druhile and P. Gibart, *J. Cryst. Growth*, **24/25**, 172 (1974).
17. M. Balog, Ph.D. Thesis, The Herew University of Jerusalem, Jerusalem (April 1975).
18. M. E. Cowher, T. O. Sedgwick, and J. Landerman, *J. Electron. Mater.*, **3**, 621 (1974).
19. G. R. Pulliam, *J. Appl. Phys.*, **38**, 1120 (1967).
20. J. E. Mee, G. R. Pulliam, J. L. Archer, and P. J. Besser, *IEEE Trans. Magn.*, **mag-5**, 717 (1969).
21. W. R. Sinclair, M. V. Sullivan, and R. A. Fastnacht, *This Journal*, **118**, 341 (1971).
22. F. G. Peters, W. R. Sinclair, and M. V. Sullivan, *ibid.*, **119**, 305 (1972).
23. A. R. Janus, *Solid State Technol.*, **16**, 33 (June 1973).
24. J. C. Viguie and J. Spitz, *This Journal*, **122**, 585 (1975).
25. K. H. Bloss and H. Lukas, *Electrodep. Surf. Treatment*, **2**, 47 (1973/1974).
26. P. Gibart, Private communication.
27. L. F. Thompson, *This Journal*, **122**, 108 (1975).
28. R. C. Fay and T. S. Piper, *J. Am. Chem. Soc.*, **85**, 500 (1963).
29. (a) R. W. G. Wyckoff, "Crystal Structures," 2nd ed., Vol. 2, p. 5, Interscience Publishers, New York (1964); (b) W. B. Pearson, Editor, "Structure Reports," Vol. 22, p. 298, International Union of Crystallographers, (1968).
30. W. B. Pearson, "A Handbook of Lattice Spacings and Structures of Metals and Alloys," Vol. 2, p. 464, Pergamon Press, Oxford (1967).
31. Landolt-Bornstein Tables, New Series, Group III, Vol. 7, Part b (III/7bl), p. 540, Springer-Verlag, Berlin (1975).
32. M. Bonnevie-Svendsen, *Naturwissenschaften*, **45**, 542 (1958).
33. L. Ben-Dor, E. Fischbein, and Z. Kaman, *Acta Crystallogr., Sect. B*, **32**, 667 (1976).
34. S. Geller, H. J. Williams, and R. C. Sherwood, *J. Chem. Phys.*, **35**, 1908 (1968).
35. R. W. Grant, S. Geller, J. A. Cape, and G. P. Espinoza, *Phys. Rev.*, **175**, 686 (1968).
36. S. Geller, *Acta Crystallogr., Sect. B*, **27**, 821 (1971).
37. S. Okamoto, *J. Am. Ceram. Soc.*, **51**, 594 (1968).
38. H. Braun and K. J. Gallagher, *Nature*, **240**, 13 (1972).
39. K. J. Gallagher, *ibid.*, **226**, 1225 (1970).
40. Yu. F. Krupyanskii and I. P. Suzdalev, *Sov. Phys. JETP (Engl. Transl.)*, **38**, 859 (1974).

An Expression for Sheet Resistivity Using Boron Nitride Source

M. Crooke

National Electrical Engineering Research Institute, Council for Scientific and Industrial Research, Pretoria 0001, Republic of South Africa

and A. G. K. Lutsch

Rand Afrikaans University, Johannesburg 2000, Republic of South Africa

ABSTRACT

From experimental data on the use of oxidized boron nitride as a source of boron, computer-derived expressions are obtained which interrelate the deposition sheet resistivity ρ_S, deposition time t, and temperature T according to functions of the form $\rho_S = f(t, T)$; $t = f(\rho_S, T)$; and $T = f(\rho_S, t)$. The resulting expressions fit the experimental data to within the accepted reproducibility limits of the four-point probe and thus provide a useful method of estimating the values of these variables for purposes of processing or design.

Solid oxidized boron nitride, one of the newer sources of semiconductor dopant, has certain advantages over the older liquid and gaseous sources. These advantages include improved stability and reproducibility, which are such that it is possible to attempt to describe source behavior in mathematical terms. The purpose of this paper is to derive equations describing the interrelationships between the sheet resistivity ρ_S ($\Omega/\square$), time t (min), and temperature T (°C), which can be used for estimating the third variable when the other two are known.

* Key words: boron nitride, boron deposition, sheet resistivity.

Experimental

Grade M26 boron nitride disks (The Carborundum Company, Niagara Falls, New York) recommended (1)

for use in the temperature range 975°-1100°C, were precleaned, oxidized, and stabilized in accordance with the suggested procedure (1). The disks were stored in the mouth of the furnace tube when not in use (2).

The product material used throughout the exercise to evaluate ρ_s was precleaned, 30-33 mm diameter n^+ (antimony) substrates containing a n(phosphorus) epitaxial layer of thickness 18-28 μm and resistivity 4-6 Ω cm.

The sheet resistivity of deglazed samples was measured using an A. & M. Fell linear four-point probe with a probe spacing of 1.67 mm; a current source accurate to ±0.1% of the setting in the range of interest, containing a current-reversal facility to monitor contact resistance; and a high impedance digital voltmeter capable of resolving 0.01 mV.

Furnace temperatures were maintained flat to within ±0.5°C over a minimum length of 250 mm. The furnace ambient employed was 99.995% plus purity argon at a flow rate of 500 cm^3/min, in a 60 mm internal diameter quartz tube, as previous experimental work (2) had proved results to be more consistent when argon was used instead of nitrogen of the equivalent purity.

The experimental results given in Fig. 1 show the logarithm of the sheet resistivity plotted *vs.* deposition times varying between 10 and 60 min, in the 900°-1100°C temperature range, the curves being separated by temperature steps of 50°C.

In view of the close approximation to linearity exhibited in the curves of log ρ_s plotted (3) *vs.* $1/T$ or T (Fig. 2), and the plot of log ρ_s against $1/t$ (Fig. 3), obtained from data extracted from Fig. 1, it is possible to derive an expression relating ρ_s to t and T. The first plot provides $\ln \rho_s = A(T) + C$ for constant t, say $\ln \rho_s = A(T) + f_1(t) + c_1$; and the second $\ln \rho_s = B(1/t) + D$ for constant T, say $\ln \rho_s = B(1/t) + f_2(T) + c_2$. Combining both equations we get $\ln \rho_s = A(T) + B(1/t) + c = f(t, T)$. By manipulation, similar functions can be derived for t and T: $t = f(\rho_s, T)$ and $T = f(\rho_s, t)$.

When the coefficients are calculated manually, without rounding off, these expressions become: $\rho_s = \exp [10.84t^{-1} - (1.43 \times 10^{-2}T) + 17.178]$, $t = [10.84 (\ln \rho_s + 1.43 \times 10^{-2}T - 17.178)^{-1}]$, and $T = [(-69.93 \ln \rho_s) + (7.58 \times 10^2 t^{-1}) + 12.013 \times 10^2]$ (with ρ_s in $\Omega/\square$, t in min, and T in °C).

These results agree fairly well with those of Fig. 1 and confirmed the validity of a general expression of the form

$$\rho_s = \exp (Pt^{-1} + QT + R) \qquad [1]$$

Computer-derived equations were then sought for the information contained in Fig. 1 and several runs

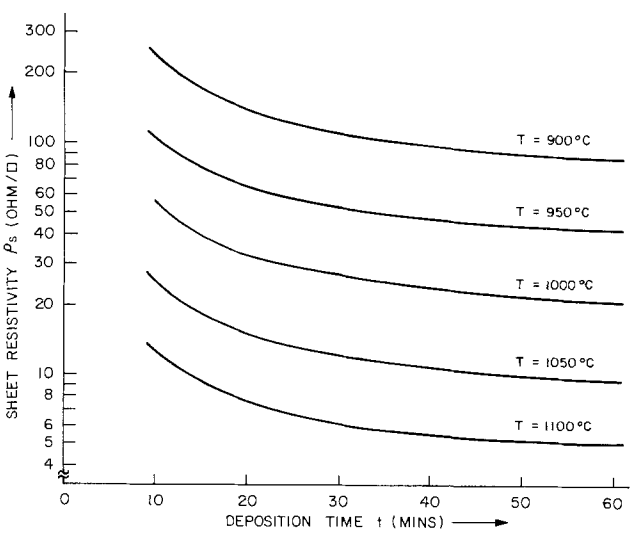


Fig. 1. Log sheet resistivity-deposition time plot using oxidized boron nitride disks as a source of boron.

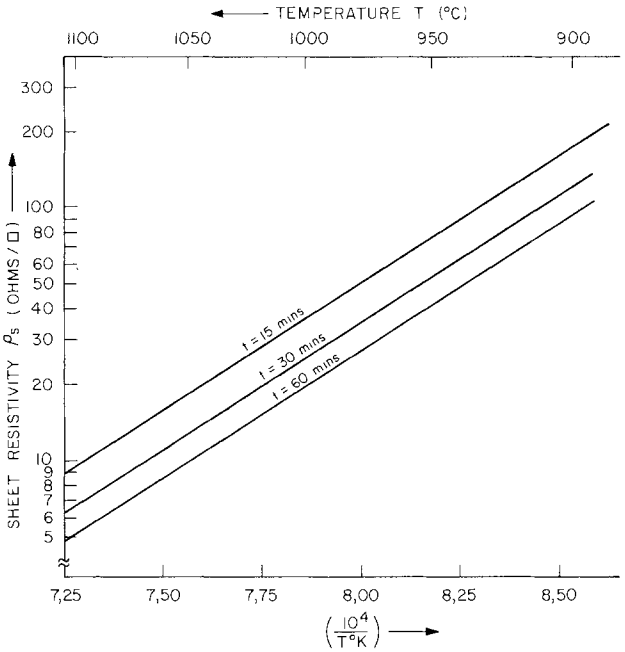


Fig. 2. Log sheet resistivity-temperature/reciprocal absolute temperature plot.

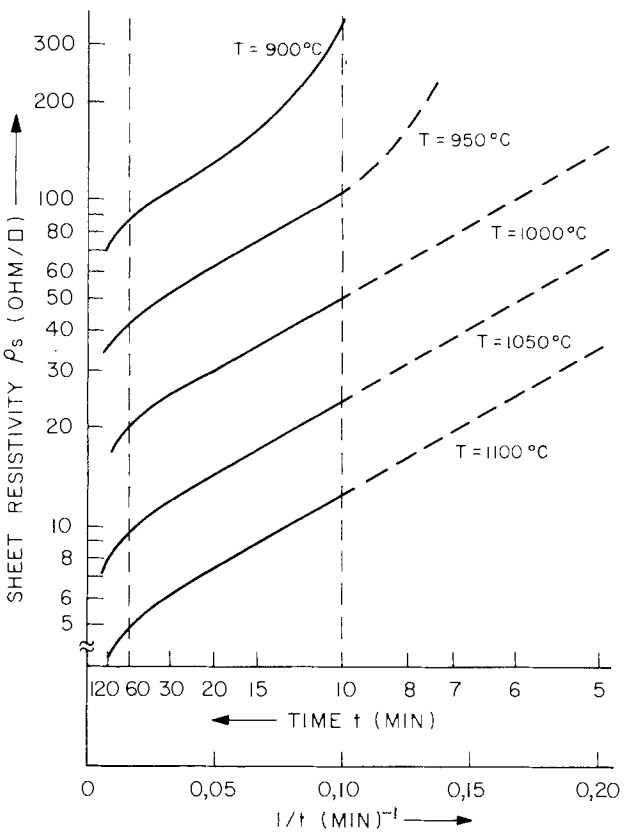


Fig. 3. Log sheet resistivity-reciprocal time plot

were made with slight computer program variations in order to determine the best fit to the experimental data. The final computer-derived equations considered acceptable were those in which the experimental ρ_s data were initially subjected to a smoothing technique and in which it was assumed that t could be better described by the addition of a constant to the experimental t value. These procedures are briefly described below.

Smoothing of the experimental data in Fig. 1 was based on Eq. [1] where, for a given value of t, say t_1, the corresponding values of T are T_1 and T_2, and ρ_{s1} and ρ_{s2} are the values of ρ_s corresponding to T_1 and t_1;

and T_2 and t_1, respectively, so that $\ln \rho_{s1} = (P/t_1) + QT_1 + R$ and $\ln \rho_{s2} = (P/t_1) + QT_2 + R$ and therefore $\ln \rho_{s1} - \ln \rho_{s2} = Q(T_1 - T_2)$. An estimate of the value of Q was made using the experimental data available. Before further calculations were attempted all the experimental values of ρ_s were adjusted to satisfy this formula, and in such a way that for each value of t the rms of the adjustments was a minimum.

The assumption regarding t is based on the consideration that the value of t used in Eq. [1] is in error and a system-dependent characteristic value (Z) must be added according to a formulation of the type $t^* = t + Z$. The value of Z is peculiar to a given experimental system and is dependent on the conditions applicable to that deposition system and may include factors such as the source-silicon spacing, thermal mass of the source holder, etc. Equation [1] can be rewritten as

$$\rho_s = \exp(Pt^{*-1} + QT + R)$$
$$= \exp[P(t + Z)^{-1} + QT + R] \quad [2]$$

An estimate of Z for any boron nitride deposition system is obtained by expanding $P(t + Z)^{-1}$ in a series of ascending powers of t which will provide an approximation to any required degree of accuracy. Thus

$$P/t^* = P/(t + Z) = P/t\left(1 + \frac{Z}{t}\right)$$
$$= (P/t)\left(1 + \frac{Z}{t}\right)^{-1}$$
$$= (P_1/t) - (P_2/t^2) + (P_3/t^3) + \ldots$$
$$(\text{where } P_2 = P_1Z, P_3 = P_1Z^2, \ldots)$$

so that the general expression of Eq. [2], using only the first two terms of this series expansion, is modified to

$$\rho_s = \exp(P_1t^{-1} - P_2t^{-2} + QT + R) \quad [3]$$

Using the smoothed (adjusted) ρ_s data, the method of least squares is used to compute the coefficients P_1, P_2, Q, and R. From the computed values of P_1 and P_2 the required estimate of Z is obtained for Eq. [2], *viz.*, $Z = (P_2/P_1)$. Using this value of Z in the new general expression

$$\rho_s = \exp(P't^{*-1} + Q'T + R') \quad [4]$$

where $t^* = (t + Z)$, and applying the method of least squares to determine the value of the coefficients P', Q', and R', the full expressions relating ρ_s, t^*, and T to each other for any system can be computed.

Under the conditions applicable to our deposition system, solution of Eq. [3] with smoothed (adjusted) ρ_s data (seven points per curve) yielded $P_1 = 16.278$ and $P_2 = 44.215$ and, therefore, $Z = P_2/P_1 = 2.72$. [Since the experimental t (Fig. 1) varies from 10 to 60 min, Z/t, ranging from 0.27 (*i.e.*, 2.72/10) to 0.045 (*i.e.*, 2.72/60) with these data, is not very small, and therefore this value of Z can only be an approximation.] The full expressions, with coefficients not rounded off, interrelating ρ_s, t^*, and T for our system are given by

$$\rho_s = \exp(15.363\, t^{*-1} - 1.44 \times 10^{-2} T + 17.219) \quad [5]$$

$$t^* = (9.4 \times 10^{-4} T + 6.509 \times 10^{-2} \ln \rho_s - 1.121)^{-1} \quad [6]$$

$$T = -69.24 \ln \rho_s + 1063.75\, t^{*-1} + 1192.29 \quad [7]$$

(with ρ_s in $\Omega/\square$, t in min, and T in °C).

Using the smoothed ρ_s values at the given experimental values of t and T of Fig. 1, the percentage error between the calculated t using Eq. [6] and the experimental t, varied between −3.17 and +3.24%, with +3.24% representing a maximum absolute error of 1.9 min in 60 min; while the percentage error between the calculated T using Eq. [7] and the experimental T, varied between −0.085 and +0.161%, with +0.161% representing a maximum absolute error of +1.5°C.

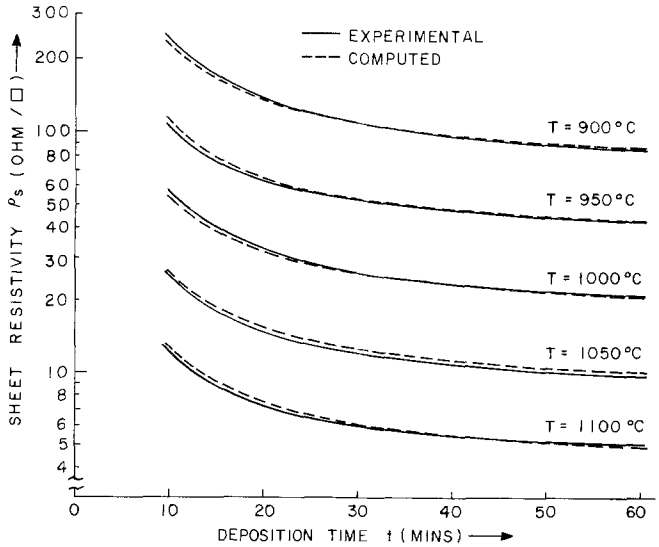


Fig. 4. Log sheet resistivity-deposition time plot. Comparison of experimental and computed data.

The percentage error between the smoothed ρ_s data and that calculated from Eq. [5] varied between −1.09 and +2.23%; while the percentage error in ρ_s between the experimentally determined ρ_s and that calculated from Eq. [5], which is of more practical interest, varied between −8.21 and +5.48%. This latter percentage error is within the accepted reproducibility limits (4-6) of ±10% for routine in-line linear four-point probe measurements. The experimental and computed data for our system are compared in Fig. 4, which shows that there is good agreement.

The indication from computer runs embodying the assumption of an error in experimental t which can be manipulated into an expression for t in ascending powers of t, is that even better fits to the experimental data, especially in t and T, would be obtained if higher powers of t were employed, but considering the reproducibility limits of the four-point probe, such accuracy was not considered warranted.

Conclusion

From experimental data obtained from any given boron nitride deposition system, equations can be computed which relate ρ_s, t, and T and form a basis for the prediction of the third variable when the remaining two are known. In view of the errors inherent in the system of four-point probe resistivity measurement, these predicted values more closely approach best estimates, and, as such, the computed equations form a satisfactory basis for the formulation of a process or design guide for the estimation of ρ_s, t, or T.

Acknowledgments

The authors would like to thank Mr. H. van Eeden for help with the experimental work, Mr. J. D. Stulting for his general assistance, and Miss J. Hewitt of NRIMS for drawing up the computer program and suggesting improvements. The authors acknowledge the support of the C.S.I. R.

Manuscript submitted Aug. 19, 1976, revised manuscript received Nov. 3, 1976.

Any discussion of this paper will appear in a Discussion Section to be published in the December 1977 JOURNAL. All discussions for the December 1977 Discussion Section should be submitted by Aug. 1, 1977.

Publication costs of this article were assisted by the National Electrical Engineering Research Institute.

REFERENCES
1. Technical Bulletin No. 1, A-2289, The Carborundum Company, Latrobe, Pennsylvania (Oct. 1974).
2. J. D. Stulting, M.Sc. Thesis, Rand Afrikaans University (1975).
3. M. Crooke and A. G. K. Lutsch, *Microelectronics*, **7**, 49 (March 1976).
4. K. E. Borbye, Bulletin No. 472-15, Haldor Topsoe, Frederiks-sund, Denmark.
5. P. P. Clerx, *Solid State Technol.*, **12**, 6 (June 1969).
6. J. K. Hargreaves and D. Millard, *Br. J. Appl. Phys.*, **13**, 231 (May 1962).

The High Temperature Oxidation of Plutonium-3.3 a/o Gallium

J. L. Stakebake

Rockwell International, Atomics International Division, Rocky Flats Plant, Golden, Colorado 80401

ABSTRACT

Oxidation of plutonium-3.3 atomic percent (a/o) gallium in air was studied over the temperature range 250°-400°C. A paralinear oxidation process was observed at all temperatures although not clearly defined at 400°C. The temperature dependence of the oxidation rates indicated a change in the oxidation mechanism between 350° and 400°C. This was attributed to the selective formation of PuO or Pu_2O_3 at the metal interface in this temperature range during the parabolic stage and film cracking or nonisothermal oxidation in the linear region. Increasing the water concentration from 7 to 160 ppm resulted in increased oxidation at 350° and 400°C but had no detectable effect at 250° and 300°C.

Plutonium metal is extremely susceptible to oxidation, making it difficult to store and nearly impossible to obtain a clean metal surface. The rate of oxidation depends strongly on three parameters: moisture, metal purity, and temperature. During the last 30 years the effects of these parameters on the oxidation of pure plutonium have been studied by a number of workers (1-10). These studies showed that small changes in low level moisture concentrations have very significant effects on the low temperature oxidation rate. For example, Schnizlein and Fischer (4) found that at 190°C an increase in the moisture content of oxygen from 21 to 180 ppm resulted in a rate increase of from 1.2 to 1.5 $\mu g/cm^2 \cdot min$. By further increasing the moisture content to 510 ppm, they found the oxidation rate increased to 3.4 $\mu g/cm^2 \cdot min$. Thompson (5) found that at 85°C an increase in the moisture content of an oxygen atmosphere from 1.5 to 35 ppm resulted in an oxidation rate increase from 19.1 to 38.6 $\mu g/cm^2 \cdot hr$.

Based on this earlier work, the accelerating effect moisture has on plutonium oxidation appeared limited to temperatures below about 200°C. The only published work which has evaluated the effect of moisture at elevated temperatures was that by Schnizlein and Fischer (4) using unalloyed plutonium. Their experiments, performed with less than 5 ppm moisture in oxygen at 300° and 400°C, produced essentially the same rates as those performed with a few hundred parts per million. Two experiments were also carried out with 20,000 ppm moisture in air at 430°C with no evident effect on the oxidation rate. They concluded that the presence of moisture had no effect on the oxidation rate above 215°C.

When considering plutonium oxidation it has generally been found that impurities, particularly if they are metallic, reduce the rate of oxidation. It follows then that plutonium alloys should oxidize slower than the pure metal. Those metals which reduce oxidation when alloyed with plutonium include cerium, hafnium, zinc (2), aluminum (2-3), and gallium (6). The addition of gallium to plutonium has been used primarily to extend the stability of the metal in the delta phase. The fact that it also confers a degree of protection against oxidation is an added bonus. Only a few studies have been made at temperatures below 100°C to evaluate the decreased oxidation resulting from the presence of gallium. Waber (7) investigated the effect of various concentrations of gallium on the rate of oxidation of plutonium at 75°C in both dry air and air containing 50% relative humidity. Figures 1 and 2 show the results for alloys containing 0.7, 2.1, and 3.4 a/o gallium. The addition of gallium had only a minimal effect on the oxidation in dry air but it became significant in the presence of moisture.

At low temperatures water vapor is the major contributor to high oxidation rates. However, with current technology plutonium would rarely be exposed to a high humidity environment. On the other hand, plutonium and plutonium alloys are repeatedly exposed to high temperatures during annealing and homogeniza-

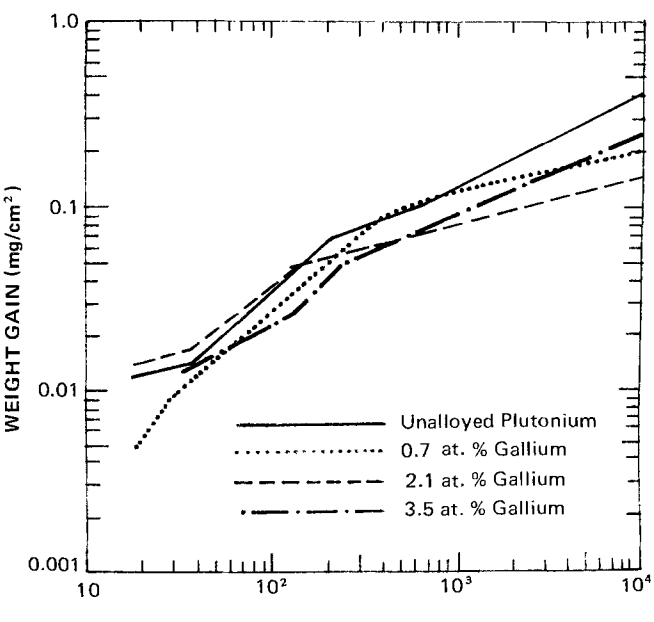


Fig. 1. The effect of gallium concentration on the rate of plutonium oxidation in dry air at 75°C (7).

Key words: corrosion, plutonium oxidation, metal oxidation.

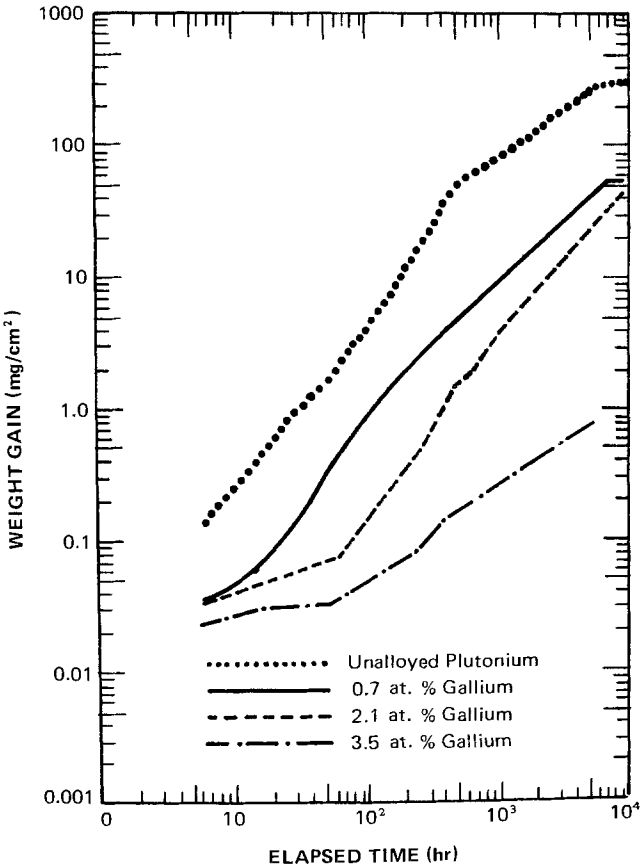


Fig. 2. The effect of gallium concentration on the rate of plutonium oxidation in air containing 50% relative humidity at 75°C (7).

tion. The only work concerned with the high temperature oxidation of a plutonium-gallium alloy was performed by Wright and Waber (6). Their data showed that the addition of 3.5 a/o gallium did confer protection against oxidation in the temperature range 276°-400°C. In all of the runs made by these workers, the oxidation reaction underwent an arrest, the duration of which was temperature dependent. Following the arrest an accelerating rate was observed.

The present investigation was carried out to provide additional information on the high temperature oxidation of plutonium alloys. For this study a plutonium-3.3 a/o gallium alloy was examined. Oxidation kinetics were determined in air from 250° to 400°C. The effect of low moisture concentrations on the high temperature oxidation of this plutonium alloy was also evaluated.

Experimental

Apparatus.—The experimental system used in this investigation is shown in Fig. 3. A Cahn Model RG recording microbalance was used to continuously monitor the reactions. The balance was contained in a glass chamber which was attached to a metal vacuum system. Since plutonium is radioactive, additional precautions were required to prevent the release of any radioactive contamination. These included mounting the entire experimental system in a hood with a high velocity air flow and special sample handling procedures. The working pressure within the system could be varied from 10^{-4} Pa (10^{-6} Torr) to 6.7×10^4 Pa (500 Torr) and was measured with either an ionization gauge or a capacitance manometer. The sample was heated with a resistance heater controlled with a power proportioning programmer. Actual sample temperatures were continuously recorded using a thermocouple located adjacent to the sample inside the hangdown tube. Moisture was monitored with a Panametrics hygrometer with the probe located within the system.

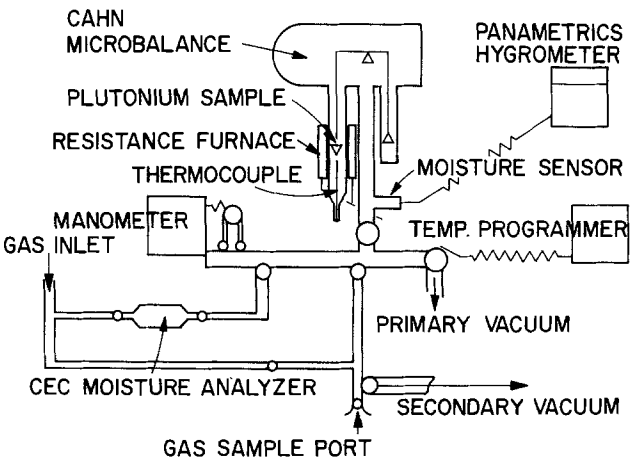


Fig. 3. Experimental system for the study of metal oxidation

Samples.—A plutonium-3.3 a/o gallium alloy was used for these oxidation studies. The presence of gallium stabilized the plutonium in the delta phase and enhanced its desirable metallurgical properties. The concentration of impurities in the alloy totaled 674 ppm_w. Results from a spark source mass spectrometer analysis of the sample are tabulated in Table I. Specimens averaging 1 cm^2 in total surface area were cut from a sheet 0.8 mm thick. This sheet was prepared by cold-rolling a sheet about 3 mm thick. Coupons were individually prepared for oxidation by mechanically abrading with 600 grit SiC paper.

Procedure.—Immediately after abrading, the samples were loaded on the balance and the system was evacuated. The samples were maintained under a dynamic vacuum of 4×10^{-4} Pa for about 20 hr. Following evacuation the sample was heated to the desired temperature and the system was backfilled to 4×10^4 Pa (300 Torr) with air.

Oxidation runs were made at 250°, 300°, 350°, and 400°C. One of the problems encountered in using the microbalance at high temperatures is thermal instability. For the temperatures used in this study, 4×10^4 Pa was the maximum pressure which could be used without creating intolerable thermal effects.

Oxidation was carried out in dry air obtained commercially. The significant difference between the two cylinders of air used for this study was the moisture content. Moisture analyses were made under flowing conditions using both the Panameterics hygrometer and a CEC moisture analyzer. 2 hr were allowed under the flowing conditions for the sensors to reach equilibrium. From these measurements the moisture levels in the air cylinders were determined to be 7 ppm for cylinder D and 160 ppm for cylinder W.

Data from the oxidation runs were processed using a digital computer curve fitting program (11) to determine the best equation for the data. In many cases, it was difficult to fit the data to any one simple rate equation because changes during the oxidation runs were frequent. For this study the first 100-200 min of the oxidation were fit to the parabolic rate equation while the last 200-400 min of the reaction were fit to a linear equation.

Table I. Mass spectrometer analysis of the bulk Pu-3.3 a/o Ga alloy

Element	Al	C	Cr	Cu	Fe	Mg	Mn	Ni	Np	O
Concentration, ppm_w	42	71	27	14	204	2	9	61	20	33

Element	P	Si	Sn	Ta	U	Zn	Other	Total
Concentration, ppm_w	7	60	6	14	76	12	16	674

Results and Discussion

Oxidation kinetics.—Initially, two different sets of apparatus were used to make triplicate runs at each temperature. However, results from one system could not be reproduced on the other balance even though the results for each system were reproducible. These variations were attributed to two possible causes: temperature variations between the two systems and different moisture concentrations in the two cylinders of air being used. In order to attain reproducibility and also evaluate the effect of low moisture concentrations, all runs reported here were made using the same experimental system.

Oxidation curves for runs made in air between 250° and 400°C are shown in Fig. 4-6. Each curve represents the fit obtained from two or more experimental runs. In Fig. 4 oxidation data from the runs in air containing 7 or 160 ppm water vapor were combined in a single curve. Examination of these curves indicated that the reaction kinetics might best be described by using a combination of parabolic and linear rate equations. Runs at 250°, 300°, and 350°C all showed an initial parabolic behavior which transformed into a linear rate as the run progressed (Fig. 4, 5). At 400°C several different factors appeared to be involved. Initially, the accelerating rate suggested that nucleation was the controlling factor during the first 5-6 min. This was not surprising considering the fast reaction rate and the lack of a perfectly clean surface prior to starting the run. The type of nucleation involved is uncertain. It could involve the growth of new oxide crystals on an oxide base film or merely the cracking of the initial oxide film present on the sample. After the first 6 min it was difficult to tell from the kinetic data alone whether the rate was parabolic as it appeared. The rate process could be linear with the decreasing rate caused by a decreasing sample size. The final sample size was calculated from the total amount of oxide formed. The reduced size did contribute to the decrease in rate but was not significant enough to cause the observed effect.

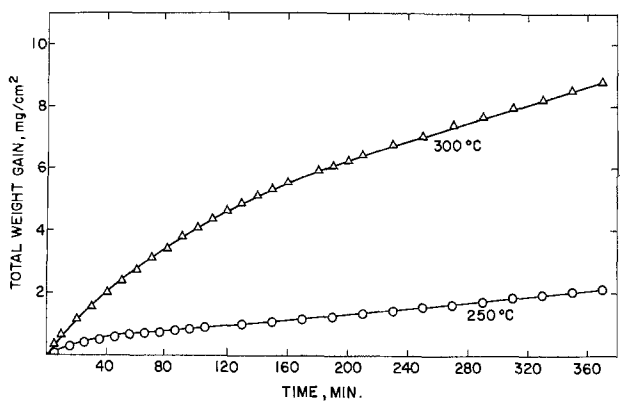


Fig. 4. Oxidation of plutonium-3.3 a/o gallium at 250° and 300°C in air containing 7 or 160 ppm water.

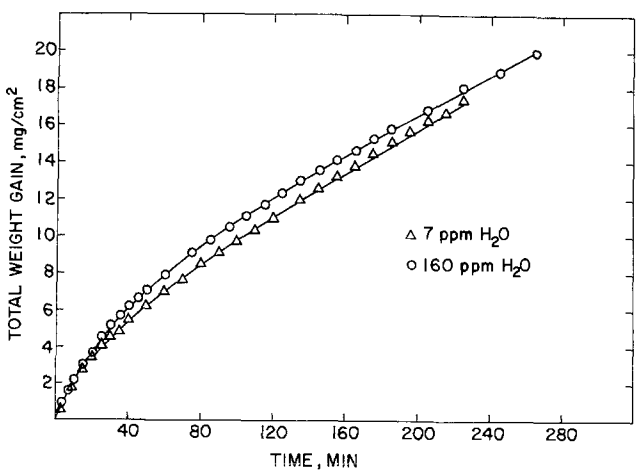


Fig. 5. The effect of low level moisture concentrations on the oxidation of plutonium-3.3 a/o gallium in air at 350°C.

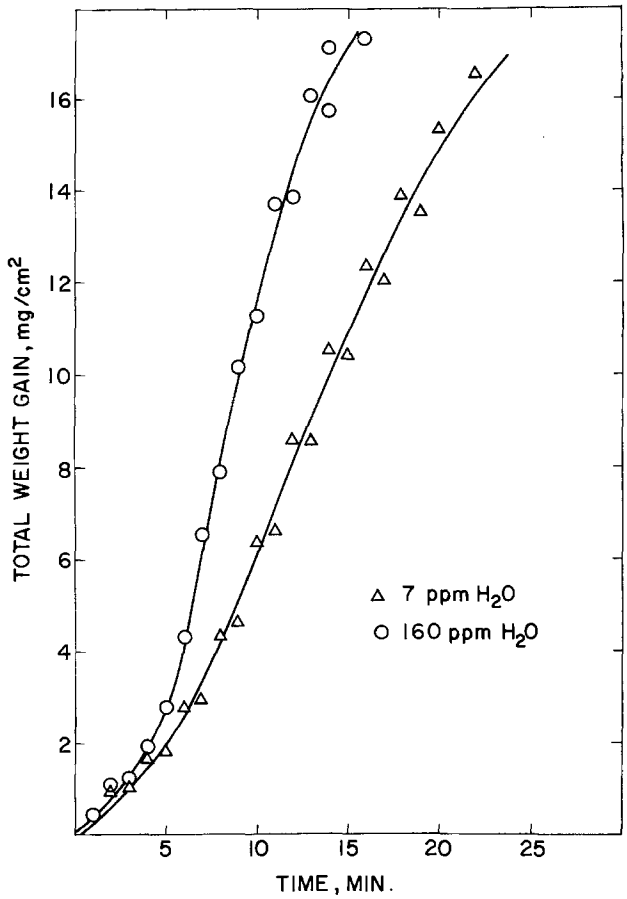


Fig. 6. The effect of low level moisture concentrations on the oxidation of plutonium-3.3 a/o gallium in air at 400°C.

Parabolic kinetics.—Oxidation data for all of the runs were evaluated using the equation $x = kt^{1/2} + c$. A plot of the data obtained in air with 7 ppm water using this equation is shown in Fig. 7. These data are for time intervals up to 400 min. Beyond about 200 min, however, the rate law begins to change from parabolic to linear. The initial portion of these runs deviated from the parabolic rate. This is most likely the result of interface-controlled reactions occurring before the diffusion controlling film forms. A similar set of curves can be obtained for the runs in air with 160 ppm of water. Rate constants for the parabolic portion of all experimental runs were obtained from a computer fit of the data to the above equation and are tabulated in Table II.

The activation energy for the parabolic rate process can be calculated using the Arrhenius equation

$$k = Ae^{-\Delta H/RT}$$

Since the parabolic equation used for this study was in the form $x = kt^{1/2} + c$, a plot of 2 ln k *vs.* $1/T$ is required to satisfy the Arrhenius equation (13). Such a plot is shown in Fig. 8 for the runs in air with both 7 and 160 ppm water vapor. A single curve could not be satisfactorily fit through all the data, thus resulting in two activation energies for the parabolic process. Between 250° and 350°C the activation energy was calculated to be 33 kcal/mole. This value can be compared with the value of 29.2 kcal/mole observed for unalloyed plutonium over the same temperature range (4).

Between 350° and 400°C there was a break in the Arrhenius plot indicating a possible change in the reaction mechanism. The parabolic activation energy was

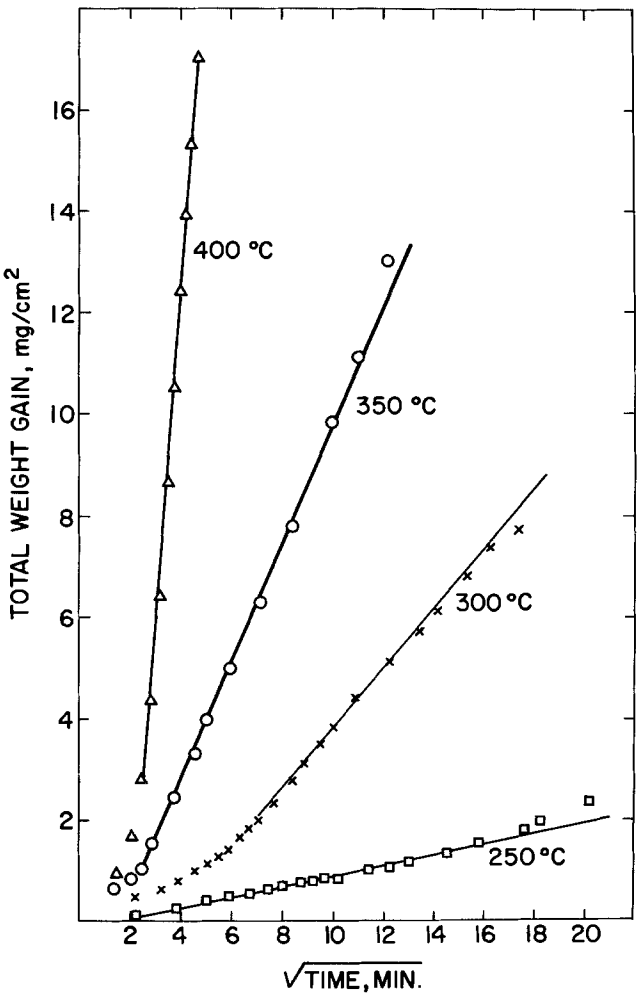


Fig. 7. Parabolic plots of the oxidation data obtained in air with 7 ppm water.

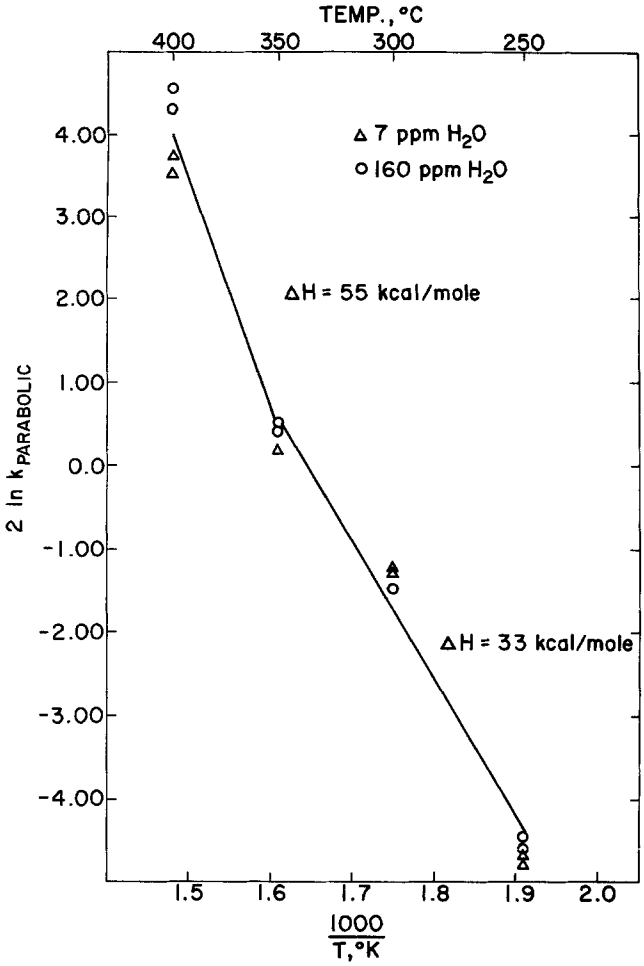


Fig. 8. Arrhenius plot of the parabolic rate constants obtained for runs in air with 7 or 160 ppm water.

calculated to be 55 kcal/mole. This value was significantly higher than the previously reported value of 38 kcal/mole for unalloyed or alloyed plutonium (4).

Linear kinetics.—Following the initial film formation resulting in parabolic kinetics, the oxidation process became linear. Linear rate constants were calculated for each run beginning after about 200 min had elapsed. In the case of the runs at 400°C, data from the last half of the runs were used. Table II tabulates the rates obtained from a least squares fit of the data to the linear equation.

The activation energy for the linear oxidation was obtained from the Arrhenius plot shown in Fig. 9. As in

Table II. Oxidation rates for the oxidation of Pu-3.3 a/o Ga in air

Run	Temperature, °C	Moisture, ppm	Rate constants: Parabolic, mg/cm²min^1/2	Rate constants: Linear, mg/cm²min
250-1D	250	7	0.089	0.0032
250-3D	250	7	0.097	0.0049
250-1W	250	160	0.108	0.0054
250-2W	250	160	0.100	0.0055
300-1D	300	7	0.52	0.013
300-3D	300	7	0.54	0.014
300-4D	300	7	0.53	0.014
300-1W	300	160	0.52	0.014
300-2W	300	160	0.48	0.013
300-3W	300	160	0.52	0.014
350-1D	350	7	1.13	0.064
350-2D	350	7	1.12	0.061
350-3W	350	160	1.28	NA
350-4W	350	160	1.30	0.047
350-5W	350	160	1.24	0.054
400-1D	400	7	6.43	0.85
400-2D	400	7	5.77	0.86
400-1W	400	160	9.89	1.53
400-2W	400	160	8.60	1.16

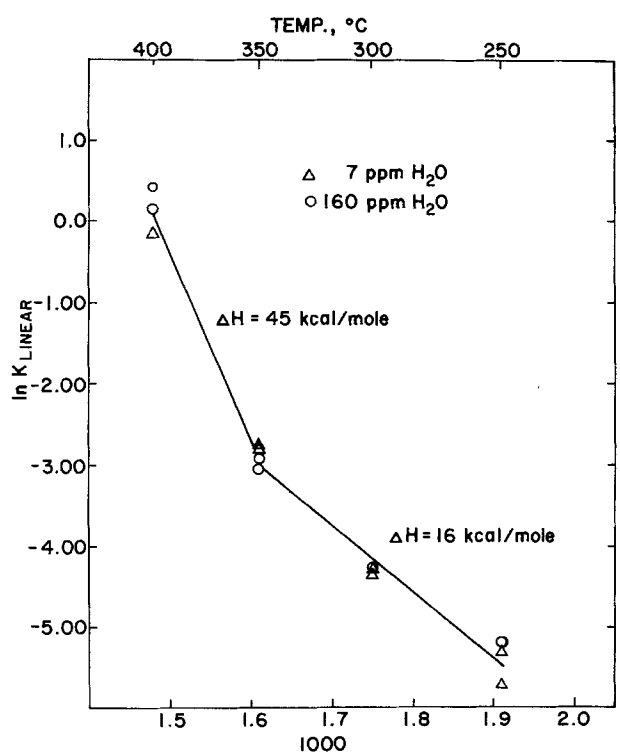


Fig. 9. Arrhenius plot of the linear rate constants for runs in air with 7 or 160 ppm water.

the case of the parabolic oxidation, there was a break in the curve indicating a change in mechanism. Between 250° and 350°C, the activation energy was 16

kcal/mole. This is the same value as reported for unalloyed plutonium for the same temperature range. Above 350°C, the activation energy increased to 45 kcal/mole. Again, this activation energy was significantly higher than that previously reported for a linear process.

Oxidation Mechanism

Paralinear kinetics have been observed for the oxidation of a number of metals (12) as well as plutonium (4). The mechanism which explains this behavior suggests an initial growth of a compact adherent oxide film of a limited thickness. This growth process, which is diffusion controlled, results in a parabolic rate law. Following the initial parabolic rate process, the reaction rate becomes linear. The change from a parabolic to a linear rate law can result from several processes. These include: phase boundary processes involving metal/oxide or oxide/oxide interfaces or diffusion through an oxide film of constant thickness. Fracture of the oxide film is still another cause for the change from parabolic to linear rates. Formation of a porous oxide, resulting in a reaction at the adherent oxide/porous oxide interface is probably the most common explanation. This porous oxide can be formed by further oxidation or recrystallization of the adherent oxide film.

Loriers (13) has attributed the paralinear oxidation of cerium to the growth of a porous CeO_2 on a compact layer of Ce_2O_3. Plutonium also forms multiple oxides including PuO, Pu_2O_3, and PuO_2. Terada *et al.* (15) have shown that under vacuum, above 200°C, the PuO_2 film is very rapidly reduced by the metal to α-Pu_2O_3. Furthermore, above 350°C one might expect almost equal amounts of PuO and α-Pu_2O_3 to be present in the oxide film. The proposed reaction sequence is

$$Pu + 3PuO_2 \rightarrow 2\alpha\text{-}Pu_2O_3 \quad [1]$$

$$\alpha\text{-}Pu_2O_3 + Pu \rightarrow 3PuO \quad [2]$$

These oxides have been found to be protective toward further oxidation (16, 17). In the present investigation the samples were heated in vacuum for periods of 10-15 min prior to the start of the run. This would be sufficient time to assure the presence of a layer of PuO or α-Pu_2O_3 on the surface. A compact layer of these oxides would result in a diffusion-controlled parabolic oxidation rate. Further oxidation of PuO or Pu_2O_3 produces PuO_2 which is porous and less coherent. The linear oxidation rate then results from the oxidation of the lower plutonium oxides.

Lindsay *et al.* (17) found that at 175°C the protective film of α-Pu_2O_3 initially increased and then decreased producing an accelerated rate as it was oxidized to PuO_2. Under these conditions it was reported that the α-Pu_2O_3 was completely depleted by oxidation and did not reform. The temperature at which the present runs were made was in the range 250°-400°C where both PuO and α-Pu_2O_3 form more rapidly. During the course of the runs there was no accelerating rate, except at 400°C, which would be expected if the surface film were being depleted. The linear reaction, therefore, is assumed to result from and be controlled by oxidation at the oxide/oxide interface. Additional work is required to identify the oxide film present at the metal/oxide interface.

Calculations of activation energies are frequently useful for evaluating the mechanism of oxidation. During parabolic oxidation the reaction is controlled by the inward diffusion of oxygen ions. The activation energies calculated for parabolic oxidation changed from 33 kcal/mole to 55 kcal/mole at about 350°C. The magnitude of these values is on the order of that expected for diffusion process. The break in the Arrhenius curves which results in the activation energy increasing to 55 kcal/mole is indicative of a mechanism change. This observation is not unusual. It could be caused by two different protective oxides, such as in the case of copper (18). For plutonium, the monoxide, PuO, may be significantly involved at these higher temperatures. However, PuO has not been prepared in bulk and little is known about its behavior. Furthermore, a complete explanation of the role of diffusion requires a knowledge of the defect structure of the protective plutonium oxides. Here again, little information is available on this subject and what work that has been done has been in the single phase region of PuO_2 (3).

During linear oxidation the formation of the nonuniform layer of PuO_2 predominates. The volume ratio of this oxide indicates that it is the least protective of all the plutonium oxides. Since this oxide is porous and allows free access of oxygen to the protective oxide layer, the linear process is controlled by the oxide (PuO + Pu_2O_3)/oxygen interface reaction.

The Arrhenius plot of the linear rate constants gave two straight lines with activation energies of 16 and 45 kcal/mole. At temperatures up to 350°C it is proposed that the activation energy of 16 kcal/mole is associated with the oxidation of the suboxides. There are two possible causes for the observed change in the temperature dependence of the oxidation rate. First is the breakdown of the protective oxide layer and the continuous exposure of fresh metal. The second possible cause is the amount of heat produced by oxidation. When a metal oxidizes linearly, large quantities of heat are produced per unit time. Above a certain temperature the amount of heat produced will exceed the amount conducted away to the surroundings. Therefore, the temperature rises progressively and the oxidation reaction becomes self-accelerating. This type of behavior has been observed for cerium (19) (above 290°C) and thorium (20) (above 500°C). Very likely both of these causes are involved in the oxidation of plutonium above 350°C.

Effect of moisture.—The role of water in the low temperature oxidation of plutonium has frequently been reported (9, 10). At temperatures greater than 100°C, however, the information is very limited. It is generally agreed that moisture will increase the oxidation rate, at least up to 200°C (4). Above 215°C, however, moisture was reported to have no effect on the oxidation of unalloyed plutonium (4). From the present work, runs at 250° and 300°C (Fig. 4) were unaffected by moisture variations of 7-160 ppm. At 350°C (Fig. 5) the difference between oxidation in air with 7 and 160 ppm water appeared to become significant. The error bars for these two curves are smaller than the data points shown on the figure. The parabolic oxidation rate increased from 1.12 to 1.27 mg/cm^{2}min$^{1/2}$ with the moisture increase of from 7 to 160 ppm. At 400°C (Fig. 6) the effect was even more pronounced. The parabolic oxidation rate increased from 6.1 to 9.2 mg/cm^{2}min$^{1/2}$ with the increase of 153 ppm of water.

Water vapor did not appear to significantly affect the linear oxidation process until the temperature was above 350°C. At 250°C there was a slight rate increase, however at 300°C there was no rate change, and at 350°C the oxidation rate actually decreased with the addition of moisture. The linear rate at 400°C began to increase significantly when the moisture level went from 7 to 160 ppm. Under these conditions the rate increased from 0.86 mg/cm^2 to 1.34 mg/cm^2.

Results from this study cannot be considered all inclusive with respect to the effects of water vapor, but they do indicate that water vapor does influence the high temperature oxidation of plutonium. Furthermore, the accelerating effects of very low moisture concentrations increased with temperature beginning at about 350°C.

Conclusion

The oxidation of a plutonium-3.3 a/o gallium alloy was investigated in air between 250° and 400°C. Oxidation kinetics were paralinear with a mechanism change occurring at 350°C. This change was attributed to the formation of plutonium suboxides, probably

PuO, during parabolic oxidation and either nonisothermal oxidation or film cracking in the linear oxidation stage. The temperature dependence of the oxidation rate as derived from the Arrhenius equation resulted in four expressions. Below 350°C the parabolic rate constant is defined as

$$k_{\text{parabolic}} = 8.5 \times 10^{11} [\exp(-33{,}100/RT)] \text{mg/cm}^2\text{min}^{1/2}$$

The linear rate constant between 250° and 350°C was

$$k_{\text{linear}} = 2.9 \times 10^{4} [\exp(-16{,}400/RT)] \text{mg/cm}^2\text{min}$$

Above 350°C the parabolic rate constant could be expressed as

$$k_{\text{parabolic}} = 4.7 \times 10^{19} [\exp(-55{,}400/RT)] \text{mg/cm}^2\text{min}^{1/2}$$

while the linear rate became

$$k_{\text{linear}} = 4.0 \times 10^{14} [\exp(-45{,}000/RT)] \text{mg/cm}^2\text{min}$$

These rate expressions represent average values and no attempt was made to distinguish between the 7 or 160 ppm moisture levels. Above 350°C some accelerating effects on the oxidation rate due to the increased moisture were noted. At 400°C this slight increase in moisture was sufficient to increase the oxidation rate from 6.1 to 9.2 mg/cm^{2}min$^{1/2}$. The greatest deviation from the generalized rate equations was observed at 400°C where the moisture effect was most prominent. All of the reactions were smooth and continuous with no evidence of a reaction arrest.

Acknowledgments

This work was performed under the auspices of the Energy Research and Development Administration Contract E(29-2)-3533.

Manuscript submitted July 20, 1976; revised manuscript received Nov. 15, 1976.

Any discussion of this paper will appear in a Discussion Section to be published in the December 1977 JOURNAL. All discussions for the December 1977 Discussion Section should be submitted by Aug. 1, 1977.

Publication costs of this article were assisted by Rockwell International.

REFERENCES

1. J. L. Stakebake, *J. Nucl. Mater.*, **38**, 241 (1971).
2. O. J. Wick, Editor, "Plutonium Handbook," Vol. 1, Gordon and Breach, Science Publishers, New York (1967).
3. C. A. Colmenares, in "Progress in Solid State Chemistry," Vol. 9, J. McCaldin and G. Somorjai, Editors, Pergamon Press, New York (1974).
4. J. G. Schnizlein and D. F. Fischer, *This Journal*, **114**, 23 (1967).
5. M. A. Thompson, in "Plutonium Handbook," Vol. 1, O. J. Wick, Editor, p. 155, Gordon and Breach, Science Publishers, New York (1967).
6. E. S. Wright and J. T. Waber, "High Temperature Oxidation of Plutonium and a Plutonium-Gallium Alloy," USAEC Report LA-1593, Los Alamos Scientific Laboratory (1953).
7. J. T. Waber, in "Plutonium Handbook," Vol. 1, O. J. Wick, Editor, p. 156, Gordon and Breach, Science Publishers, New York (1967).
8. D. T. Larson and D. L. Cash, *J. Phys. Chem.*, **73**, 2814 (1969).
9. J. L. Stakebake and L. M. Steward, *This Journal*, **119**, 730 (1972).
10. J. B. Raynor and J. F. Sackman, in "Plutonium 1965," A. E. Kay and M. B. Waldron, Editors, p. 575, Chapman and Hall, London (1967).
11. R. W. Loser, Private communication (1971).
12. O. Kubaschewski and B. E. Hopkins, "Oxidation of Metals and Alloys," p. 35, Butterworths, London (1962).
13. J. Loriers, *C. R.*, **229**, 547 (1949); USAEC Transl. HW-61492.
14. P. Camagni, A. Manara, and E. Landais, *Surf. Sci.*, **10**, 332 (1968).
15. K. Terada, R. L. Meisel, and M. R. Dringman, *J. Nucl. Mater.*, **30**, 340 (1969).
16. C. E. Holly, Jr., R. N. R. Mulford, E. J. Huber, Jr., E. L. Head, E. H. Ellinger, and C. W. Bjorklund, Proceedings of the 2nd ICPUAE, Vol. 5, p. 215, Geneva (1958).
17. J. W. Lindsay, K. Terada, and M. A. Thompson, *This Journal*, **119**, 726 (1972).
18. R. F. Tylecote, *J. Inst. Met.*, **78**, 259 (1950).
19. J. Loriers, *Rev. Metall.*, **49**, 801, 883 (1952).
20. P. Levesque and D. Cubicciotti, *J. Am. Chem. Soc.*, **73**, 2028 (1951).

Technical Notes

Some Observations Concerning GaAs Anodic Oxides

S. Szpak*

Electronic Material Sciences Division, Naval Electronics Laboratory Center, San Diego, California 92152

J. L. Tomlinson

Department of Chemical and Materials Engineering, California State Polytechnic University, Pomona, California 91768

and G. Hari Narayanan

Department of Materials Science, University of Southern California, Los Angeles, California 90007

The efficiency of anodic oxide formation, ϵ_{ox}, on n-GaAs in an electrolyte formulated by Hasegawa and Hartnagel (1) depends on the applied current density (2). In contrast, there is no evidence of parasitic reactions associated with the semiconductor-oxide interfacial charge transfer (2, 3), hence the faradaic efficiency, $\epsilon_F = 1$. The less than 100% efficiency of the growth process may be attributed to: (*i*) transport of reaction product(s) to bulk electrolyte prior to completion of surface coverage (1, 2), (*ii*) dissolution of oxide layer on contact with an electrolyte (1, 2) and (*iii*) transport of nonparticipating species across the growing oxide layer into the bulk electrolyte (2).

This preliminary note is concerned with the effect of growth rate on the accumulation of diffusing substances in the oxide layer and on the oxide structure.

Experimental

Anodic oxides were grown galvanostatically, employing standard procedures and apparatus. Potential decays on open circuit, following current interruption, were displayed on a Hewlett-Packard, Model 7001 AM X-Y recorder. Oxide layers were examined with a Hitachi HU-125 electron microscope operated at 125 kV. Specimens for the microscopic examination were prepared by ion milling from the GaAs substrate side until a small hole was observed. Areas around the hole were sufficiently thin to yield good images.

Results and Discussion

Electrode behavior on approach to V_{rest}.—An approach to the electrode rest potential upon the termination of oxide layer growth to a predetermined thickness, as a function of growth rate, is illustrated in Fig. 1. Qualitatively, the difference in the electrode transient behavior between the fast (solid lines) and the slow (dashed lines) growth rates increases with an increase in the oxide layer thickness. The slow approach to V_{rest} and its dependence on the oxide layer thickness rules out the participation of potential affecting processes within both the electric double layer and the depletion and/or space charge layer. Consequently, the processes responsible for the observed behavior ought to be confined to the oxide layer.

It was shown (2) that anodic oxidation of n-GaAs obeys a relationship

$$j = A \exp(\beta E/RT) \qquad [1]$$

The empirical constant A is related to molecular diffusion, *i.e.*, to a random walk in the absence of field, so that the total current, j, in Eq. [1] is due to a random walk perturbed by an applied electric field, E (β in Eq. [1] contains the jump distance). Thus, upon removal of the applied field, processes operative within the oxide layer are expected to be governed by diffusion. How the driving force, *e.g.*, the concentration or the electrochemical potential gradients needed for the diffusional transport is generated, has not yet been established. It may arise if: (*i*) the electric field is not uniform—presumably not a very likely situation, since the galvanostatic oxide formation is a constant field process, if Eq. [1] is obeyed; (*ii*) there is coupling between the various transports; (*iii*) a reaction of the type: $OH^- + L = O^{-2}L + H^+$ is operative (4); or (*iv*) the dielectric constant of the oxide layer depends on composition which, in turn, may lead to case (*i*).

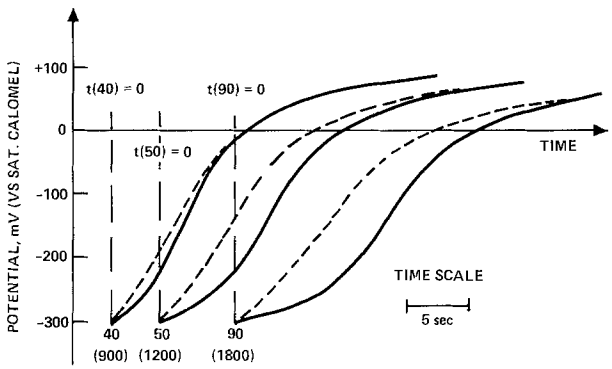


Fig. 1. Approach to electrode rest potential upon interruption of anodic current. Solid lines: $j = 2.25$ mA cm^{-2}; dashed lines: $j = 0.9$ mA cm^{-2} (numbers alongside curves denote cell terminal voltage: 40, 50, 90V or oxide layer thickness 900, 1200, and 1800 in amperes).

The observed potential difference between the initial value of -300 mV and the final value of about $+130 \pm 10$ mV, attained after approximately 30 min, is not unusually large. The approach to the rest potential may be viewed in terms of potential components within the semiconductor-oxide-electrolyte interphase, shown in Fig. 2. During the growth of the oxide layer practically all the potential drop occurs in the oxide with insignificant potential drops in the depletion and/or inversion regions, as well as in the electric double layer. On the open circuit, however, the measured potential is a sum of potentials in the space charge region, V_{sc}, and in the electric double layer, V_{el}, may be affected

* Electrochemical Society Active Member.

Key words: gallium arsenide, anodic oxide, oxide structure, rest potential, growth rate, process efficiency.

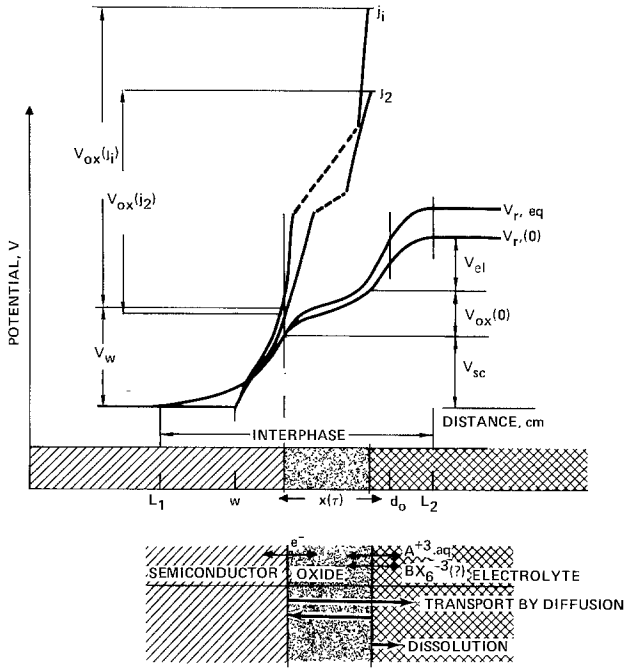


Fig. 2. Schematic representation of various electrical conditions of the semiconductor-oxide-electrolyte interphase. w, depletion region; sc, space charge region; ox, oxide; L_1 and L_2, Debye lengths in semiconductor and electrolyte; d_o, Helmholtz layer; x(τ) oxide layer thickness at current interruption. Potential components and processes indicated.

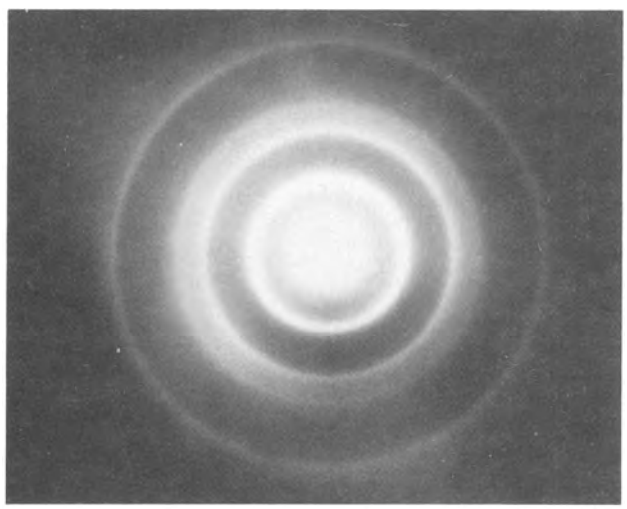
by diffusion of charged species to and from respective interfaces.

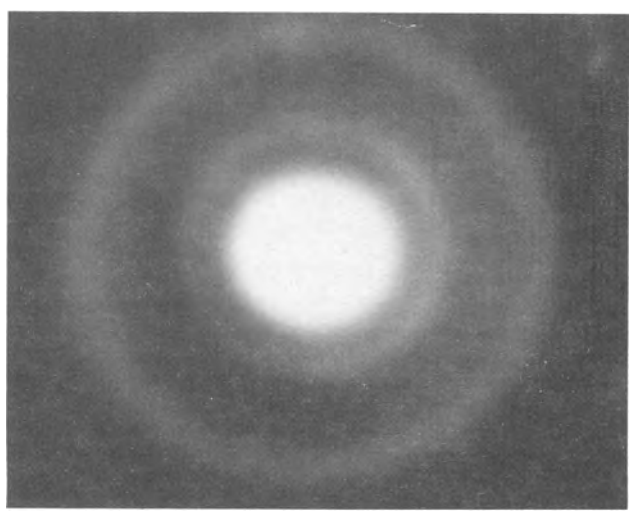
Evidently the electrode potential is not affected by the growth rate immediately after current interruption or after attainment of a stationary state. The latter situation is expected, since it may be viewed as mixed potential due to oxide dissolution on contact with an electrolyte. The former also indicates some kind of a stationary state. The approach to the rest potential if, in fact, diffusion controlled, implies a flat concentration profile of diffusing species, except close to the interface. At high rates a flat profile farther removed from the interface may be postulated as if the oxide growth has overtaken the outward migration of the potential determining species generated at the advancing oxide-semiconductor interface.

Growth rate and oxide structure.—Although no exact relation has been established between growth rate and oxide morphology even for the much studied anodic oxides on Al, nevertheless, it appears that the more severe the anodizing conditions, the more open the oxide structure (5). This observation can be extended to the far less investigated structures of anodic oxides on Si (6).

The structural and chemical properties of anodic oxides formed by the so-called AGW-process (1), were recently discussed by Weiss (7). He reported that bulk oxides were amorphous with crystalline β-Ga_2O_3 on the GaAs surface. Although not specifically stated, it is presumed that the anodizing current density did not exceed 1 mA cm^{-2}.

In an effort to shed additional light on the electrode open-circuit behavior as a function of growth rate, the





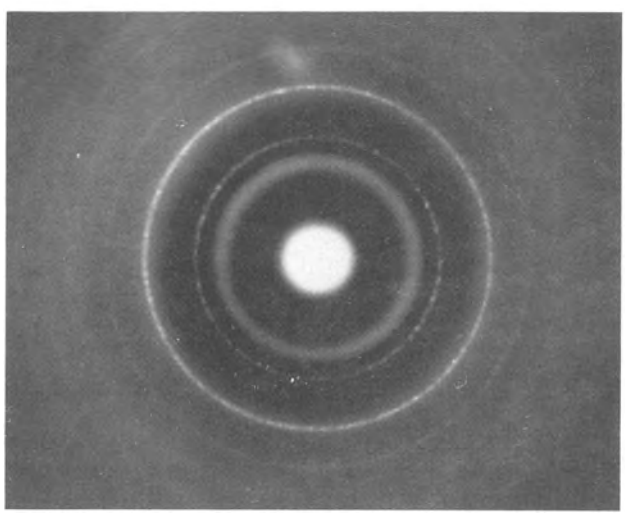


Fig. 3. Diffraction pattern of anodic oxides. (a, above left) Oxide grown at $j = 12$ mA cm^{-2}; (b, above right) oxide grown at $j = 0.25$ mA cm^{-2}; (c, left) effect of heat-treatment on oxide grown at $j = 0.25$ mA cm^{-2}.

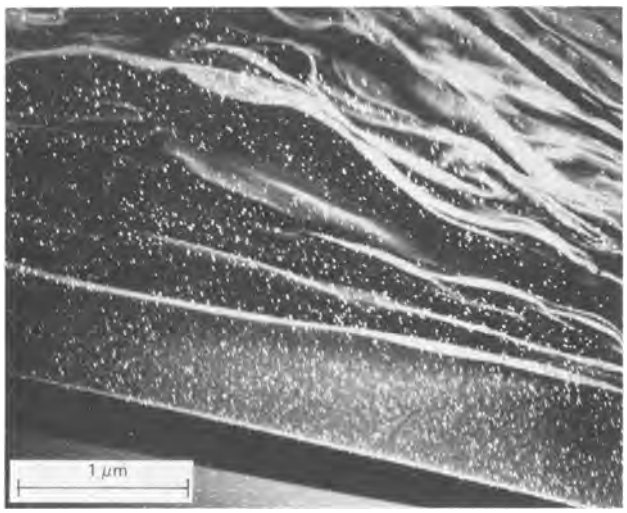


Fig. 4. Electron photomicrograph showing individual crystallites in heat-treated oxide layer imaged by darkfield technique.

bulk oxide grown at high rates ($j = 12$ mA cm^{-2}) and at low rates ($j = 0.25$ mA cm^{-2}) were compared by electron diffraction. As seen in Fig. 3a, oxide grown at high current density (C.D.) differs structurally from that grown at low C.D., Fig. 3b. In the first case, the diffraction pattern consisted of a number of rather sharp rings, while in the second case only few diffuse rings were observed. Thus, oxide grown at low C.D. is less orderly in atomic arrangement than when grown rapidly where well-defined diffraction rings with the absence of spots indicate structurally ordered regions or grains less than approximately 10 nm in size. To distinguish between these structures, we refer to them as amorphous and polycrystalline.

An initially amorphous sample heated in an argon atmosphere showed the diffraction pattern consisting of at least six well-defined rings. As seen in Fig. 3c, these rings are quite spotty, indicating a structure which is even more orderly than either one described previously. This structure is definitely polycrystalline. A dark field transmission electron micrograph, imaged from one of the diffraction spots, is shown in Fig. 4. An abundance of a particular crystallographic orientation of crystallites is evident. The folds or wrinkles in the oxide film are due to distortion induced by heating by the electron beam. Evidently, the initially amorphous oxide layer became, on heating, polycrystalline with randomly oriented grains. However, an attempt to identify the nature of oxides failed. A comparison with ASTM powder diffraction data was not consistent with lattice spacing for either α-, β-, ϵ-Ga_2O_3, or As_2O_3. The diffraction pattern d-spacings and those of respective oxides are shown in Table I. It is possible that, on heating, suboxides or mixed oxides of Ga and As were formed.

Table I. Diffraction pattern d-spacings for heat-treated anodized GaAs in angstroms

Anodic oxide*	α-Ga_2O_3**	β-Ga_2O_3**	ϵ-Ga_2O_3	As_2O_3**
2.50	3.630	5.600	6.420	6.496
2.11	2.651	4.650	4.670	4.924
1.49	2.491	3.660	3.240	4.277
1.22	2.233	2.967	3.170	4.118
1.06	2.177	2.924	2.926	3.717
0.95	2.052	2.816	2.693	3.586
0.86	1.814	2.673	2.528	3.454
	1.665	2.547	2.434	3.356
	1.565	2.396	2.328	3.328
	1.466	2.103	2.250	3.245
	1.438	2.020	2.220	3.129
	1.325	1.978	2.170	2.771

* Observed.
** From ASTM powder diffraction data.

Conclusion

The growth rate of anodic oxides on GaAs in a mixed electrolyte consisting of an aqueous solution of tartaric acid and propylene glycol, affects the growth mechanism. This conclusion is reached by observing the electrode approach to its rest potential and by examining the oxide structure. It is, therefore, suggested that the dependence of the process efficiency on the growth rate is related to, and probably governed by, transport phenomena within the growing layer modified by the oxide structure.

Acknowledgment

One of us (JLT) is indebted to the Department of Materials Science, University of Southern California, for the hospitality extended to him during his stay. This work was supported in part by the Office of Naval Research and in part by the Naval Electronics Laboratory Center Independent Research Program, Z102.

Manuscript submitted Aug. 5, 1976; revised manuscript received Nov. 12, 1976.

Any discussion of this paper will appear in a Discussion Section to be published in the December 1977 JOURNAL. All discussions for the December 1977 Discussion Section should be submitted by Aug. 1, 1977.

Publication costs of this article were assisted by the Naval Electronics Laboratory Center.

REFERENCES

1. H. Hasegawa and H. Hartnagel, *This Journal*, **123**, 713 (1976).
2. S. Szpak, *ibid.*, **124**, 107 (1977).
3. H. Gerischer, *Ber. Bunsenges.*, **69**, 578 (1965).
4. T. P. Hoar and N. F. Mott, *J. Phys. Chem. Solids*, **9**, 97 (1959).
5. G. C. Wood, in "Oxides and Anodic Films," J. W. Diggle, Editor, Marcel Dekker, Inc., New York (1973).
6. A Politycki and E. Fuchs, *Z. Naturforschg.*, **14a**, 271 (1959).
7. B. L. Weiss, in "Final Technical Report," University of Newcastle upon Tyne, Grant No. DA-ERO-75-G-038, 1976.

Accurate Determination of Shallow Zn-Diffusion Profiles in GaP and $GaAs_{0.1}P_{0.9}$ Using Anodic Oxidation and a Double Radioactive Tracer Technique

J. C. Verplanke

Philips Research Laboratories, Eindhoven, The Netherlands

The diffusion of Zn in the system GaP-GaAs is of considerable technological importance for devices.

In light emitting diodes (LED's), the Zn diffusion normally has a depth up to about 10 μm. Not much is known about the actual shape of the Zn profiles in LED's, however, although such knowledge is required in a detailed analysis of their properties. Moreover, a better understanding of the Zn diffusion mechanism might be obtained from accurate data on shallow profiles.

Essentially all the published studies concerning the diffusion of Zn in GaP, GaAs, etc. relate to deep (50-500 μm) profiles (1-9). Mostly parallel sections were removed using lapping techniques or chemical etching. With such methods it is difficult to remove accurately thin ($\sim$0.1 μm) parallel sections, this being a prerequisite for measuring shallow and steep profiles. Thus for the study of such profiles other techniques have to be found. Logan *et al.* (10) mentioned anodic oxidation as a possible method for diffusion studies.

By using anodic oxidation in combination with a double radioactive tracer technique, we were able to remove and analyze thin parallel sections of about 0.1 μm. Diffusions were performed with radioactive ^{65}Zn. Prior to the anodic oxidation, the diffused slice was irradiated with thermal neutrons in order to activate P to radioactive ^{32}P which activity was used for the determination of the removed layer thickness.

Experimental Method

Zn diffusion was carried out into layers of GaP and $GaAs_{0.1}P_{0.9}$, grown by means of vapor phase epitaxy on GaP substrates. No further surface preparation was applied.

The diffusions were performed at 675°C for periods of between 2.5 and 16 hr in 10 cm^3 silica capsules, evacuated to 10^{-5}-10^{-6} Torr, using an alloy source composed of 70% by weight radioactive Zn and 30% Ga. The radioactive isotope was ^{65}Zn (half-life 244 days; gamma energy 1115 keV) and the specific activity was about 100 mCi g^{-1}. Direct contact between diffusion source and sample material was avoided by interposing a perforated piece of silica between them.

After the diffusion the sample was etched in 2*N* HCl for some minutes. Afterward the edges and the back were removed and the sample together with two non-diffused pieces of GaP as standards were irradiated in a thermal neutron flux of about 5×10^{13} n cm^{-2} sec^{-1} for 5 min. During this irradiation the major components of the sample were activated, *e.g.*, Ga to radioactive ^{72}Ga (half-life 14.1 hr) and P to radioactive ^{32}P (half-life 14.3 days). The thickness of the removed layers was calculated from the ^{32}P activity in those layers, the ^{32}P activity in the standards (GaP), and the weight of the standards. In this way very thin layers, *i.e.*, about 0.1 μm, can be measured accurately in the region where direct thickness measurement and weighing are less accurate or unpractical and time consuming. Another advantage is the possibility of continuing the removal of the layers without interruption for measurements of the thickness or weight loss of the sample. The specific activity of Zn increased by less than 0.1% during the irradiation so no correction had to be applied.

Key words: anodic oxidation, Zn diffusion, GaP, $GaAs_{0.1}P_{0.9}$, III-V compounds, radioactive tracer.

After the ^{72}Ga had decayed, parallel layers were removed by means of an anodic oxidation technique. For this purpose the sample was attached to a glass strip. An electric contact was made on the back of the sample to enable a voltage to be applied to it. The part of the contact situated below the liquid level during the anodization was covered with lute. Small parallel layers were now removed as follows:

1. An isolating oxide layer was grown on the surface by means of anodic oxidation in the following bath (11): one volume part of a 3% citric acid solution whose *p*H was adjusted to 6.0 using ammonia and two volume parts of ethylene glycol. The anodic oxidation was carried out by slowly increasing the applied voltage, taking care meanwhile that the current did not surpass a few mA cm^{-2}. As soon as the desired voltage (150V) was reached, it was maintained at this value for 3 min, while the current dropped quickly.
2. The anodization was then stopped and the formed oxide layer was dissolved in warm 10% phosphoric acid.

Using this anodization procedure at an applied voltage of 150V, layers of about 0.10, 0.14, and 0.23 μm were removed for GaP, $GaAs_{0.1}P_{0.9}$, and GaAs, respectively. The removed layer thickness is proportional to the applied voltage. It is recommended, however, not to surpass 150V because above this voltage the surface condition may deteriorate. Sometimes the anodization stopped suddenly, in which case the process was continued by illuminating the sample homogeneously.

After the anodization and dissolution of the oxide layer, two sample fractions have to be measured, *viz.*, the anodization bath and the dissolution bath.

The removed layer thickness was determined by measuring in both fractions the ^{32}P activity in the case of GaP and $GaAs_{0.1}P_{0.9}$. The ^{32}P activity was measured by means of its Čerenkov radiation in an aqueous solution using a liquid scintillation analyzer. The ^{32}P activities of the simultaneously irradiated standards were also measured. In this way very thin removed layers (*e.g.*, 0.1 μm or less) can be measured fairly accurately, *i.e.*, with a precision, expressed as two times the standard deviation, of 3% or better. The systematic error was estimated not to exceed 3%.

The Zn contents of the removed layers were determined by measuring the ^{65}Zn activities in the sample fractions. For this purpose we used high resolution gamma spectrometry with a Ge(Li) detector coupled to a 2048-channels analyzer as well as measurement of the ^{65}Zn spectrum from 1000 to 1250 keV with a NaI(Tl) scintillation detector. The accuracy of the latter method is better on account of better counting statistics due to its higher efficiency for absorbing the 1115 keV gamma rays of ^{65}Zn. At low Zn content, however, fluctuations in the background activity are very critical, so in those cases only results of mea-

surements with the Ge(Li) detector were available. The contribution of the ^{32}P activity to the Zn measurements proved to be negligible.

The precision of the Zn contents, *i.e.*, the possible error due to random variations, expressed as two times the standard deviation, was about 5%. For low Zn concentrations, however, this value could rise to 30%. The systematic error was estimated not to exceed 3%.

From the measurements we found that about 5% of the total removed ^{32}P activity was present in the anodization bath and about 70% of the removed ^{65}Zn activity.

Results

Figures 1 and 2 show examples of diffusion profiles of Zn in GaP and $GaAs_{0.1}P_{0.9}$, respectively, determined in the above-described way.

The first 500Å show a peak in the Zn concentration. This phenomenon might be ascribed to a transition state between the vapor phase with a relatively high Zn activity and the solid phase with a low Zn activity. Except for this peak the profiles can be described rather well by a diffusion coefficient proportional to the square of the Zn concentration. The solid curves show such theoretical profiles.

Thus the interstitial-substitutional diffusion mechanism, which can explain deeper diffusion profiles in GaAs (6) and GaP (4), applies equally well to shallow diffusions in GaP and $GaAs_{0.1}P_{0.9}$.

From the two theoretical profiles, the values of D_o, *i.e.*, the diffusion coefficient at the theoretical surface concentration, were calculated. For GaP we found $D_o = 4.3 \times 10^{-12}$ cm^2 sec^{-1} ([Zn] = 2×10^{18} at · cm^{-3}) and for $GaAs_{0.1}P_{0.9}$ $D_o = 6.5 \times 10^{-12}$ cm^2 sec^{-1} ([Zn] = 2.7×10^{18} at · cm^{-3}). Normalizing D_o to [Zn] = 10^{18} at · cm^{-3}, adopting the proportionality of D_o with [Zn]^2, gave $D_o = 1.1 \times 10^{-12}$ cm^2 sec^{-1} and $D_o = 8.9 \times 10^{-13}$ cm^2 sec^{-1} for GaP and $GaAs_{0.1}P_{0.9}$, respectively.

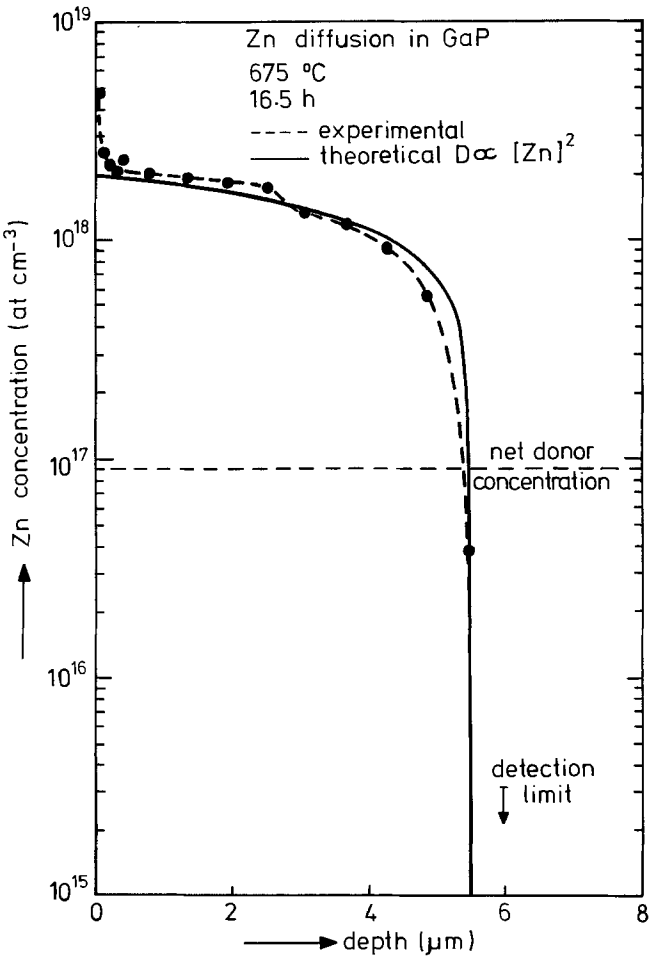


Fig. 1. Zn diffusion profile in GaP. The sample area was 0.57 cm^2. The precision of the lowest Zn concentration is about 20%, that of the other concentrations is about 5%. The indicated detection limit resulted from a 65 hr measurement with a Ge(Li) detector.

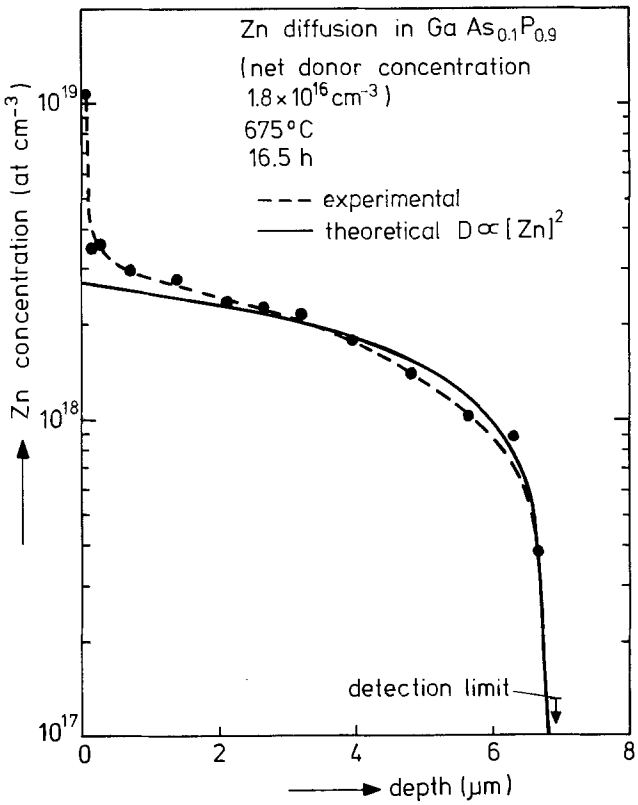


Fig. 2. Zn diffusion profile in $GaAs_{0.1}P_{0.9}$. The sample area was 0.175 cm^2. The precision of the lowest Zn concentration is about 30%, that of the other concentrations is about 10%. The indicated detection limit resulted from a 65 hr measurement with a Ge(Li) detector.

The very good resolution of the present method was confirmed as follows. From the measured profile in GaP, we calculated a gradient of the Zn concentration at the p-n junction of 1.1×10^{22} at · cm^{-4}. This is in good agreement with that obtained from capacitance-voltage measurements, *viz.*, $(1.3 \pm 0.3) \times 10^{22}$ at · cm^{-4} (12). The latter measurements were interpreted by assuming a "mixed graded-abrupt profile" (13), which is indeed the kind of near-junction profile to be expected (14).

The resulting profiles show that the described analyzing method for such shallow Zn diffusion profiles is a very useful technique. Further results will be presented in a later paper.

Acknowledgments

The author would like to thank C. Damen, F. Kuijpers, R. Oostindie, C. van Opdorp, and A. Vink for their help and discussions during this work.

Manuscript submitted Sept. 13, 1976; revised manuscript received Nov. 16, 1976.

Any discussion of this paper will appear in a Discussion Section to be published in the December 1977 JOURNAL. All discussions for the December 1977 Discussion Section should be submitted by Aug. 1, 1977.

Publication costs of this article were assisted by Philips Research Laboratories.

REFERENCES

1. S. R. Showan and D. Shaw, *Phys. Status Solidi*, **32**, 97 (1969).
2. D. Shaw and S. R. Showan, *ibid.*, **32**, 109 (1969).

3. H. C. Casey, M. B. Panish, and L. L. Chang, *Phys. Rev.*, **162**, 660 (1967).
4. L. L. Chang and G. L. Pearson, *J. Appl. Phys.*, **35**, 1960 (1964).
5. L. L. Chang and G. L. Pearson, *ibid.*, **35**, 374 (1964).
6. L. R. Weisberg and J. Blanc, *Phys. Rev.*, **131**, 1548 (1963).
7. M. A. H. Kadhim and B. Tuck, *J. Mater. Sci.*, **7**, 68 (1972).
8. B. Tuck and M. A. H. Kadhim, *ibid.*, **7**, 581 (1972).
9. B. Tuck, *J. Phys. Chem. Solids*, **30**, 253 (1969).
10. R. A. Logan, B. Schwartz, and W. J. Sundburg, *This Journal*, **120**, 1385 (1973).
11. H. Hasegawa, K. E. Forward, and H. Hartnagel, *Electron. Lett.*, **11**, 53 (1975).
12. C. van Opdorp, Private communication.
13. C. van Opdorp, *Solid State Electron.*, **11**, 397 (1968).
14. C. van Opdorp, *J. Appl. Phys.*, **38**, 5411 (1967).

Low Temperature Diffusion of Boron from Diborane Using Carbon Dioxide as Oxidant

Krishna C. Saraswat* and James D. Meindl*

Department of Electrical Engineering, Stanford University, Stanford, California 94305

Boron is widely used to dope p-type silicon. Diborane (B_2H_6) is one of the most widely used sources for thermal diffusion of boron in silicon. The usual technique for open-tube boron diffusion is to pass a mixture of B_2H_6 and O_2; N_2 being the carrier gas (1, 2). The resultant chemical reaction is

$$B_2H_6 + 3\,O_2 \rightarrow B_2O_3 + 3H_2O \qquad [1]$$

Boron trioxide is then deposited on the surface of silicon and acts as a further source of diffusion. B_2O_3 has the following reaction with Si at the B_2O_3-Si interface

$$2B_2O_3 + 3Si \leftrightarrows 4B + 3SiO_2 \qquad [2]$$

The H_2O generated by reaction [1] also reacts with B_2O_3 to form HBO_2 which subsequently reacts with Si to form elemental boron and SiO_2 (1)

$$B_2O_3 + H_2O \rightarrow 2HBO_2 \qquad [3a]$$

$$2HBO_2 + 2Si \rightarrow 2SiO_2 + 2B + H_2 \qquad [3b]$$

The elemental boron produced by reactions [2] and [3] then reacts with silicon to form a Si-B compound known as boron skin (3)

$$Si + nB \leftrightarrows SiB_n \qquad [4]$$

n usually ranges from 4 to 6.

Apart from this, the silicon is directly oxidized by the oxygen

$$Si + O_2 \rightarrow SiO_2 \qquad [5]$$

From Eq. [2], [3a], and [5], it is clear that a layer of SiO_2 is formed. Because of the presence of this layer, further diffusion of boron is impeded. At high temperatures this is not a problem because B_2O_3 penetrates through this layer of SiO_2 very quickly and thus reactions [2] and [4] keep taking place. However, at lower temperatures the situation changes. B_2O_3 cannot readily penetrate through the oxide layer and thus the boron skin (SiB_n) is not formed. Presence of boron skin is essential to get solid solubility. Therefore, at lower temperatures the diffusion becomes nonuniform and irreproducible. Slight changes in oxygen concentration cause large changes in diffusion profile (3).

An alternative system has been suggested by Nakamura (4) in which CO_2 rather than O_2 is used as the oxidant. The intent here is to study this system in more detail. In this diffusion system, CO_2 oxidizes B_2H_6 to produce B_2O_3 analogous to reaction [1]

$$B_2H_6 + 6CO_2 \rightarrow B_2O_3 + 6CO + 3H_2O \qquad [6]$$

The diffusion of boron then proceeds according to reactions [2], [3], and [4].

* Electrochemical Society Active Member.

Key words: boron diffusion, silicon, diborane, carbon dioxide.

Experimental Results

In the experiments performed, the material used was 1-2 Ω-cm, phosphorus-doped, <100> oriented silicon. The diffusion system consisted of a 6 cm diam, 1m long quartz tube, and 15 cm long × 5 cm wide quartz boat. In a series of experiments 30 min predepositions were done. The oxidant (CO_2 or O_2) and B_2H_6 were switched on at least 30 min before the predeposition to ensure the stability of the gas flow. After the predeposition the wafers were etched in dilute HF and sheet resistance was then measured with a four-point probe. Since the junctions involved were very shallow, osmium tip probes with a low force of 45g were used. In all of the experiments the total flow of gases was kept at 2.5 liter/min.

In the first experiment at a temperature of 850°C, keeping diborane at 130 ppm, carbon dioxide was varied from 0.2 to 1.2%. The results of 30 min predepositions are shown in Fig. 1. It seems that around 0.4-0.8% CO_2 gives the lowest sheet resistance.

In the second experiment at the same temperature of 850°C, carbon dioxide was kept at 0.6% and diborane was varied from 25 to 200 ppm. The results of 30 min predepositions are shown in Fig. 2. It seems that 80-160 ppm B_2H_6 gives the best results. In both of these experiments it was found that for correct amounts of CO_2 and B_2H_6 the thickness of boron glass was so small

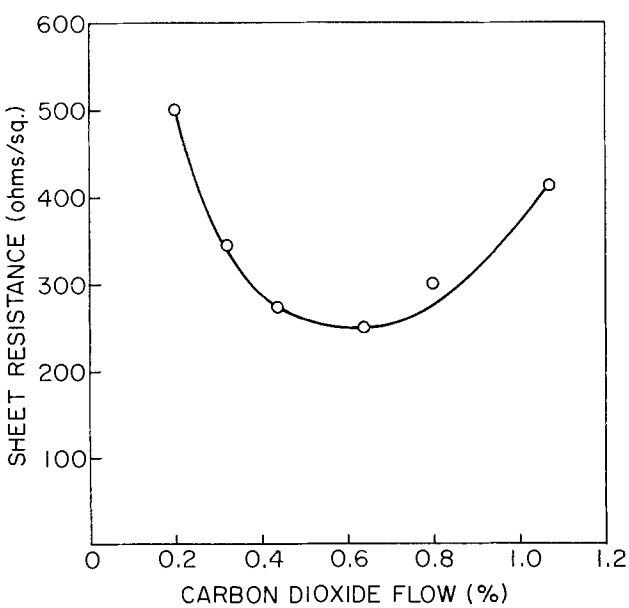


Fig. 1. Effect of CO_2 variation on sheet resistance of 30 min predeposition: T = 850°C, B_2H_6 = 130 ppm.

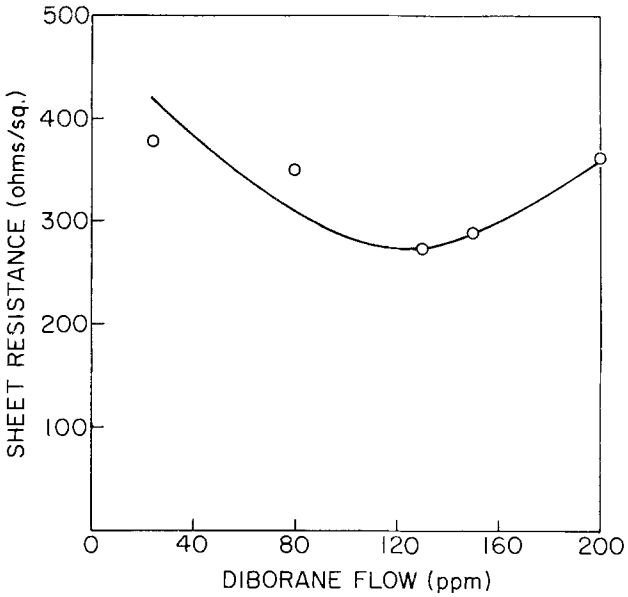


Fig. 2. Effect of B_2H_6 variation on sheet resistance of 30 min predeposition: $T = 850°C$, $CO_2 = 0.6\%$.

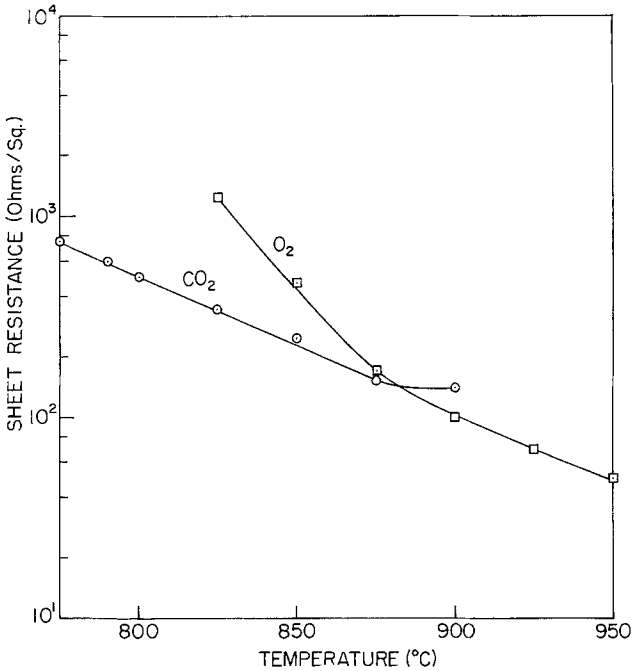


Fig. 3. Effect of temperature variation on sheet resistance of 30 min predepositions: $B_2H_6 = 130$ ppm, $CO_2 = 0.6\%$, $O_2 = 0.2\%$.

that it took only 5-10 sec to etch it using 2% HF in water. However, if too high or too low CO_2 flow or too high B_2H_6 flow was used, deposits of milky color were found on the Si surface. For low and medium flow of B_2H_6 no milky deposits were found. The milky deposits were always associated with higher sheet resistance.

In the third experiment 0.6% carbon dioxide, 130 ppm diborane, and the rest nitrogen were used and 30 min predepositions were done in a temperature range of 775°-900°C. The same experiment was repeated, replacing carbon dioxide with 0.2% oxygen, in the temperature range of 825°-950°C. The results of these experiments are shown in Fig. 3. The flow rates for the B_2H_6-O_2 experiment were optimized to get the lowest sheet resistance (5). Again, it was observed that for the B_2H_6-CO_2 system at temperatures higher than 900°C, milky deposits were found on the surface for all combinations of gas flow and the sheet resistance was very high and uncontrollable.

Discussion

Looking at Fig. 3 it is evident that at temperatures lower than 875°C the B_2H_6-CO_2 system gives much better results than the B_2H_6-O_2 system. However, at higher temperatures the B_2H_6-O_2 system gives better results. As we discussed above, the formation of a SiO_2 barrier between B_2O_3 and SiB_n takes place. Evidently, at temperatures higher than 875°C, in the B_2H_6-O_2 system the B_2O_3 penetrates through this barrier and formation of SiB_n is continuous. However, below 875°C the rate of formation of SiO_2 is faster than the rate of B_2O_3 penetration through it, leading eventually to the disappearance of SiB_n. This results in the reduction of surface concentration of boron (3). This is reflected by a sharp increase in sheet resistance as seen in Fig. 3.

In the B_2H_6-CO_2 system the only oxygen present is because of reduction of CO_2 to CO and O_2

$$2CO_2 \leftrightarrows 2CO + O_2 \qquad [7]$$

However, only 10^{-5} to 10^{-3} of CO_2 decomposes by the above reaction in the temperature range of 800°-1000°C (4). Therefore, the oxidation of SiB_n is negligible. This allows the silicon surface to be saturated with boron. This is reflected in the temperature range of 775°-875°C shown in Fig. 3. At higher temperatures CO decomposes to elemental carbon and oxygen, and carbon deposition on the silicon surface probably changes the diffusion properties of boron

$$2CO \rightarrow C + O_2 \qquad [8]$$

Conclusion

The B_2H_6-O_2 diffusion system for boron diffusion is limited to temperatures higher than 875°C because of a strong oxidizing ambient created by O_2. By replacing O_2 with CO_2, the range of diffusion in the above experiments has been lowered to 775°C. The use of the B_2H_6-CO system allows work at solid solubility. Therefore, the reproducibility of the process is better.

Manuscript submitted Jan. 19, 1976; revised manuscript received July 1, 1976.

Any discussion of this paper will appear in a Discussion Section to be published in the December 1977 JOURNAL. All discussions for the December 1977 Discussion Section should be submitted by Aug. 1, 1977.

REFERENCES

1. M. S. R. Heynes, *Electrochem. Technol.*, **5**, 25 (1967).
2. M. C. Duffy, D. W. Foy, and W. J. Armstrong, *ibid.*, **5**, 29 (1967).
3. E. Arai, H. Nakamura, and Y. Terunuma, *This Journal*, **120**, 980 (1973).
4. H. Nakamura, *Jpn. J. Appl. Phys.*, **11**, 761 (1972).
5. K. C. Saraswat, R. Anderson, and J. D. Meindl, EE-412 Integrated Circuits Laboratory Report, Stanford University, California (April 1974).

Characterization of Microplasma Sites in Silicon n^+-p Junctions

C. Donolato, P. G. Merli, and I. Vecchi

C.N.R.-LAMEL, 40126 Bologna, Italy

A major requirement for the production of avalanche photodiodes with large active area and high gain is the elimination of microplasmas, *i.e.*, small defective areas with lower breakdown voltages than that of the junction as a whole (1).

Many properties of microplasmas in p-n junctions have been investigated [for a review see (2)], but only in a few cases has the detailed structure of the defect causing premature breakdown been stated. Recently, defects causing excess reverse leakage currents in boron-diffused silicon p-n diodes have been characterized in detail (3, 4).

This note reports the identification and crystallographic characterization of defects associated with microplasma sites in phosphorus-diffused silicon avalanche photodiodes, employing scanning and transmission electron microscopy. The defects are shown to consist in SiP precipitates surrounded by a dislocation network.

Experimental

Polished <111> low dislocation p-type Si wafers with 0.5 Ω-cm resistivity (nominal) were used for diode fabrication. The diode structure was of the type described by Goetzberger *et al.* (5); the active area was a circle 60 μm diameter, surrounded by a diffused guard ring 8 μm deep; the junction was formed by a shallow phosphorus diffusion about 0.3 μm deep with an integrated P concentration $Q = 5.7 \times 10^{15}$ cm^{-2}. The sequence of the main processing steps is listed in Table I.

The diodes were observed first by an optical microscope under reverse bias at high currents (up to 5 mA) to detect the localized light emission typical of microplasmas; subsequently the *I-V* characteristics were examined on a Tektronix Type 576 curve tracer to check the electrical influence of the defects. Some of the diodes were also analyzed by a scanning electron microscope (SEM) in the electron beam induced current mode (EBIC) (3, 6), at beam energies between 2.5 and 20 keV, to obtain a map of the electrical activity of single defects at high magnification. Finally a structural analysis at high resolution was carried out on some representative diodes with the transmission electron microscope (TEM) at 200 keV after jet chemical thinning of the active area of the diode.

Results and Discussion

Figure 1 is an optical micrograph of the active area of a typical defective diode under reverse bias, showing two bright spots in the diffused recombination radiation of the junction. The *I-V* characteristic of this diode up to 1.5V before bulk breakdown ($V_B \approx 30$V) is like that of a defect-free diode, with a reverse current lower than 20 nA. The microplasmas exhibit their influence only in the breakdown region with the presence of of two kinks in the characteristic (Fig. 2).

The same diode was also examined by SEM in the EBIC mode at bias voltages near V_B (at low bias no contrast was observable) using different beam energies. The resulting images always showed two current enhancement spots at positions where microplasmas emission did, indicating that the sites of high radiative recombination are also sites of localized current multiplication (2, 7).

Figure 3 reports the EBIC image at high magnification of a single microplasma site at a reverse bias just below the turn-on voltage and indicates that the current enhancement is not uniform across the defect showing some points of lower current multiplication. A beam energy of 2.5 keV was selected as it allowed

Key words: phosphorus, precipitation, defects, diode breakdown.

Table I. Main processing steps for fabrication of avalanche photodiodes

Junction	Process	Temperature	Time
Guard ring	Oxidation (steam)	1100°C	1 hr
	Predeposition ($POCl_3$)	1000°C	12 min
	Drive-in (dry O_2)	1100°C	9 hr
Active junction	Predeposition ($POCl_3$)	920°C	7 min

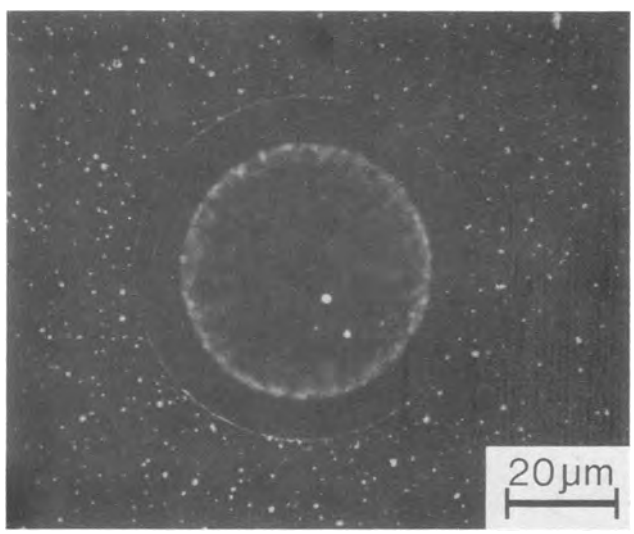


Fig. 1. Optical image of the active area of a defective diode under reverse bias, showing two microplasmas. ($V = V_B$; $I = 2$ mA).

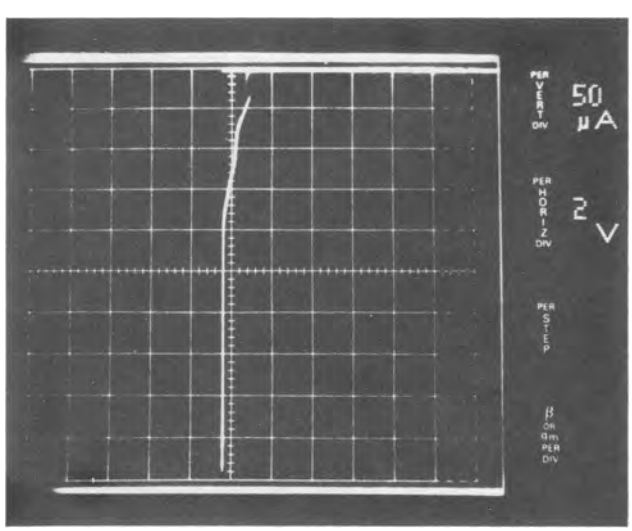


Fig. 2. *I-V* characteristics in the breakdown region of the diode of Fig. 1.

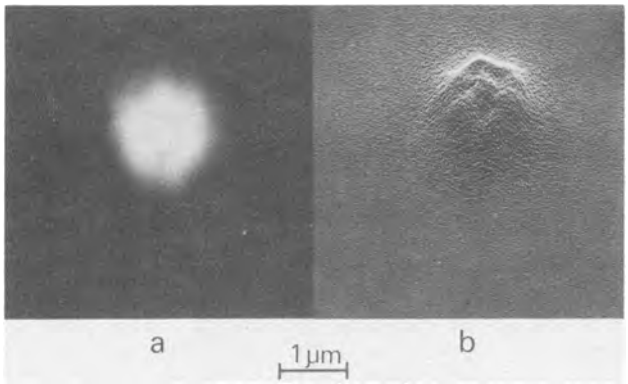


Fig. 3. Microplasma as observed by SEM in the EBIC mode at high reverse bias: (a) normal image, (b) Y-modulation image.

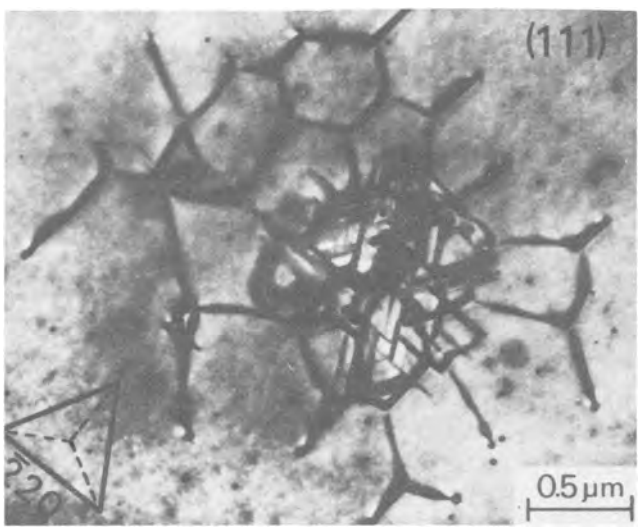


Fig. 4. TEM micrograph of a typical defect corresponding to a microplasma site, showing an aggregate of precipitates surrounded by dislocations.

sufficient carrier injection and the the best spatial resolution; in fact, increasing beam energy reduced the detail of the features of Fig. 3.

To identify the structure of the defects associated with microplasmas, some diodes were also analyzed by TEM. These observations indicated that the defects corresponding to microplasma sites had essentially the same crystallographic structure. The transmission electron micrograph of a typical defect is reported in Fig. 4. The micrograph shows that the defect consists of an aggregate of rodlike precipitates surrounded by a dislocation network. These precipitates, recently studied in detail (8), were found to be SiP orthorhombic crystals aligned with the <110> direction of silicon parallel to the sample surface and lying on the inclined {111} planes. The dislocations of Fig. 4 are of three different kinds, each being in one of the three <211> directions in the (111) plane of the sample; these dislocations are edge-type with Burgers vectors lying in the <110> directions of the sample plane.

It would be interesting to correlate the electrical activity of microplasmas with their crystallographic structure; no simple correspondence, however, appears from Fig. 3 and 4, although the features displayed are typical of all defects. Recent observations (9) showing the vanishing of EBIC dislocation contrast at high reverse bias suggest that the image contrast of Fig. 3 is essentially due to precipitates. Their presence in the space charge region produces a local enhancement of the electric field responsible for the high multiplication effects observed.

For a better understanding of the relationship between electrical activity and structure of a particular defect, images of the same defect by SEM and TEM would be required. Besides the practical difficulties in achieving these results, the much lower resolution of the SEM in the EBIC mode in comparison with the TEM sets definite limits to the detail of the correspondence. This limitation evidences the interest of other techniques which may provide a direct observation of the interaction between a particular defect and the depletion field of the p-n junction (10).

The present observations, however, have established the microstructure of defects causing microplasmas in shallow-diffused n^+-p junctions; their nature indicates that they are related to phosphorus precipitation. Further investigations on the processing step responsible for their nucleation are in progress.

Acknowledgments

We thank for their kind collaboration Prof. G. Soncini and the technical staff of this laboratory. Thanks are also due to Siemens Italia S.p.A. for technical support.

Manuscript submitted Sept. 9, 1976; revised manuscript received Dec. 2, 1976.

Any discussion of this paper will appear in a Discussion Section to be published in the December 1977 JOURNAL. All discussions for the December 1977 Discussion Section should be submitted by Aug. 1, 1977.

Publication costs of this article were assisted by C.N.R.

REFERENCES

1. H. Melchior and W. T. Lynch, *IEEE Trans. Electron Devices*, **ed-13**, 829 (1966).
2. H. Kressel, *RCA Rev.*, **28**, 175 (1967).
3. K. V. Ravi, C. J. Varker, and C. E. Volk, *This Journal*, **120**, 533 (1973).
4. C. J. Varker and K. V. Ravi, *J. Appl. Phys.*, **45**, 272 (1974).
5. A. Goetzberger, B. McDonald, R. H. Haitz, and R. M. Scarlett, *ibid.*, **34**, 1591 (1963).
6. A. J. Gonzales, in "Scanning Electron Microscopy," pp. 942-948, ITT Research Institute, Chicago (1974).
7. N. F. B. Neve, K. A. Hughes, and P. R. Thornton, *J. Appl. Phys.*, **37**, 1704 (1966).
8. M. Servidori and A. Armigliato, *J. Mater. Sci.*, **10**, 306 (1973).
9. D. B. Holt and R. Ogden, *Solid-State Electron.*, **19**, 37 (1976).
10. P. G. Merli, G. F. Missiroli, and G. Pozzi, *Phys. Status Solidi A*, **30**, 699 (1975).

JOURNAL OF THE ELECTROCHEMICAL SOCIETY

ELECTROCHEMICAL SCIENCE AND TECHNOLOGY

APRIL 1977

Kinetics and Mechanism of Oxygen Film Electroformation up to a Monolayer Thickness at the Pt/$KHSO_4$ (Melt) Interface and Its Relation with the Electroreduction Process

J. O. Zerbino, N. R. de Tacconi, A. J. Calandra, and A. J. Arvia*

Instituto de Investigaciones Fisicoquímicas Teóricas y Aplicadas, Sucursal 4, Casilla de Correo 16, 1900 La Plata, Argentina

ABSTRACT

The potentiodynamic E/I response of the Pt/$KHSO_4$(melt) interface in the potential range of the oxygen monolayer electroformation and electrodissolution under different perturbation conditions is investigated. Both the anodic and cathodic experimental results are satisfactorily explained by a reaction model involving different surface species which are formed either in successive electron transfer steps or by simple chemical processes, including the aging of the oxygen-containing species formed as reaction intermediates.

Oxide monolayers, either adsorbed or chemisorbed, can be electroformed under different potential conditions on various noble metal electrodes immersed in both aqueous acid and molten electrolytes (1-10). These monolayers, which involve different oxygen-containing species, can be also quantitatively electroreduced under properly chosen experimental conditions. The electrode processes, either anodic or cathodic, are far more complex than previously thought (7), since the different reacting species and intermediates undergo surface-state transformations and, occasionally, dissolution processes which were overlooked for a relatively long time. The existence of intermediate species was evidenced by means of the modulated voltammetry technique (10).

Nevertheless, under certain circumstances it is possible to keep the chemical transformations (aging) under control and to obtain then reproducible and coherent kinetic data related to a particular process, which can be interpreted in mechanistic terms. In this way the electroreduction of a surface oxygen atom monolayer at the Pt/bisulfate (4, 5, 10) and Au/$HClO_4$ and Au/H_2SO_4 interfaces (11, 12) were better understood, once both the aging and the chemical dissolution were kept under a certain control (4, 5). The situation, however, turned more difficult for the monolayer electroformation since in this case, although the chemical dissolution can be disregarded, the aging occurs simultaneously with the proper electrochemical reaction and it becomes practically impossible to separate the individual contributions into the over-all anodic reaction.

The present report attempts precisely to gain further knowledge about the possible mechanism of the electrochemical reactions occurring at the Pt/$KHSO_4$(melt) interface particularly for the anodic process, taking into account the conclusions derived from the theoretical reaction mechanisms previously discussed (13). The postulated complex reaction pathway explains the various E/I profiles, either anodic or cathodic, resulting under different potential perturbation conditions. Moreover, the electroreduction of the aged surface oxygen-containing species, which has been more extensively studied, can also be interpreted through the same reaction pathway.

* Electrochemical Society Active Member.
Key words: monolayer, film, oxygen, melts.

Experimental

The experimental setup and the working conditions for the Pt/$KHSO_4$(melt) and Pt/$NaHSO_4$ + $KHSO_4$ (1:1) (melt) interfaces were the same as described previously (4, 5). Experiments were made at temperatures between 223° and 257°C. The potentials are referred to the Pt/H_2(1 atm)/$KHSO_4$(melt) electrode. Two basic experimental techniques are used, namely, either the linear potential sweep (LPS) or the triangular potential sweep (TPS) techniques employing different potential/time perturbation functions, as described elsewhere (12), and the triangular modulated linear potential sweep technique (TMLPS) (14).

The corresponding circuitry is essentially that already referred to in previous publications (11, 12) including a fast risetime potentiostat (Tacussel Type PIT 20-2X, risetime = 0.2 μsec) and an ohmic drop compensator (Tacussel Type CDCO).

Results and Interpretation

When the Pt/$KHSO_4$(melt) interface is perturbed with a symmetric TPS from E_i = 0.2 to 0.6V at potential sweep rates, v, between 10 and 150 mV/sec, the E/I displays, apart from the double layer charging and discharging (Fig. 1), show, as already known, an anodic current region involving the formation of an oxygen monolayer on the metal and a cathodic current region corresponding to its electroreduction. The E/I profiles show a broad anodic current peak and a cathodic current peak, the latter being narrower and more symmetric in shape than the former. The potential of the anodic current peak becomes more positive when

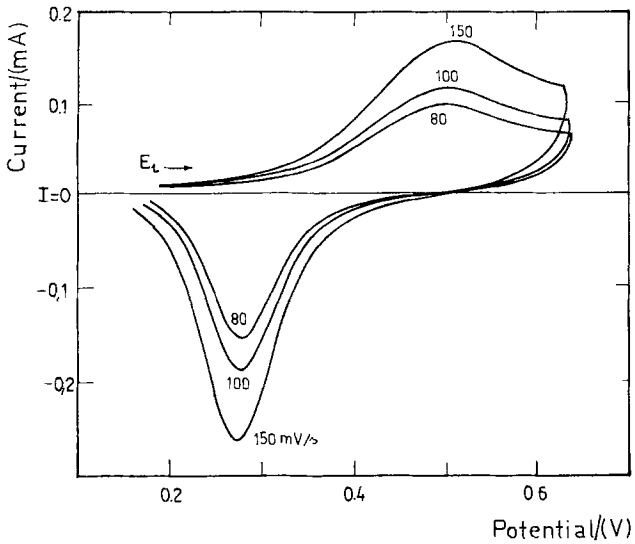


Fig. 1. Single triangular potential sweep voltammograms run at different potential sweep rates ($v_a = v_c$), starting from E_i toward anodic potentials. $KHSO_4$ at 229°C.

v increases. Its rate of shift is, however, small $(d(E_a)_p/d \ln v) = 3$ mV at 257°C. The anodic charge decreases when v increases. The potential of the cathodic current peak depends simultaneously on the various parameters as already discussed (4).

Voltammograms run with a TPS from E_i up to various anodic potential limits at two different v (Fig. 2) show that at a constant potential the initial portion of the cathodic E/I profile exhibits a cathodic current which increases as v increases. This reveals that the characteristics of the reacting species involved in the electroreduction depend on the time spent for its anodic formation.

The E/I display obtained between $E_i = 0.2$ and 0.7V with a TMLPS employing a guide ramp at $v_g = 1.5$ V/sec and a superimposed triangular modulating signal at $v_s = 20$ V/sec, and a potential amplitude $A_s = 60$ mV (Fig. 3) presents well-defined anodic and cathodic contours and an intermediate gap related to double layer charging and discharging due to the modulating signal. The lines corresponding to each modulating half-cycle all along the upper anodic contour are practically straight lines while those corresponding to the lower cathodic contour exhibit at the end a clear curvature. This effect is more remarkable at lower potentials and suggests that the reaction initially exhibits a rather reversible behavior.

When a triangular modulated triangular potential sweep (TMTPS) is used ($v_g = 1$ V/sec, $v_s = 10$ V/sec, $A_s = 40$ mV), the E/I displays corresponding to the anodic and the cathodic scans are completely different (Fig. 4). Thus, while the modulated anodic scan exhibits together with the anodic current a net cathodic contribution, the modulated cathodic scan presents along the whole potential range only a cathodic current.

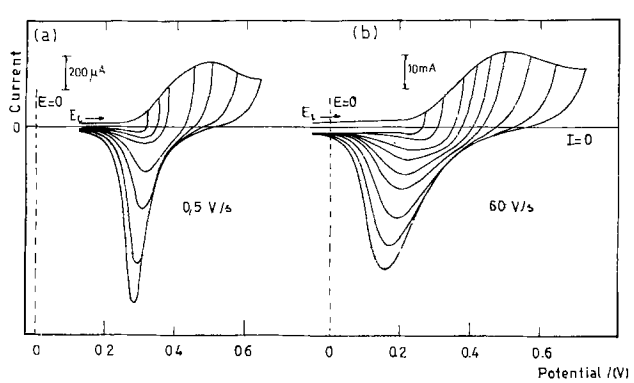


Fig. 2. Single triangular potential sweep voltammograms started at E_i and covering different potential amplitudes. $KHSO_4$ at 256°C. (a) $v_a = v_c = 0.5$ V/sec. (b) $v_a = v_c = 60$ V/sec.

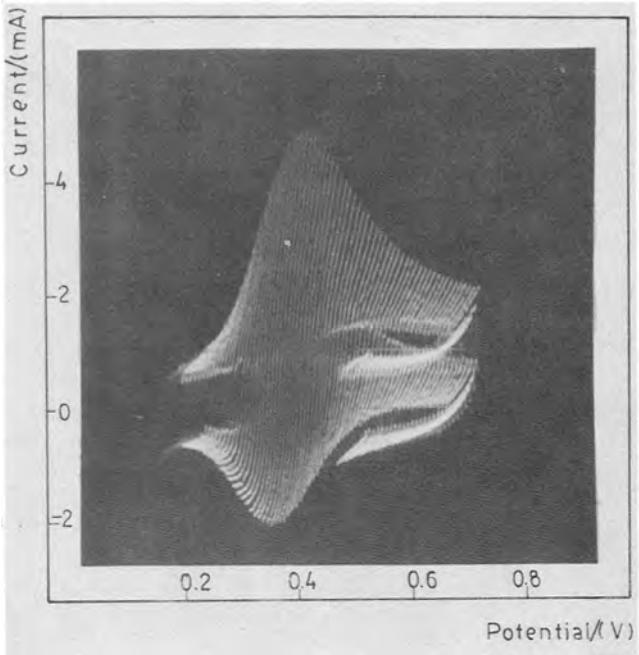


Fig. 3. E/I profile obtained with a triangular modulated linear potential sweep, $v_g = 1.5$ V/sec. $v_s = 20$ V/sec, $A_s = 0.06$V, electrode area 0.5 cm². $KHSO_4$ at 257°C.

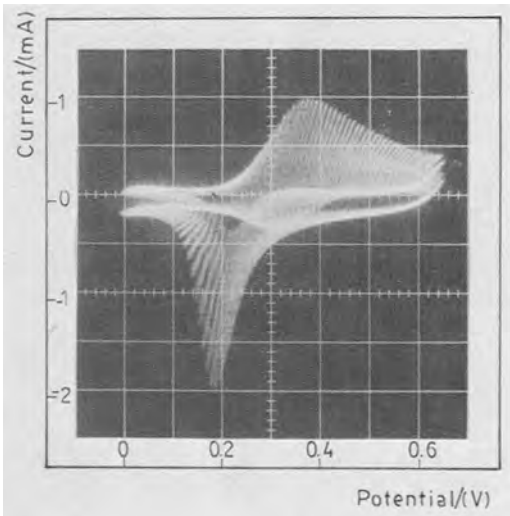


Fig. 4. E/I profile obtained with a triongular modulated triangular potential sweep, $v_g = 1$ V/sec, $v_s = 10$ V/sec, $A_s = 0.04$V, electrode area 0.5 cm². $KHSO_4$ at 223°C.

The experiments run with TMLPS covering increasing amplitudes and keeping both v_g and v_s constant show (Fig. 5) the increase of Q, the total charge, as well as Q_a, the anodic charge, and Q_c, the cathodic charge, although the Q_a/Q_c ratio increases. These results imply a certain degree of irreversibility of the over-all process (13). On the other hand, the cathodic scan exhibits a larger anodic current contribution when the amplitude of the modulating signal increases. In the anodic potential sweep at low anodic potentials, that is, on the very initial portions of the E/I envelope, any change of the amplitude of the modulating signal has no appreciable effect, as should occur for a reversible electrochemical system. But the situation is different at higher anodic potentials, as the difference between the anodic and the cathodic current peak potentials increases with the amplitude of the modulating

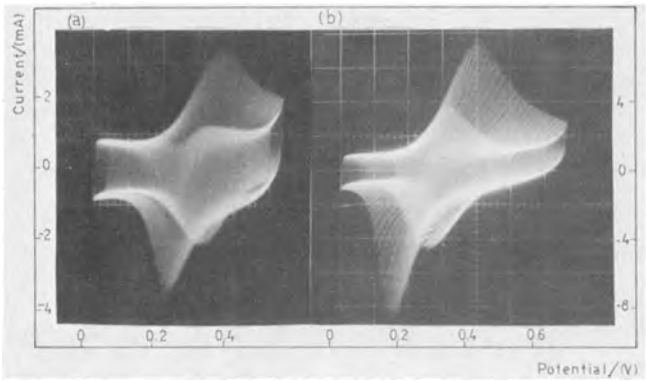


Fig. 5. *E/I* profiles run with a triangular modulated triangular potential sweep. $KHSO_4$ at 250°C. (a) $v_g = 1.5$ V/sec, $v_s = 50$ V/sec, $A_s = 0.045$V. (b) $v_g = 1.5$ V/sec, $v_s = 50$ V/sec. $A_s = 0.180$V.

signal. This indicates the contribution of an irreversible electrochemical process at higher anodic potentials.

Figure 6 shows *E/I* profiles obtained with different potential/time programs as indicated for each run. Thus, the display shown in Fig. 6a, which exhibits only a single electroreduction current peak, entails an initial linear anodic potential scan covering a relatively small amplitude, so that only a fraction of the monolayer is formed, then the system is potentiostated for 5 sec at E_f, and finally the cathodic potential scan is run. The *E/I* record depicted in Fig. 6b comprises a 5 sec aging time at E_f as before, but immediately after, the anodic scan is continued a few millivolts beyond E_f, followed by the reverse cathodic scan. The *E/I* display now exhibits two cathodic current peaks, one at lower potentials which coincides with that already described in Fig. 6a, and another one at higher potentials, corresponding to the electroreduction of the most reactive product of the anodic reaction.

An increase of the interruption time during the anodic potential sweep implies the formation of a relatively larger amount of the more stable species (Fig. 7a), as seen through the charge increase of the cathodic current peak located at more negative potentials. Under a STPS the same effect is noticed when the anodic limit of the potential excursion increases (Fig. 7b). The potential associated with the more cathodic current peak becomes more negative as the anodic charge increases and simultaneously the cathodic contour becomes wider since it includes at least the electroreduction of different species anodically formed. For a constant charge, the larger the time the system is

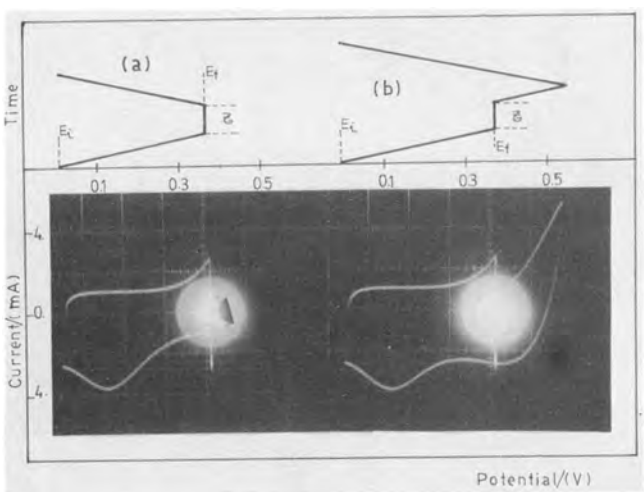


Fig. 6. *E/I* profiles obtained with potential/time programs involving potentiostating at E_f, as indicated in the figure. $v_a = v_c = 80$ V/sec, $\tau = 5$ sec. $KHSO_4$ at 225°C.

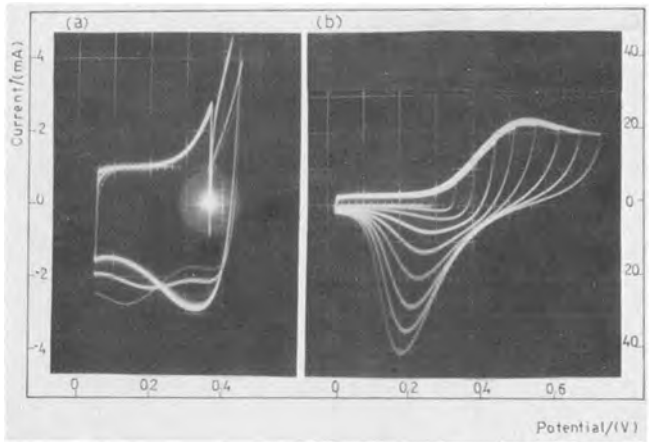


Fig. 7. Comparison between potentiodynamic *E/I* profiles involving different aging times (a) and single triangular potential sweep *E/I* displays of different potential amplitudes (b). $KHSO_4$ at 225°C. (a) $v_a = v_c = 80$ V/sec, $\tau = 5$, 5×10^{-1}, and 5×10^{-3} sec. (b) $v_a = v_c = 80$ V/sec.

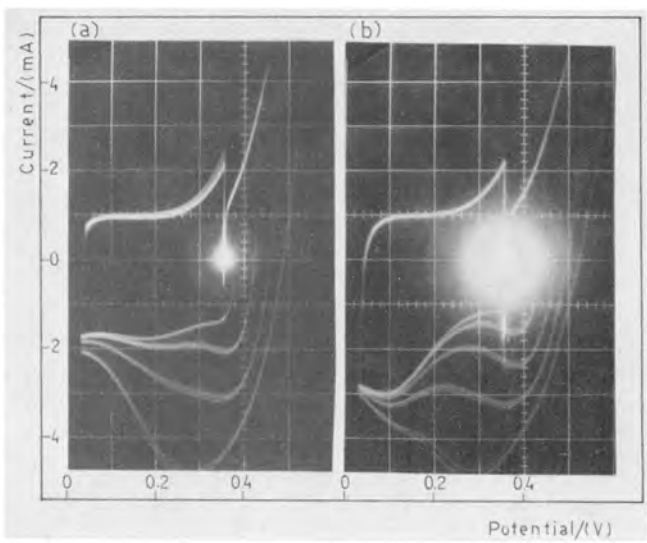


Fig. 8. *E/I* profiles obtained with the potential/time program indicated in Fig. 6b, covering different potential amplitudes. $KHSO_4$ at 225°C. (a) $v_a = v_c = 80$ V/sec $= 5 \times 10^{-2}$ sec. (b) $v_a = v_c = 80$ V/sec, $\tau = 5$ sec.

maintained at E_f, the better the definition of the single cathodic current peak situated at lower potentials.

The *E/I* profiles resulting when the anodic potential scan continues to larger anodic potentials after potentiostating the system (Fig. 8), imply that, during the cathodic scan, an increasing contribution of the electroreduction process is associated with the more reactive species produced during the electro-oxidation. Therefore, the initial species accumulated during the electrooxidation can be reversibly electroreduced before it undergoes a transformation into a more stable state. Hence, if the electroreduction of the anodic species occurs very rapidly, the cathodic *E/I* profile approaches a reversible response. This behavior, in principle, is independent of the surface coverage degree and of the aging time of the anodic product initially formed.

Discussion

The results obtained with the different potentiodynamic techniques reveal that at least two species participate in the over-all electrode process. The different voltammograms can be satisfactorily compared with those derived from a reaction model involving, for the anodic process, two consecutive electron transfer steps, each one involving the formation of surface covering species, coupled to a parallel chemical transformation

of the surface species formed during the first step into the surface species formed during the second step. In terms of the simplest chemical equations the reaction scheme postulated for the anodic reaction is

$$\mathrm{Pt} + \mathrm{H_2O} \xrightarrow{k_1} \mathrm{Pt(OH)} + \mathrm{H^+} + e^- \qquad [1a]$$

$$\mathrm{Pt(OH)} \xrightarrow{k_2} \mathrm{Pt(O)} + \mathrm{H^+} + e^- \qquad [2a]$$

$$\mathrm{Pt(OH)} + \mathrm{Pt(OH)} \xrightarrow{C_3} \mathrm{Pt(O)} + \mathrm{H_2O} + \mathrm{Pt} \qquad [3]$$

where the rate of step [1a] is larger than the rate of step [2a].

The same reaction model applies to the electroreduction of either the monolayer or a fraction of it (13). So the cathodic process corresponds to a first electron transfer involving the electroreduction of the more stable surface species into the more reactive one followed by a second electron transfer step where the latter is further electroreduced to leave finally a clean metal surface. Thus, the simplest cathodic reaction scheme is

$$\mathrm{Pt(O)} + \mathrm{H^+} + e^- \xrightarrow{k_{-2}} \mathrm{Pt(OH)} \qquad [2c]$$

$$\mathrm{Pt(OH)} + \mathrm{H^+} + e^- \xrightarrow{k_{-1}} \mathrm{Pt} + \mathrm{H_2O} \qquad [1c]$$

where step [2c] is now slower than step [1c].

In the following θ_1 and θ_2 refer to the degree of surface coverage by Pt(OH) (species 1) and Pt(O) (species 2), respectively. In principle, the energetic configuration of these species might depend both on the total surface coverage degree and on the rate of the potential perturbation applied to the metal/electrolyte interface.

The reaction pathway involving steps [1] and [2], the former being slower than the latter ($k_{-2} > k_{-1}$), was already postulated as an attempt to explain the cathodic potentiodynamic E/I profile obtained with the Pt/H_2SO_4(aq) interface at room temperature (16). However, when this reaction model is tried with the present results it fails to give a satisfactory explanation of the over-all E/I characteristics. The anodic reaction scheme implies a decrease of the total anodic charge on increasing v at a constant potential amplitude. The slow rate of the second step causes the amount of electro-oxidation product to decrease as the rate of the potential perturbation increases, because the rate of the reaction which produces it is unable to keep along with the rate of the potential perturbation. This effect, however, does not necessarily imply a shift of the anodic current peak potential toward more anodic potentials as one would expect for a simple irreversible process (15).

The existence of a second electrochemical step, which is more irreversible than the first one, requires that the anodic side of the TMLPS voltammogram involving the first reversible couple, at v_g and v_s, be matched to the anodic over-all TPS E/I profile at $v = v_g + v_s$ (13) (Fig. 9). The extent of the contribution of the first reversible process depends, however, on the anodic potential limit. As the latter becomes more anodic the amount of the second species, which is bound to the slower electrochemical reaction, also increases.

A further comparison between the experimental results and the response of the different reaction models to potential perturbations (13) shows that the existence of cathodic current maxima at the end of each triangular modulating cycle in the TMLPS confirms the reversible characteristics of step [1]. Moreover, the occurrence of step [2] at a rate slower than that of step [1] promotes an increase of the Q_a/Q_c ratios above unity and a separation of the corresponding anodic and cathodic current peak potentials. A comparison of the cathodic current maxima of the initial portions of the

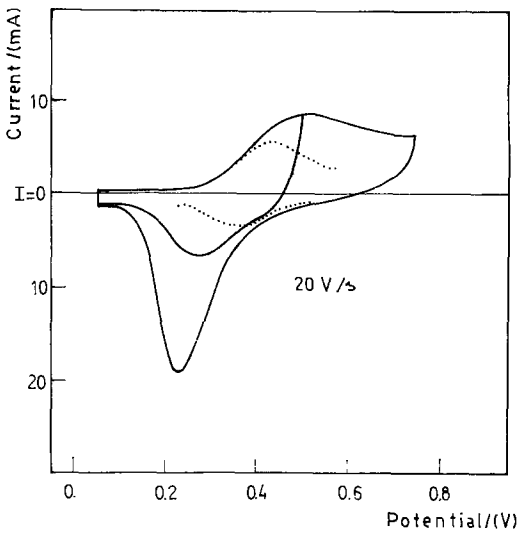


Fig. 9. Comparison between a STPS voltammogram run at 20 V/sec and a TMLPS E/I display run at $v_g = 1.5$ V/sec, $v_s = 20$ V/sec, $A_s = 0.06$V. $KHSO_4$ at 257°C. Full lines correspond to the TPS and dotted lines correspond to the envelopes of the TMLPS.

experimental E/I display with the theoretical one recorded under the same perturbation conditions and involving just only one surface coverage species, permits the estimation of the lower limiting value of the rate constant at equilibrium of step [1]: $k_1 = 2 \times 10^2$ mA/cm^2. Nevertheless, the slope of the E/I line at the inversion of the modulating signal in the potential region of the current peak yields $k_1 = 10^2$ mA/cm^2. The lower value is obviously influenced by the occurrence of step [2]. The slope of the E/I lines decreases due to the change of coverage from θ_1 to θ_2.

The appearance of a single anodic and a single cathodic current peak during the triangular potential excursion suggests that E_D, the potential difference between the equilibrium potentials of step [1] and step [2], is either zero or negative. Complementary kinetic information can be gained through the influence of the amplitude of the modulating signal in the TMLPS experiments as it can be seen in Fig. 5. Thus, during the initial portion of the cathodic E/I profile the anodic contribution increases with the amplitude of the modulating signal since the partial modulating potential excursion goes through a potential region sufficiently cathodic allowing, thus, the electrochemical conversion from a surface covered by species 2 into a surface covered by species 1. This process is assisted both by the fast first electron transfer step and by the potential which is cathodic with respect to the equilibrium potential of step [1]. Consequently, the reaction yields a relatively large extent of bare metal surface, which in the subsequent partial anodic half-cycle is covered through step [1]. Under these conditions the modulating potential scan covers the equilibrium potential of step [1], and species 1 which behaves as a reversible intermediate is, therefore, electrochemically caught up.

The cathodic E/I profile observed for the largest amplitude of the modulating signal (Fig. 5b) shows a double E/I profile, in good correspondence with the maxima of the envelope of the modulated anodic potential scan. This double E/I profile necessarily implies for the cathodic process a slow first reaction step [2c] followed by the more reversible step [1c] whose equilibrium potential either coincides with the equilibrium potential of step [2], or is more anodic than that of the latter (13). The anodic E/I envelope, recorded during the cathodic excursion with a TMTPS, is smaller than the envelope recorded during the anodic excursion, because the surface during the former potential excursion is mainly covered by species 2. The latter hinders the θ_1 to θ_2 transformation and, consequently,

species 1 accumulates on the rest of the metal surface during the cathodic potential excursion.

The mechanism involving three reaction steps explains now why the anodic *E/I* profile under a STPS becomes practically independent of v, namely, the anodic process apparently behaves as a quasi-equilibrium process, while the cathodic scan results are much more irreversible (13). During the anodic reaction steps [1a] and [3] are much faster than step [2a] while the cathodic process is mainly controlled by step [2c]. Nevertheless, the reaction mechanism should be still completed to include the aging of the surface species.

The aging effect must be related to a physicochemical change of species 2, attaining a more stable configuration at the electrode surface. The over-all aging can be formally written as follows

$$\mathrm{Pt(O)} \rightarrow [\mathrm{Pt(O)}]^* \qquad [4]$$

where the asterisk refers to the aged component.

As far as the anodic process is concerned the aging process as well as step [3] occur simultaneously along with the electroformation of the monolayer. The aging has no appreciable influence on the Q_a/Q_c ratio, obtained from the single TPS records. This ratio is always practically one if any chemical dissolution of the oxide film is restrained. The occurrence of step [4] means that the electroreduction may start either from Pt(O) or from [Pt(O)]* and during the potentiodynamic transient, the rate of the over-all process should depend on the relative ratio of those species.

In the quantitative evaluation of the experimental *E/I* profiles the aging effect can be formally taken into account through a time-dependent k_{-2} rate constant, which diminishes as the time elapsed between the anodic and the cathodic processes increases, since any aging of species 2 implies a decrease of the surface activity of the latter. Hence, the rate constant becomes a complex function of θ_1, θ_2, and E.

The former assumption is equivalent to a shift of $(E_{eq})_2$ toward more negative potentials as the electrochemical reaction proceeds, since the rate constant of step [3] should be, in principle, regarded as time independent. Either the k_{-2} time dependence or the shift of $(E_{eq})_2$ when the reaction proceeds, explains the small potential shift of the cathodic current peak when the aging process is uncontrolled. These assumptions, however, are still insufficient to explain why the anodic current peak becomes practically independent of v. To reproduce the whole voltammograms within the range of experimental errors under any perturbation conditions, the reaction model must include the assumption that the rate of any reaction yielding species 2 slows down when the contribution of the aging process increases. Whatever the case the net effect of aging corresponds to a decrease of the rate of the over-all anodic process.

The voltammograms calculated for the reaction pathway just discussed are depicted in Fig. 10. For the sake of simplicity, the rate constant of step [2c] is regarded as independent of θ and E, but it depends on t following an exponential law. The rate of step [2c] is numerically calculated as the sum of the partial rates, $v_{-2} = k_{-2}(t)\Delta\theta_2 \exp[f(E,\theta)]$, the time t is taken from the instant when $\Delta\theta_2$ becomes positive, while the rate constant of step [3] decreases with time analogously as k_{-2}.

Under the experimental conditions of Fig. 10a, the largest θ_1 value ($\sim$0.1), during the anodic scan is observed at 0.006V. This coverage by species 1 is evidenced during the partial cathodic scans of lower potential amplitude giving a rather reversible initial *E/I* response. The electroreduction of freshly formed species 2 which remains unaged, also contributes, although to a lesser extent, to the reversible initial *E/I* profile just described. The *E/I* profiles thus calculated are satisfactorily coincident with the experimental ones, taking into account the small potential shift

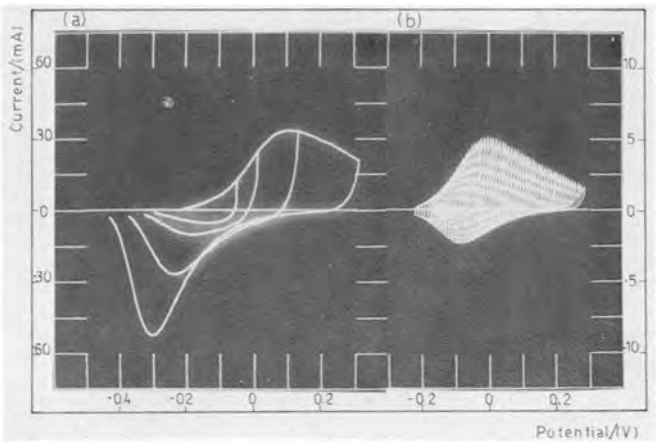


Fig. 10. Theoretical *E/I* displays calculated with the following parameters. $k_1 = k_{-1} = 10^3$ mA/cm^2; $k_2 = 0$; $k_{-2} = a[1 + b\exp(-ct)]$, where $a = 3$ mA/cm^2, $b = 7.5$, and $c = 120$ sec^{-1}; $C_3 = 3 \times 10^3$ sec^{-1}; k (one electron per particle) $= 0.21$ mC/cm^2; $\alpha_1 = \alpha_2 = \beta_1 = \beta_2 = 0.5$; Temkin factors: $g_1 = 10$, $g_2 - g_1 = -2$. T = 240°C. (a) STPS at $v = 60$ V/sec. (b) TMLPS at $v_g = 1.5$ V/sec, $v_s = 20$ V/sec, $A_s = 0.06$V.

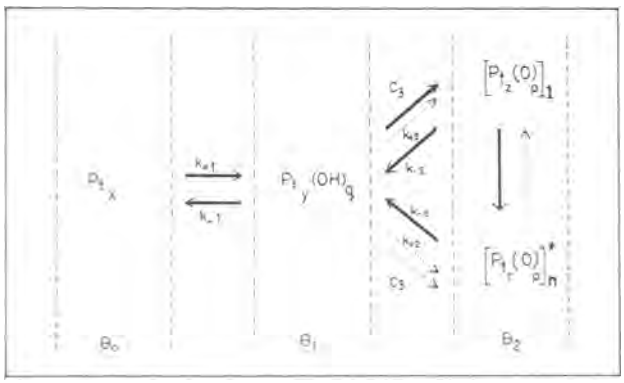


Fig. 11. Scheme of the reaction pathway and definition of the kinetic parameters. $(x + y + z)\theta = 1$; lim $\Sigma(p + q) \rightarrow 1$; $0 < (p/z) \leq 1$; $0 < (q/y) < 1$.

either of the anodic and cathodic current peaks with the potential sweep rate, depending on the perturbation conditions. The simplified diagram of Fig. 11 illustrates the possible reaction pathway involved in both the anodic and cathodic processes.

Although the coincidence between the reaction model and the experimental results is reasonably good, the oversimplification of any reaction model based upon a reduced number of possible reacting intermediates should be emphasized. On dealing with these processes in mechanistic terms one refers to reaction sequences with simple particles which remain unaltered during the course of the reaction. Undoubtedly the interpretation of these processes would be more realistic if it were based upon a continuity of states related to the species existing on the surface either for the anodic or the cathodic reactions. When a monolayer film is either formed or destroyed there is a continuous change of the surface composition between $\theta = 0$ and $\theta = 1$ or vice versa, respectively. This means that the surface energy distribution and the interaction terms, as well as the number of available sites on the surface, should change during the course of the reaction. Therefore, no simple stoichiometries are really representing the actual atom to atom ratio, but a continuous series ranging, for the anodic process, from a O/Pt ratio equal to zero up to a O/Pt ratio equal to 1, and vice versa for the cathodic process. Certainly, some of them may approach relative stable configurations which can be roughly compared to simple chemical stoichiometries of single molecules, as it has been

discussed for the case of gold oxide monolayers formed at the $Au/H_2SO_4(aq)$ and $Au/HClO_4(aq)$ interfaces (11, 12).

Acknowledgments

The Institute (INIFTA) is patronized by the following institutions: Universidad Nacional de La Plata, Consejo Nacional de Investigaciones Científicas y Técnicas, and Comisión de Investigaciones Científicas (Pcia. de Bs. As.). This work is partially supported by the Regional Program for the Scientific and Technological Development of the American State Organization. The cooperation and facilities of the Centro de Técnicas Analógico-Digitales (Ing. A. Quijano) is acknowledged.

Manuscript submitted June 17, 1976; revised manuscript received Nov. 12, 1976. This was Paper 390 presented at the Washington, D. C., Meeting of the Society, May 2-7, 1976.

Any discussion of this paper will appear in a Discussion Section to be published in the December 1977 JOURNAL. All discussions for the December 1977 Discussion Section should be submitted by Aug. 1, 1977.

REFERENCES

1. S. Gilman, in "Electroanalytical Chemistry," A. J. Bard, Editor, Vol. 2, M. Dekker, New York (1969).
2. A. Damjanovic, in "Modern Aspects of Electrochemistry," Vol. 5, J. O'M. Bockris and B. E. Conway, Editors, chap. 5, Plenum Press, New York (1969).
3. K. J. Vetter and J. W. Schulze, *J. Electroanal. Chem.*, **34**, 131 (1972); *ibid.*, **34**, 141 (1972).
4. N. R. de Tacconi, A. J. Calandra, and A. J. Arvia, *ibid.*, **51**, 25 (1974).
5. N. R. de Tacconi, A. J. Calandra, and A. J. Arvia, *ibid.*, **57**, 325 (1974).
6. J. O. Zerbino, A. J. Calandra, N. R. de Tacconi, and A. J. Arvia, *ibid.*, In press.
7. W. Boeld and M. Breiter, *Electrochim. Acta*, **5**, 145 (1961); M. Breiter and J. Weininger, *This Journal*, **109**, 1135 (1962); M. Breiter, *J. Electroanal. Chem.*, **7**, 38 (1964).
8. H. Angerstein-Kozlowska, B. E. Conway, and W. B. A. Sharp, *ibid.*, **43**, 9 (1973).
9. S. Schuldiner, B. J. Piersma, and T. B. Warner, *This Journal*, **113**, 573 (1966).
10. N. R. de Tacconi, A. J. Calandra, and A. J. Arvia, *J. Electroanal. Chem.*, **57**, 267 (1974).
11. C. M. Ferro, A. J. Calandra, and A. J. Arvia, *ibid.*, **55**, 291 (1974).
12. C. M. Ferro, A. J. Calandra, and A. J. Arvia, *ibid.*, **65**, 963 (1975).
13. N. R. de Tacconi, J. O. Zerbino, and A. J. Arvia, *ibid.*, In press.
14. B. E. Conway, H. Angerstein-Kozlowska, F. C. Ho, J. Klinger, B. MacDougall, and S. Gotresfeld, *Faraday Discuss. Chem. Soc.*, **56**, 210 (1973).
15. S. Srinivasan and E. Gileadi, *Electrochim. Acta*, **11**, 321 (1966).
16. A. J. Appleby, *This Journal*, **120**, 1205 (1973).

Electrochemical Studies of Oxide Ions and Related Species in Molten Fluorides

D. L. Manning

Oak Ridge National Laboratory, Analytical Chemistry Division, Oak Ridge, Tennessee 37830

and G. Mamantov*

Department of Chemistry, University of Tennessee, Knoxville, Tennessee 37916

ABSTRACT

The electrochemistry of oxide ions was studied in molten $LiF-BeF_2-ZrF_4$ [65.6-29.4-5.0 mole percent (m/o)] and $LiF-BeF_2-ThF_4$ (72-16-12 m/o) at gold, iridium, and glassy carbon electrodes in the temperature interval 500°-710°C. Well-defined and reproducible voltammograms could be obtained only at gold electrodes. Cyclic voltammetric and chronopotentiometric results indicate the following electrochemical reaction pathway

$$O^{2-} = O + 2e$$

$$O + O = O_2$$

$$O + O^{2-} = O_2^{2-}$$

Some evidence for adsorption of O_2 was obtained. O_2^{2-} ions are oxidized further producing a voltammetric postwave which increases with Na_2O_2 additions. O_2^{2-} ions gradually decompose in these media; this decomposition is more rapid in Zr(IV)-containing melts as compared to the Th(IV)-containing melts. NaO_2 additions result in the same voltammetric results as obtained upon the addition of Na_2O_2, indicating that O_2^- ions are more unstable in these melts than in the previously studied LiF-NaF-KF eutectic. The results obtained provide the basis for an *in situ* electrochemical determination of small amounts of dissolved oxide.

The electrochemical behavior of oxide ions and related species in molten chlorides has been studied previously by several workers (1-8). However, only a limited amount of work on the electrochemistry of oxygen-containing species has been performed in molten fluorides other than cryolite (9) [for a brief summary see (10)]. Mathews and Baes (11) have studied the equilibria $H_2O + F^- = OH^- + HF$ and $H_2O + 2F^- = O^{2-} + 2HF$ in molten $LiF-BeF_2$ [66-34 mole percent (m/o)]. Whiting *et al.* (12, 13) have obtained Raman and u.v. spectra of the unstable superoxide (O_2^-) ion in molten LiF-NaF-KF (46.5-11.5-42.0 m/o).

* Electrochemical Society Active Member.

In this work we report studies on the electro-oxidation of oxide ions in molten LiF-BeF_2-ZrF_4 (65.6-29.4-5.0 m/o) and LiF-BeF_2-ThF_4 (72-16-12 m/o), melts in which insoluble oxides, such as ZrO_2, ThO_2, and BeO, are known to form (14). The main purpose of this research was to develop the basis for an *in situ* electroanalytical method for determining low levels of soluble oxide in molten salt streams of interest to the Molten Salt Reactor Program (15). We were also interested in establishing the electro-oxidation pathway for oxide ions in fluoride melts. In this connection we also looked at the electrochemical behavior of peroxide and superoxide ions in these melts. It is worth stressing that a controversy exists regarding the electrochemistry of the "oxygen electrode" in the most commonly studied melt, the LiCl-KCl eutectic. Inman and Weaver (7) state that a clear choice cannot be made from anodic chronopotentiometry between reversible reactions: (*a*) $O^{2-} + MO \overset{-2e}{\rightleftarrows} MO\text{—}O$ $2\,O \rightleftarrows O_2$ (O_2 electroinactive) where MO is the metal surface (platinum or gold) partly covered with oxygen atoms, or (*b*) $O_2^{2-} \overset{-2e}{\rightleftarrows} O_2$ (assumed to occur on a surface covered with oxygen atoms).

Good evidence for the formation of anodic films on both noble metals was provided (7). More recently, Kanzaki and Takahashi (8) from cyclic voltammetry concluded that at platinum, rhodium, and palladium electrodes, oxide is oxidized in one step according to $O^{2-} \rightarrow O + 2e$, $O + O \rightarrow O_2$. They observed a two-step process at gold and favor the following mechanism: $O^{2-} \rightarrow O^- + e$ (first wave), $O^- \rightarrow O + e$, $O + O \rightarrow O_2$. Formation of anodic films on platinum was later considered by Takahashi *et al.* (16).

Our results in fluoride melts containing either Zr(IV) or Th(IV) differ from those in molten LiCl-KCl as is shown below.

Experimental

The experimental setup and procedures have been described previously (10, 17). The melts were prepared and purified by the Salt Production Group, MSR Program, Oak Ridge National Laboratory. These melts were contained in glassy carbon crucibles (obtained from Beckwith Carbon Corporation, Van Nuys, California). Gold, iridium, and glassy carbon unsheathed working electrodes were used. Only at gold electrodes reproducible voltammograms were obtained for the oxidation processes involving oxide and related species. Therefore, the results reported below were obtained at gold wire electrodes (diameter 0.1 cm, typical area 0.25 cm^2). Iridium quasi-reference (10) electrode was employed; the glassy carbon crucible was used as the counterelectrode. Oxide was added as either sublimed Al_2O_3 (18) or "low-temperature fired" BeO (19). The peroxide and superoxide were added as high purity Na_2O_2 and NaO_2, respectively.

Results and Discussion

Typical voltammograms of the prominent anodic wave ($E_p \sim$ 1.1-1.4V, not corrected for iR drop) observed at gold electrodes in molten LiF-BeF_2-ZrF_4 are shown in Fig. 1 and 2; similar results were obtained in LiF-BeF_2-ThF_4. Residual oxide values obtained by chemical analysis were approximately 240 ppm (3.4×10^{-2}M) for LiF-BeF_2-ZrF_4 and 110 ppm (2.3×10^{-2}M) for LiF-BeF_2-ThF_4. Additions of oxide as either Al_2O_3 or BeO produced increases in the peak current of the anodic wave at 650°C, a temperature at which we were not limited by the solubility of BeO and/or ZrO_2 or ThO_2 (20). We, therefore, attribute this wave to the oxidation of oxide ions (free or complexed) in these melts. It is of interest that the oxidation potential of O^{2-} ions is approximately 1.2V positive with respect to the reduction of Ni^{2+} in the same melts.

Scan rate studies are shown in Fig. 2. The postwave following the major anodic peak was generally more prominent at relatively fast (≥1 V/sec) scan rates; it tended to merge with the main wave at 650°C. The prepeak observed at ~+0.6V at fast scan rates (Fig. 2) was not identified. The characteristics of the prepeak varied from one gold electrode to another; its peak current generally increased with scan rate. The prepeak could be minimized by prior cycling of the electrode. The sharp increase in anodic current at ~1.8V represents the anodic limit of the melt (probably the oxidation of the gold electrode). On reverse scans, essentially no cathodic current was seen at slow scan

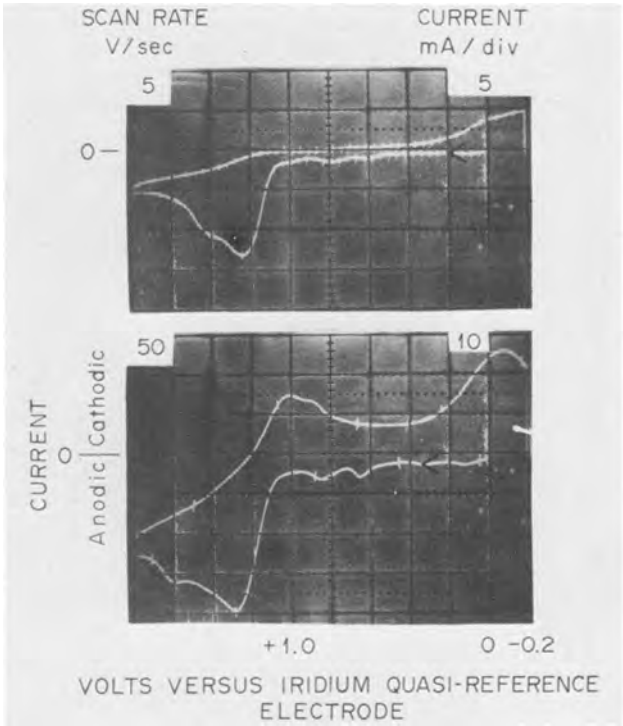


Fig. 1. Single scan cyclic voltammograms for the oxidation of O^{2-} ions in molten LiF-BeF_2-ZrF_4 (65.6-29.4-5.0 m/o). Au working electrode ($A \approx$ 0.25 cm^2), t = 500°C; melt saturated with O^{2-} ions.

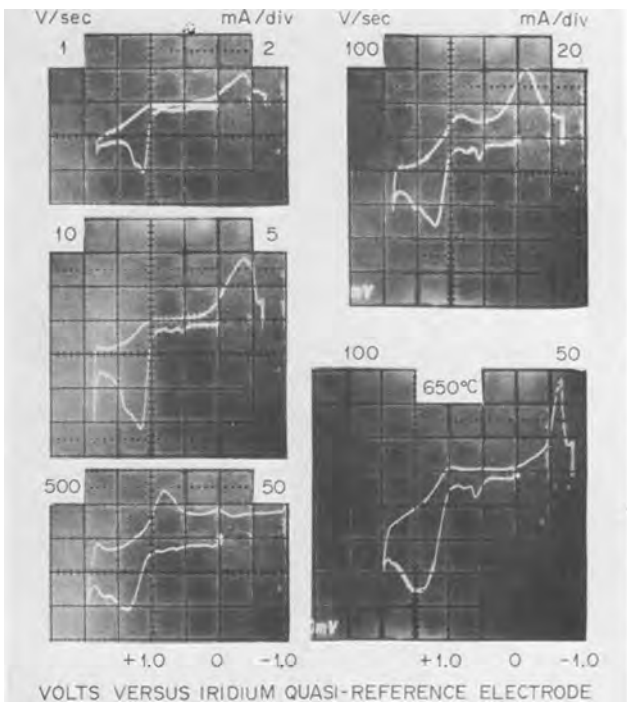


Fig. 2. Effect of scan rate and temperature on cyclic voltammograms for the oxidation of O^{2-} ions in molten LiF-BeF_2-ZrF_4. t = 500°C except where noted. Other parameters same as for Fig. 1.

rates (<0.1 V/sec); at intermediate scans (0.1-10 V/sec), a cathodic peak was observed between 0 and —0.5V. It was also observed that at fast scan rates, if the scan was reversed just after the major anodic peak but before the postwave, the cathodic peak at ~+1.0V became more pronounced while the cathodic peak at ~—0.2V became smaller. For the main anodic wave, current reversal chronopotentiograms showed that $\tau_f/\tau_r >> 3$ (21). These results suggest that we are observing an electrode reaction in which an unstable intermediate is generated which reacts to produce a more stable product.

It was attempted to compare the shape of experimental anodic voltammograms with that of the theoretical ones corresponding to case VI of Nicholson and Shain (22) (a charge transfer followed by an irreversible chemical reaction). Comparisons were made for anodic waves recorded at 0.5 V/sec to minimize iR drop after adjusting the potential-related scale to 650°C and appropriate n value and then normalizing the current function maximum to the peak current on the voltammogram. The best fit was realized at a $k_f/a \sim 4$ (22) and $n = 2$, although the shape of the theoretical waves was rather insensitive to changes in k_f/a. A more sensitive parameter is the peak potential which shifted anodically with increasing scan rate (smaller k_f/a values), although the shift was larger than the theoretical ~78/n mV/decade at 500°C (22). This discrepancy was probably caused, in part, by the large iR drop at fast scan rates.

The separation of the peak and half-peak potentials for the anodic wave, for $n = 2$, case VI of Nicholson and Shain (22), is calculated to be ~70 mV at 500°-550°C. Experimental values in both melts were in the range of 50-70 mV. The agreement is believed to be reasonable in view of the more complicated behavior of the products of the electrode reaction in the melts compared to the theoretical treatment. An $n = \sim 2$ value was also obtained from the ratio of the voltammetric $i_p/v^{1/2}$ and the chronopotentiometric $i\tau^{1/2}$ as defined by the Randles-Sevcik and Sand equations, respectively (21).

Based on these results. we postulate the following reaction pathway

$$O^{2-} \rightarrow O + 2e \quad [1]$$

$$O + O \rightarrow O_2 \quad [2]$$

$$O + O^{2-} \rightarrow O_2^{2-} \quad [3]$$

Thus, the prominent anodic wave represents the oxidation of oxide ions to atomic oxygen. The postwave, seen only at relatively fast scan rates, most likely results from the oxidation of the unstable (at least at the electrode surface) peroxy intermediate. The cathodic peak at ~+1V seen only at fast scan rates is believed to be caused by the reduction of atomic oxygen while the peak at ~—0.2V represents the reduction of molecular oxygen. Both forms of oxygen probably exist as chemisorbed species at the surface of the electrode.

The reactions

$$2\,O^{2-} \rightarrow O_2^{2-} + 2e \quad [4]$$

$$O_2^{2-} \rightarrow \tfrac{1}{2}\,O_2 + O^{2-} \quad [5]$$

appear to be ruled out by the approximate constancy of the parameter $i_p/v^{1/2}$ over a wide range of scan rates [for example, for a typical run at 650°C $i_p/v^{1/2} = 21.9 \pm 3.1$ mA sec$^{1/2}$/V$^{1/2}$ over the range of scan rates 0.1-100 V/sec; for a catalytic case, involving regeneration of reactant, a large increase in $i_p/v^{1/2}$ with decreasing v is expected (22)] and by the separation of $E_{p/2}$ and E_p (23). Although an approximately 10% decrease in the parameter $i_p/v^{1/2}$ is expected over the complete range of scan rates for case VI of Nicholson and Shain (22), the precision of our measurements (see above) is insufficient to utilize this criterion effectively. Thus, the experimental results agree best with the electrode reaction which proceeds first order in oxide with $n = 2$.

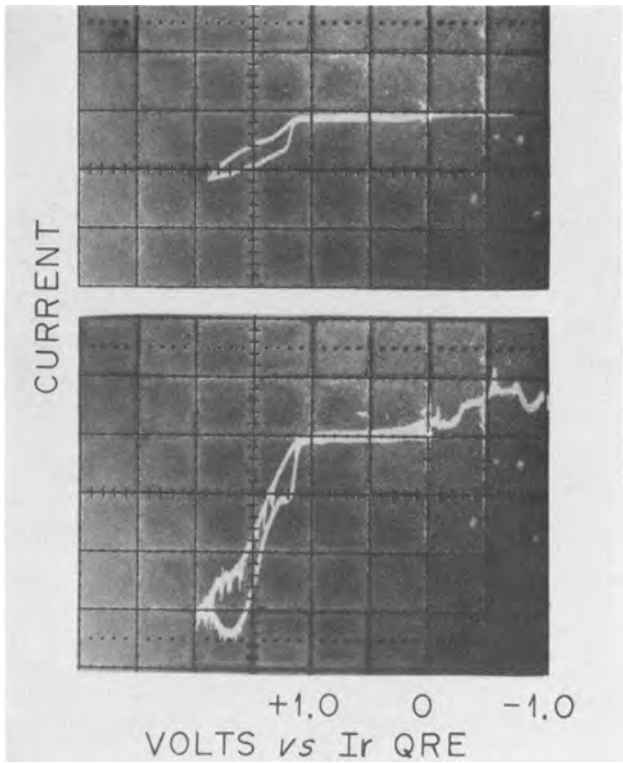


Fig. 3. Effect of Na_2O_2 additions on the height of the postwave in molten LiF-BeF_2-ThF_4 (72-16-12 m/o). Scan rate 0.1 V/sec. Upper curve, before addition; lower curve, after addition of ~3g of Na_2O_2 to ~850g of melt. t = 550°C. Au electrode ($A \approx 0.25$ cm^2). Current: 5 mA/div.

Peroxide additions resulted in a pronounced increase in the height of the postwave for both melts. The increase observed for molten LiF-BeF_2-ThF_4 is shown in Fig. 3. Similar results were obtained for molten LiF-BeF_2-ZrF_4. The equilibrium potential shifted anodically (melt became more oxidizing) and gradually approached the original value as the peroxide decomposed. Within a few hours, the peroxide decomposed from the molten LiF-BeF_2-ZrF_4 as evidenced by the cathodic shift in the equilibrium potential and decrease in wave height of the postwave. The peroxy species appeared much more stable, however, in the thorium-containing melts, taking several days to reestablish background conditions. At this time both melts were saturated in oxide; therefore, no significant changes in the main anodic wave were detected following peroxide additions. No additional reduction wave following Na_2O_2 additions was observed. Superoxide (NaO_2) exhibited the same behavior as peroxide. Apparently the NaO_2 decomposed to peroxide ($2NaO_2 \rightarrow Na_2O_2 + O_2$) and other products immediately after contacting the melts. One may speculate that the greater stability of O_2^- ions in the LiF-NaF-KF eutectic (12, 13) as compared to the melts employed in this study is due to the presence of large alkali counterions, such as K^+ ions in the alkali fluoride eutectic. It is well known (24) that the superoxides of the larger alkali ions are more stable.

The peak height of the reduction wave at ~—0.2V did not change significantly with increasing potentiostatic formation time at ~1.7V. This suggests that a chemisorbed film is formed on the electrode, after which the excess O_2 escapes from the melt. A film "aging" effect (7), however, was observed. Galvanostatic stripping curves following short formation times (5-20 sec) exhibited increasingly cathodic reduction potentials. An approximately constant $i\tau$ product was obtained which also indicates reduction of a surface film rather than a diffusing species.

In conclusion, we have shown that the electro-oxidation of soluble oxide species at gold electrodes in fluoride melts, such as LiF-BeF_2-ZrF_4 and LiF-BeF_2-ThF_4, provides the basis for an *in situ* determination of small amounts of dissolved oxide. The electro-oxidation results in atomic oxygen which rapidly recombines to form chemisorbed O_2 or reacts with the reactant O^{2-} forming O_2^{2-} which is oxidized further.

Acknowledgment

This research was sponsored by the Energy Research and Development Administration under contract with Union Carbide Corporation.

Manuscript submitted Aug. 30, 1976; revised manuscript received Oct. 27, 1976.

Any discussion of this paper will appear in a Discussion Section to be published in the December 1977 JOURNAL. All discussions for the December 1977 Discussion Section should be submitted by Aug. 1, 1977.

Publication costs of this article were assisted by Oak Ridge National Laboratory.

REFERENCES

1. H. A. Laitinen and B. B. Bhatia, *This Journal*, **107**, 705 (1960).
2. G. Delarue, *J. Electroanal. Chem.*, **1**, 285 (1959-1960).
3. R. Littlewood and E. J. Argent, *Electrochim. Acta*, **4**, 114 (1961).
4. A. M. Shams El Din, A. A. El Hosary, and A. A. A. Gerges, *J. Electroanal. Chem.*, **6**, 131 (1963).
5. N. S. Wrench and D. Inman, *ibid.*, **17**, 319 (1968).
6. D. Inman, in "Electromotive Force Measurements in High-Temperature Systems," C. B. Alcock, Editor, pp. 174-178, Institution of Mining and Metallurgy, London (1968).
7. D. Inman and M. J. Weaver, *J. Electroanal. Chem.*, **51**, 45 (1974).
8. Y. Kanzaki and M. Takahashi, *ibid.*, **58**, 339 (1975).
9. E. W. Dewing and E. T. van der Kouwe, *This Journal*, **124**, 58 (1977).
10. G. Mamantov, in "Molten Salts: Characterization and Analysis," G. Mamantov, Editor, pp. 540-543, M. Dekker Inc., New York (1969).
11. A. L. Mathews and C. F. Baes, Jr., *Inorg. Chem.*, **7**, 373 (1968).
12. F. L. Whiting, G. Mamantov, and J. P. Young, *J. Inorg. Nucl. Chem.*, **34**, 2475 (1972).
13. F. L. Whiting, G. Mamantov, G. M. Begun, and J. P. Young, *Inorg. Chim. Acta*, **5**, 260 (1971).
14. C. F. Baes, Jr., in "Reprocessing of Nuclear Fuels; Nuclear Metallurgy," Vol. 15, P. Chiotti, Editor, pp. 615-644, AEC Division of Technical Information (1969).
15. M. W. Rosenthal, P. N. Haubenreich, and R. B. Briggs, ORNL Report 4812 (August 1972).
16. M. Takahashi, Y. Katsuyama, and Y. Kanzaki, *J. Electroanal. Chem.*, **62**, 363 (1975).
17. G. Mamantov and D. L. Manning, *Anal. Chem.*, **38**, 1494 (1966).
18. B. Gilbert, G. Mamantov, and G. M. Begun, *Inorg. Nucl. Chem. Lett.*, **10**, 1123 (1974).
19. C. E. L. Bamberger, H. F. McDuffie, and C. F. Baes, Jr., *Nucl. Sci. Eng.*, **22**, 14 (1965).
20. B. F. Hitch and C. F. Baes, Jr., ORNL Report-4046, pp. 19-20 (Dec. 31, 1966).
21. P. Delahay, "New Instrumental Methods in Electrochemistry," Interscience, New York (1954).
22. R. S. Nicholson and I. Shain, *Anal. Chem.*, **36**, 706 (1964).
23. M. S. Shuman, *ibid.*, **41**, 142 (1969).
24. F. A. Cotton and G. Wilkinson, "Advanced Inorganic Chemistry," 3rd ed., p. 417, Interscience, New York (1972).

Film Breakdown on Nickel under Transpassive Dissolution Conditions in Sodium Nitrate Solutions

Madhav Datta and Dieter Landolt*

Materials Department, Swiss Federal Institute of Technology, Lausanne, Switzerland

ABSTRACT

Film breakdown phenomena leading to transpassive high rate dissolution of nickel in nitrate electrolytes were investigated under controlled flow conditions. Current efficiencies for metal dissolution were determined as a function of current density at different pH, temperature, and nitrate ion concentration. Initiation of film breakdown was investigated by performing experiments at very small dissolution times using polycrystalline and single crystal anodes and observing the resulting surface textures by means of optical and scanning electron microscopes. Results indicate that during high rate nickel dissolution, current efficiency is mostly governed by anode potential and nitrate ion concentration while bulk electrolyte pH and temperature have relatively little effect. Transpassive dissolution is initiated by local breakdown of the passive film. Dissolution takes place at the activated sites from a few well-defined crystal planes. With increasing time, these sites grow until they merge together resulting in an etched surface microtexture. Similarities between observed film breakdown phenomena leading to high rate dissolution at potentials above those for oxygen evolution and the pitting behavior of passive metals under corrosion conditions are discussed.

The importance of passivation phenomena in affecting electrochemical machining (ECM) operations has been demonstrated in many publications (1-16). In so-called passivating electrolytes, ECM takes place in the transpassive potential region where the protective property of passive films formed at the anode at low potentials is destroyed. Anodic reactions occurring in the transpassive potential region during high rate dissolution of steel and nickel have been studied by several authors (6-16). In all these studies, oxygen evolution was found to be the predominant anodic reaction at relatively low current densities in the transpassive potential region. At higher current densities, however, the relative amount of metal dissolution increased with increasing current density. Mao (6) investigated high rate dissolution of steel in sodium chlorate and sodium nitrate solutions under ECM conditions. The current

* Electrochemical Society Active Member.
Key words: film breakdown, transpassive dissolution, pitting, nickel, electrochemical machining.

efficiency for metal dissolution was measured while simultaneously the anodically evolved gas was collected and analyzed. The total current efficiency for divalent iron formation and anodic oxygen evolution added up to 100%. Similar results have been reported by Datta and Landolt (8) and LaBoda *et al.* (14) for high rate nickel dissolution in chlorate electrolytes where divalent nickel formation and oxygen evolution were found to account for all charge passed. Recently high rate transpassive dissolution of nickel in concentrated nitrate electrolytes has been studied by the present authors under controlled flow conditions (10). Current efficiency for nickel dissolution was found to increase with increasing current density until a maximum value close to 100% was reached. At current densities below the maximum an etched surface texture resulted from dissolution. Metal dissolution efficiency at low current densities was influenced relatively little by flow conditions, but the current density corresponding to maximum efficiency was higher the higher the flow rate. Anodic brightening occurred at current densities above the maximum. The phenomena of anodic brightening and the factors governing the transition from etching to brightening have been discussed in detail (10, 11). In the present study, attention is focused on the phenomena leading to film breakdown and anodic dissolution in the etching region.

Relatively little is known about the phenomena of film breakdown leading to high rate dissolution under ECM conditions, although different theories have been proposed in the literature. According to Mao (6), the oxide film formed on steel in chlorate solution dissolves under conditions of low *p*H at the electrode resulting from oxygen evolution. However, in a later work Mao, LaBoda, and Hoare (9) explained the dissolution mechanism of steel in different passivating electrolytes in terms of an ion exchange model already mentioned by Hoar (17). According to the model, anions adsorbed on the film are exchanged with the oxygen ions of the oxide matrix which eventually breaks down and dissolves resulting in film thinning leading to high rate dissolution. Recently, Chin and Mao (12) reported that oxide film on steel is ruptured by intergranular attack and high rate dissolution takes place from the underlying bare metal surface.

In order to better define the phenomena of breakdown in the transpassive potential region, high rate dissolution of nickel in nitrate electrolytes has been investigated in the present study under controlled flow conditions. One part of the experimental program consisted of determining the experimental variables which govern nickel dissolution efficiency. For that purpose, metal dissolution efficiencies were determined as a function of current density at different *p*H, temperature, and nitrate ion concentration. In the second part a microscopic study of surfaces of polycrystalline and single crystal anodes having been subjected to short anodic pulses was carried out to further investigate the breakdown mechanism.

Experimental

The experimental apparatus has been described elsewhere in detail (18). It consisted of a rectangular flow channel 3.2 mm wide and 0.5 mm high through which the electrolyte was pumped at a constant linear velocity of 1000 cm/sec corresponding to turbulent flow conditions. In a first series of experiments aimed at the study of current efficiency for metal dissolution, rectangular electrodes epoxy cast into a cylindrical PVC holder were used. Anodes and cathodes were 3.2 mm wide and 10 mm long. They were made of nickel 200 and positioned flush with the channel wall. Before each experiment, the anode was mechanically polished on 600 carborundum paper, degreased with benzene, and cleaned with soap solution and distilled water. It was then subjected to cathodic pretreatment in 1M NaOH solution at 20 mA/cm^2 for 30 sec followed by rinsing with distilled water. In order to maintain the cell geometry, only small amounts of metal were dissolved. All experiments were performed galvanostatically by passing a constant charge of 60 C/cm^2 corresponding to a maximum dissolution depth of 20 μm. During the experiments, current and time were monitored on a digital oscilloscope (Nicolet Type 109). Current densities applied ranged up to 30 A/cm^2. The anode was carefully weighed before and after each experiment using an analytical balance having a precision of 0.01 mg (Sartorius Model 2474.). Before weighing, the samples were cleaned with acetone and dried with air.

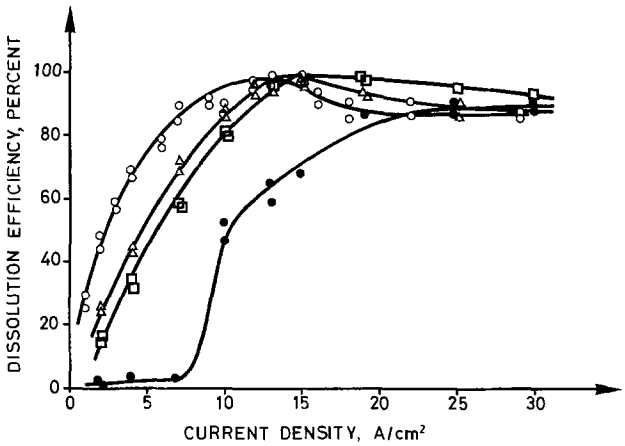


Fig. 1. Influence of electrolyte *p*H on current efficiency for nickel dissolution in 6M nitrate solution. 5M $NaNO_3$ + 1M HNO_3 (○), 5.9M $NaNO_3$ + 0.1M HNO_3 (△), 6M $NaNO_3$ + 0.1M NaOH (□), 6M $NaNO_3$ + 1M NaOH (●).

A second series of experiments was aimed at investigating the initiation of film breakdown leading to high rate dissolution. For that purpose, experiments were carried out at very small dissolution times using 10 mm diameter cylindrical electrodes which could be easily removed from the electrode holder for scanning electron microscope studies. Only a part of the anode corresponding to the width of the channel (3.2 mm) was exposed to the electrolyte while the remaining part was insulated by the Teflon spacer constituting the flow channel. Polycrystalline nickel anodes were machined from a bar of high purity nickel[1] (99.95%). Some experiments were carried out with [111] oriented single crystal[1] (99.95%) anodes. The different electrode assemblies have been described elsewhere in detail (16). Before each experiment nickel anodes were fixed in a plastic mold and the flat part was mechanically polished to 0.25 μm finish using diamond paste. Polished anodes were taken out of the plastic mold, cleaned, and pretreated as before. A test experiment was carried out with an electropolished single crystal anode to assure that the mechanical polishing procedure did not affect obtained results (16).

Electrolyte solutions were prepared from analytical grade chemicals and distilled water. Temperature of the electrolyte was maintained by means of thermostat. Unless otherwise indicated, experiments were performed at 25°C.

Results and Discussion

Current efficiency.—The influence of electrolyte *p*H on current efficiency for nickel dissolution in 6M nitrate solution is shown in Fig. 1 giving data obtained in 5M $NaNO_3$ + 1M HNO_3, 5.9M $NaNO_3$ + 0.1M HNO_3 (*p*H = 0.5), 6M $NaNO_3$ + 0.1M NaOH (*p*H = 12.2), and 6M $NaNO_3$ + 1M NaOH. From anodic weight loss measurements an apparent current efficiency for anodic dissolution was computed on the basis of Ni^{2+} formation (10). The data indicate that in the *p*H range 0.5-12, metal dissolution efficiency is relatively little influenced by *p*H of the electrolyte. In strongly alkaline

[1] Supplier: Cristal Tec, Grenoble Cedex, France.

solutions, on the other hand, transpassive nickel dissolution sets in at much higher current densities only. The observed behavior can be explained by considering the local pH change at the anode due to oxygen evolution. An estimation of H^+ ion buildup at the anode indicates that the local pH can indeed be neutral or acidic even in a slightly alkaline bulk solution (6M $NaNO_3$ + 0.1M NaOH). In a strongly alkaline solution, however, the local pH at the anode remains alkaline and metal dissolution is, therefore, inhibited, *i.e.*, oxygen evolution takes place over a wide range of current density. The results lead to the conclusion that in ECM practice, where neutral electrolytes are commonly used, small changes in electrolyte pH should not affect machining performance.

Figure 2 shows the influence of electrolyte temperature on the metal dissolution efficiency. These data were obtained at 5°, 25°, and 40°C in 5M $NaNO_3$ + 1M HNO_3. Results indicate that at low current densities where metal dissolution efficiency is an increasing function of current density, the electrolyte temperature has little influence on metal dissolution efficiency. This is in contrast with the previously observed dependency of surface brightening on temperature (11).

The influence of bulk nitrate ion concentration on metal dissolution efficiency is shown in Fig. 3 which gives data obtained in 5M $NaNO_3$ + 1M HNO_3, 3M $NaNO_3$ + 1M HNO_3, and 1M $NaNO_3$ + 1M HNO_3. Due to migration, the nitrate ion concentration at the anode surface at a given current density is different from that in the bulk. For a given flow condition, the nitrate ion concentration at the anode increases with increasing current density and it is higher the higher the bulk nitrate concentration. A quantitative estimation of the degree of local nitrate ion buildup is difficult because of gas evolution and because of the use of concentrated multicomponent electrolytes. However, qualitatively, the data of Fig. 3 show that a clear relationship exists between local anion concentration, anode potential (current density), and metal dissolution efficiency. Passive film breakdown is, therefore, favored by high nitrate ion concentration and high anode potential.

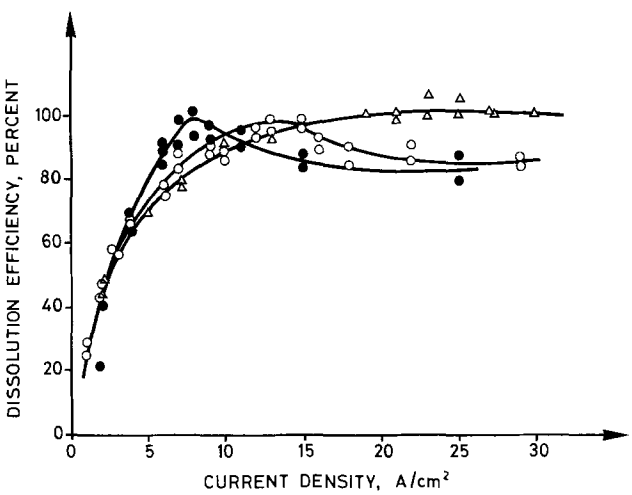


Fig. 2. Influence of electrolyte temperature on nickel dissolution efficiency in 5M $NaNO_3$ + 1M HNO_3. 5°C (●), 25°C (○), 40°C (△).

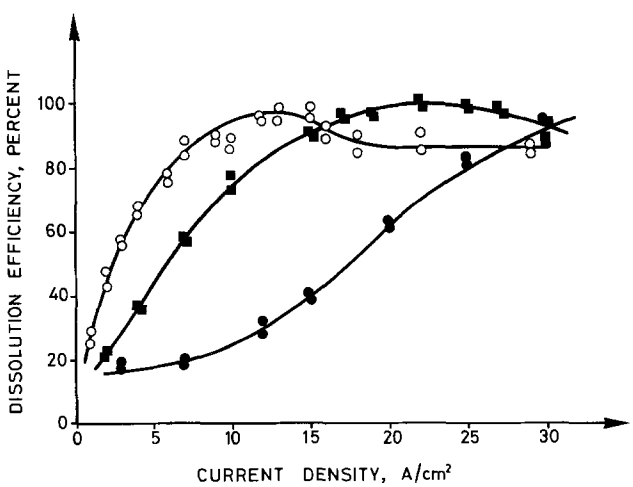


Fig. 3. Effect of bulk nitrate ion concentration on nickel dissolution efficiency. 5M $NaNO_3$ + 1M HNO_3 (○), 3M $NaNO_3$ + 1M HNO_3 (△), 1M $NaNO_3$ + 1M HNO_3 (●).

The behavior presents some analogy to well-known film breakdown phenomena in chloride solutions leading to pitting. For example, the critical pitting potential of stainless steel was found to be strongly dependent on chloride ion concentration by Leckie and Uhlig (19) and more recently by Broli *et al.* (20). The pitting potential was also reported to be independent of pH in the range 1-7 but for pH values higher than 7, the OH^- ions acted as pit inhibitor (19). Similar results were obtained by Venu *et al.* (21) and Rajagopalan *et al.* (22) who reported that the presence of NaOH inhibited passivity breakdown on steel in NaCl solution. Except at very low temperatures, the critical pitting potential was reported to be little influenced by increasing temperature (19).

Because of large ohmic drops associated with high current densities, it was not possible to determine the actual anode potentials in the present study. However, dissolution efficiency in these experiments can be taken as a measure of the stability of the film, *i.e.*, oxygen evolution takes place on stable films whereas increasing metal dissolution efficiency indicates film breakdown. The obtained results for metal dissolution efficiency as a function of pH, temperature, and nitrate ion concentration, therefore, suggest that a pitting-type mechanism leads to high rate dissolution in passivating ECM electrolytes.

Microscopic studies.—To investigate further the above hypothesis, surfaces resulting from dissolution were studied microscopically. The experiments described in the previous section involved passage of 60 C/cm^2 and anodes after dissolution in the ascending part of the current efficiency *vs.* current density curve exhibited an etched surface texture similar to that described in Ref. (10). To study the development of surface roughness experiments at smaller dissolution times were performed in 5M $NaNO_3$ + 1M HNO_3 solution.

On application of a very short current pulse, the anode surface looked unaltered to the naked eye even at a high current density. Under an optical microscope, however, localized breakdown sites resembling etch pits could be seen. Initiation and growth of these dissolution sites were studied as a function of dissolution time and current density.

Figure 4 shows the effect of dissolution time on surface attack at a current density of 3 A/cm^2. Figure 4(a) corresponds to a charge of 1 C/cm^2. It shows that initiation of dissolution occurs at discrete sites which are randomly distributed. With increasing dissolution time, grain boundaries become severely attacked and the dissolution sites grow giving rise to characteristic dissolution patterns which are oriented in definite directions. Figure 4(c), for example, shows three grains and their boundaries. The dissolution lines are pointed toward a particular direction which is different in different grains. The directional growth of the dissolution sites must, therefore, be related to grain orientation.

The surface attack at 5 A/cm^2 corresponding to a higher dissolution efficiency is shown in Fig. 5. For the same charge, the number of dissolution sites here is much higher than at 3 A/cm^2. As before, the breakdown sites grow bigger with time and the whole surface becomes densely covered with small etch pits. The

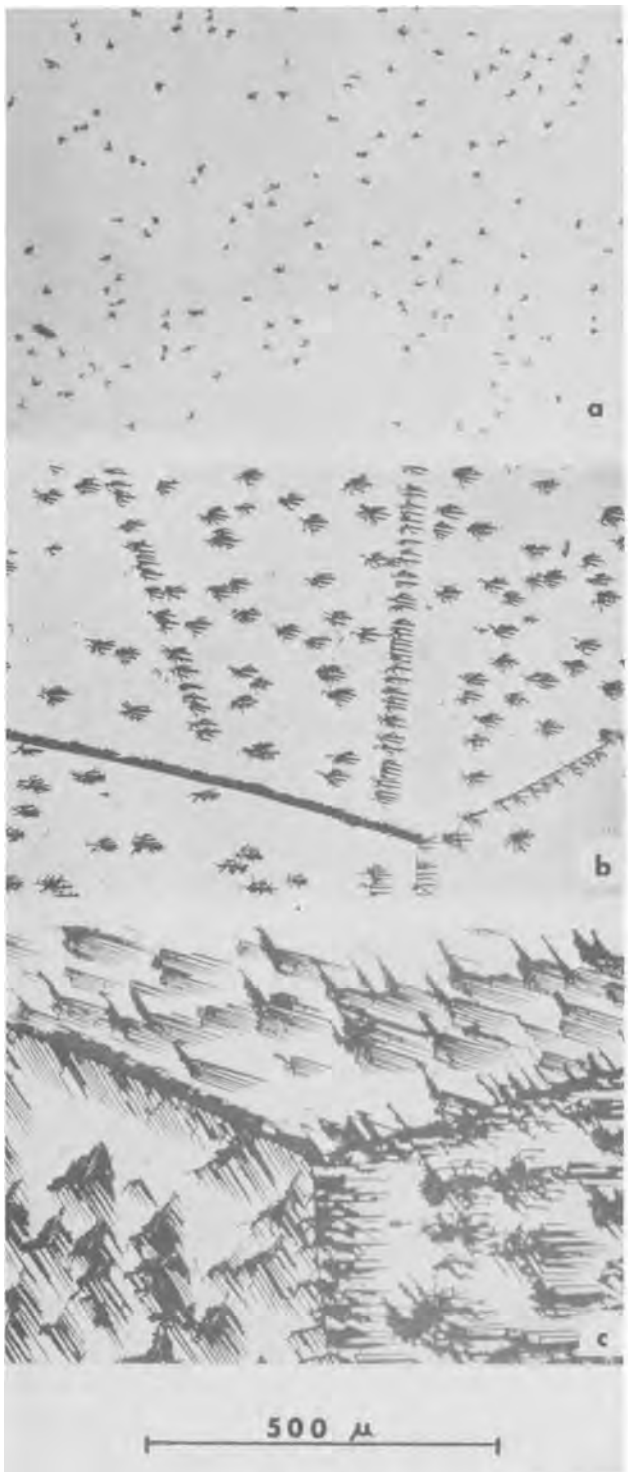


Fig. 4. Effect of dissolution time on surface attack: (a) 0.32 sec, (b) 0.85 sec, (c) 2.97 sec; current density, 3 A/cm^2.

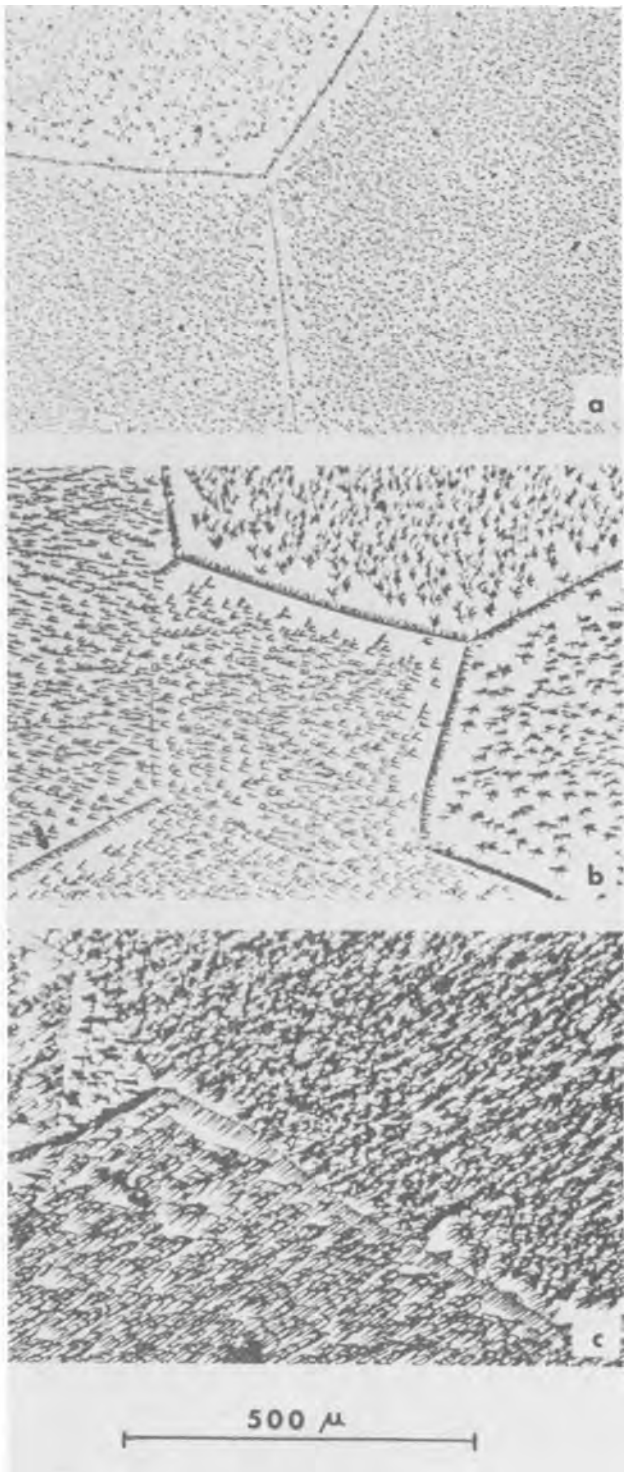


Fig. 5. Effect of dissolution time on surface attack: (a) 0.22 sec, (b) 0.49 sec, (c) 1.01 sec; current density, 5 A/cm^2.

same behavior is also seen in Fig. 6 which represents dissolution experiments performed at a constant current density of 7 A/cm^2. At this current density, even at the smallest dissolution time employed, the surface is fully covered with etch pits. With increasing time of dissolution, they grow in size and finally merge together giving rise to an etched surface appearing black to the naked eye. It is interesting to note that under a given dissolution condition, the number of dissolution sites and their size are different in different grains (cf. Fig. 5 and 6b, 6c) indicating that different crystals in a polycrystalline nickel anode dissolve at different rates. Dissolution efficiency should, therefore, be related to the crystal orientation.

To further illustrate initiation and growth of dissolution sites, surface textures resulting from dissolution were examined under a scanning electron microscope (SEM). SEM pictures of samples obtained from experiments performed at 3 A/cm^2 and different dissolution times are shown in Fig. 7-9. The SEM micrographs presented in Fig. 7 demonstrate that initiation of dissolution is highly localized, *i.e.*, dissolution pits with sharp boundaries are apparent in an otherwise intact passive film on which probably oxygen is evolved. The pits are randomly distributed and their shape is also random. At very high magnification (Fig. 7b) submicroscopic steps are visible within the pit indicating that dissolution proceeds from preferred crystallographic planes similar to active dissolution.

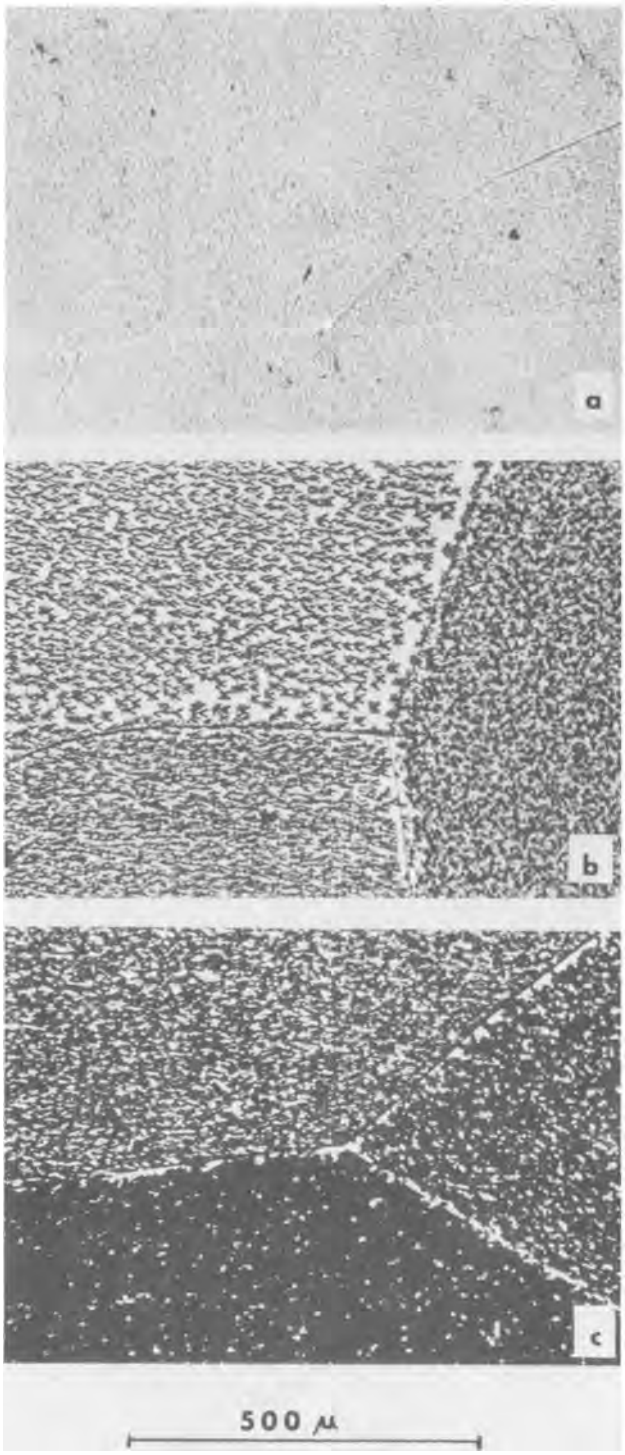


Fig. 6. Effect of dissolution time on surface attack: (a) 0.12 sec, (b) 0.49 sec, (c) 0.74 sec; current density, 7 A/cm^2.

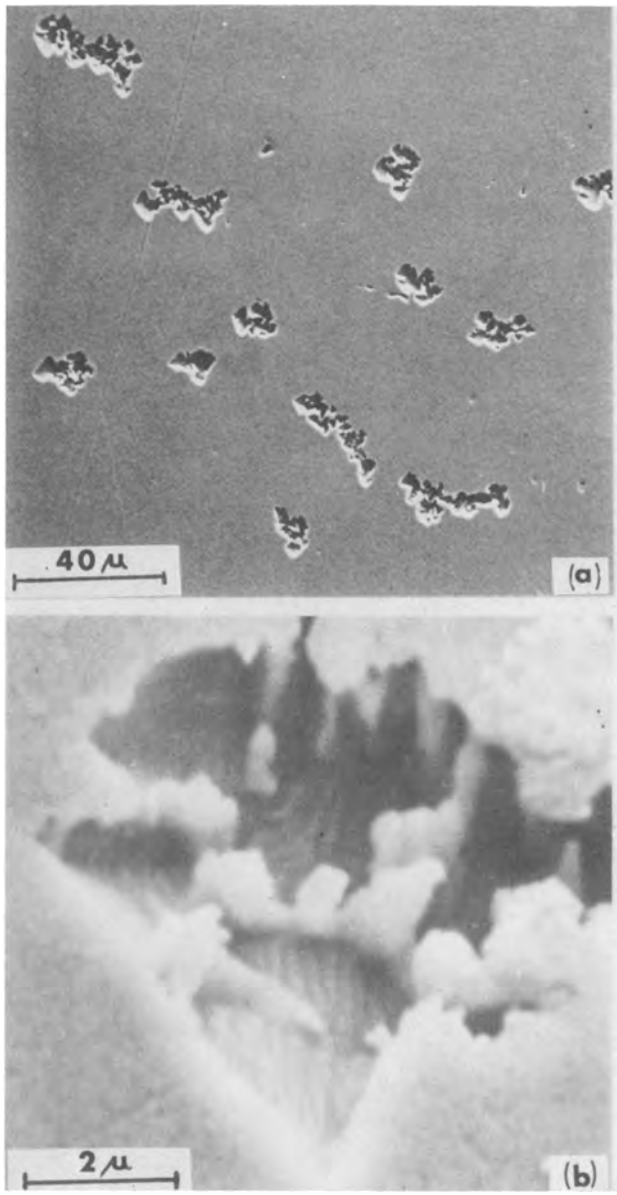


Fig. 7. SEM photographs showing dissolution pits on a polycrystalline nickel anode after a dissolution time of 0.32 sec; current density, 3 A/cm^2.

Figure 8 shows that with increasing dissolution time, the randomly shaped pits grow in certain specific directions giving rise to parallel ditches. Submicroscopic steps are again visible on the side walls. Figure 9 shows that with increasing dissolution time the ditches may grow to considerable length without getting broader. Growth direction is different for different grains but within a single grain growth is usually in the same direction. This confirms that dissolution occurs from a few particular crystal planes.

To further investigate the influence of crystallographic orientation on the dissolution process, experiments were performed using a single crystal with [111] orientation. Figure 10 shows SEM photographs of a surface resulting from dissolution at 3 A/cm^2. Dissolution proceeds in three directions oriented approximately 120° to each other corresponding to the [111] projections. This gives rise to Y-shaped dissolution sites, all oriented in parallel. The behavior further confirms that the process of dissolution is related to grain orientation and probably proceeds from close-packed planes. Some undercutting of the film is observed. This is particularly evident in Fig. 10 (b) which indicates that mechanical removal of the film may be possible under certain conditions. Since oxide film on nickel is in general very thin, such a mechanism should not affect the dissolution efficiency significantly, however.

The different microphotographs clearly demonstrate that transpassive dissolution of nickel in nitrate solution is initiated by local breakdown of the passive film and, therefore, presents some analogies to the pitting behavior of passive metals in aggressive media under corrosion conditions. The process of nucleation and growth of corrosion pits and the electrochemical conditions within pits have been widely studied (17, 23-30) but the mechanism of nucleation is not yet understood. Hoar *et al.* (24) proposed that preferential nucleation occurs on those parts of the film overlying grain boundaries and dislocations and suggested a mechanical

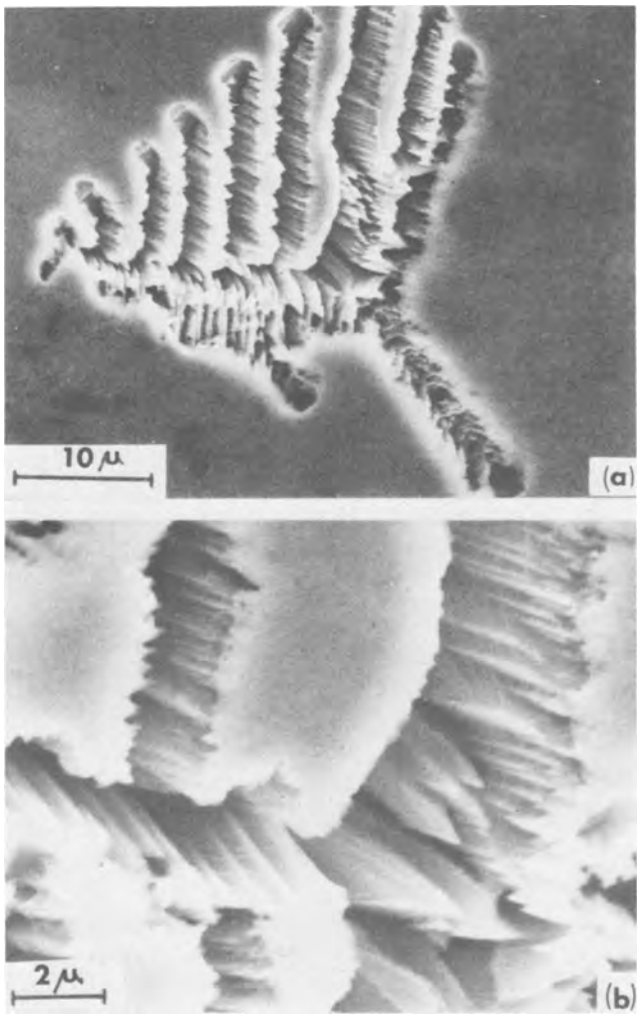


Fig. 8. SEM photographs showing dissolution pits on a polycrystalline nickel anode after a dissolution time of 0.85 sec; current density, 3 A/cm^2.

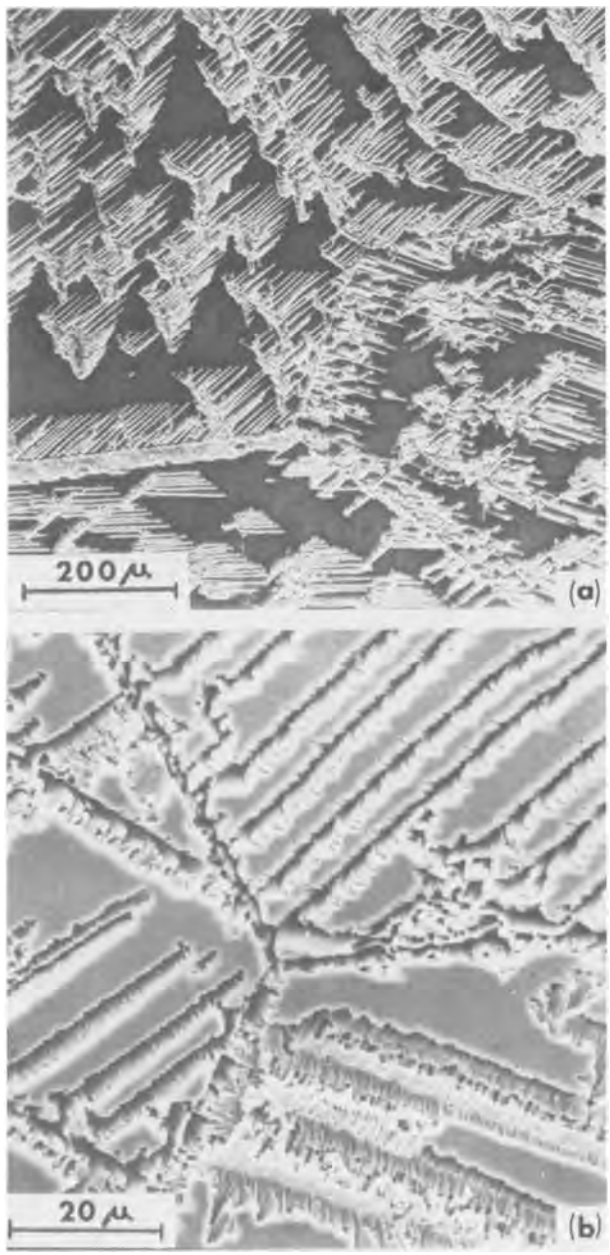


Fig. 9. SEM photographs showing dissolution pits on a polycrystalline nickel anode after a dissolution time of 2.97 sec; current density, 3 A/cm^2.

mechanism for anion penetration into the passive film (17). Smialowska and co-workers (25, 26) studying the pit morphology on stainless steel showed that pits may also nucleate at inclusions in the metal. According to Vetter and Strehblow (27, 28), Sato (29), and Galvele (30), the breakdown of the anodic oxide film is controlled not only by the electrochemical reactivity of the aggressive ions but also by mechanical and dielectric properties of the film itself. Similar factors may play a role in breakdown processes leading to local breakdown and high rate dissolution under ECM conditions but a detailed mechanistic description cannot be given at present.

Conclusions

The results of the present study show that high rate transpassive dissolution of nickel in sodium nitrate is initiated by local breakdown of the passive film and, therefore, presents many similarities with conventional pitting phenomena well known, *e.g.*, in chloride media. For nickel in sodium nitrate film breakdown causes a change from anodic oxygen evolution to high rate metal dissolution. Breakdown is favored by high current density and high anode potential and by high nitrate ion concentration. On the other hand, it depends relatively little on electrolyte temperature and on bulk electrolyte *p*H as long as the latter does not become strongly alkaline. Photomicrographs show that film breakdown is initiated at randomly distributed discrete sites the number of which increases with increasing current density. The nucleation sites grow in distinct directions by anodic dissolution from a few well-defined crystal planes. Eventually they merge together yielding a rough and etched microtexture. It appears that high rate transpassive dissolution at steady state involves a delicate balance between depassivation and repassivation phenomena which govern the extent of the anode surface covered by the passive film and thus determine current efficiency.

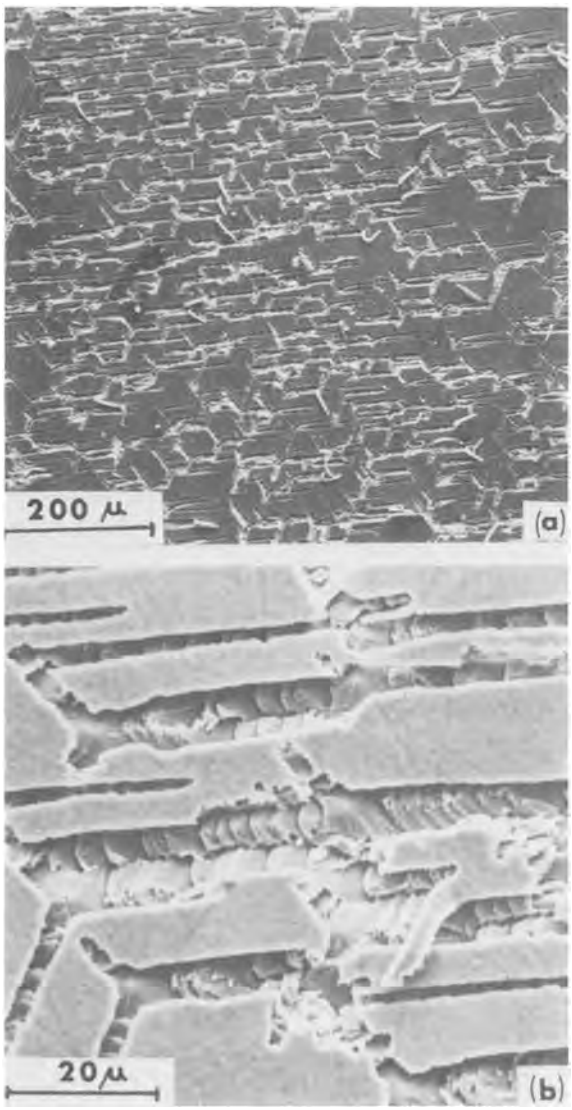
Acknowledgment

This work was supported by the "Fondation pour l'Encouragement des Recherches Scientifiques (FERS)," Bern, Switzerland.

Manuscript submitted Oct. 26, 1976; revised manuscript received Dec. 1, 1976.

Any discussion of this paper will appear in a Discussion Section to be published in the December 1977 JOURNAL. All discussions for the December 1977 Discussion Section should be submitted by Aug. 1, 1977.

Publication costs of this article were assisted by the Swiss Federal Institute of Technology.



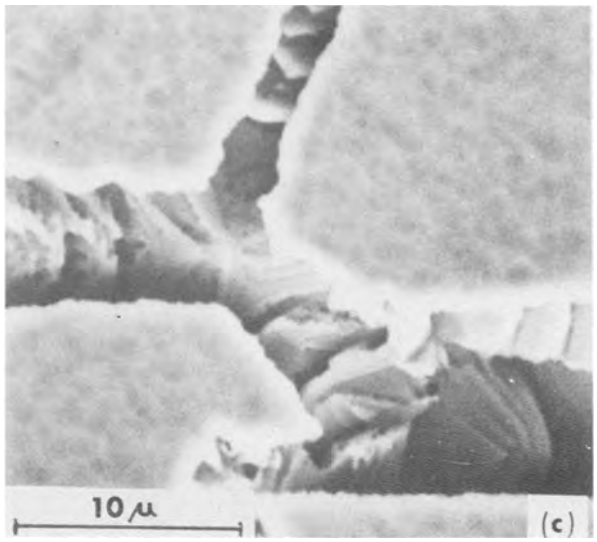


Fig. 10. SEM photographs of surface attack resulting from dissolution of a [111] oriented single crystal nickel anode; current density, 3 A/cm^2; dissolution time, 2.66 sec.

REFERENCES

1. M. A. LaBoda and M. L. McMillan, *Electrochem. Technol.*, **5**, 340 (1967).
2. J. P. Hoare, M. A. LaBoda, M. L. McMillan, and A. J. Wallace, *This Journal*, **116**, 199 (1969).
3. P. A. Brook and Q. Iqbal, *ibid.*, **116**, 1458 (1969).
4. D. Landolt, R. H. Muller, and C. W. Tobias, *ibid.*, **116**, 1384 (1969).
5. D. Landolt, R. H. Muller, and C. W. Tobias, *ibid.*, **118**, 36 (1971).
6. K. W. Mao, *ibid.*, **118**, 1870 (1971); *ibid.*, **118**, 1876 (1971).
7. D. Landolt, *ibid.*, **119**, 708 (1972).
8. M. Datta and D. Landolt, *Corros. Sci.*, **13**, 187 (1973).
9. K. W. Mao, M. A. LaBoda, and J. P. Hoare, *This Journal*, **119**, 419 (1972).
10. M. Datta and D. Landolt, *ibid.*, **122**, 1466 (1975).
11. M. Datta and D. Landolt, *J. Appl. Electrochem.*, To be published.
12. D. T. Chin and K. W. Mao, *ibid.*, **4**, 155 (1974).
13. K. W. Mao and D. T. Chin, *This Journal*, **121**, 191 (1974).
14. M. A. LaBoda, A. J. Chartrand, J. P. Hoare, C. R. Weise, and K. W. Mao, *ibid.*, **120**, 643 (1973).
15. J. P. Hoare and C. R. Weise, *Corros. Sci.*, **15**, 435 (1975).
16. M. Datta, Doctoral Thesis, EPF Lausanne, Thesis No. 222 (1975).
17. T. P. Hoar, *Corros. Sci.*, **7**, 341 (1967).
18. D. Landolt, *Rev. Sci. Instrum.*, **43**, 592 (1972).
19. H. P. Leckie and H. H. Uhlig, *This Journal*, **113**, 1262 (1966).
20. Aa. Broli, H. Holtan, and T. B. Andreassen, *Werkst. Korros.*, **27**, 497 (1976).
21. K. Venu, K. Balakrishnan, and K. S. Rajagopalan, *Corros. Sci.*, **5**, 59 (1965).
22. K. S. Rajagopalan and K. Venu, *ibid.*, **8**, 557 (1968).
23. H. H. Strehblow and J. Wenners, *Z. Phys. Chem., (N. F.)*, **98S.**, 199 (1975).
24. T. P. Hoar, D. C. Mears, and G. P. Rothwell, *Corros. Sci.*, **5**, 279 (1965).
25. Z. Szklarska-Smialowska, *ibid.*, **11**, 209 (1971).
26. A. Szummer, Z. Szklarska-Smialowska, and M. Janik-Czachor, *ibid.*, **8**, 833 (1968).
27. K. J. Vetter and H. H. Strehblow, *Ber. Bunsenges. Phys. Chem.*, **74**, 449 (1970).
28. K. J. Vetter and H. H. Strehblow, in "Localized Corrosion," R. W. Staehle, B. F. Brown, J. Kruger, and A. Agarwal, Editors, p. 240, NACE-3, Houston (1974).
29. N. Sato, *Electrochim. Acta*, **16**, 1683 (1971).
30. J. R. Galvele, *This Journal*, **123**, 464 (1976).

The Composition of Passive Films on Ferritic Stainless Steels

A. E. Yaniv

Israel Ministry of Defense, Scientific Department, Tel-Aviv, Israel

and J. B. Lumsden and R. W. Staehle*

Department of Metallurgical Engineering, The Ohio State University, Columbus, Ohio 43210

ABSTRACT

Auger electron spectroscopy has been used to investigate the influences of pH, Cl^- addition, and potential on the composition of passive films on Fe-Cr-Mo ferritic stainless steels. It was found that the improved corrosion resistance properties obtained by the addition of molybdenum cannot be explained by its enrichment of the protective film. Molybdenum was not found in the film even at those potential and pH values at which its oxide is the stable species. However, the relative iron and chromium content in the film followed predictions based on their solubilities in aqueous solutions. These results also indicate changes in bonding in the film as a function of distance from the substrate.

The development of high purity Fe-Cr-Mo ferritic stainless steels of low interstitial content stimulated the commercial use of ferritics after the results of several studies demonstrated the excellent corrosion resistance of this class of alloys. The improved corrosion resistance is derived mainly from the addition of molybdenum.

The beneficial effect of molybdenum on austenitic stainless steels in increasing its resistance to attack by chloride and acid solutions has been known for many years. Molybdenum- and silicon-containing austenitic stainless steels were investigated by Streicher (1) and by Rhodin *et al.* (2, 3). Bond and Lizlovs (3-7) have extensively studied the corrosion properties of molybdenum-containing ferritic stainless steels exposed to chloride solutions. Besides a substantial increase in pitting potential, the addition of 5% Mo to 13, 18, and 25% Cr alloys produces over an order of magnitude decrease in the critical current density. Further, the effect of molybdenum depends upon the chromium level: the higher the chromium content the greater the effect. Thus, molybdenum interacts synergistically with chromium. The function of Mo, or for that matter Cr, in improving resistance to halide solutions is not understood.

Ambrose and Kruger (8) have presented evidence that Mo increases the passivation rate; they suggest that in the presence of chloride ions the film is constantly breaking down and being repaired. Whether or not pitting occurs depends upon the rate at which the film repairs itself. Uhlig explains the beneficial effects of Mo and Cr using a competitive adsorption model (9). He rationalizes the effects of Cr by its greater affinity for oxygen than Fe and that of Mo by its lower affinity for chloride than Cr.

Rhodin (2,3) found that the improved corrosion behavior of the austenitic stainless steels correlated with the enrichment of silicon and molybdenum and the depletion of iron in the surface films. He used a film-stripping procedure in which an aggressive reagent (an anhydrous methanol bromide solution) was employed to attack the metal and float the film away. The isolated film was then chemically analyzed. However, Lumsden and Staehle (10, 11), using Auger electron spectroscopy (AES), found no enrichment of molybdenum or silicon in the films on these alloys. To the contrary, a depletion was observed.

* Electrochemical Society Active Member.

Key words: passivity, corrosion, molybdenum, Auger electron spectroscopy.

The work reported herein was undertaken to determine correlations between film composition and its protective quality. Auger electron spectroscopy was used to determine film compositions on Fe-Cr-Mo ferritic stainless steels as a function of pH and chloride content.

Experimental

The alloys used were high purity ferritic stainless steels provided by Climax Molybdenum Company with chromium contents of 13, 17, and 25% and with varying additions of molybdenum. They were prepared by induction melting and vacuum casting. The chemical compositions are given in Table I. The surfaces studied were mechanically polished by standard metallographic techniques (12) to ¼ μm diamond paste. Prior to polarization, the specimens were washed in a mild detergent, rinsed in double distilled water, and finally cleaned ultrasonically in methanol.

Polarization was carried out in a glass cell of standard design (13), which was open to the air. Initially, polarization curves were determined potentiodynamically at a scan rate of 0.55 mV/sec to establish the active, passive, and transpassive regions.

Films were formed potentiostatically in 1*N* H_2SO_4, 1*N* Na_2SO_4 + H_2SO_4 (pH 3), 1*N* NaCl + H_2SO_4 (pH 3.45), and pH 14 NaOH at 60, −150, −150, and −700 mV (NHE), respectively. Prior to anodic polarization the specimens were cathodically polarized at −750 mV (NHE) for 1 hr. The alloys were passivated for 1 hr.

Table I. Composition and heat-treatment of the ferritic stainless steels used

Alloy	Cr	Mo	C	N	Ni	Condition (°C,1 hr WQ)
1	13.68	0.08	0.003	0.004		815
2	13.14	1.04	0.005	0.004		815
3	13.60	1.88	0.002	0.004		815
4	12.95	3.48	0.003	0.004		980
5	13.04	4.77	0.003	0.003		980
6	17.35	<0.01	0.002	0.003		815
7	17.35	1.14	0.003	0.004		815
8	17.61	2.02	0.004	0.004		815
9	17.58	3.52	0.005	0.004		815
10	17.38	4.75	0.004	0.004		980
11	25.66	0.002	0.002	~0.015		815
12	25.26	2.05	0.002	0.017		815
13	25.25	5.25	0.002	0.013		980
14	25.66	0.002	0.002	0.015	0.13	980
15	26.15	0.99	0.003	0.016	0.1	980
16	25.26	2.05	0.002	0.017	0.13	980
17	25.58	3.49	0.002	0.015	0.13	980
18	25.25	5.24	0.002	0.013	0.13	980

After removal from the electrolyte, the specimens were washed in double distilled water and placed immediately in the vacuum system.

Polarization in a NaOH *p*H 14 solution was carried out in an open-to-the-air polypropylene beaker using a Hg/HgO/NaOH reference electrode and a zirconia bridge. The reference electrode was constructed of a platinum wire embedded in a shrinkable Teflon tube which was mounted in the end of a zirconia tube. The zirconia tube contained mercury and HgO on the bottom covered with a mixture of ZrO_2 particles and NaOH. A bridge was made of a ¼ in. Teflon tube filled with the same mixture as the reference electrode and closed on both ends with a porous ZrO_2 plug.

Selected specimens were also passivated in a HNO_3 solution using the same procedure as that employed by Nielsen and Rhodin (2, 3). The surface preparation consisted of first mechanically polishing as above followed by pickling in a 10% HCl solution at 80°C for 1 min. Then the surfaces were passivated by immersion in a 5% HNO_3 solution at 60°C for 30 min. The alloys were subsequently rinsed in demineralized, double distilled water.

Auger analysis was performed using a Varian cylindrical mirror analyzer (14) with a coaxial electron gun. Before analysis the system was pumped to 8×10^{-10} Torr or less using nonmechanical pumping. No bakeout was used in order to avoid changing the composition of the films.

The composition of the passive films was determined using the profiling technique (15, 16). This consists of simultaneous etching by argon ion bombardment and AES analysis. A 600 eV ion beam was used having an ion current density of approximately 1 $\mu A/cm^2$. The Auger spectra were taken using a 2 kV, 50 μA electron beam (static) having a diameter of approximately 50 μm. A 17 kHz modulation frequency was used with a modulation amplitude of 2V (p-p).

Results

The composition profiles are given as plots of normalized peak heights *vs.* sputtering time. The Auger peak heights have been normalized to the sum of those for iron and chromium in order to compensate for any change in surface and experimental conditions which affect the Auger signal. Due to the uncertainty in the sputtering rate, the sputtering time is given rather than the thickness of the film removed; however, the rate of film removal has been estimated to be approximately 3 Å/min before submonolayer coverage is reached. This was determined by sputtering and Auger analyzing oxide films which were formed by exposing iron to chromate solutions. The thickness was determined using an ellipsometer. After coverages of less than a monolayer are attained, the sputtering rate decreases exponentially since the rate at which an element is sputtered is proportional to its surface concentration.

Preliminary experiments were carried out to find the effect of the mechanical surface preparation on the film composition. A chromium deficiency was found in the film.

Figure 1 gives the composition of the passive film formed on the Fe-25.25Cr-5.24Mo alloy which had been exposed to the *p*H 3 sulfuric acid solution and polarized to a potential of −150 mV (NHE) for 1 hr. The Auger peaks used for all profiles were the O 510 eV, Fe 703 eV, Cr 529 eV, Mo 221 eV, S 152 eV, C 272 eV, and Cl 181 eV lines.

The results given in Fig. 1 are typical of those obtained for all the alloys exposed to the *p*H 3 solution. In addition to oxygen and the alloying elements, sulfur was present in appreciable amounts but was localized in the outermost layers and was easily sputtered off. Carbon, which was present in large quantities on the surface, was rapidly removed and reached a level slightly above its content in the steels after 5-10 min of sputtering. Its presence on the surface was probably due to atmospheric contamination. The relative amount

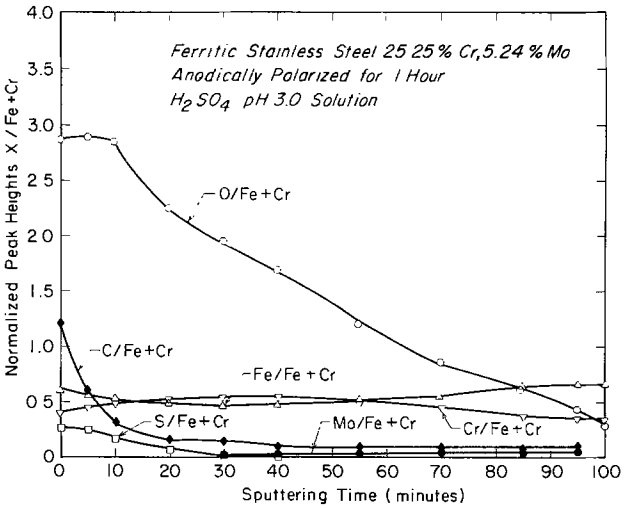


Fig. 1. Normalized Auger peak heights *vs.* sputtering time for the passive film on Fe-25Cr-5Mo ferritic stainless steel.

of molybdenum in the film was the same as that described in previous publications (10, 11), *i.e.*, no molybdenum in the outermost layers of the films and no enrichment in the films. Finally, chromium enriches the film with a corresponding depletion of iron.

The effects of heat-treatment on the anodic film composition were evaluated using alloys 11, 12, 14, and 16 in Table I. No effect was observed, but it should be emphasized that only 25% Cr steels heat-treated at 815° and 980°C were available.

The surfaces of the alloys which were polarized in the *p*H 3.45 chloride solution were examined optically and no attack was observed. The lowest pitting potential, 295 mV (NHE), was obtained for the Fe-13Cr alloy. The potential applied to the alloys exposed to the chloride solution was −150 mV (NHE). This potential is well below the pitting potential of all of the alloys used in this investigation.

The analysis of the film formed on the Fe-25.25Cr-5.24Mo alloy at −150 mV (NHE) exposed for 1 hr to a H_2SO_4-1.0*N* NaCl solution is shown in Fig. 2. The compositions were similar to those obtained for films formed in the *p*H 3 solution without chloride. In all cases the enrichment of chromium in the passive film was observed reaching the highest value for the 25% Cr steels and proportionally lower for the 17 and 13% Cr steels (Fig. 3). Molybdenum was not detected in the surface and near-surface layers nor did it enrich. Chlorine was detected in the surface and near-surface

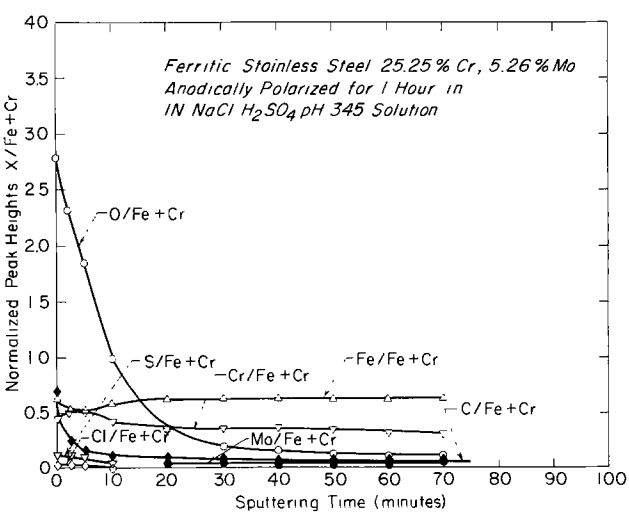


Fig. 2. Composition of passive film formed on Fe-25Cr-5Mo alloy after anodic polarization in a *p*H 3.45 chloride solution.

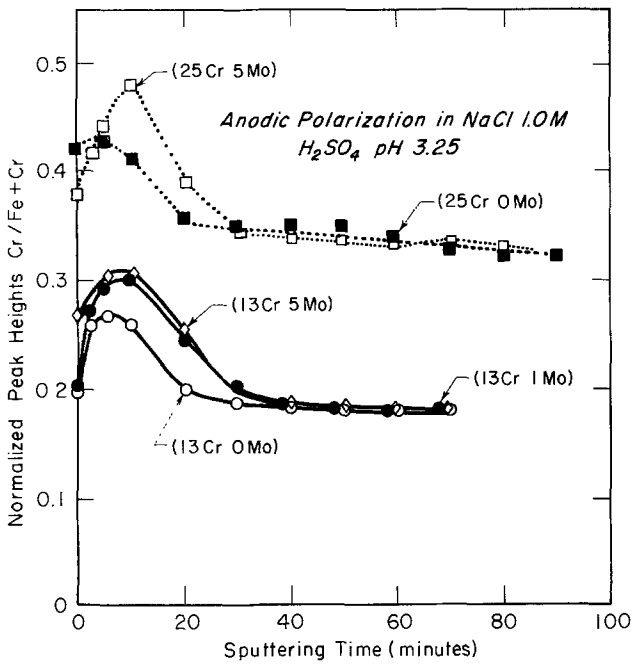


Fig. 3. Relative chromium composition of passive films on ferritic stainless steels formed by anodic polarization in a pH 3.45 chloride solution.

layers only. Also, there was no significant difference in the thickness of the passive film on the alloys as deduced from the sputtering time necessary to reach the substrate.

Typical results for alloys exposed to 1*N* H_2SO_4 are given in Fig. 4. This is the composition profile of the film on Fe-25.25Cr-5.24Mo which had been polarized at 60 mV (NHE) for 1 hr. Chromium enrichment was found to coincide with a decrease in the iron content in the film. The molybdenum content was the same as that observed previously.

For comparison. an AES analysis was performed on surfaces which had been passivated by immersion in nitric acid. The film compositions resulting from passivation in nitric acid (Fig. 5) differed from those formed anodically only in the chromium content. Whereas anodic polarization resulted in films with varying amounts of chromium enrichment depending upon the chromium content of the alloy, the amount of chromium enrichment which resulted from passivation in nitric acid did not change in either the 17% or the 25% Cr steels with or without molybdenum; the 13% Cr steels were attacked by the 10% nitric acid solution.

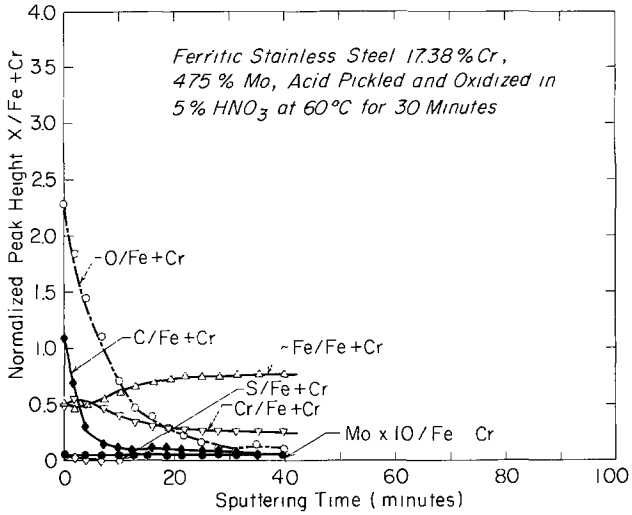


Fig. 5. Passive film composition on 17Cr-5Mo ferritic stainless steel after passivation in 5% HNO_3 at 60°C for 30 min.

The films formed on 13, 17, and 25% Cr alloys (with 0 and 5% Mo) exposed to the *p*H 14 NaOH solution were analyzed. In every case a depletion of Cr and an absence of Mo was observed in the films. An enrichment in iron was found corresponding to the chromium depletion. As the film was sputter etched, the iron and chromium contents uniformly approached the alloy levels. This is shown in Fig. 6.

The effects of potential were determined for alloys exposed to the H_2SO_4-NaCl solution. Figure 7 shows the film composition of the 18% Cr 5% Mo alloy obtained by polarization in the transpassive region at 1250 mV (NHE). For all of the alloys investigated there was a depletion of chromium in the film and an enrichment of iron relative to the bulk composition. Molybdenum was detectable in the surface layers of the film on those alloys in which it was present; however, the depletion-enrichment type of behavior of chromium and iron was independent of its existence in the alloy. Figure 8 shows the Auger results for the 25% Cr 5% Mo stainless steel which had been polarized cathodically at −1150 mV NHE. The film compositions on the ferritic stainless steels which had been polarized cathodically were identical to those resulting from polarization in the transpassive region.

Thus, these results suggest that cathodic polarization changes the surface composition of the alloy. It is not conclusive, however, that the observed film is that

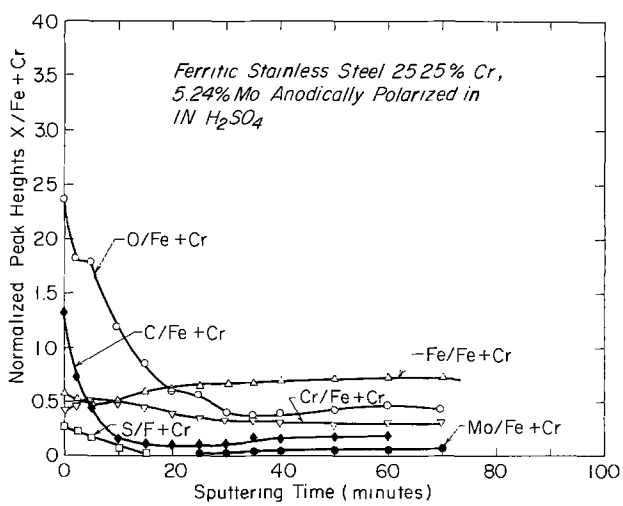


Fig. 4. Auger results for the passive film on Fe-25Cr-5Mo formed by anodic polarization in 1*N* H_2SO_4.

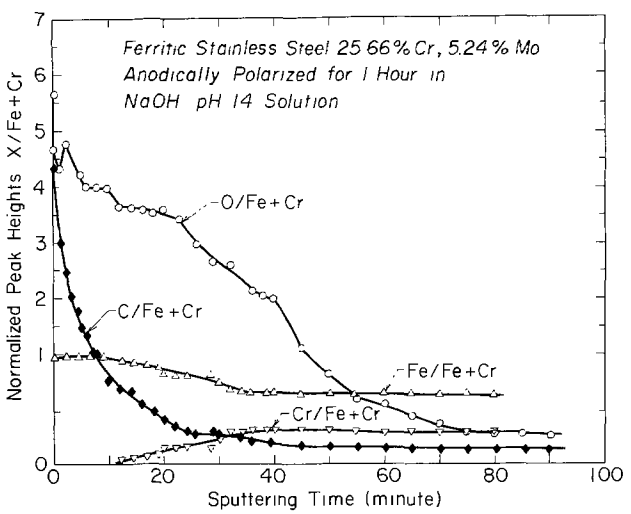


Fig. 6. Composition of the film formed in a pH 14 NaOH solution.

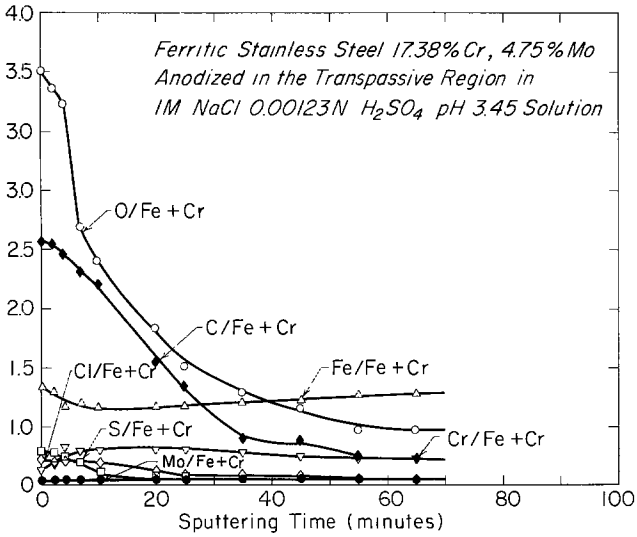


Fig. 7. Auger results for the film formed on 17% Cr 5% Mo stainless steel polarized in the transpassive region.

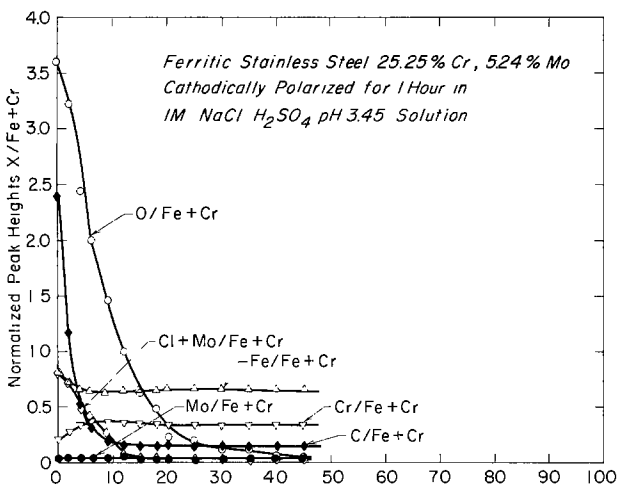


Fig. 8. Effects of cathodic polarization of the film composition on 25% Cr 5% Mo alloy.

which exists on the alloy in solution. If the air-formed film is removed by cathodic reduction, then oxidation would occur when the alloy is taken out of solution and exposed to the air. However, the air-formed film on the alloys used in this investigation is always enriched in chromium; therefore, air oxidation of an unaltered surface would not produce a film depleted of chromium.

Figures 9-13 show the Auger spectra at various depths in the passive film on the Fe-25.25Cr-5.25Mo alloy which had been passivated in the HNO_3 solution. Each figure has two spectra. One is the complete spectrum showing all of the Auger lines from the constituents of the film; the other is the low energy or valence band spectrum from iron. For the latter, two of the electrons involved in the Auger transition are in the valence band. Thus, these Auger electrons are very sensitive to changes in bonding. Figure 9 shows the spectra which result after 5 min of sputtering. The film for the most part is an iron oxide with only a small amount of Cr. The valence band spectrum shown is that of iron; this is the type of spectrum which results when iron is in the ferric state as reported previously (17). The spectra in Fig. 10 were taken after 10 min of sputtering. Here, a substantial amount of Cr appears in the film; whereas the oxygen and iron content remains approximately the same as that in the previous spectrum. Molybdenum also begins to become detectable. The lower energy peak in the valence band spectrum has shifted in energy; this is the same type of valence band

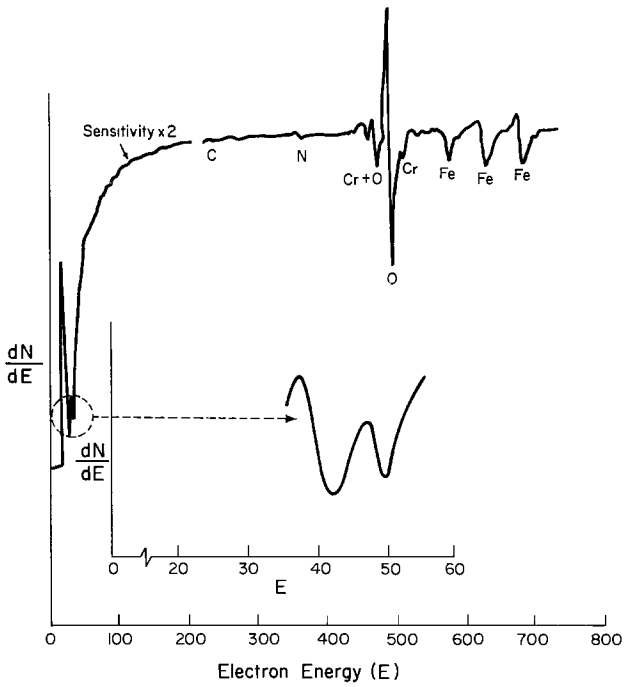


Fig. 9. Auger spectra of the passive film on Fe-25Cr-5Mo after 5 min of sputtering.

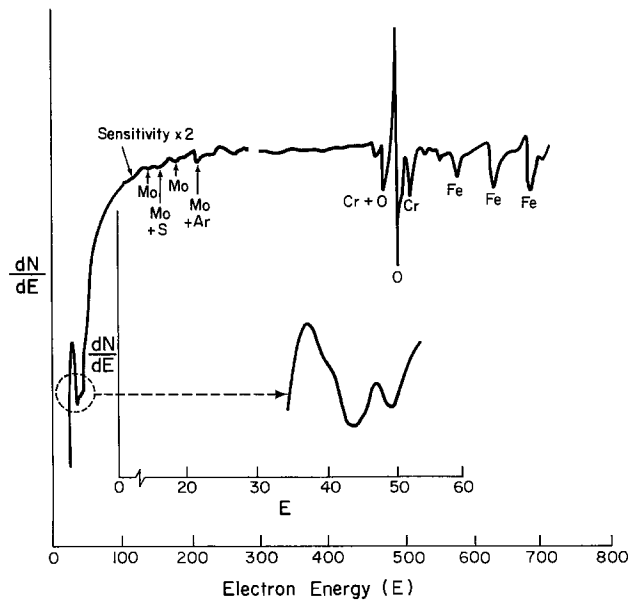


Fig. 10. Auger spectra of the passive film on Fe-25Cr-5Mo after 10 min of sputtering.

spectrum which was observed from Fe in the ferrous state. Figure 11 shows the spectra which resulted after 15 min of sputtering. The valence band spectrum for Fe at this depth is the same as that obtained for a Fe free surface although a substantial amount of oxygen remains here after the film has been sputtered for 15 min. The implication of the latter result is that oxygen is bonded to the Cr with iron being in the metallic state. The spectra obtained after 20 min of sputtering are given in Fig. 12. These spectra are essentially the same as those in Fig. 11 except that the oxygen level has substantially decreased and the Fe lines have increased in amplitude. Figure 13 summarizes the above results. This pattern was also observed for films formed by anodic polarization.

Discussion

The role of alloying elements in improving corrosion resistance properties is frequently interpreted in terms of the relative range of the thermodynamic stability,

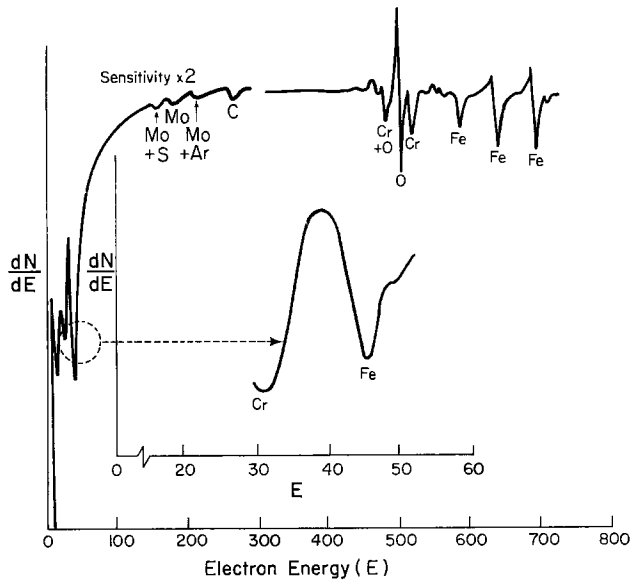


Fig. 11. Auger spectra of the passive film on Fe-25Cr-5Mo after 15 min of sputtering.

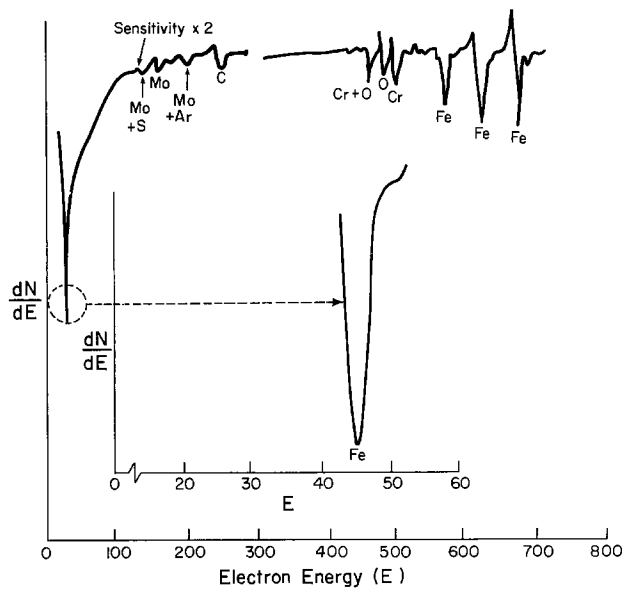


Fig. 12. Auger spectra of the passive film on Fe-25Cr-5Mo after 20 min of sputtering.

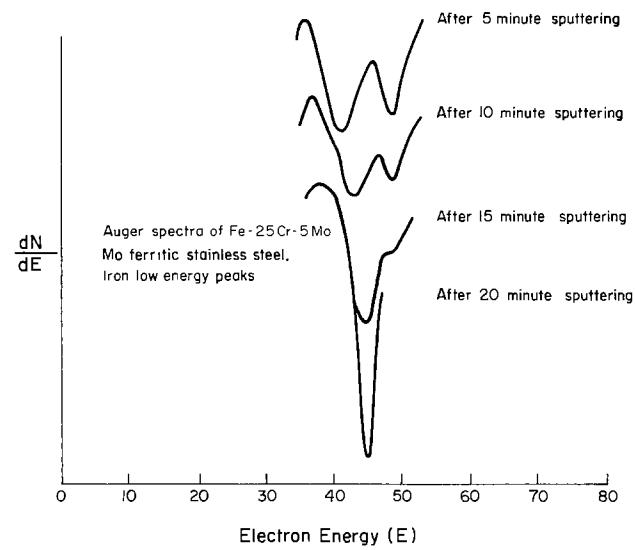


Fig. 13. Valence band spectra of Fe in the passive film on Fe-25Cr-5Mo after various sputtering times.

with respect to pH and potential, of their insoluble species. Thus, the effectiveness of chromium and molybdenum as alloying elements in iron is interpretable in terms of the broader range of acid stability of Cr_2O_3 and MoO_2. This argument can also be extended to rationalize the increased effectiveness of alloys containing chromium and molybdenum in resisting attack in chloride solutions if pitting is assumed to be a result of localized acidification (18).

Using solubility arguments for the effects of alloying on corrosion properties, one can obtain an "enrichment model." According to this concept, in the passive region the oxide or hydroxide of highest solubility selectively dissolves at the film-solution interface. The film then becomes enriched in the more stable species and this oxide or hydroxide governs the rate of dissolution. Thus, the improved corrosion properties in acid and chloride environments obtained by alloying stainless steels with molybdenum could be explained by an enrichment of molybdenum oxide in the passive film. However, no evidence for this was found using AES; on the contrary, a depletion of molybdenum was found in the surface and near-surface layers of the passive film (see Fig. 4). This was the case even for the pH 3 and 3.45 solutions in which the films were formed under conditions at which MoO_2 is thermodynamically stable [see the Pourbaix diagram (19) in Fig. 14]. The same general trends were found for passive films formed in the pH 3.5 sulfate solution with and without chloride ions (Fig. 1 and 2). Thus, the presence of chloride ions in solution had no effect on film composition in the passive region.

Although thermodynamics could not be used successfully to predict the relative amount of molybdenum in the protective film, the general trend of the chromium content followed thermodynamic predictions. Chromium was found to enrich in the passive film under those conditions where Cr_2O_3 was stable (Fig. 14). However, the Pourbaix diagrams are overly pessimistic in the acid region since a passive range was obtained in 1*N* H_2SO_4 although the hydroxides and oxides of iron, chromium, and molybdenum are not the stable phases in this region. This also applies to unalloyed iron and chromium because both have a passive range in H_2SO_4. Since these diagrams were calculated from known thermodynamic data for bulk compounds, either these thin oxide films are a different

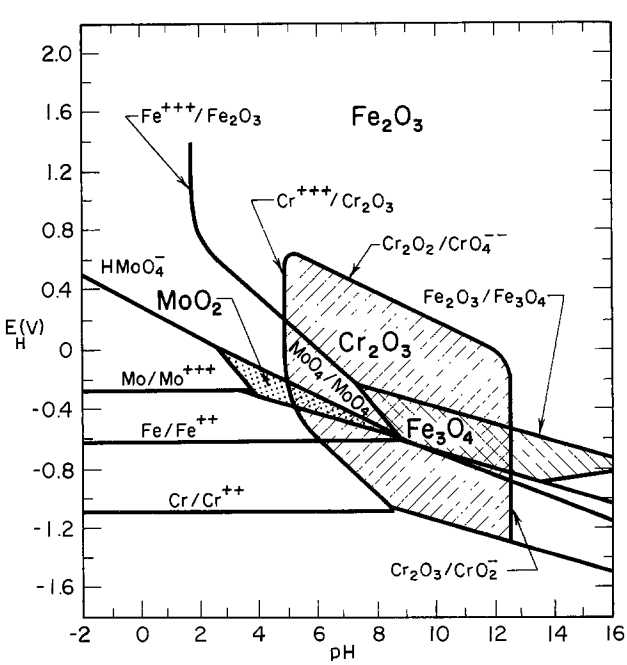


Fig. 14. Superposition of Pourbaix diagrams for chromium, molybdenum, and iron showing the insoluble products and some of the equilibria defining the phase boundaries.

phase or compound whose bulk properties are not known or one must consider the kinetics. The films formed at pH 14 were found to be depleted of chromium; this is consistent with the potential-pH diagram if the insoluble product is considered to be Cr_2O_3. The vertical line representing the boundary between passivity and corrosion, *i.e.*, $[CrO_3^{---}] = 10^{-6}$, is located at approximately pH 12.5 for Cr_2O_3.

The influence of potential on the chromium and iron content of the film is also predictable from thermodynamics. At 1250 mV (NHE) soluble chromate ions and insoluble Fe_2O_3 are the stable species (Fig. 7). The results obtained after cathodic polarization should be compared with those obtained in caustic solutions since the evolution of hydrogen at the electrode is accompanied by the generation of hydroxide ions. This raises the pH at the electrode surface. Both cathodic polarization in the pH 3.5 solution and anodic polarization in pH 14 solution (compare Fig. 6 and 8) resulted in a chromium depleted-iron enriched film.

Legitimate questions can be raised about the effectiveness of the Auger technique in detecting molybdenum since it seems inconceivable that an alloying addition which can increase the pitting potential over 500 mV would not be a major constituent of the film. Yet the Auger results for the relative amounts of chromium and iron in the passive films were consistent with solubility arguments. Thus, one would suspect that if the technique were altering the composition of metal ions in the film, it would be manifested in the behavior of these constituents as well as molybdenum.

A further question is whether or not the electron and ion beams are volatilizing the molybdenum oxide. Figure 15 shows the Auger spectra of a cathodically deposited molybdenum oxide film (from a molybdate solution). This film has a substantial amount of molybdenum and a small amount of iron, thus duplicating a passive film on an iron base alloy enriched in molybdenum. The spectrum remained unchanged after 5 and 15 min bombardments by the electron gun. Figure 16 shows spectra taken before and after 40 min of sputtering. Again, there were no anomalies. Although the carbon and nitrogen levels decrease substantially after 40 min of sputtering, there were only slight changes

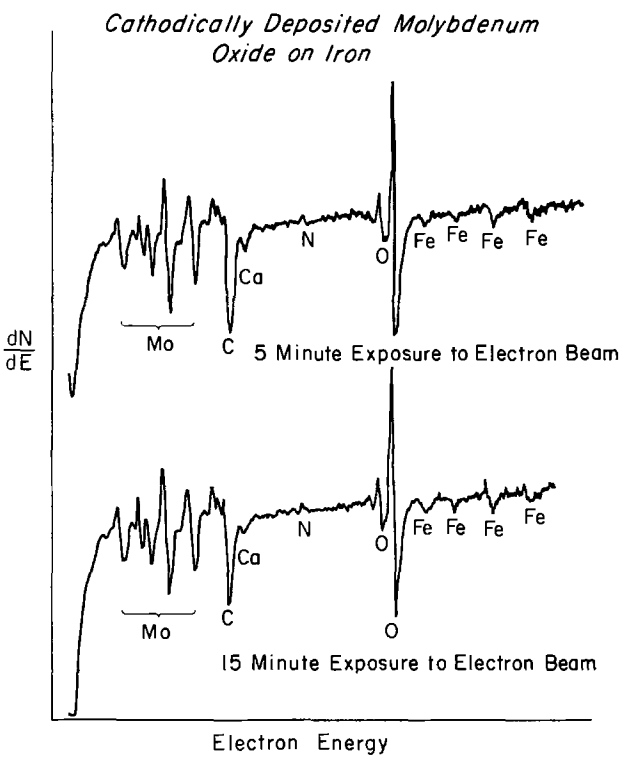


Fig. 15. Effect of electron beam on cathodically deposited molybdenum oxide film.

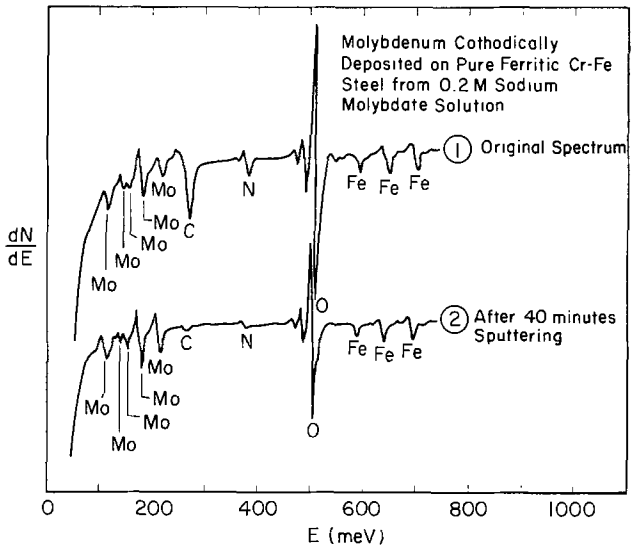


Fig. 16. Effect of sputtering on cathodically deposited molybdenum oxide film.

in the peak height ratios of the other elements. These changes could be due to the removal of adsorbed molybdate ions and water from the surface or due to an inhomogeneous film. However, the important point is that molybdenum is not preferentially removed by sputtering. Thus, these results suggest that if molybdenum is, in fact, enriched in the film, the Auger technique would detect it.

One of the inherent uncertainties in the profiling technique is the possible occurrence of differential sputtering. This arises because elemental sputtering yields are different, which results in an altered surface layer enriched in the element with the lower sputtering yield. Frankenthal and Malm (20) have concluded that films formed on iron-chromium alloys during mechanical polishing are not differentially sputtered. It is uncertain whether these results can be applied to this investigation since a different ion beam energy was used; however, when a 600 eV ion beam is used to sputter a mechanically polished surface, the Auger results are similar to the results of Frankenthal and Malm. Also, there is no evidence that large differences in the elemental sputtering rates exist. For example, if this phenomenon were causing an apparent enrichment of chromium in the films, then one would expect to observe an enrichment in those films in which chromium was depleted from the surface layers.

Carbon contamination was found on all surfaces. This was probably from hydrocarbon or carbon dioxide which was adsorbed when the specimens were transferred from the cell to the vacuum system. The varying concentrations of these overlayers cause the difference in behavior of the oxygen peak decline in Fig. 1, 2, and 7.

When the oxygen level is large relative to that of chromium, the oxygen line (510 eV) causes some distortion in the chromium line (529 eV). Coad and Cunningham (21) have analyzed iron and chromium mixed oxides using both XPS, in which there is no interference between lines, and AES. These results indicate that the errors caused by the distortion are not significant.

The Auger results for the composition of passive films differ substantially from those obtained by chemical analysis. Perhaps the high silicon and molybdenum content found by Rhodin and Nielsen (2, 3) occurs because the film-stripping procedure created an altered layer. It is conceivable that such a layer would contain undissolved silicon and molybdenum from the alloy.

The Auger results eliminate from consideration the enrichment idea for explaining the improved quality

of the protective film derived from the presence of molybdenum in the alloy. Other possibilities for rationalizing the effects of molybdenum include an increased repassivation rate (8) or the prevention of localized acidification (19) by altering the corrosion potential or anodic dissolution kinetics. Electrochemical results indicate that indeed, both the corrosion potential and the potential necessary to maintain the high current density required to sustain pit growth increased with increased molydenum content in the ferritic stainless steels (22).

Perhaps molybdenum exerts its beneficial effects by improving the quality of the bonding at the metal-oxide interface creating a barrier layer. There are two possible interpretations of the results shown in Fig. 9-13. One is metallic iron which is present in a chromium oxide matrix (possibly two-dimensional). The other is that there is a chromium oxide layer adjacent to the substrate. The presence of molybdenum in the layer could have a substantial influence on the quality of the bond.

Acknowledgments

The authors gratefully acknowledge support from the National Science Foundation, Grant No. DMR74-08061, and from the American Iron and Steel Institute, Grant No. 61-244.

Manuscript submitted Sept. 13, 1976; revised manuscript received Dec. 6, 1976.

Any discussion of this paper will appear in a Discussion Section to be published in the December 1977 JOURNAL. All discussions for the December 1977 Discussion Section should be submitted by Aug. 1, 1977.

Publication costs of this article were assisted by The Ohio State University.

REFERENCES

1. M. A. Streicher, *This Journal*, **103**, 375 (1958).
2. T. N. Rhodin, *Corrosion*, **12**, 465t (1956).
3. N. A. Nielsen and T. N. Rhodin, *Z. Electrochem.*, **62**, 707 (1958).
4. E. A. Lizlovs, *Corrosion*, **22**, 297 (1966).
5. E. A. Lizlovs and A. P. Bond, *This Journal*, **116**, 574 (1969).
6. E. A. Lizlovs and A. P. Bond, *ibid.*, **119**, 22 (1971).
7. E. A. Lizlovs, ASTM STP 516, 250 (1972).
8. J. Kruger and J. R. Ambrose, NBS Report NBSIR 74-583 (September 1974).
9. H. H. Uhlig, Joint Japan-USA Seminar on Passivity and Its Breakdown on Iron and Iron Base Alloys, NACE, Houston, Texas (1976).
10. J. B. Lumsden and R. W. Staehle, *Scr. Metall.* **6**, 1205 (1972).
11. J. B. Lumsden and R. W. Staehle, ASTM SPT 596 (1976).
12. "Metals Handbook," Vol. 8, pp. 44-26, ASM, Metals Park, Ohio (1975).
13. N. D. Greene, "Experimental Electrode Kinetics," Rensselaer Polytechnic Institute, Troy, New York (1965).
14. P. W. Palmberg, G. K. Bohn, and J. C. Tracy, *Appl. Phys. Lett.*, **15**, 254 (1969).
15. P. W. Palmberg, *J. Vac. Sci. Technol.*, **9**, 160 (1972).
16. P. W. Palmberg, in "Electron Spectroscopy," D. A. Shirley, Editor, North Holland Publishing Company, Amsterdam (1972).
17. M. Seo, J. B. Lumsden, and R. W. Staehle, *Surf. Sci.*, **50**, 541 (1976).
18. J. R. Galvele, *This Journal*, **123**, 464 (1976).
19. M. Pourbaix, "Atlas of Electrochemical Equilibria in Aqueous Solutions," Pergamon Press, New York (1966).
20. R. P. Frankenthal and D. L. Malm, *This Journal*, **123**, 186 (1976).
21. J. P. Coad and J. G. Cunningham, *J. Electron Spectrosc. Relat. Phenom.*, **3**, 435 (1974).
22. J. R. Galvele and J. B. Lumsden, To be published.

Oxidation of Copper-Containing Films at Room Temperature

Charles B. Greenberg

PPG Industries, Incorporated, Glass Research Center, Pittsburgh, Pennsylvania 15238

ABSTRACT

In a previous publication, formation of a novel, copper-containing, electroless-replacement film was described. Partial replacement of electroless copper was from an aqueous Ag^{+}-$S_2O_8^{-2}$ solution. The emphasis was on an accompanying, accelerated oxidation reaction in the air, which was also shown to occur after electroless copper was exposed to a solution containing only sodium thiosulfate. Additional data are herein described to elaborate the synergistic dependence of the oxidation of Cu in these films on two impurities, one probably a sulfide, and the other H_2O from the air. These new data show that oxidation in air can be very much inhibited by prior exposure to extra dry O_2 despite the otherwise very strong propensity for oxidation. This suggests some probable mechanisms relative to cationic diffusion and the Cabrera-Mott model for oxide growth.

The oxidation in air and O_2 of metals, including copper, at various temperatures has been seriously discussed since at least the 1940's. Attempts have been made to fit oxidation, for example, to the kinetics of electron tunneling and ionic diffusion through the growing oxide. The complexity of this problem is suggested by the numerous rate equations in the literature, including inverse logarithmic, direct logarithmic, linear, parabolic, and cubic. Apparently, the fit for a particular rate equation varies at least with the temperature and the thickness of the particular metallic oxide. The history and status of this important area of activity have been reviewed by Rönnquist and Fischmeister (1), Fehlner and Mott (2), and Lawless (3).

The focal point for much of recent thinking is an early paper by Cabrera and Mott (4). It forms the basis for the concept of oxide growth at room temperature by ionic diffusion in the growing oxide film. In the case of copper, growth is by cationic diffusion in Cu_2O. Lawless (3, 5) especially, but also Fehlner and Mott, emphasized that the ease of oxidation is very much dependent on impurities, defect structure, and grain boundaries. An impurity may enhance ionic diffusion by promoting a defect structure; it may promote crystallization or recrystallization which hinders or favors grain boundary diffusion. It is, however, usually difficult to identify an impurity or assign a clear role to it. In an earlier publication by this author (6),

impure electroless copper films and copper contained in films made by successive electroless copper deposition and partial silver replacement were shown to oxidize at an unusually rapid rate in air at 24°C. Water vapor was necessary with O_2 in the surrounding gas phase, and a poorly crystallized, sulfur-containing component, probably Cu_2S, was necessary in the films. In each case, copper sulfide had formed by reaction with $S_2O_3^{-2}$. Electroless copper films were treated with aqueous $S_2O_3^{-2}$ solution; $S_2O_3^{-2}$ was contained in the replacement solution. The phenomenon proved to be interesting and of practical value for architectural films; it was explained by invoking the Cabrera-Mott model and assuming favorable defects or grain boundaries.

In the present publication the intent is to elaborate this unusually rapid oxidation of Cu, easily observed by monitoring decreasing specular reflectance. The accompanying increase of luminous transmittance for electroless copper supports the assumption of oxidation; there is no indication of any light scattering. Further observations which have been made with similarly treated electroless copper and electroless-replacement films conform to the hypothesis of ionic diffusion. They illustrate the formation, under adverse conditions, of a thin passivating layer, apparently Cu_2O with a very low defect density, when such fresh films are permitted to first "see" dry O_2 before the ambient air. The conditions are adverse in the sense that all films are prepared from aqueous solutions and therefore hardly free of H_2O at first. They also contain the sulfide impurity.

Experimental Procedures

Sample preparations.—Thin films were deposited on one surface of commercially available soda-lime-silica float glass, 0.6 cm thick, by either electroless deposition or a sequence of electroless and replacement deposition. All sample preparations were carried out at room temperature with demineralized water by puddling each solution on the horizontally positioned substrate (6). Electroless copper films were deposited, after conventional palladium activation, using the solutions and reagent grade chemicals shown in Table I. Film deposition was terminated at a luminous transmittance (T) of 0.23; response was CIE standard C. Spot to spot variations in reflectance within the sample were within ± 0.005 of the center; this is a relatively small variation. Sample area was about 25-50 cm^2. To introduce the sulfide impurity and promote subsequent oxidation, electroless copper was treated at room temperature for 50 sec with an aqueous solution containing 3.0 g/liter $Na_2S_2O_3 \cdot 5H_2O$. This was done after rinsing away the residual coppering solution with water and was done prior to a final rinse, followed by drying with compressed air.

The electroless-replacement films, partial copper replacement by silver, were deposited in the way previously described for the replacement solution shown in Table I. The coppering solution was compositionally different than that used for the above electroless copper but kinetically similar. Final rinsing was with either water or methanol. The latter had been used at times with the intent to inhibit oxidation during rinsing (7); it proved to have no obvious influence at all on oxidation. The $S_2O_3^{-2}$ in the replacement solution, as previously, was the source of sulfide in these films.

Monitoring film oxidation.—The method for monitoring relative reflectance in various environments was also used previously. For purposes of clarity a schematic illustration is shown in Fig. 1. The coating-up sample was placed in a stationary position inside the glass enclosure within about 15 sec of drying. The glass enclosure was over the open port of the head of a gain-modified Gardner precision glossmeter Model GG-9100, precision about ± 0.002. The optics of this system were altered by the necessary reduction of gain and the glass

Table I. Coating solutions

A. SENSITIZER	0.5 g/l $SnCl_2 \cdot 2H_2O$ 0.5 cm^3/l HCl (Conc)	
B. ACTIVATOR		
a. for electroless film	0.1 g/l $PdCl_2 \cdot 2H_2O$ 0.1 cm^3/l HCl (Conc)	
b. for electroless–replacement film (typical solution), to T = 0.80	1.1 g/l $AgNO_3$ 5.0 cm^3/l NH_4OH (28-30% NH_3) 0.16 g/l NaOH 1.3 g/l Dextrose	
C. COPPERING	a. for electroless film to T = 0.23	b. for electroless–replacement film to T = 0.30–0.33
	7.6 g/l $CuSO_4 \cdot 5H_2O$	3.8 g/l
	2.5 g/l $NiSO_4 \cdot 6H_2O$	1.3 g/l
	59.0 cm^3/l HCHO (with Methanol)	29.0 cm^3/l
	36.3 g/l $KNa\ C_4H_4O_6 \cdot 4H_2O$	12.1 g/l
	11.1 g/l NaOH	11.1 g/l
D. PARTIAL REPLACEMENT FOR 50 SEC	0.67 g/l $AgNO_3$ 0.67 cm^3/l NH_4OH (28-30% NH_3) 2.0 g/l $Na_2S_2O_3 \cdot 5H_2O$	

plate supporting the sample. The reflectance, although therefore not a CIE response, is in the visible portion of the spectrum. Prior to positioning the sample, the bottled O_2 or N_2 gas lines had been purged for at least 10 min through valve no. 1. Thereafter this valve was closed while maintaining a slightly positive pressure preceding it. When the sample was placed over the light source and the glass lid placed over the glass plate, valve no. 2 was opened. Valve no. 3 being closed, a negative pressure was attained so as to bring oxidation of the film to a virtual halt within 30 min. Silicone grease between the lid and plate was used to minimize ingress of air. Thereafter the roughing pump was isolated at the source, valve no. 1 was opened, and

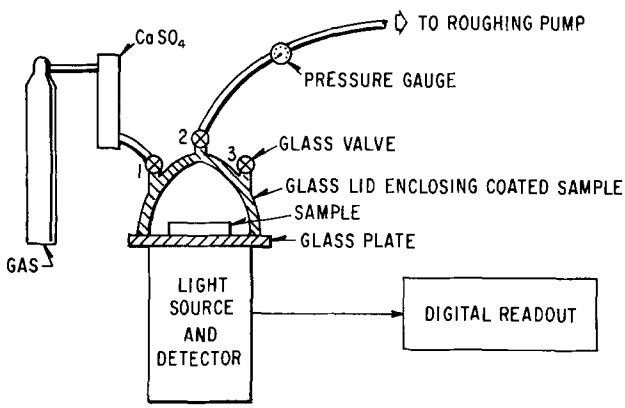


Fig. 1. Schematic diagram of system for monitoring reflectance changing as a function of time. The tungsten light source and selenium detector define an angle of incidence of 20°. The resultant spectral response of the optical head, with internal filtering, but excepting the external glass plate, is a very close approximation to the CIE Standard Co.

the flow of gas was increased until atmospheric pressure was reached. As the pressure became slightly positive, valve no. 3 was opened as an exhaust. The flow of bottled gas was maintained for 30 min, after which time valve no. 1 was closed, and ambient air was drawn through the chamber with the roughing pump.

The bottled gas was extra dry O_2 from Matheson Gas Products, or, in one reference experiment, N_2 from Linde Air Products. In two instances an analysis was supplied for O_2 intentionally doped with CO_2, in one case with 1 ppm by volume and in the other 284 ppm. This was done to determine the importance of CO_2 in the oxidation reaction. In one instance O_2 was passed over water contained at room temperature in an Erlenmeyer flask which took the place of the dryer. This was done to confirm the role of H_2O. One other variation is the position of the pressure gauge. It was either as shown or in the gas line for the same purpose. Purging with dry O_2 may have been more complete having it as shown in Fig. 1.

The ambient conditions were not significantly variable from time to time. The temperature was 22°-26°C, and the relative humidity was approximately 45-65%.

At the end of an experimental run the instrument was checked to be sure that no significant drift had occurred. Only in one instance was the drift observable; this was a shift in the relative reflectance of −0.01. This occurred when monitoring electroless copper. It is a relatively small error in any event but even less significant, as it turned out, in view of the result obtained for that experiment.

Results and Discussion

Inhibition of copper oxidation in extra dry O_2.—The two curves shown in Fig. 2 illustrate film passivation. In contrast to what happens in the ambient after being in N_2, the copper-containing replacement film is passivated by prior exposure to extra dry O_2. This means that a "first-formed" oxide can be protective for the copper component of this film at room temperature, as aluminum oxide is, for example, for aluminum. This oxide must be assumed to be cuprous oxide, in the absence of identification during prior work of other compounds by electron diffraction. When the film has first been exposed to N_2, this oxide growth is inhibited. Thereafter, when growing in the ambient, the oxide which forms is apparently a better medium for cationic diffusion. There is an apparent sensitivity to the water vapor in air, and perhaps CO_2.

The same conclusion follows from inspection of Fig. 3. In this case an electroless copper film, free of silver, is shown to be passivated by exposure to dry O_2. The

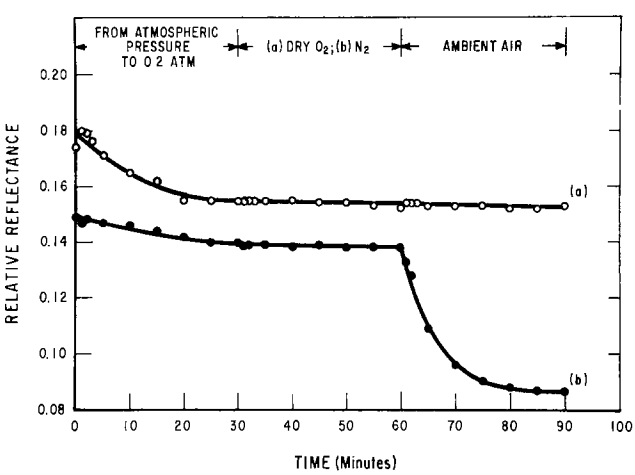


Fig. 2. Relative reflectance from the glass-film interface for two similar copper- and sulfur-containing, electroless-replacement films undergoing successive exposures to indicated environments. The dry O_2 contained 1 ppm in volume percent of CO_2.

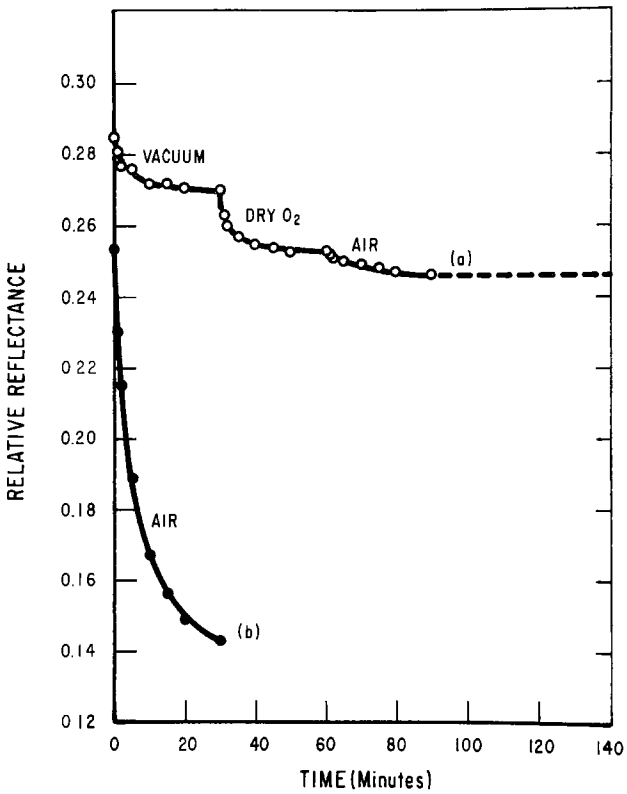


Fig. 3. Relative reflectance from the glass-film interface for two similar electroless copper films immediately after treatment for 50 sec in an aqueous solution of 3.0 g/liter $Na_2S_2O_3 \cdot 5H_2O$. No analysis for CO_2 in O_2.

small decrease in reflectance within the first minutes of exposure to dry O_2 may be a result of an inadequate purge or a momentary leak to the ambient. Nevertheless, there is passivation. The extrapolation of the uppermost curve (a), as indicated by the dashed line, is based on measurements after the conclusion of the 90 min experiment. Approximately 1 hr after the run, the reflectance was unchanged. On the following day there was a decrease of only −0.006. The sample monitored in the air without prior exposure to dry O_2, curve (b), was considerably oxidized after only 30 min. This sample was monitored while it was on the glass plate shown in Fig. 1, so as to preserve the comparison.

It should be pointed out that at the point of switching from one environment to another, a few seconds were consumed in operating valves. This time was not counted so there is some small, but insignificant, error in time in experiments such as those in Fig. 2 and 3. Within each figure the differences in reflectance between curves (a) and (b) at 0 min resulted from uncontrollable variations in sample preparation, exacerbated by the ongoing oxidation during film processing. It is only by chance that (b) in each case has a slightly lower reflectance at the beginning of the experiment.

Role of H_2O and CO_2.—In Fig. 4 there are two curves shown which point directly to water vapor as a necessary impurity. In dry O_2 doped with CO_2 to an extent close to that for dry ambient air (8) it is still evident that the passivating film forms. On the other hand, by passing otherwise dry O_2 over water, the formation of this passivating film is prevented. It cannot be excluded that CO_2 dissolved in the water is synergistic with H_2O, but it is at least clear that H_2O is necessary.

Qualitative mechanism and implications.—When exposed to air without prior exposure to $S_2O_3^{-2}$ or dry O_2, copper, perceived as a film or a component in a film, simply has a thin cuprous oxide growth on it. It is easiest to refer to the case of the electroless, silver-free film to visualize what happens in both types of films cited in this work. The prior treatment in $S_2O_3^{-2}$ re-

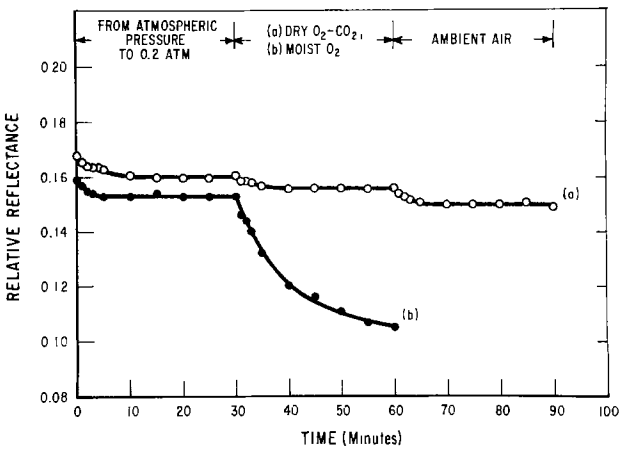


Fig. 4. Relative reflectance from the glass-film interface for two similar copper- and sulfur-containing, electroless-replacement films undergoing sucessive exposures to indicated environments. For sample (a), 284 ppm in volume percent of CO_2 in dry O_2.

sults in the formation of an apparently poorly crystallized sulfide by reaction with Cu^+ at the film surface. Subsequent rapid oxidation in air must proceed by cationic diffusion through the sulfide film, which is probably easy. More than that, however, it must be especially easy in the growing oxide. This would be so if the sulfide film favorably influenced the defect structure and/or morphology of the oxide. This seems very likely because the oxide is growing on a surface other than crystalline copper. Bunn (9) has suggested that impurities may be the cause for inconsistencies between the shape of cuprite crystals and cuprite's atomic structure from x-ray analysis. A further requirement, however, for rapid growth, is that the oxide be "immediately" contaminated by H_2O. Whether H_2O produces favorable defect sites in bulk or in dislocations and/or influences crystallinity or morphology is a speculative matter. The anhydrous oxide being so markedly resistant to further growth confirms, according to the following line of reasoning, that it is at least structurally freer of bond-disruptive hydroxide. By the Cabrera-Mott model, assuming a continuous Cu_2S layer

$$\frac{1}{2}O_2 \xrightarrow{Cu_2S} O^{-2} + 2\,Cu_{\square} + 2e_{\square} \qquad [1]$$

The cationic vacancies, $Cu_{\square}$, and electron holes, $e_{\square}$ are generated after adsorption of O_2. At the Cu_2S-Cu interface there occurs

$$Cu + Cu_{\square} + e_{\square} \rightarrow Cu^+ \qquad [2]$$

This is possible because Cu_2S is a p-type semiconductor and deficient in Cu^+. The cation diffuses to the Cu_2S-O^{-2} interface where the oxide forms. It is driven by the field existing across the Cu_2S film. The over-all reaction is

$$\frac{1}{2}O_2 + 2Cu \rightarrow Cu_2O \qquad [3]$$

Growth of Cu_2O, also a p-type semiconductor, requires continued adsorption of O_2 on the growing oxide and migration of cations. With adsorbed H_2O also present, it is possible that, concomitantly

$$Cu_2O + H_2O \rightarrow 2CuOH \quad (\text{or } Cu_2O \cdot nH_2O) \qquad [4]$$

Two forms of cuprous oxide are recognized, based on colors ranging from red to yellow (10). It is suspected that the yellow is probably of smaller particle size, but it may also exhibit a different growth habit. It has also been mentioned as a hydrated version of the red. These have not been distinguished by x-ray diffraction; therefore, the yellow form might have a different habit but could only contain amorphous hydroxide or a content outside the limits of detection. By flame emission spectroscopy, CuOH has been identified, but this from atomized salt solutions (11). There is, therefore, no real evidence for the existence of CuOH in the solid state; nevertheless, it does not preclude existence in the thin film. Oxide structure and morphology are already established in a favorable way for oxidation in air because of the underlying Cu_2S and its following oxygenated, aqueous rinse. Dehydration of adsorbed water from one crystal face or another in dry O_2 could not affect subsequent growth in air unless the anhydrous oxide which forms is structurally different and passivating; otherwise, rapid oxidation would always occur in air. This is not simple adsorption of H_2O with an electrochemical reaction. By implication, it seems probable that H_2O becomes part of and disrupts the growing oxide lattice. Migration of Cu^+ is thereby promoted, accounting for results herein. To conclude more than this, however, would require knowledge about how traces of hydroxide fit in Cu_2O structurally. However this may be, the significant acceleration of copper oxidation in air after $S_2O_3^{-2}$ treatment, coupled with the need for water vapor, is testimony to the important influence which these impurities have.

Summary

Using electroless copper films and electroless-replacement films containing copper, the rate of oxidation at room temperature has been discussed in terms of a probable sulfide impurity in the films and water vapor in the air. Together, these accelerate oxidation considerably. However, when a fresh film of either type is exposed to dry O_2, prior to the ambient, it is passivated for oxidation in air. Implicit in these data, first of all, is the conclusion that the over-all kinetics of oxidation of copper can be governed by the presence, or temporary denial, of an impurity, in a very significant way. Also, in light of exposure to the growth-promoting $S_2O_3^{-2}$ solution, preceding exposure to dry O_2, it is further concluded that the anhydrous oxide is remarkably resistant to further growth. Finally, while it is certainly not a new idea that impurities influence the kinetics of oxidation, these data provide evidence for behavior that suggests an interesting synergism. The sulfide impurity probably promotes a favorable structure and/or morphology for growth by oxidation; adsorbed H_2O apparently promotes cationic migration by entrainment and hydration in the oxide lattice.

Acknowledgments

The writer is again grateful to Mr. P. P. Harmon for his technical assistance and to Mrs. J. O. Bookmyer for information retrieval.

Manuscript submitted Oct. 4, 1976; revised manuscript received Dec. 9, 1976.

Any discussion of this paper will appear in a Discussion Section to be published in the December 1977 JOURNAL. All discussions for the December 1977 Discussion Section should be submitted by Aug. 1, 1977.

Publication costs of this article were assisted by PPG Industries, Incorporated.

REFERENCES

1. A. Rönnquist and H. Fischmeister, *J. Inst. Met.*, **89**, 65 (1960-61).
2. F. P. Fehlner and N. F. Mott, *Oxid. Met.*, **2**, 59 (1970).
3. K. R. Lawless, *Rep. Prog. Phys.*, **37**, 231 (1974).
4. N. Cabrera and N. F. Mott, *ibid.*, **12**, 163 (1948-49).
5. K. R. Lawless and D. F. Mitchell, *Colloq. Int. CNRS*, **122**, 27, (1965).
6. C. B. Greenberg, *This Journal*, **123**, 337 (1976).
7. J. Kruger, *This Journal*, **106**, 847 (1959); *ibid.*, **108**, 503 (1961); *ibid.*, **111**, 1038 (1964).
8. "Handbook of Chemistry and Physics," 53rd ed., p. 174, The Chemical Rubber Co., Cleveland (1972).
9. C. W. Bunn, "Chemical Crystallography," 2nd ed., p. 270, Oxford University Press, Oxford (1961).

10. M. C. Sneed, J. L. Maynard, and R. C. Brasted, "Comprehensive Inorganic Chemistry," Vol. 2, p. 66, D. Van Nostrand Company, Inc., New York (1954); M. Straumanis and A. Cirulis, *Z. Anorg. Chem.*, **224**, 107 (1935); P. Bévillard, *Bull. Soc. Chim. Fr.*, **1950**, 561.
11. E. M. Bulewicz and T. M. Snyder, *Trans. Faraday Soc.*, **52**, 1475, 1481 (1956).

Studies on the Oxide-Coated Metal Anodes for Chlor-Alkali Cells

F. Hine,* M. Yasuda, and T. Yoshida*

Nagoya Institute of Technology, Nagoya 466, Japan

ABSTRACT

Formation of the mixed oxide consisting of RuO_2 and TiO_2 was studied by the DTA/TGA technique and x-ray diffraction. The coating agent containing $RuCl_3$ and tetra-n-butyl titanate converted into the mixed oxide of RuO_2 and TiO_2 at about 400°C on the Ti substrate, and the reaction was exothermic. The electric resistance through the oxide film depends much on the fire temperature, and an optimum condition arises between 450° and 500°C. The solution composition and the time of preparation are also important factors. The anodic polarization behavior in the NaCl solution was also affected by the material or the condition of preparation of the oxide-coated Ti electrode.

Since the dimensionally stable anode (DSA®) has been developed by de Nora, many chlorine engineers have been interested in the metal anodes (1, 2). About 30% of the total chlorine in Japan is being produced by modern amalgam cell plants with DSA and replacement of graphite anodes is continuing.

Some papers on this material have been published, but details are still unclear (3-9). According to Beer's patent (10), the titanium substrate is painted with the coating agent containing $RuCl_3$ and tetra-butyl titanate, $Ti(OBu)_4$, and is fired at 400°-600°C in air for a few minutes.

The properties of the mixed oxide of RuO_2 and TiO_2 is important, also the interface between the Ti substrate and the oxide layer should be clarified in detail. Therefore, the coating agent was dried, fired, then powdered to yield samples for various examinations: the differential thermal analysis (DTA), the thermogravimetric analysis (TGA), and x-ray diffraction.

The polarization measurements of the oxide-coated titanium electrode (OCTE) in chloride solution were carried out by the current interruption technique.

The electric resistance through the interface between Ti and the oxide layer was determined.

Experimental Procedure

The composition of the coating agents examined are listed in Table I. Of these, type 10 was used only several times as reference because of weak adhesion with Ti substrate. The number of the type in this table corresponds to the mole ratio of Ru to Ti in the solution, *e.g.*, Ru/Ti = ½ for type 12, and the same code number is used as the type of OCTE when it is painted on the Ti substrate.

The coating agent was dried to solid at 100°C for about 24 hr and was powdered with an agate mortar. $Ti(OBu)_4$ was also powdered as reference, but $RuCl_3$ was avoided because of its hygroscopic behavior.

A Ti plate 20 mm wide, 22 mm long, and 0.5 mm thick was cleaned with 10% oxalic acid at 80°C for about 3 hr. The chemical composition of the Ti substrate is as follows: 0.071% Fe, 0.0055% N, 0.091% O, 0.0014% H, and 99.86% Ti. Coating was repeated until the oxide layer deposited enough for examination, from 4 to 80 coats. The average increments of weight and thickness per coating are shown in the last column of Table I. It was evaluated from the data of a thick oxide layer (80 coats), while the thickness depends on the viscosity of the coating agent.

The samples, both powdered and OCTE, were baked in an electric furnace under given conditions of the oxygen partial pressure (mostly in air) in the temperature range of 300°-700°C. Most samples were prepared at 300°, 450°, and 600°C.

The sample 20 mm wide and 22 mm long for the conductivity measurements of the interface was prepared in the same manner, while Pt plate was also employed as substrate.

Silver was vapor-plated on the oxide coat of 0.5 cm^2 area under 5-8 $\times$ 10^{-5} mm Hg vacuum, then Ag electroplating was carried out on it in a usual cyanide bath

* Electrochemical Society Active Member.

Key words: chlorine overvoltage, oxide-coated Ti anode, thermal decomposition, DTA and TGA technique.

Table I. Composition of coating agents employed

Type	$RuCl_3 \cdot H_2O$* (g)	$Ti(OBu)_4$** (ml)	36% HCl*** (ml)	n-C_4H_9OH (ml)	Mole ratio† Ru/Ti	Thickness of oxide layer‡ mg/cm^2	Thickness of oxide layer‡ microns
10		0.00			1/0	0.117	0.45
11		1.34			1/1		
12	1	3.00	0.4	6.2	1/2	0.218	0.64
14		5.36			1/4		
15		6.68			1/5	0.295	1.29

* Ruthenium chloride, 99.9%.
** Tetra-n-butyl titanate monomer.
*** Hydrochloric acid, analytical grade.
† Mole ratio, Ru/Ti, corresponds to the type of coating agent, and also to the type of electrode when it is painted on Ti substrate.
‡ Average increments of weight and thickness of the mixed oxide (RuO_2 + TiO_2) on Ti substrate per coating. It has been evaluated with the samples of 80 coats.

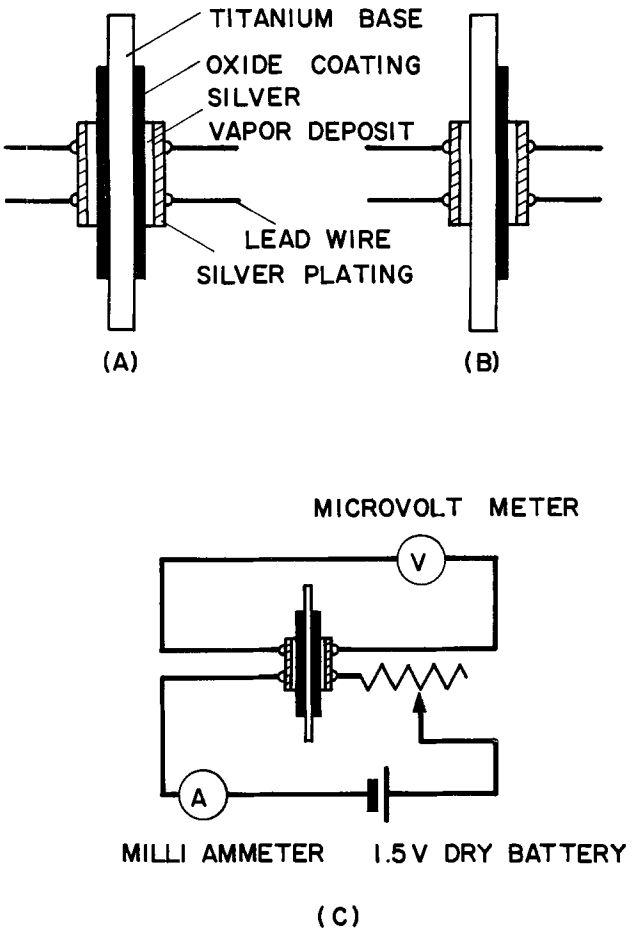


Fig. 1. Specimens and circuit for conductivity measurement

(36 g/liter AgCN, 60 g/liter KCN, and 45 g/liter K_2CO_3 at room temperature) at 10 mA/cm² for 1 hr, so as to prepare the terminal for the resistance measurements. Unplated surface was insulated with PVC. Copper lead wires were soldered as shown in Fig. 1. We had trouble with mode B, which was one-side coated, because Ti was oxidized during firing at high temperature, and the resistance of the oxidized Ti substrate increased considerably. Therefore, mode A was normally used. It was confirmed that there was no rectification at the interface consisting of metal and oxide. The resistivity measurements were carried out by means of the four-probe method as shown in Fig. 1. The data obtained with specimens of 0.5 cm² were listed and plotted directly instead of the usual presentation in ohms per unit area.

Results

DTA and TGA.—Figures 2-4 are the data of DTA and TGA obtained in air atmosphere. The upper curve is the DTA and the lower the TGA. All samples showed the exothermic change with weight loss. The chemical formula indicated in the figure, such as RuO_2, was identified by x-ray diffraction. TiO_2(A) and TiO_2(R) indicate the anatase- and rutile-type titanium dioxide, respectively. The x-ray chart for the sample prepared at 300°C showed amorphous structure because the temperature was too low. The percent at the right-hand side in the chart shows the weight loss due to firing at 700°C.

Figure 2 shows the data of $RuCl_3$. Some changes at about 100°C would be due to vaporization of water from the sample. While $RuCl_3$ is hygroscopic material, it changes to fine powder by heating and loses its wettability. The data with acidified samples showed small effect of addition of HCl.

A large exothermic change was observed at about 420°C when butanol was added (curve A-2).

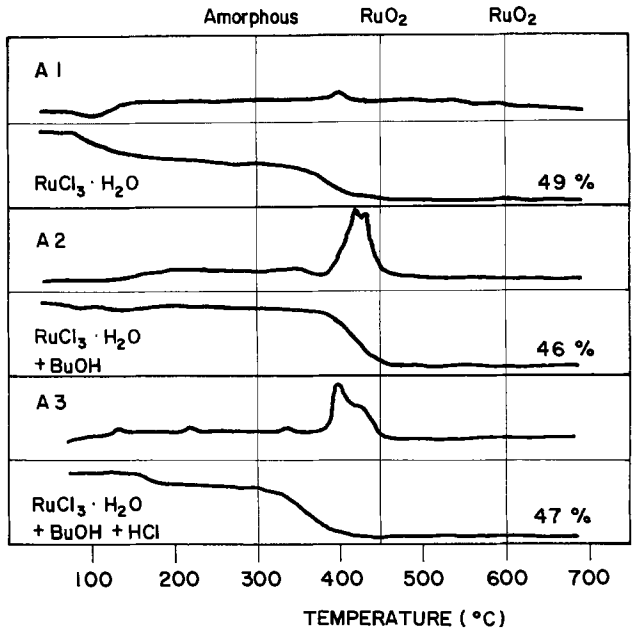


Fig. 2. DTA and TGA curves

The specimen for curve A-3 consists of $RuCl_3 \cdot H_2O$, HCl, and butanol (type 10). Small changes at 140°, 220°, 340°C were observed and a large peak on the DTA curve appeared at about 420°C.

The data of $Ti(OBu)_4$ are shown in Fig. 3. It is evident that the reaction is affected very much by addition of HCl and butanol. A large peak on the DTA curve at about 520°C diminished when HCl was added.

Figure 4 shows the data of the mixture of $RuCl_3$ and $Ti(OBu)_4$. These data showed a large change at relatively low temperatures. The mole ratio of Ru to Ti was widely varied, while only three samples are shown here. The highest peak on the DTA chart moved with the mole ratio in the temperature range between 300° and 400°C (Fig. 5).

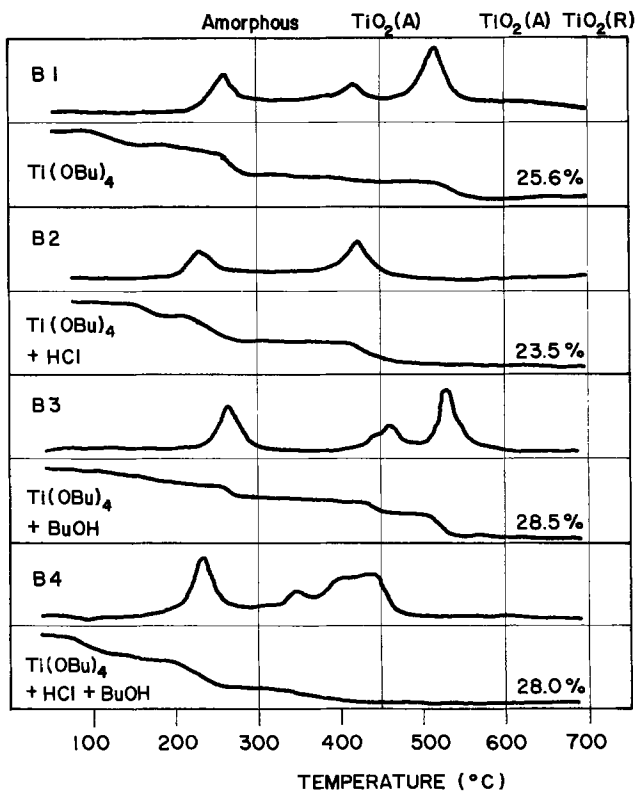


Fig. 3. DTA and TGA curves

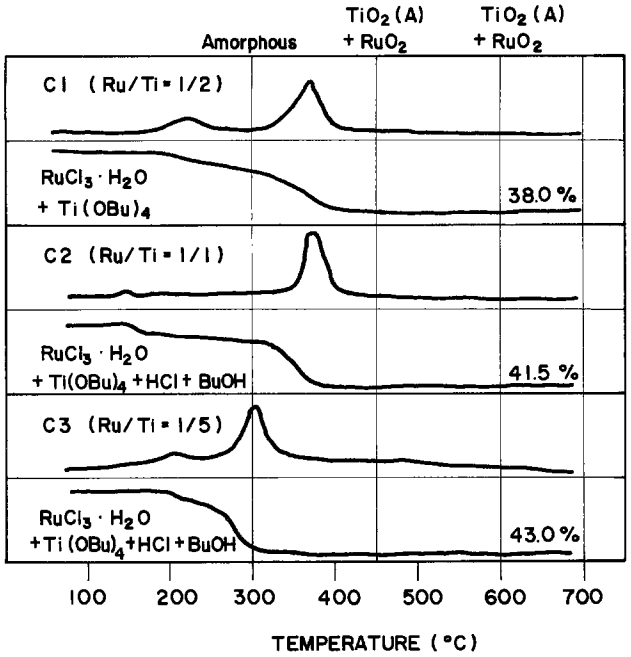


Fig. 4. DTA and TGA curves

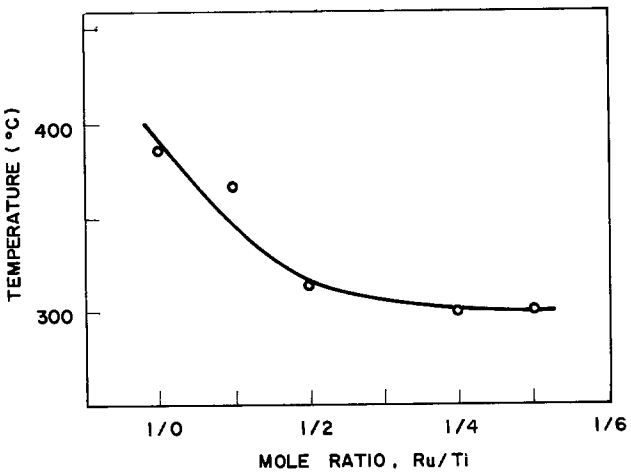


Fig. 5. Peak temperature of the DTA chart as a function of the mole ratio of Ru to Ti.

The experiment with the sample containing Ti powder (100 mesh) was carried out, and no significant effect was found. The chemical composition of Ti powder made by Osaka Titanium Manufacturing Company was as follows: 0.024% Fe, 0.010% Si, 0.030% Cl, 0.002% Mn, 0.009% Mg, 0.015% N. 0.008% C, 0.0078% H, 0.30% O, and more than 99.2% Ti.

X-ray diffraction.—The data for Ru powder fired at 700°C for about 60 min showed some oxidation of RuO_2. It changed completely at 1200°C. Dried then powdered $RuCl_3$ also changed to RuO_2 in the range 450°-600°C, and was not affected by either HCl or butanol.

$Ti(OBu)_4$ converted to TiO_2(A) when it was heated at 450°-600°C for only a few minutes in air. TiO_2(A) became TiO_2(R) at 700°C.

It is interesting to know the behaviors of the specimen painted on Ti substrate. Acidified $Ti(OBu)_4$ on Ti plate changed to TiO_2(A) at 600°C, then to TiO_2(R) at 700°C.

Other samples were prepared with the solutions of types 12 and 15 with Ti substrate at 450°C for 10 min. The x-ray data showed the oxide mixture consisted of RuO_2 and TiO_2(R) instead of anatase (Fig. 6). Its mixed oxide would be a solid solution having the rutile configuration.

It was confirmed that the oxide deposited on a glass plate consisted of RuO_2 and TiO_2(A). Therefore, the

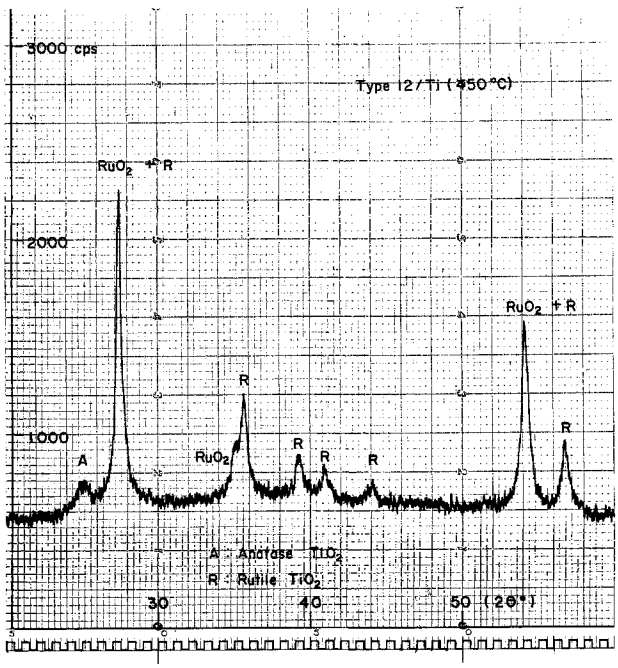


Fig. 6. Type 12 on Ti substrate fired at 450°C for 10 min in air atmosphere.

effect of Ti metal on the formation reaction of oxide is appreciable.

The sample prepared with powdered $Ti(OBu)_4$ and Ti powder consisted of TiO_2(A). On the other hand, the mixture of the powder of type 12 with a small amount of Ti powder converted to the rutile-type oxide mixture with some TiO_2(A) by heating at 450°C (Fig. 7). When the sample was heated at high temperature such as 700°C ,the peak for TiO_2(A) on the x-ray chart lowered gradually, and the peak split: $2\theta = 27°$-$28°$ and 35°-36°, as shown in Fig. 8.

Resistivity measurements.—The resistivity through the oxide layer measured at room temperature is a function of the conditions of preparation such as the mole ratio of Ru to Ti, the number of coating or the thickness of the oxide layer, the fire temperature, the time of firing, and the oxygen partial pressure. It is impor-

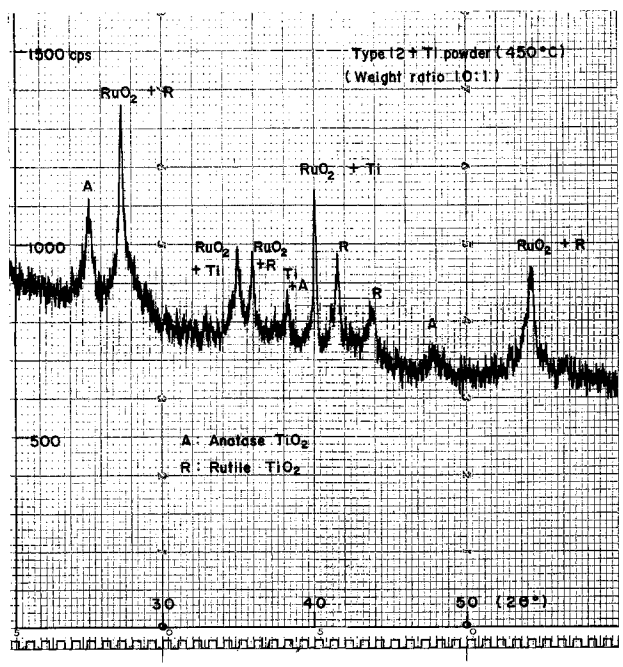


Fig. 7. Type 12 with Ti powder fired at 450°C for 10 min in air atmosphere.

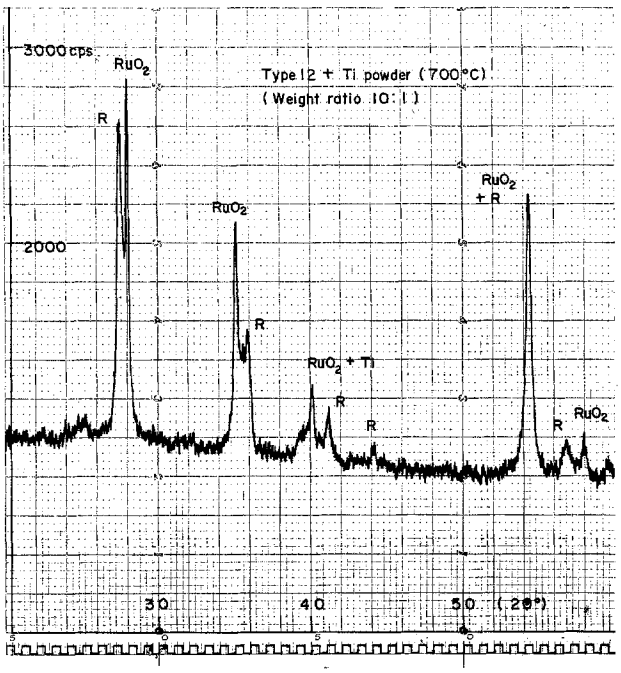


Fig. 8. Type 12 with Ti powder fired at 700°C for 10 min in air atmosphere.

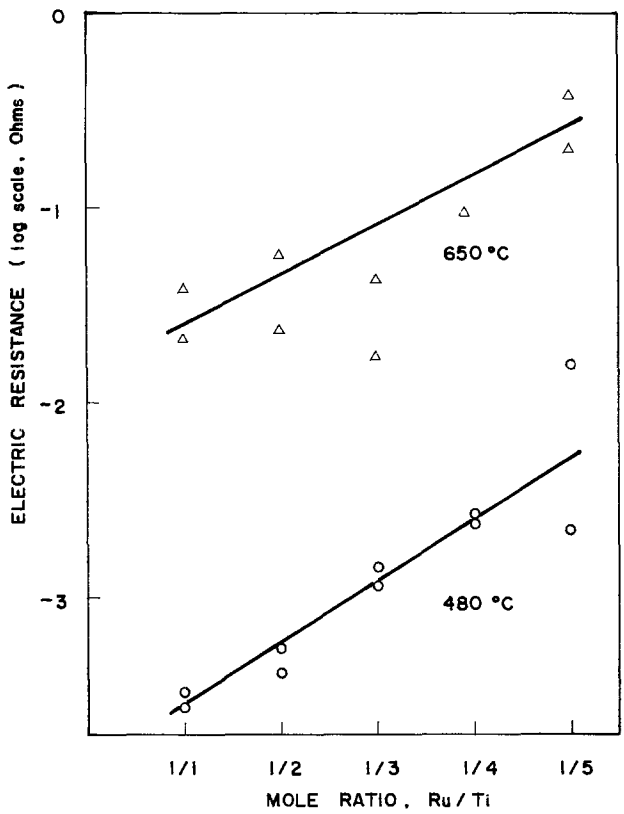


Fig. 9. The electric resistance at room temperature as a function of the mole ratio of Ru to Ti. The fire temperature is shown in the figure. The OCTE, 4 coats, was fired for 5 min.

tant to note that the larger the Ti content the larger is the resistivity (Fig. 9). As shown in Fig. 10, there is an optimum temperature of firing between 350° and 450°C.

When the specimen is fired at low temperatures, say 400°C, for relatively long time such as 30 min, the Ti substrate is oxidized gradually by oxygen passing through the oxide layer and the resistivity increases. Therefore, the heat-treatment should be carried out within a few minutes.

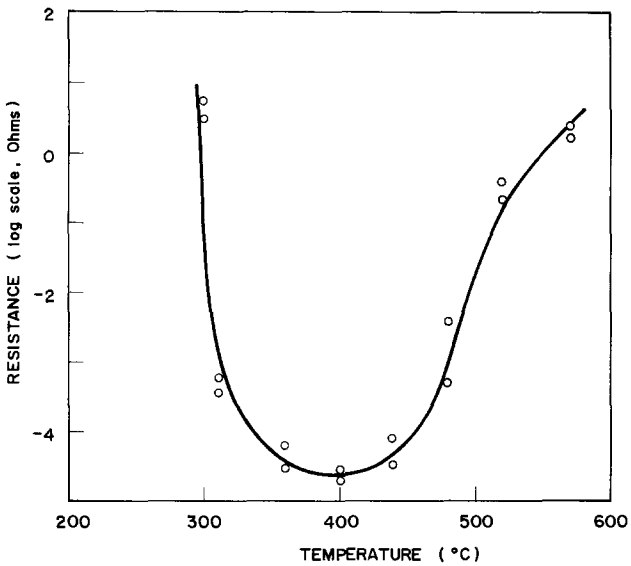


Fig. 10. The electric resistance at room temperature as a function of the fire temperature (type 15). The OCTE, 4 coats, was fired for 5 min.

The specimen prepared under oxygen showed almost the same properties as the specimen fired in air.

Figure 11 shows the electric resistance as a function of the temperature of measurement in a range −50° to 150°C. The temperature coefficient of the resistivity is observed to be negative, which is discussed later. But it is important that it is a typical property of semiconducting materials.

Polarization measurements.—The polarization curves of the specimens of different composition (fired at 450°C for 10 min) in saturated NaCl ($pH = 0.9$) with dissolved chlorine at 40°C are shown in Fig. 12. The specimen, type 10, was avoided because of its weak strength as anode. It is obvious that the curve is almost independent of the oxide composition within the range of our experiment.

It is interesting that the polarization depends so much on the fire temperature as shown in Fig. 13, where the solid line and the dashed line show the data with type 12 on Ti and Pt as substrates, respectively.

The OCTE, type 12, prepared at 400° and 500°C shows relatively low chlorine overvoltage.

The overvoltage of the specimen prepared at 300°C is high, probably due to insufficient thermal decomposition of $RuCl_3$ to oxide.

The Ti substrate is oxidized at temperatures higher than 600°C, and hence, the overvoltage becomes high. At temperatures higher than 700°C, the DTA and the x-ray data show significant crystallization of the oxide.

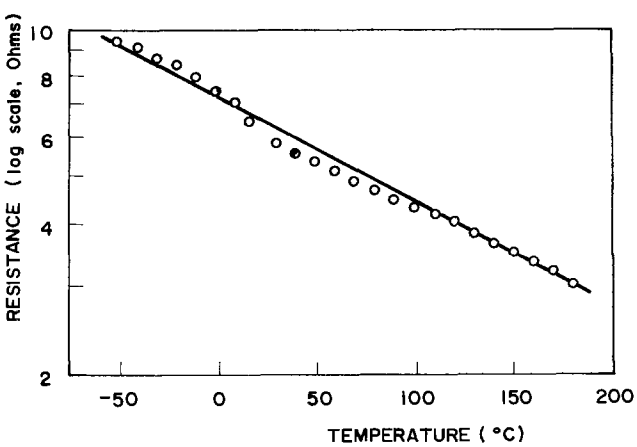


Fig. 11. The electric resistance vs. temperature curve (type 12). The OCTE, 5 coats, was fired at 550°C for 20 min.

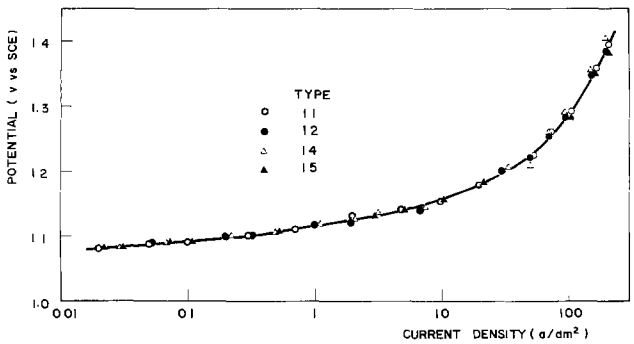


Fig. 12. The anodic polarization curves in saturated NaCl (pH 0.9) at 40°C. The OCTE, 4 coats, was fired at 450°C for 10 min.

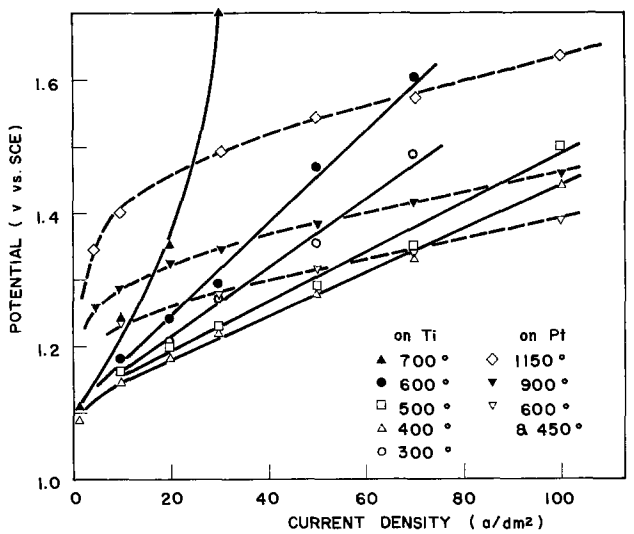


Fig. 13. The anodic polarization curves of type 12 painted on Ti and Pt substrates in saturated NaCl (pH 0.9) at 40°C as functions of the fire temperature. The specimens with Ti and Pt substrates were painted 4 and 8 times, respectively, and were fired for 10 min.

The polarization data of those specimens show poor activity as the chlorine electrode, even when Pt is employed as substrate instead of Ti.

Figure 14 is the summary of the polarization of the specimens prepared at various temperatures. The ordinate is the slope of the polarization curve shown in Fig. 13. The curve shows a minimum resistivity in the temperature range between 400° and 500°C.

Discussion

The active material on the OCTE invented by Beer consists of the mixture of RuO_2 and TiO_2, and is strong under severe conditions of service as chlorine electrode (10). We made a RuO_2 deposited on Ti, and polarized it in a saturated NaCl solution (pH = 2-3) at about 90°C under 100-150 A/dm² for few days. A single oxide (RuO_2) peeled off considerably and failed during electrolysis, whereas a mixture of RuO_2 and TiO_2 was no problem.

The DTA/TGA data of the coating agent without Ti powder show that a large exothermic change in a range 300°-400°C, depending on the composition of the coating agent, appears (Fig. 2-4). At high temperatures (450°-600°C), the peaks for RuO_2 and TiO_2(A) on the x-ray chart are clearly separated from each other.

The DTA/TGA data are not affected by the presence of Ti, either plate or powder. On the other hand, the x-ray data of the sample consisting of the mixed oxide with Ti prepared at 450°-600°C show the peaks of RuO_2 and TiO_2(R).

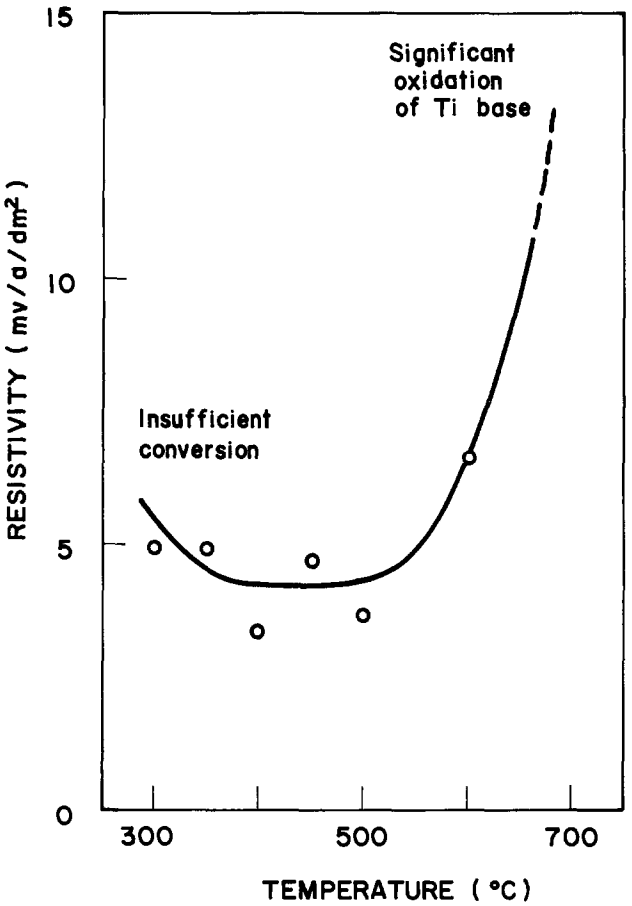


Fig. 14. The polarization resistance as a function of the fire temperature.

Adhesiveness between the oxide mixture and Ti substrate becomes excellent.

The coating agents shown in Table I were dried at 100°C and powdered, with Ti in some cases. The samples were heated at 450°-600°C. The x-ray data describe that three components, *i.e.*, $RuCl_3$, $Ti(OBu)_4$, and metallic Ti, are necessary to form rutile oxide. The TiO_2(A) will form by heating if one of those components is eliminated. In other words, we could obtain a suitable material as anode when we paint Ti substrate with the mixed solution of $RuCl_3$ and $Ti(OBu)_4$.

We require the anode material to have low resistivity, good electrochemical activity, corrosion resistance, and geometrical stability under service conditions.

The experimental data show that the larger the Ru/Ti ratio the lower is the electric resistance. The temperature of firing is also a factor of the resistivity. A preferable material can be obtained at the temperature just beyond the peak of the DTA/TGA chart at about 400°C.

It is assured that the TiO_2 layer on the substrate sustains a major part of the electric resistance through the metal-to-oxide. It is well known that Ti is covered with an oxide layer, and thermal oxidation to TiO_2(R) proceeds at relatively low temperatures such as 400°C (11-14). We experienced difficulty with making measurements of electric resistance with the specimen mode B in Fig. 1, due to significant oxidation of the bare surface of Ti. Even with mode A, the resistivity increased considerably when the specimen was heated at 400°C for 30 min or more.

The x-ray data of the specimen, which was prepared with the coating agent, type 12, on Pt sheet instead of Ti under various temperatures (450°, 620°, 900°, and 1150°C) for 10 min, showed RuO_2 + TiO_2(R). The resistivity of those specimens was one to two orders lower than that of the minimum of OCTE shown in Fig. 10. Those results suggest that increase in the re-

sistivity of the material with Ti substrate is caused by oxidation or diffusion of oxygen through the oxide coat during heat-treatment (15, 16), but the resistivity is a small function of the degree of crystallization.

The temperature coefficient of the resistivity of OCTE is negative as shown in Fig. 11, and agrees with reference data (9). It is said that the single crystal of RuO_2 has the characteristics of metal-like conductivity (17-19), and TiO_2(R), which is also single crystal, behaves like an oxygen-defective n-type semiconductor (20). The behavior of OCTE as a semiconductor has been reported by several authors (7, 21), but only with the experimental data of the resistivity measurements.

The anodic polarization curves of the OCTE prepared at 450°C for 10 min are also independent of the Ru/Ti ratio in the range 1/1-1/5. The polarization behavior of the OCTE has been reported (5, 7). Generally, the electrochemical activity is said to decrease with increase in the Ti content in the active materials. Of course, the polarization behavior is a factor in practice, but the Ru/Ti ratio of 1/2 seems to be optimum from the viewpoint of economical consideration (10).

The scanning electron microscopic observation shows the rough surface of the OCTE and the roughness factor is 80-200 (7, 9, 22). Therefore, it would also be a large factor of low chlorine overvoltage in concentrated NaCl solution, while the relationship between the chlorine overvoltage and the surface roughness has not been clarified yet in detail.

The Tafel slope of the anodic polarization curve shown in Fig. 12 at relatively low current densities is about 40 mV/decade, but the overvoltage increases quickly at high current density ranges. Those phenomena have been described by Kuhn *et al.* (7), who have tried to apply the theory of semiconductors (23). As shown in Fig. 13 and 14, the chlorine overvoltage of the specimen prepared at temperatures higher than 500°C is high, probably due to failure in activity and oxidation of substrate.

The specimen with Pt substrate has the polarization behavior shown by the dotted line in Fig. 13. As described above, the substrate does not oxidize by heating in this case. Therefore, increase in the overvoltage by firing at high temperatures would be due to failure in the electrochemical activity or crystallization of the oxide layer.

According to the x-ray diffraction, the active material prepared with $RuCl_3$ and $Ti(OBu)_4$ consists of the solid solution of the rutile-type mixed oxide of Ru and Ti, while RuO_2 prepared from $RuCl_3$ by firing is a nonstoichiometric compound containing Ru(III) (8).

The crystal size depends on the preparation temperature, *e.g.*, 115 and 201Å at 400° and 500°C, respectively (9). From those reference data and our experiments, the active material deposited on Ti substrate would be a solid solution of the rutile-type oxide of Ru and Ti, which has an oxygen-defective and mosaic structure.

Crystallization proceeds firing at temperatures higher than 700°C, and the peaks of TiO_2(R) and RuO_2 on the x-ray chart split off. The electrochemical activity of such a material is poor.

Acknowledgment

The author wishes to express many thanks for support of Olin Research Center, New Haven, Connecticut, also for useful suggestions of Professor Toshio Takada, Research Institute of Chemistry, Kyoto University. A part of this work was covered by Ministry of Education, 743016.

Manuscript submitted July 19, 1976; revised manuscript received Nov. 27, 1976.

Any discussion of this paper will appear in a Discussion Section to be published in the December 1977 JOURNAL. All discussions for the December 1977 Discussion Section should be submitted by Aug. 1, 1977.

Publication costs of this article were assisted by the Nagoya Institute of Technology.

REFERENCES

1. O. de Nora, *Chem.-Ing.-Tech.*, **42**, 222 (1970); *ibid.*, **43**, 182 (1971).
2. J. Horacek and S. Puechaver, *Chem. Eng. Prog.*, **67** (3), 71 (1971).
3. G. Faita and G. Fiori, *J. Appl. Electrochem.*, **2**, 31 (1972).
4. A. T. Kuhn and C. J. Mortimer, *ibid.*, **2**, 283 (1972).
5. E. A. Kalinovskii, R. U. Bonder, and N. N. Meshkova, *Sov. Electrochem.*, **8**, 1430 (1972).
6. R. C. Érenburg, L. I. Krishtalik, and V. I. Bystrov, *ibid.*, **8**, 1690 (1972).
7. A. T. Kuhn and C. J. Mortimer, *This Journal*, **120**, 231 (1973).
8. D. Galizzioli, F. Tantardini, and S. Trasatti, *J. Appl. Electrochem.*, **4**, 57 (1974).
9. K. J. O'Leary and T. J. Navin, Abstract 257, p. 603, The Electrochemical Society Extended Abstracts, Spring Meeting, San Francisco, California, May 12-17, 1974.
10. British Pat. 6490/67; Belgian Pat. 710,551; Japanese Pat. 46-21884.
11. J. W. Hickmann and E. A. Gulbransen, *Anal. Chem.*, **20**, 158 (1948).
12. P. Kofstad, "High-Temperature Oxidation of Metals," p. 170, John Wiley & Sons, Inc., New York (1966).
13. P. Kofstad, K. Hauffe, and H. Kjollesdal, *Acta Chem. Scand.*, **12**, 259 (1958).
14. P. H. Morton and W. M. Baldwin, *Trans. ASM*, **44**, 1004 (1952).
15. K. Hauffe, *Arch. Eisenhüttenwes*, **24**, 161 (1953).
16. P. Kofstad, P. B. Andersen, and O. J. Krudtaa, *J. Less Common Metals*, **3**, 89 (1961).
17. J. M. Fletcher, W. E. Gardner, B. F. Greenfield, M. J. Holdway, and M. H. Rand, *J. Chem. Soc. A*, **1968**, 653.
18. D. B. Rogers, R. D. Shannon, A. W. Sleight, and J. L. Gillson, *Inorg. Chem.*, **8**, 841 (1969).
19. W. D. Ryden and A. W. Lawson, *Phys. Rev. B*, **1**, 1494 (1970).
20. D. C. Cronemeyer, *Phys. Rev.*, **87**, 876 (1952).
21. G. Bianchi, *J. Appl. Electrochem.*, **1**, 231 (1971).
22. W. O'Grady, C. Iwakura, J. Huang, and E. Yeager, Abstract 315, p. 753, The Electrochemical Society Extended Abstracts, Spring Meeting, San Francisco, California, May 12-17, 1974.
23. A. K. Vijh, "Electrochemistry of Metals and Semiconductors," Marcel Dekker, New York (1973).

The Anodic Formation of Cu_2O in Alkaline Solutions

V. Ashworth and D. Fairhurst[1]

Corrosion and Protection Centre, University of Manchester Institute of Science and Technology, Manchester, England

ABSTRACT

Chronopotentiometry has been used in conjunction with electron microscopy to investigate the anodic formation of Cu_2O on copper electrodes immersed in aqueous sodium hydroxide solutions (0.01-1M). The anodic transition time τ for Cu_2O formation is related to the applied current density, i_1, by the relationship

$$i_1\tau^{1/2} = \text{a constant}$$

A nucleation and growth model of film formation is proposed which is in good agreement with the experimental results. The rate-determining step is the formation of a soluble copper(I) species, film growth taking place by precipitation from solution.

It is generally considered that cuprous oxide, Cu_2O, is the first product of the anodic oxidation of copper in alkaline solutions (1-14). In the case of electrochemical reaction in aqueous sodium hydroxide this has been confirmed by electron diffraction (5). Until recently, however (11), very little attention has been focused upon the mechanism by which the reaction proceeds. More importance has been attached to the formation of copper(II) species during subsequent electrochemical oxidation reactions. According to the various sources, cupric oxide, CuO (2, 5, 6, 8, 9), cupric hydroxide, $Cu(OH)_2$ (3-8), and a soluble species thought to be the bicuprite anion, $HCuO_2^-$ (7, 10), may be formed. Nevertheless, there appear to be several conflicting opinions in the literature as to whether these divalent species form in consecutive or concurrent electrode reactions. Further, the knowledge that the treatment of alkaline solutions containing cupric ions with strong oxidizing agents can yield salts of copper(III) (15) has been linked with the possible formation of Cu_2O_3 at potentials somewhat lower than those at which oyxgen evolution occurs at a copper anode (7, 10).

Chronopotentiometry has proven to be the important technique used to investigate the reactions taking place at a copper electrode. In both anodic and cathodic polarization stages the presence of a potential arrest in the potential-time (E-t) behavior of the copper electrode has been linked to the formation, or reduction, of one of the species identified above.

Until very recently it had been considered that Cu_2O forms without appreciable formation of a soluble copper(I) species in accordance with the known instability of the copper(I) aquo ion (16) and the insolubility of Cu_2O (17). Dignam and Gibbs (11) have confirmed this view in experiments in borate solutions (pH 9.19) where the cathodic reduction of an anodically formed Cu_2O film proceeds with a current efficiency[2] of 100%, *i.e.*, there is no charge inbalance brought about by the diffusion of a soluble species away from the electrode surface. Similar conclusions have been drawn from comparable results obtained in 0.1M sodium hydroxide (7) although the electrode potential arrests associated with the electrochemical reduction of Cu_2O to the metal are not so well defined as in borate solutions and the calculations are therefore less precise. Unfortunately the majority of workers who have used chronopotentiometry to investigate the reactions taking place on copper have always reversed the direction of the applied current after the onset of oxygen evolution. The cathodic reduction of higher valent copper species formed anodically up to the oxygen evolution potential renders it impossible to determine the current efficiency for Cu_2O formation and reduction under these circumstances.

Recent work, however, indicates that in concentrated alkali a soluble copper(I) species has a more important role to play in Cu_2O formation than was previously considered (10, 14). Using a rotating split ring-disk electrode, Miller (10) showed that during the chronopotentiometric formation of a Cu_2O film at the copper disk in 1M sodium hydroxide a soluble copper(I) species could be detected by its simultaneous one electron potentiostatic oxidation [to copper(II)] and reduction [to copper(0)] at the gold half-rings. Furthermore, during controlled positive-going potentiodynamic sweeps on the copper disk Miller observed a ring current maximum corresponding to the oxidation of soluble copper(I) species to copper(II) at disk potentials negative to the Cu-Cu_2O active-passive transition. Ambrose *et al.* (14) also recorded that during high rate potentiodynamic sweeps upon a stationary copper electrode in 1M potassium hydroxide a small but definite current peak can be observed at potentials more negative than that attributable to Cu_2O formation and concluded that a soluble copper(I) species is generated prior to the appearance of any Cu_2O. Finally a recent Japanese publication (18) reports that the results of ellipsometric and chronopotentiometric studies, carried out *in situ*, are consistent with the anodic formation of Cu_2O in alkaline solutions by a dissolution-precipitation mechanism.

In the past, chronopotentiometric studies of the anodic reactions taking place at a copper electrode have been carried out at relatively high current densities (>0.5 mA/cm^2). Under these conditions only small quantities of Cu_2O are formed prior to the appearance of copper(II) species, and investigations of the initial oxidation stage are therefore difficult. This paper describes an investigation based upon low current density chronopotentiometry and electron microscopy into the anodic formation of Cu_2O in alkaline solutions. A nucleation and growth model of Cu_2O film formation is proposed which is in good agreement with the experimental results obtained.

Experimental

Chronopotentiometry.—Copper specimens were cut from 0.94 mm thick deoxidized high conductivity copper sheet (Henry Righton and Company, Limited). After annealing at 750°C *in vacuo* the specimens were used to fabricate spade electrodes having an exposed

[1] Present address: The International Paint Company, Felling, Gateshead, England.

[2] Current efficiency = $\frac{\text{charge passed along the cathodic potential arrest}}{\text{charge passed along the anodic potential arrest}} \times 100\%$.

Key words: chronopotentiometry, dissolution-precipitation, nucleation, film growth.

surface area of approximately 430 mm^2. The electrodes were electropolished using Powers' method (19) and, immediately prior to use, were etched in alcoholic ferric chloride (20). It was found that the reproducibility of the results was significantly enhanced by using electropolished and etched, rather than abraded or electropolished, surfaces (21).

The electrochemical cell used for the polarization studies consisted of a 1000 cm^3 reaction vessel with a tightly fitting lid. The working electrode was located centrally within the cell and was surrounded by a cylindrical platinum sheet counterelectrode (110 mm circumference, 35 mm high). A Luggin capillary probe provided electrolyte contact between the working and reference electrodes. All electrode potentials were measured with respect to a saturated calomel electrode (+244 mV *vs.* SHE), but are reported in this paper on the standard hydrogen scale. The electrochemical cell was completed by gas inlet and outlet tubes and an inlet for the introduction of the electrolyte solution. The cell was mounted in a thermostatically controlled water bath maintained at 30° (±0.1°C).

Sodium hydroxide solutions were used as the test environment. Approximately 750 cm^3 of test solution were deaerated by an evacuation and sparging procedure as follows. The solution was placed in a 1000 cm^3 conical flask which was evacuated until there was no further visible evidence of gas disengagement from the solution. Atmospheric pressure was then restored within the flask by allowing hydrogen gas to enter. The solution was sparged subsequently with hydrogen for 30 min before being pumped into the electrochemical cell under hydrogen pressure and without air exposure. (The electrochemical cell had been flushed previously with hydrogen.) For the duration of each experiment hydrogen gas was passed over the surface of the test solution to prevent the ingress of atmospheric oxygen.

The constant current was supplied from a stabilized power supply (Type C346, Wareham Measuring Systems Limited) and measured using a Universal avometer (±2% f.s.d.). The electrical circuit incorporated a reversing switch that enabled polarity reversals to be made in the reaction vessel without altering the direction of the current through the avometer. The electrode potential of the working electrode was measured using a *p*H meter (Model 290, Pye Electronics Limited) and its variation with time monitored on a potentiometric recorder (Speedomax XL681, Leeds and Northrup Limited).

Following the complete assembly of the cell, the working electrode was cleaned cathodically at a current density of 10 $\mu A/cm^2$. Once a sharp fall in potential had indicated the onset of hydrogen evolution on the surface of the working electrode, the current was adjusted to the level required for a particular experiment and reversed, *i.e.*, the specimen was anodically polarized. Similarly as soon as the start of a rapid rise in electrode potential became evident beyond the first anodic potential arrest, the polarity of the cell electrodes was reversed once more causing the anodically formed Cu_2O layer to be reduced.

Electron microscopy.—To examine the morphology of the Cu_2O films, experiments were interrupted at the positive limit of the anodic potential arrest, *i.e.*, the cell current was switched off, the specimen removed from the cell, and, after rinsing and drying, examined electron-optically. Both scanning and transmission electron microscopy were used for this purpose. To employ the former technique, it was necessary to coat the specimens with gold to prevent charging of their surfaces during direct examination. The use of conventional transmission electron microscopy was made possible by preparing positive replicas of the specimen surfaces using the two-stage method (22). This involved preparing an initial negative replica in plastic (M280-D blue replicating material, P.E. Electron Microscope Accessories Limited) onto which was evaporated a thin layer of carbon. The replica was then shadowed with a gold palladium alloy to improve contrast. After dissolving the plastic in acetone, the shadowed positive carbon replica was mounted on a copper grid for examination in the transmission electron microscope.

Results

The *E-t* curves recorded during cathodic cleaning of the copper specimens at a constant current density of 10 $\mu A/cm^2$ indicated that the freshly prepared specimens carried a Cu_2O film between 70 and 300Å thick. Since a 20-40Å thick film is reported to form rapidly upon a clean copper surface when the metal is exposed to air or oxygen at room temperature (23, 24), the thicker films reported here reflect a reasonably high surface roughness introduced by the electrode pretreatment.

A distinctive feature of the *E-t* variation during the anodic formation of Cu_2O was the appearance of a "potential overshoot" which immediately preceded the establishment of the anodic arrest, *i.e.*, the region of constant potential was approached from a more noble potential. As Fig. 1-3 show, the "overshoot" became more pronounced with increasing sodium hydroxide concentration and less pronounced with increasing current density. Furthermore, it was found that the anodic transition time diminished progressively with increasing current density in the same solution although at comparable current densities it increased with an increase in the concentration of sodium hydroxide (Table I).

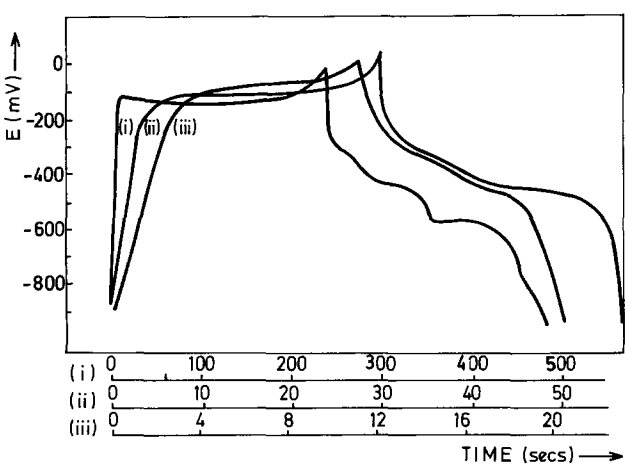


Fig. 1. Chronopotentiometric polarization curves for a copper electrode in 0.01M NaOH (i) 29.8 $\mu A/cm^2$, (ii) 101 $\mu A/cm^2$, (iii) 227 $\mu A/cm^2$.

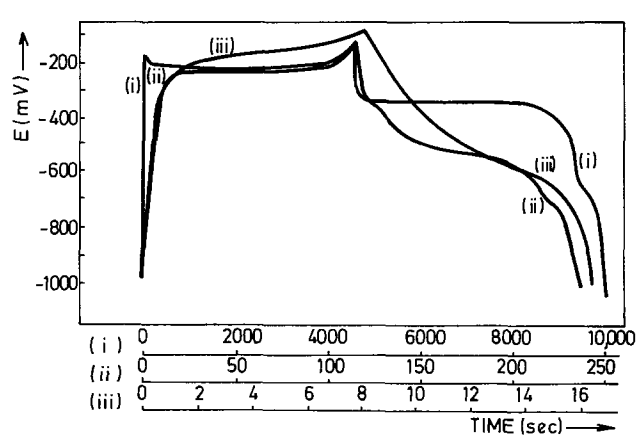


Fig. 2. Chronopotentiometric polarization curves for a copper electrode in 0.1M NaOH: (i) 25 $\mu A/cm^2$, (ii) 120 $\mu A/cm^2$, (iii) 399 $\mu A/cm^2$.

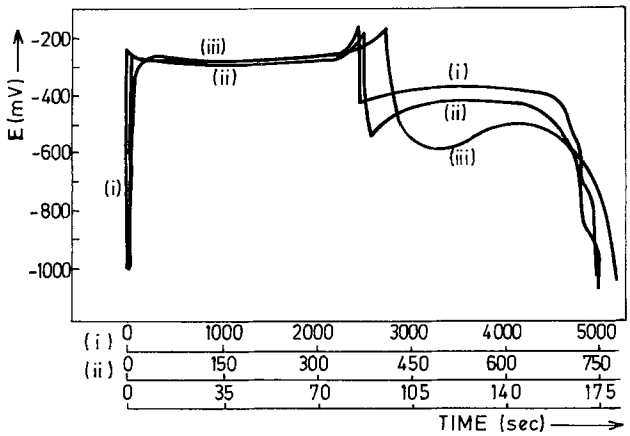


Fig. 3. Chronopotentiometric polarization curves for a copper electrode in 1M NaOH: (i) 91.1 μA/cm^2, (ii) 305 μA/cm^2, (iii) 513 μA/cm^2.

The term "transition time" is most commonly used to describe the duration of an arrest appearing in the chronopotentiogram. Since double layer charging makes a contribution to the apparent transition time in a chronopotentiogram, several methods of determining the real transition time relating to a specific electrochemical reaction have appeared in the literature. However, according to Bos and van Dalen (25), it makes little difference which method is used when carrying out experiments in solutions containing greater than 10^{-3}M of the reactant since above this concentration the charging affects are vanishingly small. In the experiments described here, it was confirmed that the actual method of transition time determination had little bearing upon the over-all results. Thus the τ values in Table I were determined using a simple graphical method similar to that described by Russell and Petersen (26) and attributed to Kuwana.

As can be seen from Fig. 1-3, the cathodic E-t curves were generally more complicated than their anodic counterparts particularly at low current densities. In 0.1 and 1.0M sodium hydroxide solutions, cathodic potential overshoots were sometimes discernible.

Table I. The effect of sodium hydroxide concentration and anodic current density on transition time (τ), film thicknesses, and the current efficiency of the formation and reduction of Cu_2O

Current density (μA/cm^2)	Transition time (sec)	Estimated film thickness (Å)	Current efficiency (%)
	0.01M NaOH		
12.9	972	155	122
20.4	359	91	113
29.8	223	82	105
45.5	105	59	100
101	26.6	33	91
150	12.8	24	100
227	7.8	22	90
	0.1M NaOH		
25.0	4560	1414	115
40.0	2097	1040	115
50.0	1836	1138	112
67.1	456	379	101
75.0	687	638	118
120	114	169	100
150	106	197	106
201	59.0	147	98
309	20.3	78	100
399	7.8	39	101
	1M NaOH		
65.5	5100	4142	104
91.1	2478	2799	101
120	1872	2785	99
150	1755	3264	105
175	1188	2578	96
305	372	1407	98
356	300	1324	97
513	93	592	93
558	108	713	91

The current efficiencies determined by comparing the charge passed in the cathodic E-t curve with that passed in the corresponding anodic curve are compiled in Table I. Measurements of the current efficiency were based on the anodic charge passed up to polarity reversal and the cathodic charge passed subsequently in attaining -956, -1056, and -1106 mV in 0.01, 0.1, and 1.0M sodium hydroxide solutions, respectively. As shown in Table I, these efficiencies varied considerably between 90 and 120% depending on both the electrolyte concentration and the applied current density.

Discussion

The anodic potential overshoot.—None of the existing literature concerning the anodic behavior of copper in alkaline solutions shows any evidence of anodic potential overshoots in the chronopotentiograms. This is not surprising since in the majority of cases experiments were carried out at higher current densities than those employed here. The experimental results showed clearly a progressive diminution in the magnitude of the overshoot with increasing current density. Comparable anodic potential overshoots have been observed during anodic film formation upon a number of metals exposed to a variety of different environments; these results have been summarized by Vermilyea (27). The same author suggests that the phenomenon arises from the additional overpotential required to produce nuclei of the anodic product on the metal surface. Once nucleation has occurred, it is envisaged that the overpotential falls due to the growth of the nuclei being a comparatively facile process.

According to Ambrose *et al.* (14) the growth of a Cu_2O film in 1M potassium hydroxide solution is preceded by the formation of a soluble copper(I) species for which the formula $Cu(OH)_2^-$ has been suggested. By analogy with the explanation put forward by Vermilyea (27), it might be argued that the anodic potential overshoot reported here is due to the kinetically easier formation of the $Cu(OH)_2^-$ ion during the early stages of anodic polarization. The overshoot is thus an indication of the need to supersaturate the solution prior to the initiation of Cu_2O formation. It is conceivable that for an electrochemical dissolution-chemical precipitation mechanism of film growth, continued growth of the Cu_2O nuclei requires saturation and not supersaturation of the electrolyte. Consequently the electrode potential falls as a steady-state situation becomes established.

The solubility of Cu_2O in water has been determined as 6.99×10^{-7} g-moles/liter (17) and one must assume a similarly low value for this compound in alkaline solutions as no data are readily available in the literature. In view of the suggested formula (14) for the copper(I) solution species, the solubility of Cu_2O in alkaline solutions can be expressed as

$$Cu_2O + 3H_2O \rightarrow 2Cu(OH)_2^- + 2H^+ \qquad [1]$$

Thus, assuming, as Eq. [1] implies, that the solubility of Cu_2O in alkaline solutions follows the same trend as CuO and $Cu(OH)_2$ (17), *i.e.*, it increases with increasing *p*H, the more pronounced anodic potential overshoot at higher hydroxyl ion concentrations can be explained.

The possibility that the solution could contain more copper(I) species in solution with increasing alkalinity is supported by the current efficiencies in Table I. The current efficiencies for the anodic formation cathodic reduction of Cu_2O at low current densities in 0.01 and 0.1M sodium hydroxide solutions were found to exceed 100% to a substantial extent, an observation that can be attributed to the simultaneous reduction of dissolved oxygen at the copper electrode. With the counterelectrode surrounding the working electrode, it is to be anticipated that some oxygen generated during the anodic polarization of the counterelectrode should diffuse to the working electrode and be reduced elec-

trochemically. The decrease in oxygen solubility with increase in sodium hydroxide concentration (28) ensures that less cathodic charge is consumed in the reduction of oxygen. Therefore it might be expected that lower current efficiencies, but never less than 100%, would be observed from this source in concentrated solutions. Thus a current efficiency of 91% recorded at 558 $\mu A/cm^2$ in 1M sodium hydroxide clearly shows the involvement of a copper(I) solution species. This particular experiment was repeated a number of times on separate specimens, but with the current being reversed at different points along the anodic Cu_2O potential arrest. The current efficiencies for the different time intervals of anodic polarization prior to current reversal are shown in Table II. The results indicate that the proportion of escaping soluble copper(I) generated remained effectively constant throughout the Cu_2O formation step. This is in agreement with the results of Miller's (10) split ring-disk experiments where, although a maximum in the concentration of soluble copper(I) at very short times (<2 sec) was observed, at longer times the concentration of this species became relatively constant.

Thus the appearance of anodic potential overshoots, becoming more predominant with increasing sodium hydroxide concentration, and the current efficiencies of substantially less than 100% are both consistent with the formation of a soluble Cu(I) species and suggest that the anodic formation of Cu_2O in alkaline solutions may take place by a mechanism of electrochemical dissolution followed by chemical precipitation.

The anodic transition time and its dependence on current density.—The diffusion model.—The empirical relationships between the experimentally determined anodic transition time τ and the applied current density i_l were found to obey the general formula

$$i_l\tau^{1/m} = K \qquad [2]$$

$$\text{units} - (\mu A/cm^2)\ (\text{sec})^{1/m}$$

The values of K and m for the experimental results are compiled in Table III. It can be seen that in all three solutions the value of the index m was close to 2. For this value, Eq. [2] coincides with the fundamental equation of chronopotentiometric analysis for an electrochemical reaction where the over-all rate is determined by the slow diffusion of a solution species (29), *viz.*

$$i_l\tau^{1/2} = \tfrac{1}{2}n\pi^{1/2}\mathbf{F}D_o^{1/2}C_o^b \qquad [3]$$

(n is the number of electrons involved in the electrochemical reaction, $\mathbf{F}$ the Faraday constant, and D_o and C_o^b the diffusion coefficient and bulk concentration, respectively, of the diffusing species). A comparison of experimental results with Eq. [3] has been used by previous workers to argue the role of diffusion in determining the rate of anodic film formation (30). However, the implications behind a compliance of the experimental results with Eq. [3] in a film-forming situation require further consideration.

The electrochemical reduction of a species Ox to a second species Red can be represented as

$$\text{Ox} + ne \rightarrow \text{Red} \qquad [4]$$

Now assuming both Ox and Red are soluble and can undergo unhindered diffusion to or from reaction sites situated upon a plane metal electrode, and that the driving force for diffusion in both cases is the existence of concentration gradients, Fick's laws of diffusion can be used to derive expressions for the time dependence of the interfacial concentrations, C_o^i and C_R^i of the oxidized and reduced species, *i.e.*

$$C_o^i = C_o^b - \frac{2i_l t^{1/2}}{\pi^{1/2}n\mathbf{F}D_o^{1/2}} \qquad [5]$$

and

$$C_R^i = \frac{2i_l t^{1/2}}{\pi^{1/2}n\mathbf{F}D_R^{1/2}} \qquad [6]$$

It is clear that Eq [3] follows directly from Eq. [5] by assuming that at time $t = \tau$ the interfacial concentration of Ox, C_o^i, is zero. Clearly, for an anodic reaction involving soluble reactants and products, an identical treatment to that given above will apply; the time dependence of the interfacial concentration of the reactant being given by Eq. [5] and that of the product by Eq. [6].

However, it may be anticipated that the above expressions may not hold for an anodic reaction producing an insoluble species. Nevertheless, in a number of instances the observation of a direct proportionality between i_l and $\tau^{-1/2}$ for the anodic passivation of metals in sodium hydroxide solutions has been explained as arising from the slow diffusion of hydroxyl ions to the metal surfaces (30). In Fig. 4 i_l has been plotted against $\tau^{-1/2}$ for the results given in Table I. Figure 4 shows that in each solution in which experiments were carried out an i_l *vs.* $\tau^{-1/2}$ relationship can be claimed. Furthermore, the results confirm to some extent those obtained by El Din and El Wahab (7) who passivated copper electrodes under similar experimental conditions. These authors claim that in their experiments the product $i_l\tau^{1/2}$ was approximately proportional to the concentration of the hydroxyl ions in solution. By comparison with Eq. [3], the immediate conclusion from their results is that the diffusion of hydroxyl ions to the metal surface is the slow step in the over-all electrode reaction. However, the best fit slopes of the plots in Fig. 4 are given in Table IV. Although the data indicate a correspondence between the product $i_l\tau^{1/2}$ and the sodium hydroxide concentration, the function does not change by orders of magnitude as Eq. [3] would suggest. Thus rate control by the slow diffusion of hydroxyl ions does not explain the linear i_l *vs.* $\tau^{-1/2}$ relationship recorded here.

There are, of course, good reasons why an i_l *vs.* $\tau^{-1/2}$ relationship arising from diffusion limitations to reaction rate should not be observed at all. Equations [3], [5], and [6] were derived by assuming that the contribution to the mass transport of the reacting species by migration under the influence of the electric field which exists between the counter and working electrodes is negligible (29). This assumption is only valid if the reacting species is accompanied by an excess of a supporting electrolyte such that the transport number of the former is vanishingly small. The as-

Table II. Chronopotentiometric current efficiency following current reversal after different intervals along Cu_2O arrest

Current density ($\mu A/cm^2$)	Time to current reversal (sec)	Current efficiency (%)
562	25	89
554	51	92
563	76	94
558	108 (completion)	91

Table III. Values of the constants m and K in Eq. [2]

NaOH concentration (M)	m	K
0.01	1.70	624
0.1	2.26	1100
1.0	1.86	2416

Table IV. Slope of i_l vs. $\tau^{-1/2}$ plots shown in Fig. 4

NaOH concentration (M)	Slope ($\mu A\ cm^{-2}\ sec^{-1/2}$)
0.01	620
0.1	1142
1.0	5357

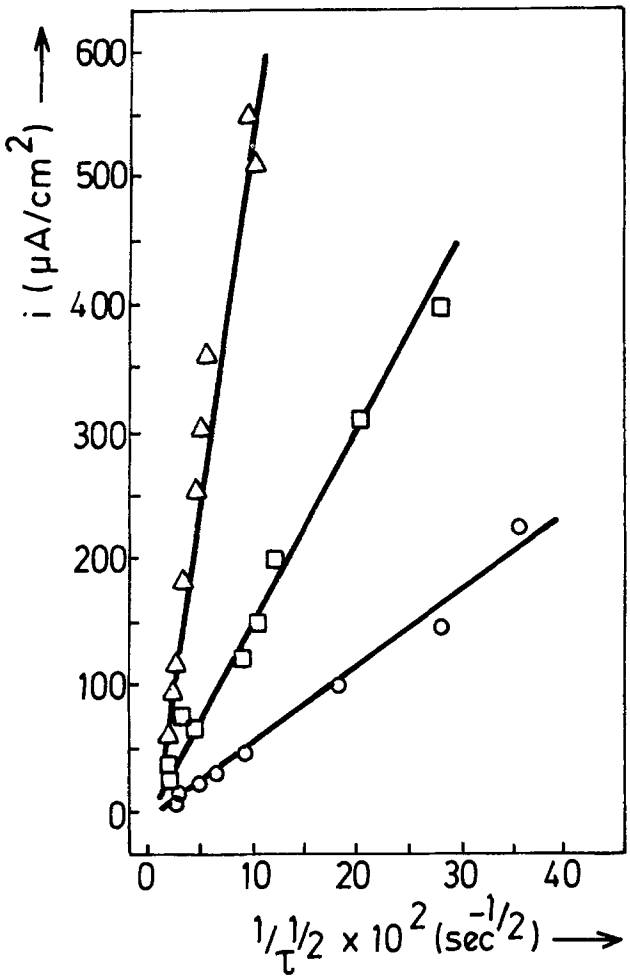


Fig. 4. Plots of i_l vs. $1/t^{1/2}$ for the anodic formation of Cu_2O in sodium hydroxide solutions: ○ 0.01M NaOH, □ 0.1M NaOH, △ 1.0M NaOH.

sumption is acceptable here, although in the general case of experiments made in dilute electrolyte solutions and at high current density it is inappropriate. It is further assumed in the derivation of Eq. [3], [5], and [6] that during the course of the reaction there is no progressive barrier introduced at the metal surface by the reaction products. For the formation of a sparingly soluble compound which accumulates at the metal-solution interface, there must necessarily be some hindrance to the movement of solution species between the bulk of the electrolyte and the metal surface except perhaps where the films formed are very thin (31, 32).

In view of the first objection and the observed $i_l\tau^{1/2}$ relationship, it might be argued that if the Cu_2O film forms by anodic dissolution followed by chemical precipitation it is the slow movement of the soluble copper (I) species between the dissolution sites and the growing Cu_2O nuclei which is rate determining. Under these circumstances the large excess of sodium hydroxide would act as the supporting electrolyte and the soluble copper(I) species might be expected to diffuse solely under the influence of the concentration gradient. By analogy with Eq. [6], Eq. [3] would then become

$$i_l\tau^{1/2} = \tfrac{1}{2}\pi^{1/2}n\mathbf{F}D^{1/2}_{Cu(I)}C^*_{Cu(I)} \qquad [7]$$

where C^* is the maximum concentration of soluble copper(I) attainable at the metal-solution interface. Assuming a diffusion coefficient $D_{Cu(I)}$ of 10^{-5} cm²/sec comparable to that of the Cu^{2+} ion, it is possible to estimate values for $C^*_{Cu(I)}$ from the data of Table II; these values are compiled in Table V. The increase in $C^*_{Cu(I)}$ with increasing alkalinity is in agreement with the trend in the solubility of Cu_2O suggested earlier.

Table V. Estimated solubility of Cu(I) species based on Eq. [7]

NaOH concentration (M)	$C^*_{Cu(I)}$ (g ions/liter)
0.01	3.24×10^{-5}
0.1	5.96×10^{-5}
1.0	28.00×10^{-5}

Furthermore the value for $C^*_{Cu(I)}$ in 1M sodium hydroxide solution is comparable to that estimated by Miller (10) using a rotating split ring-disk electrode system in the same solution (1×10^{-4} g-ions/liter). Nevertheless, from the basic assumptions of the diffusion model it should be added that the Cu_2O film would need to maintain a substantial degree of porosity during its growth. Since the quantity of charge and hence the Cu_2O film thickness was found to vary considerably and in a particular solution was dependent upon the applied current density (see Table I), it is to be anticipated that the mass transport of solution species to and from the metal-solution interface is hindered to an extent which will in turn depend upon the applied current density. It can also be added that with the growth of the Cu_2O film progressively diminishing the metal solution interfacial area, the actual current density at the metal surface must increase correspondingly. It is difficult, therefore, to envisage how this alternative model based upon the rate-limiting diffusion of a soluble copper(I) species would give rise to the observed linearity between i_l and $\tau^{-1/2}$.

The nucleation and growth model.—Apart from the classical interpretation of the $i/\tau^{1/2}$ relationship observed in chronopotentiometry, it is also possible to derive, theoretically, an identical relationship for anodic film formation if there exists a simple dependence upon current density of the number of nuclei formed initially. This alternative model makes two assumptions. First, that τ coincides with the complete coverage of the metal surface by the oxide film. Second, that essentially all of the nuclei that grow are formed instantaneously. In the latter assumption the model follows that put forward by Dignam and Gibbs (11) to explain the formation of Cu_2O in sodium tetraborate solutions (pH 9.2). Nevertheless, it does require some justification.

The initial stage in the growth of the anodic film is the formation of discrete growth centers or nuclei. The total number of nuclei N contributing to the growth of the film is given by the time dependence of the nucleation process. This is normally expressed (27) as

$$N = N_0(1 - \exp(-AT)) \qquad [8]$$

where N_0 is the total number of nucleation sites available and A the nucleation rate constant. If A is large, all the sites are converted to nuclei and we can write $N = N_0$.

According to Fleischmann and Thirsk (33) the nucleation rate constant A is a function of the overpotential η as follows

$$A = Ki_0 \exp\frac{(-k_2\sigma^3)}{\eta^2} \qquad [9]$$

where K is a frequency factor, i_0 the exchange current density, σ the surface free energy of the nucleus, and k_2 is a constant. The relationship between A and η as given by Eq. [9] has been verified for the growth of MnO_2 crystallites upon a platinum substrate (34). Thus it may be assumed that in the present work the formation of nuclei of Cu_2O occurred essentially within the duration of the anodic potential overshoot; the number of nuclei formed at longer times being small by comparison due to the lower overpotential and the substantial decrease in the number of nucleation sites available.

Thus, assuming the near-instantaneous nucleation of N hemispherical nuclei which grow at equal rates in

three dimensions, the volume of oxide V at time t is given by

$$V = \frac{2}{3} N\pi r^3 \qquad [10]$$

where r is the radius of the nuclei.

Now assuming negligible loss of charge due to solubilization, V will be proportional to the total charge passed and we can write

$$\frac{2}{3} N\pi r^3 = k_1 i_1 t \qquad [11]$$

where k_1 is a constant and i_1 the applied current density. On rearranging, Eq. [11] becomes

$$r = \left(\frac{3k_1 i_1 t}{2N\pi} \right)^{1/3} \qquad [12]$$

Since the nuclei are hemispherical, the area of the electrode surface covered is $N\pi r^2$, or from Eq. [12]

$$\text{surface area covered at time } t = N\pi \left(\frac{3k_1 i_1 t}{2N\pi} \right)^{2/3} \qquad [13]$$

If the total surface area of the electrode is S_o square centimeters, then it follows that at time $t = \tau$

$$S_o = N\pi \left(\frac{3k_1 i_1 \tau}{2N\pi} \right)^{2/3} \qquad [14]$$

and rearranging

$$N^{1/2} i_1 \tau = \frac{2S_o^{3/2}}{3\pi^{1/2} k_1} \qquad [15]$$

or

$$N^{1/2} i_1 \tau = \text{constant} \qquad [16]$$

Experimentally $i_1 \tau^{1/2}$ was found to be a constant. Thus

$$\underline{i_1 \propto N^{1/2}} \qquad [17]$$

That is, a plot of i_1 *vs.* $\tau^{-1/2}$ will be linear if the number of instantaneously formed nuclei is directly proportional to the square of the current density.

Figures 5 to 9 show both scanning and transmission electron micrographs of anodically oxidized metal surfaces. As can be seen from Fig. 6 and 7, the Cu_2O films formed in 0.1M sodium hydroxide were comprised of a great many cubic crystallites which entirely cover the surface of the metal. It can be said also that in 0.01M sodium hydroxide the Cu_2O films had a similar morphology (Fig. 5), but due to the small quantities of Cu_2O formed in the most dilute solution it was difficult to obtain highly resolved and informative micrographs from these specimens.

For the purpose of examining the extent to which Eq. [17] is applicable to the results obtained in 0.1M sodium hydroxide it should be noted that an identical result to Eq. [17] is obtained if a cubic rather than hemispherical growth form is assumed. From Fig. 6 it can be estimated that the majority of the cubes formed at 25 μA/cm^2 in 0.1M sodium hydroxide have sides approximately 2500Å in length. Similarly, from Fig. 7(a) the corresponding cubes have sides of approximately 600Å. From the initial assumption that at time $t = \tau$ the metal surface is completely covered by cubes of Cu_2O, the number of nuclei N formed upon 1 cm^2 of surface is given by

$$N = \frac{10^{16}}{a^2} \qquad [18]$$

where a^2 is the area of metal surface (square angstroms) occupied by a single cube. Thus

$$\frac{N_{25}}{N_{67.1}} = \frac{(600)^2}{(2500)^2} = 0.0576 \qquad [19]$$

and from Eq. [17] we also have

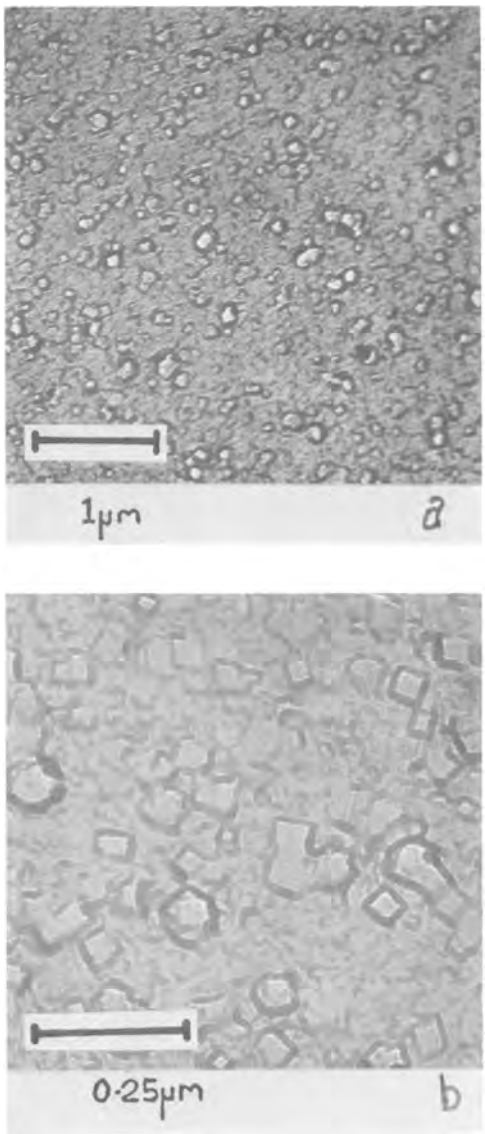


Fig. 5. Transmission electron micrographs of the Cu_2O film formed in 0.01M NaOH at 10 μA/cm^2.

$$\frac{N_{25}}{N_{67.1}} = \left(\frac{25}{67.1} \right)^2 = 0.139 \qquad [20]$$

The agreement here is not particularly good although the values obtained in Eq. [19] and [20] are of a comparable magnitude.

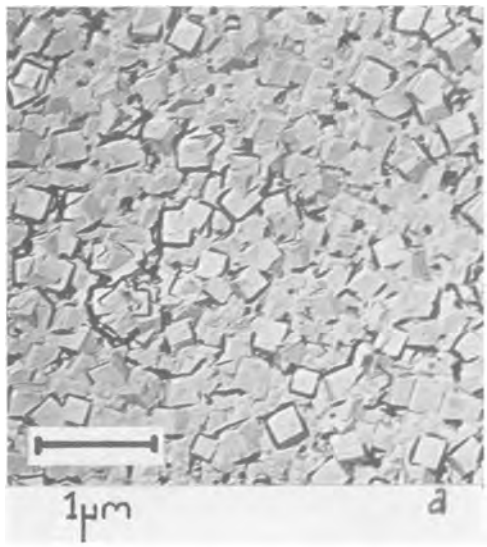
Figures 8 and 9 show that in contrast to the Cu_2O films formed in 0.01 and 0.1M sodium hydroxide the individual crystallites formed in 1M solutions were polyhedral. Similar polyhedral growth of Cu_2O upon copper single crystals exposed to solutions containing cupric ions has been the subject of a series of reports appearing in the literature (35). However, the electron micrographs (Fig. 8 and 9) show that it is permissible to repeat the above calculations, in this case treating the polyhedra as hemispherical crystallites. From the micrographs

$$\frac{N_{90}}{N_{350}} = \left(\frac{800}{3750} \right)^2 = 0.046 \qquad [21]$$

and from Eq. [17]

$$\frac{N_{90}}{N_{350}} = \left(\frac{90}{350} \right)^2 = 0.066 \qquad [22]$$

The agreement here is closer than that obtained from the micrographs of the Cu_2O films formed in 0.1M sodium hydroxide. It can therefore be said that the





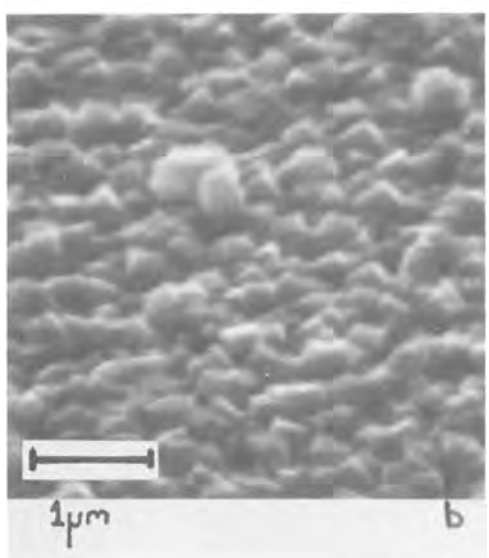
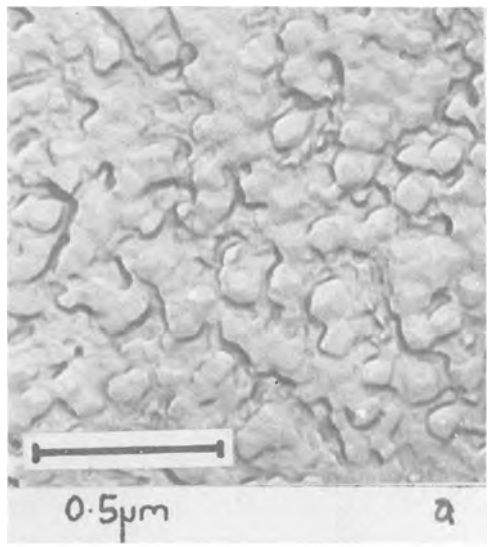


Fig. 6. (a) Transmission electron micrographs of the Cu_2O film formed in 0.1M NaOH at 25 $\mu A/cm^2$. (b) Scanning electron micrograph of the Cu_2O film formed in 0.1M NaOH at 25 $\mu A/cm^2$.

micrographs of Fig. 6-9 do show some evidence that a dependence of N upon i_l^2 does exist during anodic Cu_2O film formation.



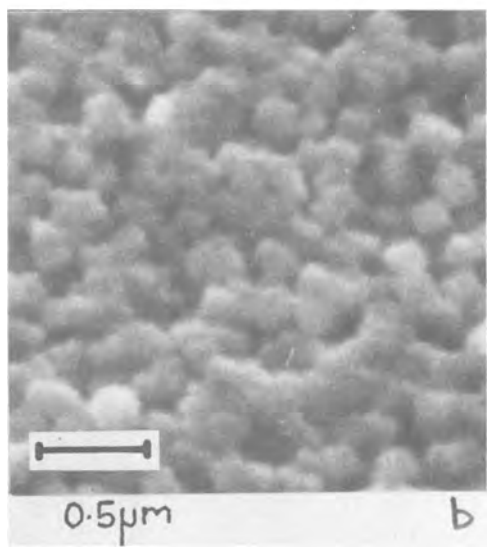
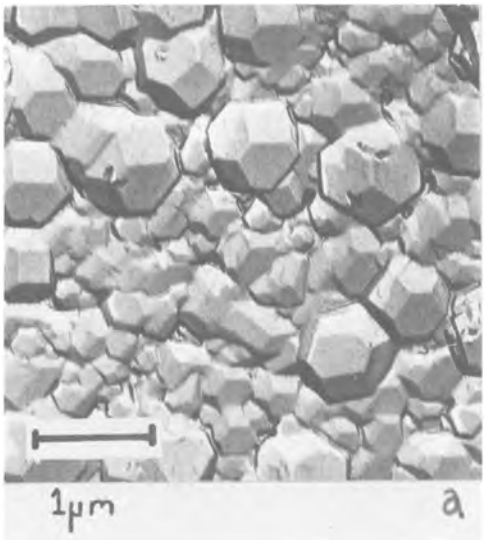


Fig. 7. (a) Transmission electron micrograph of the Cu_2O film formed in 0.1M NaOH at 67.1 $\mu A/cm^2$. (b) Scanning electron micrograph of the Cu_2O film formed in 0.1M NaOH at 60 $\mu A/cm^2$.

In summary, the results suggest that the dependence of the transition time upon the square of the current density, observed during the chronopotentiometric formation of Cu_2O in sodium hydroxide solutions, arises from the influence of the magnitude of the applied current density upon the number of Cu_2O nuclei formed initially. They further suggest that the i *vs.* $\tau^{-1/2}$ relationship is not due to rate limitations imposed by the slow diffusion of a solution species as put forward by earlier workers to explain similar results obtained during anodic film formation under comparable conditions.

The anodic arrest potential and its dependence on current density.—In Fig. 10 the anodic arrest potential E is shown as a function of the applied current density at each of the three sodium hydroxide concentrations in which experiments were carried out. Despite some scatter of the experimental points in the 0.01 and 0.1M solutions, there appears to be a linear relationship between E and i_l at low values of i_l. With the exception of the results obtained at the two lowest current densities in 1M sodium hydroxide, the linearity between E and i_l was found to extend over the entire range of current densities examined. The scales of overpotential given on the right-hand side of Fig. 10 were derived by obtaining a least squares fit of the linear data extrapolating to zero and using the intercept value of E as the "equilibrium" value for the reaction taking



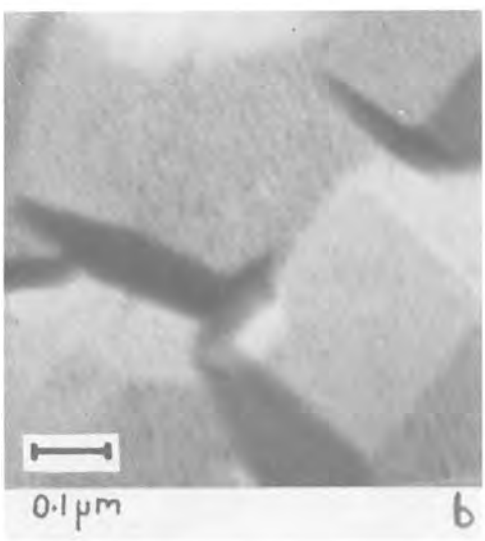
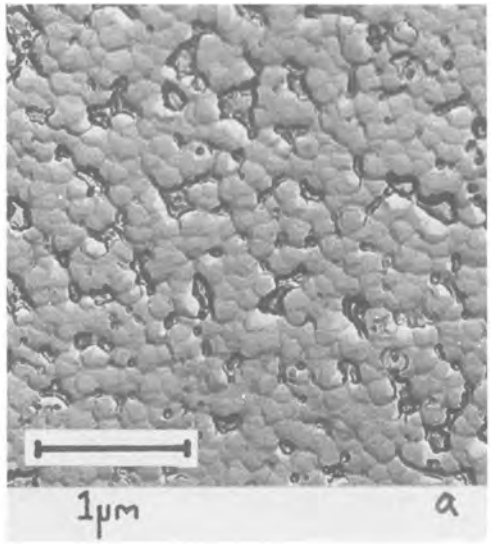


Fig. 8. Transmission electron micrographs of the Cu_2O film formed in 1M NaOH at 90 $\mu A/cm^2$.



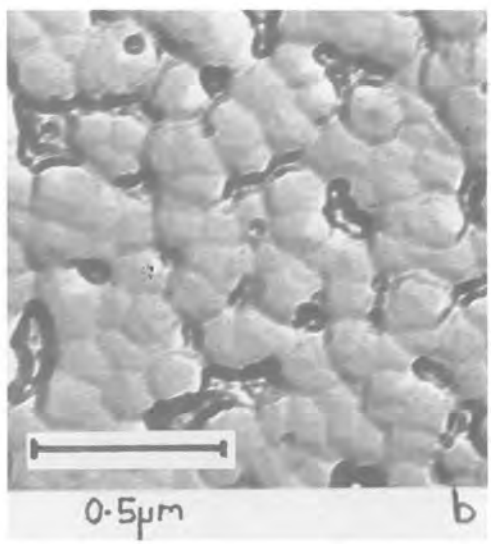


Fig. 9. Transmission electron micrographs of the Cu_2O film formed in 1M NaOH at 350 $\mu A/cm^2$.

place. With the linear plots confined to low overpotentials (< 30 mV), the dependence of E on i_l resembles that predicted by a limiting case of the Butler-Volmer equation (36).

For an electrochemical reaction in which electron transfer is slow due to the transfer taking place via the formation of a high energy intermediate, theory (36) predicts that where a single electron is involved in this, the rate determining step, the current is given by

$$i_l = i_o \left\{ \exp\left[\frac{(1-\beta)\mathbf{F}\eta}{RT}\right] - \exp\left[-\frac{\beta\mathbf{F}\eta}{RT}\right] \right\} \quad [23]$$

where β is the symmetry factor and describes the profile of the energy barrier that must be surmounted for the reaction to proceed, and i_o is the exchange current density. Expanding Eq. [23] and restricting its application to low overpotentials (20-30 mV) gives

$$i_l = \frac{i_o \mathbf{F}\eta}{RT} \quad [24]$$

and substituting for $\mathbf{F}$, R, and T (303°K) yields

$$i_o = \frac{0.026\, i_l}{\eta} \quad [25]$$

Values of i_o calculated by applying Eq. [25] to the linear portions of the curves shown in Fig. 10 are shown in Table VI. According to Ambrose (14), the dissolution of copper(I) in alkaline solutions proceeds by the electrochemical reaction

$$Cu + 2\,OH^- \rightarrow Cu(OH)_2^- + e \quad [26]$$

At low overpotentials metal dissolution is commonly activation controlled, the magnitudes of i_o and β being characteristic of a particular metal-electrolyte system (37). By applying simple kinetic considerations to Eq. (26), it can be shown that the exchange current density i_o for the reaction is given by (21)

$$i_o = K_a [Cu(OH)_2^-][OH^-]^{2\beta} \quad [27]$$

where K_a is a constant. If it can be assumed that the change in $Cu(OH)_2^-$ ion concentration is small compared to the tenfold variations in OH^- ion concentration, then a plot of $\log_{10} i_o$ *vs.* $\log_{10} [OH^-]$ should be linear. This is confirmed for the experimental results by Fig. 11 in which the slope of the curve gives $\beta =$

Table VI. Values of exchange current density (i_o) obtained from Eq. [25]

NaOH concentration (M)	i_o (A/cm²)
0.01	2.90×10^{-5}
0.1	1.53×10^{-4}
1.0	4.33×10^{-4}

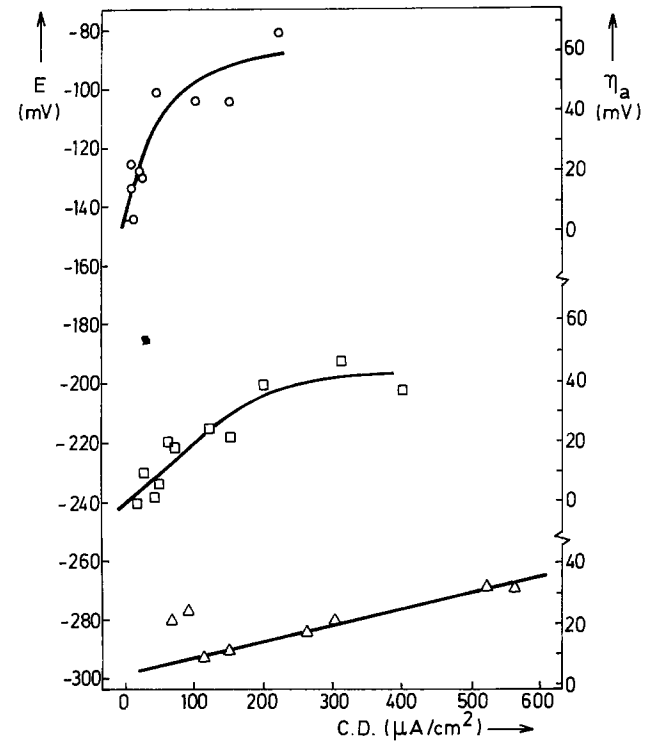


Fig. 10. The variation in the anodic arrest potential with applied current density: ○ 0.01M NaOH, □ 0.1M NaOH, △ 1.0M NaOH.

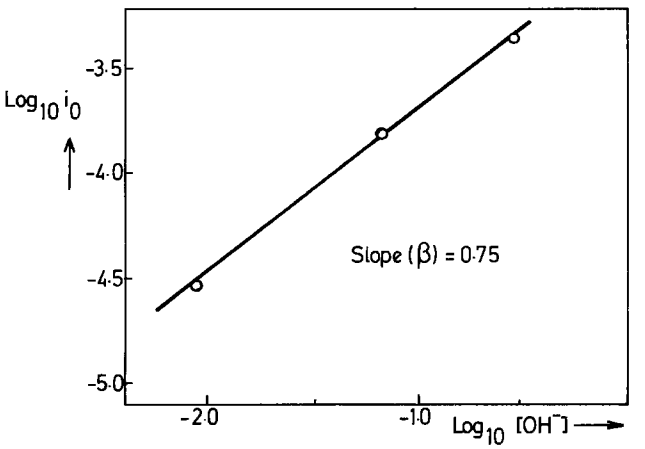


Fig. 11. Exchange current density as a function of hydroxyl ion concentration.

0.375. It should be noted that for this value of β, Eq. [25] is only valid when η is less than 20 mV.

During steady-state galvanostatic polarizations of copper electrodes in sodium hydroxide solutions (pH 12.05-13.06), Kim and Nobe (38) recorded two separate regions of potential in which the overpotential was directly proportional to the logarithm of the applied current density. Applying the Butler-Volmer equation, Eq. [23], to the lower region, attributable to the copper-copper(I) reaction, a somewhat lower value of 0.152 for β is obtained. By way of further comparison, tables of kinetic data show values lying between 0.26 and 0.65 for metal dissolution in aqueous solutions (37). The value of β determined in the present experiments clearly lies well within this range.

From the foregoing mathematical treatment of the experimentally recorded variation in the anodic arrest potential with the applied current density, it can be said that the results are consistent with a model in which the rate-determining step is charge transfer. This suggests that for an electrochemical dissolution-chemical precipitation mechanism of Cu_2O formation in alkaline solutions, which has been previously put forward in the literature (18), it is the former step which is slow and determines the over-all reaction rate. Clearly this would not be consistent with an interpretation of the $i\tau^{1/2}$ relationship based on a model invoking diffusion control.

The anodic potential-time curve profiles.—Low current densities.—From Eq. [14] the area of the electrode surface covered by the anodic film at time t (S_f) after commencement of nucleation is given by

$$S_f = (3/2\, N^{1/2}\pi^{1/2}k_1 i_1 t)^{2/3}$$

Therefore S_t, the area of metal surface remaining uncovered at time t is given by

$$S_t = S_o - (3/2\, N^{1/2}\pi^{1/2}k_1 i_1 t)^{2/3} \qquad [28]$$

S_o being the original surface area of the film-free metal. If the applied current I is concentrated at the exposed areas of the metal surface where metal dissolution is taking place, the actual current density, i_t will be given by

$$i_t = \frac{I}{S_t} \qquad [29]$$

Now I is equal to $i_1 \times S_o$, *i.e.*, the product of the applied current density (relative to a film-free surface) and the original surface area of the film-free metal. Since S_t is given by Eq. [28], we can write for i_t

$$i_t = \frac{i_1 S_o}{S_o - (3/2N^{1/2}\pi^{1/2}k_1 i_1 t)^{2/3}} \qquad [30]$$

or, substituting for S_o from Eq. [14]

$$i_t = \frac{i_1}{1 - (t/\tau)^{2/3}} \qquad [31]$$

with $\tau \propto 1/i_1^2$ we also have

$$i_t = \frac{i_1}{1 - (Ki_1^2 t)^{2/3}} \qquad [32]$$

Equation [32] shows that as a consequence of progressive Cu_2O film formation the actual current density is dependent on both the magnitude of the applied current density and the time from the commencement of Cu_2O nucleation.

Using Eq. [24] and [31], it is now possible to derive a theoretical relationship between the overpotential η and the time t. From Eq. [24] we have at low overpotentials (<20 mV)

$$\eta = \frac{RT}{F}\frac{i_1}{i_o} \qquad [33]$$

Consequently, the change in the overpotential with time follows the same profile as the current density, which is given by Eq. [31]. Thus, letting $i = i_t$ in Eq. [31] we obtain

$$\eta = \frac{RT}{F}\frac{i}{i_o}\left(\frac{1}{1 - (t/\tau)^{2/3}}\right) \qquad [34]$$

Using a simple curve-fitting procedure (21), the curve predicted by Eq. [34] was compared with the experimentally recorded E-t curves. It was found that Eq. [34] gave an exceptionally good description of the rise in electrode potential with time recorded in 0.1M sodium hydroxide at 120 μA/cm² (τ = 111 sec) [see Fig. 12(b)]. At lower current densities in the same solution, the agreement was not quite as good mainly due to the influence of nucleation and the accompanying anodic potential overshoot [see Fig. 12(a)]. As shown in Fig. 13 and 14, an equally satisfactory correspondence with Eq. [34] was also observed in 0.01M sodium hydroxide and in the higher current density experiments in 1M solutions. A significant divergence of the experimental curves from the theoretical E-t profiles as t approached τ that was occasion-

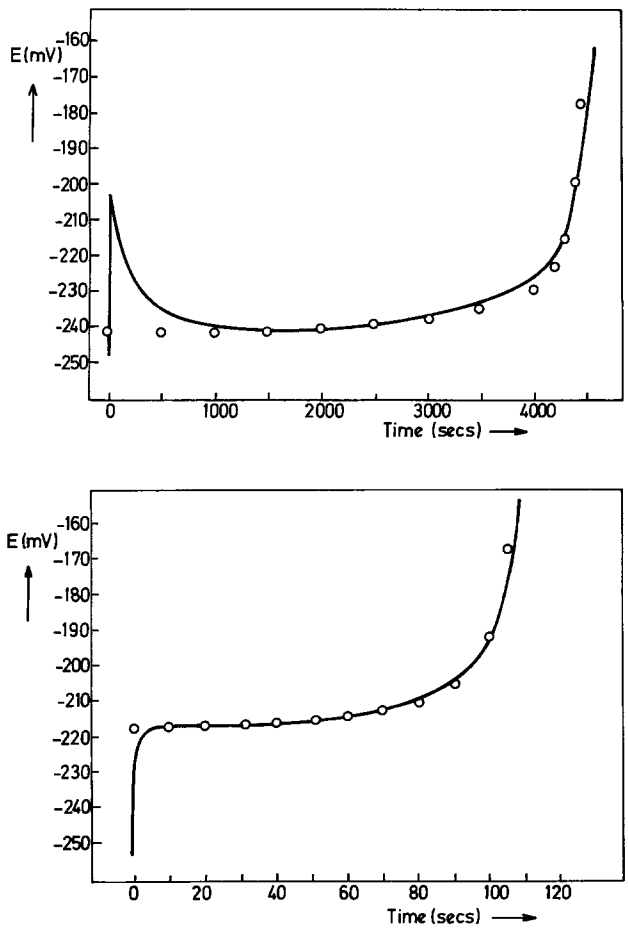


Fig. 12. A comparison of experimental and theoretical *E-t* curves in 0.1M NaOH: ○ theoretical points, — experimental curve; (a) 25 $\mu A/cm^2$, $\tau = 4560$ sec; (b) 120 $\mu A/cm^2$, $\tau = 111$ sec.

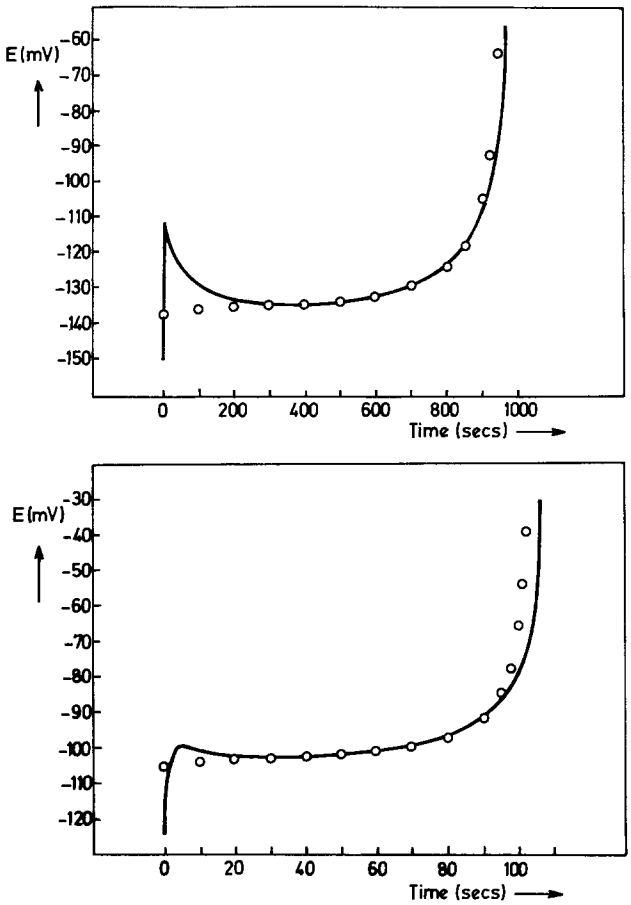


Fig. 13. A comparison of experimental and theoretical *E-t* curves in 0.01M NaOH: ○ theoretical points, — experimental curve; (a) 12.9 $\mu A/cm^2$, $\tau = 972$ sec; (b) 45.5 $\mu A/cm^2$, $\tau = 105$ sec.

ally observed is attributed to two main factors. First, Eq. [34] was derived for overpotentials of below 20 mV. From the experimental results η must necessarily have exceeded this limit as t approached τ. Second, with the very thick films formed at low current densities in 0.1 and 1M solutions, some contribution to the reaction rate from the slow diffusion of the solution species is anticipated at $t \rightarrow \tau$. Nevertheless the excellent agreement between the predicted and the determined curves provides further evidence for the role of charge transfer as the rate-determining step in the reaction which leads to film formation.

High current densities.—As shown in Fig. 10, the linear relationship between the arrest potential and the applied current density broke down in 0.01 and 0.1M sodium hydroxide solutions at current densities greater than 45.5 and 201 $\mu A/cm^2$, respectively. Correspondingly, it was found that above these limits the observed rapid rise in electrode potential with time during Cu_2O formation could not be represented by Eq. [34]. Here the experimental curves were very similar to those derived theoretically by Meyer and his collaborators (31) (Fig. 15) for the anodic formation of a thin film under conditions of rate control by the slow mass transport of a single reacting species. For comparison, the anodic *E-t* curves recorded in this work at 227 $\mu A/cm^2$ in 0.01M and 399 $\mu A/cm^2$ in 0.1M sodium hydroxide have been reproduced in Fig. 16. Both these experimental curves have τ values of 7.9 sec and it is evident from Fig. 16 that they have almost identical profiles. Implicit in Meyer's derivations was the assumption that the growing anodic film in no way affects the rate of electrochemical reaction at the metal-solution interface. In view of the relatively large quantities of Cu_2O formed here and the morphological characteristics of the films (see the electron micrographs of Fig. 5-9), this assumption cannot be applied with any degree of satisfaction here.

At large overpotentials (>60 mV), the second term in the Butler-Volmer equation (Eq. [23]) is negligible compared to the first. Thus, considering only the first term of Eq. [23] and rearranging we obtain

$$\eta = \frac{2.3RT}{(1-\beta)\mathbf{F}} \log_{10} \frac{i}{i_o} \qquad [35]$$

Allowing $i = i_t$ and substituting for i_t from Eq. [31], Eq. [35] becomes

$$\eta = \frac{2.3RT}{(1-\beta)\mathbf{F}} \left\{ \log_{10} \frac{1}{1-(t/\tau)^{2/3}} + \log_{10} \frac{i_l}{i_o} \right\} \qquad [36]$$

i.e.

$$\eta = 0.096 \left\{ \log_{10} \frac{1}{1-(t/\tau)^{2/3}} + \log_{10} \frac{i_l}{i_o} \right\} \qquad [37]$$

The theoretical curves corresponding to i_l/i_o ratios of 1, 5, and 10 and described by Eq. [37] are shown in Fig. 17. It is clear that these curves predicted by Eq. [37] differ very little from those derived theoretically by Meyer (31). Consequently, it is no simple task to decide which of two possible mechanisms of rate control is operating by a direct comparison of the profiles of the experimental curves with those predicted by the theory appropriate to either mechanism. However, it has been shown previously that a nucleation and growth mechanism of film formation in which the number of instantaneously formed nuclei is directly proportional to the square of the applied current density can give rise to the observed i_l *vs.* $\tau^{-1/2}$ relationship. Further, at low current densities the dependence of the arrest potential upon the applied current density is consistent with a model involving a charge transfer rate-determining step. Finally, and most important, in direct contrast with the mathematical treatment of dif-

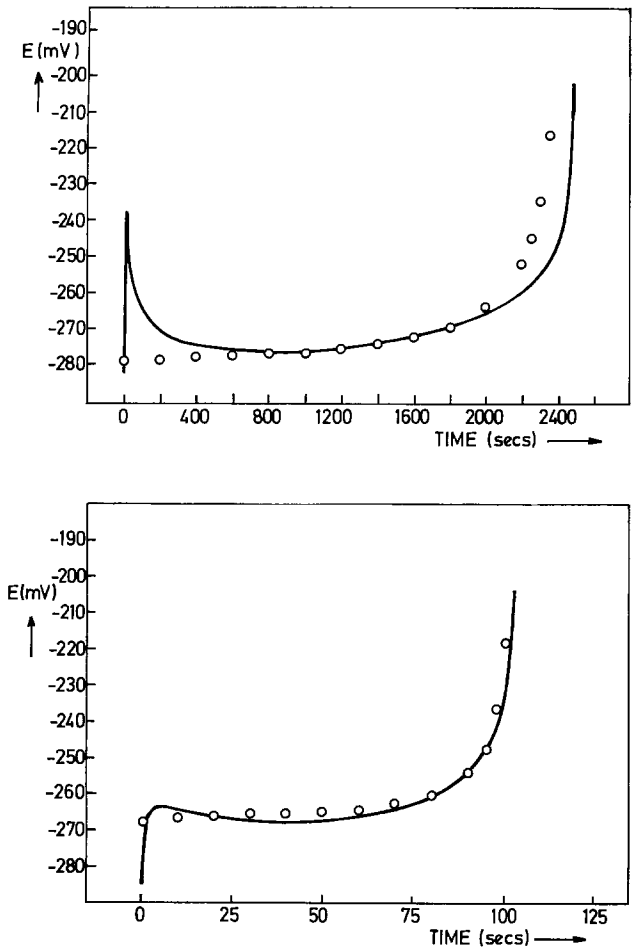


Fig. 14. A comparison of experimental and theoretical *E-t* curves in 1M NaOH: ○ theoretical points, — experimental curve; (a) 91.1 μA/cm^2, τ = 2478 sec; (b) 305 μA/cm^2, τ = 103.5 sec.

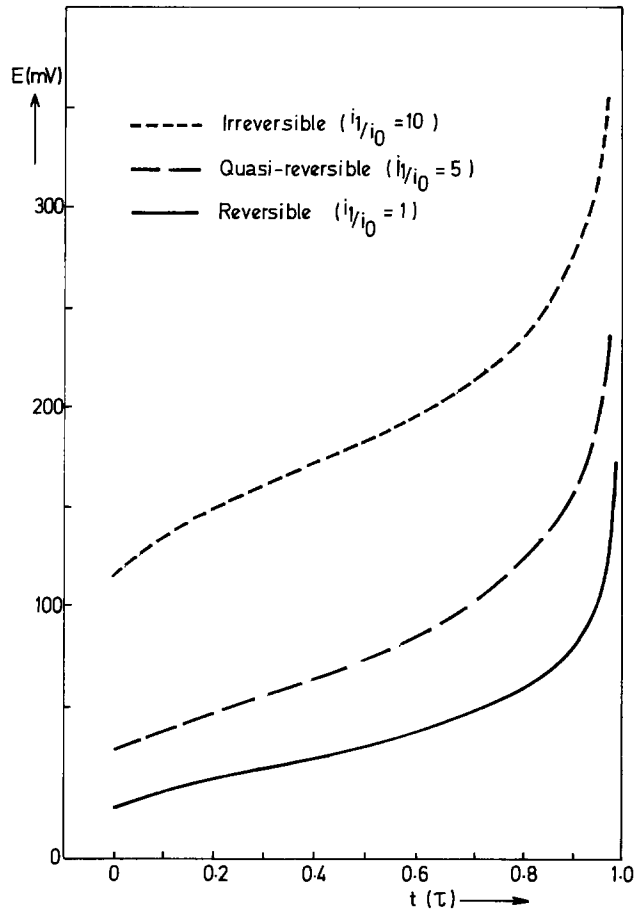


Fig. 15. Theoretical chronopotentiometric curves for rate control by diffusion [after Meyer (31)].

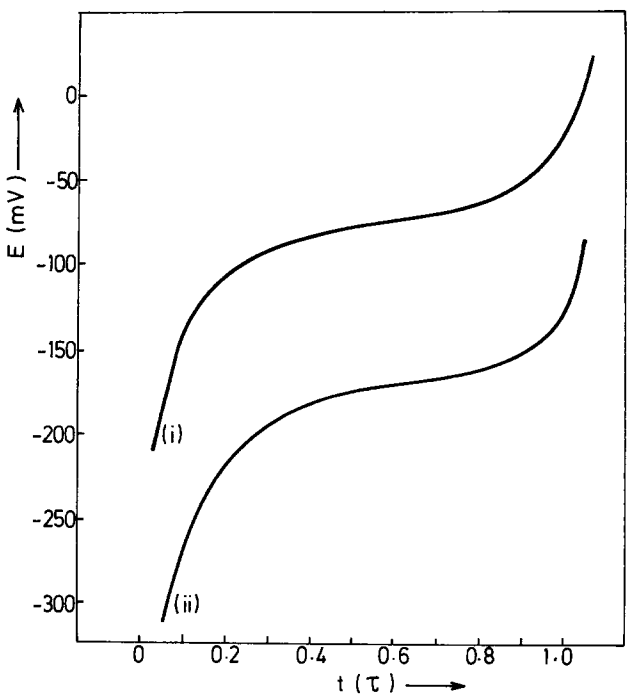


Fig. 16. Anodic polarization curves at high current densities: (i) 0.01M NaOH, 227 μA/cm^2, τ = 7.8 sec, (ii) 0.1M NaOH, 399 μA/cm^2, τ = 7.8 sec.

fusion control, the model proposed here does not disregard the effect of the progressive buildup of reaction product on the rate of electrochemical reaction at the metal-solution interface. Indeed, it is this which indirectly determines the *E-t* curve profiles. It is therefore considered that the *E-t* curve profiles recorded at high current densities in 0.01 and 0.1M sodium hydroxide solutions are more likely to arise from a slow charge transfer step in the over-all electrochemical dissolution-chemical precipitation mechanism of anodic Cu_2O film formation.

Conclusions

It has been found that the results obtained during the chronopotentiometric formation of Cu_2O upon a copper electrode in sodium hydroxide solutions are in good agreement with an electrochemical dissolution-chemical precipitation mechanism of film growth as follows

electrochemical dissolution

$$Cu + 2\,OH^- \rightarrow Cu(OH)_2^- + e$$

chemical precipitation

$$2Cu(OH)_2^- + 2H^+ \rightarrow Cu_2O + 3H_2O$$

The results suggest that it is the slow transfer of charge during the initial dissolution stage which governs the over-all reaction rate. Nuclei of Cu_2O form instantaneously and grow until the metal surface is entirely covered by the Cu_2O film; the transition time, τ then coincides with complete coverage of the metal surface. The observation of a direct i *vs.* $\tau^{-1/2}$ relationship during anodic film formation has on several previous occasions been taken as an indication of rate control by the slow mass transport of a solution species involved in the over-all electrode reaction. For a number of reasons which have been stated, this interpretation is inadequate. It has been shown that an i *vs.* $\tau^{-1/2}$ relationship will be observed if the number of instantaneously formed oxide nuclei is directly proportional to

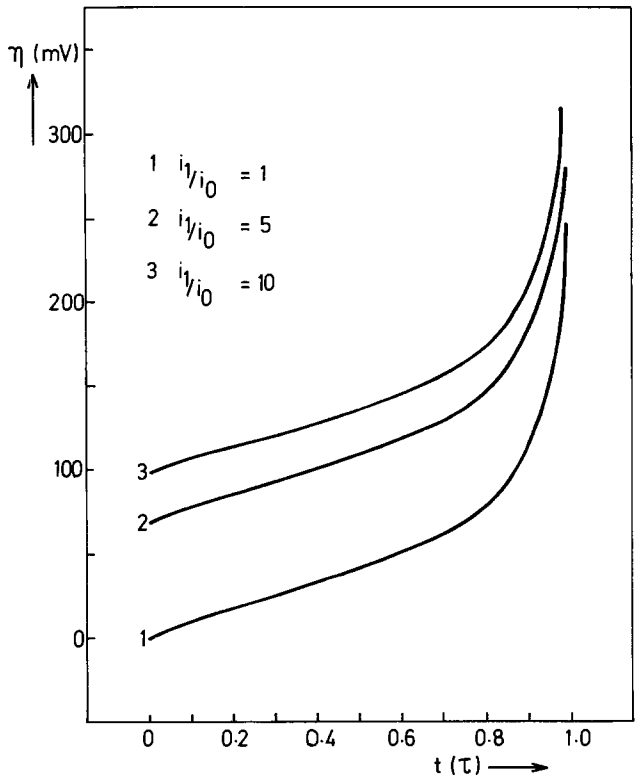


Fig. 17. Theoretical chronopotentiometric waves for a charge transfer controlled reaction at large overpotentials.

the square of the applied current density. Electron micrographs of chronopotentiometrically formed Cu_2O films lend support to this, a more plausible interpretation of the experimental results.

Acknowledgments

The authors wish to thank Professor G. C. Wood for provision of laboratory facilities. One of us (D.F.) is indebted to the Science Research Council for financial support.

Manuscript submitted Sept. 13, 1976; revised manuscript received Dec. 14, 1976.

Any discussion of this paper will appear in a Discussion Section to be published in the December 1977 JOURNAL. All discussions for the December 1977 Discussion Section should be submitted by Aug. 1, 1977.

LIST OF SYMBOLS

A	nucleation rate constant
C_x^i	interfacial concentration of species x
C_x^b	bulk concentration of species x
D_x	diffusion coefficient of species x
E	electrode potential
$\mathbf{F}$	Faraday's constant
I	applied current
i	current density
i_l	applied current density
i_o	exchange current density
i_t	current density at exposed metal surface
K, k, k_1, k_2, k_a	various constants
N	number of instantaneously formed nuclei
N_o	number of nucleation sites
n	number of electrons involved in electrochemical reaction
R	gas constant
r	radius of the nuclei
S_o	total surface area of film-free metal
S_f	area of surface covered by film after time t
S_t	area of surface free of film after time t
T	temperature
t	time
V	total volume of oxide at time t
β	symmetry factor
η	overpotential
σ	surface free energy of nucleus
τ	transition time

REFERENCES

1. W. Feitknecht and H. W. Lenel, *Helv. Chim. Acta*, **27**, 775 (1944).
2. A. Hickling and D. Taylor, *Trans. Faraday Soc.*, **44** 262 (1948).
3. L. de Broukere and F. Bouillon Nyssen, *Bull. Soc. Chim. Belg.*, **60**, 26 (1951).
4. S. E. S. El Wakkad and S. H. Emara, *J. Chem. Soc.*, **1953**, 3508.
5. J. S. Halliday, *Trans. Faraday Soc.*, **50**, 171 (1954).
6. R. W. Ohse, *Z. Phys. Chem. (N.F.)*, **21**, 406 (1959).
7. A. M. Shams El Din and A. El Wahab, *Electrochim. Acta*, **9**, 113 (1964).
8. V. A. Plokhov and V. N. Flerov, *Z. Priklad. Khim.*, **40**, 325 (1967).
9. S. Ya. Lanina and Z. A. Iofa, *Electrokhimya*, **5** (3), 359 (1969).
10. B. Miller, *This Journal*, **116**, 1675 (1969).
11. M. J. Dignam and D. B. Gibbs, *Can. J. Chem.*, **48**, 1242 (1970).
12. H. P. Leckie, *This Journal*, **117**, 1478 (1970).
13. N. A. Hampson, J. B. Lee, and K. I. McDonald, *J. Electroanal. Chem.*, **32**, 165 (1971).
14. J. Ambrose, R. G. Barradas, and D. W. Shoesmith, *ibid.*, **47**, 47, 65 (1973).
15. G. Rozovskis, *Liet. T S R Mokslu Akad. Darb. Ser. B*, **1963**, 19: *ibid.*, **1964**, 25.
16. M. Pourbaix, "The Atlas of Electrochemical Equilibria in Aqueous Solutions," chap. 29, section 29H, Pergamon Press, Oxford (1966).
17. W. F. Linke, "Solubilities, Inorganic and Metal Organic Compounds," Van Nostrand, New York (1958).
18. T. Yoshimura, Y. Imanaka, and M. Yamashita, *Chem. Abstr.*, **81**, 20085g (1974).
19. R. W. Powers, *Electrochem. Technol.*, **2**, 274 (1964).
20. G. L. Kehl, "The Principles of Metalographic Laboratory Practice," 3rd ed, McGraw-Hill, New York (1949).
21. D. Fairhurst, Ph.D. Thesis, University of Manchester, Manchester, England (1975).
22. V. E. Coslett, "Practical Electron Microscopy" Butterworth, London (1951).
23. R. H. Lambert and D. Trevoy, *This Journal*, **105**, 18 (1958).
24. V. A. P'Yovkov and A. P. Kostyuk, *Met. Abst.*, **30**, 386 (1963).
25. P. Bos and E. van Dalen, *J. Electroanal. Chem.*, **45**, 165 (1973).
26. C. D. Russell and J. M. Petersen, *ibid.*, **35**, 467 (1963).
27. D. A. Vermilyea, in "Advances in Electrochemistry and Electrochemical Engineering," Vol. 3, P. Delahay and C. W. Tobias, Editors, chap. 4, John Wiley & Sons, New York (1963).
28. National Research Council, "International Critical Tables" (1929).
29. P. Delahay, "New Instrumental Methods in Electrochemistry," John Wiley & Sons, New York (1954).
30. S. Khalafella *et al.*, *J. Phys. Chem.*, **62**, 1307 (1958); *ibid.*, **63**, 1252 (1959); *ibid.*, **65**, 1484 (1961).
31. R. E. Meyer, F. A. Posey, and P. M. Lantz, *J. Electroanal. Chem.*, **19**, 99 (1968).
32. M. C. Banta, R. E. Meyer, and F. A. Posey, *ibid.*, **47**, 223 (1973).
33. M. Fleischmann and H. R. Thirsk, in "Advances in Electrochemistry and Electrochemical Engineering" Vol. 3, P. Delahay and C. W. Tobias, Editors, chap. 3, John Wiley & Sons, New York (1963).
34. M. Fleischmann, H. R. Thirsk, and I. M. Tordesillas, *Trans. Faraday Soc.*, **58**, 1865 (1962).
35. G. T. Miller *et al.*, *This Journal*, **106**, 854 (1959); *ibid.*, **113**, 415, 421, 528, 883 (1966).
36. J. O'M. Bockris and D. Drazic, "Electrochemical Science," chap. 3, John Wiley & Sons, New York (1972).
37. N. Tanaka and R. Tamamushi, *Electrochim. Acta*, **9**, 965 (1964).
38. C. P. Kim and K. Nobe, *Corrosion*, **27**, 382 (1971).

Variational Approximations to Current Distribution Problems

The Rotating Disk Electrode

S. H. Glarum

Bell Laboratories, Murray Hill, New Jersey 07974

ABSTRACT

A variational function for electrolytic cells of arbitrary geometries and overpotential functions is presented, and low order approximations for the rotating disk electrode (RDE) are examined. A simple analytical solution for the total RDE current exists when the overpotential function is linear, and is used in the analysis of time-dependent boundary condition problems. Nonlinear overpotential functions may often be effectively linearized, leading again to analytical solutions. The influence of periodic reverse plating on the mean current distribution is analyzed in this approximation.

The determination of current distributions in electrolytic cells remains one of the pivotal problems of electrochemical technology. It demands the solution of Laplace's equation within arbitrary volumes with arbitrary, and generally nonlinear, boundary conditions. Analytical solutions of primary current distributions (fixed boundary conditions) are possible for those geometries amenable to conformal or imaging transformations to simpler configurations (1-3). Analytic techniques have been suggested for situations in which boundary conditions are linear, but few solutions are available (2, 4). The development of numerical computational techniques utilizing high speed computers currently makes possible the solution of specific problems but, because of the large number of parameters entering into such calculations, specific solutions are necessarily limited in their application (5). The developing interest in problems with time-dependent boundary conditions further complicates numerical procedures.

In other areas of science and engineering, variational analysis has provided a powerful tool for seeking approximate solutions to complex problems. Although the applicability of variational analysis to current distribution problems is recognized, it is doubtful that the power of this technique has been adequately exploited (6). Certainly a major virtue of the variational approach is its ability to yield a first-order solution with a modicum of effort, and to improve systematically this approximate solution by passing to more involved calculations.

The rotating disk electrode (RDE) is presently one of the more useful tools for the study in the laboratory of metal deposition phenomena. Its properties reflect not only the microscopic aspects of this process, but also the macroscopic effects of nonuniform current distributions and hydrodynamic flow. Although the latter effects are sometimes considered a hindrance, limiting the usefulness of the RDE, they should be realistically viewed as an advantage, making possible controlled studies of the combined effects of microscopic and macroscopic processes, provided one can easily determine their interaction and unravel their influence upon experiments.

It is the intent of this paper to demonstrate the use of variational analysis for the study of current distributions in electrolytic cells by considering its specific application to the RDE. Although the geometry of this system is trivial in the sense that the mathematics reduce to a one-dimensional problem, we believe the analytic simplicity of the results derived is of value to users of the RDE, and the approach is strongly suggestive of procedures by which more difficult problems may be attacked. Numerical solutions to a variety of RDE problems have been presented by Newman and colleagues and afford a basis for judging the accuracy of variational approximations (7-11). It should be clear that our purpose is not to find approximate answers to problems already adequately solved, but to explore the usefulness of approximate solutions in analyzing current distribution problems.

Key words: variational analysis, current distributions, rotating disk electrodes.

A Variational Function

Let us examine the function

$$W(\phi) = \kappa \int_\tau d\tau\, \underline{\nabla}\phi \cdot \underline{\nabla}\phi + 2\int_s ds\, f(s) \int_0^{\phi_0(s)-\phi} d\theta\, F(\theta) \qquad [1]$$

where the first integral extends over a volume τ enclosed by the surface s. The functions $\phi_0(s)$, $f(s)$, and $F(\theta)$ are assumed given, κ is a constant, and ϕ is an arbitrary function of τ. Taking the first variation with respect to ϕ yields

$$\delta W = -2\kappa \int d\tau\, \delta\phi \nabla^2\phi + 2\int ds \left[\kappa \frac{\partial \phi}{\partial n} - f(s)\, F(\phi_0 - \phi) \right] \delta\phi \qquad [2]$$

where $\partial/\partial n$ denotes a derivative with respect to the outward normal at the surface. The condition that W be stationary for arbitrary variations in ϕ thus requires

$$\nabla^2\phi = 0 \qquad \text{in } \tau$$

$$\mathcal{I}(s) \equiv \kappa \frac{\partial \phi}{\partial n} = f(s)\, F(\phi_0 - \phi) \qquad \text{on } s \qquad [3]$$

Taking ϕ to be the potential and κ the bulk conductivity the latter expression then defines the current density, $\mathcal{I}(s)$, on the surface. When applied to the electrolytic cell, it is evident that $f(s)$ vanishes on insulating portions of the bounding surface, that it reflects the concentrations of electroactive species on the electrode surfaces, and that $F(\theta)$ is an overpotential function. In a complete solution $f(s)$ is dependent upon the particulars of mass transport and the current distribution, and a general procedure requires iterative calculations, first assuming an approximate $f(s)$, determining ϕ variationally, recalculating $f(s)$, etc.

For linear boundary conditions, $F(\theta) \propto \theta$, the stationary value of W becomes

$$W_s = \kappa \int ds\, \phi_0(s) \frac{\partial \phi_s}{\partial n} \qquad [4]$$

and the total energy dissipation in the combined sur-

face-volume system is stationary (actually a minimum) for the specified $f(s)$. In particular, for a two-electrode system the total electrode current is a minimum. In problems where linear boundary conditions exist, variational calculations should be especially helpful in determining this most often measured experimental parameter. The accuracy in determining the total current at a given level of approximation will significantly exceed that of the current distribution itself.

When boundary conditions are nonlinear and mass transport effects are important, the total current is no longer a minimum. One may often, nevertheless, linearize these effects in an initial approximation and obtain useful results. Variational analysis remains applicable under all circumstances, but the procedure is certainly more demanding when linearization is inadequate.

The RDE Variational Function

Levich and Newman have derived basis functions appropriate for the RDE (6, 7). For purposes of completeness and definition, we shall here summarize their derivations and introduce this functional set into the variational equation. The RDE consists of a circular electrode, radius r_o, flushly imbedded in an infinite insulating mantle. The exposed half-space is filled with electrolyte, and the potential in this space vanishes as r and z (cylindrical coordinates) become infinite. With the transformation to coordinates ξ and η defined by

$$z = r_o\xi\eta$$
$$r^2 = r_o^2(1 + \xi^2)(1 - \eta^2) \quad [5]$$

the Laplacian is separable, yielding

$$\frac{\partial}{\partial\eta}(1-\eta^2)\frac{\partial F_l(\eta)}{\partial\eta} = -l(l+1) = -\frac{\partial}{\partial\xi}(1+\xi^2)\frac{\partial G_l(\xi)}{\partial\xi} \quad [6]$$

where

$$\phi_l = F_l(\eta)G_l(\xi) \quad [7]$$

These differential equations are recognized as those of Legendre, and a particular solution for ϕ is of the form

$$\phi = [AP_l(\eta) + BQ_l(\eta)][CP_l(-i\xi) + DQ_l(-i\xi)] \quad [8]$$

where P_l and Q_l are Legendre functions of the first and second kinds. For ϕ to be well behaved as $\eta \to 1$ and vanish as $\xi \to \infty$ requires $B = C = 0$, while the boundary condition upon the insulating mantle is fully satisfied if l is restricted to positive even integers or zero. A general solution to the potential distribution for the RDE is therefore

$$\phi = \sum_l{}' a_l P_l(\eta) Q_l(-i\xi) \quad [9]$$

where the summation prime indicates that l is restricted to the values 0, 2, 4. 6, ... This function satisfies the conditions that $\nabla^2\phi = 0$ in τ and $\partial\phi/\partial n = 0$ on the mantle. The coefficients a_l can only be found when the remaining boundary conditions on the electrode are known.

At the electrode surface ($\xi = 0$)

$$\phi = \sum_l{}' c_l P_l(\eta)$$
$$\frac{\partial\phi}{\partial n} = -(r_o\eta)^{-1}\left(\frac{\partial\phi}{\partial\xi}\right)_{\xi=0} = (2/\pi r_o\eta)\sum_l{}' c_l[P_l(0)]^{-2}P_l(\eta) \quad [10]$$

where

$$c_l = (i\pi/2)P_l(0)a_l = (2l+1)\int_0^1 d\eta\,\phi(\eta)P_l(\eta) \quad [11]$$

and the value for $Q_l(-0i)$ has been introduced.

Substitution into the variational function finally yields

$$W = 4\kappa r_o\sum_l{}'(2l+1)\left\{\int_0^1 d\eta[P_l(\eta)/P_l(0)]\phi(\eta)\right\}^2 + 4\pi r_o^2\int_0^1\eta d\eta\, f(\eta)\int_0^{\phi_o-\phi(\eta)} d\theta\, F(\theta) \quad [12]$$

In this expression ϕ is an arbitrary function, and solution of the RDE problem reduces to finding that ϕ which minimizes W, given $f(\eta)$, $F(\theta)$, and ϕ_o. The total electrode current

$$I = 2\pi\kappa r_o^2\int_0^1\eta d\eta\frac{\partial\phi}{\partial n} \quad [13]$$

is more conveniently given by

$$I = 4\kappa r_o\int_0^1 d\eta\,\phi(\eta) \quad [14]$$

Linear Solutions

RDE solutions to problems with linear boundary conditions, *i.e.*

$$f(\eta)F(\theta) = \theta/z \quad [15]$$

z being the normalized surface impedance, are readily handled variationally, and are of especial importance in that convenient analytical expressions can be derived to achieve any reasonable degree of accuracy. A natural choice for ϕ is

$$\phi(\eta) = \sum_l{}' c_l P_l(\eta) \quad [16]$$

in which case

$$I = 4\kappa r_o c_0 \quad [17]$$

Substitution of this expansion, together with the linear boundary value condition, into Eq. [12], followed by setting $\partial W/\partial c_l = 0$, gives the set of linear equations

$$g_l\Gamma c_l + \sum_{l'}{}' K_{ll'}c_{l'} = K_{0l}\phi_o \quad [18]$$

where

$$g_l = [2(2l+1)P_l(0)^2]^{-1} \quad [19]$$
$$K_{ll'} = \int_0^1\eta d\eta\, P_l(\eta)P_{l'}(\eta)$$

and

$$\Gamma = 4\kappa z/\pi r_o = (z/\pi r_o^2)/(4\kappa r_o)^{-1} = Z/R_\infty \quad [20]$$

Z is the total impedance associated with the electrode surface and R_∞ is the high frequency or primary resistance of the cell. The parameter Γ is thus the reciprocal of ρ as defined by Albery and Hitchman, or equal to $(4/\pi J)$ in Newman's notation (7, 12). The convention adopted here simplifies the form of following expressions.

Clearly the ratio I/ϕ_o is constant for this problem and we may define a total cell impedance

$$\begin{aligned} Z_{tot} \equiv \phi_o/I &= R_\infty|g_l\Gamma\delta_{ll'} + K_{ll'}|/|g_l\Gamma\delta_{ll'}(1-\delta_{l,0}) + K_{ll'}| \\ &= R_\infty + Z\,g_0|g_l\Gamma\delta_{ll'} + K_{ll'}|'/|g_l\Gamma\delta_{ll'}(1-\delta_{l,0}) + K_{ll'}| \\ &= R_\infty + Z_{eff} \end{aligned} \quad [21]$$

where the prime on the determinant indicates that l and l' are restricted to values 2, 4, 6, ... Both determinants yield polynomials of the same degree in Γ, and in the limit $\Gamma \to \infty$, $Z_{eff} \to Z$. The ratio for Z_{eff} may be rewritten as

$$Z_{eff} = Z\left[1 + \sum_i\frac{\alpha_i}{1+\Gamma\beta_i}\right] \quad [22]$$

Solutions for α and β may be found from the roots, Γ_i, of the determinantal equation

$$|g_l\Gamma\delta_{ll'} + K_{ll'} - 2K_{ol}K_{ol'}|' = 0 \quad [23]$$

Thus

$$\beta_i = 1/\Gamma_i$$
$$\alpha_i = \frac{-|g_l\Gamma_i\delta_{ll'} + K_{ll'}|'}{\Gamma_i(\prod_{l\neq 0} g_l)\prod_{j\neq i}(\Gamma_i - \Gamma_j)} \quad [24]$$

The order of solution is equivalent to the number of roots found. In a trivial first approximation $(\alpha, \beta) = (1/3, 64/15)$. For second and third approximations $(\alpha, \beta) = (0.1250, 3.251)$, $(0.4083, 9.752)$ and $(0.1197, 3.238)$, $(0.1053, 5.978)$, $(0.4511, 17.330)$, respectively.

In a finite approximation, truncation of this series gives a constant limiting value as $\Gamma \to 0$. In fact, the sum diverges logarithmically. A practical lower limit to the useful range of Γ for a particular order of approximation is set by its smallest root. For the first three orders of approximation this is equivalent to the condition that no more than 77, 90, or 94% of the monitored potential drop occurs within the electrolyte.

The difficulties encountered as $\Gamma \to 0$ occur because the current distribution approaches the primary distribution, with a singularity at the electrode's edge, and its representation by a low order polynomial is inadequate. Newman has discussed this difficulty when the surface impedance is capacitive (8). We can estimate the asymptotic behavior of Z_{eff}/Z as $\Gamma \to 0$ by supposing

$$1 + \sum_i \frac{\alpha_i}{1 + \Gamma\beta_i} = -\frac{1}{4}\ln\Gamma + A + B(\Gamma)^{1/2} + C\Gamma + D(\Gamma)^{3/2} + \ldots \quad [25]$$

The left-hand expression is valid when Γ is large, while the right-hand side is correct for small Γ. The logarithmic term and the expansion in $\sqrt{\Gamma}$ are suggested by Newman's analysis. We assume that both series converge in the vicinity of some intermediate value. From a comparison of derivatives in this region one can then deduce $A, B, C, \ldots$. As the accuracy of the left-hand side improves, the range of Γ broadens, and $A, B, C, \ldots$ become insensitive to the choice of Γ. When the third-order expansion is employed, the coefficients are stationary for $\Gamma \simeq 0.6$, giving

$$-\frac{1}{4}\ln\Gamma + 0.562 + 0.637\,\Gamma^{1/2} - 0.138\,\Gamma + 0.008\,\Gamma^{3/2} \quad [26]$$

Newman's numerical calculation for the constant yields 0.623, when the factor of $4/\pi$ relating Γ to his variable is taken into account (8). A higher order solution is presumably required to achieve a more accurate set of coefficients. In the real world, when Γ is very small, the properties of electrolytic cells are sensitive to deviations from the assumed geometry, and precise expressions are more of theoretical than practical interest.

It should be duly noted that the system of linear equations here solved is equivalent to that used by Newman and later by Nisancioglu and Newman in studying frequency dispersion at the RDE (8, 9). Thus the coefficients β_i approach the eigenvalues $\pi\Lambda_i/4$ in the latter work as the order of approximation increases. We would emphasize, however, that Eq. [22] constitutes a general solution to all linear RDE problems. If Γ is frequency dependent, one can easily use this equation to find the behavior of the RDE, and the electrode's response in the time domain is given by a straightforward Fourier transform. It is apparent from the variational origin of our analysis that an approximate or truncated solution for Z_{eff} will always be less than its correct value when Γ is real.

Newman has solved these equations to high order for the case $\Gamma = i\omega CR_e\pi r_o^2$, where C is the double layer capacitance per unit area (8). Results are expressed in terms of an effective series resistance and capacitance, *i.e.*

$$Z_{tot} = R_{eff} + (i\omega\pi r_o^2 C_{eff})^{-1} \quad [27]$$

Our interest here is in examining the usefulness of low order approximations. Results are plotted in Fig. 1 and 2 for the first three orders of approximation and compared with Newman's calculations. Low order approximations appear sufficient for the interpretation of all but the most precise data. With a second-order approximation, the error in the effective capacitance is less than 4% in a region where the capacitive current itself is but 10% of the total current.

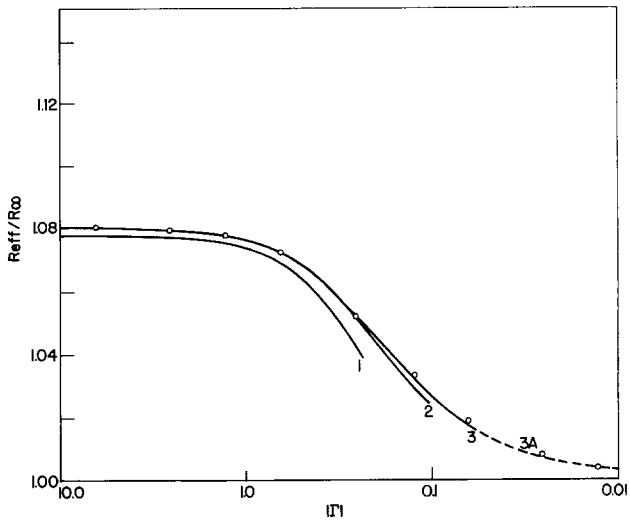


Fig. 1. Dispersion of effective series resistance for RDE calculated to first, second, and third order. Curve 3A is obtained from the low Γ asymptotic expansion. Exact values are indicated by circles.

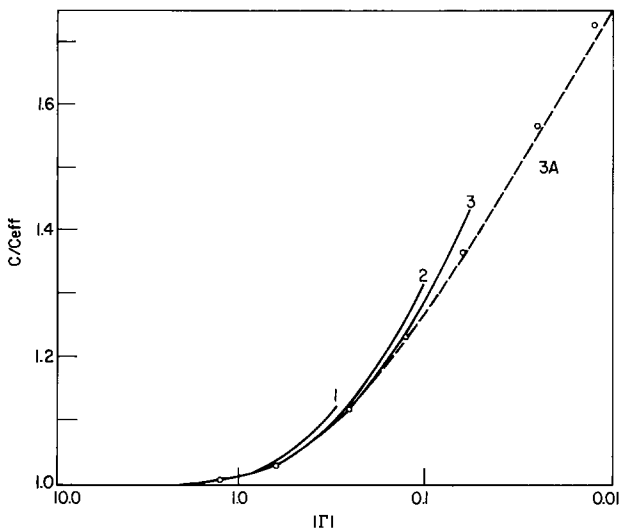


Fig. 2. Dispersion of effective series capacitance for RDE calculated to first, second, and third order. Curve 3A is obtained from the low Γ asymptotic expansion. Exact values are indicated by circles.

Complex plane plots are becoming a useful means for studying electrode reactions. The effects of nonuniform current distributions at the RDE on such measurements are readily gauged by letting

$$\Gamma = \Gamma_o/(1 + i\omega\tau) \quad [28]$$

Then, for a normalized dispersion

$$Z_{eff}/Z_o = (1 + i\omega\tau)^{-1} + \sum [\alpha_i/(1 + \Gamma_o\beta_i)][1 + i\omega\tau/(1 + \Gamma_o\beta_i)]^{-1} \quad [29]$$

In addition to the leading term for a uniform current distribution, a series of additional relaxation times appears. Actual plots are shown in Fig. 3. The major distortion introduced by these relaxations is an enlargement of the over-all dispersion, and a slight flattening of the plot when $\omega\tau > 1$. The maximum remains close to $\omega\tau = 1$. These observations apply even when

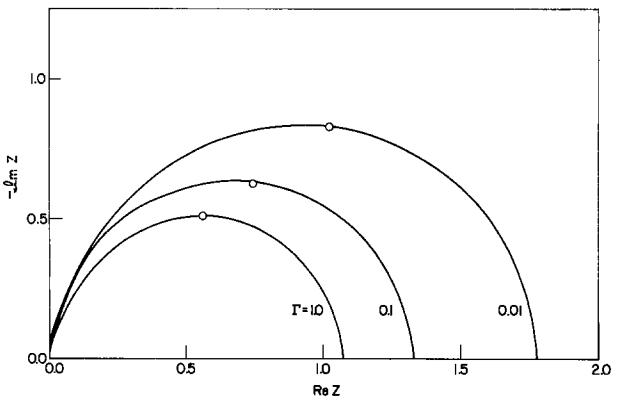


Fig. 3. Complex impedance plots for a simple double layer dispersion. Circles show points for $\omega\tau = 1$.

the asymptotic expansion ($\ln + A$) is used, as shown by the plot for $\Gamma = 0.01$. We may conclude that, at least for linear systems, qualitative interpretations of complex impedance plots obtained with the RDE are not seriously complicated by nonuniform current distributions. For the quantitative analysis of high frequency data, however, the use of Eq. [22] can prevent erroneous interpretations of high frequency dispersions.

Returning to Eq. [18], this set of equations may also be solved for c_l, and the current density distribution is then given by

$$\mathcal{I}(\eta) = (1/z)\left[\phi_0 - \sum\nolimits' c_l P_l(\eta)\right] \qquad [30]$$

Second-order approximations for current distributions are shown in Fig. 4. The agreement with exact results is adequate for $\Gamma > 0.5$ (7). Because of the variational basis for our analysis, it is to be expected that the current distribution will be given less accurately than the total current, and that the calculation weights most heavily those regions of the electrode where the current density is greatest. As $\Gamma \to 0$ the current density at the electrode's boundary becomes infinite, and its central area is of lesser importance. The apparent minimum seen when Γ is small is an artifact of trying to approximate a steeply rising function by a fourth-order polynomial.

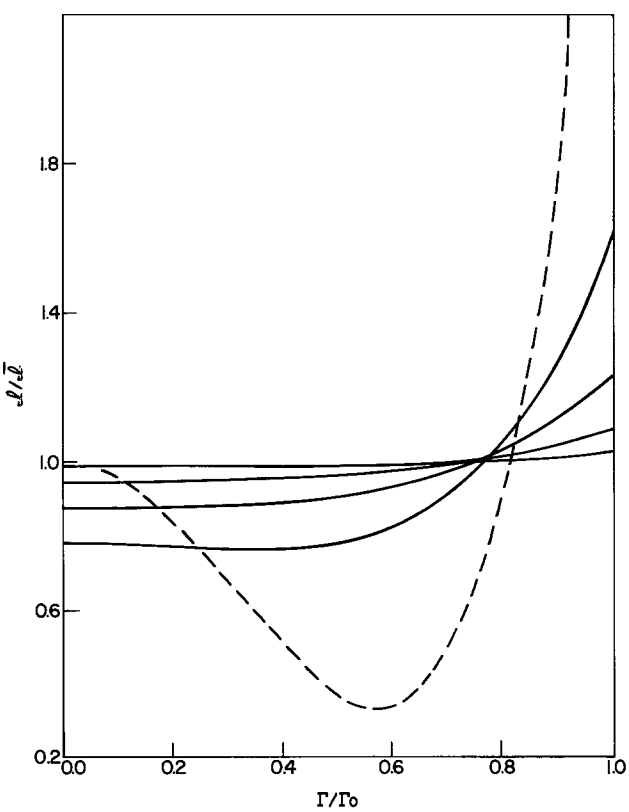


Fig. 4. RDE current distributions calculated to second order (quartic approximation) for linear polarization. Values for Γ are 10, 3, 1, 0.3, and 0.0, with uniformity increasing with Γ.

Alternating current distributions are of growing interest in electrodeposition studies. Qualitatively, one anticipates that at high frequencies the current distribution should become less uniform, approaching the primary distribution. If we let

$$1/z = (1/r) + i\omega C = (1/r)(1 + i\omega\tau)$$

$$\Gamma = \Gamma_0/(1 + i\omega\tau) \qquad [31]$$

assume faradaic current flows only through r, and use a first-order solution

$$\mathcal{I}_F = (1/r)\phi_0 e^{i\omega t}\Gamma \frac{64\Gamma + 30(1 - \eta^2)}{64\Gamma^2 + 84\Gamma + 15} \qquad [32]$$

For a linear system the time average $\mathcal{I}_F$ vanishes, and no influence upon the macroscopic aspects of electrodeposition would be expected. An a-c current may nevertheless have an influence, of currently unknown origin, upon the microscopic properties of an electrodeposit, and this calculation provides an estimate of the spatial uniformity of this influence. The modulus of $\mathcal{I}_F$ is readily found, and in Fig. 5 the ratio $\mathcal{I}_F(\eta = 1)/\mathcal{I}_F(\eta = 1/\sqrt{2})$ is plotted as a function of frequency. This ratio may be viewed as a measure of the uniformity of the a-c current distribution. As expected, this ratio increases with frequency, and the worse the initial distribution, the more rapidly nonuniformity rises.

Nonlinear Solutions

Let us choose as an expression for the potential

$$\phi = \sum\nolimits' c_l P_l(\eta) \qquad [33]$$

The condition that the variational function (Eq. [12]) be stationary with respect to variations in c_l is

$$\frac{4\kappa}{\pi r_0} g_l c_l - \int_0^1 \eta d\eta\, f(\eta)\, P_l(\eta)\, F(\phi_0 - \phi) = 0 \qquad [34]$$

When $F(\theta)$ is a general function, exact solutions can only be found by numerical integration. One can, however, linearize these expressions within a limited domain. Let us suppose that $\phi(\eta)$ is a slowly varying function over the electrode surface so that we may expand $F(\phi_0 - \phi)$ about a mean function $\bar{\phi}(\eta)$

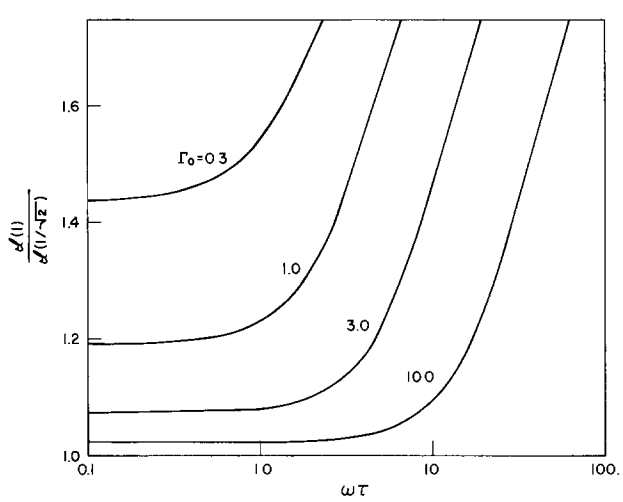


Fig. 5. Variation with frequency of the ratio of the current density at $r/r_0 = 1$ to that at $r/r_0 = 1/\sqrt{2}$ for linear a-c polarization.

$$F[\phi_o - \phi(\eta)] = F[\phi_o - \bar{\phi}(\eta)] - F'[\phi_o - \bar{\phi}(\eta)]\,\Delta\phi(\eta) \quad [35]$$

and let

$$\bar{\phi} = \sum_l{}' \bar{c}_l P_l(\eta)$$

$$\Delta\phi = \sum_l{}' \Delta c_l P_l(\eta) \quad [36]$$

For a first-order linearization

$$c_0 = \bar{c}_0 + \Delta c_0$$
$$c_l = \Delta c_l \qquad l \neq 0 \quad [37]$$

These substitutions then give ($f(\eta) = 1$)

$$\frac{4\kappa}{\pi r_o}\bar{c}_0 = F(\phi_o - \bar{c}_0)$$

$$\Gamma g_l c_l + \sum_{l'} c_{l'} K_{ll'} = K_{0l}(1 + \Gamma)\bar{c}_0 \quad [38]$$

where

$$\Gamma = 4\kappa/[\pi r_o F'(\phi_o - \bar{c}_0)] \quad [39]$$

The equations to be solved involve one nonlinear expression for $\bar{c}_0$, and a set of linear expressions equivalent to those encountered in our discussion of the linear boundary value problem. The differences are only that Γ is now a function of $\bar{c}_0$, and ϕ_o has been replaced by $(1 + \Gamma)\bar{c}_0$. As Eq. [17] for the total current still applies, using our previous solution to the linear problem we obtain

$$I_{TOT} = \pi r_o^2 F(\phi_o - \bar{c}_0)(1 + \Gamma)/\left[1 + \Gamma\left(1 + \sum \frac{\alpha_i}{1 + \Gamma\beta_i}\right)\right] \quad [40]$$

Formally, linearization may be carried to second order by solving parametric expressions for $\bar{c}_0$ and $\bar{c}_2$. The remaining linear equations are no longer those previously encountered, and, when first-order linearization is inadequate numerical procedures appear more appropriate.

A conventional nonlinear overpotential function is the exponential one

$$F(\theta) = i_o[\exp(\theta/\lambda) - \exp(-\theta/\lambda)] \quad [41]$$

where $\lambda \sim kT/e$. Calculated current-voltage curves are plotted logarithmically in Fig. 6 for various values of γ, where γ is given by

$$\Gamma = 2\gamma \exp[(\phi_o - \bar{c}_0)/\lambda] + \exp[-(\phi_o - c_0)/\lambda] \quad [42]$$

Thus γ is the value of Γ in the linear regime about $\phi_o = 0$. These plots are of little value in estimating Tafel parameters when $\gamma < 100$. From our discussion of linear solutions, however, it should be apparent that the major correction involves linear IR_∞ compensation. Applying such a correction shows that useful information can be extracted even when $\gamma = 1$ (Fig. 7).

Current distributions are found when the equations are solved for the coefficients c_l. It is easily shown that when the expanded overpotential function is employed

$$\mathcal{I}(\eta) = F(\phi_o - \bar{c}_0) - F'(\phi_o - \bar{c}_0)\sum_l \Delta c_l P_l(\eta) \quad [43]$$

one obtains a spatial distribution identical to that for the linear problem with the same Γ value. When this approximation suffices, Newman's numerical calculations for linear and Tafel polarization should coincide for equal values of his indexing parameter (7, 12). The similarity is striking.

As a better estimate we might instead evaluate

$$\mathcal{I}(\eta) = F\left[\phi_o - \sum_l c_l P_l(\eta)\right] \quad [44]$$

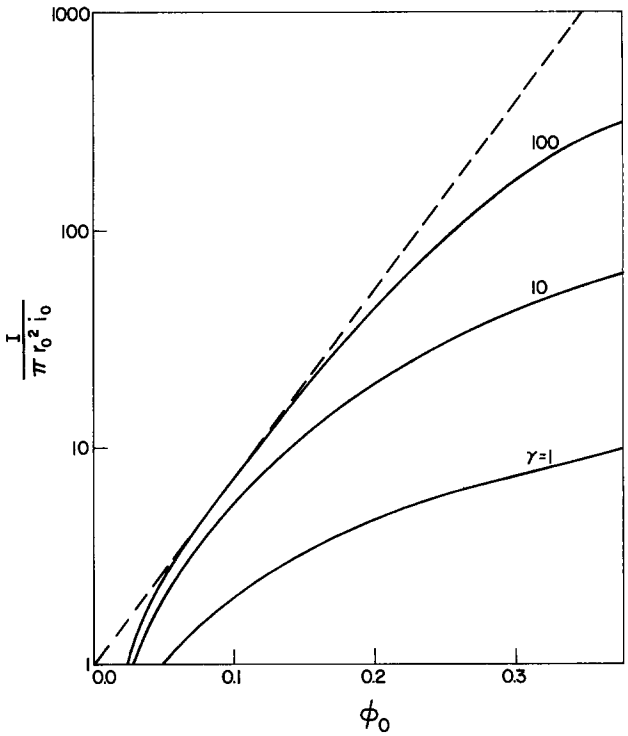


Fig. 6. Tafel plots for an exponential overpotential function with finite electrolyte conductivity. ($\lambda = 0.05$).

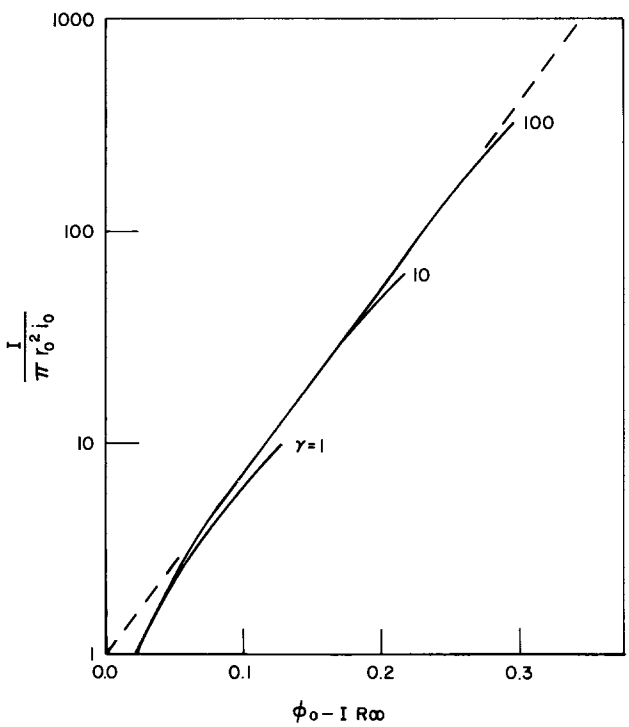


Fig. 7. The data of Fig. 6 replotted with an IR_∞ correction.

When a specific example is considered, say the point for $\phi_o = 0.2$V on the $\gamma = 1$ curve in Fig. 6 ($\Gamma = 0.386$), both functions give similar results differing by typically 3% for a second-order solution.

This analysis has useful implications for periodic reverse plating (13). In this process one plates out metal under conditions giving a nonuniform distribution. The current is then reversed, and a portion of the plated metal is removed. If the current distribution on the anodic portion of the cycle is less uniform than on the cathodic portion, macroleveling can be achieved. We have found that the distribution is determined by a parameter Γ which may be evaluated for each point

on a current-voltage curve. Therefore, if the value of Γ at the cathodic operating point is greater than its value at the anodic operating point, leveling occurs. If it is less, the resulting distribution will be less uniform than if no reversal had been employed. In the special case of a symmetric current-voltage curve for which Γ continually decreases as $|\phi|$ increases (Eq. [41]), the magnitude of the anodic potential must always exceed that of the cathodic potential to obtain a more uniform distribution of metal.

By way of illustration we shall take as a specific example cathodic deposition at a potential of -0.2V for $\gamma = 10$ with $F(\theta)$ given by Eq. [41]. The cathodic operating point may be found in Fig. 6. The anodic and cathodic periods are assumed to be sufficiently long that transient processes may be safely ignored. The anodic duty cycle is adjusted to give a constant mean current which is taken as 50% of the cathodic current. Current distributions are plotted in Fig. 8 for different anodic potentials, ϕ_a. When $0 < \phi_a < |\phi_c|$ periodic reversal leads to a less uniform deposit. For $\phi_a = 0.38$V one finds a uniform distribution, and for more anodic potentials the distribution is reversed.

In this example the current distribution is sufficiently uniform that a first-order approximation suffices. In more general instances multilevel anodic waveforms can be envisioned to suppress higher order terms. Chemistry sets a practical limit to periodic reversal. Its successful application requires rather large anodic potentials, and the chemistry which actually occurs in this region may be considerably different from that in the cathodic region. Only when one can anodically etch away deposited metal with no complications from metal oxide film formation does periodic reversal appear to be a viable technique for producing more uniform electrodeposits.

Discussion

The ease with which we have found solutions for the problems considered in the preceding sections testifies to the usefulness of variational analysis for the study of current distributions in electrolytic cells. The examples given required handling of only 2×2 or 3×3 determinants, and can be (and were) solved with a pocket calculator. A minor amount of computer time would obviously yield more exact answers.

The RDE is a particularly useful tool, both theoretically and experimentally, for the study of electrode processes and current distributions. Mathematically, it has a hydrogenic simplicity, while manifesting all the complications of "real" cells. When total electrode currents are measured, the stricture that meaningful results can be had when $\Gamma > 10$ is unduly severe (12). This limit can easily be extended by two orders of magnitude with minor corrections, because the total current in linear systems is a stationary quantity, and insensitive to first-order variations in the current distribution. For nonlinear systems this is not precisely true, but, barring pathological examples, the total current is still less sensitive to the current distribution than is the distribution itself. For linear problems an arbitrarily precise solution exists for the total current. This solution can be especially useful in analyzing time-dependent phenomena.

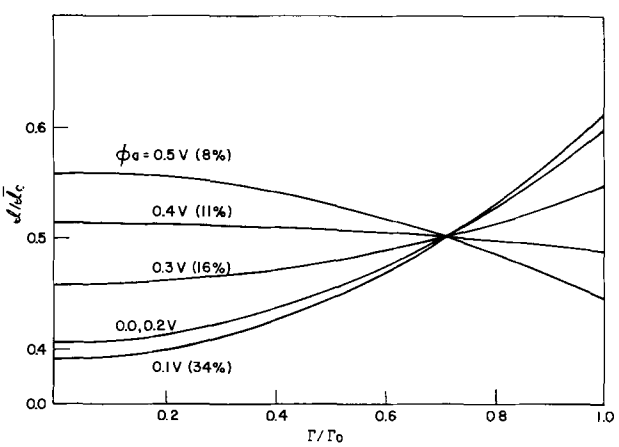


Fig. 8. Current density distributions calculated to first order for period reverse plating on a RDE. Anodic potentials and duty cycles are indicated on each curve. A symmetric exponential overpotential function is assumed, with cathodic deposition occurring at -0.2V.

Several RDE problems remain to be scrutinized in greater detail. We have not considered the influence of mass transport on current distributions, other than to indicate how it can be formally introduced into these problems. As an approximation one might neglect concentration correlations across the electrode, in which case a spatially independent $F(\theta)$ can be defined as a function of bulk concentration and hydrodynamic layer thickness. At no point could the current density exceed a defined limit, and a uniform distribution would imply a uniform potential outside the double layer. Neither consequence holds for an exact solution (7). Proper consideration of mass transport in RDE problems necessitates replacing the matrix elements K_{ll}, by

$$\sum_{l''} b_{l''} \int \eta d\eta \, P_l(\eta) \, P_{l'}(\eta) \, P_{l''}(\eta) \qquad [45]$$

where the coefficients $b_{l''}$ need be found by iterative procedures.

A second problem for analysis is the interaction of a-c and d-c current distributions in nonlinear systems. For quasi-static conditions our treatment of periodic reverse plating illustrates a limiting behavior. Frequency-dependent effects are more complex. A portion of the a-c current will be rectified, contributing to the d-c current. Both the a-c current distribution and its rectification efficiency will be spatially and frequency dependent. Proper solution requires expansion of $\Gamma(t)$, $\bar{c}_0(t)$, and $c_l(t)$ to second order when the a-c modulation is small and is beyond the scope of this presentation.

The determination of current distributions in real plating bath geometries can present greater difficulties. The art of variational analysis is in finding a tractable set of basis functions which closely approximate the real solution. It is obviously desirable, and not difficult, to find sets satisfying Laplace's equation. The variational equations then reduce to surface integrals.

A distinction is often drawn in the literature between primary and secondary current distributions. This nomenclature is perhaps unfortunate, for it bears the implication that the primary distribution must first be found before the real or secondary distribution can be deduced. The primary distribution possesses nontrivial singularities at edges and corners. Unless these singularities are carefully incorporated into variational functions, very high order approximations are necessary. This is evident from our discussion of linear solutions to the RDE as $\Gamma \to 0$. By contrast, in respectable plating baths these singularities are erased by electrode polarization, and the current distribution at edges and corners can be effectively described by variational functions which are not exact in these regions. The determination of secondary current distributions is thus a simpler problem than finding primary distributions (4).

There is no obvious reason to suppose that our conclusions regarding time-dependent effects on current distributions at the RDE are not also relevant to more general geometries. Thus, periodic reverse plating should only lead to more uniform macrodeposits when rather stringent requirements are met. The conditions under which time-dependent currents produce salubrious results on the microscale remain to be examined. These may not depend explicitly upon nonlinear proc-

esses, and a linear approximation can then be used to deduce the spatial distribution of microscopic changes.

Manuscript received Aug. 2, 1976.

Any discussion of this paper will appear in a Discussion Section to be published in the December 1977 JOURNAL. All discussions for the December 1977 Discussion Section should be submitted by Aug. 1, 1977.

Publication costs of this article were assisted by Bell Laboratories.

LIST OF SYMBOLS

A, B, C, D	linear coefficients
a_l, c_l	linear coefficients
F_l, G_l	see Eq. [7]
$F(\theta)$	overpotential function
$f(s)$	surface function
g_l	see Eq. [19]
I	total current
$\mathcal{I}(s)$	surface current density
$K_{ll'}$	see Eq. [19]
n	normal surface coordinate
P_l, Q_l	Legendre functions
R_∞	primary resistance
r_0	disk radius
r, z	cylindrical coordinates
s	surface coordinates
W	variational function
Z	surface impedance
z	normalized surface impedance (ohm-cm^2)
α_i, β_i	coefficients (Eq. [22])
Γ	see Eq. [20]
$\delta_{ll'}$	Kronecker delta function
η, ξ	see Eq. [5]
θ	overpotential parameter
κ	volume conductivity
τ	volume coordinate
ϕ	potential function

REFERENCES

1. J. Newman, "Electrochemical Systems," chap. 18, Prentice-Hall, Englewood Cliffs, N.J. (1973).
2. C. Kasper, *Trans. Electrochem. Soc.*, **77**, 353, 365 (1940); *ibid.*, **78**, 131, 147 (1940); *ibid.*, **82**, 153 (1942).
3. J. Newman, *This Journal*, **113**, 501 (1966).
4. C. Wagner, *ibid.*, **98**, 116 (1951).
5. J. A. Klingert, S. Lynn, and C. W. Tobias, *Electrochim. Acta*, **9**, 297 (1964).
6. V. G. Levich, "Physicochemical Hydrodynamics," section 49, Prentice-Hall, Englewood Cliffs, N.J. (1962).
7. J. Newman, *This Journal*, **113**, 1235 (1966).
8. J. Newman, *ibid.*, **117**, 198 (1970).
9. K. Nisancioglu and J. Newman, *ibid.*, **120**, 1339 (1973).
10. K. Nisancioglu and J. Newman, *ibid.*, **120**, 1356 (1973).
11. K. Nisancioglu and J. Newman, *ibid.*, **121**, 523 (1974).
12. W. J. Albery and M. L. Hitchman, "Ring-Disc Electrodes," chap. 4, Oxford University Press, Oxford (1971).
13. C. C. Wan, H. Y. Cheh, and H. B. Linford, *Plating*, **62**, 559 (1974).

Technical Notes

Observation of a Substructural Network in the Positive Plates of Lead-Acid Storage Batteries

J. Perkins and M. T. Coyle

Materials Science Group, Naval Postgraduate School, Monterey, California 93940

In terms of realizing capacity, most contemporary lead-acid batteries are positive limited, *i.e.*, reach a fully discharged state in a given cycle when the capacity of the positive plate is exhausted, while the negative plate at that point is not fully discharged. Furthermore, the positive plates typically realize only about 50% of their theoretical capacity, and are prone to a variety of deterioration modes during cyclic service. These facts are well known, and there has been considerable effort to improve the lead-acid system by means of analyses of the performance of the positive plate. Among these studies have been a number of investigations that have emphasized the importance of the microstructural features of the active material. The morphological state of the positive plate is of great importance, particularly with respect to mechanical stability of the active material mass and realization of capacity. The microstructure of lead-acid positive plates has been widely studied in the past utilizing cross-sectional optical microscopy (1, 2) and replica transmission electron microscopy (3-7). These studies have been reviewed by Burbank *et al.* (8) and Perkins (9). The present paper reports on the results of a detailed scanning electron microscopy investigation into the substructural evolution of positive plate microstructures. The results of the present investigation correlate with previous results by other microscopic methods, and add to the understanding of these microstructures and their significance.

Experimental

The observations reported here are based on cycling of laboratory lead-acid cells in a trickle-discharge routine. The cells were constructed from 12 cm square sections of standard full-size lead-calcium-grid submarine (TLX-39B) battery plates, received from Gould, Incorporated in the formed and dried condition. The cells were loaded for positive plate limitation, with two negative and one positive plate per cell, and a large electrolyte reservoir. Microporous rubber separators and fiberglass retainer mats were used. The cells were prepared and cycled in accordance with rather standard procedures for this type of lead-acid cell (10, 11). The cells were first filled with 1.255 specific gravity electrolyte, and prior to initial charge were allowed to stand for 15 hr in order to cool. An initial constant current (500 mA) charge was carried out for at least 65 hr and continued until cell voltage and specific gravity stabilized at 2.32-2.36 and 1.295-1.275, respectively. The trickle-discharge routine consisted of a full charge, trickle discharge at a rate of 50 mA for 96 hr, recharge

to full cell voltage, and a capacity test discharge at a nominal 3 hr rate of 4500 mA, terminated when cell voltage reached 1.6V. A constant potential charging method was utilized, according to standard procedures (11), with a 800 mA constant current finishing rate for these cells; limited overcharge was allowed.

At selected intervals, cells were removed from the cycling. The positive plates were carefully removed and washed, first by immersion for 5 min in cold tap water, then by rinsing with a gentle stream of water over each face. No mechanical cleaning or blotting was used. After washing, the plates were allowed to dry for 24 hr in an oven at 70°C. The plates were sectioned with a jeweler's saw and active material was selectively broken away from grid bars, or fractured through, or razor-cut wedge sections were removed. The samples were observed in a Cambridge S4-10 scanning electron microscope operated at 20 kV. No conductive coating was necessary for observation, and good resolution was obtained at magnifications up to 20,000×.

It should be noted that in related work, float and deep discharge routines were also imposed on cells, and lead-antimony-grid batteries were also evaluated. This comprehensive work will be reported in a future paper. The present paper reports only on observations on the structure of trickle-discharged Pb-Ca positive plates.

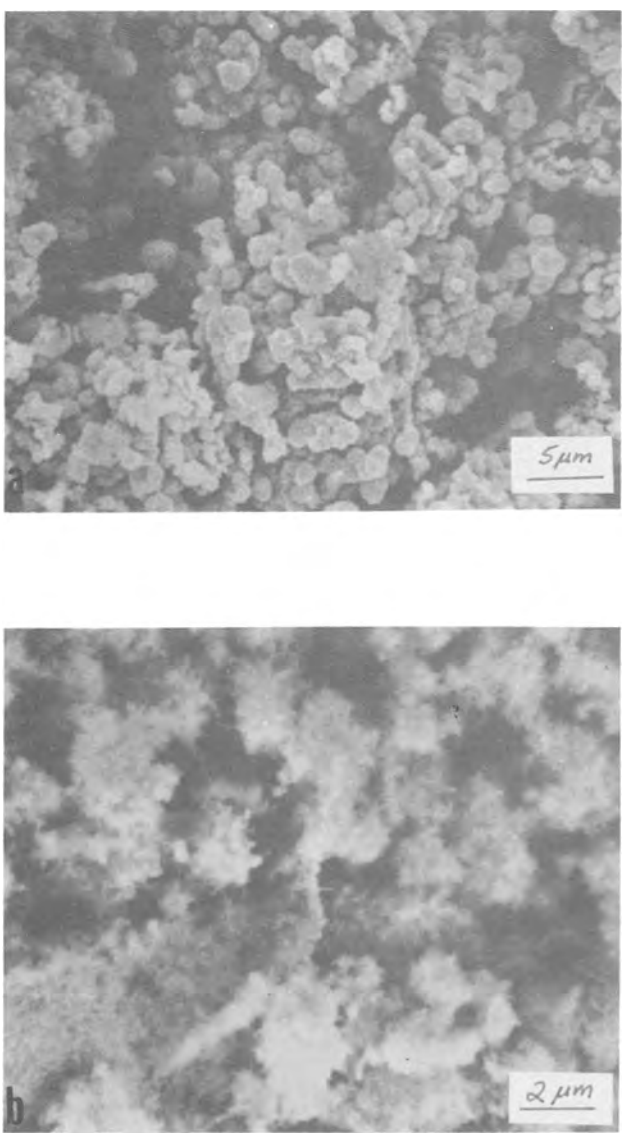


Fig. 1. Initial microstructure of positive plate in formed condition: (a) regular arrangement of nodular masses averaging about 2 μm in diameter, (b) fine structure on the surface of the nodules, consisting of a field of short whisker crystals averaging less than 0.5 μm in length.

Results and Discussion

The initial, as-formed microstructure of the positive plate active material is shown in Fig. 1, and can be described as an aggregate of small (2 μm) nodular masses in a regular arrangement, with limited structural contiguity. The surface of the individual nodules, when observed at higher magnification, shows a fine whiskerlike substructure (Fig. 1b); the majority of these whiskerlike microcrystals are a few tenths of a

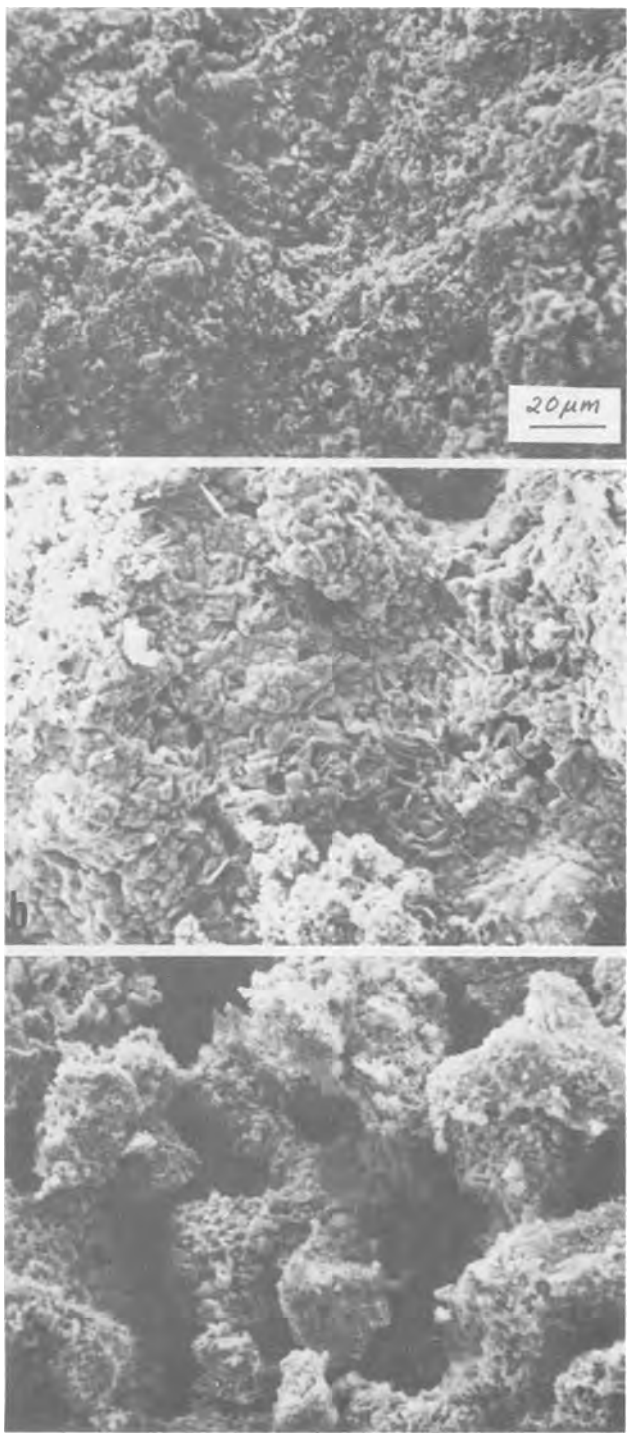


Fig. 2. Active material microstructural changes with cycling. (a) 5 cycles: regular and uniform distribution much like initial microstructure, (b) 13 cycles: agglomeration into more consolidated masses with less uniform distribution, (c) 60 cycles: fully developed "coralloid" labyrinth structure with large open spaces. All plates observed in the charged condition. All photos same magnification.

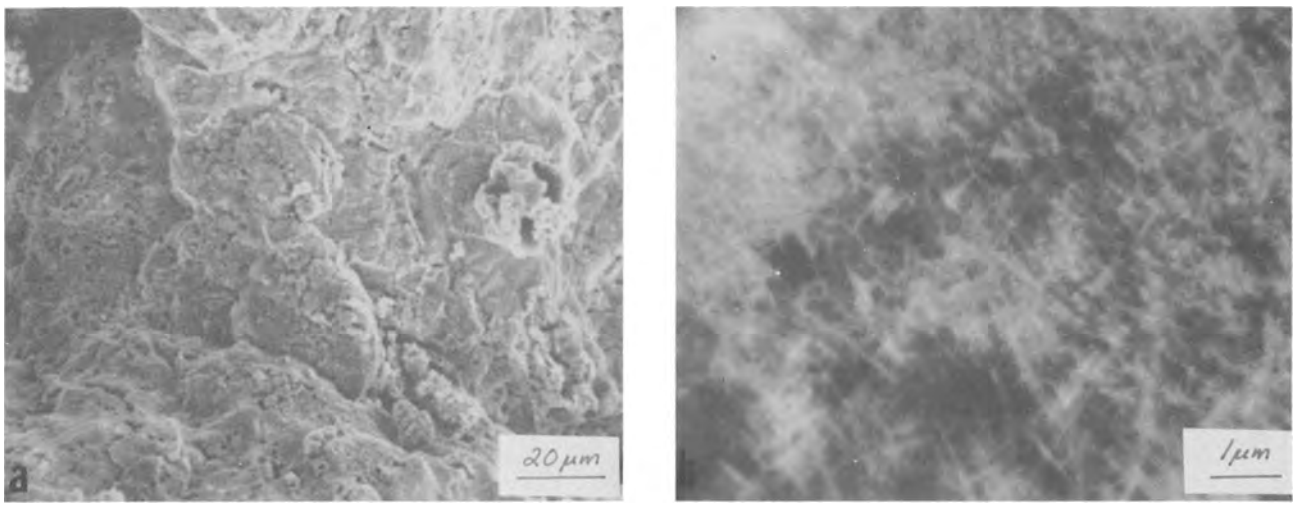


Fig. 3. Submicrostructure observed in active material after about 10 cycles: (a) structure observed developing near middle thickness layer of active material pellets which appears, at low magnification, as a coating over the active material particles, (b) at high magnification is seen to consist of a very fine whisker like network.

micron in length. In addition, there are some more distinct "spiny" crystal arrays, which average about 1.5 μm in length. This substructure resembles certain PbO_2 morphologies reported by other workers, based on observations by less distinct microscopic techniques. Burbank and Ritchie (3) described branched prismatic crystals of PbO_2 which existed individually and clustered together in "Christmas tree" dendrites, together with more complex aggregates composed of compound spikes of dendritic growth, covered with so-called sessile (static, unchanging) crystallites of varying sizes. It is believed that these are the same sort of structures as seen in Fig. 1.

Microstructural changes in the active material with cycling, for plates subjected to the trickle-discharge routine, are shown in Fig. 2. The originally regular nodular array gradually evolves into a more consolidated labyrinth structure containing large open spaces. Simon and co-workers observed similar microstructural developments during continuous charge/discharge cycling, and termed the three-dimensional structure a "coralloid" structure (12).

A more subtle development noticed with cycling is illustrated by Fig. 3. At relatively low magnification, this appears as an apparently dense layer that coats the surface of the PbO_2 crystals in the recharged positive plate. At this point in the cyclic history (13 cycles), this structure was found only near the middle thickness plane of the active material pellets in the grid. At higher magnification, the substructure of this layer is revealed, and is seen to be made up of the same sort of fine whiskerlike crystalline forms previously described.

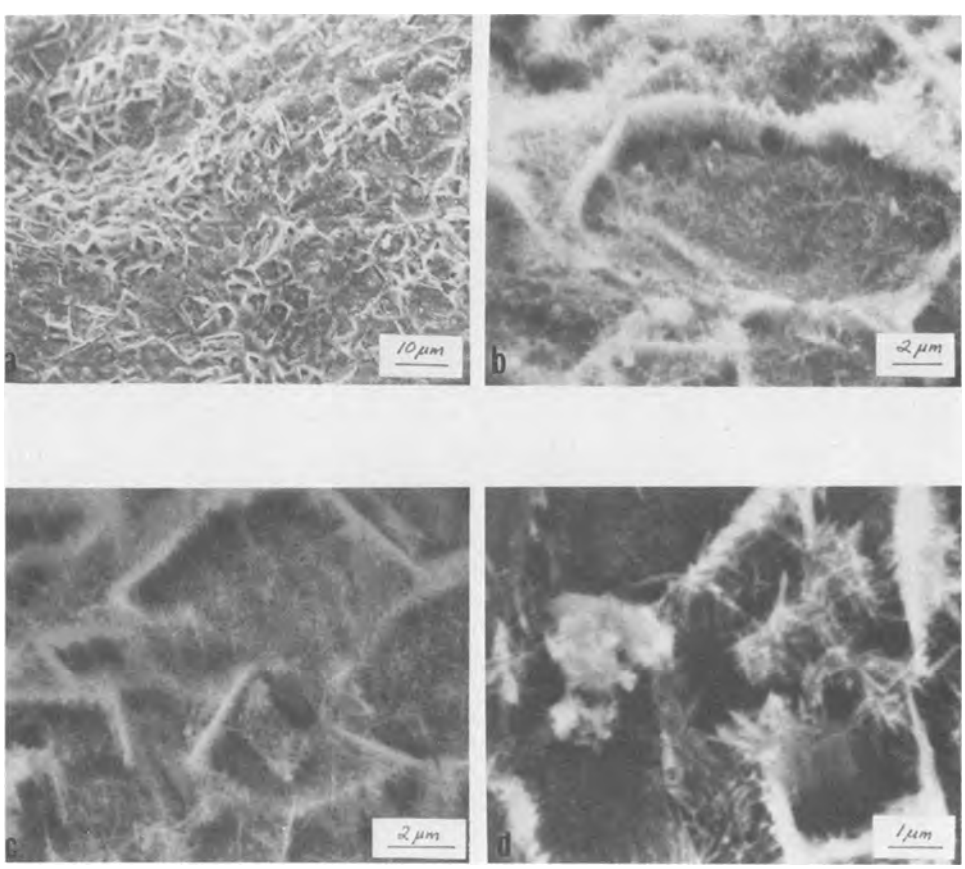


Fig. 4. (a) Patterned imprint of cell-like substructural network observed on grid surface when active material broken away. (b) ond (c) Higher magnification views showing rectilinear outlines consisting of denser whisker network. (d) Very high magnification view, showing dendritic crystals.

More of the larger, linear spiny crystals are evident, now developed into a branching network extensive enough to completely blanket the underlying nodular aggregate.

Further indication of the evolution of an extensive substructural network during trickle-discharge routine is seen on the surface of the grid as a patterned structure when the active material is broken away (Fig. 4). What appears at lower magnification as a white pattern against the grid surface is made up, on the fine scale, of a whisker network similar to those already described. The pattern of "walls" typical of this structure can also sometimes be revealed within the active material mass, as seen in Fig. 5, when the active material pellets are fractured through. It is obvious that the patterns observed on various two-dimensional surfaces represent a structure that is part of a cell-like three-dimensional distribution throughout the active material mass. Furthermore, when the two-dimensional patterns are studied, it is obvious that the shapes of the spaces mapped out represent the outlines of polyhedral lead sulfate crystals which have since transformed to PbO_2 during recharging (oxidation). The cell-like three-dimensional network structure, composed of a dense weave of whiskerlike crystals, extends throughout the charged positive plate, with the regions of greatest density determined by the prior location of the edges of the polyhedral lead sulfate crystals in the discharged plate.

This hypothesis is confirmed by Fig. 6, which shows an area on the grid surface, at a point of incomplete recharge, where some $PbSO_4$ crystals exist in a state of partial transformation. The correspondence between the slow dissolving edges of these crystals and the patterned outline observed for the fully charged condition is quite vivid.

Therefore, the mechanism of formation of the substructural network is based on the transformation of fairly large $PbSO_4$ crystals formed during the trickle-discharge routine. These are transformed in a typical preferred crystallographic sequence, with the edges of the polyhedra transformed more slowly than the planar faces, so that the crystal faces and interior are consumed first, leaving behind a "framework" structure of the edges. This final framework eventually converts to PbO_2, but forms a denser array of whiskers arranged in cell walls that correspond to the prior $PbSO_4$ crystal edges. At the grid surface and other surfaces within the active material mass, this structure can be seen as a sort of imprinted pattern. The exact genesis of the fine whiskerlike form which makes up the substructural network is not known, but obviously is a preferred morphological form of PbO_2 associated with $PbSO_4$ transformation under particular electrochemical conditions. It seems that the size and spacing of these whiskers decreases as the rate of oxidation decreases, *i.e.*, such as at the end of a recharging procedure on the positive plate. X-ray diffraction indicates the presence of only β-PbO_2 in these networks.

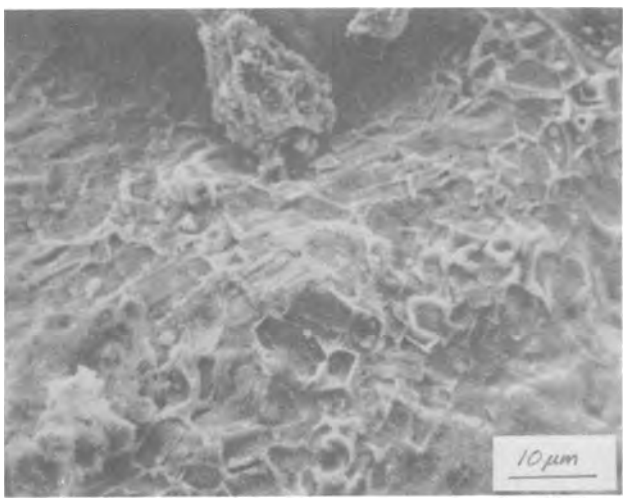
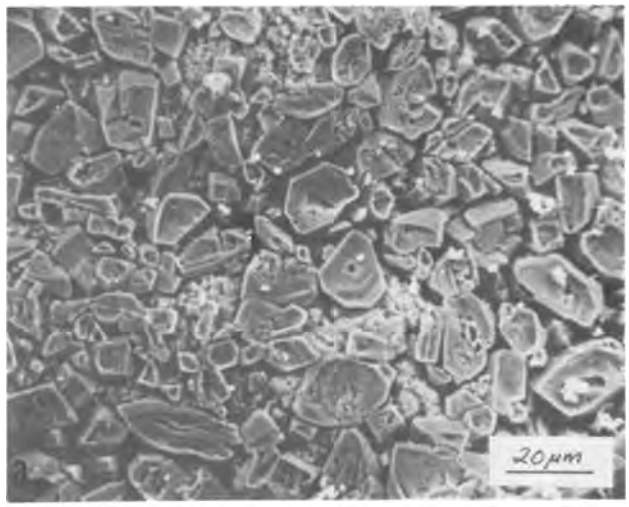


Fig. 5. Cell-like pattern of the substructural network observed within the active material mass when a pellet is cracked open.



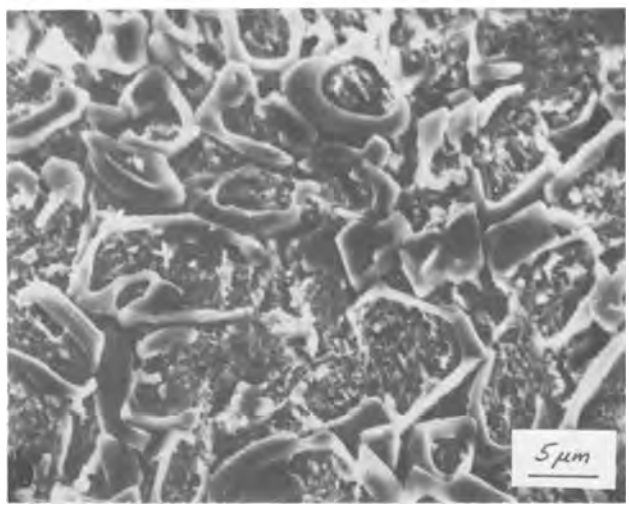


Fig. 6. (a) Array of lead sulfate crystals beginning to transform during charging. Compare the shapes of these polyhedra with the patterns seen in Fig. 4a and 5. (b) Array of almost fully transformed lead sulfate crystals, indicating the correspondence between the slow transforming edges of the polyhedra and the denser rectilinear regions of the whiskerlike substructural network.

Conclusions

The extensive fine scale whiskerlike network of PbO_2 observed in these trickle-discharged plates is considered to impart both favorable electrochemical characteristics and structural integrity to the active material mass of the positive plate. This structure is apparently the same structure observed by Simon (13) using light microscopy, and referred to as a "reticulate" structure. This structure was observed by cross-sectional optical microscopy to be arranged in a cell-like network with generally rectilinear sides (13). The present observations also correlate with the replica electron microscope work of Burbank (7), which revealed branched prismatic crystals in satisfactorily floated positive plates, whereas the crystal morphology in unsatisfactory plates was nondescript. Simon was also able to notice fine prismatic crystals in association with the reticulate structure (13). It was suggested that the reticulate structure serves as a sort of "microgrid," from both an electrical and mechanical standpoint. This proposal is supported in this study by observation of

the three-dimensional form of the structure. In a later paper, which will compare the structure of trickle-discharged and floated plates, it will be shown that these structures are indeed correlated with more satisfactory performance, particularly in association with capacity retention in repeatedly cycled plates.

Acknowledgments

The interest and support of the Energy Conversion Division of the Naval Sea Systems Command, the Surface Chemistry Branch of the Naval Research Laboratory, and the Division of Energy Storage Systems of ERDA are gratefully acknowledged. Some materials were supplied by Mare Island Naval Shipyard, California and by Gould, Incorporated.

Manuscript received Nov. 2, 1976.

Any discussion of this paper will appear in a Discussion Section to be published in the December 1977 JOURNAL. All discussions for the December 1977 Discussion Section should be submitted by Aug. 1, 1977.

Publication costs of this article were assisted by the Naval Postgraduate School.

REFERENCES

1. A. C. Simon and S. M. Caulder, *This Journal,* **118**, 659 (1971).
2. A. C. Simon, C. P. Wales, and S. M. Caulder, *ibid.*, **117**, 987 (1970).
3. J. Burbank and E. J. Ritchie, *ibid.*, **116**, 125 (1969).
4. J. Burbank, *ibid.*, **111**, 1112 (1964).
5. W. O. Butler, C. J. Venuto, and D. V. Wisler, *ibid.*, **117**, 1339 (1970).
6. J. Burbank, *ibid.*, **111**, 763 (1964).
7. J. Burbank, in "Batteries," D. H. Collins, Editor, p. 43, Pergamon Press, Oxford (1963).
8. J. Burbank, A. C. Simon, and E. Willihnganz, in "Advances in Electrochemistry and Electrochemical Engineering," Vol. 8, P. Delahay and C. W. Tobias, Editors, p. 157, John Wiley & Sons, New York (1970).
9. J. Perkins, *Mater. Sci. Eng.,* To be published.
10. "Naval Sea Systems Command Manual 0962-073-4010," Service Manual for U.S. Submarine Main Storage Battery Guppy 1 Mod C Type TLX-39B, (April 1973).
11. "Naval Ships Technical Manual," Chapter 9623, (June 1973).
12. A. C. Simon, S. M. Caulder, and J. T. Stemmle, *This Journal,* **122**, 461 (1975).
13. A. C. Simon, NRL Report 6292, Washington, D.C. (June 1965).

Anodization Constants for Tantalum

L. Young*

Department of Electrical Engineering, The University of British Columbia, Vancouver, British Columbia, Canada V6T 1W5

In device applications of anodic oxide films, it is common practice to use so-called "anodization constants" (in units of angstroms per volt) to predict the thickness of oxide which will be produced by anodizing at constant current until a chosen voltage, V, is reached and then holding at this constant voltage for a fixed time ("soaking"). In experimental determinations of anodization constants, plots of film thickness D *vs.* V are prepared, a straight line is drawn, and the slope dD/dV is taken as the anodization constant.

It is interesting to relate anodization constants to the published kinetic data for steady-state anodization at constant current density. These data give the ionic current density J as a function of the field in the oxide ($E = V/D$) and the temperature. [Here, V is strictly the overpotential for oxide production less a correction for interfacial overpotential which turns out (1, 2) to be negligible.] The expression $J = J_0 \exp(-W/kT) \exp BE$ was used in earlier work but it was found that B was not inversely proportional to temperature if taken as independent of E. It was later proposed (1) that data for constant current anodization of tantalum in dilute sulfuric acid could be fitted by

$$J = J_0 \exp(-W/kT) \exp(q(\alpha E - \beta E^2)/kT) \quad [1]$$

where $J_0 = 10^{8.24}$ A cm^{-2}, $W = 2.185$ eV, $\alpha = 6.995$Å, $\beta = 3.35$ Å/(10^7 V cm^{-1}), $q = 5e$, and k = Boltzmann's constant. The thicknesses of oxide were determined optically and were based on a value of refractive index which later work has confirmed to within about 1%. Dreiner and Tripp (3) in a detailed study over an extended temperature range have confirmed the need for either an expression of the form of Eq. [1] or a Schottky expression as used by Young and Zobel (4). Their data seem also to be in excellent numerical agreement. This paper may be consulted for references to further work not quoted here, including Dignam's work on aluminum. We are not concerned here with the theoretical basis of Eq. [1]. This is discussed, for example, by Dell'Oca *et al.* (5). Siejka Nadai, and Amsel (2), using nuclear microanalysis of oxygen, determined fields for current densities of 10 and 1 mA cm^{-2} which agreed within 1%, provided the density was as assumed below. The earlier data of Vermilyea (6) were based on an assumed density of 8.74 g cm^{-3} and agree within a few percent after correction to $p \simeq 8$ g cm^{-3}, although fitted to a different form of expression.

The ionic current density which is produced by a given field depends, in general, on the history of previous currents of fields which have been applied. However, Young and Zobel (4) found that their experimental data on J as a function of E obtained during constant voltage anodization agreed within experimental error with the data (Eq. [1]) obtained at constant current. We can, therefore, use this expression for the constant voltage part of the anodization as well as for the constant current part. We assume that the current efficiency is 100% during the constant current anodization. As far as is known, the current efficiency during the constant voltage part does not affect the result.

With the expression of Eq. [1], numerical methods become necessary and the University of British Columbia Computing Centre's Runge-Kutta routine (7) with error correction was used to calculate D after a fixed time at constant voltage with initial conditions $D = D_0 = V/E_0$, where E_0, is the constant field during the initial constant current phase, and with $dD/dt = \chi J$, where $\chi = M/\rho 10\mathbf{F}$, J being given by Eq. [1] with $E = V/D$, M = molecular weight of Ta_2O_5, ρ = density of oxide, and $\mathbf{F}$ = Faraday's constant. The density was taken as 7.93 g cm^{-3}. This value (8) was given as ±3% but agrees within 1% with the more accurate value of 8.03 ± 0.04 g cm^{-3} (for formation in 0.1% H_3PO_4) given by Schrijner and Middelhoek (9). Even

* Electrochemical Society Active Member.
Key words: thin films, anodic oxide films, tantalum.

Table I. Computed thicknesses at listed voltages. Formation is at constant current density J_1 giving field E_0 until the voltage V is reached and then at constant voltage V

	Thickness (Å)			
Voltage	J_1 = 1.55 mA cm^{-2} $1/E_0$ = 16 Å/V 238°K 20 min soak	J_1 = 13.5 mA cm^{-2} $1/E_0$ = 15 Å/V 298°K 20 min soak	J_1 = 13.5 mA cm^{-2} $1/E_0$ = 15 Å/V 298°K 60 min soak	J_1 = 11.5 mA cm^{-2} $1/E_0$ = 15 Å/V 296°K 60 min soak
10	198.5	198.5	204.6	203.3
50	949.9	949.8	978.8	973.1
100	1864.0	1863.8	1920.8	1909.9
150	2765.2	2764.8	2849.4	2833.4
200	3658.1	3657.3	3769.4	3748.1

with an error of ±3%, since the constant voltage phase accounts for only 15-20% of the final thickness, the extra error would be ±0.6%.

Some typical calculated thicknesses are given in Table I, both for a 20 min soak as used by Schwartz *et al.* (10, 11) and for a 1 hr soak which is believed to be typical of some device applications. Data are given for different initial current densities and one column is for 296°K rather than 298°K. More figures are given than are absolutely significant in order that relative trends may be seen.

We note first that D is not linear in V. This fact turns out to cause surprise, even disbelief, and to require discussion. It may be explained as follows. A given ionic current density gives a fixed dD/dt independent of D but $dE/dt = -(V/D^2)dD/dt$ at constant voltage. At the start of the soak, the current density is independent of thickness. Therefore, the field starts to fall at a rate which is initially inversely proportional to thickness. The ionic current density decreases less rapidly the thicker the film but this only partially compensates, so that the final field, which might be regarded as a reciprocal of the anodization constant, will still be bigger the smaller the voltage.

The nonlinearity might escape notice in a plot of D *vs.* V but is apparent in a plot of D/V *vs.* V. (Fig. 1). The anodization constant which would be found from a plot of D *vs.* V would, of course, tend to be determined by the larger values of D. The dependence on the value of the initial current is slight (up to 0.1% for the example chosen), the temperature dependence would be quite appreciable for some applications (*e.g.*, up to 0.6% for a 2°C change in the examples chosen).

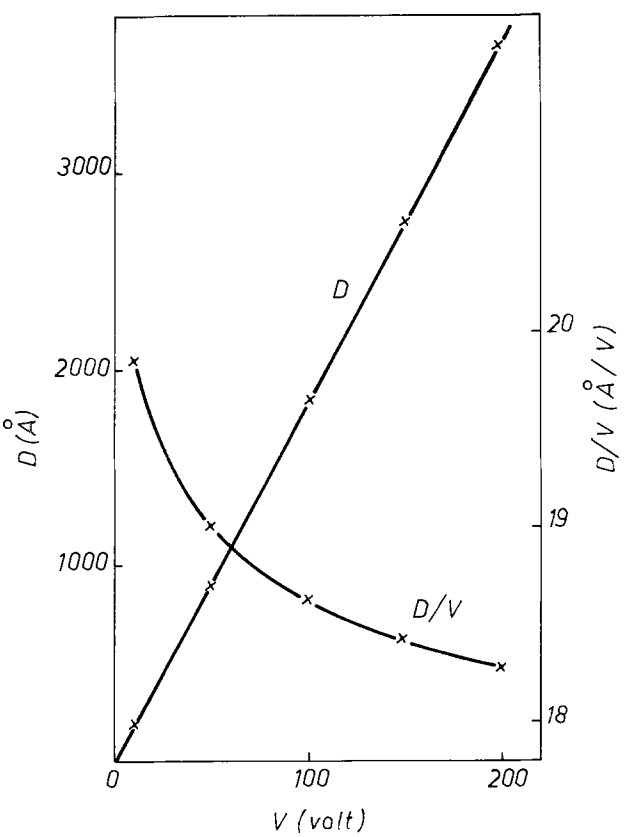


Fig. 1. Plot of D and D/V vs. V from data in first column of Table I.

Experimentally determined anodization constants have been compared with reciprocal fields for constant current formation, even for current densities as high as 10 mA cm^{-2}. To confuse the two concepts is greatly to underestimate the accuracy with which film thickness should be predictable. This should be of the order ±1% with a reproducibility much better than this if the second electrode has a defined potential. Muth's angstroms per volt values (12), which receive some use as anodization constants, are for constant current formation in dilute citric acid (17-15.6 Å/V for 0.1-1 mA cm^{-2}). The angstroms per volt value found by Klerer (13) (16 Å/V ± 3.2%) and his widely quoted dielectric constant (21.2 ± 3.3%) seem low. He used sputtered tantalum films (14) but this may or may not account for the difference. Mills, Young, and Zobel (15) found that the permittivity of the oxide formed on sputtered tantalum was close to that of films formed on bulk tantalum. It should be added that the electrolyte can have a strong effect on anodization constants, even in dilute solutions. Take-up of electrolyte tends to reduce thickness and permittivity together, so that the capacitances of films formed to a given potential in different solutions tend to be less different than the thicknesses. In some practical applications, the capacitance rather than the thickness is to be controlled.

Manuscript submitted Oct. 7, 1976; revised manuscript received Nov. 30, 1976.

Any discussion of this paper will appear in a Discussion Section to be published in the December 1977 JOURNAL. All discussions for the December 1977 Discussion Section should be submitted by Aug. 1, 1977.

Publication costs of this article were assisted by The University of British Columbia.

REFERENCES

1. L. Young, *Proc. R. Soc. London, Ser. A*, **258**, 496 (1960).
2. J. Siejka, J. P. Nadai, and G. Amsel, *This Journal*, **118**, 727 (1971).
3. R. J. Dreiner and T. B. Tripp, *ibid.*, **117**, 858 (1970).
4. L. Young and F. G. R. Zobel, *ibid.*, **113**, 277 (1966).
5. C. J. Dell'Oca, D. L. Pulfrey, and L. Young, *Phys. Thin Films*, **6**, 1 (1971).
6. D. A. Vermilyea, *Acta Metall.*, **1**, 282 (1953).
7. Due to C. M. Lee. See any text on numerical methods.
8. L. Young, *Proc. R. Soc. London, Ser. A*, **244**, 41 (1958).
9. A. J. Schrijner and A. Middelhoek, *This Journal*, **111**, 1167 (1964).
10. R. L. Ruth and N. Schwartz, *ibid.*, **123**, 1860 (1976).
11. P. J. Silverman and N. Schwartz, *ibid.*, **121**, 550 (1974).
12. D. G. Muth, *J. Vac. Sci. Technol.*, **6**, 749 (1969).
13. J. Klerer, *This Journal*, **112**, 896 (1965).
14. W. D. Westwood, N. Waterhouse, and P. S. Wilcox, "Tantalum Thin Films," Academic Press, New York (1975).
15. D. Mills, L. Young, and F. G. R. Zobel, *J. Appl. Phys.*, **47**, 1821 (1966).

Potassium Ion-Selective Electrode

Potassium Zinc Ferrocyanide in a Silicone Rubber Matrix

Peter A. Rock,* Terry L. Eyrich,[1] and Steven Styer[2]

Department of Chemistry, University of California, Davis, California 95616

We report here a new Pungor-type, potassium ion, heterogeneous membrane electrode in which the active material is potassium zinc ferrocyanide imbedded in a silicone rubber matrix. The electrode responds to potassium ion in a Nernstian manner over the concentration range 1 to 10^{-3}M; the electrode is operational down to 10^{-4}M. The K^+/Na^+ ion selectivity of the electrode is comparable to commercially available cationic glass electrodes. The electrode is simple and inexpensive to fabricate from readily available materials. A simple and effective procedure for the preparation of leak-free, reproducible, heterogeneous rubber matrix membranes is also described.

Experimental

The procedure used to prepare the heterogeneous salt-plus-silicone rubber membrane disks is as follows. The dried salt is thoroughly mixed with silicone rubber. The salt-plus-rubber mixture is then cured in the barrel of a disposable plastic syringe from which the tip end has been cut off with a razor blade. Fresh membrane disks of the desired thickness are cut with a razor blade from the end of the cured cylinder after extrusion with the syringe plunger. This simple procedure greatly facilitates the preparation of leak-free and reproducible membrane disks. The membrane disk is glued with rubber cement to the end of a glass tube. Several centimeters of 0.1M KCl is placed in the tube and a silver-silver chloride (thermal-electrolytic type) electrode (1) is inserted into the KCl solution. The electrode lead wire is then glued in place with a plug of silicone rubber at the upper end of the tube; the resulting electrode is rugged and insensitive to moderate shock. The electrode is represented diagrammatically as

$$\mathrm{Ag(s)\,|AgCl(s)\,|KCl(aq)\,|KX(memb)} \qquad [1]$$

where KX is a water-insoluble potassium salt. Several potassium salts were investigated including $KB(C_6H_5)_4$, KUO_2AsO_4, and potassium metal ferrocyanides (iron, manganese, cobalt, copper, and zinc). The best electrode performance was obtained with the salt $K_2Zn_3[Fe(CN)_6]_2 \cdot 8H_2O$ which was prepared as described in the literature (2). Electrical measurements were made using a Keithley 602 electrometer as a unity gain amplifier in conjunction with a Leeds and Northrup K-3 potentiometer. The reported voltages are the average of five readings taken at 2 min intervals during a period after the cell voltage stabilized (usually 3 to 5 min). The weight percentage of salt in the mixture was varied over the range 40-80%; the best results were obtained with *ca.* 55 weight percent (w/o) of $K_2Zn_3[Fe(CN)_6]_3 \cdot 8H_2O$.

Results

The cells used to study the potassium electrodes were of the type

$$\mathrm{Ag(s)\,|AgCl(s)\,|KCl(aq, M)\,|KX(memb)\,|KCl(aq,\ M_1),NaF(aq, M_2)\,|Hg_2Cl_2(s)\,|Hg(l)} \qquad [2]$$

for which, with M held constant

$$\mathcal{E} = \mathcal{E}^\circ - \frac{RT}{\mathbf{F}} \ln [a_{K^+}\, a_{Cl^-} + k_{K^+,Na^+}\, a_{Na^+}\, a_{F^-}] \qquad [3]$$

with $M_2 = 0$, we have

$$\mathcal{E} = \mathcal{E}^\circ - \frac{2RT}{\mathbf{F}} \ln M_1 \gamma_\pm \qquad [4]$$

and therefore the theoretical Nernst slope is 118 mV/decade at 25°C.

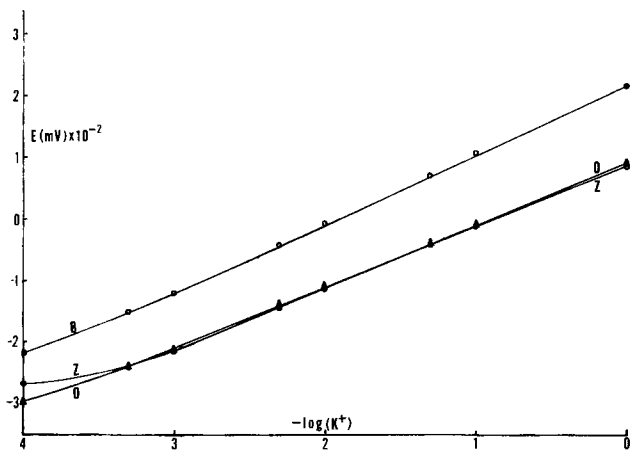


Fig. 1. Plot of voltage *vs.* $-\log (K^+)$ for a potassium zinc ferrocyanide/silicone rubber membrane electrode (Z), an Orion potassium ion electrode (O), and a Beckman cationic glass electrode (B). The cell solutions are KCl(aq) of the indicated concentration in contact with a calomel electrode (25°C).

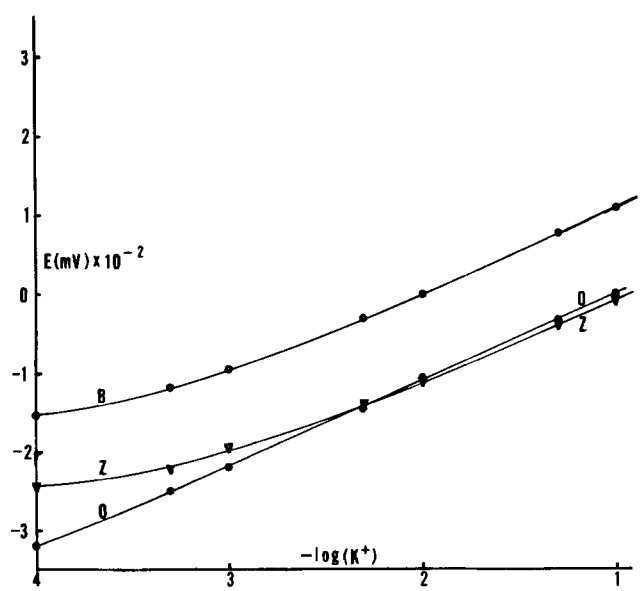


Fig. 2. Plot of voltage *vs.* $-\log (K^+)$ for a potassium zinc ferrocyanide/silicone rubber membrane electrode (Z), an Orion potassium ion electrode (O), and a Beckman cationic glass electrode (B). The cell solutions are KCl(aq) of the indicated concentration plus 0.010M NaF(aq) in contact with a calomel electrode (25°C).

* Electrochemical Sociey Active Member.
[1] Present address: Department of Chemistry, Merced Junior College, Merced, California 95340.
[2] Present address: Department of Chemical Engineering, University of California, Berkeley, California 94720.
Key words: potassium, ion-selective, electrode, membrane.

Figures 1 and 2 show the results of a comparison between $K_2Zn_3[Fe(CN)_6]_2 \cdot 8H_2O$/silicone rubber heterogeneous membrane electrode (Z), an Orion liquid ion-exchanger potassium selective electrode (O), and a Beckman (39137) cationic glass electrode (B). The comparison is made for both KCl(aq) and KCl(aq) in the presence of 0.010M NaF(aq). The test solutions were in contact with a Hills and Ives type calomel electrode (3). For the KCl(aq) solutions the slopes (millivolt/decade) (uncorrected for activity coefficients) over the range 1 to 10^{-3}M for three electrodes are: 101 mV (Z), 102 mV (O), and 112 mV (B). Correction for activity coefficients gives an observed slope of 116 mV for the potassium zinc ferrocyanide electrode. The selectivity coefficient for the $K_2Zn_3[Fe(CN)_6]_2$ electrode can be estimated by the extrapolation-intersection method (4) from the data in Fig. 1 as $k_{K^+,Na^+} \approx 0.10$, which is about the same as that for the cationic glass electrode. In contrast to the above results we found that although several other insoluble potassium salts in silicone rubber responded satisfactorily to the activity of potassium ion in aqueous solution, their selectivity characteristics were not as good as the potassium zinc ferrocyanide membrane. For example, $k_{K^+,Na^+} = 0.5$ for $KB(C_6H_5)_4$ (50 w/o) in silicone rubber.

Acknowledgment

This research was supported by UCD Committee on Research and by the Chancellor's Patent Fund.

Manuscript submitted Sept. 30, 1976; revised manuscript received Nov. 22, 1976.

Any discussion of this paper will appear in a Discussion Section to be published in the December 1977 JOURNAL. All discussions for the December 1977 Discussion Section should be submitted by Aug. 1, 1977.

Publication costs of this article were assisted by the University of California.

REFERENCES

1. D. J. G. Ives and G. J. Janz, "Reference Electrodes," p. 179, Academic Press, New York (1961).
2. P. A. Rock and R. E. Powell, *Inorg. Chem.*, **3**, 1593 (1964).
3. G. J. Hills and D. J. G. Ives, *J. Chem. Soc.*, **1951**, 311.
4. IUPAC, Information Bulletin No. 43 (1975), IUPAC Secretariat, Cowley Center, Oxford OX4 3YF, United Kingdom.

Brief Communication

Catalysis of Oxygen Cathodic Reduction in Cobalt Ammoniacal Solutions

A. Bettelheim and J. Manassen[1]

Atomic Energy Commission, Nuclear Research Centre-Negev, Beer-Sheva, Israel

Oxygen electrodes, which can reach nearly reversible behavior, are important for fuel cell research. Usually these electrodes are coated with catalytic layers (1-3) or are immersed in catalytic suspensions (4, 5) to overcome their great deviation from thermodynamic reversibility. The homogeneous catalysis of the oxygen electrode is treated in previous studies (6, 7).

The electrocatalytic influence of iron-phthalocyanine (Fe-PhC) on oxygen cathodic reduction in KOH and H_2SO_4 aqueous solutions is known (1-3). Manassen (1) found that the electrocatalytic effect of Fe(II)-phthalocyanine (Fe(II)-PhC) equals that of Fe(III)-phthalocyanine (Fe(III)-PhC).

In a previous work (8), we have shown that use of the peroxo complex $[(NH_3)_5Co\text{-}O_2\text{-}Co(NH_3)_5]^{+4}$ increases the limiting current of oxygen reduction on a platinum electrode without decreasing the overpotential. This homogeneous effect was explained as an increase of dissolving oxygen capacity of the cobalt-ammoniacal solution. In the present work, reduction of oxygen on Fe-PhC electrodes was studied in cobalt-ammoniacal solutions.

Two types of electrodes (1.0 × 2.8 cm each) were prepared (1): the noncatalytic electrode (type A) was a Ni gauze on which carbon was deposited, and the catalytic one (type B) was a similar electrode but impregnated with Fe(III)-PhC. The instrumentation is described elsewhere (6, 8).

The Fe(III)-PhC electrode catalyzes oxygen reduction in ammoniacal solutions by reducing the overvoltage by about 350 mV. This heterogeneous effect

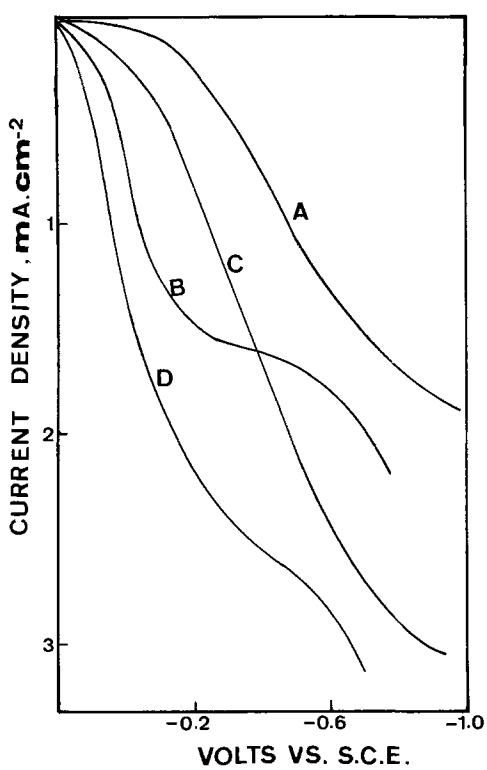


Fig. 1. Potentiostatic voltammograms (voltage sweep rate: 200 mV · min^{-1}) of oxygen reduction in oxygen-saturated solutions containing NH_3 (6.3M) and NH_4Cl (1M) (pH: 10.3). A, Type A electrode; B, type B electrode; C, type A electrode with $CoCl_2$ (10^{-2}M); D, type B electrode with $CoCl_2$ (10^{-2}M).

[1] Present address: The Weizmann Institute of Science, Rehovot, Israel.

Key words: catalysis, oxygen, cobalt-ammonia.

is demonstrated by comparing curves A and B in Fig. 1: For a type B electrode, a current density of 1 mA · cm^{-2} is obtained at −0.15V, whereas the same current density is reached at −0.50V for a type A electrode. Addition of Co(II) ions to the ammoniacal solution causes an increase of current, on type A as well as on type B electrodes (Fig. 1, curves C and D). A Fe-PhC cathode in a cobalt-ammoniacal solution will improve the performance of the oxygen electrode by reducing its overvoltage and increasing the cathodic current. A combination of homogeneous and heterogeneous effects, as shown here, may be useful in fuel cell research.

Manuscript received Nov. 19, 1976.

Any discussion of this paper will appear in a Discussion Section to be published in the December 1977 JOURNAL. All discussions for the December 1977 Discussion Section should be submitted by Aug. 1, 1977.

REFERENCES

1. J. Manassen, *J. Catal.*, **33**, 133 (1974).
2. A. Kozawa, V. E. Zilionis, and R. J. Brodd, *This Journal*, **117**, 1470 (1970).
3. A. Kozawa, V. E. Zilionis, and R. J. Brodd, *ibid.*, **118**, 1705 (1971).
4. H. Alt, H. Binder, and G. Sandstede, *J. Catal.*, **28**, 8 (1973).
5. M. Caselli, G. Scarano, and A. Traini, *Electroanal. Chem. Interfac. Electrochem.*, **44**, 91 (1973).
6. A. Bettelheim, M. Faraggi, I. Hodara, and J. Manassen, *J. Chem. Soc., Faraday Trans. 1*, To be published.
7. F. Hine, S. Yoshizawa, K. Yamakawa, and Y. Nakane, *Electrochem. Technol.*, **4**, 555 (1966).
8. A. Bettelheim, M. Faraggi, I. Hodara, and J. Manassen, *J. Chem. Soc., Faraday Trans. 1*, **73**, 143 (1977).

Photoelectrochemical Energy Conversion and Storage

The Polycrystalline CdSe Cell with Different Storage Modes

Joost Manassen and Gary Hodes

Department of Plastics Research, The Weizmann Institute of Science, Rehovot, Israel

and David Cahen

Department of Structural Chemistry, The Weizmann Institute of Science, Rehovot, Israel

The photoelectrochemical cell (PEC) furnishes an alternative to the commercially available photovoltaic cells for the direct conversion of sunlight into electrical energy (1, 2). As we have indicated previously (3), it has the distinct advantage over a photovoltaic cell in that storage of the converted energy is possible *in situ*.

We want to discuss here some general principles connected with storage in a PEC and to give experimental evidence that, after due development, this mode may be able to compete with the combination photovoltaic cell/storage battery.

In Fig. 1(a) the PEC is schematically indicated. P is the photoelectrode, in our experiments a polycrystalline layer of CdSe on titanium metal, which is obtained by electrolytic codeposition of Cd and Se, which combine *in situ* to give CdSe. Subsequent heating in an inert atmosphere improves the performance of the electrode considerably. C is the counterelectrode which is prepared by applying an aqueous paint of high surface area carbon, cobalt(II) acetate and Teflon suspension onto a stainless steel gauze and subsequent sintering in an inert atmosphere at ~300°C. The electrocatalytically active species is presumably the cobalt sulfide which is formed when this electrode is immersed in the electrolyte. This electrode is only slightly polarized with the currents to be expected in a solar cell exposed to nonconcentrated sunlight (4). The cell is filled with an aqueous solution, which is typically 1M in OH^-, S^{--}, and sulfur. On illumination with light, sulfide is oxidized to sulfur at P and electrons flow over the load L to C, where sulfur is again reduced to sulfide. Typical open-circuit voltages are greater than 0.5V and typical short-circuit currents more than 10 mA/cm^2 (AM1 sunlight).[1]

Key words: photoelectrochemistry, energy conversion, energy storage.

[1] In more recent experiments stable cells have shown open-circuit voltages up to 0.67V, short-circuit currents up to 12 mA/cm^2, and fill factors up to 40%, in laboratory tests.

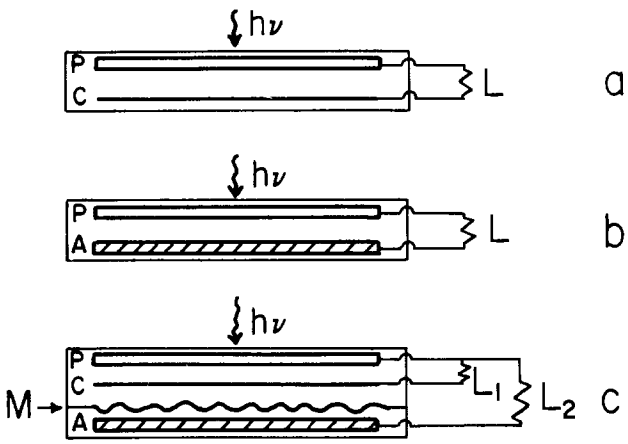


Fig. 1. (a) A photoelectrochemical cell without the possibility of *in situ* storage. (b) A photoelectrochemical storage cell with two electrodes. (c) A photoelectrochemical storage cell with three electrodes.

In order to convert such a PEC into a storage cell, C is replaced by a storage electrode A as pictured in Fig. 1b. A must be capable of undergoing a reversible chemical change, which schematically can be indicated as

$$AX + ne^- \rightleftharpoons A + X^{n-} \qquad [1]$$

where X is a solute present in the electrolyte. If the redox potential of reaction [1] is intermediate between the potential of P during illumination and that of the redox potential of the S/S^{--} couple, equilibrium [1] moves to the right under illumination, consuming electrons. In the dark it produces electrons by reaction in the opposite direction. A typical example is Ag_2S, which reacts according to

$$Ag_2S + 2e^- \rightleftharpoons 2Ag + S^{--} \qquad [2]$$

A cell using the arrangement of Fig. 1b has some serious disadvantages, however, which make it unsuitable for practical use. On current inversion, which occurs in the dark, P now serves as the counterelectrode, and sulfur is reduced to sulfide at its surface. As we have pointed out before (5), this reaction should be minimized at P in order to obtain maximum efficiency during illumination. Therefore an efficiently working photoelectrode makes a poor counterelectrode and in the arrangement of Fig. 1b it will severely limit the back current in the dark. The second disadvantage is that since A should have a reasonably high surface area if it is to be used efficiently, then it will also act as a good counterelectrode. Thus it will not only give reaction [2] under illumination, but will also reduce sulfur from the solution to sulfide resulting in a loss of storage capacity. These disadvantages can be overcome by using the arrangement pictured in Fig. 1c.

A cation-specific membrane M separates the compartment containing A from that containing P and C. In the present case cation-exchange membranes containing sulfonic acid groups bound to various polyaromatic matrixes were used.[2] The membrane was held in place between the two cell compartments by two rings of Parafilm on either side, which were pressed into an annular groove in one compartment of the glass vessel by a Viton O-ring from the other side. Sulfide as well as sulfur may be absent from the storage compartment and other redox couples which do not pass the membrane may be added. According to our experience neither sulfur nor sulfide passes through the membrane. The loads L_1 and L_2 can be chosen in such a way that during illumination part of the current produced flows over L_1 to C and can be used, while part flows over L_2 to A where it is stored. In the dark, current flows over L_2 and L_1 from A to C and the direction of the current over L_1 does not change. The fact that P is a bad counterelectrode is now turned to advantage and, according to our experience, less than 10% of the dark current flows to P if C is properly constructed. By the use of a relay or photosensitive switch, the arrangement of Fig. 1c can be refined even further.

In Fig. 2 the current-voltage characteristics are given of a CdSe cell used by us, and on the vertical axis the potentials of some redox couples are indicated, taken from Ref. (6). When no current is drawn under illumination (open circuit) the potential of P is about −1.0V *vs.* NHE, while the potential of C is that of the S/S^{--} couple (−0.48V *vs.* NHE). When current is drawn from the system the potential of P moves gradually towards that of C, an undesirable feature of the PEC which will have to be improved. Also indicated is the voltage-current behavior of a typical solid-state cell, which it is hoped will be obtained for a PEC in the future.

If a silver/silver-sulfide electrode is added to a cell of the type of Fig. 1c and when no sulfur is present in the storage compartment, almost theoretical storage efficiencies can be obtained, but the open-circuit potential of the storage cell is only −0.69 + 0.48 = −0.21V, which is rather low. Such a low voltage not only decreases the conversion efficiency of the cell, but also excessive quantities of the expensive silver are needed to store a reasonable amount of electrical energy. Mercury suffers from the same disadvantage, but can be useful for the amalgamation of other electrodes. Iron sulfide is cheap and can be used, but it gives unwanted side reactions. When sulfur as well as sulfide is omitted from the storage compartment, redox couples other than those containing sulfide can be used, but here other complications occur. When, for instance,

[2] These membranes are under investigation at this Institute and their long-term performance and comparison to the behavior of other commercial membranes in this system will be the subject of a later report. We thank Dr. Gerald Tanny for supplying the membranes and advice in their use.

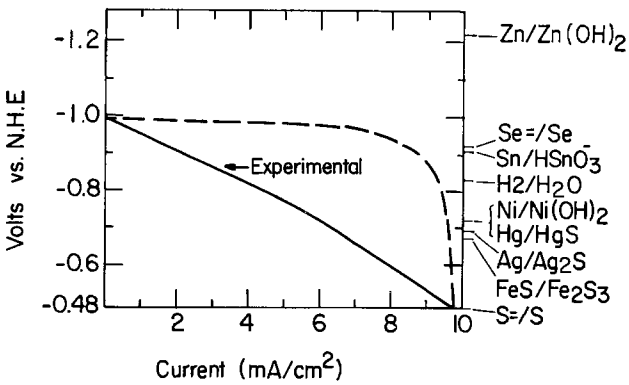


Fig. 2. The current/voltage characteristics of a working CdSe cell. On the vertical axis the redox potentials (pH 14) of some possible storage systems are indicated. The dotted line shows the I-V characteristic of a good solid-state cell.

a porous nickel electrode is used in a storage compartment, free from sulfur as well as sulfide, hydrogen evolution can be observed at its surface, when the cell is illuminated, in spite of the fact that the potential of the $Ni/Ni(OH)_2$ couple is more positive than that of hydrogen formation (at *p*H 14). This imposes another restriction, *viz.*, the material of which the storage electrode is made should have a high overpotential for hydrogen evolution.

If the current-voltage characteristics of the PEC were better, *i.e.*, less voltage drop under load, tin could be used. With the PEC in its present state, the charging current with a tin storage electrode is too low (see Fig. 2) and an arrangement with two PEC's in series is necessary. The experimental arrangement is pictured in Fig. 3. A is a strip of tin foil immersed in an alkaline solution. R is a recorder, L a variable load. K_1 and K_2 are on/off switches. The other symbols have their usual meaning. The light intensity of the lamps illuminating P_1 and P_2 was regulated such that with K_1 closed and K_2 open a current of 2 mA flowed by way of R to A. When the lamps were switched off, K_1 opened and K_2 closed automatically and L was chosen such that a current of also 2 mA flowed from A over R to C_2. 12 hr cycles of illumination and dark

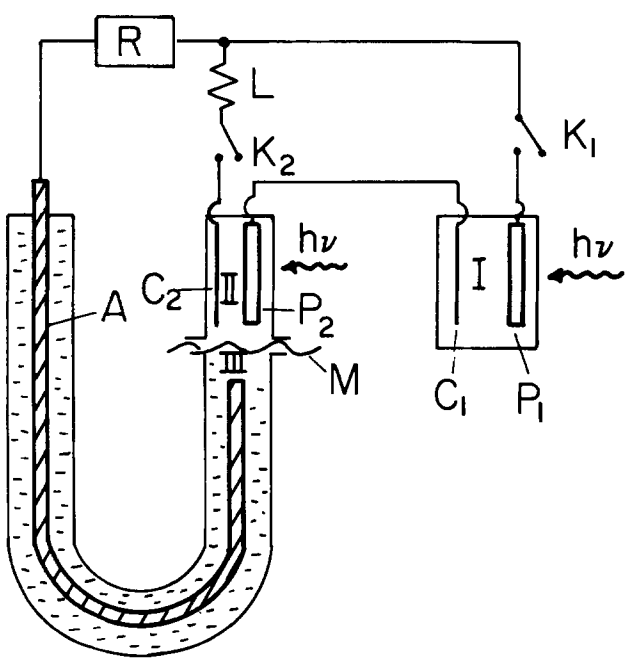


Fig. 3. The experimental setup for testing storage electrode materials as a function of time. I and II contain $S^=$, sulfur as well as alkali; III only alkali.

periods were used and the arrangement worked uninterrupted for three weeks. The quantity of tin taken was 0.4g and fifteen 12 hr periods at a current of 2 mA would have sufficed to consume the tin entirely, were no recharge to have taken place.[3] During the illumination period the tin crystallized at the side nearest to the membrane, where it assumed a porous structure. Open-circuit voltages in the dark were near to theoretical and no hydrogen evolution was observed. The same experiment was repeated with zinc instead of tin. A piece of foil weighing 0.2g was taken and this cell also worked uninterrupted for three weeks. The crystal growth was much more dendritic than in the case of tin and traces of hydrogen evolution could be observed.

Tin seems to be the suitable material for the idealized cell (indicated in Fig. 2), which also under load keeps its voltage of 0.5V. The dark voltage of $-0.91 + 0.48 = 0.43$V is only 14% lower than the voltage under illumination, which is a realistic loss for a storage operation. Zinc is attractive because of its low price, low molecular weight, and high dark voltage of $-1.24 + 0.48 = -0.76$V.

To supply an average power of 1 mW during 30 hr, a theoretical quantity of ~80 mg of tin[3] would be needed and only 50 mg of zinc. Both quantities fall well within economical and constructional possibilities. An alternative possibility which was only superficially checked is to add a redox couple to the storage compartment using an inert electrode. The Se/Se^{--} couple has the right redox potential for such a system. It appeared, however, that the dissolved selenium underwent too many side reactions. It is clear that there is scope here for the use of good water soluble coordination complexes, which have to be charged in order to ensure impermeability through an ion-selective membrane and which have a suitable redox potential.

A practical system for the conversion of solar energy to electrical energy should also include storage capacity. Therefore the economic feasibility of using photovoltaic cells must be considered together with that of using storage batteries. In a PEC the addition of one electrode and a membrane may be compared with that of a complete storage battery to a solid-state cell. From the preliminary results presented here, it is clear that the future prospects for a practical PEC are enhanced considerably by its capability of storing the converted energy without the need for a separate external storage device.

[3] Here, a four-electron change is assumed for tin, corresponding to the $Sn/HSnO_3^-$ couple.

Manuscript submitted Oct. 6, 1976; revised manuscript received Dec. 12, 1976.

Any discussion of this paper will appear in a Discussion Section to be published in the December 1977 JOURNAL. All discussions for the December 1977 Discussion Section should be submitted by Aug. 1, 1977.

REFERENCES

1. A. Fujishima and D. Honda, *Nature*, **238**, 37 (1972).
2. H. Gerischer, *J. Electroanal. Chem.*, **58**, 263 (1975).
3. G. Hodes, J. Manassen, and D. Cahen, *Nature*, **261**, 403 (1976).
4. G. Hodes, J. Manassen, and D. Cahen, *J. Appl. Electrochem.*, To be published.
5. J. Manassen, D. Cahen, G. Hodes, and A. Sofer, *Nature*, **263**, 97 (1976).
6. W. M. Latimer, "The Oxidation States of the Elements and Their Potentials in Aqueous Solutions," 2nd ed., p. 346, Prentice-Hall, Inc., Englewood Cliffs, N.J. (1953).

Determination of Ion Complexation Constants in Electrochemical Double Cells Without Liquid Junction

Arnold Z. Gordon*,[1] and Peter A. Rock**

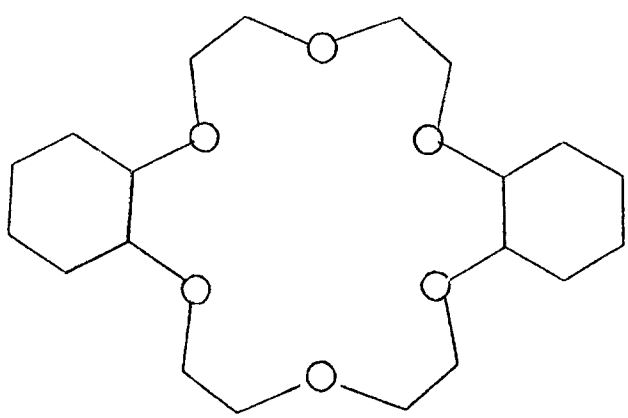
Department of Chemistry, University of California, Davis, California 95616

We have developed a novel electrochemical method for the study of ion complexation reactions. The method employs electrochemical double cells without liquid junction for which the ion complexation reaction of interest is the net cell reaction. The method involves setting up two electrochemical cells in series opposition that are the same except that one cell contains the complexing agent in the cell electrolyte.

This communication outlines the general method and reports the use of the electrochemical double cell

$$Pb(Hg,2\text{-phase})\,|PbCO_3(s);\ BaCO_3(s)\,|BaXCl_2(aq,m),X(satd)\,|Hg_2Cl_2(s)\text{-}Hg(l)\,|Hg_2Cl_2(s)\,|BaCl_2(aq,m)\,|BaCO_3(s);\ PbCO_3(s)\,|Pb(Hg,2\text{-phase}) \quad [1]$$

where X is the crown ether dicyclohexyl-18-crown-6 (1)



to determine the equilibrium constant for the complexation of $Ba^{2+}(aq)$ by dicyclohexyl-18-crown-6.

* Electrochemical Society Student Member.
** Electrochemical Society Active Member.
[1] Present address: Department of Chemistry, University of California, Santa Cruz, California 95060.

Key words: cell, complexation, crown, barium, electrode.

Experimental

Because of the sensitivity of the two-phase lead amalgam [~5 weight percent (w/o) Pb] to oxygen, the entire cell was set up on a high vacuum line; all cell components were introduced to the cell under oxygen-free conditions (2). The $Pb(Hg)\,|PbCO_3(s);$

$BaCO_3(s)|Ba^{2+}(aq)$ and $Hg(l)|Hg_2Cl_2(s)|Cl^-(aq)$ electrodes were prepared as recommended in the literature (3, 4). The $PbCO_3$ was freshly precipitated from dilute aqueous solution and authenticated by x-ray powder pattern and electron microprobe analysis. The reagent grade $BaCO_3(s)$ was covered with distilled water and held at *ca.* 80°C for about a week. The dicyclohexyl-18-crown-16 (technical grade) was obtained from the Aldrich Chemical Company. All other chemicals used were reagent grade. The cell electrolytes were deoxygenated with argon prior to introduction to the cells. Emf measurements were made with a Keithley 630 potentiometric electrometer which was calibrated against a certified Leeds and Northrup K-3 potentiometer. The cells attained a stable voltage (± 0.5 mV) within a few hours and maintained a stable voltage for over 48 hr. Voltage vs. current reversibility checks showed no evidence of a hysteresis loop.

Results

The electrode reactions for cell [1] are

$$Pb(Hg) + BaCO_3(s) + X(s) = PbCO_3(s) + BaX^{2+}(aq) + 2e^-$$

$$Hg_2Cl_2(s) + 2e^- = 2Hg(l) + 2Cl^-(aq)$$

$$2Hg(l) + 2Cl^-(aq) = Hg_2Cl_2(s) + 2e^-$$

$$PbCO_3(s) + Ba^{2+}(aq) + 2e^- = BaCO_3(s) + Pb(Hg)$$

and the net cell reaction is

$$BaCl_2(aq) + X(s) = BaXCl_2(aq) \qquad [2]$$

Application of the Nernst equation to reaction [2] yields

$$\mathcal{E} = \mathcal{E}^\circ - \frac{RT}{2\mathbf{F}} \ln \left\{ \frac{a_{BaX^{2+}} a^2_{Cl^-}}{a_{Ba^{2+}} a^2_{Cl^-}} \right\} \qquad [3]$$

$$\mathcal{E} = \mathcal{E}^\circ - \frac{RT}{2\mathbf{F}} \ln \left\{ \frac{[BaX^{2+}][Cl^-]^2}{[Ba^{2+}][Cl^-]^2} \cdot \left(\frac{\gamma_{BaX^{2+}} \gamma_{Cl^-}{}^2}{\gamma_{Ba^{2+}} \gamma_{Cl^-}{}^2} \right) \right\} \qquad [4]$$

The cells are set up with $[BaCl_2]_{total} = [BaXCl_2]_{total}$ and, thus, if the complexation equilibrium is such that in the presence of excess X, $[BaX^{2+}] >> [Ba^{2+}]$ (strong complexation), then Eq. [4] reduces to $\mathcal{E} \simeq \mathcal{E}^\circ$ (assuming that the activity coefficients are the same for dilute solutions of $BaCl_2(aq)$ and $BaXCl_2(aq)$ of equal concentrations), and $K_{comp} \simeq \exp(2\mathbf{F}\mathcal{E}^\circ/RT)$. If the above assumptions are valid, then the observed voltage of cell [1] should be independent of the concentration of $BaCl_2$. For cell solutions with barium chloride concentrations (the two cell electrolytes are taken from the same stock solution, and one is then saturated with the crown ether) of 0.476, 3.00, and 4.69 mM, the observed cell voltages (22° ± 1°C) were 62.0 ± 0.6, 58.2 ± 1.0, and 61.2 ± 0.5 mV, respectively. The average of these $\mathcal{E}^\circ$ values (60.5 ± 1.3 mV) yields a value of $K = (1.16 \pm 0.18) \times 10^2$ (22°C) for the reaction

$$Ba^{2+}{}_{(aq)} + X(s) \rightleftharpoons BaX^{2+}(aq) \qquad [5]$$

where X is dicyclohexyl-18-crown-6. The value of K for reaction [5] can be combined with the solubility of the crown ether in water of about 0.038M (22°C) (1) to yield a value of $K = 3.1 \pm 0.5 \times 10^3$ for the reaction

$$Ba^{2+}(aq) + X(aq) = BaX^{2+}(aq) \qquad [6]$$

Izatt *et al.* (5) report values of K for reaction [6] of 2.0×10^3 and 4.0×10^3 for the two conformational isomers of dicyclohexyl-18-crown-6. Since our sample of the crown ether is a mixture of the two isomers, the agreement between our calculated value of K for reaction [6] and the measured values of Izatt *et al.* is within the experimental uncertainty.

The method outlined above for the determination of complexation constants has definite advantages over conventional techniques. The double cell method gives $\mathcal{E}^\circ$ directly from a single measurement, rather than as a small difference between two large numbers, and the minimization of activity coefficient effects is accomplished automatically by the manner in which the cell solutions are prepared.

Acknowledgment

Acknowledgment is made to the donors of the Petroleum Research Fund, administered by the American Chemical Society, for support of this research.

Manuscript received Sept. 20, 1976.

Any discussion of this paper will appear in a Discussion Section to be published in the December 1977 JOURNAL. All discussions for the December 1977 Discussion Section should be submitted by Aug. 1, 1977.

Publication costs of this article were assisted by the Petroleum Research Fund.

REFERENCES

1. C. J. Pedersen, *J. Am. Chem. Soc.*, **89**, 7017 (1967).
2. G. Singh, J. C. Hall, and P. A. Rock, *J. Chem. Phys.*, **56**, 1855 (1972).
3. B. Jakuszewski and S. Taniewska-Osinska, *Rocz. Chem.*, **36**, 329 (1962).
4. G. J. Hills and D. J. G. Ives. *J. Chem. Soc.*, **1951**, 311.
5. R. M. Izatt, J. H. Rytting, D. P. Nelson, B. L. Haymore, and J. J. Christensen, *Science*, **164**, 443 (1969); *J. Am. Chem. Soc.*, **93**, 1619 (1971).

JOURNAL OF THE ELECTROCHEMICAL SOCIETY

SOLID-STATE SCIENCE AND TECHNOLOGY

APRIL 1977

Ionic Conduction in Ternary Chalcogenides

B. Tell and Sigurd Wagner

Bell Laboratories, Holmdel, New Jersey 07733

and H. M. Kasper*

Bell Laboratories, Murray Hill, New Jersey 07974

ABSTRACT

Ionic conduction has been discovered in the chalcopyrite-type semiconductors $CuGaS_2$, $AgGaS_2$, and $AgGaSe_2$, in $LiInS_2$, and in the cation-deficient chalcogenides $CuGa_5S_8$, $CuGa_5Se_8$, and $AgGa_5S_8$.

In a recent study (1) the n into p interdiffusion coefficient in the chalcopyrite-type semiconductor $CuInSe_2$ was determined as $D(cm^2\ sec^{-1}) = 164 \exp [-1.19\ (eV)/kT]$. The magnitude of the preexponential term was taken as an indication for concentrations or mobilities of point defects substantially above those of the related II-VI compounds. If these point defects carry electrical charge, their migration will lead to ionic conduction. It is therefore tempting to investigate the ionic conductivity of I-III-VI_2 compounds especially since ZnS and CdS under certain conditions have been found to be ionic conductors (2).

In electronically highly conducting chalcopyrites such as $CuInSe_2$, ionic conduction will make an insignificant contribution to the total conductivity, *i.e.*, the ionic transference number $t_i = \sigma_i/(\sigma_e + \sigma_i)$ will be small (σ_i and σ_e denote the ionic and the electronic conductivity, respectively). However, it is known that several I-III-VI_2 chalcopyrites can only be prepared with high electronic resistance, and that others can be made electronically resistive by appropriate anneals (3). These compounds may, like $CuInSe_2$, contain point defects in large concentration or with high mobility, and may therefore be predominantly ionic conductors. With experiments described below we have, in fact, detected ionic conduction in single crystals of $CuGaS_2$, $AgGaS_2$, and $AgGaSe_2$.

Because of the current interest in electrolytes containing IA metals for high emf, we have also investigated cells with a $LiInS_2$ electrolyte. This compound is a ternary tetrahedrally coordinated chalcogenide with the rhombohedral $BeSiN_2$ structure, a superstructure of wurtzite.

Taking our considerations a step further, we have sought, and found, evidence for ionic conduction in single crystals of several ternary chalcogenides of the composition I-III_5-VI_8, *i.e.*, in $CuGa_5S_8$, $CuGa_5Se_8$, and $AgGa_5S_8$. In the notation of Parthé (4) these compounds are written as $1_3{}_5 0_2 6_8$. Each formula unit includes two metal vacancies, 0. In general, the metal atoms seem to be randomly distributed leading to a zinc blende type structure. With a quarter of the metal sites vacant, a high mobility can be expected for defects. This class of ternary chalcogenides is closely related to the well-known ionic conductors α-Cu_2HgI_4 and α-Ag_2HgI_4 (5), $1_2 2 0 7_4$-compounds in the Parthé notation. These iodides also contain a quarter of vacant metal sites; the metals are also randomly distributed over the metal sublattice leading to a zinc blende structure; $1_3{}_5 0_2 6_8$ and $1_2 2 0 7_4$ compounds equally have a valence electron concentration of 4.57.

We have measured the open-circuit emf and the two-point a-c resistance of galvanic cells incorporating the ternary compounds as electrolytes, the corresponding Group I metal as one electrode, and a mixture of the appropriate Group VI element with carbon powder as the other electrode. These cells may be represented as (−Pt) I|I-III_a-VI_b|VI,C (Pt+) with Pt lead wires on both sides. The polarities shown are those developed during discharge of the cell. The observed open-circuit emf, E, is related to the thermodynamic value E_o for the formation of the appropriate I_2-VI compound, *viz.*, Cu_2S (6), Cu_2Se (7), Ag_2S (6), Ag_2Se (6), and Li_2S (8) by the relationship $E = E_o t_i$ where t_i is the ionic transference number as previously defined (9).

Not-intentionally-oriented platelets were cut 0.5-1.0 mm thick from melt-grown crystals, polished, and cleaned with organic solvents in an ultrasonic bath. On one face (5-10 mm^2) metal electrodes were applied by evaporation followed by electroplating. After cementing the other face onto the flat-ground ends of high melting glass tubes (3 mm^2 open area), the latter were filled with the chalcogen-carbon mixture. With Pt wires connected to both electrodes, these were sealed for protection from the atmosphere. A schematic cross section of a cell is shown in Fig. 1. The cells, provided with iron-constantan thermocouples, were kept in a resistance-heated oven for experiments between room temperature and ~250°C.

The Li/$Li_{1.1}InS_2$/S,C cells were prepared by cementing glass tubes to both faces of $LiInS_2$ platelets, filling one with Li metal and the other with the sulfur-carbon mixture. Both tubes were closed with carbon piston contacts and then sealed.

Table I shows the principal experimental results. EMF's were measured with a Keithley Model 610B electrometer, and the 1 kHz a-c resistances R with a General Radio Model 1650A impedance bridge. We have listed the highest measured emf, E, of the one to three cells prepared with each electrolyte, in the range

* Electrochemical Society Life Member.

Key words: ionic conductor, ternary chalcogenide, battery.

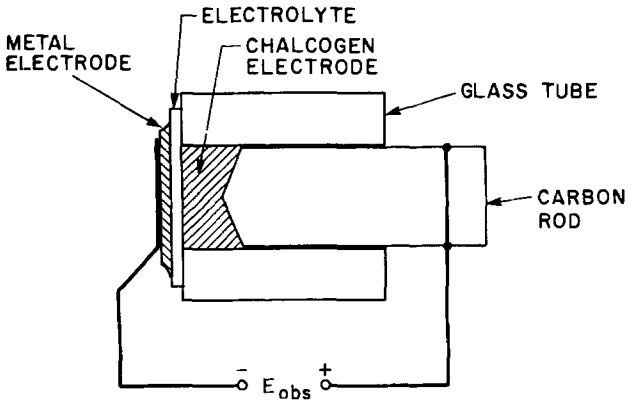


Fig. 1. Schematic cross section of a cell with a copper or silver electrode. Not shown is the sealant which covers the electrode, the electrolyte, and part of the carbon rod at the end of the glass tube.

of temperature investigated. E is compared to the thermodynamic value, E_o, that corresponds to the formation of I_2-VI compounds. The ionic transference number t_i is also tabulated.

The highest emf's of cells incorporating $AgGaS_2$ or $AgGa_5S_8$ lay above E_o. It is difficult to locate the source of this excess emf, E-E_o. $E_o(Ag_2S)$ used in Table I is the maximum value, *i.e.*, that for Ag_2S in equilibrium with saturated sulfur vapor (9). Any other composition of Ag_2S would lead to an even lower value for $E_o(Ag_2S)$ and thus would raise E-E_o. A shunt path within the cell would reduce E below the open-circuit value. The temperature along the cell being uniform within 2°C, thermal gradients cannot significantly contribute to E. It is possible that the excess emf results from the dissolution of silver and sulfur in the ternary electrolytes.

The 1 kHz cell resistances, R, reflect the combined ionic and electronic resistances of the ternary electrolytes. Because of the two-point measurement technique, R also contains contact and electrode resistances.

In several compounds the ionic and electronic conductivities are of comparable magnitude which reduces t_i to values below unity. Evidence presented in Fig. 2 suggests that σ_i/σ_e can be raised to achieve $t_i = 1$. Figure 2 displays the emf as a function of reciprocal temperature for three lithium-doped $AgGaS_2$ samples, one cut from boule No. 606, and two from boule No. 782. In sample No. 606 σ_i is evidently much greater than σ_e at all temperatures. In samples No. 782A and B $\sigma_e < \sigma_i$ near room temperature but $\sigma_e > \sigma_i$ at 250°C. The solid line for samples 782A and B is a least squares fit to the experimental data of the form $E = E_o[1 + (\sigma_e^o/\sigma_i^o) \exp(-\Delta\epsilon_A/kT)]^{-1}$, with $\sigma_e^o/\sigma_i^o = 2.8 \times 10^3$ and $\Delta\epsilon_A = 0.29$ eV.

By adding iodine to the anode compartment of the $AgGaS_2$ and $AgGaSe_2$ cells we have reached emf's of 0.5-0.6V at temperatures above 100°C compared to 0.7V, the theoretical voltage for the formation of AgI. We

Table I. Experimental data on cells containing ternary chalcogenide electrolytes

Electrolyte	E (V)	E_o (V)	t_i	R (10^6 Ω)	T (°C)
$CuGaS_2$	0.03	0.47	0.06	0.5	250
$CuGa_5S_8$	0.34	0.47	0.72	18	220
$CuGa_5Se_8$	0.18	0.35	0.51	2.5	230
$AgGaS_2$	0.26	0.24	1.0	3	270
$AgGa_5S_8$	0.26	0.24	1.0	1	270
$AgGaSe_2$	0.22	0.25	0.68	200	20
$LiInS_2$	2.20	2.45	0.94	100	200

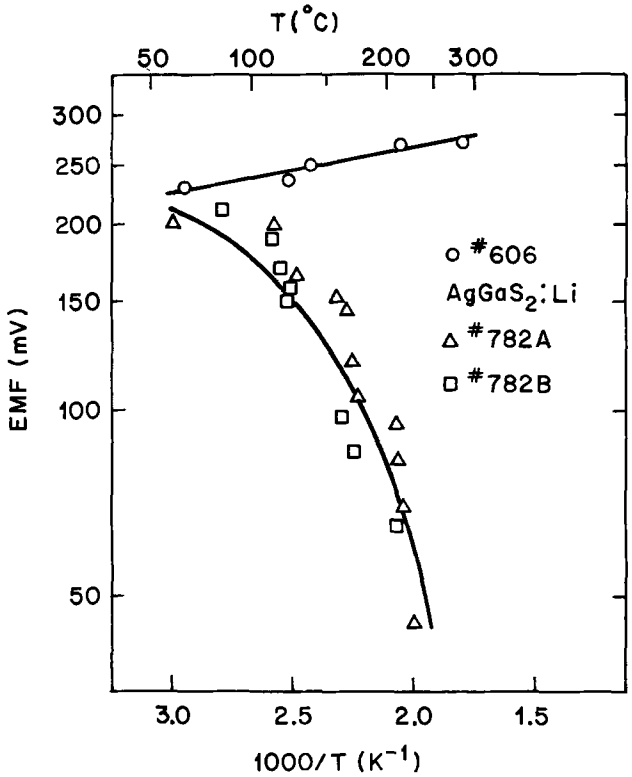


Fig. 2. EMF as a function of inverse temperature for three lithium-doped $AgGaS_2$ samples cut from two different boules.

believe that a leaky AgI layer, which passes mainly Ag^+ ions, forms on the $AgGaS_2$ or $AgGaSe_2$ and that the result of this experiment demonstrates that Ag^+ is the principal mobile ion in $AgGaS_2$ and $AgGaSe_2$.

Acknowledgments

We would like to thank Dr. K. D. Becker, Ruhr University, Bochum, for helpful discussions, and D. H. Olson and L. M. Schiavone for the application of metal electrodes.

Manuscript submitted Sept. 23, 1976; revised manuscript received Dec. 3, 1976.

Any discussion of this paper will appear in a Discussion Section to be published in the December 1977 JOURNAL. All discussions for the December 1977 Discussion Section should be submitted by Aug. 1, 1977.

Publication costs of this article were assisted by Bell Laboratories.

REFERENCES

1. B. Tell, S. Wagner, and P. M. Bridenbaugh, *Appl. Phys. Lett.*, **28**, 454 (1976).
2. R. Galli and F. Garbassi, *Nature*, **253**, 720 (1975).
3. B. Tell, J. L. Shay, and H. M. Kasper, *J. Appl. Phys*, **43**, 2469 (1972).
4. E. Parthé, "Cristallochimie des Structures Tetraédriques," Gordon and Breach, New York (1972).
5. For an unconventional but stimulating discussion of these and of other ionic conductors see J. C. Phillips, *This Journal*, **123**, 934 (1976).
6. T. B. Reed, "Free Energy of Formation of Binary Compounds," M.I.T. Press, Cambridge, Massachusetts (1971).
7. D. D. Wagman, W. H. Evans, V. B. Parker, I. Halow, S. M. Bailey, and R. H. Schumm, "Selected Values of Chemical Thermodynamic Properties," NBS Technical Note 270-4, U.S. Government Printing Office, Washington, D.C. (1969).
8. O. Kubaschewski, E. Ll. Evans, and C. B. Alcock, "Metallurgical Thermochemistry," Pergamon Press, London (1967).
9. C. Wagner, *Z. Phys. Chem. B*, **21**, 25 (1933).

Single Carrier Steady-State Theory for Formation of Anodic Films Under Conditions of High Space Charge in Very Large Electric Fields

A. T. Fromhold, Jr.*

Department of Physics, Auburn University, Auburn, Alabama 36830

ABSTRACT

The kinetics of growth of anodic films are modeled in the high space charge limit; the predictions of the model are examined analytically and numerically. The results illustrate that space charge due to the mobile ionic species can lead to a marked retardation of the rate of growth as measured under constant voltage conditions. Time increases by factors as large as 3000 are found to be required for growth to a given thickness. For a given film thickness the time factors are somewhat greater at larger voltages; at a given voltage the time factors increase nearly linearly with increasing thickness. These observations lead to the following major conclusion: Space charge effects do not disappear and do not saturate with increasing electric field value; on the contrary, the space charge retardation is even more pronounced in the realm of very high electric fields, large applied voltages, and very thick anodic films. For the case of growth under constant current conditions in the presence of space charge, a given growth rate was found to require a significantly larger voltage than would be predicted in the usually considered homogeneous field limit; however, the increase in voltage is relatively less in the higher voltage regime (*e.g.*, a factor of 2) than it is for growth at very low voltages (where factors as large as 10 to 100 are not uncommon). The voltage at constant current was found to increase quasi-linearly with thickness in the thick film high voltage realm, whereas at low voltages the space charge produced marked curvature in the voltage-thickness plots. The quasi-linear variation of voltage with thickness found for the thick film high voltage realm constitutes proof *sine qua non* that present experimental data in the literature indicating experimental constancy of the field at constant current cannot be employed to disqualify anodic film growth models having uncompensated space charge.

The experimental situation.—There have been a number of experimental studies carried out which have a direct bearing upon various aspects of transport during growth (1) of anodic films. Pringle (2, 3) has done a series of beautiful inert marker experiments in order to deduce the transport numbers of the mobile metal species and the mobile oxygen species during the anodic oxidation of tantalum. In one series of experiments (2), for example, radioactive noble gases were implanted by means of a mass separator into thin films of anodic tantalum oxide. The transport numbers for the tantalum and the oxygen were found to be 0.243 and 0.757, respectively, thus leading to the conclusion that it is the oxygen species which is the more mobile under the conditions for that experiment. The noble gas concentration profiles were found to broaden on further anodization, and this was interpreted as being due to the simultaneous movement of tantalum and oxygen atoms during the charge transfer event. In a later series of experiments (3), Pringle measured ^{18}O concentration profiles in thin anodic tantalum oxide films by combining a sectioning technique for locating the isotope with a nuclear technique based on proton bombardment of the ^{18}O and counting of the emitted neutrons in the $^{18}O(p,n)^{18}F$ reaction in order to detect the ^{18}O. The results could be interpreted very well ". . . in terms of a forced diffusion (under the influence of the electric field during anodization) from a constant source (the electrolyte) into a semi-infinite medium (the oxide) . . . ."

Agius and Siejka (4) investigated the passivity of iron by nuclear microanalysis using the $^{16}O(d,p)^{17}O$ reaction, and found that the relationship between the number of oxygen atoms and the potential is approximately linear in the passive region. The results agreed satisfactorily with corresponding data taken by Foley, Kruger, and Bechtoldt (5) by ellipsometry and the data of Frankenthal (6) based on coulometric measurements. It is definitely not clear whether or not sufficient data have been taken over an extended thickness range (several decades) for any given anodic system to be able to say with any degree of certainty whether or not a small curvature (as predicted by the present analysis) exists or not. It is hoped such studies will be undertaken by competent experimentalists in the not-too-distant future.

Rigo and Siejka (7) have carried out interesting Rutherford backscattering studies using 1.8 MeV He ions in order to characterize the long range migration of niobium during the anodic oxidation of tantalum and aluminum on niobium, and Cherki and Siejka (8) have utilized the method of nuclear microanalysis of stable oxygen isotopes by the reactions $^{16}O(d,p)^{17*}O$ and $^{18}O(p,\alpha)^{15}N$ to investigate the mechanisms of growth, dissolution, and transport associated with oxygen during the formation of porous anodic layers $\lesssim$ 7000Å in thickness on aluminum. It was concluded by means of ^{18}O tracer techniques that the growing oxide layer is formed at the metal-oxide interface by oxygen transport through the base layer. The isotope analysis of oxygen at various depths in anodic layers was developed by Amsel and Samuel (9) to investigate migration mechanisms of ionic charge carriers during the growth of compact anodic aluminum oxide films. The method consists of an analysis of the excitation curve as a function of bombarding energy in the vicinity of a narrow resonance of the $^{18}O(p,\alpha)^{15}N$ reaction measured for the sample under investigation.

Earlier studies on anodic films have been summarized in the review by Vermilyea (10) and in Young's classic book (11). A thoughtful review of many of the major

* Electrochemical Society Active Member.

theoretical ideas which developed over the years, together with some extension into the realm of two-carrier transport, has been given by Young (12).

Present work.—Without a doubt, the simultaneous migration of two charged ionic species as observed by Pringle is a much more complex situation than the simple case of one charged ionic species. The *raison d'être* of the present approach, based as it is on the theoretical and numerical analysis of a single uncompensated ionic charge carrier, is to carry out, first, the simplest calculation in order to develop some intuitive understanding of space charge effects, and at some later time to try to do the more complex numerical problem involving two species. Moreover, there may well exist experimental systems where a single mobile ionic species predominates, and in such cases the present analysis will be immediately applicable. This is an exciting area of present-day research, with many types of experiment being developed all the time for deducing new information on the microscopic processes operative during anodic growth. It is anticipated that new theoretical approaches will need to be developed as our understanding of the experimental situation continues to broaden.

The effects of single carrier space charge and defect concentration gradients on anodic film formation have already been examined in an earlier study (1) for the limit of thin anodic films and low voltages. Discrete hopping equations were utilized to take into account the atomic nature of the diffusion medium and to include high field current nonlinearities. One of the most important conclusions of the earlier work (1) is that, for a fixed voltage, the uncompensated space charge of the mobile ionic species can be a critical factor in retarding the growth rate of the anodic film. The question of whether or not this effect persists in the higher electric field, higher space charge, and thicker film domains is an interesting and a critical one, and it is to answer this question that the presently reported work was undertaken.

First of all, new calculations utilizing the earlier numerical approach are illustrated briefly in the present paper. This serves to review the major effects predicted at lower voltages and thinner anodic films, and extends the results to situations involving higher valence and larger space charge. Next, the analytical development constituting the major thrust of the present paper is presented. This development is appropriate for very high electric fields and very thick anodic films. This development is followed by specific numerical evaluations of the analytically derived equations. These include the single carrier diffusing defect and electric field profiles, the kinetics for constant voltage growth, and the thickness dependence of the voltage for constant current growth. Conclusions are then summarized.

Numerical Evaluation of Space Charge Effects at Low Voltages in the Thin Film Limit

Previous work.—The published computations of Fromhold and Kruger (1) for thin anodic film growth utilized an iterative scheme developed for the domain of electric field strength for which the electric-field-produced current contributions were generally of the same order as the concentration-gradient-produced current contributions. The relevant microscopic equations for this space charge gradient model (1) include the potential well to potential well hopping current and Poisson's equation in discrete form, and the computations were carried out in the steady-state limit. To supplement these published calculations, to test their generality, and to explore the effects of increasing the charged defect concentration by an order of magnitude and the valence by a factor of 2, a set of calculations has been carried out utilizing the new parameter values as listed in Table I.

Table I. Values utilized for parameters in numerical computations for transport through a passive* anodic oxide film layer. (These values are appropriate for Fig. 1 through 12.)

Symbol	Terminology	Value	Units
n_0	Areal defect density of mobile species at position $x = 0$	10^{12}	no./cm^2
n_N	Areal defect density of mobile species at position $x = L$	10^{10}	no./cm^2
W	Activation energy for diffusion of mobile ionic defect species	0.5	eV
T	Temperature	300	°K
ν	Attempt frequency of mobile ionic defect species	10^{13}	sec^{-1}
$2a$	Lattice parameter of anodic oxide	3.2	Å
Z	Valence of diffusing species determining its charge	−2	—
ϵ	Relative dielectric constant of anodic oxide (in units of ϵ_0, the permittivity of free space)	6	—
R	Volume of oxide per ionic defect transported through the anodic film	25	Å^3

* The author is indebted to Dr. J. Kruger of the National Bureau of Standards for his aid in choosing a set of parameters which should be fairly typical for the anodization of iron.

Particle currents.—Although the complete results are presented elsewhere (13), the essential retarding effects of the space charge on the ionic current can be noted directly from Fig. 1. The solid curves constitute logarithmic plots of current *vs.* thickness for several voltages with space charge effects included. The dashed curves show the corresponding results when space charge is neglected. It can be seen that at a given thickness, such as 100 monolayers, the current at a given voltage is decreased by orders of magnitude by the space charge.

The curvature in the very thin film region exhibited by both the solid and dashed curves is a manifestation of the nonlinear diffusion effects (14) attributable to very large electric field values. The breakaway between the pairs of solid and dashed curves at a given voltage occurs because of the space charge, and it can

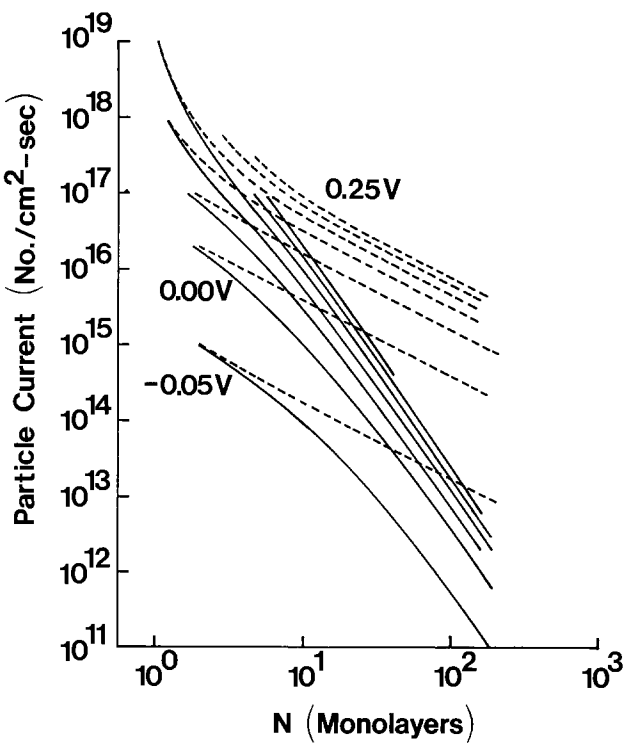


Fig. 1. Logarithm of the defect particle current *vs.* logarithm of the anodic oxide thickness for growth with space charge (solid curves) under constant electrostatic potentials ranging from −0.05 to 0.25V in increments of 0.05V. (Microscopic parameter values are listed in Table I.) Dashed curves illustrate the corresponding homogeneous field calculations.

Table II. Particle current densities J_0 associated with a given curve number in Fig. 2, 3, and 4 for the low voltage anodization regime

Curve No.	Particle current density J (No./cm²-sec)
1	1×10^{11}
2	5×10^{11}
3	1×10^{12}
4	5×10^{12}
5	1×10^{13}
6	5×10^{13}
7	1×10^{14}
8	5×10^{14}
9	1×10^{15}
10	5×10^{15}
11	1×10^{16}
12	5×10^{16}
13	1×10^{17}
14	5×10^{17}
15	1×10^{18}

be noted that the separation between the two curves in each pair increases markedly with increasing thickness. The greater slopes of the solid curves relative to the dashed curves reflect the greater limiting-thickness behavior of growth kinetics for the space-charge-modified situation relative to the homogeneous-field case. The slopes of the thicker film portions of the dashed curves in Fig. 1 are approximately 1, whereas the slopes of the solid curves in this figure range as high as 2.8. Such slopes lead to semiempirical growth laws $L(t) \propto t^{1/n}$, with $n \simeq 4$ for the later stages of space-charge-modified growth. It is interesting to compare these slopes with those in the very thin film growth stages where nonlinear electric field effects are very pronounced and the resulting growth kinetics are sharply rate limiting, as follows from considerations quite analogous to those of Cabrera and Mott (15) for thermal oxidation. In this thickness region the slope in Fig. 1 has values as large as 5, corresponding to $n \simeq 6$ in the corresponding semiempirical growth law $L(t) \propto t^{1/n}$. As a final word on the kinetics in this low voltage regime, it should be pointed out that the -0.05V curve in Fig. 1 represents anodization produced by the ionic concentration gradient under reverse bias conditions for the voltage.

Defect profiles.—A series of constant current anodization curves was computed for the new set of microscopic parameter values listed in Table I, with the several currents utilized listed in Table II. The computed diffusing areal defect density profiles for this set of computations including space charge effects are illustrated in Fig. 2; the corresponding defect profiles as computed in the homogeneous-field limit are illustrated in Fig. 3. The key relating curve number to current density is given in Table II. A comparison of Fig. 2 and 3 shows that the qualitative and quantitative differences between the space-charge-modified profiles and the homogeneous field profiles are quite pronounced

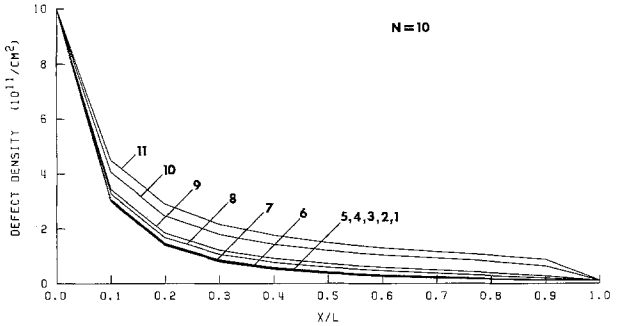


Fig. 2. Defect density for a 10-monolayer anodic oxide film computed with space charge effects *vs.* normalized position x/L for several values of the current. (Microscopic parameter values are listed in Table I and particle current densities for the several curves are listed in Table II.)

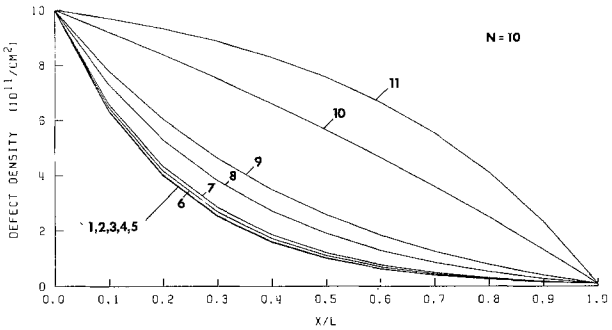


Fig. 3. Defect density for a 10-monolayer anodic oxide film computed in the homogeneous field limit *vs.* normalized position x/L for several values of the current. (Microscopic parameter values are listed in Table I and particle current densities for the several curves are listed in Table II.)

even for thicknesses as small as 10 monolayers. This reflects the very large space charge values chosen for the present set of computations. [An areal density $n_0 = 10^{12}/\text{cm}^2$ with $2a = 3.2$Å as listed in Table I corresponds to the value $C(0) = 3.125 \times 10^{19}$ cm^{-3} for the bulk density of charged defects near the interface.] Note that the ionic defect densities are significantly less for the case of space charge (Fig. 2) than in the corresponding homogeneous-field limit (Fig. 3). One can argue qualitatively that the reason the defect density is relatively lower for the ionic space-charge-modified profile (as compared to the homogeneous field profile) is the following: The space charge of the single diffusing species gives rise to large forward values for the electric field, so the defect density must drop accordingly to maintain the fixed value chosen for the presently considered forward hopping current. This reasoning neglects several factors, including concentration gradient effects and the reverse hopping current. The qualitative argument is actually independent of the particular transport equation employed for the field-modified diffusion, just as long as the transport current increases locally with an increase in the local value of the diffusing defect density and with an increase in the local value of the electric field.

Voltage under constant current growth.—The voltage *vs.* thickness curves computed for the series of currents listed in Table II are shown in Fig. 4. The upper set constitutes the space-charge-modified sequence, whereas the lower set is the homogeneous field sequence computed for comparison purposes. The concave curvature so evident in the upper sequence in the thicker film growth region is quite characteristic of the presence of space charge; on the other hand, the homogeneous field curves in the lower sequence are very closely linear for thicknesses beyond those where the concentration gradient gives rise to some initial convex curvature. It can also be noted from Fig. 4 that a given current at a given thickness requires a much larger voltage with space charge than is the case in the absence of space charge.

The consideration of space charge effects for the opposite extreme limiting case of high voltage anodization in the thick film region is now examined. The approach utilized is basically analytical, but with numerical evaluations of the resulting equations carried out to obtain qualitative insight into the predictions of the model.

Analytical Formulation for Evaluation of Space Charge Effects at High Voltages in the Thick Film Limit

Particle current.—As a starting point, it is convenient to utilize a very high field equation closely analogous to the one employed by Dewald (16)

$$J_0 = (D/2a)C(x) \exp [ZeE(x)a/kT] \qquad [1]$$

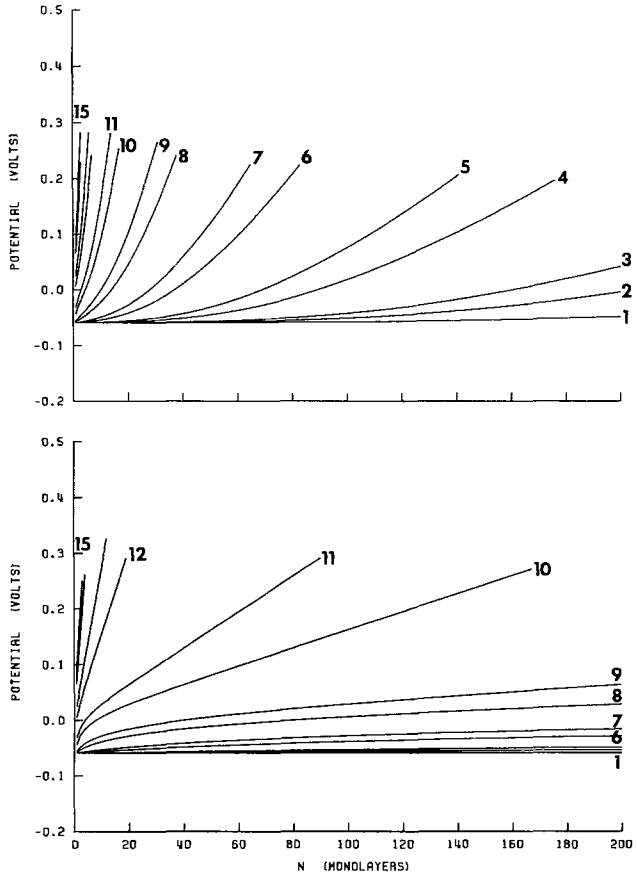


Fig. 4. Comparison of homogeneous field results (lower portion) with computations including space charge (upper portion) for electrostatic potential vs. thickness in monolayers for a growing anodic film. (Microscopic parameter values are listed in Table I and particle current densities for the several curves are listed in Table II.)

where J_0 is the steady-state particle current through the existing anodic oxide film, $C(x)$ is the bulk defect concentration of the uncompensated charged diffusing ionic species at position x in the oxide, $E(x)$ is the macroscopic electric field at position x, D is the diffusion coefficient, $2a$ is the hopping distance between potential minima within the oxide for the diffusing species, Ze is the charge per particle of the diffusing ionic species, and kT is the thermal energy at temperature T involving the Boltzmann constant k. The origin of Eq. [1] can be easily traced to the microscopic hopping model (13-17) and the assumption that the electric field is so large that the forward hopping current so greatly exceeds the reverse hopping current that the latter can be entirely neglected (13). The essential point involves the ratio of the electrostatic energy difference $ZeE(x)a$ between a potential energy minimum and the adjacent potential energy barrier maximum to the thermal energy kT. A sufficient condition for the validity of Eq. [1] is that $|ZeE(x)a/kT| >> 1$, but as a practical matter Eq. [1] can generally be utilized whenever the ratio exceeds 2 or 3. The complete development of Eq. [1] from the consideration of the hopping of defects over field-modified potential energy barriers in the anodic oxide, together with the specific conditions of applicability, can be found in a review article (13) on anodic oxidation.

Electric field.—The electric field $E(x)$ must be obtained from Poisson's equation of electrostatics

$$E(x) = E_0 + (4\pi/\epsilon) \int_0^x ZeC(x)dx \qquad [2]$$

where E_0 is the surface charge field at the interface at $x = 0$, and the term involving the integral of the charge density $ZeC(x)$ of the uncompensated mobile ionic defect species in transit represents the total space charge contribution to the electric field. The parameter ϵ is the static dielectric constant of the anodic oxide. Differentiation of Eq. [2] gives

$$\frac{dE(x)}{dx} = \frac{4\pi Ze}{\epsilon} C(x) \qquad [3]$$

Solving for $C(x)$ from this equation and substituting into Eq. [1] gives

$$J_0 = (D/2a)(\epsilon/4\pi Ze) \exp[ZeE(x)a/kT] \frac{dE(x)}{dx} \qquad [4]$$

This constitutes a differential equation for the electric field, with all of the remaining quantities being position-independent parameters and physical constants. To solve Eq. [4], it is convenient to change variables by defining

$$\beta(x) \equiv \exp[ZeE(x)a/kT] \qquad [5]$$

It follows directly that

$$\frac{d\beta(x)}{dx} = \frac{Zea\beta(x)}{kT} \frac{dE(x)}{dx} \qquad [6]$$

Equations [5] and [6] are sufficient to convert Eq. [4] to the form

$$J_0 = (D/2a)(\epsilon/4\pi Ze)(kT/Zea) \frac{d\beta(x)}{dx} \qquad [7]$$

Equation [7] can be integrated immediately to give

$$J_0 x = (D/2a)(\epsilon/4\pi Ze)(kT/Zea)[\beta(x) - \beta_0] \qquad [8]$$

where

$$\beta_0 = \exp[ZeE_0 a/kT] \qquad [9]$$

It is convenient to introduce a parameter λ

$$\lambda \equiv 4\pi(Ze)^2 a/\epsilon kT \qquad [10]$$

which has the dimensions of an area. Equation [8] then can be written simply as $J_0 x = (D/2a\lambda)[\beta(x) - \beta_0]$, from which we obtain

$$\beta(x) = \beta_0 + (2a\lambda J_0/D)x \qquad [11]$$

The definition for $\beta(x)$ (Eq. [5]) then leads to the electric field

$$E(x) = (kT/Zea)\ln[\beta_0 + (2a\lambda J_0/D)x] \qquad [12]$$

Defect profile.—The defect profile obtained from Eq. [3] and [12] is

$$C(x) = (\epsilon/4\pi Ze)(kT/Zea)\left(\frac{(2a\lambda J_0/D)}{\beta_0 + (2a\lambda J_0/D)x}\right) = \frac{2aJ_0/D}{\beta_0 + (2a\lambda J_0/D)x} \qquad [13]$$

where Eq. [10] has been employed.

By utilizing Eq. [1] as evaluated at $x = 0$

$$J_0 = (D/2a)C(0)\exp(ZeE_0 a/kT) = (D/2a)C(0)\beta_0 \qquad [14]$$

Eq. [13] can be written as

$$C(x) = \frac{C(0)\beta_0}{\beta_0 + \lambda C(0)\beta_0 x} = \frac{C(0)}{1 + \lambda C(0)x} = \frac{C(0)}{1 + (x/x^*)} \qquad [15]$$

where

$$x^* \equiv [\lambda C(0)]^{-1} \qquad [16]$$

The parameter x^* will be referred to as the "space charge screening parameter" because it is the distance in which the concentration $C(x)$ in Eq. [15] falls to one-half of its largest value $C(0)$. It should be strongly emphasized, however, that the space charge is not actually "screening" the surface charge field E_0 in the

usual physical sense of the word[1] because the charge density $ZeC(x)$ is of the same sign as the surface charge density which is the source of the surface charge field E_o.

Alternate electric field expressions.—Equations [14] and [16] allow us also to simplify Eq. [12] to the form

$$\begin{aligned} E(x) &= (kT/Zea)\ln[\beta_o + \beta_o\lambda C(0)x] \\ &= (kT/Zea)\ln\beta_o + (kT/Zea)\ln[1 + (x/x^*)] \\ &= E_o + E^*\ln[1 + (x/x^*)] \end{aligned} \quad [17]$$

where Eq. [9] and [16] have been used for β_o and x^*, and the parameter E^* (which can be called the thermal fluctuation field) is defined by

$$E^* \equiv kT/Zea \quad [18]$$

Electrostatic potential and voltage.—The electrostatic potential follows from the electric field expression

$$V(x) \equiv -\int_0^x E(x)dx \quad [19]$$

Substituting Eq. [17] into Eq. [19] gives

$$\begin{aligned} V(x) = &- E_o x + E^* x \\ &- E^* x^*[1 + (x/x^*)]\ln[1 + (x/x^*)] \end{aligned} \quad [20]$$

One of the most useful quantities is the total voltage $V(L)$ across the anodic film. This follows directly by evaluating Eq. [20] at $x = L$

$$V(L) = -E_o L + E^* L \ln \mathcal{Q} \quad [21]$$

where

$$\ln \mathcal{Q} \equiv 1 - (x^*/L)[1 + (L/x^*)]\ln[1 + (L/x^*)] \quad [22]$$

The parameter $\mathcal{Q}$ contains the essential space charge modification of the voltage. In the absence of space charge effects, $x^* \to \infty$, $\ln \mathcal{Q} \to 0$, and $\mathcal{Q} \to 1$, as shown in Appendix A. Since $\mathcal{Q}$ is film thickness dependent, the voltage under constant current conditions has a complex dependence on thickness which is examined numerically in the next section. To obtain the voltage $V(L)$ *vs.* thickness L under constant current conditions, the following procedure is employed. For the current J_o in question, the surface charge field is first obtained from Eq. [14]

$$E_o = E^* \ln[2aJ_o/DC(0)] \quad [23]$$

where E^* is determined from Eq. [18]. This expression for E_o is substituted into Eq. [21] to give the voltage

$$V(L) = -E^* L \ln[2aJ_o/\mathcal{Q}DC(0)] \quad [24]$$

Then $V(L)$ can be evaluated numerically for a series of film thicknesses, utilizing Eq. [22] to determine $\mathcal{Q}$ for each thickness.

Particle current under constant voltage conditions.—To obtain the current J_o *vs.* thickness L under constant voltage conditions, the following procedure is employed. For the fixed voltage $V(L)$ in question, the surface charge field is determined by Eq. [21] for any film thickness L

$$E_o = E^* \ln \mathcal{Q} - [V(L)/L] \quad [25]$$

with $\ln \mathcal{Q}$ given by Eq. [22]. The required parameters x^* and E^* are given by Eq. [16] and [18], respectively. This value of E_o is substituted into Eq. [14] to give the current

$$\begin{aligned} J_o &= (D/2a)C(0)\exp(E_o/E^*) \\ &= [\mathcal{Q}DC(0)/2a]\exp[-V(L)/(E^*L)] \end{aligned} \quad [26]$$

and J_o can then be evaluated for a series of film thicknesses. Alternatively, this expression for the current can be substituted directly into the growth rate expression

$$\frac{dL(t)}{dt} = RJ_o \quad [27]$$

to give

$$\begin{aligned} \frac{dL(t)}{dt} &= [\mathcal{Q}RDC(0)/2a]\exp[-V(L)/(E^*L)] \\ &= (\mathcal{Q}RDC(0)/2a)\exp[L^*/L] \end{aligned} \quad [28]$$

where L^* is the positive quantity

$$L^* \equiv -V(L)/E^* = -ZeaV(L)/kT \quad [29]$$

and R is the volume of new oxide formed per ion which is transported through the anodic film.

Approximate forms for the growth rate expression.—Although $\mathcal{Q}$ is a sufficiently complicated function of L so that an exact integration of the above growth rate expression will generally require numerical techniques, there are two important limiting cases which can be solved analytically. These limiting cases are the zero space charge (homogeneous field) limit and the opposite extreme of the very large space charge limit. For the homogeneous field limit, $x^* \to \infty$ and $\mathcal{Q} \to 1$, as shown in Appendix A, so that the above growth rate expression [28] reduces in this limit to

$$\frac{dL(t)}{dt} = \Theta\exp(L^*/L) \quad \text{(zero space charge)} \quad [30]$$

where

$$\Theta \equiv RDC(0)/2a = R[4a^2\nu\exp(-W/kT)]n_o/4a^2 \quad [31]$$

On the other hand, for the very large space charge limit, $x^* \to 0$ and $\mathcal{Q} \to \infty$ asymptotically as $(2.718x^*/L)$, as shown in Appendix B, so that the growth rate expression [28] reduces in this limit to

$$\frac{dL(t)}{dt} = (\gamma^*/L)\exp(L^*/L) \quad \text{(large space charge)} \quad [32]$$

where

$$\gamma^* = 2.718x^*\Theta = 2.718RDC(0)x^*/2a \quad [33]$$

Rate laws.—The limiting case growth rate expressions [30] and [32] can be integrated to obtain growth laws. The integral forms are, respectively

$$\Theta t = \int_0^L \exp(-L^*/L')dL' \quad [34]$$

and

$$\gamma^* t = \int_0^L L'\exp(-L^*/L')dL' \quad [35]$$

Changing dummy variables from L' to η according to the definition

$$\eta \equiv L/L' \quad [36]$$

$$\begin{aligned} d\eta &= -[L/(L')^2]dL' \\ &= -(1/L)\eta^2 dL' \end{aligned} \quad [37]$$

lead to the expressions

$$\begin{aligned} \Theta t &= \int_\infty^1 \exp(-\eta L^*/L)[-(L/\eta^2)]d\eta \\ &= L\int_1^\infty \eta^{-2}\exp(-\eta L^*/L)d\eta \\ &= L\mathcal{E}_2(L^*/L) \quad \text{(zero space charge)} \end{aligned} \quad [38]$$

and

$$\begin{aligned} \gamma^* t &= \int_\infty^1 (L/\eta)\exp(-\eta L^*/L)[-L/\eta^2]d\eta \\ &= L^2\int_1^\infty \eta^{-3}\exp(-\eta L^*/L)d\eta \\ &= L^2\mathcal{E}_3(L^*/L) \quad \text{(with space charge)} \end{aligned} \quad [39]$$

[1] Usually the word "screening" denotes an assembly of mobile charge in the neighborhood of some fixed source charge of opposite sign, in which case the "screening charge" reduces the electric field in the surrounding region over the value it would have in the absence of screening.

Table III. Values of space charge parameters and ionic diffusion coefficient computed from the microscopic physical parameter values listed in Table I

Symbol	Definition	Terminology	Value	Units
$C(0)$	$n_0/2a$	Bulk defect density at $x = 0$	3.125×10^{19}	no./cm^3
λ	$4\pi(Ze)^2a/\epsilon kT$	Parameter	7.47×10^{-15}	cm^2
x^*	$[C(0)\lambda]^{-1}$	Space charge screening parameter	4.28	Å
E^*	kT/Zea	Thermal fluctuation field	-8.08×10^5	V/cm
D	$4a^2\nu\exp(-W/kT)$	Ionic diffusion coefficient	4.08×10^{-11}	cm^2/sec
θ	$RDn_0/4a^2$	Homogeneous field preexponential growth factor	99.46	Å/sec
γ^*	$2.718\ x^*\theta$	Space-charge-modified preexponential growth factor	1159	Å^2/sec

The quantities $\mathcal{E}_2(L^*/L)$ and $\mathcal{E}_3(L^*/L)$ are the second and third order exponential integrals (18). Recurrence relations and polynomial approximations are readily available (18) so that numerical evaluations of these limiting high field growth expressions can be carried out. The domain of validity of the growth expressions is specified in Appendixes A and B, respectively. The results of such numerical evaluations are presented in the following section.

Numerical Evaluation of Analytical Expressions for High Voltages and Thick Films

Parameter values.—To gain the desired insight into the predictions of the equations derived in the last section for the high voltage thick film limit, a numerical evaluation has been carried out with an HP-65 programmable electronic calculator. The values chosen for the primary microscopic physical parameters are those listed in Table I which were utilized for the low voltage computations illustrated above. This, of course, facilitates a comparison of our results for the low voltage and the high voltage limits. The values of the secondary space charge parameters depending only on the microscopic parameter values listed in Table I are given in Table III.

Let us consider a 1000Å anodic oxide film having the microscopic parameters listed in Table I. With an applied voltage of 100V, the average field[2] $\langle E\rangle = -V(L)/L$ has the enormous value of -10^7 V/cm, so that the condition [B-9] given in Appendix B for the very high field limit might be expected to be well met, since $Ze\langle E\rangle a/kT \simeq 12.4$. The self-consistency of this assumption for all values of the field throughout the film will be tested shortly. The value $n_0 = 10^{12}$/cm^2 leads to a defect concentration $C(0) = n_0/2a = 3.125 \times 10^{19}$/cm^3. The value of the parameter λ defined by Eq. [10] is 74.71×10^{-14} cm^2, and the value of the space charge screening parameter x^* defined by Eq. [16] is 4.2832Å. The thermal fluctuation field defined by Eq. [18] is $E^* = -8.0785 \times 10^5$ V/cm. The value of $\ln \mathcal{Q}$ defined by Eq. [22] is -4.4807 which gives $\mathcal{Q} \simeq 1.1326 \times 10^{-2}$. Substituting these values into Eq. [21] gives the surface charge field $E_0 = -6.3803 \times 10^6$ V/cm. These values, which of course are specific to the film thickness and voltage under consideration, are listed for reference purposes in Table IV. Since $ZeE_0a/kT \simeq 7.90$, the very high field condition [A-11] given in Appendix A is definitely met in the region $x \simeq 0$. The space charge is negative since $Z < 0$, so that the field can only increase in magnitude from $x = 0$ to $x = L$. Therefore the very high field condition is met throughout the anodic oxide film, and the equations developed are thus applicable to the presently considered situation.

[2] Since $V(x) \equiv -\int_0^x E(x)dx$, the average field $\langle E\rangle$ in the oxide, defined as $\int_0^L E(x)dx/\int_0^L dx$, is simply equal to $-V(L)/L$.

Table IV. Values of space charge parameters computed from microscopic physical parameter values listed in Table I and the computed parameters listed in Table III when a voltage $V(L) = 100$V is impressed across an anodic film of thickness $L = 1000$Å. (These values are appropriate for Fig. 5-7.)

Symbol	Definition	Terminology	Value	Units
$\ln \mathcal{Q}$	Eq. [22]	Parameter defined by $1 - (x^*/L)[1 + (L/x^*)] \ln [1 + (L/x^*)]$	-4.48	—
$\mathcal{Q}$	$\exp\{\ln \mathcal{Q}\}$	Space charge growth retardation parameter	1.13×10^{-2}	—
E_0	—	Surface charge electric field as obtained from Eq. [21]	-6.38×10^6	V/cm
ZeE_0a/kT	—	Ratio of electrical energy between barrier minimum and barrier maximum to thermal energy	7.90	—
L^*	$-ZeaV(L)/kT$	Critical thickness parameter	12,380	Å

Profiles.—The concentration profile (solid curve) for these parameters as given by Eq. [15] including space charge effects is illustrated in Fig. 5. The corresponding homogeneous field concentration profile (again not explicitly including any imposed concentration gradient) is illustrated by the dashed curve in this figure. The marked difference between the two is especially noteworthy, since it highlights the very important point that the space charge will greatly modify the defect distribution in a growing anodic film. Were the concentration gradient to be included in the computations, the fixed lower defect density at the outer interface would cause a rapid drop-off of the dashed curve near that interface, so in one sense the constant value dashed curve illustrated in Fig. 5 is not actually physically meaningful. The distinction between the solid and dashed curves is, however, very illuminating, since it delineates specifically the effect of the space charge. The rapid falloff of the solid curve near the high defect density interface is required if the current is to remain position independent (*i.e.*, independent of x) in the film, since the increasingly larger values of electric field (see Fig. 6) at larger x values represent larger and larger values of the driving force per particle, which requires in turn smaller and smaller numbers of mobile particles at larger x values to maintain a fixed value for the current.

The integral of the defect distribution of Fig. 5 gives the total defect density as a function of position within the anodic film, which in turn determines the spatial variation of the electric field, as illustrated in Fig. 6.

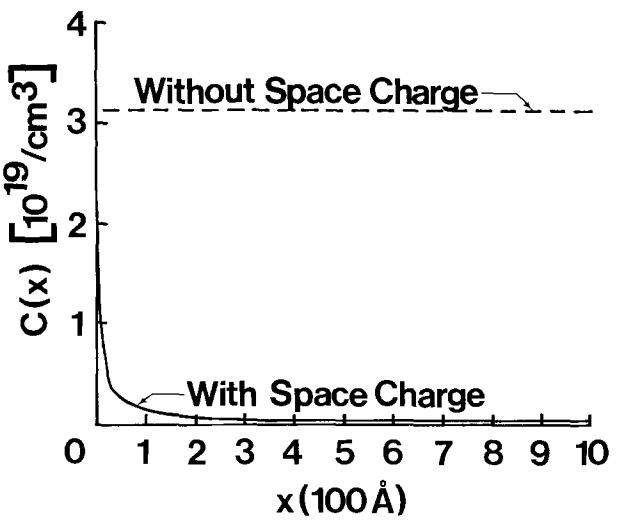


Fig. 5. Defect concentration profile in the large space charge very high field limit for a 1000Å anodic film with an impressed potential of 100V. (Microscopic parameter values are listed in Tables I, III, and IV.)

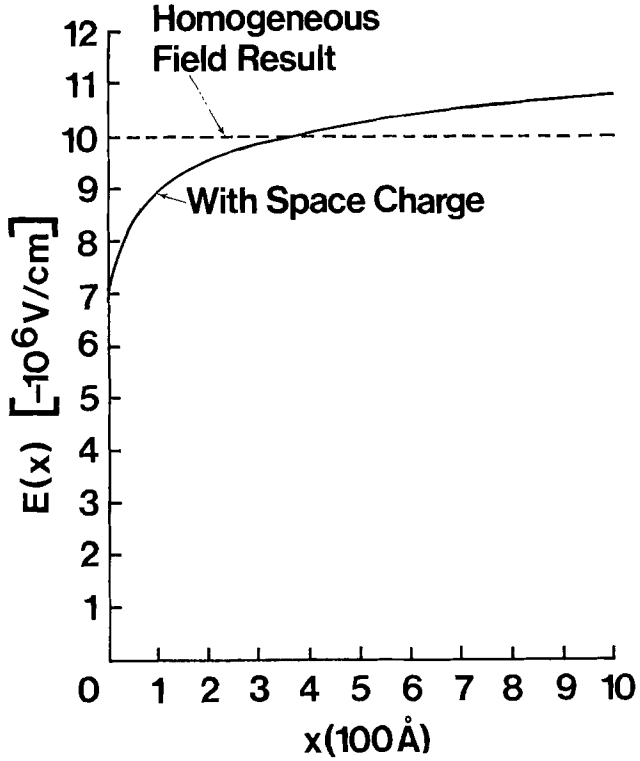


Fig. 6. Electric field profile in the large space charge very high field limit for a 1000Å anodic film with an impressed potential of 100V. (Microscopic parameter values are listed in Tables I, III, and IV.)

This quantity is obtained from Eq. [12]. The departures from the corresponding homogeneous field, as also illustrated in this figure, are noteworthy. Two points should be noted, namely, that the uniform (homogeneous) field approximation would be quite poor, and the high field limit is a poorer approximation with space charge because near $x = 0$ the field is significantly less than it would be in the homogeneous field limit.

The electrostatic potential (Eq. [20]) for the present situation is illustrated in Fig. 7. It is interesting that the electrostatic potential variation within the film in the presently considered very high field situation does not depart greatly from a linear variation appropriate

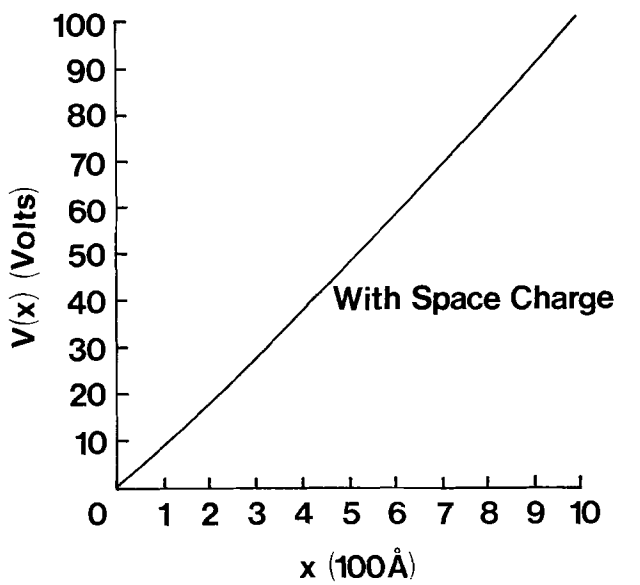


Fig. 7. Electrostatic potential profile in the large space charge very high field limit for a 1000Å anodic film with an impressed potential of 100V. (Microscopic parameter values are listed in Tables I, III, and IV.)

for a homogeneous field. The reason is that the space charge is so large that the space charge screening parameter $x^* \simeq 4.3$Å is only a tiny fraction of the film thickness $L = 1000$Å; thus the defect density drops to very low values throughout most of the anodic film (*cf.* Fig. 5), with the consequence that the electric field over the major portion of the anodic film is indeed approximately homogeneous. For example, the defect density in the center of the film given by the computations leading to Fig. 5 is 2.65×10^{17} cm^{-3}, which is a factor of 0.848×10^{-2} below the fixed value at the interface chosen for the calculations. This drop in space charge density to a value below 1% of the interfacial value means that the defect density is lower deep within the anodic film because of space charge effects, and the electric field varies much more slowly deep within the anodic film than it does near the fixed defect density interface. Figure 6 shows that the variation of the electric field is less than 10% over the latter 70% or so of the film. It is interesting to compare the potential distribution illustrated in Fig. 7 with that of Fig. 12 in Ref. (1). The greater curvature manifested in the 160 monolayer film in Fig. 12 of Ref. (1) is due primarily to the lower defect density with the accompanying larger value for the space charge screening parameter. [Figure 12 of Ref. (1) is based on the microscopic parameter values listed in Table I of Ref. (1), which lead to the value $x^* = 286$Å, whereas the curves illustrated in that figure are for thicknesses of 80 and 640Å.] In this way we see a resolution of a seemingly paradoxical situation in which moderate space charge densities introduce large changes in the potential distribution within the film whereas large space charge densities lead to a potential variation which is not too different from that expected in the homogeneous field limit. That the situations of zero space charge and large space charge are nevertheless quite different can be inferred from a comparison between the defect profiles shown in Fig. 5. The kinetics of anodic film growth are also quite different in the two situations, as has already been verified by computations for the current (*cf.* solid and dashed curves in Fig. 1). [The computations illustrated in Fig. 1 are comparable to those shown in Fig. 16 and 17 of Ref. (1) for a lower space charge density. The high voltage thick film limit space charge computations have also been carried out for the parameter values utilized in Ref. (1), but the results will not be presented since they are qualitatively the same (though not quite so pronounced) as the space-charge-modified results presented herein.]

Anodic film growth under constant current conditions.—For constant current growth, the surface charge field E_0 for the presently considered situation is independent of thickness, according to Eq. [14]. Equations [15], [12], and [20] then show, respectively, that at a given position x within the anodic film the defect concentration, the electric field, and the electrostatic potential will be essentially independent of anodic film thickness in the very high field limit. (The total electrostatic potential difference across the oxide film, *i.e.*, the voltage, does of course depend upon the thickness.) The further limit of considering a homogeneous field ($\epsilon \to \infty$, $\lambda \to 0$, $x^* \to \infty$) for these profile equations yields $C(x) \to C(0)$, $E(x) \to E_0$, and $V(x) \to -E_0 x$, as shown in Appendix B.

The most important result for growth under constant current conditions is the relation for the total electrostatic potential, *i.e.*, the voltage, developed across the anodic film *vs.* the thickness given by Eq. [21]. This is the very high field analog of the numerically computed curves illustrated in Fig. 4. Whereas the homogeneous field voltage $V(L) = -E_0 L$ increases linearly with thickness, Eq. [21] predicts a logarithmic modification which is introduced by the space charge. This logarithmic factor might be expected to give rise to a noticeable curvature in the voltage *vs.* film thickness plot at constant current. Numerical computations to

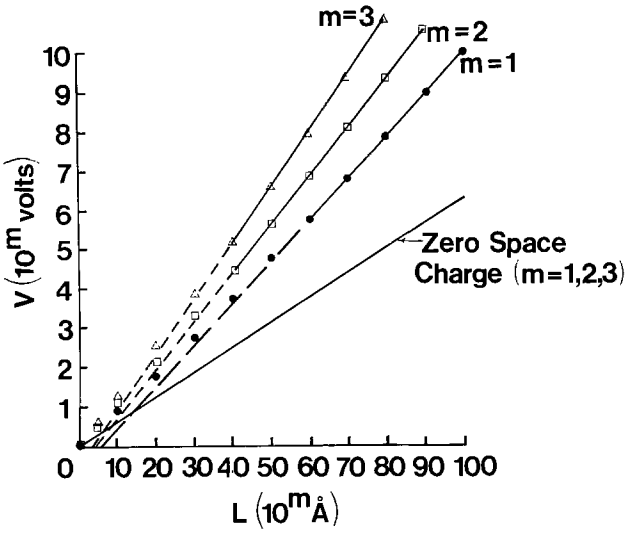


Fig. 8. Voltage vs. thickness over three decades for anodic film growth with space charge for a constant current ($J = 1.071 \times 10^{20}$ cm^{-2}-sec^{-1} for the value of the diffusion coefficient listed in Table III) and comparison with zero space charge results. (Microscopic parameter values are listed in Tables I and III.)

delineate this effect are illustrated in Fig. 8. It is very interesting that the curvature present in the computed voltage *vs.* thickness curves is not pronounced enough to be noticeable over a limited range of film thicknesses, although it is evident from the lack of superposition of the curves $m = 1$, 2, and 3 for the three successive decades shown in Fig. 8 that indeed there is a nonlinearity in the voltage-thickness relationship. This nonlinearity, however, is not nearly as pronounced for the presently considered high voltage limit as it is for the corresponding low voltage limit illustrated in Fig. 4. Therefore a great deal of care is needed in taking experimental data in order to avoid missing the curvature. Otherwise, one could very easily conclude (erroneously) on the basis of sparse data points taken over a limited thickness range that current is simply a linear function of voltage. This in turn might lead one to interpret experimental results (again erroneously) as indicating a strictly homogeneous field, and on this basis deduce entirely wrong values for the microscopic physical parameters for transport through the anodic film.

The voltage has been examined above at some length for the presently considered situation of growth under constant current conditions because it contains the experimentally measurable effects of space charge on the kinetics. The anodic film thickness itself simply increases linearly with time for this case.

The growth kinetics under constant voltage conditions.—Even though anodic film growth is often carried out under constant current conditions, at other times anodization is carried out with a fixed voltage drop across the film. For a given voltage $V(L)$, the values of the time t corresponding to a given value of thickness L can be obtained from Eq. [38] and [39], and then kinetics curves $L(t)$ *vs.* t at constant voltage $V(L)$ can be plotted for the cases of zero and nonzero space charge, respectively. The process can be repeated successively for different voltages $V(L)$ to give a family of growth curves. Such curves should be terminated with (or before) $L = L^*$, as indicated in Appendixes A and B. The value of L^* increases linearly with applied potential, according to Eq. [29]. It is also important to verify that E_0 does not drop below the magnitude required for validity of the very high field approximation. A typical family of curves computed for the homogeneous field case is shown in Fig. 9. The corresponding growth curves computed with space charge effects are shown in Fig. 10.

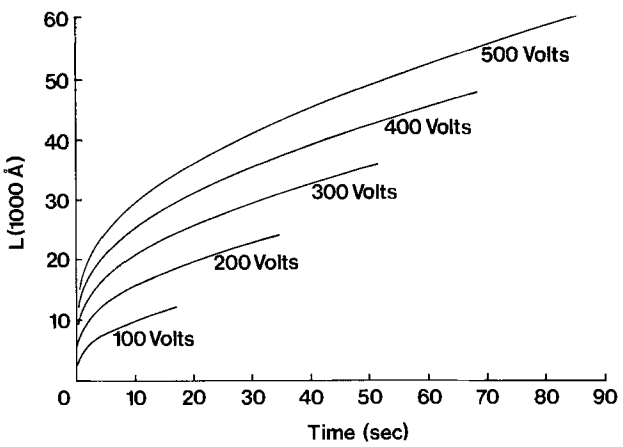


Fig. 9. Constant voltage growth kinetics in the homogeneous field limit for very high electric fields. Microscopic parameter values are listed in Tables I and III.

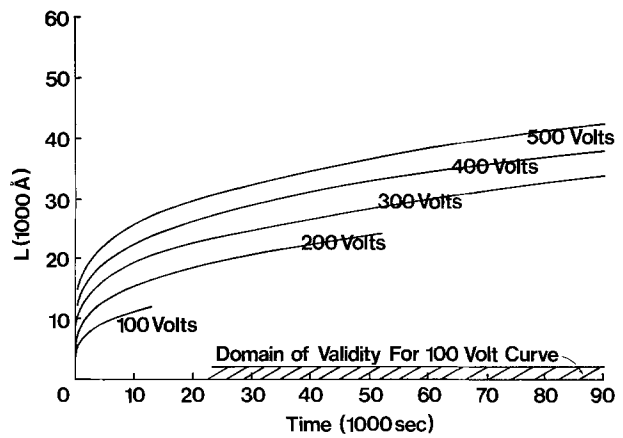


Fig. 10. Constant voltage growth kinetics in the large space charge very high field limit. Microscopic parameter values are listed in Tables I and III.

The curves in these two figures represent the growth of an anodic oxide film having the microscopic parameter values listed in Table I under several different applied voltages, namely 100, 200, 300, 400, and 500V. The quantities which are determined by the microscopic physical parameters of Table I are listed in Table III. The defect profile, the electric field profile, and the electrostatic potential profile have already been illustrated for a 1000Å film at 100V for the set of parameters listed in Table I (*cf.* Fig. 5-7). The diffusion coefficient defined (19) by $D = 4a^2\nu \exp(-W/kT)$ has, for the microscopic parameter values listed in Table I, the value 4.0778×10^{-11} cm^2/sec. Utilizing the value $R = 25$Å^3, as would be appropriate for either Fe_2O_3 or Fe_3O_4 to an accuracy of 1% or so, the value of γ^* defined by Eq. [33] is 1.159×10^{-13} cm^2/sec, and the value of Θ defined by Eq. [31] is 99.56×10^{-8} cm/sec. The parameter L^* defined by Eq. [29] for this case varies linearly with the voltage; it has the value 12,380Å for $V(L) = 100$V. Several interesting features emerge from a comparison of Fig. 9 and 10. Qualitatively the homogeneous field kinetics curves (Fig. 9) do not bend over quite so sharply as the kinetics curves including space charge (Fig. 10), thus illustrating the tendency of space charge to increase the limiting-thickness character of the growth kinetics. The splitting between the several curves for different voltages is greater in the homogeneous field limit than in the more exact nonhomogeneous field situation. Both of these effects are quite analogous to the results noted above for the exact numerical computations for lower voltages and thinner films. Thus the marked effects of space charge on the kinetics persist throughout the entire domain of film thickness. The retardation effect of

Table V. Values of the t_{sc}/t_{nsc} ratio evaluated from the computations illustrated in Fig. 9 and 12 which indicate the increase in time required to grow anodic films of various thickness when space charge effects are important

Voltage (V)	Thickness 10,000Å	20,000Å	30,000Å	40,000Å	50,000Å
100	651				
200	706	1300			
300	736	1370	1950		
400	754	1410	2020	2600	
500	768	1450	2080	2680	3250

space charge on the growth rate is especially evident when the time scales of Fig. 9 and 10 are compared, since it can be noted that there is a difference of a factor of 1000. For example, a 40,000Å film for the microscopic parameter values in question requires in excess of 70,000 sec for growth at 500V, whereas in the homogeneous field limit the growth time would be of the order of or less than 30 sec. It is perhaps unnecessary to emphasize that this is an enormous effect.

It is of some interest to understand the decrease in current at a given voltage and thickness when space charge is present. Equation [1], evaluated at $x = 0$, indicates that the current depends exponentially on the surface charge field E_o. Since $|E_o| < |\langle E \rangle|$ to the extent that space charge is present, the current will drop accordingly.[3]

[3] The reason the surface charge field at fixed voltage drops in the presence of space charge is due to the following fact: The space charge itself produces a contribution to the voltage, and this contribution is of the same sign as the surface charge field contribution; therefore the surface charge field must be lower in magnitude to maintain the fixed voltage. One can easily develop a qualitative understanding of these effects by carrying through a very simple analysis based on the oversimplified model of a uniform space charge C_o, in which case the surface charge field E_o takes the form $\langle E \rangle - (2\pi Ze C_o/\epsilon)L$.

The ratio t_{sc}/t_{nsc} of the time required for the anodic film to achieve a given thickness when space charge is present to the corresponding time computed in the homogeneous field limit indeed provides a good measure of the retarding effects of space charge. Table V lists this ratio deduced in the computations leading to Fig. 9 and 10. The ratio is plotted as a function of voltage for several thicknesses in Fig. 11, and it is plotted as a function of thickness for different voltages in Fig. 12. It can be noted (Table V) that the time factors range from 600 to 3000 for films 10,000-50,000Å in thickness under applied voltages of 100-500V. For a given film thickness, the time factors are somewhat greater at larger voltages (Fig. 11). At a given voltage, the time factors increase nearly linearly with increasing thickness (Fig. 12).

Although Fig. 9 and 10 serve the purpose of illustrating the predictions of the kinetics equations [38] and [39] for growth in the homogeneous field and large space charge limits, respectively, it should be pointed out that Fig. 10 does not provide a good representation of the kinetics over the entire film thickness domains illustrated for the several voltages. The reason for this is peculiar to space charge, in that the electric field in some regions of the film can differ markedly from the average electric field obtained from taking the ratio of voltage to film thickness. If the electric field in any portion of the anodic film drops below the magnitude required for validity of the very high field limit, then the equations for this limit become inapplicable to the situation at hand. Since the electric field for single species anodic film growth generally has its lowest magnitude at $x = 0$, namely $|\langle E \rangle| > |E_o|$, it is necessary to test to see whether E_o as obtained from Eq. [21] for a given voltage and film thickness remains sufficiently large to satisfy the very high field criterion

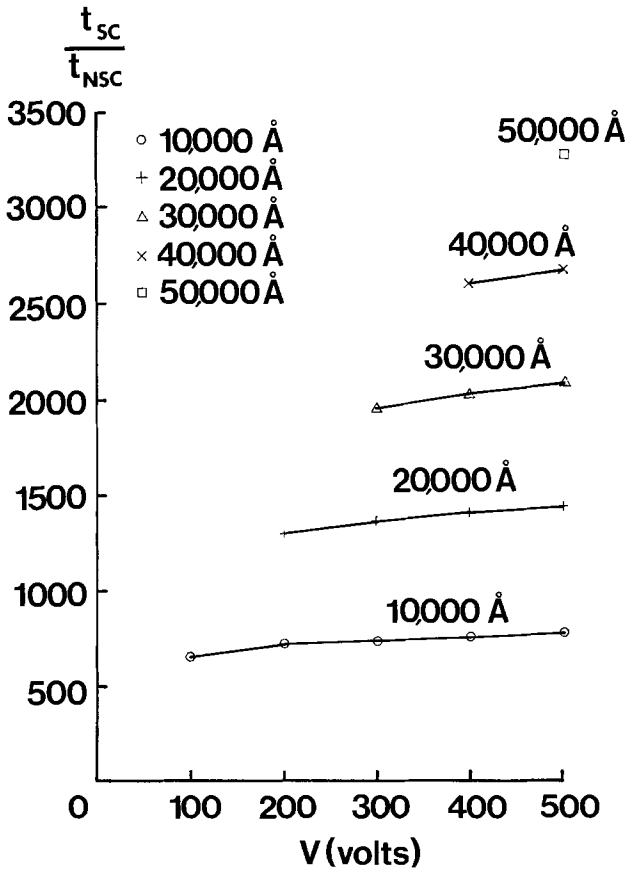


Fig. 11. Ratio of time t_{sc} required to grow an anodic film of several specified thicknesses with space charge to corresponding time t_{nsc} without space charge vs. anodizing voltage. Microscopic parameters are listed in Tables I and III.

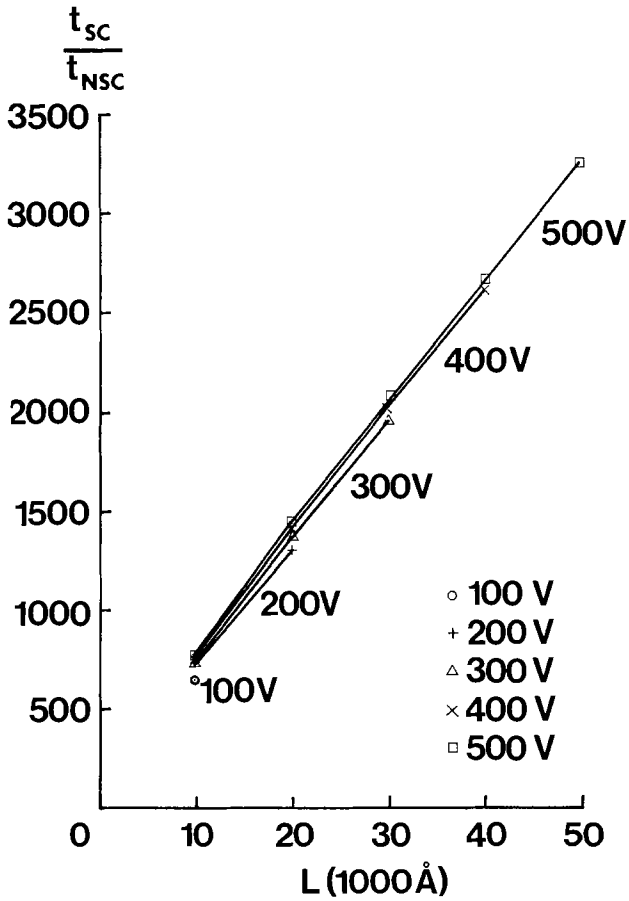


Fig. 12. Ratio of time t_{sc} required to grow an anodic film with space charge at several specified voltages to corresponding time t_{nsc} without space charge vs. anodic film thickness. Microscopic parameters are listed in Tables I and III.

(listed in Appendix B) with increasing values of the film thickness. It is indeed found that $|E_0/E^*|$ drops below unity for the presently considered parameter values whenever the film thickness exceeds 2000Å or so with an applied voltage of 100V. (This contrasts with the homogeneous field case illustrated in Fig. 9 for which $|E_0/E^*|$ exceeds unity over the entire range of the illustrated growth curve.) The major portion of the growth curve illustrated in Fig. 10 therefore represents only an upper limit to the actual thickness, since the consideration of some reverse hopping (13-17) against the applied field in the thicker film lower field domain means that the actual growth rate will be even slower than illustrated in Fig. 10. This additional space charge effect is also in the retarding direction, thus yielding an even greater tendency towards limiting-thickness-type growth. This means that the time factors listed in Table V and illustrated in Fig. 11 and 12 are overly conservative, since the other space charge retarding effects mentioned above will yield longer times for growth under space charge conditions, thus leading to somewhat larger values for the concomitant time factors. Although Fig. 10 could have been restricted to contain only the lower thickness portions of the kinetics curves for which the high field condition $|E(x)/E^*| \gtrsim 1$ is well met throughout the anodic film, the curves are illustrated in their entirety to emphasize the fact that much greater caution is required in utilizing equations for the very high field limit when space charge is present than is required in the homogeneous field limit, due to the fact that the large field limit is violated earlier when space charge is present.

Summary and Conclusions

An analytical development for single carrier steady-state ionic transport and anodic film growth valid in the "very high field" limit with space charge of the mobile ionic species included has been carried out to complement published (1) "intermediate field" numerical computations which utilized a space charge gradient model. The published intermediate field computations illustrated that the growth rate is significantly retarded by space charge of the diffusing ionic species producing film growth. The purpose of the presently reported work was to examine whether or not this pronounced space charge retardation of the growth rate would persist at higher electric fields, and if so, whether it would constitute a larger or a smaller effect relative to the situation at intermediate field strengths. The results of the present analytical development lead to the following major conclusion: Space charge effects do not disappear and do not saturate with increasing electric field value; on the contrary, the space charge retardation is even more pronounced in the realm of very high electric fields, large applied voltages, and very thick anodic films. It is convenient to consider the results in terms of time factors, where a given time factor is defined as the ratio of the time required for the anodic film to grow to a given thickness under a given applied voltage when space charge effects are included to the corresponding time which would be required in the absence of space charge retardation effects. A specific evaluation of the derived analytical expressions for anodic film growth times with and without space charge effects yields time factors ranging from 600 to 3000 for films 10,000-50,000Å in thickness under applied voltages of 100-500V. For a given film thickness the time factors are somewhat greater at larger voltages; at a given voltage the time factors increase nearly linearly with increasing thickness.

Acknowledgments

The author wishes to thank Dr. Charles H. Holmes for his long-term interest in this research on space charge effects, for his frequently enlightening technical discussions on scientific topics and areas of broader mutual interest, and for providing the programmable HP 65 electronic calculator utilized in carrying out the numerical work presented herein for the high voltage thick film limit. The author also acknowledges the support of the Auburn University Computer Center in carrying out the low voltage thin film computations, and wishes to thank the personnel for their cooperation.

Manuscript submitted May 10, 1976; revised manuscript received Oct. 18, 1976. This was Paper 86 presented at the Toronto, Canada, Meeting of the Society, May 11-16, 1975.

Any discussion of this paper will appear in a Discussion Section to be published in the December 1977 JOURNAL. All discussions for the December 1977 Discussion Section should be submitted by Aug. 1, 1977.

Publication costs of this article were assisted by Auburn University.

APPENDIX A

Limiting Case of a Homogeneous Field

The homogeneous field approximation consists of neglecting the space charge contribution to the electric field. From Eq. [2] it can be noted that this is easily simulated from a mathematical standpoint by taking the limit

$$\epsilon \to \infty \qquad [A\text{-}1]$$

since then $E(x) \to E_0$. This leads to the corresponding limiting values

$$\lambda \to 0 \qquad [A\text{-}2]$$

$$x^* \to \infty \qquad [A\text{-}3]$$

as obtained from Eq. [10] and [16]. The limiting value of the space charge parameter $\mathcal{Q}$ follows from Eq. [22] by employing l'Hospital's rule for evaluating indeterminant forms. The algebraic details are worthwhile from the standpoint of those who may be unfamiliar with the various rules and procedures for the evaluation of indeterminant forms

$$\ln \mathcal{Q} = \lim_{x^* \to \infty} \{1 - (x^*/L)[1 + (L/x^*)]\ln[1 + (L/x^*)]\}$$

$$= 1 - \lim_{x^* \to \infty} \ln[1 + (L/x^*)] - \lim_{x^* \to \infty} \left(\frac{\ln[1 + (L/x^*)]}{L/x^*} \right)$$

$$= 1 - 0 - \lim_{x^* \to \infty} \frac{\frac{d}{dx^*}\ln[1 + (L/x^*)]}{\frac{d}{dx^*}\left(\frac{L}{x^*}\right)}$$

$$= 1 - \lim_{x^* \to \infty} \left[\frac{-L/(x^*)^2}{\frac{1 + (L/x^*)}{-L/(x^*)^2}} \right]$$

$$= 1 - \lim_{x^* \to \infty} \left[\frac{1}{1 + (L/x^*)} \right] = 1 - 1 = 0 \qquad [A\text{-}4]$$

Therefore

$$\mathcal{Q} = e^{\ln \mathcal{Q}} \to e^0 = 1 \qquad [A\text{-}5]$$

(zero space charge limit)

This leads to a very interesting result, namely that the ratio of the growth rate (Eq. [28]) with space charge to that computed without space charge at a given thickness and voltage is simply

$$\frac{(dL/dt)|_{\text{with space charge}}}{(dL/dt)|_{\text{zero space charge}}} = \frac{(QRDC(0)/2a)\exp(L^*/L)}{(1RDC(0)/2a)\exp(L^*/L)} = \mathcal{Q} \qquad [A\text{-}6]$$

(constant or fixed voltage)

where $\mathcal{Q}$ must be computed from Eq. [22] for the value of x^* given by Eq. [16] (together with Eq. [10]) and the thickness in question. Table III, for example, gives the value $\mathcal{Q} \simeq 0.0113$ for a typical set of parameter values, whereas the value of $\mathcal{Q}$ for another typical set of parameter values, *viz.*, those used in Ref. (1), is approximately 0.393.

Utilizing the above value $x^* = \infty$ appropriate for the homogeneous field limit in Eq. [15], [17], and [20] then yields for the concentration, electric field, and electrostatic potential profiles the following limiting values

$$C(x) \to C(0) \qquad [A\text{-}7]$$

$$E(x) \to E_o \qquad [A\text{-}8]$$

and

$$V(x) \to -E_o x \qquad [A\text{-}9]$$

The first two relations follow directly, but to obtain the last relation it is necessary to evaluate an indeterminant form in Eq. [20]

$$\begin{aligned} V(x) &\to \lim_{x^* \to \infty} \{-E_o x + E^* x \\ &\quad - E^* x^* [1 + (x/x^*)] \ln [1 + (x/x^*)]\} \to -E_o x \\ &\quad + E^* x - E^* x \lim_{x^* \to \infty} \{\ln [1 + (x/x^*)]\} \\ &\quad - E^* \lim_{x^* \to \infty} \left[\frac{\ln [1 + (x/x^*)]}{(1/x^*)} \right] \to -E_o x \\ &\quad + E^* x - 0 - E^* x = -E_o x \end{aligned} \qquad [A\text{-}10]$$

where the evaluation proceeds along the same lines as Eq. [A-4].

The validity of Eq. [1] utilized in the present analytical development of high voltage thick film expressions hinges on the assumption of very large forward fields, as discussed in the text following Eq. [1]. In the presently considered homogeneous field limit this requires

$$|ZeE_o a/kT| \gtrsim 1 \qquad [A\text{-}11]$$

which, with the aid of Eq. [29] and the homogeneous field voltage expression $V(L) = -E_o L$, can be written in the form

$$|L^*/L| \gtrsim 1 \qquad [A\text{-}12]$$

Hence the domain of the high field growth expressions in the absence of space charge is

$$L \lesssim L^* \qquad [A\text{-}13]$$

APPENDIX B

Limiting Case of Very Large Space Charge

The effect of space charge on the electric field can be noted from Eq. [2] to be enhanced for lower values of the dielectric constant ϵ. Therefore the large space charge limit can be simulated mathematically by taking the limit

$$\epsilon \to 0 \qquad [B\text{-}1]$$

This leads to the corresponding limiting values

$$\lambda \to \infty \qquad [B\text{-}2]$$

$$x^* \to 0 \qquad [B\text{-}3]$$

as obtained from Eq. [10] and [16]. The limiting value of the space charge parameter $\mathcal{Q}$ follows from Eq. [22] by employing l'Hospital's rule for evaluating indeterminant forms. The evaluation proceeds as follows

$$\begin{aligned} \ln \mathcal{Q} &= \lim_{x^* \to 0} \{1 - (x^*/L)[1 + (L/x^*)] \ln [1 + (L/x^*)]\} \\ &= 1 - \lim_{x^* \to 0} \left[\frac{\ln [1 + (L/x^*)]}{(L/x^*)} \right] \\ &\quad - \lim_{x^* \to 0} \{\ln [1 + (L/x^*)]\} \\ &= 1 - \lim_{x^* \to 0} \left[\frac{-L/(x^*)^2}{\dfrac{1 + (L/x^*)}{-L/(x^*)^2}} \right] \\ &\quad - \lim_{x^* \to 0} \{\ln [1 + (L/x^*)]\} \\ &= 1 - 0 - \infty = -\infty \end{aligned} \qquad [B\text{-}4]$$

Therefore

$$\mathcal{Q} = e^{\ln \mathcal{Q}} \to e^{-\infty} = 0 \qquad [B\text{-}5]$$

and the current and growth rate given by Eq. [26] and [28] approach zero in this limit. Prior to reaching this extreme, however, a good asymptotic expression for $\ln \mathcal{Q}$ follows from Eq. [22] by neglecting 1 relative to L/x^*, in which case

$$\ln \mathcal{Q} \simeq 1 - (x^*/L)(L/x^*) \ln (L/x^*) \simeq 1 - \ln (L/x^*) \qquad [B\text{-}6]$$

and

$$\mathcal{Q} = e^{\ln \mathcal{Q}} \simeq e^{1 - \ln (L/x^*)} \simeq 2.718\,(x^*/L) \qquad [B\text{-}7]$$

This provides the approximation needed to deduce an analytical expression for the growth law from Eq. [28].

It should be noted that the limiting expression for $\mathcal{Q}$ deduced above involves the approximation

$$L/x^* >> 1 \qquad [B\text{-}8]$$

which in some sense requires a large thickness L. On the other hand, the validity of Eq. [1] hinges on the requirement of very large forward field, which requires

$$|ZeE(x)a/kT| \gtrsim 1 \qquad [B\text{-}9]$$

as discussed in the text following Eq. [1]. In addition, as already shown in a footnote in the text, $\langle E(x) \rangle = -V(L)/L$, so the inequality [B-9] certainly requires

$$|-ZeV(L)a/kTL| \gtrsim 1 \qquad [B\text{-}10]$$

which, with the aid of Eq. [29], can be written in the form

$$|L^*/L| \gtrsim 1 \qquad [B\text{-}11]$$

Hence the domain of applicability of the high space charge growth equations deduced herein is fixed by

$$x^* << L \lesssim L^* \qquad [B\text{-}12]$$

LIST OF SYMBOLS

Lower case English characters

a	half of the hopping distance for defects in anodic film ($2a$ is the lattice parameter or the nearest neighbor distance)
e	electronic charge magnitude
k	Boltzmann's constant
m	power exponential ($m = 1, 2, 3$) in 10^m
n	power in n^{th} root growth law ($L(t) \propto t^{1/n}$)
n_N	areal defect density at anodic oxide interface located at $x = L$
n_o	areal defect density at anodic oxide interface located at $x = 0$
t	time
t_{sc}	time to grow anodic film under a given set of conditions with space charge effects included
t_{nsc}	time to grow anodic film under a given set of conditions in the homogeneous field limit
x	position in anodic film
x^*	space charge screening parameter defined by $[\lambda C(0)]^{-1}$

Upper case English characters

C_o	hypothetical uniform charged defect density
$C(0)$	bulk defect density of the mobile ionic species at $x = 0$
$C(x)$	bulk defect density of the mobile ionic species at position x
D	ionic diffusion coefficient
$E(x)$	electric field at position x in anodic film
$\langle E \rangle$	average electric field in the anodic oxide defined as

$$\int_0^L E(x)\,dx \Big/ \int_0^L dx = -V(L)/L$$

E^* thermal fluctuation field defined by kT/Zea
E_0 surface charge electric field (*i.e.*, the electric field at position $x = 0$ in the anodic film)
J_0 particle current of the mobile ionic defect species in the anodic film
L^* critical thickness parameter defined as $-ZeaV(L)/kT$
L' dummy variable of integration
$L(t)$ anodic film thickness in units of distance
N thickness of anodic film in monolayers (and total number of barriers across the film)
R volume of oxide per ionic defect transported through the anodic film
T temperature
$V(L)$ total electrostatic potential across the anodic film (equal in magnitude to the voltage across the anodic film)
$V(x)$ electrostatic potential at position x in anodic film defined by $V(x) = -\int_0^x E(x)\,dx$
W zero field activation energy for motion of mobile ionic defect species
Z charge per particle of mobile ionic defect species (in units of e)

Upper case English script characters

$\mathcal{E}_n$ nth order exponential integral ($n = 1, 2, 3$)
$\mathcal{Q}$ space charge growth retardation parameter given by $e^{\ln \mathcal{Q}}$
$\ln \mathcal{Q}$ parameter defined by $\{1 - (x^*/L)[1 + (L/x^*)] \ln[1 + (L/x^*)]\}$

Lower case Greek characters

β_0 parameter defined by $\exp(ZeE_0a/kT)$
$\beta(x)$ variable defined by $\exp(ZeE(x)a/kT)$
ϵ static dielectric constant of anodic film (in units of ϵ_0, the permittivity of free space)
η dummy variable of integration
γ^* growth rate preexponential parameter (for growth with space charge) defined as $[2.718\,RDC(0)x^*/2a]$
λ parameter defined by $4\pi(Ze)^2a/\epsilon kT$
ν attempt frequency of mobile ionic defect species
π 3.14159...

Upper case Greek character

Θ growth rate preexponential parameter (for homogeneous field limit) defined as $[RDC(0)/2a]$

REFERENCES

1. A. T. Fromhold, Jr. and J. Kruger, *This Journal*, **120**, 722 (1973).
2. J. P. S. Pringle, *ibid.*, **120**, 398 (1973).
3. J. P. S. Pringle, *ibid.*, **120**, 1391 (1973).
4. B. Agius and J. Siejka, *ibid.*, **120**, 1019 (1973).
5. C. L. Foley, J. Kruger, and C. J. Bechtoldt, *ibid.*, **114**, 994 (1967).
6. R. P. Frankenthal, *Electrochim. Acta*, **16**, 1845 (1971).
7. S. Rigo and J. Siejka, *Solid State Commun.* **15**, 259 (1974).
8. C. Cherki and J. Siejka, *This Journal*, **120**, 784 (1973).
9. G. Amsel and D. Samuel, *J. Phys. Chem. Solids*, **23**, 1707 (1962).
10. D. A. Vermilyea, in "Advances in Electrochemistry and Electrochemical Engineering," Vol. 3, C. Tobias and P. Delahay, Editors, chap. 4, Interscience Publishers, New York (1963).
11. L. Young, "Anodic Oxide Films," Academic Press, New York (1961).
12. L. Young, *Can. J. Chem.*, **37**, 276 (1959).
13. A. T. Fromhold, Jr., in "Oxides and Oxide Films," Vol. 3, J. W. Diggle and A. K. Vijh, Editors, pp. 1-272, Marcel Dekker, Inc., New York (1976).
14. A. T. Fromhold, Jr., "Theory of Metal Oxidation," Vol. I, chap. 8, see especially p. 272, North-Holland Publishing Co., Amsterdam, (1976).
15. N. Cabrera and N. F. Mott, *Rep. Prog. Phys.*, **12**, 163 (1949).
16. J. F. Dewald, *This Journal*, **102**, 1 (1955).
17. A. T. Fromhold, Jr., *Phys. Lett. A*, **28**, 176 (1968).
18. "Handbook of Mathematical Functions," M. Abramowitz and I. A. Stegun, Editors, Applied Mathematics Series, No. 55, p. 227, U.S. Department of of Commerce, National Bureau of Standards, Washington, D.C., (1964).
19. See, for example, A. T. Fromhold, Jr. and E. L. Cook, *J. Appl. Phys.*, **38**, 1546 (1967).

The Phase Transformation during Crystallization of ZnS

M. Sakaguchi, M. Ohta, M. Satoh, and T. Hirabayashi

Department of Applied Chemistry, Faculty of Engineering, Niigata University, Nagaoka, Niigata, Japan

ABSTRACT

In order to investigate the cubic → hexagonal transformation during crystallization of ZnS, microcrystalline ZnS and microcrystalline ZnS containing CdS or Cu_2S with various ratios were thermally treated at 850° or 1150°C in atmospheres of He, HCl, H_2S, or their mixtures, and the cubic content in the crystals obtained was estimated by the x-ray powder diffraction method. The cubic →hexagonal transformation in ZnS crystal containing CdS was promoted with a certain amount of blended CdS at 850°C in all atmospheres. In HCl, the percent cubic in unblended ZnS decreased rapidly in the initial stage, then increased over 0.5 hr ("retransformation"). The percent cubic in blended samples also decreased temporarily but the degrees of retransformation decreased with increasing CdS content. In H_2S, unblended ZnS remained cubic, while it transformed to hexagonal due to blending with CdS. The transformation reaction in the (0.95)ZnS-(0.05)CdS sample was followed by using a high temperature x-ray diffractometer. The result showed that the cubic peak intensity for CdS decreased with temperature and disappeared near 550°C, while the hexagonal peak intensity for the solid solution emerged near 650°C. The cubic → hexagonal transformation in microcrystalline ZnS containing Cu_2S was inhibited with the amount of blended Cu_2S at 1150°C in all atmospheres.

In the phase transformation reaction of ZnS crystals, an important role is played by a trace of foreign ions (1-8). McKeag *et al.* (1), Aven *et al.* (2), Nickerson *et al.* (3), and Gashurov *et al.* (4) have found that the hexagonal → cubic transformation in ZnS crystals was promoted by a trace of copper, and recently Kozielski (5) has reported that the "hexagonality" of (Zn, Cd)S solid solution increased with Cd concentration.

It has also been found that the transformation reaction was affected by the presence of a foreign anion. That is, Skinner *et al.* (6) have noted that the cubic → hexagonal transformation occurred readily below its normal temperature when O_2 was occluded in the crystals, and Bansagi *et al.* (7) and Sakaguchi *et al.* (8) have found that the transformation rate is affected by the adsorption of anion on the crystal surface during the transformation reaction. Although several studies have been done on the effect of individual foreign ions on the transformation reaction in ZnS, no work has been reported on the combined effect of promotive and inhibitive ions on this reaction.

In this paper, the ZnS crystal containing CdS (hexagonal at low temperature) or Cu_2S (cubic at high temperature) is thermally treated in atmospheres of He, HCl, H_2S, or their mixtures, and then the combined effect of promotive and inhibitive factors on the transformation phenomena of ZnS crystals is discussed.

Experimental

The starting materials used in this study were unblended ZnS powder and blended samples as follows, *viz.* $(1-x)$ZnS-(x)CdS samples and $(1-y)$ZnS-$(y)Cu_2S$ samples. Samples of $(1-x)$ZnS-(x)CdS and $(1-y)$ZnS-$(y)Cu_2S$ compositions were prepared by carefully blending the microcrystalline ZnS powder with ratios of $0 \leq x \leq 0.5$ microcrystalline CdS powder and $0 \leq y \leq 0.01$ microcrystalline Cu_2S powder, respectively.

He was of high purity purified by passage through a glass tube containing the molecular sieve 5A at −196°C. HCl and H_2S were pure materials for the preparation of semiconductors, further purified by vacuum distillation using both dry ice alcohol and liquid O_2 baths.

The apparatus for heating by a static method was constructed of borosilicate glass, except for the reaction tube which was made of quartz. Dead space of the reaction system was about 100 ml. The heating temperature was detected by a Pt-Pt 13% Rh thermocouple and maintained constant to ±1°C by an automatic controller, and the thermocouple was checked at the melting points of Sn (231.9°C), Zn (419.5°C), and Cu (1083°C) before and after the experiments.

The starting material (2.0g) was initially evacuated in high vacuum for 30 min at 25°C, then heated for 0-3 hr at 850° or 1150°C in each ambient gas (1 atm). The time interval required to reach the heating temperature was adjusted to be 30 min in all cases, and the heating time denoted as zero, meaning that the heating was stopped instantly at the given temperature. After heating the sample was rapidly cooled at the rate of ~200°C/min.

The crystal structure of the heated samples was examined by x-ray powder diffraction using Cu(Ni)K_α radiation, and the cubic content (percent cubic) was determined by the method reported by Bansagi *et al.* (7). High temperature x-ray measurements were done in a special high temperature diffractometer attachment equipped with a wide-angle goniometer (Rigaku Denki Company, Limited Type SG-7).

Results

The effect of ambient gases on the sintering reaction during crystal growth of microcrystalline ZnS is shown in Fig. 1. The BET surface area of the ZnS heated at 850°C showed a remarkable drop during the initial stage of heating, especially in H_2S atmosphere, indicating that considerable sintering occurred.

To observe the effects of both the ambient gas and the presence of CdS on the transformation reaction, $(1-x)$ZnS-(x)CdS samples were heated for 1 hr at 850°C in He, H_2S, or HCl. The results are shown in Fig. 2. The percent cubic in unblended ZnS decreased in the order of H_2S, He, and HCl, although at lower than the normal transition point. These results suggest that the cubic → hexagonal transformation was promoted by HCl and inhibited by H_2S relative to He. On the other hand, the percent cubic in the blended samples decreased considerably with the amount of CdS, and no cubic structure was detectable in HCl above 10 mole percent (m/o) CdS, while the cubic form still remained in H_2S and He above 50 m/o CdS.

Figure 3 shows the dependence of cubic structure on heating time when the sample is heated in the promo-

Key words: phase transformation, zinc sulfide, copper(I) sulfide, solid solution.

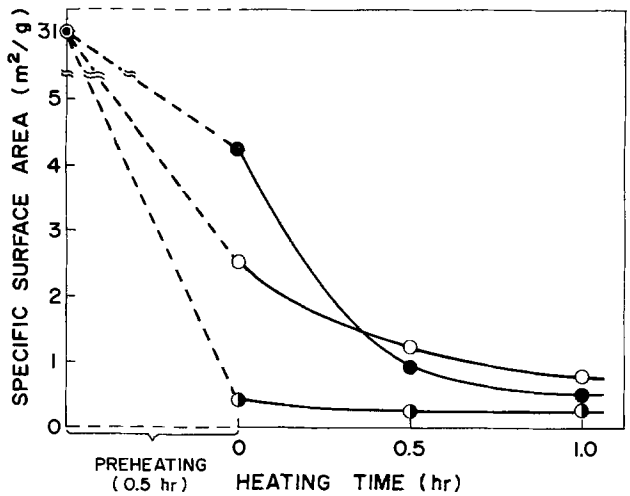


Fig. 1. Dependence of heating time or specific surface area of ZnS crystal heated at 850°C: ○, in He; ◑, in H_2S; ●, in HCl; ◉, starting material.

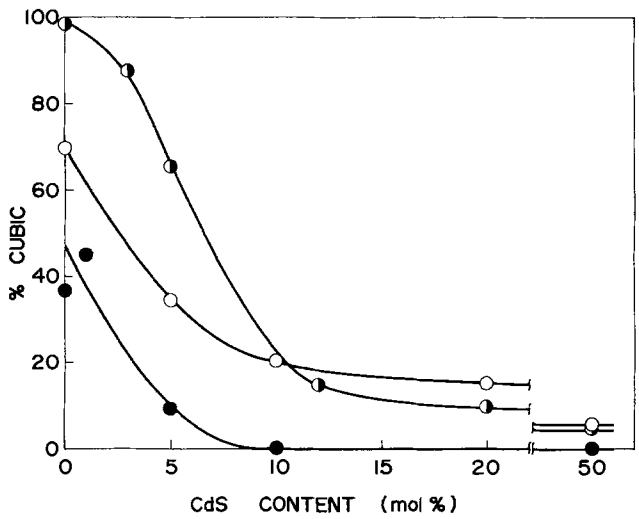


Fig. 2. Effect of CdS content on percent cubic of (1 — x)ZnS-(x)CdS samples heated for 1 hr at 850°C: ○, in He; ◑, in H_2S; ●, in HCl.

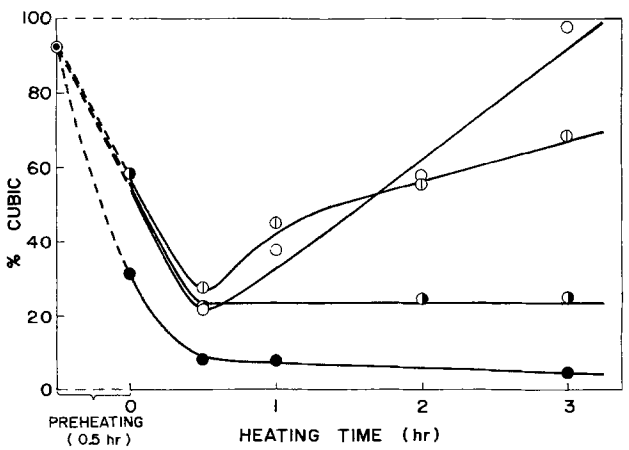


Fig. 3. Relation between heating time and percent cubic of (1 — x)ZnS-(x)CdS samples heated at 850°C in HCl: ○, x = 0; ◑, x = 0.01; ◑, 0.03; ●, x = 0.05; ◉, starting materials.

tive atmosphere of HCl. The percent cubic in unblended ZnS decreased rapidly in the initial stage, then increased after 0.5 hr. This reversal in behavior indicates that the crystal structure reverted to cubic ("retransformation"), which is the stable form at this temperature. Similarly, the percent cubic in blended samples also decreased temporarily, but the degree of retransformation decreased with increasing CdS content.

Figure 4 shows a similar plot for the sample heated in the inhibitive atmosphere of H_2S. The inhibitive effect of H_2S decreased with the amount of CdS.

The transformation reaction in the (0.95)ZnS-(0.05)CdS sample as a function of temperature was followed by using a high temperature x-ray diffractometer. Figure 5 shows that the cubic peak intensity for CdS decreased with temperature and disappeared near 550°C, while the hexagonal peak intensity for the solid solution emerged near 650°C. The latter peak intensity was constant above 800°C. It is interpreted, therefore, that CdS dissolved readily in ZnS.

Similar experiments were done on (1 — y)ZnS-(y)Cu_2S samples; the cubic structure of Cu_2S is stable at high temperature in contrast to CdS. Figure 6 shows percent cubic *vs.* Cu_2S content for such samples heated in H_2S or HCl for 1 hr at 1150°C. Under these conditions the unblended ZnS transformed completely to hexagonal. On the other hand, ZnS blended with Cu_2S was more effectively returned to cubic by H_2S than by HCl, depending on the amount of Cu_2S present. The cubic → hexagonal transformation was inhibited more effectively by a smaller amount of Cu_2S than the amount of CdS required to promote the reaction at 850°C.

Table I shows the effect of ambient gas on the structural transition of (0.999)ZnS-(0.001)Cu_2S at 1150°C. The inhibitive effect due to Cu_2S was greatly enhanced by heating in H_2S; no effect was observed after heating for 1 hr in HCl, but the inhibitive effect emerged after 3 hr heating. These results suggest that the transforma-

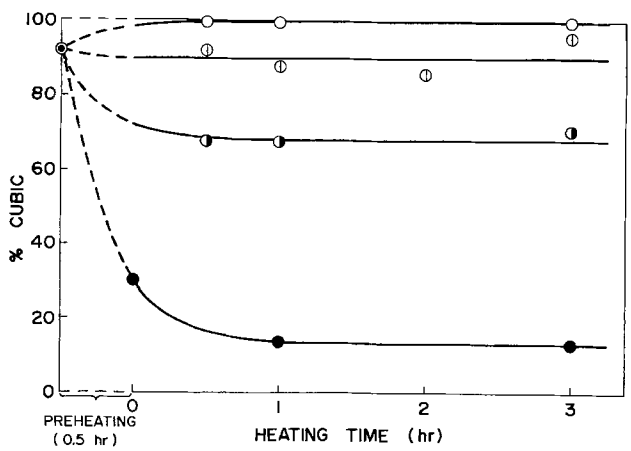


Fig. 4. Relation between heating time and percent cubic of (1 — x)ZnS-(x)CdS samples heated at 850°C in H_2S: ○, x = 0; ◑, x = 0.03; ◑, x = 0.05; ●, x = 0.10; ◉, starting materials.

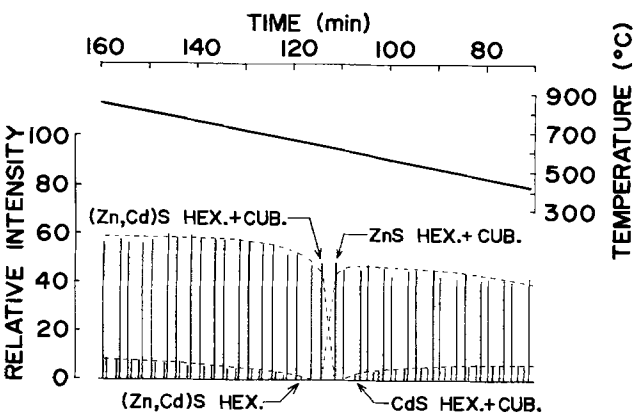


Fig. 5. High temperature x-ray diffractometer trace of (0.95)ZnS-(0.05)CdS sample in an He flow of 100 ml/min at 2θ region of 25.0° ~30.0°, and at a heating rate of 5.5°C/min.

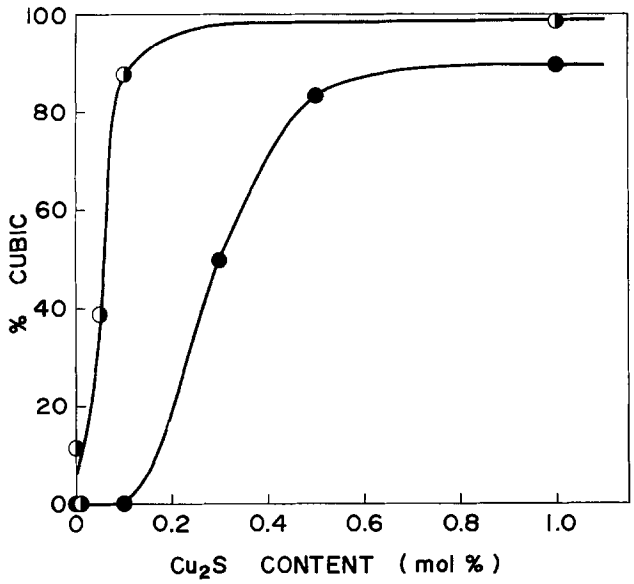


Fig. 6. Effect of Cu_2S content on percent cubic of (1 —y)ZnS-(y)Cu_2 samples heated for 1 hr at 1150°C: ◑, in H_2S; ●, in HCl.

tion reaction during the crystallization of the microcrystalline ZnS powder was noticeably affected not only by the presence of a second component (CdS or Cu_2S) in the solid phase but also by the ambient gases (HCl, He, or H_2S).

Experiments were also carried out to observe the influence of mixed gases, that is, H_2S mixed in various ratios with HCl. These results of mixed gases on unblended ZnS and (0.95)ZnS-(0.05)CdS sample are shown in Fig. 7. In Fig. 7 a sharp increase in cubic content occurred in the unblended ZnS by mixing HCl with a small amount of H_2S, while the cubic content increased gradually in the blended sample.

Similar examination of the unblended ZnS and (0.999)ZnS-(0.001)Cu_2S sample was carried out in H_2S-HCl mixtures at 1150°C. The results in Fig. 8 are in distinct contrast to the $(1-x)$ZnS-(x)CdS samples at 850°C. That is, the effect on the unblended ZnS was slight with the variation of gas composition, while the effect on the blended sample showed a strong dependence on the partial pressure of H_2S.

Discussion

The phase transformation phenomena observed during crystallization of the microcrystalline ZnS blended CdS reported herein showed a similar tendency to earlier reports (5, 10).

The promotive effect of CdS on the cubic →hexagonal transformation in ZnS crystals as shown in Fig. 2 and 5 results from the formation of a solid solution of CdS in ZnS prior to the transformation step, *i.e.*, each individual ZnS-CdS solid solution had an inherent transition point. Furthermore, the effectiveness of the CdS presence was enhanced in HCl, and was rather depressed in H_2S compared with He.

The combined effect resulting from the presence of promotive and inhibitive factors can be explained as follows. The original microcrystalline ZnS precipitated

Table I. Percent cubic of (1 — y)ZnS-(y)Cu_2S samples heated at 1150°C in various ambient gases

Sample	Heating conditions: Ambient gas (1 atm)	Time (hr)	Percent cubic
ZnS	H_2S	1	12.3
(0.999)ZnS-(0.001)Cu_2S	H_2S	1	87.5
(0.999)ZnS-(0.001)Cu_2S	HCl	1	0
(0.999)ZnS-(0.001)Cu_2S	HCl	3	52.3
(0.999)ZnS-(0.001)Cu_2S	He	3	70.0

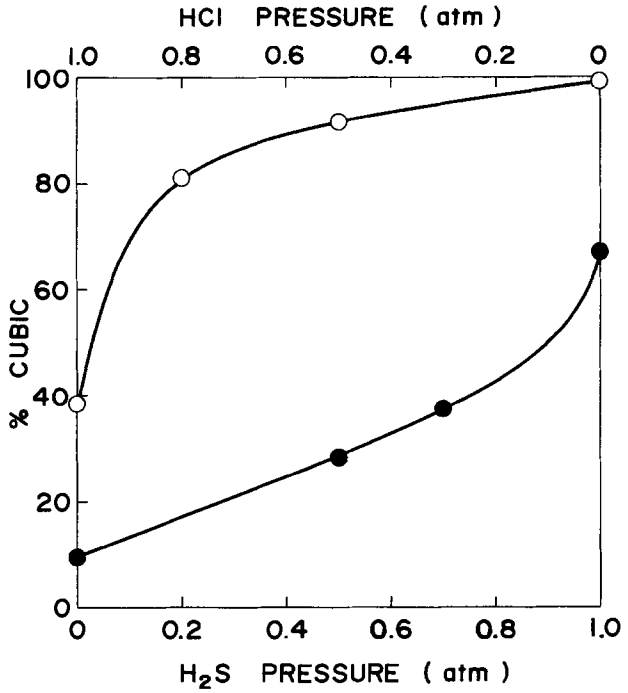


Fig. 7. Relation between composition of ambient gases and percent cubic of (1 — x)ZnS-(x)CdS samples heated for 1 hr at 850°C: ○, $x = 0$; ●, $x = 0.05$.

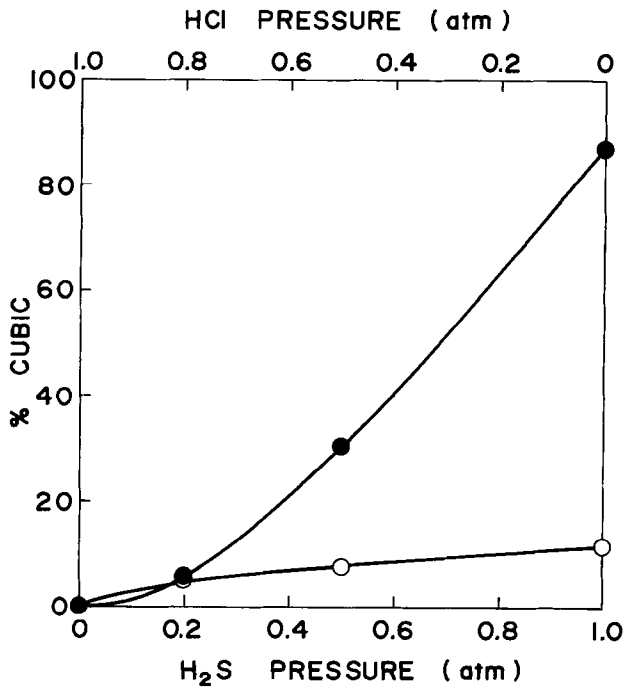


Fig. 8. Relation between composition of ambient gases and percent cubic of (1 — y)ZnS-(y)Cu_2S samples heated for 1 hr at 1150°C: ○, $y = 0$; ●, $y = 0.001$.

from aqueous $ZnSO_4$ with H_2S can hardly avoid the inclusion of SO_4^{2-} (as $ZnSO_4$) even after most careful washing. Therefore, on heating at 850°C the contamination of the sintered ZnS with oxygen is expected even in He, where the incorporated $ZnSO_4$ would decompose to ZnO.

An earlier study (6) has reported that the hexagonal structure of ZnS crystals was stabilized by the included oxygen below the normal transition point. Accordingly, although ZnS was unblended the crystal obtained by heating in He will be transformed to about 30 m/o hexagonal (Fig. 2).

The deoxidization occurred as soon as ZnS was heated in H_2S where H_2S is expected to react rapidly

with $ZnSO_4$ prior to sintering, therefore, a higher cubic content resulted. In HCl atmosphere, however, $ZnSO_4$ should remain in the sintered samples as would be expected in the case of He; HCl cannot react directly with $ZnSO_4$, but $ZnCl_2$ produced by the reaction between HCl and ZnO formed by thermal decomposition would sublime. Accordingly the "retransformation" or reversion to the stable cubic form may occur progressively with heating time.

In Fig. 7, the increase in cubic content of the unblended ZnS is due to the presence of H_2S, which is expected to deoxidize the included $ZnSO_4$. On the other hand, the cubic content of the blended sample decreased in the gas mixtures more than was estimated from Fig. 2. From these results it can be assumed that the solubility of oxygen in the ZnS crystals increased in ZnS-CdS solid solution, but a more detailed discussion must await further work.

The unblended cubic ZnS transformed completely to hexagonal on heating in H_2S or HCl at 1150°C. On the other hand, blending ZnS with a trace amount of Cu_2S, the cubic content was remarkably increased by heating in H_2S (*i.e.*, copper sulfide-induced transformation), but no detectable change was observed in HCl (Fig. 6, Table I). This behavior can be explained by postulating that the effective force for a copper sulfide-induced transformation was damaged by the presence of SO_4^{2-}, which was initially present in the sintered samples heated in HCl. The increase in cubic structure content with heating time in HCl gas was coincident with oxygen removal as ZnO, resulting from the thermal decomposition of the $ZnSO_4$ and the reaction with HCl. Furthermore, this discussion of Table I is supported by the data in Fig. 8 where the percent cubic of the Cu_2S blended sample increased in a linear relation with the partial pressure of H_2S, a deoxidizing agent for $ZnSO_4$.

Manuscript submitted Aug. 11, 1976; revised manuscript received Oct. 26, 1976.

Any discussion of this paper will appear in a Discussion Section to be published in the December 1977 JOURNAL. All discussions for the December 1977 Discussion Section should be submitted by Aug. 1, 1977.

Publication costs of this article were assisted by Niigata University.

REFERENCES

1. A. H. McKeag and E. G. Steward, *This Journal*, **104**, 41 (1957).
2. A. Addamiano and M. Aven, *J. Appl. Phys.*, **31**, 36 (1960).
3. J. Nickerson, P. Goldberg, and D. H. Baird, *This Journal*, **110**, 1228 (1963).
4. G. Gashurov and E. Banks, *ibid.*, **114**, 1143 (1967).
5. M. J. Kozielski, *J. Cryst. Growth*, **30**, 86 (1975).
6. B. J. Skinner and P. B. Barton, *Am. Mineral.*, **45**, 612 (1960).
7. T. Bansagi, E. A. Secco, O. K. Srivastava, and R. R. Martin, *Can. J. Chem.*, **46**, 2881 (1968).
8. M. Sakaguchi and T. Hirabayashi, *J. Appl. Phys.*, **44**, 2530 (1973).
9. M. Sakaguchi, T. Hirabayashi, and H. Kasahara, *Nippon Kagaku Zasshi*, **89**, 258 (1968).
10. T. Lukaszewicz and J. Kalicinska-Karu, *Acta Phys. Pol.*, **A45**, 721 (1974).

Preparation and Fluorescent Properties of Lithium Rare Earth Phosphate Phosphors

Y. Tsujimoto, Y. Fukuda, and M. Fukai

Matsushita Electric Industrial Company, Limited, Central Research Laboratories, Moriguchi, Osaka 570, Japan

ABSTRACT

Efficient emission has been found in the phosphate phosphors, $LiY_{1-x}Tb_xP_4O_{12}$ and $LiY_{1-y}Eu_yP_4O_{12}$ under u.v. excitation. For the preparation of these phosphors, an appropriate firing temperature must be selected in regard to the ionic radius of rare earth ions. The luminescence intensity changes little over the wide range of activator concentration, The rare earth metaphosphate phosphors such as $Y_{1-x}Tb_xP_3O_9$ and $Y_{1-y}Eu_yP_3O_9$ were found to show similar properties. Under vacuum u.v. excitation by Xe lamp, the brightness of $LiY_{0.1}Tb_{0.9}P_4O_{12}$ exceeds that of Zn_2SiO_4:Mn. The enhancement of Tb^{3+} emission by Ce^{3+} ions was found in both $LiTb_{1-x}Ce_xP_4O_{12}$ and $Tb_{1-y}Ce_yP_3O_9$.

In usual phosphate phosphors, the increase of an activator concentration over several percent results in a quenching of fluorescence. In recent years, however, phosphate compounds which contain Nd^{3+} as a cation have attracted special interest as low threshold laser materials. First, Danielmeyer and Weber proposed NdP_5O_{14} (1) in 1972 and then Yamada *et al.* found $LiNdP_4O_{12}$ (2) in 1974. Hong analyzed the crystal structures of a series of phosphates (3-6) including neodymium metaphosphate and made clear that those low threshold laser materials had a crystal structure favorable for suppressing the interactions between Nd^{3+} ions and thus concentration quenching was reduced. One of the merits of the above-mentioned materials is that they have a very high concentration of luminescent centers. This fact suggests to us the application of these phosphates to a visible light emitting phosphor activated with rare earth ions.

Key words: rare earth luminescence, photoexcitation, high activator concentration, sensitization.

The present work is an extended application of $LiLnP_4O_{12}$ and LnP_3O_9 (Ln = rare earth ions) phosphors in which the preparation method, fluorescent properties of Tb^{3+} and Eu^{3+} centers, and sensitization of Tb^{3+} emission by Ce^{3+} ion are related.

Experimental

Preparation of phosphors.—Phosphors were prepared from intimate mixtures of high purity raw materials by conventional solid-state reactions in air. Starting materials were ≧ 99.99% rare earth oxides and reagent grade Li_2CO_3 and $NH_4H_2PO_4$. For the preparation of $LiLnP_4O_{12}$ (Ln = rare earth elements) 150% Li_2CO_3 and 110% $NH_4H_2PO_4$ were weighed, compared with the stoichiometric ratio. In firing the LnP_3O_9, 110% $NH_4H_2PO_4$ was used and 0.2 mole fraction of LiF was added as a flux. Fired samples were washed in hot water to remove unreacted lithium and phosphorous compounds.

Measurements.—Emission and excitation spectra were obtained with the aid of a grating monochrometer whose blaze wavelengths were 500 and 300 nm, respectively. A hydrogen discharge lamp was used as a u.v. excitation source. A photomultiplier with S-4 sensitivity was applied as the detector. Calibration of the spectral response of the apparatus used was not made. Vacuum ultraviolet (v.u.v.) excitation spectra were measured by the double beam method with a Hinteregger type hydrogen lamp and concave grating monochrometer.

Two kinds of relative brightness are obtained with the photomultiplier of S-4 response coupled with a Wratten 106 filter. One is by excitation with 254 nm of a mercury discharge lamp and the other is with a xenon lamp which has emission in the v.u.v. region from 150 to 200 nm.

Fluorescence decay times were measured by exciting the samples with a short time pulse (~4 nsec) from a deuterium flash lamp and observing the luminescence decay on an oscilloscope.

All measurements were carried out at room temperature.

Results and Discussions

Sample preparation conditions.—For the preparation of $LiLnP_4O_{12}$, the firing temperature must be below a critical value which related to the Ln^{3+} ionic radius. Above this critical temperature, resulting material was found to become Li-free rare earth metaphosphate. Figure 1 shows the relation between the ionic radius of Ln^{3+} ion and the temperature at which this transformation occurs. When the ionic radius of Ln^{3+} ion was larger than that of Tb^{3+} (1.09Å), rare earth metaphosphate did not appear within the temperature studied. At the critical firing temperature, which is shown by triangles, two compounds, $LiLnP_4O_{12}$ and LnP_3O_9, exist.

This critical temperature might change with the mole ratio of starting materials. Detailed experiments, however, have not been carried out. Sample firings were made at temperatures ranging from 750° to 850°C in regard to the average ionic radius of Ln^{3+} ion. Firing periods were 3-17 hr.

Obtained powder samples showed the same x-ray diffraction pattern as monoclinic $LiNdP_4O_{12}$. Under the firing conditions of 850°C and 3 hr, rare earth metaphosphate has an orthorhombic or monoclinic structure depending on whether the Ln^{3+} ion is larger than Eu^{3+} (1.13Å) or smaller than Gd^{3+} (1.11Å) (6).

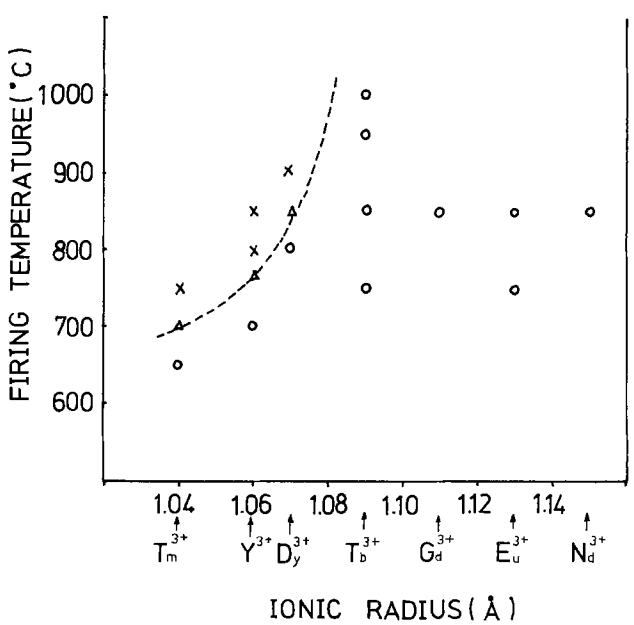


Fig. 1. Relation between the ionic radius of Ln^{3+} ion and the compounds obtained in regard to the firing temperature. Mole fractions of the starting materials of Li_2CO_3, Ln_2O_3, and $NH_4H_2PO_4$ are 1.5, 1.0, and 8.8, respectively: x rare earth metaphosphate, ○ lithium rare earth metaphosphate, △ mixture of the two phosphates.

Emission and excitation spectra.—All the phosphors investigated show emission lines characteristic of Eu^{3+} and Tb^{3+}. The emission spectra of $LiEuP_4O_{12}$ and $LiTbP_4O_{12}$ under 254 nm excitation are given in Fig. 2. In the rare earth metaphosphate. emission spectra of Eu^{3+} and Tb^{3+} are essentially similar to those of Fig. 2, except that the emission line corresponding to the $^5D_0$-$^7F_2$ transition of Eu^{3+} is stronger than that in $LiEuP_4O_{12}$.

Excitation spectra of Tb^{3+} fluorescence in $LiGd_{1-x}Tb_xP_4O_{12}$ when x is varied, are given in Fig. 3. Judging from the variation of excitation intensity *vs.* Tb^{3+} concentration, the excitation band at about 225 nm can be attributed to host excitation and those in longer wavelength rather than that of the f-f and the f-d excitation bands. In this longer wavelength region, bands at 240 ~ 270 nm are estimated to belong to the 4f-5d transition, since the ratio of magnitude variation of 4f-5d bands with Tb^{3+} concentration is smaller than that of 4f-4f bands (7).

The excitations at wavelengths of 273 and 312 nm seem to originate from a Gd^{3+} center whose energy is transferred to the Tb^{3+} center, since these excitations are not observed in $LiY_{1-x}Tb_xP_4O_{12}$ and the peak intensities increase with increased Gd^{3+} concentration. The similar behavior of these two peaks is observed in $Gd_{1-x}Eu_xP_3O_9$ as well. This suggests that energy transfer from Gd^{3+} to Eu^{3+} is also operative.

The excitation spectra of $LiY_{1-x}Tb_xP_4O_{12}$ and $LiGd_{1-x}Tb_xP_4O_{12}$ in the v.u.v. region are given in Fig. 4 together with that of Zn_2SiO_4:Mn for comparison. Zn_2SiO_4:Mn is known as a good phosphor for v.u.v. excitation (8, 9). From Fig. 4, however, $LiY_{0.1}Tb_{0.9}P_4O_{12}$ is found to have higher emission intensity than Zn_2SiO_4:Mn in the wavelength region longer than 160 nm. When it was excited by a Xe lamp the brightness was 115% of that of Zn_2SiO_4:Mn (Fig. 7).

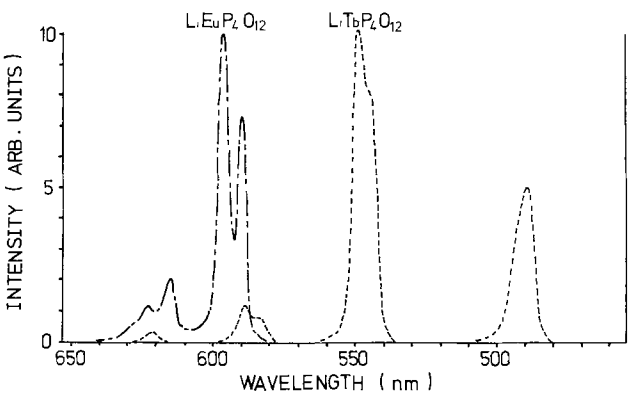


Fig. 2. Emission spectra of $LiTbP_4O_{12}$ and $LiEuP_4O_{12}$ under 254 nm excitation.

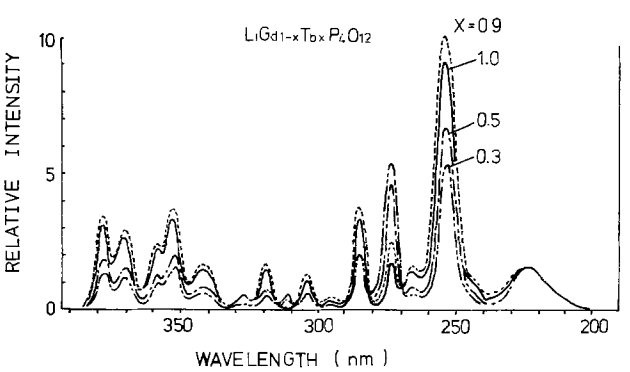


Fig. 3. Excitation spectra of $LiGd_{1-x}Tb_xP_4O_{12}$

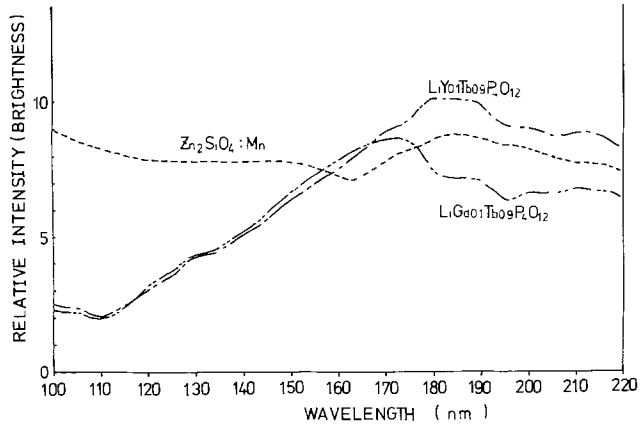


Fig. 4. Vacuum ultraviolet excitation spectra of $LiY_{0.1}Tb_{0.9}P_4O_{12}$ and $LiGd_{0.1}Tb_{0.9}P_4O_{12}$ compared with that of Zn_2SiO_4:Mn.

Emission intensity.—The dependences of relative brightness of each phosphor on activator concentration are given in Fig. 5-7. The curves in Fig. 7 are the results obtained under v.u.v. excitation and the rest are those obtained under 254 nm excitation. What is common to all the curves in Fig. 5-7 is that there is little concentration quenching of emission even at the highest activator concentration.

In the case of $LiLnP_4O_{12}$, this is due to the crystal structure in which the Ln^{3+} ion shares no O^{2-} atom and interactions between the Ln^{3+} ions are considered to be weak (3, 4). As mentioned previously, rare earth metaphosphate shows two kinds of crystal structure, *i.e.*, orthorhombic and monoclinic. In the former structure each Ln^{3+} atom shares two O^{2-} atoms with one of the neighboring Ln^{3+} atoms and two other O^{2-} atoms with another Ln^{3+} atom, which seems to enhance Ln^{3+}-Ln^{3+} pair interaction (5). The latter structure, however, has LnO_6^{9-} octahedra which are isolated from each other with no atom common to any two Ln^{3+} atoms (6) and less interaction between Ln^{3+} ions is expected.

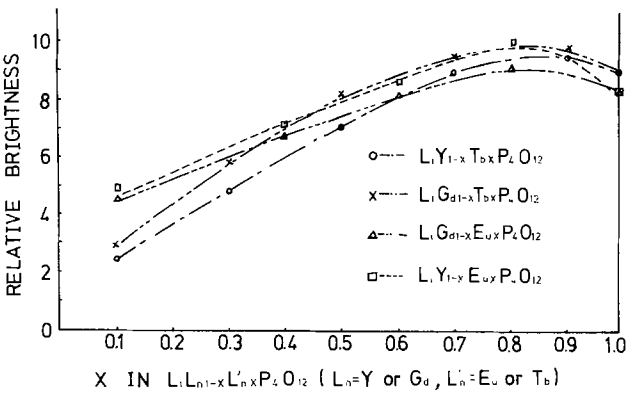


Fig. 5. Relative brightness of lithium rare earth metaphosphate activated with Tb^{3+} or Eu^{3+} vs. activator concentration (254 nm excitation).

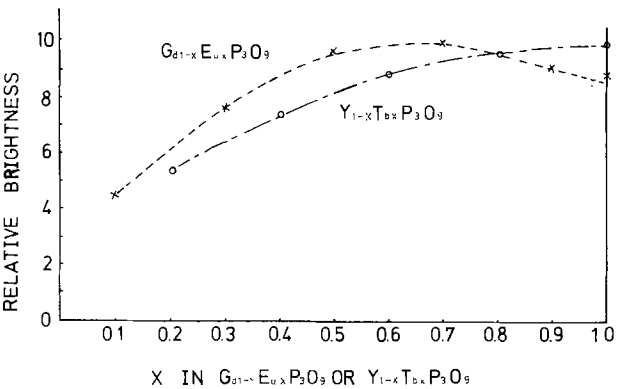


Fig. 6. Relative brightness of rare earth metaphosphate activated with Tb^{3+} or Eu^{3+} vs. activator concentration (254 nm excitation).

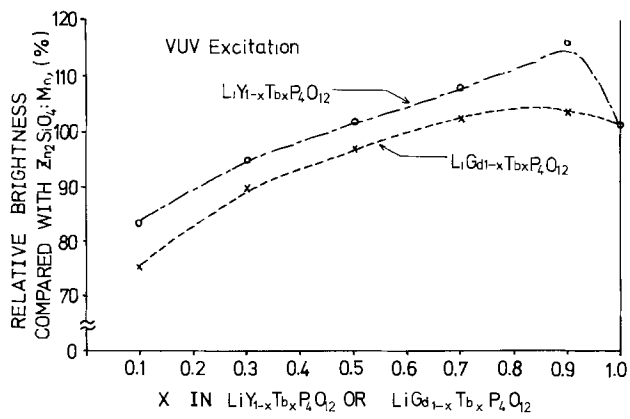


Fig. 7. Relative brightness of Tb^{3+} activated lithium rare earth metaphosphate compared with that of Zn_2SiO_4:Mn under v.u.v. excitation.

From the results in Fig. 5 one could expect the gradual variation of emission decay time. In Fig. 8 decay rates of $LiY_{1-x}Tb_xP_4O_{12}$ are given and a weak dependence on Tb^{3+} concentration is observed. These decay rates are affected by the sample preparation conditions rather than Tb^{3+} concentration. A low firing temperature for short period, *e.g.*, 750°C, 3 hr, results in a light brown coloration of samples and a decrease in decay time. The light brown body color suggests the existence of Tb^{4+} and this acts as an energy acceptor (12). The decay rates of colored $LiTbP_4O_{12}$ samples are shown in Fig. 8 by the vertical bar. Under the firing conditions of 750°C and 18 hr, $LiTbP_4O_{12}$ has a slight body color and shows the decay rate corresponding to the top of the bar in Fig. 8. Samples fired at higher temperature show longer decay times. These values of the samples fired at 850°C are given by the dashed curve in Fig. 8. At this temperature, however, samples tend to change to rare earth metaphosphates

Though not so obvious, $Gd_{1-x}Eu_xP_3O_9$ with orthorhombic structure shows a little concentration quenching, while $Y_{1-x}Tb_xP_3O_9$ with monoclinic structure indicates no quenching even at 100% Tb^{3+} replacement. This difference can be partially explained by the above-mentioned fact. The degree of quenching of Eu^{3+} emission is small compared with, for example, $La_{1-x}Nd_xP_3O_9$ (10) which is isomorphous with $Gd_{1-x}Eu_xP_3O_9$. This indicates that exchange coupling between Eu^{3+} ions is weak (11).

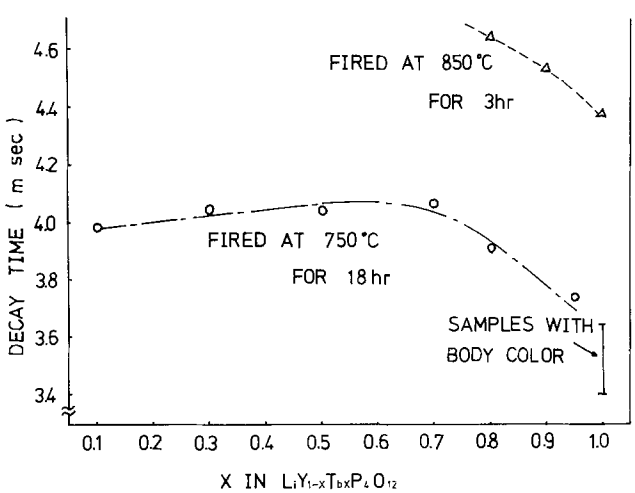


Fig. 8. Luminescence decay times of $LiY_{1-x}Tb_xP_4O_{12}$ when x is varied.

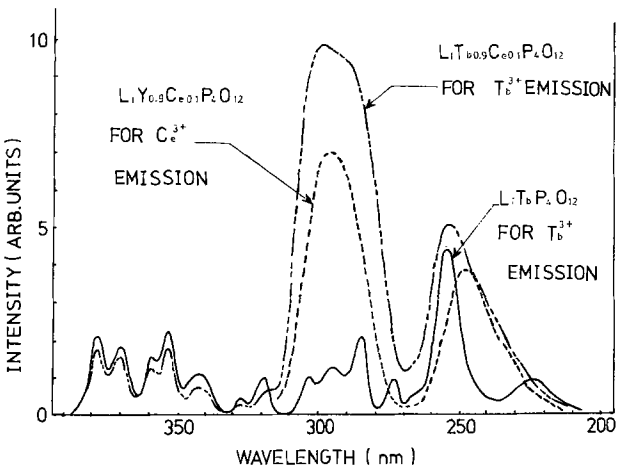


Fig. 9. Excitation spectra of Ce^{3+} emission in $LiY_{0.9}Ce_{0.1}P_4O_{12}$ and of Tb^{3+} emission in $LiTb_{0.9}Ce_{0.1}P_4O_{12}$ and $LiTbP_4O_{12}$.

with increasing Y^{3+} concentration, so data are taken only to the concentration of 20% Y^{3+}. The increase of decay rate is probably due to the decrease of some defects which acts as energy acceptor.

Sensitization.—It is well known that Tb^{3+} emission is enhanced by Ce^{3+} ion (13, 14). Even in $LiLnP_4O_{12}$ and LnP_3O_9, strong interaction between the d state of Ce^{3+} ion and the f state of Tb^{3+} ion compared with the interaction between f-f states of Tb^{3+} ions can be expected. In $LiTb_{1-x}Ce_xP_4O_{12}$ and $Tb_{1-x}Ce_xP_3O_9$, this sensitization was observed. In Fig. 9 three kinds of excitation spectra are shown for comparison. The solid curve is the already stated excitation spectrum of $LiTbP_4O_{12}$. When a portion of Tb^{3+} is replaced by Ce^{3+}, excitation intensity at about 300 nm increases greatly. This is given by the dot-dashed curve. Maximum enhancement is obtained at 5% Ce^{3+} replacement. The dashed curve is the excitation spectrum of $LiY_{0.9}Ce_{0.1}P_4O_{12}$ when a longer wavelength side of Ce^{3+} emission is monitored. As can be seen from these spectra, the excitation curve overlaps with that of Tb^{3+} emissions. This indicates efficient energy transfer from Ce^{3+} to Tb^{3+}. The same kind of excitation spectra were observed in $Tb_{1-x}Ce_xP_3O_9$.

Two broad excitation bands at 300 and 250 nm of Ce^{3+} emission in Fig. 9 can be attributed to the 4f-5d transitions of Ce^{3+} ions. These bands are assigned as the excitation from ground $^7F_{5/2}$ state to the $^5D_{5/2}$ and $^5D_{3/2}$ manifold.

To see how the energy transfer from Ce^{3+} to Tb^{3+} occurred, the relative intensity of Ce^{3+} emission under 254 nm excitation was compared when the Ce^{3+} concentration was fixed at 10% and the Tb^{3+} concentration was varied. The results are shown in Fig. 10 together with the excitation spectrum of Tb^{3+} emission of $LiTbP_4O_{12}$. The emission intensity of Ce^{3+} is, of course, decreased with increasing Tb^{3+} concentration, but its shape is not affected by the Tb^{3+} excitation spectrum, that is, by the absorption of Tb^{3+} ions. If there is radiation transfer, one would expect that in the emission spectrum of Ce^{3+} some dips at the location of Tb^{3+} absorption lines would appear together with the decrease of emission intensity. The results of Fig. 10 mean that the mechanism of energy transfer from Ce^{3+} to Tb^{3+} is of the nonradiative type (13).

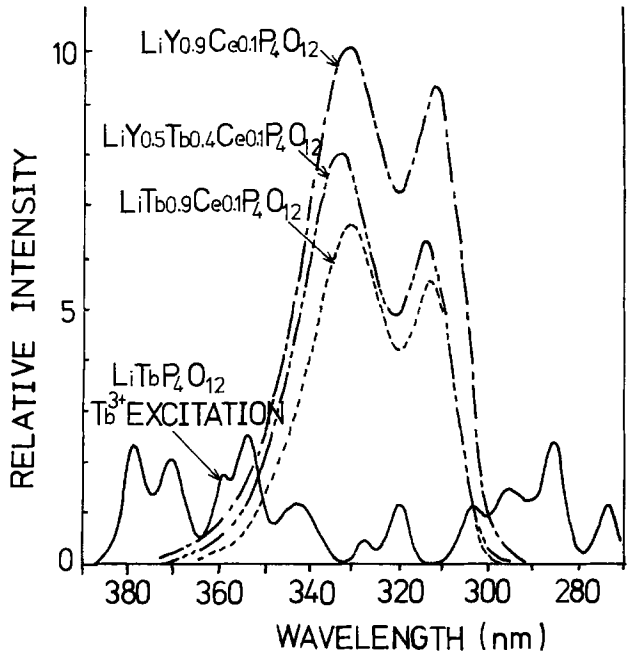


Fig. 10. Variation of intensity of Ce^{3+} emission in $LiY_{0.9-x}Tb_xCe_{0.1}P_4O_{12}$ when x is varied (254 nm excitation).

When Tb^{3+} was replaced by Eu^{3+} ion, the sensitization of Eu^{3+} emission by Ce^{3+} ion was not observed.

Acknowledgment

The authors wish to thank Y. Takesako for preparing samples and taking measurements.

Manuscript submitted Sept. 3, 1976; revised manuscript received Dec. 13, 1976. This was Paper 159 presented at the Washington, D.C., Meeting of the Society, May 2-7, 1976.

Any discussion of this paper will appear in a Discussion Section to be published in the December 1977 JOURNAL. All discussions for the December 1977 Discussion Section should be submitted by Aug. 1, 1977.

Publication costs of this article were assisted by Matsushita Electric Industrial Company, Limited.

REFERENCES

1. H. G. Danielmeyer and H. P. Weber, *IEEE J. Quantum Electron.*, **qe-8**, 805 (1972).
2. T. Yamada *et al.*, *J. Appl. Phys.*, **45**, 5096 (1974).
3. H. Y.-P. Hong, *Mater. Res. Bull.*, **10**, 635 (1975).
4. H. Y.-P. Hong, *ibid.*, **10**, 1105 (1975).
5. H. Y.-P. Hong, *Acta Crystallogr., Sect. B*, **30**, 468 (1974).
6. H. Y.-P. Hong, *ibid.*, **30**, 1857 (1974).
7. T. Hoshina, *J. Chem. Phys.*, **50**, 5158 (1969).
8. J. D. Kingsley and G. W. Ludwig, *This Journal*, **117**, 353 (1970).
9. E. R. Ilmas and T. I. Savikhina, *J. Lumin.* **1,2**, 702 (1970).
10. H. Y.-P. Hong and K. Dwight, *Mater. Res. Bull.*, **9**, 775 (1974).
11. M. V. Weber, *Phys. Rev. B*, **4**, 2932 (1971).
12. B. Blasse and A. Bril, Philips *Res. Rep.* **22**, 481 (1967).
13. S. Shironoya and E. Nakazawa, *Appl. Phys. Lett.*, **6**, 118 (1965).
14. G. Blasse and A.Bril, *J. Lumin.*, **3**, 18 (1970).

Liquid Crystal Alignment Produced by RF Plasma Deposited Films

G. J. Sprokel* and R. M. Gibson

IBM Research Division, San Jose, California 95193

ABSTRACT

Exposure of surfaces to the reaction products of an rf plasma induces specific aligning properties for smectic and nematic liquid crystals. Oxygen etched indium-tin oxide (ITO) films and surfaces on which SiO_2 or SnO_2 is deposited show strong parallel alignment. ITO surfaces exposed to a CF_4 plasma or surfaces on which a polyfluorocarbon film is deposited by a C_2F_4 plasma show strong perpendicular alignment.

Plasmachemistry has found application in many fields and a monograph on the subject is now available (1). In the semiconductor industry one application, photoresist "ashing," is now quite common (2). In principle the organic layer is oxidized in an O_2 rf plasma leaving a clean surface provided the resist is metal free (3). The method can be applied to transparent conducting films of indium-tin oxide (ITO) deposited on glass. It was found that such "oxidized" surfaces cause parallel alignment for cyanobiphenyls in particular if the sample is placed outside the plasma region avoiding surface damage by electron or ion bombardment. However, there is an undesirable side effect: The resistivity of the ITO film increased by one or two orders of magnitude. It was found that this can largely be overcome by exposure to a hydrogen plasma after the O_2 etching. Nevertheless the method is only applicable to ITO and glass surfaces. A method was developed to deposit SiO_2 or SnO_2 on almost any surface and it was found that such layers, although extremely thin, cause the same parallel orientation found for glass or ITO surfaces. In principle the deposition consists of establishing an O_2 plasma and introducing a sufficiently volatile organo-silicon or organo-tin compound in the plasma. Complete oxidation to SiO_2, that is, SnO_2, must be obtained and the oxides are carried by the gas stream onto the substrate. Again, the substrate is placed well outside the plasma region.

An rf plasma system operated in this way can also produce films which cause perpendicular alignment. Exposing glass or ITO surfaces to the fragments produced in a CF_4 plasma, mainly $F\cdot$ and $CF_3\cdot$, causes removal of Si and the resulting F-rich surface induces perpendicular alignment. Again the resistivity of ITO layers was found to increase but, as in the case of O_2 etching, the resistance can be reduced again by exposure to a H_2 plasma. For surfaces other than glass, a CF_4 plasma has little effect. However, if the CF_4 gas is replaced by C_2F_4 one can deposit a polyfluorocarbon film (4) which again causes perpendicular alignment for smectic or nematic alkylcyanobiphenyls. The oxide layers as well as the polymer layers conform to surface topology. They stick well and are stable in time. No long term change has been noticed in cells stored at 100°C.

Little prior literature exists on alignment by rf plasma polymerized films. Dubois *et al.* (5) found perpendicular alignment for films produced by glow discharge polymerization of hexamethyldisiloxane. The organo-silicon polymer is produced in the discharge region which usually leads to polymers which cannot be identified. The oxide films produced in the present work are essentially free of C-H bonds.

The subject of this paper is the production and characterization of oxide and polymer films which have strong aligning properties. The properties of the aligned liquid crystals have been discussed elsewhere (6). This separation is made possible by the nature of continuum theory which is essentially thermodynamic. The observed alignment is introduced as an energy term and does not require specification of the surface forces. Reference (6) can be summarized as follows: Data on the alignment are obtained by measuring the permittivity of the liquid crystal layer as a function of temperature while the sample is subjected to a strong magnetic field. One single compound, n-octylcyanobiphenyl, was used to compare the surface aligning effects. This compound is convenient because it is smectic A at room temperature and has a nematic phase between 32° and 40°C. In the smectic phase, the surface forces determine the alignment regardless of the previous history of the sample. In the nematic phase, if the magnetic field direction is parallel with the direction of the surface forces no additional alignment is observed. If the magnetic field is orthogonal to the direction of the surface forces, only incomplete alignment is obtained in the H direction. For parallel as well as for perpendicularly aligned cells the threshold is increased and the slope of the $\epsilon(H)$ curve near threshold is steeper. The energy stored in the liquid crystal layer in producing the alignment is of the same order of magnitude as the differential surface tension for cells up to 10 μm thick.

Plasma Deposited Layers

Table I summarizes the plasmas which have been used and the type of alignment caused by the deposited film. The plasma equipment is a modified Tegal (7) plasma-etcher. The pumping system was changed to avoid pump oil contamination and a manifold was made to mix gases outside of the system. Metalorganics are contained in vials which can be heated to obtain the desired vapor pressure. For SiO_2 deposition a number of silanes or siloxanes are suitable. Bis (dimethylamino) dimethylsilane (Silar No. 1420) has about the desired vapor pressure at room temperature. There are, however, many others which can be used. For SnO_2 deposition tetrabutyl tin was used as it affords better control than $Sn(CH_3)_4$. Gas pressures are in the 0.1-0.5 Torr range. Exposure time is ¼-½ hr; deposition rate 2-5 Å/min, film thickness 100Å.

Deposited films are analyzed by infrared and x-ray fluorescence (ESCA). All ESCA data were obtained by

Table I. Plasma conditions and liquid crystal alignment

Plasma		Substrate	Alignment
O_2	Etch	Glass, ITO	Parallel
O_2 + silane	Deposit	Glass, ITO, Cr/Au, Al	Parallel
O_2 + Sn (bu)$_4$	Deposit	Glass, ITO, Cr/Au, Al	Parallel
CF_4	Etch	Glass, ITO	Perpendicular
C_2F_4	Deposit	Glass, ITO, Cr/Au, Al	Perpendicular

* Electrochemical Society Active Member.

D. W. Rice of this laboratory. Infrared did not show hydrocarbons in oxide films supporting the contention that the oxide film is indeed SiO_2, that is, SnO_2, rather than a polymer. ITO films exposed to an O_2 plasma followed by CF_4 have approximately the composition $In_{0.22}Sn_{0.01}F_{0.24}O_{0.54}$ as calculated from ESCA data. Comparing this to the original stoichiometry, $In_{0.36}Sn_{0.03}O_{0.60}$ it is seen that the ratio O/In has increased from 1.67 to 2.45. The F/O ratio is 0.44, thus O is incorporated by the O_2 plasma and some of it is replaced by F during the CF_4 plasma. If ITO samples are exposed to a C_2F_4 plasma after a brief O_2 plasma etch, the ESCA spectra indicate a fluorocarbon surface with $^{-}CF_2$ and $^{-}CF_3$ peaks. Only traces of In^{III} are left even if the film is only approximately 50Å thick. CF_4 etched glass or ITO shows fluorine as F^{-}; the polyfluorocarbon film has covalent F exclusively. Since both surfaces cause the same type of alignment ionic interaction must be excluded Figure 1 shows the F^{-} peaks for CF_4 etched glass or ITO and the covalent F found in a film deposited by a C_2F_4 plasma Figure 2 shows the hydrocarbon on a ITO surface prepared by rf sputtering after a few weeks storage in a container but exposed to laboratory air. These CH_2 peaks disappear after O_2 etching. The top part of the figure shows the relative intensities of CF_2 and CF_3 peaks in a polyfluorocarbon film. Thus, in summary, it is seen that parallel aligning layers are oxides such as SiO_2, SnO_2, or In_2O_3. Perpendicular alignment is obtained by using polyfluorocarbon films or F-rich ITO or glass. Other oxides have not been investigated. Cells are usually completed and filled shortly after the aligning layers have been deposited, however, storing the substrates at this state has not shown adverse effects. Completed cells have been aged at 80°C for several months without change in alignment.

Permittivity Measurements

Permittivity is the ratio of the capacitance of the filled cell to that of the empty cell, both corrected for stray capacitance. The capacitance is measured by a gain-phase technique rather than a standard R-C bridge. The stray capacitance can be kept to a minimum and data can be obtained over an extended range of frequencies. It has been shown (8) that a liquid crystal cell can be represented by a parallel R-C circuit only in the middle of the audio range. At very low frequencies the electrode space charge causes the cell to resemble a series circuit C_s-R, where C_s is much larger than the capacitance of the liquid crystal layer. In addition, aligning layers are blocking layers and cause phase shift. Such cells are best represented by two R-C circuits in series. The time constants are quite different and one can separate the effects by taking data over a wide frequency range. Cells prepared by oxygenation or fluoridation of ITO behave as series R-C circuits where R represents the resistance of the layer rather than the cell. Again one can separate the contributions from gain-phase data taken over a wide frequency range.

Figure 3 shows the measuring circuit and an exploded view of the cell. The cell, represented by R_1C_1 is placed in a double-walled thermostat. A strip heater between the walls and an external control circuit regulates the cell temperature to about 0.05°C between 25° and 150°C. One side of the cell is connected to a low impedance audio oscillator, the other to a fast operational amplifier connected as source follower. R_2 is a standard resistor in the range of 10 kΩ to 1 MΩ. C_2 represents the stray capacitance, a small standard capacitor is sometimes added. The circuitry is packaged in a rectangular aluminum box which fits between the

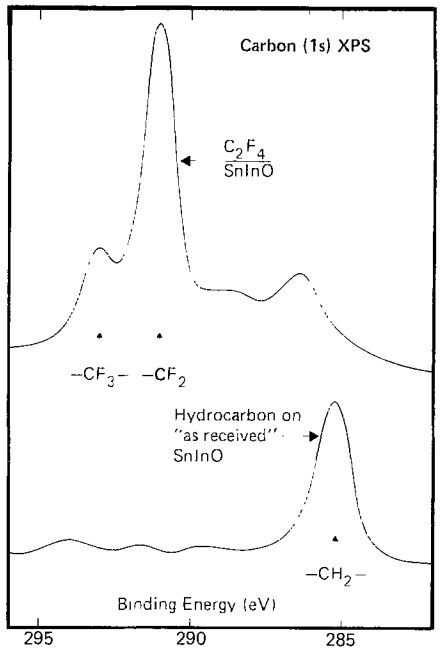


Fig. 2. $^{-}CF_2$ and $^{-}CF_3$ peaks for a polyfluorocarbon film deposited by a C_2F_4 plasma.

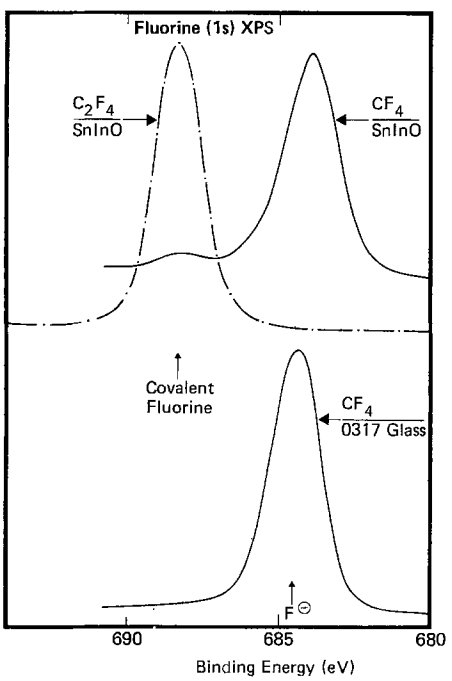


Fig. 1. Details of XPS spectra showing F^{-} peaks for CF_4 etched glass and ITO and F peaks for a polyfluorocarbon film deposited by C_2F_4 plasma.

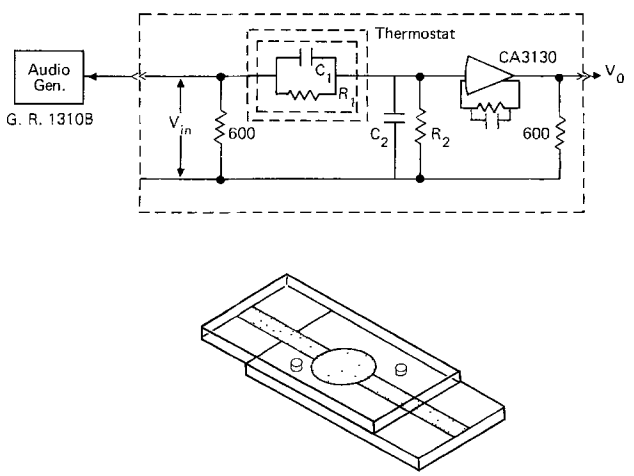


Fig. 3. Schematic circuit for measuring the impedance of a liquid crystal cell by a gain/phase technique; insert is a typical cell configuration.

poles of a 12 in. Varian magnet. The operational amplifier compartment can be cooled with dry nitrogen.

The phase shift in the operational amplifier can be neglected for frequencies up to 500 kHz. The gain and phase for the series circuit R_1C_1-R_2C_2 is determined by

$$\frac{V_o}{V_i} = \left| \frac{Z_2}{Z_1 + Z_2} \right| \exp j(\omega t + \phi) \qquad [1]$$

The experiment yields data for the phase angle ϕ and the gain q at the measuring frequency

$$q = \left| \frac{V_o}{V_i} \right| = \left| \frac{Z_2}{Z_1 + Z_2} \right| \qquad [2]$$

From Eq. [1] and [2] an explicit form for the cell parameters is obtained

$$X_1 = \omega R_1 C_1 = \frac{1}{q_o} \cdot \frac{q}{\sin\phi} - \frac{1}{tg\phi} \qquad [3]$$

where

$$q_o = \frac{R_2}{R_1 + R_2} \qquad [4]$$

As stated above, in general q_o cannot be obtained from d-c measurements. In a frequency range where R_1 and C_1 are independent of frequency, q_o is calculated from

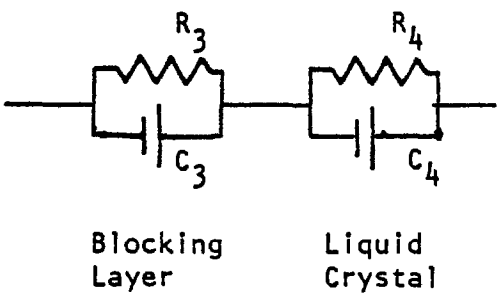
$$\frac{1}{q_o} = \frac{\frac{1}{\nu_1} \cdot \frac{1}{tg\phi_1} - \frac{1}{\nu_2} \cdot \frac{1}{tg\phi_2}}{\frac{q_1}{\nu_1 \sin\phi_1} - \frac{q_2}{\nu_2 \sin\phi_2}} \qquad [5]$$

where the indexes refer to the two frequencies. For hand calculation it is advantageous to choose the frequency ratio large, say $\nu_2/\nu_1 > 50$. Then the low frequency data dominate and Eq. [5] simplifies to

$$\frac{1}{q_o} \approx \frac{\cos\phi_1}{q_1} \qquad [6]$$

For computer calculations the simplification is immaterial.

For high resistivity liquid crystal material ($\rho \approx 10^{11}$ Ω-cm) and cells with metal electrodes q_o is constant down to a few hertz. For cells with blocking layers q_o decreases with frequency below about 200 Hz depending on the thickness of the blocking layer and the permittivity of the liquid crystal material. Cells with blocking layers must be represented by two R-C circuits:



This readily converts to a single parallel R-C circuit but the resulting parameters R and C are now frequency dependent. If the index 3 represents the blocking layer and 4 the liquid crystal, R_1 in Fig. 3 is now determined by

$$R_1 = R_4 \cdot \frac{\left(\frac{R_3 + R_4}{R_4}\right)^2 + X_4^2 \left(\frac{R_3}{R_4} + \frac{X_3}{X_4}\right)^2}{\frac{R_3 + R_4}{R_4} + X_4^2 \left(\frac{R_3}{R_4} + \left(\frac{X_3}{X_4}\right)^2\right)} \qquad [7]$$

For $\omega \to 0$, $R_1 \approx R_3 + R_4$. For $X_3 >> \frac{R_3 + R_4}{R_4}$, $R_1 \approx R_4$ since $C_3/C_4 >> 1$.

Experimentally R_3 and R_4 are of the same order of magnitude although the blocking layer is much less than 1% of the cell thickness. Thus R_1 in Eq. [4] starts to increase at the frequency where X_3 is of the order of unity. Permittivity data for cells with blocking layers are obtained in a frequency range such that the calculated R and C change by less than 1% over the range. Then the low frequency data are used to calculate the resistance of the blocking layers. An abnormally low value usually indicates pinholes. The resistivity of oxide blocking layers is at least 10^{12} Ω-cm; fluorocarbon films usually have higher resistivities.

Finally, for completeness, Eq. [8] and [9] list the empty cell capacitance and the stray capacitance

$$\omega R_2 C_0 = \frac{q}{\sin\phi} \qquad [8]$$

$$\omega R_2 C_s = \frac{1}{tg\phi} - \frac{q}{\sin\phi} \qquad [9]$$

R_2 is the standard resistor, C_0 the capacitance of the empty cell, C_s the total stray capacitance at the junction. C_0 is about 50 pF for 10 μm cells. C_s is about 10 pF including the input capacitance of the operational amplifier.

Electrical Effects of Plasma Etching of ITO

As was shown above, exposure of ITO to the products of an oxygen or CF_4 plasma leads to incorporation of O and F in the ITO layer. This has a profound effect on the resistivity of the film. Figure 4 shows the increase in resistivity of a number of test samples after exposure to a pure O_2 plasma. As before the sample is downstream from the plasma and not subjected to ion bombardment. Test samples are prepared by photolithography from rf sputtered ITO coatings 700-1000Å thick. The test pattern is a stripe, 1 × 0.050 in., with the usual four contacts. The sheet resistance of the coating is 0.5-1.5 kΩ/sq. Each data point in Fig. 4 represents one test sample. The ratio of the sheet resistance after exposure and the original resistance is plotted *vs.* the exposure time. Notice that for short exposure times, say up to 30 min, the data agree reasonably well but for longer exposure time there is considerable deviation. This is probably caused by

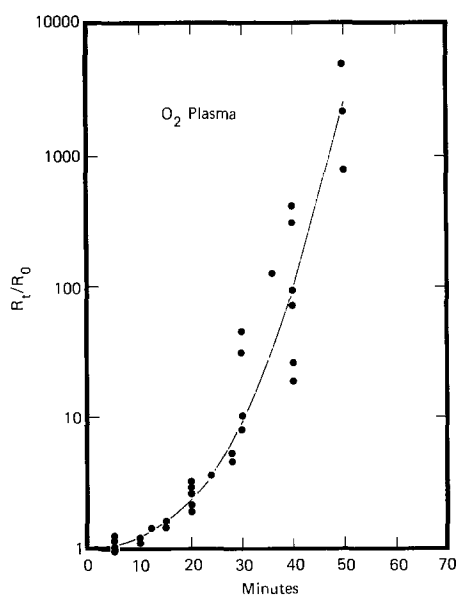


Fig. 4. Increase in sheet resistance vs. exposure time to an O_2 plasma. Each data point represents one sample.

thickness variations along the stripe. (30 min is enough to obtain alignment.)

It is generally assumed that Sn^{IV} acts as a donor center in the oxide semiconductor In_2O_3 (9). Thus, oxygen incorporated in the film removes donor centers or acts as a trap. Assuming that the decrease in carrier concentration is proportional to the increase in oxygen one can regard the process as oxygen diffusion and calculate the diffusion coefficient of O into the ITO film. Numerical values for D calculated from data in Fig. 4 are $D = 3\text{-}8 \times 10^{-15}$ cm^2 sec^{-1}. The process is likely to be more complicated than simple diffusion but the accuracy of the data does not permit evaluation of a two-parameter model. The numerical value for D is about the same as that for P diffusion in silicon at 1000°C. The inverse process is exemplified in Fig. 5. Exposure to forming gas plasma (95% N_2, 5% H_2) removes bound oxygen and creates new carriers. Thus the sheet resistance can be reduced to approximately the starting value and this will not affect the aligning properties of the surface.

Alignment by ITO Films

The alignment produced by oxide or polyfluorocarbon films has been discussed elsewhere (6). In this section we compare the alignment produced by O_2 etched ITO films and that obtained if the O_2 exposure is followed by reduction in a H_2 plasma. Figures 6 and 7 list the observed permittivity of n-octylcyanobiphenyl as a function of temperature while the sample is held in a magnetic field aligned parallel with the surface-induced orientation or orthogonal to it. Figure 6 refers to a cell after exposure to an O_2 plasma. Figure 7 shows data for a cell exposed to a H_2 plasma after the O_2 treatment. In the smectic phase both samples are aligned parallel to the electrode surface, $\epsilon_1 \approx 5.1$. If the sample is heated without a magnetic field or with a 14 kG field directed parallel to the surface, ϵ changes slowly and continuously with temperature until the transition to isotropic is reached. In particular there is no discontinuity at 32°C, the SmA → N transition temperature. Thus the alignment remains controlled by the surface throughout the nematic phase and a magnetic field does not cause additional alignment. If the sample is heated in a magnetic field orthogonal to the surface-induced alignment, a sharp increase in ϵ occurs at 32°C and ϵ is about 10 throughout the nematic region. In the isotropic phase ϵ decreases to the same value as before. Figures 6 and 7 are almost identical and it is concluded that exposure to H_2 plasma does not change the surface alignment. At this stage of knowledge these results cannot be taken for granted, *e.g.*, exposure to CF_4 would have produced a perpendicularly aligned cell.

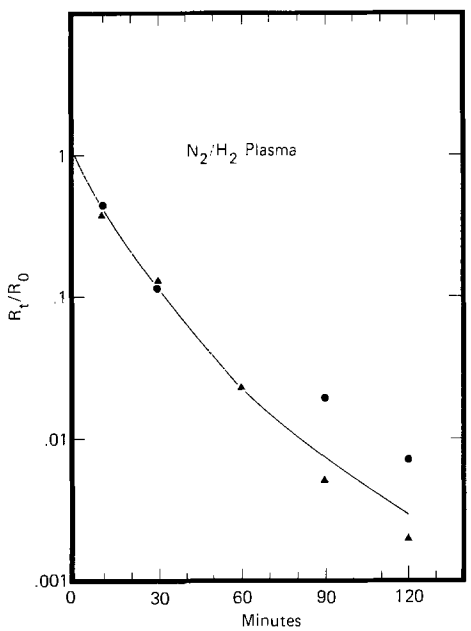


Fig. 5. Decrease in sheet resistance vs. exposure time to an N_2/H_2 plasma. Data points represent two samples previously exposed to an O_2 plasma.

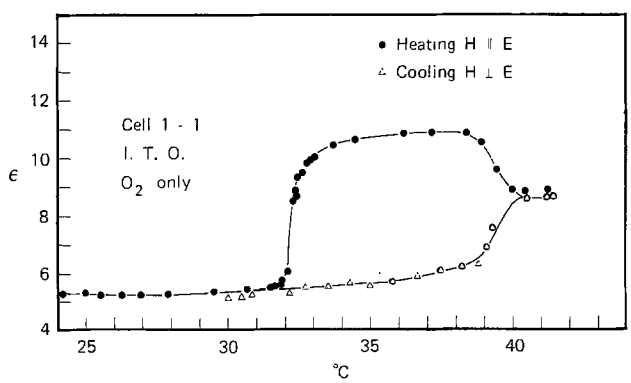


Fig. 6. Permittivity vs. temperature for OCBP in a cell having ITO electrodes exposed to an O_2 plasma for 20 min.

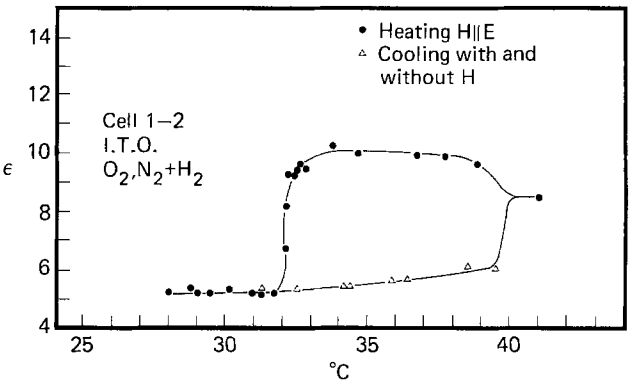


Fig. 7. Permittivity vs. temperature for OCBP in a cell having ITO electrodes exposed to O_2 plasma followed by exposure to N_2/H_2 plasma for 30 min.

Summary

Plasma etching and deposition techniques can be used to obtain aligned liquid crystal cells. Oxygen etched glass or ITO surfaces, and surfaces on which SiO_2 or SnO_2 is deposited show strong parallel alignment. Glass or ITO surfaces exposed to CF_4 plasma or surfaces on which a polyfluorocarbon film is deposited by a C_2F_4 plasma show strong perpendicular alignment. The alignment is permanent and the cells can be temperature cycled at will without changing the original alignment. The composition of the surface layer was studied using electron spectroscopy (XPS). The electrical characteristics of the deposited films were obtained by R-C measurement.

Acknowledgment

We thank D. W. Rice of this laboratory for the surface analysis by ESCA and Vance Hoffman of Varian for preparing the ITO films.

Manuscript submitted Oct. 12, 1976; revised manuscript received Nov. 24, 1976.

Any discussion of this paper will appear in a Discussion Section to be published in the December 1977 JOURNAL. All discussions for the December 1977 Discussion Section should be submitted by Aug. 1, 1977.

Publication costs of this article were assisted by IBM Corporation.

REFERENCES

1. J. R. Hollahan and A. T. Bell, in "Techniques and Applications of Plasmachemistry," John Wiley & Sons, Inc. (1974).
2. R. W. Kirk, in *ibid.*, chap. 9.

3. H. G. Hughes, W. L. Hunter, and K. Ritchie, *This Journal*, **120**, 97 (1973).
4. M. Millard, in Ref. (1), chap. 5.
5. J. C. Dubois, M. Gazard, and A. Zann, *J. Appl. Phys. Lett.*, **24**, 297 (1973).
6. G. J. Sprokel, Paper C1-9 6th International Liquid Crystal Conference, Kent State University, 1976 (to be published in *Mol. Cryst.*).
7. Tegal Corporation, Richmond, California.
8. G. J. Sprokel, *Mol. Cryst. Liq. Cryst.*, **26**, 45 (1974).
9. D. B. Fraser and H. D. Cook, *This Journal*, **119**, 1368 (1972).

Analysis of Transport Processes in Vertical Cylinder Epitaxy Reactors

C. W. Manke* and L. F. Donaghey**

Materials and Molecular Research Division, Lawrence Berkeley Laboratory and Department of Chemical Engineering, University of California, Berkeley, California 94720

ABSTRACT

Momentum, heat and mass transfer processes were studied in a vertical cylinder reactor for the epitaxial growth of Si from $SiCl_4$ in H_2 by chemical vapor deposition. An analytical solution to the problems of heat and mass transfer in a tapered annulus is presented based on constant transport properties and fully developed laminar flow. The mean gas-phase temperature and deposition rate distribution of silicon are calculated within the reactor using a developing temperature model. Results of experimental studies of silicon deposition from $SiCl_4$ in H_2 at 1200°C in a vertical cylinder reactor are compared with the analytical results and with other models of diffusion-controlled chemical vapor deposition. This study provides an analytical method for calculating epitaxial deposition rate distributions in vertical cylinder reactors, and for designing reactors to improve the yield and uniformity of epitaxial growth.

Vertical cylinder (barrel) reactors have been developed recently for the epitaxial growth of semiconductor layers by chemical vapor deposition (CVD). This type of reactor has already demonstrated the potential for scale-up of the epitaxial growth process. The increased throughput of the vertical cylinder reactor as compared to the horizontal reactor is particularly important in the semiconductor industry where high volumes of silicon bipolar devices are involved.

Growth rate uniformity of epitaxial silicon by CVD is of great importance for semiconductor applications. The yield of finished devices is sharply diminished by nonuniformity of the thickness of the epitaxial silicon layer either on the individual wafers or from wafer to wafer within the processing batch. Growth rate uniformity, of course, must be accomplished using an economical quantity of reactant gas. Successful processing, therefore, requires the development of reactor design principles for achieving optimum growth rate uniformity at reasonable reactant flow rates. The development of mathematical models for the description of transport processes and the deposition rate distribution of silicon in the vertical cylinder reactor is examined in this paper.

Models for the CVD rate of silicon have been studied by a number of investigators. Eversteyn and coworkers (1, 2) and Rundle (3, 4) have developed models for the growth rate of silicon in horizontal reactors based on diffusion through a laminar sublayer adjacent to the susceptor, and on diffusion in a fully developed laminar flow, respectively. Fujii *et al.* (5) developed a quantitative model of silicon deposition rates in vertical cylinder reactors, and quantitative studies were reported by Dittman (6).

In the above works, the gas temperature profile was considered to be constant over the entire length of the reactor. In a real reactor, however, the temperature, velocity, and concentration profiles can be expected to change rapidly in the entrance region near the leading edge of the constant-temperature susceptor before achieving the constant, or fully developed distributions assumed by the above models.

Several of the above models recognize the need for incorporating boundary layer theory into a growth rate model. For example, Eversteyn assumes a boundary layer thickness equal to a fraction of the channel width. Dittman used a modified form of the Chilton-Colburn analogy to obtain properties of boundary layer flow over a flat plate. Unfortunately, the geometry and transport phenomena of the vertical cylinder reactor are not well described by either of these models. It is shown in this paper that mass transfer analogies based on turbulent flow over a flat plate do not give a satisfactory prediction of the silicon growth rate in the vertical cylinder reactor, and that what is needed is a method for predicting the growth rate based on the theory of developing heat and mass transport in the laminar flow regime, the Graetz problem in an annular passage.

Important theoretical methods for assessing transport in a fluid in fully developed laminar flow can be found in the fluid mechanics literature. Graetz (7) solved the problem of developing heat transfer in tubes by means of an eigenfunction expansion. Nusselt (8) improved the accuracy of Graetz's calculation of the first three eigenvalues. Brown (9) solved the Graetz problem in a flat duct, and the extension to a right circular annulus has been studied by Hatton and Quarmby (10), and by Reynolds and co-workers (11, 12).

In this paper, a solution to the Graetz problem of heat transfer in an annular passage is used to demonstrate that the mean gas temperature in the vertical cylinder reactor increases with distance over a significant portion of the axial susceptor length, and that a fully developed temperature profile is not attained under typical operating conditions for silicon deposition. Mass transfer is shown to have a positive temperature dependence resulting in enhancement of the growth rate as temperature increases. A method for calculating the growth rate is presented which takes into account the effects of the developing heat and mass transfer

* Electrochemical Society Student Member.
** Electrochemical Society Active Member.

profiles in the annular passage. The method is used to study the effects of gas flow rate and susceptor tilt angle on growth rate uniformity and reactant yield. Finally, growth rate calculations are compared to those predicted by other published models and to experimental results obtained in a commercial vertical cylinder reactor.

Theory

The vertical cylinder reactor.—For silicon epitaxial growth from $SiCl_4$, a dilute mixture of $SiCl_4$ in hydrogen is passed through an annular passage between a cylindrical outer quartz wall of the reactor and an octagonal silicon carbide-coated, graphite susceptor, idealized here as the frustrum of a cone or, in the limit of a constant inner radius, a right-circular cylinder. The vertical cylinder reactor is shown schematically in Fig. 1.

In the vertical cylinder reactor studied here, silicon substrate wafers are placed on the faces of a graphite susceptor which is radiantly heated by quartz lamps placed outside a forced air-cooled quartz cylinder which is the outer wall of the reactor. Typical operating conditions for silicon epitaxial growth from $SiCl_4$ are a susceptor temperature near 1200°C, a reactant gas mixture containing about 1% $SiCl_4$ in hydrogen, and a flow rate yielding Reynolds numbers of order 10^2. Under those conditions the fluid is in laminar flow. Shaw (13) reports that the temperature at which mass transfer control of the growth rate predominates over kinetic control is not precisely known; however, several experimental studies indicate that deposition of epitaxial silicon from a dilute $SiCl_4$ reactant is entirely diffusion controlled at 1200°C. The silicon deposition reaction is surface-catalyzed and therefore occurs only at the surface of the heated susceptor. Silicon deposition occurs on all parts of the susceptor surface. Calculation of the growth rate, then, is a matter of determining the rate of mass transfer of the reactant from the gas stream to the susceptor surface. Since the mass transfer rate is dependent on the velocity and temperature distributions in the gas phase, equations governing all three transport phenomena must be considered.

Transport equations.—The steady-state equations governing transport are the following.[1]

1. The momentum equation in the axial direction

$$\rho V_r \frac{\partial V_z}{\partial r} + \rho V_z \frac{\partial V_z}{\partial z} = -\frac{\partial p}{\partial z} + \rho g_z + \mu \frac{1}{r}\frac{\partial}{\partial r}\left(r\frac{\partial V_z}{\partial r}\right) \quad [1]$$

2. The energy equation in the axial direction

$$V_r \frac{\partial T}{\partial r} + V_z \frac{\partial T}{\partial z} = \alpha \frac{1}{r}\frac{\partial}{\partial r}\left(r\frac{\partial T}{\partial r}\right) \quad [2]$$

3. The equation for continuity of the diffusing species, in the axial direction

$$V_r \frac{\partial X}{\partial r} + V_z \frac{\partial X}{\partial z} = \mathcal{D} \frac{1}{r}\frac{\partial}{\partial r}\left(r\frac{\partial X}{\partial r}\right)$$

4. The equation of continuity

$$\frac{1}{r}\frac{\partial}{\partial r}(\rho r V_r) + \frac{\partial}{\partial z}(\rho V_z) = 0 \quad [3]$$

The fluid physical properties in the above equations, μ, ρ, α, and $\mathcal{D}$, are assumed to be constant, a necessary condition for a simplified analytical treatment.

The radial velocity distribution for fully developed laminar flow is the solution to Eq. [1]. In a cylindrical annulus the solution has the form

[1] Variables are defined in the list of symbols at the end of the paper.

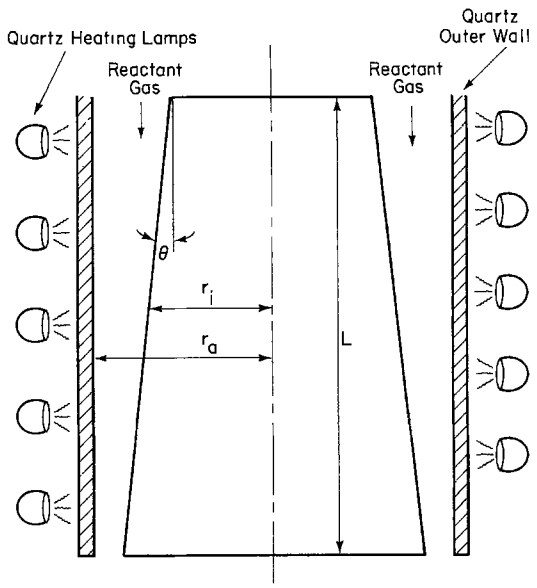


Fig. 1. The vertical cylinder reactor

$$U(\bar{r}) = \frac{2U_m}{A}(1 - \bar{r}^2 + B\ln\bar{r}) \quad [5]$$

where A and B are constants. The buoyancy term, g_z, of Eq. [1] is neglected in deriving Eq. [5]; this assumption leads to a small error at the susceptor leading edge where a large thermal gradient is present, but the omission of the buoyancy term is a simplification necessary for analytical treatment. The condition of stable, fully developed laminar flow in the reactor is the basis for the following mathematical description of transport processes.

The following dimensionless parameters are useful in reducing the transport equations to simple forms

$$\bar{r} = r/r_o$$

$$\theta(\bar{x}) = \frac{T - T_i}{T_e - T_i}, \quad \bar{x} = \frac{z}{\mathrm{Re\,Pr}\,d_h} \quad [6]$$

$$\chi(\bar{z}) = \frac{X - X_i}{X_e - X_i}, \quad \bar{z} = \frac{z}{\mathrm{Re\,Sc}\,d_h}$$

In addition, it is useful to define the bulk-mean reduced temperature and reactant mole fraction as follows

$$\theta_m = (AU_m)^{-1}\int_A U\theta\,dA$$

$$\chi_m = (AU_m)^{-1}\int_A U\chi\,dA \quad [7]$$

where the integral is over the cross-sectional area of the annulus at a given axial position.

For fully developed velocity, the energy equation, Eq. [2], can be reduced to the following dimensionless temperature equation

$$\frac{\partial^2\theta}{\partial\bar{r}^2} + \frac{1}{\bar{r}}\frac{\partial\theta}{\partial\bar{r}} = \frac{U(\bar{r})}{\alpha}\frac{\partial\theta}{\partial\bar{x}} \quad [8]$$

Using the dimensionless mole fraction defined above, the reactant mass continuity equation can be reduced to a similar form

$$\frac{\partial^2\chi}{\partial\bar{r}^2} + \frac{1}{\bar{r}}\frac{\partial\chi}{\partial\bar{r}} = \frac{U(\bar{r})}{\mathcal{D}}\frac{\partial\chi}{\partial\bar{z}} \quad [9]$$

The boundary value problems for solving Eq. [8] and [9] can be made homogeneous by subtracting the fully developed solutions which are valid as $\bar{x}$ and $\bar{z}$

tend to infinity. The complete solutions to Eq. [8] and [9] can then be solved by separation of variables in the form

$$\theta = \theta_{fd} + \sum_{n=0}^{\infty} C_n F_n \exp(-\lambda_n \bar{x}) \quad [10]$$

where the functions F_n satisfy a differential equation of the Sturm-Liouville type.

Solution of the transport equations for developing flow is a difficult problem. Reynolds, McCuen, and Lundberg (11, 12) have obtained solutions for the coefficients C_n by numerical integration using an iterative method developed by Berry and de Prima (14). As a result of their work, θ_m and the Nusselt number, Nu, (and by analogy χ_m and Sh for mass transfer) can be obtained for several types of boundary conditions in an annular passage. These functions will be used in a differential expression for material balance to calculate the growth rate of silicon in the vertical cylinder reactor, taking into account the effects of developing heat and mass transfer in a fully developed velocity distribution.

Boundary conditions and initial values.—Heat transfer.—Heating of the susceptor in the vertical cylinder reactor is typically achieved with rf or quartz-iodide lamp heating, which hold the entire susceptor at a constant temperature. The outer quartz wall is air-cooled but subject to radiant heating from the hot susceptor (and from the quartz lamps) as well as to convective heating both inside and outside the reactor. As a result the boundary condition at this wall is quite difficult to determine. Experimental measurements of the outer wall temperature indicate that the quartz wall reaches a temperature near 500°C over the major portion of the wall (15). Therefore the temperature boundary condition can be approximated by assuming the entire outer wall to be at a constant temperature of 773°K. Thus

$$T = \begin{cases} 1473°K, \ r = r_i, \ 0 < z & [11] \\ 773°K, \ r = r_o, \ 0 < z & [12] \end{cases}$$

Since the gas enters the reactor at room temperature, the initial value is taken as 298°K.

For the boundary conditions of specified temperatures at both walls of the annulus, the mean temperature of the gas at a downstream location is determined from dimensionless temperature functions according to the following equation

$$T_m(\bar{x}) = T_e + \theta_{mi}(\bar{x}) \cdot (T_i - T_e) + \theta_{mo}(\bar{x}) \cdot (T_o - T_e) \quad [13]$$

Mass transfer.—The boundary condition for mass transfer at the susceptor surface is specified by chemical reaction equilibria at the temperature of the susceptor, since for susceptor temperatures near 1473°K the growth rate is limited by diffusion rather than by the kinetics of the surface reactions. The deposition reaction is

$$SiCl_4 + 2H_2 = Si_{(c)} + 4HCl \quad [14]$$

In addition, other gas phase species are formed by reactions such as

$$SiCl_4 + H_2 = SiCl_3H + HCl \quad [15]$$

$$SiCl_4 + H_2 = SiCl_2 + 2HCl \quad [16]$$

Sirtl, Hunt, and Sawyer (16) indicate that other species are negligible. A very low partial pressure of $SiCl_4$ (10^{-5}) exists in the equilibrium composition at 1473°K for the Si-H-Cl system at low values of the Cl/H ratio (0.02327 for 1.15% $SiCl_4$ in H_2). Since the driving force for diffusion of the reactant to the susceptor surface is the difference between the partial pressure in the bulk gas stream (10^{-2}) and the partial pressure at the susceptor surface (10^{-5}), the boundary condition for mass transfer at the inner surface can be approximated very well by taking the reactant concentration to be zero. Since deposition does not occur at the outer wall, a flux equal to zero is specified. The boundary conditions for mass transfer are then

$$X = 0, \ r = r_i, \ z > 0 \quad [17]$$

$$\frac{dX}{dr} = 0, \ r = r_o, \ z > 0 \quad [18]$$

For an inlet gas containing 1.15% (volume) $SiCl_4$, the initial condition is

$$X = 0.0115 \text{ at } z = 0 \text{ and } r_i \leq r \leq r_o \quad [19]$$

Thermodynamic yield from reactant gas.—While Eq. [14] is the principal reaction for silicon deposition, the gas species $SiCl_3H$ and $SiCl_2$ will also be formed in an equilibrium mixture by the competing side reactions given in Eq. [15] and [16]. The yield of epitaxial silicon produced from the reactant diffusing to the susceptor will be reduced if these as well as other species are formed in significant quantities. Sirtl *et al.* report the equilibrium yield of solid silicon from $SiCl_4$ as a function of the $SiCl_4$ mole fraction. For a $SiCl_4$ mole fraction of 0.0115 and a temperature of 1473°K, the yield of silicon is approximately 70% (16). To account for the reduction in deposition efficiency caused by the side reactions forming vapor species other than $SiCl_4$, HCl, or H_2, the fluxes of $SiCl_4$ to the susceptor surface must be multiplied by the deposition efficiency, η, to obtain the yield of deposited silicon from the reactant gas. Since reaction kinetics are assumed to be very fast at the temperature of the susceptor, 1473°K, the deposition efficiency used in this study is the equilibrium yield for a $SiCl_4$ mole fraction of 0.0115, which is 0.70.

Growth rate equation.—The dependence of the growth rate on axial distance can be easily developed by taking a material balance on a differential ring element of the reactor annulus. The molar flow rates of reactant entering and leaving the element are $\dot{M}\bar{X}|_z$ and $\dot{M}\bar{X}|_{z+\Delta z}$, respectively. The molar flux to the susceptor surface of a differential element $2\pi r_i \Delta z$ is

$$2\pi r_i \Delta z \, Sh \frac{\mathcal{D}}{d_h} (\bar{X} - X_i) p/(RT_m) \quad [20]$$

where $X_i = 0$. By balancing the above rates one obtains the differential equation for the reactant concentration

$$-\dot{M} \frac{d\bar{X}}{dz} = \frac{p 2\pi r_i \, Sh \, \mathcal{D}}{d_h RT_m} \bar{X} \quad [21]$$

After integration this equation becomes

$$\bar{X} = X_o \exp\left\{ -\frac{2\pi p}{\dot{M}R} \int_0^z \frac{r_i \, Sh \, \mathcal{D}}{d_h T_m} dz \right\} \quad [22]$$

The flux to the surface is then given by

$$\frac{p}{RT_m} \mathcal{D} \frac{d\bar{X}}{dr}\bigg|_{r=r_i} = \frac{p}{RT_m} Sh \frac{\mathcal{D}}{d_h} (\bar{X} - X_i) \quad [23]$$

From Eq. [22] and [23] and the deposition efficiency, η, the linear growth rate expression in μm/min becomes

$$G = 6 \times 10^5 \frac{M_{Si}}{\rho_{Si}} \frac{p \, Sh \, \mathcal{D} \eta}{RT_m d_h} X_o \exp\left\{ -\frac{2\pi p}{\dot{M}R} \int_0^z \frac{r_i \, Sh \, \mathcal{D}}{d_h T_m} dz \right\} \quad [24]$$

Equation [24] can be used together with values of Sh and T_m resulting from the solution of the transport equations to predict the variation of growth rate with axial position in the reactor.

Transport properties.—Transport properties are functions of both temperature and composition. Since these properties are taken to be constants in the transport equations, however, they must be evaluated at a composition and temperature representative of average conditions in the reactor. Since the reactant mixture is dilute, the choice of the inlet composition for evaluation of properties should not lead to significant errors. A simple choice of a representative temperature is the mean cross-sectional temperature, T_m, from Eq. [13], with reduced distance, $\overline{X}$ evaluated using transport properties at the inlet temperature. The length-averaged value of T_m can then be calculated and used as the representative temperature for evaluation of mean transport properties.

Transport properties evaluated for the composition of the inlet gas containing 1.15% $SiCl_4$ and 98.85% H_2 on a molar basis are summarized in Table I. For heat transfer, the viscosity, density, thermal conductivity, and heat capacity of the above mixture are evaluated at 298°K. An important result of the evaluation of properties for heat transfer is that the Prandtl number for the mixture is 0.44 at 298°K, much lower than the value of 0.7 usually found for pure gases. For the growth rate equation, properties are evaluated at average temperatures which were determined from the results of the heat transfer calculation. Viscosity, density, and the diffusion coefficient are given at different temperatures in Table I.

Equations used to determine the values of transport properties were obtained from experimental data and from Reid and Sherwood (17). A complete description of the evaluation methods for transport properties is given in the Appendix.

Temperature dependence of the growth rate.—The temperature dependence of the transport coefficients can be utilized to estimate the dependence of the growth rate on temperature. As explained in the Appendix, the diffusion coefficient for $SiCl_4$ in H_2 is calculated by the equation

$$\mathcal{D} = 7.0861 \times 10^{-9} T^{3/2} \Omega_o^{-1} p^{-1} \qquad [25]$$

The approximate temperature dependence of the diffusion coefficient in the temperature range of interest is $T^{1.674}$. If the effect of the exponential term in Eq. [22], the reactant depletion term, is neglected, the temperature dependence of the growth rate equation, Eq. [24], is $T^{0.674}$. The growth rate will therefore be enhanced as the temperature increases. A limit to this increase is established by thermodynamic conditions, however, since the amount of $SiCl_3H$, $SiCl_2$, and other species in the vapor phase increase with temperature, causing the thermodynamic yield to reach a maximum at about 1430°K.

Results and Discussion

Flow regime.—The range of Reynolds numbers for the operating conditions considered in this study is from 50 to 500. Bird *et al.* (18) indicate that laminar flow will prevail in annular passages for Reynolds numbers less than 2000. Flow instability in the presence of a large thermal gradient can occur even in laminar flow, however. Curtis and Dismukes (19) and Fujii *et al.* (5) discuss this possibility and conclude that flow instabilities do not occur for hydrogen-rich systems under the conditions for epitaxial silicon deposition.

Temperature variation along the susceptor.—The variation of the mean temperature of the gas as a function of the axial position along the susceptor is shown in Fig. 2, for a pressure of 1 atm (101.325 kPa) and Reynolds numbers of 50, 100, 250, and 500 at 1 atm, and for an initial gas temperature of 298°K. All of the curves in Fig. 2 show the characteristics of developing heat transfer. In a region near the leading edge of the susceptor, the temperature of the gas increases very rapidly with distance. The rate of increase of temperature with distance becomes more gradual at increasing distances from the leading edge. As shown in Fig. 2, the axial mean temperature gradient becomes small, corresponding to the approach of the fully developed temperature distribution, only for low Re numbers and large axial distances. For the barrel reactor in the present study, the fully developed value of the mean temperature is 1088°K. The calculated mean temperature of the gas is less than 90% of the fully developed value on the first 10 cm of the susceptor at Re = 50, and on the first 20 cm of the susceptor at Re = 100. For Reynolds numbers of 250 and 500, the mean temperature is well below the fully developed value on the entire 40 cm length of the susceptor. As these results indicate, entry region temperature development occurs over a significant portion of the susceptor at Reynolds numbers greater than 50. Since the growth rate is roughly proportional to $T^{0.674}$, the effects of axial temperature variation on growth rate are expected to be large.

Qualitative effects of entry region temperature development on growth rate.—Because of the positive temperature dependence of the growth rate, entry region temperature development can be expected to affect the growth rate in three important ways:

1. Over-all growth rates will be lower than those predicted by theories which consider temperature to be at the maximum, fully developed value.
2. Lower than average temperatures at upstream positions and higher than average temperatures at downstream locations will enhance deposition on the downstream portion of the susceptor, partially compensating for the negative effect of reactant depletion on growth rate. Deposition will therefore be more uniform than predicted by growth rate models which evaluate gas temperature at the fully developed value or a constant length averaged value.

Table I. Transport coefficients for a reactant mixture of 1.15% $SiCl_4$-98.85% H_2

T (°K)	μ_{mix} (μ-poise)	ρ (g/m^3)	$\mathcal{D}$ (m^2/sec) × 10^4	Sc
298	97.9	1.511		
592	161.1	0.7606	1.162	1.823
726	187.0	0.6202	1.648	1.830
912	219.5	0.4937	2.426	1.833
997	2337.0	0.4516	2.818	1.836

Molecular weight of mixture: 3.695.
Thermal conductivity of mixture at 298°K = 0.38 J/(m-sec °K).
Heat capacity of mixture at 298°K = 29.45 J/(g-mol °K).
Pr at 298°K = 0.44.

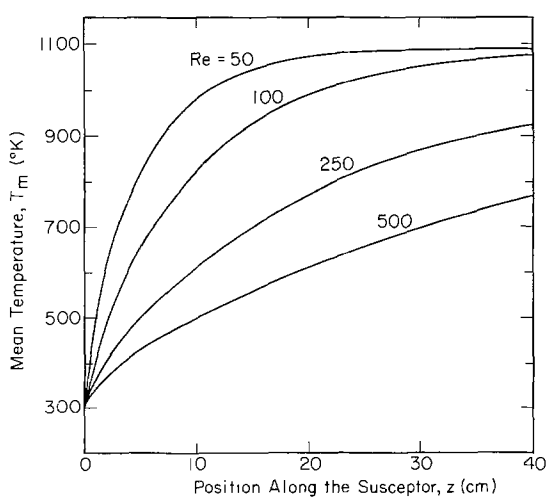


Fig. 2. Variation of the mean temperature of the gas with position along the susceptor.

3. In spite of the decrease in reactant depletion with increased velocity, the over-all growth rate should reach a maximum value as velocity is increased and then decrease with further increases in velocity due to the decrease in average gas temperature. These three effects are discussed further as quantitative growth rate expressions and experimental results are presented.

A constant temperature method for growth rate calculation.—Because of the similarity between the heat and mass transfer equations discussed in the theory section, the dimensionless heat transfer solutions of Reynolds *et al.* (11, 12) can be applied directly in the calculation of the growth rate using Eq. [24]. With this analogy, developing mass transfer rates in the annular passage are determined subject to the conditions of laminar flow, constant fluid and transport properties, and a fully developed velocity field. Results are shown in Fig. 3 for Reynolds numbers 50, 100, 250, and 500. High deposition at upstream susceptor positions and low deposition at downstream positions are characteristic of all of the predicted curves. At the lower Reynolds numbers of 50 and 100, the decrease in growth rate with distance is largely a result of reactant depletion. For the higher Reynolds numbers, however, reactant depletion is a less important factor. Lower resistance to radial diffusion is reflected in high values of the Sherwood number in the leading edge region and is expected to produce higher growth rates on the front portion of the susceptor, especially at high flow velocities. A major limitation of the above method of calculating mass transfer rates is that it does not include the effect of the simultaneously developing temperature profile in the reactor.

The developing temperature model for growth rate calculation.—The heat transfer solutions of Reynolds *et al.* (11, 12) are valid only for constant property flow. Strict application of these solutions to Eq. [24] requires that all parameters be evaluated at a constant temperature as described above. The heat transfer calculation, however, indicates that the temperature will increase with downstream position. An approximate calculation of the growth rate with variable temperature can be made by using Eq. [24] with $\mathcal{D}$ and T_m evaluated at the local value of T_m in the gas. The basis for this approximation is the assumption that the Sherwood number at a downsteram location for flow with changing properties will be nearly equal to the value evaluated at the length averaged mean temperature defined by

$$T_{mL} = L^{-1} \int_0^L T_m dz \qquad [26]$$

The assumption should be fairly good if the temperature variation in the region of interest along the susceptor is small, but less accurate as temperature variation from the length average value increases. For this reason, the developing temperature model is expected to work best for low gas velocities, but the model cannot be expected to give accurate results in the leading edge region of the susceptor where the rate of temperature change with axial position is extreme. Since the leading edge region is extended as the Reynolds number is increased, the developing temperature model becomes less accurate in the leading-edge region as the Reynolds number increases. Nevertheless, over the susceptor region of commercial interest, the model is expected to give reasonable accuracy.

The accuracy of this method is supported by experimental studies in the barrel reactor carried out at a Reynolds number of 92.6, as is shown below.

The results of growth rate calculations using the developing temperature model are shown in Fig. 4. Lower temperatures in the upstream region of the reactor result in calculated growth rates which are lower than those predicted by the constant property method. Deposition in the downstream region is higher because the temperature is greater than the length averaged value and because the lower predicted values in the upstream portion result in a smaller depletion of the reactant in that region of the reactor.

A comparison of the developing temperature model to the constant temperature method is shown in Fig. 5 for high and low flow rates. The difference between the two methods is more pronounced at the higher flow rate since the variation of the local temperature from the length average value is greater. For Re = 50, flow is close to being fully developed and the growth rates predicted by the two methods are similar. As expected the variable temperature method predicts a more uni-

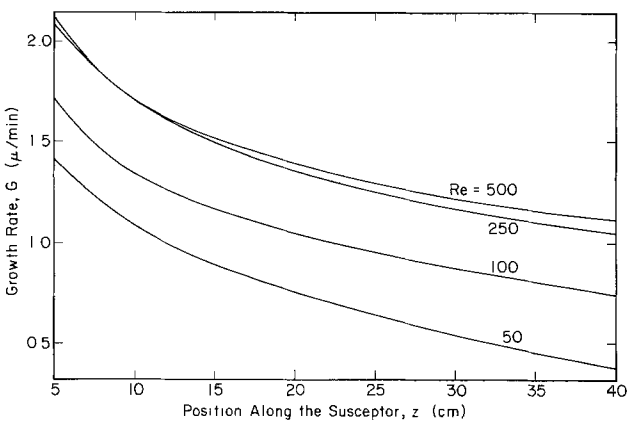


Fig. 3. Variation of growth rate with position along a constant diameter susceptor according to the constant temperature model. Transport properties are evaluated at the average mean temperature of the gas.

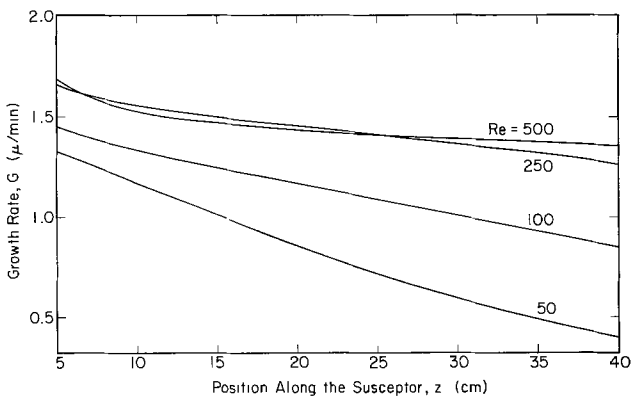


Fig. 4. Variation of growth rate with position along a constant diameter susceptor according to the developing temperature model.

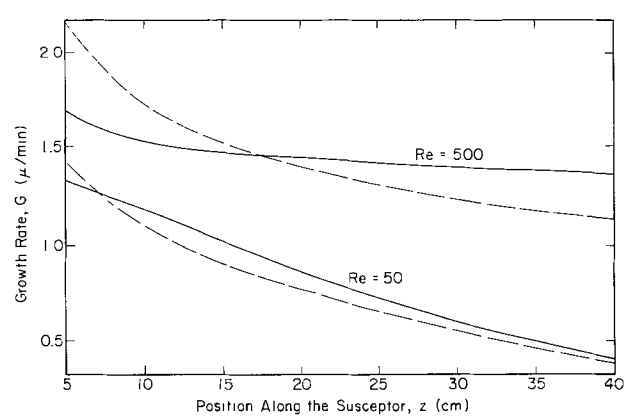


Fig. 5. Comparison of the growth rate variation predicted by the constant temperature modes (– – –) and the developing temperature modes (———).

form growth rate distribution than the constant temperature method.

An assumption of the present study is that there is no preheating of the gas entering the vertical cylinder reactor. Depending on the reactor design, some preheating could occur by radiative heat transfer or by convection via recirculation currents. The effect of reactant gas preheating would be to raise the mean temperature and decrease the temperature gradients in the region near the leading edge of the susceptor, from those shown in Fig. 2. Reactant gas preheating therefore increases the deposition rates near the leading edge of the susceptor. Thus, the growth rates predicted by the developing temperature model, shown in Fig. 5, would then be brought closer to the growth rates predicted by the constant temperature model.

Near the leading edge of the susceptor, the developing temperature model predicts deposition rates which are lower than the experimental values, because the gas phase region adjacent to the susceptor has the greatest influence on thermally activated CVD reactions. This error in the method becomes the error introduced by using a cross-stream average temperature in mass transfer calculations diminishes with increasing distance from the susceptor leading edge. A correction of the model in the region near the susceptor leading edge is not needed if substrate wafers are excluded from this part of the reactor.

Growth rates for a reactor with a tapered susceptor.—The Sherwood number varies slowly with the parameter, r_i/r_0. If the taper angle is small, the approximate growth rate for a tapered susceptor reactor can be calculated by Eq. [24] using the Sherwood number distribution for the average value of r_i/r_0. Growth rates for a reactor with an average inner diameter of 8.25 cm and a taper angle of 3.58° are presented in Fig. 6. Growth rates were calculated by the variable temperature method. Mass transfer to the susceptor is enhanced by the increasing inner radius. For Re of 250 and 500, the predicted deposition rate is higher at downstream positions. For Re of 100, enhancement of the growth rate due to the increasing inner radius offsets the effect of reactant depletion and a nearly uniform growth rate distribution is predicted. The constant diameter growth rate is shown for comparison. The Re value of 100 is very close to the design flow for the reactor for which Re is 92.6. At Re = 50 the enhancement due to taper angle is insufficient to compensate reactant depletion and the growth rate declines with distance.

Yield, over-all growth rate, and growth rate nonuniformity.—Table II summarizes yield, over-all growth rate, and growth rate nonuniformity predicted by the developing temperature method. Values are calculated

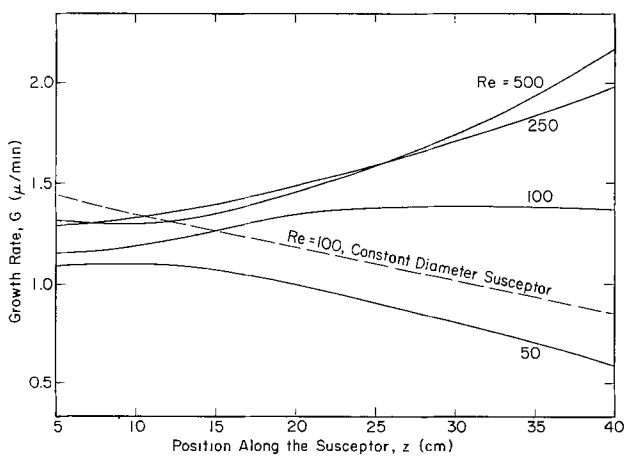


Fig. 6. Variation of growth rate with position along a tapered susceptor (taper angle = 3.58°) according to the developing temperature model.

Table II. Yield, over-all growth rate, and growth rate nonuniformity

Susceptor diameter	Re_{298}	Yield (%)	$\bar{G}$ (μmin^{-1})	$\Delta G/\bar{G}$ (%)
		Constant diameter susceptor		
Constant	500	7.42	1.43	10.8
Constant	250	14.5	1.42	13.2
Constant	100	29.8	1.13	25.9
Constant	50	42.7	0.81	53.0
		Tapered susceptor		
Tapered 3.58°	100	33.7	1.25	5.9
Tapered 3.58°	92.6	35.5	1.21	4.7

for ($5 \leq z \leq 40$), the approximate useful area of the susceptor. Growth rate nonuniformity is evaluated by Eversteyn's method (1)

$$\Delta G = \frac{G_{max} - G_{min}}{G_{max} + G_{min}} \times 100\% \qquad [27]$$

For a constant diameter susceptor, deposition uniformity is achieved by increasing the flow rate at the expense of reactant yield. Predicted results indicate low growth rate nonuniformities at Re = 250 and 500, but very poor reactant yields. The choice of flow rate for a constant diameter reactor would involve a compromise between the cost of higher reactant throughput at low reactant yield and the added cost of reduced yield of finished devices due to nonuniform epitaxial layer deposition. The tapered susceptor reactor offers an attractive alternative to this compromise. Using this innovation, the taper angle can be set to minimize growth rate nonuniformity at a specified velocity. The predicted growth rate nonuniformity for the tapered susceptor reactor at Re = 100 is much smaller than that for the constant diameter reactor at Re = 500. At the design value, Re = 92.6, growth rate nonuniformity is further reduced. With the tapered susceptor, predictions indicate that a small growth rate nonuniformity (4.73%) can be attained at an acceptable reactant yield (35.5%).

Comparison to experimental results and other growth rate models.—The growth rate predicted by the developing temperature method for a tapered susceptor reactor is compared to the calculations of other models and to experimental values in Fig. 7.

Experimental data were taken for a commercial barrel reactor, the AMT 740, of the dimensions shown in Fig. 1, with a susceptor taper angle of 3.58°. A flow of

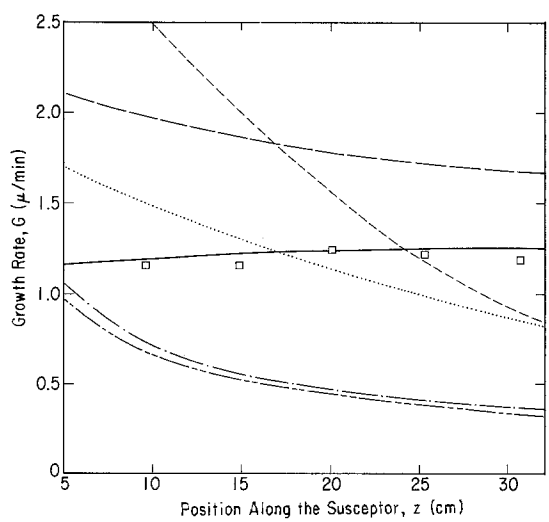


Fig. 7. A comparison of growth rate models and experimental data. (——) Developing temperature model, this work; (— — —) Eversteijn and Peek; (— —) Fujii et al.; (· · · ·) Rundle; (—·—) Dittman; (——— — ———) Chilton-Colburn analogy. Squares are experimental data.

112 liters/min (1867 cm^3/sec) of reactant gas containing 1.15% $SiCl_4$ in H_2 was introduced at the top of the reactor by entrance tubes which were adjusted to the optimum orientation. The deposition rates of epitaxial silicon were measured at multiple points on each wafer. Values were then azimuthally averaged for each axial position. The values shown in Fig. 7 are the average values at the substrate wafer centers. The theoretical predictions are based on a reactor of the same dimensions as the experimental reactor with the same initial $SiCl_4$ mole fraction, with Re = 92.6, corresponding to a flow rate of 112 liters/min in the experimental reactor. The growth rate is predicted by the developing temperature method for a tapered annulus. Agreement between the theoretical prediction and the experimental data is excellent, as shown in Fig. 7.

Fujii's model for the growth rate in a barrel reactor with a tapered susceptor predicts values which are higher than the observed values, especially for the first 20 cm of the susceptor. This result is expected, as mentioned earlier, because Fujii's growth rate equation is for the fully developed temperature. The fact that Fujii's growth rate equation contains adjustable parameters which were optimized for a barrel reactor of different dimensions could also be partly responsible for the high growth rates obtained using his method. A comparison of Fujii's model to the results of this work shows that the developing temperature method of this work is more accurate in both predicting values for the growth rate and in representing the variation of growth rate with susceptor position.

Dittman's correlation and the Chilton-Colburn analogy to flow over a flat plate both fail to represent the data quantitatively or qualitatively. Dittman's correlation is based on experimental data taken on a reactor with a very short susceptor and a large separation between the susceptor and reactor wall. Apparently, neither Dittman's correlation nor the Chilton-Colburn analogy to flow over a flat plate provided a realistic description of the growth rate distribution in a reactor of industrial dimensions.

Of the horizontal reactor models. Rundle's method gives growth rates which compare closest with the experimental data. Eversteyn's stagnant layer model predicts growth rates which are much higher than the experimentally observed values for the barrel reactor. Rundle's model, based on a laminar, parabolic velocity distribution is apparently much more representative of flow in the vertical cylinder reactor than is the turbulent-flow stagnant-sublayer model. This again confirms the need for applying laminar flow transport theory to the vertical cylinder reactor.

Of the models examined, the developing temperature method proposed in this work gives the best agreement with the experimental data. It is the only model which predicts the observed lower growth rate values at upstream positions on the susceptor. The developing temperature method incorporates two features not found in the other models studied: It accounts for the effect of increasing temperature on growth rate distribution and it accounts for the reduction in deposition efficiency due to side reactions. The excellent agreement between the developing temperature method and the experimental growth rates demonstrates the importance of considering these effects in developing an accurate method for growth rate prediction.

After comparing the results of several models to experimental data, the three predicted effects of developing heat transfer can be further examined. Experimental growth rates and growth rates predicted by the developing temperature method are both lower than those for Fujii's barrel reactor model in which temperature is considered to be fully developed. This comparison confirms the first prediction, that the over-all growth rates are lower than those predicted for constant, fully developed temperature. Since Fujii's model predicts less uniform growth than either values predicted by the developing temperature method or those observed experimentally, the second expected effect is confirmed. The third expected effect is that the over-all growth rate should reach a maximum value and then decrease as the flow rate is increased. The decline in growth rate does not occur in the range of Reynolds numbers 50-500, studied in this paper. Fujii *et al.* (5) have reported experimental results which show that the over-all growth rate does decrease at high flow rates.

Conclusion

Calculation of heat transfer using the solution by Reynolds *et al.* (11, 12) for developing heat transfer in an annular passage indicates that entry region temperature development will occur over a significant portion of the susceptor in a barrel reactor at Reynolds numbers greater than 50. Since barrel reactors typically operate at Reynolds numbers of order 10^2, the assumption of a constant temperature or constant temperature profile throughout the reactor is clearly unsatisfactory.

Due to the positive dependence of the silicon growth rate on mean gas temperature, over-all growth rates are expected to be lower than those predicted by models which incorrectly assume the temperature of the gas to be fully developed throughout the reactor. Furthermore, growth rates are expected to be more uniform than predicted by fully developed temperature models. The enhancement of mass transfer rates which accompanies the increase in temperature with downstream position helps to offset the decrease in growth rate caused by reactant depletion. The decline in over-all growth rate at very high reactant flow rates observed experimentally by Fujii *et al.* (5) is also a consequence of developing heat transfer and the positive temperature dependence of growth rate. As the reactant flow rate is increased beyond flow rates for which reactant depletion is significant, the mean temperature of the gas becomes the primary factor influencing growth rate. Further increase in the flow rate results in extension of the entry length for heat transfer and a lower length average mean gas temperature for the reactor, hence a lower over-all growth rate.

The developing temperature model for growth rate calculation proposed in this work gives a growth rate temperature dependence of $T^{0.674}$. The developing temperature method predicts growth rates which are in excellent agreement with experimental data obtained for a commercial barrel reactor. The model gives a more satisfactory description of the growth rate in a barrel reactor than any of the previously published models studied. Among the previously published models, Rundle's model for a horizontal reactor seems to give the best comparison to experimental growth rate values. The model based on the Chilton-Colburn analogy to boundary layer flow over a flat plate gave a particularly poor comparison to the experimental growth rates. This comparison confirms that the analogy to flow over a flat plate is an unsatisfactory representation of the geometry and boundary conditions for mass transfer in a barrel reactor of commercial dimensions.

The developing temperature model was used to study the effects of reactant flow rate and susceptor tilt angle on growth rate uniformity and reactant yield. For reactors with nontapered susceptors it was found that high reactant flow rates would be required to obtain growth rate nonuniformity of 10% or less. With the susceptor tilted slightly to an angle of 3.58°, however, an optimum growth rate nonuniformity of about 5% could be achieved at a much lower reactant flow rate. Reactant yield was found to drop off sharply with increased flow rate; therefore the over-all performance of the tapered susceptor reactor is expected to be far superior to that of the nontapered reactor. This exercise demonstrates the usefulness of the developing temperature model in evaluating process design alternatives in addition to giving the specific result described

above. It is hoped that this work will be useful as a process design tool as well as a contribution to the understanding of transport processes in the vertical cylinder reactor.

Acknowledgment

This report was done with support from the United States Energy Research and Development Administration.

Manuscript submitted June 24, 1976; revised manuscript received Nov. 15, 1976.

Any discussion of this paper will appear in a Discussion Section to be published in the December 1977 JOURNAL. All discussions for the December 1977 Discussion Section should be submitted by Aug. 1, 1977.

Publication costs of this article were assisted by the University of California.

APPENDIX

Transport Properties

Viscosity.—H_2.—The viscosity of pure H_2 was calculated by the equation of Maitland and Smith (20)

$$\ln(\mu/S) = A\ln(T) + B/T + C/T^2 + D \quad [A\text{-}1]$$

where $A = 0.68720$, $B = -0.61732$, $C = -111.49$, $D = -3.9001$, and $S = 88.0$, and where μ is given in μ-poise.

$SiCl_4$.—Viscosity of pure $SiCl_4$ was obtained from the corresponding state method of Stiel and Thodos (21-23)

$$\mu = \begin{cases} (34.0)(10^{-1})\,T_r^{0.94}, & T_r \leq 1.5 \\ (17.78)(10^{-1})(4.58\,T_r - 1.67)^{5/8}, & T_r > 1.5 \end{cases} \quad [A\text{-}2]$$

where $\xi = T_c^{1/6}/M^{1/2}p_c^{2/3}$, $T_r = T/T_c$, T_c = critical temperature = 506°K, p_c = critical pressure = 37.1 atm (3.76 MPa), and M = molecular weight of $SiCl_4$ = 169.9.

$SiCl_4$-H_2 mixture.—The viscosity of the gas mixture is calculated by Wilke's method (24)

$$\mu_{mix} = \sum_{i=1}^{n} \mu_i \Big/ \left[1 + \sum_{\substack{j=1 \\ j=i}}^{n} \phi_{ij}(y_j/y_i)\right] \quad [A\text{-}3]$$

where $\phi_{ij} = [1 + (\mu_i/\mu_j)^{1/2}(M_j/M_i)^{1/4}]^2/(8 + 8M_i/M_j)^{1/2}$, y_i = mole fraction of i, and M_i = molecular weight of i.

Mixture density.—The density of the mixture is calculated according to the ideal gas law

$$\rho_{mix} = \frac{p}{RT}\sum_{i=1}^{n} y_i M_i \quad [A\text{-}4]$$

Heat capacity.—Heat capacity data for each of the components is given in Ref. (25). These data were fit to a quadratic form

$$C_p = A + BT + CT^2 \quad [A\text{-}5]$$

Constants for Eq. [A-5] are as follows: for H_2; $A = 14{,}534$, $B = -0.4023$, and $C = 9.816\ (10^{-4})$, and for $SiCl_4$; $A = 561.4$, $B = 6.417\ (10^{-2})$, and $C = -8.640\ (10^{-6})$. Heat capacity is given in units of J/(kg°K).

The heat capacity of the mixture is determined by adding the component heat capacities weighted according to mole fractions

$$C_{pmix} = \sum_{i=1}^{n} y_i C_{pi} \quad [A\text{-}6]$$

Thermal conductivity.—H_2.—Experimental data from the literature has been fit to the following second order polynomial

$$k = 0.080796 + 3.7312(10^{-4})T - 7.4683(10^{-9})T^2 \quad [A\text{-}7]$$

where k is given in J/(m-sec °K).

$SiCl_4$.—Euken's method (17) is used to relate thermal conductivity to viscosity

$$k = (C_{pSiCl_4} + 61.18)\,\mu_{SiCl_4} \quad [A\text{-}8]$$

$SiCl_4$-H_2 mixture.—The mixture thermal conductivity is calculated by the Mason and Saxena (26) formulation of the Wassiljewa equation

$$k_{mix} = \sum_{i=1}^{n} k_i \left[1 + \sum_{j=1}^{n} A_{ij}(y_j/y_i)\right]^{-1} \quad [A\text{-}9]$$

The parameter A_{ij} can be taken as equal to the parameter ϕ_{ij} used in Wilke's equation (6) for the mixture viscosity.

Binary diffusion coefficients.—Binary diffusion coefficients are estimated using the equation deduced from kinetic theory (17).

$SiCl_2$-H_4.—Using the combined potential parameters

$$\sigma_{12} = 4.31\text{Å}$$

$$\frac{\epsilon_{12}}{k} = 144\text{°K}$$

the theoretical equation gives

$$\mathcal{D}_{SiCl_4\text{-}H_2} = 7.0861\ (10^{-9})\,T^{3/2}/\Omega_{\mathcal{D}} \quad [A\text{-}10]$$

in units of $m^2\ sec^{-1}$.

The collision integral $\Omega_{\mathcal{D}}$ can be evaluated from tabulated values or from Ref. (27)

$$\Omega_{\mathcal{D}} = \frac{A}{BT^*} + \frac{C}{\exp(DT^*)} + \frac{E}{\exp(FT^*)} + \frac{G}{\exp(HT^*)} \quad [A\text{-}11]$$

where $T^* = kT/\epsilon_{12}$, $A = 1.06036$, $B = 0.15610$, $C = 0.1930$, $D = 0.47635$, $E = 1.03587$, $F = 1.52996$, $G = 1.76474$, and $H = 3.89411$.

Reduced transport parameters.—Reynolds number

$$Re_{mix} = \frac{\rho_{mix} d_h v}{\mu_{mix}} \quad [A\text{-}12]$$

Prandtl number

$$Pr_{mix} = \frac{\dfrac{C_{pmix}}{(M_{mix})}\mu_{mix}}{k_{mix}} \quad [A\text{-}13]$$

Schmidt number for $SiCl_4$-H_2

$$Sc_{SiCl_4\text{-}H_2} = \frac{\mu_{mix}}{\rho_{mix}\mathcal{D}_{SiCl_4-H_2}} \quad [A\text{-}14]$$

LIST OF SYMBOLS

A	$1 + (r_i/r_o)^2 - B$
B	$[(r_i/r_o)^2 - 1]/\ln(r_i/r_o)$
C_p	heat capacity, J/(g-mole °K)
$\mathcal{D}$	diffusion coefficient, m^2/sec
d_h	hydraulic diameter; $d_h = 2(r_o - r_i)$, cm
g_z	gravitational constant, 980 cm/sec^2
G	linear growth rate, μ/min
$\overline{G}$	average linear growth rate, μ/min
ΔG	growth rate nonuniformity, μ/min
h	$-k[T_i - T_o]^{-1}\partial T/\partial r\|_{r=r_i}$
k	thermal conductivity, J/(m-sec° K)
k_x	$-\mathcal{D}[X_m - X_i]^{-1}\partial X/\partial r\|_{r=r_i}$
M_{Si}	molecular weight of silicon, 28 g/mole
$\dot{M}$	total molar flow rate, mole/sec
Nu	Nusselt number, Nu = hd_h/k
p	pressure, atm (101.325 kPa)
Pr	Prandtl number, Pr = $Cp\mu/k$
$\bar{r}$	r/r_o
r	radial distance, cm
r_i	inner radius, cm
r_o	outer radius, cm
R	gas constant, R = 82.06 atm-cm^3
Re	Reynolds number, Re = $\rho d_h v/\mu$
Sc	Schmidt number, Sc = $\mu/\rho\mathcal{D}$
Sh	Sherwood number, Sh = $k_x d_h/\mathcal{D}\ p/RT$
T	temperature, °K

T_i	inner wall temperature, °K
T_o	outer wall temperature, °K
T_e	entrance temperature, °K
T_m, $T_m(x)$	mean temperature, °K
U, $U(r)$	velocity, cm/sec
U_m	mean velocity, cm/sec
v	velocity, cm/sec
v_r	component of velocity in radial direction, cm/sec
v_z	component of velocity in axial direction, cm/sec
x	axial distance, cm
$\bar{x}$	x/d_hRePr
X	mole fraction $SiCl_4$
$\bar{X}$	mean mole fraction $SiCl_4$
X_i	mole fraction $SiCl_4$ at inner radius
X_e	initial mole fraction $SiCl_4$
z	axial distance, cm
$\bar{z}$	z/d_hReSc
α	thermal diffusivity $= k/(\rho C_p)$
θ	dimensionless temperature function
θ_{mi}, θ_{mo}	dimensionless mean temperature functions
μ	absolute viscosity, μ-poise
χ	dimensionless concentration function
χ_m	mean dimensionless concentration function
ρ	density, g/cm³
ρ_{Si}	density of silicon, 2.33 g/cm³
Ω_D	collision integral for diffusion

REFERENCES

1. F. C. Eversteyn, P. J. W. Severin, C. H. J. v. d. Brekel, and H. L. Peek, *This Journal,* **117**, 925 (1970).
2. F. C. Eversteyn and H. L. Peek, *Philips Res. Rep.,* **25**, 472 (1970).
3. P. C. Rundle, *Int. J. Electron.,* **24**, 405 (1968).
4. P. C. Rundle, *J. Cryst. Growth,* **11**, 6 (1971).
5. E. Fujii, H. Nakamura, K. Haruna, and Y. Koga, *This Journal,* **119**, 1106 (1972).
6. F. W. Dittman, in "Chemical Reaction Engineering II," H. M. Hulburt, Editor, pp. 463-473, Advances in Chemistry Series 133, American Chemical Society, Washington, D.C. (1974).
7. L. Graetz, *Ann. Phys. (Leipzig),* **18**, 79 (1883); *ibid.,* **25**, 337 (1885).
8. W. Nusselt, *Z. Ver. Dtsch. Ing.,* **67**, 206 (1923).
9. G. M. Brown, *AIChE J.,* **6**, 179 (1961).
10. A. P. Hatton and A. Quarmby, *Int. J. Heat Mass Transfer,* **5**, 973 (1962).
11. W. C. Reynolds, R. E. Lundberg, and P. A. McCuen, *ibid.,* **6**, 483 (1963).
12. R. E. Lundberg, P. A. McCuen, and W. C. Reynolds, *ibid.,* **6**, 495 (1963).
13. D. W. Shaw, in "Crystal Growth, Theory and Techniques," Vol. 1, C. H. L. Gordon, Editor, pp. 1-48, Plenum Press, London-New York (1974).
14. V. J. Berry and C. R. dePrima, *J. Appl. Phys.,* **23**, 195 (1952).
15. R. Rosler, Private communication.
16. E. Sirtl, L. P. Hunt, and D. H. Sawyer, *This Journal,* **121**, 919 (1974).
17. R. C. Reid and T. K. Sherwood, "The Properties of Gases and Liquids," 2nd ed., McGraw-Hill, New York (1966).
18. R. B. Bird, W. E. Stewart, and E. N. Lightfoot, "Transport Phenomena," John Wiley & Sons Inc., New York (1960).
19. B. J. Curtis and J. P. Dismukes, *J. Cryst. Growth,* **17**, 128 (1972).
20. G. C. Maitland and E. B. Smith, *J. Chem. Eng. Data,* **17**, 2 (1972).
21. L. I. Stiel and G. Thodos, *AIChE J.,* **7**, 611 (1961).
22. L. I. Stiel and G. Thodos, *AIChE J.,* **10**, 266 (1964).
23. L. I. Stiel and G. Thodos, "Progress in International Research on Thermodynamics and Transport Properties," pp. 352-365, Academic Press, New York (1962).
24. C. R. Wilke, *J. Chem. Phys.,* **18**, 517 (1950).
25. JANAF Thermochemical Tables, D. R. Stull and H. Prophet, Editors National Bureau of Standards, Washington, D.C. (1971).
26. E. A. Mason and S. C. Saxena, *Phys. Fluids,* **1**, 361 (1958).
27. P. D. Neufeld, A. R. Janzen, and R. A. Aziz, *J. Chem. Phys.,* **57**, 1100 (1972).

An Examination of the Product Catalyzed Reaction of Trimethylgallium with Phosphine and the Mechanism of the Chemical Vapor Deposition of Gallium Phosphide and Gallium Arsenide

D. J. Schlyer and M. A. Ring

Department of Chemistry, San Diego State University, San Diego, California 92182

ABSTRACT

The formation of GaP via reaction of Me_3Ga with PH_3 was examined. The reaction follows a Langmuir-Hinshelwood mechanism (adsorption of both reagents prior to reaction). The GaP surface was also found to catalyze the unimolecular decomposition of PH_3 and Me_3Ga. These results and similar ones for the reaction of Me_3Ga with AsH_3 are discussed.

The chemical vapor deposition (CVD) of single crystal layers of III-V semiconductor compounds, such as GaAs, from the reaction between Group III organometallics and Group V hydrides has now been well established (1-9). The mechanism involved in these potentially very important processes or in similar processes [i.e., formation of II-VI semiconductor compounds (10)] is not understood and has only been briefly discussed (1, 5, 11).

Key words: CVD, GaAs, GaP.

We have recently reported (12) our results on the reaction of $(CH_3)_3Ga$ [trimethylgallium (TMG)] with AsH_3 over the product surfaces $[(CH_3)_{3-x}GaAsH_{3-x}$, $x = 1.1$ to 2.2]. In this paper we report results for reaction of TMG with PH_3 over our GaP surfaces $[(CH_3)_{3-x}GaPH_{3-x}$, where x averaged 2.8] as well as for some experiments for the TMG-AsH_3 system. In the discussion section we incorporate these results with those reported by other groups. While the surfaces present in our investigations were not identical to those

present in the chemical vapor deposition (CVD) processes, the fact that the apparent activation energy for our reactions and those for the CVD GaAs process were identical suggests that the mechanism may be similar.

We have examined these reactions at lower temperatures than those used in the CVD processes. This was necessary to allow for reactant adsorption on the surfaces to effect the kinetics so that these adsorptions could be detected in an effort to understand the mechanisms.

Experimental

Pyrolysis apparatus.—The experiments listed in Tables I and II were carried out in an 80 cm^3 Pyrex reaction vessel wrapped with a heating tape and heavily insulated to stabilize temperature. The temperature of the vessel was monitored by a Chromel-Alumel thermocouple inserted into a well which extended to the center of the vessel. A U trap with an attached 200 cm^3 expansion bulb was connected to this vessel. This assembly was incorporated into the standard high vacuum system. Pressures were measured with a mercury manometer read through a traveling telescope which gave an accuracy of 13 Pa (0.1 mm Hg). The interior of the vessel was coated with the solid product from previous experiments at 240° or 270°C which, as is explained later, can be described as $(CH_3)_{3-x}GaPH_{3-x}$, where x averaged about 2.9 at 270°C and about 2.7 at 240°C.

Kinetic runs.—In a typical experiment, TMG (1.0 mmole) was expanded into the 200 cm^3 expansion bulb. The pressure was noted, the Teflon valve to the bulb was closed, and the TMG removed from the rest of the system. Phosphine (2.5 mmoles) was expanded into the trap which gave a higher pressure of PH_3 in the trap than of TMG in the bulb. The Teflon valve connecting the trap to the bulb was then opened for 5 sec, and the hydride was allowed to flow into the bulb. During this interval, the pressure in the two parts came to equilibrium, and the pressure was read to obtain the ratio of the two reactants. It was assumed that no TMG was lost from the bulb by diffusion. Control experiments were carried out to show that this was the case. The PH_3 left in the trap was removed and the two reactants allowed to stand for about 1 min to ensure that complete mixing had taken place. This mixture was then expanded into the reaction vessel and the temperature and pressure were noted. From these data, it was possible to calculate the number of millimoles of each reactant in the vessel.

After the reaction was completed, the products were toepler pumped into a known volume and a pressure reading taken. The products were then recirculated through a −78°C trap and again toepler pumped into the known volume. The pressure was read and the amount of TMG removed determined by difference. It was determined by infrared spectral analysis that a −78°C trap would quantitatively separate TMG from PH_3 in this system. The remaining products were recirculated through a −196°C trap to remove the PH_3 for quantitative determination. The noncondensable products were then toepler pumped into the same vol-

Table I. Reactions of $(CH_3)_3Ga$ with PH_3 at 270°C

	Initial pressure × 10^{-3} (Pa)*		Consumed, mmole		Produced, mmole		
Expt.	$(CH_3)_3Ga$	PH_3	$(CH_3)_3Ga$	PH_3	M**	D†	M/D‡
1	5.00 (37.5)*	4.77 (35.8)*	0.0492	0.0225	0.0275	0.0156	1.76
2	4.95 (37.1)	5.12 (38.4)	0.0451	0.0213	0.0541	0.0143	3.76
3	4.94 (37.0)	4.72 (35.4)	0.0455	0.0234	0.0541	0.0164	3.31
4	4.78 (35.9)	4.56 (34.2)	0.0443	0.0250	0.0574	0.0176	3.27
5	4.89 (36.7)	4.52 (33.9)	0.0447	0.0254	0.0475	0.0188	2.53
6	4.96 (37.2)	2.49 (18.7)	0.0389	0.0160	0.0328	0.0111	2.96
7	4.97 (37.3)	2.47 (18.5)	0.0410	0.0168	0.0311	0.0119	2.60
8	5.00 (37.5)	2.51 (18.8)	0.0389	0.0188	0.0389	0.0135	2.88
9	4.94 (37.0)	2.48 (18.6)	0.0402	0.0160	0.0369	0.0111	3.31
10	4.92 (36.9)	4.71 (35.3)	0.0352	0.0246	0.0492	0.0184	2.66
11	2.52 (18.9)	4.85 (36.4)	0.0188	0.0168	0.0361	0.0111	3.24
12	2.51 (18.8)	4.95 (37.1)	0.0188	0.0143	0.0295	0.0086	3.45
13	2.48 (18.6)	4.95 (37.1)	0.0164	0.0184	0.0361	0.0135	2.68
14	2.48 (18.6)	5.26 (39.5)	0.0176	0.0168	0.0340	0.0254	2.86
15	2.56 (19.2)	5.06 (38.0)	0.0217	0.0188	0.0369	0.0131	2.81
16	4.98 (37.4)	4.77 (35.8)	0.0303	0.0225	0.0443	0.0156	2.84
17	2.51 (18.8)	4.97 (37.3)	0.0193	0.0188	0.0361	0.0123	2.95
18	5.04 (37.8)	4.86 (36.3)	0.0328	0.0250	0.0443	0.0176	2.52

* Pressure in pascals (mm Hg in parenthesis).
** M = methane − $\frac{[(CH_3)_3Ga \text{ consumed} - D]}{2}$.
† D = PH_3 consumed − 2/3H_2.
‡ See text.

Table II. Reactions of $(CH_3)_3Ga$ with PH_3 at 240°C

	Initial pressure × 10^{-3} (Pa)*		Consumed, mmole		Produced, mmole		
Expt.	$(CH_3)_3Ga$	PH_3	$(CH_3)_3Ga$	PH_3	M**	D†	M/D‡
1	4.83 (36.3)	4.79 (35.9)	0.0348	0.0328	0.0410	0.0172	2.39
2	4.89 (36.7)	4.76 (35.7)	0.0352	0.0246	0.0451	0.0176	2.57
3	4.84 (36.3)	4.79 (35.9)	0.0336	0.0217	0.0377	0.0160	2.35
4	4.85 (36.4)	4.80 (36.0)	0.0307	0.0242	0.0426	0.0180	2.35
5	4.84 (36.3)	4.77 (35.8)	0.0311	0.0205	0.0377	0.0152	2.47
6	4.80 (36.0)	2.39 (17.9)	0.0299	0.0127	0.0221	0.0078	2.84
7	4.75 (35.6)	2.43 (18.2)	0.0328	0.0180	0.0385	0.0115	3.36
8	4.77 (35.8)	2.40 (18.0)	0.0279	0.0135	0.0238	0.0086	2.74
9	2.44 (18.3)	4.86 (36.3)	0.0168	0.0172	0.0320	0.0107	2.98
10	2.43 (18 2)	4.88 (36.6)	0.0160	0.0168	0.0303	0.0115	2.66
11	2.43 (18 2)	4.84 (36.3)	0.0172	0.0172	0 0320	0.0111	2.91
12	4.79 (35.9)	2.41 (18.1)	0.0316	0.0143	0.0275	0.0205	2.91
13	4.88 (36.2)	2.43 (18.2)	0.0287	0.0172	0.0320	0.0119	2.67

* Pressure in pascals (mm Hg in parenthesis).
** M = methane − $\frac{[(CH_3)_3Ga \text{ consumed} - D]}{2}$.
† D = PH_3 consumed − 2/3H_2.
‡ See text.

ume and measured. A sample of the noncondensable gases was taken, and a mass spectrum obtained. This spectrum was compared with that of a known standard to determine the relative quantities of H_2 and CH_4.

Results

The results reported for the reaction of PH_3 with TMG were carried out over the product surfaces. The bulk product had the formula $(CH_3)_{3-x}GaPH_{3-x}$, where x averaged 2.9 at 270°C and 2.7 at 240°C. The data for these analyses are presented later.

Control reactions and heterogeneous nature.—The only volatile products from the TMG-PH_3 [and TMG-AsH_3 (12)] reaction were CH_4 and H_2. In control experiments we observed that our product surfaces $[(CH_3)_{3-x}GaPH_{3-x}]$ prepared at 270°C catalytically decomposed both TMG and PH_3 to form CH_4 and H_2, respectively. These decompositions occurred at 240°C and pressures similar to those in Tables I and II. These decompositions were not observed over a silicon surface (for PH_3) or an arsenic surface (for TMG) at higher pressures and temperatures up to 340°C. Similar catalytic results were observed for AsH_3 and TMG over their product surfaces $(CH_3)_{3-x}GaAsH_{3-x}$, where x averaged 1.1 at 203°C and 2.2 at 259°C (12).

The results of the reactions of TMG with PH_3 over the product surfaces are listed in Tables I and II. The minimum set of equations required to explain our data are as follows

$$PH_3 \rightarrow 1/4\,P_4 + 3/2\,H_2 \qquad [1]$$

$$2(CH_3)_3Ga \rightarrow \text{product} + CH_4 \qquad [2]$$

$$(CH_3)_3Ga + PH_3 \rightarrow (CH_3)_2GaPH_2 + CH_4 \qquad [3]$$

$$(CH_3)_2GaPH_2 \rightarrow (CH_3)GaPH + CH_4 \qquad [4]$$

$$(CH_3)GaPH \rightarrow GaP + CH_4 \qquad [5]$$

The product in reaction [2] was not identified. It could be $(CH_3)_2GaCH_2Ga(CH_3)_2$.

The initial results indicate a need to follow reaction [3] by some variable other than the consumption of TMG or PH_3 or the production of CH_4 or H_2. We have found the most reliable value to be the PH_3 consumed corrected for the PH_3 decomposed via reaction [1]. We have defined a term D, where

$$D = (PH_3 \text{ consumed} - 2/3\,H_2 \text{ produced}) \qquad [6]$$

It is possible that some hydrogen-containing polymer may remain after the reaction. However the correction ($-2/3$ H_2 produced) was small, so that a small error in the correction would only result in a very small error in D.

The rate of the reaction between TMG and PH_3, determined by D, was obtained at 190°C over surface areas of 130 and 305 cm^2. The relative rate of reaction increased by 2.1 ± 0.2 as the surface area increased by 2.3. Thus this reaction was essentially heterogeneous under these conditions. Similar results were found for the TMG-AsH_3 reaction at 260°C (12).

Solid product.—In principle, the average value of x in the solid product, $(CH_3)_{3-x}GaPH_{3-x}$, can be determined from the value of D and the CH_4 produced only from reactions [3]-[5]. We have defined a term M, which is the CH_4 produced from reactions [3]-[5]. The term M has been set equal to the total CH_4 production $-$ $[(CH_3)_3Ga$ consumed $- D/2]$. The CH_4 correction attempted to account for the CH_4 formed by reaction [2]. The ratio of CH_4 formed to TMG consumed in the TMG heat decompositions averaged close to 0.5.

The value of x in the solid product $(CH_3)_{3-x}GaPH_{3-x}$ would be equal to M/D. Thus the results in Tables I and II indicate that x averaged 2.9 at 270°C and 2.7 at 240°C. The solid products were obtained as very thin films and were not examined. It is unlikely that our product films were of uniform composition.

Reaction order and mechanism.—The results listed in Tables I and II can be used in an effort to elucidate aspects of reaction [3] [*i.e.*, formation of $(CH_3)_2GaPH_2$]. The rate of reaction [3] was followed by the quantity D.

Rate control for heterogeneous reactions can be due to five factors: (*a*) diffusion of reactants to the surface, (*b*) adsorption of the reactants (this is an activation energy of adsorption and not the heat of adsorption which is usually not rate controlling), (c) reaction on the surface, (*d*) desorption of the products (heat of adsorption equal to heat of desorption, and (*e*) diffusion of products from the surface. In our unpacked reaction vessel, gaseous diffusion to and from the surface would be fast and not rate controlling. The adsorption process is usually fast compared to the surface reaction. Thus, rate control will only depend on the surface activation energy and the heats of adsorption of the reactants and products.

Bimolecular heterogeneous reactions can occur by the adsorption of both reagents on the surface followed by the surface reaction (Langmuir-Hinshelwood mechanism) or by the adsorption of one reagent and reaction with the other in the gas phase (Rideal-Eley mechanism). These two mechanisms can be distinguished by the kinetic reaction orders.

The general form for the rate of a heterogeneous reaction (Langmuir-Hinshelwood mechanism) for a two-site model will take the form of Eq. [7] (13)

$$\text{rate} = \frac{k b_a b_b p_a p_b}{(1 + b_a p_a)(1 + b_a p_a)} \qquad [7]$$

where p_a is the pressure of species a and b_a is the equilibrium adsorption constant for species a. This equation is based on Langmuir adsorption isotherms which assume all similar catalytic sites are equivalent. This form appears generally valid even though Langmuir isotherms are not generally obeyed. Equation [7] assumes that product desorption does not effect the rate. This was the case for our system where the rate did not change when excess CH_4 was added initially to the reaction system. The Langmuir-Hinshelwood mechanism is operative when the reaction orders of both reagents are less than one. This lower reaction order can be due to reactant poisoning (when $bp > 0.05$) or to lower values of the adsorption equilibrium constants. b, at higher pressures.

The reaction orders with respect to PH_3 and TMG for reaction [3] were determined by the change in ln D with respect to ln p of PH_3 or TMG while the pressure of the other reagent was held constant. The reaction orders for PH_3 were 0.6 ± 0.2 and 0.8 ± 0.2 at 270° and 240°C, respectively, while those for TMG were 0.5 ± 0.2 and 0.6 ± 0.2 at 270° and 240°C, respectively. Since these reaction orders are clearly less than one, the reaction occurs via the Langmuir-Hinshelwood mechanism (*i.e.*, adsorption prior to reaction).

The reaction orders obtained for the TMG-AsH_3 reaction were clearly less than one for TMG but only slightly less than one for AsH_3 (12). This result again demonstrated that TMG was adsorbed prior to reaction; however, the AsH_3 could have reacted in the gas phase with adsorbed TMG. We did demonstrate the AsH_3 adsorbed on our surfaces and was catalytically decomposed by these surfaces at 172°C (12). These results suggested that AsH_3 adsorbed prior to reaction with TMG. It would appear that both reactions (TMG with AsH_3 or PH_3) occur by similar mechanisms since they have very similar activation energies. Thus we suggest that the TMG-AsH_3 reaction also occurs via a Langmuir-Hinshelwood mechanism.

Activation energy.—The apparent activation energy for the TMG-PH_3 reaction obtained from the data in Tables I and II was about 54 kJ/mole. The rate was followed by the term D. The apparent activation energy, E_a, is related to the activation energy of the surface reaction, E_s, by Eq. [8] (13)

$$E_a = E_s + Q_{TMG} + Q_{PH_3} \quad [8]$$

where Q_i is the heat of adsorption of the species i at the same surface coverage present during the kinetic runs.

The apparent activation energy for the TMG-AsH_3 reaction was also about 54 kJ/mole (12).

Reaction of PH_3 and AsH_3 with the solid products.— The solid products from our TMG-AsH_3 reactions were $(CH_3)_{3-x}GaAsH_{3-x}$, where x averaged 1.1 at 203°C and 2.2 at 259°C (12). When these solid products were heated to 420°C for 18 hr, CH_4 and H_2 were produced. However the values of x for the new solid products were only about 1.3 and 2.6 (12). We have now examined the reaction of AsH_3 with the initial product surface. In a typical experiment, TMG (0.0820 mmole) and AsH_3 (0.0783 mmole) were expanded into a vessel at a temperature of 364°C. This gave a pressure in the vessel of 9917 Pa (74.4 mm Hg). The reaction was allowed to proceed for 10 min at which time the products were removed and analyzed. The quantity of TMG consumed was 0.0553 mmole and the quantity of AsH_3 consumed was 0.0734 mmole. After correction for H_2 produced, this gave a value of 0.0434 mmole for D. The corrected quantity of CH_4 produced was 0.1106 mmole giving x a value of 2.5. When the product surface was then exposed to 0.218 mmole of AsH_3 at a pressure of 13,500 Pa (101.3 mm Hg) for the same time and at the same temperature as the initial run, 0.0209 mmole of CH_4 was produced, while 0.0635 mmole of AsH_3 was consumed. Therefore, the total CH_4 produced from both the initial reaction and exposure to AsH_3 was 0.1316 mmole. The value of x now becomes 0.1316/0.0434 = 3.0. This titration of the surface shows that there were methyl groups remaining on the surface after the initial reaction was complete. It also demonstrates that AsH_3 reacts with $(CH_3)_{3-x}GaAsH_{3-x}$ to form GaAs. It should be noted that the solid products represented as $(CH_3)_{3-x}GaEH_{3-x}$ (E = P or As) could in reality be $(CH_3)_{3-x}GaEH_{3-y}$, where $y > x$.

In one experiment, where AsH_3 and TMG (0.027 mmole each) were allowed to react at 365°C at a total pressure of 3332 Pa (25.0 mm Hg) for 15 min over "GaAs"; the ratio, M/D was 2.94. When this solid was treated with AsH_3 at 365° only a trace of CH_4 was produced.

A similar experiment was carried out for $(CH_3)_{3-x}GaPH_{3-x}$ prepared at 270°C on a silica gel (30/60 mesh) supported surface with a $(CH_3)_{3-x}GaPH_{3-x}$ surface area of 320 m^2 as determined by the BET method (14). When the product surface was exposed to PH_3 at 270°C, the quantity of CH_4 produced was sufficient to account for a 3% coverage of the Ga sites by methyl groups. Thus, the surface contained a small number of methyl groups as suggested by the M/D ratios in Table I.

Discussion

The CVD formation of GaAs and GaP via reaction of TMG with AsH_3 or PH_3 can now be examined. Manasevit and Simpson (1) prepared high quality single crystal thin films of GaAs and GaP from reaction of TMG with AsH_3 or PH_3 in H_2 flow. The hydride to TMG partial pressures used were about 10/1. It was suggested that AsH_3 and TMG react in the gas phase and that reaction with TMG prevents its thermal decomposition.

Ito, Shinohara, and Seki (5) found a transition from p-type product GaAs to n-type GaAs when the AsH_3/TMG ratio reached about 10/1. They proposed a mechanism involving the gas phase reaction of TGM with H_2 to yield CH_4 and Ga which was adsorbed on the surface. This Ga then reacted with surface bound As from the gas phase decomposition of AsH_3.

Petzke, Gottschalch, and Butler (11) have drawn several conclusions regarding the kinetics of the reactions in the $(CH_3)_3Ga$-AsH_3-H_2 system from an analysis of data reported by Manasevit and Simpson (1) and that of Inoue and Asahi (15). Petzke *et al.* found that (*i*) the reaction was first order in TMG and (*ii*) the apparent activation energy was 54 kJ/mole. From these observations, they concluded that the reaction must be heterogeneous, since the third Ga-CH_3 bond dissociation energy is $\approx$ 322 kJ/mole.

From our data, we have calculated an apparent activation energy of 54 kJ/mole for the reaction of TMG with both AsH_3 and PH_3. This suggests that the process occurring in our low temperature reaction may be similar to the process occurring during the deposition as carried out by Manasevit and Simpson (1).

From the surface to volume studies, we can eliminate any mechanism which involves reaction completely in the gas phase. This view is also supported by Petzke *et al.* (11) who also found the reaction to be heterogeneous. On the basis of the heterogeneous character of the reaction, we cannot exclude the possibility of the formation of a gas phase complex which then diffuses to the surface and reacts. However, we were unable to detect any gas phase complex formation even at room temperature where complex formation would be greatest.

We, therefore, propose a mechanism we feel is consistent with all the data for both systems

$$(CH_3)_3Ga_{(g)} + S1 \rightleftharpoons \underset{I}{(CH_3)_3Ga \cdot S1} \quad [9]$$

$$AsH_{3(g)} + S2 \rightleftharpoons \underset{II}{AsH_3 \cdot S2} \quad [10]$$

$$I \rightarrow \frac{1}{2} CH_{4(g)} + \text{products} \quad [11]$$

$$II \rightarrow \frac{3}{2} H_{2(g)} + As_4 \quad [12]$$

$$I + II \rightarrow (CH_3)_2GaAsH_2 + CH_{4(g)} \quad [13]$$

$$(CH_3)_2GaAsH_2 \rightarrow (CH_3)GaAsH + CH_{4(g)} \quad [14]$$

$$(CH_3)GaAsH \rightarrow GaAs + CH_{4(g)} \quad [15]$$

Those species not subscripted are solid phase, I and II are surface complexes of $(CH_3)_3Ga$ and AsH_3, respectively, and S1 and S2 are two different types of sites.

The mechanism above is written with two types of sites. The same conclusions would be made for a one-site mechanism. We have proposed a two-site mechanism since AsH_3 (and PH_3) are good Lewis bases and TMG is a good Lewis acid. The As (or P) site would be a good Lewis base site (to complex TMG) and the Ga Lewis acid site should complex AsH_3 or PH_3 very well.

The consequences of the above mechanism have significance to the process of chemical vapor deposition. The most important point to be made is that care must be taken to remove all CH_3 groups from the surface before they are buried by further deposition. Buried CH_3 groups could then thermally decompose via reaction [16]. When this occurs

$$H_3CGaAs \rightarrow CGaAs + 3/2\, H_2 \quad [16]$$

an arsenic atom would be replaced by a carbon atom with one less electron in the outer shell which would result in a p-type site. The H_3CGaAs group could be formed via reaction [17]

$$H_3CGaAsH \rightarrow H_3CGaAs + 1/2\, H_2 \quad [17]$$

since the As-H bonds are relatively weak. In fact, it is not unlikely that the solid products described as $(CH_3)_{3-x}GaEH_{3-x}$ (where E is P or As) should be described as $(CH_3)_{3-x}GaEH_{3-y}$, where $y > x$. We have demonstrated that AsH_3 and PH_3 can remove CH_3 groups bound to gallium. This result coupled with the reactions represented by Eq. [16] and [17] can explain the results of Seki and co-workers (5) who found a

transition from p-type to n-type GaAs at a mole ratio of AsH_3 to $(CH_3)_3Ga$ of 10/1.

Acknowledgment

The authors are indebted to the San Diego State University Foundation for partial financial support.

Manuscript submitted July 12, 1976; revised manuscript received Nov. 29, 1976.

Any discussion of this paper will appear in a Discussion Section to be published in the December 1977 JOURNAL. All discussions for the December 1977 Discussion Section should be submitted by Aug. 1, 1977.

REFERENCES

1. H. M. Manasevit and W. I. Simpson, *This Journal*, **116**, 1725 (1969).
2. H. M. Manasevit, *ibid.*, **118**, 647 (1971).
3. H. M. Manasevit, F. M. Erdmann, and W. I. Simpson, *ibid.*, **118**, 1864 (1971).
4. B. J. Baliga and S. K. Ghandhi, *ibid.*, **121**, 1642 (1974).
5. S. Ito, T. Shinohara, and Y. Seki, *ibid.*, **120**, 1419 (1973).
6. H. M. Manasevit, *J. Cryst. Growth*, **22**, 125 (1974).
7. C. C. Wang and S. H. MacFarlane III, *ibid.*, **13-14**, 262 (1972).
8. C. C. Wang, I. Landany, S. H. MacFarlane III, and F. C. Dougherty, *ibid.*, **24-25**, 239 (1974).
9. C. C. Wang and S. H. MacFarlane III, *Thin Solid Films*, **31**, 3 (1976).
10. H. M. Manasevit and W. I. Simpson, *This Journal*, **118**, 644 (1971).
11. W. H. Petzke, V. Gottschalch, and E. Butler, *Krist. Tech.*, **9**, 763 (1974).
12. D. J. Schlyer and M. A. Ring, *J. Organomet. Chem.*, **114**, 9 (1976).
13. S. J. Thompson and G. Webb, "Heterogeneous Catalysis," chap. 4, John Wiley & Sons, Inc., New York (1968).
14. A. W. Adamson, "Physical Chemistry of Surfaces," 2nd ed., p. 577, John Wiley & Sons, Inc., New York (1961).
15. M. Inoue and K. Ashai, *Natl. Tech. Rep. (Jpn.)*, **18**, 303 (1972).

AL/Si and Al/Poly-Si Contact Resistance in Integrated Circuits

H. M. Naguib* and L. H. Hobbs

Bell-Northern Research, Ottawa, Ontario, Canada K1Y 4H7

ABSTRACT

This paper presents results on the effects of sintering temperature, sintering time, and contact geometry on Al/Si and Al/poly-Si contact resistance. At sintering temperatures >450°C the resistance of p-type contacts is virtually constant and independent of time. The resistance of n-type contacts, particularly to poly-Si, increases with increasing sintering temperature for $T > 450$°C. This is attributed to the precipitation of a p-type (Al-doped) layer on n-contacts during sintering. The interface resistance of both Al/Si and Al/poly-Si contacts is independent of the length of the contact and inversely proportional to the width of the contact.

It is widely recognized that Al is the most suitable contact material for conventional integrated circuits with junction depths of ~1.5 μm (1). Typically Al films for this purpose are deposited onto the Si wafers by electron beam evaporation to a thickness of the order of 1 μm. To form a low resistance ohmic contact, it is standard practice to follow the deposition of the Al layer by a heat-treatment cycle at temperatures below the Al-Si eutectic point (*i.e.*, <577°C). This is usually referred to as "sintering." However, at temperatures well below the eutectic, excessive dissolution of Si into Al films at the contact windows can be observed (2-4) which can lead to a vertical or lateral shorting of a junction. It has also been reported (5) that Al films in contact with polycrystalline silicon (poly-Si) layers, as in Si-gate MOS devices (6) or poly-Si resistors (7), could induce dissolution and recrystallization of the Si at temperatures as low as 400°C. Accordingly, it appeared desirable to carry out the sintering cycle at temperatures as low as possible, consistent with achieving ohmic contacts to both single crystal Si substrates and poly-Si layers.

In this work we have measured the contact resistance at Al/Si and Al/poly-Si interfaces after various sintering cycles in order to establish the optimum cycle for producing reliable, low resistance contacts in integrated circuits. We have also investigated the effect of contact geometry on the contact resistance so as to achieve optimum design for integrated circuit resistors.

Experimental Determination of Contact Resistance

The main problem in the experimental determination of contact resistance is the separation of the metal-semiconductor interface resistance, R_c, from the semiconductor bulk resistance, R_s. Recently, various methods of measuring contact resistance have been analyzed (8). The method developed by Berger (9, 10) and Murrman and Widman (11, 12), provides a high degree of measurement accuracy using the resistor structure shown in Fig. 1. Three contacts are made to a rectangular diffused region, where the width of the contact (ω) is, as nearly as possible, equal to the full width of the diffused region (W). Two of the contacts are spaced closely together at a distance l_1, while the third contact is located at a much greater distance l_2

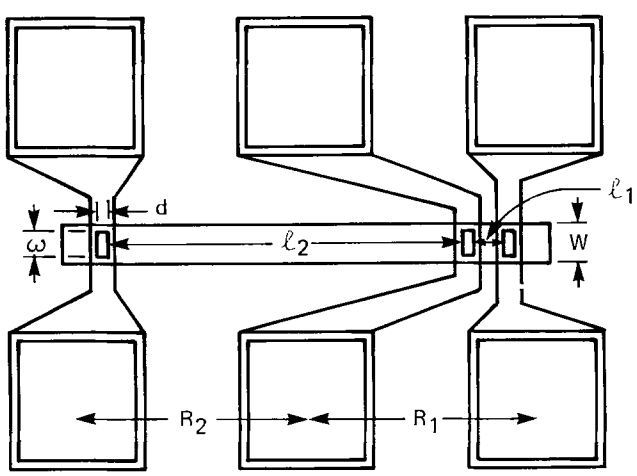


Fig. 1. Typical resistor structure used in the determination of R_c and R_s.

* Electrochemical Society Active Member.

Key words: aluminum metallization, contact characterization, ohmic contacts, silicon technology.

from the central contact ($l_2/l_1 \geq 10$). To exclude any contact resistance introduced by the probes, the current probes are separated from the voltage probes as shown in Fig. 1. The total resistance, R_{total}, between any two contacts can be expressed as

$$R_{total} = R_s \cdot \frac{l}{W} + 2R_c \quad [1]$$

Applying Eq. [1] to the separately measured resistance values R_1 and R_2 leads to

$$R_c = \frac{R_1 l_2 - R_2 l_1}{2(l_2 - l_1)} \quad [2]$$

and

$$R_s = \frac{(R_2 - R_1)W}{l_2 - l_1} \quad [3]$$

Using the resistor structure shown in Fig. 1, Si and poly-Si resistors with various contact configurations were fabricated on Si wafers which were subjected to the diffusion, oxidation, and passivation processes used in conventional MOS Si-gate technology. The preparation of the contacts involves: opening windows in the pyroglass passivation layer overlying the wafer, electron beam evaporation of a pure Al film onto the wafer, photoengraving and etching of aluminum interconnect patterns, and a subsequent sintering cycle. A typical process sequence is shown in Table I.

After sintering, the dimensions l_1, l_2, ω, W, and d were measured at several locations on each wafer using a Leitz digital microscope. It was found that the average error in these measurements was <1 μm. The electrical measurements were carried out on a large number of chips using an Electroglas Model 103 automatic wafer prober. One probe was placed on each of the six bonding pads associated with each resistor (cf. Fig. 1). The prober was connected to a Hewlett Packard 3050A automatic data acquisition system including a Model 9830A programmable calculator to control a Model 3490A digital multimeter, Model 9866A printer, and a Leeds and Northrup 2740 scanner. The computer controlled automatic tester measured R_1 and R_2, calculated R_c and R_s (Eq. [2] and [3]) for all resistors on each wafer, and printed out statistical information of the results. Following each sintering the resistivity data were collected using 2-3 wafers prepared at different runs.

Results and Discussion

The effect of sintering on Al/Si contact resistance.— Si-diffused resistors prepared as described in Table I were sintered for various periods of time (5-60 min) at temperatures varying between 300° and 560°C. The average sheet resistance of the Si substrates in these experiments was 9 Ω/sq for phosphorus-doped resistors and 40 Ω/sq for boron-doped resistors. After sintering,

Table I. Process flow sheet

(a) Si resistors	(b) Poly-Si resistors
Material	Material
(*i*) n-type, <111>, 8-12 Ω-cm	n-type, <111>, 4.5-9.5 Ω-cm
(*ii*) p-type, <100>, 8-12 Ω-cm	
Initial oxidation (~1 μm)	Initial oxidation (~1 μm)
Photoengraving of diffusion wells	Poly-Si deposition (CVD), ~0.3 μm)
Boron deposition and drive-in for material (*i*)	Photoengraving of poly-Si islands
Phosphorus deposition and drive-in for material (*ii*)	Boron or phosphorus deposition and drive-in

Pyroglass deposition and phosphorus gettering
Contact window photoresist and etch
Preevaporation cleaning (40 sec, 50:1 H_2O:buffered HF
6 sec, 50:1 H_2O:HF)
Al deposition (~1 μm, electron beam evaporation $<10^{-6}$ Torr, unheated substrate)
Al photoresist and etch
Al sintering (in N_2 as described in the text)
Resistivity measurements (constant current of 1 mA)

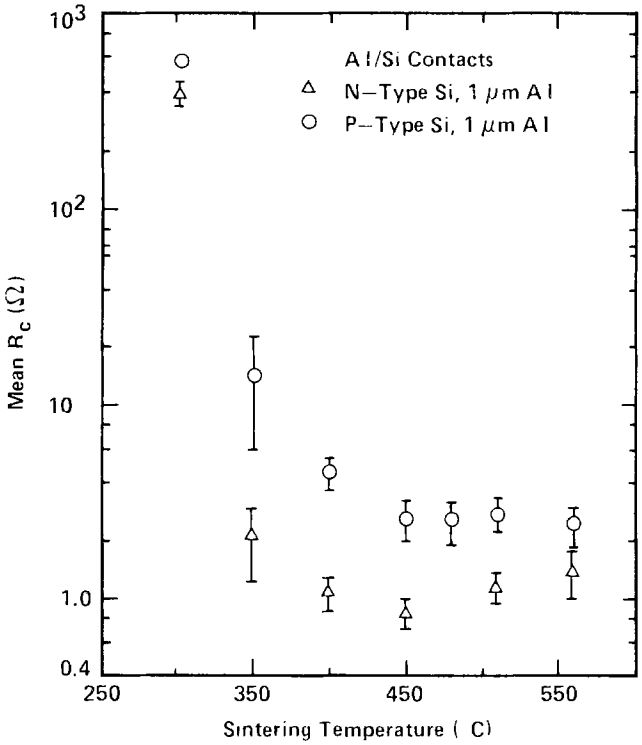


Fig. 2. Al/Si contact resistance, R_c, as a function of sintering temperature. The sintering was carried out for 5 min in N_2.

the contact resistance of resistors having contact windows of 12 × 10 μm were measured.

Using a 5 min sintering, a major drop in R_c values was observed at 350°C as shown in Fig. 2. This drop in R_c represents the first stage of the contact formation as the Al penetrates through the barrier layer at the Al/Si interface. Until recently, it was usually assumed that this barrier was a thin SiO_2 film formed on the Si surface over the contact base prior to evaporation. However, the penetration rate of Al into SiO_2 at 350°C is $\simeq 6 \cdot 10^{-4}$ Å/min (1). Therefore, a film of SiO_2 approximately 15Å thick, which is normally formed on Si at room temperature, would be penetrated in $\simeq$17 days during a 350°C sintering cycle. However, recent work indicated (13) that the film present on a freshly etched Si surface is primarily an oxidized impurity film rather than a pure SiO_2 film. Since, as yet, no attempt has been made to measure the penetration rate of Al through such impurity films, the initial stage of Al/Si contact formation remains poorly understood.

R_c values continue to decrease slowly between 350° and 450°C. At temperatures $\geq$450°C, R_c values for boron-doped (p-type) resistors are virtually constant and also found independent of sintering time between 5 and 60 min. Si in solid solution with Al has relatively little effect on the electrical conductivity of the resultant alloy (14). Therefore, once Al penetrates through the barrier layer in the contact area to form an ohmic contact with the Si, further interaction of Al and Si has a minor effect on the Al/Si contact resistance. For phosphorus-doped (n-type) resistors a gradual increase in R_c at temperatures >450°C is observed. This may be the result of an interaction between the aluminum, which is a p-type dopant, and the n^+-doped layer at the contact. Such an interaction is discussed in more detail in connection with phosphorus-doped poly-Si resistors.

Some data on the effect of various sintering conditions on Al/Si contact resistance have been previously reported (15-17). However, a direct comparison of the present results with the previously reported ones is not possible. Measurements reported by Hopper *et al.* (15, 16) were obtained on contact areas ~10^4 times larger than those used in our diffused resistor structures and, therefore, the dependence of R_c on process

differences and on Si surface doping is probably significantly different. In the work of McNeil (17) the measuring technique did not separate R_c from R_s and consequently the measured resistivities were much higher (10-100 times) than those reported here. However, in agreement with the present results, McNeil did report an increase in contact resistance for n-type Si resistors at sintering temperatures >500°C.

Berger (8) showed that the Al/Si contact resistance decreased with increasing substrate doping level. The surface dopant concentration for our Si-diffused resistors was ~6.5 × 10^{20} atoms/cm³ for n-type resistors and ~8 × 10^{19} atoms/cm³ for p-type. The contact resistivities (ρ_c) for these resistors following a 400°C/30 min sintering cycle was 1.3 × 10^{-6} and ~4 × 10^{-6} Ω · cm², respectively. These values are in good agreement with Berger's results obtained in sintering cycle of 400°C/20 min.

The effect of sintering on Al/poly-Si contact resistance.—In this series of experiments the contact resistance of poly-Si resistors, with a contact window size of 12 × 10 μm was measured before and after 5 min sintering at temperatures varying between 300° and 560°C. The average sheet resistance of the poly-Si used in these experiments was 26 Ω/sq for phosphorus-doped resistors and 56 Ω/sq for boron-doped resistors.

As shown in Fig. 3 the effect of sintering on Al/poly-Si contact resistance is strongly dependent on whether the dopant is n- or p-type. A 5 min sintering of boron-doped resistors at temperatures between 300° and 560°C always results in a reduction in the contact resistance: the percentage reduction varies between 55% at 300°C to 69% at 560°C. Values of R_c of the p-type resistors decline slowly between 300° and 450°C and then become constant at temperatures >450°C. After sintering current-voltage measurements at 1 mA have shown that the contacts are ohmic.

Using a sintering time of 5 min a reduction of ~31% in the contact resistance of phosphorus-doped resistors is observed between 300° and 350°C. The reduction decreases at higher sintering temperatures and changes to an increase in R_c at temperatures >450°C. Resistors sintered at 560°C for 5 min showed an increase of ~900% in Al/poly-Si contact resistance. Values of R_c increase slowly between 300° and 450°C for these n-type resistors followed by a sharp increase in R_c at sintering temperatures >450°C. Current-voltage measurements have shown that the contacts are ohmic except at 560°C sintering where the measurements became irreproducible, particularly at currents higher than 0.2 mA.

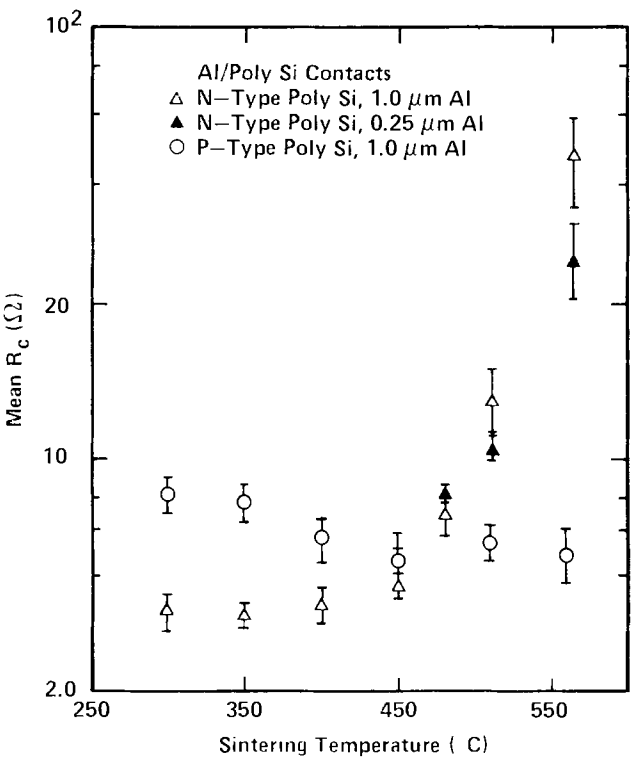


Fig. 3. Al/poly-Si contact resistance, R_c, as a function of sintering temperature. The sintering was carried out for 5 min in N_2.

The substantial increase in contact resistance of phosphorus-doped poly-Si resistors, particularly at temperatures >450°C, can be attributed to the formation of what might be termed a "quasi-Schottky diode." During sintering, Si dissolves into the aluminum to the solubility limit at that sintering temperature. On cooling the dissolved Si precipitates onto the n-Si substrate as a thin, electrically active, p-type (Al-doped) layer. The formation of such a layer on n-contacts has been confirmed recently using scanning electron microscopy (18, 19) and in-depth Auger analysis (20). Also, it has been shown (21) that the formation of a p-layer on n-type Si is responsible for the increase in Schottky barrier heights, ϕ_B, of Al/Si junctions during low temperature heat-treatments (<600°C). It is interesting to note that the increase in ϕ_B (22) occurs at 450°C, the same temperature at which the increase in contact resistance of n-type contacts was observed in our work. In addition, the magnitude of ϕ_B is known to be dependent on the amount of Al available for reaction, as determined by the thickness of the Al metallization (20). We have also found that Al/n-poly-Si contact resistance increases with increasing thickness of the Al metallization, particularly at temperatures >500°C, as shown in Fig. 3.

In another series of experiments Al/poly-Si contact resistance was investigated as a function of poly-Si doping level, as measured by dopant deposition time. The results are summarized in Table II. In general, the contact resistance decreased with increasing doping level. However, it appears that the sintering temperature is the dominant effect in determining R_c values rather than the effects of the dopant concentration.

The effect of contact geometry.—We have also examined the effect of contact geometry on the contact resistance of both Si and poly-Si resistors following a sintering cycle of 450°C/5 min. The contact window dimensions of these resistors are shown in Fig. 4. The aluminum was evaporated on unheated wafers to a thickness of 1 μm. The results are summarized in Tables III and IV. These results are compared with Berger's (9,10) and Murrman and Widman's (11, 12) theoretical analysis.

These authors have shown that a contact to a planar device can be described in terms of a "transmission line

Table II. The effect of dopant deposition time on Al/poly-Si contact resistance

(a) Boron-doped poly-Si

Deposition time (min)	Sheet resist R_s (Ω)	Contact resistance R_c, (Ω) Before sintering	After 510°C/5 min
7	96.74	70.68	11.99
12	86.87	22.90	10.18
17	69.82	21.14	7.57
22	55.59	16.31	6.41
27	59.00	11.00	5.22

(b) Phosphorus-doped poly-Si

Deposition time (min)	Sheet resist R_s (Ω)	Contact resistance R_c, (Ω) Before sintering	After 450°C/ 5 min	After 510°C/ 5 min
9	60.63	11.89	10.88	23.96
14	48.32	7.13	7.72	23.55
19	35.26	6.56	5.79	15.88
24	26.30	4.66	4.08	11.77
29	28.42	4.53	5.48	13.30

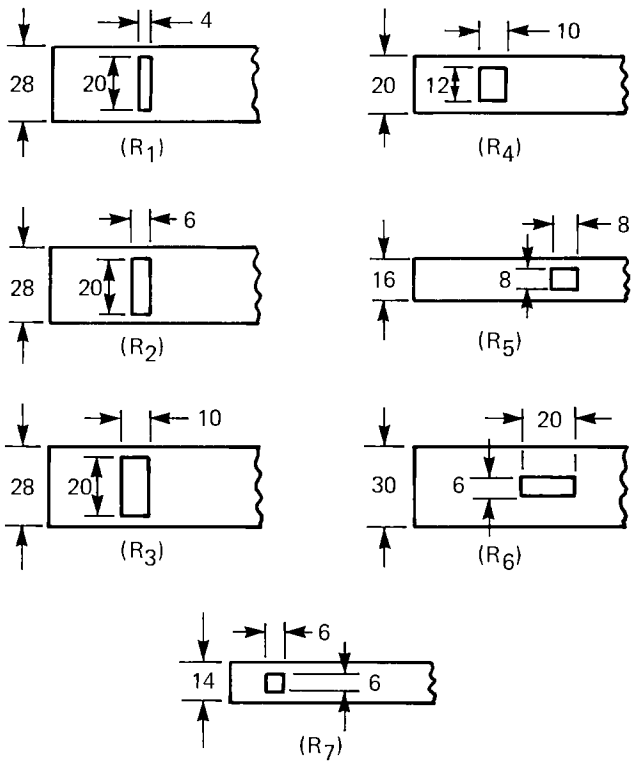


Fig. 4. The end structures of resistors used to determine the effect of contact geometry.

model" (TLM) and may be characterized by; the geometry, the semiconductor sheet resistance R_s beneath the contact, and the contact resistivity, ρ_c. According to the TLM model, R_c is given by the following expression

$$R_c = Z \coth \alpha d \quad [4]$$

where

$$Z = \frac{\sqrt{R_s \cdot \rho_c}}{\omega} \quad [5]$$

and

$$\alpha = \sqrt{R_s/\rho_c} \quad [6]$$

The parameter α can be determined from the equation

$$\frac{R_s \cdot d}{R_c \cdot \omega} = \alpha d \tanh d \quad [7]$$

where R_c, R_s, d, and ω are known. Values of the contact parameter αd calculated for various resistors used in the present investigation are given in Table III and IV.

The TLM model assumes that the contact extends over the total resistor width, *i.e.*, $\omega = W$ and, therefore, it neglects the effect of the crowding resistance,, R_d, which should be considered when $\omega << W$. Ting and Chen (23) have calculated R_d and their results may be written in the following form

$$\frac{R_d}{Z} = \frac{\omega}{2\pi}\left(\frac{1}{k}\ln\frac{k+1}{k-1} - \ln\frac{k^2}{k^2-1}\right) \quad [8]$$

where

$$k = \frac{\omega + 2\delta}{2\delta}$$

$$\delta = \frac{W - \omega}{2}$$

Here, δ is the distance between the contact edge and the resistor edge and is determined by mask alignment and etching tolerances. Taking $\delta = 12$ μm for resistor R_6 and $\delta = 3.75$ μm for all other resistor structures, R_d was calculated for all the resistors, using Eq. [8]. The results are also shown in Tables III and IV.

Within experimental error, the results shown in Tables III and IV are, at least qualitatively, in good agreement with the TLM model. As predicted in this model, for "electrically long contacts" ($\alpha d \geq 2$) of the same contact width, such as resistors R_1, R_2, and R_3, R_c is independent of the contact length. On the other hand, comparison of R_c values for resistors of the same contact length, such as R_2 and R_7, clearly indicate the dependence of R_c on the width of the contact, again as predicted by the TLM model. The dependence of R_c on ω can also be illustrated by comparing resistors R_4 and R_2 which have the same area (120 μm^2), but different geometries.

Except for resistor R_6, where $W >> \omega$, the estimated values of the crowding resistance, R_d for Si and poly-Si resistors, seems to be too small to have a significant influence on the results.

Conclusions

The main conclusions of the present investigation are the following:

1. Sintering at 450°C gives the lowest Al/Si and Al/poly-Si contact resistance for integrated circuit device applications.
2. At sintering temperatures >450°C, the contact resistance for boron-doped resistors is independent of temperature.
3. Phosphorus-doped resistors, particularly poly-Si ones, show a gradual increase in the contact resistance at temperatures >450°C. This is attributed to the precipitation of a p-type (Al-doped) layer and the formation of Schottky diodes on n-contacts during sintering.

Table III. Contact resistance, R_c, vs. contact window size for Si resistors sintered at 450°C for 5 min in N_2

Res. No.	Contact size $\omega(\mu m) \times d(\mu m)$	Mean* $R_c(\Omega)$	Std dev	αd	δ (μm)	k	$\frac{R_d}{Z \cdot \alpha}$	$Z \cdot \alpha$	R_d (Ω)
			(a) Boron-doped Si resistors (R_s = 40 $\Omega/\square$)						
R_1	20 × 4	1.25	0.29	6.40	3.75	3.67	0.24	2.0	0.48
R_2	20 × 6	1.38	0.23	8.70	3.75	3.67	0.24	2.0	0.48
R_3	20 × 10	1.54	0.36	12.98	3.75	3.67	0.24	2.0	0.48
R_4	12 × 10	2.61	0.53	12.77	3.75	2.60	0.29	3.34	0.97
R_5	8 × 8	3.40	0.70	11.76	3.75	2.07	0.31	5.00	1.55
R_6	6 × 20	4.88	1.48	27.32	12.00	1.25	0.70	6.67	4.67
R_7	6 × 6	2.99	1.27	13.38	3.75	1.80	0.31	6.67	2.07
			(b) Phosphorus-doped Si resistors (R_s = 9 $\Omega/\square$)						
R_1	20 × 4	0.56	0.15	3.21	3.75	3.67	0.24	0.45	0.11
R_2	20 × 6	0.51	0.08	5.29	3.75	3.67	0.24	0.45	0.11
R_3	20 × 10	0.56	0.07	8.04	3.75	3.67	0.24	0.45	0.11
R_4	12 × 10	0.95	0.11	7.89	3.75	2.60	0.29	0.75	0.22
R_5	8 × 8	1.30	0.24	6.92	3.75	2.07	0.31	1.13	0.35
R_6	6 × 20	1.35	0.17	22.22	12.00	1.25	0.70	1.50	1.05
R_7	6 × 6	1.63	0.27	14.67	3.75	1.80	0.31	1.50	0.47

* Average number of measurements ≈250.

Table IV. Contact resistance, R_c, vs. contact window size for poly-Si resistors sintered at 450°C for 5 min in N_2

Res. No.	Contact size $\omega(\mu m) \times d(\mu m)$	Mean* $R_c(\Omega)$	Std dev	αd	δ (μm)	k	$\frac{R_d}{Z \cdot \alpha}$	$Z \cdot \alpha$	R_d (Ω)
			(a) Boron-doped poly-Si resistors (R_s = 56 Ω/□)						
R_1	20 × 4	2.94	0.51	3.81	3.75	3.67	0.24	2.80	0.67
R_2	20 × 6	2.56	0.51	6.56	3.75	3.67	0.24	2.80	0.67
R_3	20 × 10	2.72	0.48	10.26	3.75	3.67	0.24	2.80	0.67
R_4	12 × 10	4.93	0.80	9.46	3.75	2.60	0.29	4.67	1.35
R_5	8 × 8	6.56	1.01	8.54	3.75	2.07	0.31	7.00	2.17
R_6	6 × 20	8.53	1.26	21.88	12.00	1.25	0.70	9.34	6.54
R_7	6 × 6	8.01	1.27	6.99	3.75	1.80	0.31	9.34	2.90
			(b) Phosphorus-doped poly-Si resistors (R_s = 26 Ω/□)						
R_1	20 × 4	2.85	0.66	1.83	3.75	3.67	0.24	1.30	0.31
R_2	20 × 6	2.45	0.45	3.18	3.75	3.67	0.24	1.30	0.31
R_3	20 × 10	1.32	0.76	7.14	3.75	3.67	0.24	1.30	0.31
R_4	12 × 10	3.74	0.46	5.79	3.75	2.60	0.29	2.17	0.63
R_5	8 × 8	5.51	1.12	4.72	3.75	2.07	0.31	3.25	1.00
R_6	6 × 20	6.24	0.81	13.98	12.00	1.25	0.70	4.34	3.04
R_7	6 × 6	7.54	1.23	3.47	3.75	1.80	0.31	4.34	1.35

* Average number of measurements ≈190.

4. The use of low sintering temperatures and thin Al metallization minimizes the thickness of the p-type layer precipitated on n-contacts and reduces the contact resistance.

5. For contacts most frequently used in integrated circuit devices, the contact resistance is independent of the length of the contact and approximately inversely proportional to the contact width, in agreement with the theoretical predictions of the transmission line model.

Acknowledgments

We wish to acknowledge R. Poulsen for his contribution in designing the test masks and in setting up the computer program used in this work. We also thank R. J. Kriegler for suggesting this investigation and for a critical review of the manuscript. Useful discussions with A. Aitken, J. White, D Colton, and A Ibrahim at BNR are also sincerely appreciated.

Manuscript submitted July 27, 1976; revised manuscript received Nov. 23, 1976. This was Paper 94 presented at the Washington, D. C., Meeting of the Society, May 2-7, 1976.

Any discussion of this paper will appear in a Discussion Section to be published in the December 1977 JOURNAL. All discussions for the December 1977 Discussion Section should be submitted by Aug. 1, 1977.

Publication costs of this article were assisted by Bell-Northern Research.

REFERENCES

1. E. Philofsky and E. L. Hall, *IEEE Trans. Parts, Hybrid Packaging*, **php-11**, 281 (1975).
2. P. A. Totta and R. P. Sopher, *IBM J. Res. Dev.*, **13**, 226 (1969).
3. R. J. Anstead and S. R. Floyd, *IEEE Trans. Electron Devices*, **ed-16**, 381 (1969).
4. C. H. Lane, *Metall. Trans.*, **1**, 713 (1970).
5. K. Nakamura, M.-A. Nicolet, J. W. Mayer, R. J. Blattner, and C. A. Evans, Jr., *J. Appl. Phys.*, **46**, 4678 (1975).
6. F. Faggin and T. Klein, *Solid-State Electron.*, **13**, 1125 (1970).
7. F. D. King, J. Shewchun, D. A. Thompson, H. D. Barber, and W. A. Pieczonka, *ibid.*, **16**, 701 (1973).
8. H. H. Berger, *This Journal*, **119**, 507 (1972).
9. H. H. Berger, *Solid-State Electron.*, **15**, 145 (1972).
10. H. H. Berger, *Dig. Tech. Papers ISSCC*, p. 160 (1969).
11. H. Murrman and D. Widman, *ibid.*, p. 162.
12. H. Murrman and D. Widman, *IEEE Trans. Electron. Devices*, **ed-16**, 1022 (1969).
13. S. I. Raider, R. Fitsch, and M. J. Palmer, *This Journal*, **122**, 413 (1975).
14. L. W. Kempf, in "Metals Handbook," 1948 ed., T. Lyman, Editor, p. 805, ASM, Cleveland, Ohio.
15. R. C. Hopper and L. E. Sharif, in Proceedings of Engineering Seminar on Electrical Contacts, Electrical Contacts, p. 45 (1965).
16. R. C. Hopper, J. A. Cunningham, and J. G. Harper, *Solid-State Electron.*, **8**, 831 (1965).
17. G. McNeil, *This Journal*, **116**, 1311 (1969).
18. H. Sankur, J. O. McCaldin, and J. Devaney, *Appl. Phys. Lett.*, **22**, 64 (1973).
19. T. M. Reith and J. D. Schick, *ibid.*, **25**, 524 (1974).
20. H. C. Card, in Proceedings IEEE Electron Device Meeting, Washington, D.C., p. 288 (December 1975).
21. J. Basterfield, J. M. Shannon, and A. Gill, *Solid-State Electron.*, **18**, 290 (1975).
22. K. Chino, *ibid.*, **16**, 119 (1973).
23. C. Y. Ting and C. Y. Chen, *ibid.*, **14**, 433 (1971).

Cathodic Mapping of Leakage Defects

S. M. Hu

IBM System Products Division, East Fishkill Facility, Hopewell Junction, New York 12533

ABSTRACT

A new method for diagnosing integrated circuits by mapping leakage defects has been developed. It is based on the cathodic plating of metallic ions, such as nickel, on leaky devices. The method is simple, reliable, and nondestructive, and makes defects easy to spot. Also, it avoids many of the drawbacks of the anodic method of defect mapping. Correlation with *I-V* characteristics is shown. The method has been applied to the study of transistor pipes and swirl defects in silicon substrates. In particular we have used this method to demonstrate that dislocations in silicon can lead to transistor leakage but not necessarily always through enhanced diffusion. The method is complementary to the anodic mapping method; for many applications, each of the methods has its limitations.

Excessive leakage currents in transistors and diodes constitute an important yield detractor in integrated circuits. They may be caused either by the generation of electron-hole pairs at some metallic precipitates at the reverse-biased p-n junctions, or by pathological conductive paths between the emitters and the collectors of transistors. Leakage diagnosis is often important in the development of new processes for manufacturing integrated circuits. *I-V* characterization by direct probing of devices would serve well but for the small size of modern devices, which makes this method not only excessively laborious, but usually impractical. One practical method of diagnosis resorts to certain test vehicles, such as kerf transistors. However, the probabilities of defects on the large test devices and on the actual devices are often not identical. Therefore, a simple method of mapping leaky transistors is needed. The anodic method, though widely used in one version or another, has its drawbacks, and in certain cases does not work at all. The present paper introduces another method, cathodic mapping, which was developed to avoid such drawbacks and limitations.

Anodic Method

To help the reader choose between the two methods, anodic and cathodic, let us begin with a review of the anodic method. Currently there are three variations. In Plantinga's original method (1), the silicon wafer is made an anode by the application of 4V across the cell, and is placed in an electrolyte, the Sirtl etch. Leaky emitters are etched much faster and hence deeper than the nonleaky transistors. The principle of this method is diagrammed in Fig. 1, in which the two main causes of leakage currents are shown to effect charge transfer in the electrochemical reaction

$$Si \rightleftarrows Si^{4+} + 4e \qquad [1]$$

This method, however, is destructive, and the difference between the etch depths of leaky and nonleaky emitters does not lend itself to easy visual recognition in the rapid scan under the microscope that is necessary in examining a large number of transistors on a wafer.

In a modification of the anodic method, described by Kulkarni *et al.* (2), an electrolyte containing no HF (*e.g.*, a solution of 10% $NaClO^4$) is used, and thus the dissolution of silicon is replaced by the oxidation of silicon

$$Si + 2\,O^{=} \rightleftarrows SiO_2 + 4e \qquad [2]$$

This method, although a small layer of silicon is consumed, is less destructive than Plantinga's anodic etching method. A serious drawback is that the anodically grown SiO_2 film has an insulating property. It quickly takes up the major part of the applied voltage; eventually, at a thickness that depends on that voltage, it stops the current flow and ceases to grow. The leakage criterion is usually defined at certain current levels and at an applied voltage of one to a few volts. In the method of Kulkarni *et al.*, the initial applied voltage is 3V, which allows only 200Å of SiO_2 to be grown anodically; such a film on a silicon substrate is, in effect, invisible. It is then expedient to gradually increase the applied voltage stepwise, say at 3 V/min, to 19V; hold it constant for half an hour; and then increase it again steadily to 30V in order to reach a visible oxide about 500Å thick. In the course of these increases, the normally nonleaky transistors will also start to leak at some points, with the result that the devices become covered by SiO_2 of different thicknesses and colors. Since the mapped devices are not clear-cut black-and-white cases, defect counting is inconvenient and sometimes discretional, making the operator hesitate.

Seto *et al.* (3) describe a third variation of the anodic method. By aluminum evaporation and photolithography, thin aluminum pads are formed on the contact areas (*e.g.*, emitter windows). Then the wafer is placed in an electrolyte, an aqueous solution of 8% sulfuric acid, and acts as an anode with an applied voltage of 2.5-5V. If a device has a leakage current above a cer-

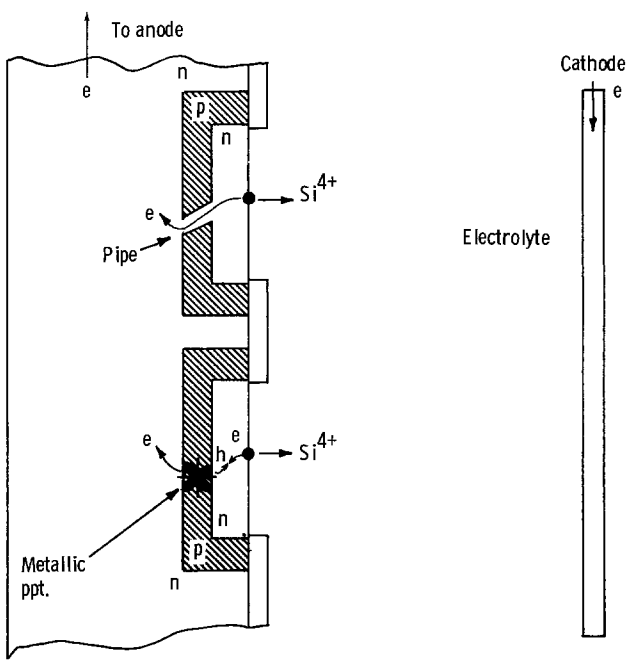


Fig. 1. Anodic etching of leaky transistors. The top transistor is "piped," the bottom one contains a generation-recombination defect.

Key words: electrical leakage, semiconductor devices, defect diagnostics, cathodic plating, pipes, swirl defects.

tain level, the aluminum pads (instead of the silicon) on the device contacts will be oxidized

$$2Al + 3\,O^{=} \rightleftarrows Al_2O_3 + 6e \qquad [3]$$

This version is a vast improvement over the two preceding versions, in two respects. First, the high contrast in reflectivity between the unoxidized and the oxidized aluminum pads makes excellent visibility for rapid scanning of leaky units. Second, the anodic aluminum oxide films, which are electrically fairly leaky by comparison with anodic SiO_2 films, take up very little of the voltage drop across the devices and thus make possible the use of a constant applied voltage. As a result, the oxidized and unoxidized aluminum pads are immediately distinguishable, leaving no need for discretion and hesitation. A drawback of this method is that it requires two extra processing steps, aluminum evaporation and photolithography. Another is that under certain evaporation conditions, the aluminum pads do not anodize at the set voltage. A possible explanation of this peculiarity is that presumably the anodic films formed of aluminum having suitable grain structure are leaky enough to keep the applied voltage almost wholly across the reverse-biased junctions of the devices, whereas the anodic oxide films formed of aluminum having larger grain structure are better insulators and soon become blocking to anodic reactions.

The anodic method, in all three of these versions, has one important limitation: it does not work in certain cases such as n-on-p diodes or multiple emitters with a very large common base. When the substrate is made anodic, the junctions of n-on-p diodes are forward biased, with the result that all the diodes are anodized, whereas we should be interested only in the reverse leakage of the diodes. For multiple-emitter transistors, a very large common base brings a high probability of leakage defects somewhere at the base-collector junction; that is, a very large base-collector junction is most often leaky. This then leads to a case of n-on-p diodes, as illustrated in Fig. 2. In fact, it was the author's experience of such a case that motivated the development of the cathodic leakage-mapping method.

Cathodic Method

In the cathodic leakage-mapping method, the emitter-base junctions are reverse biased, and the leakage

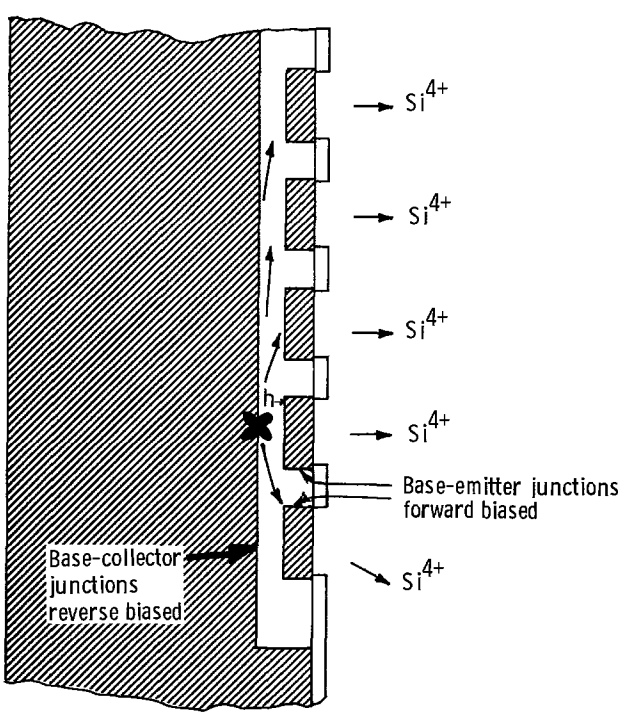


Fig. 2. In the anodic method, a single defect in a large common base-collector function will cause all the emitters in the large common base to be mapped out.

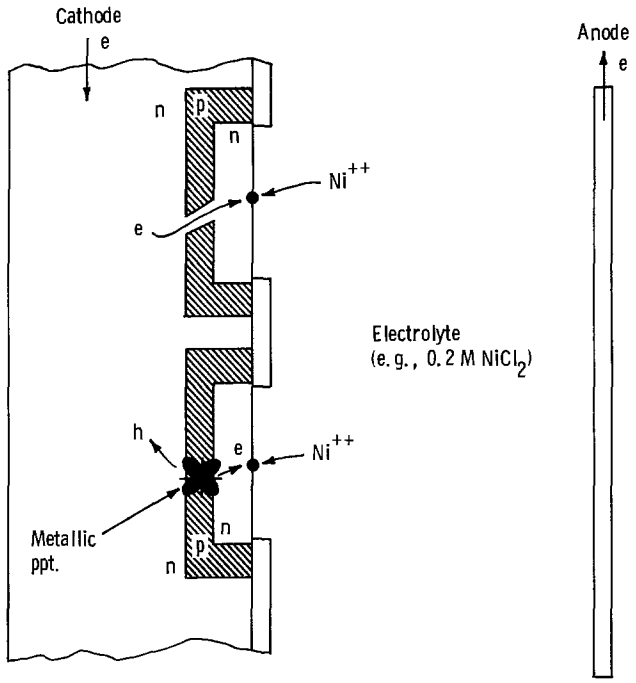


Fig. 3. Cathodic plating of suitable metallic ions, such as nickel, on leaky transistors. The top transistor is "piped," the bottom one contains a generation-recombination defect.

is accompanied by a reverse flow of electrons, which leads to the electrode reaction (Fig. 3). This method is far simpler than the anodic method. The wafer is simply made a cathode with respect to a platinum electrode in a suitable electrolyte containing suitable cations. We found that a 0.2M aqueous solution of nickel chloride with 0.1% of 47% HF gave good results. Other metallic ions having oxidation potentials close to that of nickel can also be used. Ions with low oxidation potentials, such as copper, are not suitable; they tend to plate out automatically even without an externally applied voltage. This tendency, however, can be suppressed by adding a suitable sequestering agent. We have also tried electrophoresis of positively charged colloidal particles, which have the promise of being colored easily; but the results were not quite satisfactory.

Next, a voltage of 2-5V, depending on the particular criterion of leakage current, is applied across the electrodes. Because the nickel films plated on the leaky transistors are highly conductive, the voltage across the device junctions remains essentially constant throughout the mapping operation. This is an important factor in contributing to reliable results by keeping the basis of the leakage criterion constant.

For good visibility, the plated nickel films should be at least 200Å thick. The plating time (in seconds) should then be about $0.03/j$ or longer, where j is the leakage current density (in amperes per square centimeter of emitter area) chosen to distinguish between leaky and nonleaky devices. A longer plating time, for improved visibility, would cause the nominally nonleaky devices to be plated too, with the result that in the neighborhood of the defined leakage criterion, the shade of the mapped emitters might undergo continuous variation. The experimenter would then have to exercise some degree of discretion to count the leaky devices, and the resolution would necessarily be poor. Fortunately, this case has not arisen in the author's experience. There are two possible reasons for this. The first, somewhat speculative, is that this mapping method may have benefited from the overpotential phenomenon (in some ways analogous to the Schottky barrier). Usually, an overpotential develops between an electrode and an electrolyte and is dependent on the electrode material. It appears that the overpotential on a semiconductor silicon surface is high when the sur-

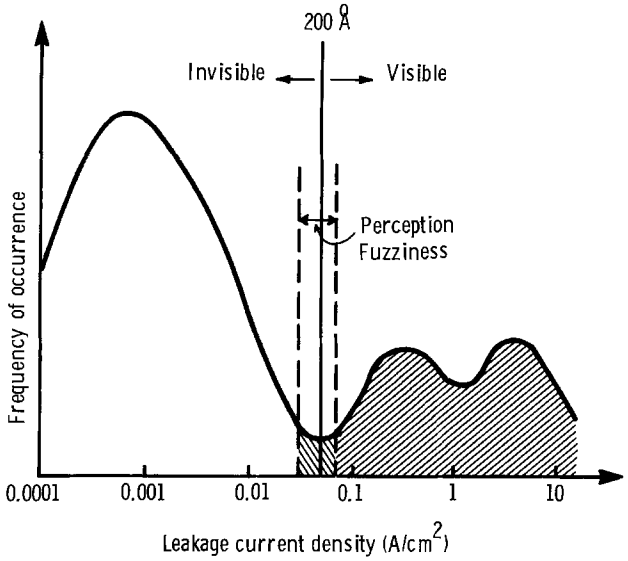


Fig. 4. Schematic illustration of a trimodal leakage current distribution in transistors, fairly representative of actual cases. It is seen that when the cathodic plating voltage and the plating time are so adjusted as to separate the modes, the resulting error due to fuzziness in visual perception will be a very small percentage even without the benefit of the overpotential phenomenon.

face is bare but is suddenly lowered when it is plated with a thin layer of nickel. Once this overpotential is lowered or removed, the plating increases much faster. Thus, for the leaky transistors that have plated past the incubation period, the plated film will be massive and easily distinguishable both from those that are still within the incubation period and from those that will not plate. The second reason, which also helps in reducing the resolution problem, is that in general the leakage current densities of devices carry over many decades in their statistical distributions. Thus, a ±100Å fuzziness in visual perception constitutes a leakage current range that comprises a very small percentage of the devices, particularly if this leakage range is chosen to fall at some node in a multimodal distribution. This is illustrated in Fig. 4.

The cathodic method is nondestructive; the plated nickel films can later be removed, if desired, by placing the wafer in, for example, nitric acid.

Correlation of Cathodic Mapping and *I-V* Characteristics

To demonstrate the correlation between the cathodic mapping and the *I-V* characteristics of devices, and to establish experimental conditions suitable for cathodic mapping, we used a test vehicle consisting of multiple emitters on a common base. The base was formed by blanket diffusion of boron into a n-type, 0.1 Ω-cm substrate. The emitters were formed by diffusion of arsenic through photolithographically defined SiO_2 emitter openings of various sizes. The wafer was placed in a 0.2M $NiCl_2$ solution (with the back side insulated from the solution). Then a voltage of 2.5V was applied between the electrodes, with the silicon wafer as the anode, for 5 min. After being rinsed with deionized water and dried, the wafer was ready for the usual visual counting of leaky devices under a microscope (special chip layouts are usually needed so that the leaky units can be checked conveniently). For correlation, photomicrographs were taken. A plated map is shown in Fig. 5. The appearance of the plated films depends on the additives in the solution and on how the wafer surface has been prepared; they may show up as areas of dark color, as in Fig. 5, or of bright metallic luster. In either case, the contrast with an unplated silicon surface is very strong.

I-V curves were then taken on some of the large devices, both plated and unplated. Only large emitters are accessible to probing. Units 1, 2, 3, and 7 in Fig. 5 measure 125 × 175 μm, and units 5 and 6 measure 75 × 550 μm. Panels of *I-V* curves for units 1-7 are placed alongside the cathodically mapped devices for comparison.

Application of Cathodic Mapping to Defect Study

Study of transistor pipes.—Although the transistor pipe is often discussed, its physical identity and the mechanism of its formation remain unresolved. It is generally thought to be caused by enhanced diffusion of either emitter or subcollector dopant along a segment of dislocation traversing the transistor base. As an example of the application of the cathodic method, we now report an experiment designed to demonstrate that dislocations traversing transistors can cause leakage, but not necessarily only through enhanced diffusion.

We again used a test vehicle with multiple emitters on a large common base. After blanket diffusion of boron into n-type, 0.1 Ω-cm substrate, and photolithographic opening of emitter windows in the SiO_2 film, the sample was given a series of indentations, with a 20g load at 600°C. The apparatus and the procedure of indentation are described elsewhere (4). Two zigzag rows of indentations were made. Each indentation produced an indentation dislocation rosette, whose structure has been described elsewhere (5). Briefly, the rosette consists of four columns of triangular dislocation half-loops, moving parallel to the surface plane of a (001) substrate, as well as four columns of prismatic loops moving down at an angle to the surface. After cleaning, the wafer was given an arsenic emitter diffusion. The cross section of the device is now as shown in Fig. 6, where an inset shows the structure of an indentation dislocation rosette. We may expect that any dislocation segments traversing the transistors will either become pipes by enhanced arsenic diffusion along their length, or accumulate metallic impurities such as copper, nickel, and iron. In either case, the transistors

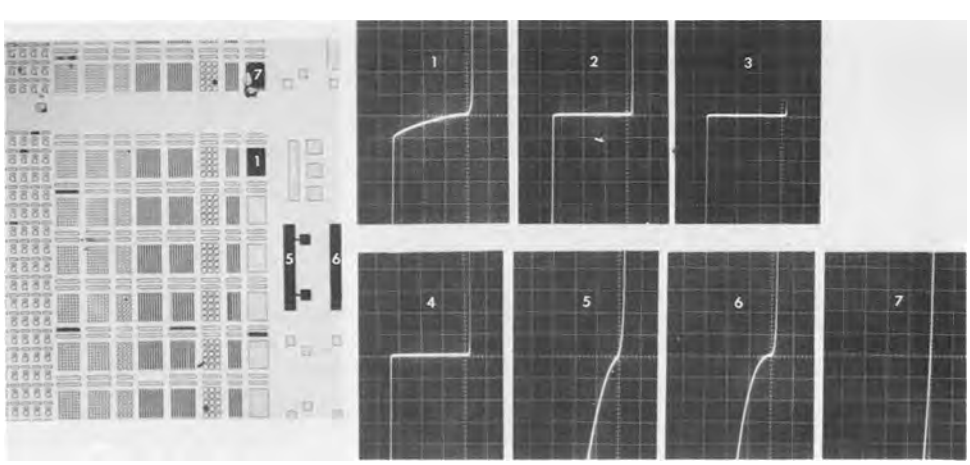


Fig. 5. Correlation between cathodic mapping of leakage defects and *I-V* characteristic. The left-hand side is a photomicrograph of a test chip consisting of multiple emitters of various sizes sitting on a blanket base-collector junction. The darkened units are the leaky units that had been nickel plated. Scales for the *I-V* curves for the corresponding numbered units on the right-hand side are: vertical, 10 μA/div; horizontal, 2V/div.

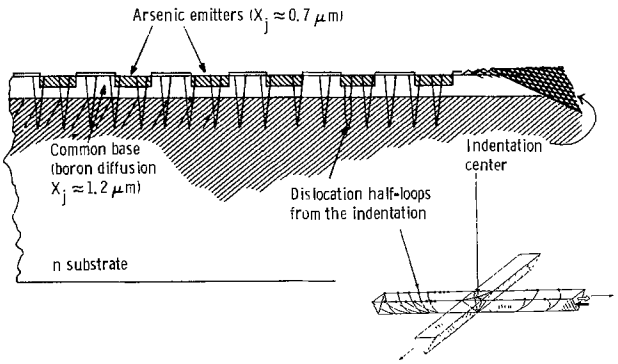


Fig. 6. Schematic illustration showing a number of emitters sitting on a blanket base which have been traversed by a column of dislocation half-loops that had emanated from the indentation center at the right. The emitter diffusion was done after the formation of the indentation dislocation rosette so that there was a chance for enhanced arsenic diffusion along the dislocations. The inset shows a schematic structure of the dislocation rosettes.

traversed by the dislocation half-loops should become leaky. One would then expect the cathodic mapping to reveal these leaky transistors clustered in a pattern of crosses. This was what was observed, as is seen in Fig. 7, showing the results of two separate experiments. The figure serves also to show the possible variation in the texture of plated nickel films.

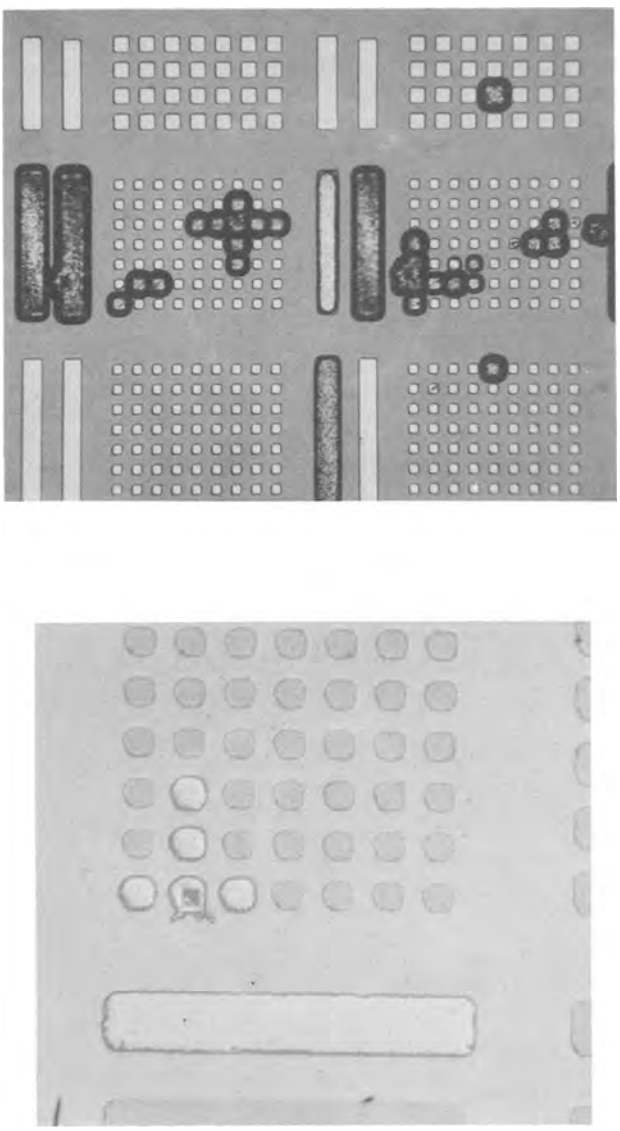


Fig. 7. Photomicrographs showing that the emitters which were traversed by dislocation half-loops in the indentation dislocation rosettes were decorated with high contrast nickel films after cathodic mapping.

To investigate whether the leakage mechanism is enhanced arsenic diffusion (pipe) or an accumulation of metallic precipitates at the dislocations, we applied nitric acid to remove the nickel films plated on the emitters of the leaky transistors. Then a proprietary method of gettering was applied to the back side of the wafer, which, after being annealed in nitrogen at 900°C for 1 hr, was subjected to cathodic mapping for the second time. This time, only the indentations themselves were plated; the emitters in the previously decorated arms of the rosettes were not decorated. This result indicated that the leakage mechanism in the present case is the precipitation of fast diffusing and hence getterable metallic impurity, not the enhanced diffusion of the slow diffusing and hence ungetterable arsenic. It is prudent to add that, though this is true for this particular case of transistor geometrical dimensions and processing parameters, it need not be generally true for other cases. Further study of this subject is being considered.

Leakage from swirl defects.—A second leakage phenomenon is known to be associated with "swirl" defects. In particular, leaks in vidicon diodes reveal themselves as swirls of bright spots (6). Swirl defects are clusters of point defects or microdislocation loops, which are frozen in during the crystal growth but usually are transformed and interact with high temperature processes such as oxidation to produce oxidation stacking faults, etc. The nature of swirl defects is beyond the scope of this paper; here we merely want to demonstrate dramatically, by means of cathodic mapping, that they can lead to junction leakage in devices.

The test vehicle was the same as that described earlier in this paper; here, however, since the occurrence of swirls is very much dependent on the conditions of crystal growth and the particular position in a crystal from which the wafer was cut, the wafer had to be specially chosen. After the device processing and cathodic mapping described earlier, the plated emitters, on n-on-p diodes, were found to cluster in a swirl as shown in Fig. 8. This particular mapping results in highly reflective nickel films on the leaky units, which make the form of the swirl pattern readily visible to the naked eye. Note that in the quarter wafer shown in Fig. 8, a small corner segment of the sample was placed above the electrolyte and hence was not cathodically mapped.

Conclusion

This paper has introduced a new method for diagnosing integrated circuits and their test vehicles by mapping leakage defects. The method is very convenient and simple to use, in contrast with the anodic method.

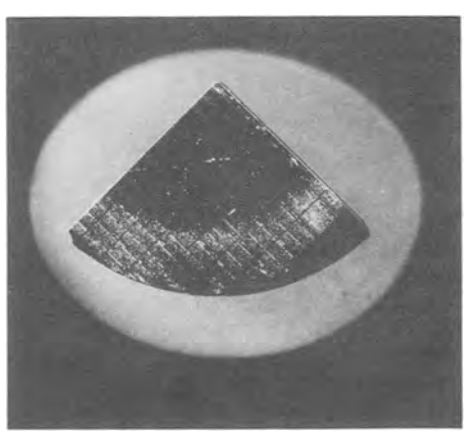


Fig. 8. Cathodic mapping of leakage transistors that images swirl defect distribution (bright band) in a silicon wafer quarter.

It makes the mapped leaky devices highly visible, it is free from the drawbacks associated with the anodic method, it is nondestructive, and it lends itself to repeated use on the same sample. It keeps the voltage drop across the devices constant, thus leading to reliable and interpretable results. It makes for clear distinction between leaky and nonleaky devices, probably because overpotential is reduced once a thin film of nickel has been plated; this effect is in direct contrast with the effect of the insulating anodic oxide film formed in the anodic method.

After mentioning all these virtues of the cathodic method, we must conclude by mentioning its limitation, which is essentially complementary to that of the anodic method. Specifically, it cannot be applied to n-p-n transistors that are completely isolated from the substrate. In modern integrated circuits, many transistors are so isolated. In such cases, the cathodic method would be useful in mapping, for example, leakage in the isolation itself. Another of the numerous possible applications would be the mapping of n-channel FET integrated circuits.

Acknowledgments

The author thanks Mr. Paul R. Poponiak for his skillful experimental assistance and Dr. T. H. Yeh for useful discussions.

Manuscript submitted Aug. 31, 1976; revised manuscript received Nov. 29, 1976. This was Paper 451 RNP presented at the Washington, D.C., Meeting of the Society, May 2-7, 1976.

Any discussion of this paper will appear in a Discussion Section to be published in the December 1977 JOURNAL. All discussions for the December 1977 Discussion Section should be submitted by Aug. 1, 1977.

Publication costs of this article were assisted by the IBM Corporation.

REFERENCES

1. G. H. Plantinga, *IEEE Trans. Electron Devices*, **ed-16**, 394 (1969).
2. M. V. Kulkarni, J. C. Hasson, and G. A. A. James, *ibid.*, **ed-19**, 1098 (1972).
3. D. K. Seto, F. Barson, and B. F. Duncan, in "Semiconductor Silicon 1973," H. R. Huff and R. R. Burgess, Editors, pp. 651-657, The Electrochemical Society Softbound Symposium Series, Princeton, N.J. (1973).
4. S. M. Hu, *J. Appl. Phys.*, **46**, 1465 (1975).
5. S. M. Hu, *ibid.*, **46**, 1470 (1975).
6. For example, see A. J. R. deKock, *Appl. Phys. Lett.*, **16**, 100 (1970). See also H. Shiraki, J. Matsue, and T. Kawamura, Proceedings of the Second Conference on Solid State Devices, Tokyo (1970).

Four-Point Sheet Resistance Measurements of Semiconductor Doping Uniformity

David S. Perloff, Frederick E. Wahl, and James Conragan

Signetics Corporation, Research and Development Laboratory, Sunnyvale, California 94086

ABSTRACT

A system is described for automatically measuring the sheet resistance of doped semiconductor wafers using either a conventional four-point probe or microelectronic van der Pauw resistors. Graphic display formats useful for conveying information about doping uniformity are discussed, and the tendency of random measurement error to degrade equivalue contour maps is illustrated. Excellent agreement is observed for sheet resistance data obtained from van der Pauw resistors which differ in area by more than three orders of magnitude. It is shown experimentally that the four-point probe and van der Pauw resistors may be used interchangeably for doping uniformity measurements.

The spatial uniformity of the processes employed in semiconductor microcircuit fabrication is an important determinant of the matching of components and of the yield of functional circuits. Even a highly controlled doping process such as ion implantation may be subject to intrinsic sources of variability which can adversely affect component matching (1, 2).

Parameters such as sheet resistance and film thickness have been shown to vary systematically over the surface of a processed silicon wafer (3, 4). The equivalue contour maps (topographs), which were used in Ref. (4) for exhibiting spatial variations, summarize a great deal of information in a compact and easily comprehended format. This method of display is, however, extremely sensitive to random measurement error, particularly when such error becomes comparable to the difference in parametric values at adjacent test sites.

In this paper, four-point sheet resistance measurement techniques are described which provide data sufficiently free of random error to justify the use of equivalue contour maps. It will be shown that the four-point probe (FPP) (5, 6) and van der Pauw resistors (7), although sampling areas of the wafer which differ by as much as five orders of magnitude, nevertheless provide comparable information about the spatial distribution of impurities.

Key words: four-point probe, resistor, silicon.

Data Acquisition System

A general-purpose system for the acqusition of four-point sheet resistance data is shown schematically in Fig. 1. This system consists of a standard X-Y probing apparatus, data terminal, recording devices, prober control, and sequencing and interface modules. Two of the four sample probes carry current supplied by a Keithley Model 225 constant (±0.005% stability) current supply; potential differences[1] are measured across the remaining two probes with a resolution of 10 μV by a Nonlinear Systems Corporation Model MX-1 digital voltmeter. The magnitude of the measurement current is adjusted to achieve a potential difference in the range of 30 ± 10 mV for both FPP and van der Pauw resistor measurements.

A rectangular array of up to 99 rows and 99 columns is employed for one-dimensional profiling as well as two-dimensional mapping of wafers. The wafer probe

[1] The polarity of the current supply is reversed and readings of the potential difference averaged to eliminate small offset voltages associated either with thermoelectric effects or instrumentation.

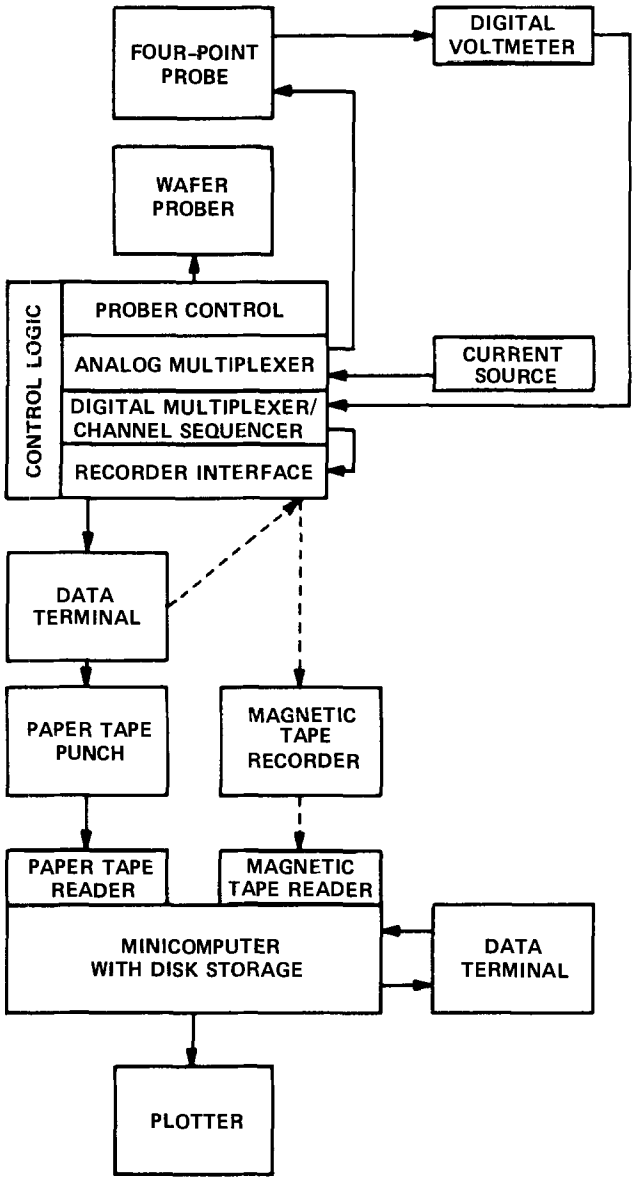


Fig. 1. Data acquisition system

step-and-repeat distances ΔX and ΔY may be varied between 10 and 999 mil in increments of 1 mil along both the X and Y axes of movement. At each test site, an analog multiplexer is used to switch analog signals. For each analog channel, a digital multiplexer and its associated digital channel sequencer select up to nine channels for transfer by the interface system to the recording device (paper tape punch or incremental magnetic tape recorder).

Data are analyzed off-line by a Digital Equipment Corporation Model PDP 11/40 minicomputer with associated system and program disk drives, tape reader, and terminal. Conventional disk management and program overlay techniques make it possible to handle an extensive data base. The hard copy output device (Versatec Incorporated "Matrix") may be operated as a conventional line printer or as a high resolution plotter. In the latter mode, images are built up and stored on disk until the analysis has been completed, then printed continuously.

Presentation of Data

There are a number of alternatives for displaying the spatial variation of sheet resistance data. These include one-dimensional profiles, two-dimensional maps (1, 4, 6, 8-10), and three-dimensional perspective drawings (3, 9, 10). Discussion in this section is restricted to the one- and two-dimensional formats, since these are considered by the authors to be more easily interpreted than perspective drawings, particularly for smoothly varying data.

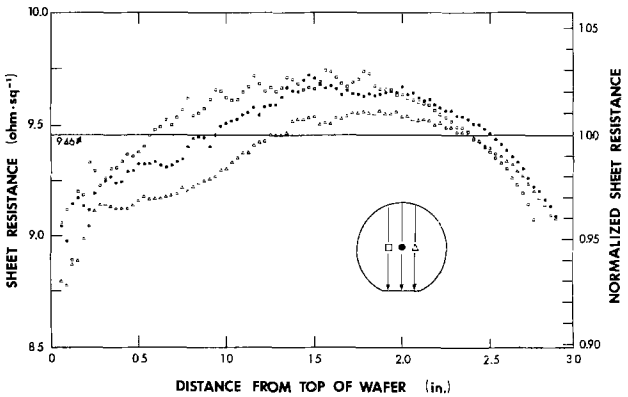


Fig. 2. One-dimensional FPP sheet resistance profiles for a phosphorus-diffused wafer ($\bar{\rho}_s$ = 9.46 Ω/sq and $\sigma^*(\%)$ = 2.47%).

One-dimensional profiles.—Figure 2 illustrates the variation in sheet resistance from top edge to bottom edge of a 3 in. diameter p-type silicon wafer doped with phosphorus from a phosphine diffusion source. Three parallel profiles (ΔX = 444 mil, ΔY = 30 mil) have been obtained using an in-line FPP (11) oriented perpendicular to the direction of travel. The solid line (9.46 Ω/sq) represents the mean sheet resistance as determined by averaging data from 118 sites on the wafer, as described below. The scale on the right side of the figure represents the fractional deviation from the wafer mean and permits comparison with the equivalue contour map discussed below.

One-dimensional profiles provide detailed information concerning the point-to-point variation in doping across the surface of a semiconductor wafer. They are particularly useful for exhibiting rapid local fluctuations such as are known to occur in ion-implanted wafers (1).

Two-dimensional maps.—The method of mapping sheet resistance variations employed by the authors involves measurements at 118 standard test sites located on the square grid shown in Fig. 3a. The distance between grid points is L = 222 mil for a 3 in. diameter wafer. The mean sheet resistance $\bar{\rho}_s$ and standard deviation σ are given by the expressions

$$\bar{\rho}_s = \frac{1}{118} \sum_{i=1}^{118} (\rho_s)_i \qquad [1]$$

and

$$\sigma^2 = \frac{1}{117} \sum_{i=1}^{118} [(\rho_s)_i - \bar{\rho}_s]^2 \qquad [2]$$

For an ideal gaussian distribution, ~95% of the data fall within two standard deviations of the mean. For this reason, the authors employ as a quantitative measure of the doping uniformity $\pm 2\sigma^* \times 100\%$, where the relative standard deviation σ^* is defined by the relation

$$\sigma^* = \frac{\sigma}{\bar{\rho}_s} \qquad [3]$$

After evaluating $\bar{\rho}_s$ and σ, the 118 sheet resistance values are displayed in one of the three formats which will now be described.

Deviation maps.—Figure 3b is an example of a deviation map for the same wafer for which one-dimensional profiles are plotted in Fig. 2. Deviations from $\bar{\rho}_s$ are computed according to the formula

$$\Delta_i(\%) = [(\rho_s)_i/\bar{\rho}_s - 1] \times 100\% \qquad [4]$$

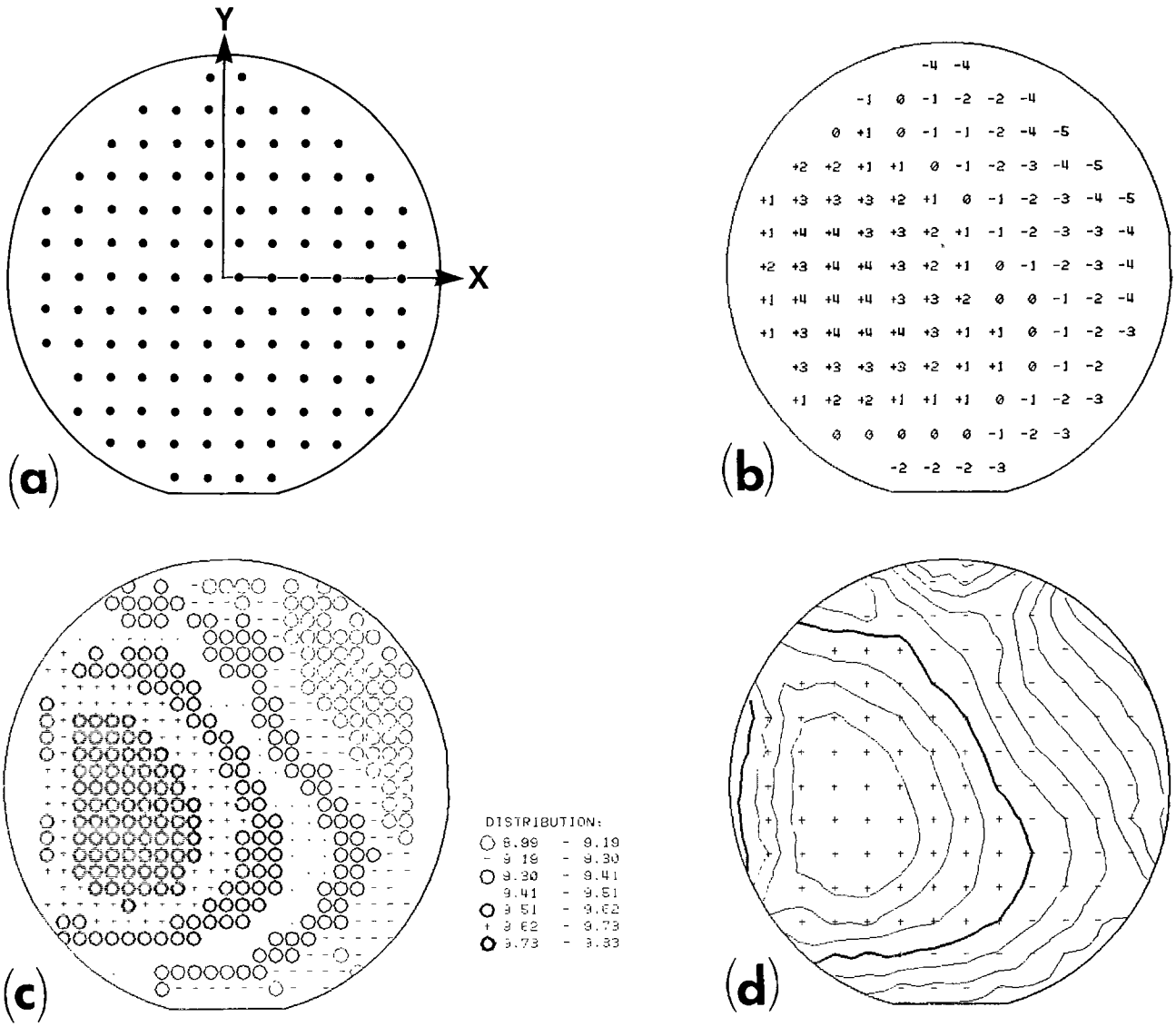


Fig. 3. Methods of displaying spatial sheet resistance variations: (a) standard 118 test site configuration; (b) percent deviation map; (c) histograph; (d) equivalue contour map. The data were obtained from FPP measurements of the wafer of Fig. 2.

rounded to the nearest integer value and plotted at the appropriate test site locations.

This display format requires the least amount of computation and can be implemented with a standard line printer. The underlying pattern of variation (Fig. 3c and 3d) may be observed by drawing smooth contour lines which enclose equal values of $\Delta_i(\%)$. (These contours may be drawn automatically using the graphic display techniques described in this paper.)

Histographs.—It is common practice to employ histograms to summarize the distribution of data over a range of values. Figure 3c is a histograph (two-dimensional histogram) which associates each measured value, and the interpolated values discussed below, with one of seven intervals into which the full range of experimental data has been divided. These intervals, each of which contains an equal number of values, are identified by circles of various line thicknesses and the symbols +, ·, and −. Unlike the deviation map, for which the + (−) sign identifies values which are above (below) the wafer mean, this method of display identifies values which are above (below) the wafer median.

The histograph succeeds in revealing the underlying pattern of variation by separating the data into seven bands of alternating character density.[2] In order to obtain continuous bands, it was necessary to first subdivide the initial network (Fig. 3a) by employing an interpolation scheme (described below) which results in a fourfold increase in the density of grid points. The distance between subgrid points for a 3 in. diameter wafer is 111 mil.

Equivalue contour maps.—Figure 3d shows an equivalue 1%-contour map obtained from the same data used for Fig. 3b and 3c. The heavy contour represents the mean sheet resistance $\bar{\rho}_s$, computed using Eq. [1], while the lighter contours differ from $\bar{\rho}_s$ in increments of $0.01\ \bar{\rho}_s$. The symbols + (−) identify experimental values which are greater (less) than $\bar{\rho}_s$. A curve representing the variation of ρ_s along any particular direction (as in Fig. 2) may be constructed by determining the points of intersection with the equivalue contours.

As in the case of the histographs discussed above, interpolation has been used to increase the density of grid points. This procedure assures that the contours, which are constructed from discrete line segments, will appear smoothly varying to the eye. In addition, a linear extrapolation scheme is utilized which allows contours to extend to the edge of the map.[3] These refinements help, in the opinion of the authors, to make

[2] A similar approach is employed in Ref. (10), in which the magnitude of a parameter is indicated by the darkness of the position characters.

[3] The contours drawn near the edge of the map may not be quantitatively correct since resistance values may change more rapidly near the edge of the wafer than over its interior. The extrapolation procedure is justified, however, as an aid to achieving a qualitative appreciation of the spatial variation of the parameter.

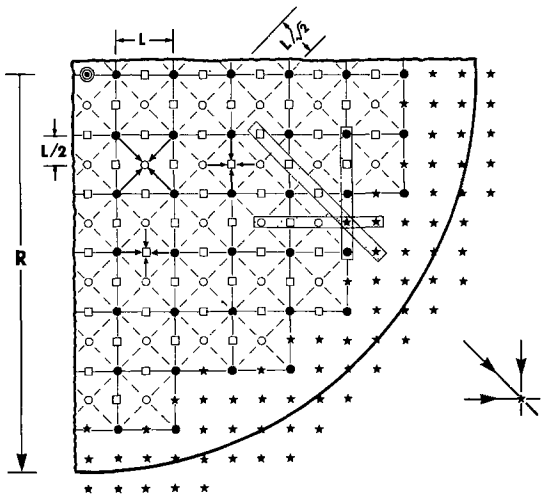


Fig. 4. Interpolation and extrapolation of data in the lower right quadrant of the wafer. The principal directions along which extrapolation is carried out are shown at the lower right.

equivalue contour maps the most effective means of displaying the patterns of spatial variation which are characteristic of semiconductor doping processes.

Interpolation and extrapolation of data.—Figure 4 illustrates the manner in which interpolation is carried out in the lower right quadrant of the wafer. A subgrid with cell parameter $L/2$ is obtained from the initial network of data points (●) in two stages. The first stage involves averaging the four experimental data points at the corners of the original grid cell to obtain the values represented by the symbol ○. This procedure results in a new grid rotated through 45° and having a cell parameter $L/\sqrt{2}$. The second stage involves averaging the four values at the corners of each $L/\sqrt{2}$ grid cell to obtain new values identified by the symbol □.

At the periphery of the expanded data array, extrapolation is used to obtain those subgrid values (★) which cannot be generated by the four-corner averaging technique described above. One estimate at an empty subgrid site is obtained by employing a least squares linear fit to a set of four nearby data points lying along one of the principal directions shown in Fig. 4. Using estimates obtained for the other two principal directions, one computes an average value for the sheet resistance at that point on the wafer. An example of this treatment of the data is shown in Fig. 4 for the case of the empty site nearest the center of the wafer. (In this instance, only three values are used along two of the principal directions, since the fourth value corresponds to an empty site.) This procedure is carried out, one site at a time, always filling the empty site nearest to the center of the wafer. Off-wafer sites are also filled in order to allow equivalue contours to extend to the wafer boundary, thereby significantly improving the comprehensibility of the contour map.

Measurement error.—The influence of random measurement error on the one-dimensional profiles in Fig. 2 is revealed by the scattering of data points. In a two-dimensional equivalue contour map, random error is manifested by irregular, distorted, or—in extreme cases—isolated contours. A technique for experimentally determining random error and the effect of such error on equivalue contour maps will now be discussed.

Experimental assessment.—The most direct way to assess random error is to determine the variation among a series of independent measurements of the sheet resistance. The procedure employed by the authors is illustrated in Table I, which summarizes a series of independent FPP (11) sheet resistance measurements made at nine different locations in a 3 × 3 square array ($\Delta X = \Delta Y = 120$ mil) centered on the phosphorus-diffused wafer for which data are presented in Fig. 2 and 3. After recording the first ($j = 1$) set of nine readings (probes along the X axis), the FPP is returned to its initial position, displaced 2 mils along the X axis, and a second ($j = 2$) set of nine readings recorded. This procedure is repeated until five readings have been obtained at each location. Each set of five readings is in turn used to compute a local standard deviation given by the expression

$$(\sigma_e)_i^2 = \frac{1}{4}\sum_{j=1}^{5}[(\rho_s)_{ij} - (\bar{\rho_s})_i]^2 \qquad [5]$$

where $(\bar{\rho_s})_i$, the local mean sheet resistance, is

$$(\bar{\rho_s})_i = \frac{1}{5}\sum_{j=1}^{5}(\rho_s)_{ij} \qquad [6]$$

These nine standard deviations are then used to compute an average standard deviation of the measurement error according to the formula

$$\sigma_e^2 = \frac{1}{9}\sum_{i=1}^{9}(\sigma_e)_i^2 \qquad [7]$$

When comparing values of σ_e for wafers of different sheet resistance, it is convenient to employ the relative standard deviation of the measurement error

$$\sigma_e^* = \frac{\sigma_e}{(\bar{\rho_s})_e} \qquad [8]$$

where $(\bar{\rho_s})_e$ is the average sheet resistance for the 45 measurements. The value $\sigma_e^*(\%) = 0.136\%$ obtained from Table I is typical of the random measurement error which the authors experience with a 25 mil FPP assembly on layers having sheet resistance ≤ 500 Ω/sq.

Effect on contour maps.—The effect of measurement error on a two-dimensional display format may be simulated by systematically introducing randomness into a set of data, $P(X, Y)$, whose relative standard deviation is $\sigma_P^* = \sigma_P/\bar{P}$. The influence of measurement

Table I. An example of the determination of FPP measurement error for the phosphorus-diffused wafer of Fig. 2 and 3. According to Eq. [7], $\sigma_e^*(\%) = 0.136\%$.

Probe location† X (mils)	Y (mils)	i	$(\bar{\rho_s})_i$ (Ω/sq)	$(\sigma_e^*)_i$ (%)	$(\rho_s)_{i1}$ (Ω/sq)	$(\rho_s)_{i2}$ (Ω/sq)	$(\rho_s)_{i3}$ (Ω/sq)	$(\rho_s)_{i4}$ (Ω/sq)	$(\rho_s)_{i5}$ (Ω/sq)
−120	120	1	9.696	0.131	9.717	9.690	9.700	9.686	9.690
0	120	2	9.681	0.187	9.691	9.653	9.680	9.679	9.701
120	120	3	9.647	0.103	9.657	9.634	9.653	9.652	9.639
−120	0	4	9.707	0.095	9.691	9.711	9.706	9.714	9.711
0	0	5	9.698	0.168	9.685	9.693	9.685	9.702	9.724
120	0	6	9.675	0.100	9.663	9.686	9.667	9.677	9.680
−120	−120	7	9.719	0.123	9.709	9.724	9.705	9.733	9.725
0	−120	8	9.720	0.189	9.700	9.709	9.718	9.725	9.748
120	−120	9	9.703	0.071	9.699	9.714	9.700	9.705	9.696

† The location $X = 0$, $Y = 0$ represents the center of the wafer.

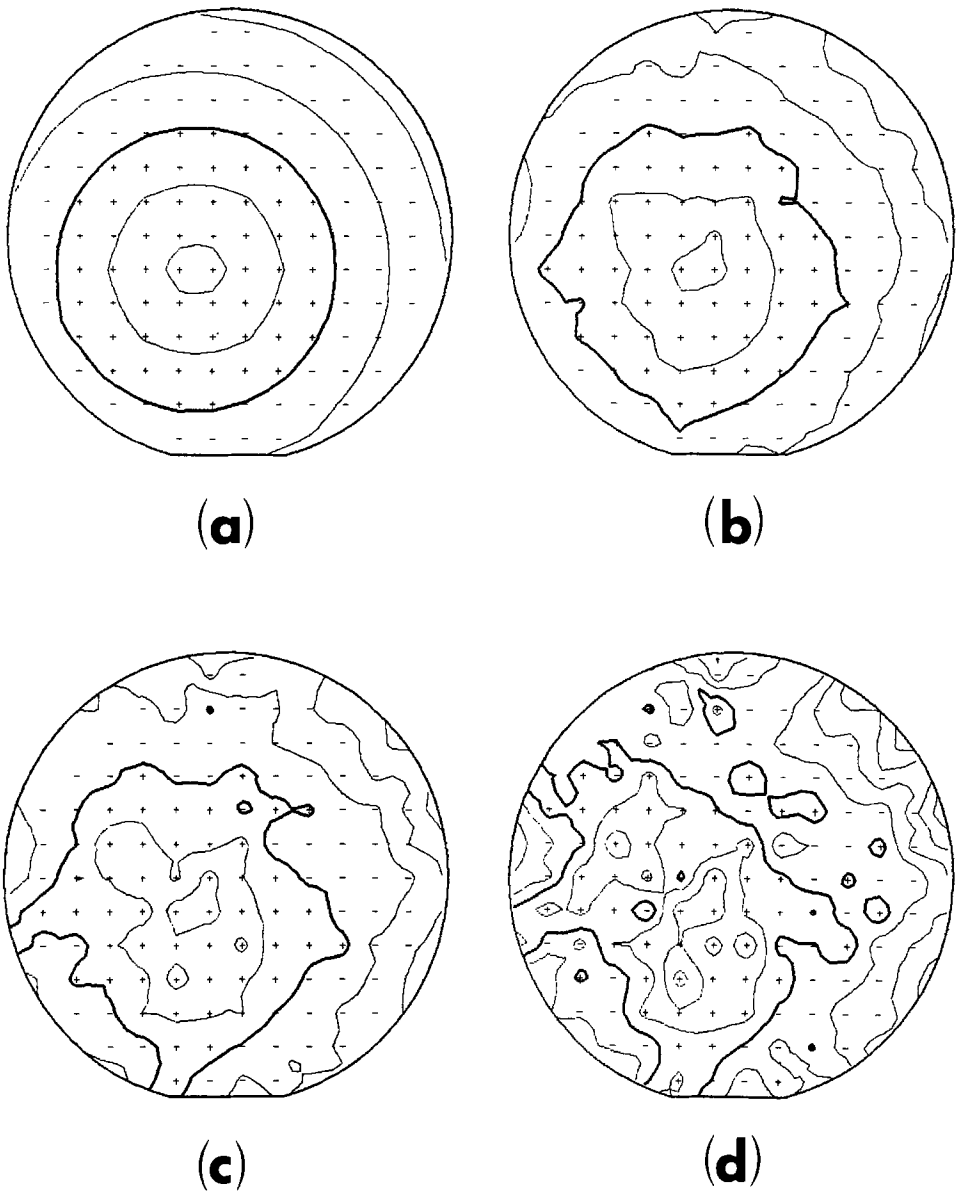


Fig. 5. The effect of random error of magnitude $\sigma_\epsilon^*(\%)$ on a hypothetical distribution for which the over-all uniformity is $\sigma_P^*(\%) = 1.00\%$: (a) $\sigma_\epsilon^*(\%) = 0$; (b) $\sigma_\epsilon^*(\%) = 0.25\%$; (c) $\sigma_\epsilon^*(\%) = 0.50\%$; (d) $\sigma_\epsilon^*(\%) = 1.00\%$.

error is simulated by adding to each of the 118 $P(X, Y)$ values a random number $\epsilon(X, Y)$ selected from a normal distribution with a nominal mean of 0 and a relative standard deviation $\sigma_\epsilon^* = \sigma_\epsilon/\bar{P}$.

Examples of this procedure for various values of σ_ϵ^* are shown in Fig. 5a-5d for the case of a pattern of concentric circles (note similarity to Fig. 3d) for which $\sigma_P^*(\%) = 1.00\%$. As σ_ϵ^* increases in magnitude, the contours become progressively less regular until a point is reached at which it is no longer possible to recognize the underlying pattern of variation shown in Fig. 5a. This point appears to occur when $\sigma_\epsilon^*(\%) \approx 0.50\%$, since the underlying pattern, which can be detected in Fig. 5b despite the irregular contours, can no longer be identified in Fig. 5c. Figure 5d illustrates the consequences of the measurement error becoming comparable to the intrinsic variability of the data. Not only have the circular contours become so distorted that they reach the edge of the wafer map, but many isolated regions have appeared as a result of large excursions from the correct local behavior.

Measurement Techniques

In this section the FPP and van der Pauw resistors are discussed from the perspective of producing data suitable for mapping sheet resistance variations. A special test mask is then described which incorporates both vehicles on the same wafer, making it possible to carry out a direct experimental comparison.

FPP measurements.—It is common practice to employ an in-line FPP, as shown in Fig. 6, for characterizing the sheet resistance of doped semiconductor wafers (5, 6). If the probe separation distance s is at least twice the thickness of the layer being measured, then

$$\rho_s = k\frac{\Delta V}{I} = kR \qquad [9]$$

where k is a geometrical correction factor which depends on the location of the probes and the shape of the sample, I is a current through two of the probes, ΔV is the potential difference measured between the remaining two probes, and the resistance R is defined

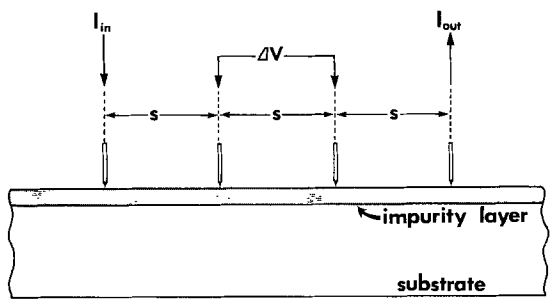


Fig. 6. Conventional current/voltage configuration for an in-line FPP array.

as $\Delta V/I$ (12). Ordinarily, the outer two electrodes of the in-line FPP carry current and the inner two electrodes are used to measure voltage since, for an FPP having equal distances of separation between the probe needles, this assignment results in the largest value of ΔV (13).

Logan (14) has shown that a circular sample doped on both sides (such as the phosphorus-diffused wafer described above) should behave as if its front surface were part of a continuous infinite sheet. Thus the correction factor is a constant value ($k = \pi/\ln 2 = 4.532$), independent of the location of the FPP. In contrast, a thin circular sample doped on one side will require knowledge of the orientation and position of the probe array in order to utilize Eq. [9]. General expressions have been derived for the case of the FPP oriented along the radius (14) and for the FPP oriented perpendicular to the radius (15) of a thin circular sample. Perloff (6) has derived expressions for the FPP oriented at an arbitrary angle with respect to the wafer radius, making it possible to employ automatic wafer probing equipment for evaluating doping uniformity.

An alternative approach to FPP measurements, which is particularly useful for ion-implanted wafers, involves the application of photolithographic techniques to define rectangular regions of sufficient size to accommodate the FPP array, as shown in the cross-sectional view of Fig. 7a. If an automatic wafer probing apparatus is employed to position the FPP so that it occupies the same relative location in each pattern (Fig. 7b), k will assume a constant value over the entire wafer. When the FPP is positioned equidistant from the edges of a rectangular test pattern (RTP), the solution furnished by Smits (12) may be employed to compute the correction factor. Figure 8 is a plot of k *vs.* $b/3s$ for the case of an in-line FPP, probe separation s, situated symmetrically within RTP's of length b and width a. The magnitude of k, for fixed values of the ratio $b/3s$, decreases rapidly as the aspect ratio b/a increases. Experimental points were obtained for

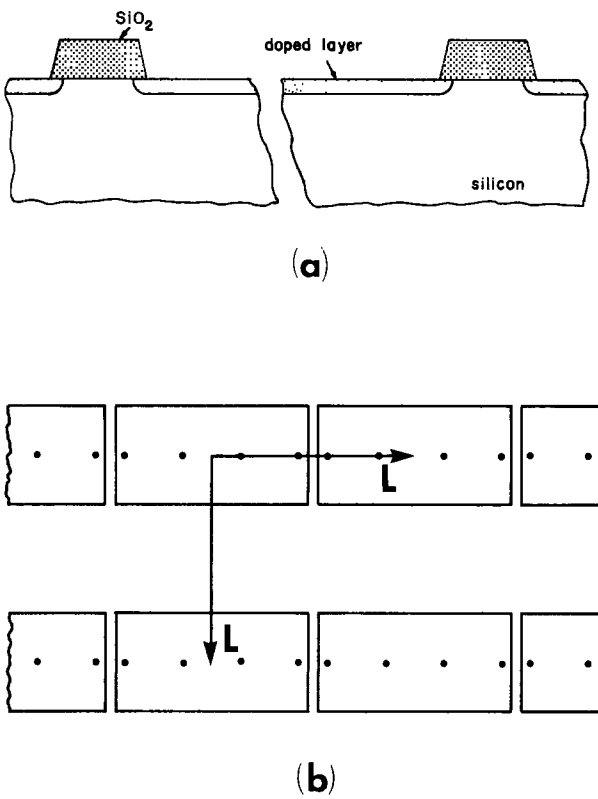


Fig. 7. Rectangular test patterns used in conjunction with an in-line FPP to eliminate variations in correction factor: (a) cross section through test pattern; (b) arrangement of patterns on a square grid (L = 222 mil for a 3 in. diameter wafer).

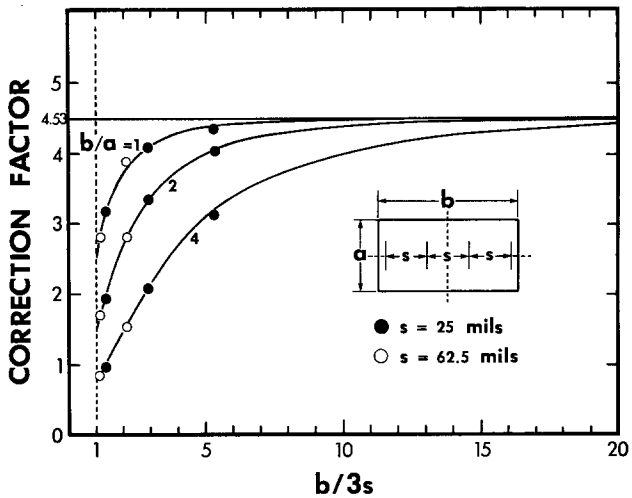


Fig. 8. Correction factor k *vs.* $b/3s$ for a FPP symmetrically positioned within a rectangular test pattern of length b and width a.

various size RTP's using FPP assemblies for which s = 25 and 62.5 mil.

The sensitivity of the FPP to small doping variations is illustrated in Fig. 9a which represents a typical pattern of variability obtained for a 3 in. diameter n-type silicon wafer implanted with boron in a mechanically scanning implantation system (1). (These data were obtained by employing an s = 62.5 mil FPP in conjunction with 220 × 110 mil^2 RTP's.) Figure 9b represents the pattern predicted on the basis of small changes in the linear velocity of the wafer as it traverses a stationary ion beam. This pattern, which is unique to the Ferris wheel mechanism employed for moving the wafers, corresponds extremely well to the experimental results of Fig. 9a. The irregularity in the contours of Fig. 9a is, as discussed above, a consequence of random error in the experimental sheet resistance data. The effect is not, however, significant enough to impair the interpretation of the resulting contour map.

The use of the FPP for evaluating the sheet resistance of junction isolated implanted layers has been discussed by Stephen (16) who identified the following sources of error when making such measurements: surface effects, junction leakage, geometrical factors, magnitude of the measuring current, probe loading, and ambient temperature. In practice, by employing commercially available "precision" probe assemblies and restricting the measurement to layers greater than 2000Å in thickness and less than 500 Ω/sq, one can achieve an absolute accuracy of ±1% and a $\sigma_e^*(\%) \leqq 0.5\%$. The primary source of error, under these circumstances, is associated with variation in the distances between adjacent probe needles due to mechanical tolerances of the probe assembly (17).

Van der Pauw resistor measurements.—The FPP cannot conveniently be used to evaluate a series of doping steps on the same test wafer, as would be desirable when examining the spatial variation of device parameters. Van der Pauw (7) has described a resistor geometry which can be fabricated simultaneously with active devices and should be insensitive to variations in both the photomask and the exposure and etching steps used to delineate the pattern. The sheet resistance of a van der Pauw resistor is determined from the relation

$$\rho_s = \frac{\pi}{\ln 2}\,\frac{R_a + R_c}{2}\,f(R_a/R_c) \qquad [10]$$

where, with reference to Fig. 10, $R_a = \Delta V_{23}/I_{14}$, $R_c = \Delta V_{43}/I_{12}$, and the function $f(R_a/R_c)$ satisfies the transcendental expression

$$\frac{R_a/R_c - 1}{R_a/R_c + 1} = \frac{\cosh^{-1}[(1/2)\exp(\ln 2/f)]}{\ln 2/f} \qquad [11]$$

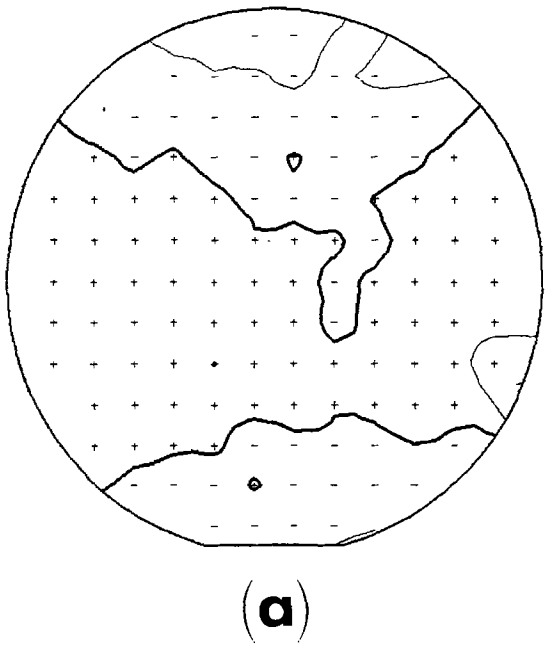


Fig. 9. Pattern of variation for a wafer implanted in a mechanically scanning system: (a) experimental results ($\sigma^*(\%) = 0.50\%$, $\bar{\rho}_S = 34.5$ Ω/sq; (b) predicted behavior ($\sigma^*(\%) = 0.35\%$).

A third current/voltage configuration, $R_b = \Delta V_{24}/I_{13} = R_a - R_c$, is ordinarily used for Hall effect measurements. For a symmetric pattern and symmetrically arranged contacts, one has that $R_a = R_c$ and consequently $f(R_a/R_c) = 1$.

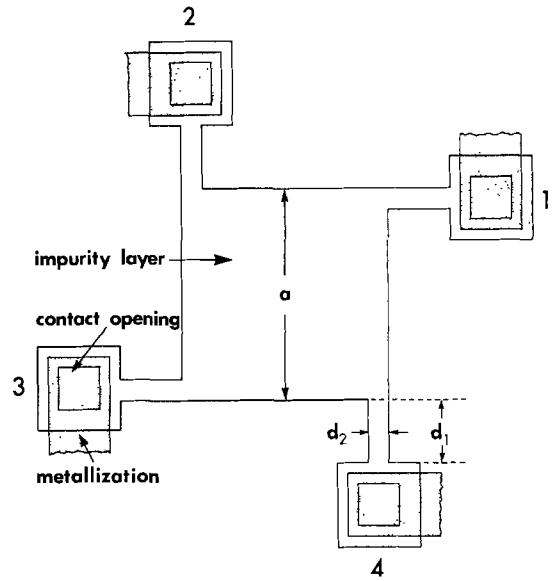


Fig. 10. Van der Pauw four-point resistor structure

Van der Pauw's analysis is based on the assumption of point contacts. In practice, however, one is obliged to make contact to the body of a van der Pauw resistor through arms of finite width. David (18) has determined the error associated with measuring the sheet resistance of a structure with orthogonal boundaries and finite-width contact arms. For the offset quadrate cross shown in Fig. 10, which is the geometry employed in the National Bureau of Standards process evaluation mask set (NBS-3) (19), Eq. [10] is correct to better than 0.1% as long as the requirement $d_1/a \geq d_2/a$ is fulfilled.

Comparison of FPP and van der Pauw measurements. —In order to compare directly FPP and van der Pauw measurements, the authors have employed a specialized test mask which permits both types of measurements to be made at each of the 118 standard test sites shown in Fig. 3a. A 212 × 50 mil² RTP, designed to accommodate a 62.5 mil FPP, and four different size van der Pauw resistors of the design shown in Fig. 10 are employed for this comparison. For each size van der Pauw resistor, three identical structures are clustered as close together as possible to facilitate a determination of random measurement error.

Table II summarizes the results of an evaluation of a 3 in. diameter boron-implanted (150 keV, 5×10^{14} cm^{-2}) n-type silicon wafer. The excellent agreement among values of ρ_S and $\sigma^*(\%)$, for structures varying in area over almost five orders of magnitude, is typical of the comparative behavior observed by the authors at impurity concentrations above ~10^{18} cm^{-3}. Figure 11 compares equivalue contour maps constructed from data for (a) the 10 × 10 μm² van der Pauw resistor, (b) the 100 × 100 μm² van der Pauw resistor, and (c) the 5400 × 1260 μm² = 212 × 50 mil² RTP. These maps, which convey essentially identical information about

Table II. Comparison of FPP and van der Pauw resistor† data for a boron-implanted n-type silicon wafer

Test pattern	a (μm)	b (μm)	$A = a \times b$ (μm)²	$\bar{\rho}_S$ (Ω/sq)	$\sigma^*(\%)$	$\sigma_e^*(\%)$ 1-config.	$\sigma_e^*(\%)$ 2-config.
vdP-1	10	10	1.0×10^2	168.91	1.55	0.832§	0.020§
vdP-2	35	35	1.2×10^3	167.99	1.48	0.292	0.046
vdP-3	100	100	1.0×10^4	168.95	1.47	0.267	0.021
vdP-4	500	500	2.5×10^5	168.70	1.45	0.078	0.057
RTP‡	1260	5400	6.8×10^6	167.62	1.56	0.057	—

† The van der Pauw geometry is shown in Fig 10. The arm length $d_1 = 30$ μm and the arm width $d_2 = 10$ μm for each of the four patterns.
‡ Data obtained using a 62.5-mil FPP.
§ Cf. Table III.

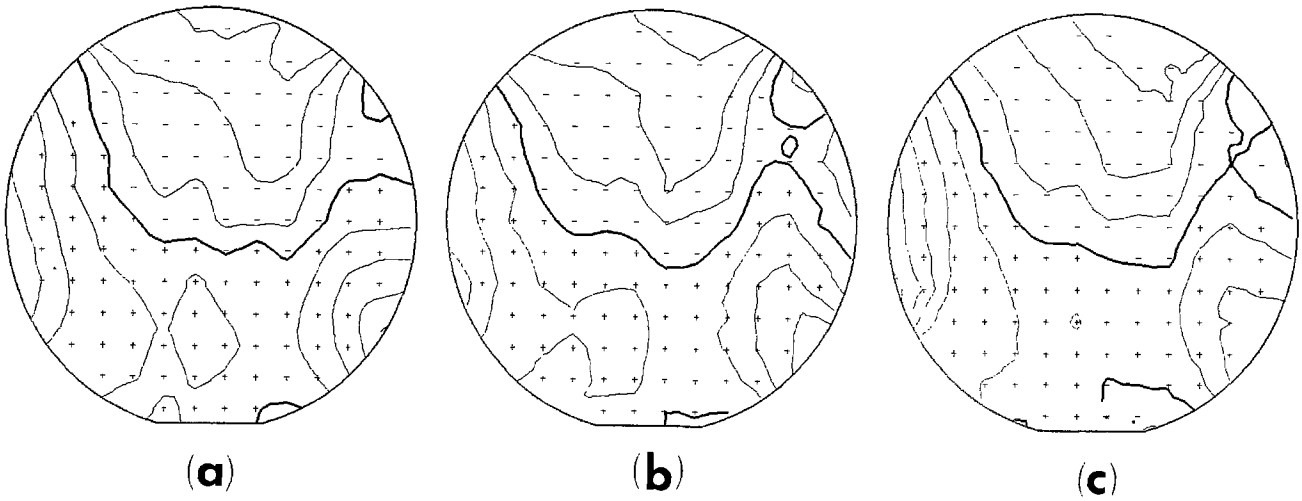


Fig. 11. Two-configuration equivalue contour maps for the boron-implanted wafer of Table II: (a) 10 × 10 μm^2 van der Pauw resistor; (b) 100 × 100 μm^2 van der Pauw resistor; (c) 5400 × 1260 μm^2 rectangular FPP test pattern.

the spatial variation of sheet resistance, demonstrate conclusively that the FPP and van der Pauw resistors may be used interchangeably. [Changes in the velocity of the wafer in a mechanically scanning implantation system employing track-mounted wafer carriers are responsible for the distinctive pattern (1).]

As discussed in the preceding section, random error plays an important role in determining the visual quality of equivalue contour maps. Table II provides results for $\sigma_e^*(\%)$ for the five different test structures. The van der Pauw resistor data were obtained by measuring the three "identical" structures for each of the four resistor sizes at nine different wafer locations. The FPP data were obtained by performing five independent measurements on each of nine different RTP's.[4] It is clear that the use of two independent current/voltage configurations leads to a dramatic reduction in $\sigma_e^*(\%)$ for each size van der Pauw resistor but particularly for the 10 × 10 μm^2 resistor, for which the one-configuration value is 0.832% and the two-configuration value is 0.020%. It is noteworthy that even the 500 × 500 μm^2 van der Pauw resistor is influenced by geometric variations to a small extent as evidenced by the one-configuration value of 0.078% *vs.* the two-configuration value of 0.057%. The value of 0.057% for the FPP measurements compares favorably with the two-configuration values for the van der Pauw resistors.

The importance of using two-configuration data for small van der Pauw resistors may be appreciated by comparing the maps of Fig. 12, representing $4.532R_a$ and $4.532R_c$ data for the 10 × 10 μm^2 resistor, with the map of Fig. 11a, which was constructed by combining these data in accordance with Eq. [10]. The contour maps of Fig. 12 exhibit the influence of random error as irregular contours and isolated features, just as occurs in the measurement error simulations of Fig. 5c and 5d.

Table III summarizes the measurement error data used to compute $\sigma_e^*(\%)$ for the 10 × 10 μm^2 van der Pauw resistor. The large variation among the one-configuration values $(\rho_s)_{i1}$, $(\rho_s)_{i2}$, and $(\rho_s)_{i3}$ is attributed to fluctuations in photolithography and etching which cause the dimensions of nominally identical structures to vary randomly. The variability which still remains in the two-configuration data is associated, at least for the 10 × 10 μm^2 resistor, with the finite resolution of the digital voltmeter and stability of the current supply. This conclusion is based on the fact that, irrespective of resistor size, repeated measurements of the same van der Pauw resistor lead to values of $\sigma_e^*(\%)$ in the range 0.015-0.020% for both the one- and two-configuration cases. Additional sources of variability are attributed to local gradients in sheet resistance, junction leakage current, and changes in ambient temperature. Some of these effects may be influencing σ_e^* for the larger van der Pauw resistors, particularly local resistivity gradients, since these would be expected to become more important as the center-to-center spacing between patterns increases.

Conclusion

The results of this investigation demonstrate that both the conventional FPP and van der Pauw resistors of microelectronic dimensions are suitable for use with automated wafer probing equipment for characterizing the doping uniformity of semiconductor wafers. Both vehicles are capable of providing sheet resistance data sufficiently free of random measurement error to

[4] The FPP was displaced in 2 mil increments parallel to the 212 mil side of the RTP, with the third repetition corresponding to the symmetry position. The geometric error inherent in this choice of probe locations is not a significant contribution to the measured value of σ_e^*.

Table III. An example of the determination of measurement error for resistor vdP-1 of Table II. According to Eq. [7], $\sigma_e^*(\%) = 0.832\%$ for the one-configuration case and 0.020% for the two-configuration case.

Probe location†			1-configuration					2-configuration				
X (mils)	Y (mils)	i	$(\overline{\rho_s})_1$ (Ω/sq)	$(\sigma_e^*)_1$ (%)	$(\rho_s)_{i1}$ (Ω/sq)	$(\rho_s)_{i2}$ (Ω/sq)	$(\rho_s)_{i3}$ (Ω/sq)	$(\overline{\rho_s})_1$ (Ω/sq)	$(\sigma_e^*)_1$ (%)	$(\rho_s)_{i1}$ (Ω/sq)	$(\rho_s)_{i2}$ (Ω/sq)	$(\rho_s)_{i3}$ (Ω/sq)
−222	222	1	172.15	0.763	170.94	173.55	171.96	171.93	0.022	171.96	171.90	171.95
0	222	2	172.82	0.619	173.32	173.55	171.59	171.09	0.019	171.11	171.08	171.08
222	222	3	170.09	1.069	168.45	172.05	169.78	170.01	0.027	170.00	169.97	170.05
−222	0	4	172.51	0.453	173.18	171.65	172.70	171.81	0.015	171.84	171.79	171.80
0	0	5	170.88	0.540	171.90	170.60	170.12	171.46	0.000	171.45	171.46	171.46
222	0	6	170.87	0.901	170.66	172.50	169.44	170.72	0.014	170.71	170.71	170.74
−222	−222	7	169.83	1.272	170.18	171.79	167.51	171.19	0.032	170.24	171.12	171.20
0	−222	8	170.50	0.653	170.88	169.24	171.37	171.03	0.000	171.03	171.01	171.05
222	−222	9	169.87	0.898	171.00	170.49	168.14	170.69	0.022	170.71	170.64	170.70

† The location $X = 0$, $Y = 0$ represents the center of the wafer.

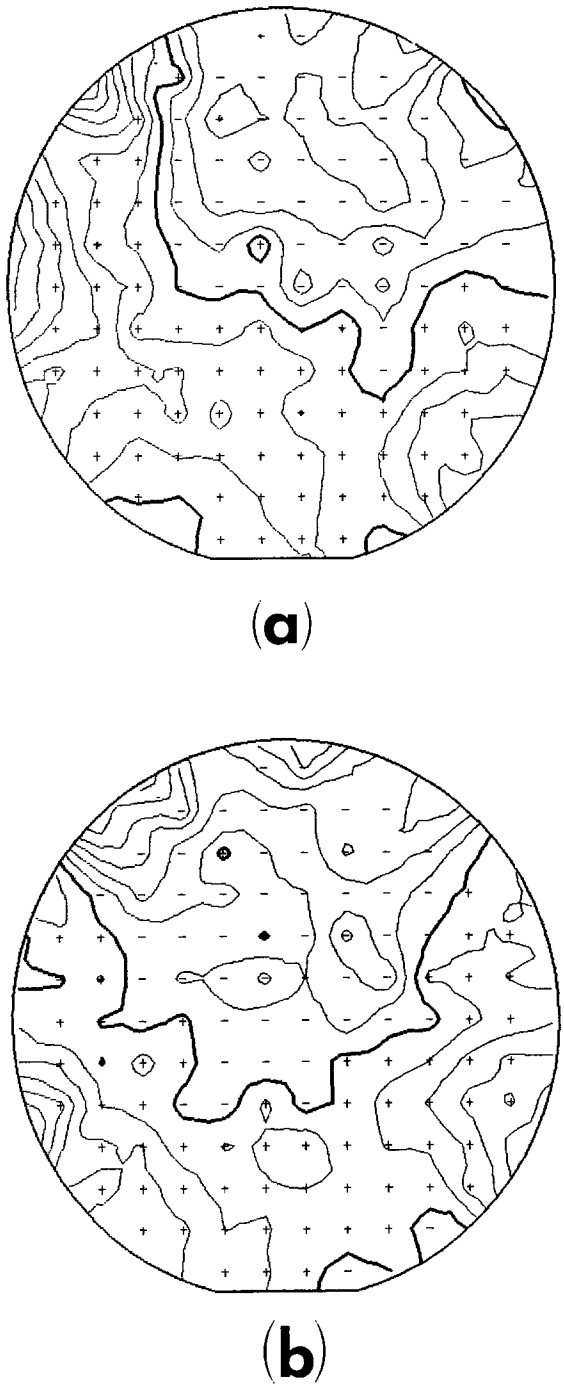


Fig. 12. One-configuration equivalue contour maps for the 10 × 10 μm^2 van der Pauw resistor corresponding to the two-configuration map of Fig. 11a.

justify the use of high resolution two-dimensional graphic display techniques.

The procedure employed for assessing the random error associated with four-point resistance measurements may be applied to any device or process parameter for which it is possible to carry out a series of independent measurements at various locations on the semiconductor wafer. By evaluating the relative measurement error in this way, one may predict the extent to which graphic display techniques will be an effective means of exhibiting spatial variations.

Acknowledgments

The authors wish to acnowledge the able assistance of Mr. D. Mar in the areas of mask design and wafer characterization. Technical discussions with Mr. J. D. Reimer, Dr. J. T. Kerr, Dr. J. A. Marley, Dr. S. W. Mylroie, Dr. H. J. Sigg, and Dr. M. G. Buehler (National Bureau of Standards) have been extremely valuable both in carrying out this investigation and preparing the results for presentation.

Manuscript submitted Oct. 4, 1976; revised manuscript received Nov. 6, 1976.

Any discussion of this paper will appear in a Discussion Section to be published in the December 1977 JOURNAL. All discussions for the December 1977 Discussion Section should be submitted by Aug. 1, 1977.

Publication costs of this article were assisted by Signetics Corporation.

REFERENCES

1. D. S. Perloff, F. E. Wahl, and J. T. Kerr, in Proceedings of 7th International Conference on Electron and Ion Beam Science and Technology, Washington, D.C., 1976.
2. G. Kelson, H. H. Stellrecht, and D. S. Perloff, *IEEE J. Solid-State Circuits*, **sc-8**, 396 (1973).
3. P. A. Crossley and W. E. Ham, *J. Electron. Mater.*, **2**, 465 (1973).
4. D. S. Perloff, F. E. Wahl, and J. D. Reimer, *Solid State Technol.*, **20**, 31 (Feb. 1977).
5. L. B. Valdes, *Proc. Inst. Radio Engrs.*, **42**, 420 (1954).
6. D. S. Perloff, *This Journal*, **123**, 1745 (1976).
7. L. J. van der Pauw, *Philips Res. Rep.*, **13**, 1 (1958).
8. M. G. Buehler and W. R. Thurber, *IEEE Trans. Electron Devices*, **ed-23**, 968 (1976).
9. G. Wolfe, *Circuits Manufacturing*, **16**, 48 (April 1976).
10. W. E. Ham, *Nat. Bur. Stand. Spec. Publ. 400-15*, pp. 25-34 (January 1976).
11. Manufactured by A. M. Fell Ltd., London, England.
12. F. M. Smits, *Bell Syst. Tech. J.*, **37**, 711 (1958).
13. R. Rymaszewski, *J. Sci. Instrum.*, **2**, 170 (1969).
14. M. A. Logan, *Bell Syst. Tech. J.*, **40**, 885 (1961).
15. L. M. Swartzendruber, *Solid-State Electron.*, **7**, 413 (1964).
16. G. Dearnaley, J. H. Freeman, R. S. Nelson, and J. Stephen, "Ion Implantation," North Holland, Amsterdam (1973).
17. F. E. Wahl and D. S. Perloff, Unpublished results.
18. J. M. David, *Nat. Bur. Stand. Spec. Publ. 400-19*, p. 44 (April 1976).
19. M. G. Buehler, *Nat. Bur. Stand. Spec. Publ. 400-15*, pp. 35-46 (January 1976).

Boron Autodoping during Silane Epitaxy

Paul H. Langer*

Bell Laboratories, Allentown, Pennsylvania 18103

and Joseph I. Goldstein

Lehigh University, Bethlehem, Pennsylvania 18015

ABSTRACT

In order to calculate the redistribution of boron in silicon by both diffusion and autodoping during epitaxial growth, certain materials parameters must be known as a function of temperature. The parameters are the diffusion coefficient of boron, the evaporation coefficient of boron from silicon, and the silicon evaporation rate in a hydrogen ambient. The value of the diffusion coefficient of boron is already well known while the values for the other two parameters have not been determined over the temperature range usually used for epitaxial growth. The evaporation coefficient of boron in silicon in a hydrogen ambient was experimentally determined to be $h = 1.674 \times 10^7 e^{-2.48/kT}$ where h is in microns per minute, the energy is expressed in electron volts, and temperature is in degrees Kelvin. The evaporation rate of silicon in a hydrogen ambient was measured as 0.013 ± 0.003 microns/min in a hydrogen ambient. These results were obtained in the temperature range from 1190° to 1380°C. These results allowed the accurate prediction of boron back surface "autodoping" effects during epitaxial growth using a numerical solution to Fick's second law. Radial as well as in-depth concentration *vs.* distance plots were experimentally determined illustrating boron autodoping for both lightly and heavily doped substrates. Reduction of boron autodoping was obtained by the addition of HCl to the ambient during epitaxial growth, permitting the growth of lightly doped layers on heavily boron-doped substrates.

In order to calculate the impurity redistribution during epitaxial growth or other high temperature semiconductor device processing steps, accurate values of the diffusion coefficient, segregation coefficient, and evaporation coefficient must be known for each of the dopant elements in silicon. Any time a lightly doped region is exposed to a heavily doped region transport of dopant will occur both through the solid and gaseous phases. The transport of dopant from one wafer to another or from one region on a wafer to another region on the same wafer has been known as "autodoping." The presence of excess dopant via autodoping in regions where it is unwanted leads to the inability to fabricate certain types of transistors and integrated circuit structures. The epitaxial growth process has long been the principal processing step in which autodoping may occur. Especially in the fabrication of integrated circuits, autodoping must be suppressed or at least controlled.

The purpose of this paper is to first obtain the physical constants necessary to characterize boron autodoping. With these constants available, predictions of the boron distribution during epitaxial growth are made. These predictions are then compared with experiments as an over-all test of the mathematical model being employed.

Background: Epitaxial Growth

The existence of dopant in an epitaxial layer over and above that dopant which was transported by solid-state diffusion from the substrate has been a subject of interest from the earliest work on epitaxial deposition. Thomas *et al.* (1) and Grossman (2) explain the existence of this extra dopant by a mechanism which involves transfer of dopant from the front surface of the wafer, mixing of this dopant with the gas phase, and reincorporation of some fraction of the dopant in the gas phase back into the wafer. Thomas worked exclusively with arsenic-doped substrates. Since solid-state diffusion was ignored in this model, application near the substrate-layer interface was difficult. Another approach to the autodoping problem was developed separately by Rice (3) and Grove *et al.* (4). They proposed that solid-state diffusion alone was the only mechanism for dopant transport from the substrate into the layer. They neglected the effects of the ambient gas phase. Abe *et al.* (5), studying arsenic autodoping with the aid of a numerical model, also ignored the ambient gas phase. The third approach to the explanation of the source of the unwanted dopant was put forward by Joyce *et al.* (6), Shepherd (7), and Skelly (8). These authors showed that dopant from the back of the wafer could also be a source of added impurity to the growing layer. Langer and Goldstein (9) developed a mathematical model of the process that essentially combines all three effects. Their model was solved numerically using a program called "CASPER" (9) (computer aided semiconductor processing and epitaxial redistribution). They proposed that while all of the autodoping mechanisms may be operative simultaneously their relative importance varies with the dopant species under consideration.

Using the evaporation coefficient of boron estimated by Grove (4), predictions were made for layer autodoping. It was calculated that, while no measurable effect could be detected in the transition region between the substrate and the epitaxial layer, a very sizable effect on the mean layer doping would occur once this transition region was past. Grove had not observed this predicted effect.

Theory

A model developed by Langer and Goldstein (9) solved Fick's second law using the implicit Crank-Nicolson method (CNM)

$$\frac{\partial C(x,t)}{\partial t} = D \frac{\partial^2 C(x,t)}{\partial x^2} \qquad [1]$$

in one dimension. They assumed that the diffusivity, D, is independent of the concentration $C(x,t)$, where x and t are the spatial and time variables, respectively. The boundary conditions at the front surface of the wafer are as follows

* Electrochemical Society Active Member.

Key words: silicon, semiconductor, deposition, autodoping.

$$D\frac{\partial C(i,t)}{\partial x} = h[C(i,t) - k_e C_m(t)] + v[C(i,t) - k_g C_m(t)] - fh[C(b,t) - k_e C_m(t)] \quad [2]$$

where i is the instantaneous position of the front gas-solid interface, h is the evaporation coefficient, $C_m(t)$ is the mean gas phase concentration, f is the fraction of back or side area acting as an autodoping source, k_e is the effective segregation coefficient between the gas and the solid, k_g is an arbitrary constant that will depend upon the gas velocity distribution in the boundary layer and relates the mean gas phase concentration to the concentration near the interface, v is the velocity of movement of the interface, while $C(b,t)$ represents the concentration at the back or side of the wafer.

At the back surface the boundary condition is

$$D\frac{\partial C(b,t)}{\partial x} = h[C(b,t) - k_e C_m(t)] \quad [3]$$

Figure 1 schematically shows the various sources of dopant in an epitaxial reactor. Autodoping during the growth cycle in an epitaxial reactor occurs principally from three major sources. The sources may vary in their contribution of dopant at any one point in the reactor. The three sources are: (*i*) the edges and back of the wafer, (*ii*) dopant from edges and backs of other wafers either down or upstream from the wafer of interest, and (*iii*) dopant from the susceptor coating.

In order to apply Eq. [1] along with the boundary conditions to an autodoping problem, the evaporation coefficient, h, of boron from silicon must be determined. In order to determine the evaporation coefficient, the evaporation rate of silicon in a hydrogen ambient must first be ascertained.

Experimental

Evaporation experiments.—Evaporation of silicon.— Figure 2 is a schematic of the reactor system that was used to perform the high temperature cycling for the evaporation experiments. This reactor was of circular cross section and was water cooled. The inner tube was 60 mm ID fused quartz. Power was supplied using a 450 kHz radio-frequency generator. The susceptor consisted of a graphite slab 25 cm long by 4.8 cm wide. The slab was made from General Electric pyrolytic infiltrated graphite. The susceptor was used uncoated after a 1 hr bakeout at 1450°C in hydrogen. The susceptor was supported in the reactor on a fused quartz sled. The specimens used were (111) oriented silicon wafers, 1.5 in. in diameter. Two wafers per run were placed in the reactor shown in Fig. 2.

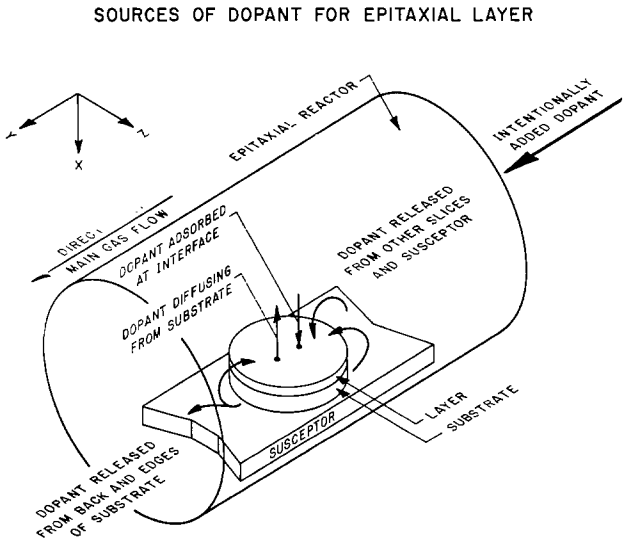


Fig. 1. Schematic representation of an epitaxial reactor showing sources of dopant.

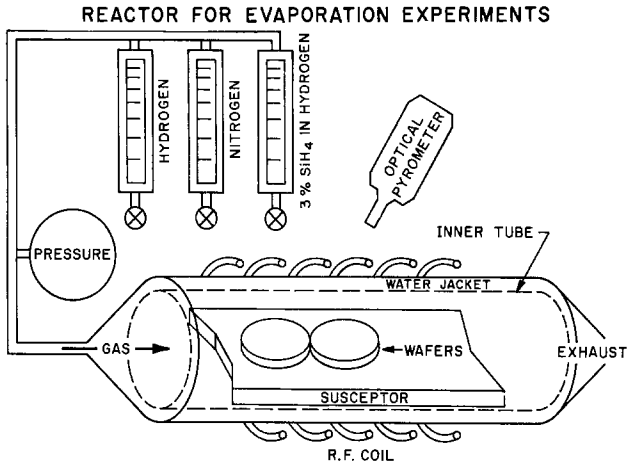


Fig. 2. Schematic of epitaxial reactor system

The standard cycle consisted of the following: 10 min nitrogen, 10 min hydrogen, raise power and stabilize (10 min), 1 hr at temperature in 20 liters/min of hydrogen, lower power, 10 min hydrogen, 20 min in nitrogen. Precautions were taken to prevent moisture from condensing inside the tube when it was opened for loading or unloading of wafers. No cooling water was run through the system when the reactor was open. The flush schedule was arranged so that at least 300 volume changes of dry gas (~1 ppm water) were passed through the reactor before the temperature was raised. Even with these precautions, pitting of the silicon surface was observed when the wafers were heated above 1050°C. Therefore silane was introduced during the initial nitrogen flush cycle to getter any residual water that may have been condensed on the reactor walls or the susceptor. This technique proved completely successful in eliminating the pitting of the silicon surface.

All evaporation samples were held at temperature for 1 hr. The temperature was recorded using a Leeds and Northrup (L&N) automatic optical pyrometer (Model No. 8641) which had been calibrated by L&N at five temperatures against a high precision automatic optical pyrometer traceable to the National Bureau of Standards. The adsorption corrections for the two thicknesses of fused quartz, the cooling water, and the plexiglass safety shield were determined experimentally in the following manner. A graphite block with two holes in it was placed in a resistance-heated diffusion furnace. In one hole a Pt-Pt-10%Rh thermocouple was placed and the pyrometer was sighted on the interior of the second hole. The block was brought to temperature and the fused quartz and plexiglass were placed between the heated block and the pyrometer while the optical temperature was determined. The quartz and plexiglass were withdrawn and the optical temperature was again determined. This procedure was repeated at temperatures from 900° to 1350°C. It was found that a constant adsorption correction of 25°C was sufficient over the experimental range of temperatures used for the evaporation and growth procedures. Emissivity corrections were made using Allen's (10) values for a polished silicon surface in vacuum.

To determine the evaporation rate of silicon in a hydrogen ambient the following procedure was used. A lightly boron-doped wafer [~10 parts per billion atomic (ppba)] with 7000A of thermally grown oxide was etched in a buffered hydrofluoric acid solution to remove the oxide film covering one-half of the front surface. The rest of the oxide was protected by Kodak metal etch resist during the etch. The photoresist was then removed and the wafers were cleaned using a mixture of nitric and sulfuric acids followed by a rinse in deionized water. The wafers were then scrubbed using a mild detergent, and rinsed again and spun dry.

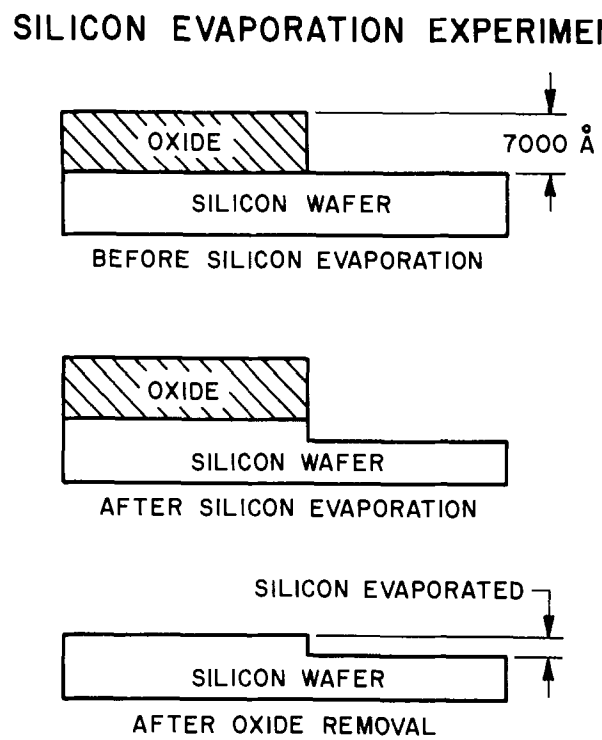


Fig. 3. Silicon evaporation experiment

Following the drying, the wafers were heated in the reactor for a period of 1 hr.

After the high temperature cycle, the remaining oxide was completely removed by a buffered HF etch. The step height was then measured between the area protected by the oxide during the high temperature treatment and the area that had been exposed to the ambient (20 liters/min hydrogen stream). This height measurement was performed using a Talysurf profilometer.[1] Figure 3 schematically shows the evaporated and protected parts of the silicon surface and exactly what quantities were measured in the determination of the evaporation rate. A control was run with no thermal treatment to check for the attack of the buffered hydrofluoric acid solution on the silicon wafer surface. Etching of the silicon by the buffered solution was 0.05 μm or less. Therefore the measured step height was due entirely to the evaporation of silicon. It was assumed that no reaction occurred under the oxide since the thickness of the oxide did not change during the thermal treatment.

Evaporation of boron.—Once the evaporation rate of the silicon had been determined, the next step was the determination of the boron evaporation coefficient. This was acomplished by measuring the concentration distribution of the boron in the silicon wafer after evaporation had been allowed to occur. This boron distribution was then fitted to calculated boron concentration distributions in which the only variable was the evaporation coefficient of the boron. The procedure that was used to determine the actual boron concentration distribution in the wafer is given below.

The wafers used to determine the evaporation coefficient of boron had to be doped enough that the surface concentration after evaporation was still above the background of the reactor. A 10 min deposition run was made at a rate of 0.4 μm/min to determine the reactor background concentration. The resultant resistivity measured by four-point probe on the epitaxial structure showed the system background concentration to be 2 ppba n-type. Therefore, wafers doped to 4 ppma with boron were chosen for the evaporation study. These wafers were grown by the Czochralski method and were oriented in the (111) direction. The wafers

[1] Commercial diffusion height gauge.

RADYNE REACTOR
WAFER POSITION FOR BORON AUTODOPING EXPERIMENTS

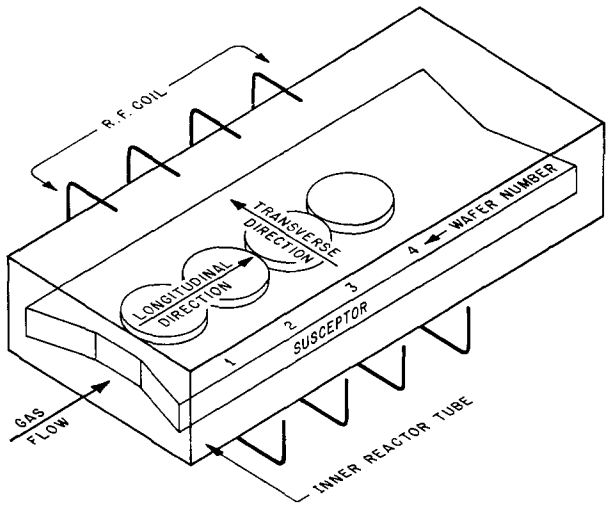


Fig. 4. Radyne reactor

were sawed, chemically etched, and then polished with Syton.[2] The cleaned wafers were subjected to 1 hr at temperature in a 20 liters/min hydrogen ambient. The range of temperature used was 1190°-1380°C. After the evaporation heat-treatment, the resultant wafers were angle lapped at a nominal 0.5° angle using Linde A abrasive on a glass plate, followed by a quick polish with Syton abrasive on a plexiglass plate. The prepared samples were measured on a Solid State Measurements ASR-100 spreading resistance probe test set to obtain plots of spreading resistance *vs.* depth from the wafer top surface. This data was then fed into a computer program containing the empirical calibration data and was converted to uncorrected resistivity. The Schumann (11) multilayer correction modified by Morris (12) was applied to the uncorrected resistivity before conversion to carrier concentration was made. Resistivity values were converted to concentration using Lee's polynomial fit (13).

Boron autodoping experiments.—A second epitaxial reactor was used for the boron "back" surface autodoping studies. It was a commercial Radyne unit shown schematically in Fig. 4. It differed from the first system in two major respects: the cross section was rectangular (38 × 76 mm), and the gas flow used was 108 liters/min (76 cm/sec). The susceptor was 9.5 mm thick and tilted at an angle of 1.5° from the horizontal. These two factors result in greater uniformity of deposition rate in both the longitudinal direction (direction of the gas flow), and in the transverse direction (perpendicular to the gas flow) as shown by Takahashi (14). The susceptor used in this case was silicon-carbide-coated graphite with a layer of undoped silicon covering all surfaces. Two consecutive runs were made of 10 min each. Arsine was introduced during the deposition cycle to achieve a n-type doping level in the growing epitaxial layer of about 10 ppba. Both runs were made with four 32 mm diameter wafers placed near the center of the susceptor as shown schematically in Fig. 5. A deposition rate of 0.92 μm/min was achieved in both runs at a temperature of 1120°C. No preheat, HCl etch, or postepitaxial growth heat cycle was employed. The wafers in the first run were all lightly doped p-type (100 ppba). In the second run the first and third wafers were also lightly doped, while the second and fourth wafers (position relative to gas inlet end) were heavily doped with boron to about 200 ppma. It was these heavily doped wafers that would become the autodoping source. After the layer was

[2] Syton is a commercially available silicon polishing compound manufactured by the Monsanto Chemical Company.

deposited, all wafers were measured at 25 μm intervals across the surface both in the direction of the gas flow and in a direction 90° to the gas flow. All measurements were made using an automatic spreading resistance probe (20) with on-line correction capabilities. Selected wafers were also profiled in depth for concentration.

Results and Discussion

Boron evaporation.—The evaporation coefficient of boron from silicon was determined over the temperature range from 1190° to 1380°C. The measured evaporation coefficient enables one to calculate the movement of boron across gas-solid interfaces so that doping and autodoping during epitaxial growth may be accurately predicted. The folowing equation derived by Grove (4) gives the value of the evaporation coefficient, h, at a boundary ($x = i$), in terms of the concentration at the boundary $C(i,t)$, the flux of dopant, $D\frac{\partial C(i,t)}{\partial x}$, and the boundary velocity, v

$$h = \frac{D}{C(i,t)}\frac{\partial C(i,t)}{\partial x} - v \qquad [4]$$

Equation [4] assumes that the gas phase concentration of boron is negligible compared to the value in the solid, $C(i,t)$. Therefore, the evaporation coefficient can be measured if the velocity of movement of the boundary, v, and the concentration gradient as a function of distance into the solid is determined. During the evaporation experiments, v is simply the evaporation rate of the silicon. If h is large compared to v, v may be neglected. For some elements such as antimony, arsenic, and phosphorus, this is the case. However the evaporation rate of silicon was measured experimentally and found to be significant, in the determination of the boron evaporation coefficient. The evaporation rate of silicon was determined to be 0.013 $\pm$ 0.003 μm/min over the temperature range from 1190° to 1380°C. This measured value is much smaller than the value of 0.023 $\pm$ 0.005 μm/min determined by Tung (15). Tung observed gross nonuniformity of the evaporation effect and his samples may have experienced etching by residual water vapor in the system. This form of attack had been eliminated in this work by the addition of 3% silane to the room temperature nitrogen flush.

The measured boron concentration was normalized to a concentration determined deep into the wafer ($\sim 3\sqrt{Dt}$), where the concentration gradient was almost zero. The depth was normalized ($x/2\sqrt{Dt}$) using the published diffusivity of boron (16). This normalization was performed so that comparison between experimental and calculated results for the concentration *vs.* depth distribution of boron could be easily accomplished in order to graphically determine the boron evaporation coefficient. The rate of silicon evaporation was also normalized using the diffusivity of boron, D_B, in the following manner

$$v_n = \frac{v}{\sqrt{D_B/t}} \qquad [5]$$

Solutions of concentration *vs.* distance were then obtained to Fick's second law for various assumed values of the normalized evaporation coefficient, h_n, where

$$h_n = \frac{h}{\sqrt{d_B/t}} \qquad [6]$$

These normalized solutions were then plotted with respect to the experimental data that had also been normalized. When a graphical fit was obtained between calculated and experimental concentrations, a value of h_n was determined from the closest curves. The calculated and normalized concentration *vs.* depth values for different values of the evaporation coefficient are plotted in Fig. 5 as solid lines at 1263°C (real). The solid circles (Fig. 5) are the experimental data. The experimental data fit the calculated curves quite well. The normalized values of h_n were then converted to evaporation coefficients by mutliplying by $\sqrt{D/t}$, and these results are summarized in Table I, over the temperature range from 1205° to 1382°C.

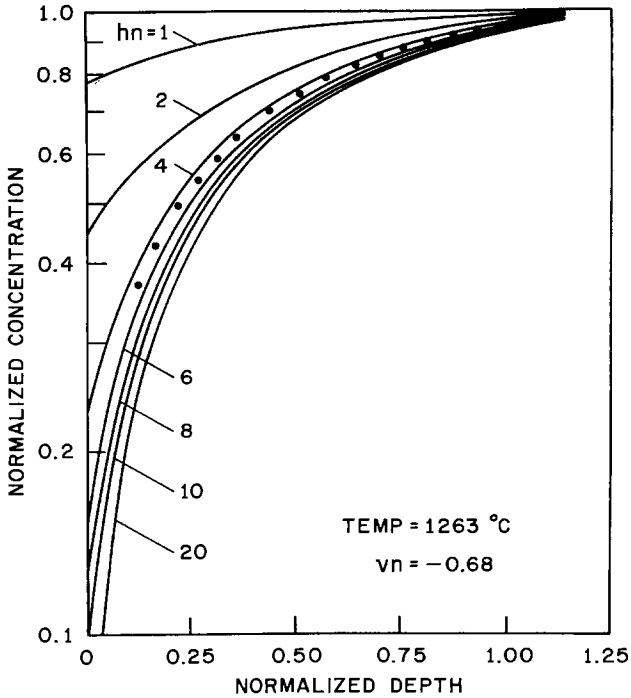


Fig. 5. Experimental values of normalized concentration *vs.* depth plotted along with analytical solution (solid line). Time: 1 hr, temperature: 1263°C, normalized silicon etch rate: —0.7 μm/min, dopant: boron.

The experimentally determined values of h are plotted against the reciprocal of the temperature in Fig. 6. A least square first order polynomial was fit to an Arrhenius type of equation to produce

$$h = 1.674 \times 10^7 e^{-2.48/kT} \qquad [7]$$

where h is given in units of microns per minute, the energy is in electron volts, the temperature in degrees Kelvin, and the value of k used is 8.62×10^{-5} eV/°K.

Values of $h_n > 20$ cannot be determined by the above technique. This is not a serious drawback since $h_n > 20$ is very close to the diffusion-limited case (all dopant reaching the surface by diffusion evaporates). Very little difference can be seen in the calculated concentration distributions for $h_n = 20$ and $h_n = \infty$.

Boron autodoping.—To completely test the numerical model, the contribution to layer doping from dopant escaping from the back and edges of the wafer was calculated and is shown in Fig. 7. The numerical model predicts that when a heavily doped boron substrate (200 ppma) is used, a level of about 120 ppba is predicted for the epitaxial layer. A major difficulty arises when trying to simulate back surface (back and sides) autodoping, *i.e.*, one does not know what fraction of

Table I. Boron evaporation data

Temp (°C)	Run/ wafer	$\sqrt{D/t}$	$-V_n$	h_n	h (μm/min)
1188	23D	0.011	1.15	4.4	0.048
1206	29U	0.013	1.05	5.0	0.065
1246	31D	0.025	0.80	5.0	0.095
1263	31U	0.110	0.68	5.0	0.110
1305	30D	0.034	0.43	5.0	0.170
1322	30U	0.036	0.32	5.1	0.184
1365	32D	0.050	0.05	10.0	0.500
1382	32U	0.057	0	10.0	0.570

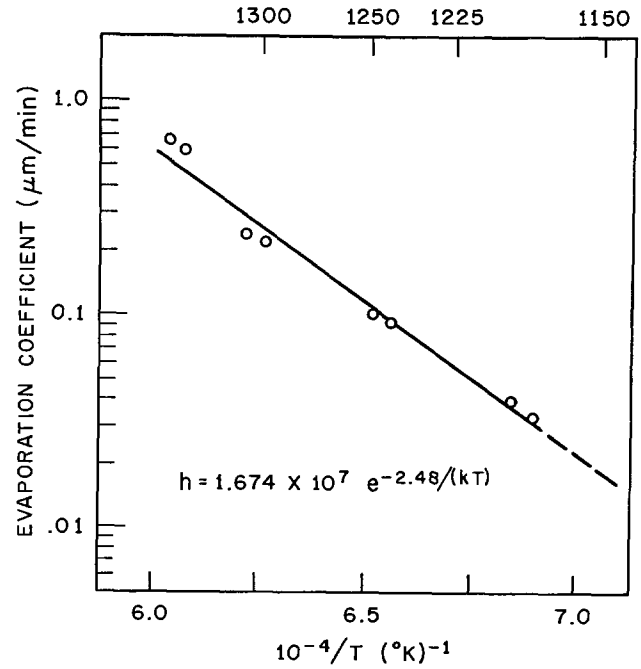


Fig. 6. Experimentally determined boron evaporation coefficient vs. reciprocal of temperature in degrees Kelvin.

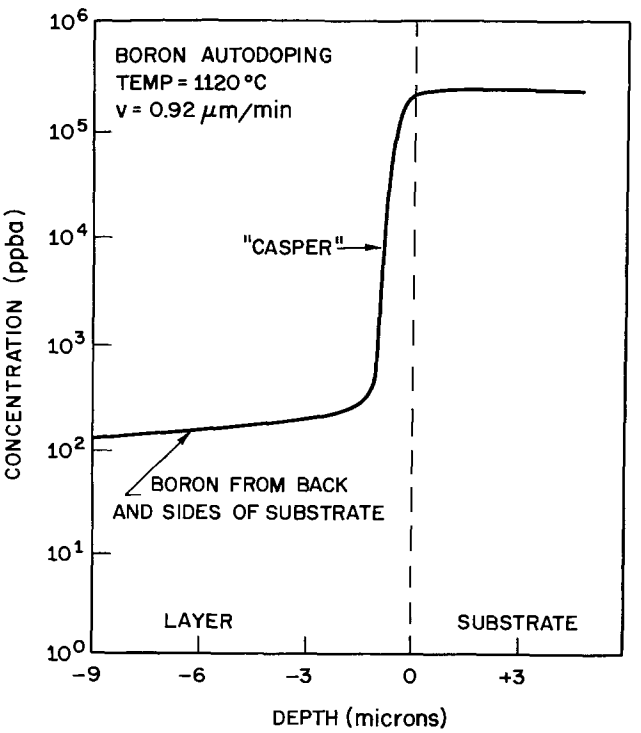


Fig. 7. Plot of concentration vs. depth or the autodoping contribution from a heavily doped boron substrate. Time: 10 min, temperature: 1120°C, growth rate: 0.92 μm/min, silicon source: silane.

the back surface (effective area) of the wafer is contributing dopant to the gas stream. This fraction has been estimated by other workers studying arsenic as between 0.9 (8) and 4% (7). The smaller value of effective area (8) represents work done using silane in a single wafer reactor at 1050°C. Since only one wafer was present, it was impossible to assess the results of the evaporated dopant on other wafers in the system. The authors also used a rather small total gas flow, *i.e.*, 2 liters/min. The larger value of effective area (7) represents the results of multiwafer system using silicon tetrachloride at 1200°C. Both heavily and lightly doped substrates were present in the system. According to the method of Shepherd (7), the effective source area for back surface autodoping would increase as the number of wafers in the system increased. All of the Shepherd data were taken at the center of the wafers.

Two factors had been neglected by the previous authors in their treatment of back surface autodoping. The first factor is that dopant released from the sides of the wafer must also be considered as a potential autodoping source, since this side area represents 2-4% of the wafer-to-surface area for normal semiconductor wafers. The second factor is the size of the source of the autodoping species (edges and back of the wafer) relative to the size of the sink for this dopant (front surface of the wafer). This size difference results in a decrease in transferred dopant as one moves further from the source. This decrease in dopant can result in a large radial concentration gradient if the intentional doping level is small. If diffusion was the only transport mechanism in the gas phase adjacent to the wafer, then the radial concentration profile (from the center of a given wafer out in any direction) of transferred dopant would be the same in any direction relative to the gas flow. If other dopant transport mechanisms are present, dopant from upstream wafers would affect the ambient gas phase concentration and appear to give effects similar to intentionally added dopant with the effect increasing in the downstream direction.

To assess the validity of the back autodoping model using the experimentally determined value of the evaporation coefficient of boron, consecutive epitaxial runs were made. The first run (control run) contained only lightly doped wafers (0.1 ppma). The first and third wafers in the second run were also lightly doped while the second and fourth wafers were heavily doped with boron to a level of about 200 ppma. The surface concentration results across all wafers in the direction of the gas flow for the first run (all lightly doped substrates) are plotted in Fig. 8. The results in Fig. 8 were obtained by spreading resistance measurements from the upstream (inlet) edge of wafer No. 1, going in the direction of the gas flow. to the downstream edge of wafer No. 4 (exit end of reactor). Data were taken

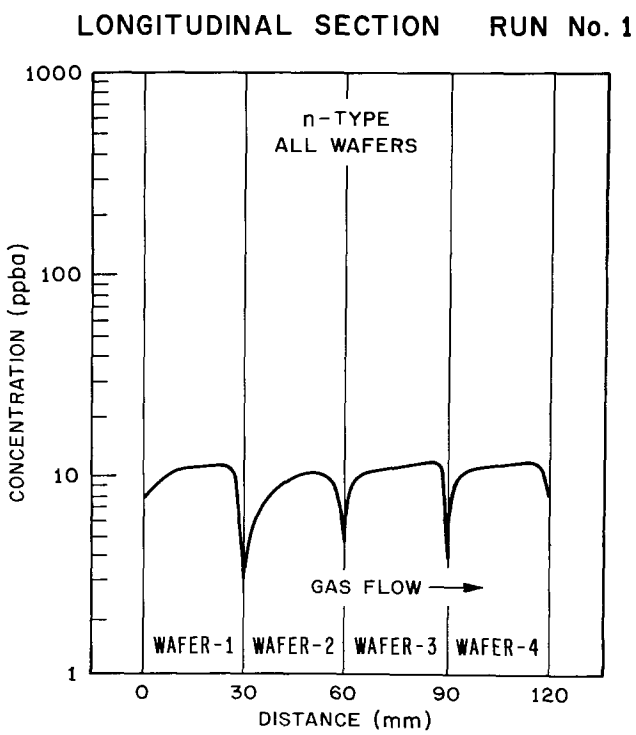


Fig. 8. Composite plot over all four wafers of surface concentration vs. distance of first epitaxial deposition run. All substrates lightly doped. Temperature: 1120°C, time: 10 min, growth rate: 0.92 μm/min, dopant: arsine, silicon source: silane.

every 25 μm at the surface of the 9.2 μm thick epitaxial layer. For this section longitudinal or axial will mean in the direction of the gas flow (inlet to outlet), while transverse will refer to data obtained perpendicular to the gas flow across the center of a given wafer. The concentration results displayed in Fig. 8 for run No. 1 show a level of about 10-12 ppba, n-type, with a small rise in the dopant level from the leading edge of each wafer. This decrease in concentration at the edges of the wafers may be caused by boron autodoping from the lightly doped substrates or contamination from the susceptor. Figure 9 is a transverse surface section taken across the center of the third wafer, and shows about a 20% difference in concentration from the center to the edge of the wafer. These results will be compared to the results of the second run, and the differences in concentration level and type will be used to characterize any autodoping that is present.

The second run (wafers No. 1 and 3 lightly doped, wafers No. 2 and 4 heavily doped) showed some very interesting autodoping effects. The longitudinal concentration profile across all the wafers on the susceptor is shown in Fig. 10. The first wafer is n-type until about 8 mm from its trailing edge (Fig. 10). The concentration level over the first 20 mm (in the direction of the gas flow) shows no signs of autodoping and is characteristic of the results of the first epitaxial run (control run). It establishes that the intentionally added dopant is n-type. Continuing across wafer No 1 in the direction of the gas flow, a p-n junction is encountered. The concentration then rises above 200 ppba, p-type, as one approaches the boundary between the first and the second wafer.

The second wafer (heavily doped) is completely p-type with extremely high values of concentration seen at both the leading and trailing edges. It appears that dopant released at the leading edge of the wafer is swept downstream across the wafer by the ambient gas because the autodoping effect is much more pronounced in the direction of the gas flow. Therefore, diffusion is not the only mechanism for the transport of dopant in the gas phase. Looking at the transverse concentration profile (Fig. 11) across the center of wafer No 2, one again sees an autodoping effect at both edges

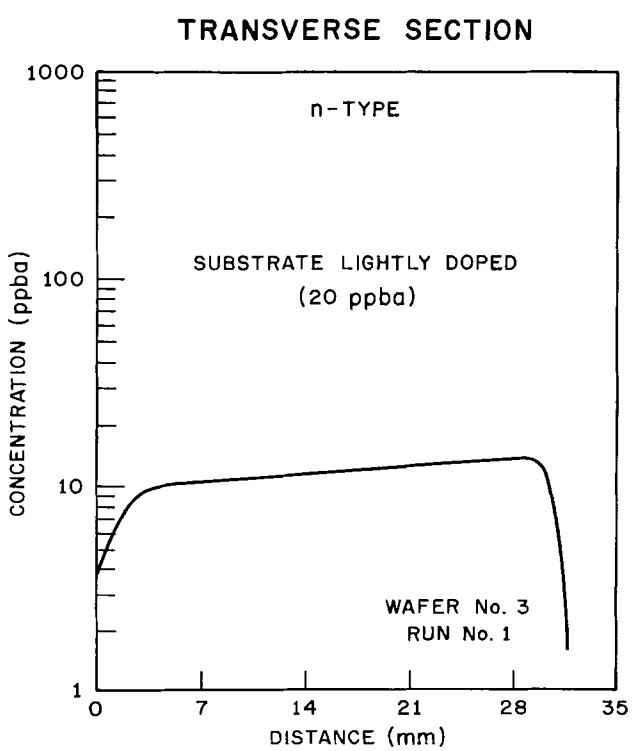


Fig. 9. Transverse plot of surface concentration vs. distance for the third wafer in run No. 1.

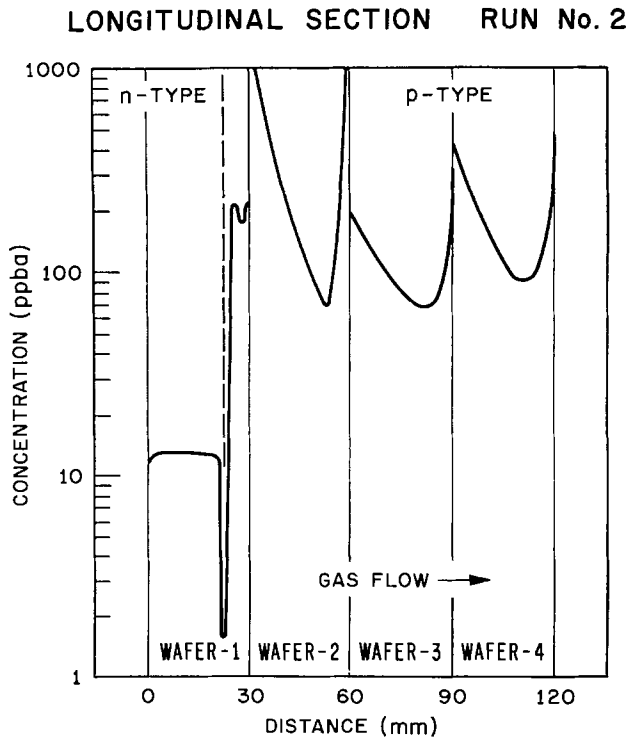


Fig. 10. Composite plot over all four wafers of surface concentration vs. distance in the second epitaxial run. Substrates one and three were lightly doped with boron while two and four were heavily boron doped. Temperature: 1120°C, time: 10 min, growth rate: 0.92 μm/min, gas phase dopant: arsine, silicon source: silane.

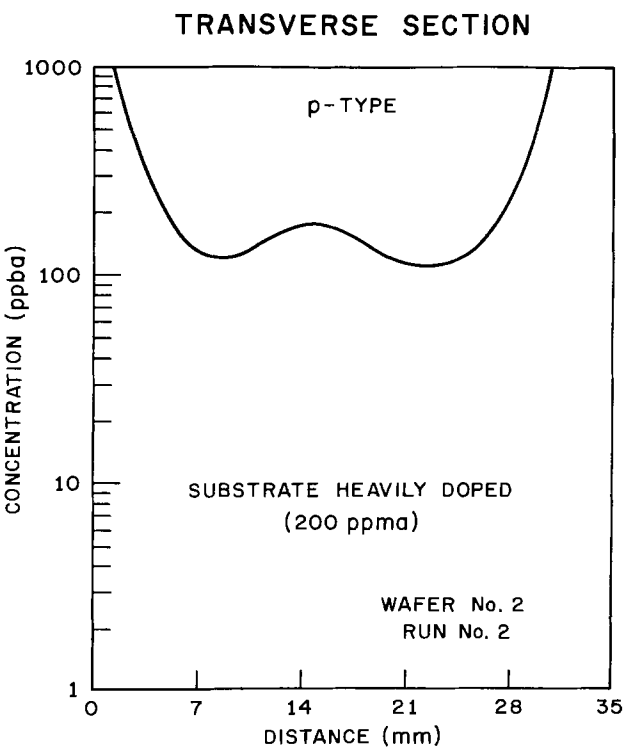


Fig. 11. Transverse plot of surface concentration vs. distance for the third wafer in run No. 2.

of the wafer and a small peak in concentration in the central region. The transverse section does not exhibit the large directional effect seen in the longitudinal profile. Also, the boron concentration at the edges of the transverse section are similar to the size of the autodoped region at the trailing edge. This indicates that the effect of the gas flow on diffusion of released dopant is negligible. The implication of this result is

that dopant released at an edge goes into the mean gas phase well above the surface of the wafer where the temperatures are lower and the gas velocities higher. The shape of the transverse profile (Fig. 11) near the center of the wafer may be due to the transverse variation in gas velocity above the susceptor (18). The increased concentration near the edges (Fig. 11) is due to dopant transported from the back and sides of the wafer and diffusing perpendicular to the gas flow during epitaxial growth of the layer. The concentration above the surface of the third wafer (lightly doped) which does not contribute boron to the reactor ambient is also completely p-type. Again, one sees the smearing of dopant (Fig. 10) from the leading edge toward the downstream end of the wafer. The transverse profile (Fig 12) of this wafer (No. 3) does not show an increased edge concentration. This is expected since this wafer is lightly doped and therefore cannot contribute dopant to the gas stream for reincorporation through the autodoping process. The p-type dopant in this layer comes from wafers No. 2 and No. 4. At the trailing edge of wafer No. 3, dopant released from wafer No. 4 and diffusing upstream against the gas flow is present. The maximum concentration at both the leading and trailing edges of the wafer is less than on either of the heavily doped structures. The fourth wafer (heavily doped) also shows the smearing effect of the autodoped species. Also, the minimum concentration found on the wafer is higher than the minimum concentrations found on any of the previous wafers. This is further evidence that dopant released from the sides and the back of the heavily doped upstream wafer (No. 2) is also affecting the mean gas phase concentration downstream from the source.

The experimental concentration *vs.* depth plot (open circles) taken at a point 15 mm from the leading edge on wafer No. 4 parallel to the gas flow is shown in Fig. 13 along with the results of the numerical simulation using "CASPER" (solid line). The simulation was performed assuming 1% of the back and side area was acting as a source of the autodoping species. Errors in the simulation involve not only the source area but also the effective distribution coefficient between the gas and the solid as well as the value of the evaporation coefficient. Even though agreement between calculations and experimental results (Fig. 13) is excellent, the presence of the large transverse and longitudinal concentration gradients tends to complicate the interpretation. Calculations were also made at 8 and 24 mm (dashed lines, Fig. 13) from leading edge of wafer No. 4 using 4 and 0.8% for the side and back area. The effect of this area factor shows almost a linear relationship to the average layer doping, *i.e.*, the concentration gradient in the layer is the same except that the levels are different. As one can see from Fig. 10 (wafer No. 2), the concentration at the surface varies by a factor of ten from the leading edge of wafer to a point about 20 mm downstream. Therefore, the problem can no longer be described by a one-dimensional model and a more complex interpretation is needed. One could empirically determine f (the fraction of effective area acting as a source) as a function of position in the reactor. This approach could give a reasonable first approximation to the concentration profiles measured. A one-dimensional approach would still be valid in systems (antimony substrates) that do not exhibit large transverse and longitudinal concentration gradients.

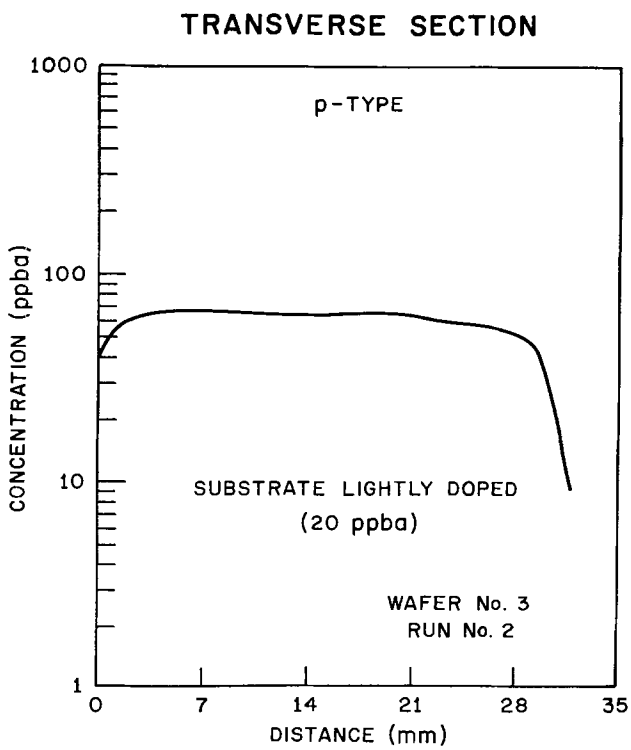


Fig. 12. Transverse plot of surface concentration vs. distance for third wafer in run No. 2.

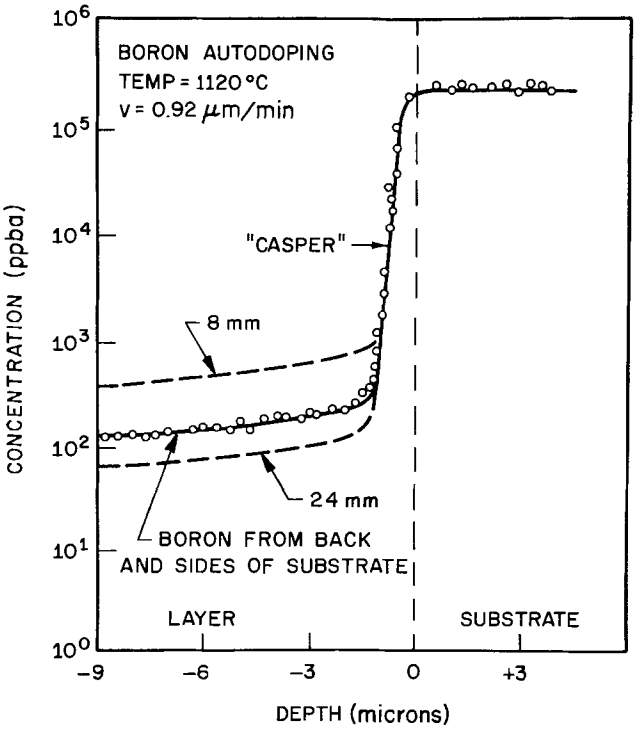


Fig. 13. Plot of concentration vs. depth 15 mm from leading edge of wafer No. 4 in the second run. "CASPER" simulation (solid line) is plotted along with the experimental results (open circles). Other "CASPER" calculations (dashed lines) at 8 and 24 mm.

The concentration gradient over the top few microns of the layer for a multiwafer system may also vary as a function of position from the source of the autodoping species. This is due to the fact that the time rate of change of the mean gas phase autodoping component is different from that dopant that is transferred without going through the mean gas phase. Therefore downstream wafers should show a smaller slope in the gradient near the surface than upstream wafers due to the larger component of the mean gas phase effect with downstream position. This change in slope was experimentally observed even within one wafer.

These results are not valid as a check on the evaporation coefficient determined in the previous series of experiments due to the presence of the large transverse and longitudinal concentration gradients. These autodoping results do indicate that the product, $k_e \cdot f \cdot h$ was chosen correctly as can be seen from the agreement between theory and data in Fig. 13.

Effect of HCl on boron autodoping.—The extension of these results to a system in which chlorine atoms are present during the deposition cycle (*e.g.*, silicon tetrachloride, or dichlorosilane) is not straightforward. Bloem (17) has shown that additions of HCl or water vapor to a reactor ambient will result in decreased doping efficiency of diborane. He postulates the formation of a stable boron chloride compound which ties up some of the available boron that would normally be available for doping or autodoping. This may explain why Grove (4), using silicon tetrachloride as his silicon source, did not report any autodoping when using heavily boron-doped substrates. Oxide masking may not be as effective in preventing autodoping of boron as with n-type elements since the segregation coefficient for boron between the oxide and the silicon is about 4 to 5 (18). Therefore, the concentration of boron in the oxide layer would be larger than in the silicon. Depending on the relative diffusivity of boron in the oxide to the evaporation rate of boron from the oxide, one might even postulate that an oxide layer would act as a larger source of dopant during the initial stages of epitaxial growth than the exposed silicon wafer back and edges. In order to establish whether HCl additions during epitaxial growth would reduce or eliminate boron autodoping, a third run was made. Substrate wafer doping levels were the same as in run No. 2. The HCl to silane ratio was maintained at unity. Figure 14 is an in-depth concentration profile on wafer No. 4 taken at the center. As one can see, the layer is n-type and no autodoping is evident. Traces of autodoping were still found near the edges of the wafers extending in 1-2 mm. Therefore, addition of HCl to the ambient during epitaxial growth over heavily doped boron substrates will significantly reduce the boron autodoping effects and will allow one to grow a lightly doped layer over a heavily doped boron substrate (2000 ppma).

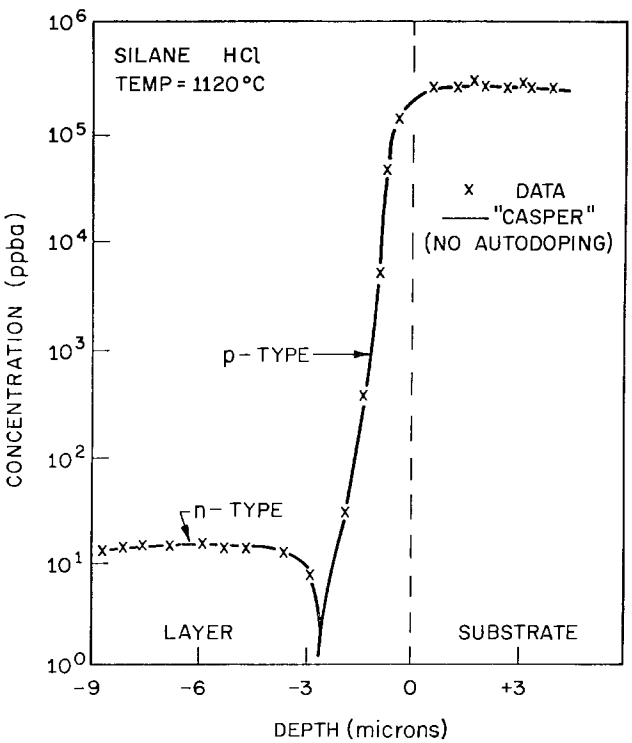


Fig. 14. Plot of concentration *vs.* depth showing reduction of boron autodoping with HCl addition to gas phase.

Summary

In summary, a set of equations [1]-[3] has been used to describe the redistribution of dopant (autodoping) in a silicon wafer during epitaxial growth. The evaporation rate of silicon and the evaporation coefficient of boron were determined as a function of temperature and these experimental results were used to predict the autodoping contribution from heavily doped boron substrates. Though the numerical model was unsuccessful in characterizing the distribution of dopant over the entire wafer diameter due to the large longitudinal and transverse concentration gradients, it was very successful in predicting the in-depth distribution at the center of the wafer where these gradients were negligible. Boron autodoping during silane epitaxy can be suppressed using a low concentration of HCl added to the gas phase during epitaxial growth.

Manuscript received Dec. 9, 1976.

Any discussion of this paper will appear in a Discussion Section to be published in the December 1977 JOURNAL. All discussions for the December 1977 Discussion Section should be submitted by Aug. 1, 1977.

Publication costs of this article were assisted by Bell Laboratories.

REFERENCES

1. C. O. Thomas, D. Kahng, and R. C. Manz, *This Journal*, **109**, 1055 (1962).
2. J. J. Grossman, *ibid.*, **110**, 1065 (1963).
3. W. Rice, *Proc. IEEE*, **52**, 284 (1964).
4. A. S. Grove, A. Roder, and C. T. Sah, *J. Appl. Phys.*, **36**, 802 (1965).
5. T. Abe, Y. Nishi, K. Sato, and N. Oi, *Denki Kagaku*, **35**, 142 (1967).
6. B. A. Joyce, J. C. Weaver, and D. J. Maule, *This Journal*, **112**, 1100 (1965).
7. W. H. Shepherd, *ibid.*, **115**, 652 (1968).
8. G. Skelly and A. C. Adams, *ibid.*, **120**, 116 (1973).
9. P. H. Langer and J. I. Goldstein, *ibid.*, **121**, 563 (1974).
10. F. G. Allen, *J. Appl. Phys.*, **28**, 1510 (1957).
11. P. A. Schumann and E. E. Gardner, *Solid-State Electron.*, **12**, 371 (1969).
12. B. L. Morris, P. H. Langer, and J. C. White, Spreading Resistance Symposium, National Bureau of Standards, Gaithersburg, Maryland (June 1974).
13. T. P. Lee, *IEEE Trans. Electron Devices*, **ed-13**, 881 (1966).
14. R. Takahashi, Y. Hoga, and K. Sugawara, *This Journal*, **119**, 1406 (1972).
15. S. K. Tung, in "Metallurgy of Semiconductor Materials," J. Schroeder, Editor, p. 95, Interscience, New York (1961).
16. D. L. Kendall and D. B. DeVries, in "Semiconductor Silicon," R. R. Haberecht and E. L. Kern, Editors, p. 358, The Electrochemical Society Softbound Symposium Series, New York (1969).
17. J. Bloem, *This Journal*, **118**, 1837 (1971).
18. L. E. Katz and J. C. Colby, Paper 60 presented at The Electrochemical Society Meeting, San Francisco, California, May 12-17, 1974.
19. F. A. Trumbore, *Bell Syst. Tech. J.*, **39**, 205 (1960).
20. J. E. White, Spreading Resistance Symposium, National Bureau of Standards, Gaithersburg, Maryland (June 1974).

Oxynitride Deposition Kinetics in a SiH_4-CO_2-NH_3-H_2 System

A. K. Gaind,* G. K. Ackermann, V. J. Lucarini,* and R. L. Bratter
IBM System Products Division, East Fishkill Facility, Hopewell Junction, New York 12533

ABSTRACT

Silicon oxynitride films ($Si_lO_mN_p$) have been deposited from SiH_4-CO_2-NH_3-H_2 chemical system in a vertical, cold-wall, multiple wafer, barrel-type reactor. The kinetics of SiH_4-CO_2 and SiH_4-NH_3 reactions, both in H_2, have also been studied in the same reactor. All three reactions are first order with respect to SiH_4 under conditions of "isolation technique." Within the selected experimental range, the SiO_2 deposition rate is independent of CO_2 concentration, the Si_3N_4 deposition rate is independent of NH_3 concentration, and the $Si_lO_mN_p$ deposition rate is nearly independent of both CO_2 and NH_3 concentrations. The deposition rate of SiO_2, Si_3N_4, and $Si_lO_mN_p$ are not dependent on the H_2 flow rate in the experimental range of 60-130 liters/min; thus all three reactions are chemical-surface rate limited within the experimental range. The activation energies are 23.5, 24, and 29 kcal/g-mole for $Si_lO_mN_p$, SiO_2, and Si_3N_4, respectively. An anomalous effect of deposition temperature on silicon oxynitride refractive index (composition) was discovered and has been explained by the use of adsorption theory.

Silicon oxynitride films ($Si_lO_mN_p$) are of interest in large scale integration (LSI) fabrication because they can be employed, for example, as barriers to diffusion and oxidation in the field region of integrated field effect transistor (FET) circuits and in the gate region as part of the metal-oxynitride-oxide-silicon structure. Other attractive properties and uses of $Si_lO_mN_p$ films have been reported (1-5).

Many chemical systems have been used for chemical vapor deposition (CVD) of silicon oxynitride (4, 6-10), of which all are SiH_4 based except for that of Koltsov *et al.* (9) who used $SiCl_4$. We preferred SiH_4 because it eliminates the possibility of NH_4Cl formation and associated difficulties (11). NH_3 is used as the nitriding agent without exception. Various oxidants have been used; *i.e.*, O_2 (7), N_2O (8), and NO (4, 6). Nutall *et al.* (10) used a mixture of O_2 and CO_2 as an oxidant at high temperatures (900°-1100°C), but abandoned the use of CO_2 after they determined there was no advantage in adding CO_2 to O_2. Thus, chemical systems for silicon oxynitride deposition which use SiH_4 as the silicon-bearing compound encounter two common conditions: (*i*) Very high NH_3/oxidant ratios ($\sim$ 50 to $\geq$ 5000) are required during the gas phase to produce films with refractive indexes $\geq$ 1.73; and (*ii*) the oxidation and nitriding reactions, when considered independently of each other, have very different activation energies ($\geq$ 12 kcal/g mole). The oxidation reaction has the lower activation energy, and is faster (6).

The first condition leads to poor process control, especially in forming Si_3N_4-rich $Si_lO_mN_p$ films. To improve the process control, we sought an oxidant such that the rates of oxidation and nitriding reaction (or activation energies) would be nearly equal. Reported activation energies of the SiH_4-CO_2 reaction (12) and the SiH_4-NH_3 reaction (6) are within 2 kcal/g mole of each other. Thus, silicon oxynitride of 1.73 refractive index was deposited with an NH_3/CO_2 ratio of $\sim$ 6 at 900°C, using the SiH_4-CO_2-NH_3-H_2 system.

Despite the fact that the silicon oxynitride deposition was reported in the literature as early as 1968, to the best of our knowledge no successful attempts have been made to extract a rate expression or to obtain an activation energy for silicon oxynitride deposition. Therefore, purposes of our study were to: (*i*) investigate deposition kinetics of silicon oxynitride films and empirically derive a rate expression; and (*ii*) examine the kinetic relationship between SiO_2 and Si_3N_4 rate expressions on the one hand, and the silicon oxynitride rate expression on the other.

* Electrochemical Society Active Member.

Key words: thin films, chemical vapor deposition, deposition kinetics.

The underlying principles described in this paper and used in this study are of fundamental importance. With slight modifications, they could be used to analyze other complex CVD depositions which are limited by surface chemical reaction rates. This is especially true if the objective is to obtain empirical rate expressions, the importance of which, from an engineering point of view, cannot be overemphasized. The isolation of an empirical rate expression, however, does not automatically lead to a reaction mechanism, and we will not attempt to postulate any. However, from data analysis we did discover a mutual chemical interference phenomenon which gives some insight into the reaction mechanism of SiO_2, Si_3N_4, and $Si_lO_mN_p$ formation.

Experimental

Equipment.—The equipment used for this investigation was a vertical, cold-wall, barrel-type, induction-heated, multiple wafer reactor which has been previously described (12, 13). Figure 1 is a schematic cross-sectional view of the reactor.

Temperatures were measured by optical pyrometer;[1] all reported values have been corrected for system transmission losses and emissivity (14). Gases (carrier and reacting) were introduced at the top of the reactor. All gases were metered by calibrated rotameters, except SiH_4 (5% in H_2), which was controlled by a mass-flow controller.

Deposition conditions and measurement techniques.—Three 57 mm diameter Si, 11-25 Ω-cm, p-type <100> wafers were usually processed in each experimental

[1] Temperature along the susceptor length is $\leq \pm 10$°C of any reported value.

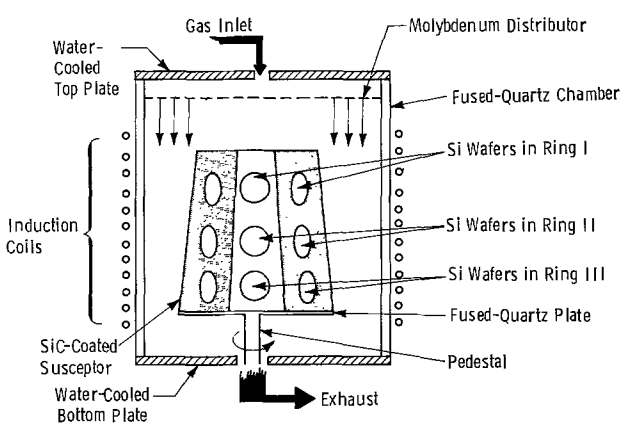


Fig. 1. Cross section of the reactor

run. One wafer each was placed in ring 1, 2, or 3 (Fig. 1) at a predetermined, fixed position. The remaining positions on a susceptor were filled with dummy wafers to protect the susceptor. Before being loaded in the reactor, wafers were cleaned ultrasonically in deionized water for 5 min, followed by a 3:1 H_2SO_4/HNO_3 at 120°C cleaning (10 min). The wafers were then dipped in 10:1 dilute HF and rinsed in running deionized water (5 min) and subsequently spin dried. After this cleaning procedure, the wafer surface is hydrophobic.

During the experimental work, the H_2 flow rate was typically 110 liters/min, SiH_4 (5% in H_2) $\sim$ 200 cm³/min ($\sim$ 10 cm³/min pure SiH_4). The sum of CO_2 and NH_3 flow rates was kept constant at $\sim$ 2.3 liters/min.

The deposited film thicknesses were measured by either constant angle reflection interference spectroscopy (CARIS) (15) or ellipsometry, whereas the refractive index was always measured by ellipsometry.

The typical deposition uniformity within a run (*i.e.*, all three wafers) was $\sim \pm$ 5% at 1000°C. The worst-case uniformity was $\leq \pm$ 15% at any deposition temperature in the 850°-1050°C experimental range. Because of nearly uniform deposition within a run, we used average deposition rates (an average of three rings). Thus, as a first approximation the silane concentration variations along the susceptor length were not taken into account.

Results

The units of deposition rate used throughout this paper are in moles per minute rather than the usual angstroms per minute because material thicknesses of varying density and molecular weight cannot be compared directly. Silicon oxynitride density, molecular weight, and composition were assumed to vary with the refractive indexes. For justification of these assumptions, refer to Appendix A.

Deposition rate vs. effective silane concentration.—Figure 2 is the log-log plot of effective SiH_4 concentration inside the reactor *vs.* deposition rate at 900° and 1000°C. The effective SiH_4 concentration, C_{SiH_4}, is defined as the product of SiH_4 feed concentration, $C^0_{SiH_4}$, and $(1 - Y_{SiH_4})$, where Y_{SiH_4} is the fraction of SiH_4 converted to deposit (see Appendix B for a detailed derivation and explanation of terms).

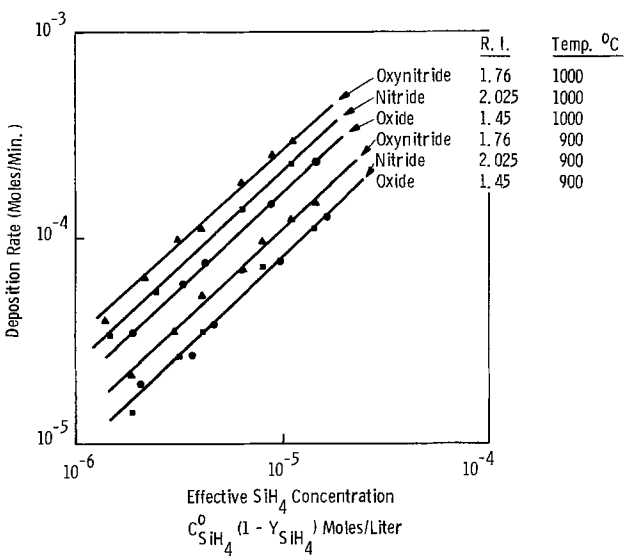


Fig. 2. Deposition rate as a function of effective SiH_4 concentration. The H_2 flow rate constant is $\sim$ 110 liters/min. For oxynitride the NH_3 + CO_2 flow rate constant is 2.3 liters/min. For nitride the NH_3 flow rate constant is 750 cm³/min. For oxide the CO_2 flow rate constant is 750 cm³/min.

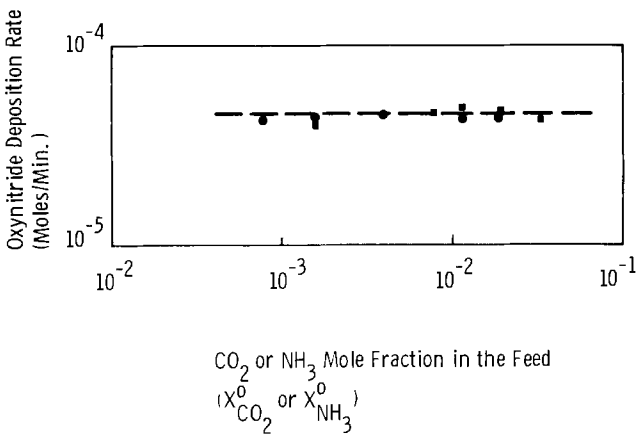


Fig. 3. Oxynitride deposition rate as a function of CO_2 or NH_3 mole fraction. SiH_4 mole fraction in feed ($X^0_{SiH_4}$) = 7.1 × 10⁻⁵. ● = $X^0_{NH_3}$ constant at 5.93 × 10⁻³, $X^0_{CO_2}$ variable. ■ $X^0_{CO_2}$ constant at 5.93 × 10⁻³, $X^0_{NH_3}$ variable. H_2 flow rate 110 liters/min, deposition temperature 1000°C.

In Fig. 2 note: (*i*) The slope of all the curves is nearly unity in all cases; *i.e.*, the order of the reaction is one with respect to SiH_4 for SiO_2, Si_3N_4, and $Si_lO_mN_p$;[2] (*ii*) the deposition rates of oxide and nitride are nearly identical for a fixed effective SiH_4 concentration at 900°C; (*iii*) silicon oxynitride deposition rates are larger than either Si_3N_4 or SiO_2 deposition rates at both temperatures; (*iv*) the silicon oxynitride deposition rate is less than the sum of the deposition rates of SiO_2 and Si_3N_4.

Deposition rate vs. CO_2 or NH_2 mole fraction.—The deposition rate of the silicon oxynitride films as a function of CO_2 mole fraction, with NH_3 mole fraction constant at 5.93 × 10⁻³, is shown in Fig. 3. For this experiment, the deposition temperature was kept constant at 1000°C as was the H_2 flow (110 liters/min) and SiH_4 mole fraction in the feed ($\sim$ 7.1 × 10⁻⁵). The above experiment was then repeated with the exception that the CO_2 mole fraction was kept constant (5.93 × 10⁻³) with NH_3 mole fraction as a variable. The results are also shown in Fig. 3.

The refractive index of silicon oxynitride films deposited during the above experiments changed from 1.5 to 1.82. As can be seen from Fig. 3, the silicon oxynitride deposition rate as a first approximation is independent of NH_3 or CO_2 concentration. These results are consistent with the "isolation technique" (16); *i.e.*, since both CO_2 and NH_3 concentrations used here are considerably larger than SiH_4 concentration, the rate of silicon oxynitride deposition should be independent of NH_3 and CO_2 concentrations.

Similarly the deposition rates of SiO_2 and Si_3N_4 are independent of CO_2 and NH_3 concentrations when the CO_2:SiH_4 and NH_3:SiH_4 ratios are kept larger than 7:1 and 5:1, respectively (12, 17). These results were verified during the course of this investigation.

Deposition rate vs. flow rate.—Deposition rate was nearly a constant ($\sim \pm$ 4%) for SiO_2, Si_3N_4, and $Si_lO_mN_p$ for a fixed SiH_4 feed rate (mole fraction), when the H_2 flow rate was varied from 60 to 130 liters/min. The ratios of SiH_4:CO_2, SiH_4:NH_3, and SiH_4:NH_3:CO_2 were kept constant, respectively, for SiO_2, Si_3N_4, and silicon oxynitride deposition. The experiment clearly showed that the reactions in all three cases are surface-chemical rate limited in the flow range of interest here (see Appendix C for additional justification).

[2] Though only one oxynitride (*i.e.*, n = 1.76) is shown, identical behavior is observed for all oxynitrides in the 1.5-1.9 refractive index range.

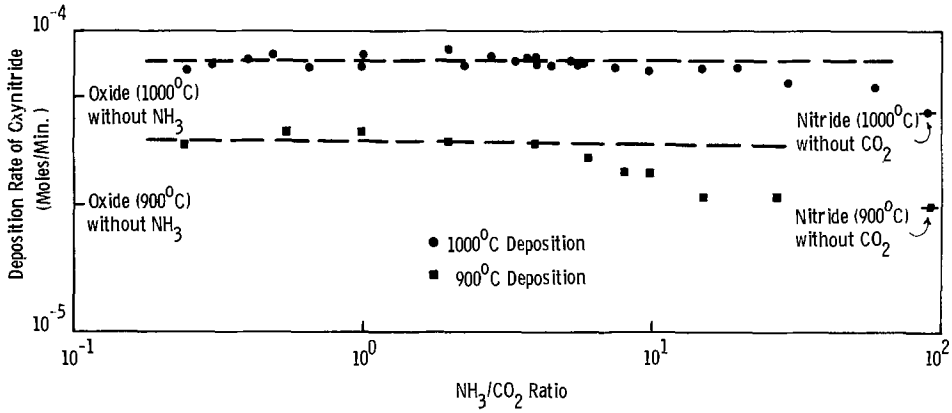


Fig. 4. Oxynitride deposition rate as a function of NH_3:CO_2 ratio. H_2 flow rate constant at ~ 110 liters/min, $NH_3 + CO_2$ flow rate constant at ~ 2.3 liters/min, 1000°C data reproduced at $NH_3 + CO_2$ flow rate of ~ 3.9 liters/min. SiH_4 mole fraction in the feed ($X^o_{SiH_4}$) = 9.3×10^{-5}.

Deposition rate of oxynitride vs. NH_3:CO_2 ratio.— The deposition rate of silicon oxynitride is independent of the NH_3:CO_2 ratio, as a first approximation (Fig. 4). However, at a high NH_3:CO_2 ratio (*i.e.*, > 10) the silicon oxynitride deposition rate appears to approach the deposition rate of Si_3N_4, both at 900° and 1000°C, as can be seen from the data in Fig. 4. The difference between the experiment of Fig. 4 and that of Fig. 3 is that the sum of NH_3 and CO_2 flow rates were kept constant at ~ 2.3 liters/min in the experiment of Fig. 4, whereas that was not the case in the experiment of Fig. 3. The feed mole fraction of SiH_4 is also higher in Fig. 4.

Refractive index vs. NH_3:CO_2 ratio.—The refractive index and, hence, the composition of deposited silicon oxynitride films (see Appendix A) is a function of NH_3:CO_2 ratio as shown in Fig. 5. The change of deposition temperature from 1000° to 900°C produced anomalous and unexpected results. These results, however, have been reproduced several times and, thus, the phenomenon of higher refractive index for oxynitrides deposited at 900°C than those deposited at 1000°C for a fixed NH_3:CO_2 ratio is quite real. However, because of the data presented in Fig. 2, we expected that the silicon oxynitride at 1000°C would have higher refractive index for a fixed NH_3:CO_2 ratio because the deposition rate of the Si_3N_4 is higher than the SiO_2 at 1000°C. Thus, the results of Fig. 5 cannot be explained by separately studying the deposition rates of the Si_3N_4 and the SiO_2.

We attempt to explain this anomalous effect of deposition temperature on silicon oxynitride composition later in this paper.

Theory and Calculations

The reaction for formation of silicon oxynitride can be stoichiometrically expressed as follows

$$1\,SiH_4 + mCO_2 + pNH_3 \xrightarrow{k_{on}} Si_lO_mN_p + mCO + \left(2l + \frac{3}{2}p\right) H_2 \quad [1]$$

Knowing that the above reaction is surface-chemical rate limited, a rate expression is formulated, as shown below, following the general procedure used for heterogeneous reaction (18)

$$r_{oxy} = k_{on}\theta^{n_1}_{SiH_4}\theta^{n_2}_{NH_3}\theta^{n_3}_{CO_2} \quad [2]$$

where r_{oxy} is the rate of deposition of silicon oxynitrides in moles/minute, θ_{SiH_4}, θ_{NH_3}, and θ_{CO_2} are the fractions of the surface (on which reaction is occurring) covered by SiH_4, NH_3, and CO_2, respectively, and k_{on} is the surface-chemical rate constant for the silicon oxynitride formation in moles/minute. The order of reaction with respect to SiH_4, NH_3, and CO_2 is given by n_1, n_2, and n_3, respectively. These orders will vary from 0 to 1 (18). Zero order implies strong adsorption by a given reactant (*i.e.*, $\theta = 1$), a fractional order implies that the reactant dissociates during the reaction (18, 19). If the reaction order is 1 with respect to a given reactant, then that reactant participates in the reaction as a whole; *i.e.*, without dissociation (18).

Since the fractional surface coverage by any chemical species is proportional to its partial pressure which in turn is proportional to the concentration of that species in gas phase inside the reactor, Eq. [2] can be rewritten as

$$r_{oxy} = K'_{on}C^{n_1}_{SiH_4}C^{n_2}_{NH_3}C^{n_3}_{CO_2} \quad [3]$$

where C_{SiH_4}, C_{NH_3}, and C_{CO_2} are, respectively, the concentrations of SiH_4, NH_3, and CO_2 inside the reactor.

We have intentionally used considerably higher concentrations of NH_3 and CO_2 with respect to SiH_4 (*i.e.*, isolation technique). This was done due to four reasons: (*i*) to prevent the formation of silicon-rich films; (*ii*) to make the deposition of silicon oxynitrides dependent on as few variables as possible; (*iii*) to minimize refractive index (composition) variations within a run; and (*iv*) to facilitate data analysis from a kinetic point of view. Thus, under the conditions of isolation technique, C_{NH_3} and C_{CO_2} (also θ_{NH_3} and θ_{CO_2}) are nearly constant, and therefore the deposition rate of silicon oxynitride would be independent of NH_3 and CO_2 concentration. This is indeed the case as shown in Fig. 3 and 4.

Thus, Eq. [3] reduces to

$$r_{oxy} = K''_{on}C^{n_1}_{SiH_4} \quad [4]$$

Following similar reasoning and under the conditions of isolation technique, the rates of Si_3N_4 and SiO_2 can be expressed as follows

$$r_n = K''_nC^{n'_1}_{SiH_4} \quad [5]$$

$$r_{ox} = K''_{ox}C^{n''_1}_{SiH_4} \quad [6]$$

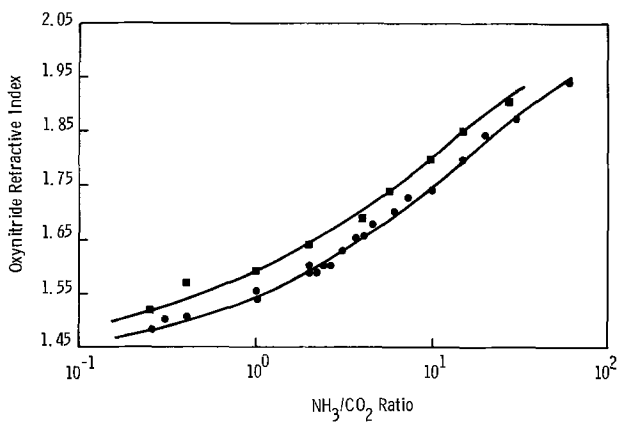


Fig. 5. Oxynitride refractive index as a function of NH_3:CO_2 ratio at two deposition temperatures. ■ = 900°C deposition, ● = 1000°C deposition. Rest of the condition some as Fig. 4.

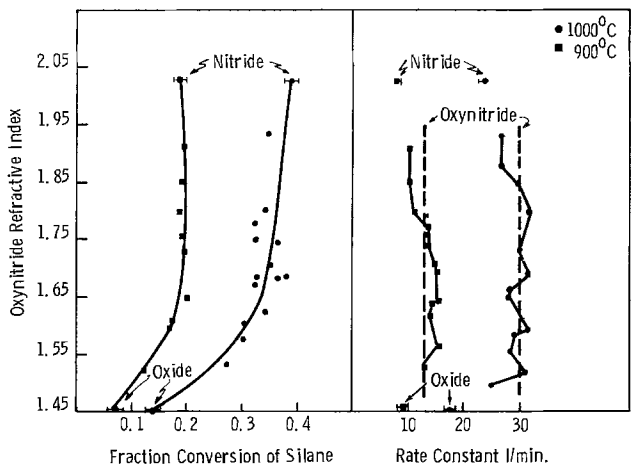


Fig. 6. Fractional conversion of silane and rate constants for oxide, nitride, and oxynitride as a function of refractive index (composition). ■ = 900°C deposition, ● = 1000°C deposition.

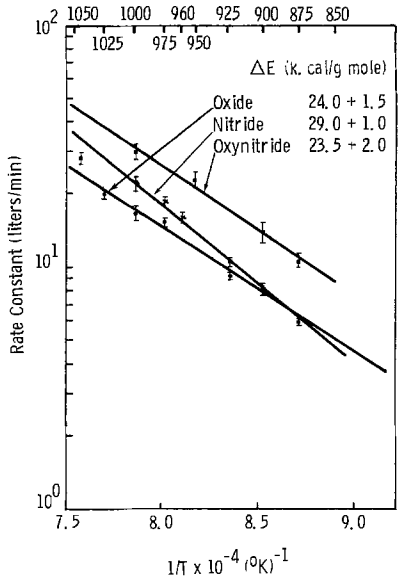


Fig. 7. Rate constant as a function of $1/T$ for SiO_2, Si_3N_4, and $Si_lO_mN_p$.

where r_n and r_{ox} are the rates of Si_3N_4 and SiO_2 deposition, respectively, in moles/minute, K''_n and K''_{ox} are the respective rate constants, and where C_{SiH_4} is the effective SiH_4 concentration in the reactor. From Fig. 2 it is seen that n_1, n'_1, and n''_1 are all equal to 1, thus showing that SiH_4 participates in these three reactions as a whole; *i.e.* without dissociation.

Evaluation of rate constants.—The rate constants of $Si_lO_mN_p$, Si_3N_4, and SiO_2 can be readily calculated from Eq. [4] through [6] provided the SiH_4 concentration inside the reactor is known. Since C_{SiH_4} is equal to $C^0_{SiH_4}(1 - Y_{SiH_4})$ as shown in Appendix B, knowledge of fractional conversion (Y_{SiH_4}) is important. Y_{SiH_4} can be readily obtained by mass balance (cf. Appendix B). In Fig. 6 the rate constants and fractional conversion of SiH_4 are shown as a function of the refractive index at two deposition temperatures of 900° and 1000°C. Note that the silicon oxynitride rate constants are nearly independent of the silicon oxynitride refractive index (1.5-1.93). Similar results are obtained at all temperatures in the experimental range of 850°-1000°C.

Since both NH_3 and CO_2 are present in the reactor during the deposition of silicon oxynitride, one may hypothesize that SiH_4 oxidation and nitriding reactions proceed simultaneously and in parallel without mutual interference. If this were the case, then

$$r_{oxy} = r_{Si_3N_4} + r_{SiO_2} \qquad [7]$$

From Eq. [4], [5], and [6], with n_1, n'_1, and n''_1 equal to 1, we have

$$K''_{on}C_{SiH_4} = (K''_n + K''_{ox})C_{SiH_4} \qquad [8]$$

Thus due to above hypothesis, K''_{on} should be equal to $K''_n + K''_{ox}$. This is not the case as can be seen in Fig. 6. Therefore, one is forced to accept the converse hypothesis; *i.e.*, the simultaneous presence of NH_3 and CO_2 changes either the oxidation rate constant or the nitriding rate constant, or both. These possibilities are investigated further on in this paper.

Rate expression (empirical).—The rate constant for any surface-chemical reaction can be expressed as a product of a frequency factor and an exponential term; *i.e.*, $K = Ae^{-\Delta E/RT}$, where A is the frequency factor, ΔE the activation energy in cal/g mole, R is the gas constant (1.98 cal/g mole °K), and T is the temperature in °K. The activation energies of SiO_2, Si_3N_4, and silicon oxynitride reactions are determined in Fig. 7 by the usual Arrhenius plot of logarithm of rate constant *vs.* inverse absolute temperature. The calculated values of frequency factors are shown in Table I.

Thus, under the conditions of isolation technique, the rate expressions for all three materials (*i.e.*, SiO_2, Si_3N_4, and silicon oxynitride) may be expressed as follows

$$r_{ox} = 2.4 \times 10^5 \exp[-24 \times 10^3/RT]C_{SiH_4} \qquad [8]$$

$$r_n = 22.3 \times 10^5 \exp[-29 \times 10^3/RT]C_{SiH_4} \qquad [9]$$

$$r_{on} = 3.5 \times 10^5 \exp[-23.5 \times 10^3/RT]C_{SiH_4} \qquad [10]$$

Equations [8] through [10] are applicable within the temperature range of 850°-1050°C and in those reactors where the flow of gases is nearly parallel to the wafer surface.

Investigation of anomalous temperature effect on refractive index.—In Fig. 5 we have shown that the refractive index of silicon oxynitride is higher at 900°C than at 1000°C for a fixed NH_3:CO_2 ratio. We pointed out earlier that these results were anomalous and cannot be explained by separately investigating the deposition rates of the Si_3N_4 and SiO_2. We now show that this phenomenon is explainable.

Expressing oxynitride deposition rate as a sum of equivalent Si_3N_4 ($r'_{Si_3N_4}$) and SiO_2 (r'_{SiO_2}) deposition rates (cf. Appendix A)

$$r_{oxy} = r'_{Si_3N_4} + r'_{SiO_2} \qquad [11]$$

where $r'_{Si_3N_4}$ is not equal to $r_{Si_3N_4}$ and r'_{SiO_2} is not equal to r_{SiO_2}. The $r_{Si_3N_4}$ and r_{SiO_2} are defined by Eq. [5] and [6].

Now

$$r'_{Si_3N_4} = K_1\theta_{SiH_4}\theta^{m_1}_{NH_3} \qquad [12]$$

and

$$r'_{SiO_2} = K_2\theta_{SiH_4}\theta^{m_2}_{CO_2} \qquad [13]$$

Considering Eq. [12] only for the present, one can write an expression for θ_{NH_3} in a multicomponent system using Langmuir adsorption theory (19); *i.e.*

$$\theta_{NH_3} = \frac{b_{NH_3}p_{NH_3}}{1 + b_{NH_3}p_{NH_3} + b_{CO_2}p_{CO_2} + b_{H_2}p_{H_2} + b_{SiH_4}p_{SiH_4}} \qquad [14]$$

Table I. Frequency factors for SiO_2, Si_3N_4, and silicon oxynitride. Applicable temperature range 850°-1050°C

Material	A (liters/min)* ($\times 10^5$)
SiO_2	2.4 (±0.3)
Si_3N_4	22.3 (±2.5)
$Si_lO_mN_p$	3.5 (±0.4)

* Values in parenthesis are twice the standard deviation.

where various b's are the ratio of adsorption and desorption rate constants for a given gas and p's are the respective partial pressures.

Assuming that NH_3 and CO_2 adsorb more strongly than the other components, *i.e.*

$$b_{NH_3}p_{NH_3} + b_{CO_2}p_{CO_2} >> 1 + b_{H_2}p_{H_2} + b_{SiH_4}p_{SiH_4} \quad [15]$$

Equation [14] then reduces to

$$\theta_{NH_3} \approx \frac{b_{NH_3}p_{NH_3}}{b_{CO_2}p_{CO_2} + b_{NH_3}p_{NH_3}} = \frac{p_{NH_3}}{K_3 p_{CO_2} + p_{NH_3}} \quad [16]$$

where $K_3 = b_{CO_2}/b_{NH_3}$. Substituting Eq. [16] in Eq. [12] and noting that partial pressures are equal to mole fraction, provided the total pressure is 1 atm, which is the case here, Eq. [12] becomes

$$r'_{Si_3N_4} = K_1\theta_{SiH_4}\left[\frac{X_{NH_3}}{K_3X_{CO_2} + X_{NH_3}}\right]^{m_1} \quad [17]$$

where X_{NH_3}, X_{CO_2} are mole fractions of NH_3 and CO_2, respectively.

Now if an experiment is performed such that the partial pressure of SiH_4 is kept constant and the NH_3:CO_2 ratio varied keeping the $NH_3 + CO_2$ partial pressure constant, the resulting silicon oxynitride deposition rate is first normalized for changes in SiH_4 fractional conversion as the film composition changes (cf. Fig 6 and Appendix B), and then it is separated into equivalent Si_3N_4 and SiO_2 deposition rates (cf. Appendix A). Equation [17] can then be used to predict the variation of equivalent Si_3N_4 deposition rate as a function of NH_3:CO_2 ratio depending on one of the following two limiting conditions

(*i*) If $K_3X_{CO_2} > X_{NH_3}$, then

$$r'_{Si_3N_4} \approx K'_1\left[\frac{X_{NH_3}}{X_{CO_2}}\right]^{m_1} \quad [18]$$

(*ii*) If $X_{NH_3} > K_3X_{CO_2}$, then

$$r'_{Si_3N_4} \approx K''_1 \quad [19]$$

The expected trends from Eq. [18] and [19] show excellent agreement with the experiment as shown in Fig. 8. Note that $r'_{Si_3N_4}$ first increases as a function of NH_3:CO_2 ratio and then saturates to a constant value according to Eq. [19]. The value of m_1 obtained from this experiment is 0.6.

Following similar development as with Eq. [12], Eq. [13] modifies to

$$r'_{SiO_2} = K_2\theta_{SiH_4}\left[\frac{X_{CO_2}}{K_4X_{NH_3} + X_{CO_2}}\right]^{m_2} \quad [20]$$

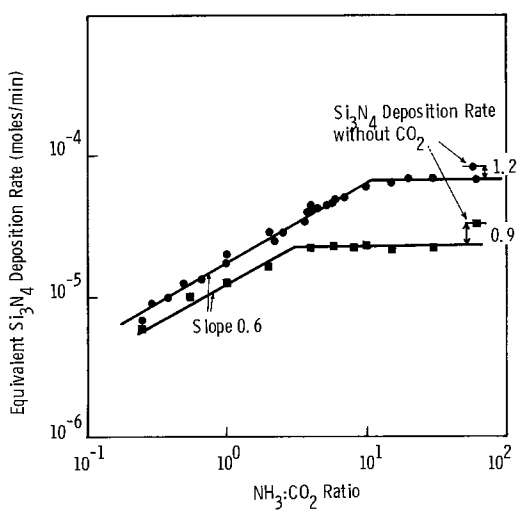


Fig. 8. Deposition of "equivalent" Si_3N_4 in the oxynitride films *vs.* NH_3:CO_2 ratio. ● = 1000°C deposition, ■ = 900°C deposition. H_2 flow rate ~ 110 liters/min, $NH_3 + CO_2$ flow rate constant at 2.3 liters/min. Effective SiH_4 concentration in the reactor (C_{SiH_4}) ~ 3.75 × 10^{-6} moles/min.

Equation [20] can then be used to predict the variation in deposition rate of equivalent SiO_2 as a function of CO_2:NH_3 ratio depending on one of the following two limiting conditions

(*i*) If $K_4X_{NH_3} > X_{CO_2}$, then

$$r'_{SiO_2} \approx K'_2\left[\frac{X_{CO_2}}{X_{NH_3}}\right]^{m_2} \quad [21]$$

(*ii*) If $X_{CO_2} > K_4X_{NH_3}$, then

$$r'_{SiO_2} \approx K''_2 \quad [22]$$

Thus, the deposition rate of equivalent SiO_2 would increase first as a function of CO_2:NH_3 ratio (*i.e.*, Eq. [21]) and finally saturating according to Eq. [22]. Figure 9 shows this behavior is in excellent agreement with the theory. The value of m_2 obtained from the above experiment is 0.5.

The purpose of generating the above theoretical analysis and Fig. 8 and 9 is to compare the saturation value of $r'_{Si_3N_4}$ with $r_{Si_3N_4}$ and r'_{SiO_2} with r_{SiO_2}.

The values of $r_{Si_3N_4}$ and r_{SiO_2} are shown for both 900° and 1000°C on Fig. 8 and 9, respectively. Note that the saturation value of $r'_{Si_3N_4} < r_{Si_3N_4}$ and $r'_{SiO_2} > r_{SiO_2}$. The above facts lead us to the conclusion that the simultaneous presence of NH_3 and CO_2 changes both the oxidation and nitriding rate constants. This is consistent with the hypothesis previously accepted that the simultaneous presence of NH_3 and CO_2 changes the rate constants of both nitriding and oxidation reactions.

The above changes in the rate constants of Si_3N_4 and SiO_2 deposition are the root cause of the phenomenon of temperature dependence of refractive index at a fixed NH_3:CO_2 ratio. These changes are the reason why the data of Fig. 2 could not predict the results of Fig. 5. The impact of alteration of the rate constants is best seen if the ratio of equivalent Si_3N_4 to equivalent SiO_2 (from Fig. 8 and 9) is plotted against the NH_3:CO_2 ratio. This is done in Fig. 10. Note $r'_{Si_3N_4}/r'_{SiO_2}$ ratio is higher for 900°C deposited films; *i.e.*, higher relative amount of Si_3N_4 is formed in the films deposited at 900°C than at 1000°C in the presence of CO_2. This is precisely the reason for observing a higher refractive index at 900°C than at 1000°C for a fixed NH_3:CO_2 ratio.

Discussion

We have shown that SiH_4-CO_2-NH_3 reaction, which leads to the deposition of silicon oxynitride films, is first order with respect to SiH_4. This was determined by using the isolation technique (16); *i.e.*, NH_3 and CO_2 concentrations (mole fractions) were considerably larger than SiH_4 in the gas phase.

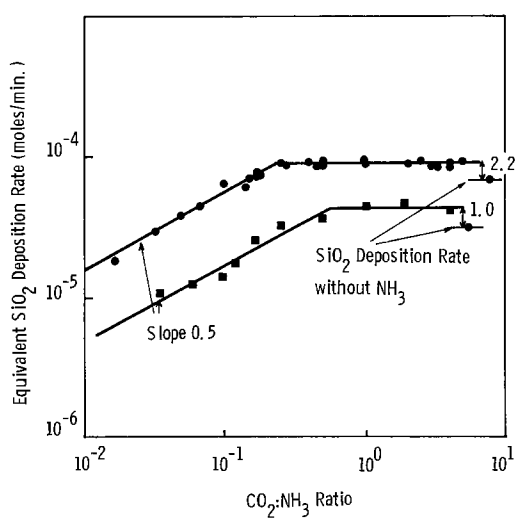


Fig. 9. Deposition rate of "equivalent" SiO_2 in oxynitride films *vs.* CO_2:NH_3 ratio. ● = 1000°C deposition, ■ = 900°C deposition. Rest of the condition the same as Fig. 8.

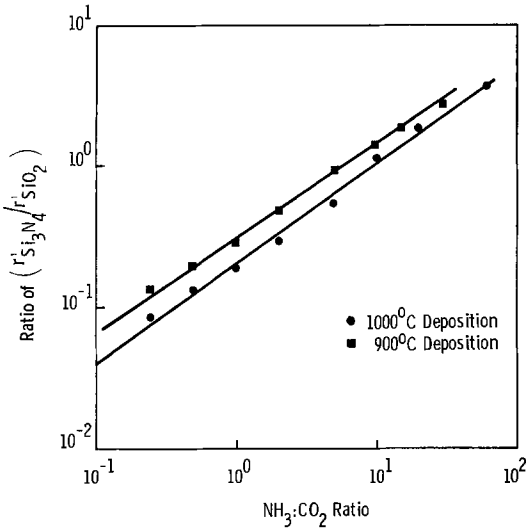


Fig. 10. The ratio of "equivalent" Si_3N_4 to SiO_2 in oxynitride at two deposition temperatures, showing a higher relative amount of nitride incorporation in the oxynitride films at 900°C than at 1000°C for a fixed NH_3:CO_2 ratio.

The same technique (*i.e.*, isolation) cannot be used to isolate the orders of reaction with respect to CO_2 and NH_3 since this would involve using larger concentrations of SiH_4 than CO_2 or NH_3, which in turn leads to the deposition of silicon-rich films. However, in the process of explaining the anomalous deposition temperature effect (Fig. 5) on the silicon oxynitride refractive index, we did indirectly discover the order of reaction with respect to both NH_3 and CO_2 (Fig. 8 and 9). We have shown that the rate of equivalent Si_3N_4 deposition first increases as a function of NH_3:CO_2 ratio with an order of 0.6 (Fig. 8) and then saturates when $X_{NH3} > K_3X_{CO2}$. In the region where the $r'_{Si_3N_4}$ is still increasing as a function of NH_3:CO_2 ratio, the CO_2 mole fraction, X_{CO2}, is larger than the NH_3 mole fraction, X_{NH3}. Thus, as compared to X_{NH3}, the X_{CO2} is approximately a constant; therefore, the order of reaction with respect to NH_3 is 0.6 for the nitrogen incorporation in silicon oxynitride films. Similarly, from Fig. 9 we deduce that the order of reaction with respect to CO_2 for oxygen incorporation, in the silicon oxynitride films, is 0.5. Since fractional orders imply decomposition (18, 19) we conclude that both NH_3 and CO_2 decompose prior to participating in the reaction with SiH_4.

The above analysis and inferences not only provide some insight into SiH_4-NH_3-CO_2 reaction, but also increase our understanding of SiH_4-CO_2 and SiH_4-NH_3 reactions. Take, for example, Si_3N_4 and $Si_lO_mN_p$. Assuming that the nitrogen incorporation follows similar reaction paths in both cases, we can conclude that NH_3 first dissociates into possibly $NH_2\cdot$ and $H\cdot$. Then $NH_2\cdot$ reacts with SiH_4 to form a substitutional compound where all hydrogen atoms are replaced by $NH_2\cdot$. This reaction will probably involve many steps, only one of which will be rate controlling, such that the first-order participation of SiH_4 is satisfied. The substituted silane compound then decomposes to Si_3N_4 (in the absence of CO_2) or forms a silicon, nitrogen, and oxygen "polymer" in the presence of CO_2.

Similarly, if we assume that the oxygen incorporation in $Si_lO_mN_p$ and SiO_2 follow similar paths, then we conclude that CO_2 first dissociates into CO and O. The oxygen reacts with SiH_4 to form SiO_2 in the case of SiH_4-CO_2 reaction, possibly in more than one step, one of which will be rate controlling. In the presence of NH_3 (or $NH_2\cdot$), the atomic oxygen reacts with the substituted SiH_4, leading to silicon, oxygen, and nitrogen polymer. Note that we have not mentioned the role of the so-called "water-gas" reaction for the oxygen incorporation in $Si_lO_mN_p$ films. We have done this because of two reasons: (*i*) the water-gas reaction is very slow and would be rate controlling; and, if that were the case, the order of the reaction with respect to CO_2 should have been 1 (20); (*ii*) much evidence has been generated against water-gas reaction mechanism when we investigated the SiH_4-CO_2-H_2 reaction (12).

In Fig. 2 we show that when investigated independently the SiH_4-CO_2 and SiH_4-NH_3 reactions result in equal deposition rates at 900°C. Why then is a NH_3:CO_2 ratio of $\sim$ 6 required in the gas phase to produce silicon oxynitride composition of Si_2ON_2 at 900°C? The answer lies in Fig. 8 and 9. The presence of CO_2 retards the rate of nitrogen and the presence of NH_3 enhances the rate of oxygen incorporation, respectively, in the silicon oxynitride films. Now the questions become: (*i*) Why should CO_2 retard the nitrogen incorporation rate? (*ii*) Why should NH_3 enhance the oxygen incorporation rate? The answers probably are that the CO_2 adsorbs more strongly than the NH_3 (*i.e.*, $K_3 > 1$, Eq. [17]). Since K_4 (Eq. [20]) is the reciprocal of the K_3, it must be less than 1, and thus the enhancement of oxygen incorporation in the presence of NH_3 (*i.e.*, Eq. [20]). The above analysis, of course, is correct in the region before $r'_{Si_3N_4}$ and r'_{SiO_2} have reached the saturation values. Figures 8 and 9 support the point that $K_3 > 1$ and $K_4 < 1$. The saturation value of $r'_{Si_3N_4}$, being less than $r_{Si_3N_4}$, is consistent with the explanation that the CO_2 adsorbs more strongly than NH_3. However, the role of NH_3 in the enhancement of the saturation value of r'_{SiO_2} is unclear and not understood at present.

Despite the fact that the chemical reactions involved here are very complex, we have nonetheless gained some insight into reaction mechanism of $Si_lO_mN_p$, Si_3N_4, and SiO_2.

Summary and Conclusions

Much is known about silicon oxynitride properties (1-10); however, to the best of our knowledge, nothing exists in the literature regarding the kinetics of oxynitride deposition from any chemical system. We have thus attempted to bridge the knowledge gap between oxynitride properties and kinetics.

During this study we have obtained the empirical rate expressions for SiO_2, Si_3N_4, and $Si_lO_mN_p$. Despite the fact that these rate expressions were obtained under somewhat restricted experimental conditions, they should nonetheless be widely applicable. This especially holds for those multiple wafer reactors where the flow of the gases is nearly parallel to the wafer surface and the objective is to deposit uniform and stoichiometric (nonsilicon rich) films.

Some of the fundamental concepts used in this paper are quite general and important since they increase the understanding of complex chemical reactions. These concepts are: (*i*) The use of moles/minute as unit of deposition rates. This approach permits the comparison of the deposition rates of materials which are changing in composition, density and molecular weight. (*ii*) The simple, yet powerful, concept of fractional conversion and its use in the correction of the SiH_4 concentration. The direct comparison of chemical reactions with differing efficiency (*i.e.*, fractional conversion) was made possible by the correction of SiH_4 concentration. (*iii*) The use of the absorption theory in theoretical descriptions of surface-chemical rate-limited chemical reactions. It is our hope that the use of these concepts will increase the understanding of CVD reactions in general.

The use of CO_2 as an oxidant for the deposition of silicon oxynitride is quite novel and has not been previously reported. In our experience the use of CO_2 leads to significantly better process and film property control than when other oxidants, such as N_2O or O_2, are used. The above is especially true when high deposition temperatures (*i.e.*, $\sim$ 1000°C) are used for $Si_lO_mN_p$ deposition. The key advantage of using the SiH_4-CO_2-NH_3-H_2 system, however, is the ability of this chemical system

to deposit silicon oxynitride films with refractive index larger than 1.73 with relative ease, especially at high deposition temperatures.

We have also analyzed and discussed the anomalous effect of deposition temperature on silicon oxynitride composition. In the process of this analysis we have discovered some fundamental facts regarding the mechanism of SiH_4-CO_2, SiH_4-NH_3, and SiH_4-NH_3-CO_2 reactions, even though it was not our purpose to unravel the mechanism of these reactions.

Finally it is our hope that this paper will help in the transition of chemical vapor deposition from an art into a science.

Acknowledgments

Our thanks are due to Dr. W. A. Pliskin for extensive discussions and assistance during the course of this study. Contributions of V. L. Elliott, in the preparation of samples, are also gratefully acknowledged.

Manuscript submitted May 20, 1975; revised manuscript received Sept. 15, 1976.

Any discussion of this paper will appear in a Discussion Section to be published in the December 1977 JOURNAL. All discussions for the December 1977 Discussion Section should be submitted by Aug. 1, 1977.

Publication costs of this article were assisted by IBM Corporation.

APPENDIX A

Refractive index vs. infrared absorption maxima.—Figure 11 presents the infrared absorption maxima as a function of refractive index. The infrared spectra was taken in transmission; *i.e.*, the silicon wafers with deposited films were broken in half, and one-half was used in sample beam and the other half was stripped of its deposit in HF and used in the reference beam. Similar data is presented for the SiH_4-NO-NH_3-N_2 system (4). Note that the two systems (*i.e.*, CO_2-NH_3 and NO-NH_3) follow the same curve, indicating similarity of the deposited films. We also observed weak absorption bands $\sim$ 3380 cm^{-1} and a very weak and broad absorption at $\sim$ 1200 cm^{-1} (4). The absorption maxima at $\sim$ 3380 and $\sim$ 1200 cm^{-1} were not present when SiO_2 was deposited from SiH_4-CO_2-H_2. The 3380 cm^{-1} band is attributed to N-H stretching.

Note that the absorption maxima are only a function of refractive index and not a function of deposition temperature. Though we only show the data points of two temperatures, the absorption maxima of all silicon oxynitride films deposited at any temperature within the 850°-1000°C experimental range fall on the same general curve as shown in Fig. 11. Thus, we conclude that the composition and structure of oxynitride films are only dependent on refractive index and are independent of deposition temperature and the chemical system used to produce them.

Composition vs. refractive index.—The interdependence of the composition and the refractive index for oxynitride has been established previously (4, 6). For

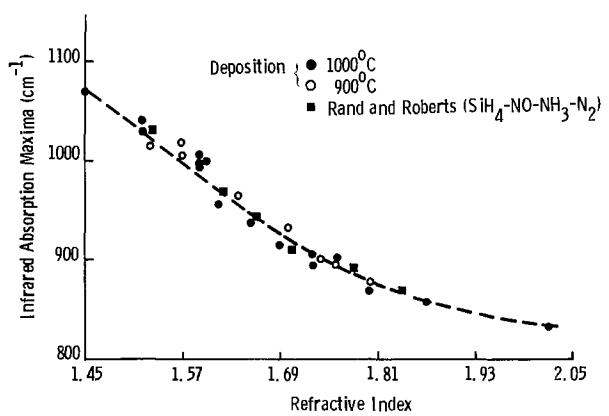


Fig. 11. Infrared absorption maxima as a function of refractive index.

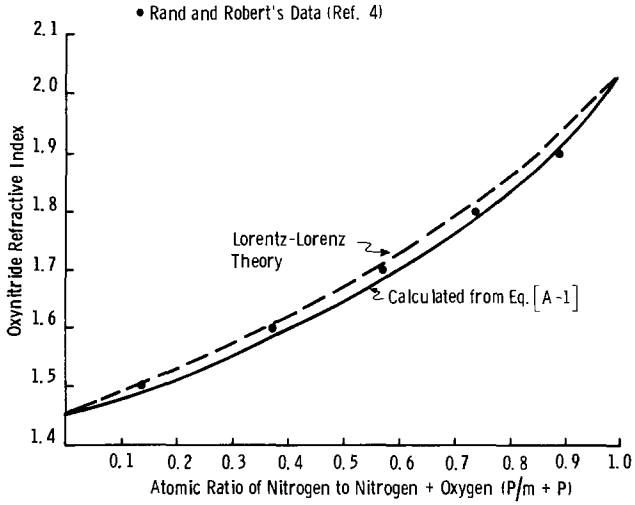


Fig. 12. Plot of refractive index vs. the ratio of atomic nitrogen to the sum of atomic nitrogen and oxygen in silicon oxynitrides.

ease of calculation, we have chosen to represent oxynitride films ($Si_lO_mN_p$) as $xSiO_2 \cdot ySi_3N_4$, where x and y are mole fractions. It should be clearly understood that by representing silicon oxynitride as $xSiO_2 \cdot ySi_3N_4$ we are not implying any structure. It is merely a convenient mathematical representation. The obvious relationships between l, m, p and x and y are $x + 3y = l$, $2x = m$, and $4y = p$, whereas $x + y = 1$.

For the purposes of calculating x and y we have used two methods: (*i*) Lorentz-Lorentz theory (21-24), and (*ii*) the oxynitride refractive index (n_{on}) is assumed to vary linearly with the refractive indexes of SiO_2 ($n_{ox} = 1.45$) and Si_3N_4 ($n_n = 2.025$) as shown in Eq. [A-1] (24)

$$n_{on} = n \cdot n_{on} + y \cdot n_n \qquad [A\text{-}1]$$

Once x and y are known, calculations of l, m, and p are a trivial matter. Figure 12 is a plot of refractive index *vs.* the ratio of atomic nitrogen to the sum of atomic nitrogen and oxygen in silicon-oxynitrides. Data of Rand and Roberts' (4) is provided for comparison. Note the excellent agreement between either method and the experimental data. Throughout this paper we have used the mean value of the composition calculated by the methods described above.

Density and molecular weight vs refractive index.—Once the composition of oxynitride is known as outlined above, the calculation of molecular weight is straightforward. Then, by the use of Lorentz-Lorenz theory (21, 24) the molar refractivity and density can be computed. The results of these computations are shown in Table II.

Conversion of deposition rate units.—By direct thickness measurements, and knowing the deposition time, we obtained the deposition rates in Å min^{-1}. The deposition rates in the units of moles min^{-1} were obtained as shown in Eq. [A-2]

$$r = \frac{\rho \times A_s \times r' \times 10^{-8}}{M} \qquad [A\text{-}2]$$

where r is deposition rate in moles min^{-1}, r' the deposition rate in Å min^{-1}, A_s the susceptor area (1058

Table II. Oxynitride, molecular weight, molar refractivity, and density as a function of refractive index

Refractive index	Molecular weight	Molar refractivity	Density
2.025	140	23.03	3.09* (Si_3N_4)
1.9	121.6	19.46	2.91
1.8	106.4	16.51	2.75
1.7	92.0	13.71	2.59
1.6	78.4	11.07	2.42
1.5	66.4	8.74	2.23
1.45	60	7.50	2.15* (SiO_2)

* Experimental determination.

cm^2), ρ and M the density (g cm^{-3}) and the molecular weight (g $mole^{-1}$) of the deposited film, respectively.

APPENDIX B

Silane concentration along the length of the susceptor is assumed to be constant.

Effective concentration of SiH_4 along the susceptor is defined as

$$C_{SiH_4} = \frac{N}{V} \text{constant} \qquad [B\text{-}1]$$

where N is the number of molecules of SiH_4 and V is the volume of reacting mixture. At feed conditions the concentration of SiH_4 is given by

$$C^o_{SiH_4} = \frac{N^o}{V^o} \qquad [B\text{-}2]$$

where O superscript represents the feed conditions. Due to deposition, the Y_{SiH_4} fraction of SiH_4 is converted to deposit, then

$$N = N^o\,(1 - Y_{SiH_4})$$

and $$V = V^o\,[1 + \phi(Y_{SiH_4})] \qquad [B\text{-}3]$$

But since the reacting mixtures are mostly H_2 in every case, therefore $V^o \sim V$.

Thus

$$C_{SiH_4} = \frac{N^o(1 - Y_{SiH_4})}{V^o} = C^o_{SiH_4}\,(1 - Y_{SiH_4}) \qquad [B\text{-}4]$$

Y_{SiH_4} can be readily calculated by mass-balance, *i.e.*

$$Y_{SiH_4} = \frac{l \times \text{moles of deposit/min}}{\text{moles of silane/min}}$$

The value of l varies between 1 (for SiO_2) and 3 (Si_3N_4), and can be readily calculated by the procedure described in Appendix A knowing the refractive index of a given oxynitride film.

APPENDIX C

For any heterogeneous reaction which is only dependent on the concentration of a single reactant, the rate of reaction may be written as (25)

$$r = \frac{h_G K_s}{h_G + K_s} C_A \qquad [C\text{-}1]$$

where h_G is the mass transfer coefficient, K_s is the surface-chemical reaction rate constant, and C_A is the concentration of the reactant in gas phase. Now, if the reaction rate was mass transfer limited (*i.e.*, $K_s > h_G$), then Eq. [C-1] would reduce to

$$r \approx h_G C_A \qquad [C\text{-}2]$$

For any condition of flow and temperature distribution within a reactor the mass transfer coefficient may be expressed as follows (26)

$$N_{Nu} = a N_{Re}^{n} N_{sc}^{n'} \qquad [C\text{-}3]$$

where N_{Nu} = dimensionless number (Nusselt) = $h_G L/D$, where h_G is mass transfer coefficient, L length of reaction zone, D the diffusivity of the reactant; N_{Re} = dimensionless number (Reynolds) = $\rho VL/\mu$, where ρ is density of the gas, V flow velocity, L the length of reaction zone, μ the viscosity of the gas; N_{sc} = dimensionless number (Schmidt) = $\mu/\rho D_G$, symbols have same meaning as before; n, n', and a are dependent on reactor shape, temperature profile, and flow profile.

From Eq. [C-3] we se that

$$h_G \propto N_{Re} \propto \text{velocity} \propto \text{flow rate}$$

Thus, from Eq. [C-2], if the reaction is mass transfer limited, the reaction rate must increase in proportion to flow rate. We have shown that the reaction rate is independent of flow rate (60-130 liters/min) for Si_3N_4, SiO_2, $Si_lO_mN_p$; therefore, all three reactions are independent of mass transfer coefficient.

The question may arise as to what happens to deposition rate when the flow rate is decreased to a very low value of, say, ~20 liters/min or increased to a very high value of, say, ~200 liters/min. In both cases the average deposition rate over three rings (Fig. 1) is less than the one obtained in the flow range of 60-130 liters/min. This is due to the SiH_4 depletion as indicated by extreme nonuniformity within a run ($> \pm 50\%$).

For multiple wafer reactors, the criterion of mass transfer limited *vs.* surface-chemical reaction rate-limited regions must take into account the deposition uniformity. Since nonuniform depositions are of little practical value, the flow rate range used to check the validity of Eq. [C-2] must be such that the deposition uniformity within a run is at least $\pm 15\%$. This is indeed the case for Si_3N_4, SiO_2, and $Si_lO_mN_p$ depositions in the flow range of 60-130 liters/min at 1000°C. Under identical flow conditions and uniformity constraints the deposition rate of silicon epitaxy, deposited from $SiCl_4$-H_2 reaction, increases as a function of flow rate at 1150°C. Thus, the deposition of silicon epitaxy from $SiCl_4$ and H_2 is a mass transfer limited reaction, whereas the depositions of the Si_3N_4 from SiH_4-NH_3, the SiO_2 from SiH_4-CO_2, and the $Si_lO_mN_p$ from SiH_4-CO_2-NH_3 are surface-chemical reaction rate limited within the appropriate experimental constraints of this study.

REFERENCES

1. C. M. Drum and M. J. Rand, *J. Appl. Phys.*, **39**, 4458 (1968).
2. P. F. Schmidt, M. J. Rand, J. P. Mitchell, and J. D. Ashner, *IEEE Trans. Nucl. Sci.*, **ns-16**, 211 (June 1969).
3. P. F. Schmidt and J. D. Ashner, *ibid.*, **ns-17**, 11 (June 1970).
4. M. J. Rand and J. F. Roberts, *This Journal*, **120**, 446 (1973).
5. R. L. Bratter and A. K. Gaind, U.S. Pat. 3,886,000 (1975).
6. D. M. Brown, P. V. Gray, F. K. Heumann, H. R. Phillipp, and E. A. Taft, *This Journal*, **115**, 311 (1968).
7. T. L. Chu, J. R. Szedon, and C. H. Lee, *ibid.*, **115**, 318 (1968).
8. N. C. Tombs, F. A. Sewell, Jr., and J. J. Comer, *ibid.*, **116**, 862 (1969).
9. Y. I. Kol'tsov, N. G. Kol'tsov, G. I. Zhuravlev, and I. V. Korobov, *Izv. Akad. Nauk SSSR, Neorg. Mater.*, **7**, 521 (1971).
10. Ferranti Limited, Annual Report on Research Project RP-1-55, AD-827049 (1967).
11. M. J. Grieco, F. L. Worthing, and B. Schwartz, *This Journal*, **115**, 525 (1968).
12. A. K. Gaind, G. K. Ackermann, V. J. Lucarini, and R. L. Bratter, *ibid.*, **123**, 111 (1976).
13. A. K. Gaind, G. K. Ackermann, A. Nagarajan, and R. L. Bratter, *ibid.*, **123**, 238 (1976).
14. F. G. Allen, *J. Appl. Phys.*, **28**, 1510 (1957).
15. F. Reizman and W. Van Gelder, *Solid-State Electron*, **10**, 625 (1967).
16. G. W. Castellan, "Physical Chemistry," p. 607 Addison-Wesley Publishing Co., Inc. (1964).
17. V. Y. Doo, D. R. Kerr, and D. R. Nichols, *This Journal*, **115**, 61 (1968).
18. S. Glasstone, "Textbook of Physical Chemistry," D. Van Nostrand Co., Inc., New York (1946).
19. G. C. Bond, "Catalysis by Metals," p. 73, Academic Press (1962).
20. G. L. Tingey, *J. Phys. Chem.*, **70**, 1406 (1966).
21. M. Born and E. Wolf, "Principles of Optics," 5th ed., p. 87 (1975).
22. K. L. Chopra, S. K., Sharma, and V. N. Yadava, *Thin Solid Films*, **20**, 209 (1974).
23. R. Jacobson, in Proceedings of Symposium on Optical Properties of Dielectric Films, Boston, Massachusetts, 1968.
24. A. K. Gaind and E. W. Hearn, To be published.
25. O. Levenspiel, "Chemical Reaction Engineering," p. 335, John Wiley & Sons, Inc., New York (1967).
26. J. R. Welty, C. E. Wicks, and R. E. Wilson, "Fundamentals of Momentum Heat and Mass Transfer," p. 558, John Wiley & Sons, Inc., New York (1969).

Gas Phase Composition Considerations in the Thermal Oxidation of Silicon in Cl-H-O Ambients

R. E. Tressler,* J. Stach,* and D. M. Metz

Departments of Materials Science and Electrical Engineering, The Pennsylvania State University, University Park, Pennsylvania 16802

ABSTRACT

The improved electrical stability and accelerated growth kinetics of thermal SiO_2 grown in oxygen ambients containing Cl_2 and HCl have been well documented, but the mechanisms of this improvement are still poorly understood. This paper presents calculations of equilibrium partial pressures of the possible gaseous species in the Cl-H-O system under thermal oxidation conditions. These results are correlated with published results on (*i*) oxidation kinetics; (*ii*) detrimental effects of water vapor in the growth ambient; and (*iii*) chlorine content in the as-grown oxide.

It is well known that silicon thermal oxidations performed in HCl- or Cl_2-containing ambients result in an improvement in the control of mobile sodium ions which are major contributions to the instabilities as observed in bias temperature stressed MOS structures (1-3). The oxidation kinetics in these environments are modified (much more rapid than in dry O_2), indicating that the incorporation of a chlorine species modifies the transport rate of oxidant species to the Si-SiO_2 interface, at least in the parabolic growth rate regime (4-7). Clearly, solute chlorine species also interact with the sodium ions to produce the passivation effect.

This analysis was undertaken in an attempt to correlate the observed solute effects on the parabolic oxidation rate with the observed solute effects on the sodium ion passivation process. To fundamentally analyze the physical chemistry of this process, the composition of the gas phase in equilibrium with the growing oxide and the corresponding solubilities of the gaseous species in the oxide must be known. Unfortunately, most of the published studies do not give the partial pressures of the gaseous species or enough data to calculate these equilibrium pressures. The ability to depth profile SiO_2 films for chlorine concentrations is a rather recent and less-than-routine technique using nuclear backscattering spectroscopy (2) or ion machining coupled with Auger spectroscopy (8).

In this paper the results of equilibrium gas phase composition calculations in the Cl-H-O system are presented in conjunction with some correlations that have been made of these compositions with published kinetic results, elemental analyses, and electrical measurements on oxides.

Thermodynamic Calculations

Equilibrium partial pressures of the various gaseous species in the Cl-H-O system were calculated using a modified SOLGAS program (9). The calculations were performed from 700° to 1300°C for given ratios of the input gases holding the total pressure at 1 atm.

In Fig. 1 the equilibrium partial pressures in HCl-O_2 ambients as a function of temperature are presented for two HCl concentrations. For the ratio R = H/O = Cl/O, R = 0.10 corresponds to 20 volume percent (v/o) HCl and R = 0.01 corresponds to 2 v/o of HCl in the input mixture. The predominant species are HCl and O_2 plus Cl_2 and H_2O from the reaction $2HCl + 1/2\ O_2 \rightarrow Cl_2 + H_2O$. It can be seen that for a given R the Cl_2 and H_2O partial pressures (p_{Cl_2}, p_{H_2O}) decrease with increasing temperature although it has been reported that the chlorine concentration in the SiO_2 layers increases with temperature (2). This reported chlorine increase with temperature indicates that the solubility of Cl_2 in SiO_2 increases more rapidly with temperature than its partial pressure decreases with temperature at a given input composition. The partial pressures of HOCl, ClO, and HO are at somewhat lower pressures and increase with temperature at a given input composition.

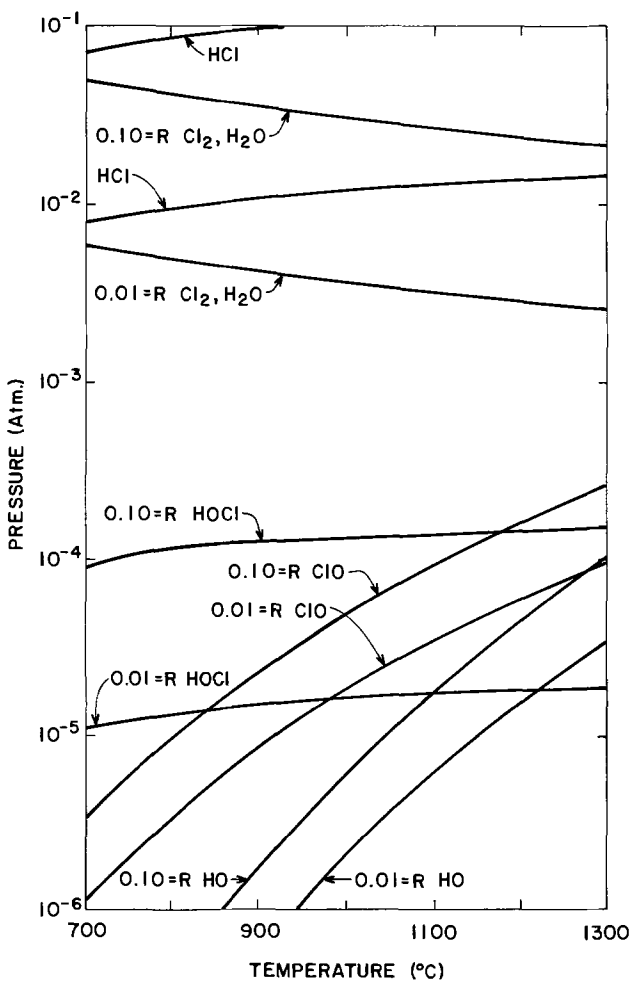


Fig. 1. Equilibrium partial pressures in HCl-O_2 ambients *vs.* temperature and H/O or Cl/O atom ratios. R = H/O = Cl/O. Total pressure = 1 atm.

* Electrochemical Society Active Member.

Key words: silicon dioxide, chlorine, hydrogen chloride, passivation, mobile ions.

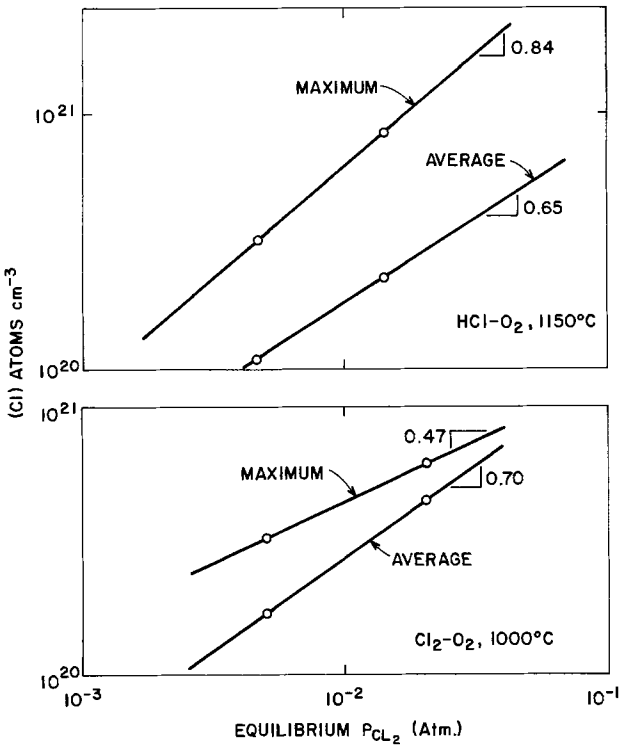


Fig. 2. Chlorine concentration in SiO_2 vs. equilibrium chlorine pressure in HCl-O_2 and Cl-O_2 oxidation ambients [after van der Meulen et al. (2)]. Maximum and average concentrations are shown.

To complete the equilibrium considerations the concentrations of the gaseous species in the growing oxide in equilibrium with the particular gas phase composition are needed. Although published data are scarce, van der Meulen *et al.* (2) have reported the chlorine concentrations in SiO_2 grown in HCl-O_2 and Cl_2-O_2 ambients. Figure 2 shows a plot of chlorine concentration as a function of equilibrium Cl_2 partial pressure calculated from the input gas compositions from the experimental data of van der Meulen *et al.* (2). Very few data points are available and maximum and average Cl concentrations, which reflect a nonuniform distribution in the SiO_2 layer, are plotted. From the equilibrium constant for Cl_2 dissolution in SiO_2 as a monatomic species, the slope of the chlorine concentration *vs.* equilibrium pressure of Cl_2 plot should be 1/2. Note that the tentative straight lines produce slopes that do not all agree with a slope of 1/2. Ideally, one must have similar plots for $(OH)^-$ (or H^+) as a function of H_2O partial pressure, and likewise for the other possible species, including Cl over much larger ranges of T and p_{Cl_2}, to fully characterize the equilibrium situation.

Growth Kinetics

The survey (1-7) of oxidation kinetics in Cl-H-O environments indicates certain trends in rate constants in the parabolic oxidation regime, where diffusion of the oxidant species is generally accepted to be rate limiting. Of particular interest are the p_{Cl_2} effects on the parabolic rate constant B (1-3) for HCl-O_2 and Cl_2-O_2 ambients.

From the data of Kriegler *et al.* (1), it is obvious that the parabolic rate constant is not directly dependent on the total concentration of chlorine in the gaseous ambient since the rate constant for 2.5% Cl_2 is much larger than the rate constant of 5% HCl. This result suggests that B may be directly related to p_{Cl_2} (or p_{ClO} since both quantities show similar trends). In Fig. 3, the parabolic rate constant is plotted as a function of equilibrium p_{Cl_2} at 1100° and 1150°C showing an obvious increasing trend with the chlorine partial pressure rather than the total concentration

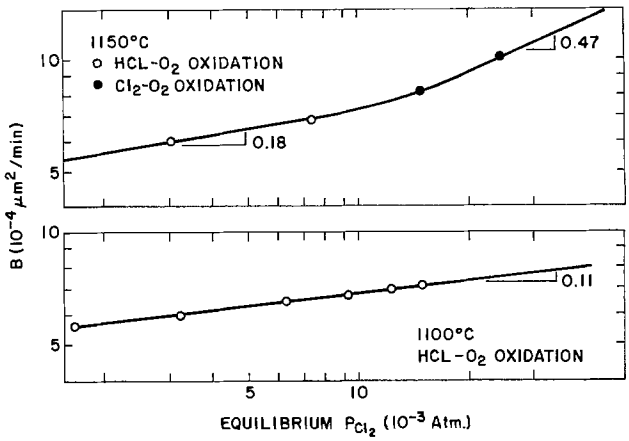


Fig. 3. Log of the parabolic rate constant vs. log of the equilibrium chlorine pressure, at 1150°C [rate constants determined from Kriegler et al. (1)] and 1100°C [rate constants from Hirabayashi and Iwamura (3)].

of chlorine species which suggests that the HCl molecules are not directly involved in the reaction of HCl/O_2 ambients with SiO_2. However, the change in B cannot be simply related to the incorporation of chlorine via the reaction $Cl_2 \rightarrow 2Cl$, assuming that the dissolved Cl controls the oxidation at the Si-SiO_2 interface by some undetermined mechanism, since the slope of the B *vs.* p_{Cl_2} plot is not 1/2 as predicted by the parameters included in B (4). If the partial pressure of H_2O affects the oxidation kinetics, which is well known to be the case for H_2O-O_2 ambients, the magnitude of the effect cannot be assessed at this point; since experimental data are not available for H_2O-O_2 ambients at 1100° and 1150°C in the compositions of interest. Clearly, much additional experimentation is required to elucidate the precise mechanism(s) by which the p_{Cl_2}, p_{H_2O}, or p_{ClO} controls the oxidation of Si in H-Cl-O ambients.

Electrical Properties of Oxides

In order to interpret the electrical characteristics observed by Kriegler (10), his data were replotted as a function of p_{Cl_2}. Figure 4 shows mobile ion density as a function of log p_{Cl_2} as a result of varying the initial HCl/O_2 ratio. It can be seen that above a critical

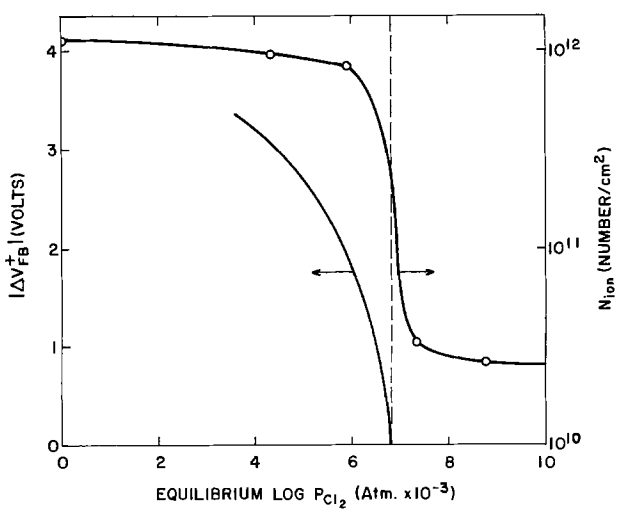


Fig. 4. Number of mobile ions and flatband voltage shift vs. equilibrium chlorine pressure for (100)Si, 1150°C HCl oxidation [after Kriegler (9)]. In the upper curve p_{Cl_2} variations are the result of variations in the initial HCl/O_2 ratio. In the lower curve, p_{Cl_2} variations are due to added H_2O vapor in a 6% HCl/O_2 oxidation ambient. The range of added water vapor to produce the 4-7 $\times$ 10^{-3} range of p_{Cl_2} was 5-25 Torr H_2O.

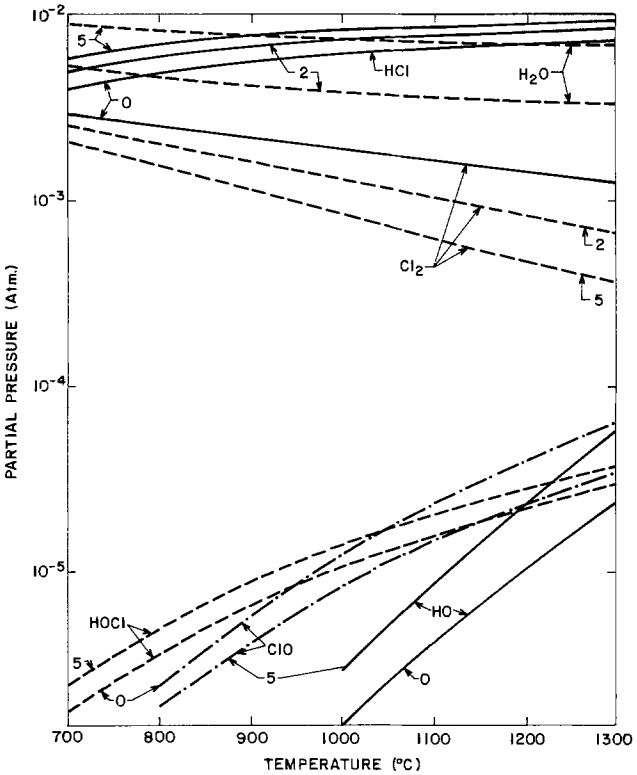


Fig. 5. Simulation of HCl-O ambient with added H_2O vapor. Cl/O atom ratio = 0.005. Total pressure = 1 atm. The numbers indicate the level of added H_2O in Torr.

$p_{Cl_2} \sim 7 \times 10^{-3}$ atm (for this particular total Na concentration), the mobile ion density approaches a lower level of $5 \times 10^{10}/cm^2$. One can also reduce the p_{Cl_2} at a given HCl-O_2 ratio by introducing H_2O. In Fig. 5, the calculated equilibrium partial pressures of gaseous species in HCl-O_2 ambients with added H_2O partial pressures of 2 and 5 Torr are presented. Note that at 1150°C with 5 Torr of added H_2O the p_{Cl_2} drops to ~20% of the corresponding partial pressure in dry O_2. Also, plotted in Fig. 4 is the flatband voltage shift, $|\Delta V^+_{FB}|$, as a function of p_{Cl_2} where p_{Cl_2} was decreased in a 6% HCl-O_2 ambient by adding H_2O to the atmosphere. These data show that $|\Delta V^+_{FB}|$ is also minimized at $p_{Cl_2} \sim 7 \times 10^{-3}$ atm.

From this preliminary analysis, it becomes clear that the partial pressures of the gaseous species in equilibrium with the growing thermal oxide determine the kinetics of growth and also determine the concentration of "passivating" species in the oxide. The suggestion is made that trends in growth constants and electrical characteristics are related to the partial pressure of Cl_2 (or ClO) in the gas phase and not the total chlorine content of the gas phase. Extensive experimentation with oxides grown in systematically varied compositions in the Cl-H-O system over a wide range of temperatures is necessary to unequivocally establish the nature of the gas/solid interaction and the mechanism of passivation.

Acknowledgments

This research was partially funded by the Advanced Research Projects Agency Order 2397 through the National Bureau of Standards Semiconductor Technology Program Contract 5-35717.

Manuscript submitted Sept. 19. 1975; revised manuscript received Sept. 15, 1976. This was Paper 137 presented at the Dallas, Texas, Meeting of the Society, Oct. 5-9, 1975.

Any discussion of this paper will appear in a Discussion Section to be published in the December 1977 JOURNAL. All discussions for the December 1977 Discussion Section should be submitted by Aug. 1, 1977.

Publication costs of this article were assisted by The Pennsylvania State University.

REFERENCES

1. R. J. Kriegler, Y. C. Cheng, and D. R. Colton, *This Journal*, **119**, 388 (1972).
2. Y. J. van der Meulen. C. M. Osburn, and J. F. Ziegler, *ibid.*, **122**, 284 (1975).
3. K. Hirabayashi and J. Iwamura, *ibid.*, **120**, 1595 (1973).
4. B. E. Deal and A. S. Grove, *J. Appl. Phys.*, **36**, 3770 (1965).
5. J. R. Ligenza and W. G. Spitzer, *J. Phys. Chem. Solids*, **14**, 131 (1960).
6. W. A. Pliskin, *IBM J. Res. Develop.*, **10**, 198 (1966).
7. B. E. Deal, *This Journal*, **121**, 198 (1974.)
8. N. D. Chou, C. M. Osburn, Y. J. van der Meulen, and R. Hammer, *Appl. Phys. Lett.*, **22**, 380 (1973).
9. G. Eriksson, *Acta Chem. Scand.*, **25**, 2651, (1971).
10. R. J. Kriegler, in "Semiconductor Silicon 1973," H. R. Huff and R. R. Burgess, Editors, p. 372, The Electrochemical Society Softbound Symposium Series, Princeton, New Jersey (1973).

Ionic Conductivity of Cuprous Chloride Containing Cuprous Sulfide

Tsuneo Matsui[1] and J. Bruce Wagner, Jr.*,[1]

Materials Research Center and Department of Materials Science and Engineering, Northwestern University, Evanston, Illinois 60201

ABSTRACT

The electrical conductivity of undoped cuprous chloride and cuprous chloride containing cuprous sulfide as an impurity in concentrations between 0.20 and 1.0 mole percent (m/o) has been measured as a function of temperature between 60° and 370°C using the a-c method. The results have been analyzed to obtain the values of the energies of formation and migration, mobility of copper interstitial ions, and concentrations of Frenkel defects. The solubility limit of cuprous sulfide in cuprous chloride has also been determined by using electrical conductivity measurements and x-ray diffraction.

Electrical conductivity measurements of cuprous chloride have been measured (1, 2). However, information on the concentration and mobility of ionic defects in cuprous chloride has not yet been reported. The predominant lattice defects in ionic crystals have been conveniently investigated by measuring the ionic conductivity of samples containing known concentrations of aliovalent cations (3-8). However, there is virtually no solid solution between cuprous chloride and divalent metal chlorides [for example $PbCl_2$ (9), $ZnCl_2$ (9), $CaCl_2$ (10), and $MgCl_2$ (10)]. Hsueh and Christy measured the electrical conductivity of CuCl doped with $PbCl_2$, $CaCl_2$, $CdCl_2$, and $ZnCl_2$ but they could not obtain information about the concentration and mobility of lattice defects because of the limited solubility (11).

In this paper the ionic conductivity of pure CuCl and CuCl doped with Cu_2S has been measured. The experimental results are analyzed to obtain the value of the migration energy and mobility of copper interstitial ions, and formation energy and concentrations of Frenkel defects.

Theory

It has been recently found that cuprous chloride is predominantly an ionic conductor above 100°C (2). Several different investigations (1, 11, 12) indicate that the predominant intrinsic defects in copper halides are Frenkel cation pairs (*e.g.*, copper interstitial, $Cu^{\cdot}_i$, and copper vacancy, V'_{Cu}). The ionic conductivity, σ, may be written as

$$\sigma = Nq\,(x_v u_v + x_i u_i) \qquad [1]$$

where N is the number of copper ions per unit volume, u the mobility, q the absolute electronic charge, x the molar fractions of defects, and the subscripts v and i refer to vacancy and interstitial copper ions, respectively. Using the notation of Kröger and Vink (13), the reaction equation and the law of mass action for Frenkel defects may be written as

$$Cu_{Cu} = V'_{Cu} + Cu^{\cdot}_i \qquad [2]$$

and

$$x_v \cdot x_i = K_F \equiv x_0^2 \qquad [3]$$

where x_0 is the molar fraction of the intrinsic defects. By doping Cu_2S in CuCl, copper interstitials are produced as follows

$$Cu_2S = Cu_{Cu} + S'_{Cl} + Cu^{\cdot}_i \qquad [4]$$

The condition of electroneutrality requires that

$$x_i = C + x_v \qquad [5]$$

where C is the molar fraction of cuprous sulfide. Thus Eq. [3] becomes

$$x_i(x_i - C) = x_0^2 \qquad [6]$$

or

$$x_i = \frac{C}{2}\left\{1 + \left(1 + \frac{4x_0^2}{C^2}\right)^{1/2}\right\} \qquad [7]$$

Substituting Eq. [3] and [7] into Eq. [1], we have

$$\sigma = Nq\,x_0\,(u_v + u_i)\left\{\sqrt{\left(\frac{C}{2x_0}\right)^2 + 1} - \left[\frac{C}{2x_0}\cdot\frac{\phi - 1}{\phi + 1}\right]\right\} \qquad [8]$$

where

$$\phi = u_v/u_i \qquad [9]$$

For undoped crystals, the electrical conductivity is written as

$$\sigma_0 \equiv Nq\,x_0\,(u_v + u_i) \qquad [10]$$

Thus, the conductivity isotherm is expressed as

$$\frac{\sigma}{\sigma_0} = \left\{\sqrt{\left(\frac{C}{2x_0}\right)^2 + 1} - \left[\frac{C}{2x_0}\cdot\frac{\phi - 1}{\phi + 1}\right]\right\} \qquad [11]$$

When $C >> x_0$, Eq. [11] may be written as

$$\frac{\sigma}{\sigma_0} = \frac{C}{x_0(1 + \phi)} \qquad [12]$$

For any constant temperature, a plot of σ *vs.* C should be linear for extrinsic conduction. For cuprous halides, $\phi << 1$ (14) and from Eq. [10], the slope can be written as

$$\frac{\sigma_0}{x_0\,(1 + \phi)} \cong \frac{\sigma_0}{x_0} = Nq\,u_i \qquad [13]$$

By using Eq. [13], we can calculate the mobility of copper interstitials and concentrations of intrinsic Frenkel defects for each temperature.

Experimental

Sample preparation.—The samples used in this study were sintered pellets of pure CuCl and CuCl doped with Cu_2S. For pure CuCl, ultrapure anhydrous CuCl powder (99.999% Semi-elements Incorporated) was used without further purification. Doped samples were made by mixing the ultrapure CuCl powder with the appropriate amount of Cu_2S powder (99.0% Alfa Products, Ventron Corporation, with the major impurity being Fe and Ni) from which some of the absorbed water had previously been removed by heating at about 110°C in a Vycor glass tube connected to a vacuum pump.

* Electrochemical Society Active Member.
[1] Present address: Center for Solid State Science, Arizona State University, Tempe, Arizona 85281.
Key words: copper interstitial mobility, Frenkel defects.

The Cu_2S was added in concentrations of 0.20, 0.30, 0.40, 0.70, and 1.0 m/o. These undoped and doped powders were pressed at 75,000 psi in a 0.319 in. diameter steel die. The freshly prepared pellets were sealed in an evacuated Vycor glass and then sintered at 390°C for 72 hr. After the first sintering, the pellets were pulverized, pressed, and again sintered in an evacuated Vycor glass tube at 390°C for 96 hr. The sintering conditions were strictly controlled so as to produce final sintered densities in a narrow range (in this study, 88-89% of the theoretical value of pure CuCl) so that a valid comparison could be made from one pellet to another. After sintering, the size of the pellets was about 8 mm in diameter and about 2 mm long. The pellets were then polished and washed in acetone.

Total conductivity measurements.—To make the conductivity measurements, the sample was sandwiched between reversible copper electrodes which were 99.999% pure copper rod obtained from American Smelting and Refining Company, and electrical contact was ensured by applying a slight pressure by means of springs. The sample was annealed at 370°C for 2 hr prior to measurements to ensure a good interface contact. Copper halides, when equilibrated with copper electrodes, exhibit virtually 100% ionic conduction (1), just as the silver halides equilibrated with silver electrodes (15). The electrical conductivity was mainly measured using a General Radio a-c bridge (1650A) at 1000 Hz. It was also measured in the frequency range 0.80-20 kHz by using audio oscillator Model 202D (Hewlett-Packard Company). For pure CuCl, 0.30, 0.70, and 1.0 m/o samples at 153°, 250°, and 302°C there was no frequency dependence. Conductivity values were calculated from resistance measurements, pellet dimensions, and density. Correction for porosity was made by the following equation (16)

$$\sigma_t = \sigma_m\left(1 + \frac{P}{1 - P^{2/3}}\right) \qquad [14]$$

where σ_t is the conductivity after correction, σ_m the conductivity before correction, and P the porosity.

Electronic conductivity measurements.—Electronic conductivity was measured by using Wagner's polarization cell where a sample was sandwiched between a reversible electrode, copper, and a blocking electrode, graphite (pyrolytic graphite from the Union Carbide Company). Before measurements the polarization cell was annealed at 370°C for 2 hr. Wagner (17) showed that the total electronic current I_T passing through a cell under steady-state conditions is given by

$$I_T = RTA/L\mathbf{F}\{\sigma_{\ominus}^{\circ}[1 - \exp(-EF/RT)] + \sigma_{\oplus}^{\circ}[\exp(+EF/RT) - 1]\} \qquad [15]$$

where A is the cross section area of the interface between graphite and the sample, L the thickness of the samples, $\mathbf{F}$ Faraday's constant, $\sigma_{\ominus}^{\circ}$ electronic conductivity due to excess electrons in the sample coexisting with copper, and $\sigma_{\oplus}^{\circ}$ electronic conductivity due to excess electron holes in the sample coexisting with copper. The other symbols have their usual meanings. If $\sigma_{\oplus}^{\circ} >> \sigma_{\ominus}^{\circ}$, $I_{\oplus}$ becomes

$$I_T \simeq I_{\oplus} = RTA/L\mathbf{F}\{\sigma_{\oplus}^{\circ}[\exp(E\mathbf{F}/RT) - 1]\} \qquad [16]$$

and when $E >> RT/\mathbf{F}$, Eq. [16] can be written as

$$I_{\oplus} = RTA/L\mathbf{F}\{\sigma_{\oplus}^{\circ}\exp(E\mathbf{F}/RT)\} \qquad [17]$$

By using Eq. [17], we can determine the electronic hole conductivity from a plot of the log $I_{\oplus}$ *vs.* E, the applied potential. A Keithley 260 nanovolt source was used to apply various stable d-c potentials, and the current was measured by reading the voltage drop across a series resistor with a Doric Digital microvoltmeter.

Both total electrical conductivity and electronic conductivity measurements were carried out under a slow flow rate of purified argon gas (about 0.2 cm/sec). A Marshall resistance furnace was used in a horizontal position. The temperatures were controlled to ± 1°C by Leeds and Northrup Electromax controller and temperature was measured by Doric Digital voltmeter using Chromel-Alumel thermocouple. The thermocouple was calibrated by using the phase transition temperatures of CuI (14).

X-ray diffraction analysis.—The x-ray diffraction patterns of the pure and doped CuCl were obtained at room temperature by using a Philips diffractometer with CuKα radiation through a Ni filter.

Results

Measurements of the total electrical conductivity of a pure CuCl sample and five doped samples containing different concentrations of Cu_2S have been carried out in the temperature range of 60°-370°C. The results are shown in Fig. 1. The previous data on the total electrical conductivity of polycrystalline (1) and single crystalline (2, 11) CuCl are also shown in Fig. 1. The total electrical conductivity increased with increasing concentration of Cu_2S.

Electronic conductivity measurements were carried out on one sample doped with 0.70 m/o Cu_2S. The results are shown in Fig. 2. The previous data on partial electronic hole conductivity of pure CuCl (single crystal) by Joshi and Wagner (2) are also shown in Fig. 2. Polarization curves are also shown in Fig. 3. Between 0.2 and 0.4V, the theoretical slope based on Wagner's theory (17) fitted the experimental results. But when higher polarization potentials were applied, slopes with less value than the theoretical value were obtained. This anomalous behavior may be attributed

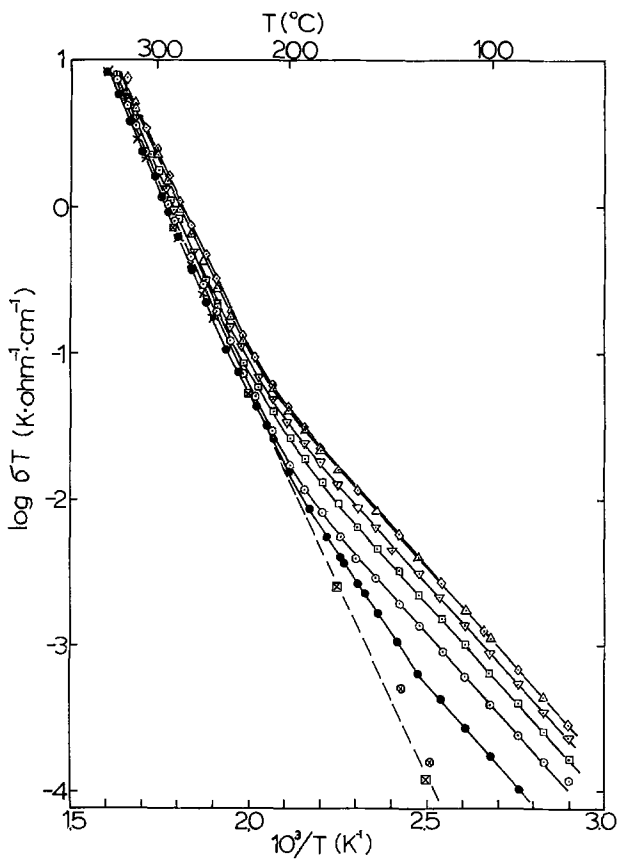


Fig. 1. The temperature dependence of the electrical conductivity of pure CuCl and CuCl-Cu_2S. This study: ●-●-● pure CuCl, ⊙-⊙-⊙ 0.20 m/o Cu_2S, ⊡-⊡-⊡ 0.30 m/o Cu_2S, ▽-▽-▽ 0.40 m/o Cu_2S, △-△-△ 0.70 m/o Cu_2S, ◇-◇-◇ 1.0 m/o Cu_2S. Pure CuCl: x-x-x Wagner and Wagner (1), ⊗-⊗-⊗ Joshi and Wagner (2), ⊠-⊠-⊠ Hsueh and Christy (11).

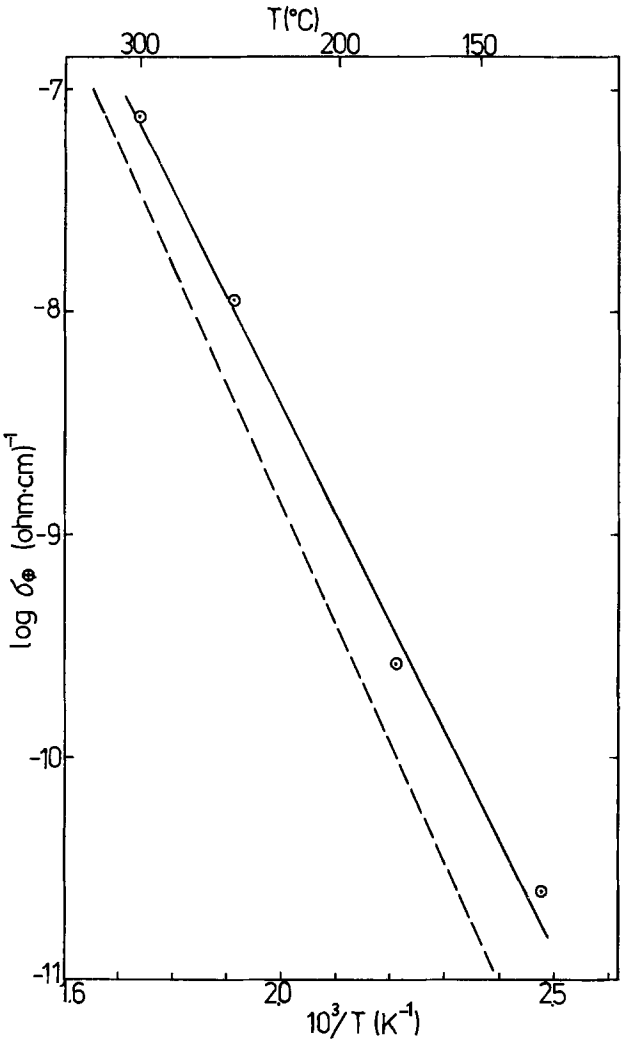


Fig. 2. The temperature dependence of the electronic hole conductivity equilibrated with a copper electrode: - - - CuCl by Joshi and Wagner (2), ⊙ CuCl + 0.70 m/o Cu_2S in this study.

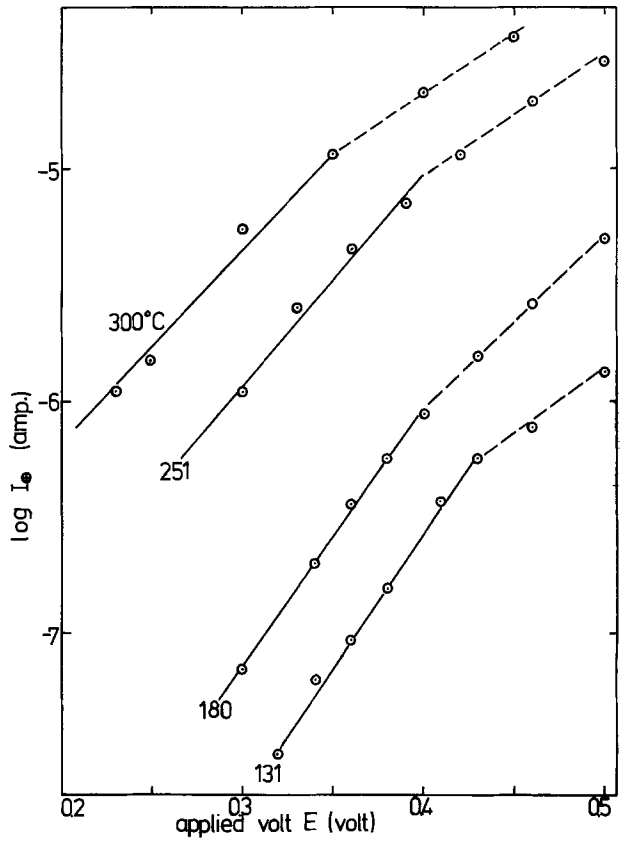


Fig. 3. Logarithm of electronic hole current vs. applied potential in CuCl doped with 0.70 m/o Cu_2S: —— theoretical slope.

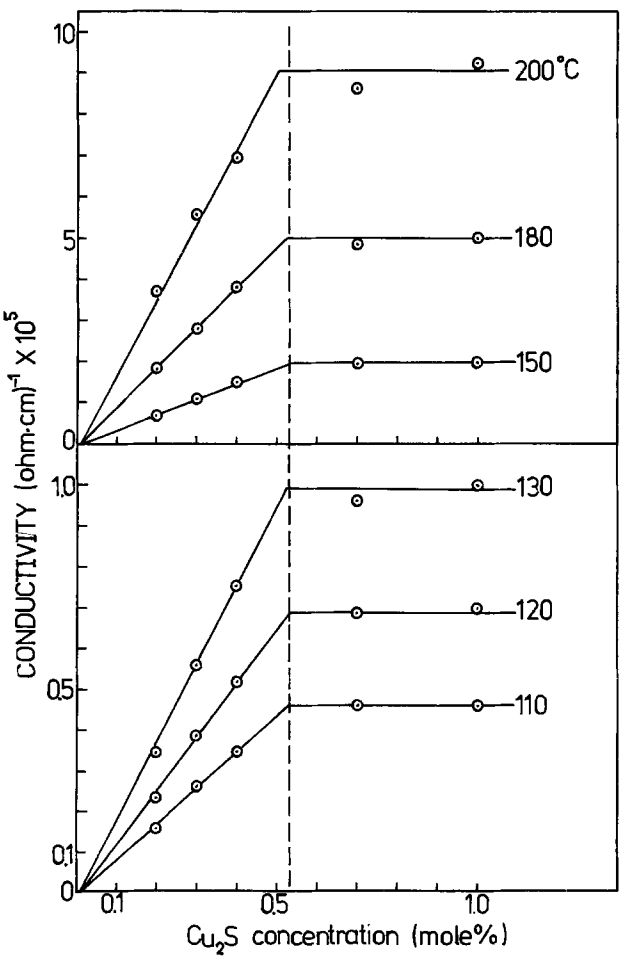


Fig. 4. The electrical conductivity vs. concentration of Cu_2S: - - - - solubility limit (0.53 m/o Cu_2S).

to the high concentration of electron holes at the electrolyte/blocking electrode interface resulting from the high polarization potential. The same phenomena were obtained in the case of PbF_2 by Joshi and Liang (18). From Fig. 1 and 2, it is concluded that the electron hole contribution to the total electronic conductivity can be neglected, *i.e.*, the total conductivity of doped samples is virtually ionic conductivity which is the same as pure CuCl.

In the doping studies, association or precipitation appeared to steepen the slope of log σT *vs.* $1/T$ in the extrinsic region and affect the conductivity values (7, 8). To eliminate this error, the limits of simple extrinsic conduction and solubility limits were determined by applying Eq. [12], which shows that the σ *vs.* concentration isotherm should be linear (Fig. 4). As seen in Fig. 4, the solubility limit of Cu_2S in CuCl was 0.53 ± 0.03 m/o and did not change from 110° to 200°C within experimental error.

We also have checked the solubility limit of Cu_2S in CuCl by means of x-ray diffraction at room temperature. The x-ray diffraction peaks of all doped samples were the same as that of pure CuCl (19), and no other diffraction peaks were observed.

However, the solubility limit could be determined from the concentration dependence of lattice constants based on the electrical conductivity data. The x-ray data are shown in Fig. 5. It can be seen that the solubility limit found by x-ray diffraction at room temperature is consistent with electrical conductivity results. The solubility limit at high temperatures could not be determined since even by quenching from 200°C

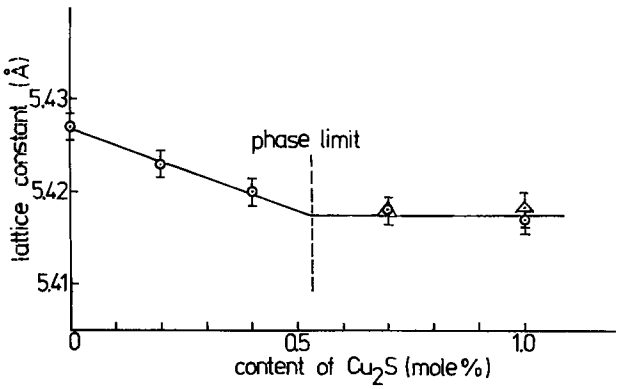


Fig. 5. Lattice constant vs. concentration of Cu_2S at 22°C: ⊙ annealed sample, △ sample quenched from 200°C.

to ice water the lattice constant was almost the same as that at room temperature, which indicated the difficulty of quenching.

Discussion

The increased conductivity observed when CuCl was doped with Cu_2S is due to an increase in ionic conductivity since the electronic hole conductivity is far below (five or six orders lower) the total electrical conductivity, and the ionic conductivity of CuCl increased monotonically with increasing dopant concentration of Cu_2S. These indicate that the predominant defects in the extrinsic region below 230°C are copper ion interstitials according to Eq. [4]. Above 230°C the steeper slope, shown in Fig. 1, represents the change from the extrinsic region to the intrinsic region where the Frenkel defects (copper ion interstitials and copper ion vacancies) are thermally generated in greater concentration than the defects introduced by the Cu_2S ($x_0 >> C$).

At higher temperatures, our results of the electrical conductivity on polycrystalline CuCl are in good agreement with the previous data on polycrystalline (1) and single crystalline (2, 11) CuCl, but in the extrinsic region below 230°C our conductivity values are higher than the single crystal data (2, 11, 20). To check the effect of short-circuit paths such as grain boundaries on the conductivity values, two samples with different densities (82 and 88%) each containing the same dopant concentration (0.30 m/o Cu_2S) were studied. The conductivity values of these two samples and their temperature dependence were in good agreement with one another within experimental error (± 3%) after correcting for porosity using Eq. [14]. Generally, in the pure single crystals of alkali halides and silver halides a knee in the conductivity curve is exhibited at low temperature, below which the conductivity is affected by very small amounts of impurities (extrinsic region) which are accidentally present (6-8, 21-23). The electrical conductivity of pure single crystal CuI which exhibits the same crystal structure as CuCl at low temperature has been also studied by Jow and Wagner (24). According to their data, curvature of an Arrhenius plot of the electrical conductivity of CuI was obtained for all temperatures below 369°C. The difference between the conductivity data for the single and polycrystalline samples may be inferred to be due to the small amount of impurities present in the polycrystalline samples.

As seen in Fig. 1, activation energies of pure CuCl ($90° \leq T \leq 130°C$) and doped samples ($60° \leq T \leq 200°C$) in the extrinsic region did not change (12.5 ± 0.5 kcal/mole) with increasing the dopant concentrations. Thus, the basic assumption which is made in doping studies that the mobility does not change with doping level holds in this case.

By using Fig. 4 the mobility and migration energy of copper interstitial ions, and the concentration and formation energy of Frenkel defects were then calculated.

Table I. Mobility of copper interstitial ions and concentration of Frenkel defects at various temperatures for CuCl

Temperature (°C)	u_i (cm²/Vsec)	x_0 (mole fraction)
110	$(2.34 \pm 0.37) \times 10^{-7}$	$(5.83 \pm 0.93) \times 10^{-5}$
120	$(3.52 \pm 0.67) \times 10^{-7}$	$(8.96 \pm 1.70) \times 10^{-5}$
130	$(4.98 \pm 0.64) \times 10^{-7}$	$(1.34 \pm 0.17) \times 10^{-4}$
150	$(9.73 \pm 1.30) \times 10^{-7}$	$(2.88 \pm 0.38) \times 10^{-4}$
180	$(2.46 \pm 0.18) \times 10^{-6}$	$(7.63 \pm 0.58) \times 10^{-4}$
200	$(3.85 \pm 1.84) \times 10^{-6}$	$(1.45 \pm 0.69) \times 10^{-3}$

The data between 0.20 and 0.40 m/o and between 110° and 200°C which exhibited linear isotherms were used. The calculated data of the mobility of copper interstitial ions and concentrations of Frenkel defects are summarized in Table I and Fig. 6. The migration energy of copper interstitials was 12.1 ± 0.9 kcal/mole, and the formation energy of Frenkel defects was 5.6 ± 0.2 kcal/mole.

Another important feature of the extrinsic isotherms in Fig. 4 was that they were all extrapolated to the same finite concentration of Cu_2S. This is evidence for a common level of impurity binding a fixed amount, 0.01 m/o, of Cu_2S. This may account for the difference between the electrical conductivity of polycrystalline undoped CuCl in this study and the data obtained previously on single crystalline CuCl (2). A similar effect has been also observed for NaCl doped with $MgCl_2$ (7, 25) and NaCl doped with $CdCl_2$ (8, 26).

Summary

Conductivity measurements have been performed on undoped CuCl and CuCl doped with different concentrations of Cu_2S. The mobility and migration energy (E_m) of copper interstitial ions, and concentrations and formation energy (E_f) of Frenkel defects were calculated: $E_m = 12.1 \pm 0.9$ kcal/mole and $E_f = 25.6 \pm 0.2$ kcal/mole.

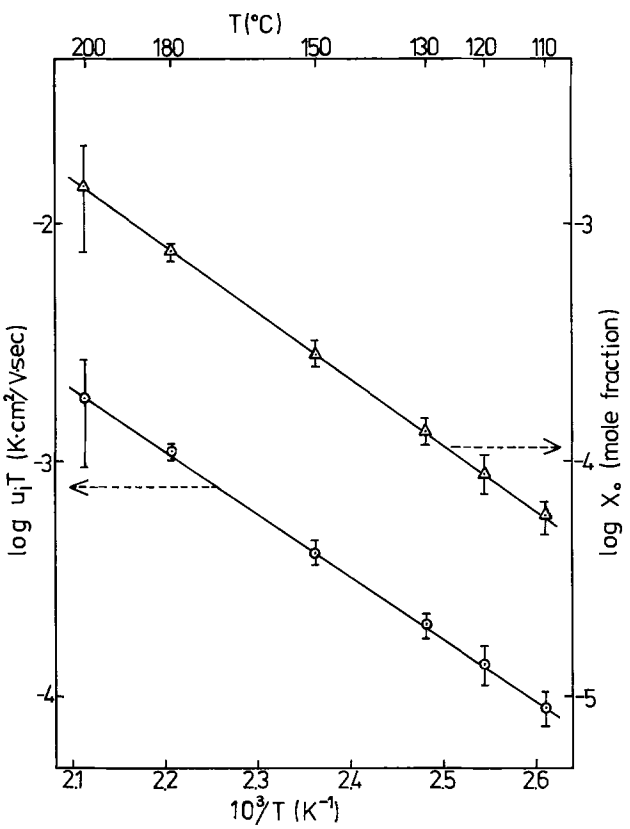


Fig. 6. The temperature dependence of the mobility for copper interstitial ions and of the concentration of Frenkel defects in CuCl: ⊙ mobility (u_i), △ concentration (x_0).

The solubility limit of Cu_2S in CuCl was found to be 0.53 ± 0.03 m/o from room temperature to 200°C by using x-ray and electrical conductivity measurements.

Acknowledgments

This work was supported by the Advanced Research Projects Agency of the Department of Defense and was monitored by the Office of Naval Research through the Materials Research Center of Northwestern University under Contract No. N00014-75-C-1116.

Manuscript submitted Aug. 23, 1976; revised manuscript received Nov. 15, 1976.

Any discussion of this paper will appear in a Discussion Section to be published in the December 1977 JOURNAL. All discussions for the December 1977 Discussion Section should be submitted by Aug. 1, 1977.

REFERENCES

1. J. B. Wagner and C. Wagner, *J. Chem. Phys.*, **26**, 1597 (1957).
2. A. V. Joshi and J. B. Wagner, Jr., *This Journal*, **122**, 1071 (1975).
3. J. Teltow, *Ann. Phys. (Leipzig)*, **5**, 63, 71 (1949).
4. I. Ebert and J. Teltow, *ibid.*, **15**, 268 (1955).
5. E. Koch and C. Wagner, *Z. Phys. Chem. (B)*, **38**, 295 (1937).
6. A. B. Lidiard, "Handbuch der Physik," Vol. 20 p. 246 (1957).
7. D. L. Kirk and P. L. Pratt, *Proc. Br. Ceram. Soc.*, **9**, 215 (1967).
8. H. W. Etzel and R. J. Maurer, *J. Chem. Phys.*, **18**, 1003 (1950).
9. G. Herrmann, *Z. Anorg. Chem.*, **71**, 262 (1911).
10. O. Menge, *ibid.*, **72**, 189 (1911).
11. V. W. Hseuh and R. W. Christy, *J. Chem. Phys.*, **39**, 3519 (1963).
12. T. E. Mayer and R. B. Levy, *ibid.*, **1**, 647 (1933).
13. F. A. Kröger and H. J. Vink, "Solid State Physics," Vol. 3, p. 588, Academic Press, New York (1956).
14. T. Matsui and J. B. Wagner, *This Journal*, **124**, 300 (1977).
15. B. Ilschner, *J. Chem. Phys.*, **28**, 1109 (1958).
16. H. W. Russel, *J. Am. Ceram. Soc.*, **18**, 1 (1936).
17. C. Wagner, Proceedings of the 7th International Committee for Electrochemical Thermodynamics and Kinetics, London, 1955, Butterworths, London (1957).
18. A. V. Joshi and C. C. Liang, *J. Phys. Chem. Solids*, **36**, 927 (1975).
19. A.S.T.M.Card 6-0344, N.B.S. Circular 539 IV, 35 (1953).
20. J. Rivera, L. A. Murray, and P. A. Hoss, *J. Cryst. Growth* **1**, 17 (1967).
21. T. G. Stoebe and P. L. Pratt, *Proc. Br. Ceram. Soc.*, **9**, 181 (1967).
22. E. Barsis, E. Lilley, and A. Taylor, *ibid.*, **9**, 203 (1967).
23. L. Heyne, *Electrochim. Acta*, **15**, 1251 (1970).
24. T. Jow and J. B. Wagner, To be published.
25. G. D. Watkins, *Phys. Rev.*, **113**, 1 (1959).
26. A. B. Lidiard, *ibid.*, **94**, 29 (1954).

Polycrystalline Aluminum Oxide Anodization on Silicon

Kiyoto Iida

Nippon Electric Company, Limited, I.C. Division, Nakaharaku, Kawasaki, Japan

ABSTRACT

Anodization of aluminum oxide, deposited by $AlCl_3$ hydrolysis on silicon, is investigated in various electrolytes and a new selective etching technique is studied. Polycrystalline aluminum oxide is converted into amorphous film by anodization. The anodized film is soluble in various acidic solutions. At a specific anodizing stage, anodic current shows an abrupt change under a fixed anodic voltage. Characteristics of current density *vs.* anodizing time are successfully explained by the solubility of the anodized aluminum oxide in the electrolyte and by the formation of new anodic SiO_2. Anodization effects on electrical properties of MA(O)S structures with the anodized film are investigated.

Recently, there has been an increasing interest in the use of aluminum oxide as gate-insulator and passivating dielectric for MIS (metal-insulator-silicon) devices. The charge storage phenomenon of this film is especially interesting, regarding its memory application (1, 2). For forming this film, chemical vapor deposition technique is ordinarily used, because a uniform film of excellent quality can be obtained at relatively low temperatures. The electrical properties of MA(O)S (metal-aluminum oxide-(silicon dioxide)-silicon) structures with CVD aluminum oxide are sensitive to the thermal history, ambient gases, and various other processing factors of aluminum oxide formation. Among these factors, oxygen heat-treatment has an especially large influence on $Si\text{-}Al_2O_3$ structure, for it forms a new silicon dioxide underneath the original aluminum oxide (3, 4).

In the anodization of preexisting dielectric film on silicon substrate, an interesting feature is that a change in the chemical composition of the film depends on the mobile species. In the case of amorphous silicon nitride films on a silicon substrate, it has been shown that conversion of the nitride film to anodic SiO_2 occurs by oxygen ions replacing nitrogen. Here, oxygen ion migration through amorphous silicon nitride would change its composition (5). Schmidt and Wonsidler (5) reported that in the anodization of polycrystalline α-alumina films on silicon substrate in aqueous borate solution, growth of new oxide occurred at the oxide-silicon interface, increasing the total film thickness. They reported that, in the preexisting aluminum oxide anodization, silicon ion migration changes the chemical composition of the film, whereas oxygen ion migration does not. Kamoshida and Mayer also studied aluminum oxide film anodization on a silicon substrate and observed the formation of anodic SiO_2 using MeV $^4He^+$ ion backscattering spectra (6).

In the present work, it was found that, in the anodization of preexisting aluminum oxide on a silicon substrate, polycrystalline aluminum oxide is converted into amorphous aluminum oxide and the anodized film becomes soluble in various acidic solutions. Anodization effects on electrical properties of MA(O)S structures with the anodized aluminum oxide film

Key words: anodization, aluminum oxide, physicochemical properties, conversion, selective etching technique.

were studied. Furthermore, the anodization process is applied for opening windows in Si-Al_2O_3-SiO_2 structures.

Experimental

Aluminum oxide films were deposited by the reaction of $AlCl_3$ with CO_2 and H_2 onto 3 ~ 4 Ω-cm, p-type silicon substrates. The temperature of the silicon substrate during deposition was kept at 850°C to give a deposition rate of 100 Å/min. Thickness of the film was extended from 500 to 2500Å, which was measured by ellipsometry. The film has polycrystalline form and was hardly soluble in acidic solutions, except by hot H_3PO_4. Detailed descriptions of film preparation and physicochemical and electrical properties of the film appear in previous papers (3, 4, 7). After deposition of aluminum oxide film onto silicon substrates, the film was covered with chemically vapor deposited silicon dioxide. Windows were then opened in the silicon dioxide to expose a part of the aluminum oxide surface. The back side of the wafer was also covered with silicon dioxide. The layers of silicon dioxide served as an electrically insulating barrier to anodization.

Both ammonium borate dissolved in ethylene glycol and 2 volume percent (v/o) sulfuric acid were used for electrolytes. Anodizations were performed at various anodic voltages in an open vessel at room temperature. Anodic current was measured relative to a platinum cathode.

Thicknesses of converted film and remaining aluminum oxide film after anodization were measured by taking advantage of the great difference in solubility of the film in H_2SO_4. Film thickness was measured by ellipsometer with 5461Å of Hg lamp. Infrared absorption spectrum was recorded on a grating spectrophotometer, and a 100 Ω-cm silicon substrate was used as a spectrum reference. For evaluation of anodization effects on electrical properties of the anodized film, MA(O)S devices were constructed by evaporation of aluminum electrodes onto the film. Capacitance-voltage (*C-V*) measurements were made at 1 MHz at 25°C and automatically plotted on an X-Y recorder.

Results

Typical anodic current *vs.* electric field, which is applied to polycrystalline CVD aluminum oxide film on silicon, is shown in Fig. 1, where ammonium borate in ethylene glycol is used as an electrolyte. Anodic voltage is continuously applied to samples with a constant sweep rate of 3 V/sec. In the anodization of 730Å aluminum oxide, anodic current begins to flow through the film at an electric field of 1.3×10^7 V/cm. In an electric field above 1.7×10^7 V/cm, anodic current increases exponentially with electric field, due to an anodic oxidation of silicon substrate. In the anodization of 1280 and 1850Å aluminum oxides, current density *vs.* electric field continues to show deviation from an exponential curve until higher electric fields are reached.

Figure 2 shows that the electric field (*Ei*), at which anodic current begins to flow through aluminum oxide, depends on aluminum oxide film thickness. These values correspond to dielectric breakdown field strength in the film. When an electric field above *Ei* is applied to a sample, the aluminum oxide surface begins to react with an electrolyte. Interference color of the top surface of the anodized aluminum oxide changes with anodizing time, indicating an increase in total film thickness.

Physicochemical properties of the anodized aluminum oxide are entirely different from those of the original oxide. Figure 3 shows the electron diffraction patterns of the original CVD aluminum oxide (Fig. 3a) and the anodized aluminum oxide in ammonium borate in ethylene glycol (Fig. 3b). In the

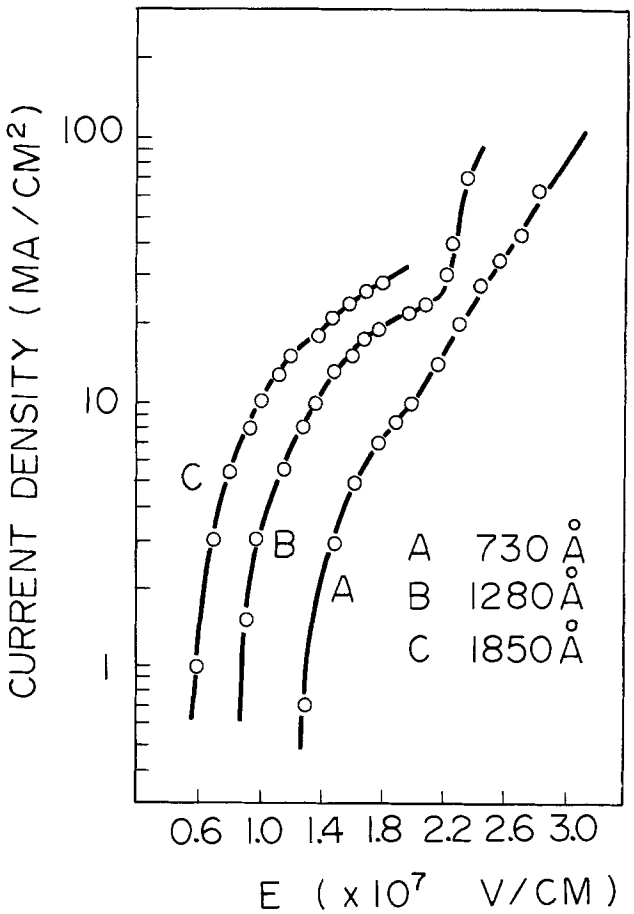


Fig. 1. Current and electric field relation for polycrystalline Al_2O_3 anodization in ammonium borate in ethylene glycol electrolyte.

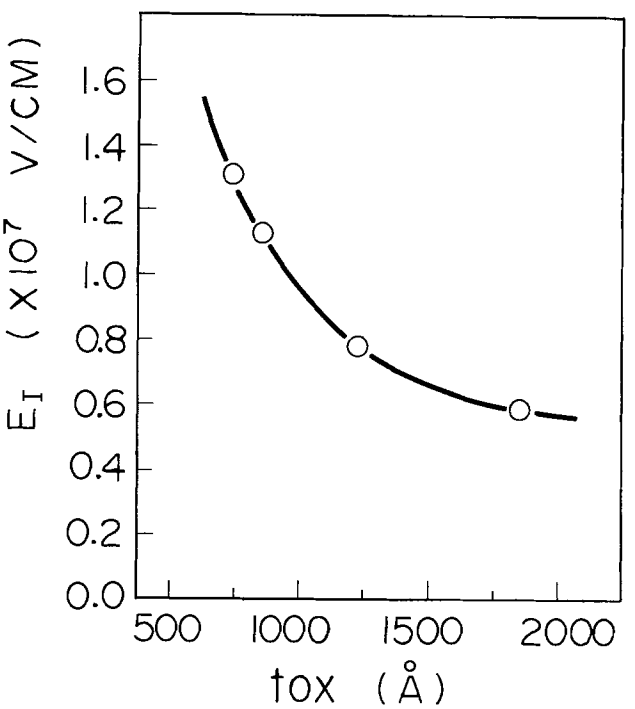


Fig. 2. Relationship between *Ei* and film thickness. *Ei* is the electric field at which anodic current begins to flow through the film.

case of the original aluminum oxide, Debye rings are observed, typical of polycrystalline material, while the anodized film gives amorphous signature.

Table I summarizes physicochemical properties of the anodized aluminum oxide and the original poly-

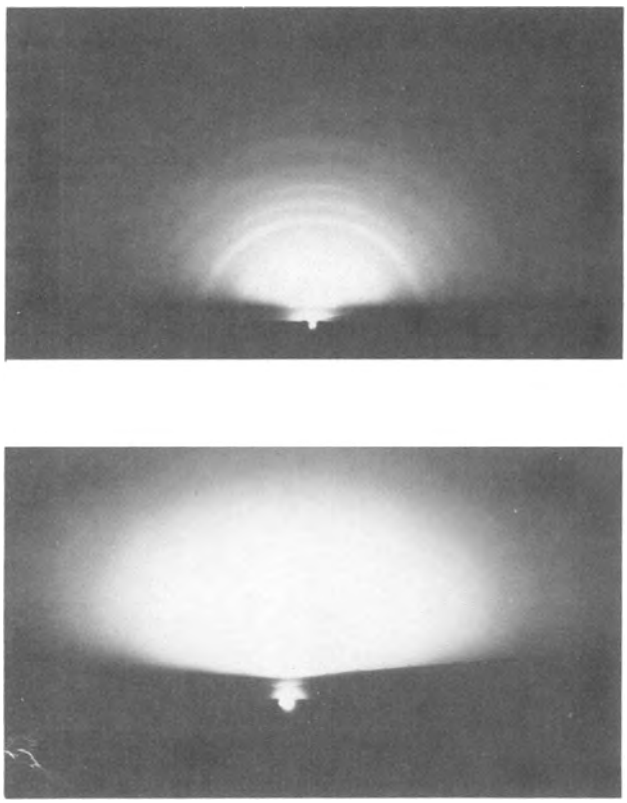


Fig. 3. Al_2O_3 electron diffraction patterns: (a, top) original CVD Al_2O_3, (b, bottom) anodized Al_2O_3 in ammonium borate in ethylene glycol electrolyte.

crystalline CVD aluminum oxide for comparison purposes. The anodized film is easily soluble in various acidic solutions, and is partly soluble even in boiling water. The anodized aluminum oxide, however, is hardly soluble in organic solutions, such as acetone or trichloroethylene or the electrolyte of ammonium borate in ethylene glycol. The anodized aluminum oxide is very susceptible to scratching or to mechanical stresses. Anodized aluminum oxide density and refractive index are 2.1 ± 0.2 and 1.45 ± 0.05, respectively. These values are smaller than those of the original oxide.

Figure 4 shows changes in aluminum oxide film thickness with anodizing time, where a sample with 1100Å thick CVD aluminum oxide is anodized at a fixed voltage of 180V ($E = 1.65 \times 10^7$ V/cm) in ammonium borate in ethylene glycol electrolyte. t_{ANOD} indicates the total film thickness after anodization. t_{ANOD} increases with increasing anodizing time. For investigating the amorphous film thickness (t_{AMOR}) converted by anodization, the anodized aluminum oxide was dipped into boiling H_2SO_4 solution at 100°C. Then, the remaining aluminum oxide thickness (t_{REM}) was measured. t_{AMOR} indicates the film thickness which is etched out by boiling H_2SO_4 solution

Table I

	Anodized Al_2O_3	C.V.D Al_2O_3
Etchant Applicability		
Buffered HF	Yes	No
H_3PO_4	Yes	50-70Å/MIN(160°C)
H_2SO_4	Yes	No
HNO_3	Yes	No
Density	2.1±0.2	2.9±0.2
Refractive Index	1.45±0.05	1.76±0.02

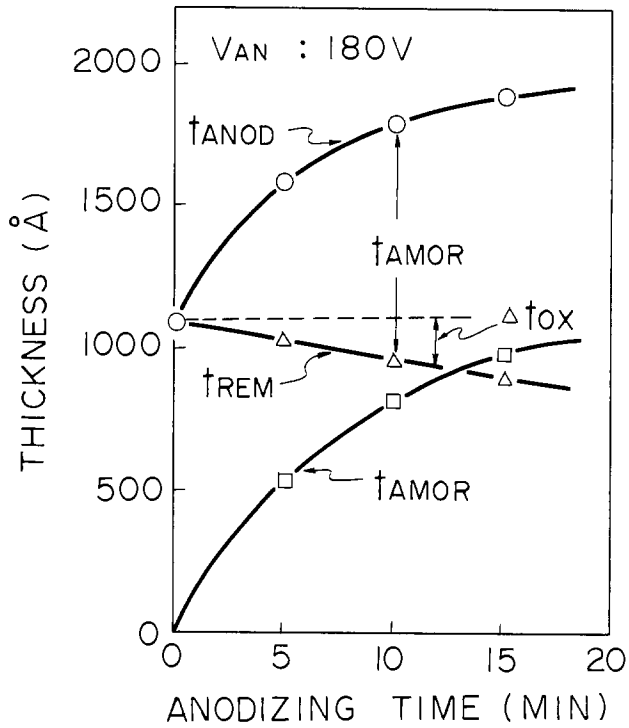


Fig. 4. Total anodized Al_2O_3 thickness (t_{ANOD}) and the amorphous film thickness (t_{AMOR}) as a function of time during Al_2O_3 anodization on Si.

$$t_{AMOR} = t_{ANOD} - t_{REM}$$

t_{AMOR} increases with increasing anodizing time, approximately in proportion to the square root of time. Polycrystalline CVD aluminum oxide is converted into amorphous film from the top surface of the film by anodization.

Figure 5 shows t_{ANOD} and t_{AMOR} *vs.* initial polycrystalline CVD aluminum oxide thickness or *vs.*

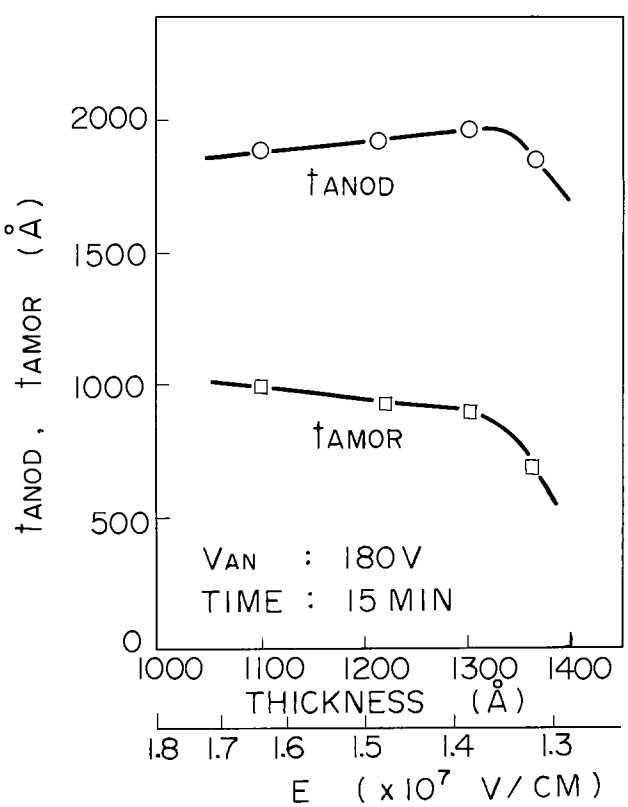


Fig. 5. t_{ANOD} and t_{AMOR} *vs.* initial polycrystalline Al_2O_3 thickness, or *vs.* electric field.

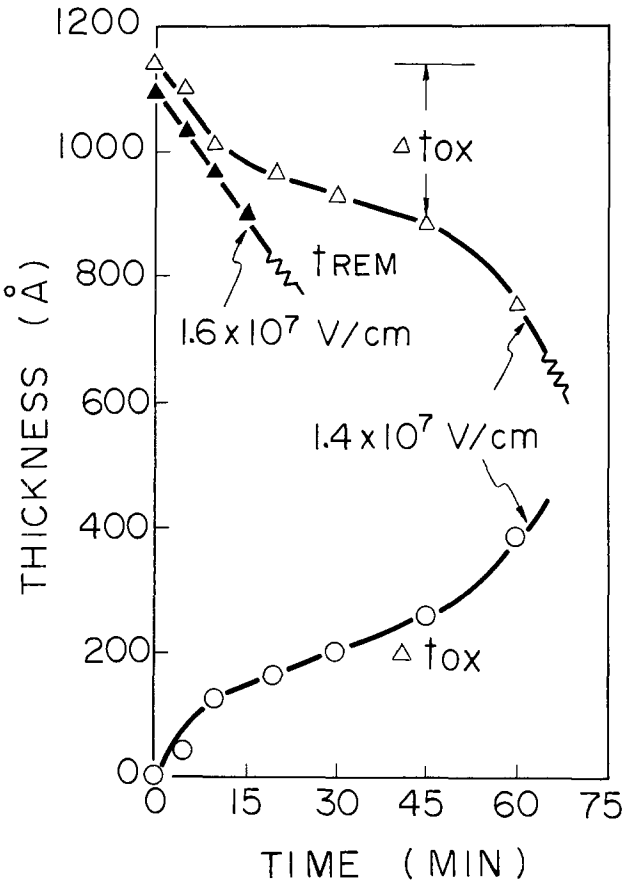


Fig. 6. t_{REM} and Δt_{ox} vs. time

electric field, where anodization is carried out at 180V for 15 min. Converted amorphous film thickness (t_{AMOR}) decreases with decreasing electric field. t_{ANOD}, however, gradually increases with decreasing electric field until lower electric fields are reached. At an electric field lower than 1.3×10^7 V/cm, t_{ANOD} as well as t_{AMOR} abruptly decreases with decreasing electric field.

Figure 6 shows t_{REM} and Δt_{ox} *vs.* anodizing time, where Δt_{ox} indicates that the thickness difference between initial polycrystalline CVD aluminum oxide (t_{ox}) and remaining film dipped into boiling H_2SO_4 solution (t_{REM})

$$\Delta t_{ox} = t_{ox} - t_{REM}$$

Δt_{ox} increases with anodizing time, approximately in proportion to the square root of time for a relatively short duration. However, at a longer anodization Δt_{ox} abruptly increases with anodizing time, and destructive breakdown of dielectric film is observed. The higher the electric field, the earlier the destructive breakdown occurs. In this case, destructive breakdown means lack of surface uniformity of the anodized film.

Figure 7 shows dependence of electric field on Δt_{ox}, where 1220Å thick polycrystalline CVD aluminum oxide is anodized at various voltages for 30 min. At an electric field lower than 1.1×10^7 V/cm, Δt_{ox} is negligibly small. Destructive breakdown of the anodized film occurs at an electric field higher than 1.7×10^7 V/cm.

Typical current density *vs.* anodizing times under various fixed anodic voltages for a 1280Å CVD aluminum oxide film are shown in Fig. 8, where ammonium borate in ethylene glycol is used as an electrolyte. In anodization at 190V ($E = 1.48 \times 10^7$ V/cm), the anodic current gradually decreases with increasing anodizing time. Here, polycrystalline CVD aluminum oxide reaction with the electrolyte gradually proceeds with anodizing time. Microscope examination

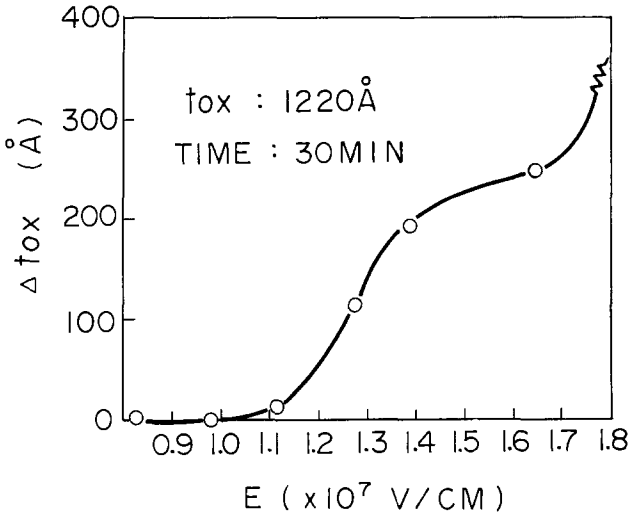


Fig. 7. Electric field dependence on Δt_{ox}

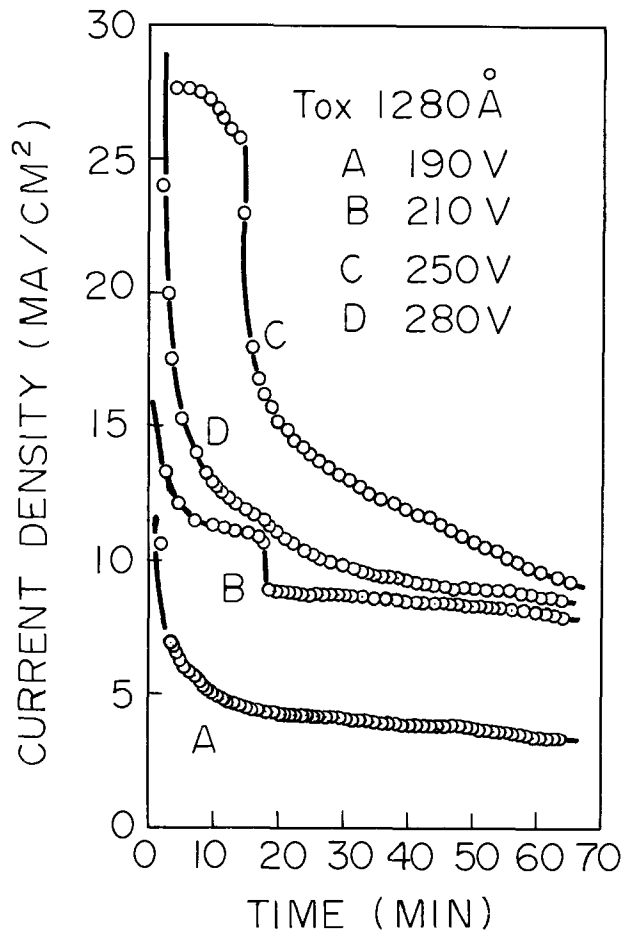


Fig. 8. Current density *vs.* time under various fixed anodic voltages, using ammonium borate in ethylene glycol electrolyte.

showed surface uniformity. In an anodization at 210V ($E = 1.6 \times 10^7$ V/cm), an abrupt anodic current change is observed immediately after 18 min of anodizing time. After the abrupt change of anodic current, it gradually decreases with anodizing time again. The higher the anodic voltage, the earlier the abrupt anodic current change appears. In an anodization at 250V (1.95×10^7 V/cm), it appears in 15 min of anodizing time. After the abrupt change, the surface of the film becomes nonuniform and formation of anodic silicon dioxide is observed. In an anodization at 280V ($E = 2.19 \times 10^7$ V/cm) anodic current decreases abruptly in the beginning stage. No distin-

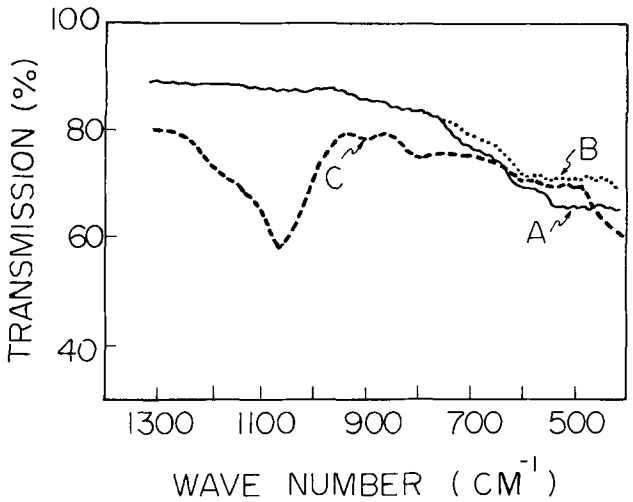


Fig. 9. Infrared absorption spectra of the anodized aluminum oxide: A, as-grown polycrystalline Al_2O_3; B, before current density vs. time transition; C, after current density vs. time transition.

guishable critical abrupt change is observed because the reaction at the surface of the film is violent.

Figure 9 shows the infrared absorption spectra of the anodized samples, compared with an as-grown one, before and after the abrupt change in anodic current. The spectrum of the anodized sample before the abrupt current change (sample B) is similar to that of an as-grown one (sample A), except for smaller absorption below 700 cm^{-1} in wave number. After the abrupt anodic current change, an absorption of 1070 cm^{-1} in wave number is observed (sample C), which is related to Si-O stretching band (8). Formation of anodic silicon dioxide follows the complete conversion of a polycrystalline aluminum oxide to an amorphous aluminum oxide since no Si-O stretching band is present in the spectrum at an incomplete conversion stage (sample B).

When polycrystalline aluminum oxide anodization is carried out at relatively low voltages (*e.g.*, below 2.0×10^7 V/cm in electric field for 1300Å aluminum oxide), the film surface converts to the anodized film uniformly. When anodized at higher anodic voltages and/or longer anodizing time, the aluminum oxide surface becomes nonuniform. Figure 10 shows photographs of an aluminum oxide surface anodized at a high voltage. Small holes are first observed in the film (Fig. 10a). Anodic silicon dioxide is formed at the holes by continued anodic oxidation of the silicon substrate. After longer anodization, the hole size increases and the region covered with anodic silicon dioxide expands to the entire area of the wafer (Fig. 10b).

Figure 11 shows typical current density *vs.* anodizing time under various fixed anodic voltages using 2% sulfuric acid as an electrolyte. Initial aluminum oxide thickness is 1280Å. In contrast with that of ammonium borate in ethylene glycol electrolyte, a current peak is observed at a specific anodizing time. The higher an applied anodic voltage, the earlier a peak appears. In an anodization in 2% sulfuric acid, the anodized aluminum oxide is etched out by the electrolyte during anodization and a decrease in the aluminum oxide thickness is observed. Later, as the silicon substrate is anodically oxidized, the total thickness of the oxide film increases with anodizing time. The polycrystalline aluminum oxide anodizing rate is faster and occurs at lower voltage in 2% sulfuric acid electrolyte than in ammonium borate in ethylene glycol electrolyte.

The anodization process can be used to open windows in polycrystalline aluminum oxide in Si-Al_2O_3-SiO_2 structures. Figure 12 shows sequential steps for opening windows in polycrystalline aluminum oxide.

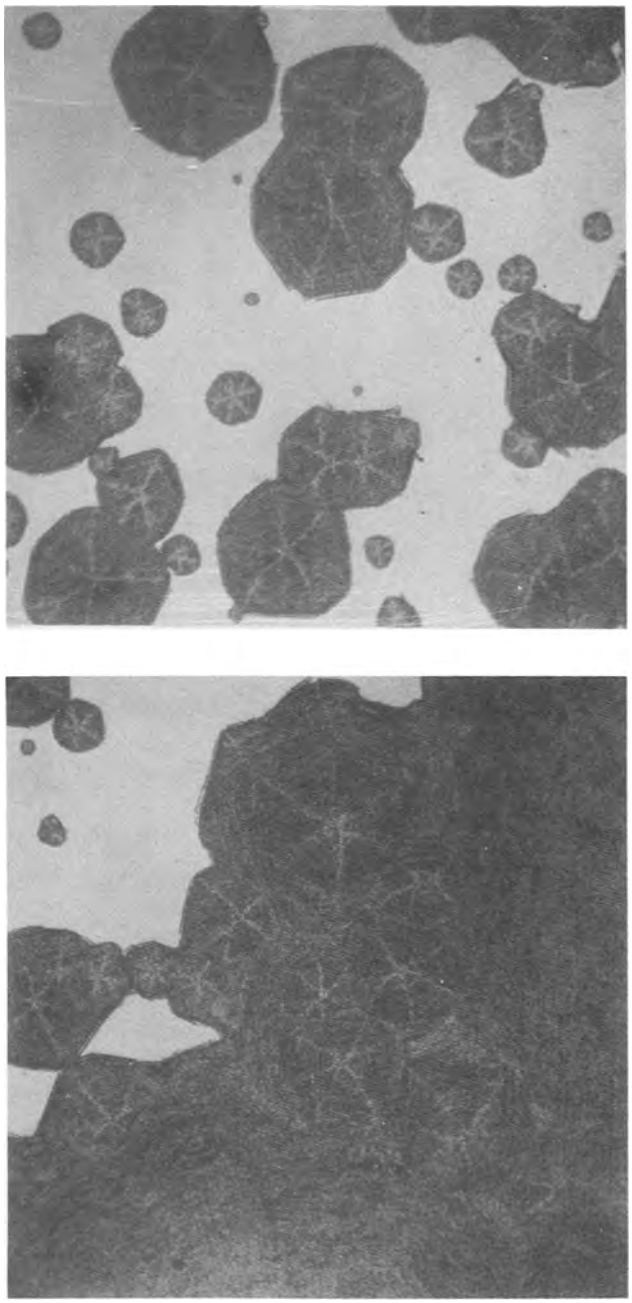


Fig. 10. Photographs of the surface of Al_2O_3 anodized at high voltage.

The technique principle involves anodized aluminum oxide solubility in various acidic solutions, as shown in Table I. During anodization, the silicon dioxide and/or photoresist serves as a mask confining anodization to the open window areas of the silicon dioxide.

Anodization effects on electrical properties of MAS structures were studied using *C-V* characteristics. Figure 13 compares MAS diode *C-V* characteristics with 1100Å thick as-grown aluminum oxide with diodes using oxide films anodized at 50 and 100V in ammonium borate in ethylene glycol electrolyte. Anodization causes electrical instability at the aluminum oxide-silicon interface, and broadening and negative shift of the *C-V* curve are observed. The capacitance decrease in accumulation region for a sample anodized at 100V indicates that the aluminum oxide thickness (t_{ANOD}) increases due to anodization, as shown in Fig. 4.

Figure 14 shows V_{FB} shift of *C-V* curve *vs.* anodic voltage in MAS diodes. Negative V_{FB} shift depends

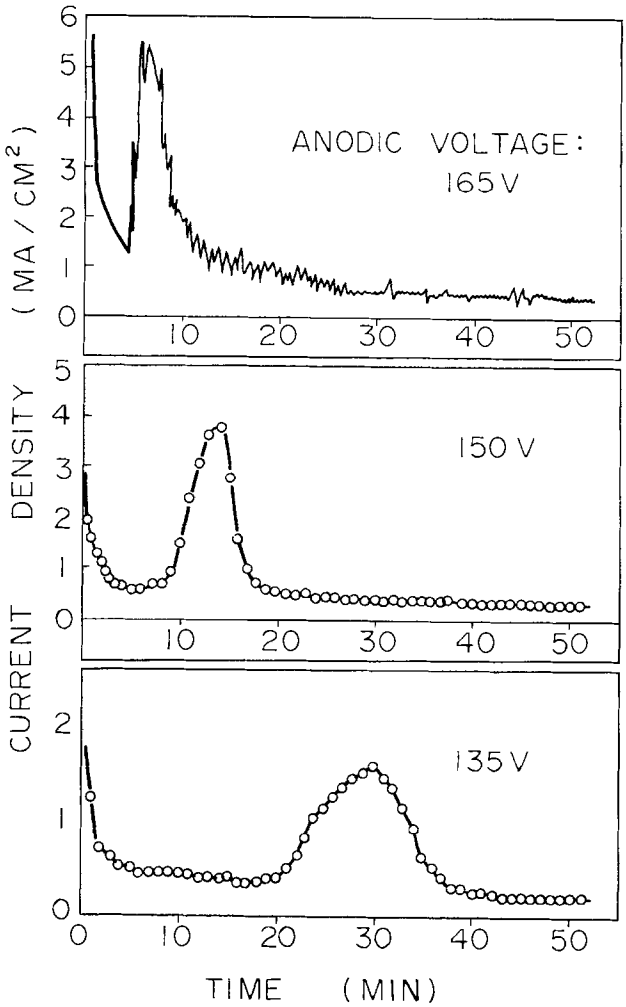


Fig. 11. Current density vs. time under various fixed anodic voltages using 2% sulfuric acid electrolyte.

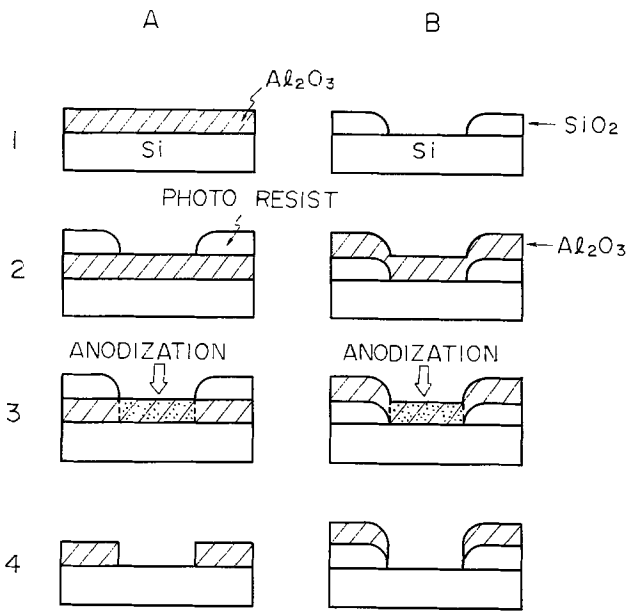


Fig. 12. Sequential steps for opening windows in polycrystalline Al_2O_3 by anodization.

on the anodic voltage magnitude. No V_{FB} shift in positive direction is observed.

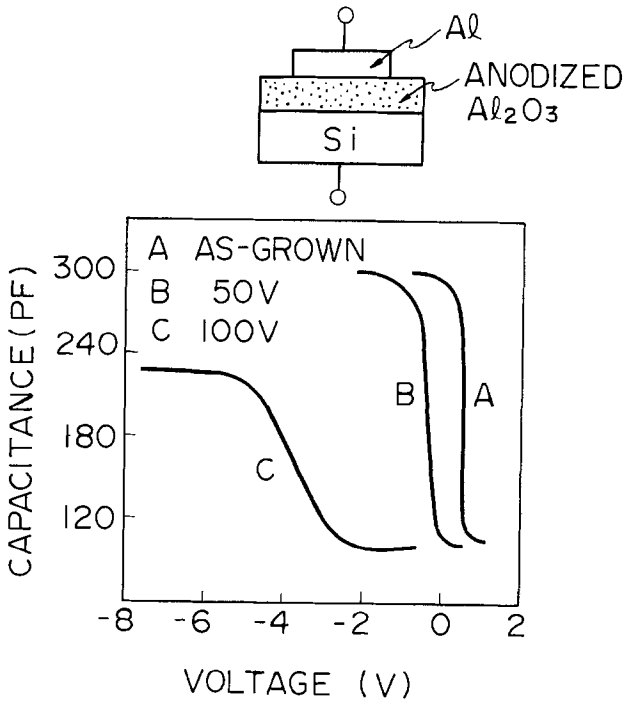


Fig. 13. MAS diodes C-V curves with anodized Al_2O_3

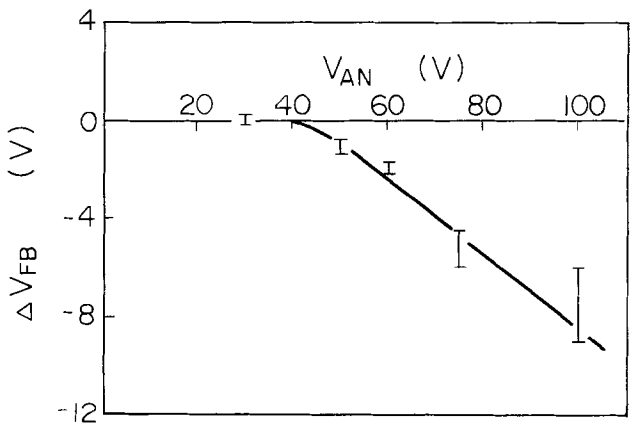


Fig. 14. V_{FB} vs. anodic voltage in MAS diodes with anodized Al_2O_3

Figure 15 shows an anodization etching effect on electrical properties in MAS diodes. The V_{FB} shift characteristics with applied voltage on gate electrode in MAS diodes were similar to those in previous papers (7, 9). The sample etched by anodization process, shown in Fig. 12, initially has a negative V_{FB}, in contrast to that in the sample etched by hot phosphoric acid solution.

Electrical instabilities generated by anodization shown in Fig. 13-15 are completely recovered by additional heat-treatment. Figure 16 shows an effect of heat-treatment on C-V characteristics in a MAS diode etched by anodization process. C-V characteristic in a sample heat-treated at 400°C in nitrogen ambient after anodization is almost the same as that in the sample etched by hot phosphoric acid solution. The V_{FB} shift characteristics in the heat-treated sample were also the same as that in the sample etched.

Discussion

Polycrystalline CVD aluminum oxide physicochemical properties are changed by anodization from the top surface of the film. As shown in Fig. 3b the film anodized gives an amorphous signature. The film is soluble in various acidic solutions, as shown in Table I. Although anodization changed the properties of aluminum oxide, no special infrared absorption band,

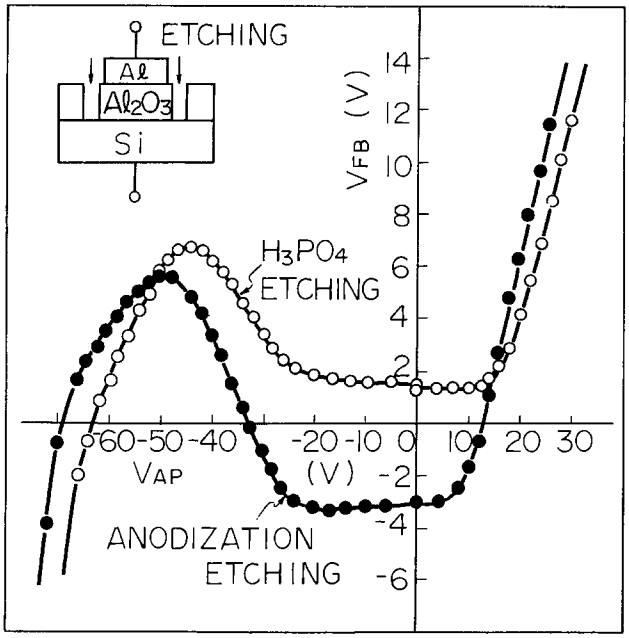


Fig. 15. C-V shift characteristics of MAS diodes etched by hot phosphoric acid and by anodization technique.

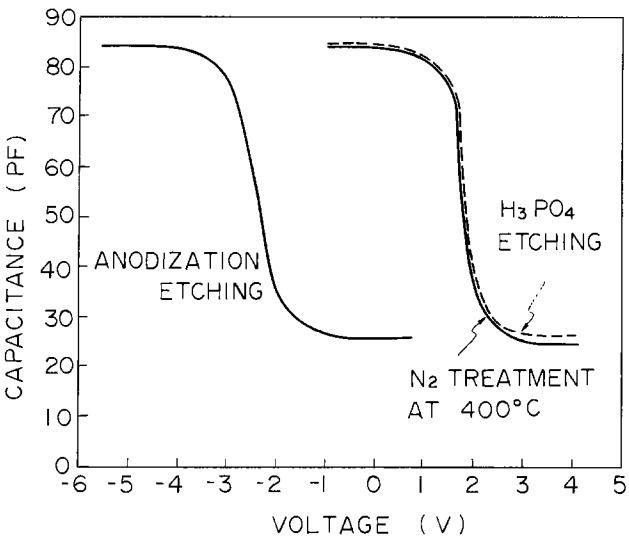


Fig. 16. Heat-treatment effect on C-V curve in a MAS diode etched by anodization technique. Heat-treatment was performed in nitrogen ambient at 400°C for 30 min.

except for aluminum oxide, could be detected, as is shown in spectrum B in Fig. 9. Anodized aluminum oxide physicochemical properties are relatively similar to those of a film deposited at low temperatures (4). Judging from the properties of the anodized film, it is assumed that the bond between Al and O atoms is weaker than that of the original film.

Anodized aluminum oxide thickness (t_{ANOD}) increases with anodizing time, in proportion to square root of time, as shown in Fig. 4. This depends on the structural conversion from the top surface of the anodized film, resulting in t_{AMOR} increase with anodizing time. t_{ANOD} may be determined by the conversion rate (Δt_{AMOR}/time) and the solubility of the anodized film by ammonium borate in ethylene glycol electrolyte during anodization. The anodized aluminum oxide is not soluble in the electrolyte at room temperature. However, it is slightly soluble at high temperature. In the t_{ANOD} dependence on electric field shown in Fig. 5, the higher the electric field, the smaller the observed t_{ANOD}, until lower electric fields are reached. This dependence may be caused by anodized film solubility at high electric field because of the reaction heat.

At later stages of anodization and/or under high voltage application to a sample, aluminum oxide is broken down in dielectric. Silicon substrate is anodized forming anodic silicon dioxide in locations of holes in the aluminum oxide and/or underneath the anodized aluminum oxide. Formation of anodic silicon dioxide is detected by the infrared absorption spectrum shown in Fig. 9 (sample C), and by viewing through an optical microscope shown in Fig. 10.

Characteristics of current density *vs.* electric field (Fig. 1) and of current density *vs.* anodizing time (Fig. 8 and 11) can be successfully explained by the structural conversion of polycrystalline CVD aluminum oxide to amorphous film due to anodization and by the solubility of the anodized film in the electrolyte. In the case of electrolytes, which have no solvent action with the anodized aluminum oxide, such as ammonium borate in ethylene glycol, anodized aluminum oxide thickness increases with increasing anodizing time, as shown in Fig. 4. The rapid anodic silicon dioxide formation at later anodization stages leads to an abrupt decrease in current density, as shown in Fig. 8. Exponential current density increase in the higher electric field region shown in Fig. 1 (sample A) is due to an anodic silicon substrate oxidation. The deviation from an exponential curve shown for 1280 and 1850Å aluminum oxide shown in Fig. 1 results from the fact that the thicker films have not yet broken down to allow silicon dioxide formation. With an anodized aluminum oxide-dissolving electrolyte such as sulfuric acid, a peak of current density is observed as shown in Fig. 11. Decrease in aluminum oxide thickness during anodization leads to an increasing current density. The abrupt current density decrease from the peak indicates the rapid anodic silicon dioxide formation. Schmidt (5) and Kamoshida (6) did not observe the conversion of aluminum oxide to amorphous film in their examinations. This lack may be caused by the use of anodized aluminum oxide-dissolving electrolyte in the anodization.

The electrical instabilities caused by anodization, shown in Fig. 13 and 14, are similar to those of negative bias application to MA(O)S structures. In MA(O)S structures with aluminum electrodes, C-V curve broadening or distortion, as well as positive and following negative V_{FB} shifts, are often observed after negative bias application to the electrode (9, 10). When evaporated Au is used as a MA(O)S structure electrode, electron injection from the electrode and positive V_{FB} shift is rarely observed (11, 12). In anodization of aluminum oxide on silicon, the electrolyte takes the role of an electrode and a positive bias is applied to the substrate. A negative bias, therefore, is applied to the electrode of the electrolyte. Electrical instabilities caused by anodization may be caused by hole injection from the silicon substrate into the film. In anodization of aluminum oxide on silicon, ionic current from the electrolyte to the silicon substrate through the film becomes dominant. Consequently, lack of shift of V_{FB} in the positive direction is a reasonable result, as no electron injection from the electrode to the film occurs during the anodization. These instabilities generated by anodization are completely recovered by additional heat-treatment, as shown in Fig. 16.

Anodization process can be used to open windows in polycrystalline aluminum oxide in Si-Al_2O_3-SiO_2 structures. The technique principle involves anodized aluminum oxide solubility in various acidic solutions, as shown in Table I. During anodization, the silicon dioxide or photoresist serves as a mask, confining anodization to the open window areas of the silicon

dioxide. In selective etching of polycrystalline aluminum oxide less than 500Å thick, conventional photoresist can be used for the dielectric anodization mask.

Conclusions

Anodization of aluminum oxide, deposited by aluminum trichloride hydrolysis on silicon, has been investigated in various electrolytes. As an application of this result, a new polycrystalline aluminum oxide selective etching technique has been studied. A series of experiments on aluminum oxide anodization on silicon has shown that the film changes its physicochemical properties from the top surface of the film, and the anodized film becomes easily soluble in various acidic solutions. Anodized film thickness increases with anodizing time, approximately in proportion to the square root of the time involved. At later anodization stages, the silicon substrate is anodized as well and anodic SiO_2 is formed. Oxidizing species penetrate through the anodized aluminum oxide to form anodic SiO_2 but do not penetrate through the original film, directly. The anodized aluminum oxide has an amorphous structure and is very susceptible to scratches or mechanical stresses, as well as to chemical solvents. In the current density *vs.* anodizing time characteristics in ammonium borate in ethylene glycol electrolyte, an abrupt change in anodic current is observed. This is in contrast with the characteristic in the 2% sulfuric acid electrolyte, where an anodic current peak appears. These current density *vs.* anodizing time characteristics can be successfully explained by the fact that the anodized film is not soluble in the former electrolyte during anodization while it is soluble with the latter case. In the study of MA(O)S structure electrical properties with as-anodized aluminum oxide, broadening and negative C-V curve shifts were observed. These instabilities, however, are completely recovered by additional heat-treatment. Electrical instabilities by anodization may be caused by hole injection from the silicon substrate to the film. The anodization process is applied for opening windows in polycrystalline aluminum oxide in Si/Al_2O_3/SiO_2 device structures. In selective polycrystalline aluminum oxide etching, an etching operation preceded by anodic conversion is more practical and useful than the conventional method using hot H_3PO_4 etchant.

Acknowledgments

The author wishes to thank Drs. Y. Matsukura, S. Nakanuma, and O. Kurakami for their encouragement, and Drs. M. Kamoshida and M. Nakagiri for many stimulating discussions.

Manuscript submitted March 6, 1976; revised manuscript received Dec. 7, 1976. This was Paper 45 presented at the Washington, D.C., Meeting of the Society May 2-7, 1976.

Any discussion of this paper will appear in a Discussion Section to be published in the December 1977 JOURNAL. All discussions for the December 1977 Discussion Section should be submitted by Aug. 1, 1977.

Publication costs of this article were assisted by the Nippon Electric Company, Limited.

REFERENCES

1. S. Nakanuma T. Tsujide R. Igarashi, K. Onoda, T. Wada, and M. Nakagiri, *IEEE J. Solid-State Circuits*, **sc-5**, 203 (1970).
2. D. F. Bentchkowsky, *ibid.*, **sc-6**, 301 (1971).
3. K. Iida, *Jpn. J. Appl. Phys.*, **11**, 288 (1972).
4. K. Iida and T. Tsujide, *ibid.*, **11**, 840 (1972).
5. P. F. Schmidt and D. R. Wonsidler, *This Journal*, **114**, 603 (1967).
6. M. Kamoshida and J. W. Mayer, *ibid.*, **119**, 1084 (1972).
7. K. Iida, T. Tsujide, and M. Nakagiri, *Jpn. J. Appl. Phys.*, **11**, 1153 (1972).
8. K. Sato, *This Journal*, **117**, 1065 (1970).
9. F. B. Micheletti, P. W. Norris, K. M. Schlesier, and J. M. Shaw, *Solid State Technol.*, **14**, 37 (Dec. 1971).
10. K. Iida, *Jpn. J. Appl. Phys.*, **12**, 807 (1973).
11. P. Balk and F. Stephany, *This Journal*, **118**, 1634 (1971).
12. T. Tsujide and K. Iida, *Jpn. J. Appl. Phys.*, **11**, 600 (1972).

Technical Notes

Oxidation of Ni_3Sn_4, Metastable SnNi, Ni_3Sn_2, and Ni_3Sn

H. G. Tompkins and J. E. Bennett

Bell Laboratories, Columbus, Ohio 43213

The equiatomic metastable tin-nickel alloy is being considered for use as an underplate for connector contacts. This electrodeposited material has been shown to be exceptionally passive in various atmospheres and aqueous solutions (1). A previous paper by the authors (2) considered the nature of its passive film. One of the tentative conclusions of that work was that the passivity may not depend on the metastable nature of the alloy. The purpose of this work was to further investigate that tentative conclusion. It is generally accepted that the passivity of a material in the presence of various atmospheric and aqueous corrodants is somehow related to the oxide film which forms on the surface. Although it is essential, for completeness, to study the effects of the various corrodants on the material, the first efforts, it seems, should be directed toward understanding the nature of the oxide film. Upon heating or aging above certain temperatures, the metastable alloy transforms to a mixture of Ni_3Sn_2 and Ni_3Sn_4 (3). In this work, the low temperature (room temperature and 156°C) oxidation of the separate alloys Ni_3Sn_4, metastable tin-nickel, Ni_3Sn_2, and Ni_3Sn_1

was investigated using Auger electron spectroscopy to determine the effect of a range of compositions on the nature of the oxide film.

Experimental

The metastable equiatomic alloy was prepared by electrodeposition, as described in a previous paper by the authors (3). Verification of the metastable structure was made by x-ray diffraction using both diffractometer and powder techniques as also previously reported (3). The Ni_3Sn_4, Ni_3Sn_2, and Ni_3Sn_1 equilibrium compounds were prepared by induction melting of 99.999% pure nickel rod (Research Organic/Inorganic Chemical Corporation) and 99.999% pure tin sheet (Ventron Corporation) in the proper proportions. The compounds were double melted and solidified under flowing helium. After cooling, the compounds were placed in a resistance tube furnace and given a homogenizing anneal of 5 hr at 500°C in flowing hydrogen. They were withdrawn from the hot zone and allowed to cool in flowing hydrogen. Slices from each ingot were analyzed by x-ray diffraction and found to be essentially the desired compounds.

Flakes from the electrodeposited alloy and slices from the compound ingots were used for the Auger analysis.

The samples were initially sputtered clean to remove all effects of the sample fabrication (diamond saw cutting, lubrication, etc.). In all subsequent experiments, a reproducible surface condition was obtained by sputtering with the same argon ion energies. Although the surface generated was not quite representative of the bulk due to preferential sputtering, it was, in the authors' opinion, the closest representation of the bulk which could be obtained and was quite reproducible. After a half-hour equipment cool-down time at a pressure on the low 10^{-8} Torr range, the system was backfilled to atmospheric pressure with O_2. After 1 hr the O_2 was pumped out and the system pumped to the low 10^{-8} Torr range (pumping time, 3 hr). For the 156°C oxidation the samples were removed from the system and placed in a small oven (Pyrex tube wrapped with heating tape) for the allotted time. The atmosphere in these cases was room air.

The Auger analysis was done with a commercial instrument purchased from Physical Electronics Industries using a 3 kV, 1 μA incident electron beam. The sputtering was done with a 1 kV argon ion beam operated at 4.7 $\mu A/cm^2$. In a separate experiment in the same vacuum system, sputtering yields of 2.93 and 2.3 atoms/ion were measured for Sn and Ni, respectively, by sputtering through a known thickness of material. This gives a sputtering rate between 7.6 and 8.2 Å/min for all of the alloys studied.

Results and Discussion

A typical spectrum is shown in Fig. 1 (in this case, Ni_3Sn_2 after 1 hr of exposure to O_2 at room temperature). Profiles (peak-to-peak height plotted *vs.* sputtering time) were obtained and typical ones are shown in Fig. 2. The relative magnitude of the tin and nickel

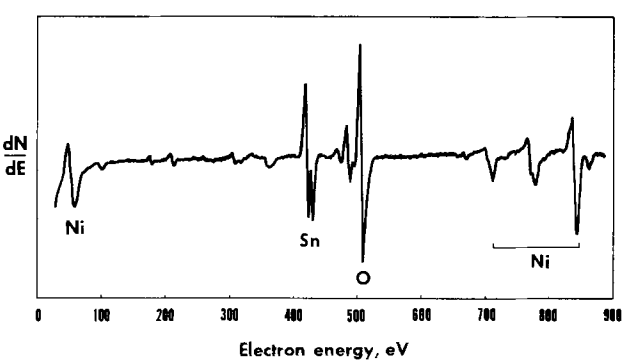


Fig. 1. Typical Auger spectrum (in this case, Ni_3Sn_2 after 1 hr exposure to O_2 at atmosphere pressure at room temperature).

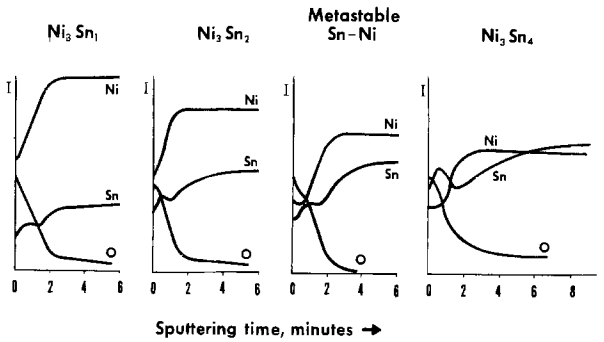


Fig. 2. Profiles of the passive films on Ni_3Sn_4, Sn-Ni, Ni_3Sn_2, and Ni_3Sn_1. Sputtering rate was about 7.9 Å/min.

signals is not normalized, but instrumental magnifications of two for nickel and one for tin were used. This gives a signal ratio which is roughly proportional to the relative concentration of tin and nickel. The profiles were obtained under identical sputtering conditions. Although the peak heights in the bulk (after the profiles leveled off) were different, illustrating the different bulk compositions, the films which formed on these materials showed similar features. These are that the tin profiles showed an initial rise, followed by a decline, followed in turn by an increase to the bulk value. The nickel profile increased to slightly above the final bulk value and then gradually decreased to the bulk value with the increase somewhat lagging the initial tin signal increase. The oxygen profile decreased monotonically. These features occurred in all four materials. Using the sputtering time for the oxygen to decrease to half its original value, and a sputtering rate of 7.9 Å/min, we see that the thickness of the film for all of the material was from 8 to 14Å. The previous work (3) pointed out that a nonzero value for nickel before sputtering does not necessarily imply nickel on the surface, since the escape depth of the high energy nickel peak used here is 11Å. The profiles clearly illustrate the similarity of the oxide films which form on these four materials.

After the room temperature oxidation studies were completed, sputter-cleaned samples were removed from the system and heated at 156°C in air for 1 hr and then analyzed. Following this analysis, samples were removed from the system, heated to 156°C in air for 5 days, and again analyzed. For both of these treatments the profiles obtained were essentially identical with the ones shown in Fig. 2, obtained after 1 hr in oxygen at room temperature. Specifically, no additional film growth was observed. In contrast, the oxide film on a pure tin coupon heated at the same time (1 hr) was about 2.5 times as thick as the film exposed to O_2 for 1 hr at room temperature. The results of Graham and Cohen (4) suggest that the film on pure nickel should be about 1.5 times as thick when heated at 150°C than when exposed at room temperature. The significant observation is that no additional oxidation of the various compounds could be detected beyond the films which form in 1 hr at room temperature, even when samples were heated at 156°C for as long as 5 days.

No specific quantitative measurements were made concerning the identity of the species making up the film. X-ray photoelectron spectroscopy (XPS) measurements have been made on the metastable alloy by Sharma and Thomas (5). Their data indicate that after 10 min at 760 Torr of O_2, the film content is a combination of nickel hydroxide and tin oxide or hydroxide with significantly more tin in the film than nickel.

These measurements, of course, say nothing about the species on the other alloys studied in this work. The similarity in film thickness and profile suggests however, that the films are, at least, not grossly different. The lack of change in the profiles after heating

at 156°C for 5 days indicates a rather strong stability of the films on all four alloys.

Manuscript submitted Nov. 1, 1976; revised manuscript received Dec. 22, 1976.

Any discussion of this paper will appear in a Discussion Section to be published in the December 1977 JOURNAL. All discussions for the December 1977 Discussion Section should be submitted by Aug. 1, 1977.

Publication costs of this article were assisted by Bell Laboratories.

REFERENCES

1. N. Parkinson, S. Britton, and R. Angles, *Sheet Met. Ind.*, **28**, 1 (1951); S. Britton and R. Angles, *J. Electrodepositors' Tech. Soc.*, **27**, 293 (1951).
2. H. G. Tompkins and J. E. Bennett, *This Journal*, **123**, 1003 (1976).
3. J. E. Bennett and H. G. Tompkins, *ibid.*, **123**, 999 (1976).
4. M. J. Graham and M. Cohen, *ibid.*, **119**, 879 (1972).
5. S. P. Sharma and J. H. Thomas, Submitted to *Anal. Chem.*

Cd(S,Se):Cu-Photoconductive Material for Electrophotography

S. Faria* and V. Chiola*

GTE Sylvania Incorporated, Towanda, Pennsylvania 18848

For almost three decades amorphous selenium and zinc oxide binder layers have dominated the field of electrophotography (1-2). The two best known electrophotographic methods are Xerography and Electrofax, where selenium and zinc oxide in a binder are the insulating photoconductive materials, respectively. A third technology, Canography, is now receiving appreciable attention and application.

In recent years numerous organic and inorganic compounds have been developed and are being field tested as potential electrophotographic materials. Wide attention has been given to polyvinylcarbazole (3), with or without trinitrofluorenone (4), as an efficient organic photoconductive material. The most investigated inorganic materials are the chalcogenides (5) of which cadmium sulfide has received considerable attention.

Claus (2) reported that early work with electrophotographic-grade cadmium sulfide was plagued by poor copy quality due to rough photoreceptor surface, poor resolution, and high background.

The purpose of this paper is to report on the electrophotographic properties of selenium-modified cadmium sulfide. This material has advantages of good resolution, high durability, and good copy quality.

Experimental

Materials preparation.—Solid solutions of cadmium sulfide and cadmium selenide were prepared from luminescent-grade materials and were activated with copper and coactivated with chlorine. Thermal treatments were conducted in inert atmospheres at temperatures between 400° and 600°C to properly diffuse the copper into the matrix and to prevent oxidation of the cadmium sulfide or selenide. Excess copper and copper sulfide are removed by washing with dilute potassium cyanide solution. Subsequent water washings were carried out to insure complete removal of ionic species from the Cd(S,Se):Cu surface.

Photoreceptor screens preparation.—Photoreceptor screens containing the cadmium-sulfoselenide, copper-activated material were prepared for evaluation of electrophotographic properties. These were made by thoroughly mixing and suspending the Cd(S,Se):Cu powder in a lacquer and depositing a 40-50 μm thick layer on a clean aluminum substrate using a conventional blading technique. The lacquer binder suspension consisted of a dibasic acid-modified vinyl chloride-vinyl acetate resin dissolved in methyl-isobutyl ketone. The photosensitive layer was air dried and then thermally bonded by lamination with a layer of transparent adhesive-backed polyester film. Figure 1 depicts the structure of the screen and its various layers.

* Electrochemical Society Active Member.

Key words: electrophotography, photoreceptor, cadmium sulfide, cadmium selenide.

Experimental Results and Discussion

Electrophotographic evaluation of Cd(S,Se):Cu.—Although there are other ways of evaluating the surface charge, for example, the revolving turntable (6, 7), for this work, we used two Saxon plain paper copying machines (PPC-1) manufactured by Copystatics Manufacturing Corporation, Division of Saxon Industries. Three screens, usually 25 × 10 cm each, were secured to the aluminum drum of the machine and their electrical properties, copying qualities, and maintenance were measured. Lifetime performance was carried to extended periods in excess of 30,000 cycles.

The principle of operation is widely known as Canography (7, 8). In operation the surface of the photoreceptive screen is charged positively in the dark with a d-c corona discharge. Negative charges injected from the aluminum layer into the CdS:Cu or Cd(S,Se):Cu layer are attracted to the interface by the positive charges on the insulating surface. The image from an original copy is then optically projected to the positively charged photoreceptive surface. Dark areas from the original, representing the letters, numbers, etc. do not dissipate the positive charges on the photoreceptor screen, while the light areas, *i.e.*, the background, tends to dispel the positive charges. The invisible electrostatic image thus formed is made visible by means of negative toner particles attracted by the positive charges. A more detailed description of this process is found in Ref. (9-10) and in Ref. (7). An electrostatic voltmeter known as a Microprobe and sold by Monroe Electronics Incorporated is placed near the surface of the drum to measure the electrostatic charge potential from both the dark and light areas. An original white sheet, one-half of which is covered with black paper served as the test pattern for measuring the electrostatic potential

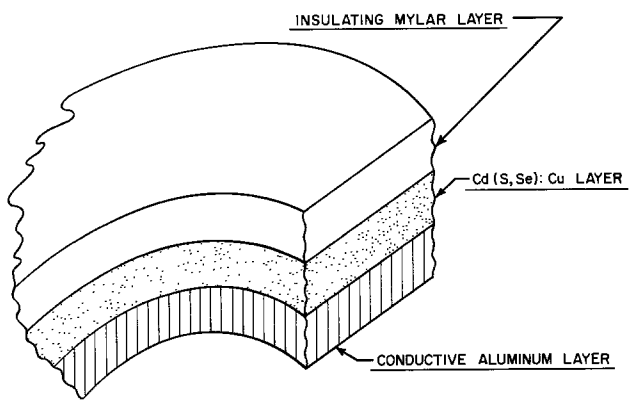


Fig. 1. Composition of photoreceptor showing the Cd(S,Se):Cu material sandwiched between the insulating and conductive layer.

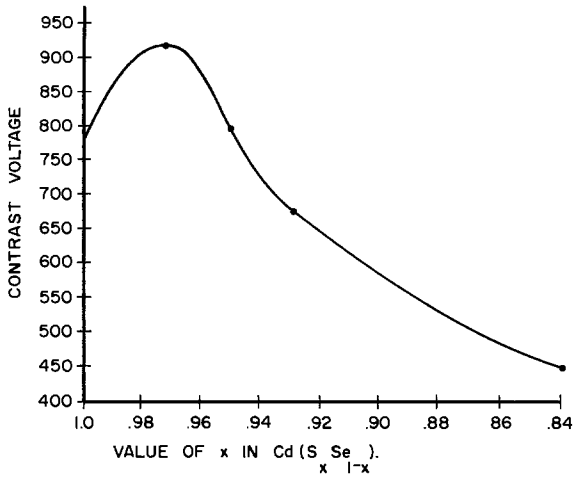


Fig. 2. Relationship of contrast voltage to CdSe addition to CdS

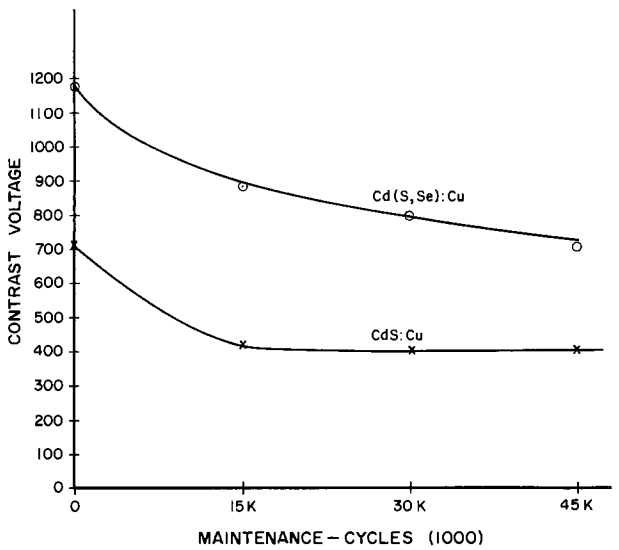


Fig. 3. Comparison of contrast voltage for the systems CdS:Cu and Cd(S,Se):Cu with maintenance.

drop between the light (background) and dark (image) areas.

The difference in electrostatic voltage between dark and light areas is known as the contrast voltage. The relationship of contrast voltage with varying amounts of CdSe addition to CdS are shown in Fig. 2. The best contrast in copy quality was obtained when a range of 0.02-0.05 moles CdSe is incorporated in CdS. Specific data showing the relationship of contrast voltage with cadmium sulfide to cadmium selenide ratio are shown in Table I.

The low negative (background) voltage indicates a strong photosensitive material. Continued light exposure and corona charging and discharging reduces the potential drop from both light and dark areas. This is shown in Fig. 3 and 4. Figure 3 shows a comparison of the electrophotographic system CdS:Cu and the Cd(S,Se):Cu. We find that the small amount of CdSe added to CdS extends the life of the photoreceptor, *i.e.*, the contrast after 30,000 copies is better than unmodified CdS:Cu. Copies of excellent contrast are not unusual after 50,000 cycles with the Cd(S,Se):Cu material.

Table I. Contrast voltage relationships to CdS-CdSe concentration

Moles CdS	Moles CdSe	Dark voltage	Light voltage	Contrast voltage
1.00	0.000	+660	−120	780
0.979	0.0210	+740	−180	920
0.957	0.0430	+700	−100	800
0.936	0.0640	+580	−100	680
0.840	0.1560	+400	−50	450

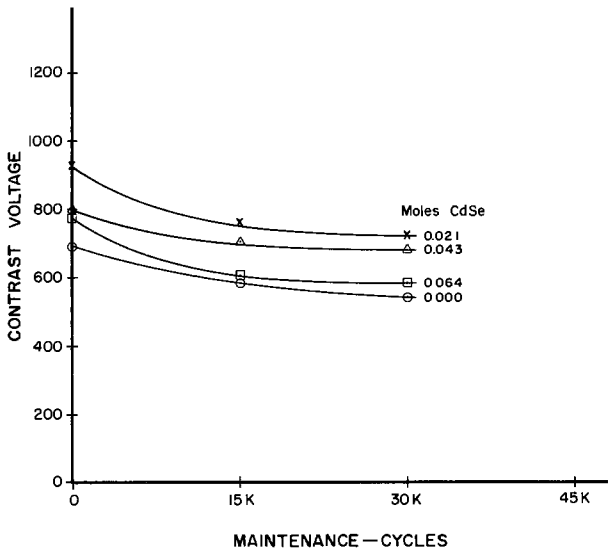


Fig. 4. Contrast voltage relationship maintenance at various CdSe additions.

Particle size.—One important requirement for smooth screen deposition is that the particle size of the Cd(S,Se):Cu be small. Two techniques of controlling particle size have been employed: (*i*) start with very small size CdS, and (*ii*) adjust the firing temperature and flux parameters. Photosensitivity is very much dependent on firing temperature and use of a correct amount of activator. High temperature increases the sensitivity but also promotes particle size growth. By controlling both the size of the starting sulfide and firing temperature, material displaying the particle size distribution shown in Fig. 5 is obtained. Most of the particles are between 2 and 4 μm. This size range material disperses well in the type of binder used for making the screens. Smaller, more uniform size, as for example 0.5 to 1 μm, would be desirable for achieving improved resolution and contrast.

Cd(S,Se):Cu spectro-response.—Figure 6 shows the photoconductivity excitation spectrum for the 46.5 moles S to Se ratio of the Cd(S,Se):Cu material as measured with a microwave photoconductive spectrometer, Model 815R, made by Micro-Now Instrument Company.

The short wavelength peak is the characteristic absorption band of CdS, while the long wavelength peak

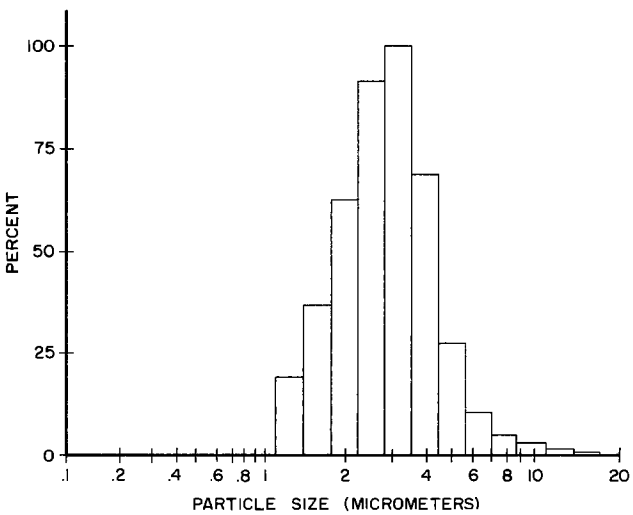


Fig. 5. Particle size distribution of Cd(S,Se):Cu as measured by the Coulter Counter method.

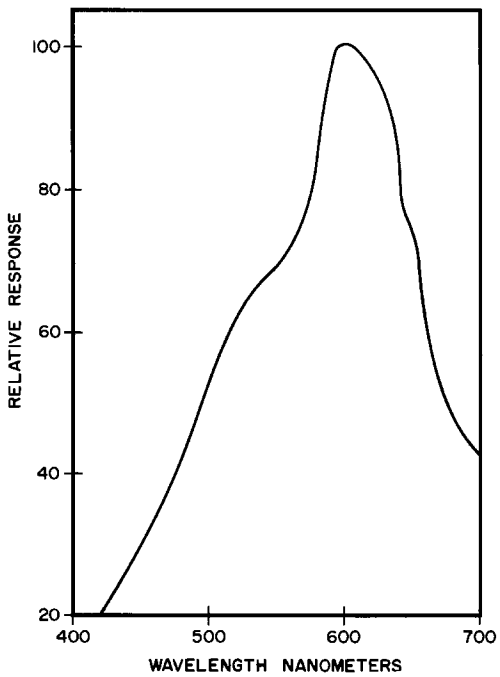


Fig. 6. Photoconductivity excitation spectrum of Cd(S,Se):Cu

is mainly due to CdSe and the effect of Cu on the matrix. Image transfer with a light source matching its emission spectrum to that of the photoconductor response will result in high contrast reproduction.

Figure 7 shows a comparison of copy quality between an image reproduced in a commercial machine and a machine using the Cd(S,Se):Cu electrophotographic material.

Conclusions

We have shown that Cd(S,Se):Cu containing a specific ratio of CdS to CdSe, when processed in a control manner, is an effective electrophotographic material. The combination of high photosensitivity, small particle size, and broad absorption response has yielded material having excellent reprographic characteristics and life or maintenance. Copying machines using Cd(S,Se):Cu and based on the Canographic technology have produced good image quality, high resolution, and exceptional life expectancy and durability.

Acknowledgments

The authors acknowledge the Copystatic Manufacturing Corporation of Miami Lakes, Florida, Subsidiary of Saxon Industries, for their support, technical assistance in measurement techniques, and the Saxon plain paper copier machines used in the measurements.

Manuscript submitted April 12, 1976; revised manuscript received Nov. 19, 1976. This was Paper 240 presented at the Washington, D. C., Meeting of the Society, May 2-7, 1976.

Any discussion of this paper will appear in a Discussion Section to be published in the December 1977 JOURNAL. All discussions for the December 1977 Discussion Section should be submitted by Aug. 1, 1977.

Publication costs of this article were assisted by GTE Sylvania Incorporated.



Fig. 7. Comparison of copy quality. Image at left is typical of that obtained from a commercial machine which does not use Cd(S,Se):Cu. Image at right was reproduced in a machine using Cd(S,Se):Cu.

REFERENCES

1. R. B. Comizzoli, G. S. Lozier, and D. A. Ross, *Proc. IEEE*, **60**, 358 (1972).
2. C. J. Claus, *Image Technol.*, Part II, (April/May 1969).
3. H. Hoegl, *J. Phys. Chem.*, **69**, 755 (1965).
4. R. M. Schaffert, *IBM. Res. Dev.*, **15**, 75 (1971).
5. D. W. Chapman and F. J. Stryker, *Photogr. Sci. Eng.*, **II**, 22 (Jan.-Feb. 1967).
6. O. C. Klein and J. G. Johnston, *J. Tech. Assoc. Pulp Paper Industry*, **50**, 39A (Feb. 1967).
7. M. J. Mitsui, *IEEE Trans. Electron Devices*, **ed-19**, 396 (1972).
8. K. Nakamura, *ibid.*, **ed-19**, 405 (1972).
9. U.S. Pat. 3,689,146 (1972).
10. U.S. Pat. 3,666,363 (1972).

Physical Contact Properties of Beryllium Metallization on Silicon Devices

J. B. Mooney[1] and J. O. McCaldin*

California Institute of Technology, Pasadena, California 91125

With the advent of electron beam lithography and associated high resolution techniques, integrated circuit device dimensions will decrease, and this will obviously increase the problems associated with contact metallization. Aluminum has been widely used in silicon devices, and, since it is a single element metallization, it has best fulfilled the requirements for device metallization

* Electrochemical Society Active Member.
[1] Permanent address: Stanford Research Institute, Menlo Park, California 94025.
Key words: Be ohmic contacts, metallization, ultramicro-devices.

(1-3). However, the solubility of Si in solid Al at device processing temperatures is significant, and the dissolution and diffusion of Si are very rapid at temperatures well below the eutectic temperature of 577°C (1-5). The results of this attack upon the Si are dissolution pits (3, 6, 7). Several remedies for this problem are in use today, particularly the inclusion of Si in the original Al metallization and the addition of barrier metals at the Al-Si interface (3). These pits are likely to become a more serious problem as device dimensions shrink, however. Most other metallization systems that have been considered are composed of multiple metal layers (8, 9) or systems based on the formation of silicides (10, 11), but the simplicity of a single metal system without compound formation has many advantages.

The elements of the periodic chart have been classified as to their chemical reaction with Si (8, 12). Table I lists those elements which do not form silicides and their melting points, eutectic temperatures, and resistivities. The elements which meet the 4 $\mu\Omega$-cm resistivity criterion of Sello (1) and are solids at reasonable device processing temperatures are Al, Au, Ag, and Be. Of these, Be has only recently been considered as a Si device metallization, possibly because of its well-known toxicity. In semiconductor processing, the existing requirements for cleanliness are such that process modification required to provide toxicity protection would be relatively minor.

As stated above, Be meets the resistivity criterion of Sello (1, 14). Also, beryllium (13) is scratch resistant, will not corrode, can withstand high temperatures, its deposition and patterning are simple processes, it is an acceptor in Si (15), and it affords a low solid solubility for Si (4). In its low solid solubility for Si and its scratch resistance, Be is superior to Al as a potential metallization for ultramicro-devices. Recently Hall, Koblinski, and Cragg (16) have reported on the electrical properties of Be and Be-Al alloys as a contact metallization for Si. It was the purpose of this study to determine the adherence of Be to Si and SiO_2 (3), and the extent of chemical attack which will occur at device processing temperatures.

Experimental

The substrates were [111] oriented Si wafers with a 4000Å thermal oxide layer. Windows of various sizes and geometries were photolithographically opened in the oxide. The wafers were prepared for Be deposition by cleaning in trichlorethylene, acetone, methanol, and deionized water, followed by a 20 sec etch in 10% HF solution and thorough rinsing with deionized water. The wafers were blown dry with a jet of dry nitrogen and immediately introduced into the evaporator which was an ion-pumped system equipped with a liquid nitrogen cryopump, an electron gun, and a quartz crystal deposition rate monitor. Evaporations were made after the Be source had been melted with a shutter shielding the substrate until the background pressure could be maintained at or below 6×10^{-5} Torr during the deposition.

Two sources of Be were used. Beryllium flake 99.99+% purity (Spex Industries, Incorporated) and Be distillate (Nuclear Metals). Although spectrographic analysis indicated that the two sources were of similar purity, processing characteristics demonstrated that the distillate was superior. The Be flake was contaminated with spectrographically undetectable gases, which evolved violently upon melting with the electron beam. Electron microprobe analysis of the Be flake showed a relatively high Cl content. Even after outgassing in the vacuum system prior to evaporation, the evaporated layers were only partially adherent. Where Be did adhere, the strain was such that the oxide was lifted from the Si in some areas. There also appeared to be some attack upon the Si substrate. When the Be flake was thoroughly melted in a W boat in an Ar stream prior to introduction into the vacuum system, the layers were comparable to the high quality layers obtained with the Be distillate. When the Be distillate was used as received, and with thorough melting by the electron beam prior to opening the shutter, good adherent layers were obtained.

The results of various heat-treatments in Ar are summarized in Table II. The lowest temperatures studied produced no detectable substrate/metal reaction, whereas at the highest temperatures gross reaction occurred. Portions of the wafer with the evaporated Be layer were introduced directly into a tube furnace at the indicated temperature. After the indicated time the sample was removed from the furnace and plunged directly into room temperature deionized water. The samples were examined by optical and scanning electron microscopy (SEM). Portions of the sample were examined as treated, after removal of Be by concentrated HCl, and after removal of Be and SiO_2 by HCl and HF. In the cases where there was sufficient reaction of the Be with the SiO_2 to produce an insoluble residue, portions of the remaining deposit were removed mechanically to observe whether the Si had been attacked by the Be. Be layers of 2500 and 5000Å thickness yielded the same results. One sample which was not cleaned prior to Be evaporation showed some lifting and cracking of the Be layer over the SiO_2 free area (scribe lines). In the other experiments with properly cleaned substrates, Be layers were adherent and did not crack. The color of the SiO_2 after removal of the Be with HCl was interpreted as a measure of the amount of SiO_2 reacting with the Be. Consistent with this interpretation is the presence of an insolube residue after higher temperature treatments and the electron microprobe results discussed next.

Table III presents the results of an electron microprobe determination of the Si content of the Be layer at a beam energy of 5 keV for which there is expected to be negligible contribution from the substrate Si. The Si signal detected over oxide-free portions of the substrate (scribe line) is mostly background, and the variation is not considered significant within the expected precision of the analytical method. However, the enhanced signal detected over the SiO_2 covered regions of the substrate (field) reflects the presence of Si in the metallization overlying these regions. These results and the observed acid insoluble residue indicate that a chemical reaction occurs between the SiO_2 and the Be.

Table I. Melting points and resistivity of nonsilicide formers (13,4)

Material	Melting point (°C)	Eutectic (°C) with Si	Resistivity $\mu\Omega$-cm (°C)
Be	1270	1090	4.0 (20°)
Ge	940	(940)*	46×10^6 (22°)
Ag	961	830	1.59 (20°)
Sb	630	630	39.0 (0°)
Al	660	577	2.65 (20°)
Zn	419	419	5.9 (20°)
Au	1063	370	2.37 (20°)
Pb	327	327	20.6 (0°)
Cd	320	320	6.83 (0°)
Tl	303	(303)	18.0 (0°)
Bi	264	264	106.8 (0°)
Sn	232	232	11.0 (0°)
In	156	156	8.37 (20°)
Ga	30	30	17.4 (20°)
Hg	−39	−39	98.4 (50°)

* Lowest temperature at which a liquid is present in this binary system.

Table II. Summary of heat-treatments of Be-metallized Si wafers

Temperature (°C)	Time (minutes)	Oxide color	Residue after HF treatment
No heat treatment		Pink	None
440	5	Pink	None
475	5	Blue tint	Trace
535	5	Green	Edges
625	5	Gray*	Insoluble
625	20	Gray-green*	Insoluble
765	5	Green*	Insoluble

* Color of insoluble residue on SiO_2 surface.

Table III. Electron microprobe results*

Heat-treatment	Scribe line (Si) counts	Field (SiO_2) counts**
535°-5 min	56.2	141
625°-5 min	70.2	352
625°-20 min	60.7	567
765°-5 min	78.7	1352

* 5 keV beam.
** Ratioed from 36,000 counts on bare Si, 1352 counts represents about 3.7% Si.

The possible reactions are

$$2SiO_2 + 2Be \rightarrow Be_2SiO_4 + Si \quad [1]$$

$$SiO_2 + 2Be \rightarrow 2BeO + Si \quad [2]$$

After HCl and HF treatment the sample which was treated at 535°C for 5 min had the insoluble residue concentrated around what had been the edges of the openings in the original SiO_2 layer. When this residue and the over-all residue remaining on samples which were treated at higher temperatures were removed by mechanical agitation, there was no evidence of attack on the Si substrate as observed with the SEM. Although there was no apparent attack upon the Si, there was a thin residue over the Si in the scribe lines after Be removal by HCl from the 625°C-20 min and 765°C-5 min samples. This residue did not dissolve after 1 hr in concentrated HCl.

Conclusions

The present investigation found that Be metallization of integrated circuits has some substantial advantages over the present widely used Al metallization. Beryllium metallization adheres to both the Si and the oxide of an integrated circuit wafer and does not crack or lift the oxide layer upon being quenched in water from temperatures as high as 765°C. There is no visible attack upon the Si substrate up to 765°C for 5 min. A definite limitation to Be metallization, however, is the reaction between Be and SiO_2 that occurs at temperatures exceeding 440°C, and at least partially converts the SiO_2 to an HF insoluble product at temperatures above 535°C.

Acknowledgments

This work was supported in part by the Office of Naval Research.

Manuscript submitted July 16, 1976; revised manuscript received Jan. 6, 1977.

Any discussion of this paper will appear in a Discussion Section to be published in the December 1977 JOURNAL. All discussions for the December 1977 Discussion Section should be submitted by Aug. 1, 1977.

Publication costs of this article were assisted by the California Institute of Technology.

REFERENCES

1. H. Sello, in "Ohmic Contacts to Semiconductors," B. Schwartz, Editor, p. 277, The Electrochemical Society Softbound Symposium Series, New York (1968).
2. H. C. Card, *IEEE Trans. Electron Devices*, **ed-23**, 538 (1976).
3. A. J. Learn, *This Journal*, **123**, 894 (1976).
4. M. Hansen, "Constitution of Binary Alloys," McGraw-Hill, New York (1958).
5. R. L. Boatright and J. O. McCaldin, *J. Appl. Phys.*, **47**, 2260 (1976).
6. John S. Best and J. O. McCaldin, *ibid.*, **46**, 4071 (1975).
7. J. R. Black, in "Ohmic Contacts to Semiconductors," B. Schwartz, Editor, p. 311, The Electrochemical Society Softbound Symposium Series, New York (1968).
8. M. P. Lepselter and J. M. Andrews, *ibid.*, p. 159.
9. J. M. Poate, P. A. Turner, and W. J. De Bonte, *J. Appl. Phys.*, **46**, 4275 (1975).
10. G. J. Van Gurp and C. Langereis, *ibid.*, **46**, 4301 (1975).
11. G. J. Van Gurp, *ibid.*, **46**, 4308 (1975).
12. J. O. McCaldin, *J. Vac. Sci. Technol.*, **11**, 990 (1974).
13. "Handbook of Chemistry and Physics," 49th ed., R. C. Weast, Editor, Chemical Rubber Company, Cleveland, Ohio (1968).
14. R. W. Powell, *Philos. Mag.*, **44**, 645 (1953).
15. E. A. Taft and R. O. Carlson, *This Journal*, **117**, 711 (1970).
16. E. L. Hall, A. N. Koblinski, and J. E. Gragg, Proceedings of the Reliability Physics Symposium (April 1976).

Optimization of Alignment Marks and Their Electron Signals in a Semiconductor Process

H. Friedrich, H.-U. Zeitler, and H. Bierhenke

Siemens AG, Research Laboratories, 8 München 80, Germany

Direct pattern generation on the wafer using an electron beam system to realize integrated circuits makes alignment and therefore alignment marks necessary. Figure 1 shows the secondary electron signal of a 1 μm oxide step covered with 0.3 μm resist. The asymmetric secondary electron signal is caused by the asymmetric collection of secondary electrons due to the position of the detector. This signal quality allows good signal detection for wafer positioning. But, when coming to thinner layers, as necessary when using the scaling principle for integrated MOS circuits (1), the signal-to-noise ratio *vs.* scaling factor α becomes worse as shown in Fig. 2. That means smaller steps lead to smaller signals, which cannot be processed in the short time necessary for automatic alignment.

But using an electron beam system means smaller structures and therefore demands a higher absolute positioning accuracy, which is approximately 20% of the smallest structure size, *i.e.*, 0.5-1 μm-structures need a positioning accuracy of about 0.1 μm and a layer thickness of about 0.2 μm. Hence it follows that the main problem to realize small structures is not only their size but also the positioning accuracy required.

These conclusions lead to demands on alignment marks which give good and exact signals for small layers and which are not affected by the manufacturing process (2).

Several suggestions for alignment marks required above have been investigated, *e.g.*, silicon and silicon dioxide steps proposed in Ref. (3). A new method will be offered here. An additional processing step has been used. Etching anisotropically (4) through a field oxide mask into a (100)-silicon substrate leads to V-grooved alignment marks which give good SEM signals. Figure 3 shows a principal cross section of such a structure and the backscattered electron signal expected. An alignment mark like this is a well-defined structure with a constant flank angle of about 55° and without appreciable edge roughness. Therefore one can use narrow grooves, *e.g.*, of a width of only 1 μm for alignment purposes.

The signal measured is a function of the number of backscattered electrons reaching the detector. Therefore the edges result in a maximum and the bottom of

Key words: electron beam writing, automatic alignment, direct pattern generation, electron detectors.

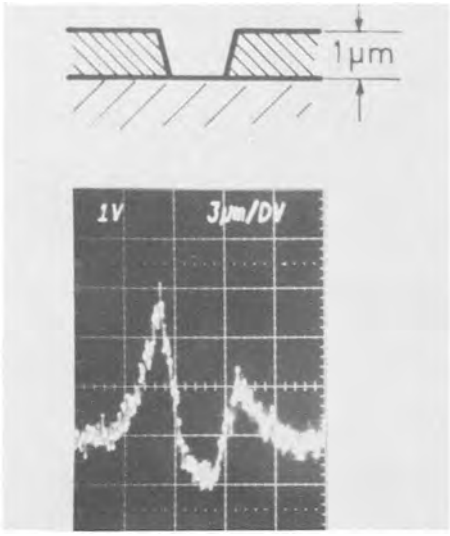


Fig. 1. Secondary electron signal of a 1 μm oxide step

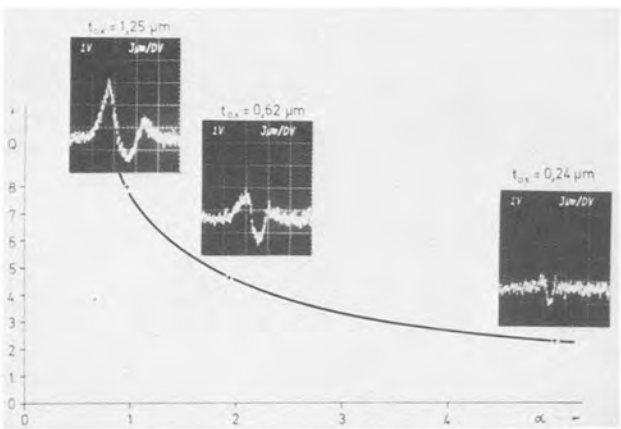


Fig. 2. Signal to noise ratio Q vs. scaling factor α

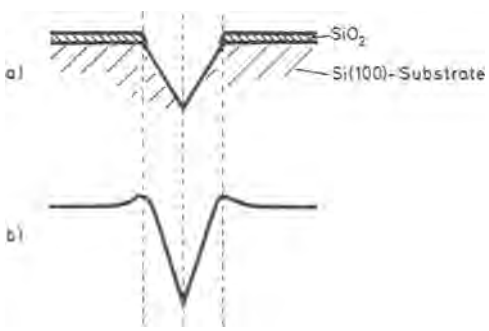


Fig. 3. Principal cross section of V-grooved alignment mark (a) and the belonging backscattered electron signal (b).

the groove gives the minimum. In Fig. 4 one can see a SEM micrograph of such a structure and of the measured backscattered electron signal which has been taken using a primary energy of 20 keV. The correspondence between the expected and the measured signal is quite good.

In the following, the signals measured at this alignment mark are shown for different important steps of an n-silicon gate process. These signals have been observed using two different electron detectors: (*i*) a conventional secondary electron detector especially sensitive for the electrons of low energies, and (*ii*) a silicon diode detector for backscattered electrons with higher energies. In every case the primary energy has been 20 keV, the slice was covered with 0.3 μm PMMA resist and the width of the structures was 1 and 2 μm, respectively.

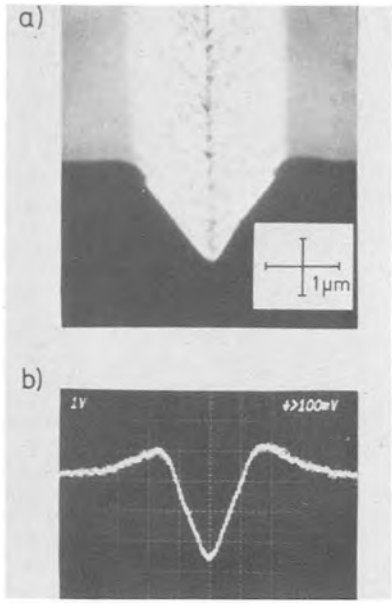


Fig. 4. SEM micrograph of V-grooved alignment mark (a) and the belonging backscattered electron signal (b).

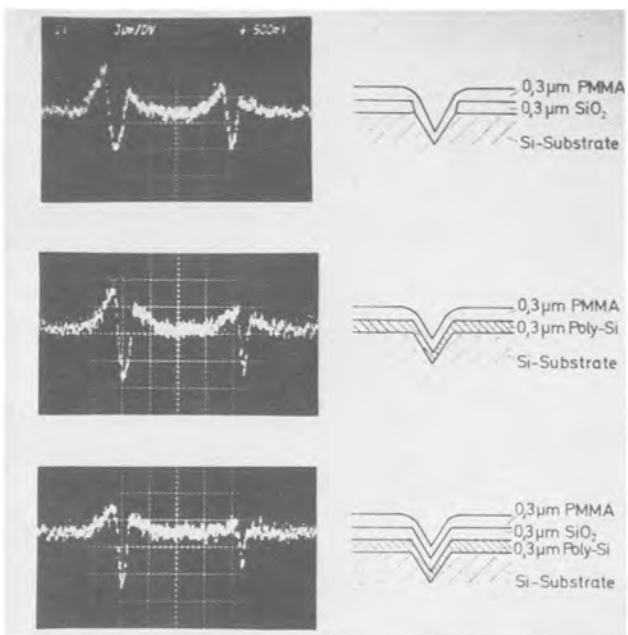


Fig. 5. Secondary electron signals for different steps of a n-silicon gate process.

Figure 5 shows these signals, measured with a secondary electron detector for a substrate covered with 0.3 μm silicon dioxide and resist, for a substrate with 0.3 μm polysilicon and resist and for a substrate with polysilicon, silicon dioxide, and resist. Even the last one gives useful signals for detection and computing.

The symmetrical silicon-diode detector for backscattered electrons consisting of four parts has been used for the signals of the same structure which are shown in Fig. 6. The signal-to-noise ratio of these signals is 18 *vs.* 9 for those shown in Fig. 5. Therefore one should use a backscattered electron detector for alignment mark detection with good signal-to-noise ratio. An additional advantage of this detector is that it is free of any potential that influences the electron beam.

The example of a n-silicon gate process for the use of those grooved alignment marks has shown that narrow structures give very good electron signals, which are insignificantly influenced by the processing steps.

For special purpose it might be necessary to decrease the primary energy. The influence of this on the de-

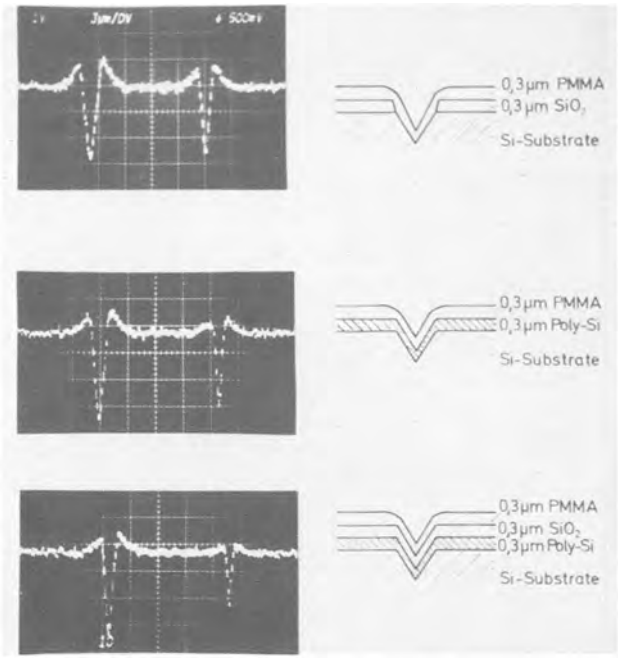


Fig. 6. Backscattered electron signals for different steps of a n-silicon gate process.

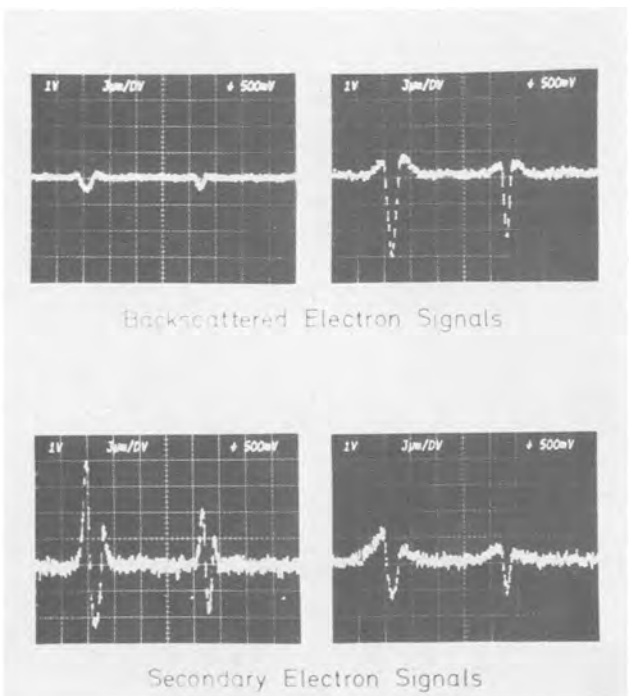


Fig. 7. Electron signals of V-grooved Si substrates with poly-Si layers for various primary energies.

tected signals is shown in Fig. 7, for 10 and 20 keV. The decrease of sensitivity for lower energies of the backscattered electron detector results in decreased backscattered signals while the higher secondary electron efficiency leads to better secondary signals.

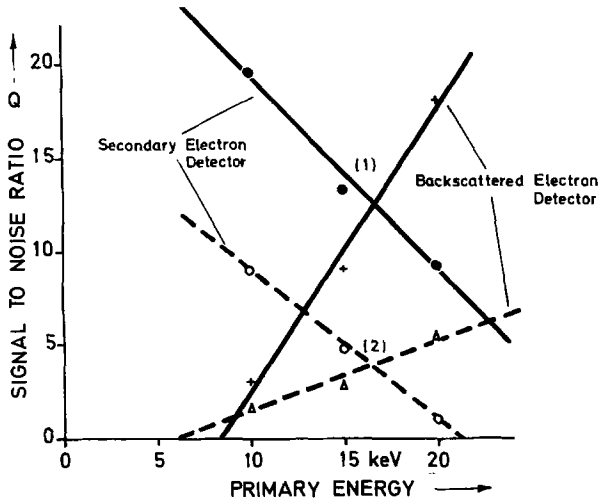


Fig. 8. Signal to noise ratio vs. primary energy with (1) and without (2) substrate etching.

Figure 8 shows a graph of the signal-to-noise ratio *vs.* primary electron energy for alignment marks with and without V-grooved substrate etching. In every case the signal quality of the substrate etched structures is much better and the selection of which detector to use for the best signal depends on the energy needed.

With these marks, described above, a positioning accuracy between two different mask levels, each adjusted to an earlier etched alignment mark level, of $\Delta x = 60 \pm 80$ nm measured with a vernier could be achieved for approximately one hundred alignments.

It has been shown in this paper that V-grooved alignment marks for a semiconductor process using electron beam technology give improved electron signals independent of the type of layer sandwich which are not affected by the process.

Acknowledgment

The authors express their appreciation to Mrs. Sylvia Henkel for providing the structures and helpful assistance during the measurements.

Manuscript submitted July 27, 1976; revised manuscript received Nov. 29, 1976. This was Paper 195 presented at the Washington, D. C., Meeting of the Society, May 2-7, 1976.

Any discussion of this paper will appear in a Discussion Section to be published in the December 1977 JOURNAL. All discussions for the December 1977 Discussion Section should be submitted by Aug. 1, 1977.

Publication costs of this article were assisted by Siemens AG.

REFERENCES

1. R. H. Dennard *et al.*, Design of Micro MOS-switching Devices, IEDM Washington, D.C. (Dec. 1972).
2. E. D. Wolf *et al.*, *J. Vac. Sci. Technol.*, **12**, 1266 (1975).
3. T. H. P. Chang, *ibid.*, **10**, 1129 (1973).
4. J. W. Faust, Jr., in "The Surface Chemistry of Metals and Semiconductors," H. C. Gatos, Editor, John Wiley & Sons, Inc., New York (1960).

Mechanism of Arsenic Diffusion into Silicon from Arsenic-Doped Oxide Source

K. D. Beyer*

IBM System Products Division, East Fishkill Facility, Hopewell Junction, New York 12533

The diffusion properties of arsenic in Si and SiO_2 for arsenic-doped oxides have been studied previously (1) by varying the arsenic concentration in the arsenic-doped glass. Ghezzo and Brown (1) found that, after the diffusion in argon, the sheet resistance of diffusions from arsenic-doped oxide sources decreased with increasing arsenic concentration in the doped oxide glass, up to a certain concentration. Above this concentration of the arsenic-doped oxide, the sheet resistance increased with increasing arsenic concentration in the doped oxide. However, this deviation from the monotonic dependence of the sheet resistance on the arsenic concentration, after arsenic-doped oxide diffusion in argon, has not been explained.

Sakurai *et al* (2) studied the effects of N_2 and O_2 atmospheres on the arsenic diffusion from arsenic-doped oxide into silicon by the backscattering method and discovered the accumulation of elemental arsenic at the interface of arsenic-doped oxide and silicon. The differences between the O_2 and N_2 diffusions of arsenic-doped oxides were attributed to the property differences of the silicon–arsenic-doped oxide interface in O_2 and N_2.

Baak (3) studied the thermodynamics of arsenic in arsenic-doped oxide and found a higher chemical stability of arsenic-doped oxides in O_2 at high partial pressure than in O_2 at low partial pressure.

To study the relationship between the properties at the arsenic-doped oxide–silicon interface and the arsenic diffusion from the arsenic-doped oxide into silicon, a neutron-activation analysis of the arsenic-doped glass and the silicon was done after diffusion as well as the measurement of sheet resistance and junction depth.

Experimental

Arsenic-doped oxides were deposited by a 30 min O_3 decomposition at 215°C of an arsenic paint-on diffusion source consisting of 1.2g polymethylsiloxane glass resin, 1.2g $As[O\text{-}Si(C_6H_5)_2Si\text{-}O]_3As$, and 10.0g n-butylacetate, and were spun at 3000 rpm for 30 sec on p-type <100> 1-2 Ω-cm silicon wafers (4). After O_3 decomposition of the film at 181°C for 30 min, the wafers were diffused at 1175°C for a total diffusion time of 140 min under the following ambient conditions: 140 min in argon, 15 min in oxygen followed by 125 min in argon, and 140 min in oxygen. After diffusion, the wafers were cut into halves. On one half, sheet resistances and junction depths were measured; on the other half, the arsenic in the doped oxide and in the silicon was profiled by the neutron-activation analysis technique.

Results

Table I shows the sheet resistance and junction depth values and the surface quality at the arsenic-doped oxide–silicon interface, after diffusion, as functions of the diffusion ambient. The quality is described in terms of the presence or absence of a residue layer at the silicon surface after removal of the arsenic-doped oxide in hydrofluoric acid.

Figures 1, 2, and 3 present the arsenic profile, taken by neutron-activation analysis, in the arsenic-doped oxide and in the silicon after diffusions in argon for 140 min, in oxygen for 15 min followed by 125 min in argon, and in oxygen for 140 min, respectively. In these figures, the arsenic concentration, measured in atoms per cubic centimeter, is plotted on a semilogarithmic scale of the ordinate. On the abscissa the thickness of the arsenosilicate glass is measured in angstroms, while the silicon depth is measured in micrometers. In these arsenic profile figures, the zero value of the abscissa is set at the interface of arsenic-doped oxide and silicon.

* Electrochemical Society Active Member.
Key words: diffusion, arsenic, doping, glass.

Table I. Sheet resistance and junction depth values and the silicon surface quality after the arsenic-doped oxide diffusion in various ambients and after doped-oxide removal by HF

Diffusion ambient	Sheet resistance (Ω/□)	Junction depth (μm)	Surface quality
140 min in Ar	44.1	1.9	Residue
15 min in O_2, 125 min in Ar	8.5	2.5	No residue
140 min in O_2	12.5	2.4	No residue

As shown in Table I, a higher sheet resistance is observed for the arsenic-doped oxide diffusion in argon than in O_2; this is in agreement with the results of previous investigations (1). A lower sheet resistance is observed for arsenic-doped oxide diffusions that received a 15 min O_2 heat-treatment, followed by a 125 min diffusion in argon, than for diffusions in O_2 for 140 min. According to Table I, a residue layer is present, after completion of the arsenic-doped oxide diffusion at the arsenic-doped oxide–silicon interface, only

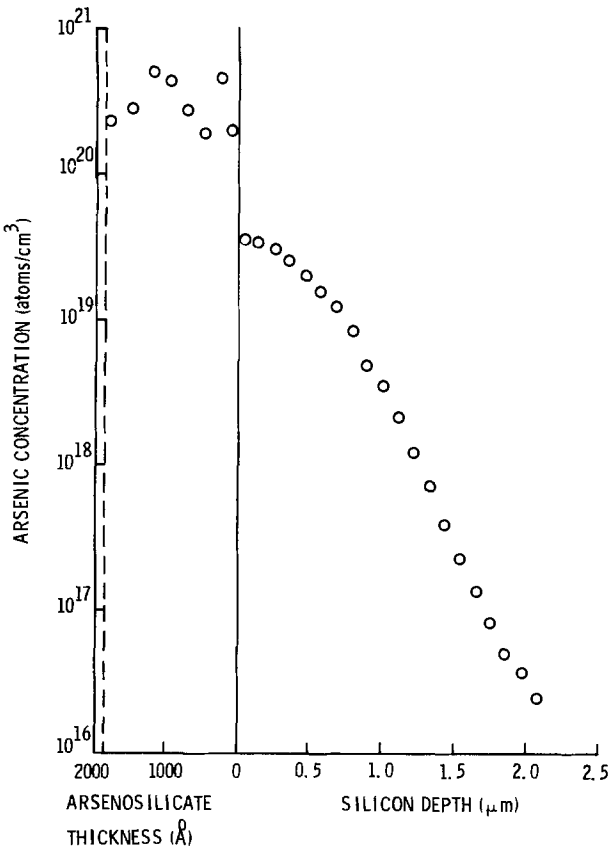


Fig. 1. Profile of arsenic concentration in the arsenic-doped oxide and in the silicon after diffusion in argon for 140 min.

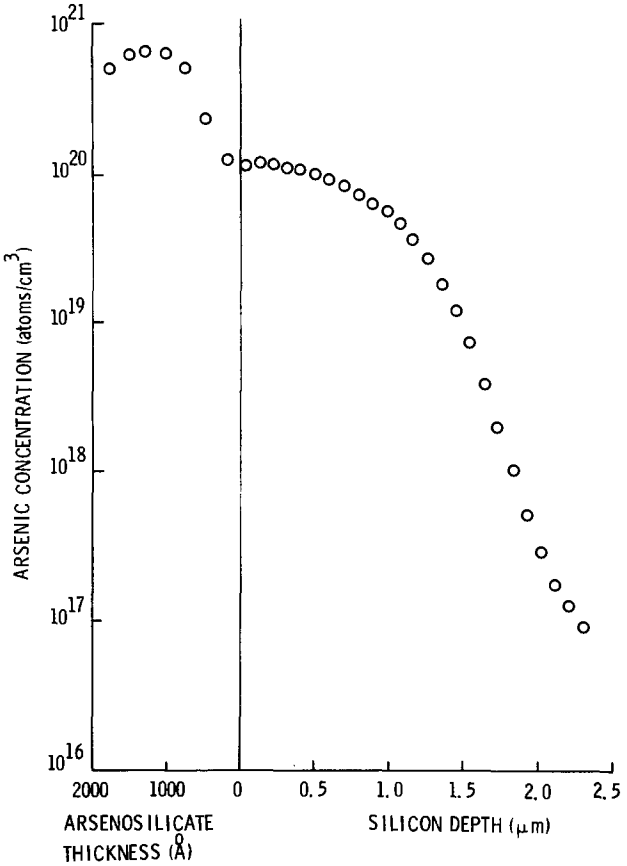


Fig. 2. Profile of arsenic concentration in the arsenic-doped oxide and in the silicon after diffusion in oxygen for 15 min followed by 125 min in argon.

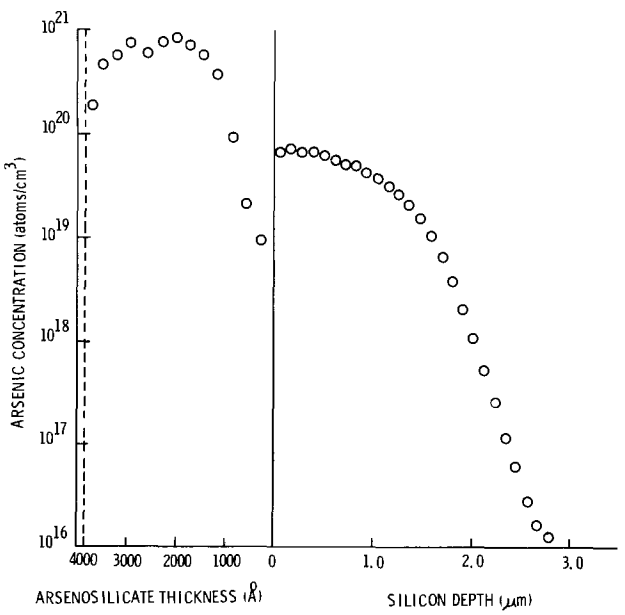


Fig. 3. Profile of arsenic concentration in the arsenic-doped oxide and in the silicon after diffusion in oxygen for 140 min.

if the whole arsenic-doped oxide diffusion is done in argon.

Figure 1 indicates that arsenic-doped oxide diffusions in argon cause an abrupt change of the arsenic concentration at the arsenic-doped oxide–silicon interface, with the arsenic concentration being one order of magnitude higher in the arsenic-doped oxide than in the silicon. For the arsenic-doped oxide diffusion with the 15 min O_2/125 min argon heat-treatment, as shown in Fig. 2, no arsenic concentration change between arsenic-doped oxide and silicon at the interface can be detected. For the arsenic-doped oxide diffusion in O_2, as seen in Fig. 3, the arsenic concentration is an order of magnitude higher in the silicon than in the arsenic-doped oxide at the arsenic-doped oxide–silicon interface.

Discussion

After the arsenic-doped oxide diffusion in argon, the arsenic concentration is an order of magnitude higher in the arsenic-doped oxide than in the silicon at the arsenic-doped oxide–silicon interface (Fig. 1). This arsenic concentration step at the arsenic-doped oxide–silicon interface can be explained by the presence of an arsenic barrier layer at the interface. Physical evidence of a layer formation at the arsenic-doped oxide–silicon interface is the residue layer which is formed after arsenic-doped oxide diffusion in argon, as shown in Table I and reported in previous investigations (1). One can assume that the residue layer is the barrier layer, which is responsible for the arsenic concentration step at the interface after the arsenic-doped oxide diffusion in argon. The higher sheet resistance value after arsenic-doped oxide diffusion in argon in comparison with the arsenic-doped oxide diffusion in O_2, as seen from Table I and as reported by other authors (1), also supports the assumption of the presence of an arsenic barrier layer at the interface after arsenic-doped oxide diffusions in argon. The formation of a residue layer was also reported when argon was replaced by N_2 as a diffusion ambient (2, 5). Sakurai *et al.* (2) pointed out that the differences between O_2 and N_2 diffusions of arsenic-doped oxides can be attributed to property differences of the arsenic-doped oxide–silicon interface. These property differences can be explained by the higher chemical stability of arsenosilicates in O_2 than in N_2 (3, 6).

The arsenic-doped oxide diffusion in O_2 followed by a 125 min heat-treatment in argon produces the same arsenic concentration in the arsenic-doped oxide as in the silicon at the arsenic-doped oxide-silicon interface (Fig. 2). Apparently, no barrier layer is present at the interface after a 15 min O_2/125 min argon heat-treatment of arsenic-doped oxides. This is confirmed by the absence of a residue layer under identical diffusion conditions. The absence of a residue/barrier layer at the interface, after a 15 min O_2/125 min argon arsenic-doped oxide diffusion, is in contrast to the presence of a residue/barrier layer at the interface after a 140 min arsenic-doped oxide diffusion in argon. Consequently, under the conditions of this experiment, such as arsenic concentration in the arsenic-doped oxide, arsenic-doped oxide thickness, and diffusion temperature and time, the choice of the diffusion ambient during the first 15 min of the diffusion heat-treatment determines whether a residue/barrier layer is formed. The diffusion in O_2 prevents the formation of a residue/barrier at the interface, while the diffusion in argon causes the formation of a residue/barrier layer at the interface during the first 15 min of the arsenic-doped oxide diffusion. The prevention of a residue/barrier layer at the arsenic-doped oxide–silicon interface in oxygen ambients can be explained by the chemical stability of arsenosilicate in oxygen during heat-treatments (3, 6). The absence of a residue/barrier layer formation at the arsenic-doped oxide–silicon interface during the 125 min argon heat-treatment, following the initial 15 min heat-treatment in oxygen, can be explained in three ways:

1. The initial O_2 heat-treatment transforms the arsenosilicate glass into the chemically stable As_2O_5-type arsenosilicate (3, 6). Upon further heat-treatment in argon, the arsenosilicate remains in the chemically stable As_2O_5-type arsenosilicate.

2. During the initial 15 min O_2 diffusion of arsenic-doped oxide, the arsenic concentration in the arsenic-doped oxide is depleted because of outdiffusion and arsenic diffusion from the arsenic-doped oxide into silicon. As low concentration arsenic-doped oxides do

not form a residue/barrier layer at the arsenic-doped oxide–silicon interface after an argon diffusion (1), the arsenic depletion of the arsenic-doped oxide during the initial O_2 heat-treatment may be sufficient to form a low arsenic concentration doped oxide that is chemically stable in an argon ambient.

3. A thin SiO_2 layer between arsenic-doped oxide and silicon (1, 7), which can be formed during the initial 15 min heat-treatment in O_2, will prevent the formation of a residue layer at the arsenic-doped oxide–silicon interface during the argon diffusion.

The first explanation, the transformation of arsenosilicate glass into the chemically stable As_2O_3-type arsenosilicate during heat-treatment in oxygen and the stability of As_2O_5-type arsenosilicate in a subsequent heat-treatment, does not account for the sheet resistance minimum of arsenic-doped oxide diffusions for longer heat-treatments in O_2 than for shorter ones (8).

For the second explanation, higher arsenic depletion of arsenic-doped oxides for oxygen than for argon during initial heat-treatments, no evidence can be found, because the arsenic concentration in the arsenic-doped oxide after diffusion is approximately equal for the 140 min argon and 15 min oxygen/125 min argon heat-treatments (Fig. 1 and 2).

The third explanation, the elimination of a residue layer at the arsenic-doped oxide–silicon interface during diffusion in argon by the presence of a thin SiO_2 layer between arsenic-doped oxide and silicon, is supported by previous experiments (1, 8). Higher sheet resistance values are observed for arsenic-doped oxides deposited on thin SiO_2 layers and diffused in argon than for arsenic-doped oxides deposited on silicon and diffused in oxygen (1, 8). This discrepancy can be explained by the lower arsenic diffusivity in undoped SiO_2 layers than in arsenic-doped SiO_2 layers (9). According to previous experiments (10), a sheet resistance minimum for arsenic-doped oxide diffusions into silicon can be obtained, not only by certain oxygen-argon or oxygen-nitrogen ambient cycles (8), but also by a certain constant ambient ratio of oxygen and nitrogen. It can be assumed that, during diffusion, such a constant ambient ratio would produce a SiO_2 layer that is sufficient to prevent a residue/barrier layer formation and that is too thin to inhibit the arsenic diffusion from the arsenic-doped oxide into silicon.

An arsenic concentration step at the arsenic-doped oxide–silicon interface, with a higher arsenic concentration in the silicon than in the arsenic-doped oxide, can be observed after a 140 min oxygen diffusion of arsenic-doped oxides, as seen in Fig. 3. During the 140 min O_2 diffusion, the film thickness of the arsenic-doped oxide increased from 2000 to 3850Å. This increase can be explained by the growth of an oxide layer at the arsenic-doped oxide–silicon interface during the 140 min oxygen heat-treatment at 1175°C.

In order to interpret the higher arsenic concentration in the silicon than in the arsenic-doped oxide after the completion of the arsenic-doped oxide diffusion in oxygen, one can assume that, during the initial oxygen heat-treatment, arsenic diffuses easily from the arsenic-doped oxide through the initially thin SiO_2 layer, formed during the oxygen diffusion at the interface of arsenic-doped oxide and silicon, into the silicon. In the late stages of the arsenic-doped oxide diffusion in oxygen, the arsenic concentration in the doped oxide near the doped oxide-silicon interface depletes and the SiO_2 layer thickness at the doped oxide-silicon interface increases. The arsenic depletion and the SiO_2 layer thickness increase cause the formation of a SiO_2 mask, which prevents further arsenic diffusion from the arsenic-doped oxide into the silicon and from the silicon into the arsenic-doped oxide.

Conclusions

During diffusions from arsenic-doped oxides, in argon, an arsenic diffusion barrier layer is formed at the arsenic-doped oxide–silicon interface. The formation of this layer can be prevented if the arsenic-doped oxide is diffused, first, in oxygen and, then, in argon. Arsenic-doped oxide diffusion entirely in oxygen causes the formation of a SiO_2 layer at the arsenic-doped oxide–silicon interface, thereby slowing the arsenic diffusion from the arsenic-doped oxide into the silicon.

Acknowledgments

The author is indebted to R. Kastl and F. V. Keicher for the neutron activation analysis and to M. Whitehill for the hot processing.

Manuscript submitted Sept. 14, 1976; revised manuscript received Dec. 28, 1976.

Any discussion of this paper will appear in a Discussion Section to be published in the December 1977 JOURNAL. All discussions for the December 1977 Discussion Section should be submitted by Aug. 1, 1977.

Publication costs of this article were assisted by the IBM Corporation.

REFERENCES

1. M. Ghezzo and D. M. Brown, *This Journal*, **120**, 110 (1973).
2. T. Sakurai, H. Nishi, T. Furuya, H. Hashimoto, and H. Shibayama, *Appl. Phys. Lett.*, **22**, 219 (1973).
3. T. Baak, *J. Am. Cer. Soc.*, **42**, 27 (1958).
4. K. D. Beyer, *This Journal*, **123**, 1556 (1976).
5. P. C. Parekh, D. R. Goldstein, and T. C. Chan, *Solid-State Electron.*, **14**, 281 (1971).
6. E. Arai and Y. Terunuma, *Jpn. J. Appl. Phys.*, **9**, 691 (1970).
7. H. Teshima, Y. Tarui, and O. Takeda, *Bull. Electrotech. Lab., Tokyo*, **33**, 631 (1969).
8. K. D. Beyer, U.S. Pat. 3,798,081 (1974).
9. J. Wong and M. Ghezzo, *This Journal*, **119**, 1413 (1972).
10. K. Reindl, *Solid-State Electron.*, **16**, 181 (1973).

Brief Communication

Current-Induced Solution Growth of Garnet Layers

L. Jastrzebski, H. C. Gatos,* and A. F. Witt*

Department of Materials Science and Engineering, Massachusetts Institute of Technology, Cambridge, Massachusetts 02139

Yttrium-iron-gallium garnet layers were grown isothermally on single crystal YIG and GGG substrates from a BaO-BaF_2-B_2O_3 solution by applying an electric current across the seed solution interface. The growth rate and composition were found to depend strongly on the current density. Growth is qualitatively explained on the basis of electromigration of charged species to the crystal-solution interface.

It has been reported (1) that growth of semiconductor compounds from solution can be initiated and sustained by passing electric current across the growth interface while the temperature of the system is maintained constant; growth, originally attributed to Peltier cooling (1), was subsequently shown to be due to electromigration of charged Group III and Group V atoms in the liquid phase (2). InSb (1), GaAs (2, 3), and GaAs (4) layers have been successfully grown by this method. In the present note experimental results are reported on the growth of $Y_3Fe_{5-x}Ga_xO_{12}$ layers.

All experiments were carried out, without substrate rotation, in a standard apparatus for epitaxial growth of garnets from solution (5); electrical contacts (with Pt) were made to the seed and the crucible. A 25 mole percent solution of oxides (37.5% Y_2O_3 + 52.1% Fe_2O_3 + 10.4% Ga_2O_3) in 41% BaO + 18% BaF_2 + 41% B_2O_3 was used; the seeds were single crystals of GGG with (111) orientation and YIG with a high index orientation. Growth was carried out at 1195°C (the equilibrium liquidus temperature 1190°C) employing current densities of 10^{-4} to 2 A/cm^2; the polarity of the seed was positive. With the electrical contacts connected to the power supply, growth was initiated by immersing the seed into the solution and terminated by withdrawing the seed while the system was at the growth temperature of 1195°C. With the above current densities, layers of $Y_3Fe_{5-x}Ga_xO_{12}$ were obtained ranging in thickness from 8 to 800 μm. The flux attached to the grown layer was removed with dilute (50%) HCl and the average thickness of the layer was determined by measuring the weight gain of the seed and optically by employing a cross section of the seed with the epitaxial layer. The grown layers were monocrystalline with inclusions identified as flux (see Fig. 1).

The average growth rate as a function of current density is plotted in Fig. 2. The normalized growth rate (growth velocity/current density) decreases with increasing current density (Fig. 2); *i.e.*, the growth efficiency decreases with increasing current density. Figure 3 shows the composition of the grown layers (determined by an electron microprobe) as a function of current density. It is seen that the Ga concentration increases significantly with increasing current density. The lattice parameter of a layer grown

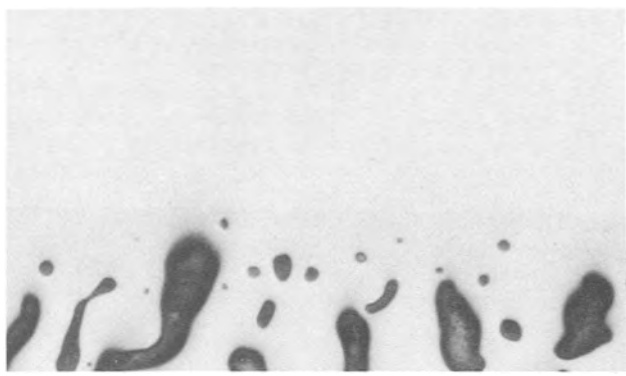


Fig. 1. Photomicrograph of a layer (lower part) grown on a YIG substrate (upper part) at a current density of 0.5 A/cm^2 (880X).

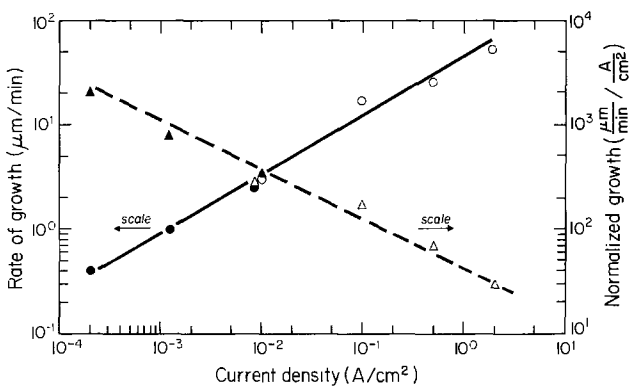


Fig. 2. Average current-induced growth rate and normalized growth rate as a function of current density; ▲, ● = GGG substrate; △, ○ = YIG substrate.

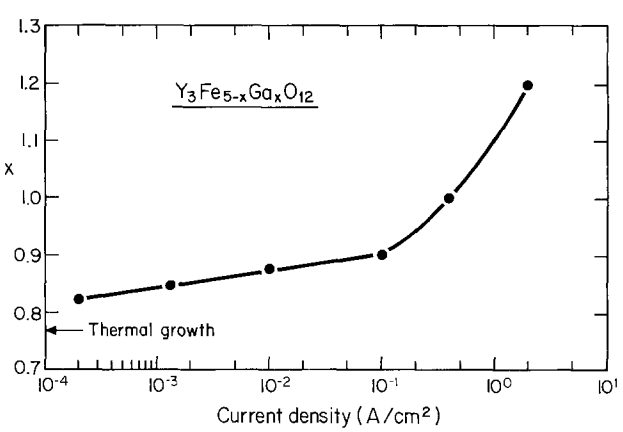


Fig. 3. Composition of the grown garnet layers as a function of current density.

* Electrochemical Society Active Member.
Key words: garnets, solution growth, current-induced growth.

at 0.5 A/cm^2 was found to be 12.360Å, which corresponds to the composition $Y_3Fe_4GaO_{12}$ (6). The composition of a thermally grown layer from the same solution (by decreasing the temperature 8°C below the equilibrium temperature) was found to be $Y_3Fe_{4.3}Ga_{0.7}O_{12}$ and the average growth rate 0.5 μm/min.

A quantitative interpretation of the experimental results is not possible since there is no detailed information available on the type of the species present in the solution, their charge, and their mobility. However, a qualitative explanation will be presented. During current flow negatively charged yttrium, iron, and gallium oxide species migrate toward the seed (positive) and charged boric oxide species migrate away from the seed. Thus, the solution becomes supersaturated at the seed-solution interface and growth takes place. The negative charge of the above three oxide species probably results from association with F^- whereas the positive charge of the boric oxide results from association with Ba^{++}. Apparently, the relatively high charge of these species and the relatively high resistance of the solution (of the order of 1Ω) are responsible for the fact that, for a current density of 1 A/cm^2, the growth rate of garnets is about three orders of magnitude higher than that reported for GaAs (2) where the resistance of the solution is about $10^{-4}\Omega$.

The increase in the gallium concentration with increasing current density (Fig. 3) is attributed to the higher mobility of the charged gallium species as compared to that of the yttrium and iron species. The observed decrease of the normalized growth velocity with increasing current density is believed to be associated with the increase in concentration of BaO and BaF_2 (with increasing current density) at the seed solution interface. Actually, at current densities greater than 10 A/cm^2 seed dissolution took place rather than crystal growth. At this current density a (positive) platinum electrode, used in the place of the seed, was attacked by the solution, apparently because the solution became depleted in boric oxide which migrated to the opposite electrode; this type of platinum attack has been reported for solutions rich in BaO and BaF_2 (7).

In summary, current-induced solution growth of garnet layers was achieved. The growth velocity and composition were found to depend strongly on current density. This dependence is qualitatively consistent with migration of charged species during current flow. The implications of the present finding to the growth and composition of oxide epilayers and crystal growth by top seeding are being pursued.

Acknowledgment

The authors are grateful to Dr. A. Linz and Mr. V. Belruss for making facilities available and for their assistance in carrying out the growth experiments, and to Prof. R. Ogilvie for the electron microprobe results. The authors are also indebted to the National Science Foundation for financial support.

Manuscript submitted July 16, 1976; revised manuscript submitted Nov. 22, 1976.

Any discussion of this paper will appear in a Discussion Section to be published in the December 1977 JOURNAL. All discussions for the December 1977 Discussion Section should be submitted by Aug. 1, 1977.

Publication costs of this article were assisted by Massachusetts Institute of Technology.

REFERENCES

1. M. Kumagawa, A. F. Witt, M. Lichtensteiger, and H. C. Gatos, *This Journal*, **120**, 583 (1973).
2. L. Jastrzebski, H. C. Gatos, and A. F. Witt, *ibid.*, **123**, 1121 (1976).
3. D. J. Lawrence and L. F. Eastman, *J. Cryst. Growth*, **30**, 267 (1975).
4. J. J. Daniele, *Appl. Phys. Lett.*, **27**, 373 (1975).
5. See for example articles in *J. Crystal Growth*, **27** (1974).
6. S. Geller, J. A. Cape. G. P. Espinosa, and D. H. Leslie, *Phys. Rev.*, **148**, 522 (1966).
7. See J. T. Carlo, Ph.D. Thesis, Department of Electrical Engineering, M.I.T., Cambridge, Mass. (1973).

Direct Observation of the Structure of Thin, Commercially Useful Silicon on Sapphire Films by Cross Section Transmission Electron Microscopy

W. E. Ham,* M. S. Abrahams, C. J. Buiocchi, and J. Blanc

RCA Laboratories, David Sarnoff Research Center, Princeton, New Jersey 08540

Observations of the defect structure in thick (8-10 μm) silicon on sapphire films by transmission electron microscopy (TEM) were recently reported by Abrahams and Buiocchi (1). These films were grown by the pyrolysis of silane on polished single crystal $(1\bar{1}02)$ sapphire substrates. Such thick films are of little practical use and it is conceivable that their defect structure does not represent the structure of the thinner SOS films normally used for device fabrication. It is therefore necessary to examine the actual films of interest in order to be confident of the defect structure existing in practical devices. The observation of thick films allows examination of only the so-called "bottom" interface of the SOS film; the top interface was not observed nor would it be of great technical interest, although the observation of the top interface in device-like composites is of great importance.

* Electrochemical Society Active Member.

Key words: TEM, cross sections, thin films, SOS, electrically active defects.

The limitation to making observations on thick films is due to the ion thinning method used for final thinning of these specimens (2). If the "top" surface is unprotected during thinning, it will be eroded. Two methods have previously been proposed to alleviate this problem: in one, two samples are sandwiched together with an intermediate aluminum layer and bonded by thermal compression (4); in the other, the sample is encapsulated in an appropriate epoxy (5). Although these are moderately successful, the former leads to the possibility of additional defects being introduced during the relatively high temperature, high stress thermal compression, and the latter still seems to have some difficulty retaining the very top surface, presumably because of differential thinning.

We have here sought another method of protection which would further minimize these problems and which also would be compatible with routine operations in the semiconductor industry. Here, we describe the successful use of a protective layer of deposited



Fig. 1. Transmission electron micrograph of thinned sapphire-silicon-deposited oxide. Some silicon has been removed entirely by the ion beam but the protection layer is still intact after approximately 25 μm of ion thinning. (Bright field image).

SiO_2 on SOS. The SiO_2 composite was then thinned in an argon ion beam by our usual techniques for transmission electron microscopy. Details of these methods may be found in Ref. (2) and (3).

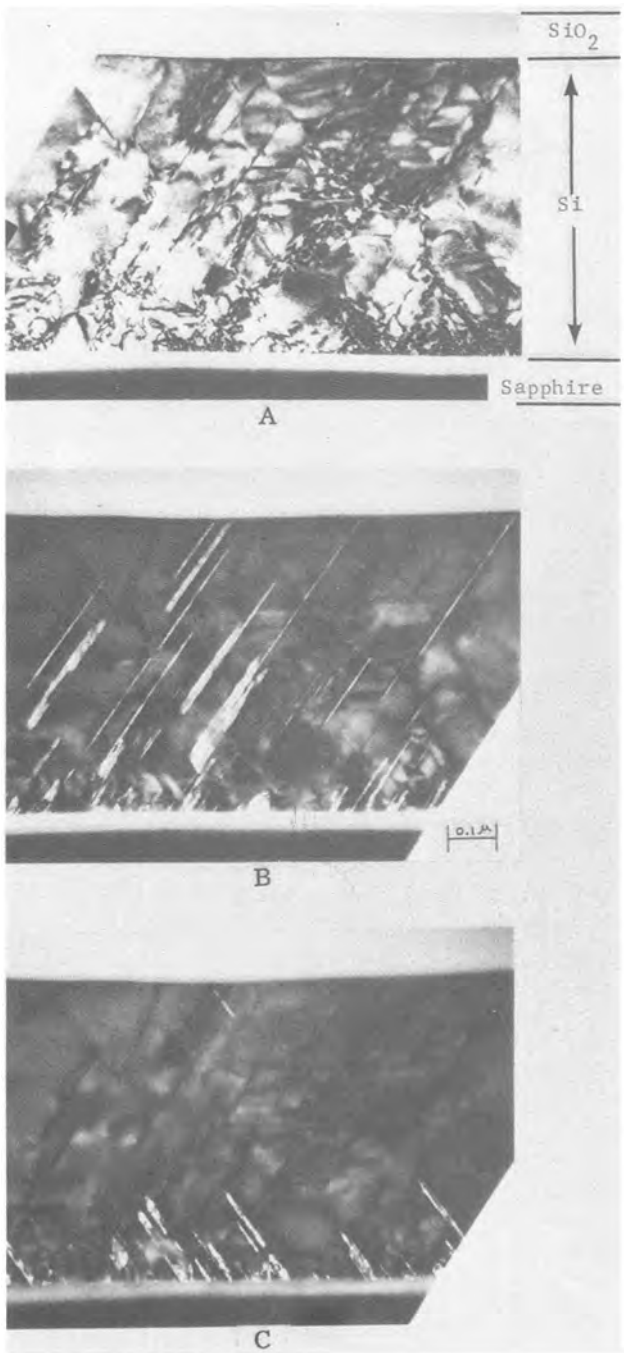


Fig. 2. Transmission electron micrographs of Al_2O_3-Si-SiO_2 composite at higher magnification. [For diffraction pattern and imaging conditions, see Ref. (1)]. (a) Many-beam bright field; (b) and (c) dark field images showing the two different sets of twins. The white band immediately below the silicon is thin sapphire; this region is free of contrast features as the substrate has very few defects.

Figure 1 shows a low magnification TEM (montage) of such a specimen. Much of the silicon above the sapphire has been eroded, but substantially all of the deposited oxide has been retained. (In the normal course of events, we would, of course, have attempted to preserve more of the silicon.) It is thus clear that a protective deposited SiO_2 layer less than 1 μm in thickness could be used.

Figure 2 shows, at higher magnification, the right-hand area of Fig. 1 where the sapphire, silicon, and deposited SiO_2 have all been preserved. Figure 2(a) shows a many-beam bright image, while 2(b) and 2(c) are dark field images showing two different sets of twins, *i.e.*, microtwins and isolated stacking faults. [For diffraction patterns and imaging conditions, see Ref. (1).] Note that in Fig. 2b, one set of twins extends from the bottom silicon-sapphire interface to the silicon-SiO_2 interface, while the second set (Fig. 2c) terminates at 2000Å from the silicon-sapphire interface. The latter may possibly have been annihilated by interaction with the first set. The defects shown in Fig. 2b closely resemble the structure proposed by Ham for electrically active defects in SOS films (6).

The defect structure shown here for a 6000Å SOS film is strikingly similar, qualitatively and quantitatively, to that previously presented (1) for a 10 μm SOS structure. This result suggests that the defects are grown in during the silicon deposition and are not produced by cooling or subsequent processing. It also shows that the twins are not annihilated by the longer times at growth temperatures required by the thick deposit, compared to the standard thickness.

Finally, the region of the film where the MOS conducting channel forms near the top interface is clearly observed to within perhaps 10Å of that interface. A clear, concise, and complete picture of films of actual technological interest has been obtained. A more detailed study of defects in such thin SOS films is in progress. It is clear, in addition, that this protective technique can be applied to other semiconductor interfaces for study by TEM.

Summary

1. It is possible to observe the structure of thin SOS layers by transmission electron microscopy including both interfaces which terminate the silicon layer.
2. The defect structure in the thin film is similar to that of the thicker films.
3. The defect structure is similar to that predicted from electrical data (6).
4. Deposited SiO_2 is a suitable protection layer for ion beam thinning processes.
5. A key step to the successful direct comparison of the structure of SOS films with their electrical properties has been developed.
6. Some effects of the defects on the surface channel conductance of MOS devices would be expected at a film thickness of 6000Å since the defects are clearly present within a few angstroms of the top surface. A sharp reduction in the channel conductance may be expected in the 2000Å thickness range where the second set of twins commences.

Acknowledgments

The authors would like to express their appreciation to A. S. Bucholz who carefully and skillfully prepared the samples for the ion thinning operation and to E. Strouse who expertly processed the SOS wafers.

Manuscript submitted Oct. 12, 1976; revised manuscript received Dec. 29, 1976.

Any discussion of this paper will appear in a Discussion Section to be published in the December 1977 JOURNAL. All discussions for the December 1977 Discussion Section should be submitted by Aug. 1, 1977.

Publication costs of this article were assisted by RCA Laboratories.

REFERENCES

1. M. S. Abrahams and C. J. Buiocchi, *Appl. Phys. Lett.*, **27**, 324 (1975).
2. M. S. Abrahams, C. J. Buiocchi, and M. D. Coutts, *Rev. Sci. Instrum.* **39**, 1944 (1968).
3. M. S. Abrahams and C. J. Buiocchi, *J. Appl. Phys.*, **45**, 3315 (1974).
4. G. R. Booker, Private communication.
5. T. T. Sheng and C. C. Chang, *IEEE Trans. Electron Devices*, **ed-23**, 531 (1976).
6. W. E. Ham, in "Heteroepitaxial Semiconductors for Electronic Devices," Springer Verlag (1976).

JOURNAL OF THE ELECTROCHEMICAL SOCIETY

REVIEWS AND NEWS

JANUARY 1977

Dielectric Isolation: Comprehensive, Current and Future

K. E. Bean* and W. R. Runyan*

Texas Instruments Incorporated, Dallas, Texas 75222

ABSTRACT

The continually increasing, widespread use of integrated circuits requires improved isolation techniques and characteristics beyond those obtainable with p-n junctions. Junction isolated planar circuits have several limitations that dielectric isolation (DI) can substantially impact. For example, DI allows increased packing density, eliminates unwanted SCR action with the substrate (particularly important in cross points and radiation hardened devices), and provides higher collector-base breakdown voltages. Unfortunately, such structures also have some limitations such as cost and manufacturing process problems. The advantages, problems, and future projections of DI circuit manufacturing are discussed following a review of the semiconductor industry's current DI processing technology.

A comprehensive paper on dielectric isolation seems fitting since 1974 marked the end of the first decade of development and production of dielectrically isolated silicon integrated circuitry. Several authors published the first papers almost simultaneously in 1964 (1-4) and originally suggested it for low capacitance, high speed circuits. It was almost immediately adapted to radiation hardened IC's because it eliminated interaction between components during gamma irradiation, and is still widely used for this purpose. It has subsequently been used for high voltage isolation, reduction of substrate parasitics, and high packing density. Table I summarizes applications that have been reported and indicates the wide potential.

Dielectric isolation (DI) is a method of fabricating integrated circuits in which the circuit components are isolated by other than p-n junctions. Figure 1 is an idealized cross section showing DI and comparing it to p-n junction isolation. Each component in the DI circuit is completely isolated by an SiO_2 film. The oxide replaces the p-n junction and the components are made in mechanically polished melt-grown material instead of in an epitaxial layer. The substrate is polycrystalline silicon rather than p-type single crystal (assuming an npn circuit). Figure 2 is a top view of an actual dielectrically isolated circuit. The SiO_2 isolation is clearly visible as the black outline around each of the components.

* Electrochemical Society Active Member.

Key words: dielectric isolation, radiation-hardened IC's, silicon orientation dependent etching, silicon circuit isolation.

Table I. DI applications

Year	Device	Feature	Ref.
1964	Simple IC	Low capacitance	(1-3)
1965	Complementary IC		(6)
1965	Radiation resistant IC	Isolation during irradiation	(3)
1969	Nixie tube driver	Selective Au doping	(42)
1969	High voltage IC's	High breakdown voltage	(42)
1972	High speed CMOS	Low capacitance	(43)
1973	Power IC	High breakdown voltage	(44)
1973	High performance op amp	Low capacitance complementary structure	(45)
1973	Thermal printer	Process control	(46)
1974	Silicon vidicon	High packing density	(47)
1974	Cross points	Substrate interaction eliminated	(48)

Despite the number of applications proposed, the percentage of integrated circuits built by full DI remains very small and for several years have been primarily for the military market [radiation hardened (5, 6)]. The reasons for the lack of growth are not that the technical advantages have been overstated,

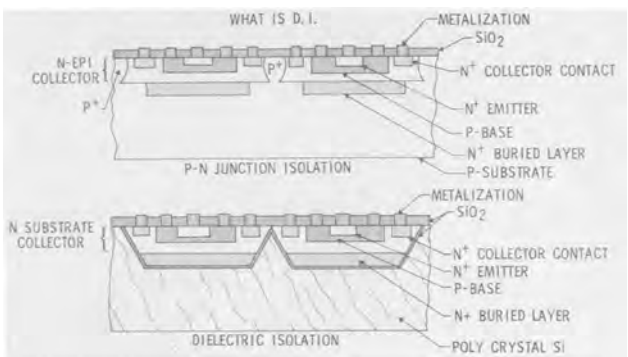


Fig. 1. Graphic comparison of junction and dielectric isolation

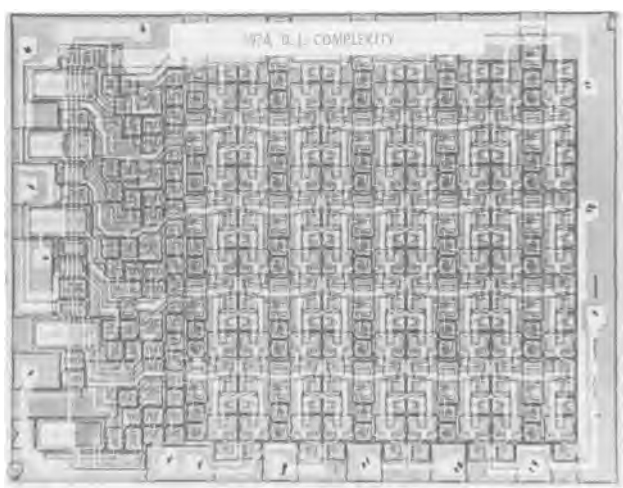


Fig. 2. State-of-the-art DI circuit complexity

but rather that it has proved exceedingly difficult to provide cost competitive products made with DI. It has continued to be used only when the designer can find no other way of achieving the desired performance and when the market is willing to pay a premium. However, it appears that some of the newer refinements described herein may allow it to be more widely used.

DI Processes

Today's DI processes may be divided into three methods: precision grind, lap, and polish (1-3, 7-12); double poly (4); and selective etch and deposition (9, 13). Each method has its own advantages and disadvantages as related to device performance and to problems of substrate fabrication. The materials have been primarily (100) and (111) orientation Si, with the early work using (111) due to its common usage at that time and the later and current work being primarily (100). The preference for (100) is due to a combination of the fourfold symmetry of the (100) system and the fast orientation-dependent (OD) etching in the [100] direction (14-24) which provides built-in process control.

Other processes considered in the past have involved the use of glass or ceramic matrix material (25-29) instead of the polycrystalline Si of Fig. 1. In addition, there are numerous composite structures in which a portion of the isolation is solid dielectric and part is p-n junction (30), or a portion is solid dielectric and a portion air (31). Some of these composites, sketched in Fig. 3, are currently receiving wide attention because of the improved packing density that they afford over junction isolation, but will not be discussed in this paper which will be devoted only to full DI.

The precision grind, lap, and polish process, sometimes referred to as single poly, with an n^+ buried layer to reduce collector saturation resistance is shown in Fig. 4. An oxide is grown on the substrate, whose resistivity is determined by the desired collector resistivity, and windows opened by conventional photolithography processing. These windows allow the isolation moats to be etched, usually with an orientation dependent etch which attacks the silicon in the <100> direction as much as 100 times faster than in the <111> direction (19, 21-23). Thus the cross section of an etched groove will appear triangular as shown in Fig. 4 if the mask is aligned on the slice so that the grooves are parallel with the traces of (111) planes. Thanks to the fourfold symmetry of the {100} system in silicon, adjacent sides of a rectangular mask can both be aligned with the traces of {111} planes on the (100) surface so that square or rectangular arrays of grooves can be etched. Due to the large difference in etch rate in the <100> *vs.* <111> directions, when the etch reaches the (111) plane intersecting the (100) surface at the edge of the mask, the etch rate becomes less than 0.03 μm/min

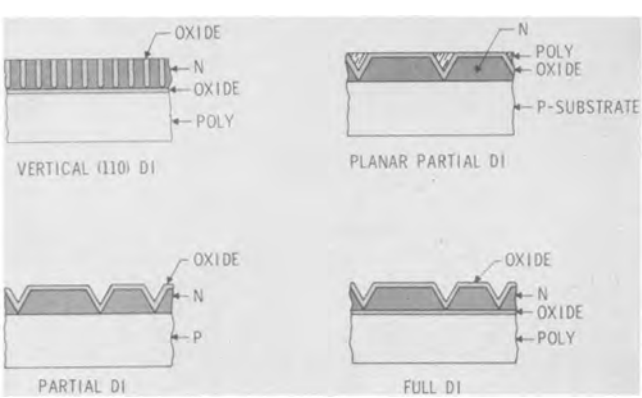


Fig. 3. Combination isolation approaches

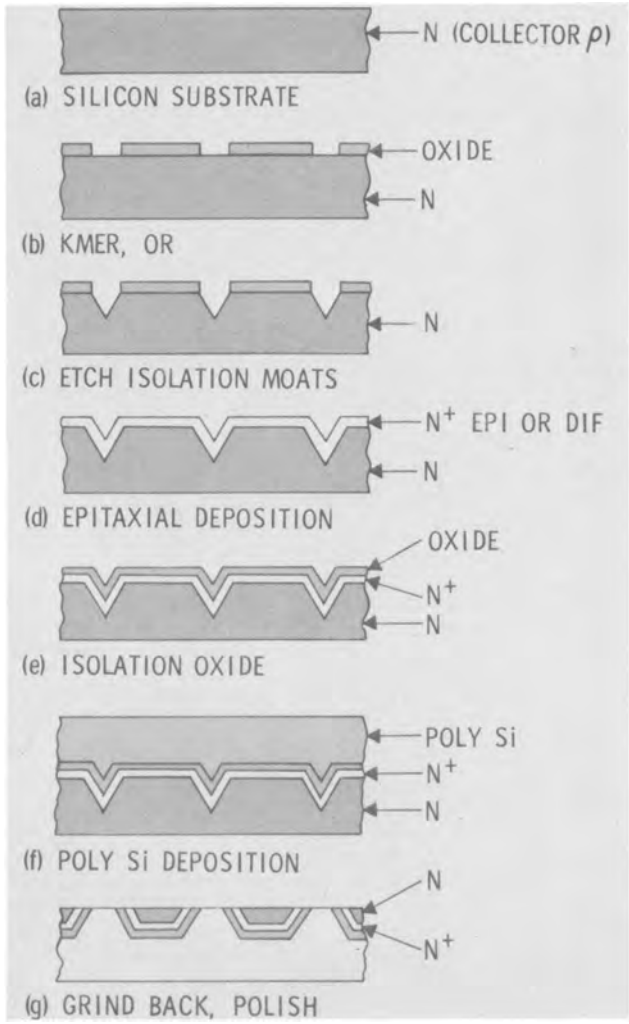


Fig. 4. Standardized DI process. Precision grind, lap, and polish method. Surface N^+ contact.

and for practical purposes, etching stops.[1] Since the {111} planes intersect the (100) surface at a fixed angle (54.74°), the width of the oxide opening determines the depth of the OD (isolation) etch moat. After the isolation moats are etched a n^+ diffusion or a heavily doped epitaxial film may be deposited across the entire surface. A thermal oxide is then grown across the top of the wafer. This oxide becomes the isolation between the single crystal and a polycrystalline silicon layer which is added next. The thickness of this layer is approximately equal to the thickness of the original slice, in general 15-20 mils. The polycrystalline silicon deposition can be made in a conventional epitaxial reactor using a silicon halide-hydrogen reduction process. For example, 10 mole percent (m/o) $SiHCl_3$ in hydrogen at 1150°C gives a deposition rate of about 10 μm of polycrystalline silicon per minute. After the polycrystalline silicon is deposited, the poly surface is ground on a Blanchard or similar type surface grinder to reestablish parallelism between the top of the slice (polycrystalline silicon) and the bottom (original single crystal silicon substrate) of the slice. Should deposition conditions be such that a polycrystalline lip is present on the single crystal side it must first be removed to allow the slice to seat well on the grinder chuck. The slice is then inverted and the original substrate is ground back far enough to reveal the isolation oxide in the deepest thickness indicators

[1] The effective mask undercutting and the measured etch rate at this point are a strong function of how carefully the mask is aligned to (111) traces. [See *e.g.*, Ref. (22)].

(which may be the scribe lines) and the single crystal islands of silicon, and then polished. After polish the slice is ready for conventional device processing except that the isolation diffusion steps are eliminated. In the process described, an n^+ surface collector contact is provided by the epi or diffused n^+ film. If a buried layer of n^+ material is desired which does not contact the top surface, the epi or diffusion may be performed prior to step b in the process. In that case the isolation moats are etched through the buried layer thus leaving it across the bottom of the final isolated tank. The precision grind and polish process is fairly simple compared to other processes but the final surface is mechanical-polished and the uniformity of the n-layer thickness across the slice is determined by how nearly parallel the final surface, after lap and polish, is with the original one.

Figure 5 shows the selective etch and deposition method. This one begins as the grind lap and polish process but has some additional steps. However the original substrate is chosen to be very low resistivity. After grind and polish-back an oxide is grown across the surface. The oxide is opened up in the areas where the individual active components are to be formed. The slice is then placed in an epitaxial reactor and the low resistivity silicon is selectively HCl vapor etched from the oxide-free areas to a depth required for the transistor collector region. An epitaxial film of the desired resistivity for the collector is redeposited *in situ* into this selectively etched region. This process gives rise to a near perfect epitaxial surface in which to build the final device and an n^+ collector contact at the surface completely surrounding the collector to provide minimum R_{CS}. Further, the thickness of the collector region is determined not by the mechanical tolerance of the lapping operation but by the etch and refill control, and is independent of any warping of the slice. The primary problem in using this process is reestablishing surface planarity in the epi refill and preventing either grooves or sharp spikes at the edges of the window. Since it is difficult to prevent the grooves/spikes formation, some process variations provide a deliberate overfill followed by a polish back. This retains some advantages, but the superior surface finish is lost.

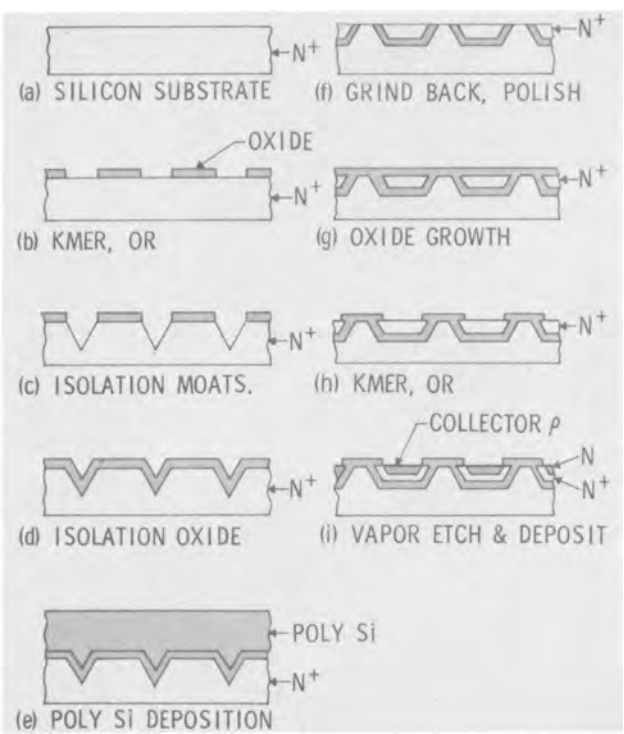


Fig. 5. Selective etch and deposition process for DI

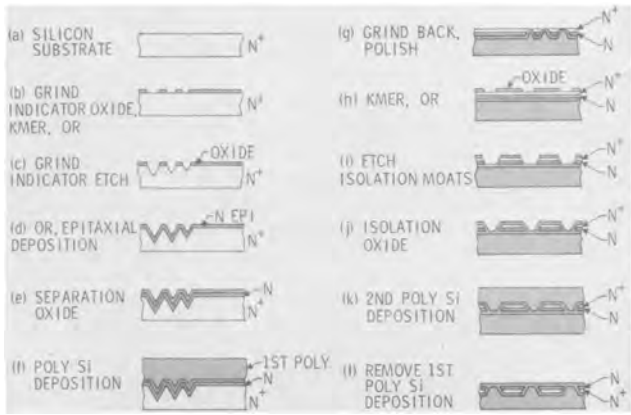


Fig. 6. Double polycrystal silicon DI process

Figure 6 shows the somewhat more complicated double poly process. To understand this process, skip to step d and neglect for the moment the grind indicators mentioned in steps b and c. An n-epi film, the thickness and resistivity determined by the collector parameters of the device or circuit to be fabricated, is deposited over the n^+ substrate. An SiO_2 layer called the separation oxide is grown or reactor deposited across the epi surface. Next a temporary polycrystalline silicon layer is grown over the oxide. The slice is inverted and ground and polished back to a thickness equal to that of the epi layer plus a suitable amount of n^+. At this point a problem arises. Unless great care is taken in keeping track of reference surfaces and the amount of material removed, there is no way of knowing when to stop lapping. To assist in this, the thickness indicator grooves shown in steps b and c of Fig. 6 are used.[2] When the grinder or polisher cuts through to them they become visible and the operator can cease grinding or polishing. There will normally be a series of grooves of increasing depth to assist in more accurate control. Assuming no mask undercutting, the depth d of an indicator groove is given by

$$d = (W/2) \tan \theta$$

where W is the width of the mask opening and θ is the angle the appropriate (111) plane makes with the surface (54.7° for a (100) surface). Typically, 6 to 8 depths will be used in an array, and the array will be placed in 5 positions over the slice for double poly process or in each circuit bar for single poly processing, as shown in Fig. 7.

Oxide is thermally grown or deposited across the surface. The oxide is opened for isolation moats as

[2] The same problem also occurs in single poly and thickness indicators are used.

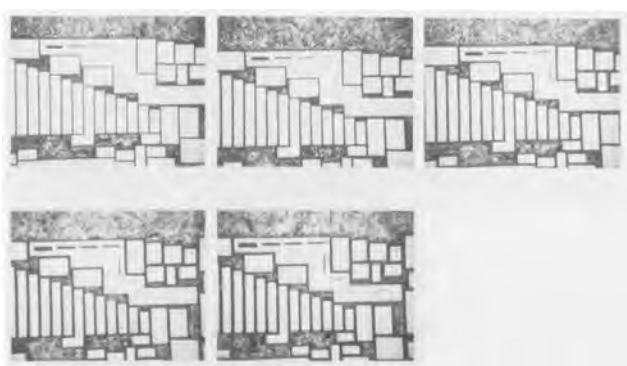


Fig. 7. Designed-in process control and monitoring through the use of OD etching of {100} silicon. Successive thickness indicator array designed into each circuit to show thickness of remaining single crystal silicon at polish back. Upper left four indicators showing. Upper right six indicator showing, etc.

in the single poly process. However, in this case, the moat depth will not be determined by the oxide opening, but by the distance to the separation oxide. An isolation oxide is then thermally grown or vapor deposited. A second poly silicon deposition is made over this isolation oxide. The slice is then inverted and the first poly silicon layer is ground, polished, and/or chemically etched back to the original epi film surface which is protected by the separation oxide. As can be seen in Fig. 6l, the resulting structure is a dielectrically isolated epitaxial film above an n^+ buried layer. This process is used in cases where very exact control of the collector thickness is required. It is quite long and costly but provides a very good surface for the fabrication of shallow devices since they are formed in an epitaxial film which has not been subjected to mechanical or wet chemical processing.

Application of Anisotropic Etching

The fourfold symmetry of {100} oriented silicon is extensively used in OD etching to provide for the very exact control of isolation pattern and thickness indicator etch widths and depths mentioned as well as to allow maximum packing density. (The ratio of active area to isolation poly area is maximized when the isolation oxide surrounding adjacent single crystal regions just touch each other and form an inverted V). Figure 8 is a scanning electron micrograph (SEM) which shows a top view and cross-sectional view of a 50 μm deep isolation moat OD etched in a {100} silicon substrate. It shows very clearly how the OD etch precisely terminates on the {111} plane which intersect the (100) surface at 54.74°.

Figure 9 is a cross-sectional view (step f, Fig. 4) after polysilicon deposition comparing the use of planar etch and a (111) surface with OD etch and a (100) surface. Note in the (111) cross section the rounded bottom shape of the planar-type etching. In this case the undercutting or lateral spreading on each side under the mask is approximately equal to the depth of the etching. However, in the (100) cross section, the undercutting is practically zero if the mask is perfectly aligned (22). Note the process control provided by OD etching of the (100) surface, and the very exact crystallographic {111} intersections which make it possible to use this phenomena for the thickness indicators previously described. Figure 10 is a photomicrograph of a section through the thickness indicators. The isolation oxide and polycrystalline silicon are also evident. The bottom photograph shows the mask used on the (100) surface to produce the thickness indicator etch. Again the depth of the etch moat is directly controlled by the width of the oxide or mask opening. At outside corners only, there is undercutting by the etch because other fast etching planes are exposed. In order to minimize this difficulty, "corner compensation" is used. That is, the masks are deliberately shaped so that after undercut, the corners are relatively sharp. Figure 11 is a top view of a (100) slice which has been etched using an oxide mask with built-in corner compensation. Here the oxide mask projecting out over the corners

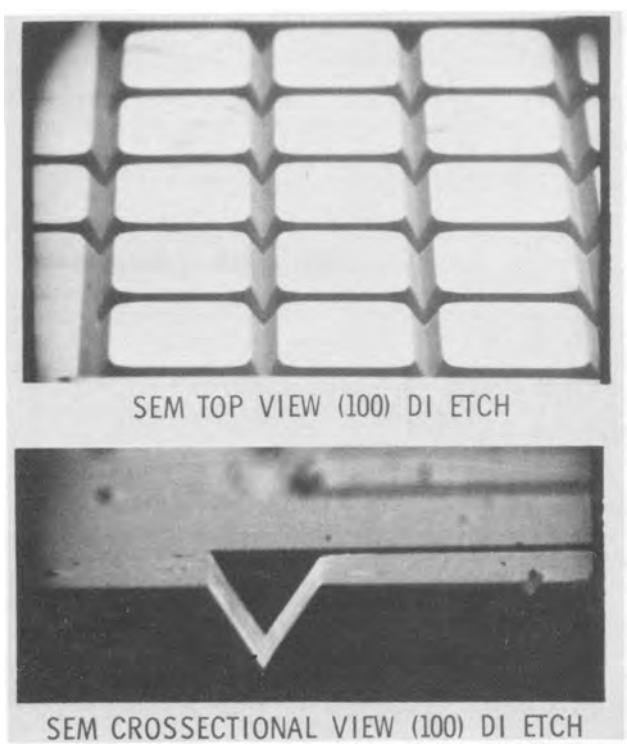


Fig. 8. (100) DI processing. OD etched isolation moat process control.

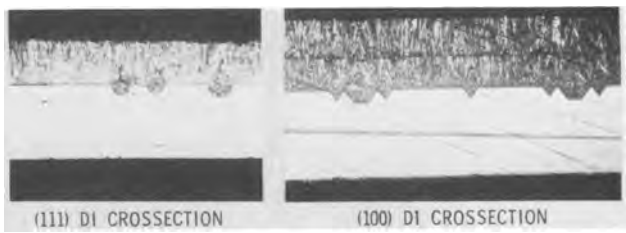


Fig. 9. DI processing (111) vs. (100) silicon

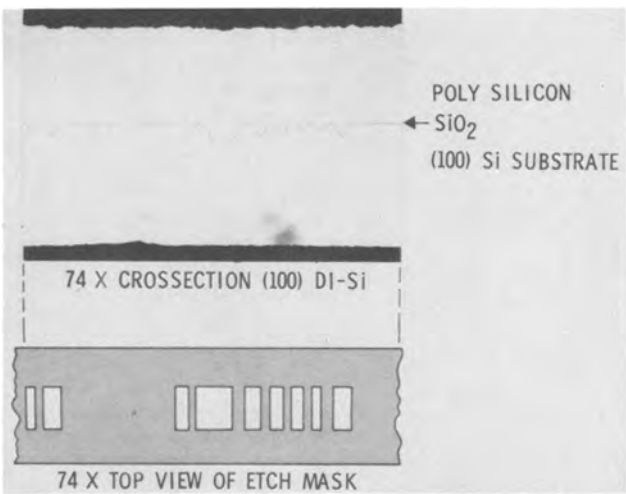


Fig. 10. Thickness indicator mask and cross section through indicator area of DI slice.

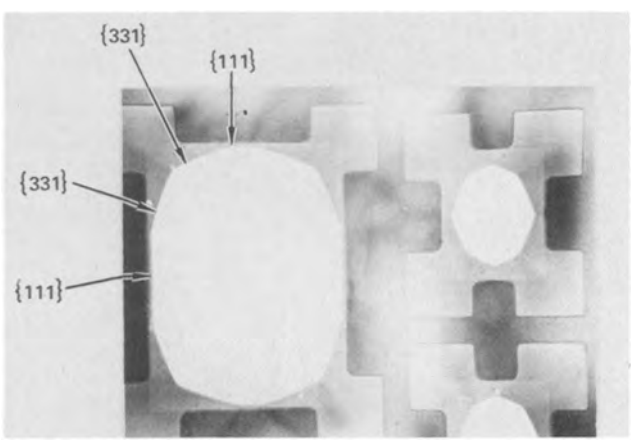


Fig. 11. Undercutting and OD etch termination planes in (100) silicon. {331} planes revealed by overetching of (100) silicon with OD etch.

of the isolation etched silicon islands can be plainly seen. This slice was purposely over etched in order to show very clearly the effect of such over etching. The corner faceting was determined to be {331} planes which etch relatively slowly but still faster than the {111} planes. This etching or undercutting at the corners is a result of the {331} planes being exposed at that point. The faster etching {331} planes also have fourfold symmetry in the {100} system; in fact they have double fourfold symmetry [the set $(\bar{1}33)$, $(\bar{3}13)$, (133), $(3\bar{1}3)$ and the set $(\bar{3}13)$, $(\bar{1}33)$, (313), $(1\bar{3}3)$], each of which intersect the (100) surface at an angle of 46.5°. One may use these shallower angle (46° *vs.* 54°) etch terminations when running metallization (leads) up and down over the sides of the moats, *e.g.*, in air isolation of Fig. 3.

In Fig. 11 the small islands on the right have undercut to the point where there is no {111} termination around the periphery of the silicon island and the entire island is bounded by {331} low angle planes. Figure 12 shows two examples of OD etch using an uncompensated mask. In Fig. 12a the etch depth is 23μm. The corner oxide undercutting can be seen and the {331} planes are well defined. In Fig. 12b the OD etch step is 54 μm and the need for corner compensation is further emphasized. Figure 13 is a top view of a properly corner compensated slice which has also been OD etched to a depth of 54 μm. The oxide compensation can be seen overhanging the four corners and near perfect 90° corners are revealed. If the compensated corner mask is used and under etching occurs, a slight projection of the silicon is left at the top in each corner. Figure 14 is a top view of two OD etched (100) silicon slices using different mask alignment. The same mask pattern was used on both slices and the slices were etched simultaneously in the same etch bath. In Fig. 14a the mask was aligned with the grooves running in a <310> direction so that etch termination occurs on the {331} planes which intersect the (100) surface at angles of 46°. Notice the exact square corners even though no corner compensation was used. In Fig. 14b the mask used was aligned with the <110> direction so that etch

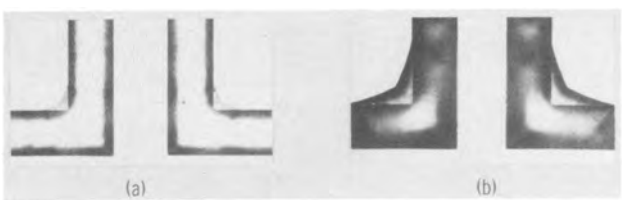


Fig. 12. Mask (outside) corner undercutting in (100) silicon *vs.* OD etch depth. (a) 23 μm etch depth. (b) 54 μm etch depth.

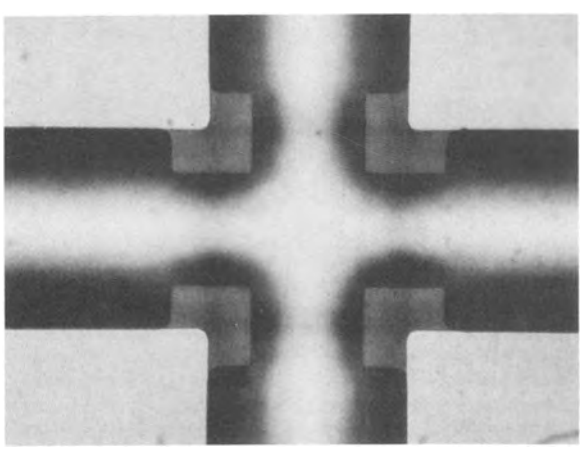


Fig. 13. Mask design compensation for OD etch corner undercutting.

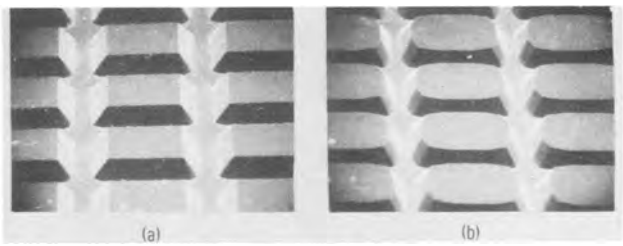


Fig. 14. OD etch pattern alignment effects in (100) silicon. (a) [310] alignment. (b) [110] alignment.

termination is on the steeper {111} planes. In this case corner undercutting occurs and the need for compensation is emphasized. As before, the lower angle <310> alignment may be desirable if one wishes to run metallization or leads up and down over islands and moats (30-31). However, the sidewall undercutting will be greater with the <310> alignment.

The OD etch used in this work was 20% KOH, 64% deionized water, and 16% normal propanol by weight (21). Other etches such as hydrazine-catechol, hydrazine-alcohol, and ethylene diamine are also very orientation dependent (14, 15, 17). The corner undercutting and faceting plane at the corners appears to be different depending on the etch used. For example corner terminations on {221} planes are reported when using hydrazine etches (17, 24).

Defects in DI (32)

Table II is a summation of some of the defects and problems which may arise during DI processing. Figure 15 is a view of two DI slices. The top portion shows a slice which was bowed before lapping so that the center portion of the slice has been polished through to the underlying oxide or polycrystalline silicon. The lower photograph shows a 100% isolated slice, with uniform depth from island to island in the single crystal tanks. Figure 16 shows the effect of nonparallelism of the top and bottom of the slice at grind and polish-back. The top view has uniform

Table II. Summation of defects

DEFECT	PROBABLE CAUSE
NON-ISOLATED REGIONS ON SLICE	SLICE BOWING OR TAPER
GAPS OR HOLES IN ISOLATION OXIDE	SLICES NOT CLEANED PROPERLY PRIOR TO OXIDATION
"COSMETIC" DEFECTS ON FINISHED DEVICES	DAMAGE TO KMER, DAMAGED MASK, POOR KMER TECHNIQUE
SMALL POLY INTRUSIONS IN SINGLE REGION	MASK DEFECT DURING ISOLATION "MOAT" ETCHING
"CROWS FEET" OR SCRATCHES ON SLICE SURFACE	POOR OR INADEQUATE POLISHING
HUMPS WHERE ISOLATION OXIDE INTERSECTS SURFACE (SINGLE POLY)	TOO SOFT AN ABRASIVE AND/OR POLISHING PAD USED DURING POLISHING
GROOVES WHERE ISOLATION OXIDE INTERSECTS SURFACE	OXIDE ETCHING STEPS DURING SUBSEQUENT PROCESSING WHICH DO NOT PROVIDE ISOLATION OXIDE MASKING
SINGLE CRYSTAL ISLANDS CHIPPING OUT	POLY SILICON GROWN IN EXTREME THERMAL GRADIENT, INCORRECT DEPOSITION PARAMETERS DURING POLY SILICON DEPOSITION, INSUFFICIENT CLEANUP PRIOR TO ISOLATION OXIDATION

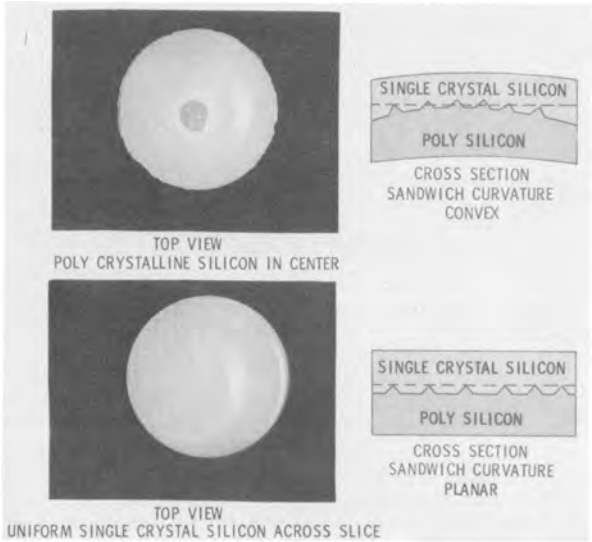


Fig. 15. DI processing problems and effect; effect of sandwich curvature on collector thickness uniformity using the DI process.

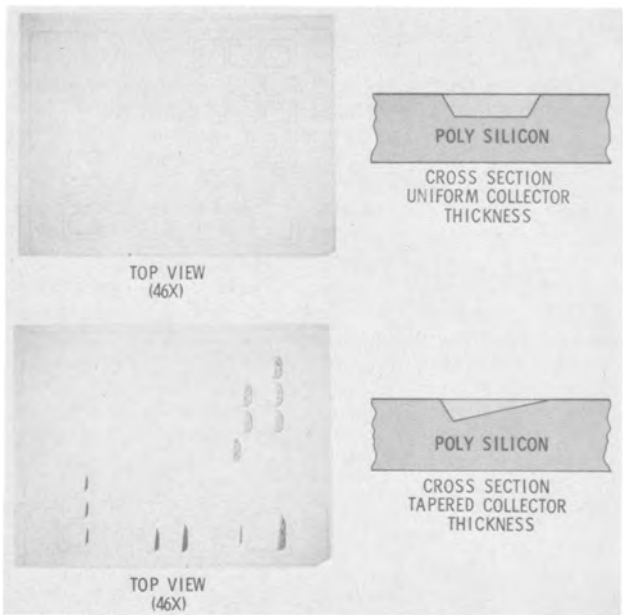


Fig. 16. DI processing problems and effect; effect of parallelism on collector uniformity.

island thickness whereas the bottom view shows a nonuniform island thickness and the effect of grinding and polishing through the single crystal region into the oxide or polycrystalline region below. Figure 17 is the top view of an integrated circuit chip along with enlarged views of two of the adjacent single crystal islands. At the upper left is a small island showing only one defect present in the top surface, whereas the figure on the right is a larger island showing many defects. This area-related defect phenomena has often been observed, it is also noted in the large peripheral area around the integrated circuit. In the bottom view one may see many defects. It is believed that these defects are mobile and move to sinks at the single crystal-oxide interface. It should be noted from the bottom photograph that only one thickness indicator is shown in the lower left portion of the array. This indicates that the slice did not have the proper polishing after grind-back, thus leaving gross damage in the surface. Figure 18 is a top view photograph of a selective etch and refill component in a DI circuit. Note the center section of the single crystal island has been selectively etched

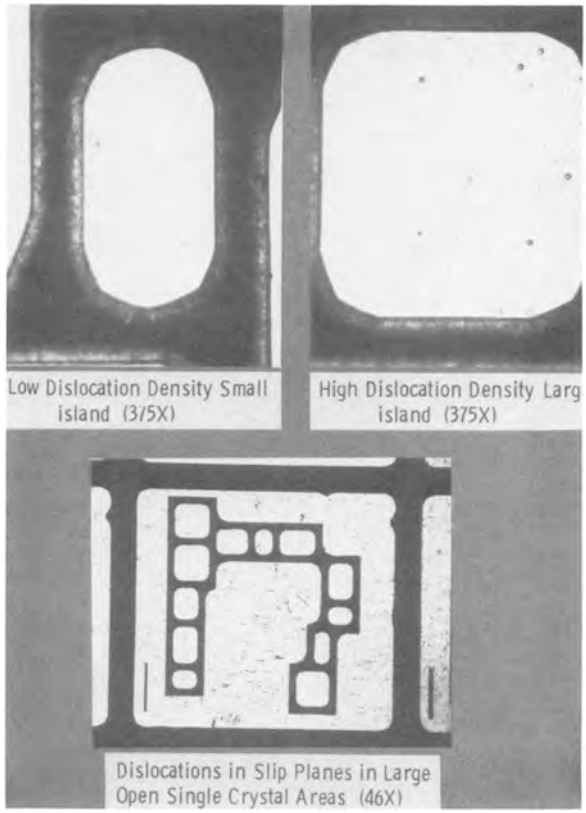


Fig. 17. DI process induced material defects; defect density vs. island size.

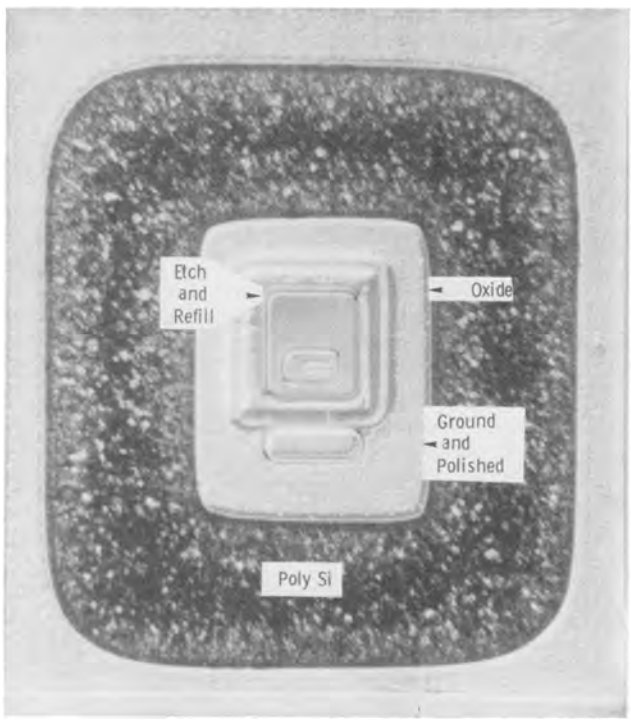


Fig. 18. DI component in integrated circuit selective etch and refill process.

out and then epitaxially regrown. It is evident that the damage in the original silicon crystal of the island after polish is much greater than that of the etch and refilled portion.

New Processes

A new process under development in several laboratories is shown in Fig. 19. One approach makes

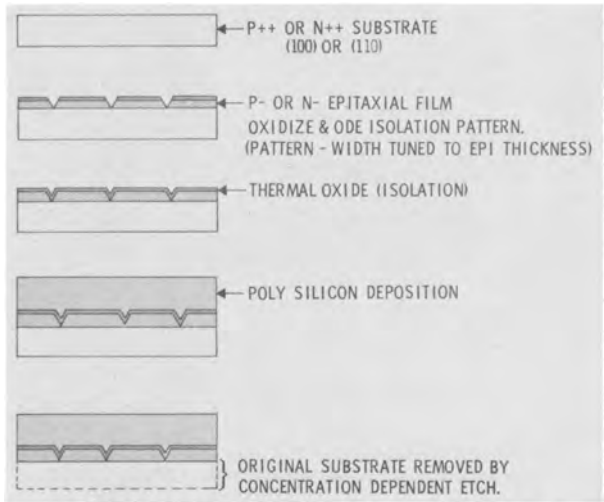


Fig. 19. Current DI development processes

use of a p^{++} or n^{++} substrate of {100} silicon with an epitaxial layer. The layer thickness is adjusted to the width of the isolation pattern mask which will be used for OD etching. That is, it is adjusted so that the OD etch will just penetrate the epitaxial film but not reach into the p^{++} or n^{++} substrate. The slice is then thermally oxidized and polycrystalline silicon deposited. Next, the polycrystalline silicon is protected by an oxide or some other media and the slice etched with a solution which attacks the p^{++} or n^{++} original substrate material but stops at the higher resistivity n or p epitaxial layer. Dash etch (1 HF, 3 HNO_3, 10 acetic) or some variant is suitable for this purpose (33, 34). Another approach makes use of an electrochemical etch which also stops at an n or p layer (35-39). Still a further approach utilizes the concentration-dependent etch of the KOH-normal propanol-water etch which does not etch a p^+ region (21, 40). Ethylene diamine-pyrocatechol-water will also stop at p^+ regions (41) and has been used as an alternate to the other etches.

This kind of process appears to have several theoretical advantages. (*i*) It eliminates mechanical polish damage inherent in present processing and allows fabrication of very shallow devices in a chemically polished surface which should be damage free. (*ii*) It reduces the critical parallelism required in the existing precision grind, lap, and polish processes, and allows a decrease in polycrystalline silicon thickness requirement. (*iii*) It provides the possibility of improved process yield due to the slice breakage which normally occurs at the (mechanical) precision grinding and polishing process. (*iv*) It provides increased packing density capability.

Another new technology which may be utilized for high packing density dielectric isolation is shown in Fig. 20. This is a SEM of a cross section of a {110} silicon slice which has been OD etched. It shows 5 μm moats etched 80 μm deep with 5 μm wide ridges between. Orientation dependent etch rate differences as great as 600:1 ([110] direction to [111] direction) have been observed in the {110} silicon slices (22). The undercutting in the etch used for {110} silicon processing is primarily a function of the mask alignment with the trace of the {111} plane at the (110) surface (22-23). The sidewalls of the moats are {111} planes perpendicular to the surface. It should be mentioned however that the intersection of the traces of the four {111} vertical planes in the (110) crystal forms a rhombus having angles of 109° and 71° rather than a rectangle. Therefore circuit designs would be layed out in rows of rhombi rather than in rectangles or squares. For cases where the moats are very narrow, the isolation oxide will completely fill in the gaps and the poly silicon will be eliminated or go only across the surface.

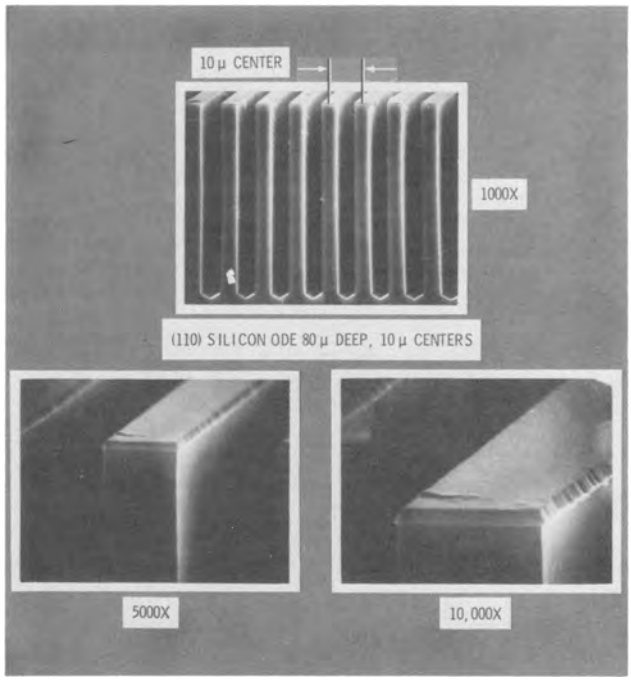


Fig. 20. Current DI development technology

Acknowledgments

The authors wish to thank Mrs. Hettie L. Smith for manuscript typing and proofing and R. L. Yeakley and the reviewers for several helpful comments and references.

Manuscript submitted Dec. 8, 1975; revised manuscript received April 26, 1976. This was Paper 138 presented at the New York Meeting of the Society, Oct. 13-17, 1974.

Any discussion of this paper will appear in a Discussion Section to be published in the December 1977 JOURNAL. All discussions for the December 1977 Discussion Section should be submitted by Aug. 1, 1977.

Publication costs of this article were assisted by Texas Instruments Incorporated.

REFERENCES

1. D. McWilliams, C. Fa, G. Larchian, O. Maxwell, and G. Leblanc, Congresso Scientifico Internazionale Per L'Elettronica, June 22-26. 1964; D. McWilliams, C. Fa, G. Larchian, and O. Maxwell, Jr., *This Journal*, **111**, 153C (1964).
2. J. Bouchard, G. F. Hammond, and F. W. Hammond, Jr., Abstract 165, p. 123, The Electrochemical Society Extended Abstracts, Fall Meeting, Washington, D.C., Oct. 11-15, 1964.
3. J. W. Lathrop, *Proc. IEEE*, **52**, 1430 (1964).
4. G. L. Schnable, A. F. McKelvey, and J. A. Hastings, *Electrochem. Technol.*, **4**, 57 (1966).
5. G. C. Messenger, *IEEE Trans. Nucl. Sci.*, **ns-13**, 141 (1966).
6. J. P. Spratt, G. L. Schnable, and J. D. Standeven, *IEEE J. Solid-State Cir.*, **sc-5**, 14 (1970).
7. D. A. Maxwell, R. H. Beeson, and D. F. Allison, *IEEE Trans. Electron. Dev.*, **ed-12**, 20 (1965).
8. B. D. Joyce, N. P. Formigoni, C. C. Roe, and F. Schliesing, *Electrochem. Technol.*, **4**, 482 (1966).
9. R. L. Petritz, *Trans. Met. Soc. AIME*, **236**, 235 (1966).
10. F. H. Lee, *IEEE Trans. Electron. Dev.*, **ed-15**, 645 (1968).
11. U. S. Davidsohn and F. Lee, *Proc. IEEE*, **57**, 1532 (1969).
12. B. L. Kravitz, *Solid-State Technol.*, **13**, 57 (1970).
13. V. Y. Doo and D. K. Seto, *Electrochem. Technol.*, **5**, 87 (1967).

14. J. M. Crishal and A. L. Harrington, Abstract 89, p. 202, The Electrochemical Society Extended Abstracts, Spring Meeting, Los Angeles, California, May 6-10, 1962.
15. R. M. Finne and D. L. Klein, *This Journal*, **114**, 965 (1967).
16. K. E. Bean and P. S. Gleim, *Proc. IEEE*, **57**, 1469 (1969).
17. D. B. Lee, *J. Appl. Phys.*, **40**, 4569 (1969).
18. A. I. Stoller, *RCA Rev.*, **31**, 271 (1970).
19. H. A. Waggener, R. C. Kragness, and A. L. Tyler, International Electron Device Conference, Washington, D.C., Oct. 18-20, 1967.
20. W. K. Zwicker and S. K. Kurtz, in "Semiconductor Silicon 1973," H. R. Huff and R. R. Burgess, Editors, p. 315, The Electrochemical Society Softbound Symposium Series, Princeton, N.J. (1973).
21. J. B. Price, in *ibid.*, p. 339.
22. K. E. Bean, R. L. Yeakley, and T. K. Powell, Abstract 23, p. 68, The Electrochemical Society Extended Abstracts, Spring Meeting, San Francisco, May 12-17, 1974.
23. D. L. Kendall, *Appl. Phys. Lett.*, **26**, 195 (1975).
24. M. J. Declercq, L. Gerzberg, and J. D. Meindl, *This Journal*, **122**, 545 (1975).
25. Anon, *Electronics*, **40**, 93 (March 20, 1967).
26. A. I. Stoller and W. H. Schlip, Jr., *RCA Rev.*, **29**, 485 (1968).
27. P. W. McMillan, G. Partridge, and F. R. Ward, *Microelectron. Reliability*, **8**, 113 (1969).
28. A. I. Stoller, J. A. Amick, and N. E. Wolff, *Electronics*, **40**, 97 (March 20, 1967).
29. T. H. Ramsey and T. Smith, International Electron Devices Conference, IEEE, p. 14, October 1966.
30. S. W. Fields, *Electronics*, **45**, 65 (July 3, 1972).
31. K. E. Bean, J. S. Crabbe, J. C. Hoffman, and F. D. Malone, in "Semiconductor Silicon 1973," H. R. Huff and R. R. Burgess, Editors, p. 880, The Electrochemical Society Softbound Symposium Series, Princeton, New Jersey (1973).
32. R. L. Yeakley, P. S. Gleim, W. R. Runyan, and K. E. Bean, Abs. 31, AIME Technical Conference on Defects in Electronic Materials for Devices, Boston (1969).
33. H. Muraoka, T. Ohhashi, and Y. Sumitomo, in "Semiconductor Silicon 1973," H. R. Huff and R. R. Burgess, Editors, p. 327, The Electrochemical Society Softbound Symposium Series, Princeton, New Jersey (1973).
34. Y. Sumitomo, T. Yasui, H. Nakatsuka, T. Oohashi, H. Tsutsumi, and H. Muraoka, Abstract 25, p. 74, The Electrochemical Society Extended Abstracts, Spring Meeting, Houston, May 7-11, 1972.
35. M. J. J. Theunissen, J. A. Appels, and W. H. C. G. Verkuylen, *This Journal*, **117**, 959 (1970).
36. H. J. A. van Dijk and J. de Jonge, *ibid.*, **117**, 553 (1970).
37. R. L. Meek, *ibid.*, **118**, 1240 (1971).
38. C. P. Wen and K. P. Weller, *ibid.*, **119**, 547 (1972).
39. T. I. Kamins, Contract No. DAHC15-72-C-0171 ARPA Order No. 2053 (February 1973).
40. G. L. Kuhn and C. J. Rhee, *This Journal*, **120**, 1563 (1973).
41. J. C. Greenwood, *ibid.*, **116**, 1325 (1969); A. Bohg, *ibid.*, **118**, 401 (1971).
42. D. F. Allison, A. P. Youmans, and T. H. Wong, *Electronics*, **42**, 112 (May 12, 1969).
43. Anon, *Electron. Design*, **22**, 87 (Oct. 26, 1972).
44. Y. Sumitomo, K. Niwa, H. Sawazaki, and K. Sakai, in "Semiconductor Silicon 1973," H. R. Huff and R. R. Burgess, Editors, p. 893, The Electrochemical Society Softbound Symposium Series, Princeton, New Jersey (1973).
45. T. R. Huffman and R. G. Daniels, in *ibid.*, p. 769.
46. T. R. Payne and H. R. Plumlee, *IEEE J. Solid-State Circuits*, **sc-8**, 71 (1973).
47. K. E. Bean and J. R. Lawson, *ibid.*, **sc-9**, 111 (1974).
48. W. R. Runyan, *Electron. Pkg. Prod.*, **14**, 162 (1974).

Report of the Electrolytic Industries for the Year 1975[1]

S. D. Argade*

BASF Wyandotte Corporation, Wyandotte, Michigan 48192

and F. B. Leitz*

Bureau of Reclamation, U.S. Department of the Interior, Denver, Colorado 80255

Chlorine—Caustic Soda

I. Production.—Chlorine production in the United States reached a level of 9,228,000 short tons in 1975, which was 14.8% below the record high 1974 output of 10,872,000 tons (1-3). Canadian production of chlorine in 1975 was 860,000 tons, representing a decrease of 19.6% from the 1974 level of 1.07 million tons (1-3). January through July of 1975, the chlorine production rates significantly dropped due to the economic downturn to the levels approaching those of 1968-1969 (1, 2, 4). The recovery from the recession in the last 5 months of the year brought the chlorine production rates back to the 1972 level in the month of December (6).

Despite the lower production rates of 1975, the U.S. chlorine production capacity increased by 7.8% in 1975. The Canadian chlorine capacity rose 13.6%. During the year 1975, a total of eleven locations in the U.S. started up new, expanded or modernized facilities. Some of the plants replaced their older facilities completely. In Canada, a new chlorine plant came on stream and another one was expanded (5) (See Table 1). The Chlorine Institute estimates that the U.S. chlorine capacity will be boosted from the present 34,600 tons per day to about 41,100 tons per day by January 1, 1978, which represents an increase of 18.8% (See Table 2). By 1980 the capacity is estimated to be 42,000 tons per day (6). Several significant expansions have been announced in Mexico, one being scheduled to start up in 1976 (5).

In 1975, 73.4% of the installed U.S. chlorine capacity was in the diaphragm cells, 21.8% in mercury cells, and 4.8% in all other production routes. In Canada, 64.6% chlorine capacity was in the diaphragm cell process and 35.4% in the mercury cell process (5).

Markets for chlorine remained in the traditional areas such as vinyl chloride monomer, other chlorinated organics, inorganic chemicals, water and waste treatment, and the rest going to numerous miscellaneous applications. Demand for chlorine was less than 70% of the capacity from March through July and the situation improved during the rest of the year (6). Chlorine prices remained at $115 per ton level on the Gulf Coast, the price that was posted in the fall of 1974,

[1] This report is sponsored by the Industrial Electrolytic Division of The Electrochemical Society. While it is primarily a summary of production and developments in the chlor-alkali industry, reports of other electrolytic industries are included.
The material presented herein has been gathered from many sources, as noted in the References, and does not necessarily represent the opinions of the authors.

* Electrochemical Society Active Member.

for most of the year as producers cut the chlorine output to match the market (7, 8). The prices for chlorine were raised toward the year end due to higher costs; for example the Gulf Coast prices were raised to $125 per ton. Elsewhere prices for chlorine were as high as $150 per ton (6).

Chlorinated organic products continued to make the news in the health and the environmental arena. Since chlorinated organic products consume a large fraction of the chlorine produced in the U.S., factors that affect these industries are in turn reflected in the chlorine industry. The potential of carcinogenesis by compounds such as vinyl chloride, chloroform, and trichloroethylene, was widely publicized (13-24). OSHA worker exposure standards for vinyl chloride monomer (VCM) became final on April 1, 1975. Since, the Supreme Court refused to review the challenges brought against the OSHA standards by the Society of the Plastics Industry and other vinyl producers (14). The polyvinyl chloride producers were able to meet the OSHA standards for 1975 with no major problems. The industry could meet the stricter 1976 standards with the workers using appropriate protection gear. The VCM producers which use mainly closed systems did not have many problems (13). The vinyl makers were also getting ready to meet the EPA requirements to limit VCM emissions to a concentration level of 10 ppm in all exhaust gases except for emergency relief valve discharges (16). The emissions control is reportedly going to be costly (16).

After some controversy over the use of chloroform in drug products, the FDA was removing chloroform from such use (17-20). The EPA found trace quantities of chloroform and other chlorinated organics in a number of city water supplies (25). Another chlorinated hydrocarbon widely used in the industry, trichloroethylene, was found by the National Cancer Institute (NCI) to cause liver cancer in mice and the NCI issued a "Statement of Concern" (21, 22). Trichloroethylene is widely used in the vapor degreasing of metal parts, and it is a very large volume chlorinated solvent (23).

The controversial issue on fluorochlorocarbons and the stratospheric ozone layer depletion continued to boil (26-32). A federal Task Force on Inadvertent Modification of the Stratosphere (IMOS) recommended that the use of fluorochlorocarbons in aerosols be banned and other uses be restricted (26). If the government were to ban the use of fluorochlorocarbons, the economic dislocations would run into billions of dollars (28). The industry proposed more research on the problem (28). The state of Oregon has already banned the use of fluorochlorocarbons (27), and a number of other states are considering it (30). If the ban on the fluorochlorocarbons were promulgated, which may be more than likely according to a study by A. D. Little, Incorporated (32), it is not known how or to what extent it would affect the chlorine industry.

According to the U.S. Department of Commerce data, the caustic soda production in 1975 reached a level of 9,266,000 short tons as 100% NaOH compared to the 1974 production of 11,189,000 short tons (33). The recent recession knocked down the caustic production significantly, and it represents the largest single drop from one year to the next in more than 25 years (9).

Markets for caustic traditionally are in the area of general chemical manufacture, pulp and paper, alunina, rayon, and cellulosics. The market breakdown is given below (9):

General chemicals	46%
Pulp and paper	16%
Alumina	5%
Rayon and cellulosics	4%
Other industries	12%
Miscellaneous and exports	17%

As in other years the supply of caustic depended on the production of chlorine. As the chlorine output was reduced in early 1975, caustic soda became tight in the market. This situation continued through the summer partly due to inventories of caustic built up at the consumer plants in anticipation of continued strong demand. The chlorinated organics and PVC markets began to recover from the recession in the fall, and as the chlorine output was increased, necessarily the caustic availability improved to the point that the caustic market softened late in the year (9). The caustic market is expected to improve as the pulp and paper and aluminum industries recover from the recession. The prices for caustic remained at the $140-160 per ton range in the first half of 1975 (11). The midyear prices were raised to $150-170 depending on the plant location (11, 12). These prices remained steady at year end, although some downward price pressure was reported as the caustic demand was relatively weaker than the chlorine demand, particularly on the Gulf Coast (9).

II. Developments.—A. Chlorine cells and components.—Conversion of chlorine cell rooms to the coated titanium anodes is continuing (see Table 1) and reportedly half of the chlorine capacity in North America will have switched over to the metal anodes (34). Corning Glass Works and Electronor Corporation, an affiliate of O. DeNora of Italy, have entered into an agreement to jointly develop new types of anodes and cathodes for electrochemical and electrometallurgical processes (35).

Commercial chlorine cells utilizing the cation exchange membranes are coming of age. Hooker Chemical and Plastics Corporation installed membrane cells

Table 1. Changes in the current chlorine operations (5)

Producer and location	Cell type/change	Capacity tons/day	Completion date
1. Canadian Industries Becancour, Que., Canada	Hooker H-2A (diaphragm)	385	October 1975
2. Diamond Shamrock Corp. LaPorte, Texas	Diamond MDC-29 (diaphragm)	1200	January 1975
3. Dow Chemical Co. Freeport, Texas	Dow (diaphragm)	1000	January 1975
4. Georgia Pacific Corp. Plaquemine, La.	Hooker H-4 (diaphragm)	800	January 1975
5. Hooker Chemical and Plastics Corp. Taft, La.	Hooker H-4 (diaphragm)	900	January 1975
6. Pennwalt Corp. Tacoma, Wash.	Glanor® 1144 (diaphragm) Conversion of cell room	200	December 1975
7. Reed Paper Co. Dryden, Ont., Canada	Hooker MX (membrane) Conversion of mercury cell room	45	November 1975
8. Vulcan Materials Co. Wichita, Kans.	Hooker H-4 (diaphragm) 25% expansion	—	December 1975
9. Weyerhaeuser Co. Longview, Wash.	Diamond MDC-29 (diaphragm) Conversion of mercury cell room and expansion	385	May 1975
10. BASF Wyandotte Corp. Wyandotte, Mich.	Conversion to metal anodes and small expansion	—	March 1975
11. Brunswick Chemical Co. Brunswick, Ga.	Conversion to metal anodes	—	December 1975
12. Georgia Pacific Corp. Bellingham, Wash.	Conversion to metal anodes	—	June 1975
13. PPG Industries New Martinsville, W.Va.	Columbia N-3 and N-6 (diaphragm) Conversion to metal anodes	—	December 1975

with a 45 tons per day chlorine capacity at Reed Paper Company's Dryden, Ontario, plant and the cells have been operating successfully since November 1975 (4, 36). Hooker Chemical and Plastics Corporation has cells using the Nafion® membranes operating at its Tacoma, Washington, facility (36, 37). Diamond Shamrock will start up a line of cells at its Muscle Shoals plant employing its modification of du Pont's Nafion® membrane (37). The Diamond Shamrock membrane cells produce high strength caustic soda with minimal salt concentration directly in the electrolyzer at high current efficiencies (36). The regular Nafion® membranes permit hydroxyl ions to migrate from the cathode compartment into the anode compartment resulting in current efficiency losses. The Hooker MX cell consumes 2800 kW-hr/ton Cl_2 compared to 2500 kW-hr/ton Cl_2 with a typical asbestos diaphragm. Finding methods to cut down this migration is the aim of the development work at du Pont, Diamond Shamrock, Hooker, and several Japanese companies who are hard at work on the membrane improvements (37).

The Japanese producers have been very active in chlorine cell development work using cation exchange membranes (37, 41). Asahi Chemical is operating a membrane cell plant of 44,000 tons per year in caustic capacity using Nafion® membranes. Tokuyama Soda is operating a 2200 tons per month plant at Tokuyama City to compare its own membranes with Nafion®. Toyo Soda hopes to build a 2200 tons per month plant at Sekata City, Honshu, by spring 1977 using Hooker MX cells. It is also testing its own membranes as well as du Pont's in a pilot plant. Asahi Glass test data from a 220 tons NaOH per month pilot plant using its own fluorinated membrane shows a 90-92% current efficiency at a caustic concentration of 40-41% and a cell voltage of less than 4V at an unknown current density (37, 38).

Du Pont is reportedly carrying out engineering design as well as development of construction cost estimates for a plant to produce the Nafion® perfluorosulfonic acid products. If demand warrants, commercial production could begin by 1980 (42, 43).

Oronzio DeNora, Italy, has patented a new electrolytic cell suitable for gas evolving electrodes. By withdrawing the generated gas behind the electrode the cell avoids increase in cell resistance resulting from gas bubbles present in the electrolyte gap between the electrodes (44).

Ionics and du Pont are offering sodium hypochlorite generating systems for destroying cyanide containing wastes in the plating industry. The cells use Nafion® membranes, and du Pont will market the systems (45).

B. Other developments.—Another large chemical company, Mond Division of ICI, Ltd., has opted for the Kel-Chlor® process for a 330 tons per day chlorine plant to recover by-product HCl. The design of this plant will use a lower pressure version (4 atm *vs.* 15 atm) of the du Pont unit that started up in 1974. The ICI plant will use lower temperatures and proprietary brick-lined process vessels rather than the tantalum-lined equipment used earlier (49, 50).

In Japan, where solid salt resources are not available, the Agency of Industrial Science and Technology is studying a process which utilizes concentration of seawater. The brine produced by electrodialysis of seawater would be used in a diaphragm cell chlorine plant (51).

Hydrogen from a chlorine plant would supply part of the hydrogen requirements of an ammonia plant. The hydrogen will be used after purification by scrubbing (52).

A highly accurate chlorine monitor sensitive to 1 ppb chlorine has been developed by the National Bureau of Standards at Gaithersburg, Maryland. The direct readout instrument measures, in addition to chlorine, hypochlorites, and chloroamines in seawater, fresh or waste waters. The instrument is based on iodide oxidation and detection with a coulometric cell (53).

After some controversy the FDA rescinded the permit for the sale of salt from the diaphragm chlor-alkali cell process as table salt. The salt produced in the caustic concentration step was found to contain asbestos fibers and hence was not suitable for food grade use (54).

OSHA is calling for a still tighter ceiling for worker exposure to asbestos, 0.5 fibers/cm^3 time averaged over an 8 hr period. This is significantly lower than 2.0 fibers/cm^3 already on the books for compliance by July 1976, and 5.0 fibers/cm^3 in effect now. The peak exposure would also be halved under the standard (to 5 fibers/cm^3 in a 15 min period). New requirements for monitoring medical surveillance and worker training would also be set. No timetable on this change has been announced (49).

A process for purifying the diaphragm cell caustic has been developed under the sponsorship of Research

Table 2. New or expanded chlorine plants planned or under construction (5, 6)

	Producer and Location	Cell type and capacity	Status	Completion date
1.	E. I. du Pont de Nemours and Co. Corpus Christi, Texas	Diamond MDC-55 (diaphragm) 1000 tons/day	Engineering	1st Quarter 1977
2.	NL Industries, Inc. Magnesium Div. Rowley, Utah	Bayer $MgCl_2$ 80,000 tons/yr	Building	
3.	Olin Corp. McIntosh, Ala.	Hooker (diaphragm) 1000 tons/day	Engineering	1st Quarter 1978
4.	Vulcan Materials Co. Geismar, La.	Diamond MDC-55 (diaphragm) 600 tons/day	Engineering	3rd Quarter 1977
5.	BASF Wyandotte Corp. Geismar, La.	Diamond (diaphragm) modest expansion	Underway	2nd Quarter 1976
6.	BASF Wyandotte Corp. Port Edwards, Wis.	DeNora (mercury) modest expansion	Engineering	1977
7.	Dow Chemical Co. Plaquemine, La.	Dow (diaphragm) expansion 1000 tons/day	Underway	1976
8.	Dow Chemical Co. Freeport, Texas	Dow (diaphragm) expansion 2000 tons/day	Underway	1977-1979
9.	Georgia Pacific Corp. Bellingham, Wash.	DeNora (mercury) 20% expansion 103 tons/day	Underway	2nd Quarter 1976
10.	Hooker Chemical and Plastics Corp. Niagara Falls, N.Y.	Hooker H4 (diaphragm) 450 tons/day expansion	Engineering	2nd Quarter 1977
11.	Hooker Chemical and Plastics Corp. Tacoma, Wash.	Hooker (diaphragm) 400-675 ton/day expansion	Engineering	4th Quarter 1977
12.	Kaiser Aluminum and Chemical Corp. Gramercy, La.	Hooker (diaphragm) 7% expansion 37 tons/day	Underway	2nd Quarter 1976
13.	Mobay Chemical Co. Baytown, Texas	Uhde (HCl) expansion 100 tons/day	Engineering	1st Quarter 1976
14.	Pennwalt Corp. Portland, Ore.	Diamond (diaphragm) expansion 200 tons/day	Building	1st Quarter 1977
15.	PPG Industries, Inc. Lake Charles, La.	Glanor® 1144 Bipolar (diaphragm) 1500 tons/day expansion	Underway	1976
16.	Stauffer Chemical Co. Henderson, Nev.	Diamond MDC-29 (diaphragm) 320 T/D conversion	Engineering	4th Quarter 1976

and Development Corporation of Japan. Mitsui Shipbuilding will construct a 10 tons per day pilot plant. Fifty per cent diaphragm cell caustic is diluted first to 40% NaOH. According to the Secondary Refrigerant Freezing Process (SRFP), 40% NaOH is cooled to precipitate the hydrate $NaOH \cdot 3.5\ H_2O$ by direct injection of a refrigerant. The crystalline caustic soda hydrate is separated in a centrifuge and is washed to give a 39% NaOH product with 0.01% NaCl. The next phase of this work would include using the hydrate system $NaOH \cdot 2H_2O$ and a solid-solid separation system since the salt will coprecipitate with caustic soda (38, 46-48). This caustic purification process could allow production of rayon grade caustic at a price comparable to the caustic from the ion exchange membrane cells (47).

C. Mercury cells.—No new mercury cell plants were built or planned for construction in 1975 in the United States or Canada. There were a few planned expansions as detailed in Table 2. The mercury cell plant at the Reed Paper Mill Company, Dryden, Ontario, was converted over to a Hooker MX membrane cell plant. The Weyerhaeuser Company's mercury cell plant at Longview, Washington, was changed over to diaphragm cells. The recession has affected the Japanese program of conversion of mercury cell plants over to the diaphragm cells. The Japanese Ministry of International Trade and Industry has now given the industry until March 1978, for completion of the conversion program and is suggesting that the industry should convert over to membrane cells rather than diaphragm cells (38). Elsewhere in the world mercury cell plants are still being planned for construction.

New treatment techniques aim to recover heavy metals from waste waters. Du Pont has a system called "Extended Surface Electrolysis." Using flow-through sandwich type porous electrodes the system can cut contamination by as much as 90% and can recover gold, silver, mercury, and lead (55). A number of selective adsorbents have been cited in the literature last year (55). Akzo Zout Chemie is offering a mercury pollution abatement package for chlor-alkali plants (56).

EPA researchers have confirmed that inorganic mercury can be transformed into toxic methyl mercury by common agricultural plants and soils (58). That transformation was once thought to be possible only under anaerobic conditions in mud and sediments of streams and lakes (57, 58). The researchers have recommended no additional major new controls on mercury. Concern is about the increasing amounts of mercury that will be emitted into the air as coal becomes a more favored fuel (58).

Total mercury consumption in the U.S. declined in 1975 by 14% from 59,500 flasks (76 pound) to 51,100 flasks. The domestic U.S. production of primary mercury totaled 6750 flasks according to the U.S. Bureau of Mines. Secondary production increased by 30%. Imports fell 14.6% to 44,500 flasks in 1975 compared to the 1974 level of 52,100 flasks. Imported mercury came mostly from Canada, Algeria, Italy, Yugoslavia, Spain, Mexico, and Peru. The chlor-alkali producers purchased 15,223 flasks of mercury in 1975 compared to 16,813 flasks in 1974 representing a decline of about 10%. Mercury prices continued their decline throughout 1975. As the year began, the New York price ranged from $190-225 per flask and the London price from $165-185 per flask. By year end, the average price had plummeted to about $117 per flask and about $75 per flask in London. Not even the organization of the largest mercury producing nations, officially formed in April 1975, could control the downslide of mercury prices (59, 60).

Other Alkalis and Electrolytic Processes

Caustic potash.—Caustic potash production in 1975 was 196,971 short tons as 88-92% liquid which represents a decrease of 4.5% over the 1975 production total of 206,252 short tons (61). U.S. demand for caustic potash for 1975 was estimated at 185,000 tons (62).

U.S. production of marketable potassium chloride, sulfate, magnesium sulfate, and manure salts was 2.5 million tons of K_2O equivalent. Domestic U.S. production of K_2O equivalents remained the same in quantity as 1974 but increased in value by 43% to about $227 million. About 84% of the production of potassium salts came from New Mexico and the rest from Utah and California (63).

The price of potassium muriate in bulk f.o.b. Carlsbad, New Mexico, and Saskatchewan, Canada, was quoted in early 1975 at 63 to 68 cents per unit of K_2O (20 lb of K_2O); in November 1975, the price was quoted at 65 to 70 cents per unit (63). Caustic potash price in early 1975 was quoted at a U.S. price for tank car quantities of $7.50 per 100 pounds, 45% basis (62).

Mississippi Chemical, a fertilizer cooperative, acquired the Teledyne potash mine in New Mexico and returned it to production after improvements (63). A multimillion dollar expansion of this Carlsbad, New Mexico, mine is planned by Mississippi Chemical with an onstream target of mid-1976 (64).

The dispute between the Canadian potash producers in Saskatchewan and the provincial government has added another twist. A Crown Corporation, the Potash Corporation of Saskatchewan, was formed in early 1975 to act as the vehicle for the province's participation in future expansions and new potash mining ventures (63). Now, the government is trying to buy a 51% holding in the Saskatchewan potash industry. If the producers refuse, a bill introduced in the legislature, would expropriate the assets at fair market value (65, 66). This action was prompted by the failure of producers to expand the output according to the Saskatchewan governor. The potash industry did not see a favorable investment climate since the tax load is 83% on pretax earnings (65-67). Regina Duval Corporation of Canada expected the Potash Corporation of Saskatchewan (the government corporation) to make a bid to acquire its 1.5 million short tons per year mine at Duval. This would be the first offer by the province in a program aimed at acquiring at least half of the potash industry by negotiated purchase or expropriation (68).

Nippon Soda Company Limited established an ion exchange membrane process for caustic potash using du Pont's Nafion® membranes (69).

Soda ash.—Production of natural soda ash increased an estimated 2% in 1975 despite an over-all soda ash production decline of about 10% (70). Natural soda ash (trona) increased from 4.05 to 4.15 million tons while synthetic or Solvay process soda ash decreased from 3.5 to 2.9 million tons (71).

The number of synthetic plants decreased from six to four with a capacity at year end of 2.85 million tons (72). Allied Chemical closed its 800,000 ton per year plant at Baton Rouge, Louisiana, in May (73). Olin Corporation shut down its Lake Charles, Louisiana, plant in September and went out of the soda ash business. This plant had produced as much as 350,000 tons per year, but recently had been operating at 80% of this rate (74). The synthetic plants are all quite old (the most recent having been built in 1935). The reason for most synthetic plant closings is the difficulty of meeting environmental standards (75). It has been predicted that all the synthetic plants would close because of energy and environmental problems, perhaps before 1980. However, the remaining synthetic producers—Allied, BASF Wyandotte, Diamond-Shamrock, and PPG Industries—say they plan to keep operating their synthetic plants for the foreseeable future (76).

All producers of natural soda ash in Wyoming and California were in the process of increasing production. The present capacity for natural soda ash production is 6.4 million tons. By 1977 the capacity of plants for which increases have been announced will be 8.75 million tons per year (72).

The current consumption of soda ash, which closely matches production, is distributed 51% to glass manufacture, 22% to chemicals, and small percentages to pulp and paper, soaps and detergents, water treatment, and other uses (72). Soda ash net exports were up from 6 to 7% (70).

Average prices of soda ash rose 20% in 1975 (70). Transportation costs are the main factor in the pricing differential between the eastern synthetic product and western trona. Producers of trona increased their price from $38 to $42 per ton on January 1, 1975 (75). In December, Allied Chemical raised bulk prices from $40 to $49 per net ton f.o.b. Green River, Wyoming, and from $59 to $71 per net ton f.o.b. Syracuse, New York (78). PPG increased the bulk price from $60 to $67 per ton (79).

In Western Europe, synthetic soda ash staged a mild comeback, taking back some of the market lost to electrolytically produced caustic soda. Local caustic soda manufacturers had reduced production because of weakness in chlorine. There are no known natural deposits of any size on the continent. Belgian Solvay is now considering making as yet unspecified investments in synthetic soda ash capacity (80).

Potential supplies of soda ash as a by-product of oil shale processing could affect the U.S. market once recovery of oil from shale reaches commercial scale (75). Use in stack gas scrubbing for removal of sulfur dioxide has the potential for becoming a major new market for soda ash (76).

Sodium chlorate.—According to the U.S. Department of Commerce data, the sodium chlorate production in the United States in 1975 amounted to 167,700 short tons (81). Estimated U.S. demand for sodium chlorate was 200,000 tons (production plus imports) (82). By 1979 the U.S. sodium chlorate demand is estimated to be 260,000 tons and growth per year for this commodity through 1979 is reported to be 3% per year. Canadian sodium chlorate production and consumption for 1975 was estimated at 140,000-150,000 tons (83).

In early 1975, the bulk price for sodium chlorate was raised to $215 per ton for the dry material (84). In mid-year, sodium chlorate on the same basis was quoted at $220-$225 per ton (82, 85) and toward the end of the year the prices were raised to $250 per ton (86).

Erco Industries, a division of Albright and Wilson Limited, started a 9000 tons per year sodium chlorate expansion at its plant in North Vancouver, Canada (87). At the same location Erco Industries will add another 10,000 tons per year capacity to come on stream in early 1977 (83). This expansion in Western Canada is coupled with a similar move by the company's chlorate plant in Buckingham, Quebec, where an expansion of 12,000 tons per year sodium chlorate is also scheduled for start up in early 1977. At that time the total production in the two plants should reach 110,000-120,000 tons per year (83).

Dow Chemical of Canada Limited is planning to build a sodium chlorate plant with an initial capacity of 30,000 tons per year expandable to 50,000 tons per year at Thunder Bay, Ontario, Canada. Completion is planned for late 1977 at a cost of $13 million (88, 89).

A sodium chlorate cell adaptable to input load variation, higher level of brine impurities, quick start ups and shutdowns is available from Diamond Shamrock Corporation. The compact unit is particularly suited for sodium chlorate needs of a pulp mill (90).

Squamish Chemicals, Limited has sold its sodium chlorate plant at Squamish, British Columbia, Canada, to Hooker Chemicals (Nanaimo) Limited a subsidiary of Canadian Occidental Petroleum, Limited. The plant has a capacity of 10,000 tons per year (91).

Aluminum.—U.S. production of primary aluminum reached 3,879,000 short tons in 1975, representing a substantial drop of 21%, compared to the record 1974 production of 4,903,000 tons. The total U.S. aluminum supply also fell 23% to 5.6 million tons in 1975, almost 1.7 million tons below the record 1974 supply. Withdrawals from the government stockpile were only 2,000 tons in 1975 compared to 500,000 tons of the stockpile material sold in 1974. Secondary aluminum recovery in the U.S. totaled 1,182,000 tons in 1975 down only 6% from 1974, according to the Bureau of Mines estimates (92, 94). The aluminum can recycling program of the aluminum industry has started to pay off. In 1975, 82,500 tons of aluminum were recovered from this source, and it represents a significant increase over that of 51,500 tons in 1974 (92).

In the aluminum industry the brunt of the production cutbacks was borne by the primary aluminum producers in the recession year 1975. The demand for aluminum started easing in late 1974 which resulted in producers cutting back the primary aluminum production rates. In March 1975, the operating rate dropped to 83% and by July to a low of 73%. A small pick-up in November brought the rate to 75% where it remained for the remainder of the year (92, 93).

U.S. primary aluminum imports fell by 75,000 tons in 1975 to 434,000 tons which was the lowest level since the 1970 recession. Due to the decreased world demand, U.S. exports of crude and semicrude primary aluminum decreased by 50% during the year. China purchased almost 90,000 tons of aluminum from U.S. producers helping the U.S. export situation, otherwise the net import balance which was 80,000 tons in 1975 would have been even greater (92).

The shortage of aluminum ended in late 1974 shortly after decontrol of aluminum prices, and aluminum was usually available below the published list prices. Markets for aluminum remain in end use areas of building and construction, containers and packaging, transportation, electrical, consumer durables, machinery and equipment, and exports. For all 1975, shipments totaled 4.95 million tons down 27% from the 1974 total of 6.81 million tons. The largest reductions in the aluminum end use markets compared to 1974 were in electrical uses including conductors, consumer durables and machinery, and equipment. The smallest reduction in shipments was in the containers and packaging area (92). By the 1977 model year the usage of aluminum will jump to 100 pounds per car making the transportation sector a significant market for aluminum, according to the Aluminum Association (95).

The U.S. domestic list price of primary aluminum ingot remained at 39 cents per pound until August when major producers increased the price to 41 cents per pound where it remained for the rest of the year. However, due to the supply-demand of 1975, producers discounted the published price during the last quarter to the 34-36 cents per pound range to encourage demand (92, 93).

Free world primary aluminum production declined 11% in 1975, compared to that of 1974, to a total 10,685,000 tons, U.S. plants accounting for much of this decline (92).

The production of bauxite in the United States declined from 2.18 million tons in 1974 to about 2.01 million tons in 1975. Total imports of dried and calcined bauxite into the United States, reflecting the aluminum production cutbacks, decreased 20% to an estimated 14.2 million tons. Jamaica, Surinam, and Guinea were the principal bauxite suppliers. Alumina imports declined slightly in 1975 to about 3.5 million short tons. Australia supplied 60% of the total alumina imported with Jamaica and Surinam providing most of the remainder. Exports of alumina from the United States increased to over 1 million tons (92, 93).

Free world alumina production fell 10% in 1975 to an estimated 24.3 million tons. The International Bauxite Association (IBA) formed in 1974 has now 11 members: Australia, Dominican Republic, Ghana, Guinea, Guyana, Haiti, Indonesia, Jamaica, Sierra Leone, Surinam, and Yugoslavia. These countries produce over 75% of the world's bauxite. Australia is the largest producer with 25% capacity followed by Jamaica with 19% of production capacity. IBA did not conclude an agreement on a uniform pricing formula for bauxite (92).

Jamaica negotiated the principles of an agreement with Reynolds Metals Company along the lines of the agreement reached with Kaiser Aluminum and Chemicals Company. The companies will sell 51% of their mining operations and land to the Jamaican government (96). Lower taxes will be levied if expansions are financed by the companies. Revere was also near a

similar agreement with the Jamaican government; however, its operations there were shut down in August 1975. Revere's capacity expansions in Jamaica were postponed due to the recession in 1975 (92, 96).

Throughout the world, a number of new and expansion projects for bauxite and alumina have been delayed in 1975. Agreements with local governments were reached by a number of aluminum producers for payment of special levies on ore in terms of a percent of the realized base price for aluminum ingot (92).

The Trombetas project in Brazil is progressing with bauxite production of 3.25 million tons per year (92). After the Brazilian government made some adjustments, the joint Japan-Brazil project is on again. An initial eight month feasibility study is planned for a 352,000 tons per year aluminum smelter in Belem in the state of Para (97). Another aluminum project with hydroelectric power may be in the making on the Brazil-Paraguay border (97, 98).

Australian authorities have given consent to a feasibility study for constructing a large aluminum smelter 600,000 tons per year on the Purari River in Papua, New Guinea. The study sponsored by Papua, New Guinea, Japan, and Australia will include a hydroelectric power plant (99).

Japanese producers signed an agreement with the Indonesian government for the Asahan hydroelectric project and aluminum project. It will consist of a 247,500 tons per year aluminum smelter on the Indonesian island of Sumatra with start up in 1981 (100).

The Bureau of Mines and ten companies are continuing a research project to recover alumina from domestic nonbauxite ores. A nitric acid leach process using kaolinitic clay was tried for one week. Hydrochloric acid leaching of clay was tested in late 1975 and a mini pilot plant is under construction (92, 93).

According to the Bureau of Mines, Colorado oil shale could prove an important source of alumina. Heat energy from the oil shale is adequate for power needs and would also yield large amounts of soda ash (101).

A 24 ton per day pilot plant to make alumina in which Southwire has a 40% interest has started using Russian knowhow after the Golden, Colorado, facility ran into trouble with the U.S. technology. Southwire assumed sole U.S. rights to sell Soviet aluminum, copper, iron, and steel processes (102).

Ash from a coal-fired 2000 MW power station in the Hot Creek area of British Columbia could provide an important source of alumina. Ash output from the power plant is expected to total 3 million tons per year containing 27-33% alumina. On the basis of 28% average alumina content the ash could yield 840,000 tons per year alumina (103).

Aluminum producers are grooming new production methods. Alcoa's new aluminum chloride process that challenges the conventional Hall process will slice electrical energy requirements to 9 MW-hr per ton and over-all lower operating costs. The other feature of the process is that it can tolerate considerable load variations. The production using this process with initial capacity of 30,000 tons per year will start up in early 1976. Alcoa will also produce more than 100,000 tons per year of aluminum chloride at the Palestine, Texas facility (104, 105). Japan Electrochemistry Association also wants to build a 15,000 tons per year pilot plant based on the aluminum chloride process developed by them (106).

Sumitomo Chemical has begun commissioning its newest aluminum plant at Toyo City on Shikoku Island in Japan. Initial capacity would be 100,000 tons per year in this plant which uses 13.5 MW-hr of electrical energy per ton of aluminum representing an energy saving of 1.5 to 2 MW-hr per ton. The process deals with more stable linings around the anodes with more stable electrode surfaces and closer electrode spacing. The cells will have a longer life of 6 years, two times the life for conventional cells. Kaiser also has a similar process (105, 107).

Tel Aviv University's researchers have developed an inexpensive aluminum electroplating method using $AlBr_3$ + KBr in aromatic hydrocarbons. The coatings are claimed to be smooth homogeneous and ductile and cost about the same as zinc electroplating (108).

Beryllium.—Data on production of beryllium metal and products are not published; however, both Kawecki Berylco Industries Incorporated (KBI) and Brush Wellman Incorporated experienced declines in beryllium product sales in 1975 (109). These companies are the only substantial producers of beryllium metal in the free world. Brush extracts beryllium from bertrandite ores [$Be_4Si_2O_7(OH)_2$] mined in Utah. KBI relies mainly on imported beryl ores.

Battelle Columbus Laboratories estimates the average consumption of beryllium in the U.S. during 1973-1975 to have been 260 tons per year (109). Of this 66-75% is used as beryllium-copper alloys, 19-25% as beryllium metal, and 6-8% as beryllium oxide. Use of beryllium was about evenly divided between electronic and electric, aerospace and mechanical, and other applications. Beryllium-copper alloys containing 0.5-2.0% beryllium have high hardness and strength after heat-treating and excellent thermal conductivity. They are used in electrical connectors, springs, bellows, clips, sensing mechanisms for seatbelts, injection molds for plastics, and nonsparking tools.

Beryllium metal is used primarily in the aerospace industry where its low density is important and for nuclear applications. Beryllium oxide is used in electronics because of its unique combination of high thermal conductivity and low electrical conductivity (110). Prices for beryllium metal, quoted as 5 in. rod, rose from $135 to $155 per pound during 1975 (111, 112). The price of imported beryl (10-12% BeO) remained steady at $30 per short ton.

The over-all production and consumption of beryllium ores was significantly lower in 1975 than in 1974 (113). No domestic beryl production was reported. An estimated 1550 tons of beryl was imported during 1975, primarily from Brazil, which accounted for 41% of imports, followed by the Republic of South Africa and Uganda. This continues the decline from the peak importation of 6422 tons in 1969 (110).

Exports of beryllium metal and alloys exceeded $1 million by the end of October, approximately the same as in 1974. The export destinations were the United Kingdom, Canada, Japan, and France (109).

As of November 30, 1975, government stockpile inventories contained 17,986 tons of beryl (11% BeO), 7,397 tons of beryllium-copper master alloy (containing about 4% beryllium) and 229 tons of beryllium metal. The stockpile objectives for both beryl and the master alloy are zero and for beryllium metal 88 tons. Although each commodity exists in surplus, the holdings have not changed in the past two years (113).

In October the U. S. Department of Labor proposed new standards which, if adopted, would reduce worker exposure to beryllium by one-half (113).

Chromium.—In 1975, as in earlier years, the United States continued to rely on imports. The imports were received mostly from South Africa, Japan, Rhodesia, U.S.S.R., the Philippines, and Turkey. Domestic production of chromite was last reported in 1961 (114, 115). Domestic consumption of chromite was 870,000 short tons in 1975, 40% lower than the 1974 level of 1,446,000 short tons, as all the three consuming industries recorded an off year. The consumption in the metallurgical industry was down 41%, in the refractory industry it was off 39%, and in the chemical industry it fell 34%. Production of chromium alloys in 1975 decreased by 42% compared to that in 1974 (114, 115).

Although consumption of chromite decreased because of slackening demand, imports of chromite in 1975 totaled 1.25 million tons, a 13% increase over that of 1974. Owing to the low demand, stocks in the consuming industries increased 74%. Ferrochromium imports in 1975 were the highest in history at 318,823 tons nearly doubling imports of 1974 (114, 115). No material from the government stockpile was available during the year because congressional legislation is

required for further stockpile disposal of chromium material (114).

Demand for chromium alloys fell substantially as stainless steel production in 1975 dropped nearly 50%. Both producer and consumer inventories of chromium alloys swelled during the year due to the large influx of imported ferrochromium and the economic recession (114, 115).

Published chromite prices rose despite the weak chromium demand. With the possibility of a new ban on the U.S. imports of chromite from southern Rhodesia, Russian and Turkish suppliers boosted their prices to almost three times the early 1974 levels. The year end price for Russian chromite (48% Cr_2O_3) was \$136 per ton. The Turkish chromite prices ranged from \$118 to \$127 per ton. The South African Transvaal chromite ranged from \$33 to \$46 per ton. South African and Phillippines suppliers were attempting to boost the prices of new contracts (114, 116).

Due to the increased ore costs despite the lower demand levels ferrochrome producers were forced to raise their prices. Low carbon ferrochrome prices were in the range \$0.92-\$1.20 per lb and the charge chrome (66-70% Cr) quotes ranged from \$0.48 to \$0.57 per pound (116).

Expectations in early 1975 were that the new Congress would repeal the 1971 Byrd amendment to the Military Procurement Authorization Act. Under the Byrd amendment, which states that if the U.S. imports a strategic material from a communist country it may not refuse it from a noncommunist country, the Southern Rhodesian chromite imports were permitted. In September, the repeal of the Byrd Amendment was defeated in the Congress by 209-187 vote (114, 116).

A number of new world chromium supply developments are continuing. African Metals plans start up of two plants producing a total of 220,000 tons per year of chrome-containing pellets in South Africa. Tubatsi Ferrochrome, a joint venture of Union Carbide and South Africa's General Mining, expects the start up of a 132,000 tons per year ferrochrome at Steelport, South Africa, in late 1976. Johannesburg Consolidated Investments is planning a 132,000 tons per year ferrochrome operation to start in late 1977. Turkey's state-owned Etibank will start a 55,000 tons per year ferrochrome plant in 1976 (116).

Millions of pounds of chromium, nickel, and molybdenum that go to waste each year during stainless steel production can be converted into a recyclable alloy by an experimental recovery process that is developed by the U.S. Bureau of Mines (117).

A new commercial chromium plating process based on trivalent chromium has been developed by Albright and Wilson Limited, of England. The system has a number of advantages over the hexavalent chromium baths. It is applicable over a wide range of current densities providing more uniform decorative deposits, at rates of 3-5 microinches/min at 100 ASF. The absence of toxic spray, improved throwing power and coverage, haze-free deposits and generation of microcracks and micropores in the coating without other additives and lower chromium concentrations in the bath are the other claimed benefits (118).

Copper.—The U. S. mine, smelter, and refinery outputs, consumption of copper, and net imports of unmanufactured copper were all substantially lower in 1975 than in 1974 (119). Supply exceeded consumption with a resultant buildup of refined copper stocks and price reduction during the year.

Production from primary materials was estimated at 1.40 million tons at smelters and 1.50 million tons at refineries, reductions of 7 and 9%, respectively, from 1974. Production of refined copper from scrap was approximately 345,000 tons compared to 497,000 tons in 1974.

While there were some production starts, the more general trend was toward trimming production schedules.

Asarco, Incorporated was scheduled to bring on stream in late 1975 or early 1976 an electrolytic refinery near Amarillo, Texas, which is to be one of the world's largest. The plant has a design capacity of 420,000 tons per year of refined copper (120).

The Lakeshore copper mine of Hecla Mining Company is coming into production. The complex is located 30 miles south of Casa Grande, Arizona. Production of sulfide and oxide ores began in September and October; full production is estimated to require an additional 6 months. The complex is designed to produce 9,000 tons per day of sulfide ore and 6,000 tons per day of oxide ore which will be treated to produce 30,000 tons per year of electrowon cathodes from the sulfide ore and 55,000 tons per year of precipitate, containing 65% copper, from the oxide ore. Total project cost, including working capital, was estimated at \$185 million early in 1975. The Lakeshore deposit is reported to contain more than 500 million tons of ores (121, 122).

Production was slated to begin in the final quarter of 1975 at the new solvent extraction electrowinning plant of Anamax Mining Company at Twin Buttes, Arizona, treating low-grade oxide ores. Construction of the \$100 million plant is a joint venture between the Anaconda Company and Amax, Incorporated (123).

Anaconda Company announced the closing of its 77 year old Raritan Copper Works in Perth Amboy, New Jersey. The plant had been Anaconda's main processor of copper from the company's properties in Chile. Copper cathode production at the plant last year totaled 113,000 tons (124). Lack of feed material, high inventories, and low prices forced the shutdown.

Anaconda Company temporarily shut down its Arbiter process plant at Anaconda, Montana, in July citing faltering prices and mechanical difficulties (125). The \$20 million plant, which went on line in September 1974, had a capacity of 36,000 tons per year of copper cathodes. The process employs an ammoniacal leach on sulfide ores and employs new technology aimed at more efficient flexible metal recovery without air pollution (126).

United States and foreign copper producers, both mine operators and smelters, began wholesale production cutbacks in December 1974 (127). These generally ranged from 10 to 20% and persisted throughout 1975 (128).

The decline in demand for copper was a reflection of general economic conditions, particularly in the large copper-consuming areas of automobiles, home construction, and utility construction. (119).

Consumption of refined copper was projected to be only 1.5 million tons, a 32% drop from 1974 and the smallest annual consumption since 1961.

The 68 cents per pound base cathode price posted December 27, 1974, was reduced again to 63 cents per pound on January 23, 1975 by major manufacturers. The U.S. market price was not strengthened by the gap, well over the usual 5 cents per pound which existed between the U.S. producer and London Metal Exchange prices (129).

Two U.S. producers lowered prices by 3 cents per pound in June (131). This was not followed by other producers and for a while there were as many as four different prices for cathode and five different prices for wirebar (132). This price cut was rescinded by the end of July. There was some enthusiasm in the market when the price on the London Metal Exchange surged to over 58 cents per pound (133). The large (world) refined copper stocks, above 1.1 million tons, and the failure of the market demand to pick up left the market in the doldrums. The year closed with the U.S. price at 63 cents per pound and the London Metal Exchange at 53-54 cents per pound. The consensus is that a significant turnaround for copper will not occur until the second quarter of 1976 (134).

Stocks of refined copper at primary producers built up rapidly from 101,000 tons at the start of the year to 225,000 tons by the end of June, then declined to 189,000 tons by the end of October. Stocks of refined copper at brass plants and wire mills were 145,000 tons at the

start of the year, peaked at 163,000 tons in March, and declined to 133,000 tons by the end of September (119). Worldwide stocks of refined copper reached 1.41 million tons which is considered to be twice the desirable level (134).

Net importation of copper is a small component of supply compared to the U.S. production. Importation of unmanufactured copper was estimated at 270,000 tons compared to 609,000 tons in 1974 while exports increased from 198,000 tons to 240,000 tons (119). There was a net exportation of refined copper as imports plunged from 340,000 tons to 85,000 tons while exports increased from 127,000 tons to 170,000 tons. Imports of blister copper dropped from 208,000 tons to 95,000 tons (119).

The attempts of the Council of Copper Exporting Countries (CIPEC) to bolster sagging prices were largely ineffective. The group, whose members, Chile, Peru, Zaire, and Zambia, have been providing approximately 37% of the free world copper mine production, agreed to cut copper exports by 10% in December 1974, and to extend the cutback to 15% in April 1975 (135).

U.S. mine production during 1975 was 1.40 million tons, 11% less than 1974 and the smallest quantity since strike-disrupted 1968. Principal copper producing states were Arizona, with 57% of the total, followed by Utah, New Mexico, Montana, Nevada, and Michigan. The weak demand and increased costs of production led to permanent closure of several underground operations, cutbacks or temporary closures at other operating properties, and a slowdown of several new developments (119).

Duval Corporation announced a substantial production cutback in February and a further cutback in September at the Mineral Park open-pit property near Kingman, Arizona. This property produced 20,000 tons of copper in 1974 (138).

A major closing announced in November to take place over a period of months affected Anaconda Company's Butte, Montana, underground mines. Lack of profitability over several years and the desire to preserve the potential of large low-grade ore zones under Butte Hill for future large-scale underground development were the reasons given for the decision (139).

Phelps Dodge reduced operating schedules at mines in Metcalf, Morenci, and Ajo, Arizona, and Tyrone, New Mexico, from 5½ days to 5 days a week. These facilities account for 97% of the company's mining output (140).

Underground mining at Phelps Dodge Corporation's Copper Queen branch at Brisbee, Arizona, was scheduled to end in June. The mines, operated since 1880, accounted for 15,000 tons of the company's total copper production of over 280,000 tons in 1974 (141).

Phelps Dodge also halted exploration at the historic Shattuck Mine in Brisbee. This decision was due to "a combination of the poor copper market and the need to conserve cash for essential expenditures, such as the Hidalgo Smelter." Company officials indicated that exploration work would be resumed someday (142).

In Canada, copper mine production for 1975 was estimated at 821,000 tons of copper in concentrate compared to 933,000 tons for 1974. Production of blister copper dropped from 602,000 tons of copper to an estimated 567,000 tons. The combination of massive tax increases and depressed metal prices has wiped out most of Canada's major mine development plans. Nearly 300,000 tons per year of new mine capacity in the development stage, all in British Columbia, has been shelved (143).

A production cut from 825,000 to 550,000 tons per year scheduled for early in October was announced for the Cobar Mine by Australia's Broken Hill South. The Port Kembla Smelter of Electrolyte Refining and Smelting Company of Australia, Limited, which treats all of Cobar's concentrates was expected to announce a similar cutback. However, Australia's two largest copper mining companies. Mount Isa Mines and Mount Lyell Mining and Railway both stated that they had no plans to decrease production (144).

Cities Service Company's Pinto Valley deep pit mine west of Miami, Arizona, is estimated to contain some 350 million tons of ore averaging 0.44% sulfide copper. The mine and mill, begun ahead of schedule in June 1974, has a design capacity of 40,000 tons per day and will recover more than 60,000 tons per year of copper. A solvent extraction electrowinning plant is under construction to be completed in mid 1976. (145).

Continental Copper is evaluating plans for a new 2000 tons per day underground mine and mill on Marble Peak near Tucson, Arizona. Continental currently estimates indicated and inferred reserves to be 12 million tons with an average of 2.2% copper. For an initial production rate of 2000 tons per day the capital cost is expected to be appreciably greater than the $8-10 million projected in 1973. Testing indicated that the mill will recover 90% of the metal values in a concentrate of 30% copper with some silver (146).

A $200 million expansion is underway at Cyprus Mines Corporation's Baghdad Mine west of Prescott, Arizona. The present 6000 tons per day concentrator will be replaced by a 40,000 tons per day system. Start up is scheduled for late in 1977 (147).

The Anaconda Company continues with its Carr Fork project in Utah. This project involves a major underground mine and a 10,000 tons per day concentrating complex. Operation of the $135 million complex is scheduled for 1979 (148).

Utah Copper Division of Kennecott Copper Corporation is having difficulties with the Environmental Protection Agency over its Garfield, Utah, smelter (149).

A $152 million complex at Khatri in Rajasthan, India, was formally opened in February. The complex includes an electrolytic refinery with a capacity of 34,000 tons, a smelter, a concentrator, and two mines. Ore reserves are estimated at 52 million tons, containing 0.72% copper at Khatri and 32 million tons of 1.56% copper at Kalihan (150).

A spokesman for Liard Copper Mines announced that drilling results at the Shaft Creek deposit in British Columbia "support a new geological concept which strongly suggests that the presently stated reserve of 300 million tons may eventually be doubled" (151).

A major copper find may be in the making in northwestern Quebec and eastern Ontario. Over 7000 claims have been filed (152).

Texasgulf, Incorporated announced that its new smelter to be built at Timmins, Ontario, will incorporate a continuous smelting process developed by Mitsubishi Metal Corporation and electrolytic refining technology used for several years by the Onahama Smelting and Refining Corporation. The company hopes to have the 130,000 tons per year, $200 million smelter and refinery on stream by 1976 (153, 154).

In a surprise move during February, Secretary of the Interior, Rogers C. B. Morton, proposed issuing permits for manganese nodule mining to U.S. companies if the United Nations fails to agree on a Law of the Sea Treaty by January 31, 1976. This move would particularly displease the developing nations who fear for the loss of any possible participation in this resource and in some cases fear loss of markets for copper, nickel, cobalt, and manganese. An excellent review of the political, economic, and technical situation is contained in Ref. (155).

A variety of advanced technologies are presently employed in working plants, being tested on pilot scale, or are under active research and development.

Solvent ion exchange is used in a small number of operating plants with a total capacity of 175,000 tons per year of cathodes, and is planned or under consideration for others. This process, pioneered at the Ranchers Exploration and Development Plant in Miami, Arizona, is highly versatile for purifying leach liquors and concentrating metal values (156).

An increased usage of titanium starter sheets in copper refineries has occurred (156). Among the advantages cited for titanium are that the oxide film on the titanium acts as an excellent parting agent and that

less distortion is observed during the start of the plating cycle.

Mechanized stripping of starter sheets, using both copper and titanium blanks, has been employed in the Pori Copper Refinery of Finland's Outokumpu Oy since 1974 (122).

At plants near Tucson, Arizona, Duval Corporation and Cyprus Mines Corporation are each testing a ferric chloride leach process. Duval operated a pilot plant for 2 years and is now building a 32,500 tons per year plant. Cyprus Mines Corporation is operating a pilot plant producing 7 tons per day of copper powder (157).

The electric furnace has been gaining a bigger role in the U.S. copper industry for smelting copper concentrates. In 1972, Cities Service installed the first electric smelting furnace in recent years. Inspiration Consolidated Copper has just completed a $54 million smelter, and the Anaconda Company is presently installing an electric furnace in its smelter in Anaconda, Montana (158).

The top blown rotary converter, developed by The International Nickel Company and Dravo Corporation, based on oxygen steel-making technology is now in use for smelting nickel concentrates at Copper Cliff, Ontario, and has been demonstrated in full scale tests on copper concentrates. The converter can produce high SO_2 exhaust gases to facilitate sulfur removal or recovery (158).

A commercial Noranda process continuous smelter came on stream at Noranda, Quebec, in March 1973, at a design capacity of 800 tons per day of copper concentrate. Kennecott Copper Corporation is installing this process at its Garfield, Utah, smelter (158).

Kennecott Copper Corporation has been experimenting with a solution mining process at its copper deposit 9 miles north of Safford, Arizona. The wells at Safford go as deep as 5000 feet and, if successful, the system could recover low grade ores that would not be economically accessible by conventional open pit or underground methods (159). Kennecott has not permanently shelved the possibility of using a nuclear blast to establish an underground leaching cavity.

Chile will test an electrolytic process to recover copper and make phosphoric acid as a by-product. The process apparently involves the reduction of copper sulfate solution with white phosphorus to obtain pure electrolytic copper. Codelco, the state copper corporation, is providing financial backing for a pilot plant (160).

Research by the Bureau of Mines suggests that sulfur in copper sulfide concentrates can be converted to insoluble anhydrite ($CaSO_4$) by roasting with lime. The calcine is then leached with HCl to take metal values into solution. An alternative process uses a ferric chloride leach to precipitate elemental sulfur (161).

Several techniques are under development to raise the current density limits above the 15-20 A/ft^2 typically observed. Successful techniques have included periodic current reversal, rapid flow of electrolyte over electrode surfaces, air agitation, high frequency sound, and use of a rotating-drum cathode (162).

Lithium.—In 1975 lithium chemicals were produced by Foote Mineral Company Lithium Corporation of America, and Kerr-McGee Corporation. At the Kings Mountain, North Carolina, mine Foote Mineral Company extracted spodumene ore to be processed into ceramic or chemical-grade spodumene concentrate. At the Silver Peak, Nevada, location Foote Mineral produced lithium carbonate from the lithium-bearing underground brine deposits. The Foote Mineral plant at Silver Peak, Nevada, is rated at 14 million pounds per year of Li_2CO_3 equivalent. Lithium Corporation of America produces a variety of lithium chemicals at its Bessemer City, North Carolina, plant which is rated at 27 million pounds per year Li_2CO_3 equivalent. At Searles Lake, California, Kerr-McGee Chemical Corporation reportedly has an annual capacity of 1 million pounds of lithium carbonate as a by-product (163, 164). In 1975 the General Services Administration sold 161 tons of lithium hydroxide monohydrate on the open market (163).

Demand for lithium products was strong until April 1975, when inventory accumulation was halted and the demand fell in response to the economic recession during the rest of the year. The largest application for lithium carbonate in the aluminum industry declined significantly since the aluminum production decreased 21% in 1975. The dramatic growth in lithium chemical usage during the 1972-1974 period did not continue through 1975 (164). Other major uses for lithium chemicals were in the manufacture of heavy duty greases, glass, ceramics, brazing fluxes, batteries, and for absorption air conditioning equipment. The ceramic industry is the second largest user of lithium ores and chemicals in applications where low thermal expansion characteristics of lithium-aluminum-silicate are required (163, 164). According to U.S. Geological Survey, conventional uses could consume currently recoverable resources by 2000 leaving nothing for the applications in the area of thermonuclear power unless new deposits are found and developed (165). There is also potential for use of lithium as the heat transfer medium in a fusion reactor (164).

In early 1975, the prices of lithium compounds were quoted at: lithium hydroxide monohydrate at $1.02 per pound, lithium fluoride at $2.22 per pound, lithium chloride at $1.47 per pound, and lithium metal ingots at $10.65 per pound (166). In November 1975, lithium chemical prices were: lithium hydroxide monohydrate $1.10 per pound, lithium carbonate at $0.84 per pound, lithium fluoride at $2.42 per pound, lithium bromide at $1.86 per pound, lithium chloride at $1.26 per pound, and the lithium metal ingots at $11.10 per pound (167).

Estimated U.S. consumption in 1975 fell to 28 million pounds of lithium carbonate equivalent from the 1974 level of 32 million pounds. The world consumption of Li_2CO_3 equivalent in 1975 was estimated at 48 million pounds and decreased from the 1974 level of 53.4 million pounds (164).

The Corporation of Development in Chile and the Foote Mineral Company announced the formation of a company to explore lithium deposits at Salar de Atacama near Antofagasta, Chile. Exploration continued in 1975 at the deposits which are similar to those at Silver Peak, Nevada (164).

The battery development using solid lithium alloy negative electrodes, iron sulfide positive electrodes, and LiCl-KCl molten electrolyte is continuing, particularly for the peak power demand in power plants. Argonne National Laboratories is working on increasing the life of the battery from five months to eight years (165, 168). If these batteries are developed, they are being groomed for the automotive applications also (168).

Magnesium.—Magnesium metal is produced in the United States by Dow Chemical Company, Freeport, Texas; American Magnesium Company, Snyder, Texas; and NL Industries, Inc., Rowley, Utah (169). Domestic production during 1975 was estimated to be 125,000 tons (170).

Both the American Magnesium Company and the NL Industries facilities employ an advanced technique using dehydrated brine for electrolyte feedstock which permits simultaneous manufacture of chlorine as a by-product. Neither plant is in full production (171). The former plant suffers from ecological problems. Although the latter plant was announced to be operating in May at a rate of 13,000 tons per year out of a capacity of 45,000 tons per year (172), the company subsequently announced suspension of production because of technical problems until late in 1976 at the least (170, 173).

The principal use for magnesium, about 45% of consumption, has been in aluminum-based alloys much of which is used for aluminum can tops. About 35% of world consumption is for structural magnesium and 20% is used for chemical, electrochemical, and metallurgical processing (171). The price of magnesium, relative to that of aluminum, is too high to permit much

penetration into the structural market (171). The price is high enough, however, to attract capital into new magnesium production facilities, which is not the case with aluminum. It has been suggested that if the price of aluminum rises sufficiently to provide a reasonable return on investment in new aluminum production facilities, the structural market should develop for magnesium (170).

In contrast to the rising trend of the last three years, magnesium prices remainded steady during 1975 at 82 cents per pound, quoted as primary ingot (174, 175).

During the period January to September, 5,214 tons of magnesium metal were imported, and 20,103 tons were exported (169). The major foreign producer is Norsk Hydro, Heroya, Norway. Together with other western European and Japanese producers, the total foreign production was estimated to be 70,000 tons (171).

Several new plants are under construction or have been announced. Northwest Alloys, Incorporated, a subsidiary of the Aluminum Company of America, is reported to be bringing its 26,000 tons per year plant at Addy, Washington, on stream in 1976. This plant is to use the French Magnetherm® process which is based on thermal reduction of dolomite with ferrosilicon. If the start up is successful, magnesium production in the western hemisphere might reach 155,000 tons per year late in 1976, a figure which includes the 5,500 tons per year capacity of Chromasco, the Canadian producer (170).

Dow Chemical has plans for a 50,000 tons per year plant to go on stream by 1978 or 1979. Abroad, Norsk Hydro has announced plans to erect a 16,500 tons per year plant at Heroya, Norway, to develop a new process before proceeding to a 55,000 tons per year plant in the early 1980's (171). The Scalistiri Group is reported to be planning a 120,000 tons per year plant on the Greek island of Euboea starting in 1978 (176).

Manganese.—According to the U.S. Bureau of Mines there was no 1975 U.S. production of manganese ore, concentrate, or nodules containing 35% or more manganese. The production of ferruginous manganese ore concentrates containing 10-35% Mn was continued in New Mexico and the Cuyuna range in Minnesota, although at a reduced rate. Most of the manganese requirements were met by imports and sales from the government stockpile (177).

U.S. production of ferromanganese (high carbon, medium and low carbon grades) amounted to 607,700 short tons in 1975. The ferromanganese stocks in 1975 reached all-time highs. Silicomanganese production was 222,772 tons and 22,114 tons of manganese metal were produced (178, 179).

The price for U.S. produced standard (minimum 78% Mn content) high carbon ferromanganese held at $393 per ton in early 1975. Imported standard high carbon ferromanganese prices slid steadily from $402-$411 per ton at the start of 1975 to $348-$370 per ton in late 1975. Cutbacks in steel production at home and abroad and consumers drawing on their inventories were factors contributing to lower prices. Imported medium carbon ferromanganese prices dropped by 2-5 cents to $0.43-$0.455 per pound in the first half of 1975 and then dropped further to $0.38-$0.44 per pound in late December 1975. Electrolytic manganese metal held at $0.54 per pound in most of 1975 but drastic production cutbacks were necessary to maintain this price level (177, 179).

Cumulative sales of government stockpile excesses in 1975 by the General Services Administration were: natural battery ore 43,700 short tons; 18,000 short tons of type B chemical ore; and metallurgical ore, 63,826 short tons of stockpile grade and 409,991 short tons of nonstockpile grade (177). In 1975 manganese ore imports returned to traditional levels after domestic producers restarted some blast furnace ferromanganese production. Imports of the manganese ore in 1975 amounted to 1,574,045 short tons compared to the 1974 total of 1,188,145 short tons (178). U.S. imports of ferromanganese in 1975 amounted to 406,922 short tons with 313,936 short tons of Mn content. The manganese ore imports in terms of Mn content were from Brazil, Gabon, South Africa, Australia, Mexico, and Zaire in decreasing order of supply. Major ferromanganese supplying countries were France, South Africa, Japan, and Norway (178).

World 1975 manganese ore production was estimated at about 24,420,000 tons (gross weight) (179). An exploration success was scored at Morro de Sete Lagoas in Uapes district in Brazil near the Venezuelan border with samples running at 47.5% Mn. Deposits of 25-30 million tons of 47-51% Mn are claimed for the find (179).

When the Trans-Gabon Railway will be completed in the 1980's it will be possible to double production of the Comilog mine to 4 million tons per year (177, 179).

The Indian state mining company, Mysore Minerals, expects to develop iron manganese deposits in Karnataka where about 1.1 million short tons of manganese mineralization has been found in association with iron ore (179).

A five nation 14 company consortium plans to develop the Tambao mine in Upper Volta by investing $24 million. Production is slated for 1980 at 625,000 tons per year (177, 179).

Union Carbide is discussing with the U.S.S.R. a possible manganese complex at Nikopol with 1.2 million tons per year ferromanganese plant (179).

Australia's Broken Hill Pty. held discussions on a possible Saudi Arabian ferromanganese plant in cooperation with the Saudi Arabian firm Petromin (179).

France's Pechiney is expanding its Saint-Beron ferromanganese plant by 11,000 tons per year and its subsidiary Eurominas is constructing a 110,000 tons per year ferromanganese plant in Portugal (179).

Satralloy Incorporated switched one of its six ferrochrome furnaces at Steubenville, Ohio, to ferromanganese production in October 1975 (177, 179).

Associated Manganese Mines of South Africa plans new furnaces at its Cato Ridge ferromanganese plant with start up scheduled for 1977.

The proliferation of multinational consortia for mining deep ocean manganese nodules continued in 1975. INCO formed a consortium, Ocean Management Incorporated, with AMR group of West Germany and Deep Ocean Mining Company, a 23 company Japanese group led by Sumitomo. A reported $30 million is budgeted for the four year project. The U.S. Department of the Interior has set up Ocean Mining Administration (OMA) to promote and encourage ocean mineral resource recovery from seabeds beyond the limits of national jurisdiction. Before ocean mining can begin, however, agreement between the developed and the developing countries will have to be reached on how to administer the seabed mining internationally. The ocean floor is considered to be the "common heritage of mankind" (180). The U.S. Government proposed to issue permits to begin ocean mining if the "Law of the Sea Treaty" in the U.N. fails to go through by January 31, 1976 (155). A 600,000 km^2 area in the coastal seabed off Western Australia has mineral nodules containing manganese, copper, nickel, uranium, and gold (182).

Manganese nodules are enlisted in boosting the upgrading of heavy petroleum fractions in work at Mobil R&D Corporation and Hokkaido University. Mobil reported that using the crushed nodules in an experimental fixed bed reactor, removal of trace metals from heavy petroleum fractions was attained with good results. Successful commercial application of the technology could mean an increased supply of low sulfur fuel oils and gasoline (177, 181).

The organometallic compound methyl cyclopentadienyl manganese tricarbonyl (MMT) can be used, according to Ethyl Corporation, to raise the octane rating of unleaded gasoline by two points at 0.125g per gallon level consumption rate. At 1980 gasoline consumption rate this would amount to 17,300 tons per year of manganese (177, 179).

Nickel.—Due to the reduction in production of specialty steels caused by the worldwide economic slump, a substantial oversupply of nickel developed during 1975. These developments of 1975 may have significant influence on the future worldwide supply-demand balance of nickel (183).

The U.S. continued to rely on foreign sources for a major portion of its nickel requirements. Domestic nickel producers increased their activity in 1975 over that in 1974 as a result of Freeport's renovated nickel-copper-cobalt refinery in Louisiana. The only domestic mine operator, Hanna Mining, produced approximately 16,500 tons of nickel from laterite ore, as measured by mine shipments. The associated smelter recovered about 13,000 tons of nickel as ferronickel. By-product plants recovered another 900 tons of nickel in various forms. Copper smelters and refiners and other manufacturing plants, including iron and steel, recovered an estimated 58,000 tons of nickel from scrap (184). Canadian production of nickel through the first 11 months of 1975 totaled 244,964 short tons and was about 7% lower than that in the corresponding period for 1974 (184). Smelter production of nickel in New Caledonia through the first 11 months of 1975 was 4% greater than that reported for the same period in 1974 and totaled 70,585 tons. Of this quantity, 52,417 tons was in ferronickel and 18,168 tons in matte nickel (184).

The nickel oversupply situation resulted from the reduced nickel consumption and the continued high level of imports in anticipation of the possibility of future price increases. The oversupply situation caused the record high levels of consumer stocks of nickel. The pattern of nickel usage was similar to that in earlier years with approximately 42% consumed in steels, 26% in nickel and nickel alloys, and 14% in electroplating. Pure unwrought nickel increased its share of the total U.S. nickel market at the expense of ferronickel and nickel oxide. Primary nickel consumption was estimated to be 144,000 tons in 1975, compared to the 1974 level of 208,107 tons (185, 186).

The price of nickel was stable at $2.01 per pound through nearly August of the year when the price was raised to $2.20 per pound. Reportedly, however, consumers were able to buy considerable quantities of nickel at the old price of $2.01 per pound for the rest of the year. Hanna Mining Company raised the price of the domestically produced ferronickel from $1.97 to $2.16 per pound of Ni content in September. The price of the imported ferronickel in the last four months of the year ranged from $2.15 to $2.19 per pound of nickel content (184).

In 1975, U.S. imports totaled 162,271 short tons of nickel compared with the 1974 imports of 221,399 tons. Canada remained the principal supplier of nickel accounting for 62% of the total. New Caledonia was the second most important supplier of nickel followed by Norway and the Dominican Republic. Imports from U.S.S.R. in 1975 were about one half the 1974 level (184, 185)

Major new nickel capacity projects expected to come on stream failed to reach the objectives. Several projects including Greenvale, Marinduque, and Selebi-Pikwe (Bostswana) experienced cost overruns and delays. A number of other projects were canceled or shelved, major reasons being inflation and adverse government policies. The capital investment for developing new nickel capacity is estimated at $10.00 per lb of annual capacity in terms of 1975 dollars (183).

Long awaited approval, on a much reduced scale however, is now foreseen for the Agnew nickel project in Western Australia in which London's Selection Trust group has a 60% stake with MIM Holdings having the remaining 40%. Plans are now for 10,000 tons per year nickel capacity starting sometime in 1978 (187).

A nickel smelting plant costing about $500 million is being planned by a group of Japanese companies in association with the Indonesian government. Indonesian Nickel Development Company will initially produce 29,200 tons of ferronickel (25% Ni) annually starting in 1980, on the Gebe Island in the Moluccas. The plant is eventually projected to produce 110,000 tons of ferronickel annually (188).

The Rhodesian Nickel Corporation Limited will start ore production early in 1976 at its third nickel mine at Epoch near Filabusi in Matabeleland. Due to inflation, the cost of the development of the mine has increased from $10 million to about $12 million (189).

Johannesburg Consolidated Investment Company Limited has started ore production from the new Shangani mine which is about 60 miles northeast of Bulawayo. Planned throughput of 75,000 tons of ore per month will be achieved in 1976 and by 1977 the annual capacity will be 5500 tons of nickel (183).

The prospects for mining asteroids for iron and nickel is being proposed by Massachusetts Institute of Technology scientists. They envision attaching an impulse generating device to an asteroid of 1 km in diameter and gradually moving it into an orbit closer to the earth. Part of the asteroid would be melted in space to shape it into a space vehicle to lower it to a landing site in the ocean. Some $140 billion worth of metals could be brought to earth annually in this fashion (190).

UOP, Incorporated has developed a nickel extraction process for a wide range of nickel laterite and other nickel-bearing ores. By adding various chemicals during the roasting step the process makes the nickel more extractable. The new hydrometallurgical/additive technique attains 90 + % yields as pyrometallurgical techniques but uses 30-50% less energy. The process is a takeoff from reductive roasting/ammoniacal leaching methods for low grade ores (191).

According to a Bureau of Mines Report of Investigations, nickel and cobalt could be recovered from low grade domestic laterites. The process involves selective reduction of oxides with carbon monoxide at 350°-600°C and extraction by multistage leaching with aqueous ammonium hydroxide and ammonium sulfate in the presence of oxygen followed by solvent extraction. Low energy requirement for the process is claimed (184).

According to a report by the National Research Council, airborne nickel and its compounds may be carcinogenic. Significantly increased incidence of lung and nasal cancers were found in workmen working in nickel smelters and refineries. The report prepared for EPA suggests how nickel should be monitored and the maintenance of comprehensive health records of nickel workers (192).

Sodium.—United States sodium metal production is showing a gradual down trend. The estimated total production for 1975 is 160,000 tons. This compares to 173,212 tons in 1974 and 173,903 tons in 1973 (193).

The total U.S. capacity is 189,000 tons per year which consists of five plants with yearly tonnages as follows: du Pont at Memphis, Tennessee, 35,000, and at Niagara Falls, New York, 42,000; Ethyl Corporation at Baton Rouge, Louisiana, 45,000, and at Houston, Texas, 30,000; and R. M. I. at Ashtabula, Ohio, 37,000 (193).

The dominant use for sodium metal has been for antiknock compounds. The increasing usage of unleaded gasoline, and the general downturn of the economy have accounted for the decreased use of sodium metal. At present 65-70% of the U.S. consumption of sodium is for making antiknock compounds like tetraethyl lead. Other uses include metal refining (particularly titanium metal) and manufacture of pharmaceuticals. A possible large scale usage is in liquid-metal-cooled nuclear reactors, but this use has not yet been realized (194).

The average annual price for sodium has shown a gradual upward trend being 15.9 cents per pound in 1970, 17.4 cents per pound in 1973, 17.9 cents per pound in 1974, and 22 to 22.5 cents per pound in 1975 (194).

The production of tetraethyl lead in 1975 was down an estimated 2% from 1974 (195). Domestic prices dropped following a drop in lead prices. Effective May 15, Ethyl Corporation, followed by du Pont cut its

quotes on antiknock mixes by 0.7 cents per pound to 56.8 cents per pound for standard tetraethyl lead mix (196).

Titanium.—The titanium industry experienced a period of reduced production and demand while the price of domestic titanium sponge rose, and prices of ores and imported sponge moved within narrow limits.

The two U.S. producers of sponge, Titanium Metals Corporation of America and R. M. I. Incorporated, have a total capacity of approximately 18,500 tons per year. Production in 1975 was 4% less than in 1974. Consumption of sponge and scrap was 17,000 tons and 7,700 tons, respectively. Sponge inventory in the hands of producers and consumers reached 6500 tons. Imports of sponge for consumption were 3425 tons at the end of September. Of this quantity, 61% was from Japan, 28% from the U.S.S.R. and 11% from the United Kingdom (197). This proportion of imports was typical of recent years except for 1974 when a disproportionately large quantity was imported from the U.S.S.R. (199).

Production of ingot was about 27,000 tons, down one third from 1974 (197). Titanium ingot melting capacity is being raised 20% in a $2 million expansion by Timet Division of Titanium Metals Corporation of America. Timet is also doubling welded tube facilities in Toronto at a cost of $1 million. R. M. I. Incorporated announced a delay in its previously publicized plan to expand the capacity of its Ashtabula, Ohio, sponge plant. Timet announced the initial operation of a commercial size cell to produce sponge by an electrolytic method (200).

Robert S. Nycum, Timet president, expects the market for titanium mill products to be about 25,000 tons by 1980 and 35,000 tons by 1985 compared to last year's record 17,500 tons. Major growth will be in industrial uses (198).

The principal consumer of titanium metal, the aerospace industry, was affected by reduced commercial aircraft production.

The price of domestic sponge rose from $2.45 per pound in January to $2.70 per pound in December (201, 202). This compares to $1.42 per pound early in 1974 (199). In a contrary action, the price of Japanese sponge decreased slightly from $2.85 to between $2.65 and $2.70 per pound.

The price of rutile (96% TiO_2), which soared from $275 per short ton in 1974, held at $710 per short ton throughout the year. Ilmenite (54% TiO_2) held at $55 per short ton and slag at $60 per short ton throughout the year (201, 202).

U.S. mine production of titanium minerals was about 640,000 tons, a decline of 16% from 1974. Ethyl Corporation completed the feasibility study of Paris Landing, Tennessee, but has postponed further action (197).

Imports of ilmenite increased to 150,000 tons, mostly from Western Australia. Imports of natural rutile were about 165,000 tons, a decrease of 15% from 1974. Imports of synthetic rutile were 50,000 tons. Imports of slag were approximately 300,000 tons, 27% more than in 1974 (197).

Australian production of rutile was estimated at 320,000 tons, continuing the decline from the peak of 405,200 tons in 1970. Australian ilmenite production was just under 900,000 tons, which is about equal to 1974 production (197).

The 1975 report of the Department of the Interior to Congress under the 1970 Mining and Minerals Policy Act voiced concern over the vulnerability of the U.S. resulting from dependence on imports. At present 97% of the U.S. demand of rutile is supplied by imports, principally from Australia and India, and 23% of ilmenite is supplied by imports, primarily from Canada and Australia (203). A report in a similar vein by the U.S. Geological Survey listed titanium as a material for which the U.S. (in 1974) was more than 90% dependent on imports for primary materials (204).

A pending shortage of rutile is one of the major problems facing the titanium industry. Best estimates place world rutile reserves at less than 10 million tons. With annual production of TiO_2 for pigments running close to 2.5 million tons, this is a fairly small supply. Alternative sources of titanium include alluvial deposits and titaniferous magnetites scattered throughout the world, which will provide a source of TiO_2 far into the future. Known reserves of pigment grade ilmenite (more than 45% TiO_2) total about 165 million tons. Lower grade ilmenite resources add about 225 million tons (205).

Demand for titanium dioxide pigment declined 38% between June 1974 and April 1975. By the end of the year, however, recovery seemed to be well established. Production for 1975 was estimated at 720,000 tons, 9% less than in 1974. Du Pont and Kerr-McGee Chemical Company have recessed plans for new construction at DeLisle, Mississippi, and Mobile, Alabama, respectively (197).

Du Pont, SCM-Glidden, and NL Industries all increased the price of titanium dioxide by 3.5 cents per pound in August. This put the new price at 43.5 cents per pound for rutile and 38.5 cents per pound for anatase (206).

Du Pont closed its 70,000 tons per year sulfate process plant at Edgemoore, Delaware, and replaced it with a 80,000 tons per year chloride process plant (207). In April the new plant was briefly closed to investigate the cause of a leak of $TiCl_4$ (208, 209). The new plant creates less than one-third the waste of the sulfate-process plant but even that amount will cause headaches for some time to come.

NL Industries announced the temporary closing of their 128,000 tons per year TiO_2 plant at Sayreville, New Jersey, for installation of pollution control equipment and routine maintenance (210).

New technology is under development for production of metallic titanium as an alternative to the presently used Kroll process (reduction of titanium tetrachloride with magnesium). Howmet Corporation of Whitehall, Michigan, is developing an electrolytic process using a fused salt bath. Timet Division of TMCA has produced 400,000 pounds of titanium electrolytically in a variety of laboratory and semiworks plants. The United Kingdom's Electricity Council Research Center in Capenhurst, Chester, is working on a plasma process employing titanium tetrachloride and sodium. Bethlehem Steel Corporation in Bethlehem, Pennsylvania, is considering a plasma process which is also at the laboratory stage (211).

Zinc.—Smelter production of primary slab zinc was 445,000 tons, down 20% from 1974, continuing the decline of zinc smelter production since 1969 (212). American Smelting and Refining closed its 50,000 ton per year zinc smelter in Amarillo, Texas, during May. The firm announced that the 50 year old smelter could not absorb the cost of being brought into compliance with air pollution standards (213). This reduced U.S. zinc smelting capacity to 680,000 tons per year, which is well below U.S. zinc consumption. Imports for consumption of slab zinc were about 375,000 tons, representing a decrease of 35% from 1974. Canada was the leading source of metal imports, providing 58% of the total, followed by Australia, Peru, Belgium, and Luxembourg.

"Zinc producers bite the bullet" fairly well summarized the market for 1975 (214). In face of a market which remained sluggish for most of the year, metal inventories increased early in the year. By mid-year, U.S. producers were curtailing production (215). Foreign production was even more dramatically reduced (216).

Producer and consumer stocks, at 256,736 tons on January 1, had climbed to 269,455 tons in April, the highest level in recent years. However, as smelter production declined and demand increased later in the year, stocks fell to a more normal level of 145,000 tons by the year end (212).

The General Services Administration delivered 5000 tons of zinc from the government stockpile. The last three quarters of the year were declared closed because of the high producer stock balance. The total amount

of zinc authorized for sale at the year end was 172,000 tons (212).

In August the President signed Public Law 94-89 suspending the duty on zinc ores, concentrates, and zinc-bearing materials until June 30, 1978 (212).

In spite of the falling demand for zinc, the U.S. producer price remained very close to 39 cents per pound for prime western zinc for essentially the whole year. This contrasts to a high of over 90 cents per pound in May 1974. New Jersey Zinc announced in September a price increase of 2 cents per pound effective October 10 but was forced to rescind the increase when other producers failed to follow (212, 217). Prices for zinc on the London Metal Exchange had dropped late in the year because of weakness of the pound sterling and unwillingness of European sellers to appear to be raising prices (217). To get out of this difficulty, most foreign producers were quoting prices in U.S. dollars at the year end (218).

Over the past several years the end use of slab zinc has remained proportionately fairly steady: 40% for die casting, 38% for galvanizing, 13% in brass, 4% as zinc oxide, 3% as rolled zinc, and 2% for other uses. The lowered demand for zinc which appeared during 1974 and continued through 1975 was largely due to weakness in the automotive industry (219). The total consumption of slab zinc in 1975 was 925,293 short tons compared to 1,310,000 short tons in 1974 and 1,504,000 short tons in 1973 (212).

Mine production was approximately 474,000 short tons, down 5% from 1974. Tennessee, Missouri, and New York account for one-half of domestic ore production. New Jersey Zinc began shipping concentrate from its new Elmwood mine in Tennessee in January. American Smelting and Refining shut down the Mascot mill in east Tennessee in October and brought its new Young mill on stream. This mill can process 20% more ore than the Mascot mill it replaced. The Park City mine in Utah began production in May. Callahan Mining Corporation and New Jersey Zinc, through a joint venture, began to develop a zinc-copper deposit in north central Virginia (212).

Imports for consumption of zinc ores and concentrates reached 428,544 short tons in 1975. Canada supplied about two-thirds of the total. Other major suppliers were Mexico, Honduras, and Nicaragua (212).

A new 50,000 tons per year electrolytic zinc refinery is under construction at Bartlesville, Oklahoma, by New Jersey Zinc. This is scheduled to come on stream by May 1976. It will replace the old horizontal retort plant in Bartlesville (212, 219).

A partnership of New Jersey Zinc and Union Miniere SA of Belgium announced plans for a 90,000 tons per year electrolytic refinery at Clarksville, Tennessee. The agreement also covers four zinc mines in mid-Tennessee. The total project will involve $190 million of which $97 million will be allocated to the refinery and $67 million to mine development and ore processing capital requirements. Construction is scheduled to begin in 1976 with completion in 1979. This project replaces the 160,000 tons per year refinery announced last year by New Jersey Zinc (220, 221).

American Smelting and Refining suspended work on its proposed 180,000 tons per year electrolytic zinc plant at Stephensport, Kentucky. The refinery and associated sulfuric acid plant will cost more than $200 million to build. Ralph L. Hennedach, the company president, cited depressed metal markets, increased inventories, steeply rising capital costs, and the difficulty in obtaining capital as reasons for the temporary suspension of the project (222).

A number of projects for development of mines and refineries in Canada and abroad are in various stages of development (223). The unfavorable market has caused postponement of some plans (224).

Texasgulf disclosed significantly higher reserves than previously announced at the Kidd Creek Mine in Timmons, Ontario. These include proven reserves of 86.1 million tons, probable reserves of 51.9 million tons, and inferred reserves of 6.4 million tons. The metal content of proven and probable reserves in 6.11% zinc and small concentrations of copper, silver, and lead (225). A series of lead, zinc, and silver occurrences has been discovered about two miles inside the proposed National Arctic Range in the Brooks Range in Alaska according to the U.S. Bureau of Mines, which calls the deposits "significant" (225).

A 60,000 tons per year refinery is being constructed in Thailand by Thai Zinc. A majority of this company is owned by New Jersey Zinc. The refinery costing $87 million is scheduled for completion in 1977. Of technical interest is the ore which consists of a 2:1 mixture of hemimorphite (zinc silicate) and smithsonite (zinc carbonate). This combination poses unique problems in separating the zinc from the silica without losing too much of the metal. A new process was developed by Electrolytic Zinc of Australia and a 1.1 tons per day pilot plant was operated by New Jersey Zinc at Palmerton, Pennsylvania (226).

The Environmental Protection Agency laid down more stringent regulations for operation of Bunker Hill Company's Kellogg, Idaho, lead-zinc smelter. The new rules require an 82% control on sulfur oxide emissions from the plant. EPA orders superseded less stringent regulations adopted by the state (227).

The Electrical Industry

It is impossible to separate the electrical industry from the over-all energy situation in the United States today. This situation is dominated by the potential shortage of petroleum and natural gas and long-term uncertainties.

The National Research Council's Committee on Mineral Resources and the Environment found it essentially impossible for the United States to achieve independence from external energy sources over the next decade by increasing domestic production of oil and natural gas. Further, if present trends of world consumption continue, the world's resources of these commodities will be substantially consumed in the next 50 years. The committee estimated total U.S. reserves, known plus undiscovered, at 150 billion barrels of oil and 600 trillion cubic feet of natural gas. Current U.S. annual consumption is about 6 billion barrels of oil and 23 trillion cubic feet of natural gas. The difficulty with raising production rapidly is that 70% of the undiscovered reserves lie under the outer continental shelf or in Alaska (228).

A petition to the president signed by 25,000 scientists and engineers claimed that increased use of coal and nuclear energy was the only way to energy independence. Use of these materials presents no problems "incapable of being solved" while alternative energy sources like geothermal, solar, and fusion suffer from geographical and technological limitations (229).

Concern was voiced that neither Congress nor the Administration had shown the required sense of urgency over energy matters. Important problems which require resolution include financing an embryonic coal conversion industry and setting guidelines for a compromise between quick action and environmental acceptability (230).

At a recent Research Directors Conference, reserved optimism was expressed that U.S. technology could overcome the pressing energy problems. Doubts were expressed about the possibility of raising the staggering amounts of capital required for development of domestic resources. Participants in the conference generally agreed that nuclear energy was a major hope for the future, if its development is not derailed by inappropriate environmental concerns, and that geothermal, solar, and other exotic electrical energy alternatives will have little impact on the energy problem for the foreseeable future although these processes may contribute to the energy pool (231).

Energy needs may produce significant shortages of engineering manpower in the near future. The Labor Task Force of Project Independence predicted that the project would create a need for 78,895 engineers, of

various backgrounds, in 1977, and 119,847 by 1990 (232).

An optimistic note is the 8% reduction in energy consumption (in 1974 compared to 1972) achieved by the 26 companies participating in the Manufacturing Chemists Association's plan to report to the Federal Energy Administration. The goal of this program is for the chemical industry to achieve a 15% reduction by 1980 (234).

The Organization for Economic Cooperations and Development has formed the International Energy Agency to deal with difficulties created by tightening fuel supplies. Stated aims include reducing dependence on oil imports and promoting cooperation between oil-producing and oil-consuming countries (235).

US power generation.—Tables 3-7 summarize the production, installed generating capacity, fuel consumption, sales to ultimate consumers, cost, and average usage of electrical energy for the period January to December 1975, except where noted. The figures are preliminary and in some cases partially estimated. For comparison, revised final figures are given for 1974 except for Table 7 where a longer time span is examined.

Table 3. Production of electrical energy* in 1975 (236)
(Billions kW-hr)

Electric utility	1974	1975	% Change
Coal-fired	829.8	844.4	+1.76
Oil-fired	299.3	292.0	−2.43
Gas-fired	319.9	297.1	−7.13
Nuclear	112.7	167.5	+48.62
Other**	2.9	3.4	+17.24
Total generated by consumable fuels	1564.6	1604.4	+2.54
Hydroelectric	260.9	268.2***	+2.80
Total	1825.5	1872.6	+2.58

* Excluding generation of approximately 100 billion kW-hr by private industry.
** Includes production from known geothermal sources, wood, and waste.
*** Estimated.

Table 4. Installed generating capacity by fuel type (236, 237)
(Millions kW)

Fuel type	1974	1975	% Change
Hydro	54.3	55.8	+2.76
Pumped storage	8.8	9.7	+10.23
Fossil fuel	336.9	351.2	+4.24
Nuclear	30.3	38.9	+28.38
Internal combustion	5.0	5.0	0
Combustion turbine	39.3	43.5	+10.69
Total	474.6	504.3	+6.26

Table 5. Fuel consumption by electric utilities (236)

Fuel	1974*	1975*	% Change
Coal, million tons	392.3	402.6	+2.63
Oil, million barrels	536.1	513.4	−4.23
Gas, billion cu ft	3429.2	3123.2	−8.91
Coal equivalent, million tons**	739.7	765.0	+3.42

* For 12 months ending November 1975.
** Includes equivalent for oil, gas, nuclear, geothermal, wood, and waste.

Table 6. Electric utility sales to ultimate consumers in 1975 (236)
(Billions kW-hr)

Consumer	1974	1975	% Change
Residential	555.0	591.1	+6.50
Commercial	392.7	421.1	+7.23
Industrial	689.4	656.4	−4.79
Other	63.7	67.3	+5.65
Total	1700.8	1735.9	+2.06

Table 7. Cost and average usage of electrical power (236)
(Cost ¢/kW-hr)

Consumer	1965	1969	1976
Residential	2.25	2.09	3.25
Commercial	2.13	1.99	3.27
Industrial	0.90	0.91	1.99

(Average use kW-hr/yr)

Consumer	1965	1969	1976
Residential	4,933	6,571	8,246
Commercial	27,399	36,950	49,313
Industrial	1,380,618	1,633,362	1,574,095

The production of electrical energy from all sources in 1975 was up slightly from 1974. This was composed of a decrease in use of gas and oil and an increase in all other sources. A notable increase was in nuclear energy which produced over 10% of the energy generated by consumable fuels.

The distribution of installed capacity shows the increase in nuclear capacity as well as significant increases in combustion turbine capacity and in pumped storage, an increasingly popular method of leveling the highly variable energy demand curve.

The data on fuel consumption, like the energy production data, reflect the decreasing use of gas and oil. They also reflect a slight decrease in the efficiency of fuel utilization. A rather disturbing fact is that during the past decade the coal rate in pounds per kilowatt has steadily increased from 0.858 in 1965 to 0.943 in 1975.

The data on sales to consumers show that residential and commercial consumption increased by about 7% for both categories while industrial consumption decreased by almost 5%.

A partial explanation of this is seen in the cost of electrical energy. The trend of average costs over the past decade is seen in Table 7. The year 1969 was the year of minimum cost when the gradual reduction of costs of electrical energy was replaced by relatively more rapid increase of costs. The policy of offering preferential rates to users of very large quantities is diminishing. In 1965 the cost to the industrial consumer was less than half that of the residential or commercial use; in 1975 it was almost two-thirds. And while everybody's electric bill had gone up, the cost per kilowatt hour to the industrial user in 1975 was more than twice what it had been in 1969 (236).

Energy from fossil fuels.—The President in his State of the Union Message asked for curtailment of the use of imported oil, for a speedy conversion from oil to coal, and for postponement of clean air standards for several years for power plants to help them convert from oil to coal. This fairly well summarized the problems in the area of fossil fuels (238).

The Supreme Court ruled in March that the U.S. Government owns the energy resources of the continental shelf, rejecting the claims of 12 Atlantic coast states (239).

A shale oil project based on Lurgi-Ruhrgas coal gasification technology was announced by American Lurgi Corporation and Dravo Corporation. A 4000 tons per day plant somewhere in the western United States is planned at a cost of $25-$30 million (240).

The Lawrence Livermore Laboratory announced an *in situ* process for removal of oil from deeply buried oil shale with minimum mining and surface disturbances. A cost of $6-$9 per barrel is claimed. The process involves rubblizing the shale in place with explosives followed by underground retorting (241).

The Organization for Economic Cooperation and Development predicted that the industrialized free world would turn more to coal as a source of electric power than to any other energy source over the next

10 years (242). They forecast that coal's share of all electricity generated in the OECD countries would jump to 2836 × 10^9 kW-hr by 1985, a full 22% higher than previous forecasts. By contrast, oil's share will decrease 57%, to 991 × 10^9 kW-hr.

The Energy Supply and Environmental Coordination Act of 1974 gave the Federal Energy Administration broad powers to reduce oil and gas consumption by directing industry to use coal. Potential oil savings, ranging from 0.85 to 1.175 million barrels of oil per day, will be realized by converting utility and industrial power plants to coal, by ensuring that central stations do not convert from coal to oil or gas and by requiring that new central stations have the capability to burn coal (243).

The United States has sufficient coal resources to allow consumption to triple, but a lack of local water resources may prove to be a major difficulty. This problem is expected to become particularly acute in the attempt to develop the largely untapped western coal reserves (245).

The Coalcon coal conversion demonstration plant will be located outside Belleville, Illinois. Coalcon is a joint venture of Union Carbide and Chemical Construction Company. The $237 million plant, financed largely by ERDA, is scheduled to start up in 1990. Some 2600 tons per day of coal will be converted to 4000 barrels of liquid and 22 million standard cubic ft of pipeline-quality gas (246).

Battelle Memorial Laboratories unveiled a new process for removing sulfur from coal. The process involves leaching the coal with sodium hydroxide, which converts both sulfur and part of the ash to soluble forms (247).

According to data released by the EPA at the end of January, electric utilities around the country are operating, building, or planning over 100 systems to control emissions of sulfur oxides from power plant stacks. Of these, the scrubber on Arizona Public Service Company's 115 MW Cholla I Station is the first to meet the National Academy of Engineering's criterion for proven, industrial scale scrubber reliability. The scrubber, developed by Research Cottrell, is a wet limestone/sludge throwaway system. Operational data include over 90% SO_2 removal, 91.5% scrubber availability with 97% boiler availability, and operating cost of 0.6 mills per kW-hr based on 3.78 mill busbar cost. Capital costs are quoted at $50-$60 per kilowatt (248).

Energy from nuclear sources.—Although the operating nuclear capacity was increased in 1975, the overall nuclear picture is mixed. By September of the year seven reactors had been completed during 1975: Calvert Cliffs 1, Annapolis, Maryland (845 MW); Hatch 1, Baxley, Georgia (786 MW); Cook 1, St. Joseph, Michigan (1060 MW); Prairie Island 2, Minneapolis, Minnesota (530 MW), Fitzpatrick, Oswego, New York (821 MW), Fort St. Vrain, Denver, Colorado (330 MW); and Rancho Seco, Sacramento, California (916 MW). Completion was expected during the remainder of 1975 on four more reactors: Brunswick 2, Wilmington, North Carolina (821 MW); St. Lucie 1, Fort Pierce, Florida (810 MW); Millstone 2, New London, Connecticut (828 MW); and Trojan, Portland, Oregon (1130 MW) (250).

The number of nuclear power plants scheduled to go on line between 1976 and 1985 is 128 with a total capacity of 139,000 MW.

During the period September 1974 to September 1975, rising costs forced cancellation or indefinite postponement of seven major plants. One of these plants, consisting of two 1160 MW high temperature gas cooled reactors, was projected to cost over $2.4 billion, or over $1000 per kilowatt. Another was shelved when the cost increase, because of a two year delay in schedule, reached about $800 per kilowatt. Seven plants with a total capacity of 8010 MW were committed during this period. This is the lowest annual figure since the industry really got off the ground (250).

A serious problem which may be hampering growth of fission energy use is the lack of acceptance of nuclear energy by the general public. Although fears of reactor safety have diminished in recent years, public apprehension is now focused on the "back end" of the cycle—the processing of spent fuel to recover plutonium and uranium and the management of radioactive wastes. Further complicating the picture is the corporate reluctance to go nuclear in view of the critical shortage of capital funds, the large investments required for nuclear facilities and the pending shortage of fissionable material, which can be avoided only with substantially increased activity in exploration, mining, and processing (251).

Even more uncertainty surrounds development of the breeder reactor. The Administration's top priority program for development and commercialization of the liquid metal fast breeder reactor is being increasingly attacked by Congress and environmentalists. At the center of the controversy is the proposed Clinch River breeder reactor demonstration plant on which construction is scheduled to start in 1976. Although admitting the value of the reactor in conserving uranium, the environmentalists would like to see the entire program delayed, for as much as 5-10 years, until problems involved in production, transportation, security, and disposal of the large quantities of plutonium involved can be resolved. There is also concern about the safety of the breeder itself (252).

Nuclear commitments outside the United States increased 34% to 294,000 net MW, between the second quarter of 1974 and the first quarter of 1975. Total commitments break down to a 20% increase in operable capacity, a 19% increase in capacity under construction, a 3% decrease in capacity on order, and a 68% increase in capacity in the planning stage (253).

According to Dr. Arnoldo Angelini, President of the National Board of Electric Power in Italy, nuclear plants will generate most of the electrical power in Europe by 1990. Power generated from fossil fuels will decrease from 80% today to less than 30%. In the next 10 years alone $100 billion will be invested in nuclear plants (254).

Other energy sources.—The largest direct hydro unit in the United States, believed to be the largest in the world, was placed in operation. The unit, the 19th generator at the Grand Coulee Dam, is certified at 600 MW but has a rated capacity of 690 MW. Two further units of similar capacity and three 805 MW units will be installed at 6 month intervals (255).

Combustion of industrial wastes and municipal refuse offers the opportunity to conserve fossil fuels and at the same time to eliminate environmental pollution. As experience is accumulated, this practice can be expected to spread. A large facility to generate electricity from municipal waste is to be built in central New Jersey. The plant, based on technology of Von Roll, Limited, of Switzerland, is designed for disposal of 4000 tons of refuse per day with a generating capacity of 110 MW (256). EPA officials have found "significant" levels of bacteria and viruses at Union Electric's prototype refuse powered plant in St. Louis, Missouri. Undaunted, the company plans to start construction on a commercial 8000 tons per day plant to be fed with solid waste (257).

Geothermal energy activities are progressing on a broad front. Activities center around a phenomenon called a geothermal anomaly, a spot in the earth's crust where temperatures are much higher than would normally be expected. Such spots are believed to be related to volcanism caused by crustal plate motion. The geothermal resource may consist of steam, hot water, a mixture of steam and water, or hot rock. Geothermal water is often much more saline than normal ground water (258).

World generating capacity from geothermal sources today is slightly more than 1000 MW. About 500 MW of that comes from one field, the Geysers, in California and most of the remainder from Italy (258).

As the value of steam produced by fossil fuels has increased, geothermal prospecting has been able to at-

tract investment capital. In the most geothermally attractive portion of the United States, the western states, the majority of the land is held by the Government. Federal lands first became available for geothermal exploration in January 1974, when the Geothermal Steam Act of 1970, Public Law 91-581, was implemented. Under this Act, lands are categorized as being either in or out of Known Geothermal Resources Areas (KGRA). Lands within KGRA's are leasable only on competitive bids. In highly prospective areas like the Geysers, industry has shown willingness to enter multimillion dollar bids. Competitive sales have been conducted in California, Utah, Oregon, and Nevada. Other areas may be leased on noncompetitive bids. In January 1974, 2456 applications for noncompetitive geothermal leases were received. While a variety of techniques of geothermal prospecting are in use, wildcat drilling is on the increase. Fuchs and Huttrer have provided a survey of activities and problems in geothermal energy (259).

A major legal difficulty is the continuing question of whether geothermal resources are water or mineral.

According to the U.S. Geological Survey, the nation has geothermal resources capable of producing about 42,000 MW centuries of electricity with recovery costs varying from present levels to more than two times higher (260).

The Electric Power Research Institute has commissioned a $595,000 study to determine whether power conversion techniques in which geothermal hot water is flashed to steam for power use can be cost competitive and still meet environmental constraints. EPRI's program manager for geothermal projects predicts that U.S. use of this resource could triple every 5 years and reach 200,000 MW by the year 2000 (261).

Geothermal energy may not be as clean as once believed. A study of the Wairakei, New Zealand, geothermal steam plant showed that the plant produced nine times the waste heat of a coal- or oil-fired plant and emitted high levels of water vapor, carbon dioxide, sulfur, arsenic, hydrogen sulfide, and mercury compounds (263).

Substantial technological problems face development of geothermal power, and this power source is admittedly not the panacea for the U.S. energy problems, but it can provide a supplemental power resource in the future.

Although radiant energy incident upon the earth from the sun far exceeds the world's present energy needs and although it was the source of much of our present energy reserves, its diffuse nature has thus far made large scale direct conversion of solar energy uneconomical.

A National Solar Energy Program has been organized by ERDA. Under this plan solar would provide 0.8% of the U.S. energy demand by 1985, 7% by 2000, and 25% by 2020. The plan is strongly dependent on progress in research and development and on economic relationships with other energy sources (264).

ERDA is funding the first large scale solar power plant, a 10 MW plant to be located in the southwestern United States within the next 5 years (265).

In a program aimed at developing low cost solar cells, ERDA has selected 16 organizations for contracts. The program is designed to foster industrial capability, by 1985, of producing silicon solar arrays at a market price of $500 per peak kilowatt in place of the $20,000 to $25,000 present day price (266).

Argonne National Laboratory has awarded contracts to seven firms for production of prototype collectors. These will be the first industrial versions of the compound parabolic concentrator being developed by Argonne. The concentrator can be used for generation either of electricity or usable heat (167).

The Solar Energy Research Institute, mandated by Congress in the Solar Energy Research, Development, and Demonstration Act of 1974, is in the process of formation. The new institute was proposed by a National Research Council committee to have a staff of 1400 with an annual budget of $48 million. This is in contrast to the recommendations of the U.S. solar industry, as surveyed by Mitre Corporation, which consists of a staff of 120 and a budget in fiscal 1976 of $6-$10 million. The committee envisions both contributive and supportive roles for SERI (268).

Recent developments in magnetohydrodynamic power indicate that it is still under active investigation in a number of countries. In the Soviet Union, a team of U.S. and Soviet engineers recently completed a continuous test of U.S. built electrodes in a Soviet built 1 MW plant. Cooperation between the United States and the U.S.S.R. began in 1973 and is intended to give U.S. researchers access to facilities not available in the United States (269).

Manuscript received June 23, 1976. This report was presented at the Industrial Electrolytic Division at the Washington, D.C., Meeting of the Society, May 2-7, 1976.

Any discussion of this paper will appear in a Discussion Section to be published in the December 1977 JOURNAL. All discussions for the December 1977 Discussion Section should be submitted by Sept. 1, 1976.

REFERENCES

1. News Release, Chlorine Institute, Feb. 4, 1976.
2. *Chemical and Engineering News*, p. 7, Feb. 9, 1976.
3. *Chemical Marketing Reporter*, p. 4, Feb. 2, 1976.
4. *Ibid.*, p. 4, Feb. 9, 1976.
5. Chlorine Institute, Pamphlet 10, North American Chlor-Alkali Industry Plants and Production Data Book, 1976.
6. *Chemical Week*, p. 7, Dec. 24, 1975.
7. *Ibid.*, p. 27, May 7, 1976.
8. *Ibid.*, p. 9, July 2, 1975.
9. *Chemical and Engineering News*, p. 14, Jan. 19, 1976.
10. *Chemical Age International*, p. 10, Dec. 12, 1975.
11. *Chemical Week*, p. 25, June 11, 1975.
12. *Ibid.*, p. 29, June 18, 1975.
13. *Chemical and Engineering News*, p. 8, Aug. 11, 1975.
14. *Ibid.*, p. 9, June 2, 1975; *Chemical Engineering*, p. 36, June 9, 1975.
15. *Chemical Week*, p. 49, May 7, 1975.
16. *Ibid.*, p. 33, Jan. 28, 1976.
17. *Chemical and Engineering News*, p. 6, March 8, 1976.
18. *Chemical Week*, p. 19, Jan. 14, 1976.
19. *Ibid.*, p. 15, March 17, 1976.
20. *Chemical and Engineering News*, p. 7, March 22, 1976.
21. *Ibid.*, p. 6, May 5, 1975.
22. *Chemical Week*, p. 16, May 7, 1975.
23. *Chemical and Engineering News*, p. 41, March 19, 1975.
24. *Ibid.*, p. 20, July 7, 1975.
25. *Chemical Week*, p. 13, May 28, 1975.
26. *Chemical and Engineering News*, p. 4, June 16, 1975.
27. *Ibid.*, p. 5, June 23, 1975.
28. *Ibid.*, p. 6, July 14, 1975.
29. *Ibid.*, p. 5, Dec. 22, 1975.
30. *Ibid.*, p. 4, Jan. 5, 1976.
31. *Ibid.*, p. 7, Jan. 19, 1976.
32. *Ibid.*, p. 5, Feb. 2, 1976.
33. Current Industrial Reports, Inorganic Chemicals, Dec. 1975, Bureau of Census, U.S. Dept. of Commerce, issued Feb. 1976.
34. *Chemical Week*, p. 9, Feb. 1976.
35. *Electrochemical Progress*, p. 5, Feb. 1976.
36. S. A. Dahl, *Chemical Engineering*, p. 60, Aug. 18, 1975.
37. *Chemical Week*, p. 33, March 24, 1976.
38. F. Hine, Chlor-Alkali Industry in Japan in 1975, Private communication, Jan. 11, 1976.
39. *Chemical Economic Engineering Review*, p. 48, May 1975.
40. *Japan Chemical Week*, p. 5, June 12, 1975.
41. *European Chemical News*, p. 46, Sept. 26, 1975; *Electrochemical Progress*, p. 11, July/Aug. 1975.
42. *Chemical Week*, p. 11, Feb. 25, 1976.
43. *Chemical Marketing Reporter*, p. 5, Feb. 23, 1976.
44. *European Chemical News*, p. 25, March 5, 1976.
45. *Electrochemical Progress*, p. 15, July/Aug. 1975.
46. *European Chemical News*, p. 42, Sept. 19, 1975.
47. *Ibid.*, p. 27, Feb. 27, 1976.

48. *Electrochemical Progress,* p. 9, Jan. 1976.
49. *Chemical Engineering,* p. 123, Nov. 10, 1975.
50. *Electrochemical Progress,* p. 7, Dec. 1975.
51. *Japan Chemical Week,* p. 1, Dec. 25, 1975.
52. *Chemical and Engineering News,* p. 21, March 22, 1976.
53. *Electrochemical Progress,* p. 11, April 1975.
54. *Chemical Engineering,* p. 60, May 26, 1975.
55. *Ibid.,* p. 30, Dec. 22, 1975.
56. *Electrochemical Progress,* p. 9, June 1975; p. 11; May 1975.
57. *Chemical and Engineering News,* p. 12, July 22, 1974.
58. *Chemical Week,* p. 31, Feb. 4, 1976.
59. Mercury in 1975, Annual Preliminary, Mineral Industry Surveys, Bureau of Mines, U.S. Dept. of the Interior, Dec. 19, 1975.
60. Mercury in the fourth quarter, 1975, Mineral Industry Surveys, Bureau of Mines, U.S. Dept. of the Interior, March 2, 1976.
61. Current Industrial Reports, Inorganic Chemicals, Jan. 1975 to Dec. 1975, Bureau of the Census, U.S. Dept. of the Interior.
62. *Chemical Marketing Reporter,* p. 9, Nov. 3, 1975.
63. Potash in 1975, Annual Preliminary, Mineral Industry Surveys, Bureau of Mines, U.S. Dept. of the Interior, Dec. 22, 1975.
64. *Chemical Week,* p. 20, June 25, 1975.
65. *Ibid.,* p. 20, July 2, 1975.
66. *Chemical Week,* p. 12, Nov. 26, 1975; *Chemical Engineering,* p. 85, Dec. 1975.
67. *Chemical Week,* p. 25, March 24, 1976.
68. *Ibid.,* p. 23, March 3, 1976.
69. *Japan Chemical Week,* p. 6, Nov. 21, 1974.
70. Sodium Compounds in 1975, Annual Preliminary, Mineral Industry Surveys, Bureau of Mines, U.S. Dept. of the Interior, Dec. 22, 1975.
71. *Chemical and Engineering News,* p. 30, Dec. 22, 1975.
72. *Ibid.,* p. 11, Feb. 24, 1975.
73. *Chemical Week,* p. 13, May 7, 1975.
74. *Ibid.,* p. 17, Aug. 13, 1975.
75. *Engineering and Mining Journal,* pp. 183-184, March 1975.
76. *Chemical and Engineering News,* p. 10, Nov. 24, 1975.
77. *Ibid.,* p. 9, Sept. 1, 1975.
78. *Chemical Week,* p. 23, Dec. 10, 1975.
79. *Ibid.,* p. 20, Dec. 17, 1975.
80. *Ibid.,* p. 45-47, Aug. 20, 1975.
81. Current Industrial Reports, Inorganic Chemicals, Bureau of Census, U.S. Dept. of Commerce, Jan. to Dec. 1975.
82. *Chemical Marketing Reporter,* p. 9, Oct. 27, 1975.
83. *Canadian Chemical Processing,* p. 10, Jan. 1976; *Chemical Marketing Reprter,* p. 3, June 2, 1975, p. 3, April 28, 1975.
84. *Chemical Marketing Reporter,* p. 21, Jan. 6, 1976.
85. *Ibid.,* p. 29, July 28, 1975; *Journal of Commerce,* p. 5, Sept. 11, 1975.
86. *Chemical Marketing Reporter,* p. 47, Nov. 17, 1976; p. 24, March 1, 1976.
87. *Chemical Industry (London),* p. 438, June 7, 1975; *Electrochemical Progress,* p. 11, July/Aug. 1975.
88. Wall Street Journal, p. 37, Sept. 11, 1975.
89. Pulp and Paper, Canada, p. 121, Nov. 1975; *Industrial Miner (London),* p. 54, Nov. 1975.
90. *Paper Trade Journal,* p. 42, Feb. 1976.
91. *European Chemical News,* p. 11, July 11, 1975; *Chemical Marketing Reporter,* p. 4, July 14, 1975.
92. *Engineering and Mining Journal,* p. 84, March 1976.
93. Aluminum and Bauxite in 1975, Annual Preliminary, Mineral Industry Surveys, Bureau of Mines, U.S. Dept. of the Interior, Dec. 16, 1975.
94. Aluminum Industry in Dec. 1975, Aluminum Monthly, Mineral Industry Surveys, Bureau of Mines, U.S. Dept. of the Interior, March 2, 1976.
95. *Chemical Week,* p. 27, March 3, 1976; *Chemical and Engineering News,* p. 26, March 10, 1975.
96. *Electrochemical Progress,* p. 6, April 1975; p. 5, May 1975.
97. *Chemical Week,* p. 31, June 11, 1975; *American Metal Market,* p. 8, Feb. 3, 1976.
98. *Chemical Engineering,* p. 71, Jan. 5, 1976.
99. *Electrochemical Progress,* p. 5, April 1975.
100. *Chemical and Engineering News,* p. 7, July 14, 1975.
101. *Chemical Week,* p. 13, April 23, 1975; p. 37, Aug. 20, 1975.
102. *Chemical Week,* p. 24, Feb. 4, 1976.
103. *Met. Bulletin (London),* p. 20, Oct. 2, 1975.
104. *Chemical Engineering,* p. 63, July 21, 1975.
105. *Chemical Week,* p. 39, Feb. 25, 1976.
106. *Met. Bulletin (London),* p. 20, March 5, 1976.
107. *Chemical Engineering,* p. 33, June 9, 1975.
108. *Electrochemical Progress,* p. 11, April 1975.
109. *Engineering and Mining Journal,* pp. 181-182, March 1976.
110. *Ibid.,* pp. 136-137, March 1975.
111. *Ibid.,* pp. 42-48, Feb. 1975.
112. *Ibid.,* pp. 52-64, Jan. 1976.
113. Beryllium in 1975, Annual Preliminary, Mineral Industry Surveys, Bureau of Mines, U.S. Dept. of the Interior, Dec. 16, 1975.
114. Chromium in 1975, Annual Preliminary, Mineral Industry Surveys, Bureau of Mines, U.S. Dept. of the Interior, Dec. 22, 1975.
115. Chromium in Dec. 1975, Chromium Monthly, Mineral Industry Surveys, Bureau of Mines, U.S. Dept. of the Interior, Feb. 25, 1976.
116. *Engineering and Mining Journal,* pp. 116-132, March 1975.
117. *American Metal Market,* p. 15, Nov. 19, 1975.
118. *Chemical and Engineering News,* p. 16, June 23, 1975.
119. Copper in 1975, Annual Preliminary, Mineral Industry Surveys, Bureau of Mines, U.S. Dept. of the Interior, Dec. 16, 1975.
120. *Engineering and Mining Journal,* p. 36, July 1975.
121. *Engineering and Mining Journal,* pp. 37-40, Nov. 1975.
122. *Ibid.,* p. 106, June 1975.
123. *Ibid.,* p. 239, Nov. 1975.
124. *Chemical Week,* p. 17, April 16, 1975.
125. *Engineering and Mining Journal,* p. 203, Sept. 1975.
126. *Ibid.,* p. 104, June 1975.
127. *Ibid.,* p. 46, Jan. 1975.
128. *Chemical Week,* p. 21, Feb. 26, 1975.
129. *Engineering and Mining Journal,* p. 40, Feb. 1975.
130. *Ibid.,* p. 58, June 1975.
131. *Ibid.,* p. 56, July 1975.
132. *Ibid.,* p. 50, Aug. 1975.
133. *Ibid.,* p. 58, Sept. 1975.
134. *Ibid.,* pp. 52-64, Jan. 1976.
135. *Ibid.,* p. 64, May 1975.
136. *Ibid.,* p. 21, Jan. 1975.
137. *Chemical Week,* p. 63, Oct. 22, 1975.
138. *Engineering and Mining Journal,* p. 193, Sept. 1975.
139. *Ibid.,* pp. 24-27, Jan. 1975.
140. *Chemical Week,* p. 19, Jan. 22, 1975.
141. *Engineering and Mining Journal,* pp. 131-132, July 1975.
142. *Ibid.,* p. 17, Nov. 1975.
143. *Ibid.,* p. 37, Jan. 1976.
144. *Ibid.,* p. 35, Oct. 1975.
145. *Ibid.,* pp. 89-91, July 1975.
146. *Ibid.,* pp. 27-31, Jan. 1975.
147. *Ibid.,* p. 289, June 1975.
148. *Ibid.,* p. 46, May 1975.
149. *Ibid.,* pp. 31-32, April 1975.
150. *Ibid.,* p. 161, April 1975.
151. *Ibid.,* p. 183, Oct. 1975.
152. *Chemical Week,* p. 17, April 30, 1975.
153. *Chemical Engineering,* p. 51, April 28, 1975.
154. *Engineering and Mining Journal,* pp. 135-136, June 1975.
155. *Ibid.,* pp. 75-86, April 1975.
156. *Ibid.,* p. 101, April 1975; pp. 100-103, June 1975.
157. *Ibid.,* p. 134, June 1975.
158. *Ibid.,* p. 136, June 1975.
159. *Ibid.,* pp. 37-38, Sept. 1975.
160. *Chemical Week,* p. 31, July 23, 1975.
161. *Engineering and Mining Journal,* p. 42, April 1975.
162. *Ibid.,* p. 138, June 1975.
163. Lithium in 1975, Annual Preliminary, Mineral Industry Surveys, Bureau of Mines, U.S. Dept. of the Interior, Dec. 1975.
164. *Engineering and Mining Journal,* p. 179, March 1975.
165. *Chemical and Engineering News.* p. 18, Jan. 26, 1976.
166. *Chemical Marketing Reporter,* p. 21, April 14, 1975.
167. *Journal of Commerce,* p. 5, Nov. 3, 1975.
168. *Chemical Week,* p. 23, May 7, 1975.
169. Magnesium and Magnesium Compounds, Annual

Preliminary, Mineral Industry Surveys, Bureau of Mines, U.S. Dept. of the Interior, Dec. 16, 1975.
170. *Engineering and Mining Journal,* pp. 160-162, March 1976.
171. *Ibid.,* pp. 184-188, March 1975.
172. *Chemical Week,* p. 29, May 21, 1975.
173. *Ibid.,* p. 13, Sept. 10, 1975.
174. *Engineering and Mining Journal,* pp. 42-48, Feb. 1975.
175. *Ibid.,* pp. 52-64, Jan. 1976.
176. *Ibid.,* p. 83, Jan. 1976.
177. Manganese in 1975, Annual Preliminary, Mineral Industry Surveys, Bureau of Mines, U.S. Dept. of the Interior, Dec. 22, 1975.
178. Manganese in Dec. 1975, Manganese Monthly, Mineral Industry Surveys, Bureau of Mines, U.S. Dept. of the Interior, Feb. 26, 1976.
179. *Engineering and Mining Journal,* pp. 135-137, March 1976.
180. *Chemical and Engineering News,* p. 10, March 24, 1975.
181. *Chemical Engineering,* pp. 51-52, Sept. 1, 1975.
182. *American Metal Market,* p. 2, Feb. 10, 1976.
183. *Engineering and Mining Journal,* p. 96 March 1975.
184. Nickel in 1975, Annual Preliminary, Mineral Industry Surveys, Bureau of Mines, U.S. Dept. of the Interior, Dec. 22, 1975.
185. Nickel in Dec. 1975, Nickel Monthly, Mineral Industry Surveys, Bureau of Mines, U.S. Dept. of the Interior, Feb. 26, 1976.
186. Report of the Electrolytic Industries for the year 1974, *This Journal,* **122**, 308C (1975).
187. Financial Times, p. 29, Feb. 17, 1976.
188. Wall Street Journal, East ed., p. 6, Feb. 11, 1976.
189. *World Miner.,* p. 37, Dec. 1975.
190. *Chemical and Engineering News,* p. 21, March 22, 1976.
191. *Chemical Engineering,* p. 60, Jan. 19, 1976.
192. *Ibid.,* April 21, 1975; *Chemical Week,* p. 24, April 30, 1975.
193. *Chemical Marketing Reporter,* p. 9, June 30, 1975.
194. Mineral Facts and Problems, Bureau of Mines, U.S. Dept. of the Interior, 1975 Chapter, In press.
195. Sodium Compounds in 1975, Annual Preliminary, Mineral Industry Surveys, Bureau of Mines, U.S. Dept. of the Interior, Dec. 22, 1975.
196. *Chemical Week,* p. 29, May 21, 1975.
197 Titanium in 1975, Annual Preliminary, Mineral Industry Surveys, Bureau of Mines, U.S. Dept. of the Interior, Dec. 22, 1975.
198. *Chemical Week,* p. 27, June 25, 1975.
199. *Engineering and Mining Journal,* pp. 134-136, March 1975.
200. *Ibid.,* pp. 162-179. March 1976.
201. *Ibid.,* pp. 42-46, Feb. 1975.
202. *Ibid.,* pp. 52-60, Jan. 1976.
203. *Ibid.,* pp. 114-115, Sept. 1975.
204. *Chemical and Engineering News,* p. 5, July 28, 1975.
205. *Engineering and Mining Journal,* p. 167, June 1975.
206. *Chemical Week,* p. 16, July 30, 1975.
207. *Ibid.,* p. 26, Jan. 1, 1975.
208. *Ibid.,* p. 17, April 30, 1975.
209. *Ibid.,* p. 29, May 21, 1975.
210. *Ibid.,* p. 31, May 14, 1975.
211. *Chemical Engineering,* p. 64, July 21, 1975.
212. Zinc in 1975, Annual Preliminary, Mineral Industry Surveys, Bureau of Mines, U.S. Dept. of the Interior, Dec. 17, 1975.
213. *Chemical Engineering,* p. 138, April 28, 1975.
214. *Engineering and Mining Journal,* p. 46, Jan. 1975.
215. *Ibid.,* p. 54, April 1975.
216. *Ibid.,* p. 40, Feb. 1975.
217. *Ibid.,* p. 44, Oct. 1975.
218. *Ibid.,* p. 49, Jan. 1976.
219. *Ibid.,* pp. 96-98, March 1975.
220. *Ibid.,* p. 178, Sept. 1975.
221. *Chemical and Engineering News,* p. 9, June 2, 1975.
222. *Ibid.,* p. 7, June 30, 1975.
223. *Engineering and Mining Journal,* pp. 73-86, Jan. 1976.
224. *Ibid.,* p. 260, Nov. 1975.
225. *Ibid.,* p. 181, Oct. 1975.
226. *Ibid.,* p. 26, Sept. 1975.
227. *Chemical Week,* p. 9, Nov. 26, 1975.
228. *Chemical and Engineering News,* p. 5, Feb. 17, 1975.
229. *Ibid.,* p. 7, Nov. 24, 1975.
230. *Ibid.,* p. 24, Dec. 22, 1975.
231. *Ibid.,* p. 23, April 28, 1975.
232. *Chemical Week,* p. 28, Jan. 22, 1975.
233. *Chemical and Engineering News,* p. 16, May 12, 1975.
234. *Ibid.,* p. 38, May 19, 1975.
235. *Power,* p. 122, Feb. 1975.
236. *Electrical World,* pp. 39-70, March 15, 1976.
237. *Ibid.,* p. 59, March 15, 1975.
238. *Ibid.,* p. 19, Feb. 1, 1975.
239. *Chemical and Engineering News,* p. 9, March 24, 1975.
240. *Chemical Engineering,* p. 81, Dec. 8, 1975.
241. *Power,* p. 151, June 1975.
242. *Electrical World,* p. 43, Feb. 15, 1975.
243. *Power,* pp. 33-35, July 1975.
244. *Electrical World,* p. 19, Feb. 1, 1975.
245. *Ibid.,* p. 39, Jan. 1, 1975.
246. *Chemical and Engineering News,* Aug. 18, 1975; *Chemical Engineering,* Dec. 8, 1975.
247. *Chemical and Engineering News,* pp. 24-25, July 7, 1975.
248. *Electrical World,* p. 21, Feb. 1, 1975; *Power,* pp. 44-46, May 1975.
249. *Chemical and Engineering News,* p. 20, May 12, 1975.
250. *Electrical World,* pp. 35-44, Oct. 15, 1975.
251. *Chemical and Engineering News,* p. 17, June 16, 1975.
252. *Ibid.,* p. 16, June 9, 1975.
253. *Ibid.,* p. 7, May 26, 1975.
254. *Ibid.,* p. 7, March 31, 1975.
255. *Electrical World,* p. 18, Nov. 1, 1975.
256. *Chemical and Engineering News,* p. 17, June 2, 1975.
257. *Chemical Engineering,* p. 81, Dec. 8, 1975.
258. *Chemical and Engineering News,* pp. 21-26, June 9, 1975.
259. *Engineering and Mining Journal,* pp. 89-93, Jan 1975.
260. *Ibid.,* pp. 29-30, Oct. 1975.
261. *Chemical Week,* p. 27, Dec. 24, 1975.
262. *Chemical and Engineering News,* p. 15, June 23, 1975.
263. *Ibid.,* p. 18, March 10, 1975.
264. *Ibid.,* p. 7, Aug. 18, 1975.
265. *Ibid.,* p. 20, June 16, 1975.
266. *Ibid.,* p. 22, Nov. 3, 1975.
267. *Ibid.,* p. 16, July 21, 1975.
268. *Ibid.,* pp. 9-23, Nov. 3, 1975.
269. *Ibid.,* p. 24, Nov. 3, 1975.

Electronegativity, Ionicity, and Effective Atomic Charges

J .P. Suchet

Laboratoire de Chimie Structurale, Université René Descartes, F-75270 Paris Cedex 06, France

ABSTRACT

This paper reviews the concepts of electronegativity and ionicity, together with the concept of effective static atomic charge which is associated with them. It is briefly recalled that the ionicity of a chemical bond has two components: a chemical component linked to the valency of the atoms and to their short distance spatial arrangement, and an electrostatic component linked to their effective charge. In solids, however, the appearance of group vibrations of the atoms also introduces the concept of effective dynamic charge, taking account of dielectric phenomena. Emission, absorption, and diffraction of x-rays are related to these two kinds of effective atomic charges and may be used for evaluating them. The substitution, in the second component of ionicity, of the dynamic charge for the static charge probably defines something different from what is usually called ionicity.

The Concept of Electronegativity

Pauling (1, 2) defined electronegativity χ as the attractive power of an atom for an excess electron with respect to its normal electronic cloud, and calculated it empirically from the bond energies prevailing between the different atoms. Shortly thereafter, Mulliken (3) defined it more rationally as the mean between the ionization potential of the first electron and the electronic affinity of the atom. He then realized that electronegativity depends on the valency and on hybridization, and then inferred that the establishment of a chemical bond between two atoms of different electronegativities gives rise to a transfer of electrons between them, namely the appearance of an effective charge (4).

Sanderson (5-7) continued the work of Mulliken and defined the relative electronegativity χ_r of an atom as the ratio of its compactness C to the compactness C_o of the atom of the isoelectronic rare gas

$$\chi_r = C/C_o = (Z/4.19r^3)/(Z_o/4.19r_o^3) = Zr_o^3/Z_or^3 \quad [1]$$

This concerns a "stability ratio," with low values corresponding to the least electronegative elements (metals), and high values to the most electronegative elements (nonmetals). This ratio naturally depends on the electrical charge supported by the atom. As Mulliken observed, an interatomic bond involves a transfer of electrons to the more electronegative atom. In these conditions, the relative compactness of the two linked atoms are certainly closer than those of the two same atoms when isolated from each other (Fig. 1). Sanderson (6, 7) thus intuitively discovered that the bond between two atoms must correspond exactly to the "equalization of electronegativities" between them. By establishing an arbitrary hypothesis on the electronic transfer occurring in the compound NaF, taken as a reference, he then suggested empirical equations for calculating the initial electronegativities of the atoms.

The importance of the concept of effective atomic charge in defining electronegativity was confirmed and intensified in subsequent investigations. Iczkowski and Margrave (8) defined the latter as the derivative of the energy of the atom with respect to its charge. Hinze and Jaffe (9) calculated the energies of promotion of valency states for a large number of atoms and ions in different states, and combined them with the ionization potentials and the electronic affinities to obtain the "orbital electronegativities" of different σ and π orbitals. Ferreira (10) employed Sanderson's principle of equalization of electronegativities to calculate "effective electronegativities" which took account of hybridization and charge transfer. This matter is dealt with further in this paper.

Key words: electronegativity, ionicity (parameter), charge (electric, effective), bond (chemical).

The Concept of Ionicity

Pauling (11) employed the very old concept of ionicity in his approach to the "valence bond" and suggested evaluating the ionic character of a chemical bond from the difference in electronegativities of the elements involved. He then determined the proportionality constant such that the atomic charges in hydracid molecules were in good agreement with their measured dipolar moment. Syrkin and Dyatkina (12), followed by Coulson (13), subsequently gave a better definition, by incorporating two standardized wave functions corresponding to purely ionic and purely covalent bonds. Hence they wrote the general wave function of a bonding electronic pair as

$$\psi = P_c(M{:}X) + P_i(M^+X^-) = P_c\psi_{cov} + P_i\psi_{ion} \quad [2]$$

where P_c and P_i are probability coefficients and the square of the second can be taken as the ionicity parameter. Equation [2] shows clearly that if one of the electrons of the pair always gravitates in the sphere of influence of the nucleus of the nonmetal X, the position of the other depends on the ionicity parameter and the choice of extreme configurations for

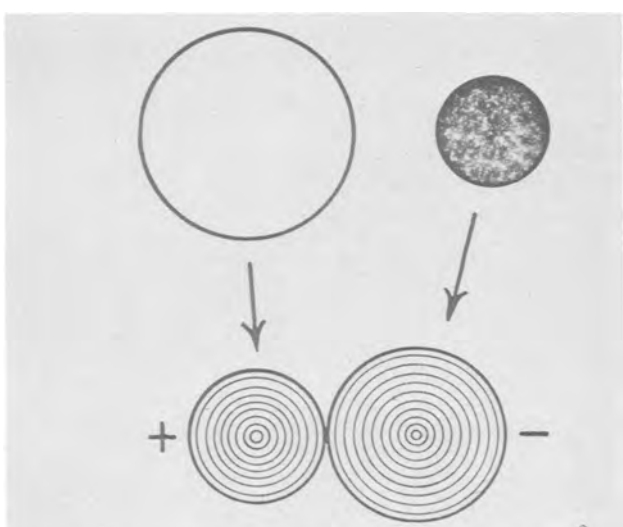


Fig. 1. Schematic representation of the combination of an atom with low electronegativity and an atom with high electronegativity, according to Sanderson (7).

which $P_i = 0$ and $P_i = 1$. The approximation embodied in the concept of effective atomic charge, while requiring the integration of these electrons in the point charges located on the nuclei M and X, establishes a simple link between the charge and the ionicity parameter. For example, in hydracid molecules, the effective charge q_p supported by the hydrogen atom is by definition the hundredth portion of the ionic character percentage mentioned by Pauling.

Nevertheless the definitions of Pauling and Coulson differ widely in the general case. The former takes as the zero ionicity state the homopolar state, in which the atoms present do not support any charge, identical to the covalent state in hydracids. In general, however, the homopolar state already incorporates a certain ionicity. Coulson's definition takes as the zero ionicity state the pure covalent state, in which the electronic distribution is rigorously identical to that of the elements of the same structure. For Pauling, an ionicity equal to zero corresponded to the configuration M^oX^o (neutral atoms) and an ionicity of 100% corresponded to the customary ionic formula $M^{+n}X^{-n}$ (elements M and X of the same valency n) (Fig. 2). During the fifties, however, certain investigations on semiconductor compounds led their authors to conclude that the figures thus determined were too low and failed to permit a satisfactory interpretation of physical properties.

The Nature of Ionicity

Goodman (14) recalled that the neutral formula Zn^oS^o of zinc blende is as divergent from a purely covalent formula $Zn^{-2}S^{+2}$ (in which the distribution of valency electrons on the hybrid orbitals sp^3 is identical to that of diamond) as from the purely ionic formula $Zn^{+2}S^{-2}$. Hence, as he stated, the neutral formula already has an ionic character of 50% as compared with the former, without mentioning the additional ionicity created by the appearance of a positive charge on the zinc atom. This observation perfectly corresponds to the definition embodied in Eq. [2], and Fig. 2 depicts the distinction between the two possible definitions of ionicity.

Suchet (15-20, 22-24) and Suchet and Bailly (21) resumed the definition of Syrkin and Dyatkina, together with that of Coulson, and simplified Eq. [2] by ignoring the permutation of the two electrons in the function ψ_{cov} and by using the monoelectronic orbital ϕ_X as a factor

$$\psi = [(1 - \lambda)^{1/2}\,\phi_M + \lambda^{1/2}\,\phi_X]\,\phi_X \qquad [3]$$

$P_c = (1 - \lambda)^{1/2}$ and $P_i = \lambda^{1/2}$ (Fig. 3). The electrons of the pair thus represented are distributed into $(1 - \lambda)$ electrons on M and $(1 + \lambda)$ electrons on X. If

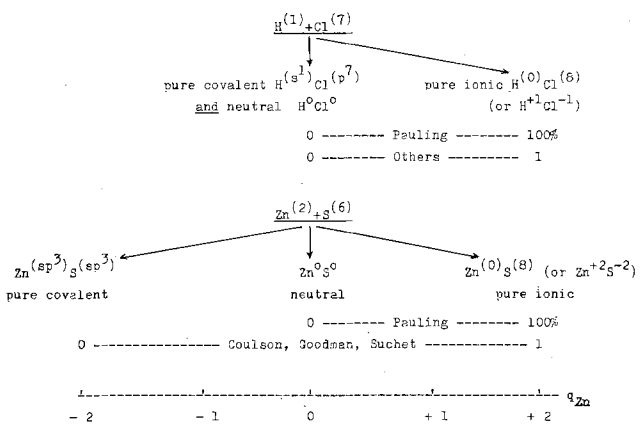


Fig. 2. Comparison of definitions of the ionic character, according to Pauling (11), and of ionicity according to Coulson (13), Goodman (14), and Suchet (15-17). Corresponding values of the charge supported by the zinc atom in the compound ZnS.

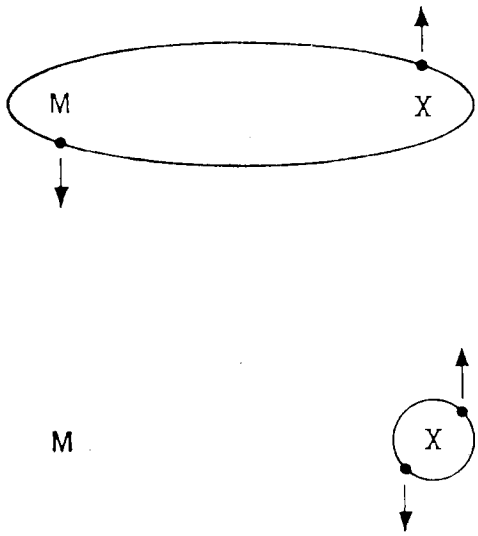


Fig. 3. Diagram showing the purely covalent distribution and purely ionic distribution of electrons in a pair of valency electrons, according to Suchet (15-17).

each atom participates in c bonding pairs, the 2c electrons of an arbitrarily isolated "molecule" MX are distributed into $c(1 - \lambda)$ on M and $c(1 + \lambda)$ on X (general formula). In the neutral or homopolar state, M possesses n electrons (those which it loses in case of ionization) and X thus possesses the remainder, namely $2c\text{-}n$. This distribution can be written as coinciding with the general formula for a special value λ_o, leading to

$$\lambda_o = 1 - n/c \qquad [4]$$

Thus the chemical ionicity of the homopolar state depends only on the positions of the elements M and X in the periodic table of elements and on the type of bond. The heteropolar state is derived from the homopolar state by transferring a certain number q of electrons to an atom X at the expense of the neighboring atoms M. The new distribution is thus $c(1 - \lambda_o) - q$ and $c(1 + \lambda_o) + q$. This can be written as coinciding with the general formula for a value λ, leading to

$$\lambda = \lambda_o + q/c \qquad [5]$$

Hence the ionicity of a bond in a molecule or a crystal is obtained by adding to the chemical ionicity an electrostatic ionicity which is proportional to the effective atomic charge. The latter ionicity corresponds qualitatively to the ionic character of Pauling. For a quantitative representation, it is better to use (25)

$$\Lambda = (\lambda - \lambda_o)/(1 - \lambda_o) \qquad [6]$$

At about the same time, Batsanov (26-27) also arrived at an ionicity composed of two components. The first only depends on the valency of the atom, and on the types and number of the orbitals. The second is linked to the effective charge. For this author, the deformation of the electronic cloud of the anion and its shift toward the cation become increasingly greater with increasing electronegativity χ of the cation and with decreasing ionization potential I of the anion. Hence, in the molecule MX, the valency electrons are thus distributed in the ratio $I/(I + \chi)$ on M and $\chi/(I + \chi)$ on X.

The Concept of Effective Charge

It has just been shown that the concept of effective atomic charge is implicit in the definition of electronegativity as well as in that of ionicity. The question arises as to whether the charge is the same in both cases. *A priori*, one is tempted to reply in the affirmative, since the chemical conception integrating these

two concepts is the same: atoms at rest (hence at low temperature) and absence of external disturbances. Furthermore, the various numerical evaluations, which roughly approach each other, do not contradict an affirmative conclusion.

Returning to the work on electronegativity, it can be seen that if the charge transfers serve to calculate the effective electronegativities of Ferreira (10), the latter can accordingly be used to calculate the effective charges

$$q_F = (\chi_X - \chi_M)/(\Delta\chi_i^+ + \Delta\chi_j^-) \qquad [7]$$

However, the variations $\Delta\chi$ incorporated in this equation can only be obtained from rarely known electronic screen constants. Nevertheless, Tables I and II provide some values of q_F for certain simple compounds. Hinze *et al.* (28) showed that the orbital electronegativity is the derivative of the energy of the atom (in the given valency state) with respect to the electronic occupation of the orbital in question (0, orbital vacant; 1, case discussed by Mulliken; 2, nonbonding pair). This is a parabolic function in which the coefficient k of the quadratic term serves to calculate the effective charge, taking account of Sanderson's principle of equalization of electronegativities

$$q_H = (\chi_X - \chi_M)/2(k_X + k_M) \qquad [8]$$

Yatsimirskii (29) fairly closely follows the reasoning of Hinze *et al.*, but prefers to employ the energy of the orbital instead of that of the atom, thus introducing a correction coefficient α, which is inversely proportional to the interatomic distance M-X

$$q_Y = (\chi_X - \chi_M)/2(k'_X + k'_M + \alpha) \qquad [9]$$

Table I mentions two values of q_Y.

Working in another direction, Suchet (16, 24) and Suchet and Bailly (21) proposed a direct semiempirical calculation of the effective charge from the ionic charge, by considering the progressive deformation of the electronic clouds of the ions M^{+n} and X^{-n} (Z and Z' electrons, ionic radii r and r') when they approach each other (Fig. 4). They inferred the appearance at b of dipoles Δ and Δ', partially neutralized at c with the interpenetration of the two clouds. By dividing the residual charge $\Delta - \Delta'$ equally between the two atoms, the calculation shows that

$$q_S = n - (\Delta + \Delta')/2 \qquad [10]$$

By assuming that the dipolar moments Δx and $\Delta' x'$ are proportional to the products of the mean fields

Table I.

	q_F	q_Y	q_{SB}	q_P
HF	0.33 and 0.45		0.57	0.60
HCl	0.16	0.39	0.18	0.19
HBr	0.12 and 0.10	0.12	0.10	0.11
HI	0.056		0.02	0.04

Table II.

	q_F	q_S	e^*
LiF	0.75	0.78	0.87†
LiCl	0.59	0.63	0.73‡
LiBr		0.27	0.68‡
NaF	0.69	0.79	0.93†
NaCl	0.54	0.71	0.74‡
NaBr	0.43	0.49	0.69†
NaI	0.38	0.27	0.71†
KF	0.70	0.75	0.88‡
KCl	0.49	0.72	0.80†
KBr		0.57	0.76†
KI	0.465	0.42	0.69†

† Szigeti (32).
‡ Hass (34).

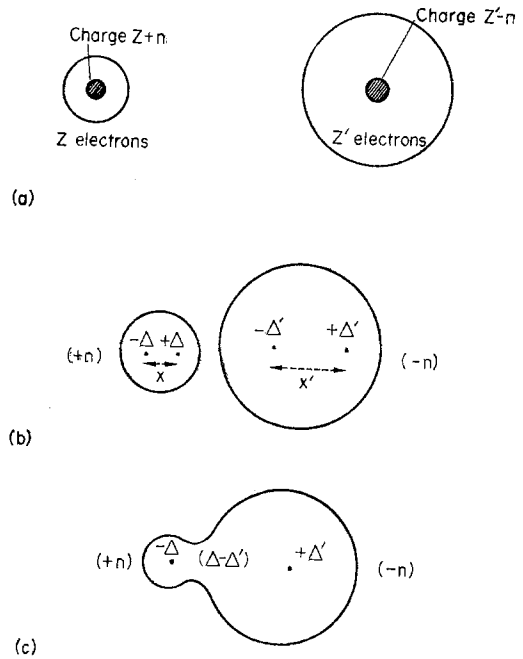


Fig. 4. Diagram showing the mutual polarization of two ions, leading to a partial return to a covalent bond: (a) no interaction, (b) slight interaction, (c) overlap, according to Suchet and Bailly (21) and Suchet (24).

n/r^2 and $-n/r'^2$ by charges Z' and Z, and that the distances x and x' are inversely proportional to r and r', this leads to

$$q_S \sim n[1 - (Z/r' + Z'/r)C^t] \qquad [11]$$

The evaluation of the constant at 0.01185 gives zero charges on the atoms of crystals of the element germanium and on those of the element tin. Suchet and Bailly (21) and Bailly (30) also derived the ionicities λ by direct calculation from the thermochemical data, so that the use of Eq. [5] in the opposite direction leads to

$$q_{SB} = c(\lambda - \lambda_o) \qquad [12]$$

Actually, the values of λ thus obtained are identical to those calculated by Eq. [5] from the charge q_S of Eq. [11], within the range of accuracy of the thermochemical data. Tables I, II, and III provide various values of q_S and q_{SB}. Table I corresponds to hydracid molecules and shows fairly good agreement with the values of q_P derived from the ionic characters of Pauling.

Effective Dynamic Charge

It was observed in the foregoing section that, on the basis of both electronegativity and ionicity, the atomic lattice considered was always at rest. This state of things corresponds to the intuitive conception of chemists, for whom solids are formed by the association of atoms whose electronic clouds undergo a temporary disturbance during the establishment of the bond, following which the nuclei and electrons reach a new equilibrium. We are obliged to say that the exchanges of energy between the solid and the exterior, whether thermal, electromagnetic, or corpuscular energy, can in no conditions be dealt with

Table III.

	q_S	e^*	e_S
InAs	0.68	0.56	0.49
GaAs	0.49	0.51	0.80
AlAs	0.28		1.00
InSb	−0.04	0.42	0.38
GaSb	−0.50	0.33	0.58
AlSb	−0.98	0.53	0.67

within such a framework. The atoms are subjected to forces which draw them away from their equilibrium positions and, owing to interatomic forces, their movements are coordinated and periodic, giving rise to group vibrations (phonons).

To simplify matters, suppose that a molecule MX is arbitrarily isolated and that the interatomic distance R of the two atoms is increased by a quantity x in the direction M-X. This might lead one to believe (31) that the effective static charge $q(0)$ supported by atom M in the initial situation is replaced, in the new situation, by a charge $q(x)$. One of the simplest relationships imaginable between $q(x)$ and $q(0)$ is

$$q(x) = q(0) + xdq/dx \qquad [13]$$

In this case, the dipolar moment can be written as the sum of the relative shift of two atoms with charges $\pm q(0)$ and the transfer of the charge dq/dx over their mutual distance R

$$P = xq(0) + xRdq/dx \qquad [14]$$

By defining an effective dynamic charge e such that $P = ex$, it can be seen that

$$e = q(0) + Rdq/dx \qquad [15]$$

Thus the new charge is due to the sensitivity of the static charge to small relative shifts of the atoms. It is still clear that more complex movements can occur, simultaneously comprising components which are parallel and perpendicular to the direction M-X, and leading to a charge of a slightly different nature. Moreover, the inertia of the nuclei and the electrons leads to a strong influence of the vibration frequency on the values of these charges. Although a single static charge is inferred by the foregoing, all these reasons indicate a large number of dynamic charges, depending on the structure of the solid, the types of vibration, and their frequency.

Comparison of Charges

The dielectric properties of crystals constitute one of the major phenomena indicating the presence of dipoles in solids. If an attempt is made to connect the dielectric constant ϵ (low frequency), ϵ_∞ (high frequency), and infrared dispersion frequencies with microscopic data, one is led to attribute the existence of dipolar moments to the deformation and movement of atoms, which introduce effective dynamic charges e. At the frequencies of visible light waves, these movements are negligible, but at lower frequencies (infrared), they must be taken into consideration.

The first rigorous analysis was the work of Szigeti (32), who employed a theorem of Lorentz relative to cubic crystalline lattices to simplify the calculation of macroscopic polarization by taking account of close neighbors only. This gave for the charge

$$e^2 = 3.4(\epsilon - \epsilon_\infty)MX/[(\epsilon_\infty + 2)/3]^2\lambda_t^2\rho \qquad [16]$$

where M and X are the atomic weights of the two elements making up the compound, ρ is its density in g/cm^3, and λ_t is the reststrahlen wavelength in μm. Equation [16] can be slightly modified if the longitudinal or transversal vibration modes are the only ones in action. This is notably the case of diffusion by optical modes (longitudinal) (33).

Table II concerning alkaline halogenides compares the numerical values given by Ferreira (10) and Suchet (16, 19, 20) for static charges q, with those given by Szigeti (32) and Hass (34) for special dynamic charges e^* derived from the study of infrared spectra. The former reveal a certain consistency, and there is a deviation between charges q and e^*.

The Role of X-Rays

About 12 years ago, Syrkin (35) remarked the difficulty of arriving at accurate values of effective atomic charges, as all the methods employed to determine them relied in various degrees on uncertain theories or empirical calibrations, and called for more direct experimental methods, such as those employing x-rays.

The first investigations carried out in this direction concerned the successive transitions of the electron expelled from layer K by an energy quantum X. In effect, these transitions occurred in the field of an atom whose initial effective charge, depending on its sign, is increased or diminished by a unit. A fine analysis of the absorption spectrum should thus permit an evaluation of this charge. However, Nefedov (36) soon discovered that the spectral shifts of **x** emission lines are far more sensitive to the value of the effective charge. Leonhardt and Meisel (37) recently indicated that the shifts obtained in the latter method by different quantum mechanics calculations using the free ion model provide consistent values, at least with respect to the satellite lines $K\alpha_1$ and $K\alpha_2$.

Sapre and Mande (38-40) observed that the K absorption discontinuity shifts toward the high energy side in certain compounds and toward the low energy side in some others, depending on whether the absorbing atom supports a positive or a negative effective charge. In a series of experiments on arsenic, selenium, gallium, and germanium compounds, they established that the shift is related to an effective static charge q and found that the charges computed by Suchet (20) give a good representation. On Fig. 5 appear three compounds where arsenic is negatively charged (InAs, GaAs, AlAs) and three where it is positively charged (As_2O_3, As_2S_3, As_2Se_3). The shift increases much faster than the charge, approximately as $aq + bq^3$ (41).

On the other hand, Sirota and Gololobov (42) employed diffraction methods to construct electronic density distribution cards for III-V compounds. A graphic integration then permitted them to plot the limits of the electronic clouds at levels below 0.03 electron/Å^3. Table III compares the numeric values given by Suchet (16, 19, 20) for static charges q, those given by Szigeti (32) for dynamic charges e^*, and those given by Sirota and Gololobov (42). It appears that the latter, while not identical to the values of e^*, are nevertheless dynamic charges, and are hence designated by the symbol e. It has already been shown that all the dynamic charges, especially when deter-

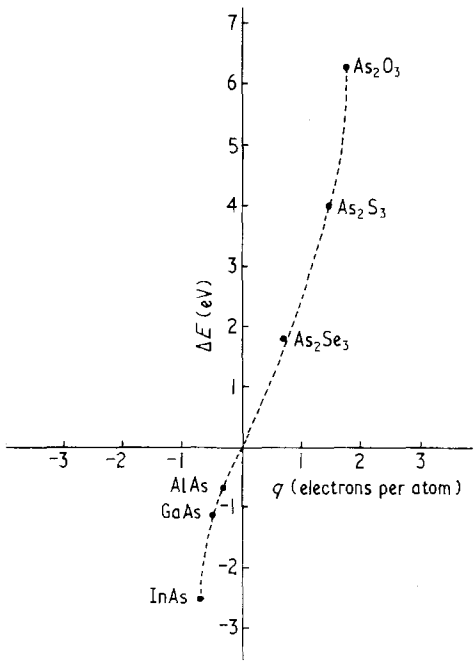


Fig. 5. Plot showing the dependence of the chemical shift ΔE on the effective static charge q_S, according to Sapre and Mande (38).

mined by different methods, are not necessarily equal in value.

Correlations with Properties

Depending on whether the physical phenomena considered leave the atoms in the lattice substantially at rest, or whether they cause them to vibrate, correlations can be found with the static charge q and the associated parameters (such as ionicities λ or Λ), or with dynamic charges such as e^* and the parameters which may be associated with them.

The pairing of ionized interstitial impurities and charged vacancies does not involve any periodic disturbance of the lattice or of the electronic distribution. The diffusion of ions Li^+ in the interstitial sites of III-V compounds reveals a pairing with a negatively charged Sb vacancy for AlSb (43) and GaSb (44), and with a negatively charged Ga vacancy for GaAs (45), indicating that the charges q carried by the metal in these compounds are negative for Al and Ga in the former and positive for Ga in the latter, respectively. Similarly, if no other factor limits the value of the mobility of the majority carriers in a crystal, this mobility must rise with decreasing elementary dipole (and charge q). Hence one can expect to find for InSb, in which the electronic mobility reaches 10^6 cm^2/Vsec, a value of q which is substantially nil, which has been confirmed by ERP (46). This also applies for HgTe. These observations, which besides form the basis of the semiempirical model of Suchet (15, 16), contributed to give the charges q_S a certain credibility from the start. The direct calculation of the ionicities of III-V compounds on the basis of thermochemical data subsequently confirmed their correct order of magnitude (21).

Correlations with static charges also exist for the magnetic interaction energy (20, 23, 47-49), and also, in a less evident manner, for the thermal conductivity of the lattice (20, 50-52) and the semiconduction excitation energy (20, 22, 23, 53).

The dielectric properties, and particularly the measurement of the dielectric constant in alternating current, provide a periodic disturbance of the position of the atoms, which are capable of shifting slightly in the field as far as the infrared frequencies, as well as that of the electronic clouds, which can follow the electrical attractions up to the ultraviolet region. The correlations with the e charges, which appeared very early (32), are in fact at the very source of their definition. This also applies to infrared absorption and emission (32), as well as to infrared reflectivity (34, 54) and piezoelectric properties (55).

The Phillips f_i Parameter

Phillips (56, 57) recently developed a semiempirical model which will not be dealt with in detail here, except to state that it is based on a parameter f_i, which is determined from the dielectric constant at optical frequencies. By his references to the work of Pauling and Mulliken, Phillips clearly showed that he considered this parameter as a classic ionicity corresponding, like the ionic character of Pauling, to the electrostatic component only of Eq. [5]. Hence, in order to compare it with the ionicity defined above, it is necessary to use the form Λ of Eq. [6], which takes, like f_i, the value 0 for the homopolar state and the value 1 for the ionic state. The correlation on which the Phillips' parameter was based, and which was responsible for its initial success, is an exact forecast of the stable region of the structures of blende and wurtzite ($f_i \leq 0.785$) and of rock-salt ($f_i \geq 0.785$) in inorganic compounds.

Table IV provides a comparison of f_i and Λ for compounds in which the nonmetal is relatively light and where the metal has substantially the same dimensions as the nonmetal. The two series of values seem to vary approximately regularly in the same direction.

Table IV.

	Λ	f_i		Λ	f_i
AlAs	0.09	0.274	LiCl	0.63	0.903
GaAs	0.16	0.310	NaCl	0.69	0.935
GaP	0.49	0.374	KCl	0.72	0.953
AlP	0.52	0.307	CaO	0.73	0.913
ZnS	0.54	0.623	MgO	0.73	0.841
CuCl	0.60	0.746	KF	0.75	0.955
			NaF	0.78	0.946
			CaS	0.82	0.902
	Zinc blende			Rock salt	

Table V.

	Λ	f_i		Λ	f_i		Λ	f_i
AlSb	−0.33	0.426	MgTe	−0.04	0.554	LiI	−0.09	0.890
GaSb	−0.17	0.261	ZnTe	−0.02	0.546	NaI	0.27	0.927
InSb	−0.01	0.321	CaTe	0.25	0.394	KI	0.42	0.950
	Zinc blende			Miscellaneous			Rock salt	

Table V, on the other hand, lists compounds in which a small metal atom is associated with a large nonmetal atom, whose electronic cloud is strongly polarizable (antimony, tellurium, iodine). These figures immediately reveal a large, significant divergence, as the periodic, highly rapid disturbances of the large electronic clouds greatly reduce their polarizability. The ionicity $\Lambda = f(q)$ calculated from a static charge reflects strong polarization, causing a return of electrons to the metal atom, this process becoming more intense as the atom is smaller and highly charged. The negative values simply imply that the compound is more covalent than the homopolar state selected as a reference (AlSb has practically four electrons per atom, like diamond). On the contrary, the Phillips parameter reflects practically no polarization. The value of 0.321 for InSb is a medium value and does not stand out in any way from that of the other III-V compounds. In the previous section, it was shown that no static electric dipole could exist in this compound. Hence the matter involves a function $f_i = f(e)$ calculated from a dynamic charge, as the author remarked recently (25). Moreover, Lawaetz (58) had emphasized the close relationship between f_i and e^*.

Conclusion

Although the physical models were greatly improved during the last fifty years, they are still unable to represent the large variety of chemical compounds (59). The concept of effective atomic charge is typically the kind of approximate model which the chemists strongly need and its future is promising because, although the static charge is derived from the old concepts of electronegativity and ionicity, the dynamic charge has several links with the new physical ideas. Equation [15] establishes between the charges q and e a simple relation which schematizes their roles.

From the point of view of effective atomic charge, the controversy prevailing a few years ago between Phillips (60) and Pauling (61) seems meaningless, as the latter used for the ionicity a function $f(q)$, although the former introduced a function $f(e)$ for which the term "dynamic ionicity" would probably be more adequate.

Manuscript received Feb. 3, 1976.

Any discussion of this paper will appear in a Discussion Section to be published in the December 1977 JOURNAL. All discussions for the December 1977 Discussion Section should be submitted by Aug. 1, 1977.

Publication costs of this article were assisted by the Université René Descartes.

REFERENCES

1. L. Pauling and D. M. Yost, *Proc. Natl. Acad. Sci. U.S.A.*, **14**, 414 (1932).

2. L. Pauling, *J. Am. Chem. Soc.*, **54,** 3570 (1932).
3. R. S. Mulliken, *J. Chem. Phys.*, **2,** 782 (1934).
4. R. S. Mulliken, *ibid.*, **3,** 573, 586 (1935).
5. R. T. Sanderson, *Science*, **114,** 670 (1951).
6. R. T. Sanderson, *J. Am. Chem. Soc.*, **74,** 272 (1952).
7. R. T. Sanderson, *J. Chem. Educ.*, **29,** 539 (1952); *ibid.*, **31,** 2, 238 (1954); *ibid.*, **32,** 140 (1955).
8. R. P. Iczkowski and J. L. Margrave, *J. Am. Chem. Soc.*, **83,** 3547 (1961).
9. J. Hinze and H. H. Jaffe, *ibid.*, **84,** 540 (1962).
10. R. Ferreira, *Trans. Faraday Soc.*, **59,** 1064 (1963).
11. L. Pauling, "The Nature of the Chemical Bond," Cornell University Press, Ithaca, New York (1945).
12. Y. K. Syrkin and M. E. Dyatkina, "Structure of Molecules," Butterworths, London (1950).
13. C. A. Coulson, "Valence," Clarendon Press, Oxford (1952).
14. C. H. L. Goodman, *Nature (London)*, **187,** 590 (1960).
15. J. P. Suchet, International Conference on Semiconductor Physics, Praha, 1960, *Czech. J. Phys.*, **11,** 904 (1961).
16. J. P. Suchet, *J. Phys. Chem. Solids*, **21,** 156 (1961).
17. J. P. Suchet, Thesis, Paris (1961).
18. J. P. Suchet, "Curso de compostos semicondutores," p. 25, Centro Tecnico de Aeronautica, Sao Jose dos Campos, S.P., Brazil (1963).
19. J. P. Suchet, Gordon Conference on Chemistry and Metallurgy of Semiconductors, Tilton, New Hampshire (1964).
20. J. P. Suchet, "Chemical Physics of Semiconductors," p. 114, Van Nostrand, London (1965). Polish Translation, P.W.N., Warshaw (1966). Russian Translation, Izd. Metallurgiya, Moscow (1969).
21. J. P. Suchet and F. Bailly, *Ann. Chim. (Paris)*, **10,** 517 (1965).
22. J. P. Suchet, Séminaires de Chimi et de l'Etat Solide," J. P. Suchet, Editor, Vol. 1, p. 37, S.E.D.E.S., Paris (1969).
23. J. P. Suchet, "Crystal Chemistry and Semiconduction in Transition Metal Binary Compounds," p. 18, Academic Press, New York, (1971).
24. J. P. Suchet, "Electrical Conduction in Solid Materials," p. 32, Pergamon Press, Oxford (1975).
25. J. P. Suchet, *C. R. Acad. Sci. (Paris)*, *Ser. C*, **278,** 1361 (1974).
26. S. S. Batsanov, "Elektrootritsatel'nost' elementov i khimicheskaya sviaz'," p. 104, Izd. sibirsk. otd. Akad. Nauk SSSR, Novosibirsk (1962).
27. I. A. Ovryannikova and S. S. Batsanov, Sb. Nauchn. Tr., Inst. Biol., Akad. Nauk B. SSR, **11,** 93 (1966).
28. J. Hinze, M. A. Whitehead, and H. H. Jaffe, *J. Am. Chem. Soc.*, **85,** 148 (1963).
29. K. B. Yatsimirskii, *Zh. Eksp. Teor. Khim.*, **1,** 41 (1965).
30. F. Bailly, *J. Phys.*, **27,** 335 (1966).
31. J. P. Suchet, *C. R. Acad. Sci. (Paris)*, **258,** 2305 (1964).
32. B. Szigeti, *Trans. Faraday Soc.*, **45,** 155 (1949).
33. H. B. Callen, *Phys. Rev.*, **76,** 1394 (1949).
34. M. Hass, *J. Phys. Chem. Solids*, **24,** 1159 (1963).
35. Ya. K. Syrkin, *Usp. Khim.*, **31,** 397 (1962).
36. V. Nefedov, *Phys. Status Solidi*, **2,** 904 (1962).
37. G. Leonhardt and A. Meisel, *J. Chem. Phys.*, **52,** 6189 (1970).
38. V. B. Sapre and C. Mande, *J. Phys. C.*: **5,** 793 (1972).
39. V. B. Sapre and C. Mande, *J. Phys. Chem. Solids*, **34,** 1351 (1973).
40. V. B. Sapre and C. Mande, *Indian J. Pure Appl. Phys.*, **12,** 74 (1974).
41. J. P. Suchet, *C. R. Acad. Sci., Ser. C*, **281,** 87 (1975).
42. N. N. Sirota and E. M. Gololobov, *Dokl. Akad. Nauk SSSR*, **156,** 1075 (1964).
43. F. Kover and A. Quilliet, *C. R. Acad. Sci. (Paris)*, **244,** 1739 (1957).
44. H. J. Hrostowski and C. S. Fuller, *J. Phys. Chem. Solids*, **4,** 155 (1958).
45. C. S. Fuller and K. B. Wolfstirn, "Proceedings of International Conference on Physics of Semiconductors," Exeter, (1962), p. 745, Inst. Phys. & Phys. Soc., London (1962).
46. M. Guéron, *Phys. Rev. A.*, **135,** 200 (1964).
47. J. P. Suchet, *C. R. Acad. Sci. (Paris)*, **253,** 2490 (1961).
48. J. P. Suchet, *J. Phys. Rad.*, **23,** 497 (1962).
49. F. Bailly and J. P. Suchet, "Séminaires de Chimi et de l'Etat Solide," J. P. Suchet, Editor, Vol. **1,** p. 65, S.E.D.E.S., Paris (1969).
50. P. Leroux-Hugon, M. Rodot, and J. P. Suchet, *C. R. Acad. Sci. (Paris)*, **254,** 1250 (1962).
51. J. P. Suchet, H. Rodot, P. Leroux-Hugon, and M. Rodot, *Adv. Energy Conv.*, **3,** 569 (1963).
52. N. Xuan Xinh, *C. R. Acad. Sci. (Paris)*, **258,** 2292 (1964).
53. J. P. Suchet, *ibid.*, **255,** 1444 (1962).
54. M. Hass and B. W. Henvis, *J. Phys. Chem. Solids*, **23,** 1099 (1962).
55. M. Zerbst and H. Boroffka, *Z. Naturforsch., Teil A*, **18,** 642 (1963).
56. J. C. Phillips, *Rev. Mod. Phys.*, **42,** 317 (1970).
57. J. C. Phillips, "Bonds and Bands in Semiconductor," Academic Press, New York (1973).
58. P. Lawaetz, *Phys. Rev. Lett.*, **26,** 697 (1971).
59. J. P. Suchet, *Bull. Soc. Chim. Fr.*, No. 1-2, 3 (1975).
60. J. C. Phillips, *Phys. Rev. Lett.*, **22,** 645 (1969).
61. L. Pauling, *ibid.*, **23,** 480 (1969).

JOURNAL OF THE ELECTROCHEMICAL SOCIETY

ELECTROCHEMICAL SCIENCE AND TECHNOLOGY

MAY 1977

The Electrochemistry of Some n-Heptylviologen Salt Solutions

Raymond J. Jasinski*

Texas Instruments Incorporated, Dallas, Texas 75222

ABSTRACT

n-heptylviologen dibromide, and other viologen derivatives, form insoluble, stable, adherent, and colored radical cation salts when reduced cathodically from aqueous solution. As a result, such compounds are under study as the basis for alphanumeric displays. The presence of bromide ion in these solutions results in a number of undesirable side effects which can be minimized, in part, by replacement of bromide with dihydrogenphosphate anions. During these experiments it was found that the anion and viologen concentrations determined the potential at which the n-heptylviologen radical cation was formed and the adherence of the film. The metal substrate influenced the kinetics of side reactions, and the film adherence. The possibility of specific chemical interaction of HPO_4^{-2} with the radical cation is suggested by the data.

The "viologens" (1) are alkyl derivatives of 4,4′ dipyridyl. The dimethyl and diethyl compounds have been used as soluble redox potential indicators in biological systems (2), and as herbicides (3, 4) (the dimethyl compound is discussed in the literature in this context under the name "paraquat"). The electrochemistries of these compounds in aqueous solution are discussed in Ref. (10)-(12), (17), and (18). The general sequence of reaction is reduction of the dication to a stable, soluble, blue radical cation, followed, at more negative potentials, by reduction of the radical cation and/or the dication to the nominally colorless compound. It was recently shown (5, 16) that cathodic reduction of the longer chain alkyl derivatives yields a colored radical cation that is also stable in water and, in particular, is insoluble, adheres to the substrate on which it was formed, and can be anodically oxidized back to the dication. A number of these compounds are now being considered as active ingredients for "electrochromic" alphanumeric displays. Cathodic reduction of N,N′ diheptyl-4,4′ dipyridinium dibromide, potassium bromide solution yields an insoluble red violet film (5, 13, 16); reduction of N,N′ di(p-cyanophenyl)-4,4′ dipyridinium dichloride solution yields an insoluble green film (6).

The present paper discusses some properties of n-heptylviologen redox processes as they are influenced by the electrolyte anion and by the metal substrate at which the charge transfer takes place. This paper does not deal with long term effects, such as aging of films, or with low temperature effects.

Experimental

The term "diradical" will be used to indicate the two-electron reduction product of the viologen dication, as it is present on the electrode surface. Little information is available in the literature on whether or not these two electrons are paired. This question, relative to soluble reduced viologens, is discussed in Ref. (18) and (20); magnetic measurements on soluble dibenzyl-viologen (21) indicated that the two-electron reduction compound was diamagnetic.

The equipment used in these studies included the following: Wenking ST72 potentiostat, Wenking VSG72 scan generator, PAR digital coulometer, Keithley 616 digital electrometer, TI No. 341 recorder, Lab Con Company glove box.

The glass test cell was of the standard three-compartment design; a glass frit separated the counterelectrode compartment from the working electrode; a capillary, within 1 cm of the working electrode, isolated the PermaProbe reference electrode. The test cell and the glove box were deaerated with nitrogen which had been passed over copper at 300°C.

Open-circuit ("equilibrium") potentials were recorded 5-7 min after depositing a nominal 2 mC/cm² of radical cation film at potentials positive to those for diradical formation. No attempt was made to control cell temperature during these studies nor to confirm the day-to-day reproducibility of the PermaProbe reference electrode.

Because of the chemical reaction between the diradical and the dication, it was not possible to obtain open-circuit potentials that were stable and were not mixed potentials. Therefore the diradical formation potential was taken from the constant current charging curves. To minimize the influence of ohmic effects, the value recorded was that potential halfway between the cathodic and anodic potential plateaus. This technique, in spite of its lack of rigor, was also found to be necessary for obtaining potentials of poorly adherent radical cation films.

The n-heptylviologen dibromide was synthesized in-house from dipyridyl and n-heptylbromide (12); NMR indicated no detectable monosubstituted dipyridyl, excess heptylbromide or dipyridyl; the infrared spectra (KBr pellets) for this synthesized viologen were identical to those taken on the small samples of purchased material.

Bromide ion was replaced with the various other anions of interest via passing an aqueous solution of the viologen dibromide down a column of anion exchange resin (Amberlite 1RA-400) in the appropriate form. We were not successful in isolating solid salts other than the bromide. The anions which were found to be compatible with the viologen and its reduction products were Br^-, $H_2PO_4^-$, SO_4^{-2}, F^-, formate, and

* Electrochemical Society Active Member.

Key words: displays, electrochromics, dipyridinium salts, radical cations, colored films.

acetate; Br^-, Cl^-, BF_4^-, and ClO_4^- viologen solutions have been studied by others (7). Bicarbonate, at pH 7.5, slowly hydrolyzed the viologen; BH_4^- and CN^- discolored viologen bromide solutions; PF_6^-, SbF_6^-, AsF_6^-, and SCN^- generated precipitates on addition to n-heptylviologen solutions. Nitrate chemically oxidized the viologen radical cation.

The metal electrodes used were platinum (Corning No. 476060), silver (Corning No. 476065), and gold foil. The gold was cleaned by anodization in KCN solution, the only procedure found effective after the viologen diradical had been deposited on the gold electrode surface in bromide solution.

The negative potential limits, at pH 5.5, were −740 mV for gold, −540 mV for platinum, and −600 mV for silver, as measured by the irreversible generation of cathodic charge. The reaction is, of course, the generation of molecular hydrogen; the H_2/H^+ electrode potential *vs.* the PermaProbe at pH 5.5 was measured (14) as −520 mV. Obviously the potential range available for studying the viologen radical cation films on platinum is limited. Nevertheless (see Table I), there is a sufficiently large potential difference between viologen reduction and hydrogen evolution, that films can be formed, at least in some electrolytes; such deposits have been reported from fluoride, Br^-, Cl^-, BF_4^-, and ClO_4^- solutions (7). It was also found here that short excursions to −1V, in the presence of n-heptylviologen dication, did not yield visible hydrogen gas or a defined plateau on the constant current charging curve. A classical technique for increasing the overvoltage for hydrogen evolution from active metals is amalgamation of the surface with mercury. This was done with platinum by cathodization in mercurous ion solution. The electrode surface so prepared did not generate hydrogen during the 24 hr hold at −600 mV, as had the original platinum electrode; radical cation films were stable on this amalgamated surface when formed within the potential range of −450 to −850 mV.

The anodic limits of these metals were set by the oxidation of the electrode rather than the electrolyte. Silver is the least noble metal studied; reaction took place at +87 mV in 0.3M KBr^-, and at +26 mV in 2M $H_2PO_4^-$. Although the silver/salt reactions were reversible, the metal-to-salt-to-metal cyclic process tarnished the silver surface via the finely divided silver so formed. The initiation of gold oxidation in the bromide and phosphate solutions occurred at nominally the same potential (+700 mV). At higher potentials, in bromide, the electrode discolored and finally bromine evolution was observed; gold did not visibly discolor in phosphate at any potential.

Results and Discussion

Shown in Table I are the reduction potentials for n-heptylviologen dication as a function of anion and metal substrate. The least negative number for each pair of potentials is the steady-state open-circuit potential for the metal coated with a film of radical cation; the more negative potential is that for the radical cation/diradical reaction; for reasons discussed above, only two significant figures are listed for the potential values.

Thus, it is the anion rather than the metal substrate which determines the redox potential; within the accuracy of the data, the potentials of the radical cation formation, for a given anion, were independent of the metal substrate on which the film was formed.

The physical properties of the radical cation film also depended on anion. For example, radical cation films generated on gold and silver from formate solution showed an obvious tendency to "recrystallize" on open circuit. The electrode initially covered uniformly with radical cation salt would, within a short time, become lighter at the edges and darker in the center of the electrode. Addition of formate to phosphate solutions resulted in radical cation formation on both gold and silver electrodes, which also showed this recrystallization effect; the effect was not observed in the original phosphate solution. (Measurements could not be taken on platinum since formate oxides at −470 mV.)

"Well-behaved" radical cation films were generated from viologen bicarbonate solutions; these were adherent, stable, and free of recrystallization effects. However, the minimum pH possible with bicarbonate was 7.5, and slow hydrolysis of the viologen dication became obvious after a few days.

Acetate was investigated briefly. Radical cation films formed from this solution were stable if the salt concentration was at or above 0.5M; films generated from 0.3M acetate slowly lost adherence and drifted off into the solution as a blue haze.

The metal was not entirely without effect however. Of interest are the observations noted in Table I for gold, platinum, and silver electrodes in fluoride and sulfate solutions of the n-heptylviologen dication. As reported by others (7), stable red violet films were obtained by reduction on platinum from fluoride solutions. We have found the same to be true for platinum and silver in sulfate solution. However, color was not found when gold was cathodized in either viologen solution, yet the charging curves showed well-defined plateaus on cathodization and on anodization. The addition of 2*N* KF to a phosphate/formate viologen solution completely suppressed the color normally generated on gold electrodes. The red violet film formed on silver from fluoride was not all that stable, slowly converting over to a blue haze which floated away from the electrode surface. This did not happen with platinum, nor was this blue material formed from a gold electrode. The mechanism involved has not been established.

Stable "well-behaved" radical cation films were obtained with phosphate solutions of the appropriate pH; the remainder of this paper discusses the electrochemistry of the n-heptylviologen/phosphate system, using the behavior of the same viologen in bromide as reference (5, 7).

Unlike the n-heptylviologen bromide electrode, the properties of n-heptylviologen phosphate are pH dependent. The trends observed in formation and equilibrium potentials were in agreement with the solubility product mechanism (7) and the sole involvement of monovalent phosphate in controlling the radical cation concentration. Fitting the measured potentials for ten viologen/dihydrogenphosphate solutions (pH 5-7.5) to the Nernst equation resulted in an E_0 of -357 ± 6 mV (average error) *vs.* PermaProbe (or −147 *vs.* NHE); K_{12} for the dihydrogenphosphate/hydrogenphosphate equilibrium was taken as 6.71 (15). The potential for the second electron reduction, yielding the neutral diradical, was in the range of −750 to −800 mV, and was independent of pH, viologen concentration, and total phosphate concentration.

The dynamics of the viologen phosphate electrode are illustrated by the charging curve shown in Fig. 1, for 0.036M viologen, 2M phosphate, pH 6 on gold at a constant 0.1 mA/cm^2. In most of its features, this curve

Table I. Reduction potentials for n-heptylviologen salts

Anion	Potentials (mV *vs.* PermaProde) Au		Pt		Ag	
Br^- (0.3M)	−420	−730	−430	(<−600)	−430	−700
$H_2PO_4^-$ (2M)	−390	−770	−390	(<−600)	−390	—
Formate (0.4M)	−570	−650			−550	−670
HCO_3^- (1M)	−490	−680			−500	−670
Acetate (0.5M)	−550	−650				
F^- (1M)*	−540 (no color)	−600	−590		−530	
SO_4^{-2} (0.3M)	−540 (no color)	−650	−570*	−620*	−520	−640

* Millimolar viologen.

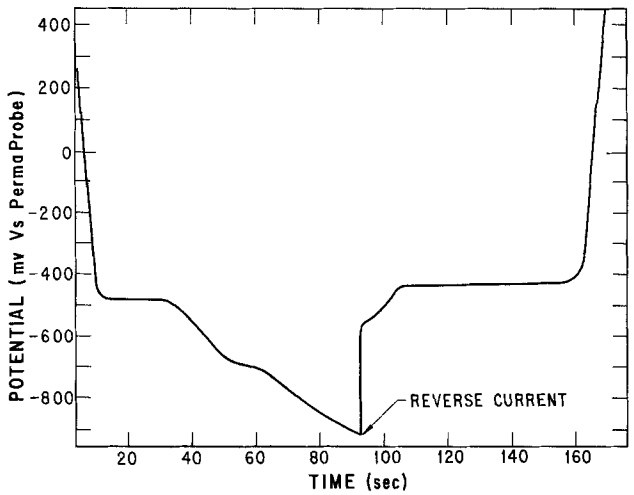


Fig. 1. Shown is a charging curve taken on gold at 0.1 mA/cm² in pH 6 molar phosphate containing 0.036M n-heptylviologen dication. At zero time the current was made cathodic; at nominally 92 sec the current direction was reversed.

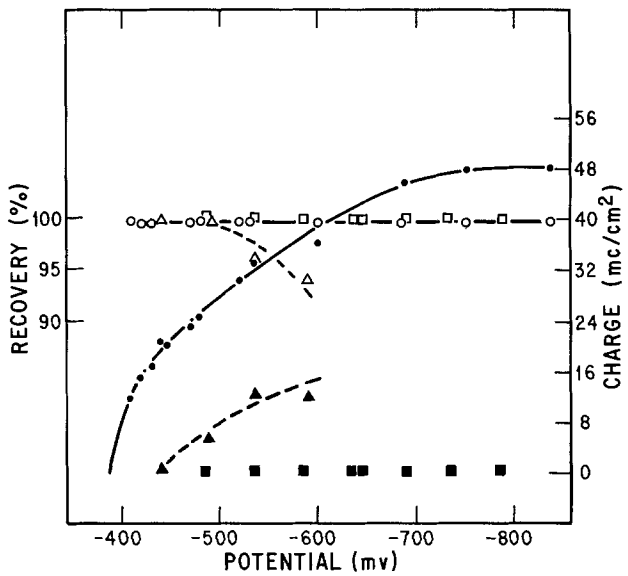


Fig. 2. Plotted vs. potential are the percent cathodic charge recovered anodically (open symbols) and the total cathodic charge passed (closed symbols). The electrode was gold, scanned at 20 mV/sec from +100 mV to the potential listed and back to +100 mV. The solutions were (○) 0.01M n-heptylviologen in 2M phosphate, pH 5.5, (△) 0.02M n-heptylviologen in 0.3M KBr, and (□) 0.2M n-heptylviologen in 0.3M KBr.

resembles closely those obtainable in KBr/viologen solutions. Two well-defined cathodic plateaus were observed, associated with the dication/radical cation and radical cation/diradical reactions. The disparity in lengths of the corresponding anodic and cathodic plateaus is due, presumably, to the intervening chemical reaction of the diradical with the dication (16); some of the remaining diradical is, obviously, oxidizable anodically. As the potential rises, here at 160 sec, the electrode cleared of the last traces of color. It is in this aspect that these phosphate charging curves differ from those taken in KBr. In bromide solution containing essentially the same amount of viologen, color remained visible to at least +300 mV and the ascending branch of the anodic curve was well spread out along the X axis. When the cathodic charging in bromide solution was restricted to the first plateau, complete erasure was obtained before the anodic curve rose to +300 mV. This restriction on potential avoided the diradical process, but also decreased the amount of charge passed into the electrode. The latter was the dominant factor as shown by the following results.

The experiment consisted of a series of cyclic voltammograms from +100 mV to a given potential and back at 20 mV/sec; the potential was then held at +100 mV until the coulometer stopped counting anodic charge for 60 sec. In Fig. 2 are six curves which relate the percent cathodic charge recovered as anodic charge (the open symbols) and the total input cathodic charge (closed symbols) with the negative potential limit of the cyclic scan.

Under these conditions, then, it was possible to anodize totally the high charge capacity radical cation films formed from the phosphate electrolyte. However, total anodization was not achieved for the radical cation films generated from 0.02M viologen/KBr, even though the negative limit of the potential sweep was kept positive of that required for diradical formation. Repeating these experiments but with a lower viologen concentration resulted in less cathodic charge (0.8 mC/cm²) and greater reversibility. Thus, within the accuracy of the coulometer and the background charge correction, the over-all reversibility of the radical cation redox process in 0.02M viologen bromide solution is more sensitive to the quantity of charge passed, *i.e.*, the thickness of the film than to the potential limit of formation.

To further test the effective reversibility of the high charge content deposits formed from phosphate solution, a series of fifteen repetitive cycles was made between +100 mV and −431, −481, and −531 mV each; no hold period was used; the total cathodic charge input per cycle was essentially as shown in the figure. Within the accuracy of the experiment, the cumulative anodic charge was equal to the total input cathodic charge.

Although anodization of the radical cation film formed out of the dilute viologen/KBr solution was essentially complete to the coulometer, and independent of the negative potential limit, a side reaction did become visible at potentials more negative than −732 mV, *i.e.* the accumulation of black spots on the gold surface. This effect is related to the formation of the diradical which occurs in this potential region (Fig. 1).

The electrode material and solution composition also affected the side reaction. This spot generation phenomenon was not observed in phosphate solution on gold over the entire potential range, or on platinum in the same bromide solution over the entire potential range.

(Repetitive scans of the phosphate solution into the diradical region did generate spots eventually. It has not yet been established whether this cosmetic effect is inherent to the gold/viologen system or whether this was due to an impurity generated electrochemically at the counterelectrode. There is some support for the latter, in that phosphate solutions cycled in the test cells described did "age," particularly when the contents of the counter and working electrode compartments were combined. In these solutions freshly cleaned gold and platinum electrodes showed the discolorations while freshly prepared phosphate solutions did not yield discoloration on the same electrodes. In any event, gold cathodized in fresh phosphate viologen solutions is less affected by side reaction discoloration than gold cathodized in fresh viologen bromide solutions.)

Positive potential excursions also had an effect on the cosmetics of the viologen redox processes. It was observed that prior oxidation of the gold electrode in KBr at +450 to +650 mV resulted in the generation of residue and spots on subsequent reduction at the dication/radical cation plateau. These spots were slow to clear on anodization and reappeared on subsequent cathodization. Similar results were observed in phosphate solutions at and above +750 mV. Degradation in

cosmetics was found in phosphate for pure and amalgamated platinum that had been anodized at potentials in excess of +600 mV. Such electrodes, subsequently cathodized, developed blue black spots and a yellow, oil-like film which could not be removed electrochemically, but could be wiped off physically. Pulsed anodization of platinum to +1.2V produced a green yellow material on the surface which was extremely adherent.

Besides potential-dependent side reactions, there are also chemical side reactions. Consider the following. The color, adherence, and general appearance of the viologen radical cation/phosphate films formed at and below pH 5.5 were comparable to those of viologen radical cation in KBr. At higher pH values this was not the case. The color of the radical cation films formed in pH 6 phosphate were lighter than at the lower pH values; no problem was noted with adherence. The electrode behavior in pH 7, molar phosphate was inferior to that at pH 6, in that, on open circuit, a blue haze slowly developed about thick deposits of radical cation film. Although the dihydrogenphosphate at pH 7 is only 34% of the total phosphate (15), the $H_2PO_4^-$ concentration was still 0.34M; at pH 6, 0.1M phosphate was sufficient to form a stable, adherent radical cation film with 0.036M viologen. At pH 7.5 [14% of the anion is the dihydrogenphosphate (15)], constant current reduction yielded a prominent blue haze; it formed more rapidly and eventually erased the red violet radical cation film from the surface of the electrode. The same results were obtained on gold and silver.

The cyclic voltammogram accompanying the effects on gold, at pH 7.5, is shown in Fig. 3 (100 mV/sec).

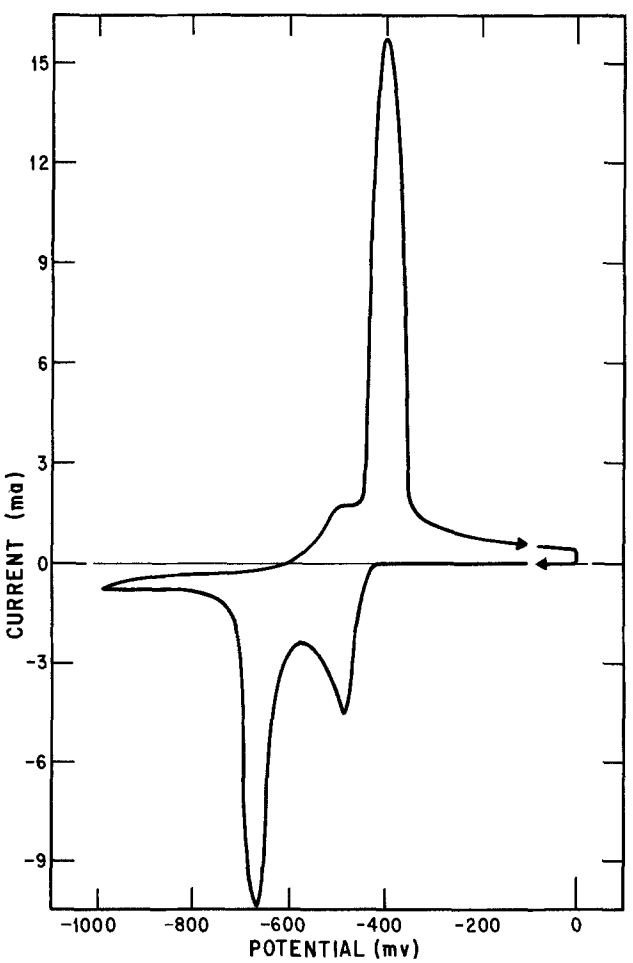


Fig. 3. Shown is a reproduction of a 100 mV/sec cyclic voltammogram, starting at 0 mV *vs.* PermaProbe. The electrode was gold immersed in pH 7.5, molar phosphate containing 0.036M n-heptyl-viologen dication.

There are distinct cathodic peaks at −485 mV and at −640 mV, the latter, associated with diradical formation, being much larger than found at lower pH values. Subsequent anodic oxidation yielded a shoulder at −510 mV, and the sharp peak at −420 mV, characteristic of radical cation oxidation.

The interpretation here is the following. Both the radical cation and the diradical form on cathodic reduction of the solution. The adherence of the radical cation is much less than at lower pH values (a blue haze was observed) so that the electrode surface does not passivate. Thus more diradical can form than at lower pH, and the diradical is held strongly to the surface; the electrode passivates. As the potential goes more positive, the diradical either reacts chemically with the dication and is oxidized via the radical cation, or it is oxidized directly in one step, accounting for the −420 mV peak. The tailing of the anodic portion of the curve could be due to the irreversibility of the diradical oxidation or to the diffusion-controlled oxidation of the "blue haze."

The effect of pH on response time is also consistent with the idea that, in phosphate, higher pH results in a less adherent radical cation film. Plotted in Fig. 4 are the current-time relationships in pH 5 and pH 6 phosphate/viologen solution for gold electrodes first pulsed cathodically (−500 mV) and then pulsed anodically (−250 mV). Obviously, the radical cation film generated out of the pH 6 solution erases (anodizes) faster than that generated out of pH 5 solution. This experiment was repeated with silver electrodes; the anodic portions of the curves were essentially identical to those obtained for gold at pH 5, *i.e.*, pH had little effect on adherence, at least in this low pH range. As mentioned both silver and gold electrodes showed the presence of blue haze at pH 7.5.

These adherence effects cannot be the result of a pH interaction with the viologen dication or radical cation; well-behaved films were generated out of viologen bicarbonate solution, pH 7.5. Nor can these effects be due to the lack of monovalent anion, as shown above. Excess divalent sulfate did not give rise to the phenomenon either with or without phosphate present (pH 6). The cause then must be the chemical properties of the HPO_4^{-2} anion. It is unlikely that this anion would

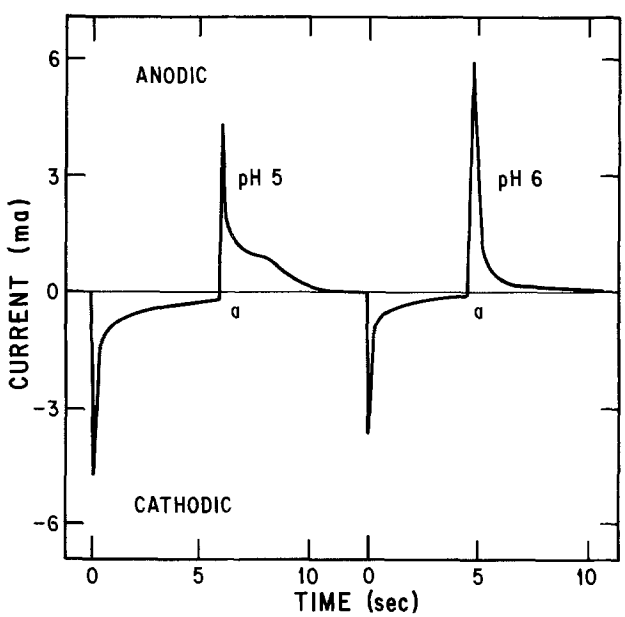


Fig. 4. Shown are the current pulses resulting from the following constant potential sequence: at time zero, −500 mV was applied to generate the cathodic currents; at time (a) the potential was increased to −250 mV to generate the anodic current. The electrode was gold in molar phosphate containing 0.16M n-heptyl-viologen dication. The pH values were 5 and 6.

specifically adsorb on the electrode surface at these negative potentials and displace the viologen radical cation film. More likely (19) is the chemical interaction of HPO_4^{-2} with the radical cation film to yield a reduced but soluble complex ion, colloid, or micelle as the blue haze. Molecular models are consistent with interaction between hydrogenphosphate ions within the radical cation film [assuming the "sandwich" structure proposed in Ref. (7)].

Summary

Thus, regarding the properties of the viologen/phosphate electrode system, (*i*) stable radical cation films can be formed on gold, platinum, and silver from $H_2PO_4^-$ solutions; (*ii*) the effective potential region available for viologen redox reaction study is greater than in bromide electrolytes; (*iii*) formation potential, adherence, erasure times are pH dependent; and (*iv*) side reactions are less significant to electrode cosmetics.

To generalize, (*i*) the equilibrium potential of the n-heptylviologen radical cation films is determined by the viologen concentration and the anion composition of the electrolytes; to this extent the electrode is an inert substrate for charge transfer, (*ii*) the metal substrate exerts an effect with regard to the kinetics of side reactions and film adherence, and (*iii*) chemical reactions can and do occur between the radical cation film and other ions in solution.

Acknowledgments

The author wishes to acknowledge the assistance of Mr. William Wasson in preparing the n-heptylviologen and Ms. Sarah Weir and Dr. Gary Rice in acquiring the experimental data.

Manuscript submitted Nov. 2, 1976; revised manuscript received Jan. 7, 1977. This was Paper 205 presented at the Las Vegas, Nevada, Meeting of the Society, Oct. 17-22, 1976.

Any discussion of this paper will appear in a Discussion Section to be published in the December 1977 JOURNAL. All discussions for the December 1977 Discussion Section should be submitted by Aug. 1, 1977.

Publication costs of this article were assisted by Texas Instruments Incorporated.

REFERENCES

1. L. Michaelis, *Z. Biochem.*, **250**, 564 (1932).
2. L. Michaelis and E. Hill, *J. Gen. Physiol.*, **16**, 859 (1933).
3. W. Boon, *Chem. Ind. (London)*, **1965**, 782; R. Homer *et al.*, *J. Sci. Food Agri.*, **11**, 309 (1960).
4. French Pat. 1,356,547 (1964).
5. H. T. van Dam, J. Ponjeé, and C. Schoot, U.S. Pat. 3,854,794 (1974); C. Schoot, J. J. Pongeé, H. T. van Dam, R. A. van Doom, and P. T. Bolwijn, *Appl. Phys. Lett.*, **23**, 64 (1973).
6. J. G. Kenworthy, Brit. Pat. 1,314,049 (1973).
7. H. T. van Dam and J. Ponjeé, *This Journal*, **121**, 1555 (1974).
8. J. Corwin, R. Arellano, and A. Chivvis, *Biochem. Biophys. Acta*, **162**, 533 (1968).
9. L. Winters, A. Borror, and N. Smith, *Tetrahedron Lett.*, **24**, 2313 (1967).
10. J. Volke and V. Volková, *Collect. Czech. Chem. Comm.*, **34**, 2037 (1969).
11. E. Kosower and J. Cotter, *J. Am. Chem. Soc.*, **86**, 5524 (1964).
12. W. Schwartz, Ph.D. Thesis, Universtiy of Wisconsin (1961).
13. K. Belinko, *Appl. Phys. Lett.*, **29**, 363 (1976).
14. R. Jasinski, *This Journal*, **121**, 1579 (1974).
15. L. Sillen and A. Martell, "Stability Constants of Metal-Ion Complexes," Special Publication 17, The Chemical Society, London (1964).
16. C. Schoot, J. J. Ponjeé, H. T. van Dam, R. A. van Doom, P. T. Bolwijn, and S. van Houten, SID International Symposium, p. 146 (1973).
17. L. Pospisil, J. Kuta, and J. Volke, *J. Electroanal. Chem.*, **50**, 217 (1975).
18. R. Elofson and R. Edsberg, *Can. J. Chem.*, **35**, 646 (1957).
19. See reference 3 in R. Dickerson *et al.*, *J. Chem. Phys.*, **25**, 606 (1956).
20. L. Michaelis, *Chem. Rev.*, **16**, 243 (1935).
21. See reference 6 in R. Elofson and R. Edsberg, *Can. J. Chem.*, **35**, 646 (1957).

Reactions in the Na_2O-NaCl System

Kurt H. Stern* and Rm. Panayappan

Naval Research Laboratory, Washington, D.C. 20375

and David R. Flinn*

U. S. Bureau of Mines, College Park, Maryland 20740

ABSTRACT

The behavior of Na_2O-NaCl melts at 830°C has been studied by three techniques: (*i*) potentiometric studies, using oxide ion specific zirconia electrodes in the reversible galvanic cell

$$Ag|AgCl, NaCl|glass|NaCl, Na_2O|ZrO_2|O_2 (Pt)$$

(*ii*) manometric experiments in which the uptake of O_2 by the melts was observed, and (*iii*) chemical analyses in which oxide and peroxide were found in quenched melts. All three kinds of experiments are thus consistent with the partial conversion of oxide to peroxide by the reaction $Na_2O + \frac{1}{2} O_2 = Na_2O_2$, but the calculated equilibrium varies with the technique employed. Both chemical and electrochemical studies indicate that the peroxide/oxide ratio does not change as the oxygen pressure is changed from 0.1 to 10^{-6} atm. Various explanations for this result are examined.

The behavior of dissolved oxides in molten salts has been a subject of continued interest since Lux (1) first studied acid-base behavior in melts during the 1930's. Knowledge of the state of dissolved oxides is required for understanding the behavior of the oxygen electrode, the solubility product of slightly soluble oxides, and the corrosion of metals.

Until Zambonin and Jordan (2) discovered that the oxide ion in molten nitrates largely transformed

* Electrochemical Society Active Member.

Key words: oxide melts, zirconia electrodes, molten NaCl, peroxides.

to peroxide and superoxide ions, the oxide ion was considered to be a stable species in molten salts. Although nitrate melts may be anomalous in this respect because the NO_3^- ion can oxidize the O^{2-} ion to O_2^{2-} and O_2^-, the absence of this phenomenon in other melts, *e.g.*, halides, sulfates, and carbonates, should no longer be taken for granted, particularly since in nitrate melts the oxidation involves molecular oxygen when that substance is present and the reduction of the melt anion by O^{2-} when O_2 is absent (3). Some evidence for the formation of peroxides and superoxides in molten chlorides has already been presented (4), but all the proposed mechanisms require the presence of molecular oxygen. Whether some lower limit for the required oxygen pressure exists has not yet been established. At any rate, on the basis of the evidence presented so far, O^{2-} would be expected to be stable in halide melts when O_2 is absent.

Most earlier studies used the oxygen electrode on platinum as an oxide ion reversible electrode. However, the nonspecificity of the platinum surface for a particular electron exchange reaction means that more than one such reaction may occur on this surface, depending on experimental conditions. For example, both one- and two-electron processes have been observed for the oxygen electrode on platinum (5). Moreover, the use of this electrode necessarily precludes studying oxides in the absence of O_2.

More recently, solid-state electrodes reversible only to oxide ions have been used in melts. These electrodes, which are generally oxide-doped zirconia, have the great advantage of serving as oxide ion specific membrane electrodes, with no electron exchange possible at the phase boundary between the solid oxide electrode and the oxide-containing melt. Such an electrode was used by Combes, Vedel, and Tremillon (6) to carry out potentiometric titrations of Cu^{++} and Ni^{++} by O^{2-} in 1:1 NaCl-KCl. We have recently used these electrodes in nitrate melts (3). However, since several reactions occur after the addition of Na_2O to these melts and their equilibria are established at different rates, it was never possible to associate a particular cell emf with an absolute oxide activity, although the correct Nernst slopes were obtained from changes in the added oxide concentration. This problem is in fact quite general. Assuming that a stable reference electrode is available, then a change in cell emf measures (through the Nernst equation) changes in the O^{2-} activity. However, even if the reference electrode is well defined and reversible so that a reversible cell reaction can be identified with an independently determined E° (a condition not commonly fulfilled), emf measurements of such a cell can only be used to determine oxide ion activities and not the mechanism by which this oxide activity arises—a characteristic of all thermodynamic measurements. A mechanistic interpretation of the potentiometric measurements thus requires extra thermodynamic assumptions and/or measurements. For example, the obtaining of the correct Nernst slope for a postulated electrode reaction is frequently taken as evidence for the correctness of the postulate. but as we have shown (3), more than one reaction may give the correct slope if several mobile equilibria are operating.

A more stringent test of a postulated reaction is obtained if, in addition to the correct slope, the correct E° is also obtained. Such a test requires that all electrode potentials, melt activities, and phase boundary potentials must be known for the cell in question. At the present state of knowledge in molten salts, such an independent calculation of E° is generally out of reach because the data obtained from a galvanic cell are themselves used to obtain E°. A more modest goal is to study a cell in which a well-defined, reversible reaction takes place, and to test the interpretation by some independent method.

In the present work we studied solutions of Na_2O in NaCl electrochemically by using oxide-doped zirconia electrodes, and manometrically in order to observe the uptake of oxygen by these melts. In addition, chemical analyses were carried out on quenched melts.

The cell used can be written formally as

$$\text{Ag}|\text{AgCl, NaCl}|\text{solid Na}^+\text{ conductor}|\text{NaCl},\ \text{Na}_2\text{O}|\text{stab. Zirconia}|\text{O}_2\text{(Pt)} \quad \text{[I]}$$

The cell reaction therefore is

$$2\text{Ag(s)} + 1/2\,\text{O}_2\text{(g)} = (2\text{Ag}^+ + \text{O}^{2-})\text{ in NaCl} \quad \text{[1]}$$

The selectivity of fused silica, a pure cation conductor, for silver ion and oxide ion is so low (7) that there is no significant contribution to the phase boundary potential across the membrane from these two ions, the only contribution to the cell emf arising from the difference in NaCl activity across the membrane. Mullite behaves similarly. The total cell emf therefore is

$$E = E^\circ - RT/2\mathbf{F}\ln[a^2_{\text{AgCl(R)}}\cdot a_{\text{Na}_2\text{O}})/p_{\text{O}_2\text{(R)}}{}^{1/2}] + RT/\mathbf{F}\ln a_{\text{NaCl(Na}_2\text{O)}}/a_{\text{NaCl(R)}} \quad \text{[2]}$$

$a_{\text{AgCl(R)}}$ and $a_{\text{NaCl(R)}}$ are the activities in the reference melt. $a_{\text{NaCl(Na}_2\text{O)}}$ is the activity of NaCl in the melt to which Na_2O is added. For the dilute solutions of Na_2O used in this work, $a_{\text{NaCl(Na}_2\text{O)}} \approx 1$. Separating out the constant terms gives

$$E = [E^\circ - RT/\mathbf{F}\ln(a_{\text{AgCl(R)}}/a_{\text{NaCl(R)}})] - RT/2\mathbf{F}\ln a_{\text{Na}_2\text{O}}p_{\text{O}_2\text{(R)}}{}^{1/2} \quad \text{[3]}$$

Since thermodynamic data for AgCl-NaCl solutions are known (8), $a_{\text{AgCl(R)}}$ and $a_{\text{NaCl(R)}}$ can be determined from the reference melt composition. $p_{\text{O}_2\text{(R)}}$ represents the oxygen pressure inside the zirconia electrode and not the pressure of O_2 above the Na_2O-NaCl melt. Suppose, for example, that in the presence of O_2 the equilibrium

$$\text{Na}_2\text{O} + 1/2\,\text{O}_2 = \text{Na}_2\text{O}_2 \quad \text{[4]}$$

is established in the melt. Then $a_{\text{Na}_2\text{O}}$ is related to the equilibrium constant for reaction [4]

$$a_{\text{Na}_2\text{O}} = a_{\text{Na}_2\text{O}_2}/K_{\text{eq}}p_{\text{O}_2}{}^{1/2} \quad \text{[5]}$$

The purpose of this work is to examine Na_2O-NaCl melts to see if reactions like [4] involving Na_2O_2 or NaO_2 occur to a significant degree and must be taken into account when these melts are used, for example, as solvents for heavy metal oxides, or when they occur in corrosive environments. Electrochemical experiments have been supplemented by manometric and chemical studies to gain information on this system.

Experimental

Experiments were carried out both in a helium-filled dry box (Vacuum/Atmospheres Corporation) with recirculating dry train in which moisture and O_2 were generally kept at the 1 ppm level and in a similar dry box in which an equally dry and CO_2-free helium-oxygen atmosphere could be maintained at approximately 10% O_2. The general methodology follows that of our earlier work (3), both for the electrochemical and manometric experiments, with some changes necessitated by the corrosive nature of Na_2O-NaCl melts. All experiments were carried out at 830° ± 5°C.

Materials.—Salts.—Reagent grade NaCl was vacuum-dried at 500°C before use. Reagent Na_2O (Alfa Inorganics) (94% Na_2O by analysis) containing ~2% Na_2O_2 impurity, and reagent Na_2O_2 were used without pretreatment. All weighing and transfer operations involving these substances were carried out in the dry boxes in which the experiments were done.

Containers.—The following crucible materials were examined as containers: high-purity alumina, magnesia, calcia-stabilized zirconia, zirconium, platinum, and gold. None were completely inert. Results are described in the next section.

Reference electrodes.—Both fused silica and mullite tubes were examined. The reference melt inside these tubes was ~10 mole percent (m/o) AgCl in NaCl, and a silver wire functioned as electrode. The potential-determining processes of the glass electrodes had previously been studied in detail (7). A comparison of fused silica and mullite in NaCl over 1-2 day periods showed the mullite electrodes to have better emf stability. Since both materials are attacked even by dilute Na_2O-NaCl melts, the electrodes were kept in the melt only during the actual measurements and just above the melt the rest of the time.

Oxide-reversible electrodes.—Three types of zirconia electrodes were studied, all made by Zircoa Corporation: CaO-, Y_2O_3-, and MgO-stabilized ZrO_2. All three function as pure oxide ion conductors and would be expected to be reversible only to O^{2-} ions in the melt. The inside of the tubes, fitted with platinum gauze and wire in contact with the ceramic, is reversible to oxygen gas. It was found that CaO-stabilized tubes frequently were so weakened by their exposure to the melt that they cracked unpredictably even when great care was taken to protect them from thermal shock. Consequently only results with MgO- and Y_2O_3-stabilized electrodes are reported. Both kinds were very stable and could be used for many experiments if they were protected from thermal shock. No systematic differences in their electrochemical behavior were found.

General procedure.—Electrochemical studies.—Crucibles to be used as melt containers were filled with NaCl and placed in an alumina crucible fitted with a fired lava stone top having holes to accommodate the salt addition tube, glass reference electrode, zirconia electrode, and Chromel-Alumel thermocouple in an alumina sheath. For experiments in the He-filled box the tops of the zirconia electrodes were fitted with ultraTorr O-ring connectors so that the oxygen gas pressure inside the tube could be adjusted through a copper tube sealed through the dry box wall. For experiments in the O_2-filled box, the electrodes were left open to the box atmosphere. The actual O_2 pressure, generally between 8 and 12%, was measured with a Beckman oxygen analyzer for each experiment. The entire cell assembly was placed in a platinum wire-wound furnace whose temperature was controlled through a thermocouple in the furnace well. The actual melt temperature was measured by a Chromel-Alumel thermocouple in an alumina tube placed directly in the melt. After this melt temperature had been reached, the thermocouple and its alumina sheath were removed from the molten NaCl to minimize contact of alkaline melts with alumina.

In order to be able to prepare very dilute Na_2O-NaCl melts, "stock melts" containing ~1 m/o Na_2O in NaCl were prepared by dissolving reagent Na_2O in NaCl at 830°C in a gold crucible, keeping the melts hot in the helium-filled dry box for several hours, pouring the melts into stainless steel trays for quenching, grinding, and analyzing by titration with standard HCl. Additions of these melts as well as of reagent Na_2O allowed oxide concentrations between $\sim 5 \times 10^{-4}$ to several mole percent to be prepared.

Some electrolysis experiments were carried out using a conventional d-c power supply, ammeter, and electronic coulometer.

Manometric studies.—Gold or platinum crucibles were sealed into a fused silica envelope of 835 ml capacity. This container had one standard taper opening through which the crucible could be filled and one attachment to the ultraTorr fitting through which gas, generally oxygen, could be passed in and out of the envelope. The lower half, containing the crucible, was placed in the furnace, the entire operation being conducted in the helium-filled dry box. The system was calibrated so that the actual number of moles of oxygen taken up or released by the melt could be measured in terms of pressure changes in the system (3).

In order to produce sufficiently large pressure changes in the system, $\sim 5 \times 10^{-2}$ mole Na_2O in ~1 mole NaCl were mixed in the container, sealed into the envelope, and attached to the measuring system and a gas reservoir of known volume from which O_2 could be metered into the cell. The mixture was heated under continuous pumping to decompose any Na_2O_2 impurity. After the final temperature had been reached, pumping was continued until no further pressure increase could be measured over a period of ~10 min. During this time a very small amount of some metal deposited on the inside wall of the cooler parts of the glass vessel. This material turned white as soon as O_2 was admitted. (The attainment of zero pressure implies that under the experimental conditions, the thermal dissociation of Na_2O is negligible compared to that of the higher oxides present as impurities, consistent with the thermodynamic stability of Na_2O.) A known amount of O_2 was then added to the system. After an initial decrease, the pressure became constant in ~30 min. The reverse process could be carried out by then pumping out the reservoir and letting the gas from the envelope expand into the reservoir. Assuming that the uptake and release of O_2 were produced by shifts in the oxide-peroxide equilibrium, the amount of peroxide dissociated could be calculated from the pressure increase. The dissociation appeared to take a little longer than the formation of peroxide, but generally not more than an hour.

Several values of the equilibrium constant could be obtained by such successive operations during one day, the length of the experiment generally being limited by the continuing vaporization of NaCl from the melt, and the corrosion of the crucibles. In fact, most experiments were done in heavy-walled platinum crucibles since a 5 m/o Na_2O-NaCl melt rapidly corrodes through gold.

Chemical studies.—Chemical analyses of melts prepared in various ways were carried out to aid in the interpretation of the electrochemical studies, primarily those done in the He-dry box. These analyses were: (*i*) titrations with standard (0.02*N*) HCl which give the sum of oxide, peroxide, and superoxide, and (*ii*) titrations with $KMnO_4$ (standardized against $Na_2C_2O_4$) in ice water which give the sum of peroxide and superoxide. Since no distinction between peroxide and superoxide is made in this work, results are calculated as peroxide. Analysis of the reagent Na_2O used showed that the actual oxide content was 94% of theoretical and that it contained 2% peroxide. Before the quenched melts were analyzed, the method was checked by analyzing synthetic unmelted NaCl-Na_2O and NaCl-Na_2O_2 mixtures of similar composition. The end point of the synthetic as well as of the melt samples was sharp at ~pH 5, indicating the absence of carbonate.

Results

General observations.—None of the container materials studied were completely inert to even dilute (<1 m/o) Na_2O-NaCl melts. Some of the changes undergone by the containers are obvious from visual examination; others can be detected from the time dependence of the emf of cell [I]. High purity Al_2O_3 dissolves slowly: $NaAlO_2$ was found in the aqueous solution of a quenched melt. MgO appeared to dissolve rapidly so that the O^{2-} concentration in the melt increased continuously. Gold crucibles, which were used in most of the experiments, produced small amounts of colloidal gold in suspension, but stable emf's could be obtained in them if the melts were dilute, and O_2 was absent. If even small amounts of reagent Na_2O were added in an O_2-containing atmosphere, corrosion was greatly accelerated and the melt leaked out through the holes thus produced. Platinum crucibles which were initially shiny bright acquired a very adherent brown-black coating, insoluble in molten NaCl, which seemed to partly protect the crucible from further attack. Results obtained in these crucibles will be described. The behavior of zirconia was more complex. Figure 1 shows the emf-time curve after sufficient reagent Na_2O (21 mg) had been added to NaCl in a CaO-stabilized zirconia crucible to make the resultant melt 3.9×10^{-4} mole fraction in O^{2-}. Over a 20 min period the O^{2-} concentration increased by a factor of 20 after the added Na_2O had already dissolved (the polarity of the ZrO_2 electrode becomes more negative with increasing O^{2-} concentration) and then decreased again over long periods of time. The sequence recurred after each subsequent addition of Na_2O. As is shown later, the decrease of O^{2-} is the phenomenon normally observed in Pt and Au containers where it is attributed to O_2^{2-} formation and vaporization of Na_2O. The increase of O^{2-} was, however, found only in ZrO_2 containers and suggests some solubility of the crucible material itself. This was of concern since zirconia electrodes were used in these experiments. The behavior of these electrodes was therefore carefully studied. The initial emf of cell [I] before the addition of NaCl was usually in the range 250-350 mV. Steady emf's were generally obtained after 1-2 hr. This emf may be associated with the solubility of ZrO_2 and/or its stabilizing agent in the melt (see below). The initial emf of cells employing electrodes used in previous runs tended to drift lower with progressive use, though rarely below 200 mV. These old electrodes were roughened and slightly whitened, indicating some attack by the alkaline melts. For runs in the O_2 atmosphere the electrodes were pulled up just above the melt to avoid contact as much as possible. For runs in the He-filled box this was not possible since the electrodes had to be attached to the O_2-containing manifold. However, stable emf's were measured when the dilute stock melt was added, indicating the stability of the electrodes at least in dilute melts.

Electrochemical studies.—Approximately 40 different runs of cell [I] were made, employing variations of container materials, electrode materials, atmosphere, and operating procedures. In all cases in which the container material was not obviously reactive, results were quite similar. Therefore, only typical results are presented.

According to Eq. [2] and [3] the emf of cell [I] should vary with O_2 pressure according to $RT/4F \ln p_{O_2}$. A test of this relation is shown in Fig. 2. Some hysteresis is noticeable before any Na_2O had been added to the melt, slightly better agreement with theory being obtained when the pressure was decreased from 1 atm.

In order to reach lower concentrations than is possible by adding pure Na_2O to NaCl, a stock melt was prepared as described previously, and analyzed for O^{2-} by titration with 0.02*N* HCl under an inert atmosphere. Under these conditions the analysis yields the sum of oxide and any peroxide and superoxide that may be present. With this stock melt it was possible to reach nominal oxide concentrations lower than 10^{-5} mole fraction. After the addition of each increment a stable emf was obtained in a few minutes both in the He and the O_2 atmospheres. As shown in Fig. 3, the initial dependence of emf on X_{O2-} is very much less than the theoretical $RT/2F$ for $X_{O2-} < 1 \times 10^{-4}$. Above this concentration, the theoretical slope was attained. Possible reasons for the low concentration curvature are discussed later. The reproducibility of the data is described by a value of X_{O2-}

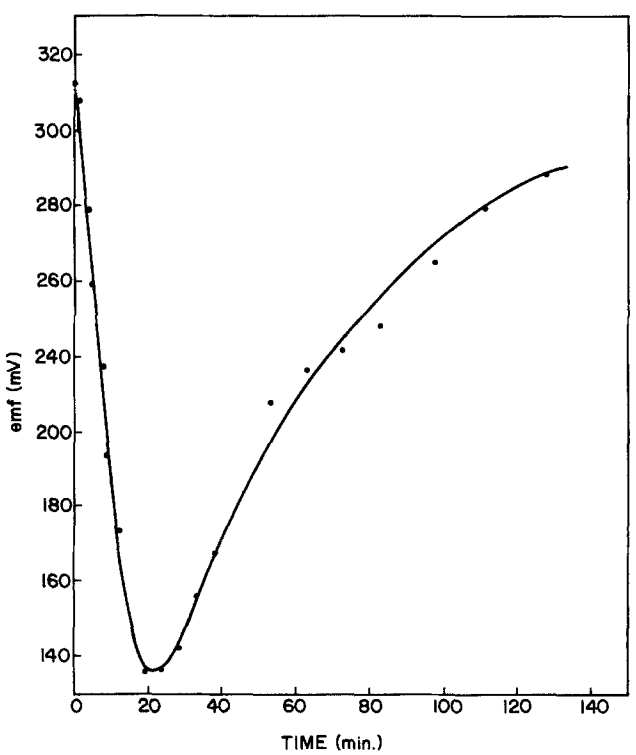


Fig. 1. Emf-time plot of cell [I] in a ZrO_2 crucible after addition of Na_2O.

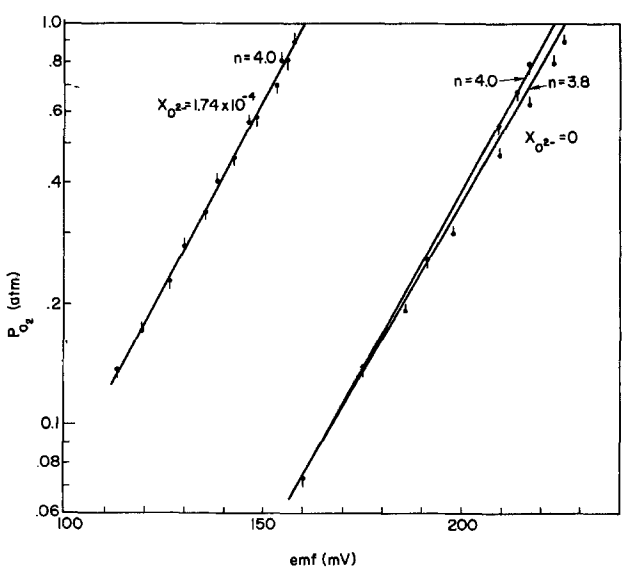


Fig. 2. Emf dependence of cell [I] on p_{O_2} in the zirconia electrode at two melt compositions.

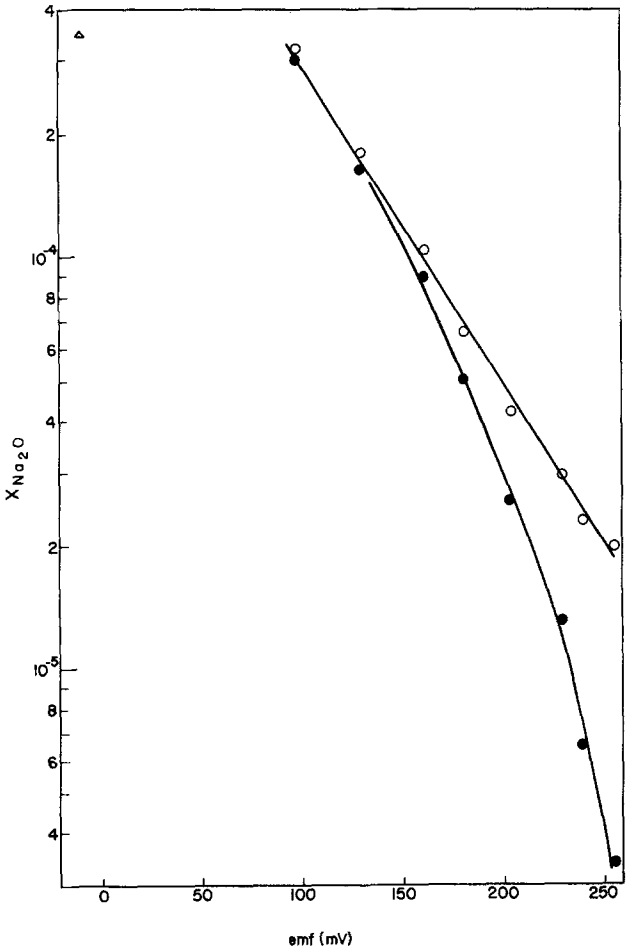


Fig. 3. Emf dependence of cell [I] on melt composition for additions of stock melt. ●, Nominal $X_{O^{2-}}$; ○, corrected for impurities; △, reagent Na_2O. For discussion, see text.

$= (4.6 \pm 2.2) \times 10^{-3}$ when $E = 0$ for seven experiments with different combinations of crucibles and electrodes.

Entirely different results are obtained, both in He and O_2 atmospheres, when reagent Na_2O is added to NaCl. The emf is not constant but becomes increasingly positive for several hours after each addition, indicating that the O^{2-} concentration is decreasing after the rapid initial change associated with solution of Na_2O in the melts. Moreover, the actual emf values are more negative by ~140 mV than would be expected on the basis of the dilute stock-melt additions. The effect is illustrated in Fig. 4 for an experiment in the He box. The filled circles represent the concentrations calculated from the stock melt; the open triangles are for additions of reagent Na_2O made so rapidly that no appreciable decrease of emf occurred. Both sets of data have a slope of $RT/2F$, but are separated by ~140 mV. In the O_2 atmosphere the decrease of emf after addition of Na_2O is so rapid that only a single point for reagent Na_2O after addition of stock melt could be obtained. If it is assumed that the addition of reagent Na_2O initially produces an equivalent O^{2-} concentration in the melt, then it follows that the O^{2-} concentration produced by addition of stock melt is considerably less than expected from the nominal concentration. The ratio between the O^{2-} concentration immediately after the addition of reagent Na_2O and the final value obtained after the emf had become approximately constant is ~7. (The emf never becomes exactly constant because of slow corrosion reactions with the container and the electrodes.) Similar results were obtained

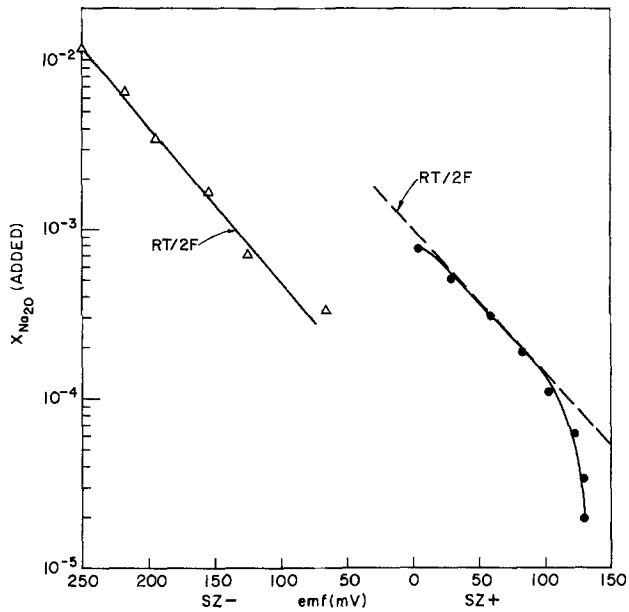


Fig. 4. Emf dependence of cell [I] on melt composition. ●, Nominal $X_{O^{2-}}$ (stock melt); △, reagent Na_2O. For discussion, see text.

in both Au and Pt crucibles. Typical data are shown for Au in Table I.

The value of X_{Na_2O} in Table I is that from the Na_2O calculated to have remained from the previous plus the new addition. It is apparent from the ratio in the next to the last column that a major part of the Na_2O added disappears. The first point is not anomalous but was reproduced in Pt as well. Apparently the first additions of Na_2O are almost entirely used up, after which the ratio becomes approximately constant. The initial portion of the emf-time curve is always linear, and the slope (last column of Table I) is, within a factor of ~3, independent of the initial O^{2-} concentration. Both of these observations are consistent with O^{2-} disappearing by a first-order reaction. The rates observed in the O_2-filled box are higher than in helium, but not by the factor of at least 10^4 by which the oxygen pressures differ. The rates are thus likely to be limited by some process in the melt.

Since corrosion reactions also lead to a decrease in the O^{2-} concentration, reproducible emf-time data are difficult to obtain and electrode kinetic techniques might prove useful. These are beyond the scope of the present paper.

On the assumption that the above results might be accounted for by peroxide formation, an attempt was made to measure emf's after addition of reagent Na_2O_2 to the melt. However, the results were the same as for the addition of pure Na_2O. Most likely solid Na_2O_2 decomposes to Na_2O before it dissolves in NaCl. Similar results were obtained for additions of NaO_2.

Table I. Ratio between $X_{O^{2-}}$ immediately after addition of Na_2O and at equilibrium

X_{Na_2O} (initial)	$E_{initial}$ (V)	E_{final} (V)	$X_{initial}/X_{final}$	dE/dt (mV/min)
5.38×10^{-4}	−0.206	+0.204	5760	2.2
2.55×10^{-3}	−0.527	−0.410	11.85	2.9
1.55	−0.496	−0.298	65.6	0.56
4.23	−0.504	−0.430	9.22	0.94
7.54	−0.486	−0.383	8.82	2.4
1.29×10^{-2}	−0.422	−0.384	3.49	0.98
2.10	−0.769	−0.672	7.76	2.8

If similar experiments are carried out with stock melts which have been heated only briefly instead of several hours, the emf is also time dependent, similar to additions of reagent Na_2O. This shows that the transformation from an unstable emf to a stable one is not a function of concentration or of the melting process, but depends on a reaction occurring in the melt itself, *i.e.*, the reagent Na_2O undergoes reaction after solution in NaCl.

Chemical studies.—Synthetic mixtures of ~1 m/o Na_2O + NaCl and 1 m/o Na_2O_2 + NaCl were melted in Pt crucibles both in the He and O_2 boxes. Samples taken at intervals for analysis by dipping cold ceramic rods into the melt and by dipping into the liquid with a thermally equilibrated Pd bucket gave the same results, showing that no phase separation occurs on quenching. Melts taken from these crucibles shortly after melting and for several hours thereafter were black; samples taken at subsequent intervals were increasingly white. Similar melts prepared in alumina crucibles were white. Spectroscopic analyses of the melts from the Pt crucibles showed ~1% Pt in the black melts and ~0.1% in the white ones. This is consistent with the observations that (*i*) the analytically determined (oxide + peroxide) concentration was always less than expected from the weighed additions, and (*ii*) that a brownish coating was always found in the crucibles at the end of the runs. Evidently the Pt first reacts with the dissolved Na_2O to produce a platinic oxide in solution which slowly precipitates out. The peroxide/oxide ratio becomes constant within ~1 hr, but the absolute values of the concentrations continue to decrease slowly over many hours, indicating slow vaporization and/or thermal decomposition. Typical results for a run in a 15% O_2 atmosphere are shown in Table II. Similar results are obtained when starting with Na_2O_2 except that the initial peroxide/oxide ratio tends to be higher and then decreases.

Since platinum is attacked by even 1 m/o Na_2O solutions, similar experiments were also run in zirconium crucibles which are commonly used for peroxide fusions. In order to duplicate concentrations used in the manometric experiments, the initial concentrations were ~5 m/o Na_2O. Duplicate experiments run in He and in 20% O_2 atmospheres gave rather different results. In He more than half the oxide added initially had disappeared in half an hour, and peroxide was virtually absent. In O_2 much more of the added oxide was retained in the melt and substantial amounts of peroxide were formed. As in the experiments done in platinum, both oxide and peroxide concentrations decreased by a factor of ~2 in 5-6 hr while the peroxide/oxide ratio remained approximately constant at $(7.2 \pm 0.8) \times 10^{-2}$. Both crucibles were covered by an adherent white coating, probably ZrO_2, slightly in the He experiment and extensively in the O_2 atmosphere. Assuming that the peroxide found in solution is formed by the reaction $Na_2O + 1/2\ O_2 = Na_2O_2$, the equilibrium constant for this reaction can be calculated from the chemical analysis. The results are summarized in Table III.

The most striking result is that in Pt the peroxide/oxide ratio is approximately independent of the oxygen pressure rather than exhibiting the expected $p_{O_2}^{1/2}$ dependence, whereas in Zr no peroxide is formed at very low p_{O_2}. In oxygen both kinds of crucibles give similar results. As expected for an equilibrium, the same peroxide/oxide ratio is obtained whether the starting material is Na_2O or Na_2O_2. The comparison of these results with those obtained from the other experiments and their interpretation are taken up in the discussion.

Table II. Analysis of a Na_2O-NaCl melt initially 1.0 m/o Na_2O; 830°C; Pt crucible; 15% O_2 in He atmosphere

t (hr)	$X_{O^{2-}}$	$X_{O_2^{2-}}$	$X_{O_2^{2-}}/X_{O^{2-}}$
0.25	5.09×10^{-3}	0.85×10^{-3}	0.167
0.75	3.50	0.71	0.204
2.0	2.83	0.38	0.133
25.0	1.09	0.12	0.114
			Avg = 0.155 ± 0.030

Table III. Oxide and peroxide analyses of quenched melts

Container	p_{O_2} (atm)	$X_{initial}$ (starting reagent)	No. of samples	$X_{Na_2O_2}/X_{Na_2O}$	K_{eq}
Pt	~10^{-6}	4.4×10^{-3} (Na_2O)	7	0.115 ± 0.050	~115
Pt	0.21	1.0×10^{-2} (Na_2O)	4	0.155 ± 0.030	0.34
Pt	0.21	1.0×10^{-2} (Na_2O_2)	6	0.103 ± 0.003	0.23
Zr	0.21	5.1×10^{-2} (Na_2O)	4	0.077 ± 0.004	0.17
Zr	~10^{-6}	5.1×10^{-2} (Na_2O)	8	—	—

All of the HCl titration curves were those characteristic of strong acid-strong base neutralization and exhibited no inflections of the type observed by Shams El Din and Hosary (9) in molten nitrates, and attributed by them to pyronitrate formation. For this reason and because of the high melt temperatures, it seems reasonable to exclude intermediate species, such as oxychlorides, as well as carbonate contamination from consideration.

Manometric studies.—The experimental procedure for determining the amount of O_2 taken up by an NaCl melt containing Na_2O has already been described. Uptake of O_2 was generally complete in 20-30 min, a period somewhat shorter than observed in the electrochemical studies. The experiment was also done by starting with Na_2O_2 which evolved O_2 rapidly, consistent with the electrochemical and chemical observations.

In all cases the amount of O_2 taken up corresponded to partial conversion of O^{2-} to O_2^{2-}. Thus, although the presence of O_2^- cannot be ruled out on the basis of these experiments, its formation is probably negligible. In all further calculations, therefore, it is assumed that the only significant reaction occurring in these melts is $Na_2O + 1/2\ O_2 = Na_2O_2$. Over the range of pressures attainable in our apparatus (0.1-1 atm), the equilibrium constant is independent of pressure. The same value is obtained from both increasing and decreasing pressure experiments, indicating that the equilibrium is mobile. Since the oxide/peroxide ratio necessarily shifts with changes in pressure, the constancy of K_{eq}, expressed in concentration units (mole fraction), indicates that the activity coefficient ratio is independent of concentration for these rather dilute melts. It was noticed that, for a given initial filling of the crucible, the value of K_{eq} obtained from successive absorptions and desorptions of O_2 tended to decrease after the first few reversals. This phenomenon, indicating the loss of O^{2-}, may be associated with the progressive corrosion observed for both crucibles and/or vaporization of Na_2O. Consequently only the first few K_{eq} in each run were used to calculate the average. This interpretation is consistent with the observation that even the initial K_{eq} values in Au are lower than those in Pt by a factor of ~2, and corrosion of Au is more rapid than that of Pt. The average of seven determinations in Pt containers and two in Au is 2.51 ± 0.76 for the equilibrium constant expressed as

$$K_{eq} = \frac{X_{Na_2O_2}}{X_{Na_2O} \cdot p_{O_2}^{1/2}} \qquad [6]$$

with p in atmospheres.

Calculation of the oxide-peroxide equilibrium constant.—On the basis of the chemical, manometric, and

electrochemical results presented in the preceding sections, it seems reasonable to suppose that, at least in the presence of oxygen, oxide ions are partly transformed to peroxide. Methods for calculating the equilibrium constant of reaction [4] from manometric and chemical data are quite straightforward. The method used to calculate the equilibrium constant from the electrochemical results is somewhat more complicated. The procedure has been described elsewhere (10). The result is that at equilibrium in the He-box (Fig. 4)

$$K_{eq}p_{O_2}^{1/2} = X_{Na_2O_2}/X_{Na_2O} = 6.83/0.98 = 6.97 \quad [7]$$

A similar experiment done at an oxygen pressure of 0.123 atm is illustrated in Fig. 3. The open circles represent the nominal oxide concentrations resulting from the addition of stock melt. The open triangle is for the addition of pure Na_2O. Using the same method described previously for the He-box experiments gives $K_{eq}p_{O_2}^{1/2} = 5.92$. This approximate constancy of $K_{eq}p_{O_2}^{1/2}$ is quite similar to that found in the chemical studies. Since the atmospheres in the two dry boxes differ by a factor of at least 10^4, the K_{eq} values differ by a factor of 100; yet for some reason the peroxide/oxide ratio appears to be independent of oxygen pressure. We note first that the equilibrium constant determined electrochemically lies close to the values of $K_{eq}p_{O_2}^{1/2}$ determined manometrically and chemically. For example, when $p_{O_2} = 0.1$ atm, $K_{eq} = 5.92/(0.123)^{1/2} = 22$, which is at least within an order of magnitude of the manometric results. Considering that the electrochemical and manometric experiments are completely independent and make different assumptions, this agreement is reasonably satisfactory. It follows that the electrochemical experiments in the He atmosphere are anomalous since K_{eq} is approximately three orders of magnitude too large. One possible resolution seemed to lie in the distinction between O_2 in the atmosphere above the melt and O_2 dissolved in the melt. As defined by Eq. [6], the standard state for O_2 is the gas at 1 atm, although the reaction can only occur through O_2 dissolved in the melt. For equilibrium conditions this is reasonable since the concentration of dissolved O_2 is proportional to p_{O_2} through Henry's law. However, as recently pointed out by Fouletier, Fabry, and Kleitz (11), oxide-doped zirconia functions as a semipermeable membrane for O_2. Thus in the He box an O_2 pressure gradient of $\sim 10^6$ exists from the inside to the outside of the electrode. If O_2 is then transported across the membrane from inside the electrode into the melt, the O^{2-} in the melt might be converted to O_2^{2-}. Such transport has in fact been measured (13), but on the basis of the activation energy for diffusion, this mode of O_2 transport should be negligible at 830°C. An experimental test carried out in a manner similar to that in Ref. (12) confirmed this conclusion.

A further source of O_2 is the impurity concentration in helium. If the partial pressure of O_2 in He is 10^{-6} atm, a simple calculation based on the kinetic theory of gases shows that 5.8×10^{-3} mole O_2 will collide with the melt surface (~ 12 cm^2) per minute. For a typical oxide content in the melt (8×10^{-3} mole) and rate (1 mV/min = 2%/min), the reaction rate is 1.6×10^{-4} mole/min. Thus, assuming that a substantial fraction of the oxygen impinging on the surface dissolves, the amount of O_2 available from the gas phase is sufficient to account for the observed decrease of the O^{2-} concentration.

To test this hypothesis, a similar experiment was carried out in a closed container of ~ 500 ml capacity. In this case the total O_2 available for reaction comes from the impurity in the helium, $\sim 10^{-8}$ mole. The decrease in the added oxide concentration should therefore be negligible and a stable emf should be observed after the addition of Na_2O. However, the emf actually still changed in the direction associated with decreasing oxide ion concentration, indicating that even in the absence of O_2, O^{2-} is not stable in NaCl, either because it reacts with the container and/or electrodes, or because of reactions in the melt not yet considered. These are discussed in the next section.

A similar experiment was carried out in a graphite crucible which would be expected to enhance the stability of O^{2-} ($C + Na_2O_2 = Na_2O + CO$). Although the concentration of O^{2-} still decreased with time, its rate of disappearance was noticeably slowed.

Finally, we consider possible reasons for the deviation from the Nernst slope observed at low oxide concentrations (cf. Fig. 3). It has been suggested (6) that stabilized zirconia might possess some selectivity for chloride ions at low oxide concentration. Alternatively, the same results might be accounted for by an oxide impurity concentration in the 1-10 ppm range. Thus, if the initial emf is considered to arise from such an impurity and the appropriate concentration is added to the purposely added (solid circles) concentration, the resulting concentrations (open circles) lie on the Nernst slope. To distinguish between these explanations, reagent NaCl was electrolyzed at 2.0V between a platinum and a zirconia electrode so that any oxide ions in the melt would be transported through the zirconia. At intervals the open-circuit voltage between the zirconia and a mullite reference electrode was measured in order to follow the oxide concentration in the melt. When the electrolysis was carried out in a platinum crucible, the initial current decreased by a factor of ten. Concomitantly, the open-circuit voltage changed from about 200 to 500 mV, corresponding to a change in the oxide concentration (open triangles in Fig. 4) from 6×10^{-7} to 1×10^{-9}. After the current flow was interrupted, the emf rose fairly rapidly toward its initial value, suggesting that the initial impurity oxide concentration arises from the solubility of the ceramic electrodes. This seems a reasonable explanation, particularly since in an alumina crucible no emf higher than 350 mV could be obtained, corresponding to an oxide concentration of 2×10^{-8}. In this case the additional oxide ions arise from the solubility of the crucible. Although the selectivity of zirconia for chloride ions cannot be ruled out entirely on the basis of these results, the contribution of Cl^- to the transport of charge through zirconia must be minor, since the current through the ceramic would not otherwise decrease so markedly in the presence of such a great excess of Cl^-.

Discussion

Because of the extremely corrosive nature of even dilute Na_2O-NaCl melts, none of the measurements reported here were entirely free of container effects. Reactions carried out in Al_2O_3, MgO, and ZrO_2 crucibles probably reflect as much the reactions of the melts with the containers as they do the interactions in the NaCl-Na_2O-O_2 system itself. Even reactions carried out in Pt and Au crucibles suffer somewhat from slow dissolutions of the metals. For this reason the precision normally expected from potentiometric measurements is probably not attainable for this system. Moreover, an interpretation of the data requires the isolation of those features which are common to all the experiments and therefore associated with interactions in the melt rather than with the containers.

We first summarize the results obtained in the various experiments.

1. Both in ~ 0.1 atm O_2 and in $\sim 10^{-6}$ atm O_2, the emf-concentration and emf-time dependences of cell

[I] are a function of the manner in which Na_2O is added: (*i*) If the Na_2O is added as an aged, dilute (~m/o Na_2O in NaCl) stock melt, stable emf's are rapidly obtained in both atmospheres after each addition and the concentration dependence is $RT/2F$. (*ii*) If the Na_2O is added as reagent material or as an unaged stock melt, the emf changes with time in a direction indicative of a decrease in O^{2-}. If the reagent Na_2O additions are taken to represent "real oxide," then the stock melt additions contain almost an order of magnitude less oxide than expected from their nominal composition.

2. The manometric experiments show that O_2 is taken up by a Na_2O-NaCl melt and that this O_2 can be removed by pumping. If it is assumed that the reaction responsible for this phenomenon is $Na_2O + 1/2\ O_2 = Na_2O_2$, then the value of K_{eq} for this reaction is 2.51 ± 0.76, independent of p_{O_2} between 0.1 and 1.0 atm.

This result can be compared with calculations based on known thermodynamic data. Using values in the JANAF tables (13), the equilibrium constant for the reaction

$$Na_2O(s) + 1/2\ O_2(g) = Na_2O_2(s) \qquad [8]$$

at 1100°K is 3.14, the value to be expected in any solvent in which Na_2O and Na_2O_2 form ideal solutions, and in excellent agreement with our experiment.

3. The chemical analyses show that both oxide and peroxide are slowly lost from the melt, whereas the oxide/peroxide ratio becomes constant after ~1 hr when starting with either oxide or peroxide.

4. All three kinds of experiments, when done in Pt or Au crucibles, show that peroxide is formed from oxide and that the steady-state peroxide/oxide ratio is independent of oxygen pressure for each kind of experiment; but agreement among the three experiments is not as good: chemical 0.1, manometric 1.1, electrochemical 7.2 (at 20% O_2).

5. Only in the manometric experiments could the pressure be varied systematically from 0.1 to 1 atm. Within this range the melt concentration ratio was consistent with the equilibrium of reaction [4].

6. The equilibrium constants for reaction [4] calculated for the three methods are: chemical 0.3, manometric 2.5, electrochemical 22.

7. At very low oxygen pressures the peroxide/oxide ratios for the chemical and electrochemical experiments are virtually the same as at higher pressures when done in Pt and Au, but no peroxide could be detected in zirconium crucibles.

We consider first possible reasons for the discrepancies between the results obtained by the three methods in oxygen. Since it was shown (by a comparison of dipped and quenched melts) that the chemical analyses represent melt compositions, we assume provisionally that the chemical analyses represent melt composition. The higher values of K_{eq} (higher peroxide concentrations) obtained by manometry and potentiometry then remain to be accounted for. In the former, K_{eq} is calculated from the manometrically observed uptake and release of O_2. Thus, if there were another reaction which also reversibly absorbs O_2, the higher K_{eq} obtained by manometry could be accounted for. The only substances present capable of reacting with O_2 are NaCl and the container material. The reaction

$$2NaCl + \tfrac{1}{2}\ O_2 = Na_2O + Cl_2$$

is slight, $K_{eq} = 4.3 \times 10^{-18}$, and can only be made to occur by bubbling O_2 through the melt (14), a procedure not employed in these experiments. The oxides of both platinum and gold exist but are considered too unstable. Nevertheless, as indicated by the extensive corrosion of the metals and the platinum found in the analyzed melts, some oxygen-containing metal species may exist and account for the higher peroxide/oxide ratio.

The electrochemical experiment is even more indirect. Here peroxide formation is inferred from a comparison of equilibrated stock melts and additions of reagent Na_2O. Thus the calculation requires the correspondences: change of emf ↔ decrease of oxide ↔ increase of peroxide to hold. From what has been observed of the zirconia electrodes, the first of these is probably correct over the period of several hours during which an experiment is carried out. The second can only hold if there exists no other path for the disappearance of oxide. As the chemical experiments have shown, however, oxide does disappear from the melt, most rapidly immediately after addition and more slowly for several hours thereafter, either by vaporization and/or by reaction with the container; yet this decrease rarely exceeds a factor of two, corresponding to a change of $(RT/2F)\ln 2 = 33$ mV, much smaller than is actually observed for the emf time dependence over a period of several hours (*cf.* Table I). Moreover, if the vaporization of Na_2O during the addition is taken into account, the peroxide/oxide ratio would be larger since the line through the triangles in Fig. 4 would shift left.

The potentiometric results show that oxide disappears not only at low (1 ppm) oxygen pressure, but even when the total amount of O_2 has been limited by working in a closed He-filled container. The chemical analyses indicate that in Pt containers peroxide is formed both at 1 ppm and at higher O_2 content, but in zirconium crucibles peroxide forms only at higher O_2 content. We note that ZrO_2 was also observed to form at 1 ppm O_2. Since this oxide is much more stable than PtO_2, it is conceivable that Zr acts as a "getter" for O_2 and keeps it from reacting with the melt, whereas PtO_2 probably can only form as an unstable intermediate in some reaction sequence.

What still requires explanation is how oxide can disappear from the melt (to a much greater extent than can be accounted for by vaporization alone) even when O_2 is absent and why the peroxide/oxide ratio is virtually independent of O_2 pressure. This is in fact the situation obtaining in nitrate melts: In the absence of O_2, NO_3^- is reduced to NO_2^- by O^{2-}. In chloride melts the anion is, however, not reducible; but the oxidation of O^{2-} could proceed if even traces of Cl_2 were present since the equilibrium constant for the reaction

$$2Na_2O(s) + Cl_2(g) = 2NaCl(l) + Na_2O_2(s) \qquad [9]$$

is 2.05×10^{17} at 1100°K (13). The only Cl_2 in the system would arise from the thermal dissociation of NaCl itself

$$NaCl(l) = Na(g) + 1/2\ Cl_2(g) \qquad [10]$$

for which the equilibrium pressure of Cl_2 is 1.8×10^{-10} atm. Assuming ideal solution behavior and substituting this value of p_{Cl_2} into

$$K_{eq} = \frac{X_{Na_2O_2}}{X^2_{Na_2O}} \cdot \frac{X^2_{NaCl}}{p_{Cl_2}} = 2.05 \times 10^{17} \qquad [11]$$

gives, for dilute solutions ($X_{NaCl} \approx 1$), $X_{Na_2O_2}/X^2_{Na_2O} = 3.7 \times 10^7$. Since p_{Cl_2} cannot exceed its equilibrium value, this is the highest possible value of the ratio. Because of the nonlinear form of the equation, the ratio $X_{Na_2O_2}/X_{Na_2O}$ increases with the concentration of added oxide, rising from 3.9 when $X^\circ_{Na_2O} = 10^{-6}$ to 430 when $X^\circ_{Na_2O} = 10^{-2}$. [Under the same conditions the sodium from the dissociation of NaCl is not sufficient to reduce Na_2O_2: for the reaction

$$Na_2O_2 + 2Na = 2Na_2O \qquad [12]$$

K_{eq} (at 1100°K) $= 1.58 \times 10^{12}$ (14). $p_{Na} = 3.6 \times 10^{-10}$

atm from which $X^2_{Na_2O}/X_{Na_2O_2} = 5.7 \times 10^2$. Thus for example, if $X_{Na_2O} = 1 \times 10^{-2}$, then $X_{Na_2O_2} = 1.8 \times 10^{-7}$ which is negligible.]

Thus, if reaction [9] actually occurred, all of the added oxide would be converted to peroxide. This is clearly not the case, probably because the concentration of dissolved Cl_2 is too low for the reaction to occur at measurable speed. At any rate, the functional relation predicted by Eq. [11] does not agree with the electrochemical results shown in Fig. 4. Thus, as can be seen from Eq. [11], the ratio $X_{Na_2O_2}/X_{Na_2O}$, and hence the ratio $X°_{Na_2O}/X_{Na_2O}$, is dependent on $X°_{Na_2O}$. For example, while $X°_{Na_2O}$ rises from 10^{-6} to 10^{-2}, X_{Na_2O} changes from 1.2×10^{-7} to 1.2×10^{-5}. Since the plotted concentrations for the stock melt (solid circles) represent $X°_{Na_2O}$, the slope for this plot should have been twice that for addition of pure Na_2O, rather than the same, regardless of O_2 pressure. This leaves the electrochemical results obtained in the closed container unexplained unless one assumes that the observed decrease of oxide is produced by vaporization and/or decomposition or that traces of O_2 were introduced each time that the container was opened to add fresh Na_2O.

The question which then remains is why the ratio $X_{Na_2O}/X°_{Na_2O}$ appears to be independent of oxygen pressure. If the decrease of O^{2-} with time is to be accounted for by reaction [4], then the ratio should vary with p_{O_2}; if by reaction [9], the ratio should vary with $X°_{Na_2O}$. Neither condition obtains, and the ratio is independent of both p_{O_2} and of $X°_{Na_2O}$. Moreover, the chemical results show that the decrease of oxide inferred from the potentiometric results is equivalent to the formation of peroxide and that the peroxide/oxide ratio is also independent of O_2 pressure, at least in Pt containers. In the presence of sufficient oxygen there is not much doubt that the results are well accounted for by reaction [4]. The anomalous results are those obtained at low oxygen pressure.

The question of superoxide (O_2^-) formation in these melts has not been addressed, not because it may not be significant, but because the present data cannot be interpreted in terms of more than one equilibrium. In fact, for the reaction $Na_2O_2 + O_2 = 2NaO_2$, $K_{eq} = 3.72 \times 10^{-3}$ at 1100°K (13), so that superoxide formation may become appreciable at higher oxygen pressures. Polarographic measurements would be helpful in providing information on this point.

We consider next the calculation of $E°$ for cell [I], *i.e.*, reaction [1].

The data presented in Fig. 3 and 4 permit the calculation of $E°$ from Eq. [3]. The composition of the reference AgCl-NaCl melt was $X_{AgCl} = 0.102$. Activity coefficients at 800° are (8) $\gamma_{AgCl} = 1.37$, $\gamma_{NaCl} = 1.00$, from which $a_{AgCl} = (0.102)(1.37) = 0.140$, $a_{NaCl} = 0.898$. Since the Na_2O concentration was generally below 0.01 mole fraction, the activity of NaCl in that melt was unity. Substituting these values into Eq. [2] gives for the $E°$ values in the 12.3% O_2 box

$$E° = E - 0.141 + 0.109 \log X_{Na_2O}$$

and in the He-filled box (p_{O_2} inside the zirconia tube = 1 atm)

$$E° = E - 0.187 + 0.109 \log X_{Na_2O}$$

assuming that Na_2O-NaCl solutions are ideal ($a_{Na_2O} = X_{Na_2O}$). Using the data shown in Fig. 3 and the procedure previously described for obtaining the real oxide concentration yields $E = -0.010$ when $X_{Na_2O} = 3.89 \times 10^{-4}$ from which $E° = -0.523$. Similarly, in the helium box, $E = 0$ when the nominal $X_{Na_2O} = 4.6 \times 10^{-3}$. From the distance between the curves in Fig. 4 we have $X_{nom.}/X_{real} = 7.81 \times 10^{-4}/0.98 \times 10^{-4} = 7.97$. Hence, $X_{real} = 5.77 \times 10^{-4}$. Therefore $E° = -0.582$V, in fair agreement with the value in the O_2-filled box.

It is interesting to compare these results with those of a previous study (15) in which the equilibrium constant of reaction [1] was determined by analysis of melts prepared by direct mixing of NaCl-AgCl and NaCl-Na_2O melts.

These earlier results resemble the present ones in that nearly the same value of $X^2_{Ag^+} \cdot X_{O^{2-}} = K_{eq} p_{O_2}^{1/2}$ was obtained in air and in a helium-filled dry box, whereas the ion product would be expected to differ by a factor of ~100 in the two atmospheres. In air the value of the ion product was 3.8×10^{-7}. Since the oxide concentration was determined by titration with HCl, it would consist of the sum of O^{2-} and the higher oxides. Applying the results of the present work, the actual oxide concentration would be

$$X_{O^{2-}} = \frac{3.8 \times 10^{-7}}{(0.140)^2(5.9)} = 4.6 \times 10^{-7}$$

from which $K_{eq} = 2.0 \times 10^{-8}$, and $E° = -0.840$V, compared with -0.523V based on the present work alone. Although this difference is too large to provide satisfactory agreement, the two studies exhibit qualitatively similar results: the independence of an oxide concentration from oxygen pressure, when a dependence is expected.

Manuscript submitted Sept. 7, 1976; revised manuscript received Dec. 20, 1976.

Any discussion of this paper will appear in a Discussion Section to be published in the December 1977 JOURNAL. All discussions for the December 1977 Discussion Section should be submitted by Aug. 1, 1977.

Publication costs of this article were assisted by the Naval Research Laboratory.

REFERENCES

1. For example, H. Lux, *Z. Electrochem.*, **45**, 303 (1939).
2. P. G. Zambonin and J. Jordan, *J. Am. Chem. Soc.*, **89**, 6365 (1967); *ibid*, **91**, 2225 (1969).
3. D. R. Flinn and K. H. Stern, *J. Electroanal. Chem.*, **63**, 39 (1975).
4. E. P. Mignonsin, L. Martinot, and G. Duyckaerts, *Inorg. Nucl. Chem. Lett.*, **3**, 511 (1967).
5. For example, D. Inman, in "Electromotive Force Measurements in High-Temperature Systems," C. B. Alcock, Editor, p. 163, Institute of Mining and Metallurgy, London (1968).
6. R. Combes, J. Vedel, and B. Tremillion, *Anal. Lett.*, **3**, 523 (1970).
7. K. H. Stern, *J. Phys. Chem.*, **72**, 1963 (1968).
8. G. J. Janz and C. G. M. Dijkhuis, "Molten Salts, Vol. 2," *National Standards Reference Series No. 28*, NBS, Washington, D.C. (1969).
9. A. M. Shams El Din and A. A. El Hosary, *Electrochim. Acta*, **12**, 1665 (1967).
10. K. H. Stern, Rm. Panayappan, and D. R. Flinn, in "International Symposium on Molten Salts," J. P. Pemsler, J. Braunstein, K. Nobe, D. R. Morris, and N. E. Richards, Editors, pp. 64-77, The Electrochemical Society Softbound Symposium Series, Princeton, N.J. (1976).
11. J. Fouletier, P. Fabry, and M. Kleitz, *This Journal*, **123**, 204 (1976).
12. S. F. Palguev, V. K. Gilderman, and A. D. Neujmin, *ibid.*, **122**, 745 (1975).
13. D. R. Stull and H. Prophet, JANAF Thermochemical Tables, NBS (1971).
14. K. H. Stern and W. E. Reid, *J. Phys. Chem.*, **66**, 1311 (1964).
15. K. H. Stern, *ibid.*, **64**, 1311 (1962).

Kinetics of Electrochemical Incorporation of Lithium into Aluminum

Carlos A. Melendres*

Argonne National Laboratory, Chemical Engineering Division, Argonne, Illinois 60439

ABSTRACT

The electrochemical incorporation of lithium into aluminum was investigated by chronocoulometric, galvanostatic, and potentiostatic techniques. Results of the chronocoulometric measurements were interpreted in terms of the theory developed by Astakhov. Incorporation of lithium to form the solid solution α-phase is limited by its rate of diffusion into aluminum, with a measured diffusion coefficient of about 4×10^{-10} cm^2/sec at 450°C. Implantation at potentials where a layer of intermetallic compound forms on the electrode surface was found to be limited initially by the reaction to form the compound LiAl (β-phase) and subsequently by the rate of lithium diffusion into the growing β-phase layer. The results of galvanostatic transient measurements indicate a diffusivity of lithium in β-LiAl of the order of 10^{-8} cm^2/sec and a fast charge transfer step. The initial steps in the formation of the intermetallic compound appear to involve typical electrocrystallization (*i.e.*, nucleation and growth) processes.

Lithium-aluminum alloys appear promising for use as negative electrodes in molten-salt-based secondary batteries which are being developed for off-peak energy storage in utility networks and for electric vehicle propulsion (1, 2). Contributions to the understanding of the electrochemical behavior of these alloy electrodes have come from the emf measurements of Yao *et al.* (3) and Selman (4) in molten LiCl-KCl; the galvanostatic and potentiostatic studies of L'vov and Gnilomedov (5) and L'vov (6); and the polarization measurements of James (7, 8). The charging of the Li-Al electrode involves phenomena collectively termed by Kabanov and his school (9) as "incorporation" or "implantation." The occurrence appears to be widespread when alkali and alkaline earth metals are electrolytically deposited onto a foreign substrate with which they can form an alloy. In an attempt to understand the overpotential behavior of Li-Al electrodes in LiCl-KCl electrolyte, interesting aspects of the kinetics of the incorporation process became evident and are presented here. The conclusions are based on the analysis of galvanostatic transients and chronocoulometric measurements.

Experimental

The electrochemical measurements were carried out in a glove box under high purity helium atmosphere. The apparatus is shown in Fig. 1. The cell consisted of three electrodes: a working electrode of aluminum wire, a counterelectrode of Li-Al alloy, 2.54 cm in diameter × 0.64 cm thick, and a reference electrode also of Li-Al alloy, 1 cm in diameter × 1.5 cm long. The aluminum wires were nominally 0.1588 cm in diameter, and were Marz grade (99.99% Al) material, obtained from Materials Research Corporation, Orangeburg, New York. The Li-Al electrodes were prepared by casting from 40 atomic percent (a/o) Li-Al powder [a composition in the $\alpha + \beta$ region of the phase diagram (10)] at ~800°C in alumina crucibles and attaching tantalum leads while the liquid metal alloy was cooling. Li-Al electrodes in the $\alpha + \beta$ composition range have been shown (3) to give a stable and reproducible emf of about 290 mV anodic of Li/Li$^+$ at 450°C. Electrodes of this type when used here as potential reference will be called the LiAl electrode. A 5.5 cm diameter alumina crucible was used as the electrolyte container. The electrolyte was polarographic grade LiCl-KCl eutectic obtained from Anderson Physics Laboratories, Champaign, Illinois.

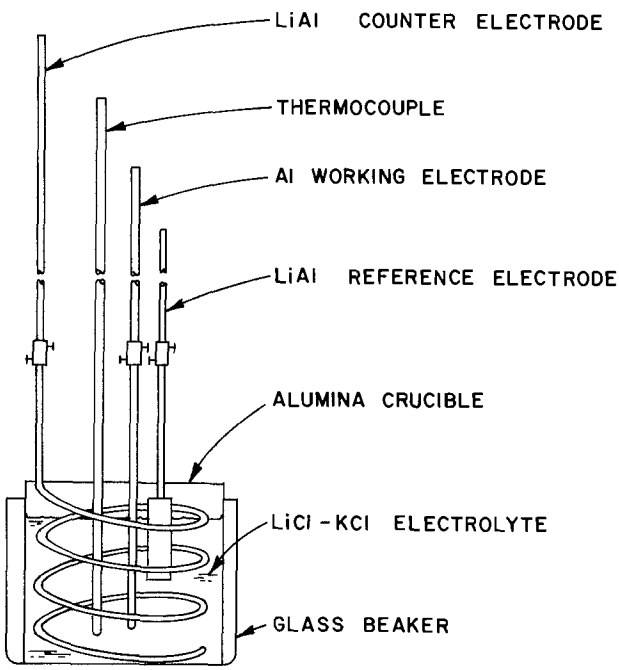


Fig. 1. Experimental apparatus

All measurements were made at a temperature of 450° ± 4°C. A potentiostat/galvanostat (Princeton Applied Research Model 173) with a risetime of about 6 μsec was used in either a constant current or a constant potential mode. Current integration was accomplished by using a digital coulometer (PAR Model 179) which plugs into the potentiostat/galvanostat. Fast transients were displayed by a Hewlett-Packard Oscilloscope, Model R5103N (equipped with a D15 single beam storage unit, 5A22N Differential Amplifier, and a 5B12N Dual Time Base) and photographed with a Polaroid camera attachment. Long-term potential-time or charge-time behavior was displayed on a Hewlett-Packard Model 7040A X-Y recorder.

Results and Discussion

Although the undervoltage deposition of metals on solid substrates with which they can form alloys or intermetallic compounds is fairly well known (11), the over-all processes which eventually lead to the implantation of the discharged atom into the electrode have

* Electrochemical Society Active Member.
Key words: lithium-aluminum electrodes, electrochemical incorporation, kinetics of incorporation.

not been extensively investigated. Kabanov *et al.* (8) first recognized (*i*) the special position that electrochemical incorporation (or perhaps a better term would be intercalation) occupies between the electrocrystallization of metals and the formation of liquid metallic solutions (or amalgams) and (*ii*) the fact that the rate of incorporation depends substantially on the microstructural condition of the electrode. The system Li-Al provides an interesting example for testing theories on incorporation. An understanding of its electrochemical behavior is also important for the further engineering development of electrochemical energy storage devices that make use of Li-Al alloys as negative electrodes (1, 2).

Incorporation at potentials anodic of LiAl.—The time development of the electrode potential that is observed on charging lithium into pure aluminum wires at constant current is illustrated in Fig. 2. As lithium is incorporated into the aluminum at low current densities, *i.e.*, < 5 mA/cm^2 (Fig. 2a), the potential decreases from the aluminum rest potential of about 1.2V *vs.* LiAl (12), and asymptotically approaches that of LiAl ($\sim$290 mV *vs.* Li/Li$^+$). At higher current densities, the cathodic polarization curve appears as in Fig. 2b. Following an initial jump, the overpotential remains roughly constant for some time then gradually increases with time. The behavior in Fig. 2a typifies the incorporation of lithium into aluminum to form the α-phase which is a solid solution of lithium in aluminum (10). During incorporation at high current densities, formation of the β-phase (an intermetallic compound of 45-55 a/o Li in Al) occurs (13). It was of interest to determine the process that limits the rate of incorporation in each case.

The onset of lithium deposition into aluminum occurs well below the reversible potential of the Li/Li$^+$ couple and the potential for the formation of the LiAl compound, as may be deduced from Fig. 2a. The incorporation rate to form the α-phase is evidently low. To investigate the rate-limiting process, potential step experiments with current integration, herein referred to as chronocoulometry [also termed the potential-step-integral method (14)], were undertaken. In this method, the potential is stepped to a desired value and the charge passed during the controlled-potential electrolysis is measured as a function of time by electronic integration of the observed current. According to Astakhov's theory (15), if the incorporation rate is limited by diffusion of lithium into the aluminum, the amount of lithium (in equivalent coulombs, Q) incorporated is proportional to the square root of the time of electrolysis, $t^{1/2}$. When the rate is limited by a reaction to form an intermetallic compound, Q is directly proportional to t, provided that the potential is held constant and no concentration polarization occurs in the solution. Figure 3 shows chronocoulometric curves obtained when the potential is stepped from the open-circuit voltage of about 1.2-0.020V *vs.* a LiAl reference electrode at 450°C. Excellent agreement with a diffusion-controlled rate is observed. From potential *vs.* time plots similar to Fig. 2a, the diffusion coefficient of lithium in aluminum may be obtained approximately (neglecting the effect of cylindrical geometry) using the Sand equation (16)

$$C(t) = C(o) + \frac{2\,i\,t^{1/2}}{F\Pi^{1/2}D^{1/2}} \qquad [1]$$

Taking $C(t)$ to be the saturation concentration of lithium in the α-phase [7.3 a/o at 450°C (10)] at the time t when LiAl potential is reached and $C(o) = 0$, a value of diffusivity, D, equal to $4.0 \pm 1.0 \times 10^{-10}$ cm^2/sec is obtained at 450°C. This is in good agreement with the value of 4.5×10^{-10} cm^2/sec measured by Costas (17) using a different technique.

Incorporation with compound formation.—At current densities where the rate of lithium deposition on the aluminum surface exceeds the diffusion flux into the interior of the electrode, accumulation of lithium in the surface layers results in the formation of the intermetallic compound LiAl. The electrode polarization is shown in Fig. 2b. Electrochemical incorporation under this condition was examined further by chronocoulometry. Potential steps from the open-circuit voltage to more negative potentials *vs.* the LiAl reference were applied to aluminum wires and the resulting current was integrated electronically over time to obtain the charge passed. Typical results are shown in Fig. 4, where it can be seen that a linear relation exists initially between Q and t, but a deviation from linearity occurs at later times. This deviation begins when the lithium charged into the electrode corresponds to about 20-30% of the theoretical capacity calculated on the basis of complete conversion of the whole wire to 45 a/o Li-Al. When the above data are replotted as Q *vs.*

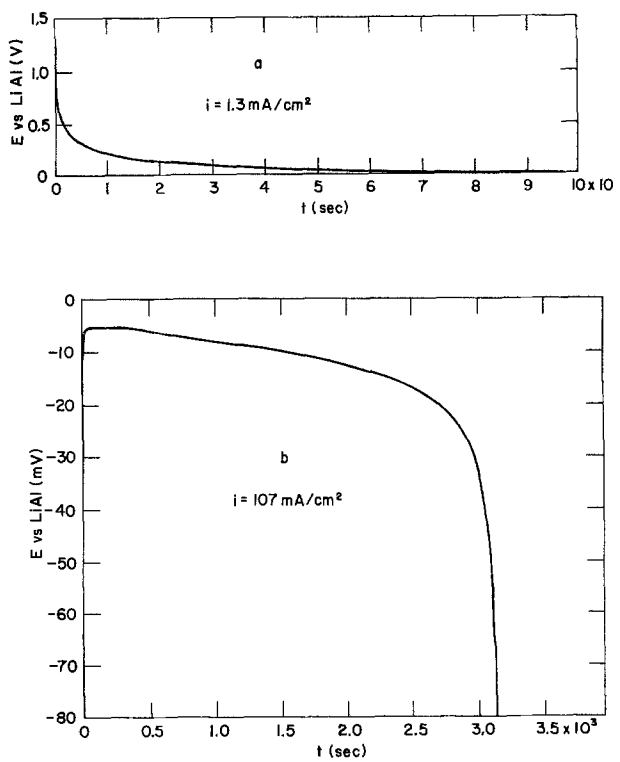


Fig. 2. Charging curves for lithium incorporation into aluminum: (a) at low current densities, (b) polarization at high current densities.

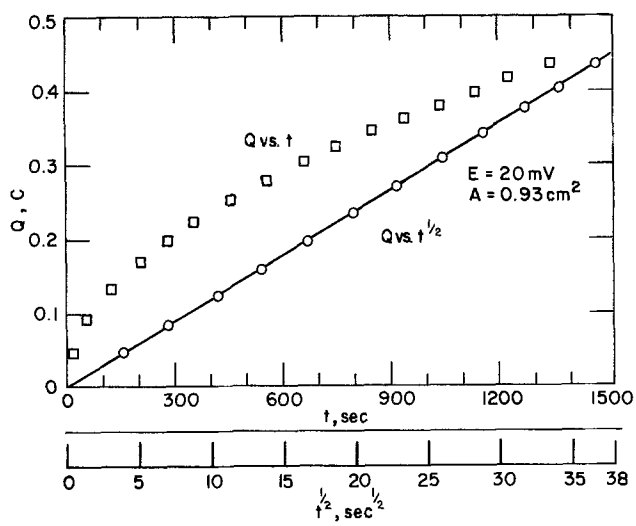


Fig. 3. Chronocoulometric curves for lithium incorporation to form the α-phase Li-Al alloy.

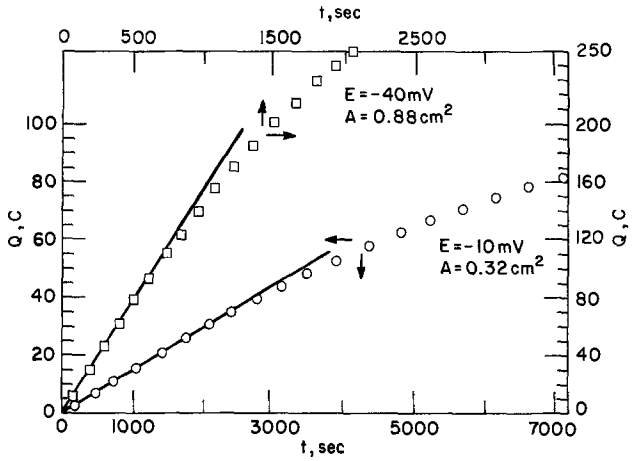


Fig. 4. Chronocoulometric curves for lithium incorporation with formation of the β-phase.

$t^{1/2}$, a linear relation is obtained for $t > 2000$ sec, as shown in Fig. 5. In line with Astakhov's theory, the rate of incorporation appears to be controlled initially by compound formation but, as the β-phase layer thickens, a transition to diffusion control occurs. The reactive propagation of the interphase between the intermetallic compound layer and α-phase depends on the diffusion rate of lithium through the growing compound layer. This diffusion is presumably through a vacancy mechanism. The rate of incorporation as measured by the initial slope of Q/A *vs.* t is found to increase with potential, as shown in Table I. The possibility was also considered that the deviation from linear behavior of the Q *vs.* t plots above roughly 20% loading may result from concentration changes in the solution in the vicinity of the electrode. To examine this, the potentiostatic charging process was interrupted for about 10-15 min, to allow solution equilibrium to be established, and then continued to completion. Again, the linear Q *vs.* $t^{1/2}$ relation was obtained with loadings above 20-30%.

Further evidence for diffusional process.—Additional experiments were conducted to confirm the existence

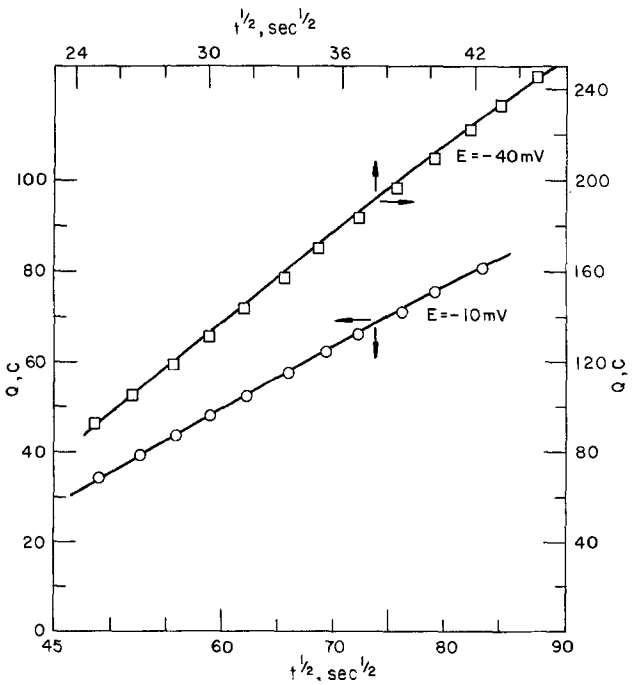


Fig. 5. Replot of later portions of chronocoulometric curves in Fig. 4.

Table I. Variation of incorporation rate with potential

E vs. LiAl (mV)	$(dQ/dt)\ 1/A^a$ (C/cm²-sec)
+20	1.03×10^{-3}
−10	4.56×10^{-2}
−20	6.11×10^{-2}
−30	1.11×10^{-1}
−40	1.74×10^{-1}

[a] A = Electrode area, cm².

of diffusional overpotential in incorporating lithium into aluminum at high rates.

In one experiment, lithium was charged galvanostatically into a wire, in selected increments, at a current density of 81.4 mA/cm² to desired loadings. Between these chargings, but after a waiting period of 15 min to allow equilibrium conditions to be reestablished, a potential step of −40 mV *vs.* LiAl was applied and the current measured after 50 sec. The results are shown in Table II. It is seen that the current remains constant initially, as is characteristic of kinetic control in a potentiostatic experiment, then decreases slowly as the amount of lithium charged increases. This decrease in current is indicative of the predominant effect of diffusion.

Galvanostatic charging curves similar to Fig. 2b also show an apparent transition time (τ) which decreases as the current density (i) increases. The difficulty in precisely defining the transition time did not, however, permit the constancy of the product $i\,\tau^{1/2}$ to be established. The existence of a transition time is nevertheless generally considered a strong diagnostic test for the existence of diffusional overpotential (18).

Finally, galvanostatic transient measurements which were undertaken to elucidate the initial steps of the incorporation process also showed diffusional behavior when the β-phase layer has thickened considerably (percent loading >20% at the current densities normally used). Typical overpotential *vs.* time curves are shown in Fig. 6. If only charge transfer and diffusional overpotentials are present, the time dependence of overpotential should follow the equation (18)

$$\eta = \frac{RT}{n\mathbf{F}}\,\frac{i}{i_o} + \frac{2}{\sqrt{\pi}}\,\frac{RT}{n^2\mathbf{F}^2}\cdot\frac{i\sqrt{t}}{C_o\sqrt{D}} \qquad [2]$$

at low overpotentials. Figure 7 shows plots of η *vs.* $t^{1/2}$ for the transients shown in Fig. 6. A linear relation is obtained. The lines pass through the origin indicating that the charge transfer component of overpotential (the first term on the right-hand side of Eq. [2]) is negligible, *i.e.*, the exchange current density is high. The overpotential is thus purely diffusional. An approximate value of the diffusion coefficient of lithium in β-LiAl may be calculated from the slope of the η *vs.* $t^{1/2}$ plots. Using C_o equal to 0.045 g-atoms/cm³ for the lithium concentration in the β-phase, and current

Table II. Incorporation of lithium at constant potential following constant current[a] charges (electrode area, 0.86 cm²)

Q total (C)	% loading[b]	I[c] (mA)
23.4	9.3	114
47.5	18.9	114
70.7	28.2	112
95.0	37.9	109
117.9	47.0	104
142.5	56.8	101
166.0	66.2	97
190.3	75.9	92
214.1	85.4	84
237.7	94.8	73

[a] −70 mA.
[b] Based on complete conversion to LiAl.
[c] Current measured 50 sec after application of constant potential of −40 mV *vs.* LiAl.

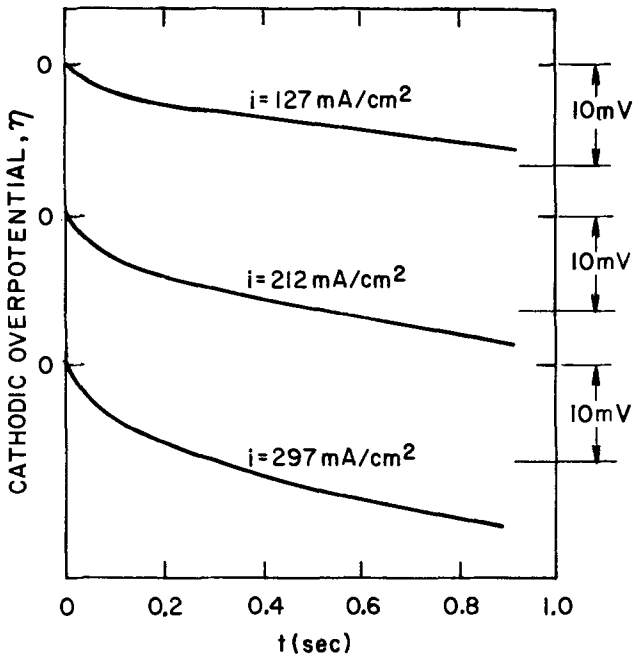


Fig. 6. Galvanostatic transients on precharged aluminum electrode (loading = 55%).

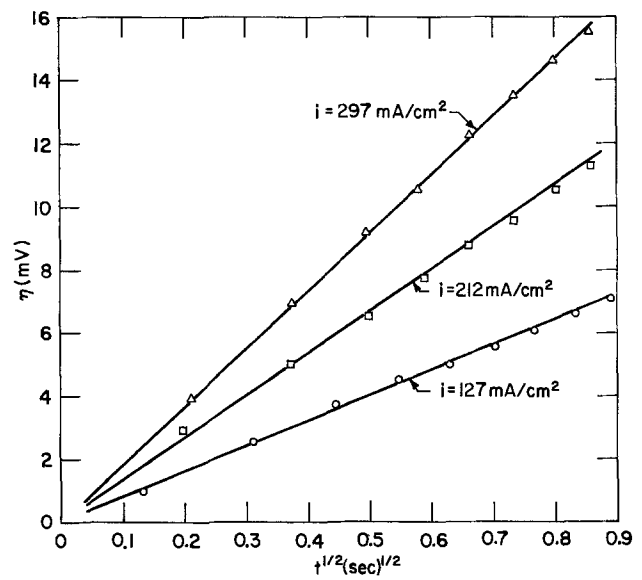


Fig. 7. Overpotential *vs.* $t^{1/2}$ plots for transients of Fig. 6

densities calculated on the basis of the wetted areas of the original wires, values of diffusivity in the order of 10^{-8} cm²/sec at 450°C are obtained. More precise numbers cannot be obtained without accurate knowledge of the electrode areas of the charged wires; the effect of the cylindrical wire geometry will also have to be considered. Differences in the present values and those given by L'vov (6) and James (7) (2×10^{-6} and 5×10^{-5} cm²/sec, respectively), which were obtained on discharge of LiAl electrodes, may be due to a difference in actual electrode areas. There may also be a real difference between the "in" and "out" diffusivities of Li in LiAl similar to what has been observed in Au-Ag alloys (19). More accurate diffusivity measurements are being attempted using a Li^6 isotope tracer and ion probe microanalysis.

The above experiments confirm the previous conclusion made based on Astakhov's theory. The deviation of the Q *vs.* t plot from linearity during incorporation at negative potentials *vs.* LiAl is due to a change in the rate-limiting mechanism from intermetallic compound formation to lithium diffusion through the thickening β-phase layer. L'vov's previous conclusion (5) that the rate is determined wholely by the first mechanism appears incorrect.

Initial steps in the formation of the intermetallic compound LiAl.—The question may be asked as to whether the mechanistic steps that lead to the building up of the crystal lattice during electrodeposition of metals on the same or a foreign unreactive substrate occur also during deposition onto a surface where alloy formation is favored. This question has not been extensively considered in works that have appeared in the open literature. Vetter (18) has summarized the prevailing ideas on the kinetics of electrocrystallization of metals on the same substrate. The analysis of galvanostatic and potentiostatic transients could lead to some understanding of the steps involved in the early stages of the incorporation process and the formation of the intermetallic compound; therefore, a study of the overpotential *vs.* time behavior was made for electrodes of pure aluminum and aluminum precharged with lithium to desired loadings. Potential-time transients following a current step were recorded over various time scales and at different current densities. Typical results are shown in Fig. 8. On deposition into pure aluminum at high current densities, a marked superpolarization (20) is observed as in Fig. 8a. Immediately after switching off the current step (which is a few hundred milliseconds duration), the electrode potential on open circuit is found to be that of LiAl. Upon standing at open circuit for a few minutes, the potential of the electrode again approaches 1.2V; application of a current step shows again a superpolarization. If, however, the step is applied while the electrode potential is still that of LiAl, the transient appears as in Fig. 8b. No superpolarization is observed but the transient is characterized by a relatively long rise time in the order of 3-60 msec. The appearance of superpolarization has been attributed by Bockris and

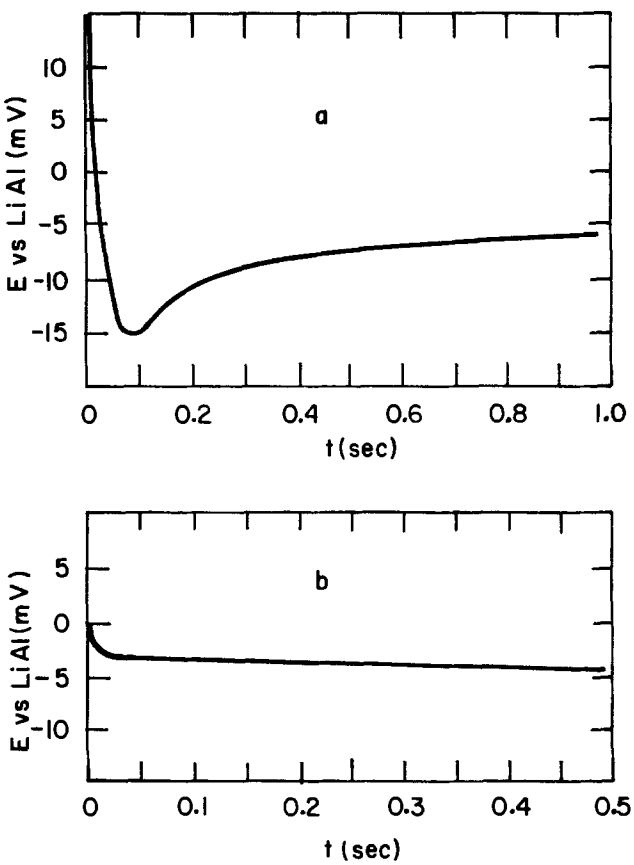


Fig. 8. Galvanostatic transients for initial charging of lithium into aluminum (i = 30 mA/cm²): (a) initial transient, (b) after predeposition of lithium.

co-workers (20) to the presence of impurities. The possibility that the superpolarization is due to an oxide film was considered. Such a film should, however, be reduced following the initial deposition of lithium so that subsequent current pulses should no longer exhibit superpolarization. This is clearly not so. Moreover, in some experiments the aluminum wires were preanodized at ~1.3V to clean up the surface. Superpolarization was also observed reproducibly with such pretreated wires indicating that oxide films are not responsible for the phenomenon. Vermilyea (21), however, has shown that such transient effects may be expected due to changes in surface configuration during electrolytic crystal growth. In the present case, the superpolarization is probably associated with the difficulty of initially forming the surface layers of β-phase LiAl, *i.e.*, it indicates the onset of electrocrystallization of the intermetallic compound and the large overpotential is due to slow nucleation (22). Calculation of the charge passed at the peak of the transient shows that the amount of lithium deposited corresponds to a few atomic layers. The superpolarization increases nearly linearly with current density from 8 mV at 20 mA/cm^2 to 25 mV at about 160 mA/cm^2. This variation indicates a dependence of supersaturation on overpotential. These values, considered as overvoltage for nucleation, are in accord with theoretical predictions (21). Following Kabanov (9), the superpolarization may also be associated with the difficulty of initially incorporating lithium atoms into the aluminum at high rates, owing to the relatively few vacancy sites available on the surface. A return of the superpolarization on standing at open circuit presumably results from diffusion and dissolution of the surface layer lithium into the interior of the electrode or chemical dissolution of lithium in the electrolyte and dissipation of the vacancies into sinks within the electrode. The time needed for the electrode potential to relax from 0 to ~1.2V *vs.* LiAl depends on the amount of charge passed, *i.e.*, the amount of lithium incorporated during the cathodic pulse.

Following the predeposition of lithium equivalent to a few atomic layers on an aluminum wire, the transient exhibits no superpolarization but rather a fairly flat overpotential with a slow risetime in the order of milliseconds (Fig. 8b). It is interesting to examine the process that gives rise to this overpotential. The slow risetime suggests that the rate-controlling step is not the charge transfer process. For the latter, the risetime, t_R is approximately

$$t_R \approx \frac{4RT}{Fi_0} C$$

e.g., t_R would be about 40 μsec for a double layer capacity, of 20 μF/cm^2 and an exchange current density, of 30 mA/cm^2 at 450°C. The large time constant can be associated with a high pseudocapacitance which may be caused by an adsorption layer on the electrode surface (23). Values of the pseudocapacitance calculated from the initial portion of the overpotential-time ($\eta - t$) curves, *i.e.*, $C = i/(d\eta/dt)_{t\to 0}$, are in the order of mF/cm^2 of apparent electrode area. One interpretation is that the discharge of Li^+ under the present condition occurs via the intermediate state of a chemisorbed lithium atom (24). The slow risetime may also be explained in terms of the high solubility of lithium in aluminum and a change of surface coverage upon switching on the current. This type of behavior is analogous to that observed for hydrogen discharge on palladium which has been postulated to occur also via an adsorbed state (18, 25, 26). The possibility of the high pseudocapacitance being due to a large surface area of the electrode cannot be ruled out at the present time. It appears unlikely, however, that the deposition of only a few atomic layers of lithium could cause such a large area change. The interpretation that appears most plausible to us is that of Rangarajan (27) who showed that a slow risetime in overpotential could arise from a slow incorporation of the discharged species at the lattice building sites. This appears more consistent with the current-potential relation (overpotential measured at 250 msec after applying the current step) shown in Fig. 9. The nonlinear behavior clearly rules out charge transfer or diffusion as the cause of the overpotential. The linear i *vs.* η^2 replot is indicative of the "square law" relation that is characteristic of electrocrystallization processes controlled by a slow lattice growth (22). The large change in lattice parameters (4.05Å for the α-phase to 6.4Å for the β) (28) and accompanying volume expansion during crystallization of the β-phase LiAl presumably are also responsible for the slow lattice growth. Further details of the kinetics of nucleation and growth of the β-phase are being investigated.

It appears that an interesting analogy exists between the process of electrochemical incorporation with compound formation to that of the high temperature oxidation of metals (29). In the latter, the chemical reaction leading to the formation of a metal oxide on the surface occurs first. Further growth and thickening of the oxide layer then occurs in many instances by the diffusion of oxygen through the oxide film and reaction at the oxide-metal interface. The parabolic law governing the rate of growth of the oxide layer is analogous to the Q *vs.* $t^{1/2}$ behavior observed in this work on electrochemical incorporation. This is not surprising, since in both cases the rates are limited by the diffusion of the reacting species. Interestingly, electrochemical incorporation appears to differ also from conventional electrodeposition in that while crystal growth occurs progressively on the surface in the latter case, it occurs at the intermetallic compound-metal interface in the former and progressively moves inward toward the center until all the aluminum is converted to the new phase.

Conclusions

From the foregoing results and discussion, the following conclusions can be made:

1. The incorporation of lithium into aluminum to form the α-phase (at potentials anodic of LiAl) is limited by the rate of lithium diffusion into the aluminum. The diffusivity of lithium in aluminum was measured to be 4.0 $\pm$ 1.0 $\times$ 10^{-10} cm^2/sec at 450°C.

2. At potentials that allow the formation of a layer of the intermetallic compound LiAl on the electrode surface, incorporation is limited initially by the reaction to form LiAl and subsequently by the rate of diffusion of lithium into the β-phase as it thickens. The apparent diffusivity of lithium in the β-phase was found to be in the order of 10^{-8} cm^2/sec.

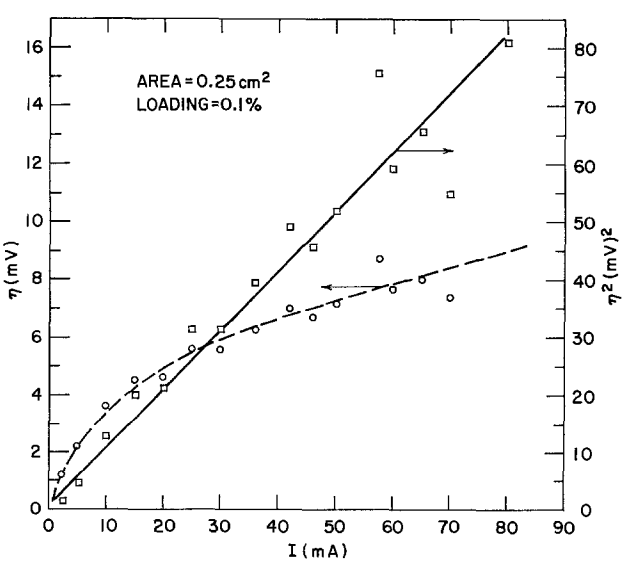


Fig. 9. Current-potential curve at short times

3. The initial steps in the formation of the intermetallic compound LiAl appear to involve typical electrocrystallization processes (nucleation and lattice growth). The process of electrochemical incorporation with compound formation bears a striking similarity to the high temperature oxidation of metals.

Acknowledgments

The author is grateful to Dr. R. K. Steunenberg and Dr. F. A. Cafasso for their continued interest in this work; also to Dr. M. F. Roche for comments on the manuscript and Gwen Kesser for editorial assistance. This work was done under the sponsorship of the U.S. Energy Research and Development Administration, Division of Physical Research.

Manscript submitted Oct. 18, 1976; revised manuscript received Jan. 5, 1977.

Any discussion of this paper will appear in a Discussion Section to be published in the December 1977 JOURNAL. All discussions for the December 1977 Discussion Section should be submitted by Aug. 1, 1977.

Publication costs of this article were assisted by Argonne National Laboratory.

LIST OF SYMBOLS

A	apparent electrode area calculated on the basis of the wetted area of the starting aluminum wire
C	capacitance
C_o	initial lithium concentration
$C(t)$	concentration of lithium at time t
D	diffusion coefficient
E	electrode potential with respect to LiAl reference
$\mathbf{F}$	Faraday constant
i	current density calculated on the basis of apparent electrode area
i_o	exchange current density
I	current
n	number of electrons transferred
η	overpotential
Q	quantity of charge passed
R	gas constant
t	time
t_R	risetime of transient
τ	transition time

REFERENCES

1. W. J. Walsh *et al.*, Proceedings of the 9th Intersociety Energy Conversion Engineering Conference, San Francisco, California, Aug. 26-30, 1974.
2. W. W. Schertz, A. A. Chilenskas, and V. M. Kolba, Proceedings of the 10th Intersociety Energy Conversion Engineering Conference, Newark, Delaware, Aug. 18-22, 1975.
3. N. P. Yao, L. A. Heredy, and R. C. Saunders, *This Journal*, **118**, 1039 (1971).
4. J. R. Selman, D. K. DeNuccio, C. J. Cajigas, and R. K. Steunenberg, Abstract 35, p. 75, The Electrochemical Society Extended Abstracts, Spring Meeting, Toronto, Canada, May 11-16, 1975.
5. A. L. L'vov and A. A. Gnilomedov, *Elektrokhimiya*, **11**, 507 (1975).
6. A. L. L'vov *et al.*, *ibid.*, **11**, 1322 (1975).
7. S. D. James *Electrochim. Acta*, **21**, 157 (1976).
8. S. D. James, Naval Ordnance Laboratory Report NOLTR-72-224 (AD-757-007), White Oak, Maryland (Jan. 1973).
9. B. N. Kabanov, I. G. Kiseleva, and I. I. Astakhov, *Elektrokhimiya*, **8**, 955 (1972).
10. M. Hansen and K. Anderko, "Constitution of Binary Alloys," McGraw Hill Book Company, New York (1969).
11. D. M. Kolb, M. Przasnyski, and H. Gerischer, *J. Electroanal. Chem.*, **54**, 25 (1974).
12. J. Plambeck, *J. Chem. Eng. Data*, **12**, 77 (1967).
13. C. A. Melendres and C. G. Sy, To be published.
14. J. H. Christie, G. Lauer, and R. A. Osteryoung, *J. Electroanal. Chem*, **1**, 60 (1964).
15. I. I. Astakhov, *Elektrokhimiya*, **8**, 1549 (1972).
16. P. Delahay, "New Instrumental Methods in Electrochemistry," Interscience, New York (1954).
17. L. P. Costas, U.S. AEC Report TID-16676 (1963).
18. K. Vetter, "Electrochemical Kinetics," Academic Press, New York (1967).
19. D. O. Raleigh and H. R. Crowe, *This Journal*, **116**, 40 (1969).
20. W. Mehl and J. O'M. Bockris, *Can. J. Chem.*, **37**, 190 (1959).
21. D. A. Vermilyea, *J. Chem. Phys.*, **25**, 1254 (1956).
22. M. Fleischmann and H. R. Thirsk, in "Advances in Electrochemistry and Electrochemical Engineering," Vol. 3, P. Delahay and C. W. Tobias, Editors, p. 123, Interscience, New York (1965).
23. E. Gileadi and B. E. Conway, in "Modern Aspects of Electrochemistry," Vol. III, J. O'M. Bockris and B. E. Conway, Editors, chap. 5, Butterworths, London (1964).
24. J. O'M. Bockris and A. K. N. Reddy, "Modern Electrochemistry," Vol. 2, p. 1026, Plenum Press, New York (1970).
25. A. Frumkin and N. Aladjalova, *Acta Physicochim. URSS*, **19**, 1 (1944).
26. R. Clamroth and C. A. Knorr, *Z. Electrochim*, **57**, 399 (1953).
27. S. K. Rangarajan, *J. Electroanal. Chem.*, **16**, 485 (1968).
28. W. B. Pearson, "A Handbook of Lattice Spacings and Structures of Metals and Alloys, Vol. 4, p. 365, Pergamon Press, New York (1958).
29. P. Kofstad, "High Temperature Oxidation of Metals," John Wiley & Sons, New York (1966).

The Determination of the Corrosion Rate of Zinc in Solution by the Differential Pulse Method

Kevin G. Boto[1] and Lindsay F. G. Williams

Department of Defence, Materials Research Laboratories, Ascot Vale, 3032 Melbourne, Australia

ABSTRACT

The electrochemical measurement of the corrosion rate of zinc in near-neutral solutions using a differential pulse polarograph has been achieved to a greatly improved accuracy compared with previous work. The perturbation of the corroding system is minimized as the potentiostatic polarizing pulse is applied for only 60 msec. The double layer charging of the electrode is monitored on an oscilloscope and the faradaic current measurements made by the normal Y recorder output of the polarograph. The iR correction facility on the polarograph is used to determine the Tafel parameters and can also be used if resistance overvoltage is a problem during the polarization resistance measurements. Four different solutions are examined where the cathodic processes are either separately or jointly oxygen reduction or hydrogen evolution. Where only one cathodic process occurs, the correlation of the weight loss with the corrosion current calculated by the Stern-Geary method is within 7%. Where two cathodic processes occur, errors of up to 15% are encountered.

Recent studies on the corrosion of zinc in aerated near-neutral aqueous solutions (1-3) highlight two important areas which have been overlooked in past investigations. The first is a comprehensive study of the cathodic reactions which control the rate of corrosion of zinc in these solutions. Despite the common use of zinc as a sacrificial coating, a thorough study of the oxygen reduction reaction on zinc has been reported only recently (1) and it is obvious from this work that a concurrent hydrogen evolution reaction occurs in near-neutral solutions. Therefore, the exact nature of the cathodic reactions on zinc still requires further investigation to determine the extent of the hydrogen evolution in near-neutral solutions.

The second area where further research is required is in the electrochemical methods for determining instantaneous corrosion rates. When studying corrosion reactions and particularly at rotating ring-disk electrodes, it is important to be able to monitor the corrosion rate of the disk because the cathodic reactions are usually surface dependent and, therefore, vary throughout the course of any one experiment. The refinement of simple methods such as linear polarization (4, 5) by Oldham and Mansfeld (6, 7) and the derivation of new methods by Barnartt (8) and others (9-11) have not produced any dramatic improvements in the correlations between electrochemically calculated corrosion currents and the weight loss for zinc freely corroding in aqueous solution. Impedance measurements (12) have been shown to yield reasonably accurate corrosion rates for steel, but they are limited to reactions where the corrosion current does not alter during the course of the experiments. In practice, this does not usually occur, particularly where corrosion products are formed on the surface.

It has been our experience with corrosion rate measurements that the inaccuracies in determining the polarization resistance, $\Delta E/\Delta i$, and Tafel parameters usually result in far greater errors than the use of the simple Stern-Geary equation (4). Standard corrosion rate measurements on zinc in aqueous solution involve a constant current and the measurement of small potential changes (2, 3, 13). The applied constant current results in drifts in the potential of the zinc particularly in the pH range where corrosion products form on the surface. When superpolarization (14, 15) does not occur, the ΔE is usually measured after a few seconds to avoid the slow polarization of the electrode. For example, when zinc is immersed in an aerated, neutral chloride solution, a typical set of ΔE values after 5, 30, 60, and 180 sec at a polarizing current of 0.11 μA/cm^2 was 1.0, 1.5, 1.8, and 2.0 mV (16). When superpolarization occurs, it is normal to allow this to decay before recording the ΔE value (2).

One way of overcoming these problems is by the use of a potentiostatic method where a potential pulse is applied to the corroding specimen for a relatively short period of time. In this way, the perturbation of the system from its corrosion potential is minimized. These measurements can be recorded using a modern polarographic analyzer with a differential pulse mode.

A previous communication (17) described the differential pulse method for corrosion rate determinations, and the present paper shows the application of the method to a number of systems where zinc is freely corroding in near-neutral aqueous solutions with oxygen reduction and hydrogen evolution as cathodic processes.

Experimental

Zinc (99.99%) specimens (approximately 5 cm^2) were machined to a cylindrical shape to fit a standard electrode assembly (18). The zinc electrode assembly, an auxiliary electrode, and a saturated calomel electrode (SCE) with a Luggin capillary were fitted through a 75 mm multisocket, flat flange lid. The lid was placed on a jacketed beaker with a capacity of 600 ml and in all experiments the temperature was maintained at 25.0°C. The lid also contained facilities for bubbling either high purity grade nitrogen or medical grade air through the solution.

The solutions used in experiments were made from either AR- or R-grade chemicals with double distilled water. A 0.1 mole/liter ethylenediaminetetra-acetic acid (EDTA) and 0.1 mole/liter sodium acetate solution was adjusted to a pH of 8.5 by additions of NaOH. Similarly, a 0.2 mole/liter succinic acid solution was adjusted to a pH of 5.6. The other solution used was an unbuffered 0.1 mole/liter NaCl solution with a pH of 6.3. The volume of solution used in each experiment was 500 ml.

The weight loss of zinc during each experiment was determined in one of two ways. Where the weight change was greater than 10 mg, the specimen was weighed before and after the corrosion experiment. In all other experiments, the solution was analyzed for zinc using a Princeton Applied Research (PAR) Model 174 polarographic analyzer in the differential pulse

[1] Present address: Australian Institute of Marine Science, Townsville 4810, Australia.

Key words: corrosion, linear polarization, differential pulse, zinc.

mode with a scan rate of 2 mV/sec, a pulse amplitude of 25 mV, and a drop time of 1 sec.

The differential pulse corrosion rate measurements were made using the PAR 174 polarograph with the following sequence. The corrosion potential (E_{corr}) of the zinc in the solution was measured using a Tacussel S70 millivoltmeter. With the polarograph in the normal mode (*i.e.*, as an ordinary potentiostat), the potential of the zinc was set at the E_{corr} value by adjustment of the initial potential settings, so that if the polarograph were disconnected there would be no change in potential of the zinc. The final adjustment of E_{corr} was achieved by zeroing the current output of the potentiostat. During all these measurements the scanning facility was not used and the operations were all conducted with the polarograph set on initial potential. The polarograph was switched to the differential pulse mode usually with an amplitude of 5 mV and a pulse frequency of 1 sec. This operation superimposed a 5 mV pulse of 60 msec duration on the E_{corr} value every 1 sec. The current response for the zinc electrode was photographed on a Tektronix oscilloscope Type 561A connected to the PAR 174/50 a-c interface unit or measured on a Moseley Model 7030A recorder.

The Tafel slopes for the anodic dissolution of zinc were determined in the N_2 saturated solutions. As there was appreciable curvature of the log *i vs. E* plots at higher current densities, the *iR* compensation facility available on the PAR a-c interface unit was used. The Tafel slope for the hydrogen evolution reaction was determined in a similar manner.

Results

The corrosion rate of zinc in solution has been measured by the differential pulse method for four different situations. They are where; (*i*) oxygen reduction is the major cathodic process; (*ii*) hydrogen evolution is the major cathodic process; (*iii*) both hydrogen evolution and oxygen reduction occur, but at a pH where no corrosion products precipitate on the surface; and (*iv*) both cathodic processes occur as in (*iii*) but corrosion products precipitate on the surface.

(i) Zinc in an aerated EDTA solution (pH = 8.5).— The results for this solution are used to demonstrate the two different methods of recording the current response to the potential pulse. The first method involves the use of an oscilloscope to display the complete current response and the clock monitor on the PAR interface unit enables the oscilloscope to be triggered just prior to the application of each pulse. The current-time profile resulting from the application of a 5 mV potential pulse of about 60 msec duration to the zinc electrode immersed in this solution is shown in Fig. 1 for both anodic and cathodic pulses. The decay in current associated with double layer charging was complete within the first 10 msec, after which a constant faradaic current was observed. At the completion of each pulse, there was a similar but inverted current decay associated with the reversion of the double layer to its previous state at E_{corr}. The frequency of the pulses could be adjusted as discussed above and in these measurements the pulse frequency was 2 sec^{-1}.

The second method of recording the current uses the current sampling system on the PAR polarograph where the current flow is measured just before the application of the pulse and again at the end of the pulse. The readout presented to the recorder is the difference between these two sampled currents. However, there is one further complication because this difference between the two currents is averaged with the previous difference readings in the PAR memory before being displayed on the recorder. Therefore, when the current response to the first pulse is measured it is displayed as an average with zero and is much less than the final reading obtained after numerous pulses. For this reason about twenty pulses are required before the recorder reaches the actual current value as

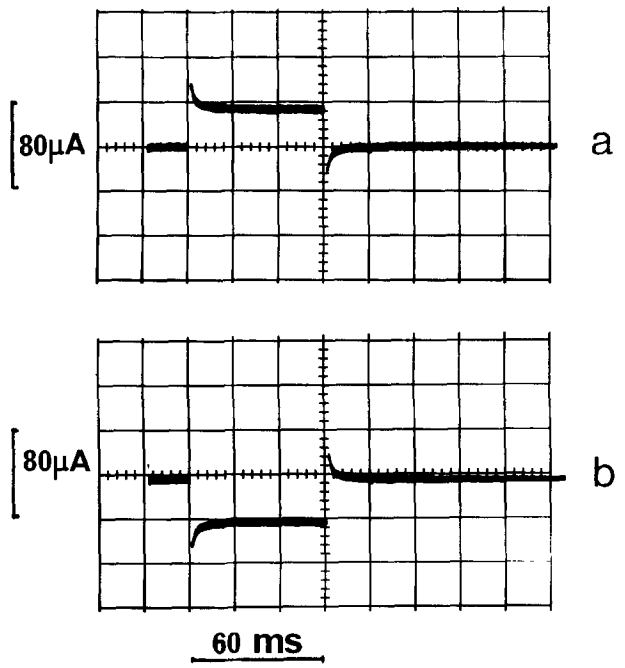


Fig. 1. Oscilloscope traces showing the current-time profiles for 5 mV pulses to a zinc electrode after 3 hr immersion in an air-saturated 0.1 mole/liter EDTA, 0.1 mole/liter sodium acetate solution at pH 8.5: (a) cathadic; (b) anodic pulses.

shown in Fig. 2 where about fifty potential pulses of 5 mV were applied in the anodic direction before inverting the pulse to make it cathodic using the scan direction switch. After another 50 pulses the potential pulse was again reversed and the procedure repeated. With a pulse frequency of 2 sec^{-1}, the total time for the recording in Fig. 2 was 100 sec. The currents re-

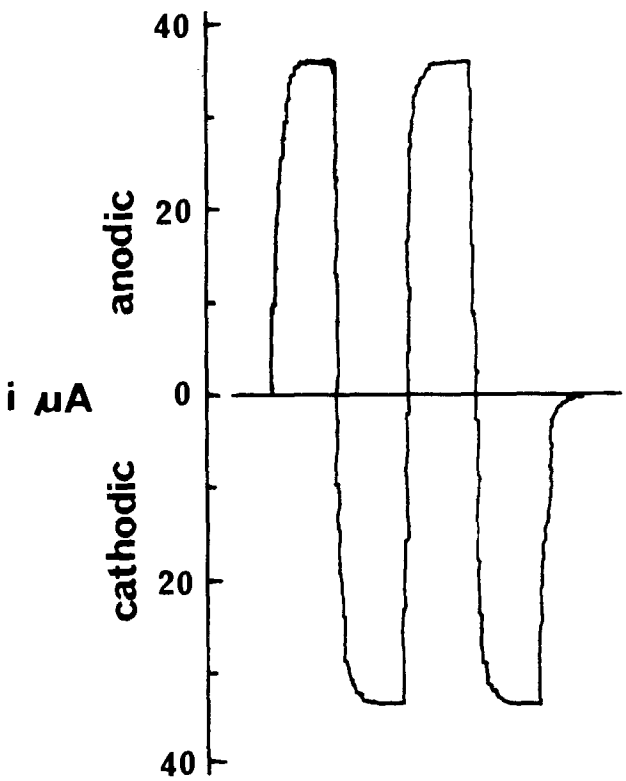


Fig. 2. Recorder trace showing the sampled current when two series (of about 50 pulses each) of anodic and two series of cathodic pulses are applied to a zinc electrode after 29 hr immersion in an air-saturated 0.1 mole/liter EDTA, 0.1 mole/liter sodium acetate solution at pH 8.5.

corded in this way agreed with those measured using the oscilloscope. In general, the oscilloscope was used to monitor the decay curves and the recorder output was used for current measurements.

The cathodic process in this solution is diffusion-controlled oxygen reduction as shown by rotating disk studies (1). Therefore, the corrosion current, i_{corr}, was calculated using the Stern-Geary equation (4)

$$\frac{\Delta E}{\Delta i} = \frac{\beta_a}{2.3\, i_{corr}} \qquad [1]$$

where β_a was the Tafel slope for the anodic dissolution of zinc in this solution. Using the iR correction facility on the PAR interface unit, the value of β_a was found to be 81 ± 2 mV. It is recognized that there is some deviation from linearity of the E *vs.* i plot with the 5 mV pulses as evidenced by the fact that anodic currents were typically 7-12% larger than cathodic currents. However, this relatively small deviation leads only to small errors in the calculated i_{corr} values. In all experiments, the corrosion potential was sufficiently different from the reversible zinc potential to be able to use Eq. [1].

The average i_{corr} value for each experiment was obtained by plotting the individual i_{corr} values against time and measuring the area under the curve. The average i_{corr} values for duplicate experiments where zinc samples were immersed in an aerated EDTA solution at pH 8.5 were 13.2 and 12.9 $\mu A/cm^2$ compared with 13.1 and 13.3 $\mu A/cm^2$ calculated from the weight loss, respectively.

As previously reported (17), the values calculated by the Barnartt method (8) were about 25% higher than those calculated as above. For the Barnartt method pulses of 10 and 25 mV were used and similar results were obtained with both pulse amplitudes.

There was some superpolarization of the zinc, usually occurring after several hours immersion in this solution. The recorder trace in Fig. 3 shows the worst case of superpolarization encountered with potentiostatic pulses of 4 sec duration. However, the differential pulse method which only permits a 60 msec polarization of the zinc does not allow sufficient time for an equilibrium value to be achieved. The presence of superpolarization effects can be identified with even 60 msec pulses by a U-shaped current trace. Superpolarization was not observed in all experiments in this solution despite the fact that there was no insoluble corrosion product.

(ii) Zinc in a deaerated succinate buffer solution (pH = 5.6).—The cathodic process in this solution was hydrogen evolution, which is an activation-controlled process as shown by rotating zinc-disk studies (1, 19).

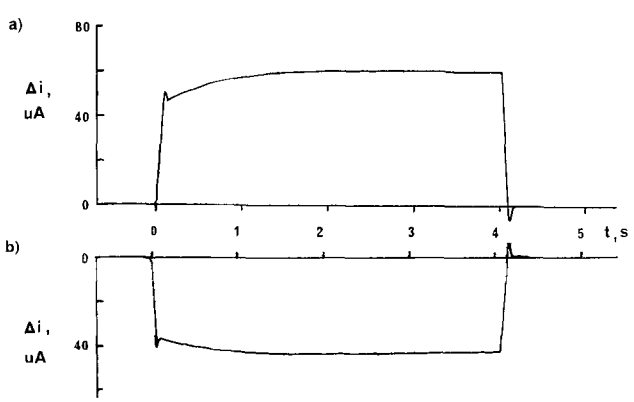


Fig. 3. Recorder traces showing the superpolarization effect in the current-time profiles for 5 mV pulses of 4 sec duration to a zinc electrode after a 4 hr immersion in an air-saturated 0.1 mole/liter EDTA, 0.1 mole/liter sodium acetate solution at pH 8.5; (a) anodic; (b) cathodic pulses.

The oscilloscope traces of current *vs.* time when 5 mV pulses were applied to the corroding zinc specimen are shown in Fig. 4. The capacitive current decay associated with the application of the potential pulse was generally complete by the time the current measurements were made. Where corrections were necessary, the current near the end of the 60 msec pulse was corrected in the following way. From the cathodic current decay after the end of the anodic pulse, the capacitive current was measured after 50 msec and subtracted from the cathodic i value. The decay curves in Fig. 4 are typical of the results for this solution and, therefore, these corrections were very minor.

The currents were generally obtained from the recorder trace and used in the Stern-Geary equation (4)

$$\frac{\Delta E}{\Delta i} = -\frac{\beta_a \beta_c}{2.3\, i_{corr}\,(\beta_a + \beta_c)} \qquad [2]$$

where β_c was the Tafel slope for the hydrogen evolution reaction. Both β_a and β_c were measured using iR correction and were 38 and −111 mV, respectively.

The i_{corr} values depended on the pretreatment of the zinc surface and this led to substantial changes in the corrosion rate during many experiments. An example of this is shown in Fig. 5 where the calculated i_{corr} values increased from 640 to 950 μA during the course of the experiment. This surface dependence of the reaction has been studied in greater detail (19). The average i_{corr} values were from the area under the i_{corr} *vs.* time plots, and two representative corrosion rate experiments resulted in average i_{corr} values of 55.0 and 782 μA compared with the i_{corr} values calculated from analysis of the zinc in the solution of 52.7 and 749 μA, respectively. The lower currents were obtained using

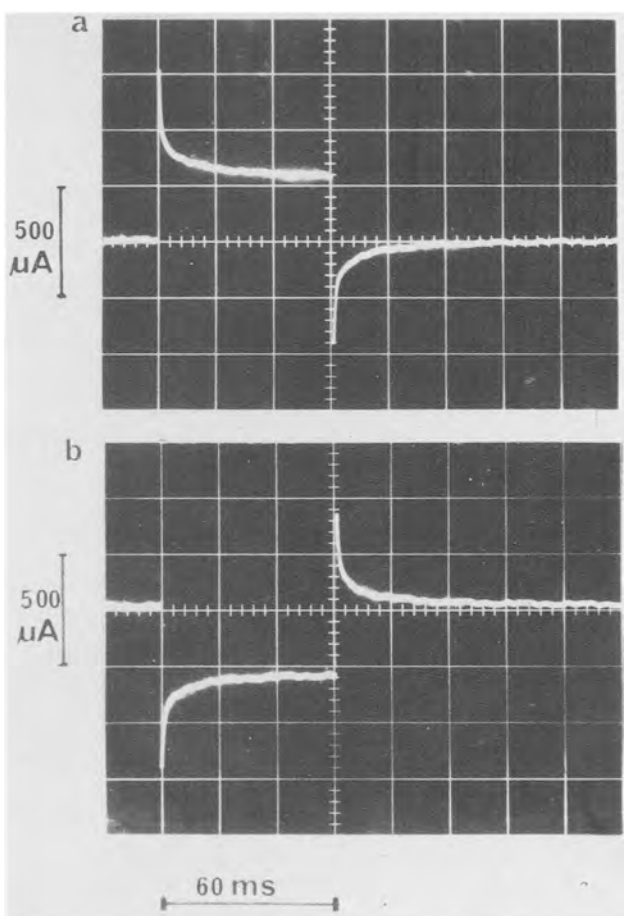


Fig. 4. Oscilloscope traces showing the current-time response to 5 mV pulses applied to a zinc electrode after 23 hr immersion in a deaerated succinate solution at pH 5.6; (a) anodic; (b) cathodic pulses.

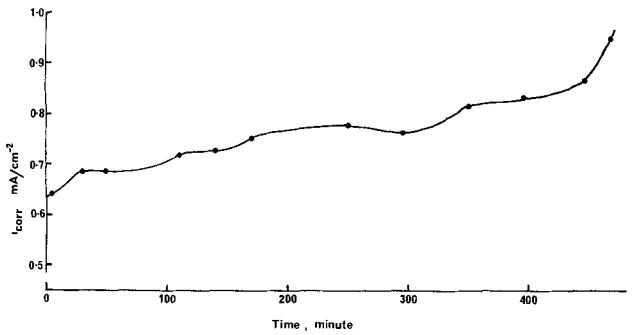


Fig. 5. Plot of the calculated corrosion current i_{corr} vs. the time of immersion of a zinc specimen in a deaerated succinate solution of pH 5.6.

a chemically polished zinc surface, while the higher currents were from the same sample after several days immersion in the deaerated succinate buffer solution.

(iii) Zinc in an aerated succinate buffer solution (pH = 5.6).—In this solution a mixed cathodic process occurs, that is, the diffusion-controlled oxygen reduction reaction and the activation-controlled hydrogen evolution reaction. Therefore, to accurately calculate i_{corr} from the measured polarization resistance values ($\Delta E/\Delta i$), the relative contribution of each process to the over-all cathodic reaction must be known. It is difficult with the present stationary electrode set up to accurately measure the contribution of each process. This is because of irreproducible stirring effects in the cells due to air bubbling which affects the rate of oxygen reduction from one experiment to the next. Also, as discussed above, the hydrogen evolution reaction appears to change drastically during the course of an experiment and thus would require continuous monitoring, *e.g.*, by deaerating the solution and measuring the change in i_{corr} to yield an accurate average value.

Instead, it was assumed that the oxygen reduction reaction was the major cathodic reaction, and hence Eq. [1] with $\beta_a = 38$ mV was used to calculate i_{corr}. As seen below, the worst correlation achieved with the weight loss value was within 7%. Thus it appears that even with this seemingly gross assumption, the method still yields reasonably accurate values of i_{corr}. The good correlation is probably due to the fact that the calculation is relatively insensitive to the contribution of each reaction as can be easily seen by simple calculations using, *e.g.*, both Eq. [1] for a diffusion-controlled reaction and Eq. [2] for an activation-controlled process with $\beta_a = 38$ mV and $\beta_c = -111$ mV and assuming a 50% contribution for each reaction. Also, as the experiments were not unduly long (only a few days), it is likely that the hydrogen evolution reaction was only a minor contribution at first and increased slowly as the experiment proceeded, giving a low average contribution over about two days.

It is recognized that the calculation accuracy is limited by this assumption and the error would probably be greater for long-term experiments. However, the correlation achieved is much better than has been obtained by other workers.

Typical anodic and cathodic current-time traces are shown in Fig. 6. In these experiments the capacitive current decay was complete within the first 15 msec and the recorder trace was used to measure the Δi values. The corrosion rate of the zinc in this solution increased for both specimens during the course of the experiments as shown in Fig. 7, even though the potential remained relatively constant for the latter part of the runs. Integration of the i_{corr} *vs.* time curves yielded average i_{corr} values of 206 and 129 μA/cm^2 for the two specimens shown, compared with the values from the weight loss measurements of 191 and 126 μA/cm^2, respectively.

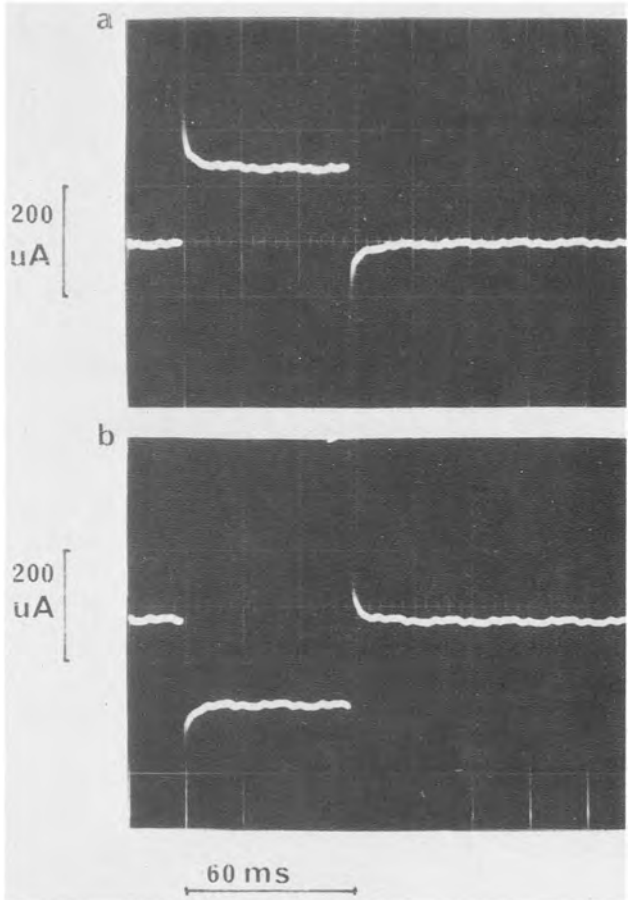


Fig. 6. Oscilloscope traces showing the current-time response to 5 mV pulses applied to a zinc electrode after 10 min immersion in an aerated succinate buffer solution at pH 5.6; (a) cathodic; (b) anodic pulses.

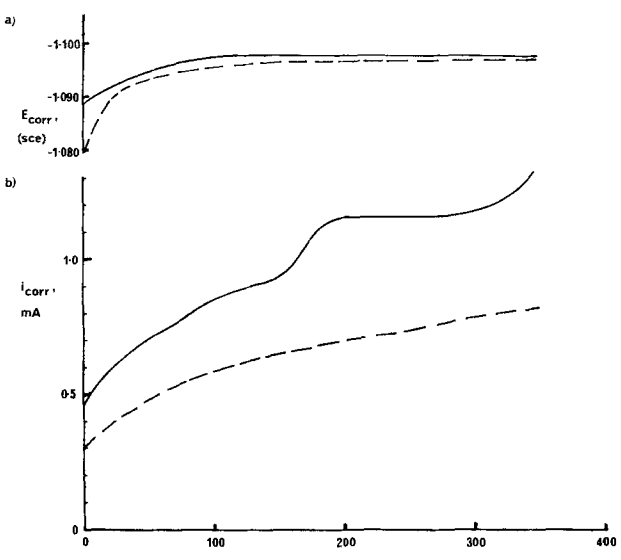


Fig. 7. Plots of (a) corrosion potential, E_{corr}, and (b) calculated corrosion currents, i_{corr}, for two experiments where zinc was immersed in an air-saturated succinate solution at pH 5.6.

(iv) Zinc in an aerated chloride solution (pH = 6.3).—In an aerated 1 mole/liter sodium chloride solution at pH 6.3, corrosion products formed on the zinc surface. Accordingly, this was the most complicated corrosion reaction studied, as there was also a mixed cathodic process. In the first part of the corrosion ex-

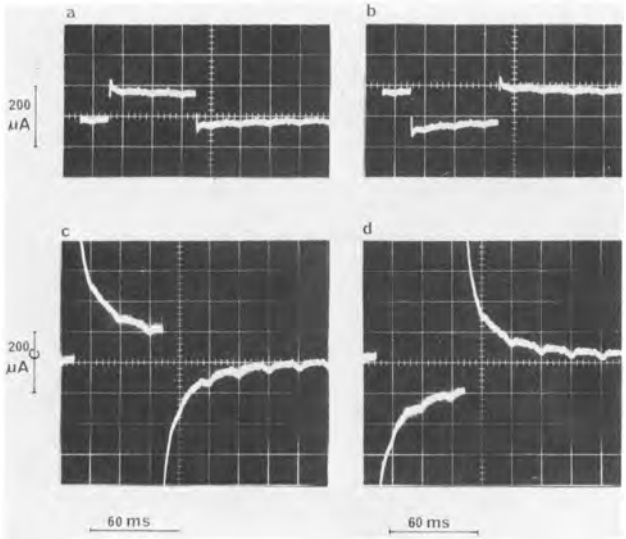


Fig. 8. Oscilloscope traces showing the current-time response to 5 mV pulses applied to a zinc electrode after (a) and (b) 20 min and (c) and (d) 24 hr immersion in an air-saturated 1.0 mole/liter NaCl solution; (a) and (c) cathodic; and (b) and (d) anodic pulses.

periments where the zinc surface remained relatively free from corrosion products, the current-time profiles were similar to those in Fig. 8 a and b for 5 mV pulses. As the experiment proceeded, the current decay associated with the double layer charging increased in magnitude and became more drawn out, as shown in Fig. 8 c and d. In the later part of these experiments, correction for the slow decay of the capacitive current was made by the methods described above.

The cathodic process in these solutions was essentially oxygen reduction and, as discussed above for the aerated pH 5.6 succinate solutions, the extent of hydrogen evolution is not known. It is likely to be less significant here because of the higher pH of the 1 mole/liter NaCl solution which being unbuffered results in an increase in the pH near the electrode surface due to the cathodic processes. Because of the buildup of corrosion product on the zinc, the reaction was not controlled simply by diffusion of oxygen through the solution to the reacting zinc surface, *i.e.*, as normally shown by rotating disk studies (1). The reaction was controlled by the rate of arrival of oxygen at the metal surface and this varied with the rate of nucleation, lateral spreading, and thickening of the films of corrosion product (20). Consequently, Eq. [1] was used to calculate i_{corr} values. The Tafel slope needed for the calculation was found to increase as the corrosion product built up on the surface. In all the Tafel plots the iR correction facility on the PAR polarograph was adjusted immediately before each polarization curve was determined. β_a was 10.7 mV initially and increased over a period of several days to 12.1 mV. The value of 10.7 was used in the calculations because most experiments only lasted one day. This value is lower than β_a values reported in the literature (3, 21) for similar solutions where no iR correction was used.

The average corrosion currents calculated from two experiments were 88 and 101 $\mu A/cm^2$ compared with the values obtained from the weight loss of 84 and 85 $\mu A/cm^2$.

Discussion

Differential pulse measurements.—The inaccuracies in most electrochemically determined corrosion rates originate from the experimental problems of measuring Tafel slopes and the polarization resistance. Without any modifications, commercial polarographs with a differential pulse mode are ideally suited to the differential pulse method of estimating the corrosion rates of metals immersed in aqueous solutions. The method results in the rapid, accurate measurement of the polarization resistance used in the calculation of corrosion rates by the Stern-Geary methods for either diffusion- or activation-controlled cathodic processes. As some polarographs are fitted with an iR correction facility, the Tafel parameters used in the equations can be determined with minimal resistance overvoltage effects. Accurate ΔE values are automatically obtained with pulses as small as 5 mV in amplitude. The errors associated with the nonlinearity of the E *vs.* i plot in the vicinity of E_{corr} is minimized by the use of small potential pulses and i_{corr} values with only small inherent errors are readily obtainable. The current ranges available on the polarographs suit slow corrosion reactions. With relatively fast corrosion reactions such as zinc in acidic solutions, the surface area of the specimen must be relatively small.

For the polarograph used in these experiments the duration of each pulse was about 60 msec and this could not be adjusted. With the corrosion reactions studied, only the neutral chloride solution resulted in decay profiles which were not essentially complete during the 60 msec. Clearly, in circumstances like this it would be advantageous to be able to extend the duration of the pulse. Nevertheless, a correction can be made by subtracting the decay associated with the end of the oppositely polarized pulse. In order to ensure that the recorded output does not suffer from inaccuracies due to slow capacitive decays, the oscilloscope should always be used to monitor the decay profile.

The amplitude of the pulse can be varied in 5 set steps for the PAR polarograph but other models offer continuous adjustment which would be better suited to examining the linearity of the E *vs.* i plot and using more complex equations for the calculation of i_{corr}. The time between pulses can be varied from 0.5 to 5 sec. The iR correction facility can be used for the Δi measurements if it is thought to be necessary (22).

Correlation of i_{corr} with weight loss.—The differential pulse method for zinc in the EDTA solution (pH 8.5) resulted in an i_{corr} value within 4% of that calculated from the weight loss as shown in the table. This was the best correlation achieved probably because the cathodic process was a simple diffusion-controlled oxygen reduction with negligible contribution from the hydrogen evolution reaction. This obviates the need to measure a cathodic Tafel slope. In addition, the electrode remained free from corrosion product and so the capacitive decay was always complete within 20 msec. Barnartt's method (8) for 10 and 25 mV pulses resulted in i_{corr} values about 25% high. However, even these results are much better than those reported by Walter using a galvanostatic technique and a similar calculation method (2) where typically the i_{corr} values were 80% higher than those calculated from chemical analysis of the zinc in solution.

In the deaerated succinate buffer solution (pH = 5.6), the cathodic reaction was hydrogen evolution. The rate of this cathodic process and, therefore, the rate of corrosion of the zinc was dependent on the surface pretreatment, with electropolished surfaces yielding very low i_{corr} values. The hydrogen evolution reaction is currently being studied (19) and is an activation-controlled process as shown by rotating disk studies. The correlation of i_{corr} in these deaerated solutions with weight loss was within 5%.

The correlations between electrochemically determined corrosion currents and the weight losses were excellent when only one cathodic process occurred. However, when oxygen reduction and hydrogen evolution occurred concurrently, the correlations in the worst figures were 7% for the succinate solution (pH = 5.6) where no corrosion products formed on the surface and about 15% in a neutral chloride solution with corrosion products present. It was not feasible in these experiments to estimate the relative contributions of

Table I. Comparison of electrochemically determined corrosion currents with those calculated by either weight loss [(a), (c), and (d)] or chemical analysis (b)

Solution	i_{corr}, μA/cm²		
	Electrochemical	Actual	% error
(a) Aerated EDTA	13.2	13.1	0.8
(pH = 8.5)	12.9	13.3	3
(b) Deaerated succinate	55.0	52.7	4
(pH = 5.6)	782	749	4
(c) Aerated succinate	206	191	7
(pH = 5.6)	129	126	2
(d) Aerated NaCl	88	84	5
(pH = 6.3)	101	85	16

the two cathodic processes but previous experience (1) indicated that hydrogen evolution was a minor contribution. If corrections for the hydrogen evolution were made it would result in lower calculated i_{corr} values. As all the i_{corr} values were too high in the solutions where both cathodic processes were occurring, a correction for the hydrogen evolution reaction would improve the correlation between the i_{corr} and weight loss.

In conclusion, the corrosion rate of zinc immersed in a number of near-neutral solutions can be accurately determined electrochemically by using iR compensation for the Tafel parameters and the differential pulse method as shown in Table I. The correlations with weight loss are an order of magnitude better than those normally experienced for zinc in near-neutral solutions. The method has been applied to rotated zinc-disk electrodes (19) and opens up great possibilities for rotated ring-disk studies on corroding metals. The use of iR correction can overcome the inaccuracies recently reported by Mansfeld (22).

Manuscript received Nov. 10, 1976; revised manuscript received Jan. 17, 1977.

Any discussion of this paper will appear in a Discussion Section to be published in the December 1977 JOURNAL. All discussions for the December 1977 Discussion Section should be submitted by Aug. 1, 1977.

Publication costs of this article were assisted by the Department of Defence of Australia.

REFERENCES

1. K. G. Boto and L. F. G. Williams, *J. Electroanal. Chem.*, **77**, 1 (1977).
2. G. W. Walter, *Corros. Sci.*, **16**, 573 (1976).
3. G. W. Walter, *ibid.*, **15**, 47 (1975).
4. M. Stern and A. L. Geary, *This Journal*, **105**, 638 (1958).
5. M. Stern, *Corrosion*, **14**, 440 (1958).
6. F. Mansfeld, *ibid.*, **29**, 397 (1973); *ibid.*, **30**, 92 (1974).
7. K. B. Oldham and F. Mansfeld, *Corros. Sci.*, **13**, 813 (1973).
8. S. Barnartt, *Electrochim. Acta*, **15**, 1313 (1970); *Corrosion*, **31**, 153 (1975).
9. D. B. Mathews, *Aust. J. Chem.*, **28**, 243 (1975).
10. R. L. Le Roy, *Corrosion*, **31**, 173 (1975).
11. M. Periassamy and P. R. Krishnaswamy, *J. Electroanal. Chem.*, **61**, 349 (1975).
12. I. Epelboin, M. Keddam, and H. Takenouti, *J. Appl. Electrochem.*, **2**, 71 (1972).
13. L. F. G. Williams, 6th International Congress on Metallic Corrosion, Sydney, Australia (1975), In press.
14. J. O'M. Bockris and H. Kita, *This Journal*, **108**, 676 (1961).
15. S. Barnartt, *ibid.*, **119**, 812 (1972).
16. Typical data from experiments in L.F.G. Williams, 6th International Congress on Metallic Corrosion, Sydney, Australia (1975).
17. K. G. Boto and L. F. G. Williams, *Corros. Sci.*, In press.
18. M. Stern and A. C. Makrides, *This Journal*, **107**, 728 (1960).
19. L. F. G. Williams, To be published.
20. C. J. Slunder and W. K. Boyd, "Zinc: Its Corrosion Resistance," Australian Zinc Development Association, Sydney (1974).
21. J. W. Johnson, Y. C. Sun, and W. J. James, *Corros. Sci.*, **11**, 153 (1971).
22. F. Mansfeld, *Corrosion*, **32**, 143 (1976).

Hardening Effect of Ultrasonic Agitation on Copper Electrodeposits

C. T. Walker[1] and R. Walker

Department of Metallurgy and Materials Technology, University of Surrey, Guildford, Surrey GU2 5XH, England

ABSTRACT

Studies have been made of the properties of copper electrodeposited from ultrasonically agitated, acid sulfate solutions. The intensity of ultrasound was measured with an acoustic calorimeter and the value for cavitation was determined. Transmission electron microscopy was used to examine annealed foil and deposits. Ultrasonic agitation was found to increase the hardness, reduce the porosity, and change the grain size. It also produced a high dislocation density compared with deposits from still or stirred baths. Hardening is considered to be due to a substantial reduction in porosity in deposits produced at low intensity and to work-hardening caused by the collapse of cavities at high intensities.

Ultrasonic agitation of the electrolyte increases the hardness of electrodeposits (1). The reason for this is not understood and the explanations so far advanced seem invalid. Thus, Müller and Kuss (2) propose that hardening is due to dislocation blocking caused by the incorporation of foreign particles in the plate. No experimental evidence supports this view; rather it has been demonstrated that deposits formed in an ultrasonic field contain fewer extraneous particles (3). According to Kochergin and Vyaseleva (3) hardening is caused by a decrease in grain size. Although some experimental results (1) appear to support this, it is more generally accepted that ultrasound in fact increases the grain size of deposits.

This paper provides a new explanation for the hardening effect of ultrasonic agitation: namely, that it is caused by work-hardening and by a decrease in porosity. In connection with the work-hardening we have previously presented experimental evidence (4) that ultrasound hardens both copper deposits plated

[1] Present address: Europäisches Institute für Transurane, Karlsruhe, West Germany.

from a stirred electrolyte and annealed copper sheet. In these cases hardening was associated with indentations in the surface caused by cavitation.

Equipment

Plating tank.—The plating solution was contained in a Perspex tank (15 × 30 × 15 cm) which was seated on the transducer probes (diameter 12.7 cm) of the ultrasonic generator; acoustic contact was made through a water layer (Fig. 1). The tank was modified to reduce the amount of ultrasonic energy lost by reflection at the water-Perspex-electrolyte interfaces formed with the base. This was effected by two acoustic windows in the base of the plating tank that were of a slightly smaller diameter (12.5 cm) so that the tank rested on top of the probes. The windows were formed by stretching a 500 gauge polythene sheet (100 μm thick) over two holes cut in the base of the tank. This material is favorable to sound transmission: its specific acoustic impedance is similar to that of water (their values are 1.85×10^6 and 1.5×10^6 kg^{-2} sec^{-1}) and it is thin compared with the wavelength of the sound used (15 cm in polythene).

Acoustic calorimeter.—The calorimeter is shown in Fig. 2. Ultrasound entered through a polythene acoustic window, J (diameter 4.8 cm), in the base. This was bonded to the body of the calorimeter and was secured by a push-fit Perspex ring, H. The Dewar flask, E (height 14 cm, ID 5 cm), ensured almost total internal reflection of sound and good thermal isolation. Castor oil, F (200 ml), was the sound absorbing fluid because it has a high sound absorption coefficient (1.85×10^{-5} neper cm^{-1}) compared with other fluids and its specific acoustic impedance (1.42×10^6 kg^{-2} sec^{-1}) is about the same as that of water.

Materials and Methods

Intensity measurement.—Calorimetry is the only reliable way of measuring the total acoustic energy dispersed in a cavitating liquid. A substitution system (5) was used in which the calorimeter was first calibrated by simulating the heating effect of ultrasound with a 1.2Ω resistance wire. Electrical power in the range 0.4-5.3W was applied to the heating coil from a d-c power pack for a fixed time of 3 min ± 1 sec. To calibrate the instrument heating curves were constructed for each power input to the coil by noting the temperature rise in the castor oil at 30 sec intervals. A calibration curve which covered the expected range of ultrasonic power in the electrolyte, was obtained from the heating curves by plotting their slopes, $d\theta/dt$, against the electrical power, I^2R, using the equation

$$\frac{d\theta}{dt} = \frac{I^2R - h}{MJS} \qquad [1]$$

where I = power pack current (A), R = heating coil resistance (Ω), M = mass of castor oil (g), S = specific heat of castor oil (cal g^{-1} °C^{-1}), J = mechanical equivalent of heat (Jcal^{-1}), and h = heat losses (W).

It can be seen from Eq. [1] that the calibration curve, $d\theta/dt$ *vs.* I^2R is a straight line with slope $(MJS)^{-1}$ and intercept $-h/MJS$. Heat losses from the calorimeter were small because the value of h, which was assumed to be independent of θ, was only 0.15W.

After calibration, the calorimeter, together with its heating coil, was transferred to the plating bath where the ultrasonic intensity in the electrolyte was measured. The ultrasonic power was estimated from the slope of each heating curve using the calibration curve and the intensity was determined by dividing the power value by the area of the acoustic window.

Although calorimetric methods of intensity measurement are generally agreed to be unreliable at low intensities, the substitutional technique gave good reproducibility on repetition of experiments and intensity values are believed accurate to better than ±10%.

Cavitation threshold intensity.—The cavitation threshold intensity in the electrolyte was determined with a piezoelectric disk connected to an oscilloscope. The disk, a PXE modified lead zirconate titanate ceramic was encapsulated in Araldite and mounted inside a plastic sleeve to avoid wetting and to give it rigid support. Initially at low intensity, the disk produced a sine wave trace on the oscilloscope, but as the intensity was increased the trace became distorted and eventually complete breakdown occurred. The cavitation threshold intensity was that at which distortion of the sine wave was first observed, and was found to be about 20 Wm^{-2}.

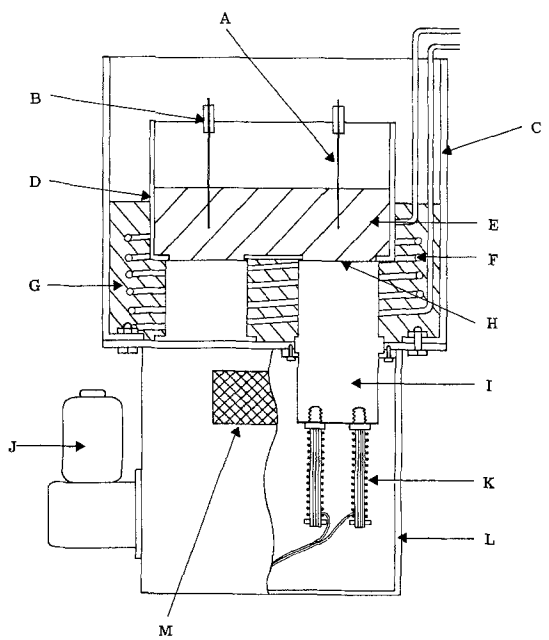


Fig. 1. Apparatus for ultrasonic agitation of the electrolyte. A, electrode; B, electrode clamp; C, stainless steel tank; D, Perspex plating tank; E, electrolyte; F, copper cooling coils; G, water bath; H, acoustic window; I, transducer probe; J, cooling fan and motor; K, transducer element; L, steel box; M, air vent; I, J, and K comprise the transducer unit.

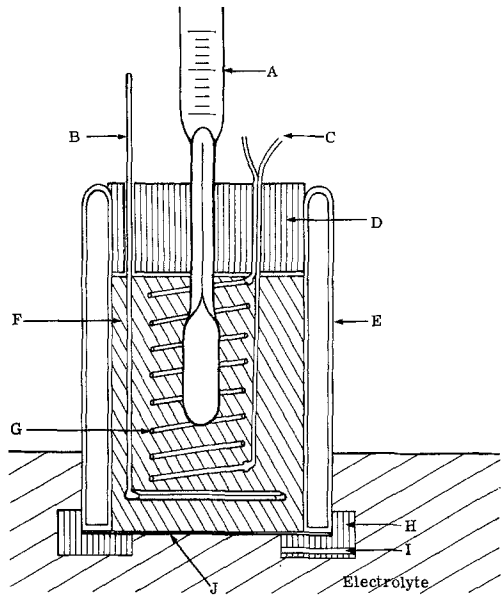


Fig. 2. Acoustic calorimeter. A, Beckman thermometer; B, glass stirrer; C, power pack lead; D, rubber bung; E, open-ended Dewar flask; F, castor oil; G, heating coil; H, Perspex L-shaped ring; I, vent hole for trapped air; J, polythene acoustic window.

General plating techniques.—Ultrasound of frequency 13 kHz was applied to a standard plating technique: namely copper deposition from an acid sulfate electrolyte. Since in ordinary industrial practice the electrolyte is stirred to increase bath efficiency and because ultrasonic agitation is often thought of only as a superior form of mechanical stirring, the properties of deposits from a stirred bath were compared with those of deposits from an ultrasonic bath and deposits from the still bath were used as a control. Electrodeposition was carried out with the three baths connected in series so that fluctuations in plating conditions such as deposition time and current density were the same. Each bath contained 4.1 of electrolyte the composition of which was $CuSO_4 \cdot 5H_2O$ 125 gl^{-1}, H_2SO_4 49 gl^{-1}. General grade chemicals and distilled water were used.

Both electrodes (15 × 5 cm) were made of copper: the anode of Analar grade foil (110 μm) and the cathode of either Analar foil or commercial grade sheet. The electrodes were placed 15 cm apart and in the ultrasonic plating tank they were above the acoustic windows parallel to the direction of sound propagation (Fig. 1). Before use the electrodes were degreased with acetone, etched in 50% HNO_3, and washed in distilled water. The backs of the cathodes were lacquered with "Lacomit" to give an electrode area of 20 cm^2 and a Perspex sheet was bonded to the back of electrodes subjected to ultrasonic intensities greater than 596 Wm^{-2}. This prevented the removal of lacquer during plating.

Deposits were produced at current densities in the range 20-700 Am^{-2}. Their thickness was fixed nominally at 78 μm and plating was performed at ambient temperature, which was 20° ± 2°C. The plate thickness was calculated from Faraday's law assuming a cathode current efficiency of 100%. Since ultrasound causes heating of the electrolyte, the above temperature was maintained in the ultrasonically agitated plating solution by copper cooling coils in the surrounding water bath (Fig. 1).

Hardness.—An Akashi microhardness machine with a diamond indenter and a 50g load was used. Because the surface of the deposits was rough (Fig. 3), before measuring the hardness it was necessary to smooth the

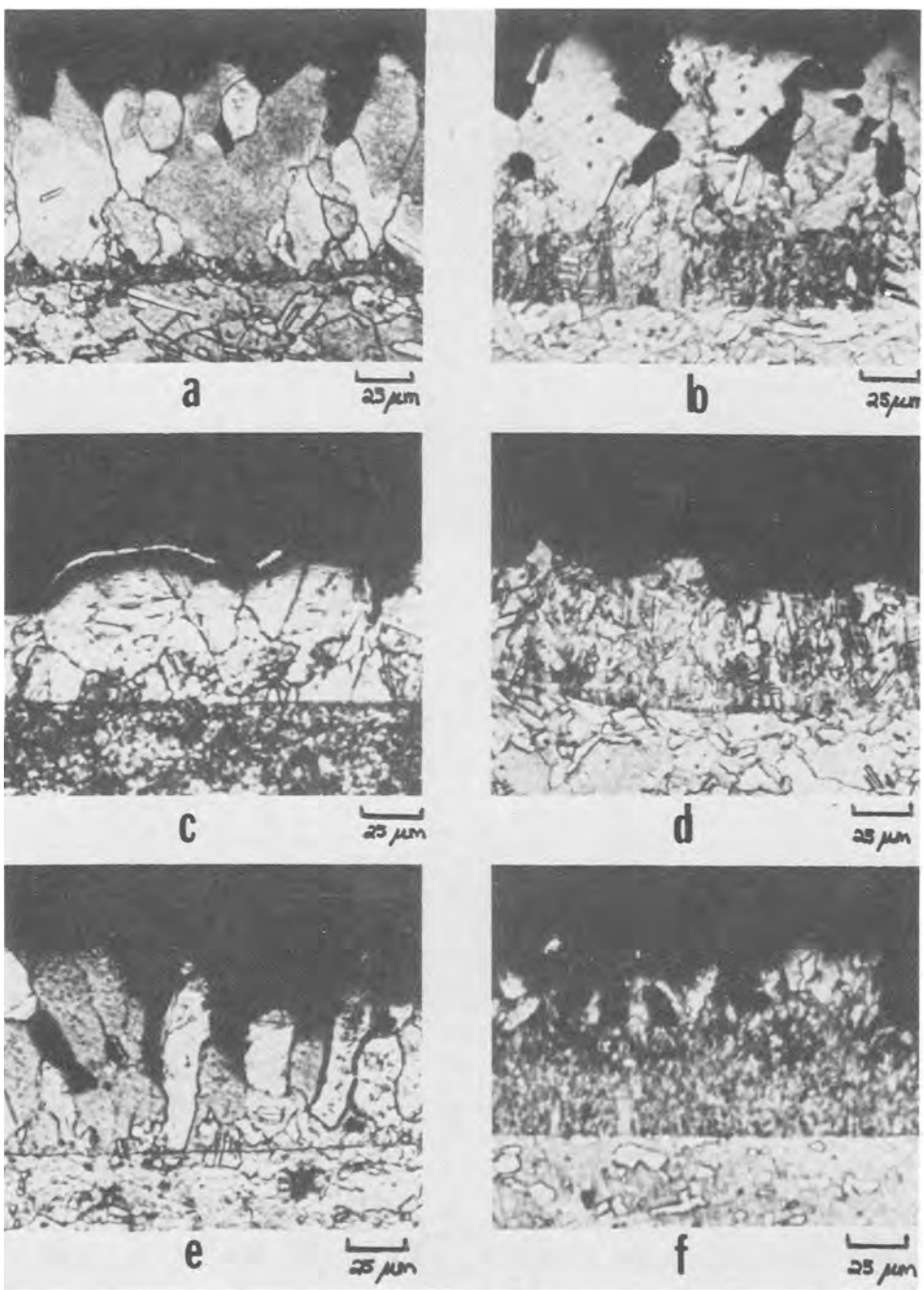


Fig. 3. Vertical sections through deposits. (a), (c), (e) Current density 100 Am^{-2}; (b), (d), (f) current density 300 Am^{-2}; (a), (b) stirred solution; (c), (d) ultrasonically agitated solution, I = 596 Wm^{-2}; (e), (f) still solution.

plate with 600 grade emery paper and lightly buff with metal polish.

Measurements were made on the surface of planar samples with the deposits attached to the cathode (copper sheet 720 μm thick). Eight determinations were carried out on each deposit (Fig. 4) and the mean and standard deviation calculated (illustrated in Fig. 5). Consistent hardness values were obtained on repetition of experiments. Thus Fig. 4 exemplifies the results from a number of observations. Since the deposit thickness was considerably more than ten times the maximum indentation depth (6.5 μm for copper of hardness 50 HV) the hardness values are unaffected by the hardness of the substrate cathode. The hardness was also unaffected by the procedure of smoothing and burnishing.

Grain size.—The linear intercept method (6) was used to determine grain size. Measurements were made on the surface of planar samples taken from the deposits used for hardness determination.

Sections of deposit with electrode were taken from the center of the cathode to avoid anomalous structures. They were mounted, ground, and polished parallel to the surface of the plate using standard metallographic techniques and etched in acidic ferric chloride solution to reveal the grains. The mean intercept length was determined from the linear distance containing about 100 grains and was measured using a Bausch and Lomb optical microscope.

In the ASTM standard (6) the correlation factor between the average intercept length and estimated grain size is about 1.12, but several other factors have been used including 1.5 (7) and 1.6 (8). To avoid confusion, therefore, the mean intercept length is reported here.

Porosity.—The porosity of plate was assessed from its density. Deposits were formed on foil cathodes at current densities of 100, 200, 300, and 400 Am^{-2} and density measurements were made with the deposits attached to the cathode. Three deposits were produced

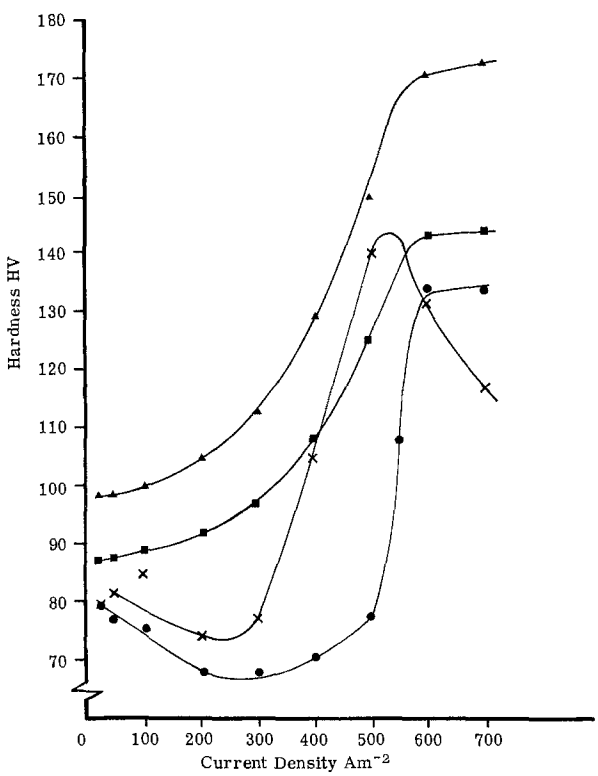


Fig. 4. Deposit hardness related to agitation and current density. ▲, Ultrasonic agitation, I = 928 Wm^{-2}; ■, ultrasonic agitation, I = 596 Wm^{-2}; X, still; ●, stirred. Each point represents the mean of eight separate determinations.

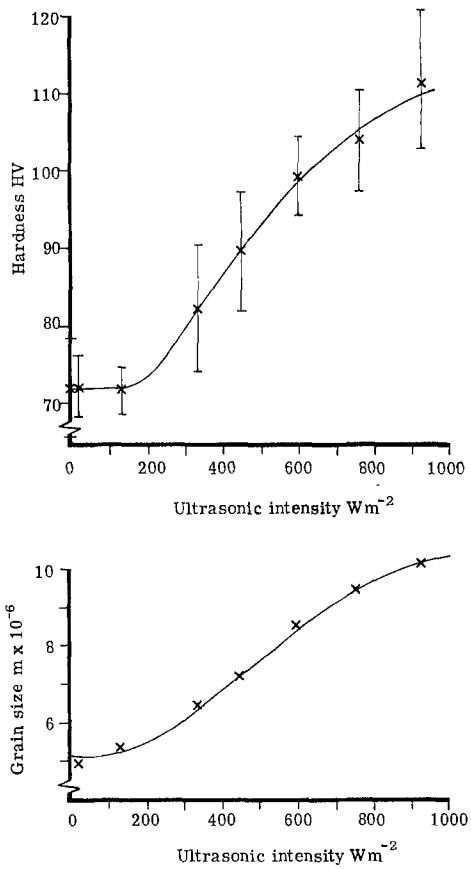


Fig. 5. Effect of ultrasonic intensity on deposit hardness and grain size, current density 300 Am^{-2}.

at each current density. The lacquer was removed from the back of the cathodes with acetone and the edges were trimmed to remove atypical structures.

Four specimens, each about 2 cm square, were cut from each cathode for density determination. The specimens were weighed in air and then in 100 ml of water containing about 0.1 ml of teepol to reduce surface tension. The deposit density, ρd, was calculated from Eq. [2] and the percentage porosity, P, from Eq. [3]

$$\rho d = \frac{T_t \rho m - T_f \rho f}{T_d} \qquad [2]$$

$$P = 100 - \left(\frac{\rho d}{\rho F} \times 100 \right) \qquad [3]$$

where T_t = total thickness of cathode foil and copper deposit, ρm = measured density, T_f = thickness of copper foil, ρf = density of copper foil, T_d = thickness of deposit, and ρF = density of the pore-free deposit.

This method gave a mean density for Analar copper foil of 8.956 gcm^{-3} which is close to the theoretical value of 8.96 gcm^{-3}. It was, therefore, accepted as a reliable method for the determination of deposit density. Deposit thickness was determined from metallographic sections, examples of which are contained in Fig. 3. Thickness values together with determined errors are reported in Table I which also lists deposit density and porosity.

Transmission electron microscopy.—A JEOL 100B electron microscope was used at 100 kV to examine the structure of: (*i*) deposits formed at a current density of 300 Am^{-2} (plating time 2 hr), (*ii*) an annealed copper foil cathode removed from a deposit after being subjected to ultrasound of intensity 596 Wm^{-2} for 2 hr, and (*iii*) an annealed copper cathode after the application of ultrasound (intensity 928 Wm^{-2}) through a continuous growing deposit.

Table I. Porosity of deposits related to agitation and current density

Current density, Am^{-2}	Thickness, μm	Measured density, gcm^{-3}	Std dev	Deposit density, gcm^{-3}	Porosity, %
		Still			
100	82 ± 12	8.85	0.03	8.70 ± 0.09 ± 0.10	2.9 ± 1.1 ± 1.0
200	80 ± 10	8.35	0.30	7.51 ± 0.76 ± 0.89	16.2 ± 9.9 ± 8.4
300	80 ± 10	8.43	0.25	7.70 ± 0.54 ± 0.75	14.1 ± 8.4 ± 6.1
400	80 ± 8	8.54	0.20	7.96 ± 0.57 ±0.54	11.3 ± 5.9 ± 6.5
		Stirred			
100	80 ± 10	8.95	0.01	8.93 ± 0.03 ± 0.02	0.3 ± 0.3
200	100 ± 7	8.75	0.01	8.52 ± 0.03 ± 0.04	4.9 ± 0.5 ± 0.3
300	112 ± 4	8.40	0.15	7.85 ± 0.28 ± 0.32	12.4 ± 3.6 ± 3.1
400	95 ± 4	8.85	0.07	8.72 ± 0.16	2.7 ± 1.8
		Ultrasonic agitation, I = 596 Wm^{-2}			
100	56 ± 4	8.95	0.01	8.93 ± 0.03	0.3 ± 0.3
200	62 ± 5	8.95	0.01	8.93 ± 0.03	0.3 ± 0.3
300	56 ± 4	8.95	0.01	8.93 ± 0.03	0.3 ± 0.3
400	58 ± 4	8.95	0.01	8.93 ± 0.03	0.3 ± 0.3

The foil cathodes were annealed at 550°C for 15 min before use. In the experiment in which ultrasound was applied to the cathode through a growing deposit (3), a Perspex sheet was bonded to the back of the cathode to stop cavitation impact from that direction.

Thin foil preparation.—Several specimens about 2 cm square were cut from each plated cathode. Before examination in the microscope they were thinned to about 1000Å to enable transmission of the electron beam. Thus, the specimens were first chemically thinned to a thickness of about 5 μm in a solution of equal parts orthophosphoric acid (sp gr 1.76), nitric acid (sp gr 1.42), and glacial acetic acid at the temperature of mixing, about 50°C. In the case of specimens from the cathodes, before thinning began, unwanted material (deposit or electrode) was removed in a solution of 50% nitric acid. Prior to immersion in the nitric acid the surface of the material required for electron microscopy was lacquered with Lacomit to protect it from chemical attack.

A potentiostatic electropolishing method (9) was used for final thinning. The polishing cell arrangement was similar to that used for conventional electropolishing, but with the addition of a calomel reference electrode between the anode and platinum cathode. The window technique (10) was used to aid perforation, and polishing was carried out at room temperature in an electrolyte consisting of 4 volumes orthophosphoric acid (sp gr 1.76), 3 volumes ethanol, and 3 volumes distilled water. The polishing potential was between 1.3-1.4V (relative to the standard calomel electrode).

Results

Hardness.—Figure 4 shows, that in general, deposit hardness increases with current density although deposits from the still and stirred baths exhibit an initial slight fall in hardness followed by a steep rise. In the still bath this is succeeded by a sharp decrease associated with the production of completely powdery, nonadherent deposits.

Mechanical stirring produces softer deposits whereas ultrasonic agitation considerably increases deposit hardness, especially at the higher intensity (928 Wm^{-2}). At the lower intensity (596 Wm^{-2}), however, there is a slight overlap in hardness with that of deposits from the still bath. The increase in hardness with rising intensity is larger at higher current densities.

The effect of increasing ultrasonic agitation at a specific current density (300 Am^{-2}) is illustrated in Fig. 5 together with the standard deviation of each reading. It is apparent that hardness inreases with a rise in intensity above about 150 Wm^{-2}. Below this value no change occurs.

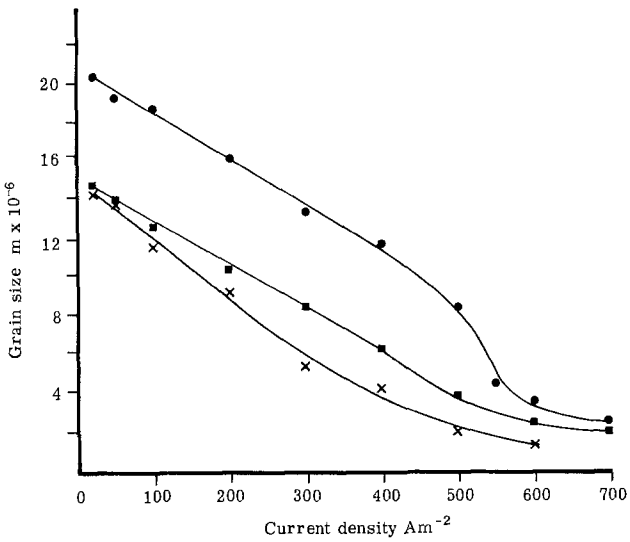


Fig. 6. Deposit grain size related to agitation and current density. ●, Stirred; ■, ultrasonic agitation, I = 596 Wm^{-2}; X, still.

Grain size.—In all three baths deposit grain size decreases with increase in current density (Fig. 6). The grains of deposits from the ultrasonic bath were larger than those of deposits from the still bath. At all but the highest current density, however, they were considerably smaller than the grains of deposits from the stirred bath. Figure 6 illustrates the effect of only one intensity on deposit grain size. The result of increasing ultrasonic intensity at a specific current density (300 Am^{-2}) is presented in Fig. 5. This shows that grain size increases with rise in intensity above 100 Wm^{-2}. Below this value no significant change occurs.

Porosity.—It is evident from Table I that plate from the ultrasonic bath is almost pore free whereas deposits from the still and stirred baths are considerably more porous with the single exception of those from the stirred bath at the lowest current density.

The porosity of still and stirred deposits, which is somewhat higher than that encountered in normal industrial practice, varies with current density and is a maximum at 200 and 300 Am^{-2}, respectively.

Structure and dislocation density.—Transmission electron micrographs (Fig. 7) show that twins are present in plates from all three baths, but they are much more numerous in deposits from the ultrasonic bath, particularly in those formed at the higher ultrasonic intensity (micrograph d). Figure 7 also shows that ultrasound of high intensity (928 Wm^{-2}) causes a significant increase in dislocation density. Further, most of the dislocations appear to be associated with twin boundaries. At the lower intensity (596 Wm^{-2}) a slight increase in dislocation density is apparent.

Effect of ultrasound on the dislocation density of annealed foil cathodes.—Figure 8 shows that ultrasound causes a considerable increase in the dislocation density of annealed copper foil cathodes and the formation of a dislocation cell structure. Moreover, micrograph c shows that an increase in dislocation content even occurs when ultrasound is applied to the cathode through a growing deposit. Dislocation tangles and the beginnings of a cell structure are exhibited. The significance of this slight increase in dislocation density is referred to later.

Discussion

Ultrasonic agitation causes an obvious increase in the hardness of deposits (Fig. 4). Further, grain size

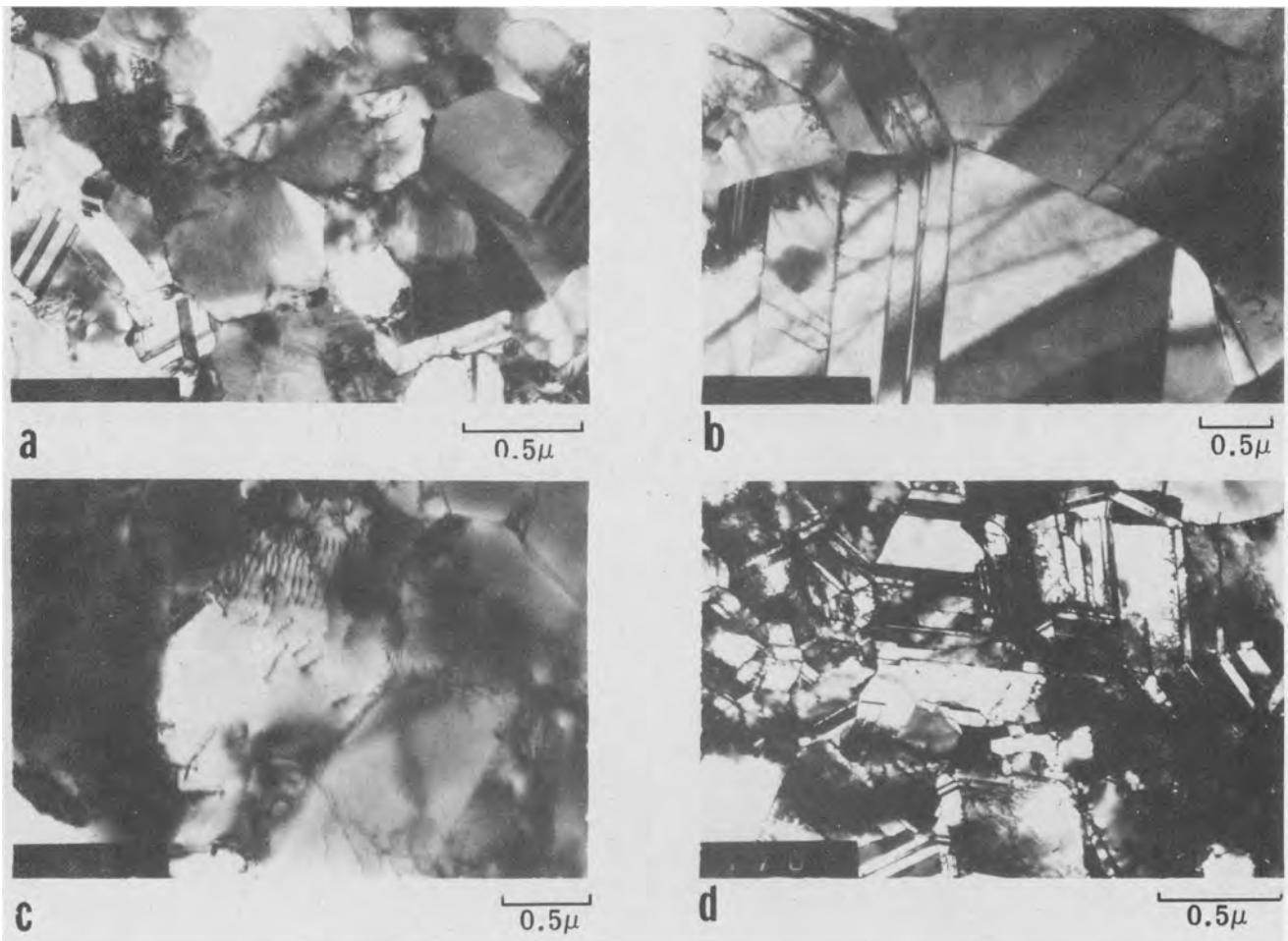


Fig. 7. Electron micrographs of deposits formed under various conditions of bath agitation. (a) Still, (b) stirred, (c) ultrasonic agitation intensity 596 Wm^{-2}, (d) ultrasonic agitation intensity 928 Wm^{-2}.

measurements, porosity determinations, and electron microscopy indicate that more than one factor is responsible.

A plot, Fig. 9, of the variation of deposit hardness with grain size for deposits from the three baths suggests that deposit grain size is the main factor determining hardness. The correlation may be explained by the fact that in small grained deposits there are many grain boundaries to block the slip planes along which deformation occurs (Petch relationship).

Decrease in grain size is largely responsible for the general increase in deposit hardness with rise in current density observed for deposits produced under all agitation conditions (Fig. 4). Thus, the steep hardness rise exhibited by deposits from the still and stirred baths results from the formation of small grains. In the still bath small grains (< 5 μm) are due to deposition under diffusion-controlled conditions. At high current densities (> 500 Am^{-2}) diffusion control (concentration polarization) leads to the formation of almost completely powdery deposits in this bath and hence a sharp fall in hardness (Fig. 4). Before the decrease occurs, however, the hardness of the plate from the still bath exceeds that of deposits formed in the low intensity ultrasonic field (596 Wm^{-2}) over a narrow range of current densities. This is because deposits from the still bath have very small grains (Fig. 5).

It can be seen from Fig. 5 that ultrasonic agitation increases both the grain size and the hardness of deposits. The large grain size results from the decrease in the concentration polarization caused by the stirring associated with the collapse of cavities. Further, the hardness of deposits from the different baths generally decreases with an increase in grain size (Fig. 9), so it is probable that in ultrasonic deposits the larger grain size reduces the hardening effect caused by other factors.

It is apparent from Fig. 9 that the hardness of still and stirred deposits is not determined by grain size alone: above a certain grain size, hardness is seen to increase with grain size. This suggests that another factor, absent in ultrasonic deposits, modifies hardness. The second factor is porosity, and its influence is such that for a specific grain size the less the porosity the higher the hardness. Since deposits from the still and stirred baths are porous (Table I) the average hardness measured is below the value for the pore-free material. Thus, a relation exists between the hardness curves in Fig. 4 and the porosity values in Table I. For instance, the current density at which the softest deposits are obtained from the still and stirred baths corresponds to that at which the most porous deposits are formed. Further, the initial slight fall in hardness with increase in current density observed for deposits from these baths is associated with an increase in porosity. Deposits from the ultrasonic bath at an intensity of 596 Wm^{-2} are almost pore free (Table I); hence, it is likely that hardening caused by low intensity ultrasound results from the decrease in porosity.

The reason for the decrease in porosity caused by ultrasonic agitation is not clear. Metallographic sections (Fig. 3) indicate, however, that porosity in deposits from the still and stirred baths is mainly caused by the failure of adjacent grains to meet during growth. If this is so, then it can be assumed that ultrasound reduces porosity by promoting the coalescence of grains. A SEM study of deposit nucleation and growth lends support to this. Ultrasound was found to

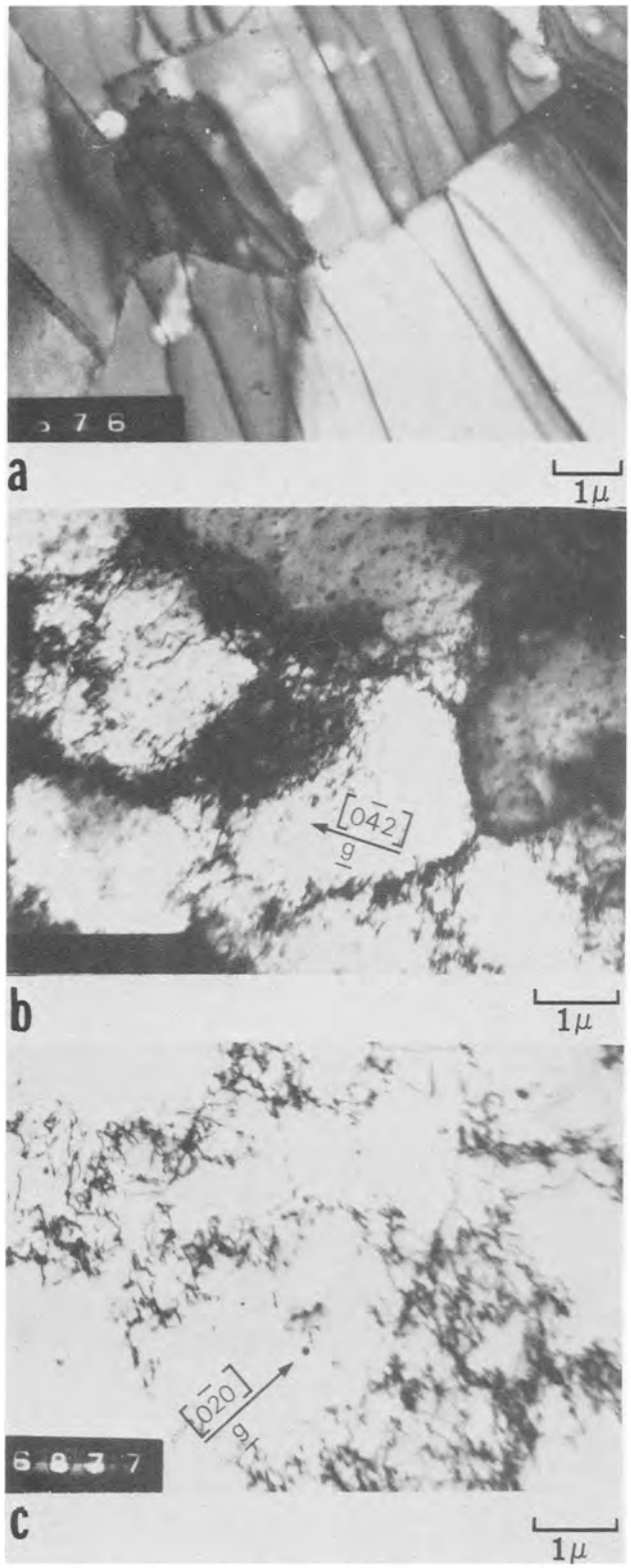


Fig. 8. Electron micrographs of foil cathodes showing the effect of ultrasound. (a) Annealed cathode, (b) same as (a) but after ultrasonic irradiation for 2 hr at an intensity of 596 Wm^{-2}, (c) same as (a) but after ultrasonic irradiation for 2 hr at an intensity of 928 Wm^{-2}. Ultrasound applied through the deposit. Back of cathode protected with Perspex sheet.

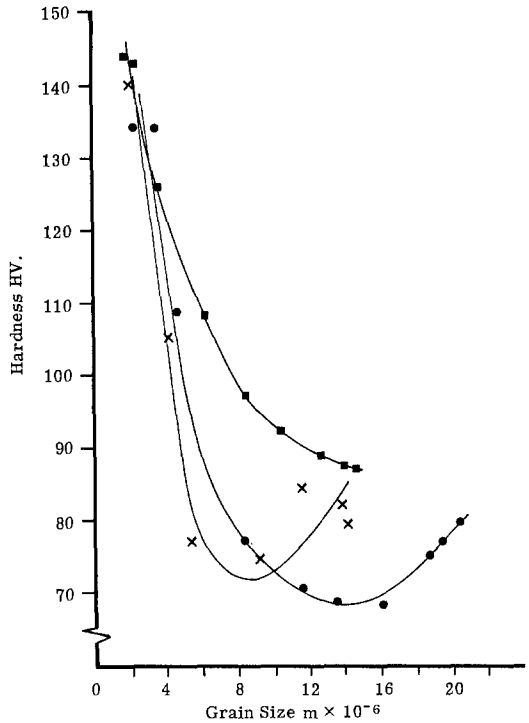


Fig. 9. Deposit hardness related to grain size. ■, Ultrasonic agitation, $I = 596$ Wm^{-2}; ●, stirred; X, still.

produce lateral growth whereas deposits from the still and stirred baths exhibit mainly three dimensional growth (Fig. 10). It is suggested that ultrasound favors such growth because cavitation removes the crystals and whiskers that grow normal to the surface (11).

The hardness of deposits from the ultrasonic bath continues to rise with increase in intensity above that at which pore-free deposits are formed (Fig. 4). Hence it is clear that a further factor is causing hardening. The hardening caused by high intensity ultrasound (> 596 Wm^{-2}) is considered to be mainly work-hardening and results from the repeated impacts of high pressure impulses caused by the collapse of cavities at the cathode. That cavitation is an important factor controlling deposit hardness is inferred from Fig. 6. The figure shows that hardness is unaffected by ultrasound of intensity below about 150 Wm^{-2}. This is probably because at such low intensities the impact pressures arising from cavitation collapse are too small either to cause work-hardening or to reduce porosity.

Electron microscopy of deposits and annealed copper cathodes confirms a high dislocation density. When an ultrasonic field of high intensity acts upon an annealed copper cathode through the growing deposit, the change in dislocation density and arrangement indicate that it is slightly work-hardened. This experiment was based on the inference that if cavitation work-hardens the cathode through the deposit then the deposit ought also to be work-hardened. The deposit removed from the cathode and other deposits formed under identical conditions contain more dislocations than deposits from the still and stirred baths (Fig. 7), but the increase alone is probably insufficient to account for the hardening observed (15 points) on raising the ultrasonic intensity from 596 to 928 Wm^{-2}. It is likely, however, that the increase in the number of growth twins contributes to the hardening, and that hardening is due to dislocation blocking by boundaries (twin and grain) rather than dislocation interaction.

Thus, the greater hardening at high current densities (28 points at 600 Am^{-2}) caused by raising the ultrasonic intensity from 596 to 928 Wm^{-2} can be explained on the grounds that more boundaries are available to block dislocation movement; although deposit grain size increases with intensity (cf. Fig. 5 and 6) the grains of deposits formed at 928 Wm^{-2} are remarkably small (not more than 4 μm).

Ultrasonic agitation increases the density of growth twins because it promotes faulting in the stacking se-

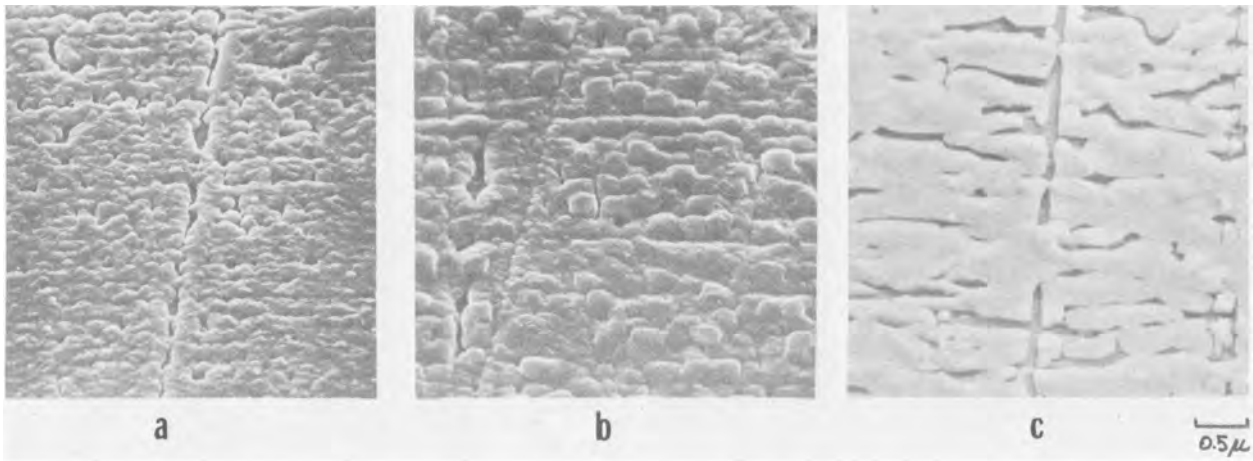


Fig. 10. Growth of deposits after 5 min. Current density 50 Am^{-2}. (a) Still solution, (b) stirred solution, (c) ultrasonically agitated solution, $I = 596$ Wm^{-2}.

quence of atoms on the {111} copper planes. Increased faulting is not surprising since, even at the lower intensity, ultrasonic energy in the electrolyte is equivalent to about 596 Jm^{-2}. If it is assumed that only 1% of this energy is transmitted to the copper deposit, the energy required to produce a coherent twin boundary, 2.0×10^{-2} Jm^{-2} (12), is still greatly exceeded. Further, the energy from cavitation implosions at the cathode will also contribute to the production of growth twins.

It is evident from a comparison of Fig. 7 and 8 that the work-hardening effect of ultrasound is greater on annealed copper cathodes than on copper deposits. For instance, plate formed at the lower intensity (596 Wm^{-2}) exhibits only a small increase in dislocation density, whereas the cathode removed from the deposit has a dislocation cell structure that is equivalent in conventional mechanical working terms to about 5% strain. This is expected because the deposits have a considerably smaller grain size than the annealed copper foil. Deposits are, therefore, intrinsically harder than annealed copper foil and have a greater resistance to cavitation impact.

It is well known that damage is caused when cavitation occurs in a liquid near a metal surface, but disagreement exists as to whether this is due to the impact of shock waves or liquid jets arising from collapse. Rayleigh (13) believes that the impact of shock waves arising from imploding cavities some distance away from the solid boundary causes damage. Parsons and Cook (14), however, suggest that the destructive action of collapsing cavities is caused by the direct impact of the liquid against the surface of the solid. Kornfeld and Suvorov (15) attributes damage to jets of liquid striking the metal surface during the asymmetrical collapse of cavities on or close to the surface. Observations by Ellis and co-workers (16, 17) and Shutler and Mesler (18) give support for the mechanism. They actually saw the formation of such jets in collapsing cavities and also damage on adjacent solid surfaces.

For cavitation to work-harden copper the impact stress at the surface due to cavitation collapse must exceed a value comparable to the hardness, which for annealed copper is about 5×10^8 Nm^{-2}. The intensity of the stress pulse on the surface of a solid exposed to cavitation appears uncertain at present, but may be expected to vary within wide limits depending on bubble size and the details of collapse.

Using the equations of Rayleigh (13) we have calculated the magnitude of the stress pulse arising from the collapse of a spherical cavity at a distance from the cathode to be 2.0×10^8 Nm^{-2}, and that due to the impact of an electrolyte jet to be 1.2×10^9 Nm^{-2}. The calculations were performed for an ultrasonic intensity of 900 Wm^{-2}, and a spherical collapse to 5% of the cavities original diameter was assumed. At an intensity of 928 Wm^{-2}, the actual stress in an acoustic wave is 5.4×10^4 Nm^{-2}, so cavitation is capable of producing a "stress concentration factor" of 4.0×10^3 to 2.0×10^4. It is to be noted that in the case of cavitation collapse at a distance from the cathode, a stress pulse of 2.0×10^8 Nm^{-2} is produced only by a bubble that is in the immediate vicinity of the cathode, and which remains spherical during collapse. In practice most bubbles undergo distortions when they collapse (15). Thus, calculation shows that the stress pulse arising from electrolyte jets is about a factor of 10 higher than that due to the collapse of spherical cavities in the electrolyte and it appears that only the stress pulse resulting from the impact of electrolyte jets is capable of causing plastic deformation of copper deposits and copper cathodes. These findings lead us to conclude that cavitation hardening is due solely to the impact of electrolyte jets arising during the asymmetrical collapse of cavities.

Conclusions

The hardness of deposits produced under all agitation conditions generally increases with rise in current density. This is accompanied by a decrease in grain size. Grain size is largely responsible for the hardness differences between deposits from the still and stirred baths, although variation in porosity with current density is also a contributing factor to the hardness of deposits from these baths.

Ultrasonic agitation increases the hardness of deposits. The change is dependent on the ultrasonic intensity; the higher the field intensity the greater the hardness. The increase in hardness caused by ultrasonic agitation is due to two factors: (*i*) a substantial reduction in deposit porosity, and (*ii*) work-hardening.

The first is the predominant factor at low intensities (below about 600 Wm^{-2}), whereas the second is the controlling factor at high intensities. Work-hardening results from repeated impacts of electrolyte jets on the surface of the deposit during the collapse of cavities. Hardening is due to dislocation blocking by twin and grain boundaries rather than dislocation interaction.

The degree of cavitation occurring in the electrolyte is the principal factor controlling the properties of deposits produced in an ultrasonic field. Cavitation influences deposit properties in two ways. Firstly it has an electrochemical effect. This causes the increase in grain size. It results from a decrease in concentration polarization caused by the stirring resulting from cavitation collapse. Secondly, cavitation has a mechanical effect, which causes the increase in hardness.

Acknowledgments

We thank Professor M. B. Waldron for research facilities at the University of Surrey and Mr. A. Grange of Ultrasonics Limited, Shipley, Yorkshire, for his interest and for providing the ultrasonic generator and Dr. A. Kelly, F.R.S. (Vice-Chancellor, Surrey University) and Dr. D. Tabor, F.R.S. (Professor of Physics, Cambridge University) for useful discussion. C.T.W. also thanks the Science Research Council for financial support.

Manuscript submitted Feb. 3, 1976; revised manuscript received Nov. 30, 1976.

Any discussion of this paper will appear in a Discussion Section to be published in the December 1977 JOURNAL. All discussions for the December 1977 Discussion Section should be submitted by Aug. 1, 1977.

REFERENCES

1. C. T. Walker and R. Walker, *Electrodeposition Surf. Treat.*, **1**, 457 (1972-1973).
2. Fr. Müller and H. Kuss, *Helv. Chim. Acta*, **33**, 217 (1950).
3. S. M. Kochergin and G. Ya Vyaseleva, "Electrodeposition in Ultrasonic Fields," 1st ed., p. 19, Consultants Bureau, New York (1966).
4. C. T. Walker and R. Walker, *Nature Phys. Sci.*, **244**, 141 (1973); *ibid.*, **250**, 410 (1974).
5. E. A. Lloyd, in "Ultrasonic Techniques in Biology and Medicine," B. Brown and M. Gordon, Editors, 1st ed., pp. 46-68, Eliffe, London (1967).
6. ASTM Standard E 112-63, Part 31, 446-460 (1968).
7. R. L. Coble, *J. Appl. Phys.*, **32**, 793 (1961).
8. R. E. Fryxell and B. A. Chandler, *J. Am. Ceram. Soc.*, **47**, 283 (1964).
9. B. J. Ginn and E. D. Brown, *Br. Weld. J.*, **12**, 90 (1965).
10. H. M. Tomlinson, *Phil. Mag.*, **13**, 867 (1958).
11. R. Walker and C. T. Walker, *Ultrasonics*, **13**, 79 (1975).
12. M. C. Inman and A. R. Khan, *Phil. Mag.*, **16**, 937 (1961).
13. J. W. S. Rayleigh, *ibid.*, **34**, 94 (1917).
14. C. A. Parsons and S. S. Cook, *Engineering*, **107**, 515 (1919).
15. M. Kornfeld and L. Suvorov, *J. Appl. Phys.*, **15**, 495 (1944).
16. C. F. Naude and A. T. Ellis, *J. Basic Eng.*, **83**, 648 (1961).
17. T. B. Benjamin and A. T. Ellis, *Phil. Trans. R. Soc., Ser. A*, **260**, 221 (1966).
18. N. D. Shutler and R. B. Meisler, *J. Basic Eng.*, **87**, 511 (1965).

Potential-Selective Deposition of Copper from Chloride Solutions Containing Iron

Ralph White,* James A. Trainham,† and John Newman†

Materials and Molecular Research Division, Lawrence Berkeley Laboratory, and Department of Chemical Engineering, University of California, Berkeley, California 94720

and Thomas W. Chapman†

Department of Chemical Engineering, University of Wisconsin, Madison, Wisconsin 53706

ABSTRACT

The hydrometallurgy of copper may involve leaching of the metal from its ore with an aqueous solution containing cupric and ferric chloride. The subsequent deposition of copper from such a process stream is modeled here in an idealized electrochemical cell with a rotating-disk electrode. The potential distribution and concentration profiles within the diffusion layer are predicted for given potential differences between the electrode and the solution. The cuprous ion, which is formed by the reduction of the complexed cupric ion at the electrode, is stabilized in the chloride solution and can react either at the electrode or with ferric species within the diffusion layer. The assumption is that this fast and irreversible homogeneous reaction generates a reaction plane, whose position is shown in the concentration and potential profiles. In addition, the position of the reaction plane is plotted as a function of the potential difference between the electrode and the adjacent solution. Predicted current-potential and current efficiency-potential curves are also reported. Finally, the iron contamination of the deposited copper is estimated to be less than 10^{-5} atom percent for some cases. Also, because some of the partial current densities are below their limiting values, the analysis is strictly valid only at the center of the disk.

Among the numerous hydrometallurgical schemes for extraction and recovery of copper currently under consideration there are several which employ an aqueous chloride solution as a lixiviant (1-11). The tendency of chloride to form metal complexes provides high metal solubilities; and, in conjunction with a suitable oxidizing agent such as chlorine, oxygen, ferric ions, or cupric ions, excess chloride facilitates rapid leaching of not only scrap metal but also sulfide ores such as chalcopyrite, $CuFeS_2$ (12-15).

* Electrochemical Society Student Member.
† Electrochemical Society Active Member.
Key words: hydrometallurgy, current efficiency, homogeneous reaction, simultaneous electrode reactions, migration effect, reaction plane, rotating-disk electrode.

The possibility of regenerating a leaching agent such as ferric ions at an anode while depositing copper cathodically makes the prospect of direct electrolysis of copper chloride leach liquors attractive. There are, however, two major difficulties with this approach. First, copper deposits from chlorides in a rough, porous, or even powdery form under most operating conditions so that the copper product would probably require remelting (11, 16, 17). The second problem is that the pregnant leach liquors may contain oxidized species that could react in the electrolysis cell and cause low current efficiencies for metal deposition. For example, iron occurring in an ore, or as the leaching agent, may appear in the electrolysis cell as ferric ion

and be reduced to ferrous ion at the cathode. This latter problem can be avoided by assuring reduction of the electrolyte prior to electrolysis, or by precipitating iron, to eliminate ferric ions, while using a diaphragm to prevent transport of ferric ions from the anode to the cathode. Nevertheless, it is interesting to investigate the quantitative effect of ferric ions on the deposition of copper from chloride solutions to determine whether removal of ferric ions prior to electrolysis is necessary. In this paper we compute the cathodic current efficiency for deposition of copper from a copper chloride solution which contains high levels of ferric ions and identify some interesting phenomena that can occur in this situation. The current efficiency for a cupric chloride solution which contains no ferric ions is considered elsewhere (18).

The process stream that results when copper ore containing iron is leached under mildly oxidizing conditions is presumed to contain the following ionic species in water at 25°C: $CuCl^+$, $FeCl^{2+}$, H^+, and Cl^-. Available stability constant data (19, 20) indicate that these are the most stable forms of the possible cupric-chloride and ferric-chloride complex ions in chloride solutions. Subsequently, these complex ions will be referred to as the cupric and ferric species, respectively.

Deposition of copper from the process stream is assumed to involve two steps. The first step is the reduction of the cupric species

$$CuCl^+ + e^- + 2Cl^- \rightarrow CuCl_3^{2-} \quad [1]$$

The second step is the reduction of the resulting cuprous-chloride complex ion (hereafter referred to as the cuprous species) to copper

$$CuCl_3^{2-} + e^- \rightarrow Cu + 3Cl^- \quad [2]$$

Stability constant data (19, 21) also indicate that this cuprous species is the most stable form of those possible in the solution considered here. It should be emphasized that the stability of the cuprous species enables it to exist at a much higher concentration than its counterpart could in other solutions, such as copper sulfate in aqueous sulfuric acid [see Ref. (22), for example].

Two additional electrode reactions are the cathodic deposition of iron

$$FeCl^+ + 2e^- \rightarrow Fe + Cl^- \quad [3]$$

by reduction of a ferrous-chloride complex ion, which is produced within the diffusion layer (see reaction [5]), and the reduction of hydrogen ions to form dissolved hydrogen gas

$$H^+ + e^- \rightarrow \frac{1}{2} H_2 \quad [4]$$

This ferrous species, $FeCl^+$, is also considered to be the most stable form that could exist in this solution (19).

One could also conceive of the direct reduction of ferric to ferrous species on the electrode, and this would occur at quite positive electrode potentials (where copper and iron would, in fact, dissolve). However, the presence of the ferric species is incompatible with the simultaneous presence of the cuprous species, and the ferric species cannot exist in the region near the electrode in the range of potentials where reactions [1] and [2] may occur. Instead, in addition to its participation in reactions [1] and [2] at the rotating-disk electrode, the cuprous species can diffuse away from the electrode and react with the ferric species, which is being transported toward the working electrode from the bulk solution, according to the following oxidation-reduction reaction

$$CuCl_3^{2-} + FeCl^{2+} \rightleftarrows CuCl^+ + FeCl^+ + 2Cl^- \quad [5]$$

This reaction occurs within the diffusion layer adjacent to the rotating-disk electrode. Since such ionic reactions are usually relatively rapid, reaction [5] is essentially equilibrated locally, and the treatment is similar to that for partial dissociation of bisulfate ions within a diffusion layer (23).

The ferrous species produced by reaction [5] diffuses back into the bulk solution and is also transported toward the electrode (where it may react according to reaction [3]).

The equilibrium constant K for reaction [5] can be estimated to be 1.55×10^5 (kg/mole)^2 by using standard electrode potentials as well as the stability constant data referred to above. Because this is a large number, the analysis can be simplified by assuming that K is infinitely large. (Further work on this problem in which K is not set equal to infinity is contemplated.) As a consequence of the assumption that reaction [5] has an infinitely large equilibrium constant, a reaction plane forms within the diffusion layer and thereby separates it into two regions (see Fig. 1). Furthermore, because of this assumption the ferric species is absent in region 1 and the cuprous species is absent in region 2.

The formation of a reaction plane by an instantaneous, irreversible bimolecular reaction was treated first by Hatta (24) within the context of simultaneous gas absorption and chemical reaction. Van Krevelen and Hoftijzer (25), Danckwerts (26), Perry and Pigford (27), Olander (28), and others have applied this concept in similar work. Recent treatment of reaction planes can be found in books by Sherwood and Pigford (29), Astarita (30), Danckwerts (31), Albery and Hitchman (32), Sherwood, Pigford, and Wilke (33), and Carberry (34). Friedlander and Litt (35) and Acrivos (36) used the reaction plane concept in their analyses of laminar boundary layer flows with a homogeneous reaction. Others (37-51) have also studied this subject.

Also of concern with this system is the possibility that the chloride complexing will stabilize the cuprous species to such an extent that iron is deposited in preference to copper. The standard electrode potentials of reactions with the chloride-complexed species were calculated from those of reactions of noncomplexed species and the stability constants from the literature. Table I shows that, at the potentials at which copper will begin to be plated, the ferrous ion is more stable than either the ferric ion or metallic iron, and this is true in both the complexed and noncomplexed systems.

The desired process in the electrochemical cell is the reduction of cupric species to deposited copper, which requires two electrons per copper atom deposited. The current efficiency will therefore be defined as the number of copper atoms deposited for each two electrons passed through the cell. The principal process which tends to reduce the current efficiency is the diffusion

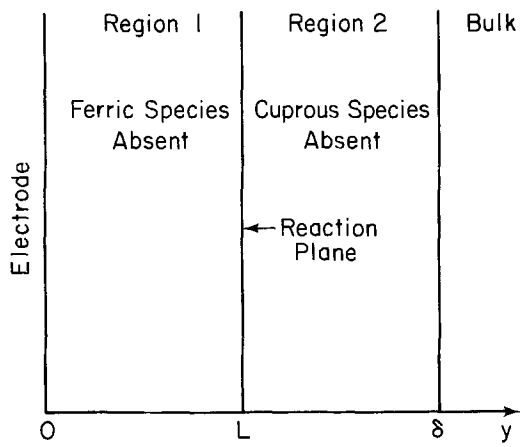


Fig. 1. The separation into regions of a diffusion layer within which a fast oxidation-reduction reaction occurs with an infinitely large equilibrium constant.

Table I. Standard electrode potentials with and without complexing by chloride, at 25°C

Reaction	U^θ, V	
	Noncomplexed	With chloride
Ferrous/ferric	0.771	0.745
Cuprous/copper	0.521	0.233
Cupric/copper	0.337	0.3355
Cuprous/cupric	0.153	0.438
Ferric/iron	−0.036	−0.0523
Ferrous/iron	−0.440	−0.451

of cuprous species back into the solution where it can escape or lead to the indirect reduction of ferric species to ferrous according to reaction [5]. Any reduction of ferrous ions to iron at the electrode will also lower the current efficiency as well as contaminate the deposit. In addition, the current efficiency is lowered by the reduction of hydrogen ions according to reaction [4].

The electrochemical cell used to model the physical phenomena discussed above consists of a rotating-disk electrode (the active portion of which is made either of copper or of an inert material such as platinum), a normal calomel reference electrode (whose standard electrode potential is 0.2676V), a distant counterelectrode, and a bulk solution of the same composition as the process stream. Deposition of copper from this electrochemical cell can be analyzed by applying dilute-electrolytic-solution theory with constant physical properties (22, 52). The results of this analysis include concentration profiles of the ionic species within the diffusion layer on the electrode, current-potential curves, and current efficiencies for this system.

For convenience, the current density distribution was assumed to be uniform on the surface of the electrode. Newman (53) showed how one should calculate the current distribution on a rotating-disk electrode, but consideration of the problem treated here at that level of sophistication is beyond the scope of this work. However, the results to be presented are applicable at the center of the disk.

Newman (54) also showed that for the rotating-disk electrode, on which one electrode reaction occurs at its limiting value, the governing equations for electrolytic mass transfer are the same as those for other flow configurations. Consequently, the assumption that the results reported here are also applicable to other flow configurations (54) should be a reasonable first approximation.

Governing Equations

Material-balance equations for species within the diffusion layer on a rotating-disk electrode are (55)

$$(D_i/D_R)c_i'' + 3\xi^2 c_i' + (z_i u_i F/D_R)(c_i\Phi'' + c_i'\Phi') = 0 \quad [6]$$

where the prime denotes differentiation with respect to the dimensionless distance ξ. For the rotating disk

$$\xi = y/\delta \quad [7]$$

where y is the normal distance from the surface and δ is the thickness of the diffusion layer, expressed as

$$\delta = \left(\frac{3D_R}{a\nu}\right)^{1/3}\left(\frac{\nu}{\Omega}\right)^{1/2} \quad [8]$$

with $a = 0.51023262$ (56). The position of the reaction plane, the ionic species concentration profiles, and the potential distribution can be determined by solution of these equations together with the condition of electroneutrality

$$\sum_i z_i c_i = 0 \quad [9]$$

and the following boundary conditions.

The boundary conditions in the bulk solution are that

$$c_i \to c_{i,\infty} \quad \text{as} \quad \xi \to \infty$$

At an arbitrary position, Φ can be specified, corresponding to the arbitrary zero of potential. At the reaction plane the boundary conditions are:

1. The total flux of each element (Cu, Fe, and Cl) as well as the flux of H^+ and dissolved H_2 is continuous.
2. The concentration of both the cuprous and the ferric species is zero.
3. The fluxes of ferric and cuprous species to the reaction plane are equal.

The boundary conditions at the rotating-disk electrode are that the normal component of the flux of species i evaluated at the electrode surface is equal to the sum of its reaction rates

$$N_i = -z_i u_i F c_i \frac{d\Phi}{dy} - D_i \frac{dc_i}{dy} = -\sum_{j=1}^{m} \frac{s_{ij} i_j}{n_j F} \quad [10]$$

where m is the number of reactions occurring at the electrode and s_{ij} and n_j are the stoichiometric coefficient of species i and the number of electrons transferred in electrode reaction j when written in the abstract form

$$\sum_i s_{ij} M_i^{z_i} \to n_j e^- \quad [11]$$

The current density due to reaction j was approximated by the Butler-Volmer equation

$$i_j = i_{oj}\left[\exp\left(\frac{\alpha_{aj}F}{RT}\eta_{sj}\right) - \exp\left(-\frac{\alpha_{cj}F}{RT}\eta_{sj}\right)\right] \quad [12]$$

where the composition dependence of the exchange current density was assumed to have the form

$$i_{oj} = i_{oj,ref}\prod_i\left(\frac{c_{i,o}}{c_{i,ref}}\right)^{\gamma_{ij}}\prod_k a_k^{\gamma_{kj}} \quad [13]$$

The symbol $i_{oj,ref}$ represents the exchange current density evaluated at the reference concentration of the ionic species, with $c_{i,ref} = 1M$, and at unit relative activity of the metallic species. In Eq. [13], i ranges over the ionic species and k over the metallic species. The relative activity of iron was taken to equal its mole fraction in the deposit, and the relative activity of copper was set equal to unity since little iron was expected to be deposited. Thus, a_{Fe} was set equal to $0.5\, i_3/i_2$, and the activity coefficient was ignored. The activity coefficient of iron should be greater than unity since iron and copper are not completely miscible, and consequently the deposition rate of iron should be even lower than that calculated here.

The transfer coefficients α_{aj} and α_{cj} are taken to sum to n_j. The exponents for both ionic and metallic species were given the values

$$\gamma_{ij} = q_{ij} + \frac{\alpha_{cj}}{n_j} s_{ij} \quad [14]$$

where $q_{ij} = -s_{ij}$ for a cathodic reactant and is zero otherwise.

The surface overpotential for reaction j is

$$\eta_{sj} = V - \Phi_o - U_{j,o} \quad [15]$$

where V is the potential of the rotating disk, Φ_o is the potential of the solution just outside the diffuse part of the double layer as measured by a reference electrode of a given kind, and $U_{j,o}$ is the theoretical open-circuit potential for reaction j at the composition prevailing at the electrode surface—again relative to the reference electrode of a given kind. For a normal calomel reference electrode

$$U_{j,o} = U^\theta_j - U^\theta_{cal} - \frac{RT}{n_j F}\left[\sum_i s_{ij}\ln\left(\frac{c_{i,o}}{\rho_o}\right) + \sum_k s_{kj}\ln a_k\right] + \frac{RT}{F}\ln\left(\frac{c^\lambda_{Cl^-}}{\rho_o}\right) \quad [16]$$

Here, $c^{\lambda}_{Cl^-}$ is the concentration of chloride ion in the reference electrode compartment, and the concentrations must be expressed in moles/liter if the usual tabulations of standard electrode potentials U^{θ}_j are to be used. Note that possible activity-coefficient corrections to the concentrations of the ionic species have been ignored.

Solution Technique

Equations [6] and [9] together with the above boundary conditions constitute a boundary-value problem involving coupled, ordinary, nonlinear, differential equations. The governing equations and boundary conditions were cast in finite-difference form accurate to order h^2, where h is the dimensionless distance between mesh points, and solved by a numerical solution technique developed by Newman (22). An interesting aspect of this problem is the unknown reaction plane position. In conditions 2 and 3 there is one more boundary condition than would be needed for a fixed plane position. Consequently, the plane position L must be treated as an unknown constant. To use the same computer subroutines, the treatment of this unknown constant was similar to that used by Newman (57) for the eigenvalues of the Graetz problem.

Parameter values used to obtain numerical results are presented in Table II. Mobilities were calculated from the tabulated diffusion coefficients by means of the Nernst-Einstein relation, $u_i = D_i/RT$. For the transfer coefficients, $\alpha_{cj} = 0.5$, and the exchange current densities, $i_{oj,ref}$, for reactions [1] and [3] were given the value 10^{-3} A/cm^2 while values of 5×10^{-3} and 5.89×10^{-7} A/cm^2 were used for reactions [2] and [4], respectively.

Results

Results are presented for four cases. In case one, only reaction [1], the reduction of the cupric species to cuprous species, is permitted to occur at the electrode (see Table II). In the remaining cases, reactions [1], [2], [3], and [4] occur at the electrode. These separate cases emphasize the significance of multiple electrode reactions and the significance of the ratio of the bulk concentration of cupric species to ferric species. Table II gives the bulk concentrations for each case.

Figure 2 displays the dependence of the electric potential Φ on the dimensionless distance from the electrode ξ for case one. Two quantities of interest, Φ_o and $\tilde{\Phi}_o$, are illustrated in this figure. The potential in the solution at the electrode surface (just outside the diffuse double layer) Φ_o and the potential of the working electrode V are used to form the potential difference $V - \Phi_o$, which is related to the driving force for the electrode reaction (see Eq. [15]).

The electric potential in the solution outside of the diffusion layer, $\tilde{\Phi}$, extrapolated to the electrode surface

Table II. Parameter values

Species	$10^5 D_i$, cm^2/sec	$c_{i,\infty}$, mole/liter		
		Cases 1 and 2	Case 3	Case 4
$CuCl_3^{2-}$	0.6*	0	0	0
$CuCl^+$	0.6*	3	2.25	1.5
$FeCl^+$	0.739**	0	0	0
$FeCl^{2+}$	0.896**	1.5	2.25	3
Cl^-	2.032†	6.1	6.85	7.6
H^+	9.312†	0.1	0.1	0.1
H_2	3.8‡	$4.155 \cdot 10^{-10}$	⟶	⟶

$T = 298.15$°K $\quad \nu = 0.010049$ cm^2/sec
$\rho_o = 0.99707$ g/cm^3 $\quad \Omega = 261.8$ rad/sec

* Taken from Ref. (58).
** Because of a lack of data, the diffusion coefficients of the ferrous and ferric species were taken to be the same as those of ferrocyanide and ferricyanide ions, respectively, as given in table 75-1 of Ref. (22).
† Taken from table 75-1 of Ref. (22).
‡ This value was arbitrarily selected for this work [see Ref. (59)].

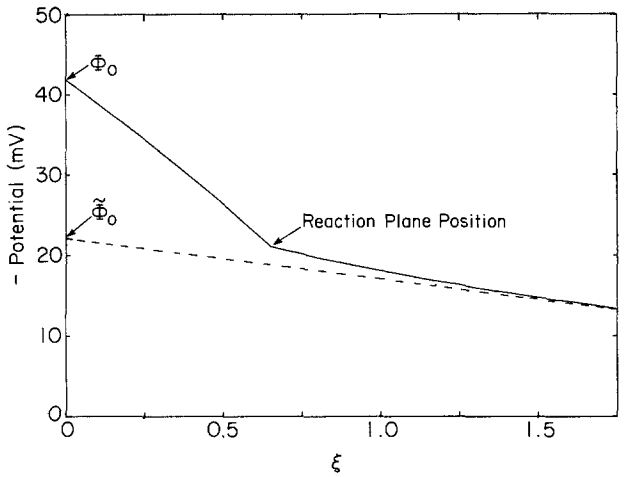


Fig. 2. Dependence of the electric potential on the dimensionless distance from the electrode when $V - \tilde{\Phi}_o = -0.3545$V and reaction [1] alone occurs at the electrode.

is designated as $\tilde{\Phi}_o$. Its value may be obtained by extrapolating Ohm's law

$$i_T = \sum_{j=1}^{m} i_j = -\kappa_\infty \frac{d\tilde{\Phi}}{dy} \qquad [17]$$

to the electrode surface from the bulk by using the previously calculated value of i_T and the conductivity κ_x of the bulk solution. The potential difference $V - \tilde{\Phi}_o$ represents an alternative driving force for the electrode reaction. We might write for the total overpotential

$$\eta_{sj} + \eta_{cj} = V - \tilde{\Phi}_o - U_{j,\infty} \qquad [18]$$

where η_{cj} is the concentration overpotential for reaction j and $U_{j,\infty}$ is the theoretical open-circuit potential for reaction j at the bulk solution composition and the alloy composition of the deposit.

There is a difference between $\tilde{\Phi}_o$ and Φ_o because the conductivity varies with position in the diffusion layer and is not equal to κ_∞ and because there exists a diffusion potential due to the concentration variations and the different diffusion coefficients of the various species [see equation 125-7 of Ref. (22)]. These factors are accounted for when one solves simultaneously the coupled Eq. [6] and [9] across the diffusion layer to obtain the potential distribution in Fig. 2.

Figure 3 depicts the calculated concentration profiles of the ionic species within the diffusion layer that were obtained at the same potential difference. In this figure, the dimensionless distance from the electrode at which the concentration of both the cuprous and the ferric species is zero indicates the position of the reaction plane.

The calculated current density due to reaction [1] alone, i_1, normalized by the current density predicted by the Levich equation (60)

$$i_{LD} = 0.62048 \frac{n_1 F c_{R_\infty}}{s_{R1}} (\Omega\nu)^{1/2} \left(\frac{D_R}{\nu}\right)^{2/3} \qquad [19]$$

is presented in Fig. 4, as a function of the potential differences $V - \tilde{\Phi}_o$ and $V - \Phi_o$.

Figure 5 displays the calculated concentration profiles for case two with $V - \tilde{\Phi}_o = -0.3493$V.

In Fig. 6 the dimensionless position of the reaction plane L/δ is presented as a function of the potential

difference $V - \tilde{\Phi}_0$ for cases 1 and 2.

The total predicted dimensionless current density for case 2 is plotted in Fig. 7 as a function of the potential difference $V - \tilde{\Phi}_0$. The current densities due to reactions [1] and [2] for case 2 are also plotted in Fig. 7. (The current density due to reactions [3] and [4] were too small to be plotted conveniently on Fig. 7.)

These calculated current densities were used to calculate the current efficiency, $100 \times 2i_2/i_T$, as a function of the potential difference $V - \tilde{\Phi}_0$, which is plotted in Fig. 8. Also shown in Fig. 8 are the current efficiencies for cases 3 and 4.

Finally, the dependence of the relative surface concentration of the cupric, cuprous, and chloride species on $V - \tilde{\Phi}_0$ is presented in Fig. 9.

Discussion

The potential profile and the concentration profiles shown in Fig. 2, 3, and 5 are not smooth at the reaction plane because of the assumption that K is infinite.

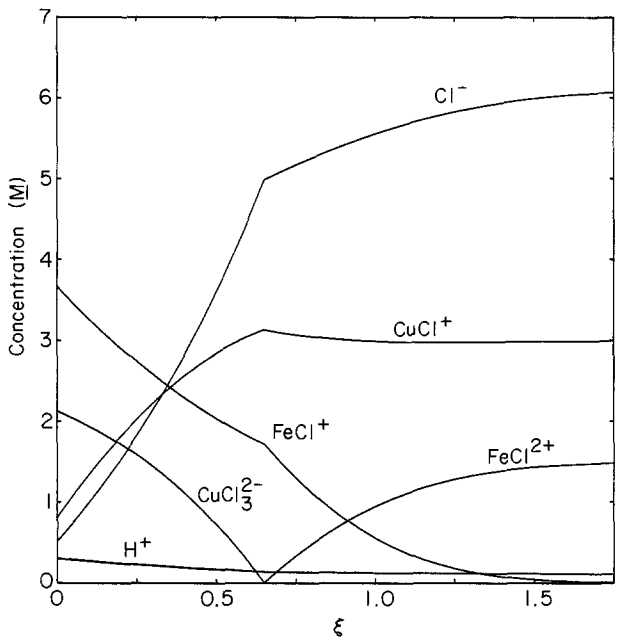


Fig. 3. Dependence of the concentration of the various species on the dimensionless distance from the electrode for case 1 with $V - \tilde{\Phi}_0 = -0.3545$V.

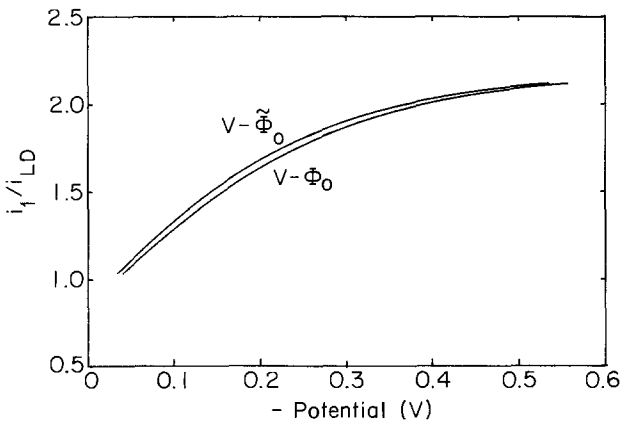


Fig. 4. The dimensionless current density when reaction [1] alone occurs at the electrode as a function of the potential differences $V - \tilde{\Phi}_0$ and $V - \Phi_0$.

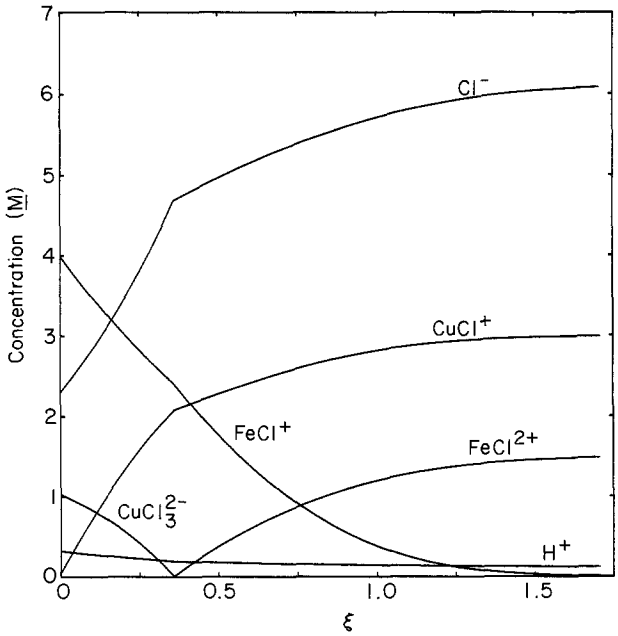


Fig. 5. Concentration profiles of the various species near the electrode for case 2 with $V - \tilde{\Phi}_0 = -0.3493$V.

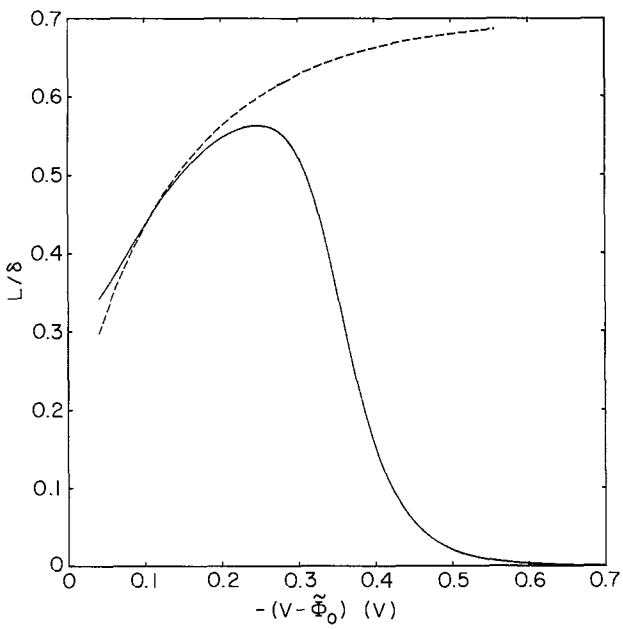


Fig. 6. Dependence of the dimensionless reaction plane position on $V - \tilde{\Phi}_0$ for cases 1 (– – –) and 2 (——).

Consider first case one, where the only electrode reaction is the reduction of cupric to cuprous ions. The latter diffuse away from the electrode to the reaction plane, where they reduce ferric to ferrous ions, with regeneration of cupric. Some of the cuprous species also escape by radial convection. The concentration profiles in Fig. 3 illustrate these processes. As the electric driving force is increased, the concentration of the limiting reactant, the cupric species, approaches zero, and the concentration of the product cuprous species at the electrode increases. Consequently, the position of the reaction plane moves away from the electrode, as also shown in Fig. 6. The position of the reaction plane is determined by a balance of the transport of cuprous species from the electrode and the transport of ferric species from infinity. The ferrous species, the product of the plane reaction, also has accumulated toward the

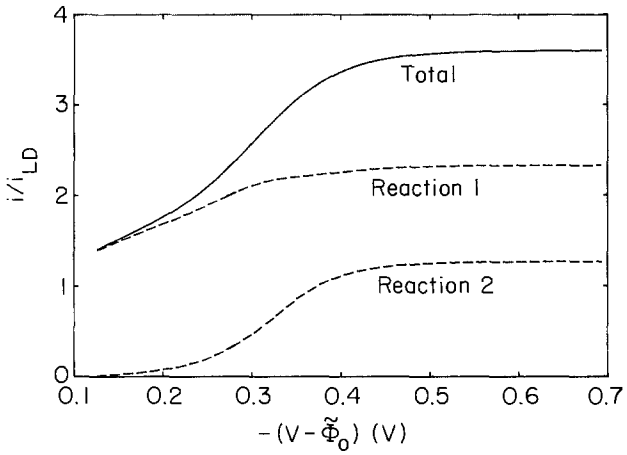


Fig. 7. Dependence of the dimensionless current densities on $V - \tilde{\Phi}_0$ for case 2.

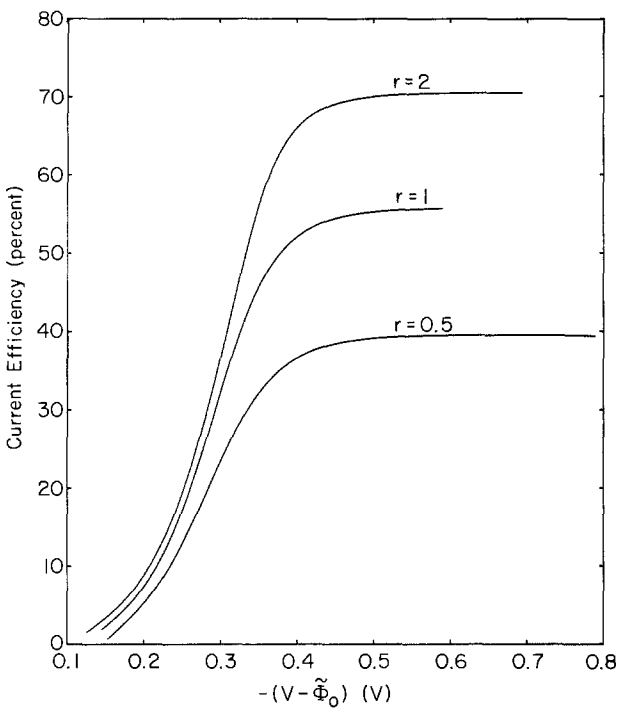


Fig. 8. Dependence of the current efficiency on $V - \Phi_0$. $r = c_{CuCl^+,z}/c_{FeCl^{+2},\infty}$. r = 2, 1, and 0.5 for cases 2, 3, and 4, respectively.

disk surface. The chloride ion is produced by reaction [5] at the plane and consumed by reaction [1] at the electrode, and the consequences of this are observed in the concentration profiles.

The current density for reaction [1] can exceed substantially the limiting value for convection and diffusion of the cupric species as given by the Levich equation. Figure 4 shows ratios as high as 2.12. This enhancement is due to ionic migration of the limiting reactant (55) and the regeneration of the cupric species at the reaction plane. Since the cupric species is positively charged, it is attracted toward the cathode according to the potential distribution in Fig. 2. This effect of migration also accounts for the maximum in the concentration of the cupric species at the reaction plane and for the increase of concentration of the ferrous species toward the electrode (see Fig. 3), where this species is neither produced nor consumed. The effect of the reaction plane is, in essence, to bring

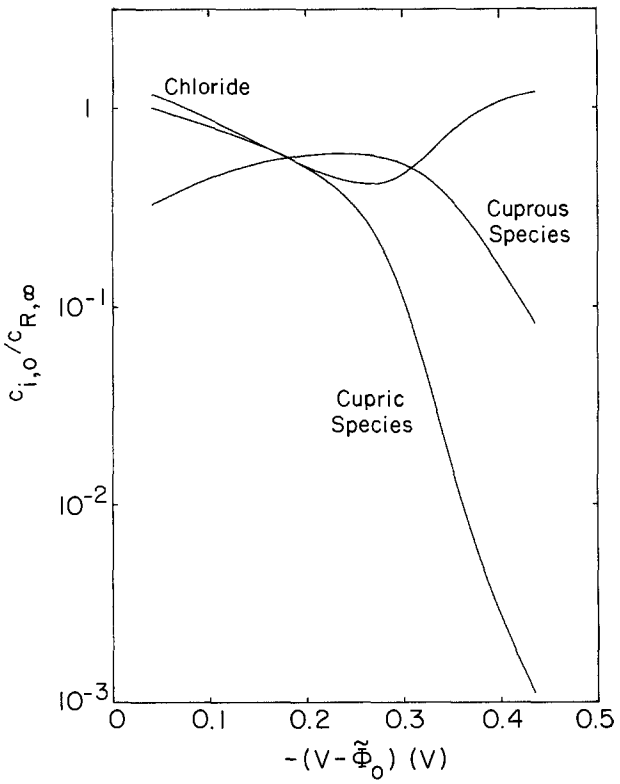


Fig. 9. Dependence of the relative surface concentration of some of the ionic species present in the system on $V - \tilde{\Phi}_0$ for case 2.

the bulk concentration of the limiting reactant closer to the electrode, since the cupric species is produced at the plane by reaction [5], and this serves to increase the concentration gradient at the electrode.

Another way to think about this effect is to realize that the reduction of ferric to ferrous, which occurs at the plane, requires a supply of electrons from the electrode. The indirect supply of these electrons through the transport of cuprous species from the electrode to the plane contributes to a higher current density for reaction [1]. In fact, the reduction of ferric to ferrous requires a smaller electric driving force than the reduction of cupric to cuprous (see Table I). When the reaction-plane distance has decreased to zero, the reduction of ferric to ferrous can proceed directly on the electrode, and the analysis would actually become simpler.

Figure 4 shows that $\tilde{\Phi}_0 - \Phi_0$, the difference between the potential drop through the diffusion layer and that obtained by extrapolation with the bulk conductivity, is relatively small compared with the scale of potentials over which the current rises toward its limiting value. For the situation in Fig. 2, $\tilde{\Phi}_0 - \Phi_0$ has the value of 19.9 mV.

For case two, we must now consider the additional effects associated with the possibility of depositing copper and iron on the electrode and also the possibility of evolving hydrogen gas at the electrode. The deposition of copper by reaction [2] consumes cuprous ions produced through reaction [1], and consequently less of the cuprous species remains to diffuse back into the solution. Comparison of the concentration profiles in Fig. 3 and 5 shows this reduction of the cuprous concentration at the surface. The reaction plane is now much closer to the electrode, as also depicted in Fig. 6. Comparison of the predicted reaction plane positions at small values of $-(V - \tilde{\Phi}_0)$ for cases 1 and 2, as shown in Fig. 6, reveals that the reaction plane is further from the electrode in case 2, a result which is

due to the dissolution of deposited copper according to reaction [2].

The current densities in Fig. 7 reflect the difference in the potentials of the two copper reactions (see Table I). The current density due to reaction [1] is well along toward a limiting current, the same limit shown in Fig. 4, before the current density due to reaction [2] becomes significant. The slight increase in the current density due to reaction [1] above the initial plateau is due to the increasingly larger concentration gradient of the limiting reactant as the reaction plane moves closer to the electrode (compare Fig. 3 and 5). The cupric species produced at the reaction plane can no longer escape by radial convection. Furthermore, the current density due to reaction [2] will increase the potential gradients and enhance further the migration of cupric ions toward the electrode from the bulk solution.

In order to avoid contamination of the deposit with iron, the electric driving force should not be made too large, according to the standard electrode potentials in Table I. For example, the current density for reaction [3] is very small and can be used to estimate that less than 10^{-5} atom percent (a/o) of the deposit is iron for values of $V - \tilde{\Phi}_o$ more positive than about -0.51V. However, this estimate is probably high because the activity of iron was taken to equal the atom fraction, with neglect of the activity coefficient. Since the activity coefficient is greater than unity, the deposition of iron would be further impeded.

For such low rates of reaction [3], the low current efficiencies in Fig. 8 are mainly due to two causes: (*i*) "leakage" of cuprous species away from the electrode by radial convection, and (*ii*) consumption of cuprous species at the reaction plane. The latter is equivalent to the indirect current required for reduction of ferric to ferrous at the plane. Because the reduction of cupric and ferric species occurs at a lower electric driving force than reaction [2], the current efficiency increases with an increase in the electric driving force and approaches about 70.5, 55.7, and 39.5% for cases 2, 3, and 4, respectively. The maximum possible current efficiency is determined mainly by the ratio of ferric and cupric concentrations in the bulk solution. At still larger values of the electric driving force, the current efficiency would decrease due to the deposition of iron by reaction [3] and the evolution of hydrogen according to reaction [4].

For some cases the range of acceptable operating potential differences may be determined by the solubility limit of the cuprous species (approximately 1*M* in the solutions studied here) and the maximum tolerable iron contamination of the deposit or hydrogen gas evolution. For case 2, Fig. 9 (also see Fig. 5) shows that operating at potential differences more positive than about -0.35V could lead to undesirable precipitation of cuprous species. (For cases 3 and 4, $\tilde{\Phi}_o - V$ should be at least 0.32 and 0.275V, respectively, to avoid CuCl precipitation.) At the other extreme in the range of acceptable operating potential differences for case 2, the current density due to reaction [3] may be used to predict that the iron contamination of the deposited alloy would exceed 10^{-5} a/o for $V - \tilde{\Phi}_o$ values more negative than about -0.52V. Further reduction of $V - \tilde{\Phi}_o$ would lead eventually to hydrogen gas evolution. (The value of $V - \tilde{\Phi}_o$ at which this may begin to occur for case 4 was predicted to be approximately -0.789V, for example.)

Another limiting situation is associated with the bulk chloride concentration. Since chloride ions are consumed and liberated at the electrode at rates which depend on $V - \tilde{\Phi}_o$, a minimum in the surface concentration of chloride ions exists, as shown in Fig. 9. The implication of this minimum is that, for some bulk compositions, the chloride ion concentration would vanish at the electrode, a condition which may be considered undesirable because the complexing of the species would be no longer ensured.

Summary and Conclusion

The results of this work are that one can predict for this system: (*i*) the location of a hypothesized reaction plane; (*ii*) reasonable concentration profiles for the ionic species; (*iii*) realistic current-potential curves; (*iv*) current efficiencies of about 70.5, 55.7, and 39.5% for cases 2, 3, and 4, respectively; and (*v*) a copper product that can be at least 99.99999% pure. Consequently, the design of an electrochemical cell to remove the copper directly from the model process stream appears to be feasible provided that problems with the physical structure of the copper deposit can be avoided.

Again, the anlaysis is strictly valid only at the center of the disk.

Acknowledgment

This work was supported by the United States Energy Research and Development Administration.

Manuscript submitted Sept. 7, 1976; revised manuscript received Dec. 20, 1976.

Any discussion of this paper will appear in a Discussion Section to be published in the December 1977 JOURNAL. All discussions for the December 1977 Discussion Section should be submitted by Aug. 1, 1977.

Publication costs of this article were assisted by the University of California.

LIST OF SYMBOLS

a	constant = 0.51023262
a_k	relative activity of metal k in the deposit
c_i	concentration of species i, mole/liter
$c_{i,o}$	concentration of species i at the electrode surface, mole/liter
$c_{i,\infty}$	concentration of species i in the bulk solution, mole/liter
$c_{i,ref}$	reference concentration of species i, mole/liter
D_i	diffusion coefficient of species i, cm^2/sec
D_R	diffusion coefficient of the limiting reactant ($CuCl^+$), cm^2/sec
$\mathbf{F}$	Faraday's constant = 96,487 C/mole
h	mesh size
i_j	current density due to reaction j, A/cm^2
i_T	total current density, A/cm^2
i_{oj}	exchange current density, A/cm^2
$i_{oj,ref}$	reference exchange current density, A/cm^2
i_{LD}	limiting current density due to diffusion (see Eq. [18]), A/cm^2
K	equilibrium constant for reaction [5], (kg/mole)^2
L	position of the reaction plane, cm
m	number of rotating-disk electrode reactions
M_i	symbol for the chemical formula of species i
n_j	number of electrons transferred in reaction j
N_i	normal component of the flux of species i, mole/cm^2-sec
R	universal gas constant = 8.3143 J mole^{-1}K^{-1}
s_{ij}	stoichiometric coefficient of species i in reaction j
T	absolute temperature, °K
u_i	mobility of species i, cm^2 mole J^{-1} sec^{-1}
$U_{j,o}$	theoretical open-circuit potential for reaction j at the surface composition, V
U^θ_j	standard electrode potential for reaction j, V
U^θ_{cal}	standard electrode potential of the calomel reference electrode, V
V	potential of the rotating-disk electrode, V
y	normal distance from the disk, cm
z_i	charge number of species i
α_{aj}	anodic transfer coefficient for reaction j
α_{cj}	cathodic transfer coefficient for reaction j
γ_{ij}	exponent in composition dependence of exchange current density
δ	diffusion layer thickness, cm
η_{cj}	concentration overpotential for reaction j, V
η_{sj}	surface overpotential for reaction j, V
κ_∞	bulk solution conductivity, ohm^{-1} cm^{-1}
ν	kinematic viscosity of the solution, cm^2/sec
ξ	dimensionless distance from the disk

ρ_o pure solvent density, g/cm^3
Φ potential in the solution, V
Φ_o potential in the solution adjacent to the electrode surface, V
$\tilde{\Phi}$ potential in the solution outside the diffusion layer, V
$\tilde{\Phi}_o$ potential in the bulk solution extrapolated to the surface of the rotating-disk electrode, V
Ω rotation speed of the disk, rad/sec

REFERENCES

1. F. P. Haver and M. M. Wong, *J. Met.*, **23**, 25 (1971).
2. F. P. Haver, R. D. Baker, and M. M. Wong, "Improvements in Ferric Chloride Leaching of Chalcopyrite Concentrate," U.S. Bureau of Mines RI 8007 (1975).
3. P. R. Kruesi, E. S. Allen, and J. L. Lake, *CIM Bull.*, **66**, 81 (1973).
4. K. N. Subramanian and P. H. Jennings, *Can. Metall. Q.*, **11**, 387 (1972).
5. C. Rampacek and J. T. Dunham, *Min. Congr. J.*, **62**, 43 (1976).
6. W. L. Chambers and R. W. Chambers, U.S. Pat. 3,692,647 (1972).
7. J. C. Paynter, *J. S. Afr. Inst. Min. Metall.*, **74**, 158 (1973).
8. K. J. Cathro, in "International Symposium on Copper Extraction and Refining," Vol. II, pp. 776-792, The Metallurgical Society of AIME, New York (1976).
9. W. W. Harvey and F. O. Dudas, SME-AIME Preprint No. 76-B-73 presented at AIME Annual Meeting, Las Vegas, Nevada, February 22-26, 1976.
10. G. E. Atwood and C. H. Curtis, U.S. Pat. 3,785,944 (1974).
11. T. D. Kaun, M.S. Thesis, University of Wisconsin, Madison (1975).
12. J. E. Dutrizac and R. J. C. MacDonald, *Miner. Sci. Eng.*, **6**, 59 (1974).
13. R. J. Roman and B. R. Benner, *ibid.*, **5**, 3 (1973).
14. D. L. Jones and E. Peters, in "International Symposium on Copper Extraction and Refining," Vol. II, pp. 633-653, The Metallurgical Society of AIME, New York (1976).
15. W. Kunda, R. Hitesman, and H. Veltman, *ibid.*, pp. 793-822.
16. M. M. Wong, F. P. Haver, and R. D. Baker, Paper presented at Annual Meeting of AIME, New York, February 16-20, 1975.
17. R. F. P. Winand, P. P. Andrianne, and J. P. Dubois, Paper presented at AIME Annual Meeting, Las Vegas, Nevada, February 22-26, 1976.
18. J. A. Trainham and T. W. Chapman, To be published.
19. L. G. Sillén and A. E. Martell, Special Publication No. 17, The Chemical Society, Burlington House, London (1964).
20. Marie-José Schwing-Weill, *Bull. Soc. Chim. Fr.*, No. 3, 823 (1973).
21. T. Hurlen, *Acta Chem. Scand.*, **15**, 1231 (1961).
22. J. S. Newman, "Electrochemical Systems," Prentice-Hall, Inc., Englewood Cliffs, N.J. (1973).
23. L. Hsueh and J. Newman, *Ind. Eng. Chem., Fundam.*, **10**, 615 (1971).
24. S. Hatta, *Tech. Rep. Tôhoku Imp. Univ.*, **8**, 1 (1928).
25. D. W. Van Krevelen and P. J. Hoftijzer, *Recl. Trav. Chim. Pays-Bas*, **67**, 563 (1948).
26. P. V. Danckwerts, *Trans. Faraday Soc.*, **46**, 300 (1950).
27. R. H. Perry and R. L. Pigford, *Ind. Eng. Chem.* **45**, 1247 (1953).
28. D. R. Olander, *AIChE J.* **6**, 233 (1960).
29. T. K. Sherwood and R. L. Pigford, "Absorption and Extraction," McGraw-Hill Book Co., New York (1952).
30. G. Astarita, "Mass Transfer with Chemical Reaction," Elsevier Publishing Co., Amsterdam (1967).
31. P. V. Danckwerts, "Gas-Liquid Reactions," McGraw-Hill Book Co., New York (1970).
32. W. J. Albery and M. L. Hitchman, "Ring-disc Electrodes," Oxford University Press, London (1971).
33. T. K. Sherwood, R. L. Pigford, and C. R. Wilke, "Mass Transfer," McGraw-Hill Book Co., New York (1975).
34. J. J. Carberry, "Chemical and Catalytic Reaction Engineering," McGraw-Hill Book Co., New York (1976).
35. S. K. Friedlander and M. Litt, *Chem. Eng. Sci.*, **7**, 229 (1958).
36. A. Acrivos, *ibid.*, **13**, 57 (1960).
37. V. G. Levich, "Physicochemical Hydrodynamics," p. 345, Prentice-Hall, Inc., Englewood Cliffs, N.J. (1962).
38. R. B. Bird, W. E. Stewart, and E. N. Lightfoot, "Transport Phenomena," John Wiley & Sons, Inc., New York (1960).
39. A. Acrivos, Editor, "Modern Chemical Engineering," Vol. 1, Reinhold Publishing Corp., New York (1963).
40. P. L. Chambré, *J. Chem. Phys.*, **25**, 417 (1956).
41. M. Jischa, *Int. J. Heat Mass Transfer*, **16**, 2261 (1973).
42. G. T. Sergeev, *Inzh.-Fiz. Zh.*, **23**, 234 (1972).
43 F. Coeuret and J. J. Ronco, *Int. J. Heat Mass Transfer*, **14**, 2017 (1971).
44. P. L. Chambré and J. D. Young, *Phys. Fluids*, **1**, 48 (1958).
45. A. V. Lykov and G. T. Sergeev, *Inzh.-Fiz. Zh.*, **26**, 807 (1974).
46. M. Jischa, *Int. J. Heat Mass Transfer*, **15**, 1125 (1972).
47. Yu. M. Gershenzon, V. B. Rozenshtein, A. I. Spasskii, and A. M. Kogan, *Dokl. Akad. Nauk SSSR*, **205**, 624 (1972).
48. K. Ueyama, J. Hatanaka, and K. Ogawa, *J. Chem. Eng. Jp.*, **5**, 248 (1972).
49. K. Ueyama, J. Hatanaka, and K. Ogawa, *ibid.*, **5**, 371 (1972).
50. N. Peters, *Int. J. Heat Mass Transfer*, **19**, 385 (1976).
51. R. B. Bird, W. E. Stewart, E. N. Lightfoot, and T. W. Chapman, "Lectures in Transport Phenomena," AIChE Continuing Education Series 4, American Institute of Chemical Engineers, New York (1969).
52. J. Newman, in "Advances in Electrochemistry and Electrochemical Engineering," Vol. 5, C. W. Tobias, Editor, pp. 87-135 (1967).
53. J. Newman, *This Journal*, **113**, 1235 (1966).
54. J. Newman, *Int. J. Heat Mass Transfer*, **10**, 987 (1967).
55. J. Newman, *Ind. Eng. Chem., Fundam.*, **5**, 525 (1966).
56. R. White, C. M. Mohr, Jr., and J. Newman, *This Journal*, **123**, 383 (1976).
57. J. Newman, in "Electroanalytical Chemistry," Vol. 6, A. J. Bard, Editor, Marcel Dekker, Inc., New York (1973).
58. P. de Voogd, Ir. (M.Sc.) Report, Technische Hogeschool Delft (1961).
59. J. Newman and L. Hsueh, *Ind. Eng. Chem., Fundam.*, **9**, 677 (1970).
60. B. Levich, *Acta Physicochim. URSS*, **17**, 257 (1942).

Etch Rates of an Electroplated Alloy (Sn-Ni) Using a Quartz Crystal Microbalance

J. H. Thomas III*

Bell Laboratories, Columbus, Ohio 43213

ABSTRACT

Etch rates for electroplated tin-nickel alloy (65 w/o Sn, 35 w/o Ni) in 10% HCl solution have been determined at 25°, 50°, and 75°C using a quartz crystal oscillator as a sensitive microbalance. Sn-Ni electrodeposits exposed to laboratory ambient for 24 hr exhibit linear etch rates (170, 290, and 540 Å/min for 25°, 50°, and 75°C, respectively). Tin nickel (SN-Ni) exposed for more than 6 weeks exhibits nonlinear etch rates initially. An induction period of 25 sec is required before etching begins in 10% HCl for the 6-week exposed samples. These effects are attributed to the presence of a passivating native oxide (30Å thick) which is not observed on the 24-hr exposed Sn-Ni.

Tin-nickel electroplated alloy is presently being investigated for use as an underplate for gold-plated electrical contacts. Many aspects of the physical properties of the polycrystalline tin-nickel deposit, such as corrosion resistance (1) and the buildup of surface passivity (2-4), are presently being investigated. In fabricating gold on tin-nickel contacts, the tin-nickel surface is usually treated in dilute HCl (10%) for a period of between 30 and 60 sec to remove possible oxide buildup prior to gold electroplating. This procedure, called activation, insures good gold film adherence. This practice stems from early investigations into the electrochemical (5, 6) and chemical (7) properties of tin-nickel. Parkinson *et al.* (7) show that the native oxide protects the metal in solutions containing Cl^- with *p*H of more than 1.3. It was also shown that HCl (both 1 and 4*N*) dissolves tin-nickel alloy at a slow rate at temperatures near room temperature. In this paper, etch rates for tin-nickel (65/35) alloy have been determined at room temperature (25°C), 50°, and 75°C using a quartz crystal oscillator as a sensitive microbalance.

Experimental

Polycrystalline tin-nickel samples were prepared by electroplating (3) ~7000Å of tin-nickel on 5 MHz AT-cut circular quartz oscillator plates (supplied by Sloan Technology Corporation, Santa Barbara, California, for use in their film thickness monitors). Quartz crystals were supplied with an evaporated gold film applied to both sides for electrical contact purposes. The gold area was ~1 cm^2 per side. Deposited film thickness is limited by the mass of the total film which subsequently causes the oscillator frequency to shift. On quartz crystal mass monitors of this type, mass loading must be limited to that which will result in less than 100 kHz frequency shift at 5 MHz (9). Frequency change is related to mass change by the following: $\Delta m = 1.77 \times 10^{-8} \Delta f$ g/cm^2 [see Ref. (9)]. To insure a maximum linear crystal response to mass loading, films were not deposited in excess of 7 kÅ per side. At this thickness, Sn-Ni is likely to be porous, but this will not significantly affect the results of this study. Some crystals were allowed to stand in unfiltered laboratory air for 24 hr while a few were aged in this manner for more than 6 weeks. Two coupons (1½ × 1½ in.) were also prepared by electroplating 3 mils of tin-nickel on clean O.F.H.C.[1] copper (supplied by M. Antler). These samples were allowed to stand in laboratory air for about 4 months, which produced a passivating native oxide.

Etch rate and mass loss measurements were performed using a Sloan Crystal thickness monitor (DTM-3) in lab air (see Fig. 1a). A Hewlett-Packard frequency counter was attached to the oscillator output to provide an accurate measurement of the oscillator frequency. Sequences of measurements were typically made to precision of about ±30 Hz.

Contact resistance measurements (10) were made using a gold wire probe (20 mils diameter) (11) at a force of 100g (see Fig. 1b). All measurements were made at a constant current of 1 mA and a maximum open-circuit voltage of 100 mV. Six probings were made for each measurement condition as described below. Contact resistance measurements were per-

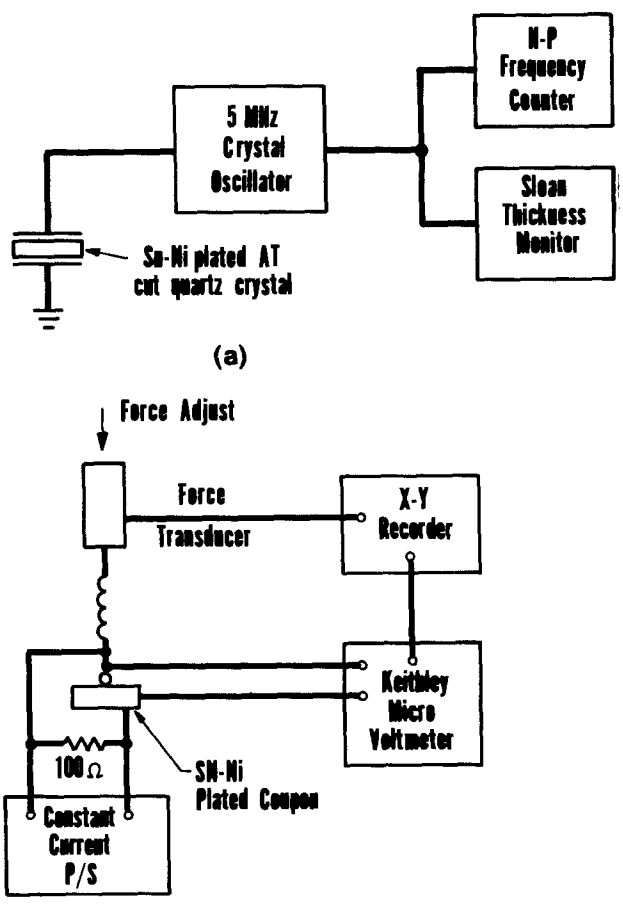


Fig. 1. (a) Block diagram of the mass loss monitor system; (b) block diagram of the contact resistance probe.

* Electrochemical Society Active Member.
[1] Trademark: American Metals Climax, Incorporated.

formed only on the electroplated copper coupons because the quartz crystals are very fragile.

The 10% HCl solution was prepared using Baker reagent grade HCl (37% HCl) and reverse osmosis deionized water with a resistivity in excess of 5 MΩ-cm. A new solution was prepared before each experiment. Above room temperature measurements were performed by heating 100 ml of solution in a covered beaker on a hot plate. Solution temperature was controlled to within ±1°C.

The following procedure was used to etch the electroplated Sn-Ni samples. The crystals were handled with semi-cleanroom procedures, that is, lint-free gloves, etc. Etching was performed by mounting the crystal (which is approximately ½ in. diameter) on a stainless steel tricep. Only the stainless steel spring fingers of the triceps holding the crystals were immersed in the etchant. During the etch, the samples were vigorously agitated by hand. Upon completion, the etched samples were rinsed in flowing water and blown dry with filtered dry air. All frequency shift measurements were made at room temperature. A similar procedure was used to etch the tin-nickel plated coupons. However, for reference purposes only half of the coupon was exposed to the etchant.

Results

Etch rate vs. temperature (samples aged for 24 hr).—The tin-nickel electroplated crystals which were exposed to lab environment for ~24 hr were used in this study. A number of crystals were etched at room temperature to check reproducibility. Crystals were etched for a given time (30 or 60 sec) using the above procedure, and frequency shift was determined after each etch period. In some cases, up to 5 min were required for the newly etched crystal to stabilize in the oscillator. Transient conditions were attributed to a temperature/humidity differential from the cleaning/drying operation to the crystal mount. Figure 2, curve A shows a typical frequency shift *vs.* etching time at room temperature. Frequency shift is converted to film thickness or mass using a computed density for tin-nickel of 8 g/cm^3 and a crystal constant of 1.77 × 10^{-5} g/cm^2/kHz (5). Mass change is indicated along the right-hand side of Fig. 2. Slight nonlinearities in etch rate (that is, deviations from a straight line in curve A) are likely due to surface contamination in handling or variations in exposure time during successive measurements. AT-cut crystals are more sensitive to mass change near the center of the disk. For these samples (curve A), the 10% HCl appears to attack the tin-nickel at an almost constant rate. When the samples were etched long enough to remove most of the Sn-Ni, the underlying gold on the crystal was exposed more or less uniformly. This indicates that the etchant etched the polycrystalline sample surface uniformly. The slope of the curve can be converted to an etch rate using the crystal constant and the density of tin-nickel. At room temperature, this particular sample etches at a rate of ~200 ± 10 Å/min. The error is estimated from the ±30 Hz inaccuracy in the data.

As mentioned earlier, the etch rate in 10% HCl solution was measured at 25°, 50°, and 75°C. Figure 3 summarizes etch or mass loss data as a function of sequential etch times at these temperatures. In all cases, etching proceeds at a nearly constant rate. Elevated etchant temperature increases the etch rate. Etch rates for the samples shown are 170, 290, and 540 Å/min at 25°, 50°, and 75°C, respectively. However, considering the manner in which etching was performed, that is, exposing the etched surface to lab air between each measurement, the discrepancy in etch rate (170 *vs.* 200 Å/min) at room temperature is not surprising.

Effects of the native oxide (samples aged more than 6 weeks).—Curve B in Fig. 2 shows a typical etch characteristic (that is, mass loss *vs.* etch time). For a crystal which had been exposed to lab ambient for >6 weeks and subsequently etched in room temperature 10% HCl for the various times, no frequency shift was noted (except some variation around the initially measured frequency) for etch times less than 25 sec. An initial etch time of >25 sec produces a measurable frequency shift (for 30 sec, Δf = ~60 Hz) indicating a mass loss. Subsequent 30 sec etches remove considerably more material and the rate becomes linear as shown in Fig. 2, curve B. The linear etch rate is similar to that of curve A indicating that Sn-Ni is being etched. Apparently, the oxide is not appreciably etched for immersion times of less than 30 sec. Unfortunately, higher time resolution measurements were not performed on the quartz crystals.

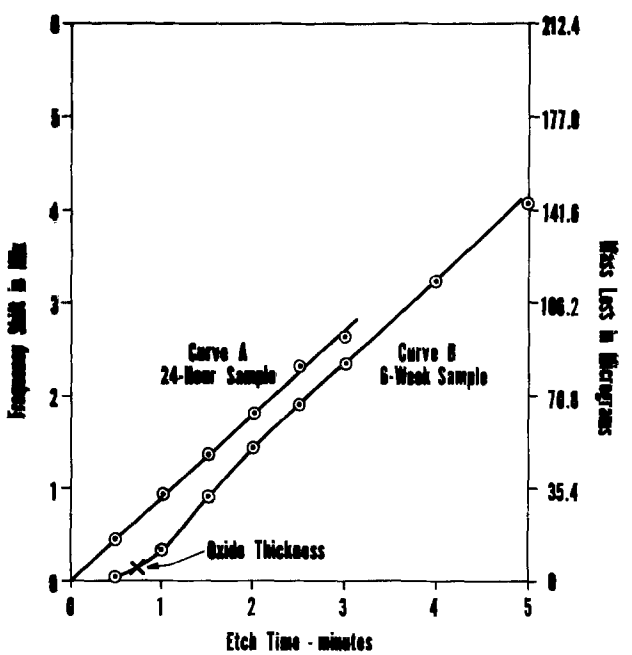


Fig. 2. Curve A: etching characteristics, frequency shift, or mass loss *vs.* etch time for a Sn-Ni sample exposed for 24 hr. Curve B: a similar characteristic for a sample exposed for > 6 weeks.

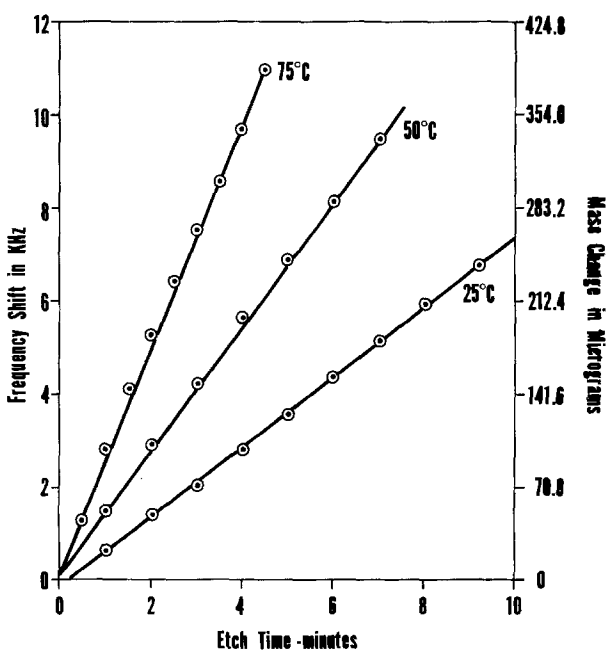


Fig. 3. Etching data, mass loss *vs.* etch time, are shown at 25°, 50°, and 75°C. Etch rates (slopes) are 170, 290, and 540 Å/min.

To study this phenomenon in more detail, contact resistance measurements were performed on a Sn-Ni plated copper coupon as a function of etch time at room temperature. The sample was cleaned and blown dry with clean air and six contact resistance measurements were made at a contact force of 100g. After making initial resistance measurements, the coupon was etched and measured sequentially for two 10 sec periods, four 15 sec periods, two 20 sec periods, and one 25 sec period. The 25 sec etch was followed by four 10 sec etches.

Etching data are summarized in Fig. 4. Bars indicate the range of the six contact resistance values and the dot indicates the median value of contact resistance. Initial contact resistance is near 1000Ω (at 1 mA constant current) and is indicative of an electrically insulating film. Immersion and subsequent etching caused a decrease in contact resistance until a contact resistance of around 100 mΩ was attained. Further etching did not reduce the contact resistance until the etch time was increased to 25 sec. After the 25 sec etch, a marked decrease in contact resistance to around 20 mΩ was observed. Etch times after the 25 sec etch were reduced and repeated until a low repeatable value of contact resistance (~6 mΩ) was attained. This resistance corresponds to a technically clean metallic surface obtained by handling in the laboratory environment. For reference, an abraded gold flat was measured and a value of 3.2 mΩ was measured repeatably.

Discussion

Figure 2, A and B show etch rate data for Sn-Ni which has been aged for 24 hr after plating and more than 6 weeks after plating, respectively. A considerable difference is observed between initial etch rate of the two samples. In the case of the newly plated samples, etching occurs at a near linear rate from the onset. Samples exposed for >6 weeks etch at a slower rate initially and eventually attain a steady etch rate. This suggests that for the samples exposed for a long time the initial nonlinearity is due to the removal of the native oxide. Thus, the oxide appears to etch at a slower rate than the Sn-Ni metal. The oxide which builds up on the Sn-Ni surface after ~24 hr exposure to lab air does not show any evidence of chemical passivity in 10% HCl. Therefore, a clear distinction exists between the long-term oxide and the short-term oxide passivity and etch characteristics. Properties and growth kinetics of both oxides were investigated through the use of analytical surface instruments (ESCA, AES, etc.) (3, 4, 12). The passive native oxide which grows on Sn-Ni was shown to be a form of hydrated nickel stannate (12).

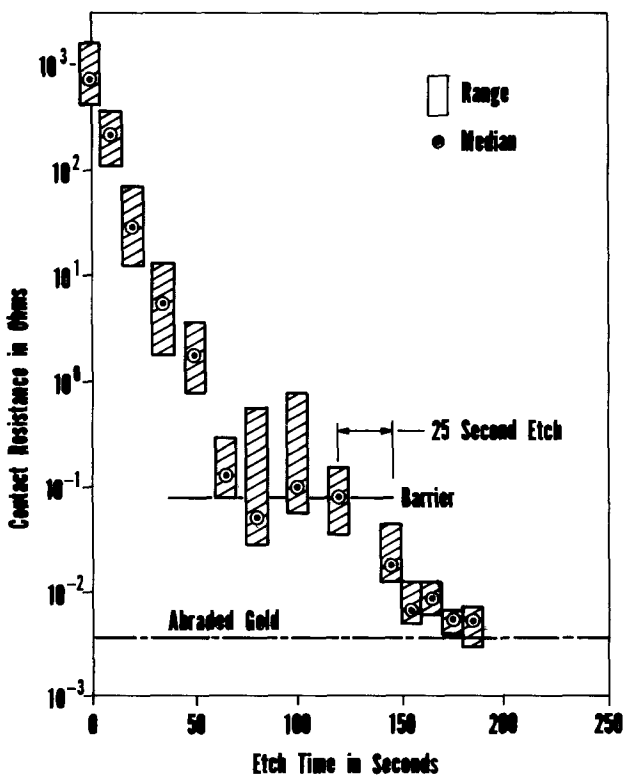


Fig. 4. Contact resistance at 100g force, 1 mA constant current, and 100 mV open-circuit voltage shown as a function of etch time.

From the data shown in curve B of Fig. 2, an approximation of the oxide thickness was made by assuming the point at which the initial slow etch rate begins to increase. A point midway between the first and second data points (indicated by "X") was chosen. Assuming the density of the oxide to be 6.85 g/cm^3 [estimated by averaging the known densities of SnO_2 and NiO (12)], the frequency shift at this point is ~100 Hz which corresponds to a film thickness of ~30Å. Contact resistance data indicate that the oxide film reaches an equilibrium thickness in ~6 weeks exposure to air (2). The thickness estimated from the etch results is in good agreement with the ESCA depth profile results discussed in Ref. (12) (~35Å thick).

Etch rate measurements at various temperatures show that after removal of the native oxide, Sn-Ni metal is removed at a more or less steady rate. The rate is observed to range from ~500 Å/min at 75°C to ~200 Å/min at 25°C. As a practical matter, 10% HCl is a very slow etchant for electroplated Sn-Ni at or above room temperature.

Contact resistance measurements (using a gold probe) show a large initial decrease in resistance with etch time in 10% HCl at room temperature. This may be due to Cl^- incorporated in the oxide which changes its conductivity and is likely related to the breakdown of chemical passivity.[2] Since weight loss was not observed on crystals etched in a similar manner, it is unlikely that the native oxide is being removed in the initial etch stages. The change in resistance is observed to reach a plateau or barrier at ~100 mΩ for etch times of <25 sec. The plateau most likely corresponds to a saturation effect in the oxide film. When the etch time is increased to 25 sec, contact resistance is decreased by a factor of five corresponding to a partial removal of the native oxide. Subsequent 10 sec etches removed the remainder of the passive oxide, exposing the metal surface. Resistance measurements stabilized at ~6 mΩ (compared with 3.2 mΩ Au-Au) at a force of 100g. Lower force contact resistance values tracked the 100g data but exhibited a larger range around the median.

Contact resistance and etch rate data clearly show, in the presence of a passivating native oxide on Sn-Ni, an induction period before which Sn-Ni metal or oxide is not etched by 10% HCl at room temperature. In the case of room temperature etching, the sample must be immersed in the HCl solution for >25 sec before any mass loss is observed. The contact resistance measurements confirm these results. It is likely that shorter times will initiate Sn-Ni etching in 10% HCl at elevated temperatures.

Conclusions

Etch rates for Sn-Ni have been determined using a quartz crystal oscillator as a microbalance. It has been shown that Sn-Ni etches at a linear rate (170, 290, and 540 Å/min, respectively) in 10% HCl solution at 25°, 50°, and 75°C. When a "thick" oxide (samples exposed >6 weeks in lab air) is present, an induction period is required before the oxide or Sn-Ni is etched, that is, the native oxide remains passive for immersion times <25 sec in 10% HCl. These results are confirmed

[2] It is a well-known fact that small quantities of impurities in normally insulating films can change their conductivity drastically. See, for example, J. J. O'Dwyer, "The Theory of Elecrical Conduction and Breakdown in Solid Dielectrics," chap. 2, Clarendon Press, Oxford (1963).

by contact resistance measurements. Room temperature etching of Sn-Ni electroplate exposed for ~24 hr and >6 weeks exhibits different initial etch characteristics. After ~1.5 min in 10% HCl, the "thick" oxide samples etched at essentially the same rate as the thin oxide sample. The initial nonlinearity in etch rate is attributed to the existence of a thick native oxide. Oxide thickness was estimated to be ~30Å.

Acknowledgments

The author wishes to thank E. T. Ratliff for plating the crystals and G. V. McIlhargie for the use of the Sn-Ni plating facility. The author is also indebted to M. Antler for his interesting discussion and the plated Sn-Ni coupons used in this study and to F. E. Bader for his critical reading of this manuscript.

Manuscript submitted Nov. 19, 1976; revised manuscript received Jan. 21, 1977.

Any discussion of this paper will appear in a Discussion Section to be published in the December 1977 JOURNAL. All discussions for the December 1977 Discussion Section should be submitted by Aug. 1, 1977.

Publication costs of this article were assisted by Bell Laboratories.

REFERENCES

1. M. Antler, M. Feder, C. F. Hornig, and J. Bohland, *Plating Surf. Finishing*, **63**, 30 (1976).
2. M. Antler, M. H. Drozdowicz, and C. F. Hornig, *Corrosion*, To be published.
3. J. E. Bennett and H. G. Tompkins, *This Journal*, **123**, 999 (1976).
4. H. G. Tompkins and J. E. Bennett, Paper presented at the American Vacuum Society Symposium, Chicago, Illinois, Sept. 21-24, 1976.
5. M. Clarke and R. G. P. Elbourne, *Corros. Sci.*, **8**, 29 (1968).
6. M. Clarke and S. C. Britton, *ibid.*, **3**, 207 (1963).
7. N. Parkinson, S. C. Britton, and R. M. Angles, *Sheet Met. Ind.*, **28**, 1 (1951).
8. W. H. King, *Res. Dev.*, **20**, 28 (1969).
9. C. S. Lu and O. Lewis, *J. Appl. Phys.*; G. Z. Sauerbrey, *Physik*, **155**, 206 (1959); also C. D. Stockbridge, "Vacuum Microbalance Techniques," Vol. 5, p. 193 Plenum Press, New York (1966).
10. M. Antler, in "Gold Plating Technology," Electrochemical Publications, Ltd., U.K. (1974).
11. J. H. Thomas III *IEEE Trans. Parts, Hybrids, Packag.*, **php-12**, 255 (1976).
12. J. H. Thomas III and S. P. Sharma, Submitted to *J. Vac. Sci. Technol.*; also, S. P. Sharma and J. H. Thomas III, Submitted by *Anal. Chem.*

A-C Impedance and Corrosion Studies on Implantable Anode Materials

H. M. Carim*,[1] and R. B. Beard*

Biomedical Engineering and Science Program, Drexel University, Philadelphia, Pennsylvania 19104

and A. S. Miller

Department of Pathology, School of Dentistry, Temple University, Philadelphia, Pennsylvania 19104

ABSTRACT

The use of heart pacemakers and other implantable electronic devices is increasing. The hybrid cell, as a power source, consisting of a sacrificial anode and a catalytic cathode for tissue oxygen reduction has been successfully employed to pace heart-blocked dogs. The life and biocompatibility of the cell are determined by the anode material loss in the recipient's body. Corrosion rates of Al anodes implanted in dogs have been studied using the d-c polarization technique of Greene and Stern. The difference in the measured apparent corrosion rates is explained. The effect of extensive pitting of Al under galvanostatic loading conditions and its effect on the linear and Tafel curves are discussed. Preliminary data from *in vivo* a-c impedance measurements are presented in an effort to correlate them to the corrosion parameters. Problems associated with the a-c bridge measurements include the elimination of the tissue impedance (exhibiting possible dielectric relaxation) between the measuring electrodes. It is shown that it is possible by careful selection of the electrode geometry to minimize the effects of tissue and auxiliary electrode impedances on the metal-tissue interface parameters of the test electrode.

Hybrid cells consisting of porous palladium black cathodes where dissolved oxygen in the body fluids is catalytically reduced by galvanic coupling to sacrificial anodes which are oxidized have been reported (1). Reduction of available energy due to large overpotentials of the cathodes has been overcome by using powder metallurgy techniques with Pd black (2, 3). Early biocompatibility studies have been previously reported (1). This paper describes further measurements of anode corrosion rates and preliminary a-c impedance studies in an effort to characterize the corroding metal-tissue interface.

* Electrochemical Society Active Members.
[1] Present address: Medical Products Division, 3M Center, St. Paul, Minnesota.
Key words: *in vivo*, aluminum, corrosion, a.c impedance, anodes.

Experimental Procedures

Corrosion studies.—Corrosion rates were determined by using the linear polarization technique (4-8); galvanostatic anodic and cathodic polarization curves. The corrosion currents were determined from (8) $I_{corr} = 0.026/R_p$ where R_p is the polarization resistance determined from the linear polarization curves.

The linear polarization technique consists of determining the Tafel slopes β_a and β_c for both anodic and cathodic processes and the polarization resistance, R_{pol}, of the corroding electrode under study. The polarization resistance is the slope of the linear portion of the polarization curve obtained by plotting overpotential *vs.* current density for the first 10-20 mV of overpotential of the electrode.

In the *in vivo* studies, the current was passed between a test electrode and a porous palladium black auxiliary electrode implanted in dogs. The potential of the test electrode was measured with respect to an Ag-AgCl reference electrode placed on the skin of the dog with conductive paste.

The procedure for obtaining a galvanostatic polarization curve was as follows. The constant current (d.c.) was incremented in equal steps (at least ten equal steps per decade on a logarithmic scale) at equal intervals of time, usually between 2-5 min. The change in potential due to the constant current increment was noted at the end of the time interval. This procedure was continued until a complete polarization curve was obtained.

A Keithley Model 225 current source with a Model 160 ammeter was used in the *in vivo* galvanostatic measurements where the current was passed through the test electrode via an auxiliary electrode (9). The electrode voltage was monitored using a Model 610C electrometer and a Digitex 268 millivoltmeter. All electrodes were sterilized in a Bard ethylene oxide gas sterilizer. Electrical connections were made by Teflon-coated multistrand stainless steel wire No. 31A.W.G. (Gooner Wire Company, California) and were percutaneously brought out of the dog. One major problem with previous implants was the permeation of fluids into and beneath the epoxy encapsulation over the sample. However, the present method of applying the epoxy resin by abrading the surface (to remove metal oxide) and the additional PVC-paraffin dip has successfully solved the problem. No ingress of fluids was observed after 5 months of implantation. The implants were given a final coating of Dow Corning medical grade silicone adhesive A for biocompatibility. All samples had a 1 cm^2 area exposed. Metals of 99.99% purity were supplied by A. D. Mackay and Company, New York. An Ag-AgCl standard 16 mm Beckman biopotential electrode was placed on the skin with conductive paste for the duration of the experiment.

Electrical impedance studies.—Test electrodes of Al were made similar to those used in corrosion studies, but of 0.22 cm^2 exposed area. These implanted "impedance cells" had the Al electrode facing, approximately 1-2 mm apart, a parallel plate porous palladium auxiliary (counter) electrode. For *in vitro* measurements, in addition to the above, electrodes of 99.99% purity Al wire 0.005 cm^2 area embedded in epoxy were used. The cross-sectional area (of the wire) was polished with 0.05 μm alumina and inspected for flaws with a low power microscope. Reagent grade chemicals and doubly distilled water were used to make the chloride solutions. The a-c bridges included the Wayne Kerr B201 for 0.1-5 MHz and B221 for 0.25-50 kHz in conjunction with a Wayne Kerr SR 268 source detector, G.R. 1312 decade oscillator, and G.R. 1232A null detector, for measurements of 20-200 Hz, with a G.R. 1608-A bridge.

The total measured impedance between the electrodes includes the solution and tissue impedance. The measuring electrodes consist of a porous palladium counterelectrode whose interfacial impedance (10, 11) is significantly lower than the test electrode. The equivalent circuit employed to represent the measured impedance Z_m is given in Fig. 1.

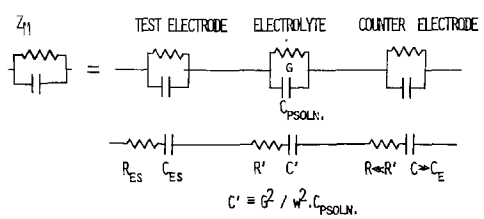


Fig. 1. Equivalent circuit used to represent measured parallel capacitance and conductance as Z_m.

Results and Discussion

Corrosion.—Gross pitting studies.—Two dogs were used with one set of samples in each, loaded to the range of current densities shown in Table I. The set S samples upon removal showed that epoxy adhesion was lost allowing fluid ingress beneath the masked area up to the lead connection. This is ascribed to electrolyte passage through the epoxy resin (12) since this set did not have the PVC-paraffin coating as on set M. In this confined region beneath the epoxy capsule, brightening of the electrode and uniform corrosion had occurred. Under a low power microscope shallow hemispherical and saucer-shaped pitting over the entire area was seen.

Three of the electrodes of set S showed the dark original oxide on the unmasked area intact with micropitting. The electrodes were presumably under cathodic protection (13) by the uniformly corroding parts elsewhere on the electrode. Three other S samples showed brightening of the exposed area as well as that masked by epoxy wherein fluids had permeated. The exposed surfaces had thick crusts of corrosion products. Some pits approximately 20 on one sample of 0.1-0.5 mm opening and up to 0.4 mm depth were present, with innumerable micropits.

The three samples in set M which were implanted and loaded to the currents shown in Table I had the epoxy well adhered. Corrosion was seen only on the exposed area where varying amounts of deep pitting were observed. The area under such macropits was roughly proportional to the loading; the rest of it was covered by the original darker oxide which had undergone micropitting of various geometrical shapes. This area was evidently acting as a cathode (13) for O_2 reduction to the anodic dissolution areas in the pits. Due to the absence of a freely flowing electrolyte in *in vivo*, the corrosion products were again deposited on the surface, especially over the pitted areas. The pits were large, up to 0.7 mm in opening and equally deep with extensive lateral growth. Ob-

Table I. Aluminum electrodes with *ca.* 1 cm^2 area implanted in dogs for 20 weeks

ELECTRODE		AVERAGE LOAD CURRENT UA.	AVERAGE POTENTIAL UNDER LOAD RELATIVE TO Ag-AgCl REFERENCE ELECTRODE. VOLTS. −VE
SET	S		
	1+	75	1.00
	2*	25–35	.67——.94
	3*	19	.70——.96
	4	18–22	.94——.97
	5*	18–21	.95——.97
	6	11–13	.84——.89
SET	M		
	0"	30–45	.62——.64
	1"	19	.64——.66
	2"	12–13	.63——.66

+ UNLOADED AFTER 80 DAYS, * LOADED AFTER 80 DAYS. ALL MEASUREMENTS ON SET S WERE MADE 80 DAYS AFTER IMPLANTATION.

"POTENTIALS WERE .9–1.0 BEFORE LOADING.

servations under a low power microscope clearly showed that the areas under crevice corrosion and the surface of the pits were totally covered with small bright hemispherical pits.

There is difference of opinion as to the morphology and initiation (14, 22) of pitting of Al in solutions containing Cl^- ions. According to Kaesche (15) and Wood *et al.* (16), Al polarized to or below the pitting potential E_p shows crystallographic pitting which turns to electropolished pits as the potential is raised (more +eV); whereas Galvele *et al.* (17) claim that brightened hemispherical pits are not a general rule. They showed the transition from purely spherical polished to a crystallographic pitting as the NO_3^-/Cl^- concentration ratio is decreased. This study shows that the pits (*i*) are crystallographically not well defined but tend to be more or less hemispherical and (*ii*) show a degree of electrobrightening described as polished pits, which is what Hoar (20) found for metals with an oxide undergoing pitting at the breakdown potential. Given Cl^- containing organic fluids as the medium (18, 19), it is not surprising to note during galvanic corrosion at constant current that Al anodes undergo severe pitting at approximately −0.62V *vs.* Ag-AgCl and show brightened hemispherical pit surfaces.

Two electrodes implanted under no load for 5 months showed very little sign of visual corrosion. One sample showed evidence of the beginning of crevice corrosion, with some micropitting and one large pit of 0.1 mm opening. The other electrode showed a similar surface with an additional 0.4 mm wide and deep pit. The exposed area showed numerous micropits of irregular shapes under a low power microscope.

A scanning electron microscope, SEM, micrograph is shown in Fig. 2 and 3. This proves that loading of the electrode results in large pits which propagate extensively with time.

Electrodes of set S of Table I were observed to have undergone uniform metal dissolution under the encapsulating epoxy due to fluid ingress because of bad epoxy adhesion, rather than deep pitting. As a result, galvanic coupling to the copper rivet for the lead wire was established, enhancing the corrosion. These samples showed more active potential (Table I); −0.9V as compared to those of set M (≈ −0.6-

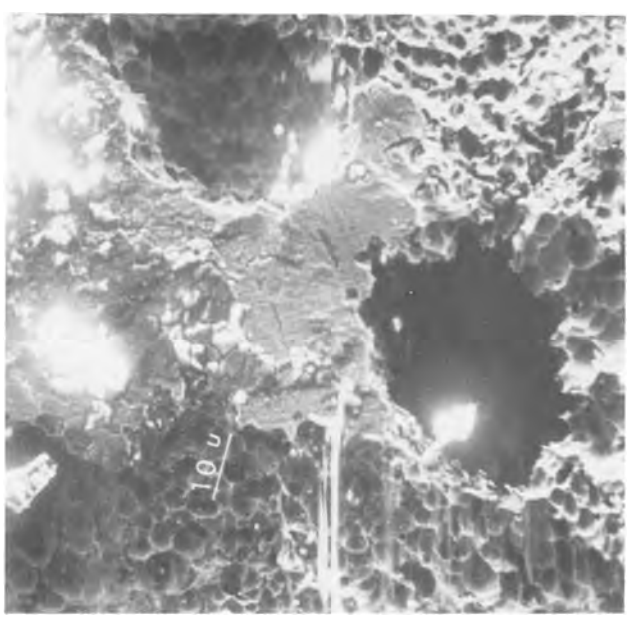


Fig. 2. Scanning electron micrograph showing brightened hemispherical pits and pit surfaces on a loaded aluminum electrode after removal.



Fig. 3. Scanning electron micrograph showing unloaded aluminum electrode surface after removal.

0.65V). Craig (21) has shown that the potential of a corroding metal is an indication of the nature of the metal dissolution process thus indicating that for the above potential ranges sets S and M were undergoing uniform and pitting attack, respectively.

Pitting potential.—Figures 4-6 show anodic polarization curves taken on Al samples *in vivo*. The curves generally do not show a linear Tafel region (see below), however, the interesting feature is the plateau region of apparent nonpolarizability, occurring at an average potential of −0.60V *vs.* Ag-AgCl. The shape of the curve with the hump before the apparently nonpolarizable region is characteristic of the type of galvano-kinetic method used (22). In this study the quasi-stationary method, where a constant current was changed stepwise and a certain rate was used.

Various investigators (34) have given an explanation of the plateau region part of the *E-I* curves. The potential maximum on the hump is called the pitting potential E_p and the potential at the plateau the pitting protection potential, E_{pp}. de Wexler and Galvele (23) have proposed from data on strained Al samples that a critical pitting potential definitely exists for Al and is independent of the oxide.

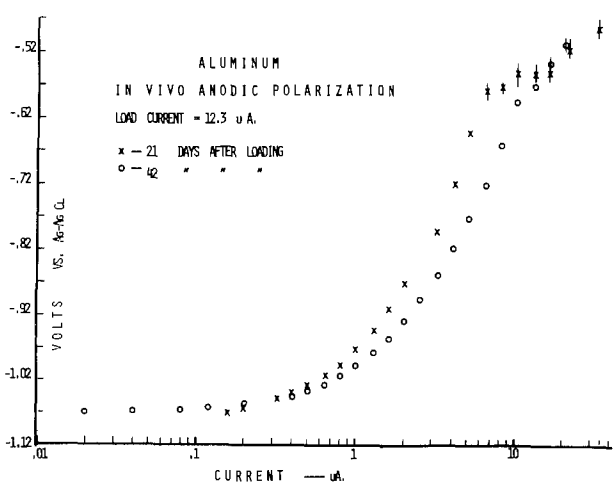


Fig. 4. Anodic polarization curves of aluminum electrodes (set M) showing changes with time under load. Vertical bars indicate oscillations of potential.

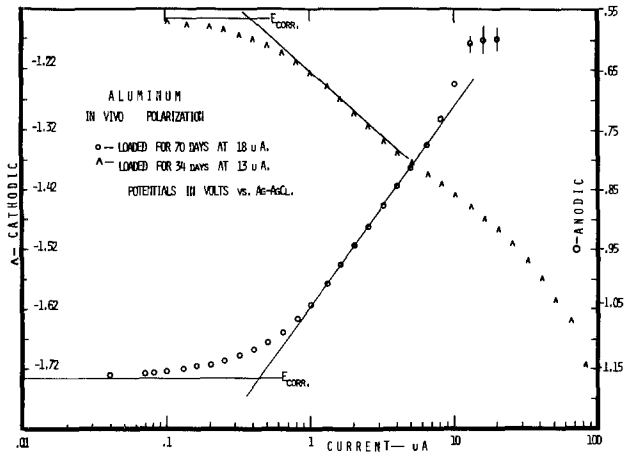


Fig. 5. Polarization curves of aluminum electrodes. ○ = anodic polarization curve taken at 5-8 min time intervals between current increments showing linear Tafel region.

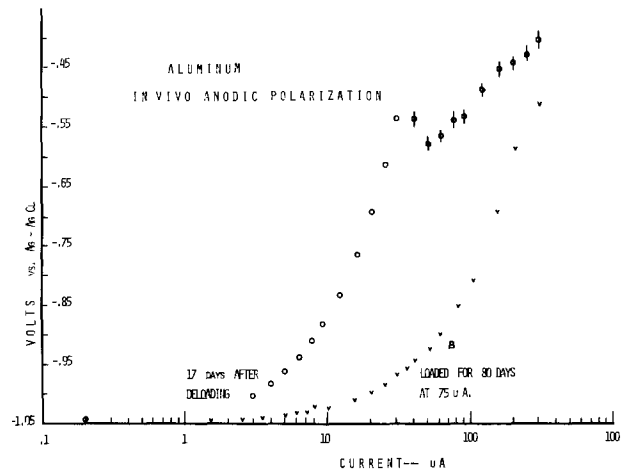


Fig. 6. Aluminum electrode (of set S) polarization curve showing effect of partial passivation due to removal of load current.

Broli *et al.* (22) have shown that there is only one critical potential of Al, and have given reasons for differing values obtained by different types of potential and current controlled *E-I* curves. According to Wood *et al.* (16) the breakdown or pitting potential only represents that stage in the pitting process at which the combined effects of increasing active surface area and decreasing ability of local cathodic activity to support that area require a sudden increase in current supply. On the other hand, Pryor (24) has claimed that at and above the critical potential the Al ions migrate through the oxide by a high field mechanism.

Figure 4 shows that with time, under load, the plateau region is somewhat shortened. This was observed in most of the loaded samples. One explanation of this nonpolarizable region is that it occurs when the external current increases at a rate proportional to the area increase due to propagating pits (15) supporting the anodic process and new pits initiated on any cathodic area. Thus a constant true anodic current density maintains the potential of the specimen constant. During polarization in the plateau region, the potential oscillates rapidly between ±100 mV. This could be due to the activation and increase in "new anodic" and cathodic areas (16) which may momentarily supply a supporting cathodic current. The new "anodic areas" could be the mentioned passive areas supporting O_2 reduction (see above) which are not activated due to breakthrough type of current across the Al oxide of ions as proposed by Pryor (24). The reduction in the nonpolarizable region with time under load is then due to a decrease in the availability of passive (cathodic) area supporting O_2 reduction since more of this area is attached by pitting with increasing time and load.

The above effect is well demonstrated in Fig. 6, where the sample is from set S. The sample had undergone uniform dissolution over its entire surface. Curve B shows no evidence of a plateau, since little or no new anodic area is available (no large pits propagating) nor oxide-covered cathodic area which could undergo breakdown. After deloading, part of the anodically active area passivates, the breakdown of which manifests as the reappearance of the apparent nonpolarizable region. Table II gives some values of the E_p which were observed. Some electrodes showed more +V values of the breakthrough potential after several weeks under load. As to why the breakdown consistently occurs in the range −0.52-0.62V *vs.* Ag-AgCl is yet unknown.

The above curves were obtained by open-circuiting the loaded electrodes, and the polarization was then begun after a time period during which the potential decreased (more −V) to a steady-state value of approximately −1.1V from the value of −0.64 under load. The decrease in potential is explained as follows. Upon removal of the load current, the anodic current density through the true dissolution area (inside pits) decreases (due to repassivation), causing a fall in E_{corr}.

Tafel regions.—The time between current increments was 1-2 min. The electrode potential had reached a near steady state in this interval. As the breakthrough potential was approached, this time was observed to be insufficient and the potential was still increasing

Table II. Values of potentials corresponding to the nonpolarizable region of the anodic polarization curves observed with time after loading. (Note zinc electrode No. 2 was not loaded, and the load on No. 3 was removed after 37 days.) All potentials are −V measured relative to Ag-AgCl reference electrode

SET M ALUMINUM ELECTRODES.			
ELECTRODE.NO.	0	1	2
	.62	.62	.62
	.59	.59	.60
	.55	.61	.62
	.58	.59	.58
	.59	-	.67
	.50	-	-

ZINC ELECTRODES. POTENTIALS CORRESPONDING TO BREAK IN POLARIZATION CURVES.			
ELECTRODE. NO.	1	2	3
LOAD CURRENT.			
AVERAGE UA.	24	0	15
	*	.93	*
	*	.92	*
	*	-	.93+
	*	-	-
	*	-	-
	*	-	-
	*	-	-
	*	-	-

* NO BREAK IN CURVE OBSERVED. - DATA NOT TAKEN
+ OBSERVED AFTER REMOVING LOAD

(→ +eV). In some cases even though 5-8 min were allowed, a steady potential was not reached, although this resulted in the appearance of a linear Tafel region as shown in Fig. 5. The breakthrough potential, however, still occurred between −0.52 to −0.62V *vs.* Ag-AgCl.

The cathodic polarization curves give β_c values between 0.2 and 0.25 while the β_a values were greater than 0.3.

Since the samples of set M had substantial areas of the original oxide on the surface intact (under cathodic protection by the pits), the curves in Fig. 4 and 5 show a smaller change with time under load as compared to those of set 5 as seen in Fig. 6.

Linear polarization and zinc electrodes.—High purity 99.99% solid zinc electrodes were also implanted and loaded. Figure 7 shows two polarization curves. The nonpolarizable plateau region is obtained for all unloaded. Zn electrodes at approximately −0.92V *vs.* Ag-AgCl (Table II). This region disappears when the electrodes are loaded, leading to the conclusion that Zn, like Al, has a protective oxide or hydroxide layer which undergoes breakdown upon anodic polarization. The unloaded zinc sample showed a layer of products of corrosion on the surface, with a few areas along the edges showing the beginning of crevice corrosion. The loaded electrode showed an uneven surface marked by large shallow pits due to random metal dissolution. Upon deloading the electrode, the polarization resistance increases with time, indicative of repassivation. It remains to be determined if this is caused by a *p*H change at the interface due to loading.

Figures 8 and 9 show the linear polarization curves for loaded Al and Zn samples. Due to loading of the

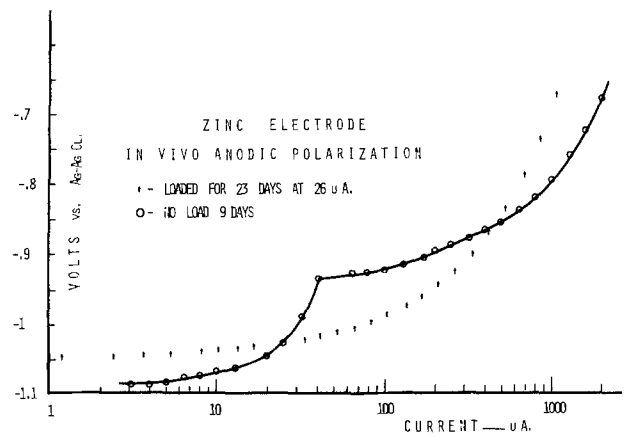


Fig. 7. Anodic polarization curves for zinc electrodes showing break in the curve for unloaded electrode at *ca.* −0.93V. Potentials measured relative to Ag-AgCl electrode.

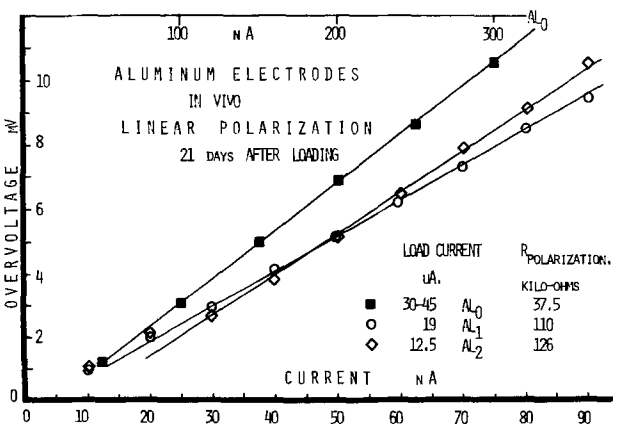


Fig. 8. Linear polarization plots for loaded aluminum electrodes

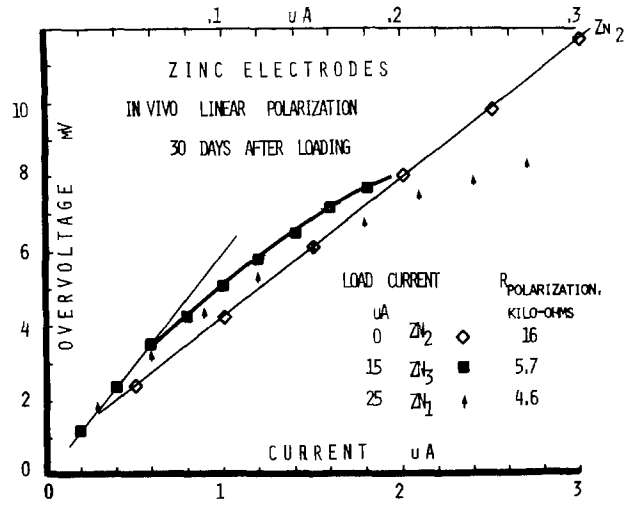


Fig. 9. Linear polarization plots for zinc electrodes showing the curvatures after first few millivolts of overvoltage.

electrodes, the time changing anodic area inside the pits and crevices caused nonlinearities in the first 10 mV of overvoltage *vs.* applied current plots. The corrosion current calculated from the data, therefore, gives an approximate value for the whole electrode (25) and not per unit area of originally exposed area. The loaded zinc electrodes showed a consistent flattening of the curve after the first few millivolts overvoltage as shown in Fig. 9. The unloaded Zn electrodes did not show this tendency. The unloaded zinc electrode polarization resistance, R_p, increased with time, due possibly to increased passivation by a layer of products of corrosion on its surface. Unloaded Al electrodes behave similarly until some large pitting starts. Due to the changing true area undergoing dissolution, the apparent R_p for Al electrodes changes with time, whereas for Zn electrodes the change in true area is not as large and therefore the R_p tends to show less change with time (see Table III).

We conclude that Al shows extensive and severe pitting of the bright hemispherical morphology when loaded. The corrosion current measured by linear polarization is approximately proportional to loading as the area under dissolution in the enlarging pits increases. During such galvanic corrosion the potential is approximately −0.64V and the anodic polarization curve shows a breakthrough or pitting propagation potential of approximately −0.60V. Due to changing area, Tafel regions are not generally obtained. Unloaded electrodes show a plateau region at approximately −0.92V. The area change is less in Zn electrodes and occluded cell pitting is not seen.

During this study the tissue surrounding the implant material was excised and histopathological studies

Table III. Linear polarization resistance changes with time after loading for aluminum and zinc electrodes

DAYS		1-7	7-14	14-21	21-28	28-35	35-42	42-49	49-56	56-63	63-70	70-77
ELECTRODE												
Al	0	30	33	38	-	36	16	-	-	-	-	-
	1	87	77	110		100	76	-	-	-	136	-
	2	80		126	109	105	88	-	-	-	-	-
Zn	1	1.7	1.2	3	4.6	5.5	4.5	-	2.6	-	5.4	-
	2	7	5.8	24.5	16	44	45	50	46	-	-	48
	3	3	5.2	5	5.7	5.8	-	-	-	-	-	-

- DATA NOT TAKEN. TIME INTERVAL IN DAYS SHOWS PERIOD DURING WHICH DATA WAS TAKEN.
ALL VALUES OF R_p IN KILO OHMS

were performed, with results similar to those previously reported (1). These results indicate that for loaded zinc electrodes there is an adverse tissue reaction characterized by dilated capillaries, infiltrate of neutrophils, lymphocytes, and plasma cells. Unloaded zinc samples that have been well passivated by the hydroxide-oxide layer on the electrode are free from macroscopic inflammation. Histologic examination of aluminum electrodes under no-load conditions revealed a well-formed relatively thick (550 μm) mature fibrous connective tissue capsule with only mild aggregate of lymphocytes. Aluminum electrodes loaded up to 18 $\mu A/cm^2$ showed little inflammatory reaction and acceptable biocompatibility. Although the body fluids buffer changes in *p*H at the site of implantation, it is to be expected that the *p*H at the metal-tissue interface will be different from neutral *p*H depending upon the rate of electrode reaction and the degree of encapsulation. The local *pH* changes at the metal-tissue interface could not be monitored. Attempts are being made to implant a *p*H sensitive electrode. In the *in vitro* experiments the *p*H was continuously monitored and adjusted if necessary by adding the appropriate acid-base solutions.

A-C electrical impedance measurements.—From the discussion on corrosion, it is evident that to characterize the metal-tissue interface it is necessary to supplement the d-c polarization data by some other technique. The linear a-c polarization technique can be used, as shown by Richardson and Wood (26) and Heine and Pryor (27).

The impedance of the test electrode was measured on a conductance-capacitance a-c bridge. A porous palladium counter (or auxiliary) electrode was implanted near the test electrode. The measurement was effected by the connection of the bridge leads to the test and auxiliary electrodes. The d-c potential of the electrode was monitored with respect to an Ag-AgCl reference electrode as described above by disconnecting the bridge leads.

The following electrode parameters determined by d-c polarization can also be obtained by linear a-c polarization impedance:

1. The d-c linear polarization resistance, R_{pol}, is equivalent to the a-c R_{pol} as the frequency approaches zero.

2. The type of electrode reaction can also be determined from the frequency variations of the a-c impedance at a given potential, *i.e.*, whether it is under activation or diffusion control. In addition, a-c linear polarization impedance measurements are sensitive to the adsorption of electroactive species.

In the particular case of aluminum electrodes, the a-c linear polarization impedance data were obtained for the equilibrium potential only, since any potentiostatic control results in a difficulty of balancing the bridge due to the fluctuations in the surface changes on the electrode caused by the breakdown-repair events of the oxide layer.

For an electrolyte such as physiological saline, the impedance is determined at a sufficiently high frequency, *e.g.*, 1 MHz, where the electrode impedances can be neglected. This value may be used to correct for the background electrolyte. A typical measured conductance *vs.* frequency curve for saline is shown in Fig. 10. The conductance reaches an asymptotic value at approximately 20 kHz, below which electrode polarization decreases the measured conductance. Figure 11 shows a similar plot for tissue excised from around an implant and measured between Pd-black electrodes.

Tables IV and V show average values of data obtained for *in vivo* Pd-Al impedance cell. It is clear that in the frequency range of interest, *i.e.*, below 20 kHz, the solution and Pd counterelectrode series

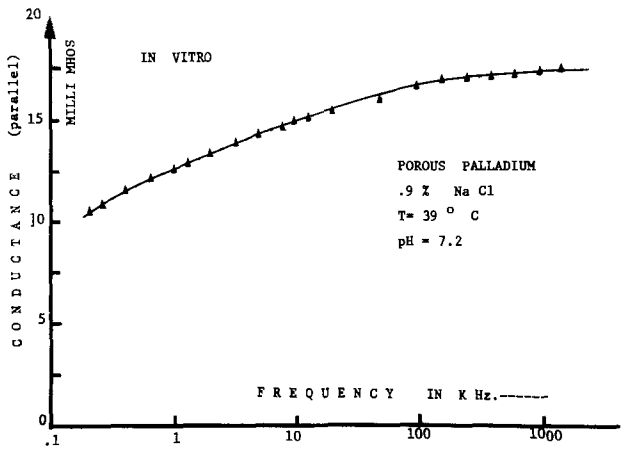


Fig. 10. Measured parallel conductance of saline solution showing frequency independence.

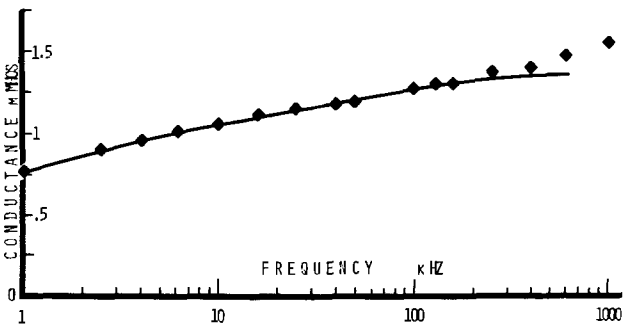


Fig. 11. Measured parallel conductance of excised tissue from capsule formed around implanted cell in dog. Tissue relaxation is observed above *ca.* 300 kHz.

capacitances may be neglected. If the solution resistance is measured accurately it can be subtracted from the measured resistance, and the Pd resistance neglected. Figure 12 shows how geometrical factors may be altered to minimize the impedance contribution of the solution and counterelectrode.

When biological tissue is the medium between the measuring electrodes, its electrical impedance has been shown (28-30) to exhibit a dielectric relaxation which extends over a wide range of frequencies. It

Table IV. *In vitro* resistance comparison

FREQ. K Hz.	Pd R_{series} ohms	SOLUTION R_{series} ohms	ALUMINUM R_{series} ohms
.40	1.79	19.77	101.8
.62	1.33	19.77	73.58
1	1.19	19.77	52.70
4	.728	19.77	18.30
10	.511	19.77	9.18
50	.24	19.77	2.40

Al=.2166 sq.cm. .9 % NaCl. T=39° C pH= 7.2

Table V. *In vitro* capacitance comparison

FREQ. K Hz.	Pd C_{series} u F	SOLUTION C_{series} u F x 10^3	ALUMINUM C_{series} u F
.4	445	16200	5.17
.62	325	6743	4.75
1	233	2592	4.35
4	88.1	162	3.28
10	41.7	25.9	2.70
50	7.45	1.03	2.11

Al =.2166 sq. cm. .9 % Na Cl. T =39° C . pH= 7.2

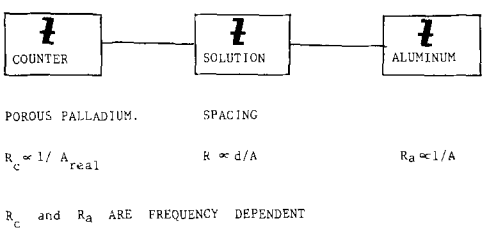


Fig. 12. The geometrical factors available to minimize the impedance of the counterelectrode and solution between it and test electrode. R_c, R_A, and R are impedances.

is, therefore, more difficult to correctly account for tissue impedance. In the implanted impedance cells, the body fluids and partial tissue ingrowth between Al-Pd electrodes did not show appreciable relaxation up to 1 MHz. The tissue parameters were, therefore, assumed to introduce little error as the series Al impedance is generally much greater at low frequencies.

The double layer capacitance, C_{dl}, is difficult to determine for pitted corroding electrodes. Heine and Pryor (27) and Wood *et al.* (16) have approximated this by C_{dl} of an equal area Pt electrode, which in our opinion is not truly representative of the C_{dl} on an oxide-coated electrode like Al of considerably lower (—V) potential.

Figure 13 shows typical data of measured parallel conductance and capacitance *vs.* frequency plotted on the complex impedance plane as developed by Sluyters and co-workers (31). It has been shown that if the measured impedance, $Z_m = A' + jZ''$, is plotted on this plane, a straight line of 45° slope is obtained at low frequencies if the electrode reaction is diffusion controlled. If the reaction is charge transfer controlled, then a semicircle is obtained with its center on the A' axis. Figures 14 and 15 show that the measured angles lie in the 60°-70° range, *i.e.*, neither of the above-mentioned mechanisms controls the reaction. For such reactions it is possible that they are adsorption controlled (11). The method of obtaining parameters for this plot derived by Timmer is given by DeRosa (11). Figure 16 shows the transformations used to obtain R_a and C_a. Figure 17 shows a polarization-capacitance curve. According to Timmer's theory, $R_a = X_a = \gamma/\omega^{1/2}$ where R_a, X_a represents the impedance due to the adsorbed species. Hence a plot of R_a, X_a *vs.* frequency produces a linear

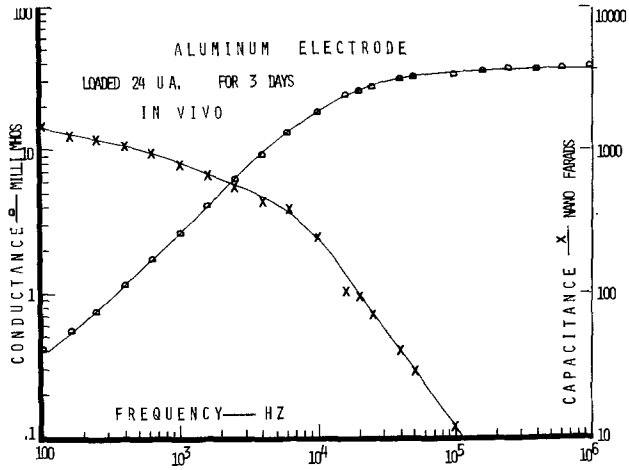


Fig. 13. Measured parallel conductance and capacitance of aluminum electrode. Note asymptotic value of conductance for frequencies greater than 100 kHz.

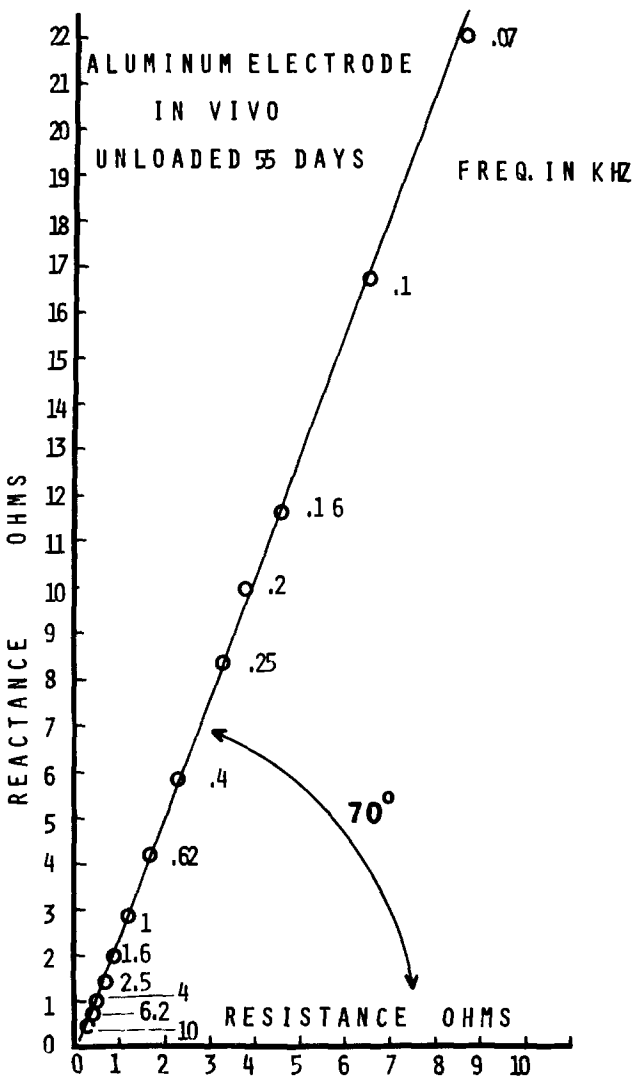


Fig. 14. Complex plane plot of electrode resistance vs. reactance. Parameter is frequency.

relationship. Figure 18 shows a plot obtained from R_a, X_a for Al *in vivo*.

The electrodes after removal showed extensive micro and large deep pitting with brightened hemispherical pitted surface. In spite of this, the complex plane plots give consistent angles of 60°-70°. Figure 18 thus

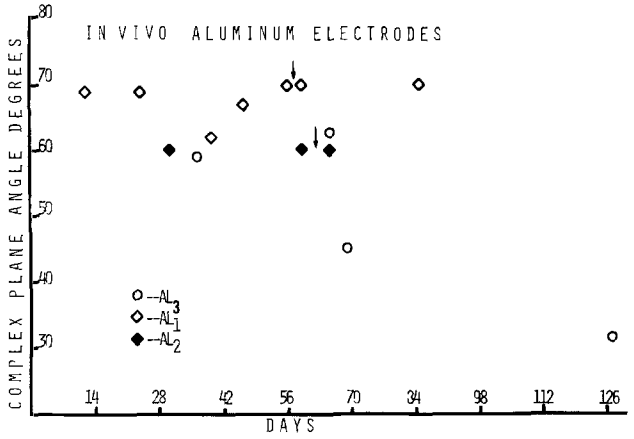
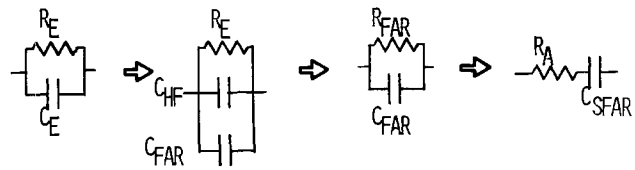


Fig. 15. Variance of complex plane angles with time. Arrows indicate day electrodes were loaded.



$$C_A = \frac{C_{SFAR}\,(C_{LF} - C_{HF})}{(C_{LF} - C_{HF}) - C_{SFAR}} \qquad R_A = X_A = \frac{\gamma}{\omega^{1/2}}$$

Fig. 16. Adsorption equivalent circuit transformations

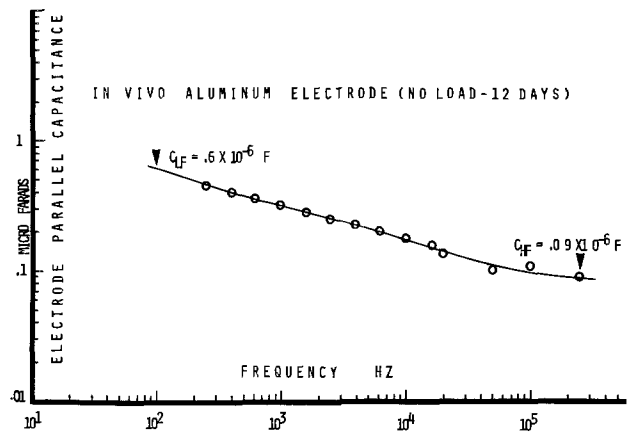


Fig. 17. Aluminum electrode parallel capacitance showing determination of C_{LF} and C_{HF}.

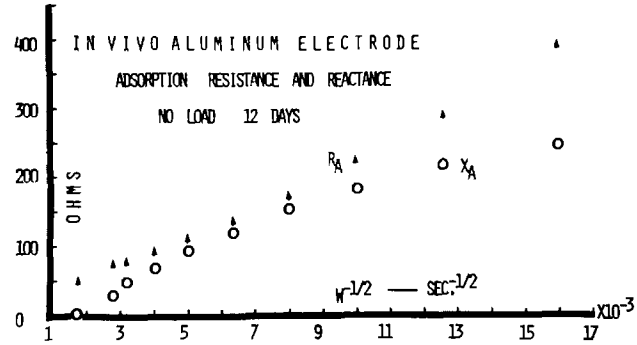


Fig. 18. Values of adsorption resistance R_a and reactance X_a showing linear relationship with $\omega^{-1/2}$ and R_a approximately equal to X_a.

shows reasonable agreement with the adsorption theory, though it remains to be determined if this is an effect of the oxide alone.

Protein combines with metal interfaces to increase the electrical resistance and decrease the exchange current. Svare (32) and Korostoff observed that cystine in physiological concentrations passivates Ni. Aragon and Hulbert (33) demonstrated that *in vivo* corrosion rates are lower than *in vitro* due to plasma and interstitial fluid constituents.

Further impedance measurements on polished Al electrodes *in vivo* and *in vitro* are in progress. For coarsely polished electrodes, complex plane angles of the data taken *in vitro* lie in the range obtained for *in vivo* measurements. Polished electrodes *in vitro* show complex plane angles of the order of 80°; the Cole-Cole plots of the parameters show a distinct relaxation phenomenon. Since the complex plane plot does not indicate an electrochemical reaction relaxation, it is likely that the air-formed oxide exhibits a dielectric relaxation of probably the inhomogeneous Maxwell-Wagner type since the conductance part of the complex dielectric constant shows a large increase as the frequency tends to zero. Present measurements are being analyzed to determine the nature of the relaxation and will be reported.

Acknowledgment

This study was partially supported by the Biomaterials Program NSF Grant GH 3378 and NHIL Training Grant HL0517.

Manuscript submitted March 15, 1976; revised manuscript received Dec. 4, 1976. This was Paper 385 presented at the Toronto, Canada, Meeting of the Society, May 11-16, 1975.

Any discussion of this paper will appear in a Discussion Section to be published in the December 1977 JOURNAL. All discussions for the December 1977 Discussion Section should be submitted by Aug. 1, 1977.

Publication costs of this article were assisted by Drexel University.

LIST OF SYMBOLS

A	geometric electrode surface area, cm²
C_{dl}	double layer capacitance, f
C_{LF}, C_{HF}	electrode parallel capacitance extrapolated to half a decade (freq) lower and higher, respectively (f)
E_{corr}	equilibrium (no-load) potential of electrode, V *vs.* Ag-AgCl
E_p	pitting propagation potential
f	a-c frequency, Hz
G, C_{psoln}	solution (electrolyte or tissue) parallel conductance (Ω) and capacitance (f)
R_a, X_a	resistance and reactance due to adsorbed species on electrode surface, Ω
R_c, R_a', R	impedance, Ω
R_F, C_F	faradaic resistance and capacitance of electrode admittance
R_p	slope of linear polarization plot, Ω
Z_m	impedance (or admittance) as measured between a-c bridge leads
β_a, β_c	anodic and cathodic polarization Tafel slopes,
γ	a constant = slope of R_a, X_a *vs.* $\omega^{-1/2}$
ω	$(2 \cdot \pi \cdot f)$ radians/sec

REFERENCES

1. R. B. Beard, H. M. Carim, S. E. Dubin, J. F. DeRosa, and A. S. Miller, *This Journal*, **121**, 1129 (1974).
2. J. F. DeRosa, R. B. Beard, and A. W. Hahn, *IEEE Trans. Biomed. Eng.*, **17**, 324 (1970).
3. R. B. Beard, J. F. DeRosa, R. M. Koerner, S. E. Dubin, and K. J. Lee, *ibid.*, **19**, 233 (1972).
4. V. J. Colangelo, N. D. Greene, D. B. Kettlekamp, H. Alexander, and C. J. Campbell, *J. Biomed. Mater. Res.*, **1**, 405 (1967).

5. N. D. Greene, "Experimental Electrode Kinetics," Rensselaer Polytechnic Institute Publications, Troy, New York (1965).
6. H. M. Carim, R. B. Beard, J. F. DeRosa, and S. E. Dubin, Paper presented at ACS Division of Organic Coatings, Symposium on Biomedical Application of Polymers, Chicago, Illinois, August 1973.
7. M. Stern, *Corrosion*, **14**, 60 (1958).
8. N. D. Greene and D. A. Jones, *J. Mater.*, **1**, 345 (1966).
9. H. M. Carim, M.S. Thesis, Drexel University (1973).
10. J. F. DeRosa, M.S. Thesis, Drexel University (1969).
11. J. F. DeRosa, Ph.D. Dissertation, Drexel University (1974).
12. E. L. Koehler, in "Localized Corrosion," p. 118, NACE. Houston, Texas (1974).
13. M. Pourbaix, *ibid.*, p. 12.
14. J. Zahavi and M. Metzger, *This Journal*, **121**, 268 (1974).
15. H. Kaesche, "Localized Corrosion," p. 519, NACE, Houston, Texas (1974).
16. G. C. Wood, W. H. Sutton, *et al.*, *ibid.*, p. 532.
17. J. R. Galvele, *et al.*, *ibid.*, p. 580.
18. H. Böhni and H. H. Uhlig, *This Journal*, **116**, 906 (1969).
19. M. A. Heine, D. S. Keir, and M. J. Pryor, *ibid.*, **112**, 24 (1965).
20. T. P. Hoar, "Localized Corrosion," p. 112, NACE, Houston, Texas (1974).
21. H. L. Craig, Jr., *ibid.*, p. 604.
22. A. Broli, H. Holtan, and K. S. Prestrud, *Corrosion*, **30**, p. 427 (1974).
23. S. B. de Wexler and J. R. Galvele, *This Journal*, **121**, 1271 (1974).
24. M. J. Pryor, "Localized Corrosion," p. 8, NACE, Houston, Texas (1974).
25. D. A. Jones and N. D. Greene, "Corrosion," p. 367, NACE, Houston, Texas (1974).
26. J. A. Richardson and G. C. Wood, *This Journal*, **120**, 193 (1973).
27. M. A. Heine and M. J. Pryor, *ibid.*, **110**, 1205 (1963).
28. H. P. Schwan, in "Physical Techniques in Biological Research," Vol. VI, Chap. 6, W. L. Nastuk, Editor, Academic Press, New York (1963).
29. H. P. Schwan, *Proc. IRE*, **47**, 11 (1959).
30. H. P. Schwan, in "Advances in Biological and Medical Physics," Vol. V, J. H. Lawrence and C. A. Tobias, Editors, Academic Press, New York (1957).
31. J. H. Sluyters, *Rec. Trav. Chim. Pays-Bas*, **79**, 1092 (1960).
32. C. W. Svare, Dissertation, University of Pennsylvania (1969).
33. P. J. Aragon and S. F. Hulbert, *J. Biomed. Mater. Res.*, **6**, p. 155-174, (1972).
34. H. P. Leckie and H. H. Uhlig, *This Journal*, **113**, 1262 (1966).

Photogalvanic Cells
II. Current-Voltage and Power Characteristics

W. J. Albery
Physical Chemistry Laboratory, Oxford OX1 3QZ, England

and M. D. Archer
Department of Physical Chemistry, Cambridge CB2 1EP, England

ABSTRACT

A general treatment is developed for the current-voltage characteristics of photogalvanic cells containing two identical electrodes and operating by virtue of the homogeneous reactions

$$A + Z \underset{\text{in dark}}{\overset{\text{in light}}{\rightleftharpoons}} B + Y$$

where A, B, and Y, Z are redox couples. The treatment is in terms of the electrode and homogeneous kinetics, the relative magnitudes of the diffusion and reaction layers, and the position of the photostationary state. Power cannot be drawn from the cell if both couples are either highly reversible or highly irreversible. The best performance is obtained if one couple (A, B say) is highly reversible, and the other (Y, Z) highly irreversible, and this case is explored in detail. If the homogeneous kinetics are rapid, we find an important contribution to the current delivered by the cell from catalytic currents due to the presence of Y and Z close to the electrode.

A previous paper (1) discussed the open-circuit potential of photogalvanic cells. In order to obtain useful work from such a cell, current must be drawn from it, and this paper explores the current-voltage power characteristics of a common type of photogalvanic cell, illustrated in Fig. 1. It contains two identical electrodes of equal area, one immersed in illuminated solution, and the other immersed in dark solution. The differentiation between the dark and illuminated solutions may be achieved either by a black barrier that permits electrical contact, as in Fig. 1, or more gradually by the absorbance of the solution itself, causing the light intensity to drop from the front to the back of the cell. We shall consider the power obtainable from such a cell in terms of the same variables as before, namely, the electrode kinetics of the redox couples, the concentrations of the redox species, and the position of the photostationary state. We do not consider the influence of the over-all cell length, but assume throughout that it is rather greater than the sum of the diffusion layers at the two electrodes. If this is so, then the cell performance is independent of cell length, except in so far as this may affect the collection efficiency, *i.e.*, the number of electrons flowing per photon absorbed. Moreover, we do not consider the variation of light intensity throughout the cell, but simply assume that the dark electrode is always genuinely in the dark and that the solution is optically fairly dilute, so that the photostationary state is uniform in the region of the illuminated electrode.

As in part I (1), the analysis assumes that the solution contains two components. A and Z, which on irradiation undergo a photoredox reaction to form B and Y. A, B, and Y, Z are redox couples. B and Y undergo a second-order thermal back reaction, to reform A and Z. The equilibrium in the dark lies heavily on the side

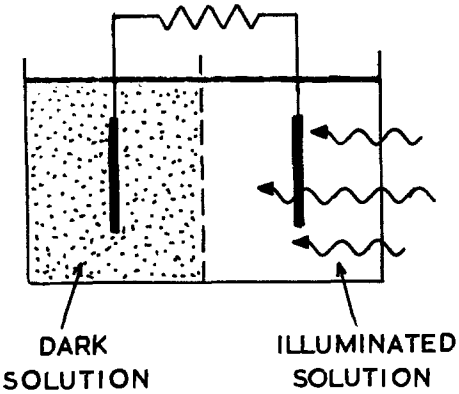


Fig. 1. The photogalvanic cell

of A and Z. The two electrodes are conventional redox electrodes.

System and Notation

We use the same system and notation as in the previous paper (1)

Solution:

$$A + Z \underset{k_{-H}}{\overset{k_H}{\rightleftarrows}} B + Y \qquad [1]$$

where $k_H << k_{-H}$ (liter mol^{-1} sec^{-1})

Electrodes:

$$A + e \underset{k_{-A}}{\overset{k_A}{\rightleftarrows}} B \qquad [2]$$

$$Y + e \underset{k_{-Y}}{\overset{k_Y}{\rightleftarrows}} Z \qquad [3]$$

where k_A, k_{-A}, k_Y, and k_{-Y} (cm sec^{-1}) are electrochemical rate constants.

Photochemistry:

$$A \xrightarrow{h\nu} A^* \xrightarrow{k_*} A$$

$$A^* + Z \xrightarrow{k_Q} B + Y$$

giving over-all

$$A + Z \xrightarrow{g} B + Y \qquad [4]$$

where g (in dimensions of concentration per unit time) is the rate at which B and Y are generated by the photoelectron transfer reaction.

Using lower case letters to denote the concentrations of the various species

$$g = \frac{I\epsilon a z k_Q}{k_* + k_Q z}$$

where I (einstein cm^{-2} sec^{-1}) is the light intensity in the region close to the illuminated electrode, and ϵ is the extinction coefficient of A. To simplify the algebra, we assume that

$$g = g'' a z$$

where

$$g'' \simeq I\epsilon k_Q / k_* \qquad [5]$$

The use of the full expression for g leads to more complicated algebra in the description of X_k but does not otherwise affect our conclusions.

We use a subscript D to denote the bulk concentrations in the unilluminated solution, and a subscript L for bulk concentrations in the photostationary state in the illuminated solution. Both electrodes will perturb the concentrations from these bulk values and we use a subscript zero for concentrations at the electrode surface and a subscript ∞ for the bulk values. Thus $c_\infty = c_L$ or c_D depending on whether the electrode is illuminated or not. The perturbations to the concentrations near the electrodes are described by a' and z'

$$a = a_\infty - a' \qquad b = b_\infty + a' \qquad [6]$$

$$y = y_\infty + z' \qquad z = z_\infty - z' \qquad [7]$$

We assume that the diffusion coefficients of all species are the same and this means that we only need two functions a' and z', since $(a + b)$ and $(y + z)$ must remain constant at all points in solution [1]. We define the following dimensionless quantities which describe the concentrations (with respect to A) of B and Y in the dark solution and Z in the illuminated solution

$$B_\infty = b_D / a_D \qquad [8]$$

$$Y_\infty = y_D / a_D \qquad [9]$$

$$Z_\infty = z_L / a_D \qquad [10]$$

Three further dimensionless quantities P, ι, and θ are used to describe the voltage, current, and power produced by the cell

$$P = \mathbf{F}(E - E^\theta_{A,B})/RT \qquad [11]$$

where $E^\theta_{A,B}$ is the standard redox potential of the A, B couple

$$\iota = i/(A\mathbf{F}Da_D X_{tr}^{-1}) \qquad [12]$$

where A is the area of the electrodes and X_{tr} is the thickness of the diffusion layer. The current is normalized with respect to a_D and X_{tr}^{-1} as the diffusion-limited currents in the cell are usually proportional to these parameters

$$\theta = |\iota \Delta P| = |\iota (P_L - P_D)| \qquad [13]$$

where P_L and P_D are the dimensionless potentials of the illuminated and dark electrodes.

The power, W, produced by the cell is given by

$$W = \theta A D a_D R T X_{tr}^{-1} \qquad [14]$$

The fractional conversion achieved by the photochemistry is described by f, where

$$a_L = a_D(1 - f) \qquad [15]$$

$$b_L = b_D + f a_D \simeq f a_D \qquad [16]$$

$$y_L = y_D + f a_D \qquad [17]$$

$$z_L = z_D - f a_D \qquad [18]$$

We have assumed that the concentration of B generated photochemically is much larger than its concentration in the dark. The relationship between f and g'' is readily found by substitution into the equation governing the composition of the photostationary state

$$(k_H + g'')az = k_{-H} by \qquad [19]$$

to be

$$g'' = \frac{f}{1 - f}\left(\frac{k_H(1 + Z_\infty) + k_{-H}(f + B_\infty + Y_\infty)}{Z_\infty}\right) \qquad [20]$$

Diffusion and Reaction Layer Thicknesses at the Electrodes

The concentration changes in the region of the two electrodes extend into the solution for a distance which may be determined by the transport of species to the electrode, or by the kinetics of the homogeneous reactions [1] and [4]. The shorter of these two will be the effective boundary layer at the electrodes. Currents at planar electrodes of large area in unstirred solutions do not decay away to zero according to the equations of semi-infinite linear diffusion but they reach a steady value. This is because natural convection maintains a reasonably uniform stagnant layer of thickness $\sim 3 \times 10^{-2}$ cm (2). At the illuminated electrode additional convection may be caused by the thermal effects of the absorbed radiation.

The kinetic length, X_k, depends upon the reaction kinetics. The general expression is

$$X_k = D^{1/2}[(k_H + g'')(a_* + z_*) + k_{-H}(b_* + y_*)]^{-1/2} \quad [21]$$

where the subscript asterisk denotes concentrations at the edge of the reaction layer. In many cases, simpler expressions for X_k suffice. For instance, in some photogalvanic solutions, one couple (A, B) is present in lower concentrations than the other (Y, Z). Moreover, $k_H << k_{-H}$. Therefore, at the dark electrode (at which $g'' = 0$)

$$X_k \simeq D^{1/2}(k_{-H}y_\infty)^{-1/2}$$

and at the illuminated electrode

$$X_k \simeq D^{1/2}(g''z_\infty + k_{-H}y_\infty)^{-1/2}$$

The reaction layer thickness may therefore be different at the dark and illuminated electrodes, and both can be varied by adjusting the concentrations of the species.

As the smaller of the two lengths X_{tr} and X_k normally determines the boundary layer across which species must diffuse to the electrodes, we consider the current-potential relationships for the cases $X_{tr} < X_k$ and $X_{tr} > X_k$ separately.

Electrode where $X_{tr} < X_k$.—We deal first with the case where $X_{tr} < X_k$. Under these conditions reactions [1] and [4] are too slow to take place to any significant extent in the diffusion layer. We normalize the electrochemical rate constants in reactions [2] and [3] by writing

$$\lambda_N = k_N X_{tr}/D \quad [22]$$

where

$$N = \pm A \text{ or } \pm Y$$

The transport of the species to the electrode is related to electrode kinetics by

$$D\left(\frac{\partial a}{\partial x}\right)_o = D\frac{a_\infty - a_o}{X_{tr}} = k_A a_o - k_{-A}b_o \quad [23]$$

and

$$D\left(\frac{\partial z}{\partial x}\right)_o = D\frac{z_\infty - z_o}{X_{tr}} = k_{-Y}z_o - k_Y y_o \quad [24]$$

In our nomenclature, these equations become

$$a'_o = \lambda_A(a_\infty - a'_o) - \lambda_{-A}(b_\infty + a'_o)$$

$$z'_o = \lambda_{-Y}(z_\infty - z'_o) - \lambda_Y(y_\infty + z'_o)$$

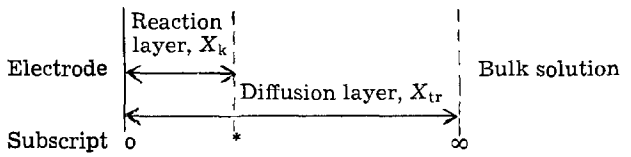
and the general expression for the current-potential curve is

$$\iota a_D = a'_o - z'_o = \frac{\lambda_A a_\infty - \lambda_{-A}b_\infty}{1 + \lambda_A + \lambda_{-A}} + \frac{\lambda_Y y_\infty - \lambda_{-Y}z_\infty}{1 + \lambda_Y + \lambda_{-Y}} \quad [25]$$

(The sign convention adopted for i and ι is positive for a cathodic current, negative for an anodic one.) The current is simply the sum of the currents due to the A, B and Y, Z couples, and both of these may be subject to diffusion control (across X_{tr}), charge transfer control, or mixed control, according to whether ($k_A + k_{-A}$) and ($k_Y + k_{-Y}$) is greater than, less than, or comparable with D/X_{tr}. In other words, the couples behave reversibly if $(\lambda_N + \lambda_{-N}) >> 1$ and irreversibly if $(\lambda_N + \lambda_{-N}) << 1$.

When no current flows, then [25] reduces to our previous result (Eq. [24] and [25] of Ref. (1)), which relate the open-circuit potential to the composition of the solution: in the dark solution, an equilibrium potential is obtained, but in the illuminated solution, a mixed potential is observed. The concentration perturbations at the illuminated electrode extend over the diffusion layer X_{tr}.

Electrode where $X_{tr} >> X_k$.—In this case there is time and space for the homogeneous reactions [1] and [4] to take place in the diffusion layer and so we must introduce a subscript asterisk to denote the concentrations at the outside edge of X_k



X_{tr} remains an important parameter even if it is much larger than X_k because, as we shall show later, supply of species to the outer edge of the reaction layer by transport across the diffusion layer can be the current-limiting process.

The differential equations describing the steady-state concentration profiles of A and Z are

$$\mathrm{Tr}(a) - (k_H + g'')az + k_{-H}by = 0$$

$$\mathrm{Tr}(z) - (k_H + g'')az + k_{-H}by = 0$$

where Tr is an operator describing transport by diffusion and possibly convection. We solve these equations by the method of Koutecky and Levich (3). Substitution from [4] and [7] gives

$$\mathrm{Tr}(a' - z') = 0 \quad [26]$$

and

$$\mathrm{Tr}(a') - (k_H + g'')(a'z_\infty + z'a_\infty - a'z') - k_{-H}(a'y_\infty + z'b_\infty + a'z') = 0 \quad [27]$$

Equation [26] has no kinetic terms and solving it with the boundary conditions that $a' = 0$ and $z' = 0$ at $x = X_{tr}$ we obtain

$$a' - z' = (a'_o - z'_o)(1 - x/X_{tr}) \quad [28]$$

Since $X_k << X_{tr}$, we can then write for $x < X_k$

$$a' - z' \simeq a'_o - z'_o \simeq a'_* - z'_* \quad [29]$$

This approximation implies that $a'_* \simeq a'_o$ and $z'_* \simeq z'_o$, or that the concentrations at the outer and inner boundaries of the reaction layer are roughly the same. This remains a good approximation even though there is a significant gradient when the small difference $c'_* - c'_o$ is divided by the small length X_k, to give the fluxes to the electrode. Equating the transport of the species to the electrode with the electrode kinetics, we obtain

$$D\left(\frac{\partial z}{\partial x}\right)_o = D\frac{a_* - a_o}{X_k} = k_A a_o - k_{-A}b_o \quad [30]$$

$$D\left(\frac{\partial z}{\partial x}\right)_o = D\frac{z_* - z_o}{X_k} = k_{-Y}z_o - k_Y y_o \quad [31]$$

These equations are similar in form to [23] and [24], but transport occurs across the reaction layer rather than the diffusion layer. In this case, we normalize the electrochemical rate constants by writing

$$\lambda_N = k_N X_k/D \quad [32]$$

and in our nomenclature, [30] and [31] become

$$a'_o - a'_* = \lambda_A(a_\infty - a'_o) - \lambda_{-A}(b_\infty + a'_o)$$

$$z'_o - z'_* = \lambda_{-Y}(z_\infty - z'_o) - \lambda_Y(y_\infty + z'_o)$$

and eliminating a'_o and z'_o between these two equations and [29] we obtain

$$\frac{\lambda_A a_\infty - \lambda_{-A}b_\infty - (\lambda_A + \lambda_{-A})a'_*}{1 + \lambda_A + \lambda_{-A}} = \frac{\lambda_{-Y}z_\infty - \lambda_Y y_\infty + (\lambda_Y + \lambda_{-Y})z'_*}{1 + \lambda_Y + \lambda_{-Y}} \quad [33]$$

Again, the couples behave reversibly or irreversibly according to whether $(\lambda_N + \lambda_{-N})$ is greater or less than one, but this time reversible behavior requires higher values of $(k_N + k_{-N})$ because X_k is smaller than X_{tr}.

The concentrations of species in the reaction layer also depend on their supply across the diffusion layer. The current is given by

$$\frac{i}{AF} = D\left[\left(\frac{\partial a}{\partial x}\right)_0 - \left(\frac{\partial z}{\partial x}\right)_0\right]$$

and differentiating [28] and using the approximation in [29] we obtain

$$\iota a_D = (a'_0 - z'_0) \simeq (a'_* - z'_*) \qquad [34]$$

A further relationship between a'_* and z'_* can be obtained from [27] by noting that outside the reaction layer, the kinetic terms are in balance and so we have

$$(k_H + g'')(a'_* z_\infty + z'_* a_\infty - a'_* z'_*) + k_{-H}(a'_* y_\infty + z'_* b_\infty + a'_* z'_*) = 0 \qquad [35]$$

Thus we now have two equations, [33] and [35], to determine the two unknowns, a'_* and z'_*, which are required to find the current from [34]. However, the general solution of the quadratic Eq. [35] does not serve either for entertainment or instruction, so we shall instead discuss various special cases in the next section. First we note that when no current flows at the electrode, $a'_* = z'_* = 0$ (from [34] and [35]) and Eq. [33] also reduces to our previous result (1). However, in this case, the concentration changes caused by the existence of partial anodic and cathodic currents at the illuminated electrode are confined to the reaction layer.

The Effect of Electrode Kinetics on Cell Performance

In part I (1), we showed that the change in potential of the open-circuit electrode on illumination of the photogalvanic solution depended on the electrode kinetics of A, B and Y, Z: No change is found if both couples are reversible, and the largest change is found if one couple is reversible and the other very irreversible. If both couples are electroactive, with different k° values, then intermediate potential changes are obtained. We now consider the effect of electrode kinetics on the closed-circuit performance of the cell for the three different cases given in Table I.

The rate constants for the electrochemical reactions [2] and [3] of the couples A, B and Y, Z are normalized by [22] or [32]; the shorter of the two lengths X_{tr} or X_k is used in this normalization. If $\lambda_N + \lambda_{-N} >> 1$, then the species will be more likely to react on the electrode than to diffuse across X_{tr} or to react in the solution within the distance X_k. The couple will be reversible and the surface concentrations will obey the Nernst equation. On the other hand for $\lambda_N + \lambda_{-N} << 1$ the electrochemical reactions do not perturb the concentrations from the values fixed by the homogeneous reactions [1] and [4]; the couple is irreversible. Figure 2 shows schematically how the concentration profiles across the cell on open and short circuit depend upon the electrode kinetics. These profiles have been drawn for the particular case where $a_D = z_D >> b_D = y_D$ and where there is a high degree of conversion in the photostationary state.

In case a, the electrode kinetics are so rapid that the photochemical perturbation to the concentrations in the bulk solution is destroyed on the illuminated electrode; the concentrations at the electrode surface return to their thermodynamic values and the electrode

Table I. Electrode kinetics

Case*	$\lambda_A + \lambda_{-A}$	$\lambda_Y + \lambda_{-Y}$
a	>>1	>>1
b	>>1	<<1
e	<<1	<<<1

* The lettering refers to our previous discussion (1).

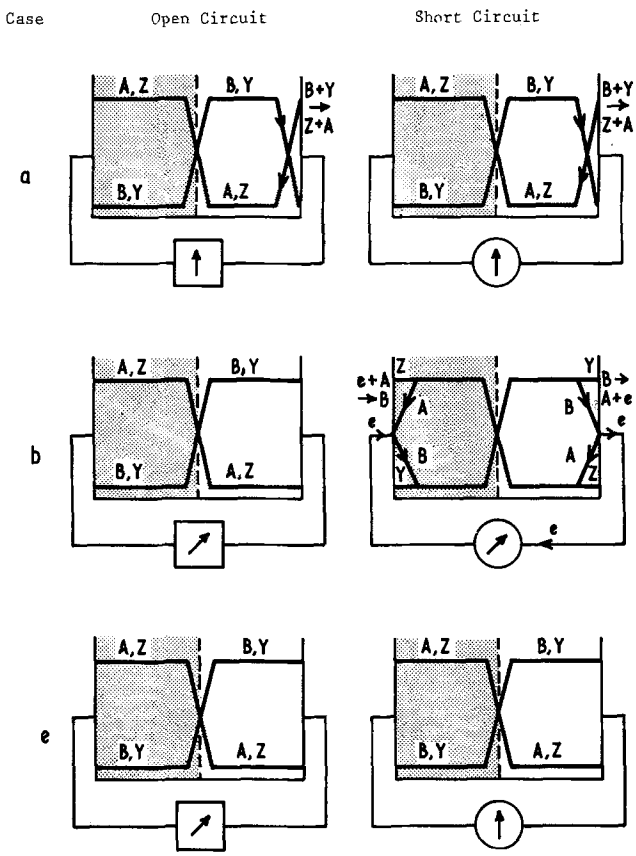


Fig. 2. Concentration profiles across a photogalvanic cell on open and short circuit for cases a, b, and e of Table I. The dark electrode is on the left and the illuminated electrode on the right. The potential difference for case b and e on open circuit is given by the Nernst equation for the A, B couple.

acts as an efficient catalyst for the reaction

$$B + Y \rightarrow Z + A$$

No power can be obtained under these conditions. This is further illustrated in Fig. 3, which shows typical current-potential curves at the dark and illuminated electrodes, when both couples are reversible. Figure 3 has been drawn for the particular case that $E^\theta_{Y,Z} - E^\theta_{A,B} = 0.2$V, so that $a_D/b_D = z_D/y_D = 50$; the composition of the photostationary state has been taken as $a_L/b_L = z_L/y_L = 0.02$. This rather symmetrical case illustrates the general conclusion clearly: The total current-potential curve is the same at the dark and illuminated electrodes, although the two are made up of different components.

In case e, a potential develops if no current is passed but the electrode kinetics are now so slow that neither couple reacts efficiently on the electrodes and hence again very little power can be obtained. This is further illustrated in Fig. 4, which is drawn for the same conditions as Fig. 3, except that A, B has been made rather irreversible ($\lambda^\circ = 10^{-2}$) and Y, Z very irreversible ($\lambda^\circ = 10^{-4}$). The total current-potential curves at the dark and illuminated electrodes differ only at extreme potentials, and negligible current is obtained in the working region of the photogalvanic cell, between E_D and E_L.

The optimal case for current production is case b, for which the A, B couple is reversible and the Y, Z couple very irreversible or better still totally unreactive at the electrodes. The electrode processes then involve only the A, B couple. As shown in Fig. 2, A is reduced to B at the dark electrode, and B is oxidized to A at the illuminated electrode.

In part I, we showed that case b was also optimal for the open-circuit potential of the cell: It is clearly

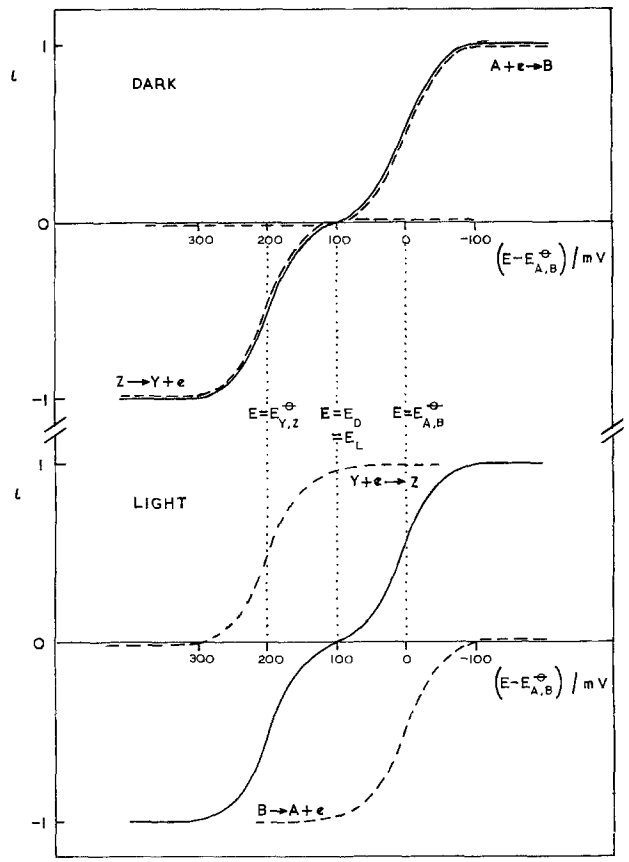


Fig. 3. An example of current-potential curves for the dark and illuminated electrode when both couples are reversible (case a, Table I); $a_D/b_D = z_D/y_D = 50$, $a_L/b_L = z_L/y_L = 0.02$. ι, the normalized current, is defined in Eq. [12]. The broken lines are for the A, B and Y, Z couples separately and the full line is the sum of these components. Note that E_D and E_L, the open-circuit potentials of the dark and illuminated electrodes, are the same for the two electrodes.

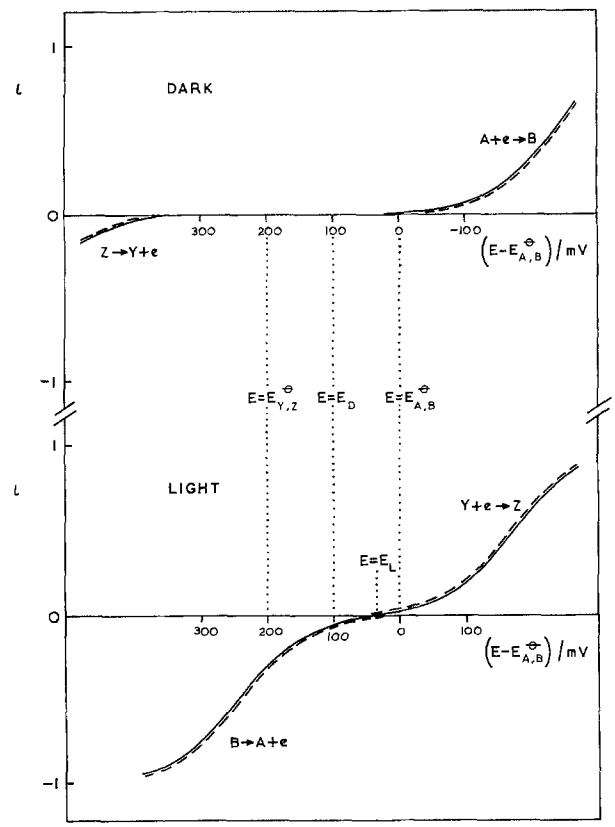


Fig. 4. An example of current-potential curves when both couples are rather irreversible (case e, Table I). $\lambda^{\circ}_{A,B} = 10^{-2}$, $\lambda^{\circ}_{Y,Z} = 10^{-4}$. Other conditions as for Fig. 3. E_L is slightly displaced from E_D, but negligible power is obtained from this cell.

therefore also optimal for power production, and we consider it in more detail in the next section.

The optimal case; A, B reversible and Y, Z irreversible.—With the approximations for case b in Table I, we obtain from [25] and [33]-[35] a general expression for the current-potential curves at both the dark and the illuminated electrodes, which covers the two different conditions $X_k > X_{tr}$ and $X_k < X_{tr}$

$$\iota a_D = S\left[\frac{1+C}{1+CX_k/X_{tr}}\right] \qquad [36]$$

where

$$S = \frac{k_A a_\infty - k_{-A} b_\infty}{k_A + k_{-A}} = -\frac{b_\infty \exp(\tfrac{1}{2}P) - a_\infty \exp(-\tfrac{1}{2}P)}{\exp(\tfrac{1}{2}P) + \exp(-\tfrac{1}{2}P)} \qquad [37]$$

and for $X_k > X_{tr}$

$$C = 0$$

while for $X_k < X_{tr}$

$$C = \frac{[(k_H + g'')z_\infty + k_{-H}y_\infty](k_A + k_{-A})}{[(k_H + g'')k_{-A} + k_{-H}k_A](a_\infty + b_\infty)} \qquad [38]$$

In deriving [36] the term in X_k/X_{tr} arises from including the x/X_{tr} term which was previously neglected in deriving [29] from [28]. In order to simplify the treatment we have assumed in Eq. [37] that the charge transfer coefficient is one-half.

Examination of the general Eq. [36] shows that, depending on the size of X_k/X_{tr}, three different cases, listed in Table II, can be distinguished and we next discuss the "simple" case.

The simple case.—When $X_k > X_{tr}$, $C = 0$ and the only term on the right-hand side of Eq. [36] is the "simple" term S. This term describes the reversible current-potential curve for the A, B redox couple. The same expression is obtained from Eq. [25] if λ_Y and λ_{-Y} are set equal to zero. At the dark electrode the ratio a_x/b_x is large; this ratio is smaller near the illuminated electrode; here its value depends on the light intensity and homogeneous kinetics according to [19].

In Fig. 5, we have plotted current-potential curves for a particular case where in the dark $B_\infty = b_D/a_D = 10^{-1}$ and in the light this ratio is reversed, $b_L/a_L = 10$ (*i.e.*, $f = 0.9$). Figure 5A shows the usual current-potential curves for each individual electrode. Power can only be obtained when a cathodic current ($A + e \rightarrow B$) flows at the dark electrode and an anodic current ($B \rightarrow A + e$) at the illuminated electrode. Hence in Fig. 5B the relevant parts of the current-potential curves are again plotted; this time a logarithmic scale is used for the current so that small currents can be displayed. Now when current flows through the cell, since we have taken the electrodes to be of equal area

$$\iota_D = -\iota_L$$

This condition is satisfied by drawing horizontal tie lines on Fig. 5B. The length of the tie line gives the

Table II. Approximations for C term in [36]

Name	Condition	$\frac{1+C}{1+CX_k/X_{tr}}$
Simple	$X_{tr}/X_k < 1$	1
Intermediate	$1 < X_{tr}/X_k < C$	X_{tr}/X_k
Catalytic	$1 < C < X_{tr}/X_k$	C

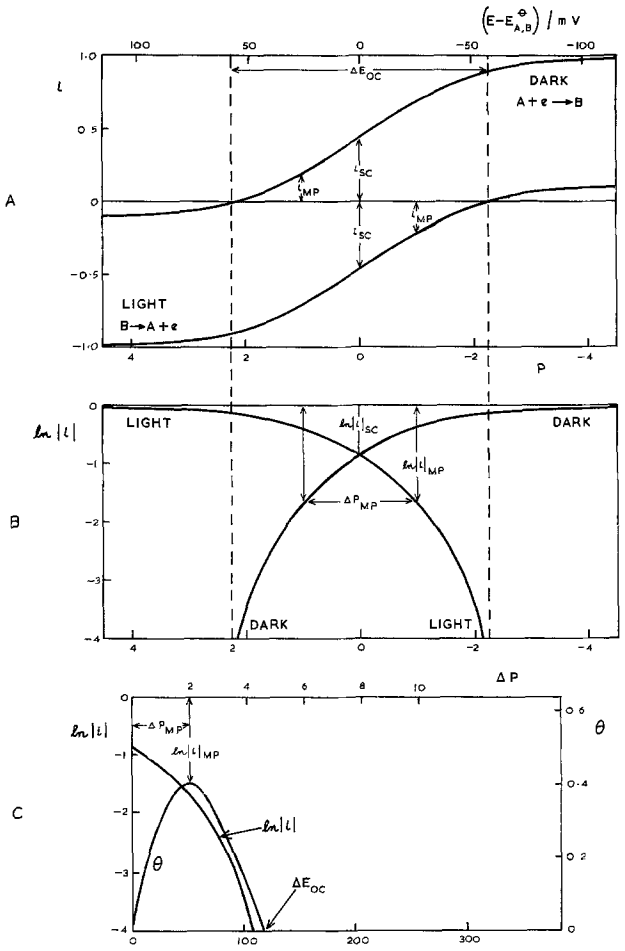


Fig. 5. Current-potential (ι-P) and (θ-P) characteristics for the simple case defined in Table II, when one couple (A, B) is reversible, the other irreversible (case b, Table I). $b_D/a_D = a_L/b_L = 10^{-1}$. The normalized current, potential, and power (ι, P, θ) are defined in Eq. [12], [11], and [13]. ΔE_{oc} = open-circuit voltage of cell, ι_{sc} = short-circuit current, ΔP_{MP} and ι_{MP} = normalized voltage and current at the maximum power point. Figures 5A and 5B display the current-potential curves for each electrode, on a linear and logarithmic scale, respectively, and Fig. 5C shows the current-voltage and power characteristics of the cell.

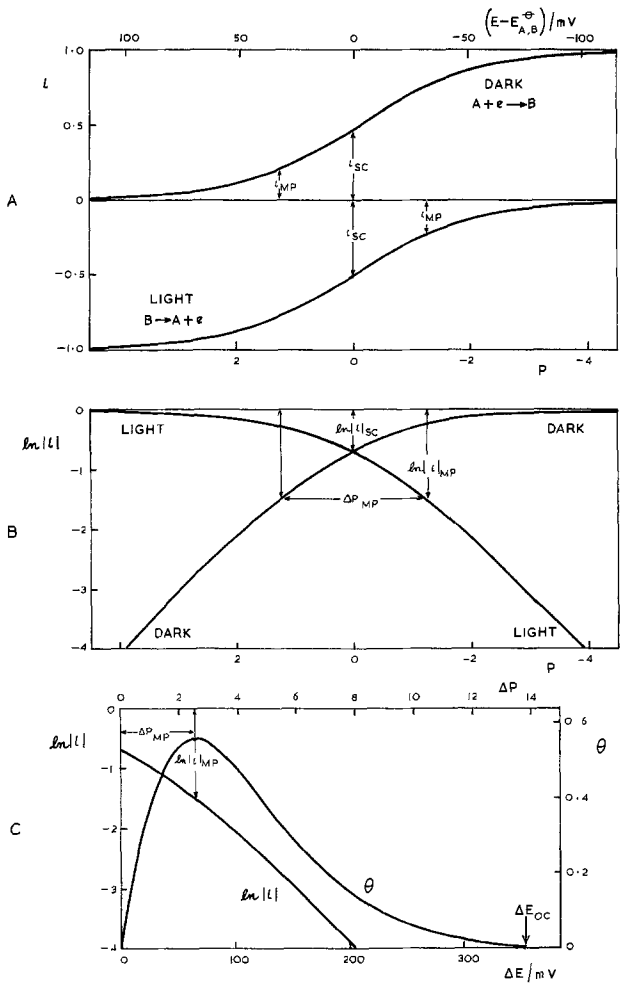


Fig. 6. Current-potential and power characteristics for the same conditions as in Fig. 5, except that $b_D/a_D = a_L/b_L = 10^{-3}$.

voltage developd by the cell. For instance where the curves intersect at the top of the "Gothic" arch we have the short-circuit condition that the equal and opposite currents are as large as possible but no voltage is developed at all. This is indicated by ι_{sc} on Fig. 5A and 5B. As $|\iota| \to 0$, ($\ln |\iota| \to -\infty$), the potential difference, ΔP or ΔE, rises to its maximum value, the open-circuit potential ΔE_{oc}, given by the zero current points in Fig. 5A, or by the distance between the asymptotes in Fig. 5B. The power developed by the cell is proportional to $\theta(=\iota\Delta P)$ and can be calculated from the curves shown in Fig. 5B. Figure 5C shows the current-voltage ($\ln|\iota|$) and power (θ) characteristics of the cell as a function of the cell voltage (ΔE). The power function passes through a maximum value of $\theta = 0.4$ and the currents (ι_{MP}) and potential difference (ΔP_{MP}) corresponding to this maximum power point are shown on Fig. 5A and 5B.

Figure 5 was calculated for moderate ratios of 10^{-1} for b_D/a_D and a_L/b_L. In Fig. 6, the same functions are plotted for the case that these ratios are equal to 10^{-3}. The open-circuit voltage of the cell is three times larger than for Fig. 5, but the power function at its maximum has only increased from 0.40 to 0.55. This is because the currents associated with the increased potential difference are small and one merely obtains a useless tail to the power function: The current-potential curves do not start to rise toward their transport limited values until the potential is in the neighborhood of $E^{\theta}_{A,B}$.

Further decrease in the ratios b_D/a_D and a_L/b_L below 10^{-3} makes no difference to the maximum in the θ function and the maximum value of θ that can be obtained is

$$\theta_m = 0.55 \qquad [39]$$

In Fig. 5 and 6 we took symmetrical examples; in Fig. 7 we show an unsymmetrical example for which $b_D/a_D = 10^{-3}$ and $b_L/a_L = 1$ (*i.e.* $f = 0.5$); the latter condition means that the illuminated solution is half-bleached in the photostationary state. For these conditions, although the open-circuit potential is greater than for the case shown in Fig. 5, the maximum value of θ is only 0.18. The performance of this cell is limited by the dark electrode, which shows severe concentration polarization in its working potential range.

It can be seen that for this type of cell the open-circuit voltage is not very relevant to the amount of power that can be obtained from the cell. Quite large potential differences can be developed by a concentration cell, providing that no current is passed, but as soon as current is drawn, concentration polarization tends to equalize the concentrations at the two electrodes and reduce the potential difference. In all cases the conditions for maximum power are found fairly close to the short-circuit condition, with a cell voltage at maximum power of only $\sim 2.5\ RT/\mathbf{F}$.

Therefore the nominal power (short-circuit current $\times$ open-circuit cell voltage) is not a good estimate for the power that can be obtained for this type of cell.

The intermediate case.—Next we consider briefly the intermediate case of Table II. In this case, the cur-

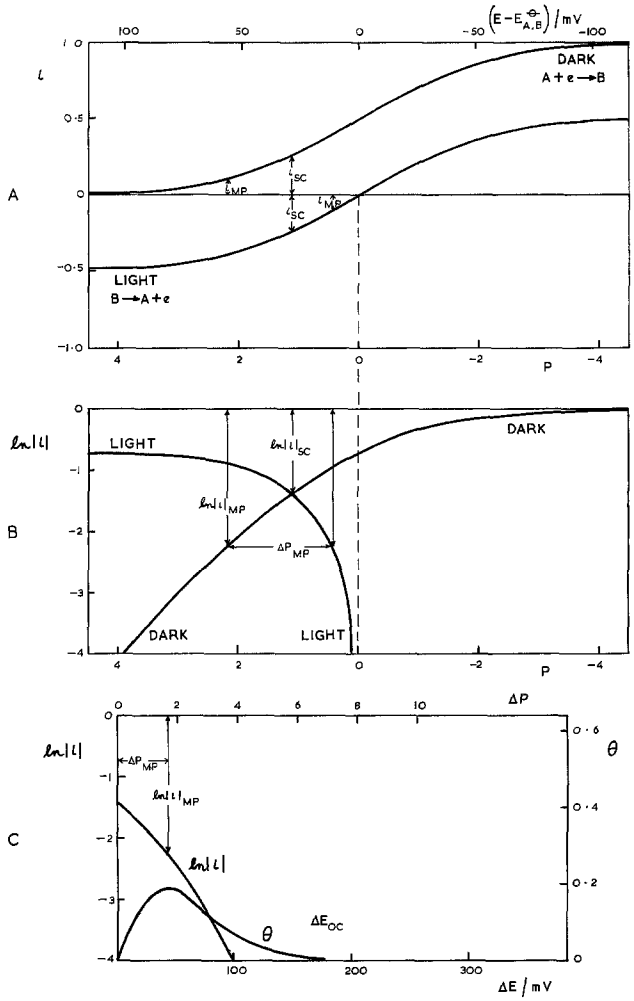


Fig. 7. Current-potential and power characteristics for the same conditions as in Fig. 5, except that $b_D/a_D = 10^{-3}$, $a_L/b_L = 1$.

rents given by [37] are merely modified by the factor X_{tr}/X_k, which is greater than 1. Hence larger currents are found than in the simple case. This is because the concentration polarization at the electrodes takes place over the smaller distance X_k defined by Eq. [21]. Apart from this factor, the shapes of the current-voltage and power characteristics are the same as for the simple case.

The catalytic case.—The current-potential curves for the "catalytic" case of Table II are rather different from those for the simple or intermediate cases. The currents are modified by the expressions for C given in Table III. In Fig. 8 we show the current-potential curves for an example of the catalytic case, in which we have taken

$$Y_\infty = y_D/a_D = Z_\infty = z_L/a_L = 10^2$$

and

$$B_\infty = b_D/a_D = (1 - f) = a_L/b_L = 10^{-2}$$

The limiting currents are 100 times larger than those

Table III. Expressions for S and C in [36]

	Dark electrode	Illuminated electrode
S	$\dfrac{1 - B_\infty \exp(P_D)}{1 + \exp(P_D)}$	$\dfrac{1 - f - f\exp(P_L)}{1 + \exp(P_L)}$
C	$\dfrac{Y_\infty(1 + \exp(P_D))}{1 + \exp(P_D - \Delta P^\theta)}$ where $\Delta P^\theta = P^\theta_{X,Y} - P^\theta_{A,B} = \ln(k_{-H}/k_H)$	$\dfrac{Z_\infty(1 + \exp(-P_L))}{f(1 + \exp(P_* - P_L))}$ where $P_* = \ln\left(\dfrac{(1-f)Z_\infty}{f(Y_\infty + f)}\right)$

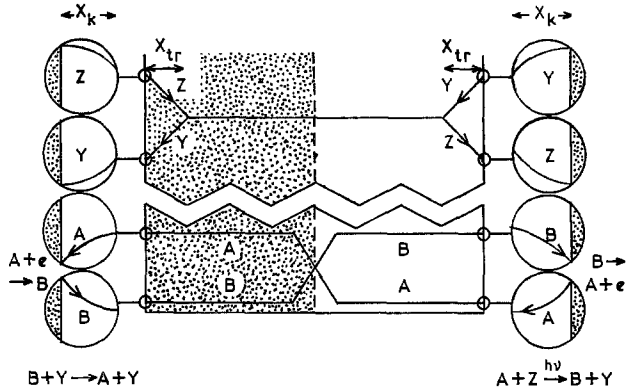


Fig. 8. Current-potential and power characteristics for the catalytic case defined in Table II. Electrode kinetics are the same as for Fig. 5-7 (case b, Table I). The concentration ratios have been taken as $y_D/a_D = z_L/a_L = 10^2$, $b_D/a_D = a_L/b_L = 10^{-2}$. Note the greatly increased values of ι and θ, compared with those in Fig. 5-7. The open-circuit cell voltage ($P = \ln 10^4$) is, however, the same as it would be in the simple case.

for the simple case, since at the electrodes, there are catalytic currents reducing Y or oxidizing Z, even though Y and Z are themselves electrochemically inactive. At the dark electrode the reduction of Y takes place by the sequence

Electrode: $e + A \rightarrow B$

Solution: $Y + B + A \rightarrow Z$

Over-all: $e + Y \rightarrow Z$ [40]

while at the illuminated electrode the oxidation of Z occurs through the sequence

Solution: $Z + A \xrightarrow{h\nu} B + Y$

Electrode: $B \rightarrow A + e$

Over-all: $Z \rightarrow Y + e$ [41]

The current-potential curves in Fig. 8B now meet in a flat arch ("Stonehenge") rather than the Gothic arches of Fig. 5 and 7. The cell voltage remains near its open-circuit value until the cell current is quite near its short-circuit value, and hence more power can be obtained than in the simple or intermediate case. The maximum value of θ of 400 is about 700 times larger than θ_m (=0.55). The current at the maximum power point is approximately 300 times larger than for the simple case and the potential difference is about 2.3 times larger, for this particular case. The reason for this great improvement is that the sequences [40] and [41] of catalytic reactions prevent the electrodes becoming polarized with respect to A and B. Figure 9 shows schematic concentration profiles for the catalytic case. Comparing these profiles with those in Fig. 2 we see that the surface concentrations of A and B remain very different at the two electrodes and this maintains the potential difference. Furthermore, the current is not limited by the transport across X_{tr} of A and B but rather by the transport of Y and Z, which for the catalytic case are present in much larger concentrations.

The General Behavior of the Current-Potential Curves

Having examined each case and shown some particular examples, in Fig. 10 we display the general behavior of current-potential curves calculated from Eq. [36] for the simple and catalytic cases. The curves are plotted in the same way as the B sections of Fig. 5-8. The current-potential curve for a dark electrode starts in the bottom left-hand corner at a potential determined by B_∞. As P becomes more negative the

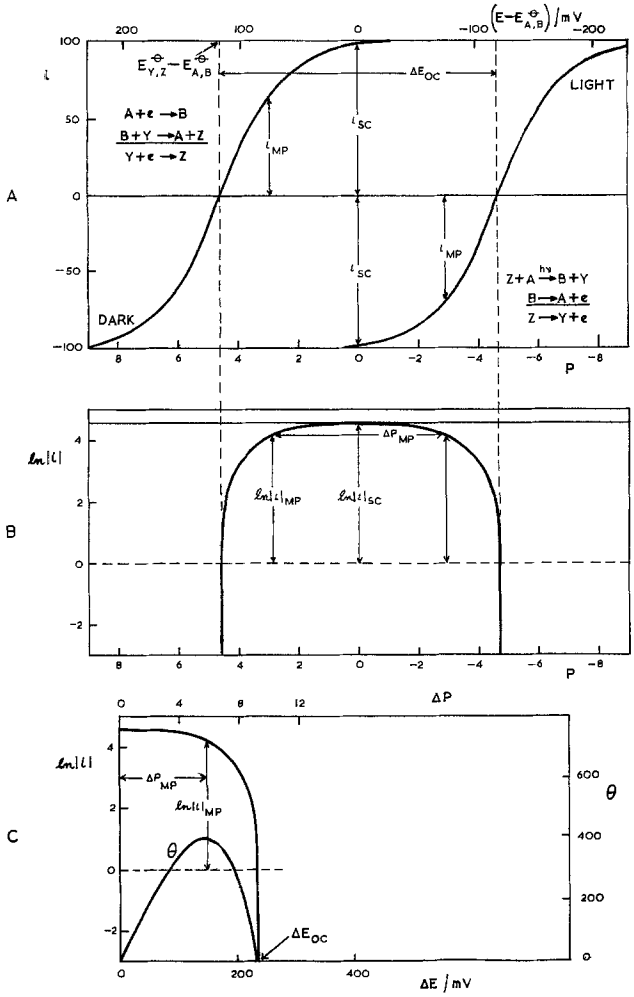


Fig. 9. Concentration profiles across a photogalvanic cell for the catalytic case where $Y_\infty = Z_\infty >> 1$ and $X_k << X_{tr}$.

dark current eventually rises to a limiting value on the right of the diagram which depends on Y_∞. For the catalytic case, the exact route for the crossover between the "vertical" asymptote on the left and the "horizontal" asymptote on the right depends on the value of Z_∞. If $Y_\infty \gtrless Z_\infty$ then the transition is sharp and almost right angled (*e.g.*, $Y_\infty = 10^2$ or $Y_\infty = 10^4$). If on the other hand $Y_\infty > Z_\infty$, then a more gradual transition is found with a region where the slope is 45° (*e.g.*, $Y_\infty > Z_\infty = 10^2$). Similarly the curves for the illuminated electrode start in the bottom right-hand corner at a potential determined by f (the fraction of A that is bleached) and they cross over to a limiting value on the left of the diagram determined by Z_∞ or f. For the catalytic case, the transition depends upon the value of Y_∞ and is sharp for $Z_\infty \gtrless Y_\infty$ (*e.g.*, $Z_\infty = 10^2$ or $Z_\infty = 10^4$) and gradual for $Z_\infty > Y_\infty$ (*e.g.*, $Z_\infty > Y_\infty = 10^2$). As in the examples we have discussed the two curves (dark and illuminated) for any particular cell creates an "arch" which determines the power characteristics of that cell. In Fig. 10 we have outlined a typical Gothic example (S) of the simple case illustrated in Fig. 5-7, and a piece of Stonehenge (C) for the catalytic case as illustrated in Fig. 8. Figure 10 displays the current-voltage behavior of a cell in such a way that the power characteristics can be easily estimated and it shows how these characteristics vary with the concentrations of the species (B_∞, Y_∞, and Z_∞) and the fraction of A that is bleached (f). The three variables B_∞, Y_∞, and Z_∞ are however not independent since they are related for $Z_\infty >> 1$ by

$$B_\infty Y_\infty / Z_\infty = \exp(-\Delta P^\theta)$$

where

$$\Delta P^\theta = (E^\theta_{Y,Z} - E^\theta_{A,B})\mathbf{F}/RT$$

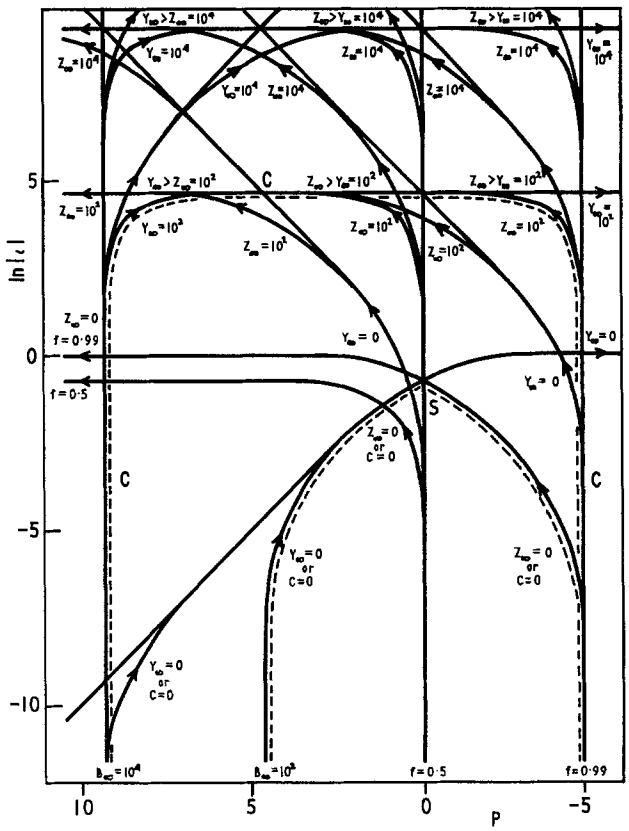


Fig. 10. Current-potential curves given by Eq. [36] for a cell containing a reversible *A, B* couple and an irreversible *Y, Z* couple. See text for discussion.

Limitations on the values of Y_∞ and Z_∞.—The theoretical behavior illustrated in Fig. 10 suggests that it would be desirable to have Z_∞ and Y_∞ as large as possible. Unfortunately there is a practical limitation. The increased performance arises from the A and B species catalyzing the reduction and oxidation of Y and Z. We have assumed that the A, B couple is reversible but there is a limit to the amount of Y or Z it can handle at each electrode. Combining the condition for reversibility ($\lambda > 1$), the definition of λ in [32], and the condition for the catalytic case in Table II, we find

$$Y_\infty \text{ and } Z_\infty < X_{tr} k^\circ_{A,B}/D < 10^2 \qquad [42]$$

The estimate of 10^2 in [42] is obtained by taking $X_{tr} = 10^{-2}$ cm, $D = 10^{-5}$ cm^2 sec^{-1}, and $k^\circ_{A,B} < 10^{-1}$ cm sec^{-1}, where $k^\circ_{A,B}$ is the standard electrochemical rate constant for the A, B couple. If Y_∞ or Z_∞ is increased above ~10^2, no improvement in cell output will result, because charge transfer overvoltage will cause power losses, unless A, B is extraordinarily reversible.

Variation of Power with X_{tr} and X_k

In our discussion so far we have been concerned with how the power varies with the load on the cell and with the electrode kinetics. We now explore how the maximum power from a cell with a matched load varies with X_{tr} and X_k. At constant X_{tr} the power, W, is proportional to θ, as shown by Eq. [14], and Fig. 11 shows the variation of θ/θ_m with (X_k/X_{tr}), where $\theta_m = 0.55$ (Eq. [39]). We have taken for the catalytic case the curve labeled C in Fig. 10, where Z_∞ and Y_∞ have their maximum value of 10^2 (Eq. [42]). Like Table II (or Gaul) the figure is divided into three parts. On the left-hand side we have the catalytic case; the homogeneous reactions are fast enough for reaction sequences [40] and [41] to take place. The difference between θ_m and the maximum value of θ for curve C ($= 852$) is shown by the vertical arrow. On the right-hand side we have the simple case. Under these

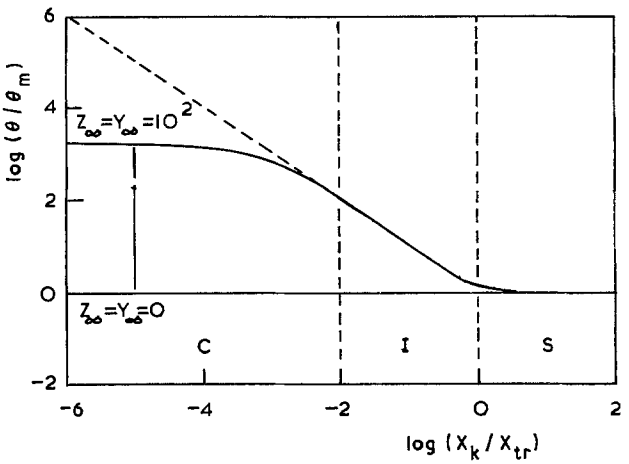


Fig. 11. Variation of maximum power with X_k. The catalytic case illustrated is for $Z_\infty = Y_\infty = 10^2$; the broken line shows the maximum possible power from [43].

conditions the homogeneous reactions are too slow for the catalytic currents to be developed in the diffusion layer. In between we have the intermediate case, for which from Table II

$$\theta = \theta_m(X_{tr}/X_k) \qquad [43]$$

Here θ decreases with increasing X_k. Under these conditions there are catalytic currents. These currents, however, are not limited by the transport of Y or Z across X_{tr} but rather by the transport and reaction of A and B in the reaction layer.

To examine how the maximum power varies with X_{tr} we have to define a new function ϕ where

$$W = \phi\theta_m A D a_D R T X_k^{-1} \qquad [44]$$

and

$$\log \phi = \log (\theta/\theta_m) - \log (X_{tr}/X_k) \qquad [45]$$

In [44] as opposed to [14] the power output, W, is normalized with respect to X_k rather than X_{tr}. Figure 12 shows how ϕ (and hence W) varies with X_{tr}/X_k. Figures 11 and 12 are complementary; the former shows the behavior for constant X_{tr} and varying X_k, while the latter shows the behavior for constant X_k and varying X_{tr}. The same catalytic case (curve C in Fig. 10) is shown.

Three regions are again found in Fig. 12. For the intermediate case from [43] and [45], $\phi = 1$. In this region the power produced is independent of X_{tr}. The reason for this is, firstly that Y and Z are not being consumed rapidly enough for their concentration polarization to be important, and secondly that the concentration profiles of A and B are determined by what happens in the reaction layer rather than by their diffusion across X_{tr}. In both Fig. 11 and 12, more power is produced the smaller is X_k or X_{tr}. In particular on the right of Fig. 12, as X_{tr} becomes large, very little power is produced. In the limit, a cell operating under conditions of semilinear infinite diffusion would not produce any power in the steady state. This is because the concentration polarization reduces the current to zero.

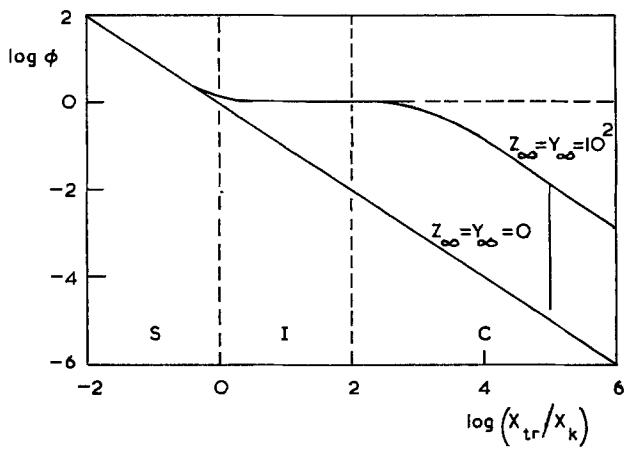


Fig. 12. Variation of maximum power with X_{tr}. The catalytic case illustrated is for $Z_\infty = Y_\infty = 10^2$; the broken line shows the maximum possible power from [43].

The broken lines in Fig. 11 and 12 show the maximum possible power that can be obtained from the intermediate and catalytic cases, even if the restriction on the size of Y_∞ and Z_∞ given in [42] was removed. The transport and reaction of the electrochemically active couple will always ultimately limit the current and the line given by [43] is the maximum value of θ that can be obtained in the catalytic case. As C is increased, although θ is larger in the catalytic region, the boundary between this region and the intermediate region moves to the left in Fig. 11, so that values of θ greater than those given by [43] cannot be found.

Photogalvanic Concentration Cells as Practical Solar Energy Converters?

The broken lines of Fig. 11 and 12, representing the maximum power that can be found, correspond to $\phi = 1$ in Eq. [44] and hence we derive the following simple expression for the maximum power obtainable from the type of photogalvanic concentration cell discussed in this paper

$$W_{max} = 0.55 A D a_D R T X_k^{-1} \qquad [46]$$

The former is limited by the solubility of A. Furthermore in deriving Eq. [46] we assumed that there was sufficient light intensity to convert nearly all the A to B in the photostationary state. The maximum conversion is given by

$$\frac{b_L}{a_L} = \frac{I_{o\epsilon}}{k_{-H}y}$$

and taking $b_L/a_L > 10$ with typical values for I_o for solar radiation of 10^{-7} E cm^{-2} sec^{-1} (4), and $\epsilon = 10^8$ cm^2 mol^{-1}, we find that

$$k_{-H}y < 1 \text{ sec}^{-1} \qquad [47]$$

But for the catalytic case we require

$$y/a_D \sim 10^2$$

and so

$$(a_D/M) < 10^{-2}(k_{-H}/\text{M}^{-1}\text{sec}^{-1})^{-1} \qquad [48]$$

If this condition is violated then sunlight will be unable to convert all the A to B in the photostationary state and less power will be obtained than predicted from Eq. [46].

Returning to consideration of Eq. [46], the other variable, X_k, will be limited by the condition in Eq. [47], giving $X_k > 3 \times 10^{-3}$ cm. Taking $D = 10^{-5}$ cm^2 sec^{-1} and $a_D = 10^{-3}$M (implying from Eq. [48] $k_{-H} \sim 10\text{M}^{-1}$ sec^{-1}) we obtain from Eq. [46]

$$W_{max}/A \sim 10^{-6} \text{ W cm}^2$$

Most real systems will not fulfill all the necessary conditions in [42], [47], and [48], and in the next paper of this series we shall explore how the power varies with the kinetics of the reaction of B and Y and with the concentrations of A and Y. However it is clear that the power output of the cell depends on a complicated interplay of the parameters describing the photochemistry, the homogeneous kinetics, the mass transport, and the electrode kinetics. Conclusions based on simple concepts like the "power conversion efficiency" may well be misleading. For instance, if the power output is limited by mass transport, increasing the light intensity will not increase the amount of power from the cell.

Conclusions

1. Photogalvanic concentration cells will be most efficient when one electrochemical couple is reversible and one irreversible.

2. As shown in Fig. 11 and 12, the efficiency of photogalvanic cells is improved by reducing both X_k and X_{tr}.

3. If $X_{tr} > X_k$, the maximum power that can possibly be obtained is given by [46]. Under these conditions the homogeneous kinetics are sufficiently rapid to suppress the concentration polarization of A and B at the electrodes and to produce catalytic currents from the larger concentrations of Y and Z. The maximum power is unlikely to be $> 10^{-6}$ W cm^{-2}, if sunlight is used to drive the cell.

In this treatment we have made the following assumptions:

(*i*) The electrodes are of the same material and are of equal area.

(*ii*) All diffusion coefficients are equal.

(*iii*) The photochemical generation obeys a relation, $g = g''az$.

(*iv*) Except for conclusion 1 the electrode kinetics follows case b in Table I, so that the A, B couple is reversible and the Y, Z couple irreversible.

(*v*) The concentration of photochemically generated B is much larger than that in the dark.

Acknowledgments

We thank Mr. Stephen Fisher for a helpful conversation, and the General Electric Company (Schenectady) for partial support of this work.

Manuscript submitted May 27, 1976; revised manuscript received Nov. 17, 1976. This Paper 217 presented at the Washington, D. C., Meeting of the Society, May 2-7, 1976.

Any discussion of this paper will appear in a Discussion Section to be published in the December 1977 JOURNAL. All discussions for the December 1977 Discussion Section should be submitted by Aug. 1, 1977.

REFERENCES

1. W. J. Albery and M. D. Archer, *Electrochim. Acta*, In press.
2. T. N. Anderson and H. Eyring, in "Physical Chemistry: An Advanced Treatise," Vol. IX A, H. Eyring, Editor, pp. 268-269, Academic Press (1970).
3. J. Koutecky and V. G. Levich, *Z. Fiz. Khim.*, **32**, 1565 (1956).
4. S. T. Henderson and D. Hodgkiss, *Br. J. Appl. Phys.*, **14**, 125 (1963) D. M. Gates, *Science*, **151**, 523 (1966).

Spectral Response and Efficiency Relations in Semiconductor Liquid Junction Solar Cells

A. Heller,* K. C. Chang, and B. Miller*

Bell Laboratories, Murray Hill, New Jersey 07974

ABSTRACT

States due to imperfections at or near surfaces of semiconductors in liquid junction solar cells can be identified by changes in the photoresponse spectra under short-circuit current conditions. These effects become dominant features in two-beam experiments with an intense pumping (laser) source and a weak modulated probing beam. The presence of these states can be correlated with drastic decreases in short-circuit currents, open-circuit voltages, fill factors, and maximum power conversion efficiencies of the cells. Elimination of the damaged surface regions by suitable etching allows AM2 solar conversion efficiencies of 1.3 and 7.2%, respectively, in the cells n-CdS/0.1F Na_2S-0.02F S-0.1F NaOH/C and n-CdSe/1F Na_2S-1F S-1F NaOH/C.

Semiconductor liquid junction solar cells (1) consist of the bulk semiconductor phase, the interface between semiconductor and solution, the redox electrolyte, and a counterelectrode. The motion of carriers in photoexcited semiconductors and in solutions and the transfer of charge at (metallic) counterelectrode interfaces are reasonably understood. The unique features and the problems of semiconductor liquid junction solar cells derive from the chemistry and physics of the semiconductor-electrolyte interface first described by Brattain and Garrett (2). The critical dependence of the stability of such cells on this interface has been discussed by Gerischer (1). That the power conversion efficiency also depends on the properties of the interface as controlled by prior chemical etching was noted by Kaiser, Ellis, and Wrighton (3) in the case of CdSe.

The importance of proper preparation of the semiconductor surface became evident to us in early phases of work on the efficiencies of both single crystal and polycrystalline semiconductor based cells. In fact, efficiencies were found to vary by as much as three orders of magnitude with the method of preparation of the semiconductor surface. Such variations were also expected from experience with solid-state cells where the loss of efficiency has been attributed to the trapping of carriers in surface states, followed by recombination (4).

The significance of surface imperfections in controlling the efficiencies made necessary a fast and simple technique for the monitoring of the quality of the semiconductor surface *in situ*. Byvik (5) recently showed the presence of states within the "forbidden" gap by measuring the photovoltaic response of semiconductors immersed in electrolyte solutions. We have observed distinct changes in the photoresponse spectra of many semiconductors *in situ* with the mode of surface preparation. These changes can be correlated with the level of power conversion efficiency of these semiconductor liquid junctions in solar cell use. The spectral response behavior provides a sensitive indicator for optimizing surface preparation conditions for given semiconductor-redox electrolyte combinations.

We present here the results for two solar cells with n-CdS and n-CdSe single crystal anodes. Similar behavior was observed with other cells utilizing both single crystal and polycrystalline electrodes.

Experimental

Hexagonal (wurtzite) n-CdS and n-CdSe single crystals cleaved into 1 mm thick plates with the surfaces perpendicular to the c axis were purchased from

* Electrochemical Society Active Member.

Cleveland Crystals Incorporated, Cleveland, Ohio. The conductivities of the crystals were at least 0.1 Ω^{-1}-cm^{-1}. Ohmic contacts were formed to the back of each plate with evaporated indium. A copper lead was attached to the indium layer with silver epoxy. Epoxy resin was used to seal the copper wire in a glass tube and to insulate all but the exposed face of the semiconductor electrode.

Pyrex test cells were equipped with Pyrex flat windows. The active crystal face was brought to 1 ± 0.5 mm of the window to minimize solution light absorption. Typical crystal area was 0.2 cm^2. The counterelectrode was a ~ 10 cm^2 geometric surface area carbon ring attached to a graphite rod. Provision was made for a calomel reference electrode. Nitrogen was bubbled through the solution which was also stirred by a magnetic bar.

The electrolytic solutions were 0.1F Na_2S-0.02F S-0.1F NaOH (CdS experiments) and 1F Na_2S-1F S-1F NaOH (CdSe experiments). A 1 mm thick layer of these solutions cuts off 50% of the light at 350 nm in the case of the first solution and at 490 nm for the second.

CdS crystals were etched for 20 sec in conc HCl and CdSe for 20 sec in 5:1 (v/v) HCl-HNO_3. The initial spectra and voltammetric characteristics of the crystals as supplied could be changed by etching and restored by polishing with Linde A (0.3μ alumina).

Current-voltage characteristics of the cells were measured with a PAR Model 173 potentiostat-galvanostat programmed by a PAR Model 175 universal programmer.

The light source was a 100W tungsten-halogen lamp (Oriel Corporation). The beam was chopped at 100 Hz with a Bulova tuning fork and then focused on the entrance slit of a 0.25m Schoeffel grating monochromator. Both entrance and exit slits were set at 0.5 mm. Part of the exit slit was masked to define a spot of 2 mm height as focused on the electrode face.

The lasers used were a Spectra Physics Model 310A argon-ion laser (10 mW at 488 nm) and a Spectra Physics Model 155 helium-neon laser (1.8 mW at 632.8 nm). The spot diameter of the argon laser was brought to 4 mm and that of the helium-neon laser to 2 mm using concave lenses. Thus the irradiance of CdS at 488 nm was about 80 mW/cm^2 and of CdSe at 632.8 nm about 60 mW/cm^2. The beam from the laser was not chopped. The image of the monochromator slit on the crystal was completely overlapped by the light spot from the laser. The irradiance of the crystals by the light that passed through the monochromator varied with wavelength but was never more than 1 mW/cm^2.

Photoresponse spectra under "short-circuit" d-c load conditions were obtained by connecting the cell electrodes to the "transformer mode" input of a PAR Model 116 differential preamplifier plugged into a PAR Model 124A lock-in amplifier. The d-c resistance of this input was measured as 2.2Ω. This synchronous detection method also served to reject the unchopped laser radiation response.

The spectra were corrected for the number of photons reaching the cell at the various wavelengths and normalized to unity at their maxima. Thus the short-circuit current photoresponse spectra represent relative quantum yields. Corrections for solution light absorption were not made.

The energy conversion efficiencies were measured using a calibrated Eppley thermopile and direct sunlight with irradiances close to 75 mW/cm^2.

Results

Figure 1 shows the normalized short-circuit current photoresponse spectra of an as polished (unetched) n-CdS electrode, with and without laser irradiation. In addition to the response at wavelengths shorter than 512 nm, the wavelength corresponding to a 2.42 eV bandgap (6), the spectrum shows a peak at 536 nm (2.31 eV) when the laser is off. Exposure of the CdS to the 488 nm laser light reduces the photocurrent almost to zero on the short wavelength side until the absorption edge is approached. The photocurrent then peaks at 512 nm (the wavelength equal to the 2.42 eV bandgap) and shows a shoulder at longer wavelengths.

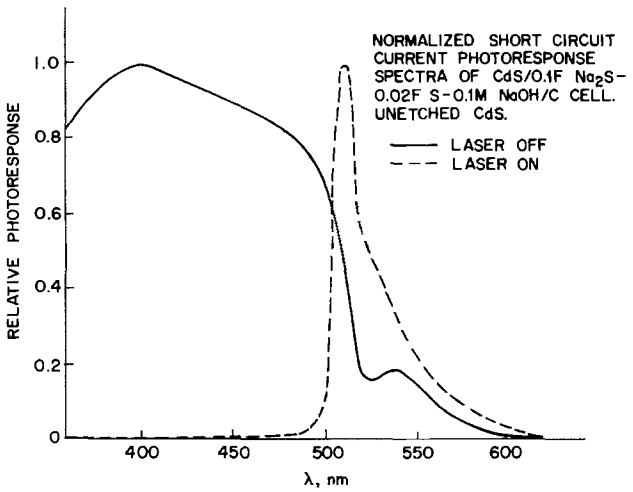


Fig. 1. Effect of laser pumping on unetched n-CdS single crystal electrode spectra.

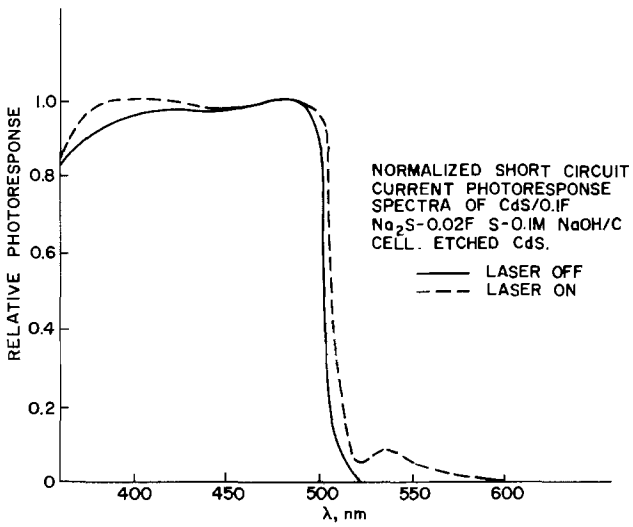


Fig. 2. Effect of laser pumping on etched n-CdS single crystal electrode spectra.

Figure 2 shows the equivalent spectra after etching of the CdS. The drastic difference between the spectra in Fig. 1 produced by the laser irradiation no longer exists. The response of the etched crystal is nearly flat at photon energies exceeding the bandgap in both Fig. 2 spectra. With the laser on a small peak at 536 nm is still observed. This reflects both the sensitivity introduced by the laser pumping and the fact that the etching step is insufficient to provide a "perfect" surface.

The spectral difference between the unetched and etched CdS without the laser irradiation is shown in Fig. 3. Two maxima are observed; 515 nm (2.407 eV) and 537 nm (2.309 eV). These correspond to transitions located 0.014 and 0.112 eV below the bandgap energy.

The current-voltage characteristics of the solar cells with unetched and etched CdS crystals, respectively, are shown in Fig. 4 for a solar irradiance of 76.6 mW/cm^2. Comparison of the performance of the unetched and the etched cells shows that the respective experimental short-circuit currents are 0.68 and 4.1 mA/cm^2. Under AM2 conditions these currents are estimated to be 0.65 and 4.0 mA/cm^2, respectively. The corresponding open-circuit potentials are 0.41 and 0.59V. The maximum power density measured for unetched CdS is 0.34 mA/cm^2 × 0.21V = 0.07 mW/cm^2, translating to an AM2 efficiency of 0.09% and to a fill factor of 0.25.

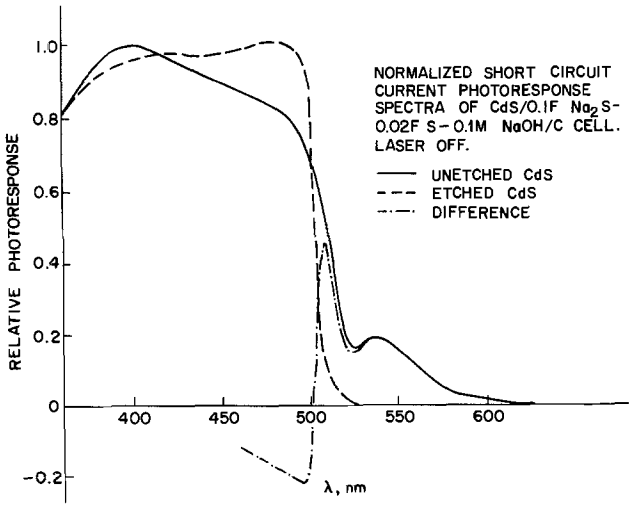


Fig. 3. Effect of surface defects on n-CdS single crystal electrode spectra. Laser off.

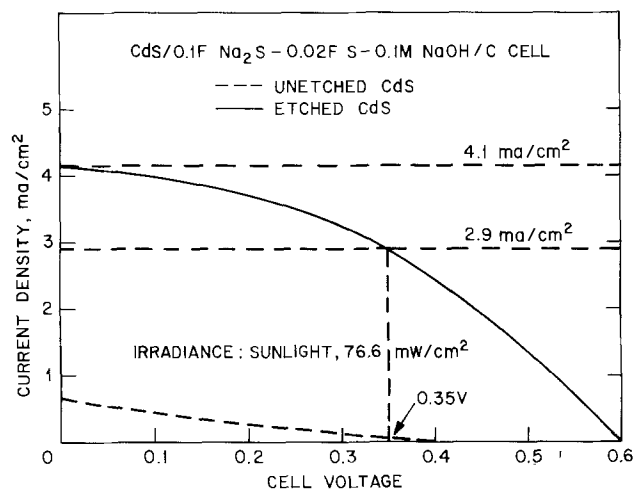


Fig. 4. Current-voltage characteristics of n-CdS/0.1F Na_2S-0.02F S-0.1F NaOH/C cell with etched and unetched n-CdS electrodes.

Etched CdS delivers 2.8 mA/cm² × 0.35V = 0.98 mW/cm² or an AM2 efficiency of 1.3% at a fill factor of 0.41.

The data for the single crystal n-CdSe electrodes are shown in Fig. 5-7. Figure 5 compares the photocurrent spectra of the polished CdSe left unetched, and the same surface etched in 5:1 HCl-HNO_3. The photoresponse of the unetched electrode extends beyond the 727 nm (1.705 eV) bandgap (7) with a maximum at

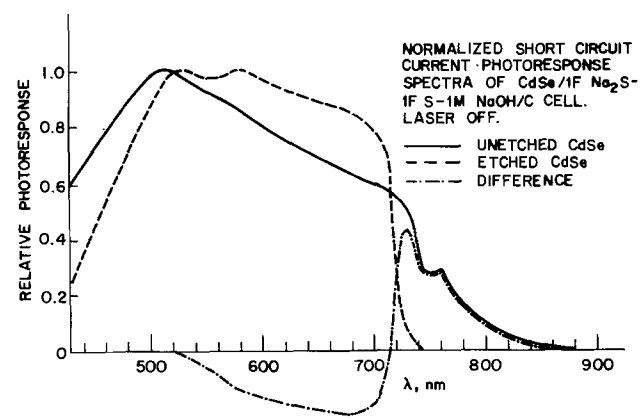


Fig. 5. Effect of surface defects on n-CdSe single crystal electrode spectra. Laser off.

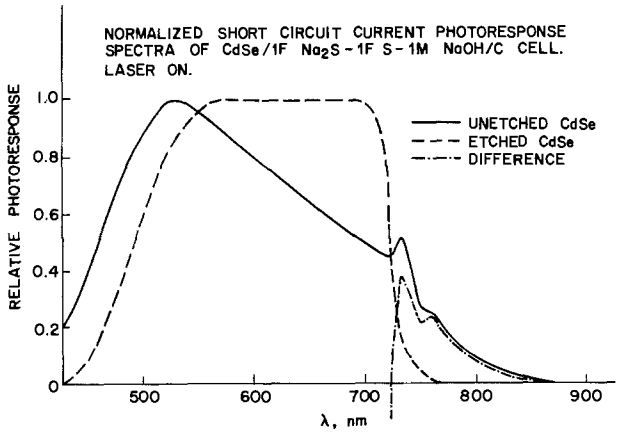


Fig. 6. Effect of surface defects on n-CdSe single crystal electrode spectra. Laser on.

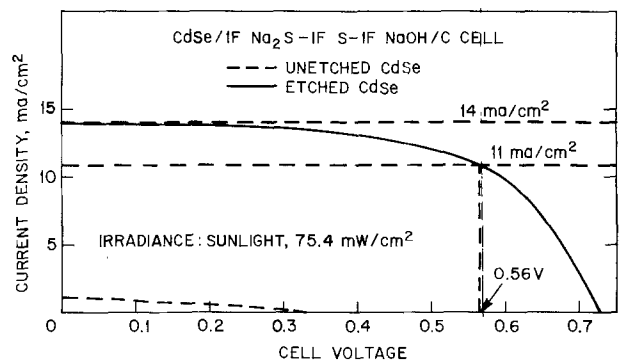


Fig. 7. Current voltage characteristics of n-CdSe/1F Na_2S-1F S-1F NaOH/C cell with etched and unetched n-CdSe electrodes.

757 nm. The difference spectrum in Fig. 5 shows two transitions; 731 nm (1.694 eV) and 757 nm (1.638 eV). These transitions define two states differing by 0.011 and 0.067 eV from the band edge.

The photocurrent spectra obtained with light from the He-Ne laser (632.8 nm) flooding the CdSe crystal are shown in Fig. 6. The etched CdSe displays a sharp band edge at 727 nm (1.705 eV) and a flat response at shorter wavelengths down to the uncorrected region of polysulfide absorption. The spectrum obtained with unetched CdSe is different, extending to longer wavelengths with a peak at 731 nm and a shoulder at 757 nm. In contrast to that of the etched CdSe, the photoresponse peaks near the polysulfide absorption region and decreases as the photon energy approaches that of the bandgap. The difference spectrum between unetched and etched CdSe also shows maxima at 731 and at 757 nm.

The current voltage characteristics of the CdSe cells are shown in Fig. 7. The measured short-circuit current density is 1.2 mA/cm² for unetched CdSe and 14 mA/cm² for etched CdSe. The open-circuit voltages are, respectively, 0.33 and 0.73V. The measured power density maximum for the unetched cell is 0.6 mA/cm² × 0.16V = 0.1 mW/cm², and the fill factor is 0.25. The corresponding values for the etched CdSe cell are 11 mA/cm² × 0.56V = 6.1 mW/cm² and fill factor 0.60. The over-all power conversion efficiency, η, for the etched electrode cell is

$$\eta = \frac{6.1 \times 100}{75.4} = 8.1\%$$

This result is the best of four obtained on different occasions with sunlight near 75 mW/cm² with four different electrodes. The data are virtually identical in short-circuit current and open-circuit voltage and vary only in fill factor to give an average η of 7.2 ± 0.7% (std dev.).

Discussion and Conclusions

The results establish a simple correlation between the presence of the states which are within the forbidden gap and the efficiency of semiconductor liquid junction solar cells. These states are responsible for the 515 and 537 nm transitions in CdS and for the 732 and 757 nm transitions in CdSe. That these states are due to imperfections near or at the surface is evident from the fact that they are removed by a brief etching. Such etching simultaneously reduces or eliminates the spectral transitions within the bandgap and increases the short-circuit current, fill factor, open-circuit voltage, and thus the over-all power conversion efficiency.

The additional states are introduced by mechanical polishing and its attendant surface or bulk dislocation generation. The fact that wurtzite actually undergoes a phase transition to sphalerite upon grinding is well known (8). Lattice defects produced by abrasion have also been reported by Gerischer *et al.* (9) in ZnO where the damage depth is found comparable to the particle size of the abrasive. Similar considerations for our experiments would produce a defect layer of 0.3μ.

Surface and near-surface defects are well known to affect the performance of solar cells by introducing states which act as carrier traps and recombination centers (10). Recombination centers lead to saturation of photocurrents at low light levels and to changes in the photoresponse spectrum both above and within the bandgap. Saturation at moderate light intensities is evident both in CdS and CdSe where laser input drops the response of the unetched crystals to the modulated beam by more than an order of magnitude. Removing the defects by etching makes the modulated photoresponse insensitive to the laser beam.

The origin of the saturation effect can be explained by assuming that the new states are traps for one of the carriers. Whether they are electron or hole traps, they are populated by exposure of the crystal to an intense beam of light. Minority carriers moving toward the interface or majority carriers moving to the bulk thus meet a greatly increased probability of recombination.

Such processes also account for the shape of the photoresponse spectra at higher light intensities in unetched CdS (Fig. 1). Light of short wavelengths is absorbed closer to the surface where the density of populated traps is high. Because of the resulting high recombination probability, such light produces virtually no photocurrent. On the other hand, light near the band edge penetrates deeper to more perfect regions of the crystal where little recombination takes place. As a consequence, substantial photocurrent is produced by wavelengths near the absorption edge.

Upon removal of the top layer with the dislocation generated recombination sites, the performance of the cells is dramatically improved. It is notable that the 4.0 mA/cm^2 short-circuit current for CdS and the 14 mA/cm^2 short-circuit current for CdSe represent 80% of the theoretical limits of these materials for AM2 conditions (11). The quantum efficiency is probably close to unity and the losses are primarily reflection losses at both the semiconductor-liquid and glass-air interfaces and solution absorption losses.

Whether the defects manifest themselves as donor or acceptor levels is not established herein but is under investigation by capacitive techniques.

It may be noted that similar photoresponse techniques with laser irradiation on anodically formed CdS surfaces (12) show the same minimal effects of the laser beam observed in studies of etched single crystals. Unlike the single crystal spectra, those obtained on anodized surfaces have a tail at wavelengths longer than 512 nm (the 2.42 eV bandgap).

The sensitivity of the technique of photoresponse spectra with superimposed laser irradiation confirms it as an excellent diagnostic tool for evaluating surface preparation methods for semiconductor electrodes in liquid junction solar cell investigations.

Manuscript submitted Nov. 12, 1976; revised manuscript received Jan. 6, 1977.

Any discussion of this paper will appear in a Discussion Section to be published in the December 1977 JOURNAL. All discussions for the December 1977 Discussion Section should be submitted by Aug. 1, 1977.

Publication costs of this article were assisted by Bell Laboratories.

REFERENCES

1. H. Gerischer, *J. Electroanal. Chem.*, **58**, 263 (1975).
2. W. H. Brattain and C. G. B. Garrett, *Bell Syst. Tech. J.*, **34**, 129 (1955).
3. A. B. Ellis, S. W. Kaiser, and M. S. Wrighton, *J. Am. Chem. Soc.*, **98**, 1635 (1976).
4. H. J. Hovel, "Semiconductors and Semimetals," Vol. 11, "Solar Cells," p. 77-82, Academic Press, New York (1975).
5. C. E. Byvik, Abstract 238, p. 584, The Electrochemical Society Extended Abstracts, Spring Meeting, Washington, D.C., May 2-7, 1976.
6. M. Balkanski and R. D. Waldron, *Phys. Rev.*, **112**, 123 (1958).
7. Y. S. Park, *ibid.*, **132**, 2450 (1963).
8. H. W. Leverenz, "Luminescence of Solids," p. 88, John Wiley & Sons, Inc., New York (1950).
9. H. Gerischer, F. Hein, M. Lübke, E. Meyer, B. Pettinger, and H. R. Schöppel, *Ber. Bunsenges. Phys. Chem.*, **77**, 284 (1973).
10. H. J. Hovel, "Semiconductors and Semimetals," Vol. 11, "Solar Cells," pp. 13,15, Academic Press, New York (1975).
11. H. J. Hovel, *ibid.*, p. 38.
12. B. Miller and A. Heller, *Nature (London)*, **262**, 680 (1976).

Current Distribution on a Rotating Ring-Disk Electrode below the Limiting Current

Peter Pierini and John Newman*

Materials and Molecular Research Division, Lawrence Berkeley Laboratory, and Department of Chemical Engineering, University of California, Berkeley, California 94720

ABSTRACT

Ring-disk electrodes have been used in the literature to simulate experimentally the nonuniform current distribution across a rotating disk electrode operated at a fraction of the limiting current. The analogy of a sectioned disk to a ring-disk electrode is difficult to substantiate since both the limiting current and primary current distributions are radically different. Thus a detailed knowledge of the distribution of current and concentrations is developed to compare rationally the differences in nonuniformity for the ring-disk and disk electrodes. Integral measures of the degree of departure from the limiting current and primary current distributions are developed and related to the measurement of throwing power.

The ring-disk electrode system is one of the most convenient arrangements of two working electrodes in a common cell. The concentric, rotating electrode structure is relatively easy to fabricate and is available commercially. The device has drawn attention recently, as both the object of theoretical analysis and experimental applications. Bruckenstein and Miller (1) and Smyrl and Newman (4) have performed experiments with ring disks to assess the nonuniform current distribution on a disk electrode utilizing the sectioned-electrode approach. Miller and Bellavance (2) have reported a number of experiments with the system, including measurement of interrupter and steady-state resistances and interactive resistances between the ring and the disk. Smyrl and Newman (3, 4) have presented data for ring-disk electrodes operated at and below the limiting current, along with a detailed analysis demonstrating the limiting current calculations. The primary current distribution was recently computed by Miksis and Newman (5). The limiting current (4, 11) and the primary current (5) densities of a ring electrode are not uniform, so the current density on a ring operated at some fraction of the limiting current, where kinetics also must be taken into account, does not approach the uniform distribution (12) that prevails near the edge of a disk electrode as the fraction of the limiting current approaches unity. The current distribution across a ring-disk electrode tends to be more nonuniform than for an equivalent disk.

Newman's (6) approach to the computation of the concentration and current density distributions across a rotating disk electrode has been applied successfully to a number of other electrode geometries (7-9, 24-26). Parrish and Newman (8) investigated the current distributions on two plane parallel electrodes in channel flow, the only application to two interactive working electrodes. The ring-disk geometry contains two working electrodes and can utilize a counterelectrode, which would be considered infinitely far from the working electrodes. The working electrodes interact through the potential distribution, which is described by an elliptic Laplacian equation giving global effects, and through the parabolic concentration boundary-layer equations which allow a downstream influence on the ring electrode by the disk. The ring implicitly affects the disk concentration profile by modifying the potential which enters into the kinetic expressions, thus changing the flux boundary conditions that would exist on the disk from the situation prevailing if no ring were present.

Current can flow between any of the three electrodes in the cell, but common experimental objectives usually attempt to limit the possibilities. The ring and the disk can be operated potentiostatically with the current from each electrode being collected by the counterelectrode. The disk can be used to produce a species not in the bulk solution which can then be collected by the ring electrode, usually one electrode being driven cathodically and the other anodically. The disk electrode can be driven as a bipolar electrode where a current loop exists in the solution over the electrode. The analysis presented here applies to all these cases, but the results are restricted to the sectioned disk, with the ring and the disk maintained at the same potential. Results for the other situations will be reported in a subsequent paper.

The kinetics of the surface reaction to be considered are of three types, a product-independent metal deposition from a single salt solution (6), a product-independent reaction with a supporting electrolyte (6), and a reaction depending on all reacting species with a supporting electrolyte (10). These reactions are representative of plating from a solution with and without a supporting electrolyte, and of redox reactions or organic synthesis with a supporting electrolyte. The analysis is restricted to laminar flows, high Schmidt numbers, and dilute solutions with constant physical properties.

The method of computing current densities and concentration profiles is developed for a ring-disk system operated potentiostatically. Integral measures of the way in which these profiles deviate from the limiting current and primary current distributions are discussed. The design of ring-disk electrodes for the purpose of measuring the throwing power is shown.

Overpotentials

Let a single electrode reaction be expressed by

$$\sum_i s_i M_i^{z_i} \rightarrow n\, e^- \qquad [1]$$

where s_i is the stoichiometric coefficient, M_i is the symbol for the chemical species, z_i is the species charge number, and n is the number of electrons participating in the reaction. The potential applied between each of the working electrodes and a single counterelectrode located at infinity is

$$V_d = U + \Phi_{o,d} + \eta_c + \eta_s \qquad [2]$$

$$V_r = U + \Phi_{o,r} + \eta_c + \eta_s \qquad [3]$$

The applied potentials are separated into the equilib-

* Electrochemical Society Active Member.

Key words: sectioned disk, throwing power, potential distribution.

rium potential U which is associated with reaction [1], a concentration overpotential η_c, a surface overpotential η_s, and an ohmic potential Φ_o for each working electrode which is extrapolated to the surface of the electrode. The expression for the concentration overpotential (13) is

$$\eta_c = -\frac{RT}{ZF}\left[\sum_i s_i \ln\left(\frac{c_{i,\infty}}{c_{i,o}}\right) - t\left(1 - \frac{c_{1,0}}{c_{1,\infty}}\right)\right] \quad [4]$$

Equation [4] applies approximately to metal deposition from a single salt where t is the transference number of the metal ion, species 1. Z is then equal to $-z_-z_+/(z_+ - z_-)$. For the case in which the reactants and products are minor components in a solution containing an excess of supporting electrolyte, t is zero, and Z is equal to $-n$. The surface overpotential can be related to the current density by

$$i = i_o\left[\exp\left(\frac{\alpha ZF}{RT}\eta_s\right) - \exp\left(\frac{-\beta ZF}{RT}\eta_s\right)\right] \quad [5]$$

The kinetic parameters α and β are determined by the reaction taking place. The local exchange current density i_o is taken to have a composition dependence given by

$$i_o = i_{o,\infty}\prod_i\left(\frac{c_{i,o}}{c_{i,\infty}}\right)^{\gamma_i} \quad [6]$$

The γ_i's are specified by the particular reaction taking place and the condition of the surface upon which the reaction occurs, and $i_{o,\infty}$ is an exchange current density evaluated at the composition of the bulk solution. The parameter γ_i can be considered a pseudo reaction order, the values are usually determined experimentally and can be fractional. Newman (27) suggests rules for the estimation of the exponents γ_i.

Potential Distribution

The potential variation in the region of constant concentration is described by a solution of Laplace's equation which matches the current at the surface of the electrode with the mass flux through the boundary layer for a faradaic process. The particular solution found to be most suited for the ring-disk configuration operated below the limiting current is (14)

$$\Phi_o(r) = \frac{2}{\pi\kappa_\infty}\int_o^{r_2}\frac{i(r')}{r + r'}K\left(\frac{4rr'}{(r + r')^2}\right)r'dr' \quad [7]$$

The integral is evaluated at all points r' on the electrode surface where there is a nonzero value of the normal component of the current density i, K is the complete elliptic integral of the first kind (15), and r is the radial position on the surface at which Φ_o is desired. The behavior of the elliptic integral K when r is equal to r' requires special care in the numerical evaluation of Eq. [7]. The integral technique for the ring-disk system when mass transfer and kinetic effects must be considered offers real computational advantages over previously used series solutions (6) and a combination of series and integrals (5).

The primary advantage in using an integral equation rather than the combination of series and integral solutions, which is also applicable, is programming efficiency and lower computing costs. However, if the current distribution on the disk approaches the primary current distribution, the series solution can be used to compute the potential without modification. The integral technique requires the same careful handling of singular points as used in Newman and Miksis (6) for the primary current on a ring. The series solution when applied across both the ring and disk electrodes suffers from the serious inability to cope with discontinuities in the current distribution where the insulator meets the active electrode in three places.

Concentration Profile

The Lighthill transfomation has been successfully applied to the problem of evaluating the concentration profile through the diffusion boundary layer in previous examples of the calculation of current distributions below the limiting current (4, 7-10, 24, 25). The flux at the electrode surface, either the ring or the disk, can be expressed by (4)

$$\frac{\partial c_{i,o}}{\partial\zeta} = \frac{-r}{\Gamma(4/3)}\int_o^r \frac{dc_{i,o}}{dr'}\frac{dr'}{(r^3 - r'^3)^{1/3}} \quad [8]$$

and inverted to give

$$c_{i,o} - c_{i,\infty} = \frac{-1}{\Gamma(2/3)}\int_o^r \frac{\partial c_{i,o}}{\partial\zeta}\Big|_{r=r'}\frac{r'dr'}{(r^3 - r'^3)^{2/3}} \quad [9]$$

Equation [8] is equated to a flux specified by Eq. [2] or [3] and Eq. [4] and [5] and then solved for the concentration at the electrode surface. Equation [9] is used to track the surface concentration variation across the insulating annulus Equation [9] can also be manipulated to yield

$$\frac{c_{i,o} - c_{i,\infty}}{c_{j,o} - c_{j,\infty}} = \frac{s_i}{s_j}\left(\frac{D_j}{D_i}\right)^{2/3} \quad [10]$$

One species can now be chosen and conveniently designated to be subscripted as i equal to 1, then Eq. [8] need be solved for only the value of $c_{1,0}$. All other surface concentrations needed in the expression of the electrode kinetics may be computed by Eq. [10] as long as the only reaction occurring is Eq. [1].

The total current or mass transfer rate to the electrode is a quantity which must be computed as accurately as possible if a good comparison with experimentally measured currents is desired. The ratio of the ring current to the disk current is very sensitive to errors in computing the integral values. A quantity, j, proportional to the total flow of a species to the electrode surface between the limits of integration, 0 and r, is

$$j = \int_o^r \frac{\partial c_{i,o}}{\partial\zeta}r'dr' \quad [11]$$

which becomes upon substitution of Eq. [8] and one integration

$$j = \frac{-1}{2\Gamma(4/3)}\int_o^r \frac{dc_{i,o}}{dr}(r^3 - r'^3)^{2/3}dr' \quad [12]$$

Equations [8] and [12] are Stieltjes integrals, so the points at the center of the disk and the leading edge of the ring must be taken into account when evaluating the integrals. Equation [12] can be easily solved by using the method of Acrivos and Chambre (19) utilizing the same mesh points that are generated in the solution of Eq. [8].

Numerical Solution

A set of equations is now established which can be solved numerically by the same techniques given in previous work (6, 8-10). The parameters that the solution depends on are α, β, γ_i, t, r_o/r_1, r_1/r_2, Z, D_j/D_i, and

$$N = -\Gamma(4/3)\frac{nFr_2i_{LIM,DISK}}{RT\kappa_\infty} \quad [13]$$

and

$$J = \frac{i_{o,\infty}r_2nF}{RT\kappa_\infty} \quad [14]$$

and

$$\delta = |i_{avg}|\frac{r_2nF}{RT\kappa_\infty} \quad [15]$$

N is referred to species 1 so $i_{LIM,DISK}$ is the limiting current density on a disk electrode for species 1. There is a δ for both the ring and the disk, with the ap-

propriate average current density being substituted in Eq. [15]. J represents a dimensionless exchange current density.

Measures of Nonuniform Current Distributions

The problem of assessing the effect of nonuniform ohmic potential drop on arbitrarily shaped electrodes has long been of interest to electroplaters. A specific solution which will deposit an even thickness of metal over a range of current densities has been the goal of many experimental investigations and is the basis of a portion of the plating industry. Haring and Blum (16) introduced the concept of defining throwing power by a well-chosen experiment. Parallel, rectangular electrodes of equal area were connected by a solution contained within insulating planes normal to the electrode surfaces, which would give a uniform primary current on the electrodes and an easily defined primary resistance. Two cells with a primary current ratio of 5 were polarized with the same voltage, and currents were measured. The throwing power can then be computed by applying (17)

$$\text{T.P.} = \frac{\frac{I_{P1}}{I_{P2}} - \frac{I_1}{I_2}}{\frac{I_{P1}}{I_{P2}} + \frac{I_1}{I_2} - 2\frac{A_1}{A_2}} \times 100 \qquad [16]$$

I_1 and I_2 are the measured currents, I_{P1} and I_{P2} are the primary currents, and A_1 and A_2 are the areas of the electrodes. This measurement does not characterize the solution independently of the measuring device. In an unstirred cell, natural convection becomes a significant factor as the current densities are increased (23). Throwing powers measured with cells having the same electrode spacing ratio but different electrode areas are usually different. The effect of natural convection can be minimized by stirring the cells, but the effect of the stirring rates must then be assessed. Studies on membranes (18) have shown that stirring can totally obscure the measurement of desired membrane properties at a surface in a well-stirred tank. Thus it seems difficult at best to describe theoretically the Haring-Blum cell well enough to measure a throwing power that could be related to solution properties only.

The throwing power is a measurement of the deviation of a current ratio from the primary current ratio on two electrodes with different geometries. A rotating ring-disk electrode system is a good device to make this type of measurement since the primary current distribution is now known (5), and the effects of stirring are well characterized by N. Figure 1 shows the radius ratios necessary to construct a ring-disk electrode with a given average primary current density ratio. The average current density ratio must be used instead of the current ratio as in the Haring-Blum cell because the electrode areas are not equal. Throwing powers for ring-disk systems can be computed as a function of the electrode and solution parameters by setting $V_r = V_d$.

Another measure of nonuniformity is a deviation from the limiting current distribution, which is uniform on the disk but not on the ring. A useful parameter f_2 can be defined (4) as the ratio of the current to the ring, divided by the area of both the ring and the insulating gap, to the average current density on the disk.

$$f_2 = \frac{I_r}{I_d} \frac{r_0^2}{r_2^2 - r_0^2} \qquad [17]$$

The value of f_2 compared to the value for the limiting current distribution

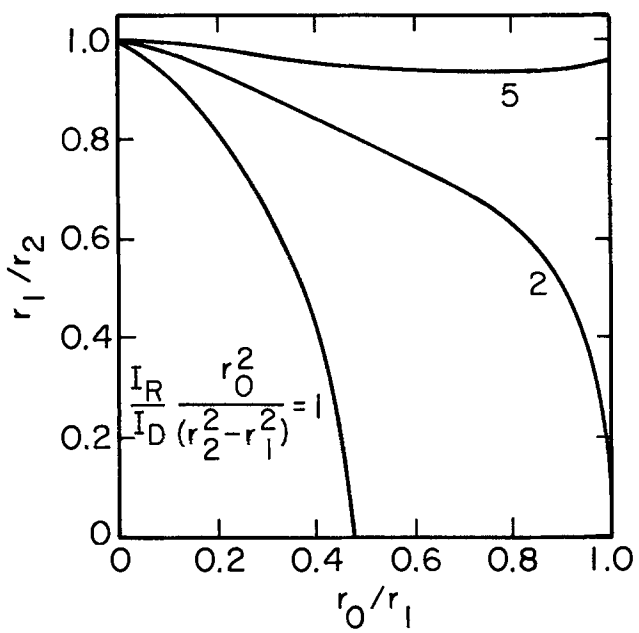


Fig. 1. Design curves for ring-disk electrodes with a given average primary current ratio.

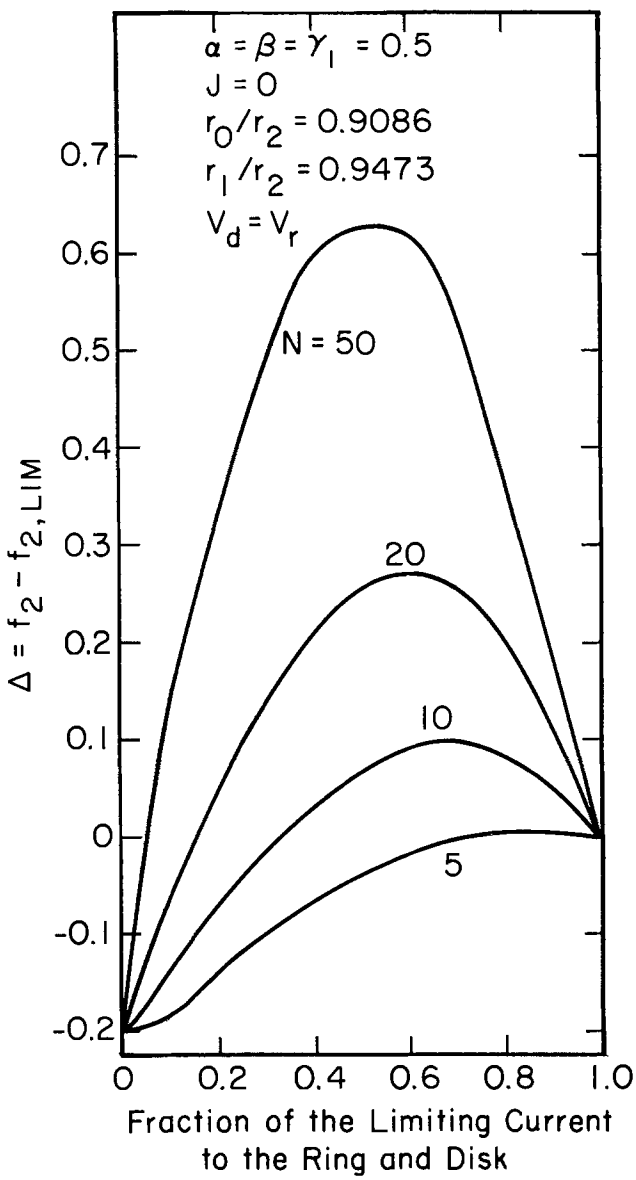


Fig. 2. The variation of Δ calculated for metal deposition from a solution with supporting electrolyte for Tafel kinetics and several stirring rates.

$$\Delta = f_2 - f_{2,\mathrm{LIM}} \qquad [18]$$

then provides the measure of deviation from the limiting distribution.

Results and Discussion

The number of possible combinations of reaction, solution, and electrode parameters is enormous. The discussion is restricted to two electrode geometries, two limiting cases, and the results of an experiment.

Tafel kinetics.—When $|i| >> i_o$, one exponential term in Eq. [5] becomes negligible in comparison to the other. For cathodic current densities, Eq. [5] may then be represented by

$$\eta_s = -\frac{RT}{\beta Z\mathbf{F}}(\ln|i| - \ln i_o) \qquad [19]$$

The other term of Eq. [5] would be retained if the current were anodic.[1] Figure 2 shows the variations of Δ for a ring-disk operated potentiostatically, with V_d set equal to V_r. At low rotation speeds or smaller values of N, little deviation from the limiting current ratios appears until the electrodes are operating appreciably below the limiting current. However, for the higher values of N, there exist large variations in Δ over the entire operating range. At very low currents, all the curves on Fig. 2 come together at $\Delta = -0.205$. Here the Tafel kinetics force the current density to be uniform and equal on the disk and ring electrodes.

Figure 3 gives the values of the throwing power for the same electrode and solution. The effect of N is reflected in the same over-all manner by Δ and by the throwing power. N becomes smaller as the electrical conductivity increases, illustrating the effect of increasing κ_∞ on the throwing power. N is proportional to r_2 and therefore gives a qualitative idea of how the characteristic dimensions of irregularly shaped objects would influence the throwing power of a given plating bath. Another interesting feature is the approximate location of the minimum in the family of throwing power curves. Limits on allowable current densities in a plating situation would be placed on either side of this point to minimize the variation of deposit thickness.

Intermediate kinetics.—The situation in which no single aspect of the concentration or surface overpotential expressions is dominant may be termed intermediate kinetics. For the same electrode used to demonstrate Tafel kinetics, a moderate dimensionless stirring rate N was chosen, and five values of the dimensionless exchange current density J were used to show the effect of concentration and surface overpotential on Δ in Fig. 4 and the throwing power in Fig. 5. When J is small and the reaction is considered slow, the current

[1] Z will be negative for reduction of an anion or oxidation of a cation. In such a case, the words anodic and cathodic should be interchanged in the text.

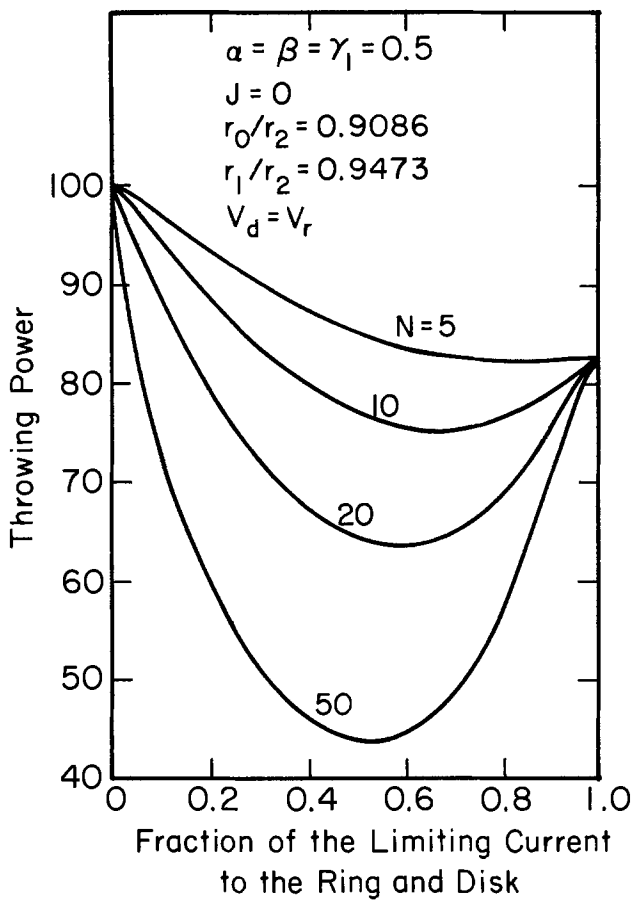


Fig. 3. The variation of the throwing power calculated for metal deposition from a solution with supporting electrolyte for Tafel kinetics and several stirring rates.

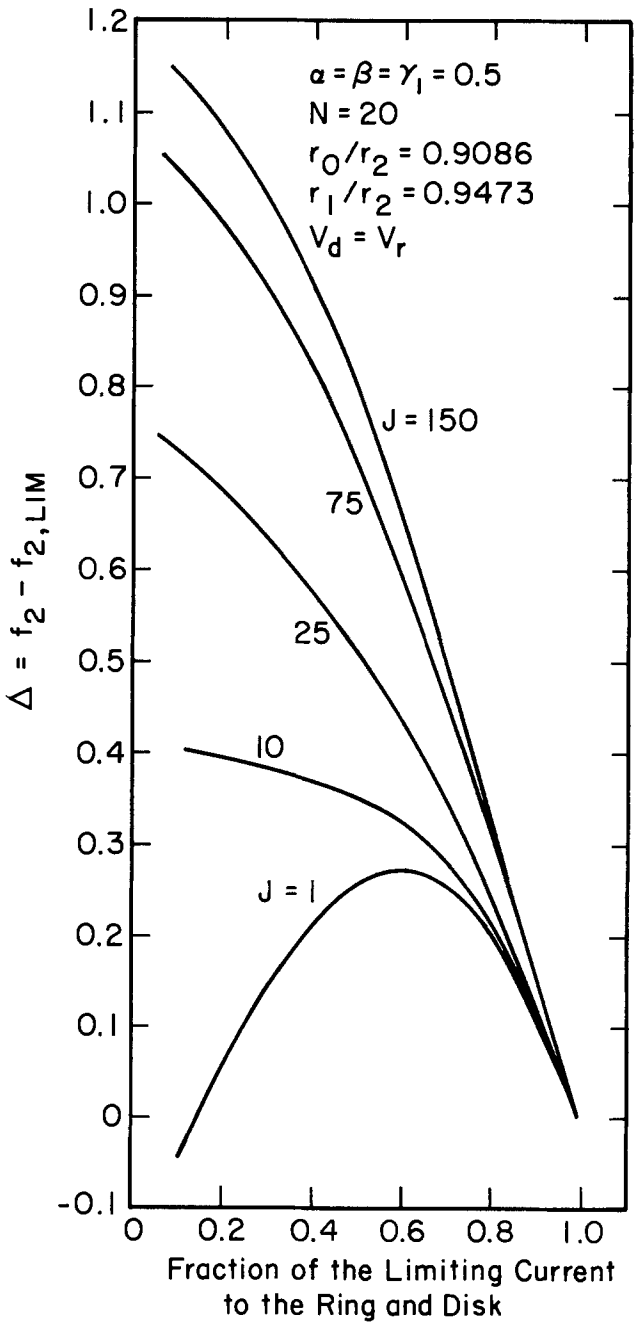


Fig. 4. Computed values of Δ for metal deposition from a solution with supporting electrolyte for a fixed stirring rate and for five values of the dimensionless exchange current density.

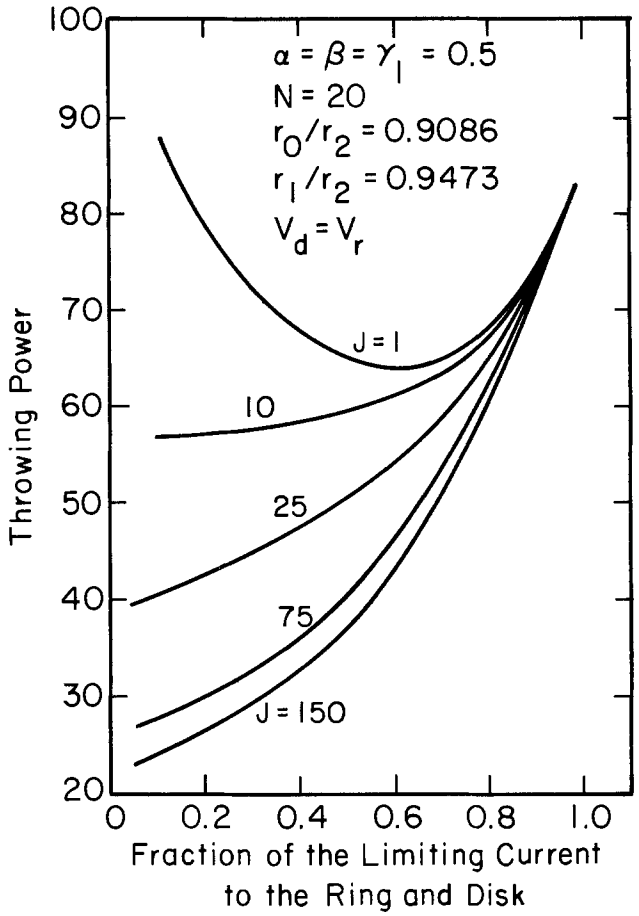


Fig. 5. Computed values of the throwing power for metal deposition from a solution with supporting electrolyte for a fixed stirring rate and for five values of the dimensionless exchange current density.

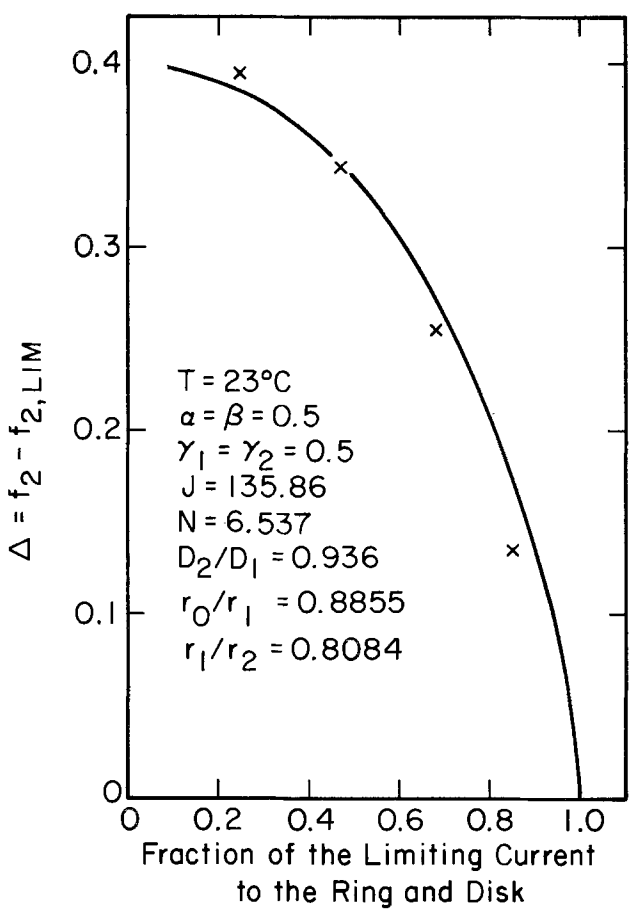


Fig 6. Δ shown as a function of the fraction of the limiting current with $V_d = V_r$. Points are measured and the smooth curve computed for a 1M KNO_3, 0.05M $K_3Fe(CN)_6$, 0.05M $K_4Fe(CN)_6$ solution. Ferrocyanide is the reference species and is being oxidized at the electrodes.

distribution is quite uniform for small fractions of the limiting current. This corresponds to $\Delta = -0.205$ for this geometry. For larger values of J, the surface overpotential becomes less important. The current distribution would approach a primary distribution for smaller values of the average current (and high rotation speeds). This corresponds to $\Delta = 1.977$ and a throwing power of zero for this geometry. The behavior at high average currents is determined more by the effect of mass transfer, and the influence of kinetic parameters decreases.

Comparison with experiment.—The smooth curve in Fig. 6 is the computed variation of Δ for curve A of Fig. 1 in the work of Smryl and Newman (4), and the points are experimentally determined (20). The values of α, β, γ_1, and γ_2 are taken from the literature (21) for the ferricyanide-ferrocyanide redox couple. The value of the exchange current density used to compute J was estimated with Eq. [6] from the experimentally determined value reported by Vetter (22). The conductivity of the bulk solution was determined to be 0.0894 Ω^{-1}-cm^{-1} in our laboratory, thus yielding a somewhat different value of N from that estimated earlier (4). The remaining parameters were measured (20). Good agreement between the computation and the experiment is shown.

Acknowledgments

This work was supported by the United States Energy Research and Development Administration.

Manuscript submitted Sept. 16, 1976; revised manuscript received Jan. 12, 1977.

Any discussion of this paper will appear in a Discussion Section to be published in the December 1977 JOURNAL. All discussions for the December 1977 Discussion Section should be submitted by Aug. 1, 1977.

Publication costs of this article were assisted by the University of California, Berkeley.

LIST OF SYMBOLS

English characters

A_1, A_2	area of electrode 1 or 2, cm^2
a	0.51023
c_i	concentration of species i, mole/cm^3
$c_{i,o}$	concentration of species i at the electrode surface, mole/cm^3
$c_{i,\infty}$	concentration of the ith species in the bulk solution, mole/cm^3
D_i	diffusion coefficient of the ith species, cm^2/sec
f_2	dimensionless ratio of ring to disk current densities, see Eq. [17]
$f_{2,LIM}$	Eq. [17] applied to the limiting current distribution
F	Faraday's constant, 96,487 C/equiv.
i	normal current density at the electrode surface, A/cm^2
i_o	local exchange current density, A/cm^2
$i_{o,\alpha}$	characteristic exchange current density, A/cm^2
$i_{LIM,DISK}$	limiting current density for species 1 on a disk electrode, A/cm^2
I_{P1}	primary current for electrode 1, A
I_{P2}	primary current for electrode 2, A
I_1	current to electrode 1, A
I_2	current to electrode 2, A
j	proportional to the average or total mass transfer rate, mole/cm
J	dimensionless exchange current density
M_i	chemical symbol for the species i
N	dimensionless stirring rate
n	number of electrons in reaction

R universal gas constant, 8.3143 J/mole-°K
r radial coordinate, cm
r_o radius of disk electrode, cm
r_1 inner radius of ring electrode, cm
r_2 outer radius of ring electrode, cm
s_i stoichiometric coefficient of ith species
t transference number of reactant
T absolute temperature, °K
T.P. throwing power, see Eq. [16]
U open-circuit potential, V
V_d potential applied between the disk and the counterelectrode, V
V_r potential applied between the ring and the counterelectrode, V
y normal distance from the surface, cm
z_i charge number of ith species
Z $-n$ or $-z_+z_-/(z_+ - z_-)$

Greek characters

α, β parameters in Eq. [5]
γ_i parameters in Eq. [16]
δ dimensionless average current density
Δ dimensionless deviation of f_2 from limiting current f_2, see Eq. [18]
ζ dimensionless normal distance from surface, $y(a_\nu/3D_i)^{1/3}(\Omega/\nu)^{1/2}$
η_c concentration overpotential, V
η_s surface overpotential, V
κ_∞ electrical conductivity of the bulk solution, Ω^{-1}-cm^{-1}
ν kinematic viscosity
Φ_o potential extrapolated to the surface, V
Ω rotation speed, rad/sec

REFERENCES

1. S. Bruckenstein and B. Miller, *This Journal*, **117**, 1044 (1970).
2. B. Miller and M. I. Bellavance, *ibid.*, **120**, 42 (1973).
3. W. H. Smryl and J. Newman, *ibid.*, **119**, 208 (1972).
4. W. H. Smryl and J. Newman, *ibid.*, **119**, 212 (1972).
5. J. J. Miksis, Jr. and J. Newman, *ibid.*, **123**, 1030 (1976).
6. J. Newman, *ibid.*, **113**, 1235 (1966).
7. W. R. Parrish and J. Newman, *ibid.*, **116**, 169 (1969).
8. W. R. Parrish and J. Newman, *ibid.*, **117**, 43 (1970).
9. K. Nisancioğlu and J. Newman, *ibid.*, **121**, 241 (1974).
10. P. Pierini, P. Appel, and J. Newman, *ibid.*, **123**, 366 (1976).
11. V. G. Levich, "Physiochemical Hydrodynamics." p. 107, Prentice-Hall, Englewood Cliffs, N.J. (1962).
12. V. G. Levich, *Acta Physiochim. URSS*, **17**, 257 (1942).
13. J. Newman, *Int. J. Heat Mass Transfer*, **10**, 983 (1967).
14. J. Newman, in "Electroanalytical Chemistry," Vol. 6, A. J. Bard, Editor, p. 326, Marcel Dekker, New York (1973).
15. M. Abramowitz and I. A. Stegun, Editors "Handbook of Mathematical Functions," p. 608, National Bureau of Standards, Washington, D.C. (1964).
16. H. E. Haring and W. Blum, *Trans. Electrochem. Soc.*, **44**, 313 (1923).
17. T. P. Hoar and J. N. Agar, *Discuss. Faraday Soc.*, **1**, 162 (1947).
18. C. K. Colton and K. A. Smith, *AIChE J.*, **18**, 958 (1972).
19. A. Acrivos and P. L. Chambre, *Ind. Eng. Chem.*, **49**, 1025 (1957).
20. W. H. Smryl, Private communication (1975).
21. F. A. Posey and S. S. Misra, *This Journal*, **113**, 608 (1966).
22. K. J. Vetter, "Electrochemical Kinetics," p. 493, Academic Press, New York (1967).
23. Ch. W. Tobias and R. Hickman, *Z. Phys. Chem.*, **229**, 145 (1965).
24. R. V. Homsy and J. Newman, *This Journal*, **121**, 1448 (1974).
25. R. Alkire and A. A. Mirarefi, *ibid.*, **120**, 1507 (1973).
26. R. Cabán and T. W. Chapman, *ibid.*, **123**, 1036 (1976).
27. J. Newman, "Electrochemical Systems," p. 174, Prentice-Hall, Englewood Cliffs, N.J. (1973).

Electrochemical Removal of Silver Ions from Photographic Fixing Solutions Using a Porous Flow-Through Electrode

John Van Zee and John Newman*

Department of Chemical Engineering, University of California, Berkeley, California 94720

ABSTRACT

Silver ions were removed from a simulated photographic fixing solution by using a porous flow-through electrode. A feed of 1000 mg/liter of silver was reduced to less than 1 mg/liter in a 5.5 cm thick bed and to less than 10 mg/liter in a 4.0 cm thick bed. The flow rate in both cases was 22 cm^3/min across a superficial area of 61 cm^2. Side reactions reduced the current efficiency to 45% at these low product concentrations. Optimization of incremental power costs and recovered silver value suggests that further reduction of silver concentration is economical.

Motion-picture laboratories remove silver from fixing baths by electrochemical methods because (*i*) the operations can handle large volumes, (*ii*) the fixer can be reused, and (*iii*) the recovered silver is of high purity. Existing electrolytic systems categorized as low current density operations (about 0.1 mA/cm^2) require extensive space to accommodate large volumes of fixing solution. So-called high current density systems (about 10 mA/cm^2) require additional electricity for solution agitation; this agitation is produced by internal paddles, external pumping, or moving electrodes.

Although not specifically investigated here, waste-stream quality standards provide another incentive for silver recovery. Current practice (1) is to dump effluent stream with a silver concentration of up to 100 mg/liter while existing California standards (2) specify 0.02 mg/liter. Hence economical recovery of silver to satisfy this thousandfold discrepancy would be welcome.

The use of porous, fixed, flow-through electrodes for trace metal recovery is suggested by Bennion and Newman (3). The porous electrode provides a large plating area per unit volume with flakes and chips of graphite. A low flow rate allows the solution to be gravity fed. The application of the porous elec-

* Electrochemical Society Active Member.
Key words: waste-water treatment, metal recovery.

trode to silver recovery in motion-picture laboratories realizes the space advantages of high density systems without requiring operating expense for agitation.

Design Problem

It is desirable to maintain the silver concentration of fixing baths below 5000 mg/liter, and many present-day systems are capable of maintaining a concentration of 500 mg/liter. Tailing cells are used to reduce the 500 mg/liter to less than 100 mg/liter in the plant effluent. Thus, a reasonable cell design objective is the reduction of silver ion concentration from 1000 to 10 mg/liter.

Current efficiencies of 75% are considered high in existing operations due to the presence of side reactions. The silver deposition reaction

$$Ag(S_2O_3)_2^{-3} + e^- + 2H^+ \rightarrow 2HS_2O_3^- + Ag \quad [1]$$

must compete with reduction of thiosulfate (4)

$$S_2O_3^{-2} + 8e^- + 8H^+ \rightarrow 2HS^- + 3H_2O \quad [2]$$

which may lead to an alternative mechanism of silver removal

$$HS^- + 2Ag(S_2O_3)_2^{-3} + 3H^+ \rightarrow Ag_2S + 4HS_2O_3^- \quad [3]$$

To reduce the occurrence of the side reactions, the porous electrode is designed for a specified ohmic potential drop in the solution phase. A value of -0.1V is used in the following design calculation. The electrode is designed by using the equations of Bennion and Newman (3) and the parameters in Table I. The Wilson and Geankoplis correlation (5) is used for calculation of the mass-transfer coefficient. The design results are also shown in Table I.

Experimental Equipment and Procedure

The experimental cell used varies only in size from the porous electrode built by Bennion; the bed diameter is 8.8 cm. The cathode was packed with irregularly shaped carbon particles (Union Carbide granules plus powder, GP-22), and the anode was packed with a mixture of carbon and copper powder. Two sheets of Whatman 40 filter paper backed the feed-side Plexiglas plates and facilitated tight packing of the beds.

A saturated calomel cell was used for measurement of the potential between the reduced silver product stream and the cathode (VDP). The circuit consisted of a d-c power supply with the ground attached to the cathode. The power lead went to a 1Ω resistor and then to the cell anode. The potential drop across the resistor was measured and recorded on a strip-chart recorder. The potential drop between the dilute product stream and the cathode (VDP) was measured and recorded on another strip-chart recorder. A multimeter was used to measure the potential drop across the power supply. A digital voltmeter was used to verify and calibrate the recorders and multimeter. The two recorders were used to observe trends and to establish when steady state was attained.

Flow rates of the feed, reduced silver product, and anolyte streams were controlled with needle valves. Float-type glass flowmeters were used to measure relative fluctuations in the flow rate. A graduated cylinder and a stopwatch were used for verification of the reported flow rate. The cathode flow rate was about 99% of the feed flow rate. Flow was induced by gravity. The room temperature fluctuated between 21° and 25°C.

Table I. Sample design calculation

Input parameters		Design results
c_{in} = 1000 mg/liter	ρ = 1.18 g/cm³	v = 7.9 × 10⁻³ cm/sec
c_{out} = 10 mg/liter	D = 10⁻⁵ cm²/sec	L = 1.32 cm
κ_0 = 0.123 mho/cm	μ = 0.018 g/cm-sec	Re = 0.087
ϵ = 0.3	ρ_{Ag} = 10.5 g/cm³	t = 0.7 day
$\Delta\Phi_2$ = −0.1V	M_{Ag} = 107.87 g/mol	k_m = 1.10 × 10⁻³ cm/sec
a = 25 cm⁻¹	Sc = 1525	

Table II. Feed composition

	Grams
Sodium thiosulfate ($Na_2S_2O_3 \cdot 5H_2O$)	20
Sodium bisulfite ($NaHSO_3$)	1
Silver nitrate ($AgNO_3$)	0.16
Sodium bromide (NaBr)	0.13
Water (78.9 ml)	78.7

The feed composition is listed in Table II. Actual fixing baths contain gelatin due to dissolution of film material. If actual bath solutions cause plugging of the porous electrode, it would be necessary to use a filter in the feed line. Nitrate ions, which were introduced with the silver when preparing the simulated photographic fixing solution, are not present in typical commercial fixing baths.

The feed and product concentrations were analyzed with a Perkin Elmer Model 303 atomic absorption spectrophotometer. Concentrations below 20 mg/liter were measured directly. Concentrations above 20 mg/liter were diluted by volume to the 20 mg/liter range. Two samples were analyzed for each run, and the maximum variation was ±3%.

In all experimental runs the cell was oriented with the cathode above the anode. The cell was inverted to change the cathode thickness from 5.5 to 4.0 cm. The cell was inverted after all the initially packed copper powder had been dissolved and the oxidation of thiosulfate ($S_2O_3^{-2}$) to tetrathionate ($S_4O_6^{-2}$) dominated the anode reaction for eight runs. By inverting the cell, the feasibility of a third anode reaction, dissolution of silver metal, was verified.

Results

Figure 1 shows the relationship of total cell current and VDP for the two bed thicknesses. Dilute product concentrations (in milligrams of Ag/liter) are shown below the experimental points. The theoretical limiting current is sketched to illustrate the

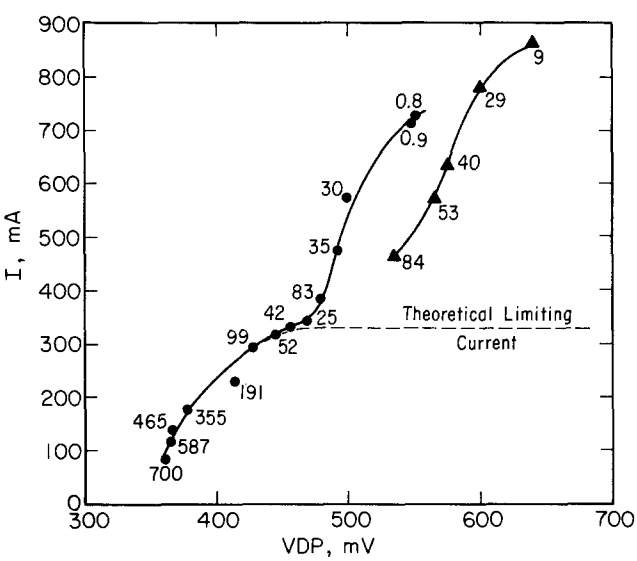


Fig. 1. Current-voltage curves. Superficial electrode area = 61 cm². Flow rate = 22 cm³/min. Electrode thickness: ● = 5.5 cm, ▲ = 4.0 cm. Feed concentration = 1000 mg Ag/liter. Numbers below points are dilute product concentration in milligrams of Ag/liter. VDP is the potential of a saturated calomel cell in the dilute product stream vs. the cathode.

extent of side reactions. The feed concentration increased by 6% due to evaporation losses. Approximately 2 hr were required to reach steady state after each change in the power source potential. Steady state was observed when the total current and VDP remained constant for 1/2 hr.

Discussion

The current-voltage curves for both thicknesses display the same general shape. The large VDP shift between the curves is unexplained at present. The interruption of decreasing dilute product concentrations between VDP of 460 and 490 mV is also unexplained.

The extent of side reactions is shown by the graph of current efficiency *vs.* total current (Fig. 2). (The current required by reaction [1] is calculated from the measured inlet and outlet concentrations of silver and the flow rate. The ratio of this result to the total current is the current efficiency.) The general shape of the graph is expected; that is, current efficiency drops as total current is increased. Current efficiencies greater than 1 may point to inaccuracies in velocity, concentration, or current measurements.

The specific side reactions were not identified; however, no gassing was observed, and hence evolution of hydrogen is doubtful. Reaction [2] has been cited in the literature. The characteristic black suspension of silver sulfide (Ag_2S) was not evident in the dilute product stream. It is possible that Ag_2S was filtered from the dilute product stream by the graphite bed. There was no discernable adverse plugging of the electrode. Another possible side reaction is the reduction of thiosulfate to $S_2O_4^=$.

It is feasible to calculate the superficial area per unit volume, a, by using the correlation of Wilson and Geankoplis, Bennion and Newman's limiting current expression, and the experimental data. With $D = 10^{-5}$ cm²/sec. the value of a ranged from 8 to 13 cm^{-1}. This is about half the value assumed in the design calculation. Another interpretation is that the correlation of Wilson and Geankoplis predicts too high a value of the mass-transfer coefficient, at least for deep beds where aL is greater than 100. The design equations used by Bennion and Newman actually give values of a closer to 25 cm^{-1}.

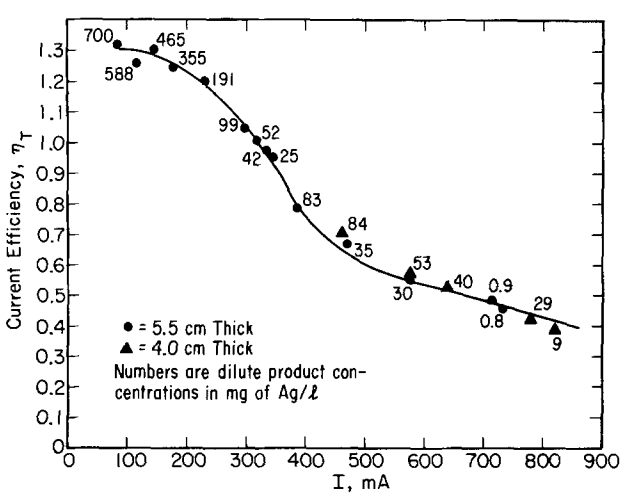


Fig. 2. Current efficiency-total current curves

Optimization.—The presence of nongassing side reactions permits an interesting optimization of the operating current such that incremental power costs are just balanced by the incremental value of recovered silver. The optimum current can be determined by differentiation of the total cost, with the result

$$C_p d(VI) = -C_{Ag} Q d(c_{out}) \quad [4]$$

where C_p = power costs (\$/J), C_{Ag} = silver value (\$/g), Q = flow rate (cm³/sec), VI = power applied to cell (W), and c_{out} = effluent Ag concentration (g/cm³).

The resistance of the cell was on the order of 5Ω; that is, $V = 5I$. An optimum current greater than 2A was determined from the experimental flow rate and typical costs. This optimum indicates that the effluent silver concentration can be economically reduced further despite the low current efficiencies.

Mauscript submitted Nov. 5, 1975; revised manuscript received Nov. 22, 1976.

Any discussion of this paper will appear in a Discussion Section to be published in the December 1977 JOURNAL. All discussions for the December 1977 Discussion Section should be submitted by Aug. 1, 1977.

LIST OF SYMBOLS

a	effective interfacial area of electrode packing per unit volume of electrode, cm^{-1}
c_{in}	inlet concentration of silver
c_{out}	concentration of silver in effluent stream
C_{Ag}	value of silver recovered, \$/g
C_p	electric power cost, \$/J
D	diffusion coefficient of soluble silver species, cm²/sec
I	cell current, A
k_m	mass transfer coefficient between electrode and flowing stream, cm/sec
L	electrode thickness, cm
M_{Ag}	molecular weight of silver, g/mole
Q	volumetric flow rate, cm³/sec
Re	$= v\rho/a\mu$, Reynolds number
Sc	$= \mu/\rho D$, Schmidt number
t	time required to plug electrode, days
v	superficial flow velocity, cm/sec
V	cell potential, V
ϵ	porosity or void volume fraction of electrode
κ_0	conductivity of feed solution, Ω^{-1}-cm^{-1}
μ	viscosity of feed solution, g/cm-sec
ρ	density of feed solution, g/cm³
ρ_{Ag}	density of metallic silver, g/cm³
$\Delta\Phi_2$	allowed variation of potential of the solution within the electrode, V

REFERENCES

1. M. L. Schreiber, *J. Soc. Motion Pict. Eng.*, **74**, 505 (1965).
2. "Water Quality Control Plan, Ocean Waters of California," State Water Resources Control Board, Chapter IV, Table B, Effective July 1972
3. D. N. Bennion and J. Newman, *J. Appl. Electrochem.*, 2, 113 (1972).
4. K. Hickman, W. Weyerts, and O. E. Goehler, *Ind. Eng. Chem.*, 25, 202 (1933).
5. E. J. Wilson and C. J. Geankoplis, *Ind. Eng. Chem., Fundam.*, 5, 9 (1966).

Current Distribution on a Continuous Moving Sheet Electrode

K. Viswanathan* and D-T. Chin†

Department of Chemical Engineering, Clarkson College of Technology, Potsdam, New York 13676

ABSTRACT

A theoretical study has been made to characterize the electrochemical behavior of a continuous moving flat surface. The current distribution on the electrode is calculated by taking into account concentration polarization, activation overpotential, and ohmic potential drop in the electrolyte. Numerical results are presented for the Butler-Volmer electrokinetics. It is shown that the current distribution depends on the magnitude of the limiting current. A uniform current distribution can be achieved if the current level is less than 78.5% of the limiting current.

Continuous moving electrodes are used in moving cathode processes such as electrolysis of brine and in electroplating of sheet metals and wires (1). The flow on a continuous moving sheet electrode is of a novel type which has characteristics opposite to the boundary layer on a stationary flat plate (2). The rate of laminar mass transfer to the electrode is proportional to the square root of the Schmidt number instead of a cube root relationship for most known electrolyte flow systems (3). This gives the continuous moving electrodes a higher limiting current density at large Schmidt numbers; at Sc = 1000, for example, the limiting current is enhanced by a factor of $Sc^{1/6} = 3.2$. In this study the nature of a continuous moving sheet electrode is further characterized with a theoretical study. Using the method illustrated by Newman (4), the surface concentration and the potential and current distribution on a continuous moving sheet electrode have been calculated on a digital computer. Numerical results are presented for the Butler-Volmer electrokinetics. This paper describes the details of the study.

Mathematical Analysis

To set up a mathematical model for current distribution we consider one side of a continuous flat sheet electrode which is moving with a constant velocity U_s through an otherwise undisturbed electrolyte as shown in Fig. 1. The velocity of the electrode is high such that the boundary layer approximation can be used to describe the flow of electrolyte near the electrode surface. The counterelectrode is located at a distance b from the moving electrode, and the cell walls are made of an insulation material. To simplify the analysis, we shall make the following assumptions: (*i*) The continuous moving electrode and the counterelectrode are of equal potential bodies; (*ii*) the concentration overpotential and the activation overpotential at the counterelectrode are zero; (*iii*) there is a supporting electrolyte present in the solution so that migration of the reactive ions is negligible; (*iv*) the ohmic potential drop across the concentration boundary layer is negligibly small compared to the ohmic potential drop across the bulk of the electrolyte; (*v*) the electrolyte flow in the vicinity of the moving electrode is laminar in nature; (*vi*) the presence of the cell wall and the counterelectrode does not affect the flow boundary layer on the continuous moving electrode; and (*vii*) the physical properties of the electrolyte are constant. The governing equations describing an electrochemical process at the continuous electrode are

voltage balance

$$E = \eta_a + \eta_{conc} + \phi_{ohm} \qquad [1]$$

Butler-Volmer equation of electrode kinetics

$$i = i_0\left(\frac{C_s}{C_\infty}\right)^\gamma \left[\exp\left(\frac{\alpha n\mathbf{F}}{RT}\eta_a\right) - \exp\left(-\frac{\beta n\mathbf{F}}{RT}\eta_a\right)\right] \qquad [2]$$

concentration overpotential

$$\eta_{conc} = \frac{RT}{n\mathbf{F}} \ln \frac{C_s}{C_\infty} \qquad [3]$$

Here E is the difference between the applied cell voltage and the thermodynamic equilibrium cell voltage, i_0 is the exchange current density based on the bulk concentration of the reacting ion. All the other notations have their usual meanings.

To calculate the surface concentration C_s one needs a convective diffusion equation to describe the transport of the reactive ion from the bulk to the electrode surface

convective diffusion

$$U\frac{\partial C}{\partial x} + V\frac{\partial C}{\partial y} = D\frac{\partial^2 C}{\partial y^2} \qquad [4]$$

The boundary conditions are

$$C = C_\infty \quad \text{at} \quad x = 0 \quad \text{and} \quad y = \infty \qquad [5]$$

$$\frac{\partial C}{\partial y} = \frac{i}{n\mathbf{F}D} \quad \text{at} \quad y = 0 \qquad [6]$$

Here x is the surface distance from the inlet of the continuous moving sheet electrode, y is the perpendicular distance from the electrode surface, U and V are the velocity components of the electrolyte along the x and y directions, respectively. Equations [4]-[6] would give a variable surface concentration along the x direction. The standard procedure for the solution is (*i*) to obtain a solution for the case of a constant surface concentration, *i.e.*, a solution with Eq. [6] replaced with $C = C_s$ at $y = 0$ for all x; and (*ii*) to apply a superposition integral to the resulting equation to obtain a solution for variable surface concentrations. Chin (3)

* Electrochemical Society Student Member.
† Electrochemical Society Active Member.
Key words: convective diffusion, limiting current, electrode kinetics.

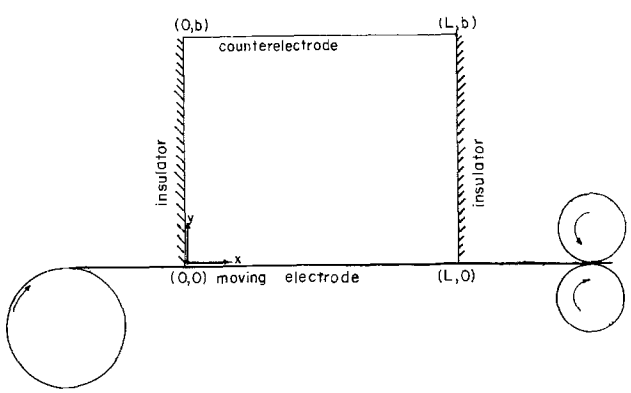


Fig. 1. Schematic diagram of the continuous moving sheet electrode.

has obtained an asymptotic solution of Eq. [4] for the uniform surface concentration conditions. At high Schmidt numbers, his result can be expressed as

$$C = C_\infty + (C_s - C_\infty)\,\mathrm{erfc}\left(\frac{y}{2}\sqrt{\frac{U_s}{Dx}}\right) \qquad [7]$$

(for uniform surface concentration and Sc >> 1) where erfc designates the complementary error function. It is interesting to note that this result coincides with the well-known penetration theory of a falling liquid film (5). By applying Duhamel's superposition integral theorem (6) to Eq. [7], one has a pair of stieltjes integrals

$$i(x) = n\mathbf{F}\sqrt{\frac{U_s D}{\pi}}\int_0^x \left(\frac{dC_s}{dx}\right)_{x=t}\frac{dt}{\sqrt{x-t}} \qquad [8a]$$

or

$$C_s(x) = C_\infty + \frac{1}{n\mathbf{F}\sqrt{\pi U_s D}}\int_0^x i(t)\,\frac{dt}{\sqrt{x-t}} \qquad [8b]$$

(for variable surface concentrations and Sc >> 1). Here i is the local current density at the electrode surface and t is a dummy variable.

In addition, one needs a Laplace equation to calculate the ohmic potential drop in the cell, ϕ_{ohm}

Laplace equation

$$\frac{\partial^2\phi}{\partial x^2} + \frac{\partial^2\phi}{\partial y^2} = 0 \qquad [9]$$

The boundary conditions are

$$\left.\begin{aligned} \phi &= 0 && \text{at } y = b \\ \frac{\partial\phi}{\partial x} &= 0 && \text{at } x = 0 \text{ and } x = L \\ \frac{\partial\phi}{\partial y} &= -\frac{i}{\kappa} && \text{at } y = 0 \end{aligned}\right\} \qquad [10]$$

where ϕ is the electric potential in the electrolyte, κ is the electrolyte conductivity, b is the distance between the moving and the counterelectrodes, and L is the length of the moving electrode inside the cell. It should be noted that the boundary conditions are so chosen that ϕ_{ohm} is equal to $\phi(x, 0)$. Equations [9] and [10] have been solved with the method of separation of variables. The solution for the ohmic potential drop across the cell can be expressed in terms of a Fourier cosine series

$$\phi_{ohm}(x) = \frac{b}{L\kappa}\int_0^L i(t)\,dt + \sum_{m=1}^{\infty}\frac{2}{m\pi\kappa}\tanh\frac{m\pi b}{L}\cos\frac{m\pi x}{L}\int_0^L i(t)\cos\frac{m\pi t}{L}\,dt \qquad [11]$$

We now have five equations to describe the electrochemical reaction at the continuous moving sheet electrode. They are Eq. [1], [2], [3], [8], and [11]. These equations are strongly coupled and simultaneous solution is required to find the five unknowns, *i.e.*, the activation overpotential η_a, the concentration overpotential η_{conc}, the ohmic potential drop ϕ_{ohm}, the surface concentration C_s,and the local current density at the electrode i. In order to obtain a more generalized solution and to reduce the number of parameters for the calculation, we introduce the following dimensionless quantities

$$X = x/L; \qquad b^* = b/L; \qquad C_s^* = C_s/C_\infty$$

$$\eta_a^* = \frac{n\mathbf{F}}{RT}\eta_a; \quad \eta_{conc}^* = \frac{n\mathbf{F}}{RT}\eta_{conc}; \quad \phi_{ohm}^* = \frac{n\mathbf{F}}{RT}\phi_{ohm}$$

$$E^* = \frac{n\mathbf{F}}{RT}E; \qquad i^* = \frac{n\mathbf{F}}{RT}\frac{L}{\kappa}i \qquad [12]$$

Substituting Eq. [12] into Eq. [1], [2], [3], [8], and [11] we have

voltage balance

$$E^* = \eta_a^* + \eta_{conc}^* + \phi_{ohm}^* \qquad [13]$$

Butler-Volmer's rate expression

$$i^* = \xi C_s^{*\gamma}[\exp(\alpha\eta_a^*) - \exp(-\beta\eta_a^*] \qquad [14]$$

concentration overpotential

$$\eta_{conc}^* = \ln C_s^* \qquad [15]$$

surface concentration

$$i^* = N\int_0^X \left(\frac{dC_s^*}{dX}\right)_{X=t}\frac{dt}{\sqrt{X-t}} \qquad [16]$$

ohmic potential drop

$$\phi_{ohm}^* = b^*\int_0^1 i^* dt + \sum_{m=1}^{\infty}\frac{2}{m\pi}\tanh(m\pi b^*)\cos(m\pi X)\int_0^1 i^*\cos(m\pi t)\,dt \qquad [17]$$

Here t is a dummy variable. The transfer coefficients α and β are usually equal to 0.5. For the first-order electrochemical reactions the parameter γ is equal to 0.5. There are two significant parameters in the above equations; they are

average dimensionless limiting current density

$$N = \frac{n^2\mathbf{F}^2 DC_\infty}{RT\kappa\sqrt{\pi}}\sqrt{\mathrm{Re_L Sc}} = -\frac{1}{2}\int_0^1 i_{lim}^*\,dX \qquad [18]$$

dimensionless exchange current density

$$\xi = \frac{n\mathbf{F}L}{RT\kappa}i_o \qquad [19]$$

where $\mathrm{Re_L} = U_s L/\nu$ and $\mathrm{Sc} = \nu/D$.

The average limiting current density N represents the ratio of ohmic potential drop to the concentration overpotential at the electrode. A large value of N implies that the ohmic resistance tends to be the controlling factor for the current distribution. For small values of N, the concentration overpotential is large and the mass transfer tends to be the rate-limiting step of the over-all process. The dimensionless exchange current density ξ, on the other hand, represents the ratio of the ohmic potential drop to the activation overpotential. When both N and ξ approach infinity, one obtains the geometrically dependent primary current distribution.

Numerical Results and Discussion

Using the method illustrated by Newman (4), we have solved Eq. [13]-[17] numerically on an IBM 360/44 digital computer for the unknowns η_a^*, η_{conc}^*, ϕ_{ohm}^*, C_s^*, and i^*. We considered a simple first-order cathodic reaction with $\alpha = \beta = \gamma = 0.5$.

Figures 2 and 3 show the current and the surface concentration distributions for various current levels at the leading edge for $N = 50$, $\xi = 1$, and $b^* = 1$. The vertical axis in Fig. 2 is the local current density divided by the geometric average limiting current density at the electrode. The horizontal axis is the dimensionless surface distance from the entrance point of the continuous moving electrode. The average current density of these curves is also shown in the figure. It is seen that at a low current level of $i/(i_{lim})_{avg} = 0.096$, the current profile is almost flat. This is because the concentration polarization is small, and one has a secondary current distribution which is uniform for this geometry. As the average current density increases, the profile has a pronounced steep region near the leading ($X = 0$) and the trailing ($X = 1$) edges. The current density is highest at the leading edge where the concentration boundary layer is thin and the rate of mass

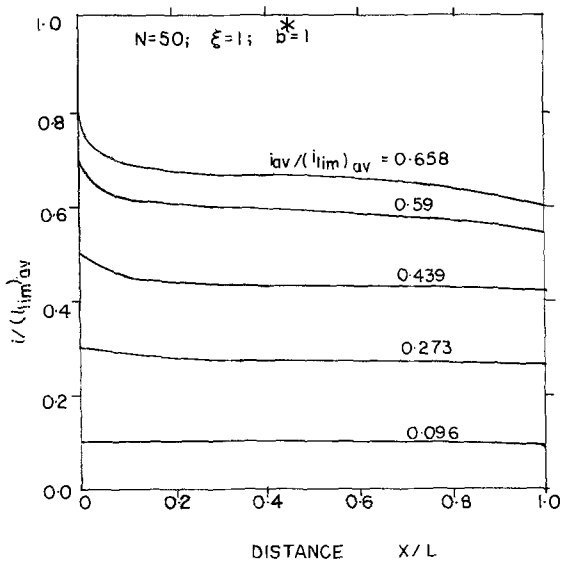


Fig. 2. Current distribution for $N = 50$; $\xi = 1$; and $b^* = 1$ at various specified current levels.

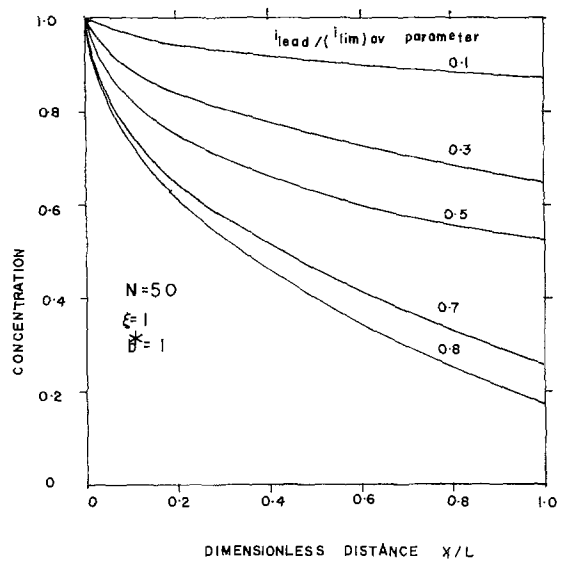


Fig. 3. Surface concentration distribution for $N = 50$; $\xi = 1$; $b^* = 1$ at various specified current levels.

transfer is high. At the trailing edge, the effect of concentration polarization is important, and the current density becomes smaller than the average value. Figure 3 shows that the surface concentration is equal to the bulk concentration at the leading edge and decreases sharply with increasing distance along the electrode surface. As expected, the surface concentration distribution is most uniform for the smallest current level.

Figure 4 shows the effect of N on the current distribution for $\xi = 100$, $i(0)/i(_{\text{lim}})_{\text{avg}} = 0.8$, and $b^* = 1$. Also shown in the figure is a limiting current curve designated by $i_{\text{avg}}/(i_{\text{lim}})_{\text{avg}} = 1$. It is interesting to note that for large values of N, the current densities exceed the limiting current density locally near the trailing edge. The same phenomena is also reported for the rotating spherical electrode (7). As the value of N increases, the mass transfer proceeds faster, and the current distribution becomes more uniform.

For this geometry, the primary current distribution is uniform; the secondary current distribution which is obtained by letting $N \to \infty$ is also uniform. As a consequence, the dimensionless exchange current density ξ, is not an important parameter. Our calculation for different values of ξ ranging from 0.0001 to 100 in-

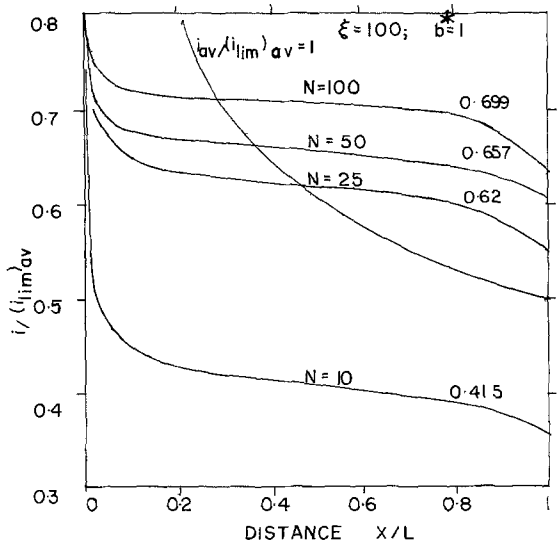


Fig. 4. Current distribution for $\xi = 100$ and $b^* = 1$ for various values of N when $i_{\text{leading}}/(i_{\text{lim}})_{\text{avg}}$ was set equal to 0.8.

dicates that the current distribution is virtually independent of ξ at $N = 100$. For smaller values of N, the effect of ξ is greater; in general, the smaller the value of ξ, the more uniform is the current distribution. The effect of electrode spacing on the current distribution at the continuous moving electrode is shown in Fig. 5. It is seen that the current density becomes more uniform as the value of b^* increases. This is because the ohmic drop in the solution tends to be the dominant term when the electrode spacing is large. The effect is more pronounced when N is large. For smaller values of N, the process tends to be mass transfer limited and the concentration overpotential becomes more important.

Conditions for uniform current distributions.—The results shown in Fig. 4 suggest that a uniform current

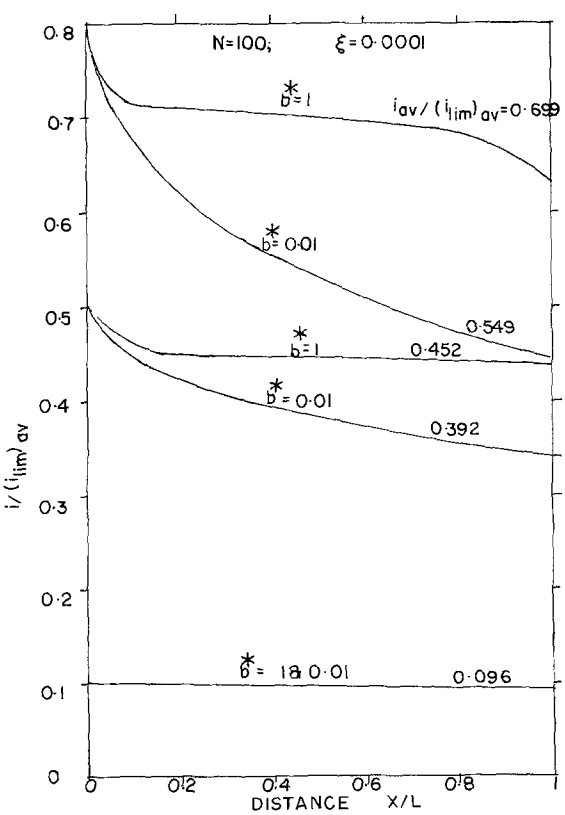


Fig. 5. Effect of electrode spacing on current distributions

distribution can be achieved at the continuous moving sheet electrode when the values of N are large. It can be shown from Eq. [8b] that at a constant flux condition, the surface concentration is described by the following relation

$$C_s^* = 1 - \frac{4}{\pi} \frac{i^*}{(i_{lim}^*)_{avg}} \sqrt{X} \qquad [20]$$

Here $(i_{lim}^*)_{avg}$ is the geometric average of the dimensionless limiting current density; according to Eq. [18], it is numerically equal to $-2N$. Since C_s^* cannot have negative values, there is a limited distance from the leading edge over which i^* can be maintained at a constant value. Letting $C_s^* = 0$ at $X = 1$, we have

$$\frac{i^*}{(i_{lim}^*)_{avg}} \leq \frac{\pi}{4} = 0.7854 \qquad [21]$$

Equation [21] suggests the possibility of attaining a uniform current flux if $i^*/(i_{lim}^*)_{avg} \leq 0.7854$. If this condition is not met, the surface concentration C_s^* becomes zero at a certain value of $X = X_c$, beyond which the current is limited by mass transfer due to zero concentration at the surface. The value of X_c can be determined by letting $C_s^* = 0$, in Eq. [20], and solving for X. To calculate the current distribution in the region between $X = X_c$ and $X = 1$, we evaluate dC_s^*/dX from Eq. [20], substituting it into Eq. [16], and evaluate the integral for $X \geq X_c$. The result can be arranged to give

$$i^*(X) = \frac{2}{\pi} i^*(X_c) \sin^{-1} \sqrt{\frac{X_c}{X}} \qquad [22]$$

(for $X_c \leq X \leq 1$). Numerical results calculated from Eq. [22] are plotted in Fig. 6 for various constant current levels. It is seen that the uniform current distribution cannot be achieved if the current level is greater than 78.5% of the average limiting current density. It should be noted that the results in Fig. 6 are given for $N \to \infty$. Most industrial electrochemical processes are carried out under the condition of large N. This condition is imposed by a low electrolytic conductivity

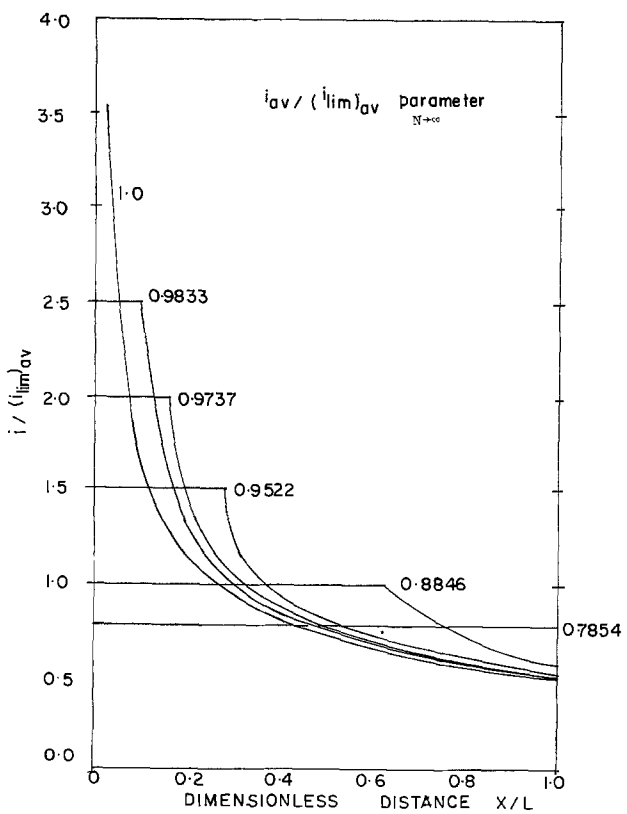


Fig. 6. Current distribution for high values of N

and a high limiting current density. A typical acid copper sulfate bath, for instance, contains 0.75M $CuSO_4$ and 1M H_2SO_4 with a specific conductivity of 0.4 mho/cm (8) at room temperature. The diffusivity of cupric ion in dilute sulfuric acid has been found to be 5.2×10^{-6} cm²/sec (9) at 25°C, giving the Schmidt number of the system equal to 2000. Thus at an operating Reynolds number of 10^5 (corresponding to a typical cell of 4m long and a sheet velocity of 0.026 m/sec), the value of N for the copper deposition reaction on the continuous moving electrode can be calculated to be 1610 at 25°C. This is a large value and can be considered to be close to infinity. Our calculation indicates that Eq. [20]-[22] give a good approximation for the system with N greater than 100.

Conclusions

A theoretical study has been made for the current distribution on a continuous moving sheet electrode. Numerical results are presented for the first-order electrokinetics. It is shown that the current distribution depends strongly on the magnitude of the limiting current. A uniform current distribution can be achieved if the average current density at the electrode is less than 78.5% of the average limiting current density.

Acknowledgment

This study was supported by Engineering Research Funds, Clarkson College of Technology. One of the authors (K.V.) received part of his stipends from a Merck industrial gift during the period of the study.

Manuscript submitted July 28, 1976; revised manuscript received Nov. 27, 1976. This was Paper 271 presented at the Washington, D.C., Meeting of the Society, May 2-7, 1976.

Any discussion of this paper will appear in a Discussion Section to be published in the December 1977 JOURNAL. All discussions for the December 1977 Discussion Section should be submitted by Aug. 1, 1977.

LIST OF SYMBOLS

b	distance between the counter and the continuous moving sheet electrode, cm
b^*	dimensionless electrode distance defined as b/L
C	concentration of the reacting ion, g-mole/cm³
C_s	surface concentration of the reacting ion, g-mole/cm³
C_s^*	dimensionless surface concentration, C_s/C_∞
C_∞	bulk concentration of the reaction ion, g-mole/cm³
D	diffusion coefficient of the reacting ion, cm²/sec
E	difference between the applied cell voltage and the thermodynamic equilibrium cell voltage, V
E^*	dimensionless applied cell voltage defined as $n\mathbf{F}E/RT$
$\mathbf{F}$	Faraday constant, 96,500 C/g-equiv., or 23,060 cal/(g-equiv.)(V)
i	local current density at the electrode, A/cm²
i^*	dimensionless local current density, $n\mathbf{F}Li/RT\kappa$
i_{avg}	geometric average current density, A/cm²
i_{lim}	local limiting current density, A/cm²
$(i_{lim})_{avg}$	geometric average limiting current density, A/cm²
i_{lim}^*	dimensionless local limiting current density, $n\mathbf{F}Li_{lim}/RT\kappa$
i_o	exchange current density based on the bulk concentration, A/cm²
K	geometric average mass transfer coefficient, cm/sec
L	length of the continuous moving sheet electrode passing through the cell, cm
n	number of electrons transferred in the electrode reaction, g-equiv./g-mole
R	universal gas constant, 1.987 cal/(g-mole)(°K)
Re_L	Reynolds number defined as U_sL/ν, dimensionless
Sc	Schmidt number defined as ν/D, dimensionless

T absolute temperature, °K
U velocity component of the electrolyte along the x direction, cm/sec
U_s velocity of the continuous moving sheet electrode, cm/sec
V velocity component of the electrolyte along the y direction
x surface coordinate measured from the point of inlet of the continuous moving sheet electrode, cm
X dimensionless surface coordinate, x/L
y a coordinate perpendicular to the surface of the continuous moving sheet electrode, cm
α, β transfer coefficients, dimensionless and $\alpha + \beta = 1$
γ an electrokinetic parameter related to the order of reactions, dimensionless
η_a activation overpotential, V
η_a^* dimensionless activation overpotential defined as $n\mathbf{F}\eta_a/RT$
η_{conc} concentration overpotential, V
η_{conc}^* dimensionless concentration overpotential, $n\mathbf{F}\eta_{conc}/RT$
κ conductivity of the electrolyte, mho/cm
ν kinematic viscosity of the electrolyte, cm²/sec
ξ dimensionless exchange current density, $n\mathbf{F}Li_o/RT\kappa$
ϕ electric potential of the electrolyte, V
ϕ_{ohm} ohmic potential drop in the electrolyte, V
ϕ_{ohm}^* dimensionless ohmic potential, $n\mathbf{F}\phi_{ohm}/RT$

REFERENCES

1. C. L. Mantell, "Electrochemical Engineering," McGraw-Hill Book Co., New York (1960).
2. B. C. Sakiadis, *AIChE J.*, **7**, 26 (1961).
3. D-T. Chin *This Journal*, **122**, 643 (1975).
4. J. Newman, "Electrochemical Systems," Prentice-Hall, Englewood Cliffs, N. J. (1973).
5. R. B. Bird, W. S. Stewart, and E. N. Lightfoot, "Transport Phenomena," John Wiley & Sons, Inc., New York (1965).
6. F. B. Hildebrand, "Advanced Calculus for Applications," Prentice-Hall, Englewood Cliffs, N. J. (1976).
7. K. Nisancioglu and J. Newman, *This Journal*, **121**, 241 (1974).
8. F. A. Lowenheim, Editor, "Modern Electroplating," John Wiley & Sons, Inc., New York (1963).
9. A. R. Gordon and A. Cole, *J. Phys. Chem.*, **40**, 733 (1936).

Mass Transfer to a Continuous Moving Surface

D-T. Chin,* K. Viswanathan,† and R. Gutowski

Department of Chemical Engineering, Clarkson College of Technology, Potsdam, New York 13676

ABSTRACT

Asymptotic correlations are presented for the rate of mass transfer to a continuous moving flat surface in laminar flow. A laboratory cell has been developed to test the theory for uniform surface concentrations. The limiting current measurement was carried out for the reduction of ferricyanide ion over the range of $1,500 < Re < 70,000$ and $1,800 < Sc < 29,300$. The experimental value agrees well with the theory for $Pe < 1.5 \times 10^8$.

The continuous moving surface is widely used in the manufacture of sheet glasses, fabrication of steel sheets, extrusion of thin films and fibers, drying of papers, and electroplating of metallic sheets and wires. Sakiadis (1-3) and Koldenhof (4) calculated velocity profiles for the system. Numerical solutions of laminar thermal boundary layers were obtained by Tsou *et al.* (5), Erickson *et al.* (6), and Rhodes and Kaminer (7) for continuous moving flat plate, and by Rotte and Beek (8) for continuous cylinders. A mass transfer correlation was obtained by Chin (9) for the condition of constant surface concentrations. For electrochemical applications, mass transfer under a condition of varying surface concentrations has been treated numerically by Viswanathan and Chin (10) for a continuous flat surface and by Alkire and Varjian (11) for a continuous resistive wire. The theory suggests that the rate of mass transfer is proportional to the square root of the Schmidt number when the value of the Schmidt number is large. This is in contrast to the cube root relationship for the other geometries such as pipe flow, flat plate, and rotating disk (12).

There have been few heat and mass transfer experiments reported for the continuous moving surface. Griffin and Throne (13) used the Schmidt shadowgraph method to observe the thermal boundary layer on a continuous moving flat belt in ambient air. Their results indicate that the rate of heat transfer is proportional to $Pr^{1/3}$ when the Prandtl number is in the neighborhood of 0.7. Tvarusko (14) and Rott, Tummers, and Dekker (15) have made the limiting current measurements for the continuous moving cylindrical wire. Tvarusko's result for the deposition of copper from an acid cupric sulfate solution is an order smaller than the theory prediction. Rott *et al.* measured the limiting current for the reduction of ferricyanide at two Schmidt numbers: $Sc = 700$ and $Sc = 1800$. Their result indicates that the theory for the continuous flat plate is also valid for the continuous cylinders, if the wire diameter is large. For smaller size wires, their data are 10-15% lower than the theory prediction.

In this study, we have extended Chin's asymptotic correlation (9) to the case of a constant flux at the surface. This condition is prevalent at the surface of a continuous moving sheet electrode if the reaction rate is below 78.5% of the limiting current (10). It is also of interest to heat transfer engineers. Experimentally, we developed a laboratory cell to determine the rate of mass transfer to the continuous moving sheet electrode at a constant surface concentration. The limiting current is measured for the reduction of ferricyanide ion over a wide range of Schmidt numbers from 1,800 to 29,000. The data agree with the laminar theory for $Pe < 1.5 \times 10^8$. This paper summarizes the results of these studies.

Analysis

Under the steady-state conditions, the convective diffusion equation takes the form

* Electrochemical Society Active Member.
† Electrochemical Society Student Member.
Key words: convective diffusion, limiting current, asymptotic analysis.

$$U\frac{\partial C}{\partial x}+V\frac{\partial C}{\partial y}=D\frac{\partial^2 C}{\partial y^2} \quad [1]$$

in the laminar boundary layer of a continuous moving flat plate, where x is the axial distance from the leading edge of the boundary layer, y is the perpendicular distance from the continuous surface, and U and V are the velocity components of the fluid along the x and y directions, respectively. For the case of a constant surface concentration, Chin (9) has made a curve fitting of Sakiadis' (2) tabulated stream function and substituted it into Eq. [1] to obtain a mass transfer correlation. His results can be summarized as

$$\mathrm{Sh}=\mathrm{Re}^{1/2}\mathrm{Sc}^{1/2}\left(0.56419-\frac{0.094167}{\mathrm{Sc}^{1/2}}-\frac{0.030573}{\mathrm{Sc}}+\frac{0.0035082}{\mathrm{Sc}^{3/2}}\right) \quad [2]$$

(uniform surface concentration)

For mass transfer under the uniform flux at the wall, Eq. [1] may be reduced to an ordinary differential equation with similarity transformations

$$\frac{d^2\phi}{d\eta^2}+\frac{1}{2}\mathrm{Sc}\left[f(\eta)\frac{d\phi}{d\eta}-f'(\eta)\phi\right]=0 \quad [3]$$

$$\phi'(0)=-1 \quad [4]$$

$$\phi(\infty)=0$$

where

$$\phi=\frac{(C-C_\infty)\sqrt{\frac{U_w x}{\nu}}}{\frac{j_w x}{D}} \quad [5]$$

$$\eta=y\sqrt{\frac{U_w}{\nu x}} \quad [6]$$

$$\frac{df(\eta)}{d\eta}=f'(\eta)=\frac{U}{U_w} \quad [7]$$

The stream functions $f(\eta)$ can be represented by the following relation (9)

$$f(\eta)=1.61605[1-e^{-\eta}(1+0.381207\eta+0.0185019\eta^2-0.00543507\eta^3)] \quad [8]$$

To obtain an analytical solution for Eq. [3] and [4], we assume that the dimensionless concentration, ϕ, can be expanded in an asymptotic series of Sc

$$\phi=\mathrm{Sc}^{1/2}\phi_0(\xi)+\phi_1(\xi)+\frac{1}{\mathrm{Sc}^{1/2}}\phi_2(\xi)+\frac{1}{\mathrm{Sc}}\phi_3(\xi)+\cdots \quad (\mathrm{Sc}\gg 1) \quad [9]$$

where

$$\xi=\mathrm{Sc}^{1/2}\eta=y\sqrt{\frac{U_w}{Dx}} \quad [10]$$

Substituting Eq. [8]-[10] into Eq. [3], expanding the functions $f(\eta)$ and $f'(\eta)$ in Taylor series, and equating the terms having the same power of Sc, we have

$$\frac{d^2\phi_0}{d\xi^2}+\frac{1}{2}\xi\frac{d\phi_0}{d\xi}-\frac{1}{2}\phi_0=0 \quad [11]$$

$$\frac{d^2\phi_1}{d\xi^2}+\frac{1}{2}\xi\frac{d\phi_1}{d\xi}-\frac{1}{2}\phi_1=0.113938\xi^2\frac{d\phi_0}{d\xi}-0.221854\phi_0 \quad [12]$$

$$\frac{d^2\phi_2}{d\xi^2}+\frac{1}{2}\xi\frac{d\phi_2}{d\xi}-\frac{1}{2}\phi_2=0.113938\xi^2\frac{d\phi_1}{d\xi}-0.221854\phi_1 \quad [13]$$

$$\frac{d^2\phi_3}{d\xi^2}+\frac{1}{2}\xi\frac{d\phi_3}{d\xi}-\frac{1}{2}\phi_3=0.113938\xi^2\frac{d\phi_2}{d\xi}-0.221854\phi_2-0.00580312\xi^4\frac{d\phi_0}{d\xi}+0.0232125\xi^3\phi_0 \quad [14]$$

$$\left.\begin{aligned}\phi_0'(0)=-1,\ \phi_1'(0)=\phi_2'(0)=\phi_3'(0)=0\\ \phi_0(\infty)=\phi_1(\infty)=\phi_2(\infty)=\phi_3(\infty)=0\end{aligned}\right\} \quad [15]$$

Equations [10]-[14] have been integrated numerically on a digital computer. The results for the local mass transfer coefficient at the wall may be given as

$$\mathrm{Sh}=\frac{\mathrm{Re}^{1/2}\mathrm{Sc}^{1/2}}{1.12838+\frac{0.135623}{\mathrm{Sc}^{1/2}}+\frac{0.0530111}{\mathrm{Sc}}+\frac{0.0117658}{\mathrm{Sc}^{3/2}}} \quad [16]$$

(uniform wall flux)

where Sh and Re are the local Sherwood and the Reynolds numbers, respectively, based on the distance from the leading edge of the boundary layer.

Numerical solutions of thermal boundary layers have been obtained by Tsou *et al.* (5) and Rhodes and Kaminer (7) for laminar flow on a continuous flat surface. Figure 1 is a comparison between the present results and those of the previous computations. The asymptotic results of Eq. [2] and [16] are plotted in the figure $(\mathrm{Sh}/(\mathrm{ReSc})^{1/2}$ *vs.* Sc) as the solid curves; the dashed lines are the numerical solution. It is seen that the agreement between the solutions is excellent except in the region of low Schmidt numbers. Although the present analysis is based upon $\mathrm{Sc}\gg 1$, the theory does not deviate from the numerical solution until the Prandtl number becomes less than 0.7. At Sc = 0.7, the difference between the two solutions is less than 0.8%.

Experimental

At large Schmidt numbers, Eq. [2] can be integrated to give the average Sherwood number

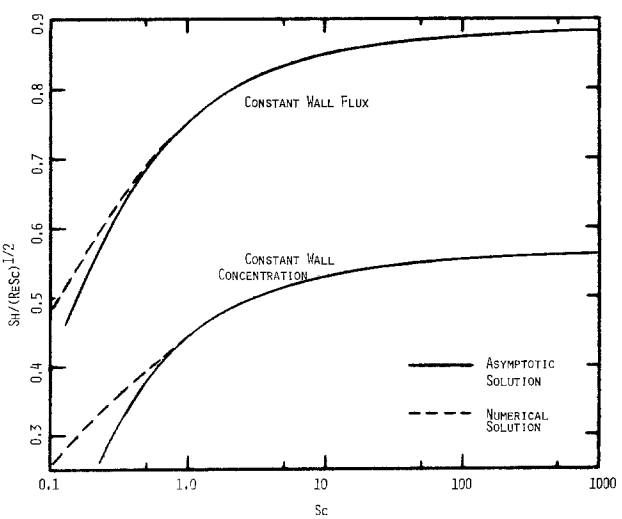


Fig. 1. A comparison between the asymptotic results and those of the numerical solutions.

$$Sh_{avg} = \left(\frac{Kx}{D}\right) = 1.128 Re^{1/2} Sc^{1/2} \quad (\text{for } Sc >> 1) \text{ [17]}$$

Here K is the geometrical average mass transfer coefficient; it is related to the average limiting current density by

$$K = \frac{(i_{lim})_{avg}}{nFC_\infty} \quad [18]$$

In this study, the square root dependence of the Schmidt number has been further tested over a wider range of Schmidt numbers. We used a rotating cylinder to simulate the flow over the continuous moving surface. As shown in Fig. 2B, the working electrode was a metallic cylinder rotating inside a cylindrical container and against a stationary skimmer plate made of an insulation material. The flow near the inner cylinder is similar to that induced by the continuous moving surface. The effect of curvature can be neglected if the cylinder diameter is much greater than the thickness of the concentration boundary layer. Such a system has been used successfully by Tsou, Sparrow, and Goldstein (5) to determine the thermal boundary layer and the velocity profile on the continuous moving surface. The rotating bipolar electrode recently developed by Nadebaum and Fahidy (16) also has a similar arrangement. Their results indicate that the rate of mass transfer is enhanced by the presence of the skimmer plate.

Figure 2A is a schematic diagram of our experimental setup. The working electrode was a piece of copper tubing, 5.08 cm OD and 2.82 cm high, embedded on a Teflon rod of the same diameter. The Teflon rod was placed vertically inside a cylindrical Plexiglas cell container of 19 cm ID and 18 cm deep. It was held by two ball bearings, one on the top plate and the other on the bottom plate of the container, which permitted the rod to rotate smoothly without oscillation. The top of the Teflon rod was attached to a brass shaft-timing pulley assembly and powered with a d-c motor (Minarik 3/4-56C). The electric contact to the working electrode was made by two carbon brushes as shown in the figure. Within the cell container, a spring-loaded Teflon skimmer plate of 1.3 cm thick and 18 cm high, was fastened on the container wall. The skimmer pressed tightly against the Teflon rod and the working electrode while in operation. The counterelectrode was a stainless steel screen located at the container wall; it had a surface area much greater than the working electrode. A saturated calomel electrode inserted through a hole on the top plate into the cell container was used as the reference electrode.

The system was originally designed to measure the limiting current for the reduction of cupric ion to copper at the working electrode, with a copper plate of a large surface area used as the anode. The subsequent experiments with a solution containing 1.5M H_2SO_4 and 0.05M $CuSO_4$ were not successful. The reproducibility for the limiting current measurements was very poor. A careful examination revealed that the copper deposited at the limiting current densities gave a rough coating to the working electrode, which in turn scraped off Teflon particles when rotating against the Teflon skimmer plate. Thus the surface of the working electrode became contaminated, and no accurate measurement was possible.

A ferricyanide-ferrocyanide system with sodium sulfate as the supporting electrolyte was found satisfactory for the limiting current measurement. The reaction at the working electrode was the reduction of ferricyanide to ferrocyanide ions. It was found that a prolonged exposure of the copper working electrode to the solution leads to the corrosion of copper with the formation of brown precipitates. The problem was alleviated by making the solution slightly alkaline. A typical solution used for the experiments was: potassium ferricyanide, 0.01M; potassium ferrocyanide, 0.01M; sodium sulfate, 0.5M; sodium hydroxide, 0.01M; glycerol, 0-5.1M; kinematic viscosity, 0.00983-0.0333 cm/sec; and diffusivity of ferricyanide ion, 5.40-1.139 $\times 10^{-6}$ cm^2/sec. To change the Schmidt number of the system, glycerol was added to the solution to increase the solution viscosity and to decrease the diffusivity of ferricyanide ion. The concentration of glycerol was varied from 0 to 5M; this covered the range of the Schmidt numbers from 1,800 to 30,000 at room temperatures. If the concentration of sodium hydroxide was too high, the copper electrode would become black due to the formation of copper oxide on the electrode surface; also glycerol would react with ferricyanide ions. With 0.01M sodium hydroxide, there was no change of ferricyanide concentration during the run.

For each run the concentration of ferricyanide ion was determined with an iodometric titration. The solution viscosity was measured with an Ostwald viscometer, and the density with a specific gravity bottle. A rotating disk electrode was used to determine the diffusivity of ferricyanide ions. The limiting current measurement was performed with a Wenking HP 72 potentiostat. All the runs were made at a constant room temperature of 22°C.

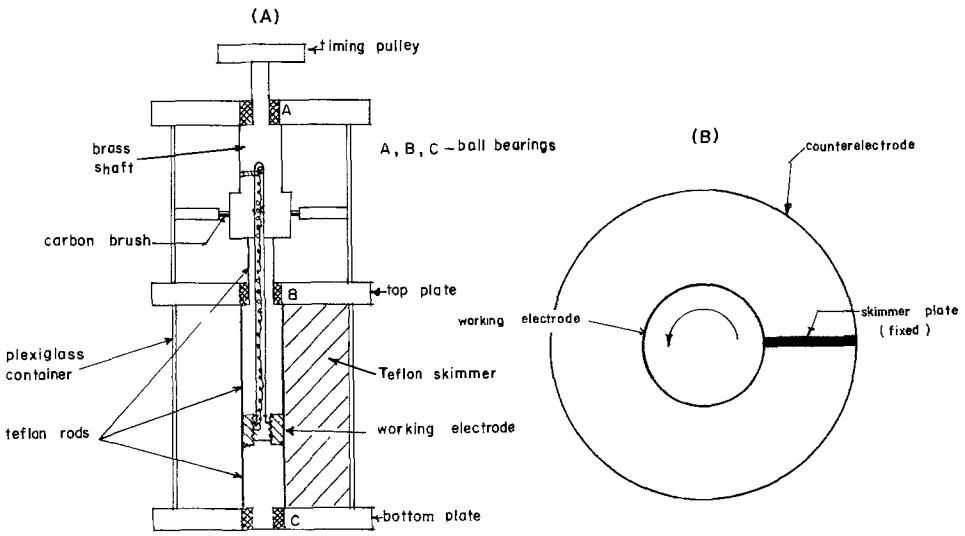


Fig. 2. Schematic diagram of the experimental apparatus.

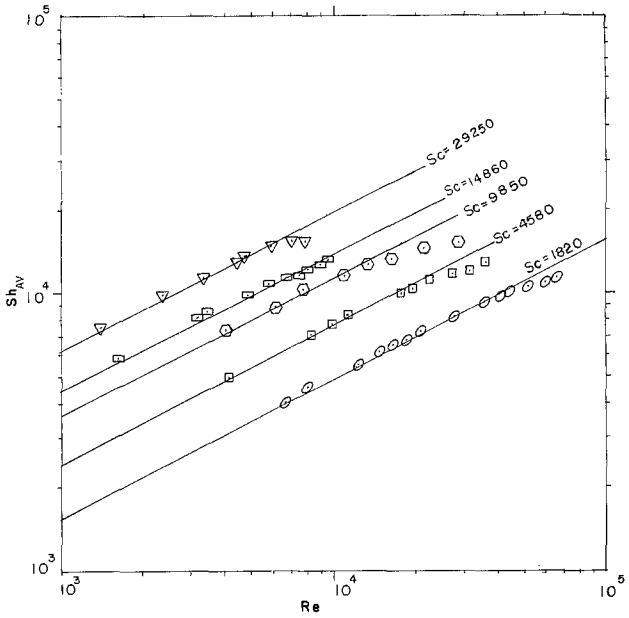


Fig. 3. Results of the limiting current measurement presented in the form of Sh_{avg} *vs.* Re.

Results and Discussion

The results of the limiting current measurements are given in Fig. 3, where the average Sherwood number is plotted against the Reynolds number in a log-log scale for five different Schmidt numbers. For each Schmidt number, the data exhibit a linear relation in the low Reynolds number region with a slope equal to one-half. The data deviate from the linear portion at higher Re. The point of deviation depends on the Schmidt number. The higher the Schmidt number, the earlier is the deviation.

In accordance with Eq. [17], these data are replotted logarithmically in Fig. 4 in the forms of Sh *vs.* Pe. Here the Peclet number, Pe, is the product of the Reynolds number and the Schmidt number. In this way, all the data points as represented by various hollow symbols converge into a single curve. The solid line in the figure is the theoretical prediction as calculated from Eq. [17]. The points of deviation from the theory for various Schmidt numbers also converge into a common point; it takes place approximately at Pe = 1.5×10^8. The agreement with the theory in the linear portion is found to be better than 97%. For comparison, the data of Rott *et al.* (15) obtained with the continuous cylindrical wires are also plotted in the figure as the solid dots. It is seen that their data continue to agree with the theory for Pe greater than 1.5×10^8.

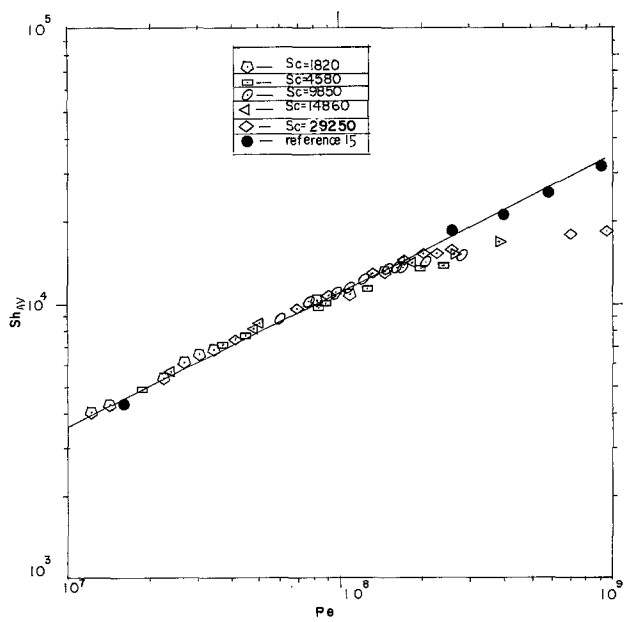


Fig. 4. Comparison with the laminar mass transfer theory. The solid line in the figure is the theory prediction of Eq. [17].

It is interesting to note that for the Peclet number greater than 1.5×10^8, the present experimental mass transfer rates are consistently less than the theory prediction. If the deviation was caused by the transition from laminar to turbulent flow, one would expect the experimental points lying above the laminar theory. Also, the point of deviation should occur at a fixed critical Reynolds number, not the Peclet number. If this was due to the effect of the surface curvature of the experimental device, one would expect that the disagreement takes place in the region of low Peclet numbers not at high Peclet numbers. This is because the thickness of the concentration boundary layer decreases with increasing Peclet number, and the effect of surface curvature is greater if the boundary layer is thick. We exclude the possibility that this might be caused by the chemical nature of the redox reaction or passivation of the copper working electrode. It was found that in the flatten region of Fig. 4, the polarization curves were well behaved and had clear-cut limiting current plateaus for the reduction of ferricyanide ions. One possible explanation is that according to the theory, the thickness of the concentration boundary layer is inversely proportional to the square root of the Peclet number

$$\delta = \frac{1.77x}{\sqrt{\mathrm{ReSc}}} = \frac{1.77x}{\sqrt{\mathrm{Pe}}} \qquad [19]$$

Here δ is the local thickness of the Nernst diffusion layer. The concentration boundary layer at the trailing edge would become thinner and thinner as the Peclet number increased. Eventually, the thickness became smaller than the physical gap between the working electrode and the Teflon skimmer. When this happened, the concentration boundary layer at the trailing edge would be carried by the rotating copper cylinder across the gap to the leading edge of the flow boundary layer. The thickness of the concentration boundary layer near the leading edge region would then be increased by this carry-over effect, and the over-all mass transfer rate would be decreased. For the present apparatus, the surface distance between the leading and the trailing edges was 15.96 cm. Using the value of Pe = 1.5×10^8 as the point of deviation in Fig. 4, the thickness of the Nernst diffusion layer at trailing edge can be calculated to be 0.002 cm when the carry-over phenomena started to affect the limiting current measurement. Whether the apparatus was able to maintain a gap less than 0.002 cm between the working electrode and the stationary skimmer when the electrode is rotating at high speeds, remains to be determined. The analysis, nevertheless, indicates that the discrepancy might be caused by the mechanical tightness of the apparatus rather than a breakdown of the mass transfer theory in the laminar region. It seems that further investigation is necessary to resolve the problem

Conclusions

1. Asymptotic correlations are presented for predicting the rate of mass transfer to a continuous moving flat surface. The result is valid for laminar flow over a range of Schmidt numbers from 0.7 to infinity. The maximum error which occurs in the neighborhood of Pr = 0.7 is less than 0.8%.

2. A laboratory cell has been used to test the theory for uniform surface concentration. The limiting cur-

rent was measured for the reduction of ferricyanide ion over a range of Reynolds numbers from 1,500 to 70,000 and Schmidt numbers from 1,800 to 29,300. The data agree with the theory for $Pe < 1.5 \times 10^8$. The deviation above $Pe = 1.5 \times 10^8$ was probably caused by a mechanical flaw of the experimental cell rather than the breakdown of the theory in the laminar region.

Acknowledgment

This study was supported by Engineering Research Funds, Clarkson College of Technology. One of the authors (K. V.) received part of his stipends from a Merck industrial gift during the period of the study. The experiments in acid copper sulfate solutions were carried out by C. H. Tsang.

Manuscript submitted July 28, 1976; revised manuscript received Nov. 27, 1976. This was Paper 271 presented at the Washington, D. C., Meeting of the Society, May 2-7, 1976.

Any discussion of this paper will appear in a Discussion Section to be published in the December 1977 JOURNAL. All discussions for the December 1977 Discussion Section should be submitted by Aug. 1, 1977.

LIST OF SYMBOLS

C	concentration of the diffusing species, g-mole/cm^3
C_∞	bulk concentration, g-mole/cm^3
D	diffusivity of the diffusing species, cm^2/sec
$\mathbf{F}$	Faraday constant, 96,500 C/g-equiv.
f	dimensionless stream function defined in Eq. [7]
$(i_{lim})_{avg}$	geometric average limiting current density, A/cm^2
K	geometric average mass transfer coefficient, cm/sec
k	local mass transfer coefficient, cm/sec
n	number of electrons transferred in electrode reaction, g-equiv./g-mole
Pe	Peclet number defined as ReSc, dimensionless
Re	local Reynolds number, $U_w x/\nu$, dimensionless
Sc	Schmidt number, ν/D, dimensionless
Sh	local Sherwood number, kx/D, dimensionless
Sh_{avg}	average Sherwood number, Kx/D, dimensionless
U	velocity component along the x direction, cm/sec
U_w	velocity of the continuous moving surface, cm/sec
V	velocity component along the y direction, cm/sec
x	distance from the leading edge of the boundary layer and measured along the direction of motion of the continuous surface, cm
y	perpendicular distance from the continuous moving surface, cm
δ	thickness of the Nernst diffusion layer, cm
η	a similarity coordinate defined as $y\sqrt{U_w/\nu x}$, dimensionless
ν	kinematic viscosity of the fluid, cm^2/sec
ξ	a dimensionless coordinate defined as $Sc^{1/2}\eta$ or $y\sqrt{U_w/Dx}$
ϕ	dimensionless temperature defined by Eq. [5] for the case of uniform heat flux at the wall
ϕ_1	the zeroth-, the first-, the second-, and the third-order solutions of ϕ, as defined in Eq. [9]

REFERENCES

1. B. C. Sakiadis, *AIChE J.*, **7**, 26 (1961).
2. B. C. Sakiadis, *ibid.*, **7**, 221 (1961).
3. B. C. Sakiadis, *ibid.*, **7**, 467 (1961).
4. E. A. Koldenhof, *ibid.*, **9**, 411 (1963).
5. F. K. Tsou, E. M. Sparrow, and R. J. Goldstein, *Int. J. Heat Mass Transfer*, **10**, 219 (1967).
6. L. E. Frickson, L. T. Fan, and V. G. Fox, *Ind. Eng. Chem. Fundam.*, **5**, 19 (1966).
7. C. A. Rhodes and H. Kaminar, Jr., *AIAA J.*, **10**, 331 (1972).
8. J. W. Rotte and W. J. Beek, *Chem. Eng. Sci.*, **24**, 705 (1969).
9. D-T. Chin, *This Journal*, **112**, 643 (1975).
10. K. Viswanathan and D-T. Chin, *ibid.*, **124**, 709 (1977).
11. R. Alkire and R. Varjian, *ibid.*, **124**, 388 (1977).
12. V. G. Levich, "Physicochemical Hydrodynamics," Prentice-Hall, Englewood Cliffs, N. J. (1962).
13. J. F. Griffin and J. L. Throne, *AIChE J.*, **13**, 1210 (1967).
14. A. Tvarusko, *This Journal*, **119**, 43 (1972).
15. J. W. Rotte, G. L. J. Tummers, and J. L. Dekker, *Chem. Eng. Sci.*, **24**, 1009 (1969).
16. P. R. Nadebaum and T. Z. Fahidy, *This Journal*, **122**, 1035 (1975).

Technical Notes

Dibasic Lead Sulfate in Lead-Acid Battery Pastes

B. P. Varma* and C. W. Fleischmann*

Eltra Corporation, C & D Batteries Division, Plymouth Meeting, Pennsylvania 19462

The process is well known by which commercial lead oxides are partially sulfated to form stiff pastes for subsequent application onto metallic grids to compose electrodes for lead-acid cells. After pasting, and prior to electrochemical formations, these electrodes are allowed to stand or "cure" to develop various basic sulfates and to oxidize any free lead (1). The cured pastes, in addition to the unreacted starting materials, principally PbO, may contain the monobasic lead sulfate, $PbO \cdot PbSO_4$, and the tribasic lead sulfate hydrate, $3PbO \cdot PbSO_4 \cdot nH_2O$ (1-6). Depending on the composition of the starting commercial oxides, unreacted metallic lead or Pb_3O_4 may also be present (1-6). In pastes cured at higher temperatures (>70°C) and humidities, the tetrabasic species, $4PbO \cdot PbSO_4$, is developed in significant amounts (1, 2). It will also form slowly at lower temperatures (5, 7, 8). The dibasic lead sulfate, $2PbO \cdot PbSO_4$, is a well-recognized high temperature phase (9-11), but it has been discounted in battery pastes on the basis of thermodynamic arguments (3). Nevertheless, it has been reported at times (5, 12).

In the course of our investigations on lead-acid battery pastes (13), dibasic lead sulfate was observed in pastes. These observations are discussed.

Experimental

Pastes were prepared from the three commercial oxides described briefly in Table I by blending 9.07 kg of the oxide with 1-1.3 liters water and then slowly adding 460-960 ml 7.02M H_2SO_4. The pastes were subsequently cured at low temperatures (25°-55°C) and over a wide range of humidities (cure I) or, alternatively, for 3 hr at higher temperatures (80°-85°C) in steam (cure II). The compositions of the oxides and the cured plates were determined by comparing their x-ray diffraction patterns to published data (9, 11, 14). The free lead content of pastes made from leady oxides was reduced to 0.5-5% during cure I, depending on the particular conditions, and to 1-2% during cure II. The free lead content was determined by wet methods.

Results and Discussions

Cure I products.—The pastes cured via cure I and humidities were found to contain tribasic lead sulfate, monobasic lead sulfate, and tetragonal lead oxide, PbO(t). Dibasic lead sulfate was not found in any of the cured pastes.

Orthorhombic lead oxide, PbO(o), was not detected in any of the cured pastes including the paste made from oxide A, which contained PbO(o) as a component. The absence of orthorhombic PbO in the pastes after curing is in accordance with past reports (15, 16) that this phase converts to the tetragonal phase in the presence of moisture and/or mechanical working.

Cure II products.—The products found in pastes cured via cure II are given in Table II. The composition depended on the starting oxides, but every cured paste contained both tetrabasic lead sulfate and tetragonal PbO. Differences, however, were observed as to the development of the other basic sulfates. The paste of oxide A also developed both monobasic and tribasic lead sulfates, whereas the cured pastes of the other three oxides contained dibasic lead sulfate. Dibasic lead sulfate was found in one of the leady oxides (oxide C) but not in the other (oxide A). All the literature reports (5, 12) in which the dibasic species was observed were for pastes prepared from leady oxides. Oxides B and D, both nonleady oxides, however, also developed the dibasic species. Hence, the presence of free lead in the starting oxide does not appear to be a requirement for the formation of dibasic lead sulfate.

Table I. Compositions of starting oxides

Oxide	Description	Compositions as found by chemical analysis	Compositions* as found by x-ray diffraction
A	A commercial leady oxide, Barton process	PbO 80.93% Pb 19.07%	PbO(o) PbO(t) Pb
B	A commercial nonleady oxide, followed by mechanical furnace	PbO 90.54% Pb_3O_4 9.46%	PbO(o) PbO(t) Pb_3O_4
C	A commercial leady oxide, Ball-Mill process (Schimadzu)	PbO 76.66% Pb 23.34%	PbO(t) Pb
D	Tetragonal PbO, laboratory preparation	PbO 100%	PbO(t)

* PbO(o) indicates orthorhombic modification.
* PbO(t) indicates tetragonal modification.
* Pb indicates free bulk particles of lead.

Table II. Products after steam curing

Oxides	Products
A	$4PbO \cdot PbSO_4$ $3PbO \cdot PbSO_4 \cdot nH_2O$ $PbO \cdot PbSO_4$ PbO(t)
B, C, D	$4PbO \cdot PbSO_4$ $2PbO \cdot PbSO_4$ PbO(t)

Double cure II products.—A double cure by cure II for pastes made from oxide A changed the principal products to $4PbO \cdot PbSO_4$, PbO(t), and $2PbO \cdot PbSO_4$. These products were the same as those which developed after one cure in the pastes made from the other oxides.

Several mechanisms may be suggested for the formation of dibasic in the pastes. It may develop as a result of tribasic disproportionation on extended cure II conditions. If that is the case, however, it is not immediately apparent why the pastes of oxide A should have

* Electrochemical Society Active Member.
Key words: lead oxides, basic lead sulfates, tetragonal PbO, orthorhombic PbO.

behaved differently than the others. Perhaps the mechanism involves PbO, which is known to have different reactivities depending on both the polymorph and its past history. The effects of the polymorph on the product basic sulfates have been reported by Bode and Voss (17), Ikari *et al.* (18), and Biagetti and Weeks (19). Effects of mechanical working on the reactivity (15, 20) and structure (21) of PbO(t) are also known. Since both oxides B and C were mechanically worked during preparation, the nature of the products formed in the cured pastes may be a function of the distortion, hence the activity, of the PbO(t) in these oxides. Further research is needed to define the reaction mechanisms occurring in battery pastes during curing.

Conclusion

Although dibasic lead sulfate is not commonly reported in battery pastes, it may develop under some curing conditions which also develop $4PbO \cdot PbSO_4$.

Acknowledgments

This work was supported in part by the Prestolite Battery Division of the Eltra Corporation, and the authors are grateful to Ken Borror and Paul Reeme of that division for obtaining the x-ray diffractograms. The authors are also grateful for the suggestions and comments of the reviewers.

Manuscript submitted Nov. 30, 1976; revised manuscript received Jan. 10, 1977.

Any discussion of this paper will appear in a Discussion Section to be published in the December 1977 JOURNAL. All discussions for the December 1977 Discussion Section should be submitted by Aug. 1, 1977.

Publication costs of this article were assisted by Eltra Corporation.

REFERENCES

1. G. W. Vinal, "Storage Batteries," 4th ed., pp. 30-36, John Wiley & Sons, Inc., New York (1967).
2. H. B. Stephensen, C. L. Hixon, H. S. Long, J. S. Bryson, J. D. Purdum, and E. J. Ritchie, Final Report LE-82/LE-84, International Lead Zinc Research Organization, New York (1971).
3. S. C. Barnes and R. T. Mathieson, "Batteries 2," Proceedings of the 4th International Symposium at Brighton, September 1964, p. 41, Pergamon Press, New York (1965).
4. J. Armstrong, I. Dugdale, and W. J. MuCusker, in "Power Sources 1966," D. H. Collins, Editor, p. 163, Pergamon Press, New York (1967).
5. E. Skoluda, S. Olszanski, B. Szczesniak, H. Handrysiak, and S. Tabat, *Przem. Chem.*, **53**, 624 (1974).
6. G. L. Clark, J. N. Mrgudich, and N. C. Schlietz, *Z. Anorg. Allg. Chem.*, **119**, 145 (1921).
7. J. N. Mrgudich, *Trans. Electrochem. Soc.*, **81**, 165 (1942).
8. T. G. Chang and M. M. Wright, Paper 13 presented at The Electrochemical Society Meeting, Las Vegas, Nevada, Oct. 17-22, 1976.
9. H. W. Billhardt, *This Journal*, **117**, 690 (1970).
10. J. J. Lander, *J. (and Trans.) Electrochem. Soc.*, **95**, 174 (1949).
11. J. D. Esdaile, *This Journal*, **113**, 71 (1966).
12. D. Pavlov, G. Papazov, and V. Iliev, *ibid.*, **119**, 8 (1972).
13. C. W. Fleischmann and W. J. Schlotter, *ibid.*, **123**, 969 (1976).
14. Joint Committee on Powder Diffraction Standards, Index to the Powder Diffraction File, **26**, (1976).
15. E. J. Ritchie, in "Lead Oxides," Section II, p. 19, Independent Battery Manufacturers Association Inc., Largo, Florida (1974).
16. M. Leblanc and E. Eberius, *Z. Phys. Chem., Abt. A*, **160**, 69 (1932).
17. H. Bode and E. Voss, *Electrochim. Acta*, **1**, 318 (1959).
18. S. Ikari, S. Yoshizawa, and S. Okada, *J. Electrochem. Soc., Jpn.*, **27**, E167 (1959).
19. R. V. Biagetti and M. C. Weeks, *Bell Syst. Tech. J.*, **49**, 1305 (1970).
20. A. V. Pamfilov, E. G. Ivancheva, and A. G. Ivancheva, *Zh. Obshch. Khim.*, **16**, 325 (1946).
21. G. L. Clark and S. F. Kern, *J. Am. Chem. Soc.*, **64**, 1637 (1942).

Suppression of Surface Dissolution of CdS Photoanode by Reducing Agents

Tooru Inoue, Tadashi Watanabe, Akira Fujishima, and Ken-ichi Honda

Department of Synthetic Chemistry, Faculty of Engineering, The University of Tokyo, Hongo, Bunkyo-ku, Tokyo 113, Japan

and Koichi Kohayakawa

Department of Applied Chemistry, Faculty of Engineering, Kanagawa University, Rokkakubashi, Kanagawa-ku, Yokohama 221, Japan

Electrochemical photocells (1-21) have recently drawn the attention of a number of investigators primarily in connection with solar energy conversion. The following three criteria appear to be of crucial importance for a semiconductor material to be used as a photoanode in an electrochemical photocell: (*i*) sufficient stability, (*ii*) sufficient light absorption in the visible wavelength region, and (*iii*) sufficient band bending under the conditions used. The third point implies that the flatband potential is sufficiently cathodic, and has been emphasized in several papers (13-15). At stable photoanodes such as TiO_2 (1-12), $SrTiO_3$ (13-15), SnO_2 (16, 17), $KTaO_3$ (18), WO_3 (19, 20), and Fe_2O_3 (20, 21), the electrode reaction is the direct oxidation of water resulting in oxygen evolution by the action of holes produced in the valence band. However, these semiconductors possess relatively wide bandgaps (exceeding 3.0 eV) except WO_3 and Fe_2O_3 and hence do not efficiently utilize solar energy. In this respect, cadmium sulfide (CdS) seems to be a promising material since it shows a strong absorption of wavelengths shorter than 520 nm. However, the anodic reaction at illuminated CdS electrode is the dissolution of the electrode surface (22-24) according to

$$CdS + h\nu \rightarrow h^+_{val} + e^-_{cond} \quad [1]$$

$$2h^+_{val} + CdS \rightarrow S_{ad} + Cd^{2+} \quad [2]$$

where h^+_{val}, e^-_{cond}, and S_{ad} denote a hole in the valence band, an electron in the conduction band, and a sulfur atom deposited on the electrode surface, respectively. For the application of CdS as a photoanode in an electrochemical photocell, the dissolution process [2] should be minimized. This problem has been

Key words: electrochemical photocell, semiconductor electrodes, solar energy, rotating ring-disk electrode.

partly solved by adding appropriate reducing agents such as I^- (25), hydroquinone (26), and S^{2-} (27, 28) into the electrolyte solution. Attempts have also been reported on the dissolution suppression of CdSe (27), Bi_2S_3 (28), and CdTe (29) photoanodes by addition of S^{2-}, Se^{2-}, and Te^{2-}, respectively. However, a more systematic investigation appeared necessary for a better choice of the reducing agent applicable to a practical electrochemical photocell. In the present study we investigated the photoelectrochemical processes at CdS single crystal electrode, mainly focusing upon the suppression of its dissolution, by addition of a variety of reducing agents differing widely in their redox potentials. The rotating ring-disk electrode (RRDE) technique served as a useful tool for the *in situ* determination of the dissolution rate of the electrode surface.

Experimental

The CdS single crystal (n-type) (Teikoku Tsushin Kogyo Company, Limited) employed in the present study was undoped, with the carrier density of 7.4×10^{16} cm^{-3} (determined by measurement of the Hall effect by this company). The crystal was shaped into a disk 6.0 mm in diameter and 1.0 mm in thickness. Indium was vacuum-evaporated onto a face of the crystal in order to insure an ohmic contact with the conducting wire. Then, the CdS disk was assembled in a Teflon rod using epoxy resin together with an amalgamated Cu ring 7.0 mm in inner diameter and 9.0 mm in outer diameter, thus constructing a ring-disk electrode. The (0001) crystal face of CdS exposed to the electrolyte solution was polished with alumina powder, etched in concentrated HCl for 10 sec, and then washed with water. The ring-disk electrode thus prepared was set in a RRDE measurement system (Nikko Keisoku) as is schematically shown in Fig. 1. The potentials of the disk and ring electrodes were controlled independently by means of a dual potentiogalvanostat (Nikko Keisoku). The light source was a 500W high pressure mercury arc lamp and the wavelength of the illuminating light was fixed at 440 nm with an interference filter (Koshin Kogaku) having a peak transmittance of 40% and the half-band width of 10 nm. The CdS-electrolyte interface was uniformly illuminated through a quartz window attached at the bottom of the cell. The supporting electrolyte was 0.2M Na_2SO_4 and all the reducing agents used were reagent grade. In most of the RRDE experiments, the potential of CdS disk electrode was kept at 1.0V *vs.* SCE where a saturation photocurrent occurs, and the potential of the Cu(Hg) ring electrode was swept at a rate of 30 sec/V in order to analyze the products of the photoelectrochemical reaction on the CdS disk electrode. The rotation rate of the RRDE was set at 1000 rpm.

Results and Discussion

Figure 2 shows the currents at the CdS disk and Cu(Hg) ring electrodes as a function of the ring potential, with and without illumination. I_D, I_R, and V_R denote the disk current, the ring current, and the ring potential, respectively. In the dark, the disk current is negligibly small at the fixed potential of 1.0V *vs.* SCE, and hydrogen evolution occurs at potentials more cathodic than −1.5V *vs.* SCE at the Cu(Hg) ring electrode. Under illumination in the absence of a reducing agent, SO_3^{2-} in the present case, an anodic photocurrent flows at the CdS disk electrode. At the same time, a reduction current appears at the Cu,(Hg) ring electrode in the potential range more cathodic than *ca.* −0.6V, which corresponds to the reduction of Cd^{2+}. By addition of Na_2SO_3 into the electrolyte solution, the magnitude of the disk photocurrent undergoes practically no change, whereas that of the ring current for Cd^{2+} reduction shows a decrease. In what follows, the limiting current at the ring electrode corresponding to the reduction of Cd^{2+} is expressed as $I_{R,Cd}$ for the electrolyte containing a reducing agent, and as $I°_{R,Cd}$ for that free of reducing agents. For the SO_3^{2-}-free electrolyte solution, it was found that the ratio of the magnitude of $I°_{R,Cd}$ to that of the anodic photocurrent at the CdS disk coincides fairly well with the theoretical collection efficiency for the RRDE employed. This implies that in this case the dissolution of the CdS electrode surface due to reaction [2] is totally responsible for the anodic photocurrent. From this it follows that the value of $(I°_{R,Cd} - I_{R,Cd})/I°_{R,Cd}$ represents the fraction of the anodic photocurrent by which the reducing agent is being oxidized in competition with the reaction [2]. Below we call the quantity 100 $(I°_{R,Cd} - I_{R,Cd})/I°_{R,Cd}$ the percentage of dissolution suppression.

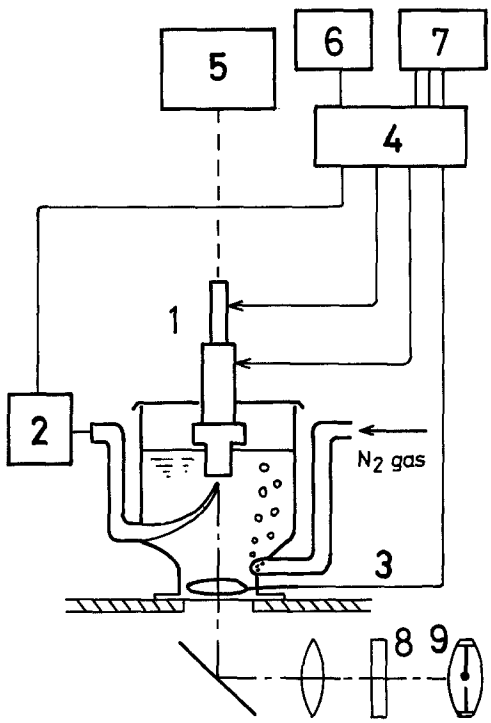


Fig. 1. Experimental setup. 1, RRDE; 2, SCE; 3, Pt counterelectrode; 4, dual potentiogalvanostat; 5, speed controller; 6, potential sweeper; 7, X-Y-Y' recorder; 8, interference filter; 9, light source.

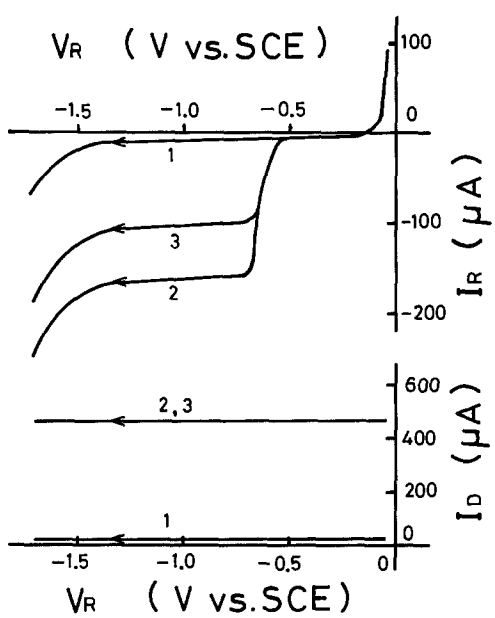


Fig. 2. Dependences of (a) ring current at Cu(Hg) and (b) disk current at CdS, on the ring potential. The disk potential is fixed at 1.0V *vs.* SCE. 1, In darkness. 2, CdS illuminated; $[SO_3^{2-}] = 0$. 3, CdS illuminated; $[SO_3^{2-}] = 10^{-3}$M.

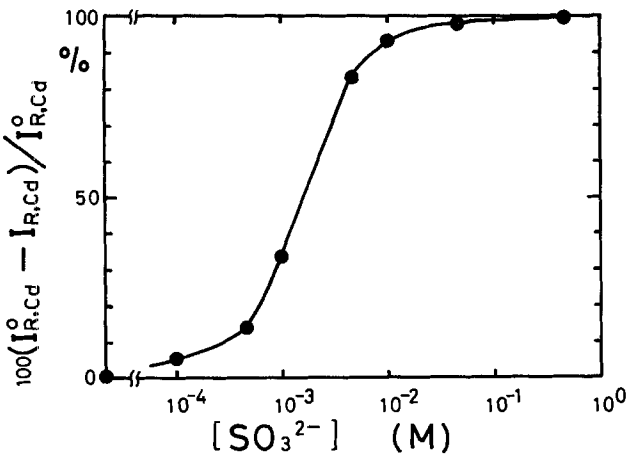


Fig. 3. Percentage of dissolution suppression as a function of SO_3^{2-} concentration.

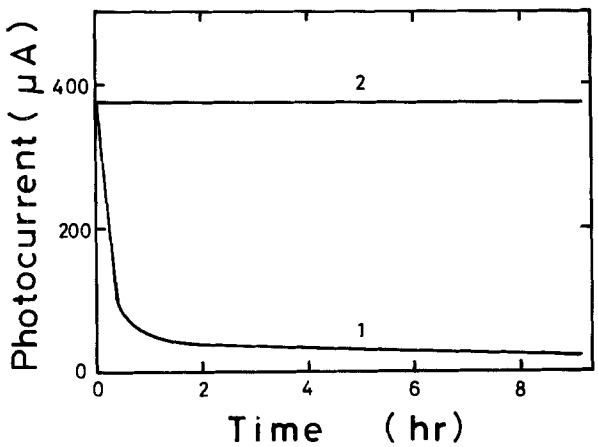


Fig. 4. Decay characteristics of the photocurrent at CdS electrode. 1, In 0.2M Na_2SO_4; $[SO_3^{2-}] = 0$. 2, In 0.2M Na_2SO_4; $[SO_3^{2-}] = 1.0$M.

For SO_3^{2-}, $S_2O_3^{2-}$, and S^{2-}, the determination of $I_{R,Cd}$ was straightforward, since their oxidation products did not undergo reduction at the ring electrode, due presumably to the irreversibility of the oxidation process (*e.g.*, Eq. [3] and [4] below). With Cl^-, Br^-, Fe^{2+}, I^-, and $Fe(CN)_6^{4-}$, on the contrary, the reduction of both Cd^{2+} and the oxidized species of these reducing agents proceeded at the Cu(Hg) ring electrode, and hence a double reduction wave was recorded as the ring current. In this case a simple subtraction was required for the determination of the value of $I_{R,Cd}$.

Figure 3 shows the percentage of dissolution suppression by added SO_3^{2-} as a function of its concentration. Note that the suppression efficiency increases with increasing concentration of the reducing agent, and is almost complete at concentrations above 0.1M.

In the absence of reducing agents in the electrolyte solution, the photocurrent at CdS single crystal electrode usually shows an abrupt decay with time. This phenomenon is attributed to the deposition of sulfur, which acts as a light filter on the electrode surface, produced according to reaction [2]. If the dissolution process [2] is suppressed by added reducing agents, the decay characteristic is also expected to decrease. This is shown in Fig. 4, where the current-time curves for electrolyte solution with and without 1.0M Na_2SO_3 are illustrated.

Concerning the oxidation reaction of SO_3^{2-}, which should proceed in competition with the dissolution of the CdS surface, the following two mechanisms are equally possible

$$2SO_3^{2-} + 2h^+_{val} \rightarrow S_2O_6^{2-} \qquad [3]$$

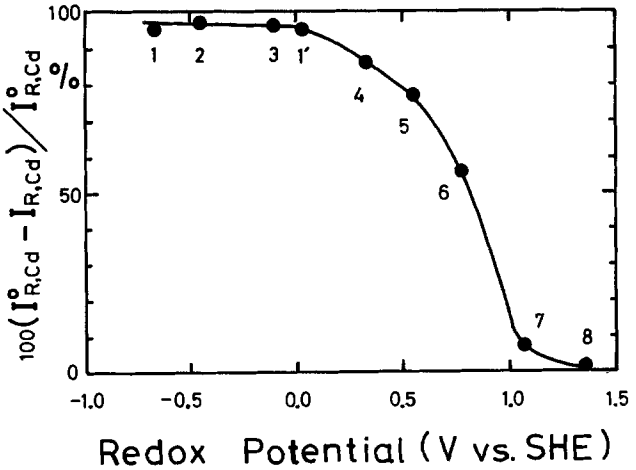


Fig. 5. Percentage of dissolution suppression by reducing agents (0.01M) as a function of their redox potential. 1, SO_3^{2-}/SO_4^{2-}; 1', $SO_3^{2-}/S_2O_6^{2-}$; 2, S^{2-}/S; 3, $S_2O_3^{2-}/S_4O_6^{2-}$; 4, $Fe(CN)_6^{3-/4-}$; 5, I^-/I_2; 6, $Fe^{2+/3+}$; 7, Br^-/Br_2; 8, Cl^-/Cl_2.

$$SO_3^{2-} + 2\,OH^- + 2h^+_{val} \rightarrow SO_4^{2-} + H_2O \qquad [4]$$

These schemes have been confirmed by a number of authors (30-32) in aqueous alkaline solution such as that used in the present study (pH 9.3).

Gerischer and Meyer (22) demonstrated that in the case of I^- one of the reaction products (I_3^-) attacks the electrode and causes a chemical dissolution of the CdS surface, according to

$$CdS + I_3^- \rightarrow Cd^2 + S + 3I^- \qquad [5]$$

Based upon the results shown in Fig. 3 and 4, however, we conclude that such a chemical dissolution is impossible, or at least sufficiently slow, for the present CdS/SO_3^{2-} system. If a reaction similar to [5] occurs effectively, the percentage of dissolution suppression cannot reach almost 100%, and the decay characteristic of photocurrent would appear, even for the case of a concentrated sulfate electrolyte solution.

Measurements of the percentage of dissolution suppression were carried out for a total of eight reducing agents differing widely in their redox potentials: SO_3^{2-}, S^{2-}, $S_2O_3^{2-}$, $Fe(CN)_6^{4-}$, I^-, Fe^{2+}, Br^-, and Cl^-. The results are summarized in Fig. 5. Two different redox potentials were taken for SO_3^{2-} ($SO_3^{2-}/S_2O_6^{2-}$ and SO_3^{2-}/SO_4^{2-}), since two oxidation processes are possible, as mentioned above. From this figure it is seen that the reducing agent whose redox potential is more negative suppresses more effectively the dissolution of the CdS surface. In particular, the percentages of dissolution suppression by SO_3^{2-}, S^{2-}, and $S_2O_3^{2-}$ are quite high, exceeding 95% at such a relatively low concentration.

The flatband potential of CdS single crystal electrode (and hence the vicinity of the conduction band edge of CdS in an energy level diagram) is situated in the potential region around −0.5V *vs.* SHE (33). Therefore, the results given in Fig. 5 are rather surprising, since the interfacial charge transfer concerned (oxidation of reducing agents) may proceed via the valence band by the action of photogenerated holes, and not via the conduction band. However, recently using TiO_2 electrode in acetonitrile with a large number of electroactive compounds, Frank and Bard (34) detected intermediate energy levels between the conduction and valence bands capable of mediating electron transfer. It is felt that further investigations will be necessary for a quantitative interpretation of our experimental results.

Above we have investigated the stabilization of the surface of CdS photoanode by the addition of suitable reducing agents to the electrolyte solution. For a practical application of such systems in the electrochemical

photocell, however, the effect of additives on the cell performance must be clarified. An investigation along this line has been reported by Gerischer and Gobrecht (35), who studied the power characteristics of CdS electrochemical photocell containing $Fe(CN)_6^{4-/3-}$ and $S_2O_3^{2-}/S_4O_6^{2-}$ as redox couples. They found a smaller photo-emf for the latter redox couple than the former, and elucidated such a result on the basis of the difference between the redox potential of the additive and the Fermi level of CdS. Taking these findings into account, we feel that detailed investigations will be required before an ideal electrochemical photocell is realized.

Acknowledgment

The authors are grateful to Allen J. Bard, The University of Texas, for the stimulating suggestions and discussions.

Manuscript submitted Nov. 29, 1976; revised manuscript received Jan. 4, 1977.

Any discussion of this paper will appear in a Discussion Section to be published in the December 1977 JOURNAL. All discussions for the December 1977 Discussion Section should be submitted by Aug. 1, 1977.

Publication costs of this article were assisted by The University of Tokyo.

REFERENCES

1. A. Fujishima and K. Honda, *Nature*, **238**, 37 (1972).
2. A. Fujishima, K. Kohayakawa, and K. Honda, *This Journal*, **122**, 1487 (1975).
3. A. Fujishima, K. Kohayakawa, and K. Honda, *Bull. Chem. Soc. Jpn.*, **48**, 1041 (1975).
4. M. S. Wrighton, D. S. Ginley, P. T. Wolczanski, A. B. Ellis, D. L. Morse, and A. Linz, *Proc. Natl. Acad. Sci. U.S.A.*, **72**, 1518 (1975).
5. K. L. Hardee and A. J. Bard, *This Journal*, **122**, 739 (1975).
6. J. Keeney, D. H. Weistein, and G. M. Haas, *Nature*, **253**, 719 (1975).
7. A. J. Nozik, *ibid.*, **257**, 383 (1975).
8. W. Gissler, P. L. Lensi, and S. Pizzini, *J. App. Electrochem.*, **6**, 9 (1976).
9. J. H. Carey and B. G. Oliver, *Nature*, **259**, 555 (1976).
10. D. Laser and A. J. Bard, *This Journal*, **123**, 1027 (1976).
11. T. Ohnishi, Y. Nakato, and H. Tsubomura, *Ber. Bunsenges. Phys. Chem.*, **79**, 523 (1975).
12. H. Yoneyama, H. Sakamoto, and H. Tamura, *Electrochim. Acta*, **20**, 341 (1975).
13. T. Watanabe, A. Fujishima, and K. Honda, *Bull. Chem. Soc. Jpn.*, **49**, 355 (1976).
14. M. S. Wrighton, A. B. Ellis, P. T. Wolczanski, D. L. Morse, H. B. Abrahamson, and D. S. Ginley, *J. Am. Chem. Soc.*, **98**, 2774 (1976).
15. J. G. Mavroides, J. A. Kafalas, and D. F. Kolesar, *Appl. Phys. Lett.*, **28**, 241 (1976).
16. H. Kim and H. A. Laitinen, *This Journal*, **122**, 53 (1975).
17. M. S. Wrighton, D. L. Morse, A. B. Ellis, D. S. Ginley, and H. B. Abrahamson, *J. Am. Chem. Soc.*, **98**, 44 (1976).
18. A. B. Ellis, S. W. Kaiser, and M. S. Wrighton, *J. Phys. Chem.*, **80**, 1325 (1976).
19. G. Hodes, D. Cahen, and J. Manassen, *Nature*, **260**, 312 (1976).
20. K. L. Hardee and A. J. Bard, *This Journal*, **124**, 215 (1977).
21. K. L. Hardee and A. J. Bard, *ibid.*, **123**, 1024 (1976).
22. R. Williams, *J. Chem. Phys.*, **32**, 1505 (1960).
23. H. Gerischer and E. Meyer, *Z. Phys. Chem. (N.F.)*, **74**, 302 (1971).
24. H. Gerischer, *J. Electroanal. Chem. Interfacial Electrochem.*, **58**, 263 (1975).
25. A. Fujishima, E. Sugiyama, and K. Honda, *Bull. Chem. Soc. Jpn.*, **44**, 304 (1971).
26. F. Sitabkhan, *Ber. Bunsenges. Phys. Chem.*, **76**, 389 (1972).
27. A. B. Ellis, S. W. Kaiser, and M. S. Wrighton, *J. Am. Chem. Soc.*, **98**, 1635 (1976).
28. B. Miller and A. Heller, *Nature*, **262**, 680 (1976).
29. A. B. Ellis, S. W. Kaiser, and M. S. Wrighton, *J. Am. Chem. Soc.*, **98**, 6418 (1976).
30. F. Foerster and A. Friessner, *Ber. Bunsenges. Phys. Chem.*, **35**, 2515 (1902).
31. A. Friessner, *Z. Elektrochem.*, **10**, 265 (1904).
32. F. Yokosuka, A. Okuwaki, and T. Okabe, *Nippon Kagaku Kaishi*, **1975**, 1722.
33. R. A. L. Vanden Berghe and W. P. Gomes, *Ber. Bunsenges. Phys. Chem.*, **76**, 481 (1972).
34. S. N. Frank and A. J. Bard, *J. Am. Chem. Soc.*, **97**, 7427 (1975).
35. H. Gerischer and J. Gobrecht, *Ber. Bunsenges. Phys. Chem.*, **80**, 327 (1976).

Brief Communication

The Thermodynamics of Arsine Evolution

H. J. Davis*

Noranda Research Centre, Pointe Claire, Quebec, Canada H9R 1G5

The widely published and accepted values for the arsine evolution potential in acid solutions appear to be in error. In view of the very hazardous nature of arsine and the industrial significance of arsenic cementation and removal by electrolysis, a reassessment of the available thermodynamic data relating to this process has been undertaken.

Latimer (1), de Bethune and Loud (2), and Pourbaix (3) give the standard aqueous electrode potential for the reaction

$$As + 3H^+ + 3e^- = AsH_3(g)$$

as -0.608V. This result is based on a value of 42 kcal/mole for the free energy of formation of AsH_3 calculated from an enthalpy of formation of 41 kcal/mole at 298.2°K (4) and an estimate of 52 cal/mole deg for the standard entropy (1). [This value for the enthalpy is based upon the work of Ogier (5) in 1878 and its validity was questioned by Latimer (1)]. These data give the arsine evolution potential at 298.2°K as

$$E_{298.2} = -0.608 - 0.0591\,pH - 0.0197 \log pAsH_3 \quad [1]$$

More recent data on the enthalpy of formation of $AsH_{3(g)}$ have been obtained as follows:

$$\Delta H^\circ_{f298} = 18{,}000 \pm 1{,}500 \text{ cal/mole (1956) (6)}$$

* Electrochemical Society Active Member.
Key words: arsine, standard potential, arsenic, safety.

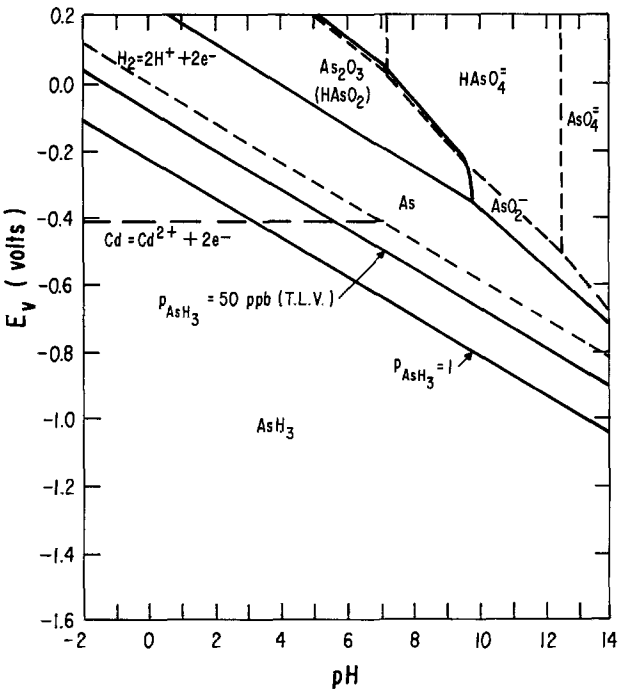


Fig. 1. Potential-pH equilibrium diagram for the system arsenic-water at 25°C, showing voltage-pH ranges capable of giving rise to arsine generation in excess of the threshold limit value.

$$\Delta H°_{f298} = 15{,}870 \pm 250 \text{ cal/mole (1960) (7)}$$

$$\Delta H°_{f298} = 15{,}000 \text{ cal/mole (1961) (8)}$$

$$\Delta H°_{f298} = 14{,}900 \pm 400 \text{ cal/mole (1972) (9)}$$

The standard entropy of arsine has been obtained as follows

$$S°_{298}(AsH_{3(g)}) = 53.21 \pm 0.1 \text{ cal/mole deg (1955) (10)}$$

$$S°_{298}(AsH_{3(g)}) = 53.22 \pm 0.1 \text{ cal/mole deg (1961) (11)}$$

From the above, values of 15,000 cal/mole for the standard enthalpy of formation of arsine and of 53.2 cal/mole deg for the standard entropy of arsine have been used to recalculate the standard free energy of formation of arsine from solid arsenic and gaseous hydrogen. Using a value of 8.4 ± 0.2 cal/deg mole for the standard entropy of arsenic (11) and the accepted value of 31.2 cal/deg mole for the standard entropy of hydrogen (4), the standard free energy of formation for arsine according to the following equation

$$As_{(s)} + 3/2\ H_2 \rightarrow AsH_{3(g)}$$

is given by

$$\Delta G°_{f(AsH3)} = \Delta H°_f - T\Delta S°_f$$

$$= 15{,}000 - 298.2\ (-2.0)$$

$$\Delta G°_{f(AsH3)} = 15{,}596 \text{ cal/mole}$$

This value is lower than the value of 26.4 kcal/mole given by Gunn *et al.* (7) and quoted by Dewalens *et al.* (12). The difference is due to the necessity of using solid arsenic as representative of its standard state at 25°C, Gunn *et al.* (7) apparently using the entropy of arsenic vapor in their calculation of $\Delta S°_f$. The value of 15,596 cal/mole for the free energy of formation of arsine agrees well with the data published by Hopper *et al.* (13) on the free energy of arsine as a function of temperature.

Using this value for $\Delta G°_{o(AsH3)}$ the standard aqueous electrode potential for the arsine/arsenic couple in acids is given by

$$E°_o = \frac{-15{,}569}{3 \times 23{,}060} = -0.225\text{V}$$

At other pH and arsine partial pressures, the reversible potential at 25°C for the reaction

$$As + 3H^+ + 3e^- = AsH_3(g)$$

is given by

$$E_o = -0.225 - 0.0591\ pH - 0.0197 \log p(AsH_3)$$

Figure 1 shows the modified pH-potential diagram for arsenic reduction in aqueous solutions at 25°C. It is now apparent that arsenic cementation with such metals as iron or cadmium does not preclude the evolution of arsine and recent suggestions in the literature (14, 15) that cadmium can be used to safely cement arsenic are not consistent with the data presented here and must be viewed with extreme caution.

Manuscript received Dec. 6, 1976; revised manuscript received Jan 7, 1977.

Any discussion of this paper will appear in a Discussion Section to be published in the December 1977 JOURNAL. All discussions for the December 1977 Discussion Section should be submitted by Aug. 1, 1977.

REFERENCES

1. W. M. Latimer, "Oxidation Potentials," Prentice-Hall, New York (1952).
2. A. J. de Bethune and N. A. S. Loud, "Standard Aqueous Electrode Potentials and Temperature Coefficients at 25°C," Clifford A. Hempel, Skokie, Illinois (1960).
3. M. Pourbaix, "Atlas of Electrochemical Equilibria in Aqueous Solutions," Pergamon Press, Oxford (1966).
4. F. D. Rossini, D. D. Wagman, W. H. Evans, S. Levine, and I. Jaffe, "Selected Values of Chemical Thermodynamic Properties," N.B.S. Circular 500 (February 1972).
5. M. J. Ogier, *C. R.*, **87**, 210 (1878).
6. S. M. Ariya *et al.*, *Zh. Obshch. Khim.*, **26**, 1813 (1956).
7. S. R. Gunn *et al.*, *J. Phys. Chem.*, **64**, 1334 (1960).
8. F. E. Saalfeld and H. J. Svec, U.S.A.E.C. Report IS-386 (November 1961).
9. S. R. Gunn, *Inorg. Chem.*, **11**, 796 (1972).
10. R. H. Sherman and W. F. Giauque, *J. Am. Chem. Soc.*, **77**, 2154 (1955).
11. K. K. Kelley and E. G. King, U.S. Bureau of Mines, Bulletin 592 (1961).
12. J. Dewalens, L. Heerman, and L. V. Simaeys, *This Journal*, **122**, 477 (1975).
13. J. R. Hopper, H. S. M. Setty, E. M. Swinderman, and C. L. Yaws, *Solid State Technol.*, **18**, 47 (1974).
14. B. R. Palmer, G. Gutierrez Menendez, and M. C. Fuerstenau, *Metall. Trans. B*, **6**, 557 (1975).
15. B. R. Palmer, F. Nami, and M. Fuerstenau, *ibid.*, **7**, 385 (1976).

Thermal Desorption of Hydrogen Electrochemically Adsorbed on a Carbon Electrode

W. Warren and J. T. Kummer

Ford Motor Company, Engineering and Research Staff, Dearborn, Michigan 48121

A completely inert electrode (one that does not react with water or chemisorb H_2) charged in a dilute acid solution (HCl, H_2CO_3) to some voltage less than the hydrogen evolution voltage will, in addition to neutral adsorbed species, consist of excess electrons in the electrode surface together with the compensating positive charge due to an excess of hydrated protons at or near the solution electrode interface. Upon removing from solution and heating to a sufficiently high temperature the excess hydrated protons will dehydrate, combine with the excess electrons in the electrode, and, if they are sufficiently mobile, combine and be evolved as hydrogen gas.

Satisfactory inert electrodes would be gold or mercury since they are inert to water and do not chemisorb hydrogen. We are dealing with a surface phenomenon so that the magnitude of any experimental results will increase linearly with the surface area of the inert electrode. High surface area gold electrodes stable toward sintering at high temperature (up to 1000°C) are not available. Experimental work with gold electrodes of low surface area would require sensitive hydrogen detection equipment and equipment to monitor the cleanliness of the gold surface. Since this type of equipment is not available to us, we have used high surface area carbon as the electrode. This simplifies the analytical problems but complicates the interpretation of the results because the electrode is not inert to water and hydrogen. Using carbon electrodes, we have nevertheless obtained results that are consistent with an explanation based on proton dehydration and these results are the subject of this brief note.

Experimental

The carbon electrode used (~0.6 × 0.6 × 5 cm) was obtained from Stackpole Carbon Company, St. Marys, Pennsylvania. It weighed ~2g and its surface area was ~200 m^2/g. The electrode was treated with concentrated HCl + HF at 100°C and then, after washing, with hydrogen at 800°C before use in order to reduce oxygenated surface groups. The ash content was <0.2 weight percent (w/o).

The apparatus used is shown in Fig. 1. For these experiments a 0.5M HCl solution was used as an electrolyte, and helium gas was used to manipulate the solutions and also as a carrier gas for the evolved hydrogen when the carbon electrode was heated. The helium carrier gas was analyzed for hydrogen and other constituents by a Consolidated Engineering Corporation 615 mass spectrometer constructed for continuous on-stream analysis.

Procedure

Before the run, the apparatus and solutions were purged with helium. With stopcock A and B closed, the top part of the apparatus was evacuated through stopcock C to a few Torr and then the degassed HCl solution was allowed to rise and cover the electrode. The evacuation is importnt in order to allow the solution to penetrate the carbon. The carbon electrode was charged by a variable voltage d-c source in an arrangement that permitted continuous monitoring of the current and of the potential difference between the carbon and calomel electrode. The electrolyte resistance and the small overvoltage of the calomel electrode as a function of current had been previously determined so that the zero current potential of the carbon electrode *vs.* the calomel electrode as a function of coulombs charged could be obtained. The charging current was typically between 0.5 and 1 mA. The charging time was overnight. During charge the carbon electrode was negative and the calomel electrode positive.

After charging was completed, the electrolyte was drained away from the charcoal and a helium flow of about 30 cm^3/min was established. The charged electrode was dried by heating to about 120°C for at least 15 min, followed by heating to about 250°C for at least 10 min. Longer heating did not produce any additional removal of electrolyte from the electrode. The helium

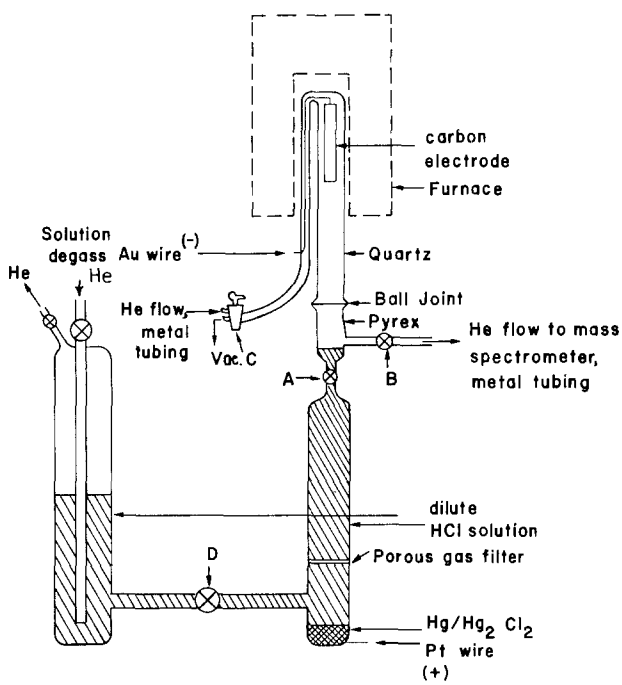


Fig. 1. Apparatus used for the experiments

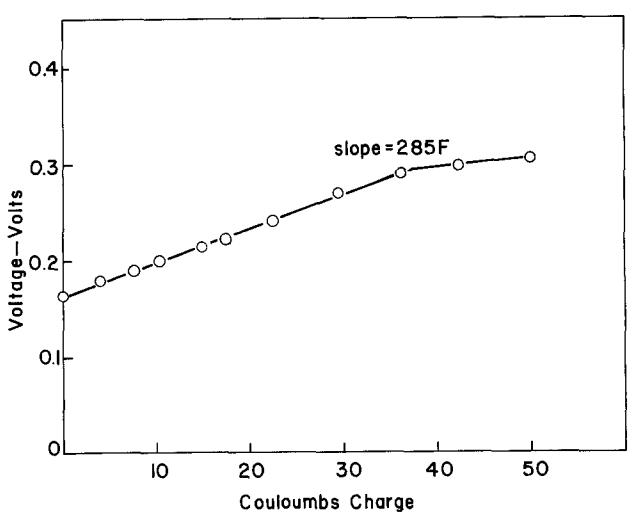


Fig. 2. Open-circuit voltage vs. charge during charging

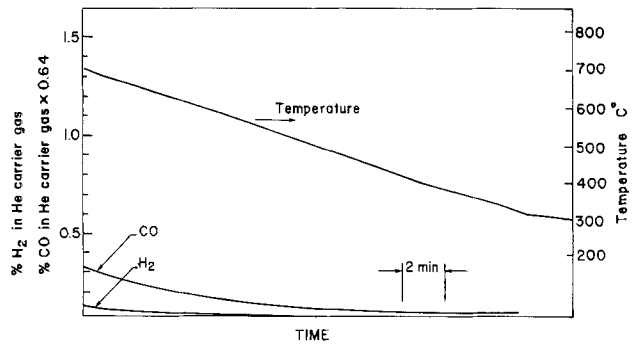


Fig. 3. Thermal desorption of an uncharged electrode

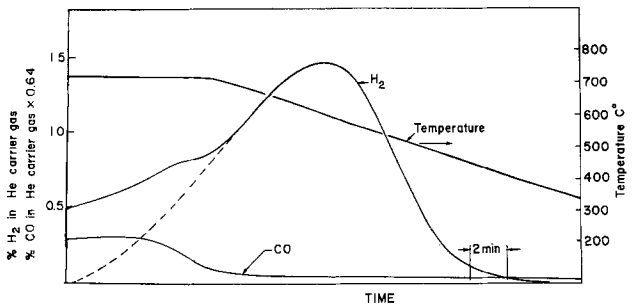


Fig. 4. Thermal desorption of a charged electrode

flow was then continuously sampled by a Consolidated Electrodynamics mass spectrometer as the electrode was heated by a small furnace controlled by a linear programmer. The temperature was generally raised from about 250° to about 700°C in ~15 min, and was constantly monitored by a thermocouple wrapped around the apparatus less than 5 mm away from the surface of the charcoal. The electrode could then be cooled and recharged without ever exposing it to the atmosphere.

Temperatures much greater than ~700°C were avoided since at 650°C the water-gas reaction was found to be measurable and the expected proton dehydration will produce water vapor. Above 600°-700°C CO was evolved from the carbon.

Results

After a helium purge at 700°C, the voltage of the uncharged carbon electrode with respect to the calomel electrode was from −0.13 to −0.16V. This, according to Frumkin *et al.* (1) is the potential of zero charge. The charging curve of voltage *vs.* charge was linear in all cases up to ~ −0.30V. The calculated hydrogen evolution voltage (1 atm H_2) is ~ −0.33V. See Fig. 2 for a representative charging curve. The electrode behaved as a nearly perfect capacitor up to ~0.30V or up to a charge of 30-35C. It was possible to raise the carbon electrode potential past that voltage but deviation from ideal capacitor behavior was observed and became quite pronounced with increasing charge. The average of five runs showed an implied capacitance of 290 ± 20 farads. The total H content of the carbon electrode before use was 0.2 w/o and after eight runs, during which a total charge of 400C was passed, was 0.4 w/o.

During the heating process, the mass spectrometer was used to check all mass numbers from 12 to 100, as well as mass number 2. However, with few exceptions the only mass numbers that showed any temperature variation corresponded to hydrogen and carbon monoxide. Although water was certainly present at some temperatures, it was trapped out with Dry Ice before reaching the mass spectrometer so that any HCl evolved would not corrode the machine. Methane peaks were also occasionally detected, but the total amount of methane given off in any single run never exceeded about 0.1 ml. Similarly, small amounts of CO_2 were sometimes seen.

Evolution of hydrogen and carbon monoxide followed a constant pattern. See Fig. 4. CO evolution began when the electrode reached about 600°C. Hydrogen evolution began around 350°-400°C, reached a peak between 500°-550°C, and began to rise again around 650°C as CO evolution began.

A blank run made by heating the carbon electrode after exposure for 16 hr to the dilute HCl solution in the apparatus of Fig. 1, but without charging, did not evolve H_2 below 600°C, (2) and only small amounts at 650°-700°C. See Fig. 3. When the electrode was charged, evolution of hydrogen at <600°C was observed. See Fig. 4. The results of four charging runs are shown in Table I. In calculating the total amount of hydrogen evolved, the hydrogen evolution during the last part of the run at high temperatures was estimated using the dashed line, as illustrated in Fig. 4. After several charging runs in which ~100C of charge had been passed, the HCl electrolyte was analyzed for total carbon content (not CO_2) and found to contain only 0.37 mg C.

Discussion

The evolution of hydrogen, upon heating, by the charged electrodes but not by the uncharged electrode shows that hydrogen is evolved thermally as a result of the prior electrochemical process. At the end of charge, a measured number of electrons have been moved into the carbon electrode and an equal number of Cl^- ions removed as Hg_2Cl_2 from solution at the mercury electrode (very visible). As a result, at the carbon electrode, there will be an excess of hydrated H^+ ions over the anions present at or near the electrode surface, or there will be neutral chemisorbed H species on the electrode surface of various kinds produced from the solution protons, or there will be produced compensating anions in solution ($HCOO^-$, for example) produced from neutral species at the carbon electrode surface. These are required because of the necessity of charge neutrality. A hydrogen ion, even in a tight double layer, would be hydrated because a proton has essentially no size and because the hydration is thermodynamically necessary in order for the H^+ to exist at the usual electrochemical voltages (3). The hydrated hydrogen ions could be electrostatically attracted to the basal and prismatic planes of the carbon as a result of the excess electrons in the electrode. On an inert electrode that does not chemisorb hydrogen, and at a volt-

Table I. Results obtained by heating a charged carbon electrode

Run*	Coulombs added	H_2 expected, cm³ STP	Voltage relative to calomel: Before charging	After charging	After heating	H_2 evolved to 700°C, cm³ STP	CO evolved to 700°C, cm³ STP	H_2 evolved as % of H_2 expected
3	40.7	4.73	−0.15	−0.28	−0.16	3.3	<1	70
4	38.6	4.48	−0.16	−0.30	−0.04	3.2	<1	71
8	43.3	5.03	−0.13	−0.30	−0.17	3.1	1.5	62
6	117	13.59	−0.14	−0.41**	−0.16	8.6	1.5	63

* In runs 1, 2, and 5 the electrolyte drained from electrode during the charging due to leaky stopcock so results are not included.
** A small amount of H_2 evolution during charge observed.

age less than the thermodynamic hydrogen evolution voltage and in the presence of H_2 gas this is what occurs.

If a hydrogen atom can form a stable covalent bond to the carbon electrode surface (or to an O atom chemically bound to the surface) then the hydrogen can exist as an essentially neutral (modified by its dipole behavior) surface chemisorbed species after charge. On carbon these chemisorbed H atoms would probably occur at the prismatic faces where there are unsaturated valences rather than on the basal planes (4). These could be formed at less than the evolution voltage if their free energy of formation were negative. Since the voltages we used on charge are just less than sufficient to produce H_2 molecules (not H atoms) in a thermodynamic sense, then we can assess the probability of chemisorbed H species occurring by measuring the chemisorption of H_2 on degassed carbon when exposed to molecular H_2 under conditions where the chemisorption is not rate limited. Hydrogen chemisorption on degassed carbon at 350°C has been observed by Boudart and co-workers (5) so that this type of surface species could be present on our carbon surface after charge. From Boudart's work one could estimate that ~10% of the graphite crystal edge atomic sites could be covered with chemisorbed hydrogen atoms if there were no kinetic inhibitors to this process. One cannot say from Boudart's work if the chemisorbed H would form in the presence of water or that they would evolve H_2 in the temperature range that we observed. The apparent capacitatorlike behavior of the charging curves would argue for electrostatically adsorbed hydrated hydrogen ions rather than the formation of a covalent surface compound, but the present experiments are not conclusive in this respect.

The formation of acid anions in water solution free from the electrode in the absence of O_2 appears chemically unlikely (6). In addition, the absence of significant amounts of carbon compounds in the electrolyte would argue against such an interpretation.

The low yield of hydrogen (~60-70%) with respect to the charge passed has been of great concern to us. It is possible that, upon heating, some H atoms are incorporated into the carbon lattice rather than combining with another H atom. This is qualitatively consistent with hydrogen analysis data of the carbon before and after use. It is also possible that our inability to experimentally observe hydrogen evolution from the electrochemical process above 700°C could be important. As stated before, however, the fact that carbon is not inert to hydrogen and water makes precise quantitative results difficult to obtain.

On the onset of this work, which was a summer project for an undergraduate student, it was hoped that we could determine if the temperature required for hydrogen evolution was affected by the final charging voltage. This might be expected from thermodynamic considerations. Such data may help in understanding electrode processes, and could conceivably be of practical interest in the production of H_2 from a part electrochemical, part thermal process. Because of time limitation and the difficulty of working with carbon, this goal was not realized.

Manuscript submitted Nov. 1, 1976; revised manuscript received Jan. 5, 1977.

Any discussion of this paper will appear in a Discussion Section to be published in the December 1977 JOURNAL. All discussions for the December 1977 Discussion Section should be submitted by Aug. 1, 1977.

Publication costs of this article were assisted by the Ford Motor Company.

REFERENCES

1. A. N. Frumkin, E. A. Ponomarenko, and R. Kh. Burshtein, *Dokl. Akad. Nauk* SSSR, **149**, 1123 (1963); *CA*, **61**, 2194-C.
2. Balwant Rai Puri and R. C. Bansal, *Carbon*, **1**, 451 (1964).
3. H. F. Halliwell and S. C. Hyburg, *Trans. Faraday Soc.*, **59**, 1126 (1963).
4. Yu A. Zarifyany, V. F. Kiselev, N. N. Leyhnev, and O. V. Nikitina, *Carbon*, **5**, 127 (1967).
5. A. Robell, E. V. Ballow, and M. Boudart, *J. Phys. Chem.*, **68**, 2748 (1964).
6. J. S. Mattson and H. B. Mark, Jr., "Activated Carbon," Marcel Dekker Inc., New York (1971).

JOURNAL OF THE ELECTROCHEMICAL SOCIETY

SOLID-STATE SCIENCE AND TECHNOLOGY

MAY 1977

The Speed of Response of Solid Electrolyte Galvanic Cells for Gas Sensing

L. Heyne* and D. den Engelsen

Philips Research Laboratories, Eindhoven, The Netherlands

ABSTRACT

The factors affecting the speed of response of solid electrolyte gas sensors are considered. The uptake or release of sample material (gas) by such cells is the main reason for sluggishness in response and for variation with time in the emf developed. Special attention is given to the effect on the emf caused by the presence of a second phase with electrical properties different from those of the main material. For a model cell, consisting of a solid electrolyte containing an intergrain phase with mixed conductor properties, the diffusion equation is solved numerically. The ambipolar diffusion coefficient is used in the calculations. The numerical parameters required for the calculation of concentration profiles and emf as a function of time are those of a typical calcia-stabilized zirconia. The results have a more general validity.

When the concentration of the active component at one of the electrodes of an electrochemical concentration cell is suddenly altered, the response of the open-cell voltage on this change shows some delay. One common reason for such a delay is that a certain, finite, amount of material is taken up (or released) by the electrolyte-electrode system, and it takes some time before the material required is supplied (or extracted) by the medium to be measured. During this transition period the emf developed by the cell may have a value deviating from that in the final stationary state. This represents a slow electrical response.

In the idealized galvanic cells usually considered in textbooks only the extra material adsorbed on the surface of electrolyte and electrode is involved, inducing a change in double layer charge. But with practical electrolytes there is also penetration into the electrolyte because its composition depends on the pressure of the active component of the gas sample. In solid electrolyte cells the active component usually forms a main constituent of the electrolyte material. Consequently, variations in gas concentration induce changes in the composition of the electrolyte. These compositional changes give rise to small deviations from the exact stoichiometric ratio.

During each transition from one concentration in the medium to another one, the amount of material equivalent to the aforementioned changes must be supplied (or taken up) by the medium. Although these amounts usually are very small, they nevertheless may give rise to an appreciable sluggishness in response if the supply is hampered in one way or another.

So we recognize the two key parameters which determine the speed of response. The first is the amount of active material involved in the change from one condition to the other. The second is the density of material flux with which the required amount can be supplied. In each of the several mechanisms that may be speed limiting for the emf response, we have to consider the nature and magnitude of these two key parameters.

It is the aim of the present paper to study the influence on the emf of the takeup of active material by the electrolyte and its diffusion into the bulk of the electrolyte. Therefore, we neglect other factors such as adsorption and double layer charging. In the first instance we further assume that the rate of the material takeup is determined by internal diffusion only ("reversible" electrodes). Later on we relax these restrictions and discuss the influence of polarization effects.

The diffusion in the bulk of the electrolyte is an example where the model of so-called ambipolar diffusion can be applied. In this concept two types of charged particles flow simultaneously with their fluxes adapted in such a way that no net charge transport takes place. Consequently, the resulting mass transport represents the flow of a neutral chemical component only. This type of diffusion is also known as chemical diffusion to stress the difference with self-diffusion or tracer diffusion, where only one particle type is involved and where no "chemical" concentration gradients exist.

In the following, calculations are made for several models of the solid electrolyte in a galvanic gas sensor. The cell considered is schematically represented in Fig. 1a: A sample gas space and a reference gas space are separated by a solid electrolyte which is provided with porous inert electrodes on both sides. Figure 1b illustrates the penetration of the active species into the electrolyte when, after a long period of equal partial pressures at both sides, the sample pressure is suddenly increased. Since, as is shown below, the effective diffusion coefficient is concentration dependent, exact integration of Fick's diffusion laws presents difficulties. Although some methods for dealing with these problems are treated in the literature (1, 2), we preferred to use a numerical integration method right from the start. This has the advantage that not only the exact law for the concentration dependence of the diffusion coefficient can be used, but also any nonuniformity in the

* Electrochemical Society Active Member.

Key words: diffusion, lattice defect, electrode polarization, zirconia, oxygen.

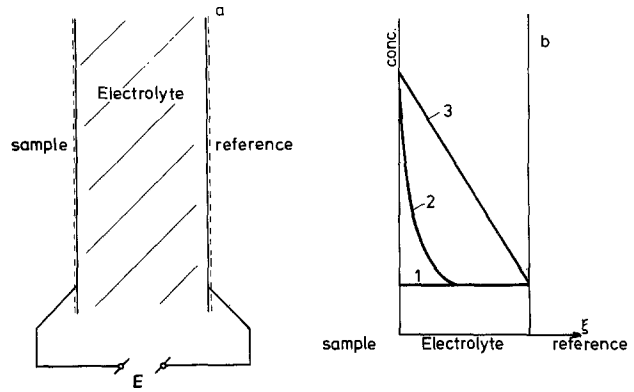


Fig. 1. Schematic representation of electrochemical gas sensor with solid electrolyte. a, Physical lay-out. b, Concentration profiles in electrolyte after a sudden increase in partial pressure in sample space. Curve 1, initial distribution; curve 2, intermediate distribution; and curve 3, final steady-state distribution.

electrolytic properties can be introduced at will. In this way it became possible to study the influence of a foreign compound with mixed conductor properties present within the electrolytic sample at grain boundaries.

Basic Equations

There exist two methods that give a simple quantitative description of the combined diffusive motion of two types of charge carriers. One is due to Wagner and stems from his treatment of the growth of "scaling layers" on metal surfaces (3-5); the other is the so-called "ambipolar" treatment which is used extensively in many fields, such as semiconductors, gas discharges, and electrolytic solutions (6). We quote only the results of both descriptions and show that for the case of interest here they lead to practically the same value for the effective diffusion constant. A more detailed analysis of the assumptions and approximations involved will be given in a separate paper.

The formulas take a simple form if transport numbers t_k are introduced where index k indicates the type of charge carrier. They are defined as the ratio of partial conductivity σ_k and total conductivity as follows

$$t_k = \frac{\sigma_k}{\sigma_1 + \sigma_2} \quad \text{where} \quad k = 1, 2$$

Using the proportionality between mobility and diffusion coefficient D_k (Einstein relation) these equations can also be written as

$$t_k = \frac{z_k^2 c_k D_k}{z_1^2 c_1 D_1 + z_2^2 c_2 D_2} \quad \text{where} \quad k = 1, 2 \qquad [1]$$

Here c_k and z_k denote charge carrier concentration and relative charge, respectively.

In the ambipolar treatment the diffusion process is described as the simultaneous flow of the two types of charge carriers. Their local concentrations are adapted to each other by the condition of electroneutrality. The expression arrived at for the common effective diffusion coefficient is

$$\tilde{D} = \frac{(z_1^2 c_1 + z_2^2 c_2) D_1 D_2}{z_1^2 c_1 D_1 + z_2^2 c_2 D_2} \qquad [2]$$

Identifying index 1 with electronic carriers and 2 with ionic defects and introducing transport numbers according to Eq. [1] yields

$$\tilde{D} = t_e D_{ion} + t_{ion} D_e = t_e D_{ion} + (1 - t_e) D_e \qquad [3]$$

This ambipolar diffusion coefficient refers to the neutral combination of ionic defects and electronic carriers and thus to the neutral active component considered earlier. In solid electrolytes or mixed conductors t_{ion} is not very small and, since usually electronic charge carriers are much more mobile than ionic defects ($D_e >> D_{ion}$), the second term in Eq. [3] dominates strongly. Therefore this equation can be written

$$\tilde{D} \approx t_{ion} D_e \qquad [4]$$

Wagner's type of treatment leads to an effective diffusion coefficient which can be written in the form

$$\tilde{D} = t_{ion} D_e \left(\frac{1}{kT} \frac{\partial \mu}{\partial \ln \tilde{c}} \right) \qquad [5]$$

Here μ is the chemical potential per atomic unit of one (neutral) component of the substance considered, $\tilde{c}$ the excess concentration over the stoichiometric composition of the same component (in atomic units), and k and T have their usual meaning. For solid electrolytes and mixed conductors with high ionic defect concentrations, the factor in parenthesis, the so-called thermodynamic factor, appears to be close to unity, so that Eq. [5] becomes identical with Eq. [4]. For such materials the ionic conductivity is independent of the components' chemical potential (partial pressure), so the transport numbers t_e and t_{ion} are only variable through the variation of the electronic conductivity σ_e.

Numerical Method

In this section it will be shown how the diffusion process following a jump in sample pressure as indicated in Fig. 1b can be evaluated numerically and how the resulting emf changes with time.

To avoid unnecessary complexity of the presentation, we restrict our considerations to oxidic materials with mixed conduction, where electron holes and oxygen vacancies are the relevant charge carriers. In concordance with the final remark of the previous section, the concentration V of the latter type of charge carriers is independent of oxygen pressure (chemical potential), and consequently independent of position in a diffusion experiment. We restrict oxygen pressure variations to that range, where the electronic conductivity always remains p-type.

However, it must be recognized that these choices do not represent a restriction of the applicability of the method to be discussed. With the appropriate, and straightforward, modifications it can be applied at oxygen pressures where the conductivity is n-type, or to galvanic cells with different types of electrolytes of mixed conductors as well.

The concentration of holes h is a measure of the deviation of stoichiometry (excess oxygen).[1] It will be considered as the time and position dependent variable in Fick's second diffusion law. To obtain this parameter in a dimensionless form it is expressed in units of the hole concentration at a certain standard condition (h_{st}), for instance that prevailing in the equilibrium state before the jump in sample pressure took place

$$c_\xi(t) = h(t, \xi)/h_{st} \qquad [6]$$

where t denotes time and ξ is the one-dimensional position coordinate.

Because of the defect mechanism postulated (V = constant), see for instance (8), h depends on the oxygen partial pressure p_{ox} as a quarter-power law

$$h \sim p_{ox}^{1/4} \qquad [7]$$

So, *e.g.*, a jump by a factor 10 in c corresponds to a jump by a factor of 10,000 in the oxygen partial pressure.

Solution of Fick's second diffusion law, which in one dimension reads

[1] Stoichiometry is defined as that composition where the charges of all constituent positive and negative ions, in their normal valency state, balance to zero.

$$\frac{\partial c}{\partial t} = \frac{\partial}{\partial \xi}\left(\tilde{D}\frac{\partial c}{\partial \xi}\right) \qquad [8]$$

can be done by replacing it by the following difference equation

$$\Delta c = \frac{\Delta t}{(\Delta \xi)^2}\Delta(\tilde{D}\Delta c) = \Delta(\tilde{D}'\Delta c) \qquad [9]$$

Here Δt and $\Delta \xi$ denote small steps in time and in position and

$$\tilde{D}' = \tilde{D}\cdot\frac{\Delta t}{(\Delta \xi)^2} \qquad [10]$$

is a normalized dimensionless diffusion coefficient. Here ξ-space is thought to be divided into a grid of integer ξ-values, denoted by x, ranging from 0 to n (the sample boundaries) and spaced by $\Delta\xi$ cm. Expression [9] allows one to calculate a new concentration distribution c_x^{new} at time $t + \Delta t$ from a known one c_x at time t

$$c_x^{new} = c_x + \Delta c = c_x + \tilde{D}'_{x+1}(c_{x+1} - c_x) - \tilde{D}'_x(c_x - c_{x-1}) \quad x = 1, 2 \ldots (n-1) \qquad [11]$$

The indexed values of c and $\tilde{D}'$ denote concentrations and normalized diffusion coefficients at the position indicated by the index.[2] At the boundaries ($x = 0$ and $x = n$) the concentration values are kept fixed; c_0 at the value corresponding to the new oxygen pressure in the sample atmosphere, c_n at the value equivalent with the reference pressure (see Fig. 1). From the new values of c_x, new local transport numbers can be computed according to Eq. [1] and, using Eq. [3], new local diffusion coefficients can be found also

$$t_{h,x}^{new} = \frac{c_x^{new} h_{st} D_h}{c_x^{new} h_{st} D_h + 4VD_V} \quad x = 0, 1 \ldots n \qquad [12]$$

$$\tilde{D}_x^{new} = t_{h,x}^{new} D_V + (1 - t_{h,x}^{new}) D_h \quad x = 0, 1 \ldots n \qquad [13]$$

Here the values 1 and 2 have been introduced for z_1 and z_2 of Eq. [1].

It has been indicated in a previous paper (9) that a second phase between the grains of a ceramic electrolyte sample may have a pronounced effect on its transient behavior used as a galvanic cell. This is so because oxygen potential drops over such second-phase layers give rise to emf contributions different from that of a good electrolyte. A second phase can be introduced in the present model calculations in a very straightforward way. The constants h_{st}, V, D_h, D_V of Eq. [12] and [13] are given values different from those of the main compound in a certain, limited region of x-values. In this way a layer of different properties is simulated. The set of values chosen for the calculations to be presented below are also indicated in Table I.

For each concentration profile calculated using Eq. [11], the emf developed can be calculated from the well-known equation (3)

$$E = -\frac{1}{ze}\int_{'}^{''} t_{ion}\, d\mu \qquad [14]$$

Using the relative hole concentrations $c_x(t)$, Eq. [7], and assuming ideal thermodynamic behavior of holes this equation here takes the form

$$E = \frac{kT}{e}\sum_{x=0}^{n-1}(1 - t_{h,x})(\ln c_{x+1}(t) - \ln c_x(t)) \qquad [15]$$

To enable a simple comparison with the value expected from the ideal Nernst law, we introduced a temperature of 1008°K which with $t_V = 1$ yields an emf value of exactly 200 mV per decade in c_0 (50 mV per decade in p_{ox}).

A sequence of computations was started by setting all concentrations c_x equal to unity except the first one, c_0, which was set corresponding to the new situation in the sample space [for instance (10)]. To illustrate this procedure a simplified example is shown in Fig. 2 for the special case that $\tilde{D}' = 1/2$ (and thus is constant), and for only five values of x. Here the initial and right-hand boundary concentrations are taken as zero, the left-hand boundary is set at unity. It can be easily shown, that as long as $\tilde{D}' \leq 1/2$ such a repetitive process yields smooth solutions. However, if $\tilde{D}' > 1/2$ gradients develop into steeper ones during successive steps and numerical "explosion" results, see for instance Ref. (11). However, this restriction presents no difficulties, because by choice of $\Delta\xi$ and Δt, see Eq. [10], $\tilde{D}'$ can always be made smaller than 1/2 so that good convergence is obtained and, as practice shows, with reasonable computing time. To obtain sufficient accuracy, the calculations reported below have been carried out using 50 values for x and 3200-9600 concentration profiles were calculated successively.

Numerical values for material parameters and experimental conditions are required for the calculations. Such parameters are well known for calcia-stabilized zirconia, and, moreover, cells in which this compound is used are of great practical importance. As our model electrolyte we therefore chose a ceramic containing this compound as its main constituent. Its relevant data are represented in the left-hand column of Table I.

[2] The $\tilde{D}'$ values are chosen as the values at the right-hand side of each grid element instead of averages over the elements to simplify introduction of an inhomogeneity.

Table I. Data used for calculations at $T = 1008°K$

	Stabilized ZrO_2 at $p_{ox} = 1$ bar (10)	Second phase at standard condition (c = 1)
σ_{ion}, Ω^{-1}-cm^{-1}	10^{-3}	2×10^{-5}
σ_h, Ω^{-1}-cm^{-1}	2×10^{-7}	4×10^{-5}
t_h	2×10^{-4}	0.67
V, cm^{-3}	5×10^{21}	5×10^{19}
D_V, cm^2-sec^{-1}	3×10^{-8}	5.4×10^{-8}
h, cm^{-3}	10^{18}	10^{19}
D_h, cm^2-sec^{-1}	10^{-7}	22×10^{-7}
$\tilde{D}$, cm^2-sec^{-1}	10^{-7}	7.6×10^{-7}

	$C_x^{new} = 1/2\,(C_{x-1} + C_{x+1})$				
$t < 0$	0	0	0	0	0
$t = 0$	1	0	0	0	0
$t = \Delta t$	1	1/2	0	0	0
$t = 2\Delta t$	1	1/2	1/4	0	0
$t = 3\Delta t$	1	5/8	1/4	1/8	0
$t = \infty$	1	3/4	1/2	1/4	0

Fig. 2. Simplified example of numerical method. Numbers represent excess concentrations over the original value, upper row, at 5 positions in sample. Boundary values are 1 (first column) and 0 (fifth column). New c-values are obtained by taking the average of the neighboring previous values as indicated by the arrows. This corresponds to $\tilde{D}' = 1/2$ in Eq. [11].

They were taken from our earlier work (10) and have been confirmed, at least in order of magnitude, by later research [see for instance the recent surveys by Fouletier *et al.* (12) and by Fischer and Jahnke (8)].

Note that, because t_V is very close to unity, $\tilde{D} = D_h$ (see Eq. [4]). Consequently, both $\tilde{D}$ and $t_V = t_{ion}$ are independent of the oxygen pressure, and the latter parameter is irrelevant as far as the stabilized zirconia part of the ceramic electrolyte is concerned (staying always in the p-type region).

If a second phase is simulated in the model electrolyte, the set of values given in the second column of Table I is used for that region. These values are not based on actual measurement, but are postulated as possible values. They were intentionally chosen in such a way that the results from the calculations showed interesting features. This aspect is discussed more extensively later on.

The calculations are carried out with a dimensionless parameter x for position. To keep a link with practice, a value of 5 μm was chosen for $\Delta\xi$ to convert the dimensionless x-values to realistic position coordinate values ξ. A time interval of $\Delta t = 0.1$ sec in Eq. [10] then yields $\tilde{D}'$ values below 1/2 when c_0 (the left-hand boundary value after the pressure jump) is kept below 10 and when the data of Table I are introduced via Eq. [12] and [13].

Results

In Fig. 3 and 4 the results of such model calculations for a uniform zirconia sample are given as direct computer plots for a few profiles. The curves are constructed by drawing straight connections between the 50 calculated concentration values. Since in this case the diffusion coefficient is constant and the material uniform, the well-known error function or Fourier's series solution of the diffusion equation (13) could be used to check the accuracy of the result. It appeared that as long as the kinks in the curves are not obvious, the accuracy of the graph is better than the line width of the drawing. Only at the start of the calculation the gradients at the left-hand boundary are so steep that kinks are visible and appreciable errors occur.

In Fig. 5 the curves numbered 1 show that the emf developed is constant and has the value corresponding with Nernst's law right from the beginning. This is so notwithstanding the fact that a diffusion process is still

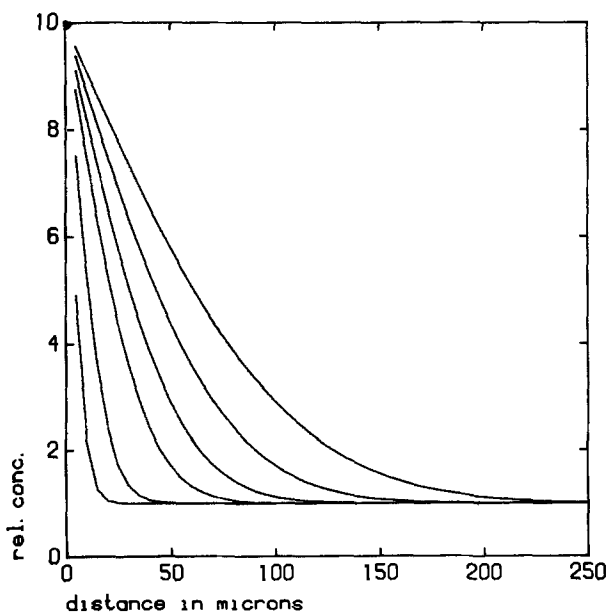


Fig. 3. Concentration profiles in pure stabilized zirconia 2, 10, 40, 80, 160, and 320 sec after a pressure increase at left electrode by a factor of 10^4.

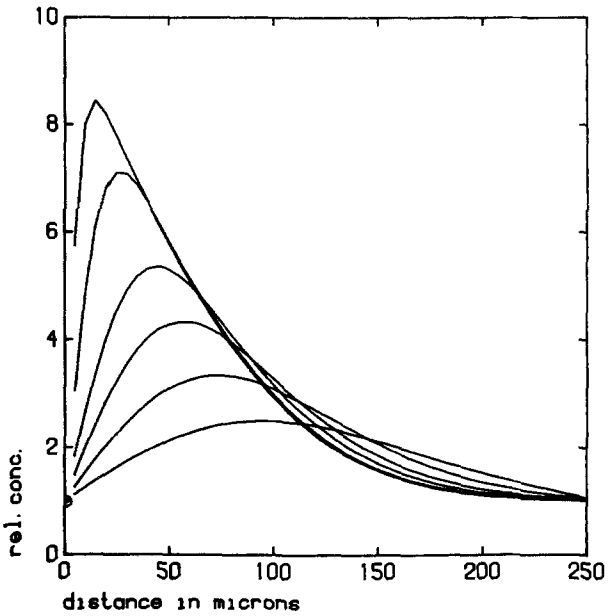


Fig. 4. Concentration profiles 2, 10, 40, 80, 160, and 320 sec after a return to original pressure at left electrode directly after the last profile of Fig. 3.

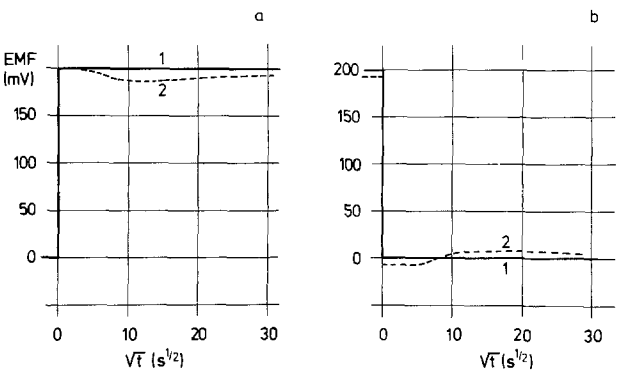


Fig. 5. Time response of emf ($-E$) after pressure increase a, and return to original pressure b. The square root time scale is chosen to be able to span a large period without losing the zero point. Curves 1, pure electrolyte, correspond to profiles of Fig. 3 and 4. Curves 2, zirconia with second phase, correspond to profiles of Fig. 7 and 8.

going on, and that a stationary state has not been established even at the times of the last profiles shown. The reason is that t_{ion} in Eq. [14] is constant, in fact equal to unity, and can be put in front of the integral. Consequently E becomes independent of the μ-distribution (or c_x-distribution) and is determined by the boundary values only. It is important to realize that these boundary values are assumed to be constant and are determined by the fixed oxygen content of the neighboring gas atmospheres by a gas-solid equilibrium. This equilibrium situation is only present if the contacts behave as perfectly reversible electrodes. The latter may not be true in many practical situations however. If the electrodes are not ideally reversible, then the oxygen flux, caused by the concentration gradient inside the solid, leads to a difference in chemical potential of oxygen at both sides of the gas-solid interface. This is larger in the beginning, because of the steep gradients present then, see Fig. 3. In the situation of Fig. 4 fast desorption takes place in the beginning. For a given gradient the oxygen flux can be calculated from Fick's first law. Figure 6 gives this takeup as a function of time expressed in terms of the equivalent electrical current. The infinite value which theoretically should occur at $t = 0$ is not pictured due

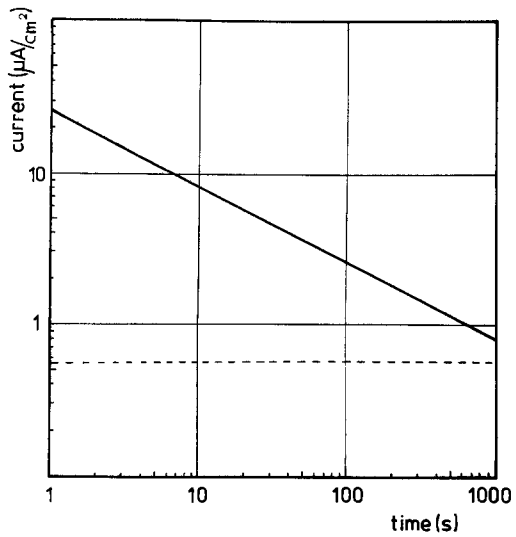


Fig. 6. Uptake of oxygen expressed in terms of current density for uniform zirconia sample and a pressure increase equivalent to a hole concentration rise from 10^{17} to 10^{18} cm^{-3} (10^{-4} to 1 bar in p_{ox}). The dashed line gives the steady-state penetration level for 250 μm sample thickness.

to the logarithmic scales chosen. In the final steady state a linear concentration profile is established leading to a permanent oxygen penetration through the electrolyte wall (8, 10, 12, 14). Its value corresponds to 0.57 μA in the case considered and is also indicated in the figure. Polarizable electrodes generate overvoltages as a result of this flux which, at the left-hand electrode, are large at short times and which modify the emf measured. The resulting time response curves then take the shape of those shown in Fig. 13 (to be discussed later on) instead of the fast response curves 1 of Fig. 5.

The results of calculations on a more complicated model are represented in Fig. 7 and 8. In the ξ-range between 50 and 75 μm the material properties are taken different from those of zirconia according to Table I. The emf shown in Fig. 5a, curve 2 starts with the ideal Nernst value. But as soon as the diffusion front reaches the "second phase," which occurs after about 16 sec, the latter starts to contribute to the emf and deviations

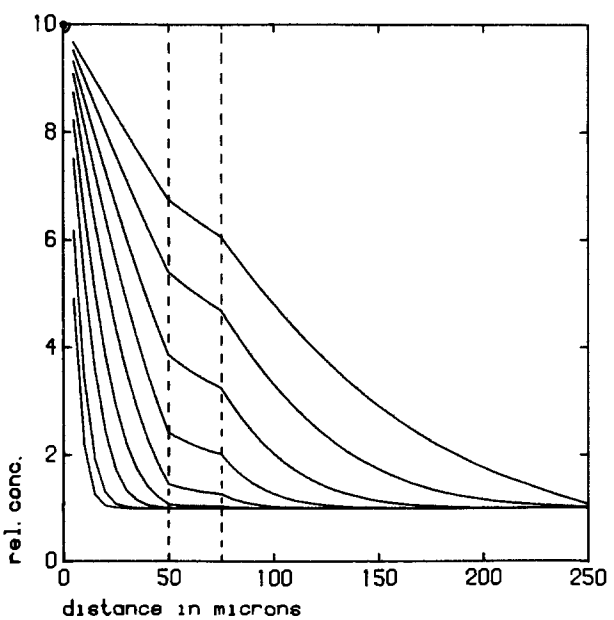


Fig. 7. Concentration profiles in electrolyte with second phase layer with mixed conduction in region indicated by dotted lines. Time after pressure increase at left electrode 2, 4, 10, 20, 40, 80, 160, 320, and 640 sec.

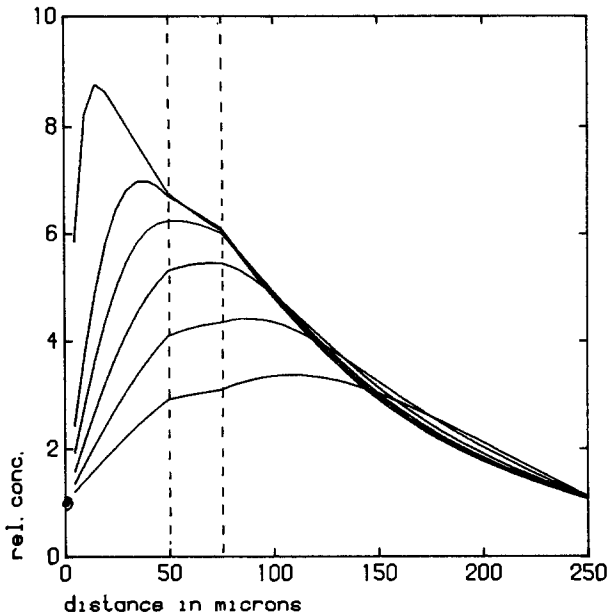


Fig. 8. Concentration profiles 2, 20, 80, 160, and 320 sec after return to original pressure at left electrode directly after last profile of Fig. 7.

occur because the ionic transport number is lower than unity. The deviations grow as the gradient in this region increases; they fall again when the steady state is approached. This is so because the effective diffusion coefficient of the second phase is somewhat higher than that of the electrolyte proper at the concentration occurring in the steady state.

When after 640 sec the sample pressure is returned to its original value (Fig. 8), the first drop in concentration takes place in the electrolyte again. The resulting emf drop is thus exactly 200 mV, the Nernstian value, which means that the voltage starts below zero volts, Fig. 5b, curve 2. It remains practically stationary during the first 20 sec, but then the profile in the second-phase region becomes affected again and slow changes in emf take place. Eventually the concentration drop over the region becomes zero and a point of zero deviation from Nernst's law occurs, which means that the emf passes through zero after about 30 sec. But later on the gradient inverts and a positive error builds up which reaches a maximum. Only after a very long time, of the order of 1 hr, which is much longer than that covered by the computation, zero is approached again. Then the excess concentration built up inside the electrolyte wall has leveled out completely.

Since the effective diffusion constant and transport numbers of the mixed conductor depend strongly on the oxygen pressure, we expect an influence of the pressure range where the electrochemical cell is used. To see this effect a calculation was made with the same parameters as before, but representing a jump down in the oxygen pressure of the sample atmosphere, followed by a return to the original value. A factor of 10 in c is used again corresponding to 10^4 in oxygen pressure. Figure 9 gives the resulting concentration profiles, Fig. 10 the corresponding emf responses after the jump. It is obvious that the effects on the emf are much smaller than in the previous case, the reason why the voltage scale has been expanded. But the same trend and the same time delay are found again. On jumping back to the original pressure a behavior similar to that depicted by curve 2 in Fig. 5b is found. Again the deviations from Nernst's law are smaller but the time delay is the same. The effects are so small because the concentration profiles in the second-phase region stay almost horizontal and this must be a consequence of a higher effective diffusion coefficient.

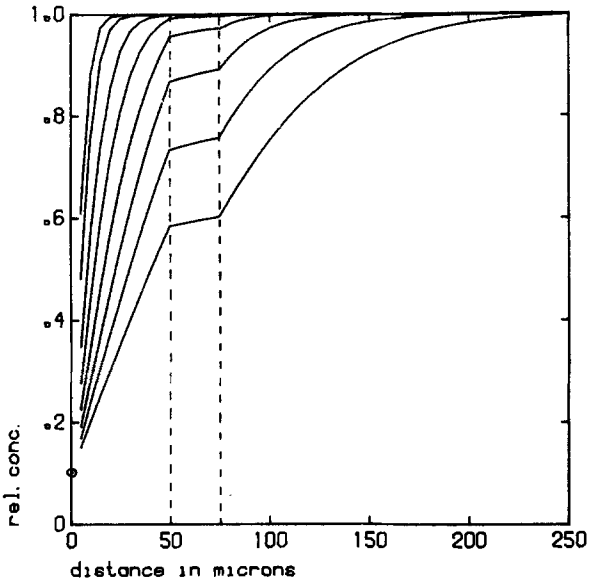


Fig. 9. Concentration profiles in electrolyte with second phase layer 2, 4, 10, 20, 40, 80, 160, and 320 sec after a pressure decrease at left electrode.

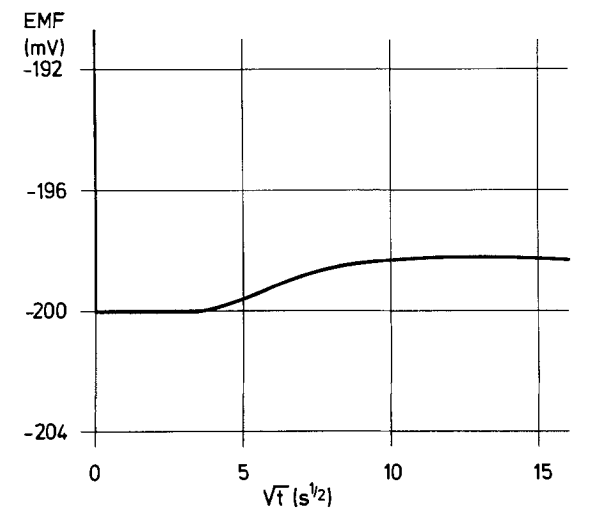


Fig. 10. Time response of emf after pressure decrease corresponding to Fig. 9.

That this is the case can be seen from the values given in Table II which were calculated with Eq. [12] and [13] for hole concentrations a factor 10 higher or lower than the standard value used in all calculations as the starting condition. We see that the transport numbers also contribute to make the error small at lower oxygen pressures; t_{ion} is closer to unity then.

So far the presence of a second phase has been introduced into the model in the form of a layer of mixed conductor properties at some distance from the surface only. The surface itself was considered free from such a contamination. In Fig. 11 and 12 the opposite case is shown; a mixed conductor layer of the same properties and thickness as before is now thought to be present on the surface only. Since the concentration

Table II. Concentration dependence of t_h and $\tilde{D}$ in second phase material

c	0.1	1	10
t_h, %	17	67	95
$\tilde{D}$, 10^{-7} cm^2-sec^{-1}	18.2	7.6	1.6

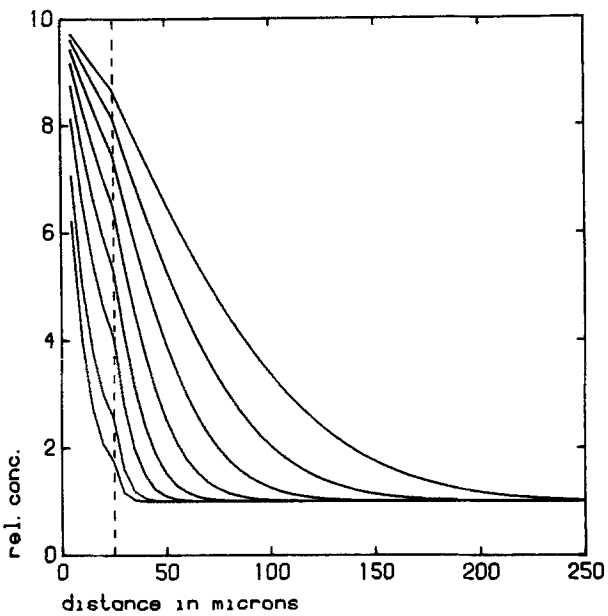


Fig. 11. Concentration profiles in electrolyte with mixed conductor region near the surface 2, 4, 10, 20, 40, 80, 160, and 320 sec after pressure increase at left electrode.

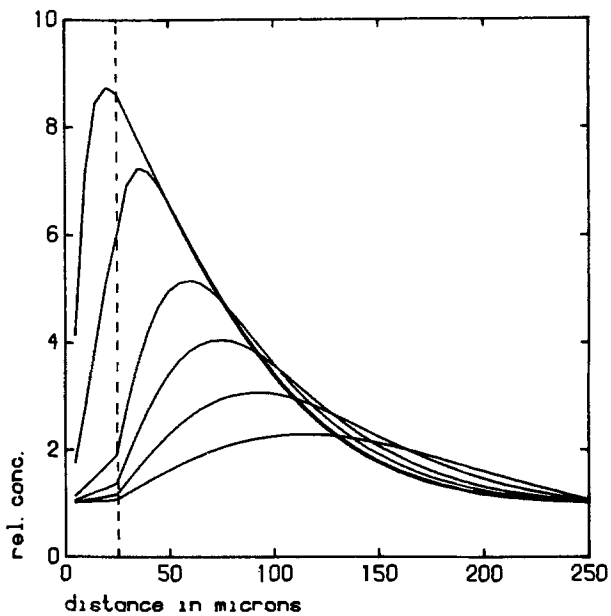


Fig. 12. Concentration profiles in electrolyte with mixed conductor region near the surface 2, 4, 10, 20, 40, 80, 160, and 320 sec after return to original pressure at left electrode following the last profile of Fig. 11.

changes occur in the mixed conductor region right from the beginning, the emf curves represented in Fig. 13 start with deviations from Nernst's law. These diminish in the course of time when the gradient flattens out, and the curves display a typical slow response. This contrasts with the overshoot behavior found before when the second phase is present in the interior of the sample. If the surface layer had been given such properties that no contribution was made to the emf at all (t_{ion} very small), it would have acted as a plain diffusion barrier. Qualitatively the emf response curves would not have changed in this case as calculations, not presented here, showed. The deviation from the ideal response can then be considered as the polarization of a surface layer belonging to the electrode. In fact the foreign layer on top of the electrolyte might be the electrode metal itself, which in that case is no longer considered as ideally porous. In this way the

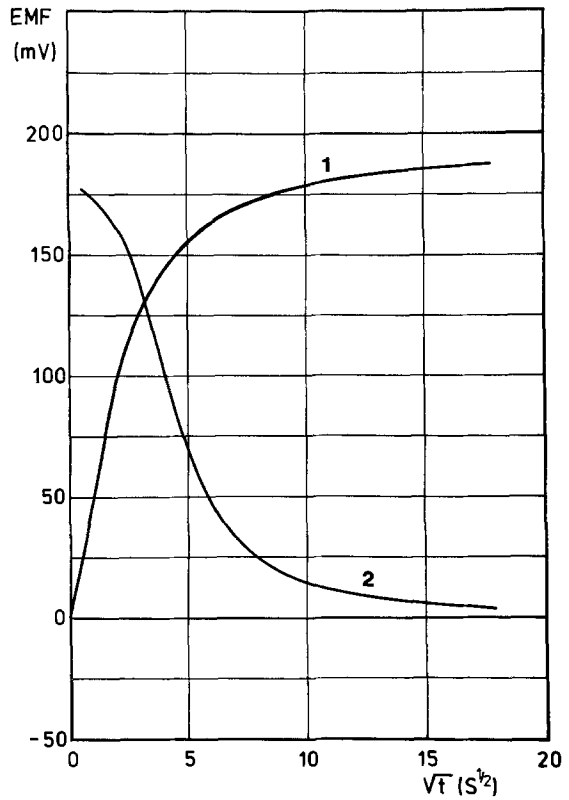


Fig. 13. Time response of emf after pressure increase, curve 1, and return to original, curve 2, corresponding to the profiles of Fig. 11 and 12. Curves of similar shape are found in the case that the surface layer is a mere diffusion resistance, for instance a metal (electrode).

nonreversible electrode qualitatively discussed before in connection with the oxygen uptake, can be introduced into our method of analysis in a quantitative manner.

The results given so far represent only a small part of the computations actually carried out. These covered a wider range of material parameters; also a pressure dependence corresponding to n-type conductivity (low pressure for zirconia) was included. However, since only changes in the magnitude but not in the character of the effects were encountered, the material was restricted to that given above. It demonstrates all typical features.

Discussion

The calculations presented in the previous section clearly illustrate several typical aspects of voltaic measuring cells with solid electrolytes, which, although recognized by those who have practical experience in building such galvanic cells, have never been discussed in much detail in the literature. One of the main points is that there is a large difference in the speed of the emf response and the speed by which processes inside the electrolyte lead to a steady state. That in satisfactorily working cells the output voltage reaches a stationary value very soon does not say that the diffusional process of adaptation of the interior of the electrolyte to the gas atmosphere has come to an end. In practical cells the latter process may take several hours. During the internal diffusion in zirconia, an oxygen flux is present in order to supply the amount of oxygen required for the readjustment of the local deviation from stoichiometry. This oxygen flux is a combination of a flow of oxygen vacancies and electron holes as described in the section Basic Equations. It gives rise to secondary effects, which may result in an emf deviating from Nernst's theoretical value.

We next discuss the following secondary effects: gas uptake (or release), electrode polarization, and intergrain polarization. To be able to do this we first discuss the parameters which determine the intensity of the flux in the final stationary state as well as during the transient.

In heterogeneous systems with only a small amount of second phase between the grains of solid electrolyte, the material flow is mainly determined by the latters' properties. Since t_{ion} is very close to unity, only the concentration and diffusion coefficient of the electronic charge carriers are relevant, see Eq. [3]. The effective diffusion coefficient equals the electronic one, so that no concentration dependence exists. It determines the time scale of the diffusion process.

The steady-state permeation flux density is proportional to the electronic component of the conductivity and can be written as (10)

$$j(\infty) = eD_h(h_o - h_{st})/l \qquad [16]$$

where the flux is expressed in terms of the equivalent electrical current.

The transient flow follows from the concentration profile existing at a certain moment. If we use the error function approximation, which is valid at short times (13) we have

$$h_\xi(t) - h_{st} = (h_o - h_{st}) \operatorname{erfc} \xi/(2\sqrt{D_h t}) \qquad [17]$$

By differentiation with respect to ξ and multiplication by eD_h we obtain the flux which for $\xi = 0$ corresponds to the gas uptake

$$j(t) = e\sqrt{D_h}\,(h_o - h_{st})/\sqrt{(\pi t)} \qquad [18]$$

We see a different functional dependence of the steady state, [16], and the transient, [18], gas flows. This difference allowed to determine both D_h and h separately in the past (10), so that their values, as given in Table I, can be used in the present calculations with faith.

Since the transient processes of gas uptake or release are large in magnitude and last over extended periods, they may be more disturbing in many practical applications than the steady-state penetration. Measures to reduce the latter, for instance by increase of the wall thickness l, see Eq. [16], or by the use of a guard atmosphere (14), therefore help only in such cases where only very slow pressure variations take place, so that the steady state is approached closely.

Gas uptake.—In the beginning it was stressed that the speed of response of cells is determined by the combination of the amount of gas required, and the ease by which the required amount can be supplied. So it depends on the medium to be measured, and on its connection to the galvanic cell, whether this gas uptake will give rise to measuring errors or not. If the geometry is unfavorable or the concentration low, so that the supply by diffusion is hampered, such errors occur. They are large in the beginning (see Fig. 6) but may be negligible in the steady state when only the steady-state gas permeation value counts. In such a case the speed of response is determined by the slow internal diffusion processes.

Electrode polarization.—The same type of slow response occurs if the limitation in the gas supply rate is not situated in the medium to be measured, but in the cell proper in the form of a polarizable electrode. This case was discussed in connection with Fig. 13. It explains the well-recognized experimental fact that the type, thickness, and way of application of the metal electrode are of utmost importance for the speed of response of the type of cells discussed (9, 15). In this respect it is not relevant if the polarization results from a diffusional or reaction kinetic type of limitation. From a practical point of view it is important to be aware of this requirement of reversibility. It means that the quality of electrodes for emf cells can be checked by electrical current techniques (9, 16, 17) such as voltage recording after a galvanostatic pulse

or impedance measurement at the low frequency end of the frequency domain.

Intergrain polarization.—Intergrain polarization gives rise to overshoot effects rather than to delay in the response, see Fig. 5. Such effects have been observed in practical cells with zirconia (9) and were originally appreciated as long termed creeping effects in the emf or drift in the zero voltage. The usually small effects seem irreproducible as long as it is not recognized that very long time constants are involved and that pressure variations of hours ago, or even of previous days if cells are cooled down in between, still exert their effect. These effects are typical results of the combination of the mixed conductor properties of the second phase between the grains and the chemical diffusion characteristics of the electrolyte proper. No effect is observed at all if the ionic transport number in the second phase is also near unity, or if the effective diffusion coefficient is much larger than that of the grains. In the latter case no concentration gradient is built up over the second phase. On the other hand, if the oxygen diffusivity is very low, the sample would show a high electrical resistance and would be disregarded as a suitable electrolyte right from the start. Thus, only if the ionic transport number is sufficiently different from zero to give a reasonable effective diffusion constant, Eq. [3], and at the same time sufficiently different from unity to yield emf errors, the phenomena are exhibited. It appeared that the silicate-rich phases that are often found in commercial zirconia samples have parameters in this range. The values used in the calculations, see Table I, were intentionally chosen to demonstrate the effect. From the discussion above it will be clear that the values are not as arbitrary as they might seem at first glance. This is also illustrated by the great change in the magnitude of the effects when a different average oxygen pressure range is used, modifying the parameters only slightly (Fig. 9 and 10).

Influence of doping.—From the previous discussion it is clear that if the flux is appreciable all types of polarization discussed (concentration, electrode, and intergrain polarization) are comparatively high. The question arises what material parameters can be varied to reduce the flux.

The electronic charge carrier concentration can in principle be modified by doping. However, it must be borne in mind that in many solid electrolytes this has been done already, with the aim to increase the concentration of mobile ionic defects. For instance, from the defect chemistry of stabilized zirconia it can be inferred that the adding of more acceptor-type dopants (Ca or Y for example) increases both the oxygen vacancy and the free hole concentrations (18). Consequently, at moderate oxygen pressures, which means p-type electronic conductivity, a smaller dopant concentration would be favorable for low fluxes in both the transient and the steady-state situation. However, in a pressure region with n-type electronic conductivity a high doping would be better because this would at the same time reduce the electron concentration and increase the vacancy concentration. Moreover, high doping also shifts the detection limit to lower pressures. The optimum doping thus depends on the requirements imposed by the type of application.

We now consider the influence of additional dopants of other elements, possibly inadvertently present as impurities, in concentrations low as compared to the main dopant discussed above.

Here, and also in electrolytes with a high intrinsic structural disorder, we do not expect an appreciable effect on the free carrier concentrations. However, such impurity content may be important for "trapping" phenomena. As was shown earlier (10) in zirconia, the capture of holes by multivalency impurity centers like Fe^{2+}, converting them into Fe^{3+},[3] reduces the diffusion coefficient $\tilde{D}$ by a large factor, the so-called "trapping" factor, which is proportional to the trap concentration. This is so because the deviation from stoichiometry now corresponds to the sum of both free and trapped electronic carriers and, at a given free carrier concentration, is consequently enlarged. The fluxes are still determined by the free carriers and their concentration gradients and are therefore not affected by trapping phenomena. Since more material has to be transported (gas absorbed) by fluxes of the same magnitude, this automatically means slowing down of the transient processes under influence of trapping.

Concluding, it can be stated that the use of "purer" zirconia, which in this context means containing fewer traps, results in cells exhibiting the same steady-state oxygen permeation rate. If transient effects are observable they have the same magnitude but occur on a shorter time scale.

[3] Free ion notation is used here. In Kroger and Vink's defect notation the centers should be indicated by Fe_{Zr}^{2-} and Fe_{Zr}^{1-}, respectively.

Conclusion

Although the discussion referred mainly to stabilized zirconia in a certain oxygen pressure range, the method of calculation, as well as the physicochemical interpretation, have a much wider scope. They can be extended to systems with any other type of solid electrolyte for which data on defect concentrations and diffusion coefficients are available. We think of sensors using silver or lead halides, calcium or lanthanum fluoride, etc.

In all such systems a small electronic conductivity component gives rise to a material (gas) flux which, depending on electrode and intergrain properties, may cause secondary effects observable in the emf behavior. In the transient situation this flux is higher than in the steady state, so that deviations from the ideal emf are more pronounced shortly after abrupt pressure changes. Such deviations take the form of a slow response when the electrodes show some degree of polarization; overshoot behavior can be expected from intergrain phases with mixed conductor properties.

The time behavior of these secondary effects is determined by that of the flux and thus is a function of the solid-state properties of the electrolyte material itself. These properties depend on purity and doping. The magnitude of the secondary effects depends also on the special properties of the electrode or the intergrain phase.

Manuscript submitted Aug. 23, 1976; revised manuscript received Dec. 7, 1976. This was Paper 77 presented at the Washington, D.C., Meeting of the Society, May 2-7, 1976.

Any discussion of this paper will appear in a Discussion Section to be published in the December 1977 JOURNAL. All discussions for the December 1977 Discussion Section should be submitted by Aug. 1, 1977.

Publication costs of this article were assisted by Philips Research Laboratories.

LIST OF SYMBOLS

- c_k concentration of particle species k
- c_x dimensionless hole concentration h/h_{st} at position x
- $\tilde{c}$ excess concentration over stoichiometric composition
- D_e diffusion coefficient of electronic charge carriers
- D_{ion} diffusion coefficient of ionic defects
- D_k diffusion coefficient of particle species k
- $\tilde{D}$ effective ambipolar diffusion coefficient of neutral component
- $\tilde{D}'$ dimensionless effective diffusion coefficient: $\tilde{D}' = \tilde{D}\,\Delta t/(\Delta\xi)^2$
- e absolute value of electronic charge
- E cell emf
- h hole concentration
- h_{st} hole concentration at standard condition

k Boltzmann's constant
l sample thickness
p_{ox} oxygen partial pressure
t time coordinate
t_e electronic transport number
t_{ion} ionic transport number
t_k transport number of species k
T absolute temperature
V vacancy concentration
x integer position coordinate
z_k relative charge of particle species k
Δt time step between successive calculations
$\Delta\xi$ spacing of ξ-values in position coordinate grid
μ chemical potential of component per atomic unit
σ_k partial conductivity of species k
ξ position coordinate

REFERENCES

1. C. Wagner, *J. Chem. Phys.*, **18**, 1227 (1950).
2. A. D. Pelton and T. H. Etsell, *Acta Metall.*, **20**, 1269 (1972).
3. C. Wagner, *Z. Phys. Chem., Ser. B*, **21**, 25 (1933).
4. C. Wagner, *ibid.*, **32**, 447 (1936).
5. C. Wagner, in "Atomic Movements," p. 153, American Society for Metals, Cleveland, Ohio (1951).
6. W. van Roosbroeck, *Phys. Rev.*, **91**, 282 (1953); F. Helfferich, "Ion Exchange," p. 269, McGraw-Hill Book Co., New York (1962).
7. J. W. Patterson, E. C. Bogren, and R. A. Rapp, *This Journal*, **114**, 752 (1967).
8. W. A. Fischer and D. Jahnke, "Metallurgische Elektrochemie," chap. 5.4.3, Verlag Stahleisen m.b.H. Düsseldorf, Springer, Berlin (1975).
9. N. M. Beekmans and L. Heyne, *Electrochim. Acta*, **21**, 303 (1976).
10. L. Heyne and N. M. Beekmans, Meeting of British Ceramic Society, Basic Science Section on "Mass Transport in Non-Metallic Solids," London, Dec. 17-18, 1969: *Proc. Br. Ceram. Soc.*, **19**, 229 (1971).
11. See, *e.g.*, R. D. Richtmyer, "Difference Methods for Initial-Value Problems," Interscience Publishers, New York (1957).
12. J. Fouletier, P. Fabry, and M. Kleitz, *This Journal*, **123**, 204 (1976).
13. J. Crank, "Mathematics of Diffusion," Clarendon Press, Oxford (1956).
14. J. Fouletier, H. Seinera, and M. Kleitz, *J. Appl. Electrochem.*, **5**, 177 (1975).
15. N. M. Beekmans and L. Heyne, *Philips Tech. Rev.*, **31**, 112 (1970).
16. L. Heyne, in "Mass Transport in Oxides," J. B. Wachtman and A. D. Franklin, Editors, p. 158, National Bureau of Standards, Spec. Publ. No. 296, Washington, D.C. (1968).
17. J. E. Bauerle, *J. Phys. Chem. Solids*, **30**, 2657 (1969).
18. L. Heyne, in "Fast Ion Transport in Solids," W. van Gool, Editor, p. 123, North Holland, Amsterdam (1973).

Kinetics of the Thermal Oxidation of Silicon in O_2/HCl Mixtures

D. W. Hess* and B. E. Deal*

Fairchild Camera and Instrument Corporation, Research and Development Laboratory, Palo Alto, California 94304

ABSTRACT

The thermal oxidation kinetics of silicon in O_2/HCl mixtures were studied as a function of HCl concentration, oxidation temperature, and silicon orientation, and the results compared to those obtained for oxidation of silicon in dry oxygen. The effective parabolic rate constant B generally showed a linear increase with increasing HCl concentration, while the effective linear rate constant B/A showed essentially no increase after a substantial increase for a 1% HCl addition. Possible explanations for such effects are considered. Activation energy plots for the rate constants were not linear, suggesting that several reaction mechanisms may be operative during silicon oxidation in O_2/HCl mixtures.

One of the most significant developments in the passivation of silicon surfaces during the fabrication of integrated circuits over the past several years has been the addition of a chlorine species during thermal oxidation. It has been demonstrated (1-3) that such additions result in improved threshold stability and increased dielectric strength. In addition, it has been observed that chlorine additions increase the rate of silicon oxidation (4-6), but extensive data for widely varying oxidation conditions have not been reported. Therefore, in this investigation the thermal oxidation kinetics of silicon in O_2/HCl mixtures are characterized as a function of oxidation temperature, HCl concentration, and silicon orientation, and the results are compared to those obtained from silicon oxidations performed in a dry oxygen atmosphere.

Experimental

The silicon wafers used in this study were 4-6 Ω-cm, phosphorus doped, with (100) and (111) orientations. The cleaning procedure as well as the oxidation system utilized has been previously described (7). The HCl was of 99.99% purity and was used as obtained from the manufacturer. The oxygen and nitrogen were from a liquid source and were further dried and filtered by passage through a Matheson Model 451 gas purifier. The wafers were rapidly pushed into the furnace in oxygen at the oxidation temperature, preheated for 15 sec, and a certain volume percent HCl added. After the allotted oxidation time, the O_2/HCl was turned off, and after a 2 min nitrogen purge, the wafers were pulled out of the furnace at the rate of ~15 cm/min.

The flowmeters utilized in this investigation were calibrated as described in Ref. (7). For the HCl, the flowmeters were calibrated with nitrogen, and the flows subsequently corrected for the density and viscosity of HCl.

The oxide thicknesses were measured with a Rudolph Model 436-200E ellipsometer with a helium-neon laser source. The reproducibility of the oxide thickness over the range investigated was ±3%.

The contamination level in the oxides was determined by bias-temperature stressing MOS capacitor structures under fields of $+5 \times 10^5$ and -3×10^5

* Electrochemical Society Active Member.
Key words: HCl/O_2 oxidation, silicon oxidation kinetics, silicon dioxide.

V/cm at 300°C for 3 min. The mobile ion charge density was typically found to be $<2 \times 10^{10}$ cm^{-2}.

Data Evaluation

The oxidation rate data were evaluated using the general relationship for the thermal oxidation of silicon as developed by Deal and Grove (8)

$$x_o^2 + Ax_o = B(t + \tau) \quad [1]$$

where x_o = oxide thickness in μm, A = constant in μm, B = parabolic rate constant in μm^2/hr, B/A = linear rate constant in μm/hr, t = oxidation time in hr, and τ = correction factor which accounts for an observed initial accelerated growth rate in dry oxygen, in hr.

Since the parabolic rate constant B depends on the partial pressure of oxidant in the oxidizing ambient, the solubility of the oxidizing species in SiO_2, and the effective diffusion coefficient of the oxidizing species in SiO_2 (8), there should be no variation of B with silicon orientation. On the other hand, the linear rate constant B/A involves the reaction rate constants at the SiO_2 surface and at the silicon surface, so that any orientation dependence of the oxidation rate should appear in this term via the constant A.

Since the method of analysis utilized depends on the correction factor τ, which is determined by extrapolation (8) and is thus prone to some error, oxidation times at least three times greater than the τ value for any set of oxidation conditions were generally used for the determination of B and B/A. In this way, any error in τ should have little effect on the calculated values of B and B/A.

Activation energies were obtained by fitting the data for B and B/A to an Arrhenius equation of the form

$$k = k_o e^{-E_a/RT} \quad [2]$$

where E_a = activation energy, T = temperature in °K, and R = gas constant.

Results and Discussion

Rate constants.—Log-log plots of oxide thickness *vs.* oxidation time for the thermal oxidation of (100) and (111) oriented silicon in O_2/HCl mixtures at temperatures of 900°, 1000°, and 1100°C, are shown in Fig. 1, 2, and 3, respectively. It is clear from the figures that the (111) silicon always oxidizes faster than does the (100). Also, it can be seen that the effect of HCl addition is to increase the oxidation rate relative to oxidation in dry oxygen. In particular, a relatively large increase in the oxidation rate occurs with the initial 1% HCl addition. Subsequent additions have a somewhat smaller effect, but the over-all rate is systematically increased. In addition, it can be observed in Fig. 1-3 that the over-all increase in oxide thickness for a particular oxidation time upon increasing the HCl concentration from 0 to 10%, is larger for (100) than for (111) oriented silicon. Although we can presently offer no explanation for this observation, it may be related to the silicon etching phenomenon mentioned below. It should be noted that very few data points are plotted for oxidations carried out at 1100°C with HCl concentrations greater than 1%. This is due to silicon etching and oxide bubble formation which occurs at the Si-SiO_2 interface during silicon oxidation with O_2/HCl mixtures at 1100°C (5, 6, 9, 10).

In order to separate the effects of HCl on the parabolic B and linear B/A rate constants, and thus obtain some indication of the role HCl plays in silicon oxidation, Eq. [1] was utilized. It should be mentioned that during the determination of τ, x_i was assumed to be essentially constant at 160 ± 40Å for all oxidation conditions investigated ($x_i = x_o$ at $t = \tau$). Although x_i should decrease with HCl addition due to water vapor generation as per the reaction of O_2 and HCl

$$4HCl + O_2 \rightarrow 2H_2O + 2Cl_2 \quad [3]$$

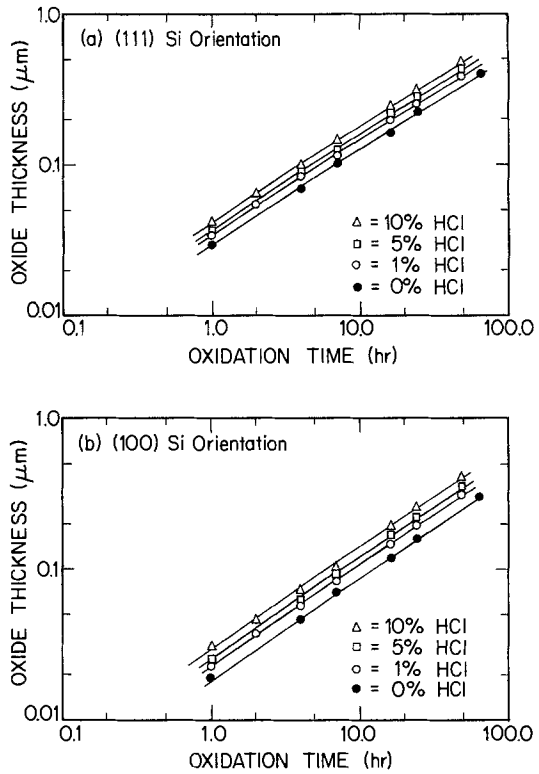


Fig. 1. Oxide thickness *vs.* oxidation time for the oxidation of (111) and (100) oriented n-type silicon in various O_2/HCl mixtures at 900°C.

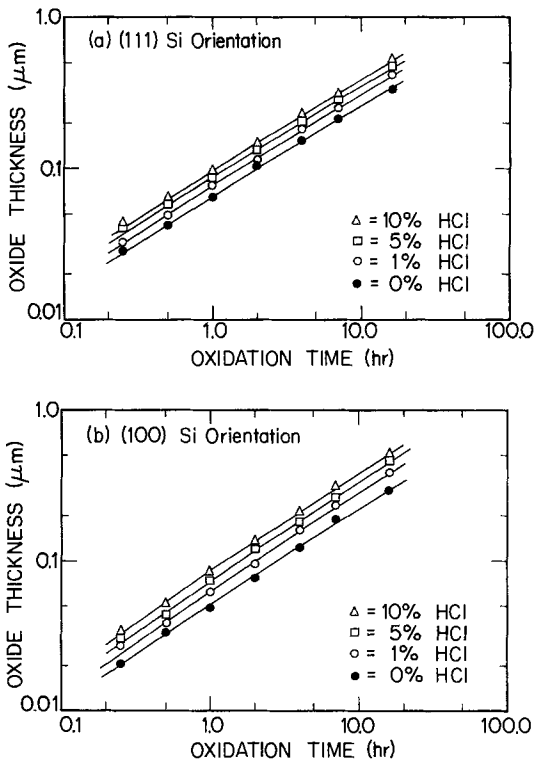


Fig. 2. Oxide thickness *vs.* oxidation time for the oxidation of (111) and (100) oriented n-type silicon in various O_2/HCl mixtures at 1000°C.

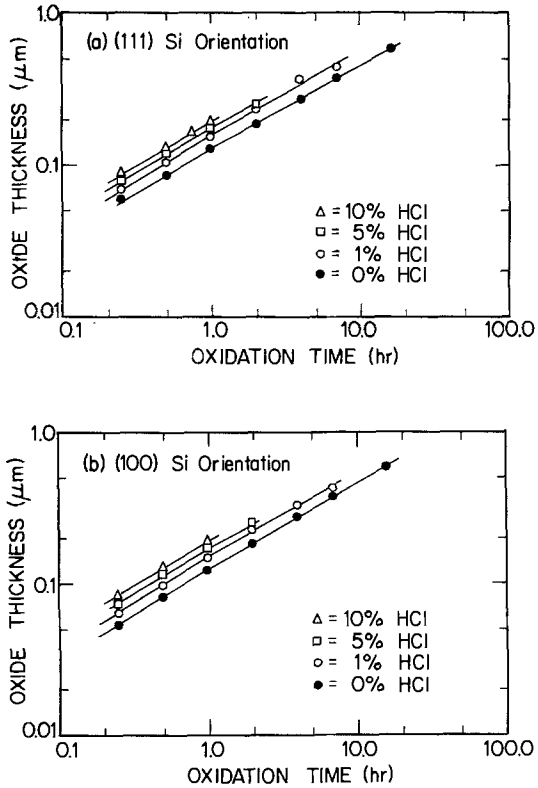


Fig. 3. Oxide thickness vs. oxidation time for the oxidation of (111) and (100) oriented n-type silicon in various O_2/HCl mixtures at 1100°C.

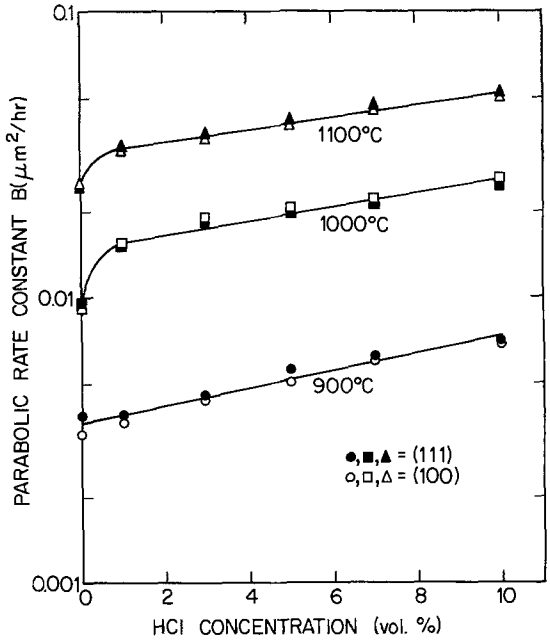


Fig. 4. Parabolic rate constant vs. % HCl concentration for (111) and (100) oriented n-type silicon at 900°, 1000°, and 1100°C.

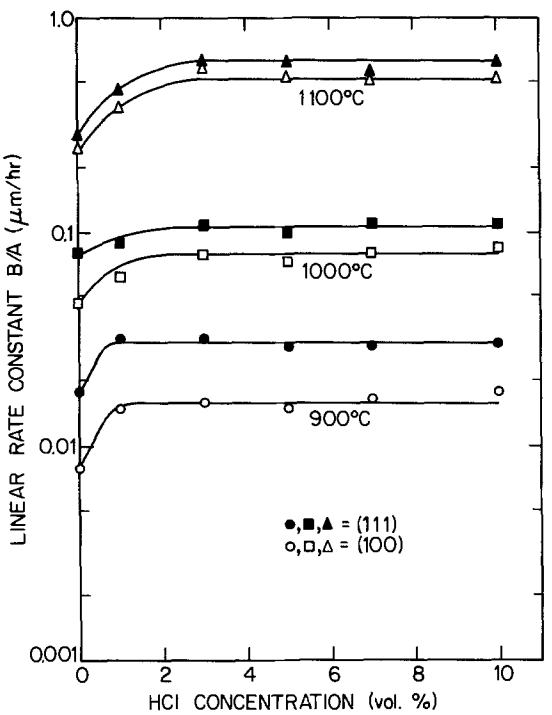


Fig. 5. Linear rate constant vs. % HCl concentration for (111) and (100) oriented n-type silicon at 900°, 1000°, and 1100°C.

the extrapolations performed to determine x_i and thus τ could not detect small changes in x_i. Nevertheless, since τ depends upon x_i, B, and B/A, a decrease in τ was observed upon HCl addition, probably in part as a result of water generation, since x_i and therefore τ are zero for oxidation in a steam ambient (8).

The results of least squares analyses on the data shown in Fig. 1-3 are summarized in Fig. 4 and 5, which are semilog plots of the effect of HCl concentration on the parabolic and linear rate constants, respectively. It should be noted that the rate constants generated via Eq. [1] and plotted in Fig. 4 and 5 are effective rate constants, in that they represent the combined effects of oxygen, water, and chlorine species on B and B/A.

Figure 4 shows that essentially no orientation effect is observed in the parabolic rate constant B, in accordance with theory. Also, increasing the HCl concentration above 1% results in a linear increase in B (the plots are put on a semilog scale for convenience). The increase in B going from 0 to 1% HCl in dry oxygen is not as consistent among the three temperatures, however. For 1000° and 1100°C, a large increase in B due to 1% HCl addition occurs, whereas this trend is not observed at 900°C. These observations are in agreement with previous work which showed a linear increase of B with 0-9% HCl addition at 900°C (6) and a large increase in B due to 1% HCl addition at 1100°C (5). Presumably, the large increase in B, as well as the linear increase with subsequent HCl additions are at least in part due to water generation as described in Eq. [3], since it is well known that small amounts of water in oxygen increase the thermal oxidation rate of silicon relative to that of dry oxygen (11). However, as pointed out by van der Meulen and Cahill (6), gas phase thermodynamic equilibrium calculations indicate that the amount of water generated via Eq. [3] cannot account for the observed increase in oxidation rate. This is consistent with the published results that Cl_2 addition to a dry oxygen atmosphere yields a considerably higher silicon oxidation rate than the same volume percent HCl addition at 1150°C (14), suggesting that the chlorine species, rather than the water generated, may be primarily responsible for the increase in oxidation rate at high temperatures. However, since it is difficult to obtain Cl_2 which contains less than 3 ppm water, some effect, although small, would be anticipated from the water present.

In regard to the above argument concerning the amount of water generated via Eq. [3], it should be pointed out that thermodynamic calculations such as those in Ref. (6) give only the idealized gas phase equilibrium conditions. The presence of a surface

(especially one such as SiO_2 which is useful for catalytic purposes) could shift the equilibrium, and thus alter the amount of water generated and incorporated into the oxide surface.

Some insight can be gained into the silicon oxidation regime affected by water or chlorine (as generated via Eq. [3]) from consideration of the definitions of the parabolic (B) and the linear (B/A) rate constants. The definitions are as follows (8)

$$B \equiv 2D_{\text{eff}}C^*/N_1 \qquad [4]$$

where D_{eff} = effective diffusion coefficient, C^* = maximum solubility of oxidant in oxide, and N_1 = number of oxidant molecules incorporated into a unit volume of oxide

$$B/A \equiv \frac{C^*}{N_1\left(\frac{1}{k}+\frac{1}{h}\right)} \qquad [5]$$

where k = surface reaction rate constant, and h = gas phase transport coefficient.

Inspection of these definitions along with comparison of Fig. 4 and 5 suggests that the monotonic increase in B with HCl concentration is related to the effective diffusion coefficient D_{eff}, since this term does not appear in the expression for B/A. Likewise, it appears that the rapid initial increase in B and B/A might be related to the solubility of the oxidizing species in the oxide film. Although the latter conclusion could be explained by water addition, this explanation would not account for the increase in D_{eff}, since this parameter is known to decrease with water addition (8).

In light of the above arguments, the gradual increase of the parabolic rate constant with increasing HCl concentration could be partially related to a chlorine species, since it has been established that a higher concentration of chlorine is incorporated into the silicon dioxide film as the HCl concentration and/or the silicon oxidation temperature are increased (12). Consequently, it might be anticipated that increasing the chlorine concentration would cause the SiO_2 lattice to be strained (especially near the interface), thus allowing diffusion of oxidant to occur more easily, and thereby increase the oxidation rate as observed in the oxidation of heavily boron-doped silicon (13). Since the ionic radius of boron when substituted for silicon in a silicon lattice (which should be close to the radius of boron substituted for silicon in SiO_2) is 0.88Å (14), while the ionic radius of chlorine is 1.8Å (15), it would be expected that the SiO_2 lattice expansion would be even greater in the case of chlorine as compared to boron. This speculation is also consistent with the previously mentioned observation that Cl_2 additions result in higher silicon oxidation rates than do HCl additions at high temperatures, since more chlorine is apparently incorporated into the SiO_2 with O_2/Cl_2 than with O_2/HCl mixtures (12).

Inspection of Fig. 5 reveals a strong orientation effect on the linear rate constant B/A, which apparently decreases with increasing temperature. This observation is discussed in more detail in the next section. Also, as generally found for B, an initial rapid increase in B/A is observed upon increasing HCl concentration in the oxygen atmosphere from 0 to 1%. However, further increase of the HCl concentration resulted in essentially no change in B/A. Although an explanation for these observations is not apparent, it is conceivable that the breaking of Si-Si bonds could be promoted by etching of the silicon substrate which is known to occur with the use of HCl (5, 6, 9, 10) so that an increase in the linear rate constant might result. However, increased HCl concentrations should then further increase B/A, unless an equilibrium between oxidation and etching is established. Clearly, additional investigation of this phenomenon is needed if we are to understand the mechanism involved. It should be mentioned that preliminary results obtained in this laboratory with O_2/Cl_2 oxidation atmospheres substantiate the above interpretation, in that relatively large increases in B/A due to Cl_2 addition at 1100°C were observed, with considerably smaller increases noted for B.

Activation energies.—An Arrhenius plot of the parabolic rate constant B for the thermal oxidation of silicon in O_2 and several O_2/HCl mixtures is shown in Fig. 6. Since essentially no orientation effect was observed for B, only the (111) orientation is plotted. A least squares analysis of the data for dry oxygen (0% HCl) gave a value of 1.2 eV (28 kcal/mole), which agrees well with previously determined values for the thermal oxidation of silicon in dry oxygen (8, 16), as well as for the diffusivity of oxygen through fused silica (17). It can be seen from Fig. 6 that HCl addition to the dry oxygen atmospheres resulted in a convex curvature (relative to dry oxygen oxidation) of the Arrhenius plot.

An Arrhenius plot of the linear rate constant B/A for the thermal oxidation of silicon in O_2 and several O_2/HCl mixtures is shown in Fig. 7. A least squares analysis of the data for dry oxygen (0% HCl) oxidation of (111) oriented silicon yielded a value of 2 eV (47 kcal/mole), which is in close agreement with the energy required to break a Si-Si bond (18). However, determination of the activation energy for (100) oriented silicon affords two choices as seen in Fig. 7. If the data from 900° to 1200°C are analyzed, and the low temperature points neglected due to less certainty of the data which might result from the long oxidation times necessary to obtain kinetic data at these low temperatures, a value of 2.5 eV (57 kcal/mole) is obtained, *i.e.*, an increase of ~25% over that for (111). This increase was predicted by Ligenza from consideration of steric hindrance in the (100) and (111) planes of silicon during thermal

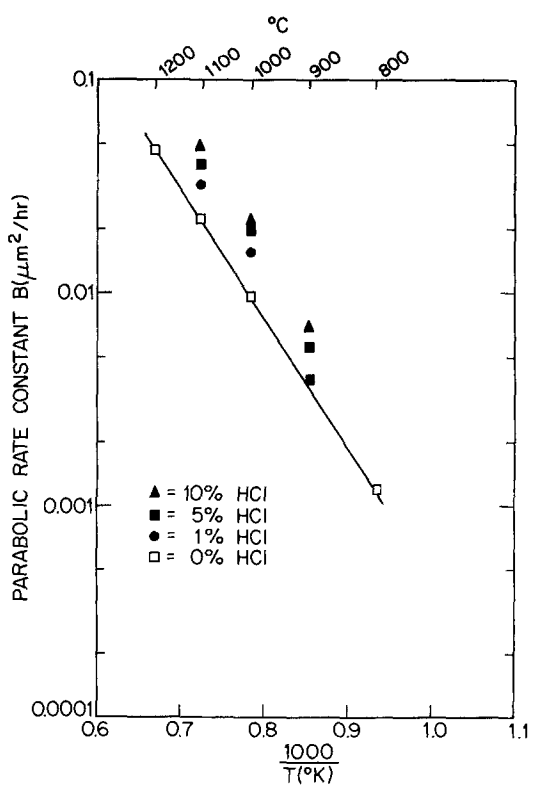


Fig. 6. Arrhenius plots of the parabolic rate constants for silicon oxidized in various O_2/HCl mixtures. Silicon orientation is (111).

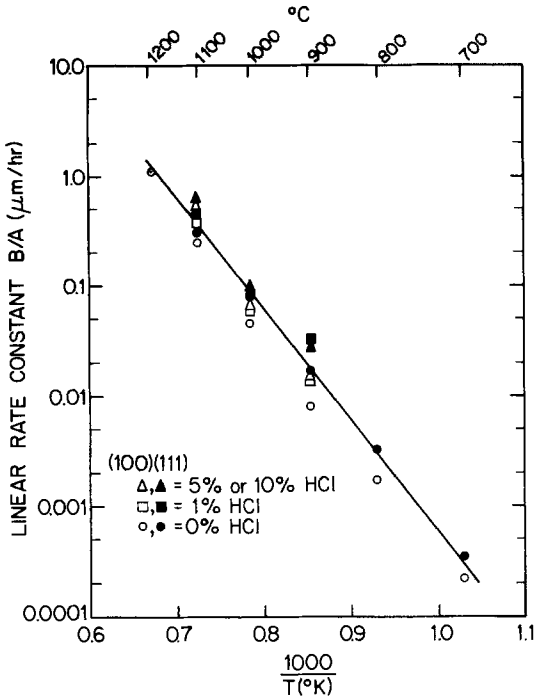


Fig. 7. Arrhenius plots of the linear rate constants for (111) and (100) oriented silicon oxidized in various O_2/HCl mixtures.

oxidation (19). On the other hand, if the data from 700° to 1200°C are analyzed, the 900°, 1100°, and 1200°C points could be considered as scatter from a line drawn parallel to the one for (111) orientation, passing through the 700°, 800°, and 1000°C points, thereby resulting in the same activation energy as (111) oriented silicon. Indeed, some faith could be put in such an assumption, since the 700°C data give B/A directly from a plot of x_o *vs.* t, which was found to be linear for this temperature. Thus, one could argue that the higher temperature analyses might be in error due to the inaccuracy in determining A from a plot of x_o *vs.* $(t + \tau)/x_o$. The slopes of these lines (B) are quite large, therefore a small change in the slope would shift the intercept (A), and thus B/A, considerably. At present, it is not known which of the above alternatives is the better one.

As in the case of the parabolic rate constant, the Arrhenius plot of the linear rate constant for HCl/O_2 mixtures (Fig. 7) is curved. In this instance, the curvature is concave relative to dry oxygen oxidation. Upon consideration of Eq. [3], it is not surprising that Arrhenius plots of the rate constants for the oxides grown in HCl atmospheres should result in curved lines. Certainly more than one activated process is occurring, *e.g.*, the oxidation due to oxygen and water vapor, along with several possible effects due to chlorine, as mentioned above. As the oxidation temperature is changed, the relative importance of these activated processes may also change. Thus it becomes necessary to separate out the effects of water and chlorine on the silicon oxidation rate. Toward this end, experiments are currently being performed to investigate the oxidation rate of silicon in O_2/H_2O and O_2/Cl_2 mixtures.

Summary

The thermal oxidation kinetics of silicon in O_2/HCl mixtures were characterized as a function of HCl concentration, oxidation temperature, and silicon orientation, and in each instance were compared to results obtained for the oxidation of silicon in dry oxygen. The effective parabolic rate constant B was found to increase linearly with HCl additions, except for an initial large increase when comparing oxidation in dry O_2 to a 1% HCl/O_2 mixture at 1000° and 1100°C. The observed increase in B could be due in part to water generation from the reaction of O_2 and HCl which would increase the solubility of oxidant in the oxide and in part to a straining of the SiO_2 lattice due to the presence of chlorine. The linear rate constant B/A showed an initial increase due to the addition of 1% HCl to the dry oxygen atmosphere, but further HCl additions had essentially no effect on B/A. Such behavior might be related to enhanced Si-Si bond breaking due to etching by a chlorine species. Arrhenius plots of the rate constants for the O_2/HCl oxidations were not linear, suggesting that more than one process was occurring during silicon oxidation in these mixtures.

Acknowledgments

The authors would like to thank Julia Bien for conducting most of the experimental procedures. A portion of this work was supported by ARPA Contract No. DAABO7-75-C-1344.

Manuscript submitted Oct. 6, 1976; revised manuscript received Jan. 11, 1977.

Any discussion of this paper will appear in a Discussion Section to be published in the December 1977 JOURNAL. All discussions for the December 1977 Discussion Section should be submitted by Aug. 1, 1977.

Publication costs of this article were assisted by Fairchild Camera and Instrument Corporation.

REFERENCES

1. R. J. Kriegler, *Denki Kagaku*, **41**, 466 (1973).
2. R. S. Ronen and P. H. Robinson, *This Journal*, **119**, 747 (1972).
3. C. M. Osburn, *ibid.*, **121**, 809 (1974).
4. R. J. Kriegler, Y. G. Cheng, and D. R. Colton, *ibid.*, **119**, 388 (1972).
5. K. Hirabayashi and J. Iwamura, *ibid.*, **120**, 1595 (1973).
6. Y. J. van der Meulen and J. G. Cahill, *J. Electron. Mater.*, **3**, 371 (1974).
7. D. W. Hess and B. E. Deal, *This Journal*, **122**, 579 (1975).
8. B. E. Deal and A. S. Grove, *J. Appl. Phys.*, **36**, 3770 (1965).
9. R. J. Kriegler, "Semiconductor Silicon 1973," H. R. Huff and R. R. Burgess, Editors, p. 363, The Electrochemical Society Softbound Symposium Series, Princeton, N.J. (1973).
10. D. W. Hess and R. C. McDonald, To be published in *Thin Solid Films*.
11. E. A. Irene, *This Journal*, **121**, 1613 (1974).
12. Y. J. van der Meulen, C. M. Osburn, and J. F. Ziegler, *ibid.*, **122**, 284 (1975).
13. B. E. Deal and M. Sklar, *ibid.*, **112**, 430 (1965).
14. Helmut F. Wolf, "Semiconductors," p. 199, John Wiley & Sons, Inc., New York (1971).
15. A. F. Wells, "Structural Inorganic Chemistry," p. 68, Oxford University Press (1962).
16. A. G. Revesz and R. J. Evans, *J. Phys. Chem. Solids*, **30**, 551 (1969).
17. F. J. Norton, *Nature*, **171**, 701 (1961).
18. F. Pauling, "The Nature of the Chemical Bond," 3rd ed., Cornell University Press, Ithaca, N.Y. (1960).
19. J. R. Ligenza, *J. Phys. Chem.*, **65**, 2011 (1961).

Effect of Chlorine on the Negative Bias Instability in MOS Structures

Dennis W. Hess*

Fairchild Camera and Instrument Corporation, Research and Development Laboratory, Palo Alto, California 94304

ABSTRACT

The effect of the chlorine concentration in silicon dioxide films thermally grown in HCl/O_2 or Cl_2/O_2 atmospheres on the negative bias instability of the effective oxide charge ($Q_{ss} + N_{st}$) has been investigated at elevated temperatures. Also considered were the effects due to silicon orientation, silicon conductivity type, and silicon oxidation temperature. The effective oxide charge increased with increasing chlorine concentration, the Cl_2/O_2-grown oxides showing larger increases than the HCl/O_2-grown oxides. Distortions in the capacitance-voltage curves were found to be more prevalent for structures prepared using n-type silicon substrates than for p-type. For the (100) oriented samples, essentially the entire increase observed was eliminated by a heat-treatment at 500°C in nitrogen with aluminum present on the oxide surface, whereas only 90% of the effect was removed in the case of (111) oriented wafers which underwent the same treatment.

One of the current trends in the manufacture of silicon integrated circuits is toward thinner gate dielectrics (1). This trend necessitates improved breakdown characteristics, particularly for the most widely used gate dielectric, silicon dioxide. In order to attain the dielectric strength needed to meet these requirements, as well as to getter and passivate against mobile ions, a chlorine species is often added to the silicon oxidation atmosphere (2, 3). Such additions typically result in a chlorine concentration "peak" in the silicon dioxide near the $Si-SiO_2$ interface (4). Thus, it might be anticipated that the density of certain oxide charges originating in the region near the silicon surface could be affected by the chlorine species. For instance, the negative bias instability observed primarily with p-channel MOS devices at slightly elevated temperatures has been well characterized in the case of thermal oxides without chlorine incorporation (5-11). A proposed model for this instability involves an increase in fixed oxide charge (Q_{ss}) and in interface state density (N_{st}) arising from additional bond breakage at the already strained interfacial region (10,12). A large concentration of chlorine near the $Si-SiO_2$ interface could enhance such an effect, and, indeed, flatband shifts have been found to increase with increasing chlorine concentration in the thermally grown silicon dioxide layer of MOS capacitor structures during room temperature stress measurements under negative bias (4). The present study characterizes the effect of chlorine concentration on this negative bias instability at elevated temperatures. The effects of silicon orientation, silicon conductivity type, and silicon oxidation temperature were also considered.

Experimental

The silicon wafers used in this investigation were 4-6 Ω-cm phosphorus or boron doped, with (100) and (111) orientation. The cleaning procedure, as well as the oxidation system utilized, has been previously described (13). The HCl and the Cl_2 were of 99.99% and 99.9% purity, respectively, and were used as obtained from the manufacturer. The wafers were rapidly pushed into the furnace in oxygen, preheated for 15 sec, and a certain volume percent (v/o) HCl or Cl_2 was added. After oxidation at 1100°C to a thickness of ~1100Å, the O_2/HCl or O_2/Cl_2 flow was discontinued, the wafers were annealed in nitrogen for 15 min, and were subsequently allowed to cool in nitrogen.

After the anneal, the oxide thicknesses were measured using a Rudolph Model 436-200E ellipsometer with a helium-neon source. The oxides were then stripped from the backs of the wafers. Aluminum dots (0.076 cm diameter) were evaporated through metal masks, and the backs of the slices were coated with aluminum, using an unheated-substrate electron beam evaporation. The wafers were then annealed for 5 min in dry nitrogen at 500°C, and the MOS capacitors were evaluated using the capacitance-voltage technique at

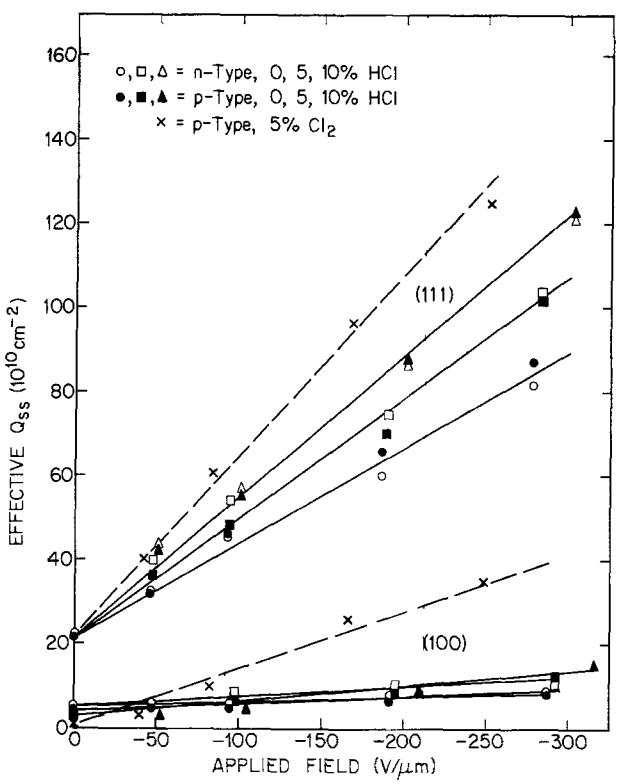


Fig. 1. Saturation values of effective oxide charge ($Q_{ss} + N_{st}$) as a function of applied negative fields for oxides thermally grown on (100) and (111) oriented silicon at 1100°C in various chlorine-containing dry oxygen atmospheres. Solid lines are for oxides grown in HCl/O_2 atmospheres, while the dotted lines are for oxides grown in Cl_2/O_2 atmospheres. The ($Q_{ss} + N_{st}$) value at zero applied field is the value prior to negative bias stressing.

* Electrochemical Society Active Member.

Key words: chlorine oxidation, negative bias instability, oxide charge, interface states, MOS.

a frequency of 1 MHz (14). The work function differences for n- and p-type silicon were taken to be +0.1 and −0.6V, respectively (15). The mobile ionic contamination (Q_o) present in the samples was found to be less than 3×10^{10} cm^{-2} in all cases.

The MOS capacitor structures were stressed under negative fields at 400°C for 5 min in air [which was a sufficient time for the fixed charge (Q_{ss}) and interface state density (N_{st}) to reach saturation], and the samples were cooled under bias. This latter procedure was found to be necessary, since even a very short time (<5 sec) at 400°C without bias resulted in a decrease of effective Q_{ss}, *i.e.*, $Q_{ss} + N_{st}$. The reproducibility of the effective Q_{ss} values was found to be $\pm 3 \times 10^{10}$ cm^{-2}.

Results and Discussion

A plot of the effective Q_{ss} *vs.* applied negative field for oxides grown in 0, 5, or 10 v/o HCl or 5 v/o Cl_2 is shown in Fig. 1. Only results for p-type silicon substrates in the case of oxides grown in O_2/Cl_2 atmospheres are plotted in Fig. 1 due to distortions observed in the *C-V* characteristics for n-type samples. This observation is discussed in more detail below. For the (111) silicon orientation, it may be observed that the negative bias instability increases with HCl concentration, and is even greater for 5% Cl_2 than for 10% HCl atmospheres. Although this trend is not as apparent for (100) oriented substrates, it is still present as can be seen in Fig. 2-5. The negative field effect observed is consistent with the breaking of Si-Si or Si-O bonds near the interfacial region, since the presence of chlorine in this region might be expected to promote bond breaking due to a straining of these bonds. Thus, larger concentrations of chlorine show larger effects. Also, it is not surprising that O_2/Cl_2 atmospheres result in a larger effect than O_2/HCl atmospheres, since apparently more chlorine is incorporated in the oxide in the case of O_2/Cl_2 (4). In addition, it should be noted that very little difference is observed between n- and p-type silicon so that the major effect is due to chlorine concentration, at least when the oxides are grown at 1100°C. When the oxides were grown at 1000°C, the chlorine concentration was found to have little or no effect. In this instance, the negative bias instability as measured by the flatband shift was consistently 10-15% less for n- than for p-type silicon. Such behavior is probably related to the types of interface states present on n- and p-type silicon surfaces. This point will be discussed further in a later section. In any case, the small effect observed at 1000°C upon chlorine addition is most likely due to the smaller concentration of chlorine in SiO_2 films grown at 1000°C than in those grown at 1100°C (4).

It can be seen in Fig. 1 that the negative bias instability is considerably less for (100) oriented silicon surfaces than for (111). This is in agreement with previous data which have demonstrated the dependence of this effect on initial fixed oxide charge (and thus generally on silicon orientation) and gives further indication that this phenomenon is related to bond breaking (8-12).

As indicated above, interface state generation can play a large role in the negative bias instability. Insight into the importance of these states can be gained from inspection of Fig. 2-5. Figures 2 and 3 show the capacitance-voltage (*C-V*) curves resulting from the negative bias stressing of MOS capacitor structures fabricated on (100) n- and p-type silicon substrates, respectively, where the oxides were grown at 1100°C in a 10% HCl/O_2 atmosphere. Figure 2 shows that

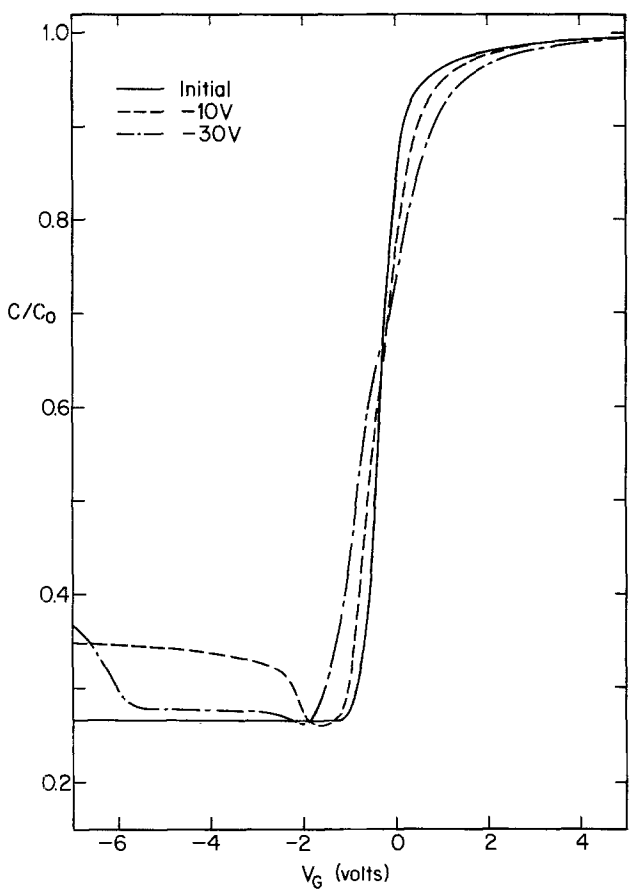


Fig. 2. Capacitance-voltage plots after negative bias temperature stress at the indicated voltages. The voltage applied to the aluminum electrode is V_G and the oxide capacitance is C_o. Oxides were grown at 1100°C in 10% HCl/O_2 on (100) oriented n-type silicon. The oxide thickness is 0.1 μm.

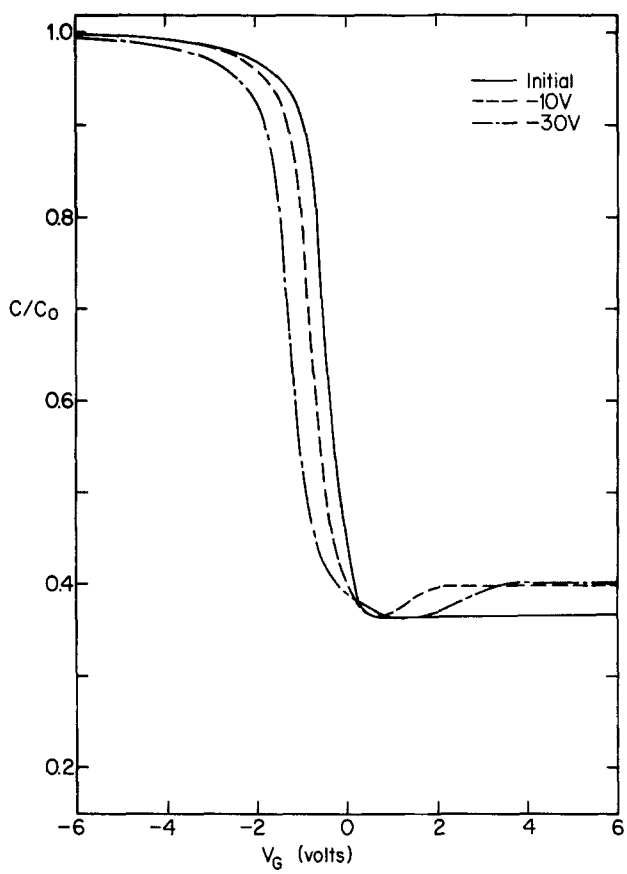


Fig. 3. Capacitance-voltage plots after negative bias temperature stress at the indicated voltages. Oxides were grown at 1100°C in 10% HCl/O_2 on (100) oriented p-type silicon. The oxide thickness is 0.1 μm.

essentially no flatband shift ($V_{FB} \simeq 0.7\ C/C_o$) occurs with the n-type substrate during bias temperature stressing, but the distortion of the C-V curves increases with applied field. However, the p-type structure (Fig. 3) exhibits a more parallel shift in the C-V characteristics, with some rounding of the curve near inversion still apparent. Although an explanation of these observations is not obvious, a qualitative description can be invoked if one assumes that at least some of the interface states formed by negative field stressing are acceptor states (electron traps) in the upper half of the silicon bandgap. These states would thus be negatively charged for n-type silicon and uncharged for p-type due to the location of the Fermi level. Therefore, these interface states would generate a shift to positive voltage (negative interface charge) for n-type silicon which would oppose any donor states (hole traps) and/or Q_{ss} generated, and a distortion of C-V curve would result. In the case of p-type silicon, the states in the upper half of the bandgap would be uncharged, so only a shift to negative voltage would be observed in the C-V curve.

It may also be noted that the inversion portion of the C-V curves has generally increased with increasing applied negative fields. This is probably due to the increased number of interface states created by the bias-temperature stress, which could act as generation sites for minority carriers.

Preliminary measurements of the interface state density utilizing the Gray-Brown technique (16) at a frequency of 1 MHz were performed on both (100) and (111) oriented n- and p-type silicon substrates which had oxides grown in 10% HCl/O_2 or 5% Cl_2/O_2 at 1100°C, and were stressed at 400°C under a negative field of ~300 V/μm. In each case, the samples showed very low concentrations of interface states ($<5 \times 10^{10}$ cm^{-2}). These results suggest that the energy levels of the interface states observed in these experiments by distortions in the C-V curves, are not located close to the silicon conduction or valence band edges. Also, the low concentration of interface states observed may be consistent with charge trapping in the oxide which occurs where bonds have been broken by negative bias-temperature stressing.

A few experiments were carried out in which positive bias (corresponding to ~200 V/μm) was applied to the MOS capacitors at 400°C. Even on (111) oriented substrates, only a very small (<0.4V) flatband shift toward positive voltage was observed, and this shift was independent of the silicon conductivity type or chlorine concentration. However, small distortions of the C-V curve were noted, primarily near the inversion point.

Figures 4 and 5 show the C-V curves resulting from the negative bias stressing of MOS capacitors fabricated on (100) n- and p-type silicon, respectively, where the oxides were grown at 1100°C in a 5% Cl_2/O_2 atmosphere. Clearly, the trends observed are identical to those for HCl oxides (Fig. 2 and 3), but are considerably more pronounced. As indicated above, this is in agreement with the larger concentration of chlorine incorporated into Cl_2/O_2-grown oxides than into HCl/O_2-grown oxides (4).

In order to determine the approximate portion of the shift in the C-V curves observed under negative bias-temperature stressing which is due to interface states, and/or oxide trapped charge which is annealable, some of the MOS capacitors were stressed under −30V at 400°C and the C-V curves recorded. The samples were subsequently heat-treated in nitrogen at 500°C for 5 min with the aluminum dots present on the oxide (anneal), since such treatments are known to reduce

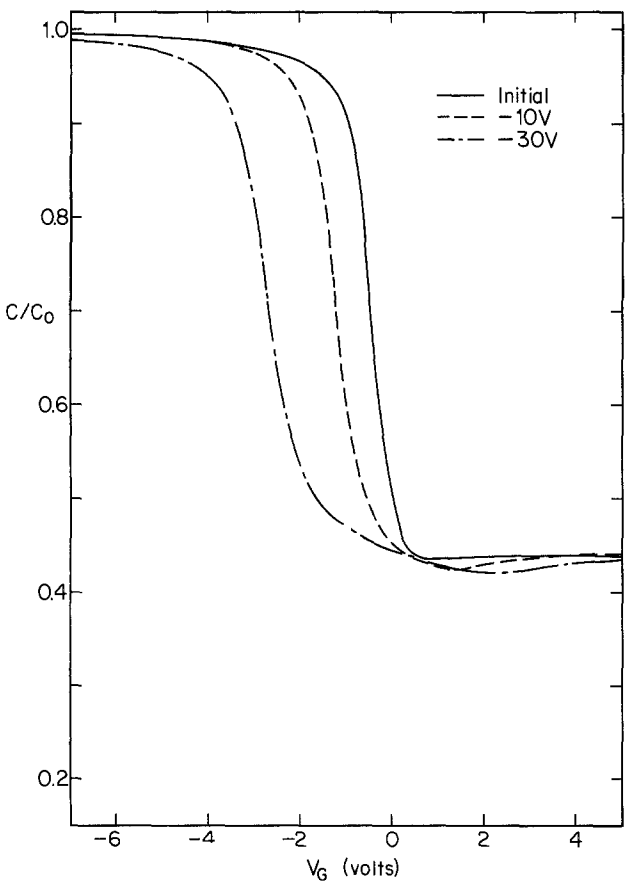


Fig. 4. Capacitance-voltage plots after negative bias temperature stress at the indicated voltages. Oxides were grown at 1100°C in 5% Cl_2/O_2 on (100) oriented n-type silicon. The oxide thickness is 0.12 μm.

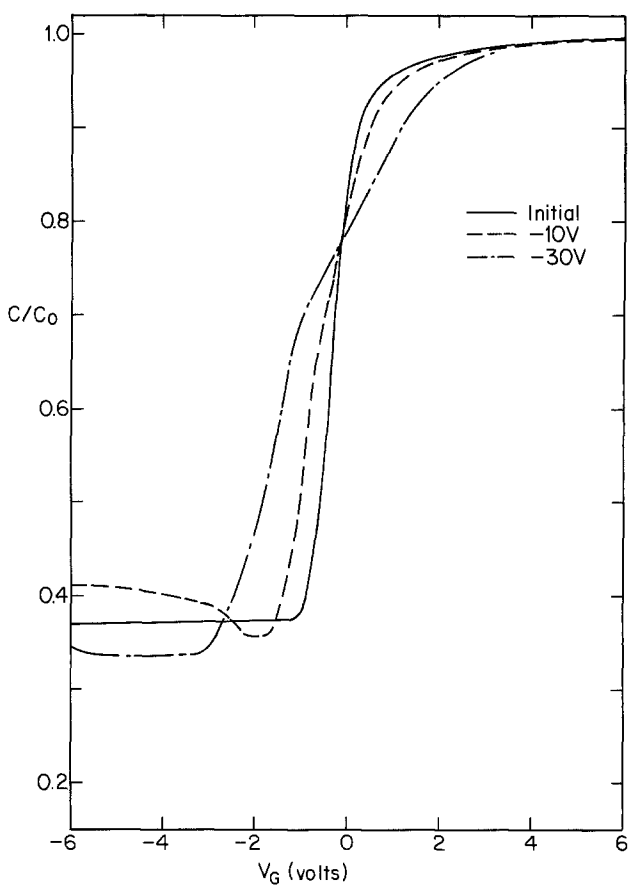


Fig. 5. Capacitance-voltage plots after negative bias temperature stress at the indicated voltages. Oxides were grown at 1100°C in 5% Cl_2/O_2 on (100) oriented p-type silicon. The oxide thickness is 0.12 μm.

the intrinsic state density (17). The resultant C-V curves indicated that essentially all of the distortions and flatband shifts had been eliminated on (100) capacitors, while ~10% of the flatband shift remained for the (111) capactiors, but all distortions had been eliminated. Also, it should be mentioned that the flatband shift was not appreciably changed with an additional 10 min N_2 treatment at 500°C. These results were independent of silicon type or chlorine concentration.

Summary

It has been demonstrated that the negative bias instability observed on MOS capacitors at elevated temperatures increases with increasing chlorine concentration in the thermally grown oxide. The effect was larger for oxides grown in Cl_2/O_2 atmospheres than for oxides grown in HCl/O_2 atmospheres. Such observations are consistent with a bond-breaking model of this phenomenon. Distortions of the C-V curves which were indicative of interface state generation and/or oxide trapped charge were most prevalent for n-type silicon, but were also observed on p-type substrates. For the structures fabricated on (100) oriented silicon, essentially the entire effect of the negative bias instability could be eliminated by a heat-treatment in nitrogen at 500°C with aluminum present on the oxide surface. However, only 90% of this effect was removed in the case of (111) oriented silicon wafers which underwent the same heat-treatment.

Acknowledgments

The author would like to thank Bruce Deal, Art Learn, and Maija Sklar for helpful discussions, and Julia Bien for experimental assistance.

Manuscript submitted Oct. 6, 1976; revised manuscript received Jan. 5, 1977.

Any discussion of this paper will appear in a Discussion Section to be published in the December 1977 JOURNAL. All discussions for the December 1977 Discussion Section should be submitted by Aug. 1, 1977.

Publication costs of this article were assisted by the Fairchild Camera and Instrument Corporation.

REFERENCES

1. R. H. Dennard, F. H. Gaensslen, H. N. Yu, V. L. Rideout, E. Bassous, and A. R. LeBlanc, *IEEE J. Solid-State Circuits*, **SC-9**, 256 (1974).
2. C. M. Osburn, *This Journal*, **121**, 809 (1974).
3. R. J. Kriegler, *Denki Kagaku*, **41**, 466 (1973).
4. Y. J. van der Meulen, C. M. Osburn, and J. F. Zeigler, *This Journal*, **122**, 284 (1975).
5. A. Goetzberger and H. E. Nigh, *Proc. IEEE*, **54**, 1454 (1966).
6. S. R. Hofstein, *Solid-State Electron.*, **10**, 657 (1967).
7. Y. Miura and J. Matukura, *Jpn. J. Appl. Phys.*, **5**, 180 (1966).
8. B. E. Deal, M. Sklar, A. S. Grove, and E. H. Snow, *This Journal*, **114**, 266 (1967).
9. A. Goetzberger, A. D. Lopez, and R. J. Strain, *ibid.*, **120**, 90 (1973).
10. M. Nakagiri, *Jpn. J. Appl. Phys.*, **13**, 1610 (1974).
11. D. J. Breed and R. P. Kramer, *Solid-State Electron.*, **19**, 897 (1976).
12. B. E. Deal, *This Journal*, **121**, 198C (1974).
13. D. W. Hess and B. E. Deal, *ibid.*, **122**, 579 (1975).
14. A. S. Grove, B. E. Deal, E. H. Snow, and C. T. Sah, *Solid-State Electron.*, **8**, 145 (1965).
15. W. M. Werner, *ibid.*, **17**, 769 (1974).
16. D. M. Brown and P. V. Gray, *This Journal*, **115**, 760 (1968).
17. P. Balk, Paper 109 presented at The Electrochemical Society Meeting, San Francisco, California, May 9-13, 1965.

Photoconductive CdS Films by a Chemical Bath Deposition Process

N. R. Pavaskar, C. A. Menezes, and A. P. B. Sinha

National Chemical Laboratory, Poona 411008, India

ABSTRACT

A new technique for the preparation of CdS thin films by chemical bath deposition is described. The CdS films prepared by this method have many of the advantages of those made by the spray deposition method, such as the ease of coating large areas and simplicity of the process. The stoichiometry is easy to maintain in both these methods. The films are formed on rotating substrates from a bath containing cadmium salt in a complex form. Electrical, photoconducting, and optical properties such as I-V characteristics, decay of photoconductivity, spectral response of photoconductivity, and optical absorption were studied. Addition of cations like Ag, Cu, In, and Zn to the deposition bath makes the films amorphous. Such amorphous layers have a density of state of the order of 10^{19}-10^{20}/cm^3/eV near the Fermi level, as determined by photodecay and field effect measurements. The films produced are strong, adhering tightly to the substrates, show little or no degradation, and are photosensitive as deposited.

Current interest in direct energy conversion devices has led to renewed research in the area of materials for such devices. In the context of the need for a simple yet reliable technique for producing large area cells of CdS of high stoichiometry, this report on the preparation of chemically bath deposited films would appear to be topical. Various factors affecting the deposition process, as well as the effect of addition of cations, have been studied in order to understand the process of deposition and thus to improve the characteristics of the films.

Key words: amorphous CdS, photoconductive decay, field effect.

We have attempted to give in some detail the procedures followed by us for the preparation of the chemically bath deposited films. The basic outline of the method is that described in Ref. (1). We have standardized the conditions under which these films can be produced with a high degree of reproducibility with respect to thickness, structure, and electrical behavior.

We must stress the fact that the chemical bath deposition technique described here is substantially different from the better known chemical spray deposition technique of Chamberlin and Skarman (2).

The chemical bath deposition technique, well known for its use in forming films of lead chalcogenides, involves a slow film deposition from a solution which contains cadmium in a complex form and an organic sulfur-containing reducing agent which react to give cadmium sulfide in thin film form. Two essentials mark the difference between the two techniques: (*i*) In the bath deposition method, the cadmium is in a complex form; in the spray method, it is ionized Cd salt solution. (*ii*) In the bath deposition method, the film forms comparatively slowly with the advantages of better orientation of crystallites and improved grain structure unlike in the spray technique where the film formation is almost an instantaneous process.

However, the bath deposition method has a limitation regarding the temperature of deposition. By its very nature, this temperature is normally restricted to about 100°C, while in the spray technique, the initial temperature may be as high as 400°C.

Experimental

Preparation.—In this study, thin films of cadmium sulfide have been prepared by reaction of thiourea with cadmium tetraammonium sulfate.

The apparatus shown in Fig. 1 consists, in essence, of an oil bath whose temperature can be controlled, and an electrically driven stirrer, using a synchronous motor to obtain constant speed. The glass substrates to be coated are suspended in pairs from the stirrer shaft. It was found that the following conditions were most suitable for obtaining uniform and sensitive films:

1. The temperature of the oil bath was maintained at 100°-110°C so as to keep the temperature of the mixture at about 80°-90°C.

2. Freshly prepared doubly distilled water was used to prepare the solutions and to clean the glass slides used as substrates. These slides were initially cleaned by "Niogen C. S." detergent solution and were boiled several times in doubly distilled water. Some metal substrates were also used, *e.g.*, nickel, aluminum, copper, Kovar, etc. These were initially cleaned with dilute acid and then were boiled several times in doubly distilled water. Finally the substrates were cleaned for a few minutes in an ultrasonic cleaner. Careful cleaning is essential for obtaining uniform films.

3. The pair of substrates was kept rotating in the reaction mixture at a constant speed of 100 rpm. This stirring action which continuously exposes the substrates to a fresh body of reactants is important for uniform deposition of the films.

For each deposition, 10 cm^3 of 1 mole cadmium sulfate solution and 50 cm^3 of 2 mole ammonia solution were mixed in a 150 cm^3 beaker to form the complex compound. To this solution was added 10 cm^3 of 1 mole thiourea solution. The reaction vessel was heated to 80°-90°C for 30 min. The cleaned pair of substrates was kept rotating approximately 2.5 cm below the surface of the solution. The films formed were washed several times with distilled water, dried, and preserved in a dark dessicator.

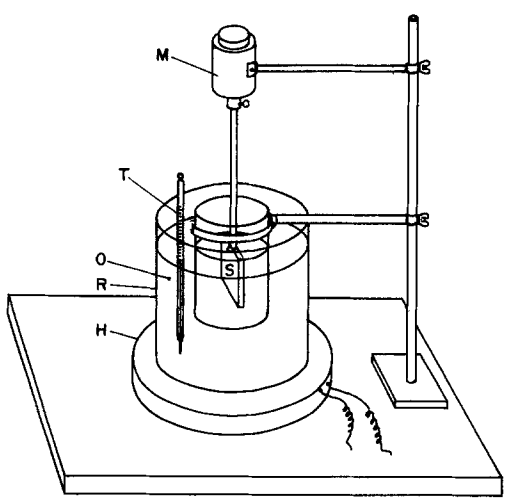


Fig. 1. Experimental setup for the deposition of the CdS layers. H, Heater; R, reaction vessel; S, substrate; O, oil bath; T, thermometer; M, synchronous stirrer motor.

A reaction mechanism for the formation of CdS based on the deposition kinetics of thin films of PbSe by Lundin (3), is suggested below:

1. Cadmium salt reacts with ammonia to form the complex compound

$$CdSO_4 + 4(NH_3) \rightarrow (Cd(NH_3)_4)SO_4$$

2. Diffusion of the complex ion, OH^-, and thiourea to the catalytic surface of CdS.

3. Dissociation of the thiourea on the CdS catalytic surface in an alkaline medium

$$\begin{matrix} H_2N & & NH_2 \\ & \diagdown \quad \diagup & \\ & C & \\ & \| & \\ & S & \end{matrix} + OH^- \rightarrow CH_2N_2 + H_2O + HS^-$$

4. Formation of bivalent sulfide ions

$$HS^- + OH^- \rightarrow S^{--} + H_2O$$

5. Formation of CdS

$$Cd(NH_3)_4^{++} + S^{--} \rightarrow CdS + 4NH_3$$

The sensitivity and the dark resistance of CdS films have traditionally been controlled by the addition of copper, which acts as electron acceptor. In our process copper is incorporated in two ways: (*i*) by addition of a copper salt (CuI, 0.1% by weight) to the bath solution, or (*ii*) by embedding the film in CdS powder to which approximately 0.1% CuI was added and baking at 100°C for 4 hr in a dry and oxygen-free nitrogen atmosphere. Films prepared by double deposition and doped with copper by the second method were used for the Hall measurements. For the study of the other properties, Cu was introduced in the films by the first method.

The thickness of the films was estimated by a method in which the area and the weight of the film were determined; the thickness deduced from this is between 0.8 and 1 μm. The surface structure of these films was examined by x-ray and electron diffraction methods.

Contacts.—It is known that In and Ga make good ohmic contacts with CdS. In and Ag were successively evaporated in vacuum (10^{-5} mm of Hg) onto a masked sample plate. The portion of the film where the contacts were to be made was kept exposed. Leads of 46 gauge silver-copper wires were soldered to the silver deposit.

The nature of the contacts was checked by the potential probe method and by measuring the current-voltage characteristics for a number of samples in the dark as well as with different illumination intensities. The potential probe method utilizes the principle that if the contacts are ohmic no abrupt potential drop should exist at the metal-semiconductor contacts.

About 3-4 mm wide electrode (In-Ag) strips were deposited at both ends of the sample. Also perpendicular to its length were deposited 1 mm wide (In-Ag) electrode strips at a distance of approximately 3 mm, leaving the CdS strip open at the center. Leads of 46 gauge silver-copper wire were soldered to each electrode strip. The sample was mounted in a shielded metal box and was connected to a multipoint rotary switch. A 90V d-c battery with a resistance in series was used as a voltage supply. Voltage drop across the length of the sample at different points was measured with a high impedance Cary 31 electrometer amplifier.

Rise and decay transients.—The rise and decay of photoconductivity includes the contributions of trap filling and emptying. The photoconductive rise and decay transients were studied with a view to finding the nature of the traps or trap levels.

The general procedure is to induce a change in the signal at a set repetition rate and observe it by a detector which is sensitive to that frequency. For this measurement of rise and decay transients the following method has been used (4).

A chopped light having chopping frequency of 14 Hz and intensity 2.4×10^{20} photons cm^{-2}-sec^{-1} was used to illuminate the sample. Consequently the current in the circuit is modulated in the same way, inducing a modulated voltage across a load resistor. The induced voltage corresponding to the change in the sample's conductance was fed to an oscilloscope (Tektronix Model 515-A) directly. An all-metal cryostat was used to mount the sample. This sample cryostat and the optical box were properly grounded to avoid stray electrical signals.

Field effect measurement.—The arrangement of the field effect experiment is presented in Fig. 2. A thick Teflon block was used as a base for mounting the sample. A layer of silver was deposited over the central portion of this which was used as a field electrode B. Electrodes A and A' are In-Ag electrodes to which aluminum pressed contacts were applied. A sweep voltage $V_{AA'}$ was applied across these electrodes and the sweep current through this circuit may be measured by a series ammeter. Sandwiched between the film surface and the field electrode B is a dielectric, such as a thin mica sheet (0.0025 cm thick). All these were maintained in position by means of side screws through the Perspex block placed on the sample. The whole assembly was fixed in a thick sheet-aluminum box to minimize stray electrical signals. A glass window was provided to illuminate the sample.

The field effect is the conductance change observed in the semiconductor when it is subjected to a transverse field (V_B). This conductance change in the sweep circuit is sometimes very small because of a large density of localized states which makes it difficult to move the Fermi level through more than a few kT. Thus detecting the field effect by measuring the conductance change is not a sensitive technique. Hence a sensitive field effect bridge was designed by us. Here the sample forms one of the arms of the bridge. With V_B kept at zero, the bridge is balanced by the variable ten-turn resistor so that the electrometer (Orion) reads zero voltage. As soon as V_B is applied to the field electrode (B, in Fig. 2), the sample conductance changes and the bridge becomes unbalanced. This imbalance voltage read by the electrometer is fed to a strip chart recorder (Varian, G-10) and may be related to the conductance change.

Spectral response of photoconductivity and optical absorption.—For the spectral response measurement, the sample was mounted in the cryostat mentioned earlier. Spectral response was measured as a photocurrent change in arbitrary units by an electrometer (EA 810 A). A calibrated Hilger monochromator with 500W projection lamp was used as a light source. Measurements were carried out at 300° and 93°K. The optical absorption was studied in the range 4000-7000Å, using a Unicam SP-600 spectrophotometer at 300°K. The absorption coefficient was calculated.

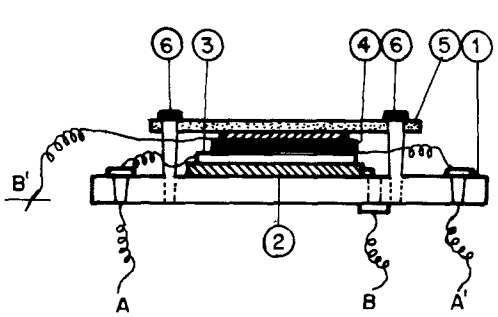


Fig. 2. Experimental arrangement of field effect specimen. 1, Teflon block; 2, silver electrode; 3, mica spacer; AA', sweep field; 4, sample; 5, Perspex block; 6, fixing screws; BB', transverse field.

Hall measurements.—As the films have high resistivity and low mobility, Hall measurements were possible only under white light illumination (10^{20} photons/cm^2/sec). The electrode arrangement required was obtained by deposition of the electrodes through a molybdenum mask which gave a distance of 10 mm between end electrodes and a length to breadth ratio of ~ 4. A special all-metal cryostat was used in which two soft iron pole pieces entered through O ring seals in the wall. Thus a small pole gap of ~ 1.5 in. could be maintained across the sample. Light coming from the source was focused on the sample by lenses. The magnetic field used was about 9000G.

Results

Preparation and structure.—CdS films prepared by the chemical bath deposition technique are uniform, adhere tightly to the substrate, and resist abrasion. These films appear to have some advantages over those prepared by other techniques, *e.g.*, their properties are relatively insensitive to oxygen and moisture. They are reproducible in structure, thickness, and electrical and photoconducting properties. We studied undoped films and films doped with indium, silver, arsenic, and copper in the form of halides, for their structure. Films deposited without dopants are polycrystalline. Films grown with dopants present during deposition are amorphous, while the precipitate obtained during the reaction is always polycrystalline irrespective of whether it is doped or undoped. Variation of temperature, speed of rotation, and composition of electrolyte do not affect these results. The ratio of resistivity in dark to that under illumination is lower for films doped with indium, silver, and arsenic than copper-doped or undoped films.

Study of the x-ray diffraction patterns shows that undoped films consist of a mixture of approximately 90% β-cubic and approximately 10% α-hexagonal forms of CdS, which was confirmed by electron diffraction measurements.

In-Ag evaporated contacts studied by the potential probe method show no major contact resistance. Current-voltage characteristics show linear behavior in the dark as well as with illumination which is characteristic of good ohmic contacts. No self-capacitance is observed at the frequencies at which the measurements were carried out.

Photoconductivity rise and decay was studied as a function of temperature in the range 130°-310°K. The dark conductivity and the steady-state photoconductivity curves as a function of temperature are given in Fig. 3. Here the steady-state photoconductivity is the conductivity corresponding to the initial value of the decay curve. The decay curves are exponential in nature over the temperature range studied. The density of states near the Fermi level was computed from the decay curves at various temperatures using the following expression (5)

$$N(E_F) = F\tau_0/kT \qquad [1]$$

where $N(E_F)$ is the density of traps at the quasi-Fermi level, F is the photoexcitation rate, and τ_0 is a photoconductivity decay response time. The density of states thus calculated is of the order 10^{19}-10^{20} cm^{-3} eV^{-1}.

The analysis of the field effect data for the estimation of the density of states at the Fermi level follows the method suggested by Arnoldussen (6, 7) with the assumption that the density of states at the surface is not very much different from that in the volume. The den-

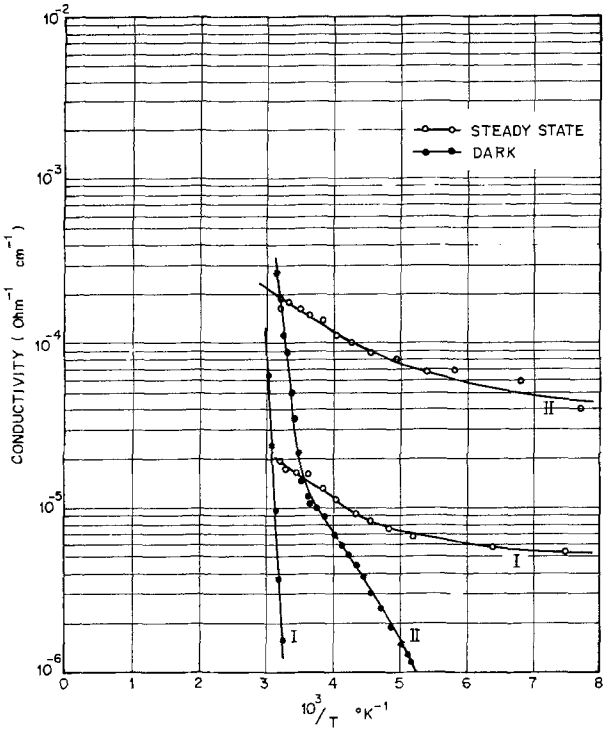


Fig. 3. Temperature dependence of dark conductivity and steady-state photoconductivity obtained from transient decay curves for CdS chemically deposited thin film: I, undoped and II, doped.

sity of states at the Fermi level, as it is moved by the applied field V_B, was calculated from

$$N[E_F(V_B)] = \frac{Q}{eDKT} \cdot \frac{G_o}{\Delta G} \qquad [2]$$

where Q is the induced charge by V_B, D is the thickness of the film, G_o is the sweep conductance measured with no field voltage applied, and ΔG is the change in the sweep conductance when the field voltage V_B is applied. This above formula is valid only in the case when $V_B \to 0$, and the shift in E_F is of the order of kT or less than kT.

The density of states at the no-field Fermi level E_{F_o} (*i.e.*, $V_B \to 0$) calculated for both the doped and the undoped films is of the order 10^{20} cm^{-3} eV^{-1}.

Figures 4 and 5 show the field effect conductance change, ΔG, as a function of field voltage V_B in the dark and under illumination for the undoped and the doped films.

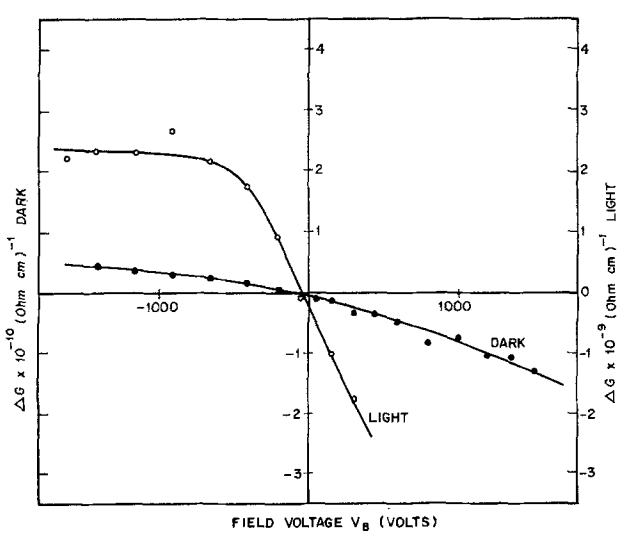


Fig. 4. Field effect conductance change as a function of field voltage in undoped CdS chemically deposited thin film.

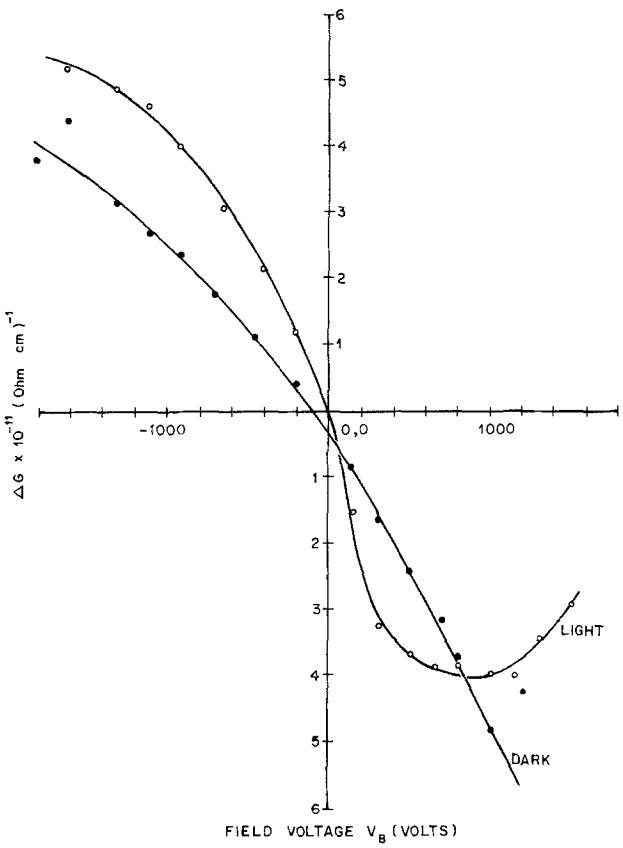


Fig. 5. Field effect conductance change as a function of field voltage in doped CdS chemically deposited thin film.

The field effect signals were recorded for different light intensities keeping the field voltage constant. Thus the density of states at the quasi-Fermi levels was calculated, which is found to remain more or less constant at 10^{20} cm^{-3} eV^{-1}.

From the observed absorption data it is found that plots of $(\alpha h\nu)^2$ *vs.* $h\nu$ (Fig. 6) for undoped and doped films gave fairly good straight lines indicating that the

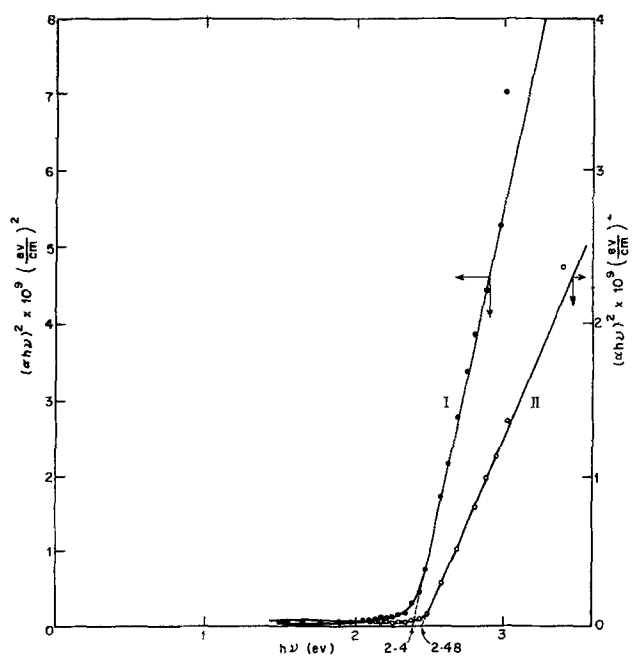


Fig. 6. Variation of $(\alpha h\nu)^2$ as a function of $h\nu$ for CdS chemically deposited thin film: I, undoped and II, doped.

transitions were direct and allowed. Besides the absorption coefficient, α, was high, of the order of 10^{-4} cm^{-1}, suggesting direct transitions. These observations are in agreement with the fact that the material is known to be a direct gap material. The plot of $(\alpha h\nu)^2$ against $h\nu$ for undoped film extrapolates to $(E_g)_{opt.} = 2.40$ eV, while that for the doped amorpous film extrapolates to $(E_g)_{opt.} = 2.48$ eV.

Spectral dependence of these films for excitation of photoconductivity at 300° and 93°K are presented in Fig. 7 and 8, respectively. At 93°K it shows a peak in the region of 480 nm for undoped samples and at 460 nm for copper-doped films. The values show that these films have a greater blue response than the corresponding CdS crystal, doped or undoped. The spectral response at 300°K gives a peak at 520 nm for undoped films and at 456 nm for doped films.

The Hall voltage for these CdS films was measured at room temperature under photoexcitation with white light (2.4×10^{20} photons/cm^2/sec) for three different magnetic fields and the Hall constant R and the mobility μ_H, were calculated; μ_H and n thus obtained are 5 $cm^2/V \cdot sec$ and $\simeq 10^{14}/cm^3$, respectively.

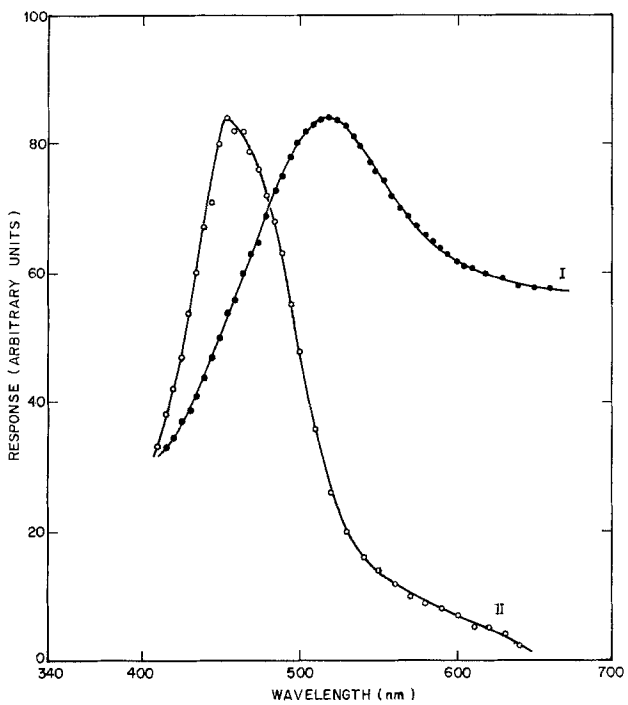


Fig. 7. Spectral response curves for CdS chemically deposited thin film at 300°K; I, undoped and II, doped.

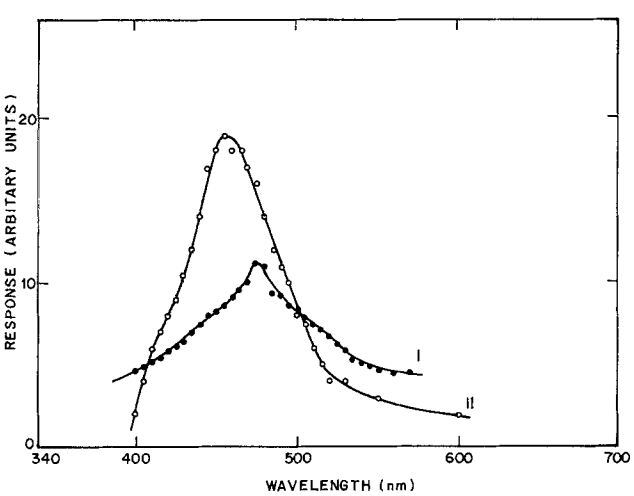


Fig. 8. Spectral response curves for CdS chemically deposited thin film at 93°K: I, undoped and II, doped.

Discussion

One of the most interesting observations related to this study is that the trace addition of cations like copper, silver, indium, etc. make the layers amorphous (as judged from x-ray and electron diffraction data). This phenomenon can be explained on the basis of adsorption and its effects on crystal growth as observed by Kennan and France (8). Thus we attribute the lack of polycrystalline form when copper (for example) is added during deposition, to the adsorption of copper ions at the surface of a growing CdS microcrystal. This then prevents the microcrystals from growing larger along the plane of the substrate (and perpendicular to it). This is also substantiated by the observed fact that layers made with copper addition during deposition are thinner than those made without it.

This result makes it possible to grow and study both amorphous and polycrystalline photoconductive chemically deposited layers. This is particularly relevant to the current interest in the preparation and properties of amorphous materials. A further inference of the mechanism of deposition may be made: that it is the slow growth of the film on the substrate alone that is controlled by the addition of cations like copper or silver. This we deduce from the observation that even when the deposited film is amorphous in structure, the precipitated cadmium sulfide which is a by-product of the process is still crystalline. Thus the adsorption mechanism which inhibits crystal growth through the agency of cations like copper etc. must involve the substrate surface and not the crystal growth face itself. This aspect has not been pursued further in this work, but left open as an avenue of future investigation.

Let us now consider the decay of photoconductivity when the photoexciting radiation is interrupted. Though the decay curves, when replotted as a function of time give nearly a straight line plot of log $\Delta\sigma$ against time indicating that the decay process is more or less exponential, the plot of log τ_0 against $1/T$ gives a straight line with very small slope indicating nearly temperature-independent behavior. This suggests that there is a uniform distribution of traps close to the conduction band. The experimental data also indicate that though a uniform distribution of traps exists, the time constant of decay is nearly the same for all the trap levels. The density of states distribution in the bandgap calculated from the decay of photoconductivity confirms those obtained by the field effect measurement.

Study of the field effect conductance ΔG as a function of field voltage in the dark shows that the conductance increases with negative field voltage and decreases with positive field voltage for undoped as well as doped samples. This indicates that: (*i*) The material is n-type; either the free electron concentration or mobility is very much greater than the free hole concentration or mobility or both. (*ii*) The bands are flat at the surface. (*iii*) ΔG against field voltage curves are close to linear which suggests that the field effect is due to change in electron concentration and not due to change in mobility μ. If the field effect were due to the change in mobility, these graphs would be sharply nonlinear since mobility depends exponentially on ϕ, the barrier height (9). This is contrary to the observation by Waxman *et al.* (10) who observed a field dependence of mobility in the case of evaporated CdS thin films.

The photofield effect conductance as a function of field voltage indicates that in the presence of light the electron and hole concentrations and/or the mobilities are not greatly different.

A plausible explanation for a shift in bandgap (2.40 for crystalline and 2.48 for amorphous) is along the lines suggested by Lehman (11). He studied optical absorption as a function of impurity concentration for In-doped CdS. He found that the quantum energy corresponding to the edge increases steadily with increasing impurity concentration up to a certain limit, then

onwards it remains constant. The explanation suggested is as follows. Any disorder in crystal causes a tailing-off of the density of allowed states below the bottom edge of the conduction band. This tail is probably strong in all conventional II-VI compounds as indicated by the observed exponential dependence of the absorption constant on the quantum energy near the edge (12). Hence a measured α in the order 100 cm^{-1} probably does not correspond to an electron transition into the conduction band but into the tail below the conduction band. Thus the band-to-band transition energy is increased due to splitting off of the levels from the conduction band.

The highlights of our experimental investigations of the study of CdS chemically deposited films are: (*i*) a photo-Hall mobility of 5-10 cm^2/V-sec at 300°K, and (*ii*) an electrical conductivity of 10^{-8} Ω^{-1}-cm^{-1} at 300°K. We now proceed to the description of a suitable model for the situation of the gap states and the relation between the conduction band and the valence band and these states, based on our experimental data.

In discussing the behavior of such a material, the role of traps and trapping centers assumes great importance, especially because of the active part which these play in determining free lifetimes. The values of carrier densities which we have found, 10^{14}-10^{15} cm^{-3} and the mobility, 5-10 cm^2/V-sec seem appropriate to a picture of a polycrystalline material with a high density of interband states and a mobility limited by intergrain boundaries.

The high density of state at the Fermi level ($\simeq$ 10^{19}-10^{20} cm^{-3} eV^{-1}) indicates that the Fermi level is effectively pinned somewhere in the bandgap and that the distribution of states between the Fermi level and the conduction band is more or less uniform. We now consider the additional support to this model from the field effect and photofield effect data.

Field effect measurements carried out on the two types of specimens have shown that one can sample the localized states by moving the Fermi level through a few kT using either an electric field or light. This, therefore, offers a means of checking our earlier hypothesis that the Fermi level is pinned in the bandgap close to the bottom of the conduction band.

Field effect data show that the density of state at E_F is 10^{19}-10^{20} cm^{-3} eV^{-1} when E_F is moved by $\simeq$ 3 kT from its equilibrium value.

The field effect also indicates that the bands are flat at the surface which further supports our model. We now come to the problem of determining the quasi-Fermi level. Assuming an electron effective mass ratio $= 0.2$ and taking a free carrier concentration $n = 1.04 \times 10^{14}$ cm^{-3} as obtained from the photo-Hall effect, the quasi-Fermi level is found to be 0.25 eV below the conduction band at an excitation intensity of about 10^{20} photons/cm^2/sec at 300°K.

This again gives additional support to our model in which we assumed that the Fermi level was effectively pinned down by a cluster of gap states, with a high density, at the Fermi level. The amount that the quasi-Fermi level moves up in response to the photoexcitation is easily known from the ratio of light to dark conductivity and was found to be of the order of 0.08 eV. Thus, to a first approximation, we may determine the position of the Fermi level by adding the amount of light-activated Fermi level shift (0.08 eV) to the value of quasi-Fermi level as determined by photo-Hall measurements. This places Fermi level of $\simeq$ 0.33 eV below the conduction band.

Having determined that the Fermi level lies fairly close to the conduction band, the high density of state would then appear to be more of a tail of conduction band states caused by localization of these states.

The merit of this model is that it satisfactorily reconciles the data obtained on our chemically deposited layers through photo-Hall, decay characteristics, field effect, and optical absorption measurements.

Acknowledgment

This is Communication No. 2036 from the National Chemical Laboratory, Poona, India.

Manuscript submitted Sept. 28, 1976; revised manuscript received Dec. 20, 1976.

Any discussion of this paper will appear in a Discussion Section to be published in the December 1977 JOURNAL. All discussions for the December 1977 Discussion Section should be submitted by Aug. 1, 1977.

REFERENCES

1. B.I.O.S. Final Report No. 530, Item No. 9.
2. R. R. Chamberlin and H. S. Skarman, *This Journal*, **113**, 86 (1966).
3. A. B. Lundin, *Izv. Akad. Nauk SSSR Neorg. Mater.*, **1**, 2107 (1965).
4. S. M. Ryvkin, "Photoelectric Effects in Semiconductors," chap. II, Consultants Bureau, New York (1964).
5. R. H. Bube, "Photoconductivity of Solids," p. 279, John Wiley & Sons, Inc., New York (1960).
6. T. C. Arnoldussen, C. A. Menezes, Y. Nakagawa, and R. H. Bube, *Phys. Rev. B*, **9**, 3377 (1974).
7. T. C. Arnoldussen, Private communication.
8. F. G. Kennan and W. G. France, *J. Am. Ceram. Soc.*, **10**, 821 (1927).
9. B. A. Nesterenko, *Sov. Phys. Solid-State (Engl. Transl.)*, **5**, 2341 (1964).
10. A. Waxman, V. E. Henrich, F. V. Shallcross, H. Borkan, and P. K. Weimer, *J. Appl. Phys.*, **36**, 168 (1965).
11. W. Lehman, *This Journal*, **112**, 1150 (1965).
12. T. S. Moss, "Optical Properties of Semiconductors," p. 38, London (1961).

Dependence of WO_3 Electrochromic Absorption on Crystallinity

O. F. Schirmer, V. Wittwer, G. Baur, and G. Brandt

Fraunhofer-Gesellschaft, Institut für Angewandte Festkörperphysik, D-7800 Freiburg, Federal Republic of Germany

ABSTRACT

The optical absorption of amorphous WO_3 electrochromic display layers is explained as small polaron absorption. The necessary W^{5+} 5d-electron localization is favored by the lattice disorder. This is concluded from the change of the optical properties to free-electron-like behavior upon crystallization of the layers. The increased electrocoloration stability of amorphous layers and the blue shift of the absorption peak in Mo-doped WO_3 films can also be explained within the model given.

It is established by now that the electrochromic coloration of evaporated WO_3 layers (1) to be used for display applications proceeds by the formation of tungsten bronzes A_xWO_3 (2, 3) (A = H°, Li°, etc.). The electrons entering the layers from the cathode are distributed over the WO_3 part of the lattice and are accommodated in W^{5+} 5d orbitals (2). The coloration is due to a broad absorption band peaked at energies near 1.2 eV (1), somewhat depending on the method of layer preparation and coloration. Such a peak is not typical for the optical behavior of crystalline tungsten bronzes; their reflectivity spectra can be explained roughly by assuming Drude-type behavior of electrons predominantly having banding character (5). On this basis one would expect to observe no or a less pronounced peak in the absorption of the electrons in the tungsten bronze of an electrochromic device. It is shown here that the optical absorption of such layers can still be understood as that of W 5d electrons in the tungsten bronzes if the disorder present in amorphous layers generally used for electrochromic display devices is considered. This will favor localization (4) of the electrons, breaking the translational symmetry of the lattice. In this way, the formation of W^{5+} d-electron bands will be hindered and the electron-phonon interaction can then cause an additional stabilization at the respective tungsten sites.

The electron together with its accompanying lattice distortion can be called a small polaron. It will be shown that the optical absorption of the amorphous films can be explained as that of small polarons. If such layers are transformed to a crystalline state, a different absorption with less pronounced peak structure is observed which shows features of banding electrons. Thus, the amorphous state is a necessary condition for the observation of electrochromic absorption bands near 1.2 eV in the tungsten bronzes. The increased stability of electrocoloration in amorphous layers can also be attributed to the disorder present. The experiments herein support an earlier proposal by Faughnan *et al.* (2) that the band absorption in electrochromic WO_3 is caused by intervalence transfer (6). The underlying physics of this model is simlar to that of small polaron absorption.

Experimental

WO_3 layers were evaporated at room temperature onto glass substrates, which were either covered with a SnO_2 film or uncovered. Layer thicknesses were between 0.4 and 1 μm, leading to weak interference structure in the optical spectra. Electrolytic coloration of the SnO_2-covered specimens with a H_2SO_4 solution as anode and the SnO_2 film as cathode resulted in the absorption and reflection spectra shown in Fig. 1; coloration of the SnO_2-free layers by applying an electric field along the plane of the film (1) led to the somewhat narrower absorption curves of Fig. 2.

Heating the WO_3 layers to 340°-400°C in air or N_2 gas and cooling in the same ambience resulted in crystallization of the layers, as demonstrated by their x-ray diffraction peaks shown in Fig. 3a. Such reflexes were completely absent in as-evaporated material, Fig. 3b. From the crystallized specimens, electrolytically colored in H_2SO_4, absorption and reflection spectra as shown in Fig. 4 were observed.

After coloration, the absorbance of the crystallized layers decreased with time and shifted to longer wave-

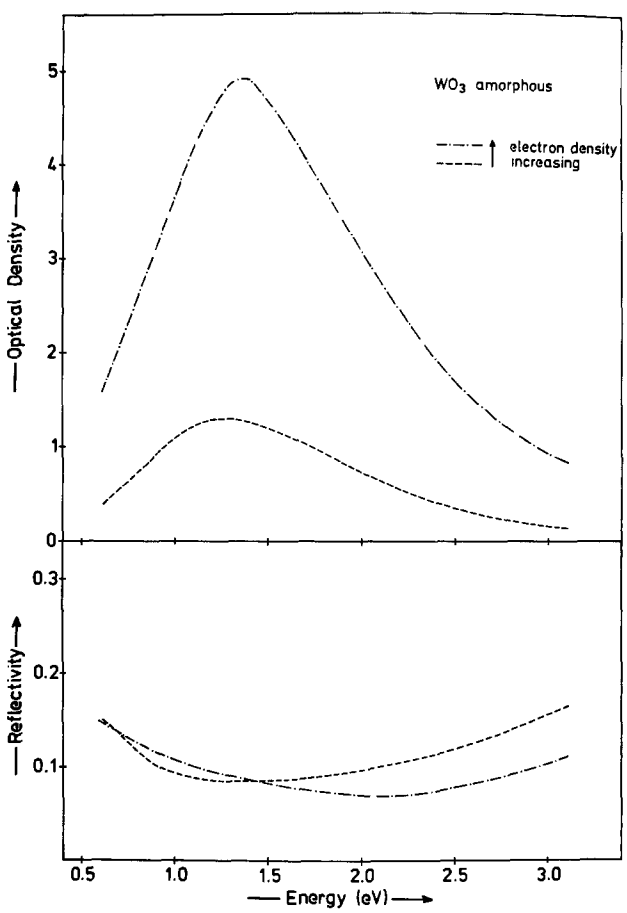


Fig. 1. Optical absorption (upper part) and reflection (lower part) of as-evaporated amorphous WO_3 layers, colored electrolytically. Spectra for two degrees of coloration are given.

Key words: tungsten trioxide, electrochromism, small polaron absorption, amorphous semiconductor, potential fluctuations.

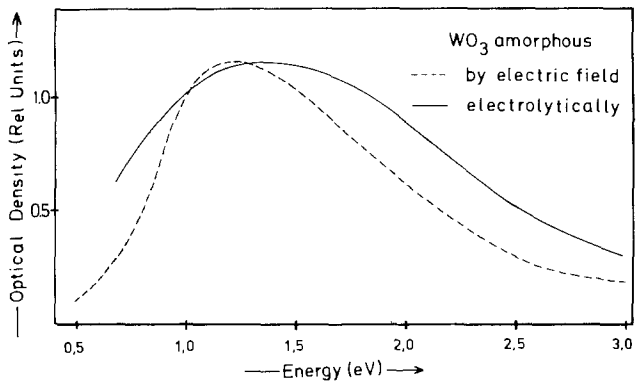


Fig. 2. Optical absorption of electrolytically colored amorphous layers, compared with that of samples colored by an electric field in the layer plane.

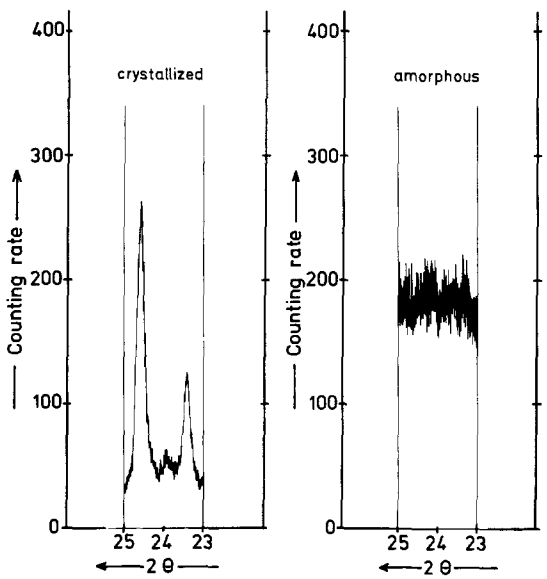


Fig. 3. Characteristic x-ray diffraction peaks observed from crystallized (left) and amorphous (right) WO_3 layers.

length as indicated in Fig. 5. The samples annealed in N_2 atmosphere were bluish before electrolytic coloration; in this state the absorption was lower but of the same wavelength dependence as after coloration (Fig. 6). After coloration layers annealed in N_2 or air essentially showed the same wavelength dependence of the absorption. Figure 6 also demonstrates the striking difference in absorbance between crystallized and amorphous layers.

The oxygen content of the layers changed upon annealing in air and N_2 atmosphere, respectively. This was checked with x-ray fluorescence: the counting rates for O and W, respectively, showed a ratio of 2.75 for air-treatment and 2.60 for N_2 annealing, *i.e.*, 5% change in the oxygen content. Since there are some ambiguities in calibrating the relative counting rates to the absolute O/W content of the layers, these ratios do not necessarily correspond to the actual stoichiometry of the specimens. The oxygen content of evaporated WO_3 layers apparently is increased by air-treatment and not lowered by N_2 annealing, as might be inferred from the above ratios; for specimens annealed in N_2 after air-treatment did not show a change in the O/W counting rate ratio.

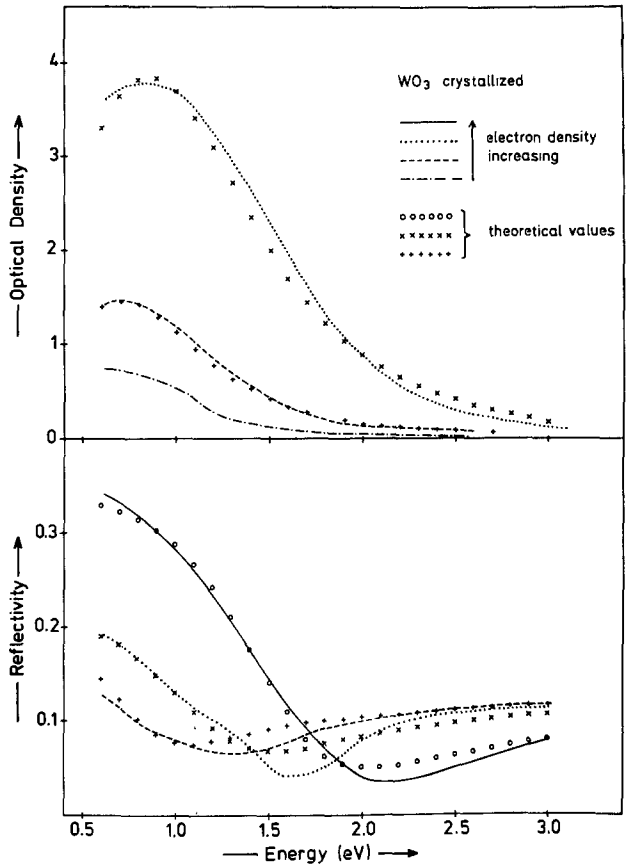


Fig. 4. Optical absorption (upper part) and reflection (lower part) of crystallized WO_3 layers, colored electrolytically. Spectra for several degrees of coloration are shown.

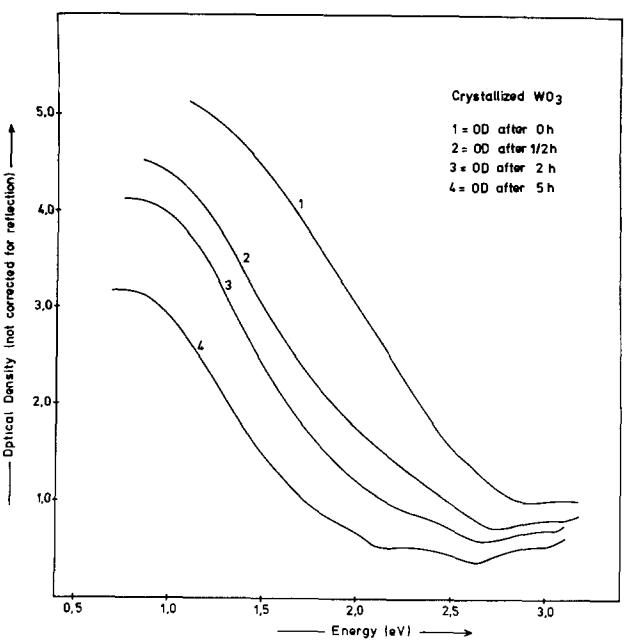


Fig. 5. Time dependence of the absorbance decay of electrolytically colored crystallized WO_3 layers.

Discussion

Amorphous material.—We shall explain the narrower band in Fig. 2 as small polaron absorption. A small polaron is formed if the interaction of a charge carrier with the surrounding lattice localizes the carrier to essentially one lattice site (7-9). The corresponding breaking of translational symmetry is favored, if the charge carrier banding, determined by the transfer integral J, is small or if its effect is suppressed by

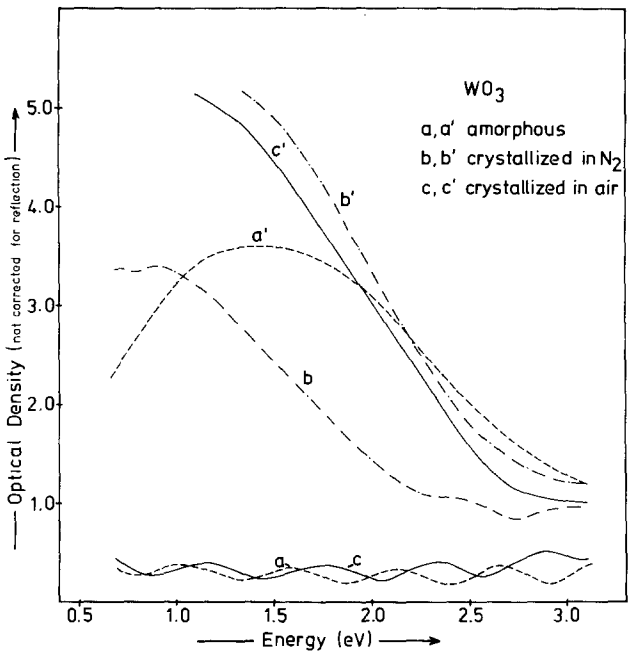


Fig. 6. Optical density (uncorrected for reflection) of WO_3 layers under the following conditions: a, a' amorphous, as-evaporated; b, b' annealed in N_2 gas; c, c' annealing in air. Primed letters refer to electrolytically colored samples, unprimed ones to the respective states before coloration.

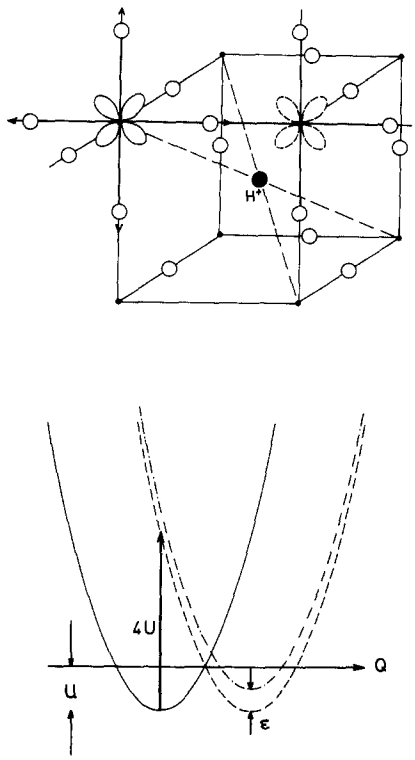


Fig. 7. Upper part: Expected effect of accommodating an electron into the shown W^{5+} 5d orbital on the lattice of an H_xWO_3 bronze. Lower part: Electronic energy vs. lattice configuration coordinate. Upon trapping the electron, the energy U is gained. A possible inequivalence of lattice sites may lead to the potential difference ϵ. The arrow marks the expected optical transition.

fluctuating local potentials. Disorder in the lattice reduces the mean free carrier path length to one lattice constant (4), if the energy range within which the local potential fluctuates is large compared to J. In the most simple approach, the carrier-induced lattice distortion is represented in a diagram showing the potential energy of electron and lattice depending on a single, one-dimensional lattice configuration coordinate, Fig. 7. The fluctuation of the local electron potential is considered by the inclusion of its difference, ϵ, between the two sites shown in Fig. 7. It has long been realized (9, 10) that optically induced transitions between two such sites can be considered as Franck-Condon transitions, indicated by the vertical arrow in Fig. 7. Recently, a simple formulation for the optical absorption band shape expected from such a system has been given (11)

$$\alpha(\hbar\omega) \propto \hbar\omega \exp\left(-w(\hbar\omega - \epsilon - 4U)^2\right) \qquad [1]$$

with $w^{-1} = 8U \cdot \hbar\omega_0$, $\hbar\omega_0$ being the energy of the representative vibration quantum. A least squares fit of this expression to the low energy onset of the optical absorption is shown in Fig. 8, where $\epsilon = 0$ was assumed. The case where $\epsilon \neq 0$ is considered below. It is seen that the low energy wing of the band is well reproduced with the parameters $U = 0.275$ eV and $\hbar\omega_0 = 0.098$. Discrepancies at energies beyond the peak energy like that in Fig. 8 have generally been noticed in small polaron absorptions (12, 13). Formerly, they have been attributed to electron transfer transitions into higher lying orbitals at neighboring sites (11, 12). They can occur since transitions are allowed to all orbitals having finite admixture to the original one by the corresponding transfer integral (11). It seems likely that the same explanation applies also here. The vibrational energy $\hbar\omega_0$, 0.098 eV, is close to that of LO phonons in WO_3 (14). This is reasonable because it is expected that the corresponding W-O spring in the lattice is strained by the electron-phonon interaction forming the small polaron. The polaron stabilization energy U, 0.275 eV, obtained from fitting the spectrum in Fig. 8, is somewhat higher than in other d-electron systems, typically 0.2 eV (12, 13). It must be considered, however, that the influence of ϵ will make the

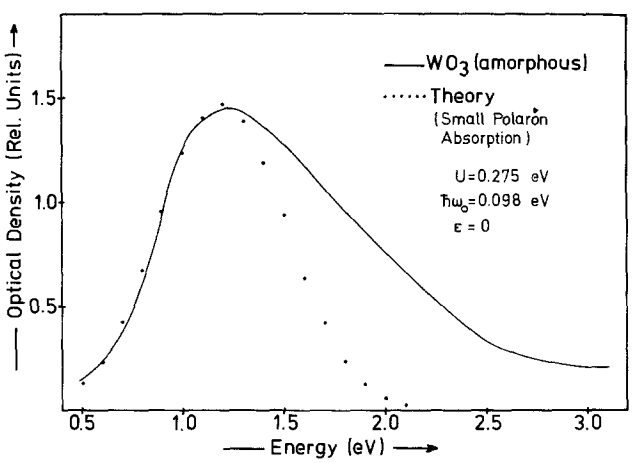


Fig. 8. Least squares fit of the low energy onset of the narrow band in Fig. 2 with the expression in Eq. [1], resulting in the fitting parameters in the upper right.

U determined for $\epsilon = 0$ an upper limit to the actual one. Since the trapped electron will tend to settle at the lowest possible potential, ϵ in Eq. [1] will be positive and U will be lower than that derived above. The observed absorption curve will then in fact be a superposition of a multitude of Gaussian bands. Since part of the apparent width of the absorption band will be caused by this superposition, the determined representative vibration frequency will also be somewhat too high.

It should be added that the rather high intensity of the electrochromic absorption band is also in accord with the model. Resonance admixture of orbitals at neighboring sites to the original one can lead to considerable transition moments (10, 11).

The appearance of a corresponding absorption band in the transmission spectrum of finely ground sodium tungsten bronze powder, pressed in thin pellets (5), can also be attributed to the presence of potential fluctuations, caused by mechanical damage during grinding.

Crystallized material.—The absorption and reflection spectra observed from crystallized layers show features different from those of amorphous specimens. The absorption now reaches a less pronounced maximum at lower energy (Fig. 4) than in the amorphous case, and the reflection spectra now show more narrow minima and an over-all behavior reminiscent of that of a plasma of free electrons. In fact the gross features of these optical properties can be explained under this assumption, provided the scattering of the electrons by optical phonons and/or lattice defects is taken into account. Expressions for absorption and reflection are obtained from the real, n, and imaginary, k, part of the complex refractive index of a plasma (15)

$$n^2 - k^2 = \epsilon_\infty - \frac{\omega_p{}^2 t^2}{1 + \omega^2 t^2}$$

$$2nk = \frac{\omega_p{}^2 t}{\omega(1 + \omega^2 t^2)}$$

ω_p being the plasma frequency.

In order to include scattering by impurities and/or phonons, we introduce a frequency-dependent relaxation time $t \propto \omega^x$, where x has to be determined from the experimental spectra. The absorption coefficient is given by (15)

$$\alpha(\omega) = \frac{2nk\omega}{c}$$

whereas

$$R(\omega) = \frac{(n-1)^2 + k^2}{(n+1)^2 + k^2}$$

determines the reflectivity. With these expressions, the absorption and reflection spectra in Fig. 4 could be fitted simultaneously using the following parameters. ϵ_∞ was set equal to 4.4, consistent with the refractive index WO_3 in the relevant frequency range (1). Depending on the coloration intensity, $\hbar\omega_p$ lies between 0.5 and 2.4 eV. Assuming an effective mass of $\sim 1 m_e$, this corresponds to carrier densities in the correct order of magnitude ($\sim 10^{21}$-10^{22}/cm^3). Plasma energies in the same range have been found by Scott *et al.* (16) for crystalline tungsten bronzes. The best simultaneous fits of reflection and absorption curves were obtained with $x = 1.1$, which leads to a high frequency asymptotic behavior of the absorption $\omega^{-3.1}$. This exponent lies between those characteristic for LO phonon scattering, $\omega^{-2.5}$ (17), and ionized defect scattering, $\omega^{-3.5}$ (18). So one might infer that the charge carriers in the crystallized layers interact both with defects and LO phonons. This result is reasonable since LO phonon interaction is also responsible for the observed formation of small polarons.

So it turns out that the optical behavior of 5d electrons, electrically injected into crystallized WO_3 layers, is consistent with the electronic properties of crystalline tungsten bronzes. 5d electrons in nonstoichiometric WO_3 crystals have been found to behave as large polarons with a coupling strength $U/\hbar\omega_0$ of ~ 3 (19). The upper limits of the corresponding values of U and $\hbar\omega_0$ inferred above from the small polaron absorption of the amorphous material with $\epsilon = 0$ are consistent with this ratio Since $\epsilon \neq 0$ will lead to a reduction of both values (see above), the actual ratio in amorphous material will still be of the same order. This means that in this intermediate coupling range the introduction of sufficiently large potential fluctuations can transform a large polaron to a small one with essentially the same coupling strength.

As shown above, the electrochromic coloration of crystallized WO_3 layers is independent of the annealing conditions, oxidizing, or reducing. Therefore, oxygen deficiency alone cannot be the cause of the 1.2 eV band in amorphous layers, as proposed in Ref. (1). The influence of disorder on the formation of this band is accounted for in a natural way by the model given above.

Additional Observations

The model presented above is supported by the observation that the addition of MoO_3 to the evaporating WO_3 material causes a blue shift of the electrochromic absorption (Fig. 9). From ESR investigations (20), one knows that electrons in such a mixed MoO_3/WO_3 compound are preferentially trapped at Mo sites. For low Mo concentrations these will be surrounded mostly by W ions. The electron capture at a Mo site will thus lead to an additional lowering of the initial state, *i.e.*, a larger effective ϵ (Fig. 7), and consequently to an absorption band peaked at higher frequency, *i.e.*, in a region of higher display efficiency. The same observation has been made independently by Faughnan (21).

The increased stability of electrochromic coloration in amorphous layers can be made plausible with the same model. Due to the potential fluctuations, electrons in not too high concentration will be more tightly bound in such layers. Oxidation of the layers by the surrounding O_2. *i.e.*, a removal of H^o, will thus be hindered, because a proton will have to capture an electron out of a deeper level, before it can escape as H^o. Of course, it is also expected that proton or H^o diffusion in an amorphous layer will be slower than in a crystalline compound.

Electrolytic coloration of amorphous WO_3 layers leads to broader absorption bands (Fig. 2) than coloration by an electric field in the layer plane. This is apparently due to a superposition of several bands corresponding to the occurrence of a higher spread of ϵ values. One must then conclude that electrons injected into WO_3 in an electrolytic experiment are accommodated in regions of high local disturbance. Since they will be captured close to the protons entering from the electrolyte, proton diffusion along highly disturbed parts of the amorphous network seems to take place. Electron injection by an electric field parallel to the layers apparently is compensated by protons sitting at less disturbed sites of the structure.

Conclusion

We have shown in this paper that the amorphous structure of evaporated WO_3 layers is a necessary

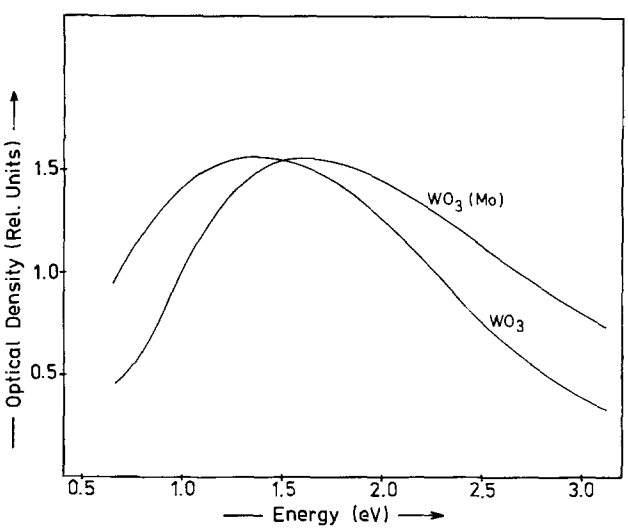


Fig. 9. Effect of adding 25 m/o MoO_3 to the WO_3 evaporating material on the electrochromic absorption.

condition for the appearance of stable electrochromic absorption bands, to be explained by intervalence or small polaron optical transfer. Otherwise an unstable free-electron-like absorption and reflection is observed, consistent with the known electronic properties of crystalline tungsten bronzes. The special behavior of the amorphous layers can be attributed to the potential fluctuations in the material caused by its disorder.

Acknowledgments

We gratefully acknowledge several discussions with Prof. H. G. Reik. Thanks are due to Mrs. C. Vogel for skilled experimental assistance, and to Dr. W. Rothemund and Mr. K. H. Schmidt for taking the x-ray fluorescence spectra. This paper is based on work supported by Bundesministerium für Forschung und Technologie under Contract NT. 647.

Manuscript submitted Oct. 28, 1976; revised manuscript received Dec. 18, 1976. This was Paper 201 presented at the Las Vegas, Nevada, Meeting of the Society, Oct. 17-22, 1976.

Any discussion of this paper will appear in a Discussion Section to be published in the December 1977 JOURNAL. All discussions for the December 1977 Discussion Section should be submitted by Aug. 1, 1977.

Publication costs of this article were assisted by Fraunhofer-Gesellschaft.

REFERENCES

1. S. K. Deb, *Philos. Mag.*, **27**, 801 (1973).
2. B. W. Faughnan, R. S. Crandall, and P. M. Heyman, *RCA Rev.*, **36**, 177 (1975).
3. H. N. Hersh, W. E. Kramer, and J. H. McGee, *Appl. Phys. Lett.*, **27**, 646 (1975).
4. P. W. Anderson, *Phys. Rev.*, **109**, 1492 (1958).
5. P. G. Dickens, R. M. P. Quillian, and M. S. Whittingham, *Mater. Res. Bull.*, **3**, 941 (1968).
6. N. S. Hush, in "Progress in Inorganic Chemistry," Vol. 8, F. A. Cotton, Editor, p. 391, Interscience, New York (1967).
7. T. Holstein, *Ann. Phys.*, **8**, 343 (1959).
8. J. Appel, *Solid State Phys.*, **21**, 193 (1968).
9. I. G. Austin and N. F. Mott, *Adv. Phys.*, **18**, 41 (1969).
10. P. Gerthsen, E. Kauer, and H. G. Reik, in "Festkörperprobleme," Vol. 5, F. Sauter, Editor, p. 1, Vieweg, Braunschweig (1966).
11. O. F. Schirmer, K. W. Blazey, W. Berlinger, and R. Diehl, *Phys. Rev. B*, **11**, 4201 (1975); O. F. Schirmer, *Z. Phys. B*, **24**, 235 (1976).
12. E. K. Kudinov, D. N. Mirlin, and Y. A. Firsov, *Sov. Phys. Solid State (Engl. Transl.)*, **11**, 2257 (1970).
13. E. V. Bursian, Y. A. Girshberg, and E. N. Starov, *Phys. Status Solidi B*, **46**, 529 (1971).
14. E. Salje, *Acta Crystallogr., Sect. A*, **31**, 360 (1975).
15. J. M. Ziman, "Principles of the Theory of Solids," p. 239, Cambridge University Press, Cambridge (1964).
16. J. F. Scott, R. F. Leheny, J. P. Remeika, and A. R. Sweedler, *Phys. Rev. B*, **2**, 3883 (1970).
17. S. Visvanathan, *Phys. Rev.*, **120**, 376 (1960).
18. H. Y. Fan, W. Spitzer, and R. J. Collins, *ibid.*, **101**, 556 (1956).
19. J. M. Berak and M. J. Sienko, *J. Solid State Chem.*, **2**, 109 (1970).
20. S. K. Deb, To be published; R. Gazzinelli, O. F. Schirmer, and V. Wittwer, To be published.
21. B. W. Faughnan, Paper 422 presented at The Electrochemical Society Spring Meeting, Washington, D.C., May 2-7, 1976.

The Al-Ga-Sb Ternary Phase Diagram and Its Application to Liquid Phase Epitaxial Growth

K. Y. Cheng[1] and G. L. Pearson

Stanford Electronics Laboratories, Stanford University, Stanford, California 94305

ABSTRACT

The ternary phase diagram of the Al-Ga-Sb system was established in the Ga-rich region. Liquidus isotherms at 400°, 450°, 500°, and 550°C and solidus isotherms at 500° and 550°C were determined experimentally. Under the assumptions that the ternary liquid is a simple solution and that the AlSb-GaSb solid forms an ideal solution, excellent agreement was obtained between the calculated liquidus and solidus isotherms and experiment. The compositional variation of the $Al_xGa_{1-x}Sb$ epitaxial layers during growth was delineated.

The $Al_xGa_{1-x}Sb$ system, which has a close lattice match between the AlSb and GaSb binary compounds, is a potential candidate for various optoelectronic applications. However, only limited experimental pseudobinary data (1-3) and liquidus and solidus data at 600°C (4) have been reported. In order to control the composition of mixed crystals grown by liquid phase epitaxy (LPE), the Al-Ga-Sb ternary phase diagram must be established in the region of interest. In this work, the liquidus data along the 400°, 450°, 500°, and 550°C isotherms were obtained by the saturation technique and the corresponding solidus data at 500° and 550°C were determined. A simple thermodynamic model (5, 6) was used to analytically fit the measured liquidus and solidus results, and then to generate the Al-Ga-Sb ternary phase diagram in the Ga-rich region. Such a semiempirical approach was used since no theoretical model can exactly describe the thermodynamic behavior of the ternary system without some adjustments. The phase diagram was then applied to LPE growth to predict conditions such as the liquid and solid compositions at given temperatures and the variation of composition in grown layers.

Experimental Procedures and Results

A saturation technique was used to determine the liquidus data along the 400°, 450°, 500°, and 550°C isotherms in the Ga-rich region of the Al-Ga-Sb system. In this study, a vertical LPE dipping system similar to that described by Wu and Pearson (7) was used to obtain the liquid compositions as well as

[1] Present address: Electrical Engineering Department, Chung-Cheng Institute of Technology, Ta-Hsi, Tao-Yuan, Taiwan (335), Republic of China.

Key words: thermodynamics, simple solution, liquid phase epitaxy.

for LPE growths. Essential components of the system are a vertical tubular furnace, a quartz reaction tube through which a palladium-purified H_2 flow is maintained, and a quartz dual seed holder.

In each saturation cycle, the ternary solution was prepared by accurately weighing appropriate amounts of 6-9's Ga and Al into the Al_2O_3 crucible along with polycrystalline GaSb. Typically, 5g of Ga were used for each run. In order to remove surface oxides from the Ga solution, it was baked out in the crucible under H_2 flow at 850°C for several hours prior to adding Al and GaSb. An additional GaSb source and a pair of back-to-back substrates, with polished (111)B surfaces oriented toward the outside, were clamped in the seed holder and positioned in the cold zone of the furnace. Prior to raising the temperature, the system was evacuated and repeatedly backfilled with purified H_2. After the system had been heated and stabilized at the desired saturation temperature, which was monitored with a calibraed Pt *vs.* Pt-13% Rh thermocouple situated beneath the crucible, the GaSb source was dipped into the solution for at least 30 min to provide saturation. The dipping time was long enough to reach true equilibrium in the ternary melt. This was verified by dipping for longer periods of time and noting that the weight loss of the GaSb source changed very little. Upon completion of the saturation cycle, the GaSb source was retracted. At this time, the growth cycle was initiated by dipping the substrates into the saturated solution and the system was cooled several degrees at a rate of 0.25°C/min. Growth was terminated by raising the substrates out of the ternary solution.

The liquid composition at the saturation temperature was determined by measuring the weight loss of the GaSb source material along with the amount of Ga, Al, and GaSb in the presaturated solution. At these low temperatures no corrections were made for evaporation of Sb from the solution. The experimental solubility data of Sb at 400°, 450°, 500°, and 550°C are listed in Table I and presented in Fig. 1 as a function of Al concentration. The solid lines are calculated isotherms to be discussed in the following section. The over-all accuracy of the liquidus data is estimated to be better than ±2°C.

The solid compositions were determined on cleaved and polished edges of $Al_xGa_{1-x}Sb$ layers, which had been grown on GaSb substrates, by electron microprobe analyses. Measured intensities of the Al-Kα, Ga-Lα, and Sb-Lα lines were converted to compositions with a correction computer program (8). In all Ga-rich layers, the Al concentration was found to decrease from its maximum value near the $Al_xGa_{1-x}Sb$-GaSb interface toward the surface as a result of the depletion of Al in the solution during growth. On the other hand, when $x \geq 0.60$, the Al concentration increased from the interface toward the surface. Thus the Al concentration measured near the $Al_xGa_{1-x}Sb$-GaSb interface was taken to be the equilibrium solid composition with an accuracy of the order of 2% (absolute). The experimental solidus results at 500° and 550°C are listed in Table I and displayed in Fig. 2 together with the calculated isotherms.

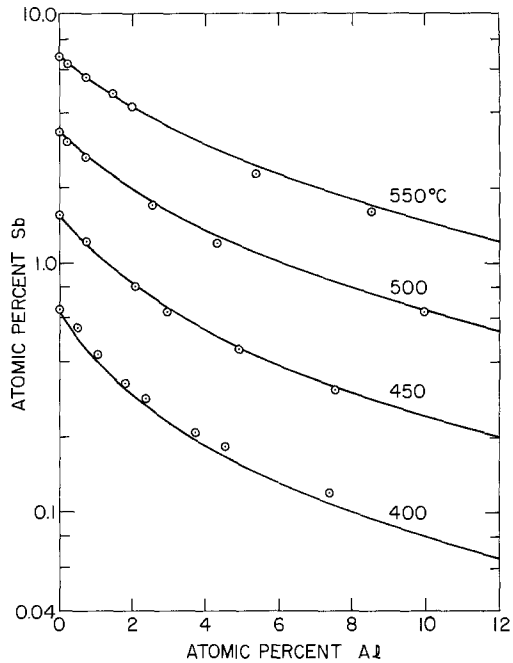


Fig. 1. Liquidus isotherms in the Al-Ga-Sb system at 400°, 450°, 500°, and 550°C. Solid lines are calculated isotherms using the parameters of Table II. The experimental data points are from Table I.

Table I. Experimental liquidus data at 400°, 450°, 500°, and 550°C and the corresponding solidus data at 500° and 550°C of the Al-Ga-Sb system

Liquidus temperature, T(°C)	Liquidus composition (atom %)		Solidus composition x (mole %)
	N_{Al}	N_{Sb}	
400	0	0.648	0
400	0.458	0.544	—
400	1.040	0.428	—
400	1.800	0.330	—
400	2.330	0.283	—
400	3.714	0.208	—
400	4.506	0.183	—
400	7.393	0.120	—
450	0	1.540	0
450	0.718	1.220	—
450	2.040	0.800	—
450	2.948	0.637	—
450	4.868	0.446	—
450	7.488	0.308	—
500	0	3.362	0
500	0.195	3.063	5.4
500	0.719	2.656	19.6
500	2.519	1.696	50.7
500	4.260	1.199	65.8
500	9.959	0.634	84.4
550	0	6.789	0
550	0.220	6.358	5.5
550	0.735	5.570	16.6
550	1.450	4.802	28.5
550	1.987	4.215	35.2
550	5.357	2.275	67.1
550	8.504	1.602	78.5
550	18.654	0.801	90.5

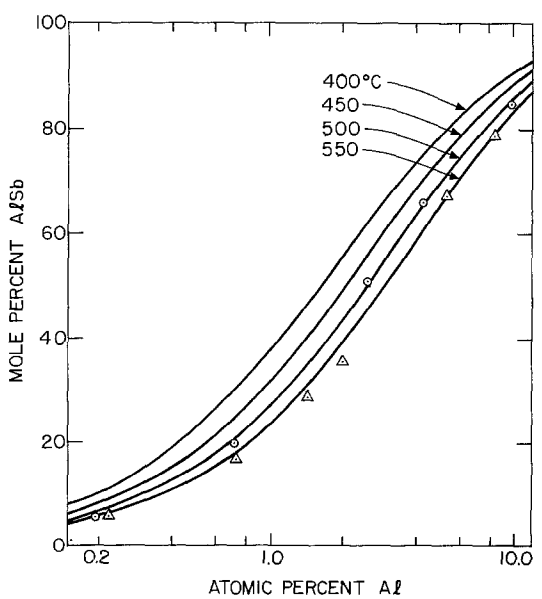


Fig. 2. Solidus isotherms in the Al-Ga-Sb system at 400°, 450°, 500°, and 550°C. Solid lines are calculated isotherms using the parameters of Table II. Experimental data: 0, 500°C; Δ, 550°C.

Calculation and Discussion

The calculation technique for determining the Al-Ga-Sb ternary phase diagram is based on the thermodynamic model established by Ilegems and Pearson (5) and Panish and Ilegems (6). When applied to the Al-Ga-Sb system, the basic model equations are

$$\gamma_{AlSb}{}^{x} = \frac{4\gamma_{Al}\gamma_{Sb}}{\gamma_{A}{}^{sl}\gamma_{Sb}{}^{sl}} N_{Al}N_{Sb} \exp\left[\Delta S^{F}_{AlSb}(T^{F}_{AlSb} - T)/RT\right] \quad [1]$$

and

$$\gamma_{GaSb}{}^{(1-x)} = \frac{4\gamma_{Ga}\gamma_{Sb}}{\gamma_{Ga}{}^{sl}\gamma_{Sb}{}^{sl}} N_{Ga}N_{Sb} \exp\left[\Delta S^{F}_{GaSb}(T^{F}_{GaSb} - T)/RT\right] \quad [2]$$

where γ is the activity coefficient of the indicated element in the liquid or compound in the solid, T^F and ΔS^F are the temperature and entropy of fusion of the indicated pure binary compound, x is either the mole or atomic fraction of AlSb in the solid, and N is either the mole or atomic fraction of the indicated element in the liquid which follow the relation

$$N_{Al} + N_{Ga} + N_{Sb} = 1 \quad [3]$$

The superscript sl refers to the stoichiometric liquid. By solving these equations the ternary liquidus and solidus isotherms can be calculated, provided the parameters γ, ΔS^F, and T^F are known or can be satisfactorily estimated.

The activity coefficient γ, which is a measure of nonideality of the liquid or solid solution, is expressed in terms of interaction parameters and concentrations in this model. In the Ga-Sb binary liquid, γ_{Ga} and γ_{Sb} are related to the interaction parameter α_{GaSb} by equations of the form

$$RT \ln \gamma_{Ga} = \alpha_{GaSb}N_{Sb}{}^{2} \quad [4]$$

and

$$RT \ln \gamma_{Sb} = \alpha_{GaSb}N_{Ga}{}^{2} \quad [5]$$

and similarly for the liquid solution of Al and Sb. In the ternary solid solution, the activity coefficients have the same forms as Eq. [4] and [5] with an interaction parameter $\alpha^{s}_{AlSb\text{-}GaSb}$. For the ternary liquid solution the activity coefficients are related to the interaction parameters by (9)

$$RT \ln \gamma_{Al} = \alpha_{AlSb}N_{Sb}{}^{2} + \alpha_{AlGa}N_{Ga}{}^{2} + (\alpha_{AlSb} + \alpha_{AlGa} - \alpha_{GaSb})N_{Ga}N_{Sb} \quad [6]$$

$$RT \ln \gamma_{Ga} = \alpha_{GaSb}N_{Sb}{}^{2} + \alpha_{AlGa}N_{Al}{}^{2} + (\alpha_{GaSb} + \alpha_{AlGa} - \alpha_{AlSb})N_{Al}N_{Sb} \quad [7]$$

and

$$RT \ln \gamma_{Sb} = \alpha_{AlSb}N_{Al}{}^{2} + \alpha_{GaSb}N_{Ga}{}^{2} + (\alpha_{AlSb} + \alpha_{GaSb} - \alpha_{AlGa})N_{Al}N_{Ga} \quad [8]$$

In a previous study (5), the Al-Ga system was found to be near-ideal and the interaction parameter was approximated by a strictly regular solution in which $\alpha_{AlGa} = 104.0$ cal/mole. The ternary solid solution is considered to be ideal based on the fact that the lattice constants of AlSb and GaSb are nearly equal (10). Therefore the solid interaction parameter $\alpha^{s}_{AlSb\text{-}GaSb}$ was taken to be zero (11) and both γ_{AlSb} and γ_{GaSb} were set equal to 1.

The liquidus interaction parameters for III-V binaries have been observed to be slowly varying functions of temperature of the form $a + bT$ (12). We follow Vieland (13) in treating the GaSb binary solution which yields

$$\alpha_{GaSb} = -RT[\ln 4N_{Ga}N_{Sb} + \Delta S^{F}_{GaSb}(T^{F}_{GaSb} - T)/RT]/[2(0.5 - N_{Ga})^{2}] \quad [9]$$

Taking $\Delta S^{F}_{GaSb} = 15.80$ eu/mole (14), $T^{F}_{GaSb} = 985°K$ (14), and the experimental liquidus data, which are consistent with the recent redetermined liquidus of Maglione and Potier (15), the best linear fit for α_{GaSb} is $3425 - 5.13T$ cal/mole.

For the Al-Sb system, the same procedures for obtaining the liquidus interaction parameter as in the Ga-Sb system were followed. Using the experimental liquidus data of Urazov (16), the best linear fit for α_{AlSb} is $12{,}300 - 10.0T$ cal/mole as reported by Panish and Ilegems (6). Recently measured AlSb liquidus data at temperatures below 950°C give $\alpha_{AlSb} = 19{,}400 - 15.6T$ cal/mole (17). In both cases, the experimentally determined $\Delta S^{F}_{AlSb} = 14.74$ eu/mole (14) was used. With this value of α_{AlSb} together with other pertinent thermodynamic parameters, calculated ternary phase diagrams are in apparent disagreement with experiment. These discrepancies can be understood easily. Since the temperature range used in this study was below the heats of fusion of the two constituents Al (660°C) and Sb (630.5°C), the derivation of α_{AlSb} from Sb solubilities in Al as shown above was inapplicable. It was decided, therefore, to obtain α_{AlSb} by fitting the experimental ternary data of Panish *et al.* (6). In view of the usual trend in III-V binaries with the simple solution approximation, an α_{AlSb} of the form $a + bT$ was assumed in the calculations. Furthermore, ΔS^F, T^F, and the other interaction parameters are either good experimental results or well-established values, and they can only be adjusted in a limited range. Based on these assumptions, the calculated ternary phase diagram showed systematic deviations from the experimental data. Ilegems *et al.* (18) found that ΔS^{F}_{AB} and α_{AB} are interdependent values for a binary system A-B, and that they can be adjusted by changing the value of either one. In this case, ΔS^{F}_{AlSb} is the good experimental value. We decided to retain ΔS^{F}_{AlSb} and adjust α_{AlSb} only. We then found that a concentration-dependent term must be added to α_{AlSb} in order to obtain a calculated-experimental matched ternary phase diagram. A similar form of composition-dependent α has been used to describe In-Ga (7) and several other III-V binary systems (19). The experimental data were put into Eq. [1] through [8] in order to calculate α_{AlSb} at various temperatures and compositions. The best fit value was found to be $\alpha_{AlSb} = 1590 - 4.0T - 18.0T\,N_{Al}$ cal/mole.

The best fit parameters together with the other thermodynamic constants used in calculating the ternary phase diagram are listed in Table II. With the aid of a computer, the liquidus isotherms were obtained by eliminating x between Eq. [1] and [2] while elimination of T between these same equations gave the solidus isotherms. The resulting calculated liquidus and solidus isotherms at 400°, 450°, 500°, and 550°C are plotted together with the experimental data in Fig. 1 and 2, respectively. The agreement between the calculated and experimental data in the Ga-rich region of the Al-Ga-Sb ternary phase diagram is significant. However, incorporation of the semiempirical composition-dependent α_{AlSb} in the calculations contradicts the basic requirement of the simple solution model where α's are constant or a function of temperature only. Moreover, the inter-

Table II. Parameters for calculation of the Al-Ga-Sb phase diagram

	T^F (°K)	ΔS^F (eu/mole)	α(cal/mole)
Ga-Sb	985 (13)	15.80 (13)	$3425 - 5.13T$
Al-Sb	1330 (13)	14.74 (13)	$1590 - 4.0T - 18.0TN_{Al}$
Al-Ga			104 (5)
AlSb-GaSb			0

action parameter of the form $a + bT$ in the simple solution model is nonphysical (11). Thus, we conclude that although the simple solution model and the curve fitting technique are adequate to describe the Al-Ga-Sb system in the Ga-rich region, the parameters determined by curve fitting have no thermodynamic significance.

Application to Liquid Phase Epitaxy

A major application of the Al-Ga-Sb phase diagram is in predicting conditions for LPE growth. Based on the ternary phase diagram, a desired crystal composition can be obtained from an equilibrium solution at a specific growth temperature. In this work, following the calculated liquidus and solidus isotherms, reproducible homogeneous $Al_xGa_{1-x}Sb$ layers with composition $0 \leq x \leq 0.92$ were grown on (111) oriented GaSb substrates. In general, as-grown surfaces were shiny and smooth. Under the microscope, the cleaved edges of the $Al_xGa_{1-x}Sb$ epitaxial layers with large values of x appear darker than the GaSb substrate. Layers with Al composition $x > 0.8$ have a hygroscopic property similar to pure AlSb. The surface turns brown when exposed to air and must therefore be stored in a desiccator. This property is similar but less serious than that in $Al_xGa_{1-x}As$. For $x < 0.27$, the epilayer can be delineated by etching in a 10% A-B solution (20) for a few seconds.

An Al concentration gradient exists in the grown layer as a result of Al depletion in the solution during growth. This can be evaluated from the phase diagram. Under the assumptions that the growth rate is slow enough such that the liquid and solid remain in continuous equilibrium and that the solid precipitates only on the growth surface of the substrate, the compositional variation during the growth can be calculated. For a 5g Ga solution and a 0.5 cm^2 substrate growth area, the variation in layer composition as a function of normalized layer thickness during cooling from 550° to 450°C was calculated and is shown in Fig. 3. From this figure we can predict the layer thickness and composition during growth between these given temperatures. The composition in the growth direction was determined by electron microprobe analyses on cleaved and polished epilayers. The measured Al composition *vs.* distance from the $Al_xGa_{1-x}Sb$-GaSb interface in seven samples grown at starting temperatures of 500° and 550°C are compared with theory as shown in Fig. 4. The calculations were normalized to 5g of Ga solution

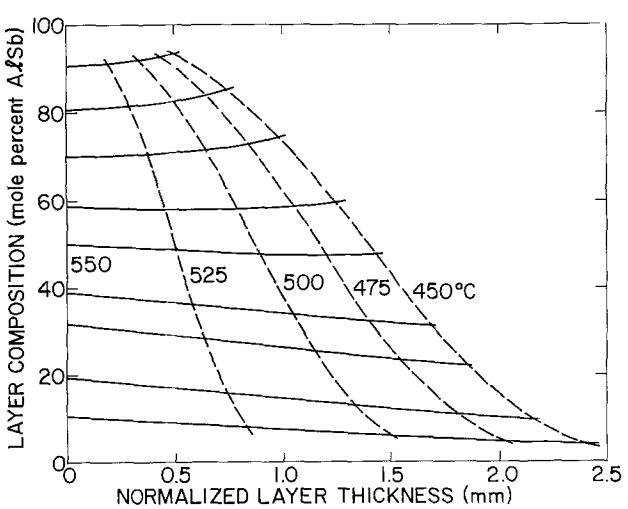


Fig. 3. Layer composition as a function of layer thickness normalized to a 5g Ga solution and a 0.5 cm^2 substrate area. Dashed lines are liquidus isotherms. The 550°C isotherm is superimposed on the ordinate axis.

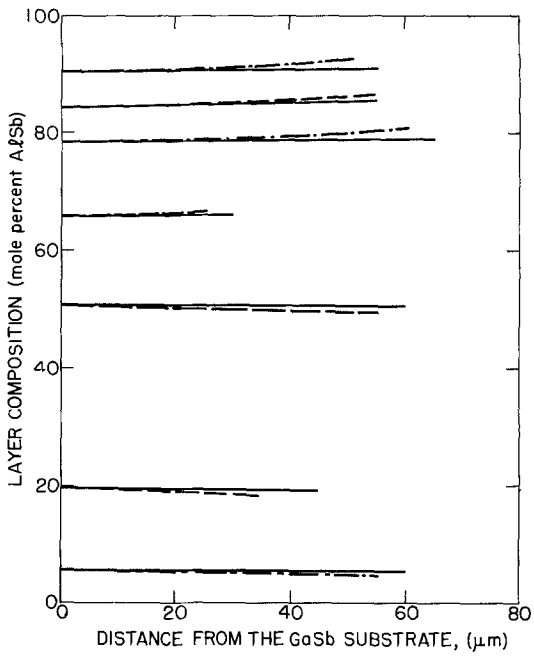


Fig. 4. Variation in layer composition for seven $Al_xGa_{1-x}Sb$ samples. Solid lines are calculated variations and dashed lines are experimental results at starting growth temperatures of 500° (– – –) or 550°C (—· —·).

and a 1 cm^2 substrate which are close to those used in this study. It was found that the Al concentration along the growth direction is constant only when $x \cong 0.6$ and increases or decreases as x becomes larger or smaller than 0.6, respectively. This property is due to the compositional dependency in the distribution coefficient of Al in the Al-Ga-Sb ternary solution.

The differences between experimental and computed values are attributed to the following two main factors neglected in the calculations. First, under the assumption of continuous equilibrium growth, the cooling rate is set equal to zero and the melt must be perfectly stirred. In this study, a cooling rate of 0.25°C/min was used and a depletion layer was formed near the interface. For Ga-rich layers, the distribution coefficient of Al is greater than or of the same order of magnitude as the Sb coefficient, so that Al segregation governs the growth. This leads to a decrease in the Al composition of the ternary solid as compared with the perfectly stirred case. The situation is reversed for Al-rich layers. This same property was observed in $Al_xGa_{1-x}As$ (21) and $Ga_xIn_{1-x}Sb$ (22). Second, we assumed that the solid precipitates only on the growth surface of the substrate. However, preferential growth on the edges of the substrate (23) and nucleation in the ternary liquid (24) cannot be neglected in LPE growth. These extra growths decrease the compositional gradient of solutes in the melt and the growth rate (24). Thus the variation of solid composition tends to be large at the end of the growth. In Al-rich layers, this property is much more severe due to the larger distribution coefficient of Sb which depletes very fast. In conclusion, the experimental results are generally in good agreement with the calculations.

Acknowledgment

This work was supported by the Joint Services Electronics Program at Stanford University through Contract NONR-0044.

Manuscript submitted May 3, 1976; revised manuscript received Dec. 6, 1976.

Any discussion of this paper will appear in a Discussion Section to be published in the December 1977

JOURNAL. All discussions for the December 1977 Discussion Section should be submitted by Aug. 1, 1977.

Publication costs of this article were assisted by Stanford University.

REFERENCES

1. I. I. Burdiyan and A. S. Borschkevski, *Sov. Phys.-Tech. Phys. (Engl. Transl.)*, **3**, 2451 (1958).
2. A. S. Borschkevski, I. I. Burdiyan, E. Yu. Lubenskaya, and E. V. Sokolova. *Russ. J. Inorg. Chem. (Engl. Transl.)*, **4**, 1306 (1959).
3. J. F. Miller, H. L. Goering, and R. C. Himes, *This Journal*, **107**, 527 (1960).
4. S. M. Bedair, *ibid.*, **122**, 1150 (1975).
5. M. Ilegems and G. L. Pearson, in "Proceedings of the 1968 Symposium on GaAs," The Institute of Physics and The Physical Society, p. 3, London (1969).
6. M. B. Panish and M. Ilegems, in "Progress in Solid-State Chemistry," Vol. 7, p. 39, Pergamon Press, Inc., Oxford (1972).
7. T. Y. Wu and G. L. Pearson, *J. Phys. Chem. Solids*, **33**, 409 (1972).
8. J. W. Colby, in "Advances in X-ray Analysis," Vol. 11, p. 286, Plenum, New York (1968).
9. I. Prigogine and R. Defay, "Chemical Thermodynamics," p. 257, Longmans, Green and Co., London (1965).
10. G. Giesecke and H. Pfister, *Acta. Crystallogr.*, **11**, 369 (1958).
11. G. B. Stringfellow, *J. Crystal Growth*, **27**, 21 (1974).
12. C. D. Thurmond, *J. Phys. Chem. Solids*, **26**, 785 (1965).
13. L. J. Vieland, *Acta Metall.*, **11**, 137 (1963).
14. B. D. Lichter and P. Sommelet, *Trans. AIME*, **245**, 99, 1021 (1969).
15. M. H. Maglione and A. Potier, *J. Chim. Phys. Chim. Biol.*, **65**, 1595 (1968).
16. G. G. Urazov, *Izv. Inst. Fiz.-Khim. Anal., Akad. Nauk SSSR*, **1**, 461 (1921).
17. J. S. Harris, Private communication.
18. M. Ilegems and M. B. Panish, *J. Crystal Growth*, **20**, 77 (1973).
19. M. V. Roa and W. A. Tiller, *J. Phys. Chem. Solids*, **31**, 191 (1970).
20. G. H. Olsen and M. Ettenberg, *J. Appl. Phys.*, **45**, 5112 (1974).
21. I. Crossley and M. B. Small, *J. Crystal Growth*, **15**, 268 (1972).
22. A. Joullie, R. Aulombard, and G. Bougnot, *ibid.*, **24**, 276 (1974).
23. I. Crossley and M. B. Small, *ibid.*, **11**, 157 (1971).
24. H. Ijuin and S. Gonda, *This Journal*, **123**, 1109 (1976).

A New Preferential Etch for Defects in Silicon Crystals

Margaret Wright Jenkins*

Motorola Incorporated, Motorola Semiconductor Products Group, Phoenix, Arizona 85008

ABSTRACT

A new preferential etch for (100) and (111) oriented, p- and n-type silicon has been developed. Oxidation-induced stacking faults, dislocations, swirl, and striations are clearly defined with minimum surface roughness or extraneous pitting. A relatively slow etch rate (~1 μm per min) at room temperature provides etch control. The long shelf life of this etch allows the solution to be stored in large quantities.

The development of a rapid and reliable method of evaluation of defects in silicon crystals is of major importance to crystal growth technology, wafer preparation, and processing. The electrical effects of crystal imperfections on device characteristics have recently been reviewed by Lawrence (1). Chemical etching is the simplest means of detecting the presence of defects in silicon crystals. An improved preferential etch which reveals defects precisely and in a more controlled manner has been developed.

The most common preferential etches presently in use are those of Sirtl (2), Dash (3), and Secco (4). Sirtl etch has been used to delineate defects on most crystal orientations, however, it favors the (111) orientation. Although the Dash etch reveals defects on all planes, the 4-16 hr etch time required is unsuitable for rapid evaluation of material. The Secco etch produces elliptical shaped dislocation pits on both (100) and (111) planes making orientation determination by etch pits more difficult.

The need for an etch which delineates defects on most orientations at a reasonable etch rate and with good definition gave rise to the development of the present etch. This etch solution preferentially delineates defects on (100) and (111) orientations of p- and n-type crystals over a wide range (0.02-20 Ω-cm) of resistivities.

A comparison of common defects delineated by this etchant and previously established etchants is given. The variation in etch rates among different material types and among the available preferential etchants is also discussed.

* Electrochemical Society Active Member.
Key words: silicon, preferential etch, defect delineation.

Experimental

The silicon material used in this work was cut from Czochralski and float zone crystals with (100) and (111) growth orientations. Both p- and n-type crystals were used with resistivities ranging from 0.02 to 20 Ω-cm. All wafers were chemically thinned on both sides and chemically slurry polished on one surface. All wafer cleaning consisted of the following steps: (*i*) 30 sec dip in 50:1, H_2O:HF; (*ii*) 5 min rinse in ultrapure deionized (UPDI) H_2O; (*iii*) 10 min boil in 7:3, H_2SO_4:H_2O_2 at 110°C; and (*iv*) 5 min rinse in UPDI water. All oxidations were performed at 1200°C in steam for 75 min. Etch rates were determined by measuring the loss in weight of the sample after each etch period (increment) and calculating to corresponding surface removal in micrometers as follows

$$\text{mass} = \text{volume} \times \text{density} \quad [1]$$

The volume of a wafer is determined by the expression

$$V = \pi r^2 t \quad [2]$$

thus

$$m = \pi r^2 t \rho \quad [3]$$

where m is the mass, π is a constant, r is the radius of the wafer, t is the thickness, and ρ is the density of Si. The change in thickness, Δt, is expressed as

$$\Delta t = \frac{\Delta m}{\pi r^2 \rho} \quad [4]$$

The actual etch rate, which is the change in thickness from one surface, is determined by the expression

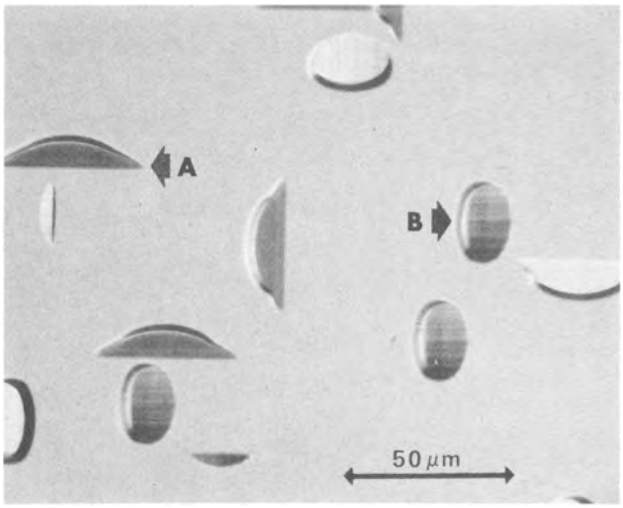


Fig. 1. Oxidation-induced stacking faults on a (100), 7-10 Ω-cm, boron-doped wafer after 30 min Wright etch. (A) Surface faults, (B) bulk faults.

$$\text{etch rate} = \frac{\Delta t}{2} = \frac{\Delta m}{2\pi r^2 \rho} \qquad [5]$$

The composition of this etch, which is known as Wright etch, is as follows: 60 ml conc HF (49%), 30 ml conc HNO_3 (69%), 30 ml of 5*M* CrO_3 (1g CrO_3/2 ml H_2O), 2g $Cu(NO_3)_2 \cdot 3H_2O$ (reagent grade), 60 ml conc acetic acid (glacial), and 60 ml H_2O (deionized). In mixing the solution, the best results are obtained by first dissolving the $Cu(NO_3)_2$ in the given amount of H_2O, otherwise the order of mixing is not critical.

Some of the etching processes were conducted according to the ASTM standard method (5). The wafer was placed with the polished surface upward, in the bottom of a plastic beaker. The etchant was added until the surface was covered with approximately 1 cm of solution. The wafer was etched with manual agitation (in a manner such that the dissolved silicon is moved away from the wafer surface) for the desired length of time (1-5 min or the removal of 1-5 μm of material for surface defects, and ~20 min or the removal of ~1 mil of material for bulk defects). The etchant was flushed from the beaker with distilled water and the wafer was rinsed thoroughly (~5 min). Batch etching was used when two or more wafers were being compared and when extended etch periods were required to reveal bulk defects. The wafers were loaded vertically into a Teflon cleaning boat and placed in an HF resistant container. The amount of etchant added was sufficient to cover the wafers (the wafers may also be immersed in the etch solution). The wafers were etched for the desired length of time and rinsed by quickly removing wafers from the etch solution and placing them under running deionized (DI) water or in a DI rinsing tank for ~5 min. Agitation was not deemed necessary in the batch etching process due to the vertical position of the wafers. However, when the wafers are in a horizontal plane, agitation is necessary to prevent the formation of surface deposits which result in etch artifacts. After rinsing, the wafers were dried and examined with the optical microscope using Nomarski differential interference contrast.

Results and Discussion

Robbins and Schwartz (6-8) described chemical etching of silicon in detail using an HF, HNO_3, and H_2O system and an HF, HNO_3, H_2O, and $HC_2H_3O_2$ system. Briefly, during chemical etching the silicon is dissolved by the etchant in a two-step process. First, the silicon is converted into a soluble oxide by a suitable oxidizing agent(s). Then the resulting oxide is removed from the surface by dissolution in a suitable solvent, usually HF. In order to delineate a crystal defect, the defect area must be oxidized at a faster or slower rate than the surrounding area forming a pit or mound.

In the present system, the silicon is oxidized with HNO_3, CrO_3 solution ($Cr_2O_7^=$), and $Cu(NO_3)_2$. The $Cr_2O_7^=$, a strong oxidizing agent, is considered to be the principal oxidizing species. The ratio of HNO_3 to CrO_3 solution stated in the formula produces a superior etched surface. Other ratios and the use of larger quantities of one of the oxidizing agents produce less desirable finish. With the addition of a small amount of $Cu(NO_3)_2$, the definition of the defect was enhanced. Therefore, it is believed that $Cu(NO_3)_2$ affects the localized differential oxidation at the defect site. The addition of the acetic acid gave the background surface of the etched silicon a smooth finish. It is theorized that this effect is attributed to the wetting action of the acetic acid which prevents the formation of bubbles during etching.

There are several characteristics of the Wright etch which offer distinct advantages over the existing preferential etchants: (*i*) improved defect delineation which facilitates defect identification, (*ii*) background surface smoothness after etching which also aids in defect identification and distribution determination, (*iii*) crystallographic etching which provides for orientation

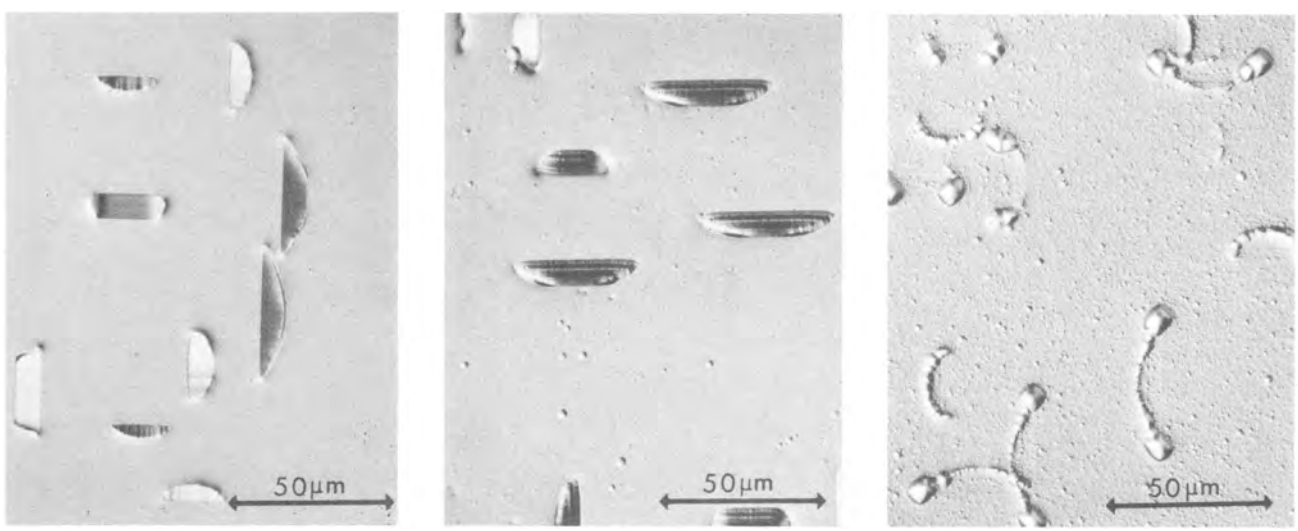


Fig. 2. A comparison of stacking fault delineation and surface condition of a (100) oriented, 1-5 Ω-cm, phosphorus-doped wafer after preferential etching. (a) After 15 min Wright etch, (b) 10 min Secco etch, and (c) 6 min Sirtl etch. Etch times were selected according to etch rates to remove similar amounts of silicon.

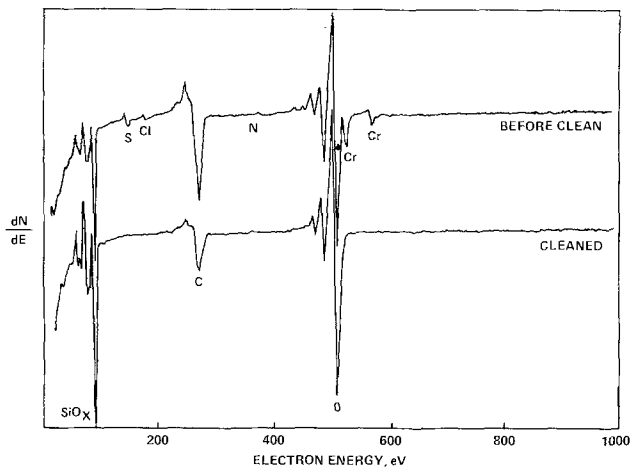


Fig. 3. Auger spectra of a Wright etched sample before and after cleaning. A copper peak at 920 eV is not seen. Other metals are removed after cleaning.

determination by the geometric shape of the etch figure, and (*iv*) a relatively slow etch rate which provides for etch control.

Oxidation-induced stacking faults, dislocations, swirl, and striations are clearly defined by this etchant with minimum surface roughness or extraneous pitting. It works exceptionally well in revealing stacking faults. Figure 1 shows surface and bulk stacking faults on a (100) oxidized surface. The stacking fault and the partial dislocation around the fault are etched at approximately the same rate, producing a flat, well-defined figure. The morphology of the faults revealed by this etch is geometrically similar to the diffraction contrast images of stacking faults obtained with the transmission electron microscope (TEM). The surface faults produce an etch figure similar to an extended partial disk while bulk faults are revealed as full loops. Bulk stacking faults that are 1 mil in diameter are shown. This is considered to be an advantage over TEM analysis where the geometry of the fault as viewed is limited to the thickness of the sample, which is typically 0.5 μm for a 100 keV beam.

A comparison of stacking fault delineation and surface condition after preferential etching is shown in Fig. 2. Portions of a (100) oxidized wafer were etched as follows: (a) Wright etch, (b) Secco etch, and (c) Sirtl etch. The definition of the defects and the background surface quality of sample (a) which was treated with Wright etch are superior to those of the Secco and Sirtl etched samples. In using this new etch, there is no excessive gas evolution (bubbles) which usually re-

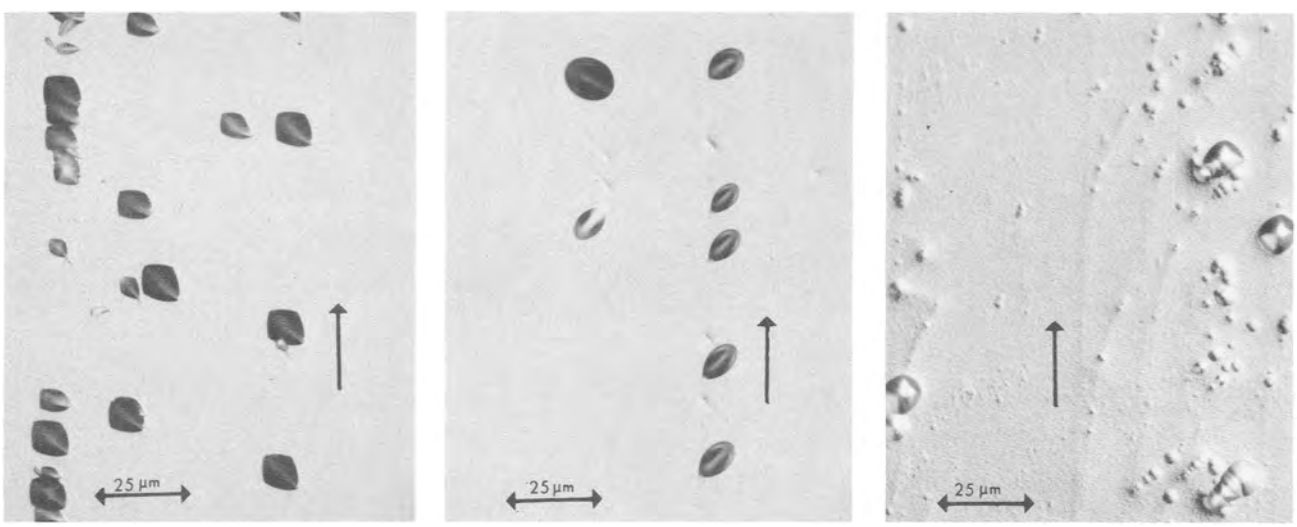


Fig. 4. A comparison of dislocation delineation on a (100) oriented, 10-20 Ω-cm, phosphorus-doped wafer after oxidation and preferential etching. (a) After 20 min Wright etch, (b) 10 min Secco etch, and (c) 6 min Sirtl etch. Arrows indicate slip directions.

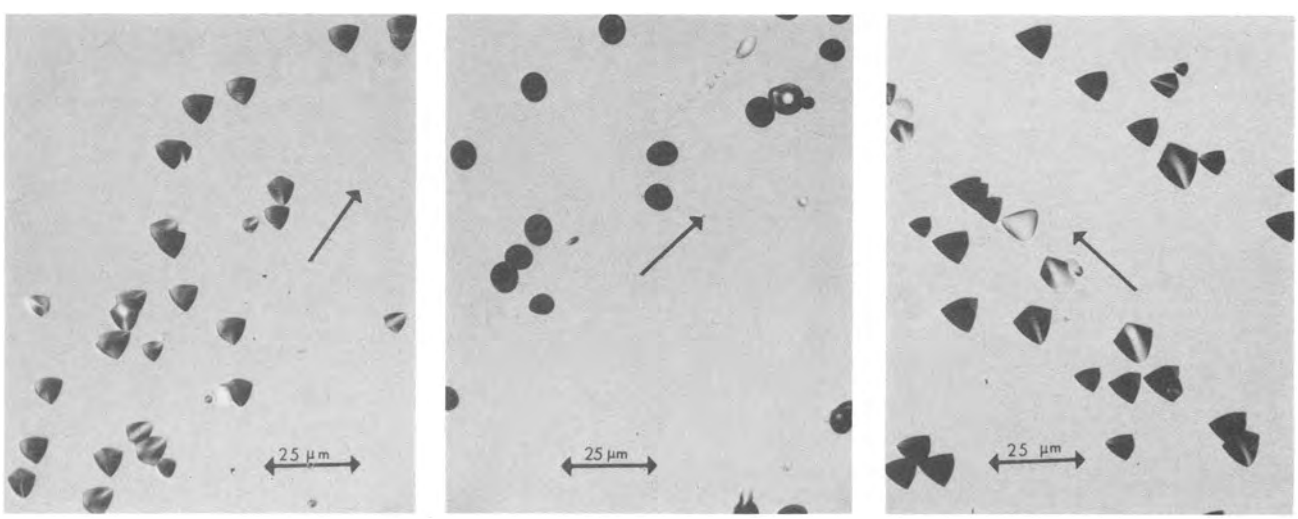


Fig. 5. A comparison of dislocation delineation on a (111) oriented, 10-20 Ω-cm, boron-doped wafer after oxidation and preferential etching. (a) After 10 min Wright etch, (b) 10 min Secco etch, and (c) 3 min Sirtl etch. Arrows indicate slip directions.

sults in nonuniform surface etching. This is often observed on Secco etched samples.

There are no surface copper deposits detected after Wright etching. Auger analyses of etched surfaces were performed to evaluate surface contamination. Figure 3 shows Auger spectra of Wright etched samples before and after cleaning. A copper peak (at 920 eV) was not revealed. The minimum detectable limit of copper by Auger analysis is 10^{12} atoms/cm^2. Other contaminants (Cl, S, N, and Cr) were removed during cleaning.[1] Heat generation is also minimized which allows large numbers of wafers to be etched in batches. In batch etching however, it should be noted that the etch rate increases with the number of wafers being etched in a given amount of solution. This is due to the exothermic nature of the etching process. As the number of wafers being etched is increased, the amount of heat generated is also increased. This raises the temperature of the solution which in turn increases the apparent etch rate. When 10-3 in. wafers (20 mils thick, n-type 7-10 Ω-cm) were batch etched in 2 liters of Wright etch for 10 min, the temperature of the solution increased only 2°C, from 25° to 27°C, and the etch rate remained constant. When 25-3 in. wafers were batch etched in 2 liters of Wright etch for 20 min continuously, the temperature of the solution reached 102°C and 2 mils of surface were removed. In this case, the over-all etch rate is more than a factor of two greater than that at room temperature. A sufficient volume of etch solution

[1] See cleaning procedure in experimental section.

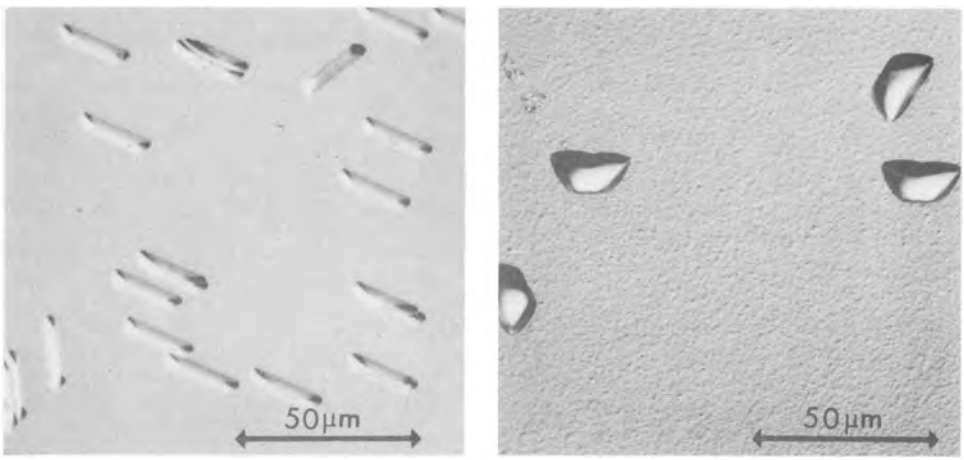


Fig. 6. a and b. Oxidation-induced stacking faults on (111) oriented surfaces after 5 min Wright etch; (a) is antimony-doped material to 0.02 Ω-cm and (b) boron-doped material to the same resistivity.

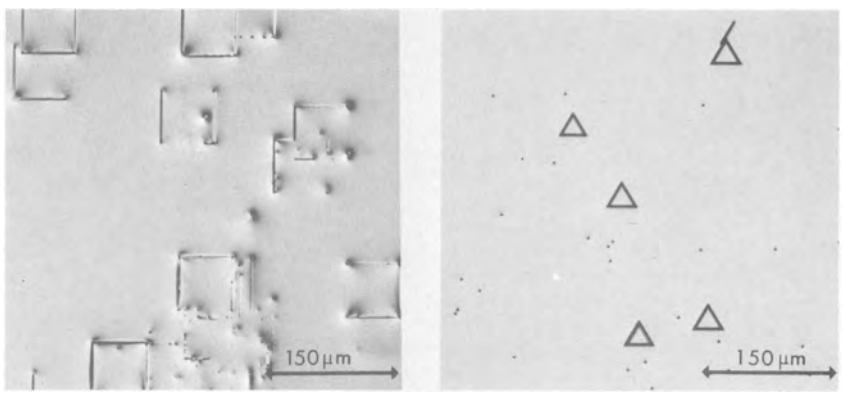


Fig. 7. a and b. Stacking faults in epitaxial layers of (100) and (111) orientations, respectively, after 5 min Wright etch.

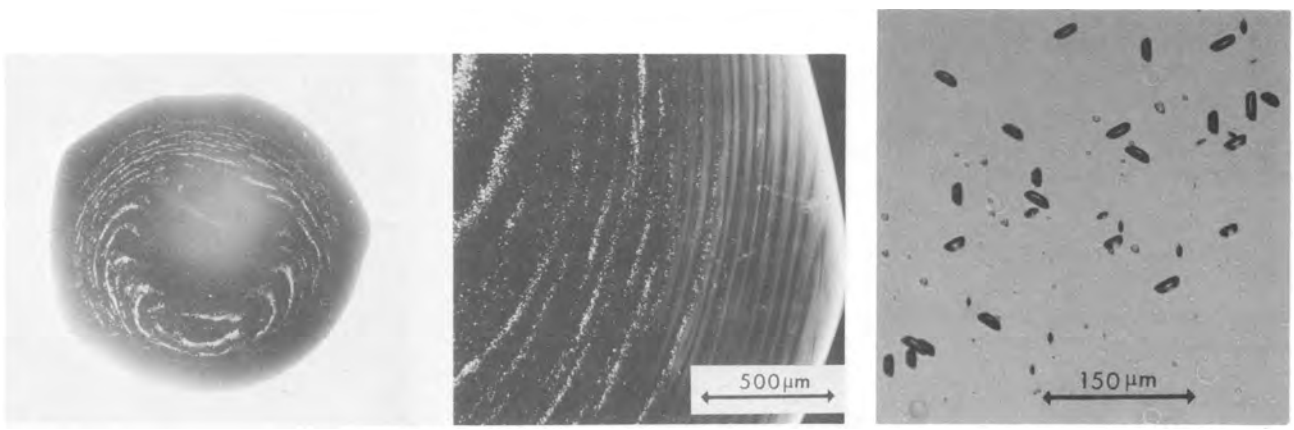


Fig. 8. a and b. Swirl distribution of defects on a flat zone, (111) oriented, 1-3 Ω-cm oxidized wafer after 20 min Wright etch. (a) Reveals "swirl" and striations at higher magnification, (b) reveals stacking faults and dislocations in the swirl pattern.

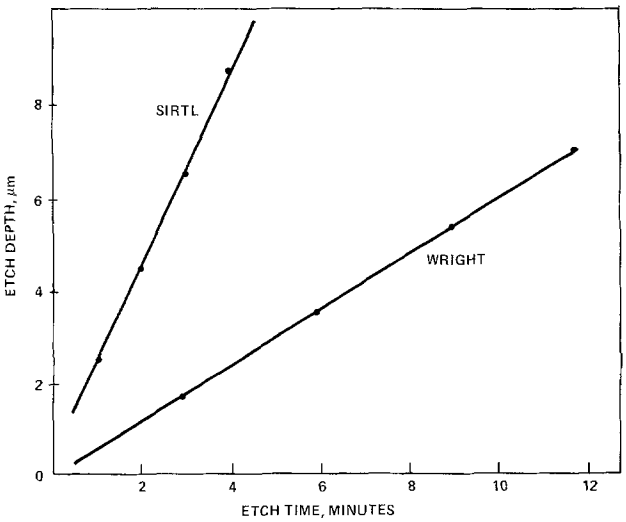


Fig. 9. A comparison of the etch rate of Wright etch with that of Sirtl etch. Sirtl is shown to have an etch rate three times that of Wright etch. A (100), 1-3 Ω-cm, phosphorus-doped oxidized wafer was used in this measurement.

to wafer surface ratio, 200 ml of solution per 3 in. wafer, will minimize heat generation and the corresponding increase in etch rate. In revealing bulk defects (*i.e.*, dislocations) where long etch periods (~20 min) are required, step etching is encouraged. Step etching (~5 min increments) will prevent over etching which may be encountered due to the variation in etch rates between different material types. Generally, boron-doped material etches faster than phosphorus-doped material. Low resistivity material tends to etch faster than that of higher resistivity for the same dopant type. However, this does not necessarily mean that the preferential differentiation of defects is greater. High index oriented planes, *e.g.*, (111), tend to etch faster initially than planes of a lower index, *e.g.*, (100).

The anisotropic crystallographic characteristics of Wright etch is demonstrated in Fig. 4a and 5a. Dislocations along slip lines on a (100), phosphorus-doped surface (4a) reveal well-defined pits with a square geometry with no extraneous pitting or surface roughness. The slip dislocations on the (111) surface (5a) show approximately triangular geometry. The Secco etch reveals the dislocations on both (100) and (111) surfaces as elliptical shaped pits (4b and 5b). The Sirtl etch reveals dislocations on a (100) surface as mounds with approximately square geometry (4c). The background surface is also shown to be textured. However, dislocations on (111) surfaces are revealed as well-defined triangular pits by Sirtl etching (5c). The background surface is also smooth.

Figure 6a and b show oxidation-induced stacking faults on (111) surfaces after 5 min of Wright etch. Figure 6a is of antimony-doped material to 0.02 Ω-cm while 6b shows boron-doped material of the same resistivity. Both samples received the same oxidation cycle. The enlarged size of the stacking faults and the textured background surface of the boron-doped sample indicate a faster etch rate than the antimony-doped sample.

Figure 7a and b show stacking faults in epitaxial layers of (100) and (111) orientations, respectively, after 5 min of Wright etch. Figure 8a shows a swirl distribution of defects on a float zone, (111) oriented, 1-3 Ω-cm oxidized wafer. Figure 8b reveals swirl and striations at higher magnification. Figure 8c reveals stacking faults and dislocations in the swirl pattern.

The relatively slow rate of this etchant provides more etch control. In Fig. 9, the etch rate is compared to that of Sirtl etch. The etch rate of Sirtl etch is shown to be approximately three times greater than that of Wright etch. The former solution etches at a rate of 3 μm per min while the latter has a rate of 1 μm per min. These etch rates were determined by weight loss measurements as described above. Etching for these measurements was performed at room temperature with manual agitation. The slope of the etch rate curves, Fig. 9, is linear with relatively no scatter in data points. These etch rates are reproducible and correspond within 10% of those determined by the direct thickness measurement method. The etch rate of Secco etch, which is not shown, is reported to be approximately 1.5 μm per min (4)

The Wright etch has a long shelf life (~6 weeks). The chemical stability of the solution permits mixing and storing in large quantities. It provides highly reproducible etch results and allows the solution to be reused. Used etch may be stored in a separate container and reused until it becomes saturated with silicon. A saturated solution is characterized by discoloration (4) and the formation of artifacts on etched surfaces. Artifacts are noncrystallographic etch features that are not reproduced on clean surfaces when properly etched in a fresh solution. Figure 10a-c show portions of a wafer that were etched with a freshly mixed solution, a 4 week old solution, and a 6 week old used solution. There is no noticeable difference in defect delineation and surface condition among the three samples. However, the etch rate of 1μ per min for the freshly mixed solution and the 4 week old solution is approximately 40% higher than that for the 6 week old used solution which contained ~4 mg of dissolved silicon per milliliter. The difference in etch rates is also evinced by the width of the stacking fault etch figures after a 5 min etch period for each solution.

Summary

The Wright etch consistently produces well-defined etch figures of common defects on silicon surfaces. It has been demonstrated that Wright etch is superior in revealing oxidation-induced stacking faults. Dislocation etch figures on (100) surfaces are shown to have superior crystallographic etch features when compared with

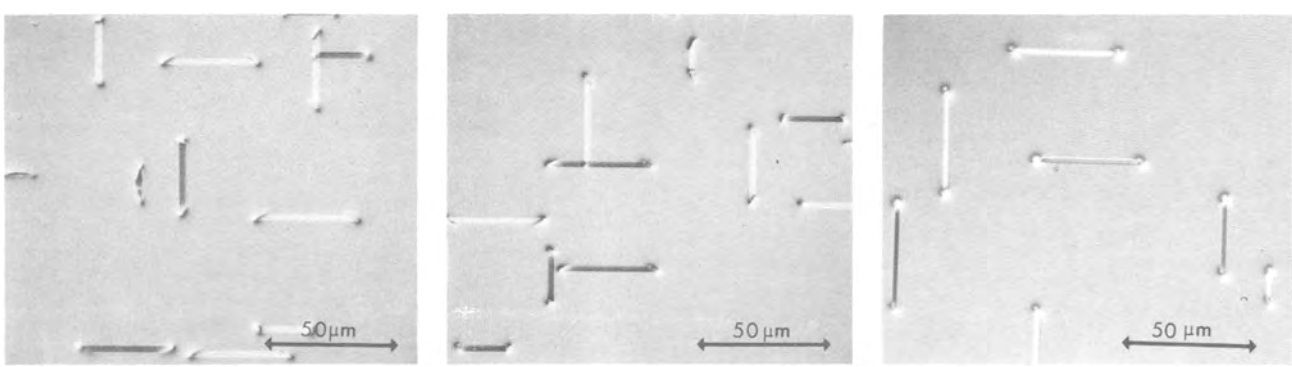


Fig. 10. Stacking faults on a (100), 1-3 Ω-cm, n-type wafer after 5 min Wright etch. (a) A freshly mixed solution, (b) a 4 week old solution, and (c) a 6 week old used solution. Stacking fault delineation and surface quality are not degraded by aging of the solution.

those revealed by Sirtl and Secco etching. The dislocation etch figures on (111) surfaces are comparable to those revealed by Sirtl etching and superior to those revealed by Secco etching. The etch rate of Wright etch (approximately 1 μm per min at room temperature) is slower than that of Sirtl and Secco etchants which provides for more etch control. The background surfaces after etching are smoother than those produced by the previous etchants. Large numbers of wafers may be etched in batches, in a sufficient amount of solution, without excessive heat generation, and the etchant may be reused without loss of defect definition.

Acknowledgment

The Auger analysis shown in this work was provided by Dr. Simon Thomas and the oxidation was conducted by Ed Reed. Their assistance is gratefully appreciated.

Manuscript submitted Aug. 27, 1976; revised manuscript received Dec. 16, 1976. This was Paper 118 presented at the Washington, D. C., Meeting of the Society, May 2-7, 1976.

Any discussion of this paper will appear in a Discussion Section to be published in the December 1977 JOURNAL. All discussions for the December 1977 Discussion Section should be submitted by Aug. 1, 1977.

Publication costs of this article were assisted by Motorola Incorporated.

REFERENCES

1. J. E. Lawrence, in "Semiconductor Silicon, 1973" H. R. Huff and R. R. Burgess, Editors, The Electrochemical Society Softbound Symposium Series, Princeton, N. J. (1973).
2. E. Sirtl and A. Adler, *Z. Metallkd.*, **52**, 529 (1961).
3. W. C. Dash, *J. Appl. Phys.*, **27**, 1193 (1956).
4. F. Secco d'Aragona, *This Journal*, **119**, 948 (1972).
5. Annual Book of ASTM Standards, Part 8, Designation F47-70.
6. H. Robbins and B. Schwartz, *This Journal*, **106**, 505 (1959).
7. H. Robbins and B. Schwartz, *ibid.*, **107**, 108 (1960).
8. H. Robbins and B. Schwartz, *ibid.*, **108**, 365 (1961).

Diffusion and Incorporation of Aluminum in Silicon

P. Rai-Choudhury,* F. A. Selim,* and W. J. Takei

Westinghouse Research Laboratories, Pittsburgh, Pennsylvania 15235

ABSTRACT

Aluminum is used as a p-type dopant in the manufacture of high power devices. The results of thermodynamic and experimental studies of the Al-Si-H-O system are discussed. Reaction with the quartz wall and moisture in the closed tube diffusion of aluminum causes the source to oxidize and reduces the aluminum partial pressure. Solutions to these problems are discussed. Heat-treatment of diffused wafers under various temperature-time conditions followed by Hall effect and resistivity measurements are performed to study possible formation of donor complexes.

The interest in Al diffusion into Si is primarily because of its use as a p-type dopant for the fabrication of high voltage junctions, and due to its role in silicon-on-sapphire film processing. For high power device fabrication, Al is preferred due to its fast diffusion in Si. The ionic radius of Al^- is close to the tetrahedral covalent radius of Si and it has a low solubility limit, and therefore dislocation generation is reduced. Also, Al does not form any intermetallic compounds with Si. Al diffusion, however, suffers from a few disadvantages because of its high reactivity with oxygen, moisture, and quartz walls. When diffusion is carried out in a sealed system under vacuum or an inert ambient, the presence of oxygen and moisture in the closed tube causes the Al source to oxidize, thus preventing transport of the dopant atoms. Reaction of the quartz walls further reduces the Al partial pressure in the system. The diffusion often results in a low surface concentration and nonreproducible shape of the impurity profile.

The diffusion of aluminum in silicon has been studied by Goldstein (1), Fuller *et al.* (2-4), Miller *et al.* (5), and Y. C. Kao (6). The surface concentrations of aluminum in silicon, found in both the experiments of Fuller *et al.* (2) and Goldstein (1) are in rough agreement but are two orders of magnitude less than the solid solubility of Al in Si. The aluminum (Al) surface concentrations in Fuller's results are below the aluminum solid solubility as their diffusions were made in quartz tubes. This permits the aluminum and quartz to react and reduce the partial pressure of aluminum significantly below the pressure to be expected in the absence of quartz. The interaction between oxygen and aluminum in silicon crystals giving rise to donor complexes and the stability of these complexes at various temperatures have been discussed by Fuller *et al.* (3, 4). Results showing electrical inactivity of Al in Si were reported by other workers. Schink and Warrick (7) have found by wet chemical methods in several silicon crystals an aluminum content of 10^{17} cm^{-3} without any influence on the n-type conductivity. In view of these discrepancies and uncertainties, it is worthwhile to reinvestigate the problem of Al diffusion in Si. The purpose of this study is to discuss sealed-tube Al diffusion and the formation of Al diffused junction, and the conditions under which the Al source remains effective throughout the diffusion cycle, to study the relevant thermodynamic data for the Al-O-H-Si system, and to determine the role and electrical activity of Al in Si.

Experimental Procedures

The silicon wafers used for sealed-tube Al-diffusion were 60-150 Ω-cm, n-type, float-zoned (111) crystals. The lapped wafers were cleaned with detergents, degreased, chemically etched, and chelated before loading in the sealed tube. The diffusion source consists of high purity aluminum pellets that are degreased, etched in NaOH, rinsed in acids and methanol. Quartz tubes were baked under heat lamps or in a 1000°C furnace before loading the source and wafers. Sealing of the quartz ampul was done either under vacuum or argon backfilled conditions. Diffusion was carried out for the desired temperature and time. At the end of the diffusion cycle the furnace was slow cooled at 0.2°-2.0°C/min to about 600°C and then the ampule was with-

* Electrochemical Society Active Member.

Key words: aluminum, junction, silicon, thermodynamics, Hall effect.

drawn from the furnace. The impurity profiles were then measured by the spreading resistance technique.

To study the reactions of Al with oxygen in silicon crystals we used both homogeneously Al-doped Czochralski silicon crystals (Al added to the melt) and Al-diffused wafers after being oxidized at different temperatures. The Al concentration in these Czochralski grown crystals varied from 5.4×10^{16} to 1×10^{18} cm^{-3}. Heat-treatment of these samples was done in N_2 atmosphere for different temperatures (400°-1100°C) and annealing times (16-300 hr), followed by either quenching or slow cooling. In a number of runs the samples were heat-treated at 1270°C for 20 min then rapidly cooled to room temperature. Thus, the high temperature equilibrium is frozen in. This was done to remove any "growth history," *i.e.*, to eliminate processes which may cause atomic defect formation, *e.g.*, precipitates, during the cooling following crystal growth. Hall effect and resistivity measurements on these samples before and after heat-treatment were conducted to check the change in carrier concentrations, conductivity type, and resistivity. Transmission electron microscopy was used to reveal the presence of any precipitates.

Sealed-Tube Aluminum Diffusion and Thermodynamics of the System Al-O-H-Si

In a sealed-tube aluminum diffusion we are dealing with quartz walls, aluminum diffusion source, oxygen and moisture (residual after high vacuum), and the silicon wafers to be diffused. Some of the possible reactions at a typical diffusion temperature in such a system are

$$2Al(g) + \frac{3}{2}O_2(g) \rightarrow Al_2O_3(s), \quad \Delta G_{1500°K} = -286 \text{ kcal} \qquad [1]$$

$$4Al(g) + 3SiO_2(s) \rightarrow 2Al_2O_3(s) + 3Si(s), \quad \Delta G_{1500°K} = -170 \text{ kcal} \qquad [2]$$

Reactions [1] and [2] have negative free energies and show that in the presence of oxygen and quartz the aluminum will be oxidized to form a stable Al_2O_3 (oxide) skin to seal or consume the aluminum source, *i.e.*, aluminum will not be available to transport and diffuse into the silicon wafers.

An examination of the thermochemistry of the Al-O-H-Si system provides information regarding the transporting species, their vapor pressures, and the feasibility of using those volatile species as diffusion sources. Figure 1 shows the thermochemical data for the aluminum-oxygen-hydrogen system at a typical diffusion temperature of 1500°K. The necessary free energy data for these calculations were obtained from the JANAF Thermochemical Tables (8). The ordinate shows the pressures (in atmospheres) of the various volatile species on a log scale while the abscissas show the equilibrium oxygen pressures (upper scale) and the equilibrium hydrogen-water vapor ratios (lower scale) on a log scale. The vertical line in the figure shows equilibrium data for liquid aluminum and solid aluminum oxide (Al_2O_3), while horizontal lines show simple vapor pressure data. The lines of various slopes to the left of the vertical line for the solid oxide show equilibrium data for the volatile oxides, hydrides, and hydroxides over liquid aluminum. The lines to the right of the vertical lines show equilibrium data for the volatile species over solid aluminum oxide. To the right of the vertical line, transport of Al is feasible in the presence of water vapor in the low parts per million range only. As the water vapor content reaches the parts per million level or higher, the partial pressures of the volatile species become extremely low and the liquid aluminum source will form an oxide skin. Under these conditions the aluminum source remains active only during the initial period of the diffusion cycle. To the left of the vertical line (*i.e.*, water vapor in the parts per billion range), liquid Al is stable, and the primary transporting species are Al and AlH. The Al source remains active throughout the diffusion cycle.

Since aluminum diffusion is normally carried out in a sealed quartz tube system, an examination of the silicon-oxygen-hydrogen system is also necessary. Figure 2 shows the thermochemical data for the silicon-quartz-water vapor system. Here again the vertical line defines equilibrium between solid silicon and solid silicon dioxide. If we operate to the left of the vertical line, oxidation of silicon wafers is not favored and the quartz would tend to reduce to SiO. In regions of practical interest, SiO is the dominant species which will react with aluminum when it is present as a diffusion source. The ideal procedure for aluminum diffusion is, therefore, not to use any quartz but instead materials such as alumina and zirconia.

When aluminum is included in the silicon-oxygen-hydrogen system, the equilibrium is shifted toward lower partial pressures for the oxides of silicon. Figure 3 shows the thermochemical data for this system at different temperatures. Here the system is allowed to reach equilibrium so that both liquid aluminum and solid alumina can coexist at a given temperature, which then determines the required ratio of p_{H_2}/p_{H_2O}. Figure 3 indicates that if the residual water vapor can be reduced to below 0.01 ppm (log $p_{H_2}/p_{H_2O} \sim 8$), a lower diffusion temperature is favored. This would maintain a low SiO pressure and minimize source oxidation. If, on the other hand, the quartz diffusion system has a high water vapor content, a higher diffusion temperature is preferable, although the aluminum source will oxidize and create a reproducibility problem.

Results and Discussions

Sealed tube aluminum diffusion.—In general, the surface concentration of aluminum diffused in silicon is about two orders of magnitude less than that at the

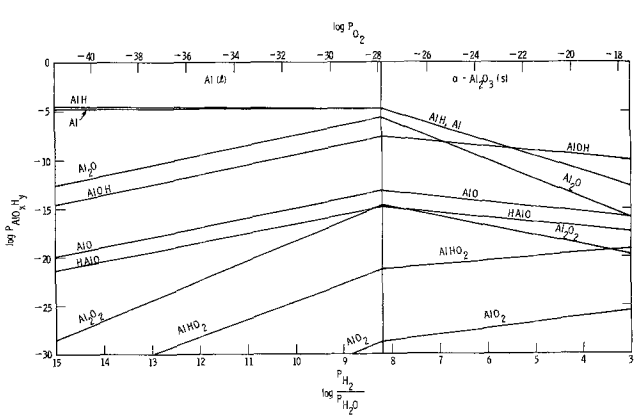


Fig. 1. Thermochemical data for aluminum-oxygen-hydrogen system at 1500°K.

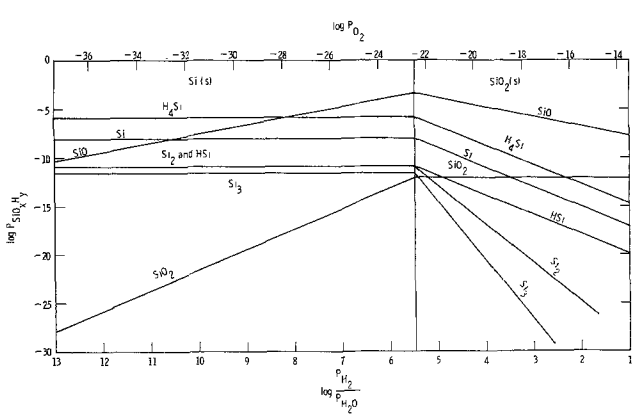


Fig. 2. Thermochemical data for silicon-oxygen-hydrogen system at 1500°K.

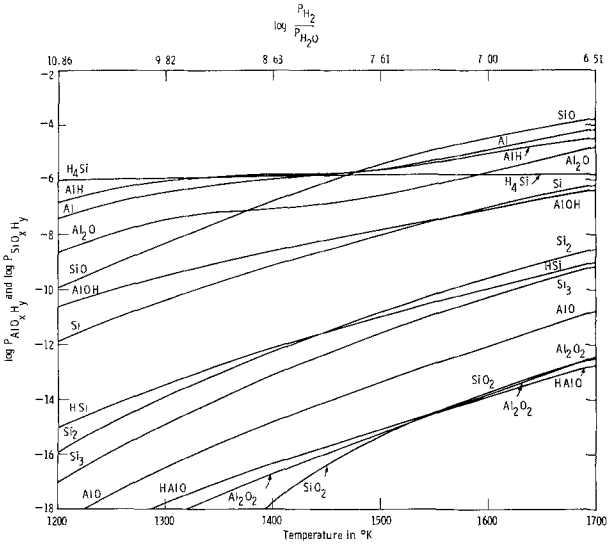


Fig. 3. Thermochemical data for silicon-oxygen-hydrogen-aluminum system at different temperatures.

solubility limit. Such a result may be expected when the experiment is carried out in a quartz system. Goldstein (1), Fuller and Ditzenberger (2), and Pavlov *et al.* (9) all performed their diffusions in quartz systems and were limited to a surface concentration of aluminum below 10^{17} cm^{-3}. Kao (6) has achieved surface concentrations near the solid solubility limit in a quartz system by allowing the quartz to be passivated by the formation of a layer of silicon and Al_2O_3. The aluminum source was maintained active during the passivation process by alloying aluminum with silicon so that no impervious skin is formed at the surface of the diffusion source.

In a quartz system, aluminum and quartz are certain to react and reduce the partial pressure of aluminum below the pressure expected in the absence of the quartz phase. In this regard, the total pressure at which diffusion is carried out is important. Under vacuum conditions the evaporated Al molecules leaving the crucible (assuming the crucible material does not react with Al) could travel considerable distances without undergoing any collisions, most of which occur at the quartz tube wall. Thus a layer of Si and Al_2O_3 builds up on the quartz wall, which becomes passivated. This is only possible if the system has a sufficiently low oxygen and moisture content, so that no impervious skin is developed at the aluminum source surface. When the quartz tube is filled with argon (necessary to prevent the tube from collapsing) to provide about 1 atm pressure at the diffusion temperature, the mean free path of the evaporated aluminum molecules is reduced to about 1 μm. Thus, the Al molecules suffer numerous collisions in the gas phase and with the crucible walls. Interaction with the quartz walls is only possible by Al transport through molecular diffusion. Since there is sufficient SiO partial pressure in equilibrium with quartz (see Fig. 2), Al will react with SiO in the crucible and not be available either to passivate the wall or to deposit on a silicon wafer.

In order to explore the effects of crucible material, quartz, polysilicon, and alumina crucibles were examined. In runs JS-3 and O218Q, aluminum pellets were placed inside a cavity in a silicon disk which were then placed in a quartz crucible. In runs O218S and O223S, aluminum pellets were in direct contact with the polysilicon crucible, whereas in Al3A, the pellets were in contact with an alumina crucible. Unfortunately, diffusions were performed under different conditions because of the need to fabricate different types of devices. Table I summarizes some typical results. The surface concentration (C_o) of aluminum is lowest (1.5×10^{16} cm^{-3}) when an argon backfilled quartz system is used. C_o increases to about $3\text{-}4 \times 10^{16}$ cm^{-3} if argon is replaced by vacuum. Use of a polysilicon liner together with flame baking of the quartz tube provided a higher C_o. When alumina is used as a liner and crucible material, C_o's as high as 8×10^{17} cm^{-3} are obtained under otherwise poor conditions, *i.e.*, argon backfilled. Experiments under vacuum conditions using an alumina liner were not performed because of practical limitations at the time. These results are consistent with the thermodynamic expectations. One of the possible reasons for lower surface concentration in run O2185 with polysilicon liner is that the aluminum source and the silicon wafers were not isolated as effectively from the quartz as in run A13A. The aluminum concentrations in these runs should be compared with the solid solubility limit of about 1×10^{19} cm^{-3}.

The analysis of the phases present in the diffusion sources was made by glancing incidence x-ray diffraction. A portion of the source was mounted in a 114.6 mm powder camera in such a position that the beam struck the diffusion source surface. Thus the technique is primarily sensitive to the phases present within about 0.1 mm of the surface. The only phases which could be detected were polycrystalline silicon, aluminum, and the corundum form of Al_2O_3. The polycrystalline silicon would arise from the formation of a Si-Al eutectic by reaction between the Al source and the Si support disk (except run AL3A where Al was placed directly on the alumina crucible). Typical patterns are shown in Fig. 4 and the results are listed in the last column of Table I.

In run AL3A, the Al source was placed in an alumina crucible, which, in turn, was placed inside an alumina cylinder open at one end only. The silicon wafers were loaded in the cylinder and an alumina cup was used to close the cylinder fairly tightly in an argon ambient. The conditions were apparently sufficiently good to provide fairly high Al surface concentrations. Figure 5 shows the impurity profile from such a run. As can be seen from Table I, the source Al remained unoxidized during the diffusion cycle. For comparison purposes, a typical profile from an all-quartz system under vacuum is shown in Fig. 6. Diffusion sources from such runs frequently will be covered with Al_2O_3.

Table I. Sealed-tube aluminum diffusion conditions

Source	Ambient	Liner inside quartz	Quartz bakeout conditions before sealings	Diff. temp (°C)	Diff. time (hr)	Surface concentration (cm^{-3})	Junction depth (μm)	Phases present in source after diffusion
JS-3	Ar, 1/3 atm	None	Dried under heat lamp	1245	8	1.5×10^{16}	49	Si, Al_2O_3, Trace Al
O218Q	Vacuum, ~10^{-6} Torr	None	Furnace-baked ~1000°C, 30 min	1200	64	2.8×10^{16}	84	Si, Al_2O_3
O218S	Vacuum, ~10^{-6} Torr	Poly-Si tube	Furnace-baked ~1000°C, 30 min	1200	64	3.5×10^{16}	90	Si, Al, Al_2O_3
O223S	Vacuum, ~10^{-6} Torr	Poly-Si tube	Flame-baked for 30 min	1175	64	6.0×10^{16}	51	Si, Al, Al_2O_3
Al3A	Ar, 1/3 atm	Alumina tube	Furnace-baked ~1000°C, 30 min	1245	8	8.0×10^{17}	63	Al
Al-alloy	Ar, 1/3 atm	None	Furnace-baked ~1000°C	1245	8	8×10^{17}	52	—

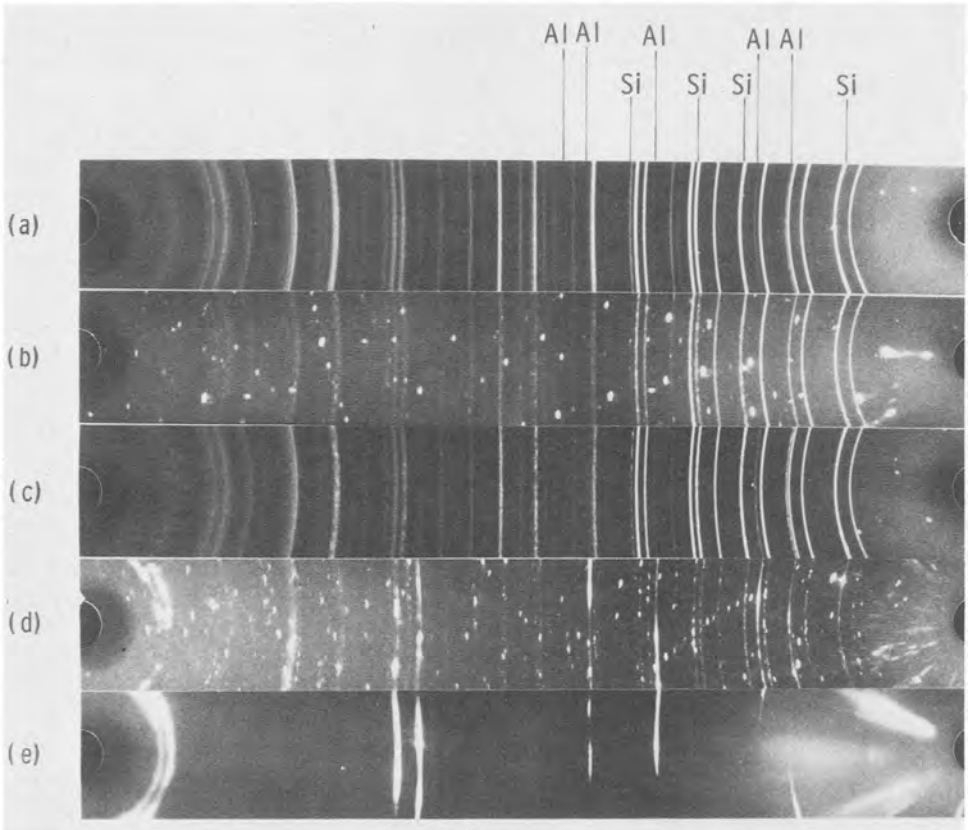


Fig. 4. X-ray diffraction patterns from Al diffusion sources: (a) run JS-3, (b) run O218Q, (c) run O218S, (d) run O223S, (e) run AL3A.

Electrical activity of aluminum in silicon.—Aluminum is known to give p-type conductivity in silicon. Heat-treatment studies by Fuller *et al.* (3, 4) show that in the presence of oxygen (10^{18} cm^{-3}) aluminum-doped silicon (3×10^{17} cm^{-3} Al) converts from p- to n-type upon reaction at a temperature 500°-900°C. The formation of aluminum-oxygen donor complexes, *i.e.*, ($SiO_4^+Al^-SiO_4^+$) or ($AlO_4SiO_4^+$), was suggested as a possible explanation in the study.

In principle, Al in Si can form two basic defects (10): interstitial aluminum atoms (Al_i), a single, double, or triple donor; or substitutional aluminum atoms (Al_{Si}), a single acceptor. In addition, complexes of these species with ionized defects such as SiO_4 donors may occur, giving rise to complexes such as ($SiO_4^+Al^-SiO_4^+$) or ($AlO_4SiO_4^+$); or neutral complexes, *e.g.*, ($Al^-SiO_4^+$).

Our studies on Al-doped samples have not revealed any conversion in conductivity from p- to n-type upon heat-treatment for different temperatures and times, indicating no formation of such donor complexes as majority species. A comparison of acceptor concentrations before and after annealing of Al-doped silicon is shown in Table II. It is seen that all samples remained p-type with no large change in resistivity after heat-treatment. In few cases we found the resistivity of some samples (No. 1) to increase by more than a factor of two. The acceptor concentrations of

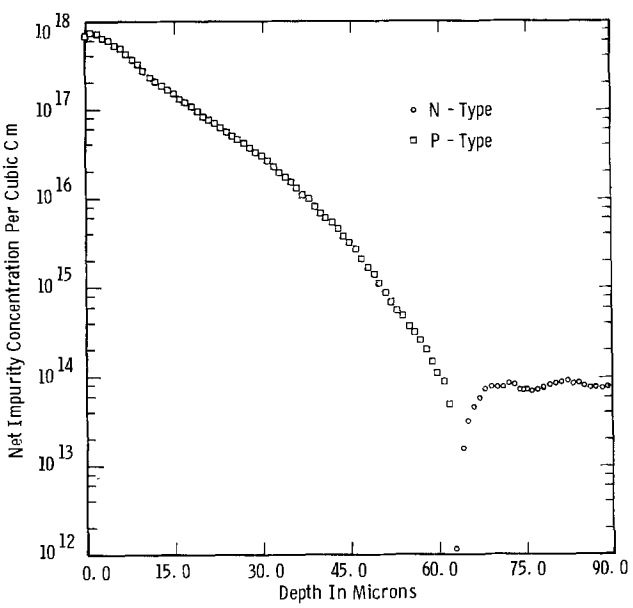


Fig. 5. Typical aluminum diffusion profile from run AL3A using alumina tubing in an argon backfilled ambient; diffusion temperature 1245°C, time 8 hr.

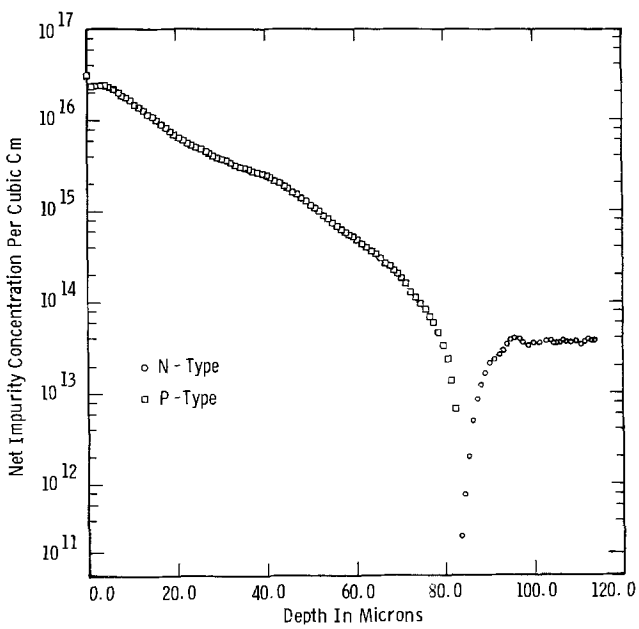


Fig. 6. Typical aluminum diffusion profile from run O218Q using an all-quartz system under vacuum.

Table II. Comparison of acceptor concentrations† before and after annealing of Al-doped silicon

Crystal No.	Anneal T(°C)	Anneal t(hr)	Original ρ(Ω-cm) p-type	Final ρ (Ω-cm) p-type	Original $N_A \times 10^{17}$ (cm^{-3})	Final $N_A \times 10^{17}$ (cm^{-3})
1*	600	112	0.129	0.315	3.2	1.3
2*	600	115	0.072	0.0673	5.6	5.5
3*	1020	16	0.654	0.655	0.62	0.6
4**	600	112	0.064	0.068	6.4	6.4
5***	550	300	0.44	0.44	0.95	0.9

† Calculated from Hall effect measurement and/or four-point probe resistivity assuming a mobility of 150 $cm^2\ V^{-1}\ sec^{-1}$ for holes as found in most of these p-type samples.
* Czochralski crystal, Al doped in the melt.
** Czochralski crystal, Al diffused.
*** Float-zoned crystal, Al diffused, and then oxygen diffused.

these samples changed from 3.2×10^{17} to 1.3×10^{17} cm^{-3}. This change corresponds to a formation of 9.5×10^{16} cm^{-3} donors compensating an equal number of acceptors reducing the acceptor concentration by an amount of 1.9×10^{17} cm^{-3}. This reduction could also be due to Al precipitation during cooling or to formation of 1.9×10^{17} cm^{-3} Al neutral complexes or deep levels. Slow or fast cooling of such samples showed no effect on resistivity, and transmission electron microscopy studies showed no evidence of observable precipitates. This suggests that the reduction in acceptor concentrations in this sample is due to formation of aluminum neutral complexes or deep levels or donor complexes as a minority species which cannot be revealed by room temperature Hall measurements.

Summary

When Al is diffused into silicon in an all-quartz system, the surface concentration of aluminum is low ($\sim 10^{16}$ cm^{-3}) due to an effective reduction of aluminum partial pressure through interactions with SiO_2, SiO, residual moisture, and oxygen. When alumina is used as a liner and crucible material, surface concentrations as high as $\sim 10^{18}$ cm^{-3} are obtained under otherwise poor conditions (*i.e.*, argon backfilled). No evidence of the interaction between Al and O giving rise to Al-O donor complexes as majority species was found.

Acknowledgments

The authors wish to thank R. F. Yut for assistance with the experimental work and A. F. Lovas for making the Hall measurements.

Manuscript submitted Oct. 11, 1976; revised manuscript received Jan. 20, 1977. This was Paper 117 presented at the Washington, D.C., Meeting of the Society, May 2-7, 1976.

Any discussion of this paper will appear in a Discussion Section to be published in the December 1977 JOURNAL. All discussions for the December 1977 Discussion Section should be submitted by Aug. 1, 1977.

Publication costs of this article were assisted by Westinghouse Research Laboratories.

REFERENCES

1. B. Goldstein, *Bull. Am. Phys. Soc., Ser. II*, **1**, 145 (1956).
2. C. S. Fuller and J. A. Ditzenberger, *J. Appl. Phys.*, **27**, 544 (1956).
3. C. S. Fuller and F. H. Doleidon, *ibid.*, **28**, 1264 (1958).
4. C. S. Fuller, F. H. Doleiden, and Katherine Wolfstirn, *J. Phys. Chem. Solids*, **13**, 187 (1960).
5. R. C. Miller and A. Savage, *J. Appl. Phys.*, **27**, 1430 (1956).
6. Y. C. Kao, *Electrochem. Technol.*, **5**, 90 (1967).
7. E. Spenke, in "Semiconductor Silicon," R. R. Haberecht and E. L. Kern, Editors, p. 15, The Electrochemical Society Softbound Symposium Series, New York (1969).
8. JANAF Thermochemical Tables, NSRDS/NBS 37 (1971).
9. P. V. Pavlov and E. V. Dobrokhotor, *Sov. Phys. Solid State (Engl. Transl.)*, **16**, 1 (1974).
10. F. A. Kröger, "The Chemistry of Imperfect Crystals," Vol. 2, 2nd ed., p. 11, North Holland/American Elsevier Publishing Company, Amsterdam and New York (1973).

Phase Diagram of the $(CuGaTe_2)_{1-x}$-$(2CdTe)_x$ System and Semiconducting Properties of $CuCd_2GaTe_4$

A. Aresti, L. Garbato, P. Manca, and A. Rucci

Istituto di Fisica dell'Università, Gruppo Nazionale di Struttura della Materia, C.N.R., 09100 Cagliari, Italy

ABSTRACT

The system $(CuGaTe_2)_{1-x}$-$(2CdTe)_x$ was investigated by microstructure, DTA, and x-ray examinations. The analysis of the phase diagram shows, in the range $0.33 \leq x \leq 1$, the existence of a continuous series of solid solutions of sphalerite-type structure, the lattice parameter of which varies coherently with microhardness. The main physicochemical and transport properties of the $CuCd_2GaTe_4$ composition are reported.

Structural and microscopic examinations, carried out on the middle composition of $A^{I}C^{III}D_2^{VI}$-$B_2^{II}D_2^{VI}$ systems (A^I = Cu, Ag; B^{II} = Zn, Cd; C^{III} = Ga, In; and D^{VI} = Se, Te), have shown that the characteristics of homogeneity and single phase seem to be restricted to copper ($CuB_2^{II}C^{III}D_4^{VI}$) and silver ($AgCd_2InTe_4$) based compositions, the main physicochemical properties of which have been investigated (1). Experimental research in this field is generally concerned with the determination of regions of mutual solubility in tetrahedral four-component systems of the type $A^{N-1}C^{N+1}D_2^{8-N}$-B^ND^{8-N} (N = 2, 3) (2-19) or, more particularly, with the synthesis and crystal growth techniques of quaternary phases with general composition AB_2CD_4 (19-26), which can be considered as the structure analogous to binary and ternary normal tetrahedral compounds.

In this paper, as a part of intensive and systematic studies on synthesis processes, stability, and structural

Key words: diamondlike quaternary semiconducting phases.

characterization of $A^IB_2^{II}C^{III}D_4^{VI}$ quaternary phases, we report the phase diagram of the $(CuGaTe_2)_{1-x}$-$(2CdTe)_x$ system, in order also to define the region of interest for semiconductor-device metallurgy.

Experimental Procedure and the Phase Diagram

The alloys in the system $(CuGaTe_2)_{1-x}$-$(2CdTe)_x$ were obtained both by direct synthesis of elements (Johnson-Matthey "Specpure") and by starting from varying amounts of the terminal points of the diagram. Samples, sealed in quartz ampuls under high vacuum (10^{-5} Torr), were heated for 3 days at about 1160°C with a continuous mechanical vibration and then quickly quenched in an ice water bath. The synthesis process was carried out with an accurate temperature program, because of the relatively high vapor pressures of cadmium and tellurium (a heating rate of about 1°C/min was found to be the most suitable). In these conditions there was no evidence of distillation and thus the starting composition was insured for all samples.

The phase diagram (Fig. 1) is the result of microstructure, DTA, and x-ray investigations, carried out systematically on different samples, taking 0.08 as the average step in x. No differences were observed in the ingots obtained by the two above-mentioned synthesis methods. The left-hand side of the diagram ($x < 0.33$), with an exception of a small range of solubility in the chalcopyrite structure, is characterized as a heterogeneous region with two distinct phases melting at about the same temperature (850°C). All DTA transitions below the solidus curve disappear near the $x = 0.33$ composition. Microstructural examinations on etched surfaces of samples of this range provided a constant value of microhardness (about 340 kg/mm²) on both phases and x-ray diffractograms clearly revealed a mixture of tetragonal (chalcopyrite) and cubic (sphalerite) structures. The latter result, at least for the range $0 < x < 0.33$, agrees with a previous roentgenographic investigation (11).

In the single phase region ($0.33 \leq x \leq 1$) the analysis of thermograms points out that no detectable heat effects due to solid-solid phase transitions appear for these alloys. X-ray diffractograms can be systematically indexed as a cubic cell of sphalerite structure. This latter result suggests that the cationic sites, for all compositions of the solid solutions, are randomly occupied by the A^I, B^{II}, and C^{III} atoms, the disorder leading consequently to an isotropic sphalerite-type cell.

Figure 2 shows the variation of both microhardness and lattice parameter *vs.* composition. It is interesting to note that the lower limit of solubility occurs for the nominal composition $CuCdGaTe_3$ (equimolar ratio of $CuGaTe_2$ and CdTe), which exhibits the maximum

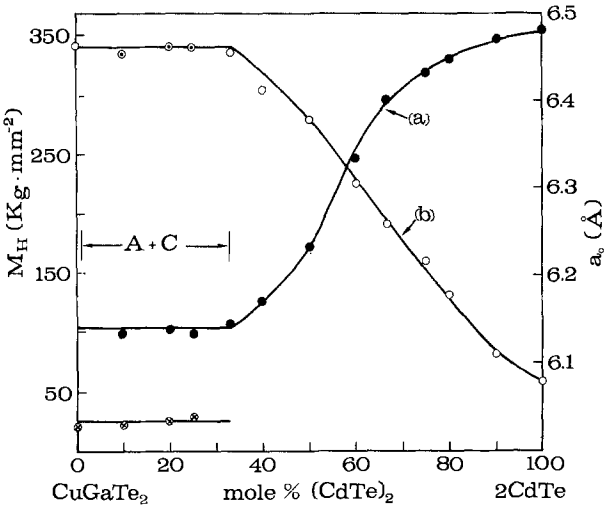


Fig. 2. Lattice parameter (a) and microhardness (b) *vs.* composition. ● zinc blende; ⊗ chalcopyrite [$a_o = (a^2c/2)^{1/3}$]. The symbol ⊙ of curve (b) refers to microhardness prints of cubic and tetragonal phases.

value of microhardness and the minimum one of lattice parameter. Such behavior seems to be characteristic of alloys whose anions are on the average surrounded by an equal number of cations (14).

Fundamental Properties of the $CuCd_2GaTe_4$ Phase

We consider the composition $x = 0.5$ ($CuCd_2GaTe_4$) in the $(CuGaTe_2)_{1-x}$-$(2CdTe)_x$ system as a relevant term of the phase diagram, because of its close analogy with $B^{II}D^{VI}$ semiconducting compounds of sphalerite structure.

Thermal conductivity (K) and thermoelectric power (α) measurements (80°-300°K, Fig. 3) were carried out on cylindrical polycrystalline samples (1.75 cm long and 1.0 cm in diameter) by using a previously reported (27) steady-state method (28). The room temperature values (Table I) are of the same order of those reported (14, 25) for some homologous quaternary phases and represent an average between the K and α values (29-31) of the terminal points of the phase diagram. A similar conclusion can be drawn for the value of magnetic susceptibility (χ_{mol}), which can be compared with the sum of the values of $CuGaTe_2$ (32) and CdTe (33). The samples grown are p-type, as shown by thermoelectric emf measurements.

The figure of merit $Z = \alpha^2\sigma/K$ at room temperature is found to be about 10^{-5} °K^{-1}. The optical gap at room

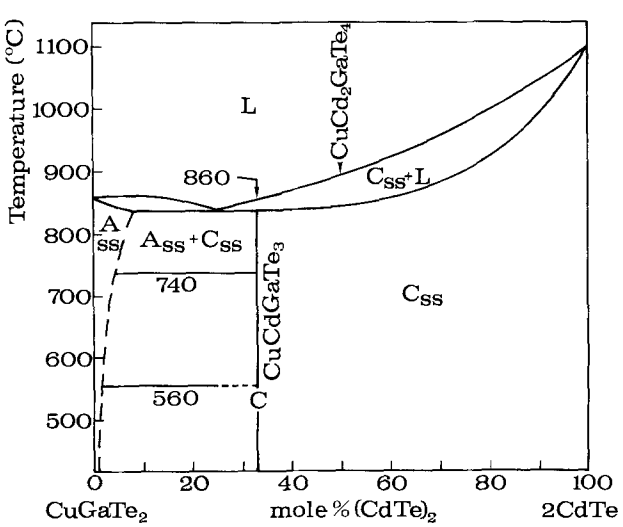


Fig. 1. Phase diagram of the $(CuGaTe_2)_{1-x}$-$(2CdTe)_x$ system

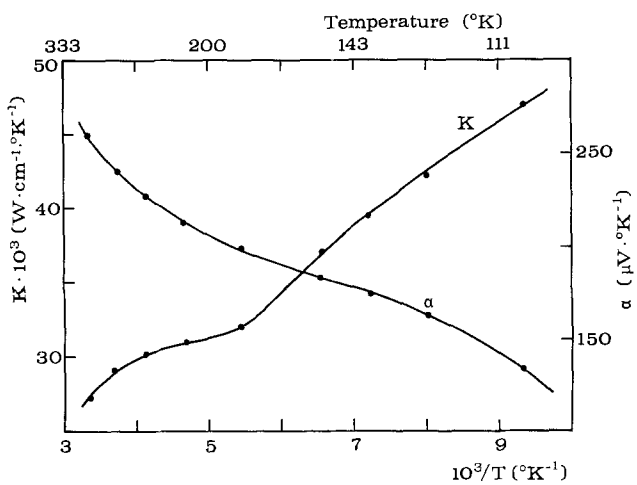


Fig. 3. Seebeck coefficient (α) and thermal conductivity (K) *vs.* temperature.

Table I. Fundamental properties of $CuCd_2GaTe_4$ phase at 300°K

Optical energy gap, eV	Electrical conductivity $(\Omega\text{-cm})^{-1}$	Hall constant, cm^3/C	Carrier concentration, cm^{-3}	Hall mobility, $cm^2/V\text{-sec}$	Thermoelectric power, $\mu V/°K$	Thermal conductivity, $mW/°K\text{-cm}$	Thermoelectric figure of merit, $°K^{-1}$	Molecular magnetic susceptibility, 10^{-6} emu/mole
1.1	7.7	1.5	$5 \cdot 10^{18}$	11	260	28	10^{-5}	−246

temperature, as deduced from absorption and reflectivity spectra (Fig. 4), is 1.1 eV. This result is in agreement with the values obtained by Woolley and Williams (11) for other quaternary phases of the Cu-Cd-Ga-Te system, but sensibly deviates from the data reported (25) for some $A^{I}B_2^{II}C^{III}D_4^{VI}$ homologous compositions. The gap 1.1 eV of $CuCd_2GaTe_4$ can be compared with the values 1.3_1 and 1.4_7 eV found (1) for the isocationic phase $CuCd_2GaSe_4$ in the zinc blende and wurtzite structures, respectively.

Electrical conductivity measurements were made by a conventional d-c method, with ohmic contacts obtained by spark-soldering thin Pt wires or by four pressed graphite probes. The experimental results, obtained on a number of different samples in the range 170°-630°K, reveal the existence of an impurity level at about 0.1 eV. All $\sigma = \sigma(T)$ curves are reproducible up to 370°K. The high concentration of impurities and the probable onset of an irreversible change above 370°K make it impossible to determine the electrical energy gap of these samples. However, thermogravimetric analysis does not show loss of weight up to 750°K and microscopic examinations do not reveal any phase change in samples after electrical conductivity measurements. Therefore, the difference in electronic properties of recycled samples might be due to a random rearrangement of the Cu, Cd, and Ga atoms in the cationic sites of the sphalerite structure.

Manuscript submitted July 12, 1976; revised manuscript received Dec. 8, 1976.

Any discussion of this paper will appear in a Discussion Section to be published in the December 1977 JOURNAL. All discussions for the December 1977 Discussion Section should be submitted by Aug. 1, 1977.

Publication costs of this article were assisted by the Universita di Cagliari.

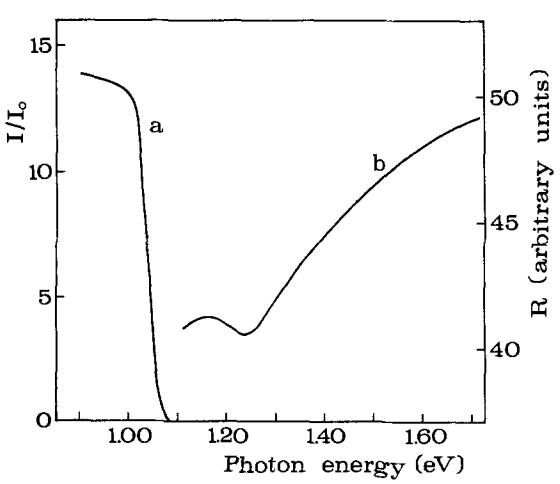


Fig. 4. Absorption (a) and reflectivity (b) spectra for the $CuCd_2GaTe_4$ phase.

REFERENCES

1. L. Garbato and P. Manca, *Mater. Res. Bull.*, **9**, 511 (1974).
2. E. F. Apple, *This Journal*, **105**, 251 (1958).
3. H. Rodot, Proceedings of Fifth International Conference on Semiconductor Physics, Prague 1960, p. 1010, Academic Press, New York (1961).
4. N. A. Goryunova and V. D. Prochukhan, *Sov. Phys. Solid State (Engl. Transl.)*, **2**, 161 (1960).
5. C. Giesecke and H. Pfister, *Acta Crystallogr.*, **14**, 1289 (1961).
6. S. Mamaev, D. N. Nasledov, and V. V. Galavanov, *Sov. Phys. Solid State (Engl. Transl.)*, **3**, 2473 (1962).
7. D. N. Nasledov, S. Mamaev, and O. V. Emelyenko, *ibid.*, **5**, 104 (1963).
8. H. Borchers and R. G. Maier, *Metallurgiya*, **8** (17), 775 (1963).
9. H. Borchers and R. G. Maier, *ibid.*, **10** (17), 1006 (1963).
10. J. Rupprecht and R. G. Maier, *Phys. Status Solidi*, **8**, 3 (1965).
11. J. C. Woolley and E. W. Williams, *This Journal*, **113**, 899 (1966).
12. A. S. Borshchevskii, N. A. Goryunova, F. P. Kesamanly, and D. N. Nasledov, *Phys. Status Solidi*, **21**, 9 (1967).
13. C. C. Y. Kwan and J. C. Woolley, *Can. J. Phys.*, **48**, 2085 (1970).
14. V. P. Chernyavskii, N. A. Goryunova, and A. S. Borshchevskii, in "Chemical Bonds in Solids," N. N. Sirota, Editor, Vol. 4, p. 66, Consultants Bureau, New York (1972).
15. V. G. Lambrecht, Jr., *Mater. Res. Bull.*, **7**, 1411 (1972).
16. M. Robbins and M. Miksovski, *J. Solid State Chem.*, **5**, 462 (1972).
17. V. G. Lambrecht, Jr., *Mater. Res. Bull.*, **8**, 1383 (1973).
18. M. Robbins and V. G. Lambrecht, Jr., *J. Solid State Chem.*, **6**, 402 (1973).
19. P. C. Donohue and P. E. Bierstedt, *This Journal*, **121**, 327 (1974).
20. H. Hahn and H. Schulze, *Naturwissenschaften*, **52**, 426 (1965).
21. R. Nitsche, D. F. Sargent, and P. Wild, *J. Crystal Growth*, **1**, 52 (1967).
22. V. V. Ilyukhin, A. V. Nikitin, and N. V. Belov, *Sov. Phys. Dokl. (Engl. Transl.)*, **11**, 1035 (1967).
23. E. Parthé, K. Yvon, and R. H. Deitch, *Acta Crystallogr., Sect. B.*, **25**, 1164 (1969).
24. C. A. Joubert-Bettan, R. Lachenal, E. F. Bertaut, and E. Parthé, *J. Solid State Chem.* **1**, 1 (1969).
25. J. J. Curry and S. R. Pollack, *J. Phys. Chem. Solids*, **31**, 1235 (1970).
26. W. Schafer and R. Nitsche, *Mater. Res. Bull.*, **9**, 645 (1974).
27. A. Congiu, L. Garbato, P. Manca, and S. Serci, *This Journal*, **119**, 280 (1972).
28. M. V. Klein and R. F. Caldwell, *Rev. Sci. Instrum.*, **37**, 1291 (1966).
29. D. P. Spitzer, *J. Phys. Chem. Solids*, **31**, 19 (1970).
30. V. P. Zhuse, V. M. Sergeeva, and E. L. Shtrum, *Sov. Phys. Tech. Phys. (Engl. Transl.)*, **3**, 1925 (1958).
31. H. Rodot, "Les Materiaux Semiconducteurs," Dunod, Paris (1965).
32. L. Garbato, P. Manca, and A. Spiga, *Nature Phys. Sci.*, **239**, 156 (1972).
33. M. Matyas, *Czech. J. Phys.*, **B12**, 838 (1962).

Oxidation Behavior of Chromium Between 300° and 600°C

D. J. Young* and M. Cohen*

National Research Council of Canada, Division of Chemistry, Ottawa, Ontario, Canada K1A 0R9

ABSTRACT

Oxidation kinetics of high purity polycrystalline Cr were measured at $p_{O_2} = 0.53$ Pa and $300° \leq T \leq 600°C$. The reaction proceeded in two stages: an initial period of growth, in which the kinetics could be described with the Cabrera-Mott theory, was followed by an abrupt transition to a lower growth rate and parabolic kinetics. The kinetic transition was accompanied by a change in diffraction pattern of the oxide from that characteristic of a random orientation of very fine grained Cr_2O_3 to a pattern indicating a strongly preferred fiber texture. The oxide film formed in the pretransition region was flat whereas that formed in the posttransition region was composed of ridges and nodules separated by a very thin oxide film. Activation energies in both kinetic regions were much less than that found for self-diffusion in Cr_2O_3. It is concluded that the rate-controlling process throughout the reaction is metal transport via preferred pathways, such as grain boundaries, through the oxide film. In the pretransition region the density of such pathways is high, leading to uniform film thickening. In the posttransition region the density of such pathways is low, leading to localized transport and hence localized oxide growth.

The reaction of chromium with oxygen has been studied extensively. Attention has been directed to two aspects: thick scale formation at high temperatures, and initial oxygen uptake on bare metal surfaces at relatively low temperatures. Thermogravimetric and marker studies (1-4) of the high temperature reaction have established that chromium grows a scale of Cr_2O_3 by outward diffusion of cations with some contribution from inward anion diffusion (2, 3, 5). Kinetics are parabolic until the temperature exceeds 900°C where Cr vaporization becomes important (6).

Investigations of initial oxygen uptake on clean, single crystal surfaces have focused on structural aspects (7-9) and the observation of Cr_2O_3 nucleation. Changes in surface potential (10, 11) have been measured during oxygen uptake on evaporated metal films, indicating that a potential drop was set up between the metal (positive) and adsorbed oxygen. Subsequent oxide film growth at low and intermediate temperatures has receiveed relatively little attention.

Alessandrini and Brusic (12) examined the oxidation of polycrystalline Cr at temperatures of 400°-600°C and at a pressure of 1 atm O_2. Their ellipsometric measurements indicated kinetics which were described as initially linear and finally parabolic. Depending on temperature, the initial linear period was up to 10 min long and the thickness of oxide formed in that time varied between ~40 and ~100Å. The subsequently observed parabolic reaction had an activation energy of 96 ± 2 kJ. These results were interpreted in terms of an initial stage in which oxide nucleation was rate determining, followed by diffusion limited growth.

Hope and Ritchie (13) have studied the oxidation of vacuum-deposited Cr films in 1 atm O_2 and $250° \leq T \leq 450°C$. Resistance marker experiments indicated that mass transport through the oxide was achieved by metal movement. An electrostatic field was applied across the growing oxide using a vacuum-deposited porous Pt counterelectrode. When the Cr-oxide interface was made positive with respect to the oxide-counterelectrode interface, the rate was enhanced; reversal of the field polarity led to a reduction in rate. The authors interpreted this result as indicating rate control by ion transport. The technique employed by Hope and Ritchie of measuring the rate of increase of resistance of a thin evaporated film, while sensitive to relative changes in reaction rate, does not yield accurate kinetics.

* Electrochemical Society Active Member.

Key words: oxidation kinetics, Cabrera-Mott equation, morphological development, ion transport.

It is evident from the above that a thorough understanding of the Cr oxidation mechanism cannot be achieved until more precise kinetic information is available. This paper presents new data in the 300°-600°C region together with a structural and morphological description of the oxide. A mechanism for oxide growth is proposed.

Experimental

Kinetics were measured manometrically in an ultrahigh vacuum system which has been described previously (14). Experiments were initiated by heating the Cr sample to temperature in a dynamic vacuum ($\sim 10^{-5}$ Pa). After times of up to 20 min, the sample was isolated from the pumps. An oxygen dose at a known pressure was then allowed to expand into the reaction chamber. Subsequent pressure changes were measured with a differential capacitance gauge which yielded a sensitivity corresponding to less than a monolayer coverage of the sample. Successive doses of oxygen were used to maintain the pressure within ±10% of the nominal value. Because the gas admission valve was relatively slow opening, the kinetics of gas uptake in the first 1-2 sec were lost.

The temperature of the metal sample was measured and controlled to within ±2°C. Representative samples were examined before and after reaction by reflection electron diffraction and electron microscopy. Moderately thick oxide films (>300Å) could be dry-stripped from the metal. Thinner films could not, and their morphology was studied by replica electron microscopy. A two-stage carbon replication technique was used.

Materials.—Polycrystalline chromium sheet was supplied by the Australian Aeronautical Research Laboratories. On analysis it was found to contain as major impurities (in parts per million atomic) O 800, C 39, N 31, Si 18, Fe 13, and S 10. This material contained inclusions which were identified by electron diffraction as Cr_2O_3. Rectangular samples of surface area ~5 cm^2 were prepared by mechanically polishing all surfaces to a 3 μm diamond finish and subsequently electropolishing in 5 volume percent (v/o) solution of $HClO_4$ in CH_3COOH at 16°C at a current density of ~0.5 A-cm^{-2}, in 10 sec bursts. The thickness of material removed mechanically was about 10 μm and electrochemically about 8 μm. The grain size of the Cr was ~0.1 mm, elongated slightly in the rolling direction. Spectroscopically standardized oxygen (<70 vpm impurities) supplied by the Baker Chemical Company was employed.

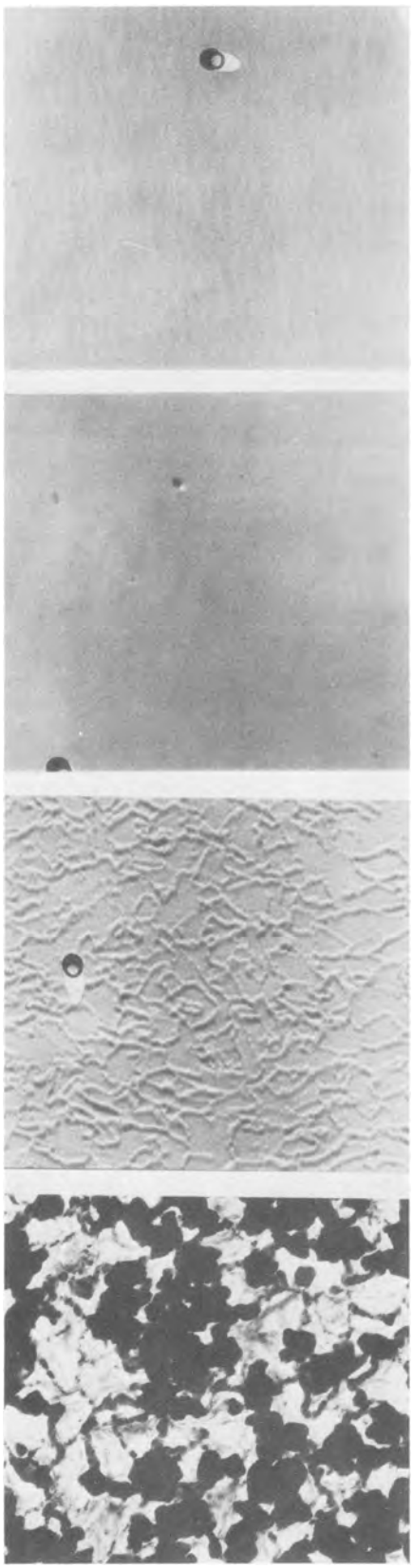


Fig. 1. Electron micrographs of oxide surface replicas. Top to bottom: (a) Replica of electropolished Cr prior to oxidation. (b) Replica of oxide grown in 150 sec at 330°C; $X = 50$Å. (c) Replica of oxide grown in 325 min at 400°C; $X = 115$Å. (d) Dry-stripped oxide grown in 395 min at 490°C; $X = 410$Å. All micrographs 30,000X; latex spheres are 910Å in diameter.

Results

Kinetics.—All kinetic experiments were carried out on samples which had already grown an oxide film during and after the electropolishing step. The thickness of this prior oxide film was measured by soft x-ray excitation (15) and found to be 16 ± 2Å. The only significant impurity was C at a concentration corresponding to ~1 monolayer. Examination of the film surface by replica transmission electron microscopy revealed the smooth, slightly rippled topography shown in Fig. 1a. Reflection electron diffraction revealed no structure at all. It is concluded that the prior oxide film is amorphous Cr_2O_3. Alessandrini and Brusic (12) estimated the thickness from ellipsometric measurements as 20 ± 4Å, while an earlier report (16) estimates the thickness of air-formed oxide as 15Å.

The rate of gas uptake at a pressure of 0.53 Pa and $300° \leq T \leq 600°C$ is shown in Fig. 2. Gas uptake has been converted to increase in average oxide film thickness on the assumption of a roughness factor equal to one and a Cr_2O_3 density of 5.25 g-cm^{-3}. The quantity plotted, X, is the actual film thickness, *i.e.*, the sum of the prior film thickness and the measured increase. The kinetics at all temperatures are characterized by an initial period of very rapid reaction followed by a much slower rate. This effect is shown more clearly in the semilogarithmic plots of Fig. 3 where an abrupt transition between the two regimes of kinetic behavior is apparent. As the temperature is increased, the transition occurs sooner but at greater film thicknesses. The

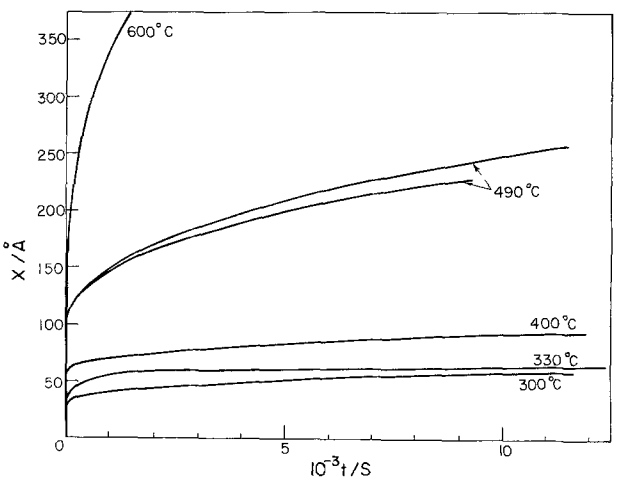


Fig. 2. Oxidation kinetics of chromium at $p = 0.53$ Pa. Oxygen uptake has been converted to average oxide film thickness as explained in text.

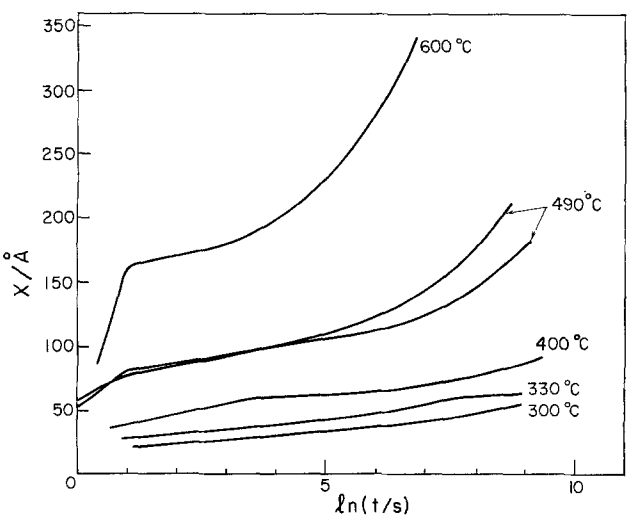


Fig. 3. Oxidation kinetics replotted to accentuate the kinetic transition.

Table I. Pretransition kinetics as described by the various rate equations

T/°C	Standard deviations in film thickness in A			
	Eq. [1]	Eq. [2]	Eq. [3]	Eq. [4]
300	3.2	2.4	2.1	2.0
330	2.6	1.7	1.4	1.5
363	2.1	1.6	0.8	0.8
400	1.6	2.3	0.6	0.6

two regimes will be referred to as pre- and posttransition.

Only at the lower temperatures are extensive data available for the early stage kinetics. Regression analysis has been performed on pretransition data obtained at temperatures up to 400°C for a logarithmic rate equation

$$X = A_1 + B_1 \ln (t + 1) \quad [1]$$

a parabolic rate equation

$$X = A_2 + B_2 t^{1/2} \quad [2]$$

and two modified (17) forms of the Mott-Cabrera rate equation

$$dX/dt = A_3 \sinh (B_3/X) \quad [3]$$

$$dX/dt = (A_4/X) \sinh (B_3/X) \quad [4]$$

where A and B are constants. A comparison of the resulting standard deviations in film thickness is shown in Table I and reveals that the best description is found in either Eq. [3] or [4]. Regression lines for Eq. [4] are shown in Fig. 4. Arrhenius plots for A_3 and A_4 were constructed and that for A_4 is shown in Fig. 5.

The posttransition kinetics are best described by a modified parabolic rate equation

$$X = k_p^{1/2}(t - t_T)^{1/2} + C \quad [5]$$

where k_p and C are constants, and t_T is the time at which the transition occurs between kinetic regimes and is determined from Fig. 3.

Data for the second stage kinetics are plotted according to Eq. [5] in Fig. 6. Parabolic rate constants found from Eq. [5] are displayed in an Arrhenius plot in Fig. 7. The activation energy is deduced therefrom to be 150 ± 13 kJ.

Morphology and structure.—In a series of experiments conducted at 330°C, samples were oxidized for different periods of time. Growth kinetics observed in these experiments are shown in Fig. 8 where the reproducibility is seen to be good. The thickness, morphology, and structure of the resultant oxide films were subsequently examined.

Average oxide thicknesses were determined by oxygen K_α x-ray excitation (15). Thicknesses determined in this way are plotted against net oxygen uptake (as

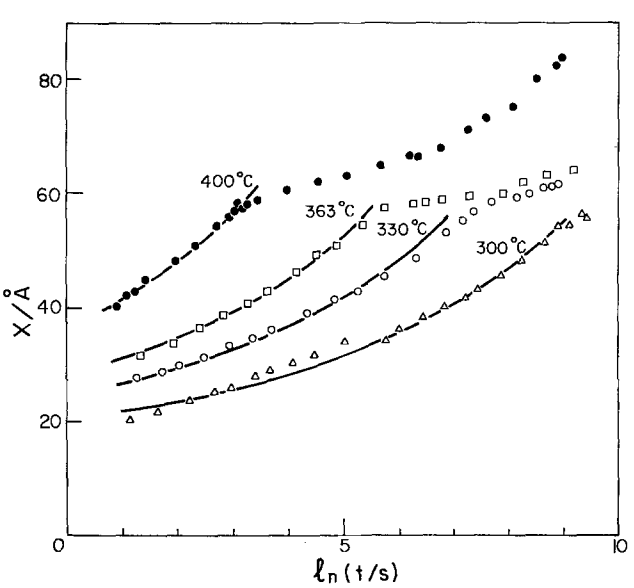


Fig. 4. Oxidation kinetics at low temperatures. Lines of best fit found from Eq. [4].

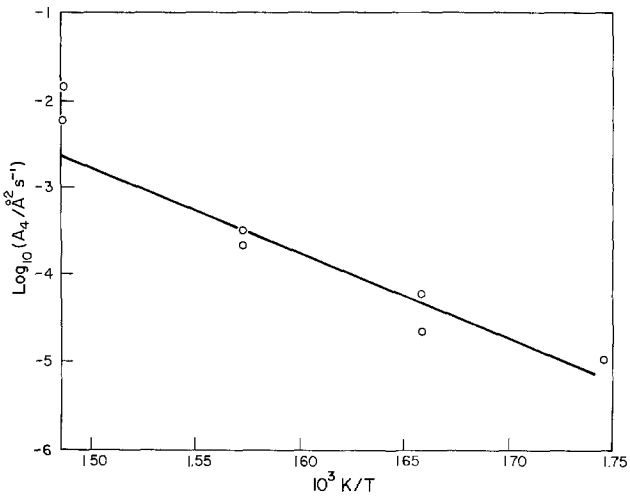


Fig. 5. Temperature dependence of parameter A_4

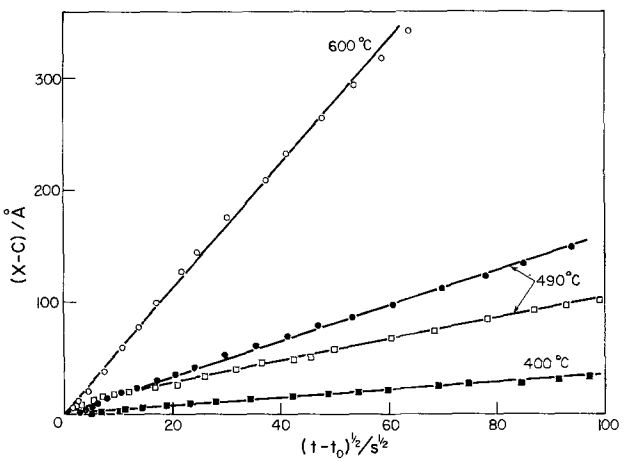


Fig. 6. Posttransition kinetics. Continuous lines are regression lines found from Eq. [5].

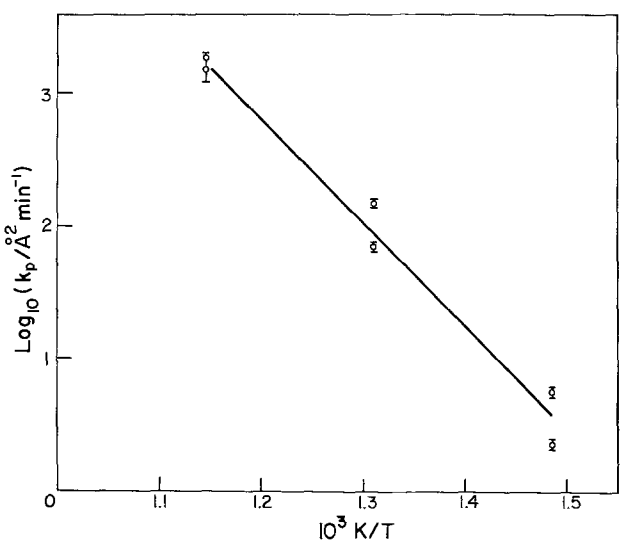


Fig. 7. Temperature dependence of posttransition parabolic rate constant, k_p.

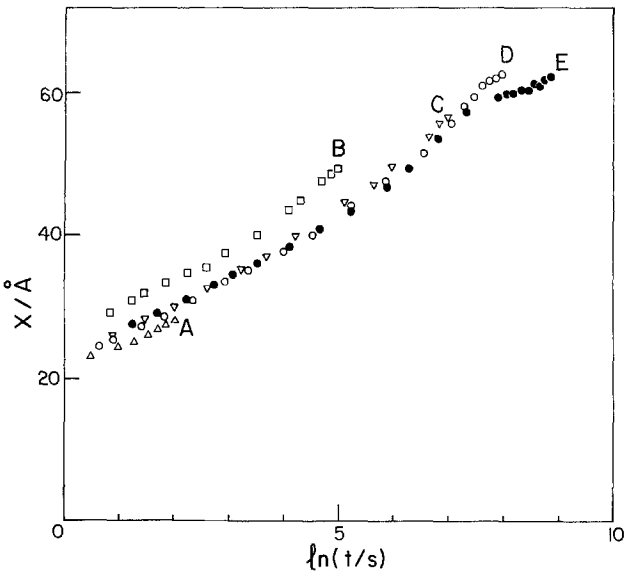


Fig. 8. Oxidation kinetics at 330°C interrupted after different periods of time. Letters identify samples subsequently used in electron diffraction experiments.

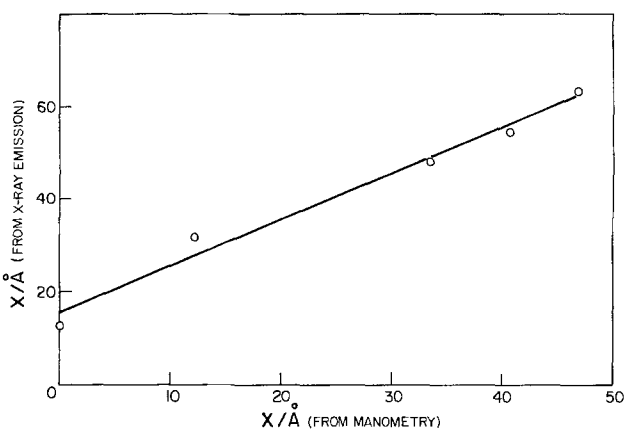


Fig. 9. Average oxide film thicknesses of samples shown in Fig. (8), as determined by O K_α x-ray excitation.

measured manometrically) in Fig. 9 where the linearity of the results is seen to be excellent. The straight line shown was found by regression, and corresponds to a prior air-formed oxide film thickness, X_o, of 16 ± 2Å.

RHEED patterns were obtained for a Cr sample which had been held at 330°C for 30 min in a dynamic vacuum and for oxidized samples for periods indicated as A-E in Fig. 8. The vacuum heat-treatment and the two short-term oxidation treatments, A and B, all produced structures which exhibited two diffuse halos attributable to Cr_2O_3. Each of samples C, D, and E produced the same diffuse spot pattern in which the diffuse spots changed to arcs as the extent of oxygen uptake increased (see Fig. 10 a-c). The pattern corresponds to two fiber orientations of Cr_2O_3: in one the (006) plane is parallel to the metal surface, in the other it is the (0.2.10) plane.

Thicker oxide films grown at higher temperatures were also examined. A film grown at 400°C to an average thickness of 50Å (*i.e.*, oxide growth was terminated in the pretransition region) yielded a diffuse halo pattern identical to the one found from samples oxidized in the pretransition region at 330°C. A RHEED pattern obtained from a 115Å film grown at 400°C is shown in Fig. 10d. The fiber orientations found at 330°C are again present although the arcs are now much broader. This orientation was preserved in all thicker oxide

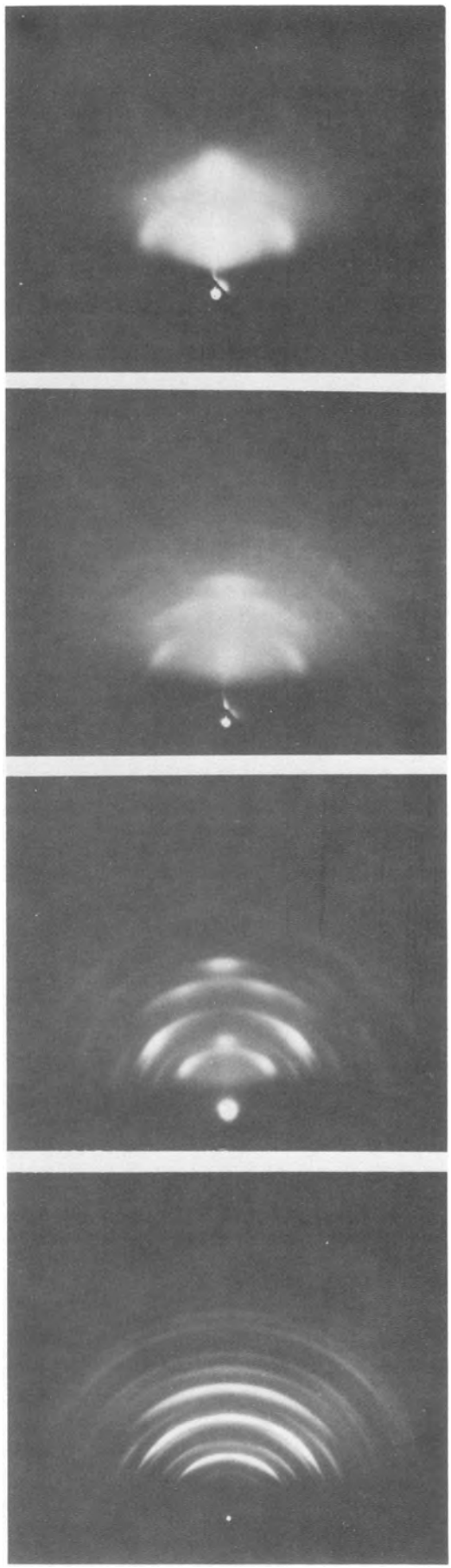


Fig. 10. Reflection high energy electron diffraction patterns. Top to bottom: (a) sample C of Fig. 8; (b) sample D of Fig. 8; (c) sample E of Fig. 8; (d) oxide grown at 400°C, X = 115Å.

films examined (up to $X \sim 1000$Å): the arcs became no broader and the only change observed was the development of higher order diffraction lines with increase in oxygen uptake.

Replica transmission micrographs showed all the oxide films produced at 330°C to have flat, featureless surfaces. An example is shown in Fig. 1b. A film grown at 400°C in the pretransition region had the same appearance. Another film grown at 400°C to an average thickness of 115Å is seen in Fig. 1c to have developed a structure of raised oxide ridges separated by regions of flat-surfaced oxide. A film of average thickness 395Å grown at 490°C was dry-stripped from the metal and a transmission micrograph is shown in Fig. 1d. The ridges seen at 400°C are again apparent and, in addition, thick nodules of oxide are now evident. The flat-surfaced oxide film which covers the metal between these features appears to be very thin.

For the reaction times used (up to 4 hr), the surface area fraction covered by ridges and nodules was approximately constant at a given temperature and varied from 0.5 at 400°C to 0.7 at 600°C. From a measurement of shadow lengths it was found that the thin portion of these posttransition oxide films accounted for <5% of the total oxygen uptake.

Discussion

The pretransition and posttransition domains of chromium oxidation behavior differ in their reaction rates, in kinetic functional form, in the activation energy of their kinetics, and in the morphology of the oxide film produced. It is evident that the two regions are characterized by different reaction mechanisms. They will therefore be discussed separately.

Pretransition kinetics.—Oxide films formed in the early stage reaction were found to possess a uniformly flat surface. The diffuse halo diffraction pattern which they yielded indicates a very fine grain structure. The film is therefore a close approximation to the theoretical model of a parallel-sided, essentially structureless oxide slab. Under these conditions and for the film thickness range in question ($X < 60$Å), the most generally useful kinetic theory of oxidation is that of Cabrera and Mott (18). This theory assumes that electronic equilibrium is established across the growing film. The resultant electrostatic potential drop across the film provides the driving force for transport of ionic defects through the film and hence for film growth. It may be shown (17) that space charge effects in such a system will generally be small. The expression for the rate of film thickening predicted by this model is

$$dX/dt = 4a\nu n_0 \Omega \exp(-U/kT) \sinh(|qa\phi|/kTX) \quad [6]$$

where Ω is the volume of oxide formed per ion, n_0 the concentration of mobile ionic defects at the interface at which they are generated, U the height of the activation barrier to their movement, a the activation distance, ν the attempt frequency on the barrier, q the charge on the ions, and ϕ the electrostatic potential drop across the film.

The evaluation of the quantity n_0 above has been treated elsewhere (17) via a steady-state kinetic approach in which n_0 is related to the surface concentration of species responsible for defect injection. In the case of metal interstitials, these latter species are taken to be metal atoms (concentration N cm^{-2}) at the metal-oxide interface, and in the case of transport by cation vacancies they are taken to be adsorbed anions (concentration σ cm^{-2}) residing on the gas-oxide interface. It seems likely that in the case of interstitials, n_0 is nearly independent of film thickness and is given by

$$n_0 \simeq [N \exp(-W/kT)]/2a \quad [7]$$

where W is the heat of solution of an interstitial cation. Combination of Eq. [6] and [7] leads to Eq. [3] with

$$A_3 = 2\Omega\nu N \exp[-(W+U)/kT] \text{ and } B_3 = |qa\phi|/kT \quad [8]$$

In the case of cation vacancy migration, no such simple relationship exists as σ_0 is proportional to $|\phi|/X$ and hence varies with film thickness. A general relationship between n_0 and σ_0 has been derived (17), but for present purposes it is sufficient to take the limiting case where X is small which leads to Eq. [4] with

$$A_4 = \Omega\nu\epsilon\phi [\exp(-Q/kT)]/2\pi q_0 \quad [9]$$

where ϵ is the dielectric constant of the oxide, Q is the height of the activation barrier to ionic movement at the oxide-gas interface, and q_0 is the charge on the surface adsorbed species.

In fitting kinetic data to Eq. [3] and [4], it has been assumed that ϕ is independent of X. It may be shown (17) that this is a reasonable approximation for $X >$ 20Å. The parameter values A_3, B_4, and A_4 derived from these fits are to be compared with the predictions of Eq. [8] and [9]. It will be assumed that the effective charge of the mobile ionic defect is ± 3 and an average value of $a = 1.47$Å will be adopted.

In principle, a value for ϕ may be calculated from an equilibrium adsorption model but the requisite thermodynamic data are lacking. However, surface potential measurements (10, 11) yield values of 2.1-2.4V at 25°C and at oxygen pressures between 1.3×10^{-3} and 13.3 Pa. Data fitting to Eq. [3] produce an estimate of 2.8 ± 0.8V, and to Eq. [4] of 2.4 ± 0.5V, both estimates being temperature independent. Since the potential drop is expected (17) to exhibit negligible temperature dependence, these values are in reasonable accord with the surface potential measurements. In view of the fact that the oxide thickness present during those measurements was unknown, the agreement is regarded as satisfactory.

Arrhenius plots for A_3 and A_4 yielded

$$A_3 = 2.21 \times 10^3 \exp[-177 \pm 24\,(\text{kJ})/RT] \text{cm sec}^{-1}$$

$$A_4 = 7.78 \times 10^{-5} \exp[-187 \pm 43\,(\text{kJ})/RT] \text{cm}^2 \text{sec}^{-1}.$$

Substituting the values $\Omega = 4.81 \times 10^{-23}$ cm^3, $\nu = 10^{12}$ sec^{-1}, $\phi = 2.4$V and the estimate $\epsilon = 5$ into Eq. [9] yields a value for the preexponential factor in A_4 of 6.4×10^{-4} cm^2 sec^{-1} on the assumption of singly charged adsorbed anions. Agreement with the empirical value is reasonable. Comparison of the theoretical expression and experimental value for A_3 results in an estimate of $N \simeq 5 \times 10^{13}$ cm^{-2}. This implies that about 5% of the surface metal atoms is in a position to enter the oxide if Eq. [3] represents the mechanism. Again, this is a reasonable result.

The activation energies deduced from the application of the two models are now considered. Since excess metal cations and cation vacancies are probably accommodated on the same sublattice in Cr_2O_3 (octahedral interstices in an approximately hexagonal close-packed array of oxygen), the activation energy for their movement will be the same. Self-diffusion data obtained (19, 20) at temperatures above 1100°C show an activation energy of 420 kJ. The very much lower value observed in the present work suggests that ionic motion is not occurring via sites in the Cr_2O_3 lattice but rather along favorable paths for transport through the film. The very small grain size of the oxide suggested by its diffuse diffraction pattern would provide a very high concentration of grain boundaries which would act as preferred transport paths. Under these conditions, it is not possible to distinguish between mass transport via excess cations or via cation vacancies.

Posttransition kinetics.—Films formed in the posttransition or parabolic growth stage are characterized by the existence of thick nodules and ridges of oxide separated by areas of very thin film. The oxygen uptake measured in this region is an approximate mea-

sure of the extent of growth of the nodules and ridges since the intervening film remains very thin. It follows that it is the nodules and ridges which grow according to parabolic kinetics. Since the surface area fraction occupied by nodules and ridges is approximately constant through the course of the reaction, the observed parabolic kinetics describe oxide thickening.

Parabolic kinetics can arise through diffusion under an activity gradient when local equilibrium is attained or, in the absence of local equilibrium, it can arise through migration under an electrostatic potential gradient. In the latter case which is expected to obtain in relatively thin films (18), the preexponential portion of the parabolic rate constant is given by $2\Omega_v s q a \phi / kT$ where s is the surface concentration of species responsible for defect injection, *i.e.*, either N or σ. Comparison with the quantity deduced from an Arrhenius plot yields $\phi s \simeq 1 \times 10^{11}$ V-cm^{-2}. As this is a reasonable result, the possibility of this model being applicable cannot be dismissed. Thus the kinetic measurements do not provide a basis on which to distinguish between diffusion under an activity gradient and migration in an electric field as the mode of mass transport.

The activation energy of 150 kJ found for the parabolic rate constant is much less than that for self-diffusion in Cr_2O_3 and is also less than the estimate of ~250 kJ found (5, 21) for oxidation at higher temperatures. It is concluded that preferred transport paths facilitate mass transport in the posttransition region of behavior also.

Structural development.—The transition between the two regions of kinetic behavior is accompanied by changes in the structure and morphology of the film. The initial fine-grained randomly oriented oxide begins to show preferred fiber texture at the time of the kinetic transition. During subsequent oxide growth this epitaxial relationship is preserved while the oxide grain size increases, as evidenced by the sharpening of the diffraction patterns and the appearance of higher order diffractions. Ridges and nodules of oxide are developed during this phase of growth.

During the pretransition period of growth, the very fine-grained structure provides a large number of grain boundaries which may serve as preferred transport paths. The density of these paths is so high that an approximately uniform film thickening results. This stage of oxidation terminates abruptly when the oxide undergoes a transformation. One of the products of this transformation is the very much more perfect fiber-oriented oxide seen in Fig. 10. Mass transport through this oxide will be much slower than along grain boundaries and oxide growth will virtually cease in the areas where this oxide covers the metal. It is therefore concluded that the thin film regions observed in posttransition oxides are areas of this more perfect oxide. Another product of the oxide transformation is polycrystalline oxide. The grain boundaries present in this material provide preferred pathways for mass transport. Thus metal ion transport and hence oxide growth will occur in the regions of polycrystalline oxide. Since these are localized, the development of oxide ridges and nodules is explained.

The transformation in oxide structure is explicable if the pretransition oxide is regarded as amorphous and therefore metastable. The provision of sufficient energy to the oxide will therefore bring about its crystallization. Although the present experiments do not reveal the source of this energy, we may surmise that stress within the growing oxide is the cause.

Summary

The oxidation kinetics of chromium show an abrupt transition between two distinct regions of behavior. The pretransition reaction proceeds according to the model of Mott and Cabrera. The evidence for this conclusion is as follows:

The kinetics of the reaction conform closely to those predicted by the model.

An assumption of the model is that electronic equilibrium is established across the growing film. The agreement between estimates for the potential drop across the film obtained from fitting kinetic data to the Mott-Cabrera equations and from independent, direct measurements of the quantity provides considerable support for the assumption.

The preexponential factors deduced from fitting data to the Mott-Cabrera model are in reasonable accord with those calculated from physical and system constants.

Posttransition kinetics are parabolic and reflect the growth of oxide ridges and nodules.

In both kinetic regimes, mass transport occurs via preferred paths through the film. In the pretransition regime the density of such paths is high, resulting in the growth of a uniform film. In the posttransition regime the density of grain boundaries is much lower, leading to the localized growth of ridges and nodules. The transition in kinetic behavior is ascribed to a transformation in oxide structure.

Manuscript submitted Nov. 1, 1976; revised manuscript received Jan. 24, 1977.

Any discussion of this paper will appear in a Discussion Section to be published in the December 1977 JOURNAL. All discussions for the December 1977 Discussion Section should be submitted by Aug. 1, 1977.

Publication costs of this article were assisted by the National Research Council of Canada.

REFERENCES

1. W. C. Hagel, *Trans. Am. Soc. Met.*, **56**, 583 (1963).
2. D. G. Barnes, J. M. Calvert, K. A. Hay, and D. G. Lees, *Philos. Mag.*, **28**, 1303 (1973).
3. J. Stringer, A. Z. Hed, G. R. Wallwork, and B. A. Wilcox, *Corros. Sci.*, **12**, 625 (1972).
4. D. Caplan, A. Harvey, and M. Cohen, *ibid.*, **3**, 161 (1963).
5. D. Caplan and G. I. Sproule, *Oxid. Met.*, **9**, 459 (1975).
6. E. A. Gubransen and K. F. Andrew, *This Journal*, **104**, 334 (1957).
7. S. Ekelund and C. Leygraf, *Surf. Sci.*, **40**, 179 (1973).
8. H. M. Kennet and A. E. Lee, *ibid.*, **33**, 377 (1972).
9. C. A. Haque and H. E. Farnsworth, *ibid.*, **1**, 378 (1964).
10. C. M. Quinn and M. W. Roberts, *Trans. Faraday Soc.*, **60**, 899 (1964).
11. W. A. Crossland and H. T. Roettgers, *Phys. Failure Electron.*, **5**, 158 (1966).
12. E. I. Alessandrini and V. Brusic, *J. Vac. Sci. Technol.*, **9**, 83 (1972).
13. G. A. Hope and I. M. Ritchie, *Thin Solid Films*, **34**, 111 (1976).
14. M. J. Graham and M. Cohen, *This Journal*, **119**, 879 (1972).
15. D. F. Mitchell and P. B. Sewell, *Thin Solid Films*, **23**, 109 (1974).
16. Gmelin, "Handbuch der Anorganische Chemie," Vol. 52B, 8th ed., Verlag Chemie GmbH, Weinheim, Germany (1962).
17. D. J. Young and M. J. Dignam, *J. Phys. Chem. Solids*, **34**, 1235 (1973).
18. N. Cabrera and N. F. Mott, *Rep. Prog. Phys.*, **12**, 163 (1948).
19. R. Lindner and Å. Åkerström, *Z. Phys. Chem. (N.F.)*, **6**, 162 (1956).
20. W. C. Hagel and A. U. Seybolt, *This Journal*, **108**, 1146 (1961).
21. P. Kofstad, "Nonstoichiometry, Diffusion, and Electrical Conductivity in Binary Oxides," p. 208, John Wiley & Sons, Inc., New York (1972).

Pressure Effects in the Oxidation of Chromium

D. J. Young* and M. Cohen*

National Research Council of Canada, Division of Chemistry, Ottawa, Ontario, Canada K1A 0R9

ABSTRACT

The effect of oxygen pressure in the range 5.3 × 10^{-2}-13.3 Pa on the oxidation kinetics of polycrystalline Cr was investigated at temperatures of 300°, 400°, 490°, and 600°C. Results were obtained by comparing reaction rates of samples oxidized at different pressures and also by observing the effect of abrupt changes in pressure during the course of a reaction. The two types of experiment yielded the same result. At 300°C the pressure exponent in the expression: rate $\propto p^r$, is small and positive, decreasing in magnitude with increasing film thicknesses. At T = 400°, 490°, and 600°C it was found that $r = -0.34 \pm 0.19$, -0.36 ± 0.10, and -0.40 ± 0.08, respectively. The positive pressure exponent at low temperature which accompanies thin film formation, is consistent with the Mott-Cabrera theory of oxidation, as modified to include adsorption equilibria. The negative pressure exponent, which accompanies parabolic kinetics, is described in terms of an adsorption model in which different adsorbed species are responsible for electrostatic field production and for point defect formation within the oxide.

It has been shown (1) that the oxidation of polycrystalline chromium in the range 300° ≤ T ≤ 600°C is characterized by an abrupt transition in kinetic behavior. The pretransition kinetics may be described with the aid of a Mott-Cabrera model (2, 3) which states that the rate is controlled by ion migration in an electric field

$$dX/dt = 4a\nu n_o\Omega \exp(-U/kT) \sinh(|qa\phi|/kTX) \quad [1]$$

where X is the average oxide film thickness, t the time, Ω the volume of oxide per ion, n_o the concentration of mobile ionic defects at the film interface at which they are generated, q their charge, U the activation energy for defect movement, a the activation distance, ν the kinetic frequency term, ϕ the potential drop across the oxide film, and k and T have their usual meanings. Posttransition kinetics are parabolic and are described by

$$X = k_p{}^{1/2} (t - t_T)^{1/2} + C \quad [2]$$

where t_T is the time at which the transition occurs between kinetic regimes, k_p and C are constants. Again, mass transport was deduced to be rate controlling but the possibilities of diffusion under a concentration gradient or ohmic conduction could not be distinguished.

The oxide morphology changes at the time of the transition in kinetic behavior (1). In the pretransition region a uniform film of oxide is formed whereas in the posttransition region oxide nodules and ridges grow, the intervening metal surface being covered by a thin, uniform oxide film. A diagrammatic cross section of the latter film is shown in Fig. 1. Since the fraction of total oxide accounted for by the regions of thin film is small it may be ignored and the approximation $X_n \propto X$ employed.

In order to probe further the nature of the oxidation mechanism, a study of the effect of oxygen pressure variation has now been made. Only one other study on chromium oxidation appears to have been reported for the presently considered temperature range. Hope and Ritchie (4) report a small, positive pressure effect within the range 250° ≤ T ≤ 450°C.

The results of pressure effect studies for both kinetic regimes are here reported. Pressure effects on posttransition kinetics were investigated at temperatures of 400°, 490°, and 600°C. For pretransition kinetics, experiments were carried out at 300°C.

* Electrochemical Society Active Member.

Key words: kinetics, adsorption, ion transport.

Experimental

High purity, polycrystalline chromium was oxidized in dry oxygen in the pressure range 5.3 × 10^{-2}-13.3 Pa and at temperatures of 300°, 400°, 490°, and 600°C. Kinetic measurements were made manometrically. Details of the technique and the materials used have been described previously (1).

Pressure effects on the reaction rate were investigated using two different methods. The first method was the standard one of oxidizing different Cr samples at different oxygen pressures. During the course of these experiments, the oxygen pressure was maintained within 10% of its nominal value except for the initial few seconds of an experiment when oxygen was being admitted to the reaction vessel and the pressure change was consequently very rapid. Due to the uncertainty arising from this initial period of ill-defined pressure, and also in order to investigate the possibility that pressure effects are dependent on the extent of reaction, an alternative technique was adopted.

In the second technique the oxygen pressure was altered rapidly to a new value during the course of a reaction. After a period of 20-40 min during which the reaction rate was measured, the pressure was again altered suddenly. Alternate increases and decreases in pressure were continued throughout the experiment, the higher pressure being from 10 to 40 times the lower value. Instrumental blanks were performed in which the sequence and duration of the different oxygen exposures were carefully duplicated. This technique of comparing reaction rates obtained in the course of a single experiment largely eliminates the difficulties commonly experienced in attempting to compare results obtained on different samples. However, the need to achieve a large number of pressure changes during the course of an experi-

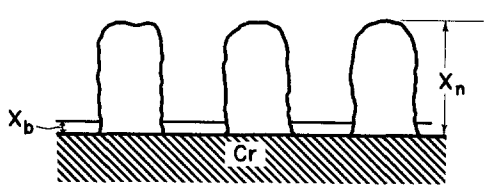


Fig. 1. Diagrammatic representation of a cross section of the oxide film formed in the posttransition reaction. The regions of thin film have a low density of favorable paths for transport whereas the thick nodules have a high density of such paths.

ment means that the periods of isobaric conditions are necessarily short. The precision with which the kinetics are measured is consequently lessened.

Results

Pretransition kinetics.—Isobaric experiments at 300°C showed the pressure effect to be smaller in absolute magnitude than the experimental errors. The reaction rate is very slow at this temperature and the reproducibility could not be improved enough to resolve any pressure effect with this technique. Pressure change experiments, however, revealed a small effect.

An increase in pressure during the course of a reaction at 300°C always caused an increase in rate and a decrease in pressure always caused a decrease in rate. If the kinetics of isobaric periods in this experiment are approximated as linear, then it is found that

$$\ln(R_1/R_2) = r \ln (p_1/p_2) \qquad [3]$$

where $R = dX/dt$, p is the oxygen pressure, and the subscripts 1 and 2 indicate successive periods of reaction. Values of r deduced therefrom are plotted as a function of X in Fig. 2. Experimental scatter is large but it may be concluded that r is small and positive, and decreases in magnitude with increasing X. A value of $r \simeq 0.35$ was found by Hope and Ritchie (4) at 300°C.

Posttransition kinetics.—Isobaric experiments were carried out at 400°, 490°, and 600°C. Parabolic rate constants were obtained from linear regression on Eq. [2] and are displayed as a function of oxygen pressure in the log-log plots of Fig. 3. From the empirical relationship

$$k_p = k_p' p^r \qquad [4]$$

where k_p' is a constant, it was found that at 600°C $r = -0.40 \pm 0.08$, and at 490°C $r = -0.36 \pm 0.10$. Data obtained at 400°C were of much lower quality and yielded $r = -0.34 \pm 0.19$.

Pressure change experiments confirmed that the pressure exponent is negative. Figure 4 shows the rate of oxygen uptake as affected by sudden changes in oxygen pressure at 600°C. It is evident that, after a short delay period, an increase in pressure always causes a decrease in rate and that a decrease in pressure always causes an increase in rate. This pattern of behavior was observed at 490°C also. The pressure effect produced by a sudden change in pressure was deduced from the reaction rates and pressures before and after the change as follows.

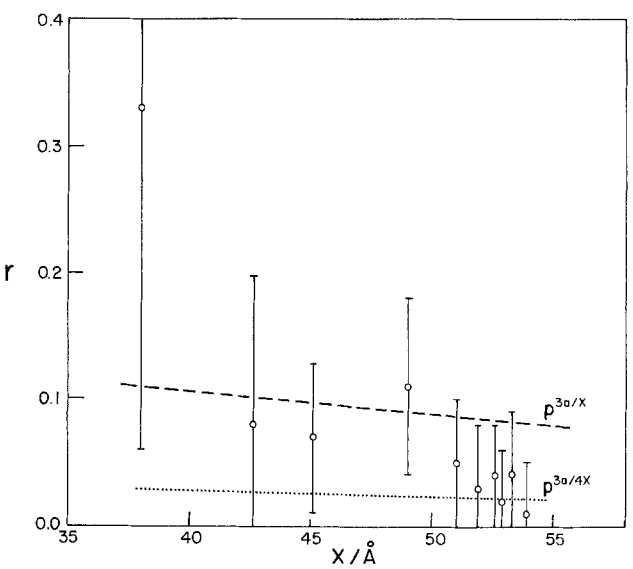


Fig. 2. Pressure exponent, r, as a function of oxide film thickness at 300°C. Also shown are pressure dependencies predicted from the Mott-Cabrera model of thin film oxidation where it has been assumed that $z = 3$ and that the predominant adsorbed species is O'' ($p^{3a/4X}$) or O_2' ($p^{3a/X}$).

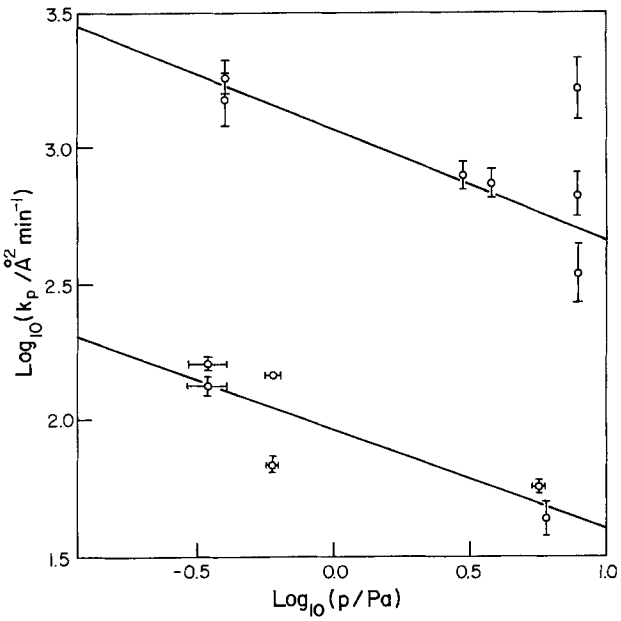


Fig. 3. Log-log plots for pressure dependence found from isobaric experiments at 600°C (upper line) and 490°C (lower line).

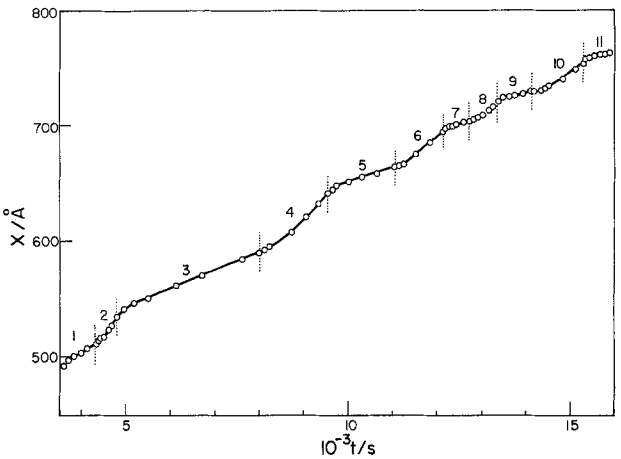


Fig. 4. Oxygen uptake with time at 600°C showing the effect of pressure changes. Numbers indicate the following pressures: 9.07, 8.5 × 10^{-1}, 8.93, 5.9 × 10^{-1}, 9.13, 6.0 × 10^{-1}, 9.07, 5.2 × 10^{-1}, 11.12, 5.1 × 10^{-1}, 12.23 Pa.

Substitution of [4] into [2] followed by differentiation yields for the reaction rate

$$R = \frac{dX}{dt} = \frac{k_p'}{2(X - C)} p^r \qquad [5]$$

Denoting by subscripts 1 and 2 the reaction before and after the pressure change, then, to a first approximation

$$\ln(R_1/R_2) = \ln[(\overline{X}_2 - C)/(\overline{X}_1 - C)] + r \ln(p_1/p_2) \qquad [6]$$

where the bars indicate average values for the periods of reaction concerned. For the short reaction periods employed, it was sufficient in evaluating dX/dt to approximate the rate as linear.

Values of the pressure exponent, r, found in this way are shown as a function of average oxide film thickness for temperatures of 600° and 490°C in Fig.

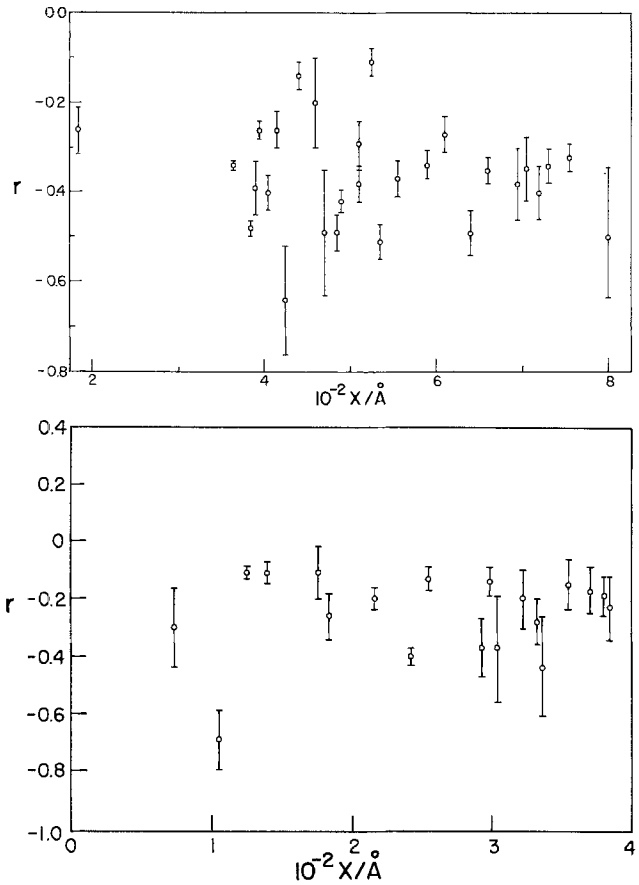


Fig. 5. Pressure exponent, r, as a function of average oxide film thickness at 600°C (upper graph) and 490°C (lower graph).

5. The results of several experiments have been summarized in this figure. Average values were found for r of -0.35 ± 0.12 at 600°C and -0.25 ± 0.14 at 490°C. These values are in reasonable accord with those deduced from the isobaric experiments. Data obtained at 400°C was again of lower quality, yielding $\bar{r} = -0.13 \pm 0.28$.

The thickness dependence of r was investigated by linear regression on the empirical equation

$$r = bX + c$$

where b and c are constants. Values of $b = (1.4 \pm 1.6) \times 10^{-4}$ and $(1.3 \pm 3.4) \times 10^{-4}$ Å^{-1} were found for data obtained at 600° and 490°C, respectively. It is therefore concluded that $r \neq f(X)$ at these temperatures.

Discussion

The previously deduced (1) mechanism for chromium oxidation of rate control by mass transport across the growing oxide film necessarily implies that both electron transport across the film and gas adsorption achieve equilibrium. Since pressure effects arise through the interaction of oxide and gas, these equilibria will now be examined.

Adsorption equilibria.—A description of adsorption equilibrium has been provided by Grimley and Trapnell (5) who considered the surface equilibria processes

$$\tfrac{1}{2}\,O_2(g) + S = O|S \qquad [7]$$

$$O|S + e' = O'|S \qquad [8]$$

$$O'|S + e' = O''|S \qquad [9]$$

where $O|S$ represents an adsorbed atom, together with the assumption of electron equilibrium across the growing oxide film

$$[e] = K_e \exp(-q_e\phi/kT) \qquad [10]$$

Here square brackets denote concentration, K_e is a constant, and q_e the electron charge. This model, together with the assumption of a fixed concentration, M, of surface adsorption sites, yields, to a close approximation (3), the results

$$[O'|S] = MK_7K_8K_ep^{1/2}[\exp(-q_e\phi/kT)]/(1 + K_7p^{1/2}) \qquad [11]$$

$$[O''|S] = [O'|S]K_9K_e \exp(-q_e\phi/kT) \qquad [12]$$

where K_7, K_8, K_9 are the equilibrium constants for the processes [7], [8], [9]. Substitution of [11] and [12] into Gauss' theorem

$$E = 4\pi|q_e|([O'|S] + 2[O''|S])/\epsilon \qquad [13]$$

where E is the electric field in the direction of metal transport and ϵ the oxide dielectric constant, together with the homogeneous field approximation

$$E = -\phi/X \qquad [14]$$

leads to an expression for ϕ. Two limiting cases are of interest: for $[O'|S] >> [O''|S]$ and $q_e\phi \gtrsim 4kT$

$$\exp(-q_e\phi/kT) = \frac{\epsilon kT(1 + K_7p^{1/2})}{4\pi(q_e)^2XMK_7K_8K_e\,p^{1/2}} \qquad [15]$$

whereas for $[O''|S] >> [O'|S]$ and $q_e\phi \gtrsim 4kT$

$$\exp(-q_e\phi/kT) = \left\{\frac{\epsilon kT(1 + K_7p^{1/2})}{16\pi(q_e)^2XMK_7K_8K_9(K_e)^2\,p^{1/2}}\right\}^{1/2} \qquad [16]$$

If adsorption involves the charged molecular species $O_2'|S$ and $O_2''|S$ then the required solutions are obtained by substituting p for $p^{1/2}$ in [11]-[16]. It is evident that at high coverages ($K_7p^{1/2} > 1$) no pressure dependence of ϕ is found. Accordingly, low coverages ($K_7p^{1/2} < 1$) will be assumed and Eq. [15] and [16] approximated accordingly.

Concentrations of adsorbed species are obtained by substitution from [15] or [16] (or the molecular oxygen analogues) into [11] and [12]. Examination of the various possibilities reveals an inverse p-dependence for the concentration of a species having more charge per atom than does the predominant adsorbed anion. Consider, for example, the case of $O'|S$ and $O''|S$, where $[O'|S] >> [O''|S]$ is assumed. An increase in p causes an increase in $[O'|S]$ and, according to Gauss' theorem, an increase in $|\phi|$. The concentration of free electrons obeys the Boltzmann distribution law and is therefore greatly reduced. The net result, as seen in Eq. [12], is a reduction in $[O''|S]$.

Pretransition kinetics.—The Mott-Cabrera model applies to the pretransition reaction and kinetics are described by Eq. [1]. The pressure dependence is therefore found from the way n_0 and ϕ are related to p. In the case of a metal excess oxide, defects originate at the metal-oxide interface and their concentration, n_0, is likely constant (3) and therefore pressure independent.

In the case of a metal deficit oxide, vacancy defects originate at the gas-oxide interface where they are formed in the region of a surface adsorbed anion species (3, 6). In the range of film thickness applicable to the pretransition region, injection of vacancies at the interface is likely rate controlling. A steady-state treatment (3) of this situation yields

$$n_0 = s/2a \qquad [17]$$

where s is the concentration of the particular surface anion species responsible for vacancy injection and is, in general, pressure dependent. In deriving [17] it has been assumed that the energy barrier to defect

movement across the interface is of the same height and width as the analogous barriers separating sites within the oxide lattice.

Pressure effects on reaction rate arising through the dependence of ϕ on p are found as follows. For small values of X the hyperbolic function in Eq. [1] may be approximated as

$$2\sinh(qa\phi/kTX) \simeq \exp(qa\phi/kTX) \qquad [18]$$

Substitution in [1] of [18] and [15] or [16] yields, for low surface coverages, pressure dependencies of the form

$$dX/dt = n_0 f(X) p^{za/lX} \qquad [19]$$

where $z = |q/q_e|$ and the value of l is characteristic of the predominant adsorbed anion species. For a metal excess oxide $n_0 \neq f(p)$ and the kinetic p-dependence is given directly by Eq. [19]. For a metal deficit oxide the p-dependence is found from Eq. [17] and [19] together with the appropriate expression for s given by the adsorption equilibria above. Results for both types of oxides are summarized in Table I.

Figure 2 shows a comparison of experimental results with the pressure dependencies $p^{3a/X}$ and $p^{3a/4X}$ where the value $a = 1.47$Å has been assigned. It is evident that the data can be described by any of the metal excess oxide models and by those of the metal deficit oxide models which involve as defect injecting anions and as predominant adsorbed anions species having the same number of electrons per atom. The other possibilities may be rejected. The only other model known to the authors which predicts a film thickness dependent pressure exponent is that of rate control by a surface ionization process (7) in which case

$$r = \frac{b}{X} - \tfrac{1}{2}$$

where b is an activation distance. This possibility must also be rejected.

It is therefore concluded that the pretransition reaction proceeds according to the Mott-Cabrera model as modified to include surface adsorption effects. The identity of the surface adsorbed species cannot, however, be determined.

Posttransition kinetics.—The oxide morphology characteristic of the posttransition regime is shown in Fig. 1 and it is to be noted that the nodules and ridges constitute ~95% of the total amount of oxide and cover *ca.* 50% of the surface. The observed kinetics, therefore, reflect the growth of these localized regions. The parabolic nature of the oxidation kinetics suggests that the reaction may be diffusion controlled. However, the Wagner model (8) of ambipolar diffusion coupled with local equilibrium cannot explain a negative pressure exponent. An alternative description is now proposed.

It was deduced earlier (1) that the posttransition oxide film shown in Fig. 1 consists of ridges and nodules of polycrystalline oxide separated by very thin film regions of a more perfect oxide. It was concluded that mass transport was confined to the grain boundaries of the polycrystalline oxide. It will now be assumed that electron equilibrium is achieved across the thin film portions of the oxide layer but not across the thick oxide nodules. In that case the adsorption equilibrium model employed above describes the concentration of species on the thin film surface. Assuming now that surface diffusion is rapid, it follows that the concentration of species adsorbed on the surface of nodules, where oxide growth is occurring, is also controlled by the electron equilibrium across the thin oxide film regions. Thus charge transfer between the underlying metal and the nodule surface occurs via the thin film region and subsequent surface diffusion of anions. Mass transport is assumed to occur via cation vacancy movement through the nodule. For the nodule thicknesses in question, the linear transport equation is appropriate

$$J = -D\frac{\partial n}{\partial x} - nu\frac{\partial \phi}{\partial x} \qquad [20]$$

Here J is the flux of defects having diffusion coefficient D and mobility u, and x is the position coordinate such that $x = 0$ at the oxide gas interface and $x = X$ at the oxide-metal interface. It may be shown (9) that for $|q\phi| \gtrsim 4kT$, the electrical potential gradient constitutes the major part of the driving force for ionic transport and Eq. [20] may be adequately approximated by

$$dX/dt = \Omega J = \Omega n_0 u|\phi|/X \qquad [21]$$

and parabolic kinetics are predicted.

The concentration of vacancies near the oxide gas interface, n_0, is found from the assumption of local equilibrium between adsorbed anions, $A^{m'}|S$, and the oxide

$$iA^{m'}|S = iS + jV^{mi'/j}Cr \qquad [22]$$

and hence

$$n_0 = K_{22}([A^{m'}|S]/[S])^{i/j} \qquad [23]$$

where the defect notation of Kroger and Vink (10) has been employed, and i and j serve to define the reaction stoichiometry. According to the postulate of rapid surface diffusion, the surface concentrations of species adsorbed on the nodules are proportional to those of species adsorbed on the thin film regions. Since the thickness of this film is practically constant, surface concentrations are a function of p but not of X. Substitution for n_0 in [21] from [23] and from the adsorption description of Eq. [11]-[16] yields the p-effect on the reaction. Results are summarized in Table II. As noted before, when the defect-producing species has more electrons per oxygen atom than

Table I. Values of pressure exponent, r, for low adsorption coverages and thin films

	Predominant adsorbed anion $O' \mid S$	$O'' \mid S$	$O_2' \mid S$	$O_2'' \mid S$
Metal excess oxide:	$\frac{za}{2X}$	$\frac{za}{4X}$	$\frac{za}{X}$	$\frac{za}{2X}$
Metal deficit oxide: Defect-injecting species				
$O' \mid S$	$\frac{za}{2X}$	$\frac{za}{4X} + \frac{1}{4}$	$\frac{za}{X} - \frac{1}{2}$	$\frac{za}{2X}$
$O'' \mid S$	$\frac{za}{2X} - \frac{1}{2}$	$\frac{za}{4X}$	$\frac{za}{X} - \frac{3}{2}$	$\frac{za}{2X} - \frac{1}{2}$
$O_2' \mid S$	$\frac{za}{2X} + \frac{1}{2}$	$\frac{za}{4X} + \frac{3}{4}$	$\frac{za}{X}$	$\frac{za}{2X} + \frac{1}{2}$
$O_2'' \mid S$	$\frac{za}{2X}$	$\frac{za}{4X} + \frac{1}{2}$	$\frac{za}{X} - 1$	$\frac{za}{2X}$

Table II. Values of pressure exponent, r, for posttransition kinetic model

Defect-injecting species	Predominant adsorbed anion $O' \mid S$	$O'' \mid S$	$O_2' \mid S$	$O_2'' \mid S$
$O' \mid S$	0	$\frac{i}{4j}$	$-\frac{i}{2j}$	0
$O'' \mid S$	$-\frac{i}{2j}$	0	$-\frac{3i}{2j}$	$-\frac{i}{2j}$
$O_2' \mid S$	$\frac{i}{2j}$	$\frac{3i}{4j}$	0	$\frac{i}{2j}$
$O_2'' \mid S$	0	$\frac{i}{2j}$	$-\frac{i}{j}$	0

does the predominant adsorbed anion, then the required negative pressure exponent results.

Comparison of experimental results with the predicted values for n shown in Table II yields estimates for i/j for the different cases. One reasonable possibility is the reaction

$$O''|S = S + O_o^x + V_{Cr}'' \quad [24]$$

together with either $O'|S$ or $O_2''|S$ as the predominant adsorbed anion species. The predicted pressure exponent is -0.5, in fair agreement with observation. However, independent evidence of the applicability of Eq. [24] is lacking.

In order to explain the change in pressure dependence which accompanies the transition in kinetics, it has been necessary to invoke a change in the nature of the surface equilibrium process. Since this transition is accompanied by a change in oxide structure (1), the requisite change in surface properties of the oxide may well be occurring, but no detailed description can as yet be formulated.

Summary

The pressure effects observed in the pretransition kinetic regime are in accord with the predictions of the Mott-Cabrera model thereby confirming the applicability of that model. However the data do not allow a distinction to be made between metal excess and metal deficit oxide.

The negative pressure exponent found in the posttransition kinetic regime is ascribed to an equilibrium process which is controlled by electron equilibrium across the thin portions of the film. Since these thin regions do not thicken appreciably during the posttransition reaction, the adsorption equilibrium is independent of time. The surface anions thus produced migrate rapidly to the surface of growing oxide nodules where they control the concentration of cation vacancies within the oxide. Nodule growth is controlled by conduction of these vacancies through the oxide and parabolic kinetics result.

Manuscript submitted Nov. 1, 1976; revised manuscript received Jan 24, 1977.

Any discussion of this paper will appear in a Discussion Section to be published in the December 1977 JOURNAL. All discussions for the December 1977 Discussion Section should be submitted by Aug. 1, 1977.

Publication costs of this article were assisted by the National Research Council of Canada.

LIST OF SYMBOLS

X	average oxide film thickness
t	time
a	activation distance for movement of cation defect in Cr_2O_3
ν	kinetic frequency term for cation defects
n	concentration of cation defects
Ω	volume of Cr_2O_3 per cation
U	activation energy barrier to cation movement in Cr_2O_3
k	Boltzmann's constant
q	charge on cation defect
ϕ	electrostatic potential drop across oxide films
k_p	parabolic rate constant
p	pressure of O_2
r	kinetic pressure exponent
S	oxide surface site
$A\|S$	species A adsorbed on S
e	electron
K	equilibrium constant
E	electrostatic field strength
ϵ	dielectric constant of oxide
q_e	charge on electron
M	total concentration of surface adsorption sites
s	concentration of surface anion species responsible for defect injection
z	effective valence of cation defect
D	self-diffusion coefficient for cation defect
u	mobility of cation defect
x	position coordinate within oxide film
J	flux of cation defects
V_{Cr}	vacancy on Cr site in Cr_2O_3
i, j	constants defining stoichiometry of defect injection equilibrium

REFERENCES

1. D. J. Young and M. Cohen, *This Journal*, **124**, 769 (1977).
2. N. Cabrera and N. F. Mott, *Rep. Prog. Phys.*, **12**, 163 (1948).
3. D. J. Young and M. J. Dignam, *J. Phys. Chem. Solids*, **34**, 1235 (1973).
4. G. A. Hope and I. M. Ritchie, *Thin Solid Films*, **34**, 111 (1976).
5. T. B. Grimley and B. M. W. Trapnell, *Proc. R. Soc. A*, **234**, 405 (1956).
6. N. Cabrera, *Philos. Mag.*, **40**, 175 (1949).
7. D. J. Young, *ibid.*, **31**, 953 (1975).
8. C. Wagner, in "Atom Movements," p. 153, A.S.M., Cleveland, Ohio (1951).
9. W. W. Smeltzer and D. J. Young, *Prog. Solid State Chem.*, **10**, 17 (1975).
10. F. A. Kroger and H. J. Vink, *Solid State Phys.*, **3**, 307 (1956).

Development of Sodium Contamination in Semiconductor Oxidation Atmospheres at 1000°C

Santos Mayo

Electronic Technology Division, Institute for Applied Technology, National Bureau of Standards, Washington, D.C. 20234

and William H. Evans

National Bureau of Standards, Physical Chemistry Division, Institute for Materials Research, Washington, D.C. 20234

ABSTRACT

The thermodynamic equilibria established in fused silica oxidation tubes operated at 1000°C are analyzed. Transparent fused silica tubes used for thermal oxidation of silicon contain about 10 ppm sodium impurity. At oxidation temperatures sodium diffuses in fused silica, evaporates into the oxidation ambient, and reacts with residual water contaminating the oxidation atmosphere. During the oxidation cycle enough sodium is incorporated into the growing oxide film to be detected later by capacitance measurements in metal oxide semiconductor (MOS) structures. Reactions taking place during currently used *in situ* furnace cleaning procedures are analyzed. Calculations indicate that the amount of sodium removed from the fused silica tube wall through chlorine or hydrogen chloride cleaning is substantial. The reaction rate is regulated by diffusion of sodium in the fused silica. The use of iodine and hydrogen iodide as cleaning agents is discussed.

Oxidation of silicon has been the subject of many investigations aimed at understanding metal oxide semiconductor (MOS) device instabilities caused by the action of mobile ion impurities localized in the oxide film (1). Test vehicles in the form of simple MOS capacitors built on silicon dioxide films 50-100 nm thick are frequently used to study ionic contamination in thermal silicon dioxide. The mobile ion density in the oxide film can be calculated from capacitance measurements after thermal cycles have been applied to the device (2).

Several contamination sources may contribute impurities to the oxide film. Due to their high natural abundance, alkali species are the most common impurities likely to contaminate silicon dioxide. Sodium, potassium, and lithium may cause ionic-type instabilities in the oxide. Sources of alkali contamination can be classified according to their origin as: (*i*) bulk and surface impurities already contained in the silicon wafer before oxidation, (*ii*) impurities introduced into the oxide film during silicon high temperature oxidation and annealing, and (*iii*) impurities introduced after oxidation through metallization (3).

Considerable research has been done to determine the presence of impurities in microelectronic process materials. Analytical techniques such as flame emission, atomic absorption, resonance fluorescence, neutron activation, and others have been used for trace contamination detection (4-6). Metallization of microelectronic devices has also received a great deal of attention regarding the introduction of ionic contamination in the oxide film from both the evaporation process used and contamination in the metal (7). These results show that impurities may be introduced through several processing steps and play a significant role in determining the electrical properties of the device.

During oxidation of silicon, sodium impurity contained in fused silica oxidation tubes evaporates from the tube wall into the oxidation ambient. In typical oxidation facilities, furnaces employing fused silica tubes are operated at about 1000°C (or 1300°K for the purpose of this paper). The oxidation atmosphere generally consists of pure dry oxygen flowing along the tube with laminar flow at about 4 cm^3/sec (equivalent to 0.5 std ft^3/hr). Transparent commercial fused silica tubes currently used for this purpose generally have an average sodium content of 10 ppm (8-9). Sodium in the tube bulk diffuses easily [diffusion coefficient in SiO_2: 2×10^{-6} cm^2/sec (10)] to the tube wall surface. This in turn causes the appearance of contamination in silicon dioxide films grown in the oxidation tube (11).

The purpose of this work is to study the oxidation atmosphere used to grow thermal silicon dioxide films as a source of sodium contamination introduced into the film during the growing cycle. The thermodynamic equilibria established in fused silica oxidation tube atmospheres at 1300°K were considered.

Reactions Occurring in Fused Silica Oxidation Tubes

The thermodynamics of sodium vaporization from sodium silicate-silica glasses has been previously studied in the temperature range of 1200°-2000°K where the equilibrium constant of the reaction $Na_2O \cdot SiO_2$ (in SiO_2) $\rightarrow 2Na(g) + \frac{1}{2} O_2(g) + SiO_2$ (c or glass) has been measured (12). Values of $K = p^2(Na) \cdot p^{1/2}(O_2)[\alpha(SiO_2)/\alpha(Na_2O \cdot SiO_2)]$ were reported for molar ratios of SiO_2 to Na_2O varying from 1.69:1 to 3.88:1, where the α's (activities) were expressed in terms of mole fractions. The results indicated Raoult law behavior was approximated in the higher ratio solutions. On this basis, extrapolation to larger ratios, *i.e.*, 10^5 (about 10 ppm sodium in the silica) leads to the value $K = 2.5 \times 10^{-19}$ at $T = 1300$°K. Using this value and thermodynamic data from Table VII we obtain $\Delta H°_{f298}(Na_2O \cdot SiO_2[10^{-5}$ mole fraction in SiO_2 gls]) $= -376.8$ kcal/mole. This value is in reasonably good agreement with the corresponding JANAF (13) value for $Na_2O \cdot SiO_2$(gls) of -373.2 kcal/mole. The difference between these values can be considered a measure of the solution effects, such as formation of $Na_2O \cdot x\ SiO_2$ species, and the difference between the properties of the simple compound as a glass and the same species in solution. For this reason the use

Key words: fused silica, oxidation furnace, semiconductor processing, silicon dioxide, thermal oxidation.

Table 1. Equilibrium atmosphere in fused silica dry oxidation tube at 1300°K. Sodium content in fused silica bulk is 10 ppm, oxygen at 1 atm.

	Reaction	K	p(atm)	N(cm^{-3})
[1]	$\frac{1}{2}O_2(g) \rightarrow O(g)$	1.76×10^{-7}	$p(O) = 1.76 \times 10^{-7}$	
[2]	$Na_2O \cdot SiO_2$ (in SiO_2) $\rightarrow Na_2O(g) + SiO_2(c)$	7.9×10^{-20}	$p(Na_2O) = 7.9 \times 10^{-25}$	
[3]	$Na_2O \cdot SiO_2$ (in SiO_2) $\rightarrow 2Na(g) + \frac{1}{2}O_2(g) + SiO_2(c)$	2.5×10^{-19}	$p(Na) = 1.6 \times 10^{-12}$	9×10^{6}
[4]	$Na_2O \cdot SiO_2$ (in SiO_2) $\rightarrow Na(g) + NaO(g) + SiO_2(c)$	9.1×10^{-20}		
[5]	$Na_2O(g) + \frac{1}{2}O_2(g) \rightarrow 2NaO(g)$	0.42	$p(NaO) = 5.7 \times 10^{-13}$	3.2×10^{6}
[6]	$Na_2O \cdot SiO_2$ (in SiO_2) $+ \frac{1}{2}O_2(g) \rightarrow 2NaO(g) + SiO_2(c)$	3.3×10^{-20}		

Total sodium density: 1.2×10^{7}

of the former value (−376.8 kcal/mole) derived from measurements (12) was preferred, assuming that any systematic errors in the calculations would be partially compensated.

A number of reactions take place in fused silica oxidation tubes operated at 1300°K. Table I shows the equilibrium[1] atmosphere resulting from 1 atm dry oxygen reacting with the tube wall. The partial pressure corresponding to atomic oxygen resulting from equilibrium dissociation of the oxygen molecule is shown through reaction [1][2] as $p(O) = 1.76 \times 10^{-7}$ atm indicating that reactions with atomic oxygen are not significant. The evaporation reactions [2], [3], and [4] show that sodium in the oxidation atmosphere is present as both atomic (Na) and molecular (Na_2O, NaO) species. Reaction [5] shows the conversion of Na_2O into NaO through interaction with oxygen. These results indicate that in a dry oxidation atmosphere atomic sodium is about three times more abundant than molecular sodium compounds. The total number of sodium atoms in the equilibrium oxidation atmosphere is 1.2×10^{7} cm^{-3} (both atomic and molecular species included).

Table II shows the equilibrium atmosphere resulting in fused silica oxidation tubes at 1300°K when water is added.[3] The reaction system [7] shows that water is more stable than OH by factors ranging from 20 to more than 100 times as humidity in the oxidation ambient increases. For increasing water content the most significant changes are seen in $p(Na_2(OH)_2)$ and p(NaOH) as resulting from reactions [8] through [11]. The sodium number density for 1 ppm water impurity goes to 3.3×10^{8} cm^{-3} or a factor 27 higher than the dry oxidation condition. If 30 ppm water is present in the oxidation ambient the sodium number density at equilibrium raises to 1.7×10^{9} cm^{-3} or a factor 142 higher than the dry oxidation condition. Table III and Fig. 1 summarize these results.[4]

The above calculations show that sodium contamination developed in oxidation atmospheres could be explained in terms of contamination in the bulk fused silica even if the furnace tube wall surface were perfectly clean. To reduce sodium density in oxidation atmospheres, it is necessary that the bulk tube material itself be sodium free. Two different approaches have been tried: (*i*) use of a sodium-free tube wall, or (*ii*) use of sodium-leaching agents to deplete a region just under the inner wall surface prior to oxidations. The first approach is based on the well-known fact that polycrystalline silicon tubes can be produced with 1000 times less sodium content than found in silica tubes (17). Empirical results indicate that oxide films grown on silicon using recently installed silicon oxidation tubes produce cleaner films (lower sodium content) than similar oxides prepared in fused silica tubes.

Polycrystalline silicon tubes develop, however, observable sodium contamination after being in operation for several months, when the use of sodium-leaching agents is then required. This contamination, developed under strictly controlled production-oriented environments, could be explained by assuming that during tube operation at oxidation temperature sodium arising from external sources reaches the oxidation chamber by diffusion through the tube wall. The contamination source could be located in furnace refractories surrounding the oxidation tube (11). Once the tube wall becomes loaded with sodium above a critical level, evaporation into the oxidation atmosphere starts to predominate. This is a slow process that may take a long time (several months) in continuous operation depending on environmental conditions (18).

Reactions Occurring When Cleaning Fused Silica Tubes

Cleaning of oxidation tubes is a frequent operation in processing facilities. At room temperature, the clean-

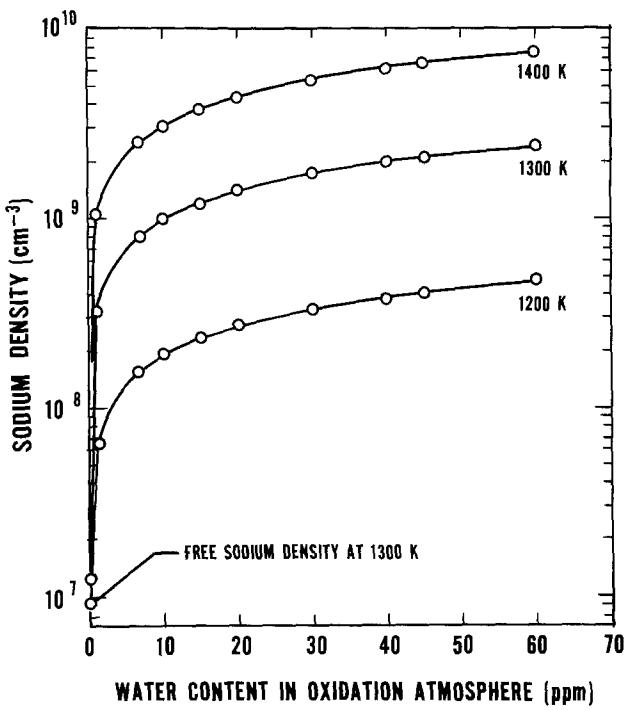


Fig. 1. Total sodium density [cm^{-3}] at equilibrium in fused silica oxidation tube atmosphere as a function of temperature and water impurity. The sodium concentration in silica is assumed 10 ppm, $p(O_2)$ is 1 atm.

[1] All calculated values presented in this work refer to equilibrium conditions and represent limiting values for the actual systems because of kinetic and diffusion factors.

[2] Data used to calculate reaction equilibrium constants are listed in Table VII. The actual calculation scheme is illustrated in the Appendix.

[3] Experimental evidence shows that in a typical "dry" oxidation atmosphere the water content is in the 20-30 ppm range (14). Moreover at oxidation temperatures in the range 900°-1300°C it was reported that water and/or hydrogen from the external ambient can diffuse through the silica tube wall into the oxidation chamber (15).

[4] Because of errors and approximations involved in thermodynamic data used to evaluate the equilibrium results, an absolute error of ±50% could be expected in these calculations. The relative error is much smaller. Resonance fluorescence measurements showed that in open fused silica oxidation tubes no free sodium was detected (16). This experimental result can be understood in terms of calculations shown in Fig. 1. For sufficiently high water content in the oxidation atmosphere the amount of free sodium detectable through resonance fluorescence technique could be substantially reduced due to sodium reactivity with excess water. Thus, free sodium is converted into compound sodium and consequently becomes not detectable by the above-mentioned technique.

Table II. Equilibrium atmosphere in fused silica oxidation tube at 1300°K. Sodium content in fused silica bulk is 10 ppm, oxygen at 1 atm.

	Reaction	K	Water content in oxygen:1 ppm		Water content in oxygen:30 ppm	
			p(atm)	N(cm^{-3})	p(atm)	N(cm^{-3})
[1]	$\frac{1}{2}\,O_2(g) \rightarrow O(g)$	1.76×10^{-7}	$p(O) = 1.76 \times 10^{-7}$		$p(O) = 1.76 \times 10^{-7}$	
[2]	$Na_2O \cdot SiO_2$ (in SiO_2) $\rightarrow Na_2O(g) + SiO_2(c)$	7.9×10^{-26}	$p(Na_2O) = 7.9 \times 10^{-25}$		$p(Na_2O) = 7.9 \times 10^{-25}$	
[3]	$Na_2O \cdot SiO_2$ (in SiO_2) $\rightarrow 2Na(g) + \frac{1}{2}\,O_2(g) + SiO_2(c)$	2.5×10^{-19}	$p(Na) = 1.6 \times 10^{-12}$	9×10^{6}	$p(Na) = 1.6 \times 10^{-12}$	9×10^{6}
[4]	$Na_2O \cdot SiO_2$ (in SiO_2) $\rightarrow Na(g) + NaO(g) + SiO_2(c)$	9.1×10^{-26}				
[5]	$Na_2O(g) + \frac{1}{2}\,O_2(g) \rightarrow 2NaO(g)$	0.42				
[6]	$Na_2O \cdot SiO_2$ (in SiO_2) $+ \frac{1}{2}\,O_2(g) \rightarrow 2NaO(g) + SiO_2(c)$	3.3×10^{-20}	$p(NaO) = 5.7 \times 10^{-13}$	3.2×10^{6}	$p(NaO) = 5.7 \times 10^{-13}$	3.2×10^{6}
[7]	$H_2(g) \rightarrow 2H(g)$	1.2×10^{-32}	$p(H) = 3 \times 10^{-13}$		$p(H) = 1.7 \times 10^{-12}$	
	$H_2O(g) \rightarrow H(g) + OH(g)$	1.54×10^{-14}	$p(H_2) = 8 \times 10^{-14}$		$p(H_2) = 2.4 \times 10^{-12}$	
	$2H_2O(g) \rightarrow H_2(g) + 2\,OH(g)$	2×10^{-16}	$p(OH) = 5 \times 10^{-8}$		$p(OH) = 2.7 \times 10^{-7}$	
	$H_2O(g) + \frac{1}{2}\,O_2(g) \rightarrow 2\,OH(g)$	2.5×10^{-9}	$p(H_2O) = 10^{-4}$		$p(H_2O) = 3 \times 10^{-5}$	
[8]	$Na_2O \cdot SiO_2$ (in SiO_2) $+ H_2O(g) \rightarrow 2NaO(g) + H_2(g) + SiO_2(c)$	2.8×10^{-27}	$p(NaO) = 5.7 \times 10^{-13}$		$p(NaO) = 5.7 \times 10^{-13}$	
[9]	$Na_2O \cdot SiO_2$ (in SiO_2) $+ H_2O(g) \rightarrow Na_2(OH)_2(g) + SiO_2(c)$	1.5×10^{-3}	$p(Na_2(OH)_2) = 1.5 \times 10^{-20}$	3.2×10^{8}	$p(Na_2(OH)_2) = 4.5 \times 10^{-19}$	
[10]	$Na_2O \cdot SiO_2$ (in SiO_2) $+ H_2O(g) \rightarrow 2NaOH(g) + SiO_2(c)$	3.1×10^{-30}	$p(NaOH) = 5.6 \times 10^{-11}$		$p(NaOH) = 3 \times 10^{-10}$	1.7×10^{9}
[11]	$NaO(g) + H_2O(g) \rightarrow NaOH(g) + OH(g)$	4.7				
			Total sodium density: 3.3×10^{8}		Total sodium density: 1.7×10^{9}	

ing can be accomplished using conventional acid solutions. At oxidation temperatures, the cleaning is made *in situ* by using 5-10% chlorine or hydrogen chloride diluted in an inert gas carrier. This treatment removes sodium contained in the tube inner "skin" down through a convenient depth. A typical cleaning action of this kind requires up to 20 hr of continuous treatment flushing the cleaning gas at about 4 cm^3/sec (0.5 std ft^3/hr). The several reactions taking place during this process are summarized in Table IV.

Reactions [16], [17], and [18] are solved as a simultaneous system. The resulting sodium number density at equilibrium in the tube atmosphere goes to 8.8×10^{16} cm^{-3} or a factor 7.3×10^{9} higher than the equilibrium sodium number density in a dry oxidation atmosphere. Reactions [16], [19], and [20] show similar results due to hydrogen chloride cleaning. The increase in sodium number density with respect to the dry oxidation condition is also in the 10^9 range. Microdroplets of liquid sodium chloride, if formed on the tube wall hot zone, would be removed by the gas stream and transported to a cooler tube zone where sodium chloride precipitates on the wall (sodium chloride melts at 801°C). This "transpiration mechanism" continues while sodium in the hot zone is available for reaction. It should be mentioned that sodium chloride formed in the gas phase is carried down the flushing gas stream and condenses also at the cooler zone where the temperature is appropriate. The cleaning action can be interpreted in terms of relocating sodium in the tube, depleting the hot zone, and enriching the exhaust tube end where the wall temperature is appropriate for condensation.

Stoichiometric equilibria in reactions [17] through [20] require the use of about 1.5g of chlorine or hydrogen chloride per gram of extracted sodium. Assuming that the oxidation tube wall surface is about 4000 cm^2 and the reaction depth in the wall is 10^{-3} cm, the total reacting volume is 4 cm^3 or about 10g fused silica. Assuming 10 ppm sodium content in the fused silica, the amount of sodium reacting is 10^{-4}g which requires the use of 1.5×10^{-4}g of chlorine or hydrogen chloride for complete reaction equilibrium. The density of 10% chlorine at 1300°K is 6.74×10^{-5} g/cm^3. At 4 cm^3/sec flow, the chlorine mass transported through the oxidation tube is 2.7×10^{-4} g/sec. This shows that the reaction rate is regulated by diffusion of sodium in the fused silica. When sodium in the wall bulk diffuses to the wall surface, the reaction with chlorine takes place immediately. In practice, a cleaning period of about 20 hr is used to deplete the tube wall. The longer the cleaning period, the longer the oxidation tube can later be operated under acceptable oxide growing conditions. These calculations indicate that the amount of sodium removed from the fused silica tube wall through chlorine or hydrogen chloride cleaning is substantial and that such cleaning certainly reduces the sodium content in the inner tube wall surface.

Iodine or hydrogen iodide can also be used for *in situ* oxidation tube cleaning. The relevant reactions taking place are summarized in Table V. Reactions [25] through [28] show the effectiveness of this type of cleaning indicating that iodine or hydrogen iodide could be used instead of chlorine or hydrogen chloride. However, due to economic reasons, the latter are more extensively used in practice. Since thermodynamic data are not available to the desired extent, similar calculations are not presented here for bromine and hydrogen bromide. However, bromine should have an intermediate behavior between chlorine and iodine according to the pattern of the members of the halogen family.

Table III. Equilibrium sodium densities in fused silica oxidation ambient at 1300°K. Oxygen at 1 atm.

Compound	Water content in oxygen: 0		Water content in oxygen: 1 ppm		Water content in oxygen: 30 ppm	
	p(atm)	N(cm^{-3})	p(atm)	N(cm^{-3})	p(atm)	N(cm^{-3})
Na	1.6×10^{-12}	9×10^{6}	1.6×10^{-12}	9×10^{6}	1.6×10^{-12}	9×10^{6}
NaO	5.7×10^{-13}	3.2×10^{6}	5.7×10^{-13}	3.2×10^{6}	5.7×10^{-13}	3.2×10^{6}
Na_2O	7.9×10^{-25}	—	7.9×10^{-25}	—	—	—
NaOH	—	—	5.6×10^{-11}	3.2×10^{8}	3×10^{-10}	1.7×10^{9}
$Na_2(OH)_2$	—	—	1.5×10^{-20}	—	4.5×10^{-19}	—
Sodium number density		1.2×10^{7}		3.3×10^{8}		1.7×10^{9}

Table IV. Equilibrium reactions in fused silica tubes at 1300°K when cleaning with 10% Cl_2 or HCl in N_2 carrier at 1 atm.

	Reaction	K	p(atm)	N(cm^{-3})
[12]	$Cl_2(g) \rightarrow 2Cl(g)$	1.6×10^{-4}	$p(Cl) = 4 \times 10^{-3}$ $p(Cl_2) = 9.8 \times 10^{-2}$	
[13]	$HCl(g) \rightarrow H(g) + Cl(g)$	1×10^{-12}	$p(HCl) \cong 0.1$ $p(Cl) = 3.2 \times 10^{-7}$	
[14]	$HCl(g) \rightarrow \frac{1}{2} H_2(g) + \frac{1}{2} Cl_2(g)$	7.5×10^{-5}	$p(Cl_2) = 7.5 \times 10^{-6}$	
[15]	$NaCl(l) \rightarrow NaCl(g)$	1.25×10^{-2}	$p(NaCl) = 1.25 \times 10^{-2}$	(vapor pressure)
[16]	$2NaCl(g) \rightarrow Na_2Cl_2(g)$	27.1	$p(NaCl) = 1.01 \times 10^{-2}$	5.7×10^{16}
[17]	$Na_2O \cdot SiO_2$ (in SiO_2) + $Cl_2(g) \rightarrow 2NaCl(g) + \frac{1}{2} O_2(g) + SiO_2(c)$	6.4	$p(Na_2Cl_2) = 2.76 \times 10^{-3}$	3.1×10^{16}
[18]	$Na_2O \cdot SiO_2$ (in SiO_2) + $Cl_2(g) \rightarrow Na_2Cl_2(g) + \frac{1}{2} O_2(g) + SiO_2(c)$	174	$p(O_2) = 3.9 \times 10^{-3}$ Sodium number density	8.8×10^{16}
[16]	$2NaCl(g) \rightarrow Na_2Cl_2(g)$	27.1	$p(NaCl) = 4.1 \times 10^{-3}$	2.3×10^{16}
[19]	$Na_2O \cdot SiO_2$ (in SiO_2) + $2HCl(g) \rightarrow 2NaCl(g) + H_2O(g) + SiO_2(c)$	0.42	$p(Na_2Cl_2) = 4.6 \times 10^{-4}$	5.2×10^{15}
[20]	$Na_2O \cdot SiO_2$ (in SiO_2) + $2HCl(g) \rightarrow Na_2Cl_2(g) + H_2O(g) + SiO_2(c)$	11.4	$p(H_2O) = 2.5 \times 10^{-3}$ Sodium number density	2.8×10^{16}

Table V. Equilibrium reactions in fused silica tubes at 1300°K when cleaning with 10% I_2 or HI in N_2 carrier at 1 atm.

	Reaction	K	p(atm)	N(cm^{-3})
[21]	$\frac{1}{2} I_2(g) \rightarrow I(g)$	0.467	$p(I) = 1.0 \times 10^{-1}$ $p(I_2) = 4.5 \times 10^{-2}$	
[22]	$2HI(g) \rightarrow H_2(g) + I_2(g)$	0.0501	$p(I) = 3.57 \times 10^{-2}$ $p(I_2) = 5.8 \times 10^{-3}$	
[23]	$2HI(g) \rightarrow H_2(g) + 2I(g)$	0.0109	$p(H_2) = 2.36 \times 10^{-2}$ $p(HI) = 5.22 \times 10^{-2}$	
[24]	$NaI(l) \rightarrow NaI(g)$	7.06×10^{-2}	$p(NaI) = 7.06 \times 10^{-2}$ *	(vapor pressure)
[25]	$Na_2O \cdot SiO_2$ (in SiO_2) + $I_2(g) \rightarrow 2NaI(g) + \frac{1}{2} O_2(g) + SiO_2(c)$	9.3×10^{-5}		
[26]	$Na_2O \cdot SiO_2$ (in SiO_2) + $2I(g) \rightarrow 2NaI(g) + \frac{1}{2} O_2(g) + SiO_2(c)$	4.3×10^{-4}	$p(NaI) = 9.3 \times 10^{-5}$ * Sodium number density	5.3×10^{14}
[27]	$Na_2O \cdot SiO_2$ (in SiO_2) + $2I(g) + H_2(g) \rightarrow 2NaI(g) + H_2O(g) + SiO_2(c)$	4.9×10^{3}		
[28]	$Na_2O \cdot SiO_2$ (in SiO_2) + $2HI(g) \rightarrow 2NaI(g) + H_2O(g) + SiO_2(c)$	54.2	$p(NaI) = 1.4 \times 10^{-2}$ * Sodium number density	7.9×10^{16}

* $p(Na_2I_2)$ can be estimated about 0.5 p(NaI) from similar results obtained with the chlorine system. No thermodynamic data are available for Na_2I_2.

The Oxidation Atmosphere as a Sodium Contamination Source

An experimental test was made to check the validity of assuming that sodium becomes trapped in an oxidation tube due to the evaporation-transpiration-condensation cycle mentioned above. In a fused silica tube operated at 1000°C "dry" oxygen[5] was allowed to flow at a rate of 4 cm^3/sec for 120 hr. The exhaust gas was passed through a 5% hydrochloric acid solution. After this period the solution was analyzed by flame emission spectrometry. The detection limit for sodium in the solution was 10^{-10} g/cm^3. No evidence of sodium was detected in the solution after correcting for evaporation of the liquid. This test was repeated twice with consistently negative results. Consequently, it was concluded that sodium is not carried out of the oxidation tube.

There is no apparent way of extracting from a furnace tube a representative sample of the oxidation atmosphere. Other analytical techniques operating on gas samples removed from the oxidation atmosphere, such as mass spectrometry, are not appropriate to detect sodium due to condensation as the temperature decreases. On the other hand, any analytical instrumentation if introduced into the oxidation tube could change the oxidation atmosphere equilibrium adding extra contamination, thus perturbing the measurements.

[5] Electronic grade oxygen typically contains about 5 ppm water and 20 ppm hydrocarbons measured as methane.

Contamination of Thermally Grown Silicon Dioxide Films

The results of Tables I and II indicate that in typical fused silica oxidation tubes the equilibrium atmosphere contains atomic and molecular sodium species resulting in a sodium number density in the 10^7-10^9 cm^{-3} range, depending on the amount of water present. Due to the low density, sodium atoms and molecules contained in the oxidation ambient can be considered as ideal gases. The number of collisions per unit time sodium executes per unit area on the wafer surface is expressed as (19)

$$\nu = 0.25\, Nv$$

where N is the sodium number density in the oxidation atmosphere, $v = (8\ kT/\pi m)^{1/2}$ is the average molecular velocity at temperature T, k is the Boltzmann constant, and m is the weight of the sodium species. The resulting value of ν for $T = 1300$°K is 10^{12} cm$^{-2} \cdot$ sec^{-1} for $N = 5 \times 10^7$ cm^{-3}. The presence of oxygen (1 atm) in the tube slightly modifies this number due to collisions with sodium atoms and molecules.

A number of reactions can take place between the growing silicon dioxide film and the impinging sodium molecules as shown in Table VI. Sodium silicate is formed by reactions [29] through [35] which have high equilibrium constants. As sodium from the oxidation atmosphere becomes incorporated into the oxide

Table VI. Impurity reactions with SiO_2 films in fused silica oxidation tube atmospheres at 1300°K

	Reaction	K
[1]	$\frac{1}{2}O_2(g) \rightarrow O(g)$	1.76×10^{-7}
[7]	$H_2(g) \rightarrow 2H(g)$	1.2×10^{-12}
	$H_2O(g) \rightarrow H(g) + OH(g)$	1.54×10^{-14}
	$2H_2O(g) \rightarrow H_2(g) + 2\,OH(g)$	2×10^{-16}
	$H_2O(g) + \frac{1}{2}O_2(g) \rightarrow 2\,OH(g)$	2.5×10^{-9}
[29]	$Na_2O(g) + SiO_2(c) \rightarrow Na_2O \cdot SiO_2$ (in SiO_2)	1.3×10^{19}
[30]	$2Na(g) + \frac{1}{2}O_2(g) + SiO_2(c) \rightarrow Na_2O \cdot SiO_2$ (in SiO_2)	4×10^{18}
[31]	$Na(g) + NaO(g) + SiO_2(c) \rightarrow Na_2O \cdot SiO_2$ (in SiO_2)	1.1×10^{19}
[32]	$2NaO(g) + SiO_2(c) \rightarrow Na_2O \cdot SiO_2$ (in SiO_2) $+ \frac{1}{2}O_2(g)$	3×10^{19}
[33]	$2NaO(g) + H_2(g) + SiO_2(c) \rightarrow Na_2O \cdot SiO_2$ (in SiO_2) $+ H_2O(g)$	3.6×10^{26}
[34]	$Na_2(OH)_2 + SiO_2(c) \rightarrow Na_2O \cdot SiO_2$ (in SiO_2) $+ H_2O(g)$	6.7×10^{8}
[35]	$2NaOH(g) + SiO_2(c) \rightarrow Na_2O \cdot SiO_2$ (in SiO_2) $+ H_2O(g)$	3.2×10^{9}

film, more sodium from the tube wall evaporates into the atmosphere, maintaining the equilibrium.

There are not enough kinetic data available to estimate precisely the actual amount of sodium incorporated into the silicon dioxide film during the oxidation cycle. The typical dry oxidation period used to grow a 100 nm thick oxide film on a (100) sample of silicon at 1000°C is about 200 min. During this period the oxide film is subjected to about 10^{16} sodium collisions per square centimeter. Parameters such as the wafer temperature, oxygen flow, and the water content in the tube certainly influence the oxide film contamination level. At equilibrium, the sodium concentration in the oxide film grown on silicon should be similar to that in the oxidation tube wall bulk, *i.e.*, 10 ppm ($\sim 10^{17}$ cm^{-3}). This consideration clearly establishes that dry oxidation of silicon made in fused silica tubes produces oxide films with a significant amount of sodium included; the upper limit is determined by the impurity level in the fused silica bulk. Whether or not this sodium which has chemically reacted with silica to form sodium silicate in the film (Table VI) influences the electrical and radiation properties of MOS devices is a matter that needs detailed examination.

It has been reported that structurally included sodium atoms in silicon dioxide films behave like immobile ionic contamination. Capacitance measurements on MOS capacitors with a dielectric of silicon dioxide doped with sodium to density of 10^{20} cm^{-3} showed that most of the included sodium is inactive from the viewpoint of both surface-state density and ionic migration under high electric field at elevated temperature (15). However, instability of semiconductor devices due to sodium mobility in thermal silicon dioxide films has been largely recognized as a central problem in semiconductor technology. Sodium was shown to cause instability under bias-temperature stress in silicon devices made by planar technology. Thermally stimulated ionic conductivity measurements made on MOS capacitors using aluminum or gold as the gate metal have shown that in sodium-doped gate oxide films with surface concentrations in the 10^{11}-10^{13} cm^{-2} range, sodium moves at temperatures above 200°C under electric fields as low as 1.2×10^5 V/cm (20).

In practice instabilities due to sodium can be eliminated either by stringent cleanliness during oxide processing or by the formation of a protective layer such as phosphosilicate glass which can trap sodium (20).

An experimental test was made in a carefully controlled fused silica tube operated at 1000°C and periodically cleaned *in situ* with chlorine. Silicon dioxide films 50-100 nm thick were grown on (100) n-type silicon surfaces using dry electronic grade oxygen and annealed *in situ* after oxidation in dry nitrogen for 30 min. The metal gate was applied by evaporation of 1 μm thick aluminum film in an electron-gun evaporator. MOS capacitors were prepared and capacitance measurements were made at room temperature before and after stressing the capacitors at 300°C for 5 min with electric field of 10^6 V/cm (2). The results indicate a clear correlation between cleaning of the fused silica oxidation tube and the total mobile ion surface density in the oxide film. These measurements indicate that oxide films grown in recently cleaned tubes show mobile ion densities in the 10^{10} cm^{-2} range.

Assuming uniform contamination film in the measurements, these "clean" oxides exhibit an impurity number density in the 10^{15} cm^{-3} range. This contamination level is caused by impurities accumulated during the device preparation process. It has been shown that radiation sensitivity of gate oxide films has no correlation with the mobile ion content in the oxide as measured by MOS capacitance measurements after bias temperature stressing or high temperature ramping (21). However a correlation of total sodium content with radiation sensitivity in the oxide of various MOS devices has been reported (22). These considerations suggest that sodium contamination introduced in the oxide film during oxidation and metallization may play a prominent role in determining the device radiation resistance. Phosphorus gettering of the gate region or hydrochloric acid passivation increases the radiation sensitivity of MOS devices. Hence to obtain reliable, radiation-stable MOS devices in the absence of gettering it has been suggested that high standards of cleanliness should be maintained (21). This is specially applicable to the oxidation step. Alkali impurity introduced through metallization should also be minimized by careful investigation of the mechanisms through which such contamination is introduced.

Conclusions

The results of the present thermodynamic calculations show that sodium included in the bulk of fused silica oxidation tubes is a significant source of contamination in oxidation atmospheres, even if sodium surface contamination produced by external agents in the tube is negligible. The presence of water in the oxidation atmosphere produces a rapid buildup of the sodium number density from the 10^7 cm^{-3} range, corresponding to dry oxidation, of up to two orders of magnitude greater for water concentrations of a few parts per million. During the oxidation cycle, sodium is incorporated into the oxide film as sodium silicate developing a significant contamination level which can be potentially harmful for MOS device radiation resistance. Water may be incorporated in the oxidation atmosphere through trace water or hydrogen from hydrocarbon impurities included in oxygen, and by ambient water that diffused into the oxidation chamber through the fused silica tube wall.

Preparation of clean oxide films requires the control of sodium impurity in the oxidation atmosphere. This in turn imposes a strict control of the tube material and appropriate care concerning the environmental conditions during wafer processing.

Acknowledgment

Thanks are due to T. C. Rains from the Analytical Chemistry Division for the results on flame emission

spectrometry. The collaboration of T. F. Leedy and R. Y. Koyama of the Electronic Technology Division in preparing MOS capacitors and in measuring their electrical properties is highly appreciated. This work was conducted as part of the Semiconductor Technology Program at the National Bureau of Standards and was supported in part by the Defense Nuclear Agency (IACRO 76-816) and the NBS.

Manuscript submitted Aug. 3, 1976; revised manuscript received Dec. 20, 1976.

Any discussion of this paper will appear in a Discussion Section to be published in the December 1977 JOURNAL. All discussions for the December 1977 Discussion Section should be submitted by Aug. 1, 1977.

Publication costs of this article were assisted by the National Bureau of Standards.

APPENDIX[6]

Calculation of Equilibrium Reaction Constant from JANAF Data

For a reaction $xX + yY \rightarrow wW + zZ$ the thermodynamic equilibrium constant may be written as

$$K = \frac{\alpha^w(W) \cdot \alpha^z(Z)}{\alpha^x(X) \cdot \alpha^y(Y)}$$

where $\alpha(X)$ is the activity of compound X. For calculations involved in this work (dealing with very dilute gaseous species), the activity may be taken as the partial pressure of the vapor phase (measured in atmospheres). The activity of a solid phase such as $SiO_2(c)$ is taken by convention as unity. For Na_2SiO_3 solid solution in SiO_2 the activity is taken as the mole fraction (10^{-5} in the present work). For the reaction

$$Na_2O \cdot SiO_2(gls) + \tfrac{1}{2}O_2(g) \rightarrow 2NaO(g) + SiO_2(c)$$

the equilibrium constant is expressed as

$$K = p^2(NaO) \times 10^5/p^{1/2}(O_2)$$

To evaluate K at a particular temperature T (measured in Kelvin) the following relations are used

$$\Delta G_T = -RT \ln K$$

$$\Delta G_T = \Delta H^\circ_{298} + T(\Sigma(G^\circ_T - H^\circ_{298})/T)$$

where ΔH°_{298} is the heat of reaction, calculated from standard heats of formation as

$$\Delta H^\circ_{f298} = \Sigma\, \Delta H^\circ_{f298}(\text{products}) - \Sigma\, \Delta H^\circ_{f298}(\text{reactants})$$

[kcal/mole]

and $\Sigma(G^\circ_T - H^\circ_{298})/T$ is calculated from Gibbs energy function in the standard state at temperature T

$$\Sigma(G^\circ_T - H^\circ_{298})/T = \{\Sigma(G^\circ_T - H^\circ_{298})/T\}_{\text{products}} - \{\Sigma(G_T - H_{298})/T\}_{\text{reactants}} \quad [\text{cal}/^\circ\text{K mole}]$$

[6] This calculation follows standard thermodynamic formalism [see Ref. (23)].

Table VII. JANAF thermodynamic data used to calculate equilibrium conditions at 1300°K for reactions listed in Tables I-VI

Compound	ΔH°_{f298}* (kcal/mole)	$-(G^\circ_T - H^\circ_{298})/T$** (cal/°K mole)
$H_2O(g)$	−57.798	51.136
$H(g)$	52.1	30.879
$OH(g)$	9.432	48.877
$O(g)$	59.559	42.044
$O_2(g)$	0	54.283
$H_2(g)$	0	36.130
$Na(g)$	25.755	40.201
$NaOH(g)$	−50.4	63.786
$NaO(g)$	20.0	60.896
$Na_2(OH)_2(g)$	−154.8	89.141
$Na_2O \cdot SiO_2$ (in SiO_2)	−376.8†	50.565
$SiO_2(c)$ (quartz)	−217.7	19.918
$Na_2O(g)$‡	8.7	72.3
$HCl(g)$	−22.063	49.624
$Cl_2(g)$	0	59.318
$Cl(g)$	28.922	43.226
$NaCl(g)$	−43.36	61.099
$NaCl(l)$	−92.237	32.199
$NaCl(c)$	−98.26	26.479
$Na_2Cl_2(g)$	−135.3	91.387
$I(g)$	25.537	46.671
$I_2(g)$	14.924	68.559
$HI(g)$	6.3	54.425
$NaI(g)$‡	−22.7	64.8
$NaI(l)$	−63.695	38.532
$NaI(c)$	−68.8	32.856

* ΔH°_{f298} = standard enthalpy of formation.
** $(G^\circ_T - H^\circ_{298})/T$ = Gibbs energy function in the standard state at temperature 1300°K.
† The value of ΔH°_{f298} for $Na_2O \cdot SiO_2$ (in SiO_2) was calculated using the equilibrium constant from reaction [3] Table I [see Ref. (12)]. The free energy function was assumed to be that of $Na_2O \cdot SiO_2$ (gls) given by the JANAF tables.
‡ The Na_2O data were estimated from various lithium, sodium, and potassium oxides data given in the JANAF tables. The NaI data are likewise estimated using the available alkali halide data.

REFERENCES

1. S. Schlegal, *IEEE Trans. Electron Devices*, **ed-14**, 728 (1967); *ibid.*, **ed-15**, 951 (1968).
2. K. H. Zaininger, *RCA Rev.*, **27**, 341 (1966).
3. R. J. Kriegler, "12th Annual Proceedings, Reliability Physics 1974," IEEE Catalog No. 74CHO839-1 PHY, pp. 250-258 (1974).
4. B. Yurash and B. Deal, *This Journal*, **115**, 1191 (1968).
5. W. R. Knolle, *ibid.*, **120**, 987 (1973).
6. W. R. Knolle and T. F. Retajczyk, Jr., *ibid.*, **120**, 1106 (1973).
7. K. G. Aubuchon, *IEEE Trans. Nucl. Sci.*, **ns-18**, No. 6, 117 (1971).
8. G. Hetherinngton, G. W. Stephenson, and J. A. Winterburn, *Electronic Eng.*, **41**, No. 495, 52 (1969); *ibid.*, **41**, No. 496, 44 (1969).
9. A. E. Owen and R. W. Douglas, *J. Soc. Glass Technol.*, **43**, 159T (1959).
10. H. F. Wolf, "Silicon Semiconductor Data," pp. 526-527, Pergamon Press, Oxford (1969).
11. D. R. Fewer and W. L. Gill, Tech. Rep. No. RADC-TR-66-345, pp. 33-49 (1966); also available as NTIS Document AD-489-969.
12. G. L. Vidale, General Electric Co., Technical Information Series, R60SD390 (1960).
13. JANAF Thermochemical Tables, D. R. Stull and H. Prophet, Editors, 2nd ed., NSRDS-NBS 37 (1971).
14. E. A. Irene, *This Journal*, **121**, 1613 (1974).
15. A. G. Revesz and R. J. Evans, *J. Phys. Chem. Solids*, **30**, 551 (1969).
16. S. Mayo, R. A. Keller, J. C. Travis, and R. B. Green, *J. Appl. Phys.*, **47**, 4012 (1976).
17. W. Dietze, L. P. Hunt, and D. H. Sawyer, *This Journal*, **121**, 1112 (1974).
18. D. H. Sawyer, Private communication.
19. S. Dushman, "Scientific Foundations of Vacuum Technique," 2nd ed., p. 14, John Wiley & Sons, Inc., New York (1962).
20. T. W. Hickmott, *Appl. Phys. Lett.*, **22**, 267 (1973); *Phys. Rev. Lett.*, **32**, 65 (1974); *J. Appl. Phys.*, **46**, 2583 (1975).
21. B. L. Gregory, *IEEE Trans. Nucl. Sci.*, **ns-22**, No. 6, 2295 (1975).
22. H. Hughes, R. D. Baxter, and B. Phillips, *ibid.*, **ns-19**, No. 6, 256 (1972).
23. G. N. Lewis and M. Randall, "Thermodynamics," 2nd ed., chap. 15, McGraw Hill Book Co., New York (1961).

Analysis of the Chemical Vapor Deposition of Titanium Diboride

I. Equilibrium Thermodynamic Analysis

Theodore M. Besmann[1] and Karl E. Spear[2]

Materials Research Laboratory, The Pennsylvania State University, University Park, Pennsylvania 16802

ABSTRACT

A thermodynamic analysis of the chemical vapor deposition (CVD) of TiB_2 from gaseous $TiCl_4$, BCl_3, and H_2 was performed using a general computer program for the calculation of heterogeneous equilibrium compositions. The conditions for the deposition of single phase TiB_2 and for the codeposition of TiB_2 plus boron were determined. Condensed TiB and titanium metal phases were determined to be unstable when the above reactants are used. The gas composition in equilibrium with the deposited solid was computed as a function of the CVD parameters of deposition temperature, total pressure, and B/(B + Ti) and Cl/(Cl + H) fractions in the reactant gas. The gaseous species generally present in greatest abundance were $TiCl_3$, $TiCl_4$, BCl_3, H_2, $HBCl_2$, and HCl. Theoretical TiB_2 deposition efficiencies were also calculated as a function of CVD parameters. The most efficient deposition was calculated to occur (*i*) at temperatures <1500°K, (*ii*) under reduced pressures, and (*iii*) in the presence of an excess of hydrogen. Equilibrium calculations coupled with experimental results were also used to determine limits on the enthalpies of formation of TiB and TiB_2.

The diboride of titanium is a refractory material with metallic properties such as high thermal and electrical conductivity. It is quite stable with respect to oxidation and chemical attack and, like all boron-containing substances, has potential for use as a neutron absorber. Present commercial interests in TiB_2 center on its use as an abrasive, as a protective coating, as a potential high temperature electrode in the refining of aluminum, and as a component in TiB_2-BN composites used for aluminum evaporator boats.

The refractory nature of TiB_2 makes the synthesis of samples with a specified composition and purity difficult. Possible means of production are discussed by Powell (1), and include synthesis from the elements, fused salt electrolysis, reduction of metal oxides with boron, carbothermic reduction of metal oxide-boron mixtures, reduction of boron halides or pyrolysis of borohydrides on a metal substrate, and finally, the technique discussed in this work, the reduction of boron and metal halides on an inert substrate.

All methods of preparation tend to have problems such as interactions with container materials and background gases, preferential vaporization of titanium or boron, or inclusion of solvent when the boride is precipitated out of solution. Chemical vapor deposition (CVD) was investigated to produce well-defined specimens of high purity. In CVD gaseous reactants pass over a heated substrate where chemical reactions occur and condensed phases deposit. The technique controls reactant concentrations through manipulation of reactant partial pressures. Because relatively low temperatures are required, problems of container interactions and sample evaporation are reduced.

Diboride shapes are now produced by powder metallurgy techniques (1), but are limited in size, shape, and density. In many cases, CVD may substitute for powder metallurgical techniques to prepare dense TiB_2 coatings and bulk materials. Its feasibility has already been investigated to some extent (2-8).

Tailoring of a CVD process to yield a desired product under optimum operating conditions requires the use of a predictive model developed from a basic understanding of the chemistry of the system, the equilibrium thermodynamic limits of the process, possible chemical kinetic rate-limiting mechanisms, and mass transport limitations. An equilibrium thermodynamic analysis provides the limiting equilibrium composition of the gas phase, limiting deposition rates, and an identification of the phase(s) which can deposit under this limiting equilibrium state.

Chemical kinetic mechanisms have often been found to limit deposition rates and influence the morphology of the deposit. These mechanisms can be elucidated only from the experimental results obtained by operating the CVD system of interest. The transfer of reactants from the bulk gas to the substrate surface, and the transfer of reaction products back into the bulk gas stream also influence both the efficiency of deposition and the deposit morphology. A complete predictive model of a CVD system must therefore consider chemical, thermodynamic, chemical kinetic, and mass transfer relations.

The present comprehensive study of the CVD of TiB_2 is described in three separate papers. The morphology of CVD TiB_2 has been described and correlated with specific deposition conditions in a previous paper (9). The present paper describes an equilibrium thermodynamic analysis of the system as a function of the same deposition conditions. An accompanying paper (10) discusses the mass transport and chemical kinetics involved, and compares the experimental rates with those calculated using a predictive model.

Except for the present study, the only other equilibrium thermodynamic analysis of the CVD of TiB_2 was a very limited attempt by Peshev and Niemyski (7). They computed the standard free energy change for the over-all reaction

$$TiCl_{4(g)} + 2BCl_{3(g)} + 5H_{2(g)} = TiB_{2(s)} + 10\,HCl_{(g)} \quad [1]$$

as a function of temperature. These values were compared to the standard free energy changes for similar CVD reactions forming elemental titanium and boron. Thus they considered only the gaseous species $TiCl_4$, BCl_3, H_2, and HCl and the three condensed phases.

In contrast to Peshev and Niemyski's (7) work, the present study is a complete equilibrium thermodynamic analysis of the CVD process. All conceivable gaseous species, a total of 21, are included with the

[1] Present address: Oak Ridge National Laboratory, Chemical Technology Division, Oak Ridge, Tennessee 37830.
[2] Also a member of the Ceramic Science Section of the Material Sciences Department, The Pennsylvania State University.
Key words: chemical vapor deposition, titanium diboride, equilibrium thermodynamic analysis.

condensed phases in calculating the equilibrium composition of the system as a systematic function of the CVD variables of temperature, total pressure, and reactant concentrations.

Calculational Technique

Chemical equilibrium calculations involve the computation of the composition of a system, subjected to certain constraints, which contains the minimum free energy. The constraints in CVD systems are the preservation of the masses of each element present, constant temperature, and constant total pressure.

Numerous methods have been reported for computing thermodynamic equilibrium compositions, but all the techniques are based on the methods of either Brinkley (11-12) or White *et al.* (13). The method first outlined by Brinkley (11-12) is the older and more indirect technique. It requires the writing of a series of chemical reactions and the computation of their respective equilibrium constants. These are then used with the constraints mentioned above to solve for the equilibrium composition.

White *et al.* (13) developed a relatively simple and direct method for computing chemical equilibria. Their technique involves minimizing the summation of the free energies of all the species. Eriksson (14) extended the method to include systems containing more than one condensed phase and developed a computer program, SOLGAS, for performing the calculations. To prevent the omission of an important species, the program can consider all conceivable gaseous species and condensed phases in a single calculation. Unstable condensed phases are rejected from the calculation. The computer program SOLGAS was modified for convenient use with CVD systems and then used to perform the calculations in the present study.

Results

The thermodynamic analysis which follows considers equilibrium in a system in which condensed phases are deposited from initial gaseous reactants of $TiCl_4$, BCl_3, and H_2. The equilibrium was calculated as a function of the CVD variables of deposition temperature, total pressure, and the fractions B/(B + Ti) and Cl/(Cl + H) in the reactant gas. All conceivable gaseous species in the Ti-B-Cl-H system were included and are listed in Table I along with their respective thermodynamic values. The only condensed phases confirmed to exist in the binary Ti-B system (18) are Ti, TiB, TiB_2, and B.

The equilibrium calculations were initially used to develop what are termed CVD phase diagrams, of which Fig. 1 is an example. These plots of computed phase boundaries as functions of CVD variables show ranges of input conditions under which specific condensed phases are the equilibrium products.

The deposition of either $Ti_{(s)}$ or $TiB_{(s)}$ was not predicted under any of the CVD conditions investigated. This is a result of the high stabilities of TiB_2 and gaseous titanium chlorides as compared to Ti and TiB, and the fact that only fully chlorided titanium and boron were used as reactants.

Detailed information on the system's equilibrium gas composition as a function of the CVD parameters is given in Fig. 2. In each plot, both the reactant gas species partial pressures and the computed equilibrium partial pressures are graphed *vs.* a specific CVD parameter while all other parameters were held constant at an arbitrary set of standard conditions.

The standard conditions chosen were: temperature = 1523°K, total pressure = 0.263 atm, B/(B + Ti) = 0.667, and Cl/(Cl + H) = 0.333.

The four graphs in Fig. 2 show that $TiCl_3$, $TiCl_4$, BCl_3, $HBCl_2$, H_2, and HCl are the major gaseous species. The equilibrium partial pressures of the titanium- and boron-containing species are greater than 10% initial input reactant gas values even at high temperatures. The relationships shown in Fig. 2 are of importance in understanding the kinetics and mechanisms of deposition (10).

Table I. Thermodynamic data for the CVD of TiB_2*

	$\Delta H°_{f,1600°K}$ (kcal/mole)	$S°_{1600°K}$ (cal/mole-°K)
Gaseous species		
B	132 ± 4	45.0 n.g.**
B_2	191 ± 6.4	62.0 n.g.
BCl	32 ± 4	65.2 n.g.
BCl_2	−21.8 ± 20	86.4 n.g.
BCl_3	−96.8 ± 0.5	99.5 n.g.
B_2Cl_4	−117 ± 1.2	132 n.g.
B_2H_6	5.84 ± 4	100 n.g.
B_5H_9	10.5 ± 1.6	147 n.g.
Cl	30.1 ± 2	48.4 ± 0.01
Cl_2	0.0	68.0 ± 0.01
H	53.8 ± 0.001	35.7 n.g.
H_2	0.0	43.2 ± 0.01
HCl	−22.8 ± 0.05	57.0 n.g.
$HBCl_2$	−61.0 ± 1	90.8 n.g.
H_2BCl	−18.1 n.g.***	76.6 n.g.***
Ti	109 ± 1	52.0 n.g.
TiCl	34.1 ± 10	76.4 ± 2
$TiCl_2$	−59.4 ± 3	91.0 ± 3
$TiCl_3$	−130 ± 1.5	109 ± 1.0†
$TiCl_4$	−183 ± 0.9	127 ± 0.7
Ti_2Cl_6	−295.9 n.g.	166.7 n.g.
Condensed phases		
B	0.0	9.92 ± 0.01
Ti	0.0	19.4 ± 0.02
TiB	−40.4 ± 9	27.2 ± 1.5
TiB_2	−78.4 ± 0.9‡	34.23 ± 0.1

* Unless indicated otherwise, values are taken from the JANAF Tables (15).

** n.g. indicates error limit not given in the reference.

*** Estimated from (2/3) $\Delta H°_{f,1600°K}$ (BH_3) + (1/3) $\Delta H°_{f,1600°K}$ (BCl_3) = $\Delta H°_{f,1600°K}$ (H_2BCl) and (2/3) $S°_{1600°K}$ (BH_3) + (1/3) $S°_{1600°K}$ (BCl_3) = $S°_{1600°K}$ (H_2BCl).

† Derived from the values for $TiCl_{3(g)}$, $\Delta H°_{298°K} = -40.6$ kcal/mole, and $\Delta S°_{298°K} = -36.4$ kcal/mole-°K and $\Delta C°_p = 4$ kcal/mole-°K determined by Sibbing and Schäfer (16) for the reaction $2TiCl_{3(g)} = Ti_2Cl_{6(g)}$.

‡ The value of $\Delta H°_{f,1600°K}$ (TiB_2) was derived from $\Delta H°_{f,298°K}$ (TiB_2) = −77.4 ± 0.9 kcal/mole determined by Huber (17) and the heat capacity, $C°_p$, reported in the JANAF Tables (15).

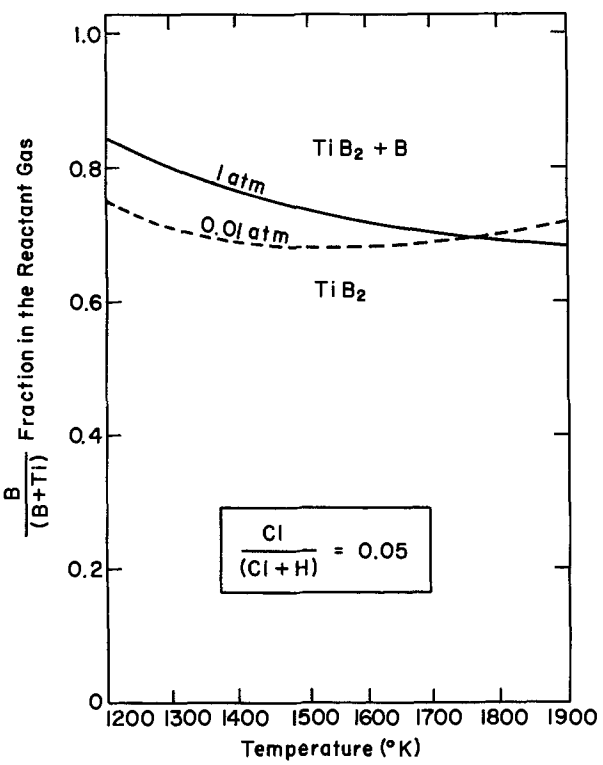


Fig. 1. CVD phase diagram based on thermodynamic equilibrium calculations. The B/(B + Ti) fraction in the reactant gas is plotted vs. the deposition temperature at two different pressures, 0.01 and 1.0 atm, and a Cl/(Cl + H) = 0.05 fraction in the reactant gas. The phase boundaries separate ranges of conditions under which either TiB_2 + B codeposits or single phase TiB_2 forms.

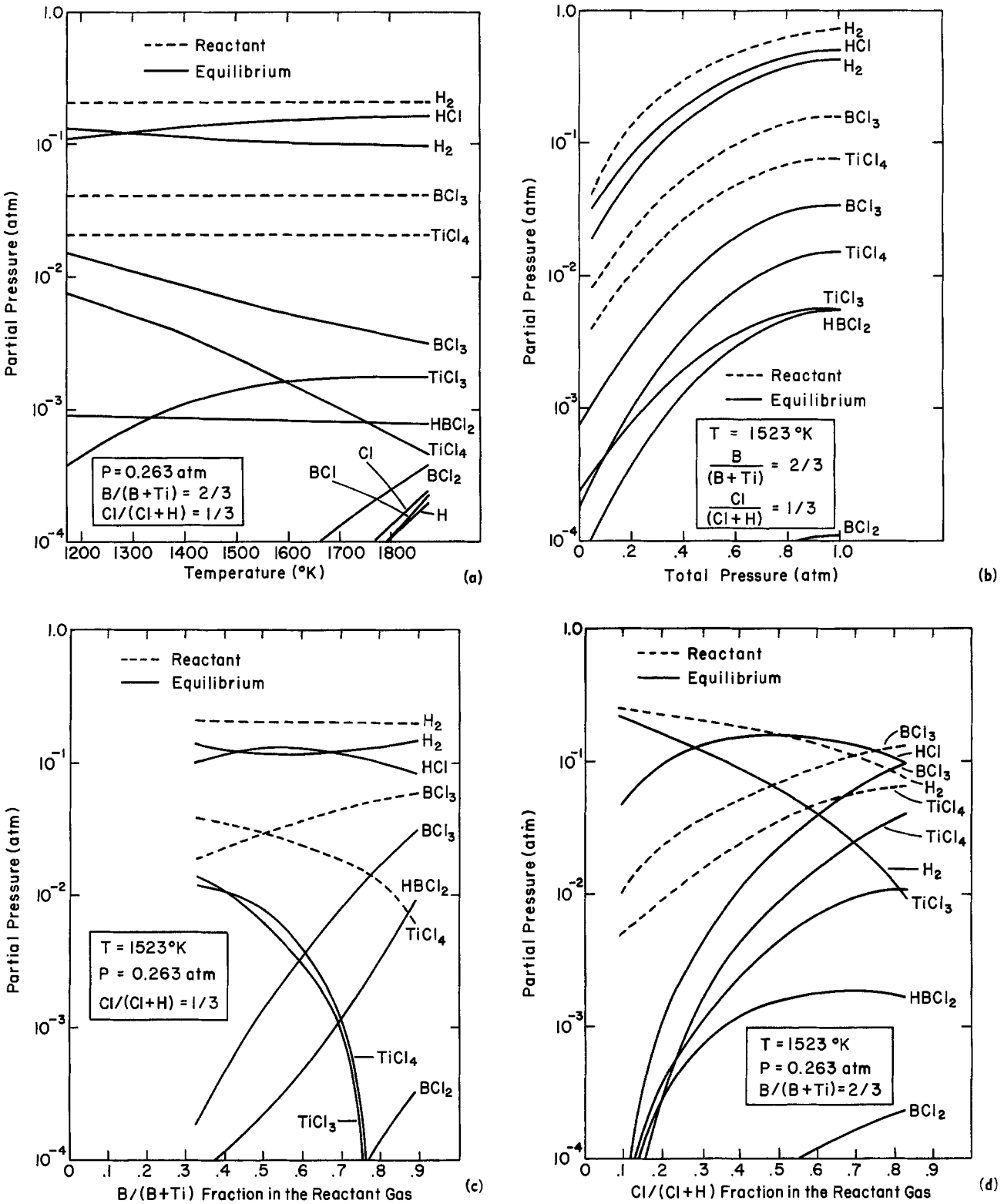


Fig. 2. Reactant and equilibrium partial pressures of the species present in the CVD system as a function of temperature (a), total pressure (b), B/(B + Ti) fraction in the reactant gas (c), and Cl/(Cl + H) fraction in the reactant gas (d).

The thermodynamic equilibrium calculations can also be used to determine theoretical deposition efficiencies. These efficiencies are defined as the moles of TiB_2 computed to deposit at equilibrium divided by the moles of diboride which could deposit if the reactants formed the maximum amount of TiB_2, *i.e.*, the amount which can form independent of any kinetic or thermodynamic limitations. Figure 3 contains plots of theoretical efficiency *vs.* deposition temperature for a series of deposition conditions. The CVD of TiB_2 is thermodynamically favored at elevated temperatures, reduced pressures, and low Cl/(Cl + H) fractions.

The equilibrium rate of formation of TiB_2 is sensitive to the value of the enthalpy of formation of TiB_2. The JANAF Tables (15) report the rather uncertain value of $\Delta H°_{f,298°K}(TiB_2) = -66.8 \pm 4$ kcal/mole. Their value is considerably more uncertain and based on older and less precise sources than is the value $\Delta H°_{f,298°K}(TiB_2) = -77.4 \pm 0.9$ kcal/mole reported by Huber (17). This more negative value is also in agreement with the recent value of Akhachinski and Chirin (19) of -76.1 ± 0.85 kcal/mole, and the values of -78.0 and -80.3 kcal/mole tabulated by Wagman *et al.* (20) for the analogous phases ZrB_2 and HfB_2, respec-

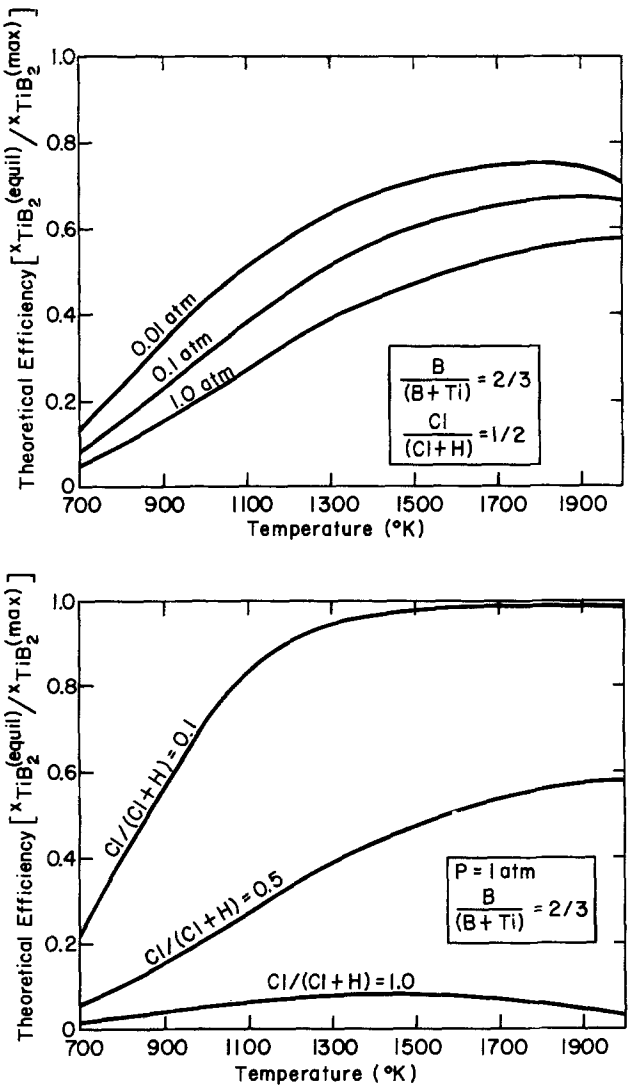


Fig. 3. Theoretical efficiencies of deposition vs. deposition temperature for total pressures of 0.01, 0.1, and 1.0 atm (a, top) and Cl/(Cl + H) fractions of 0.1, 0.5, and 1.0 in the reactant gas (b, bottom).

tively. Thermodynamic equilibrium calculations on the CVD of TiB_2 performed using the −66.8 kcal/mole value result in equilibrium deposition rates almost equal to several experimentally observed rates (10). This more positive JANAF value can therefore be considered the most positive limit for the enthalpy of formation since more positive values would yield calculated equilibrium rates lower than those observed experimentally.

The JANAF Tables (15) give an even larger uncertainty in the reported enthalpy of formation for TiB, $\Delta H°_{f,298°K}(TiB) = -38.3 \pm 9$ kcal/mole. Under experimental conditions favoring the formation of the monoboride, *i.e.*, a low B/(B + Ti) fraction in the reactant gas, the phase was not observed to form (10). These CVD conditions [$T = 1523°K$, $P = 0.263$ atm, $B/(B + Ti) = 0.333$, and $Cl/(Cl + H) = 0.333$] were used as data in thermodynamic equilibrium calculations in which the enthalpy of formation of TiB was allowed to vary. The enthalpy at which the TiB was computed to just begin to form is considered the maximum negative enthalpy of formation for the phase. This calculated limit of $\Delta H°_{f,1523°K}(TiB) > -55$ kcal/mole is consistent with the high temperature value of $\Delta H°_{f,1523°K}(TiB) = -41.0$ kcal/mole derived from the JANAF Tables (15).

Discussion

The oversimplified thermochemical logic used by Peshev and Niemyski (7) can yield misleading results. They state that if the standard free energy change ($\Delta G°$) for Eq. [1] is negative, and if the over-all reactions forming titanium and boron have more positive $\Delta G°$'s, TiB_2 should form readily. If Eq. [1] had not been the dominant over-all reaction, *e.g.*, $TiCl_3$ rather than TiB_2 had been the major product, their calculations would not have been meaningful. Only a complete thermodynamic analysis similar to that presented here would indicate the most important species. Additionally, Peshev and Niemyski ignored the possibility of the deposition of more than one condensed phase. For the conditions shown in Fig. 1, boron can codeposit with the diboride at a B/(B + Ti) as low as 0.65 in the initial reactant gases.

The trends in theoretical efficiency exhibited in Fig. 3 are easily explained by simple thermochemical logic since only one chemical reaction (Eq. [1]) is dominating. Assuming the condensed phase activity for TiB_2 is unity, the equilibrium constant, K, for Eq [1] is expressed by

$$K = \frac{p^{10}_{HCl}}{p_{TiCl_4} p^2_{BCl_3} p^5_{H_2}}$$

where the partial pressures, p's, are in atmospheres. The equilibrium constant can also be written as a function of the mole fraction of each species, x, and the total pressure, P

$$K = P^2 \frac{x^{10}_{HCl}}{x_{TiCl_4} x^2_{BCl_3} x^5_{H_2}} \qquad [2]$$

K is a constant defined by

$$K = \exp\left(\frac{-\Delta G°}{RT}\right)$$

where $\Delta G°$ is the standard free energy change for Eq. [1], R is the ideal gas law constant, and T is the absolute temperature. The data in Table I yield

$$\ln K = 31.32 - \frac{35{,}330}{T} \qquad [3]$$

The trend toward increased deposition efficiency with increasing temperature seen in Fig. 3 is now apparent from Eq. [3]. Higher temperatures yield larger values of K resulting in increased deposition.

The requisite that K in Eq. [2] must equal a specific constant at a specific temperature explains the pressure-dependent behavior of deposition efficiency observed in Fig. 3a. As P decreases, the ratio of the moles of product to the moles of reactants in Eq. [2] must increase to maintain K at the constant value. Increasing deposition efficiency thus accompanies decreasing total pressure, as seen in Fig. 3a.

Figure 3b can be explained similarly since increased amounts of hydrogen, a reactant, must cause increased amounts of product to form if K is to remain constant.

From Fig. 3 it appears that maxima in efficiency occur which shift toward lower temperatures under reduced pressures and increased Cl/(Cl +H) fractions. This is caused by the increased stability of gaseous species which form at the expense of TiB_2 at higher temperatures and under reducing conditions. Figure 2a shows that the partial pressure of $TiCl_3$ increases with increasing temperature, and thus suppresses the formation of TiB_2 at high temperatures. These phenomena cannot be predicted by the simplified thermodynamic analysis of Peshev and Niemyski (7).

Conclusions

Under all CVD conditions investigated, the thermodynamic equilibrium calculations indicate that TiB_2 and boron are the only solids which can deposit from the reactant gases of $TiCl_4$, BCl_3, and H_2. The theoretical efficiency of deposition appears to generally increase with increasing deposition temperature, although maxima appear to exist at high temperature.

Small Cl/(Cl + H) fractions in the reactant gas and small total pressures also favor higher efficiencies.

The gaseous species present in greatest abundance at equilibrium are $TiCl_3$, $TiCl_4$, BCl_3, H_2, $HBCl_2$, and HCl, and these probably play the most important mechanistic roles in the CVD of TiB_2. The present studies indicate that a $\Delta H°_{f,298°K}(TiB_2)$ of about −66 kcal/mole is the most positive value for the diboride that is still consistent with the experimental results. This limit is in agreement with later reported values which yield a $\Delta H°_{f,298°K}(TiB_2) \approx -77$ kcal/mole. Employing experimental results (10) and thermodynamic equilibrium calculations, a maximum negative limit of $\Delta H°_{f,298°K} = -55$ kcal/mole was computed for the enthalpy of formation of TiB.

The conclusions demonstrate the value of thermodynamic calculations in determining which equilibrium phases can form in a CVD system and in pointing the way toward optimizing deposition conditions. Published papers on CVD show that most studies omit such calculations or do not include all important species in their analysis. The procedures outlined in this paper are equally applicable to other CVD systems, as is the modified version of the computer program SOLGAS.

Acknowledgments

The authors are indebted to their colleagues, and especially to John H. Blanks, at the Materials Research Laboratory, The Pennsylvania State University, for helpful discussions and advice. This work was supported by the NSF under Grant No. DMR72-03133 (formerly GH-34515). This paper is based in part on the Ph.D. thesis by T. M. Besmann submitted to The Pennsylvania State University, 1976.

Manuscript submitted Sept. 3, 1976; revised manuscript received Dec. 6, 1976.

Any discussion of this paper will appear in a Discussion Section to be published in the December 1977 JOURNAL. All discussions for the December 1977 Discussion Section should be submitted by Aug. 1, 1977.

Publication costs of this article were assisted by Oak Ridge National Laboratory.

REFERENCES

1. C. F. Powell, in "High-Temperature Materials and Technology," I. E. Campbell and E. M. Sherwood, Editors, p. 349, John Wiley & Sons, Inc., New York (1967).
2. K. Moers, *Z. Anorg. Allg. Chem.*, **198**, 243 (1931).
3. C. F. Powell, in "High-Temperature Technology," I. E. Campbell, Editor, p. 131, John Wiley & Sons, Inc., New York (1956).
4. K.-Th. Wilkie, *Z. Phys. Chem. (Leipzig)*, **220**, 137 (1962).
5. R. E. Gannon, R. C. Folweiler, and T. Vasilos, *J. Am. Ceram. Soc.*, **46**, 492 (1963).
6. J. J. Gebhardt and R. F. Cree, *ibid.*, **48**, 262 (1965).
7. P. Peshev and T. Niemyski, *J. Less-Common Met.*, **10**, 133 (1965).
8. J. Cueilleron, G. Lahet, F. Thevenot, and R. A. Pâris, *ibid.*, **24**, 317 (1971).
9. T. M. Besmann and K. E. Spear, *J. Cryst. Growth*, **31**, 60 (1975).
10. T. M. Besmann and K. E. Spear, *This Journal*, **124**, 790 (1977).
11. S. R. Brinkley, *J. Chem. Phys.*, **15**, 107 (1947).
12. S. R. Brinkley, *ibid.*, **14**, 563 (1946).
13. W. B. White, W. M. Johnson, and G. B. Dantzig, *ibid.*, **28**, 751 (1958).
14. G. Eriksson, *Acta Chem. Scand.*, **25**, 2651 (1971).
15. D. R. Stull and H. Prophet, "JANAF Thermochemical Tables," Second Edition, U.S. Government Printing Office, Washington, D.C. (1971).
16. E. Sibbing and H. Schäfer, *Z. Anorg. Allg. Chem.*, **410**, 67 (1974).
17. E. J. Huber, Jr., *J. Chem. Eng. Data*, **11**, 430 (1966).
18. E. Rudy, AFML-TR-65-2, Part V (1969).
19. V. V. Akhachinski and N. A. Chirin, in Proceedings of Symposium on the Thermodynamics of Nuclear Materials, 1974, IAEA, Vienna (1974).
20. D. D. Wagman, W. H. Evans, V. B. Parker, I. Halow, S. M. Bailey, R. H. Schumm, and K. L. Churney, NBS Technical Note 270-5 (1971).

Analysis of the Chemical Vapor Deposition of Titanium Diboride

II. Modeling the Kinetics of Deposition

Theodore M. Besmann[1] and Karl E. Spear[2]

Materials Research Laboratory, The Pennsylvania State University, University Park, Pennsylvania 16802

ABSTRACT

Deposition rates and efficiencies for the chemical vapor deposition (CVD) of TiB_2 from $TiCl_4$, BCl_3, and H_2 were experimentally determined as a function of CVD variables. These results, coupled with previously determined thermodynamic equilibrium compositions and deposit morphologies, were used to develop models for the deposition process. At high temperatures the principal rate-limiting mechanism is the diffusion of gaseous species through a gas boundary layer above the deposition surface. However, low Cl/(Cl + H) or high B/(B + Ti) fractions in the reactant gas cause a chemical kinetic mechanism to become rate limiting. At lower deposition temperatures equilibrium no longer appears to exist at the substrate surface and a chemical kinetic rate-limiting mechanism becomes important. A simple linear rate expression was used to calculate an activation energy of 40 ± 12 kcal/mole for the chemical kinetic mechanism.

As has been previously discussed (1-2) there is considerable interest in the process of chemical vapor deposition (CVD) and in TiB_2 as a material. The CVD of TiB_2 has been successfully attempted by several researchers (3-9), but little has been done to elucidate the deposition processes and in CVD in general. This is not surprising since developing an understanding of complex CVD processes involves understanding chemical thermodynamic, mass transfer, and chemical kinetic

[1] Present address: Oak Ridge National Laboratory, Chemical Technology Division, Oak Ridge, Tennessee 37830.
[2] Also a member of the Ceramic Science Section of the Material Sciences Department, The Pennsylvania State University.
Key words: chemical vapor deposition, titanium diboride, kinetics, gaseous diffusion.

phenomena. Studies of the deposition of silicon, gallium arsenide, and tungsten represent the major published attempts to thoroughly understand CVD processes (10).

An earlier paper in the present series on the CVD of TiB_2 has described the thermodynamic analysis for the deposition of TiB_2 from the reactant gases $TiCl_4$, BCl_3, and H_2 (1). The identity of the condensed phases which form and the equilibrium partial pressures of the various gaseous species were calculated as a function of the CVD variables of temperature, total pressure, and the fractions B/(B + Ti) and Cl/(Cl + H) in the reactant gas. Only TiB_2 and boron were predicted to deposit under the conditions investigated. At equilibrium the most abundant gaseous species present are $TiCl_3$, $TiCl_4$, BCl_3, H_2, $HBCl_2$, and HCl. Equilibrium calculations were also used to determine theoretical TiB_2 deposition efficiencies, *i.e.*, the TiB_2 deposition rate at equilibrium divided by the deposition rate in the absence of any thermodynamic or kinetic limitations.

The morphologies of the TiB_2 deposits were previously correlated with the deposition parameters of substrate temperature, total pressure, total gas flow rate, and the B/(B + Ti) and Cl/(Cl + H) fractions in the reactant gas (2). Most diboride deposits were adherent, coherent coatings with preferred orientations such that the c-direction of the hexagonal TiB_2 was parallel to the substrate surface. As the deposition temperature increased, the deposits transformed from relatively smooth, nodular surfaces to faceted coatings. Increased B/(B + Ti) fractions in the reactant gas caused the growth of platelike crystallites several square millimeters in area fixed normal to the substrate surface. Low Cl/(Cl + H) fractions yielded irregular crystallites with decreased preferred orientation. Reduced total pressure yielded coatings having increased crystallite size, and higher gas flow rates resulted in decreased perfection in the crystallite faces of faceted coatings.

This paper describes a kinetic study of the CVD of TiB_2 in which deposition rates were systematically determined as a function of the deposition variables of temperature, total pressure, total flow rate, and the B/(B + Ti) and Cl/(Cl + H) fractions in the reactant gas. These results, along with equilibrium calculations (1) and observed deposit morphology (2), are used to model the deposition processes in an attempt to comprehend the underlying principles involved in CVD.

Peshev and Niemyski (8) also reported kinetic data on the CVD of TiB_2. Their study likewise used the over-all reaction

$$TiCl_{4(g)} + 2BCl_{3(g)} + 5H_{2(g)} = TiB_{2(s)} + 10\,HCl_{(g)} \quad [1]$$

They investigated the efficiency of deposition as a function of substrate temperature, total gas flow rate, and reactant gas Cl/(Cl + H) fractions. Their results are compared to the present study in the discussion section.

Modeling CVD Kinetics

The ultimate limit on the rate of CVD of any material is the rate of input of the reactants coupled with the system's thermodynamic equilibrium composition. This limit is rarely achieved in dynamic CVD systems and kinetic factors usually govern the deposition rate behavior. In a general review of CVD, Jones and Shaw (10) have delineated the general mass transfer and chemical kinetic processes involved in CVD. These include the flow of reactants and gaseous products through the system, the transport of chemical species from the bulk gas to the deposition surface, the transport of product gases from the surface to the bulk gas, and the chemical reactions occurring at the deposition surface.

A relatively simple model has been assumed for the transport of gaseous species between the bulk gas (where the gas flow is parallel to the substrate surface) and the deposition surface. It is envisioned that between the turbulent bulk gas and the deposition surface lies a laminar boundary layer, and that the diffusion of gaseous species through the laminar boundary layer is a possible rate-limiting step.

It is useful to assume that the diffusion of species i through the boundary layer is equivalent to the diffusion of i in a binary gas mixture containing the carrier gas j. Fick's first law yields

$$J_i = D_{ij}\left(\frac{{}_bp_i - {}_sp_i}{\delta RT}\right) \quad [2]$$

where J_i = flux of species i through the boundary layer, D_{ij} = binary diffusion coefficient for the species, ${}_bp_i$ = partial pressure of species i in the bulk gas, ${}_sp_i$ = partial pressure of species i at the deposition surface, δ = boundary layer thickness, R = ideal gas constant, and T = absolute temperature.

The functional relationships of the various parameters in the diffusion relation provide a valuable model for understanding the effects of experimental variables on the deposition rates. Jones and Shaw's (10) expression for the binary diffusion coefficient is

$$D_{ij} = \frac{AT^{1.75}}{P}\left(\frac{1}{M_i} + \frac{1}{M_j}\right)^{1/2} \quad [3]$$

where A = proportionality constant, P = total pressure, and M = molecular weight.

Bennett and Myers (11) show that for flow across a semi-infinite flat plate, laminar boundary conditions yield

$$\delta = 5\left(\frac{\mu L}{\rho v}\right)^{1/2}$$

where μ = fluid viscosity, L = distance from the leading edge of the plate, ρ = fluid density, and v = linear velocity of the fluid.

Assuming the flow across the CVD substrate region is analogous to flow across a flat plate, the functional relationship

$$\delta \propto \left(\frac{\mu}{\rho v}\right)^{1/2} \quad [4]$$

can be used. Jones and Shaw note that

$$\mu \propto T^m \quad [5]$$

where m is an empirical constant which varies between 0.6 and 1.0. Density is, assuming the gas is ideal, proportional to the total pressure and inversely proportional to temperature, and linear velocity is proportional to the volumetric flow rate and inversely proportional to density. Substituting the above relationships including Eq. [2]-[5] into Eq. [2] yields

$$J_i = \frac{ZF^{1/2}T^{(3/4-m/2)}}{P}({}_bp_i - {}_sp_i) \quad [6]$$

where Z = mass transfer coefficient (proportionality constant), and F = input volumetric flow rate at STP.

Since the diffusive flux, J_i, is directly proportional to the deposition rate, Eq. [6] can be considered as also containing the functional relationships for the CVD rate.

In applying Eq. [6] to a CVD system it is necessary to predict or experimentally determine both ${}_bp_i$ and ${}_sp_i$. A simplifying assumption is that ${}_bp_i$ is the species partial pressure in the reactant gas, although a knowledge of ${}_bp_i$ as a function of the distance from the leading edge of the substrate would yield more accurate results.

The partial pressures of species at the deposition surface, ${}_sp_i$, can be governed either by thermodynamic equilibrium or by chemical kinetic mechanisms. The equilibrium partial pressures can be calculated relatively easily. The kinetically fixed partial pressure dependencies must be experimentally determined for each system.

Table I. Standard TiB_2 CVD conditions

	This study	Peshev and Niemyski (8)
Deposition temperature, °K	1523	1673
Total pressure, atm	0.263	1.0
Total input flow rate (STP), cm³/min	462	2580
B/(B + Ti)	0.667	0.667
Cl/(Cl + H)	0.333	0.143

Two limiting cases can be of interest. The first case is where equilibrium exists at the deposition surface and the partial pressures of the reactant species at equilibrium are very small. The rate-limiting process for deposition is the diffusion of the reactant gases through the boundary layer. The diffusion rates, and thus deposition rates, are directly proportional to the bulk partial pressures.

The opposite situation arises when chemical kinetic steps are slow and the concentrations of reactants at the surface approach the partial pressures in the bulk. Diffusion is very slow due to small partial pressure gradients between the bulk gas and deposition surface and the slowest chemical kinetic step is rate limiting.

Experimental Procedure

Experimental deposition rates of TiB_2 as a function of temperature, pressure, total flow rate, and B/(B+Ti) and Cl/(Cl + H) fractions in the reactant gas have been determined. One parameter was varied while all other parameters were held constant at the arbitrary set of standard conditions listed in Table I. Also listed are the standard conditions used by Peshev and Niemyski (8) in their similar study. Individual flow rates can be easily derived from total flow rates and B/(B + Ti) and Cl/(Cl + H) fractions.

Figure 1 is a schematic of the CVD system which is similar in design to those employed by other researchers (6-8). Boron trichloride[3] and hydrogen[4] gases were metered into the system through float-type flowmeters. The $TiCl_4$,[5] which is a liquid at room temperature, was injected into a vaporizer at a constant predetermined rate by a syringe pump equipped with a gas-tight syringe. The corrosive gases were only in contact with Teflon lines and Monel valves and connections. Helium was used to purge the system.

The vaporizer was a round-bottom flask covered by a heating mantle maintained at temperatures greater than 409.4°K, the atmospheric boiling point of $TiCl_4$. The hydrogen stream flowed to the vaporizer where it mixed with the tetrachloride and passed on to a Pyrex-Vycor nozzle to mix with the BCl_3 stream. The line between the vaporizer and nozzle was wrapped with heating tape to maintain the $TiCl_4$ as a vapor.

[3] 99% purity, Stauffer Chemical.
[4] 99.95% purity, Air Products and Chemicals.
[5] 99.9% purity, Fisher Scientific.

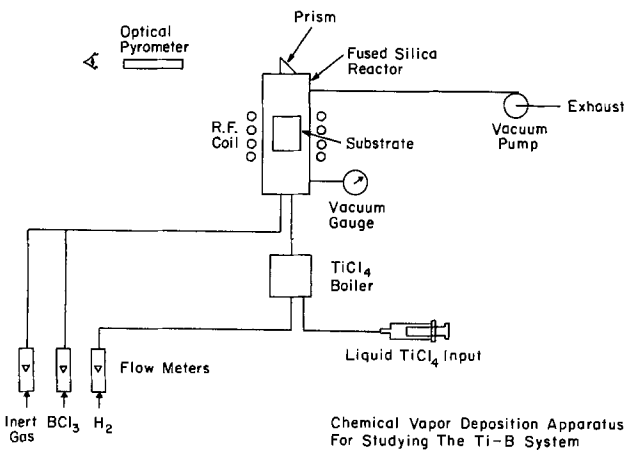


Fig. 1. Flow chart of the TiB_2 CVD system

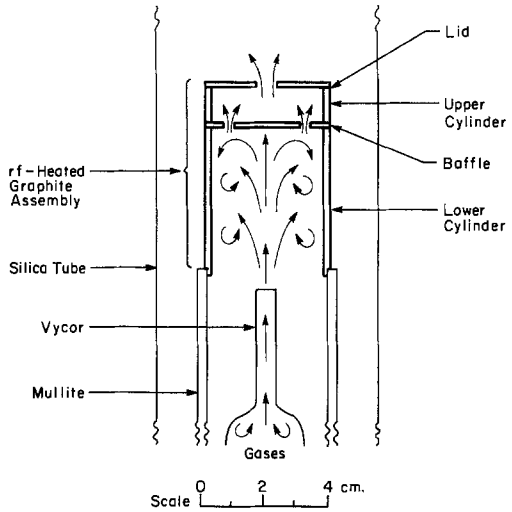


Fig. 2. Schematic of the graphite assembly in position in the CVD system. Not included in the sketch is a second mullite cylinder containing molybdenum foil shields whch surround the graphite assembly, and two molybdenum foil shields positioned on top of the lid.

Figure 2 is a sketch of the nozzle and CVD reactor setup. The gases flowed into a lower graphite cylinder which was supported by a mullite cylinder. The graphite was heated to temperature by a 10 kW, 450 kHz rf induction generator. To increase mixing and to help maintain a constant temperature in the lower cylinder, a baffle with exhaust holes was placed on top of the cylinder, a short graphite cylinder (upper cylinder) with a lid was positioned above the baffle, and a larger mullite cylinder and molybdenum foil thermal radiation reflectors were placed around the cylinders. Unreacted and product gases departed the system through a liquid-jet vacuum pump.

The CVD reactor consisted of a fused silica tube 6 cm in diameter and 25 cm tall with a Monel plate 2 cm thick and 15 cm in diameter sealing each end. The plates were held in place by four nylon dowels positioned around the periphery of the plates and outside the fused silica tube. The nozzle entered the reactor through a 2.5 cm diameter hole in the bottom plate. The top plate contained a 2.5 cm diameter Pyrex tube with a window for viewing the top of the graphite assembly. This plate also had two lines penetrating it, one leading to the vacuum pump and the other to the vacuum gauge. All penetrations of the Monel plates were sealed by compressed Teflon O-rings, and the plates were sealed to the main silica reactor tube with intervening Teflon gaskets.

For each experimental run a fresh graphite assembly was positioned above the nozzle. The system was then sealed and evacuated. Next a flow of helium was started and the substrate was brought to temperature. After the temperature had stabilized at the desired level, the helium was shut off and the reactant gases were allowed to flow through the graphite assembly. The system was usually operated for about 1 hr with constant monitoring and occasional adjustment of temperature, flow rates, and total pressure.

The deposition temperature was measured with a disappearing filament-type optical pyrometer by viewing the inner surface of the graphite cylinder through a small hole in the lid which was in line with a small hole in the baffle. The temperature of the graphite assembly was maintained by adjusting the power to the induction coil. The temperature was uniform over the length of the cylinder from the baffle to within a few millimeters above the mullite cylinder. The pressure was measured with diaphragm-type vacuum gauge and was held constant by manually opening or closing a valve in the line between the reactor and the vacuum

pump. Maintaining the total pressure constant often required adjustments during a run because the chloride species tended to condense in the exhaust line. The flow rates were set by adjusting a valve on the exit side of each flowmeter and by presetting the $TiCl_4$ injection rate. At the end of a run the gases were shut off and the system purged with helium. The induction generator was turned off and the assembly cooled to below red heat in about 5 min.

The deposition rates were determined by difference in mass of the lower graphite cylinder and baffle before and after a run. The mass in milligrams was divided by the run duration in minutes and by the inner surface area of the cylinder and baffle in square centimeters. The deposition rates ranged from about 0.5 to 1.5 mg/cm^2-min. The uncertainties associated with the measurement of temperatures, total pressure, and input flow rates were determined to average between 0.02 and 0.03 mg/cm^2-min. The mass of material deposited on surfaces not in the deposition zone and the change of mass of the graphite substrate were experimentally determined to be insignificant.

Results and Analysis

To try to elucidate the mechanisms involved in the CVD of TiB_2, the observed deposition rates have been compared with those due to strict compliance with (*i*) complete thermodynamic equilibrium, or (*ii*) gaseous diffusion (Eq. [6]) where equilibrium is assumed to exist at the deposition surface. Similar comparisons have been made using deposition efficiencies to provide another means for looking at the data. Efficiency is defined as the deposition rate divided by the rate at which the diboride would deposit in the absence of any thermodynamic or kinetic limitations. Changes in morphology correlated with rate and efficiency data aided in understanding deposition mechanisms.

In all cases, the experimental TiB_2 deposition rates were less than those calculated for thermodynamic equilibrium. Other mechanisms must therefore be limiting the deposition rates.

Temperature.—Figure 3 contains an Arrhenius plot of the logarithm of the observed deposition rate as a function of reciprocal temperature. As the temperature increases the rate goes from a strong to a weak function of temperature with a large change in slope.

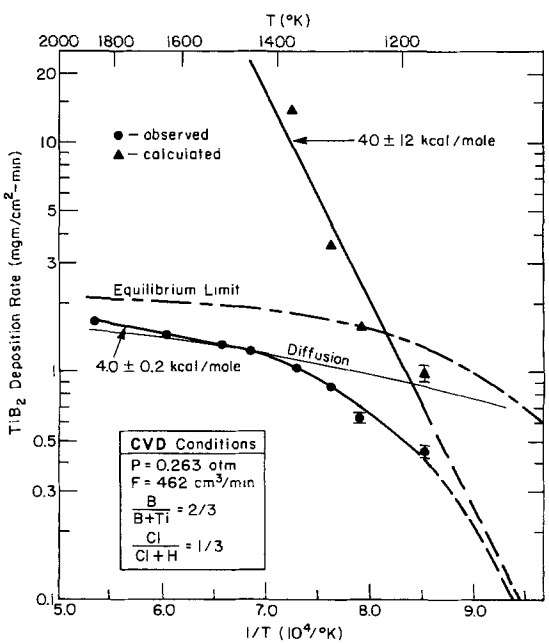


Fig. 3. Arrhenius plot for the deposition of TiB_2, including observed rates and calculated equilibrium-limited, diffusion-limited, and chemical kinetic-limited rates.

This indicates that more than one mechanism is likely to be rate controlling in the temperature range studied.

Chemical reaction rates usually increase exponentially with increasing temperature, and eventually become faster than mass transport rates. Figure 3 indicates that the present system changes from chemical kinetic to mass transport rate-limiting processes with increasing temperature. Above 1373°K the mechanism has an apparent activation energy (E_a) of 4.0 ± 0.2 kcal/mole which is significantly smaller than the 10-50 kcal/mole typical of a chemical kinetic process, but is characteristic of a gas diffusion rate-limiting process.

The experimental conditions of the present study would result in laminar flow if the substrate were an idealized smooth tube of infinite length. However, temperature gradients cause thermal convection, and the baffle in the present system and substrate end effects cause turbulence. In developing a mass transport model for the present experimental system, it is assumed that the bulk gas is turbulent, but that a laminar boundary layer exists adjacent to the substrate surface.

The mass transport model described by Eq. [6] was used to calculate diffusion-controlled deposition rates. It was assumed that the bulk gas partial pressures were equivalent to those in the input reactant gas. Thermodynamic equilibrium was assumed to exist at the deposition surface and the surface partial pressures were found from the equilibrium pressures calculated previously (1). Utilizing the partial pressures of titanium-bearing species, the temperature dependence of diffusion-limited deposition can be derived from Eq. [6] as

$$r \propto T^{(3/4-m/2)}({}_{rn}p_{Ti} - {}_{eq}p_{Ti}) \qquad [7]$$

where r = deposition rate, ${}_{rn}p_{Ti}$ = partial pressure of $TiCl_4$ in the input reactant stream, and ${}_{eq}p_{Ti}$ = sum of the equilibrium partial pressures of Ti-bearing species.

The use of boron-bearing species partial pressures would yield equivalent results.

Using the mean value of 0.8 for m, Eq. [7] is normalized to the observed deposition rate at the standard conditions and then plotted in Fig. 3. This diffusion curve generally follows the observed temperature dependence above 1373°K.

Below 1373°K the deposition rate is more dependent on temperature. A chemical rate-limiting mechanism is assumed to significantly influence the over-all rate since equilibrium is not established at the substrate surface. It is believed that the deposition rate is a function of the inherent rates of diffusion and of the slowest chemical kinetic process occurring at the deposition surface. The partial pressures at the surface are governed by the rate-limiting chemical kinetic process. This governs ${}_sp_i$ in Eq. [6] and, in turn, determines the diffusion rate. The over-all deposition rate can thus be expressed by the diffusion relation and the rate expression for the controlling chemical kinetic process.

Experimental data on the dependencies of the deposition rate on the partial pressures of the various species are not available in the lower temperature region, and so the diffusion and rate relations cannot be defined. A simple linear model can be used to sum the contributions of diffusion and chemical kinetic rate-limiting processes at temperatures below 1373°K. This model assumes that the rate is limited by (*i*) the diffusion of a reactant species through a boundary layer to the equilibrated deposition surface, and/or (*ii*) a chemical kinetic step that is a linear function of the partial pressure of the limiting species, *i.e.*, a first-order reaction. Thus it is possible to write the expression

$$\frac{1}{r} = \frac{1}{r_1} + \frac{1}{r_2}$$

where r_1 is the deposition rate controlled by the diffusion of reactants to an equilibrated deposition surface, and r_2 is the deposition rate controlled by a

chemical kinetic process when the reactant species partial pressures at the deposition surface are equal to those in the input gas.

Using the deposition rates experimentally determined at 1373°K and lower (r), and the respective diffusion-controlled deposition rates plotted in Fig. 3 (r_1), four points for r_2 were calculated and are also shown in Fig. 3. A straight line least squares fit to these points is the temperature dependence of the chemical kinetic process and from its slope an $E_a = 40 \pm 12$ kcal/mole was calculated. This relatively high E_a is typical of a chemical kinetic process.

Total pressure.—The high temperature region has been studied more closely and the influence of the total system pressure on the observed deposition rate and efficiency at 1523°K is shown in Fig. 4. From Eq. [6] and the assumptions described above, the total pressure dependence of diffusion-controlled deposition is

$$r \propto \frac{({}_{rn}p_{Ti} - {}_{eq}p_{Ti})}{P} \qquad [8]$$

Equation [8] normalized to the observed deposition rate at 0.263 atm, the standard value, is also plotted in Fig. 4 along with the equivalent curve for diffusion-controlled deposition efficiency. Agreement with the observed rate and efficiency curves indicates that gaseous diffusion through a boundary layer, with equilibrium at the deposition surface, is probably the rate-limiting mechanism.

Flow rate.—The gas flow rate influences diffusion by changing the laminar boundary layer thickness (Eq. [4]). Again from Eq. [6] the flow rate dependence of the deposition rate can be found and is

$$r \propto F^{1/2}$$

Observed deposition rates and efficiencies agree reasonably well with the diffusion curves normalized to the observed deposition rate and efficiency at the standard conditions as shown in Fig. 5.

B/(B + Ti).—Figure 6 exhibits plots of deposition rates and efficiencies *vs.* the B/(B + Ti) fraction in the reactant gas. The diffusion rate-limiting curves were

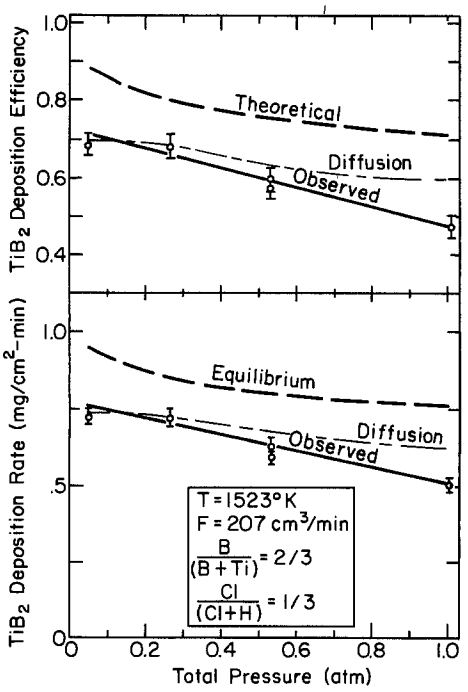


Fig. 4. Deposition rate and efficiency *vs.* total pressure including observed data plus calculated equilibrium-limited and diffusion-limited curves.

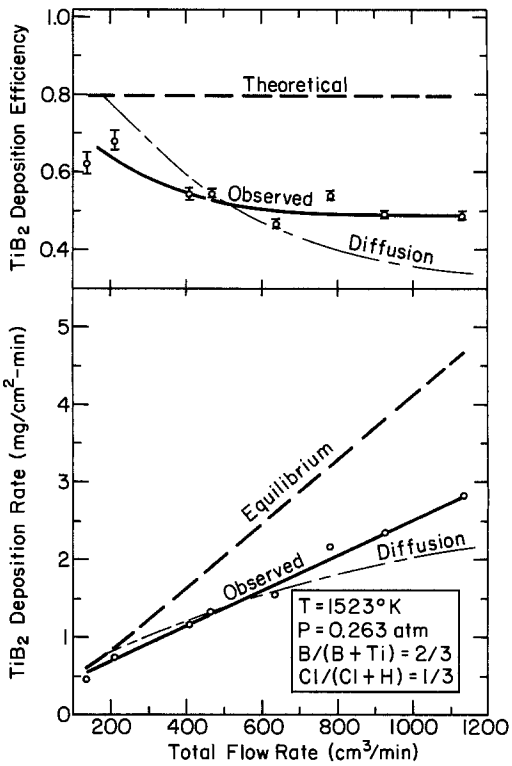


Fig. 5. Deposition rate and efficiency *vs.* total reactant gas flow rate including observed data plus calculated equilibrium-limited and diffusion-limited curves.

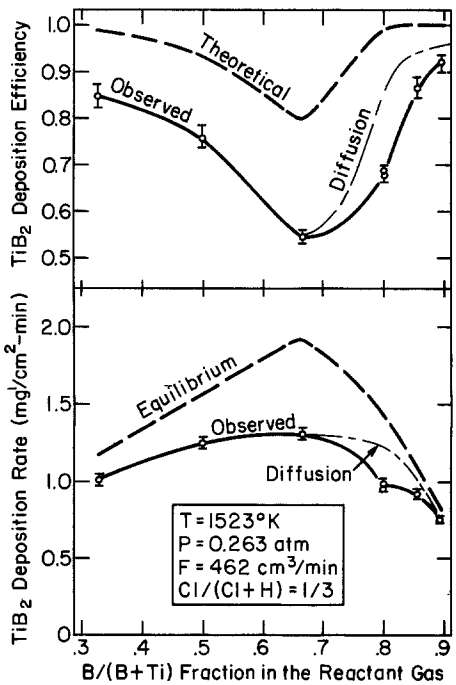


Fig. 6. Deposition rate and efficiency *vs.* reactant gas B/(B + Ti) fraction including observed data plus calculated equilibrium-limited and diffusion-limited curves.

calculated from the equation

$$r \propto ({}_{rn}p_{Ti} - {}_{eq}p_{Ti}) \qquad [9]$$

normalized to the deposition rate at the standard conditions. It is observed that the experimental deposition rate generally follows the calculated diffusion-controlled rate until B/(B + Ti) > 2/3. At these boron-rich compositions the experimental rate becomes significantly less than the diffusion rate. At B/(B + Ti)

> 2/3 it is also observed that TiB_2 no longer grows as a coherent coating. At B/(B + Ti) = 0.8 a small area of the substrate exhibits platelike crystallites oriented normal to the substrate surface, with the c-direction normal to the platelet surface (2). For B/(B + Ti) > 0.8 the TiB_2 grows exclusively as platelets indicating that a chemical kinetic mechanism is rate limiting by suppressing growth in certain crystallographic directions. At these high B/(B + Ti) fractions, boron or boron-containing species may adsorb on the crystal faces normal to the c-direction and poison the growth on these faces. The deposition surface is no longer at equilibrium and the resulting drop in deposition rate and efficiency is observed.

The shoulder in the plot of deposition rate *vs.* B/(B + Ti) in Fig. 6 is due to the change in deposit morphology. The platelike crystallites promote growth by protruding into the boundary layer, disturbing it, and increasing the reactant concentrations near the growth surface. A simple calculation of the average boundary layer thickness using Eq. [2], a typical deposition rate of about 1 mg/cm²-min, and standard conditions for determining the partial pressures of the input gas and equilibrium gas at the substrate yields a thickness of about 1 mm, which is about the same as the dimensions of many of the platelet crystallites.

Cl/(Cl + H).—Figure 7 shows the deposition rates and efficiencies as a function of the Cl/(Cl + H) fraction in the reactant gas. Equation [9] normalized to the deposition rate at the standard conditions was again used to calculate the diffusion curves. At Cl/(Cl + H) < 1/3 the experimental deposition rate is anomalously greater than that predicted from the gaseous diffusion model with equilibrium at the deposition surface. Apparently, at low Cl/(Cl + H) fractions this simple model is no longer sufficient. The large changes in average molecular weight of the gas which accompany variations in the Cl/(Cl +H) fraction change the flow characteristics of the gas. If molecular weight terms were included in Eq. [9] (and Eq. [6]), the system would be more accurately modeled.

At low Cl(Cl + H) fractions the observed deposition efficiency decreases as the theoretical efficiency continues to increase. Under these conditions a chemical kinetic process may be rate limiting and equilibrium may not exist at the deposition surface. This idea is enhanced by the fact that at low Cl/(Cl + H) fractions the coating formed is no longer faceted and coherent, but is made up of irregular crystallites which have little preferred orientation (2). Partially reduced molecular species or hydrogen may strongly adsorb on the reaction surface and slow growth. Equilibrium calculations indicate that the partial pressure of $HBCl_2$ approaches that of BCl_3 at low Cl/(Cl + H), and $HBCl_2$ may play a role in a chemical kinetic step.

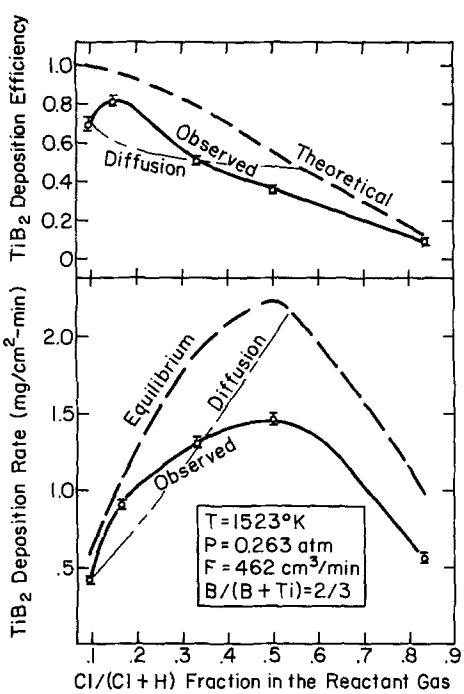


Fig. 7. Deposition rate and efficiency *vs.* reactant gas Cl/(Cl + H) fraction including observed data plus calculated equilibrium-limited and diffusion-limited curves.

Discussion

Peshev and Niemyski (8) have also reported efficiency data for the CVD of TiB_2. Although their system differed significantly, a comparison of the results is possible. The higher temperature and lower Cl/(Cl + H) fraction in the reactant gas used by Peshev and Niemyski (see Table I) increased their standard condition efficiency over that of this study, as expected. The influence of the different flow rates is difficult to compare because of different reactor and substrate configurations.

Figure 8 is a plot of efficiency *vs.* deposition temperature for the data generated in both studies. Peshev and Niemyski's (8) results indicate that the diffusion rate-limiting region, where equilibrium is presumed to exist at the deposition surface, occurs at temperatures greater than 1673°K as compared to a transition temperature of 1373°K for the present system. Lower Cl/(Cl + H) fractions in the reactant gas probably caused their system to remain chemical kinetic rate limited to higher temperatures. Their two highest temperature data points, however, yield an apparent activation energy of about 6.8 kcal/mole, which may indicate that both mass transport and chemical kinetic effects are important.

Deposition efficiencies for both studies are plotted *vs.* total flow rate in Fig. 9. The relation for calculating the efficiency curves was derived from Eq. [6]

$$\text{efficiency} = \frac{J(\text{diffusion})}{J(\text{input})} \propto \frac{F^{1/2}}{F} = F^{-1/2}$$

The curves were normalized to the deposition rates at the respective standard conditions. Agreement between the diffusion-limited and observed deposition efficiencies is fair and the efficiency of Peshev and Niemyski appears linear rather than proportional to $F^{-1/2}$.

The efficiencies as a function of reactant gas Cl/(Cl + H) ratio for both studies are compared in Fig. 10. Peshev and Niemyski (8) increased the hydrogen flow rate to vary the Cl/(Cl + H) fraction instead of varying input flow rates of $TiCl_4$, BCl_3, and H_2. To compare results it is necessary to remove the total flow rate dependence from Peshev and Niemyski's data by dividing each point by its experimental efficiency for the corresponding total flow rate. The results multipled by the efficiency at 2580 cm³/min are shown in Fig. 10.

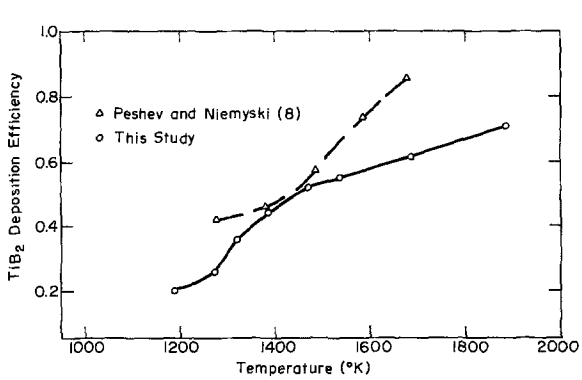


Fig. 8. Deposition efficiency *vs.* deposition temperature for Peshev and Niemyski's (8) data and that of the present study.

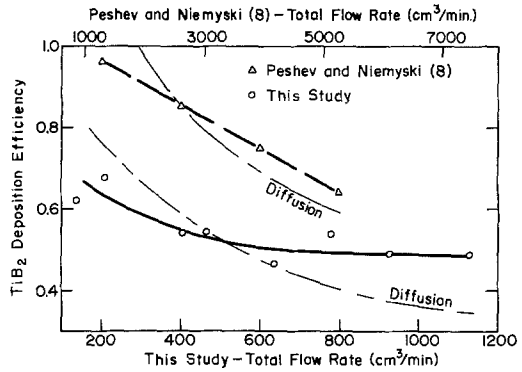


Fig. 9. Deposition efficiency vs. reactant gas flow rate for Peshev and Niemyski's (8) data and that of the present study. Included are diffusion-limited curves normalized to the deposition rates at the standard conditions of each respective study. The differences in flow rate scales should be noted.

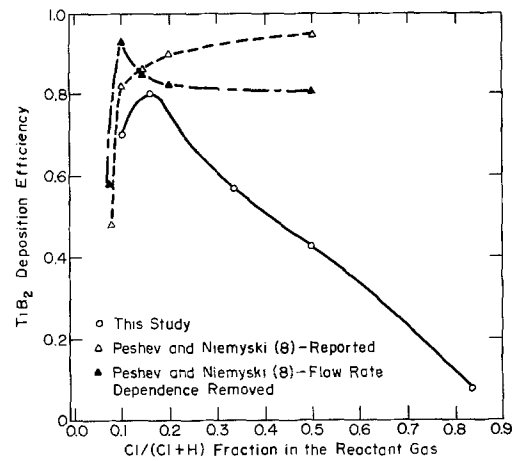


Fig. 10. Deposition efficiency vs. reactant gas Cl/(Cl + H) fraction for Peshev and Niemyski's (8) data and that of the present study. A curve derived from Peshev and Niemyski's data by removing the total flow rate dependence from their efficiencies is also shown.

The general shape of the derived flow rate-independent curve of Peshev and Niemyski (8) is similar to that found in the present study. Both curves show a significant drop in efficiency at low Cl/(Cl + H). This supports the conclusion that a chemical kinetic mechanism becomes rate limiting and reverses the trend toward increasing efficiency that is expected from equilibrium calculations (theoretical curve in Fig. 7).

Mehalso and Diefendorf (12) have recently reported a study of the CVD of boron by the hydrogen reduction of BCl_3. Their analysis was similar to that presented here, but they only considered the gaseous species BCl_3, H_2, and HCl. Their substrate consisted of a heated filament oriented parallel to the gas flow. Deposition rates were determined as a function of deposition temperature, total flow rate, and HCl concentration at, apparently, 1 atm total pressure.

They agree with the model of mass transfer across a laminar boundary layer described above and postulate the diffusion of HCl is rate limiting at lower gas flow rates. As the gas flow rate was increased to a maximum of ~4000 cm³/min they noted that the boundary layer became smaller and the rate of gaseous diffusion thus increased. At gas flow rates > 1000 cm³/min the deposition rate appeared limited by a chemical kinetic mechanism. They believe that the mechanism is the first-order desorption of HCl from the deposition surface and have calculated from an Arrhenius plot an activation energy of 52 kcal/mole. This value is similar to the

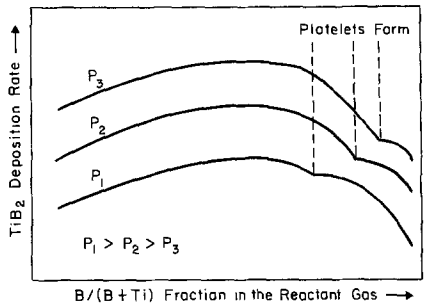


Fig. 11. Predicted relative curves for the TiB_2 deposition rate vs. reactant gas B/(B + Ti) for three different pressures.

40 ± 12 kcal/mole presently determined for the first-order, low temperature chemical kinetic rate-limiting mechanism in the CVD of TiB_2. It is possible that a single mechanism common to both the deposition of boron and the diboride of titanium, such as the desorption of HCl, may be an important rate-limiting process in the CVD systems.

The various rate relationships experimentally determined in the present study can be used to develop families of curves such as those in Fig. 3-7. As an illustration, a group of curves was developed for predicting the deposition rate as a function of reactant gas B/(B + Ti) ratio at three different total pressures. Figure 11 shows that the general shape of the predicted deposition rate curves follows that of the observed deposition rate curve in Fig. 6. From the pressure dependence of the deposition rate it was observed that the rate increases with decreasing pressure and the predicted curves show lower relative rates for higher pressures.

At high B/(B + Ti) fractions the observed rate drops below that predicted to be due to gaseous diffusion with equilibrium assumed to exist at the deposition surface, although a shoulder appears with increasing B/(B + Ti). The appearance of TiB_2 platelike crystallites, which accompanies the decreasing deposition rate, indicates that a chemical kinetic mechanism has become rate limiting. It is hypothesized that the TiB_2 platelets are formed by the adsorption of species on certain crystallite faces. At high pressures the concentrations of the gaseous species are greater and, therefore, adsorption takes place to a larger extent. As a result, at higher pressures the chemical kinetic mechanism becomes rate limiting at smaller B/(B + Ti) fractions yielding the TiB_2 platelets. The shoulder thus appears at lower B/(B + Ti) fractions and this is indicated in Fig. 11. In this manner a relationship determined with parameters held constant at specific values can be extended to other values of those fixed parameters.

Conclusions

The CVD of TiB_2 was studied by determining the deposition rates as a function of deposition temperature, total pressure, total reactant gas flow rate, and B/(B + Ti) and Cl/(Cl + H) fractions in the reactant gas. Either or both of the possible rate-limiting mechanisms of mass transfer and chemical kinetics appeared limiting under various deposition conditions. Above 1373°K rates often appeared to be limited by the diffusion of reactant species through a gas boundary layer to the deposition surface where chemical equilibrium was achieved. Below 1373°K a chemical kinetic mechanism dominates the TiB_2 deposition. An activation energy of 40 ± 12 kcal/mole was calculated for the process by using a simple linear rate expression. Changes in the composition of the reactant gas changed the rate-limiting mechanisms at 1523°K. Indications are that at B/(B + Ti) > 2/3 or at Cl/(Cl + H) < 1/3, the deposition surface is not at thermodynamic equilibrium and chemical kinetic mechanisms govern the deposition.

The model developed for the nigh temperature CVD of TiB_2 appears applicable to CVD systems operated under conditions in which chemical kinetic processes are rapid in comparison to gaseous diffusion. Mass transport models, such as the one discussed in the present paper, can be quantitatively applied to other CVD systems. The model presented here is simple, however, and involves a significant number of assumptions. The assumptions include the use of a simple expression for the binary diffusion coefficient, even though the present system contains more than two gaseous species. Hydrogen was generally present in excess, so the approximation that the other species are diffusing through pure hydrogen is probably good. The model also considers the boundary layer thickness to vary in a manner similar to that for flow across a semi-infinite flat plate.

The conclusions about the rate-limiting mechanisms and the effect of the deposition parameters on the deposit character made it possible to develop a preliminary model of the deposition processes. Such a model may allow the prediction of optimum conditions for the production of a desired deposit. Studies like this one can help provide the necessary knowledge to more thoroughly understand CVD processes in general.

Acknowledgments

The authors are indebted to their colleagues and especially to John H. Blanks at the Materials Research Laboratory, The Pennsylvania State University, for helpful discussions and advice. This work was supported by the National Science Foundation under Grant No. DMR 72-03133 (formerly GH-34515). This paper is based in part on the Ph.D. thesis by T. M. Besmann submitted to The Pennsylvania State University, 1976.

Manuscript submitted Sept. 3, 1976; revised manuscript received Dec. 6, 1976.

Any discussion of this paper will appear in a Discussion Section to be published in the December 1977 JOURNAL. All discussions for the December 1977 Discussion Section should be submitted by Aug. 1, 1977.

Publication costs of this article were assisted by Oak Ridge National Laboratory.

REFERENCES

1. T. M. Besmann and K. E. Spear, *This Journal*, **124**, 786 (1977).
2. T. M. Besmann and K. E. Spear, *J. Cryst. Growth*, **31**, 60 (1975).
3. K. Moers, *Z. Anorg. Allg. Chem.*, **198**, 243 (1931).
4. C. F. Powell, "High-Temperature Technology," I. E. Campbell, Editor, p. 131, John Wiley & Sons, Inc., New York (1956).
5. K.-Th. Wilkie, *Z. Phys. Chem. (Leipzig)*, **220**, 137 (1962).
6. R. E. Gannon, R. C. Folweiler, and T. Vasilos, *J. Am. Ceram. Soc.*, **46**, 496 (1963).
7. J. J. Gebhardt and R. F. Cree, *ibid.*, **48**, 262 (1965).
8. P. Peshev and T. Niemyski, *J. Less-Common Metals*, **10**, 133 (1965).
9. J. Cueilleron, G. Lahet, F. Thevenot, and R. A. Pâris, *ibid.*, **24**, 317 (1971).
10. M. E. Jones and D. W. Shaw, "Treatise on Solid State Chemistry, Vol. 5, Changes of State," N. B. Hannay, Editor, p. 283, Plenum Press, New York (1975).
11. C. O. Bennett and J. E. Myers, "Momentum, Heat, and Mass Transfer," p. 115, McGraw-Hill Book Co., New York (1962).
12. R. M. Mehalso and R. J. Diefendorf, in "Chemical Vapor Deposition, Fifth International Conference," J. M. Blocher, Jr., H. E. Hintermann, and L. H. Hall, Editors, p. 84, The Electrochemical Society Softbound Symposium Series, Princeton, N.J. (1975).

Chemical Vapor Deposition of Titanium Nitride on Iron in an Ultrasonic Field

Takehiko Takahashi* and Hideaki Itoh

Department of Applied Chemistry, Faculty of Engineering, Nagoya University, Nagoya 464, Japan

ABSTRACT

An adherent film of TiN up to 160 μm was obtained on an iron substrate by chemical vapor deposition (CVD) in an ultrasonic field in the temperature range of 900°-1100°C, using a reactant gas mixture of $TiCl_4 + N_2 + H_2$. Ultrasonic vibrations of the iron substrate were found to improve adherence and toughness of the film, but had a minor effect on the growth rate and the deposition temperature. The Vicker's microhardness of TiN obtained in the ultrasonic field was 1600-2000, and the film was confirmed to have a strong <220> orientation. The CVD of TiN on iron was considered to proceed by a two-step mechanism.

Titanium nitride (TiN), one of the typical interstitial compounds, has a melting point of 2950°C, a microhardness of 1400-2000, and a high chemical stability in acid or alkali solution (1). Films or whiskers of TiN have been noted in recent years as a protective and decorative coating material on metals, or as a reinforced composite material (2, 3).

Film growth and whisker growth of titanium nitride on a graphite substrate by chemical vapor deposition (CVD) from the reactants $TiCl_4 + N_2 + H_2$ were reported in detail by Synielnikowa *et al.* (4), the authors (5), and Kato and Tamari (6). Münster and Ruppert (7) studied the CVD of TiN coatings with the same reactants on an induction-heated iron substrate and obtained a TiN film of about 100 μm thick. The adherence of the deposited TiN on an iron substrate is weak when the thickness exceeds 100 μm (4). A stress is developed at the interface between TiN and Fe due to the difference in their thermal expansion coefficient. Preelectrodeposition of cobalt on an iron substrate prior to the CVD of TiC (8) or TiB_2 (9) was investigated by the authors to improve the adherence between the deposited layer and the substrate. Similar techniques to form such an interlayer have been developed by others (10).

Application of an ultrasonic field to CVD processes has not been reported. Some chemical uses of ultra-

Electrochemical Society Active Member.
Key words: chemical vapor deposition, TiN, ultrasonic field, protective coating.

sound have been investigated in the field of ultrasonics in electroplating (11), metallurgy (12), and crystallization (13). In the present study, we investigated in detail the effect of ultrasonics on CVD of TiN using a gas mixture of $TiCl_4 + N_2 + H_2$. The goal was to obtain an adherent and dense thick film of TiN on an iron substrate and to investigate the growth mechanism of the TiN film.

Experimental

The flow system of the experimental apparatus is shown in Fig. 1. An oscillator and vibrator with frequency 19 kHz and power 10-20 W/cm², were used as an ultrasound source. The ultrasonic vibrations were applied to the substrate in the reactor through a cone and horn mechanical system. The reactant gas mixture is composed of $TiCl_4$, N_2, and H_2. The $TiCl_4$ vapor is carried with hydrogen gas from the $TiCl_4$ saturator which is heated at room temperature to 70°C. Hydrogen and nitrogen gases are purified by passing them through activated copper and silica gel columns. The flow rates of H_2 and N_2 gases at room temperature are measured by flowmeters.

Figure 2 shows the schematic diagram of the vertical reactor. The ultrasonic vibration horn is inserted into the quartz reactor (inside diameter: 25 mm), and a low carbon steel substrate (carbon content: about 0.3%) is silver-soldered at the tip of the horn. The tip diameter of a nailheaded substrate is 7 mm. The vinyl chloride flange between the horn and the reactor helps to prevent the ultrasonic power from being absorbed by the reactor wall. The substrate was polished by 800 mesh emery paper and cleaned in CH_3OH and HCl aqueous solutions, before being heated for a reaction run by an rf induction coil in the temperature range of 700°-1150°C. Hydrogen gas (flow rate: 7.0 ml/sec) is introduced at the top of the reactor to prevent overheating of the horn, and the reactor wall is water-cooled by copper pipe. The temperature of the substrate is measured by an optical pyrometer through the observation window. The reactant gas is introduced at the bottom of the reactor, and the residual gases are exhausted above the sample.

Results

Deposition condition of titanium nitride.—According to the authors' study (5), the deposition process of TiN is less affected by the gas flow rates of $TiCl_4$, N_2, and H_2 than by deposition temperature. The flow rates were fixed in the present experiment in a narrow range: $TiCl_4$, 0.9-1.0 ml/sec; H_2, 7.4 ml/sec; and N_2, 2.0-5.0 ml/sec.

Figure 3 shows the relation between the growth rate of the TiN film and the substrate temperature at constant gas flow rates with and without ultrasound. The

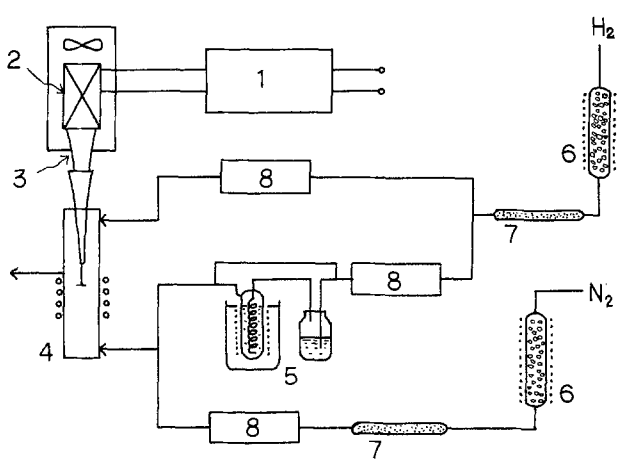


Fig. 1. Flow system of experimental apparatus. 1, Oscillator; 2, vibrator; 3, cone; 4, quartz reactor tube; 5, $TiCl_4$ saturator; 6, activated copper; 7, silica gel; 8, flowmeter.

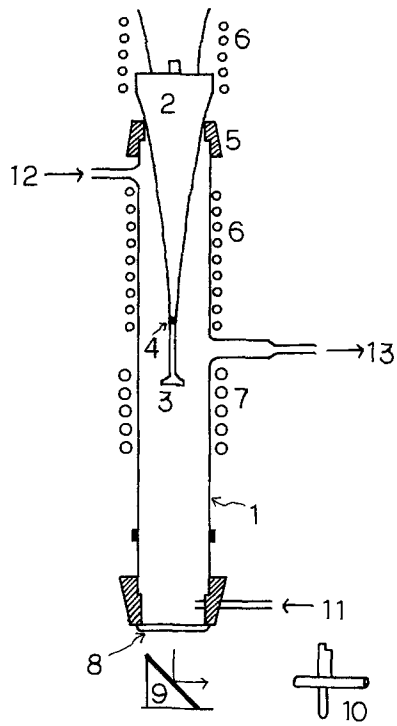


Fig. 2. Schematic diagram of reactor. 1, Quartz reactor tube; 2, horn; 3, substrate; 4, silver solder; 5, flange; 6, cooling pipe; 7, rf induction coil; 8, observation window; 9, mirror; 10, pyrometer; 11, $TiCl_4 + H_2 + N_2$; 12, H_2; 13, outlet.

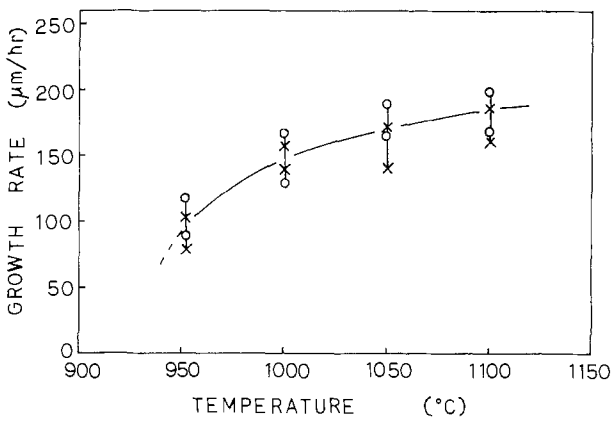


Fig. 3. Growth rate vs. substrate temperature. o—o Ultrasound applied, x—x no ultrasound. Reaction time, 60 min. Gas flow rates: N_2, 3.8 ml/sec; H_2, 7.4 ml/sec; $TiCl_4$, 1.0 ml/sec. The temperature of $TiCl_4$ saturator, 70°C.

growth rate is apparently zero at temperatures less than 900°C. The growth of titanium nitride is initiated rapidly at 950°C, above which the growth rate increases progressively with the increase of temperature. A film of about 180 μm was obtained at a substrate temperature of 1100°C with a reaction time of 60 min. The film growth rates are not significantly changed when ultrasound is applied.

Structure of vapor-deposited titanium nitride.—Figures 4a and b show the surface appearances of the deposits on a carbon steel substrate which were obtained at a substrate temperature of 1050°C, with and without ultrasound. Normally the deposited film tends to peel off partially from the substrate even with a little pat of the surface (see Fig. 4a). This probably occurs because of the stress at the TiN-Fe interface in the cooling process of the specimen. In the case of CVD with ultrasound the deposit is quite adherent to the substrate, as shown in Fig. 4b. This can be verified by

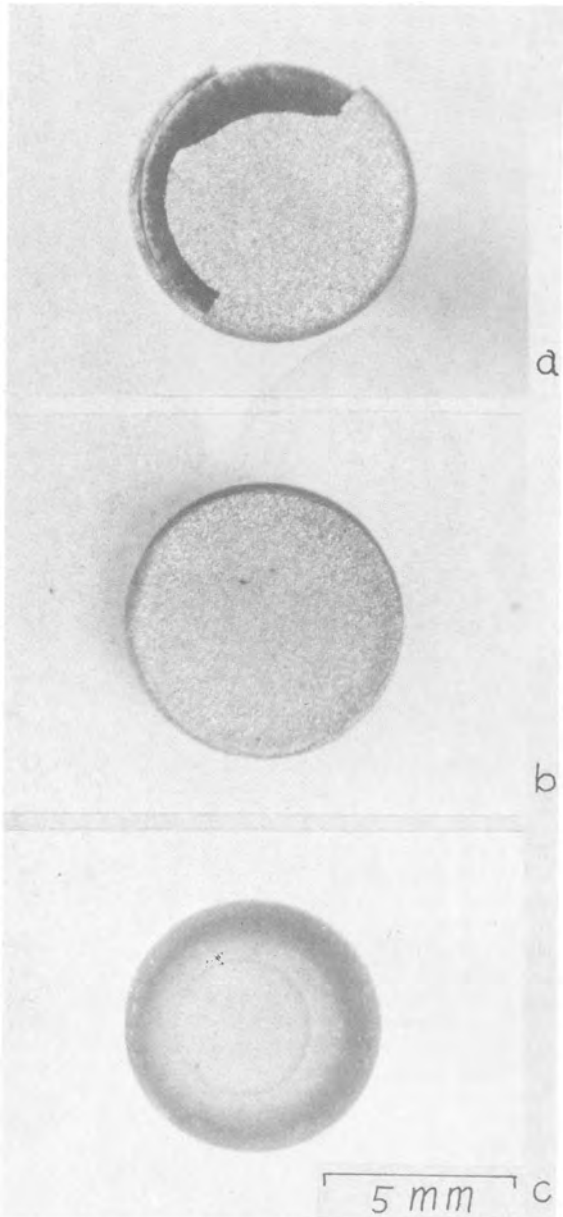


Fig. 4. Micrographs of surface appearance. (a) Temperature, 1050°C; reaction time, 60 min; no ultrasound. (b) Temperature, 1050°C; reaction time, 60 min; ultrasound applied. (c) Temperature, 950°C; reaction time, 13 min; ultrasound applied.

a hammering test, when only the rimmed part of the deposited film has some small cracks.

Figure 5 shows a typical microstructure of the vapor-deposited TiN film obtained at 950°C. A thick, golden yellow film of TiN is obtained with a 60 min reaction time. For CVD with no ultrasound, a sharply cracked line is observed as in Fig. 5b, and relatively large crystallites having glossy facets are obtained. A smooth deposit results from applying ultrasonic vibration to the substrate (see Fig. 5a).

Micrographs of cross sections etched by nital solution ($C_2H_5OH:HNO_3 = 100:5$) are shown in Fig. 6. Cracks or pores normally can be observed at the nonadherent film of TiN on the carbon steel substrate (see Fig. 6a). By CVD in an ultrasonic field a uniform and adherent film with a thickness of 100-160 μm can be obtained in a wide temperature range: 950°-1050°C (see Fig. 6b and c).

Figure 7 shows the variation of x-ray diffraction patterns of the surface of specimens deposited at substrate temperatures of 950°, 1000°, and 1050°C with ultra-

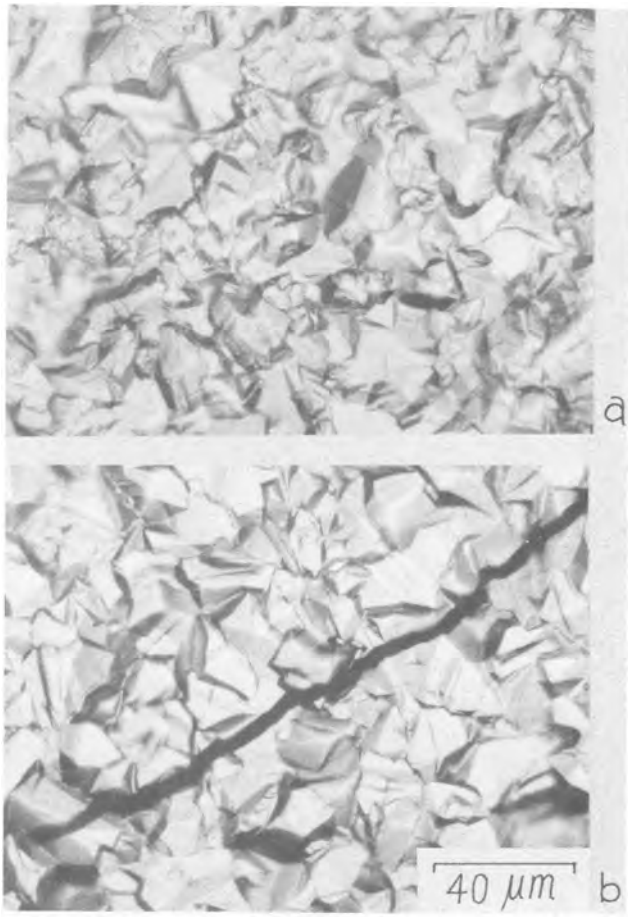


Fig. 5. Micrographs of vapor-deposited TiN. (a) Ultrasound applied. (b) No ultrasound. Substrate temperature, 950°C; reaction time, 60 min.

sound. The film had a <220> crystallographic preferred orientation (4) in the temperature range of 950°-1050°C. This result differs from vapor-deposited TiN films on graphite substrates (5), where a strong (220) line was observed only above a deposition temperature of 1200°C. Münster and Ruppert (7) found a <100> or <111> preferred orientation on an iron substrate which was considered to depend on the substrate texture. The x-ray Laue pattern of our TiN films showed a strong (220) diffraction ring which was composed of homogeneous fine Laue spots. This suggests that the crystallites are aggregated at random, independent of the orientation of the base material. The x-ray patterns having a <220> orientation were similar for specimens obtained without ultrasound.

Some properties of TiN film grown in the ultrasonic field.—Figure 8 shows a cross section of a TiN film obtained at a temperature of 1000°C in an ultrasonic field. A large microhardness indentation (300g load) at the interface between TiN and the carbon steel substrate confirms the improved adherence, since the TiN film is not peeled off from the substrate. The toughness of the deposited film seems to be high, since no cracks can be observed between five small indentations (100g load) on the cross section of TiN layer. The Vicker's microhardness was 1600-1750, comparable with the reported values (1, 15). The microhardness of the surface was 1900-2000 which is higher than that of the cross section. The hardness may be considered to be affected by the anisotropy of the TiN texture.

Figure 9 shows the etching figures of a cross section of the TiN film deposited in an ultrasonic field. Nital etching (Fig. 9a) for 30 sec shows that the texture of the carbon steel substrate near the interface does not

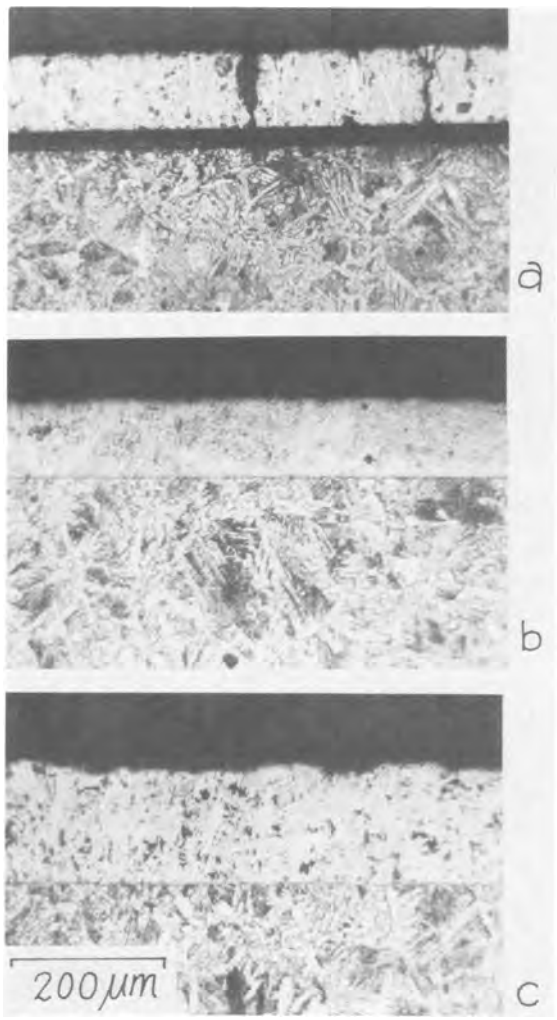


Fig. 6. Micrographs of the cross section etched by nital solution. (a) No ultrasound; temperature, 950°C. (b) Ultrasound applied; temperature, 950°C. (c) Ultrasound applied; temperature, 1000°C.

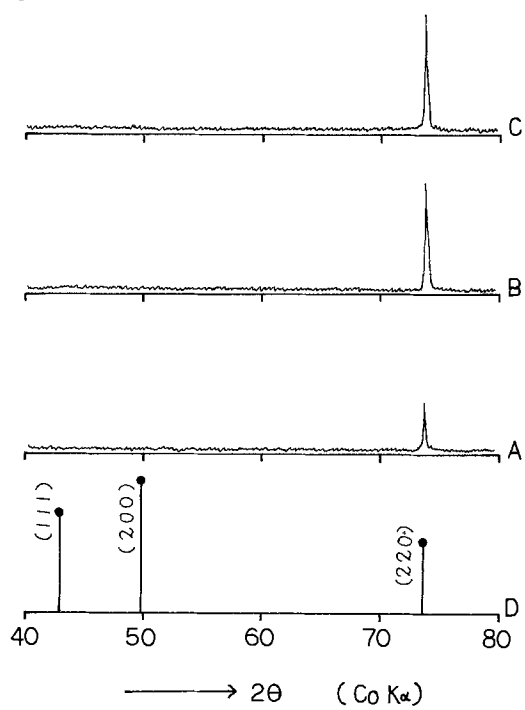


Fig. 7. X-ray diffraction patterns of deposits. Substrate temperature. A, 950°C; B, 1000°C; C, 1050°C; D, ASTM TiN (14). Reaction time, 60 min.

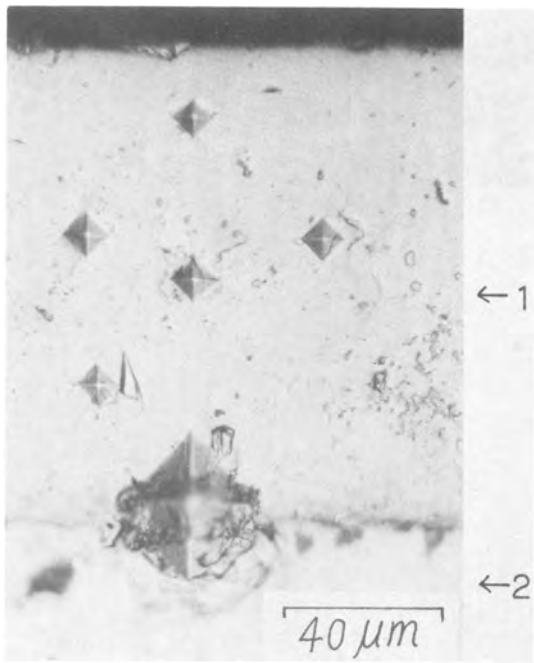


Fig. 8. Cross section of TiN film with microhardness indentations under 100 and 300g load. 1, TiN layer; 2, carbon steel substrate.

change (ferrite + perlite), but a 2-3 μm thick layer can be observed at the boundary region. Similar layers were obtained under ordinary CVD, although the adherence was not good. Figure 9b shows the TiN layer after etching by a hot aqua regia solution for 10 min. The carbon steel was etched entirely away, and very minor attack of the TiN film indicates a high chemical stability of TiN layer for hot aqua regia. The fine columnar texture can be seen in the TiN layer, which demonstrates the dense aggregation of crystallites, while a broad columnar texture was observed on the etching figure of the TiN deposited by CVD with no ultrasonic field (see Fig. 9c).

Discussion

Effect of ultrasound on CVD process.—From thermodynamic (7) and the experimental (5) data, the chemical reaction is the determining step in the formation of TiN in the temperature range of 900°-1100°C. Therefore, the effect of ultrasound on the reaction process is considered to be minor. Figure 3 shows that ultrasonic vibration does not affect the growth rate or the deposition temperature. If the process was diffusion limited such as at higher temperatures, the growth rate could be affected by ultrasonic vibration.

The development of film toughness and adhesion, however, was improved by using the ultrasonic field, as shown in Fig. 4, 5, 6, 8, and 9. The nucleation process may be promoted by activated molecular motion in the boundary region, so that the crystallite size is smaller and a dense layer of TiN was grown. Some similar characteristics of the crystallization process in an ultrasonic field have been found in the growth of crystals from the melt or solution (13). The adherence of the TiN film to the substrate was also considered to be promoted by the improved deposit properties.

Deposition mechanism of TiN on iron substrate.—The intermediate layer in Fig. 9a suggests a special growth mechanism for TiN at the initial stage of reaction. In fact, a coaxial growth layer of TiN can be observed in Fig. 4c, which was obtained at a reaction time of 13 min and a deposition temperature of 950°C. The deposition of TiN is found to be initiated radially from the center of the substrate surface. It takes 30 min at 950°C and 10 min at 1000°C, until the covering of all the substrate surface with a TiN layer is completed.

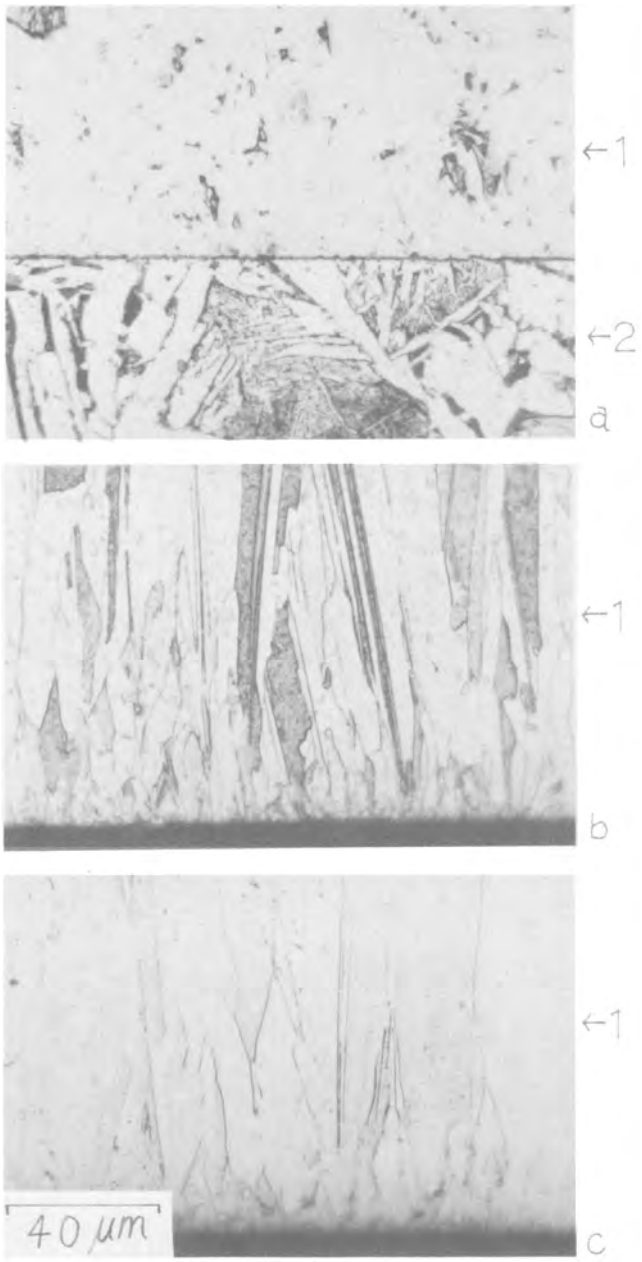


Fig. 9. Etching figures of cross section. (a) Etched by nital solution (b) Etched by hot aqua regia for 10 min, ultrasound applied. (c) Etched by hot aqua regia for 10 min, no ultrasound. 1, TiN film; 2, carbon steel substrate.

Figure 10 shows the variation of x-ray diffraction patterns with reaction time when the substrate temperature was 950°C. At a reaction time of 13 min, the strong α-Fe and weak isotropic TiN lines occur (14). Anisotropic TiN, which has a <220> preferred orientation, is apparent as the reaction time increases. Only the (220) line of TiN occurs after a reaction time of 60 min (see Fig. 7a). Figure 11 shows electron microprobe scans of the cross section, where a mixed region of Ti and Fe cannot be confirmed except at the boundary between Fe substrate and TiN film. Figures 7, 9a, 10, and 11 suggest that the reaction process is not in disagreement with the two-step process proposed by Münster and Ruppert (7). The initial displacement reaction

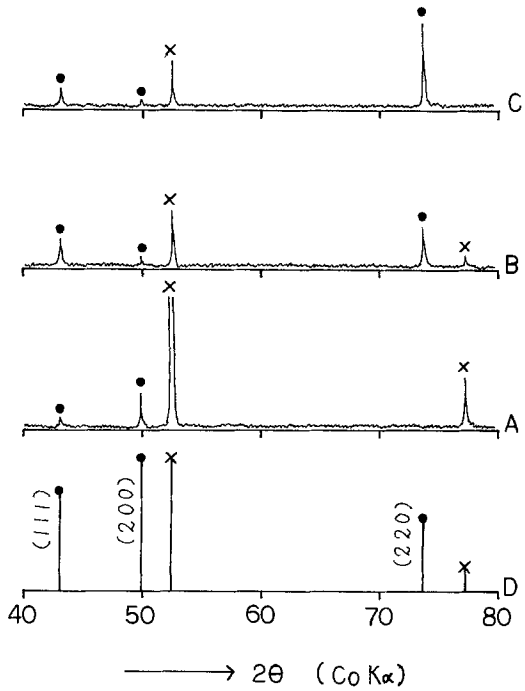


Fig. 10. Variation of x-ray diffraction patterns with reaction time. Reaction time; A, 13 min; B, 20 min; C, 33 min; D, ●; ASTM TiN (14); X, ASTM Fe (14). Substrate temperature, 950°C.

$$TiCl_4(g) + 2Fe(s) + \tfrac{1}{2}N_2(g) \rightarrow \text{isotropic-TiN}(s) + 2FeCl_2(s) \quad [1]$$

may not occur below 950°C, probably because of the substrate surface being covered with molten $FeCl_2$. After the initial stage the following deposition reaction might proceed

$$TiCl_4(g) + 2H_2(g) + \tfrac{1}{2}N_2(g) \rightarrow \text{anisotropic-TiN}(s) + 4HCl(g) \quad [2]$$

Acknowledgments

The authors wish to thank Mr. K. Terashima and Mr. H. Kamiya for XMA analysis and helpful discussions.

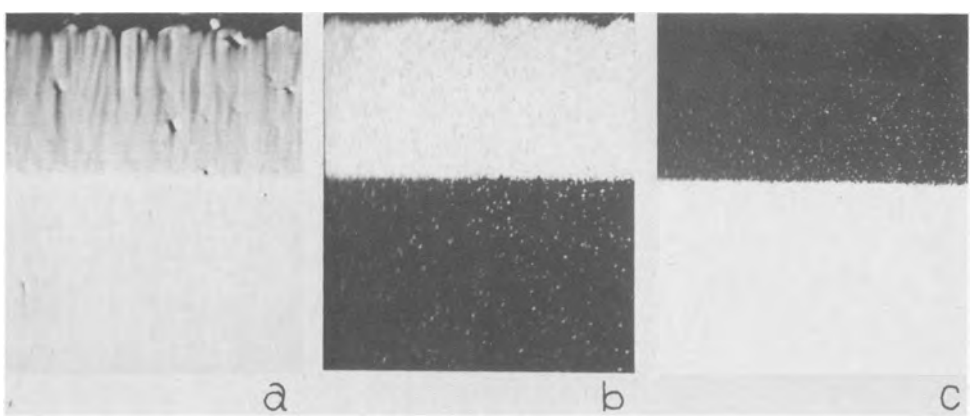


Fig. 11. Electron microprobe scans of cross section. (a) Reflected electron beam image. (b) X-ray image for TiKα. (c) X-ray image for FeKα.

Manuscript submitted Oct. 20, 1976; revised manuscript received Jan. 5, 1977.

Any discussion of this paper will appear in a Discussion Section to be published in the December 1977 JOURNAL. All discussions for the December 1977 Discussion Section should be submitted by Aug. 1, 1977.

Publication costs of this article were assisted by the authors.

REFERENCES

1. Kirk-Othmer, "Encyclopedia of Chemical Technology," Vol. 13, p. 819, John Wiley & Sons, Inc., New York (1967).
2. L. Aggour, E. Fitzer, and W. Weisweiler, *High Temp.—High Pressures*, **6**, 73 (1974).
3. R. Warren and M. Carlsson, in "Chemical Vapor Deposition, Fifth International Conference," J. M. Blocher, Jr., H. E. Hintermann, and L. H. Hall, Editors, pp. 611, 623, The Electrochemical Society Softbound Symposium Series, Princeton, N.J. (1975).
4. W. Synielnikowa, T. Niemyski, J. Panczyk, and E. Kierzekpecold, *J. Less-Common Met.*, **23**, 1 (1971).
5. T. Takahashi and Y. Suzuki, *Nippon Kagaku Kaishi*, 1043 (1974).
6. A. Kato and N. Tamari, *J. Cryst. Growth*, **29**, 55 (1975).
7. A. Münster and W. Ruppert, *Z. Elektrochem.*, **57**, 558, 564, 571 (1953).
8. T. Takahashi, K. Sugiyama, and K. Tomita, *This Journal*, **114**, 1230 (1967).
9. T. Takahashi and H. Kamiya, *J. Cryst. Growth*, **26**, 203 (1974).
10. W. Ruppert, "Proceedings of the 3rd International Conference on Chemical Vapor Deposition," p. 340, American Nuclear Society (1972).
11. S. Kochergin and G. Vyaseleva, "Electrodeposition of Metals in Ultrasonic Fields," Consultants Bureau Enterprises, New York (1966).
12. A. Crawford, *Metallurgia*, **47**, 109 (1953).
13. A. Kapustin, "The Effects of Ultrasound on the Kinetics of Crystallization," Consultants Bureau Enterprises, New York (1963).
14. L. Berry *et al.*, "Inorganic Index to the Powder Diffraction File," File No. 6-0642 and 6-096, Joint Committee on Powder Diffraction Standard, Easton (1971).
15. S. Motojima, K. Baba, K. Kitatani, Y. Takahashi, and K. Sugiyama, *J. Cryst. Growth*, **32**, 141 (1976).

Technical Notes

The Analysis of Anodic Oxide Films on GaAs and GaP by Means of Radioactive Tracer Techniques

J. C. Verplanke and R. P. Tijburg

Philips Research Laboratories, Eindhoven, The Netherlands

In III-V compound device technology native oxide films are becoming of practical interest. The importance of the native oxide on GaP and GaAs has been demonstrated by Spitzer *et al.* (1) and Schwartz *et al.* (2). Hasegawa and co-workers (3) published some promising results with GaAs MOS capacitors made with anodic oxide films. Logan *et al.* (4) suggested the use of anodic oxidation for the removal of thin predetermined layers in diffusion studies.

There have already been several studies aimed at determining the composition of the anodic oxide films (5) using for example Rutherford backscattering, Auger electron spectroscopy, combined with ion beam sputtering, and the electron beam microprobe. We analyzed anodic oxide layers made on GaAs and GaP with radioactive tracer techniques. The layers measured were as grown, as well as annealed at temperatures between 200° and 600°C. As well as the average composition we also determined the composition of anodic oxide layers on GaAs as a function of thickness.

Experimental Techniques

The compounds were activated in a thermal neutron flux prior to the oxidation step. The flux was about 3×10^{11} neutrons cm^{-2} sec^{-1} for 2 hr. The main nuclear reactions taking place are (n, γ) reactions

Key words: gallium phosphide, gallium arsenide, oxidation, radioactive tracer analysis.

$^{69}Ga(n,\gamma)^{70}Ga$ ($T_{1/2}$ = 20 min; low gamma abundance)

$^{71}Ga(n,\gamma)^{72}Ga$ ($T_{1/2}$ = 14.1 hr; main gammas 630 and 834 keV)

$^{75}As(n,\gamma)^{76}As$ ($T_{1/2}$ = 26.4 hr; main gammas 559 and 657 keV)

$^{31}P(n,\gamma)^{32}P$ ($T_{1/2}$ = 14.3 days; only betas E_{max} = 1.7 MeV)

^{72}Ga and ^{76}As can be used to analyze the oxide on GaAs and ^{72}Ga and ^{32}P for that on GaP. The half-life of ^{70}Ga is too short to be useful for analysis purposes. After activation of the starting material the anodization step is performed. Then the oxide layer is stripped off in warm diluted (10%) phosphoric acid. The activities are measured in both the anodization bath and the etching bath. ^{72}Ga and ^{76}As (GaAs) are measured simultaneously with a Ge(Li) semiconductor detector and a 2048 channel analyzer. The ^{72}Ga activity of GaP is measured with a NaI (Tl) scintillation detector and a 400 channel analyzer and the ^{32}P activity, after the ^{72}Ga has decayed, by means of its Čerenkov radiation in an aqueous solution, using a liquid scintillation analyzer. The measured activities are converted to mass by means of a standard of GaAs or GaP which is irradiated simultaneously and after that dissolved in aqua regia + some HBr. An aliquot part is pipetted and measured. The masses found in both the anodization bath and the etching bath are added in order to

determine the total layer thickness that was removed during the anodization and subsequent etching step. By adding the mole fractions of the III element in the two solutions and the mole fractions of the V element in the two solutions one has a check that no important errors have been made. The analyzing method for each element involved has an inaccuracy of less than 5%.

Sample Preparation

All our experiments were performed on (100) oriented GaAs and GaP slices with an n-type dopant between $5 \cdot 10^{17}$ and $1 \cdot 10^{18}$ atoms cm^{-3}, and having bright, etched surfaces. The anodic oxide layers are grown in a mixture consisting of one volume part of a 3% citric acid solution, with the *p*H adjusted to 6.0 with ammonia, and two volume parts of ethylene glycol (6). The samples were held in an aluminum clamp, upon which an oxide layer is formed as well. During the anodization the applied voltage is increased slowly until the desired value is obtained. The sample is held for 2 min at the maximum desired voltage during which time the current decreases to nearly zero. The oxide layer is etched off in diluted (10%) hot (80°C) phosphoric acid. Several oxide layers on GaAs were etched stepwise to check whether there is a gradient of Ga or As in the layer. The composition of that stripping solution is 20 volume parts methanol and 1 volume part phosphoric acid. The etch rate of this solution is about 50 Å/min.

Annealing of anodically oxidized layers above 300°C gives a change in color of the layer. In order to know whether this color change has to be correlated with a change in composition we analyzed samples which had been heated in evacuated capsules at different temperatures. The capsules, with a diameter of 1 cm and a length of 50 cm, were placed in a furnace. The samples were placed at the highest temperature of the capsule and radioactive material could sublime to colder parts of the capsule without causing environmental contamination.

Because anodic oxide layers contain a certain amount of water (1) the slices were heated slowly to 200°C in air (heating rate 1°C/min) and held at that temperature for 16 hr before being heated in the capsule. This treatment did not change the Ga and As content of the layers.

After annealing the oxide layers were stripped off in phosphoric acid and the etching solutions were treated as described above.

Results

The layer thickness of GaAs consumed during anodic oxidation is about twice as large as that of GaP at the same voltage (15 and 7.2 Å/V, respectively). Our data on GaAs agree with those given by Hasegawa *et al.* (6). As a function of time the growth of the layer on GaAs is somewhat faster than the growth on GaP. After 2 min 96 and 90% of the ultimate thicknesses (*i.e.*, after 20 min) are reached, respectively.

During the anodic oxidation almost twice as much gallium is lost in the oxidation bath for GaP as for GaAs (40 and 25%, respectively): The phosphorus and arsenic losses are low, however, 1.5 and 5%, respectively. In the anodic oxide layer on GaAs the average As/Ga ratio is thus 1.3 and in the anodic oxide layer on GaP the average P/Ga ratio is 1.6. This last result agrees reasonably with the results of Poate *et al.* (5), measured with Rutherford backscattering, who gave a P/Ga = 1.5. Stepwise etching of the anodic oxide layer shows that the outermost surface of the layer is Ga rich despite an As-rich gross composition, see Table I and Fig. 1. In Fig. 1 the As/Ga ratio is plotted as a function of the distance from the original surface of the layer.

Annealing was, as already described, performed in an evacuated and sealed capsule. Annealing at 400° and 500°C gave some problems in dissolving the remaining oxide layer. Now a hot, 10% water/90% phosphoric acid mixture was used. However some brownish stains could not be removed from the slices.

During annealing at these temperatures a mirrorlike deposit developed in the cold end of the capsule. Only ^{76}As activity could be detected (As, As_2O_3) in this deposit.

In Table II the results of the annealing experiments are summarized. Annealing at 300°C gives a slight decrease of the As content of the oxide layer. At 400°C (15 min and 1 hr) the As disappears very rapidly from the oxide while further oxidation clearly takes place, since more As is evaporated than the original amount in the oxide layer. The ^{72}Ga activity was now used to determine the total oxidized layer thickness because

Table I. Composition of the anodic oxide layer on GaAs as a function of thickness determined by stepwise etching of the layer

Sample	Consumed layer thickness, Å	Etching time, min	Etched percentage of the layer	Atomic ratio As/Ga
6-11	1940	1	2.1	1.20
		3	8.1	1.37
		6	19.2	1.36
		Remainder	70.6	1.38
12-10	1410	0.5	0.33	0.71
		3	6.6	1.29
		6.5	17.0	1.37
		Remainder	76.1	1.39
17-1	2290	0.5	0.51	0.73
		1	1.17	1.17
		5	8.32	1.33
		0.5	1.21	1.24
		1	1.57	1.36
		5	8.32	1.34
		Remainder	78.8	1.34
17-2	2240	0.5	0.15	0.75
		1	1.28	1.23
		5	7.71	1.37
		0.5	1.06	1.26
		1	1.82	1.28
		5	8.36	1.38
		Remainder	79.6	1.35

Table II. Average composition of the anodic oxide layer on GaAs as a function of the annealing time and temperature

Sample No.	Anneal temp, °C	Anneal time, hr	Atomic ratio As/Ga	Percentage As evaporated compared to original amount of As
3	25	—	1.35	0.0
6	192	16	1.33	1.6
7	300	1	1.28	5.1
13	400	0.25	0.22	86
10	400	1	0.26	104
12	500	1	0.29	118

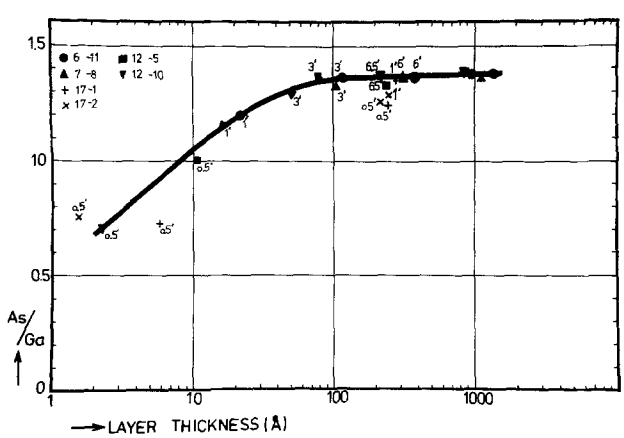


Fig. 1. In this graph the As/Ga ratio of anodic oxide layers on GaAs is plotted as a function of the distance from the original surface of the layer. The etching times used are indicated in minutes. Not all the data plotted in the figure are given in Table I.

the vapor pressure of Ga_2O_3 at these temperatures is very low.

Discussion

The ratio As/Ga >1 observed for the oxide layer differs clearly from data presented earlier in the literature. Guenther *et al.* (7) observed with Auger sputter etching technique an As/Ga ratio <1 in almost the whole film. Chang *et al.* (8) presented very recently data on the composition of anodic oxide layers. A substantial part of the studied layers was Ga rich. Only a few hundred angstroms close to the GaAs interface was As rich. The fact that, in contrast to Ref. (7) and (8), we found our anodic oxides to be As rich cannot be due to a preferential solubility of gallium oxide in our stripping solution because we found that the sum of the amounts of arsenic present in the anodizing and the stripping bath is about equal to the sum of the amounts of gallium in both solutions. This is also true for the total amounts of gallium and phosphorus detected after oxidation and dissolution of the oxide of GaP in the two solutions. For GaAs and GaP the ratios of total As/Ga and total P/Ga found for each layer are 0.95 and 1.05, respectively. This indicates that possibly a slight systematic error is made.

We conclude that the reason why our anodic oxides have a different composition from those presented in Ref. (7) and (8) must be traced back to the fact that we anodized in a glycol-based bath, whereas the authors of Ref. (7) and (8) used aqueous electrolyte. Apparently a glycol-based anodizing bath shows preferential solubility for Ga oxide and an aqueous bath preferentially dissolves arsenic oxide. Indications that oxide compositions depend on the nature of the electrolyte have already been observed by other authors (6, 9).

The top of the anodic oxide layer shows a markedly different composition compared with the bulk of it. The observed As/Ga ratio, however, is not completely independent of the etching times used. Etching times of 1 min or less give an As/Ga ratio which is somewhat lower than that observed with longer etching times. See samples 17-1 and 17-2 in Table I and Fig. 1 in which the etching time is indicated for each measuring point. An etching time of half a minute gives an As/Ga ratio of <1 on the top of the layer but of about 1.25 in the middle of it.

This indicates that there is a difference in the kinetics of the dissolution of gallium oxide and arsenic oxide, but this difference is not sufficient to account for the deviating composition of the top layer.

The reproducibility of anodization is given in Ref. (6). The reproducibility of the etching can be seen in Fig. 1 where data of many measurements fit quite well on the curve; the reproducibility depends slightly on the quality of the materials used. Dislocation-rich material shows pitting after ten or more oxidations. On good material more oxidation steps are possible with conservation of a smooth surface. At voltages higher than 150V pitting of the surface will occur very fast.

Concluding we can say that it is not possible to speak of the composition and the profile of an anodic oxide layer on GaAs since both are strongly dependent on the anodization bath used.

Manuscript submitted Sept. 27, 1976; revised manuscript received Jan. 6, 1977.

Any discussion of this paper will appear in a Discussion Section to be published in the December 1977 JOURNAL. All discussions for the December 1977 Discussion Section should be submitted by Aug. 1, 1977.

Publication costs of this article were assisted by Philips Research Laboratories.

REFERENCES

1. S. M. Spitzer, B. Schwartz, and M. Kuhn, *This Journal*, **120**, 669 (1973).
2. B. Schwartz, J. C. Dyment, and S. E. Haszko, in "1972 Symposium on GaAs and Related Compounds, Conf. Series 17, pp. 187-195, The Institute of Physics, London (1972).
3. H. Hasegawa, K. E. Forward, and H. Hartnagel, *Appl. Phys. Lett.*, **26**, 567 (1975).
4. R. A. Logan, B. Schwartz, and W. J. Sundburg, *This Journal*, **120**, 1385 (1973).
5. J. M. Poate, T. M. Buck, and B. Schwartz, *J. Phys. Chem. Solids*, **34**, 779 (1973).
6. H. Hasegawa, K. E. Forward, and H. Hartnagel, *Electron. Lett.*, **11**, 53 (1975).
7. C. S. Guenther, P. V. S. Rao, S. Thomas, and W. Paulson, Paper 159 presented at the Electrochemical Society Meeting, Dallas, Texas, Oct. 5-9, 1975.
8. C. C. Chang, B. Schwartz, and S. Murarka, Paper 350 presented at The Electrochemical Society Meeting, Las Vegas, Oct. 17-22, 1976.
9. B. Schwartz, *This Journal*, **118**, 657 (1971).

Properties of Cadmium Stannate Thin Film Electrodes and Their Use in Photogalvanic Cells

Dale Hall

Exxon Research and Engineering Company, Solar Energy Conversion Unit, Linden, New Jersey 07036

Cadmium stannate has recently been prepared as sputtered thin films displaying high transparency to visible light and exceptionally low sheet resistance (1). In CdS-Cu_2S photovoltaic cells, Cd_2SnO_4 has been used as a transparent, conducting substrate to permit backwall illumination (2). With suitable postdeposition heat-treatment, Cd_2SnO_4 films have exhibited sheet resistances of about 1 Ω/□ and ~90% visible light transmission from 500 to 650 nm. For applications requiring the highest possible conductivity and transparency, Cd_2SnO_4 appears to offer significant advantages over materials such as indium/tin oxide or tin oxide doped with antimony.

These unusual properties suggest that cadmium stannate may be a useful optically transparent electrode for research and photoelectrochemical energy conversion. The thin layer iron-thionine photogalvanic cell is a specific photoelectrochemical system in which the above-described properties of Cd_2SnO_4 can be used to advantage. Recently, a multilayer iron-thionine cell was described (3) which employed indium/tin oxide cathodes. However, Cd_2SnO_4 offers both higher light transmission and conductivity than indium/tin oxide.

The present communication reports the electrochemical behavior of Cd_2SnO_4 in sulfuric acid electrolyte. Photogalvanic short-circuit currents and open-circuit

voltages from cells using Cd_2SnO_4 cathodes are compared to outputs from cells using other cathode materials. In addition, compound transparent electrodes have been prepared with Cd_2SnO_4 thin film underlays. Data are presented to show that SnO_2/Cd_2SnO_4 photogalvanic cell anodes produce higher power outputs than identically prepared SnO_2 anodes lacking the underlay. The selectivity exhibited by the SnO_2 anode in the iron-thionine cell (3) is maintained and the electrode resistance is greatly reduced.

Electrochemical Properties

Cadmium stannate is a large bandgap [E_g ~2.9V after postdeposition heat-treatment (1)] n-type semiconductor. Charge carriers are provided by oxygen vacancies and interstitial cadmium donors in the sputtered films. Charge carrier densities of approximately 10^{21} cm^{-3} have been reported, with conductivities on the order of 6×10^3 Ω^{-1} cm^{-1}.

The Cd_2SnO_4 electrodes used in the present study were 1 × 1½ in. films sputtered on Corning 7059 glass. The sheet resistances of these films were all approximately 3 Ω/□. The electrodes were used as received for photogalvanic cell measurements, and were cut to smaller size for capacitance and current *vs.* potential measurements.

Capacitance *vs.* potential curves were recorded in sulfuric acid electrolyte at several acid concentrations. Schottky-Mott plots of $1/C^2$ *vs.* E were linear, and the flatband potential in 0.01*M* H_2SO_4 was about +0.45V *vs.* SCE (samples varied). The dielectric constant is necessary to calculate charge carrier density from Schottky-Mott plots, but could not be found in the literature. Using $\epsilon = 5$ [low frequency limit of refractive index ~2 (4)], charge carrier densities of about 10^{21} cm^{-3} were obtained for most Cd_2SnO_4 samples, with some as high as 5×10^{21} cm^{-3}. These results agree with the above-reported values based on Hall effect measurements (1).

Cadmium stannate films were initially quite hydrophobic; continued exposure to electrolyte caused a noticeable increase in wettability. Similar behavior is observed (5) for SnO_2 thin film electrodes, and has been attributed to the formation of surface hydroxyl groups (6).

Slow potential sweeps in 0.05*M* H_2SO_4 initially showed an ideally polarizable region extending from approximately +1.5 to −0.3V *vs.* SCE (Fig. 1A). After continued contact with the electrolyte, a small irregular reduction wave appeared at about +0.4V *vs.* SCE (Fig. 1B). A slight increase in anodic current appeared on the reverse scan at about +0.5V.

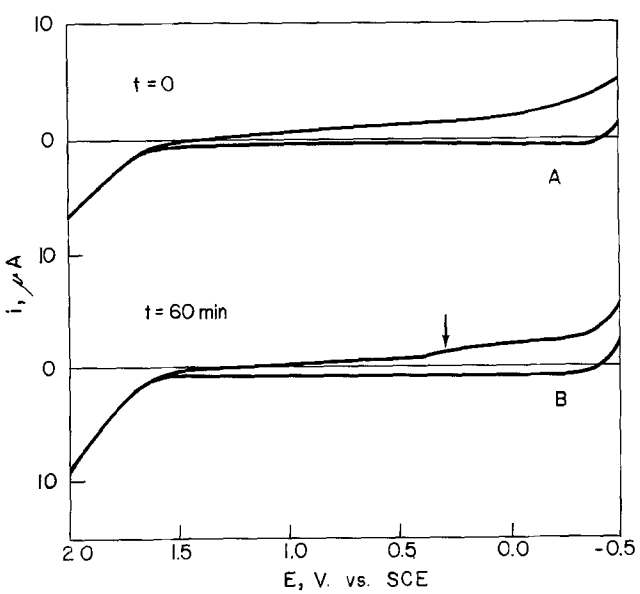


Fig. 1. Current *vs.* potential curve of Cd_2SnO_4 in 0.05*M* H_2SO_4. Electrode area = 0.35 cm^2, E_{FB} = +0.47V *vs.* SCE, n_D = 4.0 × 10^{21}, scan rate = 10 mV sec^{-1}.

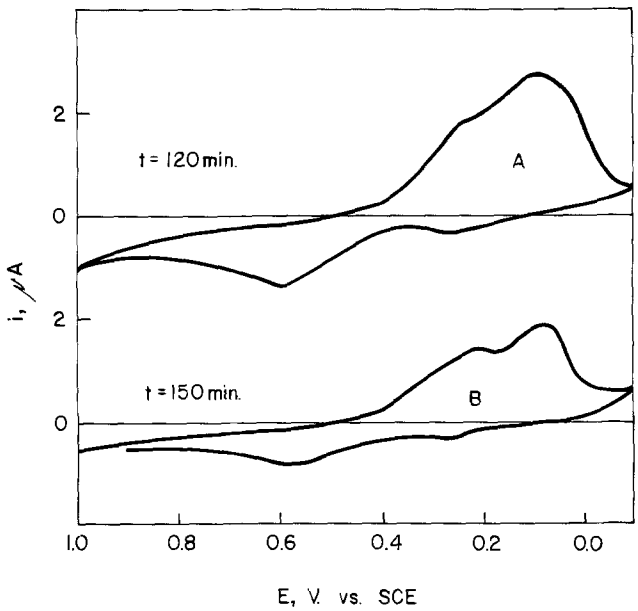


Fig. 2. Same conditions as Fig. 1, with scan rate = 2 mV sec^{-1}

A well-defined double reduction wave was observed after 2 hr of exposure to the electrolyte, with peak potentials at +0.25 and +0.1V *vs.* SCE (Fig. 2). A corresponding double oxidation wave was observed on the reverse scan. Prolonged cycling with the negative switching potential between +0.4V and the breakdown limit at −0.3V caused visible etching of the Cd_2SnO_4 film.

The cadmium, tin, and oxygen content of Cd_2SnO_4 films was examined by ESCA, both before and after exposure to sulfuric acid electrolyte. The ratio of both cadmium and oxygen content to tin content was substantially lower after use in the electrochemical cell.

The above behavior was verified with several Cd_2SnO_4 electrodes in H_2SO_4 concentrations ranging from 10^{-3} to 0.25*M*. However, one Cd_2SnO_4 sample showed an immediate and extensive reaction in 0.25*M* H_2SO_4 (Fig. 3). The symmetry of the anodic current peak and the first cathodic peak indicate that current flow is associated with surface electrolysis of the Cd_2SnO_4 film. This phenomenon has also been described elsewhere for other systems (7, 8).

The potential difference between the first cathodic peak and the anodic peak increased from 0.13V at a

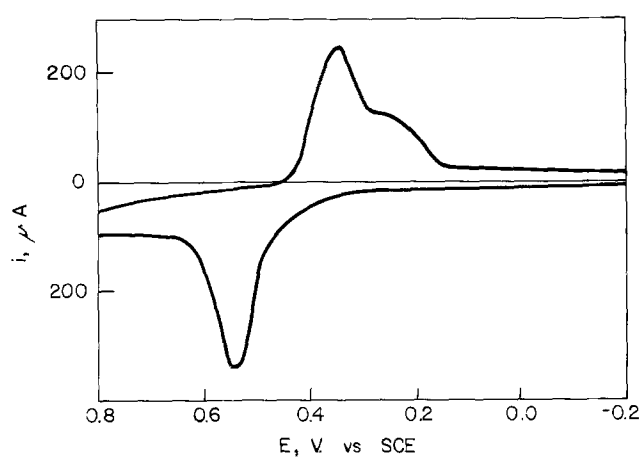


Fig. 3. Current *vs.* potential curve of Cd_2SnO_4 in 0.25*M* H_2SO_4. Electrode area = 0.7 cm^2, scan rate = 100 mV sec^{-1}.

Table I. Comparison of Cd_2SnO_4 and Pt cathodes

Anode	Cathode	V_{OC} (V)	I_{SC} (mA)
SnO_2(1)	Pt	0.147	0.40
	Cd_2SnO_4	0.128	0.30
SnO_2(2)	Pt	0.156	0.57
	Cd_2SnO_4	0.132	0.38

Cell area = 5.5 cm^2; photogalvanic solution and illumination described in Ref. (3).

sweep rate of 20 mV sec^{-1} to 0.20V at 100 mV sec^{-1}, indicating a slow electrochemical process. Rapid etching of the Cd_2SnO_4 film during the potential sweeps made further analysis impossible.

Cd_2SnO_4 as an Iron-Thionine Cell Cathode

Cd_2SnO_4 thin films were used as cathodes in iron-thionine photogalvanic cells. The usual cathode in single layer cells is an opaque sputtered platinum film. The multilayer cell, recently described (3), employed transparent films of indium/tin oxide (ITO). However, as pointed out above, Cd_2SnO_4 offers significant advantages over ITO.

Photogalvanic cell short-circuit current and open-circuit voltage measurements, comparing the performance of Cd_2SnO_4 and Pt cathodes, are shown in Table I. Cell solutions and measurement conditions were identical to those described previously (3). Some voltage and current loss was caused by the use of Cd_2SnO_4 cathodes. In spite of the lower resistance of Cd_2SnO_4, similar cells employing ITO cathodes gave comparable outputs. A partial explanation for this result is obtained from potential sweeps of the Fe^{+2}/Fe^{+3} and thionine/leucothionine (TH^+/TH_3^+) couples at Cd_2SnO_4. The expected similarity between Fe^{+2}/Fe^{+3} current-potential curves at platinum [or ITO (3)] and cadmium stannate electrodes was not observed (Fig. 4). The reduction of Fe^{+3}, which occurs at the photogalvanic cell cathode, is shifted to much more negative potentials at Cd_2SnO_4, and currents are considerably lower. The lack of Fe^{+2}/Fe^{+3} reactivity at Cd_2SnO_4, in spite of the high charge carrier density of Cd_2SnO_4 and the favorable relationship of flatband potential with the Fe^{+3}/Fe^{+2} redox potential, is the major cause of output losses in iron-thionine cells containing Cd_2SnO_4 cathodes.

A comparison of TH^+/TH_3^+ voltammetry at SnO_2 and Cd_2SnO_4 electrodes (Fig. 5) shows that the well-defined, closely spaced current peaks obtained at SnO_2 are replaced by a less reversible, partially rectifying current-potential characteristic at Cd_2SnO_4. The low reactivity of TH^+/TH_3^+ is desirable at the photogalvanic cell cathode; theoretical studies (9, 10) have shown that perfect selectivity, whether achieved by selectively permeable membranes or differential electrode reaction rates, provides optimum output in the totally illuminated cell. However, this desirable feature is more than offset by the lack of Fe^{+2}/Fe^{+3} reactivity at Cd_2SnO_4.

Cd_2SnO_4 Conductive Underlays

Electrochemical studies using resistive semiconductor thin films are often performed using conductive underlays to lower the over-all electrode resistance. Frequently, the underlay of an oxide semiconductor is the fully reduced metal, as in the combinations TiO_2/Ti (11, 12) and WO_3/W (13). Noble metal underlays have also been used [SnO_2/Pt (5) and WO_3/Au (13)]. Where transparency of the compound electrode is necessary, combinations such as TiO_2/SnO_2 (12) have been employed.

The properties of cadmium stannate appear to offer significant advantages over other transparent underlay materials, provided that those properties are not altered by overlay deposition. As part of this work, the use of Cd_2SnO_4 underlays with SnO_2 photogalvanic cell anodes was investigated. Two SnO_2 films were sputtered under identical conditions, one upon a glass

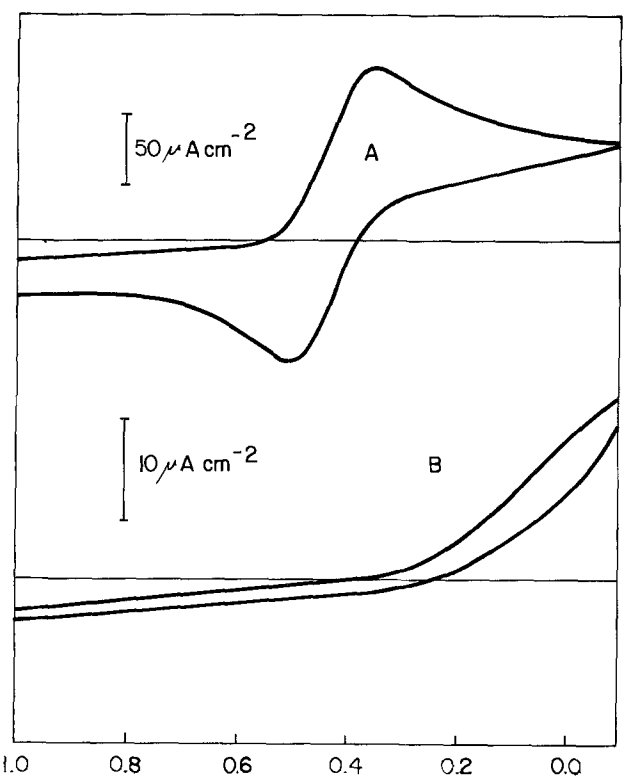


Fig. 4. Voltammetry of 1 mM Fe^{+2}/Fe^{+3} in 10^{-2}M H_2SO_4. Scan rate = 10 mV sec^{-1}; A, platinum thin film electrode; B, Cd_2SnO_4 electrode.

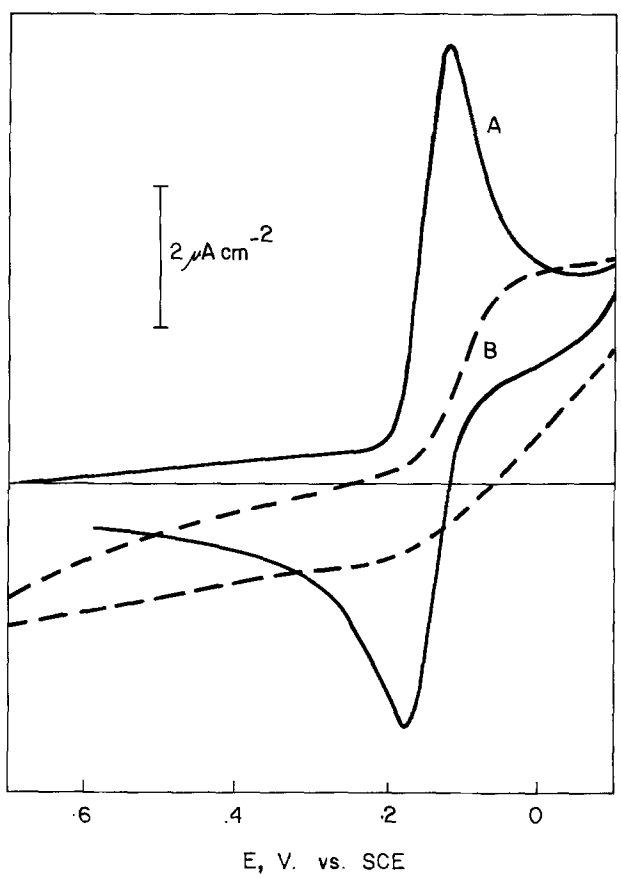


Fig. 5. Voltammetry of 4.4 × 10^{-5}M thionine in 10^{-2}M H_2SO_4. Scan rate = 10 mV sec^{-1}; A, SnO_2 electrode; B, Cd_2SnO_4 electrode.

Table II. Effect of Cd_2SnO_4 underlay on SnO_2 anode performance

Anode	Condition	R_S (Ω/□)	V_{OC} (V)	I_{SC} (mA cm^{-2})
SnO_2	Initial	850	0.112	0.023
SnO_2/Cd_2SnO_4	Initial	5	0.135	0.072
SnO_2	Reduced	840	0.175	0.027
SnO_2/Cd_2SnO_4	Reduced	5	0.163	0.138

Cells contained Pt cathode; solution and illumination as in Table I. SnO_2 was sputtered at 400°C in 85% argon/15% hydrogen. Reduction was for 10 hr at 400°C under flowing hydrogen.

substrate and the other over a Cd_2SnO_4 film (Table II). SnO_2 deposition was performed at temperatures below those which affect the properties of the Cd_2SnO_4 film during postdeposition heat-treatment (1, 2). The underlay greatly reduced electrode resistance. In addition, photogalvanic power outputs were markedly higher using the SnO_2/Cd_2SnO_4 anode, with the major difference being the increased short-circuit current.

Reduction of the SnO_2 surfaces by hydrogen causes an increase in charge carrier density at the electrode surface due to greater oxygen deficiency. The slight change of sheet resistance upon reduction indicates that only a small fraction of film depth was affected. Outputs from both the SnO_2 and SnO_2/Cd_2SnO_4 electrodes were higher after reduction, with the greatest increase occurring in the short-circuit current for the compound electrode.

The usual SnO_2 photogalvanic cell anodes (3) are obtained commercially. Sheet resistances are typically 30-100 Ω/□. The relative improvement in cell output using Cd_2SnO_4 underlays with SnO_2 of this quality would almost certainly be less than reported here. However, for systems using semiconductor electrodes with substantially lower charge density than those used in the iron-thionine cell (10^{20}-10^{21} cm^{-3}) and where thin film, transparent electrodes are desirable, Cd_2SnO_4 appears to be an excellent choice as an underlay.

Summary

Cadmium stannate electrodes initially show a large ideally polarizable region similar to that of other large bandgap oxide semiconductors. Exposure to acid electrolyte eventually causes a reductive decomposition of the Cd_2SnO_4 film. Unfortunately, this reduction occurs in the potential region in which the iron-thionine cell cathode must function (3). Hence, although reasonable outputs are obtained from cells with Cd_2SnO_4 cathodes, the response slowly declines as the cathode is consumed. This suggests that electrode stabilization by the method of Murray and co-workers (14) may be useful in practical applications of cadmium stannate electrodes.

The lack of redox reactivity at Cd_2SnO_4 is not satisfactorily explained. Cadmium stannate appears to present the unusual case of a highly doped semiconductor at which redox couples react with difficulty, even when flatband and redox potentials are favorably aligned. This should prove an interesting topic for further research.

Cadmium stannate should prove valuable in studies at optically transparent electrodes when a highly conductive substrate is necessary, if the electrode material of interest can be deposited without damaging the Cd_2SnO_4 film. The resistance of SnO_2 thin film electrodes has been successfully reduced in this way. However, it is not known whether other electrodes requiring higher deposition temperatures (*e.g.*, commercially prepared SnO_2) can be overlaid successfully.

Acknowledgments

This research was performed under Grant No. SE/AER/72-03529 of the National Science Foundation's Research Applied to National Needs Program, awarded to Boston University. We are grateful to Dr. G. Haacke of the Chemical Research Division, American Cyanamid Company, for generously furnishing cadmium stannate electrodes, and to Mr. A. Candusso, Exxon Research and Engineering Company, for preparation of SnO_2 sputtered films.

Manuscript received Dec. 13, 1976.

Any discussion of this paper will appear in a Discussion Section to be published in the December 1977 JOURNAL. All discussions for the December 1977 Discussion Section should be submitted by Aug. 1, 1977.

Publication costs of this article were assisted by the Exxon Research and Engineering Company.

REFERENCES

1. G. Haacke, *Appl. Phys. Lett.*, **28**, 622 (1976).
2. L. C. Burton, T. Hench, G. Storti, and G. Haacke, *This Journal*, **123**, 1741 (1976).
3. D. E. Hall, J. A. Eckert, N. N. Lichtin, and P. D. Wildes, *ibid.*, **123**, 1705 (1976).
4. A. Nozik, *Phys. Rev. B*, **6**, 453 (1972).
5. D. Elliott, D. L. Zellmer, and H. A. Laitinen, *This Journal*, **117**, 1343 (1970).
6. F. Möllers and R. Memming, *Ber. Bunsenges. Phys., Chem.*, **76**, 469 (1972).
7. H. A. Laitinen, C. A. Vincent, and T. M. Bednarski, *This Journal*, **115**, 1024 (1968).
8. T. O. Rouse and J. L. Weininger *ibid.*, **113**, 184 (1966).
9. R. Gomer, *Electrochim. Acta*, **20**, 13 (1975).
10. C. Lin and N. Sutin, *J. Phys. Chem.*, **80**, 97 (1976).
11. K. L. Hardee and A. J. Bard, *This Journal*, **122**, 739 (1975).
12. F. Möllers, H. J. Tolle, and R. Memming, *ibid.*, **121**, 1160 (1974).
13. G. Hodes, D. Cahen, and J. Manassen, *Nature*, **260**, 312 (1976).
14. P. R. Moses, L. Wier, and R. W. Murray, *Anal. Chem.*, **47**, 1882 (1975).

JOURNAL OF THE ELECTROCHEMICAL SOCIETY

ELECTROCHEMICAL SCIENCE AND TECHNOLOGY

JUNE 1977

EST

MnO_2 Cathodes for Seawater Cells

Charles P. Wales*

Naval Research Laboratory, Washington, D.C. 20375

ABSTRACT

Electrolytic MnO_2, carbon, and a binder were pressed onto conductive grids. Cells containing these cathodes and Al alloy A6 anodes gave an open-circuit potential of about 2.0V after adding seawater. Potential dropped rapidly in the early part of a discharge. During constant current discharges at the 15 day and 10 hr rates the average potential of these cells was 1.35 and 1.16V, respectively, with MnO_2 giving 80 and 65% of its theoretical capacity. A cell can be discharged over a period of months since the self-discharge rate of MnO_2 was low in seawater.

The AgCl-Mg seawater battery has probably been the most widely used type of seawater battery, even though it does have several disadvantages. Silver chloride is an expensive material and its use involves loss of the silver, except when recovery from the sea and salvage are feasible. Since the self-discharge or corrosion rate of Mg is large in seawater, it is not practical to use AgCl-Mg batteries over extended periods of time. Output voltage and useful capacity are lowered as Mg becomes passivated by insoluble precipitates which form on the surface of the Mg. If the cells are designed with openings so that motion of the seawater can wash the precipitates away from the Mg, then stray electrical currents can flow between the cells, resulting in another source of self-discharge.

One substitute for the AgCl cathode is CuCl (1) but this hydrolyzes readily and, therefore, is practical only when discharges are completed within a few hours after filling the cells. Successful seawater batteries have been made using $PbCl_2$ cathodes and Mg anodes (2, 3) as well as cathodes containing a mixture of $PbCl_2$ and CuCl (4). Even though the potential of $PbCl_2$ is lower than that of CuCl, $PbCl_2$ is more practical for many purposes because it does not hydrolyze readily.

Manganese dioxide is an attractive cathode material in several ways, having a high potential and being insoluble and readily available at low cost. It is likely that putting MnO_2 into the oceans would be environmentally acceptable because seawater already contains dissolved manganese. Since MnO_2 has a high ohmic resistance, the MnO_2 must be formed into electrodes of reasonably low resistance before MnO_2 can be used successfully.

A seawater cell using MnO_2 cathodes and Mg anodes has been proposed at least twice over the past thirty years (5, 6). Probable reasons why this cell has not been produced include difficulty in making suitable MnO_2 electrodes, and the choice of Mg as the anode. Experience with Mg in seawater cells indicates that Mg performs best at high rates of discharge, while it is well known that MnO_2 in Leclanché cells performs best at much lower rates of discharge, although MnO_2 has good high rate characteristics in alkaline MnO_2 cells. One would not expect MnO_2 to give a particularly good high rate performance in seawater, since the salts in seawater have a total concentration of only about 0.6 normal, and thus seawater should have a much higher electrical resistance than the electrolyte used in other cells.

* Electrochemical Society Active Member.

Key words: seawater battery, water-activated cell, manganese dioxide, discharge capacity, voltage.

Experimental

Rectangular flat plates were the most practical shape of cathode to use in the experimental cells. In order to obtain good MnO_2 electrodes three conditions had to be met: the MnO_2 needed to be in reasonably good electrical contact with the conducting grid that was in the electrode, the active material mix had to have sufficient strength to remain on the grid during discharge, and the mix had to be porous so that it could be penetrated readily by seawater.

A number of ways were investigated for achieving these conditions. The cathodes all contained electrolytic MnO_2 (Tekkosha Company Limited, content about 91% MnO_2) and a conductive grid 36 × 36 mm with an 11 mm wide lead extending 44 mm up from one corner. The grids were cut from expanded Ag, Cu, and 304 stainless steel (all size 3/0, Exmet Company), from Pt gauze, from woven carbon fiber having a polyacrylonitrile base (made by Fiberite using Thornel 300), and from multilayered sheets of graphite foil (Grafoil of Union Carbide Corporation). Metal grids often had the lower half of their leads coated with silicone rubber for protection. Corrosion of grid metal tended to be worse near the seawater-air interface, which was about 12 mm above the 36 mm square part of the grid. Good conductivity within the active material mix was obtained by adding either UCET acetylene black or 615P graphite (both Union Carbide Corporation).

Several bonding methods were tried. The preferred way of binding the active material together was a modification of the polymer bonding method given by Weininger and Secor (7). The binder was Neoprene AD-20 (du Pont) dissolved in toluene. This neoprene is a chloroprene polymer intended for use in adhesive cements. Merely pasting a mix of MnO_2, carbon, and neoprene solution onto a grid was not satisfactory. If the carbon was in the form of graphite the electrode made by pasting was fairly strong but had rather high

resistance. Acetylene black gave lower resistance but the active material cracked as the toluene evaporated and electrodes were weak. Electrodes were much improved by making a mixture too dry for pasting and then pressing this onto the grid. Electrodes were air dried at room temperature after pressing. Cathodes made this way had a lower resistance, smaller volume, and greater strength than the pasted cathodes. Resistance between two points on the surface of a cathode decreased over the first 10-25 days. The amounts of neoprene and toluene used depended on the form of conductive carbon and the amount of pressure.

Six parts by weight electrolytic MnO_2 were mixed with one part acetylene black. Sufficient 10% neoprene solution was added so that the neoprene weight in the mix was usually 35% (but a few times 40-50%) as much as the acetylene black weight. This mix was pressed onto a conductive grid at 1.5 kg mm^{-2}. The MnO_2:acetylene black ratio was not varied. Therefore the value of 6:1 may not be the best proportion to use. After air drying for at least one week the electrodes were weighed and the amount of MnO_2 present was calculated. The electrodes contained about 5g of electrolytic (91%) MnO_2, which means between 4.5 and 4.6g MnO_2. The average thickness of the active material after pressing and drying was 2.85 mm, with approximately half on each side of the grid. Total electrode thickness was in the range 2.8-3.8 mm, depending on grid thickness.

Another method for making MnO_2 cathodes used an aqueous dispersion of finely divided Teflon as the binder. To a mixture of 7 parts by weight electrolytic MnO_2 and 3 parts graphite was added 2.0 parts Teflon 30B (du Pont) diluted with 0.85 parts water. This mix was pressed onto the grid at 7 kg mm^{-2} and dried at 80°-120°C. It was necessary to use higher pressures than when using neoprene and to use graphite instead of acetylene black. Only a few electrodes were made with Teflon since this method was more difficult and resulted in cells not quite as good as those obtained with the neoprene binder.

Since the MnO_2 performed best at medium to low discharge rates, the chosen anode should also be able to discharge slowly. Alloys of aluminum with zinc have been shown to give good results at medium to low discharge rates (8), suggesting that various aluminum alloys might be suitable. Two alloys of aluminum were tried. One alloy contained 5.2 weight percent (w/o) zinc. The other was a proprietary alloy called A6, developed at Olin and now owned by Conalco. Pryor, Keir, and Sperry reported the beneficial effects of alloying high purity Al with a small amount of Sn, with the alloy usually containing one or more additional elements (9-11). The results of spectrochemical analysis indicated that alloy A6 was relatively high purity Al containing on the order of 0.1% Sn, 1% Mg, and 0.1% Ga. Anodes were usually 36 × 36 mm with a lead 7 or 11 mm wide extending 44 mm up from one corner, although some anodes of A6 alloy were 40.5 × 40.5 mm. The lower part of the leads and the top 1-2 mm of the square portion of the anodes were given a protective coating of silicone rubber. The A6 aluminum alloy was 0.18 mm thick, while the Al-Zn alloy was 1.58 mm thick.

A cell contained one MnO_2 cathode in a loosely covered beaker, two anodes of aluminum alloy placed about 30 mm apart with one on each side of the cathode, a porous inert separator between each electrode, and a reference electrode of Ag/AgCl. A cell was activated by adding 150 ml simulated seawater (Sea-Salt of Lake Products Company with *p*H adjusted to 8.2). Cells had a large excess of anode active material so discharges were always limited by capacity of the MnO_2 cathodes. Cells were discharged at room temperature (19°-24°C) using constant current. Unless stated otherwise discharges began 1 hr after adding seawater.

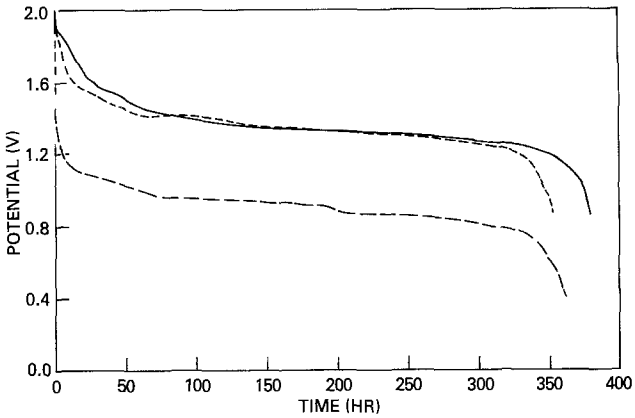


Fig. 1. Solid line, cell potentials when MnO_2 on woven carbon fiber grid was discharged in seawater at 3 mA vs. anode of Al alloy A6; line of short dashes, same except MnO_2 on Ag grid; line of long dashes, MnO_2 on Ag grid discharged vs. Al-Zn alloy.

Results and Discussion

Potentials for discharges of three cells are shown in Fig. 1. The difference in discharge lengths was not significant, representing random variation among the electrodes. Cells that contained A6 aluminum alloy gave a considerably higher potential than cells with Al-Zn alloy. The difference typically was about 0.47V for long discharges such as those in Fig. 1. Cells using the Al-Zn anodes had a continuously decreasing potential during the early part of a discharge, while potentials of cells using A6 anodes increased during the first few minutes of a discharge. Changes in cell potentials can be taken to represent changes in the MnO_2 cathode during the entire discharge when using Al-Zn anodes, and during all except the first 5% of a discharge using A6 anodes.

Reference electrode measurements indicated that anode potentials were relatively constant except at the beginning of a discharge. Potentials of the A6 anodes became increasingly negative during the first few seconds of a discharge, reaching a negative peak 3-10 min after a discharge began. These changes are indicated by the upper two cell potentials given in Fig. 1 rising to 2.0V after starting at 1.84 and 1.65V. Following this, A6 anode potential approached its normal value and became relatively constant. Potentials of the Al-Zn anodes were much more constant, usually varying less than 0.02V.

When the MnO_2 electrodes contained Ag grids the cell potential declined more rapidly during the first part of a discharge than when MnO_2 electrodes contained carbon grids (Fig. 1). The difference was caused by AgCl that formed on the Ag as a result of attack by seawater. Calculations indicated that the equilibrium potential for Ag/AgCl is $E_H = 0.245V$, assuming a chloride activity of 0.38 in seawater. Various potentials have been reported for MnO_2 depending on its source, previous treatment, and the cations in solution. Measured equilibrium potentials for MnO_2 usually fall between 0.55 and 0.63V on the hydrogen scale at *p*H 8.2 (12-14). The initial cathode potentials observed in the present work often exceeded these MnO_2 values. As a result of the MnO_2 potential being above the Ag/AgCl potential, AgCl can form on the Ag grid during a stand or in the early part of a discharge, until cathode potential drops to the Ag/AgCl value.

Figure 2 shows the way discharge potential and capacity were affected by rate of discharge. The cathodes were made with the usual 6:1:0.35 mix of MnO_2, acetylene black, and neoprene, pressed on carbon fiber grids. The discharge currents of 3, 12, and 48 mA amounted to 0.663, 2.63, and 10.5 mA g^{-1} of MnO_2. Since potential of A6 Al only changed about 0.01V when current was varied over this range, the displacements in the discharge potentials shown in Fig. 2 rep-

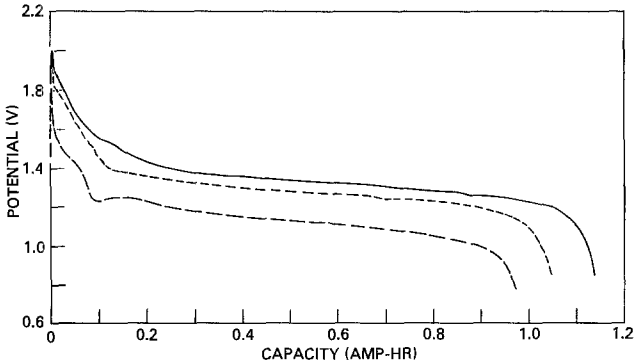


Fig. 2. Potentials when cells containing anodes of Al alloy A6 and MnO_2 cathodes with carbon fiber grids were discharged in seawater. Discharges were at 3 mA (solid line), 12 mA (line of short dashes), and 48 mA (line of long dashes).

resent the effect of discharge rate on the MnO_2 cathode. If the cells had been discharged through a fixed resistance load instead of using a controlled constant current, then the discharge potentials would have been more flat because of current falling as voltage decreased.

The effect of discharge rate on cell potential is shown in Fig. 3 with discharge length on a log scale. Cathodes made with the woven carbon fiber grids showed lower potentials, particularly at the higher rates of discharge. This potential difference was the result of resistance of the carbon fiber grid being about 2Ω, while resistance of the Ag grid was near zero. The lower curve in Fig. 2 would have been about 0.1V higher if Ag grids had been used.

According to information available the carbon fibers had been coated with an epoxy silane finish in order to improve handling characteristics before weaving. This finish was removed from one piece of the carbon fiber by soaking in acetone to dissolve most of the finish and then heating at about 315°C to burn off any residual coating. Two electrodes made using this uncoated carbon fiber gave lower potentials than the original coated material, indicating that resistance had increased.

The ampere-hour efficiency for constant current discharges of MnO_2 in seawater is given in Fig. 4 with time on a log scale. There was no significant difference between efficiency obtained from electrodes made with expanded Ag grids and those with carbon fiber grids. The straight line was fitted by the method of least squares using the combined data.

The MnO_2 electrodes in seawater did not exhibit nearly as rapid a drop in efficiency with increasing current as did Leclanché cells. Calculations based on data given by Huber [see p. 146 and 170 of Ref. (14)],

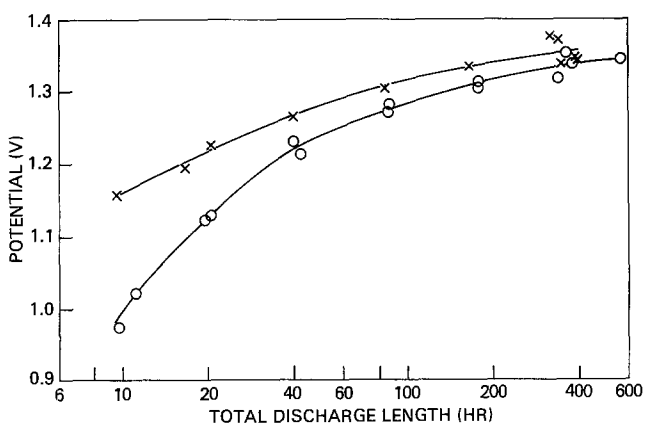


Fig. 3. Cell potentials when discharges of MnO_2 cathodes were 50% completed. Potentials are given vs. Al alloy A6. ○ cathodes contained carbon fiber grids; × cathodes contained Ag grids.

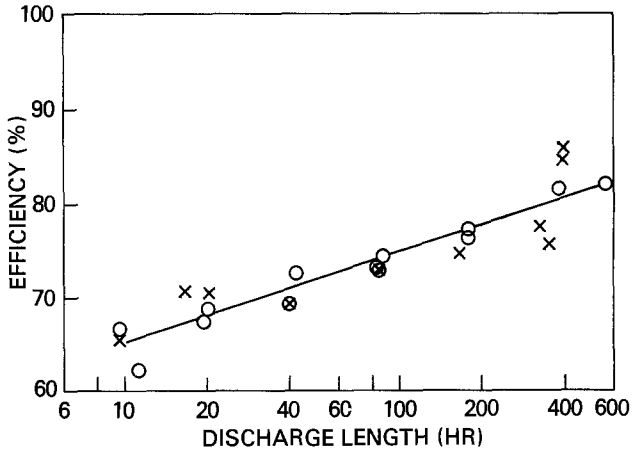


Fig. 4. Ampere-hour efficiency for discharge of MnO_2 in seawater based on the weight of MnO_2 present in the cathodes. ○ carbon fiber grids; × Ag grids.

indicated that size D or R20 dry cells gave about 30-45% efficiency when discharged in 10 hr (constant load of about 4.5-6Ω) while MnO_2 in seawater gave 62-67% (Fig. 4). On the other hand, Leclanché cells gave about 84-90% efficiency when discharged in 15 days (load of 70-80Ω) but the seawater cells gave 76-85%.

Stands in seawater.—Some cells were allowed to stand in seawater for 30 to 90 days before being put on discharge. The different behavior of the two Al alloys during a stand can be seen by comparing the upper and middle lines of Fig. 5. Potential of the A6 alloy soon became unsteady during a stand in seawater, while the Al-Zn alloy gave a relatively steady potential, only changing a few millivolts. Since the Al-Zn anodes gave an almost constant potential, the middle line in Fig. 5 indicates the way that potential of the MnO_2 cathode containing carbon fiber grids declined at a gradually decreasing rate during a stand in seawater.

When MnO_2 cathodes containing Ag grids were put in seawater their potential had an abrupt drop after about half a day (lower line in Fig. 5). After one day in seawater the potential of MnO_2 electrodes containing Ag grids was within a few millivolts of the potential of the Ag/AgCl reference electrode, indicating that the Ag grids had become covered with AgCl.

Figure 6 gives the discharge potentials for the three cells whose 30 day stands were shown in Fig. 5. When the cell with anodes of A6 alloy was put on discharge the anodic potential initially became about 0.8V less negative, which caused cell potential to fall to 1.12V (solid line in Fig. 6). After about 30 sec the anodic potential began to improve. Cell potential reflected the

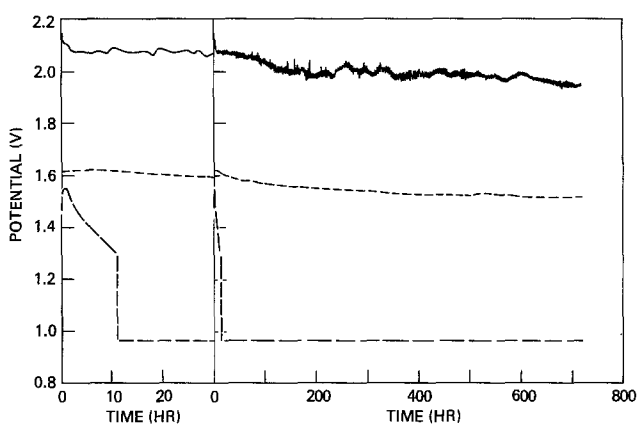


Fig. 5. Potentials during 340 day stands in seawater at room temperature. Time scale is expanded at the left. Solid line, MnO_2 on carbon fiber grid vs. A6 Al; line of short dashes, MnO_2 on carbon fiber grid vs. Al-Zn; line of long dashes; MnO_2 on Ag grid vs. Al-Zn.

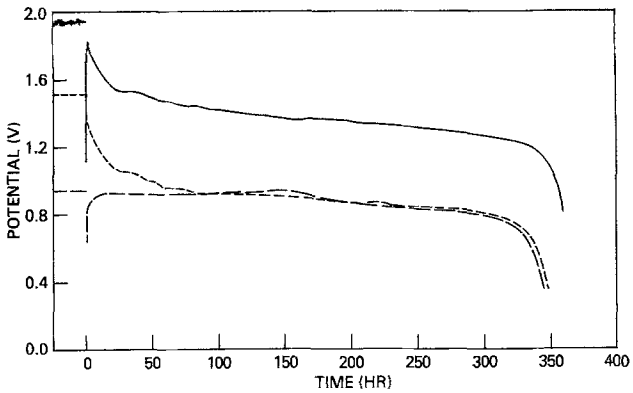


Fig. 6. Potentials during the last day of 30 day stand and during the subsequent discharge at 3 mA. See Fig. 5 for description of cells. Cathodes contained about 5g electrolytic (91%) MnO_2.

change, reaching a maximum of 1.84V after 24 min as A6 anode potential became 0.75V more negative. In this initial 24 min of discharge after a 30 day stand the MnO_2 cathodes that contained carbon fiber grids showed a potential decrease of only 0.05V from the open-circuit value. The MnO_2 potential dropped steadily during the early part of the discharge, falling 0.42V during the first day. After the first hour of discharge all changes in cell potentials shown in Fig. 6 can be considered to indicate changes in the MnO_2 potential since the anodes had relatively small potential changes beyond this point.

After a 30 day stand in seawater a cell with Al-Zn anodes had a much smaller potential change when put on discharge than did cells with anodes of the A6 alloy. Potential of the Al-Zn anodes initially became about 0.1V less negative than the stand value and then recovered 0.05V in the first 30 min of discharge and another 0.05V in the next 4 or 5 days, giving the stand potential for the rest of the discharge. The variation between the two anode alloys, as indicated by the difference in behavior of their potentials during the stand and also at the beginning of the discharge, may have resulted from the A6 alloy developing a coating that had a higher ohmic resistance. The fluctuations in stand potentials suggest continual cracking of the coating on the A6 alloy, followed by formation of a new coating.

The sharp initial drop in potential observed when the cell containing MnO_2 on the Ag grid was put on discharge after a 30 day stand (line of long dashes, Fig. 6) was attributed to resistance of the AgCl film that had formed on this grid. Potential subsequently rose in the early part of the discharge as the AgCl was reduced to Ag and resistance at the grid decreased. After these low rate discharges were 20-25% complete there was little difference between the potential of cathodes with Ag grids and those with carbon fiber.

Figure 6 can be compared with Fig. 1 to see the effect that a 30 day stand has on discharges. Both figures include one cell with a carbon fiber grid and A6 alloy anodes as well as one cell with MnO_2 on Ag and with Al-Zn anodes. Cell potentials were lower in the early part of a discharge following a stand, but these differences gradually decreased. After a discharge was about 25% complete potentials were about the same whether or not a cell had been standing 30 days in seawater.

There was no significant difference among the values obtained for the utilization of MnO_2 when using grids of woven carbon fiber, graphite foil, expanded Ag, or Pt gauze. For five cells given 30 day stands (two with carbon fiber grids and one cell containing each of the other three grid materials) the discharge efficiency for MnO_2 was in the range 73-78%, average 75%. The same discharge current gave an efficiency of 76-86% when discharges began after 1 hr in seawater (Fig. 4, hours 330-400) averaging 81%. Thus, after a 30 day stand the MnO_2 cathodes still gave about 93% of the capacity normally obtained. An efficiency of 73% was obtained when one cell with MnO_2 on Ag stood 90 days in seawater before discharge, suggesting that the loss after 90 days was not much greater than after 30 days. Discharge potentials after the 90 day stand with the Ag grid were much like those shown in Fig. 6, except that potential remained in the range 0.80-0.81V for the first 3 hr of discharge before rising to 0.9V, probably because of the larger amount of AgCl present.

Conductive grids.—Grid corrosion becomes a problem when most metals are held at the potential of MnO_2 in an electrolyte. Platinum was an excellent grid material, undergoing no corrosion after a 30 day stand in seawater followed by a discharge at the 15 day rate. But Pt is impractical considering its cost.

Type 304 stainless steel showed no attack after the bare metal had been standing in seawater for a week, but corroded very rapidly when used as a grid for a MnO_2 electrode. Potential dropped rapidly when seawater was added, and after 10 min of standing in seawater the potential was fluctuating in the range 1.08-1.16V in a cell with Al-Zn anodes. The stainless steel grid broke apart after the electrode had stood 20 days in seawater.

The corrosion rate of copper in seawater was low enough that copper could be used as the grid material if a discharge was completed within one or two days after adding seawater. The initial discharge potentials of MnO_2 cathodes containing Cu grids were not significantly different from those containing Ag grids, but potentials soon became lower because of the formation of resistive corrosion products. For example, when the MnO_2 was discharged at the 11 day rate the potential using a Cu grid was 0.08V lower after one day than the potential using Ag, and 0.15-0.20V lower from four days to the end of the discharge. Another disadvantage to using Cu grids was that potentials became unsteady after standing 14 hr or after discharging two days. Corrosion of Cu was faster during stands because the Cu was at a higher potential. After a 60 day stand in seawater the resistance of a Cu grid had become sufficiently high that cell potential fell to zero when a discharge was attempted at the 15 day rate.

Silver grids corroded more slowly than copper and could be used where cells were to be in seawater for several months, although initial discharge potentials of MnO_2 cathodes with Ag grids were lower than those obtained with carbon grids (Fig. 1, 6). Perhaps Ag or a more inert metal such as Pt or Rh could be plated on Cu in order to avoid the high cost of grids made from silver or a more noble metal, while retaining the advantage that a conductive metal has over a nonmetal such as carbon in giving higher discharge potentials (Fig. 3).

Successful MnO_2 cathodes were made using two forms of thin carbon as the conductive grid. Neither woven carbon fiber nor graphite foil underwent any noticeable attack after 30 days standing in seawater followed by discharges lasting 14-15 additional days. Reference electrode measurements indicated that after a 30 day stand in seawater the MnO_2 cathodes began discharging at a potential only 0.01-0.02V below the final stand potential. Such a small potential drop indicated that there was no formation of a highly resistive film during the stand, in contrast to the results when grids of Cu or Ag were used under similar conditions. Since MnO_2 has a low self-discharge rate in seawater, and carbon grids were apparently unattacked, it is believed that a MnO_2 cathode containing a carbon grid could be discharged continuously or intermittently and give good service over a period of one or more years.

One cathode was made by electrodepositing MnO_2 onto sheet graphite under conditions described by Storey *et al.* (15). Following the electrodeposition the cathode was washed in water and dried at room temperature. The deposit was somewhat irregular, having an average thickness of 1.2 mm. After 1 hr in seawater

this cathode gave an open-circuit potential of 2.00V in a cell with the Al-Zn alloy or 1.029V *vs.* the Ag/AgCl reference. This was about 0.35V higher than the potential obtained from the other carbon grids, perhaps indicating oxygen adsorbed on the graphite. A discharge at the 5 day rate gave a continuously decreasing potential and only 11% efficiency. Reduction of the MnO_2 apparently took place primarily next to the graphite. Then the remaining MnO_2 lost contact with the graphite, as indicated by the tendency for the MnO_2 to fall off of the graphite during the discharge. Ferrell and Vosburgh reported a similar loss of contact when using MnO_2 electrodeposited on graphite rods and reported that a layer of MnO_2 about 5×10^{-6}m thick was the maximum thickness that could be discharged completely in 2M ammonium salt solution (16).

Anodes.—Although the experimental work was designed for studying the cathodes, some information on the anodes was obtained at the same time. The efficiency with which the anodes were consumed during discharges in seawater is given in Fig. 7. Since the discharge conditions were not identical for the two alloys some caution should be used in interpreting Fig. 7. The values for the Al-Zn alloy were taken from earlier work (8) in which anodes were discharged until potential changes indicated that a discharge had ended. The results for alloy A6 come from the present work, with discharge length determined by the MnO_2 cathode. The two A6 anodes in a cell had a total theoretical capacity of 2.4 or 3.0 times the theoretical capacity of the MnO_2 cathode, depending on the particular anode size used. Therefore, the maximum discharge length of the anodes can be roughly estimated to be 2.4-3 times the discharge length measured for the cathodes. However, this does not take into account the differences between efficiency of the cathode and the anode, nor the likelihood that pieces of Al would become separated from the anode in the last half of the discharge and shorten the discharge, as was noted in the earlier work where the 5.2% Al-Zn alloy only gave 50-60% of the capacity theoretically possible (8).

The change in efficiency with discharge length (Fig. 7) indicated that a larger proportion of the A6 anodes was consumed during slow discharges. About 30% of the exposed metal in the A6 anodes having the smaller dimensions had been consumed during a discharge at the 10 hr rate and 53% at the 15 day rate, while 23 and 41% of the larger A6 anodes had been consumed at the same rates. The condition of these anodes when a discharge was ended depended on the discharge rate. During discharges at what was the 10 hr rate for cathodes many small holes 0.3-1.5 mm diam appeared in the A6 anodes. As discharge rate lengthened the holes tended to be larger but fewer in number. For example, at the 40 hr rate most of the holes were 2-4 mm diam, while at the 180 hr rate the holes were 5-11 mm in their largest dimension but only 1-3 holes were present. As the number of holes had decreased, the amount of material removed from the sides and bottom had increased. The appearance of the Al-Zn alloy after a discharge has already been described (8).

Both Al alloys gave potentials that were relatively flat during most of a discharge, so the potential when an anode was 50% discharged represented its average potential quite well (Fig. 8). The values reported here for the A6 alloy were the potentials given as the discharges of the cathodes came to an end. These potentials only differed an average of 4 mV from the anodic potentials when discharged half this much, with some potentials having risen and some fallen.

Potential of the A6 alloy changed only about 0.02V over the current density range from 0.1 to 4 mA cm^{-2}, while potential of the Al-Zn alloy changed by 0.17V over the same range (Fig. 8). Because of these potential changes a cell using the A6 alloy gave a potential that was 0.47V larger than a cell using the Al-Zn alloy at the lower current density cited and 0.61V at the higher current density. The A6 alloy was clearly the preferred alloy of the two at the higher discharge rates because of its higher cell potential and efficiency under these conditions. For very long discharges the extensive corrosion of the A6 alloy can be a problem, because it causes unsteady potentials on open circuit (Fig. 5) or when current is very low, and low initial potentials when a discharge is begun after corrosion has taken place, although it still has the advantage of soon giving a higher discharge potential.

Conclusions

The MnO_2 cathodes performed quite well in seawater, giving less of a capacity decrease with increasing discharge current than did Leclanché cells, and having a low capacity loss while standing after activation. About 93% of normal capacity was obtained following a 30 day stand in seawater. A 90 day stand before beginning a discharge gave little additional loss, indicating that the cell can be used over a period of many months.

Carbon was a good grid material when cathodes were to undergo stands or low rate discharges since carbon was not attacked by seawater when held at the MnO_2 potential. During rapid discharges the highest potentials were obtained when using conductive grids of low resistance such as Ag, but Ag cathodes gave lower potentials in the early part of a discharge because of AgCl formation. The average cathode potential was about 0.1 or 0.2V below the Ag/AgCl equilibrium potential when MnO_2 was discharged at the 7 day or 20 hr rates, respectively, so formation of AgCl was not a problem during most of a discharge. The corrosion

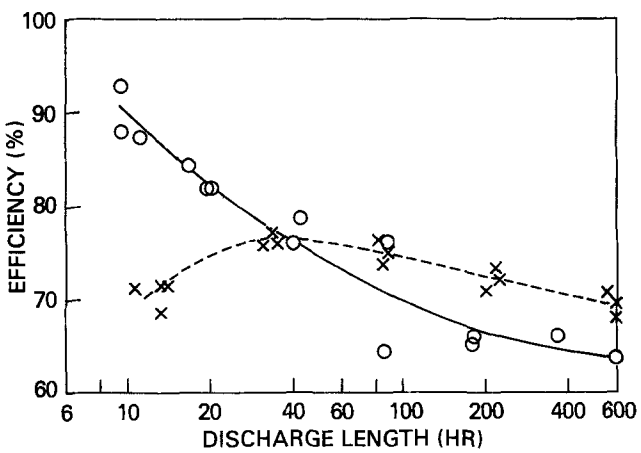


Fig. 7. Efficiency with which Al alloys were converted into current, based on weight loss during discharge. ○ Al-Sn-Mg-Ga alloy A6; × Al alloyed with 5.2% Zn.

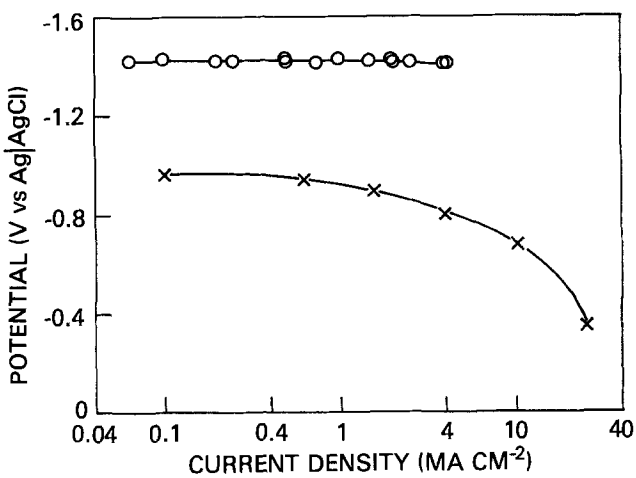


Fig. 8. Potentials when Al anodes were 50% discharged. ○ Al-Sn-Mg-Ga alloy; × Al-Zn alloy.

rate of Cu grids was low enough that they could be used in cathodes if a discharge was completed within one or two days after adding seawater.

The cathodes gave good results when coupled with anodes made from Al alloys. Of the two alloys used, the A6 Al (Al-Sn-Mg-Ga) was preferred over the Al-Zn because it gave higher cell potentials. Cells containing MnO_2 cathodes and A6 anodes gave an open-circuit potential of about 2.0V after adding seawater. Potential dropped rapidly in the early part of a discharge. Most of a discharge took place between 1.4 and 1.1V. Discharges lasting 15 days gave an average potential of 1.35V and those lasting 10 hr gave 1.16V when using grids of low resistance.

Acknowledgments

I wish to thank Dr. J. L. Weininger for providing information concerning neoprene as a binder in electrodes. The electrolytic MnO_2, acetylene black, and graphite were supplied by Union Carbide Corporation with the kindness of Dr. R. J. Brodd. Thanks are also due to E. I. du Pont de Nemours & Company for the samples of neoprene and aqueous Teflon dispersion, and to Conalco, Incorporated for providing some A6 aluminum alloy. Mr. S. H. Cress performed the spectrochemical analysis.

Manuscript received Nov. 16, 1976; revised manuscript received Dec. 27, 1976. This was Paper 65 presented at the Las Vegas, Nevada, Meeting of the Society, October 17-22, 1976.

Any discussion of this paper will appear in a Discussion Section to be published in the December 1977 JOURNAL. All discussions for the December 1977 Discussion Section should be submitted by Aug. 1, 1977.

Publication costs of this article were assisted by the Naval Research Laboratory.

REFERENCES

1. L. E. Pucher, *This Journal*, **99**, 203C (1952).
2. J. R. Coleman, *J. Appl. Electrochem.*, **1**, 65 (1971).
3. J. R. Coleman, in "Power Sources 4," D. H. Collins, Editor, p. 33, Oriel Press, Newcastle upon Tyne, England (1973).
4. T. J. Gray and J. Wojtowicz, in "Marine Electrochemistry," J. B. Berkowitz, M. Banus, M. J. Pryor, R. Horne, P. L. Howard, G. C. Whitnack, and H. V. Weiss, Editors, p. 141, The Electrochemical Society Softbound Symposium Series, Princeton, N.J. (1973).
5. I. C. Blake, L. H. Harriss, and J. B. Mullen, U.S. Pat. 2,491,640 (1949).
6. J. B. Ockerman, U.S. Pat. 3,433,678 (1969).
7. J. L. Weininger and F. W. Secor, *This Journal*, **121**, 1541 (1974).
8. C. P. Wales, A. C. Simon, and S. Schuldiner, *Electrochim. Acta.*, **20**, 895 (1975).
9. M. J. Pryor, D. S. Keir, and P. R. Sperry, U.S. Pat. 3,240,688 (1966).
10. D. S. Keir, M. J. Pryor, and P. R. Sperry, *This Journal*, **114**, 777 (1967).
11. D. S. Keir, M. J. Pryor, and P. R. Sperry, *ibid.*, **116**, 319 (1969).
12. N. C. Cahoon, *Trans. Electrochem. Soc.*, **68**, 177 (1935).
13. N. C. Cahoon, *This Journal*, **99**, 343 (1952).
14. R. Huber, in "Batteries," Vol. 1, K. V. Kordesch, Editor, p. 36, Marcel Dekker, New York (1974).
15. O. W. Storey, E. Steinhoff, and E. R. Hoff, *Trans. Electrochem. Soc.*, **86**, 337 (1944).
16. D. T. Ferrell and W. C. Vosburgh, *This Journal*, **98**, 334 (1951).

The Anodic Oxidation of Tungsten in Aqueous Base

G. Stephen Kelsey

Department of Chemistry, University of Missouri-Columbia, Columbia, Missouri 65201

ABSTRACT

The kinetics of the anodic oxidation of tungsten metal in basic aqueous solution has been investigated using galvanostatic polarization. Anodic Tafel slopes were constant over all concentrations of hydroxide at 0.136 V/decade. Cathodic Tafel slopes ranged from 0.069 to 0.197 V/decade, increasing with hydroxide ion activity. Anodic exchange current density, obtained by extrapolation, averaged $5 \pm 3 \times 10^{-8}$ A/cm^2. Single ion activities, estimated by Harned's rule, in sodium hydroxide solutions buffered with sodium nitrate to constant ionic strength, yielded rate data indicating first-order dependence on hydroxide ion activity over a concentration range of 0.02-6.00M OH^-. A mechanism commensurate with the observed behavior is proposed involving oxidation to intermediate tungsten oxides, followed by nonelectrochemical dissolution to form the soluble tungstate anion. A brief discussion of the data for the hydrogen evolution reaction is also presented, in the light of recent studies on tungsten covered by oxide layers.

In recent years much work has appeared in the area of metal/metal ion electrode behavior in aqueous solutions (1-21). Within this broad area, investigations have focused on the kinetics of the anodic oxidation/cathodic reduction mechanisms (1-9), on the initial oxidation state of the anodic oxidation product [coulometric n value (10-12)], or on the application of the anodic generation of the metal ion to coulometric analysis (13-21). Development of a theoretical basis for activation-controlled electrode kinetics (22, 23) has enabled the oxidation/reduction mechanisms of several metals to be elucidated (5-9). The comparison of experimental results with theoretical calculations has been most successful in the case of solutions where the metal/metal ion couple is reversible and the parameters of exchange current density, i_o, and reversible potential, E_R, have their true meaning. In the case of metals which do not have reversible couples, or which form oxidation products which cannot be electrodeposited on the parent metal (such as Cr/CrO_4^{2-}, *e.g.*), the interpretation of potentiodynamic or galvanostatic data is less obvious.

The anodic behavior of metals, viz., dissolution, must be at least reproducible in order to utilize the anodic oxidation of pure metals for the purpose of titrant generation (20, 21) or for the coulometric preparation of standard solutions of low concentration. Because the stability of tungstate ion is greatest in basic medium,

Key words: Tafel, dissolution, tungstate, galvanostatic polarization.

conditions for precise current efficiency for its generation were sought in sodium hydroxide solutions.

Previous studies of the hydrogen evolution reaction (HER) on tungsten (24, 25,) while contradictory in part, lend most support for an oxide surface reduction of solvent. Results for the HER in this work are confined to Tafel data, which were collected to help complete the anodic part of the study.

Work by Johnson and Wu (26) (and references cited therein) indicated that Tafel slopes for anodic dissolution in basic solution have been observed over a significant range of values. The lack of agreement concerning the anodic reaction prompted the kinetic study.

Experimental

Apparatus.—All electrochemical measurements were obtained using a PAR 173 potentiostat/galvanostat (Princeton Applied Research Corporation, Princeton, New Jersey) equipped with a Model 179 digital coulometer. Electrochemical cells employed were Metrohm EA 880 Universal titration vessels of 20 ml initial volume, and jacketed for temperature control. Tungsten electrodes used in the study consisted of ¼ in. diameter rod, fixed in a demountable holder, suitable for purposes of weighing prior to and following polarization. Platinum foil counterelectrodes of about 1.5 cm^2 area were used inside isolation tubes inserted in the cell cap. A saturated calomel electrode (SCE) of the high impedance type was used as a reference electrode with a salt bridge in connection with a PAR Model 178 electrometer probe. This, in turn, was connected to the potentiostat and completed the three-electrode cell circuit. Solution temperature was thermostatted to 25.00° ± 0.05°C.

Tungsten metal was obtained as 99.95% pure ¼ in. diameter rod from A. D. Mackay, Inc., New York. Electrolytes were all reagent grade chemicals. Solutions were prepared from distilled deionized water and were purged with prepurified nitrogen prior to all experiments.

Anodic and cathodic current-potential (i-E) data were obtained under galvanostatic conditions, *i.e.*, as $E = f(i)$. Currents from $\pm 1 \times 10^{-5}$ to $\pm 5 \times 10^{-1}$A were applied to the working/counterelectrode pair and the potential of the tungsten electrode against SCE was recorded after it stabilized (a period not exceeding 30 sec, except for the first several measurements). These data points were then used to construct E *vs.* log i, Tafel plots for subsequent study. Current densities were calculated from the applied current and the geometric area of the immersed portion of the electrode, without regard for surface roughness. The technique used to obtain current-potential data (*vide supra*) was such as to minimize area changes during an experiment except at very high applied currents, where the real surface area exceeds the geometric one due to corrosion.

Electrode pretreatment was as follows: Tungsten rods were clamped in a chuck and rotated by an electric motor, while wet-sanded with 320 grit SiC paper, followed by 400 grit, and finally wet polished with 600 grit SiC paper; pretreatment was completed by thorough rinsing with distilled deionized water (27). The final sanding and rinsing were followed by careful wiping with tissue to remove any residual SiC fines or powdered metal. After this last step was repeated, the electrode was examined under magnification to insure that no pits or other irregularities were evident, and was oven-dried at 110°C for 5 min before weighing.

The electrolyte solutions.—Eleven solutions were prepared for the study, whose compositions are described in Table I. All solutions were prepared with a total molar ionic strength of 6.00 where ionic strength is given by

$$I(M) = \tfrac{1}{2} \sum_i M_i z_i^2 \qquad [1]$$

Table I. Composition, concentration, and ionic strength data for the applied solutions

Soln. No.	Molarity, M			Molality, *M*			
	NaOH	Na_2WO_4	$NaNO_3$	NaOH	Na_2WO_4	$NaNO_3$	I(*M*)
I	2.00	0.05	3.85	2.14	0.057	3.26	7.04
II	2.00	0.10	3.70	2.14	0.113	3.17	7.02
III	2.00	0.20	3.40	2.12	0.217	2.95	6.95
IV	2.00	0.50	2.50	2.08	0.487	2.29	6.82
V	2.00	1.00	1.00	2.02	0.829	1.00	8.80
VI	0.20	0.10	5.50	0.246	0.120	4.33	7.48
VII	0.02	0.10	5.68	0.025	0.121	4.43	7.52
VIII	5.00	0.20	0.40	4.35	0.198	0.406	6.32
IX	6.00	0.00	0.00	6.21	0.000	0.000	6.21
X	1.00	0.00	5.00	1.16	0.000	4.01	7.32
XI	0.10	0.00	5.90	0.125	0.000	4.56	7.57

The concentrations of the various components are also reported in molality, calculated from the measured densities of the solutions at 25°C. Because of the high ionic strength of these solutions, activity coefficient data for the electrolytes were obtained graphically by interpolation (the case for sodium hydroxide) or extrapolations of mean molal activity coefficient data from tables by Parsons (28) and Robinson and Stokes (29). Because of the lack of data for sodium tungstate, the data for sodium chromate solutions of like molality were substituted. The assumption that the activity coefficients of these two compounds (and later, their osmotic coefficients) behave in a closely similar manner is an uncertainty in the derived activities. However, both chromate and tungstate salts are two-to-one electrolytes which undergo a base hydrolysis reaction in pure water and possess similar solubilities.

The estimation of activity coefficients for the three electrolytes was based on Harned's rule, expressed in Eq. [2], for a general three-component solution

$$\log \gamma_2 = \log \gamma_{2(0)} - \alpha_{23} M_3 - \alpha_{24} M_4 \qquad [2]$$

$$\alpha_{23} = (\Phi_3 + \Phi_2)/2.303M \qquad [3]$$

Values for α pertain to the total molality of the mixture and, for a multielectrolyte solution with a common ion, are given by Eq. [3]; again, Φ, the osmotic coefficients, are values at the total solution molality. The activity coefficients and calculated mean ionic activities are given in Table II. Because of the success of Harned's rule at high ionic strength compared to other methods of estimating single ion activities (30), it was chosen for use in the present work. Listed in Table II are the activities for water, which were obtained by extrapolation of a_{H_2O} *vs.* M data from Robinson and Stokes (29); the last column is the $-\log a_{H^+}$, which was calculated from Eq. [4]

$$K_w = \gamma_{H^+} M_{H^+} \gamma_{OH^-} M_{OH^-} / a_{H_2O} \qquad [4]$$

The value for K_w at 25°C was obtained from Hurlen (5).

The variation in the activity of hydroxide ion among solutions of equal hydroxide molarity is the probable cause of scatter in certain correlations among solutions I through V (*vide supra*), but the use of least squares analysis revealed correlation coefficients usually exceeding 0.99.

There was no attempt made to compensate for liquid junction potentials between saturated KCl and the electrolyte solutions. The Henderson equation (31) indicates that for the present solutions the junction potential could easily reach about 70 mV. More importantly, regardless of its magnitude, the liquid junction potential is a sensitive function of solution composition and probably varied quite a bit over the range of sodium hydroxide concentration (0.02-6.00M).

Results

Anodic dissolution of tungsten.—Figure 1 shows the anodic Tafel data from seven solutions covering a range of hydroxide concentration of over two orders of

Table II. Thermodynamic activity data for the applied solutions

Soln. No.	log γ			Activity, a				−log a_{H^+}
	NaOH	Na_2WO_4	$NaNO_3$	NaOH	Na_2WO_4	$NaNO_3$	H_2O	
I	0.3629	0.4334	−0.5823	4.947	0.154	0.854	0.707	15.01
II	0.3554	0.4236	−0.5845	4.852	0.299	0.824	0.708	15.00
III	0.3371	0.3903	−0.5868	4.615	0.533	0.765	0.712	14.98
IV	0.2872	0.3111	−0.5985	4.035	0.997	0.576	0.719	14.92
V	0.4085	0.5642	−0.6065	5.166	3.039	0.202	0.606	15.09
VI	0.4507	0.5563	−0.5132	0.694	0.432	1.328	0.684	14.17
VII	0.4593	0.5687	−0.5044	0.072	0.447	1.387	0.683	13.19
VIII	0.1596	0.0817	−0.6703	6.282	0.239	0.087	0.745	15.09
XI	0.1335	0.0484	−0.7416	8.447	0.000	0.000	0.749	15.22
X	0.4241	0.5236	−0.5419	3.085	0.000	1.152	0.694	14.81
XI	0.4708	0.5880	−0.5007	0.369	0.000	1.439	0.680	13.90

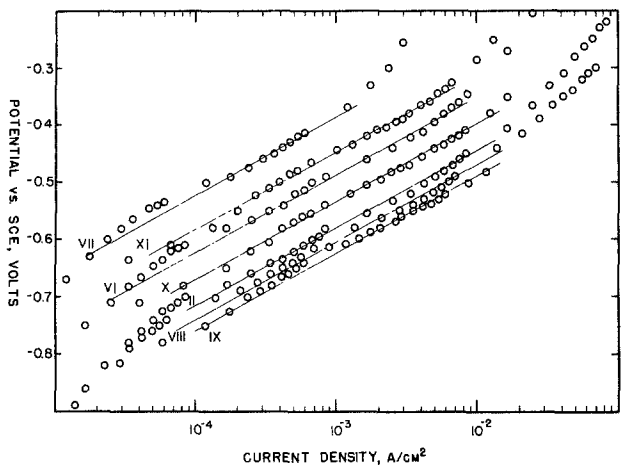


Fig. 1. Tafel diagram for the anodic dissolution of tungsten

magnitude (solutions II, VI-XI). In general, the linear portion extends for two decades of current density, nominally 5×10^{-5} to 5×10^{-3} A/cm². The solid lines are drawn with a slope of 4.606 *RT*/**F**. Slight dislocations were observed with changes in current ranges, but these discontinuities were attributed to an artifact of the potential display circuitry of the Model 173 since they appeared in both anodic and cathodic Tafel plots at regular intervals. A small uncertainty, about 2-5 mV, is due to the graduation of the voltage meter, from which potential readings were taken.

The direct dependence of anodic current (rate) on hydroxide concentration is evident from Fig. 1. A graph of log *i* *vs.* log a_{OH^-} is given in Fig. 2; data points are taken at two potentials in the linear portion of the Tafel diagrams. The solid lines in the figure represent a slope of +1, indicative of a first-order rate dependence on hydroxide ion activity. The least squares slope calculations were +1.09 and +0.91 for potentials of −0.50 and −0.60V *vs.* SCE, respectively, which illustrates, perhaps indirectly, the degree of success of Harned's rule in estimating activities in high ionic strength solutions. Graphs analogous to Fig. 2 for the other components of the solutions revealed no correlation between observed rate (current density) and activity.

The anodic Tafel plots for solutions I-IV (constant sodium hydroxide molarity), with varying amounts of sodium tungstate in them, were, within experimental error, superimposable. There seems to be no dependence on tungstate ion activity for the anodic reaction.

Coulometric experiments carried out both potentiostatically and galvanostatically revealed data consistent with those of Johnson (26) and are the subject of a separate communication. The six electron stoichiometry of Eq. [5] was observed in all solutions

$$W + 8\,OH^- \rightarrow WO_4^{2-} + 6e^- + 4H_2O \qquad [5]$$

Hydrogen evolution reaction.—The reduction of tungstate ion was not observed in any of the solutions containing the ion, and so the hydrogen evolution reaction appears to be the only one occurring during cathodic polarization. No weight changes were detected for even extended polarizations under potentiostatic conditions. Data for solutions I-V are depicted in Fig. 3. The solid lines represent a Tafel slope of 4.606 *RT*/**F**. Figure 4 represents the Tafel behavior of solutions II, VI-XI, where the hydroxide ion dependence of the reduction potential is evident.

Discussion

An exact quantitative understanding of the reversible potential and exchange current density of this system is hampered by the uncertainty of the liquid junction potential between the saturated calomel electrode and the electrolyte solutions. However, in the light of this uncertainty, the following observations are made.

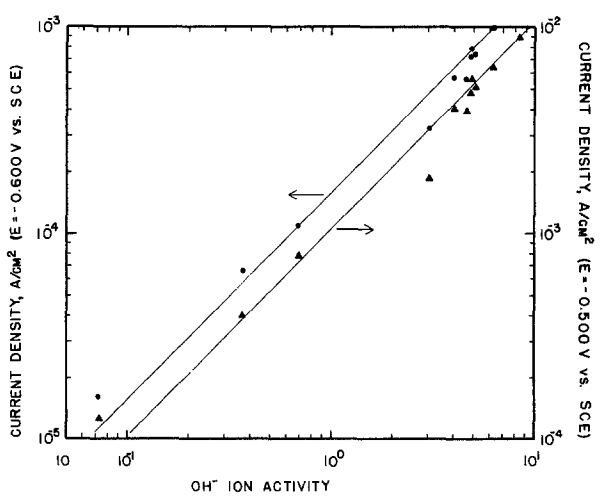


Fig. 2. Log anodic current density as a function of log hydroxide ion activity at constant potential.

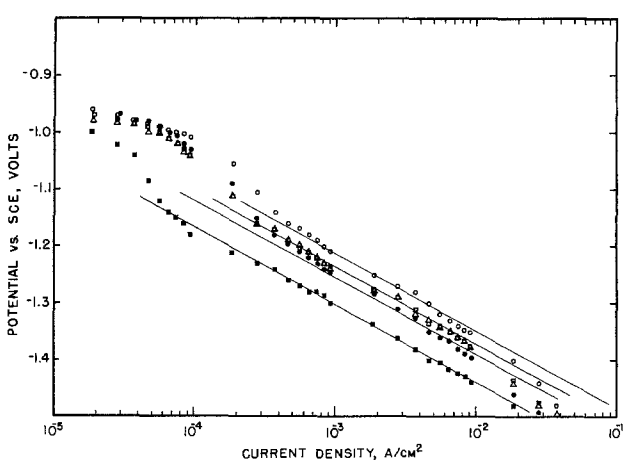


Fig. 3. Tafel diagram for the cathodic hydrogen evolution reaction in solutions I-V. ○, Solution I; □, solution II; △, solution III; ●, solution IV; ■, solution V.

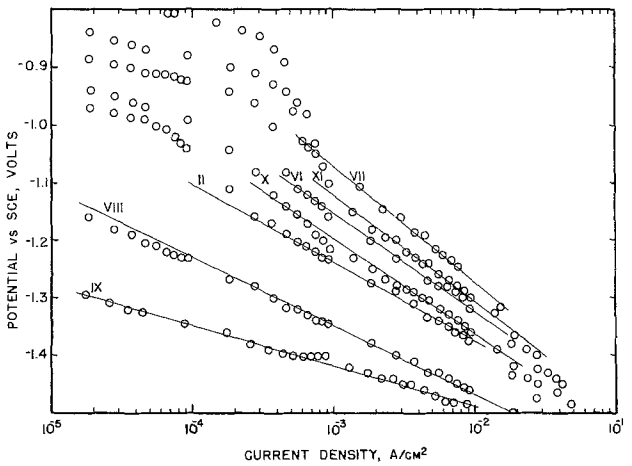


Fig. 4. Tafel diagram for the cathodic hydrogen evolution reaction in solutions II, VI-XI.

Extrapolation of the linear anodic and cathodic Tafel lines to intersection was done mathematically using the least squares values for those slopes. Values obtained in this way for the reversible potential, E_R, because of the irreversible nature of the redox system, do not have their usual meaning. In this instance the potential is more properly a corrosion potential, E_{corr}, and the exchange current density, i_o, a corrosion current density, i_{corr}. Table III contains E_{corr} and i_{corr} values, as well as open-circuit "rest" potentials obtained prior to current application in polarization experiments. Unlike earlier findings (26) the present results seem to indicate that the reaction taking place at rest involves a 2:1 ratio of OH^- to electrons. The slope of the E_{rest} *vs.* log a_{OH^-} plot in Fig. 5 is -0.123 ± 0.015 V/decade but also has sufficient scatter to cast doubt on the relationship. In the author's mind, the question of the rest potential requires a separate study to resolve the discrepancy.

The stoichiometric reaction for the oxidation of tungsten in basic solution as given by Eq. [5] masks what is doubtless a very complex mechanism. The determination of kinetic parameters involves the knowledge of the dependence of the rate-determining step on various species in solution. This unit reaction (rds) is repeated a number of times (the stoichiometric factor, ν) to produce Eq. [5]. Unfortunately, the calculation of ν is based on reversibility, requiring both anodic and cathodic Tafel slopes (22, 23). Some help, however, is gotten from a consideration of the product of the transfer coefficient, α, and the number of electrons involved in the rds as given by [6]. In work with chromium, Heumann (3) and Schwabe (4) chose values of n which yielded 0.5 for α, viz.

$$b_a = 2.303\,RT/\alpha n\mathbf{F} \qquad [6]$$

$n = 3$ and $n = 2$, respectively. From the anodic Tafel slope in the present work a transfer coefficient of 0.5

Table III. Open-circuit rest potentials, corrosion potentials, and corrosion current density data

Soln. No.	E_{rest}*	E_{corr}*,†	$-\log i_{corr}$†
I	−0.936	−0.899	5.3
II	−0.940	−0.907	5.4
III	−0.940	−0.910	5.5
IV	−0.941	−0.905	5.5
V	−0.954	−0.944	5.6
VI	−0.861	−0.818	5.4
VII	−0.790	−0.728	5.5
VIII	−1.025	−0.975	5.8
IX	−0.962	−1.018	5.9
X	−0.870	−0.866	5.4
XI	−0.740	−0.788	5.5

* Volts *vs.* SCE.
† Based on extrapolation of anodic and cathodic Tafel lines to intersection.

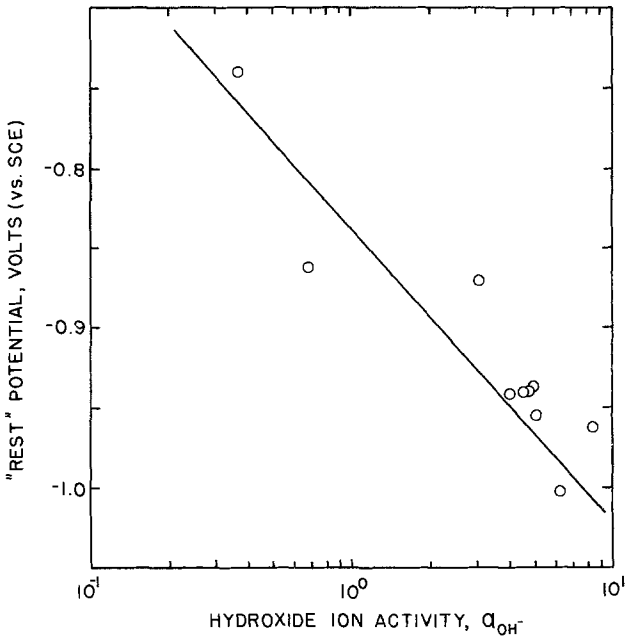


Fig. 5. Tungsten electrode rest potential as a function of log hydroxide ion activity.

yields a value of 1 for n, the number of electrons given up by tungsten in one rate-controlling event.

The sole reactant rate dependence observed gotten from Eq. [7]

$$(\partial\Delta\Phi/\partial \log a_{OH^-})_{i,T,a_{i\neq j}} = 2.303\,q'\,\nu RT/\beta n\mathbf{F} \qquad [7]$$

was for hydroxide ion, where $\Delta\Phi$ is the anodic potential at a constant current; q' is the order of the observed rate with respect to hydroxide ion ($q' = 1$, as in Fig. 2); $n = 1$; β, a symmetry factor, is taken as 0.5. The fit of these parameters to the experimental data is represented in Fig. 6. The least squares calculated slopes for the two current densities averaged 0.112 V/decade. From the measured slope, Eq. [7] was solved for ν, the number of times the rds occurs in the course of the over-all stoichiometry. A value of 1 was obtained. The deviation from the expected slope of 0.120V is actually not excessive since the activities of all the other ionic

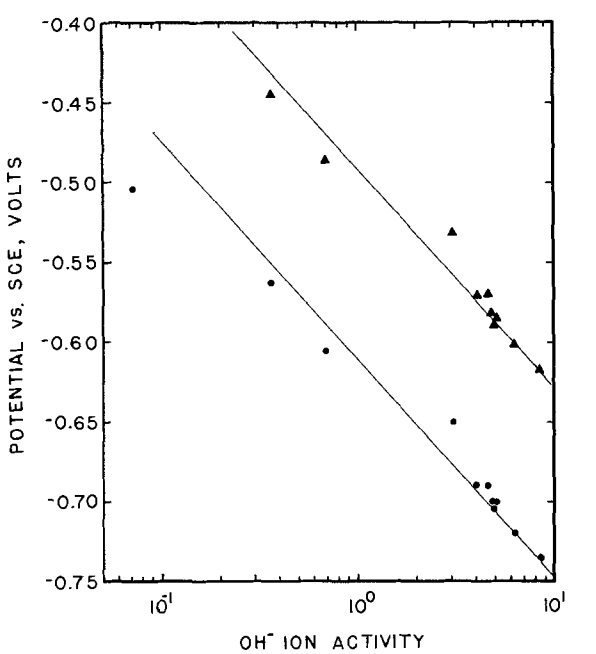


Fig. 6. Anode potential as a function of log hydroxide ion activity at constant current. ▲, Current density of 10 mA/cm²; ●, current density of 1 mA/cm².

constituents of the solutions and the activity of the water itself are not perfectly constant. The agreement with 4.606 $RT/\mathbf{F}$ is adequate, however, to corroborate the first-order dependence on hydroxide ion.

The proposed mechanism which fits the observed data is given below in six steps, four of them electrochemical

$$W_{(s)} + 2\,OH^- \rightarrow WO^+{}_{(s)} + 3e^- + H_2O \quad [9]$$

$$WO^+{}_{(s)} + 2\,OH^- \rightarrow WO_{2(s)} + e^- + H_2O \quad [10]$$

$$WO_{2(s)} + OH^- \xrightarrow{\text{rds}} WO_3H_{(s)} + e^- \quad [11a]$$

$$WO_3H_{(s)} + OH^- \xrightarrow{\text{fast}} WO_{3(s)} + e^- + H_2O \quad [11b]$$

$$WO_{3(s)} + OH^- \rightarrow HWO_4^-{}_{(aq)} \quad [12]$$

$$HWO_4^-{}_{(aq)} + OH^-{}_{(aq)} \rightleftharpoons WO_4^{2-}{}_{(aq)} + H_2O \quad [13]$$

The mediation of anodic and cathodic kinetics on tungsten by oxide formation has been suggested by other investigators (25, 26) and this metal is not unique in Group VI in this respect (32, 33). In the present work evidence of oxide behavior was found in cathodic polarizations (*vide infra*). Indeed, the electrode pretreatment procedure employed also favors air oxidation of the surface and thus one or both of the steps preceding the rds may have taken place before polarization. While parts of the final dissolution reactions are common to Johnson's work (26), the electrochemical kinetic data here indicate a rds which is first order in hydroxide ion and at the same time involving a one-electron oxidation. Equation [11a] clearly fulfills these observed requirements as does [11b]. Since the oxidation potentials for the W(IV) → W(V) and W(V) → W(VI) steps are so similar, it is difficult to choose one over the other on that basis. The oxides WO_2 and WO_3 crystallize in the same manner; both have tetragonal and rhombic space groups. In fact, the coordination of tungsten in both oxides is octahedral and magnetic susceptibility data (34) indicate that the substoichiometric oxides between WO_2 and WO_3 are perhaps best represented by a surplus of free electrons in the conduction band from defects or vacancies in the WO_3 structure. Thought of in these terms, no monomeric representation of the W(V) intermediate could correctly describe it. The fact that Hull (33) observed soluble Mo(V) species at the ring electrode indicates that it is possible to remove a W(V) complex from the lattice. However, with a following one-electron oxidation to WO_3, [11b], this possibility is less likely. The choice of [11a] as rds is also consistent with the low overpotential region wherein the Tafel relationship was observed. Besides avoiding the necessity of invoking some complex dimeric species formation (26) the new kinetic data account for the observed first-order hydroxide ion dependence and apparent one-electron charge transfer in the rds.

The reactions subsequent to [11] are chemical dissolution steps with the final [13] equilibrium attained in the bulk solution. In the concentration polarization region (high overpotentials beyond Tafel linearity), where hydroxide ion is used up as fast as it arrives, the oxides become insoluble (low pH) and current flow is limited. In the present work, the concentration of hydroxide was high enough that the double layer region never became acidic enough for passivation to occur.

The sum of reactions [11a] through [13] gives a relation which fits the observed rest potential relationship of Fig. 5 and is given in Eq. [14]

$$WO_{2(s)} + 4\,OH^- \rightarrow WO_4^{2-}{}_{(aq)} + 2e^- + 2H_2O \quad [14]$$

It describes a potential derived from the irreversible dissolution of the oxide film in the presence of base, with the 2:1 hydroxide to electron ratio. It certainly represents a mixed potential since the deposition of tungsten from tungstate ion was never observed in the course of the present work.

The cathodic polarization plots reveal the expected cathodic shift with increasing hydroxide ion activity. The Tafel lines in Fig. 3, however, do not verify the expected anodic shift V > I > II > III > IV, based on increasing OH^- activity. A factor which was not accounted for in these five solutions, though, is the hydrolysis of tungstate [15] which might help explain the observed order I > II ~ III > IV > V

$$WO_4^{2-} + H_2O \rightleftharpoons HWO_4^- + OH^- \quad [15]$$

Because several of the lines are only separated by 50 mV or less, the observed dependence can only be described as qualitative.

Figure 4 reveals that in all solutions except VIII and IX, a dislocation occurred at low current densities. This behavior has been observed by other investigators (1, 5, 34) and has been attributed to the influence of the potential of zero charge (pzc) of the metal (35). The author is unaware of data for this medium for tungsten, so that no firm conclusion here is possible. The inflection occurs at −1.00 to −1.05V *vs.* SCE in all solutions for which data were taken in that potential region.

Data from two constant current densities, 1 and 10 mA/cm², were used, together with values for E_R(cath) gotten by least squares extrapolation to the potential for the HER in each solution, to obtain overpotentials, η; $\eta = E - E_R$. Figure 7 depicts η *vs.* log a_{H^+} at the two current densities. The slopes of −0.074 and −0.118V were gotten by regression analysis. The potential data used in computing the former slope covered a range of potentials from −1.1 to −1.4V *vs.* SCE, while the latter slope was gotten from potentials of −1.3 to −1.5V *vs.* SCE. If the pzc for tungsten is responsible for the inflection at *ca.* −1.05V *vs.* SCE, then the slope difference in Fig. 7 would be attributable to the fact that the electrode potential in the former case is within 300 mV of the pzc (23), and lies between −2.303 and −4.606 $RT/\mathbf{F}$.

Finally, the observed range of cathodic Tafel slopes in Fig. 4 (−0.197V/decade at 0.02M NaOH to −0.069V/decade at 6.00M NaOH) are in qualitative agreement with Ammar's (25) dual-barrier model of reduction of solvent at a thin oxide film.

Summary

The electrochemical oxidation of tungsten metal in basic solution has been found to proceed smoothly to tungstate ion over a large range of current densities and hydroxide ion activities. Formation of the oxide film, known to exist on the metal, and allowed to occur in the present study, has been incorporated into the assigned mechanism. In addition, the data for the

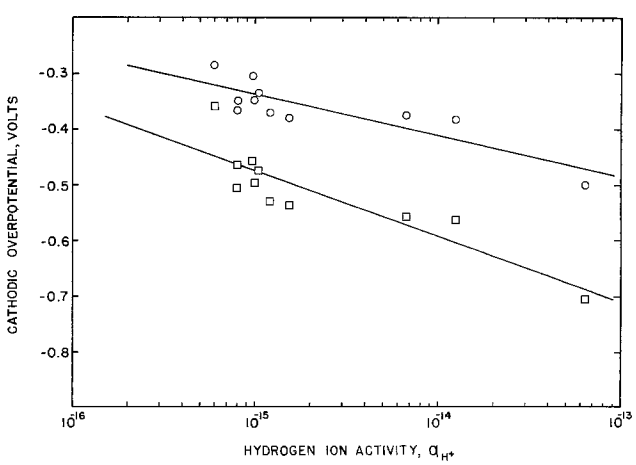


Fig. 7. Cathodic overpotential as a function of log hydrogen ion activity.

HER have also been reconciled with the oxide barrier model.

An average value for the corrosion current density of $10^{-5.5}$ A/cm^2 was obtained. The open-circuit rest potential can be described by an anodic exchange reaction involving WO_2 oxidation to tungstate ion and a cathodic solvent reduction reaction. Finally, the behavior of tungsten appears to closely resemble that of molybdenum in basic solution, with intermediate oxide species implicated in its redox chemistry.

Manuscript submitted Nov. 8, 1976; revised manuscript received Jan. 24, 1977.

Any discussion of this paper will appear in a Discussion Section to be published in the December 1977 JOURNAL. All discussions for the December 1977 Discussion Section should be submitted by Aug. 1, 1977.

REFERENCES

1. M. L. Kronenberg, J. C. Banter, E. Yeager, and F. Hovorka, *This Journal*, **110**, 1007 (1963).
2. Von T. Heumann and F. W. Diekötter, *Z. Elektrochem.*, **62**, 745 (1958).
3. Von T. Heumann and W. Rösener, *ibid.*, **59**, 722 (1955).
4. K. Schwabe, K. Müller, and A. Loge, *Electrochim. Acta*, **8**, 193 (1963).
5. T. Hurlen, *Acta Chem. Scand.*, **14**, 1533 (1960).
6. T. Hurlen, *ibid.*, **14**, 1564 (1960).
7. T. Hurlen, *ibid.*, **16**, 1337 (1962).
8. T. Hurlen, *ibid.*, **16**, 1346 (1962).
9. T. Hurlen, *ibid.*, **15**, 630 (1961).
10. M. E. Straumanis and M. Dutta, *Inorg. Chem.*, **5**, 992 (1966).
11. M. L. Rumpel, A. W. Davidson, and J. Kleinberg, *ibid.*, **3**, 935 (1964).
12. M. L. Rumpel, A. W. Davidson, and J. Kleinberg, *ibid.*, **2**, 810 (1963).
13. A. I. Kostromin, P. K. Agasyan, and V. N. Basov, *Zh. Anal. Khim.*, **25**, 216 (1970).
14. A. I. Kostromin and L. L. Makarova, *ibid.*, **29**, 1294 (1974).
15. A. I. Kostromin and R. M. Badakshanov, *ibid.*, **27**, 2046 (1972).
16. A. I. Kostromin, V. V. Mosolov, and G. Z. Badretdinova, *ibid.*, **28**, 222 (1973).
17. A. I. Kostromin, A. A. Akhmetov, and L. N. Orlova, *ibid.*, **25**, 195 (1970).
18. A. I. Kostromin, A. A. Akhmetov, and L. N. Burygina, *ibid.*, **27**, 315 (1972).
19. A. I. Kostromin, A. A. Akhmetov, and V. V. Mosolov, *ibid.*, **25**, 847 (1970).
20. A. I. Kostromin, V. V. Mosolov, and L. L. Makarova, *ibid.*, **27**, 2114 (1972).
21. G. S. Kelsey and H. W. Safford, *Anal. Chem.*, **46**, 1585 (1974).
22. R. Parsons, *Trans. Faraday Soc.*, **47**, 1332 (1951).
23. J.O'M. Bockris, in "Modern Aspects of Electrochemistry," J.O'M. Bockris and B. E. Conway, Editors, Chap. 4, Butterworths, London (1954).
24. A. M. Azzam and J. O'M Bockris, *Nature*, **165**, 403 (1950).
25. I. A. Ammar, S. Darwish, and R. Salim, *J. Electroanal. Chem.*, **52**, 443 (1974).
26. J. W. Johnson and C. L. Wu, *This Journal*, **118**, 1909 (1971).
27. American Society for Testing and Materials G 5-72, "Standard Reference Method for Making Potentiostatic and Potentiodynamic Anodic Polarization Measurements," ASTM, Philadelphia (1972).
28. R. Parsons, "Handbook of Electrochemical Constants," pp. 24-28, Academic Press, Inc. (1959).
29. R. A. Robinson and R. H. Stokes, "Electrolyte Solutions," Appendix 8.10, Butterworths, London (1955).
30. J. E. Hawkins, *J. Am. Chem. Soc.*, **54**, 4480 (1932).
31. D. T. Sawyer and J. L. Roberts, Jr., "Experimental Electrochemistry for Chemists," p. 61, John Wiley & Sons Inc., New York (1974).
32. L. L. Wickstrom and K. Nobe, *This Journal*, **116**, 525 (1967).
33. M. N. Hull, *J. Electroanal. Chem.*, **38**, 143 (1972).
34. M. J. Sienko and B. Banerjee, *J. Am. Chem. Soc.*, **83**, 4149 (1961).
35. J. M. West, "Electrodeposition and Corrosion Processes," pp. 56-58, Van Nostrand (1965).

Anodic Corrosion of Zinc Alloys in Seawater

Jeff Perkins, W. H. Luebke, K. J. Graham, and J. M. Todd

Materials Science and Chemistry Group, Naval Postgraduate School, Monterey, California 93940

ABSTRACT

Zinc alloys are widely used as sacrificial anodes in cathodic protection systems. In order to better understand the corrosion performance of these alloys the structure and morphology of corrosion products have been studied under laboratory conditions as a function of time, potential, current density, temperature, and velocity. Polarization curves have been determined and scanning electron microscopy, energy-dispersive x-ray microanalysis, and x-ray diffraction have been utilized to identify and characterize surface corrosion. Nucleation and growth processes for the primary anodic electrocrystallization product, ZnO, have been determined. A dissolution-precipitation mechanism is postulated, which describes the development of network arrays of zinc oxide platelets. The relationship of anodic corrosion to microstructural features of the bulk alloy is also described, including the role of grain boundaries and second-phase particles. Conditions leading to formation of passivating thick films are discussed.

The typical corrosion product structure formed on a sacrificial anode zinc material when coupled with mild steel in still seawater for 100 hr is shown in Fig. 1. X-ray diffraction of the as-corroded surface reveals that the primary compound seen here is zinc oxide (ZnO) (1). Morphologically, the corrosion product consists of an array of discrete single crystal plates of zinc oxide. These plates are about 30 μm average diameter, with a hexagonal plate shape, and there are about 10^6 plates per square centimeter zinc surface area (1, 2). The plates are obviously forming by a dissolution-precipitation mechanism (3, 4), developing a three-dimensional network array that is porous on the microscale. This porosity is a desirable feature since it allows free access of the electrolyte to the base anode surface and allows the sacrificial anode to corrode. This point emphasizes the impetus for the present studies, namely, decreased efficiency of sacrificial anodes due to passivation.

Key words: cathodic protection, morphology, passivity, velocity effects.

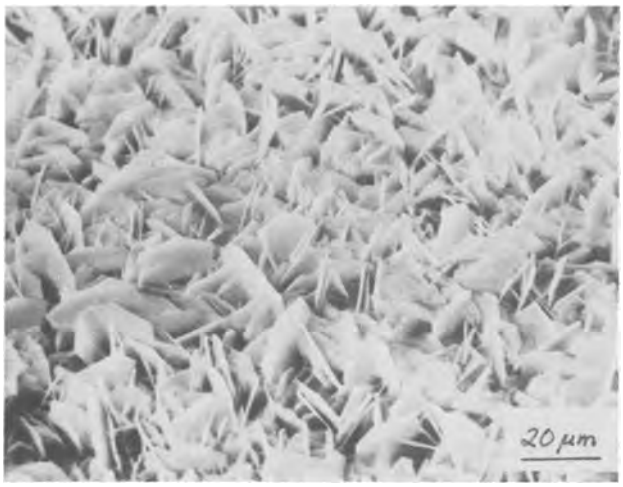


Fig. 1. Typical corrosion product structure formed on sacrificial zinc anode when coupled with steel in seawater for 100 hr. The discrete plates are ZnO crystals.

Zinc alloys have long been used as sacrificial galvanic anodes for cathodic protection. A common problem associated with this usage has been the development of apparent anode passivity and, therefore, loss of current-providing capability. This phenomenon is, of course, attributed to the development of dense, adherent corrosion product structures, unlike that seen in Fig. 1. Due to this passivation problem, extensive research was conducted in the 1950's and 1960's, leading to present specifications for ships' hull zincs (5). These specifications place impurity limitations on the zinc compositions, largely as a result of various empirical corrosion-rate studies (6-9). In order to develop better understanding of compositional influences on the corrosion performance of zinc-based materials, studies were initiated at the Naval Postgraduate School several years ago (1-4). These studies were intended to develop a fundamental understanding of composition specifications. The present studies have emphasized microscopic aspects of corrosion product formation and the influence of base metal microstructural features such as the distribution of alloying elements in the microstructure. Surface microanalytical beam techniques such as scanning electron microscopy and energy dispersive x-ray spectroscopy have been utilized extensively.

This paper summarizes several aspects of zinc anodic corrosion product formation, including (*i*) nucleation and growth sequence under stationary conditions, (*ii*) effects of base metal microstructure on the form and distribution of corrosion products, (*iii*) velocity effects, and (*iv*) current density effects. From these observations we have isolated conditions under which passivating thick films are favored.

Experimental

In previous work (1-4), when "natural" unbiased zinc-steel couples were used, they had an effective surface area ratio of about 1:50 (zinc to steel), which approximates the area ratio typical for ship hull protection. For this situation the anodic current density is about 1.5 mA/cm^2. This value is a useful reference point for comparison with imposed galvanostatic exposures reported here. Note that this current density is derived for static (no-flow) conditions at room temperature for natural couples in aerated synthetic seawater at short exposure times.

The experimental apparatus for dynamic galvanostatic experiments consisted of a cylindrical tank, rotating-disk assembly, galvanostatic power source, digital voltmeter, and frequency counter. The exposure tank was Plexiglass, 46 cm diam filled to a level of approximately 29 cm to hold 48 liters of synthetic seawater. A system of plastic baffle strips was installed within the tank volume and along its interior and bottom to keep the electrolyte as stationary as possible during traveling-electrode experiments. The tank bottom was also fitted with an embedded, 35.5 cm diam aeration canal which allowed compressed air to be bubbled through the liquid from an array of 12 air holes spaced 30° apart to ensure that the electrolyte was saturated with oxygen. The bubbling also provided a vertical circulation pattern to eliminate potential concentrations of corrosion products in the solution during tests.

The rotating-disk assembly (Fig. 2) consisted of a 30.5 cm diam, 1.27 cm thick Plexiglas disk suspended 20 cm below the electrolyte surface by a 2.54 cm diam Plexiglas shaft. The shaft was connected via a pulley arrangement to an electric motor, with variations in pulley size allowing disk speed to be varied. A single zinc sample was located in the disk underside in a small rectangular slot near the disk perimeter, 14.5 cm from the disk center. The slot was carefully machined to accommodate the 1.1 × 1.1 × 0.5 cm specimens with close tolerances, so that once in place they were flush with the disk surface and clearance between the sides of the zinc sample and the Plexiglas slot was minimized. The sample was held in place with a plastic setscrew threaded into a tapped hole in the back of each sample, as seen in Fig. 3.

The anodic zinc current was controlled using an impressed galvanostatic current system. Electrical contact was accomplished by using a brass ring in the inner wall of the setscrew hole in the disk. As the speci-

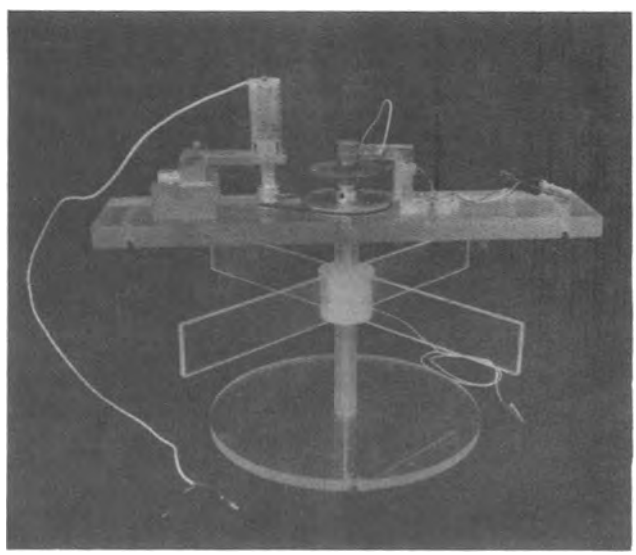


Fig. 2. Rotating-disk assembly

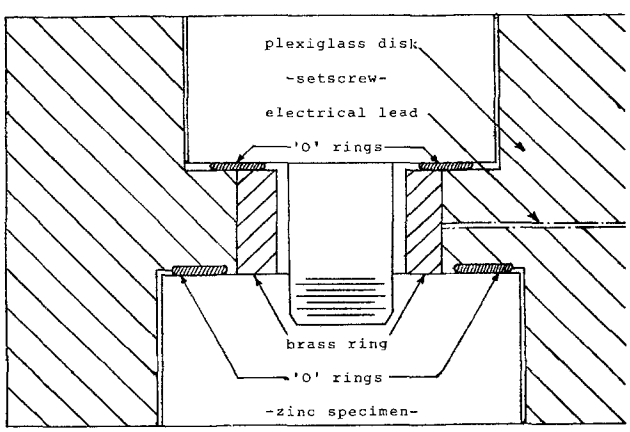


Fig. 3. Schematic detail drawing of specimen arrangement in rotating disk.

men was secured into the slot it was forced against the brass ring to complete the circuit. Two rubber "O" rings were used to isolate the brass/zinc connection from the electrolyte; one under the setscrew head and one around the outer perimeter of the brass/zinc interface. Current was delivered by a wire running into the hollow drive shaft through a watertight route along the disk radius. At the top of the shaft were fitted the drive mechanism and counting apparatus. A copper pickup brush positioned against a brass pickup ring on the shaft allowed current control to the zinc anode at velocity. The cathode was a 3.8 cm diam platinum disk positioned on top of the tank bottom baffles at the center of the tank approximately 3.2 cm below the plastic disk. As with the zinc electrode, construction was such as to ensure that the platinum disk was the only cathode in the tank during experimentation. Current output to the zinc specimen was governed by voltage selection across precision resistors in series with the load; maximum current available was 0.75A (7.50V with a 10Ω resistor). The dynamic response of this configuration was on the order of 15 μsec and over-all regulation was 0.1% of full scale of the selected range. It was possible to control specimen current to ± 2 μA regardless of anode velocity.

Zinc samples used in experimentation were machined from a standard 48.5 kg zinc alloy slab obtained from Mare Island U.S. Navy Shipyard, Vallejo, California. This was nominally a MIL-specification (5) material intended for cathodic protection use as a ship hull anode. Chemical analysis confirmed the alloy as conforming to Military Specification A-18001H, being approximately 99.99% zinc with trace amounts of lead, iron, cadmium, aluminum, copper, and silicon (5). Prior to exposure, the surface of each specimen underwent a standard preparation sequence, being sanded to a 600 grit finish, rinsed with tap water and alcohol, then dried with a jet of freon gas. Unless otherwise noted, the initial surface of samples is this uniformly sanded 600 grit finish; however, some samples were prepolished and etched to make base metal microstructural correlations. All experiments were performed with synthetic seawater electrolyte prepared using the formula and procedure developed by Kester *et al.* (10). Before each experiment the solution was tested and, if necessary, adjusted for *p*H and conductivity to meet the specifications (*p*H of 8.0-8.4 and resistivity between 22 and 24 Ω-cm): usually only small additions of distilled water, to compensate for evaporation losses, were needed to bring the seawater quality within the desired limits. Of course, the synthetic seawater electrolyte used in these experiments presents conditions which differ from natural seawater in terms of organic constituents, metallic ions, and temperature fluctuations. All of these factors can be imagined to affect the microscopic aspects of zinc corrosion, which are the subject of this paper. For example, organic impurities can participate in adsorption/desorption phenomena, noble metallic impurities may participate in local displacement reactions with zinc, and temperature affects the solubility of corrosion product compounds. However, these kinds of effects are not considered substantial in view of previous work where natural and synthetic seawater exposures were compared and microscopic corrosion observations were essentially identical (1).

Once a specimen was fastened into the rotating-disk slot, but before being lowered into the electrolyte, checks were made to ensure that the corrosion current delivered would be that actually prescribed by the experimental plan and procedures were employed to avoid current surges during circuit completion. For tests involving a stationary anode, the desired value of impressed current was applied within 10 sec of immersion. Under rotating conditions the time elapsed was approximately 20 sec because the necessary assembly rpm could not be achieved instantaneously; no current was applied until anode velocity was stable. A detailed analysis of relative velocity distribution of the electrolyte has not been attempted. In all rotating-disk mechanisms, such as used here, there is an inherent radial flow over the disk surface as well as the tangential velocity component. Mathematical solutions exist which can provide the net velocity vector under these general conditions, but the computational efforts required were considered to exceed the utility of the solutions in this case. For convenience, relative anode velocities are expressed here simply as disk rpm, and for reference corresponding approximate tangential relative velocities in cm/sec and knots are given where of interest. For example, a disk rpm of 60 rpm corresponds to a relative tangential velocity component of about 100 cm/sec or about 2 knots.

Once each corroded specimen was removed from the tank, but prior to being loosened from the disk slot setscrews, its surface was immediately rinsed by immersion in distilled water. This procedure has been shown to induce no disturbance to the corrosion product structure, while thoroughly washing away electrolyte salts. Specimens were subsequently removed from the slot, rinsed again, and allowed to dry naturally in air. After corrosion exposure, the surface of each sample was studied using a Cambridge S4-10 scanning electron microscope (SEM) equipped with a Princeton Gamma-Tech PGT-1000 energy-dispersive x-ray spectrometer.

Results and Discussion

Nucleation and growth sequence.—For natural zinc-steel couples in still seawater, an incubation time of about 7.5 min is observed prior to the formation of initial corrosion product crystals by a dissolution-precipitation mechanism (4). The nucleation and growth sequence of the network array is shown in Fig. 4. In controlled galvanostatic anodic exposures in still sea-



Fig. 4. Nucleation and growth sequence of network array of ZnO platelets on zinc in natural galvanic couple with steel in still seawater; (a) 10 min, (b) 12 min, (c) 20 min, (d) 25 min, and (e) 30 min.

water an $i \times t$ product of about 15 mA min/cm^2 is obtained, for current densities in the range 0.775-7.75 mA/cm^2. This correlates with measurements indicating that the typical current density experienced in natural galvanic couples at short terms is on the order of 1.5 mA/cm^2. Quantitative microscopic determinations of the time variation of average plate diameter in the array shows that an approximately parabolic function is followed.

Effects of base metal microstructure.— The microstructure of zinc samples employed in these studies is shown in Fig. 5. This shows a noncorroded polished and etched surface, which is not the surface condition generally employed in corrosion experiments, although some prepolished and etched samples were corroded to make better base metal microstructural correlations. The microstructure reveals grain boundaries, twin boundaries, and a distribution of apparently less conductive inclusions. Base metal grain boundaries and twin boundaries have virtually no effect on the nucleation and growth of individual ZnO platelets, as seen in Fig. 6 for a prepolished and etched sample. A narrow region free of dissolution pits is observed adjacent to the grain boundaries, perhaps indicating that the grain boundaries act as dislocation sinks in these alloys, but this heterogeneity in dissolution has no apparent effect on corrosion product formation, which is oblivious of the presence of these boundaries. On the other hand, impurity-based inclusions have a distinct effect on the distribution of dissolution and corrosion product formation. Inclusions which are microcathodic with respect to the zinc matrix cause accentuated zinc dissolution and corrosion product formation around their periphery, leading to locally denser arrays (see Fig. 7). These microstructural observations were made on prepolished and etched surfaces exposed for relatively brief periods in natural couples with mild steel under static conditions.

In controlled galvanostatic exposures at low current densities (less than natural galvanic values of about 1.5 mA/cm^2), for both static and moderate flow conditions, "ribbonlike" bands of corrosion product define interfaces between microscopic anodic and cathodic areas on the sample surface, as seen in Fig. 8a. These structures appear in the early stages of corrosion exposure, prior to the precipitation of individual ZnO platelets (*i.e.*, at $i \times t$ products less than 15 mA min/cm^2). They are firmly bonded to the base metal surface and consist of dense wall formations of zinc oxide (Fig. 8b). These walls typically encircle areas of higher dissolution (Fig. 8c), *i.e.*, locally microanodic regions. The encircled regions often, but not always, show the

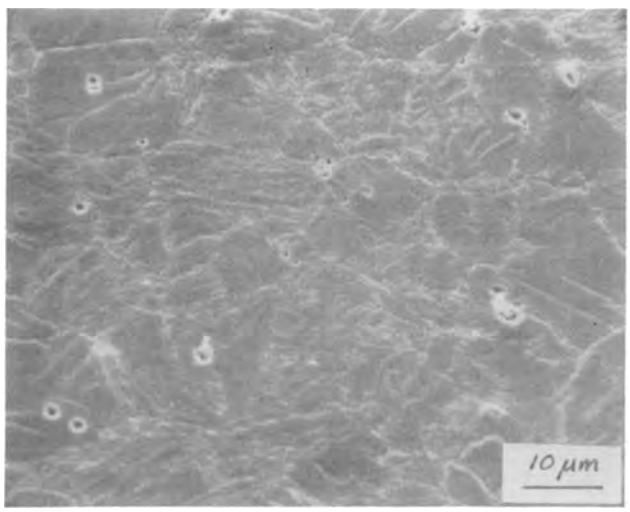


Fig. 5. Base metal microstructure of zinc samples employed in these studies. Note that this does not represent the typical surface condition employed, but was used in certain cases to make base metal microstructure; corrosion product correlations.

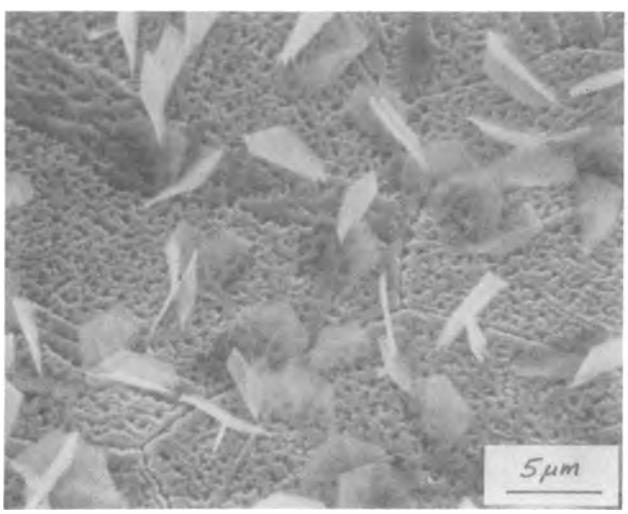
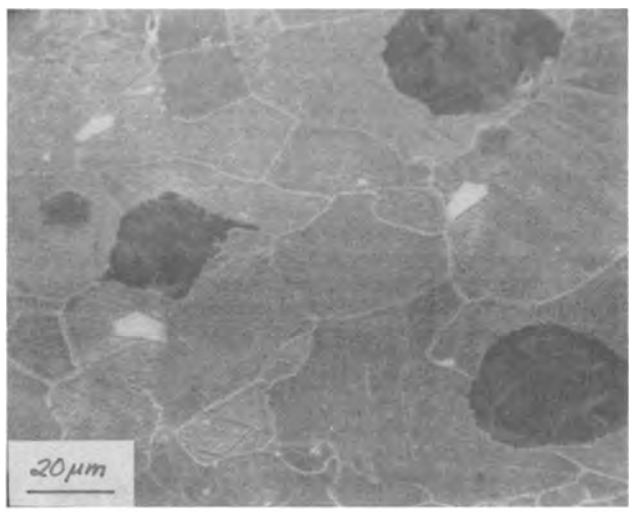


Fig. 6. Corrosion product on prepolished and etched surface shows that base metal grain boundaries and twin boundaries have virtually no effect on corrosion product distribution or orientation on specimen surface. Note dissolution pit-free region adjacent to grain boundaries.



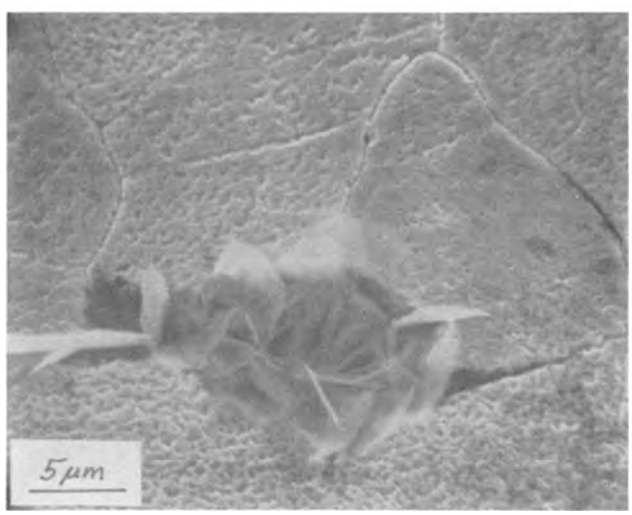


Fig. 7. Effect of base metal inclusions which are microcathodic relative to the matrix (a) accentuated zinc dissolution around such inclusions (b) pronounced corrosion product outgrowth over a grain-boundary situated particle.

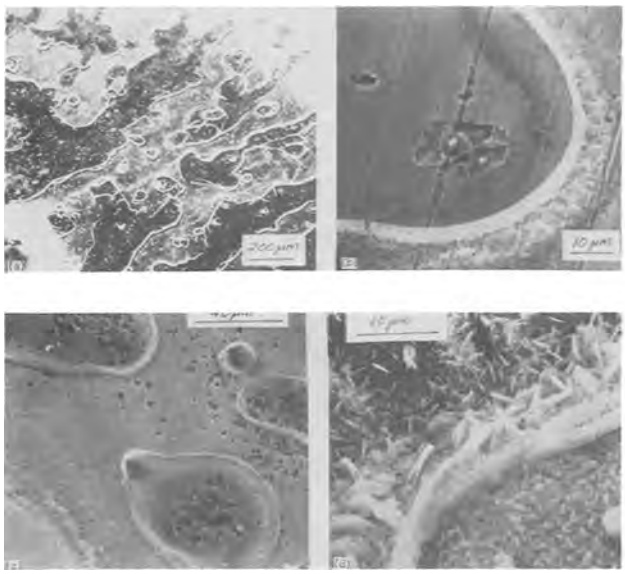


Fig. 8. Ribbonlike walls of corrosion product define interfaces between microscopic anodic and cathodic regions on the specimen surface at low galvanic current density (a) 5 min exposure at 0.775 mA/cm^2 current density and 25 cm/sec relative velocity; (b) 2 min exposure at 0.0775 mA/cm^2, stationary; (c) 2 min exposure at 0.155 mA/cm^2, stationary; (d) 40 min exposure at 1.55 mA/cm^2, 100 cm/sec.

presence of microcathodic inclusions at their centers (Fig. 8d).

Growth of these ribbonlike structures seems to continue until the walls have a given height and thickness, and they are eventually overgrown by a general network of ZnO platelets. The initial individual ZnO platelets form just to the inside of the walls encircling the dissolution pits (Fig. 8d). and in the early stages platelet nucleation is abruptly less pronounced outside the ribbon-encircled regions.

Velocity effects.—At a given current density, increased relative anode velocity leads to an increase in the number of dissolution sites per unit surface area, as seen in Fig. 9. Streaks originate from small local areas which have undergone a large amount of dissolution relative to the surrounding surface. Figure 9d shows one dissolution site at higher magnification. Increases in relative velocity increase the number of dissolution sites and associated streaks, and there is a decrease in the size of individual sites and the width of streaks.

Fluid dynamics has an important role in these changes in distribution of dissolution sites. This can be explained by considering the interaction between the hydrodynamic boundary layer and the electrochemical double layer (11). The hydrodynamic boundary layer constitutes a necessary transition layer in a fluid when there is relative motion between an object and that fluid. The fluid just next to the solid surface adheres to it without relative motion or slippage. Moving away from the surface, the relative fluid velocity changes until, at the extreme of the boundary layer, the free-stream condition of the bulk electrolyte is obtained. The electrochemical double layer refers to the distribution of ions which arises due to dissolution of the anode surface. With each added increment of relative velocity the velocity gradient in the hydrodynamic boundary layer is greater, and shear stresses at the specimen surface increase. Considering the observed increase in dissolution sites with increasing velocity, it may be inferred that increasingly irregular removal of metal ions to the hydrodynamic boundary layer occurs, leading to variable ionic concentration from place to place along the surface. Note that the role of physically microcathodic microstructural features is

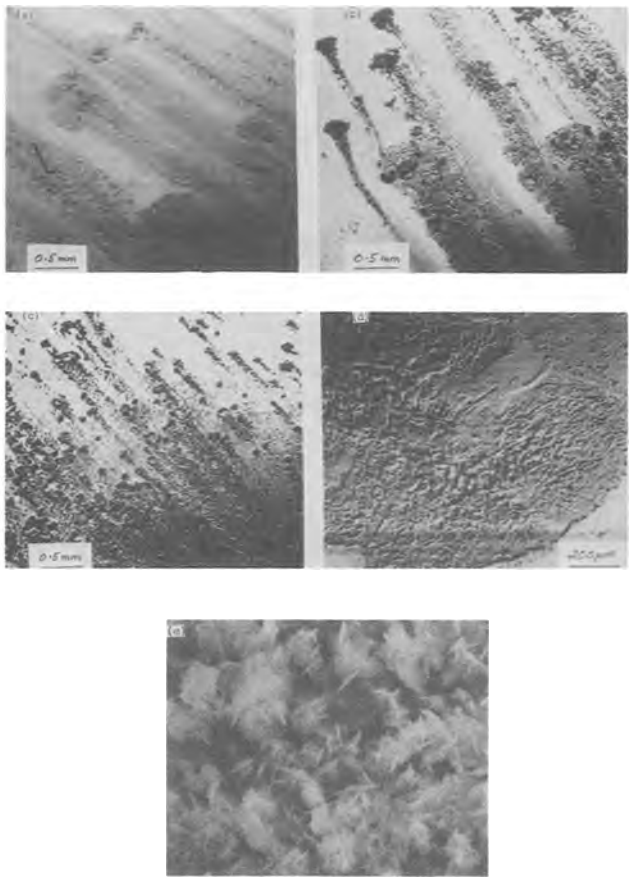


Fig. 9. Effect of relative anode electrolyte velocity on dissolution; all exposures 40 min at 1.55 mA/cm^2: (a) 50 cm/sec; (b) 125 cm/sec; (c) 150 cm/sec; (d) detail of dissolution site at 50 cm/sec; (e) high magnification view of platelet precipitation within dissolution site.

apparently reduced under dynamic conditions, as they do not seem to be preferred sites. To check the hypothesis that dissolution sites in dynamic situations are essentially independent of minor variations in surface character of the metal, artificial pits and scratches were cut into the specimen surface prior to corrosion; dissolution streaks were observed to pass over these features. They were not used as preferred nucleation sites for dissolution, whereas grinding scratches typically serve as preferred nucleation sites in static exposures. Therefore, the distribution of dissolution sites in dynamic exposures is considered to represent instabilities in the hydrodynamic boundary layer, rather than a base metal microstructural effect.

With respect to the precipitation step, the formation of ZnO platelets depends on the degree of metallic ion supersaturation in the electrolyte layer immediately above the anodic area on the surface. Figure 9e, which is a high magnification view of the dissolution site shown in Fig. 9d, shows a fine-scale platelet network, illustrating that supersaturation is still achieved and precipitation occurs under hydrodynamic conditions.

Farmer and Webb have considered the dependence of anodic zinc corrosion on electrolyte velocity with the aid of diffusion theory (12). They point out that development of a passivating film is dependent on attaining a certain critical concentration of zinc ions immediately at the electrode surface rather than in the electrolyte above it, so that passivation depends on the difference between the rate of ion formation and the subsequent rate of ion removal by the electrolyte. Ion transport from the surface can be described by reference to a hypothetical "diffusion layer" of electrolyte adjacent to the anode surface. A thick diffusion layer, such as would be expected to exist under more stagnant conditions, would inhibit ion removal and favor

passivating film growth, since ionic diffusion is relatively slow. Under laminar conditions (low relative anode velocity) the diffusion layer thickness can be assigned a value, δ, which is related to the hydrodynamic boundary layer thickness, δ_o, as: $\delta = \delta_o/Pr^{1/3}$, where Pr is the Prandtl number associated with ionic diffusion. For the particular electrolyte environment under consideration in these studies $Pr \approx 10^3$, so that $\delta \approx 0.1\delta_o$. The hydrodynamic boundary layer thickness in lamellar flow over a flat surface is inversely proportional to the square root of the relative free-stream velocity, so that both it and the diffusion layer decrease in thickness as the velocity increases. Therefore, the critical ionic diffusion path and the passivation tendency will decrease with relative velocity. Note that because of the inverse square root relationship passivation time will decrease and become less sensitive to velocity as velocity increases.

For flow conditions produced at higher relative velocities (>150 cm/sec in these studies) for current densities of natural galvanic values, the typical open network arrays of ZnO platelets are not favored, and instead, a thin compact film forms over an underlying fine-scale network array (Fig. 10). This film is quite fragile, however, and because of a cyclic film formation-cracking sequence, permanent anodic passivation does not occur under these conditions. Figure 10b reveals the sublayer present under a spalled area of the compact film. The boundary layer formed at this disk speed is probably turbulent. Turbulent boundary layers, of course, exhibit marked differences from laminar ones, with regions of intense fluid particle mixing and high shear stress on the surface. Rapid and uniform dispersion of zinc ions is inevitable under these conditions; in a sense this represents the limiting case for the observed increase in dissolution sites with boundary layer instability. It may be that because of the lack of supersaturation three-dimensional nucleation of ZnO platelets cannot occur, so that a two-dimensional lateral-growth mechanism gives rise to the more compact corrosion film. Therefore, it is likely that the observed undergrowth network was formed subsequent to formation of the compact film. As mentioned earlier, a tendency for this film to crack and spall was evident, indicating poor adhesion. It is likely that due to this cracking and loss of contact between the compact film and base metal surface, the platelet network is able to nucleate and grow under the film, where velocity effects would not be felt and supersaturation could easily be obtained. In fact, as the platelet network grows it may contribute to the tendency for the compact film to spall.

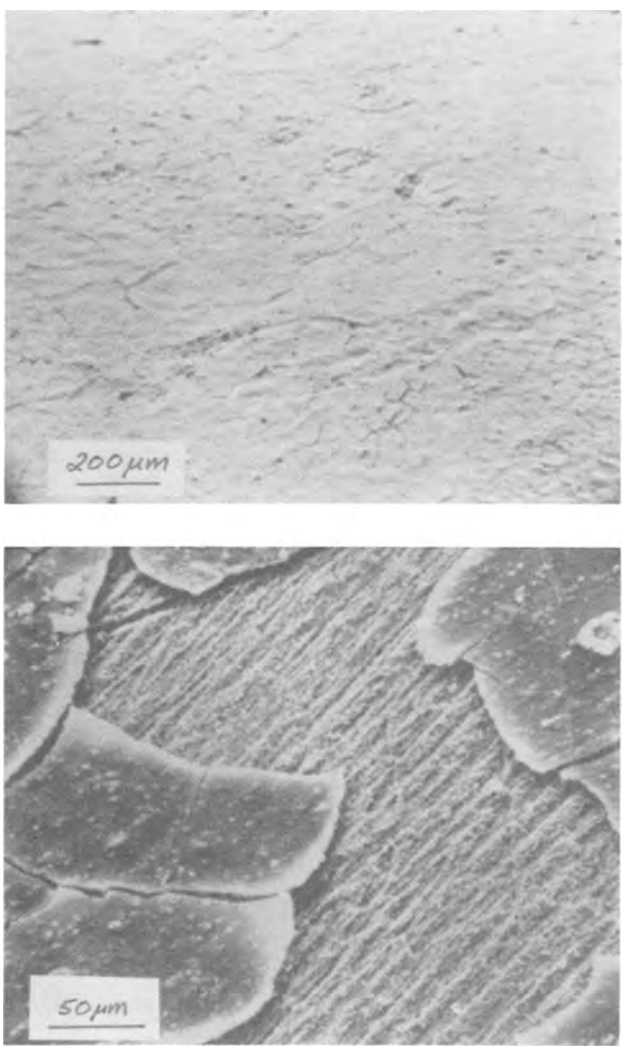


Fig. 10. (a) Fragile compact film formed under turbulent flow conditions; (b) fine network sublayer formed below compact film.

It should be noted that all the velocity effects discussed in this section refer to specimens galvanostatically corroded at a current density of 1.5 mA/cm^2, a value close to the experimentally determined approximate "natural galvanic" value. Later discussion of high current density effects will also include some consideration of the interaction between velocity and dissolution/precipitation processes.

Current density effects.—In galvanostatic exposures at zero relative anode velocity, increased current density yields more dissolution sites per unit surface area, thus leading to faster and more uniform corrosion product formation. This is illustrated in the series of photomicrographs in Fig. 11 for a given exposure time of 4 hr at zero velocity. The current densities in this series of exposures represent 1, 2, 3, and 5 times the typical natural galvanic values. Note that the exposures represent $i \times t$ products that also increase in this ratio. However, it is variation in the scale of the corrosion product network which is most notable. Keeping in mind magnification differences for the series of photomicrographs in Fig. 13, one can easily discern that the network structure nearest the base metal surface is finer for higher current densities, and that after this network is complete a secondary network is formed which commences at earlier times for higher current densities and attains a larger scale of size for a given time. Figure 12 schematically presents a model for the effect of current density on corrosion product structure.

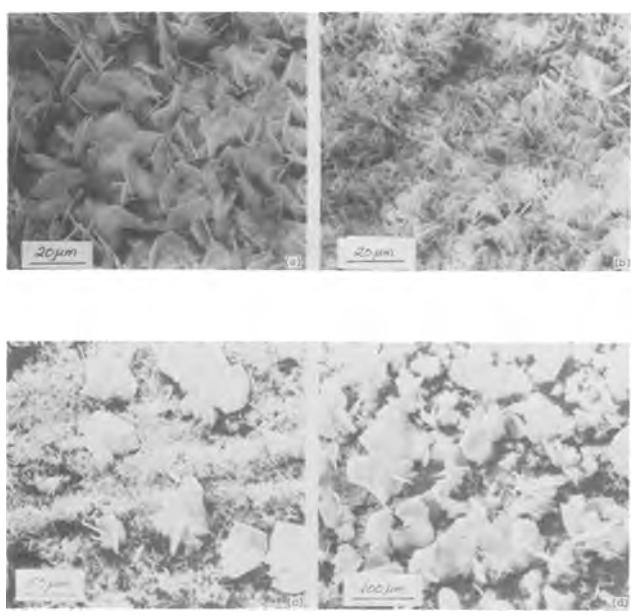


Fig. 11. Effect of current density for static exposures of 4 hr duration (a) 1.55 mA/cm^2; (b) 3.10 mA/cm^2; (c) 4.65 mA/cm^2; (d) 7.75 mA/cm^2.

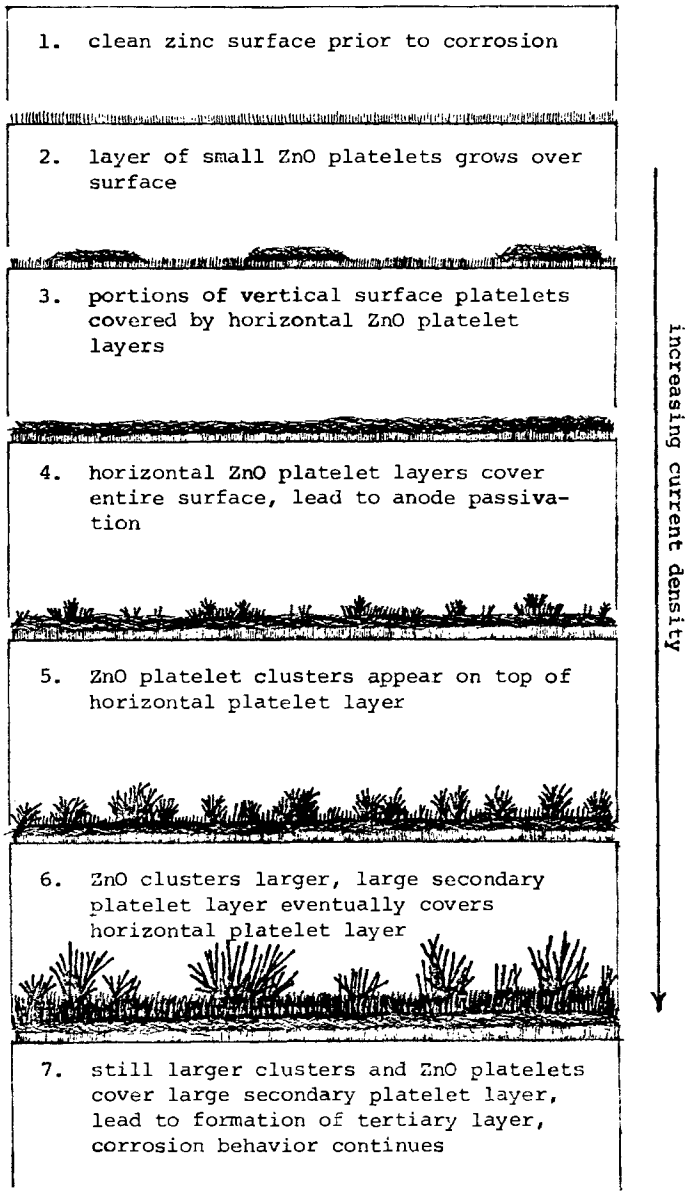


Fig. 12. Schematic model for the effect of current density on the development of corrosion product structure under static conditions.

Note that high impressed current density conditions do not lead to passivation in stationary exposures. The entire corrosion product structure consists of platelet networks with the outer networks increasing in scale, but with the entire structure microscopically porous and therefore nonpassivating. It is also noticed that as current density is increased velocity effects tend to be less evident. For example, at very high current densities (20 times natural galvanic values) high velocities had virtually no effect on the development of corrosion product structures. This is illustrated in Fig. 13, where the sequence of corrosion product formation with increasing time (at 31 mA/cm^2 and 200 cm/sec) is typical of what is observed under static conditions at lower current densities, *i.e.*, a sequence showing ribbons/dissolution pits (Fig. 13a-13c) and ZnO platelet network overgrowth (Fig. 13d). It was surprising that these fragile-appearing platelets sustain the turbulent high velocity conditions with virtually no damage. However, sections of the structure eventually do spall away, revealing the underlying ribbon structures still adhering to the base metal surface (Fig. 13e).

Conditions favoring passivating thick films.—From these studies the particular conditions favoring passivating corrosion product formation have become evident, as well as those conditions which tend to discourage passivation. The toughest, most compact films are favored by low current density, long-time exposures under static (no-flow) conditions. The film formed under these conditions consists of a layer of zinc oxide platelets compacted parallel to the anode surface over an underlying platelet network. It was shown in previous studies that the initiation of compact parallel structures is favored in the vicinity of microcathodic inclusions which modify the local field lines. The present studies show that even in the absence of such sites to trigger such formations parallel overgrowth layers will always tend to form in low current density, long-time, stationary exposures. On the other hand, high impressed current densities and turbulent flow conditions, as might be expected, tend to prevent passivation. Higher impressed fields preclude the formation of surface-parallel layers, while high velocities tend to impart mechanical stresses which crack and spall corrosion product layers, particularly as their thickness increases.

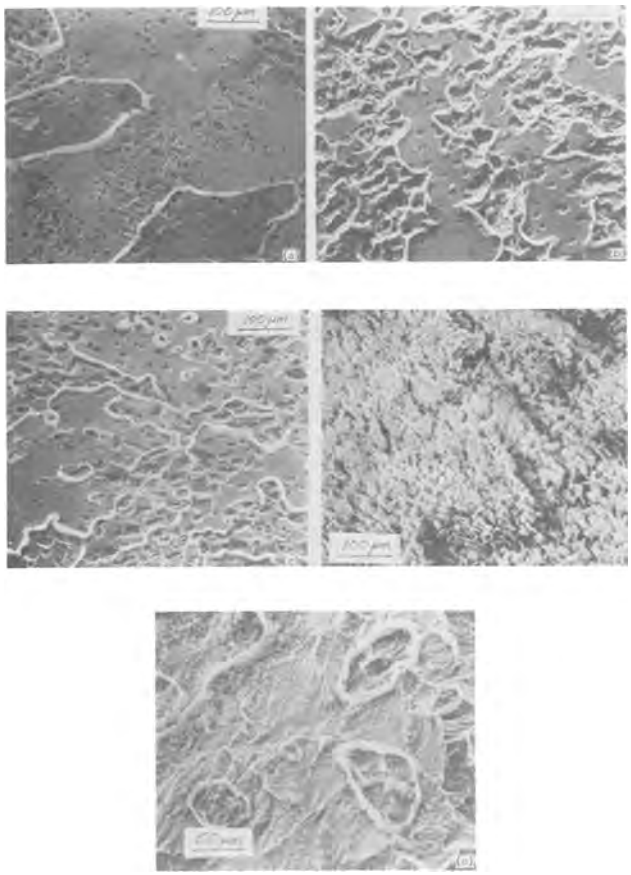


Fig. 13. High current density (31 mA/cm^2), high velocity (200 cm/sec) exposures indicates decreased velocity effect at high current density. Development of ribbon structures (a) 2 min; (b) 5 min; (c) 10 min; (d) 60 min (overgrowth of ZnO platelet network); (e) base metal surface exposed under spalled area of corrosion product formed at 60 min. Note underlying ribbon structures.

Conclusions

1. The typical structure of the corrosion product on zinc anodes in seawater consists of a three-dimensional network array of discrete single crystal ZnO (zinc oxide) plates.

2. Under galvanostatic conditions in still seawater, individual ZnO platelets initially precipitate after a current density time product of about 15 mA min/cm^2 is obtained. High current density conditions (above typical galvanic values) are not passivating in a stationary environment. These conditions promote growth of layers of primary and secondary platelet networks, with the outer layer much larger in scale.

3. Base metal microstructural inclusions which are microcathodic with respect to the zinc matrix cause ac-

centuated zinc dissolution and corrosion product formation around their periphery. The increased activity at these locations leads to locally denser corrosion product formations.

4. In galvanostatic exposures at zero relative anode velocity, increased current density yields more dissolution sites per unit surface area, thus giving faster and more uniform corrosion product formation. Turbulent flow conditions at relatively high velocities and at current densities typical of natural galvanic couples tend to disfavor the open network array typical of natural couples in still seawater, instead favoring a thin compact film over an underlying network of fine platelets. However, a cyclic film formation-cracking process prevents anode passivation under these conditions. High current density conditions (above typical galvanic values) are not passivating in a stationary environment. These conditions promote growth of layers of primary and secondary platelet networks, with the outer layer much larger in scale.

5. Compact, passivating thick films are favored by low current density, long-time exposures under no-flow conditions. The coherent film consists of ZnO platelets compacted parallel to the anode surface.

Acknowledgment

This research was supported in part by the Office of Naval Research, Metallurgy Program Office.

Manuscript received Dec. 3, 1976; revised manuscript received Feb. 17, 1977.

Any discussion of this paper will appear in a Discussion Section to be published in the December 1977 JOURNAL. All discussions for the December 1977 Discussion Section should be submitted by Aug. 1, 1977.

Publication costs of this article were assisted by the Naval Postgraduate School.

REFERENCES

1. R. A. Bornholdt and J. Perkins, *Metallography*, **8**, 401 (1975).
2. J. M. Todd and J. Perkins, *Nav. Eng. J.*, **88**, 65 (1976).
3. J. Perkins and R. A. Bornholdt, *Corros. Sci.*, Paper accepted for publication.
4. J. Perkins, *J. Cryst. Growth.*, Paper accepted for publication.
5. Military Specification MIL-A-18001H, U.S. Government Printing Office (June 28, 1968).
6. L. J. Waldron and M. H. Peterson, *Corrosion*, **16**, 375 (1960).
7. E. C. Reichard and T. J. Lennox, *ibid.*, **13**, 410 (1957).
8. R. B. Teel and D. B. Anderson, *ibid*, **12**, 53 (1956).
9. R. T. Southin, *J. Inst. Met.*, **93**, 428 (1964-1965).
10. D. R. Kester, I. W. Duedall, D. N. Conneus, and R. M. Pytkowicz, *Limnol. Oceanogr.*, **12**, 176 (1967).
11. R. White, C. M. Mohr, and J. Newman, *This Journal*, **123**, 383 (1976).
12. E. D. Farmer and A. H. Webb, *J. Appl. Electrochem.*, **2**, 123 (1972).

X-Ray Photoelectron and Auger Spectroscopic Study of the Underpotential Deposition of Ag and Cu on Pt Electrodes

J. S. Hammond[1] and N. Winograd*

Department of Chemistry, Purdue University, West Lafayette, Indiana 47907

ABSTRACT

The underpotential deposition of monolayer quantities of Ag and Cu has been studied using XPS and Auger spectroscopy. XPS chemical shifts of −0.65 and −0.95 eV *vs.* the bulk metal have been observed although no distinction was noted between the various underpotential states present in the cyclic voltammogram. The shifts were identical to vapor-deposited submonolayer films of Ag and Cu on Pt in the low coverage ($\theta \sim 0.1$) limit. A gradual shift with coverage to the bulk metal value for the vapor-deposited films and a constant shift with coverage for the underpotential deposit indicated that islanding was present only in the evaporated films. Measurement of the Cu and Ag Auger spectra gave results independent of the surface work function when compared to the XPS spectra. Interpretation of this Auger parameter is, however, at present ambiguous.

The faradaic deposition of monolayer quantities of metal cations on foreign metal substrate electrodes at potentials more anodic than the reversible thermodynamic Nernstian potential has been recognized for many years (1, 2). This underpotential deposition (UPD) phenomenon has been studied using a variety of techniques. For example, the underpotential deposition of Ag on Pt electrodes has been characterized using radioisotopic techniques (2-5), electrochemical techniques such as linear sweep voltammetry with stationary (6) and rotating ring-disk electrodes (7, 8), and specular reflection spectroscopy (9). The underpotential deposition of Cu^{2+} on Pt electrodes has also been extensively studied using linear sweep voltammetry (10), constant current coulometry (11), rotating ring-disk electrodes (12-15), and a combination of constant current coulometry and radioisotopic techniques (16, 17).

The coulometric results for Ag UPD (8) and Cu UPD (12-16) on Pt electrodes have shown that the metal ion is deposited in a zero-valent state with strong metallic bond interactions between the metallic adatoms and substrate electrode. Schultze (11), however, has concluded that copper atoms adsorbed at underpotential obey a Temkin isotherm. An electrosorption valency of $\gamma = 0.83$ was also reported where $2(1 - \gamma)$ represents the residual positive charge on the adsorbed copper atoms. The optical results of McIntyre and Kolb have also shown that the optical constants of the Ag underpotential deposit differ markedly from those of bulk silver metal (9). Further spectroscopic studies are, therefore, needed to elucidate the metallic nature of these underpotential-deposited films.

X-ray photoelectron spectroscopy (XPS or ESCA) has been established as a viable spectroscopic technique for the study of electrode surface states (18-20). The technique is well suited for analyzing the structure of the underpotential-deposited species due to its detec-

[1] Present address: Ford Motor Company, Scientific Research Laboratory, Dearborn, Michigan 48124.
* Electrochemical Society Active Member.

tion limit of 1% of a surface monolayer and its sensitivity to the electronic environment of the analyzed atom (21). A major disadvantage of the approach, however, is that the measurements must be carried out in the ultrahigh vacuum of the electron spectrometer. In this paper, we present the results of XPS analysis of underpotential-deposited Cu and Ag layers on Pt substrate electrodes. In addition, the results for *in situ* vapor phase deposition of Cu and Ag atoms on clean Pt foils are presented. The binding energies of core photoelectrons and Auger electrons show the spectral equivalence between electrochemical and vapor phase deposition of submonolayer quantities of copper and silver on platinum substrates. The observed binding energy chemical shifts conclusively reveal the metallic nature of the electrochemical UPD species.

Experimental

A potentiostat utilizing conventional operational amplifier circuitry is used to prepare the electrode samples. Electrolytes were prepared using reagent grade sulfuric and perchloric acids and water which is deionized, then doubly distilled. The electrode is a platinum plug 0.095 cm^2 in diameter press-fit into a Teflon holder 1.07 by 1.27 by 0.14 cm thick. This Teflon holder allows the electrode to be mounted onto the HP 5950A ESCA sample introduction probe and onto electrochemical cells. Due to the significant charging of photoelectron lines originating from insulating surfaces in an HP 5950A ESCA, any contamination originating from manual manipulation of the Teflon holder during transfer of the electrode from the cell to the sample probe is not observed in the XPS spectrum. Potentiostatic preparation of the electrodes was accomplished in a miniature cell of ~250 μliter internal volume (20). The typical electrolyte volume is 100-150 μliter minimizing the total dissolved contamination that could possibly adsorb on the electrode surface. If the total contaminant level is 10^{-6}M concentration in a 150 μliter electrolyte solution and all of this contaminant adsorbs on a 0.095 cm^2 geometrical surface area platinum electrode, assuming a one molecule contaminant to one platinum surface atom adsorption geometry, less than 0.7 monolayers of that contamination would appear in a subsequent XPS surface analysis. A tungsten pseudo-reference electrode is used to maintain potentiostatic control. All potentials are reported with respect to a saturated calomel reference electrode (SCE), as supplemental electrochemical experiments were carried out with the same electrolyte-working electrode combination in an electrochemical cell equipped with a SCE. Under potentiostatic control electrolyte is injected into the cell and removed using aspiration. The attenuation of the electrochemical current due to aspiration of the electrolyte from the cell occurs within the response time of the Hewlett-Packard 7035B X-Y recorder.

All experiments were completed at ambient laboratory temperature (20°-22°C). The electrodes were electrochemically cleaned by rigorous constant potential anodization at $> +2.0$V *vs.* SCE for 5-10 min. The solution was then aspirated under potentiostatic control, the potential adjusted to +1.2V, the electrolyte injected into the cell, and the electrode cycled using linear sweep voltammetry between +1.2 and 0.0V. This process was repeated until the electrode reproduced a clean *i vs. V* trace.

The XPS spectra were recorded on a Hewlett-Packard 5950A ESCA spectrometer using monochromated Al Kα x-rays. The use of monochromated x-ray flux decreases the total x-ray exposure by approximately two orders of magnitude and thereby minimizes x-ray decomposition. Platinum electrode samples were prepared in a Vacuum/Atmospheres HE 43-6 inert atmosphere box (Hawthorne, California) which encloses the ESCA sample introduction probe. A nitrogen atmosphere with a contamination level of <100 ppm was used. Details of the contamination levels observed on electrode surfaces after transfer have been reported (20). All binding energies are referenced to Au $4f_{7/2}$ at 83.8 eV. Other details concerning the ESCA sample handling system have been previously described (22).

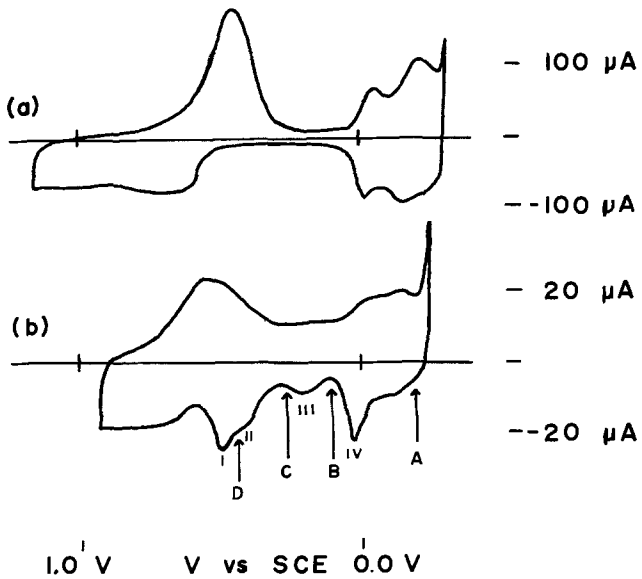


Fig. 1. Cyclic voltammograms for Cu-Pt UPD systems: (a) platinum electrode, 0.100M H_2SO_4 electrolyte, 100 mV/sec scan rate; (b) platinum electrode, 0.100M H_2SO_4 + 5 × 10^{-4} $CuSO_4$ electrolyte, 20 mV/sec scan rate. See text for explanation of I-IV and A-D designations.

Results and Discussion

The cyclic voltammograms for a Pt electrode in 0.10M H_2SO_4 and for a Pt electrode in 0.10M H_2SO_4 + 5 × 10^{-4}M $CuSO_4$ are shown in Fig. 1a and 1b, respectively. The cyclic voltammograms of the solution containing Cu(II) ions reveal four oxidation current peaks (labeled I-IV) not present in the 0.100M H_2SO_4 electrolyte. The potential associated with each peak and the potential separation between each peak and the potential for bulk anodic oxidation of copper is listed in Table I. The assignment of peak IV to the stripping of bulk copper metal can be confirmed by interrupting the potential scan at a working electrode potential of −0.25V *vs.* SCE for varying lengths of time and only the current associated with peak IV will increase during the subsequent anodic potential scan. The peak structures I, II, and III will retain their relative intensities and maximum current potential values with increasing cathodic deposition of copper(II). The assignment of peak structures I-III as the underpotential oxidation of copper on platinum agrees with previously published results (12-15).

To study the three peak structures associated with the Cu underpotential oxidation on Pt, the anodic potential scan was interrupted at the potentials designated A through D on Fig. 1b. The deposition of Cu at potential A (−0.23V *vs.* SCE) was continued for 60 sec before the solution was aspirated from the cell and the electrode removed for XPS analysis. After the anodic potential scan was interrupted at either potentials B, C, or D, the current associated with the oxidation of underpotential-deposited Cu decayed rapidly to

Table I. Peak current potentials for copper oxidation from platinum electrodes

Peak	Potential *vs.* SCE, V	Peak separation from bulk Cu oxidation
I	+0.50	+0.47
II	+0.41	+0.38
III	+0.21	+0.18
IV	+0.03	0.00

an insignificant value. If the positive potential scan was then reinitiated, the oxidative stripping peaks at potentials more positive than the interruption potential were still observed. This demonstrates the validity of interrupting the potential scan at a desired potential in order to investigate with XPS the more anodic features of the voltammogram.

The active electrochemical surface area of the platinum electrode electrochemically precleaned in 0.100M H_2SO_4 was measured by integrating the faradaic charge flow associated with hydrogen adsorption. Assuming one hydrogen atom per surface platinum atom, the electrode surface area was found to be 1.0-1.2 cm^2. By comparing the O adsorption current at +0.75V *vs.* SCE for Pt electrodes in 0.1M H_2SO_4 with and without 5×10^{-4}M Cu(II), the electrode surface area during UPD of Cu(II) was measured as 1.09 cm^2. Coulometric integration of peaks I, II, and III (Fig. 1b) averaged 271 μC or 46% of a monolayer using a value of 540 $\mu C/cm^2$ (15). The roughness factor (electrochemical surface area/geometrical surface area) of 11.3 indicates that our electrochemical cleaning produces a highly dispersed Pt surface layer in which the deposition of Cu becomes sterically hindered relative to the coulometrically measured hydrogen absorption sites. Assuming this coulometric value of 271 μC to equal one monolayer of copper UPD (12), coulometric measurement of the bulk deposition of copper for one minute at −0.17V *vs.* SCE produced a bulk deposit corresponding to a 5.8 average atomic layers of Cu. Assuming a covalent radius of 1.4Å, this bulk Cu deposit corresponds to an average thickness of 8.1Å. Coulometric measurement of peaks I and II indicates that peak III represents 10% of the total UPD Cu or an averaged thickness of approximately 0.1Å (see Table II).

The UPD Cu deposit is next transferred directly to the high vacuum environment of the XPS spectrometer. The measured binding energies of the UPD species are reported in Table II. These energies are in excellent agreement with those reported earlier (23).

The average calculated thickness of the copper adatoms on the surface of the platinum electrode can be determined from XPS spectra from the relationship

$$\frac{I_o}{I_s} = \frac{I_o^\infty}{I_s^\infty} \frac{\{1 - \exp[-d/(\lambda_o \sin\theta)]\}}{\{\exp[-d/(\lambda_o \sin\theta)]\}} \quad [1]$$

where I_o and I_s are the XPS intensities of the overlayer (o) and substrates (s), I_o^∞ and I_s^∞ are the photoelectron intensities of bulk samples of overlayer (o) and substrate (s) under an x-ray flux, d is the effective thickness of the overlayer in angstroms, and λ_o is the attenuation depth due to inelastic scattering of a particular observed photoemission core level. The sin θ term is due to the geometry of the sample and electron lens aperture. The ratio of I_o^∞/I_s^∞ for Cu $2p_{3/2}$/Pt $4f_{7/2}$ was determined empirically to be 3.07 for Cu and Pt foils which were cleaned *in situ* using Ar^+ bombardment. The attenuation depths are based on a λ $4f_{7/2}$ of Pt photoelectrons of 20Å (24) and a λ $2p_{3/2}$ of Cu photoelectrons of 12.5Å as calculated from the relationship

$$\lambda \propto \sqrt{h\nu - BE} \quad [2]$$

where $h\nu$ is the Al K_α photon energy and BE is the binding energy of the observed photoelectrons.

The calculated average thicknesses for Cu UPD on Pt electrodes at aspiration potentials A-D (Fig. 1b) are shown in Table II. The 10% decrease in the coulometric measurement of Cu UPD between aspiration potentials B-C is also reflected in the 10% average thickness decrease resulting from XPS intensity ratio measurements. However, a high degree of confidence should not be placed in the absolute calculated thickness values as significant error is to be expected from the simplicity of the homogeneous two-layer model and the exclusion of the photoelectron attenuation effects of the overlaying contamination and residual electrolyte layer (20).

The XPS binding energy shifts of the Cu $2p_{3/2}$ electrons relative to Cu $2p_{3/2}$ binding energy of bulk clean copper metal are reported in Table II for the Cu UPD electrode samples. Within the experimental uncertainty of ±0.1 eV for measuring the peak position of the Cu $2p_{3/2}$ photoelectrons, a −0.95 eV shift is observed for aspiration potentials B, C, and D. This indicates that the Cu $2p_{3/2}$ binding energy shift is not sensitive to the parameters that determine the electrochemical UPD peak structure and that the XPS core level shift is constant for coverages of Cu atoms up to an average coverage of one atomic layer. The Cu $2p_{3/2}$ binding energy shift of −0.50 eV for aspiration potential A indicates that although the electrochemical anodic stripping peaks indicate 4.8 layers of bulk Cu deposited over the UPD Cu, the XPS binding energy of these Cu atoms is still not indicative of bulk Cu metal. Further discussions of this multilayered Cu binding energy shift will be presented later. No shift of the Pt substrate photoelectron binding energies are observed.

To further characterize the Cu UPD electrodes, the $L_3M_{4,5}M_{4,5}$ Auger electrons of the Cu overlayers were measured. The Cu $L_3M_{4,5}M_{4,5}$ spectrum for bulk metallic Cu has a multipeak structure based on the multiplet splitting of the final states in the Auger electron process (25). For this reason only the binding energy equivalent of the kinetic energy of the most intense multiplet state will be used to assign the Auger binding energy. A binding energy shift of the Cu UPD Auger electrons relative to bulk Cu was not detected within the experimental uncertainty of determining the peak position (±0.2 eV).

To enhance the chemical significance of the spectral binding energy shifts for the Cu UPD electrodes, XPS data were obtained for anhydrous $CuSO_4$ CuO, and

Table II. Cu UPD on Pt electrodes

Aspiration[a] potential	Coulometric[b] surface coverage in θ	Calculated[c] average Cu thickness in Å	Cu $2p_{3/2}$[d] BE shift in eV ±0.1 eV	Cu $L_3M_{4,5}M_{4,5}$[e] BE shift in eV ±0.15 eV	Intensity ratio[f] Cu $2p_{3/2}$ / S $2p_{3/2}$	Δ BE Cu $2p_{3/2}$ − Cu $L_3M_{4,5}M_{4,5}$ eV ±0.2 eV	Δ BE Cu $2p_{3/2}$ − S $2p_{3/2}$ eV ±0.2 eV	
A	$\theta = 2.66$	12.6	−0.50	0.0	N.A.	364.5	N.A.	A
B	$\theta = 0.46$	1.0	−0.95	−0.15	9.66	364.2	763.6	B
C	$\theta = 0.41$	0.90	−0.95	+0.15	23.7	363.9	763.3	C
D	N.A.	0.2	−1.05	N.A.	N.A.	N.A.	N.A.	D
$CuSO_4$	—	—	+1.6	+1.3	9.76	365.3	766.95	$CuSO_4$
CuO[g]	—	—	+0.8	+1.1	—	364.7	—	CuO
Cu_2O[g]	—	—	−0.1	+1.9	—	363.0	—	Cu_2O
Cu metal	—	—	0.00	0.00	—	364.95	—	Cu metal

[a] Designated potentials labeled in Fig. 1b and explained in Table I.
[b] Surface coverage θ as function of full surface area measured by hydrogen absorption measurements.
[c] See text for explanation, copper covalent radius = 1.4Å.
[d] Referenced to bulk copper metal $2p_{3/2}$ at 932.8 eV.
[e] Reported in BE units with bulk copper metal $L_3M_{4,5}M_{4,5}$ at 567.85 eV.
[f] Intensity ratios based on total integrated peak intensities.
[g] Data from Ref. (26).

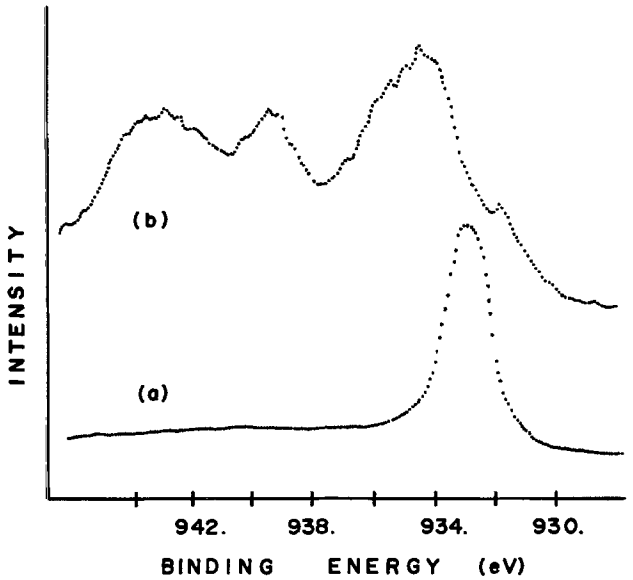


Fig. 2. Cu $2p_{2/3}$ spectra of Cu and $CuSO_4$: (a) clean Cu foil; (b) anhydrous $CuSO_4$.

Cu_2O. Figure 2, a and b, respectively, shows the Cu $2p_{3/2}$ spectra of Au^+ cleaned Cu foil and anhydrous $CuSO_4$. As noted in Table II, a +1.6 eV chemical shift is observed in the $CuSO_4$ Cu $2p_{3/2}$ binding energy relative to the clean bulk metal. A very intense Cu $2p_{3/2}$ shake-up satellite structure is also observed in $CuSO_4$ (Fig. 2b) with the satellite peaks having a binding energy separation of 4.9 and 8.5 eV from the parent peak. The satellite structure accounts for ~50% of the total Cu $2p_{3/2}$ intensity. Schön has also reported a +0.8 eV shift for the Cu $2p_{3/2}$ binding energy of CuO relative to bulk copper metal and strong satellite transitions to higher binding energy of the main parent peak (26). The appearance of strong satellite structure for Cu^{2+} species has been shown to be characteristic for a Cu d^9 compound (27). From the lack of any shake-up satellite structure and a −0.95 eV binding energy shift relative to bulk metal for the Cu UPD electrodes, the observed Cu photoelectron intensity cannot be associated with any Cu(II) species on the surface of the electrode. This eliminates any absorbed $CuSO_4$ or oxidized CuO (originating from oxidation of the electrode surface during the electrode transfer process) from being present during XPS analysis. The possibility of any Cu_2O on the surface of the electrode can be neglected due to the significant +1.9 eV binding energy shift of Cu_2O $L_3M_{4,5}M_{4,5}$ Auger electrons relative to bulk metal (see Table II). With the elimination of copper oxide or copper sulfate species as being present on the electrode surface, the binding energy chemical shift of the Cu UPD electrodes must be interpreted on the basis of a metallic structure.

In addition to the Cu adatom layer, significant quantities of residual electrolyte remain on the surface of the Pt electrode. By comparing the Cu $2p_{3/2}$/S $2p_{3/2}$ intensity ratios of pure anhydrous $CuSO_4$ with intensity ratios from the Cu UPD electrodes, and by comparing the S $2p_{3/2}$ binding energies, sufficient $SO_4^=$ is present to form a $CuSO_4$ stoichiometry (see Table II). From the separation between Cu $2p_{3/2}$ to Cu $L_3M_{4,5}M_{4,5}$ binding energies and the separation between Cu $2p_{3/2}$ to S $2p_{3/2}$ binding energies (see Table II), we can again rule out $CuSO_4$ compounds existing in the surface layer. The $SO_4^=$ or HSO_4^- is present as adsorbed electrolyte on the metallic electrode. Sulfate or bisulfate adsorption has been previously observed with XPS for Pt electrodes exposed only to sulfuric acid electrolytes (20). A similar experiment was performed by exposing unpolarized clean Pt electrode to a solution of 5×10^{-4}M $CuSO_4$ plus 0.10M H_2SO_4 for 4 min. After aspiration of the electrolyte from the electrode surface, the XPS spectral analysis of the electrode surface revealed a significant $SO_4^=$ intensity, agreeing with the previous results (20), but Cu $2p_{3/2}$ photoelectrons were not observed. This result further confirms our assignment of the XPS copper intensity recorded from Cu UPD electrodes as resulting from potentiostatic control of the electrode surface and not from extraneous deposition occurring during electrode transfer.

To complement the XPS analysis of UPD Cu on platinum electrodes, *in situ* vapor deposition of Cu on clean Pt permits the analysis of the interaction between Cu adatoms and the Pt substrate without the possible complicating influence of the residual electrolyte. The average calculated thicknesses of the Cu overlayer for several evaporations are listed in Table III. The thicknesses were calculated using Eq. [1]. The Cu $2p_{3/2}$ and Cu $L_3M_{4,5}M_{4,5}$ binding energy shifts relative to clean bulk Cu binding energy values are also listed in Table III. As with the Cu UPD electrodes, no shift of the Pt binding energies is observed due to the vapor deposition of copper adatoms. At very low coverages of copper adatoms, the Cu $2p_{3/2}$ binding energy shift matches the Cu UPD binding energy shift. As the amount of evaporated Cu is increased, however, its binding energy gradually approaches that of bulk metal at average calculated thicknesses well below monolayer coverage. In the UPD experiments, the binding energy is essentially constant with coverage until monolayer deposition is reached. We believe this discrepancy is related to the difference in the structure of the two deposited layers. In the UPD experiments, only copper ions which reduce to form a copper-platinum metallic bond can deposit at an UPD potential. This insures the formation of a complete two-dimensional monolayer of Cu adatoms before bulk Cu deposition can commence. This interpretation is consistent with the notion that Cu(o) displaces one monolayer of H in forming a uniform monolayer deposit (28). Without the electrochemical constraint on initial uniform growth, vapor phase deposition can produce a significant number of copper clusters or islands. These clusters or islands should have electronic structure approaching that of bulk Cu (29) while the XPS intensity ratios will reflect a submonolayer average thickness. The spectral convolution of these different copper geometrical groupings produced by vapor phase deposition will therefore cause a gradual increase in the Cu $2p_{3/2}$ peak binding energy with increasing calculated thickness of the vapor-deposited species.

The spectral convolution of different copper geometrical groupings can also explain the −0.5 eV Cu $2p_{3/2}$ binding energy shift for aspiration potential A (see Table II). Even though the XPS calculated average thickness of Cu is 12.6Å, a uniformly smooth nine-layer Cu adatom structure cannot be assumed. By analogy with the vapor phase deposition experiments, it seems likely that bulk electrochemical deposition of Cu proceeds through an islanding mechanism such that the aspiration potential A electrode has both thick clusters of bulk Cu and thin layers of UPD like Cu.

Table III. Vapor deposition of Cu on Pt substrates

Average[a] thickness of Cu in A	Cu $2p_{3/2}$[b] BE shift in eV ±0.1 eV	Cu $L_3M_{4,5}M_{4,5}$[c] Be shift in eV ±0.15 eV	Cu $2p_{3/2}$[d] / O 1s
0.2	−1.03	−0.05	>36
0.4	−0.80	−0.05	>36
0.5	−0.75	N.A.	>64
0.6	−0.75	N.A.	>74
0.6	−0.5	N.A.	9.8
0.7	−0.6	+0.08	>50
Cu_2O			5.56

[a] See text for calculation method.
[b] Referenced to bulk copper metal $2p_{3/2}$ at 932.8 eV.
[c] Referenced to bulk copper metal $L_3M_{4,5}M_{4,5}$ at 567.85 eV.
[d] Intensity ratios based on total integrated peak intensities.

The −0.5 eV binding energy shift is a convolution of these states.

The intensity ratios of Cu $2p_{3/2}$ to O 1s for the vapor-deposited Cu on Pt samples are listed in Table III as well as the Cu $2p_{3/2}$ to O 1s intensity ratio for Cu_2O. For all samples except one, less than one in three Cu atoms could be associated in a Cu_2O stoichiometry, even if all oxygen atoms were associated with copper atoms. The C 1s intensity was much lower than the O 1s intensity and, therefore, the binding energy shift of the Cu $2p_{3/2}$ photoelectrons must be a result of Cu-Pt interaction and not a result of copper atom interactions with other elements in the surface layer matrix. We believe that the similarity of the low coverage vapor deposition and UPD binding energy shifts is due to the same Cu-Pt interactions and that the effect of residual electrolyte on the Cu adatom is not reflected in the XPS spectrum.

We have also studied the UPD of Ag on Pt using XPS to observe specific differences between UPD and bulk silver deposition. As noted previously (8), the anodic stripping of UPD Ag occurs concurrently with the oxidation of the Pt substrate electrode. Without the use of a ring-disk type of electrode system, accurate coulometry to separate the two oxidation processes is very difficult. Therefore, the results presented in this paper will rest on the previously presented coulometric results (8) which show that the first monolayer of UPD Ag in 0.2M H_2SO_4 oxidizes over a broad potential range from 0.65 to 1.0V *vs.* SCE. The potential for maximum oxidation current of the UPD Ag occurs at approximately 0.74V *vs.* SCE. The cyclic voltammogram for a Pt electrode in 0.18M H_2SO_4 + 2×10^{-5}M Ag(I) was interrupted in the anodic scan at 0.60V *vs.* SCE by aspiration of the electrolyte. The electrode was then transferred to the XPS spectrometer. The average calculated thickness of Ag present as an UPD layer was obtained using Eq. [1] (see Table IV) Ftn[a]). The Ag present from XPS analysis corresponds to one-half to two-thirds of a monolayer. This is reasonable considering the low Ag(I) concentration and the 100 mV/sec scan speed used in the experiment.

To demonstrate that potentiostatic control of the electrode surface is maintained during aspiration of the electrolyte, electrolyte was aspirated from the microcell at a potential of +1.03V. From previous work (8) no Ag UPD adatoms should be present on the Pt surface at this oxidation potential. No trace of Ag was present in the XPS analysis with a detection limit of approximately 1% of a monolayer of Ag. In addition to cyclic voltammetry aspiration experiments, the cyclic voltammetric sweep of the Pt electrode was also interrupted in the Ag UPD region without simultaneous removal of the electrolyte from the surface of the electrode. Clean, unpolarized Pt electrodes were also exposed to the electrolyte for 4 min, the electrolyte was then aspirated and the electrodes transferred to the XPS spectrometer. The results of these experiments are listed in Table IV Ftn.[b] and [c], respectively.

The Ag $3d_{5/2}$ UPD binding energy shifts relative to clean bulk metal value of 368.2 eV average −0.65 ± 0.1 eV, a result in excellent agreement with those reported earlier (23). The Ag $M_5N_{4,5}N_{4,5}$ binding energy shifts relative to the clean bulk metal value of 1134.75 eV average 0.0 ± 0.15 eV. As with the Cu UPD electrodes, no binding energy shift of the substrate Pt photoelectrons was observed due to Ag UPD. To demonstrate that these binding energy shifts are truly representative of an Ag-Pt UPD surface state and not due to interactions with the residual electrolyte, data from samples of Ag_2SO_4, Ag_2O, and AgO are also listed in Table IV. A negative binding energy chemical shift is observed for the Ag $3d_{5/2}$ photoelectrons for these three compounds but a significant positive binding energy shift is observed for the Ag $M_5N_{4,5}N_{4,5}$ Auger electron for these same compounds. The binding energy difference between the Ag $M_5N_{4,5}N_{4,5}$ Auger electrons and Ag $3d_{5/2}$ photoelectrons indicates that the Ag UPD species is not an adsorbed Ag_2SO_4 or silver-oxide-like species. However, XPS analysis of the Ag UPD electrode surfaces reveals the presence of $SO_4^=$ or HSO_4^- ions due to the S $2p_{3/2}$ binding energy of ~168.4 eV. The intensity ratios of Ag $3d_{5/2}$ to S $2p_{3/2}$ are much lower for the electrode surfaces than for a pure sample of Ag_2SO_4. This discrepancy between the Ag $3d_{5/2}$ to S $2p_{3/2}$ binding energy separation values for the electrode samples *vs.* Ag_2SO_4 samples indicates, however, that the $SO_4^=$ or HSO_4^- is bound in the surface layer as residual electrolyte and is not interacting with the Ag atoms in an Ag_2SO_4-like compound. As was pointed out for the Cu UPD electrodes, XPS analysis of Pt electrodes exposed to H_2SO_4 electrolyte will always include a substantial $SO_4^=$ or HSO_4^- photoelectron intensity [see also Ref. (20)]. Ag atoms with an UPD-like Ag $3d_{5/2}$ and Ag $M_5N_{4,5}N_{4,5}$ binding energy shift were also observed after exposure of unpolarized electrodes to the electrolyte solution. This contrasts the absence of any XPS Ag intensity after aspiration at +1.03V *vs.* SCE and points out the validity of our aspiration technique for removing the electrolyte from the electrode surface under potentiostatic control. If electrolyte remained on the electrode surface without potentiostatic control after aspiration at +1.03V *vs.* SCE, Ag should be present in the XPS analysis.

Following a pathway analogous to the Cu experiments, we studied the *in situ* vapor deposition of silver on clean platinum. The average calculated thicknesses, based on Eq. [1], of the Ag overlayer for several evaporations are listed in Table V. The Ag $3d_{5/2}$ binding energy shifts relative to clean bulk Ag binding

Table IV. Ag UPD on Pt electrodes

Experimental conditions	Calculated[d] average Ag thickness in Å	Ag $3d_{5/2}$[e] BE shift in eV ±0.1 eV	Ag $M_5N_{4,5}M_{4,5}$[f] BE shift in eV ±0.15 eV	Intensity ratio Ag $3d_{5/2}$ / S $2p_{3/2}$	Δ BE Ag $M_5N_{4,5}N_{4,5}$ − Ag $3d_{5/2}$ in eV ±0.2 eV	Δ BE Ag $3d_{5/2}$ − S $2p_{3/2}$ eV ±0.25 eV
[a]	0.80	−0.66	−0.05	2.6	767.2	199.1
[a]	1.00	−0.72	−0.05	2.6	767.2	198.5
[b]	1.38	−0.65	N.A.	N.A.	N.A.	N.A.
[b]	0.48	−0.80	N.A.	N.A.	N.A.	N.A.
[c]	1.45	−0.42	0.0	6.97	767.0	188.4
[c]	0.66	−0.55	N.A.	3.73	N.A.	199.2
Ag_2SO_4	—	−0.25	+2.8	14.5	769.7	199.8
Ag metal	—	0.0	0.0	—	766.55	—
Ag_2O	—	−0.4[h]	+0.8[g]	—	767.75	—
AgO	—	−0.8[h]	+0.5[g]	—	767.85	—

[a] Aspiration under potentiostatic control at +0.6V *vs.* SCE.
[b] Potentiostatic control interrupted in UPD region, electrolyte not immediately removed from the electrode surface.
[c] Pt electrode exposed to electrolyte for 4 min without potentiostatic control.
[d] Calculated using Eq. [1], Ag covalent radius = 1.53Å.
[e] Referenced to bulk silver metal $3d_{5/2}$ at 368.2 eV.
[f] Reported in BE units with the bulk silver metal $M_5N_{4,5}N_{4,5}$ at 1134.7 eV.
[g] Ref. (30).
[h] Ref. (22).

Table V. Vapor deposition of Ag on Pt substrates

Average[a] thickness of Ag in Å	Ag $3d_{5/2}$[b] BE shift in eV ±0.1 eV	Ag $3d_{5/2}$[c] / O 1s
0.22	−0.7	1.9
0.78	−0.7	0.5
6.85	−0.2	24.1
Ag_2O	−0.4	7.3

[a] See text for calculation method.
[b] Referenced to bulk silver $3d_{5/2}$ at 368.3 eV.
[c] Intensity ratios based on total integrated peak intensity.

energy values are also listed in Table V. As with the silver UPD electrodes, no shift of the Pt substrate photoelectron binding energies is observed due to the vapor deposition of silver adatoms. It is noteworthy that the sample with an average calculated thickness of 6.85Å still has a −0.20 eV binding energy shift relative to bulk Ag. The tendency toward clustering exhibited in Cu vapor phase deposition could be responsible for islands of bulk silver with patches of UPD-like silver being convoluted into the Ag $3d_{5/2}$ spectrum. The intensity ratios of Ag $3d_{5/2}$ to O 1s for the evaporated silver on platinum samples do not rule out the possibility of oxide or oxygen silver atom interaction, but previous experimental data do not support the formation of such an oxide layer (22).

Comparison of the UPD species to the samples prepared by vapor deposition defines the metallic rather than ionic nature of the overlayer. The lack of movement of the peak position with surface coverage for the electrode samples also yields indirect evidence for a uniform deposit *vs.* aggregate formation in the vapor deposition experiments. The next question of interest is to elucidate the electronic properties of the adatom layer by careful examination of the observed chemical shift of the UPD species *vs.* the bulk species. It is this important question on which we now focus our attention.

The most successful progress to date in characterizing the bonding of metal adatoms on foreign metal substrates has been made by studying alkali metal adsorption on several transition metal surfaces. At low coverages, the alkali metal adatom forms a dipole with the metal surface and significant charge transfer occurs from the adatom to the substrate. The changes in the macroscopic work function and the alkali adatom energy loss spectra as a function of coverage both indicate positive charge localization on the adatom (31).

For transition metal adatoms on foreign transition metal substrates, the interpretation appears to be somewhat different. The adsorption of Hg on W(110) (32), Ni(100) (33), and Cu(111) (34) as well as solid phase Hg (35) has recently been studied by electron spectroscopy. The ultraviolet photoelectron spectra for Hg vapor adsorbed on Ni(100) reveal that there is no change in the work function between the atomically clean Ni(100) surface and the Ni surface saturated with adsorbed Hg (33). The work function remains 5.03 eV, representative of pure Ni(100), in contrast to the work function of bulk Hg of 4.49 eV (35). This differs dramatically with the results from alkali metal adsorption where the work function at monolayer coverage of alkali adatoms approaches the bulk work function of the alkali metal (31, 36). For these Hg adsorption systems, the electronic density of states of the substrate continue to define the density of the surface electrons and hence the work function stays constant.

The binding energy shifts in XPS core level spectra generally correlate with the charge density of the observed atom. However, to provide an interpretation of changes in charge density, the core level binding energy must be referenced to the vacuum level (37). For solid conducting samples, however, the experimental binding energies are referenced to the sample Fermi level, E_B^F, with the vacuum level binding energy, E_B^V, equal to E_B^F plus the bulk work function ϕ. For chemisorption studies, the relationship between E_B^F and E_B^V for the adsorbate layer has not yet been clearly defined. Several approaches have been suggested, the most recent of which is by Hagstrum who points out that the ionization energy of a surface orbital can best be approximated by the Fermi level referenced binding energy of that orbital plus the work function of the saturated uniformly covered surface (33). This relationship only holds, however, in the absence of significant adsorbate-adsorbate interactions at the full coverage limit.

One possible approach for dealing with this problem is through the use of the Auger parameter (38). The kinetic energy for a jkk Auger transition can be approximated

$$E^V(jkk) = E_B^V(j) - 2E_B^V(k) - F + 2E_R + R_e \quad [3]$$

where $E^V(jkk)$ is the vacuum level referenced kinetic energy of the jkk transition, $E_B^V(j)$ and $E_B^V(k)$ are the vacuum level referenced one electron binding energies of the j and k orbitals, F is the hole-hole interaction term due to the double ionization of the final state, $2E_R$ is the intra-atomic "static" relaxation contribution to the second $E_B^V(k)$ binding energy due to the previous creation of a k hole state, and R_e is the extra-atomic relaxation (39). The binding energy equivalent to the $E^V(jkk)$ kinetic energy is $E_B^V(jkk)$ where

$$E_B^V(jkk) = h\nu - E^V(jkk) \quad [4]$$

The Auger parameter α is then defined as

$$\alpha = E_B^V(j) - E_B^V(jkk) \quad [5a]$$

$$= E_B^F(j) - E_B^F(jkk) \quad [5b]$$

$$= 2E_B^F(j) - 2E_B^F(k) - F + 2E_R + R_e - h\nu \quad [5c]$$

The Auger parameter is, in fact, independent of the sample work function and either E_B^F or E_B^V values can be used. The difference in the Auger parameter $\Delta\alpha$ can then be defined as

$$\Delta\alpha = \alpha_{metal} - \alpha_{UPD} \quad [6]$$

where α_{metal} is the Auger parameter for the bulk metal of the UPD species and α_{UPD} is the Auger parameter for the UPD adsorbate species (38). For the Ag UPD system, $\Delta\alpha$ is +0.65 eV and for the Cu UPD system $\Delta\alpha$ is +0.95 eV.

The experimental $\Delta\alpha$ term should now be compared to the individual terms of Eq. [5c]

$$\Delta\alpha = \Delta(2E_B^F(j) - 2E_B^F(k) - F + 2E_R + R_e) \quad [7]$$

The F and $2E_R$ terms are considered atomic properties and should not vary from the bulk to UPD samples (39). From the ground-state sphere model, the relaxation contribution, ΔR_e, should be the major contribution to the $\Delta\alpha$ parameter (38). The experimental $\Delta\alpha$ values of +0.65 and +0.95 for Ag and Cu UPD therefore suggest an increase in extra-atomic relaxation for the Ag and Cu adatoms relative to bulk Ag and Cu metals, respectively.

One present theory for extra-atomic relaxation in metals is based on the formation of a semilocalized exciton (40). Coincident with core hole photoionization, the first unoccupied orbital in the photoionized atom drops below the Fermi level and is filled with an electron from the conduction band. For metal adatom adsorption on foreign metal substrates, this semilocalized exciton model predicts that the extra-atomic relaxation should be matrix independent. Therefore, either the semilocalized exciton model is inappropriate for the UPD binding energy shifts or relaxation effects are not responsible for the $\Delta\alpha$ shifts.

If we now assume that the ΔE_R term is negligible, the positive $\Delta\alpha$ values must be interpreted as shifts in the $E_B^F(k)$ terms. For Ag UPD, the $\Delta 2E_B^F(k)$ value is −0.65 eV and for Cu UPD, the $\Delta 2E_B^F(k)$ is −0.95 eV.

The ground-state sphere model assumes that the orbital separation, $E(j) - E(k)$, stays constant. One would therefore predict a $\Delta 2E_B^F(k)$ value for Ag UPD of -1.30 eV and -1.90 eV for Cu UPD. Assuming no change in relaxation, the k orbitals for Ag and Cu UPD adatoms would now appear at higher binding energies relative to the core j orbitals. It is noteworthy that a similar decrease in the core to valence level orbitals separation is observed from gaseous Hg to solid Hg (35). The relative higher binding energy of the valence level can be directly correlated with the cohesive energy of the solid Hg (35). It is tempting to use the same interpretation for the UPD spectra. The electrochemical oxidation of the UPD species at more positive potentials than bulk metal anodic stripping indicates that the cohesive energy of the UPD adatom-substrate system is higher than the bulk-deposited metal. The Auger parameter is then measuring this increase in cohesive energy.

The increase in cohesive energy as measured by $\Delta\alpha$ may now provide a comparison with the empirical correlation of Gerisher *et al.* (41, 42). The underpotential shift, ΔUp, the potential difference between bulk metal oxidation and underpotential adatom oxidation, is found to be proportional to the difference in the bulk work functions, $\Delta\phi$, of the adsorbate and substrate metals such that

$$\Delta\text{Up} = 0.5\ \Delta\phi \qquad [8]$$

where ΔUp and $\Delta\phi$ are in units of volts and electron volts, respectively. The $\Delta\phi$ may be compared with experimental increase in cohesive energy of the UPD samples. However, the experimental uncertainty in our measurements and the lack of experimental $E_B^F(k)$ values indicate that our interpretation at this time is not unambiguous and that further quantitative correlation between $\Delta\alpha$ and $\Delta\phi$ values would be highly speculative.

It is difficult to define the $E_B^F(j)$ values for the UPD adatom species. The alkali adatom adsorption experiments suggest the use of the bulk adatom metal work function. This assumption leads to a negative chemical shift for the Ag $3d_{5/2}$ photoelectrons which seems physically unreasonble. The use of the bulk Pt work function, as suggested by the Hg adsorption experiments (32-34), leads to the assignment of some partial charge on the Ag adatoms. This is more reasonable from the standpoint of increased cohesive energy influencing the initial state orbital energies. Further experimental and theoretical advances are needed to more fully elucidate this point.

Conclusion

The ESCA results indicate that in the absence of an applied electrochemical potential, binding energy shifts are observed in the core photoelectron spectra which are distinctive of the UPD adatom surface states. The binding energy shift is insensitive to the parameters responsible for the multiple UPD anodic stripping peaks and remains constant with coverage. The vapor deposition at low coverages models the UPD deposition and demonstrates the metallic nature of the UPD surface layer. The interpretation of the binding energy shifts is not without ambiguity, but is consistent with an increase in cohesive energy of the UPD surface layer. The $\Delta\alpha$ parameter permits the analysis of the binding energy shifts without requiring the determination of the sample work functions. Further study of the valence level binding energies for the UPD adatoms should be completed, however, before the interpretation of $\Delta\alpha$ values can have meaning.

Acknowledgments

This investigation was supported by National Science Foundation Grant MPS75-9308, the Air Force Office of Scientific Research Grant AF762974, and NSF-MRL Grant 7203018A4. One of us (J.S.H.) wishes to thank The Electrochemical Society for the Colin Garfield Fink Fellowship Award (1976), and one of us (N.W.) wishes to thank the Alfred P. Sloan Foundation for a Fellowship 1974-1978.

Manuscript submitted Oct. 22, 1976; revised manuscript received Feb. 14, 1977.

Any discussion of this paper will appear in a Discussion Section to be published in the December 1977 JOURNAL. All discussions for the December 1977 Discussion Section should be submitted by Aug. 1, 1977.

Publication costs of this article were assisted by Purdue University.

REFERENCES

1. M. Haissinky, *J. Chim. Phys. Phys.-Chim. Biol.*, **43**, 21 (1946).
2. L. B. Rogers, D. P. Krausse, J. C. Griess, and D. B. Ehrlinger, *This Journal*, **95**, 33 (1949).
3. J. C. Griess, J. T. Byrne, and L. B. Rogers, *ibid.*, **98**, 447 (1951).
4. J. C. Griess, J. T. Byrne, and L. B. Rogers, *ibid.*, **98**, 452 (1951).
5. J. T. Byrne and L. B. Rogers, *ibid.*, **98**, 457 (1951).
6. M. M. Nicholson, *J. Am. Chem. Soc.*, **79**, 7 (1953).
7. G. W. Tindall and S. Bruckenstein, *J. Electroanal. Chem.*, **22**, 367 (1969).
8. G. W. Tindall and S. Bruckenstein, *Electrochim. Acta*, **16**, 245 (1971).
9. J. D. E. McIntyre and D. M. Kolb, *Faraday Symp. Chem. Soc.*, **4**, 99 (1970).
10. M. W. Breiter, *This Journal*, **114**, 1125 (1967).
11. J. W. Schultze, *Ber. Bunsenges. Phys. Chem.*, **74**, 705 (1970).
12. G. W. Tindall and S. Bruckenstein, *Anal. Chem.*, **40**, 1051 (1968).
13. G. W. Tindall and S. Bruckenstein, *ibid.*, **40**, 1637 (1968).
14. G. W. Tindall and S. Bruckenstein, *J. Electroanal. Chem.*, **22**, 367 (1969).
15. S. H. Cadle and S. Bruckenstein, *Anal. Chem.*, **43**, 932 (1971).
16. B. J. Bowles, *Electrochim. Acta*, **10**, 731 (1965).
17. B. J. Bowles, *ibid.*, **15**, 589 (1970).
18. K. S. Kim, N. Winograd, and R. E. Davis, *J. Am. Chem. Soc.*, **93**, 6296 (1971).
19. T. Dickinson, A. F. Povey, and P. M. A. Sherwood, *J. Chem. Soc., Faraday Trans. 1*, **71**, 289 (1975).
20. J. S. Hammond and N. Winograd, *J. Electroanal. Chem.*, In press.
21. K. Siegbahn, C. Nordling, A. Fahlman, R. Nordling, K. Hamrin, G. Hedman, G. Johansson, T. Bergman, S. Karlson, I. Lindgren, and B. Linberg, "ESCA—Atomic, Molecular, and Solid State Structure Studied by Means of Electron Spectroscopy," Almquist and Wiksells, Uppsala, Sweden (1967).
22. J. S. Hammond, S. W. Gaarenstroom, and Nicholas Winograd, *Anal. Chem.*, **47**, 2193 (1975).
23. J. S. Hammond and N. Winograd, *J. Electroanal. Chem.*, In press.
24. C. J. Powell, *Surf. Sci.*, **44**, 29 (1974).
25. C. J. Powell and A. Mandl, *Phys. Rev. Lett.*, **29**, 1153 (1972).
26. G. Schön, *Surf. Sci.*, **35**, 96 (1973).
27. D. C. Frost, A. Ishitani, and C. A. McDowell, *Mol. Phys.*, **24**, 861 (1972).
28. S. H. Cadle and S. Bruckenstein, *Anal. Chem.*, **43**, 1858 (1971).
29. M. G. Mason and R. C. Baetzold, *J. Chem. Phys.*, **64**, 271 (1976).
30. G. Schön, *Acta Chem. Scand.*, **27**, 2623 (1973).
31. S. Anderson and U. Jostell, *Surf. Sci.*, **46**, 625 (1974).
32. W. F. Egelhoff, Jr., D. L. Perry, and J. W. Linnet, *ibid.*, **54**, 670 (1976).
33. H. D. Hagstrum, *ibid.*, **54**, 197 (1976).
34. D. R. Lloyd, C. M. Quinn, and N. V. Richardson, *J. Chem. Soc., Faraday Trans. 2*, **72**, 1036 (1976).
35. S. Srensson, N. Martensson, E. Basilier, P. Å Malmquist, U. Gelius, and K. Siegbahn, *J. Electron Spectrosc. Relat. Phenom.*, **9**, 51 (1976).
36. J. D. Levine and E. P. Gyftopoulos, *Surf. Sci.*, **1**, 171 (1964).
37. K. Siegbahn, C. Nordling, A. Fahlman, R. Nordberg, K. Hamrin, J. Hedman, G. Johansson, T. Bergmark, S. Karlsson, I. Lindgreen, and B. Lindberg, "ESCA—Atomic, Molecular and Solid State Structure Studied by Means of Electron Spec-

troscopy", p. 91, Almqvist and Wiksells, Uppsala, Sweden (1967).
38. C. D. Wagner, *Faraday Discuss. Chem. Soc.*, **60**, 291 (1975).
39. D. A. Shirley, *Phys. Rev. A*, **7**, 1520 (1973).
40. L. Ley, S. P. Kowalczyk, F. R. McFeely, R. A. Pollak, and D. A. Shirley, *Phys. Rev. B*, **8**, 2392 (1973).
41. H. Gerischer, D. M. Kolb, and M. Przasnyski, *Surf. Sci.*, **43**, 662 (1974).
42. D. M. Kolb, M. Przasnyski, and H. Gerischer, *J. Electronal. Chem.*, **54**, 25 (1974).

Iron Oxide Semiconductor Electrodes in Photoassisted Electrolysis of Water

Lun-Shu Ray Yeh* and Norman Hackerman†

Department of Chemistry, Rice University, Houston, Texas 77001

ABSTRACT

The preparation of polycrystalline n-type iron oxide electrodes by heating of iron samples in air is reported. The behavior of these electrodes in aqueous solutions of different *p*H values in the presence and absence of illumination is shown. The photocurrent response of these electrodes to all wavelengths in the visible region is seen. Photoassisted electrolysis of water occurs at these wavelengths resulting in the evolution of oxygen bubbles at the iron oxide electrodes with no noticeable corrosion problems in *p*H 4.0 acetate buffer to 5.5M KOH solutions

Recently there has been much interest in utilization of semiconductor electrodes for electrochemical studies (1-4) and for solar energy conversion by the photoassisted electrolysis of water (5-8). An electron transfer between electrode and electrolyte occurs only if either the conduction band or the valence band in the semiconductor overlap with the occupied or unoccupied states in the electrolyte. Therefore, large bandgap semiconductor electrodes have been particularly interesting in electrochemical reactions because they offer the possibilities for studies of the energy parameters of fundamental charge transfer processes. Large bandgap electrodes, such as TiO_2 (3, 5, 6, 8) (bandgap: 3.2 eV), ZnO (4, 9) (bandgap: 3.1 eV), and SnO_2 (10-12) (bandgap: 3.8 eV) have been studied considerably. On the other hand, small bandgap semiconductor electrodes are particularly useful to decompose water by utilizing solar energy.

By illuminating an n-type semiconductor with light energy greater than the bandgap of the semiconductor, holes are generated in the valence band by exciting electrons to the conduction band. These holes move to the surface of the electrode under anodic polarization where they can transfer to the electrolyte. Therefore, a suitable semiconductor electrode can be used to oxidize water to oxygen or oxidize one chemical species to the other by utilizing solar energy. In utilizing solar energy, one would like to use as much energy as possible from the sunlight. This requires a small bandgap semiconductor. Unfortunately, small bandgap semiconductors such as Si (13) (bandgap: 1.1 eV) and CdS (14) (bandgap: 2.4 eV) decompose under anodic polarization or illumination. In fact, a nondestructive or nondecomposing semiconductor is hard to obtain. Only TiO_2 (5, 6, 8), SnO_2 (11, 15), and $SrTiO_3$ (8) electrodes with bandgaps greater than 3.0 eV are known to be capable of oxygen generation from water without electrode material destruction. It is also known that only about 3% of the total solar spectra (wavelengths shorter than 400 nm) is useful for these large bandgap electrodes (7) and the rest is wasted. Therefore, in order to utilize solar energy efficiently it is important to develop a practically useful material which is nondestructive and is capable of using the greater part of the incident solar photons.

* Electrochemical Society Student Member.
† Electrochemical Society Honorary Member.
Key words: iron oxide electrodes, polycrystalline, electrolysis.

Iron oxide film semiconductor electrode has been prepared by chemical vapor deposition by Hardee and Bard (16) to observe a photocurrent response up to 550 nm. Although wavelengths greater than 550 nm, the greater part of the solar incident photons, are inefficient, the electrode does offer some advantages because of its relative stability in high *p*H solutions. We report here a simple way of electrode preparation by heating the iron samples in natural gas flame resulting in an unexpected small bandgap n-type semiconductor with an extraordinary stability in both acidic and basic solutions.

Experimental

Several iron and steel samples were used to prepare the polycrystalline semiconductor electrodes. These included zone-refined iron (generously donated by Batelle Memorial Institute), magnetic iron (obtained from Armco Steel Company, 99.9%), and cold-rolled steel (99%). The samples were cut into about 1 × 1 cm square by 2 mm thick and polished with emery paper. All samples were then cleaned in distilled water and degreased in methanol prior to use. The samples were then placed in the flame of a Fisher burner for about 15 min. The samples became red hot during this treatment and upon removal from the flame a uniform, smooth, dark gray oxide appearance was seen on the samples. An iron wire was attached to the substrate under the oxide layer by removing the oxide layer using a file around a small hole which was drilled before the substrate was heated. The iron wire was fastened on the bare metal around the hole to provide the electrical contact. The oxide layer was fairly thick and different in color than the bare metal. Silicon adhesive, from Dow Corning Company, Midland, Michigan, was used to coat the iron wire and the bare metal on the substrate. Only iron oxide, as the electrode, was exposed to the solution.

All solutions were prepared with triply distilled water, with the first distillation from potassium permanganate in deionized water, and all chemicals were reagent grade. A simple three-compartment cell containing a Luggin probe for reference electrode, platinum foil counterelectrode, and iron oxide working electrode was used for electrochemical measurements. A saturated calomel electrode (SCE) was used as the reference electrode.

The potentiostat and ramp generator used were constructed in this laboratory using Teledyne-Philbrick operational amplifiers and the design was similar to that already published (17). Data were recorded on a Moseley Autograf (Model 2DR-2) or a Hewlett-Packard (Model 7044A) X-Y recorder. For photoexcitation experiments, a 500W General Electric quartzline lamp with very little focusing was used. A 0.25m Jarrell-Ash monochromator, Model 82-410, was used to obtain the photocurrent-wavelength curves. The action spectrum was also obtained by irradiating the electrode through a circular graded interference filter (Barr and Stroud, Limited. A 5 mW spectra-Physics Stabilite™ helium-neon laser (Model 120) and exciter (Model 256) with monochromatic light output at 632.8 nm was also used for the photoexcitation experiments.

Results and Discussion

The current (i) *vs.* voltage (E) curves of iron oxide electrodes, prepared from zone-refined iron, in various solutions are shown in Fig. 1. Under the illumination there is a large rise in anodic current commencing at about +0.3V *vs.* SCE in pH 4.0 solution, at +0.15V in pH 8.4 solution, at −0.2V in pH 12.0 solution, and at −0.5V in 5.5M KOH solution. The dark current in this potential region is essentially zero. Oxygen gas evolution appears promptly with the rise of the anodic current and is quite noticeable on the electrode surface, implying that the reaction is photoassisted oxidation of water to oxygen gas. Oxygen gas evolution occurs in the dark on the iron oxide electrode at about 0.9V more positive than when the electrodes are under illumination. The oxidation in dark at high positive potentials is probably due to the result of tunneling electrons into the conduction band of the semiconductor after the band bending (18). The potential for the onset of the photocurrent shifts to more negative potentials with increasing pH values. This shift is shown in Fig. 1 with about 60 mV shift per unit pH change. The photocurrent onset potentials varied somewhat for different electrodes. Some electrodes with photocurrent onset potential occurred at about +0.5V in pH 8.4 solution, and the nonphotoassisted oxidation current at large positive potentials added to the photoassisted current to mask the appearance of photocurrent plateau. These curves are not shown here. The variation of the photocurrent onset potential from one electrode to the other (0.1-0.2V variation for most electrodes) remains unexplained in this study. Iron oxide electrodes prepared from magnetic iron or cold-rolled steel also showed similar current-voltage curves as shown in Fig. 1 with somewhat smaller current response compared to that from zone-refined iron.

The photocurrent of a semiconductor electrode depends primarily upon the intensity of the incident light providing that the incident light has an energy equal to or higher than the bandgap of the semiconductor electrode. No attempt was made to increase the focusing or the intensity of the light source. An experiment was conducted in a solution containing borate buffer (pH 8.4) with 25 mM equal molar mixture of $K_4Fe(CN)_6/K_3Fe(CN)_6$ and the result is shown in Fig. 2. In the dark the reduction current of $Fe(CN)_6^{-3}$ becomes noticeable at −0.1V and increases rapidly as the potential becomes more negative. A small oxidation current is also seen in the potential range where no oxidation current can be observed when the $K_4Fe(CN)_6/K_3Fe(CN)_6$ couple is absent. The oxidation current was also seen for Fe^{+2} at a highly doped n-type ZnO semiconductor electrode, and this was interpreted as due to the tunneling effects (19). Under illumination of the unfocused sunlight the oxidation current increases appreciably as shown in Fig. 2. This indicates that the semiconductor electrode is capable of using the sunlight in photoassisted oxidation.

The iron oxide electrodes appeared stable in all solutions from a pH of 4.0 acetate buffer to 5.5M KOH. Continuous potential scans in the range shown in Fig. 1 produced no noticeable changes in current-voltage curves or in the surface appearance of the electrode in these solutions. Also no aging effect was found in a period of 2 months. There was no detectable current change after holding the electrode for 1 hr at +1.0V in a pH of 4.0 (acetate buffer), at +0.8V in pH of 8.4 (borate buffer), at +0.6V in pH of 12.0 (phosphate buffer), or at +0.3V in 5.5M KOH solution. Under these conditions the electrode was covered with gas bubbles and gas bubbles were continuously evolved.

The photocurrent response *vs.* wavelength of the incident light is shown in Fig. 3a for iron oxide electrode prepared from zone-refined iron, Fig. 3b for that from

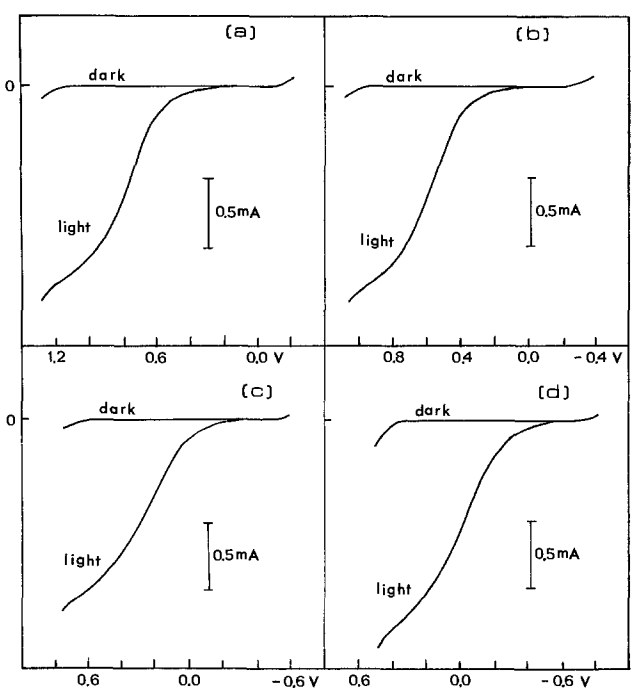


Fig. 1. Current *vs.* potential (*vs.* SCE) curves for iron oxide electrode prepared from zone refined iron with the electrode area of 1 cm^2 in 0.2M $NaNO_3$ solutions buffered to pH (a) 4.0, acetate, (b) 8.4, borate, and (c) 12.0, phosphate. Curve (d) is for 5.5M KOH.

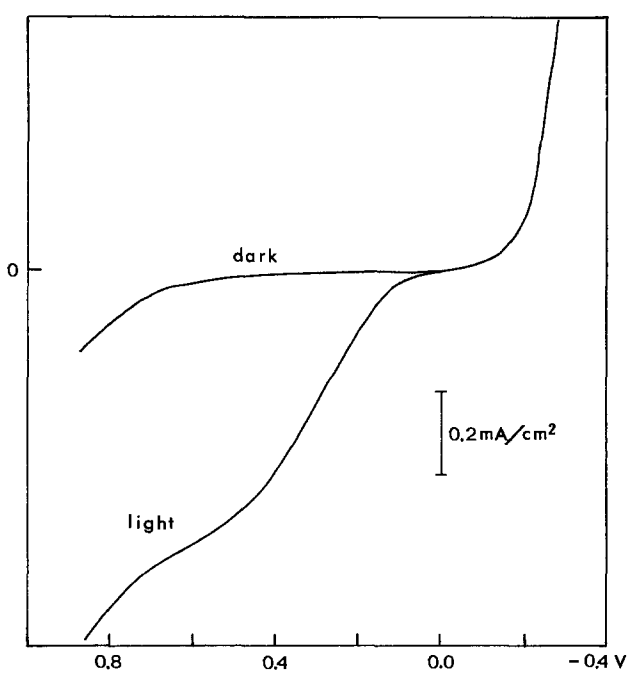


Fig. 2. Current *vs.* potential (*vs.* SCE) for iron oxide electrode prepared from zone refined iron with the electrode area of 1 cm^2 in pH 8.4 borate buffer (0.3*N*) solution containing 25 mmole equal molar mixture of $K_4Fe(CN)_6/K_3Fe(CN)_6$.

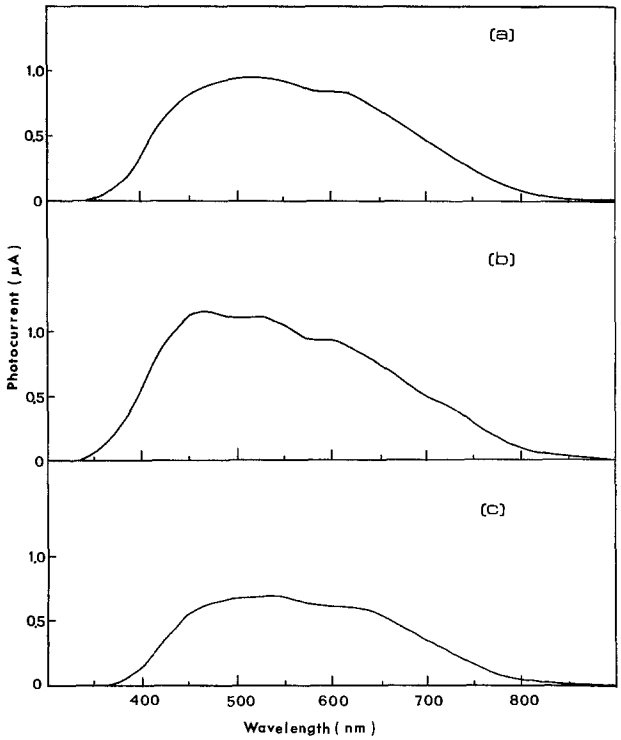


Fig. 3. Photocurrent *vs.* wavelength at a potential $E = +0.80V$ *vs.* SCE in 0.2M $NaNO_3$ solutions buffered to pH 8.4 (borate). Electrodes prepared from (a) zone refined iron, 10 nm band pass slits used for the monochromator, (b) magnetic iron, and (c) cold-rolled steel.

magnetic iron, and Fig. 3c for that from cold-rolled steel. The spectral response was recorded at $E = +0.8V$ in pH of 8.4 solutions. The incident light was not focused for these experiments and 10 nm band pass slits were used for the monochromator in Fig. 3a; no slits were used for Fig. 3b and 3c. The spectral response of all these iron oxide electrodes was essentially identical in shape and wavelength region. The coverage of all wavelengths in the visible region of these electrodes was rather unexpected, since the bandgap of Fe_2O_3 was reported to be 2.2 eV (20). This indicated that the photocurrent would decay to zero at 550 nm. Hardee and Bard (16) also observed this result for an iron oxide electrode prepared from iron acetylacetonate ($Fe(C_5H_7O_2)_3$) by chemical vapor deposition. Instead of showing no photocurrent response at 550 nm, the greater part of the incident sunlight, our electrodes showed maximal response there. The photocurrent response covered the whole visible region and extended to 850 nm. This corresponds to a semiconductor electrode with energy bandgap of 1.4 eV. Similar results were shown from different electrodes prepared here, and with excellent agreement. The extraordinarily small bandgap does provide the advantage of using the whole region of the sunlight spectra.

The photocurrent response was also performed using a 5 mW helium-neon laser with wavelength output at 632.8 nm. The result is shown in Fig. 4a to provide other evidence of the photoassisted oxidation using the low energy photons. It is interesting to point out that an anodic transient current appeared when the very weak intensity monochromatic light was turned on. These sharp anodic transients decayed fairly fast to a steady photocurrent with intensities being about a half of the peak value. When the monochromatic light was turned off a cathodic transient current with the peak about a half of the anodic transient peak was observed. However, the transients disappeared by increasing the light intensity to polychromatic light as shown in Fig. 4b. The transient response was also observed by Memming *et al.* (21) at a TiO_2 electrode when the potential was held on the rising portion of the *i-E* curve. In

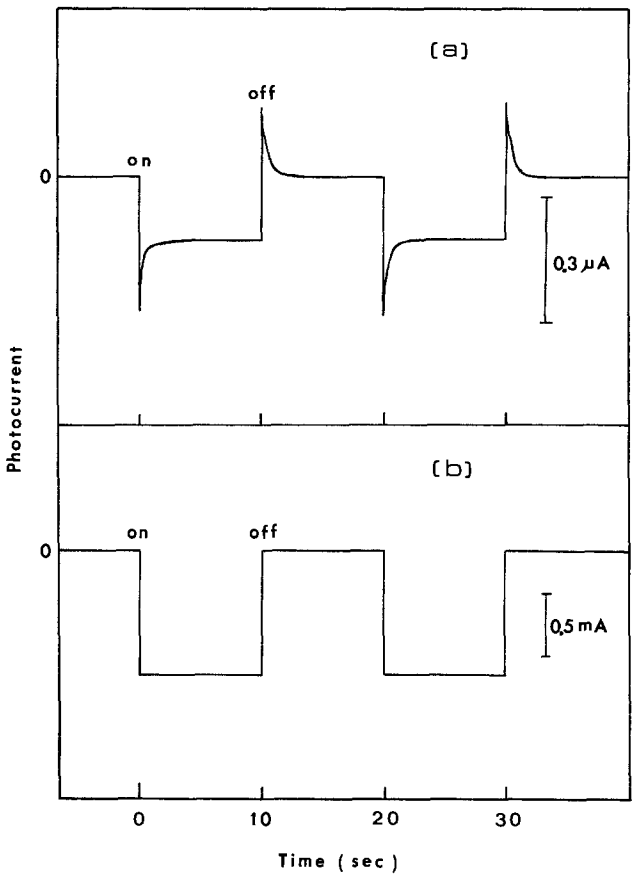


Fig. 4. Photocurrent transient (*i-t*) curves for iron oxide electrode prepared from zone refined iron in 0.2M $NaNO_3$ solutions buffered to pH 8.4 (borate) at a potential $E = +0.80V$ (*vs.* SCE) with photoexcitation source of (a) 5 mW laser monochromatic light at 632.8 nm, (b) white light.

the higher potential range at a well-defined current plateau, those transient peaks disappeared at TiO_2. Due to the lack of a well-defined current plateau at the iron oxide electrode, the whole curve is similar to the rising portion of the *i-E* curve of a conventional electrode. Therefore, the photoassisted electro-oxidation products and the intermediate species are thermodynamically reducible at these potentials. A cathodic current component is then observed by this back-reaction. Increase of the light intensity causes the transient peaks to disappear. This indicates a rather low and constant back-reaction which is undetectable at the recorder sensitivity used for the high intensity illumination. A similar light intensity effect was also observed recently by Bard and Hardee (22).

The photocurrent for the iron oxide electrode begins at 850 nm. This indicates coverage of the whole visible region in the sun spectra. Iron oxide powder was removed from an electrode and mixed with a large quantity of KBr to make a transparent pellet. An absorbance *vs.* wavelength curve, taken with a Cary 17 spectrophotometer, showed a steep rise in absorption at 850 nm with continuous rise in shorter wavelengths in the visible region. This agrees with the photocurrent experiments.

The iron oxide electrode in this study does offer advantages over large bandgap semiconductor electrodes because of its response to the whole visible region. It also offers advantages over small bandgap semiconductor electrodes because of its high stability. These advantages make it possible to be used in photoassisted electrolysis of water and in an electrochemical solar cell.

Acknowledgment

The support of this research by the Robert A. Welch Foundation of Houston, Texas is gratefully acknowledged.

Manuscript submitted Dec. 16, 1976; revised manuscript received Feb. 15, 1977. This was Paper 327 presented at the Philadelphia Meeting of the Society, May 8-13, 1977.

Any discussion of this paper will appear in a Discussion Section to be published in the December 1977 JOURNAL. All discussions for the December 1977 Discussion Section should be submitted by Aug. 1, 1977.

Publication costs of this article were assisted by Rice University.

REFERENCES

1. H. Gerischer, *Sur. Sci.*, **18**, 97 (1969).
2. M. Gleria and R. Memming, *J. Electroanal. Chem.*, **65**, 163 (1975).
3. S. N. Frank and A. J. Bard, *J. Am. Chem. Soc.*, **97**, 7427 (1975).
4. L. S. R. Yeh and A. J. Bard, *Chem. Phys. Lett.*, **44**, 339 (1976).
5. A. Fujishima, K. Kohayakawa, and K. Honda, *Bull. Chem. Soc. Jpn.*, **48**, 1041 (1975).
6. A. Fujishima, K. Honda, and S. Kikuchi, *J. Chem. Soc. Jpn. (Ind. Chem. Sec.)*, **72**, 108 (1969).
7. M. D. Archer, *J. Appl. Electrochem.*, **5**, 17 (1975).
8. M. S. Wrighton, D. S. Ginley, P. T. Wolczanski, A. B. Ellis, D. L. Morse, and A. Linz, *Proc. Natl. Acad. Sci. U.S.A.*, **72**, 1518 (1975).
9. B. Pettinger, H. R. Schöppel, and H. Gerischer, *Ber. Bunsenges. Phys. Chem.*, **78**, 450 (1974).
10. R. Memming and F. Möllers, *ibid.*, **76**, 475 (1972).
11. H. Kim and H. A. Laitinen, *This Journal*, **122**, 53 (1975).
12. H. A. Laitinen, C. A. Vincent, and T. M. Bednarski, *ibid.*, **115**, 1024 (1968).
13. T. S. Jayadevaih, *Appl. Phys. Lett.*, **25**, 399 (1974).
14. H. Gerischer and J. Gobrecht, *Ber. Bunsenges. Phys. Chem.*, **80**, 327 (1976).
15. F. Möllers and R. Memming, *ibid.*, **76**, 469 (1972).
16. K. L. Hardee and A. J. Bard, *This Journal*, **123**, 1024 (1976).
17. E. R. Brown, T. G. McCord, D. E. Smith, and D. D. DeFord, *Anal. Chem.*, **38**, 1119 (1966).
18. H. Gerischer, in "Physical Chemistry: An Advanced Treatise," Vol. 9A, H. Eyring, D. Henderson, and W. Jost, Editors, Academic Press, New York (1970).
19. B. Pettinger, H. R. Schöppel, and H. Gerischer, *Ber. Bunsenges. Phys. Chem.*, **78**, 450, 1024 (1974).
20. W. H. Strehlow and E. L. Cook, *J. Phys. Chem. Ref. Data*, **2**, 163 (1973).
21. F. Möllers, H. J. Tolle, and R. Memming, *This Journal*, **121**, 1160 (1974).
22. K. L. Hardee and A. J. Bard, *ibid.*, **124**, 215 (1977).

Study of the Critical Activation Time in the Continuous Activation of Electrode Surfaces

M. Farooque and T. Z. Fahidy

Department of Chemical Engineering, University of Waterloo, Waterloo, Ontario, Canada N2L 3G1

ABSTRACT

A method to determine the time required for the reactivation of an electrode surface exposed to oxide poisoning is illustrated in the instance of methanol oxidation in a multipolar rotating wiper-blade electrode system. The critical time can be computed by means of a mathematical model correlating electrode potential, bulk electrolyte concentration, anodization time, and experimentally determined parameters.

It has been suggested in recent research (1) on multipolar rotating wiper-blade electrodes that CH_3OH, HCHO, HCOOH, and possibly other species (such as H_2 and N_2H_4) could be continuously oxidized at a high rate on a platinum electrode. The oxide layer formed on the platinum surface, responsible for poisoning the oxidation process, is removed when the electrode passes under the wiper blade where open-circuit conditions exist. This removal is due to a chemical reaction with methanol and it ensures a higher oxidation rate than normally observed. One of the most important parameters in such oxidations is the time required for any arbitrary portion of the electrode to spend under a wiper blade at open-circuit conditions in order to become free of the "oxide" poison. This time, called the critical time, depends, for a given electrochemical system, on the potential of oxidation, the amount of oxide on the surface (which, in turn, is a function of the anodization time), and the concentration of the oxidizable species. One design criterion for a cell of this kind would be to minimize this time period, T, during which the electrode remains under the wiper blade under open-circuit conditions to ensure complete removal of the oxide layer.

In this study, a mathematical model has been developed to compute this critical time for the continuous removal of oxide poisons in the electro-oxidation of organic materials, in general, by using the methanol system as an experimental test case. Such a model could be useful in the design of continuously activated electro-oxidation processes and helpful in establishing the mechanism whereby the (O) species is removed from the electrode surface in the presence of the oxidizable species.

Key words: oxide layers, methanol oxidation, kinetics of oxide removal, electrode coverage.

Experimental

The apparatus has been previously described (1-3) in detail and its application to continuous electrode activation has been treated in the instance of the Kolbe reaction, oxygen evolution, and impurity stripping (4, 5). Experiments were performed to measure the effect of anodization time, anodization potential, and methanol concentration on the time required to free the wiped electrode of the "oxide" poison, which in this particular case was taken to correspond to the time required for the electrode potential to fall below 0.45V (NHE) after open-circuiting. This particular value is the midpoint of the 0.4-0.5V potential range which has been demonstrated (16-18) to correspond to complete oxide removal from a platinum surface.

The electrolyte was freed of oxygen by bubbling pure N_2 through it at a rate of 4.6 cm^3/sec, and in each experiment the electrode surface was prepared to the same initial state. The methanol concentrations employed were 0.9501, 0.1064, 0.0142, and 0.00683 mole/dm^3 in a 0.1 mole/dm^3 H_2SO_4 supporting electrolyte solution. The anodization potentials applied were 1.5, 1.4, 1.3, 1.2, 1.1, and 1.0V (NHE). The time of anodization was controlled by an electronic timer circuit and

was varied between zero and 1 hr. The experiments were chosen via factorial design (6) providing for two sets of replica needed in the estimation of experimental error, and conventional variance analysis was used to compute the experimental error variance and to establish the goodness of fit of the proposed model. The results of 152 experiments, replica included, are summarized in Fig. 2-5 which illustrate typical variations of the oxide-removal time. Figure 1 shows a typical oxide removal rate behavior. Note that after the anodization step there is no current flow in the circuit, hence no further oxygen adsorption. The oxide removal is due to a chemical reaction whose rate is potential independent.

Mathematical Formulation of the Critical-Time Model

Various models of growth mechanisms of thin anodic oxide films have been described in the literature and summarized in a recent review by Damjanovic and Ward (7). In the case of Pt, recent developments [*e.g.*, (8)] indicate that the oxide film is an oxide phase above approximately 1V (NHE) oxidation potential, but below this potential the film consists of reversibly chemisorbed oxygen. While the rate of oxide growth on Pt has been characterized by different mathematical "rate laws," the equation suggested by Genshaw (9) was chosen as the starting point to describe the growth rate of the conducting oxide layer formed during anodization. Genshaw's formulation yields

$$\frac{dL}{dt} = a \exp\left(-\frac{\Delta G_o^{\neq}}{RT}\right) \qquad [1]$$

where a is a proportionality constant, $\Delta G_o^{\neq}$ is the standard free energy of activation of the oxide growth, and L is the thickness of the oxide layer at time instant t of anodization. If it is assumed that the free energy of activation increases linearly with the oxide layer thickness, *i.e.*

$$\Delta G^{\neq} = \Delta G_o^{\neq} + bL \qquad [2]$$

then the appropriate form of Eq. [1] may be written as

$$\frac{dL}{dt} = a \exp\left(-\frac{\Delta G\#}{RT}\right) \qquad [3]$$

Hence, upon integration under potentiostatic conditions, one obtains that

$$L = \frac{RT}{b} \ln\left[1 + \frac{RT_a}{b} t\epsilon^{-\Delta G_o^{\neq}/RT}\right] \qquad [4]$$

by virtue of the ($t = 0$; $L = 0$) initial condition. Since the process is linked to electric discharge, its free energy must be potential dependent, which is approximated by the linear relationship

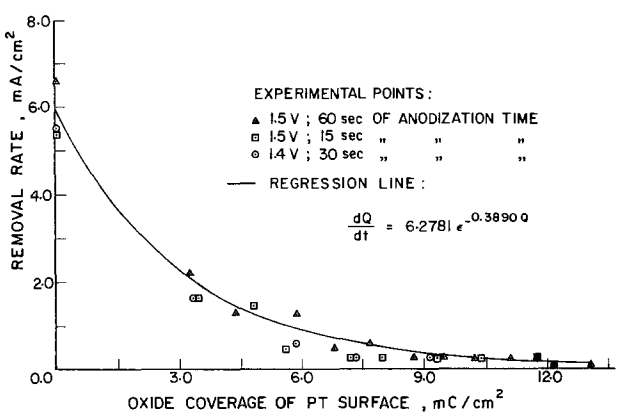


Fig. 1. Oxide removal rate as a function of oxide coverage of the electrode and anodization potential. CH_3OH: 0.035 mole/dm³, H_2SO_4: 0.1 mole/dm³; $T = 23°C$.

$$\Delta G^{\neq} = \Delta G_o - k\mathbf{F}V \qquad [5]$$

where k is a proportionality constant, $\mathbf{F}$ is the Faraday constant, and V is the electrode potential.

Let Q and Q_{ml} be the charge associated with the oxide on the surface and the monolayer, respectively, A_o the electrode area, and L_{ml} the thickness of the monolayer. Then, if q is the charge density of the oxide, one can write for θ_{ox}, the electrode coverage by oxide, the following equivalent relationships

$$\theta_{ox} = \frac{Q}{Q_{ml}} = \frac{A_o L q}{A_o L_{ml} q} = \frac{L}{L_{ml}} \qquad [6]$$

It then follows that in view of the potential effect on $\Delta G\#$ shown in Eq. [5]

$$\theta_{ox} = \frac{RT}{bL_{ml}} \ln\left[1 + \frac{RT_a}{b} t\epsilon^{-\Delta G_o/RT} \epsilon^{\frac{k\mathbf{F}}{RT}V}\right] \qquad [6]$$

which, in terms of the lumped parameters A, B, and K may be simplified to

$$\theta_{ox} = A \ln\left[1 + Bt\epsilon^{KV}\right] \qquad [7]$$

where $A \equiv \frac{RT}{bL_{ml}}$, $B \equiv \frac{RT_a}{b}\epsilon^{-\Delta G_o/RT}$, and $K \equiv \frac{k\mathbf{F}}{RT}$.

While in an earlier work (1) the rate-determining process in open-circuit oxide removal was reasoned to be the chemical reaction between Pt-O and adsorbed methanol to yield CO_2 and water, an equally plausible and more amenable assumption is that the rate of adsorption of CH_3OH on smooth Pt is the rate-controlling step. We can then characterize this process by the Roginskii-Zeldovich equation (10)

$$r_a = k_a c\epsilon^{-\alpha f\theta_{meth}} \qquad [8]$$

where r_a is the rate of adsorption, c is the methanol concentration, f is the inhomogeneity factor of the electrode surface, θ_{meth} is the coverage of this electrode surface by methanol, and $0 < \alpha < 1$. According to Beskorovainaya *et al.* (11), r_a is proportional to $c^{1.1\text{-}1.2}$ and this finding suggests a more general rate expression of the form

$$r_a = k_a' c^N \exp - [\alpha f\theta_{ox} + \alpha_{meth} f_{meth}\theta_{meth}] \qquad [9]$$

Equations [8] and [9] are isomorphic to relationships recommended in the pertinent literature (11, 19, 20); in the latter, N is an experimental constant. Since adsorbed methanol is removed from the continuously activated wiped electrode to a much larger extent than the oxide layer, it is reasonable to assume that $\theta_{ox} >> \theta_{meth}$; an alternative view would be that methanol adsorption being the rate-determining step, θ_{meth} is always smaller than θ_{ox} and varies little. It then follows that Eq. [9] may be simplified to the form

$$r_a = k_a c^N \epsilon^{-\alpha f\theta_{ox}} \qquad [10]$$

where k_a is the combination of k_a' and the essentially invariant exponential term containing θ_{meth}. Then, the rate of oxide removal may be expressed as

$$\frac{d\theta_{ox}}{dt} = -r_a = -k_a c^N \epsilon^{-\alpha f\theta_{ox}} \qquad [11a]$$

or, alternatively as

$$\frac{dQ}{dt} = -k_a Q_{ml} c^N \epsilon^{-\frac{\alpha f}{Q_{ml}}Q} \qquad [11b]$$

In Fig. 1, typical experimental observations of the oxide removal rate are shown, together with the solid line which corresponds to the statistical regression line

$$\frac{dQ}{dt} = m\epsilon^{-nQ} \qquad \begin{matrix} m = 6.2781 \\ n = 0.3890 \end{matrix} \qquad [12]$$

for c = 0.035 mole/dm³ at 23°C, in good qualitative agreement with Eq. [11b]. To obtain experimental values of Q and dQ/dt, the oxide layer was produced on the anode surface by applying a suitable potential for a given period of time, then the circuit was opened and the oxide was allowed to react with the electrolyte for a certain length of time. The remaining surface oxide was removed galvanostatically at a current density of 10 mA/cm². The charge required to lower the potential of the electrode to 0.45V was taken as equivalent to the amount of oxide present. The rate of oxide removal was obtained from the experimental Q-t plot via appropriate graphical differentiation.

Integrating Eq. [11] between the limits ($t = 0$; $\theta_{ox} = \theta_{ox}^{o}$), ($t = T$; $\theta_{ox} = 0$), and substituting Eq. [7], the expression for critical time is finally obtained as

$$T(t,V,c) = \frac{(Bt\epsilon^{KV} + 1)^{\alpha fA} - 1}{k_a \alpha f c^N} \qquad [13]$$

In Fig. 2-5 the experimentally observed oxide removal times are compared to Eq. [13]. Statistical analysis based on 152 experiments yields the least squares minimal regression line

$$T = 0.02357C^{-0.83613}[(4.78 \cdot 10^{-12} t\epsilon^{30.505V} + 1)^{0.21347} - 1] \qquad [14]$$

for the oxidation of methanol, with an error variance of 0.5227.

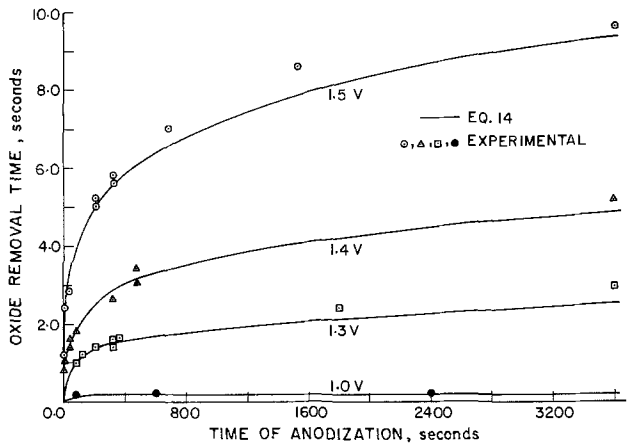


Fig. 2. Oxide removal time at open-circuit conditions as a function of anodization time and potential. CH_3OH: 0.9501 mole/dm³, H_2SO_4: 0.1 mole/dm³; T = 24°C.

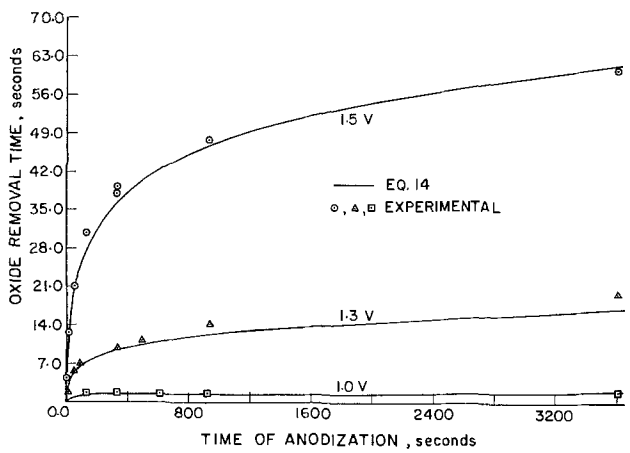


Fig. 3. Oxide removal time at open-circuit conditions as a function of anodization time and potential. CH_3OH: 0.1064 mole/dm³, H_2SO_4: 0.1 mole/dm³; T = 24°C.

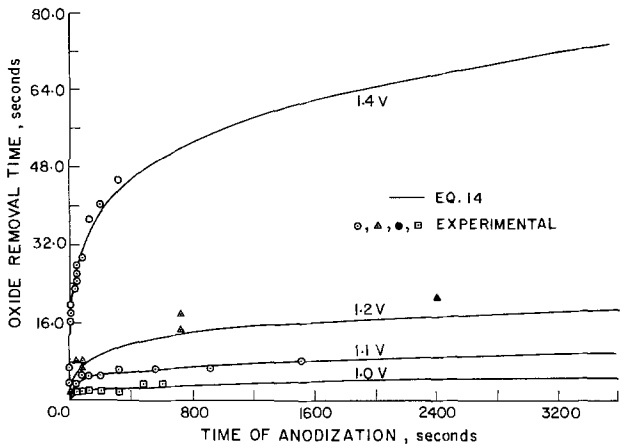


Fig. 4. Oxide removal time at open-circuit conditions as a function of anodization time and potential. CH_3OH: 0.0412 mole/dm³, H_2SO_4: 0.1 mole/dm³; T = 24°C.

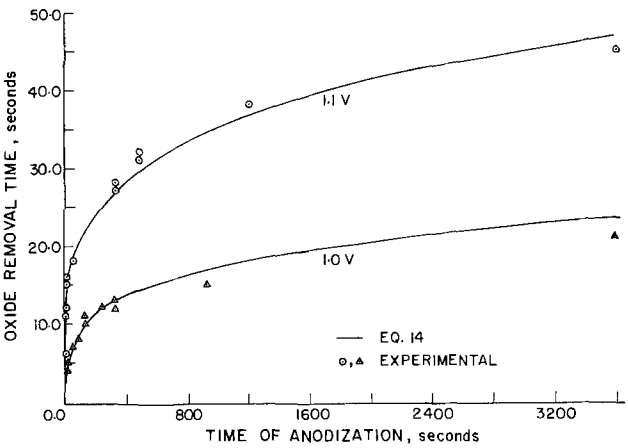


Fig. 5. Oxide removal time at open-circuit conditions as a function of anodization time and potential. CH_3OH: 0.0068 mole/dm³, H_2SO_4: 0.1 mole/dm³; T = 24°C.

Discussion

The good agreement between experimentally determined values of the oxide removal times and Eq. [13] (in 92 cases the magnitude of the relative error is less than 10% and only in 8 cases larger than 20%) indicates that the rate-determining step in the open-circuit removal of oxide from a Pt surface in the instance of methanol oxidation is the rate of methanol adsorption on the surface, followed by a chemical reaction. This finding agrees with Gromyko's report (12) about the rate-controlling behavior of CH_3OH adsorption on its electrochemical oxidation at potentials higher than 0.8V (NHE) in a different experimental apparatus.

It is instructive to compare Eq. [4] to certain relationships reported earlier in the literature for the oxide layer thickness. Using the Elovich-type expression relating the current associated with oxide growth to potential and electrode coverage, the so-called "direct logarithmic law of growth"

$$L(t) = L_0 + L_1 \log (t/t_0); \quad V = \text{const.} \qquad [15]$$

has been derived. There is some experimental evidence that Eq. [15] is obeyed on Pt anodes [*e.g.*, (13, 15)], although at the initial stage of oxide growth the layer thickness-time relationship does not follow Eq [15] [*e.g.*, (14)]. It is believed that Eq. [15] holds when either the oxide formation is the only anode reaction, or when oxide formation is a much less important process occurring in parallel with a predominant process, say, oxygen evolution. Although methanol oxidation, for example, is neither case, the degenerate forms of Eq. [4] and [15] at short times of oxide formation indicate

an essentially linear growth (*i.e.*, constant growth rate) regardless of the relative importance of the oxide formation in the over-all anodic process

$$L(t) \cong \left[\left(\frac{RT}{b}\right)^2 a\epsilon^{-\Delta G_0^{\neq}/RT}\right]t \qquad [4']$$

$$L(t) \cong [(L_0 - L_1) - L_1 \log t_0] + L_1 t \qquad [15']$$

Another interesting point would be the variation of the critical time with pertinent process parameters under galvanostatic conditions in view of the well-documented difference in the growth rate *vs.* time re-relationship with respect to potentiostatic conditions [*e.g.*, (7)], in the instance of Pt anodes. Since galvanostatic conditions are less inviting than potentiostatic conditions for a rotating wiper-blade electrode, such an investigation would be beyond the scope of our current research. The hereby presented analysis of critical time would most likely prove useful in improved design of wiper-blade electrode systems both for mechanism studies and practical oxidations at the continuously activated electrode surface, by choosing appropriate rotation rates and wiper-blade widths for a given electrode metal and specific electrochemical reactions.

Acknowledgment

This study has been supported by a National Research Council of Canada grant and a Canadian Commonwealth Fellowship and Scholarship Award.

Manuscript submitted Nov. 15, 1976; revised manuscript received Feb. 7, 1977.

Any discussion of this paper will appear in a Discussion Section to be published in the December 1977 JOURNAL. All discussions for the December 1977 Discussion Section should be submitted by Aug. 1, 1977.

Publication costs of this article were assisted by the University of Waterloo.

REFERENCES

1. M. Farooque and T. Z. Fahidy, Paper 370, Session XIV, 58th Canadian Chemical Conference, Toronto, Ont., May 1975.
2. P. R. Nadebaum, Ph.D. Thesis, University of Waterloo (1974).
3. P. R. Nadebaum and T. Z. Fahidy, *This Journal*, **122**, 1035 (1975).
4. P. R. Nadebaum and T. Z. Fahidy, *Electrochim. Acta*, **20**, 715 (1975).
5. P. R. Nadebaum and T. Z. Fahidy, *ibid.*, **20**, 721 (1975).
6. H. Scheffe, "The Analysis of Variance," chap. 8, John Wiley & Sons, Inc., New York (1959).
7. A. Damjanovic and A. T. Ward, "Electrochemistry," Series Two, Vol. 6, J. O'M. Bockris and A. D. Buckingham, Editors, Butterworths (1976).
8. L. B. Harris and A. Damjanovic, *This Journal*, **122**, 593 (1975).
9. M. A. Genshaw, "Electrosorption," E. Gileadi, Editor, chap. 4, Plenum, New York (1967).
10. S. Z. Roginskii and Ya. B. Zeldovich, *Acta Physiochem. URSS*, **1**, 554 (1934).
11. S. S. Beskorovainaya, Yu. B. Vasiliev, and V. S. Bagotskii, *Elektrokhimiya*, **1**, 1029 (1965).
12. V. A. Gromyko, *ibid.*, **8**, 707 (1972); *ibid.*, **8**, 711 (1972).
13. A. K. N. Reddy, M. A. Genshaw, and J. O'M. Bockris, *J. Chem. Phys.*, **48**, 671 (1968).
14. A. Damjanovic, A. T. Ward, B. Ulrick, and M. O'Jea, *This Journal*, **122**, 471 (1975).
15. S. Gilman, *Electrochim. Acta*, **9**, 1025 (1964).
16. L. D. Burke and A. Moynihan, *ibid.*, **16**, 167 (1971).
17. M. W. Breiter, *This Journal*, **109**, 425 (1962).
18. A. Hoffman and A. T. Kuhn, *Electrochim. Acta*, **9**, 835 (1964).
19. O. A. Petrii, in "Progress in Electrochemistry of Organic Compounds," A. N. Frumkin and A. B. Arshler, Editors, pp. 340-341, Plenum, New York (1971).
20. S. L. Kiperman, "Introduction to the Kinetics of Heterogeneous Catalytic Reactions," Izd. Akad. Nauk SSSR, Moscow (1964).

Corrosion Suppression on Rutile Anodes by High Energy Redox Reactions

L. A. Harris, D. R. Cross,[1] and M. E. Gerstner

General Electric Company, Corporate Research and Development, Schenectady, New York 12301

ABSTRACT

Rutile photoanodes are known to corrode slightly in 0.5*M* H_2SO_4. Experiments with different electrolytes show that corrosion does not occur in 9*M* H_2SO_4 or in 0.5*M* H_2SO_4 with 1*M* cobaltous ion added, though in each case water is decomposed into hydrogen and oxygen. The addition of cobaltous perchlorate to perchloric acid fails to inhibit corrosion. It is postulated that, where corrosion is suppressed, high energy intermediates are formed by single electron-transfer reactions at the electrode, and that these intermediates go on to split water in the aqueous electrolyte independently of the electrodes.

Photoelectrochemical cells, having one or both electrodes of semiconducting material are being studied as possible devices to generate electricity or to promote useful chemical reactions using the photon energy in sunlight (1-7). One of the key problems in these cells, particularly in those for decomposing water into hydrogen and oxygen, is corrosion of the semiconductor electrode (7-10).

[1] Present address: Chemistry Department, Western Maryland College, Westminster, Maryland 21157. Contributions by Dr. Cross were made during his tenure at CRD under the NSF Faculty Research Participant Program.

Key words: photoelectrochemistry, titanium dioxide, semiconductor electrodes.

It has been shown by a number of workers that introduction into the electrolyte of species that can be oxidized and reduced (redox couples) by simple electron-transfer reactions decreases electrode corrosion (11-15). In the cases reported so far, the standard redox potentials of the couples used are smaller than the potential required to decompose water (1.23V) so that it is no longer possible to split water and the cell may be used only to generate electricity at a potential determined by the redox couple, or to promote even lower energy reactions. In this report we show that higher energy redox couples can suppress the corrosion

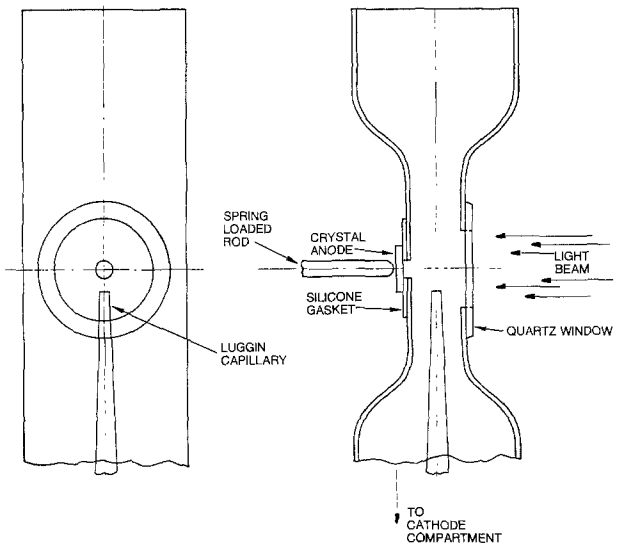


Fig. 1. The anode portion of the electrolytic test cell. The Luggin capillary leads to a saturated calomel reference electrode.

of rutile (TiO_2) and still allow the decomposition of water to taken place.

This work was done with n-TiO_2 because it is one of the few semiconducting materials with the conduction band edge located so that photogenerated holes have sufficient energy to oxidize the reduced member of redox species involved (16). It is recognized, of course, that corrosion of TiO_2 is no problem if it is used in basic electrolytes (2). But TiO_2 does corrode in 0.5*M* H_2SO_4 at a rate that can be monitored (7), so it provides a useful vehicle for this kind of study, which may have implications for the suppression of corrosion of smaller bandgap materials.

Experimental Methods

These tests were done following procedures similar to those described previously (7). The anode material was single crystal rutile cut to expose the (001) face and reduced in hydrogen at 650°C for 30 min. After reduction the surface was repolished to remove any thermal etching and to provide a high gloss surface on which corrosion would be evident. Samples were reused, without further heat-treatment, after repolishing between tests.

The cell in which the samples were tested had an anode compartment arranged as shown in Fig. 1. The rutile crystal was held against the gasketed window of the cell by a spring-loaded metal rod contacting the back of the crystal, where ohmic contact was assured by applying a paste of Ga-Ag alloy. This arrangement allowed for easy installation of the crystal and accurate weighings of the crystal before and after test. (The Ga-Ag contact is easily removed without affecting the crystal by immersing it in HCl.) The window also provided a well-defined active area (⅛ cm^2) in which the effects of corrosion contrasted with the polished surrounding area. In use, the recessed position of the anode sometimes caused bubbles to be trapped in the window. It also prevented the free convection of electrolyte past the electrode surface, making diffusion limitations more obvious than they might otherwise have been. Though the electrolyte was not stirred the volume in the vicinity of the anode surface could be flushed occasionally by a jet of solution from a dropper. No membranes or other diffusion barriers were used between the anode and cathode compartments of the cell.

The circuit used was the same as that described previously (7) except that a coulometer (VariTech Company Model VT 1176B) was inserted to record the total anodic charge passed through the rutile electrode. Illumination was provided by light from a 75W high pressure xenon lamp focused with a quartz lens to an intense but nonuniform spot of light with an intensity of about 1-1.5 W/cm^2 (10-15 times solar intensity) over the exposed sample area of 0.125 cm^2.

The samples were aged by applying enough anodic voltage (typically 1-1.5V SCE) to maintain the cell current at its saturation value. Gas evolution at the semiconductor anode and at the platinum-black cathode was observed in a qualitative fashion, but no attempt was made to measure quantitatively the amount of gas released in each case. Even though currents, charges, and weight losses were measured as accurately as possible, it would be a mistake to view most of the results as more than qualitative in nature, since quantitatively reproducible behavior of TiO_2 is difficult to achieve.

Results

The general behavior of the rutile anodes with the various electrolytes was similar to that described in the earlier paper (7) and is not described in detail here. The volt-ampere curves under full-spectrum illumination showed the same kind of changes due to aging as previously observed in 0.5*M* H_2SO_4.

The observations of principal interest for this work are summarized in Table I and are explained in more detail for each of the electrolytes in the remainder of this section.

Electrolyte 1: 0.5M H_2SO_4.—This electrolyte is the one used in our previous study in which corrosion and other aging effects were demonstrated (7). The gases liberated at the anode and cathode have previously been identified as oxygen and hydrogen, respectively. A useful indicator of hydrogen generation is polarization of the cathode to the potential expected for a hydrogen electrode at the electrolyte *p*H.

In some earlier tests using TiO_2 reduced at different temperatures average weight losses between 2 and 6 μg/C were measured after charges of 50-150C passed through the cells. If we assume that two oxygen atoms are removed with each Ti atom, these limits correspond respectively to about 410 and 140 electrons for each Ti atom removed.

After passage of 4 or 5C through the sample the corrosion is obvious to the eye; the exposed area being a velvety black in contrast to the glossy surface of the unexposed part of the crystal. The structure of the corroded surface is difficult to discern with the optical

Table I. Summary of TiO_2 electrode and cell behavior with various electrolytes

Electrolyte	1 0.5*M* H_2SO_4	2 0.5*M* H_2SO_4, 1.0*M* $CoSO_4$	3 0.5*M* H_2SO_4, 1.0*M* $Co(ClO_4)_2$	4 0.5*M* H_2SO_4, 0.58*M* K_2SO_4	5 9.0*M* H_2SO_4	6 1.0*M* $HClO_4$	7 1.0*M* $HClO_4$, 1.0*M* $Co(ClO_4)_2$
Corrosion	Yes	No	No	Yes	No	Yes	Yes
Weight loss, μg/C	3.8	0	—	3.6	0	1.1	2.3
Total charge, C	16.0	47.6	20.0	45.0	16.0	45.0	43.0
Anode bubbles	Yes	Yes	Yes	Yes	Slow	Yes	Yes
Cathode bubbles	Yes	Yes	Yes	Yes	Yes	Slow	Yes
Saturation current, mA	3.7*	2.4*	2.4	3.4	3.8	3.9	2.5
Flushing necessary	For bubbles	Yes	Yes	Yes	For bubbles	Yes	Yes
ΔI_s after cathodic run	Increases	Increases	Increases	Slightly increases	No effect	Increases	Increases

* Sequential tests on same electrode with same illumination.

microscope, but the scanning electron microscope (SEM) reveals the square tapered pits characteristic of this etching process and shown in Fig. 2a. It has already been shown that the semiconductor must be illuminated and carry a photocurrent for this etching and other effects to occur (7). To verify that simple chemical dissolution was not involved, a similar TiO_2 crystal was kept immersed in this acid for 186 hr with no detectable change in surface appearance or weight.

During photoelectrochemical aging, bubbles tended to accumulate in the anode aperture where they blocked the current. These had to be removed occasionally by flushing with a dropper, but otherwise stirring the electrolyte appeared to have little effect. After the passage of several coulombs the rate of bubble formation at the anode visibly decreased, though it remained relatively constant at the cathode. Over the same interval the saturation current increased to a peak value from which it slowly declined. The peak saturation current could not be restored by flushing the anode surface, but it was restored briefly by reversing the cell current for a minute or so and then returning to the anodic polarity. The increased current was transient, however, and in a few minutes declined to its former value. This behavior is indicated in Table I as an increase for "ΔI_s after cathodic run."

Electrolyte 2: 0.5M H_2SO_4, 1.0M $CoSO_4$.—The addition of $CoSO_4$ to the electrolyte produces a dark wine-red color characteristic of the Co^{2+} ion. Although light transmission through the solution is markedly reduced in the visible portion of the spectrum, the absorption at the shorter wavelengths needed to excite bandgap transitions in TiO_2 is not very different from that of electrolyte 1. Figure 3 shows the light transmission for 1 cm of electrolyte 2 relative to that of electrolyte 1. The total effective light reaching the sample through the cobalt-containing electrolyte, estimated by weighting the transmission values with the spectral intensity of the xenon lamp for wavelengths less than 410 nm is approximately 72% of that passing through electrolyte 1. This estimate neglects spectral variations of sample quantum efficiency. Table I shows that the saturation current with electrolyte 2 is reduced to about 63% of its former value. With both electrolytes 1 and 2, the saturation current was observed to be proportional to light intensity, which was varied by inserting calibrated neutral density filters in the optical path.

After passage of almost 50C there was no visible evidence of corrosion and no detectable weight change of the TiO_2 electrode. A slight discoloration due to a surface film on the exposed area was visible, but this did not affect the surface sheen, and no surface structure was found in the SEM.

The behavior during aging with this electrolyte differed from the first case in several respects. Though bubbles, verified by gas chromatography to be O_2, formed in the vicinity of the anode, they did not tend to adhere to the anode or block the cell current. The rate of bubble formation at the anode decreased in the same fashion as in the first case while the cathode bubbling and saturation current remained comparatively constant. After several hours, bubbles began to appear on the cell walls decreasing in density with distance from the anode.

Even when clear of bubbles, the anode had to be flushed periodically to maintain the saturation current

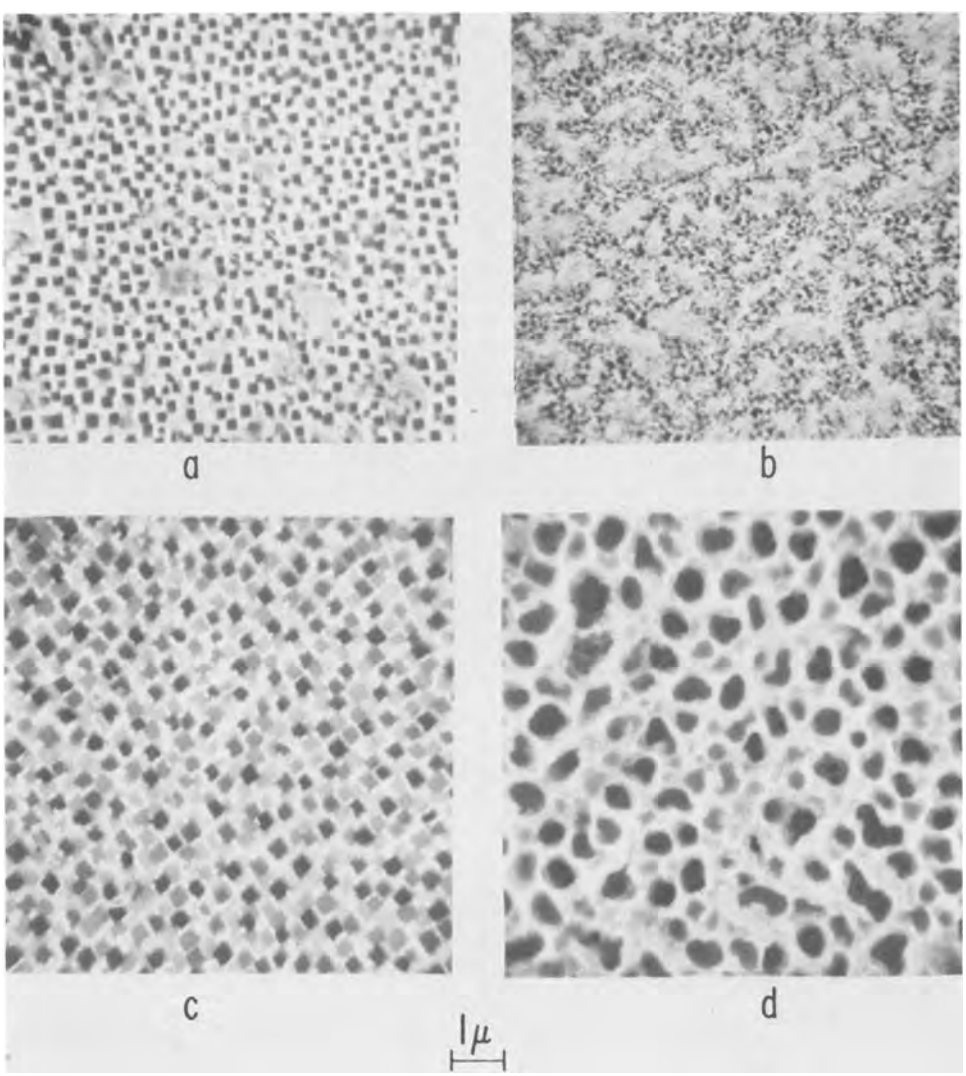


Fig. 2. Scanning electron micrographs of rutile anodes corroded in: (a) 0.5M H_2SO_4 by passage of 16C; (b) 0.5M H_2SO_4, 0.58M K_2SO_4, 45C; (c) 1.0M $HClO_4$, 45C; (d) 1.0M $HClO_4$, 1.0M $Co(ClO_4)_2$, 20C.

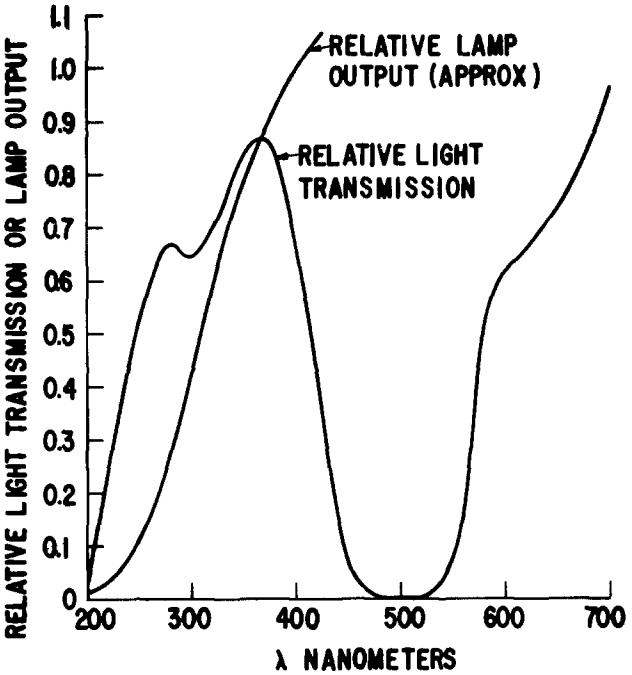


Fig. 3. Transmission of light through 1 cm of electrolyte 2 (with cobalt) relative to that through 1 cm of 0.5M H_2SO_4. Approximate spectral intensity (relative to that at 400 nm) of xenon lamp source is also shown.

level which tended to decrease, perhaps 10-30%, in a few minutes after flushing. The "flushed" value of current, however, could be increased even further by a brief cathodic run, as described for electrolyte 1.

Electrolyte 3: 0.5M H_2SO_4, 1.0M $Co(ClO_4)_2$.—Substitution of the perchlorate anion for the sulfate anion of the cobalt salt made no significant difference in cell behavior. No evidence of corrosion was found after passage of 20C. The saturation current, bubble formation, and response to flushing or reverse current were all essentially the same as for electrolyte 2.

Electrolyte 4: 0.5M H_2SO_4, 0.58M K_2SO_4.—Here the $CoSO_4$ of electrolyte 2 was replaced by as much K_2SO_4 as could be dissolved in the acid solution. This change increased the concentration of SO_4^{2-} and raised the pH from about 0.45 to 1.65.

In general this electrolyte behaved much like electrolyte 1, producing a steady flow of bubbles at the cathode and a decreasing flow at the anode. Except for clearing the aperture of bubbles flushing the anode region had little effect on the saturation current, which also matched that of electrolyte 1. The effect of a cathodic current flow, though still evident, was not so marked as in previous cases. As with electrolyte 2, bubbles eventually formed on the cell walls at an appreciable distance from the anode.

The sample lost weight at a rate comparable to that in electrolyte 1, but the SEM revealed the development of the square etch pits on a much finer scale, as shown in Fig. 2b.

Electrolyte 5: 9.0M H_2SO_4.—This strong acid did not corrode the rutile anode at all. Bubbles formed only slowly at the anode and occasionally had to be cleared away, but flushing the surface otherwise had no effect, nor did reversing the current direction in the cell. Evolution of gas at the cathode was steady and copious, consistent with the higher level of saturation current obtained.

Electrolyte 6: 1.0M $HClO_4$.—Replacing the sulfate ion of electrolyte 1 by the perchlorate ion produced little change in cell behavior. The currents were comparable, the anode had to be flushed to maintain the current, and reversing the current temporarily increased the anodic current level. As with 0.5M H_2SO_4 the sample corroded, but at a reduced weight loss per unit of charge. The corrosion pattern shown in Fig. 2c, had the characteristic square pits seen with other samples.

This electrolyte differed from the others by a somewhat reduced rate of bubble formation at the cathode.

Electrolyte 7: 1.0M $HClO_4$, 1.0M $Co(ClO_4)_2$.—Addition of $Co(ClO_4)_2$ to the perchloric acid did not prevent corrosion. Indeed the rate of corrosion, though low, was somewhat higher than with perchloric acid alone, but the pattern of corrosion was altered as Fig. 2d shows. The presence of cobalt did reduce the saturation current to a value consistent with the other cobalt-containing electrolytes. Gas was released at both electrodes.

Attempts were made to repeat some of these experiments with $MnSO_4$ substituted for $CoSO_4$, and with $CoSO_4$ dissolved in water (pH = 3.5). They could not be carried to completion because in both cases the cell currents were only transient. Initial anodic current flow soon decreased, apparently because some nonconducting species formed to block the anode. In the case of Mn, this blocking layer was visible as a brown deposit, tentatively identified as MnO_2.

Discussion

The rates of corrosion of TiO_2, in any of the electrolytes allowing this to take place, are very low since at the very least 100 electrons must transfer from the electrolyte to valence-band holes to remove one Ti atom. This fact suggests that the electrode material takes little part in the chain of chemical reactions that ultimately result in the decomposition of water. (In contrast, ZnO, which has a band structure similar to that of TiO_2, corrodes very efficiently. We observed that in a nondissolving solution of $ZnSO_4$ an illuminated ZnO anode lost one Zn atom for every two electrons transferred.)

Since each O_2 molecule requires 4 electron transfers there must be a series of intermediate activated species if the reaction is to proceed at any reasonable rate. These activated intermediates can involve chemical bonding with the electrode surface making it more susceptible to corrosion (8-10); or they can exist entirely in the electrolyte phase with the final step of O_2 formation taking place independently of the surface. In the latter case the semiconductor anode serves the purpose of oxidizing a species in the electrolyte by simple electron transfer.

The photogenerated holes in the valence band at the surface of TiO_2 are very powerful oxidizing agents having a reduction potential about 3V above that of the hydrogen electrode (16). They are thus sufficiently energetic to oxidize many species normally considered to be extremely stable in their reduced state. These high energy oxidized species can act as the intermediate in the electrolyte phase and ultimately lead to the liberation of oxygen from water, away from the electrode.

We suggest the following system of reactions as being consistent with the observed behavior of the seven different electrolytes described in the previous section. In sulfuric acid, the first reaction is

$$SO_4^{2-} + p^+ \rightarrow SO_4^- \quad [1]$$

where p^+ represents a positive hole in the valence band of the illuminated semiconductor anode. If the SO_4^- ions do not react with the material of the anode, they pair up to form the peroxydisulfate ion $S_2O_8^{2-}$

$$2SO_4^- \rightarrow S_2O_8^{2-} \quad [2]$$

The over-all reaction

$$2SO_4^{2-} + 2p^+ \rightarrow S_2O_8^{2-}$$

has a standard reduction potential of 2.01V (17), and it seems reasonable to ascribe to the first step (Eq. [1])

most of the energy to oxidize SO_4^{2-} ions. The independent, if brief, existence of the SO_4^- ion and its decay via reaction [2] have been demonstrated (18, 19).

Reaction [1] proceeds at a rate limited only by the number of photogenerated holes at the electrode surface. The negative charge on the SO_4^{2-} ion attracts it to the positive anode, and only a single electron transfers without the formation of intermediates so the reaction is unlikely to be limited by these kinetic factors. The SO_4^- so formed is an active species that can react with the electrode surface and lead to its corrosion, unless it is effectively scavenged by a competing reaction.

The principal competing reaction is the formation of $S_2O_8^{2-}$ (reaction [2]) which subsequently reacts with water independently of the electrode, and possibly assisted by the light passing the solution, by the following series of reactions (20-22)

$$S_2O_8^{2-} + H_2O \rightarrow SO_5^{2-} + SO_4^{2-} + 2H^+ \quad [3a]$$

$$SO_5^{2-} + H_2O \rightarrow SO_4^{2-} + H_2O_2 \quad [3b]$$

The peroxide can release O_2 by

$$SO_5^{2-} + H_2O_2 \rightarrow SO_4^{2-} + H_2O + O_2 \quad [3c]$$

or

$$S_2O_8^{2-} + H_2O_2 \rightarrow O_2 + 2HSO_4^- \quad [3d]$$

With high illumination levels one might expect more rapid pairing of SO_4^- ions and therefore less corrosion per unit charge transferred. In one isolated test at low light intensity the weight loss per unit charge was observed to exceed those measured at higher intensity.

In the more concentrated sulfuric acid (electrolyte 5) the concentration of SO_4^- ions is not increased because that is limited by light intensity. The reduced corrosion indicates a more effective scavenging reaction than [2]. Possible mechanisms for removal of SO_4^- from the electrode surface are simple charge exchange with other SO_4^{-2} ions

$$SO_4^- + SO_4^{2-} \rightarrow SO_4^{2-} + SO_4^- \quad [4]$$

or the formation of a triply charged peroxydisulfate ion

$$SO_4^- + SO_4^{2-} \rightarrow S_2O_8^{3-} \quad [5]$$

In either case the SO_4^- ion is prevented from reacting with the electrode and the series of reactions [3] can ultimately proceed in the volume of the cell.

When cobaltous ion is added to the electrolyte it provides another mechanism for scavenging the SO_4^- ion by the reaction

$$Co^{2+} + SO_4^- \rightarrow Co^{3+} + SO_4^{2-} \quad [6]$$

so long as $[Co^{2+}] >> [SO_4^-]$.

The Co^{3+} ion is known to release O_2 from H_2O by the over-all reaction

$$4Co^{3+} + 2H_2O \rightarrow 4Co^{2+} + 4H^+ + O_2 \quad [7]$$

which presumably involves the intermediate formation of aquated or sulfated dimeric cobalt complexes (23-27).

Direct oxidation of Co^{2+} at the electrode

$$Co^{2+} + p^+ \rightarrow Co^{3+} \quad [8]$$

is not responsible for suppressing corrosion since Co^{2+} fails to do so in the absence of the sulfate ion (electrolyte 7). The change in redox potential of the Co^{2+}/Co^{3+} couple from sulfate to perchlorate cannot be so great as to explain the difference in behavior. Nevertheless, the cobalt ion must play some part in the process since the corrosion pattern (Fig. 2d) is significantly altered. Reaction [8] seems less probable than reaction [6] because of the similar electric charge on the anode and the cobalt cation. The perchlorate ion, if oxidized at the anode surface, probably can exist only as an activated species bound to the electrode, the first step in corroding that surface.

As oxidized species tend to accumulate near the anode they limit the access of reduced species to that electrode. On flushing the anode region fresh electrolyte allows the current to increase. This diffusion limitation is assisted by the high current densities (20-30 mA/cm^2), the geometry of the cell, and the fact that reactions [3] and [7] are both relatively slow ones. It is known that reaction [7] is inhibited by the presence of H^+ ions (23), but the acid medium must be used, as insoluble $Co(OH)_2$ is formed at higher *p*H.

It is the slowness of these reactions that allows the oxidized species to diffuse out into the cell, eventually releasing oxygen in the electrolyte itself. This behavior is illustrated in electrolyte 2 by the failure of bubbles to block the anode and in electrolytes 2, 3, and 4 by the appearance of bubbles on the cell walls. It is also consistent with the observed decrease of bubble formation at the anode, as a greater proportion of the oxygen is released in the large volume of the cell where it is not so evident.

The additional increase of saturated anodic photocurrent after a brief cathodic run indicates the presence of a species bound to the electrode surface, one not readily removed by flushing the electrolyte over it. The presence of such species is confirmed by large transient sorption and desorption peaks in the voltammogram as polarity is changed. This subject has not been studied in detail and additional work is required to establish the identity of the sorbed species.

Conclusions

As noted early in this paper corrosion of TiO_2 is not a serious problem because this material can always be used in alkaline electrolytes without corroding. The qualitative observations reported here, however, do provide some insight into the nature of the electrode-electrolyte interactions that lead eventually to release of O_2 and to electrode corrosion. Hopefully some of these insights will find application to other, smaller bandgap electrode and electrolyte combinations.

To suppress corrosion and retain the ability to split water into its components a series of reaction intermediates should exist in the electrolyte so that the electrode is involved only in the first electron transfer step. The result of an electron (or hole) transfer across the interface should be the formation of a species (*e.g.*, SO_4^-) that can exist independently of the electrode long enough to react with another entity, either a different species (*e.g.*, Co^{2+} or SO_4^{2-}) or another of its own kind (*e.g.*, SO_4^-). The eventual outcome of this chain of electrolyte reactions should be the evolution of O_2 at a location removed from the electrode.

The detailed series of reactions proposed in this paper is of course a hypothetical one chosen to be consistent with known chemical reactions and the various observations reported here. Although the validity of this hypothesis will have to be determined by other more quantitative studies, the present work clearly establishes that corrosion can be suppressed by high energy redox systems which can decompose water in their turn. It appears that avoidance of a multi-electron transfer and the formation of intermediate electrode-radical species at the electrode surface provides a kinetic advantage of greater importance in suppressing corrosion than the reaction potential, provided, of course, that thermodynamic conditions are met.

Acknowledgment

The authors are grateful for useful discussions with their colleagues, J. J. Grimaldi, Jr., R. H. Wentorf, Jr., and R. H. Wilson.

Manuscript submitted Nov. 23, 1976; revised manuscript received Jan. 31, 1977. This was Paper 332 presented at the Philadelphia Meeting of the Society, May 8-13, 1977.

Any discussion of this paper will appear in a Discussion Section to be published in the December 1977 JOURNAL. All discussions for the December 1977 Discussion Section should be submitted by Aug. 1, 1977.

Publication costs of this article were assisted by General Electric Company.

REFERENCES

1. A. Fujishima and K. Honda, *Nature (London)*, **238**, 37 (1972).
2. M. S. Wrighton, D. S. Ginley, P. T. Wolczanski, A. B. Ellis, D. L. Morse, and A. Linz, *Proc. Natl. Acad. Sci.* U.S.A., **72**, 1518 (1975).
3. A. J. Nozik, *Nature (London)*, **257**, 383 (1975).
4. A. J. Nozik, *Appl. Phys. Lett.*, **29**, 150 (1976).
5. W. Gissler, P. L. Lensi, and S. Pizzini, *J. Appl. Electrochem.*, **6**, 9 (1976).
6. G. Hodes, D. Cahen, and J. Manassen, *Nature (London)*, **260**, 312 (1976).
7. L. A. Harris and R. H. Wilson, *This Journal*, **123**, 1010 (1976).
8. H. Gerischer, *Surf. Sci.*, **13**, 265 (1969).
9. H. Gerischer, *ibid.*, **18**, 97 (1969).
10. H. Gerischer and W. Mindt, *Electrochim. Acta*, **13**, 1329 (1968).
11. H. Gerischer, *Electroanal. Chem. Interfac. Electrochem.*, **58**, 263 (1975).
12. F. Sitabkhan, *Ber. Bunsenges. Phys. Chem.*, **76**, 389 (1972).
13. A. B. Ellis, S. W. Kaiser, and M. S. Wrighton, *J. Am. Chem. Soc.*, **98**, 1635 (1976).
14. G. Hodes, J. Manassen, and D. Cahen, *Nature (London)*, **261**, 403 (1976).
15. B. Miller and A. Heller, *ibid.*, **262**, 681 (1976).
16. M. Gleria and R. Memming, *J. Electroanl. Chem.*, **65**, 163 (1975).
17. J. E. Huheey, "Inorganic Chemistry, Principles of Structure and Reactivity," Table 7-6, Harper and Row Publishers, Inc., New York (1972).
18. E. Hayon and J. J. McGarvey, *J. Phys. Chem.*, **71**, 1472 (1967).
19. L. Dogliotti and E. Hayon, *ibid.*, **71**, 2511 (1967).
20. T. Moeller, "Inorganic Chemistry," p. 512, John Wiley & Sons, Inc., New York (1952).
21. C. E. Mortimer, "Chemistry, A Conceptual Approach," 2nd ed., p. 386, Van Nostrand Reinhold Co., New York (1971).
22. M. S. Tsao and W. K. Wilmarth, *Discuss. Faraday Soc.*, No. 29, 137 (1960).
23. T. Moeller, *ibid.*, No. 29, p. 301 (1960).
24. C. E. H. Bawn and A. G. White, *J. Chem. Soc. (London)*, 331 (1951).
25. M. Anbar and I. Pecht, *J. Am. Chem. Soc.*, **89**, 2553 (1967).
26. J. H. Baxendale and C. F. Wells, *Trans. Faraday Soc.*, **53**, 800 (1957).
27. R. K. Murmann, *Inorg. Chem.*, **10**, 2070 (1971).

Proton Spin Relaxation and Mobility in Hydrous Melts

J. Braunstein,* A. L. Bacarella,* B. M. Benjamin, L. L. Brown, and C. A. Girard[1]

Oak Ridge National Laboratory, Chemistry Division, Oak Ridge, Tennessee 37830

ABSTRACT

Pulse and continuous wave NMR measurements are reported for protons in hydrous melts of calcium nitrate at temperatures between −4° and 120°C. At temperatures near 50°C mean Arrhenius coefficients, ΔH_{T_1} (kcal/mole), are 7.9, 7.3, and 4.8, respectively, for melts containing 2.8, 4.0, and 8.0 moles of water per mole of calcium nitrate, compared to 4.6 kcal/mole for pure water. Temperature dependence of T_1 and T_2 in $Ca(NO_3)_2$-2.8 H_2O between −4° and 120°C are non-Arrhenius and can be represented by a Fulcher-type equation with a "zero mobility temperature" (T_0) of 225°K, close to the value of T_0 for solute diffusion, electrical conductance, and viscosity. Resolution of the relaxation rates into correlation times for intramolecular (rotational) and intermolecular (translational) diffusional motion is discussed in terms of the Bloembergen-Purcell-Pound and more recent models for dipolar relaxation.

Hydrous melts are highly concentrated aqueous electrolytes which may be characterized as molten salts containing water in amounts insufficient to form hydration shells about the ions and an intervening hydrogen-bonded solvent structure. They include the hydrate melts, which are fused stoichiometric hydrates such as $Ca(NO_3)_2 \cdot 4H_2O$ and $CaCl_2 \cdot 6H_2O$, as well as melts of nonstoichiometric composition of both higher and lower water content. Thermodynamic, transport, and theoretical investigations of hydrous melts have demonstrated the usefulness of molten salt models in understanding the behavior of concentrated electrolytes in the region where the structure is predominantly an ionic distribution perturbed by water molecules, rather than a hydrogen-bonded structure perturbed by ionic charges (1). A basic understanding of such electrolytes is important not only for theoretical reasons but also because the properties of these melts lend themselves to application in a number of developing technologies, including geothermal systems, some geothermal brines being very concentrated electrolytes; thermal energy storage with Glauber's salt or sodium thiosulfate; high temperature fuel cells (water is an anode product and a proposed cathode gas additive in molten carbonate fuel cells); interactions of water with magmas; improved water electrolyzers for hydrogen production; and thermochemical cycles for hydrogen production, in which steam-molten salt reactions may be invoked (2).

Transport studies of hydrous melts have been concerned largely with bulk properties such as the shear viscosity or electrical conductance (3). Diffusivities have been reported for dilute solute cations dissolved in hydrous melt solvents (4, 5), but little attention has been given to diffusivities or mobilities of water in hydrous melts. Proton chemical shifts have been reported for some hydrous melts (5) but these provide no information on transport properties. Nuclear spin relaxation measurements have been carried out on less concentrated aqueous electrolytes approaching the hydrous melt range (6) as well as on protons of nitric acid dissolved in molten nitrates (7) and of alkali metal ions in molten nitrates (8), but the application of this method to transport studies of hydrous melts has received little attention (9).

In this paper we report new measurements concerned with water transport properties in hydrous melts containing less than one water molecule per ion. We have determined spin-lattice and spin-spin

* Electrochemical Society Active Member.
[1] Visiting Scientist, Centre College, Danville, Kentucky.
Key words: NMR, relaxation, spin, proton mobility, diffusion, hydrous melt.

relaxation times of protons, using pulsed and continuous wave NMR measurements, as a function of water content and temperature. The temperature dependence and the dependence on water concentration are compared with those for other transport and thermodynamic properties of hydrous melts. We present preliminary results on the resolution of the observed relaxation rates in terms of correlation times for intramolecular (rotational) and intermolecular (translational) motion.

Experimental

Sample preparation.—Hydrous melt samples of $Ca(NO_3)_2$-R_{H_2O}, where the mole ratio of water, R_{H_2O} moles of water per mole salt, was between 2.8 and 16, were prepared in 5 mm NMR tubes. The melts were prepared from anhydrous salt which had been dehydrated in a desiccator containing $Mg(ClO_4)_2$ under vacuum (less than 50 μm) at ambient temperature for at least a week (10). The desired composition was prepared by the addition of a calculated amount of triply distilled water to a weighed amount of the anhydrous salt (*ca.* 10g) in a stoppered 25 or 50 ml Erlenmeyer flask. The saltwater mixture was then melted to a clear solution. The 5 mm NMR tubes were loaded with approximately 0.5 ml of the hydrous melt. Loading the tubes with the more concentrated hydrous melts, $R = 2.8$ or 4.0, required the melt, tube, and delivery tube to be heated. Prior to sealing, oxygen was removed by repeated evacuation of the samples frozen in a trichloroethylene-Dry Ice mixture (liquid nitrogen provided too great a thermal shock and led to breakage of the tubes).

Instrument.—NMR measurements were carried out with a Varian XL-100 NMR spectrometer with the Nicolet TT-100 Fourier transform accessory, with a magnetic field of 23.490 kG and a frequency of 100 MHz. Spectra were obtained at temperatures ranging from −20° to 120°C by using the variable temperature accessory for the XL-100. Spin-lattice relaxation times, T_1, were obtained from pulsed measurements with a 180°-τ-90° pulse sequence (11). Spin-spin relaxation times, T_2, were calculated from the width at half-height of continuous wave (CW) measurements (12). Precision of the reported values of T_1 and T_2 is ±10 and ±20%, respectively. Temperatures were determined from the separation of the hydrogen resonances, in ethylene glycol above 35°C, and in methanol below 35°C. It is estimated that the uncertainty in temperature is ±1°C.

Results

Relaxation times.—Values of the proton spin-latttice relaxation time, T_1, and of the spin-spin relaxation time, T_2, are listed in Table I for the melt of composition $R_{H_2O} = 2.8$ at temperatures between −4° and 120°C. Measurements at temperatures between 35° and 100°C were made also on melts of composition $R_{H_2O} =$ 4.0, 8.0, and 16.0.

Table I. Temperature dependence of proton spin-lattice (T_1) and spin-spin (T_2) relaxation times in $Ca(NO_3)_2$-2.8H_2O*

t/°C	1000°K^{-1}	T_1/sec	t/°C	1000°K^{-1}	T_2/sec
120.4	2.54	0.71	44.5	3.15	0.0315
101.2	2.67	0.43	34.7	3.25	0.0188
90.6	2.75	0.30	33.7	3.26	0.0105
84.1	2.80	0.243	27.0	3.33	0.0046
79.1	2.84	0.22	21.1	3.40	0.0047
77.9	2.85	0.21	19.4	3.42	0.0031
71.8	2.90	0.165	12.7	3.50	0.00113
69.5	2.92	0.17	12.7	3.50	0.00078
66.0	2.95	0.153	4.0	3.61	0.0003
64.8	2.96	0.125	−4.0	3.77	0.00013
61.4	2.99	0.125			
60.3	3.00	0.110			
54.9	3.05	0.110			
49.6	3.10	0.100			
47.5	3.12	0.100			
31.9	3.28	0.12			
28.4	3.32	0.09			
21.1	3.40	0.143			

* The concentrations of salt and water in moles/liter at 50°C are $C_{Ca(NO_3)_2}$ = 8.57 and C_{H_2O} = 24.00 (28).

The values of T_1 were obtained from the spectrometer's computer evaluation of the free induction decay of the signal amplitude in the 180°-τ-90° pulse sequence (11, 12). With decreasing temperature (or decreasing water content) the relaxation times decreased, and line broadening led to a decrease in sensitivity. In this region values of the spin-spin relaxation time, T_2, were calculated from the width at half-height of the continuous wave resonance peaks, a typical one being shown in Fig. 1. In this initial study, unfortunately, values of both T_1 and T_2 were not determined at the same temperatures. Nevertheless, as will be seen, the indications are that T_1 and T_2 approach equality in the high temperature (long relaxation time) region.

Composition variations.—Although the composition dependence of the relaxation times over a broad range of saltwater ratios will be dealt with in more detail in a subsequent paper, the general character of the composition dependence is similar to that reported previously for other transport properties and for thermodynamic properties (10). This may be seen in the plot in Fig. 2 of mean Arrhenius energies for spin-lattice relaxation in the temperature range 35°-100°C, obtained from best straight lines in this temperature interval where deviations from Arrhenius behavior are not pronounced. Also shown are the water concentration dependence of the diffusion coefficient (logarithmic) of dilute massive solute ions, Cd^{2+} (13); the enthalpy of vaporization of water from hydrous melts,

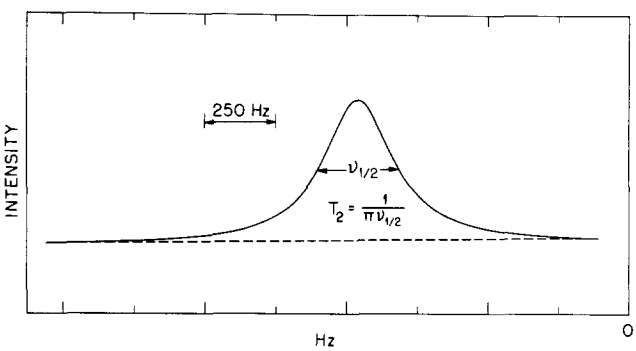


Fig. 1. Typical proton NMR CW spectrum in calcium nitrate-water mixtures, $Ca(NO_3)_2$-2.82H_2O at 287.5°K.

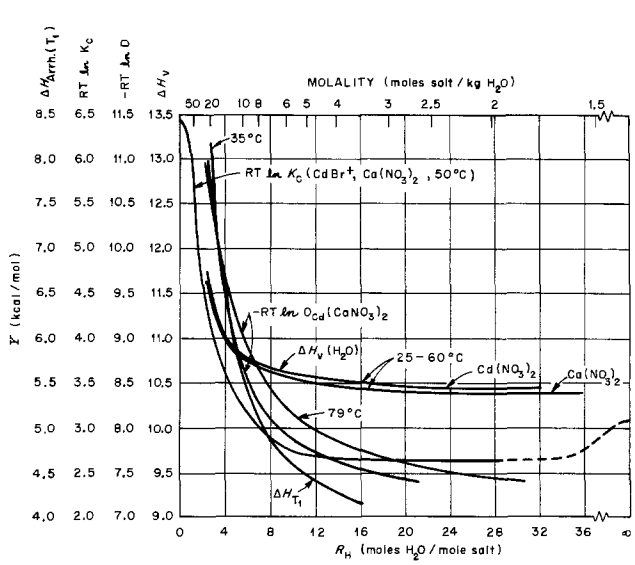


Fig. 2. Enthalpy of vaporization of water, solute association free energy, solute diffusion coefficient, and Arrhenius activation energy of the spin-lattice relaxation time (T_1) in hydrous melts of $Ca(NO_3)_2$ vs. water content.

and the free energy of association of dilute solute ions in hydrous melt solvents (10). Although a quantitative relation between the concentration dependences of the thermodynamic and transport properties may not yet be available, both reflect the change of behavior in the range of concentration between aqueous solution and molten salt. The transport properties, however, appear to show a greater variation with composition than the thermodynamic properties.

Temperature dependence.—Figure 3 shows the variation of T_1 with temperature in the melt $Ca(NO_3)_2 \cdot 4H_2O$ along with values of the fluidity (3), cadmium ion diffusivity (13), and equivalent conductance (14). The striking parallel between the behavior of the relaxation times and the macroscopic transport coefficients suggests that the same mechanism applies.

Although the Arrhenius equation can be fitted to the data over a limited range of temperature to provide mean activation energies for relaxation, measurements over an extended temperature range show marked deviations from Arrhenius behavior, as is the case for the macroscopic transport coefficients. A Fulcher-type equation (3, 13, 14) was therefore fitted to the combined spin-spin relaxation times and high temperature spin-lattice relaxation times for melts with $R_{H_2O} = 2.8$ at temperautres between −4° and 120°C, and is plotted as the solid line in Fig. 4

$$[T_1 \text{ (high temperature) and } T_2] = AT^{-1/2}e^{-\frac{k}{T - T_0}} \quad [1]$$

The parameter T_0 represents a hypothetical "zero-mobility temperature" (14). Because of the high degree of correlation of the parameter values, uncertainty about the location of the inflection, and experimental uncertainties, it was convenient to fix either k or T_0 for the T_1 data in comparing values among differing properties. The value $k = 649.5$ obtained for diffusion data in $Ca(NO_3)_2$-$4.09H_2O$ (15) leads to the values $A = 361.3 \pm 59$ and $T_0 = 224.9 \pm 0.9$ in Eq. [1] with a standard error of fit of 21.3%. This error may result in part from a slight mismatch in the joining of the high temperature T_1 data with the low temperature T_2 data as well as from the possible start of low temperature leveling off of the T_2 data, as indicated by the dashed line. The T_2 data point at the lowest temperature was excluded from the computer fit, as were the T_1 data at temperatures below 70°C.

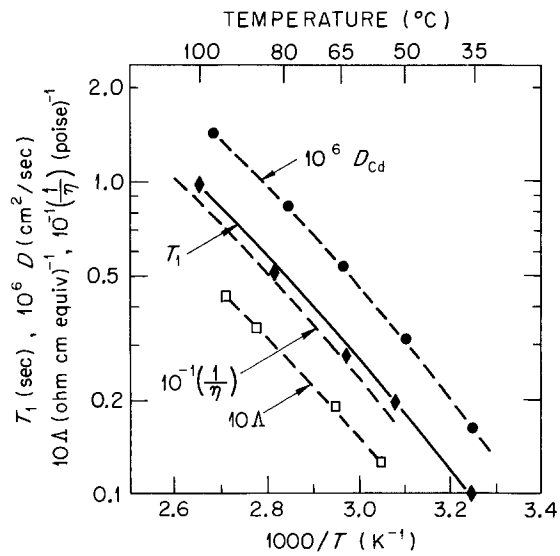


Fig. 3. Temperature dependence of proton spin-lattice relaxation time (T_1), diffusion coefficient (D) of dilute Cd^{2+}, equivalent conductance (Λ)*, and fluidity ($1/\eta$) in $Ca(NO_3)_2$-4.00 H_2O, 35°-100°C. [*$Ca(NO_3)_2$-$4.09H_2O$.]

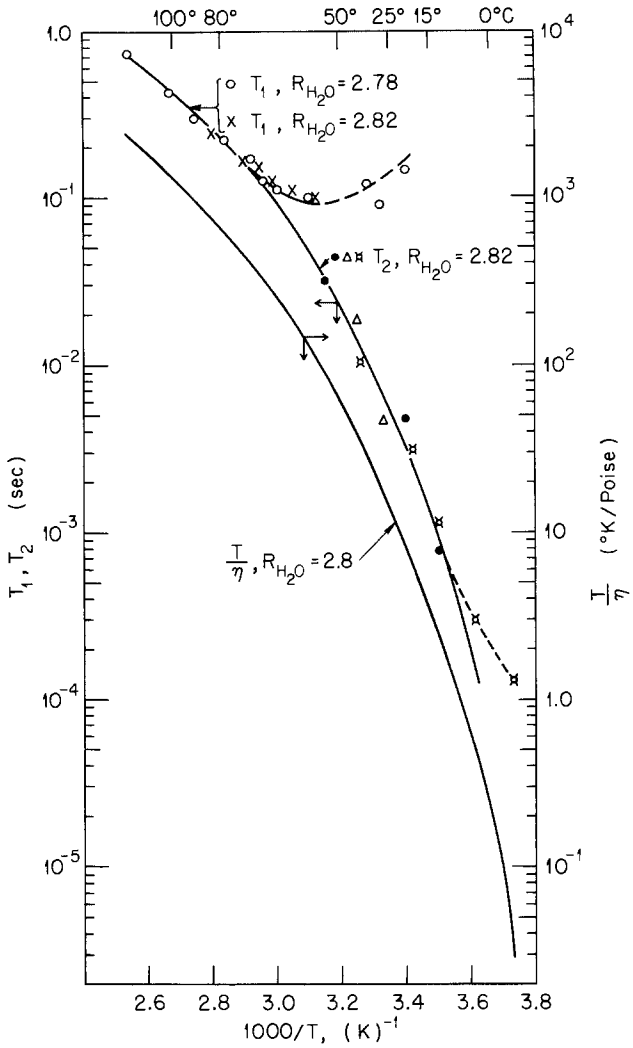


Fig. 4. Temperature dependence of proton spin relaxation times (T_1 and T_2) and of the temperature-viscosity ratio (T/η) in $Ca(NO_3)_2$-$2.8H_2O$.

Because of the experimental uncertainty in the lower temperature T_1 data, it is not certain whether the minimum and upturn indicated by the dashed line are real or an artifact, but both a minimum in T_1 and a leveling off of T_2 with increasing viscosity (decreasing temperature) would be expected from the elementary theory of nuclear magnetic relaxation via dipolar coupling, and has been observed for proton magnetic relaxation in glycerol (16). It may be seen also that the temperature dependence of the relaxation times is very close to that for the viscosities (3).

Discussion

A quantitative test of models with these preliminary results may be premature in view of some experimental uncertainty in the behavior for the shortest relaxation times and the absence of needed information on water diffusivity in the melts with water contents less than in $Ca(NO_3)_2 \cdot 4H_2O$ (9). Nevertheless, a number of qualitative conclusions may be drawn, and the application of some proposed models of relaxation may be instructive.

Grotthus mechanism.—First, the results (Fig. 3 and 4) demonstrate clearly parallel behavior of the proton relaxation times and the macroscopic transport properties. To the extent that the proton spin-lattice relaxation may be governed by the same mechanisms governing diffusion of more massive solute metal ions (such as Cd^{2+}) in the solution, our results suggest that the Grotthus chain mechanism for the anomalously high proton mobilities in aqueous solutions is not operative. This is not unreasonable since, as the water content of

a solution decreases, proton transfer could be expected to become less significant than water molecule diffusion as a mode of proton transport. Polarographic measurements of limiting currents for hydrogen reduction as compared to dilute solute metal ion reduction in concentrated lithium halide solutions are consistent with this (17). Also, experiments with hydrous melts "doped" with nitric acid (at concentrations of about 0.1M) showed little difference in the relaxation times. However, as pointed out by McCall and Douglass (18), the Grotthus mechanism applies to the mobility of excess protons over those "bound" in the water structure in dilute solutions. Since the measured relaxation time is an average for all the protons, bound and unbound, the number of excess protons may have been insufficient in our measurements to distinguish "excess" protons. Spin-echo measurements of proton diffusion coefficients in pure water are in essential agreement with tracer diffusion coefficients, but are lower than the "excess proton" diffusion coefficients calculated by application of the Nernst-Einstein equation to the limiting ionic conductance of hydrogen ions in solution. Similar behavior may occur in hydrous melts with the added complication that, in the absence of a hydrogen bonded structure, a larger concentration of excess protons may be required before a Grotthus mechanism can occur.

BPP.—A model of spin-lattice relaxation ("BPP") has been proposed by Bloembergen, Purcell, and Pound (16) for the dipole-dipole coupling mechanism for relaxation, based on a single correlation time, τ_c, proportional to the macroscopic transport properties such as the temperature reduced viscosity, η/T, or by the reciprocal diffusivity, $1/D$. This model, which is oversimplified (19) in that it assumes the Stokes-Einstein equation and neglects the possibility of a distribution of correlation times [which would correspond to a cooperative rather than to a single-event transport mechanism (20)], leads to the relation for the rotational or intramolecular part of the relaxation rate

$$(1/T_1)_{rot} = K_1 \left[\frac{\tau_c}{1 + 4\pi^2\nu^2\tau_c^2} + \frac{4\tau_c}{1 + 16\pi^2\nu^2\tau_c^2} \right] \quad [2]$$

where K_1 is a constant comprised of the nuclear spin, gyromagnetic ratio, and "molecular size" constant, ν is the radio frequency, and τ_c is the correlation time, $\tau_c \propto \eta/T \propto 1/D$. For nuclei of spin ½, like the proton in water, the dipole-dipole relaxation mechanism predominates over other modes of relaxation such as those arising from quadrupole or spin-rotational coupling, and paramagnetic impurities. In deoxygenated calcium nitrate hydrous melts, only nitrogen (besides the water protons and isotopes of H, Ca, and O) has a nuclear spin and is therefore capable of interacting with the proton nuclear spins. Equation [2], as well as a treatment of the translational or intermolecular contribution to the relaxation rate, predicts that a plot of the logarithm of the spin-lattice relaxation time *vs.* the logarithm of the correlation time (η/T, $1/D$) should have a negative slope of unity at short correlation times (high temperature, high fluidity) and a positive slope of unity at long correlation times (low temperature, low fluidity). Figures 5 and 6 are logarithmic plots of T_1 *vs.*, respectively, $1/D_{Cd}$ (in the absence of water diffusivity data, Cd^{2+} diffusivity is used for purposes of qualitative comparison) and η/T for $Ca(NO_3)_2$-$2.8H_2O$, with lines of unit slope drawn through the high temperature points. The rise at low temperatures is not well defined because of the loss of sensitivity in the measurements, but the minimum appears to occur at a relaxation time of about 0.1 sec. This is comparable with the relaxation time at the minimum in the classical measurements of proton relaxation time in glycerol by Bloembergen (when the difference of frequency is accounted for).

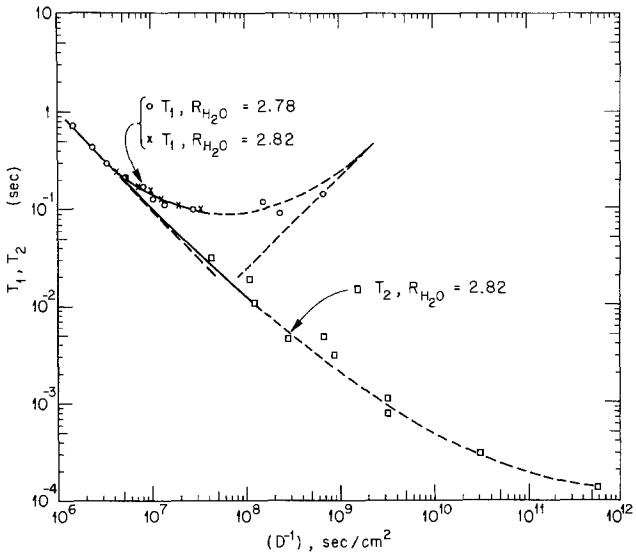


Fig. 5. Spin-lattice relaxation time (T_1) and spin-spin relaxation time (T_2) as a function of the reciprocal of the diffusion coefficient of dilute Cd^{2+} in $Ca(NO_3)_2$-$2.8H_2O$.

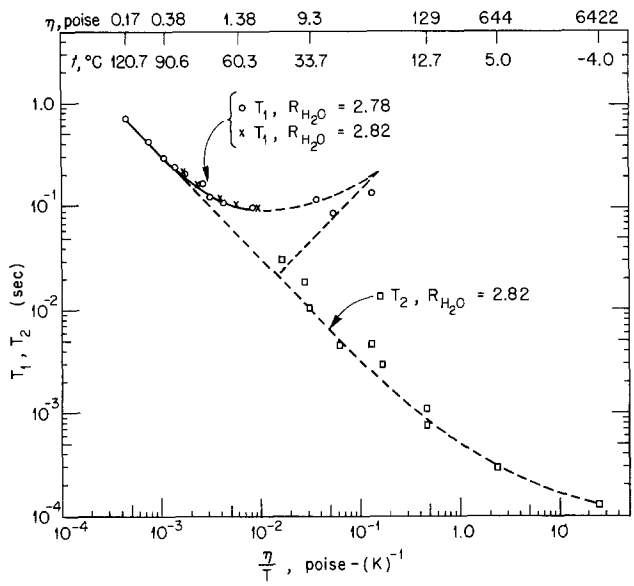


Fig. 6. Spin-lattice relaxation time (T_1) and spin-spin relaxation time (T_2) as a function of the viscosity temperature ratio (η/T) in $Ca(NO_3)_2$-$2.8H_2O$.

For the spin-spin relaxation time, the BPP model (16) leads to the equation

$$(1/T_2)_{rot} = \frac{1}{2}K_1 \left[3\tau_c + \frac{5\tau_c}{1 + 4\pi^2\nu^2\tau_c^2} + \frac{2\tau_c}{1 + 16\pi^2\nu^2\tau_c^2} \right] \quad [3]$$

which predicts a leveling off with increasing correlation times rather than a minimum. For short correlation times, T_1 and T_2 are predicted to be equal. According to BPP (16), the minimum in log T_1 occurs when $\omega_0\tau_c = 1/\sqrt{2}$, and the ratio of T_1/T_2 at this minimum is 1.6. The intersection of the T_2 slope (45°) with the T_2 plateau (0°) should occur at $\tau_c = T_2/\sqrt{2}$. If, as seems likely, there is distribution of correlation times resulting from the different molecular environments experienced by the nucleus during relaxation then the minimum value of T_1 will increase, with decreasing sharpness of the curve at the minimum point and an increased ratio of T_1/T_2. It would thus be desirable to extend the low temperature measurements in this sys-

tem to ascertain with greater accuracy the position of the minimum of T_1 and the leveling off of T_2.

Resolution of intramolecular and intermolecular motion.—Hertz (21) has discussed the interpretation of NMR relaxation measurements in terms of hydration numbers in ionic solutions. In hydrous melts such as $Ca(NO_3)_2$-2.8H_2O, where there is less than one water molecule per ion, the concept of hydration number loses significance. It is of interest however, to attempt to resolve the contributions to the measured relaxation rates of intramolecular (rotational) and intermolecular (rotational and translational motion). The BPP treatment (16) provides a starting point, although it must be recognized as only semiquantitative (22) in its use of macroscopic transport parameters, in the variety of intra- and intermolecular hydrogen distances used and in the lack of direct experimental evidence on the relative rates of the intra- and intermolecular relaxation processes (27). Modifications made by Torrey (22) (using the theory of the random walk) and others (23-26), have been discussed by Fiorito and Meister (27). Figure 7 is a plot of experimental T_1 and T_2 in $Ca(NO_3)_2$-2.8H_2O melts *vs.* several different estimates of the rotational correlation time, both from macroscopic data alone (curves III and V) and from the measured relaxation rates (curves I, II, and IV).

In curve I, T_1 is plotted against rotational correlation times, τ_{tot}, calculated from the rotational relaxation rate in the high temperature limit ($\omega\tau_{rot} << 1$) where ω is the angular frequency, $\nu/2\pi$, b is the intramolecular hydrogen-hydrogen distance, 1.52Å, γ is the gyromagnetic ratio of the proton, and $\hbar$ is Planck's constant divided by 2π

$$(1/T_1)_{rot} = \frac{3}{2}\frac{\gamma^4\hbar^2}{b^6}\tau_{rot} \qquad [4]$$

Values of $(1/T_1)_{rot}$ were obtained by subtracting the estimated intermolecular relaxation rate, $(1/T_1)_{inter}$, from the measured total relaxation rate $(1/T_1)$ (16), using the Kruger (25, 27) equations for the diffusive limit (which assumes a mean jump length much smaller than the distance of closest approach) and for the high temperature limiting case ($\omega\tau_{inter} << 1$)

$$\left(\frac{1}{T_1}\right)_{inter} = \frac{\pi\gamma^4\hbar^2N}{3dD} \qquad [5]$$

Here d is the water molecular diameter, taken as 2.76Å, and N is the spin concentration (protons per cubic centimeter). The low temperature limiting case ($\omega\tau_{inter} >> 1$) is shown in curve II with the intermolecular relaxation rate given by

$$\left(\frac{1}{T_1}\right)_{inter} = [6(5)^{1/2}/25]\frac{\pi\gamma^4\hbar^2N}{d^3}\left(\omega^{3/2}\left(\frac{d^2}{6D}\right)^{1/2}\right)^{-1} \qquad [6]$$

In the absence of water diffusivities in the melt $Ca(NO_3)_2$-2.8H_2O, D was taken as the diffusion coefficient of Cd^{2+} (13).

Curve III of Fig. 7 shows T_1 *vs.* macroscopic estimates of the rotational correlation times. The squares were calculated from the viscosity with Debye's equation for dielectric dispersion in polar liquids (16)

$$\tau_{rot} = \frac{1}{3}\tau_{Debye} = \frac{4}{3}\pi\eta a^3/kT \qquad [7]$$

assuming an H_2O molecular radius, a, of 1.38Å. The triangles correspond to estimates of the rotational correlation time

$$\tau_{rot} = a^2/6D_r \qquad [8]$$

D_r should be a rotational diffusion coefficient, but is here approximated by the Cd^{2+} diffusion coefficient (13). Correlation times were estimated also from the measured spin-spin relaxation time, T_2, with the condition of extreme narrowing, $(T_1)_{rot} = T_2$ and Eq. [4] to give the results shown on curve IV. The macroscopic τ_{rot} calculated using Eq. [7] and [8] were also plotted against T_2 as the triangles and squares on curve V.

Comparing curves I and II with III, and IV with V in Fig. 7, it is seen that the rotational correlation times calculated from the relaxation rates (Eq. [4]) are shorter than those estimated from macroscopic transport coefficients alone. Application of the BPP theory and its modifications to water at 30°C yields intramolecular correlation time estimates of 0.25×10^{-11} to 0.263×10^{-11} sec and intermolecular correlation times of 0.23×10^{-11} to 0.64×10^{-11} sec. Application to the spin-lattice relaxation times in the $Ca(NO_3)_2$-2.8H_2O melts at 121°C yields intramolecular correlation times in the range 0.318×10^{-11} to 0.802×10^{-11} sec and intermolecular correlation times of 3.62×10^{-11} to 18.4×10^{-11} sec. These preliminary results indicate that the intermolecular correlation times are greater than the intramolecular correlation times by a factor of approximately ten in $Ca(NO_3)_2$-2.8H_2O melts. Although the calculations are based on the application of macroscopic concepts of viscosity and diffusion to intermolecular motion on a molecular scale, and although correlation times for translation (motion over a distance of the order of a molecular diameter) and rotation (rotation through 180°) are not directly comparable, the order of magnitude increase of the ratio

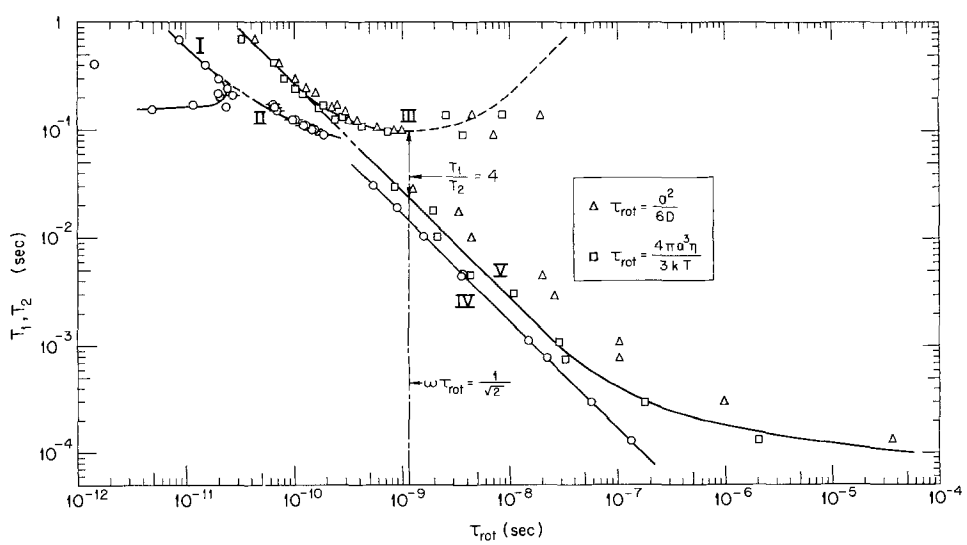


Fig. 7. Spin-lattice (T_1) and spin-spin (T_2) relaxation times as a function of correlation time (τ_{rot}) in calcium nitrate water mixtures $Ca(NO_3)_2$-2.8H_2O with τ_{rot} estimated from the relaxation rates (curves I, II, IV) and from macroscopic transport coefficients alone (curves III, V).

of intermolecular to intramolecular correlation time in the hydrous melts relative to water would appear to have at least qualitative significance. The greater freedom for rotation than from translation in melts of such high charge density suggests that the effect of electrostriction is analogous to the effect of high pressure on relaxation in liquids (28).

Conclusions

Spin-lattice and spin-spin relaxation times have been measured for hydrous melts $Ca(NO_3)_2$-R_{H_2O}, and show concentration and temperature dependences similar to those for the macroscopic transport properties. Estimates of rotational and translational correlation times, based on models for magnetic dipolar relaxation, suggest an order of magnitude greater degree of freedom for rotation than for translation in $Ca(NO_3)_2$-$2.8H_2O$ at 120°C ($\omega\tau << 1$). Low temperature results suggest that the region $\omega\tau \approx 1$ is accessible to measurement in hydrous melts, and our new techniques should provide higher precision. Additional relaxation measurements over a wide range of water contents, together with spin-echo measurements of water diffusivities, measurements with paramagnetic ions to provide shorter relaxation times, and with quadrupolar nuclei should prove useful in resolving intermolecular and intramolecular motions of water molecules in hydrous melts.

Acknowledgments

We would like to thank Professors D. H. Smith and R. Livingston for fruitful discussions of this manuscript, C. A. Angell and C. T. Moynihan for calling our attention to some valuable references, and especially R. Meister for making available a prepublication copy of Reference (9). This research was sponsored by the Energy Research and Development Administration under contract with Union Carbide Corporation.

Manuscript submitted Sept. 20, 1976; revised manuscript received Jan. 11, 1977. This was Paper 416 presented at the Washington, D. C., Meeting of the Society, May 2-7, 1976.

Any discussion of this paper will appear in a Discussion Section to be published in the December 1977 JOURNAL. All discussions for the December 1977 Discussion Section should be submitted by Aug. 1, 1977.

Publication costs of this article were assisted by Oak Ridge National Laboratory.

REFERENCES

1. J. Braunstein, in "Ionic Interactions," Vol. 1, S. Petrucci, Editor, pp. 180-260, Academic Press, New York (1971).
2. (a) M. Telkes, *ASHRAE J.*, p. 38 (September 1974); (b) A. J. Ellis, in Proceedings U. N. Symposium on the Development and Utilization of Geothermal Resources, Pisa, Italy, Sept. 22-Oct. 1, 1970, *Geothermics*, Special Issue, **2**, 516 (1970); (c) J. Millet and R. Buvet, in "Hydrocarbon Fuel Cell Technology," B. S. Baker, Editor, pp. 285-292, Academic Press, New York (1965); C. E. Bamberger and J. Braunstein, *Am. Sci.*, **63**, 438 (1975).
3. C. A. Angell and R. D. Bressel, *J. Phys. Chem.*, **76**, 3244 (1972); J. Ambrus, C. T. Moynihan, and P. B. Macedo, *This Journal*, **119**, 192 (1972).
4. J. Braunstein, L. Orr, A. R. Alvarez-Funes, and H. Braunstein, *J. Electroanal. Chem.*, **15**, 337 (1967).
5. C. T. Moynihan, C. R. Smalley, C. A. Angell, and E. J. Sare, *J. Phys. Chem.*, **23**, 2287 (1969).
6. B. F. Fabricand and S. Goldberg, *Mol. Phys.*, **13**, 323 1967).
7. L. C. Siew and B. R. Sundheim, *J. Phys. Chem.*, **73**, 4135 (1969).
8. D. Harold-Smith, *J. Chem. Phys.*, **60**, 1405 (1974); *ibid.*, **59**, 4771 (1973).
9. P. M. Gammell and R. Meister, *J. Chem. Phys.*, **64**, 4287 (1976).
10. H. Braunstein, J. Braunstein, and P. T. Hardesty, *J. Phys. Chem.*, **77**, 1907 (1973).
11. H. Y. Carr and E. M. Purcell, *Phys. Rev.*, **94**, 630 (1954).
12. T. C. Farrar and E. D. Becker, "Pulse and Fourier Transform NMR," Academic Press, New York (1971).
13. A. L. Bacarella and J. Braunstein, Chem. Div. Annual Progr. Rep., February 1976, ORNL 5111, p. 15; A. L. Bacarella, D. Brown, and J. Braunstein, Chem. Div. Annual Progr. Rep., May 20, 1974, ORNL 4976, p. 132.
14. C. A. Angell, *J. Phys. Chem.*, **70**, 3988 (1966).
15. C. T. Moynihan and C. A. Angell, *ibid.*, **4**, 736 (1970).
16. N. Bloembergen, "Nuclear Magnetic Relaxation," A reprint volume, W. A. Benjamin, Inc., New York (1961); N. Bloembergen, E. M. Purcell, and R. V. Pound, *Phys. Rev.*, **73**, 679 (1948); A. Abragam, "The Principles of Nuclear Magnetism," Clarendon Press, Oxford (1961).
17. N. K. Roberts and H. L. Northey, *J. Chem. Soc., A*, **1971**, 2572.
18. D. W. McCall and D. C. Douglass, *J. Phys. Chem.*, **69**, 2001 (1965).
19. F. Noack, "Nuclear Magnetic Relaxation Spectroscopy in NMR," Vol. 3, P. Diehl, E. Fluck, and R. Kosfeld, Editors, pp. 83-144, Springler-Verlag, New York (1971).
20. L. V. Woodcock, in, "Advances in Molten Salt Chemistry," Vol. 3, J. Braunstein, G. Mamantov, and G. P. Smith, Editors, Plenum, New York (1975).
21. H. G. Hertz, "Water," Vol. 3, F. Franks, Editor, Chap. 7, Plenum, New York (1973).
22. H. C. Torrey, *Phys. Rev.*, **92**, 962 (1953).
23. P. Hubbard, *ibid.*, **131**, 275 (1963).
24. R. Kubo and K. Tomita, *J. Phys. Soc. Jpn.*, **9**, 888 (1954).
25. G. J. Kruger, *Z. Naturforsch., Teil A*, **24**, 560 (1969).
26. J. F. Harmon and B. H. Muller, *Phys. Rev.*, **182**, 400 (1969).
27. R. B. Fiorito and R. Meister, *J. Chem. Phys.*, **56**, 4605 (1972).
28. J. Jonas, in "Advances in Magnetic Resonance," Vol. 6, J. S. Waugh, Editor, pp. 73-139, Academic Press, New York (1973).
29. W. Ewing and R. J. Mikovsky, *J. Am. Chem. Soc.*, **72**, 1390 (1950).

Corrosion of Lithium in Alkaline Solution

E. L. Littauer* and K. C. Tsai*

Lockheed Missiles & Space Company, Incorporated,
Lockheed Palo Alto Research Laboratories, Palo Alto, California 94304

ABSTRACT

The corrosion of Li was studied in 3-5M LiOH at 25°C and in 4.5M LiOH at 4°-60°C. The Arrhenius relationship is obeyed and the apparent activation energy for the Li corrosion reaction is found to be 15.5 kcal mole^{-1}. An empirical relationship is derived from which the corrosion rate v_f can be obtained at any molar LiOH. At 25°C v_f(kA m^{-2}) = 0.31(54.1 − 10[LiOH]). An equation is also given which allows calculation of the Li corrosion rate when the metal is anodically polarized. The kinetics of the H_2 evolution reaction (e.r.) on Li were determined, the transfer coefficient α has a value of 0.14. The rate-controlling process of the Li dissolution reaction is the highly polarized H_2 evolution at cathodic sites. Based on the α value obtained, the enthalpy of activation for the H_2 e.r. on Li at OCV is calculated to be 22.8 kcal mole^{-1}. It is proposed that the protective film on Li has a duplex structure with a thin oxide/hydroxide layer adjacent to the metal and an outer porous hydrated layer through which the reaction products and reactants can pass freely.

The rapid dissolution of Li in alkaline aqueous solutions can be utilized electrochemically to produce high rate battery systems (1). This is possible because the corrosion (parasitic) reaction in 3-5M LiOH can be virtually eliminated if the metal is anodically polarized by about 300 mV. It has been found that the rate of the Li dissolution reaction

$$Li + H_2O \rightarrow LiOH + \tfrac{1}{2} H_2 \qquad [1]$$

is essentially constant at constant temperature from OCV to the above-mentioned polarization level. Unlike conventional batteries, in Li-H_2O cells the current efficiency is governed by the ratio of two competing reactions, namely, the anodic dissolution reaction and the parasitic reaction (2, 3). The current efficiency increases with an increase in the anodic dissolution rate (*i.e.*, the current density), and it decreases at elevated temperatures where the corrosion reaction is stimulated. Since current efficiency is critical to cell performance, a fundamental understanding of the factors which influence the parasitic reaction is important.

No prior investigations of the corrosion of Li immersed in aqueous electrolytes have been reported. Papers on the electrochemistry of the system have been concerned with anodic passivation and mathematical modeling. This corrosion study of Li in flowing electrolyte under conditions identical to battery operation was undertaken to gain knowledge of three aspects of the Li-H_2O reaction.

(*i*) Information on the reaction at various LiOH concentrations and temperatures provides data for the determination of the reaction rate constant. This then allows calculation of corrosion rates in practical battery systems.

(*ii*) To characterize the processes which occur across the oxide/hydroxide film in a Li-H_2O cell, knowledge of the H_2O activity at the active Li surface is necessary. The assumption of the previous mathematical modeling paper (2) was that the exchange current density for the parasitic hydrogen evolution reaction is proportional to the 0.5 power of water activity at the active Li surface. This was equivalent to assuming that the transfer coefficient α is 0.5, which would be a reasonable figure in the absence of contrary experimental data. The experiments reported here have provided a precise value for α.

(*iii*) Diagnostic data from the anodic passivation studies (4, 5) led to the initial assumption on the nature of the complex film which forms on Li. Normal specimen preparation and microscopic examination of the film cannot be confidently used since reaction of occluded water with the metal on its removal from the test solution probably alters the structure. However, demonstrated correlations from this study with prior vapor phase investigations (6-8), which included visual and theoretical analyses of the film structure, would add confidence to predictions of film characteristics in the present situation.

* Electrochemical Society Active Member.
Key words: lithium, hydroxide, corrosion, hydrogen, dissolution.

Experimental

The test cell, support equipment, and procedures described previously for polarization studies of Li (4) were used for many reasons.

(*i*) The test cell is designed to insure uniform reaction across a lithium electrode of constant cross section. Even solution flow across the electrode surface is achieved because of the configuration of the ribbed steel screen flow-through matrix which acts as the counterelectrode in cell polarization experiments. This matrix is pressed against the Li surface. In alkaline aqueous solutions the Li surface is covered by a porous but protective oxide/hydroxide film.

(*ii*) Accurate potential measurements can be taken at the Li film/solution interface. The resistance of the film has been characterized and thus *IR* correction is straightforward.

(*iii*) The data obtained with this cell can be conveniently correlated with previous results.

(*iv*) Real-time corrosion rate measurements were obtained since the setup incorporated a precise hydrogen gas measuring system.

Briefly, the apparatus consisted of a circular 1.14 × 10^{-3} m^2 electrode area test cell incorporating a system to maintain constant the pressure of the ribbed screen matrix against the Li surface. In the present experiments the pressure was held at 3.5 × 10^4 Pa. Electrolyte temperature and concentration were controlled experimental variables. Solution flow rate was fixed at 0.3 m/sec. Hydrogen gas evolved during the reaction was separated from the electrolyte and measured with an American Meter Company Model 802 1 liter per revolution wet test meter. The instrument was modified with a Renco Corporation Model KT23A-500 optical encoder which, mounted on the wet test meter shaft, provided a digital signal output of 500 pulses per revolution. The encoder was mounted to eliminate the frictional drag component which would have amplified inaccuracies endemic to wet test meters at low flow rates. The encoder output was processed by an electronic digital to analog converter which provided instantaneous rate and total gas volume data. The gas rate was converted from volumetric flow rate (cubic centimeters

per second) to current (I) using the ideal gas law and Faraday's law.

Corrosion rate determinations were taken about 1 min after commencing electrolyte flow. By waiting this period of time, system stability was assured. Hydrogen evolution measurements were taken over a number of 20 sec periods. The experiments were performed in solutions of χM LiOH where $\chi = 3$, 3.5, 4, 4.5, and 5 ($\pm$ 0.05M) at 25° $\pm$ 0.1°C. The influence of temperature on the corrosion rate was determined at 4°, 15°, 25°, 35°, 45°, and 60°C in 4.5M LiOH. The corrosion potential in the same solution was determined at $T = 4°$, 15°, 25°, 35°, and 45°C. A Cd/Cd(OH)$_2$ reference ($E°_H = 0.81$) was used. This electrode has a temperature dependence of 0.14 mV/°C (9). At elevated temperatures, *i.e.*, above about 45°C, steady-state potential readings were not obtainable because of difficulties in maintaining isothermal conditions. At these high temperatures, a phenomenon referred to as thermal runaway occurs wherein the corrosion rate increases with time causing the electrode temperature to rise inconsistently. However, corrosion rate measurements could still be obtained reproducibly at up to 60°C by following a modified procedure. Here, before taking a hydrogen measurement, the anode was polarized by about 1V to temporarily suppress the parasitic reaction. On returning to OCV the electrode rapidly reverted to its active state. Its temperature remained essentially constant for about 20 sec during which time the hydrogen was monitored.

All experiments were run in triplicate. A regression analysis was performed on the data and the standard deviation was always less than 5%. Averaged values are therefore given in the figures.

Results

The corrosion rates of Li in 4.5M LiOH from 4°-60°C are shown in Fig. 1. The dramatic increase in rate above about 45°C is clearly evidenced. In this electrolyte, isothermal conditions could not be maintained for more than about half a minute, and on longer term exposure thermal runaway occurred.

The linear plot of logarithmic corrosion rate, ln v_f *vs.* $1/T$, in Fig. 2 shows that the Arrhenius relationship is obeyed for the aqueous corrosion of Li. Experiments performed in LiOH concentrations other than 4.5M (e.g., 4.0M) gave plots parallel to that shown. The apparent activation energy for the reaction $E_{act,r}$ calculated from the slope is 15.5 kcal mole^{-1}.

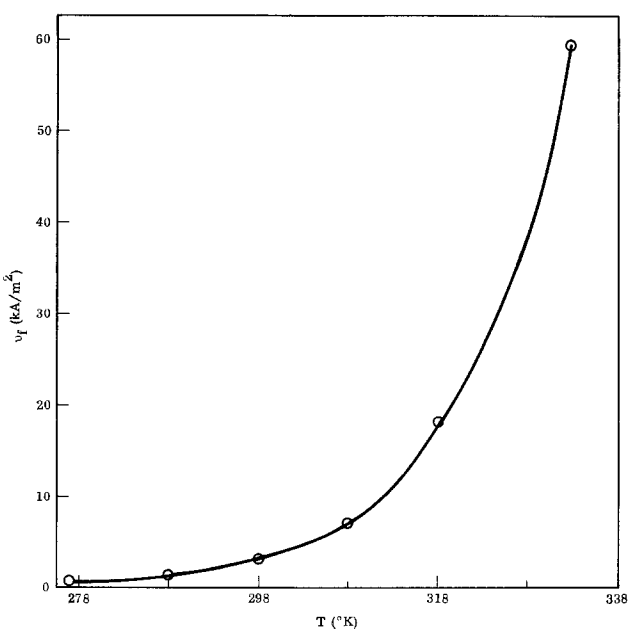


Fig. 1. Lithium corrosion rates at various temperatures in 4.5M LiOH.

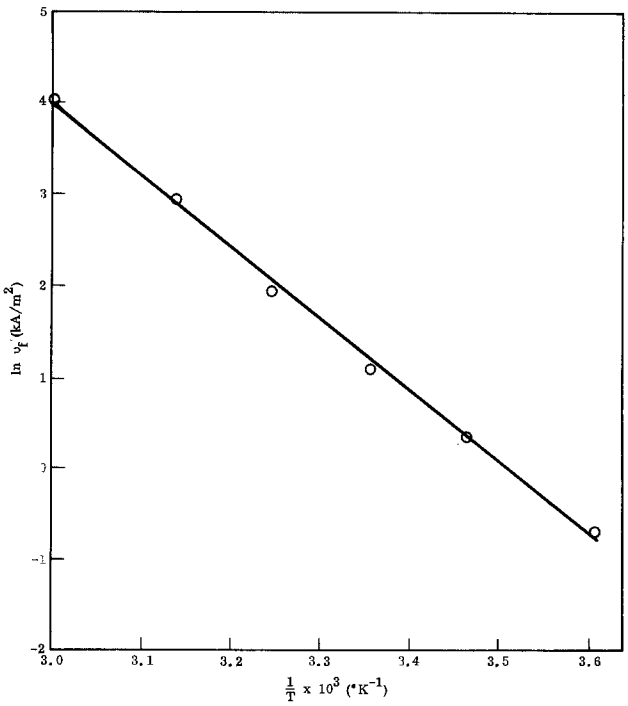


Fig. 2. Logarithmic corrosion rate (observed), ln v_f, vs. reciprocal temperature, $1/T$, (Arrhenius plot) in 4.5M LiOH.

Figure 3 indicates dependence of corrosion rate on concentration of LiOH at 25°C. This figure suggests that a linear rather than a logarithmic or parabolic relationship holds for the Li-H_2O reaction. Interestingly, extrapolation of the plot to $v_f = 0$ shows that Li would not corrode in 5.41M LiOH at 25°C. In actuality, the maximum solubility of LiOH in H_2O at that temperature is 5.3M.

Figure 4 indicates the temperature dependence of the corrosion potential, E_c, in 4.5M LiOH. The slope of the linear plot gives a value of 8 mV/°C. It was observed that the corrosion potentials under fixed experimental

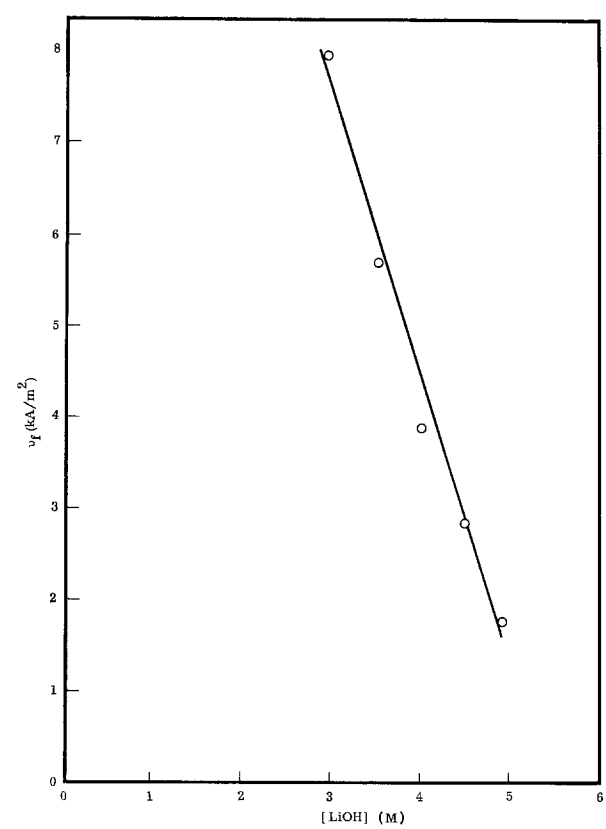


Fig. 3. Corrosion reaction rates vs. molar LiOH at 298°K

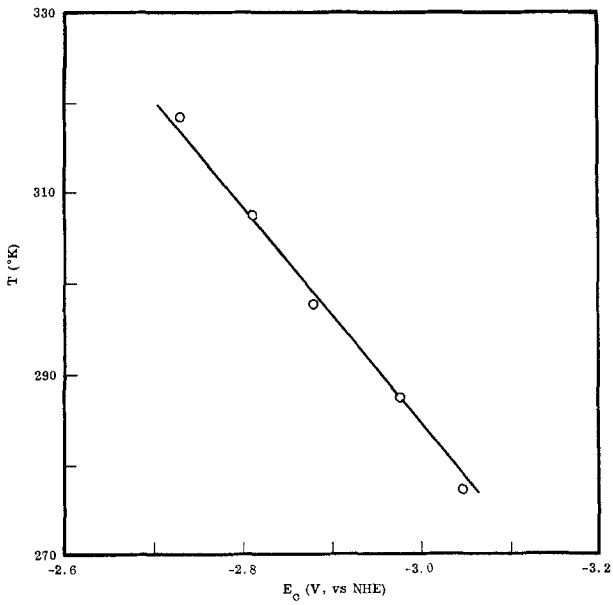


Fig. 4. Lithium corrosion potential, E_c, vs. temperature in 4.5M LiOH.

conditions were highly reproducible and remained fixed for the duration of the test, *i.e.*, >1 hr.

Discussion

Kinetics.—The chemical reaction between Li and H_2O, Eq. [1], is highly irreversible and therefore the forward reaction rate v_f may be related to the reaction rate constant k_f by

$$v_f = k_f[Li][H_2O] \quad [2]$$

It may be inferred from Fig. 2 that the Arrhenius equation is obeyed in this system. Hence

$$k_f = A \exp(-E_{act,r}/RT) \quad [3]$$

where A is the frequency factor and $E_{act,r}$ is the experimental activation energy. $E_{act,r}$ does not refer to constant absolute potential but comprises, as is discussed later, both the enthalpy of activation and a major contribution from the electric field involved (10).

Combining [2] and [3] gives the rate equation for the Li-H_2O reaction

$$v_f = A[Li][H_2O]\exp(-E_{act,r}/RT) \quad [4]$$

The rate-controlling step in the Li corrosion reaction is shown subsequently in this paper to be the reduction of H_2O at cathodic Li sites. It also represents the over-all rate of oxidation of Li in the aqueous solution.

The activity of Li at the metal surface may be assumed to be unity and pure water is 55.5 M/liter. In LiOH solution, however, the activity of H_2O is dependent on the LiOH concentration, *i.e.*

$$LiOH + nH_2O \rightleftarrows Li(H_2O)_l^+ + OH(H_2O)_m^- \quad [5]$$

where l and m represent the coordination numbers (CN) of the respective aquo complexes and $l + m = n$. Equation [4] can then be expressed

$$v_f = A(55.5 - (l + m)[LiOH])\exp(-E_{act,r}/RT) \quad [6]$$

Figure 3 plots the rates of the Li-H_2O reaction as a function of LiOH concentration and verifies the relationship given by [6]. Although the CN, m, for OH^- is unknown in LiOH solutions, the CN, l, for Li may be taken as 6 (11). Extrapolation of the plot of Fig. 3 to $v_f = 0$ gives m a value of 4. It should be pointed out that l and m represent the maximum coordination values for Li^+ and OH^- in aqueous solution. One might expect that with increasing solubility of LiOH at elevated temperatures, there would be a decrease in CN's. In practice, however, the maximum electrolyte concentration which is used in Li-H_2O cells is *ca.* 5M. Therefore this effect is unimportant here. Accordingly, $l + m$ may be set as approximately 10. Then, at 298°K, by inserting values for $E_{act,r}$ and R into [6], from the slope of the plot in Fig. 3

$$\frac{\partial v_f}{\partial[LiOH]} = -3.12 \text{ kA m}^{-2} \text{ mole}^{-1}$$

we have $A = 7.5 \times 10^{10}$ kA m^{-2} mole^{-2}. The frequency factor obtained here when put into [3] or alternately by combining [2] and [6], gives the rate constant for the Li-H_2O reaction

$$k_f = 0.31 \text{ kA m}^{-2} \text{ mole}^{-2}$$

By considering the volume fraction of LiOH solute, a modified empirical rate equation for the corrosion reaction may be obtained

$$v_f = \{a - 10[LiOH]\}\exp(b - E_{act,r}/RT) \quad [7]$$

where $a = 54.1$, *i.e.*, $10[LiOH]$ at $v_f = 0$ (extrapolated from Fig. 3) and $b = \ln A = 25.04$. This equation describes the observed linear dependency of the Li corrosion rate on LiOH conc. under conditions typical of Li/H_2O battery operation. It would appear reasonable to hypothesize that the water molecules which do not form aquocomplexes with Li^+ and OH^- play the primary role in the reaction. At elevated temperatures where isothermal conditions cannot be maintained in the system (see experimental) or in very dilute electrolytes where the corrosion rate is so high as to cause thermal runaway, this equation will not implicitly hold.

In actual practice, the rate of the Li-H_2O reaction is measured by the rate of hydrogen evolution. Reaction [1] may be regarded as a combination of two local cell reaction, *i.e.*

$$Li + OH^- \rightleftarrows LiOH_{(aq)} + e^- \quad [8]$$

$$e^- + H_2O \rightleftarrows OH^- + \tfrac{1}{2}H_2 \quad [9]$$

At OCV, [8] and [9] proceed at exactly the same forward reaction rate and the back-reaction rates are extremely small. The OCV (corrosion) potential E_c is a mixed potential representing the polarization of the Li dissolution sites and the H_2O reduction sites at the reacting surface. At 25°C in 4.5M LiOH, $E_c = -2.88$V *vs.* NHE which indicates that the H_2O reduction at the Li electrode is highly polarized. The reversible potential E_H for the H_2 e.r. in 4.5M LiOH ($pH = 14.3$) (4) = −0.84V. The electrochemical reduction of H_2O over Li may be assumed to be predominantly under activation control. The basis for this assumption is the report of prior work on the evolution of H_2 on various metals (Mg, Pb, Zn, etc.) in strongly alkaline solutions (12). The Tafel relationship is obeyed at least up to 10 kA m^{-2} and concentration polarization was found to be insignificant. Transfer coefficient, α, values reported for the H_2 e.r. on Mg, Pb, and Zn were 0.17, 0.25, and 0.32, respectively. It is assumed that the Mg and Zn electrodes, like Li, are covered with an oxide film and thus similarities would be expected in the kinetics. Then, following the model based on potential energy curves (13) the rate constant for the H_2 e.r. may be expressed

$$k_f = k \exp\left(-\frac{E - E_c}{RT/\alpha n\mathbf{F}}\right) \quad [10a]$$

and

$$k = k^\circ \exp\left(\frac{E_H^\circ - E_c}{RT/\alpha n\mathbf{F}}\right) \quad [10b]$$

where k° is the rate constant when $E = E_H^\circ$. The term $E_H^\circ - E_c$ represents the local cell potential for the Li oxidation and H_2O reduction couples. At OCV E and E_c are synonymous and [3] and [10b] will coincide. Then

$$RT \ln(A/k^\circ) = E_{act,r} + n\alpha\mathbf{F}(E_H^\circ - E_c) \quad [11]$$

and

$$\frac{\partial T}{\partial E_c} = \frac{n\alpha\mathbf{F}}{R \ln(A/k^\circ)}^{1} \quad [12]$$

The experimental data plotted in Fig. 4 of E_c *vs.* T depicts the relationship described by [11]. A straight line is observed. From the slope of this plot one could determine the H_2 e.r. rate constant k° if α were precisely known. This coefficient may be calculated as follows. By combining Eq. [2] and [10b] in the case where [Li] = 1, one obtains [13]

$$\ln v_f = \ln(k^\circ[H_2O]) + \frac{n\alpha\mathbf{F}}{RT}(E_H^\circ - E_c) \quad [13]$$

then, by plotting $\ln v_f$ *vs.* E_c/T, as in Fig. 5, the slope, 1.55×10^3, represents the term $n\alpha\mathbf{F}/R$. In the case of hydrogen evolution in alkaline solutions, $n = 1$, then α computes to 0.14. This value compares with those given above for the H_2 e.r. on Mg, Pb, and Zn.

This is perhaps a novel approach to the derivation of α. While confirmation of its magnitude from polarization curves would be desirable, in this system it is impossible to obtain discrete H_2 polarization plots because of the confounding influence of the concurrent Li dissolution reaction.

To obtain k°, we have from [11]

$$k^\circ = A \exp\left\{-\left(\frac{E_{act,r}}{RT} + \frac{E_H^\circ - E_c}{RT/n\alpha\mathbf{F}}\right)\right\} \quad [14]$$

and, at 298°K, k° computes to 5×10^{-6} kA m^{-2} mole^{-2}. With knowledge of k° and of the potential of the corroding electrode as a function of temperature, the lithium corrosion rate constant can be calculated independently from [10b] without directly measuring the H_2 evolution rate as a function of temperature.

A rate equation for the general case of H_2 evolution at a polarized electrode can be obtained where $i_{H_2} = v_f$. Combining [7] and [13] we have

$$i_{H_2} = k\{54.1 - 10[LiOH]\} \exp\left(\frac{-n\alpha\mathbf{F}(E - E_c)}{RT}\right) \quad [15]$$

and, for the special case at OCV where $E = E_c$, the corrosion current

$$i_{corr} = k(54.1 - 10[LiOH]) \quad [16]$$

Knowing the transfer coefficient also permits calculation of the enthalpy of activation for the H_2 e.r. on Li. Based on Fig. 1 and 4, Fig. 6 may be generated. A constant overvoltage has been arbitrarily taken at 25°C, *i.e.*, $\eta_{298°K} = E_H^\circ - E_c = 2.04$V. The observed corrosion rate, v_f, has been corrected to this overvoltage by $(v_f)_{\eta 298°K} = v_f \exp(\Delta E/b)$ with $b = RT/n\alpha\mathbf{F}$ and $\Delta E = E_{OBS} - E_{c(298°K)}$, where E_{OBS} is the corrosion potential at any given temperature and $E_{c(298°K)}$ is the corrosion potential at 25°C. From the slope of the plot in Fig. 6, the enthalpy of activation is

$$\Delta H^\dagger = -R\left[\frac{\partial \ln(v_f)_{\eta 298°K}}{\partial 1/T}\right]$$

and this computes to 22.8 kcal mole^{-1}.

The interconnection between the H_2 evolution and the Li dissolution reactions at OCV and also when anodically polarized is illustrated in Fig. 7. Here, the H_2 activation polarization curve, represented by curve A, has been calculated using [15]. 4.1M LiOH was selected as the solution of interest since data exist for the anodic polarization of Li in that electrolyte. The anodic curve which has been published previously in Fig. 1 of Ref. (5) is corrected here for IR and appears

[1] Actually, $k^\circ = A \exp(-E_{act,r}/RT) \cdot \exp(-n\alpha\mathbf{F}\, E_H^\circ/RT)$, but $\partial E_H^\circ/\partial T$ is effectively zero over the temperature range of concern to this study.

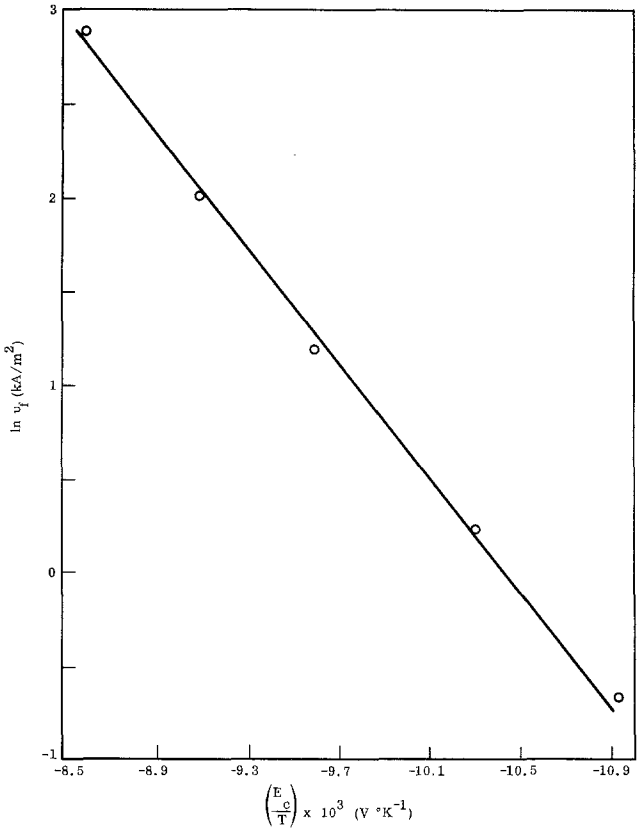


Fig. 5. Logarithmic corrosion rate, ln v_f, *vs.* E_c/T

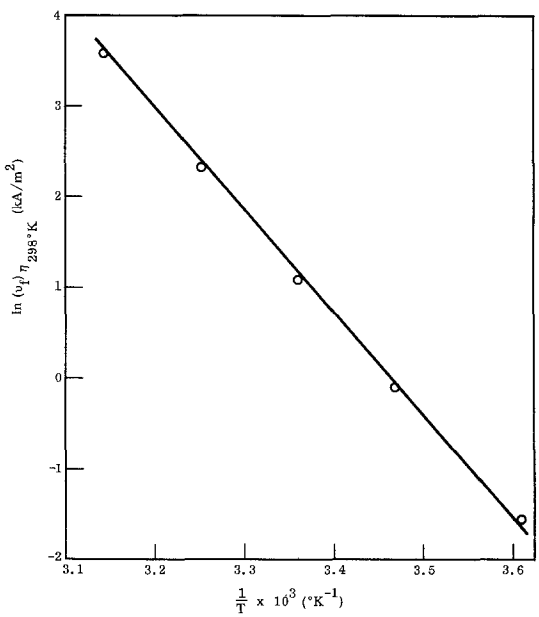


Fig. 6. Logarithmic corrosion rate (calculated) at constant overvoltage $\ln(v_f)_{\eta\ 298°K}$, *vs.* reciprocal temperature, $1/T$, in 4.5M LiOH.

as curve B. Then, by subtracting curve B from A, curve C is derived which represents the H_2-free polarization curve for Li in the solution of interest.

The E_H° for the Li dissolution reaction [1] in 4.1M LiOH ($a_{Li^+} \approx 2$) is −3.03V, while the observed OCV potential of the Li electrode E_{OBS} in that solution is −2.76V. To speculate at this time on the kinetics of the Li dissolution reaction over the narrow span $E_{Li}^\circ - E_{OBS}$ would be unwise because (*i*) no information is available on the transfer coefficient, and (*ii*) it has not been established that the Tafel relationship is obeyed for this highly energetic irreversible reaction. However, for present purposes, it is sufficient to consider the situation from −2.76V anodic as depicted in

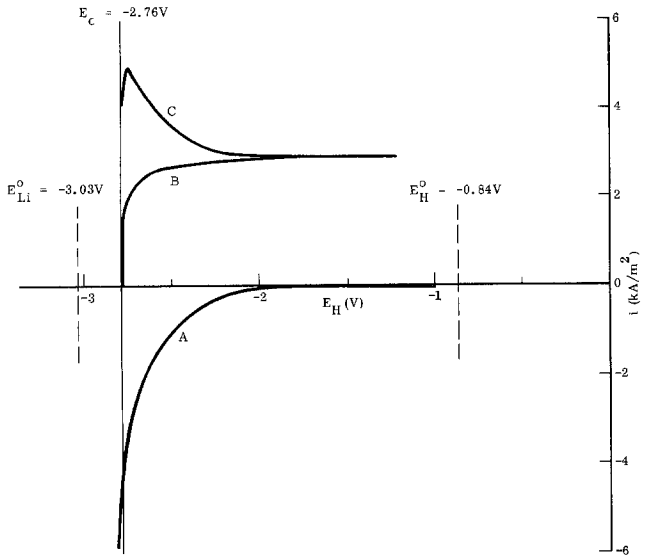


Fig. 7. Composite figure showing hydrogen evolution polarization plot on Li (curve A), actual mixed potential polarization plot for Li (curve B), and generated anodic dissolution plot of Li (curve C) in 4.1M LiOH at 298°K.

Fig. 7. Two interesting aspects are illuminated. First and most important, from the point of view of the Li/H_2O cell, is the fact that the rate-controlling process in the corrosion of Li is the polarization at the H_2 evolution reaction sites. In other words, the corrosion is under cathodic control. The activation energy for the rate-controlling step of the Li corrosion reaction as calculated above therefore clearly represents the energy for the H_2 e.r. This leads to the assumption that electrolyte additives which polarize the H_2 e.r. could significantly inhibit the corrosion reaction. The second aspect is the H_2-free polarization curve C. The configuration of this curve is quite unlike that generally observed for the anodic dissolution of metals in aqueous electrolytes. Here, the highest dissolution rate occurs in the vicinity of OCV. At about −2.2V a situation resembling a limiting current takes effect. This then defines the maximum usable current which can be drawn from the system under specific conditions of molar LiOH, solution flow rate, and temperature.

Film properties.—In the past, the high reactivity of Li with H_2O has discouraged studies of the metal immersed in aqueous solution. Experiments in saturated LiCl at low temperatures have been reported (15) but no attempt was made to examine the properties of the film. There is however information available on the reaction of Li with H_2O vapor. Irvine and Lund (6) studied the reaction at a partial pressure of H_2O vapor up to 12.6 mm Hg, and Deal and Svec (7) at 22-100 mm Hg. There is consensus that when exposed to H_2O vapor, Li becomes covered initially with a thin coherent glassy black film shown by x-ray to be LiOH. The formation of this thin film (its thickness has not been reported) follows a logarithmic rate law. Therefore it is assumed that it is protective of the underlying metal. After some hours exposure to moisture, a white layer of $LiOH \cdot H_2O$ grows over the outer surface, and the reaction rate then obeys a linear rate law. This observation at first suggests that the LiOH layer becomes permeated by cracks or pores so that the H_2O can have access to the metal. However, Evans (16) has pointed out that a linear rate law will hold during oxidation if lattice diffusion is the controlling process as long as the diffusion distance is constant. Irvine and Lund took a modified approach to this model. They proposed a duplex film where the layer adjacent to the metal remains protective and of constant thickness and, as reaction proceeds, the outer portion becomes hydrated to form the porous $LiOH \cdot H_2O$. This outer layer would then be freely permeated by H_2O and OH^-. The $LiOH \cdot H_2O$ represents the final reaction product. Eventually all the Li is converted to this form via the intermediate black film.

The reaction of Li in H_2O vapor has also been studied at elevated temperatures (8). Again, LiOH was identified as the product which forms directly adjacent to the metal with $LiOH \cdot H_2O$ as an outer layer.

Although Li immersed in aqueous LiOH poses a different situation because the reaction product can dissolve freely into the solution, certain similarities have been noted. In place of the thin shiny black film, a fairly thick dull gray covering is observed. Also, as reported in the vapor studies, a loosely adherent product which has been identified as $LiOH \cdot H_2O$ overlays some areas. This material which dissolves into the electrolyte could be considered the final reaction product. However, in contradistinction to the vapor case, it does not seem to play an important role in the reaction of the metal with aqueous solution.

Certain important differences exist between Li exposed to H_2O vapor and Li immersed in LiOH solutions. Unlike the black film, the gray film cannot be analyzed *in situ*. Although x-ray analysis shows it to be a mixture of anhydrous and hydrous LiOH, it cannot be stated categorically that morphological adjustments are absent after specimen removal from the solution or in the drying process. However, the film does not appear to change color or undergo any other alterations. More importantly, one may postulate that a duplex film exists in both systems, but in the present case the protective film directly adjacent to the metal probably comprises a very thin layer of an oxide possibly intermixed with adjacent LiOH. In a previous study of anodic passivation (4), thermodynamic considerations were given to support the proposition that Li_2O can exist at least transiently within pores in the LiOH film. Also Vermilyea (17) suggests that unstable higher oxidation states may form on metals undergoing anodic oxidation. The corrosion rate of Li in aqueous solution is so high that a situation very similar to anodic oxidation exists.

The basis for proposing the duplex film rests on the following observations. It has previously been shown that in the active polarization region, *i.e.*, from OCV to *ca.* 300 mV anodic, a linear i-η relationship is obtained (4, 5). Activation polarization for the Li dissolution reaction is negligible, and therefore the observed polarization is predominantly *IR* across the film. Recent work in these laboratories has shown that over the same polarization range, with fixed temperature and flow rate, the film thickness remains essentially constant. This thickness is in the range 6-9 $\times$ 10^{-2} cm and its value is dependent on molar LiOH (18). To support the high OCV corrosion current densities reported in this paper, in 3.5M LiOH i_{corr} = 5.92 kA m^{-2} (projected) and in 4.5M LiOH i_{corr} = 2.82 kA m^{-2} (projected), requires that the film must be permeated with electrolyte. Knowing the conductivity of the LiOH solutions, it can be calculated that approximately 5% of the projected area will comprise electrolyte. One may hypothesize that the flooded pores or fissures in the film terminate at bare Li sites, but because of the high reactivity of Li it seems logical to assume that a protective layer exists at the pore extremities. Since the actual current density within the pores must be about 20 times greater than the values given above, it follows that the protective layer must have excellent electronic or ionic conductivity. This layer (the inner portion of the duplex film) sustains such high flux rates with minimum polarization that in all likelihood it is only a few molecular layers thick. The proposed model therefore resembles that suggested by Irvine *et al.* except for differences of film thickness and perhaps morphology. The main difference is the composition of the "inner" protective layer.

In summary, a duplex film model is proposed. It comprises an outer porous layer permeated with electrolyte which provides a medium for the mass trans-

port of ions and/or gas from and to active sites. This overlays a thin inner conducting layer adjacent to the metal. The model which is based on corrosion experiments described in this paper and prior anodic polarization studies seems at the present to satisfactorily describe the system. Exact morphological and structural information about the protective film cannot be obtained by direct inspection because fine changes probably occur on removal of the specimen from solution.

Further, even if improved techniques could be developed, the film is too thick for sensitive inspection by, say, Auger or ESCA spectroscopy. Fortunately, fairly simple electrochemical experimentation gives extremely reproducible results and diagnostic techniques now being used on the system (18) may in the future provide additional insight.

Conclusions

The corrosion of Li in LiOH solutions has been considered from the point of view of the kinetics of the over-all dissolution reaction, the electrochemistry of the concurrent Li dissolution and H_2 reduction reactions, and the features of the protective film on the metal. A rate expression for the Li-H_2O reaction has been obtained, and the temperature dependence of the rate constant can be described by the Arrhenius equation. The apparent activation energy and the enthalpy of activation for the H_2 e.r. on Li are reported for the first time. It has been shown that the polarization of the H_2 evolution at the Li surface is the rate-limiting process rather than the Li dissolution reaction. The kinetic parameter, α, for the H_2 e.r. was found to compare with published values of it on metals such as Mg and Zn. Equations have been derived which permit calculation of (*i*) the OCV corrosion rate of Li in LiOH solution, and (*ii*) the corrosion rate when the metal is anodically polarized. These equations assist in the determination of optimized control points for the Li/H_2O electrochemical cell. An unusual feature of the electrochemistry of the system is revealed when the H_2-free anodic polarization curve is plotted. This curve has a configuration quite different to that normally observed for metals undergoing anodic dissolution. The effect which is reported here, but is not diagnosed in detail at this time, may perhaps be described as anodic polarization on a deenergized electrode. To account for the chemical and electrochemical characteristics of the system, a duplex film model is proposed. It comprises an "inner" presumably thin coherent layer of oxides and an outer porous layer of admixed LiOH and LiOH·H_2O. This model in conjunction with the kinetics of the H_2 e.r. helps to explain the coexistence of Li and H_2O in aqueous LiOH solution without violent reaction.

Acknowledgment

The authors wish to thank Professor E. Gileadi of Tel Aviv University for many stimulating discussions concerning this paper. This work was supported in its entirety by Lockheed Missiles & Space Company, Incorporated.

Manuscript submitted Oct. 20, 1976; revised manuscript received Jan. 21, 1977.

Any discussion of this paper will appear in a Discussion Section to be published in the December 1977 JOURNAL. All discussions for the December 1977 Discussion Section should be submitted by Aug. 1, 1977.

Publication costs of this article were assisted by Lockheed Missiles & Space Company, Incorporated.

REFERENCES

1. D. D. Kemp, E. L. Littauer, W. R. Momyer, and J. J. Redlien, Proceedings of the 11th IECEC, pp. 462-466, Lake Tahoe (1976).
2. D. N. Bennion and E. L. Littauer, *This Journal*, **123**, 1462 (1976).
3. E. L. Littauer and K. C. Tsai, Submitted to *J. Power Sources*.
4. E. L. Littauer and K. C. Tsai, *This Journal*, **123**, 771 (1976).
5. E. L. Littauer and K. C. Tsai, *ibid.*, **123**, 964 (1976).
6. W. R. Irvine and J. A. Lund, *ibid.*, **110**, 141 (1963).
7. B. E. Deal and H. J. Svec, *J. Am. Chem. Soc.*, **75**, 6173 (1953).
8. J. Besson and W. Muller, *C. R.*, **247**, 1869 (1958).
9. N. E. Khomutov, Editor, "Electrodeposition of Metals and Alloys," pp. 18-19, Russian Achievement of Science: Chemistry Series (Electrochemistry), Issue 1, Moskow (1966).
10. S. Barnartt, *Electrochim. Acta*, **13**, 901 (1968).
11. F. Basolo and R. G. Pearson, "Mechanisms of Inorganic Reactions," pp. 74-77, John Wiley & Sons, Inc., New York (1963).
12. M. D. Zhoulder, *Zh. Prikl., Khim.*, **31**, 711 (1958).
13. J. A. V. Butler, Editor, "Electrical Phenomena at Interfaces," pp. 18-24, Univ. Microfilm Inc., Ann Arbor (1951). An alternate reference is K. J. Vetter, "Electrochemical Kinetics," Chap. II, Academic Press, New York (1967).
14. K. J. Vetter, "Electrochemical Kinetics," pp. 516-536, Academic Press, New York (1967).
15. J. Ambrus, Chemistry Research Dept. Naval Ordnance Laboratory, White Oak, Md., Report No. NOL TR 72-138 (August 1972).
16. U. R. Evans, *This Journal*, **91**, 547 (1947).
17. D. A. Vermilyea, in "Advances in Electrochemistry and Electrochemical Engineering," P. Delahay and C. Tobias, Editors, Vol. III, pp. 217-219, Interscience Publishers, New York (1963).
18. E. L. Littauer, K. C. Tsai, and R. P. Hollandsworth, To be submitted to *This Journal*.

Correlations Between ^{1}HNMR Spectroscopy and Transport Properties in Molten Pyridinium Salts

David S. Newman,* Richard T. Tillack, David P. Morgan, and Wai-Ching Wan

Department of Chemistry, Bowling Green State University, Bowling Green, Ohio 43403

ABSTRACT

The equivalent conductance, viscosity, and ^{1}HNMR spectra of several molten pyridinium salts were measured as a function of temperature. The spectra of N-methylpyridinium chloride, bromide, and iodide were measured relative to an external standard of dimethylsulfone. The spectra of 4-methylpyridinium chloride and bromide were measured relative to an internal standard of hexamethyldisiloxane. No changes in chemical shifts or line widths as a function of temperature were observed, but there were significant changes in chemical shifts with change of halide ion. From correlations between these data and energies of activation for conductance and viscosity we conclude that N-methylpyridinium chloride, bromide, and iodide are most likely completely dissociated into pyridinium and halide ions, but that complex species are present in 4-methylpyridinium chloride and bromide melts.

The molten organic salts studied in this investigation were N-methylpyridinium chloride (I), N-methylpyridinium bromide (II), N-methylpyridinium iodide (III), 4-methylpyridinium chloride (IV), and 4-methylpyridinium bromide (V). They are shown in Fig. 1. These pyridinium salts are technologically and theoretically important for a variety of reasons, but especially because they are low melting, relatively stable, and can be studied by ^{1}HNMR techniques (1, 2).

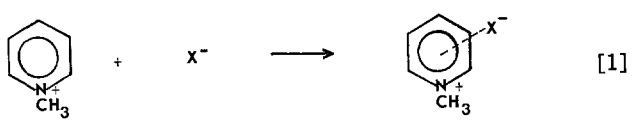
Many investigators have debated the propriety of using organic melts as general models for the molten state because of the possible presence of complex ions. In their discussion of molten alkyl ammonium salts, Janz, Reeves, and Ward (3) suggest that the rather striking similarity between the energy of activation for viscosity, E_η, and the energy of activation for equivalent conductance, E_Λ, arose from one of two causes. Either a complex was forming in the melts whose lifetime was relatively long compared with the time it took for both the electrical and mechanical stresses to relax, or steric factors, such as size, shape, and ionic orientation, made it very difficult for the ions to move past each other. The authors favored the latter explanation.

It should be kept in mind that E_η is considerably larger than E_Λ for molten alkali metal halides and many other molten inorganic halides (4). Viscosity involves the cooperative movement of both anion and cation and its energy of activation is largely determined by the ion with the greater radius. Conductance is largely due to the mobility of the smaller species and therefore requires less energy.

Lind, Abdel-Rehim, and Rudich studied another series of alkyl ammonium salts having particularly symmetrical cations and anions (Pr_4NBF_4 and Pr_4NPF_6 among others) and observed quite similar values for E_η and E_Λ in each of their melts (E_η always being slightly larger than E_Λ) (5). These authors suggested the hydrocarbon chains block or clog interstices of the melts, and cause a great deal of interionic friction. The conductance in these melts is affected to a greater extent than the viscosity because there is a transfer of neighboring ions in opposite directions during conduction while viscosity arises largely from the macroscopic movement of one layer of liquid past another with momentum transfer occurring via phonons. In other words, the alkyl chains prevent anions from passing cations, but affect the phonons to a much lesser extent.

The pyridinium salts we have chosen for study are also low melting organic compounds, but without long hydrocarbon chains. They do contain several sets of protons whose magnetic environments are vulnerable to the forces of interaction in the melts and can serve as spectroscopic probes of the molten state. We selected salts with cations and anions differing in size to foster differences between E_η and E_Λ, if they exist, and account for these differences by direct observation of changes in chemical shift of appropriate protons. On the other hand, if E_η and E_Λ were nearly equal in the pyridinium salts despite the ion size differences and the absence of hydrocarbon chains, this could be construed as a more general property of molten organic salts.

If a complex species were to form between the methylpyridinium ion and the halide ion it could do so in one of two ways. A dissociated cation and anion can combine to form an ion pair, as described by Eq. [1], or the species bonded to the nitrogen can dissociate and combine with the halide producing an R^+X^- ion pair plus a neutral picoline or pyridine as described by Eq. [2]



In either case, the magnetic environment around at least one set of protons will change as a result of com-

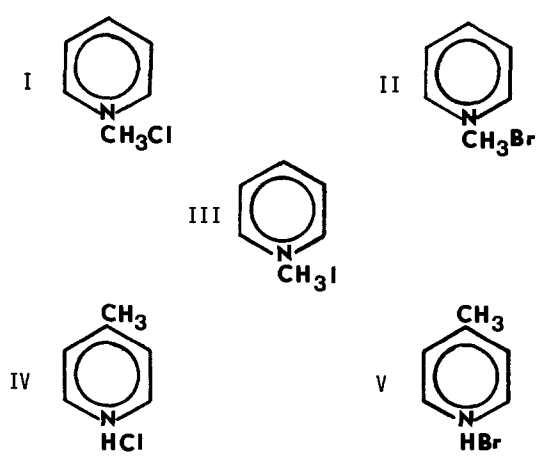


Fig. 1. N-methylpyridinium chloride (I), N-methylpyridinium bromide (II), N-methylpyridinium iodide (III), 4-methylpyridinium chloride (IV), 4-methylpyridinium bromide (V).

* Electrochemical Society Active Member.

Key words: molten pyridinium salts, conductance, viscosity, ^{1}HNMR.

plex formation and produce a temperature-sensitive ^{1}HNMR spectrum provided the energy barrier between dissociated ions and ion pairs is great enough.

Most authors divide the time scale for proton exchange into three regions. At relatively low temperatures a slow exchange region exists in which two distinct spectra, characteristic of each isolated species, are obtained. As the temperature is raised an intermediate exchange region occurs in which the peaks coalesce, broaden, and possibly change their positions making it comparatively easy to make a rough approximation of the rate constant. Finally, a fast exchange region occurs in which the coalesced peak (or peaks) narrow until a limiting single line width is reached.

In the intermediate exchange region the rate constant is given by the equation

$$k_A = \tau_A^{-1} = \sqrt{2}\pi\Delta\nu_0 \qquad [3]$$

where τ_A^{-1} is the reciprocal of the mean lifetime of the proton or protons in magnetic environment A and $\Delta\nu_0$ is the separation (chemical shift in hertz) before coalescence (9). In the fast exchange region τ_A^{-1} is given by Eq. [4]

$$\tau_A^{-1} = 4\pi n_A n_B (\Delta\nu_0)^2 (W^E - W^\circ)^{-1} \qquad [4]$$

where n_A and n_B are the concentrations of species with magnetic environments of type A and B, respectively, W° is the limiting single line width, while W^E is the line width at temperature T (10).

Since k_A (or τ_A^{-1}) is related to the enthalpy of activation by the equation

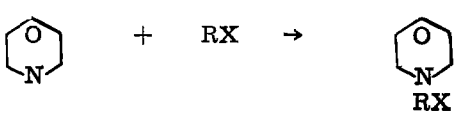
$$k_A = \left(\frac{kT}{h}\right) \exp\left(\frac{-\Delta H^\ddagger}{RT} + \frac{\Delta S^\ddagger}{R}\right) \qquad [5]$$

a measurable line width or peak position change would be expected over a 50° temperature interval if $\Delta H^\ddagger$ is 40 kJ/mole or greater and $\Delta S^\ddagger$ is not too large (11-13).

From previous data and the fact that the melt is at a relatively high temperature, we assumed our melts were in the fast exchange region and the principal experimental results, if complex species were present, would be a change of line width as temperature rose provided the lifetime, τ, of each species was long enough.

Experimental Details

Preparation of the salts.—All of the salts were synthesized in essentially the same way using a technique first described by Rozdhestvenskii and Brode (6) and modified by Newman *et al.* (1). The syntheses can all be summarized by Eq. [6]



[6]

The purity of each salt was ascertained by C, H, N analyses, infrared spectrum, and melting point.

Density measurements.—The density of each molten salt was measured as a function of temperature using a modified Lipkin bicapillary arm pycnometer. A detailed description of the density measurements appear elsewhere (7), but because the densities of salts II, III, and V are needed for the discussions that follow they are given, as a function of temperature, in Table I. The density of salt III has not been reported elsewhere.

Table I. Density as a function of temperature
$\rho(g/cm^3) = a + bT(°K)$

Salt	a	$-(b \times 10^3)$	Temperature range, °K
II	1.723	0.6528	398-468
III	1.943	0.688	390-460
V	1.703	0.7004	430-518

Viscosity measurements.—Viscosity was measured as a function of temperature using a modified Ostwald viscometer. This kind of viscometer was found to be very simple to use and precise enough for our purposes.

Dry solid salt was introduced into a large reservoir attached to one arm of the viscometer. The filled viscometer was then immersed in a constant temperature bath (± 0.10°) of Dow Corning 710 oil and the salt was allowed to melt. Viscosity readings were made at 5° intervals after allowing the bath to equilibrate for 15 min at each temperature. A minimum of two series of viscosity measurements were made with each salt.

Conductivity measurements.—The specific conductance, κ, of each salt was measured as a function of temperature using an Industrial Instruments bridge at a frequency of 1000 Hz. The salts were contained in a Pyrex capillary cell similar to the one described by Janz (8) and modified by Newman *et al.* (1). The cell constants ranged from 150 to 1500 cm^{-1} depending on the diameter of the capillary. A minimum of two series of conductance measurements was made on each of the molten salts. Conductivity readings were taken at 10° intervals over a temperature range bounded at one end by the temperature at which the melt froze (often below the normal melting point) and at the other by a temperature just below the boiling or decomposition point of the salt. The system was allowed to equilibrate at each temperature for 15 min.

^{1}HNMR spectra.—The ^{1}HNMR spectra were obtained using the variable temperature probe of a Varian A60 A NMR machine. Two techniques were used. The first employed hexamethyldisiloxane as an internal standard contained in a sealed 5 mm NMR sample tube and the second, more satisfactory technique, used dimethylsulfone as an external standard. For the external standard experiments concentric NMR tubes with circular cross-sectional area were used to contain both the external standard and sample. The capillary containing the dimethylsulfone had an ID of 1 mm and was inserted into the standard 5 mm NMR tube, surrounded by salt, in such a way that its axis was held parallel to the axis of the outer tube. This arrangement minimized errors due to differences in bulk magnetic susceptibility between sample and standard. The NMR machine maintained a temperature constant to within ± 1° during a ^{1}HNMR spectral measurement.

Results

The ^{1}HNMR spectrum of the salt III cation is shown in Fig. 2. The α, β, γ, and methyl peaks are so marked. The sweep time is 500 sec, the sweep width is 1000 sec^{-1}, and the external reference is $CH_3—\overset{\overset{O}{\|}}{\underset{\underset{O}{\|}}{S}}—CH_3$.

The chemical shifts, δ, and the difference in chemical shifts, Δ, of various sets of protons in salts I, II, and III relative to the external standard, are listed in Table II. Neither the line widths nor the chemical shifts of

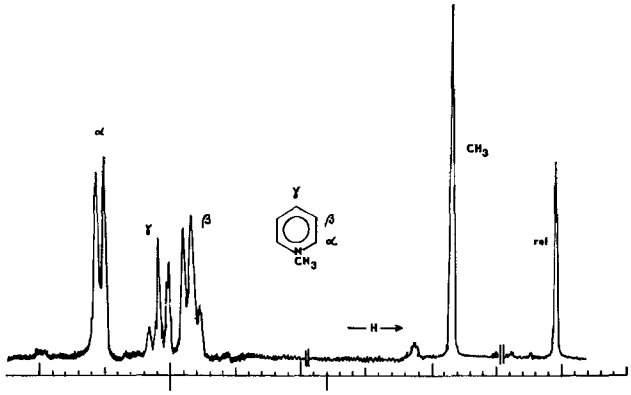


Fig. 2. The ^{1}HNMR spectrum of molten N-methylpyridinium iodide.

Table II. Chemical shift, δ, relative to the external standard $(CH_3)_2SO_2$, ppm

Salt	CH_3-N	α*	γ	β	$\Delta_{\alpha-\beta}$
III I^-	2.2	6.80	6.41	6.00	0.80
II Br^-	2.2	6.81	6.28	5.86	0.95
I Cl^-	1.5	6.2	5.6	5.1	1.1

* Measured from the large upfield peak of the doublet.

these protons were observed to change as a function of temperature so spectra at only one temperature are reported.

Table III lists δ and Δ values for the remaining two salts relative to the internal standard hexamethyl disiloxane, while the ^{1}HNMR spectrum of the 4-methylpyridinium ion is shown in Fig. 3.

The equivalent conductances of salts I-V can be described by the equation

$$\ln \Lambda = P + q/T°K \quad [7]$$

The constants, P and q, and the temperature range over which each molten salt was studied are given in Table IV.

The viscosities of salts II and III, described by the equation

$$\ln \eta = r + s/T°K \quad [8]$$

r and s together with the temperature range over which the conductance was measured are listed in Table V.

Discussion

The ^{1}HNMR spectra of salts I, II, III show a definite downfield shift in δ (*vs.* $CH_3\overset{O}{\underset{O}{S}}-CH_3$) as a function of halide ion size. Since the cation is the same in all three salts the changes in δ must be due to intermolecular interactions rather than intramolecular changes. The downfield shift (deshielding) increases as the anion radius increases which means the principal interactions are steric and not electrostatic. If they were electrostatic the downfield shift would increase in the order $Cl^- > Br^- > I^-$. Because of the strict packing requirements, we think the I^- ions passing by the methylpyridinium ions perturb the ring protons and distort the ring current by compressing the molecular orbitals. The Br^- ion is smaller than the I^- and therefore distorts the ring current and ring protons slightly less than the I^-, but considerably more than the Cl^-. The requirements for packing the Cl^- and the methylpyridinium ions in melt I are the least stringent, resulting in relatively little cation distortion. This would certainly account nicely for all of the chloride peaks being shifted upfield relative to the corresponding peaks in the bromide and iodide melts. This conjecture is strengthened by comparing the chemical shifts of the α, β, and γ peaks of salt II with the corresponding peaks of the salt dissolved in DMSO where the ionic interactions are considerably more feeble (1, 14). All of the peaks of the dissolved salt are further upfield than the corresponding peaks in the melt relative to an internal standard of TMS. The different Δ values in these melts are much more difficult to account for in detail. A plausible explanation is that in III each cation is being perturbed by at least two I^- ions, probably acting in concert. This means that the CH_3 and α protons on the nitrogen end of the molecule, where presumably the charge is located, as well as the β and γ protons on the opposite end of the molecule, are all slightly distorted by interionic interactions at any instant of time. In the chloride melt, the principal perturbation occurs at or in vicinity of the positive charge, causing a slight relative deshielding of the CH_3 and α protons, but leaving the β and γ protons relatively unperturbed. This explanation accounts for the fact that $\Delta_{\alpha\text{-}CH_3}$ is the same in all three salts, but $\Delta_{\alpha-\beta}$, $\Delta_{\alpha-\gamma}$, and $\Delta_{\beta-\gamma}$ are all larger in the chloride melt than the iodide melt. The Br^- probably perturbs both ends of the molecule simultaneously, but there is more free space at the end of the molecule opposite to the charge than in the iodide melt. Since the ions are less crowded than in III, weaker interactions occur and the values for $\Delta_{\alpha-\beta}$ and $\Delta_{\alpha-\gamma}$ will be less than in the chloride melt, but greater than in the iodide melt.

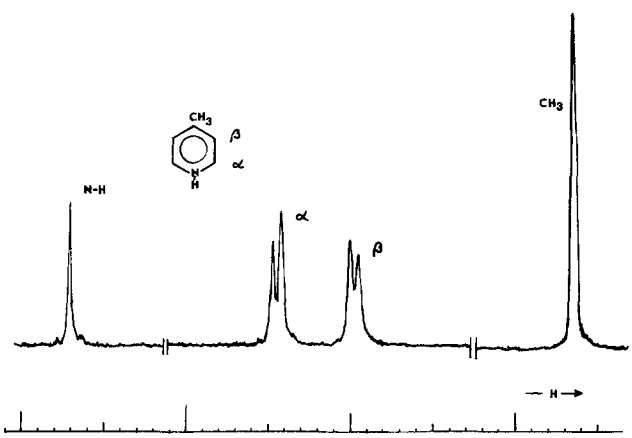


Fig. 3. The ^{1}HNMR spectrum of molten 4-methylpyridinium bromide.

Table III. Chemical shift, δ, relative to the internal standard, $(CH_3)_3SiOSi(CH_3)_3$, ppm

Salt	α	β	CH_3	H	$\Delta_{H-\alpha}$	$\Delta_{\alpha-\beta}$
V Br^-	8.98	8.03	2.61	15.30	6.32	0.96
IV Cl^-	8.16	7.16	1.66	15.36	7.20	1.0

Table IV. Equivalent conductance data
$\ln \Lambda = P + q/T$

Salt	P	$-(q \times 10^{-3})$	Temperature range, °K
I	8.818	2.747	418-463
II	8.309	2.60	433-474
III	9.47	3.15	396-450
V	7.79	2.45	435-475

Table V. Viscosity data (poise)
$-\ln m = r + s/T$

Salt	r	s	Temperature range, °K
II	9.35	-2.85×10^3	435-475
III	6.16	-3.24×10^3	400-450

The most interesting feature of the ^{1}HNMR spectra of the two 4-methylpyridinium salts is the large difference in $\Delta_{H+\alpha}$ between the Cl^- and the Br^- melts. This is especially intriguing when it is noted that the $\Delta_{\alpha-\beta}$ values are identical. We shall return to this point later.

The ^{1}HNMR spectra from all salts showed no reproducible temperature dependent chemical shift or line broadening greater than 0.03 ppm over a temperature range of at least 50°, with the possible exception of the H-N peak in salt V which narrowed approximately 0.03 ppm.

The lack of a temperature sensitive line width or δ is significant because it implies that complexes whose energy barriers are greater than approximately 40 kJ/mole cannot be present in the melt. This minimum value for the energy barrier is estimated from Eq. [5] and the fact that an A60 ^{1}HNMR machine can read 0.03 ppm at a 500 sec^{-1} sweep width. Values for $\Delta G^{\ddagger}$ ($\approx \Delta H^{\ddagger}$) are introduced into Eq. [5] and $k_A = \tau_A^{-1}$ is solved for. If τ_A is greater than 10^{-7} sec, a narrowing of

Table VI. Energies of activation

Salt	E_η (kJ)/mole	E_Λ (kJ)/mole	E_κ (kJ)/mole
N-methpyrBr	23.5	21.5	17.6
4-methpyrBr	—	20.4	17.6
N-methpyrI	26.0	25.8	24.7
N-methpyrCl	—	23.0	23.0

the band at half-height should be visible over the temperature range 400°-450°K. This idea can be seen more clearly by observing Eq. [4] which requires $W^E - W^\circ$ to approach zero as τ_A^{-1} approaches infinity.

The energies of activation for the various transport properties studied are summarized in Table VI.

A comparison of E_η with E_Λ in melt III shows that E_η is just slightly greater than E_Λ. A similar relationship between energies of activation is observed in melt II. This is the sort of behavior observed by previous workers for the alkylammonium salts and strongly suggests that it may be a general property of molten organic salts. There are no long chains to block interstices in the pyridinium melts and the Br^- and N-methylpyridinium cation differ in size, nevertheless, strong interactions and a high degree of cooperative movement are occurring.

The most striking result of our transport studies is seen by comparing Λ for 4-methylpyridinium bromide with Λ for N-methylpyridinium bromide over similar temperature ranges. It is immediately obvious that the N-methyl salt is the better conductor. At 430°K there is a 16.1% difference while at 470°K there is an 18.4% difference. We think this difference is due to the presence of complex species in melt V that are absent in melt II.

We think the chemical shift difference between salts IV and V also arises principally from complex ion formation. This conjecture is strengthened by noting that the α, β, and CH_3 peaks are upfield relative to the α, β, and CH_3 peaks of the Br^- melt, but, the $N\text{-}H^+$ peak is downfield. Moreover, Bloom and Reinsborough (15) gave strong evidence, from ultrasonic absorption studies, that molten pyridinium chloride is associated. It is reasonable to assume 4-methylpyridinium chloride behaves analogously. We think that if complexation is occurring in melt IV it is also occurring in melt V, but the complexes are more labile. The density of this salt is slightly less than the density of the N-methylbromide salt at corresponding temperatures. The only plausible explanation for the large difference in Λ that is consistent with our ^{1}HNMR data is that fewer species are present to carry the current because of complex formation between the bromide ion and either the proton or the methylpyridinium ion.

In order to further refine our model of the pyridinium melt we define a complex ion as any species in which the individual particles carry out identical translational movements while diffusing. The difference in the activation energies for equivalent conductance and specific conductance is

$$E_\Lambda - E_\kappa = \alpha RT^2 \qquad [9]$$

where α is the expansivity of the melt. To a rough approximation the energy of activation, E_κ, is equal to the energy a species must acquire to pass over an energy barrier from one site to another during translational motion in an electric field. If one assumes the Nernst-Einstein equation to hold at least approximately, this same energy is required for diffusion. Based on these ideas we make the assumption that if ΔH°_{+-}, the thermodynamic enthalpy of complex formation, is less than the enthalpy of activation for this species to diffuse, the complex will fly apart upon absorption of this amount of energy rather than pass over the barrier. The energy of activation then determines the minimum energy a complex can have and still move through the melt as a single entity. We found that in the iodide melt $E_\kappa = 25$ kJ/mole while in the bromide melt $E_\kappa = 17.5$ kJ/mole. We can therefore say, with confidence, that it is highly unlikely for complex species with ΔH°_{+-} less than 25 kJ/mole or greater than 40 kJ/mole to be present in the iodide melt. It is also very unlikely for complex species with ΔH°_{+-} less that 17.5 kJ/mole or greater than 40 kJ/mole to be present in the bromide or chloride melts. The 40 kJ/mole maximum arises from the assumption that to remain intact for approximately 10^3 diffusional jumps, or 10^{-7} sec, $\Delta H^\circ_{+-} \geqq \Delta H^\ddagger = 40$ kJ/mole. Stating it differently, no complex species are present whose lifetimes are less than approximately 10^{-10} sec in the bromide melt, 10^{-9} sec in the iodide melt, or greater than approximately 10^{-7} sec in any melt.

In salts IV and V, where there is a labile proton, it is very possible for a complex to exist that is stable enough to lower the conductivity relative to the corresponding N-methyl salt, but have a lifetime that is short compared with ^{1}HNMR resolution times. Therefore, the existence of H^+X^- ion pairs or $R\ldots H^+\ldots X^-$ ion pairs in the 4-methyl chloride and 4-methyl bromide melts is not excluded by our data.

In salts I, II, and III we think ion pairs or complex species probably do not exist. This conjecture arises from the narrow energy range allowable, the lack of a temperature sensitive peak width, the observed change in δ with change in halide ion, the near equivalence of E_η and E_Λ for both bromide and chloride melts, and the large difference in equivalent conductance between 4-methyl and N-methylpyridinium bromide.

Experimental Errors

We estimate that both the specific conductance and density data are accurate to ±1%. This figure includes errors due to impurities in the salts, decomposition products, difficulties in reading the salt level in the pycnometer, etc. This means the equivalent conductances are accurate to ±2%. We estimate the measured viscosity to be accurate to ±3% because a viscometer reading and a density reading are required. The error in the ^{1}HNMR data is difficult to ascertain. Our machine can be maintained at a constant temperature of ±1° at the elevated temperatures, but the change in noise level, variation in samples spin rate, etc. that arise near the top of the useful temperature range of the variable temperature probe of an A60 A NMR machine are uncertain. We therefore hesitate to rely on any chemical shift differences less than 0.03 ppm.

Summary and Conclusion

The equivalent conductance, viscosity, and ^{1}HNMR spectra of several fused pyridinium salts were investigated with the intention of correlating transport properties with spectral properties. From these correlations we were able to say with some assurance that 1-methylpyridinium iodide and bromide are completely dissociated, but that 4-methylpyridinium chloride and bromide probably contain complex ions. In addition, we have shown that ^{1}HNMR spectroscopy is a useful tool in elucidating the properties of molten organic salts. Finally, it seems that approximate equality of E_η and E_Λ may indeed be a property of molten organic salts.

Acknowledgment

The authors wish to thank the National Science Foundation Summer Institute for High School Teachers at Bowling Green State University for supporting this research. We also wish to thank the Faculty Research Committee at Bowling Green for contributing funds to this work. Finally, we wish to thank Ivan DenBesten and Tom Kinstle for their help with the ^{1}HNMR spectra.

Manuscript submitted July 16, 1976; revised manuscript received Jan. 11, 1977. This was Paper 384 presented at the Washington, D. C., Meeting of the Society, May 2-7, 1976.

Any discussion of this paper will appear in a Discussion Section to be published in the December 1977 JOURNAL. All discussions for the December 1977 Discussion Section should be submitted by Aug. 1, 1977.

Publication costs of this article were assisted by Bowling Green State University.

LIST OF SYMBOLS

η	viscosity
Λ	equivalent conductance
κ	specific conductance
E_i	energy of activation ($i = \kappa, \Lambda, \eta$)
k_A	rate of constant for dissociation of species A
k	Boltzmann constant
h	Planck's constant
$\Delta H^\ddagger$	enthalpy of activation
$\Delta S^\ddagger$	entropy of activation
$\Delta G^\ddagger$	free energy of activation
ΔH°	enthalpy of formation of complex
τ_A	lifetime of species A
ρ	density
δ	chemical shift
Δ	difference in chemical shift
$\Delta\nu_0$	separation of peaks before coalescence
W°	limiting single line width
W^E	single line width at temperature T
n_i	concentration of species i
α	expansivity of melt

REFERENCES

1. D. S. Newman, W. Rohr, D. Kirklin, and H. D. Frame, *This Journal*, **119**, 797 (1972).
2. V. C. Reinsborough, *Aust. J. Chem.*, **23**, 1473 (1970).
3. G. J. Janz, R. D. Reeves, and A. T. Ward, *Nature (London)*, **204**, 1188 (1964).
4. H. Bloom and E. Heymann, *Proc. Roy. Soc. London, Ser. A*, **188**, 392 (1947).
5. J. E. Lind, H. A. Abdel-Rehim, and S. W. Rudich, *J. Phys. Chem.*, **70**, 3610 (1966).
6. M. S. Rozhdestvenskii and L. M. Brode, *J. Appl. Chem. USSR*, **10**, 722 (1937).
7. D. S. Newman, D. P. Morgan, and R. T. Tillack, *J. Chem. Eng. Data*, **21**, 279 (1976).
8. G. J. Janz, "Molten Salt Handbook," Academic Press Inc., New York (1967).
9. R. G. Wilkinson, "The Study of Kinetics and Mechanism of Reactions of Transition Metal Complexes," Chap. 3, Allyn and Bacon, Boston (1974).
10. A. Allerhand, H. S. Gutowsky, J. Jones, and R. A. Meinzer, *J. Am. Chem. Soc.*, **88**, 3185 (1966).
11. J. W. Emsley, J. Feeney, and L. H. Sutcliffe, "High Resolution NMR Spectroscopy," Vol. 1, Pergammon Press (1966).
12. F. A. L. Anet and V. J. Basus, *J. Am. Chem. Soc.*, **95**, 4424 (1973).
13. F. A. L. Anet and J. J. Wagner, *ibid.*, **93**, 5266 (1971).
14. A. K. Sheinkman, L. M. Kapkan, L. G. Gahk, E. V. Titov, S. N. Baranov, and A. N. Yost, *Dokl. Akad. Nauk USSR*, **193**, 366 (1970).
15. H. Bloom and V. C. Reinsborough, *Aust. J. Chem.*, **22**, 519 (1969).

Technical Notes

Continuous Electrochemical Preparation of Chlorotrifluoroethylene

S. Wawzonek*

Department of Chemistry, The University of Iowa, Iowa City, Iowa 52242

and Stephen Willging

Loras College, Dubuque, Iowa 52001

The monomer chlorotrifluoroethylene is prepared commercially in a batch process by treating 1,1,2-trichloro-1,2,2-trifluoroethane (Freon 113) with zinc dust. The present work finds that the chemical method can be replaced by a continuous electrochemical process with over-all energy saving in the production of zinc at a cathode and with the formation of a more useful by-product, chlorine, at the anode. The cell used was similar to that described for the production of dichloroethylene from 1,1,2,2-tetrachloroethane (1). A copper wire was used as the cathode and a carbon rod was employed as the anode. The electrolyte was an aqueous solution of zinc and sodium chlorides. Deposition of the zinc on the copper cathode was followed by a reaction with Freon 113 and formation of chlorotrifluoroethylene

$$CF_2ClCFCl_2 + Zn \rightarrow CF_2{=}CFCl + ZnCl_2$$

This reaction is slow at the boiling point of Freon 113 (47.7°C) and the deposition of the zinc was therefore done intermittently; when the majority of the zinc had disappeared from the cathode, electrolysis was resumed.

The yield of the product (44%) was determined by converting the olefin to the dibromo compound which is higher boiling (92.9°C) than the olefin (−23°C). The value reported is actually a minimal one since some of the olefin is polymerized in this reaction.

Attempts were made to increase the rate of the dehalogenation of Freon 113 by forming zinc amalgam electrochemically instead of the metal. The rate proved to be very low since none of the olefin was actually isolated.

The direct electrochemical reduction of Freon 113 to chlorotrifluoroethylene was also studied. Such a reaction is reported to occur in potassium acetate solution and forms the olefin in a 74% yield (2). Using conditions which would be more suitable for the continuous formation of chlorotrifluoroethylene, the electrochemical reduction of Freon 113 was studied at a mercury cathode in 0.2*N* ammonium chloride-60% methanol. Freon 113 in this medium shows a polarographic wave at −1.34V *vs.* (Hg pool). The yield of olefin obtained under these conditions was only 5%.

* Electrochemical Society Active Member.

Key words: dehalogenation, Freon 113, zinc.

Experimental

The cell used for the zinc dehalogenation consisted of a 300 ml Berzelius beaker fitted with a rubber stopper which contained openings for a condenser, anode, cathode, and a glass tube capped with a serum cap for the introduction of Freon 113. The cathode consisted of 75 cm of 10 gauge copper wire wound as a flat spiral and placed slightly above the bottom of the beaker. The anode was a hollow carbon rod 1.5 cm in diameter sealed at the bottom with a carbon rod and perforated above the level of the electrolyte to allow the chlorine to evolve. The anode compartment consisted of a porous cup (75 × 30 mm) sealed with a rubber stopper containing the anode. The condenser was cooled with ice water and connected to two traps cooled with ice and salt and Dry Ice and isopropyl alcohol, respectively. The electrolyte consisted of an aqueous solution of 10% zinc chloride and 5% sodium chloride. The cell was maintained at the boiling point of Freon 113 with a steam bath. Freon 113 (5 ml) was injected into the cell through the serum cap. Using a voltage of 5V a current of 1.55-1.7A was obtained. After 1.5 hr the electrolysis was terminated. The zinc formed disappeared in 1.5 hr and the electrolysis of the zinc was resumed for another 2 hr. This zinc was again dissolved in a period of 1.5 hr. More Freon 113 (15 ml) was added and the intermittent electrolysis was repeated in 2 hr intervals for the next 10 hr. At the end of this time the ice salt trap contained 3 ml of Freon 113 and the Dry Ice-isopropyl alcohol trap contained 15 ml of a liquid which was converted to the dibromo compound (17.3g) in the following manner. The trap was slowly allowed to come to room temperature and the resulting vapors were passed through bromine cooled in an ice bath and then through a Dry Ice-isopropyl alcohol trap. The liquid condensed in the latter was recycled through the bromine. Excess bromine was removed by washing with a sodium bisulfite solution and the organic layer was separated, dried with anhydrous calcium chloride, and distilled. The resulting 1-chloro-1,2-dibromo-1,2,2-trifluoroethane boiled at 90°-92°C. The mass spectrum was in agreement with this formulation.

The cell for the direct reduction of Freon 113 consisted of a 1000 ml beaker which was modified in the following manner. The top was ground so that a glass cover with a similar ground surface could be used to give a gas-tight container. The glass cover contained four openings for the carbon anode, stirrer, chlorine outlet, and a condenser. A glass tube (12 mm in diameter) was connected through a glass frit to the lower part of the beaker and was used for the reference electrode (0.2*N* KCl-HgCl-Hg). The mercury pool cathode had an area of 78.6 cm^2. Contact was made through a wire sealed into the bottom of the beaker. Provisions for collecting product were similar to that given earlier.

In a typical run 50 ml of 0.2*N* ammonium chloride-60% methanol was used in the anode compartment. The catholyte consisted of 500 ml of 0.2*N* ammonium chloride-60% methanol and 15 ml of Freon 113. Electrolysis was carried out at 1.45V and gave an initial current of 0.4A. The current increased to 0.7A after 8 hr and then slowly decreased to 0.2A after 23 hr. Work-up of the material in the Dry Ice-isopropyl alcohol trap as above gave 2.1g of the dibromo compound (5%) and 3g of Freon 113.

Acknowledgment

This research was carried out under an N.S.F. undergraduate research participation program. The support is gratefully acknowledged. The research described is abstracted in part from the Senior Thesis of Stephen Willging, Loras College, 1977.

Manuscript submitted Aug. 30, 1976; revised manuscript received *ca.* Oct. 4, 1976.

Any discussion of this paper will appear in a Discussion Section to be published in the December 1977 JOURNAL. All discussions for the December 1977 Discussion Section should be submitted by Aug. 1, 1977.

Publication costs of this article were assisted by the University of Iowa.

REFERENCES

1. P. Askenasy and C. Vogelsohn, *Z. Elektrochem.*, **20**, 773 (1909).
2. Montecatini Edison, Ital. Pat. 852,487; *Chem. Abstr.*, 75, P104554y (1971).

Electrochemical Doping of TiO_2 and Fe_2O_3

D. Haneman and F. Steenbeeke

School of Physics, The University of New South Wales, Kensington, New South Wales, Australia 2033

We report electrochemical doping of TiO_2 and Fe_2O_3 with positive results for the former. The materials are of interest as electrodes in photoelectrochemical methods of solar energy conversion (1). The current work was undertaken in an effort to improve the surface region properties without using heat-treatment or ion bombardment which introduce unwanted side effects.

The doping method involves the semiconductor and a platinum strip (at 1 cm distance) as the two electrodes, the ions in solution being driven into the lattice by the applied field. Nickel and copper ions and various current densities, solution concentrations, and voltages were used, as shown in Table I. The success of the method was tested by attempting to detect the presence of the foreign atoms in the surface region of the semiconductor.

The single crystal specimen, of area approximately 1 cm^2, was pressed against a protective outer (Teflon) ring, leaving only a central disk region exposed to plating. In the case of TiO_2 a definite optical contrast was observable between the plated and protected regions. The whole specimen face was then polished away but the central disk remained detectably darker until a finite measured amount of crystal had been removed.

It was established that the persistence of the dark patch was due to alteration of the bulk, and not due to material remanent in surface valleys. When various fine paints were applied to the surface, the patch disappeared after 2 sec polishing, whereas 5 to 10 times this length of treatment was needed to remove the doped patch.

The thickness of crystal removed was measured by a weight loss method. The surface was carefully polished on a glass surface with either 1000 grade silicon carbide, or 1F compound using a uniform mechanical action and constant time periods. It was weighed periodically on a delicate balance. Reproducibility was checked by several repetitions of the treatment. The absolute thickness removed, calculated from the area,

Key words: semiconductor surfaces, solar energy, titanium oxide.

Table I. Penetration of impurities into TiO_2 during electrochemical deposition

Thickness in microns removed by polishing after which patch is		Ion used	Cell voltage (V) range	Cell current (mA) range	Time (sec) range
still visible	gone				
Several samples					30-60
range 0.3-0.6	0.4-0.7	Cu	1.8-2.1	0.55-1.0	30-60
0.4-0.7	0.5-0.8	Ni	2.3-2.7	0.5-1.0	15-30

density, and weight loss, was also checked by micrometer measurements after sufficient material was removed to make the latter measurement meaningful, and consistency was found (0.023 mm *vs.* 0.02 ± 0.005 mm by micrometer). Approximately 1 μm was removed per 30 sec of polishing.

The depths of penetration measured from disappearance of optical contrast are shown in Table I. Due to the spread in depth values, a dependence on voltage, current, time of deposition, or combinations of these parameters was not established. Over-all, the depths for Cu and Ni, for currents of 0.5-1.0 mA, voltages of around 2V, and times of about 1/2 min were close to 1/2 μm.

The concentration of dopant material in the TiO_2 lattice was estimated from the optical contrast. Considerable darkening is known to occur with approximately 0.5% doping and it is barely detectable at 10^{-2}%. Therefore our rough estimate is that the maximum initial concentration was in the region of 0.1%. Due to the diffusion profile, the concentration in the first few atomic layers is probably much higher.

The above method using optical contrast of the doped region was less effective in the case of Fe_2O_3 since it is not transparent to most of the visible spectrum, having a bandgap of about 2.2 eV. Hence the method of x-ray photoemission spectroscopy (XPS) was used.

The XPS instrument was a Varian IEE spectrometer which utilizes cylindrical samples. Hence four pieces of single crystal Fe_2O_3 were prepared which fitted together roughly to form a hollow cylinder around the central shaft of the specimen holder. The metal portions above and below the specimen were covered with Teflon and the assembly immersed in the nickel plating solution and rotated slowly with respect to the 1 cm^2 flat Pt electrode at a distance of 1 cm. In this way the specimen pieces were uniformly coated. Drying was achieved by several stages of pumping followed by air exposure, in a vacuum chamber.

The XPS spectra, which are sensitive to about the first five atomic layers, showed strong Ni peaks after the doping. However, a light rub with a paper tissue was sufficient to render the peaks completely unobservable. Hence penetration of even the first few atomic layers was less than the detection sensitivity of the instrument which we estimate in the present case as about 1% of one layer. This corresponds to a volume concentration of about 0.1%. Therefore we cannot rule out the possibility of lattice penetration but it was less than 1% of one layer in the first five layers. The indication is thus that this is less than for TiO_2 which might be expected since the latter, of tetragonal structure, has channels of about 0.15 nm diameter orthogonal to the (0001) face used (c-direction). A number of interstitial impurities show enhanced diffusion in the c-direction compared to the a-direction (3, 4). In the case of Fe_2O_3, of rhombohedral structure, such channels are not present.

The actual field at the TiO_2 surface during plating is difficult to ascertain precisely. Taking into account the resistivity and estimated surface barrier thickness of about 5 μm (5), one can calculate a field of about 2000 $V\text{-}cm^{-1}$ which is quite low. However penetration of at least 0.5 μm was achieved which is the main result of this work.

It was found that the photogalvanic current response of the TiO_2 as a function of wavelength was not affected by the doping, suggesting that impurities were in interstitial rather than substitutional positions, consistent with penetration into lattice channels. Although the method was therefore not effective in improving TiO_2 for solar energy use, it may nevertheless be useful for other materials.

Acknowledgments

The electrochemical doping method was suggested to one of us (D.H.) by Professor M. Calvin. The Fe_2O_3 samples were prepared by I. Bedwell. This work was supported by the Australian Research Grants Committee.

Manuscript submitted Jan. 4, 1977; revised manuscript received Feb. 14, 1977.

Any discussion of this paper will appear in a Discussion Section to be published in the December 1977 JOURNAL. All discussions for the December 1977 Discussion Section should be submitted by Aug. 1, 1977.

REFERENCES

1. A recent bibliography is in D. Haneman, *Proc. R. Aust. Chem. Inst.*, **44**, 37 (1977).
2. K. L. Hardee and A. J. Bard, *This Journal*, **123**, 1024 (1976); I. Bedwell, D. Haneman, and E. R. McCartney, To be published.
3. O. W. Johnson, *J. Appl. Phys.*, **35**, 3049 (1964).
4. J. L. Steel and E. R. McCartney, *Nature*, **222**, 79 (1969).
5. F. English and B. Gossick, *Solid-State Electron.*, **7**, 193 (1964).

Photochemical Studies on a Substituted Naphthalene-2,1,Diazooxide

The Formation and Identification of a Ketene from a Wolff Rearrangement

Jacob Pacansky and Duane Johnson[1]

IBM Research Laboratory, San Jose, California 95193

The use of naphthalene-2,1-diazooxides as photoresists has been reviewed by Dinaburg (1) and more recently by De Forest (2). According to these reviews, diazo compounds have been known for a long period of time but detailed studies on light decomposition of these compounds have been carried out only recently. Süs (3) was one of the first (1944) to describe the conversion of a naphthalene-2,1-diazooxide to an indene carboxylic acid by exposure to light. However, in this proposed mechanism as well as subsequent ones, intermediates were not identified. The present studies do describe the trapping of a ketene from a photoactive compound (PAC).

[1] Deceased.

Key words: photoresist, diazo, photochemistry, Wolff rearrangement, ketene.

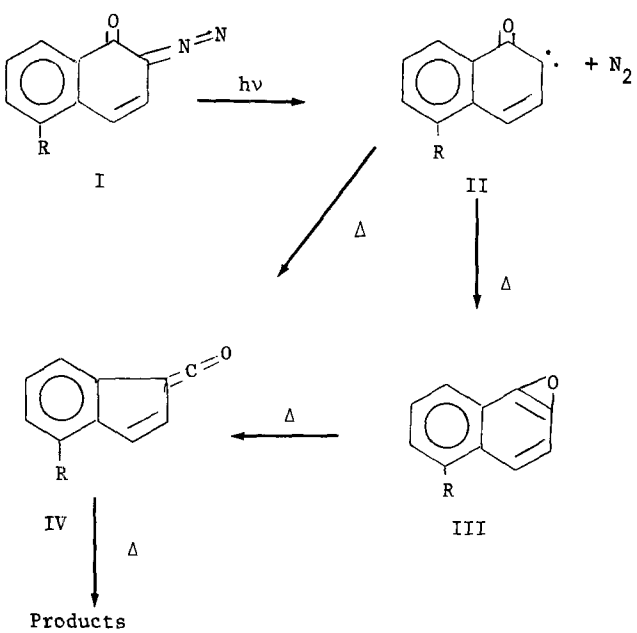
Mechanistic studies of the complex over-all processes observed when a substance is irradiated with ultraviolet light often overlook the fundamental distinction between a purely photochemical process and a complex process comprising photochemical and thermal components. It is frequently

simple photochemical process $M \xrightarrow{h\nu} M^* \longrightarrow P$

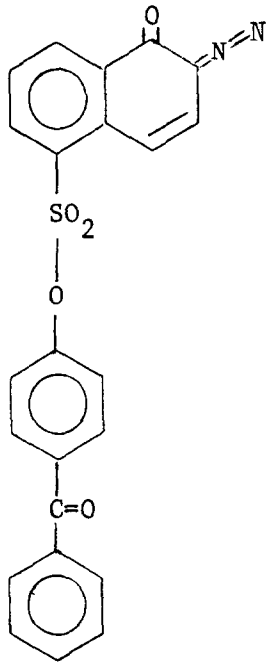
complex photothermal process $M \xrightarrow{h\nu} M^* \longrightarrow In \xrightarrow{\Delta} P$

assumed that an electronic excited state (M*) decays directly to observed product (*P*) without consideration of the possibility that a *meta*-stable ground state intermediate (*In*) may intervene. The intrusion of an intermediate can lead to serious errors in interpretation and to inordinate complexity in what is called photochemistry. Results suggest that the number of primary photochemical processes of complex molecules is rather small and that the bewildering array of products encountered in structurally similar substrates is due to a confusing overlay of thermal transformations of the initial photochemical products. The substituted naphthalene-2,1-diazooxides (**I**) are an excellent example of the confusion which has occurred.

The naphthalene-2,1-diazooxides are postulated to photodecompose by the following mechanism



Upon photochemical extrusion of N_2 from **I**, the carbene **II** is formed. The thermal transformation of **II** through the as-yet-unknown oxirene **III** or directly to the ketene **IV** is known as the Wolff rearrangement (4, 5). That this rearrangement has a very low barrier of activation was established in photochemical matrix isolation experiments on diazoketones where, in spite of the very low temperatures (below 10°K) at which the studies were performed, the rate of formation of a ketene could not be impeded (6). The success for observation of the reactive ketene intermediate, however, is not as hopeless. It may be spectroscopically identified at relatively higher temperatures (77°K), trapped, and its thermal reactions followed by warming to ambient temperatures. In light of the above discussion, we present low temperature photochemical experiments which, for the first time, show unequivocal spectroscopic and chemical evidence for a reactive ketene intermediate involved in the photolysis of the substituted naphthalene-2,1-diazooxide (4-benzoylphenyl, 6-diazo-5-oxo-5,6-dihydronaphthalene-1-sulfonate) shown below and hereafter referred to as **V**



V

A neat film of **V** was cast from a dioxane solution onto a suitable infrared transparent substrate such as CsI. The infrared spectrum of **V** at 77°K is shown in Fig. 1. The pertinent features in this spectrum are the vibrational bands due to the diazo group (the doublet at 2162 and 2118 cm^{-1}) and the carbonyl stretching frequency of the naphthoquinone at 1625 cm^{-1}.

Irradiation of **V** with u.v. light emitted from a high pressure mercury lamp and filtered to allow only light with $\lambda > 3700$Å produced total decomposition of **V** in 15 min. The infrared spectrum of **V** after photolysis at 77°K is shown in Fig. 2. It can be seen that the characteristic special features of the naphthalene-2,1-diazooxide structure (2162, 2118, and 1625 cm^{-1}) have disappeared and that many new bands appear. These are listed in Table I. In Fig. 3 are shown the results of a kinetic plot (band intensity *vs.* time) for the 1625 cm^{-1} of the starting material and the 500 cm^{-1} band of the photoproduct. (All of the bands of the starting material and photoproduct exhibit similar behavior. These two bands are picked only to be representative.) The kinetic plots clearly show that the new bands correlate with the disappearance of **V** and thus, under these conditions, the new bands appear to be due to a primary photo product.

Assignments of the new bands to a ketene structure were made on the following basis: First, ketenes characteristically have very intense absorptions at 2135 cm^{-1}. The parent ketene (7) (CH_2CO) has an intense

Table I. Bands appearing upon irradiation of V

New bands	
2135*	
2100*	(shoulder)
1495	
1460	
1435	
1310	
1145	
1095	
1040	
890	
760	
670	
615	
605	
570	
500	

* Bands characteristic of the ketene functionality.

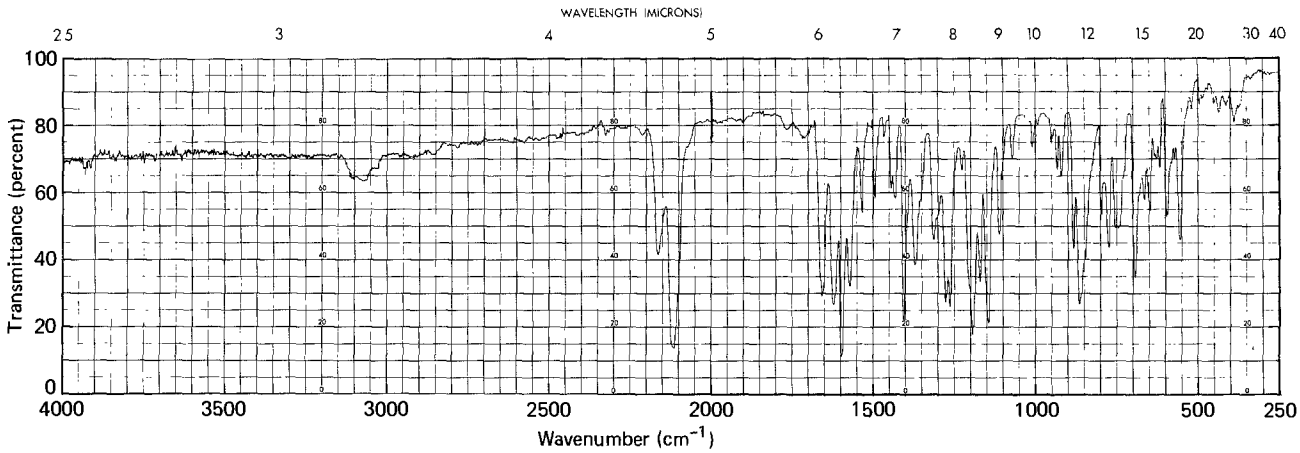


Fig. 1. The infrared spectrum of V at 77°K

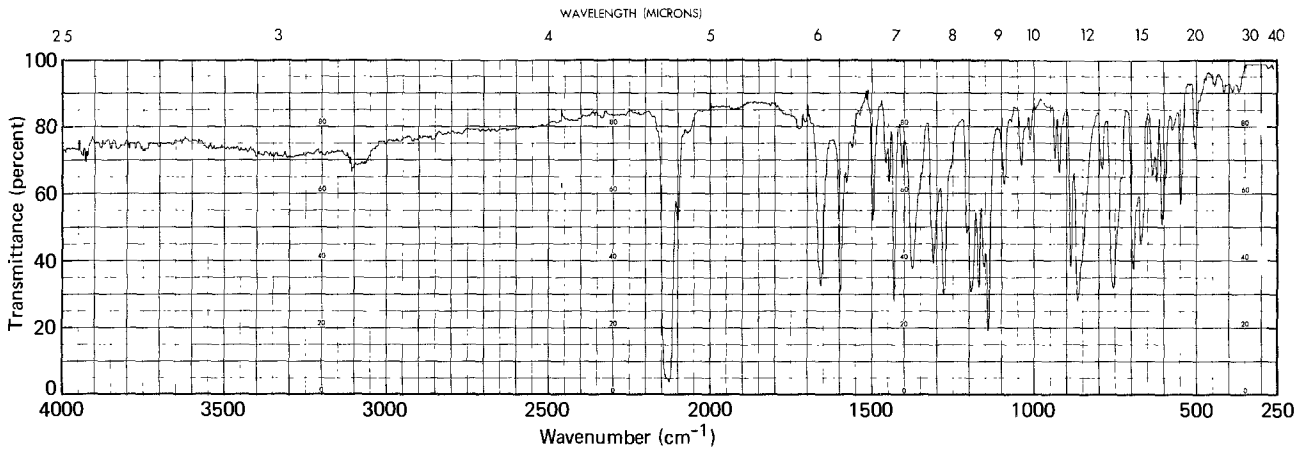
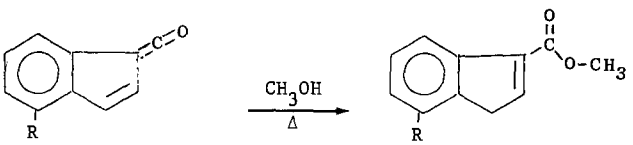


Fig. 2. The infrared spectrum of V at 77°K after irradiation with $\lambda > 3700$Å for 10 min

absorption at 2151 cm^{-1} (the CO stretch) and less intense absorptions at 1120 cm^{-1} (C=C stretch) and 588,528 cm^{-1} (C=C=O bending). The bands at 2135 and 2100 cm^{-1} are assigned to the C=O stretch of the ketene. Those at 1040, 570, and 500 cm^{-1} can only be tentatively assigned to the C=C stretch and C=C=O bending vibrations. Second, and more important, is the chemical evidence obtained from trapping experiments. Methanol was added to the PAC. After irradiation at 77°K had completely converted **V** to ketene, the temperature was allowed to rise. Synchronously the ketene and methanol disappeared with the appearance of a carbonyl band at 1720 cm^{-1} characteristic of the methyl ester,[2] the expected adduct of the trapping experiment. These results are summarized below[3]



In like manner the ketene was trapped with m-cresol. In this experiment a band appeared at 1750 cm^{-1} which could be assigned to the phenyl ester.

The ketene was further characterized by allowing a reaction with water vapor at room temperature to proceed. Compound **V** was converted to a ketene at 77°K

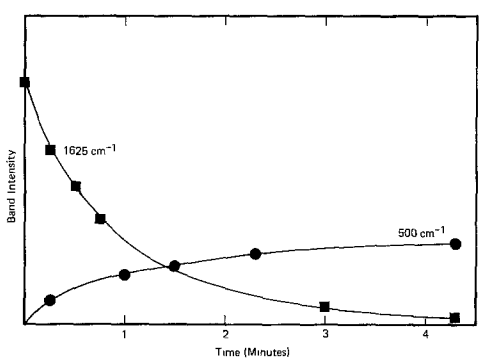


Fig. 3. Plot of band intensity of significant bands as a function of irradiation time. Substituted naphthalene-2,1-diazooxide band is 1625 cm^{-1} (■). The ketene band is 500 cm^{-1} (●).

and after allowing the temperature to rise to room temperature water vapor was introduced into the cryostat. The ketene rapidly reacted with the water vapor. The infrared spectra recorded before and after the reaction are shown in Fig. 4. At this point it should be added that the ketene at room temperature, in the absence of water vapor, is remarkably stable and will exist for hours in vacuum.

The photochemical apparatus was fitted with u.v. filters to determine the photostability of the ketene. Conversion of **V** to a ketene did not occur until a Corning No. 3-73 filter was used (0% T at 4000Å). After 20 min of irradiation, **V** was completely transformed to a ketene (T = 77°K). Irradiation with a set of filters in the high pressure mercury lamp which progressively decreased the wavelength of the light to 2900Å did not induce any phototransformations of the ketene. In fact, no changes occurred when the ketene was exposed to

[2] The methyl ester of 3-indene carboxylic acid was synthesized. The infrared spectrum of the neat liquid has a carbonyl band at 1725 cm^{-1}.

[3] Note that the methyl ester of 3-indene carboxylic acid is shown and not that of 1-indene carboxylic acid. The 3-indene acid has been misidentified as the 1-indene acid for over 60 years. This error has led to considerable confusion in unraveling the photo and thermal decomposition mechanisms of resists. To our knowledge the first study to point out this problem was the elegant work of P. Yates and E. W. Robb, *J. Am. Chem. Soc.*, 79, 5760 (1957).

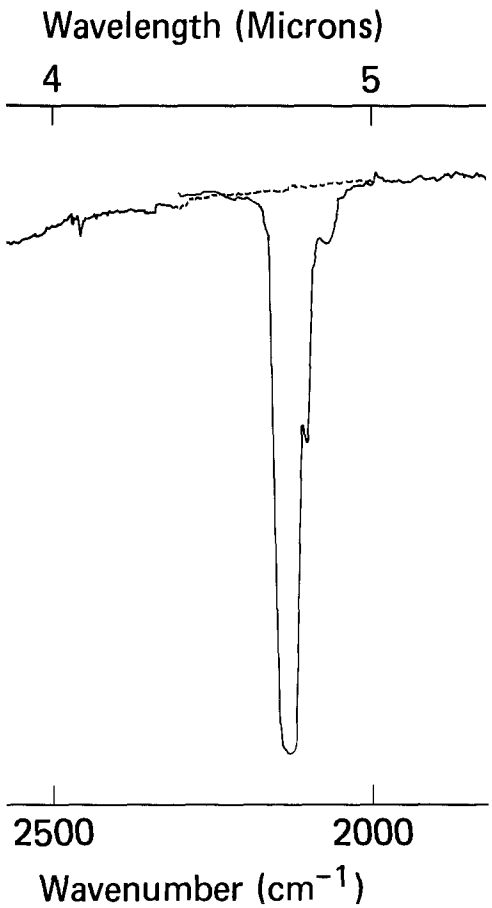


Fig. 4. The infrared spectra of irradiated V before reaction with water vapor (——) and after reaction with water vapor (– – – –).

the unfiltered high pressure mercury lamp for several hours.

In summary, the formation and identification of a ketene intermediate from a PAC used in photoresist solutions has been accomplished. The PAC was irradiated at $\lambda > 3700$Å, 77°K, and under a vacuum of 2×10^{-6} Torr. The ketene was found to be stable at ambient temperatures while still under vacuum. Infrared peak assignments have been made and a ketene trapped using methanol and m-cresol.

Acknowledgment

The substituted naphthalene-2,1-diazooxide was supplied by Nicholas Clecak. His contribution is gratefully appreciated.

Manuscript submitted Nov. 8, 1976; revised manuscript received Feb. 7, 1977.

Any discussion of this paper will appear in a Discussion Section to be published in the December 1977 JOURNAL. All discussions for the December 1977 Discussion Section should be submitted by Aug. 1, 1977.

Publication costs of this article were assisted by the IBM Corporation.

REFERENCES

1. M. S. Dinaburg, "Photosensitive Diazo Compounds," Focal Press, New York (1964).
2. W. S. De Forest, "Photoresist Materials and Processes," McGraw-Hill, New York (1975).
3. O. Sus, *Ann.*, **556**, 65 (1944).
4. W. Wolff, *ibid.*, **394**, 25 (1912).
5. R. Russell and F. S. Rowland, *J. Am. Chem. Soc.*, **92**, 7508 (1970); J. Fenwick, G. Frater, K. Ogi, and O. P. Strausz, *ibid.*, **95**, 124 (1973).
6. J. Pacansky, Unpublished results.
7. W. F. Arendale and W. H. Fletcher, *J. Chem. Phys.*, **26**, 793 (1957); C. B. Moore and G. C. Pimentel, *ibid.*, **38**, 2816 (1963).

Brief Communication

Comments Regarding Electronic Conductivity in Solid Electrolytes

John H. Kennedy*

Department of Chemistry, University of California, Santa Barbara, California 93106

The use of solid electrolyte materials in practical devices usually requires that they exhibit little or no electronic conductivity. It is simple to express conductivity as the sum of the ionic and electronic components

$$\sigma_{tot} = \sigma_i + \sigma_e \quad [1]$$

or in terms of transference numbers

$$t_i = \frac{\sigma_i}{\sigma_{tot}}, \quad t_e = \frac{\sigma_e}{\sigma_{tot}} \quad [2]$$

Investigators may make statements that $t_i > 0.999\ldots$ or that $t_e < 10^{-n}$ to indicate that the solid electrolyte will be useful in applications. Before proceeding to the point of this paper I would like to point out the obvious that in most applications the real question is the amount of charge transferred ionically with external electronic transfer (Q_i) *vs.* the amount of charge transferred by internal electronic conductivity (Q_e)

$$Q_{tot} = Q_i + Q_e \quad [3]$$

with faradaic efficiency being

$$\eta_F = \frac{Q_i}{Q_{tot}} \quad [4]$$

It is sometimes implied that t_i is related to η_F but in actual fact η_F will depend on the rate at which charge is drawn from the device. In the extreme, if a battery is not used, it will eventually completely self-discharge through even the smallest electronic path with a faradaic efficiency of 0%.

Returning to the initial expression for σ_{tot} I have noted that investigators may use a bridge method for

* Electrochemical Society Active Member.

Key words: electronic conductivity, electronic decomposition potential.

σ_{tot} and a Wagner blocking method for σ_e which is really σ^0_e. I would like to consider the difference between σ_e and σ^0_e and show that σ^0_e for hole conductivity, σ^0_+, has a different meaning in the typical galvanic cell than σ^0_e for electron carrier conductivity, σ^0_-.

Electronic conductivity is sensitive to environment, and the beauty of the Wagner technique is that it defines the conditions for which the electronic conductivity value applies. For example, in the cell Ag/AgBr/M where M is an inert blocking electrode, the value for σ^0_- refers to the electronic conductivity which would be observed in the cell Ag/AgBr/Ag. This conductivity cannot be measured directly because when a voltage is applied to the latter cell a predominantly ionic current flows. The important point to be realized is that for any electrode environment more positive than Ag the concentration of electron carriers will be lower, and σ_e will be less than σ^0_-. Electrodes more negative than Ag cannot be used since they would reduce Ag^+. Therefore, in all electrochemical cells using AgBr electrolyte the electronic transference number will be less than that calculated using σ^0_-. In other words, we are quoting the worst (highest) possible value for the electronic contribution.

However, the situation is reversed when the electrolyte is a hole conductor. Now σ^0_+ represents the conductivity in the cell M/MX/M but as the electrode potential increases the concentration of hole carriers and σ_e increase exponentially. In other words, σ^0_+ represents the minimum electronic conductivity via holes while σ^0_- represents the maximum conductivity via electron carriers.

I have found the following numerical examples instructive in appreciating this difference. Let us suppose we have an electrolyte in which σ^0_+ is $2 \times 10^{-7}\ \Omega^{-1}\ cm^{-1}$ and compare it with an electrolyte in which σ^0_- is $2 \times 10^{-7}\ \Omega^{-1}\ cm^{-1}$. For calculation purposes let us assume in both cases that $\sigma_i = 0.1\ \Omega^{-1}\ cm^{-1}$ and that the cell has an open-circuit potential of 1.0V. The expressions for the partial ionic and electronic currents [see Ref. (1) for derivation and discussion of the electronic conductivity equations], assuming no polarizations other than ohmic, are

$$I_i = \frac{V_{o.c.} - V}{l/A}\sigma_i \qquad [5]$$

$$I_+ = \frac{RT\,\sigma^0_+}{l/A\,\mathbf{F}}[\exp(V\mathbf{F}/RT) - 1]$$

$$\cong \frac{RT\,\sigma^0_+}{l/A\,\mathbf{F}}\exp(V\mathbf{F}/RT) \quad \text{when} \quad V > 0.2\text{V at } 300°\text{K} \qquad [6]$$

$$I_+ = \frac{RT\,\sigma^0_-}{l/A\,\mathbf{F}}[1 - \exp(-V\mathbf{F}/RT)]$$

$$\cong \frac{RT\,\sigma^0_-}{l/A\,\mathbf{F}} \quad \text{when} \quad V > 0.2\text{V at } 300°\text{K} \qquad [7]$$

$$I_i/I_+ = \frac{(V_{o.c.} - V)\mathbf{F}}{RT\exp(V\mathbf{F}/RT)}\left(\frac{\sigma_i}{\sigma^0_+}\right) \qquad [8]$$

$$I_i/I_- = \frac{(V_{o.c.} - V)\mathbf{F}}{RT}\left(\frac{\sigma_i}{\sigma^0_-}\right) \qquad [9]$$

where V is the voltage difference between the two electrodes. From these expressions the ratio of ionic current to electronic current can be calculated for any cell voltage and temperature. The ionic transference number (fraction of current carried ionically) increases as the cell voltage decreases but voltage efficiency decreases. In general, cells are not operated at voltages lower than the maximum powerpoint ($V_{o.c.}/2$) assuming no other polarization losses. Thus, for our example with $V = 0.5$, $T = 300°$K

$$I_i/I_+ = 0.038$$

$$I_i/I_- = 9.7 \times 10^6$$

That is, if the electrolyte is a hole conductor the current passing through the cell would be about 96% electronic. In this case, the electromigration of the holes when external current is flowing would also need to be included. On the other hand if the electrolyte is an electron carrier conductor the current would be < 1 ppm electronic. Based on the ratio σ_i/σ_e (5×10^5 in the example) one would predict the electronic current to always be smaller than the ionic current.

In a recent paper Bonino and Lazzari (2) determined the hole conductivity of nominally stoichiometric KCu_4I_5 to be $2 \times 10^{-7}\ \Omega^{-1}\ cm^{-1}$ at 281.5°C and the total conductivity to be about $0.1\ \Omega^{-1}\ cm^{-1}$, the same values as in the example above. They concluded that the electronic conductivity contribution was negligible when the electrolyte was equilibrated with copper. This statement is strictly true but could be misleading since the electronic current will not be negligible in a galvanic cell in which the cathode side is equilibrated at some positive potential compared to copper. From the equations and data given above the ratio I_i/I_+ will be 150 at 555°K (282°C) so that nearly 1% of the current would be electronic at 0.5V.

I propose that in addition to quoting σ^0_+ for hole conductors which allows calculations to be carried out, an "electronic decomposition potential" be quoted. The current-potential curve is similar in nature to an electrochemical decomposition curve, and an extrapolation back to zero current would be a helpful potential to quote. Figure 3 in Ref. (2) would indicate an electronic decomposition potential of about 0.4V. This means that the use of any cathode material more positive than 0.4V would lead to high electronic conductivity and, therefore, high self-discharge.

Another example is PbF_2 which was studied by Kennedy *et al.* (3). Data given in Fig. 8 of Ref. (3) showed that the electronic decomposition potential was 1.5-1.6V (the quoted value will vary somewhat depending on the current scale used). In agreement with that value Miles (4) found that thermodynamic potentials were achieved for cathodes of CuF_2 (0.70V) and AgF (1.30V) but the highest potential observed with PbF_4 cathodes was 1.6V instead of the thermodynamic value of 2.56V.

In conclusion, it is important to realize that a cathode material will act like the blocking electrode in a Wagner study at an applied voltage equal to the cathode potential. If an electrolyte exhibits significant hole conductivity at potentials greater than some value then all cathode materials with potentials greater than that value will self-discharge. The use of an electronic decomposition potential would alert investigators to the electrolyte's limitations much the same as the ionic domain does for oxide electrolytes (5).

Acknowledgment

The author acknowledges financial support by the National Science Foundation, Grant No. DMR 73-07507-A02.

Manuscript submitted Oct. 20, 1976; revised manuscript received Feb. 1, 1977.

Any discussion of this paper will appear in a Discussion Section to be published in the December 1977 JOURNAL. All discussions for the December 1977 Discussion Section should be submitted by Aug. 1, 1977.

Publication costs of this article were assisted by the University of California, Santa Barbara.

REFERENCES

1. D. O. Raleigh, *Prog. Solid State Chem.*, **3**, 83 (1966).
2. F. Bonino and M. Lazzari, *J. Power Sources*, **1**, 103 (1976/1977).
3. J. H. Kennedy, R. Miles, and J. Hunter, *This Journal*, **120**, 1441 (1973).
4. R. C. Miles, Ph.D. Thesis, University of California, Santa Barbara (1974).
5. J. W. Patterson, *This Journal*, **118**, 1033 (1971).

DISCUSSION SECTION

This Discussion Section includes discussion of papers appearing in the *Journal of The Electrochemical Society*, Vol. 123, No. 2, 8, 9, 10, and 12; February, August, September, October, and December 1976.

Electrochemical Semipermeability and the Electrode Microsystem in Solid Oxide Electrolyte Cells

J. Fouletier, P. Fabry, and M. Kleitz (pp. 204-213, Vol. 123, No. 2)

H.-H. Möbius and R. Hartung:[1] In Table II of this interesting article, published values of the oxygen semipermeability flux π^* and other parameters are compared. In some cases the values differ by nearly a factor of 10^4 and here one expects great measurement discrepancies. But the reasons for the differences are found in the value units used by the authors and in discrepancies of calculations. In early papers about semipermeability of solid oxide electrolytes,[2,3] results were given in cm^3O_2 (0°C, 1 atm) cm/cm^2 sec, that is cm^2 sec^{-1} (Table 1,[2] misprinted cm^2/sec^{-1}). Later we, like other authors, used for values of semipermeability the unit mole O_2 cm/cm^2 sec, that is mole cm^{-1} sec^{-1}. For a comparison it is valid: mole cm^{-1} sec^{-1} = cm^2 $sec^{-1}/2.2414 \times 10^4$ cm^3 $mole^{-1}$. The value for 1200°C from our experiments amounts to 1.6×10^{-6} cm^2 sec^{-1} (the value attributed to us in the paper of Ullmann[3] is incorrect) and after conversion 7.1×10^{-11} mole O_2 cm^{-1} sec^{-1} (the value of Ullmann 1.8×10^{-10} mole O_2 cm^{-1} sec^{-1}). The article under discussion also contains a discrepancy between the flux J defined in Eq. [17] for holes and the flux J connected in Eq. [23] with the oxygen semipermeability flux π^* of Table II without the factor 4; therefore one can expect that some values in Table II refer to mole holes ($\pi^*_h = 4\pi^*_{O_2}$).

The great deviations of equilibrium observed from Fouletier *et al.* with their original method between 1250° and 1450°C indictae a relatively high polarizability of the electrodes. The combination of the results in Fig. 7, 8, 9, 12, and 13 shows that the used platinum layer reference electrode at $p_{O_2} \approx 10^{-3}$ atm already has a polarization resistance $r_P \approx \Delta E_{ref}/JF$ of the order of 10^3 Ω-cm^2. At the same oxygen partial pressure but more than 400° lower (at 800°C) on unobjectionable operating platinum layer electrodes we measured much lower polarization resistances on the order of 10 up to the maximal 10^3 Ω-cm^2. At this point, one has to take into consideration that r_P falls exponentially with growing temperature.

Errors of potentiometric oxygen analysis with solid oxide electrolyte cells and with air at the reference electrode (because of semipermeability and therefore deviations from equilibrium) from our experience are negligible at temperatures near 800°C and oxygen partial pressure $> 10^{-6}$ atm. The polarizability of the electrodes, as well as the oxygen semipermeability, is important for errors. The polarizability of the electrodes is not only dependent on the kind of materials used, temperature, and oxygen partial pressure, but also on the conditions of preparation in thermal, electrical, and chemical treatments of the electrodes.

[1] Department of Chemistry, Ernst-Moritz-Arndt-Universität Greifswald, 22 Greifswald, German Democratic Republic.
[2] H.-H. Möbius and R. Hartung, *Silikattechnik*, 16, 276 (1965).
[3] H. Ullmann, *Z. Phys. Chem. (Leipzig)*, 237, 71 (1968).

Evaluation of Electrochemical Information Transfer System

I. Effect of Electric Fields on Living Organisms

A. A. Marino, T. J. Berger, B. P. Austin, R. O. Becker, and F. X. Hart (pp. 1199-1200, Vol. 123, No. 8)

G. E. Kaufman and M. W. Miller:[4] There are several problems with the authors' interpretation of their results as indicating that biological alterations were produced in rats by chronic exposure to a 60 Hz, 150 V/cm electric field.

For example, the authors appear to consider the slightly lower levels of serum corticoids (with no indication of statistical significance) in the exposed rats in experiments 1-3 as an indication of the general adaptation syndrome as described by Selye. However, a lower than normal level of serum corticoids would be consistent with general adaptation syndrome only if the animals were in the exhaustion phase, a possibility which is ruled out by the results of experiment 4. Also, the authors refer to "a statistically significant elevation in albumin percentage and a statistically significant decrease in gamma globulin percentage." Clearly there is no basis for determining that these differences are statistically significant since only one experimental and one control serum pool were collected in each experiment. The listed standard deviations represent only variability between replicate measurements and not variability among the individual animals comprising each pool.

Thus the only results which could conceivably be taken as indicating a statistically significant difference between exposed and control rats are the final body weights in experiments 1 and 4. However, in this regard some additional information about the reported experiments may be of interest. First, there was already a statistically significant difference in weight between the exposed and control groups in experiment 1 prior to the commencement of exposure (exposed group starting weight 60.50 ± 3.03; control group 63.58 ± 3.12; $t = 2.828$ with 31 d.f., $P < 0.01$).[5] No starting weights were available for experiment 4. Second, the exposed rats were kept one to a cage throughout the exposure period while the controls were kept three to a cage in larger cages.[6] Thus, the exposed and control conditions differed by more than the single agent being examined.

In summary, if there are any biological effects produced by exposure to a 60 Hz, 150 V/cm electric field, such effects are not apparent from the results reported by A. A. Marino *et al.*

A. A. Marino,[7] T. J. Berger,[7] B. P. Austin,[7] R. O. Becker,[7] and F. X. Hart:[8] We appreciate the interest that Kaufman and Miller have shown in our work, and we respond as follows to the four points that they have raised.

1. The average decrease in the serum corticoids of the rats which were exposed to the electric field for 1 month was about 31%. Such a decrease is entirely con-

[4] Department of Radiation Biology and Biophysics, The University of Rochester, Rochester, New York 14642.
[5] Based on starting weights given by A. A. Marino in New York State Public Service Commission (PSC) Common Hearings, Cases 26529 and 26559, Exhibit H-4, and Transcript p. 7933 (1976).
[6] A. A. Marino, *ibid.*, p. 7182 (1976).
[7] Veterans Administration Hospital and Upstate Medical Center, Syracuse, New York 13210.
[8] University of the South, Sewanee, Tennessee 37375.

sistent with the initial stages of the general adaptation syndrome.[9]

2. We thought it was apparent that the differences which we described were those between the control and experimental groups, and not differences among animals within each group. In any event, application of the electric field produced the same alteration in the distribution of serum proteins in three consecutive experiments, thereby establishing the electric field as the causitive factor.

3. There were no differences in the initial weights between the experimental and control groups in any experiment. Kaufman and Miller have performed their calculation employing weights of the experimental and control animals which were recorded on different days.

4. Other work has demonstrated that the biological effects which we observed could not possibly be attributed to any aspect of the manner in which the animals were housed.[10,11]

Investigation of Adsorbed Hydrogen on Platinum Electrode by Means of Dynamic Impedance Measurement

T. Ohsaka, Y. Sawada, T. Yoshida, and K. Nihei
(pp. 1339-1345, Vol. 123, No. 9)

R. Durand:[12] 1. The authors do not make enough distinction between two different models: the classical one of Llopis *et al.*[13]-Senda and Delahay[14] which, in the case of a single intermediate species, corresponds to their Fig. 4(c), and the model of Delahay *et al.*,[15] which does not suppose *a priori* separation of double layer charging. This last notion follows from the fact that the electrode "charge" generally depends on Γ with E constant, and it must be associated to the notion of thermodynamic charges brought by Frumkin at the same period[16] and spread out later on. In the case of one or two intermediate species, the works of Grafov *et al.*[17,18] and Barker[19] lead to equivalent circuits requiring transformers or coupling capacitors.

2. The lack of measurements beyond 2000 Hz in the paper under discussion can involve severe uncertainties for the calculations of R_E, C_D, and r: on one hand it is hardly acceptable to assume for C_D, in the "hydrogen region," a constant value obtained by extrapolation of measurements at 0.70 V_{HE}, whereas C_D strongly depends, for a well-defined pretreatment, on the value of Γ;[20-22] on the other hand, values of r per unit projected area seem to be too high for a semiactivated electrode.

3. The authors do not indicate how the experimental difficulties inherent to the use of solid electrodes were tackled: it should be necessary to investigate the influence, for instance, of the current distribution (poor in the case of a disk), of any possible electrolyte penetration between the electrode and its holder (not described), and of the surface roughness of the electrode (possibly increased by voltage scanning pretreatment) on the results, before explaining them by questionable Warburg impedance and second step (at 0.15 V_{HE}).

T. Ohsaka,[23] **Y. Sawada,**[23] **T. Yoshida,**[23] **and K. Nihei:**[24] 1. A few applications of the idea of coupling between the faradaic and nonfaradaic components have been investigated. Sluyters has treated the most convenient model using simplified procedure. Moreover, on solid electrodes it is difficult to reasonably modulate each parameter in analysis. We failed to explain our results, using Sluyters' complex plane method with coupling idea.[25] However, the results fitted well with the equivalent circuit of Fig. 4(c) in the paper under discussion. We analyzed the experimental results using the classical procedure (potential independence of C_D) combined with the equivalent circuit approach.

2. The frequency dispersion of C_p strongly depends on the value of reaction resistance r as shown in Fig. 1, assuming the equivalent circuit (a) in Fig. 4 or 9 in the paper under discussion (the results agreed with the circuit behavior especially in the high frequency range). We plotted the Bagotzky data[21] as C_p *vs.* R_p^{-1} (the relationship is similar to that found in Fig. 7 in the paper under discussion). From the linear portion [which means the assumption of equivalent circuit (a)], we estimated the value of r to be *ca.* 0.02 Ω-cm^2. This value of r gives a frequency dispersion similar to that given by Bagotzky *et al.*[21] In the case of $r = 0.58$ Ω-cm^2 which corresponds to our data in 1*N* sulfuric acid, the frequency dispersion ceases at $f > 1$ kHz. Therefore, we concluded that the dispersion of C_p may be caused largely by the difference of r which is due to the activated condition of the electrode and that the high frequency limits of 2 kHz are considered to be enough in our experiments (*cf.*, Ftn.[1] in the paper under discussion: we regret the mistake in the footnote: the sixth line should read $r = 0.58$ and $f > 1$ kHz). The reciprocal value of 0.58 Ω-cm^2 ($r^{-1} = 1.72$) is not too high a value compared to the value of r^{-1} reported by Frumkin,[26] *i.e.*, the value of r^{-1} ($r = 0.29$) in 1*N* sulfuric acid agrees approximately with our data, but not with Bagotzky's data ($r^{-1} = 50$) which is higher in magnitude. Though the double layer capacity C_D depends on Γ of adsorbed hydrogen as shown by Shuldiner[20] and Petrii,[22] C_D was determined at 0.7V in the double layer region for convenience. The assumption of the constancy of C_D does not affect so much the conditions of $C_A >> C_D$, *i.e.*, the theoretical representation of equivalent circuit (a) becomes semicircular in the complex representation and the intercepts of C_p axis show C_D and ($C_D + C_A$). In the conditions of $C_A >> C_D$, however, the representation is scarcely influenced with the change of C_D.

3. Since the change of the electrode area influenced the reproducibility and stability of the admittance data, we determined the optimum area earlier; probably this behavior is connected to the current distribution. We confirmed that there is no electrolyte penetration between electrode and its holder, from the a *vs.* i plots (where a = area of the electrode and i = current density). It is well known that the surface roughness of an electrode increases with voltage scanning (used as pretreatment). The reproducibility of surface roughness was taken care of in the present experiment by checking the shape of the i-E curves (both the general shape and magnitude of adsorbed hydrogen peak were taken into account). The scanning was always from the double layer to hydrogen

[9] H. Selye, "Stress," Acta Inc., Montreal (1950).
[10] A. A. Marino, T. J. Berger, J. T. Mitchell, R. A. Duhacek, and R. O. Becker, *Ann. NY Acad. Sci.*, 238, 436 (1974).
[11] A. A. Marino, T. J. Berger, B. P. Austin, R. O. Becker, and F. X. Hart, *Bioelectrochem. Bioenerg.*, In press.
[12] School of Electrochemistry, 38401 St. Martin d'Heres, France.
[13] J. Llopis, J. Fernandez-Biarge, and M. Perez-Fernandez, "Transactions of the Symposium on Electrode Processes, Philadelphia 1959," p. 221, John Wiley & Sons, New York (1961); *Electrochim. Acta.*, 1, 130 (1959); *ibid.*, 6, 167, 177 (1962).
[14] M. Senda and P. Delahay, *J. Phys. Chem.*, 65, 1580 (1961).
[15] K. Holub, G. Tessari, and P. Delahay, *ibid.*, 71, 2612 (1967); P. Delahay, *ibid.*, 70, 2373 (1966).
[16] A. N. Frumkin, N. A. Balashova, and V. E. Kazarinov, *This Journal*, 113, 1011 (1966).
[17] B. M. Grafov, E. V. Pekar, and O. A. Petry, *J. Electroanal. Chem.*, 40, 179 (1972).
[18] B. M. Grafov and E. V. Pekar, *ibid.*, 31, 137 (1971).
[19] G. C. Barker, *ibid.*, 40, 45 (1972).
[20] M. Rosen, D. R. Flinn, and S. Schuldiner, *This Journal*, 116, 1112 (1969).
[21] (a) V. I. Luk'yanycheva, E. M. Strochkova, and V. S. Bagotzky, *Elektrokhimiya*, 6, 701 (1970); (b) *ibid.*, 7, 267 (1971).
[22] V. A. Safonov, V. D. Dishel', and O. A. Petrii, *ibid.*, 9, 264 (1972).
[23] Department of Applied Chemistry, Waseda University, Tokyo 160, Japan.
[24] OKI Electric Industry Company, Limited, Fundamental Working Technology Laboratory, Tokyo 108, Japan.
[25] M. Sluyters-Rehback, B. Timmer, and J. H. Sluyters, *J. Electroanal. Chem.*, 15, 151 (1967); B. Timmer, M. Sluyters-Rehback, and J. H. Sluyters, *ibid.*, 15, 343 (1967); *ibid.*, 18, 93 (1968).
[26] A. N. Frumkin, in "Advances in Electrochemistry and Electrochemical Engineering," Vol. 3, P. Delahay, Editor, p. 287, Interscience, New York (1963).

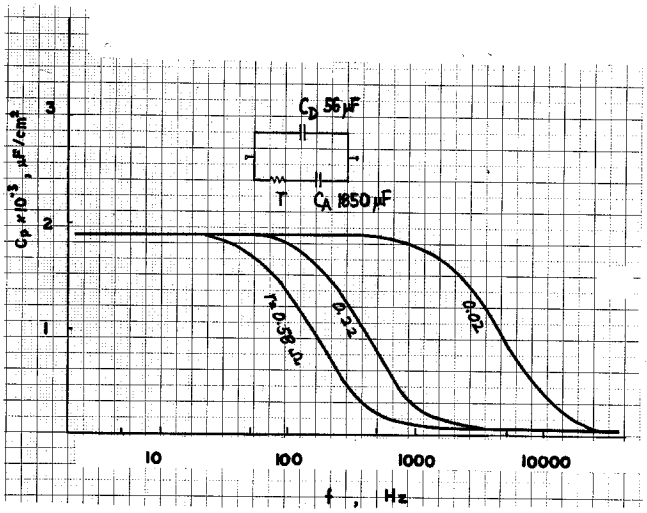


Fig. 1. Effect of the reaction resistance r on the frequency dependence of C_p with the assumption of simple circuit (a).

region, reversal of scanning was done at 0.05V. With this technique, we can get good reproducibility in our case. This is also indicated by the roughness factor which we determined to be in the range 1.7-2.5.

The Comparative Crevice Corrosion Resistance of Co-Cr Base Surgical Implant Alloys

T. M. Devine and J. Wulff (pp. 1433-1437, Vol. 123, No. 10)

P. Süry:[27] In their article (see also Ftn. [28-30]) Devine and Wulff describe the relative corrosion behavior of several surgical implant alloys in chloride-containing media at human body temperature. Special attention is paid to the relative crevice corrosion susceptibility, since this phenomenon seems to frequently initiate implant damage.

On the basis of *in vitro* electrochemical (potential time variation and polarization characteristics) and simple immersion tests on specimens with and without artificial crevice in aqueous solutions of NaCl and $FeCl_3$ + HCl, the authors have concluded that MP35N,[31] a wrought, high strength CoNiCrMoTi alloy, is less resistant to crevice corrosion in the human body than cast, cast and solutionized, and wrought CoCrMo alloy HS 21,[32] or an experimental Co base alloy with 20% Cr and 10% Mo without nickel.

We are unable to confirm these results. In a series of reports[33-36] it has been shown that MP35N exhibits strong resistance to the local breakdown of the passive oxide in general and in cases where crevice formation is to be expected. According to our findings this resistance is minimally equal to or exceeds that of cast CoCrMo. The beneficial (and theoretically expected) effect of solutionizing heat-treatment of CoCrMo reported by Devine and Wulff has also been found by us, but an improvement over wrought MP35N through heat-treatment could not be definitely deduced from *in vitro* measurements. These have so far included the following methods: "breakthrough potentials" from potentiodynamic polarization curves[33] in oxygenated and deoxygenated NaCl solutions, differential aeration cell models in Ringer's solution,[34-35] galvanostatic determination of pit repassivation potentials in Ringer's solution,[34] polarization resistance in deaerated hydrochloric acid at 50°C,[34] cyclic voltametric polarization curves with high voltage sweep rates in Ringer's and HCl solution,[34-36] immersion tests in $FeCl_3$ and $FeCl_3$ + HCl solutions with creviced and noncreviced samples,[34] potentiodynamic polarization curves in the active to passive transition region in HCl solution[35,36] potentiostatic current-time curves of creviced anchorage shafts in Ringer's solution,[35,36] and potentiostatic etching in hydrochloric acid.[35,36]

The decision to replace cast CoCrMo as a material for anchorage shafts by forged MP35N has been taken for the latter; in addition to a nondetectable loss in corrosion resistance in our experiments, it presents greatly enhanced mechanical strength and toughness, thus minimizing the risk of fatigue and corrosion fatigue. This material change was facilitated by the fact that the outstanding resistance to crevice and pitting corrosion of MP35N in polluted seawater had already been established in a four-year immersion test.[37]

In the meantime, at least two other reports have been published independently, qualifying MP35N as an implant material with high resistance to depassivation[38] and crevice corrosion[39] in saline solutions at 37°C.

In his first paper on the subject, Devine[28] pointed out that the pitting resistance of MP35N was superior to that of cast CoCrMo, while the inverse was true of crevice corrosion. From the theoretical point of view and on the basis of published data, there is no reason why this inversion should be real. It has been concluded that increasing amounts of Ni in the Co base alloy impair the resistance to crevice corrosion. With the exception of one report,[40] this effect has, to our knowledge, never been described in the literature, and there is no theoretical explanation for it.

In the course of further electrochemical studies concerning active-passive transitions of highly passive iron and cobalt base alloys in chloride media, we have come to the conclusion that it is very difficult to distinguish the different materials with the aid of only a limited number of parallel measurements. This is due to a considerable scatter of electrochemical results on such systems which, in turn, is most probably due to uncontrolled surface states and irregularities in electrode mounting procedures. The surface finish and the impurity level of the final implant should, therefore, be of great importance with respect to the actual behavior in the human body.

The weightiest evidence for the optimum combination of mechanical and corrosion properties of MP35N as a shaft material is, furthermore, the fact that our Company will soon deliver the 100,000th prosthesis based on MP35N, and that we have never heard of any crevice corrosion problem since 1972, *i.e.*, the year of the first implantation of joint endoprostheses made of MP35N.

To sum up, the results of Devine and Wulff have neither been confirmed by *in vivo* implant practice, nor verified by our own or other independent *in vitro* measurements.

T. M. Devine[41] and J. Wulff:[42] Before responding to the specific questions raised by Mr. Süry, we should first like to summarize in general terms our opinion of alloys currently employed as femoral stems in hip-joint prostheses. We do not doubt that the wrought alloy MP35N, because of its superior resistance to fatigue cracking, is more suitable for use as femoral

[27] Sulzer Brothers Limited, Department of Research and Development, CH-8401 Winterthur, Switzerland.
[28] T. M. Devine, SB-SM Thesis, M.I.T. (1971).
[29] T. M. Devine, F. J. Kummer, and J. Wulff, *J. Mater. Sci.*, 7, 126 (1972).
[30] T. M. Devine and J. Wulff, *J. Biomed. Mater. Res.*, 9, 151 (1975).
[31] Registered Trademark Standard Pressed Steel Company, Jenkintown, Pennsylvania.
[32] Haynes Stellite, Registered Trademark of Cabot Corporation, Kokomo, Indiana.
[33] C. Dockal, *Sulzer Tech. Rev.*, 54, 141 (1972).
[34] P. Suery, *Werkst. Korros.*, 26, 278 (1975).
[35] P. Suery and M. Semlitsch, *Pract. Metallogr. Spec.*, 6, 107 (1976).
[36] P. Suery, *Medita*, 6, 19 (1967).
[37] L. A. Pugliese and J. P. Stroup, *Kobalt*, 43, 69 (1969).
[38] R. Thull and M. Schaldach, *Eng. Med.*, 2, 242 (1976).
[39] W. Rostoker and C. W. Pretzel, *J. Biomed. Mater. Res.*, 8, 407 (1974).
[40] G. D. Smith, U.S. Pat. 3,356,542 (1967).
[41] General Electric Company, Research and Development Center, Schenectady, New York 12301.
[42] Department of Metallurgy and Materials Science, Massachusetts Institute of Technology, Cambridge, Massachusetts 02139.

stems of hip-joint prostheses than the cast HS21 type alloys previously used by Sulzer Brothers. We also do not doubt that wrought MP35N is superior to wrought Cr-Ni-Mo austenitic stainless steels for this purpose because of its vastly greater resistance to general and pit corrosion as well as corrosion fatigue. However, as discussed below, our data and that of others clearly show that the crevice corrosion resistance of wrought HS21 is significantly greater than that of cast HS21 which, in turn, is slightly greater than that of MP35N.

In regard to the passivation characteristics of MP35N, we agree with Mr. Süry that MP35N is similar to HS21 (*i.e.*, Co-Cr-Mo). In fact, our results as given in the paper under discussion show the passive corrosion current densities and pitting potentials of MP35N, HS25, as cast HS21, as cast and solutionized HS21, and wrought HS21 to be quite close to one another in solutions of 0.9% NaCl and 10% HCl + 1% $FeCl_3$. However, we feel that such tests as well as all the electrochemical tests cited by Mr. Süry and performed by him and his colleagues[33-36] do not evaluate the crevice corrosion resistance of an alloy. Pitting potential measurements in aqueous NaCl, for example, merely indicate the potential at which pits initiate and grow in a given solution for a given potential scan rate. Such pitting potentials are a function of the presence of pit initiation sites such as soluble inclusions, *e.g.*, sulfides.[43] Crevice corrosion is not dependent on the presence of such microscopic initiation sites since the crevice site has already been determined as the surface area containing the stagnant electrolyte. Thus, although ultrahigh purity stainless steels are immune to pitting during anodic polarization in 0.1M HCl at slow potential scan rates (60 mV/hr), they are susceptible to crevice corrosion.[44] For these reasons, we feel that electrochemical polarization tests on specimens fitted with a crevice, such as our Teflon-crevice specimens or Lizlovs'[45] glass bead crevices, are more meaningful tests of an alloy's resistance to crevice corrosion.

The results of constant potential polarization tests reported by us on creviced samples of cast HS21 and MP35N in 0.9% NaCl are completely consistent with the measurements of Rostoker and Pretzel[39] referred to by Mr. Süry. Rostoker and Pretzel[39] found MP35N and cast Co-Cr-Mo to have equivalent crevice corrosion resistance in 1% NaCl. Neither alloy underwent crevice corrosion when immersed in 1% NaCl for 100 days. Our results also showed MP35N and cast Co-Cr-Mo (HS21) to have equivalent crevice corrosion resistance in 0.9% NaCl. Both materials resisted crevice corrosion at applied potentials less than 300 mV *vs.* Ag-AgCl, but both were susceptible to crevice attack at applied potentials greater than 300 mV. In similar tests, we found MP35N to crevice corrode at lower applied potentials than cast HS21 in 10% HCl + 1% $FeCl_3$, implying that the latter is more crevice corrosion resistant than MP35N in 10% HCl + 1% $FeCl_3$. In agreement with this finding are the data reported by the Latrobe Electric Steel Company,[46] the American fabricators of MP35N, which show that MP35N is less resistant to crevice corrosion in 10% HCl + 1% $FeCl_3$ than other Co-Ni-20Cr-10Mo alloys with lower nickel contents. We were unable to crevice corrode wrought HS21 at any applied potential in either 0.9% NaCl or 10% HCl + 1% $FeCl_3$. At this point we must emphasize the distinction between cast HS21 and wrought HS21. As-cast, HS21 is highly chemically inhomogeneous.[47] Even after 24 hr at 1200°C, microprobe measurements have indicated that complete homogenization has not taken place. It does not surprise us to hear of, and in fact we ourselves have examined, castings of HS21 which, because of their casting defects and chemical inhomogeneities are of inferior corrosion resistance. As such, we feel that the wrought versions of HS21, being highly homogeneous,[47] represent a truer indication of the corrosion resistance of the HS21 composition. As additional proof of this point, Hodge and Lee[48] have recently shown that the strength and corrosion resistance of cast HS21 is much improved by hot isostatic pressing and heat-treatment which help to minimize microporosity and alloy segregation. Finally, we would like to point out that the excellent *in vivo* results achieved to date on MP35N are quite consistent with our *in vitro* results which indicate MP35N to possess excellent crevice corrosion resistance, albeit inferior to that of HS21. However, this four-year *in vivo* data presented by Mr. Süry cannot be considered as proof of the immunity of MP35N to crevice corrosion in body fluids especially since it has long been known that crevice corrosion is not a major problem in this application but is far more serious in other multipiece weight-bearing implants of the kind described by Scales.[49] Additionally, times much longer than four years are required to establish the immunity of an alloy to *in vivo* crevice corrosion.

In summary, the results of our electrochemical crevice corrosion tests are indeed consistent with the literature cited by Mr. Süry, and our ranking of the crevice corrosion resistances of all the alloys examined is in agreement with the *in vivo* results known to date as summarized in Table III of our paper. Where we disagree most certainly with Mr. Süry is that wrought HS21 is superior to cast HS21 and MP35N. In this regard, Hodge and Lee have also found that homogenization treatments improve the corrosion resistance of cast HS21. The literature Mr. Süry cites does not deal with wrought HS21 other than Smith's patent[40] of MP35N which, as Mr. Süry has mentioned, agrees with our data.

[43] G. S. Eklund, *This Journal*, **121**, 467 (1974).
[44] A. P. Bond and E. A. Lizlovs, *ibid.*, **115**, 1130 (1968).
[45] E. A. Lizlovs, *ibid.*, **122**, 589 (1975).
[46] Multiphase MP35N Technical Data, Latrobe Steel Company, Latrobe, Pennsylvania (1973).
[47] T. M. Devine and J. Wulff, *J. Biomed. Mater. Res.*, **9**, 151 (1975).

Streaming Potential Measurements of Biosurfaces

R. A. Van Wagenen, J. D. Andrade, and J. B. Hibbs, Jr.
(pp. 1438-1444, Vol. 123, No. 10)

J. J. Bikerman:[50] The Helmholtz equation for the streaming potential $E = P\epsilon\zeta/4\pi\eta K$ (P being the pressure difference, ϵ and η the dielectric constant and the viscosity of the liquid, K its electric conductivity, and ζ the electrokinetic potential) is valid only as long as the solid phase is a perfect insulator. Do the fibroblast cells used by the authors belong to this class?

Moreover, do these cells swell in the solutions used? If they do, then the above equation should be altered to $E = P\epsilon\zeta/4\pi\eta K \cdot S_1/S_2$, S_1 being the cross section (of the capillary) available to laminar flow of the liquid and S_2 the cross section available to ions.[51,52]

The authors laudably studied the effect of the capillary length and some other factors on the experimental value of E. Unfortunately, to obtain significant results, S_1, S_2, and the electric conductivity of the cells should also be known.

R. A. Van Wagenen,[53] **J. D. Andrade,**[53] **and J. B. Hibbs, Jr.:**[54] 1. It is reasonable to assume that fibroblast cells have the same general membrane structure as those commonly utilized for microelectrophoresis. The

[48] Hodge and Lee, *Corrosion*, **31**, 411 (1975).
[49] J. T. Scales, *J. Bone Jt. Surg.*, **53B**, 344 (1971).
[50] Department of Chemical Engineering, Case Western Reserve University, Cleveland, Ohio 44106.
[51] J. J. Bikerman, *J. Phys. Chem.*, **46**, 724 (1942).
[52] J. J. Bikerman, "Physical Surfaces," p. 417, Academic Press, New York (1970).
[53] Department of Material Science and Engineering, University of Utah, Salt Lake City, Utah 84112.
[54] Veterans Administration Hospital and Department of Medicine, University of Utah Medical Center, Salt Lake City, Utah 84132

transmembrane resistance is undoubtedly very high in these fibroblasts as in most cells. More important is the existence of a pronounced ionic conductance both along the plane of the cell membrane and throughout the hydrated surface of the glass substrate utilized for the fibroblast culture. The specific conductance in this region is comparable to that of bulk streaming electrolyte, but its contribution to the total conductance should be negligible at the ionic strength used in this research simply because the volume of the surface region (including cells) is so minute compared to the total volume of the capillary manifesting bulk electrolyte conductance, *i.e.*, less than 1%.

2. The medium was not isotonic, but this should not affect cell swelling since the fibroblasts were thoroughly prefixed in buffered, isotonic glutaraldehyde. The ratio S_1/S_2 should be essentially unity for capillaries of 600 μm internal diameter containing cells less than 1 μm in thickness. Also, the flow throughout the system was laminar on the basis of Reynolds number calculations determined by flow rate.

Ionic Conductivity of Some Lithium Silicates and Aluminosilicates

I. D. Raistrick, C. Ho, and R. A. Huggins
(pp. 1469-1476, Vol. 123, No. 10)

A. D. Franklin and K. F. Young:[55] Raistrick *et al.* fit their low temperature, high frequency data with an equation for the admittance which reads

$$Y^* = R_B^{-1} + j\omega C_\infty + A_B\omega^{+\beta} + jB_B\omega^{+\beta} \qquad [1]$$

This equation can be derived from an equivalent circuit for a polycrystalline ionic conductor given by Bauerle,[56] with some modification. This equivalent circuit is shown in Fig. 1, as the part labelled "low temperature high frequency" to the left of the vertical dotted line. The geometric capacitance is represented by C', while R' represents the summed internal resistance of the crystal grains, and Z^*_{gb} represents the impedance contributed by the grain boundaries. Presumably these boundaries are quite variable in their structure, composition, and properties, and Z^*_{gb} must, in general, be represented with a distribution of relaxation times. If we choose a Cole-Cole[57] distribution, which while purely empirical has been found to describe a wide variety of dielectric materials, then

$$Z^*_{gb} = \frac{\Delta Z}{1 + (j\omega\tau)^\beta} \qquad [2]$$

Under the condition that the grains are very conductive, that is, R' is vanishingly small, the admittance of this part of the circuit becomes

$$Y^* = 1/\Delta Z + j\omega C' + (1/\Delta Z)\,[(\omega\tau)^\beta \cos(\beta\pi/2) + j(\omega\tau)^\beta \sin(\beta\pi/2)] \qquad [3]$$

which is equivalent to Eq. [1] with the identifications

$$R_B = \Delta Z \qquad [4a]$$

$$A_B = (\tau^\beta/\Delta Z)\cos(\beta\pi/2) \qquad [4b]$$

$$B_B = (\tau^\beta/\Delta Z)\sin(\beta\pi/2);$$

$$C_\infty = C' \qquad [4c]$$

This equivalent circuit exhibits all of the properties discussed by Raistrick *et al.* In addition, it relates A_B, B_B, and β through

$$B_B/A_B = \tan(\beta\pi/2) \qquad [5]$$

Values of 2 arctan $(B_B/A_B)/\pi$ calculated using the data of Raistrick *et al.* for Li_2SiO_3 given in their Tables I and II are compared with their β in Table I below. The correspondence is reasonably good, although there appears to be a small but systematic difference between the two estimates of β. This discrepancy may have the following origin. In writing the Cole-Cole equation, we have applied the same exponent to j and to $(\omega\tau)$. However, this does not appear to be necessary, and Eq. [2] could be written more generally still as

$$Z^*_{gb} = \frac{\Delta Z}{1 + j^\gamma(\omega\tau)^\beta} \qquad [6]$$

The exponent γ determines how far the center of the circular arc is depressed below the real axis in the complex plane while β determines the frequency dependence. In Table I $2\arctan(B_B/A_B)/\pi$ is an estimate of γ which appears to differ a bit from the β derived by Raistrick *et al.* from the frequency dependence.

The expression for the impedance corresponding to Eq. [3] is

$$Z^* = \frac{\Delta Z}{1 + (j\omega\tau)^\beta + j\omega C'\Delta Z} \qquad [7]$$

In the complex plane this would produce a distorted arc, one that approaches the real axis at very high frequencies at an angle of $\pi/2$ and with a zero intercept, and at very low frequencies at an angle of $(\beta\pi/2)$ and with an intercept of ΔZ. A careful examination of Fig. 4 in the paper under discussion suggests just this type of asymmetry.

Turning to the high temperature, low frequency data reported by Raistrick *et al.*, we interpret their additional series element Y^*_I somewhat differently and it is illustrated to the right of the dotted line in Fig. 1. They observe that B-G (admittance) plots as a function of temperature are portions of circles that pass through the origin and have centers that lie below the real axis. As the temperature is increased the center of the circle rises until it lies upon the real axis. We suggest that this behavior can be represented with a distribution of relaxation times, but in the admittance rather than the impedance. If we again choose a modified empirical Cole-Cole[57] distribution as in Eq. [6], then the sample electrode admittance and impedance are

$$Y^* = \frac{R_B^{-1}}{1 + j^{-\epsilon}(\omega\tau)^{-\alpha}} \qquad [8]$$

$$Z^* = R_B + R_B\,[\cos(\epsilon\pi/2) - j\sin(\epsilon\pi/2)]\,(\omega\tau)^{-\alpha} \qquad [9]$$

As ϵ is allowed to go from ½ to 1, a transition from Warburg-like[58] behavior (as for a diffusion-controlled

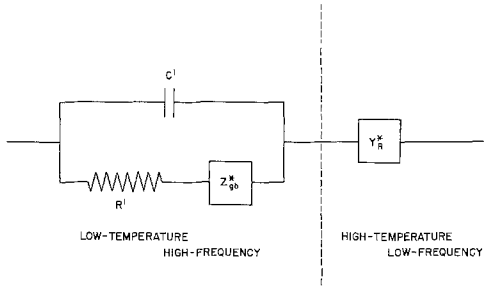


Fig. 1. Equivalent circuit for lithium silicates and aluminosilicates

[55] National Bureau of Standards, Institute for Materials Research, Washington, D.C. 20234.
[56] J. E. Bauerle, *J. Phys. Chem. Solids*, 30, 2657 (1969).
[57] K. S. Cole and R. H. Cole, *J. Chem. Phys.*, 9, 341 (1941).
[58] M. Sluyters-Rehback and J. H. Sluyters, in "Electroanalytical Chemistry," Vol. 4, A. J. Bard, Editor, pp. 16-18, Marcel Dekker, New York (1971).

Table I. Test of Eq. [5] for Li_2SiO

T, °C	$2\arctan(B_B/A_B)/\pi$	β
224	0.83	0.74
255	0.71	0.67
325	0.69	0.65
431.5	0.78	0.71
499	0.45	0.71

process) to that of a simple capacitor occurs. During this process the center of the arc in the Y^* complex plane rises toward the real axis, and the angle subtended by the Z^* line and the real axis in the Z^* complex plane increases toward $\pi/2$. This appears to match the behavior described by Raistrick *et al.*

Raistrick *et al.* represent their high temperature, low frequency sample electrode response with Z^*_I in series with the bulk resistance R_B, as

$$R_B + Z^*_I = R_B + A_I\omega^{-\alpha} - jB_I\omega^{-\alpha} \quad [10]$$

and the slope of the line in the complex impedance plane as

$$\psi_Z = B_I/A_I \quad [11]$$

which is equivalent to Eq. [9] where

$$A_I = R_B\tau^{-\alpha}\cos(\epsilon\pi/2) \quad [12a]$$

$$B_I = R_B\tau^{-\alpha}\sin(\epsilon\pi/2) \quad [12b]$$

$$\psi_Z = B_I/A_I = \tan(\epsilon\pi/2) \quad [12c]$$

Table II below shows that the estimates of ϵ from Eq. [12c] differ considerably from values of α from the frequency dependence, as given by Raistrick *et al.* Since ϵ and α are the exponents on j and $(\omega\tau)$, respectively, then it appears that they must definitely be distinguished from one another, as γ and β are in Eq. [6].

The equivalent circuit of Fig. 1, with Cole-Cole equations (modified as in Eq. [6] and [8]), describing Z^* and Y^*, is therefore an alternative to the one presented by Raistrick *et al.* This equivalent circuit fits the data equally well, and has the advantage of a more direct correspondence with expected physical processes.

I. D. Raistrick, C. Ho, and R. A. Huggins:[59] *Low-temperature-high frequency response.*—Consider the original expression for the bulk complex admittance

$$Y^*_B = A_B\omega^\beta + jB_B\omega^\beta \quad [1]$$

It may be shown by integration of either the real or the imaginary part of this expression, using the Kramers-Kronig relationship, that

$$B_B/A_B = \tan(\beta\pi/2) \quad [2]$$

and hence Eq. [1] may be rewritten as

$$Y^*_B = (jA_B'\omega)^\beta \quad [3]$$

with the identities

$$A_B = A_B'\cos(\beta\pi/2) \quad [4a]$$

$$B_B = A_B'\sin(\beta\pi/2) \quad [4b]$$

Now, taking Eq. [3] and adding a parallel resistance ΔZ to this expression gives

$$Y_B' = \Delta Z^{-1} + (jA_B'\omega)^\beta \quad [5]$$

and a corresponding impedance of

$$Z_B' = (Y_B')^{-1} = \frac{\Delta Z}{1 + \Delta Z(jA_B'\omega)^\beta} \quad [6]$$

[59] Center for Materials Research, Stanford University, Stanford, California 94305.

Table II. Test of Eq. [12c]

Compound	T, °C	$\epsilon = 2\arctan(B_I/A_I)/\pi$	α
$LiAlSi_2O_6$	692	0.68	0.85
$LiAlSi_2O_6$	786	0.54	0.73
$LiAlSi_2O_6$	931.5	0.64	0.80
$LiAlSiO_4$	667	0.66	0.79
$LiAlSiO_4$	775	0.67	0.76
$LiAlSiO_4$	923	0.47	0.70

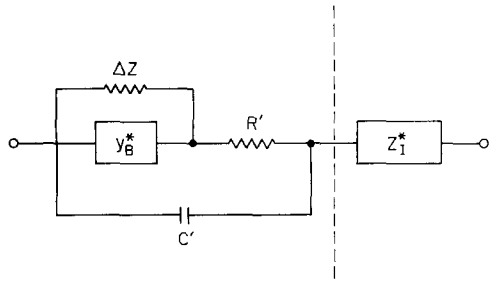


Fig. 2. Franklin and Young's equivalent circuit redrawn after separation of real and complex components of Z^*_{gb}.

This corresponds exactly to Franklin and Young's Eq. [2] with the identification

$$\tau = A_B'\Delta Z^{1/\beta} \quad [7]$$

Thus we may rewrite Franklin and Young's circuit, to the left of the dotted line, as shown below (Fig. 2). This formulation has the advantage that Z^*_{gb} has been divided into a frequency-independent (purely real) resistance, ΔZ, and a frequency-dependent (complex) admittance Y^*_B, which is identical to that proposed in our original paper.

If we then neglect R' at all frequencies, the Franklin and Young circuit is identical in all respects to our original circuit, Fig. 7a, with the identities given by Franklin and Young in their Eq. [4a]-[4c], with the additional relations given above (Eq. [4a], [4b], and [7]). The neglect of R', however, is open to question. Two points are of interest. As ω increases, Y^*_B will shunt ΔZ until R' ultimately becomes important. In the complex impedance plane the general response of the Franklin and Young circuit will be two arcs. The high frequency arc will be semicircular, the low frequency arc will have its center depressed below the real axis if $\beta < 1$. If the time constants associated with the two arcs are similar, and/or if $R' << \Delta Z$ then the Franklin and Young response will be similar to that shown in Fig. 4 of the paper under discussion. It seems, however, that the introduction of unseen circuit elements, which are then neglected, *i.e.*, R', is an unnecessary complication.

A more serious problem posed by Franklin and Young is that ΔZ is equated with an intergranular resistance rather than any kind of bulk resistance, *i.e.*, it is never possible to measure bulk conductivities in a polycrystalline material, if $R' << \Delta Z$. All that one can do is measure intergranular effects.

At the time the original paper was written, no single crystal data were available on these materials. Recently, however, measurements have been made on single crystals of β-eucryptite (β-$LiAlSiO_4$) by von Alpen *et al.*[60] $LiAlSiO_4$ is an anisotropic Li^+ conductor with the higher conductivity parallel to the crystallographic c-axis. The conductivity values perpendicular and parallel to the c-axis, lie below and above the data reported by Raistrick *et al.* and, further, the activation enthalpy perpendicular to the c-axis was identical to that which we obtained. Although certainly not definitive, this comparison suggests that we were in fact measuring a bulk conductivity rather than an intergranular effect. Further experiments on samples with a wide range of controlled concentrations of grain boundaries will be necessary to fully resolve this problem.

The modification suggested by Franklin and Young in their Eq. [6], although fitting the experimental data rather better than the original form of the admittance we used, is open to the objection that it does not conform to the general laws governing linear processes.

Expanding Franklin and Young's Eq. [6] and removing ΔZ as discussed above gives

[60] U. von Alpen, E. Schonherr, H. Schulz, and G. H. Talat, *Electrochim. Acta*, To be published.

$$Y = C\beta\omega^{\beta}\{\cos(\gamma\pi/2) + j\sin(\gamma\pi/2)\} \quad [8]$$

where

$$C = \tau/\Delta Z^{1/\beta}$$

Using the Kramers-Kronig relation

$$B(\omega) = 2\omega/\pi\int_0^{\infty}\frac{G(\nu)}{\nu^2 - \omega^2}d\nu \quad [9]$$

where B and G are the imaginary and real parts of Y, we can show, given

$$G(\omega) = (C\omega)^{\beta}\cos(\gamma\pi/2)$$

that

$$B(\omega) = (C\omega)^{\beta}\cos(\gamma\pi/2)\tan(\beta\pi/2)$$

which is not equal to

$$(C\omega)^{\beta}\sin(\gamma\pi/2)$$

unless

$$\beta = \gamma$$

In other words, the circuit element implied by Eq. [6] of Franklin and Young's discussion is nonlinear and cannot be used to describe a distribution of relaxation times.

High temperature-low frequency response.—Equations [8] and [9] of Franklin and Young are open to the same objection as their Eq. [6] discussed immediately above.

If, however, we allow ϵ to equal α, then Eq. [8] reduces to the same interface impedance formulation as was used in the paper under discussion, in series with a resistance R_B (or ΔZ).

The apparent discrepancy noted in Table II of Franklin and Young's discussion, however, remains unexplained. More careful experiments on single crystal β-PbF_2[61] have indicated rather different behavior. In this later work, much better agreement between α and the expression $2\arctan(B_I/A_I)\pi$ was obtained. Further, α appeared to be almost independent of temperature whereas B_I and A_I both appeared to follow an Arrhenius-like temperature dependence $A_I = A_I^{\circ}\exp(-\Delta H/RT)$.

As a consequence of the relationship between A_I and B_I deduced from the Kramers-Kronig relations, A_I and B_I must have the same temperature dependence if α is independent of temperature. This was confirmed experimentally. α took different values depending on the nature of the electrode preparation, and could be as low as ~0.3. This behavior cannot be explained by a simple Warburg mechanism as suggested by Franklin and Young.

Summary.—The principal points we should like to make are as follows:

First, the Franklin and Young impedance function is directly derivable from our original admittance functions, and their equivalent circuit is exactly equivalent to ours if the series resistance in their circuit is neglected, as they have done. The introduction, and subsequent neglect, of additional components which make no observable contribution to the frequency dispersion seems an unnecessary complication.

Second, Franklin and Young did this in order to arrive at an impedance function of a form analogous to the empirical relations first used by Cole and Cole to describe the complex dielectric constant. They also chose to interpret this function in terms of a distribution of relaxation times. In the paper we made a point of deliberately avoiding this interpretation. Although the complex bulk admittance appears to be associated with grain boundary effects (it was absent in the single crystal PbF_2 samples,[61] even though a complex interface impedance of the same form was still present) there appears to be no direct experimental evidence that a distribution of relaxation times is responsible, except in a formal sense.

Third, we feel that the modification of the impedance function suggested by Franklin and Young is open to the serious objection that it implies a nonlinear process.

We should like to thank Drs. Franklin and Young for their interest in our paper. The questions of interpretation raised by their comments are worthy of careful investigation in the future.

[61] I. D. Raistrick, C. Ho, Y. W. Hu, and R. A. Huggins, *J. Electroanal Chem. Interfacial Electrochem.*, To be published.

On the Differential Thermal Analysis of the Platinum-Oxygen System

J. P. Hoare, R. F. Paluch, and S. G. Meibuhr
(pp. 1821-1824, Vol. 123, No. 12)

K. Kinoshita:[62] In the paper under discussion, Dr. Hoare and co-workers reported on the application of differential thermal analysis (DTA) to identify two absorbed states of oxygen on oxidized Pt. The DTA curves for preanodized and HNO_3 treated Pt beads deserve further comment in view of the recent data obtained by the present author on the DTA of commercial PtO_2 in an inert atmosphere.[63]

Hoare and co-workers reported that two exothermic peaks were produced in the DTA scan by the desorption of oxygen species on Pt. DTA studies on PtO_2 (commercial product of Engelhard Industries, 115Å crystallite size) in flowing He by this author showed that PtO_2 decomposed to metallic Pt with an endothermic reaction at about 500°C when the sample was heated at 10°C/min. After cooling to room temperature, a second DTA curve was run and no endothermic peak was observed. Apparently, complete decomposition of PtO_2 to Pt was achieved in one heat cycle to 700°C. Weight loss measurements and x-ray diffraction analysis of the decomposition product suggested that the decomposition reaction is given by

$$PtO_2 \rightarrow Pt + O_2$$

There is evidence in the literature suggesting that the oxidation of finely divided Pt in air is an exothermic reaction.[64] For the reaction

$$Pt\ (solid) + \tfrac{1}{2}\ O_2\ (gas) \rightarrow Pt - O\ (solid)$$

the measured enthalpy at 40°C for a Pt coverage of 0.5 is −58 kcal/mole O_2,[65] which means the desorption of oxygen from Pt-O is an endothermic reaction.

The exothermic peaks in the DTA curves (Fig. 1-3 in the paper under discussion) ascribed to the desorption of oxygen from oxidized Pt beads are difficult to reconcile with the DTA results obtained on commercial PtO_2 [63] and the other results cited from the published literature.[64,65] One explanation is that the PtO_2 and Pt-O species present on the oxidized Pt beads possess thermal properties different from those found in commercial PtO_2 or Pt-O produced by the adsorption of O_2 on clean Pt.

The authors report that "the DTA curve does not return to the base line (intercept on the ΔT ordinate) between the peaks and that a long tail exists at the high temperature end of the curve." Since the specific heat capacities of the Pt sample and the Al_2O_3 reference material are not the same, this behavior in the DTA base line is generally observed. The base line would be zero only if the reference and sample parameters are identical, if heat leakage from both sample and reference thermocouples are identical, and if the sample was not undergoing a phase change or a chemical reaction.[66]

Examination of the DTA curves (Fig. 1-3) suggests another interpretation to explain the thermal analysis

[62] Argonne National Laboratory, Chemical Engineering Division, Argonne, Illinois 60439.
[63] K. Kinoshita, *Thermochim. Acta*, In press.
[64] D. J. Booth, D. Bryce-Smith, and A. Gilbert, *Chem. Ind.*, **17**, 688 (1972).
[65] J. M. Basset, A. Theolier, M. Primet, and M. Prettre, *Catal. Proc. Int. Congr. 5th*, 1972, 915.
[66] R. Melling, F. W. Silburn, and R. M. McIntosh, *Anal. Chem.*, 41, 1275 (1969).

data. Assume that the over-all shape of the DTA curve, that is, an increase in ΔT followed by a decrease in ΔT as the sample temperature increases, represents the base line characteristics. The desorption of oxygen from Pt would then produce a DTA peak which would be observed superimposed on the changing base line. If this was the case, the minimum in ΔT evident at 200°-300°C in Fig. 1-3 would be associated with the desorption of oxygen from Pt and the oxidized Pt beads would then exhibit an endothermic desorption of oxygen similar to the anticipated result based on other reports.[63-65] Furthermore, only one species of adsorbed oxygen is required to explain the endotherm rather than the two species postulated by Hoare and coworkers. Norton[67] reported evidence for the presence of two adsorbed states of oxygen on Pt, one oxygen species desorbing below 300°K and the other above 600°K. The latter oxygen species may very well be similar to the oxygen species desorbed from the oxidized Pt bead. On the other hand, two oxygen species would not be expected in the DTA curves (Fig. 1-3) since one oxygen species desorbs below 300°K and the DTA scan starts at 0°C.

There are several methods of detecting base line shifts in a DTA instrument. A DTA scan of Al_2O_3 in both the sample and reference Pt dishes should yield a ΔT of zero throughout the temperature range of the experiment. If a base line deviation exists with identical material in both the reference and sample dishes, a variety of reasons may be responsible: thermocouple placement, difference in heat leakage rates from sample and reference dishes, for example. Alternatively, oxidized Pt beads in both the reference and sample dishes should yield a base line with ΔT of zero. Finally, a DTA scan of an oxidized Pt bead in the sample dish and an untreated Pt bead in the reference dish would yield information on the presence of adsorbed oxygen species produced by the oxidation of Pt.

J. P. Hoare, R. F. Paluch, and S. G. Meibuhr:[68] We wish to thank Dr. Kinoshita for calling to our attention some interesting aspects of this DTA work and for confirming that PtO_2 is unstable. Let us point out again that the DTA peaks do not correspond to adsorbed PtO_2 because any PtO_2 formed during anodization decomposed on the Pt surface before the DTA curve could be run. Also, let us note that Booth *et al.*[64] concluded that the heat liberated during exposure of finely divided Pt or Pd to oxygen arose from the recrystallization of the Pt- or Pd-black since no oxides were detected.

According to Smith,[69] Pt is an endothermic occluder of hydrogen so that the DTA curve of the Pt-H_2 system should show an exothermic peak in agreement with Fig. 3F in the paper under discussion. Consequently, the data in our paper indicate that Pt is also an endothermic occluder of oxygen since exothermic peaks have been observed in Fig. 1-3. As stated in our paper, the peaks correspond to the adsorption of oxygen on two types of surface sites. Many other investigators have detected at least two kinds of surface adsorption sites on Pt.

Although bulk PtO_2 exhibits one endothermic peak on the DTA curve,[63] this is expected since it is the decomposition of a nonconducting compound which is certainly not the same species present on an anodized Pt sample. We plan to make some measurements on bulk PtO_2.

With regard to base line shifts, we did run DTA scans with Al_2O_3 in both pans and observed nearly flat lines. What shifts were present were always in the positive direction; we never observed a negative shift. If one superimposes an endothermic peak on a base line with a positive shift, there is no way one could observe the two humps in the curves of Fig. 1-3. Surely Fig. 3 cannot be explained by a shift in base line. Because of base line shifts, accurate measurements of the area under a given peak cannot be made, however.

We agree that using a Pt sample as a reference may give us some interesting data and we plan to carry out experiments of this type.

[67] P. R. Norton, *J. Catal.*, 36, 211 (1975).

[68] General Motors Corporation, Research Laboratories, Warren, Michigan 48090.

[69] D. P. Smith, "Hydrogen in Metals," University of Chicago Press, Chicago (1948).

JOURNAL OF THE ELECTROCHEMICAL SOCIETY

SOLID-STATE SCIENCE AND TECHNOLOGY

JUNE 1977

High Temperature Corrosion of Chromium and Chromium (III) Oxide in Chlorine and Chlorine-Oxygen Mixtures

K. Reinhold and K. Hauffe*

Institute for Physical Chemistry, University of Göttingen, D-3400 Göttingen, Germany

ABSTRACT

The chlorination kinetics of Cr between 650° and 800°C is characterized by a time-constant weight loss of the specimen caused by volatilization of $CrCl_3$ and $CrCl_4$. At low Cl_2 pressures also a scale is formed consisting of $CrCl_2$ and $CrCl_3$. The rate-determining step is the diffusion of volatile products across the laminar boundary layer. Cr_2O_3 pellets show time-constant weight loss in Cl_2 and Cl_2-O_2 mixtures. In the mixtures, the rate constant of the corrosion of Cr_2O_3 is about a hundred times smaller compared to the chlorination of Cr in the absence of O_2. It increases with the fourth root of the O_2 pressure and linearly with the Cl_2 pressure indicating that CrO_2Cl_2 seems to be the only reaction product. In a mixture of Cl_2 and O_2, the corrosion of Cr is inhibited due to formation of an outer Cr_2O_3 layer and of CrO_2Cl_2 as the only volatile product. Since Cr_2O_3 can be volatilized as described above, preoxidized samples of Cr exhibit no long-time corrosion resistance in Cl_2.

There is some interest in chemical engineering to find suitable construction material for reactions in which chlorine is involved at high temperatures. Among metals only nickel has some importance because of the comparatively low vapor pressure of $NiCl_2$. At 700°C, however, a considerable metal consumption already takes place. In a previous work Hauffe and Hinrichs (1) studied the chlorination behavior of Ni and NiO. They found time-constant weight loss of the samples due to the formation of volatile $NiCl_2$. The rate constant was proportional to the square root of the flow rate. When Ni was chlorinated, the rate constant first increased linearly with the Cl_2 pressure but became independent of the Cl_2 pressure after a critical value was reached. The authors' attempt to improve the corrosion resistance of Ni against Cl_2 by adding small amounts of O_2 to the atmosphere was not successful. While oxygen did not affect the reaction at low O_2 pressures it even caused an ignitionlike reaction above a critical pressure. This behavior may be attributed to the small difference in thermodynamic stability of $NiCl_2$ and NiO. Later on, Halfdanarson and Hauffe (2) gave a more detailed discussion of the mechanism of Ni chlorination. They were able to elucidate the rate-determining step of the reaction to be diffusion of either Cl_2 toward the sample surface or $NiCl_2$ away from it across the laminar boundary layer. They also studied the chlorination kinetics of Ni-Cr alloys. No difference was found between the rate constants of Ni and Ni-Cr alloy chlorination because of the small difference between the vapor pressure of $NiCl_2$ and $CrCl_3$ or $CrCl_4$. Preoxidized samples of Ni-Cr alloys, however, showed better resistance against chlorination than those of Ni.

In the system Cr-Cl-O, Cr_2O_3 has a much higher thermodynamic stability than the other possible products. For example the free energy of formation from the elements at 700°C is $\Delta G°_{CrCl_2(s)} = 65.7$ (3), $\Delta G°_{CrCl_3(s)} = 78.2$ (3), and $\Delta G°_{Cr_2O_3(s)} = 103.7$ (3) kcal for 1 g-atom Cr. Therefore, the aim of this investigation was the elaboration of the conditions under which inhibition by Cr_2O_3 formation takes place. This study seemed to be much more promising, since it is supported by the observation (4, 5) that the nitriding of Cr in air is inhibited by Cr_2O_3 formation. In addition, the corrosion resistance of numerous alloy systems has been considerably improved by small amounts of Cr. In the system Cr-Cl-O, however, the existence of oxyhalogenides has to be taken into consideration. It must be assumed that the extent of inhibition depends on the reactivity of Cr_2O_3 in Cl_2-O_2 mixtures. Therefore, the volatilization of Cr_2O_3 in Cl_2 and Cl_2-O_2 mixtures was investigated. Little previous work has been done. According to Moissan (6), Cr_2O_3 gives $CrCl_3$ with dry Cl_2 and CrO_2Cl_2 with wet Cl_2 at 440°C. Wasmuht (7) has found that the weight loss of Cr_2O_3 after 1 hr of chlorination at 800°C is 6.6% (no data about flow rate and chlorine pressure). If carbon is present, the reaction between Cr_2O_3 and Cl_2 starts at lower temperatures giving $CrCl_3$ (8). Recent thermodynamic investigation by Sano and Belton (9) indicates that CrO_2Cl_2 is the only reaction product in Cl_2-O_2 mixtures.

First, the chlorination kinetics of Cr had to be investigated since only little previous work was available. According to Sargent (10) the reaction between Cr and dry Cl_2 starts measurably at 300°C giving $CrCl_3$. Above 350°C, $CrCl_3$ begins to dissociate into $CrCl_2$ and Cl_2 (11). The vapor pressure equilibrium over solid $CrCl_3$ and $CrCl_2$ was thoroughly studied by Doerner (12). On the basis of these experiments he was the first to ascertain the existence of $CrCl_4$.

Experimental

Apparatus.—The weight change of the samples during corrosion was continuously followed by a quartz spiral balance. In order to avoid depletion of the reactive gases at the surface of the sample, the measure-

* Electrochemical Society Active Member.

Key words: corrosion kinetics, volatilization of reaction products, laminar boundary layer diffusion, inhibition by oxygen.

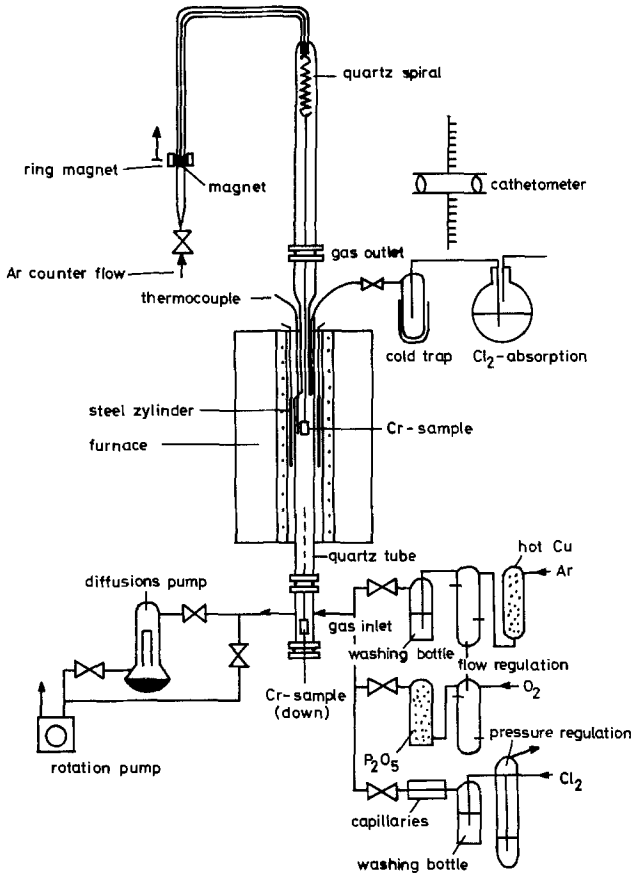


Fig. 1. Corrosion apparatus (schematic)

ments were carried out in a flow system. Argon was used as carrier gas to which oxygen and chlorine were added in suitable amounts. Thus a constant gas composition and a continuous removal of volatile products were achieved. The main part of the corrosion apparatus (Fig. 1) was the quartz reaction tube (1). The temperature in the reaction zone could be maintained to about ± 1°C. Since the upper cooling zone of the quartz tube was tapered, convective flow was avoided. A weak Ar counterflow was introduced at the top of the quartz tube to prevent precipitation of volatile products on the quartz fiber suspended from the quartz spiral balance. The dilatation of the spiral was followed by observation of a marker on the quartz fiber by means of a cathetometer. The movement of the marker could be read to ± 0.01 mm. Since the sensitivity of the spiral balance was 43 mg/cm, the accuracy of the weight determination was ± 0.05 mg.

Argon, oxygen, and chlorine of purity 99.997, 99.995, and 99.9 volume percent, respectively, were supplied by Messer-Griesheim. Small amounts of oxygen in the argon were removed by hot active copper (13), water in chlorine and oxygen was absorbed by H_2SO_4 and P_2O_5, respectively.

In order to clean the reaction chamber and dry the samples before each measurement, the apparatus could be evacuated to about 10^{-3} Torr.

Sample preparation.—Because of the brittleness of Cr no foils can be manufactured. A cylindrical ingot of 99.997% Cr, prepared by thermal decomposition of CrI_3, was supplied by General Electric, New York. This ingot was divided into smaller pieces by means of a diamond saw. From these pieces rectangular, 0.6-0.8 mm thick specimens were prepared by spark erosion. After wet grinding on 400 silicon carbide paper, the samples were polished with finest 6/0 abrasive paper and degreased in petroleum. The geometrical surface of the coupons varied from 2 to 4 cm^2 and was determined by means of a slide gauge with an accuracy of 1%. Cr_2O_3 pellets 1.5 mm thick with a diameter of 13 mm were pressed from Cr_2O_3 powder of 99.9% purity, supplied by Riedel de Haen. Before the volatilization experiments, all the samples were annealed in air at 1000°C for 24 hr.

Measuring procedure.—After the sample was suspended from the quartz fiber, its position was below the lower cooling zone of the furnace. After evacuation, argon was introduced until the pressure reached 1 atm. Now the flow rate of argon as carrier gas was regulated and adequate portions of the reactive gases added. Finally, the sample was lifted up to the reaction zone as soon as a constant gas composition was achieved (after 15 min generally). Now the dilatation of the balance was followed in suitable time intervals and thus the course of corrosion recorded. Because of initial vibrations of the spiral, caused by lifting the sample up to the reaction zone, the first reading was possible 1 min after the start. Since this time is required for the samples to reach reaction temperature, the rate of corrosion was neglected in the first minute.

Results

Chlorination of chromium, kinetics.—In the temperature and chlorine pressure region used the chlorination of Cr is characterized by a weight loss of the specimen proportional to the reaction time. Figure 2 shows a typical straight line the slope of which gives the rate constant $k = -d(\Delta m/A)/dt$, where A = geometrical surface of the sample. The rate constant does not change as long as the geometrical surface of the sample remains constant. The weight loss is caused by volatilization of the reaction products.

At low chlorine pressures also a thick scale is formed. As illustrated in Fig. 3, the mass of the scale increases linearly with time. The scale mass was determined by weighing the sample before and after scale removal. Since the inner layer of the scale is hygroscopic, the scale can be removed easily and quantitatively.

The plot in Fig. 4 gives the chlorine pressure dependence of the rate constant between 10 and 200 Torr at 700°C. Initially the rate constant is proportional to the square root of the chlorine pressure. Above the inflection point, however, (about 40 Torr) the rate con-

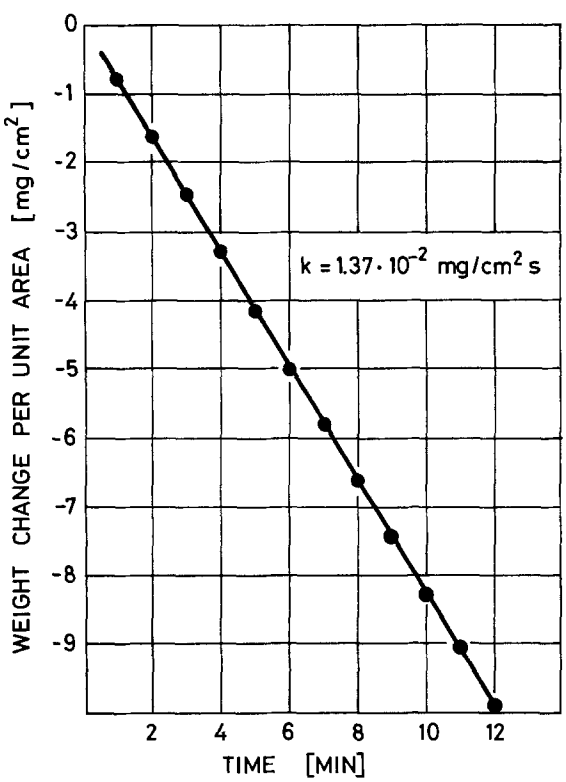


Fig. 2. Constant weight loss during Cr chlorination at T = 700°C, p_{Cl_2} = 20 Torr, and v = 1.5 cm/sec.

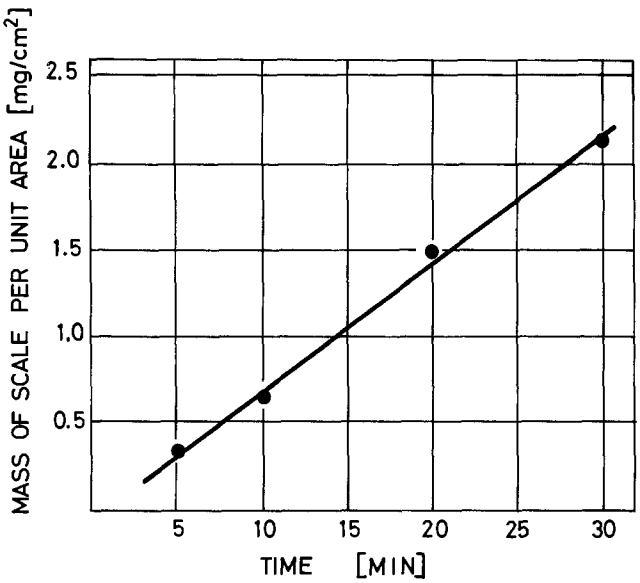


Fig. 3. Dependence of scale mass on reaction time during Cr chlorination at $T = 700°C$, $p_{Cl_2} = 20$ Torr, and $v = 1.5$ cm/sec.

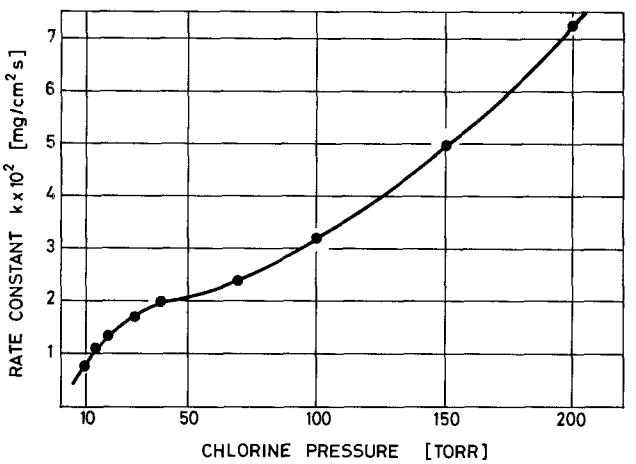


Fig. 4. Dependence of rate constant of Cr chlorination on chlorine pressure at $T = 700°C$ and $v = 1.5$ cm/sec.

stant is proportional to the second power of the chlorine pressure. For a given reaction time, the scale becomes thinner with increasing chlorine pressure. The temperature dependence of the rate constant is shown in Fig. 5. As can be seen from this plot, k initially increases exponentially. Above 750°C, however, the increase becomes smaller, caused by chlorine depletion. Above 815°C, the melting point of $CrCl_2$, the reaction could not be continuously followed anymore. As described below, the inner layer of the scale was found to be $CrCl_2$.

The flow rate is given by the equation

$$v_{(T)} = \frac{N_o}{q \cdot 60} \cdot \frac{T}{T_o} \text{ cm/sec}$$

where N_o = total gas flow at room temperature T_o in cubic centimeters per minute, q = cross section of the quartz tube in the reaction zone, and T = reaction temperature in Kelvin. This is a mean flow rate with regard to the cross section of the quartz tube. Since a parabolic flow rate profile is formed in the tube, the flow rate in the center of the tube, where the sample is located, is about two times the mean flow rate. As can be seen from Fig. 6, the rate constant follows the square root of the mean flow rate: $k \sim \sqrt{v}$.

Sample and product analysis.—The chlorination operates like a pickling procedure. After scale removal

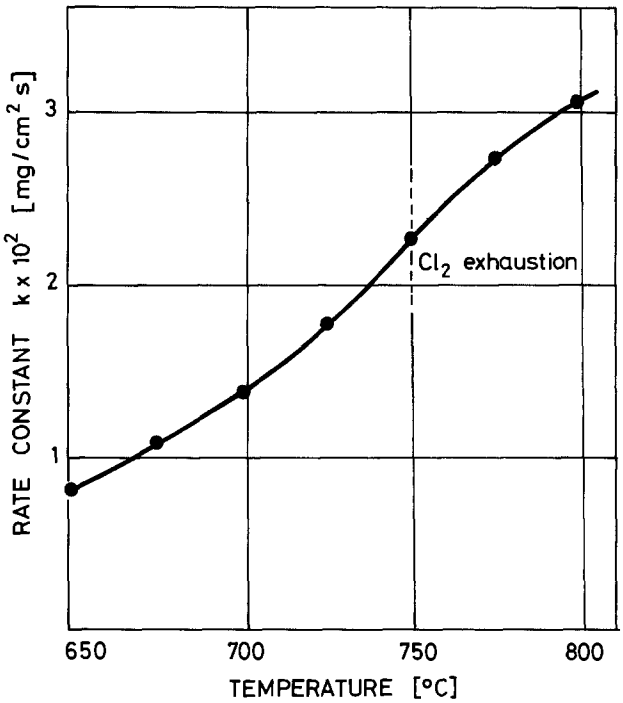


Fig. 5. Dependence of rate constant of Cr chlorination on temperature at $p_{Cl_2} = 20$ Torr, $v = 0.46 \times T/298$ cm/sec.

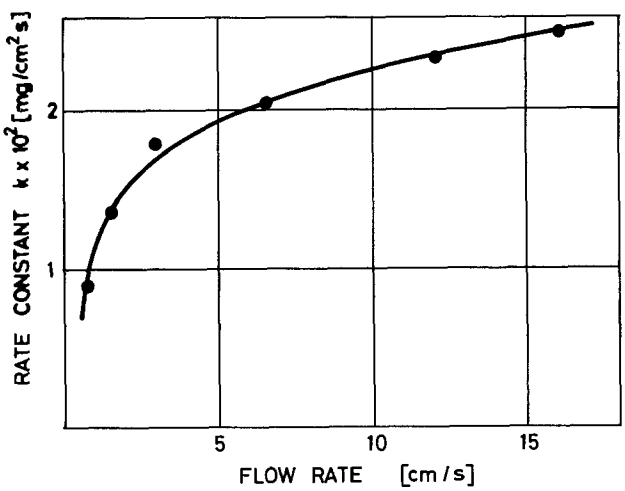


Fig. 6. Dependence of rate constant of Cr chlorination on flow rate at $T = 700°C$, $p_{Cl_2} = 20$ Torr.

the grain structure of the metal becomes visible (mean grain size = 4.8 mm²). The thickness of the metal after corrosion has decreased more markedly in the lower than in the upper part of the sample. The thickness d of the remaining metal sheet for a given reaction time t is about proportional to the square root of the distance x from the lower edge of the sample: $d \sim \sqrt{x}$.

Because of their volatility, reaction products are found not only in the scale but also as sublimates on the walls of the outlet tube. At low chlorine pressures a violet sublimate is found identified as $CrCl_3$ by chemical and x-ray analysis. At higher chlorine pressures, a dark brown precipitation is found in the cooler parts of the gas outlet. This compound decomposed rapidly in wet air under chlorine formation. We assume this product to be $CrCl_4$, since v. Wartenberg (14) who first tried to synthetize $CrCl_4$, obtained a compound of same properties.

Because of its hygroscopicity, porosity, and bad mechanical adherence, the scale was difficult to analyze. As could be concluded from qualitative and quantitative chemical analysis, the scale consists of two layers: a very thin, hygroscopic inner $CrCl_2$ phase and

a thick, porous outer layer of both $CrCl_2$ and $CrCl_3$. For microscopic investigation, the samples had to be impregnated by a transparent lacquer and embedded in epoxy resin. As was found by microscopic investigation, the thickness of the outer phase of the scale increases linearly with time. Since the thin inner $CrCl_2$ phase does not contribute to the scale mass, this result is coincident with the previous observation that the scale mass is linear with the reaction time.

Volatilization of Cr_2O_3.—The weight loss of Cr_2O_3 pellets in chlorine is linear with the reaction time. Plot a in Fig. 7 shows the chlorine pressure dependence of the rate constant between 10 and 70 Torr. The rate constants are very much smaller compared to those of Cr chlorination. Plot b in Fig. 7 shows the chlorine pressure dependence of the rate constant between 10 and 70 Torr in Cl_2-O_2 mixtures. Both in chlorine and in Cl_2-O_2 mixtures, the rate constant increases linearly with the chlorine pressure. In Fig. 8, the oxygen pressure dependence of the rate constant is represented for three temperatures. It is exactly a linear function of the fourth root of the oxygen pressure in Cl_2-O_2 mixtures. The rate constants obtained in Cl_2-O_2 mixtures are higher than in pure chlorine, but about a factor of 100 lower than the rate constants of Cr chlorination. Analogous to Cr chlorination the rate constant was found to be proportional to the square root of the flow rate.

Simultaneous attack of Cl_2 and O_2 on Cr.—Figures 9 and 10 represent the corrosion rate of Cr in several Cl_2-O_2 mixtures at 700°C. There are three typical oxygen pressure regions:

1. Between $p_{O_2} = 0$ and $p_{O_2} = 2$ Torr, a considerable initial weight loss is found. The inflection points of curves b and c are caused by precipitation of volatile chlorides as Cr_2O_3 on the quartz fiber. That could not be avoided in this oxygen pressure region. Therefore, no good reproducibility was obtained.

2. Between $p_{O_2} = 2$ and $p_{O_2} = 20$ Torr, a mass gain of the specimen was observed. After a definite reaction time (dependent on oxygen pressure) the sample mass becomes constant.

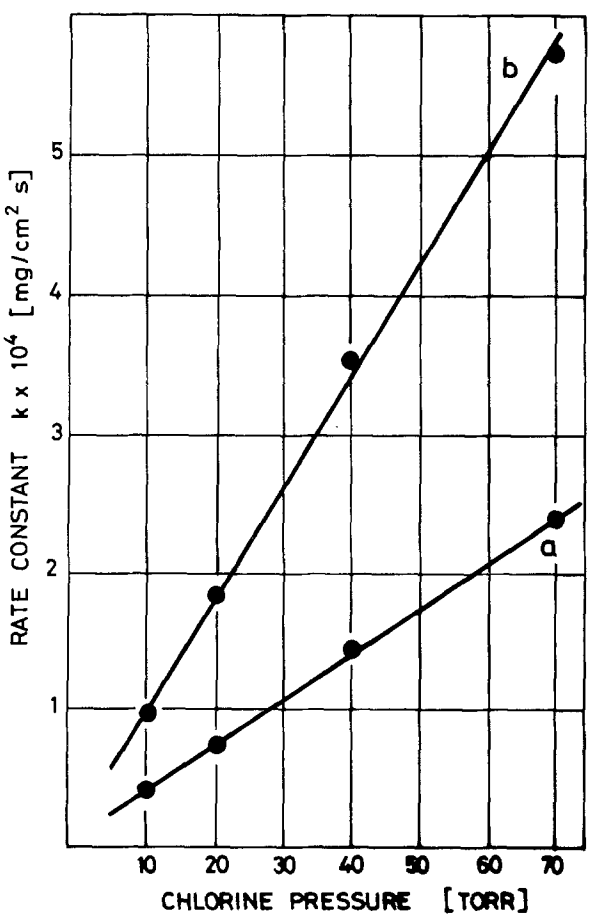


Fig. 7. Dependence of rate constant of Cr_2O_3 volatilization on chlorine pressure at $T = 700°C$, $v = 1.5$ cm/sec. Curve a, no oxygen present; curve b, $p_{O_2} = 20$ Torr.

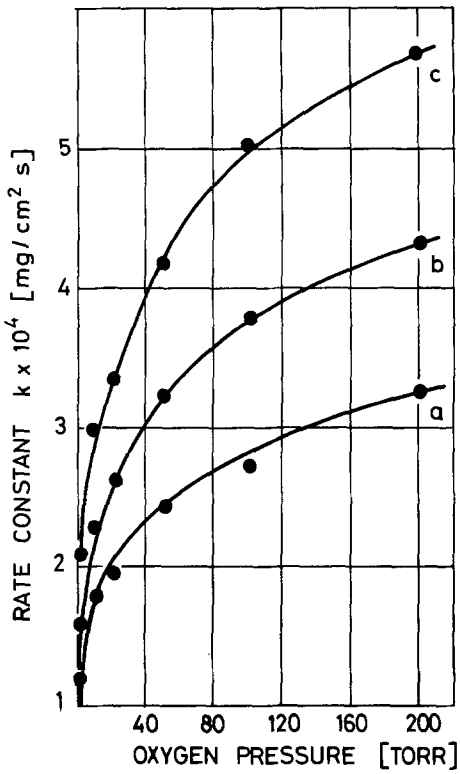


Fig. 8. Dependence of rate constant of Cr_2O_3 volatilization on oxygen pressure at $p_{Cl_2} = 20$ Torr and $v = 1.5$ cm/sec. Curve a, $T = 700°C$; curve b, $T = 750°C$; curve c, $T = 800°C$.

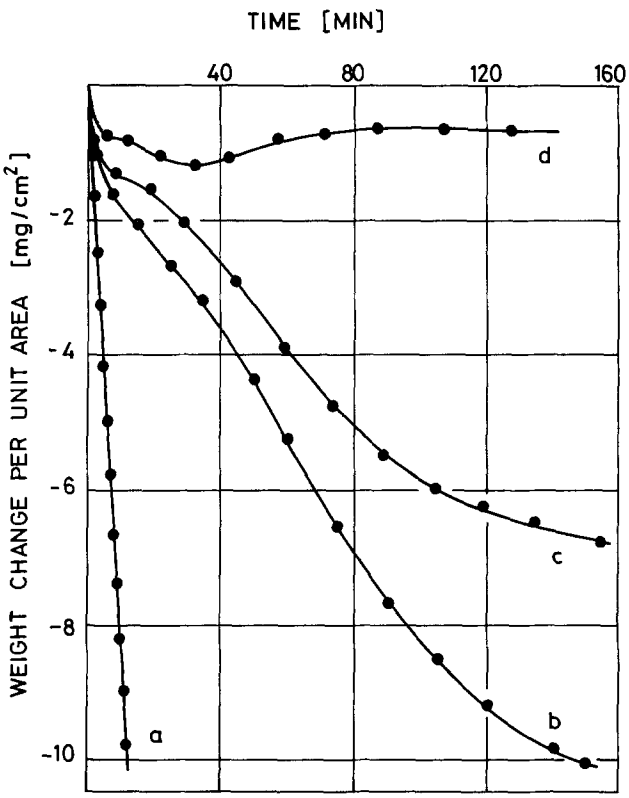


Fig. 9. Corrosion rate of Cr in Cl_2-O_2 mixtures at $T = 700°C$, $p_{Cl_2} = 20$ Torr, and $v = 1.5$ cm/sec. Curve a, no oxygen present; curve b, $p_{O_2} = 0.5$ Torr; curve c, $p_{O_2} = 1$ Torr; curve d, $p_{O_2} = 2$ Torr.

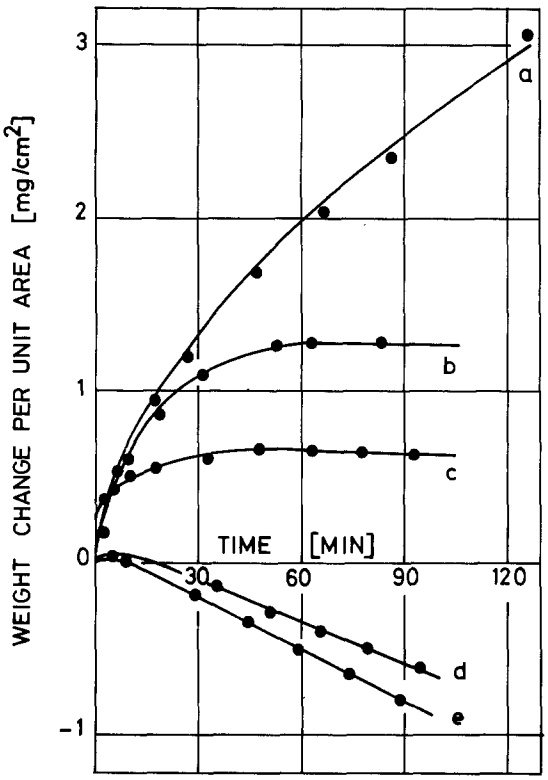


Fig. 10. Corrosion rate of Cr in O_2-Cl_2 mixtures at $T = 700°C$, $p_{Cl_2} = 20$ Torr, and $v = 1.5$ cm/sec. Curve a, $p_{O_2} = 3.5$ Torr; curve b, $p_{O_2} = 10$ Torr; curve c, $p_{O_2} = 20$ Torr; curve d, $p_{O_2} = 50$ Torr; curve e, $p_{O_2} = 100$ Torr.

3. Above $p_{O_2} = 20$ Torr, a time-constant weight loss is found again. The rate constants are $k = 1.1 \times 10^{-4}$ mg/cm² sec for $p_{O_2} = 50$ Torr and $k = 1.6 \times 10^{-4}$ mg/cm² sec for $p_{O_2} = 100$ Torr.

The influence of the oxygen pressure on scale mass and Cr consumption is shown in Fig. 11. At low oxygen pressures, there is still a high portion of volatile products after 1 hr of corrosion. With increasing oxygen pressure, the consumption of Cr decreases rapidly while the scale mass passes a maximum.

Up to $p_{O_2} = 20$ Torr the scale mass is comparable to that found for Cr chlorination. Above $p_{O_2} = 20$ Torr, however, both scale mass and Cr consumption become

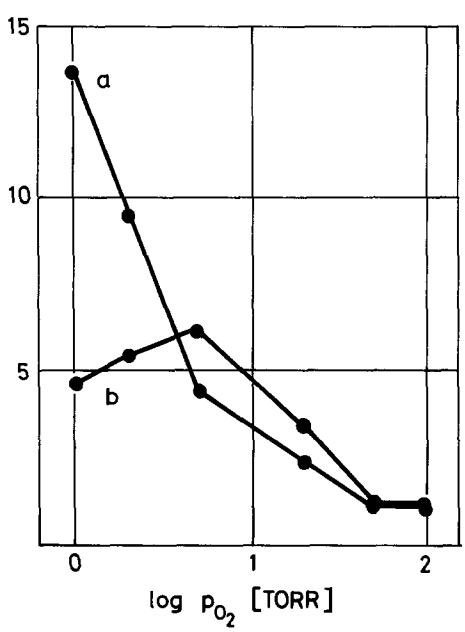


Fig. 11. Dependence of Cr consumption (curve a) and scale mass (curve b) on oxygen pressure at $T = 700°C$, $p_{Cl_2} = 20$ Torr, $v = 1.5$ cm/sec, and $t = 60$ min.

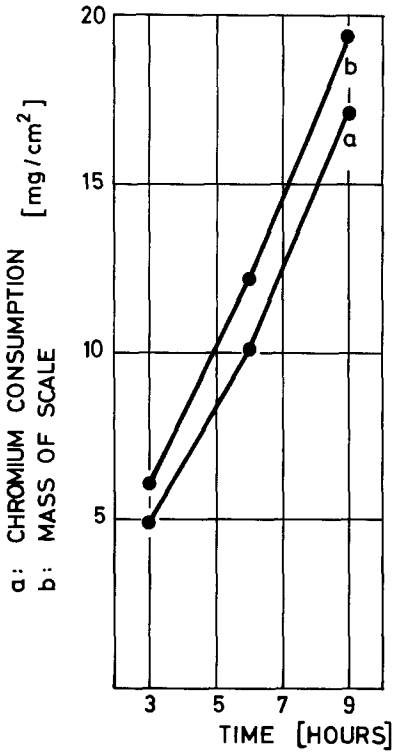


Fig. 12. Dependence of Cr consumption (curve a) and scale mass (curve b) on reaction time at $T = 700°C$, $p_{Cl_2} = 20$ Torr, $p_{O_2} = 20$ Torr, and $v = 1.5$ cm/sec.

small. As can be seen from Fig. 9 and 10, the mass of the samples attains a constant value under certain conditions. This cannot be attributed to a standstill of reaction, since Cr_2O_3 is volatilized in Cl_2-O_2 mixtures as described above. Therefore, the dependence of scale mass and Cr consumption on reaction time has been investigated. The result is given in Fig. 12. Both scale mass and Cr consumption linearly increase with the reaction time. After the sample mass has become constant, the weight gain due to formation of solid products must be equal to the weight loss caused by formation of volatile products.

Scale analysis.—Generally, the sample surfaces were completely covered by green layers. These layers were identified as Cr_2O_3 by x-ray analysis. Microscopic investigation of the samples after embedding in epoxy resin revealed a very porous and voluminous scale structure (Fig. 13). Up to $p_{O_2} = 20$ Torr the profile of the scale is as follows: $Cr/CrCl_2/CrCl_3/Cr_2O_3$. With increasing oxygen pressures, the chloride layers become thinner for a given reaction time. At $p_{O_2} = 100$ Torr, no $CrCl_3$ is detectable (Fig. 14).

Chlorination of preoxidized Cr.—The samples were preoxidized at 700°C and $p_{O_2} = 760$ Torr. After 3 hr of oxidation, a weight gain of 7×10^{-2} mg/cm² was found corresponding to an oxide layer thickness of 4200Å.

The weight loss of a preoxidized sample in chlorine at 700°C and $p_{Cl_2} = 20$ Torr is shown in Fig. 15. As can be seen from this picture, the weight loss is proportional to the second power of the reaction time: $-\Delta m/A \sim t^2$.

Discussion

By the following experimental results we may assume that transfer processes toward and away from the sample control most of the reactions described above:

1. Linear scale growth during Cr chlorination does not affect the rate constant.

2. The thickness d of the sample after scale removal is proportional to the square root of the distance x from the leading edge.

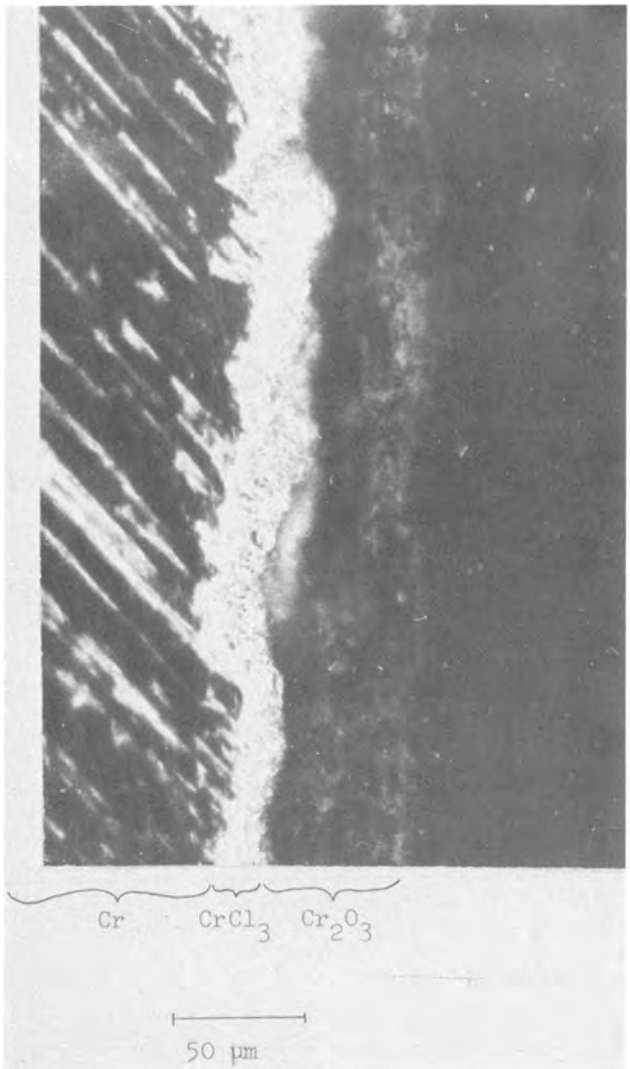


Fig. 13. Microphoto of sample profile after corrosion in a Cl_2-O_2 mixture at $T = 700°C$, $v = 1.5$ cm/sec, $p_{Cl_2} = 20$ Torr, $p_{O_2} = 10$ Torr, and $t = 60$ min.

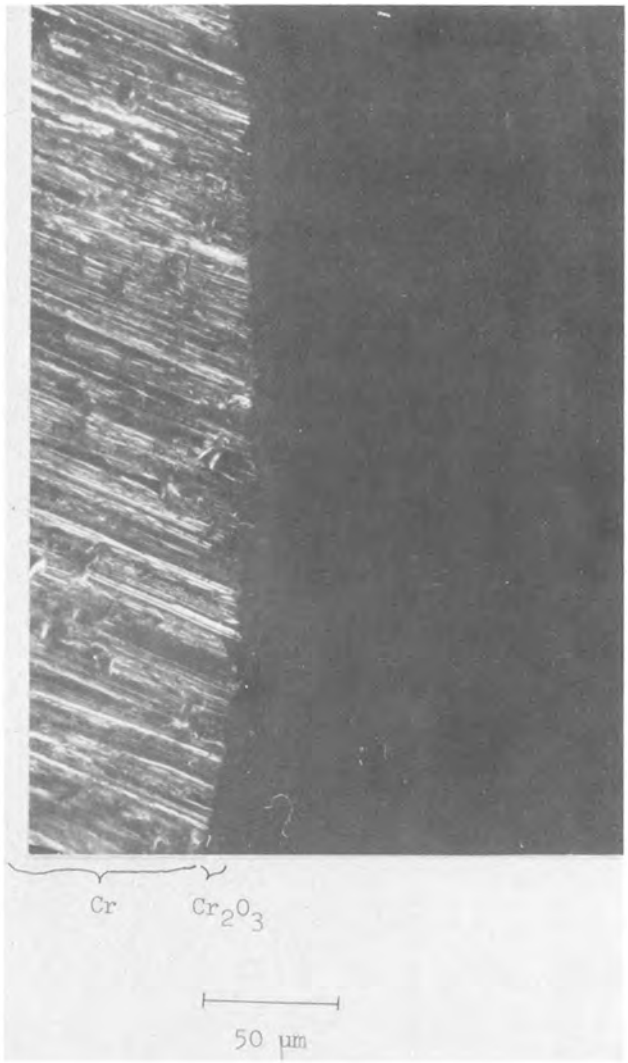


Fig. 14. Microphoto of sample profile after corrosion in a Cl_2-O_2 mixture at $T = 700°C$, $v = 1.5$ cm/sec, $p_{Cl_2} = 20$ Torr, $p_{O_2} = 100$ Torr, and $t = 60$ min.

3. The rate constants of Cr chlorination and Cr_2O_3 volatilization are proportional to the square root of the flow rate.

A Reynolds number between 1 and 10 has been calculated for the temperature and flow rate region used. Therefore, a laminar flow in the reaction tube and a laminar boundary layer at the surface of the sample are assumed. In order to simplify the solution of the Navier-Stokes equations the thickness of the boundary layer is believed to be small compared to the distance from the lower edge of the sample. In addition, the influence of mass transfer on the flow rate is neglected so that the flow equation can be solved independently of the diffusion equation.

According to Bennett, and Myers (16) the thickness of the laminar boundary layer at a flat plate is given by the equation

$$\delta = 5\sqrt{\frac{\nu x}{v_\infty}} \qquad [1]$$

where ν = kinematic viscosity, v_∞ = two times the mean flow rate, and x = distance from the lower edge of the sample. The mass transfer toward and away from the sample surface is given by the following equation (16)

$$j_A = 0.33\ (c_{A_\infty} - C_{A_0})\ \frac{D_{AB}^{2/3}}{\nu^{1/6}}\sqrt{\frac{v_\infty}{x}} \qquad [2]$$

where c_{A_∞} = concentration of A in great distance, c_{A_0} = concentration of A at the surface, and D_{AB} = diffusion coefficient of A in A + B.

The reaction between Cr and Cl_2 consists of the following steps: (*i*) transfer of chlorine toward the sample surface across the laminar boundary layer, (*ii*) diffusion of reactants across the scale, (*iii*) formation of solid products, (*iv*) formation of volatile products, and (*v*) transfer of volatile products away from the sample surface across the laminar boundary layer.

The following equilibria have to be considered: the scale formation

$$Cr(s) + Cl_2(g) = CrCl_2(s) \qquad [3]$$

$$CrCl_2(s) + \tfrac{1}{2}\,Cl_2(g) = CrCl_3(s) \qquad [4]$$

and the volatilization process

$$CrCl_3(s) = CrCl_3(g) \qquad [5]$$

$$2CrCl_3(s) + Cl_2(g) = 2CrCl_4(g) \qquad [6]$$

According to Doerner (12) the dissociation pressure of $CrCl_3$ (equilibrium [4]) is very small compared to the chlorine pressures employed in our experiments. Therefore, the scale exclusively consists of $CrCl_3$ at the interface scale/gas. From recent investigations by Oppermann (15), the data of equilibria [5] and [6] have been calculated, as shown in Tables I and II. As can be seen from these tables, the weight loss of the Cr specimen is caused mainly by the volatilization of $CrCl_4$ up

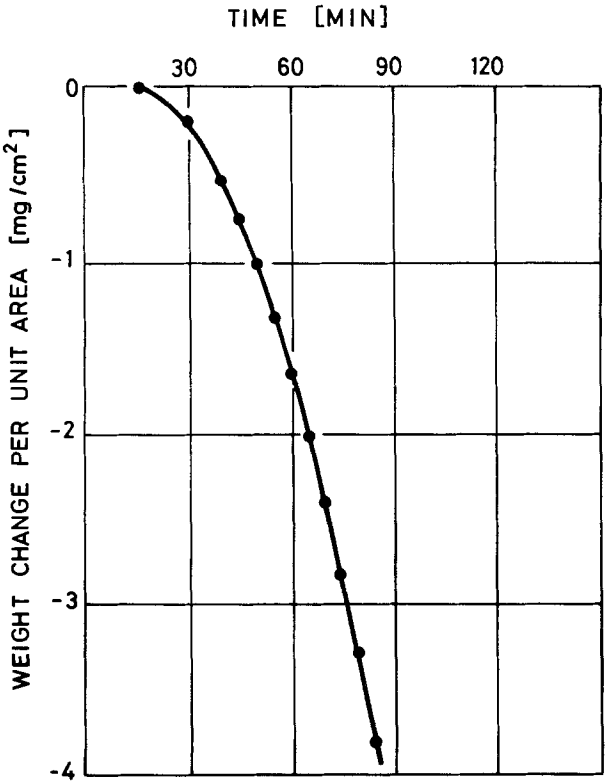


Fig. 15. Chlorination rate of a preoxidized Cr sample at T = 700°C, p_{Cl_2} = 20 Torr, and v = 1.5 cm/sec.

to 700°C. Above this temperature, however, the vapor pressure of $CrCl_3$ can be neglected no longer.

For the chlorine transfer toward the sample surface, we obtain from Eq. [2] with $c_{Cl_2 0} = 0$ and $c_{Cl_2 \infty} = p_{Cl_2}/RT$

$$j_{Cl_2} = 0.33 \cdot \frac{p_{Cl_2} D_{AB}^{2/3}}{RT\nu^{1/6}} \sqrt{\frac{v_\infty}{x}} \qquad [7]$$

The transfer of $CrCl_3$ and $CrCl_4$ away from the sample surface with $c_{CrCl_3 \infty} = 0$, $c_{CrCl_3 0} = p_{CrCl_3}/RT$, $c_{CrCl_4 \infty} = 0$, and $c_{CrCl_4 0} = p_{CrCl_4}/RT$ can be written as follows

$$j_{CrCl_3} = -0.33 \frac{p_{CrCl_3} D_{AB}^{2/3}}{RT\nu^{1/6}} \sqrt{\frac{v_\infty}{x}} \qquad [8]$$

$$j_{CrCl_4} = -0.33 \frac{p_{CrCl_4} D_{AB}^{2/3}}{RT\nu^{1/6}} \sqrt{\frac{v_\infty}{x}} \qquad [9]$$

Assuming the diffusion coefficients of $CrCl_3$ and $CrCl_4$ to be almost equal, the total mass transfer away from the chlorinated sample can be described by the sum of [8] and [9]

$$j = j_{CrCl_3} + j_{CrCl_4} = -0.33 \frac{(p_{CrCl_3} + p_{CrCl_4}) D_{AB}^{2/3}}{RT\nu^{1/6}} \sqrt{\frac{v_\infty}{x}} \qquad [10]$$

Table I. Vapor pressure of $CrCl_3$ according to Oppermann (15)

T(°C)	650	700	750	800
p_{CrCl_3} (Torr)	$2.7 \cdot 10^{-1}$	1.17	4.42	14.77

Table II. K_p for equilibrium [6] and p_{CrCl_4} for p_{Cl_2} = 20 Torr according to Oppermann (15)

T(°C)	650	700	750	800
K_p [6] (Torr)	$7.24 \cdot 10^{-1}$	3.38	13.58	47.89
p_{CrCl_4} (Torr)	3.8	8.22	16.48	30.95

The rate constant k (milligrams per square centimeter second) is correlated with the mass transfer j (mole per square centimeter second) by the following equation

$$k = -d(\Delta m/A)/dt = -j \cdot M_{Cr} \cdot 10^3 \qquad [11]$$

where M_{Cr} = atomic weight of Cr. Therefore

$$k = \frac{0.33 \cdot 10^3 M_{Cr} D_{AB}^{2/3}}{RT\nu^{1/6}} (p_{CrCl_3} + p_{CrCl_4}) \sqrt{\frac{v_\infty}{x}} \qquad [12]$$

Up to 700°C, the vapor pressure of $CrCl_3$ can be neglected (see Tables I and II). With $p_{CrCl_4} = K_{p[6]} p_{Cl_2}$ (equilibrium [6]), we obtain

$$k = \frac{0.33 \cdot 10^3 M_{Cr} D_{AB}^{2/3} K_{p[6]}^{1/2}}{RT\nu^{1/6}} \sqrt{\frac{p_{Cl_2} \cdot v_\infty}{x}} \qquad [13a]$$

or, for a given temperature

$$k = \text{constant} \cdot \sqrt{\frac{p_{Cl_2} \cdot v_\infty}{x}} \qquad [13b]$$

By this equation, the thickness profile of the metal after corrosion and the dependence of the rate constant on flow rate and chlorine pressure up to p_{Cl_2} = 40 Torr is described in accordance with the experimental results at 700°C.

By increase of the chlorine pressure, equilibrium [6] is shifted in favor of formation of more $CrCl_4$ and the thickness of the scale decreases for a given reaction time. The increase of the rate constant above the inflection point, as illustrated in Fig. 4, is not yet completely understood. For thermodynamic reasons, a direct chlorination according to

$$Cr(s) + 2Cl_2(g) = CrCl_4(g) \qquad [14]$$

should give a very much stronger increase of the rate constant than was observed. On the other hand, the rate constant is still found to be proportional to the square root of the flow rate also at high chlorine pressures.

The volatilization of Cr_2O_3 in Cl_2/O_2 mixtures between 700° and 800°C cannot be attributed to the vapor pressure of Cr_2O_3 or to formation of CrO_3. As was shown by mass spectrometry (17), the total dissociative vapor pressure over Cr_2O_3 which consists of Cr, CrO, CrO_2, O_2, and O, amounts to about 5×10^{-4} Torr at 1566°C. At 1325°C, the vapor pressure is already below 10^{-6} Torr (4). During oxidation of Cr above 1000°C, deviations from the parabolic rate law of oxidation occur. By numerous thermodynamic and kinetic investigations (4, 17-22), these deviations could be explained by oxidative volatilization of Cr_2O_3 according to

$$Cr_2O_3(s) + 3/2\ O_2(g) = 2CrO_3(g) \qquad [15]$$

From the temperature dependence of the equilibrium constant of Eq. [15], which was given by Kim and Belton (18), extrapolation to 700°C gives a CrO_3 pressure of 3×10^{-8} Torr at 76 Torr oxygen pressure. The apparent vapor pressure in the simultaneous presence of 20 Torr Cl_2, however, amounts to 1.1×10^{-1} Torr (9). Therefore, formation of CrO_3 can be neglected under these conditions. It must be concluded from our experimental results in accord with Sano and Belton (9) that CrO_2Cl_2 is the exclusive reaction product in Cl_2-O_2 mixtures. The rate constant is directly proportional to the chlorine pressure and a linear function of the fourth root of the oxygen pressure, according to

$$\tfrac{1}{2}\ Cr_2O_3(s) + Cl_2(g) + \tfrac{1}{4}\ O_2(g) = CrO_2Cl_2(g) \qquad [16]$$

The equilibrium pressure of CrO_2Cl_2 is given by

$$p_{CrO_2Cl_2} = K_{p[16]}^{1/2} p_{Cl_2} p_{O_2}^{1/4} \qquad [17]$$

Since the rate constant depends on the flow rate, diffusion of CrO_2Cl_2 across the laminar boundary layer must be assumed to be the rate-determining step of the

reaction. Taking into account that Cr_2O_3 disks, suspended so that the circular surfaces were parallel to the direction of the gas flow, have been used, Eq. [2] must be rewritten as follows

$$j_A = \text{constant}\ (c_{A_\infty} - c_{A_0}) v_\infty^{1/2} \quad [18]$$

with $c_{A_\infty} = c_{CrO_2Cl_2} = 0$, $c_{A_0} = c_{CrO_2Cl_{2_0}} = p_{CrO_2Cl_2}/RT$ and Eq. [17] we obtain

$$j_{CrO_2Cl_2} = -\text{constant} \cdot \frac{K_{p[16]}^{1/2} p_{Cl_2} p_{O_2}^{1/4} v_\infty^{1/2}}{RT} \quad [19]$$

With

$$j_{CrO_2Cl_2} = -2k/10^3 M_{Cr_2O_3} \quad [20]$$

where $M_{Cr_2O_3}$ = molecular weight of Cr_2O_3, tht rate constant k is given by the expression

$$k = \text{constant} \frac{M_{Cr_2O_3}}{2RT} 10^3 K_{p[16]}^{1/2} p_{Cl_2} p_{O_2}^{1/4} v_\infty^{1/2} \quad [21]$$

or, if all constants for a given temperature are combined

$$k = \text{constant} \cdot p_{Cl_2} p_{O_2}^{1/4} \cdot v_\infty^{1/2}$$

The volatilization of Cr_2O_3 by chlorine may be attributed to two parallel reactions

$$Cr_2O_3(s) + 3Cl_2(g) = 2CrCl_3(g) + 3/2\ O_2(g) \quad [22]$$

and

$$\tfrac{1}{2}\ Cr_2O_3(s) + Cl_2(g) + \tfrac{1}{4}\ O_2(g) = CrO_2Cl_2(g) \quad [16]$$

On the basis of the scale analysis, the corrosion characteristics (Fig. 9-10) and the volatilization experiments with Cr_2O_3 described above, the following reactions must be assumed to take place during corrosion of Cr in Cl_2-O_2 mixtures

solid products

$$Cr(s) + Cl_2(g) = CrCl_2(s) \quad [3]$$

$$CrCl_2(s) + \tfrac{1}{2}\ Cl_2(g) = CrCl_3(s) \quad [4]$$

$$2CrCl_3(s) + 3/2\ O_2(g) = Cr_2O_3(s) + 3Cl_2(g) \quad [23]$$

volatile products

$$CrCl_3(s) = CrCl_3(g) \quad [5]$$

$$2CrCl_3(s) + Cl_2(g) = 2CrCl_4(g) \quad [6]$$

$$\tfrac{1}{2}\ Cr_2O_3(s) + Cl_2(g) + \tfrac{1}{4}\ O_2(g) = CrO_2Cl_2(g) \quad [16]$$

At low oxygen pressures reactions [5] and [6] predominate and the initial weight loss of the specimen is high. Gradually, the surface is covered by Cr_2O_3 according to reaction [23] and the extent of reaction [5] and [6] decreases.

At higher oxygen pressures, from the beginning of the reaction, weight gain of the samples is observed. The tendency of the curves in Fig. 9 and 10 leads to the assumption of a maximum weight gain at a special oxygen pressure. This pressure must be high enough to prevent reaction [5] and [6] but low enough to allow formation of solid $CrCl_3$ and to keep reaction [16] small.

Figure 12 shows that the scale mass linearly increases with reaction time even after the sample mass has become constant. The scale mass which predominantly consists of Cr_2O_3 at $p_{O_2} = 20$ Torr, is very much higher than found for Cr oxidation. Gulbransen and Andrew (23), for example, found 1.4×10^{-2} mg/cm^2 weight gain after an oxidation time of 6 hr at 700°C and $p_{O_2} = 76$ Torr. As can be seen from Fig. 12, scale mass after 9 hr amounts to about 20 mg/cm^2. Therefore, a porous scale structure has to be assumed. This assumption is supported by the microscopic profile analysis shown in Fig. 13. The result for $p_{O_2} = 20$ Torr (Fig. 12) and $p_{O_2} = 10$ Torr (Fig. 13) can certainly be generalized for lower oxygen pressures, since a porous oxide structure must be assumed as long as the oxide grows on inner chloride layers. It even may be generalized for higher oxygen pressures since strong CrO_2Cl_2 formation enlarges oxide surface roughness.

Above $p_{O_2} = 20$ Torr, the corrosion is determined by reaction [16]. At $p_{O_2} = 50$ Torr and $p_{O_2} = 100$ Torr, the samples lose weight after a small initial weight gain (curves d and e in Fig. 10). The rate constants are 1.2×10^{-4} and 1.6×10^{-4} mg/cm^2 sec, respectively. Under the same conditions, the rate constants of Cr_2O_3 pellet volatilization are 1.7×10^{-4} and 1.9×10^{-4} mg/cm^2 sec, respectively (experimental values multiplied by a factor of 0.69, the portion of chromium in Cr_2O_3). The difference between the rate constant obtained for Cr_2O_3 pellet volatilization and those obtained for Cr corrosion in Cl_2-O_2 mixtures is small, indicating that the scale growth has become small above $p_{O_2} = 20$ Torr.

A real measure of inhibition found in the system Cr-Cl-O is the ratio of the consumption of Cr in Cl_2 to that in Cl_2-O_2 mixtures at constant chlorine activity. Since no difference in scale mass between Cr corrosion in chlorine and chlorine-oxygen mixtures has been found, inhibition must be mainly caused by a decreased formation of volatile products. Therefore, if the oxygen pressure is high enough to form CrO_2Cl_2 as the only volatile reaction product in Cl_2-O_2 mixtures, then the ratio of the ($CrCl_3$ + $CrCl_4$) equilibrium pressure to the CrO_2Cl_2 equilibrium pressure is a practical measure of inhibition in the system Cr-Cl-O.

The rate constant of Cr chlorination is given by the equation

$$k = \frac{0.33 \cdot 10^3 \cdot M_{Cr} \cdot D_{AB}^{2/3}}{RT\nu^{1/6}} (p_{CrCl_3} + p_{CrCl_4}) \sqrt{\frac{v_\infty}{x}} \quad [12]$$

The rate-determining step of CrO_2Cl_2 formation in the presence of oxide layers on chromium should be (analogous to Cr_2O_3 pellet volatilization) the diffusion of CrO_2Cl_2 across the laminar boundary layer

$$k' = \frac{0.33 \cdot 10^3 \cdot M_{Cr} \cdot D_{AB}^{2/3}}{RT\nu^{1/6}} p_{CrO_2Cl_2} \sqrt{\frac{v_\infty}{x}} \quad [24]$$

Under the assumption that the diffusion coefficients of the volatile molecules are almost equal, we obtain by division of the rate constant k by k'

$$k/k' = p_{CrCl_3} + p_{CrCl_4}/p_{CrO_2Cl_2} \quad [25]$$

If the corrosion is determined by reaction [16] (above $p_{O_2} = 20$ Torr), the ratio $p_{CrCl_3} + p_{CrCl_4}/p_{CrO_2Cl_2}$ can experimentally be confirmed by the ratio of the rate constants k/k'. At 700°C and $p_{Cl_2} = 20$ Torr, equilibrium pressures of $CrCl_3$ and $CrCl_4$ are 1.17 Torr (Table I) and 8.22 Torr (Table II), respectively. Using the equation

$$\log K_{p[16]} = -4750/T + 0.86 \quad [26]$$

given by Sano and Belton (9) for the temperature dependence of reaction [16], the equilibrium of CrO_2Cl_2 has been calculated to be 10^{-1} Torr at $p_{Cl_2} = 20$ Torr and $p_{O_2} = 50$ Torr. Thus

$$(p_{CrCl_3} + p_{CrCl_4})/p_{CrO_2Cl_2} = 93.9$$

In fair agreement with this ratio, it has been found experimentally for k/k'

$$k/k' = 1.37 \cdot 10^{-2}/1.2 \cdot 10^{-4} = 110$$

The weight loss of preoxidized samples of Cr cannot be explained by an exclusive volatilization of Cr_2O_3, since no straight line was obtained for the corrosion rate. From these results, we tentatively conclude that chlorine reaches the metal surface after a fast migration through the porous oxide layer enlarging the free surface for a $CrCl_3$ and $CrCl_4$ vaporization. This conclusion is supported by the presence of numerous holes

in the metal surface detected after scale removal. If we assume that

$$A' = kt \quad [27]$$

where A' = portion of the Cr_2O_3 free surface A of the sample, then we obtain with

$$-d\,(\Delta m/A)/dt = k'A' \quad [28]$$

the experimentally found relation

$$\Delta m/A = -k'' \cdot t^2 \quad [29]$$

Acknowledgment

This research was sponsored by the Arbeitsgemeinschaft Industrieller Forschungsvereinigungen (AIF), Germany. The authors are indebted to G. Romeo and W. F. Moore, General Electric Company, Research and Development Center, for the supply of the chromium used in this study.

Manuscript submitted Nov. 15, 1976; revised manuscript received Feb. 10, 1977.

Any discussion of this paper will appear in a Discussion Section to be published in the December 1977 JOURNAL. All discussions for the December 1977 Discussion Section should be submitted by Aug. 1, 1977.

REFERENCES

1. K. Hauffe and J. Hinrichs, *Werkst. Korros.*, **21**, 954 (1970).
2. J. Halfdanarson and K. Hauffe, *ibid.*, **24**, 8 (1973).
3. O. Kubaschewski and E. L. Evans, "Metallurgical Thermochemistry," 4th ed., Pergamon Press, London (1967).
4. W. C. Hagel, *Trans. ASM*, **56**, 583 (1963).
5. A. U. Seybolt and D. H. Haman, *Trans. Met. Soc. AIME*, **230**, 1294 (1964).
6. H. Moissan, *Ann. Chim. Phys.*, **21**, 199 (1880).
7. R. Wasmuht, *Z. Angew. Chem.*, **43**, 8 (1930).
8. Y. Saeki, R. Matsuzaki, and H. Movito, *Kogyo Kagahu Zasski*, **47**, 344 (1971).
9. N. Sano and G. R. Belton, *Met. Trans.*, **5**, 2151 (1974).
10. G. J. Sargent, *Trans. Am. Electrochem. Soc.*, **37**, 479 (1920).
11. P. Fireman and E. G. Portner, *J. Phys. Chem.*, **8**, 500 (1903).
12. H. A. Doerner, Bur. Mines Tech. Paper No. 577 (1937).
13. F.-R. Meyer and G. Ronge, *Z. Angew. Chem.*, **52**, 637 (1939).
14. H. V. Wartenberg, *Z. Anorg. Allg. Chem.*, **250**, 122 (1942).
15. H. Oppermann, *ibid.*, **359**, 51 (1968).
16. C. O. Bennett and J. E. Myers, "Momentum, Heat and Mass Transfer," McGraw Hill Book Co., New York (1962).
17. R. T. Grimley, R. P. Burns, and M. G. Inghram, *J. Chem. Phys.*, **34**, 664 (1969).
18. Y. W. Kim and G. R. Belton, *Met. Trans.*, **5**, 1811 (1974).
19. D. Caplan and M. Cohen, *This Journal*, **108**, 438 (1961).
20. C. S. Tedmon, *ibid.*, **113**, 766 (1966).
21. H. C. Graham and H. H. Davis, *J. Am. Ceram. Soc.*, **54**, 89 (1971).
22. C. A. Stearns, F. J. Kohl, and G. C. Fryburg, *This Journal*, **121**, 945 (1974).
23. E. A. Gulbransen and K. F. Andrew, *ibid.*, **104**, 334 (1957).

An O^{18} Study of Field-Assisted Pore Formation in Compact Anodic Oxide Films on Aluminum

J. Siejka* and C. Ortega

Groupe de Physique des Solides de l'Ecole Normale Supérieure, Université Paris VII, 75005 Paris, France

ABSTRACT

The mechanism of field-assisted pore formation in 15% wt H_2SO_4 aqueous solutions was studied by O^{18} tracing techniques. Compact base layers were first formed in an O^{18} labeled solution and further oxidized in a nonlabeled solution, leading to field-assisted pore formation. The O^{18} content and depth distribution was measured in these duplex films. It was found that the initial number of O^{18} atoms per square centimeter is conserved to within 2% and that the major part of the oxygen of the initial base layer is located on the top of the duplex film with the same O^{18} isotopic concentration. This observation shows clearly that the pore formation does not take place through a simple oxide dissolution process whether chemical or field assisted. Pore formation consists of some kind of oxide decomposition involving only cation transfer into the solution. The values of the cationic and anionic currents are calculated. Possible mechanisms for ion movement are discussed.

In our previous work (1) we found that the small values (53-64%) of the current efficiency of porous film formation are associated neither with equivalent oxygen losses following the reaction

$$Al_2O_{3oxide} + 6H^+_{sol.} \rightarrow 2Al^{3+}_{sol.} + 3H_2O$$

nor with electronic losses (1, 2). Consequently, we proposed a mechanism of direct dissolution of aluminum cations into the solution. But these experiments were not sufficiently precise to establish whether or not pore formation, which results in a decrease of the current efficiency by 14% (1), is accompanied by corresponding oxygen losses as implied by the mechanisms proposed in the literature (2, 3, 4).

The answer to this question is the main purpose of this work. The base layer thickness remains constant during the porous layer formation in "steady-state" conditions. This implies that the "dissolution" rate of the oxide at the bottom of the pores, *i.e.*, the rate of the pore depth increase, is about 10^3-10^4 Å/min under the usual formation conditions (2, 4). This rate is 10^4-10^5 times higher than the chemical dissolution rate of the oxide (1). The theories explaining this effect by an increase of the local chemical attack of the oxide due to Joule's effect, for example (3, 5, 6), have been rejected and a theory of "field-assisted dissolution of the oxide" has been proposed (4, 7). According to Ref. (4), this mechanism consists of the hydrolysis of Al-O bonds;

* Electrochemical Society Active Member.

Key words: nuclear microanalysis, O^{18} tracing, aluminum, porous oxide, sulfuric acid, dissolution current, field-assisted dissolution, oxygen movement.

the OH^- and Al^{3+} ions thus formed would pass into the solution. This kind of mechanism is tacitly accepted in the literature [*e.g.*, see Diggle *et al.* (2)].

In this work we have studied the oxygen losses during the initiation of pore formation using nuclear microanalysis and O^{18} tracer techniques (1, 8). The base layers were formed in O^{18} enriched water solution of sulfuric acid and then reoxidized in a natural solution. Following the geometrical model of Keller *et al.* (6) and of Wood *et al.* (9, 10), the volume of the pores formed through the O^{18} enriched initial layer should correspond to 14% of the volume of the oxide. According to the mechanism of chemical attack or of the "field-assisted dissolution of the oxide," a loss of O^{18} equal at least to 14% of the initial value should be observed (3, 4, 6). No oxygen losses should be observed if the mechanism of field-assisted dissolution of aluminum suggested in our previous work holds during the pore formation. This idea was recently accepted in the literature (11, 12). The mechanism of oxygen movement during the pore formation was also studied by locating in the duplex films the O^{18} atoms previously fixed in the base layer.

A second purpose of this work is to elucidate the mechanism of sulfate anion incorporation. Isotopic exchange between the oxygen of the water and the oxygen of the SO_4 anions can be disregarded (13). Consequently, the use of solutions where only water was enriched in O^{18} allowed us to measure the quantities of oxygen fixed in the oxide coming from the water and from the sulfate anions. The measurements of sulfur incorporation enabled us to establish whether the oxygen coming from SO_4^{2-} in incorporated as SO_4^{2-} anions or whether it comes from their electrochemical decomposition. This last mechanism was suggested in many papers [*e.g.*, see Ref. (14)]. From these measurements we have calculated the average charge of the oxygen atoms fixed in the oxide using coulometric measurements and the measure of oxygen content. The nature of the cation movement during the porous film formation was deduced from "pore filling" experiments (15).

Experimental Technique

We used aluminum samples (11 mm × 22 mm × 0.6 mm) pure to 99.95 or 99.999%. The preparation of the samples and aqueous solutions of sulfuric acid (15% in weight) was described in our previous paper (1). We used two solutions; s_o16 and s_o18. The s_o16 solution was made with water of natural isotopic composition, *i.e.*, containing 0.204% O^{18}. The s_o18 solution contained normalized water (*i.e.*, containing hydrogen at near-natural isotopic composition) enriched[1] to ~40% O^{18}. All the experiments were carried out at constant voltage (V = 10V) and constant temperature (14°C ± 0.5°C). The samples were left in open circuit for 1 min before each oxidation. We have observed that this process improves the reproducibility of the layer thickness.

As before (1), we used the nuclear reactions O^{16} (d, p) O^{17} [1] and O^{18} (p, α) N^{15} induced by deuteron or proton beams from a 2 MeV Van de Graaff accelerator (8) to measure the number of oxygen 16 (N_{O16}) and oxygen 18 (N_{O18}) atoms/cm² of the oxide layer. N_{O18} and $N_O{}^{16}$ have been calculated as follows

$$N_{O18} = \frac{n^{18}}{\mathcal{N}_{ref.18}} \cdot \mathcal{N}^{18}$$

and

$$N_O{}^{16} = \frac{n^{16}}{\mathcal{N}_{ref.16}} \cdot \mathcal{N}^{16}$$

where $\mathcal{N}^{16}$, $\mathcal{N}^{18}$, and $\mathcal{N}_{ref.16}$, $\mathcal{N}_{ref.18}$ are the counts measured on the sample and on the oxygen references, respectively, and n^{16} and n^{18} represent the number of oxygen 16 and oxygen 18 atoms per square centimeter fixed in the O^{16} and O^{18} references [see Ref. (8) for details]. In our experimental conditions the counts are determined with a precision of 0.2% (statistical error), whereas the values of n^{16} and n^{18} are known to within ± 3%. The O^{18} concentration profiles were estimated from the analysis of the excitation curves of the O^{18} (p, α) N^{15} reaction in the vicinity of the resonance at 629 keV, according to the method described in Ref. (1, 8). The sulfur content of the oxides was measured by the use of MeV helium backscattering techniques (1, 8).

[1] Normalized O^{18} enriched water produced at the Weizmann Institute, Rehovot, Israel.

Results and Interpretation

Oxygen 18 content of duplex films obtained by the reoxidation in s_o16 of O^{18} enriched base layers.—First we measured the values of the current density I as a function of the time t during anodic oxidation at constant voltage (Fig. 1). The $I(t)$ relationship was found to be the same for the samples oxidized in s_o16 and s_o18 solutions. Under our experimental conditions (I_o = 25 mA/cm², T = 14°C) we found t_2 = 14 sec and $t_3 \simeq$ 35 sec (see Fig. 1). According to the literature (2), the beginning of the pore formation started at time $t_1 = \frac{1}{2}t_2$. Consequently, we formed the base layer during 7 sec in s_o18 and reoxidized it in s_o16 for either 53 sec or 1 min 53 sec so that the total oxidation times were equal to 1 and 2 min.

Reproducibility of the oxygen 18 content of the base layers.—We measured the values of N_{O18} on about thirty samples formed during the time t_1. The relative spread of N_{O18} values with respect to the average was at most equal to 5%; the spread on individual sample at various points was at most equal to 1.5%. The beam diameter of the Van de Graaff accelerator was equal to 2 mm and the sample area was 2.4 cm², so measurements were made at different points on the same sample. Subsequently, each sample was cut in two parts, one (a) being reoxidized in s_o16, the other one being used as a reference (b).

Reoxidation of the base layers.—The parts (a) of the samples were reoxidized in s_o16 solution for 53 sec or 1 min 53 sec; the parts (b) were left in the same solution for the same period of time. This process allowed us to subtract the effect of the purely chemical dissolution of the oxide. The measurements of N_{O16} and N_{O18} contents were carried out on both parts of the samples. If ΔN_{O16} is the difference between the O^{16} content of the duplex layer and of the base layer, the corresponding increase $\Delta_o N_{O18}$ of the O^{18} content is equal to $2 \times 10^{-3} \times \Delta N_{O16}$ (due to the natural O^{18} content of 0.204%).

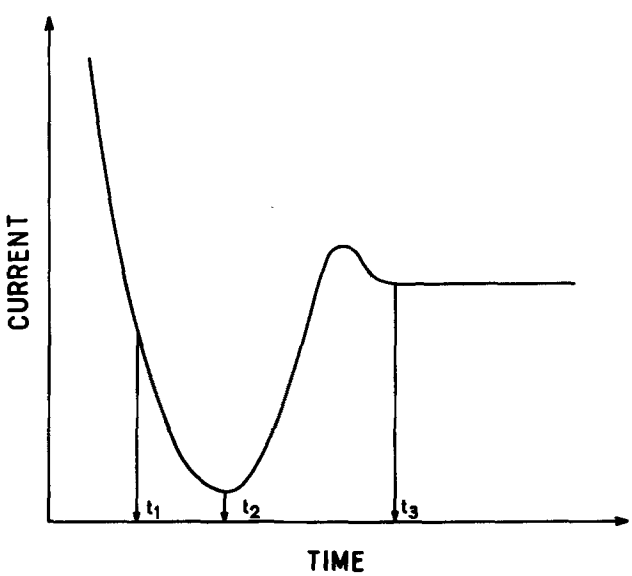


Fig. 1. Current density as a function of time during potentiostatic (V_{OX} = 10V porous film formation on aluminum; arbitrary units. Initiation of pore formation occurs at time $t_1 = \frac{1}{2}t_2$: for $t > t_3$ the oxidation takes place at steady-state conditions.

The variations of the O^{18} content due to possible oxygen losses were calculated by means of the formula

$$\Delta N_{O^{18}} = N_{O^{18}}(b) - (N_{O^{18}}(a) - \Delta_o N_{O^{18}})$$

$N_{O^{18}}(b)$ and $N_{O^{18}}(a)$ are the O^{18} contents of the barrier layers (b) and of the duplex films (a) obtained by reoxidation of (b) in s_o^{16}.

Relative oxygen 18 losses are defined, and may be written as

$$\frac{\Delta N_{O^{18}}}{N_{O^{18}}(b)} = \frac{\mathcal{N}^{18}(b) - \mathcal{N}^{18}(a)}{\mathcal{N}^{18}(b)} + 2 \times 10^{-3} \cdot \frac{n_{ref.16}\mathcal{N}_{ref.18}(\mathcal{N}^{16}(a) - \mathcal{N}^{16}(b))}{n_{ref.18} \times \mathcal{N}_{ref.16}\mathcal{N}^{18}(b)} \quad [1]$$

The first term depends only on the number of counts. The error of this term is hence of statistical origin only (0.2%). The second term depends on the number of counts and also on the absolute number of O^{16} and O^{18} atoms/cm² in the references. Thus, we find here two kinds of errors; statistical and systematic. We propose [according to Amsel (16)] the following procedure to calculate the error on the relative oxygen losses (Eq. [1]). First we calculate the standard deviation σ_{st} of all statistical terms present in Eq. [1] using the classical formula

$$\sigma_{st} = \sqrt{\sigma_1^2 + \sigma_2^2}$$

σ_1 and σ_2 being the standard deviations of statistical origin of the first and second term in Eq. [1]. The systematic error on the second term (due to the error on $q = n_{ref.16}/n_{ref.18}$ must then be expressed as a standard deviation. For this purpose we assume that the true value of q is uniformly distributed on the interval $q_o - \epsilon_{ref.}$, $q_o + \epsilon_{ref.}$, where q_o is the best estimate of q and $\epsilon_{ref.}$ the corresponding systematic error. It is readily shown that the standard deviation of q is then $\sigma q = \epsilon_{ref.}/\sqrt{3}$. In this case $\epsilon_{ref.}$ was estimated to be approximately 0.03. The over-all error in the related oxygen losses may then be estimated by inserting the above value of σq in the usual formula for calculating standard deviations.

In Table 1 we report as an example the results relating to two series of experiments in which the O^{18} concentration in the water and the sulfuric acid concentration were slightly different. As the results show, the changes of oxygen 18 contents during the reoxidation, due to possible oxygen losses, are statistically equal to zero with a maximum deviation of 2%, *i.e.*, equal to the spread of the base layer thicknesses. It must be noted that these results are related to the losses of oxygen coming from the water. The possible losses of oxygen coming from the sulfate ions will be analyzed later and will be shown to have little influence on the conclusions of these experiments.

The O^{18} distribution in the duplex films.—We estimated the O^{18} concentration profile in the duplex films by means of excitation curves as mentioned above. Figure 2 shows the typical results registered for various conditions. The fact that the various excitation curves are nearly identical indicates that most of the O^{18} atoms originally in the base layer are kept at the top of the duplex films. Moreover, a slight decrease of the maximum and a widening of the excitation curves obtained on the duplex layers is observed. Many identical experiments have been carried out and this effect was always found. This result indicates that as pores form during reoxidation the O^{18} displaced by the pores ends up in a part of the oxide just below the O^{18} en-

Table I. Measurements of $O^{18}(N_{O18})$ and $O^{16}(N_{O16})$ contents of the base layers (b) formed in s_o^{18} and of duplex films (a) obtained by reoxidation of (b) in s_o^{16}

Series	SAMPLE	Time of reoxidation in s_o^{16}	UNIT : 10^{15} at./cm²					O^{18} losses
			N_o^{18}	N_o^{16}	ΔN_o^{16}	$\Delta_o N_o^{18}$	$N_o^{18} - \Delta_o N_o^{18}$	
I	1 a	53 sec.	30.4	384	311	0.6	29.8	0 %
	b	0	29.8	73				
	2 a	53 sec.	31.0	396	322	0.6	30.4	- 0.3 %
	b	0	30.3	74				
	3 a	53 sec.	30.2	397	323	0.6	29.6	2.3 %
	b	0	30.3	74				
	4 a	53 sec.	30.0	396	322	0.6	29.4	0.3 %
	b	0	29.5	74				
	5 a	1 min. 53 sec.	30.9	794	721	1.4	29.5	- 1.7 %
	b	0	29.0	73				
	6 a	1 min. 53 sec.	30.7	794	720	1.4	29.3	0 %
	b	0	29.3	74				
	7 a	1 min. 53 sec.	31.7	823	748	1.5	30.2	0 %
	b	0	30.2	75				
II	1 a	53 sec.	35.0	428	366	0.7	34.3	- 1 %
	b	0	33.9	62				
	2 a	53 sec.	34.9	436	374	0.7	34.2	- 0.3 %
	b	0	34.1	62				
	3 a	53 sec.	34.0	529	467	0.9	33.1	0.9 %
	b	0	33.4	62				

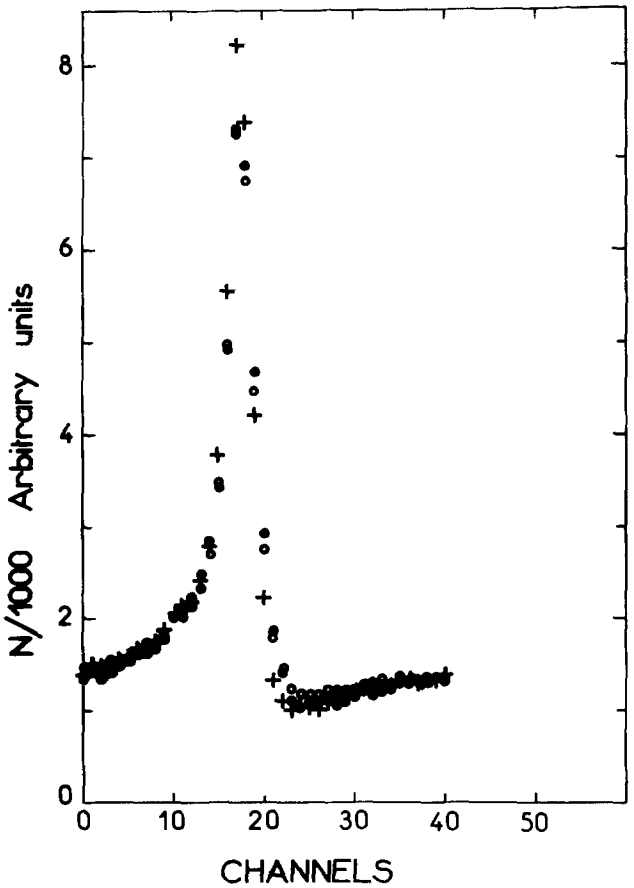


Fig. 2. Excitation curves of $O^{18}(p,\alpha)N^{15}$ reaction near the 629 keV resonance: (+), O^{18} enriched base layer formed in s_0^{18} solution; (.), (o), duplex films obtained by reoxidation of the O^{18} enriched base layer in s_0^{16} solution for 53 sec and 1 min 53 sec, respectively.

riched layer. This is in agreement with the model of the growth of porous oxides on aluminum proposed in our previous paper (1) in which the oxide is formed at the oxide/metal interface by the migration of oxygen coming from the solution and from the part of the oxide located at the bottom of the pore. To explain the inversion during growth of the order of oxygen atoms in the base layer we suggested (1) that a substructure is present in the base layer, in agreement with others (17, 18).

Current efficiency of porous layer formation.—The values of the current efficiency depend on the average charge associated with each oxygen atom fixed in the oxide. This charge is equal to -2 for oxygen coming from the electrochemical decomposition of the sulfate anion or water and -0.5 in case of SO_4^{2-} incorporation. In order to establish in which form the incorporation of oxygen coming from the sulfate anions occurs, we have measured both the sulfur and the oxygen contents. The measurements of sulfur were carried out using the backscattering method (1) and typical results are shown in Fig. 3. As in the preceding case (1), the measurement reproducibility is rather bad, with the error on these measurements estimated to be equal to ~30%. Assuming all the sulfur is incorporated in the form SO_4^{2-} the percentage of oxygen incorporated in the form of sulfates lies between 15 and 30% [(23 ± 8)%, Table II].

In a second series of experiments we calculated the percentage α of oxygen coming from the sulfate anions and incorporated in films during growth in the transitory region (from 0 to 35 sec) and during growth at steady-state condition (from 35 sec). Films were formed in s_0^{18} and α was calculated as follows

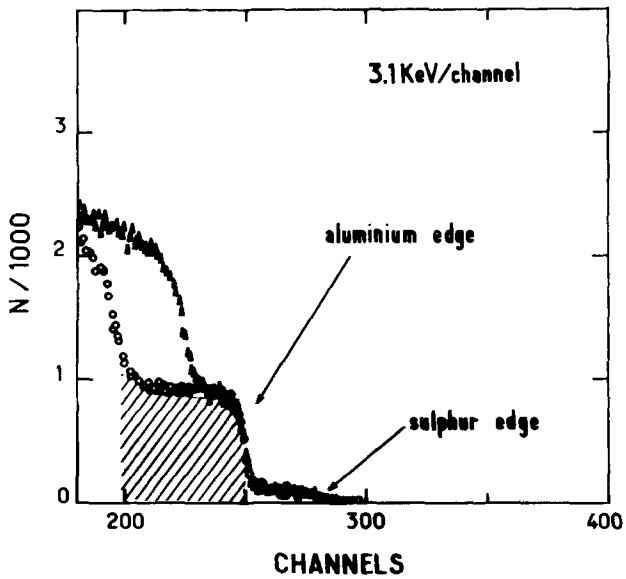


Fig. 3. Backscattering amplitude spectra for $^4He^+$ ions at 1600 keV obtained on duplex films (see Fig. 2); reoxidation during 53 sec (▲) or 1 min 53 sec (o). Shaded region represents aluminum in the oxide.

$$\alpha = \frac{C_{H2O} - C_{ox}}{C_{H2O} - C_{SO4}} \times 100\% \qquad [2]$$

where C_{H2O} and C_{SO4} represent the O^{18} concentrations of the water and the SO_4 anions (0.204%), respectively. C_{ox} represents the O^{18} concentration of the oxygen coming from the solution and fixed in films formed in the transitory region or at steady-state conditions. The O^{18} concentration of the water was deduced precisely from the measurement of the isotopic composition of an anodic oxide film of tantalum formed in this water containing a nonoxygenated salt (KCN). By using this technique [see Ref. (19)] we found an O^{18} concentration of the water equal to (42 ± 2)%. In the case of films formed in the transitory region C_{ox} was calculated by the formula

$$C_{ox} = \frac{N_{O18}(t)}{N_{O18}(t) + N_{O16}(t) - N_{O16}(i)} \qquad [3]$$

Where $N_{O18}(t)$ and $N_{O16}(t)$ represent the numbers of O^{18} and O^{16} atoms/cm^2 found on aluminum after oxidation in transitory region; $N_{O16}(i)$ represents the number of O^{16} atoms/cm^2 of the natural oxide before oxidation [$(20 \pm 5)10^{15}$ oxygen atoms/cm^2]. The number of O^{18} atoms/cm^2 of the natural oxide was neglected. In the case of films formed at steady-state conditions α was given by the formula

$$C_{ox} = \frac{N_{O18} - N_{O18}(t)}{N_{O16} - N_{O16}(t) + N_{O18} - N_{O18}(t)}$$

Where N_{O18} and N_{O16} represent the number of O^{18} and O^{16} atoms/cm^2, respectively, found on aluminum after oxidation. C_{ox} and α values are presented in Table II. From these results we can reasonably assume that α values are the same for films formed in the transitory region and at steady-state conditions. The average α from oxygen measurement is smaller than that deduced from sulfur measurement. Taking into consideration the high dispersion of sulfur measurements we cannot exclude some decomposition of SO_4^{2-}. However α values deduced from experiments with radioactive sulfur (20) were found to be equal to 10-15%. These results are in good agreement with that deduced from oxygen measurement. Consequently, we shall assume in what follows that the incorporation of sulfur occurs as SO_4^{2-}. The value of the average charge of oxygen incorporated in the oxide calculated by the formula

Table II. t_{ox} is the time of oxidation at constant voltage V = 10V. Oxides formed at steady-state conditions are oxides formed from 35 sec to 1 or 2 min

Conditions of oxides' formation	O^{18}-concentration of the oxides $\left(\frac{O^{18}}{O^{16}+O^{18}}\right)$%	Oxygen incorporated coming from SO_4^{2-} anions, expressed as % of total oxygen content (α) calculated from		Average charge (η_o) of oxygen incorporated calculated from:		Current efficiency calculated using $\eta_o = 1.80 \pm 0.05$ expressed as a % of total current
		Oxygen measurements	Sulfur measurements	Oxygen measurements	Sulfur measurements	
base layer s_o^{16}, 14°C t_{ox} = 7 sec.						
steady state conditions s_o^{16}, 14°C						61 ± 2
trans. region s_o^{18}, 14°C t_{ox} = 35 sec.	36 ± 2	$\alpha = 14 \pm 5$	$\alpha = 23 \pm 8$	−1.80 ± 0.1	−1.65 ± 0.15	
steady state conditions s_o^{18}, 14°C	36 ± 1	$\alpha = 13.5 \pm 3$		−1.80 ± 0.05		63 ± 2
base layer s_o^{16}, 15°C t_{ox} = 7 sec.						
steady state conditions s_o^{16}, 15°C						58 ± 2

$\eta = \alpha(-0.5) + (1 - \alpha)(-2)$ where −0.5 and −2 represent the average charge of oxygen incorporated as SO_4^{2-} and O^{2-}, respectively, was found to be equal to −1.80.

The measurements of the current efficiency of the porous layer formation were only performed in steady-state conditions [see Ref. (1) for details]. The values of the current efficiencies are shown in Table II. These are the same for the oxidation in s_o^{16} and s_o^{18} and do not differ from the literature data (21). The use of the value −1.80 ± 0.05 for average oxygen charge in the oxide [instead of −1.65 ± 0.1, Ref. (1)] introduces an increase of ~10% of the current efficiency with regard to the value found in Ref. (1) (see Table II).

Components of the current during the porous oxide formation in steady-state conditions.—Let us call I_{ox} the current used to form the new oxide. In our experimental conditions we found $I_{ox} = 60\% \cdot I_{tot}$ (Table II). This current may only be due to the movement of oxygenated anions (O^{2-}, SO_4^{2-}) coming from the solution. Hence the total current due to losses (I_{dis}) is equal to $40\% \cdot I_{tot}$. In the absence of oxygen losses, the pore formation process implies a movement of aluminum cations toward the solution (I_{dec}^{c}) and a movement of equivalent quantities of oxygenated anions (O^{2-}, SO_4^{2-}) towards the oxide-metal interface (I_{dec}^{o}). In steady-state conditions $I_{dec}^{c} = I_{dec}^{o}$. These currents can be calculated by the following expression (assuming there is no loss of SO_4^{2-})

$$\frac{I_{dec}^{c}}{I_{dec}^{c} + I_{ox}} = 0.14$$

where 0.14 is the ratio of the pore volume to the total volume of the oxide. We find

$$I_{dec}^{c} = 10\% \cdot I_{tot}$$

$$I_{Al} = I_{dis} - I_{dec}^{c} = 30\% \cdot I_{tot}$$

The current I_{Al} represents the current of direct dissolution of Al cations in the solution without formation of any oxide [see Ref. (1)]. The current carried by Al^{3+} cations at the oxide-solution interface is hence equal to $I_{Al} + I_{dec}^{c} = 40\% \cdot I_{tot}$. The current carried by the oxygenated anions is equal to $I_{ox} = 60\% \cdot I_{tot}$, at the oxide-solution interface, whereas inside the oxide, it is equal to $I_{ox} + I_{dec}^{o} = 70\% \cdot I_{tot}$ (Fig. 4).

Calculation of the oxygen distribution in the duplex layers.—We shall now calculate the oxygen 18 distribution in the duplex layers obtained by the reoxidation of the O^{18} enriched base layers of thickness "l" in s_o^{16} when the total thickness increases from "l" to "$4l$" (Fig. 5). We shall take as an example the O^{18} enriched base layer 5b (Table I). Let us call $(2l)^{th}$, $(3l)^{th}$, and $(4l)^{th}$, respectively, the new base layers obtained by increasing the total thickness from l to $4l$. In order to explain the SO_4^{2-} incorporation during the pore formation we have to assume that the SO_4^{2-} anions participate in the oxide growth like the O^{2-} anions. This means that I_{ox} is carried by O^{2-} and SO_4^{2-}, but taking into consideration that some SO_4^{2-} losses during the pore depth increase cannot be excluded, we shall analyze two limiting situations: (*i*) no SO_4^{2-} losses occur during the pore formation, *i.e.*, I_{dec}^{o} is carried out by SO_4^{2-} and O^{2-} anions; (*ii*) the SO_4^{2-} anions already fixed in place where the pores are formed (14% of the SO_4^{2-} content of the base layer) pass into the solution during the pore formation. In this case I_{dec}^{o} is carried out only by O^{2-} anions.

(*i*) The O^{18} concentration of the new "$2l$"th layer, *i.e.*, the new base layer, depends on the relative contribution of oxygenated anions coming from the solution (O_s), from the decomposition of the oxide at the bottom of the pores (O_p), and from their respective O^{18} concentrations. The value of (O_p) expressed as the ratio $O_p/O_p + O_s$ is equal to the volume of the pores (14% of the volume of the base layer). The O^{18} concentration of O_p depends on the part taken by the oxy-

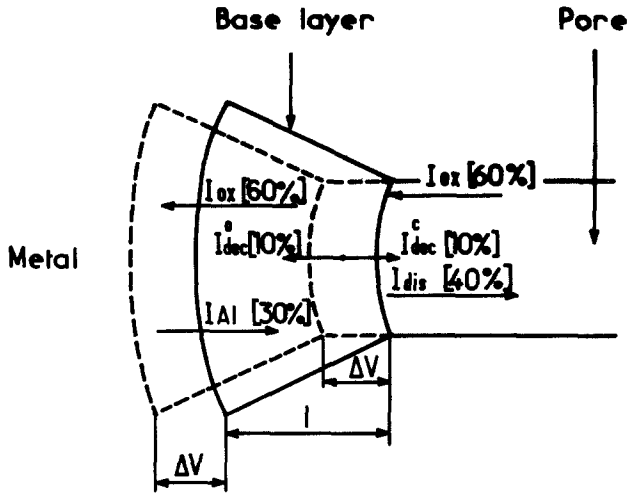


Fig. 4. Components of the current expressed as a percentage of the total ionic current flowing through the oxide during anodic oxidation at steady-state conditions; see text for definitions. l and ΔV thicknesses of the base layer and of decomposed oxide, respectively.

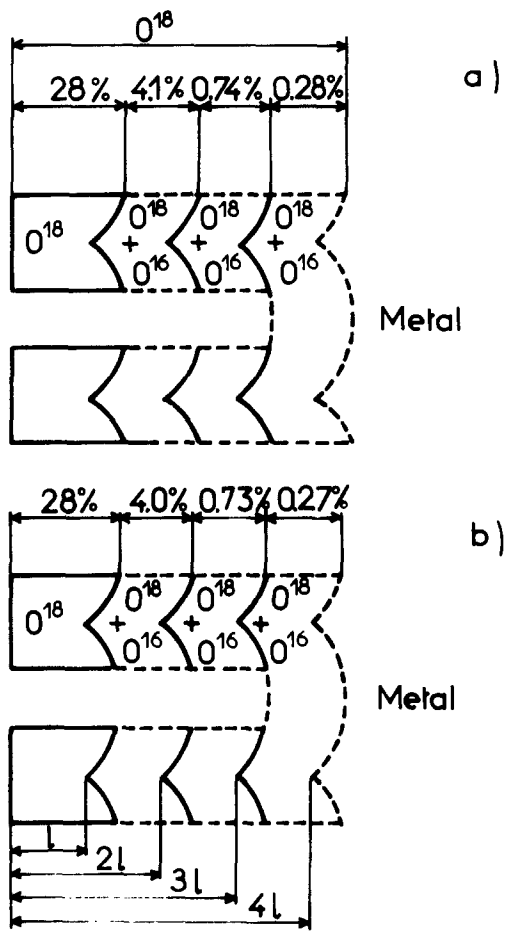


Fig. 5 Distribution of the oxygen 18 in the duplex films obtained by the reoxidation in s_0^{16} solution of O^{18} enriched base layer; "l" corresponds to the thickness of the base layer. (a) assuming that $I_{dec}°$ is carried out by SO_4^{2-} and O^{2-} anions; (b) assuming that $I_{dec}°$ is carried out only by O^{2-} anions.

gen of the natural oxide during oxide growth; either the oxygen of the natural oxide participates in the growth in the same manner as the oxygen coming from the solution or it remains at the oxide-metal interface. In the first case, assuming that the two kinds of oxygen are homogeneously distributed in the base layer, the O^{18} concentration of O_p in the base layer is equal to 28%. The O^{18} concentration of the $(2l)^{th}$, $(3l)^{th}$, and $(4l)^{th}$ layer is calculated as follows (Fig. 5a)

$$0.14 \times 28\% + 0.86 \times 0.2\% = 4.1\% \ (2l)^{th}$$

$$0.14 \times 4.1\% + 0.86 \times 0.2\% = 0.74\% \ (3l)^{th}$$

$$0.14 \times 0.74\% + 0.86 \times 0.2\% = 0.28\% \ (4l)^{th}$$

(0.2% is the natural O^{18} concentration)

If the natural oxide remains at the oxide-metal interface (taking into consideration that the number of oxygen atoms per square centimeter of the natural oxide is equal to 20×10^{15}) the O^{18} concentration of O_p is equal to 29.0/29 + 73 − 20 = 35% instead of 28%. The O^{18} concentration of the $(2l)^{th}$, $3l)^{th}$, $(4l)^{th}$ layer is equal to 5.1%, 0.88%, and 0.29%, respectively.

(*ii*) In this case the O^{16} loss is equal to $0.14 \times 14\%$ where 0.14 is the fraction of oxygen coming from SO_4^{2-}. The value of O_p is hence equal to $(1 - 0.14) \times 14\% = 12\%$. As above, the O^{18} concentration of O_p depends on the part taken by the oxygen of the natural oxide during oxide growth. If the oxygen of the natural oxide participates in the growth, O^{18} concentration of O_p is equal to the O^{18} concentration of the water (42%) diluted by the presence of 20×10^{15} oxygen atoms/cm^2 of the natural oxide.

It has been calculated as follows. Sample 5b contains 29.0×10^{15} O^{18} atoms/cm^2 and 73×10^{15} O^{16} atoms/cm^2. Subtracting 20×10^{15} oxygen atoms/cm^2 (natural oxide) we find that 82×10^{15} oxygen atoms/cm^2 come from the solution. The number of oxygen atoms per square centimeter coming from the enriched water is hence equal to

$$(1 - \alpha) \times 82 \times 10^{15} = 86\% \times 82 \times 10^{15} = 70.5 \times 10^{15}$$

It follows that the O^{18} concentration of O_p is equal to

$$(O_p) = \frac{29.0}{70.5 + 20} = 32\%$$

The O^{18} concentration of the $(2l)^{th}$ layer is equal to

$$0.12 \times 32\% + 0.88 \times 0.2\% = 4.0\% \ (2l)^{th}$$

Now we can calculate the O^{18} concentration of O_p in the $(2l)^{th}$ layer by the formula

$$4.0\% = 0.86 \times (O_p) + 0.14 \times 0.2\%$$

We obtain $(O_p) = 4.6\%$ and the O^{18} concentration of the $(3l)^{th}$ layer is equal to

$$0.12 \times 4.6\% + 0.88 \times 0.2\% = 0.73\% \ (3l)^{th}$$

From 0.73%, we deduce as above the O^{18} concentration of O_p in the $(3l)^{th}$ layer

$$(O_p) = \frac{0.73\% - 0.14 \times 0.2\%}{0.86} = 0.82\%$$

and the O^{18} concentration of the $(4l)^{th}$ layer

$$0.12 \times 0.82\% + 0.88 \times 0.2\% = 0.27\% \ (4l)^{th}$$

(see Fig. 5b)

If the natural oxide remains at the metal-oxide interface, the O^{18} concentration of O_p is equal to the O^{18} concentration of the water (42%). The O^{18} concentration of the $(2l)^{th}$, $(3l)^{th}$, and $(4l)^{th}$ layers is equal to 5.2%, 0.9%, and 0.3%, respectively. One can see that the O^{18} concentration of the duplex films is practically independent of possible losses of SO_4^{2-} incorporated anions.

The O^{18} concentration of the new oxide found at the oxide-metal interface is practically equal to the natural concentration when the total thickness is greater than $3l$. In our experimental conditions the thickness of the base layer l was equal to about 100Å^2; the total thickness of the enriched layer of the duplex film is hence equal to ~300Å. The O^{18} profiles calculated according

to the components of current (Fig. 5) are in good agreement with the form of the maximum of the excitation curves obtained on the duplex layers (Fig. 2).

Pore-filling process.—We formed a thin porous layer in s_o^{18} (t_{ox} = 35 sec) and then reoxidized it in an ammonium borate solution of natural isotopic composition to 100V (I = 1 mA/cm^2). During reoxidation the slope of the curve V(t) decreased to V $\simeq$ 60V. This well-known effect was interpreted in the literature (15) as the end of the pore-filling process. The excitation curves of O^{18} (p, α)N^{15} reactions near the resonance at 629 keV have shown that the O^{18} enriched oxide layer is completely covered by the O^{16} layer when the potential of reoxidation is greater than 60V. This implies that a part of the oxide is grown by cation movement, in agreement with Dekker and Middlehoeck (15).

Discussion

In this work we have shown that the formation of porous oxide layers on aluminum in 15 weight percent (w/o) H_2SO_4 may be explained by assuming the existence of three kinds of ionic currents I_{ox}, I_{Al}, and I_{dec} which can be expressed as percentages of the total current. The current I_{ox} is due to the movement of oxygenated anions which are transferred from the solution to the oxide-solution interface and then move through the base layer to the metal-oxide interface where the new oxide is formed. The value of this current is numerically equal to the current efficiency of porous layer formation. The current I_{Al} is due to the movement of aluminum cations going through the base layer and passing directly into the solution; the current I_{dec} is due to the movement of ions generated by the field-assisted decomposition of the oxide. I_{dec} is transported by the cations (I_{dec}^c) to the solution and by the anions (I_{dec}^o) to the metal-oxide interface. I_{dis} is the total interfacial transfer current of the cations passing into solution; $I_{dis} = I_{Al} + I_{dec}^c$ (Fig. 4). In what follows we shall discuss the mechanism of atomic movements which may account for these various kinds of currents.

The current of direct discharge of aluminum ions in the solution (I_{Al}).—The oxide-metal interface is a source of point defects for the oxide which may induce the migration of cations in the oxide by interstitial or interstitialcy mechanism or as lattice defects $(AlO)^+$ as was proposed by Dignam (22). Cation migration by vacancy motion can also occur, the injection of vacancies taking place at the oxide-solution interface by the transfer (dissolution) of the lattice cations into the solution. Let us call mechanism *A*, cation movement by interstitial or interstitialcy mechanism or as $(AlO)^+$; mechanism *B*; cation movement by vacancy motion. We do not take into account the possibility of formation of interstitial cations and vacancies in the volume of the oxide for thermodynamic reasons (22). In what follows we are going to discuss the likelihood of mechanisms *A* and *B* on the basis of our results and of the experimental data of Dekker and Middlehoeck (15) who have measured the fractional transport number of cations during the porous film formation and the pore-filling process. From measurements of the current efficiency of porous layer formation (in oxalic acid) these authors inferred that the ratio tm_1 of the interfacial transfer current of the cations passing into solution to the total current is equal to 0.33. On the other hand, they found that the fractional transport number of cations tm_2 is equal to 0.24 during the pore-filling process, *i.e.*, during the reoxidation of the porous layers in a solution of ammonium borate in glycol. The volume of the pores was found in this case to be equal to 0.12 of the total volume of the film. According to mechanism *B*, pore filling should occur without cation movement in the oxide, *i.e.*, with cation transport number equal to zero ($tm_2 = 0$), which is in contradiction with our results and those of Dekker and Middlehoeck.

Moreover, mechanism *A* is in full agreement with the experimental results of Dekker and Middlehoeck. Applying model *A* to their results (Fig. 4), using $tm_1 = 0.33$ and for volume of the pores 0.12, we can calculate the values of the various current components. It follows that

$$I_{dis} = 0.33 \cdot I_{tot} \text{ and } I_{ox} = 0.67 \cdot I_{tot}$$

From $\dfrac{I_{dec}}{I_{dec} + I_{ox}} = 0.12$ one finds that $I_{dec} = 0.09 \cdot I_{tot}$

From $I_{Al} = I_{dis} - I_{dec}$ one finds that $I_{Al} = 0.24 \cdot I_{tot}$

Thus, I_{Al} is equal to the value of tm_2 reported by these authors which suggests that mechanism *A* is valid. Moreover the current I_{Al}, which was a dissolution current during porous film formation, keeps the same value during the pore-filling process, being responsible for the oxide growth at the oxide-solution interface.

Cation movement by the lattice defects $(AlO)^+$ seems incompatible with the absence of oxygen losses, except if we assume that dissociation of the defects $(AlO)^+$ occurs before the aluminum is transferred into the solution. Moreover these defects exist only in a glass structure (22), which probably is not the case for porous aluminum oxides (23). For these reasons, we assume in what follows that cation movement occurs by interstitial or interstitialcy mechanism.

Oxygen movement (I_{ox}).—The inversion of the oxygen order in the base layer can be explained either by the migration of oxygen ions by interstitial mechanism or by migration of oxygen vacancies in "easy paths" of the oxides (1). As in the case of cationic movement, we do not take into account the possibility of the formation of interstitial oxygen anions and vacancies (Frenkel or Schottky defects) in the volume of the oxide for thermodynamic reasons (22). The two most likely kinds of oxygen migration are characterized by two different mechanisms of oxygen transfer at the oxide-solution interface, *i.e.*, injection into interstitial positions or vacancy filling. The activation energy of oxygen transfer from the solution into the oxide is much higher in the case of transfer in an interstitial position than for vacancy filling (25). Moreover, since porous oxide growth occurs only by anion migration, the most probable explanation of the observed SO_4^{2-} incorporation is the presence of oxygen vacancies at the oxide-solution interface. For these reasons, we may conclude that porous oxide growth occurs probably by migration of oxygen vacancies through "easy paths." This mechanism was also proposed by us to explain the mechanism of anodic oxidation of Zr (24). Note that such an assumption was not necessary to explain the cations movement which probably occurs by interstitial or interstitialcy mechanism.

The distance between two neighboring oxygen atoms in the molecule Al_2O_3 is the same as in the anion SO_4. This steric concordance could explain the large incorporation observed (2). However, the mechanism of movement of the adsorbed SO_4^{2-} anions through the base layer is not clear. The same difficulty of interpretation was found when studying anion impurity incorporations during the anodic oxidation of Zr, where cation movement is absent (2, 26). The latter results seem to indicate that movement of oxygen by a vacancy mechanism can introduce some anion impurity movements.

Field-assisted dissolution of the oxide (I_{dec}).—The value of I_{dec} is proportional to the rate of decomposition of the oxide at the bottom of the pores. It increases with temperature and acid concentration (2, 3). As Fig. 4 shows, the oxygen ions coming from the oxide decomposition migrate towards the oxide/metal interface and the cations pass into the solution. This effect involves the presence of a region at the oxide-solution

interface where the oxygen and aluminum ions are weakly bound, and hence more mobile than in the volume of the oxide.

Two models can be proposed to explain the presence of this region. The first model (*i*) assumes the presence of a high concentration of oxygen vacancies at the oxide-solution interface. This could be obtained by the adsorption of sulfate anions which inhibits oxygen transfer from the solution to the oxide. Then the presence of oxygen vacancies favors cation transfer into the solution. Following this model, the "field-assisted dissolution" of the oxide is a process whose rate is determined by the equilibrium between cation transfer into the solution and the reaction between oxygen and the vacancies at the oxide-solution interface. In Fig. 6 we show the diagram of the reactions which occur according to this model.

The second model (*ii*) considers that the protonization of the Al-O bonds at the surface of the oxide induces the formation of mobile $(OH^-)_s$ groups and favors cation transfer into the solution. $(OH^-)_s$ is transformed to O^{2-} and migrates by vacancy motion towards the oxide/metal interface ensuring the formation of the new oxide (Fig. 7). This is a variant of the mechanism already imagined by Hoar and Mott (27). These two mechanisms differ from one another in the mode of oxygen migration through the oxide: interstitial (Hoar and Mott); vacancy motion through "easy paths" (this work).

The density of mobile oxygen species $(OH^-)_s$ reached during porous growth depends on the chemical action of the solution and decreases with the electric field. These two models may operate simultaneously; taking into consideration that proton adsorption and diffusion in the oxide are thermally activated, the model (*i*) probably prevails at low temperature and model (*ii*) at high temperature.

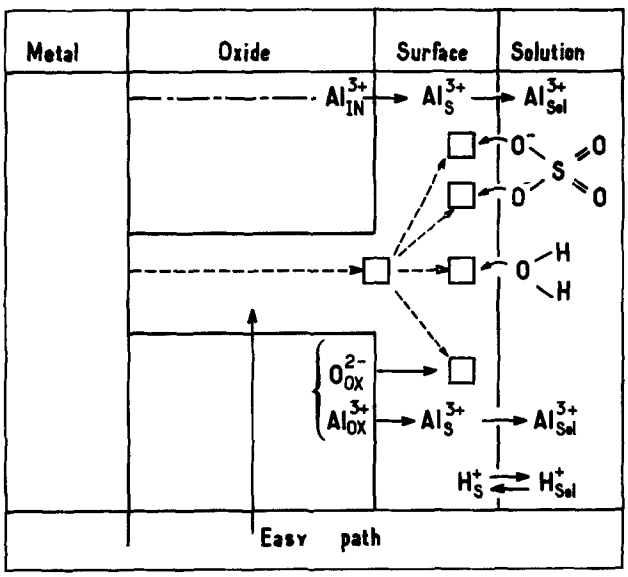


Fig. 6. Schematic presentation of the processes taking place on the surface (s) and in the volume of the base layer during the porous film formation. It is assumed that oxygen movement takes place through the base layer by "easy paths". Al_{in}^{3+} interstitial or interstitialcy movements of aluminum cations through the base layer; □ oxygen vacancy.

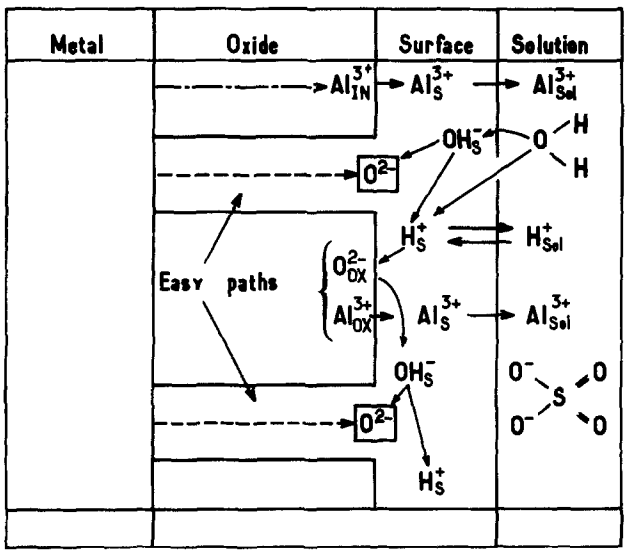


Fig. 7. See Fig. 6 for the presentation; H_s^+ and OH_s^- indicate protons and OH^- anions adsorbed on the surface of the base layer, respectively. $\boxed{O^{2-}}$ oxygen just after reaction with vacancy.

Acknowledgments

The authors wish to thank Dr. G. Amsel for enlightening discussion and Mr. A. Laurent for his technical assistance. They are also indebted to Dr. R. S. Alwitt and Professor M. Nagayama, whose very appreciated remarks have contributed to clarify the presentation of this paper. This work was supported by the Centre National de la Recherche Scientifique.

Manuscript submitted July 15, 1976; revised manuscript received Jan. 17, 1977.

Any discussion of this paper will appear in a Discussion Section to be published in the December 1977 JOURNAL. All discussions for the Dec. 1977 Discussion Section should be submitted by Aug. 1, 1977.

REFERENCES

1. C. Cherki and J. Siejka, *This Journal*, **120**, 784 (1973). J. Siejka and C. Cherki, Paper 90 presented at the Electrochemical Society Meeting, Cleveland, Ohio, Oct. 3-7, 1971.
2. J. W. Diggle, T. C. Downie, and C. W. Goulding, *Chem. Rev.*, **69**, 365 (1969). J. W. Diggle, in "Dissolution of Oxide Phases in Anodic Behaviour of Metals and Semiconductors," Vol. 2, J. W. Diggle, Editor, Chap. 4, Marcel Dekker, Inc., New York (1973).
3. T. P. Hoar and J. Yahalom, *This Journal*, **110**, 614 (1963).
4. J. P. O'Sullivan and G. C. Wood, *Proc. Roy. Soc. London, A317*, 511 (1970).
5. M. S. Hunter and P. E. Fowle, *This Journal*, **101**, 514 (1954).
6. F. Keller, M. S. Hunter, and D. L. Robinson, *ibid.*, **100**, 411 (1953).
7. J. W. Diggle, T. C. Downie, and C. W. Goulding, *ibid.*, **116**, 737 (1969).
8. G. Amsel, J. P. Nadai, E. d'Artemarre, D. David, E. Girard, and J. Moulin, *Nucl. Instrum. Methods*, **92**, 481 (1971).
9. G. C. Wood and J. P. O'Sullivan, *Electrochim. Acta*, **15**, 1865 (1970).
10. G. C. Wood, J. P. O'Sullivan, and B. Vaszko, *This Journal*, **115**, 618 (1968).
11. P. Neufeld and H. O. Ali, *ibid.*, **120**, 479 (1973).
12. J. Zahavi and M. Metzger, *ibid.*, **121**, 268 (1974).
13. T. C. Hoering and J. W. Kennedy, *J. Am. Chem. Soc.*, **79**, 56 (1957).
14. P. Lelong, R. Segond, and J. Herenguel, in "Oxydation des Metaux", Vol. 2, J. Benard, Editor, Chap. 13, Gauthiers-Villars (1964).
15. A. Dekker and A. N. Middlehoeck, *This Journal*, **117**, 440 (1970).
16. G. Amsel, Private communication.
17. La Vecchia, G. Piazzesi, and F. Siniscalco, *Electrochim. Metal*, **2**, 71 (1967).
18. J. Zahavi and M. Metzger, *This Journal*, **119**, 1479 (1972).
19. G. Amsel, "Nuclear Microanalysis of O^{16} and O^{18} in Near Surface Regions of Solids", Proceedings of an International Colloquium on Oxygen Isotopes, p. 138, Cadarache, (1972).
20. M. Nagayama, Private communication.
21. R. B. Mason and P. E. Fowle, *This Journal*, **101**, 53 (1954).
22. M. J. Dignam, in "Oxides and Oxide Films", Vol. 1, J. W. Diggle, Editor, Marcel Dekker Inc., New York.

23. G. C. Wood, in "Oxides and Oxide Films," Vol. 2, J. W. Diggle, Editor, Marcel Dekker Inc. New York (1973).
24. C. Ortega and J. Siejka, Paper 98 presented at Electrochemical Society Meeting, Toronto, Canada, May 12-16, 1975.
25. P. Kofstadt, "Nonstoichiometry Diffusion and Electrical Conductivity in Binary Metal Oxides," Wiley-Interscience, New York.
26. G. T. Rogers, P. H. G. Draper, and S. S. Wood, *Electrochim. Acta*, **13**, 251 (1968).
27. T. P. Hoar and N. F. Mott, *J. Phys. Chem. Solids*, **9**, 97 (1959).

Kinetics of Plasma Anodization of Aluminum

M. Propp, L. Young,* D. L. Pulfrey, and G. Olive*

Department of Electrical Engineering, The University of British Columbia, Vancouver, British Columbia, Canada V6T 1W5

ABSTRACT

The anodization of evaporated aluminum films in a d-c oxygen plasma has been studied using *in situ* automated ellipsometry to determine film thickness D. The aim was to investigate whether plasma anodization is analogous to solution anodization in that film growth occurs due to an ionic current produced by a high field in the oxide. Films were grown at constant total anodic current I_A, only a small part of which corresponded to film growth. The ionic current density J_i corresponding to growth was calculated from dD/dt using Faraday's law. Plots of the sample potential V (with respect to the discharge-sustaining anode) *vs.* thickness D were linear at each constant total current. The slopes dV/dD were taken as a measure of the electric field E in the oxide. The electronic current density J_e through the oxide could be represented by $J_e = J_e^o \exp CE^{1/2}$ where J_e^o varied between runs. Imposition of a chosen constant electronic current thus set the field in the oxide at a particular value in the oxide independent of thickness. By analogy with solution anodization the constant field would be expected to produce a constant ionic current. In fact, the data indicated an ionic current density J_i which decreased with increasing thickness, $J_i = (1/D)\ \alpha \exp BE$. Only if data were chosen for a narrow range of thickness was the expected relation $J_i = J_i^o \exp \beta E$ applicable, where J_i^o is constant, as found in previous work on tantalum, niobium, and aluminum. This result would be consistent with an unexpected model in which film growth involved the diffusion of some species whose surface concentration is set by the field or the electronic current. A trend of behavior with some points of similarity has previously been reported for silicon anodization in microwave-induced discharges.

In plasma anodization, a metal or semiconductor is positively biased in an oxygen plasma. This causes an oxide film to grow (1-13). It has been concluded by several authors that the process is, in principle, analogous to the process of anodic film growth in aqueous solutions. In other words, it has been believed that the applied voltage causes an electric field to be established across the oxide which draws metal or oxygen ions or both through the oxide by high field conduction. If the analogy is correct one expects (14, 15) to find a relation between the field E in the oxide and the ionic current J_i of the form $J_i = J_i^o \exp -(W - f(E)/kT)$ where W is the zero-field activation energy and $f(E)$ is αE or $\alpha E - \beta E^2$ or $\gamma E^{1/2}$. It is much more difficult to establish such relations for plasma anodizaion than it is for solution anodization. This is because the variability of plasma conditions, the problems of measuring the potential drop across the oxide, the low current efficiency, and possibly the effect of the exposure of the film to the plasma make it difficult to obtain reproducible and unscattered data. Furthermore, an oxide grows on open circuit, as first shown by Miles and Smith (3), and recently studied by Vrba and Woods (16). Conversely, the film may be simultaneously subject to erosion by sputtering (8).

Since the (supposed) ionic current density can only be determined using Faraday's laws from observed values of dD/dt (or equivalents) some *in situ* method of determining film thickness (or mass) is more or less essential for kinetic studies. Ellipsometry is suitable for this purpose (8, 9, 17, 18).

* Electrochemical Society Active Member.

The expected dependence of log J_i on E has been reported for tantalum and niobium upon anodization in a high frequency discharge (19, 20). For anodization in a d-c glow discharge results for tantalum, niobium (17, 18), and aluminum (9) gave linear relations of log J_i with E, but with values for the parameters which were outside the ranges found for anodization in various aqueous solutions. For silicon, the situation is considerably different. In the case of anodization in an rf plasma, the field has been reported to increase with thickness (21, 22), whereas, in a microwave frequency plasma growth has been attributed to diffusion, and not drift, processes (23, 24).

It will be appreciated from the foregoing that plasma anodization is a relatively complex process with the anodic film growth being affected by both the nature of the substrate and the nature and properties of the plasma. There is still very little information available on the kinetics of the film growth and it was the purpose of this work to obtain further data on the plasma anodization of aluminum in a d-c glow discharge.

Experimental Procedures

The plasma cell is shown diagrammatically in Fig. 1. It is a development of that used in our earlier work (17) and was the cell used for the work in Ref. (18). It consists of a fused silica tube with stainless steel end caps sealed with O-rings. A sorption pump and ion pump gave an ultimate vacuum (without baking) of 4×10^{-7} Torr. The specimen consisted of a silicon substrate coated on one side with a film of aluminum evaporated on to a cold substrate from high purity aluminum wire on a tungsten heater in a conventional

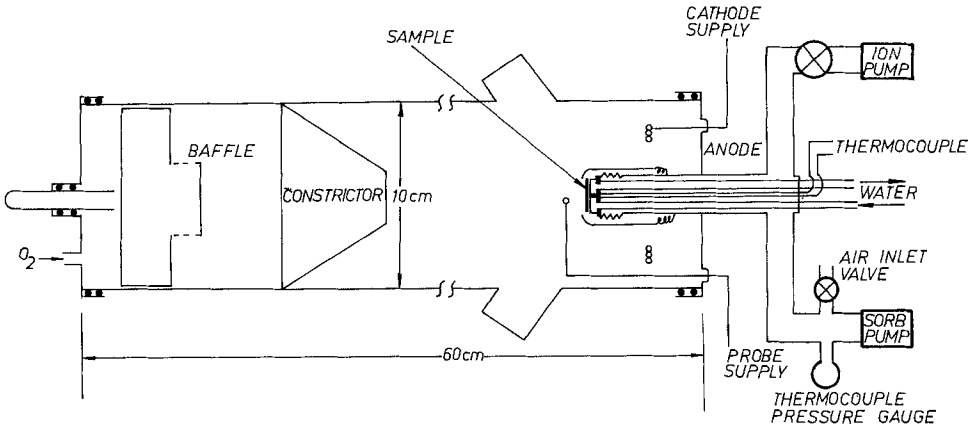


Fig. 1. The plasma anodization cell.

vacuum system. Silicon slices were used as substrates since they provided a cheap highly polished surface giving films flat enough for optical measurement. The specimen was aligned using screw adjustments, and the specimen holder was attached to the end cap with bellows. The cell and pumping system were mounted on an adjustable metal plate resting on a trolley which rode on metal rails rigidly attached to the metal frame supporting the ellipsometer. The samples were mounted in the sample holder, using silver paint on the back and a spring attachment, with a mica plate defining the area exposed to the plasma. Electrical connection was made using silver paint (not exposed to the plasma). The cell and movable ellipsometer arm were adjusted so that the light beams met the windows at normal incidence. The angle of incidence was thus set by the fixed windows and was 69.29°. The difference in zone 1 and 3 readings taken before and after insertion in the system was attributed to the window error. Changes in Δ of about 1.5° were observed with negligible change in ψ.

The pressure during runs was maintained at 100 mTorr by manual adjustment of a valve preceding the sorption pump, with high purity oxygen being supplied through a fixed valve. Water from a thermostatted bath was circulated through the sample holder. The sample temperature was assumed to be given by a Chromel-Alumel thermocouple in contact with the sample holder. The bath temperature was adjusted to maintain a constant sample temperature of 40°C. The discharge current was set at 20 mA using a variable high voltage supply with fixed series resistance. Constant currents were applied to the sample using the circuit shown in Fig. 2, while recording the specimen-discharge anode and probe-discharge anode voltages on a chart recorder. It was found that noise was reduced by using a 3-turn Al ring cathode rather than the previously used bucket cathode and constrictor arrangement. These two components were, however, left in the system, see Fig. 1. The specimen was situated in the negative glow region of the plasma. The ellipsometer is controlled by a PDP8E computer and has been described in previous papers (25, 26). It was used to track alternately in zones 1 and 3 so that readings could be averaged.

Results

Data were taken on five samples. The first three served to work out procedures and the results presented below were obtained with the last two samples.

Figure 3 shows tracings of chart recorder plots of sample voltage with respect to the discharge anode *vs.* time. On changing from a lower to a higher constant current (0.4 mA to 0.8 mA with an area of about 1 cm^2 for the cases shown) there was usually some overshoot followed by a steady constant rate of increase of voltage. The form of the transient was somewhat variable, as indicated in Fig. 3, with a tendency for the amount of overshoot to decrease with increasing thickness. These transients cannot be directly compared with the transients in solution anodization (27), because, in the plasma case, the current is mostly electronic rather than ionic, the field in the oxide sets itself at the value given by the imposed electronic current, and the observed transient is probably in electronic conductance not in ionic conductance.

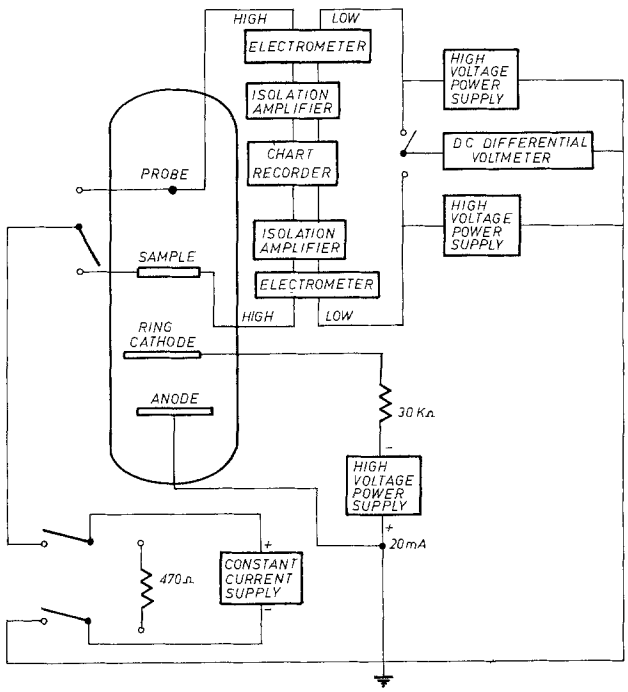


Fig. 2. The electrical circuit

Figure 4 shows plots of the ellipsometric variables ψ and Δ in $R_p/R_s = \tan \psi \exp i\Delta$ where R_p/R_s are the complex reflectivities of the oxide-coated metal in p and s light. The data shown fit a curve for a uniform film of refractive index 1.62 growing on a substrate of index 1.20 − i 6.74 up to a certain thickness beyond which one of the specimens started to diverge from the curve. Locker and Skolnick (8) found that the index of their films changed from 1.65 to 1.75 due to exposure to the plasma and possibly some effect of this kind occurred here. The films were assumed to be of uniform index through their thickness. To obtain the thickness, theoretical curves (Fig. 4b) were plotted for the fitted oxide index and for two indexes bracketing the fitted value. Contours were drawn corresponding to constant thickness. Film thicknesses were estimated from these contours and from Δ, ψ computer printouts for 0.2 nm increments in thickness.

Figure 5 shows some typical plots of thickness *vs.* time. For the times of formation involved these were linear or, particularly for thinner films, became so after some period of anodization at constant current. The slopes were calculated and converted into ionic

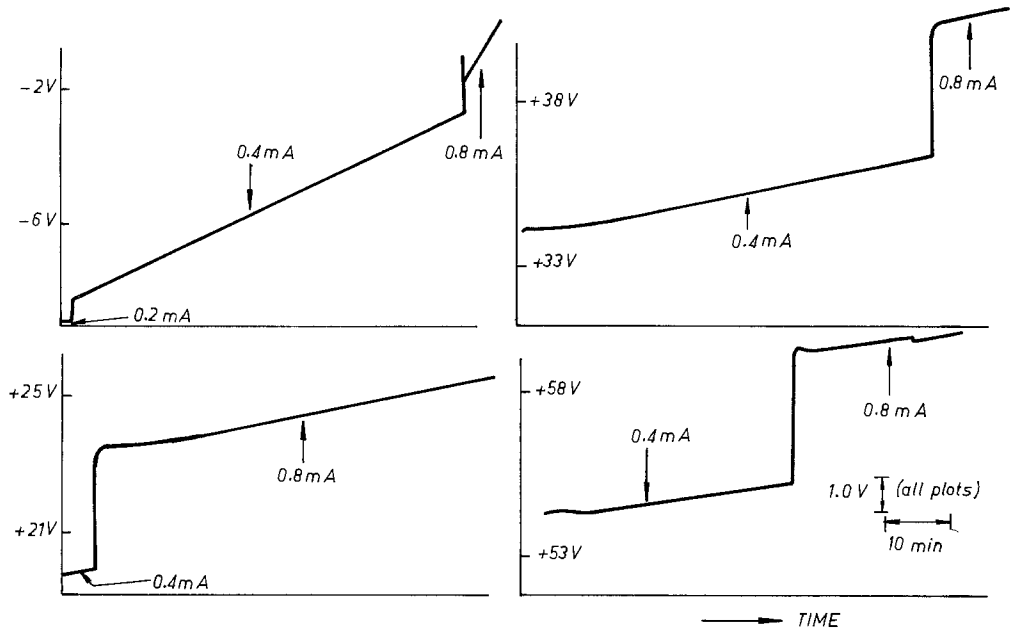


Fig. 3. Plots of sample voltage (w.r.t. discharge anode)V vs. time showing the transients on switching the anodizing current at different stages in the film growth for sample II. (The magnitude of the voltages gives an indication of film thickness.)

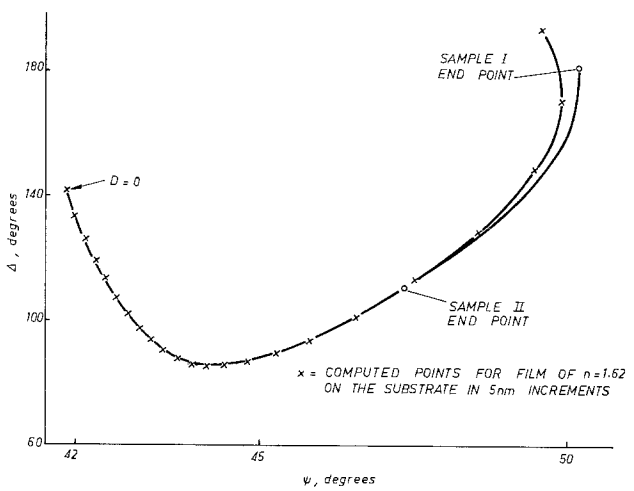


Fig. 4. a. Ellipsometry data for samples I and II

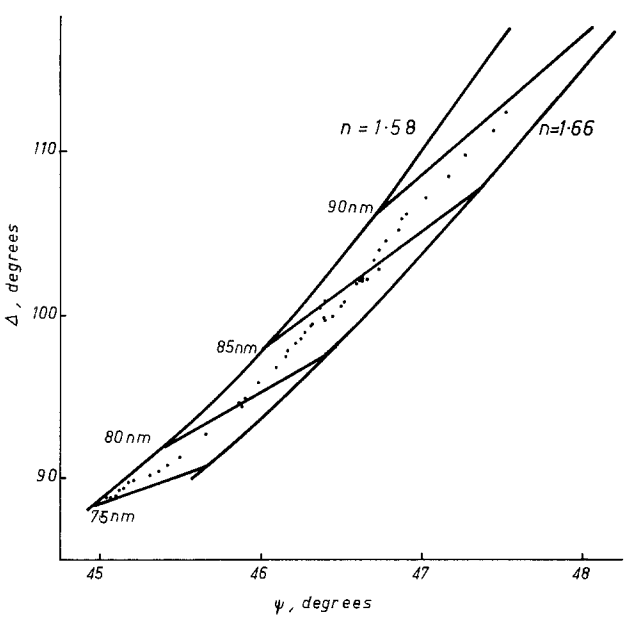


Fig. 4. b. Ellipsometry data for sample I showing the method used for estimating oxide thickness.

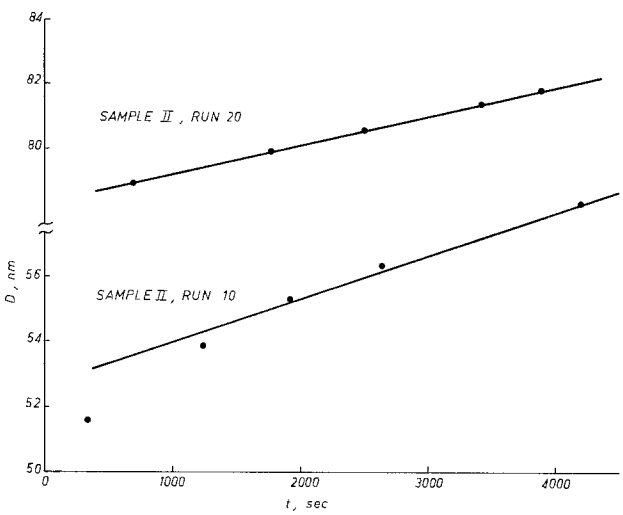
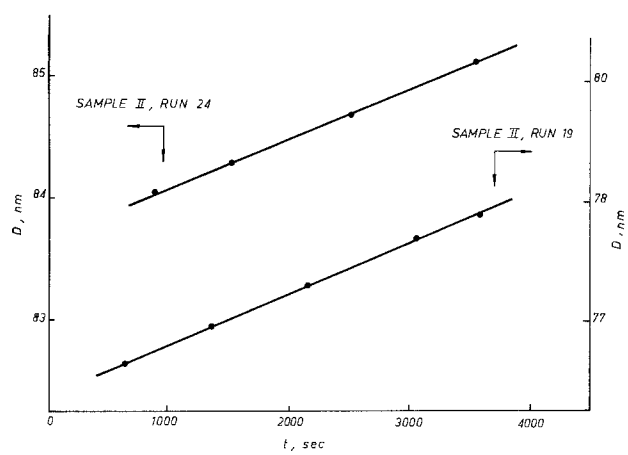


Fig. 5. Variation of oxide thickness with time of constant current anodization.

(a) I_A = 2.8 mA



(b) I_A = 1.5 mA

current density, using $J_i = (\rho 6\mathbf{F}/MW)dD/dt$ where ρ = film density [assumed (28) to be 3.1 g/cm^3], $\mathbf{F}$ = the Faraday, and MW is the molecular weight of Al_2O_3. The formations at each constant total current had to be continued for 60-70 min in order to obtain sufficient growth (*e.g.*, 1-15 nm) to give a reasonably accurate estimate of the ionic current density.

Figure 6 shows plots of voltage *vs.* thickness for the complete sequence of formations on two specimens.

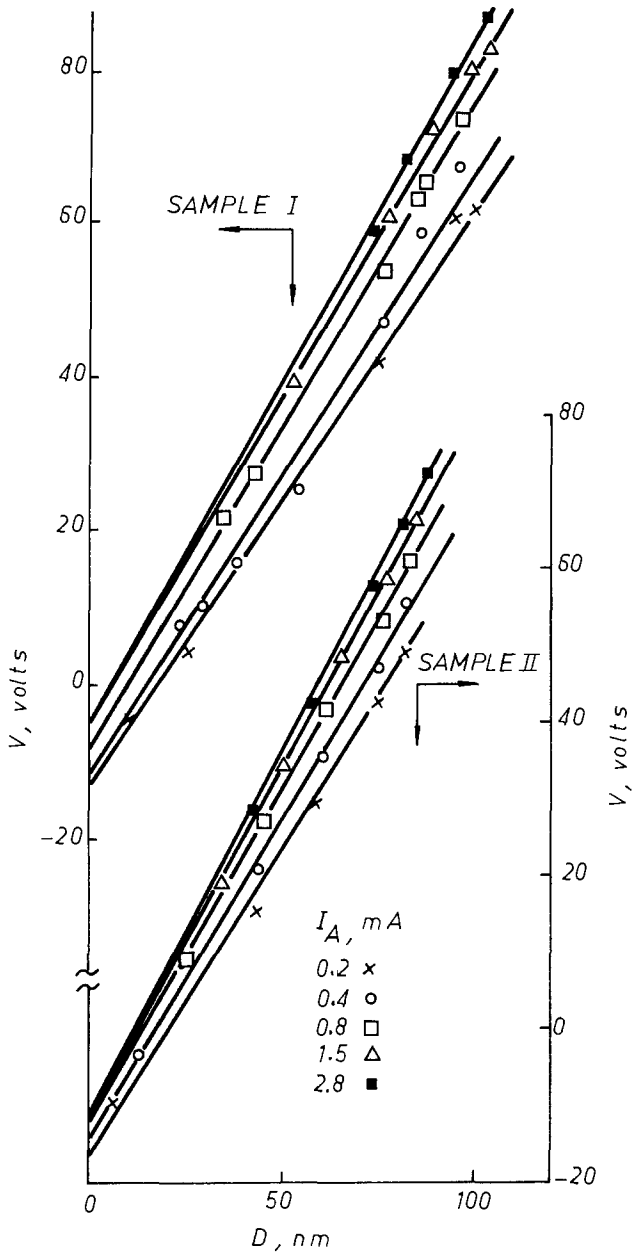


Fig. 6. Variation of V with oxide thickness

The points for each selected total current can reasonably be concluded to lie on straight lines, indicating a constant field independent of thickness at each current. The slope of the lines was taken as giving the field E in the oxide. The lines do not extrapolate to the same voltage at zero thickness. This is to be expected since the current drawn by the specimen perturbs the distribution of plasma potential (as was observed by the change in probe potential).

The dependence of E on the electronic current is explored in Fig. 7 and 8 where plots of $\log_{10}J_e$ *vs.* E and $\log_{10}J_e$ *vs.* $E^{1/2}$ are shown. Both plots gave straight lines but the Schottky plot gives more similar slopes for the two specimens. The shift in intercept between the two plots for the two specimens may be due to a difference in the distribution of plasma in the two runs. If the slope $d \log J/dE^{1/2}$ is identified as $e\sqrt{e/\pi\epsilon_0\epsilon_r}/kT$ the value of ϵ_r is found to be 8.5. The permittivity of the films at 1 kHz was measured at about 10.

Figure 9 shows a plot of $\log_{10}J_i$ *vs.* E. The fields are the average fields as derived from Fig. 6 and the result is a scatter diagram. However, from the film thicknesses shown against each point, a strong correlation is shown with thickness, the ionic current

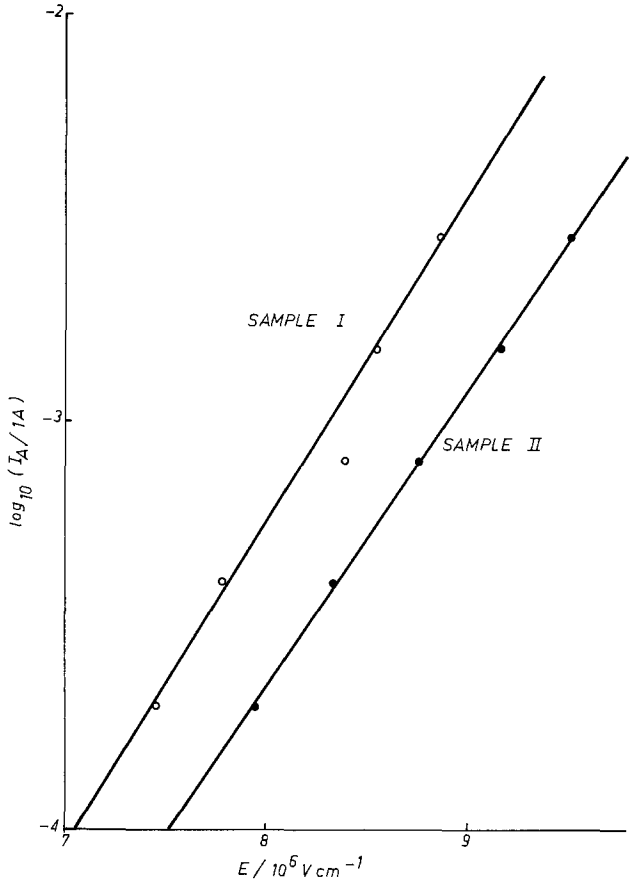


Fig. 7. Log_{10} I_A *vs.* E, with oxide field strength calculated from the slopes shown in Fig. 6.

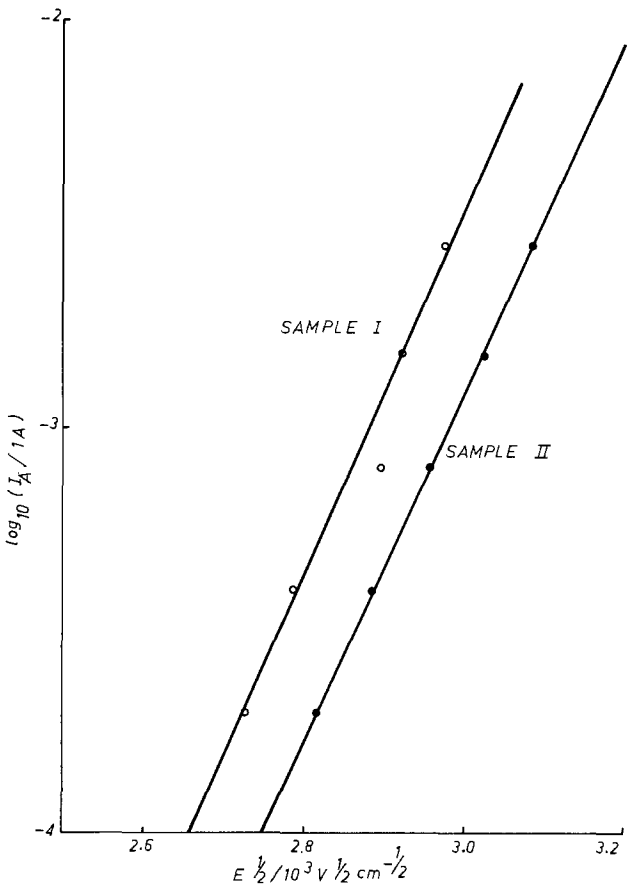


Fig. 8. Log_{10} I_A *vs.* $E^{1/2}$

tending to decrease with increasing thickness. Pursuing this correlation further, Fig. 10 shows plots of

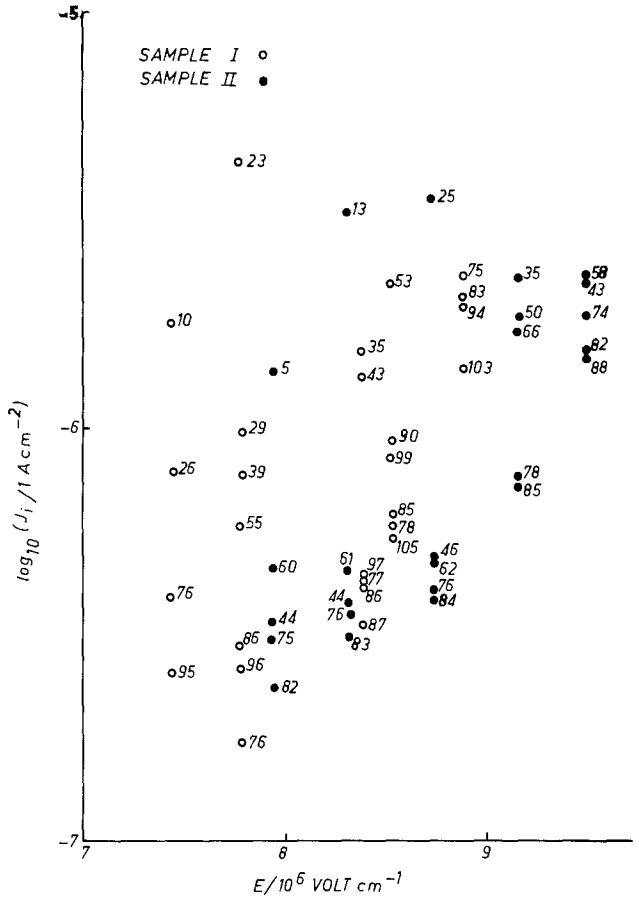


Fig. 9. Log_{10} J_i *vs.* E, with film thicknesses indicated in nanometers.

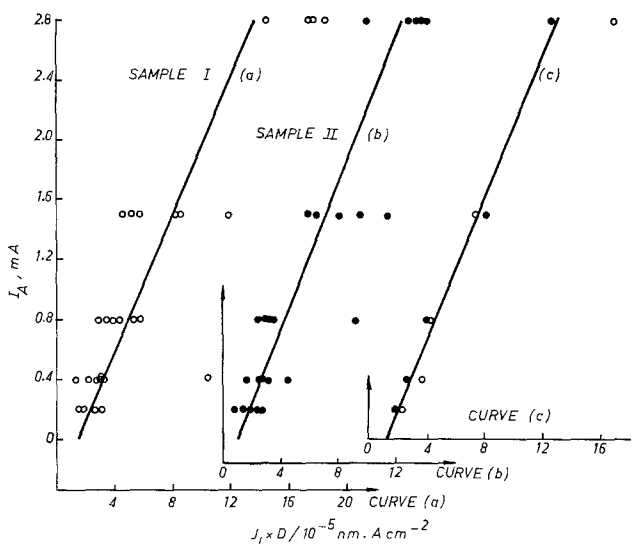


Fig. 10. Variation of ($J_i \times D$) with I_A. Curve (c) shows the average values of ($J_i \times D$) for each sample at each particular I_A.

total current *vs.* the product of thickness and ionic current. The data indicate a relation of the form $J_iD = mI_A + \gamma$ where m and γ are constants. Figure 11 shows the variation of $I_A/(J_iD - \gamma)$ where γ is the intercept in Fig. 10, over the range in D covered by the data. Further illustration of the dependence of the ionic current on thickness is given by Fig. 12 where the data for J_i *vs.* D can be compared with the curve constructed from the straight line drawn through the experimental points in Fig. 10.

Finally in Fig. 13, plots of $\log_{10}J_iD$ *vs.* E are given. Mean values of J_iD for a given total current are plotted in Fig. 14. Two lines are obtained with similar slope but different intercept, a situation similar to that for the electronic current (Fig. 7).

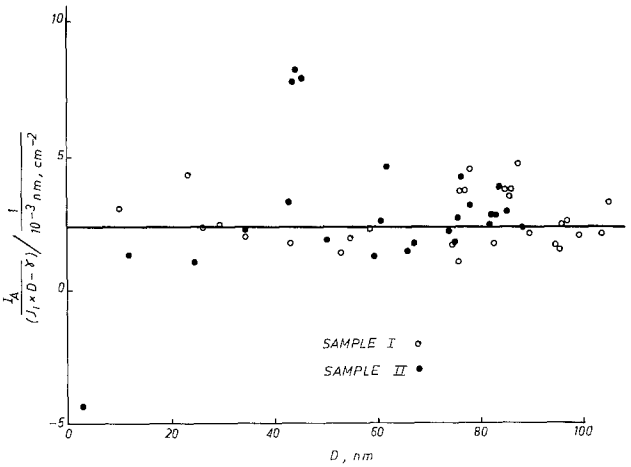


Fig. 11. Plot to examine the thickness dependence of $I_A/(J_i \times D - \gamma)$ where γ is the zero total current intercept from Fig. 10.

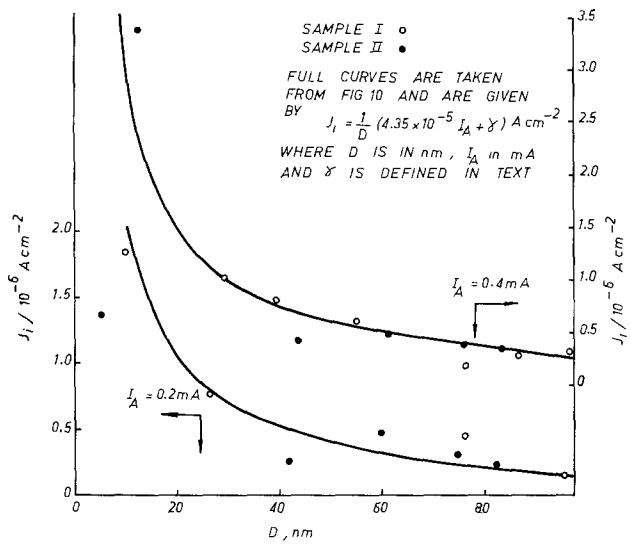


Fig. 12. Variation of ionic current density with oxide thickness, with the full curves computed from Fig. 10.

Discussion

The empirical expression $J_iD = mI_A + \gamma$ to which the data were fitted is of the form which would be given by the diffusion of a species whose concentration at the oxide/plasma interface was enhanced by the drawing of electronic current from the plasma. The relation suggests that this concentration was either linearly dependent on the electronic current or controlled by the oxide field which was determined by this electronic current. The question is whether such a model is correct or even reasonable. It is not without precedent. Previous work by Ligenza (23) and by Kraitchman (24) on the plasma anodization of silicon has indicated a diffusion process (parabolic growth law) enhanced by the plasma and applied voltage. Ligenza suggested that a mobile oxygen species was injected into the outer surface of the oxide from the plasma. The details of the observed kinetics were complex (for example, the dependence on voltage) and not fully explained by the model. In the present case, it is difficult to envisage what neutral species would be mobile in Al_2O_3 (as opposed to SiO_2) and one would expect drift to dominate over diffusion for a charged species at such high fields. Space charge effects may provide an alternative to the diffusion model. As discussed in early work on anodic oxidation (29) and recently treated numerically by Fromhold (30), space charge effects would require, in the case of transport of one ionic type without charge compensation, an increasing field with

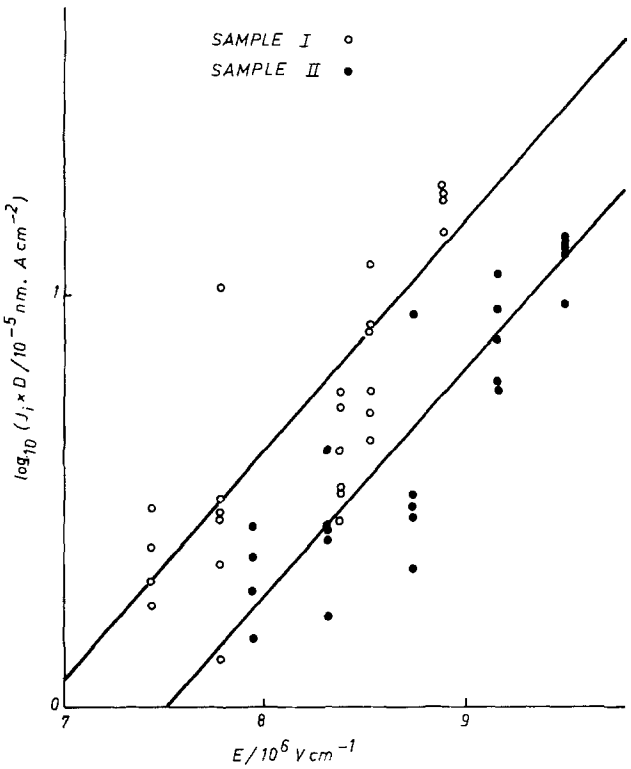


Fig. 13. Log_{10} ($J_i \times D$) vs. E for each formation but with the oxide field strength calculated from the slopes shown in Fig. 6.

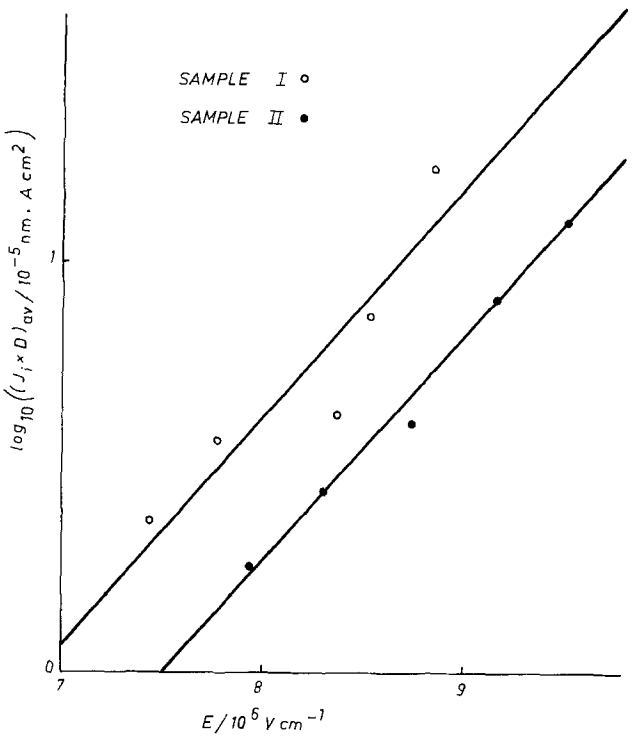


Fig. 14. Log_{10} $(J_i \times D)_{avg}$ vs. E, where the values of ($J_i \times D$) are the average values at each particular oxide field strength.

increasing thickness for high field transport at a constant ionic current. Conversely this would produce an ionic current decreasing with increasing thickness at constant average field, *i.e.*, the direction observed in the present work. In previous work on the plasma anodization of silicon in an rf plasma (21), space charge effects giving a tendency of this kind were indeed postulated. A difficulty is, then, why the electronic current should stay constant at constant average field.

Another possibility is that the mobile ions are somehow generated by the electronic current. Such an effect has been considered in connection with the stimulation of growth of anodic oxide films by u.v. radiation (31), and by Fritsche (32) in connection with the solution anodization of silicon, which occurs, like plasma anodization, at very low current efficiency. To fit the present growth law one might postulate the formation of some mobile oxygen species from absorbed oxygen at a rate proportional to electronic current.

Returning to the theory that a mobile species (or some precursor) is shot into the oxide from the plasma, work involving the application of rf + d-c voltages did not easily fit the idea that the supply of negative ions from the plasma was rate limiting (18). Arguments (2) that some plasma species (such as O_2^-) are rate limiting have often been based on reports that plasma anodization is faster in one part than another of the glow discharge. The problem is that the significance of such observations is not obvious and one must consider carefully what is being kept constant. Thus data at constant oxide field might be expected to be more significant than data at constant total current. The field to produce a given total current probably depends on the supply of electrons from the plasma. No sign of a saturation of ionic current with increasing total current has been observed.

As regards previous indications that the process of plasma anodization obeys the conventional law ($J_i \propto \exp BE$), it should be noted that, if data are taken over a range of thickness such that $1/D$ does not vary much (*i.e.*, if the thinner films are excluded), then such a law would tend to be found, particularly in view of the scatter typically shown by experimental data on plasma anodization. Perhaps the presence of this scatter, as contrasted to the extreme reproducibility of solution anodization data (where films may be made with 0.1% reproducibility of thickness) should be taken as further indication of difference in mechanism.

Acknowledgments

This work was supported by National Research Council (Canada) operating grants to L.Y. and D.L.P. Some of the equipment was constructed during a previous project supported by the USAF Avionics Laboratory, Wright-Patterson Air Force Base (Contract F33616-71-C-1886).

Manuscript submitted Oct. 13, 1976; revised manuscript received Feb. 2, 1977.

Any discussion of this paper will appear in a Discussion Section to be published in the December 1977 JOURNAL. All discussions for the December 1977 Discussion Section should be submitted by Aug. 1, 1977.

Publication costs of this article were assisted by The University of British Columbia.

REFERENCES

For reviews on plasma anodization see (1) and (2). For articles specifically on aluminum (3-13).

1. C. J. Dell'Oca, D. L. Pulfrey, and L. Young, *Phys. Thin Films*, 6, 2 (1971).
2. J. F. O'Hanlon, *J. Vac. Sci. Technol.*, 7, 330 (1970).
3. J. L. Miles and P. H. Smith, *This Journal*, **110**, 1240 (1963).
4. G. J. Tibol and W. M. Kaufmann, *Proc. IEEE*, **52**, 1465 (1964).
5. G. J. Tibol and R. W. Hull, *This Journal*, **111**, 1368 (1964).
6. G. J. Tibol, *Insulation*, **11**, 25 (June 1965).
7. L. E. Terry and E. E. Komarek, AEC Report SC-TM 397-63(14) (1964).
8. L. D. Locker and L. P. Skolnick, *Appl. Phys. Lett.*, 12, 396 (1968).
9. A. C. Nyce, Ph.D. Thesis, University of Maryland (1971).
10. P. J. Fopiano, *IEEE Trans. Parts, Mater., Packag.*, **pmp-1**, S217 (1965).
11. P. L. Worledge and D. White, *Br. J. Appl. Phys.*, **18**, 1337 (1967).

12. F. B. Micheletti, P. E. Norris, and K. H. Zaininger, *RCA Rev.*, **31**, 330 (1970).
13. J. F. O'Hanlon, *This Journal*, **118**, 270 (1971).
14. L. Young, *Proc. R. Soc. London, Ser. A.*, **258**, 496 (1960).
15. L. Young and F. G. R. Zobel, *This Journal*, **113**, 277 (1966).
16. J. Vrba and S. B. Woods, *Can. J. Phys.*, **50**, 548 (1972).
17. W. L. Lee, G. Olive, D. L. Pulfrey, and L. Young, *This Journal*, **117**, 1172 (1970).
18. G. Olive, D. L. Pulfrey, and L. Young, *Thin Solid Films*, **12**, 427 (1972).
19. E. V. Makara, V. S. Mikhalkin, and L. L. Odynets, *Elektrokhimiya*, **7**, 1096 (1971).
20. V. S. Mikhalkin and L. L. Odynets, *ibid.*, **7**, 848 (1971).
21. D. L. Pulfrey, F. G. M. Hathorn, and L. Young, *This Journal*, **120**, 1529 (1973).
22. D. L. Pulfrey and J. J. H. Reche, *Solid-State Electron.*, **17**, 627 (1974).
23. J. R. Ligenza, *J. Appl. Phys.*, **36**, 2703 (1965).
24. J. Kraitchman, *ibid.*, **38**, 4323 (1967).
25. W. D. Cornish and L. Young, *Proc. R. Soc. London, Ser. A.*, **335**, 39 (1973).
26. K. K. Yee and L. Young, *Appl. Opt.*, **14**, 1316 (1975).
27. L. Young, "Anodic Oxide Films," p. 26, Academic Press, London and New York (1961).
28. L. Young, *ibid.*, p. 219ff.
29. L. Young, *ibid.*, p. 185.
30. A. T. Fromhold, in "Oxides and Oxide Films," Vol. 3, J. W. Diggle Editor (1976).
31. L. Young, "Anodic Oxide Films," p. 138, Academic Press, London and New York (1961).
32. C. R. Fritsche, *Solid State Commun.*, **6**, 341 (1968).

Characterization of Vapor-Deposited Paraxylylene Coatings

T. E. Baker,* S. L. Bagdasarian, G. L. Fix, and J. S. Judge*

Raytheon Company, Equipment Division Laboratories, Sudbury, Massachusetts 01776

ABSTRACT

Vapor deposition and polymerization of dichloro-diparaxylylene produces a parylene polymer film whose uniqueness as a superior conformal coating can be attributed to a combination of excellent properties and high throwing power. Additional advantages for low outgassing environments have been suggested for films whose composition and structure are critically controlled. Variations in vaporization temperature, pyrolysis temperature, material charge, deposition load, and charge/load ratio were made and the resultant films analyzed. Mechanical, spectroscopic, thermal, and chromatographic analysis of these films have elucidated the dependence of their oligomeric content and structure on deposition conditions.

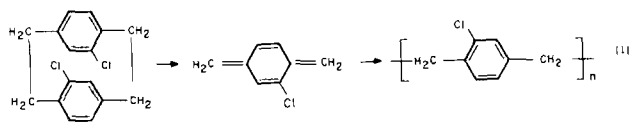
Parylene is the generic name for members of a well-known polymer series (1). Many studies have been performed on the physical and chemical properties of polymeric paraxylylene films, particularly the unchlorinated material (2-4). These films have found application as conformal coatings for electronic assemblies and have been formally approved for military applications (5). Parylene, unlike most plastics, is not sold as a polymer but is produced by vapor-phase polymerization and deposition using a special vacuum application system (6). It cannot be applied easily from solvent solutions since it is insoluble in most common solvents (7).

The process for the vapor deposition of dichloro-diparaxylylene, known as parylene C,[1] has been commercially available for several years. The existing process had been optimized to produce a conformal coating capable of protecting electronic assemblies from adverse environments. In the present application, parylene C films were needed that had an additional requirement of a minimum outgassing product under a specified thermal/vacuum environment. While low outgassing films were desired it was also necessary that the basic material integrity and inherent properties of parylene be preserved (8). To achieve this goal it would be necessary to critically control the composition and structure of these films.

Experimental

Parylene is deposited in a vacuum system from the vapor phase at a pressure around 0.1 Torr. Therefore, parylene vapor approaches the object to be coated from all directions and since deposition is not line of sight all sides of an object are coated uniformly by impinging gas molecules. This characteristic in itself is one of the primary reasons for the increasing usage of parylene within the electronics industry. A diagram of the basic process apparatus is illustrated in Fig. 1.

The process for producing parylene C films starts with the dichloro-di-p-xylylene crystalline solid dimer which is vaporized and pyrolyzed in vacuum to produce the monomeric chloro-p-xylylene. Upon entering the deposition chamber it simultaneously adsorbs and polymerizes on substrate surfaces. The formation reaction is shown schematically in Eq. [1]



The parylene C dimer was obtained from Union Carbide and an analysis report accompanied each shipment. In our investigation films were produced using a

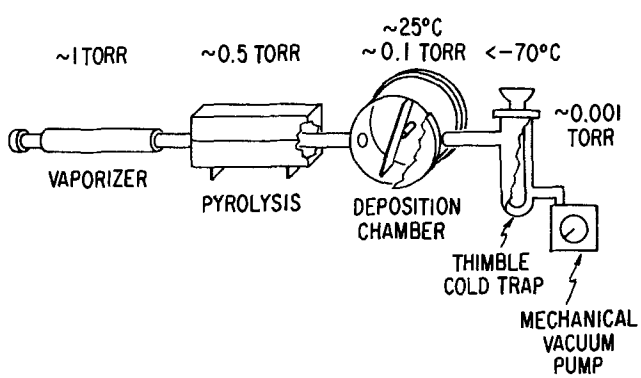


Fig. 1. Diagram of paraxylylene deposition process apparatus

* Electrochemical Society Active Member.
Key words: paraxylylene, vapor deposition, conformal coating, low weight loss, parylene, vapor phase polymerization.
[1] Tradename, Union Carbide Corporation.

Union Carbide Model No. 10C coater and deviations from the standard vaporization and pyrolysis temperatures were made. Variations in material charge, deposition load and charge/load ratio were also initially made, however, the bulk of this work was performed under constant charge/load conditions. Changes in vaporization/pyrolysis temperatures also produced changes in other dependent variables such as chamber pressure and rate of deposition.

Variations from nominal ranged from −20° to +35C° for vaporization temperature and −50° to +50°C for pyrolysis temperature.[2] This exercise was essential in determining what effects, if any, these temperature variations had on film characteristics, particularly outgassing properties, since earlier work and characteristics of other free radical processes suggest a dependence (9).

The quantitative analysis of dimer content in the resultant polymeric material has been performed previously by infrared spectroscopy (10). The infrared method has a lower detection limit of approximately 1.3% of unconverted parylene dimer in the film. The quantitative analysis of dimer content of the polymer film was performed in our laboratory by means of liquid chromatography. The polymer film was first extracted with tetrahydrofuran in a Soxhlet type extraction apparatus to remove the unconverted dimer and any additional soluble oligomers. The film weight loss was then used to calculate the percent of extractable material. This soluble fraction was analyzed by reverse phase liquid-liquid chromatography. The intensity of the major isomer peak was then compared to the intensity of the same peak in the chromatogram of a standard solution of dimer. The resultant detection limit for the determination of dimer content in a 0.5g sample of polymer by this method is approximately 0.05%.

The refractive index and the thickness of each deposited run was obtained over the 1.8-2.6 μm wavelength range utilizing a variable angle specular reflectance accessory to a Beckman ACTA MVII NIR/-VIS-UV spectrophotometer. A silicon wafer accompanied other test coupons in the deposition chamber for each run. The coated wafers were mounted on the reflectance accessory and scanned over the predescribed wavelength range and an interference pattern was generated at two incident angles, 30° and 45°.

The weight loss of the film when exposed to heat and vacuum was determined by heating the film for 2 hr at 200°C at a pressure of less than 500 μm on a Cahn Model RG electrobalance.

Results

The resultant films from variations in vaporization and pyrolysis temperatures were analyzed for relationships among percentage dimer content, percentage extractables, and vacuum weight loss. Figures 2 and 3 graphically illustrate those relationships. Applying the least squares technique to the data, it is clearly seen that monotonic relationships exist between these three measured properties. There is nearly a one to one correlation between vacuum weight loss and percent extractables: there always being slightly more soluble material than volatile material. The dimer content of the film is, on the average, about one-third of the total extracted material. The other two-thirds is apparently other oligomers. Figure 4 is an overlay of reverse phase chromatograms of dimer and extractables illustrating the predominance of dimer in the extractables as noted by the major peak.

In addition to the dimer content determination, it was originally anticipated that the same procedure could be utilized for determining the anthracene content of a polymer sample. Anthracene is utilized as a fluorescent inspection agent and is codeposited with the polymer from a dimer charge containing 0.25

[2] The nominal temperatures will vary slightly depending upon deposition equipment. For our equipment, the nominal vaporization temperature was 165°C and the nominal pyrolysis temperature was 690°C.

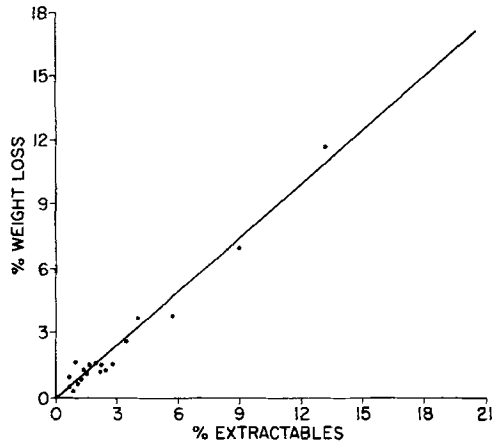


Fig. 2. Percentage weight loss as a function of percentage extractables.

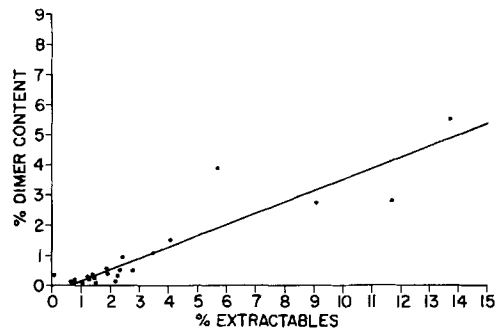


Fig. 3. Percentage dimer content as a function of percentage extractables.

weight percent (w/o) anthracene. Typically, therefore, the soluble fraction of a 0.5g sample should contain 1.25 mg of anthracene if it were incorporated into the film at its concentration in the dimer charge. Using 254 nm u.v. radiation, the detection limit for anthracene

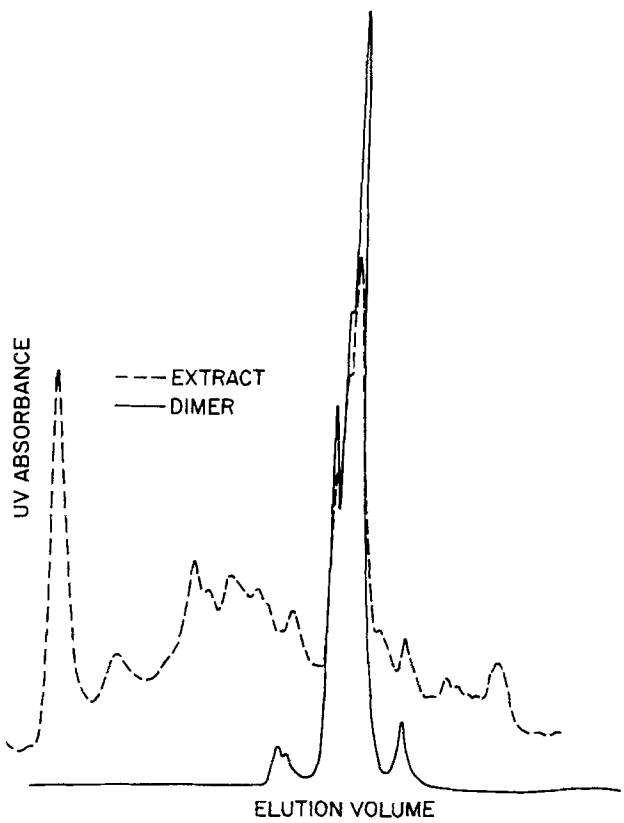


Fig. 4. Reverse phase chromatograms of dimer and extract

in the liquid chromatographic spectra of the solvent extract is such that 1/60$_{0}$0 of this amount would be detected. Surprisingly, no film extract was found to contain any detectable anthracene. This suggests that the anthracene which is incorporated into the polymer film during the CVD process is chemically combined with the matrix. Examination of the relative concentration of the three dichloro isomers present in both the dimer and polymer extracts (see Fig. 4) reveals an increase in the polymer of the dimer isomers originally present in the smallest amounts. This indicates that the reaction rates for the various isomers differ and that conditions must be optimized to assure conversion of all three isomers. Consideration of the parallel planar configuration of the parylene dimer dictates four configurational isomers with respect to the chlorine substitution. Steric hinderances probably forbid one of these configurations and, indeed, our analysis of the dimer material by reverse phase liquid-liquid chromatography reveals the predominance of three major constituents, undoubtedly the three isomers. Assuming the molar extinction coefficients of the isomers and the other impurities are equal, the three isomers typically account for 92% of the starting material. These results agree quite favorably with the 92.7% dimer reported by Union Carbide for the various lots of material used in this investigation (based on gas chromatography). The additional 8% of dimer material is reported as "other chlorinated homologs" which implies additional chlorine substitution. However, examination of the molecular weight distribution of the dimer by gel permeation liquid chromatography reveals the material to be composed of 99.2% of the di-chloro isomers.

Undoubtedly the "chlorinated homolog" content can best be attributed to noncyclic dimer formed through hydrogen abstraction having molecular weights close to that of the di-chloro isomers. Stereochemical considerations predict three noncyclic isomers and the results of reverse phase liquid chromatography analysis show three distinct minor peaks which can account for the 8% "chlorinated homolog" impurity fraction.

Somewhat surprising were the results of the electrical data obtained on the films. It was determined that the basic electrical parameters of dielectric strength, dissipation factor, and dielectric breakdown voltage did not vary significantly regardless of the process conditions. This was unexpected in that the excellent electrical properties obtained with parylene C under normal process conditions were still observed even though higher dimer and weight loss constituents were present in some films. Table I reflects the relatively high dielectric breakdown voltage strength of parylene C films produced under a wide range of process variations. Similarly, dielectric constant and dissipation factor are essentially constant despite processing variations. Examination of the data in Table II indicates that the yield stress and tensile modulus also remained relatively constant suggesting that there are no adverse effects on the mechanical properties over the variation of the deposition conditions.

Table III summarizes the effect of the various process conditions on the permeability of the film to water. It is apparent that no pronounced dependence is observed.

Table I. Variation in dielectric strength, dielectric constant, and dissipation factor as a function of deposition conditions

Vaporizer temperature (T_V) (°C)	Pyrolysis temperature (T_D) (°C)	Dielectric strength kV/mil, *ca.* 1 mil thick	Dielectric constant	Dissipation factor
165	690	10.5	2.46	0.024
165	690	10.4	2.21	0.028
185	690	10.9	2.67	0.024
165	690	12.6	2.23	0.026
200	690	13.7	2.67	0.030
145	690	13.0	2.56	0.030
165	640	12.9	2.22	0.026
165	740	13.1	2.56	0.027
200	740	14.5	2.56	0.028
165	710	13.5	2.65	0.028

Table II. Variation in yield stress and tensile modulus as a function of deposition conditions

Vaporizer temperature (T_V) (°C)	Pyrolysis temperature (T_D) (°C)	Yield stress, psi	Tensile modulus, K psi
165	690	9456	362
165	690	8933	267
165	690	9866	—
200	690	6800	350
145	690	8253	423
165	640	8610	408
165	740	8450	363
200	740	6452	321
145	640	8000	263
165	670	8075	443
165	710	8000	343

Table III. Specific permeability as a function of deposition conditions.

Vaporizer temperature (T_V) (°C)	Pyrolysis temperature (T_D) (°C)	Specific permeability mg $H_2O/cm^2/mm/24$ hr
165	690	0.012
165	740	0.015
200	740	0.012
145	640	0.022
165	670	0.013
165	710	0.013

Selected films were also studied for degree of crystallinity. Diffraction patterns were obtained using graphite-filtered copper radiation. The unannealed samples produced similar patterns with one broad peak between 14° and 15° and probably an extended "amorphous bump" from the peak, slowly decaying out to 30°-35°. Annealing produces changes in the observed patterns. The peaks are all much sharper and the slightly elevated amorphous bump disappears. The intensities increase markedly which indicates considerable enhancement of the degree of crystallinity by annealing. Table IV summarizes the intensity changes. It is apparent that initial crystallinity is relatively independent of the deposition parameters, however, crystallinity is increased upon annealing. An examination of the data on refractive index where values ranged from 1.58 to 1.80 produced no meaningful correlations with other basic material properties which were measured.

Figures 5 and 6 graphically represent the relationships between the weight percentage extractables and the variations in vaporization and pyrolysis temperatures. It is clearly evident that at the normal vaporization temperature, the weight percent extractables increases dramatically as the pyrolysis temperature is lowered even slightly. Conversely, as pyrolysis temperature is increased, the reaction tends to yield a more complete conversion of dimer to monomer prior to ultimate polymerization, and thus lower oligomeric content is found. Lowering the pyrolysis temperature or increasing the vaporization temperature tends to increase the tetrahydrofuran-extractable portion of the films. An increase in the vaporization temperature must be accompanied by a concomitant increase in pyrolysis temperature to produce minimum extractables in the resultant polymer film.

An examination of basic mechanical characteristics was made for comparison to other similar materials. A

Table IV. Crystallinity as a function of deposition conditions

Deposition temperatures		Intensity (counts/sec) x-ray diffraction	
Vaporizer T_V (°C)	Pyrolysis T_D (°C)	Before anneal	After annealing 250°C/1 hr
165	740	260	620
165	710	400	600
165	690	250	780
165	690	250	—

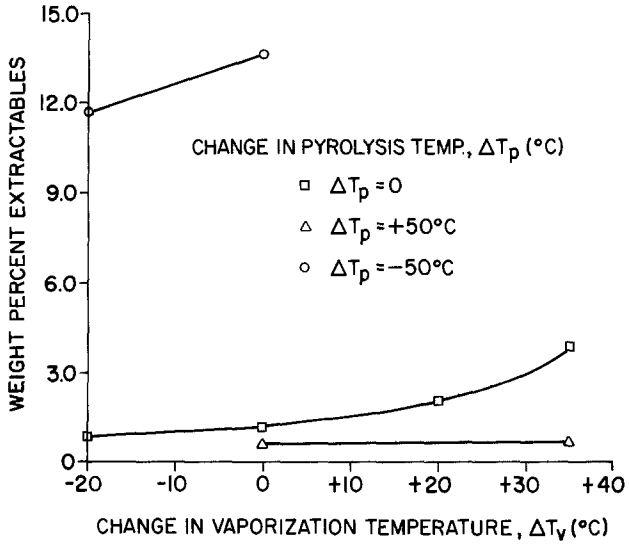


Fig. 5. Weight percent extractables as a function of vaporization temperature.

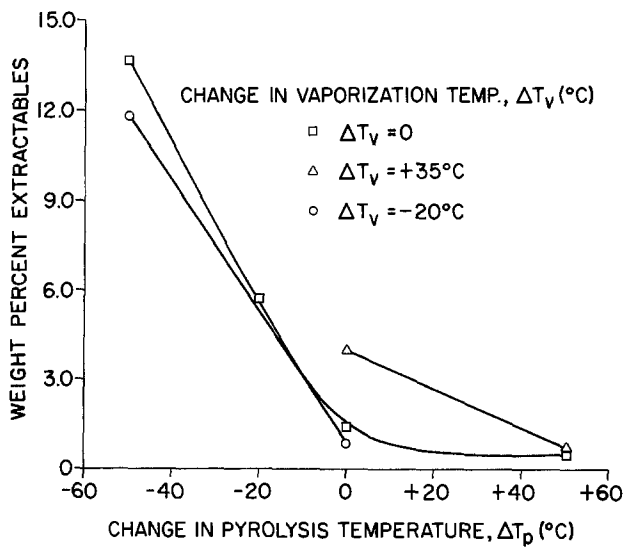


Fig. 6. Weight percent extractables as a function of pyrolysis temperature.

typical stress/strain curve for parylene C is shown in Fig. 7 (assuming constant volume or Poisson's ratio = 0.5). Parylene, like similar organic films, has a characteristic load/deflection curve (11).

The effect of aging on the yield stress and tensile modulus of parylene was also investigated. A number of samples from one deposition run were aged at 71°C in air for various times to determine if this accelerated aging had any effect on the yield stress or modulus. Contrary to previous work on parylene N, no aging effects were noted in the parylene C under these conditions (9). Since these results show that parylene is not greatly affected by aging for periods of over 10 days at temperatures up to 71°C, it may be inferred that parylene C is a relatively stable nonsensitive material. Also, no significant differences were observed in mechanical properties for films produced under the various deposition conditions.

Summary

The minimization of vacuum weight loss products in parylene C films can be achieved by critical control of the vaporization and pyrolysis temperatures. Electrical, mechanical, and physical properties of the film are essentially unchanged with minor variations in the deposition conditions which do change the films oligomeric content. Furthermore, no increase of degradation products was found in the resultant film as a consequence of increasing the pyrolysis temperature 20°C.

A more sensitive method of parylene film dimer content analysis has been developed based on liquid chromatographic analysis of solvent extracted oligomers. This analysis has demonstrated that anthracene codeposited as a fluorescent agent is chemically bound to the polymer backbone. It also suggests that the reactivities of various isomers in the starting dimer may influence the dimer content of the resultant films.

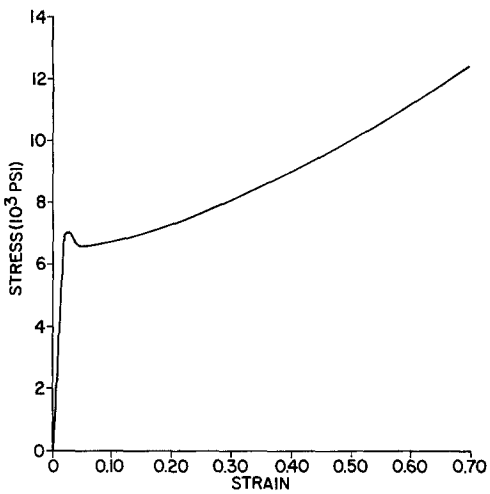


Fig. 7. Load deflection characteristics of parylene C

Manuscript submitted Dec. 21, 1976; revised manuscript received Feb. 25, 1977. This was Paper 163 presented at the Las Vegas, Nevada, Meeting of the Society, Oct. 17-22, 1976.

Any discussion of this paper will appear in a Discussion Section to be published in the December 1977 JOURNAL. All discussions for the December 1977 Discussion Section should be submitted by Aug. 1, 1977.

Publication costs of this article were assisted by Raytheon Company.

REFERENCES

1. U.S. Pat. 3,221,068; 3,288,728; and 3,342,754.
2. M. H. Kaufman, H. F. Mark, and R. B. Mesrobian, *J. Polym. Sci.*, **XIII**, 3 (1954).
3. H. H. G. Jellinek and S. H. Ronel, *ibid.*, **9**, 2605 (1971).
4. S. Kubo and B. Wunderlich, *J. Appl. Phys.*, **42**, 4565 (1971).
5. MIL-I-46058C, Insulating Compound, Electrical (For Coating Printed Circuit Assemblies), (1974).
6. W. F. Beach, Abstract 135, p. 309, The Electrochemical Society Extended Abstracts, Spring Meeting, Toronto, Canada, May 11-16, 1975.
7. L. A. Auspos, L. A. R. Hall, J. K. Hubbard, W. Kirk Jr., J. R. Schaeagen, and S. B. Speck, *J. Polym. Sci.*, **15**, 9 (1955).
8. M. A. Spivak, *Rev. Sci. Instrum.*, **43**, 985 (1972).
9. W. F. Beach, Private communication.
10. A. R. Mastro, Private communication.
11. C. A. Harper, "Handbook of Materials and Processes for Electronics," McGraw-Hill Book Company, New York (1970).

Sensitivity of Intensifying Screens to Scattered Radiation in Radiography: Physical Measurements

J. W. Castle

Eastman Kodak Company, Research Laboratories, Rochester, New York 14650

ABSTRACT

The x-ray absorption of rare earth (gadolinium-lanthanum) and medium speed calcium tungstate screens was measured in regions of high and low radiographic density of a chest phantom. The ratio of absorptions for the two regions was higher for the rare earth screens. This confirms by direct measurement that the higher observed radiographic contrast for the rare earth screens when compared to calcium tungstate screens is caused by the change in absorption of the screen phosphors with change in transmitted beam quality. The net effect in rare earth screens of this type is a reduction in the recording of scattered radiation with an increase in the percentage of information-containing (primary) radiation. The degree of this effect is a function of the amount of scattered radiation in the transmitted beam incident on the cassette.

It was suggested by Buchanan (1) that a higher radiographic contrast should be observed for x-ray intensifying screens of rare earth phosphors as compared with calcium tungstate if scattered radiation is present in the beam incident on the cassette. However, with only primary radiation the opposite effect would be expected. No difference in contrast was reported. Higher contrast for the rare earth screens was observed by Huff and Shaffer (2) for radiographs of a phantom with scattered radiation at 75-95 kVp and at 95 kVp with a grid.

In an attempt to explain this effect, screen absorption measurements were made at 60-100 kVp using 12.5 cm of plastic as the absorber. These showed the ratio of scatter/primary absorption in the screen material to be lower for rare earth screens (an 80/20 blend of the oxysulfides of gadolinium and lanthanum) than for calcium tungstate screens (3). This ratio is an indication of the relative sensitivity of a screen to scattered radiation as compared with primary. A lower ratio denotes a reduction in the recording of scattered radiation and will increase the radiographic contrast, as is evident from various other scatter reduction techniques used in radiography.

A reason for this difference in contrast is indicated in Fig. 1 which shows the absorption curves for gadolinium-lanthanum and calcium tungstate phosphors as calculated from mass energy absorption coefficients (4). Typical primary and scattered radiation spectra are included for an 85 kVp x-ray beam after passing through 12.5 cm of plastic. It can be seen that the shift of the scattered beam to lower energies results in only a minor absorption difference for the rare earth phosphors, because of the K-absorption discontinuities at 38.9 and 50.2 keV, but for calcium tungstate the shift is to a region of higher absorption.

Although the explanation for the reduction in the recording of scattered radiation seems valid, it has not been proven by measurements of a radiographic object that the ratio of total x-ray absorption by the screens in regions of high and low transmission of the radiographic object would differ for the two screens, or that the rare earth screen would have the greater difference. In fact, by the above reasoning the calcium tungstate would be expected to show higher contrast for the primary beam alone, because low density areas of the radiograph are exposed by more heavily filtered, hence harder x-rays than the higher density areas. Thus, the more rapid change in screen absorption with x-ray energy for the calcium tungstate would produce higher radiographic contrast than would be produced with the rare earth screens. However, differences in the scatter/primary beam energy ratio for the two regions could change the total beam quality as recorded by the screen/film combination and so may reverse the overall radiographic effect.

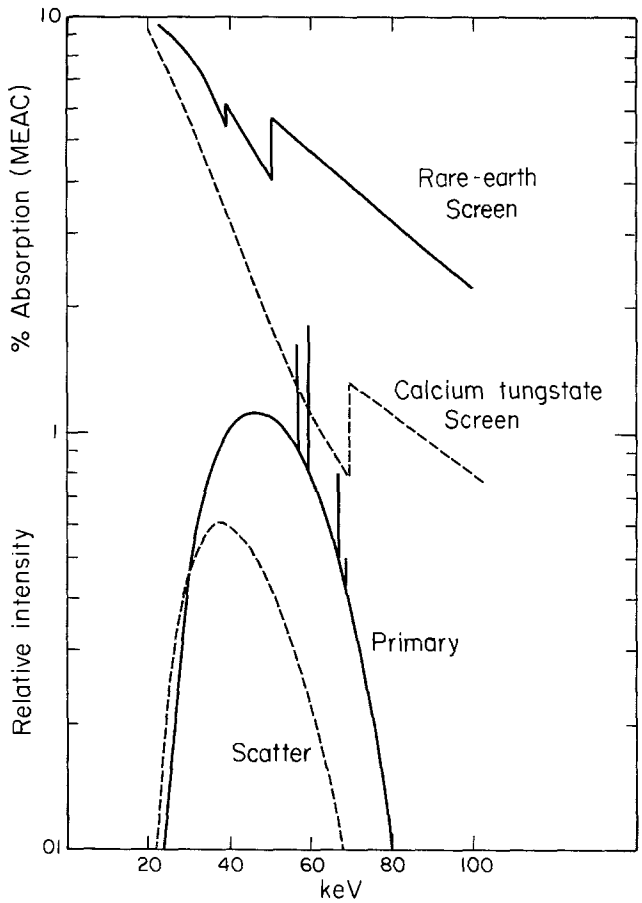


Fig. 1. Absorption curves for a rare earth screen and a medium speed calcium tungstate screen calculated from mass energy absorption coefficients. The rare earth screen is an 80/20 blend of the oxysulfides of gadolinium and lanthanum. Also shown are typical primary and scatter transmission spectra through 12.5 cm of plastic.

To obtain such data, the spectra of the primary and the scattered beams transmitted by a region of high (lung area) and low (heart area) transmission to x-rays for a chest phantom (5) were measured with an x-ray spectrometer (Fig. 2). The spectrometer has an intrinsic germanium detector feeding through a pile-up rejector/lifetime corrector, amplifier, and into a multichannel analyzer. The geometry of the detector with

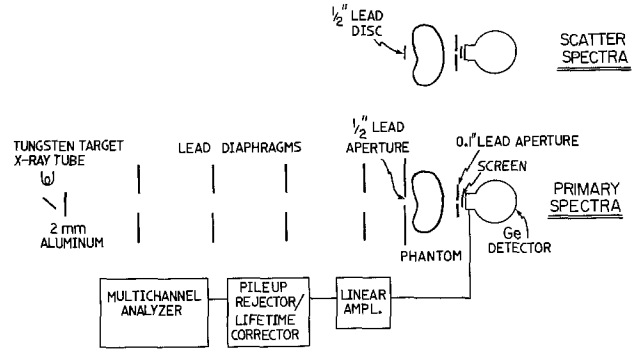


Fig. 2. Diagram of method used for measuring primary and scattered spectra through a chest phantom using a x-ray spectrometer.

its aperture is such that radiation up to 40° off axis may be recorded. Because of this the total amount of scattered radiation from an object that would be incident on a cassette is not detected. The measured spectra (Fig. 3) indicate the change in beam quality of the scattered radiation although not the total intensity. The spectra so obtained are shown in Fig. 3. From these spectra can be calculated the relative energy in the x-ray beams. The results of these calculations are shown in Table I. Although the primary beams are seen to differ in intensity by a ratio of 6.18, the total beams differ by only 3.10 for the two regions. This is because the scattered component of the total beam is nearly constant and is thus a much larger portion of the total beam through the area of the heart than through the lung.

In order to determine the energy absorbed by the screens for the different beam qualities, the screen absorption associated with the spectra for the two regions of the phantom were then measured by placing a piece of the screen over the detector and again measuring the transmission spectra. From the ratio of the energies in the transmitted beam with and without a screen, the absorption of the screens could be calculated. Table II shows the measured absorptions of the two screen pairs. For both lung and heart areas, the rare earth screens show a lower scatter/primary ratio indicating less relative sensitivity to the scattered radiation. This agrees with previously reported data in which 12.5 cm of plastic was used as the absorbing medium (3).

By combining the data of Tables I and II, we can determine the relative energies absorbed by the screens for the different conditions. The calculated energies absorbed by the two screens are shown in Table III. The absorbed energy, which is approximately proportional to the light emitted by a given phosphor, is a measure of the photographic exposure produced by a

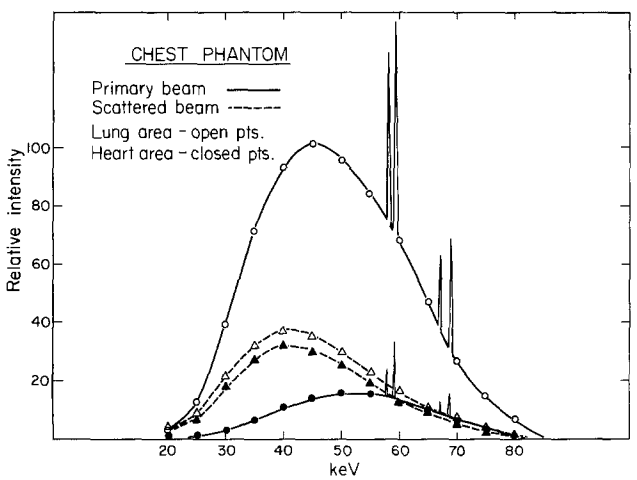


Fig. 3. Transmission spectra measured through the lung and heart area of a chest phantom at 85 kVp with 3 mm aluminum inherent filtration.

Table I. Relative measured energy of transmitted beam

	Lung area	Heart area	Ratio
Primary (P)	835	135	6.18
Scatter (S)	250	215	1.16
Total (T)	1085	350	3.10

Table II. Measured screen absorption (%)

Screen		Lung area	S/P	Heart area	S/P
Rare earth (Gd/La)	Primary (P)	62		63	
	Scatter (S)	60	0.97	60	0.95
	Total (T)	61		61	
Medium speed $CaWO_4$	Primary (P)	23		19	
	Scatter (S)	28	1.17	30	1.58
	Total (T)	24		25	

Table III. Relative beam energy absorbed by screens

Screen		Lung area	P/T	Heart area	P/T	Ratio (contrast)
Rare earth (Gd/La)	Primary (P)	515		85		6.06
	Scatter (S)	150	0.77	130	0.40	1.15
	Total (T)	665		215		3.09
Medium speed $CaWO_4$	Primary (P)	190		25		7.60
	Scatter (S)	70	0.73	65	0.28	1.07
	Total (T)	260		90		2.88

screen when irradiated with beams of different qualities. It is seen that, while the calcium tungstate has a higher ratio of absorbed energies for the primary beam through the two areas, the ratio (or contrast of the radiograph) for the total beam is higher for the rare earth screens (3.09-2.88).

Although the data confirm that for these conditions the rare earth screen would be expected to show higher contrast, this contrast difference is only a visible indication of a more fundamental difference between the two phosphors in the region of 70-120 kVp. This fundamental difference is the higher ratio of primary to total radiation absorbed in any area of a radiograph. Because of this ratio, the radiographic exposure will have a higher percentage of information-containing (primary) radiation absorbed by the rare-earth screen. This ratio is shown in the P/T columns in Table III.

To emphasize this, it is of interest to arbitrarily reduce the measured scatter from Table III by 40 and 60% (in the range of scatter reduction in some magnification techniques) and 90% (use of a grid). However, if a grid is used the primary is also reduced. For the column showing 90% scatter reduction, the primary has been reduced by 30% (6). The resulting contrast and P/T were calculated as in Table III. The results are given in Table IV. It is seen that at higher than 50% scatter reduction the contrast for the calcium tungstate screen is higher, but the rare earth screen continues to show a higher P/T ratio indicating that the rare earth screen is still recording a higher percentage of the primary radiation.

These data confirm by absorption measurements that the observed higher radiographic contrast of a rare earth screen as compared with calcium tungstate

Table IV. Effect of scatter reduction

Contrast	Screen	Percent scatter reduction 0	40	60	90
	Gd_2O_2S/La_2O_2S	3.09	3.71	4.20	5.40
	$CaWO_4$	2.88	3.62	4.27	6.25
P/T (lung)	Gd_2O_2S/La_2O_2S	0.77	0.85	0.90	0.95
	$CaWO_4$	0.73	0.82	0.87	0.93
P/T (heart)	Gd_2O_2S/La_2O_2S	0.40	0.52	0.62	0.80
	$CaWO_4$	0.28	0.39	0.49	0.68

screen is the result of change in beam quality in different areas of a radiographic object. An important corollary is the higher percentage of information-containing primary radiation absorbed by the rare earth screens.

Manuscript submitted Dec. 6, 1976; revised manuscript received Feb. 14, 1977.

Any discussion of this paper will appear in a Discussion Section to be published in the December 1977 JOURNAL. All discussions for the December 1977 Discussion Section should be submitted by Aug. 1, 1977.

Publication costs of this article were assisted by the Eastman Kodak Company.

REFERENCES

1. R. S. Buchanan *et al.*, *Radiology*, **105**, 185 (Oct. 1972).
2. K. E. Huff and E. C. Shaffer, *Proc. SPIE*, **56**, 19 (1975).
3. J. W. Castle, *ibid.*, **70**, 212 (1975).
4. E. Storm and H. I. Israel, Photon Cross Sections from 0.001 to 100 MeV for Elements 1 through 100, Report LA-3753, Los Alamos Scientific Laboratory, University of California (1967).
5. H. R. Splettstosser and H. E. Seemann, *Med. Radiogr. Photogr.*, **33**, 20 (1957).
6. G. T. Barnes *et al.*, *Radiology*, **120**, 691 (Sept. 1976).

Low Pressure Silicon Epitaxy

M. Ogirima, H. Saida, M. Suzuki, and M. Maki

Hitachi, Limited, Central Research Laboratory, Kokubunji, Tokyo, Japan

ABSTRACT

In a reduced pressure epitaxial system using SiH_4, growth parameters and autodoping from a heavily doped substrate were investigated as a function of pressure. It was found that the activation energies of epitaxial growth are about 43 and 11 kcal/mole for 80 and 760 Torr, respectively. Both vertical and lateral autodoping are remarkably reduced by epitaxial growth under low pressure. A simple one-dimensional gas diffusion model is proposed to explain the autodoping behavior in low pressure epitaxy.

The suppression of autodoping has been one of the most serious problems in epitaxial growth techniques. There are many factors which control autodoping in an epitaxial layer on a substrate with heavily doped buried layers. Autodoping from a substrate with buried layers is phenomenologically classified into two types. One is vertical autodoping and the other is lateral autodoping. The former is autodoping in an epitaxial layer on a buried layer and the latter is that on a substrate around buried layers. Vertical autodoping contains outdiffusion of impurities from buried layers in addition to autodoping from a vapor phase. Up to now, several techniques have been proposed to suppress autodoping. They are, (*i*) low temperature epitaxy, (*ii*) epitaxy using a silicon source without halogen atom, such as silane, (*iii*) two-step epitaxy, and (*iv*) low pressure epitaxy.

In comparison with high temperature epitaxy using silicon tetrachloride, low temperature epitaxy using silane has little effect on reducing lateral autodoping. Lateral autodoping has its maximum value at the interface between a substrate and an epitaxial layer. For this reason, the two-step epitaxial growth technique (1) is not an effective solution for reducing lateral autodoping.

Deines and Spiro (2) suggested the possibility of reducing autodoping by low pressure epitaxy. We therefore tried to reduce autodoping in an epitaxial layer by low pressure epitaxy and investigated the pressure dependence of autodoping in the silicon epitaxial deposition process. This paper describes some experimental results and discusses growth parameters and autodoping mechanisms of low pressure epitaxy.

Experimental

Epitaxial layers were grown in a standard horizontal reactor. Figure 1 shows the growth apparatus for low pressure epitaxy. Palladium-diffused high purity hydrogen and silane (4% in H_2) were injected into the reaction tube and reacted gas was exhausted forcibly by a mechanical oil-sealed rotary pump from the outlet of the reaction tube. Oil mist was trapped by a liquid nitrogen trap. The pressure was measured by a diaphragm-type vacuum gauge, and was controlled by varying exhaust resistance.

Key words: autodoping, growth rate, *C-V* measurements, buried layers, impurity profile.

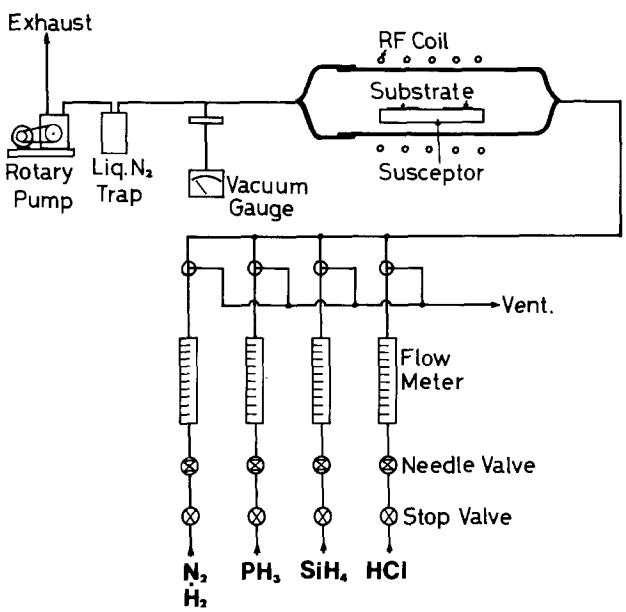


Fig. 1. Growth apparatus for low pressure silicon epitaxy

Epitaxial growth was carried out using a silicon carbide coated and RF inductively heated graphite susceptor. The inner diameter of the reaction tube was 75 mm and the susceptor could accommodate three wafers 2.5 in. in diameter. Growth temperature was always 1050°C when not indicated. After epitaxial growth, planar diodes of 300 μm in diameter were fabricated in epitaxial layers by boron diffusion. The carrier concentration was measured by the capacitance and voltage method and impurity profiles near the interface of the epitaxial layer and the substrate were obtained.

The structure of the samples for measurements of autodoping is illustrated in Fig. 2. The metallurgical in-

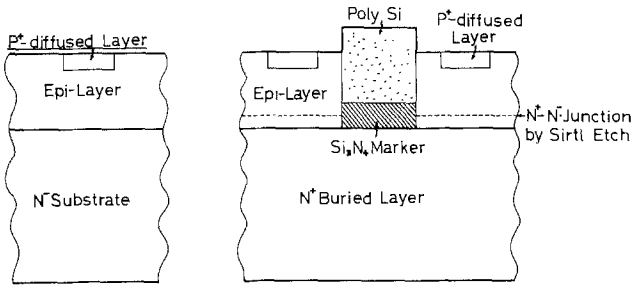


Fig. 2. Section of the samples for C-V measurements: (a, left) for lateral autodoping measurements, (b, right) for vertical autodoping measurements.

terface between an epitaxial layer and a substrate was delineated by a silicon nitride marker. After beveling a sample, n^+-n^- junction in an epitaxial layer was delineated by Sirtl etch and the shift of the junction (vertical autodoping) during the epitaxial process was measured by an optical microscope. Lateral autodoping was measured on a n^- substrate.

Results and Discussion

Growth rate.—The growth rate and uniformity of the epitaxial layer thickness are extremely dependent on the pressure in a reaction tube. Figure 3 shows the relation between growth rate and the mole ratio of SiH_4/H_2 carrier gas, which indicates that the growth rate decreases almost in proportion to the pressure. This result is reasonable because the partial pressure of silane decreases in proportion to the total pressure and is consistent with the results obtained by Henderson *et al.* (3). Figure 4 shows the temperature dependence of growth rate. For 760 and 150 Torr, an Arrhenius plot of the relation between growth rate and temperature gives an activation energy E_A of about 11 kcal/mole, but for 80 Torr, E_A is about 43 kcal/mole. This experimental fact suggests that there is a change in the reaction mechanism of silane from 150 to 80 Torr. The value 11 kcal/mole is nearly equal to that of the previous work (10 kcal/mole) by Farrow *et al.* (4), and this result indicates that surface reaction of silane is prevailing at 760 and 150 Torr. In this case, growth rate is controlled by diffusion process above 1000°C, and is almost independent of epitaxial growth temperature. On the other hand, at 80 Torr, the value of the activation energy, 43 kcal/mole, suggests that the growth rate is controlled by homogeneous nucleation in a vapor phase.

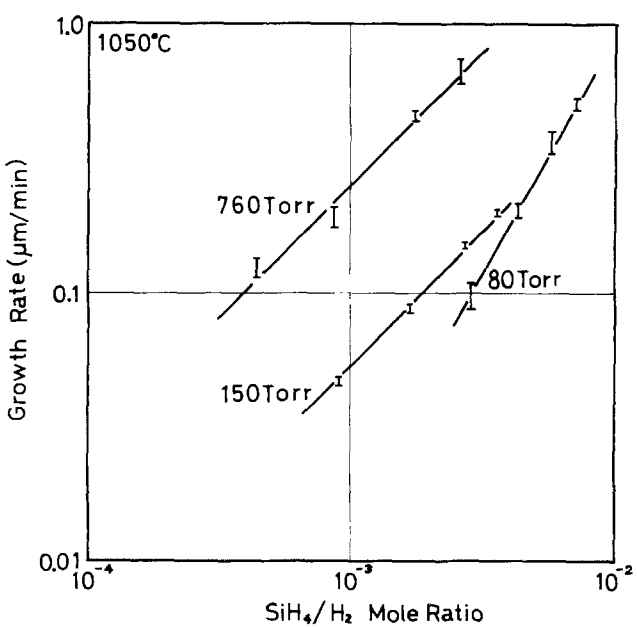


Fig. 3. Relation between growth rate and SiH_4/H_2 mole ratio

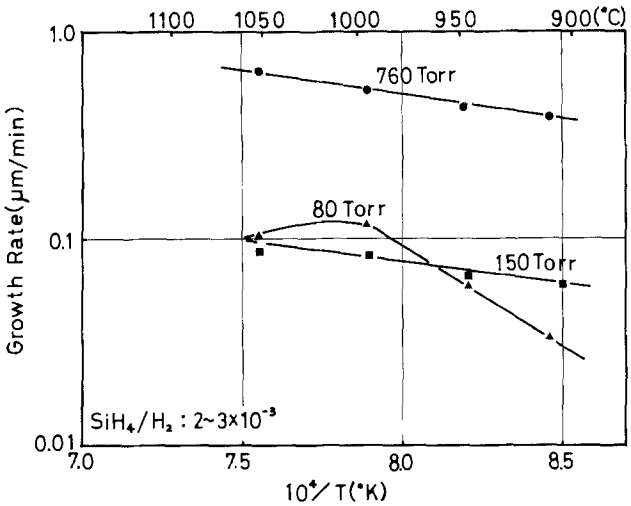


Fig. 4. Arrhenius plots of growth rate vs. growth temperature

Doping behavior is illustrated in Fig. 5 which shows that the transfer ratio (=0.56) at 80 Torr is the same as that at 760 Torr.

Autodoping.—An example of the impurity profiles near the interface is shown in Fig. 6. Parameter x is the distance of the measured diodes from the edge of the n^+ buried layer. The maximum carrier concentration is obtained at the interface between an epitaxial layer and a substrate. It is evident that the maximum impurity concentration decreases with the increase of the lateral distance x.

Photographs in Fig. 7 show the shift of the junction between the epitaxial layer and the n^+ buried layer during epitaxial growth. When epitaxial layers are grown at atmospheric pressure using silicon tetrachloride or silane, the shift of the junction, Δd, is about 0.1 or 0.2 μm at 1050°C, but, on the other hand when they

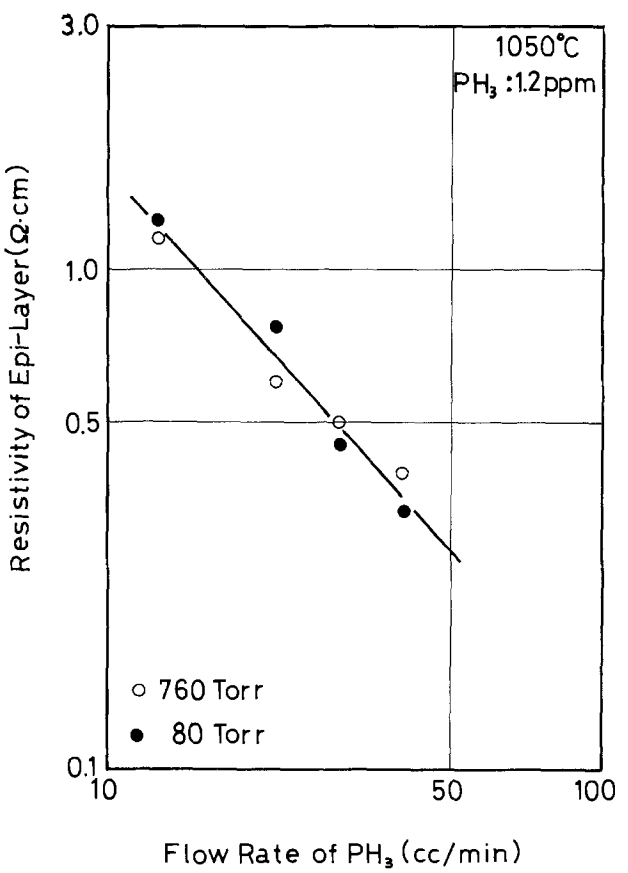


Fig. 5. Doping behavior in low pressure and atmospheric pressure epitaxy.

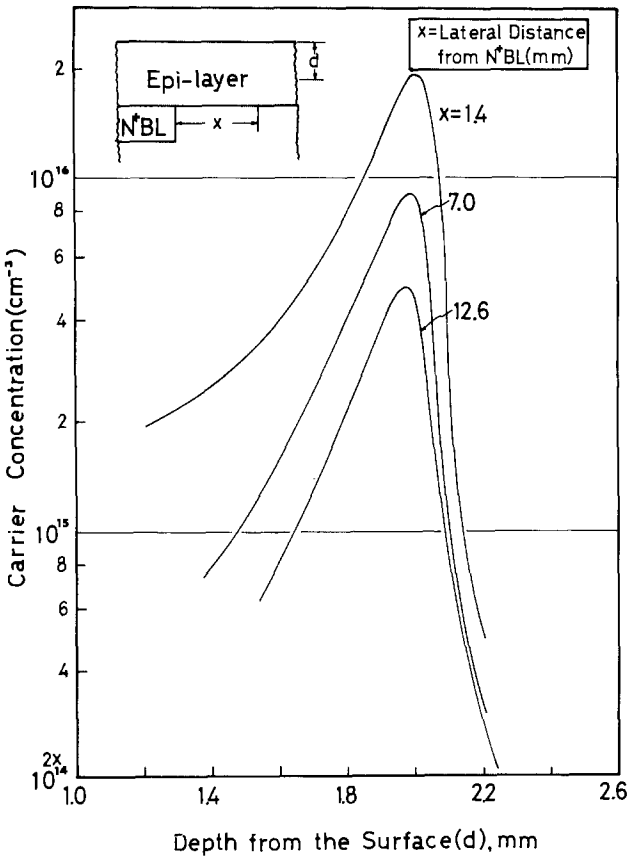


Fig. 6. Several impurity concentration profiles near the interface between an epitaxial layer and a substrate.

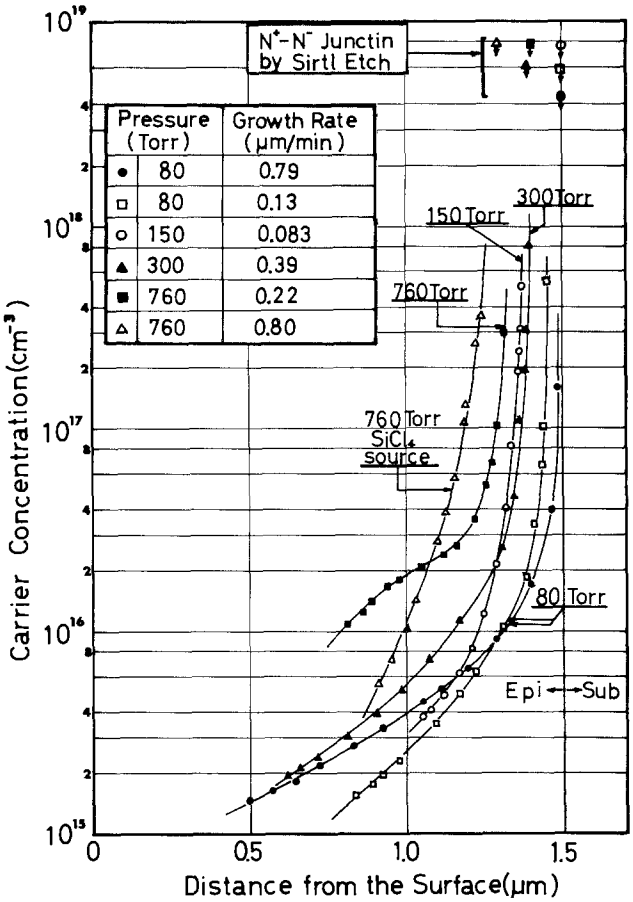


Fig. 8. Carrier concentration profiles in the epitaxial layers on n^+ burried layer.

are grown at low pressure, for example, at 150 or 80 Torr, the shift Δd is nearly equal to zero. These results are confirmed by Fig. 8. This figure illustrates the carrier concentration distribution in epitaxial layers on n^+ buried layers. The vertical line at 1.5 μm is the metallurgical interface between the epitaxial layer and the substrate. The marks at the top of the figure indicate the junction obtained from the photographs in Fig. 7. In low pressure epitaxial layers, the shift of the junction is nearly equal to zero, whereas at 760 Torr, it is about 0.2 (SiH_4 source, 1050°C) or 0.3 μm ($SiCl_4$ source, 1150°C). The shift of the junction during epitaxial growth is due mainly to two mechanisms: vertical autodoping from a vapor phase and out-diffusion in a solid from the substrate, as mentioned before. The shift of the junction by out-diffusion is calculated

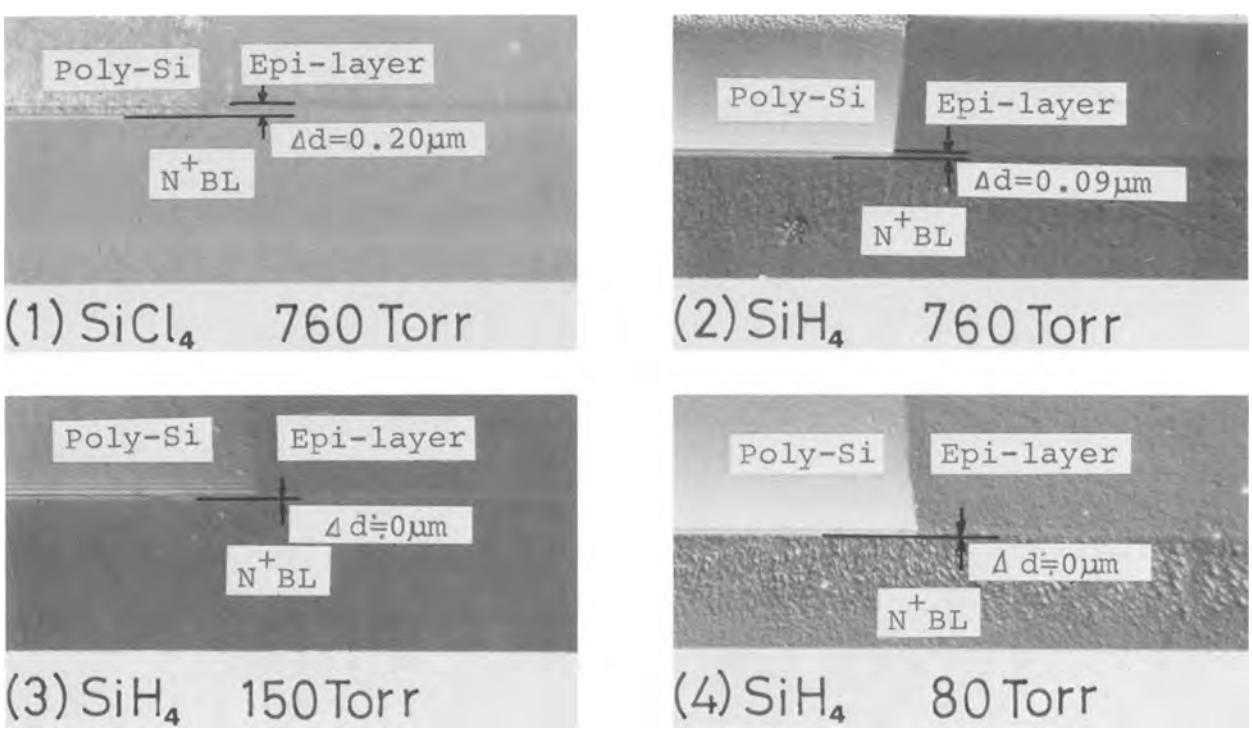


Fig. 7. Shift of the n^+-n^- junction during epitaxial growth (1050°C, 5 min)

to be about 0.025 μm when the epitaxial growth is carried out at 1050°C for 5 min. This value is comparable to the measurement error of an optical microscopic observation. Therefore, it can be concluded that in the case of low pressure epitaxy (<1050°C, <150 Torr) the decrease in vertical autodoping is due mainly to the decrease in incorporation of gaseous arsenic atoms sublimated from the n^+ buried layers.

Figure 9 shows the wafer for measuring lateral autodoping. In the central zone of the n^- substrate (20-30 Ω-·cm), there is an n^+ buried layer, 15 mm square, doped with arsenic to a concentration of 6×10^{19} cm^{-3}. In order to investigate the influence of the gas flow on lateral autodoping, the carrier concentration at the interface between the substrate and the epitaxial layer was measured as the function of the distance from the edge of the n^+ buried layer. The measurements were carried out for up-, down-, left-, and right-stream positions of the n^+ buried layer.

Figure 10 shows lateral autodoping as a function of the distance from the edge of the n^+ buried layer. Lateral autodoping is expressed by the maximum carrier concentration at the interface of an epitaxial layer and a n^- substrate. From these figures we can conclude the following three points.

1. Below 150 Torr, the dependence of lateral autodoping on the distance from the edge of the n^+ buried layer has the same tendency for down-, up-, and right (left)-stream positions.

2. Above 300 Torr, lateral autodoping is much greater in the downstream position than in the upstream position, and an epitaxial layer located in both sides of the n^+ buried layer has a middle value of the epitaxial layers located in the upstream position and in the downstream position. The curve for upstream position of atmospheric pressure epitaxy is not shown in Fig. 10a because the concentration is too high to be measured by the capacitance methods, but the concentration near the edge of the n^+ buried layer is estimated to be about 3×10^{17} cm^{-3}. It must be noted that lateral autodoping in an epitaxial layer in the upstream position for atmospheric pressure falls steeply as the distance increases, and is lower than that for 80 Torr at a point about 6 mm from the edge of the n^+ buried layer.

3. Generally speaking, lateral autodoping decreases monotonously as the pressure decreases.

The relationship between the pressure in the reaction tube and the carrier concentration at the edge of the n^+ buried layer is illustrated in Fig. 11. This figure indicates that lateral autodoping is in proportion to the nth power of the pressure p. In this case, n is about one, which suggests lateral autodoping is in proportion to the partial pressure of arsenic on the surface of the n^+ buried layer by thermal out-diffusion which is hardly affected by the pressure in the reaction tube. Then it is estimated that the partial pressure controls the equilibrium concentration of arsenic on the surface of a n^+ buried layer. As mentioned before, the transfer ratio of dopants in silicon epitaxy is independent of the pressure, and for this reason lateral autodoping is in proportion to the concentration of arsenic vapor on the n^+ buried layer. As a result, lateral autodoping is lower by about one order of magnitude in the epitaxial layer grown at 80 Torr than that at 760 Torr.

Figure 12 shows the n-channel in the p^- substrate caused by oxidizing the epitaxial layer, which demonstrates the effect of low pressure epitaxy. The distribution coefficient of arsenic in an Si/SiO_2 system is about 10 (5), the autodoped arsenic atoms in the epitaxial layer accumulate at the interface between silicon dioxide and silicon. Therefore, we can evaluate

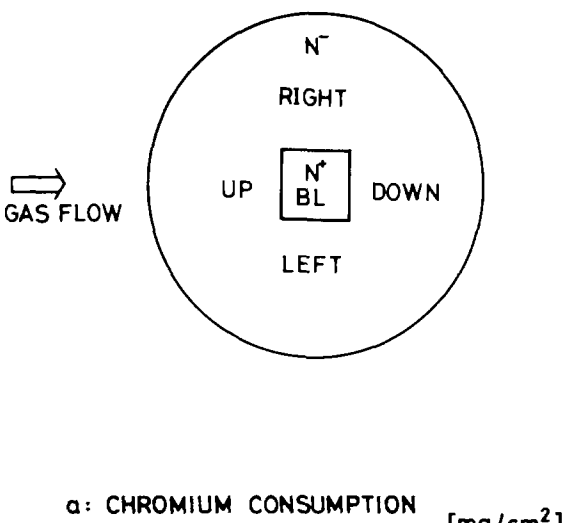


Fig. 9. Wafer for measurements of lateral autodoping

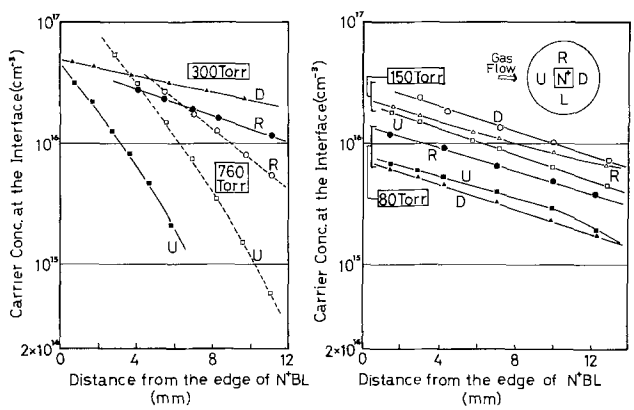


Fig. 10. Dependence of lateral autodoping on the distance from the edge of n^+ buried layer: (a, left) 760 and 300 Torr, (b, right) 150 and 80 Torr.

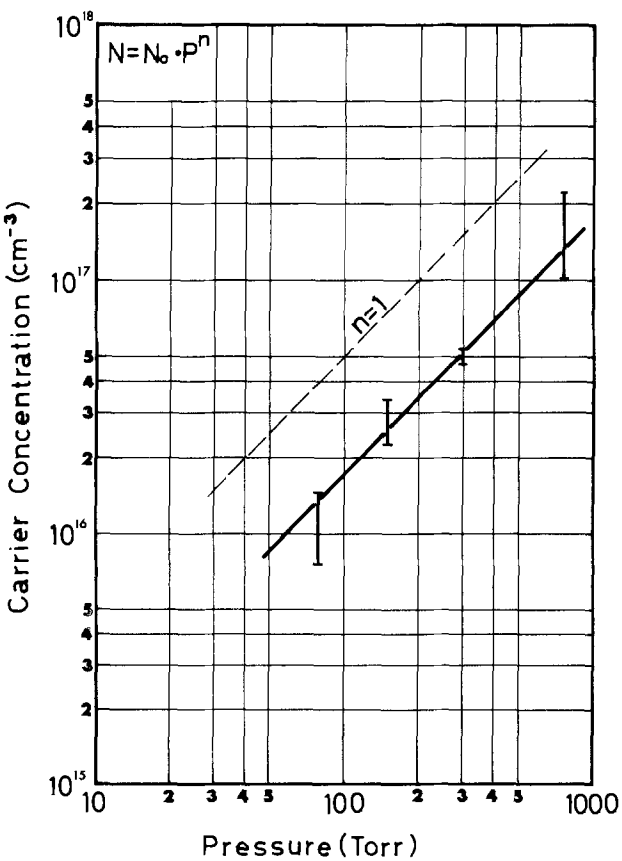
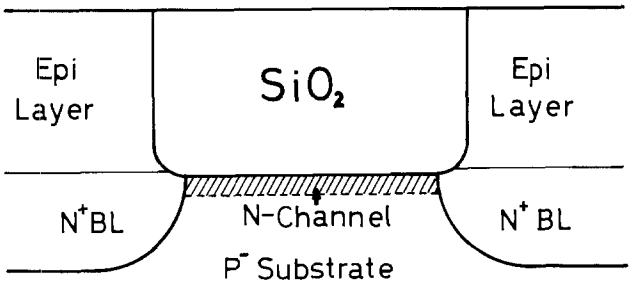


Fig. 11. Relation between lateral autodoping and pressure. Lateral autodoping is represented by maximum carrier concentration at the edge of n^+ buried layer.



Channel Conductance	
80 Torr	760 Torr
1.23 m℧	5.45m℧

Channel Length 3μm
Width 100μm

Fig. 12. n-channel in p⁻ substrate caused by oxidizing the epitaxial layer and channel conductance for low pressure (80 Torr) and atmospheric pressure (760 Torr) epitaxy.

the amount of autodoped impurities by measuring the channel conductance. As indicated in Fig. 12 the channel conductance of the epitaxial layer under an atmospheric pressure is about 5 times larger than that of low pressure epitaxial layer.

The Mechanism of Autodoping

From Fig. 10, it can be recognized that the influence of the gas flow is apparently weaker for low pressure epitaxy. For the epitaxy at an atmospheric pressure, the gas flow decreases lateral autodoping of the epitaxial layer in the upstream position and increases that in the downstream position. This fact is seen in the report by Pogge *et al.* (6). On the contrary, in the case of low-pressure epitaxy, lateral autodoping is apparently not affected by the gas flow, and is controlled only by the diffusion of arsenic atoms in the gas phase. From the direct observation of gas flow patterns in a horizontal epitaxial reactor, it is found that the gas flow pattern becomes more lamellar as the pressure decreases (7, 8). For low pressure epitaxy, we postulate that arsenic atoms diffuse laterally along the substrate surface in a stagnant layer and are hardly affected by the gas flow.

Figure 13 illustrates the schematic figure of the lateral autodoping mechanism. Let us suppose a one-dimensional diffusion model. The concentration of gaseous arsenic at a distance x from the edge of the n^+ buried layer can be denoted by C (x). Then the diffusion of arsenic in a steady state is expressed by the following differential equation

$$D\frac{d^2C}{dx^2} - v_x\frac{dC}{dx} - kC = 0 \qquad [1]$$

where v_x is the velocity of the gas flow, k is a constant, and D is a diffusion constant of arsenic in hydrogen. Using the boundary conditions

$$(x = 0,\ C = C_0) \text{ and } (x \Rightarrow \infty,\ C \Rightarrow 0)$$

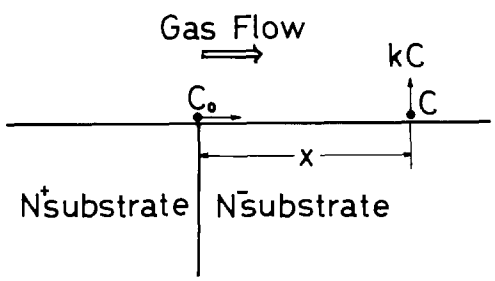


Fig. 13. One-dimensional diffusion model of lateral autodoping

the solution of Eq. [1] is in the following formulas

$$\left.\begin{aligned}&\text{(down stream)}\\ &C = C_0\exp\left(-\frac{v_x + \sqrt{v_x^2 + 4kD}}{2D}x\right)\\ &\text{(up stream)}\\ &C = C_0\exp\left(\frac{v_x - \sqrt{v_x^2 + 4kD}}{2D}x\right)\end{aligned}\right\} \qquad [2]$$

In the case of low pressure epitaxy, it is supposed that the influence of the gas flow can be neglected compared with the diffusion of arsenic atoms, that is, $v_x/D = 0$ and, formulas [2] are modified and reduce to the equation

$$C = C_0\exp\left(-\sqrt{\frac{k}{D}}x\right) \qquad [3]$$

When the transfer ratio of arsenic is m which is independent of pressure, lateral autodoping N is related to x in the formula

$$N = mC = mC_0\exp\left(-\sqrt{\frac{k}{D}}x\right) \qquad [4]$$

The natural logarithm of N varies linearly with the distance x from the n^+ buried layer, and the behavior indicated in Fig. 10 can be explained qualitatively by this one-dimensional diffusion model. Since the temperature gradient above a susceptor at 80 Torr is larger than that at 760 Torr, the buoyancy is greater at a low pressure. In addition, as arsenic atoms are much heavier than hydrogen atoms, arsenic atoms sublimated from the substrate diffuse along the wafer surface. A stagnant layer is therefore formed in low pressure epitaxy, but the thickness of the stagnant layer will be much thinner than that calculated from the experimental results by Eversteyn *et al.* (9).

Summary

Silicon epitaxial layers were grown on heavily doped (As) substrates in a reduced pressure system. Lateral and vertical autodoping was measured by the capacitance and voltage method. The following results were obtained for low pressure epitaxy.

1. Growth rate decreases with decrease of the pressure in a reaction tube.
2. The activation energy is 11 kcal/mole for the epitaxy in 760 Torr and 43 kcal/mole in 80 Torr.
3. The interface between n^+ and n^- substrate hardly moves during epitaxial growth at 1050°C for 5 min.
4. Lateral autodoping near the edge of the n^+ buried layer is in proportion to the pressure.
5. Below 150 Torr, there is little difference in lateral autodoping between the up- and downstream position of the n^+ buried layer.
6. A simple one-dimenstional diffusion model was proposed in order to explain the above results.

Acknowledgments

The authors are indebted to Messrs. M. Kawamura, K. Homma, and R. Takahashi and to Dr. O. Okada for valuable discussions related to the mechanism of autodoping.

Manuscript submitted Nov. 22, 1976; revised manuscript received Jan. 25, 1977. This was Paper 102 presented at the Washington, D. C., Meeting of the Society, May 2-7, 1976.

Any discussion of this paper will appear in a Discussion Section to be published in the December 1977 JOURNAL. All discussions for the December 1977 Discussion Section should be submitted by Aug. 1, 1977.

Publication costs of this article were assisted by Hitachi, Limited.

REFERENCES

1. T. Ishii, K. Takahashi, A. Kondo, and K. Shirahata, *This Journal*, **122**, 1523 (1975).

2. J. L. Deines and A. Spiro, Abstract 62, p. 161, The Electrochemical Society Extended Abstracts, Spring Meeting, San Francisco, California, May 12-17, 1974.
3. R. C. Henderson and R. F. Helm, *Surf. Sci.*, **30**, 310 (1972).
4. F. C. Farrow and J. D. Filby, *This Journal*, **118**, 149 (1971).
5. A. S. Grove, O. Leistico, and C. T. Sah, *J. Appl. Phys.*, **35**, 2695 (1964).
6. H. B. Pogge, D. W. Bass, and E. Ebert, in "Chemical Vapor Deposition Second International Conference," edited by J. M. Blocher, Jr. and J. C. Withers.
7. K. Sugawara, R. Takahashi, H. Tochikubo, and Y. Koga, *ibid.*
8. R. Takahashi, Y. Koga, and K. Sugawara, *This Journal*, **119**, 1406 (1972).
9. F. C. Eversteyn, C. H. J. v. d. Brekel, and H. L. Peek, *ibid.*, **117**, 925 (1970).

Chemically Bound Hydrogen in CVD Si_3N_4: Dependence on NH_3/SiH_4 Ratio and on Annealing

H. J. Stein

Sandia Laboratories, Albuquerque, New Mexico 87115

and H. A. R. Wegener

Sperry Research Center, Sudbury, Massachusetts 01776

ABSTRACT

The effects of the ammonia-to-silane ratio, R, during deposition, and of postdeposition heating on chemically bound H in 1000Å silicon-nitride films have been investigated using multiple internal reflection (MIR) spectroscopy. The films were deposited at 700°C with R equal to 10:1, 100:1, and 1000:1 in an Ar carrier gas. Vibrational modes for N-H and Si-H bonded centers show that H is incorporated into the films. The sum of the NH and SiH band intensities (total bound H) increased with R. The SiH band intensity, however, was largest in the 100:1 film. The increase in bound H with R is attributed to an increase in reactive H from NH_3 decomposition in the presence of incompletely bonded Si and N. The decrease in SiH centers when R is increased from 100:1 to 1000:1 is attributed to more complete Si-N bonding. Annealing behavior at 800°C suggests an initial transfer of H from N-H to Si-H bonds in 10:1 and 100:1 films consistent with the presence of incompletely bonded Si. Bonding of implanted H in Si_3N_4 was demonstrated by isotopic substitution of D for H, and a calibration to determine H concentrations from MIR measurements was obtained. Bond energy-limited H loss is suggested to explain an observed mass-independent annealing for implantation-produced NH and ND centers.

Thin film CVD Si_3N_4 is a technologically important material for nonvolatile MNOS (metal/Si_3N_4/SiO_2/Si) memory elements in integrated circuits. Many workers have reported on the electrical characteristics of CVD Si_3N_4, and the electrical properties are known to depend on the flow ratio, R, of NH_3 relative to SiH_4 during deposition (1). Less is known, however, about the structural or chemical compositional changes that accompany changes in R between 10:1 and 1000:1 which represent ratios of primary interest for memory-quality Si_3N_4. It is also important to know the effects of postdeposition heating on the properties of Si_3N_4 because, depending on the particular schedule for integrated circuit fabrication, the nitride may be subjected to postdeposition temperatures which are higher than that for deposition.

As a step toward an understanding of the dependence of chemical composition on the deposition parameters and on postdeposition processing, we have investigated the effects of R and of postdeposition heating upon chemically bound H in CVD Si_3N_4 films. We show that chemically bound H in thin film Si_3N_4 is readily observed by multiple internal reflection (MIR) spectroscopy, and we have used ion implantation to obtain a calibration for the concentration of H. Isotopic substitution of implanted D for H has been used to verify chemical bonding of the implanted species, and to explore the mechanism for H loss from the films caused by heating.

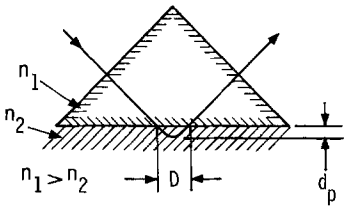
Key words: CVD silicon nitride, internal reflection spectroscopy, hydrogen bonding, nonvolatile memory.

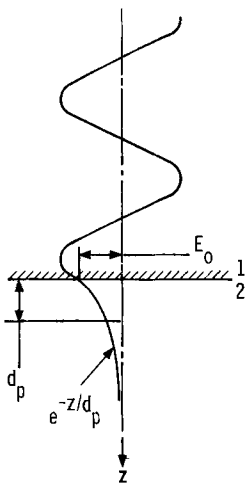
Experimental Details

Si_3N_4 films were deposited on one side of high resistivity Si MIR plates 50 × 20 × 2 mm³ with 45° end faces, and also on 1.5 in. diameter 3 Ω-cm n-type (100) Si wafers. The chemical vapor depositions were carried out at 700°C in a cold-wall horizontal reactor with an rf induction-heated graphite susceptor. The NH_3 was supplied by Air Products with a purity of 99.999+%. The ultrahigh purity (UHP) argon carrier gas and the semiconductor grade SiH_4 at 1% dilution in UHP argon were supplied by Matheson Gas Products. The SiH_4 flow rate and the total flow rates were maintained constant at 5 and 9505 cm³/min, respectively, for depositions with R equal to 10:1, 100:1, and 1000:1. The deposition rate was ~150 Å/min for all films. Thermal annealing of the films was performed with ±5°C temperature control in flowing nitrogen gas.

Index of refraction data were taken at 5461Å on a Gaertner L119 ellipsometer. A complex index of 4.050-0.028i for the Si substrate, with no corrections for a possible 10-15Å native oxide on the Si substrates, was used in determining the index of the Si_3N_4 film from Δ (change in phase) and ψ (arc-tangent of the amplitude ratio factor for polarization normal to and in the plane of incidence) measurements (2). Electrical contact was made to the nitride on the Si wafer by vapor depositing Al dots of 1 mm² through a shadow mask and then sintering at 450°C. The wafers were diced into small chips which were scrubbed onto headers

INTERNAL REFLECTION SPECTROSCOPY





(1) $d_p = \lambda/2\pi n_1 \left[\sin^2\theta - (n_{21})^2\right]^{1/2}$

$n_{21} = n_2/n_1$

λ = WAVELENGTH IN FREE SPACE

θ = ANGLE OF INCIDENCE

FOR Si_3N_4/Si AND $\theta = 45$

d_p = 3490Å FOR NH, AND 5350Å FOR SiH

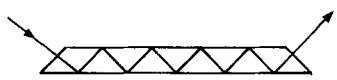
WHEN $d_{FILM} << d_p$ ($E \approx$ CONST)

(2) $d_{eff_\perp} = 4\, n_{21}\, d \cos\theta$ ($\perp$ POLARIZATION)

$= 3.30d$

(3) $d_{eff_{||}} = \dfrac{4\, n_{21}\, d \cos\theta \left[(1 + (1/n_2)^4) \sin^2\theta - (1/n_1)^2\right]}{(1 - (1/n_1)^2) \left[(1 + (1/n_1)^2 \sin^2\theta - (1/n_1)^2\right]}$

$= 3.22\, d$ (|| POLARIZATION)



MULTIPLE INTERNAL REFLECTIONS

Fig. 1. Illustration of the internal reflection technique for obtaining absorption data on thin films.

where the Al dot was wire bonded to a header post. Current measurements at a constant field were made as a function of temperature between 200° and 500°K. The temperature was increased stepwise and allowed to stabilize before each current measurement.

The MIR technique, developed by Harrick (3) and illustrated in Fig. 1, makes it possible to use infrared absorption to measure the vibrational modes for H bound to N and Si in Si_3N_4 with film thicknesses representative of those used in MNOS memory elements. Since the penetration depths, d_p, given according to Eq. [1] of Fig. 1 are significantly greater than the film thickness, the effective thickness is ~3 times the actual thickness, d, according to Eq. [2] and [3] of Fig. 1. The geometry and dimensions of the plate used in the present investigation give 12 internal reflections at the film-covered surface. In addition to the advantage of increased sensitivity compared to conventional infrared absorption, there are no interference effects in MIR. The MIR measurements for the present study were made at room temperature in a nitrogen-purged Perkin Elmer Model 221 spectrophotometer (CaF_2 prism) using a fixed angle MIR accessory in the sample beam.

Hydrogen and deuterium implantations were performed in a vac-ion pumped line of a 300 keV Accelerator Incorporated machine. Ions of 20 keV H_2^+ or D_2^+ were extracted from rf ionized sources selected and scanned across the sample through a beam-defining aperture. Secondary electrons were electrically suppressed, and the ion fluence was obtained by integrating the ion current passing through the aperture. Atomic ion energies of ≤5 keV are needed to locate H or D within the nitride film, whereas the practical lower limit for operation of the accelerator is ~20 keV. Therefore, 20 keV molecular species, which dissociate into 10 keV atomic species on encountering a solid surface were accelerated for the implantation. Implantations were made through 1000Å of Al evaporated onto the Si_3N_4 in order to reduce the energy of the atomic species to 3-4 keV before passing into the Si_3N_4.

Experimental Results and Discussion

Electrical characterization.—Electrical characteristics for Si_3N_4 films deposited for this study of chemically bound H are shown in Fig. 2 to illustrate the large R dependence of the conductance. Current densities, I, at an electric field, E, of 2.86×10^6 V/cm (metal electrode positive) for films deposited with ratios of 10:1, 100:1, and 1000:1 at 700°C are plotted as a function of reciprocal temperature. Near room temperature the current density decreases four orders of magnitude with each order of magnitude increase in R. Thermally activated transport is apparent for all films, particularly at room temperature and above. The slopes of ln

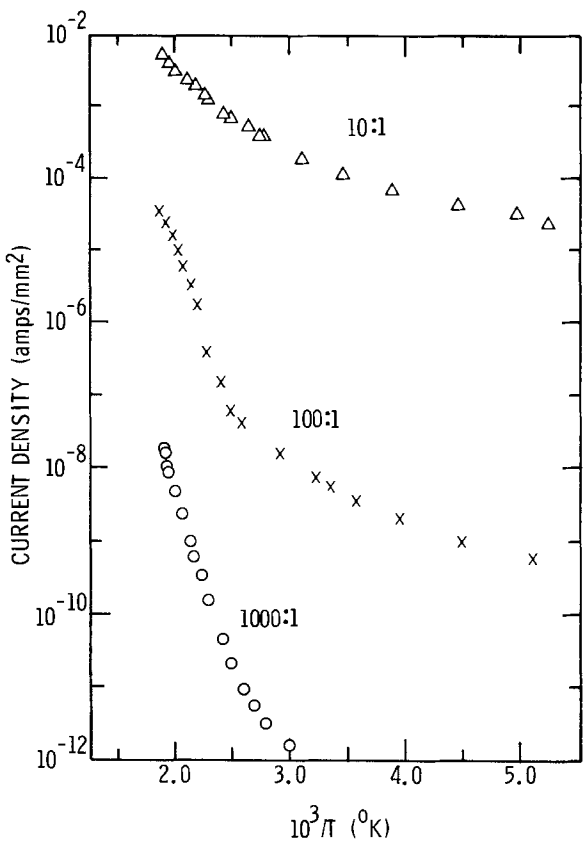


Fig. 2. Current density vs. reciprocal temperature at a constant field of 2.86×10^6 V/cm (metal electrode positive) on nitride films deposited with 10:1, 100:1, and 1000:1 NH_3/SiH_4 ratios.

current *vs.* reciprocal temperature for the 100:1 and 1000:1 films are approximately 1 eV in the region above room temperature, which implies a trap depth of ~1.5 eV when including the dielectric permittivity according to the Poole-Frenkel mechanism (4). Likewise, the smaller slope of ~0.3 eV for the 10:1 film gives an activation energy of ~0.8 eV. Shallow levels near 0.8 eV have been previously observed and attributed to Si islands (5). A 1.5 eV level has also been reported previously (5), but the centers responsible for the 1.5 eV level have not been identified.

Chemically bound hydrogen in as-deposited films.— Plotted in Fig. 3 are the optical densities measured by the MIR technique between 4000 and 2000 cm^{-1} (wave numbers) for 1000Å silicon nitride films deposited with ratios of 10:1, 100:1, and 1000:1 at 700°C. The traces are displaced relative to each other for clarity. The results show vibrational modes associated with Si-H (2160 cm^{-1}) and N-H (3335 cm^{-1}) bonding for all films (6), but the intensities of the absorption bands are dependent on R. Although searched for, there was no evidence of a band near 4160 cm^{-1} which would indicate H_2 in the films (7).

Optical densities for the peaks of the NH and SiH bands as a function of R are plotted in Fig. 4. The NH band increases with increasing R; whereas, the SiH band has a maximum intensity in the 100:1 film. Since the SiH_4 flow rate is held constant for all R, increased concentrations of NH_3 decomposition products will be the primary effect of increasing R. An increase in R should, therefore, give more complete bonding of Si to N, and give a higher probability for H bonding on remaining dangling and distorted bonds. But both NH and SiH bands are observed to increase for R equal to 100:1 relative to 10:1. Consequently, we suggest that the amount of H bound to either Si or N is limited in these two films by H available in the gaseous atmosphere. In contrast, the SiH band in the 1000:1 film is smaller than in the 10:1 and 100:1 films. This decrease in the SiH band is attributed to more complete bonding of Si to N. Simultaneously, the increased NH_3 flow causes an increase in NH bonding in the film.

The refractive index for these films decreases with increasing R as shown in Fig. 4. A high refractive index for low R has been attributed to excess Si in the films (8). If the fractional increase in refractive index is assumed to be proportional to fractional Si-Si bonding, with the refractive index for 100% Si-Si bonding taken equal to 4.05, then there is an estimated 1.5% Si-Si bonding in the 100:1 film and 7% in the 10:1 film. Backscattering measurements reported by Gyulai *et al.* (9) indicated excess Si of this magnitude and higher in films with a refractive index of 2.2. The larger SiH bands in 10:1 and 100:1 films than in the 1000:1 film discussed above is in accord with excess Si in the lower R films.

Heating above deposition temperature.—The effects of heating above the deposition temperature on chemically trapped H are shown in Fig. 5 through 7 for films deposited with R equal to 1000:1, 100:1, and 10:1, respectively. For clarity, uncertainties in the optical density are shown for the SiH band only; similar error bars apply to the NH band.

Results from isothermal annealing at 800°, 850°, and 900°C on the NH and SiH bands in the 1000:1 film are shown in Fig. 5. The data are plotted as a function of $\sqrt{\text{time}}$ because it has long been known that Si_3N_4 is an effective barrier for H diffusion at 600°C and below (10), and $\sqrt{\text{time}}$ is a commonly observed dependence for diffusion-limited loss from a medium. There is an initial rapid decrease in both the SiH and NH bands at 800°C where 0.33 of the NH band and 0.66 of the SiH band anneal out in the first 100 min. There is a further slow decrease in the bands at 850°C where the SiH band becomes unresolvable, followed by rapid decrease in the NH band at 900°C.

Annealing results for the 100:1 film in Fig. 6 show some similarities to those for the 1000:1 film, but also show a marked difference in the annealing of the SiH band. The SiH band in the 100:1 film exhibits an initial tendency to increase at 800°C and it then remains

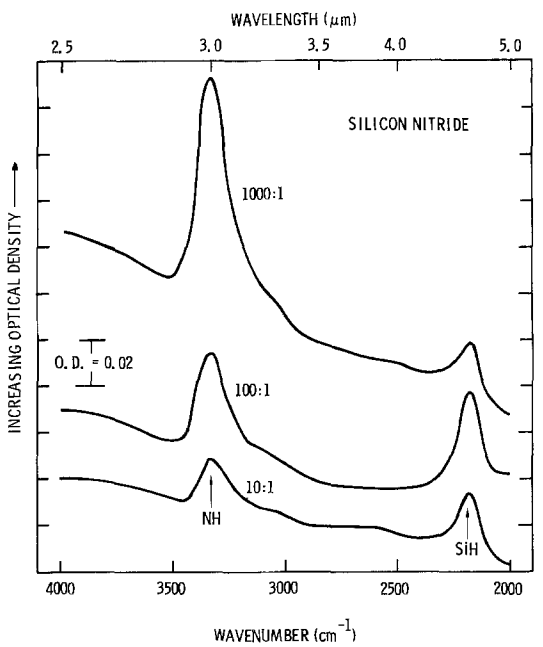


Fig. 3. Optical density vs. wave number showing NH and SiH absorption in 1000Å silicon nitride films deposited with NH_3/SiH_4 ratios of 10:1, 100:1, and 1000:1. Traces displaced relative to each other to provide clarity.

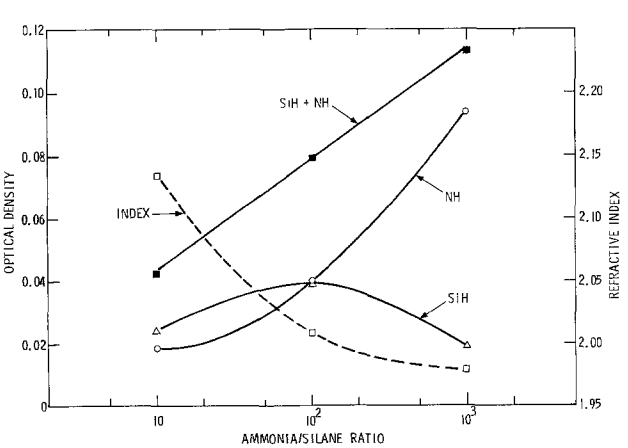


Fig. 4. Optical density for peaks of the NH and SiH bands and also refractive index as a function of NH_3/SiH_4 ratio.

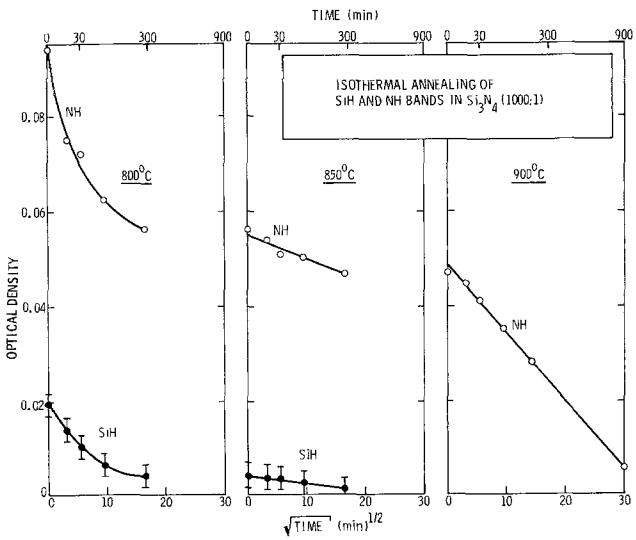


Fig. 5. Annealing behavior for the NH and SiH bands in the 1000:1 film.

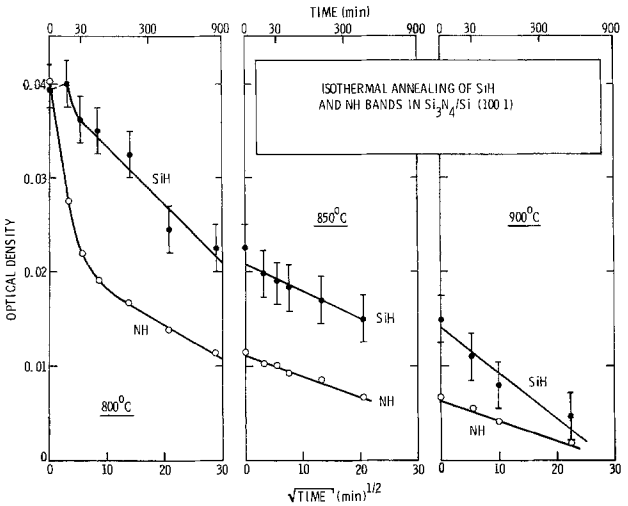


Fig. 6. Annealing behavior for the NH and SiH bands in the 100:1 film.

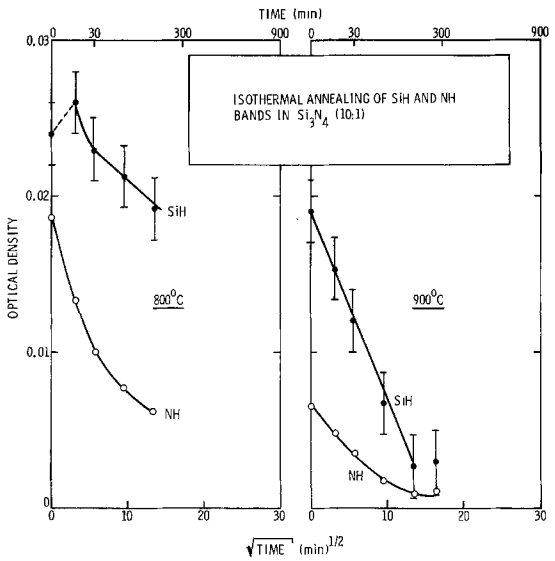


Fig. 7. Annealing behavior for the NH and SiH bands in the 10:1 film.

larger in magnitude than the NH band throughout the subsequent annealing. A more subtle difference occurs in the fractional anneal of the NH band which is 0.55 in the first 100 min in the 100:1 film compared to 0.33 of the NH band in the 1000:1 film. The *R*-dependent trend in the annealing behavior is continued in the 10:1 film as shown in Fig. 7. The 10:1 film again shows an initial increase in the SiH band intensity, and a large fractional decrease (0.60) in the NH band for the first 100 min at 800°C. These annealing results are additional evidence for incompletely bonded Si in the 10:1 and 100:1 films such that some transfer of H from N-H to Si-H bonds occurs initially at 800°C.

Bonding of implanted hydrogen and deuterium in films.—In order to obtain a calibration to determine the concentration of chemically bound H from an MIR measurement, 2×10^{16} H atoms/cm^2 were implanted through 1000Å of Al and into the 1000:1 film. Prior to implantation the film was heated at 975°C to reduce the NH band below the limit of detectability, and Al was vapor deposited on the Si_3N_4. After implantation the Al was removed and *IR* spectra were recorded as a function of annealing. The sequence for the same film was then repeated for 2×10^{16} D atoms/cm^2. Optical densities measured after implantation and heating for 10 min at the initial deposition temperature of 700°C are plotted in Fig. 8. The ratio of the frequencies 3330/2455 =

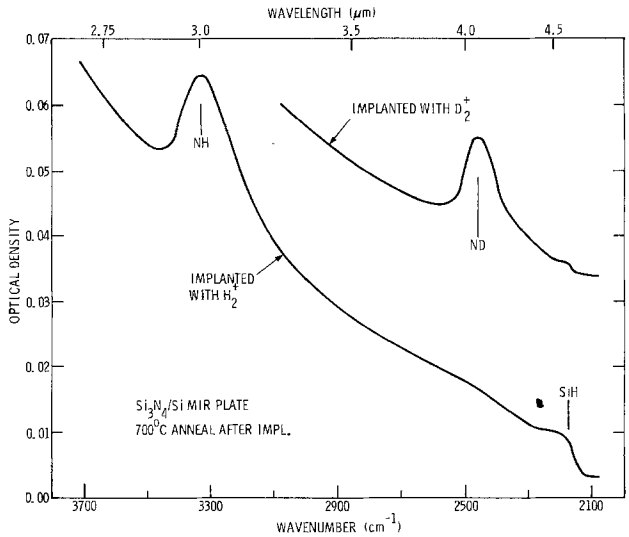


Fig. 8. NH and ND absorption bands produced by implantation of 2×10^{16} hydrogen or deuterium atoms followed by 10 min at 700°C

1.356 for the major bands observed after H and D implantation is approximately that expected for isotopic substitution of D for H in the NH molecule (7)

$$\nu_{NH}/\nu_{ND} = \sqrt{\mu_{ND}/\mu_{NH}} = 1.369$$

where μ_{NH} and μ_{ND} are the reduced masses for the atoms in the molecule according to

$$\frac{1}{\mu_{NH}} = \frac{1}{m_N} + \frac{1}{m_H}, \text{ and } \frac{1}{\mu_{ND}} = \frac{1}{m_N} + \frac{1}{m_D}$$

A similar small difference between the observed frequency shift and that expected for a free diatomic molecule was also observed for SiH and SiD band formation by ion implantation into Si (11). Consequently, the shift in vibrational frequency caused by isotopic substitution of D for H confirms chemical bonding of implanted H in Si_3N_4. The intensity of the SiH band after H implantation is ~0.2 that of the NH band. This intensity ratio is nearly equal to the ratio after deposition which suggests rebonding of implanted H at distorted or dangling bonds where H was initially bonded in the as-deposited film.

Having demontrated chemical bonding of implanted H, a calibration to relate the NH center concentration, C_{NH}, to the absorption coefficient, α, is obtained by assigning 80% of the implanted H to NH centers and 20% to SiH centers in the 1000:1 film. Since annealing of implantation-induced disorder is known to occur for temperatures $\lesssim$ 800°C (12), absorption data measured after 10 min at 800°C where the intensity of the NH band reached a maximum (see Fig. 9) was used in determining the proportionality factor between α and C_{NH}. Taking 12 internal reflections, and an effective thickness of 3*d*, the absorption cross section per NH center is

$$\sigma = \alpha/C_{NH} = \frac{\alpha d_T/d_T}{0.8(\phi)/d} = \frac{0.046/36d}{0.8(\phi)/d}$$

$$= 8 \times 10^{-20} \text{ cm}^2$$

where $d_T = 3 \cdot 12 \cdot d$ cm, $\phi = 2 \times 10^{16}$ cm^{-2} and $\alpha d_T = 0.046$. Note that *d* cancels in the above equation to make the determination of σ independent of the thickness. The cross section obtained here is in good accord with that per SiH center produced by H implantation into a thick (4500Å) oxynitride (13), and also with that per SiH center produced by H implantation into Si (11).

Annealing of implanted films.—Identification of the controlling mechanism for H loss is important since it will determine the depth distribution of chemically bound H, particularly in partially annealed films. For

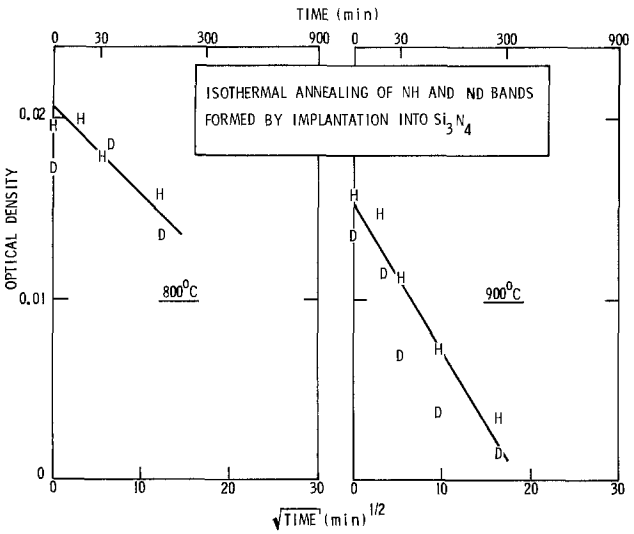


Fig. 9. Annealing behavior for implanted NH and ND bands at 800° and 900°C. H represents the NH band and D represents the ND band.

example, a diffusion-limited loss will leave a higher concentration in the center of the film than near the surfaces where H escapes, whereas bond energy-limited loss will maintain a flat profile.

Plotting the annealing results as a function of $\sqrt{\text{time}}$ (see Fig. 5 through 7 and 9) is a preliminary check for diffusion-limited behavior. However, $\sqrt{\text{time}}$ is not necessarily a valid representation of loss from a thin plane sheet (14). A comparison of NH and ND annealing is another approach for investigating the loss mechanism (15). Assuming random diffusion and no cooperative effect of the surrounding lattice, the diffusion coefficient, θ, is dependent on the jump frequency, and hence upon the isotopic mass, analogous to the vibrational frequency dependence, $\theta_H/\theta_D \approx \sqrt{m_D/m_H}$ (15). The close correspondence between the annealing of NH and ND bands shown in Fig. 9 does not support a diffusion-limited loss of H from Si_3N_4. Therefore, H loss is attributed to a bond energy-limited mechanism since the dissociation energy is only weakly dependent on the isotopic mass (16).

Summary and Conclusions

This study demonstrates that multiple internal reflection spectroscopy readily provides a measure of N-H and Si-H bonding in Si_3N_4 films which have thicknesses comparable of those for nonvolatile memory elements. Hydrogen, which is a decomposition product of the NH_3 and SiH_4 gases used for deposition, is observed in the films by way of the vibrational modes for N-H and Si-H bonded centers. Concentrations of NH and SiH centers are shown to depend on the NH_3/SiH_4 ratio, R, during deposition at 700°C.

The observed effects of R on N-H and Si-H bonding are attributed to a simultaneous increase in both H and N with increasing R. For depositions with $R \leq 100:1$ the results are interpreted to be representative of Si_3N_4 where the concentration of dangling and distorted Si and N bonds exceed the concentrations of observed NH and SiH centers such that both the NH and SiH centers increase with R. Refractive index measurements suggest that Si-Si bonds are also present in films for $R \leq 100:1$. Results for R equal to 1000:1 are interpreted to be representative of a film with nearly complete bonding of Si to N, hence small concentrations of Si-Si and Si-H bonding.

A loss of bound hydrogen from Si_3N_4, and R-dependent changes in the relative concentrations of NH and SiH centers occur on heating at temperatures between 800° and 900°C. The R-dependent changes are consistent with an excess of incompletely bonded Si in 10:1 and 100:1 film. Dissociation energy rather than diffusion is suggested as the limiting mechanism for H loss from Si_3N_4 because the loss during annealing is independent of isotopic mass for ion implantation-induced NH and ND centers. Ion implantation of hydrogen and deuterium demonstrated that these implanted species are bonded into Si_3N_4, and intensities for ion-induced absorption bands give a conversion factor to determine the concentration of chemically bound H from optical absorption measurements.

The electrical conductance of films deposited for this investigation also shows a strong dependence on R, but additional studies are required to separate H-bonding effects on film conductance from effects of Si-Si bonding.

Acknowledgment

This work was supported by the United States Energy Research and Development Administration (ERDA) under Contract AT (29-178).

Manuscript submitted Oct. 6, 1976; revised manuscript received Jan. 25, 1977.

Any discussion of this paper will appear in a Discussion Section to be published in the December 1977 JOURNAL. All discussions for the December 1977 Discussion Section should be submitted by Aug. 1, 1977.

Publication costs of this article were assisted by Sandia Laboratories.

REFERENCES

1. See for example the following reviews: J. T. Milek, in "Handbook of Electronic Materials," Vol. 3, IFI/Plenum (1971); P. Balk, in "Solid State Devices (1973)," H. Weiss, Editor, p. 51, Institute of Physics, London and Briston (1973).
2. R. J. Archer, *J. Opt. Soc. Am.*, **52**, 970 (1962).
3. N. J. Harrick, "Internal Reflection Spectroscopy," Interscience Publishers (1967).
4. S. M. Sze, "Physics of Semiconductor Devices," pp. 492-501, Wiley Interscience (1969).
5. G. A. Brown, W. C. Robinette, and H. G. Carlson, *This Journal*, **115**, 948 (1968); J. R. Yeargan and H. L. Taylor, *ibid.*, **115**, 273 (1968).
6. E. A. Taft, *ibid.*, **118**, 1341 (1971).
7. K. Nakamoto, "Infrared Spectra of Inorganic and Coordination Compounds," Wiley-Interscience (1963).
8. K. E. Bean, P. S. Gleim, R. L. Weakley, and W. R. Runyon, *This Journal*, **114**, 733 (1967).
9. J. Gyulai, O. Meyer, J. W. Mayer, and V. Rodriguez, *Appl. Phys. Lett.*, **16**, 232 (1970).
10. B. E. Deal, E. L. MacKenna, and P. L. Castro, *This Journal*, **116**, 997 (1969).
11. H. J. Stein, *J. Electron. Mater.*, **4**, 159 (1975).
12. H. J. Stein, *J. Appl. Phys.*, **47**, 3421 (1976).
13. H. J. Stein, *J. Electron. Mater.*, **5**, 161 (1976).
14. J. Crank, "The Mathematics of Diffusion," Chap. 4, Oxford University Press (1956).
15. A. V. Chadwick and J. N. Sherwood, in "Point Defects in Solids," Vol. 2, J. H. Crawford, Jr. and L. M. Slifkin, Editors, Sec. 5.2, Chap. 6, Plenum Press (1975).
16. A. G. Gaydon, "Dissociation Energies," p. 249, Chapman and Hall, Ltd. (1968).

The Dominant Recombination Centers in Electron-Irradiated Semiconductors Devices

A. O. Evwaraye and B. J. Baliga*

General Electric Corporate Research and Development, Schenectady, New York 12309

ABSTRACT

The defect states introduced by electron irradiation of silicon and the effects these defect levels have on low level minority carrier lifetimes have been studied by the capacitance transient spectroscopy and reverse recovery techniques. The E3 defect level (E_c — 0.41 eV) is the principal recombination center that controls lifetime following room temperature irradiation. As the E3 defect level anneals, however, a secondary defect level E4 emerges which then becomes the dominant recombination center. This defect level E4 is related to the electron-induced defects since it is not produced in unirradiated samples. The energy levels and capture cross sections of these electron-induced defects are reported.

In the past several years, considerable effort has been made to locate the principal recombination centers induced by either electron or gamma irradiation of silicon. The microscopic structures of these radiation-induced defects have been studied in detail with EPR by Watkins and Corbett (1-3). The dominant defect responsible for the control of minority carrier lifetime is, however, still a source of controversy in the literature. Table I summarizes the published results and the results of this work described below.

Wertheim (4, 5), using Hall effect, conductivity, and lifetime measurement techniques in his studies of electron-irradiated n-type silicon, reported a level at E_v + 0.27 eV to be the principal recombination center. He found the room temperature cross sections for this level to be 8×10^{-13} cm^2 and 9×10^{-15} cm^2 for holes and electrons, respectively. Galkin *et al.* (6), on the other hand, reported that the dominant recombination center is the level at E_c — 0.16 eV. This is presumably the A-center (oxygen-vacancy complex). They reported the room temperature cross sections for this defect level to be 4×10^{-14} cm^2 and 1.10×10^{-15} cm^2 for holes and electrons, respectively. Baicker, in his studies of electron-irradiated n-type silicon, further confused the issue (7). The results of measurements on three of his four samples agree with Galkin's conclusions, while the results on the fourth sample agree with Wertheim's measurements. Both Carter (8) and Bielle-Daspet (9) have independently reported that the principal recombination center is located at E_c — 0.17 eV. Berman *et al.* (10), investigating defects in silicon p$^+$-n junctions irradiated with gamma quanta, concluded that recombination occurs mainly at the A-centers. More recently, Rai-Choudhury *et al.* (11) concluded that the dominant center is located at E_v + 0.26 eV.

There has recently been an increased interest in the use of electron irradiation to control the recovery characteristics of power rectifiers and thyristors (12). Solar cell degradation in outer space due to radiation has also been correlated to the lifetime variation (13). Therefore, a precise determination of the principal recombination center in irradiated n-type silicon is a necessity.

In this study, the transient capacitance technique (14, 15) was used to monitor the defect concentrations as well as other changes in the spectrum as the samples were annealed. The deep level transient spectroscopy technique allows one to study each specific defect in the defect spectrum. The low level minority carrier lifetime, measured by the reverse recovery technique (16), was also monitored during the annealing process. This allowed correlation of the lifetime variation with a specific defect in the defect spectrum. Our results show that the dominant recombination center is the single negative charge state of the divacancy (17) located at E_c — 0.41 eV. During these measurements it was observed that upon annealing of this defect level the minority carrier lifetime does not recover to the preirradiation value. This is due to the emergence of a secondary defect level, E4, located at E_c — 0.35 eV, as the E3 defect level anneals out.

Table I. Summary of published results of the dominant recombination center in irradiated n-type silicon

Dominant recombination center	Measuring technique	Ref.
E_v + 0.27 eV	Hall effect	(5)
E_c — 0.16 eV	Hall effect and lifetime measurements	(6)
E_c — 0.16 eV E_v + 0.27 eV	Minority-carrier lifetime measurements	(7)
E_c — 0.17 eV	Hall effect measurements	(8)
E_c — 0.17 eV	Minority-carrier lifetime measurements	(9)
E_c — 0.17 eV	TSCAP	(10)
E_v + 0.26 eV	TSC	(11)
E_c — 0.41 eV (E3) E_c — 0.36 eV (E4)	DLTS and lifetime measurements	This work

Experimental Procedure and Results

The silicon diodes used in these studies (p$^+$nn$^+$) were fabricated from float-zone, dislocation-free, n-type silicon substrates normally used in the fabrication of commercial high voltage rectifiers and thyristors. The resistivity of the starting material was 25-35 Ω/cm. The boron-doped p$^+$ layer with a surface concentration of 10^{19} cm^{-3} and the phosphorus-doped n$^+$ layer with a surface concentration of 10^{21} cm^{-3} were obtained using conventional diffusion processing. No special care was taken to avoid the introduction of oxygen into the devices during the p$^+$ and n$^+$ diffusion cycles. These devices were then mounted on a cooling block and irradiated with 1.5 MeV electron beams to a flux of 2.8×10^{14} e/cm^2. The decrease in lifetime caused by the electron bombardment was measured by the reverse recovery technique (16). In this method, the storage time was measured for a step recovery of the diode with a forward-to-reverse current ratio of unity. These measurements were conducted over a wide range of current levels. The current level was decreased until the storage time became independent of current. The low level minority

* Electrochemical Society Active Member.
Key words: electron-induced defects, dominant recombination center, electron irradiation, gamma irradiation, defect levels.

carrier lifetime was then computed from this storage time using the relationship

$$\tau \simeq 4.38\,\tau_{sec} \qquad [1]$$

where τ is the minority carrier lifetime and τ_{sec} is the measured storage time. It must be noted that this relationship is valid only for diodes with base widths greater than twice the diffusion length. For the diodes used in this study lifetimes as high as 20 μsec could be measured without correcting for the base width. The data reported in this paper have been confined to lifetime values below this limit.

The defect spectrum was obtained by the technique of deep level transient spectroscopy (DLTS) (14, 15). Figure 1 shows the defect spectrum resulting from the 1.5 MeV irradiation. Three electron traps (E1, E2, and E3) and two hole traps (H1 and H2) were induced by radiation. The average value of the low level minority carrier lifetime immediately after room temperature irradiation was approximately 1 μsec.

The E1 defect level is the well-characterized A-center (O-V pair) located at E_c — 0.17 eV. The E2 and E3 defect levels located at E_c — 0.23 eV and at E_c — 0.41 eV, respectively, have been identified as the double negative ($[V \cdot V]^=$) and single negative ($[V \cdot V]^-$) charge state of the divacancy (17). The divacancy is known to introduce three energy levels in the bandgap (2, 18). Therefore, the presence of the divacancy would be detected by observing three activation energies with an identical introduction rate and the same annealing behavior. The microscopic structure of the H2 defect level is not known but it does not have the same introduction rate nor the same annealing behavior as E2 and E3 so that it cannot be the single positive charge state ($[V \cdot V]^+$) of the divacancy. There has been speculation that H2 is either an alternate charge state of the A-center or an interstitial related defect (19). The relationship between the A-center and H2 level is under investigation.

The H1 defect level is probably the single positive ($[V \cdot V]^+$) charge state of the divacancy. This identification is purely speculative since it was extremely difficult to follow the annealing behavior of H1 or its introduction rate because of the large concentration of H2, which tends to dominate the spectrum when minority carriers are introduced into the depletion region. If H2 is indeed a different charge state of the A-center, the use of Schottky diodes and ion-implanted junctions will reduce the concentration of both E1 and H2 defect levels. This is being tried at present.

The annealing of the samples was performed in a furnace that has been described in Ref. (17). The DLTS spectrum was recorded after each annealing step at a fixed temperature and the low level minority carrier lifetime was measured after each annealing step. From previous studies (17) it is known that the E2 and E3 levels do not significantly anneal below 280°C. So the annealing of the samples in this study was carried out at 300°, 350°, 370°, 380°, and 395°C.

Figure 2 shows the DLTS spectrum of a device after it has been annealed for 60 min at 300°C. The E3 defect level has annealed to 65% of its original value and the emergence of the E4 defect level is clearly visible. The low level minority carrier lifetime was found to increase from 1 μsec following irradiation to 1.40 μsec after 60 min of annealing at 300°C. It is seen from this figure that no other (besides E4) secondary defects appeared in the spectrum at this temperature.

Figure 3 shows the normalized DLTS signal for the E2, E3, and E4 defect levels as a function of the annealing time at 300°C. The variation of the inverse of the low level minority carrier lifetime as a function of annealing time is also shown. The accuracy of these measurements is better than ±5%. It is not surprising that the annealing of defect levels E2 and E3 follows the same simple exponential form that was previously reported (17). It is interesting to note that $1/\tau$ follows this same exponential form up to 130 min and thereafter remains essentially constant. The defect level H2 is not shown in this plot because

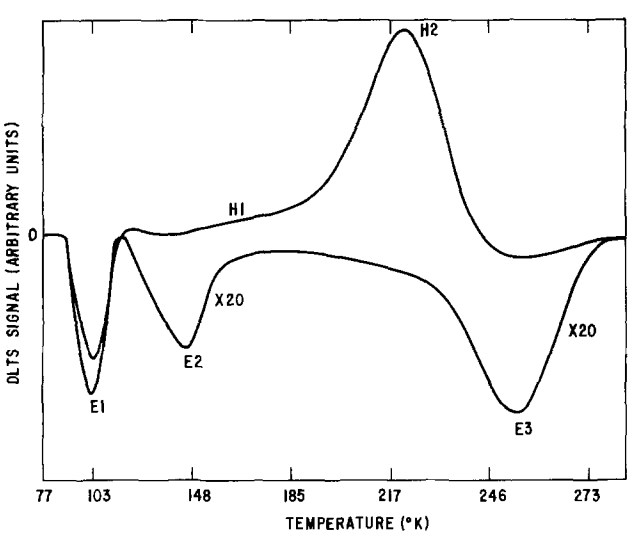


Fig. 1. DLTS spectrum of 1.5 MeV electron irradiation-induced defects in n-type silicon. E1-E3 are electron traps; H1 and H2 are hole traps.

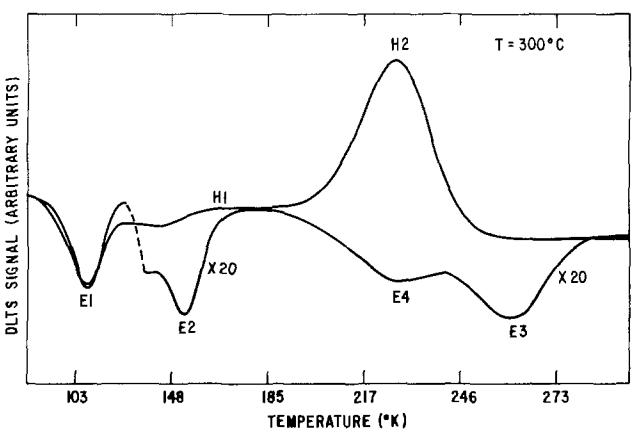


Fig. 2. DLTS spectrum of an electron-irradiated device that has been annealed at 300°C for 60 min. Note the emergence of a secondary defect E4.

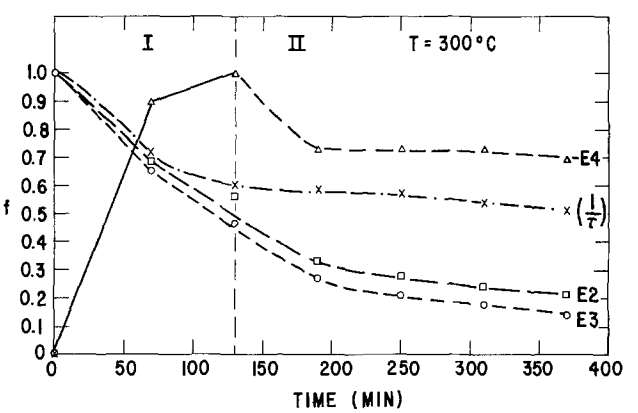


Fig. 3. The variation of the normalized concentrations of the defects E2, E3, and E4 as a function of annealing time at 300°C. Also shown is the variation of $1/\tau$ vs. annealing time. Note the two sections of the plot in which $1/\tau$ has two distinct behaviors.

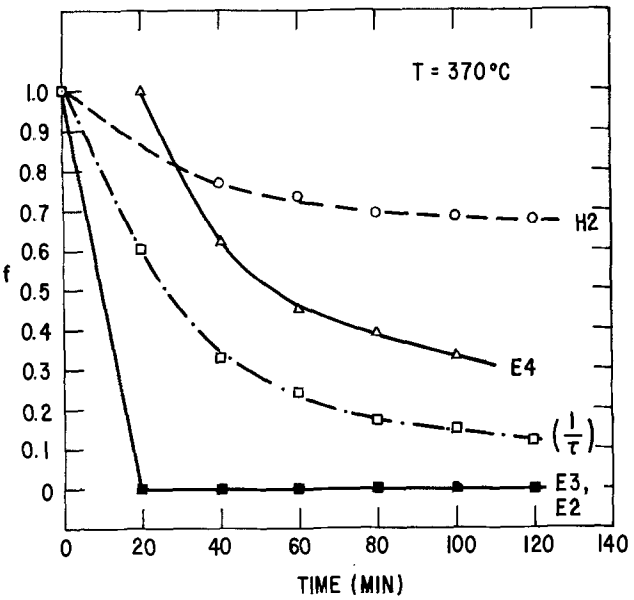


Fig. 4. The variation of the normalized concentrations of the defects E4 and H2 and the variation of the normalized $1/\tau$ as a function of annealing time at 370°C. Note that the defect levels E2 and E3 have completely annealed out after less than 20 min at this temperature.

this defect shows no measurable annealing at 300°C for these annealing times.

Figure 4 shows a plot analogous to the plot of Fig. 3 except that in Fig. 4 E3 and E2 have annealed out completely after 20 min at 370°C. It is seen from this figure that the defect level H2 is annealing but at a slower rate than E4. The variation of $1/\tau$ follows the same exponential form as the defect level E4. This suggests a relationship between the minority carrier lifetime and the defect level E4.

The electron capture cross section at E4 was determined by the usual technique of varying the majority carrier pulse duration. The electron capture cross section at E4 (σ_n^{E4}) is 4×10^{-16} cm^2, while σ_n^{E3} and σ_n^{E2} are 1.62×10^{-16} cm^2 and 0.6×10^{-16} cm^2, respectively (17).

The lifetime connected to the recombination centers produced by electron irradiation is usually expressed as

$$\frac{1}{\tau} = \frac{1}{\tau_o} + K\phi \qquad [2]$$

where τ_o is the preirradiation value of the lifetime due to the recombination centers initially present after fabrication, ϕ is the integrated electron flux, and K is the radiation damage coefficient. τ_o for most of the devices was 20 μsec and τ is about 1 μsec following room temperature irradiation to a flux of 2.8×10^{14} e/cm^2. These give a K value of 3.4×10^{-15} cm^2/e · μsec. It is realized that the radiation damage coefficient K is usually obtained from the plot of $1/\tau$ *vs.* Φ since K depends upon many variables such as the introduction rate of the recombination center (N_{TT}/Φ), the injection level, the location of the recombination center E_t, and the capture cross sections. However, the value of K obtained here agrees quite well with recent published values by Rai-Choudhury *et al.* (11). This seems to imply that in the two studies the same defect is controlling the minority carrier lifetime.

Discussion

The low level lifetime τ is given by

$$\tau = \tau_{po}\left[1 + \exp\left(\frac{E_t - E_F}{kT}\right)\right] + \tau_{no}\exp\left[\frac{2E_i - E_t - E_F}{kT}\right] \qquad [3]$$

where τ_{po} and τ_{no} are the minority carrier lifetimes in heavily doped n- and p-type silicon, respectively; E_t, E_F, and E_i are the positions of the trap level, Fermi level, and intrinsic level, respectively; k is Boltzmann's constant, and T is the absolute temperature. Substituting

$$\tau_{po} = \frac{1}{N_T <v>_p \sigma_p} \quad \text{and} \quad \tau_{no} = \frac{1}{N_T <v>_n \sigma_n} \qquad [4]$$

where N_T is the density of the recombination center, $<v>$ is the thermal velocity of the carriers, and σ the capture cross section, in Eq. [3] gives

$$\tau = \frac{1}{N_T}\frac{1}{<v>_p \sigma_p}\left[1 + \exp\left(\frac{E_t - E_F}{kT}\right)\right] + \frac{1}{<v>_n \sigma_n}\exp\left(\frac{2E_i - E_t - E_F}{kT}\right) = \frac{C}{N_T} \qquad [5]$$

where C is a constant at any fixed measurement temperature and is independent of the trap density. Thus, the low level lifetime is proportional to the reciprocal of the trap density during the annealing of a single recombination center.

From previous studies (17) and Fig. 3 we know that the annealing of the defect level E3 exhibits first-order kinetics and fits a simple exponential expression of the form

$$N_T(t) = N_T(o)e^{-t/R} \qquad [6]$$

where $1/R$ is the annealing rate of the defect. Since $1/\tau$ is proportional to N_T, then

$$1/\tau \propto e^{-t/R}$$

if N_T is the concentration of the recombination center responsible for controlling the minority lifetime.

The variation of $1/\tau$ at 300°C as a function of annealing time can be divided into two sections. The dividing line is at $t = 130$ min. In the first section $o \leq t \leq 130$ min, $1/\tau$ has the same exponential variation as E2 and E3. Since E2 is much more shallow ($E_c - 0.23$ eV) than E3 ($E_c - 0.41$ eV) and has a smaller capture cross section for electrons, it can be concluded that E3 is the dominant recombination center in Section I. It is instructive to note that in this section the defect level E4 is growing to its maximum concentration. In Section II of Fig. 3 ($130 \leq t \leq 400$ min), $1/\tau$ deviates markedly from its exponential behavior of Section I to a very little variation as a function of annealing time. At the same time the defect level E4 shows as much variation as $1/\tau$, which suggests that the defect level E3 is no longer the dominant recombination center and that E4 now controls the lifetime.

Figure 4 clearly demonstrates that the defect level E4 is the dominant recombination center after the E3 level has annealed out. Here the defect level E4 has the same exponential behavior as $1/\tau$. It is also seen from this figure that 68% of the original defect level H2 is unannealed after 120 min at 370°C, while E2 and E3 are completely annealed out after less than 20 min at this temperature. This allows the conclusion that H2 cannot be the single positive $[(V \cdot V)^+]$ charge state of the divacancy, and it not determining the lifetime.

The defect level E4 has an electron capture cross section comparable to σ_n^{E3}; it is probably as effective a recombination center as E3. It is important to point out that E4 is not formed in unirradiated devices that were annealed at these temperatures and is observed only in electron-irradiated devices, *i.e.*, the E4 defect is definitely related to the electron-induced defects.

The fact that we obtained approximately the same K value as Rai-Choudhury *et al.* (11) indicates that the same center is controlling minority lifetimes in both cases. Our results, however, do not support their

conclusion that the defect at $E_t = 0.26$ eV is the dominant recombination center. Further, our experimental results also disagree with the conclusions of Berman *et al.* and Galkin *et al.* that the A-center is the dominant recombination center. The A-center (O-V pair) is quite shallow ($E_c - 0.17$ eV) and for it to be the dominant recombination center the Fermi level would have to be above it so that it is always filled with electrons. This could conceivably happen in very heavily doped samples where the Fermi level is locked at the level due to the shallow dopants. In lightly doped samples such as the ones used in this study and those used by Berman and Galkin ($N_D \approx 10^{14}$ cm^{-3}) and like wafers used for device fabrication, the Fermi level is well below the A-center and it is usually empty. This requires that it capture electrons from the conduction band and holes from the valence band (which is 0.93 eV away). Unless the hole capture cross section is very large ($\approx 10^{-12}$ cm^2), which is highly unlikely, this center will act more like a trapping center for electrons than as a recombination center. Further, our annealing data show no correlation between the lifetime and the concentration of the A-center.

As pointed out earlier, these studies were done using 20-35 Ω/cm float-zone phosphorous-doped silicon irradiated with 1.5 MeV electrons. We have observed three electron traps E1 ($E_c - 0.17$ eV), E2 ($E_c - 0.21$ eV), and E3 ($E_c - 0.4$ eV) and two hole traps H1 ($E_v + 0.28$ eV) and H2 ($E_v + 0.42$ eV). Defect levels produced by electron irradiation of phosphorous-doped silicon with energy ranging from 0.7-10 MeV have been reported (3, 17, 19). It has been found that the same defect levels are produced over this energy range (0.7-10 MeV). In low resistivity phosphorous-doped silicon, an additional defect center due to phosphorous vacancy pairs is also observed (20, 21). However, at resistivity above 5 Ω/cm the divacancy dominates (*i.e.*, the concentration of the E-center is less than 10% of the divacancy). In the case of Czochralski-grown crystals, the same defect levels are observed with a higher concentration for the E1 ($E_c - 0.17$ eV) defect level. Since this level is much shallower than the E3 ($E_c - 0.41$ eV) defect level, we believe that the E3 defect level is also dominant in Czochralski-grown silicon. We conclude, therefore, that our results are applicable to a wide range of irradiation energy and phosphorous concentration.

Summary

We have studied the annealing behavior of the E2 and E3 defect levels as well as the variation in minority lifetimes at various temperatures; 300°, 350°, 370°, and 395°C. The dominant recombination center immediately after room temperature irradiation is the defect level E3 which has been identified as the single negative [$(V \cdot V)^-$] charge state of the divacancy. As E3 anneals out, however, a secondary defect E4 appears in the spectrum. This secondary defect then controls the minority lifetime in the n-type silicon. Our results clearly demonstrate that the dominant recombination center in high purity n-type silicon is neither the A-center (O-V pair) nor the defect level located at $E_v + 0.27$ eV, as has been assumed in the past.

Acknowledgments

The authors wish to thank Dr. D. M. Brown for his assistance in device fabrication and Dr. R. O. Carlson for his critical comments and suggestions. The assistance of L. A. Gruenke in all phases of this work is greatly appreciated.

Manuscript submitted Nov. 19, 1976; revised manuscript received Feb. 18, 1977. This was Paper 336 presented at the Las Vegas, Nevada, Meeting of the Society, Oct. 17-22, 1976.

Any discussion of this paper will appear in a Discussion Section to be published in the December 1977 JOURNAL. All discussions for the December 1977 Discussion Section should be submitted by Aug. 1, 1977.

Publication costs of this article were assisted by General Electric Company.

REFERENCES

1. G. D. Watkins and J. W. Corbett, *Phys. Rev.*, **134**, A1359 (1964).
2. G. D. Watkins and J. W. Corbett, *ibid.*, **138**, A543 (1965).
3. J. W. Corbett and G. D. Watkins, *ibid.*, **138**, A555 (1965).
4. G. K. Wertheim, *ibid.*, **105**, 1730 (1957).
5. G. K. Wertheim, *ibid.*, **110**, 1272 (1958).
6. G. N. Galkin, N. S. Rytova, and V. S. Vavilov, *Sov. Phys. Solid State*, **2**, 1819 (1961).
7. J. A. Baicker, *Phys. Rev.*, **129**, 1174 (1963).
8. J. R. Carter, Jr., *J. Phys. Chem. Solids*, **27**, 913 (1966).
9. D. Bielle-Daspet, *Solid-State Electron.*, **16**, 1103 (1973).
10. L. S. Berman, R. F. Vitman, and V. B. Shuman, *Sov. Phys. Semicond.*, **9**, 202 (1975).
11. P. Rai-Choudhury, J. Bartko, and J. E. Johnson, *IEEE Trans. Electron Devices*, **ed-23**, 814 (1976).
12. K. S. Tarneja and J. R. Johnson, 261 RNP, *This Journal*, **122**, 360C (1975).
13. W. P. Rahilly, Paper presented at the 11th IEEE Photovoltaic Specialists Conference, May 1975.
14. D. V. Lang, *J. Appl. Phys.*, **45**, 3023 (1974).
15. A. O. Evwaraye and E. Sun, *ibid.*, **47**, 3172 (1976).
16. D. C. Lewis, *Solid-State Electron.*, **18**, 87 (1975).
17. A. O. Evwaraye and E. Sun, *J. Appl. Phys.*, **47**, 3776 (1976).
18. A. H. Kalma and J. C. Corelli, *Phys. Rev.*, **173**, 734 (1968).
19. L. C. Kimerling, Proceedings of the International Conference on Radiation Effects in Semiconductors, Dubrovink, Yugoslavia (1976).
20. L. C. Kimerling, H. M. DeAngelis, and J. W. Diebold, *Solid State Commun.*, **16**, 171 (1975).
21. L. C. Kimerling, H. M. DeAngelis, and C. P. Carnes, *Phys. Rev.*, **B3**, 427 (1971).

Tapered Windows in SiO_2: The Effect of NH_4F:HF Dilution and Etching Temperature

G. I. Parisi,* S. E. Haszko, and G. A. Rozgonyi*

Bell Laboratories, Murray Hill, New Jersey 07974

ABSTRACT

Etching of windows in thermally grown silicon dioxide to achieve an approximately 45° taper edge profile has been empirically optimized using NH_4F/HF compositions and etching bath temperatures. Steeper slopes or much shallower tapers are obtainable by suitable adjustments of these two experimental parameters. The mechanism by which tapering occurs may best be described as a controlled separation of the photoresist/oxide interface which relates the lateral etch rate to the bulk etch rate. Depending on etching conditions, each beveled window edge consists of two or three distinct regions which comprise the final shape of the sloping taper. The dissolution reaction in all instances was found to be activation controlled with an apparent activation energy of 9.9 kcal/mole. Curves of etch rates as a function of temperature and HF molarity are presented and a quantitative relationship for etch rate in terms of these two parameters is given.

It has recently been shown (1-5) that dilute solutions of HF in NH_4F will produce tapered steps at the edges of windows in both thermally grown and chemically deposited SiO_2. The occurrence of a tapered step, or ramp, in place of a sharp step, or cliff, depends on the relative etch rates of the bulk oxide and the rate, be it enhanced or suppressed, at the oxide/photoresist interface. Several schemes for artificially enhancing the etch rate of the top portion of a given oxide have been reported (6-8). However, since a simple dilution of HF with NH_4F was known to produce shallow tapers it was decided to empirically optimize the etching phenomena using only two variables, etching bath temperature and NH_4F:HF concentration. In this way only the etching bath would be adjusted and the oxide materials processing would remain unchanged.

The resulting taper desired was set at ~45° (a 1:1 ramp slope) with a bulk oxide etching rate of ~1000 Å/min. It was also anticipated that a systematic study of the etching results would provide some insight into the mechanisms controlling the variable etching rates in the thickness and interfacial directions.

Experimental Procedures

Experiments were performed on thermally grown oxides of nominally 10,000Å thickness that were formed in wet oxygen at 1050°C. Kodak 747 microneg photoresist was used to generate a pattern having windows ranging in size from 8 to 40 microns. Some work was also done with Waycoat IC-III photoresist. The etchant solutions used consisted of 49% HF diluted with varying amounts of 40% by weight aqueous solutions of NH_4F. The etchant compositions ranged from 6.7:1 to 30:1 and are expressed as the volume ratios of the NH_4F solution to the HF solution. Etching solution temperatures were varied between 25° and 55°C after stabilization in a controlled temperature water bath. The volume of etchant was deliberately made large (approximately 800 ml) in order to (*i*) insure accurate composition that might otherwise not be achieved when measuring small liquid volumes, (*ii*) maintain virtually constant concentration of reactant species throughout the etching process, and (*iii*) simulate a batch processing environment capable of handling up to 20 wafers simultaneously. Both scanning electron microscopy (SEM) and Nomarski interference contrast optical microscopy were used to examine the edge profiles.

* Electrochemical Society Active Member.

Key words: beveled window etching, SiO_2 etching, dielectric films.

Results and Discussion

Qualitative observations.—The dependence of slope on etching solution at the edges of oxide windows is illustrated by the two SEM photographs in Fig. 1. A typical steep slope in an approximately 10,000Å thick oxide etched in a 6.7:1 solution is shown in Fig. 1a, while a shallow taper is obtained if a 30:1 solution is used, see Fig. 1b. Note that there are two distinct regions to the slope along each oxide edge profile. In Fig. 1a the etching rate in the depth direction, γ_d, is initially much faster than the rate, γ_l, in the lateral direction. However, the lower part of the oxide etches about the same in each direction, *i.e.*, $\gamma_d = \gamma_l$. This re-

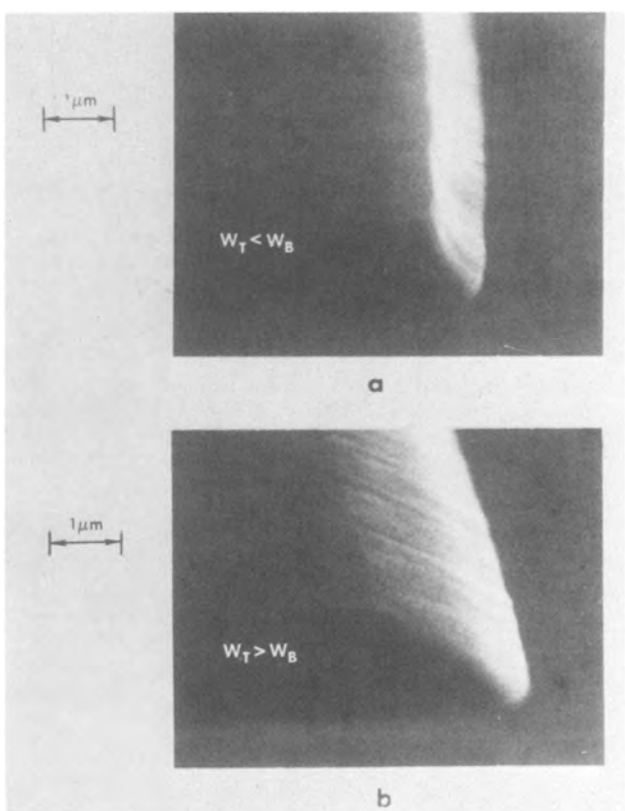


Fig. 1. Scanning electron micrographs of edge profiles etched in thermal SiO_2; magnification 14,000×. a. Steep taper slope etched with a 6.7/1 solution of NH_4F/HF at 25°C. b. Shallow taper slope etched with a 30/1 solution of NH_4F/HF at 25°C.

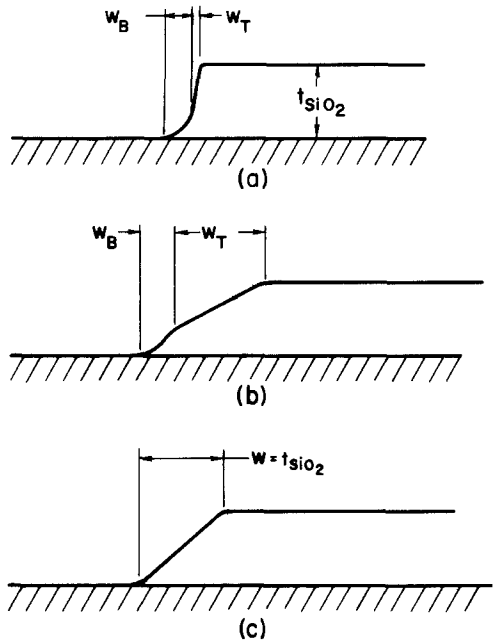


Fig. 2. Diagramatic representation of tapered oxide edges showing the different distinct regions of the profiles. a. Steep taper slope where $W_B > W_T$. b. Shallow taper slope where $W_B < W_T$. c. Ideal taper slope where $W_B = W_T = t_{SiO_2}$.

sults in a taper profile as depicted in Fig. 2a, which is very steep at the top and forms a quarter-circle at the bottom. The symbols W_T and W_B have been used for the projected width at the top and bottom of the profile since these widths are initially measured or estimated in an optical microscope. The 30:1 solution, for which $\gamma_l > \gamma_d$, see Fig. 1b, also has a final etching profile which approximates a quarter-circle as illustrated in Fig. 2b.

The differences observed for these two solutions in an optical microscope at 1000× are shown in Fig. 3. Note that the shallow taper, Fig. 3b, can be conveniently evaluated optically be measuring the number

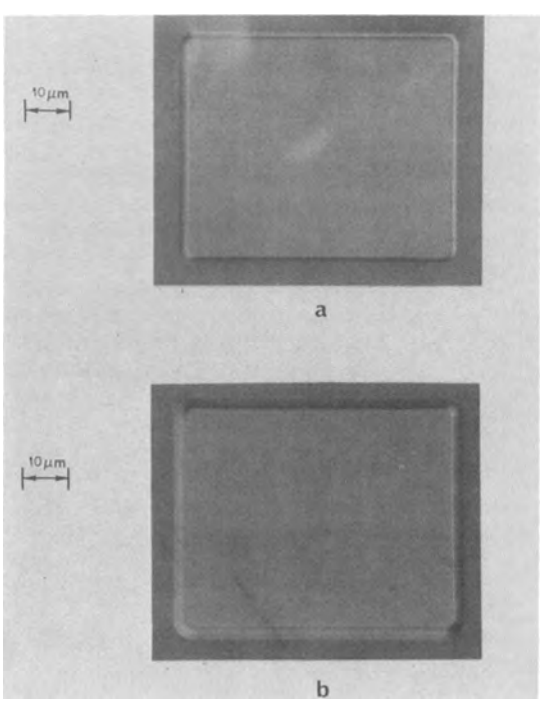


Fig. 3. Nomarski interference contrast optical micrographs of etched windows in thermal SiO_2; magnification 1000×. a. Steep taper slope showing no fringes. b. Shallow taper slope showing very discernible fringes.

and periodicity of the fringes. However, samples with taper angles greater than ~35°, *e.g.*, Fig. 1a and 3a must be examined in the SEM to obtain an unambiguous profile of the taper. Since $W_B > W_T$ for a 6.7:1 solution and $W_B < W_T$ for a 30:1 solution, dilutions intermediated to these two were investigated with the aim of obtaining a profile with $W \simeq t_{SiO_2}$ as shown in Fig. 2c.

Before extensive studies of the relative etching rates could be carried out, it was first necessary to establish that the photoresist material was not, in itself, grossly affecting the results, *e.g.*, by curling up or in some way separating from the top of the oxide surface. This was checked by examining the etched profiles of two samples (6.7:1 and 30:1) in the SEM before the photoresist was stripped. Figures 4a and 4b show that the photoresist is coherent with the oxide and behaves like a rigid cantilevered beam. However, if the undercutting is considerably more than the oxide thickness, *e.g.*, as with the 30:1 solution, see Fig. 4a, there is a tendency for the overhung part of the photoresist to lift. The photoresist undercutting was also found to be temperature independent as shown by the SEM photograph of Fig. 4b, which resulted from a 48°C etch in a 6.7:1 solution. Comparison of Fig. 4b with Fig. 1a shows that at the higher temperatures there is an increased tendency for the top of the oxide to etch faster and penetrate the photoresist/oxide interface. This indicates that the temperature dependence of γ_l is favorable for reducing the steep tapers at oxide edges.

A further proof that enhanced etching at the photoresist/oxide interface is the main factor in controlling edge tapers is illustrated by etching the oxide through a window in a Si_3N_4 mask which is known to bond very well to SiO_2 and would be expected to have a $\gamma_l < \gamma_d$. Figure 4c shows that there is very little undercutting of the nitride mask and that as a result the taper is very steep at the top of the oxide. A similar result can be obtained if the etching solution is inhibited

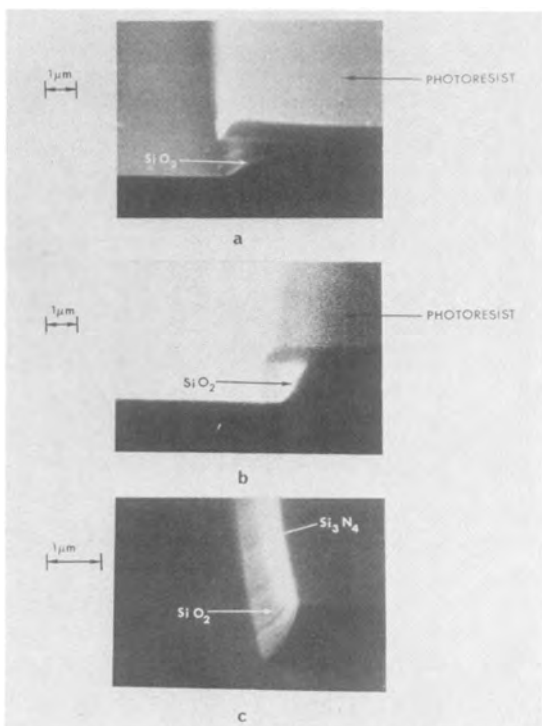


Fig. 4. Scanning electron micrographs of etched windows in thermal SiO_2 showing beveling behavior and effect of mask. a. Photoresist as a cantilevered beam after etching in a 30/1 solution at 25°C with $\gamma_l > \gamma_d$; magnification 9000×. b. Photoresist as a cantilevered beam after etching in a 6.7/1 solution at 48°C; magnification 9000×. c. Si_3N_4 as a mask bonding tenaciously to the SiO_2 and resulting in a steep taper etching in 6.7/1 solution at 48°C; magnification 16,000×.

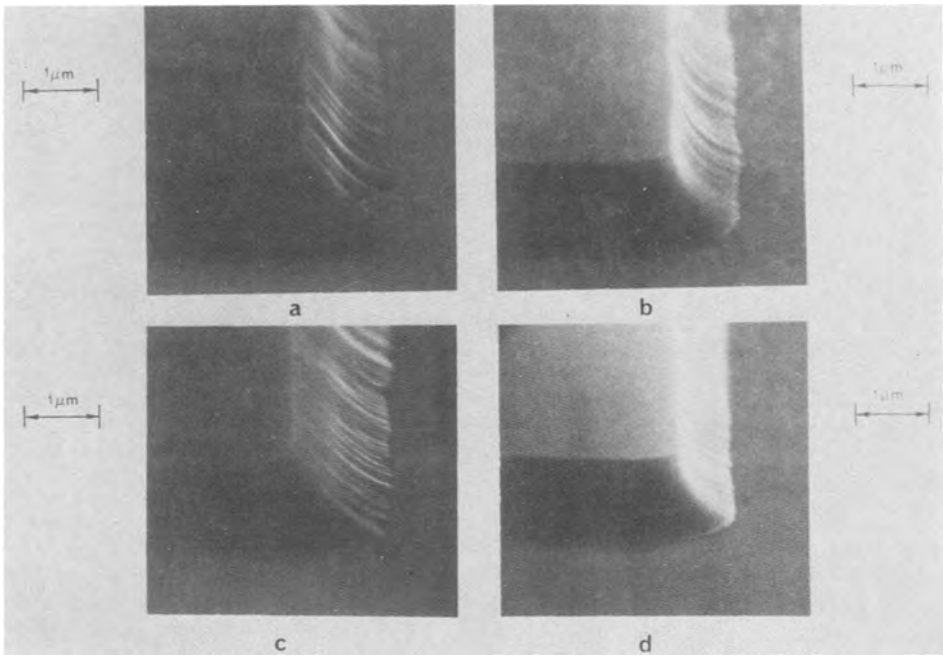


Fig. 5. Scanning electron micrographs of edge profiles showing effects of photoresist type and use of wetting agent prior to etching in 30/1 solution at 25°C; magnification 16,000×. a. Microneg 747, no wetting agent. b. Microneg 747, wetting agent predip. c. Waycoat IC-III, no wetting agent. d. Waycoat IC-III, wetting agent predip.

from attacking a photoresist/oxide interface by the use of a wetting agent prior to etching. The four SEM photographs in Fig. 5 show the tapers for two pairs of samples consisting of two different photoresists, Microneg 747, Fig. 5a and 5b, and Waycoat IC-III, Fig. 5c and 5d. A predip in a 0.2% solution of Synthrapol-N has been used for the samples shown in Fig. 5b and 5d. The gross difference in the slopes at the top of the oxides is attributed to the formation of a barrier between the interface and the etching solution. The inhibiting action of the wetting agent persists even if the samples are rinsed in deionized water following the predip and prior to etching. Oxide slopes similar to Fig. 5b and 5d continue to be obtained and are independent of the type of photoresist used. The precise role of the wetting agent is speculative. This observation, however, does suggest that a controlled separation of the photoresist/oxide interface occurs, viz., a controlled penetration of the etchant at the interface and not simply a random uncontrollable undercutting.

Figures 5a and 5c also illustrate the nature of the profile achieved when optimum etching conditions are achieved. The shape of these tapered steps, schematically shown in Fig. 6, is such that the middle region is a uniform ramp of width W_M, the bottom is arced, W_B, and concave upward, while the top, W_T, is curved and convex upward. The over-all width of the structure is approximately equal to the oxide thickness. The functional dependence of profile shape on etching solution and temperature is presented in the next section.

Quantitative rate data and profile analysis.—Etch rate in the depth direction, γ_d, as a function of HF concentration is shown in Fig. 7 for the several temperatures investigated. The compositions of the mixtures of 40% NH_4F and 49% HF have been converted to molarity of HF. Although the actual concentration of HF in these solutions is lower than that which is added, molarity has been used for preparative purposes. The corresponding equivalents are shown in Table I. The linearity of these curves suggests that the dissolution of SiO_2 in HF at any fixed temperature is a first-order reaction dependent on the concentration of HF. Since all four curves converge at the origin, the HF appears to be the sole reactive species during the etching. The other reactant is the SiO_2 which, being in the solid

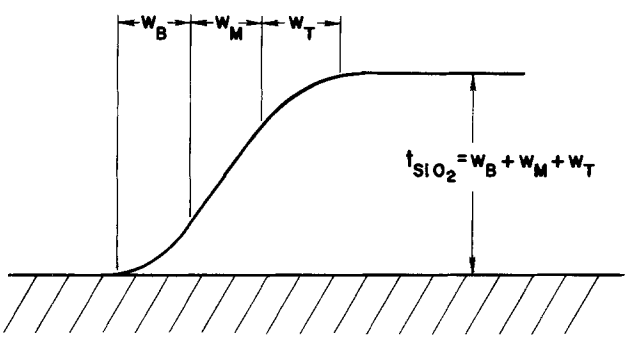


Fig. 6. Schematic representation of tapered profile for optimum etching conditions.

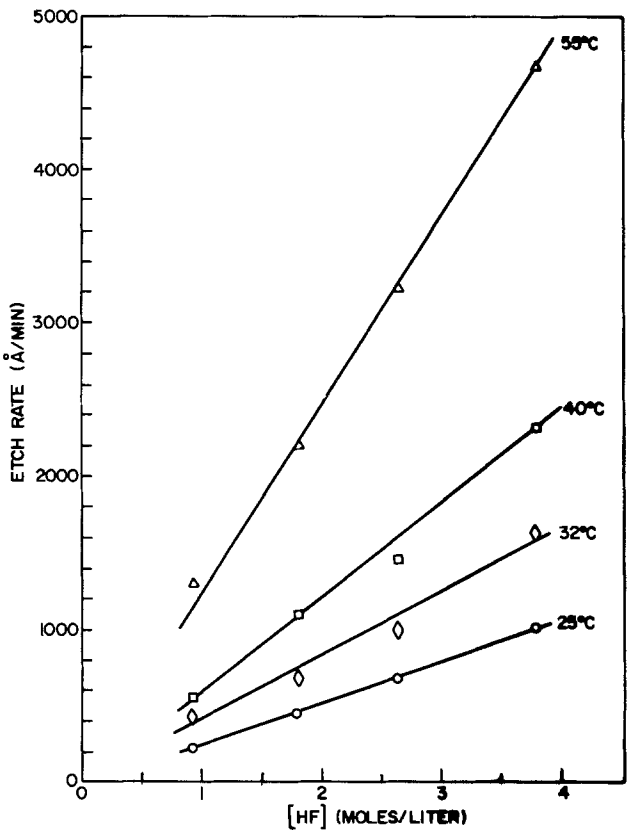


Fig. 7. Etch rate of thermal oxide as a function of HF concentration for several temperatures.

Table I.

NH_4F/HF	[HF] (moles/liter)
6.7/1*	3.8
10/1	2.6
15/1	1.8
30/1	0.9

* Commercially available buffered hydrofluoric acid (BHF) used throughout the industry is a mixture with a ratio of NH_4F:HF of 6.7:1.

phase, has a partial molar concentration of unity until such time that it is fully consumed. This dependence is, of course, a pseudolinear one that is valid within the composition range of etchants studied. It is known that etchant solutions of this type contain a large excess of F^- and hence HF_2^- which influence the reaction rate (11). From a processing consideration, however, the dependence on the HF concentration of the solutions as prepared, is followed and is useful as such.

The effect of increased temperature enhancing the etch rate is clearly evident from the steeper slopes at the higher temperatures. The dependence may be better visualized if these same etch rate data are replotted on semilogarithmic coordinates as a function of reciprocal absolute temperature. These curves are shown in Fig. 8 for the several etching solutions used. As expected, straight lines are observed, each with a negative slope typical of a single reaction mechanism. Since the slopes are all equal, the energy of activation is constant and independent of HF concentration. Clearly, the reaction mechanism is activation controlled for all of the etchant solutions investigated. These results are not completely in agreement with those reported by Lawrence (1) who proposed a diffusion-controlled mechanism for etchant solution with ratios of 20:1 or greater to explain the gradual tapered profiles obtained.

It is seen in Fig. 8 that the effect of HF concentration is to shift the position of the curves and is included in the frequency factor, A, of the rate equation

$$\text{Etch rate} = A \exp(-\Delta E/RT)$$

Using this rate equation the activation energy was calculated and found to be 9.9 kcal/mole.

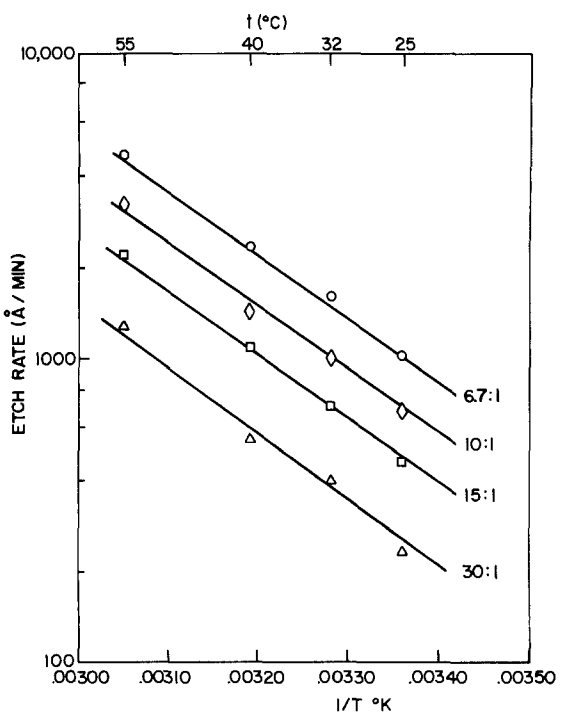


Fig. 8. Etch rate of thermal oxide as a function of temperature in several NH_4F/HF mixtures.

Both Judge (11) and Lawrence (1) have reported apparent activation energies that range from 6.7 to 11.0 and 9.2 to 11.2 kcal/mole, respectively, depending on the etchant solution composition. In both cases these authors found that the value of ΔE_{app} increases as the ratio of NH_4F to HF is increased. From these results Judge suggests several parallel reaction paths while Lawrence attributes a change in reaction type from activation controlled for low ΔE to diffusion controlled for high ΔE. Although it would appear that the relationships of ΔE with etchant composition from these two sets of data are in general agreement, an obvious discrepancy is noted for the absolute value of ΔE, if one uses a common reference point. Comparison of the value of ΔE_{app} for the commonly used buffered etch shows it to lie at the higher end of the range found by Judge (11.0 kcal/mole) whereas Lawrence's determination shows it to be at the lower end (9.2 kcal/mole). As pointed out previously, in our work, ΔE was found to lie about midway between these two values (9.9 kcal/mole) and independent of solution composition.

Finally, from our data, a simple rate equation can be formulated in which the preexponential term contains the concentration dependence. Plotting the intercepts of each of the curves of Fig. 8 as a function of HF concentration results in a straight line with slope equal to 4.50×10^9. This gives a rate equation of the following form

$$\gamma_d = 4.5 \times 10^9 \,[\text{HF}] \exp(-4980/T)$$

where γ_d = etch rate in angstroms per minute, [HF] = concentration of HF in moles per liter, and T = absolute temperature in degrees Kelvin. This expression is valid for the dissolution of thermal oxide within the range of parameter levels investigated, viz., etchant solutions between 6.7:1 and 30:1 and temperature range from 25° to 55°C. It may also hold for etchant mixtures and temperatures beyond the ranges indicated. Although the above relationship does not account for the equilibrium that exists in the etchant solutions, it is presented in the form shown for its usefulness as a processing guide.

Considering now the dependence of profile shape on temperature and etching solution, it is necessary to analyze the etching behavior in the lateral direction. Isotropic etching will, in fact, yield a quarter-circle edge profile (9). With continued etching (*i.e.*, overetching) and no photoresist lifting the quarter-circle edge profile both advances and its radius increases yielding a taper slope which becomes progressively steeper, as noted previously in Fig. 4c.

If, however, the penetration rate of etching solution at the photoresist-oxide interface, γ_l, exceeds the bulk etch rate, γ_d, of the oxide then a gradually sloping taper will be obtained that is dependent on the relative ratio of these two rates. It is this mechanism which prevails and manifests itself in giving beveled windows. The angle θ, that the taper forms with the original film surface is given by (10)

$$\sin\theta = \frac{\gamma_d}{\gamma_l}$$

For a penetration rate that is less than the bulk etch rate, ($\gamma_l < \gamma_d$) the latter, of course, is controlling and a quarter-circle with a 90° profile at the top is obtained.

A correlation of the etch or penetration rate in the lateral direction, γ_l ,as a function of temperature and HF concentration cannot be as precisely defined as the bulk etch rate, γ_d, because it is also dependent on the chemistry of the photoresist/oxide interface. Unfortunately, this interface is subject to some degree of variation due to the particular processing schedule used. Further, the undercutting is affected by the duration of etching which again is inextricably related to

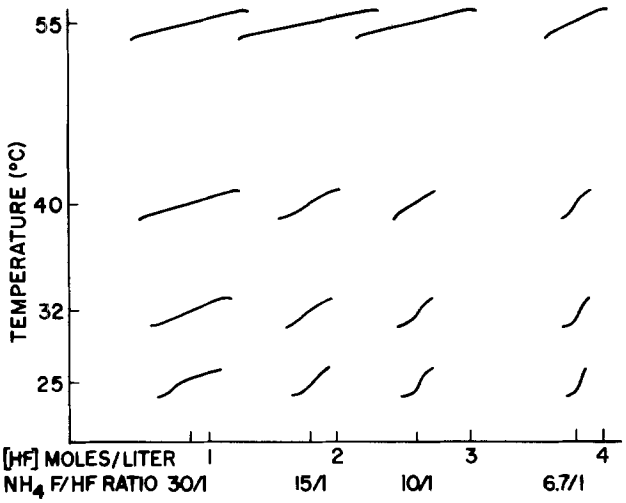


Fig. 9. Pictorial representation of normalized taper edge profiles for several temperatures and etchant compositions. Etchant composition is noted along the abscissa in both NH_4F/HF ratio and HF molarity.

temperature, etchant composition, and oxide thickness. Despite these several influencing factors, the penetration rate does, with minor exceptions, follow remarkably well the expected trend of increasing with higher temperature and higher HF molarity. A pictorial representation of the penetration rate as it relates to the profile shape is depicted in Fig. 9. Typical edge profiles for each of the temperatures and etchant compositions studied, have been taken from SEM photographs and normalized to facilitate comparison. It is important to realize that etch time has been omitted from Fig. 9 and it is merely an artifact of this representation which makes the higher penetration rates appear to have the least lateral penetration. The distinct regions to the slope along each oxide profile are clearly apparent, particularly in the lower and right portions of Fig. 9 where etching conditions are at or near room temperature and standard buffered HF concentration. The experimentally determined values of γ_I which correspond to the profiles are given in Table II. These numbers, however, are not sufficient to reveal the shape of the taper but can serve as a guide to the total penetration that occurs during etching.

For an ~45° side wall, (sin 45° = 0.707) γ_I should be equal to 1.41 γ_d. If γ_d is chosen at approximately 1000 Å/min, a good practical value for the bulk etch rate, then γ_I should be about 1400 Å/min. From either Fig. 7 or 8 and Fig. 9 it is seen that these conditions are satisfied, with some flexibility, using a 10:1 solution at 32°C.

Summary and Conclusions

The data presented in the previous section demonstrate that a wide range of options exists in applying the etchant NH_4F:HF to thermally grown SiO_2. Although we have optimized our procedures to achieve an ~45° taper with an etch rate of 1000 Å/min in a 10:1 NH_4F:HF etching bath, it is possible to obtain much shallower tapers by suitable adjustments of the temperature and NH_4F:HF ratio, as demonstrated in Fig. 9.

The advantages of the procedure are obvious when compared to the various oxide doping (7, 8), and ion implantation (6) techniques previously described, primarily because no adjustments or treatments of the SiO_2 layer need be made. In fact, introduction of the process into our device fabrication line required only the addition of a constant temperature bath. Reproducible results on large batches of wafers were obtained immediately.

Table II. Typical lateral penetration rates for thermal SiO_2 γ_I (Å/minute)

NH_4F/HF ratio	HF molarity	Temperature, °C 25	32	40	55
6.7/1	3.8	700	1600	2500	11,000
10/1	2.6	800	1300	2200	14,000
15/1	1.8	600	1200	2200	11,000
30/1	0.9	500	1200	2000	6,000

Although the etch rate *vs.* temperature or dilution curves presented in Fig. 7 and 8 are believed to be generally applicable to all steam oxides, the final shape of the etched window or step may be expected to vary depending on the type of photoresist used, or the condition of the exposed oxide/photoresist interface prior to etching. The latter problem is most evident if a wetting agent is employed as shown in Fig. 5. However, other treatments such as the influence of heating the oxide prior to photoresist application or the photoresist prior to etching, as well as the hydrophilic or hydrophobic nature of the oxide surface did not appreciably influence the taper profiles.

The mechanism by which tapering occurs may best be referred to as a controlled separation of the photoresist/oxide interface. It is completely dependent on the combined effects of the photoresist, etchant composition, temperature, and duration of etching in a reasonably uniform and controllable manner. The dissolution reaction per se we have found to be entirely activation controlled and in no case diffusion limited as suggested by Lawrence (1).

Acknowledgments

The authors gratefully acknowledge the assistance of C. J. Mogab, without which this project could not have been executed. His contributions both in thought and tangible help were vital to the successful completion of the project. The authors are also indebted to R. S. Wagner for his keen interest in this work and to H. J. Levinstein for many stimulating discussions and guidance throughout this study.

Manuscript submitted Oct. 4, 1976; revised manuscript received Feb. 4, 1977. This was Paper 182 presented at the Toronto, Canada, Meeting of the Society, May 11-16, 1975.

Any discussion of this paper will appear in a Discussion Section to be published in the December 1977 JOURNAL. All discussions for the December 1977 Discussion Section should be submitted by Aug. 1, 1977.

Publication costs of this article were assisted by Bell Laboratories.

REFERENCES

1. J. Lawrence, Abstract 191, p. 466, The Electrochemical Society Extended Abstracts, Fall Meeting, Miami Beach, Florida, Oct. 8-13, 1972.
2. G. I. Parisi and S. E. Haszko, Unpublished work.
3. R. A. Haken, I. M. Baker, and J. D. E. Beynon, *Thin Solid Films*, **18**, S3 (1973).
4. J. C. Colwell and T. E. McGahan, Private communication.
5. G. Bell and J. Hoepfner, in "Etching," H. G. Hughes and M. J. Rand, Editors, p. 47, The Electrochemical Society Softbound Symposium Series, Princeton, N. J. (1976).
6. R. A. Moline, R. R. Buckley, S. E. Haszko, and A. U. Mac Rae, *IEEE Trans. Electron Devices*, **ed-10**, 840 (1973).
7. W. Kern, J. L. Vossen, and G. L. Schnable, Proceedings of the Reliability Physics Conference, p. 214 (1973).
8. L. H. Hall and D. L. Crosthwait, *Thin Solid Films*, **9**, 447 (1972).
9. R. G. Brandes and R. H. Dudley, *This Journal*, **120**, 140 (1973).
10. T. Yanagawa and I. Takekoshi, *IEEE Trans. Electron Devices*, **ed-7**, 964 (1970).
11. J. S. Judge, *This Journal*, **118**, 1772 (1971).

Anodic Oxide on GaAs: Quantitative Chemical Depth Profiles Obtained Using Auger Spectroscopy and Neutron Activation Analysis

C. C. Chang, B. Schwartz,* and S. P. Murarka*

Bell Laboratories, Murray Hill, New Jersey 07974

ABSTRACT

The growth of oxides on GaAs, with the required properties for semiconductor applications, has obvious uses in passivation, masking, as a dielectric, etc. One promising method is anodization, and in order to assist in refining this technique, the chemistry and structure of 2500Å anodic oxides, before and after 250° and 650°C treatments in 1 atm nitrogen, have been investigated using neutron activation analysis and Auger spectroscopy combined with ion milling. The Auger data were normalized and corrected for Auger sensitivity and differential sputtering to provide profiles estimated to be quantitative within ±10%. All the oxide films investigated had compositions close to $x Ga_2O_3 + y As_2O_3$ except at the oxide-GaAs interface. Hydrogen was not detectable and was ignored. The as-anodized oxide displayed four distinct layers; these are in order, starting from the oxide surface: I, ~400Å, highly arsenic-deficient layer; II, ~1700Å, moderately arsenic-deficient layer; III, ~300Å, arsenic-rich transition layer; and IV, ~400Å, arsenic-rich interface to GaAs. The over-all As/Ga ratio in the oxide was 0.68. After 250°C anneal, only small changes in the depth profiles were observed. After 650°C anneal, most of the arsenic and some gallium were lost, and the arsenic excess near the oxide-GaAs interface was greatly reduced.

The ability to grow native oxides on GaAs has obvious implications for GaAs device technology. However, methods for growing oxides on GaAs with the necessary properties for semiconductor applications have not been perfected. One promising technique is anodization (1-3), and in order to understand the chemical and physical processes involved in the oxide growth, it is desirable to know the oxide chemistry and depth profile after anodization and after various heat-treatments. Therefore, chemical depth profiles from anodized and subsequently heat-treated GaAs have been obtained using Auger spectroscopy combined with argon ion milling. Neutron activation analysis was utilized for a quantitative calibration of the Auger data.

Experimental

Oxide films were grown on GaAs by anodization (3) in dilute aqueous solutions of H_3PO_4 at a pH of 2.5-3.5. Five samples were organic solvent degreased, bromine-methanol polished, and then anodized at 150V to grow 2500-3000Å oxides; the oxide thickness was determined by the voltage and dopant dependence of the oxide growth (3). The samples are listed in Table I, together with descriptions of the heat-treatments.

Chemical analyses were performed by measuring the surface composition using Auger electron spectroscopy (4, 5); the spectra were obtained with a cylindrical analyzer (Varian, 3 kV electrons). Depth profiles were obtained by measuring the surface composition while simultaneously milling the surface with an Ar ion gun (PHI, 1 kV argon ions).

The chemical compositions were calculated from the Auger data using the equation for the normalized Auger signal (5)

$$A_i = \alpha_i I_i / \Sigma_j \alpha_j I_j \qquad [1]$$

where $100A_i$ is the concentration of element i in atom percent (a/o), I is the Auger current determined from the peak-to-peak heights of $dEN(E)/dE$-type spectra and j runs over all elements detected. Hydrogen was not detectable and its possible presence was ignored. The small amounts of argon (several percent) implanted during ion milling were also ignored.

* Electrochemical Society Active Member.

Table I. List of samples

Sample no.	Heat-treatment	Orientation	Doping	Oxide thickness (Å)
1	None	$(\bar{1}\bar{1}\bar{1})$	5×10^{16}/cm³, Zn	2500
2	None	$(\bar{1}\bar{1}\bar{1})$	5×10^{16}/cm³, Zn	2500
3	250°C, 2 hr, 1 atm N_2	$(\bar{1}\bar{1}\bar{1})$	5×10^{16}/cm³, Zn	2500
4	250°C, 2 hr, 1 atm N_2	(100)	9×10^{17}/cm³, Si	3000
5	250°C, 2 hr, 1 atm N_2 plus 650°C, 15 min, 1 atm N_2	$(\bar{1}\bar{1}\bar{1})$	5×10^{16}/cm³, Zn	2500

The inverse Auger sensitivity factors α_i for gallium and arsenic were determined from ion-mill-cleaned GaAs, as described elsewhere (5, 6). The α_0 for oxygen was determined from a single crystal of Ga_2O_3. This crystal was prepared by melting commercial Ga_2O_3 powder in an iridium crucible by rf heating and then cooling to room temperature; x-ray diffraction analysis showed this crystal (after pulverization) to be β-Ga_2O_3; no other material was detected. The Auger transition energies and the α_i are listed in Table II.

Table II. Auger transition energies, inverse sensitivity factors α_i, and preferential sputtering coefficients, s

Element	O	Ga	As
Energy (eV)	507	1067	1228
α_i (in GaAs)	—	3.7	5.7
α_i (in oxide)	1.4	2.2	3.3
s	1.0	1.0	1.6

The α's and s's apply under the following conditions: a-c modulation 2 5 V_{p-p}, incident electrons at 3 kV, 50 μA, analyzer resolution 0.8%.

The "preferential sputtering coefficient" s includes the effects of both the electron and ion beams. When the electron beam is turned off, the value of s changes, so that the contribution from the electron beam alone is not negligible and in fact may be larger than that from the ion beam alone (6).

Preferential sputtering effects[1] were next considered. The chemical composition of a cleaved surface of Ga_2O_3 was measured before and after ion milling and was found to be the same within ±3%, so that there was no detectable preferential sputtering; *i.e.*, the differential sputtering coefficient of oxygen, referenced to gallium, was $s(O/Ga) = 1$ for Ga_2O_3.

The differential sputtering coefficient[1] for arsenic in Ga-As-oxide, referenced to gallium $s(As/Ga)$, was determined by first measuring the As/Ga concentration ratio in the anodic oxide using neutron activation analysis. Sample no. 1, which was an as-anodized specimen, was irradiated for 1 hr in a thermal neutron flux of $\sim 3 \times 10^{13}/cm^2$ sec. After 24 hr, the oxide was dissolved in a known volume of 1:1 $HCl:H_2O$. A precise volume of this solution was then transferred to a 2 in. diameter filter paper since the lithium drifted germanium detector was calibrated for this geometry. Counting was performed as a function of time to determine the half-life of the detected radiation (isotopes Ga-72 and As-76), and the concentrations of gallium and arsenic were then calculated using known efficiencies. This procedure was repeated several times and the results are presented in Fig. 1. The amount of gallium was constant with time but the amount of arsenic decreased, possibly due to loss of arsenic as chlorides, since some arsenic chlorides are relatively volatile. Contributions from other radioisotopes causing this decrease in the amount of arsenic are highly unlikely because we have carefully monitored all five gamma-ray emissions designated to radioactive As-76 and results were identical. We used the As/Ga concentration ratio at the time of dissolution as the value in the oxide, which assumes no precipitation in the HCl solution, no concentration change in the 24 hr after irradiation, and no preferential absorption at container walls. The As/Ga concentration ratio was 0.68, indicating a large arsenic deficiency immediately after anodization. This sample had an area of 0.3 cm^2, and an estimate of the total number of Ga + As atoms from the oxide thickness, assuming a composition of $xGa_2O_3 + yAs_2O_3$, gave $1.4_4 \times 10^{17}$ atoms which compares well with the neutron activation analysis result of $1.5_3 \times 10^{17}$ atoms in Fig. 1.

Chemical depth profiles of sample no. 2 are displayed in Fig. 2-4 which illustrate the data reduction process. Figure 2 shows the Auger peak heights, Fig. 3 displays the normalized Auger signal, and Fig. 4 exhibits the final depth profile corrected for differential sputtering. The ternary differential sputtering problem in Ga-As-oxide was reduced to a binary problem by assuming that both the gallium and arsenic oxides sputtered off stoichiometrically, as was the case for Ga_2O_3 described above. The corrected gallium and arsenic concentrations, x and y, respectively (Fig. 4), were calculated from the initial uncorrected values x', y' (Fig. 3) using the renormalized equation

$$x = \frac{x'(x' + y')}{x' + sy'} \quad \text{for gallium} \qquad [2]$$

and

$$y = \frac{sy'(x' + y')}{x' + sy'} \quad \text{for arsenic} \qquad [3]$$

so that $y/x = sy'/x'$. s was then evaluated by dividing the As/Ga concentration ratio from neutron activation analysis $y/x = 0.68$, by the ratio of areas under the arsenic and gallium curves of Fig. 3, which was $y'/x' = 0.44$, giving $s(As/Ga) = 1.6$ in the oxide. This correction was then applied, assuming it to be independent of composition. This completes the evaluation of the preferential sputtering coefficients which are listed in Table II.

[1] Includes electron beam desorption during Auger analysis; the separate contributions from the electron and ion beams were not differentiated in this work.

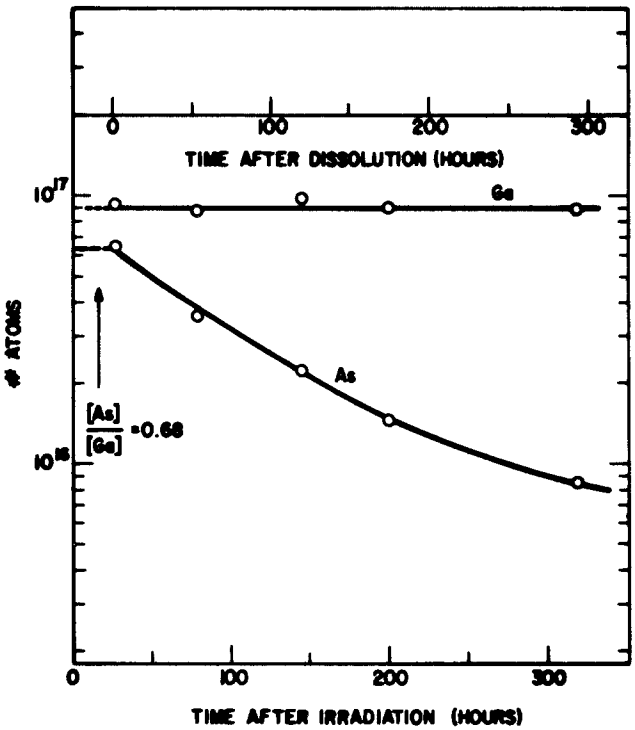


Fig. 1. Neutron activation analysis of the gallium and arsenic content of anodic oxide on GaAs. Note the gradual loss of arsenic with time after dissolution, sample no. 1.

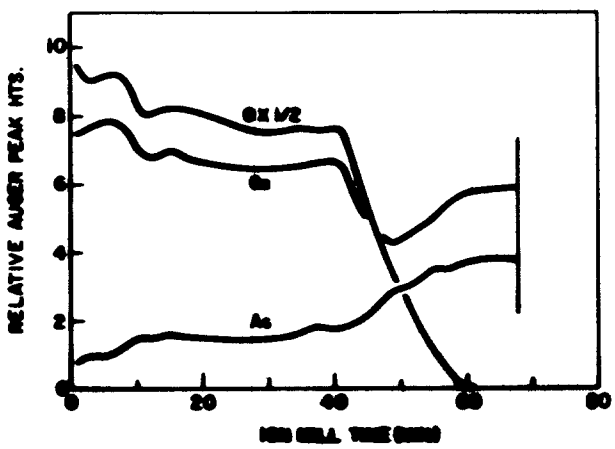


Fig. 2. Plot of Auger peak heights *vs.* ion-milling time. Reveals only the chemical constituents [*i.e.*, gallium (Ga), arsenic (As), oxygen (O)] and qualitative trends, sample no. 2, as anodized.

When measuring the As/Ga ratio in the oxide from Fig. 3, it is necessary to subtract the contribution from any GaAs that might be present, at the oxide-GaAs interface. This subtraction was accomplished by measuring the plasmon loss peak height, using the GaAs plasmon loss peak (7) about 16 eV below the main gallium Auger peak at 1067 eV. This plasmon loss peak is negligibly small in spectra from the oxide, as demonstrated in Fig. 5 where the Auger peak shapes near the gallium 1067 eV transition are displayed for spectra from the oxide (top), the oxide-GaAs interface (center), and GaAs (bottom). The plasmon loss peak is identified in Fig. 5 and the height of this peak, normalized to 50 a/o so as to be directly comparable with gallium and arsenic concentrations, is also indicated in Fig. 3 and 4 (dashed lines).

Equations [2] and [3] are valid at any given depth in the depth profile, but do not provide the correction

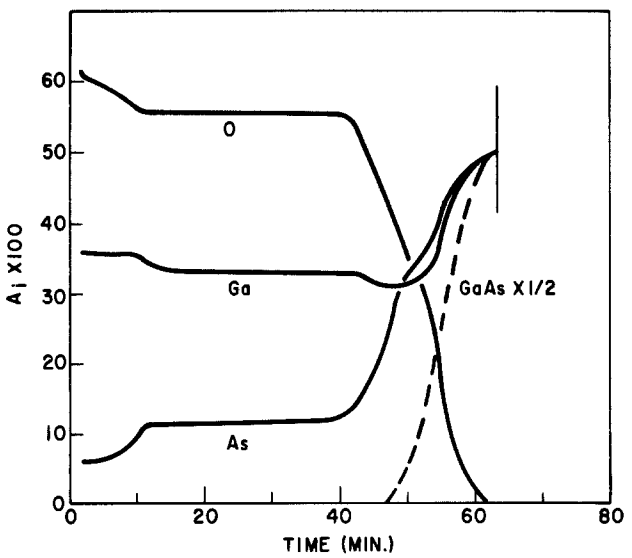


Fig. 3. Data of Fig. 2 after correction for Auger sensitivities and normalization. Amount of GaAs estimated from the plasmon loss peak height of the gallium Auger peak is also shown (dashed).

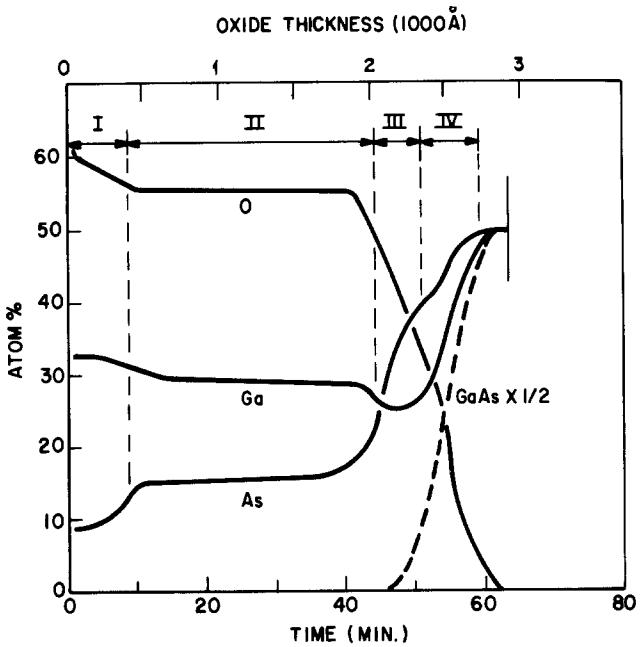


Fig. 4. Data of Fig. 3 after correction for differential sputtering. The oxide has four distinct regions. An approximate linear thickness scale is shown at the top, scaled to 2500Å at the point of 50% GaAs.

for the change in sputtering rate with change in composition. If we assume that the sputtering rate is linearly related to x, y, and s, *i.e.*, that the differential material sputtered, dm, is given by

$$dm \propto (x\rho_x + sy\rho_y)\,dt \qquad [4]$$

where ρ is the density and t is time, then our value of s(As/Ga) = 1.6 for the as-anodized oxide is too large (by ~7%). Clearly, Eq. [2] and [3] apply only to a differential depth, and for a more accurate analysis, the changes in sputtering rate with composition must be properly taken into account. A simple alternative for a more accurate determination of s is the use of an oxide whose composition is constant throughout its thickness; then the sputtering rate changes become negligible.

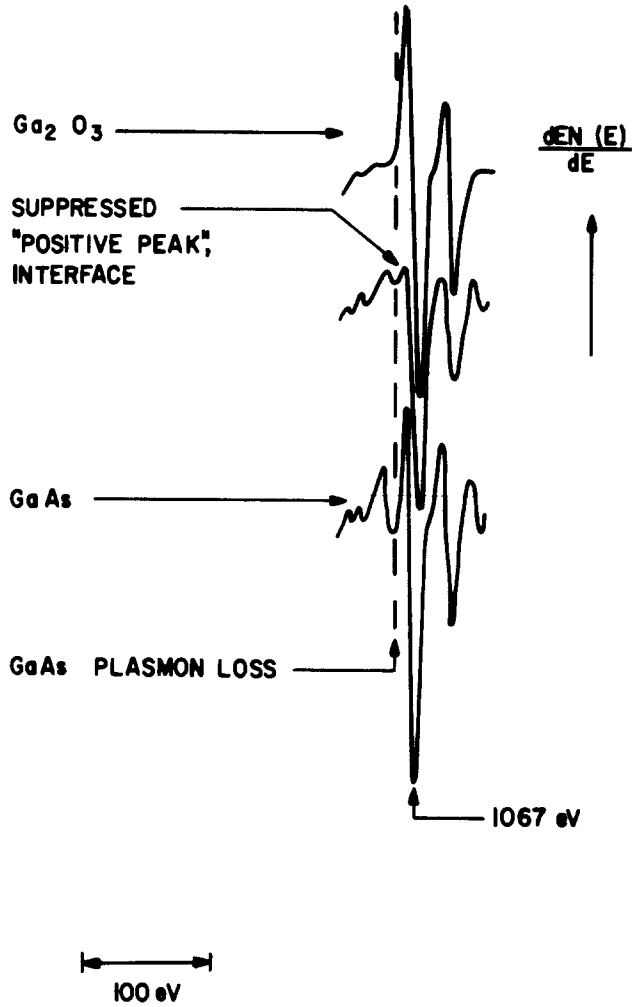


Fig. 5. The gallium Auger spectra near 1067 eV from: top, Ga_2O_3; center, region III of Fig. 4; and bottom, GaAs. The plasmon loss peak 16 eV below the main 1067 eV peak is indicated. The top two peaks have been displaced horizontally to coincide at 1067 eV.

Results

Some qualitative features of the chemical composition can be seen from a simple plot of the Auger peak heights (Fig. 2), but the quantitative information is not immediately obvious and there are several unexplained humps and dips. Many of the latter features disappear in the normalized data of Fig. 3, which is more quantitative, but without the differential sputtering correction. The curves of Fig. 4 are quantitative depth profiles which reveal the details of the arsenic deficiency in the oxide and the arsenic excess at the oxide/GaAs interface.

The as-anodized oxide of Fig. 4 has four distinct regions. The first, I, is an arsenic-deficient layer near the surface, ~400Å thick, with only ~10 a/o arsenic, an average Ga/As ratio of 2.9, and O/(Ga + As) ratio of 1.4. The second layer, II, is ~1700Å thick and has a nearly constant composition with depth; it is arsenic deficient, with a Ga/As ratio of 1.8 and an O/(Ga + As) ratio of 1.2[2]. The next two layers, III and IV, comprise the transition region from the oxide to GaAs. Region III is ~300Å thick, has a rapidly decreasing oxygen and a rapidly increasing arsenic gradient. and is arsenic rich. Region IV is the interface to GaAs; it is arsenic rich and is ~400Å thick.

The transition layers III and IV extend over a large thickness range in the depth profile; since the ideal depth resolution of the ion-mill Auger technique at ~2500Å is < 100Å for GaAs,[2] the measured total range

[2] The oxide/GaAs transition region for a ~2500Å plasma-grown (8) oxide on GaAs was <100Å when measured using the present technique.

of the transition layer of ~700Å reflects some physical property of the oxide and is not an artifact due to insufficient depth resolution. There are four possible interpretations of such a graded depth profile: (*i*) there is indeed a graded transition layer, (*ii*) the oxide thickness varies by ±300Å within the area irradiated by the incident electron beam used for Auger analysis, (*iii*) ion milling proceeds unevenly in these oxides, and (*iv*) the particular chemistry of this region causes it to ion mill unusually slowly. We speculate that (*i*) and (*ii*) are the most important factors with negligible contributions from (*iii*) and (*iv*) for the present samples.

The gallium Auger peak in region III showed a suppressed "positive peak," a feature not found anywhere else along the depth profile. This peculiar peak shape is shown in Fig. 5 and results from a superposition of the chemically shifted peak from gallium in the oxide and the unshifted peak from GaAs. To avoid large errors from this effect, the gallium concentrations were calculated by normalizing to the negative portion of the peak which is least sensitive to this perturbation. Even with this procedure, there is still an underestimate of the gallium peak height which may be non-negligible (>5%) in a small depth range approximately ±100Å near the boundary between regions III and IV in Fig. 4 (Fig. 6 and 7, also).

There is an excess of arsenic in regions III and IV; this is one of the most important definitive results of this work, and will be further discussed below. The plasmon loss peak associated with arsenic attained its maximum value (relative to the arsenic peak height) in region III so that in this layer a large fraction of the arsenic phases are separated from, and are much less oxidized than, the gallium phases. Because the plasmon loss peaks between an atom in a semiconductor and the same atom in a metal are generally not distinguishable at the energy resolution employed in this work, the present results are consistent with the interpretation, suggested by photoemission data (6), that the excess arsenic is in elemental form. This anomalous behavior of the arsenic peak is the reason why the gallium plasmon loss peak was selected for estimating the amount of GaAs. In regions I and II, the As peaks showed no measurable plasmon loss.

Quantitative depth profiles similar to Fig. 4 are plotted for sample no. 3, after 250°C treatment, in Fig. 6. There are small changes in composition, but the total arsenic content, the O/(Ga + As) ratio, and the regions I to IV, are only slightly changed. Regions III and IV have expanded to cover almost 1000Å. Results from sample no. 4 [same treatment as no. 3, but (100) instead of (111) orientation and higher conductivity] were similar to Fig. 6, except that the oxide was thicker, about 3000Å; this increased oxide thickness is due to the higher doping level (3).

Figure 7 displays quantitative depth profiles from sample no. 5 and shows that the oxide is ~800Å thinner after 650°C treatment, due to loss of much of the arsenic, some gallium, and the associated oxygen. Note that the thickness scale of the figure has been corrected for the decrease in arsenic, which caused the ion milling rate to decrease; the new milling rate was calculated using Eq. [4]. Now the oxide displays only three distinct regions, due to loss of the central arsenic-containing layer (region II). Whether an arsenic excess still remains at the oxide/GaAs interface is now not clear. In Fig. 4, 6, and 7, the oxygen concentrations are all close to 60 a/o, so that the oxide composition is approximately equal to $xGa_2O_3 + yAs_2O_3$.

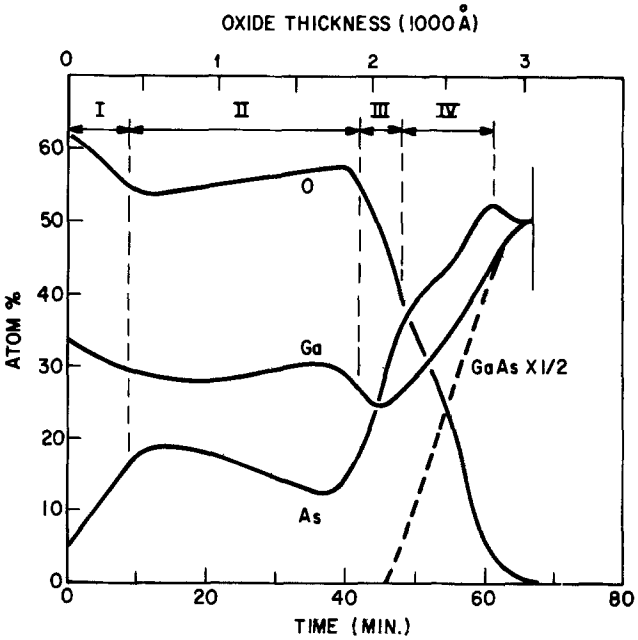


Fig. 6. Depth profile of 2500Å anodic oxide after 250°C anneal, sample no. 3.

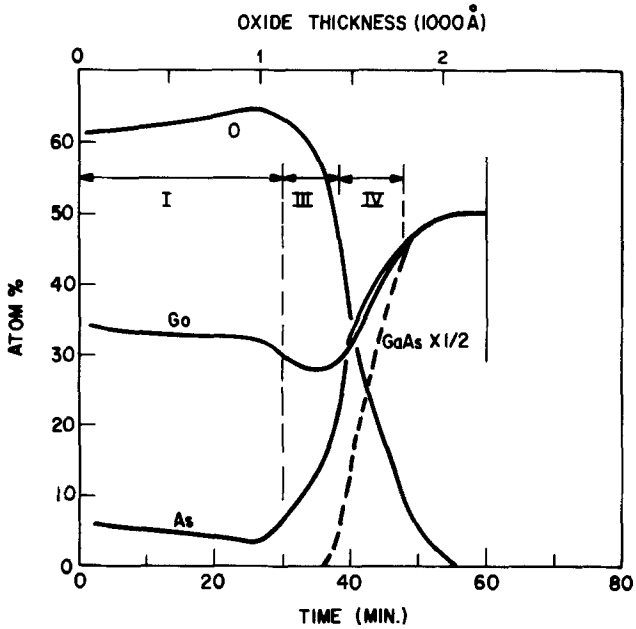


Fig. 7. Depth profile of anodic oxide after 650°C anneal; note the change in "thickness" scale due to change in composition, sample no. 5.

Discussion

The above results reveal that arsenic is preferentially lost during anodization. The arsenic deficiency near the oxide surface is probably due to preferential extraction of arsenic by the oxygen-containing species in the anodizing solution and subsequent dissolution of the molecular complex.

To explain the arsenic excess in regions III and IV, we propose that at the oxide/GaAs interface, Ga_2O_3 forms preferentially to As_2O_3 (*i.e.*, $\Delta F°$ of −238 kcal/mole for Ga_2O_3 compared to −136 kcal/mole for As_2O_3), and the arsenic is stranded as an elemental layer at the interface. The process of this and the above paragraph accounts for (*i*) the arsenic deficiency in regions I and II, (*ii*) the arsenic excess in regions III and IV, and (*iii*) the anomalously large plasmon loss peak from arsenic in region III.

Our observation of excess As at the oxide/GaAs interface is in agreement with previous ellipsometric

findings (10). The value of 0.68 for the over-all As/Ga ratio in the oxide is in fair agreement with the value of 0.77 measured using chemical analysis of an anodic oxide on GaAs formed using a different solution (11). Our depth profiles are consistent with results from ion-induced x-ray analysis (12), but the present results are much more accurate due to the higher depth resolution. Other workers (13, 14) have published Auger depth profiles of oxides on GaAs, but those results are analogous to our Fig. 2, so that the quantitative data reduction was incomplete without the three major corrections for Auger sensitivity, normalization, and differential sputtering that we incorporated into our analyses.

The most significant result of this work is the new information we obtained concerning the complex oxide-GaAs transition layer which includes regions III and IV. These transition regions are surprisingly thick and must contribute significantly to the properties of the oxide as a whole. These regions are important in determining the electronic properties of the oxide/GaAs interface, in diffusion problems, in device processing (*e.g.*, chemical etching), and for understanding the oxide growth process itself. Therefore, further experiments should be performed to (*i*) study in greater detail the oxide/GaAs interface chemistry, and (*ii*) study the interface structure by examining thin cross sections with transmission electron microscopy (15). In particular, the precise reason for the apparently diffuse oxide/GaAs interface must be elucidated. Finally, oxides on the more complex compound semiconductors, especially GaAlAs, should also be studied.

Conclusions

1. All the anodic oxides investigated in this work had compositions nearly equivalent to $xGa_2O_3 + yAs_2O_3$. The over-all As/Ga concentration ratio was 0.68 before and after 250°C treatment in 1 atm nitrogen.

2. The as-anodized oxide had four distinct layers: I, the first ~400Å at the surface, which is arsenic deficient with an average Ga/As concentration ratio of 2.9. The arsenic concentration in this layer decreased rapidly towards the oxide surface. II, a center region, ~1700Å thick with an average Ga/As ratio of 1.8 and O/(Ga + As) ratio of 1.22. III, the first transition region to GaAs where the oxygen concentration begins to decrease. This layer is arsenic rich and is ~300Å thick. IV, the interface layer to GaAs, ~400Å, which contains excess arsenic.

3. After 250°C anneal in 1 atm nitrogen, only small changes in composition were observed. After 650°C anneal, most of the arsenic, and some oxygen and gallium were lost, and the arsenic excess at the oxide/GaAs interface was greatly reduced.

Acknowledgments

The authors are grateful to M. H. Read for x-ray analysis of the Ga_2O_3 and to M. Kowalchik, who provided the Ga_2O_3 crystal.

Manuscript submitted Jan. 12, 1977; revised manuscript received Feb. 25, 1977. This was Paper 350 presented at the Las Vegas, Nevada, Meeting of the Society, Oct. 17-22, 1976.

Any discussion of this paper will appear in a Discussion Section to be published in the December 1977 JOURNAL. All discussions for the December 1977 Discussion Section should be submitted by Aug. 1, 1977.

Publication costs of this article were assisted by Bell Laboratories.

REFERENCES

1. C. J. Dell'Oca, G. Yau, and L. Young, *This Journal*, **118**, 89 (1971).
2. W. W. Harvey and J. Kruger, *Electrochim. Acta*, **16**, 2017 (1971).
3. B. Schwartz, F. Ermanis, and M. Brastad, *This Journal*, **123**, 1089 (1976).
4. C. C. Chang, in "Characterization of Solid Surfaces," P. F. Kane and G. B. Larrabee, Editors, chap. 20, Plenum Press, New York (1974).
5. C. C. Chang, *Surf. Sci.*, **48**, 9 (1975).
6. C. C. Chang, P. H. Citrin, and B. Schwartz, presented at the 4th Annual Conference on the Physics of Compound Semiconductor Interfaces, Princeton, N. J., February 1977.
7. R. Ludeke and L. Esaki, *Surf. Sci.*, **47**, 132 (1975).
8. R. P. H. Chang and A. K. Sinha, *Appl. Phys. Lett.*, **29**, 56 (1976).
9. B. Schwartz, *Crit. Rev. Solid State Sci.*, **5**, 609 (1975).
10. K. H. Zaininger and A. G. Revesz, *J. Phys. (Paris)*, **25**, 208 (1964).
11. A. G. Revesz and K. H. Zaininger, *J. Am. Ceram. Soc.*, **46**, 606 (1963).
12. L. C. Feldman, J. M. Poate, F. Ermanis, and B. Schwartz, *Thin Solid Films*, **19**, 81 (1973).
13. C. S. Guenther, P. V. S. Rao, S. Thomas, and W. Paulson, Abstract 159, p. 420, The Electrochemical Society Extended Abstracts, Fall Meeting, Dallas, Texas, Oct. 5-10, 1975.
14. C. W. Wilmsen, *J. Vac. Sci. Technol.*, **13**, 64 (1976).
15. T. T. Sheng and C. C. Chang, *IEEE Trans. Electron Devices*, **ed-23**, 531 (1976).

The Anodic Behavior of Group Six Metals in Methanolic Solution

G. Stephen Kelsey

Department of Chemistry, University of Missouri-Columbia, Columbia, Missouri 65201

ABSTRACT

The anodic behavior of chromium, molybdenum, and tungsten in aqueous solution has been the subject of considerable research. With growing interest in nonaqueous electrochemistry, a number of protic and aprotic solvents suggest themselves as suitable media for generation of soluble species from metal electrodes. The behavior of the metals was characterized by determination of current-potential data and coulometric n value determination, where n is the number of electrons lost per metal atom during the electrochemical oxidation. Data for four electrolytes were gathered: the lithium salts of chloride, methoxide, nitrate, and perchlorate. Concerted formation of Cr(III) occurs only in chloride solution. Cr(VI) forms in perchlorate and nitrate solutions, and is reduced to Cr(III) by the solvent if the methanol is allowed to acidify during the course of the electrolysis. Chromium appears to react only with traces of water in methanolic methoxide solutions, with the formation of CrO_4^{2-} ion. Molybdenum and tungsten behave similarly, forming M(VI) in chloride and methoxide solutions with high efficiency. Their behavior in perchlorate and nitrate proceeds with n values between 4 and 6, with nitrate being more conducive to a constant value over a range of current densities of 5-330 mA/cm^2. The effect of trace water contamination in the solutions was also studied, with shifts in the i-E curves observed for all three metals.

The anodic behavior of transition metals in aqueous solution has been the subject of considerable study (1-28). Both mechanistic (2-15) and analytical (16-24) implications of the electrochemical generation of dissolved species exist for the early transition metals and many of the later ones (1, 3, 11-14, 24, 26) as well. The growing importance of nonaqueous electrochemistry, both for analysis and synthesis, led us to extend the study of Group VI metals into nonaqueous solvents. By way of bridging the gap, the protic solvent methanol was chosen for study of the anodic dissolution of chromium, molybdenum, and tungsten. Of particular importance is the question of apparent oxidation state of the products often referred to as "initial valency," n (25-28).

Experimental

Apparatus.—All electrochemical measurements were obtained with PAR 173 potentiostat/galvanostat (Princeton Applied Research Corporation, Princeton, New Jersey). Accumulated coulombs were recorded with a PAR 179 digital coulometer, used in conjunction with the 173. Current-potential curves were obtained with a PAR 175 universal programmer in the single sweep mode, which applied a 1 mV/sec voltage ramp to the potentiostat. Log current-potential curves were obtained with the PAR 376 logarithmic current converter. The former data were obtained as $i = f(E)$ potentiodynamic polarization; the latter were $\log i = f(E)$. Both data fields were recorded with an Omnigraphic Model 2000, X-Y plotter (Houston Instruments, Incorporated). Electrochemical cells used were Metrohm EA 880 universal titration vessels of appropriate volume, jacketed for temperature control.

Ultraviolet-visible spectra were recorded on a Cary-14 spectrophotometer or a Perkin-Elmer 124 double-beam recording spectrophotometer.

Reagents.—Chromium metal was polycrystalline in nature, irregular in morphology, and of CP purity. Molybdenum was obtained as 0.25 in. diameter rod, 99.95%, from A. D. Mackay, Incorporated, New York. Tungsten was also 0.25 in. diameter rod, 99.95% from the same supplier.

Key words: chromium, molybdenum, corrosion, tungsten, methanol.

Methanol was reagent grade, purified by fractional distillation from magnesium ribbon through a 1m adiabatic column packed with helices, and a second distillation from 3Å molecular sieves. Karl Fischer water determinations revealed a water concentration of from 50 to 150 μg/ml.

All other chemicals used were of analytical reagent quality and used without further purification, with the exception of lithium nitrate. The as-received $LiNO_3$ (G. Frederick Smith, Columbus, Ohio) gave rise to an active/passive peak in the log i-E plots for tungsten metal. Drying at 110°C under vacuum for 8 hr removed residual water and perhaps some volatile impurities. Polarizations conducted in solutions of the reagent thus treated, yielded no such peak.

Procedure.—So-called initial valency data were obtained by careful weighing of the metal electrode before and after the passage of a fixed number of coulombs, sufficient to cause a weight loss of *ca.* 0.10g. The value of the Faraday used in the calculation of n was 96,487 C/equiv. These experiments were performed under galvanostatic conditions.

The chromium electrode, because of its polycrystalline form could not be sanded conveniently; so electrode pretreatment was restricted to immersion in 6*M* HNO_3 for 1 min followed by copious rinsing with distilled deionized water and oven drying at 110°C for 5 min. Both the molybdenum and tungsten electrodes were rotated by an electric motor while sanded in turn with wet 320, 400, and 600 grit SiC paper. This was followed by rinsing and drying as for chromium.

Column chromatographic separation of Cr(III) species was achieved by taking a 10 ml aliquot of cell solution which had previously been quantitatively transferred to a 25 ml volumetric flask and loading it onto Dowex 50-WX2 resin, 200-400 mesh in the H^+ form. The 1 cm diameter × 20 cm long column was kept at 3°C. Bands were eluted with aqueous perchloric acid solutions ranging in concentration from 0.2 to 3M. Chromium assays were done using peroxide oxidation to Cr(VI) and subsequent spectrophotometric analysis as chromate (29).

Results and Discussion

Initial experiments focused on the effects of trace water. A thorough investigation of phenomena related

to water concentration, including analytical implications will be the subject of a separate communication. Trends in i-E behavior, including the limiting cases of anhydrous methanolic solution and totally aqueous solution are depicted for each metal in Fig. 1-3. The concentration of ammonium chloride chosen represents its solubility in methanol at room temperature. The water content for the dryest case was determined by volumetric Karl Fischer titration to be 50 ± 5 mM.

The seemingly anomalous behavior of chromium is complicated by the fact that different reactions occur in the two extremes. In dry methanolic chloride, Cr(III) is formed, whereas Cr(VI) is produced in aqueous solution. The behavior of molybdenum in chloride solution of essentially neutral pH is more predictable, in that a coulometric n value of 6 was observed in all three solutions (discussed later). The cathodic shift with increasing water content has been observed at platinum electrodes by others (30). For tungsten, the aqueous chloride solution is sufficiently acidic to render the electrode passive. An extrapolation of the straight-line portion of the i-E curves for molybdenum and tungsten to zero current, yields almost identical potentials (1.12 ± 0.05V). It is interesting to note that the thermodynamic oxidation potentials for the two metals in aqueous solution are also identical (31).

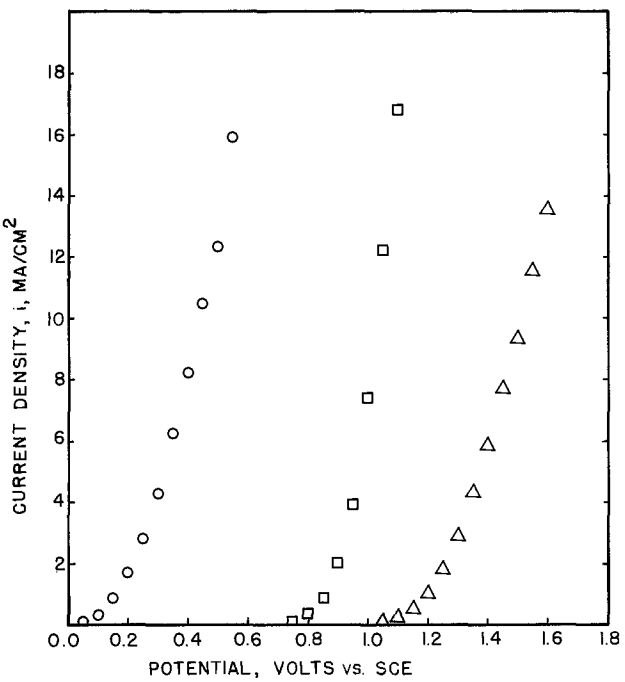


Fig. 1. Current-potential behavior of chromium in 0.43M NH_4Cl as a function of solvent composition. ○, 3 mmoles H_2O in CH_3OH; △, 4% (v/v) H_2O in CH_3OH; □, 100% aqueous.

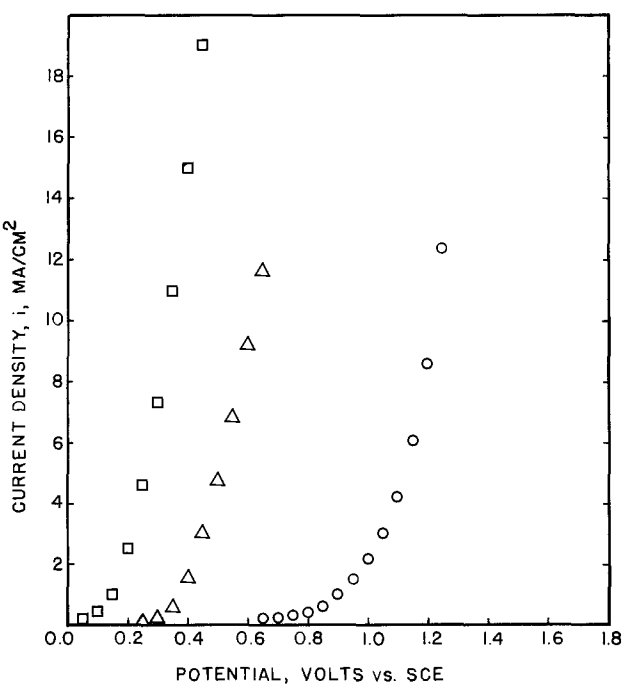


Fig. 2. Current-potential behavior of molybdenum in 0.43M NH_4Cl as a function of solvent composition. ○, 3 mmoles H_2O in CH_3OH; △, 2% (v/v) H_2O in CH_3OH; □, 100% aqueous.

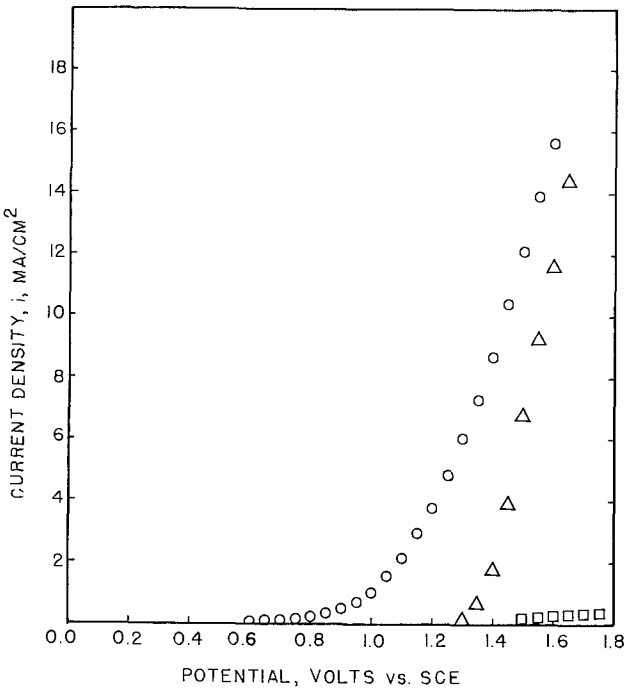


Fig. 3. Current-potential behavior of tungsten in 0.43M NH_4Cl as a function of solvent composition. ○, 3 mmoles H_2O in CH_3OH; △, 4% (v/v) H_2O in CH_3OH; □, 100% aqueous.

Because of the marked effect of water on the i-E behavior of the metals, solvent dehydration and handling were done carefully and special attempts were made to dry supporting electrolytes also. Typical water concentrations were 1-6 mM.

Chromium.—Log i-E data for the four electrolytes are given in Fig. 4-7. In general, chromium exhibits a more anodic potential at any given current density. This correlates well with potentials tabulated for aqueous solutions. The greatest difference (*ca.* +0.33V) occurs in the seemingly noncomplexing electrolytes, NO_3^- and ClO_4^-. In $LiOCH_3$ solution, which ought to

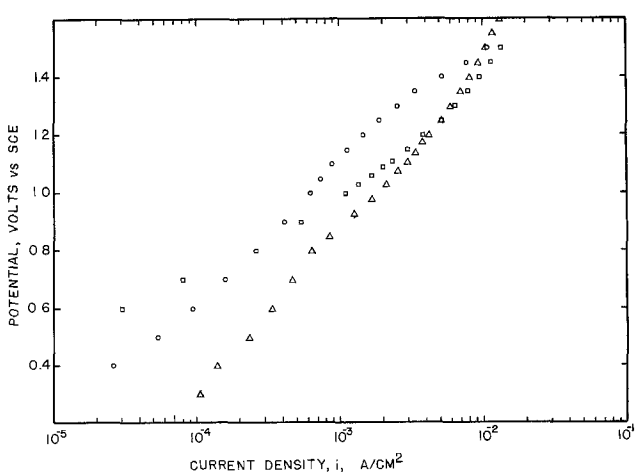


Fig. 4. Anodic polarization diagrams for 1.0M LiCl, CH_3OH. ○, Chromium; △, molybdenum, □ tungsten.

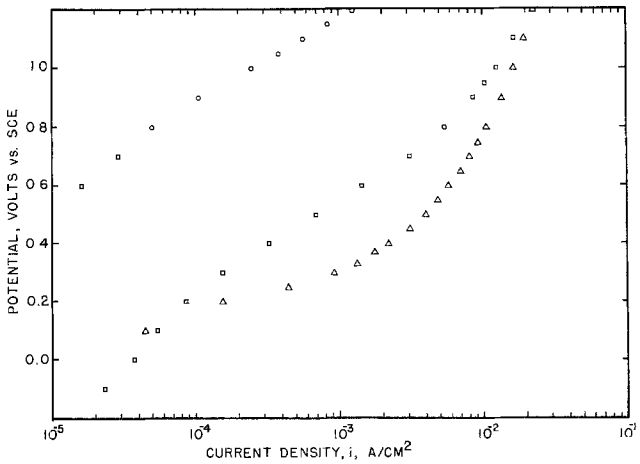


Fig. 5. Anodic polarization diagrams for 1.0M $LiNO_3$, CH_3OH. ○, Chromium; △, molybdenum; □, tungsten.

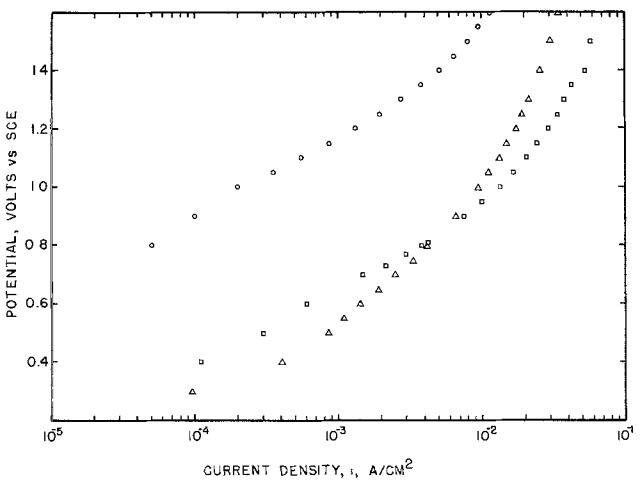


Fig. 6. Anodic polarization diagrams for 1.0M $LiClO_4$, CH_3OH. ○, Chromium; △, molybdenum; □, tungsten.

be the methanolic analog of aqueous 1M OH^- solution, chromium exhibits potentials only about 100 mV anodic of molybdenum and tungsten, whereas the standard potentials in aqueous base ($a_{OH} = 1$) reveal a 330 mV separation. Initial valency data in the OCH_3^- solutions will show that this anomaly can be explained on the basis of a Cr-H_2O or Cr-OH^- reaction in the basic methanol solution (see shift with [H_2O] in Fig. 1).

The initial valency data of Fig. 8 reveal 100% current efficiency for generation of Cr(III) in chloride solution, over a broad current density range, even in the concentration polarization region. The ultraviolet-

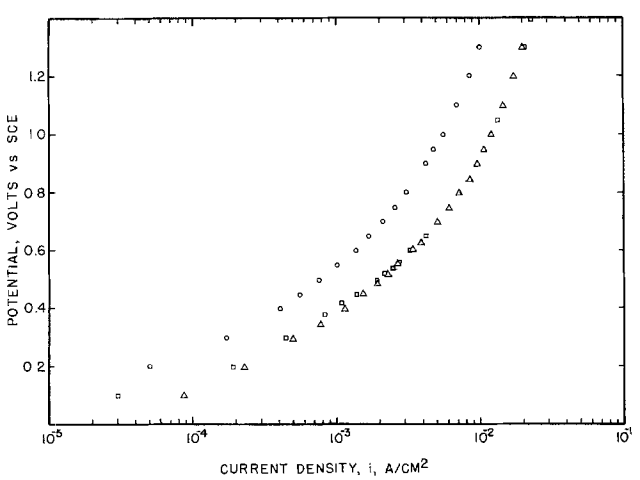


Fig. 7. Anodic polarization diagrams for 1.0M $LiOCH_3$, CH_3OH. ○, Chromium; △, molybdenum; □, tungsten.

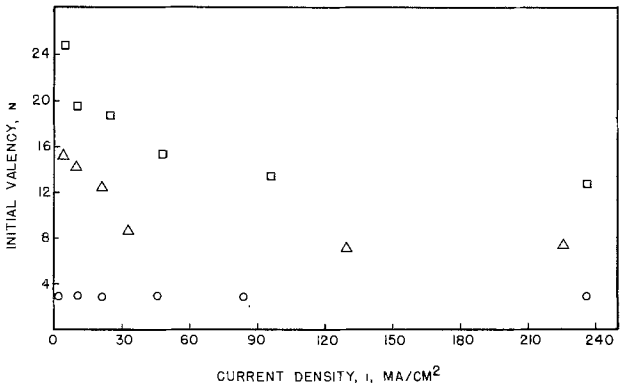


Fig. 8. Coulometric n as a function of current density for chromium. ○, 1.0M LiCl, CH_3OH; △, 1.0M $LiClO_4$, CH_3OH; □, 1.0M $LiNO_3$, CH_3OH.

visible (UV-VIS) absorption spectrum of the resulting green solution was obtained and the salient features reported in Table I. The corresponding features of a $CrCl_3 \cdot 6H_2O$ solution in 1M LiCl, CH_3OH are given for comparison. The similarities lead to the conclusion that the observed electronic spectrum is characteristic of a d^3 configuration for chromium (32). Shifts in the positions of bands are probably due to the difference in donor strength between the two hexasolvo Cr(III) species, or the presence of more than one species in the cell solution. The spectral features of species separated chromatographically from the cell solutions are in Table II, also containing eluent composition and percentages of each species. The very mixed composition of the solution casts doubt on the likelihood of a concerted "clean" oxidation mechanism. On the other hand, the substantial amounts of both mono- and dichloro complexes does not rule out a diatomic intermediate chromium species in the mechanism, as postulated for iron oxidation in aqueous solution (5). The low recovery is due to the formation of green precipitates on the frits of the cathode isolation tubes and from a highly charged species which could not be eluted in a sufficiently small volume from the ion exchange column to be spectrally analyzed. The former species could easily be polymeric oxides precipitated by the basic solution in the cathode compartments of the cell.

These results in chloride are particularly interesting in that chromium passivates in aqueous chloride (acidic) solutions (10). In water, the availability of oxygen from the solvent promotes oxidation to chromate (dichromate in acidic solution), but only in the transpassive region, at about +1.1V *vs.* SCE (18). The same investigator also observed an active region at about −0.5V *vs.* SCE, where chromium(II) was produced in HCl solution. In the present methanolic solutions, with very low concentrations of water, the available oxygen can effectively only be gotten from solvent, and unlike water, the O—CH_3 bond would be considerably more difficult to break than an O—H bond. The stablest oxidation state for chloro complexes is +3 for chromium. and in that respect the present observations are consistent.

In nitrate and perchlorate solutions, the anodic behavior of chromium was characterized by high values for initial valency. An attempt was made to ascertain whether or not this might be explained on the basis of concommitant solvent oxidation. The n and i-E data were used to extract a current-potential curve for the chromium oxidation process and a separate one for the

Table I. Absorption maxima (nanometers) for cell solutions and $CrCl_3 \cdot 6H_2O$ solution in 1M LiCl, CH_3OH

Cell solution	646	467	335(sh)	253
2.4 mmoles Cr(III)	657	472	312(sh)	245

Table II. Assay and spectral data for 1M LiCl/CH_3OH cell solution

Chromium species	Eluent	λ_{max}, nm (ϵ)	Millimoles in cell solution (%)
$(CH_3OH)_4CrCl_2^+$	0.2M $HClO_4$	—	0.294(23.1)
$(CH_3OH)_5CrCl^{2+}$	1.0M $HClO_4$	612(6.98), 431(9.06)	0.384(30.2)
$(CH_3OH)_6Cr^{3+}$(?)	2.0M $HClO_4$	—	0.245(19.3)
$[(CH_3OH)_4Cr(OCH_3)_2Cr(CH_3OH)_4]^{4+}$	3.0M HCl	—	0.197(15.6)
Total eluted Cr	—	—	1.120(88.2)
All species in cell solution	—	646(18.1), 467(~25)	1.27 (from weight loss of Cr anode)

competing reactions (33), where the sum of the current densities at each potential is equal to the observed (total) current density. One would have expected to observe essentially identical curves for the background reaction if the hypothesis were correct. However, these curves were quite different in the two electrolyte solutions, both with respect to shape and location along the potential axis. The background reaction in nitrate exhibited almost ohmic behavior and that in perchlorate exhibited a limiting current plateau. The overall oxidation in these two media is likely very complex, but some qualitative explanations are possible, based on observations made during the coulometric experiments.

he aqueous oxidation of chromium in basic solution is given in Eq. [1a]. By analogy, a simplistic methanolic stoichiometry can be written, as in Eq. [1b]

$$Cr + 4H_2O \rightarrow CrO_4^{2-} + 6e^- + 8H^+ \quad [1a]$$

$$M + 6CH_3OH \rightarrow M(OCH_3)_6 + 6e^- + 6H^+ \quad [1b]$$

Since the cathode was isolated from the anolyte during the electrolysis, the pH in the anode compartment will decrease with the passage of coulombs. As electrolysis proceeds and conditions in the cell acidify, the solvolytic reduction of Cr(VI) to Cr(III) is favored. This behavior is common for acidic Cr(VI) solutions with a variety of primary and secondary alcohols (34), wherein acid catalysis takes place. In the present case, when electrolysis began, a yellow color was imparted to the cell solution [Cr(VI)], which gradually changed to green [Cr(III)] as electrolysis proceeded, and which intensified after the cessation of current.

Additional evidence was obtained by running the same experiment in a flow cell, designed to supply fresh 1M $LiNO_3$, CH_3OH to the anode compartment at a rate of about 5 ml/min. In these experiments the anolyte was not permitted to acidify, and the resulting solutions were yellow. This color persisted after cessation of current and a spot test for Cr(VI) using a s-diphenylcarbazide was positive (35).

The electronic spectra of the green cell solutions (NO_3^- and ClO_4^- electrolytes) taken after the n experiments were qualitatively identical, the maxima and calculated average molar absorptivities given in Table III.

Table III. Absorption maxima and molar absorptivities for chromium cell solutions in 1M $LiClO_4$ and 1M $LiNO_3$, CH_3OH

	λ_{max}(nm)/ϵ(M^{-1} cm^{-1})		
$LiNO_3$	592/21.2	427/27.5	342(sh)/—
$LiClO_4$	590/18.6	425/24.9	345/—

Exhaustive electrolyses in perchlorate and nitrate solutions without isolation of the cathodes produced copious amounts of green precipitate, which seems to indicate that electrochemical reduction of Cr(VI) to Cr(III) occurred. The filtrates were yellow and also gave positive tests for Cr(VI). Comparison of the weight of recovered precipitate with electrode weight loss indicates that the precipitate could easily be Cr_2O_3 with a small amount of occluded solvent. Additional support for this oxide came from similar solubility characteristics observed.

A series of experiments in 1M $LiBF_4$, CH_3OH was performed in order to see if oxidation in the presence of an inert electrolyte which did not contain oxygen, would show significant differences. Unfortunately, the results of anodic polarization were green solutions of Cr(III), typical of a monohalo complex. Chromatographic separation of components of the solution showed at least three species, the results given in Table IV. Aside from a third band with high charge characteristics, some precipitate on the cathode compartment frits contributed to the low recovery. An interesting result is that the tetrafluoborate anion, commonly used in electrochemistry to increase the potential range in nonaqueous solvents, is not in this instance inert.

Generation of chromium in 1M $LiOCH_3$ was expected to parallel aqueous base behavior, wherein a high current efficiency for generation of Cr(VI) is observed (15). However, n data showed random scatter from 50 to 90 electrons per chromium oxidized over a current density domain of 10-190 mA/cm^2. The resulting solutions were yellow, with two absorption bands of about equal intensity at 375 and 275 nm, with respective molar absorptivities of 2200 and 1780 M^{-1} cm^{-1} (based on electrode weight loss measurements). A solution prepared from K_2CrO_4 dissolved in the electrolyte yielded an identical spectrum. Since the UV-VIS data seemed to indicate CrO_4^{2-} ion, it was thought that perhaps water contamination in the methanol might be responsible for the yellow colored solutions and very high n values. A series of galvanostatic experiments was made with various amounts of water spiked into the methanolic OCH_3^- solution. Figure 9 displays the n *vs.* water concentration relationship. It seems that the n data represent a coulometric consumption of the water present, or perhaps of hydroxide ion, depending on the position of the equilibrium in Eq. [2]. A detailed study of the water effects on these metals is underway

$$OCH_3^- + H_2O \rightleftharpoons OH^- + CH_3OH \quad [2]$$

Molybdenum.—This metal exhibits the widest variation in Tafel slope (Fig. 4-7) of the three metals, an

Table IV. Assay and spectral data for 1M $LiBF_4$/CH_3OH cell solution

Chromium species	Eluent	λ_{max}, nm (ϵ)	Millimoles in cell solution (%)
$(CH_3OH)_5CrF^{2+}$	1M $HClO_4$	615(10.5), 432(8.75), 274(6.23)	0.7187(58.4)
$(CH_3OH)_6Cr^{3+}$(?)	2M $HClO_4$	—	0.3823(26.7)
Total eluted chromium	—	—	1.047(85.1)
All species in cell solution	—	615(12.4), 435(10.7)	1.23 (wt loss)

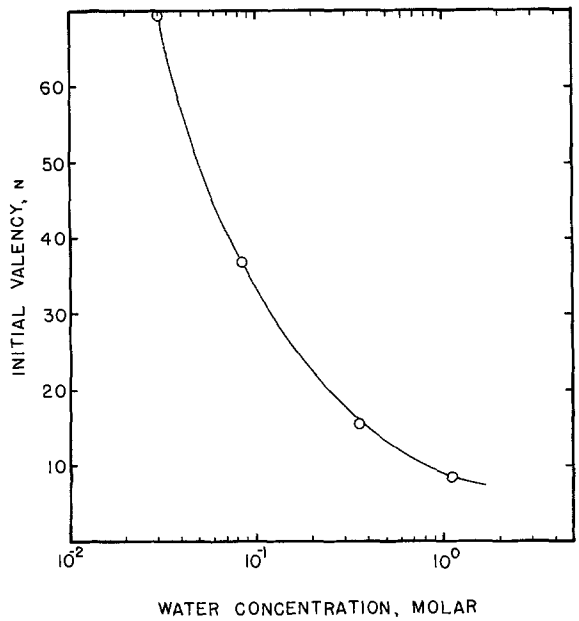


Fig. 9. Coulometric *n* as a function of water concentration in 1.0M $LiOCH_3$, CH_3OH for chromium.

observation perhaps to be expected in light of molybdenum's rich redox chemistry. Polarization in chloride solutions produced yellow colored solutions, which faded to near-colorless on standing. The former possessed a shoulder at 360 ± 10 nm on a large band in the u.v. The colorless solution had a single peak at 225 nm and a shoulder at 300 nm. These latter values agree fairly well with aqueous molybdate solutions at low pH (36). The molar absorptivity at 225 nm was 6560 M^{-1} cm^{-1} ± 1%, which is the average of five samples run at different current densities. Acid-base titrations of aliquots of cell solution taken after polarization yielded a H^+:Mo ratio of 5.7 ± 0.2, which suggests the possibility of an over-all oxidation stoichiometry approaching Eq. [1b]. Some coulombs arise from side reactions, as indicated in Fig. 10; the potentials corresponding to current densities in excess of 50 mA/cm^2 are above +1.5V *vs.* SCE and so could easily be sufficient to oxidize chloride ion to chlorine, an observation in keeping with the yellow coloration.

Generations of molybdenum in lithium nitrate solution produced both a low *n* (5.14) and a low Tafel slope (0.150V). Addition of thiocyanate to cell solutions failed to yield the characteristic red Mo(V) thiocyanate complex until stannous chloride was added, indicating

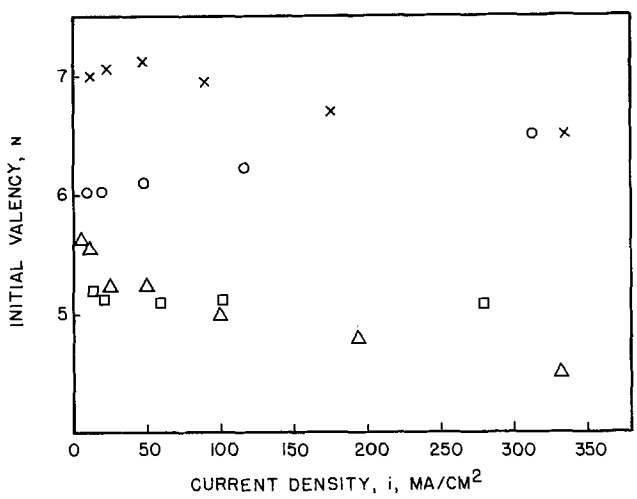


Fig. 10. Coulometric *n* as a function of current density for tungsten. ○, 1.0M LiCl, CH_3OH; △, 1.0M $LiClO_4$, CH_3OH; □, 1.0M $LiNO_3$, CH_3OH; ×, 1.0M $LiOCH_3$, CH_3OH.

that Mo(VI) was the species present in solution at the end of electrolysis. An anodic polarization in 0.5*M* KSCN, CH_3OH was made, and the yellow Mo(VI) isothiocyanate complex only was obtained (37). A similar run in 1*M* $LiNO_3$/0.1*M* KSCN, CH_3OH also gave negative results for the generation of a stable Mo(V) species, possibly because of a fast nonelectrochemical oxidation to Mo(VI) by NO_3^-. Subsequent addition of $SnCl_2$ immediately produced the intense red Mo(V) complex, which proved to be sensitive to air oxidation on standing. The suspected oxidation of Mo(V) to Mo(VI) by nitrate ion has been observed in aqueous solution with other metals (38, 39). Equation [3] is the reduction reaction in water

$$10H^+ + NO_3^- + 8e^- \rightarrow NH_4^+ + 3H_2O \qquad [3]$$

While the potential in methanolic solution would not be the same, the required acidity would be favored in the double layer where a reaction similar to [1b] would be taking place.

UV-VIS spectra of the colorless cell solutions were less satisfactory than those obtained in chloride solution, because of intense absorption by nitrate ion over most of the u.v., which prevented location of an absorption maximum. Three shoulders were observed, though, at 340, 365, and 352 nm.

Generation of Mo(VI) in lithium perchlorate occurred with high current efficiency (Fig. 10). Like nitrate, perchlorate is an oxidizing agent, and very likely responsible for the low initial valency observed at high current densities (40, 41). Equation [4] is the reduction reaction in aqueous solution

$$8e^- + 8H^+ + ClO_4^- \rightarrow Cl^- + 4H_2O \qquad [4]$$

Tests with thiocyanate for Mo(V) in the cell solutions proved negative. Acid-base titrations were complicated by decomposition of the indicator in this medium. The UV-VIS spectra were characteristic of chlorine dioxide (42). A large charge transfer band for molybdenum extended from about 460 nm to well into the u.v., with fairly well resolved shoulders at 475, 460, 445, 435, 420, 410, 400, 390, 380, 370, 360, and 350 ± 3 nm. The solution obtained from a lengthy generation was pumped under vacuum and the yellow ClO_2 trapped at liquid nitrogen temperatures. The liquid was then dissolved in pure methanol and the spectrum recorded. A maximum at 360 nm (ϵ = 1242 M^{-1} cm^{-1}) was observed. The stoichiometry of the molybdenum oxidation in this medium is very complicated and is currently under study.

The production of Mo(VI) in perchlorate and nitrate solutions is not surprising, if the analogous aqueous potential-pH diagrams have any validity (44). The absence of oxide films and passivity, however, is uncommon among data reported in nonaqueous solvents. Studies of molybdenum (14) and vanadium (45) in acetic acid solution revealed facile formation of oxide layers, with the development of intensely colored interference patterns (46). Aside from this rather unusual medium, the nonaqueous electrochemistry of molybdenum has not been heavily studied. Essential to the formation of the oxides of both of these metals is the presence of from 1 to 2*M* H_2O in the 0.02*M* $Na_2B_4O_7 \cdot 10\ H_2O$ acetic acid solution. While the present work provides oxygen in the electrolyte salts themselves (ClO_4^-, NO_3^-), every effort has been made to exclude other than trace quantities of water. Given lithium ion's affinity for water of hydration (47), it is conceivable that actual free water concentrations in these methanolic solutions could be less than the Karl Fischer titration values. This qualitative and quantitative difference, anhydrous solvent *vs.* 1*M* water, may be part of the explanation of the disparate behavior. The absence of sodium tetraborate from the present work must also represent a significant difference, in light of the fact that another valve metal, bismuth, also forms oxide layers in borate-containing aqueous solutions (48).

The oxidation products in the present work for perchlorate and nitrate solutions are soluble and if the mechanism proceeds through an oxide film as in aqueous solution (12), the rate of dissolution of the film must exceed the rate of its formation, at least under the galvanostatic conditions imposed here. And while the method of data acquisition has been shown to affect the observed overpotential parameters (49), the possibility of an ECE mechanism or another double layer oxidation step cannot be ruled out as an explanation for the low n values in these electrolytes.

Lithium methoxide proved conducive to Mo(VI) generation, analogous to the aqueous case, at all current densities. The high value of n at low current densities may be due to a slow reduction reaction occurring in the bulk solution. Evidence of this arose from observation of the yellow cell solution after electrolysis. Spectral scans were made from 600 to 300 nm immediately following electrolysis and at 15 min intervals thereafter. The charge transfer band shifted into the u.v. and a peak at 450 nm grew in. The latter band is characteristic for Mo(V) species (43), and it is possible that in strong base, methanol can be oxidized by the Mo(VI) species.

Another, though less likely explanation would be that indeed a Mo(VII) species was generated; such a permolybdate species was postulated to be stable in very basic aqueous solution at high potentials by Pourbaix (44), although such species are formed by treatment of Mo(VI) with peroxide.

Tungsten.—The behavior of this metal in methanolic chloride appears uncomplicated, and essentially represents oxidation to W(VI). Tafel linearity extends for one decade of current density (Fig. 11). Cell solutions lacked absorption characteristics in the visible spectrum and were without precipitates.

The E *vs.* log i curves in perchlorate and nitrate solutions exhibit Tafel slopes roughly parallel to those for chromium in the same media, and like chromium, were characterized by the formation of precipitates. In this instance they appeared as white dendrites on the anode itself, which proved to be freely soluble in aqueous base.

In one molar nitrate the average initial valency was 5.42 ± 0.12 and fairly constant, whereas in perchlorate solution it exhibited behavior similar to that of molybdenum, without the formation of chlorine dioxide. This range of n data would indicate that perhaps more than one oxidation mechanism is operative in ClO_4^- and NO_3^- solutions. The formation of insoluble oxidation products (probably oxides or mixed oxide esters) was observed at localized pitting sites rather than evenly over the anode surface, and could be responsible for the tendency toward lower apparent oxidation states at the higher current densities. These observations of apparent oxidation number in perchlorate and nitrate solutions are in keeping with aqueous behavior in other electrolytes for tungsten (13) and also for molybdenum (14). The rich aqueous oxide chemistry of tungsten, which includes substoichiometric oxides between WO_2 and WO_3 seems to be operative in methanolic solution also.

Lithium methoxide solution favors simple oxidation to W(VI), and the E *vs.* log i behavior is identical to that of molybdenum in this medium (Fig. 7). Evaporation of cell solutions under nitrogen produced a vitreous gel which, on exposure to air, turned to an amorphous white solid.

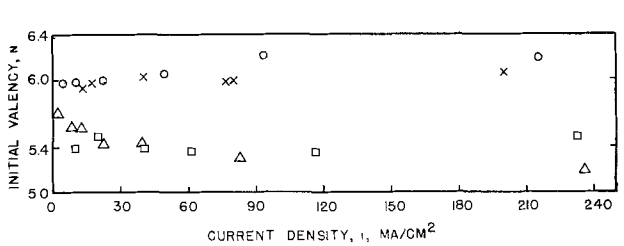


Fig. 11. Coulometric n as a function of current density for molybdenum. ○, 1.0M LiCl, CH_3OH; △, 1.0M $LiClO_4$, CH_3OH; □, 1.0M $LiNO_3$, CH_3OH; ×, 1.0M $LiOCH_3$, CH_3OH.

Summary

The anodic behavior of Group VI metals in methanolic solution has proven to be a rather dramatic function of supporting electrolyte. In parallel with established chemistry in aqueous solution, chromium shows a more recalcitrant oxidation than either molybdenum or tungsten. Only in chloride solution is oxidation to Cr(III) well behaved and 100% efficient. Oxidation to a nonintegral electrochemical valence seems to be the rule for molybdenum and tungsten in perchlorate and nitrate media, with accompanying formation of insoluble oxides.

The production of chlorine dioxide in perchlorate solutions during anodic polarization of molybdenum was noteworthy, in that previous observations were in acetonitrile at a noncorroding anode (50).

Tafel slopes for all the metals in all four electrolytes were well above 2.303 $RT/\mathbf{F}$, indicating a complex oxidation reaction.

Finally, the role of water in methanol was seen to be significant as measured in terms of shifts in the current-potential behavior along the potential axis.

The relatively straightforward aqueous electrochemistry of these metals is not retained in the protic solvent methanol; a rich redox chemistry has emerged which might have significant analytical and synthetic implications.

Acknowledgment

Much of the data for chromium and molybdenum was part of the thesis of the author and the remainder was supported by the Research Council of the University of Missouri-Columbia, under a Summer Research Fellowship.

Manuscript submitted Dec. 6, 1976; revised manuscript received Jan. 28, 1977.

Any discussion of this paper will appear in a Discussion Section to be published in the December 1977 JOURNAL. All discussions for the December 1977 Discussion Section should be submitted by Aug. 1, 1977.

REFERENCES

1. P. Brouillet, I. Epelboin, and M. Froment, C. R., **238**, 1795 (1954).
2. Von T. Heumann and W. Rösener, *Z. Elektrochem.*, **59**, 722 (1955).
3. M. Pourbaix, *ibid.*, **62**, 670 (1958).
4. Von T. Heumann and F. W. Diekötter, *ibid.*, **62**, 745 (1958).
5. T. Hurlen, *Acta Chem. Scand.*, **14**, 1533 (1960).
6. T. Hurlen, *ibid.*, **14**, 1564 (1960).
7. T. Hurlen, *ibid.*, **15**, 630 (1961).
8. T. Hurlen, *ibid.*, **16**, 1337 (1962).
9. T. Hurlen, *ibid.*, **16**, 1346 (1962).
10. K. Schwabe, K. Müller, and A. Loge, *Electrochim. Acta*, **8**, 193 (1963).
11. L. L. Wikstrom and K. Nobe, *This Journal*, **116**, 525 (1969).
12. J. W. Johnson, C. H. Chi, C. K. Chen, and W. J. James, *Corrosion (Houston)*, **26**, 238 (1970).
13. J. W. Johnson and C. L. Wu, *This Journal*, **118**, 1909 (1971).
14. C. M. Daly and R. G. Keil, *ibid.*, **122**, 350 (1975).
15. D. Monnier and P. Zwahlen, *Helv. Chim. Acta*, **39**, 1865 (1956).
16. A. I. Kostromin and A. A. Akhmetov, *Zh. Anal. Khim.*, **25**, 503 (1969).
17. A. I. Kostromin, A. A. Akhmetov, and L. N. Orlova, *ibid.*, **25**, 195 (1970).
18. A. I. Kostromin, A. A. Akhmetov, and V. V. Mosolov, *ibid.*, **25**, 847 (1970).
19. A. I. Kostromin, A. A. Akhmetov, and L. N. Burygina, *ibid.*, **27**, 315 (1972).
20. A. I. Kostromin, V. V. Mosolov, and L. L. Makarova, *ibid.*, **27**, 2114 (1972).
21. A. I. Kostromin and R. M. Badakshanov, *ibid.*, **27**, 2046 (1972).
22. A. I. Kostromin, P. K. Agasyan, and V. N. Basov, *ibid.*, **25**, 216 (1970).

23. A. I. Kostromin and L. L. Makarova, *ibid.*, **29**, 1294 (1974).
24. G. S. Kelsey and H. W. Safford, *Anal. Chem.*, **46**, 1585 (1974).
25. M. E. Straumanis, *This Journal*, **105**, 284 (1958).
26. D. T. Sorensen, A. W. Davidson, and J. Kleinberg, *J. Inorg. Nucl. Chem.*, **13**, 64 (1960).
27. M. E. Straumanis, *This Journal*, **108**, 1087 (1961).
28. M. E. Straumanis and K. Poush, *ibid.*, **112**, 1185 (1965).
29. G. W. Haupt, *J. Res. Natl. Bur. Stand.*, **48**, 414 (1952).
30. R. M. Hartman, Thesis, University of Pittsburgh, 1974, p. 62.
31. G. Milazzo, "Electrochemistry," p. 171, Elsevier Publishing Co., New York (1963).
32. F. A. Cotton and G. Wilkinson, "Advanced Inorganic Chemistry," 3rd ed., pp. 836-839, Interscience Publishers (1972).
33. J. J. Lingane, *Anal. Chem.*, **26**, 622 (1954).
34. J. D. Roberts, R. Stewart, and M. C. Caserio, "Organic Chemistry: Methane to Macromolecules," pp. 259-260, W. A. Benjamin, Inc. (1971).
35. C. E. Crouthamel and C. E. Johnson, *Anal. Chem.*, **26**, 1284 (1954).
36. A. Bartecki and D. Dembicka, *J. Inorg. Nucl. Chem.*, **29**, 2907 (1967).
37. B. J. Brisdon and D. A. Edwards, *Inorg. Nucl. Chem. Lett.*, **10**, 301 (1974).
38. E. Raijola and A. W. Davidson, *J. Am. Chem. Soc.*, **78**, 556 (1956).
39. G. P. Haight, *Acta Chem. Scand.*, **15**, 2012 (1961).
40. G. A. Rechnitz and H. A. Laitinen, *Anal. Chem.*, **33**, 1473 (1961).
41. I. M. Kolthoff and I. Hodara, *J. Electroanal. Chem.*, **5**, 2 (1963).
42. R. G. Kieffer and G. Gordon, *Inorg. Chem.*, **7**, 235 (1968).
43. S. M. Horner and S. Y. Tyree, Jr., *ibid.*, **1**, 122 (1962).
44. M. Pourbaix, "Atlas of Electrochemical Equilibria in Aqueous Solutions," pp. 275-279, Pergamon Press (1966).
45. R. G. Keil and R. E. Salomon, *This Journal*, **115**, 628 (1968).
46. M. R. Arora and R. Kelly, *ibid.*, **119**, 270 (1972).
47. B. Burrows and S. Kirkland, *ibid.*, **115**, 1164 (1968).
48. D. J. DeSmet and M. A. Hopper, *ibid.*, **116**, 1184 (1969).
49. J. L. Ord, *ibid.*, **112**, 46 (1965).
50. G. Cauquis and D. Serve, *J. Electroanal. Chem.*, **27**, App. 3 (1970).

The Thermal Decomposition of $CaSO_3$ and Its Enthalpy of Formation

D. Cubicciotti,* A. Sanjurjo, and D. L. Hildenbrand

Stanford Research Institute, Menlo Park, California, 94025

ABSTRACT

The decomposition pressure of $CaSO_3$ was measured by the torsion-effusion method over the temperature range 723°-767°K. Mass spectrometric analysis showed the effusing vapor to be SO_2 and that the decomposition/vaporization process was $CaSO_3(s) = CaO(s) + SO_2(g)$, in agreement with vapor molecular weight determinations. The observed vaporization process was not the thermodynamically most favored one, which would have produced gaseous S_2. Observed pressures were found to be dependent on the area of the effusion orifice, and the results were extrapolated to zero orifice size to derive the following equation for the equilibrium pressures of SO_2

$$\log p(\text{atm}) = -\frac{(11{,}710 \pm 600)}{T} + (9.27 \pm 0.80)$$

The standard enthalpy of formation of $CaSO_3$ at 298°K was found to be -277.0 ± 1 kcal/mole.

The reactions of lime and limestone with gaseous SO_2 are of considerable interest for the control of sulfur pollution in combustion gases. The chemistry of the absorption of SO_2 by CaO or $CaCO_3$ at high temperatures is rather complex because the reaction is heterogeneous and also because several solid phases are involved. Calcium sulfite is presumably the first solid formed in the reaction. Surprisingly, its enthalpy of formation has not been measured although a number of estimated values have been reported. In the present work, we have studied the vacuum decomposition of $CaSO_3$ to SO_2 and CaO and evaluated the enthalpy of formation of $CaSO_3$.

The high temperature equilibrium chemistry of the Ca-S-O system has been discussed recently by Tarradellas and Bonnetain (1) and by Schwitzgebel and Lowell (2). Calcium sulfite is thermodynamically unstable over the temperature range of interest, and should disproportionate by a reaction that produces no gaseous products, namely

$$4CaSO_3(s) = 3CaSO_4(s) + CaS(s) \qquad [1]$$

for which $\Delta G°$ at 700°K is -214 kcal/mole. However, that reaction is kinetically limited, presumably because it involves drastic rearrangements of the atoms in the sulfite ion.

Apparently, $CaSO_3$ can exist in a state of metastable equilibrium. No measurable disproportionation occurs when it is heated to temperatures below 775°K for periods of many hours, even though the free energy change of reaction [1] is quite negative. Tarradellas and Bonnetain (1) found from x-ray diffraction studies that disproportionation did not occur below 825°K (we presume the time of heating in their work was at least an hour). Marier and Ingraham (3) found no weight changes or thermal effects below 925°K when $CaSO_3$ was heated in N_2. Pechkovskii (4) observed some formation of $CaSO_4$ in excess SO_2 at 810°K. Foerstel and Kubel (5) observed disproportionation at 857°K, but not at 775°K when samples were heated for 2 hr in a

* Electrochemical Society Active Member.

Key words: sulfur dioxide, calcium oxide, thermodynamics, torsion effusion, gas molecular weights.

current of N_2. Low *et al.* (6) studied the infrared spectra of surface layers of $CaSO_3$ on CaO heated in vacuum. They found changes in the spectrum occurred only at temperatures of 825°K and above in 3 hr time periods.

Marier and Ingraham (3) did find endotherm and weight losses beginning about 925°K in DTA measurements on $CaSO_3$, which imply that a gaseous product is formed. They suggest the reaction was

$$CaSO_3(s) = CaO(s) + SO_2(g) \quad [2]$$

Our results, below, show that reaction [2] was the reaction that occurred under the conditions of our experiments, and probably those of Marier and Ingraham (3). At 700°K, $\Delta G°$ for that reaction is 23.9 kcal/mole. A more thermodynamically favored way of forming a gaseous product involves the formation of sulfur by the reaction

$$6CaSO_3(s) = 4CaSO_4(s) + 2CaO(s) + S_2(g) \quad [3]$$

which has $\Delta G°$ at 700°K equal to 9.5 kcal/mole, and the pressure of S_2 should be of the order of 10^{-3} atm. If both reactions [2] and [3] occurred, the equilibrium ratio of S_2 to SO_2 should be of the order of 10^5 in this temperature range. Our results show the reaction [3] did not occur.

The pressure of SO_2 for the decomposition reaction [2] would be expected to attain values in the range of $3 \cdot 10^{-7}$ atm at 750°K. Pressures in that range were too small to be measured in the manometric system used by Marier and Ingraham (3), and they observed no decomposition pressure. The present study utilized torsion-effusion measurements, which are suited to pressures of that magnitude, and mass spectrometric analysis to identify the gaseous species.

Experimental Method

Preparation.—Commercially available samples of $CaSO_3$ were not acceptable because their x-ray diffraction patterns indicated the presence of $CaSO_4$, presumably formed by air oxidation.

Samples were prepared for this work by very slow addition of aqueous Na_2SO_3 solution to $CaBr_2$ solution in aqueous ethanol. The precipitate was filtered under an N_2 atmosphere and dried in a current of argon at 675°K for 4 hr. The product was handled in a dry N_2 atmosphere. The observed x-ray pattern agreed with that reported (7) for $CaSO_3$.

Effusion measurements.—In the torsion-effusion weight-loss method (8) used here, the pressure of gas escaping through an orifice is calculated from the torque exerted on a fiber; the weight-loss information allows the molecular weight of the effusing gas to be calculated. The apparatus used has been described in earlier publications (8, 9). The effusion cells used in the present study were fabricated from high purity alumina; each cell assembly was comprised of two vertically aligned sample chambers, 3 cm long and 1 cm in diameter, mounted on either side of the suspension axis.

The sample (350 mg in each leg of the cell) was loaded under an N_2 atmosphere and the cell was quickly attached to the apparatus and evacuated. The sample was heated slowly so that the pressure in the apparatus was always less than 10^{-8} atm. At temperatures up to about 600°K some H_2O was evolved, as determined from molecular weight measurements. From about 600° to 700°K, no measurable amounts of gas were evolved. Above about 700°K, gas was evolved with a molecular weight of 64 ± 8.

Measurements were made over the range 723°-767°K. The upper temperature was chosen to avoid the disproportionation of the sample which was anticipated from the literature. After the temperature and angular deflection were steady for 1 hr at each temperature, measurements were taken. The sample was studied over a period of days during which time less than 2% of the sample had decomposed. The sample was x-rayed at the end of the run.

Table I. Cell characteristics

Cell	Orifice diameter, mm	Lever arm, mm	Wall thickness, mm	$\Sigma(Ca)$,* cm^3
1	1.048	9.744	1.083	$8.708 \cdot 10^{-3}$
2	2.095	9.949	0.966	$4.752 \cdot 10^{-2}$

* C is the Clausing factor (13) and a the area of each orifice.

Two cells were used with different effusion orifice areas. The cell geometrical constants, determined from measurements with a traveling microscope, are given in Table I. The calibration constants of the cells were checked by measuring the vapor pressure of KCl; the results were within 5% of the data reported by Pugh and Barrow (10).

The pressure of the gas effusing from the cell was calculated from the expression

$$p = \frac{2k\theta}{\Sigma afq} \quad [4]$$

where k, the torsion constant of the suspending ribbon, had a value of 0.07814 dyne-cm/rad as determined from a torsion pendulum treatment, in close agreement with the supplier's specifications. The angular displacement, θ, was measured by observation of a fixed scale reflected in a mirror attached to the suspension system. Values of f, the orifice force factor, were taken from Schulz and Searcy (11). The moment arm is q and the area of the orifice is a.

The molecular weight of the effusing gas was calculated from the expression

$$M = 2\pi RT\{[\dot{w}(\Sigma afq)]/[2k\theta(\Sigma Ca)]\}^2$$

in which $\dot{w}$ is the rate of weight loss, T the temperature, and C is the orifice Clausing factor.

Results

The pressures obtained by the torsion-effusion method are given in Table II in the chronological order in which they were obtained. Determinations of the molecular weight required that the sample be maintained at constant temperature for long times; therefore, only a few such measurements were made. The resulting molecular weights were in the range 64 ± 8

Table II. Observed pressures (p) and calculated equilibrium pressures (p_{eq}) and enthalpies of vaporization for reaction [2]

Cell	T, °K	$p \times 10^7$, atm	$p_{eq} \times 10^7$, atm	$\Delta H°_{298}$, kcal/mole
1	722.7	1.07	1.24	54.39
	725.1	1.07	1.34	54.25
	727.0	1.27	1.47	54.25
	729.8	1.49	1.73	54.22
	731.6	1.71	1.98	54.15
	734.1	1.82	2.11	54.23
	736.8	1.38	1.60	54.83
	739.0	2.23	2.58	54.29
	742.5	2.79	3.23	54.21
	743.5	2.91	3.37	54.22
	746.6	3.34	3.87	54.24
	748.7	3.67	4.25	54.24
	760.7	6.71	7.77	54.17
	767.0	8.22	9.52	54.30
				Avg 54.28 ± 0.2
2	733.2	1.08	2.01	54.74
	745.0	1.89	3.52	54.26
	741.8	1.62	3.02	54.26
	739.4	1.44	2.69	54.26
	736.7	1.27	2.37	54.25
	749.3	2.29	4.27	54.28
	751.3	2.57	4.79	54.25
	756.2	3.22	6.00	53.94
	751.8	2.60	4.85	54.26
	742.9	1.65	3.07	54.22
				Avg 54.23 ± 0.1

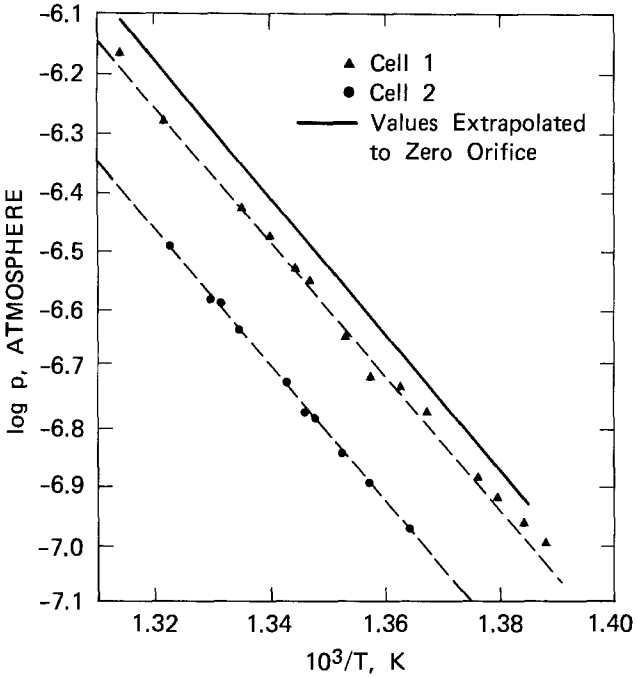


Fig. 1. Torsion effusion pressures for $CaSO_3$

and were interpreted to indicate that the effusing species was SO_2 or S_2.

The measured pressures are shown graphically in Fig. 1; higher pressures were observed with the smaller effusion orifices. Such results indicate that the rate of escape of gas from the cell was sufficiently large to perturb the rate of release of gas from the solid. That effect is not surprising in an incongruent vaporization process like the one under study. The values obtained in the two cells were analyzed by a least squares treatment, which resulted in the following equations for the apparent pressures in atmospheres

$$\text{cell 1:} \quad \log p = 8.76 - 11{,}380/T \qquad [6]$$

$$\text{cell 2:} \quad \log p = 8.71 - 11{,}500/T \qquad [7]$$

The Whitman-Motzfeldt treatment is normally applied to extrapolate effusion results to zero orifice size (9). That equation relates the measured pressure (p) to the orifice area (a), Clausing factor (C), and equilibrium pressure (p_{eq}) through a constant (β), as follows

$$\frac{p_{eq}}{p} = (1 + \beta aC) \qquad [8]$$

Thus a plot of the reciprocal of measured pressure *vs.* aC has $1/p_{eq}$ as an intercept and β/p_{eq} as a slope.

A correlation of the pressure data obtained with the two cells yielded a β value of 18 ± 1, independent of temperature. With this value of β, the equilibrium pressure (p_{eq}) was calculated for each measurement; the results are given in Table II. A least squares treatment of the equilibrium pressures for both cells gives

$$\log p_{eq}\ (\text{atm}) = -\frac{(11{,}710 \pm 600)}{T} + (9.27 \pm 0.80) \qquad [9]$$

Our initial interpretation of the results following the general tenor of the literature was that we were measuring the pressure of SO_2 generated according to reaction [2]. The molecular weight of effusing gas agreed with that of SO_2, and the enthalpy of formation derived for $CaSO_3$ was in agreement with estimated values. During our study we realized that the vaporization of $S_2(g)$ by reaction [3] was thermodynamically more favored than the vaporization of $SO_2(g)$. Thus, the partial pressure of S_2 should have been significantly greater than that of SO_2. Because the molecular weight of S_2 is the same as SO_2, the torsion weight-loss measurement of molecular weight could not distinguish between those species. Mass spectrometer studies were made to identify the gaseous species. Although the mass number of the ions produced from the two species (SO_2^+, S_2^+, or fragments) were not distinguishable in the mass spectrometer, the ions could be distinguished from their ionization efficiency curves. Thus, S_2 has an ionization potential of 9.4 eV while that of SO_2 is 12.4 eV. Therefore, measurable ion currents of parent S_2^+ would be observed at ionizing electron energies small enough so that no SO_2^+ would be formed.

A sample of $CaSO_3$ was heated in an alumina cell, with a 1.5 mm orifice, in the mass spectrometer. At 758°K, the m/e 64 signal exhibited a sharp shutter effect, indicative of an effusion cell origin, and had a threshold appearance potential of 12.6 ± 0.3 eV in agreement with that of SO_2^+. With higher sensitivity, there was no indication of S_2^+ at ionizing energies below 12.5 eV, nor were any other effusion cell species observed. A second set of observations made with a 0.3 mm diameter orifice yielded similar results. At about 900°K, well beyond the range of the torsion measurements, a small S_2^+ signal did appear below 12.5 eV, but the relative ion intensities indicated the ratio $p(SO_2)/p(S_2)$ to be greater than 20. Thus, the effusing gas was clearly identified as SO_2.

Discussion

In view of the mass spectrometer identification of SO_2 as the effusing gas, the pressures measured in the effusion studies should be interpreted according to reaction [2]. Thus, the pressures obtained from the extrapolation of the effusion pressures to zero orifice size will be taken as the equilibrium pressures for reaction [2].

The thermochemical information available for SO_2 and CaO at temperatures of interest is essentially complete and is reported in the JANAF Tables (13). For $CaSO_3$, the heat capacity up to room temperature has been measured, so the absolute entropy is known (2, 12). The heat capacity above room temperature has been estimated by extrapolation and comparison with other salts (2). The free energy function of $CaSO_3$, calculated from those values, is given in Table III.

Table III. Thermochemical data for $CaSO_3(s)$

T, °K	$C_p°$, cal/mol deg	$S°$, cal/mol deg	$-\left(\frac{G°_T - H°_{298}}{T}\right)$, cal/mol deg	$H°_T - H°_{298}$, kcal/mole	$\Delta Hf°_T$,* kcal/mole	$\Delta Gf°_T$,* kcal/mole	log K_p*
298	21.72	24.20	24.20	0.00	−277.0	−257.1	188.6
400	24.21	30.96	25.09	2.35	−277.5	−250.2	136.7
500	26.20	36.58	26.84	4.87	−277.7	−243.4	106.4
600	28.02	41.52	28.88	7.58	−277.6	−236.7	86.2
700	29.76	45.96	31.00	10.47	−277.3	−229.7	71.7
800	31.46	50.05	33.14	13.53	−290.3	−224.2	61.3
900	33.13	53.86	35.23	16.76	−289.6	−216.0	52.5
1000	34.78	57.43	37.27	20.16	−288.7	−207.8	45.4

* $\Delta Hf°_T$, $\Delta Gf°_T$, and log K_p refer to the equation for formation from the elements in their standard states as defined in the JANAF Tables.

The enthalpy change for reaction [2] at 298°K was calculated from each value of the equilibrium pressure, using the thermochemical data of Table III. The values are given in Table II. The enthalpy changes given are so-called third law values because the absolute entropies of all reactants were combined with the derived equilibrium pressures at the individual temperatures quoted. There is no drift of the enthalpies with temperature, within experimental error. The average values for each of the two cells were 54.3 ± 0.2 and 54.2 ± 0.2 kcal/mole, so that 54.3 ± 0.2 kcal/mole represents the enthalpy change at 298°K for the entire set of data.

The temperature coefficient of pressure can be used to determine a second-law value of the reaction enthalpy change. The result provides a check on the internal consistency of the data. The value calculated from Eq. [9] is 53.6 ± 2.7 kcal/mole and represents the enthalpy change for reaction [2] at 745°K. That result is converted to a 298°K value of 55.3 ± 2.7 kcal/mole by use of the heat capacity data in Schwitzgebel (2) and Table III. The result is less precise than the third law value primarily because of the short temperature range in which measurements could be made; however, the two values are in good agreement.

The standard enthalpy of formation of $CaSO_3(s)$ at 298°K was calculated from the third law value and enthalpies of formation (12) of CaO (−151.79 ± 0.2 kcal/mole) and $SO_2(g)$ (−70.95 ± 0.1 kcal/mole). The resulting value is −277.0 kcal/mole. We estimate an uncertainty of 1 kcal/mole. Table IV compares the experimental value of the enthalpy of formation of $CaSO_3$ to several estimates in the literature. The estimated values are within a few kilocalories of the experimental value obtained in the present work. A table of thermodynamic functions based on that value is given in Table III. Those functions are compatible with the JANAF Tables and can be used with them for equilibrium calculations.

Under the conditions of our experiments, the reaction that occurs, namely reaction [2], is not so thermodynamically favorable as at least two other reactions ([1] and [3]) that do not occur. That apparent anomaly must be due to kinetic effects so that under other experimental conditions one might expect different net reactions. For example, if $CaSO_3$ were heated in a closed container so that SO_2 could not escape, or if it were heated in excess SO_2 then the other reactions might begin to occur. A study of the kinetics and mechanisms of these reactions should prove fruitful.

Even without a knowledge of the detailed mechanism one might suspect that decomposition to SO_2 would be kinetically easier than the thermodynamically favored reactions.

Table IV. Estimates of enthalpy of formation of $CaSO_3(s)$ reported in the literature compared with present experimental value

Estimated $-\Delta H°_f$, 298°K (kcal/mole)	Reference
275.1 ± 2	Schwitzgebel *et al.* (14)
279 ± 2.8*	Maslov (15)
276.3 ± 1.5	Erdos (16)
275.9 ± 2.5	Lowell (2)
284.3†	Trautz and Pakeschwer (17)
277.5‡	Pechkovskii (4)
274.0	Tarradellas and Bonnetain (1)
Experimental value	
277.0 ± 1	This work

* Although Schwitzgebel *et al.* quote Maslov's value as experimental, it is really an estimate based on an extrapolation of hydrated salt values to anhydrous values.
† This value corresponds to $CaSO_4 \cdot 2H_2O$.
‡ Estimated from Pechkovskii calculations.

The formation of a molecule of SO_2 from $CaSO_3$ results from the rupture of one S—O bond, and the residual $O^=$ simply replaces the original $SO_3^=$. The formation of a molecule of S_2, on the other hand, involves rupture of six S—O bonds. Eventually, four of the oxygen atoms released become incorporated into the structure to form four $SO_4^=$ ions with a recovery of sufficient energy, including the S_2 bond energy, to make the process energetically more favorable.

The mechanism of reaction [1] is also expected to be complex. The formation of one $S^=$ ion requires rupture of three S—O bonds and redistribution of the oxygens to form three $SO_4^=$ ions. It is not surprising that the activation energies for those processes are significantly larger than that for SO_2 vaporization.

In first approximation, the β of Eq. [8] is related to the vaporization coefficient, α, and the decomposing surface area, A, by the expression $\beta = (\alpha A)^{-1}$. If A is taken to be the cross-sectional area of the cell, *i.e.*, the projected sample surface area, then $\alpha \cong 5 \times 10^{-2}$. Interestingly enough, this is close to the value $\alpha \cong 4.4 \times 10^{-2}$ found in effusion studies (13) of the decomposition process $MgSO_4(s) \rightarrow MgO(s) + SO_3(g)$, indicating that the kinetic barriers in the two processes are quite similar. Because the initial step in the decomposition processes of both $CaSO_3$ and $MgSO_4$ appears to be a rupture of an S—O bond, this similarity seems reasonable.

Acknowledgment

Financial support for this research was provided by NSF under Grant MPS 75-13751.

Manuscript submitted Dec. 13, 1976; revised manuscript received Feb. 14, 1977.

Any discussion of this paper will appear in a Discussion Section to be published in the December 1977 JOURNAL. All discussions for the December 1977 Discussion Section should be submitted by Aug. 1, 1977.

Publication costs of this article were assisted by Stanford Research Institute.

REFERENCES

1. J. Tarradellas and L. Bonnetain, *Bull. Soc. Chim. Fr.*, **6**, 1903 (1973).
2. K. Schwitzgebel and P. S. Lowell, *Environ. Sci. Technol.*, **7**, 1147 (1973).
3. P. Marier and T. R. Ingraham, Mines Branch Research Report R 222, Department of Energy, Mines and Resources, Ottawa, Canada, 1970.
4. V. V. Pechkovskii and T. G. Mal'tseva, *J. Appl. Chem. USSR*, **37**, 255 (1964).
5. F. Foerstel and K. Kubel, *Z Anorg. Allg. Chem.*, **139**, 261 (1924).
6. M. J. D. Low, A. J. Goodsel, and N. Takezawa, *Environ. Sci. Technol.*, **5**, 1191 (1971).
7. F. W. Matthews and A. O. McIntosh, *Can. J. Res.*, **268**, 747 (1948).
8. D. L. Hildenbrand and D. T. Knight, *J. Chem. Phys.*, **51**, 1260 (1969).
9. D. L. Hildenbrand and W. F. Hall, *ibid.*, **67**, 888 (1963).
10. A. C. P. Pugh and R. F. Barrow, *Trans. Faraday Soc.*, **54**, 671 (1958).
11. D. A. Schulz and A. W. Searcy, *J. Chem. Phys.*, **36**, 3099 (1962).
12. JANAF Thermochemical Tables, The Dow Chemical Company.
13. K. Lau, D. Cubicciotti, and D. L. Hildenbrand, To appear *J. Chem. Phys.*
14. K. Schwitzgebel, P. S. Lowell, T. Parsons, and K. I. Sladek, *J. Chem. Eng. Data*, **16**, 418 (1971).
15. P. G. Maslov, *Zh. Obsch. Khim.*, **29**, 1413 (1959).
16. E. Erdos, *Collect. Czech. Chem. Commun.*, **27**, 1428 (1962).
17. M. Trautz and S. Pakeschwer, *J. Prakt. Chem.*, 1922 147 (1929).

High Conductivity Cuprous Halide-Metal Halide Systems

Tsuneo Matsui[1] and J. Bruce Wagner, Jr.*,[1]

Materials Research Center and Department of Materials Science and Engineering, Northwestern University, Evanston, Illinois 60201

ABSTRACT

The a-c electrical conductivity has been measured for the systems, CuI + CdI_2, CuCl + $CdCl_2$, CuI + KI, CuI + RbI, and CuCl + RbCl and the results have been discussed in relation to phase diagrams. New highly conducting materials at room temperature have been surveyed for the system, RbCl + CuCl.

The solid electrolytes MAg_4I_5 (M = K, Rb, and NH_4) have recently been reported to have unusually high ionic conductivities (1-3). Because of the similar properties of the Ag^+ and Cu^+ ion together with the much lower cost of copper compared to silver, it is of considerable interest to synthesize copper electrolytes with high ionic conductivities analogous to those of the silver electrolytes. Copper ion high conducting materials have been recently reported (4-7). But all these materials contained organic compounds as additives. Thus some of these were somewhat unstable when used in galvanic cells (6).

In the present investigation, three methods were investigated for the preparation of new solid electrolytes with high copper ion conductivities at low temperatures. The first was the classical method of doping CuI by an aliovalent cation, in this case Cd (as CdI_2). The second was to make the different compounds by utilizing open structures. In the present study, the layered structure of $CdCl_2$ was used to make the new compound of Cu_4CdCl_6 (4 CuCl + $CdCl_2$). The third method was the preparation of a different compound by using monovalent alkali-metal halides in analogy to the highly conducting silver compounds (1-3). In the present study, KI and RbI were added to CuI, and RbCl was added to CuCl. The conducting characteristics of the compounds prepared by these three methods have been studied by using a-c conductivity measurements. The results are also discussed in relation to phase transitions.

Experimental

Materials.—The samples used in this study were polycrystalline pellets. The following materials were used: ultrapure, anhydrous CuI powder (99.9998%, Alfa Products, Ventron Corporation); ultrapure CdI_2 powder (99.998%, Alfa Products, Ventron Corporation); CuCl powder (99.999%, Semielements Incorporated); $CdCl_2$ powder (99.999%, Apache Chemicals Incorporated); KI powder (99.998%, Apache Chemicals Incorporated); and RbI and RbCl (99.9%, Apache Chemicals Incorporated). The samples were made by mixing the powders with the appropriate amounts of the halides, from which some of the water had been removed by heating at about 110°C in an evacuated Pyrex or Vycor tube before mixing.

A spark source mass spectrometric chemical analysis of $RbCu_4Cl_5$ after completion of the experiments is shown in Table I. The impurities total 0.067% by weight. The carbon most probably was introduced by the graphite electrodes used in the subsequent polarization study (23). Other impurities may have been present in the RbCl and RbI starting materials. The mixed powders were pressed at 75,000 psi in a 0.319 in. steel die at room temperature in air. The freshly prepared pellets were sintered in a sealed, evacuated quartz tube. In the case of the RbI + CuI and RbCl + CuCl systems, the halides were melted in the evacuated, sealed tubes at temperatures of 235° and 250°C, respectively (see Table I). After solidifying the material was ground, pressed, and annealed. The sizes of all the pellets were about 8 mm in diameter and 2 mm long. The detailed conditions of sample preparation and annealing conditions used in this study are presented in Table II.

Table I. Impurity concentrations in $RbCu_4Cl_5$ powder by spark source mass spectrometry* (in parts per million by weight)

Element	Detection limit	$RbCu_4Cl_5$
Li	0.001	0.003
B	0.001	0.40
C	0.01	186.0
N	0.3	0.9
O	0.1	17.0
F	0.01	84.0
Na	0.05	48.0
Mg	0.05	0.6
Al	0.1	4.7
Si	0.1	17.0
P	0.05	0.20
S	0.1	3.9
K	0.1	22.0
Ca	0.05	2.6
Ti**	0.1	11.0**
V	0.1	0.7
Cr**	0.1	40.0**
Fe**	0.1	30.0**
Mn	0.1	0.4
Ni**	0.1	23.0**
Co**	0.1	9.0**
Zn	0.1	0.7
Ga	0.05	59.0
As	0.05	7.0
Br	0.1	15.0
Se	0.1	0.9
Zr	0.3	4.0
Nb	0.1	20.0
Ru	0.1	29.0
Rh	0.1	1.6
Ag	0.5	17.0
Pd	1.0	1.0
Sn	0.5	7.0
Sb	0.3	7.0
Ce	1.0	1.0
Pr	1.0	1.3

* Analysis by Quad Group, Santa Barbara, California.
** Residual elements.
No determination for hydrogen was made.
Gold and tantalum are not reported since gold electrodes and tantalum slits are used.
Concentration of major matrix elements, Rb, Cu, and Cl are not listed.
Background lines interfere with the determination of beryllium, cesium, and germanium. Other elements not listed were not reported and have a detection limit of 1 ppma.

Conductivity measurements.—The electrical conductivity was measured by using a General Radio a-c bridge (1650A) at 1 kHz and also measured in the frequency range 1-20 kHz by audio oscillator Model 202D (Hewlett-Packard). There was no frequency dependence in this range except for the RbCl + CuCl system. All the measurements were carried out under flowing argon gas (about 0.3 cm/sec) purified by passing over heated copper turnings at about 400°C to remove trace oxygen gas and passing through a tube of silica gel to remove water vapor.

* Electrochemical Society Active Member.
[1] Present address: Center for Solid State Science, Arizona State University, Tempe, Arizona.
Key words: cuprous halide, metal halide, high electrical conductivity.

Table II. Sample preparation

Compound	Sintering condition	Annealing condition	Density (g/cm^3)
Cu_4CdI_6	320°C for 15 hr and then 420°C for 105 hr	400°C for 2 hr	4.98
Cu_2CdI_4	320°C for 15 hr and then 420°C for 105 hr	400°C for 2 hr	4.85
Cu_4CdCl_6	400°C for 93 hr	370°C for 2 hr	3.48
Cu_2CdCl_4	400°C for 93 hr	370°C for 2 hr	3.55
KCu_4I_5	After first sintering at 310°C for 71 hr, the pellet was pulverized and pressed, and then sintered again at 300°C for 115 hr	300°C for 2 hr	4.12
$RbCu_2I_3$	After melting at 335°C for 14 hr, the samples were ground and then pressed.	255°C for 16 hr	4.68
$RbCu_4I_5$			4.89
$RbCu_3Cl_5$	After melting at 250°C for 16 hr, the samples were ground and then pressed.	145°C for 16 hr	3.39
$RbCu_4Cl_5$			3.69
CuCl	After first sintering at 390°C for 72 hr, the pellet was pulverized and pressed, and then sintered at 390°C for 96 hr.	370°C for 2 hr	3.69

To make the conductivity measurements, the sample was sandwiched between copper electrodes which were 99.999% pure copper rod obtained from the American Smelting and Refining Company. Electrical contact was ensured by applying a slight spring pressure. Prior to the measurements, the cells were given a second anneal (see Table II). The annealing conditions and the densities are also summarized in Table II. Before and after measurements, there was no change in densities.

A Marshall resistance furnace was used in a horizontal position. The temperatures were controlled to ± 1°C by Leeds and Northrup Electromax controller and the temperature was measured by Doric Digital voltmeter using a Chromel-Alumel thermocouple which was calibrated by the phase transitions (369° and 407°C) of CuI.

Results and Discussion

CuI + CdI_2 system.—The crystal structure of CdI_2 is hexagonal with a layered structure, which can be viewed as more or less perfect packing of large anions with the smaller cations situated in the interstices (8). Herrmann (9) has reported that CdI_2 is soluble in CuI in all concentrations.

In the present investigation, the electrical conductivities of Cu_2CdI_4 [33 mole percent (m/o) CdI_2] and Cu_4CdI_6 (20 m/o CdI_2) samples were measured, and the results are shown in Fig. 1 and summarized in Table III. In previous studies (10), HgI_2 was used to stabilize the high temperature α-CuI phase at lower temperatures, and stabilization was achieved by formation of the compound, Cu_2HgI_4. Compared with the results on Cu_2HgI_4, our results on Cu_2CdI_4 and Cu_4CdI_6 suggest that the α-phase was not stabilized enough at lower temperatures, although the temperature above which the α-phase is stable was lowered from 407° to 308°C. This may be due to the difference in the crystal structure between Cu_2HgI_4 and Cu_2CdI_4. The crystal structure of α-Cu_2HgI_4 is the same as that of α-AgI (11), but the structure of Cu_2CdI_4 is not that of the intermediate phase, Cu_2HgI_4, but almost the same as α-CuI. This may occur because Cu_2CdI_4 is a solid solution with 33 m/o CdI_2 (7).

The transition temperatures obtained by the electrical conductivity in the present study and from previous data (9) are shown in Fig. 2. Previous results obtained by thermal analysis (9) are not sufficiently detailed to allow clarification into two (α-β and β-γ) phase transitions. Both the α-β and β-γ transition temperatures decreased with increasing concentrations of CdI_2. On the other hand, the activation energies in α-phase increased, which suggests that the mobility of copper ions was decreased by cadmium ions at normal copper lattice sites (interaction between cadmium ions and copper ions).

The electrical conductivities of Cu_2CdI_4 and Cu_4CdI_6 are higher by about one order of magnitude than pure CuI (Fig. 1) at high temperatures (200°-300°C) which may be due to the contribution of copper vacancies produced by introduction of cadmium ions. At low temperatures, the conductivities of Cu_2CdI_4 and Cu_4CdI_6 are lower than pure CuI (12). This may be due to the association (or clustering) between copper vacancies and cadmium ions.

Table III. Transition temperatures and activation energies for cuprous iodide and cuprous iodide-metal iodide system

Materials	Transition temperatures (°C) α to β	β to γ	Previous* results (9)	Activation energies (eV)**
CuI	407 ± 2	369 ± 2	414 ± 8	0.15 ± 0.03
Cu_4CdI_6	360 ± 2	325 ± 2	340 ± 6	0.33 ± 0.01
Cu_2CdI_4	308 ± 2	276 ± 4	290 ± 4	0.40 ± 0.01
Cu_2HgI_4	67 (10)	—	—	0.59 ± 0.01

* These transition temperatures previously reported are not sufficiently detailed to allow clarification into α to β or β to γ transitions (9).
** These activation energies are for the high temperature α-phases.

CuCl + $CdCl_2$ system.—The crystal structure of $CdCl_2$ is almost the same layered structure as that of CdI_2, and only differs from the CdI_2 structure in having its anions in a cubic rather than hexagonal close-packing (8). Herrmann has also studied the phase diagram of the CuCl + $CdCl_2$ system (9). According to his result, Cu_4CdCl_6 can only exist as a compound in this system.

In the present study Cu_4CdCl_6, Cu_2CdCl_4 [strictly speaking Cu_2CdCl_4 consists of two coexisting phases

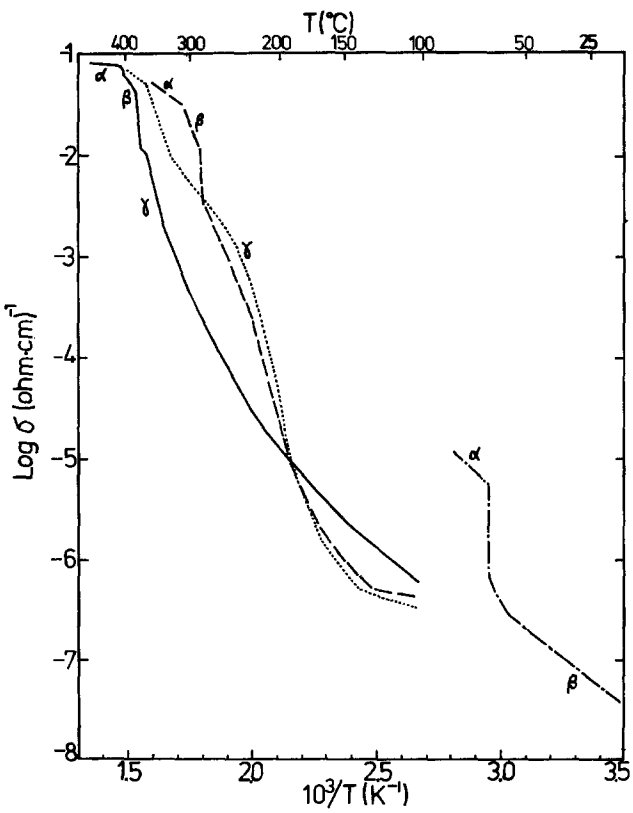


Fig. 1. The temperature dependence of the electrical conductivity of the CuI + CdI_2 system: —— pure CuI, ... Cu_4CdI_6 (20 m/o CdI_2), – – – – – Cu_2CdI_4 (33 m/o CdI_2), –·–·– Cu_2HgI_4 [Ref. (10)].

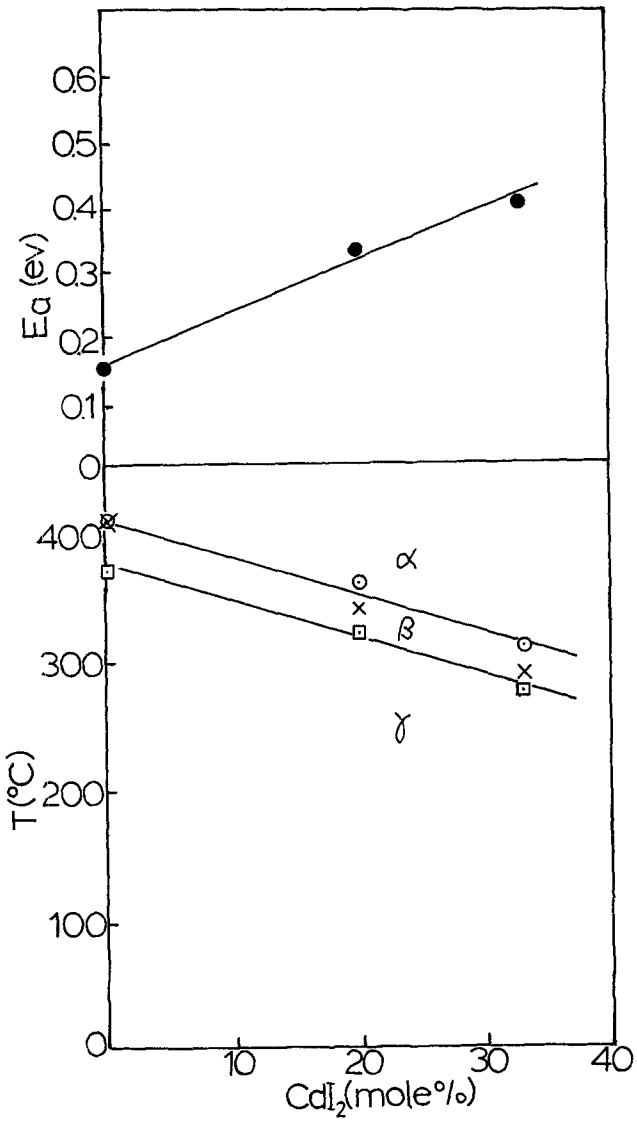


Fig. 2. Transition temperatures and activation energies vs. molar percentage of CdI_2: ● activation energy in the α-phase (this study), ⊙ transition temperatures of α-β transition (this study), ⊡ transition temperatures of β-γ transition (this study), X transition temperatures by thermal analysis (9).

of Cu_4CdCl_6 and $CdCl_2$ (9)], and pure CuCl samples were made. The conductivity results are shown in Fig. 3 and Table IV. At temperatures above 130°C, both Cu_4CdCl_6 and Cu_2CdCl_4 exhibited higher electrical conductivity than pure CuCl. This is due to the contribution of copper vacancies produced by introduction of cadmium ions. At lower temperatures there was no significant change which may be due to the precipitation of $CdCl_2$. The present data on polycrystalline CuCl are in good agreement with the data reported previously on single crystals (14, 15) and on polycrystals (16) at high temperatures (the intrinsic region). However, at low temperatures, our conductivities are higher than the previous data on single crystals (14, 17). This discrepancy may be attributed to grain boundaries or to impurities. The transition temperature of β to γ for Cu_4CdCl_6 (*i.e.*, the stable existence region of high temperature β-phase) was lowered from 407° to 330°C, and the transition temperatures obtained in the present study are in good agreement with previous data on Cu_4CdCl_6 obtained by thermal analysis (9). Both activation energies and transition temperatures of Cu_4CdCl_6 and Cu_2CdCl_4 were in good agreement with each other within experimental error. This is because Cu_2CdCl_4 does not exist as a single phase but exists as two phases of Cu_4CdCl_6 and $CdCl_2$ (9).

KI + CuI system.—The phase diagram of the KI + CuI system has been studied by Bradley and Greene

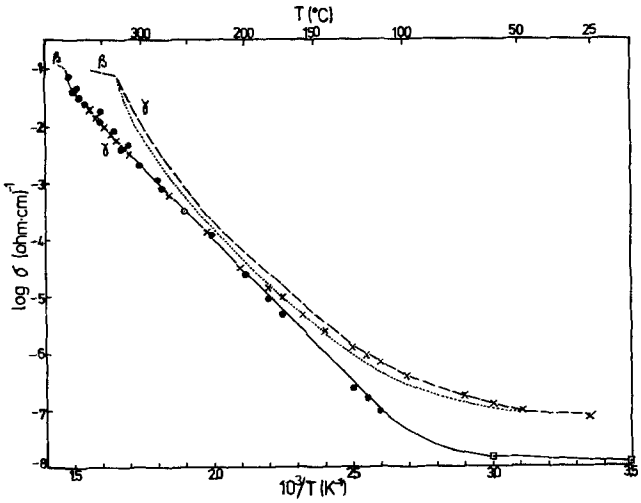


Fig. 3. The temperature dependence of the electrical conductivity of the CuCl + $CdCl_2$ system: ..... Cu_4CdCl_6 (this study), – – – – – Cu_2CdCl_4 (this study), x x x CuCl (this study), ⊙ Wagner and Wagner (16) CuCl, ⊡ Rivera et al. (17) CuCl, ● Hseuh and Christy (14) CuCl.

(2). According to their data, the KI + CuI system contains only one intermediate compound KCu_4I_5 which is stable between 257° and 332°C, the latter temperature being the incongruent melting point. However, they have not reported electrical conductivity data of KCu_4I_5. The present conductivity data are shown in Fig. 4. The temperature below which KCu_4I_5 decomposes to KI and CuI was 261° ± 2°C (see Fig. 4). This is in agreement with previous data [257°C by Bradley and Greene (2)], As seen from Fig. 4 the conductivity of KCu_4I_5 decreased abruptly by two orders of magnitude at 261°C. Above this transition, the electrical conductivity of KCu_4I_5 is about three orders of magnitude higher than that for pure CuI, although even after decomposition the conductivity of the two-phase mixture of KI and CuI was still higher than that of pure CuI. The small value of the activation energy for conduction in KCu_4I_5 suggests that the defect structure of KCu_4I_5 consists of highly disordered copper ions which, in turn, produce the high conductivity and is very similar to the MAg_4I_5 (M = K, Rb, and NH_4) compounds (1-3, 18).

CuI + RbI system.—In this system, two compounds, $RbCu_2I_3$ and Rb_2CuI_3, have been reported (2). The electrical conductivities of $RbCu_2I_3$ and $RbCu_4I_5$ (strictly speaking the latter is not a compound but consists of coexisting phases of $RbCu_2I_3$ and 2CuI) were measured between 25° and 250°C. The results are shown in Fig. 4. The electrical conductivity of $RbCu_2I_3$ was lower than pure CuI which may be due to the difference of crystal structure. The electrical conductivity of $RbCu_4I_5$ was also a little lower than pure CuI. The lower conductivity is due to the coexisting phase of CuI and the low conducting $RbCu_2I_3$, as is evident in the phase diagram (2).

CuCl + RbCl system.—In the present study the electrical conductivities of $Rb_2Cu_3Cl_5$ and $RbCu_4Cl_5$ (80

Table IV. Transition temperatures and activation energies for cuprous chloride and cuprous chloride-metal chloride system

Materials	Transition temperature (°C) β to γ	Previous results (9)	Activation energies* (eV)
CuCl	407 (13)	—	—
Cu_4CdCl_6	330 ± 2	350 ~ 310	0.26 ± 0.03
Cu_2CdCl_4	330 ± 2	319 ~ 309	0.22 ± 0.03

* These activation energies are for the high temperature β-phases.

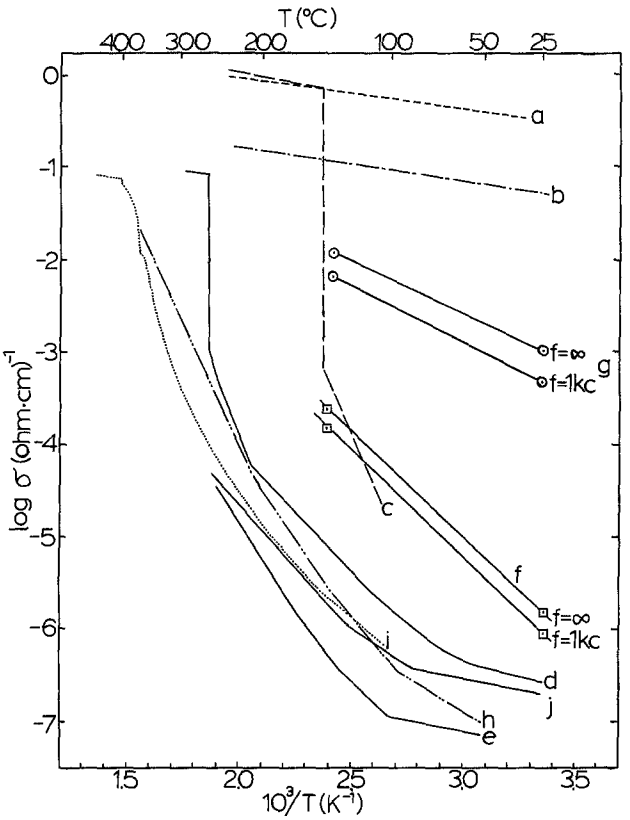


Fig. 4. The temperature dependence of the electrical conductivity of the cuprous halides and alkali halides system: (a) $RbAg_4I_5$ (18), (b) KAg_4I_5 (1), (c) AgI (22), (d) KCu_4I_5, (e) $RbCu_2I_3$, (f) $Rb_2Cu_3Cl_5$, (g) $RbCu_4Cl_5$, (h) CuCl, (i) CuI, (j) $RbCu_4I_5$.

m/o CuCl) were measured. The results are shown in Fig. 4. Sandonnini (19) has reported that the CuCl + RbCl system contains two intermediate compounds, Rb_2CuCl_3 and $Rb_2Cu_3Cl_5$, but he has not reported electrical conductivity data. These two compounds, especially the compound (80 m/o CuCl), have exceptionally high conductivity values even at room temperature. The electrical conductivity of these two samples exhibited a frequency dependence. None of the other samples exhibited such a frequency dependence. In Fig. 4, the conductivity values at 1 kHz and ∞ Hz are shown for the two samples, $Rb_2Cu_3Cl_5$ and $RbCu_4Cl_5$. Extrapolation to ∞ Hz was made to eliminate the faradaic impedance ΔR that may exist at the interface between electrode and electrolyte because the faradaic impedance is inversely proportional to the square root of frequency (20, 21). The sample containing 80 m/o CuCl [$RbCu_4Cl_5$] may be the new compound because of its high conductivity values compared to those of RbCl, CuCl, and $Rb_2Cu_3Cl_5$, and may exhibit predominantly ionic conduction just like $RbAg_4I_5$. Detailed results on the surveyed system, RbCl + CuCl will be reported in a subsequent paper (23).

The activation energies of cuprous halide and alkali-halide systems are summarized in Table V. As seen in this table, the higher the conductivity, the smaller the activation energy.

Summary

Electrical conductivity measurements on the systems CuI + CdI_2, CuCl + $CdCl_2$, CuI + KI, CuI + RbI, and CuCl + RbCl were carried out using the a-c method. The compounds KCu_4I_5, $Rb_2Cu_3Cl_5$, and $RbCu_4Cl_5$ (80 m/o CuCl) have been surveyed. These all exhibited high conductivity, especially $RbCu_4Cl_5$ which exhibited exceptionally high conductivity even at room temperature, for example, 8.25×10^{-4} Ω^{-1} cm^{-1} at 25°C and 1.14×10^{-2} Ω^{-1} cm^{-1} at 140°C. These conductivity values are higher than values reported for other copper-inorganic electrolytes and they are comparable to those previously reported for the copper-organic compounds (4-7).

Table V. Activation energies for cuprous halide-alkali halide compounds

Materials	Activation energy (eV)	References
KCu_4I_5	0.16 ± 0.02 (262° ~ 290°C)	This study
$RbCu_2I_3$	0.80 ± 0.03 (170° ~ 255°C)	This study
$RbCu_4I_5$	0.54 ± 0.02 (130° ~ 250°C)	This study
$Rb_2Cu_3Cl_5$	0.49 ± 0.02 (25° ~ 145°C)	This study
$RbCu_4Cl_5$	0.27 ± 0.01 (25° ~ 140°C)	This study
KAg_4I_5	0.14	(1)
$RbAg_4I_5$	0.07	(18)

Acknowledgments

This work was supported by the Advanced Research Projects Agency of the Department of Defense and was monitored by the Office of Naval Research through the Materials Research Center of Northwestern University under Contract No. N00014-75-C-1116.

Manuscript submitted Aug. 20, 1976; revised manuscript received Feb. 21, 1977.

Any discussion of this paper will appear in a Discussion Section to be published in the December 1977 JOURNAL. All discussions for the December 1977 Discussion Section should be submitted by Aug. 1, 1977.

REFERENCES

1. J. N. Bradley and P. D. Greene, *Trans. Faraday Soc.*, **62**, 2069 (1968).
2. J. N. Bradley and P. D. Greene, *ibid.*, **63**, 424 (1967).
3. B. B. Owens and G. R. Argue, *Science*, **157**, 308 (1967).
4. T. Takahashi, O. Yamamoto, and S. Ikeda, *This Journal*, **120**, 1431 (1973).
5. T. Takahashi and O. Yamamoto, *ibid.*, **122**, 83 (1975).
6. A. F. Sammells, J. Z. Gougoutas, and B. B. Owens, *ibid.*, **122**, 1291 (1975).
7. T. Takahashi, N. Wakabayashi, and O. Yamamoto, *ibid.*, **123**, 129 (1976).
8. R. W. G. Wyckoff, "Crystal Structures," Vol. 1, p. 266, Interscience Publishers, New York (1963).
9. G. Herrmann, *Z. Anorg. Chem.*, **71**, 296 (1911).
10. L. Suchow and G. R. Pond, *J. Am. Chem. Soc.*, **75**, 5242 (1953).
11. J. A. A. Ketelaar, *Trans. Faraday Soc.*, **34**, 874 (1938).
12. T. Matsui and J. B. Wagner, Jr., *This Journal*, **124**, 610 (1977).
13. M. R. Lorenz and J. S. Prener, *Acta Crystallogr.*, **9**, 538 (1958).
14. Y. W. Hsueh and R. W. Christy, *J. Chem. Phys.*, **39**, 3519 (1963).
15. A. V. Joshi and J. B. Wagner, Jr., *This Journal*, **122**, 1071 (1975).
16. J. B. Wagner, Jr. and C. Wagner, *J. Chem. Phys.*, **26**, 1597 (1957).
17. J. Rivera, L. A. Murray, and P. A. Hoss, *J. Cryst. Growth*, **1**, 171 (1967).
18. B. B. Owens and G. R. Argue, *This Journal*, **117**, 898 (1970).
19. C. Sandonnini, *Gazz. Chim. Ital.*, **44**, 311 (1914).
20. E. Warburg, *Ann.*, **6**, 125 (1901).
21. G. Jones and S. M. Christian, *J. Am. Chem. Soc.*, **57**, 272 (1935).
22. L. W. Strock, *Z. Physik. Chem., Abt. B*, **25**, 441 (1934).
23. T. Matsui and J. B. Wagner, Jr., *This Journal*, **124**, 941 (1977).

Investigations on a High Conductivity Solid Electrolyte System, RbCl + CuCl

Tsuneo Matsui[1] and J. Bruce Wagner, Jr.*,[1]

Materials Research Center and Department of Materials Science and Engineering, Northwestern University, Evanston, Illinois 60201

ABSTRACT

Solid electrolytes with high copper ionic conductivity and low electronic hole conductviity have been found in the RbCl + CuCl system. The highest conductivity of $RbCu_3Cl_4$ [75 mole percent (m/o) CuCl] was 2.25×10^{-3} $(\Omega\text{-cm})^{-1}$ at 25°C. The conductivity has been measured as functions of temperature and of composition. X-ray patterns and thermal analyses indicate that the material is a new compound and not a mixture of the constituents.

Solid electrolytes exhibiting high conductivity such as Ag_3SI (1, 2), MAg_4I_5 (M = K, Rb, and NH_4) (3-5), KAg_4I_4CN (6), $Ag_{19}I_{15}P_2O_7$ (7), silver organic compounds (8-11), and β-Al_2O_3 (12) have been found and all these are silver ion or alkali ion conductors. Recently, Takahashi and his co-workers (13-15) and Sammells *et al.* (16) have found new copper ion solid electrolytes with high ionic conductivity. These copper compounds were copper-organic compounds, and some are unstable when used in galvanic cells (16).

The purpose of the present study is to prepare copper solid electrolytes without organic additives. In our preceding paper (17), many kinds of compounds in the cuprous halides and metal halides systems have been examined by a-c conductivity measurements, and the new compounds with high conductivity at room temperature have been found in the RbCl + CuCl system.

In the present study, the properties of the RbCl + CuCl system were investigated in more detail by the electrical conductivity measurements and x-ray techniques.

Experimental

Materials.—Ultrapure CuCl powder (99.999%, Semi-elements Incorporated) and RbCl (99.9%, Apache Chemicals Incorporated) were used. The compounds and intermediate compositions were prepared by mixing the powders with the appropriate amounts of two kinds of chlorides, from which some of the water had been removed by heating to about 110°C in an evacuated Vycor glass tube before mixing. The preparation and annealing condition of samples have been reported in the preceding paper (17).

Conductivity measurements.—The electrical conductivity was measured by using a General Radio a-c bridge (1650A) at 1 kHz and also measured in the frequency range 1-20 kHz by audio oscillator Model 202D (Hewlett-Packard). For the electronic conductivity measurements, a constant voltage supply (099034 Leeds and Northrup Company) with a voltage divider (Gertsch Products Incorporated, Model 1001) was used to apply the polarization potentials for the Cu/electrolyte/graphite cell. The polarization potential was measured by a Keithley 610B electrometer and the current in response to the applied polarization potential was measured by reading the voltage drop across a series resistor with a Doric Digital microvoltmeter. Before measurements the polarization cell was annealed at 145°C for 16 hr.

X-ray diffraction analysis.—The x-ray diffraction patterns were obtained at room temperature by using a Philips diffractometer with $KuC\alpha$ radiation through a Ni filter.

Differential thermal analysis.—A du Pont 990 digital thermal analysis instrument was used with the various heating rates (2°-10°C/min). As the reference material α-alumina powder was used, and the measurement was carried out under the nitrogen gas flow.

Results and Discussion

In the RbCl-CuCl system, two intermediate compounds, Rb_2CuCl_3 and $Rb_2Cu_3Cl_5$, have been reported by thermal analysis (18). The compounds $Rb_2Cu_3Cl_5$ (60 m/o CuCl) and $RbCu_3Cl_4$ (67.5, 75, 80, 85, 90 m/o CuCl) were studied in the present work.

Electrical conductivity measurements.—The values of electrical conductivity at 1 kHz and ∞ Hz are summarized in Table I. Extrapolation to ∞ Hz was made to eliminate the faradaic impedance ΔR, which is inversely proportional to the square root of frequency (19, 20)

$$\Delta R = K \cdot f^{-1/2}$$

where f is frequency and K a proportionality constant. The measured resistance Rm contains both the bulk electrolyte resistance R and any faradaic impedance effects that may exist at the interface between electrolyte and electrodes. Thus

$$Rm = R + \Delta R = R + Kf^{-1/2}$$

The error caused by ΔR was minimized by extrapolating the measured resistance to infinite frequency. The typical frequency dependences are shown in Fig. 1 and 2. As shown in Fig. 1, a linear extrapolation was possible to infinite frequency. This frequency dependence changed under the different annealing conditions (at 110°C for 16 hr and at 145°C for 16 hr). This

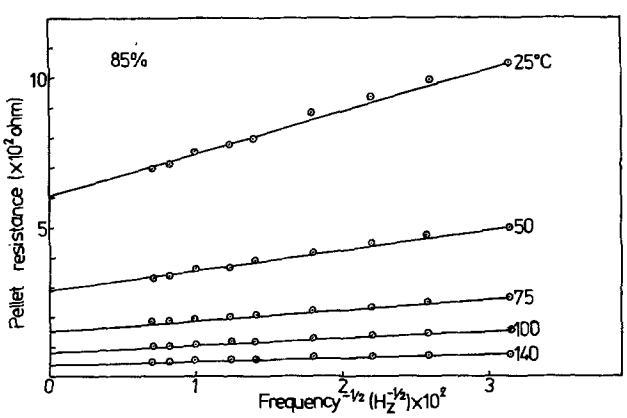


Fig. 1. Frequency dependence of the pellet resistance for the compound containing 85 m/o CuCl.

* Electrochemical Society Active Member.
[1] Present address: Center for Solid State Science, Arizona State University, Tempe, Arizona 85281.
Key words: copper electrolyte, high ionic conductivity, low electronic conductivity.

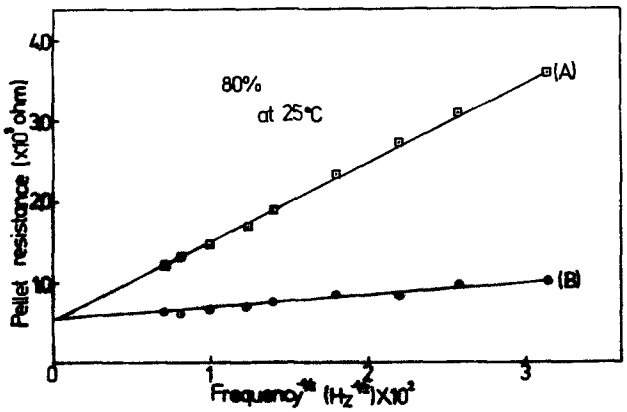


Fig. 2. Frequency dependence for the sample containing 80 m/o CuCl under the different annealing conditions: (A) annealed at 110°C for 16 hr, (B) annealed at 145°C for 16 hr.

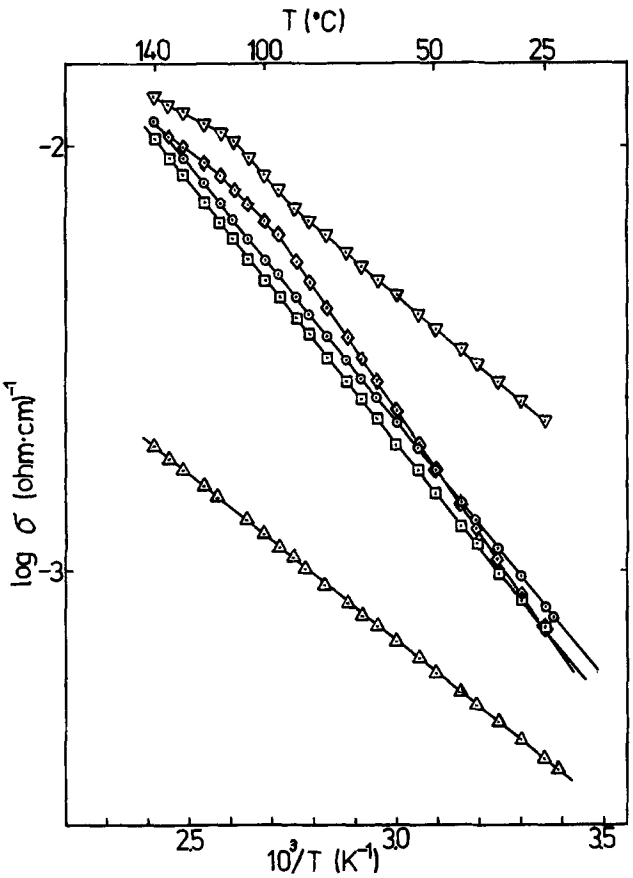


Fig. 3. Temperature dependence of the electrical conductivity for the compounds with various mole percent of CuCl at ∞ Hz: ◈ 67.5 m/o CuCl, ▽ 75.0, ⊙ 80.0, ▣ 85.0, ◬ 90.0.

behavior is probably due to the different contact conditions. However, the resistance at the infinite frequency was the same for each as is shown in Fig. 2. In this study we report the conductivities for samples annealed at 145°C for 16 hr. The temperature dependence of the electrical conductivity is shown in Fig. 3. For two samples ($RbCu_3Cl_4$ containing 75 m/o CuCl and 67.5 m/o CuCl), the changes of slope were observed at about 100° ~ 110°C. No heat change was observed near these temperatures by using the differential thermal analysis. This change in slope is unexplained at present.

The effect of composition (mole percent CuCl) upon the conductivity at room temperature (25°C) is shown in Fig. 4. The maximum value of 2.5×10^{-3} $(\Omega\text{-cm})^{-1}$ occurred at 75 m/o CuCl, which suggests the existence of a new compound whose stoichiometric composition is $RbCu_3Cl_4$. The conductivity values of the compounds from 67.5 m/o CuCl to 90 m/o CuCl were higher than that of $Rb_2Cu_3Cl_5$ by about three orders and were much higher than that of pure CuCl [polycrystalline CuCl (17) and single crystal CuCl (21)] by about four and five orders, respectively.

The activation energies of conductivity of these compounds are summarized in Table I. Note that the higher the conductivity, the smaller the activation energy.

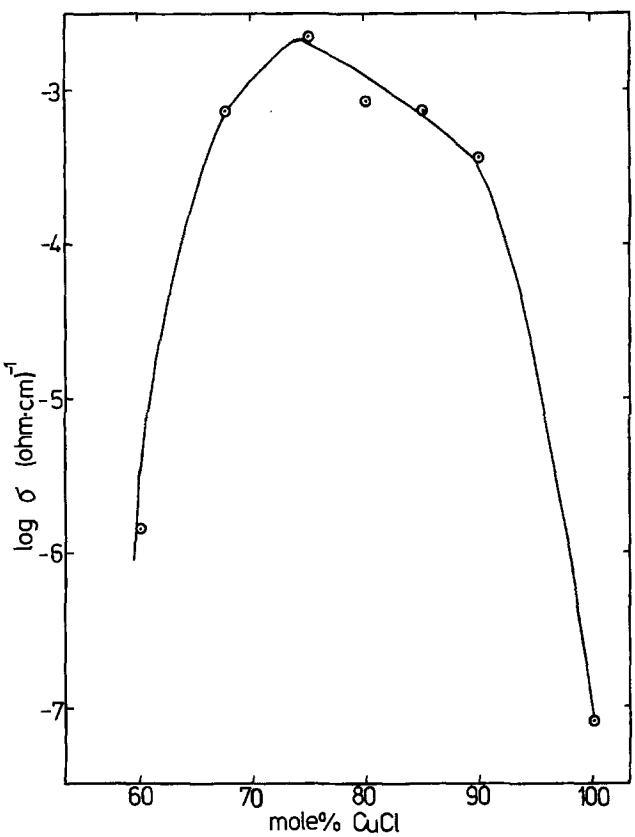


Fig. 4. Electrical conductivity extrapolated to ∞ Hz at 25°C vs. composition.

Table I. Conductivity results

Compound	m/o CuCl	Conductivity $(\Omega\text{-cm})^{-1}$ 25°C 1000 Hz (±3%)	25°C ∞ Hz (±10%)	140°C 1000 Hz (±3%)	140°C ∞ Hz (±10%)	Activation energy (eV)
$Rb_2Cu_3Cl_5$	60	8.41×10^{-7}	1.45×10^{-6}	1.41×10^{-4}	2.16×10^{-4}	0.49 ± 0.02 (25° ~ 145°C)
	67.5	3.63×10^{-4}	7.37×10^{-4}	8.42×10^{-3}	1.12×10^{-2}	0.32 ± 0.02 (25° ~ 95°C) / 0.18 ± 0.02 (115° ~ 140°C)
$RbCu_3Cl_4$	75	4.50×10^{-4}	2.25×10^{-3}	1.06×10^{-2}	1.31×10^{-2}	0.19 ± 0.02 (25° ~ 90°C) / 0.14 ± 0.02 (110° ~ 140°C)
	80	4.55×10^{-4}	3.25×10^{-4}	6.35×10^{-3}	1.14×10^{-2}	0.27 ± 0.02 (25° ~ 140°C)
	85	4.35×10^{-4}	7.35×10^{-4}	6.20×10^{-3}	1.04×10^{-2}	0.29 ± 0.02 (25° ~ 140°C)
	90	2.03×10^{-4}	3.62×10^{-4}	1.72×10^{-3}	1.98×10^{-3}	0.19 ± 0.02 (25° ~ 140°C)
CuCl*	100	8.05×10^{-8}		2.55×10^{-6}		1.00 ± 0.02 (230° ~ 370°C)

* There is no frequency dependence on pure CuCl.

Differential thermal analysis.—The melting temperature of $RbCu_3Cl_4$ (75 m/o CuCl) which exhibits the highest conductivity was measured by using DTA apparatus. An endothermic peak which is due to melting of the sample was observed for $RbCu_3Cl_4$ at 170° ± 10°C, and this melting temperature is different from the melting temperature of $Rb_2Cu_3Cl_5$ (about 150°C) reported previously (18). This also suggests the existence of a new and different compound, $RbCu_3Cl_4$.

Electronic conductivity measurements.—Preliminary electronic conductivity measurements were carried out by Wagner's polarization method (22). As was first suggested by Wagner (22) and by Hebb (23), the ionic part of the current for a two-component system can be suppressed by the use of one electrode that does not contain the constituents of the crystal. The other one may contain the constituent which is used to fix the electrochemical potentials of the electrolyte at that side of the cell, a reversible electrode. Thus, for cuprous halides, Wagner and Wagner (24) and recently Joshi and Wagner (25) have used a carbon anode and a copper cathode. However, for the ternary system, it is necessary to fix the electrochemical potential of two constituents of the electrolyte. For example, the polarization cell, $Ag|Ag_3SI|I_2 + C$, was used for Ag_3SI (26). For the RbCl + CuCl system, the polarization cell, $Cu|RbCu_3Cl_4|Cl_2 + C$, is suitable to determine the electronic conductivity. However, such a cell was difficult to construct because of the gaseous chlorine at room temperature. In the present study the cell Cu|sample (80 m/o CuCl)|graphite, was used under a very slow flow rate of argon gas (≃0.05 cm/sec). Since the activity of chlorine is not fixed in this cell, chlorine ion may migrate from the copper electrode toward the graphite electrode, which causes an ionic current in addition to the electronic current. Thus, in this cell, the chlorine evolution becomes important at higher applied voltages. As seen in Fig. 5, which shows the steady-state current as a function of polarization potential, the theoretical slope calculated by Wagner's theory could be fitted to the experimental results in the applied voltage region between 0.4 and 0.6V at all temperatures from 23° to 140°C. These experimental values were very reproducible with increasing and decreasing temperature. The reproducible data and the experimental slope which could be fitted to the theoretical slope suggested that even in this preliminary study the ionic contribution from chlorine evolution was very small compared to electronic current and also decomposition of the sample was negligibly small. Figure 5 also shows that the new compound containing 80 m/o CuCl exhibits a small electronic hole conductivity.[2] The temperature dependence of the electronic conductivity due to electron holes is shown in Fig. 6. Compared to the electrical conductivity, it is concluded that the new compound is an essentially ionic conductor.

X-ray diffraction analysis.—X-ray diffraction patterns were obtained at room temperature for all the samples containing 60-100 m/o of CuCl. The x-ray patterns of these compounds showed very different results from that of $RbAg_4I_5$ observed by Bradley and Greene (27). The comparison of d-values and intensities of some compounds in the RbCl + CuCl system and pure CuCl is presented in Table II.

[2] Electron hole conduction was inferred from the behavior of the electronic current as a function of applied voltage.

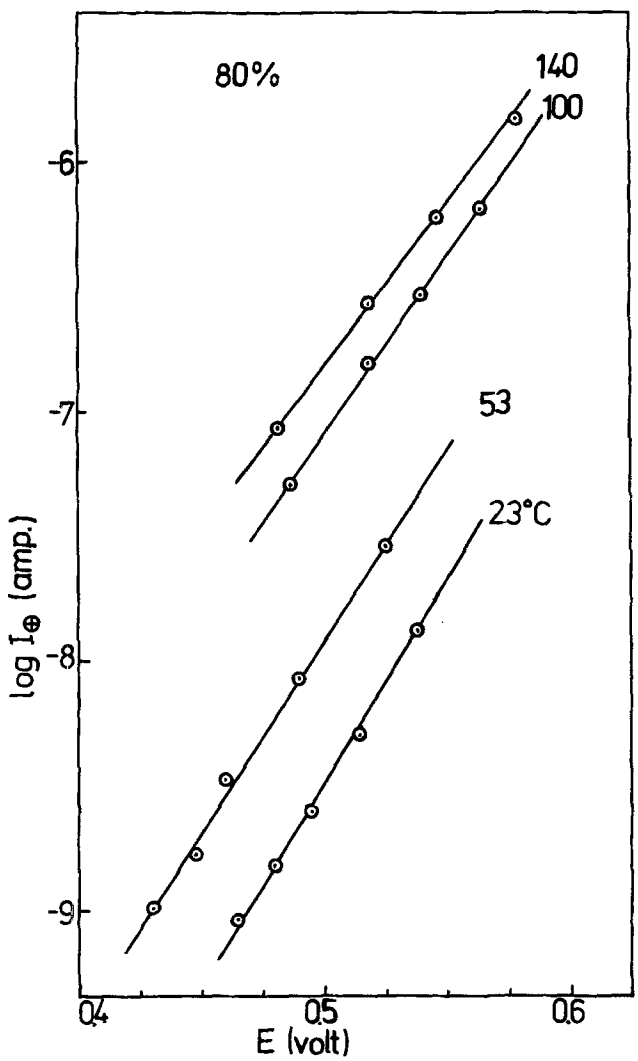


Fig. 5. Electronic hole conductivity vs. applied voltage (80 m/o CuCl).

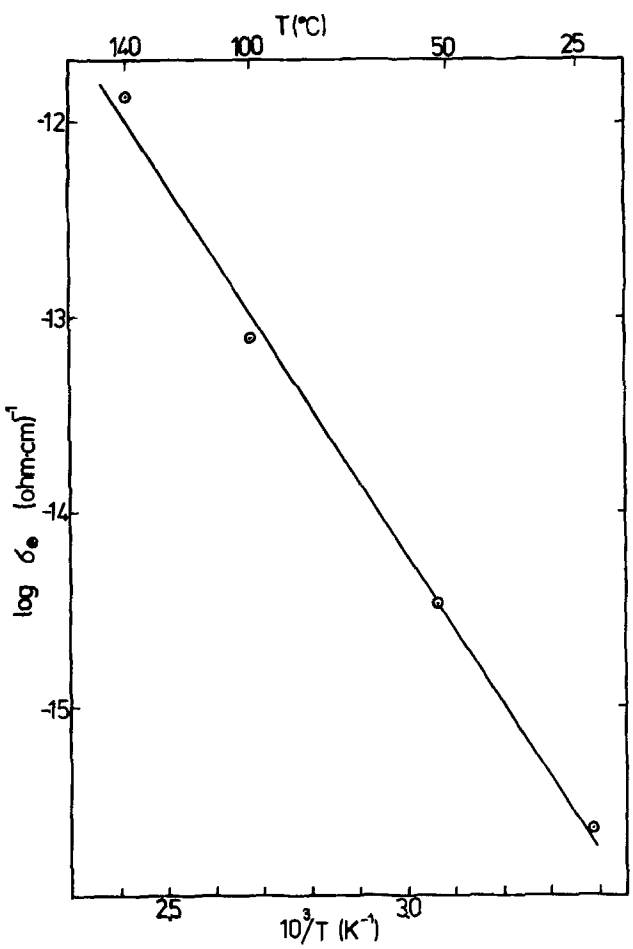


Fig. 6. Temperature dependence of the electronic hole conductivity for the sample (80 m/o CuCl).

Table II. d-values and intensities for CuCl + RbCl system at 23°C

$Rb_2Cu_3Cl_5$				$RbCu_2Cl_4$ (75 m/o CuCl)				$RbCu_4Cl_5$ (80 m/o CuCl)				γ-CuCl	
d	I	d	I	d	I	d	I	d	I	d	I	d	I
7.45	VW	2.68	M	4.53	VW	2.28	VW	4.55	VW	2.28	VW	3.11	S
6.92	VW	2.65	M	4.03	W	2.27	VW	4.04	W	2.27	VW	2.70	MW
5.61	M	2.64	M	3.89	W	2.21	W	3.89	W	2.21	MW	1.91	S
4.61	VW	2.63	M	3.84	W	2.16	VW	3.84	W	2.16	VW	1.63	MS
4.49	W	2.56	VW	3.77	W	2.14	VW	3.77	W	2.14	VW	1.35	W
4.13	MW	2.52	MS	3.69	W	2.08	VW	3.70	W	2.08	VW	1.24	MW
4.01	W	2.45	M	3.56	MS	2.06	VW	3.56	MS	2.02	W		
3.89	W	2.40	W	3.49	W	2.02	W	3.49	VW	1.96	W		
3.84	W	2.34	VW	3.45	M	1.96	W	3.45	W	1.91	S		
3.77	W	2.30	W	3.41	W	1.91	S	3.32	VW	1.88	S		
3.63	W	2.25	VW	3.31	VW	1.88	S	3.23	W	1.87	S		
3.49	M	2.23	VW	3.23	M	1.87	S	3.11	S	1.81	VW		
3.42	S	2.18	MW	3.11	S	1.81	VW	3.05	S	1.76	VW		
3.32	W	2.13	VW	3.05	S	1.76	W	2.97	VW	1.63	MS		
3.26	VW	2.10	VW	3.00	W	1.63	M	2.89	MW	1.60	M		
3.20	M	2.05	W	2.95	VW	1.60	M	2.87	MW	1.35	VW		
3.11	MS	2.02	MW	2.89	M	1.55	VW	2.86	MW	1.33	VW		
3.09	MS	1.96	W	2.86	M	1.35	VW	2.85	M	1.24	VW		
3.04	S	1.95	W	2.84	MS	1.33	W	2.78	W				
2.96	M	1.93	W	2.78	MW	1.24	W	2.77	W				
2.93	MS	1.91	VW	2.76	MW			2.73	M				
2.87	S	1.87	S	2.73	MS			2.69	MW				
2.85	MW	1.83	M	2.69	MW			2.64	MW				
2.80	MW	1.71	VW	2.64	MW			2.56	W				
2.77	VW	1.70	VW	2.56	W			2.51	VW				
2.75	MW	1.64	W	2.52	W			2.46	MW				
		1.62	W	2.46	MW			2.43	MW				
		1.60	MW	2.42	MW			2.35	W				
		1.58	W	2.35	W								
		1.40	W										

After annealing the compound at 145°C for 16 hr, the intensity of x-ray patterns increased and also the electrical conductivity increased which is similar to the behavior reported for $RbAg_4I_5$ (8).

The sample containing 67.5 m/o CuCl showed almost the same diffraction lines as those of the compound (75 m/o CuCl) together with the lines characteristic of $Rb_2Cu_3Cl_5$. The samples containing 85 and 90 m/o CuCl also showed similar diffraction lines to those of the compounds (75 or 80 m/o CuCl), but some weak lines originated from the compounds (75 or 80 m/o CuCl) disappeared and the intensity of the lines characteristic of pure CuCl increased. Although some lines characteristic of both $Rb_2Cu_3Cl_5$ and CuCl are found, the occurrence of some extra lines suggests that the compound (75 or 80 m/o CuCl) is not simply a disordered or contaminated phase but rather a separate new compound. However, the presence of CuCl and $Rb_2Cu_3Cl_5$ cannot be ruled out, indicating that the phase was not optimized to equilibrium.

From the x-ray powder data alone, no conclusions could be reached about the structure of the new compound except that the number of reflections would not be consistent with a structure of high symmetry. Further comment on the stoichiometry must await the x-ray determination on the single crystal.

Summary

New electrolytes with high copper ionic conductivity and low electronic hole conductivity were found in $RbCu_3Cl_4$ compounds. The values of the conductivity are comparable to those of organic cuprous halides previously reported by Takahashi *et al.* (13-15).

Acknowledgments

This work was supported by the Advanced Research Projects Agency of the Department of Defense and was monitored by the Materials Research Center of Northwestern University under Grant No. DAHC 1573 G-19.

Manuscript submitted Aug. 23, 1976; revised manuscript received Nov. 11, 1976.

Any discussion of this paper will appear in a Discussion Section to be published in the December 1977 JOURNAL. All discussions for the December 1977 Discussion Section should be submitted by Aug. 1, 1977.

REFERENCES

1. B. Reuter and K. Hardel, *Naturwissenschaften*, **48**, 161 (1961).
2. T. Takahashi and O. Yamamoto, *Electrochim. Acta*, **11**, 779 (1966).
3. J. N. Bradley and P. D. Greene, *Trans. Faraday Soc.*, **62**, 2069 (1966).
4. J. N. Bradley and P. D. Greene, *ibid.*, **63**, 424 (1967).
5. B. B. Owens and G. R. Argue, *Science*, **157**, 308 (1967).
6. G. W. Mellors and D. V. Louzos, *This Journal*, **118**, 846 (1971).
7. T. Takahashi, S. Ikeda, and O. Yamamoto, *ibid.*, **119**, 477 (1972).
8. B. B. Owens, *ibid.*, **117**, 1536 (1970).
9. M. L. Beradelli, C. Biondi, M. De Rossi, G. Fonseca, and M. Giomini, *ibid.*, **119**, 114 (1972).
10. B. B. Owens, J. H. Christie, and G. T. Tiedeman, *ibid.*, **118**, 1144 (1971).
11. J. Coetzer and M. M. Thackeray, *Electrochim. Acta*, **21**, 37 (1976).
12. Y. Y. Yao and J. T. Kummer, *J. Inorg. Nucl. Chem.*, **29**, 2453 (1967).
13. T. Takahashi, O. Yamamoto, and S. Ikeda, *This Journal*, **120**, 1431 (1973).
14. T. Takahashi and O. Yamamoto, *ibid.*, **122**, 83 (1975).
15. T. Takahashi, N. Wakabayashi, and O. Yamamoto, *ibid.*, **123**, 129 (1976).
16. A. F. Sammells, J. Z. Gougoutas, and B. B. Owens, *ibid.*, **122**, 1291 (1975).
17. T. Matsui and J. B. Wagner, *ibid.*, **124**, 937 (1977).
18. C. Sandonnini, *Gazz. Chim. Ital.*, **44**, 311 (1914).
19. E. Warburg, *Ann.*, **6**, 125 (1901).
20. G. Jones and S. M. Christian, *J. Am. Chem. Soc.*, **57**, 272 (1935).
21. J. Rivera, L. A. Murray, and P. A. Hoss, *J. Cryst. Growth*, **1**, 171 (1967).
22. C. Wagner, Proceedings of the 7th International Committee for Electrochemical Thermodynamics and Kinetics, Butterworths, London (1956).
23. M. H. Hebb, *J. Chem. Phys.*, **20**, 185 (1952).
24. J. B. Wagner and C. Wagner, *ibid.*, **26**, 1597 (1957).
25. A. V. Joshi and J. B. Wagner, *This Journal*, **122**, 1071 (1975).
26. T. Takahashi and O. Yamamoto, *Electrochim. Acta*, **11**, 779 (1966).
27. J. N. Bradley and P. D. Greene, *Trans. Faraday Soc.*, **63**, 2516 (1967).

On Growth and Structure of Vapor-Grown Cadmium Iodide Crystals

S. D. Sharma and Kanchan Mehrotra

Department of Physics, Indian Institute of Technology, Delhi, New Delhi 110029, India

and V. K. Agrawal

Department of Physics, Moti Lal Nehru College, New Delhi 110021, India

ABSTRACT

Cadmium iodide crystals have been grown by the vapor phase technique. Under different thermal and supersaturation conditions, cadmium iodide crystals of the same morphological form and shape, but of different size and thickness, have been obtained. No spirals are observed on the crystals which grow with their basal planes normal to the wall of the growth tube, whereas, spirals have been observed on crystals grown on a glass substrate at high supersaturation. The observations indicate that a screw dislocation mechanism is not operative in the growth of CdI_2 crystals in the present case. The growth starts with a dendritic skeleton and then changes to flat platelets by the filling in process and by two dimensional nucleation. Formation of spirals on crystals grown on glass slides has been attributed to adsorbed impurities or debris and irregularities on the substrate surface. An x-ray study of the crystals has revealed that nearly all vapor-grown crystals show the most stable basic polytype (4H) of CdI_2. Observations indicate that conditions of growth play an important role in deciding the structure.

A large number of reports on growth and polytypism (1, 2) in CdI_2 crystals have appeared in the literature; however, except for a couple of attempts by melt (3) and vapor phase (4) techniques, these crystals have been grown from solution using the isothermal evaporation technique. The growth of these crystals has often been attributed to the spiral growth mechanism. This mechanism was first proposed by Frank (5) in 1949 to explain the growth of crystals at low supersaturation. Since then spirals have been observed in crystals of many compounds during evaporation, condensation, and solidification and lend support to the Burton Cabrera, and Frank (BCF) growth theory (6). This theory has also been able to explain many of the observed effects and growth features. Frank extended the dislocation growth theory to explain the formation of polytypes (7) in a direct and simple way. The existence of polytypism in CdI_2 was predicted by Forty (8) from an optical study of the growth features on the (0001) faces of the crystals. The prediction was borne out by the x-ray investigations of Mitchell (9), who discovered 29 polytypic modifications of the compound. By combining his x-ray diffraction results with the step height measurements of Forty (8), Mitchell (9) showed that a correlation exists between the spiral step height and the unit cell height, thus supporting Frank's theory. Initial observations of growth spirals on SiC crystals by Verma (10), Amelinckx (11), and others lend support to this theory but subsequent observations of step height on solution-grown cadmium iodide crystals by Trigunayat and Verma (12) and on vapor-grown crystals by Chadha and Trigunayat (13) did not agree with the theory.

Although a large number of other theories of polytypism have been put forth, none of them explain all the observed facts. There is scattered evidence in the existing literature which indicates that conditions of growth may have an influence on polytypism.

It was felt that for a better understanding of the phenomenon of polytypism, crystals should be grown under improved and steady-state (stabilized) conditions. In the present investigation good quality CdI_2 crystals have been grown by the vapor phase technique. Optical microscope, scanning electron microscope, and x-rays were used as tools for the study. Transmission electron microscope has also been used for studying dislocation structures, the results however will be described elsewhere.

Experimental

A quartz crucible containing cadmium iodide powder of 99.5% purity was kept in the maximum temperature region (390°-420°C) of a horizontal Kanthal resistance furnace. A cross-sectional view of the experimental arrangement together with the temperature profile is depicted in Fig. 1. The crucible was enclosed in a Pyrex tube of 3.5 cm diameter, in which a vacuum of 10^{-1}-10^{-3} mm of Hg can be maintained. Glass slides are kept in the region 150°-300°C, where most of the growth is found to take place. The charge temperature was gradually increased to the desired value (390°-

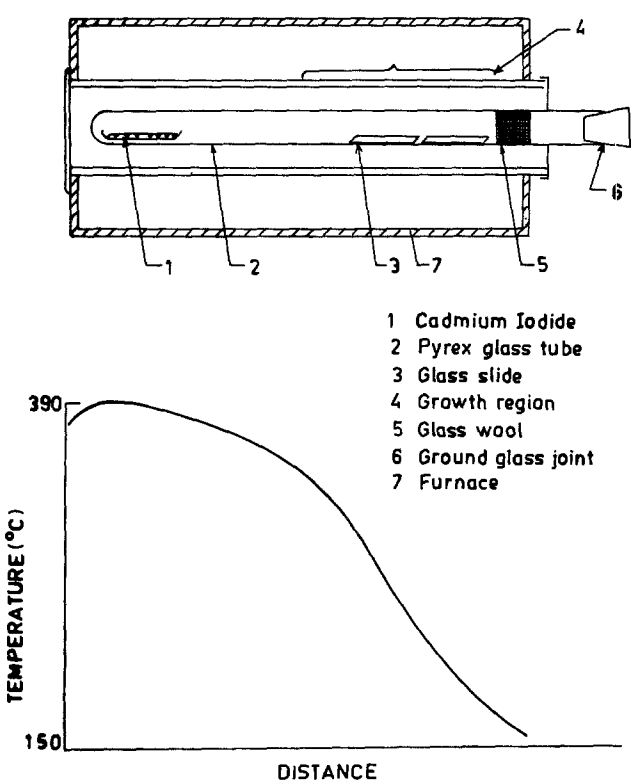


Fig. 1. Experimental arrangement for the growth of dendrites and platelets from vapor phase.

420°C) and was maintained at this value for 10-24 hr. On the completion of a growth run, the furnace was cooled to room temperature at the rate of ~ 20°C per hour. The crystals grown on slides and on the wall of the Pyrex tube were picked up and examined with a Carl Zeiss NU_2 Universal optical microscope using bright and dark field illumination and with the S4 10 Cambridge scanning electron microscope.

The as-grown crystals were also subjected to x-ray examination for structural determination. As the crystals are extremely soft, great care was exercised to ensure that they were not deformed while being taken out of the tube or during mounting on the x-ray goniometer.

Optically perfect crystals were mounted on glass fibers and were oscillated about the a-axis, the c-axis being horizontal. The range of oscillation was 15° and was adjusted to be between 55.5° and 70.5° with the incident x-ray beam. To set the a-axis of the crystal vertical, the method followed was that of Agrawal (14). After setting, the range of oscillation was taken from 33° to 48°. This range was particularly chosen to record a large number of (10.l) reflections required for the identification of polytypes. The crystals exhibiting a mixture of higher polytypes were oscillated about a*-axis in the range of oscillation between 53° and 68° for their polytypic identification (15).

The oscillation photographs of all the crystals were recorded with a camera of radius 3 cm and a collimator of aperture 0.5 mm. The size of focal spot was 1 mm^2. The photographs were taken with the Ni filtered CuKα radiation or with Cu white radiation.

Growth Observations and Mechanism

The growth of CdI_2 crystals has been examined in detail and the observations under different experimental conditions in various runs are summarized in Table I. It is evident from Table I that if the charge temperature is suitable to yield sufficient vapor, the growth of CdI_2 crystals can be classified under three groups.

1. Platelet crystals are formed at the lowest supersaturation (2-5). They invariably grow on the upper part of the growth tube with their basal faces normal to the axis of the tube.
2. Small hexagonal crystals, with their basal faces parallel to the axis of the tube, grow at intermediate supersaturation (20-100) on the glass slide substrate in the lowest part of the tube.
3. Dendrites and powderlike deposition are observed at high supersaturation (100-500).

It can be seen from Table I that the morphology of the crystals in a particular growth zone remained almost unchanged even when the charge temperature was changed from 390° to 420°C. This indicates that growth temperature is the main parameter in determining the basic morphology of the crystals. This observation is in agreement with the observation on ice (16) and ammonium chloride (17) crystals grown from the vapor phase.

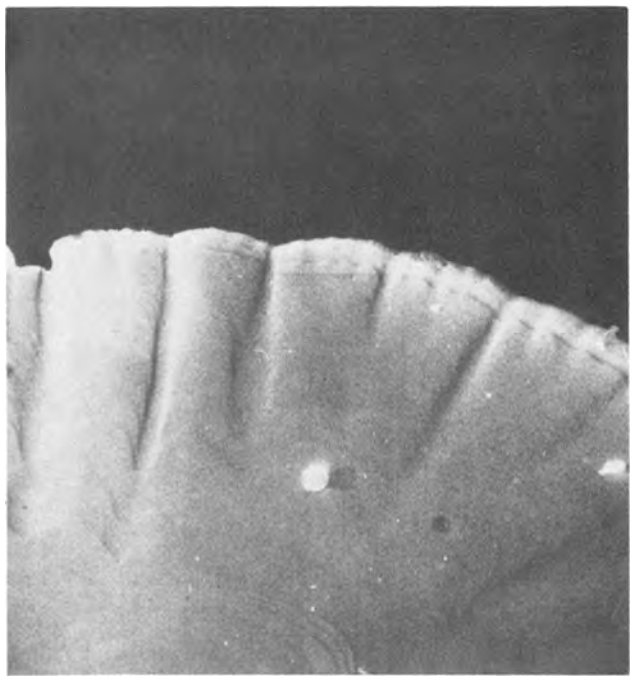


Fig. 2. SEM micrograph of a platelet which is smooth and flat in the central region and shows markings near the periphery.

The surface features of the as-grown crystals were examined in detail under high resolution optical microscopy and scanning electron microscopy.

Two principal observations were:

1. The platelets, growing with their basal faces normal to the tube axis, were smooth and flat in the central region and showed markings near the periphery (Fig. 2 and 3), and often had dendritic edges (Fig. 4). No spirals were observed on their surfaces in examination of hundreds of platelets.
2. The crystals growing in the lower part of the tube on the glass substrate often had spirals (Fig. 5 and 6) on their surfaces.

Thus the platelets growing at a lower supersaturation did not exhibit spirals while crystals from higher supersaturation areas commonly had spirals.

Burton, Cabrera, and Frank (6) have been responsible for the well-known model of spiral growth by means of the termination of a screw dislocation at the growing interface. The distinguishing features of this theory are:

1. Growth takes place under conditions of low supersaturation, less than 1%.
2. Adjacent or successive turns of the spirals should be separated by a distance of the order of $4\pi r_c$ where r_c is the radius of the critical two dimensional nucleus.
3. The step height of the spiral, at least according to the original BCF model should be monoatomic.

Table I.

Serial no	Charge temperature, °C	Period of growth, hr	Pressure of air in the tube, mm Hg	Morphology	Growth temperature, °C
1.	420	20-24	760	Platelets up to 1 cm diameter and 10 μm thick grow normal to the axis of the tube	320-390
				Small hexagonal crystals up to 4 × 4 mm on glass substrate	220-330
				Dendrites on the upper wall of the tube	190-250
				Powderlike deposition	165-200
2.	420	20-24	10^{-2}	No platelets or dendrites. Thick powder-like deposition	190-350
3.	390	20-24	760	Platelets up to 6 mm diameter and 5 μm thick grow normal to the axis of the tube	270-350
				Small hexagonal crystals up to 3 × 3 mm on glass substrate	210-290
				Dendrites on the upper wall of the tube	180-230
				Powderlike deposition	150-200
4.	390	20-24	10^{-2}	Large number of small hexagonal crystals	170-300
5.	350	20-24	760	Insufficient flux, negligible growth	

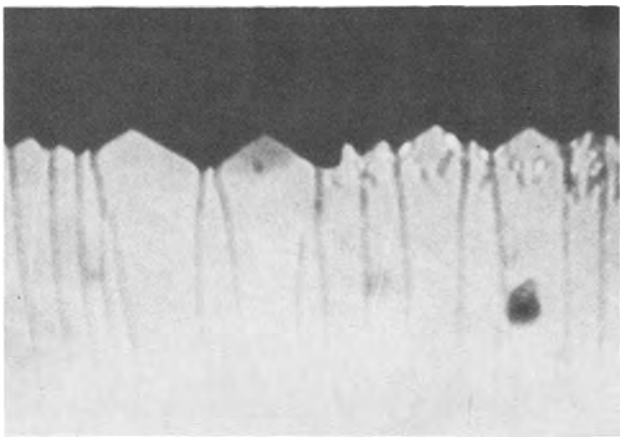


Fig. 3. Optical micrograph of a platelet which is smooth and flat in the central region and shows markings near the periphery.

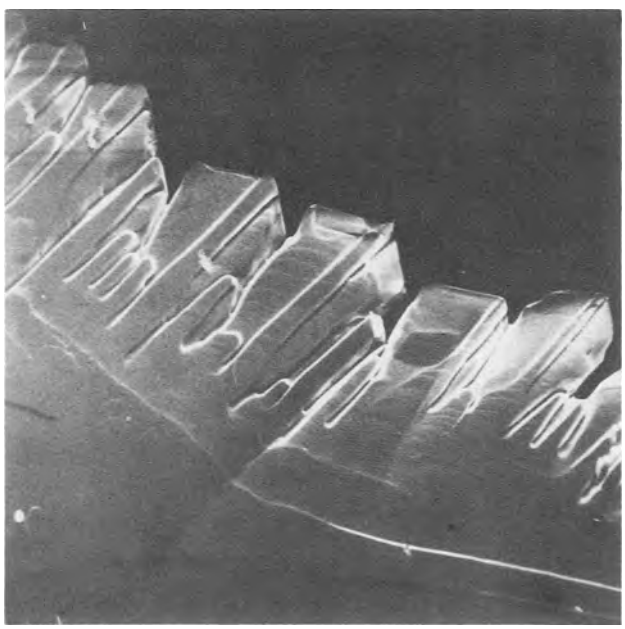


Fig. 4. SEM micrograph of a platelet having dendritic edges (X1100).

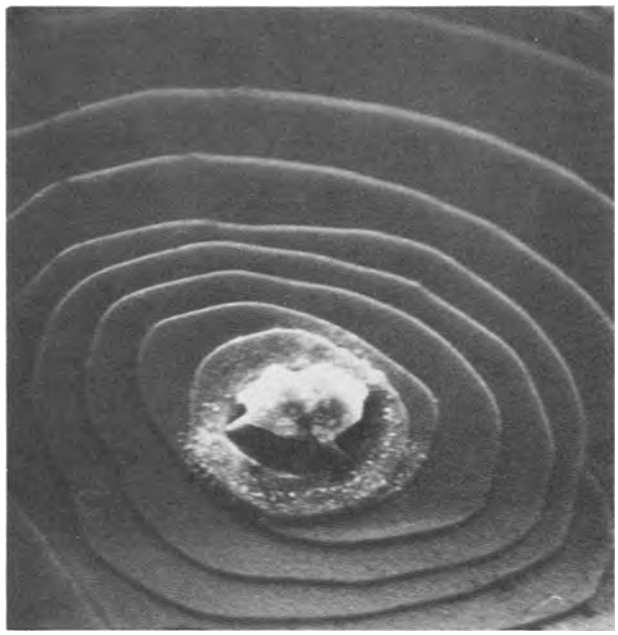


Fig. 5. SEM micrograph of the spiral on CdI_2 crystals grown on the substrate (X11,000).

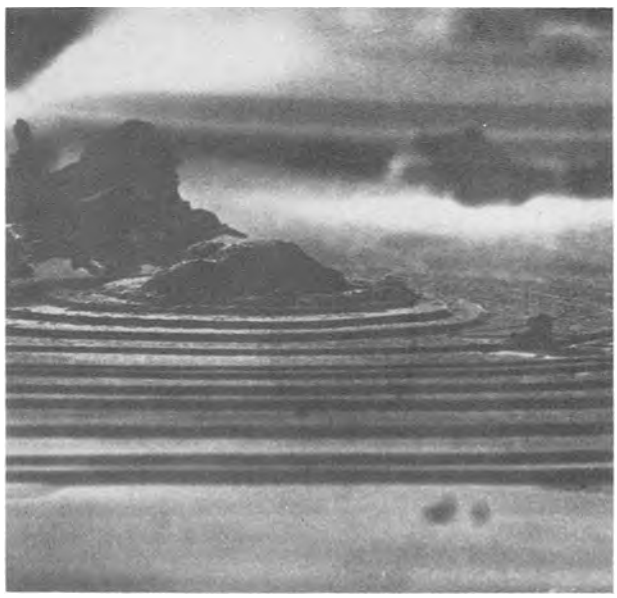


Fig. 6. SEM micrograph of the spiral of Fig. 5 after 90° rotation of the crystal (X12,000).

Furthermore, the BCF model describes only the addition of layers to an already existing layer or substrate and can operate only after this initial layer has been formed. It accounts only for growth in a direction parallel to the screw axis and does not explain the lateral growth necessary for the formation of the platelets. In the past few years a number of reports challenging the role of the screw dislocation mechanism in crystal growth have also appeared in the literature (18-25).

The observed value of pitch ($\sim 10^2$-10^3Å as is evident in Fig. 5) and the spacing of adjacent segments ($\sim 10^3$-10^5Å, Fig. 6) of the spirals and the value of the growth supersaturation (20-100) for the crystals revealing spirals are in contrast with the prediction of the BCF theory. These features combined with the fact that no spiral is observed on platelets which grow at the lowest value of supersaturation (senal nos. 2-5) clearly indicate that the formation of CdI_2 platelets in the present case does not take place by the screw dislocation mechanism and that mere observation of spirals is not sufficient evidence to attribute the growth to this mechanism.

It is felt that the spirals on crystals grown on the substrates may be due to the presence of impurity debris and/or to the irregularities on the substrate surface. To estimate the role of the debris, a few runs were performed in which a semicylindrical glass tube of external diameter equal to the internal diameter of the tube was kept in the upper region of the growth tube; only a few of the crystals, grown on the semicylindrical tube, showed spirals, whereas the spirals were again commonly observed on the crystals grown on the substrate in the lower region. These observations imply that the debris falling under gravity in the lower regions may be responsible for the formation of spirals. Again the platelets that grow in the upper region with their faces normal to the tube axis should have the minimum share of the debris and indeed no spirals were observed on them.

The formation of CdI_2 platelets has been examined in detail. It has been observed that the initiation of the growth of the platelets is dendritic (Fig. 7); this is understandable as the growth conditions, supersaturation, and the details of the growth run (Table I) are favorable for dendritic growth (26-31). The main axis of the

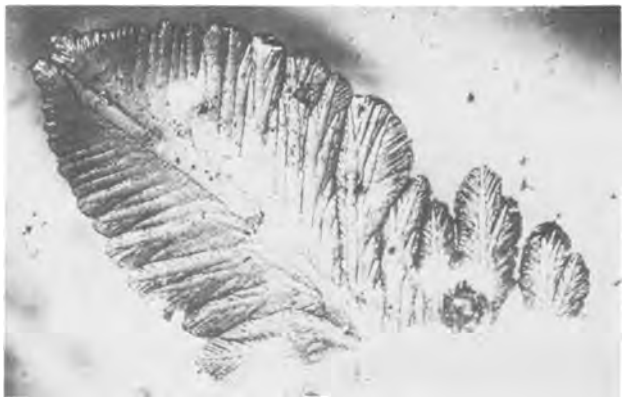


Fig. 7. View of the initial morphology of a crystal in the initial stages of growth (X220).

dendrites and its branches are found to be along $<11\bar{2}0>$, the closest packed directions.

As the growth proceeds further, more and more surface becomes available. Supersaturation is then expected to decrease and a quasi-equilibrium condition exists between growing crystals and the vapor; this results in the formation of sound crystals, *i.e.*, the dendrites grow in the fast growth direction and this stage is followed by a period during which the region between the dendritic arms is filled in (32-34). Such a transition from dendrites to platelets has been observed in a large number of crystals (Fig. 8). Figures 2, 3, and 4 show platelets which are flat and smooth in the central portion, but their edges are still dendritic; filled in portions of the dendritic arms are also evident. The growth of symmetrical crystals finally may proceed by the advance of layers, *i.e.*, layer growth is responsible for the growth of comparatively thick platelets.

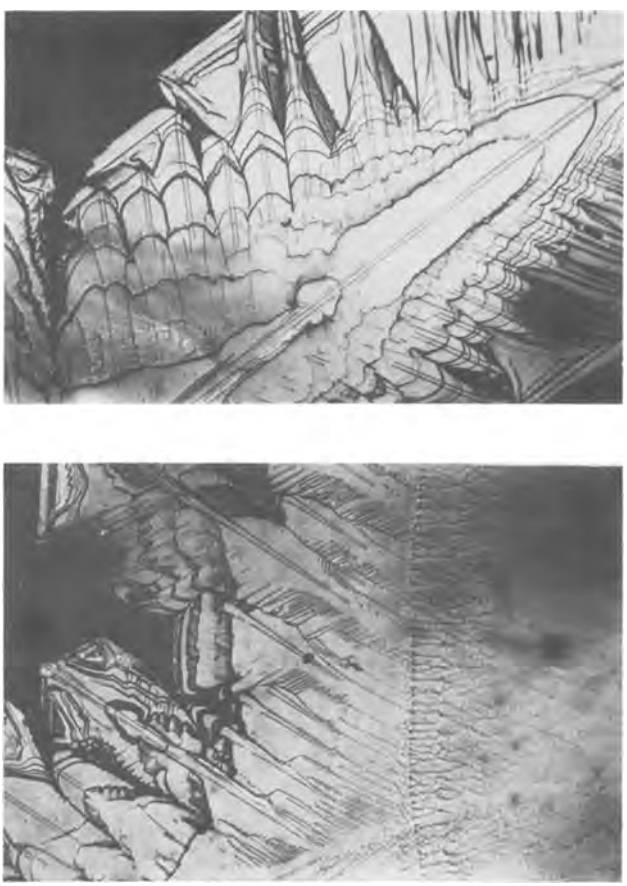


Fig. 8(a) and (b). Photographs showing dendrites changing to a platelet (X100).

X-ray Results and Discussion

Thirty-one platelets and dendrites were subjected to x-ray examination. Of these, 28 were found to be pure 4H on both the opposite basal surfaces. As the crystals sometimes displayed syntactic coalescence, diffraction spots from the two faces of a crystal were separately recorded. In two cases some unidentified polytype mixed with streaking was found on one face and the other face showed 4H. Only one crystal was found to exhibit a well-defined polytype 26H mixed with 4H (Fig. 9) on one face and a mixture of 4H, 12H and 12R on the other face (Fig. 10).

The cadmium iodide structure is made up of molecular sheets piled one on top of the other, each consisting of a layer of cadmium ions sandwiched between two layers of hexagonal close-packed iodine ions. Thus the structure of cadmium iodide permits adjacent iodine layers to slip easily with respect to one another parallel to the basal plane giving rise to stacking faults. As the faults do not involve any distortion of the nearest neighbor bonds, they have low surface energy. The effect of stacking faults is to destroy the regularity of the structure in the direction perpendicular to the layers introducing 1-D disorder in it, which gives rise to streaking on x-ray photographs. Only in a few cases streaking was observed in the vapor-grown crystals.

To explain the formation and growth of polytypic structures, Frank (6) suggested that they result from spiral growth around screw dislocations of the nonintegral Burgers vector created in certain basic structures. The absence of spirals in the present case on the

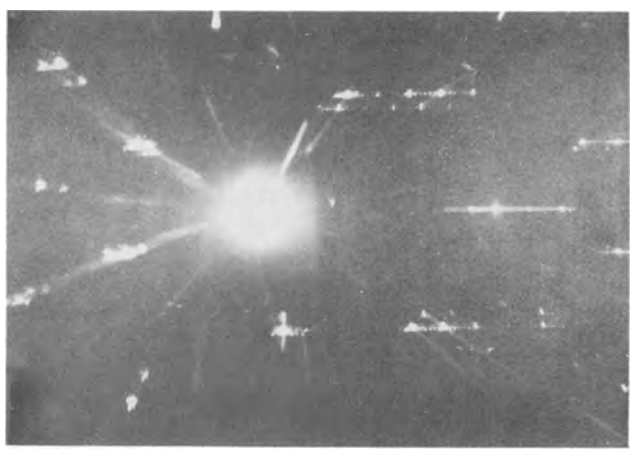


Fig. 9. a*-axis x-ray oscillation photograph of a CdI_2 crystal; the angle between incident beam and c-axis varies between 53° and 68°, Cu white radiation; camera radius 3 cm. The crystal is a mixture of polytypes 4H and 26H.

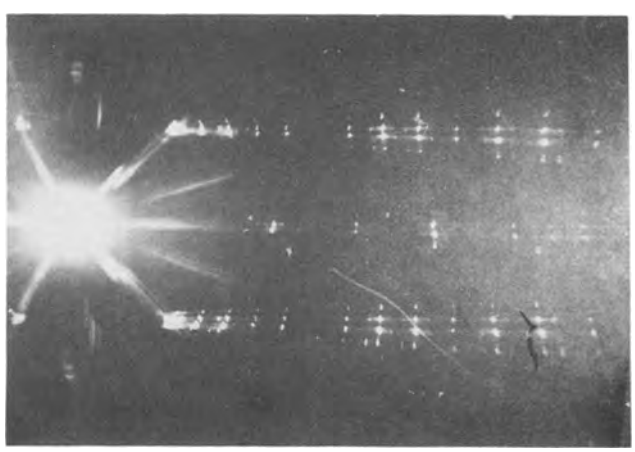


Fig. 10. a-axis oscillation photograph of the other face of the crystal in Fig. 8. The angle between the incident beam and the c-axis varies between 33° and 48°, $CuK\alpha$ radiation; camera radius 3 cm. The crystal is a mixture of polytypes 4H, 12H, and 12R.

face of nearly all platelet crystals and dendrites indicate that the polytypism and spirals are not necessarily correlated. Furthermore, the present observations on the growth of CdI_2 crystals from vapor phase have clearly demonstrated that the crystals do not grow by the screw dislocation mechanism and even the presence of spirals need not be always due to the operation of this mechanism. Thus, the formation of polytypes in the present vapor-grown CdI_2 crystals cannot be explained by Frank's theory of dislocations.

Polytypism seems to be a complicated phenomenon as the same conditions of temperature and pressure give rise to different polytypic modifications. The generally prevailing view is that the polytypes have nearly the same energy and the appearance of a particular kind of polytype is determined practically by chance. However, observations show that one particular polytype always dominates in one substance. The conditions of growth can be an important factor in determining the structure. The vapor growth under stabilized conditions indeed favors the most stable structure of the substance as is evident from the observations in the present case; whereas, the crystals of CdI_2 grown from solution (under rather undefined conditions) show a large number of polytypes (1). In solution growth the solute concentration and thus the supersaturation in different regions changes during crystallization. Variation in growth conditions may favor the nucleation of another structure; depending on conditions of growth, the crystal may develop any polytype structure. The stabilized conditions should favor the most stable polytype with least disorder, which indeed has been observed in the present case. Thus, it is evident that the growth kinetics play an important role in the formation of polytypes.

Acknowledgments

One of us (K.M.) wishes to thank the I.I.T., Delhi for the award of a research fellowship.

Manuscript submitted July 6, 1976; revised manuscript received Jan. 14, 1977.

Any discussion of this paper will appear in a Discussion Section to be published in the December 1977 JOURNAL. All discussions for the December 1977 Discussion Section should be submitted by Aug. 1, 1977.

REFERENCES

1. G. C. Trigunayat and G. K. Chadha, *Phys. Status Solidi A*, **4**, 9 (1971).
2. G. C. Trigunayat, *ibid.*, **4**, 281 (1971).
3. W. Kleber and P. Fricke, *Z. Phys. Chem. (Leipzig)*, **224**, 353 (1963).
4. G. C. Trigunayat and G. K. Chadha, *Indian J. Pure Appl. Phys.*, **2**, 392 (1964).
5. F. C. Frank, *Discuss. Faraday Soc.*, **5**, 48 (1949).
6. W. K. Burton, N. Cabrera, and F. C. Frank, *Philos. Trans. R. Soc. London, Ser. A*, **253**, 299 (1951).
7. F. C. Frank, *Phil. Mag.*, **42**, 1014 (1951).
8. A. J. Forty, *ibid.*, **43**, 377 (1952).
9. R. S. Mitchell, *Z. Kristallogr.*, **108**, 296 (1956).
10. A. R. Verma, *Philos. Mag.*, **42**, 1005 (1951).
11. S. Amelinckx, *J. Chem. Phys.*, **48**, 474 (1951).
12. G. C. Trigunayat and A. R. Verma, *Acta Crystallogr.*, **15**, 499 (1962).
13. G. K. Chadha and G. C. Trigunayat, in "Crystal Growth," H. S. Peiser, Editor, p. 313, Pergamon, Oxford (1967).
14. V. K. Agrawal, *Cryst. Lattice Defect*, **3**, 59 (1972).
15. V. K. Agrawal, *Z. Kristallogr.*, **137**, 220 (1973).
16. J. J. Gilman, "The Art and Science of Growing Crystals," pp. 15, 127, John Wiley & Sons, Inc., New York (1966).
17. S. D. Sharma and Krishna Kumar, *Jpn. J. Appl. Phys.*, **13**, 1707 (1974).
18. Chou H. Li, F. F. Y. Wang, and K. P. Gupta, *J. Appl. Phys.*, **45**, 1982 (1974).
19. C. B. Sclar and C. M. Schwartz, in "Crystal Growth," H. S. Peiser, Editor, pp. 399-403, Pergamon, New York (1969).
20. G. G. Lemmlein, M. O. Kliya, and A. A. Chernov, *Sov. Phys. Crystallogr.*, **9**, 181 (1964).
21. P. T. B. Shaffer, *Acta Crystallogr., Sect. B*, **25**, 477 (1969).
22. F. Arrese, *ibid.*, **18**, 279 (1965).
23. K. A. Jones, *J. Cryst. Growth*, **19**, 33 (1973).
24. J. Woods, *Br. J. Appl. Phys.*, **10**, 529 (1959).
25. S. D. Sharma and S. C. Kashyap, *J. Appl. Phys.*, **42**, 5302 (1971).
26. B. Chalmers, *Trans. AIME*, **200**, 519 (1954).
27. W. W. Mullins and R. F. Sekerka, *J. Appl. Phys.*, **34**, 323 (1963).
28. W. W. Mullins and R. F. Sekerka, *ibid.*, **35**, 444 (1964).
29. J. W. Cahn, in "Crystal Growth," H. S. Peiser, Editor, p. 681, Pergamon, Oxford (1967).
30. S. R. Coriell and R. L. Parker, *J. Appl. Phys.*, **37**, 1548 (1966).
31. R. F. Sekerka, *J. Cryst. Growth*, **3/4**, 71 (1968).
32. B. Chalmers, "Principles of Solidification," p. 104, John Wiley & Sons, Inc., New York (1964).
33. D. Elwell and B. W. Neate, *J. Mater. Sci.*, **6**, 1499 (1971).
34. A. Chase, in "Preparation and Properties of Solid State Materials," Vol. I., B. A. Lefever Editor, p. 183, Marcel Dekker, New York (1971).

Technical Notes

Reverse Bias Life Test Stability of Tantalum-Titanium Anodic Oxide Thin Film Capacitors

F. G. Peters and N. Schwartz*

Bell Laboratories, Murray Hill, New Jersey 07974

In a previous publication, the composition and some of the dielectric properties of tantalum-titanium anodic oxides were determined (1); this note describes some of the thin film capacitor (2) properties.

* Electrochemical Society Active Member.

It is well known that alloying of tantalum film with substitutional metals (3-5), nitrogen (6, 7), oxygen (7), or carbon (7) increases the cathodic breakdown voltage at room temperature, This increase results in near-symmetric d-c leakage characteristics compared

Table I. Time to failure of β-tantalum based TM type capacitors on anodic (9) or cathodic (10) bias at 85°C

Percent of capacitors failing	Time to failure, hr			
	+6V	−6V	+12V	−12V
2	5×10^3	1×10^3	5×10^2	5×10^1
30	5×10^7	9×10^3	8×10^6	9×10^2

to the well-known asymmetric characteristic (8). It is not clear, however, that this symmetry in room temperature d-c leakage reflects itself in increased reliability on reverse or cathodic bias.[1] This reliability is frequently evaluated at 85°C with either anodic (forward) or cathodic (reverse) bias applied. Table I indicates that, despite a high degree of conductivity symmetry near room temperature for the standard β-tantalum based TM[2] capacitor, the time to failure on anodic bias at 85°C is much larger than on cathodic bias.

In the present study, sputtered tantalum-titanium films with varying atom fractions were prepared as described earlier (1), fabricated into TM capacitors (2) by anodization to 230V in 0.01% citric acid and where the counterelectrode was evaporated Nichrome-gold film. Figure 1 shows the relative capacitance of these samples as a function of the atom fraction of titanium; the figure also gives comparable results where the alloying agent is either nitrogen (11), aluminum (12), or silicon (13). The addition of titanium to tantalum tends to maintain the capacitance density of the tantalum oxide better than either nitrogen, aluminum, or silicon. Figure 2 gives the dissipation factor at 1 kHz for the tantalum-titanium based capacitors; the dissipation factor increases with increasing titanium composition, although it is below 0.0035 for compositions below 5 atom percent (a/o) titanium.

Because of the known improvement of room temperature cathodic breakdown voltage with small additions of titanium (5), capacitors with titanium concentrations below 5 a/o were investigated with respect to cathodic life-test stability at 85°C. Fifty-six capacitors were prepared at each composition of 1.1, 1.5, 1.8, 2.5, and 3.4 a/o titanium in tantalum and fabricated into 0.1 cm^2 capacitors. The properties of these samples are relatively independent of composition, and they have been taken together as one group for the purpose of this note. The initial yield of the 280 capacitors prepared was above 93% based on a leakage criterion of 10 A/farad for a standard d-c leakage test at +50V. All of the capacitors were placed in an 85°C oven and one-half of the samples were tested at −6V for 6200 hr. At the end of this test, the other half of the samples were tested at −12V. The criterion for failure was a blown 180 mA fuse in series with the capacitor. The yield of capacitors remaining on test as a function of time is shown in Fig. 3, with a comparison to the performance (10) of standard β-tantalum based capacitors with slight nitrogen additions (14).

Figure 3 indicates that there were 2 out of 125 failures in the first 50 hr at the −6V test, and there were no other failures to the end of the test. Since these are developmental prototype samples, these initial few failures are not necessarily typical of the eventual performance of these capacitors. The failure rate at −6V is thus less than 1.6% in 6400 hr, compared to 2% in 1000 hr for standard capacitors (Table I), or 15% in 6400 hr (Fig. 3). At −12V, the tantalum-titanium based capacitors demonstrate a 30% failure rate in 4600 hr compared to the same failure rate for standard samples in only 900 hr. These results indicate that the tantalum-titanium based capacitors have a failure rate on cathodic bias at 85°C which is less than one-fifth that of the standard capacitors.

[1] The terms "anodic" and "cathodic" refer to the tantalum-based thin film electrode, equivalent to the terminology for the polarity of this electrode during the electrolytic formation at the oxide.

[2] TM is equivalent to T(tantalum-tantalum-oxide)/M(metal) capacitor structure.

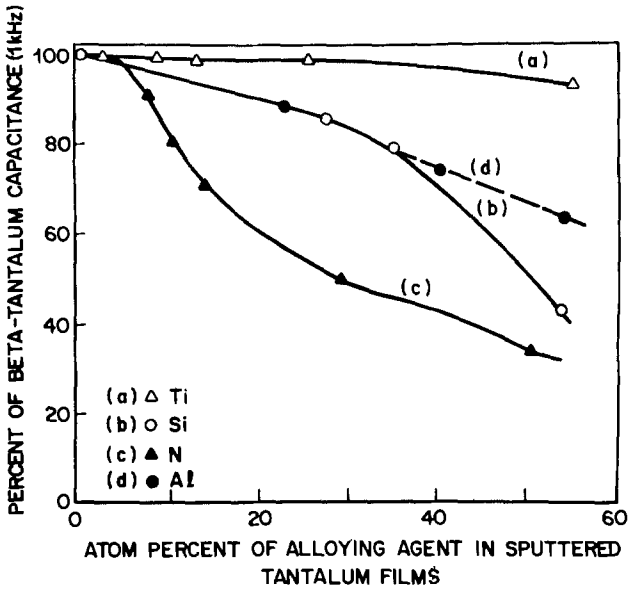


Fig. 1. Normalized capacitance at 1 kHz as a function of atom percent of alloying agent in sputtered tantalum film: Ti (this work), Si (13), Al (12), N (11).

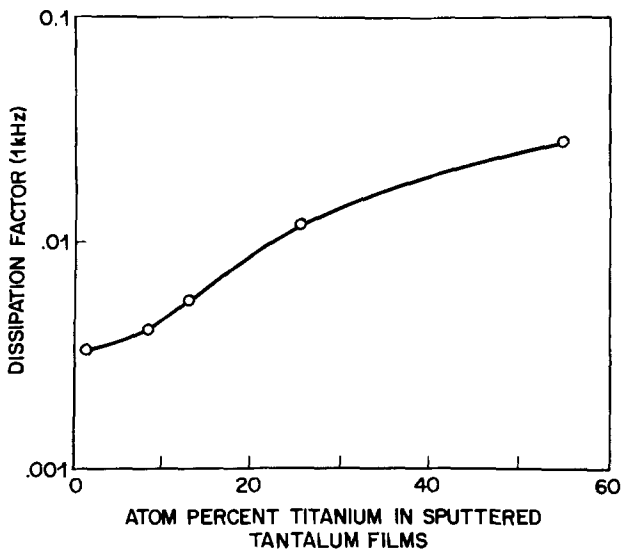


Fig. 2. Dissipation factor at 1 kHz as a function of the atom percent of titanium in sputtered tantalum films.

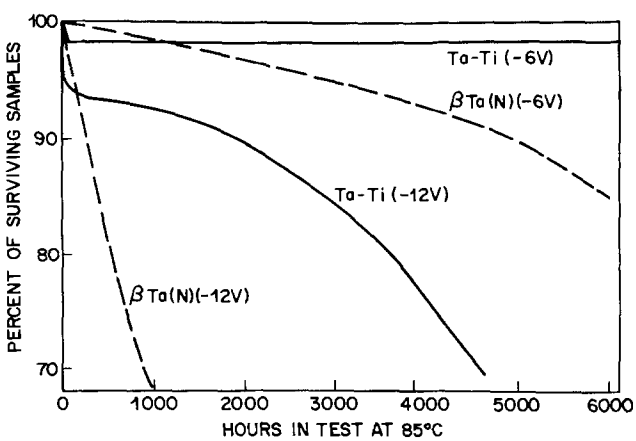


Fig. 3. Life-test stability of tantalum-titanium based capacitors at 85°C and either −6 or −12V. There were initially 125 samples on the −6V test and 121 samples on the −12V test. There were only minimal changes in capacitance and dissipation factor at the end of the −6V test, being respectively −0.15% and −0.05%.

The asymmetric room temperature d-c conductivity of the standard capacitors has been ascribed to heterogeneous conduction sites with an unknown structure (4). It has been proposed (4) that the addition of the alloying agent prevents the formation of these sites. If this model has any validity, the removal of these discrete sites has not been sufficient to improve the cathodic life-test stability so that it is equivalent to that on anodic bias (Table I). The stability of the tantalum-titanium based samples is more than adequate, however, for the cathodic bias that these components are exposed to in circuit applications.

Acknowledgments

We wish to thank W. F. McNamara for the life-test measurements.

Manuscript received Jan. 7, 1977.

Any discussion of this paper will appear in a Discussion Section to be published in the December 1977 JOURNAL. All discussions for the December 1977 Discussion Section should be submitted by Aug. 1, 1977.

Publication costs of this article were assisted by Bell Laboratories.

REFERENCES.

1. R. L. Ruth and N. Schwartz, *This Journal*, **123**, 1860 (1976).
2. W. H. Orr, D. O. Melroy, R. J. Moore, F. P. Pelletier, W. J. Pendergast, and W. H. Yocom, Proceedings of the Electronics Components Conference, May 1970.
3. N. N. Axelrod, B. H. Vromen, H. D. Guberman, D. J. Harrington, and N. Schwartz, *This Journal*, **113**, 57C (1966).
4. N. N. Axelrod and N. Schwartz, *ibid.*, **116**, 460 (1969).
5. N. N. Axelrod, N. D. Guberman, N. Schwartz, and B. H. Vroman, U.S. Pat. 3,320,500 (1967).
6. N. Schwartz, M. Gresh, and J. Deaderick, *This Journal*, **109**, 64C (1962).
7. D. Gerstenberg, *ibid.*, **113**, 542 (1966).
8. R. W. Berry and D. S. Sloan, *Proc. IRE*, **47**, 1070 (1959).
9. J. S. Fisher, Tenth Annual Proceedings Reliability Physics, 1972, Las Vegas, Nevada, p. 183 (IEEE Catalog No. 72-CHO-628-8-PHY).
10. P. W. Wyatt, To be submitted to the Proceedings of the IEEE Reliability Conference, Las Vegas, April 1977.
11. Estimated from data given in Ref. (7).
12. C. A. Steidel and D. Gerstenberg, Proceedings of the Electronic Components Conference, p. 372 (1969).
13. N. Schwartz and F. G. Peters, Proceedings of the Electronics Components Conference, p. 251 (1973).
14. H. Y. Kumagai, I. M. Fletcher, C. A. Steidel, K. L. Baurle, and J. R. Hightower, *ibid.*, p. 257 (1973).

A Method to Improve the Radial Impurity Distribution in Czochralski Silicon Crystals

Katsuro Sugawara* and Hiroo Tochikubo

Hitachi, Limited, Semiconductor and Integrated Circuits Division, Kodaira, Tokyo, Japan

The impurity distribution in Czochralski crystals should be investigated both macroscopically and microscopically. Macroscopically, the impurity distribution should be investigated both along the growth direction and along the radius, and microscopically within the growth striae (1-3). The distribution along the growth direction has been normally obtained by the "normal freezing" (4), but the radial distribution has not been quantitatively analyzed. The analyses of the radial distribution are classified as follows: (*i*) variation of the impurity distribution by appearance of (111) facets (2, 5-10), (*ii*) the distribution experimentally correlated by the growth parameters (11-12), and (*iii*) analysis of liquid flow by fluid dynamics (13-14). Recently, a novel method for obtaining uniform impurity distribution has attracted attention, using neutron activation. Float-zoned crystals of ultrahigh purity are doped by the ^{30}Si (n, γ) ^{31}P reaction (15-16). These crystals, however, are limited to high resistivities doped with phosphorus and are much more expensive than the conventionally grown crystals.

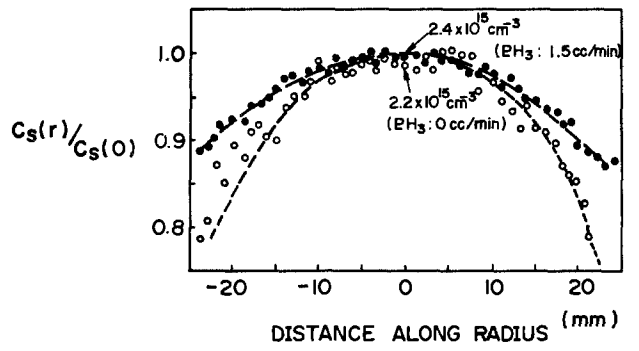
In this note, radial impurity distribution of Czochralski grown silicon crystals which are phosphorus doped from the gas phase through free melt surface in addition to the usual doping in the melt is compared with the distribution in conventionally melt-doped crystals.

The crystal growing furnace used to pull the silicon single crystals was resistance heated. A polycrystalline silicon rod of approximately 1000g in weight was charged in a high purity quartz crucible with an ID of 100 mm. After melting the polycrystalline rod, a seed crystal with (100) orientation was dipped into the melt and the single crystal of about 50 mm in diameter was pulled. The melt was doped with phosphorus to obtain a crystal of 2-3 Ω-cm resistivity; the impurity concentration ranged from 1.5×10^{15} to 2.3×10^{15} atoms/cm^3. The ambient gas was argon; the flow rate was 10 liters/min in the 300 mm diameter chamber. To investigate the effect of the phosphorus doping from the gas phase, phosphine was added to the argon. At first, the silicon single crystal was pulled up to 3 cm in length without the phosphine doping, the growth was stopped, the phosphine was added for 30 min, and then the pulling was carried out again up to 6 cm in length. This procedure was used to avoid donor formation (17) during cooling of the grown crystal by reducing the interval of heat-treatment at 450°C. The standard growth condition was a pull rate of 1.4 mm/min, and the rotation speed of the seed and that of the crucible 15 and 5 rpm (in reverse direction), respectively. The grown single crystal was cut normal to the growth axis into 5 mm thick sections at the middle of which the interface without and with the phosphine doping was located, lapped, and the resistivity measured by the four-probe method (18) at every 1 mm along the radius. Then, the impurity concentration was calibrated by using Irvin's chart (19) which shows the correlation between the resistivity and the impurity concentration of silicon. Correction of the resistivity at the edge of the silicon block along the radius was neglected, due to an error of less than 2% except for the outer 1 mm (20); the measurement of the resistivity was done by the probe with 0.25 mm spacing.

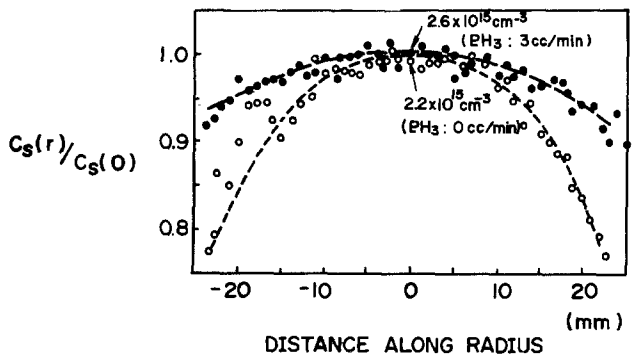
The radial impurity distribution, $C_s(r)/C_s(0)$, normalized by the value of the center, $C_s(0)$, was plotted in Fig. 1; open and closed circles show the impurity concentration without and with the phosphine doping, respectively. In the figure, the broken and solid lines represent the measured value without and with the phosphine doping. Figures 1(a), (b), (c), and (d) are the result of the phosphine doping at flow rates of 1.5,

* Electrochemical Society Active Member.

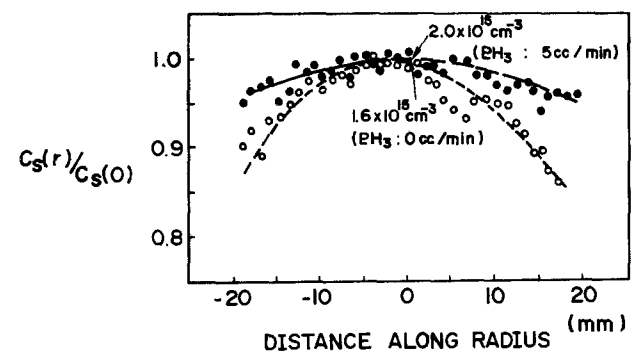
Key words: Czochralski silicon crystal, phosphorus doping, evaporation of impurity from melt, gas phase doping, segregation of impurity, radial impurity distribution.



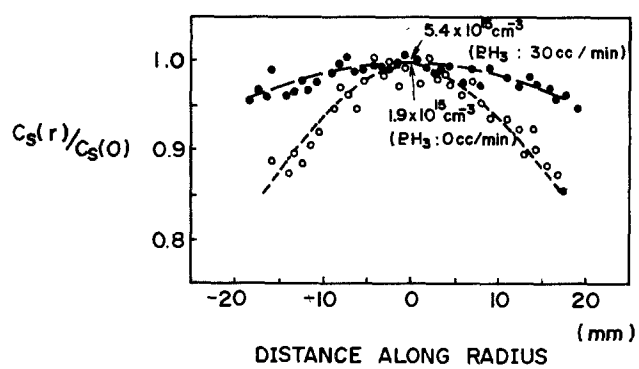
(a) PH_3 doping, 1.5 cm^3/min.



(b) PH_3 doping, 3 cm^3/min.



(c) PH_3 doping, 5 cm^3/min.



(d) PH_3 doping: 30 cm^3/min.

Fig. 1. Radial impurity distribution in Czochralski silicon crystals. Open and closed circles show the measured impurity concentration without and with the phosphine doping, respectively. — — — —, Measured value without PH_3 doping; ——, measured value with PH_3 doping.

3, 5, and 30 cm^3/min, respectively, in addition to the usual doping into the melt, together with that without the gas phase doping. The impurity distribution along the radius was generally convex and the concentration at the edge of the crystals was smaller by 20, 12, 6, 5, and 4% for the above-mentioned five cases (the phosphine flow rates of 0, 1.5, 3, 5, and 30 cm^3/min, respectively) than the corresponding concentration at the center.

Results of the computational calculation and comparison between measured and calculated values will be published in the near future.

Acknowledgment

The authors express their sincere gratitude to Dr. S. Tauchi and Mr. S. Nishida for the continued support of this work and Dr. Y. Sugita and Mr. K. Kurata for helpful discussions.

Manuscript submitted Aug. 19, 1976; revised manuscript received Feb. 4, 1977.

Any discussion of this paper will appear in a Discussion Section to be published in the December 1977 JOURNAL. All discussions for the December 1977 Discussion Section should be submitted by Aug. 1, 1977.

Publication costs of this article were assisted by Hitachi, Limited.

REFERENCES

1. P. R. Camp, *J. Appl. Phys.*, **25**, 459 (1954).
2. A. F. Witt and H. C. Gatos, in "Semiconductor Silicon," R. R. Haberecht and E. L. Kern, Editors, p. 146, The Electrochemical Society Softbound Symposium Series, New York (1969).
3. B. K. Jindal, V. V. Karelin, and W. A. Tiller, *This Journal*, **120**, 101 (1973).
4. W. G. Pfann, *Trans. AIME*, **194**, 747 (1952).
5. J. A. M. Dikhoff, *Solid-State Electron.*, **1**, 202 (1960).
6. K. Morizane, A. Witt, and H. C. Gatos, *This Journal*, **114**, 738 (1967).
7. A. F. Witt and H. C. Gatos, *ibid.*, **115**, 70 (1968).
8. K. Morizane, A. F. Witt, and H. C. Gatos, *ibid.*, **115**, 747 (1968).
9. T. F. Ciszek, in "Semiconductor Silicon," R. R. Haberecht and E. L. Kern, Editors, p. 156, The Electrochemical Society Softbound Symposium Series, New York (1969).
10. T. Abe, Paper 93 presented at The Electrochemical Society Meeting, Los Angeles, California, May 10-15, 1970.
11. K. E. Benson, *Electrochem. Technol.*, **3**, 332 (1965).
12. K. E. Benson, in "Semiconductor Silicon," R. R. Haberecht and E. L. Kern, Editors, p. 97, The Electrochemical Society Softbound Symposium Series, New York (1969).
13. J. R. Carruthers and K. Nassau, *J. Appl. Phys.*, **39**, 5205 (1968).
14. J. R. Carruthers, *This Journal*, **114**, 959 (1967).
15. M. Schnöller, *IEEE Trans. Electron Devices*, **ed-21**, 312 (1974).
16. H. A. Hermann and H. Herzer, *This Journal*, **122**, 1508 (1975).
17. W. Kaiser, *Phys. Rev.*, **105**, 1751 (1957).
18. L. B. Valdes, *Proc. IRE*, **42**, 420 (1954).
19. J. C. Irvin, *Bell Syst. Tech. J.*, **14**, 387 (1962).
20. L. J. Swartzendruber, National Bureau Standards Tech. Note 199 (April 15, 1964).

Properties of Pretilted Liquid Crystal Structures

K. Fahrenschon and M. F. Schiekel

AEG-Telefunken, Serienprodukte AG, Ulm, West Germany

This paper describes the variable control of colors in a transmissive arrangement based on the deformation of aligned nematic liquid crystal (NLC) layers between polarizers in an electrical field (DAP effect). Several authors have found different field effects which originate from different configurations of the zero-field optic axis and from use of NLC with either negative or positive values of the dielectric anisotropy $\Delta\epsilon = \epsilon_{11} - \epsilon_{\perp}$ (1-4).

We have studied a pretilted structure where the directors of NLC are well aligned within parallel planes (Fig. 1) (5). It should be mentioned that with these pretilted structures materials with either sign of the dielectric anisotropy could be used as well as materials whose dielectric anisotropy changes from positive to negative when the driving frequency changes. In this paper, however, we limit our subject to materials with a negative dielectric anisotropy, but similar results can be achieved with other materials.

In the case of the DAP effect and also with asymmetrical pretilted cells using negative anisotropic materials, an increase of the optical phase retardation is achieved with increasing cell voltage. Besides the usual measurements of the phase retardation as a function of the voltage across the cell, we also used the conoscopic observation for examining the electro-optic behavior of the LC cell. Because the reproducible and uniform generation of colors in transmissive systems is based on a uniform and well-defined deformation of the liquid crystal layer, the conoscopic method offers a quick check for the optical properties. We used a conoscopic projection method, which results in very wide angles of visual field of ±40°. Figure 2 shows the conoscopic picture of a LC cell under zero-field condition without inclination ($\bar{\theta}_0 \sim 0°$), *i.e.*, homeotropic orientation. The good zero-field orientation of this uniaxial crystal layer is marked by the sharp cross of the isogyres. Just above the threshold voltage, numerous disclinations arise, as indicated by a less-pronounced conoscopic figure. Figure 3 shows the zero-field condition of a pretilted cell with a mean pretilt angle $\bar{\theta}_0$ of about 8°, relating to an angle of incident light in air of about 12°, Note that the isogyre cross, though moving far out of the optical axis of the conoscopic system, remains sharp and that the isochromates show bright, well-defined, birefringent colors.

Figure 4 shows the state with an increased cell voltage. The isochromates in the center of the field are nearly exact straight lines. That means that within one plane, the observed color of the LC cell is independent of the angle of view. By using a stop within the projection system, which has a rectangular cross section with its longer edge perpendicular to this plane, no angular dependency arises.

The possible color range for asymmetric pretilted NLC cells is shown in the well-known charts of birefringent colors. A cell, with a mean deformation angle $\bar{\theta}_0 \sim 10°$, determined by conoscopic measurements, corresponds to an initial phase retardation of about 80 nm, which is equivalent to a dark gray instead of a black optic field.

The cells are made of 2 sheets of soda-lime glass, covered with tin-oxide or tin-indium-oxide electrodes, as usual. One electrode was then coated with a dielectric film of either silicon oxide or magnesium fluoride

Key words: liquid crystal, LCD, nematic liquid crystal.

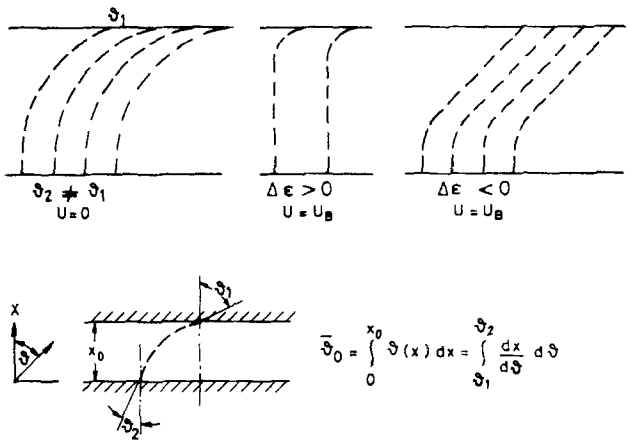


Fig. 1. Orientation of LC directors and deformation profiles in electric fields.

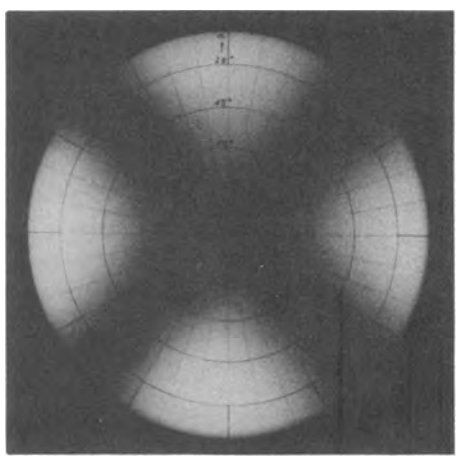


Fig. 2. Conoscopic figure of homeotropic LC layer

with a thickness of approximately 100Å. An electron beam evaporation was used, where the distance between source and target was made large enough to keep the range of deviation from the mean evaporation angle small (6). The beam angle was varied between

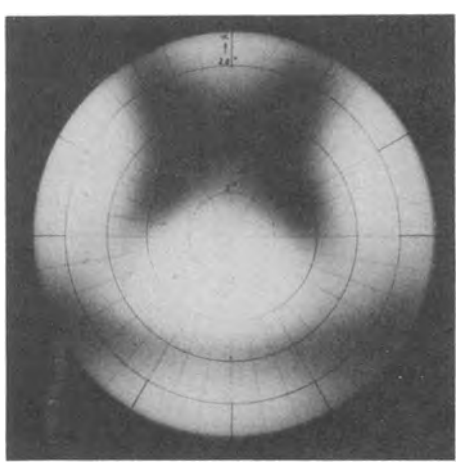


Fig. 3. Conoscopic figure of a pretilted LC cell: $\bar{\theta}_0 = 8°$, $U = 0$.

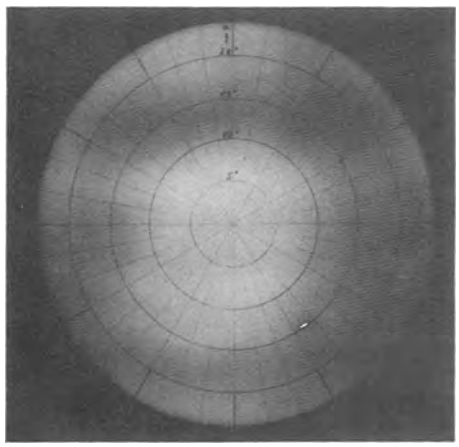


Fig. 4. Conoscopic figure of a pretilted LC cell: $\theta_0 = 8°$, $U = 5V$.

60° and 85° from the normal to the surface. The opposite electrode of the cell remained uncoated or was coated under different evaporation angles.

The LC cells used in our experiments were conventional sandwich-type cells with a thickness of the LC layer of approximately 10 μm. The glass plates with the above-mentioned electrode preparation were fitted together and sealed with glass-frit. We used two different NLC materials: N5 [an azoxy-compound made by Merck (7)] or KS 701 [a schiff-base and carbonester mixture made by Riedel de Haen (8)]. Special surfactants (9), for instance lecithines or acid "T" (Merck), were added to the bulk material in quantities < 0.5%. The additives cause the NLC directors to align perpendicular with one electrode and under a divergent angle at the opposite electrode. Thus, an asymmetric pretilted liquid crystal structure was achieved. It is obvious that the directors of the pretilted structure should always be oriented in parallel planes which are defined with respect to the plane of evaporation of the dielectric layer.

Figure 5 shows the angular transmission characteristic of a pretilted cell, measured with a He-Ne laser

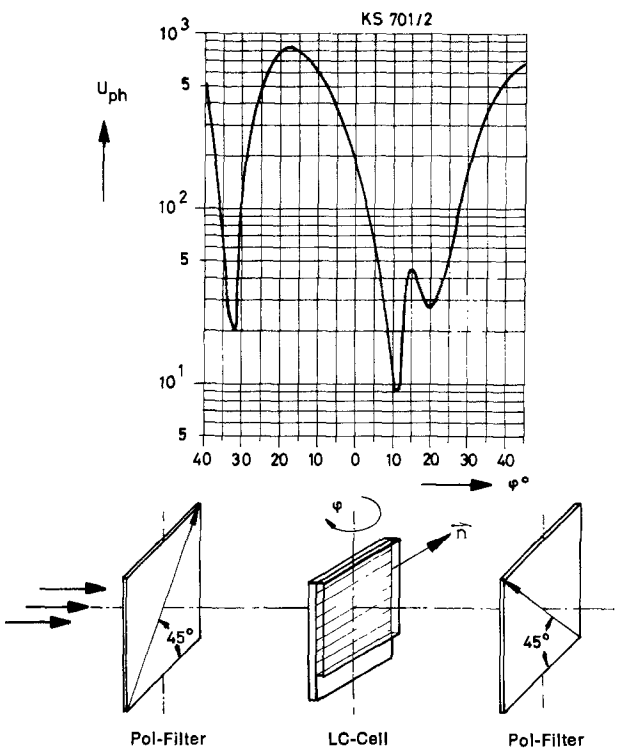


Fig. 5. Angular dependence of pretilted liquid crystals: $\vec{n}$ = projection of evaporation direction on cell surface.

($\lambda = 632.8$ nm). In Fig. 5a minimum is found, at an angle ϕ of 12°, if the axis of the cell rotation during the measurement is orthogonal to the trace of the inclined directors. Taking into account the different refractive indexes of air and the NLC, the mean pretilt angle $\overline{\theta_0}$ of the directors is calculated to be 7.5° from the normal. By conoscopic observation, an angle of approximately 8° was found, showing good agreement of both methods.

Figure 6 shows the transmission characteristic T of a NLC cell between crossed polarizers as a function of the cell voltage U. One is a homeotropic cell with $\overline{\theta_0} = 0°$ and one is an asymmetric pretilted cell with a relative large mean pretilt angle of 16°, corresponding to an initial phase retardation of 133 nm. The threshold voltage, which is about 3.8V for KS 701 in a homeotropic cell, disappeared completely with the mean pretilt of 16°. The difference in the quality of both interference curves is remarkable. For the pretilted cells, the maxima are nearly identical with the theoretical predicted values, while in the case of perpendicular orientation on both electrodes the amplitudes are much smaller due to ambiguities (or disclinations).

The dynamic behavior of a NLC cell is usually characterized by three values: delay time, turn-on time, and turn-off time. The delay time is only existing in a homeotropic layer. In a pretilted layer, only one direction is possible for a further tilt, therefore the deformation starts without any delay. The disappearance of the delay time in pretilted LC layers corresponds with the disappearance of the threshold voltage (5).

Figure 7 shows the quadratic dependence of the reciprocal turn-on time $1/t_\delta$ on the normalized cell

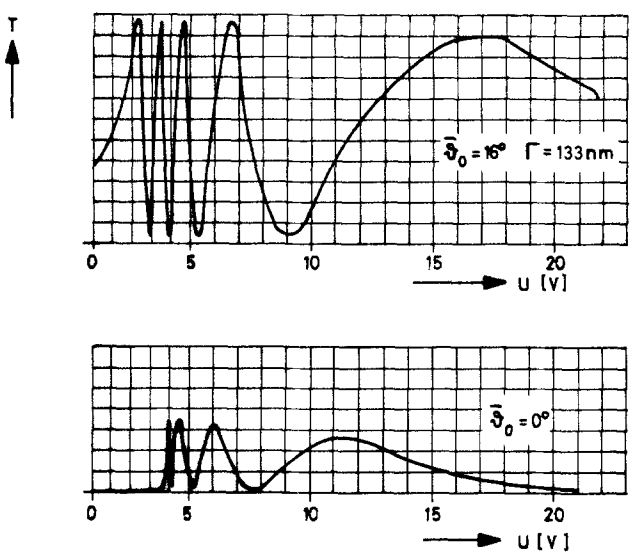


Fig. 6. Interference curves of pretilted and homeotropic cells

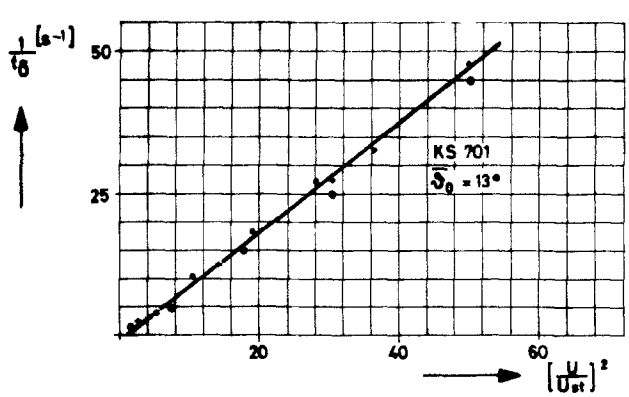


Fig. 7. Turn-on time of pretilted LC cells: t_δ = time for achieving optical retardation δ, $t \to \infty$, $U \to U_{stat}$.

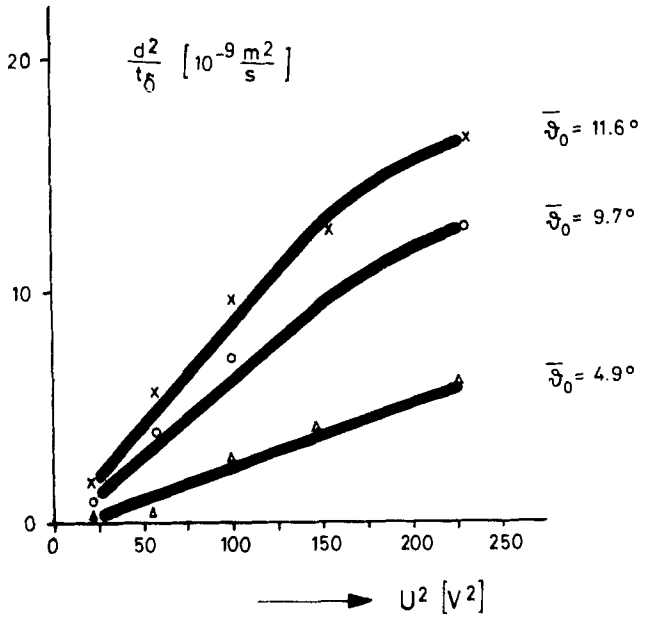


Fig. 8. Turn-on time of pretilted liquid crystal: t_δ = time for achieving optical retardation at a cell voltage U.

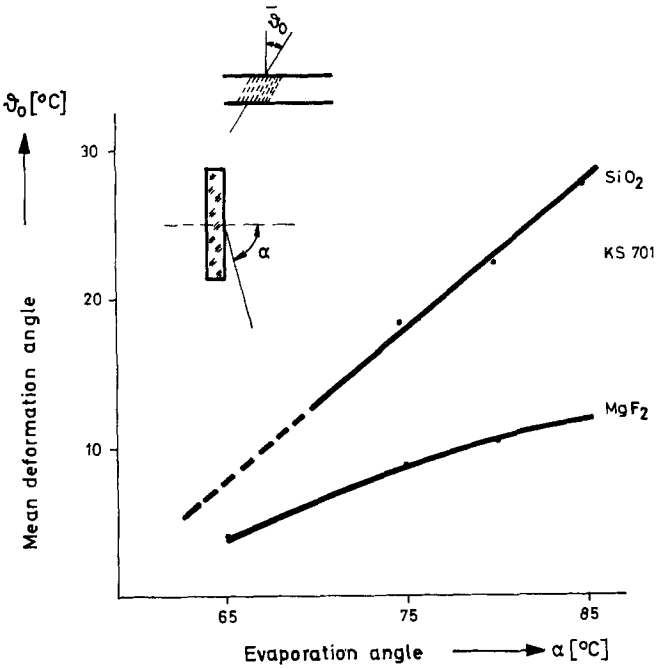


Fig. 9. Mean deformation angle of pretilted LC cells vs. evaporation angle α.

voltage U/U_{stat}. t_δ is the time during the turn-on period when a certain deformation state, characterized by a phase retardation δ, is reached. This deformation state can be achieved as equilibrium for the voltage $U = U_{stat}$ when t goes to infinity, so that the curve for $1/t_\delta = 0$ passes through $U/U_{stat} = 1$.

Figure 8 shows the dependence of the normalized reciprocal response time d^2/t_δ from the cell voltage for different values of the pretilt. With increasing mean pretilt angles $\bar{\theta}_0$ the turn-on time becomes smaller as expected. For practical applications it has a big advantage that with asymmetric pretilted cells high multiplexing ratios $Z = 100{:}1$ can be achieved, because of the large dependency of colors from the cell voltage.

The mean pretilt angle can be chosen arbitrarily by proper choice of the evaporation material and evaporation angles.

Figure 9 shows the dependency of $\bar{\theta}_0$ from the evaporation angle α in an asymmetric pretilted cell for silicon dioxide and for magnesium fluoride, using the mixture KS 701 as the liquid crystal. NLC cells with asymmetric pretilted structures are well suited as switchable color filters or as light valves for electrical and together with photoconductors for optical addressing.

Acknowledgments

This work was sponsored by the Ministry for Research and Technology, Federal Republic of Germany, Contract NT 535.

Manuscript submitted Dec. 15, 1976; revised manuscript received Feb. 22, 1977.

Any discussion of this paper will appear in a Discussion Section to be published in the December 1977 JOURNAL. All discussions for the December 1977 Discussion Section should be submitted by Aug. 1, 1977.

Publication costs of this article were assisted by AEG-Telefunken.

REFERENCES

1. V. Freedericksz and V. Zolina, *Trans. Faraday Soc.*, **29**, 917 (1933).
2. M. Schadt and W. Helfrich, *Appl. Phys. Lett.*, **18**, 127 (1971).
3. M. Schiekel and K. Fahrenschon, *ibid.*, **19**, 391 (1971).
4. A. Rapini and M. Papoular, *J. Phys. (Paris)*, **30**, C4-45 (1960).
5. K. Fahrenschon, H. Gruler, and M. Schiekel, *Appl. Phys.*, **11**, 67 (1976).
6. J. L. Janning, *Appl. Phys. Lett.*, **21**, 15 (1972).
7. R. Steinsträsser and L. Pohl, *Tetrahedron Lett.* **1971**, 1921.
8. K. Wagner, O. Liebig, and H. Kelker, Ger. Pat. 2,235,072 (1972).
9. L. A. Goodman, *RCA Rev.*, **35**, 447 (1974).

Cathodoluminescent Properties of Yttrium Terbium Aluminum Borate $Y_{1-x}Tb_xAl_3B_4O_{12}$ Phosphors

T. Takahashi* and O. Yamada

RCA Research Laboratories, Incorporated, Machida City, Tokyo, Japan

Rare earth aluminum borates, $RAl_3B_4O_{12}$, where R is yttrium or rare earth from Nd to Yb, are isostructural with huntite, $CaMg_3(CO_3)_4$ (1). The luminescent properties of the $YAl_3B_4O_{12}$ host lattice for various activators such as Eu, Cr, Tb, Ce, and Bi were investigated earlier (2-6). For a 5% Tb-doped $YAl_3B_4O_{12}$ phosphor,

* Electrochemical Society Active Member.
Key words: yttrium aluminum borate, Tb activation, coactivators.

a moderately high radiant efficiency of 5% for CR excitation was reported (4). However, no further attempt was made at that time to improve its CL properties. Because of persistent interest in good rare earth activated green emitting phosphors, it was thought worthwhile to reinvestigate this phosphor. In particular, the system $Y_{1-x}Tb_xAl_3B_4O_{12}$ is well suited to study the effect of a so-called concentration quenching on CL properties. We investigated the effects of various phosphor parameters such as preparation technique, Tb concentration, and impurities on CL properties of the phosphors. The results are discussed in this paper.

Experimental

Sample preparation.—Stoichiometric amounts of Y_2O_3, Tb_4O_7, and Al_2O_3 and 50% excess of stoichiometric amount of B_2O_3 or H_3BO_3 plus codopant in the oxide form, if desired, were mixed and ground thoroughly in a mechanically driven mortar and pestle. The mixture was placed in a Pt crucible and heated in air to 1100°C at a heating rate of 15 ~ 30°C/hr. After heating for 2 hr at 1100°C, a loosely sintered sample was immediately removed from the Pt crucible and ground by hand. It was then poured in a glass beaker half-filled with cold 1:1 HCl. After immersing in 1:1 HCl for 2 hr, the remaining powder was washed with deionized water by decantation and dried. The dried powder was mechanically reground and refired in air at 1100°C for 2 hr in a Pt crucible. The phase of powder samples was confirmed by x-ray diffraction. The Fe content of the samples was analyzed semiquantitatively by optical emission spectroscopy.

Cathodoluminescent measurements.—Sample powders were packed in shallow stainless steel dishes and were excited in a demountable cathode-ray apparatus. Most of the measurements were made at 10 kV beam voltage and about 1 $\mu A/cm^2$ beam current. Emission spectra of the phosphors were measured with a Nikon p250 grating monochrometer using HMT R376 photomultiplier as a detector. The wavelength-dependent sensitivity of the system was later corrected with a standard tungsten lamp, if necessary. The apparatus of a similar design fitted with a spectrophotometer system which gives emission spectra automatically corrected for the characteristics of the system was used in some cases. The description of the latter apparatus can be found elsewhere (7).

Results

Preparation technique and raw materials.—The preparation techniques of $Y_{1-x}Tb_xAl_3B_4O_{12}$ phosphors were checked by both x-ray diffraction and CR emission intensity. It was found that a large excess amount of B_2O_3 or H_3BO_3 (50 ~ 100% in excess of stoichiometry) was necessary to form a huntite structure single phase sample. The sample fired with 50% excess B_2O_3 became pure white after a single firing, indicating complete reduction of Tb^{4+} ions to Tb^{3+} ions, whereas the sample fired from a stoichiometric or a 1 ~ 5% excess B_2O_3 added mixture was slightly colored and also contained a small amount of an unidentified impurity phase. The leaching in cold 1:1 HCl after the first firing turned out to be quite effective to improve Tb^{3+} emission intensity under CR excitation. As much as 50% improvement over unleached samples could be achieved by this process. Such a pronounced improvement is thought to be brought about by the dissolution of B_2O_3 coating, probably in the form of glass, on $Y_{1-x}Tb_xAl_3B_4O_{12}$ particles in 1:1 HCl.

It was found that impurity Fe mainly from Al_2O_3 and B_2O_3 raw materials had a damaging effect on Tb^{3+} emission. When CP grade Al_2O_3 and/or B_2O_3 were used as raw materials, the Fe content in the phosphor was as much as 200 ppm. The use of electrolytically oxidized Al_2O_3 (99.99%) and Merck "suprapur" grade B_2O_3 or H_3BO_3 lowered the Fe content to 50 ppm or below. Approximately 15% improvement in emission intensity was attained by the use of the high purity raw materials (99.99%+).

Concentration quenching of Tb^{3+} emission.—The emission of $Y_{1-x}Tb_xAl_3B_4O_{12}$ phosphors ($x \geqq 0.05$) was due to transitions from $^5D_4$ level to the ^7F levels of Tb^{3+} ion, as was reported earlier (4). Unless otherwise stated, the effect of various parameters on CL properties was compared via the intensity of the strongest Tb^{3+} emission peak at 543 ± 1 nm due to the $^5D_4 \rightarrow {}^7F_5$ transition.

The Tb^{3+} emission intensity increases with Tb concentration up to $x = 0.3$ in $Y_{1-x}Tb_xAl_3B_4O_{12}$, but concentration quenching sets in thereafter as can be seen in Fig. 1. The tendency was unaffected by the Fe impurity level in the phosphors. In Fig. 1, the open circles are for high purity samples (Fe $\lesssim$ 50 ppm) and the closed circles are for high Fe content samples (Fe > 100 ppm) prepared from CP grade Al_2O_3 and B_2O_3.

In some Tb compounds, the quenching of Tb^{3+} emission under u.v. excitation has been successfully interpreted by the formation of Tb^{3+} ion complexes (8). The general relationship for the concentration of Tb^{3+} ions with n neighbors C_n is given by

$$C_n = [Z!/n!(Z-n)!]x^{n+1}(1-x)^{Z-n}$$

where x is the fraction of the site available to the Tb^{3+} ions and Z is the maximum number of Tb^{3+} ions in neighboring sites. In the garnet series $(Y_{1-x}Tb_x)_3Al_5O_{12}$, the quenching sets in at $x = 0.35$ where $C_0 + C_1$ takes its maximum. Such a result can be expected when single ($n = 0$) and paired ($n = 1$) Tb^{3+} ions emit with equal intensity, but more complex aggregates ($n \geqq 2$) do not.

In the $Y_{1-x}Tb_xAl_3B_4O_{12}$ system, each Y or Tb atom has six nearest Y or Tb atoms ($Z = 6$) (9), so that the maximum in $C_0 + C_1$ takes place at $x = 0.24$. Hence, even in the $Y_{1-x}Tb_xAl_3B_4O_{12}$ system under CR excitation, the formation of Tb^{3+} ion complexes with $n \geqq 2$ seems to cause the quenching.

Effect of coactivators on Tb^{3+} emisison.— A number of elements such as Bi, Sb, and Ce are known to act as sensitizers for Tb^{3+} emission under u.v. excitation (10). We also confirmed that such sensitization took place. As much as two orders of magnitude enhancement in emission intensity under 254 nm u.v. excitation was observed with a small addition of these elements (up to a few percent). However, no such sensitizing

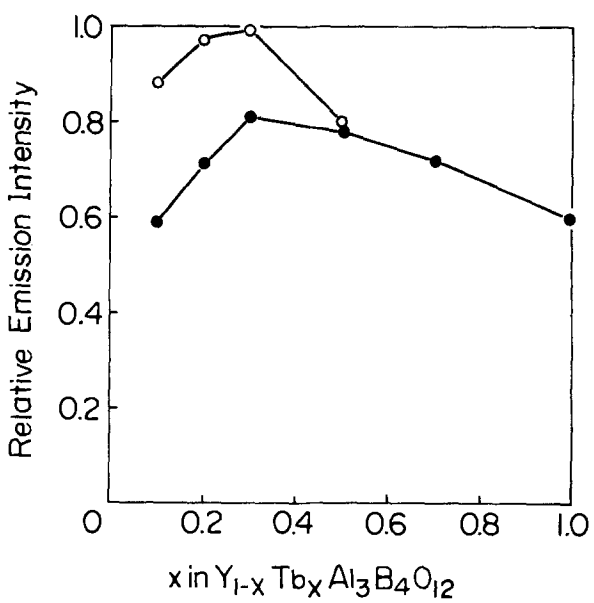


Fig. 1. Relative intensity of Tb^{3+} emission vs. Tb concentration in $Y_{1-x}Tb_xAl_3B_4O_{12}$. Open circles are for low Fe content phosphors prepared from high purity chemicals. Closed circles are for high Fe content phosphors prepared from CP grade chemicals.

Table I. Cathodoluminescent properties of green emitting phosphors*

Phosphor	Max peak wavelength λ_{max} (nm)	Relative peak output $I_{\lambda_{max}}$	Relative total output $E = \int_{400}^{700} I_\lambda d\lambda$	CE color coordinate
Zn_2SiO_4:Mn	523	100	100	X = 0.202, Y = 0.720
(Zn, Cd)S:Cu, Al	546	136	218	X = 0.354, Y = 0.591
$Y_{0.7}Tb_{0.3}Al_3B_4O_{12}$	541	179	48	X = 0.362, Y = 0.582

* Data obtained at 10 kV and about 1 $\mu A/cm^2$.

effect was observed for Tb^{3+} emission intensity under CR excitation. Figure 2 shows such a result for Bi and Sb coactivation. As can be seen, a quenching effect exists even at a very low concentration and this becomes more pronounced with increasing concentration. The quenching effect was even more marked when a small amount of other rare earth atom was added as shown in Fig. 3. In these cases, the energy lost due to quenching of Tb^{3+} emission seems to be dissipated nonradiatively. Although a small emission peak characteristic of the rare earth coactivator such as Tm, Eu, and Dy was sometimes detected, its intensity was not strong enough to compensate for the intensity loss in Tb^{3+} emission.

The quenching of Tb^{3+} emission in calcium metaphosphate glasses due to the energy transfer from Tb to a second rare earth ion under u.v. excitation has been systematically studied (11). It was found that the degree of quenching was proportional to a so-called

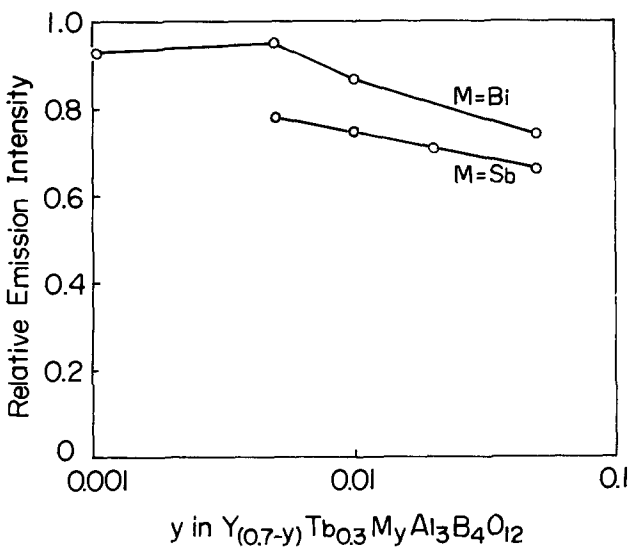


Fig. 2. Relative intensity of Tb^{3+} emission *vs.* coactivator concentration in $Y_{0.7-y}Tb_{0.3}M_yAl_3B_4O_{12}$; M = Bi or Sb.

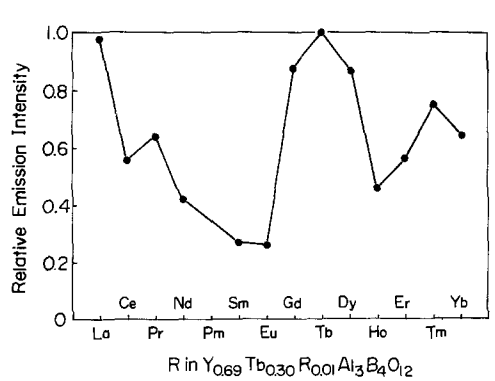


Fig. 3. Relative intensity of Tb^{3+} emission in $Y_{0.69}Tb_{0.30}R_{0.01}Al_3B_4O_{12}$.

overlap integral, $S = \int_0^\infty I(E)\sigma(E)dE$, where $I(E)$ is the emission spectrum of Tb^{3+} ion and $\sigma(E)$ is the absorption spectrum of the second rare earth ion. However, in the present case, no such systematic behavior was found to exist, indicating that the energy transfer under CR excitation is predominantly nonresonant, *i.e.*, from a higher-lying level of Tb^{3+} to a lower level of a second rare earth that is not matched in energy (8).

The case of Sm coactivation was considerably different from others and the energy transfer from Tb to Sm seems to take place quite effectively. Enhanced emission peaks of Sm^{3+} at 590 ~ 610 nm and at 640 ~ 645 nm gave rise to a yellow orange emission color. Such enhancement of Sm^{3+} emission was also observed in the series $Na_{0.5}Tb_{0.5-x}Sm_xWO_4$ only when the Sm concentration was low (12). The enhancement was believed to take place when the energy was transferred from an excited Tb to a Sm atom, rather than to a Sm-Sm or a Sm-Tb pair.

In summary, the best CL efficiency was realized in the $Y_{0.7}Tb_{0.3}Al_3B_4O_{12}$ phosphor without any coactivator. Figure 4 shows the relative peak output of the $Y_{0.5}Tb_{0.5}Al_3B_4O_{12}$ phosphor with respect to a standard Zn_2SiO_4:Mn(Pl) phosphor as a function of electron beam current density at 5 kV. As expected for rare earth activated phosphors in general, the relative efficiency gets better under the high current density operation. In Table I, the emission data are summarized for the $Y_{0.7}Tb_{0.3}Al_3B_4O_{12}$ phosphor together with the data for Zn_2SiO_4:Mn(Pl) and ZnCdS:Cu,Al(Z910). The latter is a green phosphor now in use in RCA color TV screens. It must be concluded that the $Y_{0.7}Tb_{0.3}Al_3B_4O_{12}$ phosphor is only moderately efficient as a phosphor for CRT screens.

Acknowledgments

The authors wish to thank J. Gerber and F. S. Stofko, Jr., for carrying out some of the CL measurements and H. H. Whitaker for the analysis of Fe content in the phosphors. They also wish to thank F. Okamoto and T. Oka for their technical assistance during the course

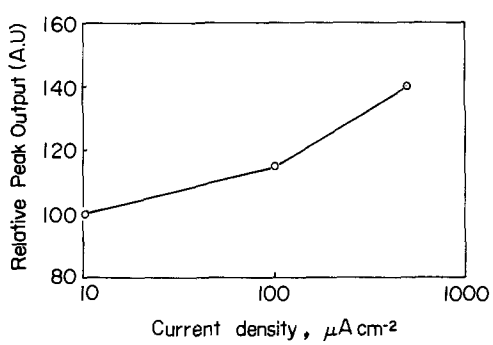


Fig. 4. Relative peak output of the $Y_{0.5}Tb_{0.5}Al_3B_4O_{12}$ phosphor with respect to Zn_2SiO_4:Mn as a function of electron beam current density. Peak output of Zn_2SiO_4:Mn at 523 ± 1 nm is taken to be 100 at each beam current density. Accelerating voltage = 5 kV.

of this work, and E. O. Johnson for critical reading of the manuscript.

Manuscript submitted Dec. 13, 1976; revised manuscript received Feb. 24, 1977.

Any discussion of this paper will appear in a Discussion Section to be published in the December 1977 JOURNAL. All discussions for the December 1977 Discussion Section should be submitted by Aug. 1, 1977.

Publication costs of this article were assisted by RCA Research Laboratories, Incorporated.

REFERENCES

1. A. D. Mills, *Inorg. Chem.*, **1**, 960 (1962).
2. G. Blasse, A. Bril, and W. C. Nieuwpoort, *J. Phys. Chem. Solids*, **27**, 1587 (1966).
3. G. Blasse and A. Bril, *Phys. Status Solidi*, **20**, 551 (1967).
4. G. Blasse and A. Bril, *Philips Res. Rep.*, **22**, 481 (1967).
5. G. Blasse and A. Bril, *J. Chem. Phys.*, **47**, 5139 (1967).
6. G. Blasse and A. Bril, *ibid.*, **48**, 217 (1968).
7. R. E. Shrader and P. N. Yocom, *J. Lumin.*, **1/2**, 814 (1970).
8. L. G. Van Uitert and L. F. Johnson, *J. Chem. Phys.*, **44**, 3514 (1966).
9. H. Y.-P. Hong and K. Dwight, *Mater. Res. Bull.*, **9**, 1661 (1974).
10. G. Blasse and A. Bril, *J. Chem. Phys.*, **47**, 1920 (1967).
11. E. Nakazawa and S. Shionoya, *ibid.*, **47**, 3211 (1967).
12. L. G. Van Uitert, E. F. Dearborn, and J. J. Rubin, *ibid.*, **45**, 1578 (1966).

Brief Communications

Control of Al_2O_3 Position in Anodic GaAs Native Oxide

B. Bayraktaroglu, S. J. Hannah, and H. L. Hartnagel

Department of Electrical and Electronic Engineering, University of Newcastle upon Tyne, Newcastle upon Tyne, NE1 7RU, England

It is shown that by careful control of kinetic growth parameters, it is possible to anodically position a thin Al_2O_3 layer in a native GaAs-oxide film either near the oxide-semiconductor interface or on the surface of the GaAs oxide. The ability to produce composite oxide structures promises several interesting advantages, such as: (*i*) stabilization of GaAs native oxide against many chemicals by placing the Al_2O_3 on the surface of the film, (*ii*) when Al_2O_3 is placed near the semiconductor surface, such a layer will be advantageous for optimum electrical characteristics due to the large bandgap of Al_2O_3 (~8 eV), and (*iii*) possible application to optical waveguides with a variation in refractive indexes of oxide layers.

Due to the difference in the threshold fields required for the activation of different anions and cations, it is possible to influence the growth mechanism of anodic oxide films, and therefore shift the effective oxide formation region anywhere from the metal-oxide interface to the oxide-electrolyte interface. For anodic Al_2O_3 films it is known (1) that the threshold field required for the activation of cations is larger than that for anions. Our findings suggest that a similar system also exists for anodic GaAs native oxides with the threshold field for cation activation again being larger than for anion activation. It is therefore possible to use a sufficiently low field so that OH^- drifts across any oxide formed to create further oxidation at the semiconductor-oxide interface, or to use a high field so that the cations become mobile which exhibit with their larger mobility a primary ion flow to the oxide surface where further oxidation occurs.

Composite oxides on GaAs have been produced by first evaporating a known thickness of Al on a polished and etched GaAs surface and then anodizing the whole structure with constant current in an electrolyte first suggested by Hasegawa and Hartnagel (2). Since the average field across the oxide during the growth is dependent on the current density, the control of growth kinetics was achieved by keeping the electrolyte temperature constant and varying the current density. The first oxide to form is always Al_2O_3 and then, depending on the current density used, GaAs native oxide can be made to form either underneath or on top of the Al_2O_3 by further anodization. Mixed oxides were previously reported under different anodic conditions without establishing or making use of the kinetic details presented here (3, 4).

If low current densities are used, *i.e.*, ~20 $\mu A/cm^2$, after the Al_2O_3 is formed, there are only anions moving across the oxide to the GaAs-Al_2O_3 interface, whereas the field at this current density is insufficient to produce mobile Ga and As ions. The oxide growth then forms GaAs native oxide underneath Al_2O_3. However, at high current densities (>2 mA/cm^2), Al_2O_3 is formed by transporting metal ions to the oxide-electrolyte interface and after all the Al is converted into Al_2O_3 the field is high enough to create Ga and As interstitial ions which are consequently transported through the Al_2O_3 layer to the oxide-electrolyte interface and hence GaAs native oxide forms on the Al_2O_3, as indicated by etch tests described below.

Although it was possible to produce thick layers of Al_2O_3 on GaAs native oxide, there is a limit to the thickness of Al_2O_3 on the GaAs surface. For Al_2O_3 thicker than ~500Å, the Al_2O_3 acts as an effective diffusion barrier for Ga and As interstitial ions and even at intermediate current densities, *i.e*, ~0.1 mA/cm^2, GaAs native oxide then still forms underneath Al_2O_3. But at higher current densities cations tend to punch through the Al_2O_3 creating locally damaged areas.

A chemical test was applied to the composite oxides using tartaric acid, which is an etchant of GaAs native oxide but not of Al_2O_3, in order to establish which oxide is on the top. When Al_2O_3 is underneath GaAs native oxide, an etching of some of the composite oxide was observed. The thickness of the oxide left behind was measured with a Dektak profile plotter.

Measured values were compared with the expected thickness of Al_2O_3 and it was concluded that the oxide left behind is, except for small traces of GaAs oxide, only Al_2O_3. For the structures grown with Al_2O_3 on top of the native oxide, no etching was observed for the same etch conditions. These results imply that in the first case practically all the Ga and As ions move across, whereas in the latter case only OH^- ions move across Al_2O_3 in the opposite direction.

It is possible to determine at which interface the Al_2O_3 layer is formed from the overpotential *vs.* time (v-t) graphs plotted during anodization. After all the Al is converted into Al_2O_3, the overpotential exhibits a temporary steep increase for the high current density case, whereas a constant potential is maintained over a short period for the low current density case. The first case corresponds to the growth of GaAs native oxide at the electrolyte interface, and the second one at the semiconductor interface.

Since most other valve metals have anodic behavior very similar to Al, it is expected that Al_2O_3 may be replaced by some other oxide systems promising wider ranges of possibilities.

Acknowledgments

The authors gratefully acknowledge financial support from the Science Research Council and the European Research Office of the U.S. Army.

Manuscript submitted Oct. 27, 1976; revised manuscript received Feb. 10, 1977.

Any discussion of this paper will appear in a Discussion Section to be published in the December 1977 JOURNAL. All discussions for the December 1977 Discussion Section should be submitted by Aug. 1, 1977.

REFERENCES

1. J. A. Davies, B. Domeij, J. P. S. Pringle, and F. Brown, *This Journal*, **112**, 675 (1965).
2. H. Hasegawa and H. L. Hartnagel, *ibid.*, **123**, 713 (1976).
3. H. L. Hartnagel, R. Singh, H. Hasegawa, and K. E. Forward, Final Technical Report, Research Grant DAJA73-74-C1703, European Research Office of U.S. Army (1974).
4. B. Schwartz *et al.*, U.S. Pat. 3,882,000 (1975).

Mask Preparation for Small Dimension Ion Milling by Two Step Lift-Off Process

O. Wada, S. Yamamoto, K. Kobayashi, A. Taguchi, and Y. Toyama

Fujitsu Laboratories Limited, Nakahara-ku, Kawasaki, Japan

The requirement for fabricating structures with dimensions smaller than a few microns has increased in recent years the need for improvements in the packing density and the operating speed of integrated circuits. The ion milling technique (1) combined with the scanning electron beam lithography (2) is very useful for this purpose because of the high resolution and the sharp edge profile of the exposed resist patterns and the small undercutting of the etched structure. In such a process, one has to prepare a mask which is resistant to the ion beam using the patterns delineated in the electron beam resist layer.

The purpose of this communication is to describe an improvement in the mask preparation in conjunction with the formation of small holes or grooves in the substrate.

In the practical fabrication processes for realizing small structures, the following subjects should be taken into consideration: (*i*) The patterns in the resist layer have to have good edge resolutions, therefore it is more useful to use the positive acting resist such as polymethylmethacrylate (PMMA) resist rather than the negative acting resist (3). (*ii*) The coverage of the exposed area in the resist layer should be minimized, because the exposure time is proportional to the area to be exposed with the scanning-type exposure system (4). (*iii*) The mask material for the ion milling should have an etching rate small enough to protect the substrate, and usually it is not easy to obtain a high yield of small structures by using the resist layer itself as an etching mask.

In the case of forming small islands, all of the conditions stated above are satisfied with the use of the so-called lift-off method (3) in which the etch-resistant metal layer is delineated using the resist pattern as a deposition mask. On the other hand, however, it is difficult to make small holes in the substrate because the exposure time for positive acting resist should be extremely long if the usual lift-off method is applied. In order to save the exposure time and simultaneously maintain the high resolution, we have introduced an improved method in which the metal patterns are delineated through a two step lift-off process. In the present method, a double metal layer structure is first patterned by the usual lift-off method with positive acting resist and the resultant structure is then used as a stencil in the subsequent lift-off process.

Key words: ion milling, two step lift-off, microfabrication.

The sequence of the processes is in the following:

1. The PMMA resist is coated on the substrate and the area under which the substrate has to be etched is exposed by the scanning electron beam system and then developed.
2. An Al layer and subsequently a Ti (first) layer are evaporated on the substrate and the resist layer is removed together with the upper Ti/Al layer by the usual lift-off method.
3. The lateral dimension of the lower Al layer is reduced using the side-etch effect of a chemical solution, in order to make an overhang structure in the double metal layer.
4. A Ti (final) layer is evaporated on the substrate and then the substrate is dipped into the Al etchant again. This results in the removal of only the Ti/Ti/Al layer and leaves behind the desired pattern in the final Ti layer.
5. The exposed area of the substrate is etched by the argon ion milling technique using the residual Ti layer as a mask.

Figure 1(a) shows the schematic illustration of the cross section of the substrate before the unwanted Ti/Ti/Al layer is removed. Prior to the evaporation of the final Ti layer, the Al layer was etched in the lateral direction by immersing in an Al etchant (3:1 H_3PO_4:-C_2H_5OH) for 60 sec. The thickness of the starting resist layer should be chosen from the required thickness of the final mask metal layer, where the thickness of the stencil Al layer should exceed the final Ti thickness, since the Al etchant has to penetrate through the gap of Ti layers. Figure 1(b) shows an example of the scan-

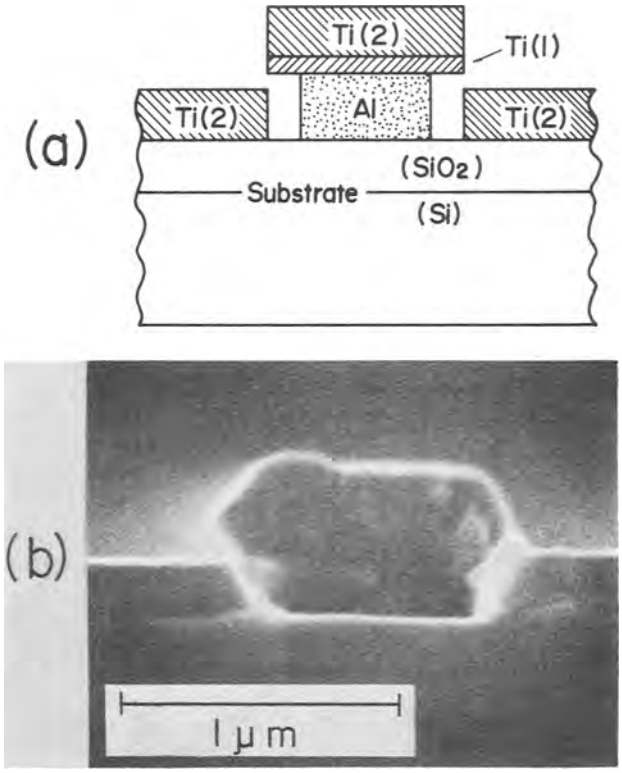


Fig. 1. (a) Schematic illustration and (b) scanning electron micrograph showing the second lift-off process. The lower Ti/Al stencil is first formed by the usual lift-off method and the chemical etching technique.

ning electron micrograph indicating the structure corresponding to Fig. 1(a). The pattern width is 1 μm, and the thicknesses of the Al, the first Ti, and the final Ti are 0.25, 0.15, and 0.18 μm, respectively. The starting resist thickness was 0.48 μm in this case. In our experiments, the removal of the unwanted Ti/Ti/Al layer was achieved in a reasonable etching time for the pattern width up to 5 μm. By increasing the starting resist layer thickness to 0.7 μm, a final Ti layer as thick as 0.48 μm was obtained. Figure 2 shows the structure revealed after the ion milling of the substrate SiO_2 to 0.5 μm depth using this 0.48 μm thick Ti mask. Because of the small etching rate of Ti layer compared with the SiO_2 layer (etching rate ratio $\simeq$0.6), deep holes and grooves with sharp edge profiles were realized.

As described above, the present method can realize a high resolution in the preparation of small holes or grooves in the substrate which are used for processes such as metallization and ion implantation. The present method together with the usual one step lift-off method are considered to be applied as complementary processes in forming structures (holes or islands) with dimensions smaller than a few microns, especially in the submicron range. Adding to the fine structure, the present method has the advantage that the final metal layer can be deposited at an elevated temperature. This is advantageous for improving the adhesion to the substrate. This feature cannot be expected for the usual lift-off method using the resist as a mask, because of the low glass-transition temperature of the resist, and therefore, the present method can also find a wide usage for patterning of high melting point metal layers.

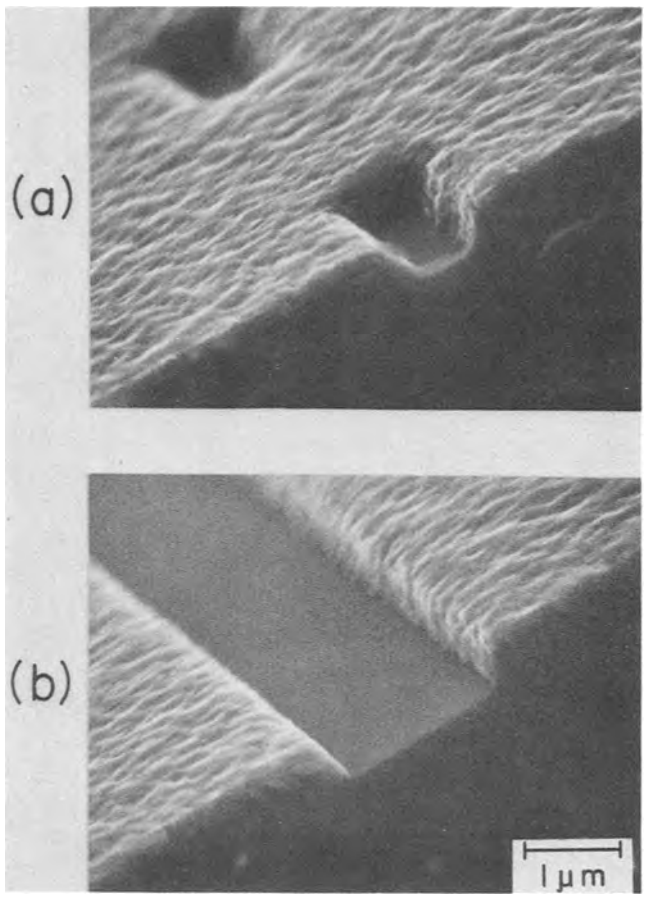


Fig. 2. Scanning electron micrographs showing (a) square holes and (b) a narrow groove both of which have been formed in the SiO_2 layer by argon ion milling technique using the patterned Ti layer as a mask.

Acknowledgment

The authors are grateful to T. Inagaki and his coworkers for exposing PMMA. They also thank S. Furuya and T. Fukuda for experimental help and T. Misugi, Y. Fukukawa, and H. Takanashi for encouragement.

Manuscript submitted Nov. 30, 1976; revised manuscript received Jan. 25, 1977.

Any discussion of this paper will appear in a Discussion Section to be published in the December 1977 JOURNAL. All discussions for the December 1977 Discussion Section should be submitted by Aug. 1, 1977.

Publication costs of this article were assisted by Fujitsu Laboratories Limited.

REFERENCES

1. E. G. Spencer, P. H. Schmidt, and R. F. Fischer, *Appl. Phys. Lett.*, **17**, 328 (1970).
2. H. N. Yu, R. H. Dennard, T. H. P. Chang, C. M. Osburn, and H. E. Luhn, *J. Vac. Sci. Technol.*, **12**, 1297 (1975).
3. M. Hatzakis, *This Journal*, **116**, 1033 (1969).
4. T. H. P. Chang, M. Hatzakis, A. D. Wilson, A. J. Speth, A. Kern, and H. Luhn, *IBM J. Res. Dev.*, **20**, 376 (1976).

A Chemical Polish for the Cadmium and Sulfur Faces of Cadmium Sulfide

A. A. Pritchard and Sigurd Wagner

Bell Laboratories, Holmdel, New Jersey 07733

In this note we report that chemical polishing with KCl buffered aqueous solutions of HCl leads to high quality finish on both the cadmium, or A, or (0001) and the sulfur, or B, or $(000\bar{1})$ surfaces of cadmium sulfide. The polishing solution is an aqueous hydrochloric acid-potassium chloride buffer with optimum *p*H values of 2.5 for the cadmium face and 1.0 for the sulfur face.

Satisfactory cadmium and sulfur surfaces have always been difficult to achieve. Three polishing procedures have been published. Warekois and co-workers (1) used a solution of $K_2Cr_2O_7$ in H_2SO_4 at 90°C to obtain a high polish, with dislocation etch pits, on the sulfur face. Sullivan and Bracht (2) chemically polished cadmium, sulfur, and prismatic faces by feeding a 30 volume percent (v/o) aqueous solution of conc HCl onto a rotating Pellon cloth. Pickhardt and Smith (3) chemo-mechanically polished cadmium faces on a Politex-Pix poromeric pad with a solution of 90 ml conc HNO_3, 300 ml precipitated silica suspension, and 10g $AlCl_3$ per 1000 ml H_2O; on sulfur faces no satisfactory finish was obtained. In an unpublished study, Polito (4) produced smooth sulfur (but not cadmium) faces with the Sullivan and Bracht technique, and smooth cadmium (but not sulfur) faces with Syton HT, a colloidal aqueous suspension of silica. The surface quality was characterized by standard incident light microscopy.

Each procedure appears to work well on only one of the two faces. In addition, the criteria for a satisfactory finish have become more stringent because the demands on surface quality have risen. Warekois *et al.* desired a visually smooth surface. Rozgonyi and Polito (5) sputtered epitaxial ZnO films on CdS for structural, electrical, and optical characterization. The CdS phonon spectrometer recently developed by Shah *et al.* (6) requires highly polished platelets. Pickhardt and Smith (3, 7) discuss the extreme surface finish of substrates needed in molecular beam epitaxy for waveguide structures.

Another explanation for the differences in polishing behavior observed in these studies may be found in the variable quality of CdS crystals. We have, for instance, observed that an acidic Syton polish can result in perfectly smooth sulfur faces in some batches while failing in others.

We now describe a procedure which reproducibly produces flat and highly polished cadmium and sulfur faces. Surfaces were inspected with a Nomarski-type incident light interference microscope at magnifications up to 1000× and with a Nomarski-type polarization interferometer ($\lambda = 546$ nm) at 125× and 290× magnification. The most satisfactory results have been obtained with batches of three CdS wafers of about 1 cm^2 area each. After string-saw cutting about 1 mm thick (0001) plates, they were etched for 2 min in 1:1 conc HCl and water in an ultrasonic bath to remove damaged surface layers and to differentiate cadmium and sulfur faces. The Cd face turns shiny while the S face remains mat (2). The first two polishing steps are carried out with Hyprez lubricant (Engis Equipment Company, Morton Grove, Illinois) on 3 μm emery paper and on 3 μm alumina paper (Ultralap, Pfizer Corporation), respectively; both papers, manufactured with self-adhesive backs, were attached to flat glass plates. The two following steps use the alumina abrasives, 0.3 μm Linde A and 0.05 μm Linde B, on Pellon cloths which also were attached to glass plates. The cloths are prepared by rubbing in the abrasive and a paraffin binder with a sapphire disk to obtain a flat surface. Before polishing, more abrasive is spread and tallow-base shaving cream is added as a lubricant. It is important to produce a smooth surface before the chemical polish is applied. Any crosshatch pattern arising from prepolishing must be removed at this point by repeating the polishing sequence with all three alumina abrasives.

Key words: crystal polishing, cadmium sulfide, buffer.

The chemical polish is an aqueous HCl/KCl buffer with *p*H = 2.5 (0.50 ml conc HCl, 13.7g KCl, 1000 ml dist H_2O) for the cadmium face; and *p*H = 1.0 (16.0 ml conc HCl, 13.3g KCl, 1000 ml dist H_2O) for the sulfur face. The solution is dripped at a rate of about 3 ml/min onto a Politex-Pix pad mounted on a motor driven (58 rpm) stainless steel plate 6 in. in diameter. To rotate the block, it is placed in a stainless steel dressing ring held by rollers near the edge of the poromeric pad. Brass weights are added to provide a pressure of 0.25-0.40 kg/cm^2 of CdS surface. Typical polishing times to reach a featureless finish are 2-4 hr.

The photoluminescence of CdS excited with a 457.9 nm argon laser beam provides a sensitive measure of the surface quality. With the absorption length for the exciting light being of the order of 0.1 μm (8), the luminescence spectrum reflects the perfection of a shallow surface layer. On vapor grown crystals or on cleaved faces the I_1 peak is narrow and intense, and the lowest background intensity between the I_1 and I_2 lines is 100-200 times smaller than that of I_1. The luminescence spectrum presented in Fig. 1 is typical of A and B faces polished with HCl/KCl buffers. This spectrum is comparable to spectra obtained on cleaved or vapor grown faces and demonstrates a damage-free finish.

Extended defects, which can be observed by focusing through the CdS crystal, always led to surface irregularities. We have also found that some crystals, especially when well conducting (~1 Ω-cm), contain entire layers of defective material. These layers seem to be (0001) oriented. When they surface it is not possible to obtain a perfect finish. One then needs to return

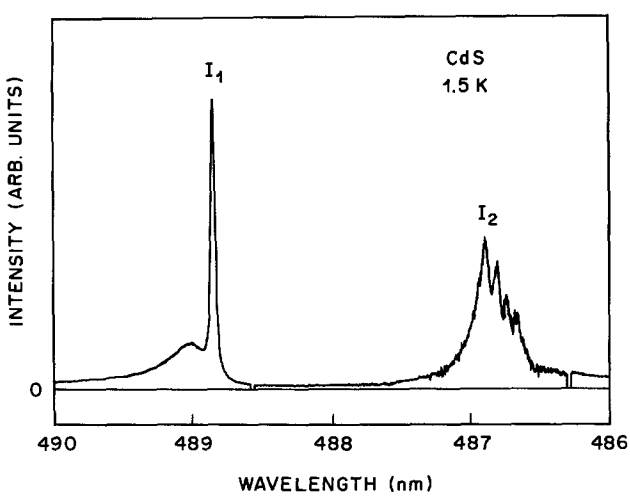


Fig. 1. I_1 and I_2 lines of the 1.5°K luminescence spectrum of polished CdS excited with 457.9 nm Ar laser light. The narrow I_1 peak and high I_1 to background (between I_1 and I_2) ratio are typical for A and B faces polished with HCl/KCl buffers.

to the alumina abrasives, remove 0.05-0.1 mm of the crystal, relap, and then repolish with the KCl/HCl buffer.

Acknowledgments

We would like to acknowledge helpful discussions with Dr. A. H. Dayem and Dr. B. I. Miller. We also thank Dr. J. Shah for providing and commenting on the luminescence spectrum.

Manuscript submitted Oct. 22, 1976; revised manuscript received Feb. 6, 1977.

Any discussion of this paper will appear in a Discussion Section to be published in the December 1977 JOURNAL. All discussions for the December 1977 Discussion Section should be submitted by Aug. 1, 1977.

Publication costs of this article were assisted by Bell Laboratories.

REFERENCES

1. E. P. Warekois, M. C. Lavine, A. N. Mariano, and H. C. Gatos, *J. Appl. Phys.*, **33**, 690 (1961).
2. M. V. Sullivan and W. R. Bracht, *This Journal*, **114**, 295 (1967).
3. V. Y. Pickhardt and D. L. Smith, *ibid.*, **121**, 1064 (1974).
4. W. J. Polito, Unpublished data (1968).
5. G. A. Rozgonyi and W. J. Polito, *J. Vac. Sci. Technol.*, **6**, 115 (1969).
6. J. Shah, R. F. Leheny, and A. H. Dayem, *Phys. Rev. Lett.*, **33**, 818 (1974).
7. D. L. Smith and V. Y. Pickhardt, *J. Appl. Phys.*, **46**, 2366 (1975).
8. B. Segall and D. T. F. Marple, in "Physics and Chemistry of II-VI Compounds," M. Aven and J. S. Prener, Editors, John Wiley & Sons, New York (1967).

DISCUSSION SECTION

This Discussion Section includes discussion of papers appearing in the *Journal of The Electrochemical Society*, Vol. 123, No. 3 and 6; March and June 1976.

A High Speed X-Ray Topographic Camera for Semiconductor Wafer Evaluation

D. L. Parker and W. A. Porter (pp. 407-409, Vol. 123, No. 3)

C. A. Wallace:[1] The experiments reported by Parker and Porter bear a close similarity to the work of Wallace, Ward, and Eastlake.[2,3] However, the vacuum chuck described does not allow the technique to be used in the transmission mode. Wallace *et al.* have developed an instrument which can be used in both the transmission (Laue) and the reflection (Bragg) modes. The crystal is mounted by an atmospheric mechanism to a plate which is subject to continuously adjustable opposed couples in a bending mechanism. In the transmission mode the direct beam is eliminated by a set of Soller slits aligned with the diffracted beam and oscillated laterally to diffuse the shadows of the diaphragms. The topograph can be viewed directly with a TV camera as an aid to alignment and for inspection of the crystals at coarse resolution.

Evolution and Current Status of Aluminum Metallization

A. J. Learn (pp. 894-906, Vol. 123, No. 6)

P. S. McLeod:[4] Table I of this article omits a rapidly developing area of sputtering commonly called planar magnetron sputtering.[5] We estimate the cost per wafer for metallization by planar magnetron sputtering to be between \$0.05 and \$0.06 for 1 μm thickness films from a five 9's pure aluminum target. This is comparable to costs for flash evaporation. We have measured static rates of deposition as high as 1.6 μm/min at 5 kW power input into a 3 1/2 $\times$ 8 1/4 in. source. This is greater than rates cited in Table II of the article and comparable to rates run at the same power from a 2 in. diameter electron beam source without a crucible liner and beam sweep. With good vacuum technique, we have made aluminum coatings with Q_0 of less than 8×10^{-3} V/PFD, and voltage shifts in C-V plots of a few hundred millivolts before annealing are typical if the sputtering voltage is kept below 500V. After annealing, evidence of damage in all cases we have seen can be eliminated by annealing for 5-10 min at 400°-450°C.

A. J. Learn:[6] Development in the area of sputtering, and plasma-related processing in general, is indeed showing rapid advancement. While magnetron sputtering is not listed in Table I of the subject article, it is, of course, referenced in the discussion of items in that table and in the concluding paragraph of the article. At the time of the paper, the published information on magnetron sputtering, was insufficient to allow full assessment of that technique as regards meeting requirements for metallization on silicon devices. This has been remedied to a large extent for general magnetron sputtering by the publications of Wilson and Terry[7] and Hoffman.[8] Similar information for planar magnetron sputtering is still lacking, although one suspects that such data are abundant, as evidenced by the unpublished results quoted above. The comparison of deposition rate for planar magnetron sputtering and other deposition methods is not entirely meaningful since the deposition geometries are typically quite different. It is noteworthy that the deposition rate for magnetron sputtering into conventional spherical rotary planetary fixturing remains relatively low at < 0.1 μm/min.[8,9] In a practical sense, presumably the throughput of silicon wafers of a given size forms a better basis for comparison. Planar magnetron sputtering is found[10] to compare favorably with other methods in this respect.

[1] Marconi-Elliott Avionic Systems, Limited, Borehamwood, Hertfordshire WD6 1RX, England.
[2] C. A. Wallace and R. C. C. Ward, *J. Appl. Crystallogr.*, **8**, 281 (1975).
[3] R. P. Eastlake and C. A. Wallace, Paper presented at the First International Congress on Crystallography, Amsterdam, August 1975.
[4] Airco Temescal, Berkeley, California 94710.
[5] P. S. McLeod and L. D. Hartsough, *J. Vac. Sci. Technol.*, **14**, (1977).
[6] Intel Corporation, Santa Clara, California 95051.
[7] R. W. Wilson and L. E. Terry, *J. Vac. Sci. Technol.*, **13**, 157 (1976).
[8] V. Hoffman, *Solid State Technol.*, **19**, 57 (Dec. 1976).
[9] P. J. Clarke, *ibid.*,, **19**, 77 (Dec. 1976).
[10] T. VanVorous, *ibid.*, **19**, 62 (Dec. 1976).

JOURNAL OF THE ELECTROCHEMICAL SOCIETY

ELECTROCHEMICAL SCIENCE
— AND TECHNOLOGY —

JULY
1977

Alkali Peroxydisulfates for Water-Activated Reserve Batteries

J. R. Dafler*,[1]

ESB Incorporated, Technology Center, Yardley, Pennsylvania 19067

ABSTRACT

Peroxydisulfates (persulfates) possess very high specific free energy changes for oxidation in aqueous systems. The alkali persulfates are very soluble and yield, in 40% aqueous systems, cell voltages, at the 4 hr rate, that exceed 2V. Persulfates are stable and can be dry-stored for long periods with little loss of oxidizing power. Used in conjunction with Mg alloy (AZ-61) anodes, persulfate cells can be activated with most common aqueous media. The $Na_2S_2O_8$/AZ-61 cell has fast start-up capability and a flat discharge characteristic at all reasonable rates of discharge. Comparisons to other battery systems at equivalent currents and rates are presented. The persulfate cell is seen as a potentially useful reserve battery for either high or low rates.

Water-activated batteries were rapidly developed during the 1940's when there was specific need for long shelf-life, higher power, reserve systems. The impetus for development came from military applications (1, 2). An early result of the intensive work done to develop such new energy sources was the silver chloride-magnesium reserve battery, which became commercially available in 1943 (3, 4). After 1946, applications for the AgCl/Mg battery grew rapidly and this system, despite its relatively high cost, became widely adopted. It has been used for weather ballons, air-sea rescue equipment, and sonobuoys, the latter application having accounted for a major fraction of production.

The cuprous chloride-magnesium reserve battery (Cu_2Cl_2/Mg) first became commercially available in 1949 (5, 6). Like the AgCl/Mg battery, it is a long shelf-life, water or seawater activated unit. It is not suitable for the same kinds of use as the AgCl/Mg battery, having lower rate capability and, generally, lower energy density.

The high cost of silver and the lower rate capabilities of Cu_2Cl_2 have led to considerable effort to find other systems suitable to replace the AgCl/Mg system. A number of water-activated systems appeared in the 1970's and deserve mention.

Aluminum/air battery.—The Furukawa Battery Company, Limited, of Tokyo introduced an aluminum/air battery in 1969 (7). It consisted of a series of closed cells containing KOH pellets and utilized a 2.54 mm thick aluminum anode and a 3.38 mm thick, porous carbon, air breathing cathode. The battery was a five-cell device activated with water poured into one cell, which then filled all five subunits through overflow connections. Sold as a low rate (0.3A) battery, this system did not fulfill its advertised energy density goals. Moreover, though sealed in water-vapor resistant PET-plastic film bags, the KOH deteriorated after 5-6 months of storage.

Cuprous fluoride/magnesium.—This cell system, Cu_2F_2/Mg (AZ-31) is a retained electrolyte cell of reasonably high power density (8). It was not, in the configurations tested here, a water-activated battery, but carried, in conjunction with its cathode/anode pouch, a plastic container filled with a strong solution of $NaClO_4$. Activation was accomplished by puncturing the electrolyte reservoir. Activation was then rapid. As with most retained electrolyte systems, this was not an "any attitude" battery such as the AgCl/Mg and Cu_2Cl_2/Mg batteries.

Lead chloride/magnesium.—Commercial samples of this system appeared in 1970-1971 as typically pasted positives in conjunction with AZ-61 anodes. The pasted positives contained $PbCl_2$ and basic Pb(OH)Cl, on an antimonial SLI grid. The system was attractive and easy to use. It yielded energy densities, in our testing, of ~66 W-hr/kg.

Coleman (9) reviewed the $PbCl_2$/Mg technology in 1971 and reported similar energy densities using Cu-mesh supports rather than typical SLI grids. Recent advances in electrode manufacture (10, 11) have made this an exceptionally attractive system, presently yielding energy densities high enough to replace AgCl/Mg in many of its applications.

Alkali peroxydisulfates.—A water-activated system designed to employ the alkali peroxydisulfates (persulfates) as a depolarizer would necessarily need to be, as in the case of the CuF_2/Mg cell, a contained electrolyte system.

The high solubilities of alkali persulfates [$(NH_4)_2S_2O_8$, 47.7 g/100 ml solution; $K_2S_2O_8$, 1.72 g/100 ml solution; and $Na_2S_2O_8$, 49.9 g/100 ml solution] can provide a reserve battery system with electrolyte of high ionic strength immediately after water activation, so that conductivity of electrolyte is never a problem. The ionic strength of persulfate depolarized batteries increases rapidly during discharge, due to the following reactions

$$Mg \rightleftarrows Mg^{++} + 2e^- \quad [1]$$

$$S_2O_8^{=} + 2e^- \rightleftarrows 2SO_4^{=} \quad [2]$$

An operating $S_2O_8^{=}$/Mg battery would be of low internal resistance, and prior to activation, should have

* Electrochemical Society Active Member.
[1] Present address: Institute of Gas Technology, Chicago, Illinois 60616.
Key words: magnesium electrodes, persulfates, water-activated batteries.

an excellent shelf-life. Alkali persulfates do not deteriorate if kept dry. They can be expected to lose ~1% of their active oxygen in one year of dry storage.

Codd (12), in 1932, reported on a $(NH_4)_2S_2O_8$ depolarized primary battery, but little seems to have come of it until 1952, when Blake (13) reported on the use of $K_2S_2O_8$ to improve the performance of AgCl/Mg water-activated batteries. Most of the experiments described were carried out using a Burgess AgCl/Mg battery (ICC40), adding $K_2S_2O_8$ or $Na_2S_2O_8$. There was improved performance (14) but this system offers no great advantage in price because the cathode material was either silver foil or silver-carbon pastes. Blake suggests that some undefined synergism makes the persulfate additive-AgCl/Mg battery perform better than either system's separate performance indicates.

Recently, primary cells with persulfate depolarizers have attracted some limited attention. Wijnen and Boter produced a flat primary system capable of driving an electric shaver (15). A semiwet system employing a feltlike absorber, saturated with alkali persulfates, this cell required clamping action to realize full current capabilities.

In 1970, Cohen *et al.* obtained some very general patents on primary cells using peroxygen chemicals as additives and as depolarizers (16). They explored the use of peroxyphosphates acting as corrosion inhibitors for the anodes used, which were either Zn or Mg and their alloys. Their embodiments, however, were cells of exceptionally low rate and capacity, even after "pro-rating' them for the quantities used.

Alkali persulfate chemistry.—Alkali persulfates, produced in enormous quantities in the United States, are widely used in the chemical and related industries. Persulfate ion is a powerful oxidant as can be seen by its standard reduction potential

$$S_2O_8^{=} + 2e^- = 2SO_4^{=} - 2.0V \qquad [3]$$

Solutions of the persulfates are intrinsically unstable, decomposing to dilute sulfuric acid and oxygen in neutral or alkaline solutions. In acidic media, the hydrolysis yields Caro's acid (H_2SO_5) and H_2O_2. The hydrolyses are

$$S_2O_8^{=} + H_2O = 2HSO_4^- + \tfrac{1}{2}\,O_2 \qquad [4]$$

in neutral media, and

$$S_2O_8^{=} + H_2O = H_2SO_5 + SO_4^{=} \qquad [5]$$

$$H_2SO_5 + H_2O = H_2O_2 + H_2SO_4 \qquad [6]$$

in acid media.

Kolthoff and Miller (17) have postulated a thermal decomposition mechanism, and report a first-order reaction rate with hydrogen ion catalyzing the decomposition. The rate is given by

$$d(S_2O_8^{=})/dt = -[k_1(S_2O_8^{=}) + k_2(H^+)(S_2O_8^{=})] \qquad [7]$$

The mechanism proposed is a chain mechanism, the uncatalyzed and catalyzed reactions being independent. The uncatalyzed chain involves the formation of labile species SO_4^- as the rate-determining step, while the formation of $HS_2O_8^-$ determines the rate of the catalyzed reaction.

Solutions of persulfates tend to become more acidic on standing, due to formation of HSO_4^-. On standing, the *p*H falls and the acid catalyzed decomposition becomes significant.

Early battery work on the alkali persulfates yielded low rate units because an effective electrode for persulfate reduction was not found. Silver, silver compounds, and silver-carbon pastes were reasonably effective but are not appropriate. The need was for a cheap, high surface area material that provided a high density of sites for decomposition. The material must also have a sufficient electrical conductivity to act as a proper electrode.

After a large number of experiments, a material was found, *i.e.*, a graphite fabric made by treating polymeric fiber cloth at high temperatures. The material has good conductivity (18), is robust, and has enough surface area to support large currents.

Experimental Procedures

Commercial samples of the alkali persulfates were used as test active material. These were supplied by the FMC Company of Princeton, New Jersey. All other chemicals used were reagent grade materials. Magnesium anode materials were supplied in the form of standard alloys such as AZ-21, AZ-31, and AZ-61. These were purchased from the Dow Chemical Company.

A standard, single cell test unit was adopted. It consisted of a small polystyrene case with plastic spacers used to adjust total cell volume. The cell finally adopted for test purposes had a volume of 22 cm^3 and used a 20 cm^3 volume of electrolyte. The separator was styrene bonded, nonwoven fiberglass mat, and electrolyte volume was defined by two negative sized pieces of corrugated, perforated PVC. The test unit exposed 39 cm^2 of Mg alloy, and 60 cm^2 of graphite cloth.

Discharges of test cells were conducted at constant currents, and ranged from 30 mA to 1.0A.

Inhibition of excess Mg alloy corrosion was done by first activating the surface with dilute HNO_3, then dipping in acidic solutions of $K_2Cr_2O_7$. Other techniques appear to be widely used (19, 20) but since they begin with a $K_2Cr_2O_7$ treatment, the simple dip treatment was used for most of the work reported here.

Treatment of data.—All discharge data was abstracted from continuous strip-chart collections, and subjected to point-by-point integration to yield point-by-point evaluation of the cell average voltage $\bar{E}$. Reference electrode discharges were followed continuously using infinite resistance linear amplifiers to prevent polarization of references. Utilization, U_T, of active material is referred to the two-electron reduction of $S_2O_8^{=}$, as indicated in Eq. [3].

A number of comparisons to other systems are presented. These are usually plotted as a dimensionless voltage [the cell terminal voltage, V, divided by the open-circuit voltage (OCV), E_{oc}] *vs.* a dimensionless capacity (the capacity, C, extracted at V, volts, divided by the total abstracted capacity, C_T).

Results and Discussion

Persulfate cell.—Sodium persulfate was quickly adopted as the material of choice. The more limited solubility of $K_2S_2O_8$ precluded use at high concentrations and $(NH_4)_2S_2O_8$ testing generally led to excessive generation of heat; high current drains often produced boiling in concentrated cells. This was due, presumably, to enhanced acid decomposition according to Eq. [7].

In a similar manner, AZ-61 was made the choice for anode. It consistently gave the highest OCV and better over-all discharge performance. AZ-61 has different corrosion characteristics than does AZ-21 or AZ-31 and, for this reason, its sludging characteristics appear superior. Robinson (21) pointed out that the higher aluminum alloys, such as AZ-61 or AZ-63, appeared to sludge and polarize less than other alloys. The films of $Mg(OH)_2$ formed are sloughed off via energetic aluminum corrosion or kept thin by hydrogen evolution and the stirring produced. Carson, Fischer, and Siewek (22) also found that, of the common alloys, AZ-61 was superior for water-activated systems. They found the sludges from AZ-21 and AZ-31 to be fluffy and slow settling, making those materials inferior to AZ-61. In this system, the *p*H is low enough to partially solubilize the $Mg(OH)_2$ formed and lower the effect of the hydroxide layer.

Table I. Summary of persulfate cell testing 22 cm³ cell at room temperature (25°C)

i_D (mA)	Concentration (g/100 ml solution)	U_T (%)	$\bar{E}$ (V)	t_D (hr)
100	10	68	1.70	3.00
	15	68	1.65	4.62
	20	68	1.98	6.10
	25	64	1.92	7.25
250	15	64	1.57	1.73
	20	65	1.74	2.35
	25	64	1.71	2.88
	30	58	1.84	3.12
	40	59	1.94	4.27

An extended series of simple experiments using increasing concentrations (g/100 ml solution) were done at two discharge currents, i_D. Electrolytes were made up as fully developed solutions and discarded daily. The data for these preliminary cell tests, using the standard cell described above, are summarized in Table I.

These tests were conducted at room temperature without inhibitor. The voltage column, $\bar{E}$, is a point-by-point integrated value preferable to the use of mid-voltage, with cells discharged to 0.5V end point.

Having achieved consistent data at reasonable discharge rates, the possible use of added, supporting electrolyte was investigated. To this end, 3% of NaCl was added to test electrolytes to simulate seawater activation. The data from these tests are summarized in Table II.

The use of 3% NaCl in conjunction with the $Na_2S_2O_8$ has led, in almost every case, to increases in performance figures for the cells (in watt hours). The increases are greater for lower concentrations of $Na_2S_2O_8$ cells than for high, and in the case of 40% solutions, the test unit without NaCl had higher operating voltages, if slightly poorer utilization and discharge time. This suggests that the value of the presence of NaCl is added initial conductivity, and the values derived from this decrease as the total concentration of electrolyte rises in the test series.

Inhibitor tests.—During discharge of a typical 40% $Na_2S_2O_8$ cell, a considerable quantity of sludge, presumably hydrated MgO is formed. There appears to be enough gassing, however, to keep the AZ-61 anode active. Control of gassing, therefore, had to be balanced with the need to keep the Mg/electrolyte interface well stirred.

The use of inhibitor as a premixed additive in the electrolyte was tried. $K_2Cr_2O_7$ or other chromate treatments appear the most recommended (19, 20) and $K_2Cr_2O_7$ was added to electrolyte solutions and tested. It was found that additions of 0.5 g/100 ml solution would effectively deactivate the cell, reducing utilization approximately to 6%. Reduction of additive inhibitor by an order of magnitude brought utilization in 20% cells up to ~73%.

A series of dip-treatment inhibitor tests were then made and these results summarized in Table III. Comparison indicated that cell voltages remained higher if the dip inhibition was used rather than the additive technique.

Table II. Summary of persulfate cell testing 22 cm³ cell at room temperature (25°C), 3% NaCl

i_D (mA)	Concentration (g/100 ml solution)	U_T (%)	$\bar{E}$ (V)	t_D (hr)	ΔW-hr* (%)
100	10	71	1.82	3.25	16.0
	15	71	1.63	4.78	2.21
	20	70	1.98	6.33	3.77
	25	67	1.95	7.50	5.06
250	10	66	1.52	1.18	
	15	68	1.66	1.82	11.2
	20	69	1.81	2.48	9.8
	25	67	1.74	2.98	5.29
	30	64	1.86	3.44	11.4
	40	60	1.87	4.28	−3.38

* ΔW-hr: percent change in watt hours, for this regime, compared to NaCl-free cells.

Table III. Summary of $K_2Cr_2O_7$ dip-inhibitor tests, i_D = 250 mA, 25°C, with and without 3% NaCl

	Concentration (g/100 ml solution)	U_T (%)	$\bar{E}$ (V)	t_D (hr)
Without NaCl	20	68	1.72	2.44
	30	69	1.81	3.72
	40	72	1.95	5.19
With NaCl	20	72	1.82	2.59
	30	69	1.85	3.72
	40	67	1.85	4.89

The inhibition treatment is effective both in suppressing gassing of Mg and in increasing the values of performance parameters. In the case of 40% units, the inhibitor treatment is seen to be quite beneficial, although the addition of NaCl and inhibitor apparently yields poorer performance than inhibitor alone. At levels of 20 and 30%, the use of inhibitor and NaCl led to increases in both utilization and average voltage.

Limited testing of longer dip treatments of the alloy negatives, and of alternate treatments was also done. Five minute dip treatments did not lead to notable increases in performance.

The long term efficacy of the $K_2Cr_2O_7$ inhibition technique was measured by discharging standard 20% cells at 30 mA. That data is shown in Fig. 1 and gives quite clear indication of the usefulness of this form of inhibitor application.

Gassing experiments, done using a modified Amlie-Ruetschi gas collecting technique (21), on electrode-sized AZ-61 pieces permitted the calculation of loss of capacity during activated, open-circuit stand. For 40% $Na_2S_2O_8$ cells with NaCl, uninhibited cells lost 0.15 A-hr/hr, and inhibited cells lost 0.077 A-hr/hr.

Work to inhibit excess gassing has led to considerable improvement of cell performance at all concentrations investigated. For low concentrations, the inhibitor + NaCl addition has led to substantial increases in U_T, E, and t_D. Added NaCl has not been beneficial for the highest percentages of $Na_2S_2O_8$.

Polarization effects.—A group of typical, standard cells were discharged in a 25°C thermostat and electrode voltages measured *vs.* SCE.

The discharges were conducted at i_D = 250 mA in inhibited anode cells with 3% NaCl added. The electrodes exhibit typical activation polarization behavior but the anode (AZ-61) does not exhibit either iR or concentration polarization. This is, of course, not unexpected. The anode reaction does not depend on the $Na_2S_2O_8$ concentration, but only on the AZ-61/H_2O interface (22, 23).

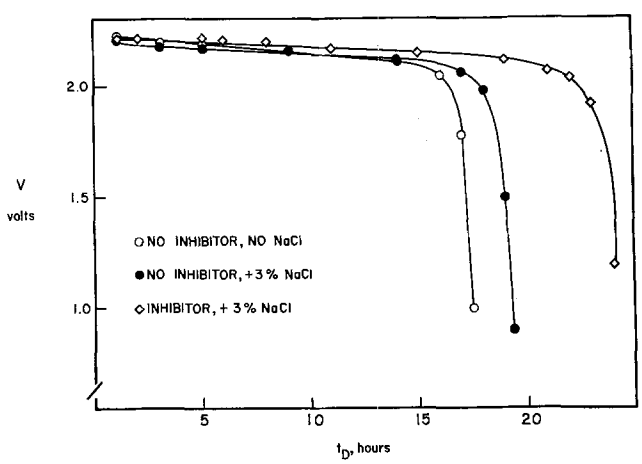


Fig. 1. Inhibitor efficiency. The dip inhibition technique was tested by using a low rate discharge over a long term. As indicated, 20% $Na_2S_2O_8$ cells were tested at discharge currents of 0.030A.

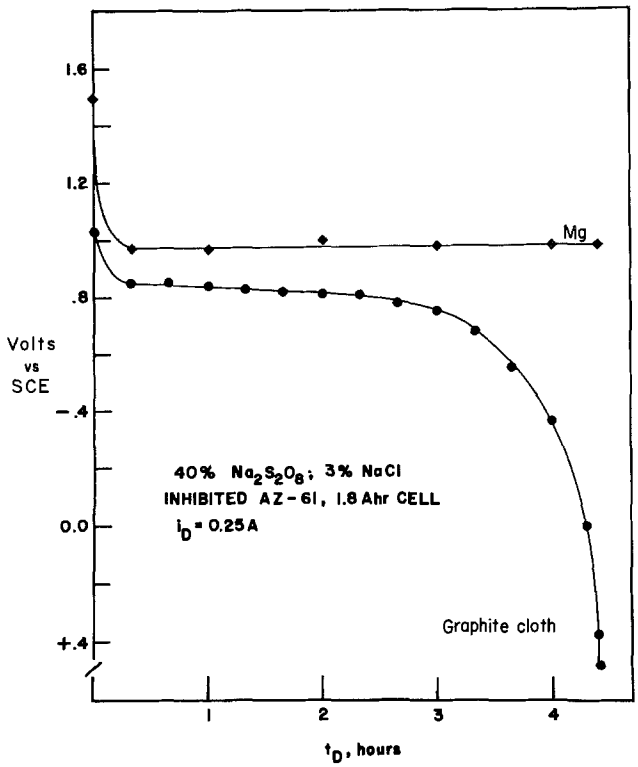


Fig. 2. Polarization of a standard 1.8 A-hr cell. A 1.8 A-hr cell was discharged at 0.25A in a 25°C thermostat. Data synthesized from six individual experiments.

The graphite cloth electrode displays typical polarization behavior, exhibiting a small activation polarization, and as the $Na_2S_2O_8$ is utilized, a very extensive, increasing, diffusion polarization. The data from a large population of experiments were synthesized and are shown in Fig. 2.

A similar series of experiments were done in a system such that the effective concentration of persulfate remained constant ($d[S_2O_8^=] = 0$). It was a well-stirred system and, as expected, there was no apparent activation polarization at the Mg electrode, with a very slight effect at the graphite cloth electrode. The iR polarization was extensive for the graphite cloth, but

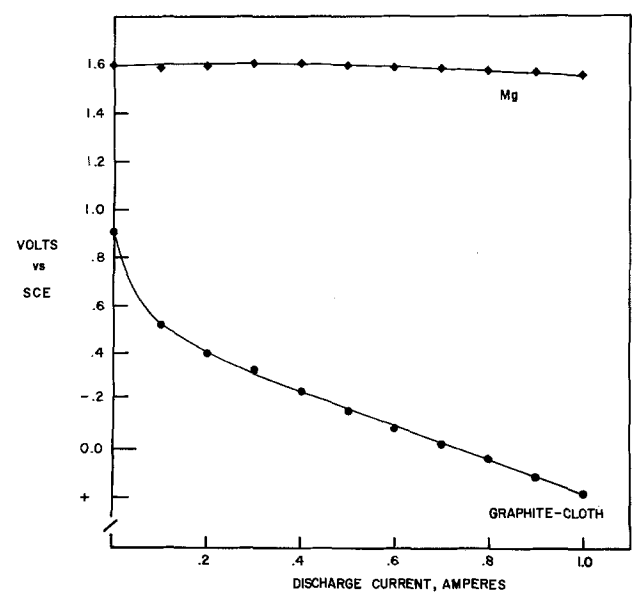


Fig. 3. Polarization effects. The elements typical of a 1.8 A-hr cell were subjected to increased polarization in an environment such that $d(S_2O_8^=) = 0$. The temperature was controlled to 25° ± 0.5°C, and the areas are: AZ-61 = 39 cm^2; graphite cloth = 60 cm^2.

the current used was not large enough to produce diffusion polarization at either electrode. The polarization data from these experiments are synthesized and displayed as Fig. 3.

The persulfate cell is a cathode-limited unit whose chemical makeup resists the onset of diffusion polarization effects. As utilization of $Na_2S_2O_8$ proceeds, the resistivity of the electrolyte drops by a factor of 4 or 5 and the ionic strength increases due to the reactions shown in Eq. [1] and [2]. A set of model solutions that represented the electrolyte at increased stages of utilization were used to collect the data shown in Fig. 4,

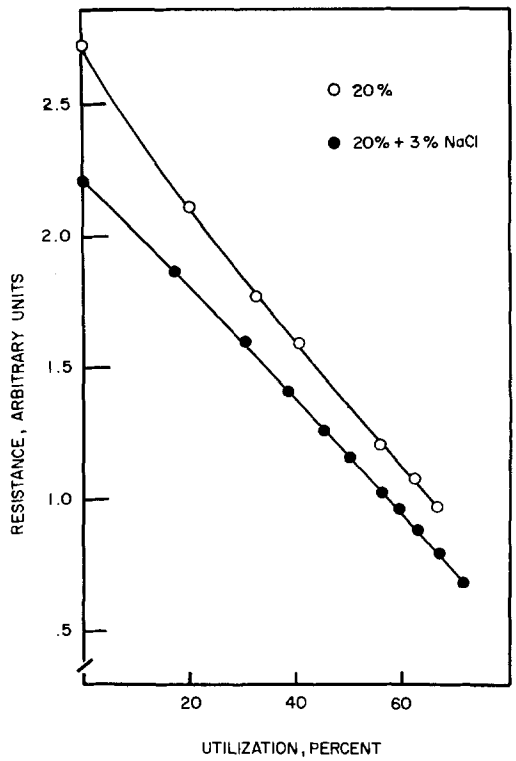


Fig. 4. Decreasing resistivity of working cells. The resistivity of the cell medium was tested by modeling the cell discharge processes as a function of U_T.

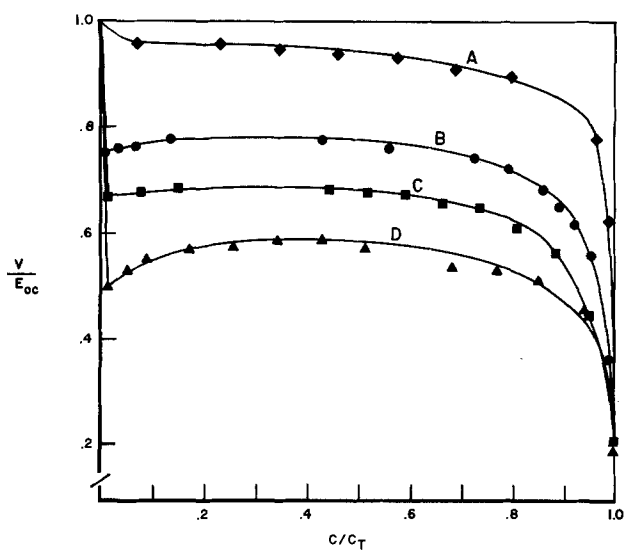


Fig. 5. Performance characteristics of persulfate cells. This dimensionless plot indicates the relative performance characteristics of 1.8 A-hr persulfate cells at increasing discharge currents. Curve A, i_D = 0.030A, $\overline{E}$ = 2.11V, C = 1.49 A-hr; curve B, i_D = 0.25A, $\overline{E}$ = 1.93V, C = 1.24 A-hr; curve C, i_D = 0.50A, $\overline{E}$ = 1.69V, C = 1.13 A-hr; curve D, i_D = 1.00A, $\overline{E}$ = 1.31V, C = 0.77 A-hr.

where the resistivity is presented as a function of utilization. At 60% utilization, the electrolyte has only 40% the resistivity of the undischarged cell.

Comparison with other systems.—The $Na_2S_2O_8$/AZ-61 cell appears to be capable of both high rate and low rate discharge. It produces a flat discharge characteristic at rates that vary from the 40 to the 1.2 hr rate. It has certain intrinsic problems because it is a "contained-electrolyte" unit and is not really suitable for intermittent service. Its over-all performance can be seen in Fig. 5, a dimensionless plot based on useful delivered capacity. Curve A, the 40 hr rate, delivers almost all its energy at voltages above 90% of OCV (2.54V). The 2 hr rate discharge, curve C, delivers its energy at ~70% of OCV. All the discharges demonstrate an attractive flat characteristic, whatever the rate.

We have compared the performance of typical 40% $Na_2S_2O_8$ cells, which have a theoretical capacity of 1.8 A-hr, to 2.0 A-hr AgCl/AZ-61 cells. The two systems were compared at i_D's of 0.25 and 0.50A. The comparisons are shown in Fig. 6, where $\overline{E}$ is plotted against time, the discharges done at room temperature. The

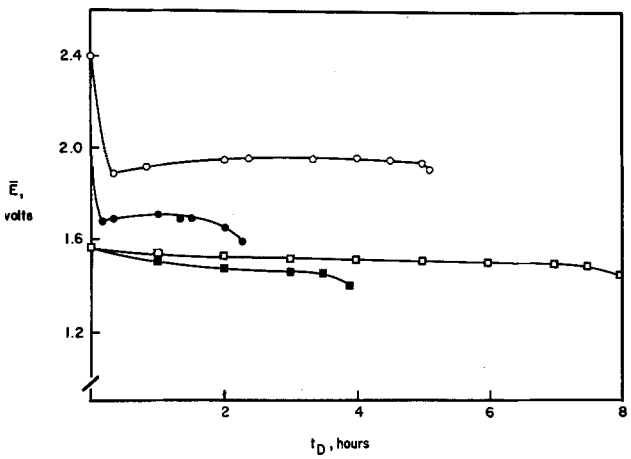


Fig. 6. Persulfate cells compared to AgCl/AZ-61. The open and filled circles represent 1.8 A-hr persulfate cells discharged at 0.25 and 0.50A, respectively. The open and closed squares represent AgCl/AZ-61 cells (2.0 A-hr) discharged at 0.25 and 0.50A, respectively.

AgCl/AZ-61 cells were discharged in 2 liter containers of artificial seawater which was stirred constantly. As the discharge curves indicate, the AgCl/AZ-61 system gives better over-all performance at lower average voltage. In the case of the $Na_2S_2O_8$/AZ-61 system, the average voltages are much higher, achieving almost 2.0V for the lower rate discharge.

A more interesting set of comparisons was made with other small systems discharged at the same current, plotted on dimensionless voltage/capacity axes, and shown as Fig. 7. All these cells have small volumes, in the neighborhood of 25 to ~ 54 cm^3. The $Na_2S_2O_8$ system is superior to all, save the Ni/Zn C-cell, which is rated almost twice the capacity. The $Na_2S_2O_8$ cell is clearly superior to both the Leclanché and alkaline MnO_2 cells though clearly operating at a much higher rate.

A final comparison was made to other systems, but at approximately the same rates, in this case, the 40 hr rate (C/40). An alkaline Ni/Zn cell and a Pb/acid battery were discharged at 0.75 and 2.0A, respectively, to achieve rate parity. An alkaline-MnO_2 cell was discharged at i_D = 0.25A, while a standard 1.8 A-hr $Na_2S_2O_8$/AZ-61 cell was discharged at 0.030A. The dimensionless variables are plotted in Fig. 8 and indicate the energy delivering capabilities of the experimental system compared to systems in current use.

Acknowledgments

The author wishes to thank ESB Incorporated for support of this effort. Susan Sharples and Jim Foley performed a large number of the discharge experiments, and D. Colbeck supplied the AgCl/AZ-61 cells for comparison.

Manuscript submitted Nov. 29, 1976; revised manuscript received Feb. 11, 1977.

Any discussion of this paper will appear in a Discussion Section to be published in the June 1978 JOURNAL. All discussions for the June 1978 Discussion Section should be submitted by Feb. 1, 1978.

Publication costs of this article were assisted by ESB Incorporated.

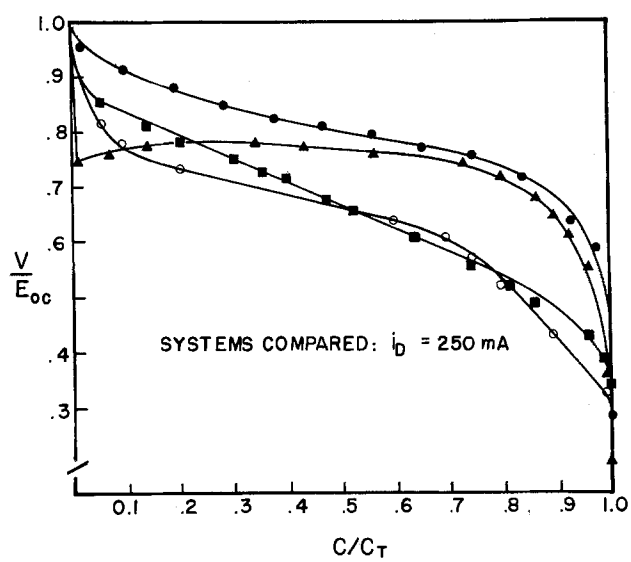


Fig. 7. Small systems compared at same current. This dimensionless plot compares the persulfate cell with other small systems: ●, 3 A-hr Ni/Zn (23 cm^3); ▲, 1.8 A-hr persulfate cell (22 cm^3); ■, 10 A-hr alkaline-MnO_2 (54 cm^3); ○, 5 A-hr industrial Leclanché cell (54 cm^3).

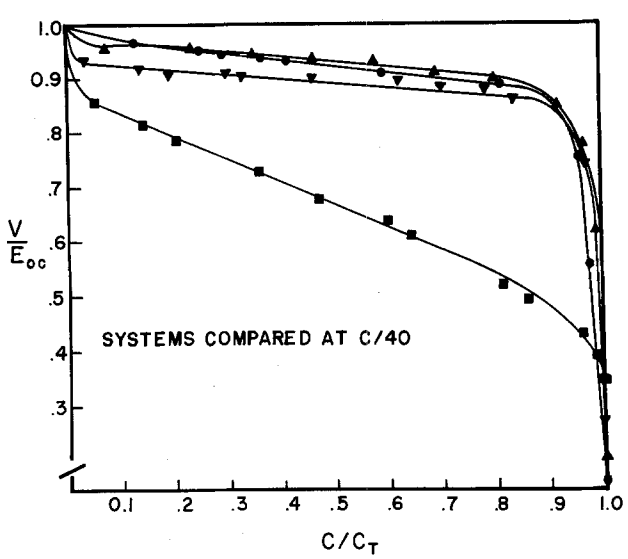


Fig. 8. Persulfate compared to other systems at C/40 rate. This is a dimensionless comparison of persulfate cells with other systems: ▼, ~3 A-hr Ni/Zn, i_D = 0.075A; ▲, 1.8 A-hr persulfate cell, i_D = 0.030A; ■, 10 A-hr alkaline MnO_2 cell, i_D = 0.25A; ●, 70 A-hr, group 27 Pb-acid automotive battery, i_D = 2.00A.

REFERENCES
1. National Defense Research Committee, Final Report on Sea Water Batteries, Bell Telephone Laboratories, Inc., New York (1945).
2. J. B. Mullen and P. L. Howard, *Trans. Electrochem. Soc.*, **90**, 529 (1946).
3. I. C. Blake, *This Journal*, **99**, 202C (1952).
4. E. H. Lawson, U.S. Pat. 2,428,850 (1947); L. H. Harriss, U.S. Pat. 2,543,106 (1951).
5. L. Pucher, *This Journal*, **99**, 203C (1952).
6. B. N. Adams, U.S. Pat. 2,322,210 (1943).
7. M. Katoh, K. Shimizer, and S. Katoh, *Denki Kagaku*, **38**, 753 (1970).
8. J. Root, U.S. Pat. 3,450,570 (1969).
9. J. R. Coleman, *J. Appl. Electrochem.*, **1**, 65 (1971).
10. H. N. Hohner, F. P. Malaspina, and W. J. Martini, U.S. Pat. 3,943,004 (1976).
11. L. I. Bintliff, F. P. Malaspina, and W. J. Martini, Br. Pat. 1,421,514 (1976).
12. A. M. Codd, *Electrical Rev.*, July 1, 1932, p. 14.
13. I. C. Blake, *This Journal*, **99**, 328 (1952).
14. I. C. Blake and J. B. Mullen, U.S. Pat. 2,534,403 (1950).
15. M. D. Wijnen and P. A. Boter, U.S. Pat. 3,444,002 (1968).
16. B. Cohen and P. Mucenieks, U.S. Pat. 3,532,552 (1970); P. Mucenieks, B. Cohen, and L. Darbee, U.S. Pat. 3,532,553 (1970); B. Cohen and P. Mucnieks, U.S. Pat. 3,532,554 (1970).
17. J. M. Kolthoff and J. K. Miller, *J. Am. Chem. Soc.*, **73**, 3055 (1951).
18. Technical Information Bulletins 464-201JG and 114BC, Union Carbide Corporation, New York.
19. R. R. Rogers, D. A. Tetu, and H. Livingstone, *Trans. Electrochem. Soc.*, **90**, 475 (1946).
20. G. T. Bakhvalov and A. V. Turkovskaya, "Corrosion and Protection of Metals," G. Isserlis, Translator, Pergamon Press, London (1965).
21. R. F. Amlie and P. Ruetschi, *This Journal*, **108**, 813 (1961).
22. H. A. Robinson, *Trans. Electrochem. Soc.*, **90**, 485 (1946).
23. W. N. Carson, W. H. Fischer, and E. G. Siwek, *Electrochem. Technol.*, **5**, 423 (1967).

Chromium Oxides as Cathodes for Secondary High Energy Density Lithium Batteries

J. O. Besenhard

Anorganisch-Chemisches Institut der Technischen, Universität München, D-8000 München 2, Germany

and R. Schöllhorn

Anorganisch-Chemisches Institut der Universität Münster, D-4400 Münster, Germany

ABSTRACT

The electrochemical reduction and reoxidation of Cr_2O_5, Cr_3O_8, thermally decomposed CrO_3, and a commercially available "CrO_3-graphite" preparation are compared in organic Li^+ electrolytes. All these cathode materials reveal an average discharge voltage of approximately 3V *vs.* a lithium anode and a maximum charge transfer exceeding one electron per Cr atom. The basic general discharge reaction is shown to be the reduction of higher chromium oxides Cr_nO_m with $1.5 < m/n < 3$. CrO_3 itself does not represent a suitable cathode material. From structural considerations it is concluded that the electrode processes are likely to be topotactic reactions of chromium oxides, yielding ternary phases $Li_xCr_nO_m$ which can be reoxidized with high coulombic efficiency.

Trioxides of Group VIa metals, particularly MoO_3 (1-6) and WO_3 (7, 8), have received considerable attention because of their potential application as cathode materials in primary and secondary organic electrolyte lithium cells. The mechanism of the MoO_3– (6, 9) and WO_3– (10) discharge reaction has been confirmed to be the reversible formation of ternary nonstoichiometric molybdenum and tungsten bronzes $A_x^{x+}[MoO_3]^{x-}$ and $A_x^{x+}[WO_3]^{x-}$, where A^+ is an alkali cation; x_{max} was found to be approximately 1.5 for Li_xMoO_3 (3, 6) and 0.5 for Li_xWO_3 (8).

Very little is known about the reduction of corresponding chromium oxides which, by virtue of their low molecular weight, should be the most interesting materials of Group VIa metal oxides. CrO_3 was repeatedly claimed to be a suitable cathode material for organic electrolyte batteries (11-13), however, this oxide is rather soluble in organic donor solvents, forming Lewis acid-base complexes CrO_3-solvent. As a substitute for free CrO_3, CrO_3 intercalated in graphite was proposed for rechargeable batteries with a solid β-alumina or organic electrolyte (13-15). It was assumed (14) that unoccupied d-orbitals of CrO_3 accept electrons from the filled p-orbitals of the sp^2 carbon atoms, thus lowering the Fermi level of graphite. Consequently, nonstoichiometric phases such as $A_x^{x+}[C_8CrO_3]^{x-}$, formed by electrochemical intercalation of an alkali metal A into C_8CrO_3 should be more stable, *i.e.*, show a more positive potential than the corresponding binary alkali metal graphites $A_x^{x+}C_8^{x-}$ (14). Indeed, a cell comprising a cathode prepared by heating (16) CrO_3 and graphite, a β-alumina solid electrolyte, and a Na anode shows an emf of 3.9V (14) and may be discharged at more than 3V, whereas the potentials of binary alkali metal graphites AC_8 are $< +$ 1V *vs.* free A (17).

From x-ray data it was however concluded in a recent publication that heating of CrO_3 and graphite does not yield a CrO_3-graphite intercalation compound but results in a mixture of unreacted graphite and the oxide Cr_3O_8 as the main thermal decomposition product of CrO_3 (18). The product formed under these conditions offers a method for the selective oxidation of primary alcohols to the corresponding aldehydes and is commercially available ("Seloxcette," Alfa products). A genuine intercalation of CrO_3 into graphite can be achieved by refluxing graphite in a solution of CrO_3 in glacial acetic acid (19) and the resulting prod-

Key words: lithium anodes, nonaqueous electrolytes, ternary phases, topotactic redox reactions.

uct is claimed to be an ionic compound, containing one CrO_4^{2-} for every three CrO_3 molecules (18). In order to elucidate the reactions of free and intercalated chromium oxides, the discharge and reoxidation behavior of CrO_3, thermally decomposed CrO_3, Cr_3O_8, Cr_2O_5, CrO_2, Seloxcette, and CrO_3-graphite prepared in acetic acid was compared in different organic electrolytes.

The most striking result of the present investigation was the observation that free CrO_3 and CrO_3-graphite prepared by the acetic acid method are practically inert *vs.* electrochemical reduction in organic Li^+ electrolytes, whereas Cr_3O_8, Cr_2O_5, thermally decomposed CrO_3, and Seloxcette behave very similarly and can be discharged at approximately + 3V *vs.* Li/Li^+. This corroborates that the reduction of chromium oxides is the essential discharge reaction in every case. Carbon present in the chromium oxide electrodes acts only as an inert electronically conducting support and can be replaced, *e.g.*, by Cu powder. The reduction of Cr_2O_5, Cr_3O_8, and Seloxcette yields more than one electron per Cr atom and can be reversed with high coulombic efficiency. The discharge mechanism of Seloxcette was assumed in an earlier publication to be the formation of a ternary phase, such as $LiCr_3O_8$ (20). The results presented here confirm this concept in principle, however, the maximum lithium content of these ternary phases and therewith the energy density of Cr_3O_8 and Cr_2O_5 cathodes were found to be much higher than was expected.

Experimental

The oxides Cr_2O_5 and Cr_3O_8 were prepared from CrO_3 (analytical grade) according to the literature (21, 22). Thin layer electrodes (approximately 10 mg cathode mixture per square centimeter geometric surface) were prepared by pressing a mixture of finely divided chromium oxide and graphite powder into Pt gauze at 5000 kg · cm^{-2}. Seloxcette, CrO_3-graphite prepared by the wet method, and CrO_2 were used without additional electronically conducting support. For the long-term galvanostatic experiments weighed pressed powder electrodes were sandwiched between porous glass to avoid losses caused by crumbling off. All measurements were carried out in a cell of the double-H type fitted with an inlet for inert gas. The working electrode was faced by two Pt counterelectrodes, separated by glass diaphragms. Instrumentation and purification of solvents and solutes have been described in former reports (23, 24).

Results and Discussion

Figure 1 shows the galvanostatic reduction and reoxidation of Seloxcette (Anal.: C = 39.5%; O = 26.0%; Cr = 34.3%, corresponding to a formal Cr/O ratio $CrO_{2.46}$) in $LiClO_4$/DME (1.2-dimethoxyethane). A cyclic voltammogram (CV) of Seloxcette in the same electrolyte (Fig. 2) demonstrates that the rate of reoxidation is slow as compared to that of the reduction. The anodic range is limited by solvent decomposition. The low coulombic efficiency of the reoxidation as calculated from the CV is not caused by irreversible side reactions but is rather due to a kinetically hindered recharging. This is evidenced by a typical reoxidation efficiency of 75-80% in low rate galvanostatic experiments (Fig. 1); values close to 100% may be found indeed for reoxidation at extremely low current density or after an incomplete discharge.

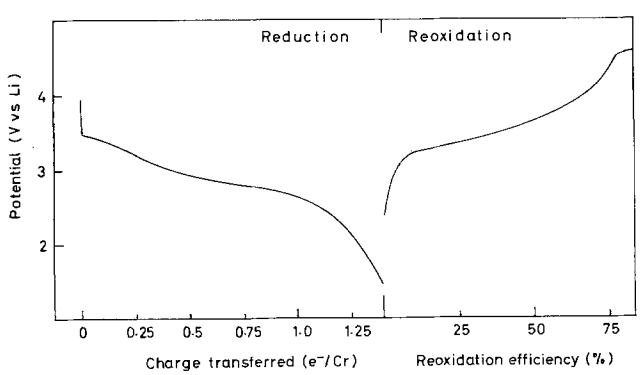


Fig. 1. Galvanostatic reduction/reoxidation of a sandwiched Seloxcette pressed powder electrode in saturated $LiClO_4$/DME; $i \approx 200$ $\mu A \cdot cm^{-2}$.

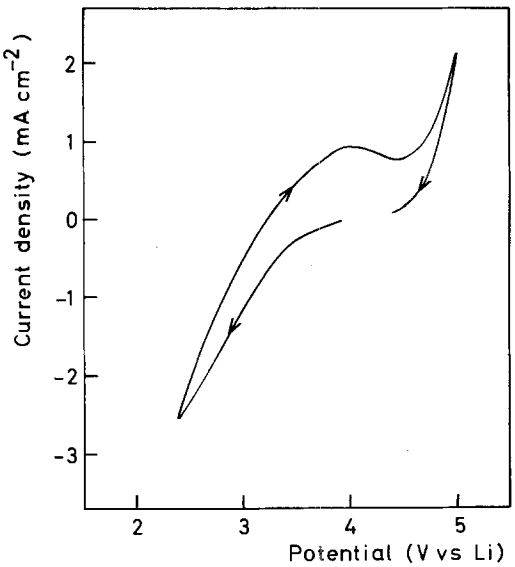


Fig. 2. Cyclic voltammogram of a Seloxcette pressed powder electrode in saturated $LiClO_4$/DME; V = 300 mV · min^{-1}.

In the range $100 < i < 1000$ $\mu A \cdot cm^{-2}$ the discharge utilization of Seloxcette depends only slightly on the current density: in 1M $LiClO_4$/DMSO (dimethylsulfoxide) a factor 2 increase of current density caused a decrease in the utilization of only about 5%. Therefore, the maximum theoretical utilization is likely to be close to 1.3 electrons per Cr atom. The current density applied cannot be lowered beyond a certain limit since the ratio discharge/background current is decreasing rapidly at low current density values.

The charge transfer observed of about 1.3 electrons per Cr atom does not correlate with the potential formation of Li_2O and Cr_2O_3 as final products, which should yield approximately 2 electrons per Cr atom. Apart from this the reversibility of the reduction may hardly be explained in terms of a rearrangement of higher chromium oxides from the insoluble insulators Li_2O and Cr_2O_3. Attempts to oxidize Cr_2O_3 in pressed powder electrodes containing Li_2O and graphite failed and there was no evidence for Cr_2O_3 formation in x-ray powder diagrams of discharged Seloxcette. A hypothetical discharge mechanism involving the reduction of CrO_3 to Cr_2O_3 was rejected earlier by thermodynamical considerations since this reaction should produce an emf of only 2V (18). The emf of Seloxcette *vs.* Li/Li^+ is +3.9V (14) and the corresponding emf data of CrO_2, Cr_2O_5, and Cr_3O_8. *e.g.*, in $LiClO_4$/DME, were found to be close to this value, however, a significant current flow does not occur above +3.6V. Supposedly an emf of +3.9V does not arise from a "bulk" reaction of the oxide crystallites but from surface products such as adsorbed oxygen. The line broadening, exhibited by the x-ray powder diagrams of the preparations used, indicates a rather small particle size and thus a high surface area of the oxides.

The maximum utilization of Cr_2O_5 and Cr_3O_8 pressed powder electrodes containing 35 weight percent (w/o) graphite powder (in $LiClO_4$/DME and $LiClO_4$/DMSO, conditions corresponding to those given in Fig. 1 and 3) was found to be close to 1.2 respective to 1.4 electrons per Cr atom. The shape of the Cr_3O_8 discharge characteristic nearly coincides with that of Seloxcette and

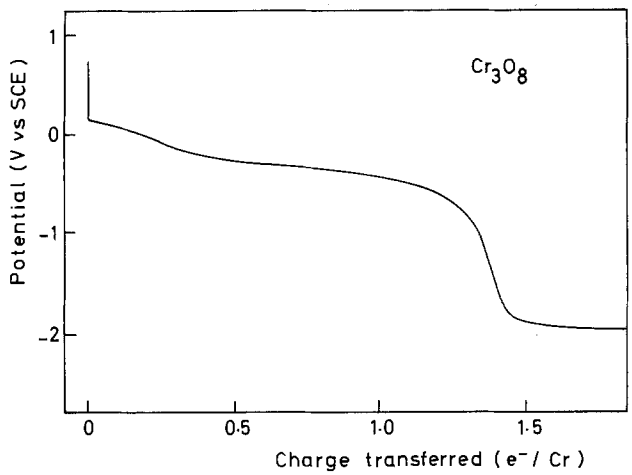


Fig. 3. Galvanostatic reduction of a sandwiched Cr_3O_8 pressed powder electrode containing 35 w/o graphite in 1M $LiClO_4$/DMSO; $i \approx 200\ \mu A \cdot cm^{-2}$, Li|1M $LiClO_4$/DMSO|SCE = −3.35V.

shows one voltage plateau at about +3V *vs.* Li/Li^+ (Fig. 3). This voltage plateau is slightly lower in the case of Cr_2O_5. An easy way to get a material which is characterized by the discharge behavior of higher chromium oxides is thermal decomposition of CrO_3. A mixture of chromium oxides with the main components according to the powder diagram being Cr_2O_5 and Cr_3O_8 (Anal.: $CrO_{2.45}$) was obtained at 300°C (18 hr, 1 Torr). Pressed powder electrodes from this material, containing graphite, Ni, or Cu powder as electronically conducting support, revealed a discharge behavior fairly similar to that of Seloxcette.

The reduction of CrO_2 also gives rise to a voltage plateau at approximately +3V *vs.* Li/Li^+ but the utilization does not exceed 0.5 electrons per Cr atom.

Preliminary experiments with CrO_3-graphite prepared by the wet method (19) (Anal.: ratio C/Cr = 15.0) gave no indication of its reduction at useful potentials. A most surprising kinetic stability toward electrochemical reduction was also observed for CrO_3 which is practically inert at a Pt electrode in $LiClO_4$/DME. Moreover, CrO_3 is not a suitable cathode material because of its high solubility in organic donor solvents.

The discharge characteristics of Seloxcette samples were not significantly affected by the type of solvent or anion of the solute, but depended strongly on the kind of cation (Fig. 4). The performance is best in Li^+ electrolytes, lower in Na^+ electrolytes; solutions of salts with cations of large ionic radii, *e.g.*, K^+, are unsuitable for the reduction of chromium oxides. Decreasing discharge voltages with increasing cation radius cannot be understood as poorer thermodynamic stability of the Na^+ and K^+ compounds as compared

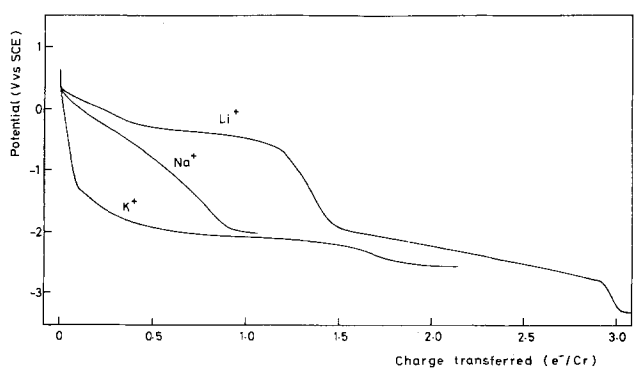


Fig. 4. Galvanostatic reduction of sandwiched Seloxcette pressed powder electrodes in 1M $LiClO_4$/DMSO, 1M $NaClO_4$/DMSO, 1M $KClO_4$/DMSO; $i \approx 200\ \mu A \cdot cm^{-2}$.

to the Li^+ compound. They are rather to be considered as increasing polarization which can be demonstrated by current interruption in the course of the galvanostatic reduction of Seloxcette. At 0.5 e^-/Cr, *e.g.*, the potential rise after current interruption is about 0.2V in the case of Li^+ but exceeds 1V in the case of K^+.

Since this potential rise is very slow and since the specific conductivities of 0.5 $LiClO_4$/DMSO and 0.5 $KClO_4$/DMSO are similar, the polarization is assumed to be caused by hindered transport in the solid phase. This behavior is similar to that observed for the reduction of the layered oxide MoO_3 (6) and is typical for a discharge mechanism involving the penetration of unsolvated alkali cations into the crystal lattice of the cathode material as the rate-determining step. On the other hand, the topotactic uptake of solvated cations [*e.g.*, intercalation of alkali cations from DMSO electrolytes into MoS_2 (23) or graphite (24)] or reactions which proceed via dissolved species (*e.g.*, the reduction of sulfur in DMSO electrolytes) in general show only little dependence of the electron acceptor utilization on cation radius. Although an interpretation of the cation dependence in terms of different solubilities of cathode material or its discharge products in different electrolytes cannot be definitely excluded, the simultaneous presence of cation dependence, efficient reversibility of the reaction, and an "odd" number of electrons transferred per Cr atom in Cr_2O_5 and Cr_3O_8 agree well with the assumption of nonstoichiometric ternary phases such as $Li_xCr_2O_5$ and $Li_xCr_3O_8$ being formed on cathodic reduction

$$xLi^+ + xe^- + Cr_nO_m \rightleftharpoons Li_xCr_nO_m \qquad [1]$$

This discharge mechanism is analogous to that of MoO_3 and WO_3 which yield ternary molybdenum and tungsten bronzes Li_xMoO_3 and Li_xWO_3.

It is obvious that structural considerations will be the crucial point for an explanation of the reaction mechanism of these electrode materials. A series of binary chromium oxides is known in the range of oxidation number +3 to +6 (21); those which are defined at least by their powder patterns are listed in Table I. The existence of additional phases has been claimed, but there is still much controversy on this point as well as on the question whether nonstoichiometric chromium oxides with notable phase ranges occur. For only four of the oxides listed in Table I, a three-dimensional structural analysis has been reported: CrO_3 which is built of infinite chains formed by the linking up of CrO_4 tetrahedra and Cr_5O_{12}, CrO_2, and Cr_2O_3 built up by three-dimensional frameworks containing either CrO_4 tetrahedra and CrO_6 octahedra or octahedra only. The structures of Cr_2O_5 and Cr_3O_8 are unknown so far. Ternary alkali chromium oxides with known structures are listed in Table II. In the series ACr_3O_8 (25) these crystallize

Table I. Binary chromium oxides

Formula	Average oxidation number (Cr)	Structure
CrO_3	+6	Chain type
Cr_3O_8	+5.4	—
Cr_2O_5	+5	—
Cr_5O_{12}	+4.8	3-dimensional framework
CrO_2	+4	Rutile type
Cr_2O_3	+3	Corundum type

Table II. Ternary phases $A_xCr_nO_m$

Formula	Structure
$Li_3Cr_3O_8$	3-dimensional framework
$NaCr_3O_8$	2-dimensional framework
KCr_3O_8	2-dimensional framework
$RbCr_3O_8$	2-dimensional framework
$CsCr_3O_8$	2-dimensional framework
$K_2Cr_8O_{16}$	Hollandite type

(depending on the type of cation) either in layer or in framework structures were built up by chromium-oxygen tetrahedra and octahedra, whereas $K_2Cr_8O_{16}$ (26) crystallized in the channel-type structure of hollandite.

It is thus apparent that a large variety of building principles is found among the binary and ternary chromium oxides. If one recalls that the maximum ratio Li/Cr taken up by the electrode materials discussed above exceeds unity, some restrictions can yet be taken into consideration as to the potential structure of the oxides investigated, if the reaction proceeds by a topotactic mechanism. As pointed out in an earlier study (6) a solid matrix with a system of interconnected and easily accessible lattice sites for guest ions is, from the viewpoint of structure, a premise in this case. For three-dimensional frameworks a relative low ratio Li/Cr should be expected; this is established by the reaction of CrO_2. Although some of the three-dimensional structures such as the hollandite type found also for $K_2Cr_8O_{16}$ have large open channels, which potentially could accommodate considerable amounts of small ions like Li^+, these phases seem not to be very stable. The lattice, *e.g.*, of those manganese oxide hydrates which crystallize in the hollandite or psilomelane structure, are known to break down easily on reduction. Rather high Li^+/metal ratios were, however, found for solids with two-dimensional or one-dimensional matrix units, *e.g.*, in the case of chain-type chalcogenides $NbSe_3$ and TiS_3 with Li/Nb respective to Li/Ti = 3 (27).

It is concluded, therefore, that the higher chromium oxides studied in this investigation are more likely to have layers or chains as structural elements, although a very open channel or zeolithe-type framework cannot definitely be excluded at this point. Detailed structural data of the oxides and Li phases under consideration have to be awaited for a final picture of the reaction mechanism.

Extended discharge of Seloxcette reveals a second voltage plateau at approximately +1V *vs.* Li/Li^+ (Fig. 4) but the length of this plateau is poorly reproducible. At approximately +1V *vs.* Li/Li^+ the intercalation of alkali cations into the graphite component of the electrode is a competing process. However, the total charge transfer of the second plateau exceeds the theoretical transfer calculated from the known stoichiometries of solvated alkali metal graphite phases (24, 28). It is more likely that irreversible processes such as solvent decomposition or further reduction of the ternary phases contribute to the electrode reaction in this discharge range.

Conclusions

The insoluble chromium oxides Cr_3O_8 and Cr_2O_5, a mixture of which can be prepared by heating of CrO_3, are suitable cathode materials for low rate secondary organic electrolyte batteries. The calculated theoretical energy density of the Li/Cr_3O_8 couple (corresponding to Eq. [1]) is 1080 W-hr · kg^{-1} (360 A-hr · kg^{-1}) based on the experimental values $x = 1.4$ and average cell voltage = 3V. The corresponding values for the Li/MoO_3 couple ($x = 1.5$, average cell voltage = 2.5V) are substantially lower with only 650 W-hr · kg^{-1} (260 A-hr · kg^{-1}). From electron transfer data, reversibility behavior and structural considerations it is concluded that the electrode processes are likely to be topotactic reactions of chromium oxides with two-dimensional or one-dimensional structural units.

Acknowledgments

The authors are obliged to Prof. Dr. H. P. Fritz, Technische Universität München, for kindly supporting the electrochemical investigations, and to BASF Ludwigshafen and AGFA-GEVAERT München for supplying CrO_2 samples.

Manuscript submitted Dec. 1, 1976; revised manuscript received Feb. 23, 1977.

Any discussion of this paper will appear in a Discussion Section to be published in the June 1978 JOURNAL. All discussions for the June 1978 Discussion Section should be submitted by Feb. 1, 1978.

Publication costs of this article were assisted by the Universität München.

REFERENCES

1. L. Campanella and G. Pistoia, *This Journal*, **118**, 1905 (1971).
2. F. W. Dampier, *ibid.*, **121**, 656 (1974).
3. N. Margalit, *ibid.*, **121**, 1460 (1974).
4. A. N. Dey, Br. Pat. 1,325,055; U.S. Pat. 3,808,052.
5. ESB Inc., Ger. Pat. 2,363,286.
6. J. O. Besenhard and R. Schöllhorn, *J. Power Sources*, In press.
7. K. F. Kamenski, U.S. Pat. 3,873,369; Ger. Pat. 2,432,269.
8. A. L. Rotinyan, S. V. Shishkina, and K. I. Tikhonov, *Sov. Electrochem. (Engl. Transl.)*, **11**, 1015 (1975).
9. R. Schöllhorn, R. Kuhlmann, and J. O. Besenhard, *Mater. Res. Bull.*, **11**, 83 (1976).
10. M. S. Whittingham, *This Journal*, **122**, 713 (1975).
11. K. H. M. Braeuer and J. A. Harvey, Report AD 654,813 (1967).
12. G. J. Methlie, U.S. Pat. 3,415,687.
13. G. Ronald, Ger. Pat. 2,502,500.
14. M. B. Armand, in "Fast Ion Transport in Solids," W. van Gool, Editor, p. 665, North-Holland, Amsterdam (1973).
15. M. B. Armand, Ger. Pat. 2,341,723.
16. R. C. Croft, *Aust. J. Chem.*, **9**, 201 (1956).
17. S. Aronson, F. J. Salzano, and D. Bellafiore, *J. Chem. Phys.*, **49**, 434 (1968).
18. L. B. Ebert, R. A. Huggins, and J. I. Brauman, *Carbon*, **12**, 199 (1974).
19. N. Platzer and B. de la Martiniere, *Bull. Soc. Chim. Fr.*, 177 (1961).
20. M. S. Whittingham, *This Journal*, **123**, 315 (1976).
21. K. A. Wilhelmi, *Acta Chem. Scand.*, **22**, 2565 (1968).
22. R. S. Schwartz, J. Fankuchen, and R. Ward, *J. Am. Chem. Soc.*, **74**, 1676 (1952).
23. J. O. Besenhard, H. Meyer, and R. Schöllhorn, *Z. Naturforsch., Teil B*, **31**, 907 (1976).
24. J. O. Besenhard, *Carbon*, **14**, 111 (1976).
25. K. A. Wilhelmi, *Chem. Commun.*, 437 (1966).
26. T. Endo, S. Kume, N. Kinomura, and M. Koizumi, *Mater. Res. Bull.*, **11**, 609 (1976).
27. D. W. Murphy and F. A. Trumbore, *This Journal*, **123**, 960 (1976).
28. J. O. Besenhard and H. P. Fritz, *J. Electroanal. Chem.*, **53**, 329 (1974).

Evidence for the Existence of Stable $CO_2^=$ Ion and Response Time of Gas Electrodes in Molten Alkali Carbonates

Alina Borucka*

Borucka Research Company, Livingston, New Jersey 07039

ABSTRACT

Experimental evidence is presented confirming the existence of a previously unknown $CO_2^=$ ion formed by the combination of CO gas and $O^=$ ion at the $CO/CO_2/Au$ electrode in molten ternary eutectic, $Li/Na/K/CO_3$. The new ion is kinetically active and its oxidation to CO_2 product is responsible for the second of two anodic processes displayed by the CO/CO_2 electrode in this melt at a half-wave potential of about +300 mV (standard CO/CO_2 reference). $CO_2^=$ has a limited solubility in the molten electrolyte and, apparently when $p_{CO}/p_{CO_2} \geq 0.25$, it decomposes to CO and $O^=$ relatively quickly: within 10 sec in the example studied. Perturbations of the standard CO/CO_2 and 1:2 O_2/CO_2 electrode equilibria by addition of solid Li_2O to the melt show that: (*a*) the response of both these electrodes to local concentration changes in the melt is very fast (0.1 sec or faster), (*b*) the carbonate dissociation equilibrium is slow, and (c) the correct forms of the Nernst equations governing the departures of the potentials of these electrodes from equilibrium are, respectively

$$E_{CO/CO_2} = E^\circ_{CO/CO_2} + \frac{RT}{2F} \ln [p_{CO_2}^2/p_{CO}]$$

$$E_{O_2/CO_2} = E^\circ_{O_2/CO_2} + \frac{RT}{2F} \ln K_p + \frac{RT}{2F} \ln [p_{O_2}^{1/2}/[O^=]]$$

Background

Previous work (1) on the kinetic behavior of the CO/CO_2 electrode in molten ternary eutectic of Li-Na-K carbonates [43.5-31.5-25.0 mole percent m/o)][1] in the temperature range of 700°-800°C led to the firm conclusion that the first oxidation wave observed was due to the reaction $CO + CO_3^= \rightarrow 2CO_2 + 2e^-$, and a tentative conclusion that the second oxidation process (see Fig. 1 and Table I) could be due to the existence of a previously unknown ionic species, $CO_2^=$, formed and oxidized as follows

$$CO + O^= \rightleftarrows CO_2^= \quad [1]$$

$$CO_2^= \rightarrow CO_2 + 2e^- \quad \text{(over-all)} \quad [2]$$

The kinetic results obtained indicated also that $CO_2^=$ has a limited solubility, as indicated by the constant value of the second limiting current when p_{CO}/p_{CO_2} ratio is equal or greater than 0.25. This was taken to indicate a saturation limit with respect to the $CO_2^=$ ion in the melt though not necessarily by way of precipitation, which in any event could not be observed under the conditions of the experiments. The tentative conclusions concerning the $CO_2^=$ ion needed further confirmation but to this date no further work on this subject has been reported.

While the thermodynamic studies of the gas electrodes in molten carbonates have been extensively reported and reviewed (5), the reliable kinetic investigations are very few and these are primarily devoted to the O_2/CO_2 reduction (6-9). The most neglected area of the kinetic and mechanistic studies in molten carbonates is still that of the anodic processes involving H_2/CO_2 and CO/CO_2 electrodes, both being of direct practical importance to the molten carbonate fuel cell and some new antipollution processes.

So far, no reliable study of any kind has been presented on the H_2/CO_2 electrode, which in these melts represents a more complex $H_2/CO/H_2O/CO_2$ system. The CO/CO_2 electrode has been evaluated fully only with respect to its thermodynamic properties (1, 6, 10) and its near-equilibrium kinetics (7), as summarized in Ref. (5). Both the prior and the present work referred to here were conducted on pure gold sheet electrodes of 1 cm^2 area, fully submerged in the electrolyte. Under unstirred conditions the CO/CO_2 gas mixture was above the melt while the stirring conditions corresponded to bubbling the gas mixture into the melt in an accurately reproducible manner (1, 5).

Present Work

The present publication reports additional experimental evidence for the existence of the $CO_2^=$ ion as the CO-carrying species (involved in the second oxidation process) and provides a basis for a more accurate kinetic and mechanistic analysis of the anodic oxidation of carbon monoxide in molten alkali carbonates.

Table I is included here because it has not been published before [other than in Ref. (1)] and because it shows the complete range of the results obtained, relating to Fig. 1 and 2 shown below.

Based on these (steady-state polarization data) (1), Fig. 1 illustrates the general character of the $CO/CO_2/CO_3^=$ system and the range of stability of the molten carbonate electrolyte under 1 atm of pure CO_2 at 800°C. The potential scale is referred to the standard CO/CO_2 electrode (p_{CO} = 0.382 atm and p_{CO_2} = 0.618 atm) and E°_B represents the limiting Boudouard potential, both previously established (1, 10). The value of E°_B shown in Fig. 1 indicates the limit to the cathodic polarization that can be applied at 800°C before carbon deposition occurs due to the Boudouard equilibrium

$$2CO \overset{K_B}{\rightleftarrows} CO_2 + C_{(solid)} \quad [3]$$

* Electrochemical Society Active Member.

Key words: $CO_2^=$ ion, molten carbonates, CO/CO_2 electrode.

[1] This eutectic composition was published by Janz and Lorenz (2) and used both in the prior and this work. While an earlier publication by Volkova (3) indicated somewhat different composition, the one quoted here was adopted because of the availability of other property data for this salt mixture [see Ref. (4)].

Table I. Steady-state polarization results for $CO/CO_2/Au$ electrodes in molten ternary eutectic: $Li/Na/K/CO_3$ at 1 atm and 800°C

Gas composition (atm) p_{CO_2}	p_{CO}	p_A	Bubbling or unstirred	Anodic limiting current density (mA/cm²) i_I*	i_{II}
0.10	0.05	0.85	U	**	0.258
			B	0.012	0.710
	0.10	0.80	B	0.026	0.745
	0.30	0.60	B	0.064	0.80
0.20	0.10	0.70	B	0.022	0.69
	0.20	0.60	B	0.046	1.030
	0.50	0.30	B	0.069	0.80
	0.80	—	U	0.070	0.344
			B	0.20	1.03
0.30	0.05	0.65	B	0.009	0.58
	0.30	0.40	B	0.054	0.86
	0.50	0.20	B	0.086	0.92
	0.70	—	U	**	0.366
			B	0.16	1.03
0.50	0.05	0.45	B	0.002	0.43
	0.20	0.30	B	0.031	0.92
	0.30	0.20	B	0.047	0.98
	0.50	—	U	**	0.286
			B	0.091	1.06
0.60	0.05	0.35	B	**	0.34
0.70	0.30	—	U	**	0.286
			B	0.037	1.06
0.80	0.05	0.15	B	**	0.29
	0.10	0.10	B	0.019	0.53
	0.20	—	U	**	0.287
			B	0.025	1.03
0.90	0.10	—	B	0.005	0.48
0.95	0.05	—	B	**	0.21

* Values of i^I correspond to estimated inflection points on polarization curves.
** Values of i^I impossible to estimate, approximately zero.

The equilibrium stability of the carbonate melt is governed by its dissociation

$$CO_3^= \overset{K_p}{\rightleftarrows} O^= + CO_2 \qquad [4]$$

which defines its oxide ion content at any given partial pressure of CO_2 gas above the melt. Without accurate control of the CO_2 component either at or above the equilibrium partial pressure, the composition of the carbonate changes with time, and gradually tends toward pure oxide. This feature can be observed in Fig. 1 by comparing the polarization curves obtained with pure argon and pure CO_2 above the melt. Under kinetic conditions with pure CO_2, the anodic stability of the ternary eutectic at 800°C extends to +800 mV before $CO_3^=$ is oxidized with evolution of oxygen while its cathodic stability, according to the reduction curve with pure argon (very low CO_2 and very high $O^=$) extends even well beyond the Boudouard potential of −204 mV.

The steady-state polarization curves for different CO/CO_2 electrodes (1) shown in Fig. 1 display two distinct oxidation stages. The lower limiting current is due to the diffusion of CO gas to the electrode surface and, as expected, shows direct proportionality to the partial pressure of CO, p_{CO}, and independence of p_{CO_2}. The upper limiting current is more complex and shows a direct proportionality to the p_{CO}/p_{CO_2} ratio.

As shown in Fig. 2, this relationship is linear up to $p_{CO}/p_{CO_2} \simeq 0.25$, above which the current remains substantially constant (its small increase with increase in p_{CO_2} being probably not significant).

The possibility of formation of the oxalate ion and its subsequent oxidation

$$CO + CO_3^= \rightleftarrows C_2O_4^= \rightarrow 2CO_2 + 2e^- \qquad [5]$$

was dismissed since this, in view of the large excess of $CO_3^=$, would require the current to be proportional to p_{CO} and independent of p_{CO_2}.

The second limiting current was interpreted as being due to the oxidation of a carrier ion $CO_2^=$ formed by the reaction [1] quoted above. While the analysis of the half-wave potentials supported the existence of the proposed ionic species, the available diagnostic criteria were not regarded as fully conclusive and the work (1) was therefore not published in open literature.

Further evidence, reported here, supports the existence of the $CO_2^=$ ion and is in agreement with a full mechanistic analysis of the oxidation of carbon monoxide in molten carbonates which will be reported separately (11).

This evidence was obtained by simple experiments consisting of: (*a*) monitoring the change in the equilibrium potential of the standard $CO/CO_2/Au$ and the 1:2 $O_2/CO_2/Au$ electrodes resulting from the addition of Li_2O solid to the molten ternary eutectic at 800°C, and (*b*) testing the response time of the 1:2 $O_2/CO_2/Au$ electrode to the sudden interruption and restoration of gas flow to the electrode.

The response time of gas electrodes in molten alkali carbonates has not been previously studied in a direct way. Equilibration studies reported for O_2/CO_2 and CO/CO_2 electrodes range from 1 to 24 hr but in view of the high exchange currents (of the order of 10^{-4} A/cm²) reported for both these electrodes (7), this seems likely to reflect the periods necessary to purge the "dead space" of the apparatus involved and the saturation time of the melt rather than the response

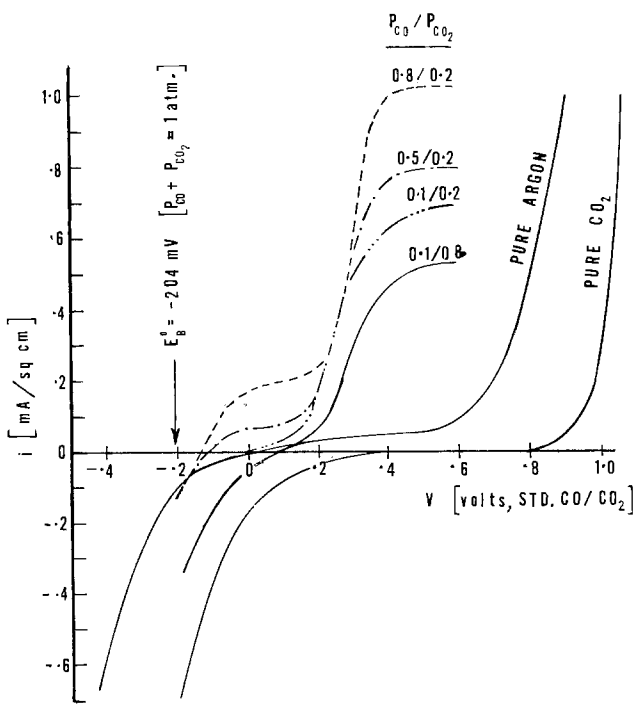


Fig. 1. General polarization characteristics for Au electrode in stirred $Li/Na/K/CO_3$ eutectic at 800°C and different gas atmospheres (p_{CO} and p_{CO_2} expressed in atmosphere units).

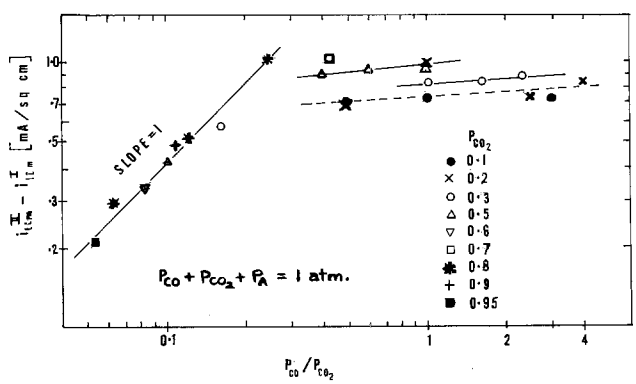


Fig. 2. Reaction order plot for $CO/CO_2/Au$ electrodes; stirred conditions, 800°C (p_{CO} and p_{CO_2} expressed in atmosphere units).

time of these electrodes in reaching their correct Nernst potentials, *i.e.*, registering the local changes in concentrations of the reacting species in the melt. The question of the response time of these electrodes is of basic and practical importance: for better understanding of the carbonate electrochemistry and for the correct use of these electrodes as accurate indicators of the local concentration changes in the melt (as demonstrated by the present study).

Experimental

The apparatus and the experimental procedure including that for outgassing and fully drying the melt and test gases were exactly the same as reported previously (6). The new tests involved only one special feature, namely, a gas- and vacuum-tight glass chamber through which accurately weighed samples of Li_2O solid (in form of pills) could be introduced into the carbonate melt. Typically, 80 mg pills of Li_2O were formed in a pill-press, subjected to drying, evacuation and equilibration with the test gas mixture before they were dropped into 200g of the melt via a 1 cm ID alumina tube serving as a guide. Both the reference and the test electrodes were of pure gold (as before) and supplied with the same gas mixture, either standard CO/CO_2 or 1:2 O_2/CO_2 to secure the lowest potential difference in the course of the experiments. Potential changes resulting from the addition of Li_2O were recorded by a Hewlett-Packard X-Y plotter Model 7035A.

Results and Discussion

In addition to the evidence for the existence of $CO_2^=$ ion shown in Fig. 1 and 2, Fig. 3 provides an additional confirmation. This shows the rate of dissolution of the Li_2O added to the melt and its effect on the equilibrium potential of the standard CO/CO_2/Au and 1:2 O_2/CO_2/Au test electrodes.

Comparison of the two sets of results in Fig. 3 shows the following interesting facts. Dissolution of Li_2O and its effect is very rapid in both cases, but its rate of reaction (as indicated by the recovery of the equilibrium potential) is much faster in the CO/CO_2 system. In this case, the effect of the added pill totally disappears in 1 min while in the case of the O_2/CO_2 electrode it disappears only after about 15 min. Additionally, Fig. 3 shows that the effect of added Li_2O on the equilibrium potential of the CO/CO_2 electrode is opposite to that shown by the O_2/CO_2 electrode and opposite to that which can be directly expected from the Nernst equation involved.

To accept the first of the above findings as meaningful, a separate test was made to establish how fast is the response of the "slower" 1:2 O_2/CO_2/Au electrode under our experimental conditions. To do so, the decay and recovery of the equilibrium potential was recorded resulting from turning the gas mixture flow to the electrode off and then on. This was done separately for the test electrode located in the bulk of the melt and then for the reference electrode enclosed in its own small separate compartment [see Ref. (10)]. The results in Fig. 4 show that both the electrodes are extremely sensitive to the local changes in concentration as affected by the supply of the gas mixture even under unstirred conditions. When the gas flow is stopped, both the electrodes drift immediately and at a rate of about 10 mV/sec. When the gas flow is again turned on, both the electrodes recover instantly to within about 20 mV of their initial equilibrium potentials. These responses may seem surprising at first but they reflect: (*a*) very fast reaction rate at the electrode (at 750°C, 1:2 O_2/CO_2 electrode has exchange current density of the order of 10^{-4} A/cm^2) (7); (*b*) very fast dissolution rate for the O_2/CO_2 gas mixture in the melt (as shown in Fig. 4 by the instantaneous recovery); and (*c*) relatively slow gas diffusion rate within the dead space of the apparatus (as shown by the potential drift of 10 mV/sec on closing the gas supply).

Additionally, the results of Fig. 4 show that the very much slower recovery of the O_2/CO_2 electrode shown in Fig. 3 is definitely not due to its inherent sluggishness.

The reasons for the changes of the equilibrium potentials of the two electrodes shown in Fig. 3 can be examined as follows. According to the dissociation equilibrium of the melt, Eq. [4] above, at any temperature T (°K)

$$O^= = \frac{K_p[CO_3^=]}{p_{CO_2}} \qquad [6]$$

which shows that for a small degree of dissociation of the $CO_3^=$ ion, a local increase in $O^=$ is effectively equivalent to a decrease in p_{CO_2} provided that the equilibrium is fast.

Because of Eq. [6], the Nernst equations for the two electrodes discussed

$$E_{CO/CO_2} = E^\circ_{CO/CO_2} + \frac{RT}{2F}\ln\left[\frac{p_{CO_2}}{p_{CO}[CO_3^=]}\right] \qquad [7a]$$

and

$$E_{O_2/CO_2} = E^\circ_{O_2/CO_2} + \frac{RT}{2F}\ln\left[\frac{p_{O_2}^{1/2}\cdot p_{CO_2}}{[CO_3^=]}\right] \qquad [8a]$$

can also be written as

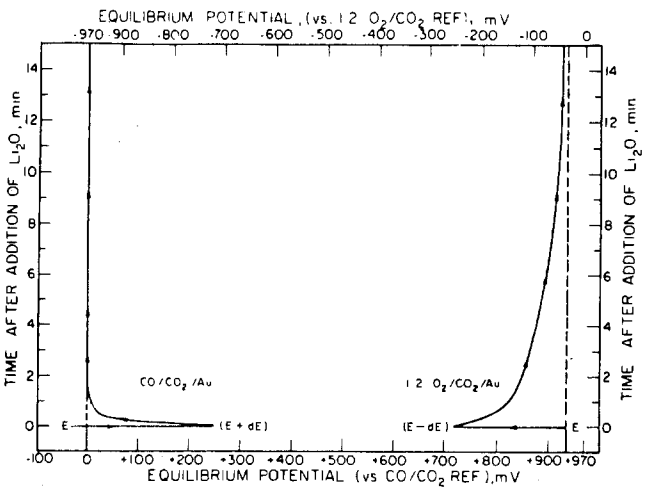


Fig. 3. Effect of added Li_2O (80 mg) on equilibrium potentials of CO/CO_2/Au and O_2/CO_2/Au electrodes (800°C; electrolyte unstirred).

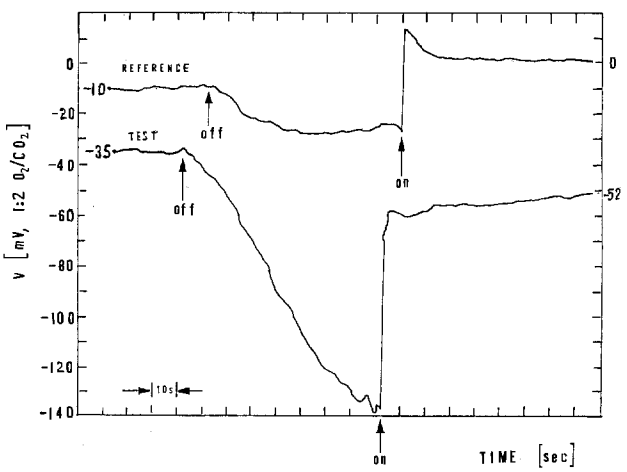


Fig. 4. Decay and recovery of equilibrium potential of 1:2 O_2/CO_2/Au electrode with gas flow off and on (750°C, unstirred electrolyte).

$$E_{CO/CO_2} = E^\circ_{CO/CO_2} + \frac{RT}{F}\ln K_p + \frac{RT}{2F}\ln\left[\frac{[CO_3^=]}{p_{CO}[O^=]^2}\right] \quad [7b]$$

and

$$E_{O_2/CO_2} = E^\circ_{O_2/CO_2} + \frac{RT}{2F}\ln K_p + \frac{RT}{2F}\ln[p_{O_2}^{1/2}/[O^=]] \quad [8b]$$

(the activity of $CO_3^=$ ion being substantially unity under conditions studied).

While at equilibrium no distinction can be made between Eq. [7a] and [7b] nor between [8a] and [8b], it is worth considering which of these truly reflect the electrode potentials under perturbed conditions such as those shown in Fig. 3.

Considering the O_2/CO_2 electrode first, we see from both the Eq. [8a] and [8b] that a sudden addition of $O^=$ ion to the melt must shift the equilibrium potential to a more negative value: $(E_{O_2/CO_2} - \Delta E)$ as it does. However, the fact that the observed shift is instantaneous while the recovery is slow suggests that Eq. [8b] more truly reflects the immediate effect of added $O^=$ and indicates that its recombination with CO_2 to form more $CO_3^=$ is rather slow. Equation [8b] therefore and not Eq. [8a] is the more correct form of the Nernst equation for the O_2/CO_2 electrode in molten carbonates.

Similarly, considering the two forms of the Nernst equation: [7a] and [7b] for the CO/CO_2 electrode and the fact that the added Li_2O causes an instantaneous positive shift of the equilibrium potential one may conclude that Eq. [7b] does not truly apply under dynamic conditions since $O^=$ shows no immediate negative effect on the equilibrium potential. Any dominating interaction between the added $O^=$ and CO_2 must also be ruled out for the same reason. Such interaction would also lead to a negative and not a positive shift in E_{CO/CO_2}.

In fact, the observed positive positive shift in E_{CO/CO_2} can presently be explained only by a very rapid interaction of the added $O^=$ with the dissolved CO and the formation of the $CO_2^=$ ion as discussed above. Formation of this ion according to reaction [1] above would cause a temporary local shortage of CO and thus shift the potential in the positive direction as observed in Fig. 3. The subsequent recovery of E_{CO/CO_2} which is relatively fast (only 1 min) is probably due to the breakdown of the new species to CO and $O^=$ which would assist in the fast recovery to the original more negative potential.

If the above, short-lived effect of added Li_2O is due to the formation of $CO_2^=$, then the following questions require answers: (*i*) In what range of potentials, if any, does it participate in the anodic or cathodic reactions of the CO/CO_2 electrode? (*ii*) Is this range of potentials the same as that indicated for the second oxidation wave in Fig. 1?

The answers to both these questions and additional evidence for the existence of the new species are shown by the results of Fig. 5. These results demonstrate dramatically how the steady-state currents of the standard CO/CO_2 electrode, potentiostated at various selected potentials, are instantly affected by the addition of a constant-weight (80 mg) pill of Li_2O.

Since the equilibrium of the CO/CO_2 electrode is governed by the reaction

$$CO + CO_3^= \rightleftarrows 2CO_2 + 2e^-$$

then, from Fig. 5, we can only conclude that the additional cathodic current observed (after addition of the pill) is due to the reduction of CO_2 being enhanced by the local shortage of CO at the electrode. The area of each cathodic peak shown in Fig. 5 is,

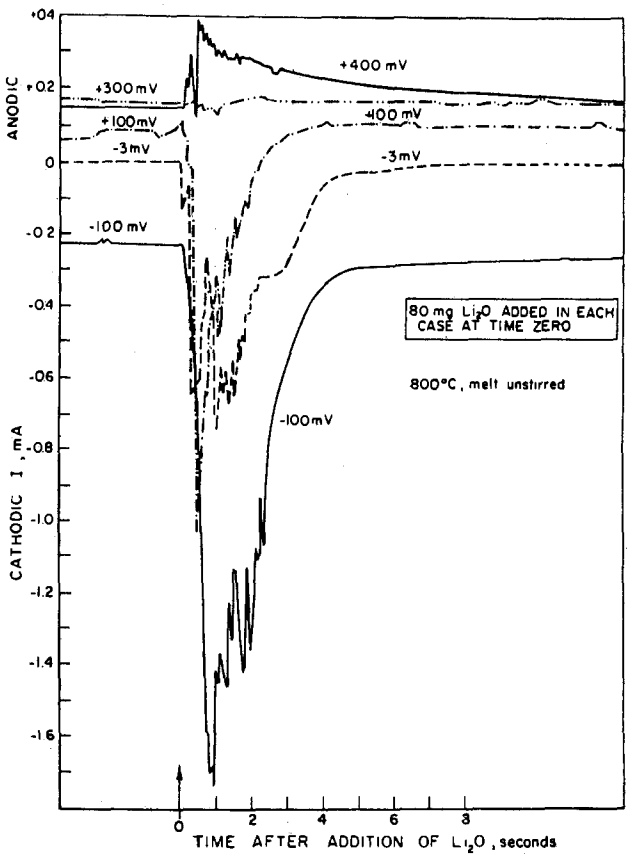


Fig. 5. Effect of added Li_2O on steady-state current of standard CO/CO_2 electrode potentiostated at different potentials (vs. standard CO/CO_2 reference).

therefore, a measure of the amount of CO_2 reduced in that period of time during which the electrode is "short" of free CO. Even at +100 mV, the steady-state current changes immediately from an anodic to a relatively cathodic value which then, in about 4 sec, returns to the original anodic level.

As the electrode is potentiostated at progressively more positive potentials, the surge of the cathodic current on addition of the same quantity of Li_2O becomes progressively smaller. The surge totally disappears at +300 mV and becomes anodic at +400 mV and higher. Evidently, at +300 mV any cathodic effect of the added Li_2O is balanced equally by the anodic oxidation of the $CO_2^=$ formed so that the net anodic current (of about 0.15 mA) remains unchanged. The fact that +300 mV is the normal half-wave potential for the second oxidation process of the CO/CO_2 electrode as shown in Fig. 1 proves that, there also, the species reacting at +300 mV must be $CO_2^=$.

With regard to the stability of the $CO_2^=$ ion, the results of Fig. 1 and 5 suggest that the species is stable but only to the extent of its limited solubility in the melt under given p_{CO}/p_{CO_2} atmosphere. Excess of it, displayed best by the curve at +400 mV, is unstable and apparently decomposes within about 10 sec.

The quantities of electricity involved at each level of potential and the effect of agitation of the electrolyte are shown in Table II. Table II shows that the rapid surge of current in each case represents no more than a few millicoulombs of total electricity and, therefore, on 1 cm^2 surface, only a few "monolayer" quantities of the reactant. ${}^uQ$ is higher than ${}^sQ$ in stirred electrolyte. This supports well the proposition that it is the cathodic reduction of CO_2 which is mainly involved, because of the shortage of CO. (With stirring, CO is more rapidly transported to the electrode and, therefore, the CO_2 current dies

Table II. Quantity of electricity and the effect of melt agitation involved in decay of current caused by addition of 80 mg of Li_2O to 200g of melt at 800°C: standard CO/CO_2 electrode potentiostated at different potentials

Constant potential, mV (*vs.* standard CO/CO_2)	Quantity of electricity, C ^sQ (stirred)	^uQ (unstirred)
−100	$\sim 1.1 \times 10^{-3}$	3.03×10^{-3}
−3	0.85×10^{-3}	1.45×10^{-3}
+100	$\sim 0.711 \times 10^{-3}$	0.894×10^{-3}
+300	~0	~0
+400	$\sim 0.133 \times 10^{-3}$	0.88×10^{-3}
+500	—	1.011×10^{-3}
+600	—	2.093×10^{-3}

out more quickly, as does also the anodic current due to $CO_2^=$.)

Since the recovery of the O_2/CO_2 electrode from the effect of added Li_2O is much slower than that of the CO/CO_2 electrode, taking about 15 min, it was of interest to check what if any effect the additive has on the cathodic reduction of oxygen. Figure 6 shows clearly that apart from the displacement of the equilibrium potential (in agreement with that shown in Fig. 3), no major kinetic effect is detected over the time interval from 2.6 to 10 min after addition of the oxide. This is in agreement with the interpretation offered above, and suggests further that the over-all oxygen reduction reaction

$$\tfrac{1}{2}O_2 + 2e^- \rightarrow O^= \qquad [9]$$

which governs the potential of the O_2/CO_2 electrode as shown above (see Eq. [8b]) does not, in fact, control its current. If it did, addition of Li_2O to the melt would reduce the cathodic current very drastically.

The results of Fig. 6 give, therefore, a broad support to the mechanism of oxygen reduction proposed by Appleby and Nicholson (8, 9) in which $O^=$ does not play any direct part. According to these authors, in the presence of oxygen, at a given partial pressure of CO_2 above the melt, fixed concentrations of peroxide, $O_2^=$, and superoxide, O_2^-, are established and these species are then, in turn, reduced in the two-step cathodic process observed.

However, since $O^=$ has clearly a major effect on the equilibrium potential of the O_2/CO_2 electrode as demonstrated by Fig. 3 yet has no apparent effect on oxygen reduction kinetics at higher overpotentials, it seems likely that its activity is restricted to the close vicinity of the equilibrium only which is neither well shown in Fig. 6 nor discussed in full detail by Appleby and Nicholson (8, 9).

The results shown in Fig. 3-6 and their analysis presented in this study demonstrate that very important diagnostic information can be gained even from very simple experiments by utilizing suitable additives to perturb the system studied.

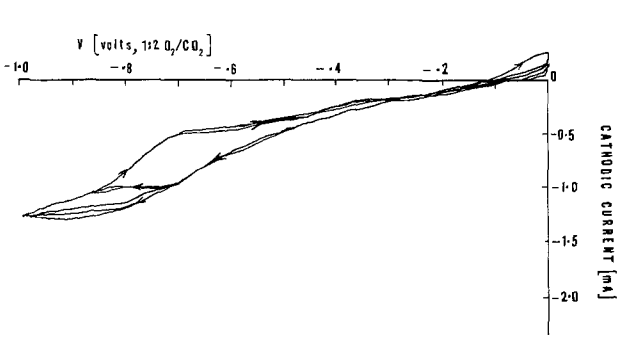


Fig. 6. Potential scans for 1:2 O_2/CO_2/Au electrode before and after addition of one 80 mg pill of Li_2O; 750°C, unstirred electrolyte, scan rate of 2500 mV/min (one scan before addition, six scans between 2.6 min and 10 min after oxide addition).

Conclusions

1. Experimental data and analysis presented confirm earlier kinetic evidence for the existence of previously unknown $CO_2^=$ ion which is formed by interaction of CO gas with $O^=$ ion in molten alkali carbonates.

2. This ion is responsible for the second of the two anodic processes displayed by the CO/CO_2 at half-wave potential of about +300 mV *vs.* standard CO/CO_2 electrode and causes a rapid positive shift in the equilibrium potential of this electrode upon addition of solid Li_2O to the carbonate melt.

3. $CO_2^=$ has a limited solubility in the melt studied and any excess of it decomposes to CO and $O^=$ relatively quickly.

4. Both CO/CO_2 and O_2/CO_2 electrodes at 800°C are extremely sensitive to local changes of concentration, whether these are caused by changes in the gas mixtures supplied or by addition of an active ionic species such as $O^=$ directly to the melt. Their response time is of the order of 0.1 sec or less.

5. In relation to the fast electrode equilibria of the standard CO/CO_2 and the 1:2 O_2/CO_2 electrodes at 800°C, the dissociation equilibrium of the ternary eutectic melt, $Li/Na/K/CO_3$ is very slow.

6. For the CO/CO_2 and the O_2/CO_2 electrodes in molten carbonates, Eq. [7a] and [8b] above are, respectively, the true Nernst equations since they reflect perturbation from equilibrium more accurately than Eq. [7b] and [8a]. (The above two sets of Nernst equations were previously regarded as equivalent since under equilibrium conditions they are not distinguishable.)

7. Contrary to the past understanding, $O^=$ ion does not play any major role in the cathodic reduction of oxygen in molten carbonates away from equilibrium in spite of its evident role in determining the potential of the O_2/CO_2 electrode at equilibrium.

Acknowledgments

Figures 3-6 presented in this paper were obtained in the course of work conducted by the author at the Institute of Gas Technology, Chicago, Illinois, as a part of the TARGET fuel cell program sponsored by Pratt & Whitney Aircraft Division of United Aircraft Corporation and published here with their kind permission. The excellent help of Mr. A. K. Robinson in preparation of this publication and helpful discussions with him and Dr. A. J. Appleby are gratefully acknowledged.

Manuscript submitted Dec. 6, 1976; revised manuscript received Feb. 24, 1977.

Any discussion of this paper will appear in a Discussion Section to be published in the June 1978 JOURNAL. All discussions for the June 1978 Discussion Section should be submitted by Feb. 1, 1978.

REFERENCES

1. A. Borucka, "Thermodynamic and Kinetic Behaviour of the CO/CO_2 Electrode in Molten Carbonate Electrolyte," Research Report, Girton College, Cambridge, England (1966).
2. G. J. Janz and M. R. Lorenz, *J. Chem. Eng. Data*, **6**, 321 (1961).
3. L. F. Volkova, *Izv. Sib. Otd. Acad. Nauk SSSR*, No. 7, 34 (1958).
4. G. J. Janz, "Molten Salts Handbook," Academic Press, New York (1967).
5. A. Borucka, in "Fuel Cell Systems II," Advances in Chemistry Series No. 90, American Chemical Society, pp. 242-268 (1969).
6. A. Borucka and C. M. Sugiyama, *Electrochim. Acta*, **13**, 1887 (1968).
7. A. Borucka and C. M. Sugiyama, *ibid.*, **14**, 871 (1969).
8. A. J. Appleby and S. Nicholson, *J. Electroanal. Chem.*, **38**, 13 (1972).
9. A. J. Appleby and S. Nicholson, *ibid.*, **53**, 105 (1974).
10. A. Borucka, *Electrochim. Acta*, **13**, 295 (1968).
11. A. Borucka and A. J. Appleby, *J. Chem. Soc., Faraday Trans.*, To be published.

Effects of Oxygen on the Mechanism of Cadmium Dissolution in Sulfate Solutions

T. N. Andersen,[1] M. H. Ghandehari,[2] E. Feng, and H. Eyring

Department of Chemistry, University of Utah, Salt Lake City, Utah 84112

ABSTRACT

The dissolution rate of cadmium was measured in various nitrogen- and oxygen-saturated acidic sulfate solutions under potentiostatic conditions. At a given potential, the dissolution rate was found to be greater in O_2- than in N_2-saturated solutions. A dissolution mechanism is proposed which explains this phenomena as well as results from tests in which potential, solution agitation, and solution composition were varied. According to this mechanism Cd^+ ions are formed as intermediates and are then oxidized to the product Cd^{+2} ions by a chemical path involving O_2 as well as by the conventional electrochemical path.

Uniform corrosion of a metal in solution is most frequently explained in terms of the electrochemical polarization curves for the independent processes, *i.e.*, metal oxidation and H^+ or O_2 reduction [*e.g.*, see Ref. (1-4)]. The polarization curves for the part reactions are added to yield that for the over-all system. This type of treatment is useful in explaining corrosion, passivation, and protection phenomena. It also has been recommended as a means for accelerated corrosion testing [*e.g.*, Ref. (2, 5)]. In the latter application the Tafel curves for one or both half-reactions (assuming one predominant cathodic and one predominant anodic reaction) are obtained by suppressing the opposite reaction. The Tafel curve is then extrapolated to the measured corrosion (mixed) potential or the two Tafel curves are extrapolated to the point of overlap to yield the corrosion current. The above superposition procedures are a means of replacing lengthy weight-loss or assay-dependent tests with one rapid electrochemical test. In order for this superposition approach to function it is necessary that the rate and kinetics of each partial reaction be independent of the other partial reaction(s) at a given potential. This independence of partial processes has been shown for several combinations of reductant (metals or hydrogen) and oxidant (5-9), and consequently would appear to be quite general. However, independence of the partial processes is not a necessary criteria for charge and mass balance across the electrode-solution interface, as suggested in some previous work (10, 12). Also an experimental attempt to obtain the corrosion rate of copper in oxygenated acid sulfate solutions by extrapolating the anodic copper polarization curve gave a corrosion rate which was erroneously low (11).[3] In the latter work (11) studies were made to determine why the partial processes were not independent when coupled, and a mechanism was proposed to explain the results.

The present study was made to investigate other systems for which the partial processes are not independent, as part of an evaluation of the superposition means of accelerated corrosion testing. Cadmium in acidic sulfate solutions was the metal chosen for study because previous work (13) suggests it dissolves as Cd^{+2} ions via a Cd^{+1} intermediate; such an intermediate offers a vehicle for interactions between the part reactions. Both H^+ ions and O_2 were studied as oxidants.

[1] Present address: Kennecott Research Center, Salt Lake City, Utah.

[2] Present address: Fansteel Research Center, Salt Lake City, Utah.

Key words: corrosion, intermediate reactions.

[3] Reference (11) attributed this failure to the mixed potential concept, but in fact should have distinguished between the law of mixed potentials ($i_{net}(E) = \sum_j i_j(E)$), which is applicable, and the superposition approach which is not applicable in this case. Donahue (12) emphasized this distinction.

Experimental

Cadmium electrodes were held at various potentials in N_2- and O_2-saturated sulfate solutions; the Cd dissolution rate and the electric current were determined for comparison in each case. All tests were made with pieces of high purity Cd sheet, 1 × 1 cm, which were covered on one side and on the edges with silicone rubber (Dow-Corning Silastic). The tests were run in a tightly covered Pyrex cell which contained 200-250 ml of H_2SO_4 acid solution of various strengths or of H_2SO_4-Na_2SO_4 mixtures. The reference electrode was a saturated calomel half-cell located in a side compartment of the main cell; it contacted the test electrode through a Luggin tube and capillary placed within a few tenths of a millimeter of the Cd surface. All potentials are reported with respect to the SCE. The counterelectrode for polarization measurements consisted of a Pt electrode, placed in a porous cup within the cell to prevent mixing of anodic and cathodic products. The solution was stirred at a constant, moderate rate with a magnetic stirrer in all cases except for those tests in which agitation was varied. The above rate is referred to throughout the remainder of this paper as "standard stirring." Oxygen or high purity N_2 was purged through the solution at approximately the same rate during each experiment. All tests were performed at 25°C.

Before each test the Cd electrode was pretreated with dilute HNO_3, then H_2O, and finally acetone to give a shiny, reproducible surface. After drying the test electrode was inserted in the cell, the open-circuit potential was measured, and polarization tests were begun. The electrode was potentiostated at various potentials near and to the positive side of the open-circuit potential, and the electric current was recorded during the entire test. Potentials were made with an electrometer voltmeter which was calibrated with a potentiometer.

Each potential was maintained at times up to 1 hr. The electrolyte was sampled several times during this test period and the Cd^{+2}-ion concentration was measured by atomic absorption to yield the rate of metal dissolution. A given electrode surface was polarized at various potentials before being withdrawn from the solution to ensure that parametric tests of potential dependence did not suffer from surface changes. Effort was concentrated near the open-circuit potential so that results would be relevant to open-circuit corrosion and so that the ohmic resistance between the Luggin capillary and test electrode would be kept negligibly small by keeping the external current moderately small. Steady-state polarization curves were obtained over a much larger range, however, to aid in establishing mechanisms.

At the end of each series of tests on a given electrode, the solution was tested for H_2O_2 concentration using the titanium sulfate colorimetric method (14).

Results and Discussion

Experimental Results

Cadmium ions (Cd^{+2}) and H_2O are the products of the reaction in oxygenated solutions. The concentrations of H_2O_2 after potentiostatic tests and even after 10 hr of open-circuit corrosion were below the detection limit of 4×10^{-5}M H_2O_2.

The Cd dissolution was linear with time (*e.g.*, Fig. 1) and the electric current was likewise nearly constant throughout each test. The dissolution data were converted to current densities on the basis that each Cd atom loses two electrons upon dissolution. The resultant dissolution current densities in N_2- and O_2-saturated solutions [$i(Cd, N_2)$ and $i(Cd, O_2)$, respectively] are shown as a function of potential in Fig. 2 and 3. Open-circuit potentials are shown also for reference purposes.

It is observed (Fig. 2) that the rate is greater in O_2- than in N_2-saturated solution at each potential for a given solution. Repeat tests with different electrodes (shown by the various points at each potential) show that this difference is statistically significant. This result is parallel to that found for Cu in dilute H_2SO_4 (11) but is unexpected in light of various other mixed potential systems (5-9). Other trends from Fig. 2 and 3 are: (*i*) Increased stirring increases the Cd dissolution current in both O_2- and N_2-saturated solutions; the effect in O_2 is shown in Fig. 3. (*ii*) The rate of dissolution of Cd is greater in M H_2SO_4 than in either 0.1M or 3M H_2SO_4. In 0.1M H_2SO_4 + 0.9M Na_2SO_4, $i(Cd, O_2)$ and $i(Cd, N_2)$ are approximately the same as in M H_2SO_4; these curves are not shown in the figures. (*iii*) The values of $i(Cd, N_2)$ and $i(Cd, O_2)$ increase with an increase in potential.

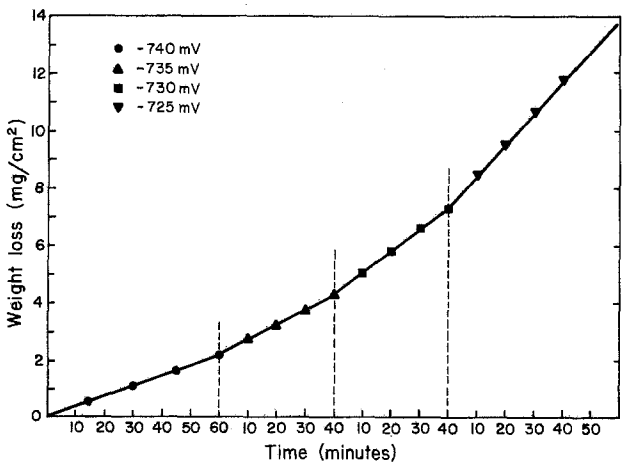


Fig. 1. Cd dissolution in O_2-saturated M H_2SO_4 at various potentials. Solution stirred at standard rate. T = 25°C.

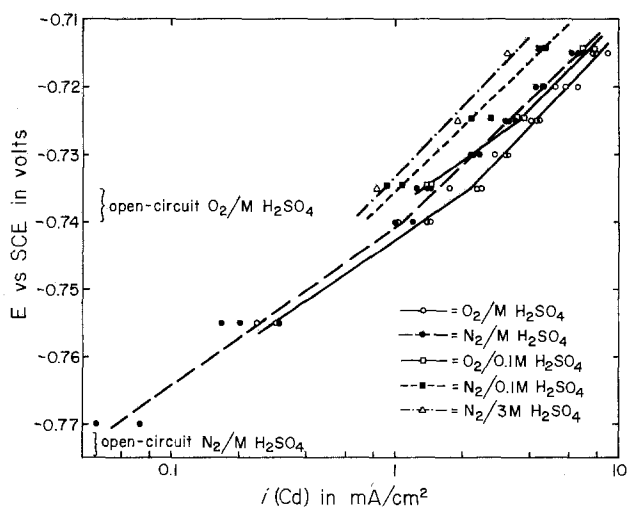


Fig. 2. Rate of Cd dissolution, i(Cd), in various O_2- and N_2-saturated solutions as a function of potential.

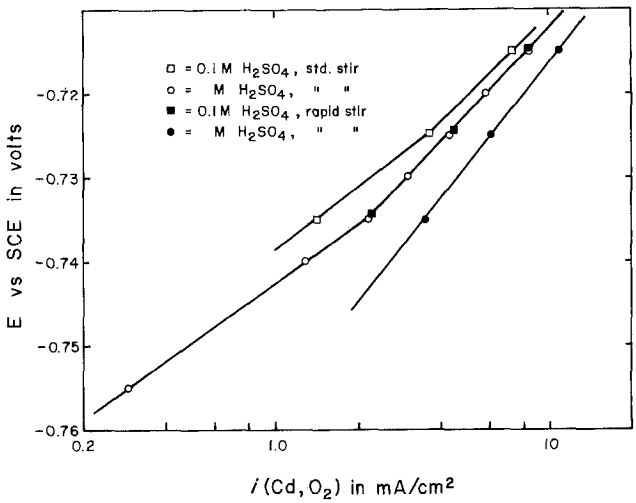


Fig. 3. Rate of Cd dissolution in O_2-saturated H_2SO_4 solutions of different strength and with varied stirring.

Further tests to expose the kinetics of the Cd dissolution consisted of determining the steady-state polarization curves for Cd dissolution in N_2-saturated solution, for H^+-ion reduction in N_2-saturated M H_2SO_4, and for O_2 reduction in O_2-saturated solutions. These curves, which are shown in Fig. 4, were determined over a much greater potential range than the dissolution rate data in Fig. 2 and 3, the purpose being to determine the kinetics of each pertinent step in the potential range of Fig. 2 and 3.

The anodic curve for Cd dissolution shows a Tafel slope over the range tested of $dE/d \log i$ = 30-35 mV. This curve shifted to higher current densities with faster stirring, which indicates that Cd dissolution is controlled both by charge transfer and mass transfer. The reduction curve in N_2-saturated solution gives a well-defined Tafel line for H_2 evolution at potentials more negative than approximately −930 mV. The shape of the curve at more positive potentials indicates the presence of a depolarizer impurity at low concentrations. Irreproducibility in the curve at the most positive potentials is further evidence that O_2 is the impurity. Oxygen reduction gives a curved E *vs.* log i plot which goes to the limiting diffusion current, $i_{l_{O_2}}$, at approximately 2.2 mA/cm², and then on to the hy-

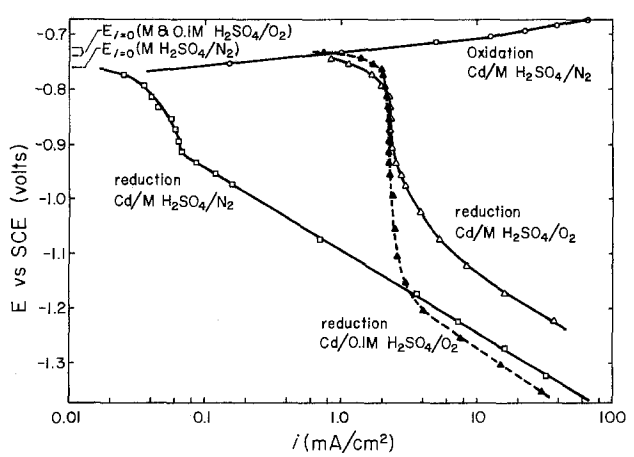


Fig. 4. Steady-state polarization curves for the reduction or oxidation at the Cd electrode in various H_2SO_4 solutions. Stirring at standard rate. T = 25°C.

drogen evolution Tafel line. At the "faster-than-standard" stirring rate $i^l_{O_2}$ was approximately 2.6 mA/cm^2.

Model to Explain Results

In N_2-saturated solution the rate of Cd dissolution accounts quantitatively for the anodic electric current. At open circuit, the measured Cd dissolution rate of approximately 0.05 mA/cm^2 appears to be balanced by H^+ ion and impurity reduction; *i.e.*, the inflection in the reduction curve in N_2/H_2SO_4 (Fig. 4) corresponds to this general current.

At or positive of the open-circuit potential in O_2-saturated solution, H^+-ion reduction is negligible, as can be seen from Fig. 4. With this fact in mind we propose the following mechanism to explain the data in Fig. 2-4

$$Cd \leftrightarrows Cd_{ad}^+ + e^- \quad [1]$$

$$Cd_{ad}^+ \leftrightarrows Cd^{+2} + e^- \quad [2]$$

$$Cd_{ad}^+ + \tfrac{1}{4}\,O_2 + H^+ \rightarrow \tfrac{1}{2}\,H_2O + Cd^{+2} \quad [3]$$

$$O_2 + 4H^+ + 4e^- \rightarrow 2H_2O \quad [4]$$

Steps [1] and [2] are assumed to be the steps for the electrochemical dissolution in N_2/H_2SO_4 [in agreement with other recent studies (13)] and step [4] is the expected reduction reaction. In addition step [3] is added because of the need for a step in which some metal dissolution occurs via a nonelectrochemical pathway, to explain the fact that $[i(Cd, O_2) > i(Cd, N_2)]_E$. Reactions [3] and [4] are irreversible whereas the reverse, as well as the forward, reactions of [1] and [2] must be considered to explain the experimental results. Monovalent Cd^+ ions are never observed in sulfate solutions (as the present faradaic dissolution results in N_2/H_2SO_4 reattest) and therefore exist only in the adsorbed state.

In N_2-saturated solution reactions [3] and [4] are negligible such that the steady-state rate of Cd dissolution is given by

$$i(Cd, N_2) \simeq i(N_2) = i_1 + i_2 = 2i_2 \quad [5]$$

When O_2 is present, reactions [3] and [4] also must be considered, which results in a steady-state electric current, $i(O_2)$, of

$$i(O_2) = i_1 + i_2 - i_4 \quad [6]$$

and a Cd dissolution rate, $R(Cd, O_2)$ (in moles/sec · cm^2), of

$$R(Cd, O_2) = R_3 + i_2/\mathbf{F} \quad [7]$$

Here R_3 is the rate of step [3] in moles Cd/sec · cm^2. Each time i_1 occurs, the resultant Cd_{ad}^+ ion is removed by step [2] or [3]. Therefore

$$i_1/\mathbf{F} = i_2/\mathbf{F} + R_3 \quad [8]$$

from which Eq. [6] becomes

$$i(O_2) = 2i_2 + \mathbf{F}R_3 - i_4 \quad [9]$$

as

$$i(Cd, O_2) = 2i_2 + 2\mathbf{F}R_3 \quad [10]$$

In addition to the above expressions one may write an equation for the balance of O_2 diffusing to the surface and the utilization of it in steps [3] and [4]; *i.e.*

$$\frac{D_{O_2}}{\delta}(a_{O_2,s} - a_{O_2,e}) = \frac{i_4}{4\mathbf{F}} + \frac{R_3}{4} \quad [11a]$$

or

$$i^l_{O_2} - \frac{4\mathbf{F}D_{O_2}a_{O_2,e}}{\delta} = i_4 + \mathbf{F}R_3 \quad [11b]$$

The subscripts s and e refer to the solution and electrode surface, respectively. Likewise a balance exists between the production of Cd^{+2} ions and diffusion of them away from the surface; this is given by

$$\frac{D_{Cd^{+2}}}{\delta}(a_{Cd^{+2},e} - a_{Cd^{+2},s}) = R_3 + \frac{i_2}{\mathbf{F}} \quad [12]$$

The parametric tests of Fig. 2 and 3 can only be rationalized and the proposed model tested (further than explaining why $[i(Cd, O_2) > i(Cd, N_2)]_E$ by assuming a specific dependence of the individual current steps on the various parameters. The present tests and information in the literature are sufficient to approximate these closely enough for the present purpose.

The fact that $i(Cd, N_2)$ depends on stirring indicates that i_1 is not rate controlling. Therefore we assume that i_2 is rate controlling and i_1 is in quasi equilibrium. Accordingly

$$i_1 = i_1^+ - i_1^- = \mathbf{F}k_1^+ \exp(\alpha_1\mathbf{F}E/RT) - \mathbf{F}k_1^- a_{Cd^+,e} \exp[-(1-\alpha_1)\mathbf{F}E/RT]\,[4] \quad [13]$$

and $i_1^+, i_1^- >> i_1$
or

$$a_{Cd^+,e} = \frac{k_1^+}{k_1^-}\exp(\mathbf{F}E/RT) \quad [14]$$

$$i_2 = i_2^+ - i_2^- = \mathbf{F}k_2^+ a_{Cd^+,e} \exp(\alpha_2\mathbf{F}E/RT) - \mathbf{F}k_2^- a_{Cd^{+2},e} \exp[-(1-\alpha_2)\mathbf{F}E/RT]\,[4] \quad [15]$$

We assume the simplest form possible for R_3, *i.e.*, that it is first order with respect to both $a_{Cd^+,e}$ and $a_{O_2,e}$. Therefore

$$R_3 = a_{Cd^+,e}a_{O_2,e}k_3 \quad [16]$$

The kinetics of Eq. [4] is known for reduction on metals in general and is of the form

$$i_4 = 4\mathbf{F}k_4 a_{O_2,e} \exp(-\alpha_4\mathbf{F}E/RT)\,[4] \quad [17]$$

Expressions [11]-[17] are sufficient to eliminate the unknown activities at the electrode surface, *i.e.*, $a_{Cd^{+2},e}$, $a_{Cd^+,e}$, and $a_{O_2,e}$, and to solve for i_2, R_3, and i_4. These are as follows

$$i_2 = \frac{(D_{Cd^{+2}}/\delta)\mathbf{F}\left(\frac{k_1^+}{k_1^-}\right)k_2^+ \exp[(1+\alpha_2)\mathbf{F}E/RT]}{\frac{D_{Cd^{+2}}}{\delta} + k_2^- \exp[-(1-\alpha_2)\mathbf{F}E/RT]} - \frac{(D_{Cd^{+2}}/\delta)\mathbf{F}k_2^- a_{Cd^{+2},s} \exp[-(1-\alpha_2)\mathbf{F}E/RT]}{\{(D_{Cd^{+2}}/\delta) + k_2^- \exp[-(1-\alpha_2)\mathbf{F}E/RT]\}}$$

$$- \frac{k_2^- i^l_{O_2} \exp[-(1-\alpha_2)\mathbf{F}E/RT]}{\left(\frac{D_{Cd^{+2}}}{\delta} + k_2^- \exp[-(1-\alpha_2)\mathbf{F}E/RT\right)\left(\frac{4D_{O_2}k_1^-}{\delta k_1 k_3^+}\exp[-\mathbf{F}E/RT] + \frac{4k_4k_1^-}{k_1k_3^+}\exp[-(1+\alpha_4)\mathbf{F}E/RT] + 1\right)} \quad [18]$$

Since the rate of Cd dissolution is expressed in Fig. 2 and 3 in terms of the equivalent current density (with two electrons per Cd atom), Eq. [7] may be rewritten

[4] The potential-independent portion of the rate constants in Eq. [13]-[15], [17] (*i.e.*, the k's) are defined such that the measured potential, E, may be used in the exponents. Therefore the k's include a constant which is a function of the standard electrode rates at the potential of the reference electrode.

$$\mathbf{F}R_3 = \frac{i^l_{O_2}}{\frac{4D_{O_2}k_1^-}{\delta k_1 k_3^+}\exp(-\mathbf{F}E/RT) + \frac{4k_4k_1^-}{k_1k_3^+}\exp[-(1+\alpha_4)\mathbf{F}E/RT] + 1} \quad [19]$$

$$i_4 = \frac{i^l_{O_2}}{1 + \frac{D_{O_2}}{k_4\delta}\exp(\alpha_4\mathbf{F}E/RT) + \frac{k_1k_3^+}{4k_1k_4^-}\exp[(\alpha_4+1)\mathbf{F}E/kT]} \quad [20]$$

The model is best tested in terms of the measured parameters, the rate of metal dissolution (i(Cd)) and the measured current density, i. The rate of Cd weight loss obtained from Eq. [10], [18], and [19] is

$$i(\mathrm{Cd}) = 2i_2 + 2\mathbf{F}R_3$$
$$= \frac{2(D_{Cd^{+2}}/\delta)\mathbf{F}(k_1^+/k_1^-)k_2^+\exp[(1+\alpha_2)\mathbf{F}E/RT]}{(D_{Cd^{+2}}/\delta) + k_2^-\exp[-(1-\alpha_2)\mathbf{F}E/RT]} - \frac{(D_{Cd^{+2}}/\delta)\mathbf{F}k_2^- a_{Cd^{+2},s}\exp[-(1-\alpha_2)\mathbf{F}E/RT]}{D_{Cd^{+2}}/\delta + k_2^-\exp[-(1-\alpha_2)\mathbf{F}E/RT]}$$
$$+ \frac{2i^l_{O_2}D_{Cd^{+2}}/\delta}{\left(\frac{D_{Cd^{+2}}}{\delta} + k_2^-\exp[-(1-\alpha_2)\mathbf{F}E/RT]\right)\left(\frac{4D_{O_2}k_1^-}{k_3\delta k_1^+}\exp(-\mathbf{F}E/RT) + \frac{4k_4k_1^-}{k_3k_1^+}\exp[-(1+\alpha_4)\mathbf{F}E/RT] + 1\right)} \quad [21]$$

In N_2-saturated solution the last term in [21] is omitted such that i(Cd) = i(Cd, N_2). Experimentally i(Cd, N_2) showed well-defined Tafel behavior with $b \simeq$ 30 mV (cf. Fig. 4). Also i(Cd, N_2) depended strongly on stirring (to approximately the same extent as the O_2 limiting current). Finally i(Cd, N_2) did not change over several orders of magnitude of $C_{Cd^{+2},s}$ (from 0 to $\sim 10^{-3}$M). These facts indicate that the second term in [21] is negligible and that $D_{Cd^{+2}}/\delta << k_2^-[\exp -(1-\alpha_2)\mathbf{F}E/RT]$ in the denominator of the first term. Thus under the present conditions i(Cd, N_2) is given by

$$i(\mathrm{Cd}, N_2) \simeq 2\mathbf{F}\frac{D_{Cd^{+2}}}{\delta}\frac{k_1^+}{k_1^-}\frac{k_2^+}{k_2^-}\exp(2\mathbf{F}E/RT) \quad [22a]$$

That this reaction is diffusion controlled was also concluded earlier (7) from studies of stirring effects on Cd dissolution.

The effect of electrolyte composition on i(Cd, N_2)$_E$ (*i.e.*, the fact that i(Cd, N_2) is greater for M H_2SO_4 than for 0.1 or 3M) appears to be due principally to electrolyte effects on the diffusion coefficient, $D_{Cd^{+2}}$, on δ, and on $k_1^+k_2^+/(k_1^-k_2^-)$. Inasmuch as $(k_1^+/k_1^-)(k_2^+/k_2^-)$ is just the equilibrium constant between metallic Cd and Cd^{+2}, ions immediately outside the metal surface (*i.e.*, inside the diffusion layer), Eq. [22a] may be rewritten as follows

$$i(\mathrm{Cd}, N_2) = 2\mathbf{F}(D_{Cd^{+2}}/\delta)(a_{Cd^{+2},e}/a_{Cd})\exp(2\mathbf{F}E/RT) \quad [22b]$$

The origin of the electrolyte effects on i(Cd, N_2) was further identified by measuring the cathodic limiting diffusion currents for Cd^{+2}-ion deposition onto Cd. These limiting currents were measured several times for deposition of Cd from 0.1, 1, and 3M H_2SO_4 which contained 2 mM $CdSO_4$. The electrode arrangement and solution agitation were identical to those in the anodic experiments, *i.e.*, Fig. 2. The resulting limiting currents were statistically equivalent (within the limit of the ± 6% reproducibility) for the three solutions. We interpret these results from the following expression

$$i^l_{Cd^{+2}} = \frac{2\mathbf{F}D_{Cd^{+2}}a_{Cd^{+2}}}{\delta} = \frac{2\mathbf{F}D_{Cd^{+2}}C_{Cd^{+2}}\gamma_{Cd^{+2}}}{\delta} \quad [23]$$

where C and γ are the concentration and activity coefficient. Since the H_2SO_4 concentration is much greater than the Cd^{+2}-ion concentration, $\gamma_{Cd^{+2}}$, $D_{Cd^{+2}}$, and δ would be determined principally by $C_{H_2SO_4}$ (rather than by small changes in $C_{Cd^{+2}}$). Because $i^l_{Cd^{+2}}$ is independent of $C_{H_2SO_4}$ at a fixed concentration of Cd^{+2} ions, it follows that $D_{Cd^{+2}}\gamma_{Cd^{+2}}/\delta$ is a constant independent of $C_{H_2SO_4}$. If this conclusion is applied to the anodic dissolution current of Eq. [22b], one concludes that i(Cd, N_2) varies with $C_{H_2SO_4}$ at constant E because $C_{Cd^{+2},e}$ varies with $C_{H_2SO_4}$. Therefore the competition between the liquid phase and the metal for the Cd^{+2} ions would appear to determine the concentration of Cd^{+2} ions ready to diffuse, $C_{Cd^{+2},e}$, in Eq. [22b].

In O_2-saturated solution both the first and last terms in Eq. [21] must be taken into account to explain the results. The last term is positive which justifies the observation that i(Cd, O_2)$_E$ > i(Cd, N_2)$_E$. The data show that the first term in Eq. [21] is the larger of the two terms, *i.e.*, (Cd, O_2)/i(Cd, N_2) in M H_2SO_4 (see Fig. 2) ranges from 1.6 at −735 mV to 1.3 at −715 mV. Therefore, the Tafel slope for i(Cd, O_2) is basically the same as for i(Cd, N_2), *i.e.*, 30 mV or 2.3 $RT/2\mathbf{F}$. After Eq. [22a] is substituted for the first two terms in Eq. [21], the ratio of Cd dissolution in O_2- to that in N_2-saturated solution is given by

$$\frac{i(\mathrm{Cd}, O_2)}{i(\mathrm{Cd}, N_2)} = 1 + \frac{i^l_{O_2}}{\frac{\mathbf{F}k_1^+}{k_1^-}k_2^+\exp[(1+\alpha_2)\mathbf{F}E/RT]\cdot B} \quad [24]$$

where

$$B = \frac{4D_{O_2}k_1^-}{\delta k_3k_1^+}\exp(-\mathbf{F}E/RT) + \frac{4k_4k_1^-}{k_3k_1^+}\exp[-(1+\alpha_4)\mathbf{F}E/RT] + 1 \quad [25]$$

As E becomes more positive, the denominator of Eq. [24] increases, so the over-all second term decreases. This is in qualitative agreement with the observed ratio, i(Cd, O_2)/i(Cd, N_2).

The value of i(Cd, O_2) increases with stirring (cf. Fig. 3), as both terms in Eq. [21] qualitatively predict.

Table I. Average rate of O_2 utilization in potentiostatic tests

Solution	E (mV)	$[i(\mathrm{Cd},O_2) - i(O_2)]_{avg}$ Standard stirring (mA/cm²)		$[i(\mathrm{Cd},O_2) - i(O_2)]_{avg}$ Rapid stirring (mA/cm²)
1M H_2SO_4	−755	1.4		
	−745	2.6		2.6
	−730	2.1		
	−725	2.2		2.5
	−720	2.3		
	−715	2.2		2.3
0.1M H_2SO_4	−735	2.2		2.8
	−715	2.6		2.7
		2.2	$i^l_{O_2}$	2.6

Table II. Open-circuit corrosion rates, i_{corr}, under various conditions

H_2SO_4	Gas	Rate of stirring	i_{corr} (mA/cm²)	Corrosion potential E_{corr} (mV)
M	O_2	Standard	1.76, 1.45, 1.75, 1.49 (1.61)*	−740
M	N_2	Standard	0.0143, 0.086, 0.084, 0.0172, 0.0465, 0.072, (0.053)	−770 to −780
M	Air	Standard	0.31, 0.49, 0.67, 0.37 (0.46)	−745 to −753
0.1M	O_2	Standard	1.63, 1.81, 1.75 (1.73)	−733
M	O_2	More rapid than standard	2.30, 2.33, 2.63 (2.42)	−740

* The average value for tests at a given set of conditions is shown in parentheses.

The increase in $i(Cd, O_2)$ with ionic strength is basically the same as for $i(Cd, N_2)$; this was discussed previously.

From the preceding paragraphs it is observed that the theoretical metal dissolution rates, $i(Cd, N_2)$ and $i(Cd, O_2)$, are qualitatively consistent with the observed dissolution rates (trends) with regard to all tested variables, *i.e.*, potential, O_2 concentration, stirring rate, and salt strength. The theory may also be tested with the measured electric current $i(O_2)$. Rather than do this directly, we note that

$$i(Cd, O_2) - i(O_2) = \mathbf{F}R_3 + i_4 \qquad [26]$$

However this is $4\mathbf{F}\cdot$ (total rate of O_2 utilization in moles cm^{-2} sec^{-1}) as shown by Eq. [11]. The experimental value for Eq. [26] is shown in Table I.

The data show that within experimental deviation, O_2 is used at a rate approximately equal to its limiting diffusion current at all conditions of stirring, solution composition, and potential with the possible exception of the potentials more negative than −735 (*i.e.*, at −755). This indicates that the second term in Eq. [11b] is much smaller than the first. It also means that the term $(4D_{O_2}k_1^-/(\delta k_1^+ k_3))\exp(-\mathbf{F}E/RT)$ in the denominator of $\mathbf{F}R_3$ (Eq. [19]) is insignificant, as is the pair of terms $1 + (D_{O_2}/(k_4\delta))\exp(\alpha_{10}\mathbf{F}E/RT)$ in the denominator of i (Eq. [20]). The O_2 utilization rate thus reduces to

$$\mathbf{F}R_3 + i_4 = i^l_{O_2}\left[\frac{1}{1+\frac{1}{a}} + \frac{1}{a}\right]$$

$$= i^l_{O_2}\left(\frac{a^2+a+1}{a+1}\right) = i^l_{O_2} \qquad [27]$$

where

$$a = \frac{4k_4k_1^- e^{-\alpha_4\mathbf{F}E/RT}}{k_1k_3^+ e^{\mathbf{F}E/RT}} \qquad [28]$$

In order for Eq. [27] to be valid, $(a + 1) >> a^2$ or, if $(a + 1) > 10a^2$ then $-0.27 < a < 0.37$. But a is just the ratio of the rates $i_4/\mathbf{F}R_3$ (cf. Eq. [16] and [17]). The applicable solution is $a < 0.37$, so the chemical step [3] utilizes a greater fraction of the O_2 than does step [4].

Application to Open-Circuit Corrosion

The open-circuit corrosion potential for Cd in the oxygenated H_2SO_4 solutions studied is approximately −740 mV. Table I shows that the O_2 utilization rate at this potential is slightly less than the limiting diffusion current for O_2, $i^l_{O_2}$. Correspondingly, the corrosion rate (see Table II) is somewhat less than $i^l_{O_2}$ (1.6 mA/cm² compared to 2.2 mA/cm² at the standard-stirring rate). Nevertheless the kinetics are substantially controlled by O_2 diffusion, so the effects of experimental parameters on the open-circuit corrosion rate should parallel those for O_2 diffusion. The corrosion data in Table II show that this prediction is borne out; *i.e.*, the corrosion rate is strongly dependent on stirring, approximately first order with respect to O_2 partial pressure, and nearly independent of the solution composition. The corrosion potential, E_c, is not the value obtained by equating $i^l_{O_2}$ and $i(Cd, N_2)$, given as −725 mV by Fig. 4. Rather E_c is more negative because of the additional "chemical" dissolution step (Eq. [3]). If the current from this step were added to the anodic electrochemical curve in Fig. 4, the resultant anodic curve would equal $i^l_{O_2}$ very near the corrosion potential.

Acknowledgments

The authors gratefully acknowledge the Army Research Office-Durham, Contract DAHC04-75-G-0019 and the Paint Research Institute for financial support.

Manuscript submitted Sept. 3, 1976; revised manuscript received Feb. 23, 1977.

Any discussion of this paper will appear in a Discussion Section to be published in the June 1978 JOURNAL. All discussions for the June 1978 Discussion Section should be submitted by Feb. 1, 1978.

Publication costs of this article were assisted by the University of Utah.

REFERENCES

1. K. J. Vetter, "Electrochemical Kinetics," chap. 5, Academic Press, New York (1967).
2. M. Henthorne, *Chem. Eng.*, **1971**, 99.
3. J. M. West, "Electrodeposition and Corrosion Processes," D. Van Nostrand Co. Ltd., New York (1965).
4. B. E. Conway, "Theory and Principles of Electrode Processes," pp. 193-195, Ronald Press, New York (1965).
5. B. Miller and M. I. Bellavance, *This Journal*, **119**, 1510 (1972).
6. C. Wagner and W. Traud, *Z. Elektrochem.*, **44**, 391 (1938).
7. G. E. Kimball and A. Glassner, *J. Chem. Phys.*, **8**, 820 (1940).
8. J. V. Petrocelli, *This Journal*, **97**, 10 (1950).
9. E. J. Kelly, *ibid.*, **112**, 124 (1965).
10. F. M. Donahue, *ibid.*, **119**, 72 (1972).
11. T. N. Andersen, M. H. Ghandehari, and H. Eyring, *ibid.*, **122**, 1580 (1975).
12. F. M. Donahue, *ibid.*, **123**, 843 (1976).
13. K. E. Heusler and L. Gaiser, *ibid.*, **117**, 762 (1970).
14. F. D. Snell and C. T. Snell, "Colorimetric Methods of Analysis," Vol. 2, p. 882, Van Nostrand Publishing Co., New York (1959).

Galvanic Cell Studies on Ionic Carbide and Nitride Solutions in Molten Salts

A. Bonomi,* M. Hadate, and C. Gentaz

Battelle, Geneva Research Center, 1227 Carouge-Geneva, Switzerland

ABSTRACT

The free energy (Gibbs) of formation of Li_2C_2, CaC_2, and Li_3N and their activities in molten salt solutions at temperatures between 823° and 973°K have been determined by using the following galvanic cells

Fe, Li-Ca (alloy) | LiCl-$CaCl_2$ eut. CaC_2 | C (s), Fe [I]

and

Fe, Li (c) | LiCl-LiF eut. Li_3N | N_2 (g,1 atm), Fe [II]

The nitrogen electrode used in cell (II) has been proved to have a Nernstian behavior by studying the dependence of emf on the partial pressure of nitrogen. The activity coefficients of CaC_2 and Li_3N in molten salts have been found to decrease with increasing concentration.

Galvanic cells using CaC_2 solutions in molten salts as electrolyte have been studied by previous authors (1-3) with unsatisfactory results as regards the possibility of determining accurately the carbon activity in iron electrodes. The reason for this lack of accuracy has been ascribed to the existence of electronic conductivity in the melt (3, 4) as a consequence of the presence of calcium resulting from the establishment of the following equilibrium

$$CaC_2 \text{ (melt)} \rightleftarrows Ca \text{ (melt)} + 2C \text{ (s)} \qquad [1]$$

Most of the previous authors (1, 3) have used pure synthetic CaC_2 prepared from the elements at a temperature near 1000°C and the physicochemical behavior of molten salt solutions prepared with the pure synthetic CaC_2 seems to be quite different from that obtained with technical grade carbide. In fact, anodic voltametric curves (5) and chronopotentiometric studies (6) carried out in solutions prepared with synthetic CaC_2 show, respectively, two waves and two transition times, the first attributed to the oxidation of calcium and the second to the oxidation of carbide ion. In the case of solutions prepared with the technical grade CaC_2, the voltametric curves show only one wave corresponding to the oxidation of carbide ion (7). Furthermore the decarburization of carbon-rich austenite samples has been reported when a low carbon steel crucible was used as electrolyte container (3) but only the carburization reaction has been observed in technical grade CaC_2 solutions even in presence of low carbon steel crucibles (7, 8).

This different behavior may be explained by assuming that the synthetic CaC_2 has a higher calcium content than the technical material and this difference in Ca content is conserved in the molten solution because equilibrium [1] is characterized by a very slow kinetic in one or both directions. Actually, the presence of calcium in synthetic CaC_2 solutions has been detected previously (9), but the analytical results show, in most cases, a much higher calcium content than the calculated values for the case of an ideal solution. Therefore, these results do not allow a conclusive opinion about the actual attainment of equilibrium [1] in molten salt solutions of CaC_2.

These preliminary considerations lead us to suppose that electrolytes based on the technical grade CaC_2 solution do not show a significant electronic conductivity. Consequently, they could be used to realize suitable galvanic cells for the activity and free energy measurements of ionic carbides in molten salt solutions. Analogously, an electrolyte based on Li_3N solution in molten salts and a nitrogen electrode have been developed in order to realize suitable galvanic cells for studying the thermodynamics of ionic nitrides in molten salt solutions.

* Electrochemical Society Active Member.
Key words: galvanic cells, calcium carbide solution, lithium nitride solution, carbon electrode, nitrogen electrode, calcium carbide, lithium nitride, free energy of formation.

Experiments

Two types of galvanic cells have been realized

Fe, Li-Ca (alloy) | LiCl-$CaCl_2$ eut. CaC_2 | C (s), Fe [I]

and

Fe, Li (c) | LiCl-LiF eut. Li_3N | N_2 (g, 1 atm), Fe [II]

the first one, corresponding to a formation cell of carbides, has been operated between 873° and 973°K, and the second one, corresponding to a formation cell of nitrides, has been operated between 823° and 973°K.

The experimental apparatus was constituted by an Inconel cell under argon (cell [I]) or nitrogen (cell [II]) atmosphere and heated by a thermoregulated furnace as described in a previous work (10). About 300g of electrolyte [30 mole percent (m/o) of $CaCl_2$ for LiCl-$CaCl_2$ eutectic, melting point 496°C or 29 m/o LiF for LiCl-LiF eutectic, melting point 485°C] was contained in an iron crucible and dehydrated by heating slowly under vacuum from room temperature to the melting point during 5 hr.

Calcium carbide or lithium nitride was added to the molten electrolyte using an iron basket that remained one night in the melt for the complete dissolution. Analytical grade $CaCl_2$ and LiCl supplied by Merck and LiF of 99.5% purity supplied by Ozark were used for the preparation of the eutectic mixtures. Technical grade CaC_2 of 80% purity, the rest being essentially CaO, and Li_3N of 94% purity supplied by Alfa Inorganics were dissolved in the electrolyte. The concentration of CaC_2 was determined by the gas volumetric analysis of the acetylene evolved by hydrolysis of bath samples as described in a previous work (11). The nitride content was determined on bath samples by the Kjeldahl method.

Using an iron crucible as anode, the pure Li or Li-Ca alloy electrode was realized by imposing a cathodic impulse to an iron microelectrode of 0.2-0.3 cm^2. The thin layer (10-100 μm) of metal deposited dissolves slowly after the pulse within a time of 5-80 min, allowing an easy recording of the emf of galvanic cells. The voltages were recorded *vs.* time using a W + W Recorder 100 and independently accurately measured on a digital voltmeter Fluke 800 A.

Table I. Solubility data for CaC_2 in molten LiCl-$CaCl_2$

Temperature (°C)	600	650	680	700
Solubility, w/o CaC_2	2.5	2.6	2.7	3.0

As it was not possible to determine directly the composition of the Li-Ca alloy produced, we have assumed a concentration of 52 atomic percent (a/o) of Ca on the basis of results reported in a previous paper (12) concerning the compositions of Li-Ca alloys obtained at the cathode by electrolysis of LiCl-$CaCl_2$ melts with different compositions.

The carbon electrode was made by a thin layer of anodic deposit of carbon on an iron pin of about 2 mm diameter and dipped about 5 mm into the bath. The nitrogen electrode was made by bubbling the gas through an iron frit or a nozzle with a 0.6 mm diameter hole. Different N_2-argon mixtures have been prepared in order to equilibrate the electrode at different nitrogen partial pressures.

Data on the solubility of CaC_2 in molten LiCl-$CaCl_2$ eutectic are not available in the literature. We have obtained the conditions of saturation adding a slight excess of CaC_2 and controlling its content at the different working temperatures. Solubility data determined in this work for CaC_2 in molten LiCl-$CaCl_2$ eutectic are given in Table I. Solubility of Li_3N in LiCl-LiF eutectic has been measured by Glemser and co-workers (13) and our chemical analysis of bath samples has confirmed the values reported by these authors.

Results

The potential decay observed after the cathodic pulse presents two plateau voltages in the case of Li-Ca electrodes and one plateau voltage in the case of Li electrodes. An example of potential decay recording obtained for the Li-Ca electrode is reported in Fig. 1.

The persistence of the plateaus has been found directly proportional to the charge used for the pulse, and decreased with the temperature. In Fig. 2, we have reported as example the time of persistence of the first plateau obtained with the carbide cell as a function of the charge used at different temperatures. The linear behavior observed confirms that the dissolution of Li or Li-Ca layers on the iron microelectrodes are the cause of the plateau voltages observed. The voltage measured at the beginning of the plateau is a function of temperature and of the CaC_2 or Li_3N content in the melt, and its reproducibility was found quite good in

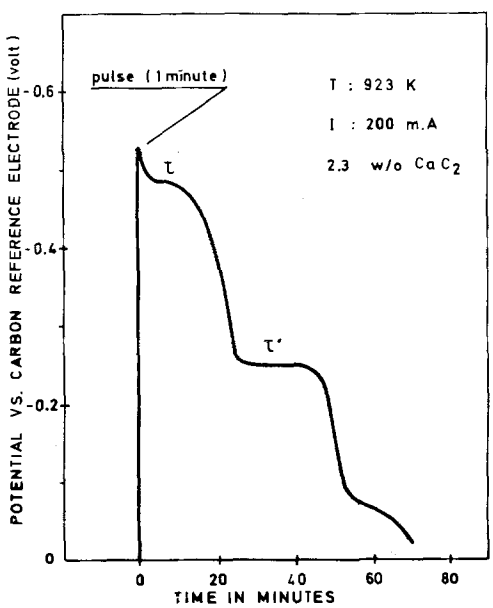


Fig. 1. Potential vs. carbon reference electrode as a function of time after 1 min of cathodic pulse.

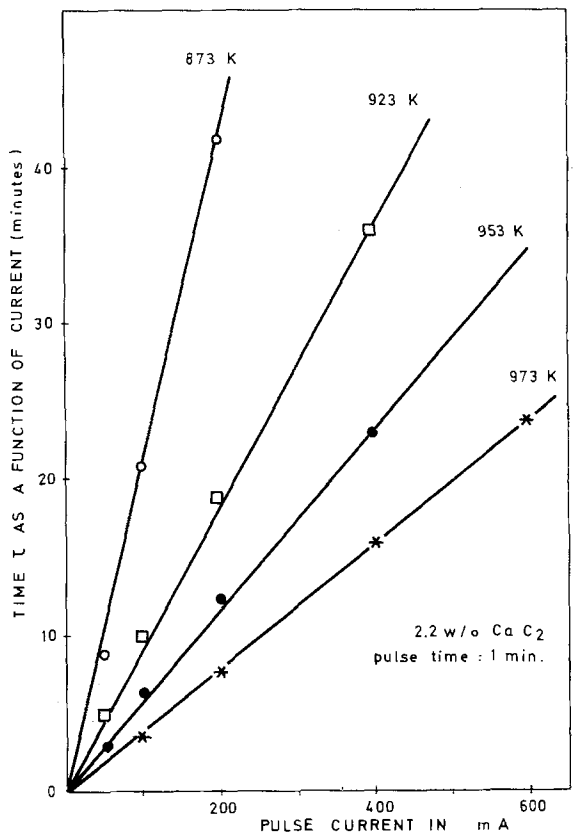


Fig. 2. Time τ as a function of pulse current at different temperatures.

the case of the nitride cell at temperatures between 823° and 973°K and for the first plateau observed with the carbide cell at temperatures between 873° and 923°K. On the other hand, a less reproducible behavior was observed in the case of the second plateau characteristic of the carbide cell and only a few values of the voltage plateau have been considered acceptable in this case.

Considering a possible composition of the Li-Ca alloy of 52 a/o Ca, from the Li-Ca phase diagram (12) at 873° and 923°K, the metal layer deposited should be formed by a two-phase system constituted by solid calcium and a liquid Li-Ca alloy. The cell voltage recorded at the beginning of the first plateau hence could be attributed to the existence of cell [I] where the negative electrode is actually constituted by the two-phase system reported above with the following cell reaction

$$Ca\ (s) + 2C\ (s) \rightarrow CaC_2\ (melt) \qquad [2]$$

As calcium is known to be much more soluble than lithium in molten salts (14), a selective depletion of Ca from the two-phase system is expected and this depletion may be the reason for the formation of the second plateau observed with the carbide cell.

After the complete depletion of Ca, we have in fact the formation of another galvanic cell [I']

$$Fe, Li\ (c) \mid LiCl\text{-}CaCl_2\ eut.\ CaC_2 \mid C\ (s), Fe \qquad [I']$$

with the following cell reaction

$$2Li\ (c) + 2C\ (s) \rightarrow Li_2C_2\ (melt) \qquad [3]$$

In the case of the nitride cell, the formation of the plateau corresponds to the existence of cell [II] with the following cell reaction

$$3Li\ (c) + \tfrac{1}{2} N_2\ (g, 1\ atm) \rightarrow Li_3N\ (melt) \qquad [4]$$

In Fig. 3 and 4 we have reported, respectively, the emf of cell [I] and of cell [II] as a function of tem-

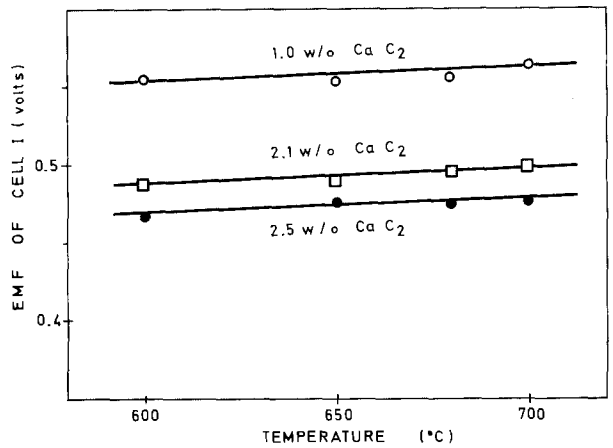


Fig. 3. EMF of cell [I] as a function of temperature at different calcium carbide concentrations.

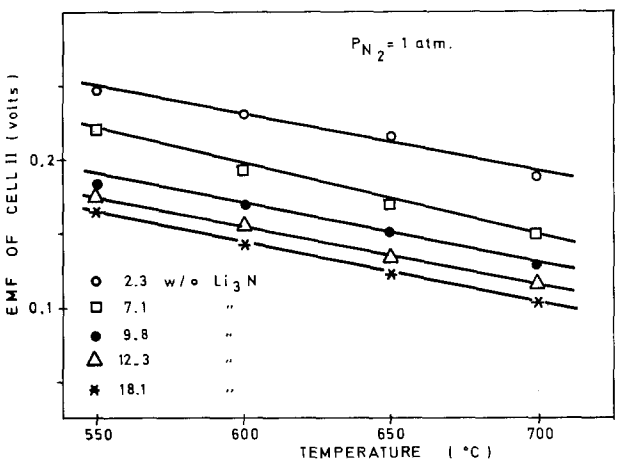


Fig. 4. EMF of cell [II] as a function of temperature at different lithium nitride concentrations.

perature at different concentrations, respectively, of CaC_2 and Li_3N.

In order to verify the thermodynamical behavior of the nitrogen electrode of cell [II], we have studied the dependence of the plateau voltage on the nitrogen partial pressure. In Fig. 5, we have reported the values of emf recorded as a function of N_2 partial pressure for two Li_3N concentrations in the melt. Then, one could remark the Nernstian behavior, being the experimental slope only 0.2 mV higher than the theoretical value calculated for a cell reaction of the type

$$3Li\ (c) + \tfrac{1}{2}\ N_2\ (g, p_x) + Li_3N\ (melt) \qquad [5]$$

Therefore, we have a good support for the possibility that our iron/nitrogen electrode could behave as a reversible nitrogen electrode with the corresponding electrode reaction

$$N^{3-}\ (melt) \leftrightarrows \tfrac{1}{2}\ N_2\ (g) + 3e^- \qquad [6]$$

in a molten electrolyte dissolving ionic nitrides.

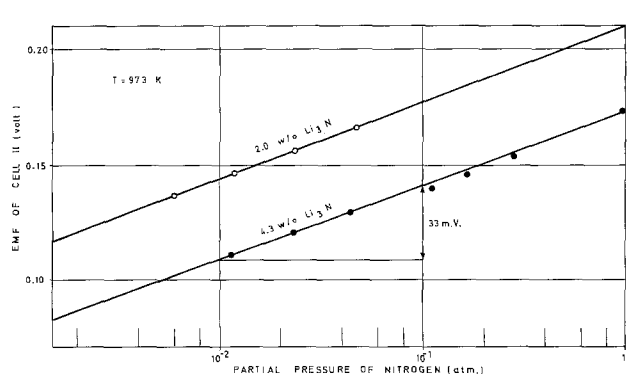


Fig. 5. EMF of cell [II] as a function of the partial pressure of nitrogen.

Discussion

As molten salt electrolytes containing CaC_2 are known to be partial electronic conductors (3, 8), the expression for the cell voltage should include a correction term involving the electron transport number (18). This partial electronic conductivity could be in addition to a simple dissolution process at the origin of the gradual depletion of Ca from the Ca-Li electrode observed in this work. However, for different reasons explained previously and concerning the behavior of technical grade CaC_2 solutions, we have considered this term reasonably small. Another source of possible partial electronic conductivity could be the metal dissolved in the melt originated by cathodic pulses on the microelectrode. In order to maintain negligible the increment of concentration of this metal and in consequence of the partial electronic conductivity we have used a great amount of electrolyte. These considerations are also valid for electrolytes containing Li_3N. Hence the same precautions have been taken experimentally and also in this case we have neglected the correction term involving the electron transport number in the expression of the cell voltage.

Galvanic cell [I].—In order to evaluate our emf data and determine the behavior of the activity coefficient of CaC_2 dissolved in molten salts, we have reported the plateau voltages of cell [I] and [I'] in Fig. 6 and 7 as a function of the logarithm of the ratio between the concentration C of CaC_2 and the value of saturation C_s at 873° and 923°K. In these figures, we have also shown for cell [I] a solid line, that indicates the emf behavior assuming the activity coefficient of CaC_2 remains constant and equal to the value existing in a saturated solution. In the same figures we have indicated the values of $E°_{CaC_2}$ and $E°_{Li_2C_2}$ calculated on the basis of the free energy of formation of the two carbides available in the literature. So we can observe the values of emf of cell [I] measured in a saturated solution of CaC_2 slightly higher (in absolute value) than those calculated from literature data and this difference in terms of free energy corresponds to about 2 kcal/mole. Nevertheless, as these data are reported with an error of ±3 kcal/mole, we consider that our experimental values are in fairly good agreement with the literature.

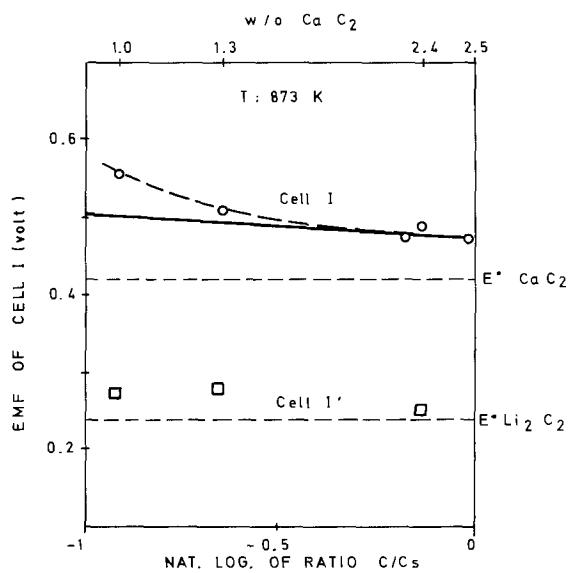


Fig. 6. EMF of cell [I] as a function of ratio C/C_s

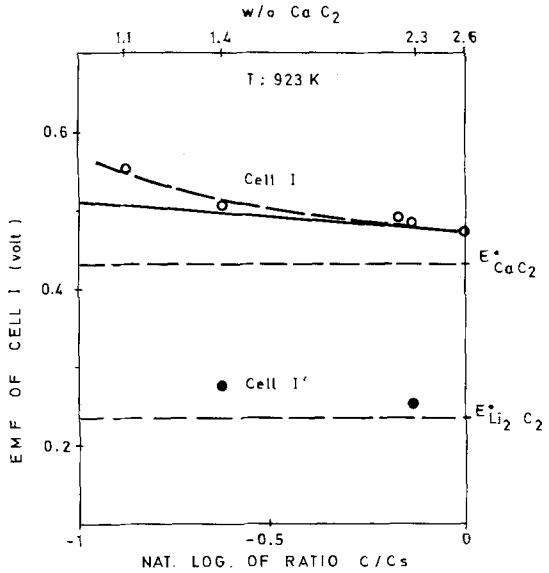


Fig. 7. EMF of cell [I] as a function of ratio C/C_S

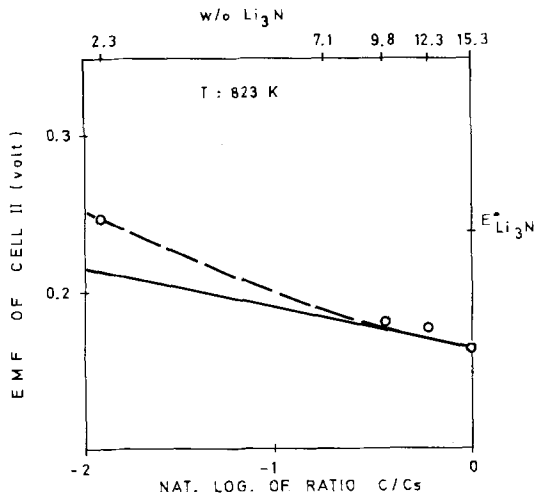


Fig. 8. EMF of cell [II] as a function of ratio C/C_S

With regard to the emf values of cell [I] reported in Fig. 6 and 7 for CaC_2 concentrations lower than the saturation, one could remark that these values are above the solid line of reference at the constant activity coefficient. This fact indicates that the activity coefficient of CaC_2 decreases slowly with the concentration.

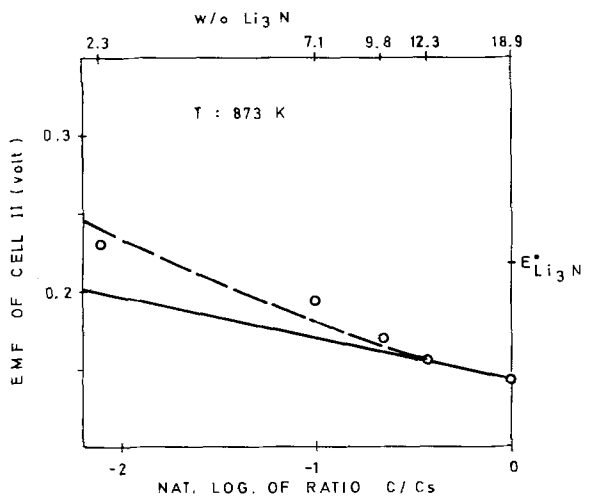


Fig. 9. EMF of cell [II] as a function of ratio C/C_S

Considering now the emf values of cell [I'] of formation of Li_2C_2, they are, as we can see in Fig. 6 and 7, in fairly good agreement with the values calculated from the literature data. However, the lack of knowledge of the solubility of Li_2C_2 in LiCl-$CaCl_2$ eutectic hinders an accurate interpretation of these data.

Galvanic cell [II].—As in the case of cell [I] we have reported the emf data of cell [II] measured at four temperatures between 823° and 973°K in Fig. 8-11

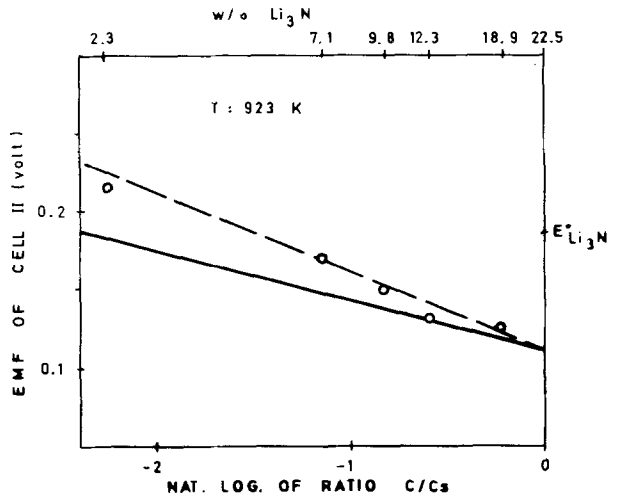


Fig. 10. EMF of cell [II] as a function of ratio C/C_S

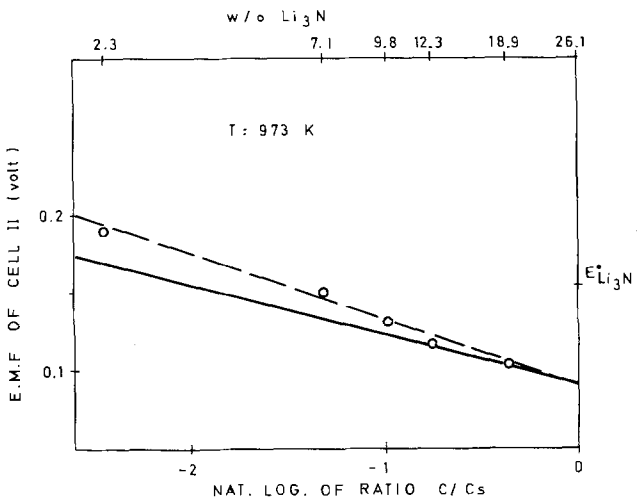


Fig. 11. EMF of cell [II] as a function of ratio C/C_S

as a function of the logarithm of the ratio of concentration C of Li_3N and the saturation value C_S. As in the analogous diagrams of Fig. 6 and 7, we have shown as a solid line the behavior of the emf for the case of an activity coefficient of Li_3N which remains unchanged and equal to the value existing in a saturated solution.

The free energy of formation of Li_3N calculated on the basis of measurements in saturated solutions are reported in Fig. 12 and compared with the values of the literature (15) and some recent data based on thermal decomposition measurements of solid Li_3N (16). Our values are about 4-5 kcal/mole lower (in absolute value) than the old literature data but in good accord with the more recent values (16). On the basis of our data, we can calculate the following free energy function valid between 823° and 973°K

$$\Delta G_{Li_3N}\ (\text{cal/mole}) = -40{,}652 + 35.2T$$

It must be remarked that our values of free energy for Li_3N are subject to uncertainty due to the fact that solid Li_3N reacts with LiCl to form a new phase $Li_9N_2Cl_3$ (17) that could be the actual compound that

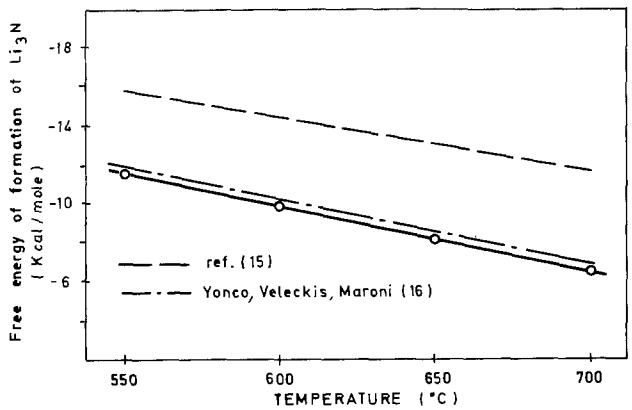


Fig. 12. Free energy ΔG of formation of Li_3N as a function of temperature.

saturates the melts used. As the reaction of formation of this phase

$$2Li_3N + 3LiCl \rightarrow Li_9N_2Cl_3$$

has probably a quite small free energy, we expect that the error affecting our data is small.

With regard to the emf of cell [II] measured for unsaturated solutions of Li_3N, one could observe in Fig. 8-11 that the values are higher than the solid line of reference at the constant activity coefficient. As in the case of CaC_2 solutions, this fact indicates that the activity coefficient of Li_3N decreases with the concentration.

Conclusion

Our results show that it is possible to realize galvanic cells giving useful results upon the free energy and the activity of ionic carbides and nitrides in molten salts, and that it is possible to realize a nitrogen electrode with a thermodynamical reversible behavior in a molten electrolyte dissolving ionic nitrides.

Manuscript submitted Aug. 5, 1976; revised manuscript received Feb. 10, 1977. This was Paper 375 presented at the Washington, D.C., Meeting of the Society, May 2-7, 1976.

Any discussion of this paper will appear in a Discussion Section to be published in the June 1978 JOURNAL. All discussions for the June 1978 Discussion Section should be submitted by Feb. 1, 1978.

Publication costs of this article were assisted by Battelle Geneva Research Center.

REFERENCES

1. G. L. Hawkes and D. R. Morris, *Trans. Metall. Soc. AIME*, **242**, 1068 (1968).
2. F. J. Salzano, L. Newman, and M. R. Hobdell, *Nuclear Technol.*, **10**, 335 (1971).
3. D. R. Morris, C. Aksaranan, B. S. Waldron, and S. H. White, *This Journal*, **120**, 570 (1973).
4. C. Aksaranan and D. R. Morris, *J. Appl. Electrochem.*, **2**, 309 (1972).
5. V. D. Dosaj, M. Sc. Thesis, Department of Chemical Engineering, University of New Brunswick, Canada (1970).
6. S. H. White, Private communication.
7. A. Bonomi and C. Gentaz, Unpublished results.
8. A. Bonomi, M. Parodi, and C. Gentaz, *J. Appl. Electrochem.*, **6**, 59 (1976).
9. C. Aksaranan, V. D. Dosaj, D. R. Morris, and S. H. White, *Can. J. Chem.*, **49**, 2014 (1971).
10. A. Bonomi, H. Giess, and C. Gentaz, *Electrodep. Surface Treat.*, **1**, 419 (1972/1973).
11. C. Gentaz, G. Bienvenu, and A. Boussiba, *Rev. Int. Hautes. Temp. Refract.*, **10**, 161 (1973).
12. Gmelins Handbuch der anorg. Chem. Calcium Teil A, System-Number 28, p. 48 (1957).
13. O. Glemser, M. Fild, and K. Kleine-Weischede, *Z. Anorg. Allg. Chem.*, **332**, 257 (1964).
14. M. A. Bredig, in "Molten Salt Chemistry," M. Blander, Editor, Interscience Publishers, New York (1964).
15. Thermodata, Bibliothèque Univ. des Sciences, B.P. 22, F-38402 St. Martin d'Hères, France.
16. R. M. Yonco, E. Veleckis, and V. A Maroni, *J. Nucl. Mater.*, **57**, 317 (1975).
17. M. Sattlegger and H. Kahn, *Z. Anorg. Allg. Chem.*, **379**, 293 (1970).
18. C. Wagner, "Advances in Electrochemistry and Electrochemical Engineering," Vol. 4, p. 1, Interscience Publishers, New York (1966).

Magnetic Field Effects on Electrochemical Reactions Occurring at Metal/Flowing-Electrolyte Interfaces

Eugene J. Kelly*

Oak Ridge National Laboratory, Chemistry Division, Oak Ridge, Tennessee 37830

ABSTRACT

A study was made to determine whether a magnetic field, such as that associated with a thermonuclear reactor, might adversely affect the corrosion behavior of metallic surfaces in contact with a flowing electrolyte. In metal/flowing-electrolyte systems, electrochemical reactions dependent on the metal/electrolyte interfacial potential difference are affected by an applied magnetic field as a consequence of the Lorentz forces acting on the charged components of the flowing electrolyte. A theoretical analysis of the magnetic field effect was developed, and its validity established by experiments involving the Ti/H_2SO_4 (H_2-saturated) system. Quantitative agreement between theoretical and experimental results was obtained for the electrochemical behavior of Ti in 1*N* H_2SO_4 (mean flow velocity: 0-650 cm/sec) over the available range of magnetic flux density (0-2.1 Tesla). Although the experimental work employed discrete Ti electrodes set in the wall of nonconducting Pyrex glass pipe, the theory was extended to include metallic pipes, *i.e.*, the "conducting-wall" case, for which case the "wall-shorting" effect was shown to be negligible. In addition to the adverse effect of a magnetic field on the "uniform" corrosion behavior of metals, the imposition of a magnetic field can also result in enhanced susceptibility to stress corrosion cracking, localized (pitting or crevice) corrosion, oxidation and reduction of solution species, and electrochemical decomposition of the electrolyte. The aforementioned processes, to name a few, are all potential dependent and, consequently, subject to the magnetic field effect.

The primary purpose of this investigation was to determine what effects a magnetic field has on electrochemical reactions occurring at metallic surfaces in contact with a flowing electrolyte. Although the study was motivated by a concern that the intense magnetic field (10-12 Tesla) associated with a Tokamak-type thermonuclear reactor might adversely affect the corrosion behavior of pipes used to transport an aqueous or molten-salt heat-exchange medium, the results are applicable to magnetoelectrochemical systems in general.

A magnetic field may affect the rates of both activation (charge-transfer) and mass-transport-controlled processes. Consider an electrochemical reaction occurring at a metal/solution interface, for example, a simple reduction reaction occurring under conditions such that the reverse reaction can be ignored

$$M^{+z} + e^- \rightarrow M^{+(z-1)} \qquad [1]$$

If the Nernst diffusion layer concept (1) is applied, the steady-state current density ($\bar{i}$) corresponding to the reduction reaction is given by Eq. [2]

$$\bar{i} = \mathbf{F}\bar{k}(D/\delta)C/[\bar{k} + (D/\delta)] \qquad [2]$$

where D and C represent the diffusion coefficient and bulk concentration of M^{+z}, respectively, δ is the Nernst diffusion layer thickness, $\bar{k}$ is the electrochemical rate constant for the charge-transfer step, and $\mathbf{F}$ is the Faraday constant. For pure mass-transport control, $\bar{k} >> (D/\delta)$, Eq. [2] reduces to Eq. [3]

$$\bar{i} = \mathbf{F}(D/\delta)C \qquad [3]$$

For pure activation control, $(D/\delta) >> \bar{k}$, Eq. [2] reduces to Eq. [4]

$$\bar{i} = \mathbf{F}kC\exp(-\alpha\lambda\mathbf{F}\Delta_{M\phi S}/RT) \qquad [4]$$

where $\bar{k} = k\exp(-\alpha\lambda\mathbf{F}\Delta_{M\phi S}/RT)$, α is the symmetry factor ($\alpha = 1/2$), λ is the charge-transfer number (in this case, $\lambda = 1$), $\Delta_{M\phi S}$ is the potential difference between the metal phase and a point just inside the electrolyte phase (the preelectrode plane or outer Helmholtz plane), and the other symbols have their conventional significance. A magnetic field can alter the hydrodynamic state within the electrolyte phase, thereby altering the value of δ and, consequently, altering the rate of a mass-transport-controlled reaction (Eq. [3]). Quantification of the effect of a magnetic field on mass-transport-controlled reactions remains a problem in classical magnetohydrodynamics and has been the subject of several recent studies (2, 3). On the other hand, the effect of a magnetic field on activation-controlled processes has not been previously quantified, and it is this phenomenon which is examined in the present report. In brief, the interfacial potential difference, $\Delta_{M\phi S}$, at a metal/flowing-electrolyte interface is altered by the presence of a magnetic field and, consequently, the rate of the charge-transfer reaction is changed (Eq. [4]). In addition to affecting the rates of activation-controlled reactions, a magnetic field may introduce mechanistic changes into the electrochemical system. For example, a metal undergoing active-state dissolution may become passive in the presence of a magnetic field. Susceptibility to localized (pitting or crevice) corrosion or stress corrosion cracking may be enhanced (or diminished). Indeed, under severe conditions, electrolytic decomposition of the electrolyte may be induced. In brief, any electrochemical process dependent on $\Delta_{M\phi S}$ may be affected by an applied magnetic field.

The electrochemical system chosen for this study, titanium in H_2-saturated 1*N* H_2SO_4, has been studied extensively in the absence of a magnetic field (4, 5), and is one in which the interfacial reactions, the oxidation of titanium to form Ti(III) ions in solution and the hydrogen evolution reaction, are both under activation control. Moreover, titanium is "nonmagnetic," *i.e.*, the magnetic permeability of titanium may be equated to that of free space.

* Electrochemical Society Active Member.

Key words: titanium, corrosion, magnetoelectrochemistry, magnetohydrodynamics, thermonuclear reactor.

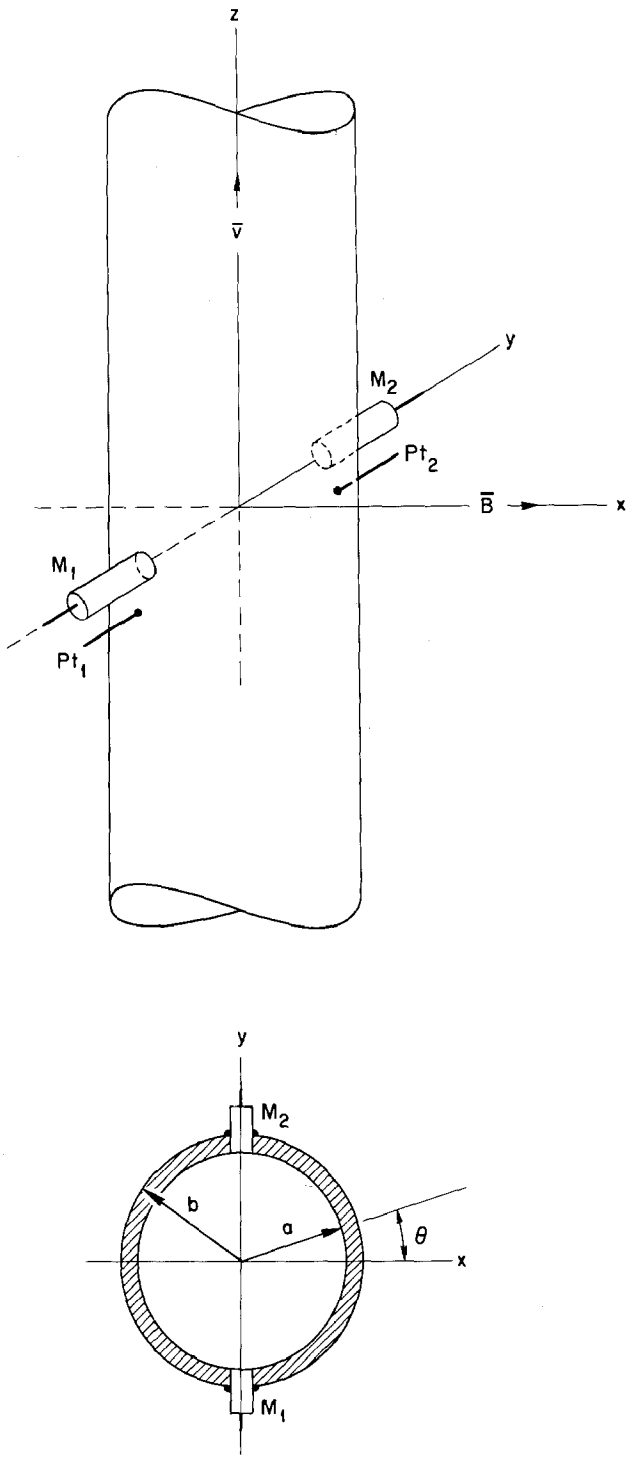


Fig. 1. Schematic drawing of the electrochemical cell segment of the forced-convection loop.

Experimental

A schematic drawing of the electrochemical cell, *i.e.*, that segment of the forced-convection loop located between the pole pieces of an electromagnet, is shown in Fig. 1. The inner and outer radii (a and b in the schematic) of the Pyrex glass pipe were 0.953 and 1.27 cm, respectively. The axis of the cylindrical cell coincided with the z axis, and the magnetic field was aligned parallel to the x axis. The fluid flow and the magnetic field were directed in the positive z and positive x directions, respectively. A pair of identical cylindrical titanium electrodes (M_1 and M_2 in Fig. 1) were located opposite one another, their common axis coinciding with the y axis. The titanium electrodes (diameter = 0.397 cm) were mounted through the wall of the pipe, and the surfaces in contact with the electrode were polished to conform to the inner surface of the pipe. Thermally collapsible polypropylene tubing was used to mask the cylindrical surfaces of the electrodes. An epoxy cement (Araldite) was used to seal the covered electrodes into slightly oversized holes in the wall. A pair of identical platinum electrodes (diameter = 0.159 cm), similarly mounted but displaced 1.27 cm along the z axis, completed the electrochemical cell.

The electrolyte (1*N* H_2SO_4) was circulated through the reservoir, pump, control valves, electrochemical cell, and back to the reservoir. The flow velocity through the cell could be varied over the range, 0-650 cm/sec. Neither the magnetic-drive centrifugal pump (March Manufacturing Company, Model TE-7R-MD), nor the polypropylene valves contained metallic parts in contact with the electrolyte. In the entire closed loop, the only metallic surfaces in contact with the electrolyte were the cell electrodes. The reservoir was made of Pyrex glass and contained 50 liters of solution. The remainder of the loop contained an additional 3 liters of solution. The temperature of the circulating electrolyte was maintained at 30.0° ± 0.1°C. In order to prevent the temperature from rising above 30°C, refrigerated water (7°C and H_2 saturated) was circulated through Teflon coils within the reservoir. Precise temperature control was then obtained with a quartz immersion heater and mercury thermoregulator located within the reservoir. A continuous stream of H_2 was maintained through the electrolyte in the reservoir. The hydrogen source was a Matheson generator which produces ultrapure gas via diffusion of electrolytically generated hydrogen through a palladium membrane.

The titanium electrodes employed in this study were made from zone-refined, polycrystalline titanium (Materials Research Corporation). The electrolyte was prepared from reagent grade H_2SO_4 and triply distilled water.

The electromagnet (Varian Associates, Twelve-Inch Electromagnet System, Model V-4012-3B with regulated power supply, Model V-2100-B) was equipped with tapered pole pieces (13.2 cm diameter at the air gap), and had a gap width of 3.2 cm. The magnetic flux density between the pole faces was variable over the range 0-2.1 Tesla (0-21 kG), and homogeneous to within 1%. Magnetic flux densities were measured with a Hall-effect gaussmeter (F. W. Bell, Incorporated, Model 610 Gaussmeter, Model STG1-0404 transverse Hall probe).

Electrochemical measurements were made with a Wenking potentiostat (Model 61 RH) used in conjunction with a Wenking electronic potentiometer (Model PPT-67) and a Hewlett-Packard/Moseley recorder (Model 7100B, Model 17501A plug-ins). A Tektronix oscilloscope (Type 533, Type D plug-in) equipped with a Polaroid camera was used for recording fast (microsecond region) potentiostatic current/time transients. The platinum electrodes (Fig. 1) served as reference (Pt/H_2) and counter electrodes.

Theory

For the configuration presented in Fig. 1 and described in the preceding section, it may be shown that, as a consequence of the Lorentz forces acting on the charged components of the electrolyte phase, a potential difference ($\Delta\phi_{MAG}$) is induced in the electrolyte phase between the two titanium (M_1 and M_2) electrodes (or between the two platinum electrodes). The magnetically induced potential difference is described by Eq. [5]

$$\Delta\phi_{MAG} = 2Ba v_m \qquad [5]$$

where a is the inner radius of the pipe, v_m is the average flow velocity [$v_m = (1/\pi a^2) \int_0^a 2\pi r v dr$], and B is the applied magnetic flux density. In the derivation of Eq. [5] (see discussion section), it will be

shown that the equation is valid for axisymmetric flow (laminar or turbulent) whether the pipe is nonconducting (Pyrex glass) or conducting (metallic). From the practical viewpoint, of course, it is the conducting-wall case which is of greatest interest. For the present, one may accept the validity of Eq. [5], and examine the electrochemical consequences of the induced potential difference.

Three potential-distance profiles for the cell shown in Fig. 1 are presented in Fig. 2. The subscripts, M and S, refer to the metal and electrolyte phases, respectively, and the subscripts, 1 and 2, designate the electrodes M_1 and M_2 located as shown in Fig. 1 or, in the case of the electrolyte phase, points just inside the electrolyte phase adjacent to M_1 and M_2. The three profiles (indicated by the subscripts a, b, and c) correspond to the following conditions: (a) Heavy line; $\Delta\phi_{MAG} = 0$ (no magnetic field present); M_1 and M_2 both at open circuit, *i.e.*, the net faradaic current at either electrode is zero. (b) Medium line; $\Delta\phi_{MAG} = 2Bav_m$ (magnetic field applied); M_1 and M_2 at open circuit. (c) Light line; $\Delta\phi_{MAG} = 2Bav_m$; M_1 and M_2 externally short-circuited to form an analogue of a metallic pipe.

The potential difference (V) between electrodes M_1 and M_2 is defined by Eq. [6]

$$V = (\phi_M)_2 - (\phi_M)_1 \quad [6]$$

and may be expressed in the expanded form

$$V = [(\phi_M)_2 - (\phi_S)_2] + [(\phi_S)_2 - (\phi_S)_1] + [(\phi_S)_1 - (\phi_M)_1] \quad [7]$$

or, for the sake of compactness

$$V = (\Delta_M\phi_S)_2 + (\Delta_2\phi_1)_S - (\Delta_M\phi_S)_1 \quad [8]$$

The change (η) in a metal/solution interfacial potential difference which accompanies a finite net faradaic current density ($\bar{i}$) at the interface is defined by Eq. [9]

$$\eta = \Delta_M\phi_S - \Delta_M\phi_S^\circ \quad [9]$$

where $\Delta_M\phi_S^\circ$ is the interfacial potential difference

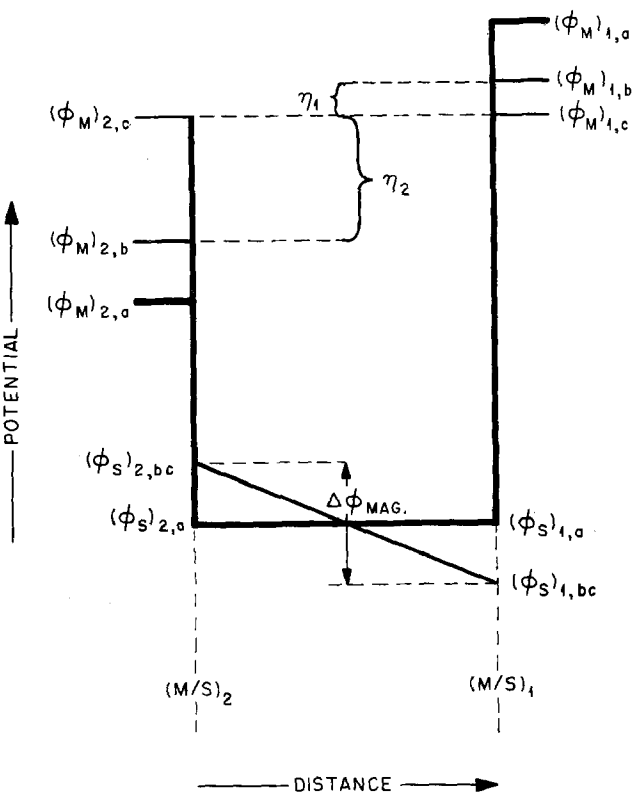


Fig. 2. Potential-distance profiles for the cell shown in Fig. See text for conditions corresponding to cases (a), (b), and (c).

when $\bar{i} = 0$. Conventional potentiostatic or galvanostatic measurements, conducted in the absence of a magnetic field, are used to determine the current densities $\bar{i}_1$ and $\bar{i}_2$, at electrodes M_1 and M_2 as function of η_1 and η_2, respectively, *i.e.*, to evaluate the functions

$$\bar{i}_1 = f(\eta_1) \quad \text{and} \quad \bar{i}_2 = g(\eta_2) \quad [10]$$

If $\Delta_M\phi_S$ from Eq. [9] is substituted into Eq. [8], one obtains Eq. [11]

$$V = \eta_2 - \eta_1 + (\Delta_2\phi_1)_S + V^\circ \quad [11]$$

where $V^\circ = [(\Delta_M\phi_S^\circ)_2 - (\Delta_M\phi_S^\circ)_1]$. For case (a) above, both electrodes are at open circuit and, consequently, $\eta_1 = \eta_2 = 0$ and no *IR* drop exists in the electrolyte phase. Therefore, with $\Delta\phi_{MAG} = 0$, it follows that $(\Delta_2\phi_1)_S = 0$ [heavy horizontal line in the electrolyte phase between the interfaces, $(M/S)_2$ and $(M/S)_1$], and Eq. [11] reduces to $V = V^\circ = (\phi_M)_{2,a} - (\phi_M)_{1,a}$. If the two electrodes are identical, then $V^\circ = 0$. In constructing Fig. 2, this assumption was not invoked, *i.e.*, $(\phi_M)_{2,a}$ and $(\phi_M)_{1,a}$ are shown to be quite different.

For case (b) above, a magnetic field is applied and, therefore, $\Delta\phi_{MAG} = 2Bav_m$. However, open-circuit conditions still apply and, consequently, the interfacial potential differences must remain the same as in case (a) ($\eta_1 = \eta_2 = 0$). This is illustrated in Fig. 2 where, for example, one observes that $(\phi_S)_{2,a}$ increases to $(\phi_S)_{2,b}$ and, in order to maintain a constant interfacial potential difference at $(M/S)_2$, $(\phi_M)_{2,a}$ increases identically to $(\phi_M)_{2,b}$. With $\Delta_2\phi_1 = \Delta\phi_{MAG}$, Eq. [11] reduces to Eq. [12]

$$V = V^\circ + \Delta\phi_{MAG} \quad [12]$$

which, in view of Eq. [5], becomes

$$V = V^\circ + 2Bav_m \quad [13]$$

Equation [13], an equation which enables one to calculate average flow velocities from open-circuit potential measurements and known values of B and a, serves as the basis for electromagnetic flow measurements (6). Moreover, according to Eq. [12], one may determine $\Delta\phi_{MAG}$ directly from potential measurements for those cases where insufficient data are available to calculate $\Delta\phi_{MAG}$ via Eq. [5], or where $\Delta\phi_{MAG}$ deviates from the value indicated by Eq. [5]. Experimental verification of Eq. [13] for the system under study is presented in the results section.

For case (c), with the magnetic field applied, electrodes M_1 and M_2 are externally short-circuited and, therefore, assuming the *IR*-drop in the highly conductive metallic phases is negligible, $(\phi_M)_{2,c}$ and $(\phi_M)_{1,c}$ must be equal. The common potential must lie somewhere between $(\phi_M)_{2,b}$ and $(\phi_M)_{1,b}$ and, consequently, it is clear from Fig. 2 that, for the system as shown, $(\phi_M)_2$ must increase from $(\phi_M)_{2,b}$ to $(\phi_M)_{2,c}$ while $(\phi_M)_1$ must decrease from $(\phi_M)_{1,b}$ to $(\phi_M)_{1,c}$, *i.e.*, η_2 becomes positive and η_1 negative. These changes in interfacial potential differences require finite faradaic currents to flow at both electrodes (Eq. [10]), *i.e.*, one electrode (M_2 for the system as illustrated in Fig. 2) must become anodically polarized (η_2 positive) while the other electrode becomes cathodically polarized (η_1 negative). Suppose, however, that M_1 and M_2 were identical electrodes, *i.e.*, $(\phi_M)_{1,a} = (\phi_M)_{2,a}$. Then, for the same $\Delta\phi_{MAG}$ shown in Fig. 2, $(\phi_M)_{2,b}$ would be greater than $(\phi_M)_{1,b}$ and, upon short-circuiting the electrodes, $(\phi_M)_2$ would necessarily decrease to the common potential while $(\phi_M)_1$ would increase to the same potential, *i.e.*, M_2 would become cathodically polarized (η_2 negative) and M_1 anodically polarized (η_1 positive). In general, if the open-circuit value of V is positive, then upon short-circuiting M_1 and M_2, electrons in the external circuit flow from M_1 to M_2, *i.e.*, M_1 becomes

the anode (net oxidation) and M_2 the cathode (net reduction). It should be noted that a reversal in the sign of the vector cross product, $\mathbf{v} \times \mathbf{B}$, resulting from a change in either the direction of the magnetic field or the fluid flow would be accompanied by a change in the sign of $\Delta\phi_{MAG}$, *i.e.*, in Fig. 2, $(\phi_S)_2 - (\phi_S)_1$ would be negative rather than positive.

The preceding discussion of the potential-distance profiles shown in Fig. 2 provides a qualitative understanding of what occurs when electrodes M_1 and M_2 are externally short-circuited in the presence of a magnetic field. A quantitative analysis of the problem follows. When M_1 and M_2 are short-circuited, the net faradaic currents at the two electrodes must be equal in magnitude and opposite in sign, *i.e.*

$$A_1\bar{i}_1 = -A_2\bar{i}_2 \qquad [14]$$

where A_1 and A_2 are the surface areas of the electrodes. According to Eq. [11], with $V = 0$ (Eq. [6], short-circuited condition) and $V^\circ = 0$ (electrodes assumed to be identical)

$$\eta_2 - \eta_1 = -\Delta\phi_{MAG} \qquad [15]$$

In writing Eq. [15], $(\Delta_2\phi_1)_S$ has been equated to $\Delta\phi_{MAG}$.[1] Equations [10], [14], and [15] are sufficient for the quantitative evaluation of the magnetic field effect on the electrochemical system. In order to illustrate the procedure, suppose the oxidation and reduction reactions occurring at the electrodes, for example, the anodic oxidation of the metal to form metallic ions in solution and the cathodic reduction of protons to form H_2, are both under activation control (as in the case of the Ti/H_2SO_4 system), and, furthermore, let it be assumed that the partial current densities corresponding to the anodic ($\bar{i}_a$) and cathodic ($\bar{i}_c$) reactions are given by Eq. [16] and [17], respectively

$$\bar{i}_a = k_a \exp(\beta_a \Delta_M\phi_S) \qquad [16]$$

and

$$\bar{i}_c = k_c \exp(-\beta_c \Delta_M\phi_S) \qquad [17]$$

where k represents a rate constant, and β represents a Tafel constant, *i.e.*, $\beta_a = (\partial \ln \bar{i}_a/\partial\Delta_M\phi_S)$. The net faradaic current density ($\bar{i}$) at the electrode is given by Eq. [18]

$$\bar{i} = \bar{i}_a - \bar{i}_c \qquad [18]$$

which, in view of Eq. [9], [16], and [17], may be rewritten in the form

$$\bar{i} = \bar{i}^\circ[\exp(\beta_a\eta) - \exp(-\beta_c\eta)] \qquad [19]$$

where $\bar{i}^\circ = \bar{i}_a^\circ = \bar{i}_c^\circ$ for $\Delta_M\phi_S = \Delta_M\phi_S^\circ$. If values of $\bar{i}_1$ and $\bar{i}_2$ from Eq. [19] are inserted into Eq. [14], a second relationship (in addition to Eq. [15]) is established between η_1 and η_2

$$A_1\bar{i}_1^\circ[\exp(\beta_{a1}\eta_1) - \exp(-\beta_{c1}\eta_1)] = -A_2\bar{i}_2^\circ[\exp(\beta_{a2}\eta_2) - \exp(-\beta_{c2}\eta_2)] \qquad [20]$$

Since $\Delta\phi_{MAG}$ is known (Eq. [5] or [12]), Eq. [15] and [20] enable one to calculate η_1 and η_2. Having determined η_1 and η_2, one may evaluate $\bar{i}_1$ and $\bar{i}_2$ by means of Eq. [19]. For illustrative purposes, suppose the two electrodes are identical, *i.e.*, $\beta_{a1} = \beta_{a2}$, $\beta_{c1} = \beta_{c2}$, and $\bar{i}_1^\circ = \bar{i}_2^\circ$. For the "small polarization" case *i.e.*, $\exp(\pm\beta\eta) \approx 1 \pm \beta\eta$, and assuming $A_1 = A_2$, Eq. [15] and [20] lead to the particularly simple result, $\eta_1 = -\eta_2 = \Delta\phi_{MAG}/2$. In actual practice, the various simplifying assumptions made above are unnecessary. In particular, a quantitative analysis requires only that the i/η polarization curves in the absence of a magnetic field be experimentally established, not that the explicit mathematical relationship between $\bar{i}$ and η be determined. The polarization curves, together with $\Delta\phi_{MAG}$ and Eq. [14] and [15], suffice to quantitatively evaluate the effect of the applied magnetic field on the electrochemical system.

In order to determine the electrochemical polarization behavior of a particular metal/electrolyte system, one employs a conventional three-electrode cell (test, reference, and counter electrodes), and measures the faradaic current at the test electrode as a function of the potential (E) of the test electrode relative to an arbitrary reference electrode (Pt/H_2, SCE, etc.). Any magnetically induced potential difference in the electrolyte phase between the test and reference electrodes ($\Delta\phi_{MAG}$) is included in E, *i.e.*

$$E = \eta + \Delta\phi_{MAG} + E^\circ \qquad [21]$$

where E°, the open-circuit potential of the test electrode when $\Delta\phi_{MAG} = 0$, depends on the specific reference electrode used, and where the IR drop in the electrolyte phase between the test and reference electrodes attributable to the faradaic current has been corrected for or, as in the present work, is negligible ($<<1$ mV). According to Eq. [21] and [10], the faradaic current density, $\bar{i} = f(\eta)$, is a function not only of E, but also of $\Delta\phi_{MAG}$. One may quantify the effect of a magnetic field on the polarization curve ($\bar{i}$ *vs.* E) by substituting η from Eq. [21] into the appropriate $\bar{i}/\eta$ equation, for example, into Eq. [19]. Again, it is not necessary to determine the explicit mathematical relationship between $\bar{i}$ and E (or $\bar{i}$ and η) in order to quantitatively evaluate the effect of a magnetic field on the polarization data. One may obtain the $\bar{i}/\eta$ polarization curve in the absence of a magnetic field by measuring $\bar{i}$ as a function of E and evaluating η in accordance with Eq. [21], *i.e.*, $\eta = E - E^\circ$. Then, if E is potentiostatically maintained at E° and $\bar{i}$ measured as a function of $\Delta\phi_{MAG}$, the identical $\bar{i}/\eta$ polarization curve must be obtained when η is again evaluated in accordance with Eq. [21], *i.e.*, $\eta = -\Delta\phi_{MAG}$. This conclusion is verified in the results section. Finally, if E_1 and E_2 refer to electrodes M_1 and M_2, respectively, in Fig. 1, then with $\eta_1 = E_1 - E_1^\circ$ and $\eta_2 = E_2 - E_2^\circ$, Eq. [15] may be rewritten in the form

$$E_2 - E_1 = -\Delta\phi_{MAG} \qquad [22]$$

In view of Eq. [22], the polarization curves, $\bar{i}_1 = f(E_1)$ and $\bar{i}_2 = g(E_2)$, measured in the absence of the magnetic field, together with $\Delta\phi_{MAG}$ and Eq. [14], enable one to quantitatively evaluate the magnetic field effect for case (c) described above.

Results

According to Eq. [13], at a constant flow velocity, the open-circuit potential difference between electrodes M_1 and M_2 (or between Pt_1 and Pt_2) in Fig. 1 should be a linear function of the magnetic flux density. A test of Eq. [13], using the two Pt electrodes, is shown in Fig. 3. Since the two electrodes are identical, $V^\circ = 0$, the straight line passes through the origin. The slope of the straight line, $(\partial V/\partial B) = 2av_m$, corresponds to an average flow velocity of 653 cm/sec. The same flow velocity measured with two Ti electrodes in positions M_1 and M_2 was 648 cm/sec, whereas, that obtained using either M_1(Ti) and Pt_2 or M_2(Ti) and Pt_1 was 650 cm/sec. Deviations in the average flow velocity over a period of 6 hr did not exceed ±0.3%.

The effect of a magnetic field on the electrochemical polarization behavior of a metal/flowing-electrolyte

[1] In the derivation of $\Delta\phi_{MAG}$ (Eq. [5]) presented in the discussion section, it will be shown that, for a metallic pipe (conducting-wall case), $(\Delta_2\phi_1)_S = \Delta\phi_{MAG}$. In the results section it will be shown that for the glass cell described above, and for the system under investigation, the IR drop in the electrolyte phase attributable to the faradaic current is entirely negligible.

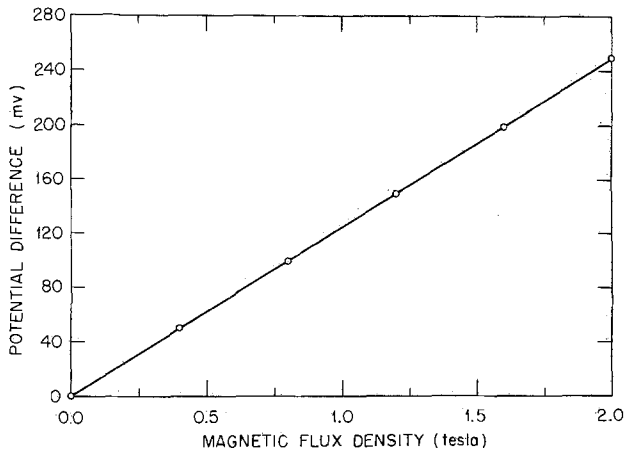


Fig. 3. Test of Eq. [13] Open-circuit potential difference between the two Pt or Ti electrodes (Fig. 1) as a function of the magnetic flux density at a constant flow velocity (v_m = 650 cm/sec).

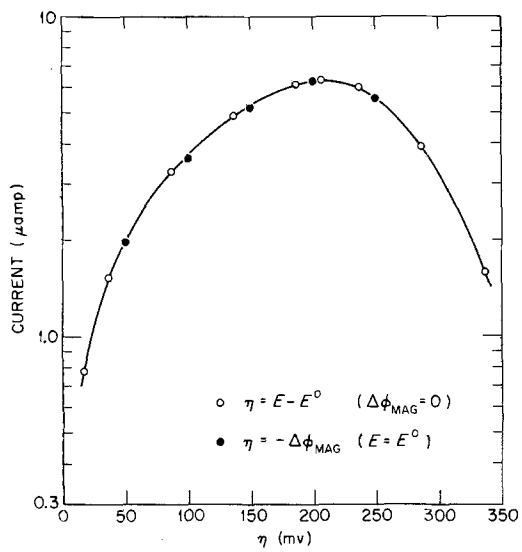


Fig. 4. Effect of magnetic field on the electrochemical polarization behavior of Ti. Test of Eq. [21]. Anodic current measured as a function of E with $\Delta\phi_{MAG} = 0$ (open circles), and as a function of the magnetic flux density at constant E and v_m, i.e., as a function of $\Delta\phi_{MAG}$ (solid circles).

system is illustrated by the results shown in Fig. 4. In the determination of the polarization curves, the titanium and platinum electrodes opposite the titanium test electrode served as the counter and reference electrodes, respectively. The anodic polarization curve for titanium, measured in the absence of a magnetic field (open circles), is independent of flow velocity, and virtually identical with results reported earlier (4, 5). As the potential of titanium is made increasingly positive relative to the open-circuit (corrosion) potential ($E°$ = −735 mV *vs.* SCE), the anodic current corresponding to the oxidation of Ti to Ti(III) ions in solution increases to a maximum at η = 205 mV (E_{MAX} = −530 mV *vs.* SCE), and then decreases as the metal is transformed from the active to the passive state. In this experiment, i was measured as a function of E, and η was calculated in accordance with Eq. 21, *i.e.*, $\eta = E - E°$. The anodic polarization curve was also determined by potentiostatically maintaining the potential of the test electrode at its open-circuit value (*i.e.*, $E = E°$), and measuring i as a function of the magnetic flux density at a constant flow velocity of approximately 650 cm/sec. Again, η was calculated in accordance with Eq. [21], *i.e.*, $\eta = -\Delta\phi_M = -2aBv_m$, and the resultant polarization curve, $i = f(\eta)$, is shown by the solid circles in Fig. 4. In agreement with the theory discussed in connection with Eq. [21], the polarization curves determined by the two methods are coincident. The potentiostat method was used to determine the resistance of the electrolyte phase between the test and reference electrodes (4). The potential of the test electrode was suddenly (<1 μsec) changed from an initial value (E_1) to a second constant value (E_2), and the resulting current-time transient was displayed on an oscilloscope and recorded on film. From an extrapolation of the current-time curve in the microsecond time region (10-100 μsec) to t = 0, the value of $(i_2)_{t=0}$, the current at E_2 for t = 0, was determined, and the electrolyte resistance (R_S) calculated by means of Eq. [23]

$$R_S = (E_2 - E_1)/[(i_2)_{t=0} - i_1] \qquad [23]$$

The solution resistance was only 8.25 ± 0.7% Ω and, consequently, even at the maximum faradaic current (6.3×10^{-6}A in Fig. 4), the IR drop in the electrolyte phase amounted to only 0.05 mV, a negligible ohmic correction. Within indicated limits of reproducibility, the solution resistance was found to be independent of the magnetic flux density (0-2.1 Tesla) over the entire range of flow velocities employed in this study.

The anodic polarization curve for the titanium electrode located in position M_1 (see Fig. 1), and the cathodic polarization curve for the titanium electrode located in position M_2, both determined in the absence of a magnetic field ($\Delta\phi_{MAG}$ = 0), are shown in Fig. 5. When the two electrodes are externally short-circuited, and a magnetic field applied to the flowing electrolyte (see Fig. 1 for the directions of v and B), the titanium electrode in position M_1 becomes anodically polarized while the electrode in position M_2 becomes cathodically polarized, the faradaic current being equal in magnitude but opposite in sign at the two electrodes. According to Eq. [22], the magnitude of the magnetically induced faradaic current may be determined by simply locating on Fig. 5 that current for which $E_2 - E_1 = -\Delta\phi_{MAG} = -2Bav_m$. Thus, the magnetic field effect may be

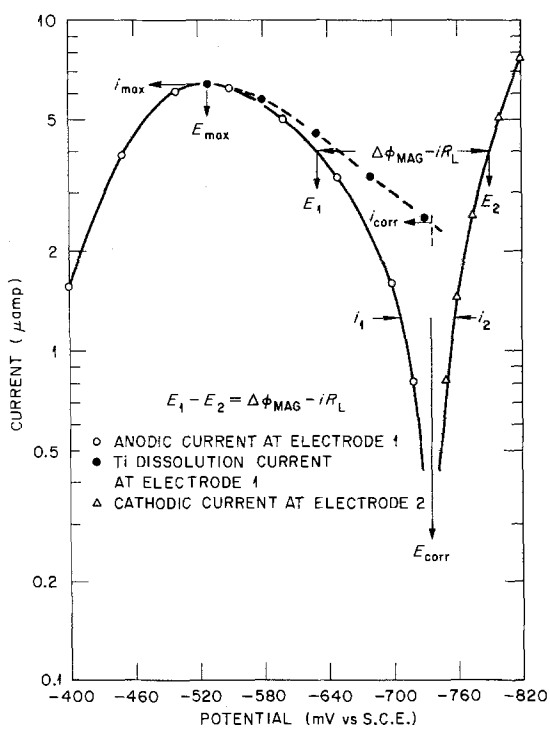


Fig. 5. Anodic and cathodic polarization curves for the two Ti electrodes, M_1 and M_2, respectively, shown in Fig. 1. Curves measured in the absence of a magnetic field ($\Delta\phi_{MAG}$ = 0). See Eq. [24].

quantitatively evaluated by a simple graphical procedure. In order to prove experimentally the validity of the theory, the two electrodes were connected through an external precision resistor (R_L), and the faradaic current determined by measuring the potential difference (IR_L) across the load resistor. Of course, Eq. [22] must be corrected to account for the potential difference appearing across the load resistor, *i.e.*

$$E_1 - E_2 = \Delta\phi_{MAG} - IR_L \qquad [24]$$

a correction indicated in Fig. 5. In Fig. 6, the net faradaic current is shown as a function of R_L at constant $\Delta\phi_{MAG}$, *i.e.*, at constant v_m and B. The open circles show the current determined by application of Eq. [24] to the net polarization curves (solid lines) shown in Fig. 5, while the solid circles show the current determined by measuring the potential difference across R_L. The results are in excellent agreement.

The currents shown by the solid curves in Fig. 5 are net currents. The partial anodic polarization curve corresponding to just the titanium dissolution reaction, *i.e.*, the net anodic polarization curve corrected for the hydrogen evolution reaction, is shown by the dashed line in Fig. 5, and was determined by measuring the concentration of Ti(III) ions in solution as a function of time at constant potential for the various potential values shown by the solid circles (5). Once E_1 and E_2 have been determined by applying Eq. [24] to the net polarization curves in Fig. 5, the actual dissolution rates at E_1 and E_2, along with the rates of the hydrogen evolution reaction, may be evaluated by means of the dashed (partial) curve. The open-circuit corrosion rate (i_{corr}) in the absence of a magnetic field is shown in Fig. 5 for comparative purposes. At E_{MAX}, the contribution of the hydrogen evolution reaction to the net anodic current is negligible (<2%), *i.e.*, the net and partial anodic currents are virtually identical. Then, a comparison of the maximum current (i_{MAX}) to i_{corr} shows that the maximum enhancement of the dissolution rate of titanium in this system is limited to a factor, (i_{MAX}/i_{corr}) = 2.5. Further increases in $\Delta\phi_{MAG}$ are accompanied by a decrease in the net current as a result of the transformation of the anode from the active to the passive state at potentials more positive than E_{MAX}.

Figure 7 shows the results of an experiment in which R_L was maintained constant at a mere 200Ω, and the current was measured as a function of the magnetic flux density at a constant flow rate. Again, the currents determined by direct measurement (solid circles), *i.e.*, by measuring the potential difference across R_L, and those determined by the application of Eq. [24] to the polarization curves shown in Fig. 5, are in excellent agreement.

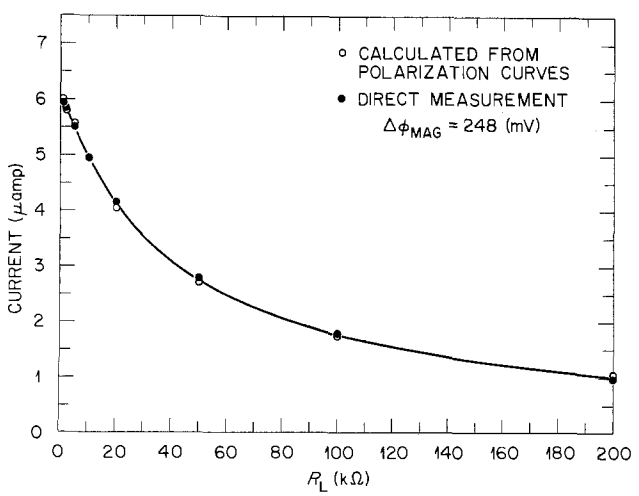


Fig. 6. Faradaic current at the Ti electrodes, M_1 and M_2 in Fig. 1, when connected through an external resistance (R_L), as a function of R_L at constant $\Delta\phi_{MAG}$. Application of Eq. [24], using the curves shown in Fig. 5.

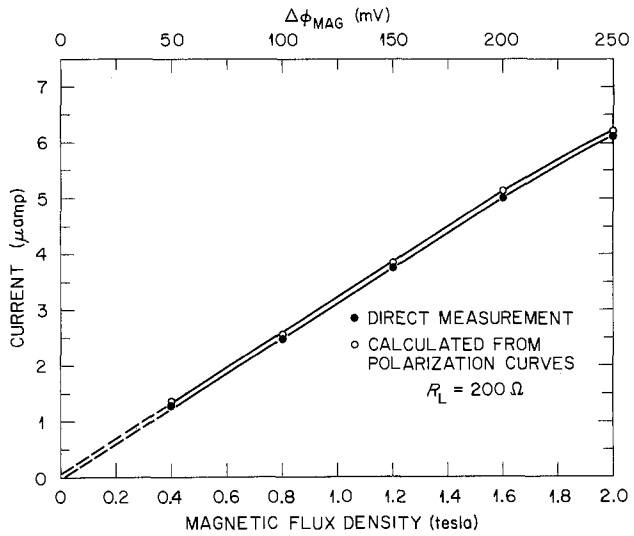


Fig. 7. Faradaic current at the Ti electrodes, M_1 and M_2 in Fig. 1, when connected through an external resistance of 200Ω, as a function of the magnetic flux density at constant v_m, *i.e.*, as a function of $\Delta\phi_{MAG}$. Test of Eq. [24].

Discussion

The experimental results presented in the preceding section establish the validity of the theoretical analysis of the effect of a magnetic field on electrochemical reactions occurring at a metal/flowing-electrolyte interface. However, the experiments necessarily involved the use of discrete electrodes set in the nonconducting wall of a Pyrex glass pipe (see Fig. 1), *i.e.*, in order to establish that the results of the short-circuit (metallic pipe analogue) experiments shown in Fig. 6 and 7 were in agreement with theoretical expectations, it was necessary to determine the anodic and cathodic polarization curves shown in Fig. 5, and the electrochemical polarization measurements, in turn, required the use of discrete electrodes in a nonconducting wall. In the following discussion, it will be shown that the analysis is equally valid for metallic pipes and, in the course of extending the theory to include the conducting-wall case, the origin and limitations of Eq. [5] will be examined. In brief, the conducting-wall case is distinguished by the wall-shorting effect, an effect which is a function of the specific conductivities of the metal and electrolyte phases, the electrochemical polarization resistance, and the inner and outer radii of the pipe. Using appropriate values of the aforementioned parameters, one finds that the wall-shorting effect is negligible for the systems of interest and consequently, the results obtained for the nonconducting-wall case apply quantitatively to metallic pipes.

The form of Ohm's law appropriate to the electrolyte phase in MHD systems is given by Eq. [25]

$$\mathbf{j}_S = \sigma(\mathbf{E} + \mathbf{v} \times \mathbf{B}) \qquad [25]$$

where, at a point in the electrolyte phase, j_S represents the current density, E is the electric field intensity, B is the magnetic flux density, v is the fluid velocity, and σ is the specific conductivity of the electrolyte. Equation [25] may be derived by expressing j_S in terms of the "drift velocities" of the ionic components of the electrolyte, and taking into account the fact that the drift velocities are proportional to the Lorentz electromagnetic forces acting on the ions and are negligibly small (drift velocities under a potential gradient of 1 V/cm, *i.e.*, conven-

tional ionic mobilities, are typically on the order of $\sim 5 \times 10^{-4}$ cm^2 sec^{-1} V^{-1}) compared to the fluid velocities of interest in this work (7). The equation is more frequently derived, however, by noting that in the coordinate system which moves with the fluid (indicated by prime marks), $\mathbf{j}_S' = \sigma\mathbf{E}'$. If the Maxwell-Lorentz transformations to the laboratory frame of reference are applied, then $\mathbf{j}_S'$ and $\mathbf{E}'$ become $\mathbf{j}_S$ and $(\mathbf{E} + \mathbf{v} \times \mathbf{B})$, respectively, and, consequently, one obtains Eq. [25] directly (8). In addition to Ohm's law, the analysis requires the use of the basic Maxwell equations

$$\nabla \times \mathbf{E} = -(\partial\mathbf{B}/\partial t) = 0 \qquad [26a]$$

$$\mathbf{E} = -\nabla\phi \qquad [26b]$$

$$\nabla \times \mathbf{B} = \mu\mathbf{j} + \mu(\partial\mathbf{D}/\partial t) = \mu\mathbf{j} \qquad [27a]$$

$$\nabla \cdot \mathbf{j} = 0 \qquad [27b]$$

where $\mathbf{D}$ is the electric displacement vector, and μ is the magnetic permeability of the medium. For the steady-state case, $(\partial\mathbf{B}/\partial t) = 0$ and $(\partial\mathbf{D}/\partial t) = 0$, Eq. [26b] and [27b] follow directly from Eq. [26a] and [27a], respectively, recalling in the latter case that div.(curl) $= 0$. For the electrolyte phase, Eq. [25], [26b], and [27b] may be combined to obtain Eq. [28]

$$\nabla^2\phi_S = \nabla \cdot (\mathbf{v} \times \mathbf{B}) \qquad [28]$$

For the geometry illustrated in Fig. 1, and transforming to the polar coordinate system shown therein, Eq. [28] may be written in the form

$$(\partial^2\phi_S/\partial r^2) + (1/r)(\partial\phi_S/\partial r) + (1/r^2)(\partial^2\phi_S/\partial\theta^2) = B(dv/dr)\sin\theta \qquad [29]$$

In writing Eq. [28] in this form, use was made of the vector identity, $\nabla \cdot (\mathbf{v} \times \mathbf{B}) = \mathbf{B} \cdot (\nabla \times \mathbf{v}) - \mathbf{v} \cdot (\nabla \times \mathbf{B})$, and the fact that $\mathbf{v} \cdot (\nabla \times \mathbf{B}) = \mathbf{v} \cdot (\mu\mathbf{j}_S) = 0$. The solution of Eq. [29] is given by Eq. [30]

$$\phi_S = \psi \sin\theta + \phi_S^0 \qquad [30]$$

where ψ is a function of r only (9). If one substitutes ϕ_S and its partial derivatives with respect to r and θ into Eq. [29], and integrates from $r = 0$ to $r = a$ (see Fig. 1), then, noting that $v = 0$ at $r = a$, one obtains the result

$$a^2\psi'_{r=a} - a\psi_{r=a} = -Ba^2v_m \qquad [31]$$

where $\psi'_{r=a}$ refers to $(d\psi/dr)$ evaluated at $r = a$, and where v_m, the average flow velocity of the fluid, was defined in the theory section. According to Eq. [25], since $v = 0$ at $r = a$, the component of $\mathbf{j}_S$ normal to the wall at $r = a$, *i.e.*, $(\mathbf{j}_S \cdot \mathbf{r}_u)_{r=a}$ is given by the expression

$$(\mathbf{j}_S \cdot \mathbf{r}_u)_{r=a} = -\sigma(\partial\phi_S/\partial r)_{r=a} = -\sigma\psi'_{r=a}\sin\theta \qquad [32]$$

where $\mathbf{r}_u$ is a unit vector normal to the wall. For a glass pipe, the nonconducting wall case $(\mathbf{j}_S \cdot \mathbf{r}_u)_{r=a} = 0$, and, therefore, $\psi'_{r=a} = 0$, *i.e.*, Eq. [31] reduces to Eq. [33]

$$\psi_{r=a} = Bav_m \qquad [33]$$

Substitution of $\psi_{r=a}$ from Eq. [33] into Eq. [30] gives the result

$$(\phi_S)_{r=a} = Bav_m \sin\theta + \phi_S^\circ \qquad [34]$$

As shown in Fig. 1, $\sin\theta$ is equal to 1 and -1 at M_2 and M_1, respectively, and therefore, according to Eq. [34], $(\phi_S)_2 - (\phi_S)_1$, *i.e.*, $\Delta\phi_{MAG}$, is given by Eq. [5]

$$\Delta\phi_{MAG} = 2Bav_m \qquad [5]$$

In order to extend the analysis to metallic pipes (conducting-wall case), it is necessary to consider a few additional equations relating to the metal phase and boundary conditions. The appropriate form of Ohm's law for the metal phase (wall at rest) is

$$\mathbf{j}_M = -\kappa\nabla\phi_M \qquad [35]$$

where κ is the specific conductivity of the metal. With $\nabla \cdot \mathbf{j}_M = 0$ (Eq. [27b]), the potential in the metallic phase is described by the Laplace equation

$$\nabla^2\phi_m = 0 \qquad [36]$$

The component of $\mathbf{j}_M$ normal to the wall at $r = b$, $(\mathbf{j}_M \cdot \mathbf{r}_u)_{r=b}$, is equal to zero, *i.e.*

$$(\mathbf{j}_M \cdot \mathbf{r}_u)_{r=b} = -\kappa(\partial\phi_M/\partial r)_{r=b} = 0 \qquad [37]$$

With this boundary condition, the solution of Eq. [36] may be written in the form

$$\phi_M = C_1[(r/b^2) + (1/r)]\sin\theta + \phi_M^\circ \qquad [38]$$

where C_1 is a constant determined by the boundary conditions at $r = a$ (9). At $r = a$, the boundary condition is $(\mathbf{j}_S \cdot \mathbf{r}_u) = (\mathbf{j}_M \cdot \mathbf{r}_u) = -i$, *i.e.*

$$\sigma(\partial\phi_S/\partial r)_{r=a} = \kappa(\partial\phi_M/\partial r)_{r=a} = \bar{i} \qquad [39]$$

For the purpose of this analysis, the linearized form of $\bar{i}$ given by Eq. [19] is used, *i.e.*, with $\exp(\pm\beta\eta) = (1 \pm \beta\eta)$, $\bar{i}$ becomes

$$\bar{i} = (1/\tau)(\Delta_M\phi_S - \Delta_M\phi_S^\circ) \qquad [40]$$

where τ, the electrochemical polarization resistance, is equal to $[i^\circ(\beta_a + \beta_c)]^{-1}$. Using Eq. [30], [31], and [38], together with the boundary conditions represented by Eq. [39] and [40], one may solve for ϕ_S at $r = a$

$$\phi_S = [(Bav_m \sin\theta)/(1 + Z)] + \phi_S^\circ \qquad [41]$$

where the dimensionless Z is given by Eq. [42]

$$Z = [(\kappa/\sigma)(b^2 - a^2)]/[(\tau\kappa/a)(b^2 - a^2) + (a^2 + b^2)] \qquad [42]$$

According to Eq. [41], the potential difference in the electrolyte phase between the points (a, θ) and $(a, -\theta)$ is given by Eq. [43]

$$(\Delta_{\theta\phi-\theta})_S = [2Bav_m/(1 + Z)]\sin\theta \qquad [43]$$

For the particular case of $\Delta\phi_{MAG}$, defined as $(\phi_S)_2 - (\phi_S)_1$, $\sin\theta = 1$ and, consequently, Eq. [43] reduces to the result

$$\Delta\phi_{MAG} = 2Bav_m/(1 + Z) \qquad [44]$$

where Eq. [44] is to be compared with Eq. [5]. The wall-shorting effect represented by the coefficient $1/(1 + Z)$ in Eq. [43] is negligible, *i.e.*, $(1 + Z) \approx 1$, for systems of interest. This may be seen by evaluating Z in accordance with Eq. [42], using the following data: $\kappa = 1.75 \times 10^6\ \Omega^{-1}$ m^{-1}, $\sigma = 22.5\ \Omega^{-1}$ m^{-1}, $\tau = 0.3\ \Omega$ m^2, $a = 9.53 \times 10^{-3}$m, and $b = 1.27 \times 10^{-2}$m. The calculated value of Z is 1.41×10^{-3} and, consequently, Eq. [43] reduces to Eq. [5]. If $\tau = \infty$, as in the case of a glass pipe, $Z = 0$ and, again, one obtains Eq. [5].

The interfacial potential difference $(\Delta_M\phi_S)$ corresponding to any value of θ is given by Eq. [45]

$$\Delta_M\phi_S = \Delta_M\phi_S^\circ - [Z\tau\sigma Bv_m/(1 + Z)]\sin\theta \qquad [45]$$

Substitution of $\Delta_M\phi_S$ from Eq. [45] into Eq. [40] gives the net faradaic current density at a point on the inner circumference of the pipe for any value of θ, *i.e.*

$$\bar{i} = -[Z\sigma Bv_m/(1 + Z)]\sin\theta \qquad [46]$$

Equation [46] shows that $\bar{i}$ varies from 0 at $\theta = 0$

to the maximum cathodic ($\theta = 90°$) and anodic ($\theta = 270°$) values at positions corresponding to M_2 and M_1, respectively, in Fig. 1. According to Eq. [9] and [40], $\bar{i}$ may be written in the form $\bar{i} = (1/\tau)\eta$, and, as was shown in the theory section, for the "small polarization" case involving short-circuited identical electrodes in positions M_1 and M_2, $\eta_1 = -\eta_2 = \Delta\phi_{MAG}/2$, *i.e.*

$$\bar{i}_1 = -\bar{i}_2 = (1/2\tau)\Delta\phi_{MAG} \qquad [47]$$

With $(1 + Z) \approx 1$, Z is virtually equal to $(a/\sigma\tau)$ and, therefore, for positions M_1 and M_2, Eq. [46] also reduces to Eq. [47]. If the values, $\Delta\phi_{MAG} = 250$ mV and $\tau = 0.3\ \Omega\ m^2$, are substituted into Eq. [47], the calculated value of $\bar{i}$ is 5.2×10^{-6} A/cm^2. The observed value is 6.2×10^{-6} A/cm^2 (see Fig. 7). The difference between the observed and calculated values of $\bar{i}$ is to be attributed to the deviation from the linearized relationship between $\bar{i}$ and $\Delta_M\phi_S$ (Eq. [40]) at high values of $|\eta|$. The assumption of a linear relationship between $\bar{i}$ and $\Delta_M\phi_S$ facilitated the analysis while not materially affecting its purpose, namely, to extend the theory to include metallic pipes and to demonstrate that the wall-shorting effect is negligible. It should be apparent that the magnetic field effect on electrochemical systems described by Eq. [19], with large values of β_a and β_c, can be very much larger than that observed in the present study of the Ti/H_2SO_4 system.

Conclusion

The results of this investigation clearly demonstrate the adverse effect of an applied magnetic field on the corrosion behavior of metals in contact with a flowing electrolyte. In the case of the Ti/H_2SO_4 system, the maximum increase in the active-state dissolution rate of the metal was limited to a factor of 2.5, a limit resulting from the passivation characteristics of titanium in 1*N* H_2SO_4. Depending on the specific metal/electrolyte system, one might expect dissolution enhancement factors many times greater than that observed in this work, all other factors remaining constant (geometry, flow velocity, magnetic flux density, etc.). Moreover, it should be emphasized that in addition to the adverse effect of a magnetic field on the "uniform" corrosion behavior of metals, the imposition of a magnetic field can also lead to enhanced susceptibility to stress corrosion cracking, localized (pitting or crevice) corrosion, oxidation and reduction of solution species, etc., and, in the limit, to electrochemical decomposition of the electrolyte. The aforementioned phenomena, to name a few, are all potential-dependent electrochemical processes and, as such, are subject to the magnetic field effect. In order to illustrate the unusual corrosion situations that could arise as a result of the magnetic field effect, consider a metal/flowing-electrolyte system which, in the absence of an applied magnetic field, exhibited an open-circuit corrosion potential corresponding to the near passive potential region, *i.e.*, to a potential somewhat positive to the active-passive transition potential region. Upon imposition of the magnetic field, one-half of the pipe would become anodically polarized as its interfacial potential difference moved in the positive (noble) direction, while the other half would become cathodically polarized. The anodically polarized section might be polarized to the transpassive potential region, and the cathodically polarized section to the active-passive transition potential region, both potential regions of enhanced susceptibility to stress corrosion cracking. Further polarization could result in activation of the once passive cathodically polarized section. The anodically polarized section, depending on the specific metal/electrolyte system, could encounter a pitting potential or a potential region of enhanced crevice corrosion. In considering the various possibilities, it should be noted that $\Delta\phi_{MAG}$ is directly proportional to the magnetic flux density and, consequently, in contrast to the relatively small value observed in the work ($\Delta\phi_{MAG} = 0.25$V at $B = 2.0$ Tesla), $\Delta\phi_{MAG}$ would attain a value of 1.5V at $B = 12$ Tesla, all other factors remaining constant. The magnetic field effect described in this paper poses potentially serious corrosion and other electrochemical problems for metal/flowing-electrolyte systems, and must be considered carefully when evaluating such systems for applications involving magnetic fields.

Acknowledgment

The author is especially indebted to Mr. A. A. Palko for his collaboration in assembling the forced-convection loop and the refrigeration system used in this program. This research was sponsored by the Materials Sciences Office, Division of Physical Research, Energy Research and Development Administration under contract with the Union Carbide Corporation.

Manuscript submitted Nov. 29, 1976; revised manuscript received March 1, 1977. This Paper 99 presented at the Las Vegas, Nevada, Meeting of the Society, Oct. 17-22, 1976.

Any discussion of this paper will appear in a Discussion Section to be published in the June 1978 JOURNAL. All discussions for the June 1978 Discussion Section should be submitted by Feb. 1, 1978.

Publication costs of this article were assisted by the Oak Ridge National Laboratory.

REFERENCES

1. K. J. Vetter, "Electrochemical Kinetics," p. 159 Academic Press, New York (1967).
2. E. Z. Gak, É. Kh. Rokhinson, and N. F. Bondarenko, *Sov. Electrochem. (Engl. Transl.)*, **11**, 489 (1975); *ibid.*, **11**, 495 (1975); E. Z. Gak, *ibid.*, **3**, 75 (1967); *ibid.*, **3**, 229 (1967).
3. T. Z. Fahidy, *Electrochim. Acta*, **18**, 607 (1973); S. Mohanta and T. Z. Fahidy, *ibid.*, **19**, 771 (1974); *ibid.*, **19**, 835 (1974).
4. E. J. Kelly, Proceedings of Fifth International Congress on Metallic Corrosion, Tokyo, 1972, p. 137, NACE, Houston (1974).
5. E. J. Kelly, *This Journal*, **123**, 162 (1976).
6. J. A. Shercliff, "Theory of Electromagnetic Flow Measurement," Cambridge University Press (1962).
7. J. O'M. Bockris and A. K. N. Reddy, "Modern Electrochemistry," Vol. 1, p. 369, Plenum Press, New York (1970).
8. W. F. Hughes and F. J. Young, "Electromagnetodynamics of Fluids," p. 33, John Wiley & Sons, Inc., New York (1966).
9. P. Franklin, "Methods of Advanced Calculus," Chap. 11, McGraw-Hill Book Co., Inc., New York (1944).

Polymer Film Coatings on Metal Electrodes Through Electroinitiated Polymerization and Their Evaluation

F. S. Teng and R. Mahalingam

Department of Chemical Engineering, Washington State University, Pullman, Washington 99164

and R. V. Subramanian and R. A. V. Raff

Department of Materials Science and Engineering, Washington State University, Pullman, Washington 99164

ABSTRACT

Adherent films of polymers on different metal surfaces are formed by the electroinitiated polymerization of acrylonitrile alone and of mixtures of acrylonitrile and acrylic acid in 0.05*N* H_2SO_4 aqueous solution. Five different metals—aluminum, nickel, copper, stainless steel and steel—are used as the cathodes for purposes of the coatings while platinum plate is the anode in each case. The electrolysis is carried out under a constant voltage. After the electrolytic runs, the coatings are scraped off the metals for infrared analysis to establish the functional groups. Furthermore, the scanning electron microscope (SEM) is used to examine the structure of the film surfaces. The effects of variable monomer concentrations and polymerization voltages on thickness and appearance of the film are also investigated. Corrosion tests are performed to compare the corrosion resistance of coated and uncoated metals in various corrosive solutions, through both the weight-loss and the electrochemical methods. It is observed that good and uniform coatings always reduce the corrosion rate of the metals (*e.g.*, coated nickel and copper). However, porous coatings are seen to accelerate the corrosion rate of the support metals (coated aluminum, for example). Also, it is observed that the monomer concentration and voltage for the electroinitiated polymerization process have some influence on the corrosion resistance of coated metals. All of these phenomena are explained through the surface structure and thickness of the coatings,

Electrocoating is a relatively new technique that was industrially initiated during the 1960's (1). In electrocoating, the object is dipped into a tank of paint and a current is passed through the system whereby the paint material is attracted to the article and is then plated out on its surface. The essential point to be noted in electrocoating is that an already formed polymer (paint) is deposited on a metal surface by employing electrophoretic processes.

Electroinitiated polymerization of monomers onto metal surface is quite different from electrodeposition. Polymerization initiated by electrolysis has been reported by some investigators (2-5). However, all these early works have been carried out with the objective of achieving polymerization within the cell solution. In the research reported here, polymerization is initiated by electrolysis as reported above but with the modified objective of depositing these polymers onto different metals to form protective films and thus resist corrosion, enabling practical use of these metals or objects. The formation of adherent films of polymer on metal electrodes by electroinitiated polymerization of monomers has been reported in earlier work from our laboratories (6, 7).

Corrosion is the destructive attack of a metal by chemical or electrochemical reaction with its environment. Reduction or practical elimination of corrosion is possible by anything that interferes with these reactions. Protective coatings such as paint can bring about this. However, the manual or mechanical application of paint or protective coating has its inherent disadvantages and gives rise to additional problems. In electroinitiated polymerization, since it is directly formed from the monomer, the film will be more economical and more uniform than other organic coatings which are obtained through electrodepositing polymers on metal surface.

Key words: comonomers, corrosion, micrographs, constant voltage, static cell.

Experimental

Materials.—Acrylonitrile (AN), a pure Aldrich product, is washed with 5% NaOH and then with 5% H_3PO_4 and dried under anhydrous Na_2SO_4 or $CaSO_4$ for several days, then stored in a refrigerator for use. Acrylic acid (AA) and N,N-dimethyl formamide (DMF) (pure Aldrich products), $NaNO_3$ (Baker) and concentrated H_2SO_4 (Mallinckrodt analytical grade) are used without further treatment.

Preparation of metal surface for coating.—An adequate preparation of the metal surface is very important for adhesive bonding. As a first step all ink markings and other foreign matter are removed from the metals by washing with soap, water and acetone, and then degreased with trichloroethylene. Different cleaning steps for different metals are then followed, as recommended in the literature (8).

Electrolytic cell and polymerization runs.—In order to obtain a coating on both sides of the metal cathode, the electrolytic cell used is a three-compartment cell separated by two sintered glass disks (7, 17, 23). The central compartment of about 500 ml capacity is used as the cathode region while the two outer compartments of about 250 ml capacity each, one on each side of the cathode, are used as the anode regions with two platinum plates as the anodes. The dimensions of anode and cathode plates are about 4 × ½ × 0.03 in. The use of the monomer is restricted to the cathode area since the coating is desired only on the cathode metal surface. The volumes of cathodic and anodic solutions are 400 ml in each compartment for all runs.

The electrical potential is applied by means of a variable direct current power supply unit (Hewlett-Packard, 6348 B). The current and voltage drop

through the cell are recorded as a function of time on a two-channel chart recorder (Hewlett-Packard, 7128 A) in series with the circuit and connected with a 10Ω shunt resistor. All electrolysis runs are carried out at room temperature. Nitrogen gas is bubbled through the solution 15 min prior to and during the process. At the end of a run, the coated metal is dipped into distilled water several times, then dried in a vacuum oven at about 40°C for 4 hr.

Infrared analysis of coatings.—The polymer coating is scraped off the metal and mixed with KBr to form a thin and transparent pellet under pressure. The instrument used is a Perkin Elmer Infrared Spectrophotometer Model 700 which automatically measures and records the transmittance of the above pellet as a function of frequency in the range of 4000-600 cm^{-1}.

Elemental analysis of coatings.—The elemental analysis of the polymer coating is carried out with a Perkin-Elmer Model 240 Elemental Analyzer.

Observation of coating surface under scanning electron microscope.—The SEM instrument used is the ETEC Auto Scan model. A small piece of coated metal is cut and a sputter coating of gold is deposited on the above specimen, in vacuum, prior to examination under the SEM.

Weight loss method for determining corrosion rates.—The test method described here is according to the steps suggested by the "Technical Practices Committees, National Association of Corrosion Engineers, NACE Standard TM-01-69" (18). The use of corrosion rates implies that all weight loss is due to general corrosion and not due to localized corrosion, such as pitting or intergranular corrosion. Assuming that localized or internal corrosion is not present, the corrosion rate expressed as mils penetration per year (mpy) is calculated by the equation

$$\text{Corrosion rate (mpy)} = \frac{\text{wt loss} \times 534}{(\text{area})\ (\text{time})\ (\text{metal density})}$$

where weight loss is in milligrams, area is square inches of metal surface immersed, and time is hours exposed.

Electrochemical method for determining corrosion rates.—Corrosion rate can be determined electrochemically by a number of methods (19) that result in a corrosion current density which is converted to corrosion rate through Faraday's law

$$\text{Corrosion rate (mpy)} = 0.1288\ I \times \frac{\text{equiv. wt}}{\rho}$$

where I = current density, $\mu A/cm^2$
ρ = specimen density, g/cm^3
equiv. wt = specimen equivalent weight, g

Corrosion currents are hence measured as a means of representing corrosion rates. The setup used here is according to ASTM designation G5-69 (20).

Results and Discussion

Current density-time relationship.—The deposition of a polymer (or copolymer) film onto a metal surface by electroinitiated polymerization can be followed on current *vs.* time curves. These curves are obtained by recording the current density through the electrolytic cell at any instant, for the duration of the experiment, on a two-channel recorder.

Some typical curves, when nickel and copper are used as cathodes and with AN in DMF solution containing $NaNO_3$ as electrolyte, are shown in Fig. 1a. It is observed that the current starts to drop off rather sharply and rapidly the moment the circuit is connected, indicating that the polymerization commences immediately and the polymer begins to deposit on the metal surface; this deposit increases the

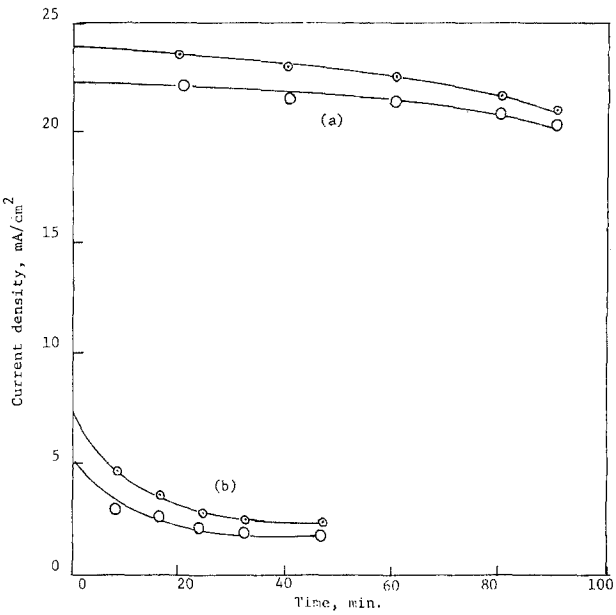


Fig. 1. Typical current density *vs.* electrolysis time curves. (a) Single monomer AN in DMF solution, (b) comonomers AN-AA in aqueous solution, (⊙) nickel electrode, (○) copper electrode.

resistance of the electrode, hence current flowing through the cell decreases gradually. However, in Fig. 1b, in which comonomer AN-AA is polymerized in 0.05*N* H_2SO_4 aqueous solution instead of in DMF solution, the current is almost constant initially, then drops off slowly and smoothly about 20 min later (depending on the metal electrode). This could be explained on the basis that the poly (AN-CO-AA) is swollen in the aqueous system, leading to greater mobility of the charge through the polymer coating. It is also observed that the curve for the thicker coating (Fig. 1a) drops off more sharply than the curve for the thinner coating (Fig. 1b), as is to be expected.

Infrared analysis of coatings.—Infrared spectroscopy is employed to prove the formation of a polymer film on each of the five different metals. For a sample of the poly (AN-CO-AA), there is an O—H band at about 3500-3400 cm^{-1} (frequency) suggesting condensed water vapor in the sample. Also, there are peaks of C—H band at about 2950 cm^{-1}, C≡N band at about 2300 cm^{-1}, C=O band at about 1700 cm^{-1}, CH_2 band at about 1450 cm^{-1}; all these prove the coatings to be the copolymer. Since the coating on aluminum includes the presence of a large amount of metal oxide, the C≡N band in the spectrum of aluminum coating is very weak. The presence of metal oxide is further confirmed through elemental analysis and SEM photographs.

The typical infrared spectrum of polyacrylonitrile film on steel when compared to the spectrum of copolymer film on steel, shows that the only difference between the two is the peak around frequency 1700 cm^{-1} which represents the C=O band; there is no C=O group in the pure PAN.

Elemental analysis of coatings.—The elemental analysis of the copolymer coating scraped off aluminum shows that the total composition of nitrogen, carbon, and hydrogen atoms is only about 11% and the color of the residue after elemental analysis is black, due to the metal oxide also being removed with the coating. However, the presence of this oxide on the metal gives rise to strongly adhering but porous coatings. In the analysis of pure polyacrylonitrile, the experimental values of nitrogen, carbon, and hydrogen composition are 24.9%, 67.1%, 5.8%, while the theoretical values should be 26.4% 67.9%, and 5.6%. The decrease in nitrogen composition may be due to condensation of water vapor and the presence of some metal oxide

Table I. Elemental analysis of poly (AN-CO-AA)[a] and polyacrylonitrile coatings on different metals

Material	Metal	% N	% C	% H	% O[b]
Poly (AN-CO-AA)	Al	2.04	7.17	1.77	—[c]
	Ni	18.47	60.83	5.96	14.74
	S-steel	20.23	59.26	8.10	12.41
PAN alone	S-steel	24.89	67.09	5.83	—

[a] Monomer mixture: 80% AN and 20% AA by volume; 30 ml monomer in 400 ml of aqueous solution, containing 0.05*N* H_2SO_4 electrolyte.
[b] The composition of oxygen is obtained by difference.
[c] Because the copolymer sample scraped off aluminum left black residue after combustion in the elemental analysis, we are unable to make the above assumption [(b)] for oxygen composition.

Table II. Comparison of coatings of polyacrylonitrile on various metal surfaces—DMF solvent

Monomer concentration	Cathode metal	Electrolyte concentration	Current density (mA/cm²) I_o	Current density (mA/cm²) I_f	Electrolysis time (min)	Thickness of coating (mg/in.²)
30 ml AN in 400 ml of DMF solution	Al	1.5g $NaNO_3$ in 400 ml of DMF solution	6.35	5.64	45	39.2
	Ni		7.52	2.41	45	54.8
	Cu		5.70	2.24	45	41.0
	S-steel		9.30	1.70	30	46.7
	Steel		8.83	3.10	30	28.4

Polymerization voltage is maintained constant at 20V for all runs.

in the tested sample. A summary of results is given in Table I.

Examination of coating surfaces under scanning electron microscope.—The photomicrographs of copolymer coatings obtained on five different metal surfaces are shown in Fig. 2a-e. The electrolyte for these is a 30 ml monomer mixture (80% AN and 20% AA) in 400 ml of 0.05*N* sulfuric acid solution; the polymerization voltage is 13V for 90 min. Next, keeping voltage, electrolysis time, electrolyte concentration, and cathode metal the same as before, the monomer mixture is replaced by monomer AN; the appearance of the film structure in this case is shown in Fig. 3a-e. It is observed that the coatings on the nickel and copper are more uniform than the coatings on the other metals. This may be due to the higher hydrogen overvoltage of copper (9) (high hydrogen overvoltage indicating hydrogen is more difficult to evolve along the metal electrode). The coating on the aluminum surface is quite rough, porous, and nonuniform although it is thicker than the other coatings. The coatings on the stainless steel and steel are not so uniform as the coatings on the nickel and copper. Also, there are some globules formed on these coatings.

SEM pictures of copolymer coatings on nickel and copper, under various polymerization voltages, are shown in Fig. 4a-d and Fig. 5a-d, respectively. It is is found that dense and uniform coatings can be obtained if the polymerization voltage is about 11-15V.

SEM pictures of copolymer coatings on nickel and copper, due to varying monomer concentrations, shown in Fig. 6a-e and Fig. 7a-e, indicate that if the monomer concentration is very low, the metal surface is not totally covered by the coating.

Influence of solvent and electrolyte on the coatings obtained through electroinitiated polymerization.—According to Funt (10) and Friedlander (11), polymers are formed on the cathode by electroinitiated polymerization in solution of AN in DMF saturated with sodium nitrate. Based on these, five different cathodes are first investigated: aluminum, nickel, copper, stainless steel, and steel, from the point of view of uniformity of the surface and thickness of the coatings. It is found that the coatings are dark yellow, uneven, nonuniform, poorly adhesive and easily dissolved in the water; however, the coatings are quite thick. A summary of these results is given in Table II. The coating thickness is based on the weight difference of the coated metal before and after polymerization, divided by the coated area and reported as milligrams per square inch. I_o and I_f are the initial and final current densities through the cell during the electrolysis process.

In order to overcome the disadvantages observed in the above coatings, the polymerization of AN and of mixtures of AN and AA in aqueous solution are tried. Although they are thin, the coatings are found to be uniform, adhesive and insoluble in the water. A summary of these results is given in Table III.

Lewis and Forrestal (12) point out that there is a polar force between nitrile C≡N and the metals, but that this force is not strong enough for the polymer to metal adhesion. Gadgieva (13) points out that in water or in humid air an oxide film on the metal surface is more easily wetted by a more polar liquid, such as water, than by a less polar hydrocarbon phase, for example, paint. The hydrogen evolved in the aqueous solution (in DMF solution there was no hydrogen evolved) will also increase the difficulties of coating. Thus, the polymer coating obtained from sulfuric acid solution is very thin, while the polymer coating obtained from DMF solutions, though thick, is more easily wetted and separated by the moisture or water.

Influence of voltage on coatings obtained through electroinitiated polymerization.—Experimental studies (2, 10, 14) show a direct proportionality between current density and polymer yield in electroinitiated polymerization. But in our work, the decrease in polymer film thickness and the increase in film defects such as pores, blisters, etc., above some voltage values require explanation. Table IV and Fig. 4 and 5 (SEM pictures) show the optimum voltage to be between 11-15V. The current density is about 20 mA/cm².

The initiation scheme for acrylonitrile in sulfuric acid solution may be free radical (14)

$$H^+ + e^- \rightarrow H\cdot$$

then

$$H + M \rightarrow M\cdot$$

or

$$H\cdot + H\cdot \rightarrow H_2$$

Table III. Comparison of coatings of poly (AN-CO-AA) and PAN on various metal surfaces

Monomer concentration	Polymer	Cathode metal	Current density (mA/cm²) I_o	Current density (mA/cm²) I_f	Electrolysis time (min)	Appearance of coating	Thickness of coating (mg/in.²)
24 ml AN and 6 ml AA in 400 ml, 0.05*N* H_2SO_4 aqueous solution	Poly (AN-CO-AA)	Al	19.8	16.7	60	Dark white, hard, porous	2.72
		Ni	23.6	21.1	90	White, uniform	0.90
		Cu	22.3	20.7	90	White, uniform	0.48
		S-steel	19.2	17.4	90	White, small bulbous	0.84
		Steel	22.5	19.7	90	White	0.76
30 ml AN in 400 ml, 0.05*N* H_2SO_4 aqueous solution	PAN	Al	21.4	19.0	60	Dark white	1.57
		Ni	23.1	22.0	90	White, not uniform	0.39
		Cu	23.7	22.5	90	White	0.29
		S-steel	18.9	17.1	90	White, uniform	0.73
		Steel	23.1	20.5	90	Little brown, white	0.71

Polymerization voltage is maintained constant at 13V for all runs.

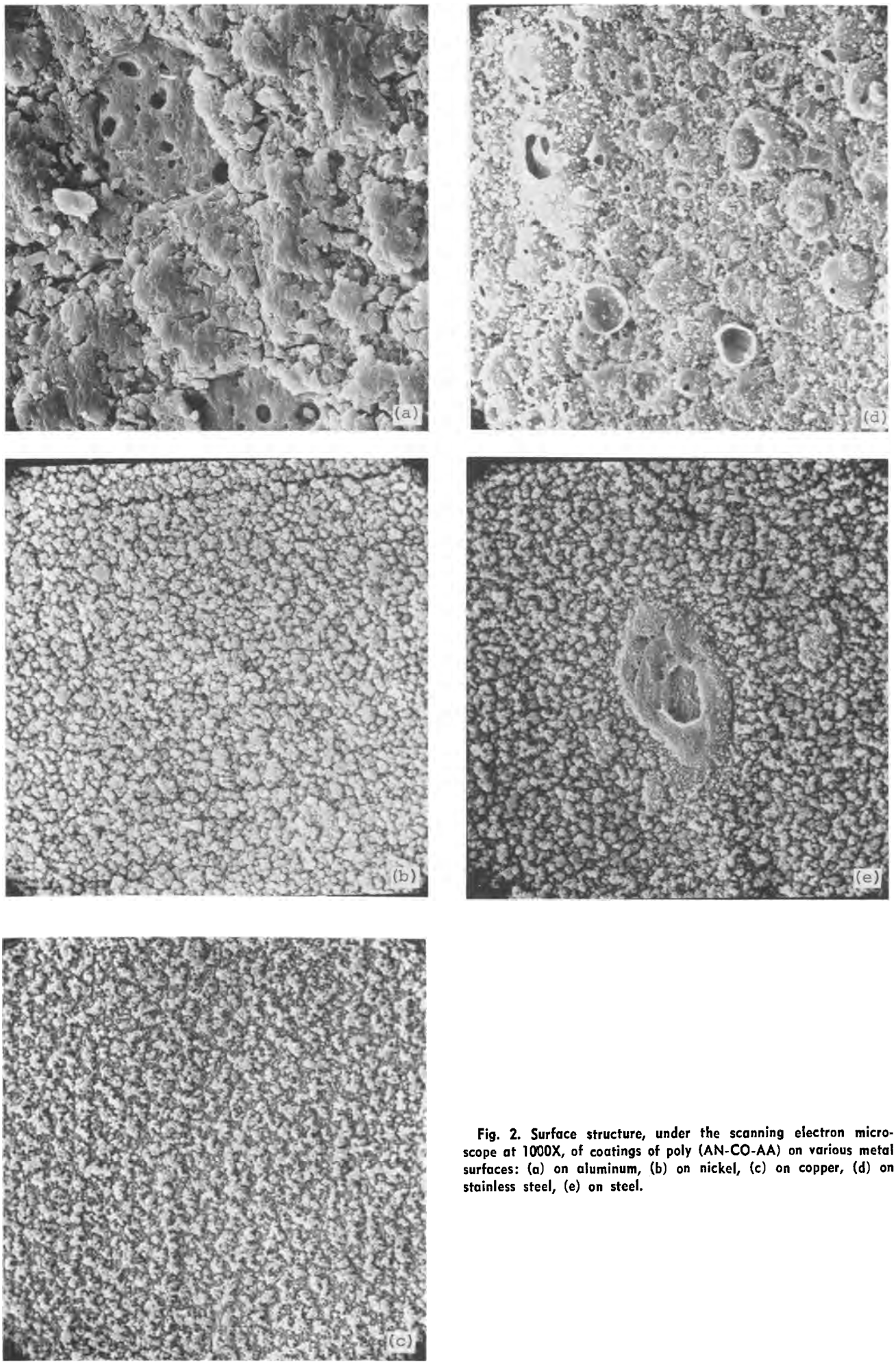


Fig. 2. Surface structure, under the scanning electron microscope at 1000X, of coatings of poly (AN-CO-AA) on various metal surfaces: (a) on aluminum, (b) on nickel, (c) on copper, (d) on stainless steel, (e) on steel.

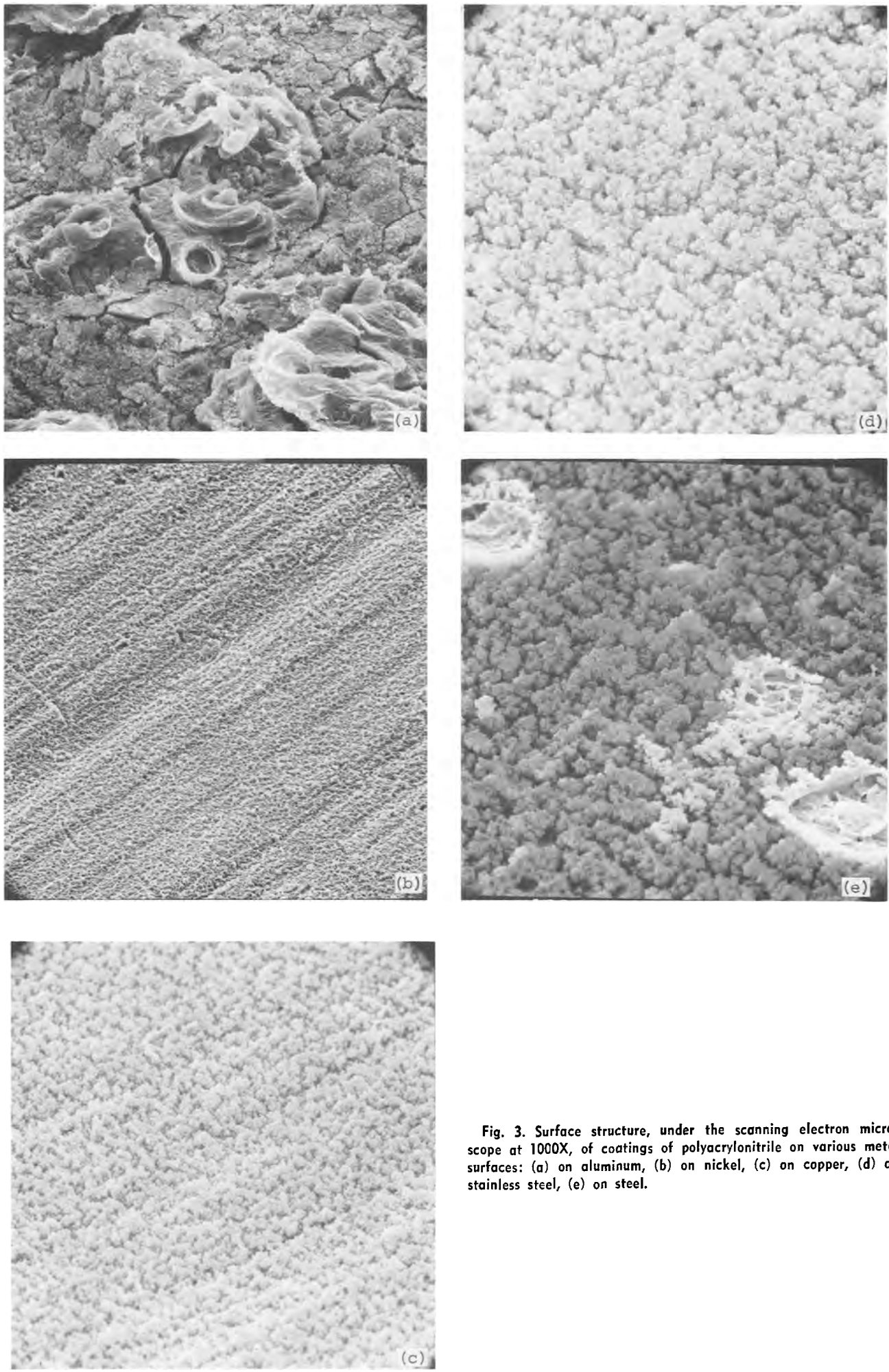


Fig. 3. Surface structure, under the scanning electron microscope at 1000X, of coatings of polyacrylonitrile on various metal surfaces: (a) on aluminum, (b) on nickel, (c) on copper, (d) on stainless steel, (e) on steel.

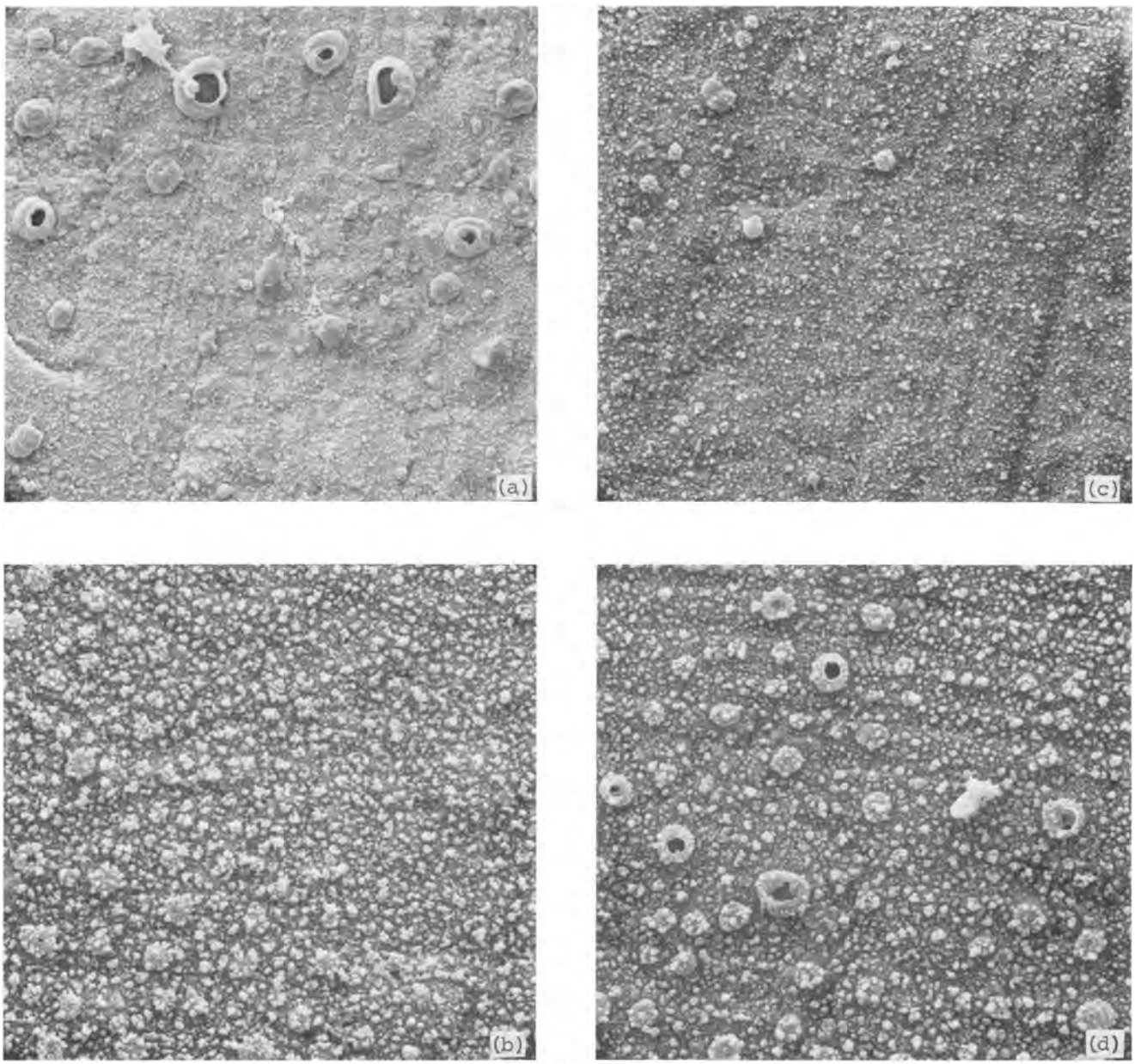


Fig. 4. Surface structure, under the scanning electron microscope at 1000X, of coatings of poly (AN-CO-AA) on nickel surface obtained at various polymerization voltages. (a) At 8V, (b) at 11V, (c) at 15V, (d) at 20V.

Table IV. Comparison of coatings on nickel and copper surfaces under various polymerization voltages

Metal	Monomer concentration	Polymer	Voltage (V)	Current density (mA/cm²) I_o	Current density (mA/cm²) I_f	Appearance of coating	Thickness of coating (mg/in.²)
Nickel	24 ml AN and 6 ml AA in 400 ml, 0.05*N* H_2SO_4 aqueous solution	Poly (AN-CO-AA)	8	12.5	10.0	White, small bulb on coating	0.52
			11	18.7	16.8	White, uniform	0.68
			13	23.6	21.1	White, uniform	0.90
			15	25.7	23.4	White, uniform	0.72
			20	32.4	27.9	White, soft	0.52
Copper	24 ml AN and 6 ml AA in 400 ml, 0.05*N* H_2SO_4 aqueous solution	Poly (AN-CO-AA)	8	17.2	15.4	White, not uniform	0.23
			11	20.3	18.8	White, uniform	0.50
			13	22.3	20.7	White, uniform	0.48
			15	25.6	23.2	White, uniform	0.45
			20	35.6	30.0	White	0.38
Nickel	30 ml AN in 400 ml, 0.05*N* H_2SO_4 aqueous solution	PAN	4	4.3	3.7	White, not uniform	0.31
			8	12.2	9.7	White, uniform	0.73
			11	18.9	16.1	White	0.47
			13	23.1	22.0	White, not uniform	0.39
			15	27.6	24.9	White, not uniform	0.36
			20	37.8	32.9	White, not uniform	0.28
Copper	30 ml AN in 400 ml, 0.05*N* H_2SO_4 aqueous solution	PAN	8	12.8	11.1	Too thin, not uniform	0.07
			11	18.3	16.5	White, not uniform	0.18
			13	23.7	22.5	White, uniform	0.29
			15	27.1	24.0	White	0.30
			20	37.6	33.5	White	0.14

Electrolysis time for each run, 90 min.

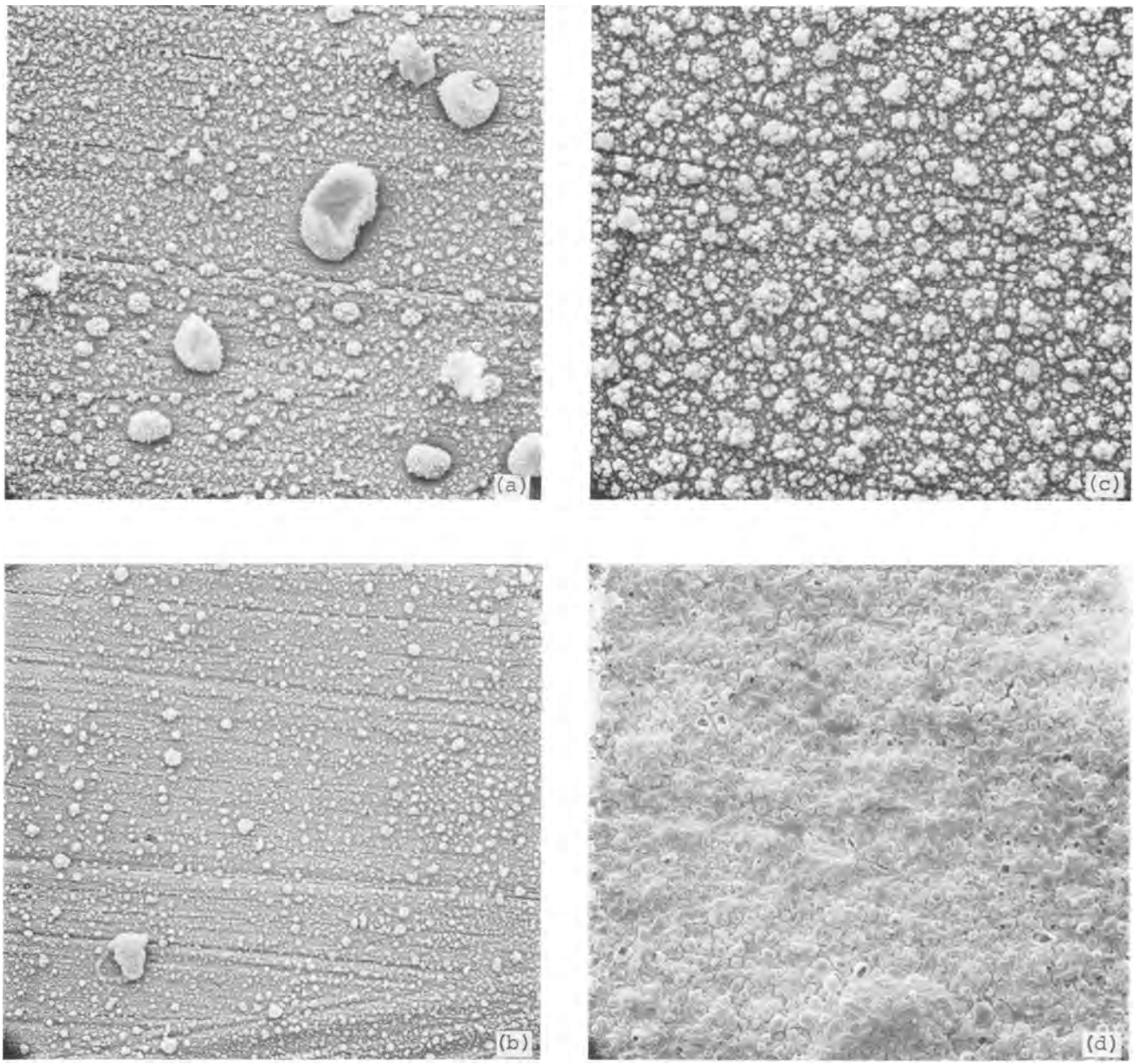


Fig. 5. Surface structure, under the scanning electron microscope at 1000X, of coatings of poly (AN-CO-AA) on copper surface obtained at various polymerization voltages, (a) At 8V, (b) at 11V, (c) at 15V, (d) at 20V.

According to this mechanism, much hydrogen is evolved along the electrodes (as has been observed during the experiments). This increases the difficulty of coating the metal. In fact, the ease of polymer deposition by electroinitiated polymerization is strongly dependent upon the hydrogen overvoltage (16) of the metal (9). If the applied voltage is too high, there is too much hydrogen evolved and water is also easily electrolyzed to form oxygen—a free radical inhibitor. In their work on electroinitiated polymerization of vinylic monomers in a polar system, Albeck, Konigsbuch, and Relis (15) point out that the decrease in polymer yield, occurring after a certain voltage value is exceeded, should be the result of the production of a free-radical suppressor by the electrolysis process.

If the voltage is too low, the current density is low, too. This will reduce the initiation rate of polymerization. It is seen that there is no polymer coating formed on the nickel surface if the voltage is less than 2V because the low voltage is actually used solely for the electrolysis of water.

Influence of monomer concentration on the coatings obtained through electroinitiated polymerization.—If the voltage, electrolyte concentration, and electrolysis time are kept constant and the monomer concentration changed, the coating thickness increases with the increase in monomer concentration. This is easily understood because initiation and propagation rates for polymerization increase as monomer concentration increases. Due to the solubility limit of acrylonitrile in water (about 7.5%), higher monomer ratios result in two-phase systems and in the nonuniformity of the coatings formed. A summary of these results is given in Table V for nickel and copper.

Comparison between corrosion rates for coated and uncoated metals, using weight loss method.—Test solutions which moderately corrode the metal specimens are used in the corrosion tests. These are 0.85% phosphoric acid, 0.27% and 0.9% ammonium hydroxide, 0.43% nitric acid, 3.55% hydrochloric acid, 5.25% and 3.15% acetic acid solution (all are weight percentage concentration) (21).

From Table VI, it is observed that the coatings on nickel and copper can prevent corrosion, based on the corrosion ratio being always greater than 1. In the case of aluminum, the coating seems to accelerate corrosion and the corrosion ratio is seen to be less than 1. From the infrared and elemental analyses and the SEM pictures, the aluminum coating is seen to be porous, rough, and nonuniform. So, the corrosion rate

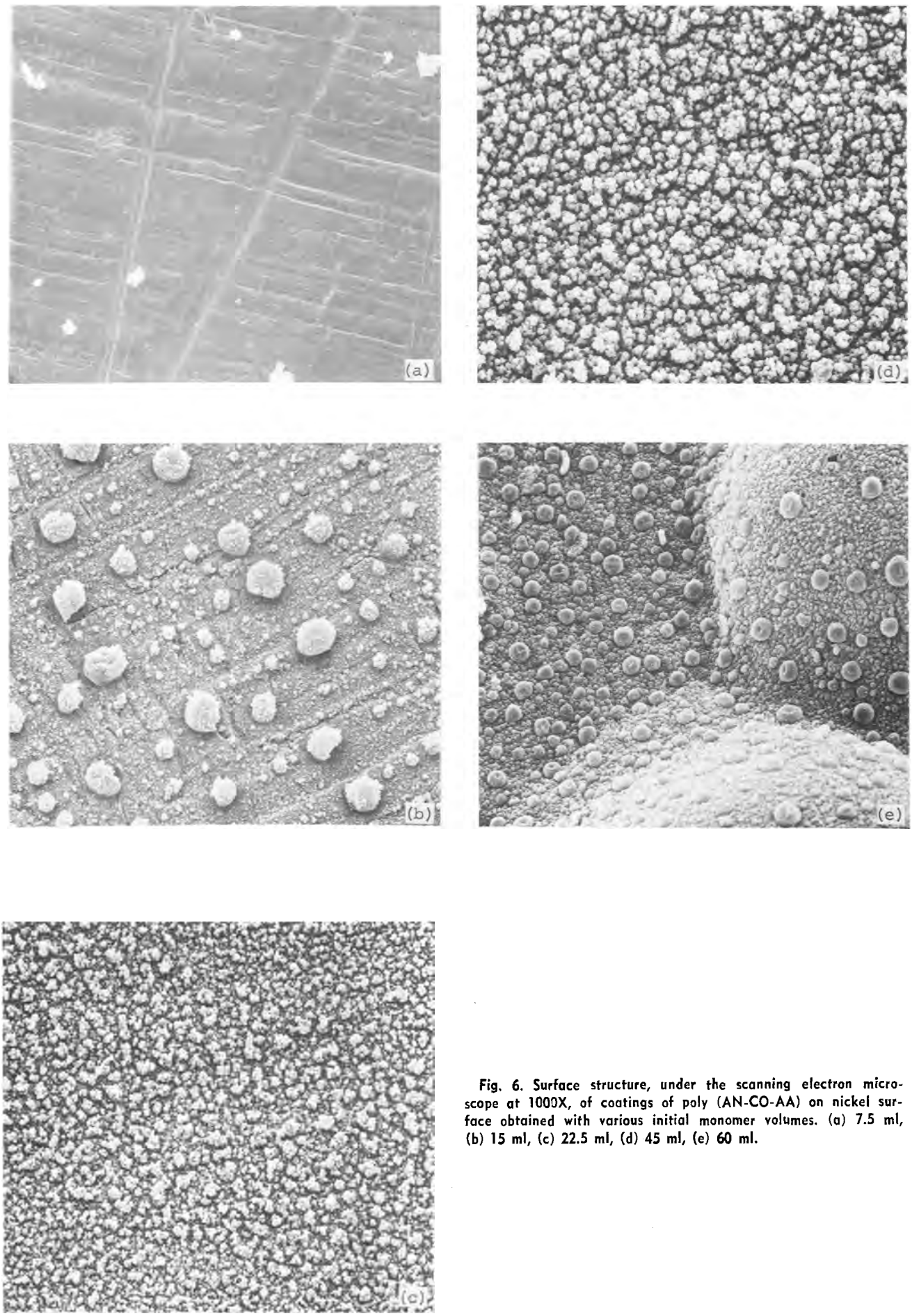


Fig. 6. Surface structure, under the scanning electron microscope at 1000X, of coatings of poly (AN-CO-AA) on nickel surface obtained with various initial monomer volumes. (a) 7.5 ml, (b) 15 ml, (c) 22.5 ml, (d) 45 ml, (e) 60 ml.

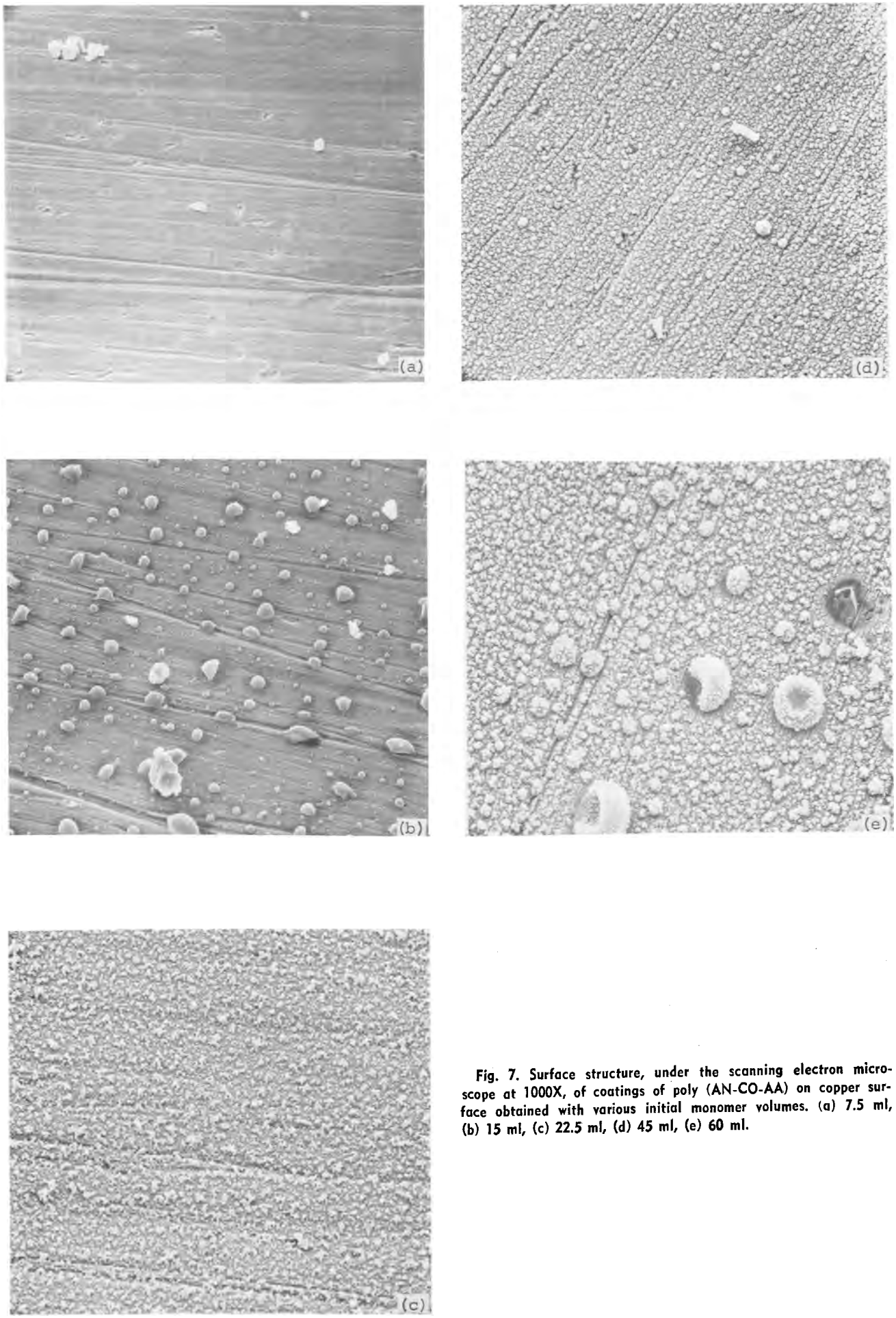


Fig. 7. Surface structure, under the scanning electron microscope at 1000X, of coatings of poly (AN-CO-AA) on copper surface obtained with various initial monomer volumes. (a) 7.5 ml, (b) 15 ml, (c) 22.5 ml, (d) 45 ml, (e) 60 ml.

Table V. Comparison of coatings on nickel and copper surfaces, with various initial monomer volumes

Metal	Initial monomer* volume† (ml)	Polymer	Current density (mA/cm²) I_o	Current density (mA/cm²) I_t	Appearance of coating	Thickness of coating (mg/in.²)
Nickel	7.5	Poly (AN-CO-AA)	22.0	21.2	White, not uniform	0.19
	15		24.3	23.2	White	0.31
	22.5		23.9	22.8	White, uniform	0.50
	30		23.6	21.1	White, uniform	0.90
	45		23.1	21.0	White, uniform	1.10
	60		23.3	20.0	White, overlap of coating	1.23
Copper	7.5	Poly (AN-CO-AA)	23.7	23.2	Not uniform	0.12
	15		23.4	22.8	White, not uniform	0.23
	22.5		24.1	23.0	White, uniform	0.33
	30		22.3	20.7	White, uniform	0.48
	45		21.5	19.7	White	0.55
	60		22.6	20.1	White, overlap of coating	0.61
Nickel	7.5	PAN	22.4	21.8	Very thin, not uniform	0.07
	15		22.0	21.5	White, not uniform	0.14
	22.5		22.7	21.9	White	0.25
	30		23.1	22.0	White	0.39
	45		23.5	22.3	White	0.53
Copper	7.5	PAN	22.5	21.8	Too thin, not uniform	0.04
	15		22.0	21.1	Not uniform	0.07
	22.5		23.2	22.0	White	0.18
	30		23.7	22.7	White	0.29
	45		23.9	22.4	White	0.33

* Monomer mixture: 80% AN and 20% AA by volume, for Poly (AN-CO-AA).
† In 400 ml of aqueous solution containing 0.05N H_2SO_4 electrolyte. Electrolysis time for each run, 90 min. Polymerization voltage is maintained at 13V for all runs.

Table VI. Comparison between corrosion rates in various media for coated and uncoated metals (Weight loss method)

Test solution	Specimen	Corrosion* rate (mpy)	Ratio*	Corrosion** rate (mpy)	Ratio**
0.85% H_3PO_4	Coated Al	55.68	0.63	64.06	0.61
	Uncoated Al	34.84		38.88	
0.27% NH_4OH	Coated Al	149.61	0.81	—	—
	Uncoated Al	120.92		—	
0.43% HNO_3	Coated Ni	21.42	1.46	—	—
	Uncoated Ni	31.15		—	
2.10% Acetic acid	Coated Ni	4.67	1.48	5.30	1.24
	Uncoated Ni	6.92		6.58	
5.25% Acetic acid	Coated Cu	2.02	1.45	2.09	1.25
	Uncoated Cu	2.93		2.61	
0.90% NH_4OH	Coated Cu	16.48	0.99	—	—
	Uncoated Cu	16.35		—	
3.55% HCl	Coated S-steel	10.51	1.02	11.85	0.90
	Uncoated S-steel	10.71		10.69	
3.15% Acetic acid	Coated steel	23.95	0.80	24.10	0.86
	Uncoated steel	19.13		20.81	

* The coating where applicable is poly (AN-CO-AA). Concentration of monomers: 24 ml AN and 6 ml AA, in 400 ml, 0.05N H_2SO_4 aqueous solution. Polymerization voltage: 13V.
** The coating where applicable is polyacrylonitrile which is obtained with 30 ml AN in 400 ml, 0.05N H_2SO_4 aqueous solution. Polymerization voltage: 13V.
Area: 1.03-2.89 in.².
Time: 23-25 hr.

of coated aluminum is increased. The coatings on nickel and copper are uniform (from the SEM pictures) and are also quite thick, especially on the nickel surface; hence, the reduced corrosion rates for nickel and copper.

Asahara, Seno, and Tsuchiya (22), in their experiments on formation of polymer film onto aluminum electrode by electrolysis of vinyl compounds, found copolymer coatings of AN-MMA, AN-MA, AN-EA, and AN-ST, etc. will cause higher hydrogen overvoltage than polyacrylonitrile alone. This accounts for the film thickness of the copolymer being thicker than of the pure polymer. In our work, it is similarly observed that the thickness of poly (AN-CO-AA) is higher than that for the pure polyacrylonitrile.. So, the corrosion rates for the copolymer coatings are less than those for PAN.

From Table IV and Fig. 4-5, it can be seen that if the polymerization voltage is changed, the thickness and surface structure of the polymer film are also changed. Also from this table, it is seen that the coating obtained at 13V is more uniform than those obtained at the other voltages. Thus, the corrosion rate of the coating corresponding to that voltage is always the smallest. Also, a thick and uniform coating on the nickel surface occurs at 8V. So, the corrosion rate for nickel with the polyacrylonitrile coating obtained at 8V is the smallest. The corrosion data are shown in Table VII.

From Table V and Fig. 6-7, it can be seen that if the monomer concentration is changed, the thickness and structure of the polymer film is also changed. As shown in Table VIII, the smallest corrosion rate occurs for the higher monomer concentration because thick and uniform coatings are obtained at the higher monomer concentrations. Also, if the monomer concentration is too low and the coating is too thin to cover the entire metal surface, the corrosion ratio is very close to 1, *i.e.*, the corrosion rates of coated and uncoated metals are almost equal.

Comparison between corrosion rates for coated and uncoated metals, using electrochemical method.—The electrochemical method is employed to cross check the corrosion rates obtained by the weight loss method. It is observed that the two methods differ within the acceptable range of less than 30% (Tables IX and X). Comparison of Tables VI and IX shows the large difference between the two testing methods occurs for nickel in 0.43% nitric acid solution and for steel in 3.15% acetic acid solution. Because it always takes a whole day for testing by the weight loss method, the nitric acid solution appears to wet the inside metal surface and loosen the bonding between polymer film and metal. The coating on the coated nickel after the corrosion test in nitric acid solution appears to swell and is easily scraped off the metal. But it takes only half an hour for testing by the electrochemical method and all coatings on the metals are found to be still strongly adhering to the surfaces after electrochemical corrosion tests.

It should be recognized that although the test corrosion media for both the methods could be considered to be moderately severe for the organic coatings developed, the amount of information developed is valuable, especially on the adherence, porosity, and uniformity of the coatings.

Conclusions

For the specimens prepared by electroinitiated polymerization, bonding between the metal and the polymer may be assumed to be through an electrostatic force between the positive metal ion in the metal oxide and the negative functional group of the polymers. The coating thickness and uniformity vary not only with the solvents, electrolytes, and electrodes, but

Table VII. Corrosion rate comparison in acetic acid solutions for nickel and copper-coatings* formed under different polymerization voltages (Weight loss method)

Metal	Polymerization voltage (V)	Polymer coating	Acetic acid concentration (%)	Corrosion rate (uncoated metal) (mpy)	Corrosion rate (coated metal) (mpy)	Ratio
Nickel	8	Poly (AN-CO-AA)*	2.1	8.38	6.39	1.31
	11			7.02	4.68	1.50
	13			6.92	4.67	1.48
	15			6.79	4.69	1.45
Nickel	4	PAN**	2.1	6.39	5.75	1.11
	8				5.01	1.28
	11				5.34	1.20
	13				5.30	1.24
	15				5.76	1.11
	20				5.98	1.07
Copper	8	Poly (AN-CO-AA)*	5.25	2.72	2.39	1.14
	11			2.44	1.53	1.60
	13			2.52	1.68	1.50
	15			2.49	1.95	1.28
	20			2.77	2.19	1.26
Copper	8	PAN**	5.25	2.61	2.80	0.93
	11				2.48	1.05
	13				2.09	1.25
	15				1.94	1.35
	20				2.58	1.01

* Concentration of monomers = 24 ml AN and 6 ml AA in 400 ml, 0.05*N* H_2SO_4 aqueous solution.
** Concentration of monomer = 30 ml AN in 400 ml, 0.05*N* H_2SO_4 aqueous solution.

Table VIII. Corrosion rate comparison in acetic acid solution for nickel and copper-coatings* formed under different initial monomer volumes (Weight loss method)

Metal	Monomer vol (ml)	Polymer coating	Acetic acid concentration (%)	Corrosion rate (mpy)	Ratio
Nickel	7.5	Poly (AN-CO-AA)	2.1	6.45	1.12[a]
	15			5.88	1.23
	22.5			5.45	1.32
	30			5.32	1.36
	45			4.58	1.57
	60			5.98	1.21
Nickel	7.5	PAN	2.1	6.81	0.97[b]
	15			6.29	1.05
	22.5			5.52	1.19
	30			5.30	1.24
	45			4.85	1.36
Copper	7.5	Poly (AN-CO-AA)	5.25	2.16	1.11[c]
	15			1.86	1.29
	22.5			1.66	1.44
	30			1.54	1.55
	45			1.20	1.99
	60			1.38	1.73
Copper	7.5	PAN	5.25	2.84	0.92[d]
	15			2.61	1.00
	22.5			2.22	1.18
	30			2 09	1.25
	45			2.01	1.30

* Coating is obtained with different monomer volumes shown in 400 ml, 0.05*N* H_2SO_4 aqueous solution. The voltage is maintained constant at 13V.
Corrosion rates for uncoated metals: [a] 7.21 (mpy), [b] 6.58 (mpy), [c] 2.39 (mpy), and [d] 2.61 (mpy).
Area: 2.47-2.83 in.^{2}.
Time: 23.0-49.5 hr.

Table X. Corrosion comparison in 5.25% acetic acid solution, for copper coated* at different polymerization voltages (Electrochemical method)

Polymerization voltage (V)	Corrosion voltage Ecorr. (V)	Corrosion current Icorr. (μA)	Area (cm^2)	Corrosion rate (mpy)	Ratio†
8	−0.08	75	16.19	2.13	1.35
11	−0.06	48	15.51	1.42	2.02
13	−0.05	56	17.26	1.49	1.92
15	−0.06	71.5	17.05	1.93	1.49
20	−0.04	85	16.84	2.32	1.24

* The coating is poly (AN-CO-AA), obtained at different voltages shown. Concentration of monomers: 24 ml AN and 6 ml AA in 400 ml, 0.05*N* H_2SO_4 aqueous solution.
† The corrosion rate of uncoated copper = 2.87 (mpy).

they are also functions of polymerization voltage and monomer concentration. It is also observed that the resistance of the coated metals to corrosion is also a function of the above variables. Since a metal oxide is present on aluminum, the coating is found to be porous, nonuniform, and having poor corrosion resistance but strongly adhesive. The optimum polymerization voltage and monomer concentration from the point of view of good corrosion resistance are found to be around 11-15V and at 45 ml monomer in 400 ml aqueous solution. Also it is found that monomer mixtures of acrylonitrile and acrylic acid are more suitable to form good corrosion resistant coatings than the monomer acrylonitrile alone.

Table IX. Comparison between corrosion rates for coated and uncoated metals (Electrochemical method)

Test solution	Specimen*	Corrosion voltage Ecorr. (V)	Corrosion current Icorr. (μA)	Area (cm^2)	Equivalent wt (g)	Corrosion rate (mpy)	Ratio
0.85% H_3PO_4	Coated Al	−0.75	1550	15.06	9.0	43.17	0.76
	Uncoated Al	−0.73	1200	15.02	9.0	32.62	
0.43% HNO_3	Coated Ni	−0.16	455	16.12	29.4	12.01	2.60
	Uncoated Ni	−0.32	1200	16.38	29.4	31.16	
2.10% Acetic acid	Coated Ni	−0.34	150	13.77	29.4	4.63	1.36
	Uncoated Ni	−0.56	290	19.54	29.4	6.31	
5.25% Acetic acid	Coated Cu	−0.05	56	17.26	31.7	1.49	1.92
	Uncoated Cu	−0.03	110	17.63	31.7	2 87	
0.9% NH_4OH	Coated Cu	−0.29	660	18.56	31.7	16.29	0.97
	Uncoated Cu	−0.44	620	18.05	31.7	15.74	
3.55% HCl	Coated S-steel	−0.26	370	18.36	27.7	9.07	1.20
	Uncoated S-steel	−0.38	450	18.58	27.7	10.89	
3.15% Acetic acid	Coated steel	−0.40	710	17.99	27.7	18.10	1.28
	Uncoated steel	−0.57	860	17.06	27.7	23.10	

* The coating is poly (AN-AA). Concentration of monomers: 24 ml AN and 6 ml AA in 400 ml, 0.05*N* H_2SO_4 aqueous solution. Polymerization voltage = 13V.

Acknowledgment

Acknowledgment is made to the Donors of the Petroleum Research Fund, administered by the American Chemical Society, for the support of this research (PRF-7491-AC5,7).

Manuscript submitted June 28, 1976; revised manuscript received Feb. 22, 1977.

Any discussion of this paper will appear in a Discussion Section to be published in the June 1978 JOURNAL. All discussions for the June 1978 Discussion Section should be submitted by Feb. 1, 1978.

Publication costs of this article were assisted by Washington State University and The Petroleum Research Fund.

REFERENCES

1. S. B. Levinson, Part I, *J. Paint Technol.*, **44**, 39 (1972).
2. N. Yamazaki, I. Tanaka, and S. Nakahama, *J. Macromol. Sci. Chem.* **A2**, 1121 (1968).
3. B. L. Funt, *Macromol. Rev.*, **1**, 35 (1967).
4. A. Kunugi, T. Tanimoto, and S. Nagaura, *Electrochim. Acta*, **17**, 3897 (1972).
5. B. L. Funt and T. J. Blain, *J. Polym. Sci.*, **8**, 3339 (1970).
6. R. V. Subramanian, R. A. V. Raff, and B. K. Garg, 172nd ACS National Meeting, San Francisco, August, 1976.
7. A. K. Julka, M. S. Thesis, Washington State University, 1974.
8. Hysol Division, the Dexter Corporation, Technical Information, Bulletin G1-600.
9. J. Oliver, *Products Finishing*, **3417**, 66 (1970).
10. B. L. Funt and F. D. Williams, *J. Polym. Sci.,/Part A2*, 865 (1964).
11. H. Z. Friedlander, *Encycl. of Polym. Sci. Technol.*, **5**, 629 (1966).
12. A. F. Lewis and L. J. Forrestal, Sixty-Sixth Annual Meeting papers for ASTM, 59 (1963).
13. R. G. Gadjieva, in Proceedings of the Fourth International Congress in Metallic Corrosion, p. 925 (1966).
14. J. W. Breitenbach and Ch. Srna, *Pure Appl. Chem.*, **4**, 245 (1962).
15. M. Albeck, M. Konigsbuch, and J. Relis, *J. Polym. Sci., Part A-1*, **9**, 1375 (1971).
16. A. F. Bogenschutz, J. L. Jostan, and W. Krusemark, *Galvanotechnik*, **60**, 750 (1969).
17. E. Dineen, T. C. Schwan, and C. L. Wilson, *Trans. Electrochem. Soc.*, **96**, 226 (1949).
18. National Association of Corrosion Engineers, *NACE Standard TM-01-69*.
19. D. A. Carter and C. C. Nathan, *Mater. Prot. Perform.*, **8**, 61 (1969).
20. American Society for Testing and Materials: G5-69.
21. M. G. Fontana and N. D. Greene, "Corrosion Engineering," pp. 342-345, McGraw-Hill Book Co., New York (1967).
22. T. Asahara, M. Seno, and M. Tsuchiya, *Kinzoku Hyomen Gijutsu*, **20**, 2 (1969).
23. F. S. Doun(Teng), M.S. Thesis, Washington State University (1976).

Evaluation of Corrosion Rates from Nonlinear Polarization Data

Rodney L. LeRoy*

Noranda Research Centre, Pointe Claire, Quebec, Canada H9R 1G5

ABSTRACT

Evaluation of corrosion rates from polarization measurements in the vicinity of the corrosion potential (the linear polarization method) depends on a knowledge of the Tafel slopes for the anodic dissolution reaction and for the corresponding cathodic process. A method is presented for derivation of these parameters from the polarization data. One calculation, based on the extent to which the polarization curve is symmetrical about the corrosion potential, yields a reliable value for the difference between the inverses of the two Tafel slopes. A second calculation computes the separate values of the parameters from this difference and measurements of the degree of nonlinearity in either the anodic or cathodic direction. This approach is presented in the form of a simple algorithm which gives Tafel constants of sufficient accuracy to make possible reliable calculation of the corrosion current from the polarization data.

Since its proposal by Stern and his co-workers (1-4), the linear polarization method has come into widespread use for determination of corrosion rates. It is common, for example, in corrosion laboratories for measurement of very low corrosion rates where conventional techniques such as weight-loss and gas-evolution measurements are insufficiently sensitive (5). Even for rapidly corroding samples, the experimental simplicity of this method and the short times required for obtaining accurate estimates of corrosion rates make it invaluable (6-8), provided that correction is made when necessary for effects of ohmic resistance (9). Several commercial corrosion rate meters are based on the linear polarization method (10), and with suitable corrections these can give good estimates of corrosion rates if the anodic and cathodic Tafel slopes are known (11).

In view of this generally recognized utility, it is surprising that the accuracy of corrosion rate measurements using the linear polarization technique has been limited by an incomplete theoretical formulation. This is true even in the simplest (and most common) case where the corrosion potential is sufficiently displaced from the reversible potentials of the anodic and cathodic reactions that competing processes can be ignored (12, 13). The principal failings relate to the assumption of linearity and to the requirement that the Tafel slopes for the anodic and cathodic processes be known in order to allow computation of the corrosion current. Recently, several authors have made contributions to the understanding of these limitations and to devising methods of overcoming them (14-22).

In the classical linear polarization method, the current density i which flows when a corroding sample is polarized to a potential ϵ from the corrosion potential is given by the linear expression

* Electrochemical Society Active Member.

Key words: Tafel slope estimation, corrosion currents, zinc corrosion, iron corrosion.

$$i = i_{corr} (\log_e 10) \left(\frac{1}{\beta_a} + \frac{1}{\beta_c}\right) \epsilon \qquad [1]$$

where i_{corr} is the corrosion current, and β_a and β_c are, respectively, the Tafel slopes of the anodic and cathodic processes. This equation is simply a linear approximation, valid for small ϵ, of the general expression for the net current which flows when competing activation-controlled anodic and cathodic reactions are taking place

$$i = i_{corr} (10^{\epsilon/\beta_a} - 10^{-\epsilon/\beta_c}) \qquad [2]$$

As was originally emphasized by Stern (4), and has been since highlighted by several other authors (15, 16), the linear approximation of Eq. [1] can rigorously be applied only to the tangent of the polarization curves at $\epsilon = 0$. Polarization data frequently exhibit significant curvature in the potential range used for these measurements, within 10-20 mV of the corrosion potential (17-22). Thus a corrosion current calculated using Eq. [1] from the best straight line which is drawn through "linear polarization" data can introduce significant errors. The magnitude of these errors and their dependence on the Tafel parameters β_a and β_c were estimated in an earlier paper (19).

It is possible to compute the corrosion current from such polarization data, however, without introducing any theoretical error, using the expression (22)

$$i_{corr} = \frac{\sum_{j=1}^{n} [i_j (10^{\epsilon_j/\beta_a} - 10^{-\epsilon_j/\beta_c})]}{\sum_{j=1}^{n} [(10^{\epsilon_j/\beta_a} - 10^{-\epsilon_j/\beta_c})^2]} \qquad [3]$$

where the anodic and cathodic Tafel constants β_a and β_c are assumed to be known. Although somewhat formidable in appearance, Eq. [3] is readily evaluated from the point-by-point polarization data using a hand calculator. The resulting corrosion current is quite insensitive to errors in the assignment of the Tafel parameters (22) although serious inaccuracy can result if approximate estimates of these parameter values are not available.

Mansfeld (20, 23), has proposed a curve-fitting procedure for determination of the anodic and cathodic Tafel slopes from nonlinearity in the vicinity of the corrosion potential. This involves computation of the polarization resistance from the tangent to the polarization curve at $\epsilon = 0$, plotting of modified polarization data ($\log_e 10 \times$ (polarization resistance) $\times i$) *vs.* the polarization ϵ, and subsequent comparison with theoretical curves calculated for various values of β_a and β_c. He also proposed (20) an elegant least squares fitting technique which requires the use of a computer. The latter of these approaches is more attractive, as it allows estimation of the corrosion current without the errors which result from drawing a tangent to the experimental data at the corrosion potential.

The purpose of this paper is to present a simple and accurate alternative approach to the estimation of Tafel parameters from the nonlinearity of polarization data. The resulting estimates, when used in Eq. [3], allow accurate evaluation of the corrosion current.

Symmetry of the Polarization Curve

An accurate relationship between the anodic and cathodic Tafel slopes can be derived from the symmetry of the polarization data about the corrosion potential. The currents which flow when a corroding sample is polarized ϵ mV in the anodic ($i_{\epsilon+}$) and cathodic ($i_{\epsilon-}$) directions are recorded and their ratio is calculated. This experimental ratio is compared with the theoretical quantity computed from Eq. [2]

$$\begin{aligned} i_{\epsilon+}/i_{\epsilon-} &= (10^{\epsilon/\beta_a} - 10^{-\epsilon/\beta_c}) / (10^{-\epsilon/\beta_a} - 10^{\epsilon/\beta_c}) \\ &= \frac{10^{\epsilon/\beta_a} (1 - 10^{-(\epsilon/\beta_a + \epsilon/\beta_c)})}{-10^{\epsilon/\beta_c} (1 - 10^{-(\epsilon/\beta_a + \epsilon/\beta_c)})} \\ &= -10^{(\epsilon/\beta_a - \epsilon/\beta_c)} \end{aligned} \qquad [4]$$

This result is conveniently rewritten in terms of the difference D of the inverse Tafel slopes

$$D = \left(\frac{1}{\beta_a} - \frac{1}{\beta_c}\right) = \frac{1}{\epsilon} \log_{10}(-i_{\epsilon+}/i_{\epsilon-}) \qquad [5]$$

Equation [5] was first derived by Reeve and Bech-Nielsen (14) and an analogous result was used by Barnartt (24).

The difference D will seldom be less than -0.035 mV^{-1} or greater than $+0.035$ mV^{-1}. The lower of these limits corresponds to a passivated surface for which the anodic Tafel slope β_a = infinity while the cathodic Tafel slope is $\beta_c = 30$ mV ($2.3\ RT/2\mathbf{F}$). The upper limit corresponds to $\beta_a = 30$ mV and β_c = infinity, for example for a diffusion-limited cathodic reaction.

The difference of the inverse Tafel slopes D is plotted in Fig. 1 as a function of the ratio $-i_{\epsilon+}/i_{\epsilon-}$. Curves are plotted for polarization values 5, 10, 15, and 20 mV from the corrosion potential. Equation [5] would, of course, be valid for much higher polarizations. However, in deriving corrosion currents it is normally desirable to restrict attention to data obtained with 10-15 mV of the corrosion potential in order to minimize possible interference effects due to competing reactions, or to modification in the mechanism of the corrosion process or its corresponding cathodic reaction.

In some instances Eq. [5] and Fig. 1 alone will suffice for definition of the Tafel parameters β_a and β_c, and for subsequent calculation of the corrosion current from Eq. [3]. An example is the analysis of the data for the corrosion of zinc in 3% sodium sulfate solution which is presented in Fig. 2. These measurements were made in a well-stirred polarization cell which was thermostated at 30°C. Potentials were measured with respect to a mercury/mercury sulfate reference electrode which was contacted to the electrolyte through a Luggin probe. The potential was scanned at a rate of 0.1 mV/sec using a Princeton Applied Research potentiostat Model 173, controlled by a Model 175 programmer. Current values obtained at plus and minus 5, 10, 15, and 20 mV are recorded in Table I, along with the corresponding calculated values of D.

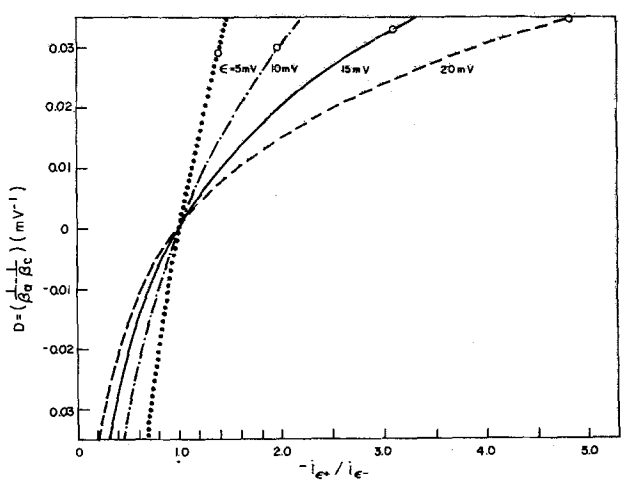


Fig. 1. Relationship between the difference D of the inverse anodic and cathodic Tafel slopes and the ratio of the net currents i which flow when a corroding sample is polarized by ϵ mV in the anodic and cathodic directions. Curves are plotted from Eq. [5] for four values of the polarization, 5, 10, 15 and 20 mV. Points indicate data obtained for zinc corroding in 3% sodium sulfate (Table I).

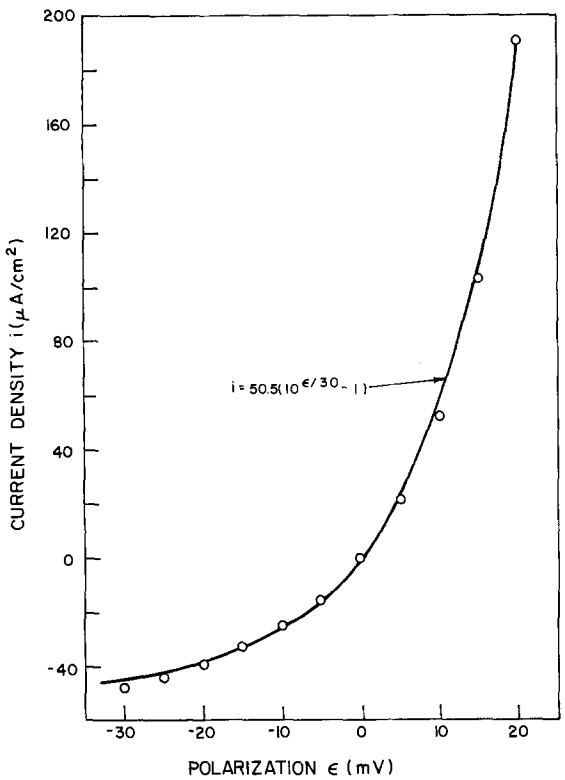


Fig. 2. Polarization data for zinc corroding in 3% sodium sulfate solution at 30°C. The solid curve is drawn from Eq. [2], for an anodic Tafel slope of $\beta_a = 30$ mV, a cathodic slope of $\beta_c =$ infinity, and a corrosion current of 50.5 μA/cm².

These values of D are indicated as data points in Fig. 1. They increase slightly with increasing polarization, but their mean value of 0.0312 mV^{-1} is a good estimate, within the required degree of accuracy (22).

Maximum Values of β_a and β_c

When the ratio of the anodic and cathodic current densities for a given polarization ϵ (the quantity $-i_{\epsilon+}/i_{\epsilon-}$ in Eq. [4] and [5]) is greater than unity, the value of the cathodic Tafel slope β_c is greater than the anodic slope, β_a. In this case, for a particular value of D there will be an upper limit on possible values of β_a, corresponding to a cathodic Tafel slope β_c of infinity. Such maximum values of β_a are plotted in Fig. 3 as a function of $-i_{\epsilon+}/i_{\epsilon-}$ for polarization values of 5, 10, and 15 mV.

For corrosion situations in which the cathodic Tafel slope is very large, Fig. 3 provides sufficient information for assignment of the Tafel slopes and for accurate calculation of the corrosion current. The data for zinc in 3% sodium sulfate solution (Fig. 2) are an example of this. The two points indicated in Fig. 3 represent maximum possible values of the anodic Tafel slope from the zinc corrosion data, for $\epsilon = 5$ and $\epsilon = 10$ mV. Both values fall close to $\beta_a = 30$ mV. The smallest value of the anodic Tafel slope normally encountered for activation controlled processes is 30 mV, corresponding to 2.3 $RT/2F$. Thus these data indicate that the anodic Tafel slope for this zinc corrosion reaction had approximately this value, 30 mV, while the corresponding cathodic Tafel slope was infinite. These assignments are consistent with the anodic dissolution parameters determined for zinc dissolution over a much wider current density range (25) and with diffusion-limited reduction of oxygen being the cathodic process.

Table I. Calculation of $D = (1/\beta_a - 1/\beta_b)$ for zinc corroding in 3% sodium sulfate solution

ϵ (mV)	$i_{\epsilon+}$ (μA/cm²)	$i_{\epsilon-}$ (μA/cm²)	$-i_{\epsilon+}/i_{\epsilon-}$	$D = (1/\beta_a - 1/\beta_c)$ (mV^{-1})
5	21.2	−15.2	1.39	0.0289
10	50.2	−25.3	1.98	0.0298
15	102.6	−32.8	3.13	0.0330
20	191.0	−39.0	4.90	0.0345
			Mean value =	0.0312

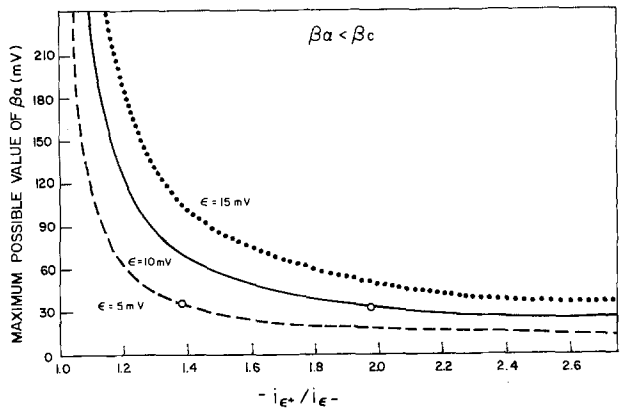


Fig. 3. Maximum possible values of the anodic Tafel slope β_a, as a function of the ratios of the net currents which flow on polarizations of $\pm\epsilon$ from the corrosion potential. The curves correspond to $\beta_c =$ infinity in Eq. [5].

Using these assigned values of the Tafel parameters ($\beta_a = 30$ mV and $\beta_c =$ infinity), the corrosion rate of zinc in the 3% sodium sulfate electrolyte was calculated directly from the polarization data using Eq. [3]. This calculation is detailed in Table II. The quantities in the numerator and denominator of Eq. [3] were calculated for each data point, and the appropriate summations were performed. The resulting value of the corrosion current was 50.5 μA/cm². Corresponding calculated current values derived from Eq. [2] are recorded in Table II, and plotted as a solid line in Fig. 2. The good agreement of the calculated curve with the experimental data suggests that "more accurate" estimation of the Tafel parameters, for example by a computer-fitting procedure, would not offer improved precision in the estimate of the corrosion current.

If the value of D calculated from Eq. [5] is negative, the value of the anodic Tafel slope β_a is greater than that of the cathodic Tafel slope, β_c. In this case a maximum possible value of the parameter β_c can be derived, corresponding to $\beta_a =$ infinity (a passive electrode). Figure 4 displays these maximum possible values for polarizations of 5, 10, and 15 mV.

Separate Estimation of β_a and β_c

The example of zinc corrosion described above was an exceptional case, in that an analysis of the symmetry of the polarization curve about the corrosion potential provided sufficient information to allow accurate computation of the corrosion current. In general, the anodic and cathodic Tafel slopes will be non-infinite, and an alternate method of calculation is required. The method used is based on the extent to which the polarization data deviates from linearity, in either the anodic or cathodic direction.

Table II. Calculation of the corrosion current for zinc in 3% sodium sulfate from Eq. [3]

ϵ_j (mV)	i_j (μA/cm²)	$i(10^{\epsilon_j/30} - 1)$ (μA/cm²)	$(10^{\epsilon_j/30} - 1)^2$	i_{calc} (μA/cm²)
20	191.0	695.54	13.261	183.9
15	102.6	221.85	4.675	109.2
10	50.2	57.95	1.333	58.3
5	21.2	9.92	0.219	23.6
0	0	0	0	0
−5	−15.2	4.84	0.102	−16.1
−10	−25.3	13.56	0.287	−27.1
−15	−32.8	22.43	0.468	−34.5
−20	−39.0	30.60	0.616	−39.6
−25	−43.9	37.46	0.728	−43.1
−30	−47.6	42.84	0.810	−45.5
		$\Sigma_j = 1136.99$	22.499	

$i_{corr} = 1136.99/22.499 = 50.5$ μA/cm²

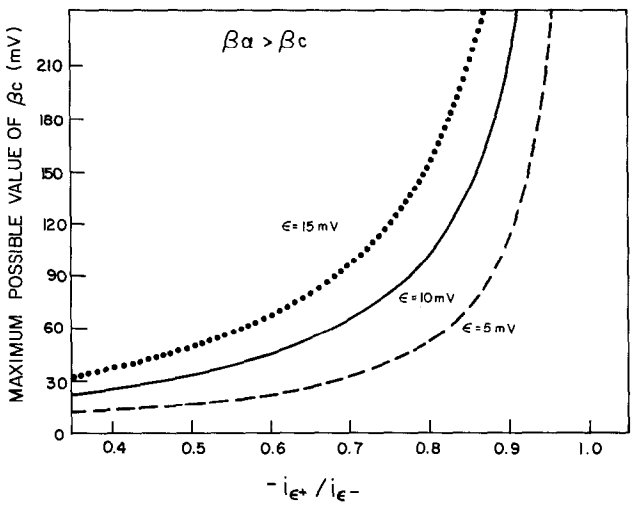


Fig. 4. Maximum possible values of the cathodic Tafel slope β_c as a function of the ratio of the currents i which flow on polarizations of $\pm\epsilon$ from the corrosion potential. The curves correspond to an anodic Tafel slope of β_a = infinity in Eq. [5].

Values of the net current which flows for polarizations of ϵ and 2ϵ from the corrosion potential are recorded, and their ratio is calculated. If the polarization data were linear, the value of this ratio would be two. In the more general case, described by Eq. [2], the value of this ratio is

$$R = \frac{10^{2\epsilon/\beta_a} - 10^{-2\epsilon/\beta_c}}{10^{\epsilon/\beta_a} - 10^{-\epsilon/\beta_c}} \qquad [6]$$

or

$$R = 10^{\epsilon/\beta_a} + 10^{-\epsilon/\beta_c} \qquad [7]$$

Using the difference D computed from the symmetry of the polarization data about the corrosion potential, the anodic Tafel slope β_a can be eliminated between Eq. [5] and [7], with the result

$$R = 10^{\epsilon D}\, 10^{\epsilon/\beta_c} + 10^{-\epsilon/\beta_c} \qquad [8]$$

Solution of this quadratic equation in $10^{\epsilon/\beta_c}$ gives the required result for the cathodic Tafel slope β_c

$$\beta_c = \epsilon/\log_{10} \frac{(R \pm (R^2 - 4 \cdot 10^{\epsilon D})^{1/2})}{2 \cdot 10^{\epsilon D}} \qquad [9]$$

The positive root is taken in Eq. [9] when the polarization from the corrosion potential, ϵ, is positive, while the negative root must be taken when the polarization is negative. The corresponding anodic Tafel slope β_a is calculated directly from the quantity D

$$\beta_a = \left(\frac{1}{\beta_c} + D\right)^{-1} \qquad [10]$$

The two Tafel parameters then allow computation of the corrosion current from Eq. [3].

Computation of values of the cathodic Tafel slope β_c from Eq. [9] and the experimental quantities R and D is facilitated by the use of Fig. 5-7, in which β_c is plotted as a function of the difference between the inverse Tafel slopes D, for different realistic values of the ratio R. Figures are drawn for lower polarization values ϵ of 5, 7.5, and 10 mV. Each of the figures has an "inaccessible region" where values of β_c would require a negative or imaginary value β_a.

Figures 5-7 are constructed for positive values of the lower polarization value ϵ. However, because of the symmetry of Eq. [2] and [5] in β_a and β_c, these figures can also be used to derive the value of the anodic Tafel slope when the polarization values ϵ and 2ϵ are negative. In this case the abscissa must be read as the negative of the difference D, $(\beta_c^{-1} - \beta_a^{-1})$.

The accuracy and utility of this method are illustrated using experimental data obtained by Mansfeld (20) for the corrosion of iron in 1*N* sulfuric acid. Comparison is made with Mansfeld's analysis of this data using both a curve-fitting procedure and a computer analysis (20, 23). The data used were obtained after the iron sample had been exposed in the sulfuric acid medium for 290 min [Fig. 3(b) of Ref. (20)].

Mansfeld's polarization data (20) are plotted in Fig. 8, and the net currents measured at polarizations of ± 5, 10, and 20 mV are recorded in Table III. Values of the difference of the inverse Tafel slopes D were calculated at each of these polarizations from Eq. [5], as described above. The resulting values were averaged to give $D = 0.0079\ \text{mV}^{-1}$.

Evaluation of the separate values of the Tafel parameters is indicated in the lower section of Table III. Calculations were carried out using the data at $\epsilon = 5$ and $\epsilon = 10$ mV, and the data at $\epsilon = 10$ and $\epsilon = 20$ mV. For example, the ratio of the positive currents measured at polarizations of 5 and 10 mV from the corrosion potential was 2.102. Substitution of this value and the mean value of $D = 0.0079\ \text{mV}^{-1}$ into Eq. [9] yielded a cathodic Tafel slope of 256 mV. The corresponding value of β_a, calculated from Eq. [10], was 85 mV. Rather than using Eq. [9], the value of β_c could have been taken with adequate accuracy from Fig. 5. This is indicated by the circle on this figure. At a value of $D = 0.0079\ \text{mV}^{-1}$, the contour for $R = 2.1$ corresponds to a value of β_c somewhat greater than 180 mV. The uncertainty in the cathodic Tafel slope β_c taken from Fig. 5 is a useful indication of the extent to which the polarization data is insensitive to the precise value of this parameter. Values of the corrosion current calculated subsequently from Eq. [3] have been shown to be correspondingly insensitive to precise assignment of such high values of the Tafel parameters (22).

The ratio of the currents flowing at negative polarizations of 5 and 10 mV from the corrosion potential was 1.962. The value of β_c calculated from this R value and the mean value of D was 62 mV, while the corresponding value of β_a (Eq. [10]) was 42 mV. These values could alternately have been derived from Fig. 5. In this case a value of β_a must be read from the graph at D = minus $0.0079\ \text{mV}^{-1}$, at a height intermediate between the contours for $R = 1.9$ and $R = 2.0$. This point is indicated by a triangle in the figure. The corresponding value of β_c was calculated using the appropriate modification of Eq. [10].

Similar evaluations of the anodic and cathodic Tafel slopes from the data at $\epsilon = 20$ and $\epsilon = 10$ mV are indicated on Fig. 7, and in Table III. The four sets of parameters determined obviously vary over a wide range. For example, the anodic Tafel slope β_a is as low as 42 mV and as high as 85 mV. However, when corrosion currents were calculated from Eq. [3] for each of the pairs of parameters, the reproduction of the polarization data was satisfactory. The data were not of sufficient accuracy to allow distinction among the different sets of Tafel parameters calculated from Eq. [9] and [10].

The parameters of the polarization curves (Eq. [2]) are summarized in Table IV, in comparison with the values derived by Mansfeld (20). The average values of the anodic and cathodic Tafel slopes and the cor-

Table III. Calculation of Tafel slopes from data for the corrosion of iron in 1*N* H_2SO_4 (20)

ϵ (mV)	$i_{\epsilon+}$ (mA)	$i_{\epsilon-}$ (mA)	$-i_{\epsilon+}/i_{\epsilon-}$	$D = (1/\beta_a - 1/\beta_c)$ (mV^{-1})
5	1.59	−1.43	1.113	0.00932
10	3.33	−2.80	1.154	0.00622
20	7.91	−5.41	1.463	0.00826
			Average =	0.0079 mV^{-1}
$R(\epsilon = 10/\epsilon = 5)$	2.102	1.962		
β_a (mV)	85	42		
β_c (mV)	256	62		
$R(\epsilon = 20/\epsilon = 10)$	2.371	1.933		
β_a (mV)	47	53		
β_c (mV)	74	92		

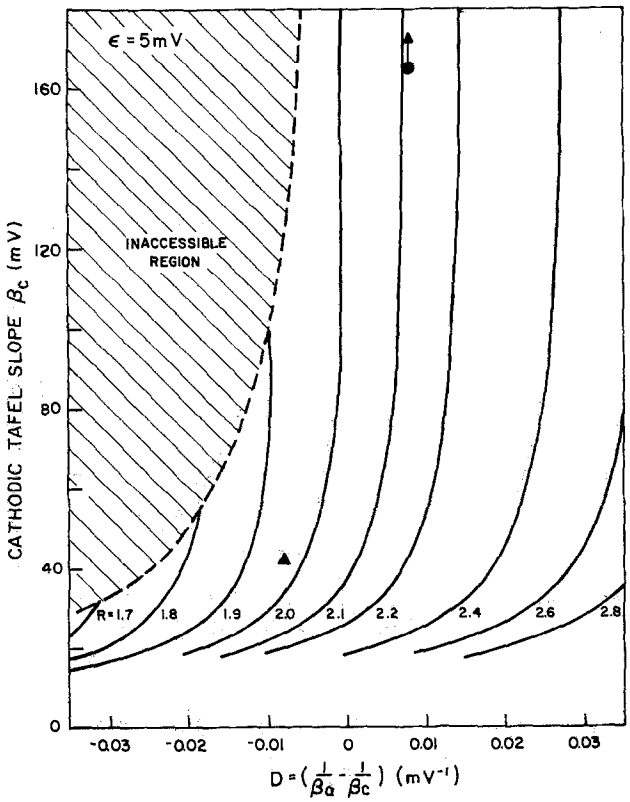


Fig. 5

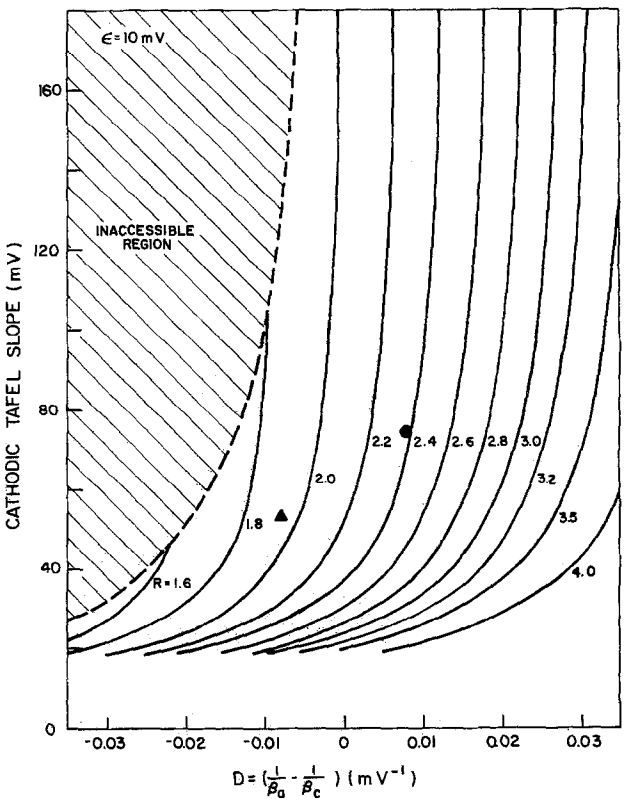


Fig. 7

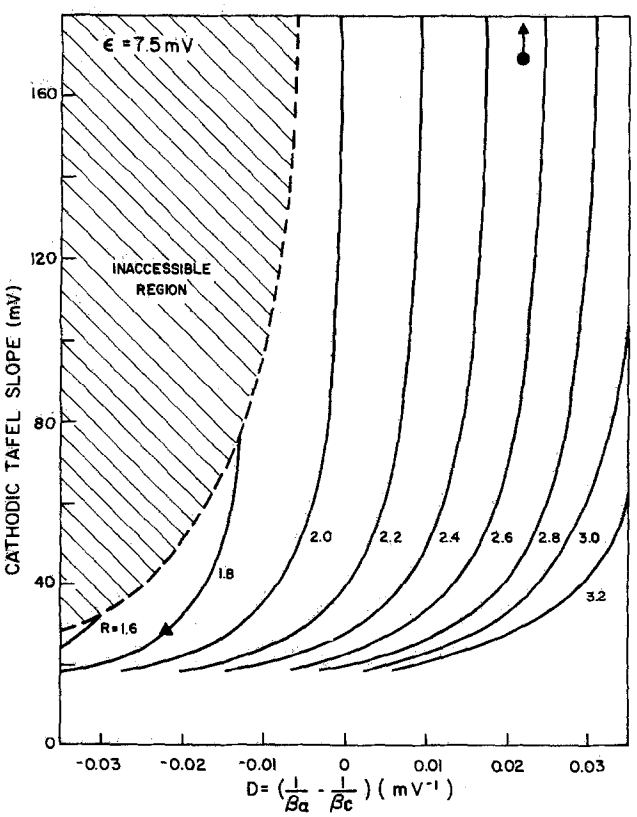


Fig. 6

Fig. 5-7. Relationships between the cathodic Tafel slope β_c and the difference between the inverse anodic and cathodic Tafel slopes. Contours are drawn for realistic values of the ratio of the net currents which flow on polarizations of ϵ and 2ϵ from the corrosion potential. The points are examples for the values of R and D calculated from the data of Tables III (Fig. 5 and 7) and V (Fig. 6). Figures 5-7 can also be used when the polarization ϵ is negative. In this case the ordinate is the anodic Tafel slope, while the abscissa must be read as the negative of D. The triangles are examples of such a determination for the data of Tables III and V.

rosion currents calculated in Table III agree closely with the values derived by the least squares computer fitting procedure. However, the corrosion currents calculated from particular results of Table III differ substantially, ranging from 3.14 to 8.74 mA. The curves corresponding to these extreme values are plotted in Fig. 8. It is apparent that in spite of the differences in the parameter values, both curves reproduce the data within its accuracy. If independent estimates of the Tafel parameters β_a and β_c are not available, the data do not allow more precise estimation of the corrosion current to be made.

The derivation of Tafel parameters which is outlined in Eq. [6]-[10] is similar to the three-point method proposed by Barnartt (24, 26). However, as applied here, these results offer a measure of the sensitivity of the resulting parameters to uncertainty in the experimental data. Furthermore, the resulting best estimates of β_a and β_c are used to calculate the best least

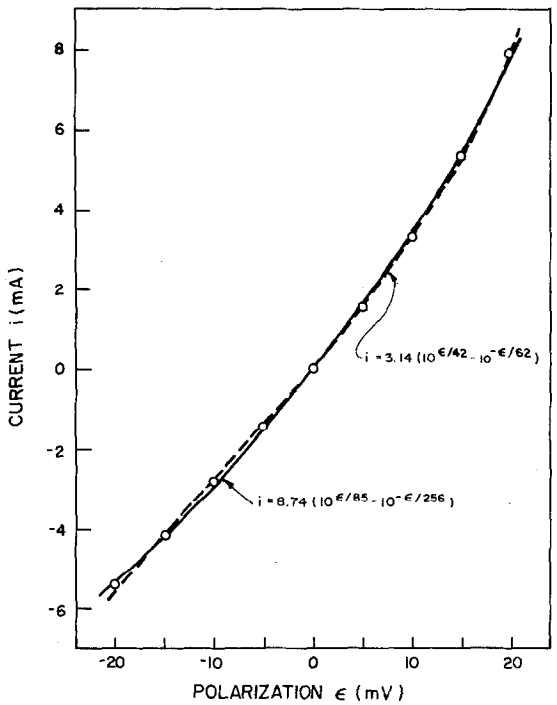


Fig. 8. Polarization data for iron corroding in 1*N* sulfuric acid after 290 min exposure (20). The solid and broken lines are drawn for the extreme values of the Tafel parameters derived from Eq. [5] and [9], as detailed in Table IV.

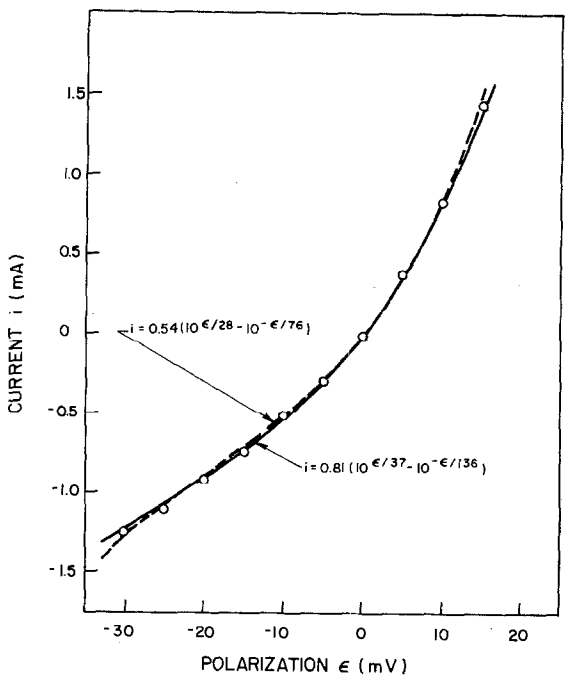


Fig. 9. Polarization data for the corrosion of iron in 1*N* sulfuric acid after 10 min exposure. The broken curve is based on Tafel parameters derived by the method of this paper (Table V), while the solid curve is plotted for the best parameter values obtained by Mansfeld (20) based on a computer analysis of this data.

squares estimate of the corrosion current from the complete experimental data, using Eq. [3].

An Algorithm for Estimation of Tafel Parameters from Nonlinear Polarization Data

The method derived in the preceding sections can be summarized as an algorithm for calculation of Tafel parameters from polarization data near the corrosion potential. The data recorded by Mansfeld (20) for corrosion of iron in 1*N* sulfuric acid after 10 min exposure are used as an example. These data are recorded in Fig. 9, and estimation of β_a and β_c values from them is summarized in Table V.

Values of the net currents flowing at polarizations of plus and minus 7.5 and 15 mV are recorded. Corresponding values of the difference D were determined from Eq. [5] at each polarization value, and their average ($D = 0.0219$ mV^{-1}) was calculated. Values of the ratio R were then calculated for the positive and negative polarizations, and the corresponding values of β_c and β_a were estimated from Fig. 6 or Eq. [9], and Eq. [10]. In the general case, the average of the resulting estimates for each of the Tafel parameters would be calculated, and the corresponding value of the corrosion current would be calculated from the polarization data using Eq. [3].

In the example considered in Table V, no real value of the cathodic slope β_c could be calculated from Eq. [9] and the experimental ratio $R = 2.315$. This indicates that the data were not consistent with the general predicted form of Eq. [2], either because of experimental error, or because the influence of some other reaction was being felt at $\epsilon = 15$ mV. Nevertheless, Tafel parameters of adequate accuracy for corrosion rate estimation could be obtained by consideration of Fig. 6. This indicates that the imaginary value of β_c determined from Eq. [9] reflected inaccuracy in the calculated value of the difference D (Table V). β_c could be taken to be infinity, with $\beta_a = 46$ mV being estimated from this value and Eq. [5]. In this example the Tafel slopes determined from the negative currents were used, $\beta_a = 76$ and $\beta_c = 28$ mV. The corresponding value of the corrosion current calculated from the data points and Eq. [3] was 0.54 mA. The predicted polarization curve (Eq. [2]) for these parameter values is compared in Fig. 9 with the curve predicted using Mansfeld's computer-fitted parameters; $\beta_a = 37$ mV, $\beta_c = 136$ mV, and $i_{corr} = 0.81$ mA. It is clear from the figure that both sets of parameters represent the data equally well within its accuracy, and improved precision in the estimate of the corrosion current is not possible without the use of additional data bearing on the Tafel parameters.

Table IV. Comparison of polarization parameters derived from the degree of nonlinearity (Eq. [9] and [10]) with parameters determined by curve fitting, for iron in 1*N* H_2SO_4 (20)

Source of data	β_a (mV)	β_c (mV)	i_{corr} (mA)
Table III, data at $\epsilon = +5$ and $\epsilon = +10$ mV	85	256	8.74
Table III, data at $\epsilon = -5$ and $\epsilon = -10$ mV	42	62	3.14
Table III, average of 4 determinations of β_c, and corresponding β_a (Eq. [10])	62	121	5.49
Mansfeld (20), curve fitting	55	105	4.86
Mansfeld (20), computer fit	64 ± 13	128 ± 43	5.76 ± 1.50

Conclusions

1. A method is presented for deriving the difference between the inverse Tafel slopes of the anodic and cathodic processes occurring on a corroding metal, based on the degree to which the polarization data is symmetric about the corrosion potential. In some cases,

Table V. Estimation of β_a and β_c values from polarization data*

ϵ (mV)	$i_{\epsilon+}$ (mA)	$i_{\epsilon-}$ (mA)	$i_{\epsilon+}/i_{\epsilon-}$	$D = (1/\beta_a - 1/\beta_c)$ (mV^{-1})
7.5	0.633	−0.416	−1.522	0.0243
15	1.440	−0.734	−1.962	0.0195
R	2.315	1.799	Averages	$D = 0.0219$ mV^{-1}
β_c (mV)	**	76	$\beta_a = 76$ mV	
β_a (mV)	**	28	$\beta_c = 28$ mV	

* Data is for corrosion of iron after 10 min exposure in 1*N* H_2SO_4 (20).
** No real solution for β_c exists for the experimental values of R and D. Values of $\beta_a = 46$ mV, $\beta_c = \infty$ could be used (Fig. 6).

when one of the two Tafel parameters is very large, this information alone suffices to completely define the corrosion current.

2. A measure of the nonlinearity of the polarization data, in either the anodic or cathodic direction, is used to calculate the separate values of the two Tafel slopes.

3. The two basic results are combined into a simple algorithm in which anodic and cathodic Tafel parameters are calculated from four current measurements around the corrosion potential. When used in a previously derived expression for the corrosion current, these parameter values allow the best possible estimate of the corrosion current to be made.

Acknowledgment

I am indebted to Mr. M. B. I. Janjua who obtained the polarization data for corroding zinc which are reported in Fig. 2.

Manuscript submitted Jan. 10, 1977; revised manuscript received Feb. 24, 1977.

Any discussion of this paper will appear in a Discussion Section to be published in the June 1978 JOURNAL. All discussions for the June 1978 Discussion Section should be submitted by Feb. 1, 1978.

Publication costs of this article were assisted by Noranda Research Centre.

REFERENCES

1. M. Stern and A. L. Geary, *This Journal*, **104**, 56 (1957).
2. M. Stern and R. M. Roth, *ibid.*, **104**, 390 (1957).
3. M. Stern, *Corrosion*, **14**, 440t (1958).
4. M. Stern and E. D. Weisert, *Am. Soc. Test. Mater. Proc.*, **59**, 1280 (1959).
5. D. A. Jones and N. D. Green, *Corrosion*, **22**, 200 (1966).
6. D. A. Jones, *ibid.*, **28**, 180 (1972).
7. A. C. Makrides, *This Journal*, **107**, 869 (1960).
8. E. McCafferty and A. C. Zettlemoyer, *J. Phys. Chem.*, **71**, 2444 (1967).
9. F. Mansfeld, *Corrosion*, **32**, 143 (1976).
10. See, for example, J. P. Frenck, U.S. Pat. 3,788,962 (1974); also U.S. Pat. 3,406,101 and 3,250,689.
11. F. Mansfeld, *Corrosion*, **30**, 92 (1974).
12. S. Barnartt, *Corros. Sci.*, **9**, 145 (1969).
13. F. Mansfeld and K. B. Oldham, *ibid.*, **11**, 787 (1971).
14. J. C. Reeve and G. Bech-Nielsen, *ibid.*, **13**, 351 (1973).
15. K. B. Oldham and F. Mansfeld, *Corrosion*, **27**, 434 (1971).
16. K. B. Oldham and F. Mansfeld, *ibid.*, **28**, 180 (1972).
17. A. C. Makrides, *ibid.*, **29**, 148 (1973).
18. G. Palombarini, L. Felloni, and G. P. Cammarota, *ibid.*, **29**, 245 (1973).
19. R. L. LeRoy, *ibid.*, **29**, 272 (1973).
20. F. Mansfeld, *ibid.*, **29**, 397 (1973).
21. F. Mansfeld, *ibid.*, **30**, 320 (1974).
22. R. L. LeRoy, *ibid.*, **31**, 173 (1975).
23. F. Mansfeld, *This Journal* **120**, 515 (1973).
24. S. Barnartt, *Electrochim. Acta*, **15**, 1313 (1970).
25. R. L. LeRoy, Submitted to *Corrosion*.
26. S. Barnartt, *Corrosion*, **27**, 467 (1971).

Electrolytic Deposition of Thin Metal Films on Semiconductor Substrates

P. Bindra, H. Gerischer,* and D. M. Kolb

Fritz-Haber-Institut der Max-Planck-Gesellschaft, 1000 Berlin 33 (Dahlem), West Germany

ABSTRACT

Electrolytic deposition of metals on semiconductor electrodes was studied by a potentiostatic pulse method. Experimental data for the deposition of Pb, Ag, and Pd on ZnO, CdS, n-GaP, n-GaAs, and SnO_2 are analyzed to obtain information regarding the mechanism of deposition and the structure of the deposits. The results suggest that the actual overpotential required for the deposition of a metal depends on the relative position of the redox potential of the metal with respect to the flatband potential of the semiconductor while the nucleation behavior of the metal is influenced by the difference in work functions of the depositing metal and the substrate.

Semiconductor substrates covered with thin metal films are of considerable scientific interest in view of their wide-spread technical application. Metal films in the thickness range of a monolayer to a few monolayers are frequently used for surface studies on semiconductors (1) and in catalysis (2), and their use is gaining increasing importance in Schottky barrier devices (3, 4) and optical energy conversion devices (5).

The deposition of metal films on semiconductor substrates can be achieved either from the vapor phase or by electrolytic deposition in a solution containing ions of the metal. Deposition from the vapor phase occurs very far from equilibrium conditions for the condensate and requires expensive and elaborate equipment. Electrolytic deposition, on the other hand, may be achieved by suitably polarizing the substrate in a solution of the metal ions in a simple electrochemical cell. Whichever method is used, the first step for phase change is the process of nucleation and the nucleation behavior is a function of supersaturation (overpotential in electrolytic deposition) and interfacial energies. The formation of a monolayer of the metal, on the other hand, requires stronger interaction between metal atom and the substrate than between the metal atoms themselves, as has been shown by studies of underpotential deposition of metals on metal substrates (6).

In this publication we present results of a study of the electrolytic deposition of metals on semiconductor electrodes by a potentiostatic pulse method. Experimental data for the deposition of Pb, Ag, and Pd on ZnO, CdS, n-GaP, n-GaAs, and SnO_2 are analyzed to obtain information regarding the mechanism of deposition and the structure of the deposits. It should be emphasized that no attempt is made to analyze the deposition mechanism in any particular system rigorously, as not enough information regarding the exact surface structures of the substrates is available. The aim in this publication is simply to show which

* Electrochemical Society Active Member.

Key words: metal deposition, growth mechanism, overpotential, work function.

factors determine the polarization behavior and the morphology of the metal deposits in electrolytic deposition of metals on semiconductor substrates.

Experimental

The electrochemical cell used was a standard laboratory type. In order to avoid contamination of the solution in the vicinity of the working electrode the cell was designed with separate compartments for the counter and the reference electrodes. The counter-electrode was a Pt foil and the reference electrode a silver wire (Ag^+/Ag) for silver deposition, or a saturated calomel electrode (SCE) for the deposition of Pb and Pd. The working electrodes were all semiconductor single crystals except for SnO_2 which was a polycrystalline film evaporated on a glass substrate. After ohmic contact was made, the crystals were embedded in Teflon cylinders using high chemical resistance Scotch Cast and polished to a mirror finish on a polishing wheel using successively finer grades of diamond paste as the abrasive. Surface damage of the crystals was then removed by subjecting the electrode surface to free chemical etching. The etchants used were 2M HNO_3 for ZnO and CdS and a solution of Br_2 in CH_3OH for n-GaP and n-GaAs. Finally, the electrodes were etched electrochemically by anodic polarization in the solutions in which the metal deposition experiments were carried out.

The solutions used were prepared with triply distilled water and Analar grade salts. The base electrolyte in each case was 1M KNO_3. Lead and silver ion solutions were made from $Pb(NO_3)_2$ and $AgNO_3$, respectively. Palladium ion solution was made by boiling PdO in concentrated nitric acid until all the salt had dissolved. The concentration of the metal ions used in the deposition experiments was 10^{-3}M in each case.

The experimental method used was the potentiostatic step method. Potential control of the working electrode was achieved using a potentiostat (PAR 173) in conjunction with a waveform generator (PAR 175 universal programmer) which was capable of providing both potentiostatic pulses and linear potential sweep profiles. The current-potential curves and the current-time transients obtained were recorded on a X-Y-t recorder.

The potential range in which metal deposition on a particular semiconductor electrode occurred was determined by obtaining current-potential curves. The capacity-potential curves for the Mott-Schottky plots were obtained by superimposing a 30 mV a-c signal of 800 Hz on the linear potential sweep.

Results

Current-time transients.—In the potentiostatic pulse method the potential of the working electrode is stepped from a potential anodic to the deposition potential for the metal to a potential range where deposition of the metal occurs. As a result, current-time transients are obtained which were compared with theoretically calculated expressions (7, 8) to ascertain the nucleation behavior and the growth mechanism for the deposition reaction.

Electrolytic deposition of metals is a highly complex process. Metal ions exist in solution as cations or complex anions and the deposition of the metal is a function of mass transfer, the charge transfer rate and its mechanism, nucleation, and crystal growth. In the case of semiconductor electrodes there is the added complication of the space charge layer inside the semiconductor which will influence the current distribution between surface parts already covered by the deposit and those which are still uncovered. Theoretical current-time curves for deposition reactions controlled by several combinations of these stages have been calculated (7, 8). When deposition of a metal is controlled by processes of nucleation and crystal growth (which is often the case on metal substrates) then rising transients of the form $i \sim t^n$ are predicted where n is a constant depending on the geometry and type of nucleation (7). Peaks in the current-time transients are predicted when two-dimensional layer growth of the metal takes place or when three-dimensional growth leading to passivation occurs (9). The falling parts of the transients are usually due to mass transport limitations.

Deposition on zinc oxide.—Lead.—The current-potential curve obtained by the application of a linear potential sweep profile for the deposition of Pb on ZnO showed that the deposition occurs at *ca.* −465 mV *vs.* SCE. The reversible potential measured for bulk lead in the same solution gave the value −460 mV/SCE. Therefore, the overpotential required for the deposition of Pb on ZnO is *ca.* −5 mV.

Current-time transients obtained for metal deposition by the potentiostatic pulse method are shown in Fig. 1. These curves have the characteristic shape often observed for the deposition of metals on metal substrates. The analysis of the rising part of the transients at higher overvoltages suggests nucleation of three-dimensional growth centers (9). At longer times the experimental curves show a falling current which is due to the onset of diffusion control.

Silver.—The deposition of Ag on ZnO requires rather high overpotentials, in the range −280 to −340 mV. The magnitude of the overpotential is explained in the discussion section in terms of the difference between the flatband potential of the semiconductor and the redox potential of the metal. Current-time transients for this deposition reaction are shown in Fig. 2. It is observed that the currents rise approximately linearly with time, the slight curvature at higher deposition potentials being due to the onset of diffusion. Clearly, these curves measure nucleation only and tell us nothing about crystal growth (10). Electron micrographs of the electrode surface showed instantaneous nucleation of three-dimensional growth centers.

Palladium.—The value of the overpotential required for the deposition of Pd on ZnO is quite high, over 400 mV. It is higher than the overpotential at which Pd deposition on palladium metal substrate occurs.

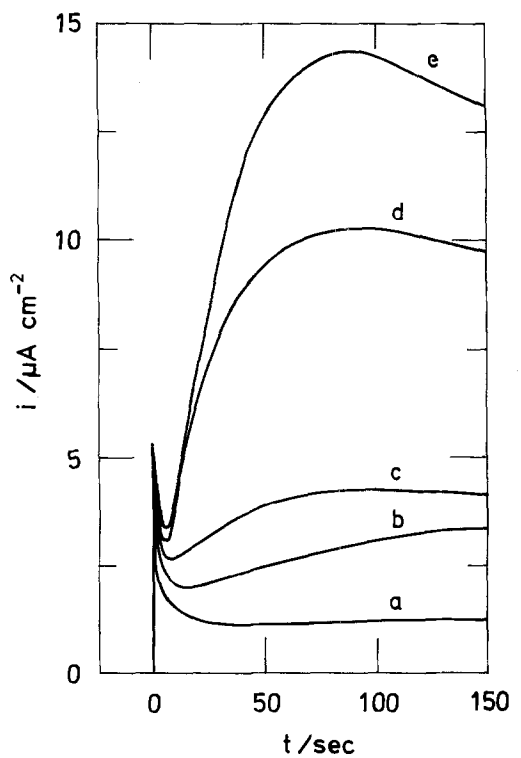


Fig. 1. Current-time transients for lead deposition on ZnO. Potentials stepped from +500 mV *vs.* SCE to (a) −520 mV, (b) −535 mV, (c) −545 mV, (d) −560 mV, (e) −565 mV.

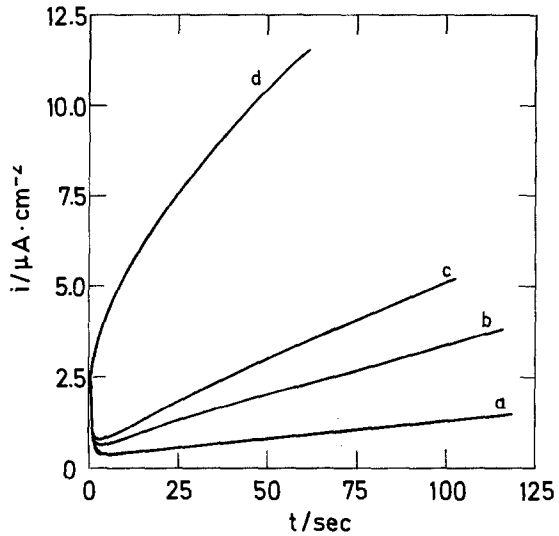


Fig. 2. Current-time transients for silver deposition on ZnO. Potentials stepped from +500 mV *vs.* Ag^+/Ag to (a) −280 mV, (b) −300 mV, (c) −320 mV, (d) −340 mV.

The acidic character ($pH = 1$) of the solution from which Pd is deposited on ZnO affects the deposition reaction in that the electrode surface undergoes chemical etching at the same time as the metal deposition occurs, thus giving rise to distorted current-time transients. The rising part of the current-time transients, shown in Fig. 3, suggests growth via progressive nucleation of three-dimensional growth centers. This growth mechanism was verified by microscopic examination of the electrode surface using a scanning electron microscope (Fig. 4). This micrograph shows nuclei of all ages (progressive nucleation) growing at the sides and the bottom of an etch pit.

Deposition on cadmium sulfide.—Lead.—The overpotential at which the deposition of Pb on CdS begins was shown by the voltammograms to be *ca.* −15 mV. Current-time transients for this deposition reaction show a slowly decaying current initially, but at longer times the current begins to rise again as processes of nucleation and crystal growth become rate determining. It is found that the deposition process is rather slow in the dark, but is strongly influenced by light with $\hbar\omega > 2.5$ eV (11).

Silver.—The transient response to the application of potential steps for the deposition of Ag on a CdS electrode is shown in Fig. 5. The reference electrode used in this case was a silver wire (Ag^+/Ag) and therefore the potentials given in Fig. 5 are the actual overpotentials. An interesting feature of this deposition reaction is seen in Fig. 5a where the deposition

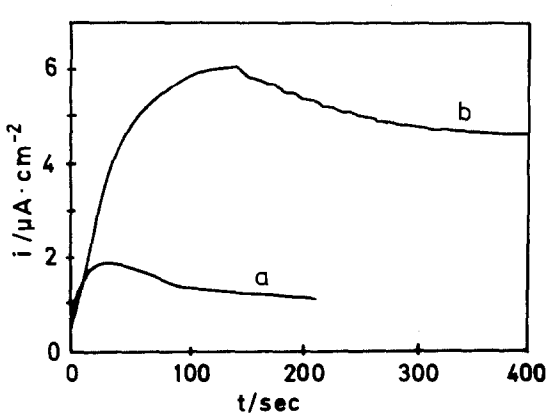


Fig. 3. Current-time transients for Pd deposition on ZnO. Potentials stepped from +1.0V *vs.* SCE to (a) +230 mV, (b) +220 mV.

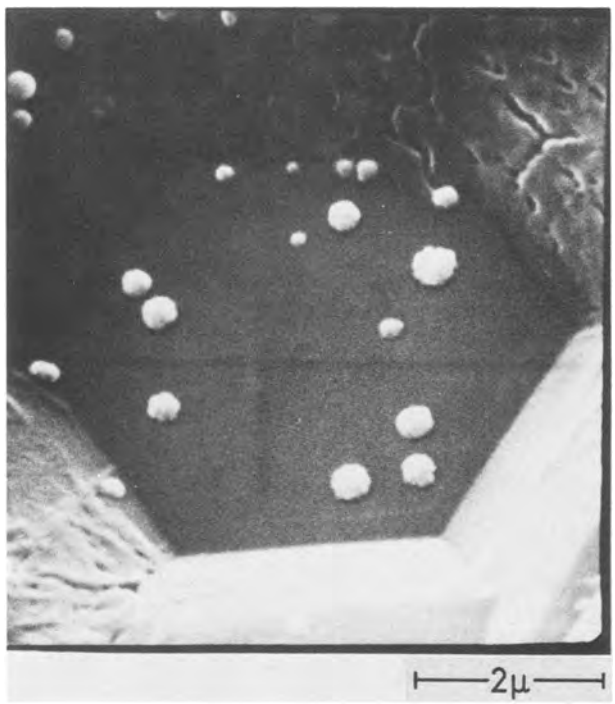


Fig. 4. Scanning electron micrograph of palladium deposited on ZnO.

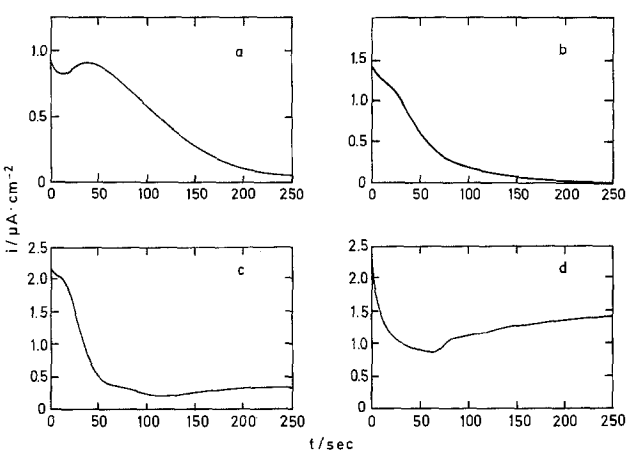


Fig. 5. Current-time transients for silver deposition on CdS. Potentials stepped from +500 mV *vs.* Ag^+/Ag to (a) +25 mV, (b) 0 mV, (c) −50 mV, (d) −100 mV.

of the metal occurs at potentials anodic to the thermodynamic reversible potential, *i.e.*, it appears as though there is underpotential deposition of Ag on CdS substrate. It is also of interest to note that the current-time transients at all overpotentials show an unsymmetrical peak of approximately constant area in the beginning. Integration of the peak shows that the charge passed is close to that required for the formation of a two-dimensional monolayer. It is very likely (7), therefore, that such a monolayer of Ag is formed on CdS when the potential is stepped to a region close to the equilibrium potential of silver.

Palladium.—The overpotential at which the deposition of Pd on CdS takes place is *ca.* −310 mV. This value still differs from the overpotentials at which Pd deposition on metal substrates occurs. Analysis of the current-time transients, shown in Fig. 6, indicates the growth of instantaneously nucleated three-dimensional nuclei.

Deposition on n-gallium phosphide.—Lead.—The current-potential curve obtained for the deposition of Pb on n-GaP showed that the deposition occurs at an overpotential of −590 mV. The current-time tran-

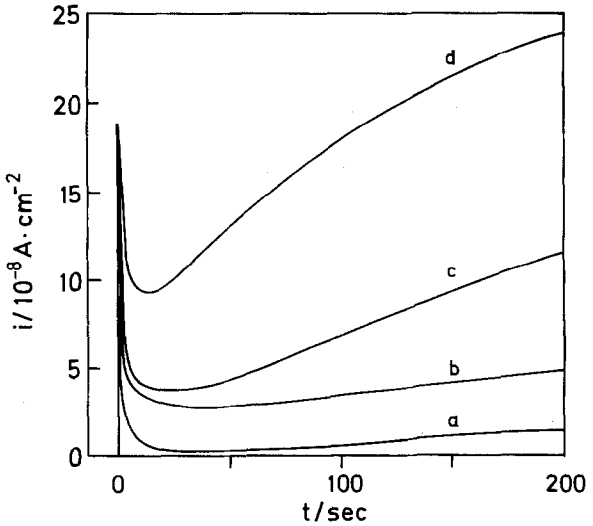


Fig. 6. Current-time transients for palladium deposition on CdS. Potentials stepped from +1.0V *vs.* SCE to (a) +337 mV, (b) +300 mV, (c) +285 mV, (d) +270 mV.

sients showed only a current decreasing with time. No characteristic features could be discerned and so the transients could not be analyzed without doing further supplementary experiments.

Silver.—The overpotential at which deposition of Ag on n-GaP occurs is *ca.* −700 mV. This is a very large overpotential in comparison with the overpotentials at which Ag deposition on metal substrates occurs. The experimental current-time transients obtained for this deposition reaction are shown in Fig. 7. The analysis of these curves shows that metal deposition occurs via instantaneous nucleation of (hemi)spherical growth centers and their subsequent three-dimensional growth controlled by transport processes (12). At short times the current increases due to the increasing area of contact between the substrate and the growing nuclei.

Palladium.—The deposition of Pd on n-GaP occurs at overpotentials greater than −800 mV. These overpotentials are much larger than the overpotential required for the deposition of Pd on metal substrates. Analysis of the current-time transients for the deposition of Pd on n-GaP at these overpotentials indicates progressive nucleation of three-dimensional growth centers. Transients at even higher overpotentials, however, indicate layer growth of the metal.

Deposition on n-gallium arsenide.—Lead.—The overpotential at which deposition of Pb on n-GaAs occurs was shown by current-potential curves to be *ca.* −160 mV. However, no additional information could be obtained from current-time transients, which had no characteristic features.

Silver and palladium.—Experiments, done with n-GaAs in solutions containing Ag^+ and Pd^{2+}, showed that deposition of these two metals also took place by simply dipping the electrode into the solution. Here, we obviously have a case of currentless deposition via hole injection by the metal ions. The analysis of current-time transients, as well as electron micrographs of these deposits, revealed layered structure. A possible explanation for the layer growth being favored in the case of hole injection into the semiconductor is given in the next section. A more extensive study on currentless metal deposition onto semiconductor electrodes will be presented later.

Deposition on tin dioxide.—Lead. —The deposition of Pb on SnO_2 starts at a low overpotential of only −2 mV. This is also the magnitude of the overpotential at which Pb deposition on metal substrates takes place. Current-time transients for the deposition reaction are shown in Fig. 8. It is observed that the form of the transients does not change over quite a large overpotential range. A peak in the transients at all overpotentials suggests a layer growth of the metal.

Silver.—The overpotential required for the deposition of Ag on SnO_2 is −35 mV. This value is similar to the overpotential at which Ag deposition on carbon (10) occurs. Potentiostatic current-time transients for the deposition of Ag on SnO_2 are similar to those for the deposition of Ag on ZnO and show that the current increases linearly with time until planar diffusion becomes rate determining. The theoretical transient for such a growth law predicts instantaneous nucleation, but, the potential dependence of the current suggests (13) that this is the case of nucleation at

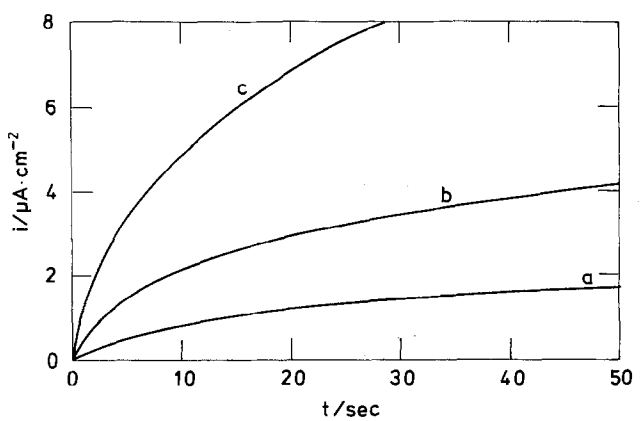


Fig. 7. Current-time transients for silver deposition on n-GaP. Potentials stepped from +500 mV *vs.* Ag^+/Ag to (a) −700 mV, (b) −733 mV, (c) −766 mV.

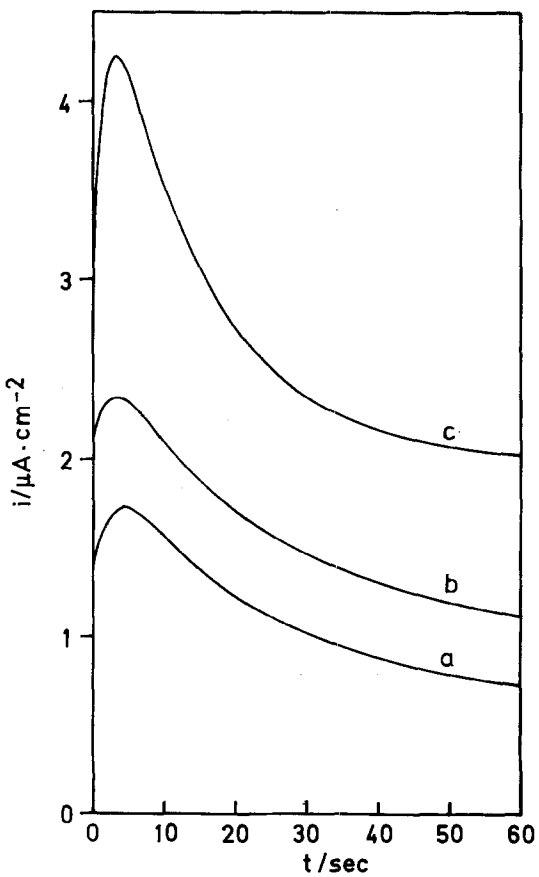


Fig. 8. Current-time transients for lead deposition on SnO_2. Potentials stepped from +500 mV *vs.* SCE to (a) −480 mV, (b) −520 mV, (c) −550 mV.

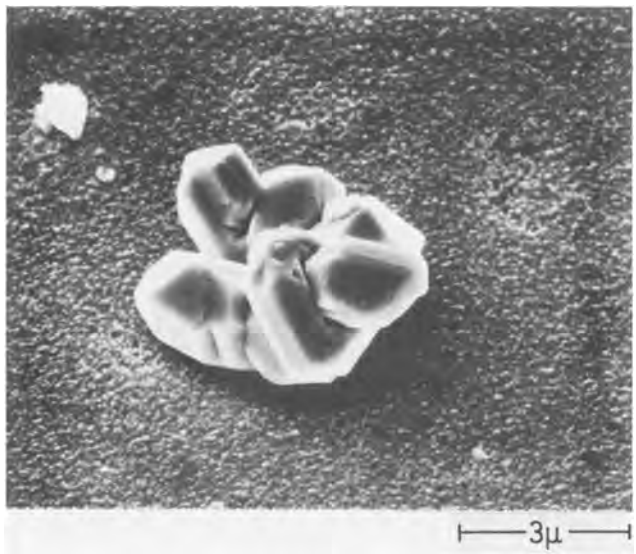


Fig. 9. Scanning electron micrograph of silver deposited on SnO_2.

the same site, *i.e.*, on top of existing nuclei. This is confirmed by the electron micrograph, Fig. 9, which shows the formation of three-dimensional single crystals of the metal.

Palladium.—Deposition of Pd on SnO_2 takes place at overpotentials below −300 mV. These values compare well with the overpotentials at which Pd deposition on metal substrates occurs. Current-time transients are shown in Fig. 10 and their analysis (Fig. 10b) indicates that Pd deposition takes place through progressive nucleation of three-dimensional growth centers whose subsequent growth is controlled by mass transfer in solution.

Discussion

The central question in the study of metal deposition on semiconductor electrodes is the extent to which the nature of the substrate influences the metal deposition reaction. The results of this investigation are discussed from two aspects: (*i*) the large overpotentials required for the deposition of some metals on semiconductor electrodes, and, (*ii*) the effect of the metal-semiconductor junction barrier on the nucleation behavior of the metal.

Metal deposition overpotential on semiconductor substrates.—The apparent overpotentials required for the deposition of Pb, Ag, and Pd on different semiconductors are summarized in Table I. It is observed that much larger overpotentials are usually required for the deposition of noble metals on semiconductors than is the case when deposition on metal substrates

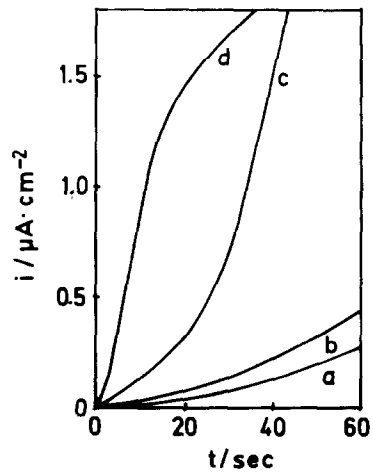


Fig. 10a. Current-time transients for palladium deposition on SnO_2. Potentials stepped from +1.0V *vs.* SCE to (a) +392 mV, (b) +385 mV, (c) +380 mV, (d) +370 mV.

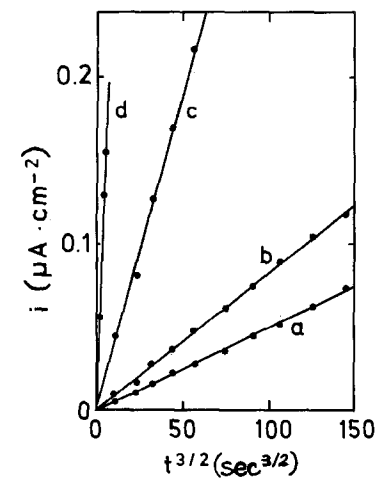


Fig. 10b. *i vs.* $t^{3/2}$ plots using data of Fig. 10a

occurs. This difference can be associated with the difference in the distributions of electronic charge at the semiconductor-electrolyte interface and the metal-electrolyte interface. A metal electrode immersed in the solution of an electrolyte develops a double layer at the metal-electrolyte interface. When a potential step is applied to such an electrode system all the charge appears at the surface and most of the potential drop occurs in the compact Helmholtz layer for solutions of high ionic strength. Electrons are always available in the surface of a metal in large enough concentrations to interact with the metal ions in solu-

Table I. Apparent overpotentials η and electron surface concentrations at the deposition potential, n_s^D, and at the equilibrium potential, n_s°, for the deposition of Pb, Ag, and Pd on various semiconductors. Work function data φ are taken from Ref. (16)

Substrate (donor concentration n_o/cm^{-3})	Flatband potential, V_{fb} *vs.* SCE pH = 5	pH = 1		Metals deposited Pb	Ag	Pd
			φ/eV	4.0	4.3	5.0
			V_o/V_{SCE}	−0.46	+0.38	+0.65
			pH	5	5	1
			η, mV	−2	−35	−260
SnO_2			n_s^D/cm^{-3}	Degenerate	10^{13}	10^{17}
(1×10^{19})	+0.02	+0.26	n_s°/cm^{-3}	Degenerate	10^{13}	10^{12}
			η, mV	−5	−280	−420
ZnO			n_s^D/cm^{-3}	Degenerate	10^{10}	10^{12}
(7×10^{15})	−0.22	+0.02	n_s°/cm^{-3}	Degenerate	10^{5}	10^{5}
			η, mV	−15	+25	−310
CdS			n_s^D/cm^{-3}	10^{13}	10^{-3}	10^{-1}
(1×10^{16})	−0.65	−0.63	n_s°/cm^{-3}	10^{13}	10^{-2}	10^{-7}
			η, mV	−590	−700	−830
n-GaP			n_s^D/cm^{-3}	10^{11}	10^{-2}	1
(4×10^{17})	−1.42	−1.18	n_s°/cm^{-3}	10^{1}	10^{-14}	10^{-14}
			η, mV	−160		
n-GaAs			n_s^D/cm^{-3}	10^{7}	Currentless by	Currentless by
(3×10^{17})	−1.22	−0.98	n_s°/cm^{-3}	10^{4}	hole injection	hole injection

tions, first for the formation of discharged atoms and then of the nuclei of the metal. Hence, for metal deposition on metal substrates only small overpotentials of a few millivolts are required to overcome the nucleation energy barrier before deposition of the metal occurs.

In the case of a semiconductor electrode the picture is totally different. As long as the semiconductor is not very highly doped, excess charge on the semiconductor electrode is distributed over an extended space charge layer. As a result the potential drop in the Helmholtz double layer can only be changed very little by the applied potential. However, due to the low density of mobile charge carriers (electrons of the conduction band in the n-type semiconductors, used in these experiments) the concentration of electronic charge carriers varies markedly with the electrode potential. Since electrons are needed for the metal ion discharge, there will be a critical concentration of electrons necessary to cause enough interaction with metal ions in solution to start nucleation of a metal deposit. The possibility of metal deposition and the overpotential required will therefore depend on the concentration of electrons in the surface of a particular semiconductor available at the equilibrium potential of the metal to be deposited. One can calculate the surface concentration of electrons for a semiconductor electrode as a function of the electrode potential V, if the flatband potential V_{fb} of the semiconductor is known. Denoting the bulk electron concentration with n_o, the approximate surface concentration of electrons, n_s, is given by

$$n_s \approx n_o \exp\left[-e_o\,(V - V_{fb})/kT\right]$$

Using this expression, we obtain a rough estimate of the surface electron concentration in the semiconductor at the equilibrium potential, V_o, of the metal and at the potential, V_D, where electrolytic deposition begins. These data are also presented in Table I for the systems studied.

The flatband potentials of the semiconductor electrodes at two different pH values are given in Table I. These values, except for SnO_2 were deduced from Mott-Schottky plots and are in good agreement with values reported by others (14). The values for SnO_2 were obtained from literature (15). In Fig. 11 the energy levels of the various semiconductors in solutions of pH = 5 and 1 are shown on the potential scale together with the equilibrium potentials of the metals deposited. These redox potentials were measured in the same cell in which deposition studies were carried out and their values agree reasonably well with literature values for metal ion concentrations of 10^{-3}M.

Inspection of Fig. 11 reveals immediately why in some cases such large overpotentials are required for metal deposition. Whenever the equilibrium potential of the metal is well below the conduction bandedge of the semiconductor, the concentration of electrons at the electrode surface is much too low to facilitate metal ion discharge. Comparing the calculated n_s values at the potentials V_o and V_D (Table I), the various systems may be separated into three groups: (*i*) the metallike substrate. When the redox potential of the metal is close to or above the conduction bandedge an accumulation layer is formed. Then enough electrons are available at V_o to allow deposition without appreciable overpotentials. This is certainly the case for the deposition of Pb on SnO_2 and ZnO, and most likely also for the deposition of Ag on SnO_2 and Pb on CdS. In these cases the overpotential is determined by the nucleation barrier of the metal and not by the semiconductor properties. This is also true for Pd on SnO_2 where the observed large overpotental is characteristic of Pd. As is seen in Table I, n_s at V_D for Pd is several orders of magnitude larger than the critical value; therefore no restrictions from the semiconductor are expected. (*ii*) Semiconductor

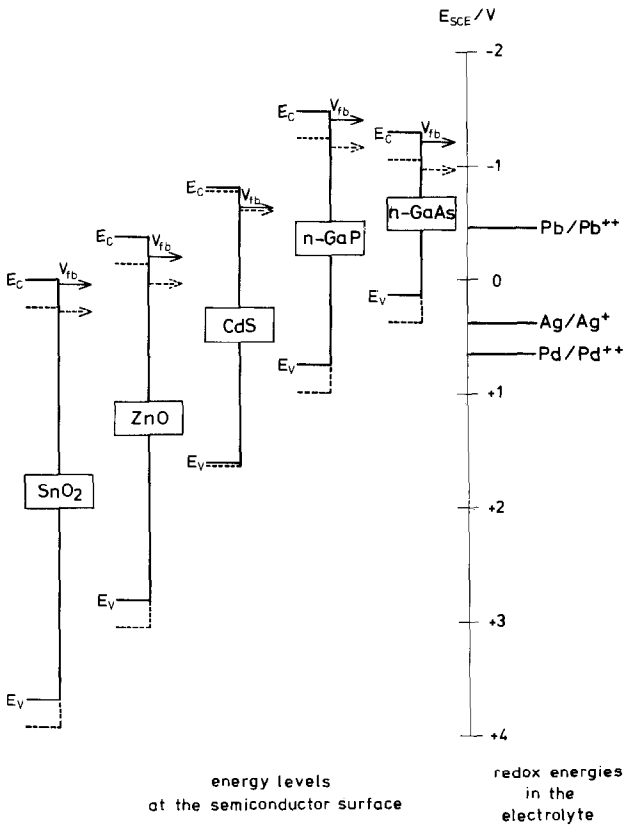


Fig. 11. Energy level diagram for the semiconductor/electrolyte interface. The flatband potentials V_{fb} of the various semiconductors are given for solutions of pH = 5 (——) and pH = 1 (– – –). The equilibrium potentials of the metals are shown on the right.

restriction due to low n_s. For Pb on n-GaAs and n-GaP, and Ag and Pd on ZnO the electron concentration at the equilibrium potential is too low to facilitate deposition. Therefore the potential has to be raised until a critical concentration of about 10^{10} electrons per cm^3 is available at the surface for all cases, before the deposition reaction can start. (*iii*) Chemical interaction with the substrate. For Ag and Pd on CdS, n-GaP, and n-GaAs the n_s values even at the deposition potentials are much too low to explain these overpotentials. Obviously in these cases a strong chemical interaction between semiconductor substrate and metal deposit helps deposition despite the low level of free electrons. This is most easily explained for Ag and Pd on n-GaAs, where currentless deposition by hole injection is possible (see Fig. 11) and indeed observed. To a much lesser extent the currentless deposition also occurs when n-GaP is brought into contact with solutions containing Ag^+ and Pd^{2+} ions. Since the hole in the semiconductor surface, describing a dangling bond, and the metal adatom are two rather reactive species, they will interact strongly with each other and form a stable bond. In the case of Ag and Pd on CdS the interaction between the metal atoms and S^{--} may lead to a polar bond, favoring the discharge of the metal ion. For Ag on CdS there is still the added complication of an exchange reaction occurring between the Cd ions in the lattice and Ag^+ in solution, forming a surface of presumably Ag_2S. This is analogous to the formation of a film of Cu_2S on a CdS crystal, when the latter is brought into contact with cuprous ions (17, 18). An investigation of this reaction has just been completed in this laboratory (19). A general consequence of the strong interaction between substrate and metal-adatom is the formation of a monolayer (6), which may manifest itself in the shape of the current-transients, in electron micrographs or in the occurrence of an underpotential deposition as in the case of Ag on CdS.

Effect of the metal-semiconductor junction barrier on the growth mechanism.—It is known from the thermodynamics of heterogeneous nucleation (20) that nucleation and growth behavior during metal deposition on a metal substrate is a function of the surface energies of the nucleate and the substrate. The experimental data obtained in this investigation, on the other hand, show that for semiconductor substrates it is the difference in work functions of the depositing metal and the substrate which mainly determines the growth behavior.

Deposition of metals on all substrates begins with the nucleation of minute clusters of the new phase formed at energetically favorable sites on the substrate. In the case of semiconductor electrodes, even small clusters consisting of only a few metal atoms in contact with the semiconductor constitute localized Schottky barriers. These contacts are in parallel to the semiconductor-electrolyte contact and thus modify the space-charge layer, which leads to a new distribution of charge at the surface as shown in Fig. 12. For a metal with a high work function the depletion layer at the contacts is extended due to charge accumulation in the deposit (see Fig. 12a), resulting in the formation of an additional barrier at the semiconductor-metal interface. Charge transfer on top of the existing metal nuclei is then more restricted by the availability of electrons so that a metal ion approaching the electrode surface would thus find it more favorable to deposit on the exposed parts of the electrode surface. That is, this system encourages progressive nucleation and therefore rapid coverage of the electrode by a layerlike growth of the metal. This is confirmed by the experimental data for the deposition of Pd on the n-type semiconductor electrodes investigated.

For a metal with a low work function (*e.g.*, Pb and Ag, see Table I) the picture is reversed. The depletion layer width at the metal-semiconductor contacts decreases so that the availability of electrons in these regions increases and the distribution of charge at the nucleus-electrolyte interface tends somewhat toward the distribution in the Helmholtz layer at a normal metal-electrolyte interface. The metal nuclei then become preferential sites for further phase change and prevent any further nucleation on the substrate. Such a system therefore encourages instantaneous nucleation. Experimental data for the deposition of Pb and Ag on the semiconductor substrates show that the metal deposition indeed occurs via instantaneous nucleation of the growth centers.

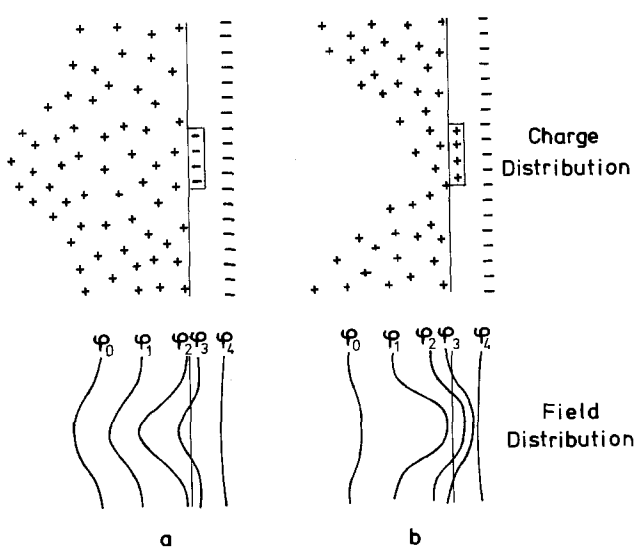


Fig. 12. Charge and field distributions in the space-charge layer of a semiconductor in contact with the nuclei of a metal with (a) high and (b) low work function.

In summary we have shown the dependency of the overpotential on the relative position of the redox potential of the metal with respect to the flatband potential of the semiconductor and the role played by the metal work function in influencing the nucleation behavior during deposition. Deviations from these observations are due to chemical interaction between the metal and the substrate and these interactions are the subject of a separate investigation in this laboratory.

Manuscript submitted Dec. 21, 1976; revised manuscript received Feb. 28, 1977.

Any discussion of this paper will appear in a Discussion Section to be published in the June 1978 JOURNAL. All discussions for the June 1978 Discussion Section should be submitted by Feb. 1, 1978.

REFERENCES

1. D. E. Eastman and J. L. Freeouf, *Phys. Rev. Lett.*, **34**, 1624 (1975).
2. H. Gerischer, B. Pettinger, and M. Lübke, in "Proceedings of the Symposium on Electrocatalysis," M. W. Breiter, Editor, p. 162 The Electrochemical Society Softbound Symposium Series, Princeton, N.J. (1974).
3. See, *e.g.*, "Proceedings of the Symposium on Electronic and Structural Properties of Interfaces," *J. Vac. Sci. Technol.*, **11** (1974).
4. A. G. Milnes and D. L. Feucht, "Heterojunctions and Metal-Semiconductor Junctions," Academic Press, New York and London (1972).
5. Y. Nakato, T. Ohnishi, and H. Tsubomuro, *Chem. Lett., Chem. Soc. Jpn.*, p. 883 (1975).
6. D. M. Kolb, M. Przasnyski, and H. Gerischer, *J. Electroanal. Chem.*, **54**, 25 (1974).
7. M. Fleischmann and H. R. Thirsk, in "Advances in Electrochemistry and Electrochemical Engineering," Vol. 3, P. Delahay and C. W. Tobias, Editors, p. 123, Interscience, New York (1963).
8. J. A. Harrison and H. R. Thirsk, in "Electroanalytical Chemistry," Vol. 5, A. J. Bard, Editor, p. 67, Dekker, New York (1971).
9. R. D. Armstrong, M. Fleischmann, and H. R. Thirsk, *J. Electroanal. Chem.*, **11**, 208 (1966).
10. M. F. Bell and J. A. Harrison, *ibid.*, **41**, 15 (1973).
11. D. M. Kolb and H. Gerischer, *Electrochim. Acta*, **18**, 987 (1973).
12. D. J. Astley, J. A. Harrison, and H. R. Thirsk, *Trans. Faraday Soc.*, **64**, 192 (1968).
13. J. A. Harrison, *J. Electroanal. Chem.*, **36**, 71 (1972).
14. W. P. Gomes and F. Cardon, *Z. Phys. Chem. NF*, **86**, 330 (1973) and references therein.
15. F. Möllers and R. Memming, *Ber. Bunsenges. Phys. Chem.*, **76**, 469 (1972).
16. S. Trasatti, *J. Electroanal. Chem.*, **33**, 351 (1971).
17. W. F. Tseng and I. G. Greenfield, *Phys. Status Solidi A*, **26**, 643 (1974).
18. J. A. Borders, *This Journal*, **123**, 37 (1976).
19. H. Gerischer and M. Lübke, In preparation.
20. R. A. Sigsbee and G. M. Pound, *Adv. Colloid Interface Sci.*, **1**, 335 (1967); D. A. Vermilyea, in "Advances in Electrochemistry and Electrochemical Engineering," Vol. 3, P. Delahay and C. W. Tobias, Editors, Interscience, New York (1963).

Solar Conversion Efficiency of Pressure Sintered Cadmium Selenide Liquid Junction Cells

B. Miller,* A. Heller,* M. Robbins, S. Menezes,
K. C. Chang, and J. Thomson, Jr.

Bell Laboratories, Murray Hill, New Jersey 07974

ABSTRACT

Pressure sintered electrodes of cadmium selenide subsequently doped with cadmium vapor have shown solar energy conversion efficiencies approaching ¾ of those of single crystal specimens in sunlight experiments. The cell CdSe/1F Na_2S-1F S-1F NaOH/C has operated at 5.1% conversion efficiency under AM2 conditions with polycrystalline electrodes. The relatively small sacrifice of efficiency from single crystal values of 7.5 ± 0.5% suggests the possibility of substantial cost advantage. The temperature and pressure conditions, cadmium doping procedure, material characterization, and the voltammetric behavior of the cell are discussed.

A major advantage of semiconductor liquid junction solar cells (1) with direct gap materials is their compatibility with polycrystalline electrodes (2-10). Since light is absorbed and holes are transferred to a solution redox couple at the same interface, high efficiency and little effect of grain boundaries are anticipated if the crystallite size is at least comparable to the light absorption depth. This dimension is of the order of 1μ for direct bandgap semiconductors (*i.e.*, those excited in transitions not involving transfer of momentum to phonons). These semiconductors include the cadmium chalcogenides, GaAs, and InP.

Since the preparation of single crystals is probably the most expensive step in producing photovoltaic cells, considerable economic advantage is expected from utilization of polycrystalline materials with efficiencies close to those of the single crystal in liquid junction based cells. Pressure sintering of semiconductor crystallites (initially prepared by conventional chemistry) is one excellent possibility for such a material. The technique can be automated, and disks or sheets of the polycrystalline material, convenient for solar energy converting electrolytic cells, can be formed.

In this work, cadmium selenide powder has been pressure sintered under controlled temperatures and pressures and doped with cadmium by heating the composite in the presence of the metal at controlled temperature. The n-type product resulting has been compared for performance relative to that of doped single crystal electrodes in the cell (11) CdSe/1F Na_2S-1F S-1F NaOH/C at typical solar irradiance levels, both in controlled laboratory and outdoor tests. Studies of CdSe photoelectrodes have been made previously (12-16).

Experimental

CdSe powder (99.999%, −325 mesh) from Alfa-Ventron was pressure sintered at temperatures in the range 925°-1100°C, usually near 10,000 psi for 2 hr. The resulting disks of about 3 mm thickness and 2.5 cm diameter were sliced in half, then annealed over Cd metal in evacuated quartz tubes at temperatures of 500°-700°C for 16-160 hr. Indium and silver epoxy electrical contacts to the sliced pellets and crystals were used. The electrode configuration, cells, and electronics were similar to those cited earlier (11, 17). The CdSe crystals were obtained from Cleveland Crystals, Incorporated as doped 1 cm^2 × 1 mm slices with resistivities in the range 1-10 Ω-cm and as a pure boule which was cut and Cd doped in the manner described for the pressed composites, but at 800°C.

The data compiled in Table I were obtained for a stationary CdSe electrode in a magnetically stirred cell with large area carbon counterelectrode. The comparable data in Table II were taken at rotating CdSe disk electrodes under three-electrode potentiostatic control where the zero cell voltage condition was that given by a carbon rod reference electrode. Thus the current-potential traces did not include any contribution from the polarization of a second carbon electrode used as a counterelectrode and were minimally affected by cell *iR* drop. We note that the latter two factors could be made very small in a suitable cell, as was the case for the one employed for Table I, in which negligible polarization of the working (large) carbon cathode relative to a carbon reference electrode was confirmed. The data of the two tables are thus equivalent in their estimate of cell efficiencies for solar conversion in spite of the operational differences. We note a higher level of efficiency for our cells [see also Ref. (11)] relative to the cell cited by Ellis, Kaiser, and Wrighton (12) where the values decline severely with light intensity as solar levels of irradiance are approached.

Polycrystalline CdSe was also formed by anodizing N5 Cd metal in 1M K_2Se-1M KOH, made by bubbling H_2Se (Matheson) in aqueous KOH. Anodization at 4 mA/cm^2 was continued for 16 hr. The electrodes were then etched in glacial acetic acid for 1 min. The anodic procedure for preparing CdSe is similar to that given by us for *in situ* formation of sulfide semiconductors (17).

All experiments were performed under argon or nitrogen atmospheres. Prior to use, all electrodes except the anodic film were etched in 3:1 or 4:1 HCl-HNO_3. All exposed electrode areas were approximately 0.3 cm^2.

The data in Table I were obtained with sunlight at approximately AM2 irradiances. Table II data were

Table I. CdSe cell performance in sunlight

CdSe sample	Solar irradiance (mW/cm²)	Short-circuit current density (mA/cm²)	Open-circuit voltage (V)	Fill factor	Overall efficiency
Crystal 1 <111> face	75	14	0.71	0.57	7.5
Pressed pellet 2	71	12	0.67	0.45	5.1
Cd(99.9%) anodized in K_2Se solution	75	4.6	0.41	0.25	0.6

* Electrochemical Society Active Member.
Key words: photoelectrochemical energy conversion, polycrystalline electrodes, semiconductors, solar cells.

Table II. Preparation and comparative performance of pressed CdSe electrode

CdSe sample	Method of preparation			Method of Cd anneal		Density, % of crystalline	Grain size, μ	Relative short-circuit* current	Relative conversion efficiency	Open-circuit voltage	Fill factor
	T, °C	p, kpsi	t, hr	T, °C	t, hr						
Crystal 1	—	—	—	—	—	—	—	1.00	1.00	0.747	0.58
Crystal 2	—	—	—	800	96	—	—	0.82	0.77	0.705	0.49
Pressed pellet 1	925	10	2	600	16	93	10-20	0.70	0.69	0.730	0.58
Pressed pellet 2	940	10	2	600	16	94	10-20	0.68	0.60	0.728	0.56
Pressed pellet 3	1100	4	1	600	17	97	10-20	0.55	0.48	0.710	0.52
Pressed pellet 4	940	10	2	700	112	94	10-20	0.68	0.70	0.755	0.49

* Unit value corresponds to ~25 mA/cm².

obtained with a 100W tungsten-halogen source, with and without a Schott KG-2 filter. This filter brings the spectrum of the source much closer to that of sunlight.

Results and Discussion

The current-voltage characteristic of a pressure sintered electrode in the CdSe/1F Na_2S-1F S-1F NaOH/C cell configuration used to obtain the data in Table I is shown in Fig. 1. The photocurrent spectrum of the etched polycrystalline CdSe does not differ substantially from that of the etched single crystal (11), and is as expected for a 1.7 eV bandgap. The over-all AM2 efficiencies, determined from Fig. 1 type curves and thermopile measurements, for single crystal, pressure sintered polycrystalline, and anodized polycrystalline electrode cells are collected in Table I, along with other pertinent data. The solar energy conversion efficiency of the cell with the pressure sintered CdSe reaches 5.1%, or 68% of the value obtained with the single crystal electrode. The lower efficiency of the anodically formed CdSe is due primarily to the limited thickness achieved by anodization under present conditions. The CdSe layer is too thin to absorb a large fraction of the incident light. No correction has been made for Fresnel reflection and solution absorbance loss: The efficiencies measured are true external conversion efficiencies and would be higher if corrected to actual photon flux reaching the electrode.

The relative efficiencies of two single crystal and four pressure sintered CdSe electrode cells are shown in Table II. The values of efficiency are normalized with respect to the crystal electrode in Table I whose origin is identical to that of crystal I in Table II. The electrodes of Table II were run under identical conditions, by fixing the lamp current and the geometry. The average short-circuit current corresponding to the unit normalized value is about 25 mA/cm², or approaching 2 AM2 solar intensities. A number of runs representing both the filter and nonfilter conditions have been averaged to obtain Table II entries. Relative results were not affected by the filter.

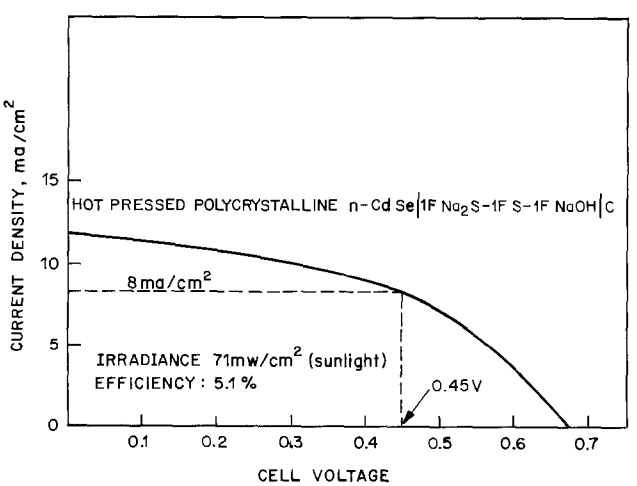


Fig. 1. Current-voltage curve for the cell n-CdSe (pressure sintered)/1F Na_2S-1F S-1F NaOH/C under sunlight.

Separate experiments in which a polycrystalline electrode was run for periods sufficient to dissolve nearly 1g of CdSe by photocorrosion showed no measurable weight loss, as also found for single crystal CdSe (12). The stability of cell currents is dependent both on average current level (light intensity) and sulfide-polysulfide concentration. Higher currents require higher concentrations to stabilize cell efficiency with time. For example, when run under tungsten illumination at short circuit initially producing a current density of 12.5 mA/cm² (~AM2 equivalence), a polycrystalline electrode dropped to 10.8 mA/cm² in 24 hr in 2F S/2F NaOH saturated with Na_2S (nearly 2F) and all the way to 0.4 mA/cm² in a 1F S/1F Na_2S/1F NaOH solution in the same time (the initial efficiencies in both solutions of the freshly etched electrodes were virtually the same). This important parameter will be discussed in detail in a future publication.

Numerous experiments have shown that the major determinant of relative performance is the etching pretreatment (11). The fill factor is sensitive to etching times, age, and preparation of the etchant. The relative efficiencies are unchanged when the fresh electrodes are etched for identical periods in identical etchants. Variation of the etching procedure changes the fill factor primarily. The fill factor entries in Table I represent the best average fill factors for the conditions used.

The flux of absorbed photons in the experiments of Table II exceeded the flux under AM2 sunlight conditions since the average short-circuit current for crystal 1 was ~25 mA/cm². The theoretical limit for 1.7 eV bandgap is 17.5 mA/cm² at AM2 sunlight (18).

The significant result is that pressure sintered specimens in Table II achieved between 48 and 70% of the solar conversion efficiency of the better of the two crystals. The second crystal, which was Cd vapor doped like the sinters, had only 77% of the efficiency of the reference crystal, and the pressed electrodes reached 90% of this level.

Sintering pressure and temperature are less critical than the doping level, which is currently being optimized. This is probably due to the large (10-20μ) grain size produced at all temperatures. (Grain sizes were measured after sintering in the plane parallel to the electrode surface.)

The doping of the samples in Table II was not ideally uniform, and there was variation in the data with the thickness of the layer removed from the surface first by mechanical abrasion, then by etching of the slices. This fact does not alter the key conclusions about the performance of the pressure sintered materials, but rather emphasizes the ease of producing polycrystalline materials with substantial conversion efficiencies.

The fact that, in these cells, the efficiencies of polycrystalline semiconductors approach those of single crystals is explained by the characteristics of the direct bandgap semiconductor-liquid junctions. These satisfy four requisites for efficient photovoltaic energy conversion with polycrystalline materials. These

requirements are that (*i*) the grain size should be sufficiently large to absorb practically all the light in the top layer of grains exposed to the electrolyte, (*ii*) the space charge layer thickness should be equal to or larger than the light absorption depth to assure rapid carrier separation (19), (*iii*) the light losses through the solution path to the semiconductor junction should be low, and (*iv*) the traps due to lattice mismatch or dislocations at or near the absorbing junction causing recombination of carriers should be minimized.

The first requirement says that L, the absorption length defined by the light absorption expression

$$I = I_0 \exp(-\alpha L)$$

must be less than the grain size. Since α for the direct gap CdSe is 10^4-10^5 cm^{-1}, grain sizes of a few microns are adequate. The 10μ grains produced by the described sintering easily satisfy this requirement. Absorption of light beyond the first layer of grains may not add to the photocurrents because of efficient trapping of the minority carriers at the grain boundary. The grain size criterion is probably also met in polycrystalline TiO_2 films in the photoelectrolysis of water (4).

In the second requirement, the thickness of the space charge layer, δ, must also be on the order of L to assure prompt separation of the carriers and thus reduce the probability of their recombination. δ is given by the equation (20, 21)

$$\delta = \left(\frac{2\epsilon\epsilon_0 \Delta\psi_{sc}}{qN_D} \right)^{1/2}$$

where ϵ is the static dielectric constant of the semiconductor [9.4 for CdSe (22)], ϵ_0 the permittivity of vacuum, $\Delta\psi_{sc}$ the voltage drop across the space charge layer (~0.7V in these cells), q the charge on the electron, and N_D the donor concentration. The latter is controlled by the time and temperature of exposure to Cd vapor in the annealing process.

For requirement (*iii*), liquid junction cells may be in a favorable position relative to p-n junction or Schottky barrier solid-state cells where light must pass through a semiconductor or metal, respectively. Many possible redox electrolytes are transparent over substantial parts of the relevant spectrum, although polysulfide solutions absorb strongly below 470 nm.

Requirement (*iv*) is inherently achieved in solid-liquid junctions where the liquid conforms to the solid. In contrast, faces of grains of two polycrystalline solids (such as two different materials of a heterojunction or even grains in a homojunction) are not easily so aligned as to match lattices. Furthermore, differences in thermal expansion coefficients at such interfaces can create stresses that result in dislocations and generate local recombination traps. Such problems do not exist at liquid-solid interfaces, and, if the grains are (operationally) single crystals, surface defects at the upper layer can be removed by etching.

Conclusion

Polycrystalline materials, as exemplified by pressure sintered CdSe, can be operated in regenerative electrolytic solar cells at substantial fractions of the respectable energy conversion efficiency of single crystal electrodes. Further optimization and control of these efficiencies appear possible and are being sought. It is anticipated that the demonstrated characteristics of these polycrystalline electrodes can be carried over to even more economic methods of manufacture. Although the problems of long term chemical stability of such liquid junction solar cells remain, a most important theoretical advantage of these systems has been further documented in this work, namely, that polycrystalline materials are not substantially inferior to single crystals.

Manuscript submitted Jan. 24, 1977; revised manuscript received March 11, 1977.

Any discussion of this paper will appear in a Discussion Section to be published in the June 1978 JOURNAL. All discussions for the June 1978 Discussion Section should be submitted by Feb. 1, 1978.

Publication costs of this article were assisted by Bell Laboratories.

REFERENCES

1. H. Gerischer, *J. Electroanal. Chem.*, **58**, 263 (1975).
2. F. Möllers and R. Memming, *Ber. Bunsenges. Phys. Chem.*, **76**, 469 (1972).
3. F. Möllers, H. J. Tolle, and R. Memming, *This Journal*, **121**, 1160 (1974).
4. K. L. Hardee and A. J. Bard, *ibid.*, **122**, 739 (1975).
5. J. G. Mavroides, D. J. Tchernev, J. A. Kafalas, and D. F. Kolesar, *Mater. Res. Bull.*, **10**, 1023 (1975).
6. H. Kim and H. A. Laitinen, *This Journal*, **123**, 53 (1975).
7. W. Gissler, P. L. Lensi, and S. Pizzini, *J. Appl. Electrochem.*, **6**, 9 (1976).
8. J. Keeney, D. H. Weinstein, and G. M. Haas, *Nature (London)*, **253**, 719 (1975).
9. M. Shiozawa, K. Narita, Y. Fujta, S. Kurita, M. Takata, and H. Yanagida, *Yogyo Kyokai Shi*, **83**, 471 (1975).
10. J. H. Kennedy and K. W. Frese, Jr., *This Journal*, **123**, 1683 (1976).
11. A. Heller, K. C. Chang, and B. Miller, *ibid.*, **124**, 697 (1977).
12. A. B. Ellis, S. W. Kaiser, and M. S. Wrighton, *J. Am. Chem. Soc.*, **98**, 6855 (1976).
13. R. Williams, *J. Chem. Phys.*, **32**, 1505 (1960).
14. G. Hodes, J. Manassen, and D. Cahen, Nature *(London)*, **261**, 403 (1976).
15. R. A. L. Vanden Berghe and W. P. Gomes, *Ber. Bunsenges. Phys. Chem.*, **76**, 481 (1972).
16. R. A. L. Vanden Berghe, W. P. Gomes, and F. Cardon, *Z. Phys. Chem. (NF)*, **92**, 91 (1974).
17. B. Miller and A. Heller, *Nature (London)*, 262, 680 (1976).
18. H. J. Hovel, "Semiconductors and Semimetals," Vol. 11, p. 38, Academic Press, New York (1975).
19. W. W. Anderson and Y. G. Chai, *Energy Conversion*, **15**, 85 (1976).
20. W. Schottky, *Z. Phys.*, **118**, 539 (1942).
21. W. W. Gärtner, *Phys. Rev.*, **116**, 84 (1959).
22. A. Manabe, A. Mitsuishi, and H. Yoshinaga, *Jpn. J. Appl. Phys.*, **6**, 593 (1967); *C.A.* 83: 199312V.

Analysis of Impedance and Admittance Data for Solids and Liquids

J. Ross Macdonald* and J. A. Garber[1]

Department of Physics and Astronomy, University of North Carolina, Chapel Hill, North Carolina 27514

ABSTRACT

Some problems of analyzing small-signal impedance data on solids or liquids are discussed. A method of using ordinary nonlinear least squares fitting procedures with minor modification to fit at the same time real and imaginary functions of the same set of unknown parameters to complex data is described in detail. This method of complex least squares fitting, which has several advantages over previous approaches, is illustrated by fitting equivalent circuit impedances to some polycrystalline β-alumina impedance data and to synthetic impedance and admittance data calculated from a theoretical model of the response of homogeneous material with completely blocking electrodes. When different physical processes yield response in overlapping frequency regions so that the different processes lead to some melding of effects in an impedance plane representation, interpretation of equivalent circuit parameters becomes difficult even when the degree of fit of the model to the data is excellent. In particular, low frequency extrapolation in the impedance plane to obtain an estimate of bulk resistance, R_x, in an overlapping completely blocking situation can yield estimates of R_x with very large errors. A method is described of avoiding such errors for both conventional and complex least squares estimation. In essence, one must find and fit the unique equivalent circuit whose elements remain related by invariant formulas to underlying microscopic parameters of the material/electrode system no matter what the degree of phenomena overlap.

Small-signal a-c impedance measurements are gaining in popularity as a technique for characterizing liquid and solid electrolytes and other materials. Analysis of small-signal data can almost always yield estimates of bulk conductivity of new materials free from the electrode polarization effects which plague steady-state d-c measurements. Under favorable conditions, detailed analysis of impedance data for homogeneous materials in terms of an appropriate model of the electrode/material system can also yield accurate estimates of microscopic parameters: mobilities, dielectric constant, electrode reaction rate constants, etc., which characterize interface and bulk behavior of the system (1-3). Even for polycrystalline materials, such as the usual form of the superionic conductor β-alumina, proper analysis may lead to valuable information about electrode reactions and intergrain and intragrain properties.

In order to carry out a meaningful analysis of impedance or admittance data, one must compare them with an analytic expression for the measured quantity, a function of frequency which generally depends on several frequency-independent parameters. Optimum characterization of the system requires that one be able to relate the gross parameters of the analytical fitting model to the microscopic parameters of interest. Sometimes, however, in the absence of a sufficiently detailed model one must be satisfied, at least for a while, with estimates of the gross parameter values, since they, and the form of the impedance expression, at least provide a concise means of representing the data. The dependence of the gross parameters, determined from several data sets, on experimental variables such as temperature may then lead to valuable insights.

It is conventional, and very desirable when possible, to approximate the analytical model of the system by an equivalent electrical circuit, preferably one which offers a useful compromise between simplicity and accuracy. It is desirable, for instance, that the equivalent circuit include as few frequency-dependent elements, such as Warburg (diffusion) impedances (1, 3), as possible. Although the basic analysis method described and illustrated herein does not require equivalent circuit representation, but only an analytical expression of the model, equivalent circuits can often clarify model behavior by clearly identifying separate phenomena which may be significant in quite different frequency ranges. Thus, most of the subsequent analysis herein will employ equivalent circuit representation. Figure 1 is a diagram which illustrates some of the important elements in the characterization process.

Once one has obtained impedance-frequency data, there are three reasonable things one can do. One can plot the impedance, Z, and/or admittance, Y, as a parametric function of frequency in the complex plane (*e.g.*, Re(Z) along the abscissa and $-\mathrm{Im}(Z)$ along the ordinate axis); one can analyze the data to obtain gross and possibly even microscopic parameters; and one can convert the data to a complex effective dielectric constant, $\epsilon^*_{\mathrm{eff}}$, and consider its frequency dependence, loss tangent, and high and low frequency limiting values. The first two approaches are often desirable; the third may not be. Whenever a system involves inhomogeneities and phase boundaries (*e.g.*, homogeneous material and electrodes or polycrystalline material with

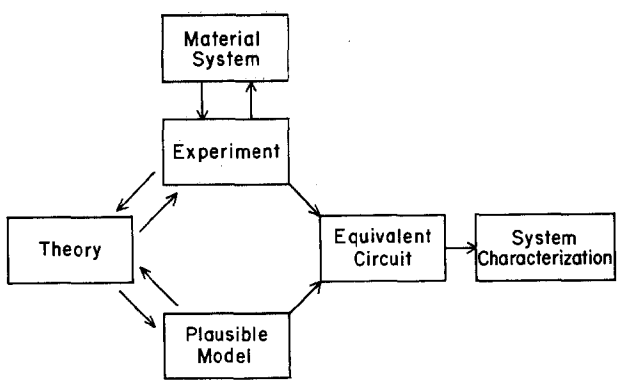


Fig. 1. Block diagram of possible system characterization elements and interactions.

* Electrochemical Society Active Member.

[1] Present address: Department of Geosciences, North Carolina State University, Raleigh, North Carolina 27607.

Key words: complex least squares, data analysis, solid electrolyte, impedance.

or without electrodes), there is a good possibility that these inhomogeneities and phase boundaries may contribute appreciably to the small-signal electrical response of the system. The derivation of an effective dielectric constant for the whole system is then undesirable since dielectric constant is properly defined in terms of an average over a possibly small but macroscopic region of a homogeneous material. Thus, the derivation of a complex dielectric constant and construction of the corresponding Cole-Cole (4) plot is appropriate for a dipolar dielectric with no mobile charge and thus no electrode space-charge or reaction effects, but both are inappropriate when mobile charge is present and electrode and/or grain boundary processes may be important. In this latter case, however, it has been found that plotting the analog of the Cole-Cole diagram, the impedance and/or possibly the admittance, in the complex plane is almost always instructive and useful (1, 3, 5, 6).

Perhaps the most subtle and difficult aspect of impedance data analysis is the development of an adequate analytical model. Some aspects of the general problem of discriminating between several models (*i.e.*, picking the most appropriate one) have been discussed elsewhere (7). One possible model (to be denoted model A) which may be appropriate for the small-signal response over a considerable range of conditions is based on the exact solution of the appropriate transport, continuity, and boundary-condition equations for instrinsic-extrinsic conduction and possible electrode reactions and adsorption (2, 8). It is particularly pertinent for conduction by ions and/or vacancies and interstitials. Some of its predictions for a simple situation are used later in this work to illustrate the analysis method described herein and to demonstrate some pitfalls in interpretation.

The present paper deals primarily with data analysis when an analytical model is available, rather than with the much more difficult problem of finding the best model. Given the model (expressed, say, as an equivalent circuit), how can one best find meaningful estimates of its parameters? One approach, recently employed by de Levie and Vukadin (9), involves a sequence of extrapolations and subtractions. As these authors point out, however, the extrapolation-subtraction method inevitably tends to accumulate (estimation) errors in the last-determined parameters, and it yields no estimates of parameter or fitting uncertainties. It would, therefore, be valuable to have a method that avoids these weaknesses. Such a method is described and illustrated below.

Complex Least Squares

When an analytic expression of a model is available, whether expressed in equivalent circuit form or not, it seems natural to consider least squares fitting of the impedance or admittance data to the impedance or admittance of the selected model in order to obtain estimates of the model parameter values. Several good nonlinear least squares (NLS) computer programs are availabe which allow fitting of real data to the model $y = f(x)$, with or without weighting of Y_i measured values. Some generalized NLS programs also allow weighting of X_i data values as well (10, 11). Impedance data and analytic expressions are of the form $Z(\omega) = \mathrm{Re}[Z] + i\mathrm{Im}(Z) \equiv u(\omega) + iv(\omega)$. Clearly, $u(\omega)$ and $v(\omega)$ will be different functions of ω but will generally both involve some or all of the same parameters. When complex data have been fitted by least squares in the past, the real $u(\omega)$ and $v(\omega)$ functions have usually been fitted separately using $\mathrm{Re}(Z)$ and $\mathrm{Im}(Z)$ data, respectively. The result of the two independent fittings is then two separate sets of different parameter value estimates.

Although the above type of fitting may be useful, it is not a simultaneous (consistent) least squares fitting of all the data, yielding one set of parameter estimates determined by all the available data taken together. Therefore, it is desirable to fit the real and imaginary parts of measured impedance to the analytical form of a model or circuit simultaneously. The only published approach of this kind known to the authors is that of Sheppard, Jordan, and Grant (12, 13). We have found, however, that the readily available generalized NLS fitting programs of Powell and Macdonald (10) and Britt and Luecke (11) may be modified very simply to allow fitting of complex data to complex functions. These modified programs seem preferable to the approach outlined by Sheppard (13).

To do complex least squares fitting with the above programs it is unnecessary to use the full theoretical analysis of Britt and Luecke, which involves an arbitrary number of different variables, any of which can be weighted, and which has not been embodied in an actual computer program in complete generality. For typical impedance or admittance data, the measured real and imaginary parts are generally uncertain, and the individual data values may need weighting to obtain the most significant statistical parameter estimates. But the frequency, f or ω, is generally measured so accurately that its uncertainties are negligible. It can then be identified with the x variable, assumed known exactly, in $y = f(x)$ real NLS fitting. Now fitting of complex data, $Z(\omega)$, can be simply reduced, as follows, to real fitting of the usual $y_i = f(x) = f(\omega_i, A_j)$ model form. Here $i = 1, 2, \ldots, n$ designates the n complex (double-valued) data points and the n real frequencies, and $j = 1, 2, \ldots, m$ denotes the m real parameters, A_j. Let us define y_k as a composite variable with $k = 1, 2, \ldots, 2n$. For $k = 1$ to n, let $Y_k \equiv \mathrm{Re}[Z(\omega_k)]$, and for $k = n + 1$ to $2n$, let $Y_k \equiv \mathrm{Im}[Z(\omega_{k-n})]$, where $\mathrm{Re}[Z]$ and $\mathrm{Im}[Z]$ are the real and imaginary measured values of Z. Now, define the analytic fitting model for impedance as $Z_m(\omega_i, A_j) \equiv u(\omega_i, A_j) + iv(\omega_i, A_j)$. The actual analytical separation of the complex Z_m function into real and imaginary parts is unnecessary; only numerical separation by the computer is needed. Thus, we let $u \equiv \mathrm{Re}(Z_m)$ and $v \equiv \mathrm{Im}(Z_m)$ be either analytical or numerical real and imaginary parts of Z_m, and let $y_k \equiv u(\omega_k, A_j)$ for $k = 1$ to n, and $y_k \equiv v(\omega_{k-n}, A_j)$ for $k = n + 1$ to $2n$. Fitting of complex data then just involves the ordinary, real NLS fitting of the real, composite Y_k data ($k = 1$ to $2n$) to the real, composite y_k model (here made up sequentially of the real and imaginary parts of the original complex model). Notice that, unlike ordinary real NLS, one is using different fitting models for the two major parts of the data. This leads to no difficulty in fitting. Since the sum of squares which is minimized by the procedure, is for unity weighting

$$S = \sum_{k=1}^{2n} [Y_k - y_k]^2 = \sum_{i=1}^{n} [(\Delta \mathrm{R}_i)^2 + (\Delta \mathrm{I}_i)^2]$$

where $\Delta \mathrm{R}_i$ and $\Delta \mathrm{I}_i$ are the real and imaginary fitting residuals, it is evident that we are minimizing the sum of squares of the $s_i = [(\Delta \mathrm{R}_i)^2 + (\Delta \mathrm{I}_i)^2]^{1/2}$, themselves the distances in the complex plane between a theoretical point and a measured data point, just as desired. Further, as we shall illustrate later, weighting of the $(Y_k - y_k)^2$ squared residuals may be introduced in the usual way. It is also worth noting that the NLS programs of Ref. (10) and (11) require no analytical expressions for function derivatives, a substantial blessing when the model expression is complicated.

The above kind of fitting yields parameter value estimates, estimates of their uncertainties, and an estimate of the standard deviation of fit, s_f. If the data determine some parameter values less precisely than others, this is immediately obvious. Further, s_f may be used to discriminate between various different possible models or equivalent circuits. We suggest that in the past the absence of such a s_f estimate has led to a proliferation of apparently different equivalent cir-

cuits not justified by the data themselves. Proper procedure should generally involve choosing that circuit or model which is best justified microscopically and which yields a minimum or at least acceptably small s_f.

Experimental Data: Fitting and Discussion

As an example of complex least squares fitting, we shall analyze the data (private communication) of Hooper, McGeehin, and Hughes (14) on polycrystalline β-alumina with silver electrodes. The 38°C data consist of twelve admittance values spanning the range from 1 kHz to 2 MHz. The corresponding impedance plane plot is shown in Fig. 2. Hooper *et al.* analyzed their data by the extrapolation method using a model equivalent to the three-time-constant Voigt circuit

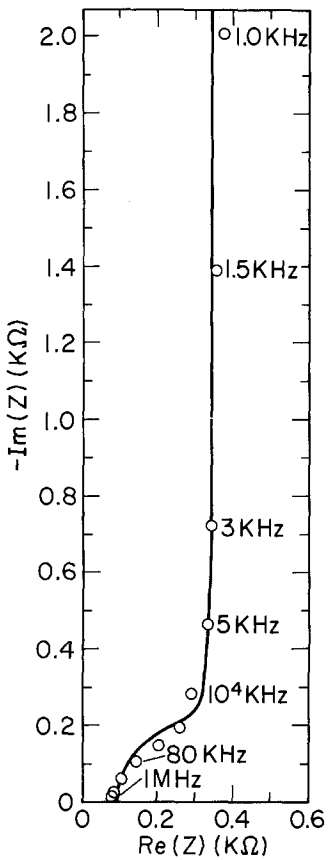


Fig. 2. Impedance plane plot of data (14) for polycrystalline β-alumina at 38°C. Experimental points, least squares line.

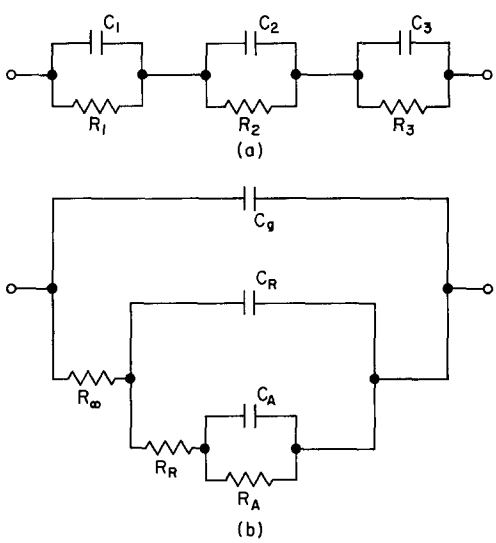


Fig. 3. Possible equivalent circuits for homogeneous and polycrystalline material/electrode systems.

(5, 6) of Fig. 3a with $C_1 = 0$ and $R_2 = \infty$. Before considering a model for least squares fitting and specific fitting results, it is useful to discuss the circuits of Fig. 3 briefly.

First, it has been shown using the exact model A results that the Fig. 3a circuit, which involves no Warburg elements, is appropriate for a homogeneous material when either the positive or the negative mobile species has a much higher mobility than the other, and pertinent time constants are separated from each other by factors of a hundred or more (2, 6). In this loosely coupled case, one can then identify R_1 and C_1 with, respectively, R_∞, the unperturbed bulk resistance of the material, and C_g, its geometric capacitance, which is, per unit area, $\epsilon/4\pi l$. Here ϵ is the bulk dielectric constant and l the electrode separation. In addition, R_2 and C_2 may be identified with the electrode reaction resistance R_R and capacitance C_R, and R_3 and C_3 with an adsorption resistance R_A and capacitance C_A. It is assumed that the reaction and adsorption processes, if present, involve the high mobility species with the one of opposite charge completely blocked at the electrodes. The reaction capacitance C_R is often found to be very nearly the double layer capacitance, C_{dl}, of two diffuse space charge layers in series, one from each electrode for identical plane parallel electrodes. Some of the possibilities following from the above are summarized in rows A-D of Table I. Note that complete blocking can occur with either R_2 or R_3 open circuited. Recent work (2) has demonstrated that for the same high mobility-ratio situation discussed above, the circuit of Fig. 3b applies exceptionally well for any ratios of the time constants, *i.e.*, for strong as well as weak coupling of the phenomena. It is therefore preferable to that of Fig. 3a for homogeneous material. Note that for loose coupling both circuits lead to three distinct, joined semicircles when impedance is plotted in the complex plane (1, 6). When a resistance is infinite, the corresponding semicircle has infinite radius.

Rows E and F apply to situations involving polycrystalline material between plane, parallel electrodes. It is assumed that the circuit of Fig. 3a is still formally applicable for such material. The bulk properties of all individual grains or crystallites contribute directly to give the over-all effective R_∞ and C_g. Because of differing grain sizes and orientations, one often finds, when measurements can be extended to sufficiently high frequencies, that the bulk semicircle in the complex impedance plane is displaced downward so that its center lies below the real axis. The R_R, C_R subcircuit, if present, may again be identified with electrode reaction/double layer effects, averaged over crystallites near the electrodes. One frequently finds nearly complete blocking again, as in system E. Farrington (15) has pointed out that adsorbed H_2O or H_2 may be expected to reduce the range over which complete blocking behavior occurs in Na-β-alumina with platinum electrodes. Finally, R_{GB} and C_{GB} are the over-all grain boundary resistance and capacitance associated with the contacts between all individual grains. As usual, one expects $R_\infty \propto l^1$, $C_g \propto l^{-1}$, and R_R and C_R independent of l, as expected for interface-related quantities. Experiment often suggests that $R_{GB} \propto l^1$ and

Table I. Identification of the R_i, C_i elements of a 6-element Voigt circuit for various systems with loose coupling. Rows A-D apply for homogeneous material and E and F for polycrystalline material.

System	Subcircuit 1		Subcircuit 2		Subcircuit 3	
	R_1	C_1	R_2	C_2	R_3	C_3
A	R_∞	C_g	∞	C_{dl}	—	—
B	R_∞	C_g	R_R	$C_R \cong C_{dl}$	—	—
C	R_∞	C_g	R_R	$C_R \cong C_{dl}$	∞	C_A
D	R_∞	C_g	R_R	$C_R \cong C_{dl}$	R_A	C_A
E	R_∞	C_g	∞	C_R	R_{GB}	C_{GB}
F	R_∞	C_g	R_R	C_R	R_{GB}	C_{GB}

$C_{GB} \propto l^{-1}$, showing these elements to exhibit bulk dependence, as one might perhaps expect for a large number of crystallites arranged in a series-parallel connection with series connections dominating. Here again, one would expect that the grain-boundary semicircle in the impedance plane would be displaced downward more often than not because of the distributed nature of the causes leading to the over-all behavior. Of course, when a semicircle is displaced, it cannot be represented adequately by means of frequency-independent elements such as the R_{GB} and C_{GB} of rows E and F. A more complicated contribution to the total impedance expression must then be employed [*e.g.*, see Ref. (6)], but again one whose parameters can best be estimated by complex least squares fitting.

Some preliminary computer modeling of the electrical properties of grains in series has been carried out by Armstrong, Dickinson, and Willis (16). It involves blocking electrodes, does not show downward displacement of semicircles, and the results appear to be representable by the circuit of row E. Further discussion of grain boundary and intragrain effects in polycrystalline β-alumina has been presented by Powers and Mitoff (17) and by Will (18). Powers and Mitoff give an equivalent circuit which agrees with that of row F except with C_g neglected and (implicitly) with little or no electrode blocking effects, so that $R_R \simeq 0$. Although specific adsorption at an electrode has not been incorporated in the circuits for systems E and F, it may sometimes be of importance and may even be the dominant process leading to nearly complete blocking behavior. Displaced semicircles and nonideal blocking and Warburg-like behavior have been recently reported for polycrystalline lithium silicates and aluminosilicates (19).

The analysis of displaced semicircles and nonideal Warburg-like data behavior in Ref. (19) employs an admittance or impedance function which can be represented by an equivalent circuit with frequency-dependent elements. Unfortunately, this particular approach, which corresponds closely to that of Jonscher in the dielectric area (20), was long ago shown to involve an impedance function associated with a physically nonrealizable system (21). The particular impedance functions used in Ref. (19) and (20) may, nevertheless, be useful empirical fitting functions if not pushed beyond their limits. On the other hand, other, somewhat empirical impedance functions have been proposed (6) which are associated with physically realizable systems, involve frequency-dependent circuit elements, and may be used to represent displaced semicircles and nonideal Warburg behavior. Although they may be formally interpreted in terms of distributions of relaxation times, they are not derived from a detailed microscopic theory of system response and, like all such semiempirical approaches, do not allow direct interpretation of impedance function parameters in terms of specific material parameters such as mobilities, reaction rates, etc. Until a theory which directly leads to nonideal behavior becomes available, circuit element characterization can only be adequately carried out for experiments which yield semicircles with little or no displacement and diffusional response close to ideal, finite-length Warburg behavior (2, 3, 6).

In β-alumina one expects to find many mobile Na^+ ions moving against a background of essentially immobile negative charges. Thus the circuits of Fig. 3 are possibly applicable for single crystal material and, with the interpretations given in rows E and F of Table I, are worth considering for polycrystalline material as well. The data of Hooper *et al.* do not extend to high enough frequencies to allow an estimate to be made of $C_1 \cong C_g$. It may be taken in the least squares fitting as fixed, indifferently, at 0 or at the value calculated from known values of area, ϵ, and l. As mentioned, Hooper *et al.* (implicitly) took $C_1 = 0$, $R_2 = \infty$, and identified R_1 and R_∞ (but including a tortuosity factor), C_2 with C_{dl}, and R_3 and C_3 with R_{GB} and C_{GB}, essentially row E of Table I with $C_1 = 0$. Since the R_{GB}, C_{GB} semicircle in Fig. 2 is not completely distinct from the C_R rise at low frequencies, it is not clear that the processes are well enough separated that the Fig. 3a circuit should necessarily be used in preference to one like Fig. 3b in interpreting the data (see later discussion). Thus, it is of interest to try fitting the data in impedance form to both the Fig. 3a circuit and that of Fig. 3b. In the latter case, since element identification is uncertain for polycrystalline data (especially where no experiments with different l's have been carried out), we shall beg the question by letting $C_g \to 0$, $R_\infty \to R_1$, $C_R \to C_2$, $R_R \to R_2$, $C_A \to C_3$, and $R_A \to R_3 \to \infty$.

The Fig. 3 impedance expressions for fitting are then

$$Z(\omega) = R_1 + (i\omega C_2)^{-1} + [R_3/(1 + i\omega R_3 C_3)] \quad [1]$$

for Fig. 3a, and

$$Z(\omega) = R_1 + \frac{1 + i\omega R_2 C_3}{(i\omega)[C_3 + C_2(1 + i\omega R_2 C_3)]} \quad [2]$$

for Fig. 3b. Fitting results yield $s_f = 15.98\Omega$ for both fits, carried out with the fixed values $C_1 = 0$ and with $R_2 = \infty$ for the first and $R_3 = \infty$ for the second. For Fig. 3a, one finds $R_1 = (96.5 \pm 7.1)\Omega$, $C_2 = (0.07734 \pm 0.00048)\mu f$, $R_3 = (248.4 \pm 9.3)\Omega$, and $C_3 = (0.0208 \pm 0.0020)\mu f$. Results for the Fig. 3b circuit were $R_1 = (96.5 \pm 7.1)\Omega$, $R_2 = (400.2 \pm 9.3)\Omega$, $C_2 = (0.0164 \pm 0.0020)\mu f$, and $C_3 = (0.06093 \pm 0.00048)\mu f$. If some of the fitting conclusions discussed in the next section apply to the present situation where different processes are not well separated in frequency, the Fig. 3b circuit element values may be more meaningful than the Fig. 3a ones. We shall not, however, pursue this subject further here.

The solid line in Fig. 2 has been drawn from the results of these fittings. It is because both circuits can, with proper element choices, represent the same impedance at all frequencies, as discussed in the next section, that fittings with them yield the same residuals and s_f values. The R_1 element, which is certainly the bulk resistance with crystallite-orientation tortuosity effects included, as stated by Hooper *et al.*, leads to a 38°C effective conductivity of about 0.00072 Ω^{-1} cm^{-1} using (private communication) $A \cong 0.44$ cm^2 and $l \cong 0.3$ cm.

While it seems reasonable to identify the R_3 and C_3 elements of Fig. 3a with R_{GB} and C_{GB}, it is clear that C_2 cannot be an ordinary diffuse double layer capacitance. Here $C_2 \simeq 0.176$ μf/cm^2 on a unit electrode area basis, a value very much smaller than would be expected if diffuse double layer theory applied to this very high Na^+ concentration situation. But diffuse layer theory ignores the finite size of charge carriers and discreteness of charge effects. Because of these effects there is a limit to how large the interfacial capacitance (without adsorption) can be (2, 22, 23), although the limit is much larger than the above value of C_2. While it is clear that C_2 is associated with the blocking character of the material/electrode interface, it is not clear from the present results whether it is an ordinary interface capacitance or is associated with pure specific adsorption (*i.e.*, $R_A \simeq \infty$ in Fig. 3b).

It will be noted that the low frequency points in Fig. 2 do not fall exactly on a vertical line. There are several sources which may lead to such a result, among which are surface roughness (16), specific adsorption (24), recombination (25), and large (but not too large) differences between the mobilities of mobile positive and negative species (1). Although a better fit of the data could be achieved were some of these effects included, possibly with the R_{GB}, C_{GB} circuit also replaced by one with a distribution of time constants (6), we are here more interested in demonstrating a fitting method and discussing the interpretation of the results than in trying to find the best model for the phenomena. In the next section, we consider in further detail

some simple fitting models for homogeneous materials and interpretation of fitting results when synthetic data are employed.

Theoretical "Data:" Fitting and Discussion

Theoretical model.—Some useful conclusions about fitting approaches and parameter interpretation can be developed by consideration and fitting of "data" derived theoretically from a known model. For present purposes it will be sufficient to use the model A already mentioned in its simplest form: an intrinsic situation where positive and negative charges have equal valences, z_e, and mobilities, μ_e; both are completely blocked at the electrodes; and there is no adsorption. Then R_x (per unit area) becomes $l/(ez_e\mu_e c_i)$, where c_i is the common equilibrium value of the positive and negative charge concentrations, and the Debye length L_D reduces to $[\epsilon kT/8\pi c_i(ez_e)^2]^{1/2}$. It will be convenient to deal with normalized quantities. Let $\tau_D \equiv R_x C_g$, the dielectric relaxation time, $\Omega \equiv \omega\tau_D$, a normalized frequency, and $M \equiv l/2L_D$. Further, normalize impedances and resistances with R_x and capacitances with C_g. Such normalization will be denoted by a subscript "N". In most experimental situations of interest for small-signal impedance measurements, $\Omega \lesssim 1$ and $M >> 1$.

For the situation defined above, the normalized total impedance of the system turns out to be (1)

$$Z_{TN} = \frac{1 + i\Omega\gamma_1}{i\Omega(1 + i\Omega)\gamma_1} = (1 + i\Omega)^{-1} - [i\Omega(1 + i\Omega)\gamma_1]^{-1}$$

$$\equiv R_{SN} + (i\Omega C_{SN})^{-1} \qquad [3]$$

where $\gamma_1 \equiv M(1 + i\Omega)^{1/2}\mathrm{ctnh}[M(1 + i\Omega)^{1/2}]$. The presence of $(1 + i\Omega)^{1/2}$ and the ctnh function are indications of the distributed nature of the system, consonant with the fact that all real systems are distributed. Their presence also means that no equivalent circuit made up only of frequency-independent circuit elements can represent the impedance of the system exactly. We shall, however, investigate the adequacy of such frequency-independent circuit approximations. Note that in normalized form, the model depends only on the single parameter M. Let us use a subscript zero to denote the limit $\Omega \to 0$. Then one finds (8) that $R_{SNO} = 1 + \{[r - 2 + \{(M)\mathrm{csch}(M)\}^2]/2(r - 1)^2\}$ and $C_{SNO} = r - 1$, where $\gamma_{10} \equiv r \equiv (M)\mathrm{ctnh}(M)$. For $M >> 1$, $R_{SNO} \cong 1 + (2M)^{-1} \simeq 1$. The total low frequency-limiting normalized parallel capacitance is $C_{PNO} = C_{SNO} + C_{gN} = r$. This result reduces to just the ordinary specific diffuse double layer capacitance for two double layers in series, one near each of the two identical electrodes, $C_{PO} = \epsilon/8\pi L_D$, for $M >> 1$.

Circuits and curves.—For the present system, the circuits of Fig. 3a and 3b reduce, respectively, to essentially those of Fig. 4a and 4c. We shall investigate the applicability of these circuits and the identity of their elements by NLS fitting of exact "data" calculated from the Eq. [3] model to the approximate models represented by these equivalent circuits. Although the Fig. 4a circuit has been widely employed for liquid, and to some extent, solid electrolyte situations, it will prove less directly applicable than that of Fig. 4c for the present homogeneous-material situation. Circuits 4a and 4c are degenerate forms of more complex equivalent circuits known as Voigt and Maxwell circuits, respectively (5, 6). The equality signs in Fig. 4 indicate that these circuits may be made to exhibit exactly the same impedance at all frequencies provided element values are chosen appropriately, as shown in the figure. Thus for example, the circuit of Fig. 4b will have the same impedance as that of 4a if the 4b element values are related, as shown, to those in 4a through the quantity μ, which involves a ratio of 4a capacitance values.

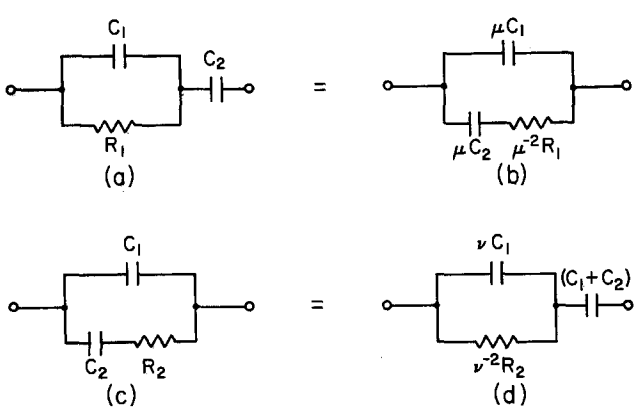


Fig. 4. Lumped-constant equivalent circuits with equal impedances when circuit (a) values are used to form $\mu \equiv C_2/(C_1 + C_2)$ and circuit (c) values are employed to form $\nu \equiv (C_1 + C_2)/C_2$.

Before considering detailed NLS fitting results, it is of interest to examine impedance and admittance plane plots following from Eq. [3]. Thus Fig. 5 and 6 show complex impedance and admittance plane plots of Z_{TN} and $Y_{TN} \equiv Z_{TN}^{-1}$ as parametric functions of Ω for several M values. As is conventional, we have actually plotted $Z_{TN}^* = \mathrm{Re}[Z_{TN}] - i\mathrm{Im}[Z_{TN}]$ in the (normalized) impedance plane. The (0,0; 1,1; 0,M) designation on the figures specifies completely blocking electrodes, equal valence numbers and mobilities, and no extrinsic conduction character. For $M >> 10^2$, Fig. 5 shows that there is present a semicircle, which is associated (in unnormalized form) with the bulk parameters C_g and R_x, and a well-distinguished vertical line, associated with the double layer capacitance. When $M \lesssim 10$, however, the bulk semicircle and the diffuse layer line begin to meld together since the frequency ranges where they occur approach each other more and more as M decreases. Qualitatively similar behavior occurs for the admittance plane results, but the semicircle there involves R_x and the double layer capacitance, and the vertical line is associated with C_g.

Were we to use NLS fitting of exact "data" derived from Eq. [3] to the Eq. [3] model itself, one would of course obtain a fit whose accuracy would be limited only by computer round-off error, and would also ob-

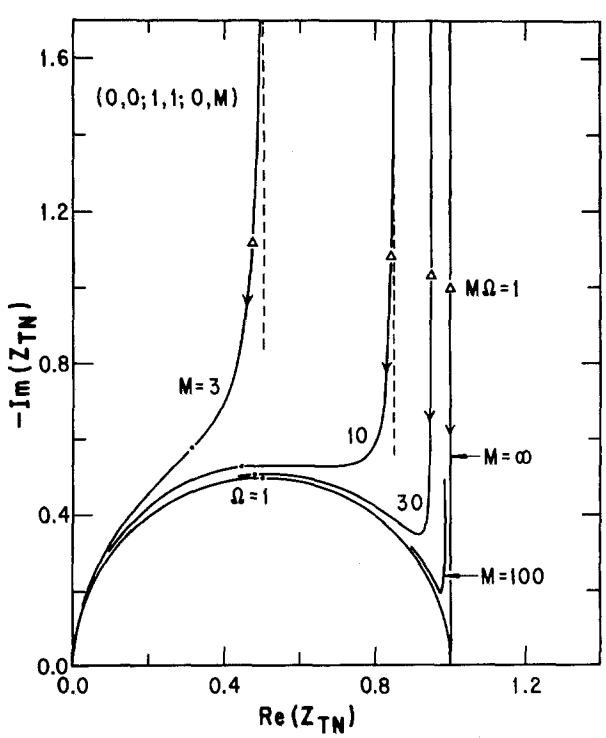


Fig. 5. Complex impedance plane plot of normalized impedance for the (0,0; 1,1; 0,M) situation.

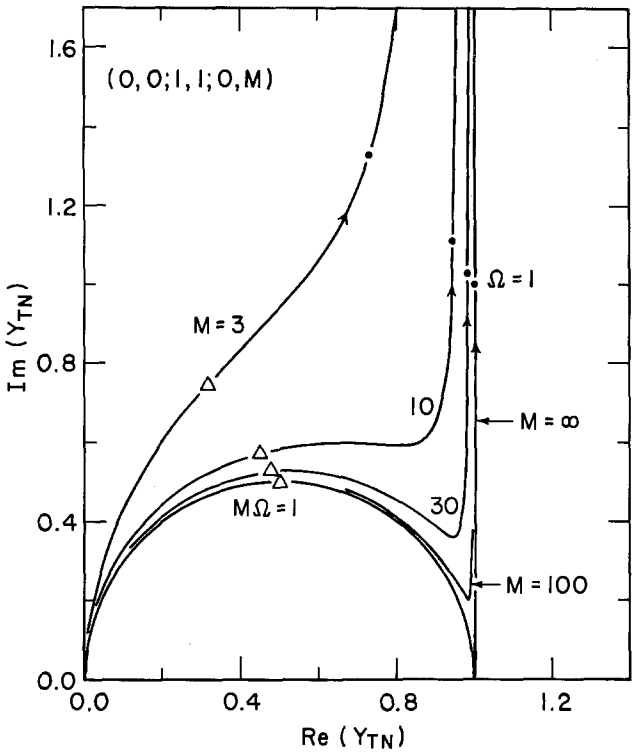


Fig. 6. Complex admittance plane plot of normalized admittance for the (0,0; 1,1; 0,M) situation.

tain a similarly accurate estimate of the single parameter M. In many experimental situations, however, one either does not have a good analytic model for fitting or finds that the appropriate analytic model is too complicated for direct least squares fitting (*i.e.*, model A in full generality). Thus one often finds an equivalent circuit approach to be useful.

Conventional analysis.—Although there is only one parameter, M, in the Z_{TN} of Eq. [3], there are three things which we want to determine from $Z_{TN}(\Omega)$ as accurately as possible. These are the normalized geometric capacitance and bulk resistance, both unity with present normalization, and M or r. If they can be well determined, we are assured that a similar procedure applied to unnormalized $Z_T(\omega)$ data will yield good values of C_g, R_∞, and C_{PO}. Since there are three distinct circuit elements in the circuits of Fig. 4a and 4c, one might expect that these elements could be related rather simply to C_g, R_∞, and C_{PO}, which are themselves expressed in terms of microscopic parameters. Consider first the usual extrapolation method applied to curves like those in Fig. 5 and 6. There is clearly no problem in obtaining estimates of C_g, R_∞, and a frequency-independent double layer capacitance, say C_{dl}, from results such as those in Fig. 5 or 6 when $M >> 10^2$. Then R_∞ (here $R_{\infty N} = 1$) may be obtained directly from the real-axis intercept of the vertical line in Fig. 5, C_{dl} from the capacitative reactance of a point on the line, and C_g from a point on the semicircle. Similarly, in Fig. 6, G_∞ (or $G_{\infty N} = 1$ here) occurs at the real axis intercept of the vertical line, C_g may be derived from the reactance on the line, and C_{dl} from a point on the admittance-plane semicircle.

Unfortunately, the situation is not so clear for relatively small M. Some authors have nevertheless used the extrapolation to the real axis of the asymptote of a curve such as that for $M = 3$ or 10 in Fig. 5 to obtain an estimate for R_∞. An extrapolation of this kind appears, for example, in Ref. (19). As Fig. 5 shows, such extrapolation can yield an R_∞ estimate incorrect by a factor of two or more for the present situation. In Fig. 6, on the other hand, all curves approach the $\mathrm{Re}(Y_{TN}) = 1$ line asymptotically, but this is by no means clear from that portion of the $M = 3$ curve shown, which might correspond to as much of an experimental curve as could be measured conveniently in a specific instance.

The determination of R_∞ from the real axis intercept of a vertical line associated with completely blocking electrode behavior corresponds to estimating R_∞ from low frequency experimental data since the impedance-plane vertical line occurs at the lowest frequencies of measurement. Alternatively, unlike such low frequency extrapolation, the determination of G_∞ from the real axis intercept of a vertical straight line in the admittance plane corresponds to high frequency extrapolation, and is in keeping with the $\omega \to \infty$ subscript of G_∞, the only conductance one expects to remain significant at sufficiently high frequencies. Similarly, C_{dl} is estimated by a low frequency extrapolation of Z_T data and C_g by a high frequency extrapolation of Y_T data. Although it is indeed much more common in liquid electrolyte work to obtain an R_∞ estimate from high rather than from low frequency extrapolation, Raistrick, Ho, and Huggins (19) have pointed out that for solid electrolytes practical frequency-range limitations often require R_∞ estimation by low frequency extrapolation (as in Fig. 5) for results obtained at low temperatures. We shall shortly demonstrate how such an estimate, which may differ appreciably from the true R_∞, may be transformed to obtain a much more appropriate estimate of R_∞.

Comparison of the shapes of the Fig. 2 curve for β-alumina and that for $M = 3$ of Fig. 5 shows considerable likeness. Since we have already seen that an extrapolation of the Fig. 5 $M = 3$ vertical asymptote to the real axis yields $R_{\infty N} \approx 0.5$ instead of the correct unity value, it is reasonable to conclude that in the case of Fig. 2, which also displays overlapping of phenomena, similar extrapolation may again lead to considerable error. Whenever this error cannot be reduced by high frequency extrapolation (because such data are lacking), it turns out, nevertheless, that it can be reduced by proper interpretation. But, as we shall see, NLS fitting of an appropriate model will always yield the most significant estimates of parameter values.

NLS analysis.—The theoretical "exact data," calculated with double precision on an IBM 370-155 computer from Eq. [3] for $M = 10^4$, 30, and 3, consisted of 25 complex Z_{TN} or Y_{TN} values and 25 Ω values. The Ω values were uniformly distributed in log Ω and covered $10^{-5} \leq \Omega \leq 10$ for $M = 10^4$ and $10^{-2} \leq \Omega \leq 10$ for $M = 30$ and 3. The data were fitted to the models of circuits of Fig. 4a and 4c

$$Z_{TN} = [R_{1N}/(1 + i\Omega R_{1N}C_{1N})] + (i\Omega C_{2N})^{-1} \quad [4]$$

and

$$Z_{TN} = [i\Omega\{C_{1N} + C_{2N}(1 + i\Omega R_{2N}C_{2N})^{-1}\}]^{-1} \quad [5]$$

respectively, with double-precision arithmetic using the present complex NLS method.

Results of fitting exact Z_{TN} "data" to the Eq. [5] model for Z_{TN} are shown in the first line of Table II for each M value. The second line presents the results of fitting exact $Y_{TN} \equiv Z_{TN}^{-1}$ "data" to the Y_{TN} following from Eq. [5]. If we identify C_{1N} as an estimator of $C_{gN} = 1$, R_{2N} as the R_{SNO} defined earlier, and C_{2N} as C_{SNO}, then the expected values of these quantities are as shown in the third line for each M choice. It is evident that these identifications are reasonable.

The $\pm$ quantities shown in the table are estimated relative standard deviations of the parameters. Had the circuit model been exactly appropriate for the data, the relative standard deviations would have arisen only from round-off error and would have been of the order of 10^{-12} or less in the present calculations. The larger values apparent here are a measure of the inexactness of the circuits employed. The larger M, clearly the better the lumped-constant approximations are to the actual distributed system. If one judged from the overall estimated standard deviation of the fit, s_f, one might

Table II. Fitting of unweighted (0,0; 1,1; 0,M) "data" to the circuit of Fig. 4c. For each M value: first line Z_{TN} fitting; second line $Y_{TN} \equiv Z_{TN}^{-1}$ fitting; third line expected value

M	Standard deviation of fit, s_f	C_{1N}	R_{2N}	C_{2N}
10^4	6.6×10^{-7}	$1.000009\ (1 \pm 7.1 \times 10^{-7})$	$1.0000498\ (1 \pm 1.5 \times 10^{-7})$	$9.999000 \times 10^3\ (1 \pm 5.5 \times 10^{-8})$
	6.0×10^{-6}	$1.000002\ (1 \pm 4.9 \times 10^{-7})$	$1.0000457\ (1 \pm 1.3 \times 10^{-6})$	$9.999000 \times 10^3\ (1 \pm 6.6 \times 10^{-6})$
	—	1	1.00005	9999
30	2.9×10^{-4}	$1.00295\ (1 \pm 2.2 \times 10^{-4})$	$1.01669\ (1 \pm 8.0 \times 10^{-5})$	$28.9965\ (1 \pm 5.9 \times 10^{-5})$
	2.3×10^{-3}	$1.00076\ (1 \pm 1.5 \times 10^{-4})$	$1.01396\ (1 \pm 5.3 \times 10^{-4})$	$28.9759\ (1 \pm 1.8 \times 10^{-3})$
	—	1	1.0166468	29
3	7.2×10^{-4}	$1.0128\ (1 \pm 7.2 \times 10^{-4})$	$1.1500\ (1 \pm 8.1 \times 10^{-4})$	$2.0021\ (1 \pm 3.6 \times 10^{-4})$
	9.1×10^{-3}	$1.0050\ (1 \pm 6.2 \times 10^{-4})$	$1.1136\ (1 \pm 3.4 \times 10^{-3})$	$1.9818\ (1 \pm 7.9 \times 10^{-3})$
	—	1	1.13603776	2.0149094698

conclude that even for M as small as 3, the lumped-constant approximation would be adequate except for the most accurate data. One must, however, consider the estimated values of the parameters themselves and must treat all standard deviations shown here with caution. Since differences between the exact result of Eq. [3] and the present circuit models are systematic rather than random in nature, the least squares fitting residuals will generally show systematic behavior and will not be randomly distributed. The standard deviations will then generally be poor approximations (usually too small) although their trends here are certainly significant.

The results of Table II show that the circuit of Fig. 4c is indeed a good approximate model for the present system. It is also evident, in accordance with the conclusions of conventional analysis discussed above, that C_{1N} is best estimated from Y_{TN} fitting and R_{2N} and C_{2N} from Z_{TN} fitting. Although the differences here are associated with systematic errors, it is likely that the same conclusions will apply to experimental data dominated by random rather than systematic errors.

For $M \gtrsim 30$, the Table II results show that the parameter estimates are highly accurate. Even the $M = 3$ results are likely to be generally adequate. But how would one proceed to obtain estimates of M, C_g, and R_∞ if these quantities were unknown and one were analyzing experimental, unnormalized data? Let us consider the worst case here, $M = 3$, and deal with the present results as actually derived from unnormalized data, *i.e.*, that for which true M, C_g, and R_∞ values are 3, 1, and 1, respectively, in appropriate units. Assume further that only the $Z_{TN} \rightarrow Z_T$ fitting results are available. Then an estimate of r is $1 + (C_2/C_1) = 1 + (2.0021/1.0128) \cong 2.9768$ and the corresponding M estimate is 2.9609, in error by about 1%. The $C_1 = 1.0128$ estimate of C_g is also about 1% in error. The above values of r and M now allow one to calculate R_{SNO}, yielding 1.13708 (instead of the correct 1.13604). Then an estimate of R_∞ is $R_\infty \cong R_2/R_{SNO} = 1.15/1.13708 \cong 1.011$, again in error by about 1%. Thus, even in the extreme high overlap case of $M = 3$, we are able to use the circuit Fig. 4c model to obtain desired parameters to about 1%.

Now what happens if exact Z_{TN} "data" is fitted to the circuit Fig. 4a model, Eq. [4]? Some results are shown in Table III. Notice that the s_f values are exactly the same as the corresponding Z_{TN} results in Table II, showing that both circuits can fit the "data" to the same degree. But it is evident that C_{1N} here is an appreciably poorer estimate of $C_{gN} = 1$ than the C_{1N} of Table II and that R_{1N}, particularly for small M, is a very poor estimate of either R_{SNO} or $R_{\infty N} = 1$. On the other hand, C_{2N} is evidently a better estimate of $C_{PNO} = r$ here than is the C_{2N} of Table II of $r - 1$. Finally, it is gratifying to note that when the parameter estimates of Table III, associated with the Fig. 4a circuit, are transformed (by the relations shown in Fig. 4) to parameter values pertaining to the Fig. 4c circuit, one obtains exactly (within round off) the values shown in Table II for all M choices.

These results and conclusions suggest that best estimates of M, C_g, and R_∞ might be obtained using a C_1 estimate obtained from admittance data fitting of the Fig. 4c circuit, a R_2 estimate from impedance fitting of the Fig. 4c circuit, and a C_2 estimate either from impedance fitting of the Fig. 4a circuit or by transformation of the Fig. 4c impedance fitting results to yield a Fig. 4a C_2 estimate. For most purposes, however, Z_{TN} fitting to the Fig. 4c circuit should be sufficient.

In the present synthetic data situation, we know for the Fig. 4c circuit that C_{1N}, which represents $C_{gN} = 1$, should be unity. Table IV presents some results obtained when C_{1N} is constrained to remain unity during NLS fitting. The first three lines in the table, for unweighted (*i.e.*, unity, weighted) residuals, show that fixing C_{1N} has increased s_f values and most of the parameter relative standard deviations but has generally improved the R_{2N} and C_{2N} estimates appreciably. Moral: use *a priori* information when available.

In some cases, it may be desirable to carry out NLS fitting with weightings different from unity. Consider

Table III. Fitting of unweighted (0,0; 1,1; 0,M) Z_{TN} "data" to the circuit of Fig. 4a

M	Standard deviation of fit, s_f	C_{1N}	R_{1N}	C_{2N}
10^4	6.6×10^{-7}	$1.0001092\ (1 \pm 7.1 \times 10^{-7})$	$0.9998498\ (1 \pm 1.5 \times 10^{-7})$	$1.00000000 \times 10^4\ (1 \pm 5.5 \times 10^{-8})$
30	2.9×10^{-4}	$1.03764\ (1 \pm 2.3 \times 10^{-4})$	$0.94985\ (1 \pm 7.8 \times 10^{-5})$	$29.9945\ (1 \pm 5.7 \times 10^{-5})$
3	7.2×10^{-4}	$1.5253\ (1 \pm 1.1 \times 10^{-3})$	$0.5071\ (1 \pm 3.6 \times 10^{-4})$	$3.01490\ (1 \pm 1.4 \times 10^{-5})$

Table IV. Fitting of (0,0; 1,1; 0,M) Z_{TN} "data" to the Fig. 4c circuit with C_{1N} fixed at unity

M	Weighting uncertainty, σ_x	Standard deviation of fit, s_f	R_{2N}	C_{2N}
10^4	1	1.4×10^{-6}	$1.0000498\ (1 \pm 3.1 \times 10^{-7})$	$9.999000 \times 10^3\ (1 \pm 1.2 \times 10^{-7})$
30	1	6.2×10^{-4}	$1.0165\ (1 \pm 1.6 \times 10^{-4})$	$28.998\ (1 \pm 1.3 \times 10^{-4})$
3	1	2.0×10^{-3}	$1.135\ (1 \pm 9.8 \times 10^{-4})$	$2.01485\ (1 \pm 5.9 \times 10^{-5})$
	$\lvert x \rvert$	1.0×10^{-2}	$1.130\ (1 \pm 2.9 \times 10^{-3})$	$2.015\ (1 \pm 3.6 \times 10^{-3})$
	$\lvert x \rvert^{-1}$	1.2×10^{-3}	$1.141\ (1 \pm 9.6 \times 10^{-4})$	$2.01490\ (1 \pm 1.5 \times 10^{-6})$
	$\lvert x \rvert^{-2}$	9.0×10^{-4}	$1.1488\ (1 \pm 9.6 \times 10^{-5})$	$2.0149093\ (1 \pm 6.9 \times 10^{-8})$
	$\lvert x \rvert^{-4}$	7.7×10^{-4}	$1.149005\ (1 \pm 2.4 \times 10^{-7})$	$2.014909468\ (1 \pm 1.4 \times 10^{-10})$

a datum value x, say the real or imaginary part of an impedance. Let σ_x be the estimated uncertainty of a given x value. Then the appropriate weighting of the squared residual corresponding to this value of x becomes $w_x = \sigma_x^{-2}$. One might know, for example, that small values of x are more uncertain than large values because of limitations in resolution of measuring techniques, etc. Then, one might take, as a first approximation, $\sigma_x = a|x|^{-1}$, where a is a constant. Then $w_x = a^{-2}x^2$, and residuals associated with larger x values are thus more heavily weighted than those associated with smaller x. The last four lines of Table IV show nonunity weighting results for $M = 3$. One notices that $|x|$ weighting is worse than unity weighting and that as weighting progressively emphasizes larger values, R_{2N} estimates degrade and C_{2N} ones improve. This trend is not surprising since at low Ω values the contribution of C_{2N} dominates the expression for Z_{TN} in the present completely blocking situation. Although such extreme weighting as $\sigma_x = |x|^{-4}$ will be inappropriate for actual experimental data, it has here allowed us to estimate C_{SNO} correct to eight or nine decimal places. For experimental situations $|x|^{-1/2}$, or possibly $|x|^{-1}$, weighting may sometimes be useful.

As we have mentioned earlier, it is often impossible or inconvenient to carry out impedance measurements to sufficiently high frequencies to cover most of the bulk-effect semicircle. Here we have indeed done so by extending the data to $\Omega = 10$ ($\omega_{max} = 10/\tau_D$). Separate fittings with $\Omega_{max} < 10$ have shown, in fact, that for the present system, parameter estimates are improved if, say, $\Omega_{max} = 0.1$ rather than 1 or 10. The choice $\Omega_{max} = 0.1$ is a high enough (normalized) frequency that C_{1N} may still be reliably estimated, but it extends less far into the region where the distributed nature of the system (not represented by our equivalent circuits), appearing through $(1 + i\Omega)^{1/2}$, is more important.

In concluding this section, we suggest that in completely blocking situations the complex NLS fitting of impedance data, extending up to perhaps $\omega_{max} \sim (10\tau_D)^{-1}$, to the circuit of Fig. 4c is most appropriate for general purpose work. Further, several weightings different from unity should be tried for the above fitting in order to find the weighting(s) which yield(s) minimum estimated standard deviations of the several parameters of interest. Even in nonblocking situations, such weighting investigation should often prove useful.

Effect of length and concentration variation.—The use of normalized quantities, as in Eq. [3] and Fig. 5 and 6, is helpful in allowing one to subsume many possible dependencies in one. Real data are initially unnormalized, however, and it is therefore of interest to examine how unnormalized impedance/admittance-plane curves corresponding to the normalized curves of Fig. 5 and 6 depend on variation of such parameters as electrode separation length and equilibrium charge concentration.

Let us consider two values of length, l_1 and l_2, and two of concentration, c_{i1} and c_{i2}. Then one readily finds from the equations and definitions above that for l and c_i variation alone, $M_2/M_1 = (l_2/l_1)(c_{i2}/c_{i1})^{1/2}$, and $R_{\infty 2}/R_{\infty 1} = (l_2/l_1)(c_{i1}/c_{i2})$. Further, $\tau_{D2}/\tau_{D1} = (l_2/l_1)^0(c_{i1}/c_{i2})$. Since $Z_T \equiv R_\infty Z_{TN}$ and $Y_T \equiv G_\infty Y_{TN}$, it is clear that R_∞ and G_∞ determine the scales of the unnormalized Z_T and Y_T curves, respectively, following from Z_{TN} and Y_{TN}, Thus, unnormalized curve size may be readily obtained from normalized results when R_∞ or G_∞ is known. But complex plane curves are parametric in frequency. Therefore, it is desirable to investigate how frequency points move their position along unnormalized curves as such quantities as l and c_i change. Figures 5 and 6 show two points with normalized frequency $\Omega = 1$ and $M\Omega = 1$. Their positions do not change much until M is considerably less than 100. But suppose we ask how the ω's involved in $\Omega \equiv \omega\tau_D$ must change as l and c_i change when we restrict attention to the same two points $\Omega = 1$ and $M\Omega = 1$ of Fig. 5 and 6. One easily obtains for $\Omega = 1$ the relation $\omega_2/\omega_1 = (l_1/l_2)^0(c_{i2}/c_{i1})$, and for $M\Omega = 1$ the result $\omega_2/\omega_1 = (l_1/l_2)(c_{i2}/c_{i1})^{1/2}$.

Table V. Effects of l and c_i variation on pertinent quantities

Variation					$\Omega = 1$	$M\Omega = 1$
M_2/M_1	l_2/l_1	c_{i2}/c_{i1}	$R_{\infty 2}/R_{\infty 1}$	$G_{\infty 2}/G_{\infty 1}$	ω_2/ω_1	ω_2/ω_1
10	10	1	10	0.1	1	0.1
	1	10^2	10^{-2}	10^2	10^2	10
	$10^{1/2}$	10	$10^{-1/2}$	$10^{1/2}$	10	1
1	0.1	10^2	10^{-3}	10^3	10^2	10^2
	10	10^{-2}	10^3	10^{-3}	10^{-2}	10^{-2}

The above relations have been employed to calculate the specific results of Table V. It shows the effects of various l and c_i variations which produce $M_2/M_1 = 10$ and 1. We see, for example, that a 10 times increase in l with no change in c_i yields unnormalized impedance plane curves 10 times larger than the normalized ones. No change occurs in the ω corresponding to $\Omega = 1$, but that corresponding to $M\Omega = 1$ occurs at one-tenth the frequency found for the original length. The ω frequency scale is thus not shifted uniformly by a change of length. On the other hand, when l and c_i change in such a way that M remains the same, the results of the bottom two lines in the table show that the frequency scale is then uniformly expanded or contracted.

Acknowledgments

We much appreciate the helpful comments of Dr. D. R. Franceschetti and the kind assistance of Dr. A. Hooper in supplying his β-alumina data for analysis. This work was supported by the U.S. National Science Foundation, Grant No. DMR 75-10739.

Manuscript submitted Dec. 14, 1976; revised manuscript received March 11, 1977.

Any discussion of this paper will appear in a Discussion Section to be published in the June 1978 JOURNAL. All discussions for the June 1978 Discussion Section should be submitted by Feb. 1, 1978.

Publication costs of this article were assisted by the National Science Foundation.

REFERENCES

1. J. R. Macdonald, *J. Chem. Phys.*, **61**, 3977 (1974).
2. D. R. Franceschetti and J. R. Macdonald, *J. Electroanal. Chem.*, To be published.
3. J. R. Macdonald, *ibid.*, **53**, 1 (1974).
4. K. S. Cole and R. H. Cole, *J. Chem. Phys.*, **9**, 341 (1941).
5. J. R. Macdonald, in "Electrode Processes in Solid State Ionics," M. Kleitz and J. Dupuy, Editors, p. 149, D. Reidel Publishing Co., Dordrecht, Holland (1976).
6. J. R. Macdonald, in "Superionic Conductors," G. D. Mahan and W. L. Roth, Editors, p. 81, Plenum Press, New York (1976).
7. J. R. Macdonald and D. R. Powell, *J. Res. Nat. Bur. Stand. (U.S.)* **75A**, 441-453 (1971).
8. J. R. Macdonald, *J. Chem. Phys.*, **58**, 4982 (1973).
9. R. de Levie and D. Vukadin, *J. Electroanal. Chem.*, **62**, 95 (1975).
10. D. R. Powell and J. R. Macdonald, *Computer J.*, **15**, 148 (1972).
11. H. I. Britt and R. H. Luecke, *Technometrics*, **15**, 233 (1973).
12. R. J. Sheppard, B. P. Jordan, and E. H. Grant, *J. Phys. D.*, **3**, 1759 (1970).
13. R. J. Sheppard, *ibid.*, **6**, 790 (1973).
14. A. Hooper, P. McGeehin, and A. E. Hughes, in "Superionic Conductors," G. D. Mahan and W. L. Roth, Editors, p. 99 (abstract), Plenum Press, New York (1976); Full details in A. Hooper, Report No. AERE-R8412, Harwell; *J. Phys. D.*, To be published.
15. G. C. Farrington, *This Journal*, **123**, 833 (1976).
16. R. D. Armstrong, T. Dickinson, and P. M. Willis, *J. Electroanal. Chem.*, **53**, 389 (1974).
17. R. W. Powers and S. P. Mitoff, *This Journal*, **122**, 226 (1975).

18. F. G. Will, *ibid.*, **123**, 834 (1976).
19. I. D. Raistrick, C. Ho, and R. A. Huggins, *ibid.*, **123**, 1467 (1976).
20. A. Jonscher, *Nature* (London), **253**, 717 (1975); *Phys. Status Solidi*, **32**, 665 (1975)
21. J. R. Macdonald, *Rev. Mod. Phys.*, **28**, 393 (1956); *ibid.*, **28**, 41 (1956).
22. R. D. Armstrong, *J. Electroanal. Chem.*, **52**, 413 (1974); *ibid.*, **66**, 148 (1975).
23. J. R. Macdonald, *ibid.*, **66**, 143 (1975).
24. J. R. Macdonald and P. W. M. Jacobs, *J. Phys. Chem. Sol.*, **37**, 1117 (1976).
25. J. R. Macdonald, D. R. Franceschetti, and R. Meaudre, *J. Phys. C.*, To be published.

The Kinetics of the Magnesium Electrode in Thionyl Chloride Solutions

E. Peled* and H. Straze

Institute of Chemistry, Tel Aviv University, Ramat Aviv, Tel Aviv, Israel

ABSTRACT

The electrochemical behavior of the magnesium electrode in thionyl chloride (TC) solutions was studied. It was found that this electrode is covered by a passivating layer which consists of some insoluble magnesium salt, probably $MgCl_2$. The properties of this layer determine the chemical and electrochemical behavior of the electrode in TC solutions. Magnesium was deposited on a nickel cathode from TC solutions containing $Mg(FeCl_4)_2$. Magnesium deposition begins after the nickel cathode is covered by a passivating layer (consisting of reduction products of TC) in which $t_{Mg^{2+}} \sim 1$. It was concluded that the rds for the deposition-dissolution process of the magnesium electrode in TC solutions is not the electron-transfer reaction, but is instead the migration of the Mg^{2+} ions through a passivating layer which covers the electrode.

There has been no report in the literature of kinetics of the deposition-dissolution process for solid magnesium metal in nonaqueous solutions. However, many papers have been published in the last fifteen years on the kinetics of alkali metals in these media. The reason for this is that magnesium is a much more difficult metal to electrodeposit than are the alkali metals. Most of the attempts to electrodeposit magnesium from nonaqueous solutions have been unsuccessful (1).

The only system in which the electrodeposition of magnesium is feasible is that of Grignard reagents with the addition of boranes in ether solutions (2).

The electrode kinetics of the alkali metals in propylene carbonate, dimethyl sulfoxide, and dimethyl sulfide is reviewed in Ref. (3-6). Most of the investigations deal with the electrochemical behavior of the lithium electrode. It was found (3-6) that: (*i*) lithium metal is chemically stable in these solutions, (*ii*) film formation on the electrode has been detected, (*iii*) trace amounts of water induce film formation, and (*iv*) the reaction $Li^+ + e(M) \rightleftarrows Li$ has a high exchange current density (1-10 mA cm^{-2}).

The rate-determining step (rds) of the deposition-dissolution process for solid alkali metals was assumed to be the electron-transfer reaction: $M^+ + e(M) \rightleftarrows M^\circ$ with a transfer coefficient (α) of 0.5-0.8 (3-6). Dey (7) indicated that in propylene carbonate solutions the lithium electrode is covered by a passive film (probably Li_2CO_3) which is formed by the reaction between lithium and propylene carbonate. He concluded that this film should be a purely ionic conductor with the Li^+ being the sole conducting species ($t_{Li^+} = 1$) (7). The same conclusion was drawn (8) for lithium electrode in thionyl chloride solutions.

In this paper the electrochemical behavior of solid magnesium electrode in thionyl chloride solution was studied. It was found that the rds of the deposition-dissolution process for magnesium metal in thionyl chloride (TC) solution is not the electron-transfer reaction but is the migration of the magnesium ions through a passivating layer which covers the electrode.

* Electrochemical Society Active Member.

Key words: passivating layer, magnesium electrodeposition, inorganic battery.

Experimental

The cell and the electrodes are shown in Fig. 1. The three electrodes were made from magnesium ribbon BDH 99.9%, 0.4 mm thick and 3 mm wide. The working and reference electrodes were parallel to each other and about 5 mm apart. They had an area of 1.4-2.5 cm^2. Each electrode was connected by a stainless steel connector to a tungsten rod sealed in the glass cap. The cell was sealed by a Viton O-ring. Connection to the vacuum line was made through a Jobling "Rotaflo" valve. The magnesium electrodes were

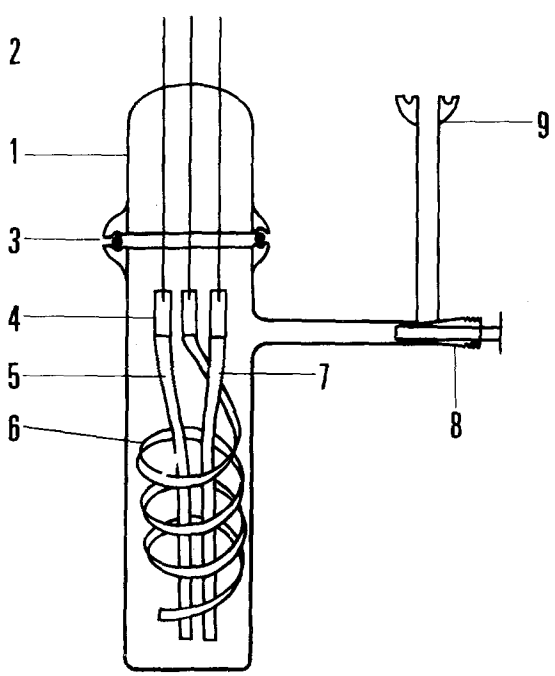


Fig. 1. The electrochemical cell. 1, Cell cap; 2, tungsten wires; 3, Viton O-ring; 4, stainless steel connectors; 5, working electrode; 6, counterelectrode; 7, reference electrode; 8, "Rotaflo" valve; 9, connection to vacuum line.

cleaned by degreasing in AR acetone, dipping in 1:4 HCl (AR Frutarom) for 15 sec, rinsing in distilled water, washing with AR acetone and drying on the vacuum line at pressure less than 10^{-4} mm Hg.

The thionyl chloride (Merck Zur Synthesis) was distilled and the first 10% and the last 20% were discarded. The middle fraction was vacuum distilled. At the end of this process a light yellow liquid was obtained.

For the preparation of $Mg(FeCl_4)_2$ solutions, weighed amounts of $FeCl_3$ (Merck Zur Synthesis) and $MgCl_2$ (Roc/Ric 98%) were transferred to a flask with a "Rotaflo" valve inside an argon-filled glove box. The flask was then attached to the vacuum line and distilled TC was transferred to it under vacuum. The salts were stirred with TC for 24 hr, and the TC was distilled. A calculated amount (for the preparation of 0.5M $Mg(FeCl_4)_2$) of twice distilled TC was transferred to this flask. The amount of $MgCl_2$ which was first introduced to the flask was always in excess (*i.e.*, for one mole of $FeCl_3$ about 0.7 mole of $MgCl_2$ was added). The exact concentrations of $FeCl_3$ and $MgCl_2$ were determined by atomic absorption spectrophotometry (Perkin Elmer, Model 403). It was found that the concentrations of $FeCl_3$ and $MgCl_2$ were 1 ± 0.1M and 0.5 ± 0.05M, respectively, in all experiments.

For the preparation of $Mg(AlCl_4)_2$ solutions the magnesium chloride was first dried in the same way as described above. Aluminum chloride (Fluka Puriss) was sublimed twice and transferred to the flask which contained the dry magnesium chloride. After this step a calculated amount of distilled TC was transferred to this flask. The magnesium chloride was always in excess (for 1 mole of $AlCl_3$ about 0.7 mole of $MgCl_2$ was employed). The solution was stirred for 48 hr to ensure complete dissolution of the magnesium chloride ($AlCl_3$ dissolved quickly in TC). It was found that the concentration of $AlCl_3$ and $MgCl_2$ were 1 ± 0.1M and 0.5 ± 0.05M, respectively, in all experiments.

All kinetic measurements were performed galvanostatically with an Elron CHG-1 galvanostat (rise time about 4 μsec). The *IR* drop was determined from the extrapolation to zero time of the fast initial jump in potential (Fig. 2).

The differential capacitance of the magnesium solution interface was calculated from the initial slope of the potential/time transient (Fig. 2) with the use of the equation

$$C = i \Big/ \left(\frac{dV}{dt}\right)_{t \to 0} \qquad [1]$$

These transients were recorded on a Tektronix Type 564 storage oscilloscope. Longer transients were recorded on a Yokogawa Type 3077 x-t recorder. Potential and current measurements were made with a Data Precision Model 245 Digital Multimeter. Electrolysis experiments were made galvanostatically with the galvanostat mentioned above.

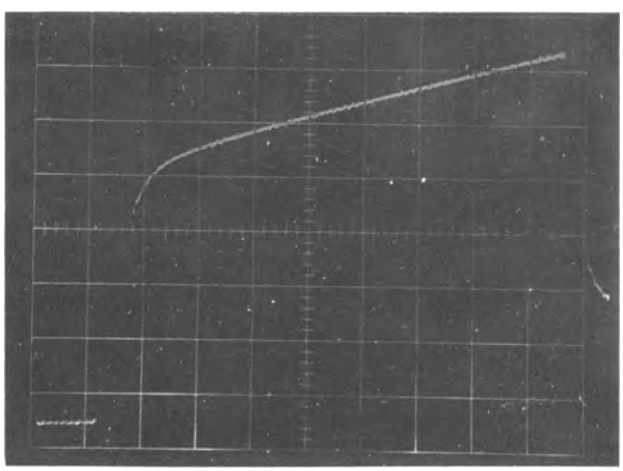


Fig. 2. Fast galvanostatic transients on Mg electrode in $Mg(AlCl_4)_2$ system. Pulse current 130 μA, electrode area 1.4 cm^2, Scale: 2 mV/div, 10 μsec/div.

Results

Reference electrode.—A magnesium ribbon dipped in the solution was used in all experiments as an indicator reference electrode. Thus, all the potentials measured during the current pulses or polarization experiments gave directly the overpotential values.

To ensure the suitability of magnesium as a reference electrode, several dozen such electrodes, in groups of three, were immersed in a saturated solution of $MgCl_2$ which contained about 1M $AlCl_3$ or $FeCl_3$. The potential difference between pairs of electrodes was recorded as a function of time. In the case of $AlCl_3$ solutions this potential difference was less than 2 mV (after a few minutes of stabilization) for a period of up to ten days. In the case of $FeCl_3$ solutions, the potential difference was unstable for the first hour, but later reached a stable value of less than 3 mV for the same lengths of time. However, in this system a bias potential of up to 25 mV was recorded in some cases for no apparent reason. This bias potential might conceivably result from impurities, particularly from penetration of traces of water into the cell. A polarizing current density of up to 500 μA cm^{-2} did not form a permanent bias potential. However, polarization with current densities of a few mA cm^{-2} sometimes caused a permanent bias potential of a few hundredths of a volt. In the case of $AlCl_3$ solutions this bias potential later disappeared.

Corrosion of magnesium in TC solutions.—The magnesium electrode corroded in 1M $AlCl_3$ TC solution forming a white film on the surface of the metal. Magnesium ribbons (0.4 mm thick) completely dissolved in the above solution within one month of storage at room temperature.

The corrosion rate in $Mg(AlCl_4)_2$ is much lower but still may be seen to take place. During the first ten minutes of the immersion of the magnesium ribbon in the system it loses its bright appearance and a black film is formed on the surface of the metal. This film then turns gray-black in color and after about 20 hr the ribbon regains its metallic appearance. After about four days of storage at room temperature a white precipitate appears at the bottom of the cell, while the light yellow color of the solution remains unchanged. After storing magnesium ribbons in this solution at 70°C for six days, they were found to be heavily corroded and a considerable amount of precipitate was found at the bottom of the cell.

The solubility of $FeCl_3$ was found to be 10^{-2}M in TC at room temperature. The color of this solution is light brown. On the addition of an excess of $MgCl_2$ it is possible to prepare 1M $FeCl_3$ TC solution which is saturated with $MgCl_2$. This solution is dark brown in color.

Magnesium ribbons kept their metallic appearance in $Mg(FeCl_4)_2$ solutions and no corrosion was detected even after one month of storage at room temperature. To ensure the chemical stability of magnesium in this solution, an acceleration corrosion test was performed at 70°C. It was found that even after storing magnesium ribbon in the above solution for a week no corrosion was apparent and the metallic appearance still remained. A magnesium ribbon which was weighed before and after six days of this treatment was found to have lost 0.3 mg cm^{-2}.

Kinetic measurements.—Two systems were studied: (*i*) $Mg(FeCl_4)_2$ and (*ii*) $Mg(AlCl_4)_2$. Several anodic (or cathodic) current pulses of 50-100 msec duration each, were applied to the magnesium working electrode at different times of immersion in the electrolyte. The shapes of the galvanostatic transients were the same in both systems. It was found that at low overpotentials

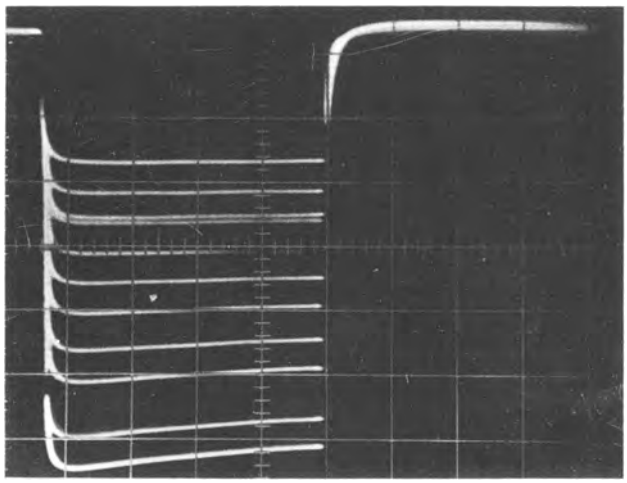


Fig. 3. Galvanostatic transients on Mg electrode in $Mg(AlCl_4)_2$ system at high anodic currents. Electrode area 2.4 cm^2. Scale: 10 mV/div, 10 msec/div, currents (μA): 206, 256, 307, 357, 408, 459, 519, 574, 662, 711.

the anodic and cathodic transients had the same shape. However, when the initial anodic overpotential was greater than about 30 mV, the potential transient had a small maximum (Fig. 3). This maximum increased in size with increasing polarizing current density. When similar polarizing cathodic current pulses were applied to the electrode, the potential did not reach a steady-state value, but increased continuously with time. The slope of the transient increased with current density. In cathodic steady-state experiments, an overpotential of 10V was obtained at a current density of 1 mA cm^{-2}.

From the data obtained in the low overpotential experiments micropolarization curves were drawn. The *IR* drop was negligible except in the cases of freshly dipped electrodes. For these electrodes, the overpotential was corrected for the *IR* drop. Typical micropolarization curves are shown in Fig. 4 and 5. The reaction resistance was calculated for both the cathodic and anodic branches. In all experiments the anodic reaction resistance ($R_{r,a}$) was 5-15% lower than the cathodic reaction resistance ($R_{r,c}$).

It was found, for both systems, that R_r increased with time of immersion of the magnesium electrode. The experimental results are summarized in Fig. 6 and 7.

In addition to the determination of R_r, the differential capacitance of the magnesium/solution interface was measured as a function of immersion time of the electrode. Identical values of capacitance were obtained from anodic and cathodic pulses. It was found that in the first day of immersion in the $Mg(AlCl_4)_2$ system the capacitance fluctuated between 1.5-4 μF cm^{-2} but later it decreased to 1 μF cm^{-2} or less. In the $Mg(FeCl_4)_2$ system the capacitance was always less than 1 μF cm^{-2}. These values of electrode capacitance are much lower than those measured in aqueous or nonaqueous solutions (9). Thus it was concluded that the electrode was covered by some passivating layer. The minimum thickness of this layer (d_{min}) was calculated from the equation (10)

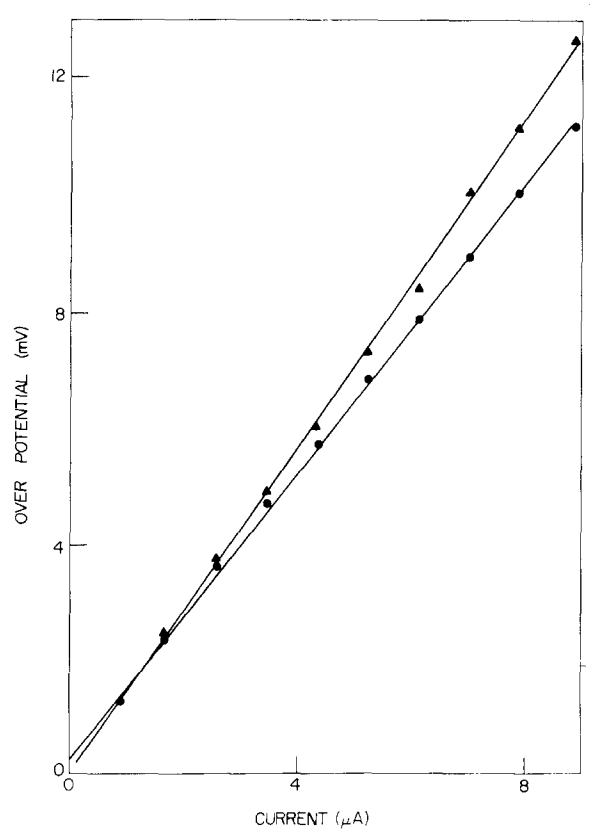


Fig. 4. Micropolarization measurements on Mg electrode in $Mg(AlCl_4)_2$ system. Electrode area 2.2 cm^2. ●, anodic; ▲, cathodic.

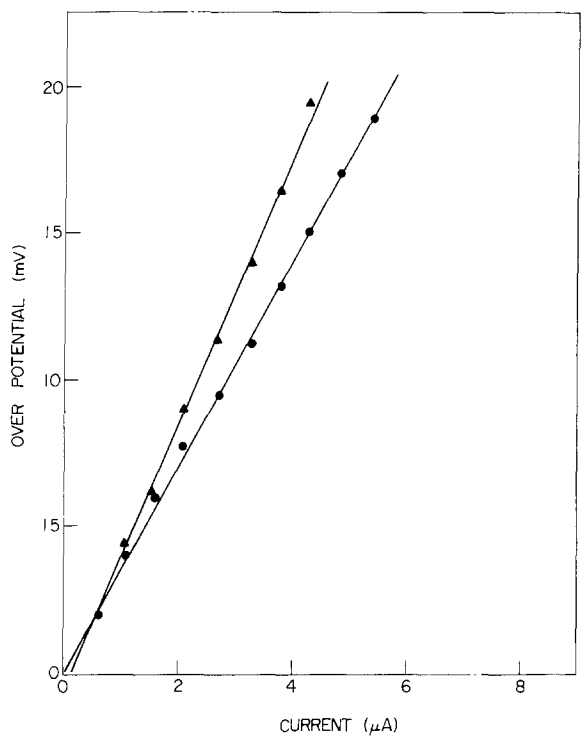


Fig. 5. Micropolarization measurements on Mg electrode in $Mg(FeCl_4)_2$ system. Electrode area 2.4 cm^2. ●, anodic; ▲, cathodic.

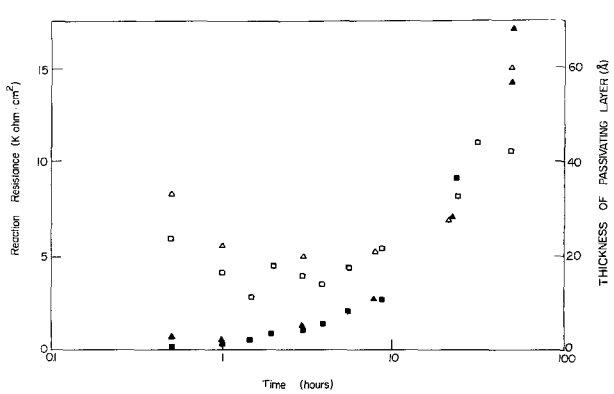


Fig. 6. The variation of $R_{r,a}$ and d_{min} with time of storage at room temperature in $Mg(AlCl_4)_2$ system. Cell 1, electrode area 2.2 cm^2; △, d_{min}; ▲, $R_{r,a}$. Cell 2, electrode area 2.4 cm^2; □, d_{min}; ■, $R_{r,a}$.

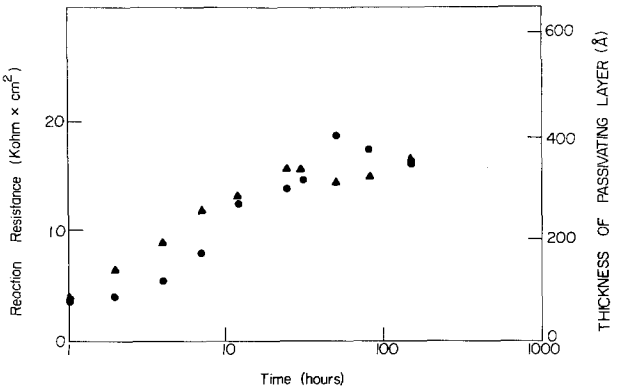


Fig. 7. The variation of $R_{r,a}$ and d_{min} with time of storage at room temperature in $Mg(FeCl_4)_2$ system. Electrode area 2.4 cm^2, ●, d_{min}; ▲, $R_{r,a}$.

$$d_{min} = \frac{\epsilon A}{C\pi\, 3.6 \times 10^{12}} \qquad [2]$$

where A = electrode area, C = differential capacitance, ϵ = dielectric constant of the passivating layers (assumed here to be 5). It was assumed that the roughness factor of the magnesium electrode was 1. The effect of immersion time on the thickness of the passivating layers is shown in Fig. 6 and 7.

A few galvanostatic experiments at various current densities were carried out in which the pulses lasted for several seconds. The micropolarization curves which were drawn from the data obtained in these experiments were similar to those obtained in the galvanostatic pulse experiments. In these cases too, $R_{r,a}$ was about 10% smaller than $R_{r,c}$. The values of R_r which were measured in steady-state experiments were 10-20% higher than those measured (for the same immersion time) by means of galvanostatic pulse techniques.

Electrodeposition of magnesium on nickel wire.—Some preliminary work was done in connection with the electrodeposition of magnesium on nickel wire in the $Mg(FeCl_4)_2$ system. The open-circuit potential (o.c.p.) difference between the nickel wire and the magnesium electrode was about 1.8V. When a C.D. of 100 $\mu A\ cm^{-2}$ was applied to the nickel working electrode, its potential (measured against a magnesium reference electrode) decreased with the electrolysis time from the o.c.p. of +1.8V to negative values. On turning off the current, the nickel potential fell immediately to a small positive value of about several hundredths of a volt, and remained there for a long time. Later, it slowly rose to 1.8V. A typical voltammogram describing this kind of experiment is shown in Fig. 8. The stabilization of the o.c.p. at about 30 mV following electrolysis indicates that magnesium metal electrodeposited on the nickel cathode. Unfortunately, this coating slowly corroded in the solution, and the nickel o.c.p. rose to its initial value.

Discussion

Solubilities and corrosion.—The halides of the alkali and alkaline-earth metals (which are donors for chloride ion) have low solubilities in TC (11). However, many Lewis acids such as $AlCl_3$, $SbCl_5$, and BCl_3 are very soluble in it (11). The solubilities of the alkali and alkaline-earth halides can be markedly increased by the addition of some Lewis acid to the TC solution. The reason for this is the formation of a large complex anion like $SbCl_6^-$, $AlCl_4^-$ or BCl_4^- (11). In this work it was found that the Mg:Al or Mg:Fe mole ratio in TC solution is about 1:2. This indicates the formation of Mg^{2+} and $AlCl_4^-$ ions in system (*i*), or Mg^{2+} and $FeCl_4^-$ ions in system (*ii*) as expected (11). However, it was found that $FeCl_3$ itself is practically insoluble in TC and we have no explanation for this.

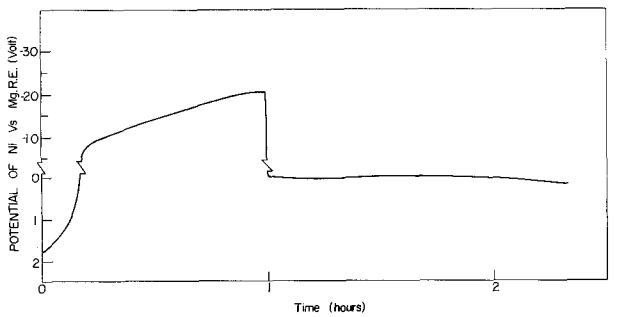


Fig. 8. Electrolysis experiment in $Mg(FeCl_4)_2$ system. Nickel cathode 1.0 cm^2, current 150 μA.

A metal will corrode if its surface has two kinds of sites: a cathodic area, where the electrons are transferred to the solution and an anodic area, where the metal ions are transferred to the solution. The rate of metallic corrosion depends on the corrosion cell potential, and on the cathodic and anodic exchange current densities (13). In the present case the corrosion cell potential is about 2V (12a). The $R_{r,a}$ for a freshly immersed magnesium electrode in the $Mg(FeCl_4)_2$ system is about 2 $k\Omega\ cm^2$ (equivalent to i_o of about 4 $\mu A\ cm^{-2}$). Thus the process responsible for the inhibition of the corrosion of magnesium in this system (even at 70°C) is the cathodic one, *i.e.*, the reduction of the solvent. However, it is well known that this solvent can be reduced and moreover it can be used as a soluble cathode for lithium (14) or magnesium (12a) batteries. Thus it can be concluded that in the $Mg(FeCl_4)_2$ system the magnesium electrode is covered by a passivating layer which is a very poor electronic conductor but is capable of conducting magnesium ions. The fact that magnesium corroded in acid solutions (containing $AlCl_3$ only) even at room temperature indicates that the passivating layer is basic and thus can dissolve in the Lewis acid. The corrosion of magnesium in $Mg(AlCl_4)_2$ system is more difficult and will be discussed later.

The composition of the passivating layer is as yet not known. It most likely consists of insoluble corrosion products. Magnesium chloride should not be soluble in this system since the latter is saturated with it. Thermodynamic considerations indicate that MgO may be soluble in this system. The standard free energy for the reaction $MgO + SOCl_2 \rightarrow MgCl_2 + SO_2$ is about -35 kcal $mole^{-1}$. Thus it is more likely that this film consists of $MgCl_2$. In any case, both $MgCl_2$ and MgO are very good electronic insulators and thus would prevent the transfer of electrons from the metal to the solution. In the case of the lithium electrode in TC solution of $LiAlCl_4$ the passivating layer was analyzed by SEM (15). It was concluded that it consists of LiCl.

Electrolysis.—Upon electrolysis of the $Mg(FeCl_4)_2$ system, the potential of the nickel cathode goes slowly from 1.8V (*vs.* MgRE) to zero within a few minutes (Fig. 8) and does not immediately jump to negative values as is the case in simple electrodeposition experiments. These phenomena can be explained as follows. When a current is passed through the cathode, its surface is in direct contact with the solution and thus can transfer electrons to the solution. In the vicinity of the o.c.p. of +1.8V, TC can be reduced but not the magnesium ions. Thus the reduction products of TC begin to accumulate near the cathode. These products may be SO_2, Cl^-, and S (16). Of these SO_2 and S are soluble in the electrolyte (16). The chloride ion concentration will exceed the solubility-product limit for $MgCl_2$ and the latter will precipitate on the cathode. In time this precipitate will prevent (or at least partially inhibit) the transfer of electrons from the cathode to the solution. From this point on, the current from the electrode to the solution will be essentially an ionic current. The magnesium ions will migrate through the passivating layer to the electrode and will be reduced to mag-

nesium atoms at the interface electrode/passivating layer. In this way the electrodeposition of magnesium continues until the current is interrupted. For the first hour the o.c.p. of the coated nickel cathode was several hundredths of a volt positive to MgRE, then it increased until it returned to its initial value of 1.8V. To explain this corrosion phenomenon it is suggested that the passivating layer which covers the magnesium deposit is not a purely ionic conductor, but, (because of impurities) it conducts electrons as well. This electron leakage through the film may also reduce the faradaic efficiency of the deposition of magnesium on nickel.

From the above, the failure of iron to undergo electroless deposition on solid magnesium electrodes in the $Mg(FeCl_4)_2$ system may be explained. As mentioned before, electrons are not transferred to the solution through the passivating layer on solid magnesium, and thus the $FeCl_4^-$ anion cannot be reduced. In addition, because of its charge and size, the iron anion cannot migrate (or diffuse) through the passivating layer (the way Mg^{2+} does). Thus it is not possible for it to reach the magnesium/passivating layer interface in order to accept electrons directly from the metal. It was found (12) that antimony and tin show the same behavior, that is, they do not undergo electroless deposition on the magnesium electrode in TC solutions when they are present as $SbCl_5^-$ and $SnCl_6^{2-}$, respectively.

The passivating-layer model.—In order to account for the observation during the chemical corrosion and electrochemical measurements of magnesium in TC solutions, a simple model is proposed in Fig. 9. The magnesium metal is covered by a passivating layer which consists of some insoluble magnesium salt, probably $MgCl_2$. The properties of this passivating layer determine the chemical and electrochemical behavior of the magnesium electrode in the TC solutions. When chemical corrosion is very slow, as in the $Mg(FeCl_4)_2$ system or in the $LiAlCl_4$ system (12), the transference number of electrons (t_e) through this layer is practically zero, and all the current is carried by ions, that is $t_{ion} \sim 1$. The value of $t_{Mg^{2+}}$ in the passivating layer in TC solutions is not known but is assumed to be close to unity. The magnesium electrode has two interfaces, the interface Mg/passivating layer in which the reaction

$$(Mg^{2+})_{pl} + 2e(M) \rightleftarrows Mg^{\circ} \qquad [3]$$

takes place, and the interface passivating-layer/solution in which the following reaction takes place

$$(Mg^{2+}(SOCl_2)_n)_{sol} \rightleftharpoons (Mg^{2+})_{pl} + n(SOCl_2)_{sol} \qquad [4]$$

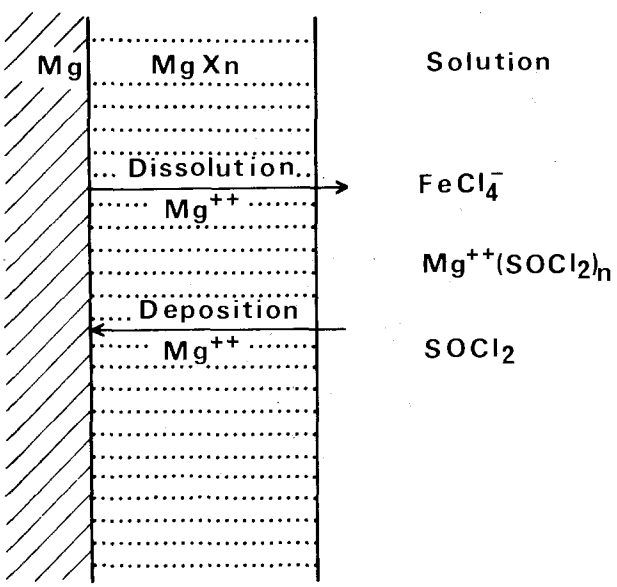


Fig. 9. Schematic model of the passivating layer on magnesium electrode in TC solutions.

The potential difference $\Delta\phi_{Mg/sol}$ contains these components

$$\Delta\phi_{Mg/sol} = \Delta\phi_{Mg/pl} + \Delta\phi_{pl} + \Delta\phi_{pl/sol} \qquad [5]$$

The first term is associated with the electron-transfer reactions, $\Delta\phi_{pl}$ is associated with the migration of magnesium cations through the passivating layer, and $\Delta\phi_{pl/sol}$ which is equivalent to the double-layer potential, is associated with the transfer of magnesium ions across the passivating-layer/solution interface.

In principle, any one of the processes associated with the three components of $\Delta\phi_{Mg/sol}$ may be the rate-determining step (rds) of the deposition-dissolution process of magnesium in TC solutions. The rds may depend on the thickness of the passivating layer, on its composition, or on the composition of the solution.

In studies of oxide films on valve metals (10) the thickness of the oxide is usually calculated from capacitance measurements. This kind of calculation is not accurate for several reasons: (*i*) The actual value of ϵ is not known. (*ii*) The passivating layer is not a single crystal. (*iii*) The roughness factor of the electrode is not precisely known and in this work is taken as unity. (*iv*) For an electrode covered by a porous passivating layer, this kind of determination of d may give values which are too small. In this work it was found that the reaction resistances which were measured in the milliseconds and in the seconds range gave similar values, and so it seems that the last quoted factor may not interfere with the determination of d_{min}.

It can be seen in Fig. 7, that in $Mg(FeCl_4)_2$ the reaction resistance of the magnesium electrode (both $R_{r,a}$ and $R_{r,c}$) and the thickness of the passivating layers (d_{min}) increase with time of immersion of the electrode. The electrical resistivity of the passivating layer (ρ_{pl}) was calculated by dividing the reaction resistance by the thickness of the passivating layer. It was found that this resistivity fluctuated between 4 and 9 $\times 10^{-9}$ Ω-cm during the time of immersion of the electrode in the solution. This indicates that the rds is the migration of the magnesium ion through the passivating layer. The rate of the electron-transfer reaction across the Mg/passivating-layer interface and the rate of transfer of Mg^{2+} ions across the passivating-layer/solution interface, should not depend significantly on the thickness of the passivating layer. It was found that $R_{r,a}$ is always smaller than $R_{r,c}$ (Fig. 4, 5). The reason for this may be as follows. Under cathodic polarization, Mg^{2+} ions must shed all its solvated $SOCl_2$ molecules before entering the passivating layer. This is a rather difficult process, the driving force for which is $\Delta\phi_{pl/sol}$ which is only a part of the total potential difference $\Delta\phi_{Mg/sol}$. In a simple aqueous electrodeposition experiment the partial discharge of the ion helps it (13); in the case at hand, partial discharge of the ion is not possible. Thus it seems that $R_{r,c}$ may include two components: the ohmic resistance to the migration of Mg^{2+} through the passivating layer and the reaction resistance for the transfer of Mg^{2+} across the passivating-layer/solution interface.

In accordance with the model the continuous increase of potential during high cathodic polarization may be ascribed to insufficient supply of Mg^{2+} ions from the solution to the passivating layer. Thus the concentration of the mobile magnesium ions in the passivating layer decreases, giving rise, in turn, to a decrease in the electrical conductivity of the layer and to an increase in the overpotential with electrolysis time (up to 10V). On anodic polarization at high current densities (C.D. > 0.5 mA cm^{-2}) the over-potential transient obtained shows a maximum (Fig. 3). This kind of transient has been observed in pulse-galvanostatic anodization experiments on valve metals in aqueous solutions (10). This phenomenon was explained (10) by an increase in the mobile-ion concentration in the oxide layer during the current pulse. It seems that this explanation applies to the present case as well.

The reason for the increase of d_{min} in this system may be a small leakage of electrons through the passivating layer. The electrons can reduce TC. At least one of the corrosion products of TC, the magnesium chloride, is not soluble in this system, and so will precipitate on the magnesium surface, giving rise to an increase in the thickness of the passivating layer. The electronic conductivity of this layer (t_e) may show the same sensitivity to impurities as does that of semiconductors. Thus in order to minimize t_e purified solutions must be used.

The magnesium electrode exhibits a more complicated behavior in $Mg(AlCl_4)_2$ system than in the previous one. The initial values of d_{min} are smaller by a factor of 2-3, while the initial R_r is 1/20 of its value in the previous system. In this system d_{min} did not increase during the first day of storage, while the reaction resistance increased by more than an order of magnitude. This process was associated with changes in the appearance of the electrode from metallic to black (fast) and then back to metallic. It is clear that during the first day of immersion the passivating layer changed. Three days later white precipitate was found at the bottom of the cell. The reason for this difference in behavior of the magnesium electrode in the two systems is not yet clear. It seems that in $Mg(AlCl_4)_2$ system t_e of the freshly found passivating layer is high, and as a result the metal corrodes. During this corrosion the passivating layer changes and a new layer with a smaller t_e is formed. This kind of behavior may result from some impurities which still stay in the solution after the present process of purification.

Summary

In the present work we found that in TC the magnesium electrode is always covered by a passivating layer. This layer cannot be completely removed and so no film-free surface can be obtained. However, it is possible to reduce the thickness of the film by anodic pulses. In the TC solutions the process of direct electron transfer from magnesium to the ions in the solution has a very low probability as the thickness of the passivating layer is higher than 20Å (after a stabilization period). The reaction resistance for the deposition-dissolution process of magnesium metal in TC solutions is mainly determined by the ionic conductivity of the passivating layer.

The model of the passivating layer proposed for the magnesium electrode in TC solutions may also be applied in the case of alkali metals in many nonaqueous systems especially those used for batteries. Under these conditions the alkali metal is usually covered with a passivating layer. When this layer is thick it is expected that the rds for the deposition-dissolution process will be the migration of metal ions through the passivating layer as was claimed by Dey (7) for lithium in propylene carbonate. However, for alkali-metal electrode covered by a thin passivating layer, the rds may be either the electron-transfer reaction

$$(M^+)_{pl} + e(M) \rightleftarrows M^\circ \qquad [6]$$

or the transfer of the alkali ions across the passivating layer/solution interface

$$(M^+ (solv)_n)_{sol} \rightleftharpoons (M^+)_{pl} + n(solv)_{sol} \qquad [7]$$

A direct transfer of electrons across the passivating layer should: (*i*) Cause a metal corrosion. (*ii*) Reduce the faradaic yield for the metal deposition as a result of simultaneous solvent reduction. Therefore it is an undesirable process in battery systems.

Acknowledgment

We are indebted to the National Council for Research and Development, Prime Minister's Office, Jerusalem, Israel for financial support of this work.

Manuscript submitted Nov. 29, 1976; revised manuscript received March 14, 1977.

Any discussion of this paper will appear in a Discussion Section to be published in the June 1978 JOURNAL. All discussions for the June 1978 Discussion Section should be submitted by Feb. 1, 1978.

Publication costs of this article were assisted by Tel Aviv University.

REFERENCES

1. A. Brenner, in "Advances in Electrochemistry and Electrochemical Engineering," Vol. 5, C. W. Tobias, Editor, Interscience, New York (1967).
2. A. Brenner and J. L. Sligh, *Trans Inst. Metal Finishing*, **49**, 71 (1971).
3. J. Jorne and C. W. Tobias, *This Journal*, **121**, 994 (1974).
4. R. Jasinski, in "Advances in Electrochemistry and Electrochemical Engineering," Vol. 8, C. W. Tobias, Editor, Interscience, New York (1967).
5. J. W. Butler, in "Advances in Electrochemistry and Electrochemical Engineering," Vol. 7, P. Delahay, Editor, Interscience, New York (1970).
6. W. H. Tiedemann and D. N. Bennion, *This Journal*, **120**, 1624 (1973).
7. A. N. Dey, Abstract 62, p. 154, The Electrochemical Society Extended Abstracts, Fall Meeting, Atlantic City, N.J., Oct. 4-8, 1970.
8. Y. Avigal and E. Peled, *J. Electroanal. Chem.*, In press.
9. R. Payne, in "Advances in Electrochemistry and Electrochemical Engineering," Vol. 7, P. Delahay Editor, Interscience, New York (1970).
10. L. Young, "Anodic Oxide Films," Academic Press, New York (1961).
11. V. Gutmann, in "Covalent Oxychlorides as Solvents in Halogen Chemistry." V. Gutmann Editor, Academic Press, New York (1967).
12. a. E. Peled, H. Straze, and M. Brand, Abstract No. 38, 26th I.S.E. Meeting, Baden, Austria, September (1975).
    b. E. Peled and H. Straze, Extended Abs. No. 127, 27th I.S.E. Meeting, Zurich, Switzerland, September (1976).
13. J. O'M Bockris and A. K. N. Reddy, "Modern Electrochemistry," Plenum Press, New York (1970).
14. J. J. Auborn, K. W. French, S. I. Lieberman, V. K. Shah, and A. Heller, *This Journal*, **120**, 1613 (1973).
15. A. N. Dey, *Electrochim. Acta*, **21**, 377 (1976).
16. D. R. Cogley and M. J. Turchan, Lithium—Inorganic Electrolyte Batteries Report ECOM-74-0030-2, May 1974; Abstract No. 28, p. 71, The Electrochemical Society Extended Abstracts, Fall Meeting, New York, Oct. 13-17, 1974.

Electrochemical Nucleation in Hydrated Melts: Electroreduction of Thallium (I) from Calcium Nitrate Tetrahydrate

Narottam P. Bansal[1] and James A. Plambeck*

Department of Chemistry, The University of Alberta Edmonton, Alberta, Canada T6G 2G2

ABSTRACT

The electroreduction of thallium(I) on a mercury electrode from its solutions in molten calcium nitrate tetrahydrate has been studied using chronoamperometry, chronopotentiometry, and cyclic voltammetry. The early stages of metal deposition are controlled by a nucleation step as indicated by the maxima in current-time transients, potential overshoots in potential-time curves, and an anodic shift of the peak potential of the reduction process in subsequent cyclic voltammetric scans. A three step mechanism has been proposed. The first step, formation of nuclei of thallium metal on the electrode surface and the growth of these nuclei into full monolayer surface coverage, is in quantitative agreement with these results.

Moynihan and Angell (1) measured the diffusion coefficient of thallium(I) in $Ca(NO_3)_2 \cdot 4H_2O$ by chronopotentiometric reduction at a mercury pool electrode. Their work has been criticized by Lovering (2), who showed that Moynihan and Angell (1) did not collect their data under diffusion-controlled conditions. Lovering (2) reported polarographic half-wave potentials and diffusion coefficients for a large number of inorganic cations in different hydrated melts. In $Ca(NO_3)_2 \cdot 4H_2O$ he reported a polarographic maximum was observed for Tl(I) reduction at concentrations above millimolar; no further details were given. In the course of a study of Tl(I) reduction by a-c chronopotentiometry in this melt unusual phenomena were noted and a full study of this electroreduction by chronoamperometry, d-c chronopotentiometry, and cyclic voltammetry was therefore carried out. The results and interpretation of that study are described below.

Experimental

A double walled, water-jacketed Pyrex cell was used for the measurements. Hot water from a constant temperature bath was constantly circulated around the cell. The temperature control was better than ±0.1°C. The bath stirrer was turned off to avoid mechanical vibrations only during the measurements. An externally driven magnetic stirrer was used for better mixing in the viscous calcium nitrate tetrahydrate melt.

Calcium nitrate tetrahydrate (B.D.H., AnalaR) and thallium nitrate (Alfa Inorganics) were used without further purification. About 80g of the melt were used for each experiment. As the solubility of oxygen is negligible in this melt (1), no precautions were taken to exclude air from the system, save for tightly capping the cell to avoid loss of water. The density of the melt without solute (3) was used in calculating the molar concentrations, as the solute concentrations used were low. All measurements were carried out at 50°C.

The cell was in a three electrode configuration. The working electrode was a P.A.R. Model 9323 hanging mercury drop electrode (HMDE) which was set up using triply distilled mercury (Engelhard). A fresh mercury drop of constant known area (0.0176 cm^2) was taken for each observation unless otherwise stated. The auxiliary electrode was a platinum flag of large area. The reference electrode was silver nitrate (0.03M in the melt)/silver which was isolated in a fritted glass compartment of porosity 10-20μ.

The constant current source for the chronopotentiometric measurements was a 225V dry battery connected in series with two potentiometers (5 MΩ and 100 kΩ) which were used as adjustable resistors to regulate the current; the switching circuitry was conventional. The potential-time curves were photographed on ASA 3000 Polaroid film using a Hewlett-Packard oscilloscope and camera (Models 175A and 196B). The chronoamperometric current-time curves and cyclic voltammograms were obtained with a P.A.R. Model 173 potentiostat/galvanostat coupled to a P.A.R. Model 175 universal programmer. The current-time curves and the voltammograms at slow scan rates (<1 V/sec) were recorded with a X-Y recorder (Houston Instrument Type 2000). The cyclic voltammograms at higher scan rates were photographed from a Tektronix Model 535A oscilloscope using the same camera.

Results

Chronoamperometry.—Some of the results for the reduction of Tl(I) on mercury in this melt are shown

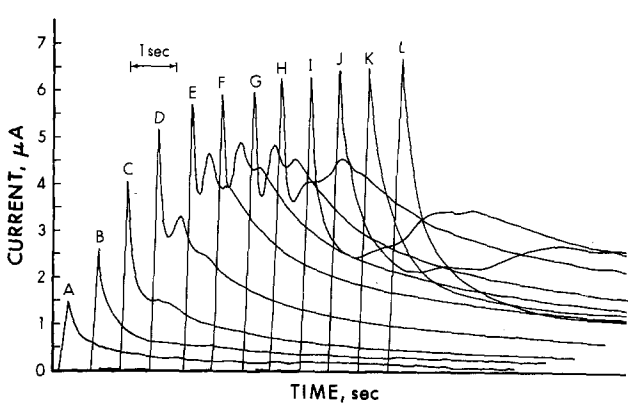


Fig. 1. Chronoamperometric curves for the Tl(I)/Tl(Hg) reduction in $Ca(NO_3)_2 \cdot 4H_2O$. Time scale arbitrarily displaced for each curve shown. Potential step (against Ag(I)/Ag reference) applied: A, −0.90V; B, −0.92V; C, −0.94V; D, −0.96V; E, −0.98V; F, −0.99V; G, −1.00V; H, −1.02V, I, −1.04V; J, −1.06V; K, −1.08V; L, −1.10V. Concentration of Tl(I) is 4.36 × 10^{-3}M. Area of HMDE, 0.0176 cm^2; temperature, 50°C. The initial potential was set at −0.2V before each run.

* Electrochemical Society Active Member.
[1] On leave of absence from the Department of Chemistry, Ramjas College, University of Delhi, Delhi 110 007, India.
Key words: chronoamperometry, cyclic voltammetry, chronopotentiometry, electrodeposition of thallium.

in Fig. 1, in which the curves clearly show maxima at potentials close to the potential of thallium(I) reduction, but are of normal shape both at potentials less cathodic than the reduction and in the region of diffusion control. The position and height of the maxima are functions of both the applied potential of the step and the concentration of Tl(I). No maxima are observed at any potential at low concentrations (below 0.459 mmole/liter); when the concentration is increased to 1.299 mmole/liter, broad maxima appear on curves whose potential step is between −0.96 and −1.02V. As the concentration is increased, the maxima become sharper, appear after shorter times, and appear at less negative potentials. When the concentration reaches 2.5 mmole/liter Tl(I) a second broad maximum appears at potentials of −0.96V; this is later than the first one which has now become sharp and appears at shorter times. When both maxima are present the shape of the curves changes as the step potential is made more cathodic; the sharpness of the second maximum increases and that of the first decreases until the two finally merge into one very broad maximum which becomes steadily less distinct. At potentials more cathodic than −1.08V the maximum can no longer be distinguished.

Polarograms can be constructed from the chronoamperometric current-time curves and are shown in Fig. 2. The presence of the maximum for all concentrations greater than 0.459 mmole/liter Tl(I) is obvious. The maximum does not affect the diffusion-limited plateau region of the polarographic curves, and the height of this plateau is directly proportional to Tl(I) concentration, as shown in Fig. 3. These composite polarograms show maxima at slightly lower concentrations than those reported by Lovering (2), whose concentration of 1.0 mmole/kg at 50°C in this melt is equivalent to 1.73 mmole/liter, while in our work a maximum is clearly apparent at 1.30 mmole/liter, which certainly confirms the maximum reported by this author.

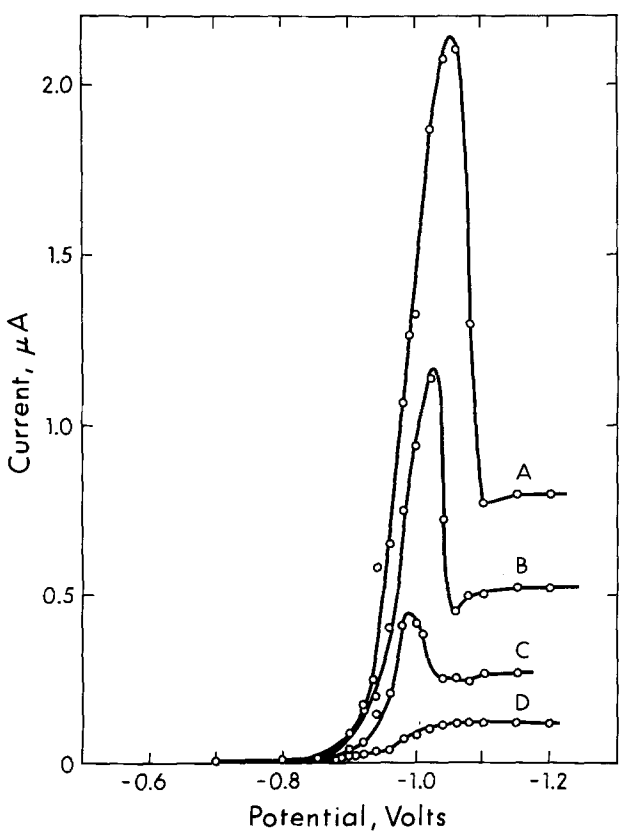


Fig. 2. Polarograms constructed from current-time curves at the HMDE. Area, 0.0176 cm². Concentration of Tl(I) in $Ca(NO_3)_2 \cdot 4H_2O$: A, 4.36 × 10^{-3}M; B, 2.56 × 10^{-3}M; C, 1.3 × 10^{-3}M; D, 4.59 × 10^{-4}M; temperature, 50°C. Current was measured 10 sec after applying the potential step.

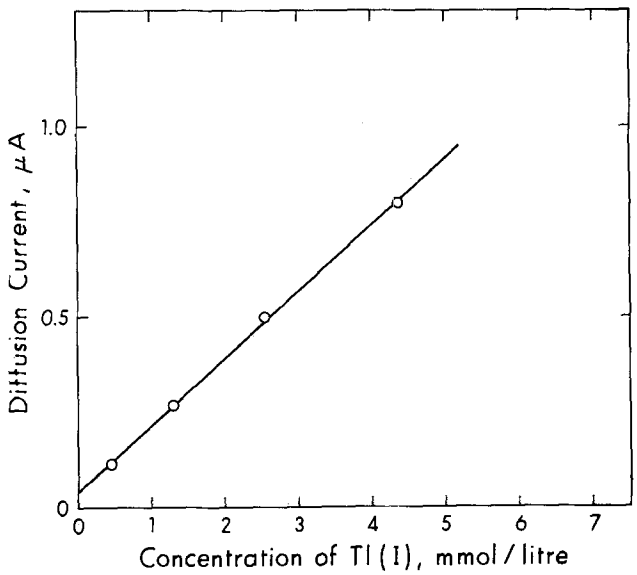


Fig. 3. Polarographic diffusion currents as a function of concentration of Tl(I) in $Ca(NO_3)_2 \cdot 4H_2O$; temperature, 50°C.

In chronoamperometry the current-time transient will follow the relationship $I = kt^{-1/2}$ when the potential is stepped to a value sufficiently cathodic of the reversible potential if semi-infinite linear diffusion controls the current. While our polarographic curves do indicate diffusion control at sufficiently cathodic potentials, the time transients are much longer than those used in cyclic voltammetric or chronopotentiometric studies and the effect of the geometry of the microelectrode may become more significant. This can be seen from the form of the equation for the current-time relationship for spherical diffusion-limited currents (4)

$$I = n\mathbf{F}AC^{\circ}D_0^{1/2}(1/\pi^{1/2}t^{1/2}) + n\mathbf{F}AC^{\circ}D_0/r_0 \qquad [1]$$

where r_0 is the radius of the spherical electrode and A, its area, is $4\pi r_0^2$. When the radius of the sphere is reasonably large, the spherical term normally will not be significant at short times. At longer times the contribution of this spherical term may become more significant. A plot of the data for thallium (I) reduction, shown in the form of a current-$t^{-1/2}$ plot in Fig. 4, indicates that our chronoamperometric data are, within experimental error, adequately described by semi-infinite linear diffusion when $t \leq 4$ sec and by spherical diffusion (dashed line) at longer times. The larger deviations at very short times are probably due to the effect of charging the double layer or to the response speed of our apparatus.

The linear portion of the I-$t^{-1/2}$ plot of Fig. 4 permits calculation of the diffusion coefficient of Tl(I) as 3.13 × 10^{-7} cm²/sec. This value, which is in good agreement with that of Lovering (2) (Table I), when inserted into Eq. [1] yields a value of 0.06 μA for the intercept rather than the 0.12 μA obtained by direct extrapolation. However, the uncertainty in the

Table I. Diffusion coefficients of Tl(I) as measured by different methods

Temperature, °C	Working electrode	$D \times 10^7$ (cm²/sec)	Technique	Reference
50.0	HMDE	3.0	Cyclic voltammetry	Present work
50.0	HMDE	3.1	Chronoamperometry	Present work
49	DME	3.3	Polarography	(2)
49.6	Mercury pool	7.0	Chronopotentiometry	(1)

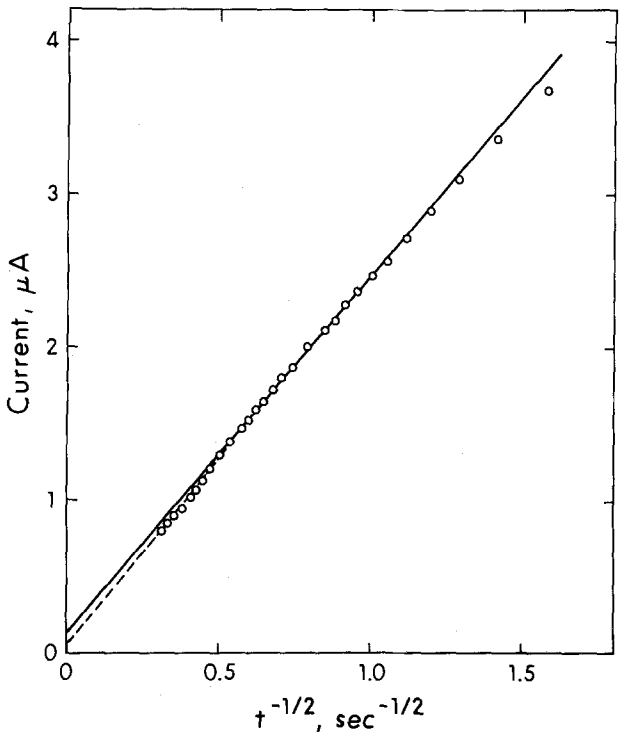


Fig. 4. Current vs. (time)$^{-1/2}$ for 4.36 × 10^{-3}M Tl(I) in $Ca(NO_3)_2 \cdot 4H_2O$ at 50°C. Area of HMDE, 0.0176 cm^2. Potential step applied, —1.20V against Ag(I)/Ag reference. The dotted curve corresponds to the values calculated from Eq. [1] for spherical diffusion.

extrapolation due to the effect of convection, which prevents acquisition of data at $t > 9$ sec even in this highly viscous melt, coupled with the observed deviation at very short times discussed above, is sufficiently large that the difference cannot be assumed to be significant.

Chronopotentiometry.—An investigation of the reduction of Tl(I) on mercury in this fused salt system by a-c chronopotentiometry was undertaken to establish the effect of markedly different diffusion coefficients of the oxidized and reduced forms of the Tl(I)/Tl(0) couple in the melt and in mercury, respectively. In the course of the investigation it was observed that transition times were sometimes unusually short and that an additional transition was sometimes present. Since the only significant advantage of a-c chronopotentiometry over d-c is better resolution of transitions, and its interpretation is otherwise less straightforward, the reduction was examined by d-c chronopotentiometry. It was found that the unusually short transitions (Fig. 5A) appeared at higher currents, while transitions were considerably longer at lower currents, although often distorted by a peak (Fig. 5B). The specific current density at which the comparatively abrupt changeover between the two types of behavior occurs is concentration dependent. The data shown in Fig. 5 are typical. It will be noted that the potential difference between the transitions is extremely small. At all concentrations the product $I_0\tau^{1/2}$ decreased with increasing current density I_0 up to the current density at which the unusually short transition appeared, which indicates that the process observed is not under normal diffusion control.

Chronopotentiometric current reversal gave values for the ratio of τ(reduction)/τ(oxidation) significantly greater than the value of 1/1 expected for a soluble product, but less than the value of 3/1 expected for soluble product.

Cyclic voltammetry.—A set of solutions of different concentrations were studied by cyclic voltammetry;

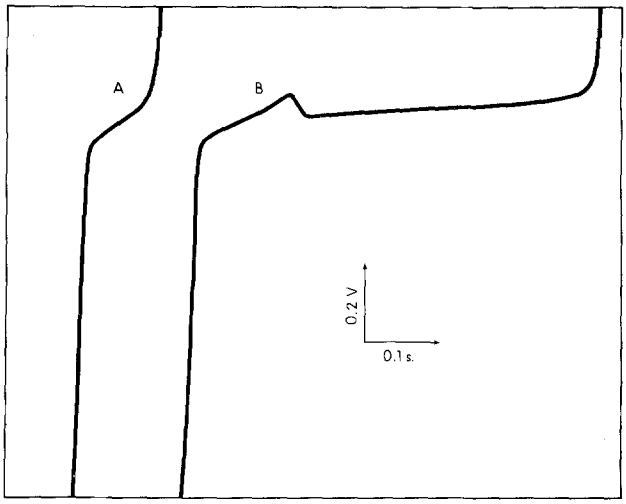


Fig. 5. Chronopotentiograms for the reduction of 10.24 × 10^{-3}M Tl(I) in $Ca(NO_3)_2 \cdot 4H_2O$ at 50°C. Area of HMDE, 0.0755 cm^2. Current applied: A, 80 μA; B, 70 μA.

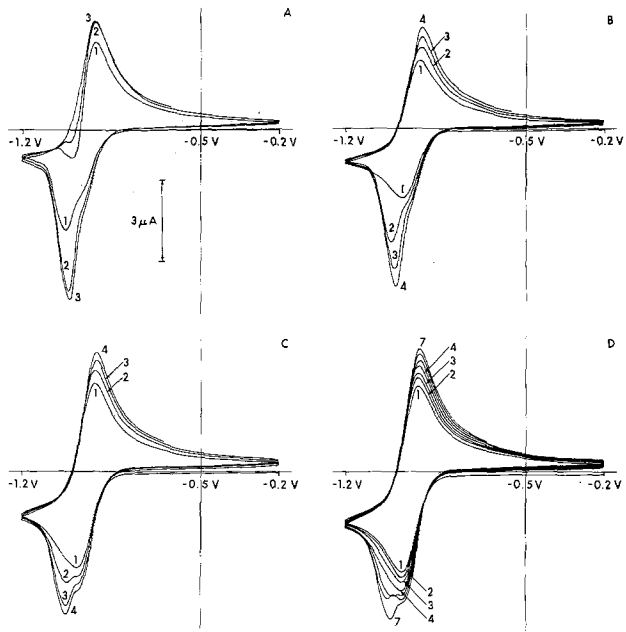


Fig. 6. Multicyclic voltammograms of 4.356 × 10^{-3}M Tl(I) in $Ca(NO_3)_2 \cdot 4H_2O$. Area of HMDE, 0.0176 cm^2. Voltage scan rate, ν: A, 50 mV sec^{-1}; B, 60 mV sec^{-1}; C, 100 mV sec^{-1}; D, 120 mV sec^{-1}. The current scale is same for all the four runs and is downward cathodic and upward anodic. Temperature 50°C.

sweep rate, ν, was varied between 0.02 V/sec and 50 V/sec. Typical cyclic voltammetric curves at several different scan rates are shown in Fig. 6, and the results are summarized in Table II. The cyclic voltammetric behavior observed depends upon both solution concentration of Tl(I) and sweep rate ν. For the two most dilute solutions, 0.459 mmole/liter and 1.299 mmole/liter, only a single cathodic peak and

Table II. Cyclic voltammetric results

Concentration Tl(I), C^o mmole/liter	$Ip\nu^{-1/2} \times 10^6$ (A $sec^{1/2}$ $V^{-1/2}$)	$Ip\nu^{-1/2}/C^o$ (A $sec^{1/2}$ cm^3 $mole^{-1}$)
0.459	1.22 ± 0.08	2.65 ± 0.18
1.299	3.32 ± 0.3	2.56 ± 0.20
2.563	6.40 ± 0.4	2.50 ± 0.15
3.538	9.43 ± 0.5	2.66 ± 0.15
4.356	10.1 ± 0.6	2.33 ± 0.13
6.582	15.9 ± 0.7	2.41 ± 0.10
9.479	22.3 ± 0.4	2.35 ± 0.04
		Mean = 2.49 ± 0.30

a single anodic peak were present over the full range of sweep rate, even in multicycle runs. These peaks, *IC* and *IA*, persisted as concentrations were increased, but at higher concentrations the curves exhibited more complex behavior which is discussed later.

The peak current, *Ip*, of the cathodic peak *IC* is directly proportional to bulk concentration of Tl(I) as shown in Fig. 7 at all intermediate scan rates (0.10 V/sec $\leq \nu \leq$ 10.0 V/sec). At these scan rates the peak current for *IC* is also directly proportional to the square root of the scan rate as shown in Fig. 8. Further, the peak potentials of *IC* and its corresponding anodic peak *IA* were independent of the scan rate, and they retained the values of -0.975 ± 0.005V and -0.910 ± 0.010V against the 0.03M Ag(I)/Ag(0) reference electrode. The separation of the cathodic and anodic peaks was constant at 70 $\pm$ 5 mV up to at least 5 V/sec but increased at higher scan rates. The ratio of the anodic peak current to the cathodic peak current was within experimental error unity at the intermediate scan rates 0.10 V/sec $\leq \nu \leq$ 10.0 V/sec, but significant deviations from unity were observed both at slower and at faster scan rates. When $\nu \leq$ 0.2 V/sec the cathodic peak current was slightly less than the anodic peak current, while the reverse is true for $\nu >$ 0.2 V/sec. All of these results would indicate a simple reversible process, at least at intermediate scan rates.

More complex behavior was first observed at a Tl(I) concentration of 2.563 mmole/liter. The simple behavior of the more dilute solutions is observed

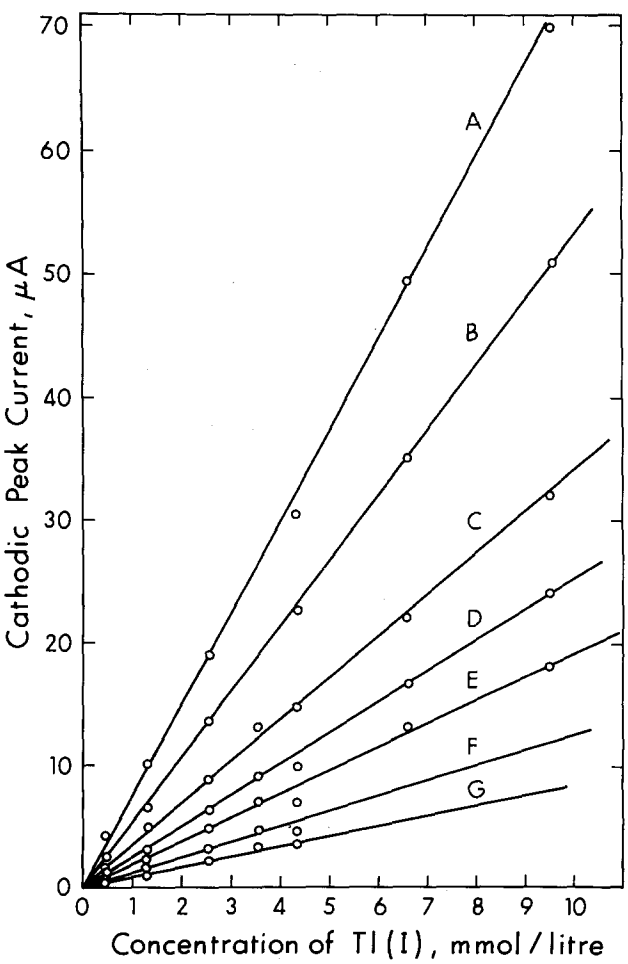


Fig. 7. Cathodic peak current *vs.* concentration of Tl(I) in $Ca(NO_3)_2 \cdot 4H_2O$ for various voltage scan rates, ν: A, 10.0 V sec^{-1}; B, 5.0 V sec^{-1}; C, 2.0 V sec^{-1}; D, 1.0 V sec^{-1}; E, 0.5 V sec^{-1}; F, 0.2 V sec^{-1}; G, 0.1 V sec^{-1}. Area of HMDE, 0.0176 cm^2, temperature 50°C.

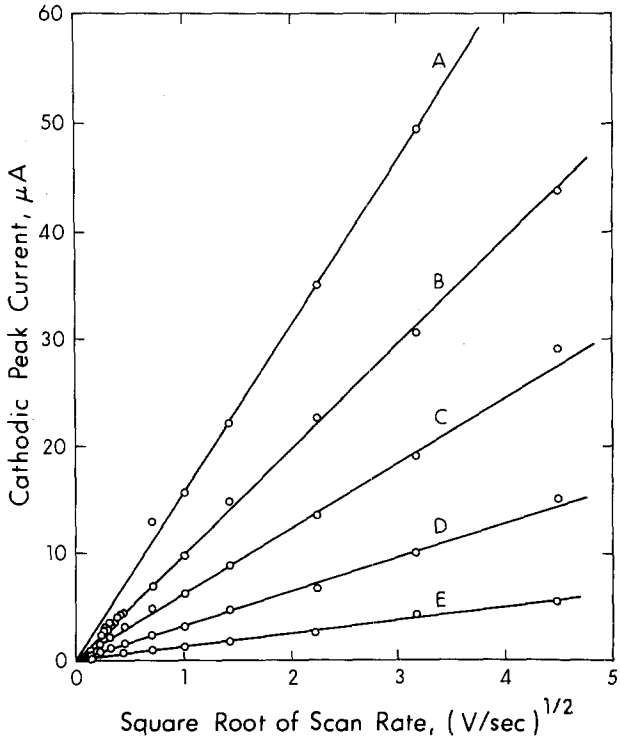


Fig. 8. Cathodic peak current *vs.* square root of voltage scan rate for the reduction of Tl(I) in $Ca(NO_3)_2 \cdot 4H_2O$ at 50°C. Area of HMDE, 0.0176 cm^2. Concentrations of Tl(I): A, 6.58 $\times$ 10^{-3}M; B, 4.36 $\times$ 10^{-3}M; C, 2.56 $\times$ 10^{-3}M; D, 1.30 $\times$ 10^{-3}M; E, 0.46 $\times$ 10^{-3}M.

at high and intermediate scan rates. However, at the slowest scan rate of 0.02 V/sec the first cycle was as expected but the second and subsequent cycles were not. In the second cycle a new cathodic peak *IIC* appeared at -0.995V and only a comparatively small shoulder appeared at the potential corresponding to cathodic peak *IC*. With additional cycles the positions of peaks *IIC* and *IC* shifted anodically and the relative magnitude of *IIC* increased while the *IC* shoulder disappeared. The height of the anodic peak *IA* increased significantly but its position did not shift with cycling.

As the concentration was further increased the complex behavior became more pronounced; the results at a Tl(I) concentration of 4.356 mmole/liter are given in Fig. 6 for several scan rates. At very low scan rates (Fig. 6A), where $\nu \leq$ 50 mV/sec, the prominent peak *IIC* appeared in the very first cycle, while at higher scan rates (Fig. 6B-6D) it appeared only in later cycles. As these typical data show, the effect of increasing scan rate is to cause the appearance of *IIC* at larger and longer numbers of cycles; this is true for all concentrations above 4.356 mmole/liter. As the concentration is increased further, the cathodic peak *IIC* becomes steadily more prominent and, at the same scan rate, appears in earlier cycles.

Determination of n.—Due to the presence of nucleation (see Discussion) during the reduction of Tl(I), no information on the number of electrons can be obtained from the slope of the polarograms or chronopotentiograms. The number of electrons can, however, be calculated when the current is controlled by diffusion. By relating the first-cycle cyclic voltammetric $Ip/\nu^{1/2}$ and chronoamperometric $It^{1/2}$, provided that the current-time curve is obtained at a potential corresponding to the diffusion plateau of the polarogram, one obtains (5, 6)

$$n^{1/2} = \frac{(Ip/\nu^{1/2})R^{1/2}T^{1/2}}{0.447\pi^{1/2}\mathbf{F}^{1/2}It^{1/2}}$$

At 50°C, this can be written as

$$n^{1/2} = 0.2106(Ip/\nu^{1/2})/It^{1/2}$$

The value of n calculated by this method, when the value of $It^{1/2}$ used was corrected for the sphericity of the diffusion field, comes out to be 0.84.

Diffusion coefficients.—The diffusion coefficients were calculated using the linear portion of the chronoamperometric I *vs.* $1/t^{1/2}$ plot obtained at plateau potentials and the mean $Ip\nu^{-1/2}/C^{\circ}$ value from the cyclic voltammetric results. The value of $n = 1$ was used in the calculations. Values of diffusion coefficients so obtained have been compared with those reported by other workers in the same melt in Table 1.

Hills *et al.* (7, 8) have reported that the presence of the nucleation process introduces discrepancies in D values. This is not reflected in our results. The values of D evaluated by the two techniques are in very good agreement not only with each other, but also with that reported by Lovering (2) using polarography. However, the value of the chronopotentiometric diffusion coefficient reported by Moynihan and Angell (1) is too high because these workers did not obtain their data under diffusion-controlled conditions (2).

In cyclic voltammetry the values of the diffusion coefficients obtained from two different runs on different days were 3.04×10^{-7} and 2.95×10^{-7} cm^2/sec, respectively. This shows the reproducibility of the results in this work.

Discussion

The unusual behavior of Tl(I) reduction in calcium nitrate tetrahydrate recorded above shows that this process is not the expected simple reversible reduction. It cannot be due simply to insolubility, since at 50°C thallium is soluble in mercury to the extent of 45 mole per cent (m/o) (9). One possible explanation would be adsorption phenomena. Lovering (10), in his study of the electroreduction of bromocadmium (II) complexes on mercury in this melt, interpreted curves showing polarographic maxima and multiple cyclic voltammetric peaks on the basis of adsorption; adsorption is well known in aqueous electrodeposition studies of many metal ions and has been demonstrated in anhydrous nitrate melts as well. The constancy of $Ip\nu^{-1/2}$ with scan rate argues against adsorption in the present case. Another possible explanation is electrocrystallization of a thallium compound on the surface of the mercury drop. This phenomenon is also known; the excellent study of Fleischmann, Pattison, and Thirsk (11) on the electrocrystallization of thin films of thallous chloride on thallium amalgam from aqueous solution shows chronoamperometric curves which are remarkably similar to those of the present work.

Yet a third possible explanation is a nucleation step. Hills, Schiffrin, and Thompson (7, 8) have shown that a nucleation step may be involved in the electrodeposition of metals from molten nitrates. This could result in large variations in the values of diffusion coefficients obtained by different workers using different techniques, perhaps as Lovering (2) and Moynihan and Angell (1) in the present case. Hills, Schiffrin, and Thompson (7, 8) studied the nucleation effects in the deposition of silver on platinum from molten $NaNO_3$-KNO_3 eutectic and also studied the aqueous electrodepositions of silver on platinum and on graphite and of mercury on graphite. These workers also have suggested that similar nucleation steps are unlikely to be observed in molten halides where predeposition reactions to form a monolayer, possibly from an adsorbed layer of metal ions, frequently occur (12). This limitation has not been substantiated. Mamantov and co-workers have observed a nucleation step in the electrodeposition of aluminum (13), zirconium (14), and iron (14) on solid microelectrodes in chloroaluminate melts. We note that initial potential overshoots very similar to those observed in the present work appear on chronopotentiograms observed during the reduction of the uranyl ion in molten NaCl-KCl (15) of Cr(II) (16) and the neptunyl ion (17) in molten LiCl-KCl, and of the chromate ion in molten LiCl-KCl in the presence of Zn(II) or Co(II) (18), all on solid electrodes, but these authors have not given an explanation of it other than overvoltage. Nucleation behavior is also known in aqueous solution, as in the electrodeposition of palladium on vitreous carbon electrodes (19).

Yet another possible explanation for these results could lie in a process which is indeed nucleation and in which the nucleation is followed not by film formation but by the formation of metal dendrites. Such phenomena have been observed by Calusaru and Kuta (20) when nitrate solutions of aqueous metal ions, including Tl(I), are reduced on the dropping mercury electrode. They state that there is a lower concentration threshold, about 18 mmole/liter for Tl(I), below which dendrite formation is not observed. This dendrite formation was favored by addition of nitrate and of gelatine. In the polarographic curves, the metal dendrite formation was observed at a potential characteristic of the metal in the diffusion-limited plateau region. This phenomenon has also been mentioned by Galus (21), who states in his review that it is sometimes observed that the deposition of aqueous metal ions on mercury electrodes gives metal which does not enter into the mercury phase; instead, it remains on the surface of the electrode in the form of a finely divided precipitate. The formation of such precipitates at the electrode surface does not appear to depend upon the normal solubility of the deposited metal since it has been observed (20, 21) both for metals that are sparingly soluble and for metals that are highly soluble in mercury.

We consider that the latter mechanism is in all probability that which prevails in the present case. Thus, the phenomena observed by us are due to the interaction of three processes. These are: (*i*) the formation of nuclei of thallium metal on the surface of the hanging mercury drop; (*ii*) the growth outward into the aqueous solution of these nuclei into dendrites of thallium; (*iii*) the dissolution of thallium on the surface into the hanging mercury drop, or the actual dissolution of the dendrite itself in the mercury drop.

The first of these steps, that of nucleation, has received considerable study in other systems. The usual effect of nucleation is the appearance of maxima in the chronoamperometric current-time curves (7, 8), as we have observed for Tl(I) reduction in this melt. These nucleation phenomena are observed in metal electrode oxidation (22-24) as well as in electrodeposition; maxima in chronopotentiometric curves (23) as well as in chronoamperometric curves (22, 24) have been reported, again in accordance with our observations. The second and third steps have been discussed qualitatively (20) but a quantitative treatment does not appear to be available. In view of the significant and thus far unpredictable change in the real area of the electrode which arises as a result of the interaction of the opposed rates of dendrite growth and dissolution, quantitative calculations appear possible only for the nucleation step. The observations are, however, in qualitative accord with these two phenomena as is discussed further below.

Quantitative study of the nucleation step can be carried out using the chronoamperometric curves given in Fig. 1. Integration of these curves from the point of origin to some arbitrarily selected time will give the total charge and enable calculation of surface coverage. In the present case integration was carried out using a planimeter. A straight line was constructed from the origin to the center of the first

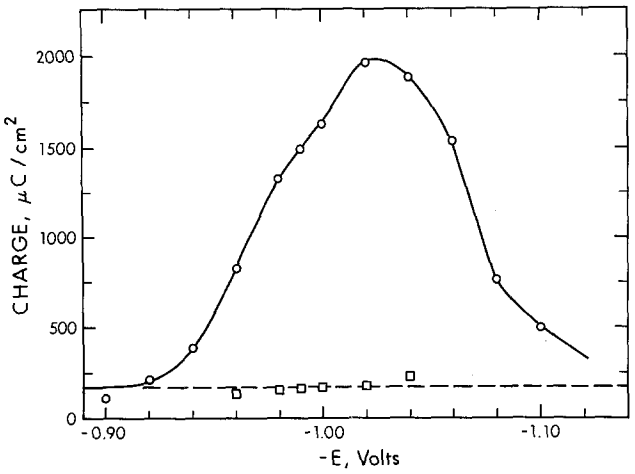


Fig. 9. Integrated area of chronoamperometric curves vs. applied potential of step. 0, Q_{total} in $\mu C/cm^2$ for charge of all processes to 14 sec from step application; □, Q_{nucl} in $\mu C/cm^2$ for charge of nucleation/nuclei growth step alone. Dashed horizontal line at 171.2 $\mu C/cm^2$ represents theoretical charge required to form monolayer of thallium metal. Area of electrode 0.0176 cm^2, HMDE.

minimum, since this is the point of initiation of nucleation (22), and the area integrated from this line to an arbitrary cutoff of 14 sec which is in all cases beyond the peak processes observed. In curves 1A, 1B, 1K, and 1L, which have no discernible minimum, the straight line was constructed through the shortest time point at which a minimum could occur, so that the areas calculated under these curves represent maximum possible values of the charge. The values of charge so calculated are shown in Fig. 9 and Table III.

It is instructive to compare these values with those which would be expected for monolayer coverage of the electrode. An expected value can be calculated from the density of metallic thallium, the atomic weight of thallium, the electronic charge, and the value of the Faraday constant; we obtain 171.2 $\mu C/cm^2$ for the charge so required. Since the maximum charge of 1.96 mC/cm^2 at −1.02V is far greater than this it is clear that the totality of the peak processes must involve far more than nucleation and must include multilayer or dendritic crystal growth. The peak processes are, however, separable into two peak processes in the chronoamperometric curves. Separation of the areas, and hence the charges, of these two processes is possible by separate integration of the area under the first peak from the initiation of nucleation, as described above, to the minimum between the two peaks, at which a perpendicular was dropped to the axis. The results of such integration are given in the last column of Table III; the values are in excellent agreement with the expected value of 171.2 $\mu C/cm^2$ for monolayer coverage and thus do reasonably correspond to a nucleation process. This argument is supported by an approximate integration of the chronoamperometric curves given in Fig. 1 of the work of Fleischmann, Pattison, and Thirsk (11), which gives values close to that of the expected monolayer for the formation of thallous chloride on thallium amalgam.

Table III. Integration of chronoamperometric curves

Curve	E, V	Q_{total}, $\mu C/cm^2$	Q_{nucl}, $\mu C/cm^2$
A	−0.90	118.0	
B	−0.92	211.9	
C	−0.94	386.6	
D	−0.96	828.8	132.9*
E	−0.98	1327.7	165.0
F	−0.99	1494.9	171.3
G	−1.00	1636.9	175.3
H	−1.02	1961.7	177.6
I	−1.04	1879.8	234.8*
J	−1.06	1543.8	
K	−1.08	766.4	
L	−1.10	499.4	

* Indicates peaks not well separated; electrode area taken as constant 0.0176 cm^2; for additional discussion see text. Q_{total} represents charge up to 14 sec, Q_{nucl} represents charge under first chronoamperometric peak.

The same paper (11) also gives an expression, derived earlier by the senior authors, for the current-time behavior expected for the instantaneous formation of N_0 nucleation centers followed by their growth as

$$i = (2z\mathbf{F}\pi hMN_0k^2t/\rho) \exp(-\pi M^2N_0k^2t^2/\rho^2) \quad [2]$$

where z is the ionic charge, $\mathbf{F}$ the Faraday constant, h the height of the nucleation centers (in centimeters), M the molecular weight, ρ the density, k the rate constant for crystal growth (in moles cm^{-2} sec^{-1}). The logarithmic form of this equation yields a plot of log (i/t) against t^2 which should be linear; as shown in Fig. 10, linear behavior is indeed obtained from the first to the second minimum in the chronoamperometric curve. This is in excellent agreement with our explanation of dendritic or multilayer growth for the subsequent peak and nucleation growing to a monolayer at the first peak.

In this model, the slope of the line should be equal to $-2.303\ \pi M^2N_0k^2/\rho^2$. For the line of Fig. 10 the slope is $-1.592\ sec^{-2}$. From this slope, using the density and molecular weight of metallic thallium, a value of 7.40×10^{-4} $mole^2$ sec^{-2} cm^{-6} can be calculated for the product N_0k^2. While these curves do not permit the separation of N_0 from k, a maximum value of k would be the diffusion-controlled limit (11) of $\pi DC_0/5h$. For this system we already know D to be 3.0×10^{-7} cm^2 sec^{-1} and C_0 for this curve is 4.35×10^{-6} mole cm^{-3}. Estimation of h as the height of a single atom using the density of thallium, the atomic weight of thallium, and Avogadro's number yields 3.0×10^{-8} cm for h, so that the maximum value of k is then 2.68×10^{-5} $mole^2$ sec^{-1} cm^{-2} and the minimum value of N_0 is 1.03×10^6 nuclei/cm^2. This minimum value of N_0 is well below the 10.7×10^{14} atom/cm^2 of the monolayer which would give 171.2 $\mu C/cm^2$ charge coverage, as is reasonable since a single nucleus may be made up of a large number of thallium atoms.

Thus the over-all electrochemical reaction which is observed in this system by any technique consists

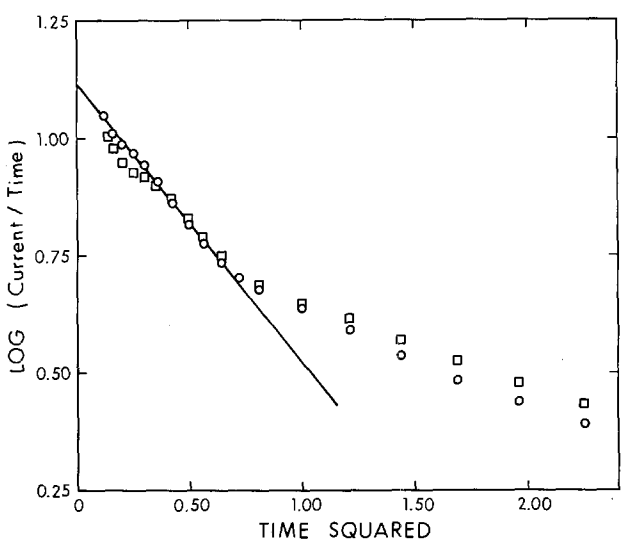


Fig. 10. Logarithmic form of Eq. [2] plotted for data of chronoamperometric curves F, 0; G, □. Values of i in μA, time in seconds.

of the three steps of nucleation, dendrite growth into solution, and dendrite dissolution in the hanging mercury drop. In the chronoamperometric curves, formation of the nuclei begins at the minimum of the current-time transient (22). As the current increases toward the maximum, perhaps the population, but at least the size of the surface nuclei, which may be visualized as monolayer islands of metallic thallium on the surface of the mercury electrode, increases. Beyond this maximum, crystal growth occurs on the surface until surface coverage is complete. The second maximum, which is observed at higher cathodic potentials and higher concentrations of Tl(I), corresponds to the formation of additional layers (11) or to initial dendritic growth.

The situation in the chronopotentiometric measurements is similar. The small overshoot occurring at the beginning of the chronopotentiometric transition (Fig. 5B) is probably the nucleation overpotential which must be achieved before bulk deposition can proceed (7, 8, 13, 14). Once nucleation has been achieved the charge transfer process is rapid and no longer requires this overpotential, so that the potential of the working electrode is seen to fall before the transient is completed with the sharp rise toward solvent reduction.

The shape of the chronopotentiometric transients was found to be a function both of current density and of bulk concentration of Tl(I). The initial potential overshoot (Fig. 5B) is observed at lower currents; as the current is increased, the overshoot disappears and the transition time becomes unexpectedly small (Fig. 5A). The abrupt disappearance of the nucleation overpotential at higher current densities may occur because at such higher current densities the transition time becomes smaller than the induction period required either to complete nucleation or to begin crystal growth. The supply of Tl(I) ions at the electrode surface is exhausted before nucleation is complete and hence the electrode potential does not fall back to the lower value characteristic of crystal growth. It is reasonable also that this change in current be small and the subsequent transition significantly longer because the dendritic growth will rapidly increase both the real area of the electrode and its outreach into solution, which will simultaneously reduce the real current density at the electrode and increase the supply of Tl(I) able to reach it to supply the current demanded.

It is further reasonable that the nucleation overpotential is smaller and the induction period for nucleation is larger when the bulk concentrations of Tl(I) are lower, because for nucleation to be completed and/or dendritic crystal growth to begin a certain minimum total amount of Tl(I) is required. Hence, in such solutions, only a single normal transition is observed.

In one experiment, the electrolysis was allowed to continue for some time after the transition time had been observed. The electrolysis current was then switched off, the solution was stirred, and allowed to stand a few minutes to ensure that uniform concentrations were achieved both in the bulk solution and in the mercury drop. A second chronopotentiometric transient was then recorded using the same mercury drop. This time the potential overshoot was very small. Since the mercury drop would still have been covered with thallium nuclei, although the dendrites may now be dissolved, nucleation should not occur and the surface layer should begin crystal growth at once. This appears to be consistent with our observation.

In the cyclic voltammetric results the appearance of the cathodic peak (*IIC*) depends upon two factors, concentration and the scan rate. It appears in earlier cycles when the concentration is high and scan rate is slow. The anodic shift of the peak potential of the reduction process in subsequent cycles has been taken (14) as the criterion for nucleation. The process of nucleation starts at the first cathodic peak (*IC*) and the population of nuclei at the electrode surface increases up to the second cathodic peak (*IIC*), when the electrode surface gets saturated; after that crystal growth takes place. The time required to complete the process of nucleation and to start crystal growth (peak *IIC*) should depend upon the concentration, the time elapsed after the nucleation has been initiated, and on the scan rate as has been experimentally observed. Thus, the cyclic voltammetric results agree well with the conclusions drawn from the other two methods, chronopotentiometry and chronoamperometry.

At the suggestion of a referee, we have attempted to compare the open-circuit potential of a HMDE upon which thallium was electrodeposited in a chronopotentiometric experiment with that of metallic thallium in the same melt. Upon cessation of the current the potential of the HMDE dropped immediately to a value identical to $E_{\tau/4}$ of the chronopotentiogram and remained constant at that potential for 5 min or more. This potential was -1.02 ± 0.01V against our Ag(I)/Ag(0) reference, while the stable potential of massive metallic thallium in the same melt was -1.20 ± 0.02V. Removal of all of the oxide from the surface of the metallic thallium was not possible, which may account for some of the observed difference, but since dissolution of thallium in mercury does occur in the third step of our proposed mechanism an exact correspondence in potential is unlikely unless the monolayer is permanently stable.

Acknowledgments

Thanks are due to Dr. G. M. Rao for his assistance during some of the experiments. This work was supported by the National Research Council of Canada through an Operating Grant.

Manuscript submitted Dec. 14, 1976; revised manuscript received March 1, 1977. This was Paper 307 presented at the Philadelphia, Pennsylvania, Meeting of the Society, May 8-13, 1977.

Any discussion of this paper will appear in a Discussion Section to be published in the June 1978 JOURNAL. All discussions for the June 1978 Discussion Section should be submitted by Feb 1, 1978.

Publication costs of this article were assisted by The University of Alberta.

REFERENCES

1. C. T. Moynihan and C. A. Angell, *J. Phys. Chem.*, **74**, 736 (1970).
2. D. G. Lovering, *Collect. Czech. Chem. Commun.*, **37**, 3697 (1972).
3. J. Timmermans, "Physical Chemical Constants of Binary Systems," Vol. 3, Interscience Pubs., Inc., New York (1960).
4. P. Delahay, "New Instrumental Methods in Electrochemistry," p. 61, Interscience Pubs., Inc., New York (1954).
5. H. Matsuda and Y. Ayabe, *Z. Elektrochem.*, **59**, 494 (1955).
6. P. Delahay, "New Instrumental Methods in Electrochemistry," p. 51, Interscience Pubs., Inc., New York (1954).
7. G. J. Hills, D. J. Schiffrin, and J. Thompson, *Electrochim. Acta*, **19**, 657 (1974).
8. G. J. Hills, D. J. Schiffrin, and J. Thompson, *ibid.*, **19**, 671 (1974).
9. M. Hansen and K. Anderko, "Constitution of Binary Alloys," p. 842, McGraw-Hill, Inc., New York (1958).
10. D. G. Lovering, *Trans. Faraday Soc.*, **67**, 2659 (1971).
11. M. Fleischmann, J. Pattison, and H. R. Thirsk, *Trans. Faraday Soc.*, **61**, 1256 (1965).
12. G. J. Hills, D. J. Schiffrin, and J. Thompson, *This Journal*, **120**, 157 (1973).

13. P. Rolland and G. Mamantov, *ibid.*, **123**, 1299 (1976).
14. B. Gilbert, G. Mamantov, and K. W. Fung, *Inorg. Chem.*, **14**, 1802 (1975).
15. R. W. Stromatt, *This Journal*, **110**, 1277 (1963).
16. D. Inman, J. C. L. Legey, and R. Spencer, *J. Electroanal. Chem.*, **61**, 289 (1975).
17. L. Martinot and G. Duyckaerts, *Inorg. Nucl. Chem. Lett.*, **5**, 909 (1969).
18. K. W. Hanck and H. A. Laitinen, *This Journal*, **118**, 1123 (1971).
19. M. F. Bell and J. A. Harrison, *J. Electroanal. Chem.*, **41**, 15 (1973).
20. A. Calusaru and J. Kuta, *ibid.*, **20**, 383 (1969).
21. Z. Galus, *CRC Crit. Rev. Anal. Chem.*, **4**, 359 (1975).
22. D. W. Shoesmith, T. E. Rummery, D. Owen, and W. Lee, *This Journal*, **123**, 790 (1976).
23. B. Behr and J. Taraszewska, *J. Electroanal. Chem.*, **19**, 373 (1968).
24. M. Fleischmann, K. S. Rajagopalan, and H. R. Thirsk, *Trans. Faraday Soc.*, **59**, 741 (1963).

Current Distribution in a Tubular Electrode under Laminar Flow: One Electrode Reaction

Richard Alkire* and Ali Asghar Mirarefi*

Department of Chemical Engineering, University of Illinois, Urbana, Illinois 61801

ABSTRACT

The reaction rate distribution along a tubular electrode was measured directly with a sectioned electrode during steady laminar flow of electrolyte through the electrode. The Fe(III)/Fe(II) redox reaction was studied at the limiting current, and the Cu(II) deposition reaction was studied at all fractions of the limiting current, The experimental conditions were systematically varied in order to determine the effect of counterelectrode placement, tube radius and length, reactant concentration, flow rate, and current density. Experimental polarization curves, limiting current, and current distribution data were compared with a theoretical model of the electrochemical system, and agreement was obtained over a wide range of parameter space. Theoretical calculations were carried out in order to make additional predictions of tubular electrode behavior at and below the limiting current.

During electrolysis, it is necessary that both chemicals and electrical energy arrive at the electrode surface in order that electrochemical reactions proceed. As a consequence, two limiting cases of current distribution phenomena arise. For example, the "limiting" current distribution may be determined without consideration of the potential field, while the "primary" and "secondary" current distributions are calculated without consideration of the mass transport of reactants to the electrode surface. In many practical situations, however, the current distribution does not conform to either simple limiting case of behavior. Interest therefore arises in analyzing the more general behavior of electrochemical systems where convective flow and electrical potential fields must be determined simultaneously. The investigation reported here (1) expands on previous work on tubular electrodes operating under steady laminar flow of electrolyte (2). In this paper, experimental and theoretical aspects were investigated in a system having a single electrochemical reaction. Next month, a similar study is described on multiple electrode reactions in a tubular electrode.

Previous Work

At limiting current conditions, the tubular electrode system is analogous to a classical problem of heat transfer through the wall of a tube held at constant temperature. Discussion of the theoretical and experimental aspects of the heat transfer problem and its mass transfer analog are commonly available for both laminar and turbulent flow situations (3). Experimental studies on tubular electrodes using the electrochemical limiting current technique have been carried out under laminar (11), turbulent (4, 5), and pulsatile forced flow (6) conditions. The role of natural convection on mass transfer in laminar flow in a straight tube has also received attention (7).

Below the limiting current condition, the reactant concentration at the tube surface varies with position and depends upon both the kinetics of the heterogeneous reaction at the wall and the potential field within the flowing electrolyte. When the potential field effect is neglected, the situation corresponds to a (nonelectrolytic) catalytic reactor problem. Chambré and Acrivos (8) developed a theoretical procedure for calculating the reactant concentration along a catalytic surface placed in a laminar flow field. Wissler and Schechter (9) used sets of orthogonal functions to evaluate the concentration profile for turbulent gas flow through a circular tube with chemical reaction at the wall. In a series of papers, Matsuda (10) analyzed a number of flow configurations and electrochemical reaction sequences including tubular electrodes with both heterogeneous and simultaneous homogeneous chemical reactions; the potential field distribution was neglected. Similarly, electroanalytical groups have investigated tubular electrodes in the presence of heterogeneous and homogeneous reactions, without consideration of the potential distribution (11, 12), *i.e.*, uncompensated resistance effects.

In order to take simultaneous account of the potential field and the concentration field, Asada *et al.* (13) developed a calculational procedure and applied it to free convection in a rectangular electrolysis cell. Newman and co-workers (14) developed and applied a related procedure to many systems having laminar forced convection. Cabán and Chapman (15) and, later, Varjian (16) showed that orthogonal collocation methods could also be used in the solution of such problems. In the tubular geometry, the only "complete" analysis (2) was carried out for laminar mass transfer in the entrance region with simultaneous consideration of a two-dimensional potential field distribution. The

* Electrochemical Society Active Member.
Key words: tubular electrode, sectioned electrode, mathematical model, copper deposition, ferric reduction, laminar flow.

work was subsequently applied to electrodeposition in circular through-holes in multilayer printed wiring boards (17, 18).

The investigation reported here (1) was intended to expand the experimental and theoretical literature on current distribution problems for currents below but at an appreciable fraction of the limiting current. An experimental system was used which enabled measurement of the local reaction rate distribution under controlled conditions (19). By systematic variation of the experimental parameters, data were obtained which were amenable to detailed comparison with theoretical calculations.

Apparatus

The experiment consisted of measuring the current distribution along a sectioned tubular electrode with steady laminar flow of electrolyte. Experiments were carried out with two different electrochemical systems: (*i*) deposition of copper from acid sulfate electrolyte, and (*ii*) reduction of ferric ions in sulfuric acid. Current distributions were measured at various fractions of the limiting current upon systematic variation of electrode geometry, flow rate, reactant concentration, and counterelectrode placement.

A diagram of the tubular electrode assembly is shown in Fig. 1. The cathode sections were fabricated by drilling out a copper rod and slicing off wafers. For studies with the Fe(III)/Fe(II) redox system, the electrode sections were platinized by a procedure described below. Electrode sections were insulated from one another with thin (0.25 mm) sheets of Teflon® having the same inner and outer radii as the copper wafers. Wafers and insulating sheets were compressed in the Plexiglas holder which had reference electrode compartments both upstream and downstream from the sectioned tubular electrode. Mercury/mercurous sulfate reference electrodes were used. The counterelectrode (not shown in Fig. 1) was placed either far upstream or far downstream from the tubular electrode, in side compartments.

The Plexiglas holder was placed in a 12 liter capacity gravity-flow system in which the hydrostatic head was kept constant by an overflow loop in the overhead reservoir. The flow rate through the cell was controlled with a needle valve and measured with precision rotameters (Gilmont No. 2-5). In order to assure fully developed laminar flow, the upstream section of the flow circuit was a smooth plastic tube in excess of 50 diameters in length.

Electrical connection to electrode sections was made through a slot in the Plexiglas holder. A potentiostatic power supply (Wenking 70TS-1 or 68TS-3) was used to control the cathode potential with respect to the reference electrode nearest the counterelectrode. Individual section currents were detected witth a multichannel zero-resistance operational amplifier device (built in-house) and displayed on a multipoint potentiostatic recorder (Leeds & Northrup Speedomax X). The total cell current was monitored with a potentiostatic strip-chart recorder (Sargent-Welch SRG). When polarization curves were measured, the potentiostat was driven at 1 mV/sec with a linear ramp generator (built in-house), and the output was displayed on an X-Y recorder (Houston 2000).

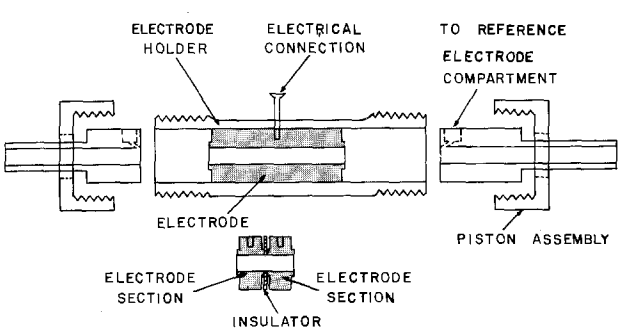


Fig. 1. Tubular electrode assembly

Experimental Procedures

Electrolytic solution was prepared from reagent grade chemicals and deionized water which had been distilled once in a tin-lined still, and which had a conductivity of 4×10^{-6} $(\Omega cm)^{-1}$. The solutions used in this study were $CuSO_4$ in 1.5M H_2SO_4 and $Fe_2(SO_4)_3$ + $FeSO_4$ in 1.5M H_2SO_4. No additives were used. The cupric concentration was measured either with a spectrophotometer (20) (Beckman Model B) or with an iodometric method (21). The ferric ion concentration was also determined by the iodometric method; the ferrous ion concentration was measured by titration with potassium permanganate (21). The conductivity of the solutions was measured with a bridge (Leeds & Northrup 4959) in a cell calibrated with 0.1 demal KCl at 26°C (29).

After assembly in the Plexiglas holder, the sectioned tubular electrode surface was polished down to 600 grade emery, then disassembled and rinsed in water. Electrode sections were scrubbed in trichloroethylene, soaked in hot phosphate/metasilicate solution, pickled in hot acidified ferric sulfate, etched in a dilute mixture of nitric and sulfuric acids, brightened in a concentrated mixture of nitric and sulfuric acids, and rinsed in distilled water. To plate platinum onto copper, the cleaned pieces were electropolished (Bath No. 200, Electro-Glo Company), gold plated (Orotemp 24, Technic Incorporated), and then platinum plated (No. 209, Engelhard). The cell was then assembled, placed in the flow circuit, and connected to the electrical circuit.

The flow rate was adjusted and the electrical circuit was energized to the desired applied potential. When steady state was reached (approximately ten residence times for low flow rates, less for higher flow rates) the applied potential, the potential difference between the upstream and downstream reference electrodes, the total current, and the section currents were measured. The applied potential was then increased and the procedure repeated until eventually the limiting current plateau was reached. The flow rate was then adjusted to another flow rate and the entire process was repeated.

Comparison of Experimental Data with Theoretical Calculations

Literature values used for the physical properties of the two chemical systems investigated are listed in Table I. In some cases, direct measurement of the properties was made; these, along with the experimental conditions for each current distribution measurement, are given in Table II. Experimental data from the copper system were compared directly with the theoretical model described in an earlier publication (2). Data for the redox system were compared with a modified version of that model (1) but, as mentioned below, only a limited number of redox experiments was carried out. Table III lists the dimensionless parameters which describe the tubular electrode model. The physical significance of these parameters has been discussed previously (2) and will be reviewed briefly in the discussion below.

Because the theoretical model is valid only in the mass transfer entrance region, or Lévêque region, the flow rate was constrained (23) to the criterion

Table I. System properties

Property	Cu system (Ref.)	Fe system (Ref.)
n	2	1
D, cm²/sec	5.0×10^{-6} (27, 28)	4.2×10^{-6} (11)
ν, cm²/sec	1.035×10^{-2} (28)	
i_o, A/cm²	0.38×10^{-3} (26)	—
α	0.75 (26)	—
β	0.25 (26)	
κ, mho/cm	0.51	

Table II. Experimental conditions

Run	System	Section length (cm)	Number of sections	Radius (cm)	Reactant concentration
63-73	Cu	0.48	9	0.635	0.1
81-83	Cu	6.0	1	0.3175	0.1
89	Cu	0.5	12	0.476	0.1
93, 94	Cu	6	1	0.476	0.013
95	Cu	5	1	0.3175	0.01
96	Cu	6	1	0.476	0.01
112	Cu	0.5	9	0.476	0.011
120-125	Fe	0.5	8	0.3175	0.04
130-140	Fe	0.5	6, 8, 11	0.476	0.02
154-167	Cu	0.45, 0.5	9, 11	0.476, 0.3175	0.0104
180	Cu	0.48	12	0.635	0.0106
181, 182	Cu	0.48	12	0.635	0.01
183	Cu	0.48	9	0.635	0.01
184-186	Cu	0.48	6	0.476	0.01
188	Cu	0.45	12	0.476	0.0106
193	Cu	2.7	1	0.476	0.01
198	Cu	0.45	9	0.476	0.0106
203	Cu	0.50	11	0.318	0.0106
204	Cu	0.50	11	0.3175	0.0106
205	Cu	0.50	8	0.3175	0.0106
210	Cu	4	1	0.3175	0.01
211	Cu	5.5	1	0.3175	0.01
212	Cu	6.0	1	0.635	0.0426
216	Fe	0.5	8	0.3175	0.008

Table III. Dimensionless system parameters

$$Z = \frac{z}{L} \qquad \gamma_O = \frac{R_o}{L}$$

$$\Phi = \frac{nF}{RT}\phi \qquad \bar{\beta} = \frac{2n\mathbf{F}L^2}{RTR_o\kappa}\langle j\rangle$$

$$J = \frac{j}{\langle j\rangle} \qquad J_N = \frac{j}{\langle j_{lim}\rangle}$$

$$\xi = \frac{2n\mathbf{F}L^2}{RTR_o\kappa} i_o \qquad N = \frac{n^2\mathbf{F}^2L^2c_{i\infty}}{-s_i\Gamma\left(\frac{4}{3}\right)RTR_o^2\kappa}\left(\frac{12QD_i^2}{\pi L}\right)^{1/3}$$

$$Q > \frac{\pi L D_i}{0.02} \qquad [1]$$

On the other hand, to conform to the requirement of laminar flow, one also has the condition

$$Q < 1050\pi R_o \qquad [2]$$

Electrodes were used only for which the aspect ratio (tube radius/length) was sufficiently small that the potential distribution within the electrolyte was essentially one dimensional. The criteria for establishing conditions of one-dimensional behavior will be discussed thoroughly in the Discussion of the Theoretical Model which follows.

Based on the simulation studies reported by Flanagan and Marcoux (22), it can be concluded that the experimental conditions studied here conform to the situation where axial diffusion is negligible, and where the velocity profile in the diffusion layer is linear.

Over-all current-potential data.—Polarization curves for both reaction systems exhibited limiting current plateaus, the plateau width being greater when the counterelectrode was upstream than when it was downstream. The average limiting current varied with flow velocity as given in Fig. 2. The dimensionless Nusselt and Graetz numbers used to correlate these data are defined as

$$\langle Nu\rangle = \frac{s_i I_{lim}}{n\mathbf{F}Dc_\infty L\pi}$$

$$Gz = \frac{Q}{DL}$$

The solid line in Fig. 2 corresponds to the solution of the convective diffusion (Lévêque) equation under limiting current conditions, that is (23)

$$\langle Nu\rangle = 1.6151\left(\frac{4}{\pi}Gz\right)^{1/3} \qquad [3]$$

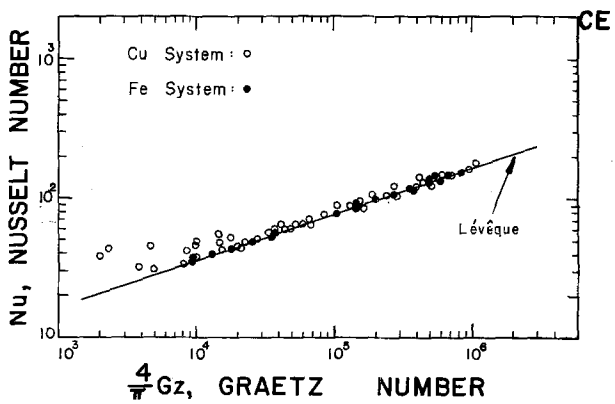


Fig. 2. Limiting current data for laminar tubular electrode

In the nomenclature given in Table III, Eq. [3] may also be written

$$\bar{\beta}_{lim} = -N \qquad [4]$$

from which it recognized [2] that the parameter N is the dimensionless limiting current density. Figure 2 indicates good agreement between data and theory at high flow rates. At lower flow rates, good agreement was found for the redox system and for dilute copper solutions (0.01M). Deviations from the theoretical correlation were observed for the more concentrated copper solutions (0.02M and above) and for tubes of large radius. These deviations have been attributed to natural convection effects superimposed on the forced flow (7); similar behavior has been observed by others (24, 25). The data in Fig. 2 have demonstrated that literature values of the system parameters can be used with the Lévêque equation to predict the average limiting current density.

Experiments below the limiting current were only carried out under those conditions for which the limiting current agreed with the Lévêque equation as judged from Fig. 2. It was found that the behavior of the redox system was not reproducible below the limiting current owing to significant variations from section to section in the rest potential of the platinum-plated electrodes. Although improvements could perhaps have been made in the plating procedures, the matter was not pursued. Rather, for comparison with theoretical calculations below the limiting current, only the copper deposition data were used.

Now let us turn to conditions far below the limiting current, under which mass transport effects play a negligible role in determining electrode behavior. Figure 3 contains current-potential data for seven electrode configurations which have been reduced to dimensionless form in accord with the definitions given

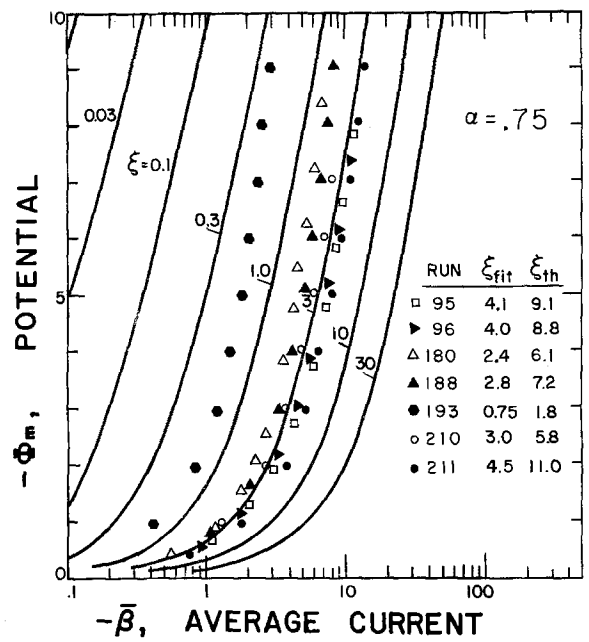


Fig. 3. Polarization data and theoretical calculations, far below limiting current (copper deposition system).

in Table III. In the absence of mass transport effects, the polarization curve should depend solely upon the dimensionless parameter

$$\xi = \frac{2nFL^2}{RTR_{o\kappa}} i_o$$

which is a dimensionless ratio of ohmic to charge-transfer resistances. The solid lines in Fig. 3 are theoretical polarization curves for various values of ξ, calculated with kinetic constants $\alpha = 0.75$, $\beta = 0.25$, and $i_o = 0.38$ mA/cm² (26). Comparison between theory and experiment is shown in the tabulated values of ξ given in Fig. 3. Based on comparison between data points and solid lines, the value of ξ which best "fits" the data is tabulated as ξ_{fit}; based on the system parameters for each run (see Tables I and II), the "theoretical" value of ξ which should characterize the data is tabulated as ξ_{th}. For the seven runs, the average value of ξ_{fit} was 43.4 ± 3.9% of ξ_{th}.

There are several reasons why the exchange current density in our flow system might be less than that measured under conditions of utmost purity (30) as cited in Ref. (26). Impurities in the flow system would be expected to reduce the exchange current density. Also, the acid concentration used here (1.5M) is greater than that used in (30) so that the i_o used here would be expected (31) to be lower. In addition, a recent examination of copper deposition kinetics in acid sulfate solutions (31) indicates that the parameters $i_o = 0.042$ mA/cm², $\alpha = 0.54$, and $\beta = 0.19$ would be consistent with the experimental conditions of the present study. Because of the consistency of the percentage difference between ξ_{fit} and ξ_{th}, it seems reasonable to conclude that the exchange current density which characterizes this experimental system is $i_o = 0.164 \pm 0.015$ mA/cm².

At intermediate fractions of the limiting current the shape of the polarization curve depends upon both ξ and N. Figure 4 gives theoretical and experimental results (polarization curves) at all fractions of the limiting current for several geometric ratios over a tenfold variation in flow velocity. The values of ξ used in calculating the lines in Fig. 4 correspond to ξ_{fit}, *i.e.*, those values which fit the data at low fractions of the limiting current. It is seen that the theory predicts correct trends upon variation of system parameters. In Fig. 4, the experimental potential is seen to be greater than the predicted value. As will be discussed below, the influence of reaction kinetics becomes minor above 60%

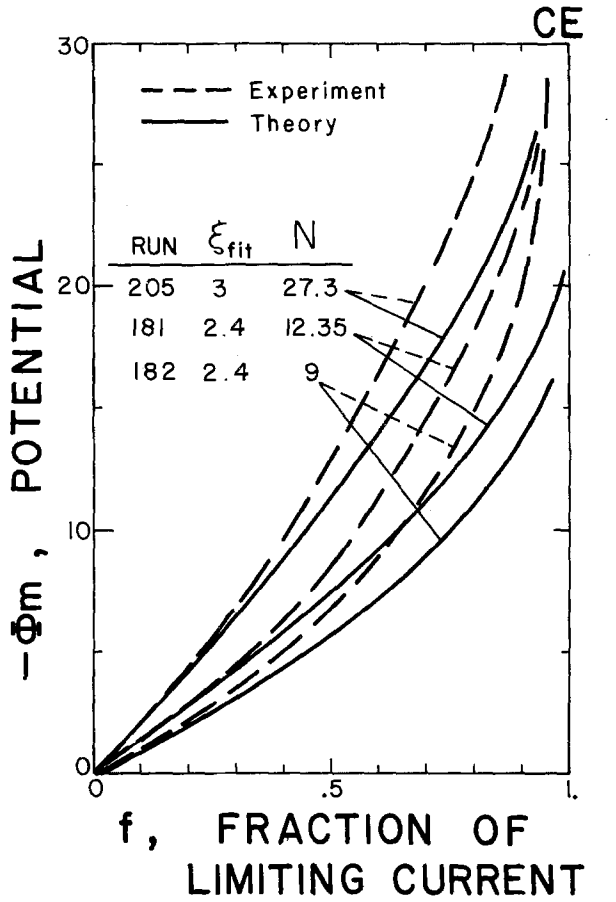


Fig. 4. Theoretical and experimental polarization curves (copper deposition system, counterelectrode downstream).

of the limiting current for the conditions given in Fig. 4; therefore the discrepancy cannot be wholly ascribed to inadequacies in the reaction rate equation. Since the mass transport measurements at the limiting current are in agreement with expectations, and since the geometry of the electrode is simple, it seems unlikely that the observed deviations could be attributed to errors in the convective diffusion or potential field aspects of the model. Whereas the source of the discrepancy remains unresolved and whereas it deserves closer attention, it seems also clear that the present model can be used to predict polarization behavior to within most engineering tolerances.

Current distribution data.—Data from current distribution measurements were reduced to dimensionless form by either

$$J = \frac{j^*}{\bar{\beta}} = \frac{j}{\langle j \rangle} \qquad [6]$$

or

$$J_N = \frac{j^*}{\bar{\beta}_{lim}} = \frac{\bar{\beta}}{-N} J = fJ \qquad [7]$$

which differ in that $\int_0^1 J \, dZ = 1$, while $\int_0^1 J_N \, dZ = f$ where f is the fraction of limiting current.

For currents far below the limiting current, the distribution should depend upon the parameter ξ such that the distribution becomes more nonuniform as ξ becomes large. Figure 5 shows typical data for three electrode lengths. The solid lines give theoretical results predicted with use of ξ_{fit} (*i.e.*, 17% of ξ_{th}), as was discussed with respect to Fig. 3. The good agreement between theory and data indicate that the model provides the correct linkage between polariation data and current distribution data. That is, once the parameter ξ_{fit} is determined from polarization curves, the model is able to predict accurately the secondary current distri-

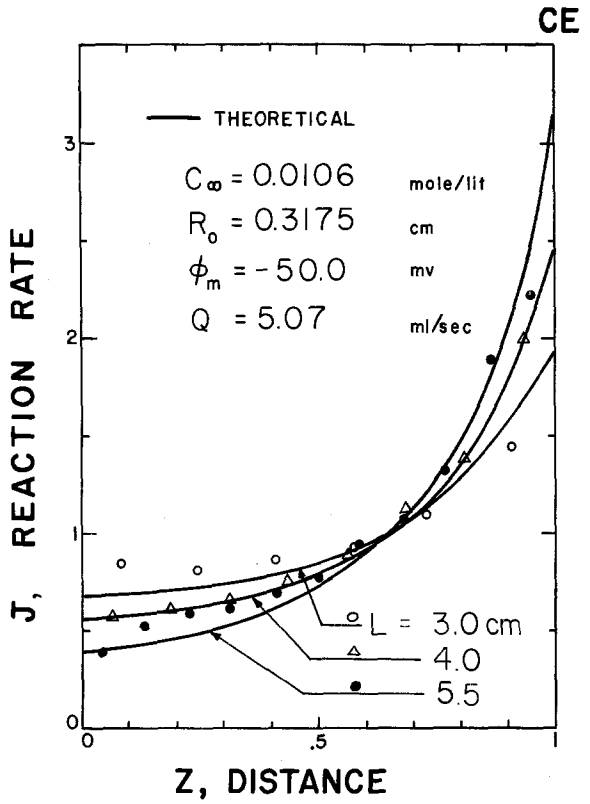


Fig. 5. Effect of electrode length on current distribution far below limiting current (copper deposition system, counterelectrode downstream).

bution. Experiments were performed with the counterelectrode either upstream or downstream; under otherwise identical conditions, the distributions were identical to within 5% and the most reactive electrode section was that nearest the counterelectrode. That is, mass transport effects did not appreciably influence the current distributions when the average current was less than about 25% of the average limiting current.

Current distributions were measured at appreciable fractions of the limiting current for the systems listed in Table II. Typical results are given in Fig. 6; experimental data are shown on the left side, and the corresponding theoretical calculations are given on the right side. Although the counterelectrode was downstream, the data at 35% of the limiting current indicate that the most reactive electrode section is the upstream section, farthest from the counterelectrode. Above 80% of the limiting current, the distribution is very similar to the limiting current distribution itself. The comparison shown in Fig. 6 indicates satisfying agreement over the entire range of f. These data indicate that once ξ_{fit} is chosen to fit polarization curves at low currents, then the model can be used to predict current distributions up to and including the limiting current.

At the limiting current, the current distribution data follow closely the distribution predicted by the Lévêque equation

$$J_{lim} = \frac{2}{3} Z^{-1/3} \qquad [8]$$

Discussion of the Theoretical Model

Since the experimental program indicated that the theoretical predictions were accurate over the range studied, it seemed worthwhile to pursue several purely theoretical aspects in order to compile salient features over a range of parameter space.

Let us first consider two aspects of behavior far below the limiting current. The first concerns the conditions under which the potential distribution within the tubular electrode can be reasonably approximated by a one-dimensional field. One basis for assessing the differences between the one- and the two-dimensional models is to compare the total currents predicted for a given applied potential, other parameters being held equivalent. Figure 7 shows the results of theoretical calculations well below the limiting current. The ordinate gives the ratio of currents predicted by the two models, and has the value of unity when the two models give identical predictions. It is seen that deviations always occur such that the two-dimensional current is less than the one-dimensional current. That is, the one-dimensional model does not account for the additional ohmic losses encountered by the radial component of current flow. Deviations from one-dimensional behavior set in for $\gamma_0 > 0.5$, that is, when the tube diameter exceeds its length. The extent of deviation becomes appreciable only over certain ranges of ξ. For small values of ξ, the applied potential is consumed primarily by charge-transfer overpotential so that geometric factors concerning the potential field are not essential. As ξ increases, deviations are observed to an extent depending upon the aspect ratio (γ_0) and owing to the nonlinear kinetics, the applied potential (Φ_m). For the experimental systems studied above, the one-dimensional model was accurate.

The second aspect of behavior far below limiting current concerns the conditions under which the current distribution in a tubular electrode is reasonably uniform. One measure of uniformity is the ratio of reaction rates at the two ends of the tube. If the distribution is uniform, then the ratio will be unity. Figure 8 gives a theoretical compilation of the reaction rate

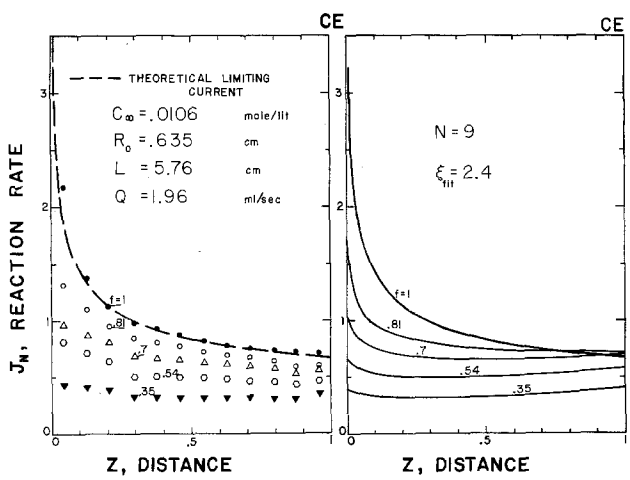


Fig. 6. Dependence of current distribution upon fraction of limiting current, experiment (left) and theory (right) (copper deposition system, counterelectrode downstream).

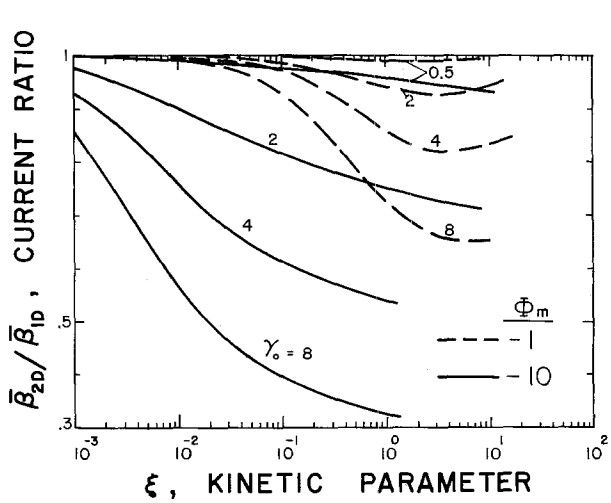


Fig. 7. Comparison between one- and two-dimensional potential field models far below limiting current.

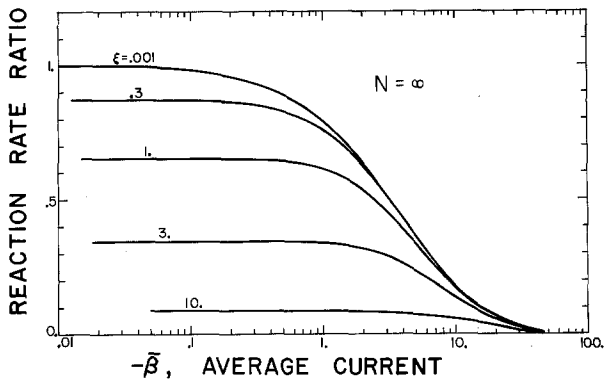


Fig. 8. Dependence of current distribution uniformness upon applied current and polarization parameter, far below limiting current.

ratio for various values of ξ and applied cathodic current $-\bar{\beta}$. It is seen that the secondary current distribution varies by less than 10% over the surface under the approximate conditions

$$\xi < 0.3 \qquad |\bar{\beta}| < 0.1 \qquad [9]$$

On the basis of discussion thus far, it would seem reasonable to suggest that Fig. 8 would apply for situations such that

$$N > 5\bar{\beta} \qquad [10]$$

At intermediate fractions of the limiting current, a more discerning criterion for evaluating the uniformity of the current distribution is

$$U = \int_0^1 |J - 1|\, dZ \qquad [11]$$

If the current distribution is uniform ($J = 1$), then $U = 0$. Figure 9 gives theoretical expectations for the current uniformity at all fractions of the limiting current for the case of a downstream counterelectrode. Far below the limiting current, it is seen that the uniformity depends upon ξ; under such conditions it is clear that the most reactive region of the electrode is the downstream end, near the counterelectrode. At the limiting current, on the other hand, the most reactive region is the upstream end where the diffusion layer is thinnest. At intermediate currents, the interaction between mass transfer and ohmic effects renders the current distribution more uniform than under either limiting condition of behavior. Were the counterelectrode upstream, no such minimum in current uniformity would be observed.

When the entire electrode operates at the limiting current, there is a characteristic potential difference between the ends of the tube which can be related to other system parameters. Knowledge of this relation is useful for designing tubular electrodes. The potential distribution when operating under limiting current is found by substituting the limiting current distribution

$$j^*_{\lim^*} = -\frac{2}{3} N Z^{-1/3}$$

into either

$$\Phi(Z) = \Phi_m - \int_Z^1 \int_0^\sigma j^*(\tau)\, d\tau d\sigma \quad \text{(downstream counterelectrode)}$$

or

$$\Phi(Z) = \Phi_m - \beta Z + \int_0^Z \int_0^\sigma j^*(\tau)\, d\tau d\sigma \quad \text{(upstream counterelectrode)}$$

and integrating. The potential difference across the

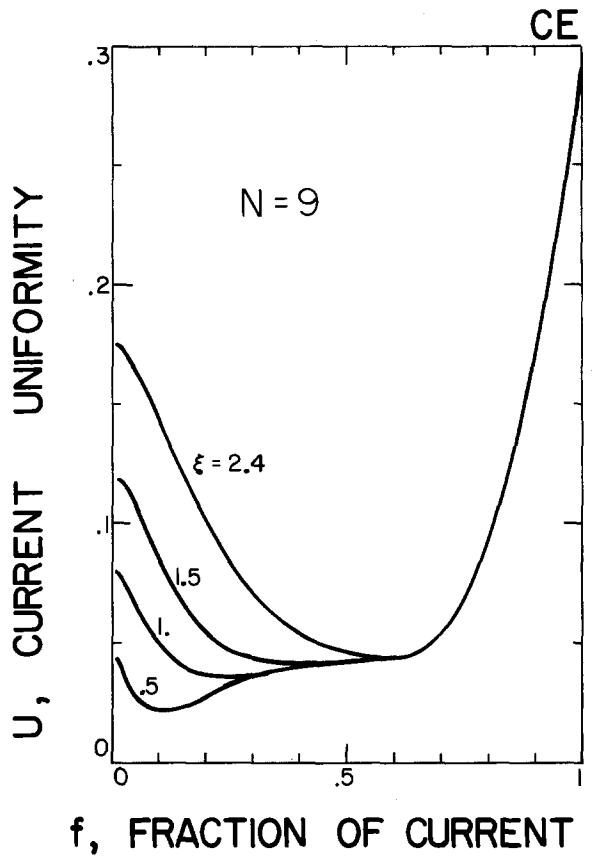


Fig. 9. Variation of current distribution uniformity upon fraction of limiting current and polarization parameter.

electrode is found to depend upon the position of the counterelectrode

$$\Delta\Phi_{\lim} = 0.4N \text{ (counterelectrode upstream)}$$
$$\Delta\Phi_{\lim} = 0.6N \text{ (counterelectrode downstream)} \qquad [12]$$

The potential drop across the tubular electrode is greater when the counterelectrode is downstream because the reaction occurs primarily on the upstream portions. This calculation illustrates why, under identical conditions of electrolysis, the limiting current plateau is wider when the counterelectrode is upstream than when it is downstream. In other words, for a given $\Delta\Phi_{\lim}$, placing the counterelectrode upstream enables the limiting current to be 50% higher. In view of the definitions of Φ and N, Eq. [12] corresponds to

$$L^5 = A \frac{1}{QD_i^2} \left[\frac{-s_i R_0^2 \kappa\, \Delta\Phi_{\lim}}{n\mathbf{F}c_{i_\infty}} \right]^3 \qquad [13]$$

where $A = 2.9128$ (counterelectrode upstream) and 0.8631 (counterelectrode downstream).

Conclusions

Because many electrochemical systems are designed to operate at appreciable fractions of the limiting current, it is often difficult to understand their behavior since competing effects tend to confound one's intuition. Continued emphasis on experimental confirmation of theoretical models therefore seems worthwhile if the advantage of using efficient models is to be practiced with confidence in engineering design work.

Whereas detailed predictions could be obtained for specific electrochemical systems, the following qualitative features seem to be characteristic of the tubular electrode geometry. For currents less than 20% of the limiting current, mass transport effects have little influence and the distribution of reaction is essentially uniform under the conditions of $\xi < 0.3$ and $\bar{\beta} < 0.1$. Above 25% of the limiting current, the current distri-

bution becomes essentially independent of the kinetics of the charge-transfer process. Appreciable mass transfer effects are encountered above 35% of the limiting current, although it is possible to maintain quite uniform current distributions by judicious placement of the counterelectrode(s). Above about 80% of the limiting current, the current distribution closely resembles the limiting current distribution and would, therefore, be influenced most by the hydrodynamic flow conditions.

The theoretical method used in this study is based on the condition that the diffusion layer is thin with respect to the tube radius; well-developed mass transfer situations cannot, therefore, be treated without additional complications.

Acknowledgments

This study was supported by the National Science Foundation (GK-36623, ENG 72-04168).

Manuscript submitted Aug. 2, 1976; revised manuscript received Feb. 1, 1977.

Any discussion of this paper will appear in a Discussion Section to be published in the June 1978 JOURNAL. All discussions for the June 1978 Discussion Section should be submitted by Feb. 1, 1978.

Publication costs of this article were assisted by the University of Illinois.

LIST OF SYMBOLS

c_∞	inlet concentration, mole/cm^3
D_i	Diffusion coefficient of species i, cm^2/sec
f	I/I_{lim}, fraction of the limiting current, dimensionless
$\mathbf{F}$	Faraday's constant, 96,500 C/equiv
Gz	Q/D_iL, Graetz number, dimensionless
I	total current, A
i_o	exchange current density, A/cm^2
j	local reaction rate, A/cm^2
$\langle j \rangle$	average reaction rate, A/cm^2
j^*	local reaction rate defined in Table III, dimensionless
J	normalized reaction rate by average current density, dimensionless
J_N	normalized reaction rate by average limiting current density, dimensionless
L	electrode length, cm
N	two-dimensional velocity parameter or average limiting current density defined in Table III, dimensionless
Nu	$2R_os_ij/n\mathbf{F}D_ic_\infty$, Nusselt number, dimensionless
Q	volumetric flow, cm^3/sec
R	universal gas constant, 8.3134 J/mole-deg
R_o	radius of the tube, cm
Re	$2Q/\pi R_o\nu$, Reynolds number, dimensionless
s_i	stoichiometric coefficient of species i in the electrode reaction
Sc	ν/D_i, Schmidt number, dimensionless
T	temperature, deg
U	measure of uniformity of the reaction rate distribution, dimensionless
Z	z/L, spatial variable in axial direction, dimensionless

Greek characters

α	anodic transfer coefficient
β	cathodic transfer coefficient
$\bar{\beta}$	average current density defined in Table III, dimensionless
γ_o	R_o/L, aspect ratio, dimensionless
$\Gamma(4/3)$	.89298, the gamma function of 4/3
κ	electrolyte conductivity, 1/Ω-cm
ξ	$2n\mathbf{F}L^2i_o/RTR_o\kappa$, kinetic parameter, dimensionless
ϕ	potential in the electrolyte, V
ϕ_m	potential at the mouth of the electrode, V
Φ	$n\mathbf{F}\phi/RT$, potential in the electrolyte, dimensionless

REFERENCES

1. A. A. Mirarefi, Ph.D. Thesis, University of Illinois, Urbana (1976).
2. R. Alkire and A. A. Mirarefi, *This Journal*, **120**, 1507 (1973).
3. W. M. Kays, "Convective Heat and Mass Transfer," McGraw-Hill Book Co. Inc., New York (1966).
4. P. Van Shaw, L. P. Reiss, and T. J. Hanratty, *A.I.Ch.E. J.*, **9**, 362 (1963).
5. E. W. Dreesen, A. Heindrichs, and W. Vielstich, *Ber. Bunsen-Ges. Phys. Chem.*, **79**, 6, 12 (1975).
6. R. D. Patel, J. J. McFeeley, and K. R. Jolls, *A.I.Ch.E. J.*, **21**, 2 (1975).
7. M. R. Goldman and R. L. Barrett, *Trans. Inst. Chem. Eng.*, **47**, T29 (1969).
8. P. L. Chambré and A. Acrivos, *J. Appl. Phys.*, **27**, 1322 (1956); A. Acrivos and P. L. Chambré, *Ind. Eng. Chem.*, **49**, 1025 (1957).
9. E. H. Wissler and R. S. Schechter, *Chem. Eng. Sci.*, **17**, 937 (1962).
10. H. Matsuda, *J. Electroanal. Chem.*, **15**, 109, 325 (1967); **21**, 433 (1969); **22**, 413 (1969); **25**, 461 (1970); **35**, 77 (1972); **38**, 159 (1972); **44**, 199 (1973).
11. W. J. Blaedel *et al.*, *Anal. Chem.*, **35**, 2100 (1963); **38**, 879 (1966); **39**, 1065 (1967); **40**, 512 (1968); **43**, 1538 (1971).
12. T. O. Oesterling and C. L. Olson, *ibid.*, **39**, 1543, 1546 (1967).
13. K. Asada, F. Hine, S. Yoshizawa, and S. Okada, *This Journal*, **107**, 242 (1960).
14. J. Newman *et al.*, *Int. J. Heat Mass Transfer*, **10**, 983 (1967); *This Journal*, **113**, 1235 (1966); *ibid.*, **114**, 239 (1967); *ibid.*, **116**, 169 (1969); *ibid.*, **117**, 43 (1970); *ibid.*, **119**, 69 (1972).
15. R. Cabán and T. W. Chapman, *This Journal*, **123**, 1036 (1976).
16. R. Alkire and R. Varjian, *ibid.*, **124**, 388 (1977).
17. T. J. Kessler and R. Alkire, *This Journal*, **123**, 990 (1976).
18. T. J. Kessler and R. Alkire, *Plating*, **9**, 22 (1976).
19. S. Szpak, J. D. Elwin, and T. Katan, *Electrochim. Acta*, **11**, 934 (1966).
20. A. R. Gahler, *Anal. Chem.*, **26**, 577 (1954).
21. I. M. Kolthoff, E. B. Sandell, E. J. Meehan, and S. Bruckenstein, "Quantitative Chemical Analysis," MacMillan Co., New York (1969).
22. J. B. Flanagan and L. Marcoux, *J. Phys. Chem.*, **78**, 718 (1974).
23. J. S. Newman, "Electrochemical Systems," p. 316, Prentice-Hall, Englewood Cliffs, N.J. (1973).
24. A. A. Wragg and T. K. Ross, *Electrochim. Acta*, **12**, 1421 (1967); A. A. Wragg, *ibid.*, **16**, 373 (1971).
25. D. J. Robinson, *ibid.*, **17**, 791 (1972).
26. J. S. Newman, "Electrochemical Systems," p. 177, Prentice-Hall, Englewood Cliffs, N.J. (1973).
27. J. Šinkovic and D. Leskovšek, *Electrochim. Acta*, **16**, 2125 (1971).
28. D. C. Carbin and D. R. Gabe, *ibid.*, **19**, 645 (1974).
29. G. Jones and B. C. Bradshaw, *J. Am. Chem. Soc.*, **55**, 1780 (1933).
30. E. Mattsson and J. O'M. Bockris, *Trans. Faraday Soc.*, **55**, 1586 (1959).
31. R. Cabán, Ph.D. Thesis, University of Wisconsin, Madison (1976).

Profile of the Refractive Index in the Cathodic Diffusion Layer of an Electrolyte Containing $CuSO_4$ and H_2SO_4

Yasuhiro Awakura, Mikio Okada, and Yoshio Kondo*

Department of Metallurgy, Kyoto University, Kyoto 606 Japan

ABSTRACT

The profile of the refractive index in the cathodic diffusion layer of a solution containing 1.85M H_2SO_4 and 0.05M $CuSO_4$ was measured by holographic interferometry. Measurement was carried out at various heights from the lower edge of the cathode and also at various cathodic current densities up to the limiting value. The theoretical expression for the difference of the refractive index between the cathode surface and the bulk electrolyte was derived assuming a uniform distribution of the local cathodic current density. Experimental results obtained at the current densities below one-half of the limiting value were in good agreement with the theoretical value. Measurement was also conducted with the solutions containing 1.85M H_2SO_4 and 0.01, 0.02, 0.03, 0.04, and 0.05M $CuSO_4$, respectively, at their cathodic limiting current densities. H_2SO_4 concentration at the cathode surface was estimated from the interferogram and $CuSO_4$ concentration at the cathode surface was presumed to be virtually zero at the limiting current. The estimated H_2SO_4 concentration was compared with the theoretical values, and it was found that they are in good agreement with each other.

During the electrodeposition of copper on a plane vertical cathode from an unstirred electrolyte, upward natural convective flow occurs along the cathode surface. This is caused by the lowered Cu^{2+} ion concentration in the cathodic diffusion layer. This natural convective flow affects the rate of electrodeposition of copper or the distribution of the cathodic current density in a vertical direction (1-3). Thus, many theoretical and experimental works have been made on the velocity profile of cathodic natural convection (4-6), on the concentration profile of solute in the cathodic diffusion layer (7-9), and on the distribution of current density on the cathode surface (10-12). Recently, two of the present authors studied the concentration profile of $CuSO_4$ in the cathodic diffusion layer during the electrolysis of aqueous $CuSO_4$ solution (13).

The industrial electrolytic refining and plating of copper are often conducted in the unstirred electrolyte containing $CuSO_4$ and H_2SO_4. Thus it is fairly important to study the concentration profiles of both components in the cathodic diffusion layer. As the first step toward the clarification of these concentration profiles, we have attempted in this paper to measure the profile of the refractive index of the solution in the cathodic diffusion layer by applying the technique of holographic interferometry, and the experimental results are compared with the theoretical values.

It is known that at the cathodic limiting current the concentration of $CuSO_4$ at the cathode surface is very close to zero (2, 14), thus the refractive index of the solution at the cathode surface is determined solely by the H_2SO_4 concentration. The concentration of H_2SO_4 at the cathode surface was estimated from the experimental results obtained at the cathodic limiting current, and the results were compared with the theoretical values.

Experimental

The profile of the refractive index in the cathodic diffusion layer was measured by holographic interferometry using the same electrodes and electrolytic cell which were described in a previous paper (13). Analytical reagent grade H_2SO_4, $CuSO_4$, and deionized water were used, and the mixed aqueous solutions of H_2SO_4 and $CuSO_4$ were prepared. The measurement was conducted at 23° ± 1°C.

First, the measurement was carried out below the limiting current. The experimental conditions are given in Table I. A solution of 1.85M H_2SO_4 and 0.05M $CuSO_4$ was used for the measurements at current densities up to the limiting value. From the current-potential curve shown in Fig. 1 it is seen that the average cathodic limiting current density of a solution of 1.85M H_2SO_4 and 0.05M $CuSO_4$ is 1.96 mA/cm². The applied cathodic current densities included 8 values up to the limiting current.

Next, the profile of the refractive index in the cathodic diffusion layer was measured at the limiting current densities with the solutions containing 1.85M H_2SO_4 and 0.01, 0.02, 0.03, 0.04, and 0.05M $CuSO_4$, respectively. The measurement was conducted at a height of 4 cm from the lower edge of the cathode. Holographic interferograms are illustrated in Fig. 2.

The profile of the refractive index of the solution was obtained from the measured interferograms as follows. The apparent profile of the refractive index in the diffusion layer, $n_f(y)$, is calculated from the holographic interferogram according to the conventional expression of

$$\frac{[{}^*n - n_f(y)]d}{\lambda'} = N \qquad [1]$$

When the incident beam is transmitted into the cathodic diffusion layer with a varied refractive index the beam is deflected toward the bulk electrolyte which has a higher refractive index. This optical distortion should be corrected. This correction involves the estimation of deflection of the incident beam, Δy, in the diffusion layer and the estimation of the position of a point at which the true refractive index of the solution is equal to the apparent refractive index at the exit point of the beam, $n_f(y_o)$. The correcting procedure described in the previous paper (13) was modified, and the following method was employed. One assumption in

Table I. Experimental conditions

Electrolyte	0.05M $CuSO_4$-1.85M H_2SO_4
Distance from the lower edge of cathode (cm)	1.0, 2.0, 4.0, 8.0
Average cathodic current density (mA/cm²)	0.236, 0.473, 0.709, 0.946 1.18, 1.42, 1.65, 1.96*

* Cathodic limiting current density.

* Electrochemical Society Active Member.

Key words: natural convection, holographic interferometry, vertical electrode, limiting current density.

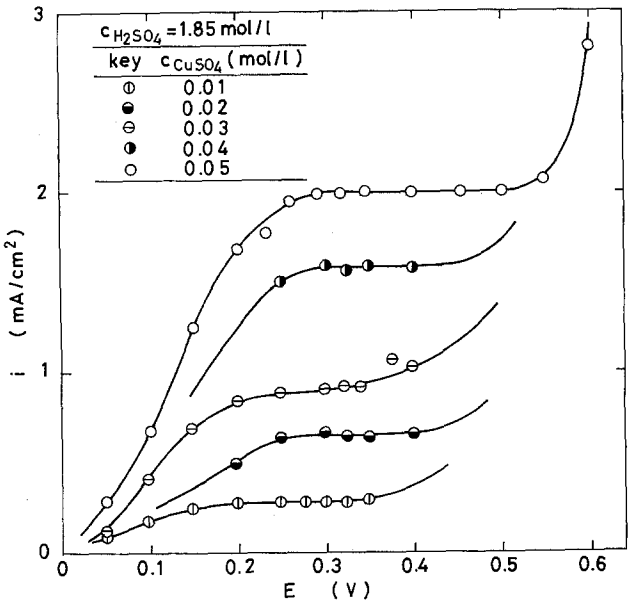


Fig. 1. Current-potential curve

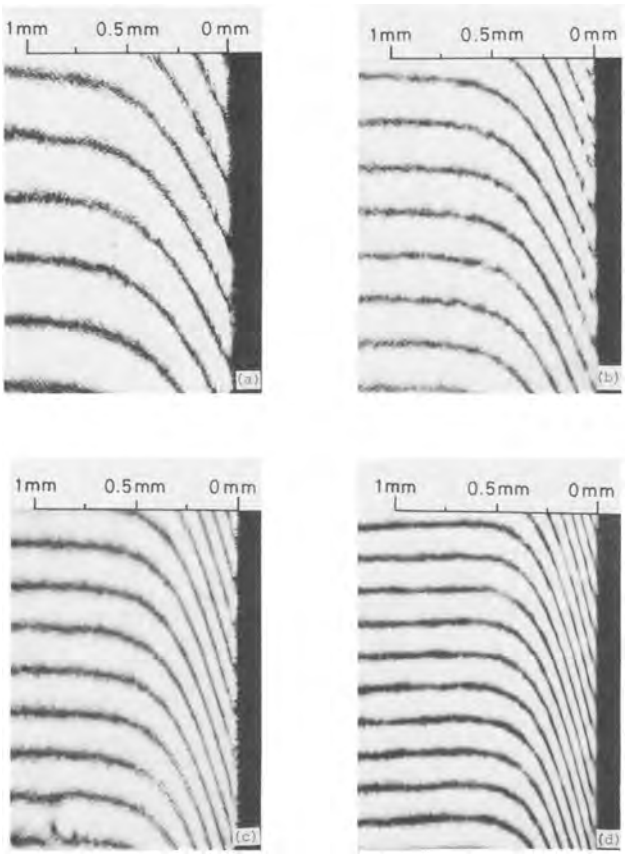


Fig. 2. Holographic interferograms of the cathodic diffusion layer at $x = 4$ cm with the solutions of (a) 0.02M $CuSO_4$-1.85M H_2SO_4, (b) 0.03M $CuSO_4$-1.85M H_2SO_4, (c) 0.04M $CuSO_4$-1.85M H_2SO_4, and (d) 0.05M $CuSO_4$-1.85M H_2SO_4 at their limiting current densities of 0.683, 0.910, 1.57, and 1.96 mA/cm², respectively.

this procedure is that the change of refractive index in the solution between the incident and exit points of the beam is approximated to be linear, as shown in Fig. 3. It is thought that the present procedure surpasses the previous one in that the employed assumption is simpler and clearer.

Under this assumption, the following expressions of the optical path length and the deflection of incident beam which passes through the solution near the

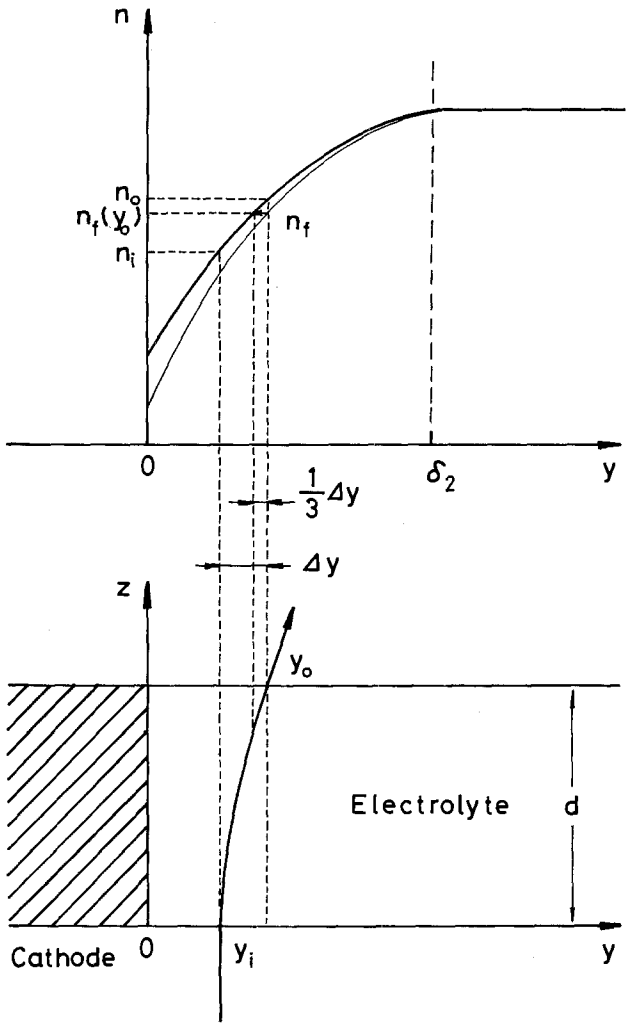


Fig. 3. Schematic illustrations of beam deflection and correction of the refractive index.

cathode surface are given by Müller (15). They are

$$p = \frac{n_i d}{2} + \frac{n_i^2}{4k} \sinh\left(\frac{2kd}{n_i}\right) \quad [2]$$

and

$$\Delta y = y_o - y_i = -\frac{n_i}{k} + \frac{n_i}{k} \cosh\left(\frac{kd}{n_i}\right) \quad [3]$$

respectively. The approximation of these equations yields

$$p = n_i d + \frac{1}{3!}\frac{2}{n_i} k^2 d^3 \quad [4]$$

$$\Delta y = \frac{kd^2}{2! n_i} \quad [5]$$

The apparent refractive index at the exit point of the beam, $n_f(y_o)$, calculated by Eq. [1] is equal to the ratio of optical path length and width of the cathode, p/d, and we have

$$n_f(y_o) = \frac{p}{d} = n_i + \frac{1}{3!}\frac{2}{n_i} k^2 d^2 \quad [6]$$

The deflection of the incident beam in the diffusion layer is about 50μ or less, and it is far less than the thickness of the diffusion layer which is about 500μ in our experiment (13). It is reasonable to assume that the change of refractive index is linear within the whole region of beam deflection, Δy. Thus we have

$$n = n_i + k(y - y_i) \quad [7]$$

By equating Eq. [6] and [7], we obtain the position of a point where the true refractive index, n, is equal to $n_f(y_o)$. It is

$$n_i + k(y - y_i) = n_i + \frac{1}{3!}\frac{2}{n_i}k^2d^2 \quad [8]$$

or

$$y - y_i = \frac{k}{3n_i}d^2 \quad [9]$$

By comparing $(y - y_i)$ with Δy of Eq. [5], we have

$$\frac{y - y_i}{\Delta y} = \frac{2}{3} \quad [10]$$

Then it can be said that $n_f(y_o)$ becomes equal to n at a point $(y_i + 2\Delta y/3)$ or $(y_o - \Delta y/3)$ under the assumption of a linear change of the refractive index between y_i and y_o.

Under the assumption of a linear change of the refractive index, Mizushina *et al.* (16) proposed the following calculating procedure of beam deflection within the diffusion layer from the apparent profile of the refractive index. When the direction of incident beam is at right angles to the inner wall of electrolytic cell, the beam trajectory within the diffusion layer is expressed by the following differential equation (17)

$$\left(\frac{dy}{dz}\right)^2 + 1 = \left(\frac{n(y)}{n(y_i)}\right)^2 \quad [11]$$

where $n(y_i)$ is the refractive index at the incident point of the beam. The integration of Eq. [11] under the boundary conditions of

$$\left.\begin{array}{ll} y = y_i & z = 0 \\ y = y_o & z = d \end{array}\right\} \quad [12]$$

yields

$$\int_o^d dz = \int_{y_i}^{y_o} \frac{n(y_i)}{\sqrt{[n(y)]^2 - [n(y_i)]^2}}\,dy \quad [13]$$

The left-hand side of this equation represents the width of the cathode, and the right-hand side can be integrated under the assumption of a linear change of the refractive index. Thus we have

$$d = \frac{n(y_i)}{\left(\frac{dn(y)}{dy}\right)_{y=y_i}} \cdot \ln\left[\frac{n(y_o) + \sqrt{[n(y_o)]^2 - [n(y_i)]^2}}{n(y_i)}\right] \quad [14]$$

The refractive indexes $n(y_i)$ and $n(y_o)$ are sufficiently close to each other, and the substitution of the approximate relationship of

$$n(y_o) + n(y_i) = 2n_f(y_o) \quad [15]$$

in Eq. [14] yields

$$\left[\frac{dn(y)}{dy}\right]_{y=y_i} = \left[\frac{n(y_o) - n(y_i) - \sqrt{2n_f(y_o)[n(y_o) - n(y_i)]}}{d}\right] \quad [16]$$

Furthermore, the deflection of the incident beam in the diffusion layer is expressed as

$$\Delta y = \frac{n(y_o) - n(y_i)}{\left(\frac{dn(y)}{dy}\right)_{y=y_i}} \quad [17]$$

From the definition of the optical path length of the incident beam in the diffusion layer, we have

$$p = \int_{y_i}^{y_o} n(y)\sqrt{1 + \left(\frac{dz}{dy}\right)^2}\,dy \quad [18]$$

Substitutions of Eq. [11] in Eq. [18] and the resultant equation in Eq. [6] yield

$$n_f(y_o) = \frac{1}{d}\int_{y_i}^{y_o} \frac{[n(y)]^2}{\sqrt{[n(y)]^2 - [n(y_i)]^2}}\,dy \quad [19]$$

Differentiation of this equation with y_o further yields

$$\frac{dn_f(y_o)}{dy_o} = \frac{1}{d}\sqrt{[n(y_o)]^2 - [n(y_i)]^2} \quad [20]$$

From Eq. [15], we have

$$n(y_o) - n(y_i) = \frac{\left[d \cdot \frac{dn_f(y_o)}{dy_o}\right]^2}{2 \cdot n_f(y_o)} \quad [21]$$

Then the deflection of the incident beam in the diffusion layer is calculated by using Eq. [16], [17], and [21], where the gradient of the apparent refractive index, $[dn_f(y_o)/dy_o]$, is obtained from the interferogram. In the calculation of $[dn_f(y_o)/dy_o]$, the measured $n_f(y_o)$ was expressed by the second-order equation of y_o by applying the least squares method. Then the correction of the profile of the refractive index is completed by transferring $n_f(y_o)$ to a position of $(y_o - \Delta y/3)$ in the direction toward the cathode surface.

Several examples of the corrected profile of the refractive index are demonstrated in Fig. 4. These profiles were obtained with a solution containing 1.85M H_2SO_4 and 0.05M $CuSO_4$ at a height of 4 cm from the lower edge of the cathode. The cathodic current density was varied between 0.236 and 1.96 mA/cm^2. The uncorrected profiles of the refractive index are also shown in the same figure. As seen in this figure, the refractive index at the cathode surface is lowered when the average cathodic current density is raised. It is also seen that the above-mentioned correction becomes more significant when the slope of the refractive index is steeper.

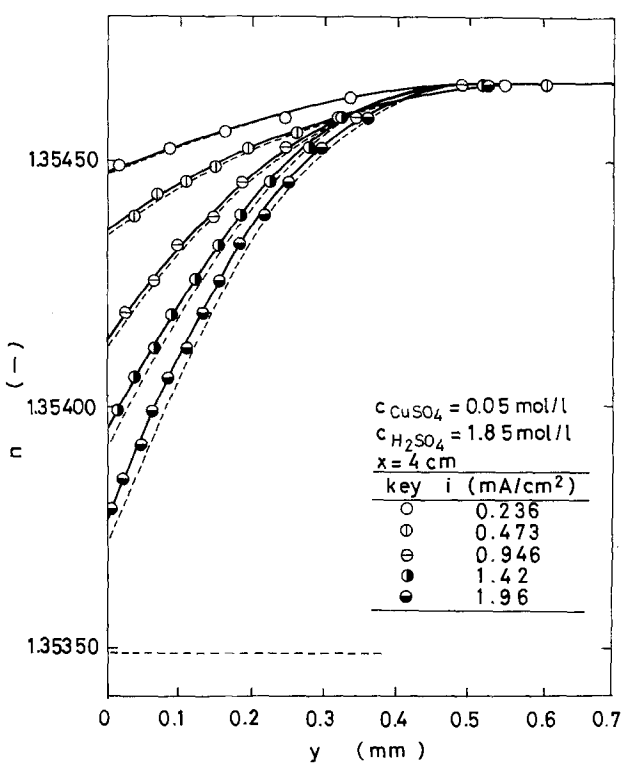


Fig. 4. Corrected profiles of the refractive index in the cathodic diffusion layer.

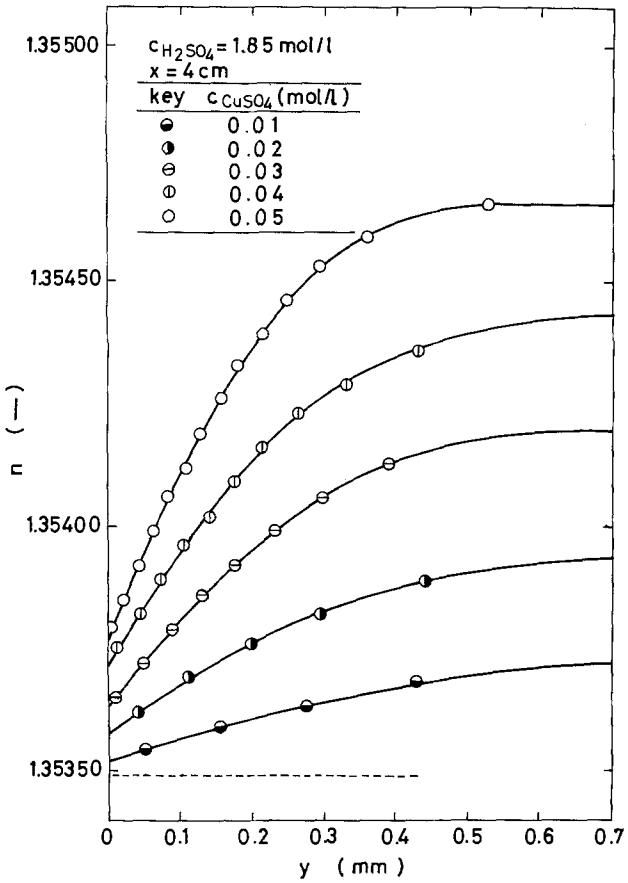


Fig. 5. Corrected profiles of the refractive index in the cathodic diffusion layer at the limiting current density.

Figure 5 demonstrates the corrected profile of the refractive index at the limiting current densities with solutions containing 1.85M H_2SO_4 and 0.01, 0.02, 0.03, 0.04, and 0.05M $CuSO_4$, respectively. As seen in this figure, the refractive index at the cathode surface decreases when the concentration of $CuSO_4$ in the bulk electrolyte is lower. The horizontal broken lines at 1.35349 in Fig. 4 and 5 represent the refractive index of aqueous 1.85M H_2SO_4 solution, respectively.

Discussion

The profile of the refractive index in the cathodic diffusion layer was measured with the solution containing 1.85M H_2SO_4 and 0.05M $CuSO_4$. In order to investigate the dependences of the difference of the refractive index between the cathode surface and the bulk electrolyte on the average cathodic current density and on the height from the lower edge of cathode, the theoretical expression was derived under the condition of uniform cathodic current density. The concentration difference of the Cu^{2+} ion, θ_1, between cathode surface and bulk electrolyte is expressed as follows (6, 13)

$$\theta_1 = \frac{\eta E}{\omega} \frac{(1 - {}^*t_1)}{z_1 F D_1} \cdot \left\{ \frac{\nu z_1 F D_1^2}{g\left(\alpha_1 - \frac{2}{3}\sigma^2\alpha_2\right)(1 - {}^*t_1)} \right\}^{1/5} \cdot i^{4/5} \cdot x^{1/5} \quad [22]$$

where

$$E = \left[\frac{\omega^2(\omega + 1)\lambda}{\eta^3 \phi} \right]^{1/5} \quad [23]$$

The symbol ϕ in Eq. [23] is

$$\phi = \frac{\lambda(\eta - 1)^{\omega+2}}{\eta^\omega(\omega + 1)(\omega + 2)} \left[\left(\frac{\eta}{\eta - 1} \right)^{\omega+2} - \frac{\lambda - 1}{\lambda e} - \frac{\omega + 2}{\lambda(\eta - 1)} - 1 \right] - \eta^{\lambda+1} B_{1/\eta}(\lambda + 1, \omega + 1) \quad [24]$$

where $B_a(b, c)$ is the incomplete beta function in the form of

$$B_a(b,c) = \int_o^a t^{b-1}(1 - t)^{c-1} dt \quad [25]$$

In addition, the concentration difference of H^+ ion, θ_2, between the cathode surface and the bulk electrolyte is related to θ_1 by taking account of the equations of mass transfer in the cathodic diffusion layer and electroneutrality in the solution as (2, 6)

$$\theta_2 = -\frac{2}{3}\sigma\theta_1 \quad [26]$$

where

$$\sigma = \frac{\delta_2}{\delta_1} \quad [27]$$

The notation σ in this equation represents the ratio of the thickness of cathodic diffusion layers of H^+ ion to Cu^{2+} ion. Its numerical value is slightly higher than unity (2). The negative sign in Eq. [26] represents the accumulation of H^+ ion in the cathodic diffusion layer which is caused by the migration of H^+ ion toward the cathode surface.

The refractive index of the solution depends not only on Cu^{2+} ion concentration but also on H^+ ion concentration. If the refractive index is expressed by a linear equation of

$$n = A + Bc_1 + Cc_2 \quad [28]$$

where c_1 and c_2 are the concentration of $CuSO_4$ and H_2SO_4, respectively, the difference of the refractive index between the cathode surface and the bulk electrolyte, Δn, is expressed from Eq. [26] and [28] as

$$\Delta = {}^*n - {}^\circ n = B\theta_1 + \frac{1}{2}C\theta_2 = \left(B - \frac{1}{3}\sigma C\right)\theta_1 \quad [29]$$

Substitution of Eq. [22] in Eq. [29] yields

$$\Delta n = \left(B - \frac{1}{3}\sigma C\right) \frac{\eta E}{\omega} \cdot \frac{(1 - {}^*t_1)}{z_1 F D_1} \cdot \left\{ \frac{\nu z_1 F D_1^2}{g\left(\alpha_1 - \frac{2}{3}\sigma^2\alpha_2\right)(1 - {}^*t_1)} \right\}^{1/5} \cdot i^{4/5} \cdot x^{1/5} \quad [30]$$

It is expected from this equation that Δn is proportional to $i^{4/5}$ and $x^{1/5}$, respectively.

The refractive index of mixed aqueous solutions of $CuSO_4$ and H_2SO_4 of various concentrations was measured at 23° ± 0.1°C. It was found that the change of the refractive index in these solutions is linear with the change of both $CuSO_4$ and H_2SO_4 concentrations in the regions from 0 to 0.27M $CuSO_4$ and from 0.8 to 2.0M H_2SO_4, respectively. The regression of the refractive index upon the concentrations of $CuSO_4$ and H_2SO_4 was calculated by the least squares method. It is as below

$$n = 1.3348 + 23.447c_1 + 10.075c_2 \quad [31]$$

The dependences of Δn on the average cathodic current density and on the height from the lower edge of the cathode shown in Eq. [30] were examined: the

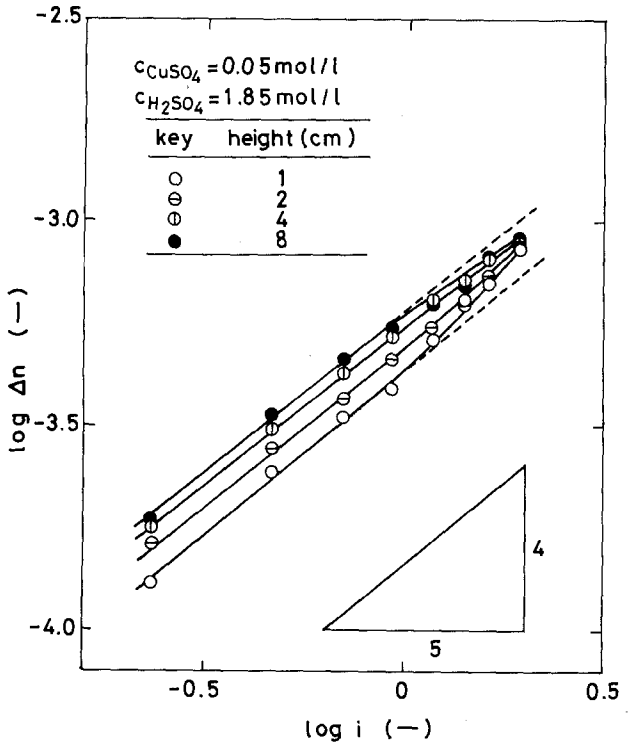


Fig. 6. Relationship between the refractive index difference and the average cathodic current density.

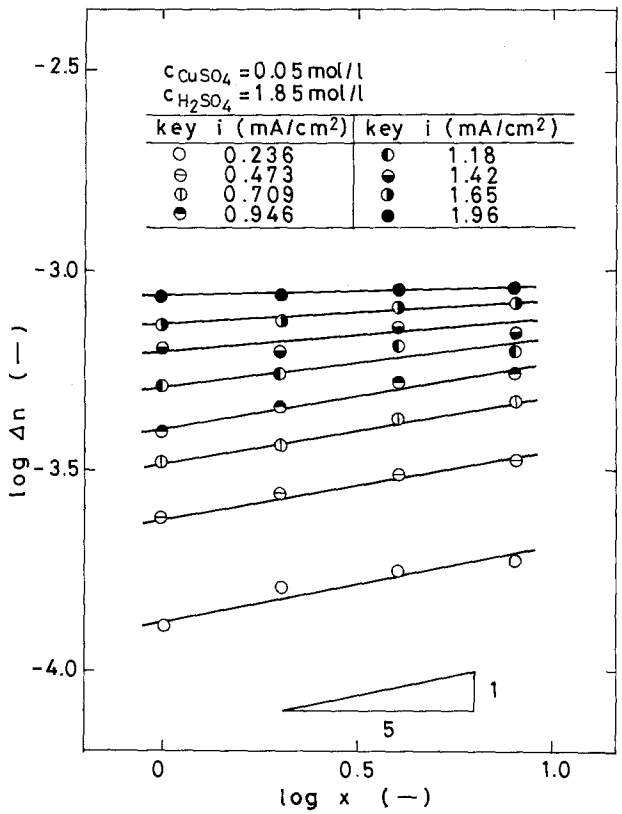


Fig. 7. Relationship between the refractive index difference and the height from lower edge of the cathode.

measured log Δn of the solution containing 1.85M H_2SO_4 and 0.05M $CuSO_4$ was plotted against the logarithmic average cathodic current density and demonstrated in Fig. 6. As seen in this figure, the slope of straight lines was obtained at 4/5, which is equal to the theoretical value of Eq. [30] when the cathodic current density is lower than the half-value of the limiting current density. Above this value of the current density, on the other hand, the Δn values start to converge into a fixed value at the limiting current density. Secondly, log Δn was plotted against log x and demonstrated in Fig. 7. By comparing the experimental slopes with the theoretical value of 1/5, it is clear that the experimental slopes are equal to 1/5 at the current densities which are less than a half of the limiting current density. They start to decrease when the average current density is raised above this half-value; it is virtually null at the cathodic limiting current density of 1.96 mA/cm².

Furthermore, the values of Δn were calculated by Eq. [30] and they were compared with the measured values. The following physical property constants and transport parameters were employed in the calculation

$D_1 = 5.74 \times 10^{-6}$ cm²/sec (19) *$t_1 = 0.0033$ (23-25)

$\nu = 1.148 \times 10^{-2}$ cm²/sec $\alpha_1 = 125$, $\alpha_2 = 26.8$ (12)

$\sigma = 1.36$ (6) $\omega = 2.3$ $\eta = 2.6$ and $E = 1.30$ (6)

Among these numerical values, ν was obtained by measuring the viscosity and density of the solution because no data were available in the literature. The results are summarized in Table II. It may be said from this table that the measured values are fairly well coincident with the calculated ones at the cathodic current denstities below 0.946 mA/cm², though the measured values are slightly lower than the calculated ones. It is also seen that the difference between the measured and calculated values becomes larger when current densities higher than 1.18 mA/cm² are applied. This difference is most significant at the height of 1 cm from the lower edge of the cathode. This may suggest that the local cathodic current density is not uniform in a vertical direction above the half-value of the limiting current density (10-12).

Following this, the difference of the refractive index between the cathode surface and the bulk electrolyte at the cathodic limiting current density was pursued; the solutions whose $CuSO_4$ concentration is varied between 0.01 and 0.05M and H_2SO_4 concentration is maintained at 1.85M were used. The logarithmic average limiting current density, log i_d, obtained with each of these solutions was plotted against the logarithmic $CuSO_4$ concentration, and it is demonstrated in Fig. 8. According to the theoretical calculations (2, 10), the

Table II. Refractive index difference in the cathodic diffusion layer of a solution containing 1.85M H_2SO_4 and 0.05M $CuSO_4$

x (cm)	1		2		4		8	
$\Delta n \times 10^4$	Meas.	Calc.	Meas.	Calc.	Meas.	Calc.	Meas.	Calc.
i (mA/cm²)								
0.236	1.31	1.20	1.63	1.37	1.79	1.58	1.84	1.81
0.473	2.43	2.09	2.78	2.40	3.11	2.75	3.40	3.16
0.709	3.35	2.88	3.71	3.31	4.33	3.80	4.72	4.76
0.946	3.93	3.63	4.62	4.17	5.28	4.79	5.56	5.50
1.18	5.24	4.34	5.58	4.98	6.59	5.73	6.38	6.58
1.42	6.54	5.03	6.28	5.77	7.32	6.63	7.00	7.61
1.65	7.15	5.69	7.47	6.54	8.27	7.51	8.39	8.59
1.96	8.62	6.51	8.70	7.48	9.12	8.59	9.37	9.86

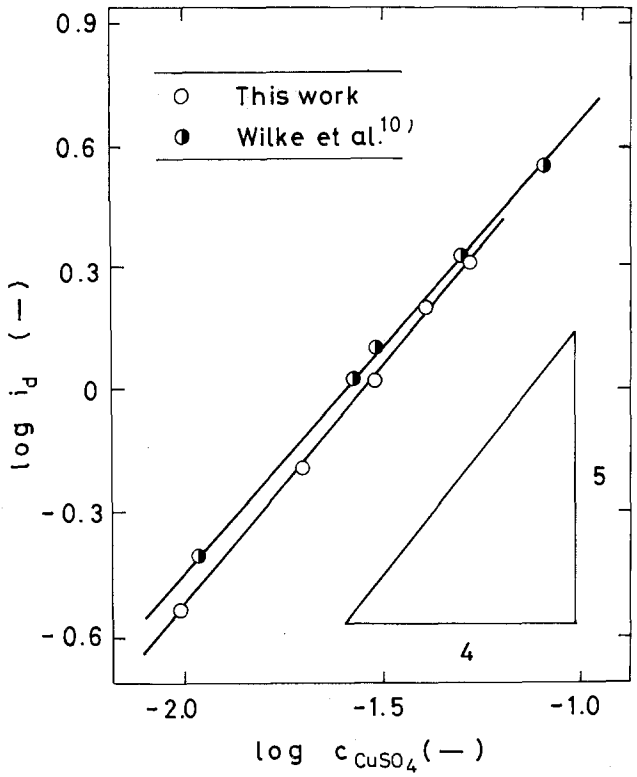


Fig. 8. Relationship between the cathodic limiting current density and the concentration of $CuSO_4$ in the bulk electrolyte.

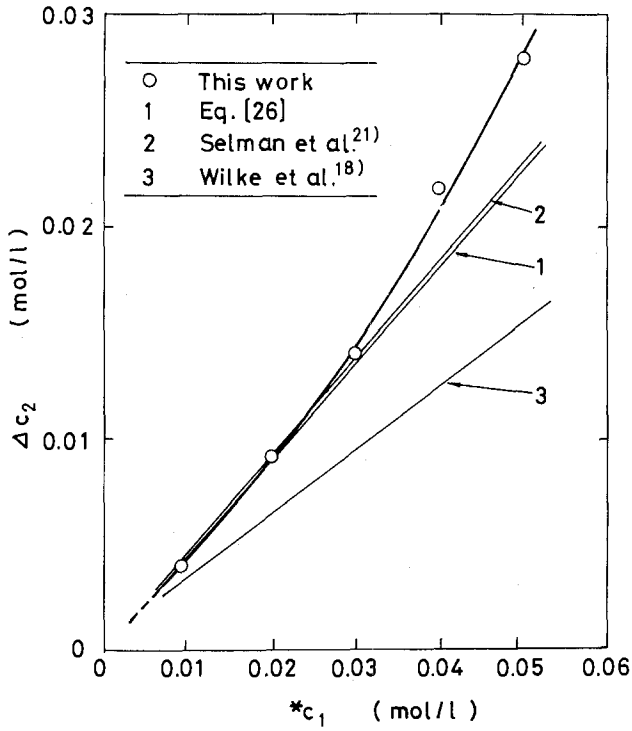


Fig. 9. Relationship between the concentration difference of H_2SO_4 (Δc_2) and the concentration of $CuSO_4$ in the bulk electrolyte ($*c_1$).

cathodic average limiting current density is proportional to the 5/4th power of $CuSO_4$ concentration in the bulk electrolyte. As seen in Fig. 8 this theoretical relationship is satisfied. For comparison, the experimental results obtained by Wilke *et al.* (10) were applied. That is, Wilke's results, where the plane vertical cathode of 3 in. height was used and the temperature was maintained at 23°C, were plotted in the same figure.

As mentioned before, $CuSO_4$ concentration at the cathode surface is regarded as zero at the cathodic limiting current density (2, 14), and the refractive index of the solution at the cathode surface shown in Fig. 5 represents the concentration of H_2SO_4. The concentration difference of H_2SO_4, $\Delta c_2 (= {}^\circ c_2 - {}^* c_2)$ between the cathode surface and the bulk electrolyte was calculated from Fig. 5, and they are plotted against the $CuSO_4$ concentration in the bulk electrolyte, respectively. It is demonstrated in Fig. 9. As seen in this figure, Δc_2 is lowered with the decrease of $CuSO_4$ concentration. This tendency is predicted in Eq. [26]. Furthermore, it is seen that the slope of Δc_2-curve decreases when the $CuSO_4$ concentration in the bulk electrolyte is lowered. This phenomenon may be explained as follows. The diffusivity of Cu^{2+} ion is lower in the solution of higher $CuSO_4$ concentrations (19, 20). When the $CuSO_4$ concentration in the bulk electrolyte becomes higher, the diffusion layer of Cu^{2+} ion, δ_1, becomes thinner (2), while the thickness of diffusion layer of H^+ ion, δ_2, is maintained to be virtually unvaried. As a result, the σ value in Eq. [27] increases, and the coefficient of $-(2/3)\sigma$ between Θ_2 and Θ_1 in Eq. [26] becomes higher when the $CuSO_4$ concentration is raised.

Brenner (7) measured the concentration of H_2SO_4 at the cathode surface by applying the freezing method during the electrodeposition of copper from a solution containing $CuSO_4$ and H_2SO_4. However, his experimental result cannot be directly compared with our experimental results because of the different electrolytic conditions. Our experimental results were compared with the following theoretical values: first, the concentration difference of H_2SO_4, Δc_2, was calculated from Eq. [26] in which Θ_2 was replaced by $2\Delta c_2$. At the cathodic limiting current density, Θ_1 is equal to the concentration of $CuSO_4$ in the bulk electrolyte, and the σ value of 1.36 was employed from our previous work (6). Selman and Newman (21), on the other hand, obtained the numerical solution for the differential equation of mass transfer at the limiting current density in the cathodic diffusion layer of a solution containing $CuSO_4$ and excessive H_2SO_4. They obtained the following expresion of Δc_2

$$\Delta c_2 = 0.46 * c_1 \qquad [32]$$

where $*c_1$ is $CuSO_4$ concentration in the bulk electrolyte. It was assumed in their calculation that the concentration of $CuSO_4$ is lower and H_2SO_4 is completely dissociated into $2H^+ + SO_4^{2-}$ ions. Furthermore, Wilke *et al.* (18) studied the mass transfer of Cu^{2+} ion in the cathodic diffusion layer by applying the technique of dimensional analysis, and they derived the following expression for the concentration difference of H_2SO_4

$$\Delta c_2 = \Delta c_1 \left[\frac{D_1'}{D_2'}\right]^{3/4} \cdot \frac{*t_2}{1 - *t_1} \qquad [33]$$

The numerical values (19, 22) of

$$D_1' = 5.74 \text{ to } 6.03 \times 10^{-6} \text{ (cm}^2\text{/sec)}$$

and

$$D_2' = 2.1 \times 10^{-5} \text{ (cm}^2\text{/sec)}$$

were employed, and the values of transference number, $*t_1$ and $*t_2$, were calculated from the mobility of each ion at the infinite dilution (23-25).

These calculated values of Δc_2 are also demonstrated in Fig. 9. It is seen that the calculated value from Eq. [33] is somewhat lower as compared with the former two calculated values and also that the measured values in the present work are in good agreement with the calculations by Eq. [26] and [32], both of which were derived from the assumption that $CuSO_4$ and H_2SO_4 in the solution are completely dissociated into $Cu^{2+} + SO_4^{2-}$ and $2H^+ + SO_4^{2-}$ ions, respectively.

Summary

It is important to pursue the concentration profiles of $CuSO_4$ and H_2SO_4 in the cathodic diffusion layer for the study of electrodeposition of copper from an unstirred aqueous solution containing H_2SO_4 and $CuSO_4$. As the first step toward this goal, the profile of the refractive index of the solution in the cathodic diffusion layer was measured by holographic interferometry at various heights from the lower edge of the cathode and at various cathodic current densities up to the limiting value.

The profile of apparent refractive index in the cathodic diffusion layer obained from the interferogram was corrected under the assumption of a linear variation of the refractive index within the region of beam deflection in the cathodic diffusion layer. The theoretical expression of the difference of the refractive index between the cathode surface and the bulk electrolyte was derived under the assumption of a uniform distribution of local current density on the cathode surface. In order to verify this theoretical relationship, the dependences of the measured log Δn on the logarithm of current density and on the logarithm of height from the lower edge of the cathode were examined. At cathodic current densities lower than the half-value of the limiting current density, these dependences were satisfied. It was also disclosed that Δn is virtually unchanged at the cathodic limiting current density along the vertical direction on the cathode surface. Both experimental and theoretical values of Δn are in good agreement with each other at the cathodic current densities less than a half of the cathodic limiting current density.

When the electrolysis takes place at the cathodic limiting current density the concentration of $CuSO_4$ at the cathode surface is regarded as virtually zero. Under this experimental condition, Δn was measured at a height of 4 cm from the lower edge of the cathode, with the solutions containing 1.85M H_2SO_4 and 0.01, 0.02, 0.03, 0.04, and 0.05M $CuSO_4$, respectively. From the above presumption that $^\circ c_1 = 0$ at the limiting current density, the concentration difference of H_2SO_4, Δc_2, is obtained from Δn. The Δc_2 value at the cathodic limiting current density decreases when $CuSO_4$ concentration in the bulk electrolyte is lowered. Furthermore, the slope of the curve of Δc_2 *vs.* $^* c_1$ decreases as $CuSO_4$ concentration in the bulk electrolyte is lowered. These experimental results were qualitatively explained from Eq. [26] and [27]. The measured Δc_2 values were compared with theoretical ones, and it was clarified that the measured Δc_2 values are in good coincidence with the calculated ones from Eq. [26] and [31].

Acknowledgments

A part of the present work was performed under the financial aid given to the authors by the Ministry of Education, to which they are grateful.

Manuscript received Aug. 2, 1976; revised manuscript received Feb. 18, 1977.

Any discussion of this paper will appear in a Discussion Section to be published in the June 1978 JOURNAL. All discussions for the June 1978 Discussion Section should be submitted by Feb. 1, 1978.

Publication costs of this article were assisted by Kyoto University.

LIST OF SYMBOLS

A	constant
B, C	constant (cm³/mole)
a, b, c	constant
c_1	concentration of $CuSO_4$ (mole/cm³)
c_2	concentration of H_2SO_4 (mole/cm³)
$^* c_1$	concentration of $CuSO_4$ in the bulk electrolyte (mole/cm³)
$^* c_2$	concentration of H_2SO_4 in the bulk electrolyte (mole/cm³)
$^\circ c_1$	concentration of $CuSO_4$ at the cathode surface (mole/cm³)
$^\circ c_2$	concentration of H_2SO_4 at the cathode surface (mole/cm³)
Δc_1	$= (^* c_1 - ^\circ c_1)$ (mole/cm³)
Δc_2	$= (^\circ c_2 - ^* c_1)$ (mole/cm³)
d	width of cathode (cm)
D_1	diffusivity of Cu^{2+} ion (cm²/sec)
D_1'	diffusivity of $CuSO_4$ (cm²/sec)
D_2'	diffusivity of H_2SO_4 (cm²/sec)
E	constant
$\mathbf{F}$	Faraday constant (= 96,500 C/g equiv.)
g	gravitational acceleration (= 980 cm/sec²)
i	current density (A/cm²)
k	gradient of the refractive index (1/cm)
n	refractive index of the solution
n_i	refractive index of the solution at the incident point of beam
$^* n$	refractive index of the solution in the bulk electrolyte
$^\circ n$	refractive index of the solution at the cathode surface
$n(y)$	refractive index of the solution at a distance y from the cathode surface
$n_f(y)$	apparent refractive index of the solution obtained from interferogram at a distance y
Δn	$= (^* n - ^\circ n)$
N	number of fringe shifts
p	optical path length along the beam trajectory (cm)
$^* t_1$	transference number of Cu^{2+} ion in the bulk electrolyte
$^* t_2$	transference number of H^+ ion in the bulk electrolyte
x	height from lower edge of the cathode (cm)
y	horizontal distance from the cathode surface (cm)
y_i	distance between the incident point of the beam and the cathode surface (cm)
y_o	distance between the exit point of the beam and the cathode surface (cm)
Δy	$= (y_o - y_i)$ (cm)
z	distance perpendicular to x- and y-directions (cm)
z_1	valency of Cu^{2+} ion (= 2 g equiv./mole)

Greek Letters

α_1	densification coefficient of $CuSO_4$, $1/\rho\ (\partial\rho/\partial c_1)$ (cm³/mole)
α_2	densification coefficient of H_2SO_4, $1/\rho(\partial\rho/\partial c_2)$ (cm³/mole)
δ_1	thickness of the diffusion layer of Cu^{2+} ion (cm)
δ_2	thickness of the diffusion layer of H^+ ion (cm)
$\epsilon, \eta, \lambda, \omega$	numerical parameter
Θ_1	concentration difference of Cu^{2+} ion between the bulk electrolyte and the cathode surface (mole/cm³)
Θ_2	concentration difference of H^+ ion between the bulk electrolyte and the cathode surface (mole/cm³)
λ'	wavelength (cm)
ν	kinematic viscosity (cm²/sec)
σ	$= \delta_2/\delta_1$

REFERENCES

1. J. N. Agar, *Discuss. Faraday Soc.*, **1**, 26 (1947).
2. C. Wagner, *This Journal*, **95**, 161 (1947).
3. G. H. Keulegan, *J. Res. Nat. Bur. Stand.*, **47**, 2240 (1951).
4. N. Ibl and R. H. Müller, *This Journal*, **105**, 346 (1958).
5. J. Selman and J. Newman, *ibid.*, **118**, 1070 (1971).
6. Y. Awakura, Y. Takenaka, and Y. Kondo, *Electrochim. Acta*, **21**, 789 (1976).
7. A. Brenner, *Proc. Am. Electroplater's Soc.*, **1940**, 95; *ibid.*, **1941**, 28.
8. T. Yannakopoulas and A. Brenner, *This Journal*, **105**, 521 (1958).
9. N. Ibl, Y. Barrada, and G. Trümpler, *Helv. Chim. Acta*, **37**, 583 (1954).
10. C. R. Wilke, M. Eisenberg, and C. W. Tobias, *This Journal*, **100**, 513 (1953).
11. N. Ibl, W. Rüegg, and G. Trümpler, *Helv. Chim. Acta*, **36**, 1624 (1953).
12. K. Asada, F. Hine, S. Yoshizawa, and S. Okada, *This Journal*, **107**, 242 (1960).

13. Y. Awakura and Y. Kondo, *This Journal*, **123**, 1184 (1976).
14. C. W. Tobias, M. Eisenberg, and C. R. Wilke, *This Journal*, **99**, 359C (1952).
15. R. H. Müller, "Advances in Electrochemistry and Electrochemical Engineering," Vol. 9, p. 281, John Wiley & Sons, Inc., New York (1973).
16. T. Mizushina, R. Ito, F. Ogino, and H. Kojima, "Proceedings of 5th Symposium of Chemical Engineering," The Society of Chemical Engineers, Japan, p. 47, Osaka (1966).
17. B. Rossi, "Optics," p. 55, Addison-Wesley Publishing Co., London (1967).
18. C. R. Wilke, M. Eisenberg, and C. W. Tobias, *Chem. Eng. Progr.*, **49**, 663 (1953).
19. Y. Awakura, A. Ebata, M. Morita, and Y. Kondo, *Denki Kagaku*, **43**, 569 (1975).
20. W. G. Eversole, H. M. Kindsvater, and J. D. Perterson, *J. Phys. Chem.*, **46**, 370 (1942).
21. J. R. Selman and J. Newman, UCRL-20322 (1971).
22. E. A. Hollingshead and A. R. Gordon, *J. Chem. Phys.*, **8**, 423 (1940).
23. R. C. Weast, "Handbook of Chemistry and Physics," 45th ed., p. D-80, The Chemical Rubber Co., Cleveland (1964).
24. E. A. Moelwyn-Hughes, "Physical Chemistry," p. 859, Pergamon Press, London (1961).
25. "Handbook of Electrochemistry," edited by The Electrochemical Soc. of Japan, p. 118, Maruzen Book Co., Tokyo (1964).

Technical Notes

Electrophoretic Mobilities in Battery Electrolytes

S. D. James*

Electrochemistry Branch, U.S. Naval Surface Weapons Center, White Oak, Silver Spring, Maryland 20910

and R. A. Neihof

U.S. Naval Research Laboratory, Washington, D.C. 20375

Surprisingly high electrophoretic mobilities were recently reported for particles of cadmium hydroxide, nickel (II) hydroxide, and silver (I) oxide in the concentrated KOH electrolytes of alkaline batteries (1). Mobilities were reported to range up to 17×10^{-4} cm^2 sec^{-1} V^{-1} in 11M KOH (43%, w/w). The validity of these data has been questioned (2) on the grounds that serious errors of both technique and calculation were involved. However, mobilities of this order could effect substantial transfer of active material through batteries. For example, in the silver-zinc torpedo battery, fields up to 0.3 V/cm exist in the electrolyte during a 6 min discharge. Suspended particles could thus, in this time, be driven a distance of 0.18 cm which is about seven times the interelectrode separation. Thus we deemed it advisable to undertake some brief experimental tests on particle mobilities in concentrated KOH. Our results support the contention (2) that the mobilities of Ref. (1) are in fact erroneous and indicate that they are too large, probably by at least two orders of magnitude.

Electrophoretic mobilities were measured directly by the microelectrophoresis method. The apparatus and technique have been described elsewhere (3). The method can detect a mobility as low as 0.1×10^{-4} cm^2 sec^{-1} V^{-1} and has yielded accurate data at quite high salt concentrations [*viz.* seawater of about 0.6 ionic strength (4)]. Measurements were made on two materials, silver (I) oxide and alumina at two KOH concentrations, 1M and 11.6M (45% w/w, a typical alkaline battery electrolyte). The silver oxide was precipitated from nitrate solution as in Ref. (1) and was a rather coarse, rapidly settling material. The alumina was a 99.99% pure, 0.05μ size powder of γ-alumina from Union Carbide, Crystal Products Division; it yielded relatively stable suspensions. The KOH contained carbonate at a level comparable with those of Ref. (1). All four measured mobilities were quite small. Only for alumina in 1M KOH did the particles move fast enough to yield a relatively accurate measurement. The alumina particles were negatively charged and an average of five determinations gave a mobility of $0.54 \pm 0.12 \times 10^{-4}$ cm^2 sec^{-1} V^{-1}. At 11.6M, the alumina had slowed down such that it was possible to say only that the particles were still negative with a mobility not exceeding 0.1×10^{-4} cm^2 sec^{-1} V^{-1}. The silver oxide particles were even slower. In 1M KOH, they appeared to be negative with a mobility no greater than 0.1×10^{-4} cm^2 sec^{-1} V^{-1}. In 11.6M KOH, the silver oxide particles had no detectable mobility. The very low mobilities found in this brief study are quite consonant with the electrokinetic literature. Although no prior data seem to exist for solutions as conductive as 1M KOH, mobilities have been reported up to the ionic strength of seawater and these diminish uniformly with increasing salt concentration (4, 5). Thus we can say that particle mobilities in the concentrated electrolytes of alkaline batteries are very unlikely to exceed 0.1×10^{-4} cm^2 sec^{-1} V^{-1} and are therefore of little or no significance in battery operation.

Acknowledgment

This work was supported by the Independent Research Program of the Naval Surface Weapons Center, White Oak, Silver Spring, Maryland.

Manuscript received March 16, 1977.

Any discussion of this paper will appear in a Discussion Section to be published in the June 1978 JOURNAL. All discussions for the June 1978 Discussion Section should be submitted by Feb. 1, 1978.

Publication costs of this article were assisted by the U.S. Naval Surface Weapons Center.

* Electrochemical Society Active Member.
Key words: electrokinetics, silver-zinc battery, nickel-cadmium battery, silver oxide, alumina.

REFERENCES
1. S. W. Mayer, *This Journal*, **123**, 159 (1976).
2. S. D. James, *ibid.*, **123**, 1857 (1976).
3. R. A. Neihof, *J. Colloid Interface Sci.*, **30**, 128 (1969).
4. R. A. Neihof and G. I. Loeb, *Limnol. Oceanogr.*, **17**, 7 (1972).
5. J. Th. G. Overbeek, in "Colloid Science," Vol. 1. H. R. Kruyt, Editor, Elsevier, Amsterdam (1952).

Cell Voltage Variation Caused by Break of Uniform Gap Distance Between the Electrodes of Mercury Cell for Brine Electrolysis

Nobuhiro Kawasaki[1] and Yasuaki Kurokami

Toyo Soda Manufacturing Company, Limited, Chlor-Alkali Section, Yokkaichi-shi, Miye-ken, Japan

The quantity of bus bar on a mercury cell for brine electrolysis increases with an increase in rated current capacity. When an anode sheet begins to get close to the mercury cathode, the electric current flowing through the bus bar, to which the anode is connected, begins to increase and the cell voltage to decrease. Therefore short circuit can be avoided if one of the two is observed all the time.

The problem is which should be observed or how they should be combined in order to prevent short circuit and prevent mechanical damage of the electrodes.

In this note, the authors are going to discuss the cell voltage and current density variations caused by a deviation from uniform gap distance between the electrodes.

In general, the cell voltage (V) can be shown within a limit range of current density (D) as follows

$$V = a + (b + cl)D \qquad [1]$$

where l is a gap distance between the electrodes, and a, b, and c are constant and determined by the operating conditions such as brine temperature, brine concentration, and amalgam concentration.

The top of Fig. 1 shows a scheme of a brine electrolysis cell having n pieces of bus bar with an anode sheet for each and uniform gap distance (l_0). One obtains the following equation as the current density dependence of cell voltage by substituting $l = l_0$ into Eq. [1]

$$V = a + (b + cl_0)D \qquad [2]$$

The total electric current in Fig. 1 is ni_0 providing i_0 for each bus bar. The cell voltage shown by V_0 becomes

$$V_0 = a + (b + cl_0)D_0 \qquad [3]$$

where D_0 is the current density corresponding to the electric current (i_0) of a bus bar.

When one of the anode sheets deviates from the uniform gap distance as the bottom of Fig. 2 shows, the cell voltage becomes

$$V = a + (b + cl_0)D' \qquad [4]$$

where D' is the current density corresponding to the electric current (i') of bus bars, and one can derive

$$D' = (nD_0 - D)/(n - 1) \qquad [5]$$

Substituting Eq. [5] into the Eq. [4], one obtains

$$V = \{a + nD_0(b + cl_0)/(n - 1)\} - D(b + cl_0)/(n - 1) \qquad [6]$$

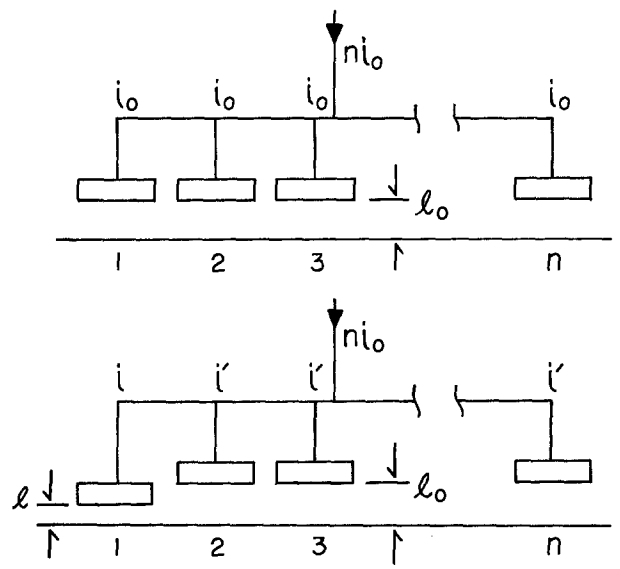


Fig. 1. Schematic brine electrolysis cells; uniform gap distance (top) and nonuniform gap distance (bottom).

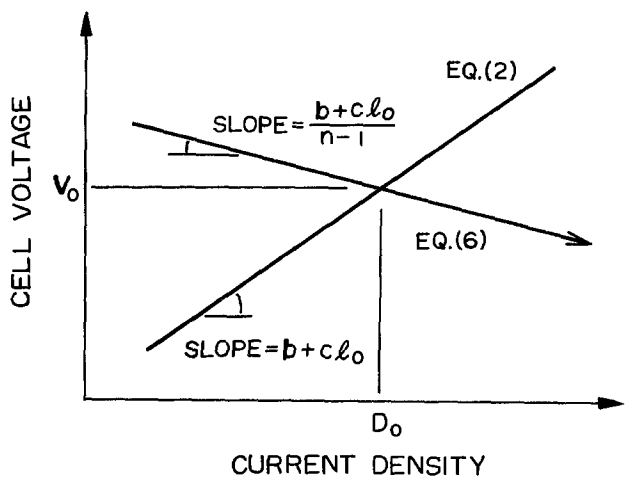


Fig. 2. Relationship between current density and cell voltage, Eq. [2] and [6] corresponding to the top and bottom of Fig. 1, respectively.

This equation is shown schematically in Fig. 2, where Eq. 2 is also shown for comparison. When one of the anode sheets breaks the uniform gap distance and gets close to the cathode, the cell voltage decreases and the current density increases in the direction shown by the arrow symbol with the slope of $(b + cl_0)/(n - 1)$. It should be noticed that the variation of cell voltage depends directly upon the quantity of bus bar.

[1] Present address: 2nd Production Division, Nanyo Plant, Toyo Soda Manufacturing Company, Limited, 4560 Tonda, Shin-nanyo-shi, Yamaguchi-ken, Japan.

Key words: cell voltage, gap distance, mercury cell, brine electrolysis.

In order to concretely understand the effect of quantity of bus bar on the cell voltage variation, the following explanation may be effective. The difference between V_0 of Eq. [3] and V of Eq. [6] is as follows

$$V_0 - V = (b + cl_0)(D - D_0)/(n - 1) \quad [7]$$

Assuming figures for both $(b + cl_0)$ and $(n - 1)$, *e.g.*, $(b + cl_0) = 0.013$ V/A · dm^2 at around 120 A/dm^2 of current density for the Olin metal anode (1) and $(n - 1) = 19$ for convenience, Eq. [6] becomes

$$V_0 - V = 0.00068\,(D - D_0) \quad [8]$$

In case the current density increases by 12 A/dm^2 corresponding to 10%, the cell voltage decreases by 0.008V. Generally the 10% increase of current density is predominant, and a certain countermeasure is taken to prevent a short circuit. On the other hand, a 0.008V variation of cell voltage is not easily detected, because this figure is within the cell voltage fluctuation due to the nonuniformity of the thicknesses of mercury cathode and iron bottom plate. Moreover, the cell voltages usually vary by more than 0.01V.

Twenty pieces of bus bar were used for the above explanation, and the cell voltage decrease was estimated to be 0.008V for a 10% increase in current density. For example, the cell voltage decrease is only 0.017V for 10 pieces of bus bar. From these examples using Eq. [7], it is apparent that the cell voltage variation caused by a deviation from uniform gap distance decreases reciprocally with an increase in the quantity of bus bar, which is related to the rated current capacity of a plant, and becomes less useful for protection of the anodes.

Acknowledgments

The authors would like to thank Mr. K. Yamori, General Manager of 2nd Production Division of Nanyo Plant, Toyo Soda Manufacturing Company, Limited for his kind comments on this study.

Manuscript submitted Dec. 13, 1976; revised manuscript received Feb. 20, 1977.

Any discussion of this paper will appear in a Discussion Section to be published in the June 1978 JOURNAL. All discussions for the June 1978 Discussion Section should be submitted by Feb. 1, 1978.

Publication costs of this article were assisted by Toya Soda Manufacturing Company, Limited.

REFERENCE

1. R. D. Burt and W. McM. Clarke, Chlor-Alkali cell section, presented at May 1970 A.I.Ch.E. Meeting in Puerto Rico.

Electrochemical Patterning of Tin Oxide Films

B. Jayant Baliga*

General Electric Company, Corporate Research and Development Center, Schenectady, New York 12301

and Sorab K. Ghandhi*

Electrical and Systems Engineering Department, Rensselaer Polytechnic Institute, Troy New York 12181

Interest in tin oxide films has grown recently because of their potential application for solar cell structures. The high conductivity of doped tin oxide, coupled with a high transmission coefficient to light from wavelengths in the violet into the infrared, makes it well suited for transparent conductive antireflection coatings and for forming heterojunctions with silicon or gallium arsenide. An additional advantage of tin oxide for such applications is its durability under harsh ambients. For example, tin oxide is not attacked at room temperature by either concentrated acids such as nitric, sulfuric, hydrochloric, and hydrofluoric acids, or by concentrated bases such as ammonium, sodium, and potassium hydroxides. However, this property makes it a difficult material to etch for the purpose of making connection patterns or test cell structures. Sputter etching (1) has been used for patterning tin oxide films, but this technique is slow and requires the dedication of an expensive vacuum system for this purpose. The only alternative technique that has been reported in the literature is the HCl-zinc powder method (2). However, this technique is difficult to use for large area structures and results in extremely poor edge definition. This note describes an electrochemical technique developed to pattern tin oxide films with resolutions limited only by the photolithographic process.

Phosphorus-doped films used in this study were deposited on polished silicon and gallium arsenide substrates by the simultaneous oxidation of tetramethyltin and phosphine gas (3). Immediately after deposition, they were covered with a thin layer of SiO_2 (usually 2000Å) grown by the oxidation of silane in the same reactor. This silica layer was patterned by conventional photolithographic techniques and used as a mask for etching the tin oxide. On all substrates a corner was also etched to expose the SnO_2 layer for contacting during the electrochemical etching.

Etching was carried out in a bath of hydrochloric acid diluted in water with a platinum anode and the tin oxide as the cathode. In this system, nascent hydrogen is generated at the cathode by the passage of current, and probably reduces the SnO_2 to tin, which is continuously dissolved in the electrolyte as etching proceeds. Figure 1 shows the etch rate as a function of the current density at the tin oxide electrode. This etch rate was measured by visually determining the time required to etch through a 2000Å film of the oxide. Etching was carried out using electrolytes with 1 part of concentrated HCl (37%) in 1-10 parts of deionized water. Concentrated HCl was not used directly due to problems with fumes attacking the etch fixtures. As can be seen in Fig. 1, the etch rate was found to be independent of dilution between HCl:H_2O ratios of 1:3 and 1:10. Higher concentrations resulted in lower etch rates.

Ammonium hydroxide was also used successfully as an electrolyte. However, continuous etching is not possible in this system due to the formation of a tin coating on the SnO_2 film. This tin coating had to be periodically removed using hydrochloric acid. Consequently, the HCl-based system is more convenient to use in practice.

Electrochemical etching of tin oxide was also achieved on insulating glass substrates. Lower current densities were preferred for these applications in order to prevent the formation of isolated unetched

* Electrochemical Society Active Member.
Key words: tin oxide, patterning, etching.

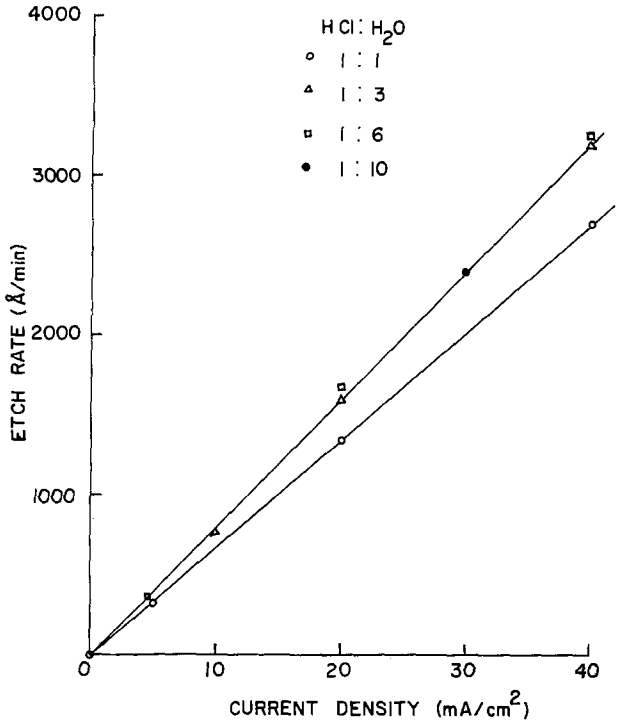


Fig. 1. Dependence of etch rate on current density and electrolyte concentration.

patches of tin oxide on the substrates. Such patches also appeared on conducting substrates at high current densities, but could be removed by prolonged etching.

In conclusion, tin oxide films can be patterned by electrochemical etching in a bath of dilute HCl, with resolutions that are typical of those obtained by photolithography. The etch rate is independent of the HCl concentration for the range of 1 part HCl (37%) diluted in 3-10 parts of water. Etching has been demonstrated to occur by the reduction of the tin oxide to tin by the generation of nascent hydrogen at the cathode (tin oxide), and its subsequent dissolution in the HCl.

Acknowledgments

The authors would like to thank P. Baliga for technical assistance and R. Rafun for assistance in manuscript preparation. This work was supported by NSF Grant No. AER 76-06186 (RANN).

Manuscript submitted Nov. 15, 1976; revised manuscript received March 1, 1977.

Any discussion of this paper will appear in a Discussion Section to be published in the June 1978 JOURNAL. All discussions for the June 1978 Discussion Section should be submitted by Feb. 1, 1977.

Publication costs of this article were assisted by Rensselaer Polytechnic Institute.

REFERENCES

1. T. Hayaski and H. Tsukamoto, *Jpn. J. Appl. Phys.*, **12**, 1457 (1973).
2. R. Muto and S. Furuuchi, *Rep. Res. Lab. Asahi Glass Co., Ltd.*, **23**, 27 (1973).
3. B. J. Baliga and S. K. Ghandhi, *This Journal*, **123**, 941 (1976).

Brief Communications

Anodic Sulfidation of Iron in Molten LiCl-KCl

C. A. Melendres,* C. C. Sy, and B. Tani

Argonne National Laboratory, Chemical Engineering Division, Argonne, Illinois 60439

Electrochemical cells in molten salt electrolytes, utilizing light metal alloys as the negative electrode and iron sulfide (either FeS or FeS_2) as the positive, are being considered for application in load leveling in electric utility systems and for electric vehicle propulsion (1, 2). An understanding of the electrochemical characteristics of the iron sulfide electrode is of interest for the further engineering development of such cells. Initial investigations on compositional changes occurring during the charging and discharging of FeS_2 and FeS electrodes have been reported (3-5). In this communication, we report on preliminary results of studies on the electrochemical formation of sulfide films on iron during electrolysis in molten LiCl-KCl eutectic containing dissolved Li_2S. This formation was established by cyclic voltammetry and controlled potential electrolysis with identification of the products formed by x-ray analysis and optical and scanning electron microscopy.

* Electrochemical Society Active Member.
Key words: iron sulfide formation, molten salt electrolyte, cyclic voltammetry of iron, film formation on iron.

The voltammetric cell consisted of a 5.5 cm diam alumina crucible to contain the electrolyte and hold the working electrode compartment. The compartment contained the Li_2S solution and was also of alumina (1 cm diam) with a 0.25 mm hole at the bottom. The working electrode was either an iron rod (0.17-0.32 cm diam) or foil (0.25 mm thick) of 99.99% purity (Marz grade material from Materials Research Corporation, Orangeburg, New York). The reference and counter-electrodes were cast lithium-aluminum alloy [40 atomic percent (a/o) Li] whose composition was in the $\alpha + \beta$ region of the phase diagram (6) and whose potential at 450°C is about 292 mV anodic of Li/Li^+ in the eutectic electrolyte (7). Polarographic grade LiCl-KCl eutectic was obtained from Anderson Physics Laboratories (Champaign, Illinois). The Li_2S was purchased from Foote Mineral Company (Exton, Pennsylvania), ground, and then vacuum dried at room temperature for several days. Li_2S material, sintered above 600°C and having an average purity higher than 99%, was obtained from Eagle Picher Industries Incorporated and also used. Solutions of the desired composi-

tion were prepared by weighing. The experiments were conducted inside a glove box under high purity helium atmosphere. Temperature control of the furnace was within 1% of the temperature setting. A potentiostat/galvanostat (Princeton Applied Research Model 173) driven by a PAR Universal Programmer (Model 175) was used for cyclic voltammetry. Voltammograms were displayed by a Hewlett-Packard Model 7040A X-Y recorder.

Cyclic voltammograms of iron were obtained in 0.005, 0.01, and 0.02*M* solutions of Li_2S in LiCl-KCl eutectic at 450°C. For the 0.01*M* solution, additional runs were made at 375° and 525°C. Typical voltammograms are shown in Fig. 1. Two anodic waves (1a and 2a) are evident at 1.4 and 1.6V *vs.* LiAl. A minor peak (3a) appears at 1.1V. The cathodic peaks 1c and 2c appear to correspond to the reduction of 1a and 2a, respectively. Wave 2a increases linearly with Li_2S concentration and temperature at a given scan rate; 1a appears to merge with 2a as the temperature increases. The wave at 1.1V also becomes more prominent at higher Li_2S concentration but the peak current decreases with temperature instead.

The shape of the voltammograms is typical of that observed for the formation and reduction of surface films (8), *e.g.*, oxides in aqueous media. The effects of increasing the switching potential for the anodic scans are an increase in the maximum peak current for the respective cathodic waves and a shift of the potential at the current maximum to more cathodic values. The former is indicative of the increase in the quantity of surface material being formed during the anodic sweep, while the latter signifies the increasing difficulty of reducing thicker and thicker layers of the surface films.

Cyclic voltammograms taken at a constant scan rate in the anodic direction while varying that in the cathodic portion are shown in Fig. 2. Integration of the areas under the cathodic peaks for scan rates from 5 to 50 mV/sec shows the charge passed to be constant at about 31 mC/cm² and 14 mC/cm² for waves 1c and 2c, respectively, regardless of the scan rate. Similarly, for an anodic scan of 5 mV/sec for wave 3, the charge under the cathodic peaks was about 3.6 mC/cm². This result implies the existence of a roughly constant quantity of material coating the electrode surface produced during the preceding anodic scan. The films are calculated to be more than a monolayer thick. The shift in cathodic peak potentials and peak currents

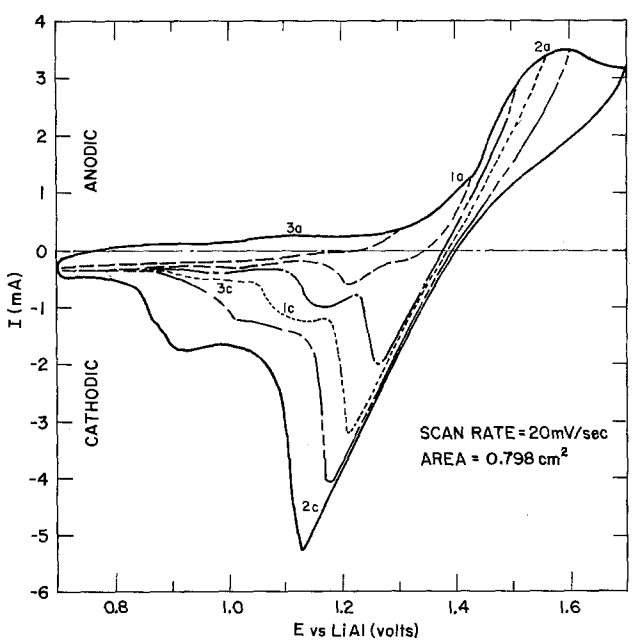


Fig. 1. Cyclic voltammograms of iron in 0.01M Li_2S solution at 450°C.

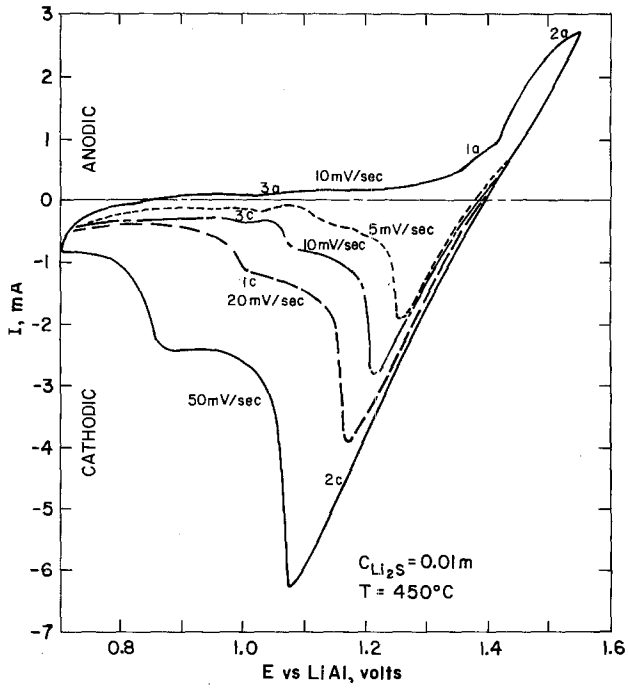


Fig. 2. Effect of scan rate on cathodic waves.

for the two waves is linear with the square root of scan rate; this is interpreted to mean that reduction of the surface films occurs under ohmic resistance control (9). The variation of peak current with the square root of scan rate for the main wave 2a is also linear. Assuming diffusion control of the process, a value of diffusion coefficient in the order of 1-4 $\times$ 10^{-6} cm²/sec at 450°C is obtained.

In order to determine the composition of the materials coating the electrode, electrolysis at various controlled potentials was undertaken at 450°C in 0.01 and 0.02*M* Li_2S solutions. Samples of the material found coating the electrode were taken and analyzed by x-ray diffraction. Results showed that FeS was present in samples anodized at potentials between 1.38 and 1.75V, while a sulfide phase of approximate composition $LiK_6Fe_{24}S_{26}Cl$ (henceforth referred to as J-phase) was found also when the potential was kept within 1.38-1.55V. Only LiCl-KCl was found at 1.2V, although the electrode appeared tarnished after the electrolysis. Examination of anodized electrodes under an optical microscope showed a coating which generally consists of a thin, grayish brown inner film and a rather thick, crystalline outer layer. This latter was identified by x-ray diffraction as either FeS, J-phase, or a mixture of both depending on the potential of anodization. Figure 3 shows an optical photomicrograph of the surface of an iron plate which has been anodized at 1.5V and subsequently washed by dipping momentarily in distilled water to remove the adhering LiCl-KCl salt layer. The black areas represent the outer layer whose composition in this particular case was determined as a mixture of FeS and J-phase by x-ray diffraction. The area of medium shade on the upper left corner corresponds to the inner film, while the light portions (bottom left) correspond to that of the iron substrate. Attempts to verify the composition of the inner film by x-ray diffraction have been unsuccessful so far; the film is very thin, making it difficult to obtain enough material, and it does not appear to be crystalline. However, elemental analysis of this inner film by an energy dispersive x-ray analyzer attached to a scanning electron microscope showed the presence of Fe and S. It is distinct from both the FeS outer layer (by the intensity ratio of Fe and S peaks) and also from the J-phase, which shows the presence of K in addition to Fe and S. Figure 4 shows the morphology of the outer layer as determined by scanning electron microscopy.

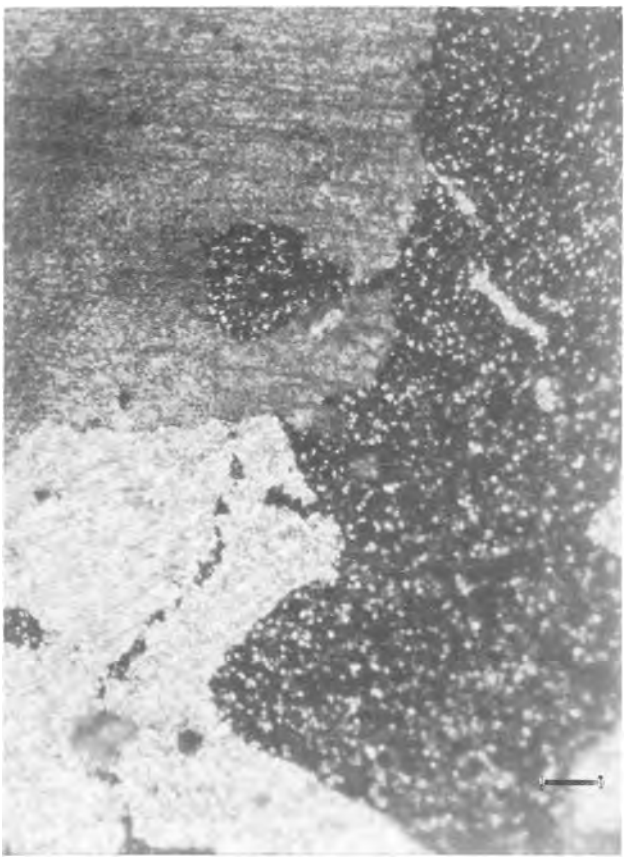


Fig. 3. Optical photomicrograph of iron electrode anodized at 1.5V (marker = 100 μm).

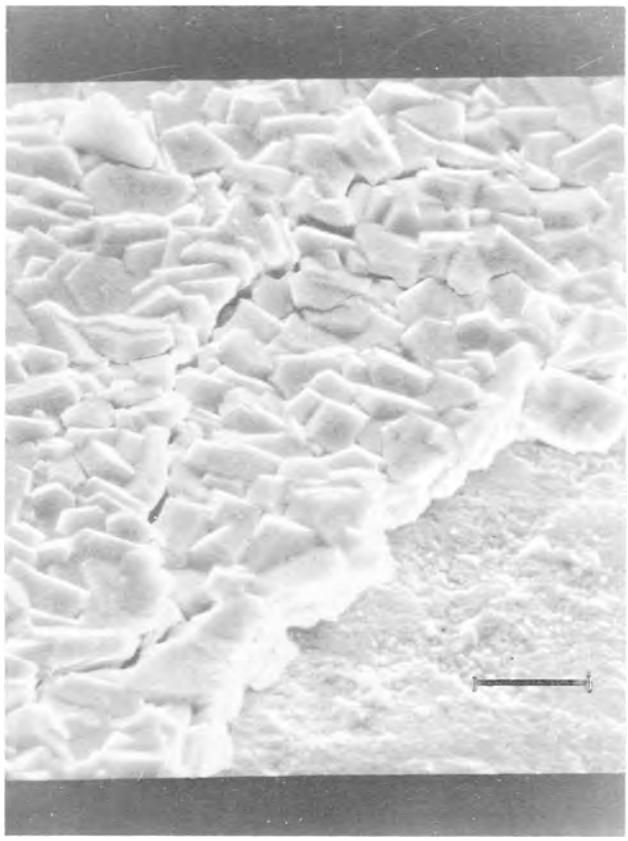


Fig. 4. Scanning electron microscope photograph of outer sulfide layer on iron electrode anodized at 1.5V (marker = 10 μm).

The hexagonal crystal habit of FeS as described in the literature (10) is not distinguishable from that of the J-phase by visual examination alone. Energy-dispersive x-ray analysis, however, shows the difference in elemental composition of the two. The cracks in the coating were inadvertently introduced during sample preparation. The coating does not seem to be very adherent, showing a tendency to peel off easily during the washing process to remove adhering electrolyte.

We consider briefly the possible reactions that could give rise to the coatings and sulfide phases. In the absence of detailed kinetic studies, any mechanistic proposal would be quite tentative. The foregoing results, nevertheless, suggest that wave 2a is due to the formation of FeS; the reaction rate at the current peak is presumably limited by diffusion of $S^=$ in the solution. The presence of wave 1a correlates well with the formation of J-phase material. The wave may be due to a change in properties of the coating because of the presence of this phase or to a distinct electrochemical reaction leading to J-phase formation. The complex composition of this phase suggests that it is probably formed by a chemical reaction following electron transfer to a precursor species. Reaction schemes that can account for the wave 1a are

Scheme (a)

$$Fe + Li_2S \rightarrow FeS + 2Li^+ + 2e^- \quad [1]$$

$$lFeS + mLi_2S + nK^+ + pCl^- \rightarrow \text{J-phase} \quad [2]$$

Scheme (b)

$$Fe + 2LiS^- \rightarrow Fe(LiS)_2 + 2e^- \quad [3]$$

or

$$Fe + 2Li_2S \rightarrow Fe(LiS)_2 + 2Li^+ + 2e^- \quad [4]$$

$$mFe(LiS)_2 + nK^+ + pCl^- \rightarrow \text{J-phase} \quad [5]$$

$$Fe(LiS)_2 + Fe \rightarrow 2FeS + 2Li^+ + 2e^- \quad [6]$$

where l, m, n, and p are integers.

For wave 2a, we propose the following

$$Fe + S^= \rightarrow FeS + 2e^- \quad [7]$$

$$J + 2Fe \rightarrow 26FeS + 4e^- \quad [8]$$

Scheme (a) suggests the possibility that FeS itself may be the precursor of the J-phase since it is found at potentials below the peak of the wave 1a. The role of Li_2S is suggested by the fact that the proportion of J-phase material formed during controlled potential electrolysis below 1.5V appears to increase with Li_2S concentration. Scheme (b) considers the possibility that another species which is directly discharged at the electrode is the precursor of the J-phase. The sulfidation reactions being proposed are analogous to the commonly observed anodic oxidation reactions of metals in aqueous alkaline solutions. The initial discharge product is thought here to be $Fe(LiS)_2$, a phase that has been found in cell studies (11). The J-phase presumably results from a chemical reaction of the $Fe(LiS)_2$ with KCl or from an inclusion of K^+ and Cl^- during formation of this stable phase. The potential dependence of the occurrence of the J-phase will be consistent with this scheme. Production of FeS from the solid phases $Fe(LiS)_2$ and J (Eq. [6] and [8]) is written in analogy with the dehydration reaction of metal hydroxide films (12). The cathodic waves would correspond to the reverse of the above reaction scheme. The nature of the reactions giving rise to waves 3a and 3c in the voltammogram has been difficult to ascertain. The peaks appear to be very symmetric and a doublet structure had been observed under high resolution. The closest separation between the anodic and cathodic portions was measured to be about 90 mV. These peaks may involve a minor species in solution which could be polysulfide; the thin inner film observed during microscopy may be due to this species or to the phase $Fe(LiS)_2$. Additional work is in progress; fur-

ther details of the present investigation also appear elsewhere (13).

Acknowledgments

The authors are grateful to Dr. R. K. Steunenberg and Dr. F. A. Cafasso for their continued interest and support of this work. We are indebted to Mr. Rudy Fuosek for assistance in electron microscopy.

This work was done under sponsorship of the U.S. Energy Research and Development Administration, Division of Physical Research.

Manuscript received Nov. 15, 1976; revised manuscript received Feb. 5, 1977.

Any discussion of this paper will appear in a Discussion Section to be published in the June 1978 JOURNAL. All discussions for the June 1978 Discussion Section should be submitted by Feb. 1, 1978.

Publication costs of this article were assisted by Argonne National Laboratory.

REFERENCES

1. W. J. Walsh, J. W. Allen, J. D. Arntzen, L. G. Bartholme, H. Shimotake, H. C. Tsai, and N. P. Yao, in Proceedings of the 9th IECEC, San Francisco, p. 911 (1974).
2. W. W. Schertz, A. A. Chilenskas, and V. M. Kolba, in Proceedings of the 10th IECEC, Newark, Delaware, p. 634 (1975).
3. A. E. Martin, R. K. Steunenberg, and Z. Tomczuk, Paper 54 presented at The Electrochemical Society Meeting, New York, New York, October 13-17, 1974.
4. F. C. Mrazek and J. E. Battles, "High Performance Batteries for Off-Peak Energy Storage and Electric Vehicle Propulsion," Progress Report for the period January-June 1974, ANL-8109, Argonne National Laboratory, p. 72 (1975).
5. Z. Tomczuk, A. E. Martin, and R. K. Steunenberg, Paper 47 presented at The Electrochemical Society Meeting, Las Vegas, Nevada, October 17-22, 1976.
6. M. Hansen and K. Anderko, "Constitution of Binary Alloys, p. 104, McGraw-Hill Book Co., New York (1969).
7. N. P. Yao, L. A. Heredy, and R. C. Saunders, *This Journal*, **118**, 1039 (1971).
8. H. Angerstein-Kozlowska, B. E. Conway, and W. B. A. Sharp, *J. Electroanal. Chem.*, **43**, 9 (1973).
9. A. J. Calandra, N. R. De Tacconi, R. Pereiro, and A. J. Arvia, *Electrochim. Acta*, **19**, 901 (1974).
10. "CRC Handbook of Chemistry and Physics," 50th ed., R. C. Weast, Editor, The Chemical Rubber Co., Cleveland, Ohio (1969).
11. P. A. Nelson, W. J. Walsh, R. K. Steunenberg, J. E. Battles, H. Shimotake, N. P. Yao, H. C. Tsai, A. E. Martin, D. R. Vissers, J. R. Birk, K. M. Myles, W. D. Tuohig, D. S. Webster, and L. Burris, "High Performance Batteries for Off-Peak Energy Storage," Progress Report for the period July-Dec. 1973, ANL-8057 (1974).
12. D. A. Vermilyea, in "Advances in Electrochemistry and Electrochemical Energy," Vol. 3, P. Delahay and C. W. Tobias, Editors, p. 264, Interscience Publishers, New York (1963).
13. C. A. Melendres and C. C. Sy, Paper 387 presented at The Electrochemical Society Meeting, Philadelphia, Pennsylvania, May 8-13, 1977.

Novel Semiconducting Electrodes for the Photosensitized Electrolysis of Water

J. Augustynski, J. Hinden, and Chs. Stalder

Laboratory of Electrochemistry and Applied Chemistry, University of Geneva, Geneva, Switzerland

The last months have seen a significant increase of interest in the utilization of semiconductor electrodes for the photoassisted electrolysis of water and in the implications of this process for solar energy conversion. As well as n-type TiO_2 (1) and SnO_2 (2), other semiconducting oxides; WO_3 (3), $SrTiO_3$ (4, 5), and Fe_2O_3 (6) have been recently proposed as possible anode materials for the photosensitized electrolysis of water. The best current-voltage characteristics have been hitherto obtained with the single crystal TiO_2 (7) and $SrTiO_3$ (4) photoanodes, although in some cases a similar behavior has been observed (8) for the polycrystalline TiO_2 electrodes. Here we report the preparation of novel semiconducting electrodes, based on polycrystalline titanium dioxide having exceptionally good current-voltage characteristics. These electrodes are formed by mixed oxide TiO_2-M_xO_y deposits on metallic titanium substrates, M being one of divalent or trivalent elements listed in Table I. The mixed oxide coatings were prepared by spraying a solution containing, for example, chlorides of both metals (elements) entering the film composition on Ti metal and heating at ~450°C in air to decompose the chlorides. Several layers, generally between 6 and 12, were deposited on each substrate. The electrodes were finally activated in argon at 600°-800°C during 30-60 min. The current-potential characteristics of the mixed oxide electrodes (area 0.9 cm^2) were measured in a two compartment cell using 1*N* sodium hydroxide solution.

Key words: semiconducting electrodes, oxide coatings, photoanodes.

Platinum foil served as the counterelectrode and a mercuric oxide electrode (HgO/Hg) was the reference electrode. All potentials are reported *vs.* normal hydrogen electrode (NHE). A 350W high pressure mercury arc lamp was used as a light source. Figure 1 shows a typical current-potential curve for a TiO_2-Al_2O_3 photoanode (electrode A, Table I) under illumination. Each point of this curve was measured after

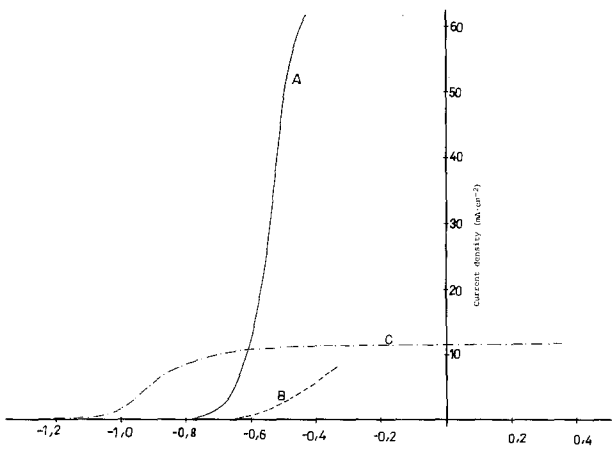


Fig. 1. Current-potential curve for a polycrystalline TiO_2-Al_2O_3 photoanode (A) illuminated by a 350W high pressure Hg lamp compared with single crystal TiO_2 (B) and $SrTiO_3$ (C) electrodes (from Ref. 7 and 4).

Table I. Some long time stability tests of mixed oxide photoanodes

	Electrode	Composition of the coating (w/o of metal)	Photoanode potential (mV vs. NHE) at 10 mA · cm^{-2}	at 20 mA · cm^{-2}	at 40 mA · cm^{-2}
A	TiO_2-Al_2O_3	94% Ti; 6% Al	−600 (−620 after 64 hr)	−570	−520 (−540 after 22 hr)
B	TiO_2-SrO	90% Ti; 10% Sr	−560	−510	−430
C	TiO_2-Ga_2O_3	94% Ti; 6% Ga	−490 (−500 after 16 hr)	−350	
D	TiO_2-Eu_2O_3	97% Ti; 3% Eu	−460	−300	
E	TiO_2-B_2O_3	94% Ti; 6% B	−530 (−500 after 15 hr)	−400 (−230 after 40 hr)	

polarization for at least 2 hr at a fixed current (controlled by a galvanostat). The current-potential characteristic of the TiO_2-Al_2O_3 photoanode is compared in Fig. 1 with those for the single crystal TiO_2 and $SrTiO_3$ electrodes (7, 4) determined under similar illumination conditions. If in the latter case the maximum anodic photocurrents observed are not higher than ~8 mA · cm^{-2} for TiO_2 and ~12 mA · cm^{-2} for $SrTiO_3$, the TiO_2-Al_2O_3 photoanode can sustain 60 mA · cm^{-2} without an excessive polarization, the potential remaining 0.85V less positive than the theoretical oxygen evolution potential in the dark. Another special feature of the TiO_2-Al_2O_3 electrode is a relatively small change in the potential with increasing anodic current as compared with the TiO_2 and $SrTiO_3$ single crystal electrodes. This difference in behavior might be attributed to the low resistivity of the mixed oxide coatings.

The good stability of the TiO_2-Al_2O_3 photoanode was confirmed by the results of long time tests given in Table I. No deterioration of the performance was observed after passage of about 6000 C · cm^{-2} corresponding to ~0.015 moles of oxygen evolved. Simultaneously there was no significant change in the weight of the electrode. As shown in Fig. 2, besides the TiO_2-Al_2O_3 electrode the best results have been obtained with a TiO_2-SrO coating. Up to ~30 mA · cm^{-2} the TiO_2-SrO electrode is nearly equivalent to the TiO_2-Al_2O_3 with respect to current-potential characteristic, but for higher current densities the TiO_2-SrO potential becomes distinctly more positive than that of TiO_2-Al_2O_3. In the case of the other two mixed oxide electrodes, TiO_2-Ga_2O_3 and TiO_2-Eu_2O_3, the current increase resulted in even larger polarization (Fig. 2), although their performances remain superior to the TiO_2 and $SrTiO_3$ single crystal electrodes. The thickness of the mixed oxide deposits being similar for all electrodes listed in Table I, the differences in their behavior must arise essentially from both unequal concentration and distribution of the oxygen vacancies in the TiO_2-M_xO_y system, resulting in the variations of conductivity. In this connection it should be stressed that the concentrations of divalent and trivalent elements in TiO_2-M_xO_y, given in Table I, are actually the mean values

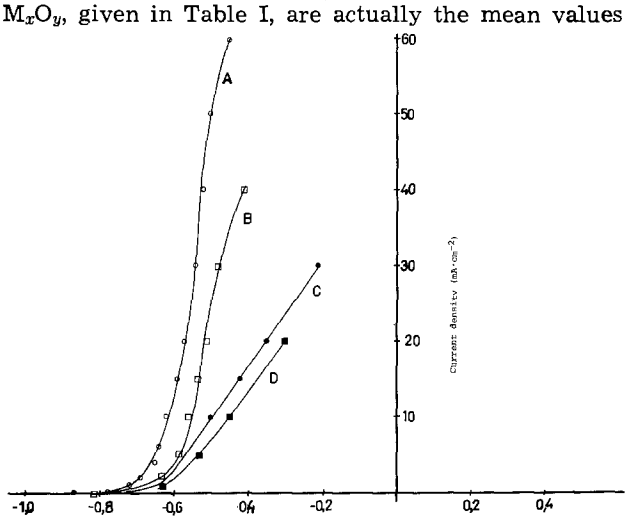


Fig. 2. Current-potential curves for different mixed oxide photoanodes: (A) TiO_2-Al_2O_3; (B) TiO_2-SrO; (C) TiO_2-Ga_2O_3; (D) TiO_2-Eu_2O_3 (the compositions of these mixed oxide coatings are given in Table I).

which can be quite different from the local concentrations through the thickness of the coating. For example, the Al^{3+} concentration in the surface region (15-20Å) of the TiO_2-Al_2O_3 electrode is much higher than the mean value of 6 weight percent (w/o), as established by the analysis performed using x-ray photoelectron spectroscopy. These changes in the concentration are certainly due to some preferential diffusion phenomena taking place during the heat-treatment of the electrodes in argon atmosphere.

One of the known features of TiO_2, having obvious implications for its utilization as photoanode, is the difficulty in making TiO_2 n-type with controlled conductivity. The latter is most likely the reason why the characteristics of the TiO_2 photoanode deteriorate during long time electrolysis despite an apparent chemical stability of this material under conditions of the oxidation of water. This deterioration which appears typically for the single crystal TiO_2 photoanodes (7) after the passage of about 1000 C · cm^{-2} was equally observed in some of our experiments carried out with no-doped, polycrystalline TiO_2 electrodes prepared in the similar way as the mixed oxide TiO_2-M_xO_y coatings. Therefore, the excellent long time characteristics of the TiO_2-Al_2O_3 photoanodes are related, in our opinion, to the fact that their initial high conductivity is not influenced by the passage of the anodic current. In other terms, the heat treatment of the mixed titanium-aluminum oxide coating deposited on Ti substrate leads to the formation of a stable TiO_{2-n}-Al_2O_3 defect structure resulting in an enhanced conductivity.

The spectral responses of the mixed oxide photoanodes listed in Table I were similar to that of the single crystal TiO_2 electrode (7), showing that the bandgap of TiO_2 is apparently not modified by the doping with Al^{3+}, Sr^{2+}, Ga^{3+}, Eu^{3+}, or B^{3+}. On the other hand, high quantum efficiencies are maintained for these electrodes up to very large current densities in contradistinction to the single crystal TiO_2 (9).

Acknowledgment

This research was supported by the Swiss National Science Foundation.

Manuscript received March 7, 1977.

Any discussion of this paper will appear in a Discussion Section to be published in the June 1978 JOURNAL. All discussions for June 1978 Discussion Section should be submitted by Feb. 1, 1978.

Publication costs of this article were assisted by Geneva University.

REFERENCES

1. A. Fujishima and K. Honda, *Nature (London)*, **238**, 37 (1972).
2. F. Möllers and R. Memming, *Ber. Bunsenges. Phys. Chem.*, **76**, 469 (1972).
3. G. Hodes, D. Cahen, and J. Manassen, *Nature (London)*, **260**, 312 (1976).
4. M. S. Wrighton, D. S. Ginley, A. B. Ellis, P. T. Wokzanski, D. L. Morse, and H. B. Abrahamson, *J. Am. Chem. Soc.*, **98**, 2774 (1976).
5. J. G. Mavroides, J. A. Kafalas, and D. F. Kolesar, *Appl. Phys. Lett.*, **28**, 241 (1976).
6. K. L. Hardee and A. J. Bard, *This Journal*, **123**, 1024 (1976).
7. H. Yoneyama, H. Sakamoto, and H. Tamura, *Electrochim. Acta*, **20**, 341 (1975).
8. A. Fujishima, K. Kohayakawa, and K. Honda, *This Journal*, **122**, 1487 (1975).
9. J. H. Carey and B. G. Oliver, *Nature (London)*, **259**, 554 (1976).

JOURNAL OF THE ELECTROCHEMICAL SOCIETY

SOLID-STATE SCIENCE
—AND TECHNOLOGY

JULY
1977

Electrical Properties of n-Type Polycrystalline Indium Phosphide Films

Tadashi Saitoh and Sunao Matsubara

Hitachi Limited, Central Research Laboratory, Kokubunji, Tokyo, Japan

ABSTRACT

Electrical properties of n-type polycrystalline indium phosphide deposited on molydenum substrates are investigated as a function of deposition conditions. For undoped films, the electron concentration is found to be 10^{15}-10^{17} cm^{-3} and tends to increase with the increase in deposition temperature. The electron mobility and resistivity are almost constant irrespective of varying deposition conditions. On the other hand, the electrical properties of sulfur-doped films are found to be strong functions of deposition conditions and doping level. A grain boundary carrier trapping model is applied to explain the electronic transport properties of the polycrystalline films. The barrier height and the density of trapping states at grain boundaries are calculated.

Polycrystalline films of various semiconductors have been used in fabricating low cost solar cells (1-3). Consequently, the growth and structure of polycrystalline indium phosphide films have been investigated by the authors (4, 5). Understanding of the electronic transport properties of polycrystalline films are considered critical to the realization of solar cells with high conversion efficiencies.

In our present study, Hall measurement was performed to gain this clear understanding of the electrical properties of n-type polycrystalline indium phosphide as a function of deposition conditions. A model including carrier trapping centers at grain boundaries (6) was utilized to obtain the barrier height and the density of trapping states at grain boundaries.

Experimental

Polycrystalline films were prepared on 50 μm thick molybdenum sheets by chemical vapor deposition (4). The molybdenum sheets were cleaned in organic solvents and subsequently etched in a $1H_2SO_4$-$1HNO_3$-$3H_2O$ solution prior to indium phosphide deposition. This etchant makes molybdenum surfaces rough and acted effectively to secure a homogeneous nucleation in the initial stage of the deposition as well as to get pinhole-free films. The deposition was carried out at substrate temperatures between 450° and 650°C. Hydrogen sulfide was used as an n-type doping gas.

Electrical properties of both undoped and sulfur-doped films were measured by the van der Pauw method (7). Specimens for the measurement were prepared as follows: First, a polycrystalline film was attached upside down to a glass plate using an epoxy adhesive. Then, the molybdenum substrate was chemically etched off except four corners. The interface between the n-type polycrystalline indium phosphide and the molybdenum was found to have an ohmic contact. Consequently, the four molybdenum corners were used as electrodes.

Key words: Hall measurement, grain boundary, crystallite, barrier height, trapping density.

The Hall voltage was measured in both current polarities and averaged to calculate the electrical properties. The observed values of electron mobility, resistivity, and electron concentration were denoted as $\bar{\mu}$, $\bar{\rho}$, and $\bar{n}$, since the values relate to both crystallites and grain boundaries.

Resistivity vertical to the film surface was measured as follows: A eutectic AuGe alloy was evaporated on the film surface, annealed at 200°C in a hydrogen gas, and mesa-etched. Then, resistivity was calculated from the linear current-voltage relationship between the AuGe electrode and the Mo substrate.

Results

Undoped films.—The grain size of the polycrystalline films depended mainly on deposition temperature and growth time and not on PCl_3 concentration in a feed gas (4). So, the electrical properties were examined with respect to the former two conditions. The electrical properties of undoped films were compared to those of undoped epitaxial layers on Cr-doped single crystal substrates. The carrier concentration of polycrystalline films was appreciably lower than that of the epitaxial ones; whereas the electron mobility was lower and hence the resistivity higher by two orders of magnitude.

Resistivity of the polycrystalline films is almost constant irrespective of varying deposition temperature, as shown in Fig. 1. Also shown in the figure is the resistivity measured in a direction vertical to the film surface. The value is in the range of 1-10 $\Omega \cdot$ cm, being one order of magnitude lower than that measured parallel to the surface. The difference in the resistivities is considered to come from the difference in the orientation of the films (4).

On the other hand, electron concentration tends to increase with increasing deposition temperature and electron mobility decreases at around 600°C, as shown in Fig. 2 and 3, respectively. Since grain sizes increase at higher deposition temperatures, the grain boundary

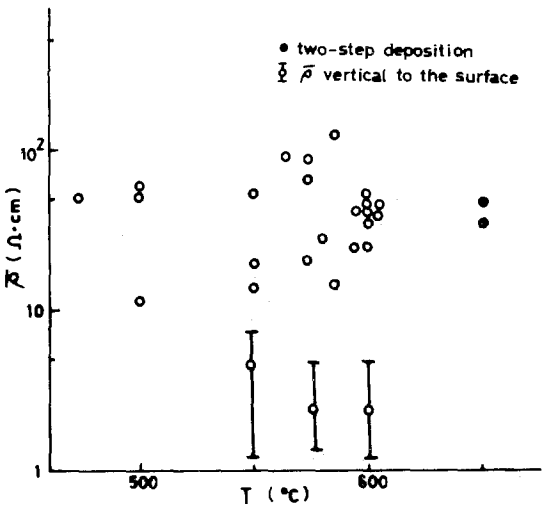


Fig. 1. Resistivity parallel and vertical to the surface vs. deposition temperature for undoped films.

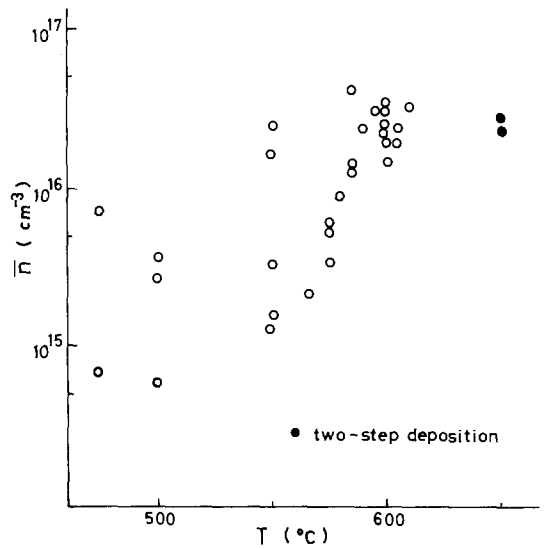


Fig. 2. Electron concentration vs. deposition temperature for undoped polycrystalline films.

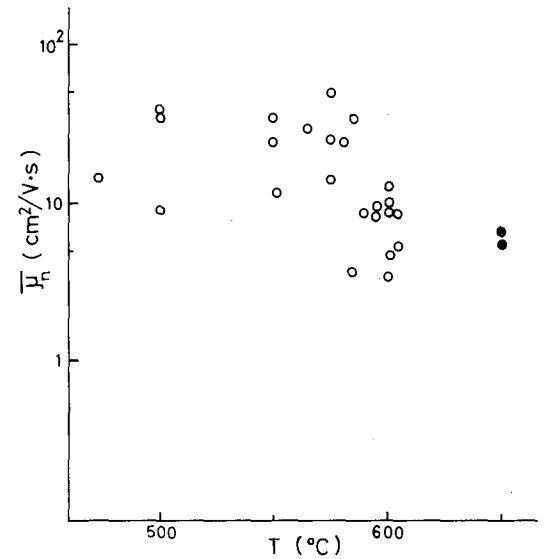


Fig. 3. Hall mobility vs. deposition temperature for undoped polycrystalline films.

area should decrease. It is assumed that a density of traps per grain boundary area remains constant. Thus, the higher the deposition temperature, the smaller the number of free carriers trapped at the grain boundary becomes causing an increase in the carrier concentration. When the deposition was carried out at more than 600°C, the deposited surface tended to become rough and have pinholes. This caused a decrease in the electron mobility of the films deposited at 600°C; probably due to the scattering of the carriers on the surfaces.

In the above figures data are also shown for two-step deposition in which a first layer was deposited at 600°C and then a second layer was deposited on it at 650°C. The observed values for the two-step deposition were similar to those of the films deposited at 600°C. This result suggests that the electrical properties of the second layers are determined mainly by those of the first layers. In other words, it indicates that each grain grows epitaxially on each of the substrates.

Furthermore, the variation of resistivity with thickness was examined. The observed values were found to be almost constant irrespective of thickness. Resistivity variation for an 18 μm thick film deposited at 575°C was also measured. It ranges from 1.2 to 4.9 $\Omega \cdot$ cm with the average value of 2.4 $\Omega \cdot$ cm.

Sulfur-doped films.—In the case of H_2S partial pressure of 6×10^{-7} atm, the carrier concentration increased with increasing deposition temperature; whereas the electron mobility increased and the resistivity decreased with the increase of deposition temperature, except around 600°C. The mobility decrease at around 600°C can be explained as the effect of free carrier scattering on the surfaces, as mentioned above.

A carrier concentration at a higher partial pressure of 3×10^{-6} atm was obtained to be about 1×10^{19} cm^{-3}, as shown in Fig. 4. It increased appreciably with deposition temperature. This suggests that saturation of the number of the carriers trapped at grain boundaries occurs. Resistivity decreased with deposition temperature, which is consistent with the increase in the grain size. In addition, electron mobility increases with deposition temperature as the value is calculated using the relationship $\bar{n}\bar{\rho}\bar{\mu} = q^{-1}$.

The variation of resistivity and electron concentration with H_2S partial pressure in the feed gas is shown in Fig. 5. It is notable that the resistivity drops rapidly at a partial pressure of 10^{-6} atm. On the other hand, the carrier concentration increased inversely. This tendency closely resembles that of polycrystalline silicon, in which the resistivity dropped drastically, about

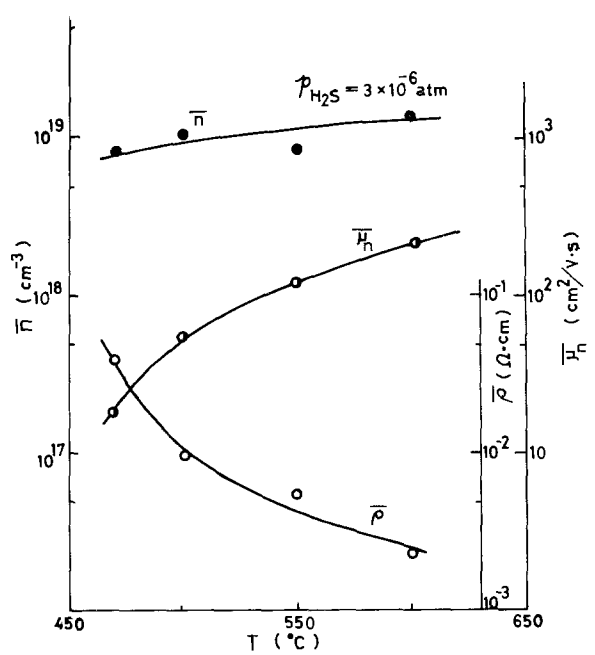


Fig. 4. Electron concentration, resistivity, and Hall mobility vs. deposition temperature for sulfur-doped films deposited at a hydrogen sulfide partial pressure of 3×10^{-6} atm.

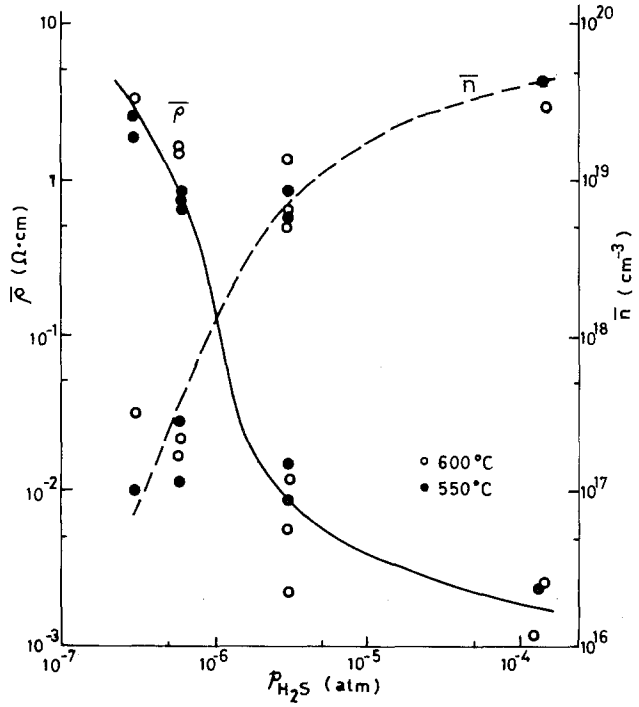


Fig. 5. Variation of resistivity and electron concentration with H_2S partial pressure in the gas phase for polycrystalline films.

five orders of magnitude (8, 9). This phenomenon can be understood as follows: As the carrier concentration decreased, the depletion-layer width around the grain boundary increased. When the depletion-layer width approached the grain size, the resistivity increased rapidly due to the trapping of almost all the carriers at the grain boundary. The smaller variation of resistivity for polycrystalline indium phosphide as compared to that of silicon is ascribed to the relatively high concentrations of residual impurities and to larger grain sizes.

The relationship between electron mobility and electron concentration for sulfur-doped films deposited at 550° and 600°C are shown as broken lines in Fig. 6. The electron mobility of polycrystalline films has a different tendency from that of the n-type single crystals shown as a solid line (10). The maximum value of the mobility is 200 cm^2/V · sec at a carrier concentration of 3×10^{19} cm^{-3}, about one-fifth that of single crystals. The lower values of the polycrystalline films deposited at 600°C than that of the films deposited at 550°C can be attributed to the scattering of the carriers at the nonuniform surfaces as already mentioned in Fig. 2.

Furthermore, the variation of the electrical properties for sulfur-doped films with thickness was measured and is shown in Fig. 7. Since the sample was attached upside down to the glass plate and etched gradually from the molybdenum side, the data at thinner thicknesses correspond to those near the as-deposited surface. As the grain size tends to increase when films become thick, the electrical properties nearer the front surface are less affected by the grain boundary. This tendency is compatible with the results shown in Fig. 7.

Barrier height at grain boundary.—In general, the electrical properties of polycrystalline films are discussed by dividing them into two regions, *i.e.*, a low resistivity region in crystallites and a high resistivity region around grain boundaries. In the case that doping level is relatively high and thus resistivity in the crystallites is sufficiently lower than that of the grain boundaries, the observed resistivity $\bar{\rho}$ is described by the following equation (6, 9, 11)

$$\bar{\rho} \propto \exp\left(\frac{\phi}{kT}\right) \qquad [1]$$

where ϕ is the barrier height.

A logarithmic plot of the resistivity *vs.* reciprocal temperature for undoped films is shown in Fig. 8. A linear relationship is obtained for samples deposited at various temperatures. Moreover, a logarithmic plot of electron mobility *vs.* reciprocal temperature was also found to vary linearly in an inverse manner. The barrier heights calculated from the figure are indicated in Table I. For films deposited at 600°C, barrier heights range from 0.2 to 0.3 eV. One barrier height for two-step deposition is almost equal to the above value. On the other hand, a smaller value of 0.081 eV is obtained for a film deposited at 500°C due to a relatively high concentration compared to other samples.

In the case of sulfur-doped polycrystalline films, a linear dependence is also obtained for a logarithmic plot of resistivity or electron mobility *vs.* reciprocal temperature. The barrier height calculated using the above equation is shown in Table I, indicating that the barrier height decreases inversely with the increase in electron concentration.

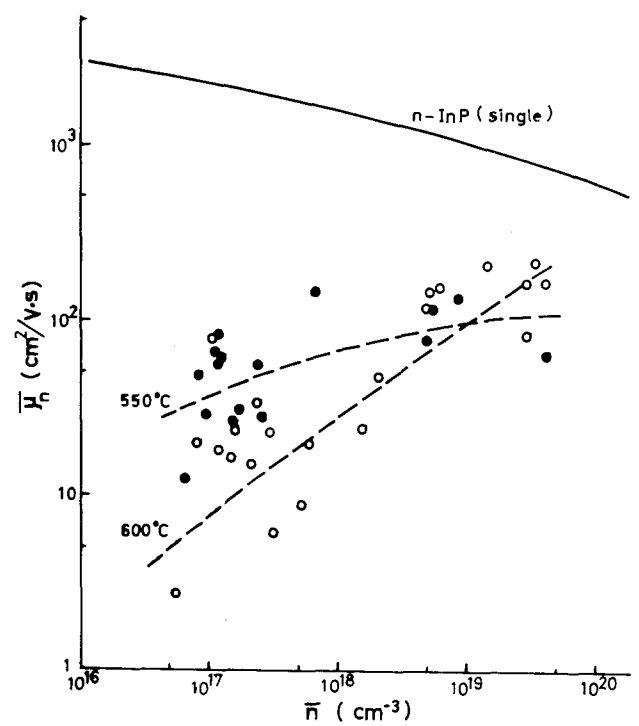


Fig. 6. Hall mobility *vs.* electron concentration for sulfur-doped polycrystalline films.

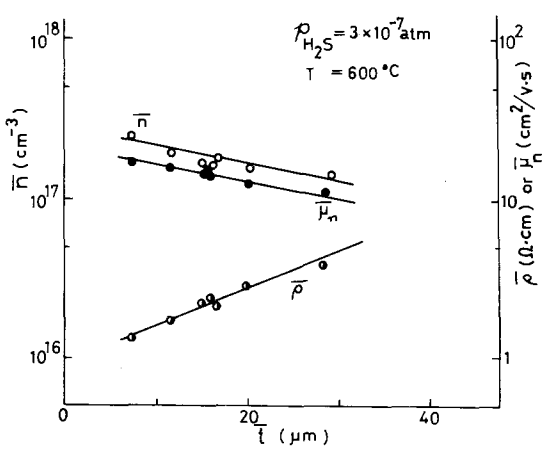


Fig. 7. Electron concentration, Hall mobility, and resistivity measured from the film surface.

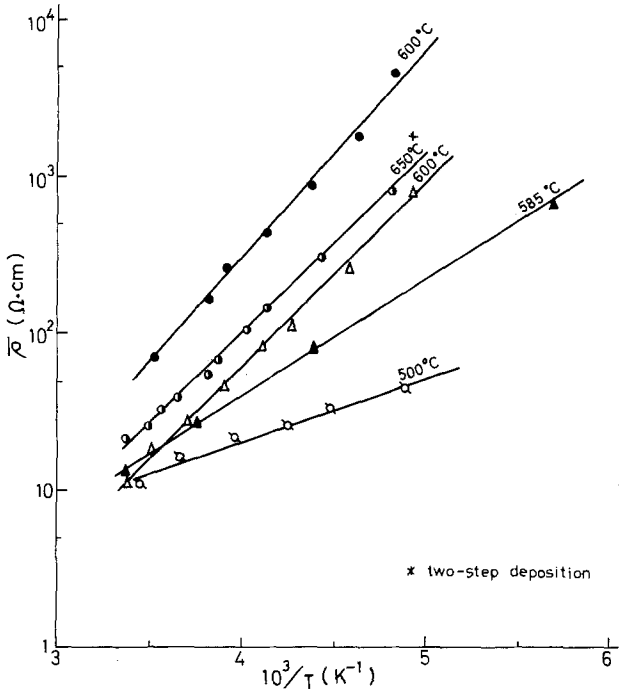


Fig. 8. Resistivity vs. reciprocal temperature for undoped polycrystalline films deposited at various temperatures.

Discussion

In general, polycrystalline films have been considered to consist of single crystallites and grain boundaries including disordered atoms. There are some different models of electronic conduction around grain boundaries, *i.e.*, grain boundaries act as a sink for impurity atoms (12) or as a trap for free carriers (6, 9). The latter model is applied for elucidating the electronic conduction properties of polycrystalline indium phosphide.

In the model, the defects at grain boundaries are assumed to generate a density of traps Nt. Therefore, free carriers are trapped, and hence grain boundaries are surrounded by a depletion region.

From Poisson's equation, assuming that only part of crystallites is depleted, the potential variation throughout the polycrystalline films can be obtained. Since the barrier height ϕ is the difference between the potential at a center of the crystallite and that at an edge of the depletion region, it can be described as (6, 9)

$$\phi = \frac{q n_t^2}{8\epsilon n_1} \qquad [2]$$

where n_1 (cm^{-3}) is the carrier concentration in the crystallite, and ϵ is the permittivity. The parameter n_t (cm^{-2}) is the number of carriers trapped at the grain boundary and is given as

$$n_t = n_1 l_2 \qquad [3]$$

where l_2 is the depletion layer width.

Kamins introduced the following equation for the observed carrier concentration $\bar{n}$ under the assumption that the Hall coefficient is additive (6)

$$\bar{n} = \frac{n_1}{1 + (l_2/l_1)^2 \exp(\phi/kT)} \qquad [4]$$

Here, l_1 is the length of the low resistivity region.

Inserting Eq. [2] and [3] into Eq. [4], the following equation concerning n_1 is obtained

$$n_1^2 - \bar{n} n_1 - A\bar{n} = 0 \qquad [5]$$

where A is

$$A = \frac{8\epsilon\phi}{e l_1^2} \exp\left(\frac{\phi}{kT}\right) \qquad [6]$$

In the case of relatively high carrier concentrations, the length l_1 corresponds to the grain size. Then, A in Eq. [6] can be calculated using observed values of grain size and barrier height. Consequently, the carrier concentration in the crystallite n_1 can also be calculated from Eq. [5] and the number of carriers trapped at the grain boundary n_t from Eq. [2].

The electron concentration in the crystallites n_1 and the number of trapped carriers n_t for undoped films are also indicated in Table I. The concentration n_1 is higher than $\bar{n}$, indicating that the carrier trapping at the grain boundary is effective. The number of carriers trapped n_t tends to increase with the carrier concentration n_1 and to saturate at about 10^{12} cm^{-2}. In addition, the depletion-layer widths l_s were found to be 1000-2000Å from Eq. [3], being approximately one order of magnitude smaller than the grain size.

On the other hand, n_1 of sulfur-doped films is almost equal to the $\bar{n}$ value, as shown in Table I. The depletion-layer widths were calculated to be far smaller than 1000Å and inversely proportional to the carrier concentrations. The number of trapped carriers n_t tends to saturate with the increase in carrier concentration and to peak at 3.3×10^{12} cm^{-2}. This value is close to that of polycrystalline silicon films (9) and is considered to be near the density of trapping states, Nt, at the grain boundary.

Summary

Electrical properties of n-type polycrystalline films have been examined using the Hall measurements. For undoped films, the carrier concentration increased with increasing deposition temperature. On the other hand, electron mobility, being about two orders of magnitude smaller than that of single crystals, was almost constant irrespective of deposition temperature and

Table I. Barrier height, electron concentration in the crystallite, and number of carriers trapped at grain boundaries for polycrystalline indium phosphide films

	Deposition temperature (°C)	Average grain size (μm)	Observed electron concentrations (cm^{-3})	Barrier height (eV)	Carrier concentrations in the crystallites (cm^{-3})	Number of electrons trapped at grain boundaries (cm^{-2})
Undoped films	600-650*	7	1.9×10^{16}	0.23	6.7×10^{16}	9.1×10^{11}
	600	7	2.3×10^{16}	0.26	9.0×10^{16}	1.1×10^{12}
	600	7	3.2×10^{16}	0.23	9.2×10^{16}	1.1×10^{12}
	585	6	1.3×10^{16}	0.15	1.8×10^{16}	3.8×10^{11}
	500	2	6.2×10^{16}	0.081	6.4×10^{16}	5.3×10^{11}
Sulfur-doped films	550	4	1.0×10^{17}	0.083	1.0×10^{17}	6.7×10^{11}
	475	1	1.6×10^{18}	0.029	1.6×10^{18}	1.6×10^{12}
	550	4	2.8×10^{18}	0.019	2.8×10^{18}	1.7×10^{12}
	600	7	2.2×10^{18}	0.019	2.2×10^{18}	1.5×10^{12}
	600	7	3.0×10^{19}	0.007	3.0×10^{19}	3.3×10^{12}

* Two-step deposition.

growth time. The resistivity parallel to the surface did not depend on deposition conditions and was one order of magnitude larger than that measured vertically to the film surface.

For sulfur-doped films, the carrier concentration increased and the resistivity decreased with increasing deposition temperature. Especially, noteworthy was the fact that resistivity increased two orders of magnitude at the H_2S partial pressure of 10^{-6} atm in the feed gas. These results are considered to be caused by the grain boundary. Electron mobility increased with the partial pressure of H_2S gas up to 200 $cm^2/V \cdot sec$ at an electron concentration of about 10^{19} cm^{-3}.

A model in which grain boundaries act as free carrier traps was utilized to elucidate the electronic transport behavior. The barrier heights for undoped films were 0.2-0.3 eV and decreased inversely with the increase in electron concentration. The density of trapping states was determined as 3×10^{12} cm^{-2}.

Acknowledgments

The authors are obliged to Dr. Takashi Tokuyama for his technical discussion and critical reading of this manuscript. This work was financed in part by the Agency of Industrial Science and Technology, Ministry of International Trade and Industry.

Manuscript submitted Aug. 31, 1976; revised manuscript received March 4, 1977.

Any discussion of this paper will appear in a Discussion Section to be published in the June 1978 JOURNAL. All discussions for the June 1978 Discussion Section should be submitted by Feb. 1, 1978.

Publication costs of this article were assisted by Hitachi, Limited.

REFERENCES

1. D. C. Reynolds, G. Leies, L. L. Antes, and R. E. Marburger, *Phys. Rev.*, **96**, 533 (1954).
2. P. Vohl, D. M. Perkins, S. G. Ellis, R. R. Addiss, W. Hui, and G. Noel, *IEEE Trans. Electron Devices*, **ed-14**, 26 (1967).
3. T. L. Chu, H. C. Mollenkopf, and S. S. C. Chu, *This Journal*, **123**, 106 (1976).
4. T. Saitoh, S. Matsubara, and S. Minagawa, *ibid.*, **123**, 403 (1976).
5. T. Saitoh, S. Matsubara, and S. Minagawa, *Jpn. J. Appl. Phys.*, **15**, 893 (1976).
6. T. I. Kamins, *J. Appl. Phys.*, **42**, 4357 (1971).
7. L. J. van der Pauw, *Philips Res. Rep.*, **13**, 1 (1958).
8. A. L. Fripp, *J. Appl. Phys.*, **46**, 1240 (1975).
9. J. Y. W. Seto, *ibid.*, **46**, 5247 (1975).
10. K. E. Brown, *Solid-State Electron.*, **17**, 507 (1974).
11. P. Rai-Choudhury and P. L. Hower, *ibid.*, **120**, 1761 (1973).
12. M. E. Cowher and T. O. Sedgwick, *This Journal*, **119**, 1565 (1972).

The Corrosion Resistance of Worn Tin-Nickel and Gold-Coated Tin-Nickel Alloy Electrodeposits

M. Antler and M. H. Drozdowicz

Bell Laboratories, Incorporated, Columbus, Ohio 43213

and C. F. Hornig[1]

Western Electric Company, North Andover, Massachusetts 01845

ABSTRACT

The corrosion resistance of electrodeposited tin-nickel alloy is due to a thin passive film, believed to be mainly tin oxide with some tin and nickel hydroxides. Thin electrodeposited gold on tin-nickel also is corrosion resistant and is of interest as an electric contact material. Presumably, a similar protective film forms on the tin-nickel layer exposed at pores in the gold. These observations have been made with deposits of both single phase (SnNi) and multiphase mixtures of SnNi, Ni_3Sn_4, and Ni_3Sn_2. The protective film can be removed by mechanical wear but will spontaneously reform, taking approximately 1500 hr in air at room temperature to reach a limiting thickness. However, the resistance of tin-nickel to many corrodents is restored in less time, after only a few days of aging. Similar observations of the development of passivity were made with freshly plated tin-nickel deposits on copper, with aged deposits on copper that were chemically etched immediately before exposure, and with newly fractured edges of tin-nickel electroforms. If the substrate is exposed by wear-through or by brittle fracture of tin-nickel the corrosion resistance of the material is determined by the substrate, and may not be restored by aging.

Electrodeposited tin-nickel alloy has considerable technological importance because of its corrosion resistance. This material is equiatomic, having the weight percent (w/o) composition, 65 Sn-35 Ni. It does not appear (1) in the equilibrium diagram for the binary tin-nickel system, which suggests that it is thermodynamically unstable. However, practical experience has shown it to be kinetically stable, even at somewhat elevated temperatures, say to 250°C (2, 3). Tin-nickel is ordinarily deposited in a single phase having the NiAs structure (2), although sound deposits that are multiphase mixtures of SnNi and the thermodynamically stable compounds (Ni_3Sn_4 and Ni_3Sn_2) have been made (4).

[1] Present address: Centronics, Hudson, New Hampshire 03051.

Key words: contact resistance, mechanical wear, oxidation, passivation, porosity.

A necessary condition for corrosion resistance when it is plated on a corrodible substrate is that the tin-nickel layer be free of transverse porosity. Corrosion resistance is shown also by gold platings on tin-nickel even when the gold is porous, for a galvanic couple does not persist at the gold to tin-nickel interface in a surprisingly wide range of atmospheres. This was established in recent studies (4) of the effects of simulated environmental pollutants on gold-plated single phase and multiphase deposits. Thus, tin-nickel alloy is a desirable underplate for gold in some electric contact applications (5) for it could permit thin (less than 1 μm), less costly gold deposits to serve in chemically aggressive atmospheres where thicker gold (6) is otherwise required. Tin-nickel without a gold overplate cannot be used in most cases because of the presence on its surface of a tough, electrically insulating film. The inertness of tin-nickel is attributable to this film (7, 8).

In exploring the contact properties of gold-plated tin-nickel, it is necessary to consider the effect on its corrosion resistance when either the gold layer or both the gold and tin-nickel layers are damaged. This could occur, for example, when it is used as a printed circuit board edge contact plating due to mechanical wear from engagement with a separable connector or from scratching caused by careless handling. There is little information on the self-healing characteristics in air of the protective oxide on tin-nickel. Indeed, the corrosion resistance of freshly plated or oxide-free tin-nickel is unknown.

The objective of this investigation was to determine whether worn tin-nickel surfaces can be corroded in a variety of environments including some in which tin-nickel has previously (4) been found to be inert. In this earlier work, the samples were prepared and stored in air between one and three months prior to exposure. In the present study, similar samples were mechanically damaged before exposure by scribing with a pointed diamond. The reactivity of damaged surfaces of tin-nickel plated copper, with and without a gold overplate, was determined as a function of time between scribing and exposure. Ancillary determinations were made of the corrosion resistance of freshly plated tin-nickel and of tin-nickel surfaces obtained by fracturing electroforms. The kinetics of contact resistance increase of chemically etched tin-nickel were also examined.

A model for wear and corrosion with gold-plated tin-nickel on a corrodible substrate such as copper is given in Fig. 1 and 2. This model postulates that wear of gold-plated tin-nickel would not lead to high contact resistance if metal loss occurs within the gold layer or if some gold is worn away, exposing only a small area of the underplate. It is apparent also that for exposed tin-nickel to not corrode, a protective film must form on it spontaneously and quickly. Exposure of a reactive substrate through wearing away of both gold and tin-nickel, or cracking of the gold-plated tin-nickel layer [both single (9) and multiphase tin-nickel electrodeposits are brittle] could be deleterious in a chemically severe environment.

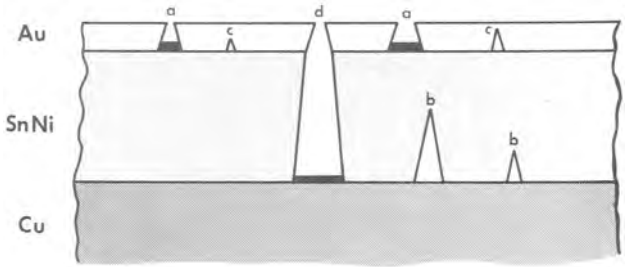


Fig. 1. Model of a plating of thin gold on tin-nickel alloy on a copper substrate: (a) designates random as-plated porosity in the gold to the underplate; (b) and (c) are internal pores in the tin-nickel and gold platings; (d) is the superposition of a pore in gold on one in tin-nickel to the substrate [adapted from Clarke and Chakrabarty (20)]. A film at the bottoms of the (a) pores inhibits corrosion of the plating. This film may be similar to that on bare tin-nickel electrodeposits. The film at the bottom of pore (d) is nonprotective. A desirable contact has few or no (d)-type pores. There is no (or little) oxide at the original interface between the gold and tin-nickel. (a)-type porosity is presumed to exist when the gold plating is thin.

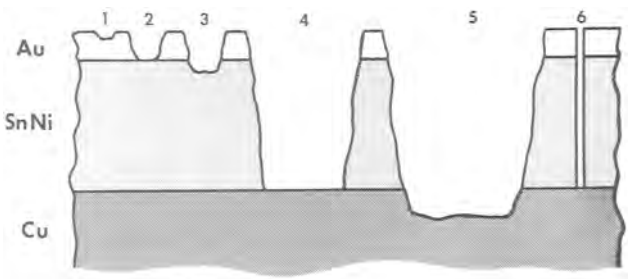


Fig. 2. Model of gold on tin-nickel plated contact after mechanical wear. Region 1 is loss of metal, localized to the gold layer; 2 is wear of gold to its interface with tin-nickel; 3 is loss of gold and tin-nickel localized to the tin-nickel layer; 4 is loss of gold and tin-nickel to its interface with copper; 5 is loss of gold, tin-nickel, and copper; and 6 is a crack through gold and tin-nickel which exposes the substrate. Condition 1 is acceptable; 2 and 3 are acceptable provided (a) that total area of material loss is small relative to the continuous gold surface in contact, (b) the sizes of individual 2 and 3 regions are small, and (c) a protective film quickly forms at the exposed surfaces of tin-nickel. Worn regions 4, 5 and cracks 6 in the plating which expose substrate would not be acceptable if they permit corrosion to occur at service conditions.

Experimental

Corrosion of Freshly Plated Tin-Nickel

Freshly plated tin-nickel can be hypothesized to be free of surface films, since it has been found to be solderable with tin-lead and mild fluxes, but this characteristic is lost if the sample is exposed in air for several hours prior to soldering (10).

The corrodibility of a tin-nickel deposit was determined by exposure for 1 hr to the vapors of concentrated (70%) HNO_3. This test is used to determine the porosity of gold on copper or nickel (11). A sample of 7 μm thick single phase (SnNi) tin-nickel plated from a fluoride bath (12) on polished copper was used, and exposure to HNO_3 commenced within 10 min of plating. This exposure produced a thin, discontinuous, light gray film on the surface. Elemental analysis of this film with an electron beam microprobe showed it to be free of copper, *i.e.*, the film was not caused by reaction with the substrate through pores in tin-nickel.

A comparison sample, plated with the first, was aged in air at 15% relative humidity (RH) for 8 days and then exposed to HNO_3 vapor in the same way. In this case, the surface on visual inspection was unattacked.

Corrosion of Fracture Surfaces of Tin-Nickel Electroforms

Additional experiments to determine whether tin-nickel alloy electrodeposits free of surface films can be corroded were made with electroformed material. Tin-nickel was plated 1.5 mm thick onto a copper tube, 4.8 mm in diameter and 33 mm long, from a fluoride bath (12). The copper was dissolved in nitric acid, leaving an intact hollow tin-nickel cylinder which then was broken into several pieces. After 3 months the pieces were cleaved again and exposed (11) within 1 min in closed vessels to the vapors of concentrated HNO_3 or to 10% SO_2 at 85% RH.

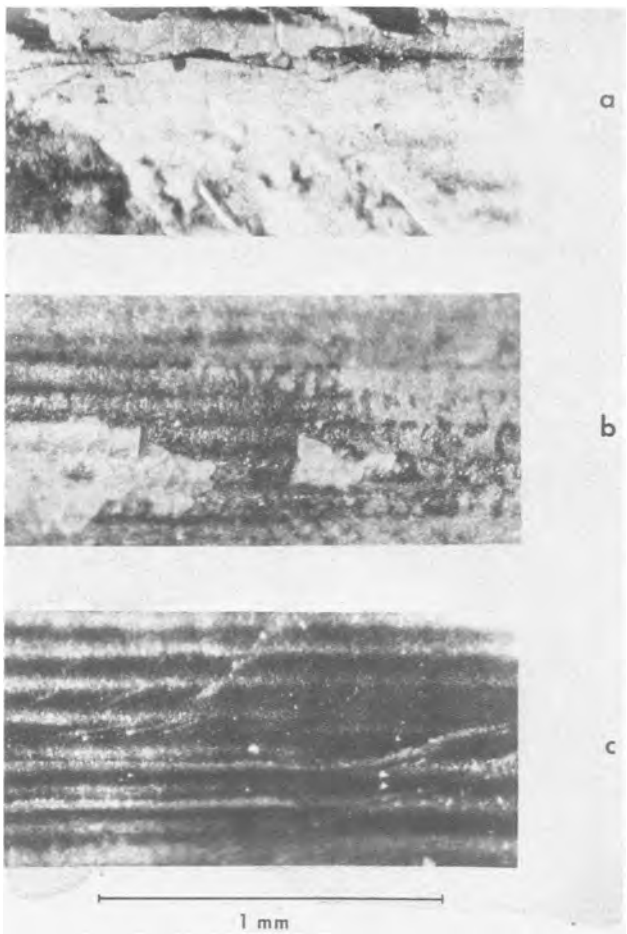


Fig. 3. Fracture surfaces of tin-nickel electroforms. (a) exposed to HNO_3 vapor for 1 hr immediately after fracture; (b) exposed to 10% SO_2 at 85% RH for 22 hr immediately after fracture; (c), same as (b), with 3 month delay between fracture and exposure. (a) and (b) are severely corroded, (c) is not corroded. Note layered structure of fractured surface. Original magnification, 70×.

It was found that the freshly fractured edges of tin-nickel were severely corroded, while the 3 month air-exposed fracture edges and the original tin-nickel electroformed surfaces were unaffected, as shown in Fig. 3. It was further established that there was visibly less corrosion on fracture edges that had been aged in air for 7 days compared to edges aged 1 day before exposure to the HNO_3 and SO_2 environments. Aging before exposure was in clean laboratory air at 25-60% RH. Additional experiments showed that 1 day air-aged fracture edges were moderately corroded when subsequently exposed at 88% RH for 27 days, while fractured samples aged for 1 week before exposure were unattacked. Other tin-nickel fracture edges aged 1 and 7 days were unchanged over flowers of sulfur for 1 week at 50°C and 85% RH. All observations were made at 70×.

It has been previously found (4) that air-aged electrodeposits of tin-nickel and porous gold plate on tin-nickel are unattacked by HNO_3 vapor, SO_2, and sulfur. Thus, both freshly fractured and freshly plated tin-nickel are corroded by some chemicals, but its usual corrosion resistance develops on aging in air. This conclusion is developed in greater detail in this paper.

Corrosion of Worn Tin-Nickel and Gold-Plated Tin-Nickel

Experimental.—Preparation of samples.—Electropolished OFHC[1] copper panels 3.8 cm square by 0.16 cm thick were plated with 12 μm of tin-nickel from a fluoride bath (12), and some of the specimens were overplated with 0.43 μm of gold from a cobalt-containing buffered acid $KAu(CN)_2$ solution. The tin-nickel samples were immersed in 18% HCl for 1 min prior to gold plating. This treatment, called "activation," common in commercial plating processes, is intended to assure good adhesion of the gold by removing any oxide that may be present on the tin-nickel surface. The cobalt content of the gold plate was 0.25 w/o. The tin content of the tin-nickel deposit was 65.2 w/o which is close to the theoretical value for the equiatomic alloy. X-ray diffraction analysis showed the tin-nickel to be single phase, having the expected NiAs structure (2). The porosity of the tin-nickel layer to the substrate was low, much less than 1 pore/cm² (except at the edges of the panels) as determined by exposure to HNO_3 vapor, SO_2, or electrography. The porosity of the gold overplating is unknown, but is presumed to be high because of its small thickness. Approximately one month elapsed between plating of the panels and the wear and electrography experiments.

Wear.—A wear machine was built which permits the sample to be moved with a weighted stylus pressed against it. The stylus was a 90° conical diamond having a rounded tip with a radius of 0.1 mm. Sliding velocity was 0.25 cm/sec. Four parallel tracks were made on each panel, 2.7-3.0 mm apart and 7 mm long, at loads of 20, 30, 50, and 100g for the tin-nickel plated samples, and at 30, 50, 100, and 200g for samples having a gold overplate.

A second set of wear tracks were made with samples lightly coated with a U.S.P. mineral white oil. This lubricant was chosen because of its purity and inertness. The appearance and reactivity to corrodents after removing the lubricant with warm reagent grade 1,1,1-trichloroethane was identical to wear without lubrication.

Additional sets of tracks were made on new areas of each sample after 23 and again after 6 more days. The panels were then aged another day before exposure to the environments numbered 1-5 in Table I and II.

[1] Trademark of American Metal Climax, Incorporated.

Table I. Corrosion of worn tin-nickel plating*,†

Environment	Temp, °C	% RH	Time of exposure	Aging time in air before exposure (days)		
				1	7	30
1. HNO_3 vapor (conc sol.)	25		1 hr	D	D	A
2. 10% SO_2	25	85	24 hr	D	D	A
3. Air	25	88	27 days	B	B	A
4. Sulfur vapor	50	85	7 days	A	A	A
5. Out-of-doors, sheltered, Columbus, Ohio	−10 to 15 (est.)	45 to 100 (est.)	30 days	A	A	A
				27	33	57
6. Electroplating plant; proximate to copper- and gold-plating tanks	25	50-70 (est.)	55 days	B	B	A
7. Factory; light assembly area	25	10-30 (est.)	55 days	A	A	A

* Worn at 20 and 30g. Results identical at both loads.
† The severity of corrosion is expressed on a scale of A-D, based on visual and microscopic examination of the panels after exposure. A, no corrosion at 460×; B, corrosion observed at 460×; C, corrosion observed at 70×; D, corrosion evident with unaided eye.

Table II. Corrosion of worn gold on tin-nickel plating*

Environment	Temp, °C	% RH	Time of exposure	Aging time in air before exposure (days) Worn at 30g			Worn at 50g		
				1	7	30	1	7	30
1. HNO_3 vapor (conc sol.)	25		1 hr	A	A	A	B	B	A
2. 10% SO_2	25	85	24 hr	B	B	A	C	C	A
3. Air	25	88	27 days	A	A	A	A	A	A
4. Sulfur vapor	50	85	7 days	A	A	A	A	A	A
5. Out-of-doors, sheltered, Columbus, Ohio	−10 to 15 (est.)	45 to 100 (est.)	30 days	A	A	A	A	A	A
				27	33	57	27	33	57
6. Electroplating plant, proximate to copper- and gold-plating tanks	25	50-70 (est.)	55 days	B	B	A	B	B	A
7. Factory, light assembly area	25	10-30 (est.)	55 days	A	A	A	A	A	A

* Severity of corrosion expressed in scale of A (none)-D (evident to unaided eye). See footnote † of Table I.

Thus, the ages of wear tracks were 1, 7, and 30 days on exposure. In the cases of environments 6-7 in the tables, the ages of the tracks were 27, 33, and 57 days. Aging was conducted in clean laboratory air that varied from 25-60% RH. Individual panels with tin-nickel and gold on tin-nickel platings were prepared for exposure in each environment.

Corrosion studies.—Corrosion testing was done in both artificial and field environments, described in Table I and II. Exposure to HNO_3 vapor was over the concentrated acid in a desiccator (11). The 10% SO_2 test was over a mixture of $Na_2S_2O_3$, H_2SO_4, and water (11). The 88% RH test was made with a slurry of $BaCl_2$ in water which provided constant humidity. The sulfur test was made by suspending the samples over flowers of sulfur and a constant humidity solution using KNO_3. The chamber was held in an oven at 50°C for 1 week.

The out-of-doors exposure was in a louvered cabinet for 30 days during November-December 1975. The surfaces were observed to be sometimes wet during rapid temperature changes during this test. Factory exposures were in an electroplating plant and in a mechanical assembly area.

Electrographic testing.—In addition to the corrosion exposures, the samples were tested for porosity by a direct printing electrographic method (13). Dye transfer paper was soaked for 30 min in a solution of 20 g/liter of the disodium salt of dimethylglyoxime and 20 g/liter of NaCl. Applied pressure was approximately 50 kg/cm² (700 psi) and current was passed through the specimen and paper for 1 min at a constant voltage of 2.0V. The appearance of red in the electrograph indicates nickel, and green signifies copper. The prints were examined at 10×.

Copper was present in the wear tracks of coupons at the two higher loads, 50 and 100g for tin-nickel, and 100 and 200g for gold-plated tin-nickel. The green lines in the electrographs were continuous in tracks at the highest loads, and nearly continuous at the second highest loads. There was no red in the tracks. As shown later, the appearance of copper originated in minute cracks through the gold and tin-nickel layers produced by the wear experiment.

The electrograph of the large unworn regions of the tin-nickel plated panel was very faint pink. Thus, aged tin-nickel alloy is not significantly affected in electrographic testing by this procedure.

To determine whether the nonreactivity of electroplated tin-nickel was due to its protective surface film, a portion of a tin-nickel panel was lightly abraded with 600 grit metallographic paper and immediately electrographed. There was reaction, with the red coloration indicating nickel.

Confirmation of this result was obtained by electrographic testing a freshly plated tin-nickel deposit. A copper panel having 7 μm of tin-nickel was electrographed within 10 min of plating. A uniform bright red color appeared in the print except for a few, scattered, more deeply colored, small red spots. Thus, unaged tin-nickel is attacked in the electrographic test. a result consistent with the experiments using aged and freshly abraded samples if it is assumed that an air-formed protective film is responsible for the chemical inertness of tin-nickel.

Results of corrosion studies and discussion.—*Wear.*—Figure 4 shows wear tracks on tin-nickel and gold-plated tin-nickel panels. Deposit adhesion was excellent at both the tin-nickel to copper and the gold to tin-nickel interfaces.

Tin-nickel shows some plastic deformation in the wear tracks. At 50g there is slight cracking, and at 100g cracks appear at the sides of the track. From the electrographic study, the cracks in tin-nickel extend to

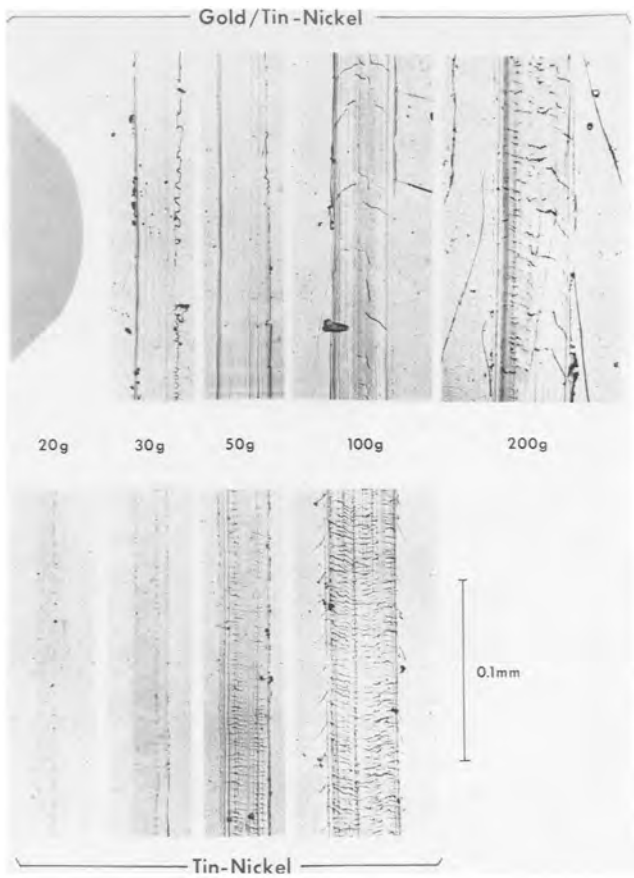


Fig. 4. Wear tracks in 12 μm thick tin-nickel electrodeposits on copper with and without a 0.43 μm thick gold overplate. Made with a diamond at loads from 20 to 200g. Shape and dimensions of conical diamond with a rounded end at top left (to scale). Direction of movement of samples, away from reader. Cracks in the platings are evident at 50 and 100g for tin-nickel and 100 and 200g for gold-plated tin-nickel. Original magnification, 460×.

the substrate. The orientation of the cracks is typical of brittle fracture wear (14) with a solid having a small tensile compared to its compressive strength.

There is no cracking at 30 and 50g with gold-plated tin-nickel, but at 100 and 200g cracks are plainly evident. The crack incidence at 100g is less with gold-plated tin-nickel compared to tin-nickel alone, but the individual cracks are larger. The electrographs show that the cracks at 100 and 200g extend to substrate copper, and that no copper is exposed in the tracks made at 30 and 50g.

Another feature of Fig. 4 concerns the removal of gold from the tin-nickel plating. Examination at 460× clearly reveals that gold has been worn from the wear tracks to an increasing degree with increasing load. This varies from none at 30g to about 25%, 70%, and 90% at 50, 100, and 200g.

The model of surface damage in Fig. 2 is therefore reasonable, except that there is no evidence from this work of significant tin-nickel removal by a smooth stylus at the loads used.

Reactivity to corrodents.—The reactivity of worn surfaces to various environments, summarized in Table I and II, is based on visual and microscopic examinations. Figures 5, 6, and 7 are typical observations.

Figure 5 is a worn tin-nickel plated panel after exposure to 10% SO_2. Corrosion is severe, especially at 50 and 100g where copper was exposed, except for tracks 11 and 12 in the photograph. With the latter, which were uncorroded, surface damage is confined to the tin-nickel layer and 30 days elapsed between wear and exposure.

Figure 6 illustrates worn gold-plated tin-nickel at 30g after SO_2 exposure. The beneficial effect of air



Fig. 5. Worn thick tin-nickel electrodeposit on copper after exposure to 10% SO_2 at 85% RH for 24 hr. Panel hung vertically. Upper row, unlubricated wear. Lower row, worn after coating with mineral oil. Lubricant removed after wear before each aging interval and before SO_2 exposure. Loads for tracks 1, 5, 9: 100g; 2, 6, 10: 50g; 3, 7, 11: 30g; 4, 8, 12: 20g. Groups of wear tracks were aged in air before SO_2 exposure as follows: 1-4, 1 day; 5-8, 7 days; 9-12, 30 days. All tracks display corrosion films except 11 and 12. Note that corrosion in tracks 3, 4, 7, and 8 is of SnNi, and in tracks 1, 2, 5, 6, 9, and 10 is of both substrate copper and tin-nickel. Original magnification, 2×.

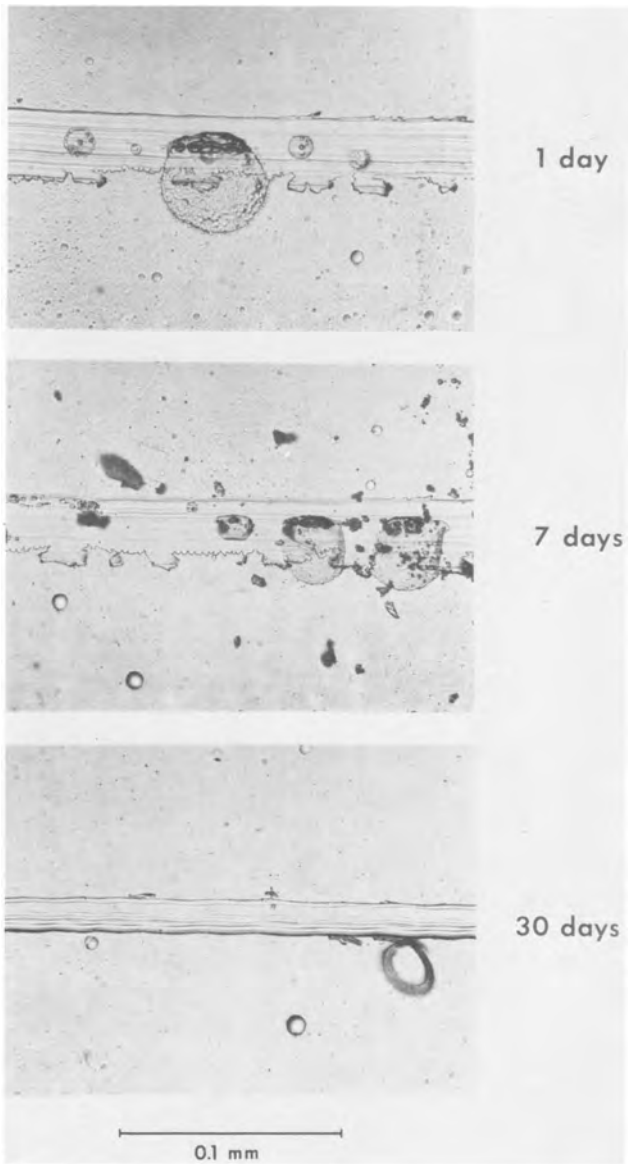


Fig. 6. Worn surface of thick tin-nickel electrodeposit plated with 0.43 μm of gold. Load: 30g. Exposed to 10% SO_2 at 85% RH for 24 hr. Aged in air before exposure for the lengths of time indicated. Original magnification, 460×.

aging before exposure is seen; there is no corrosion after 30 days, while corrosion occurs after 1 and 7 days. The volume of corrosion produced is greater in wear tracks made at 50g (Table II), because more tin-nickel was exposed than at 30g.

Figure 7 shows wear tracks made at 20g on the tin-nickel plated panel after exposure to HNO_3 vapor. There is corrosion in wear tracks after 1 and 7 days of aging prior to HNO_3 treatment. The extent of corrosion diminishes with aging, and after 30 days a film can no longer be detected on the surface. The severity of attack is less than with SO_2.

Many of the environments were corrosive to exposed copper in the wear tracks at the higher loads, as shown with SO_2 in Fig. 5. Copper does not possess the marked passivating tendency of tin-nickel.

Kinetics of Repair of Passive Film on Tin-Nickel from Contact Resistance Determinations

It is possible to determine the growth of an insulating film on a metal surface by monitoring the increase in contact resistance with time. A method for doing this has been described previously (15). Contact resistance at 100g was determined without wipe with a smooth hemispherically ended solid gold probe of 3.2

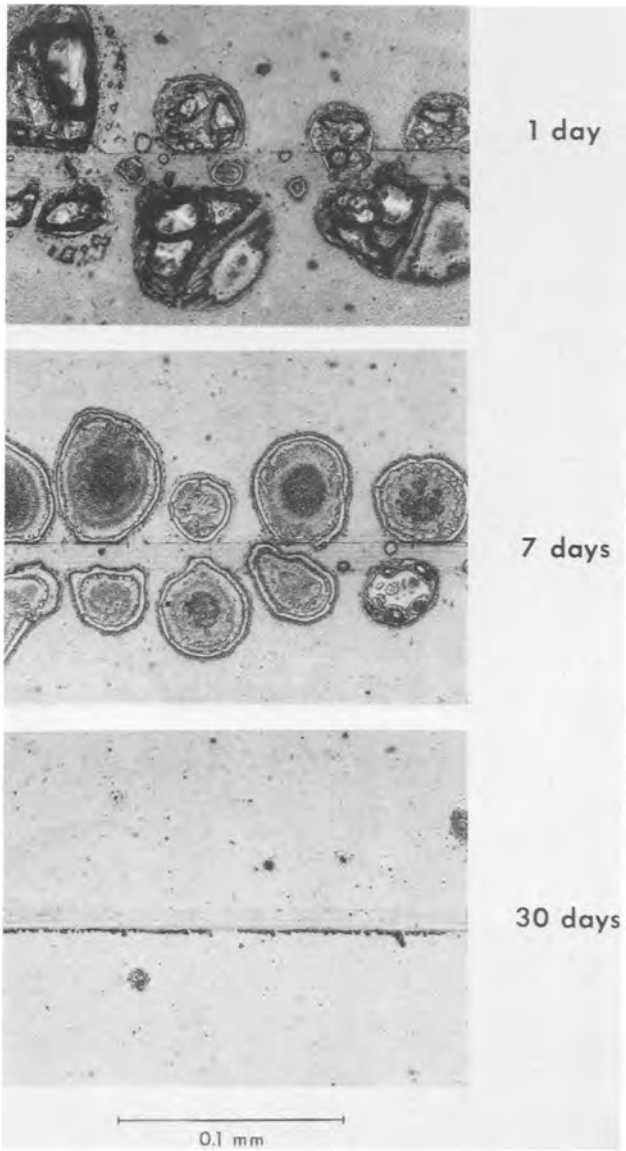


Fig. 7. Worn surface of thick tin-nickel electrodeposit after exposure to HNO_3 vapor for 1 hr. Load: 20g. Aged in air before exposure for the lengths of time indicated. Severity of corrosion diminishes with aging time. Original magnification, 460×.

mm diameter and an applied potential of 28 mV maximum. Since the contact resistance of a film-covered surface is strongly dependent on its roughness (16), a chemical method rather than mechanical wear was employed for film removal. A degreased tin-nickel plated panel was immersed in 18% HCl (1:1 mixture of water and concentrated HCl, sp gr = 1.18) for 1 min, during which there was gassing at the surface, thoroughly washed in distilled water, and dried in a stream of nitrogen. The surfaces were not visibly changed by etching. This procedure is used to activate tin-nickel prior to gold plating (see above).

The sample was probed at nine places from 0 to 200g with continuous measurement of contact resistance. Probing commenced within 6 min of etching, and was completed in 15 min. The median contact resistances at 50, 100, and 200g were 8.4, 5.4, and 3.3 mΩ. An auxiliary measurement of the contact resistance of a freshly plated tin-nickel sample, obtained within minutes of plating, showed it to be comparably low. Aging at 15-20% RH was continued to a total elapsed time of 1 hr from etching, and the median contact resistances rose to 14, 8.2, and 5.0 mΩ at the three loads. Aging continued in this environment for 1500 hr (*ca.* 63 days) with periodic probing.

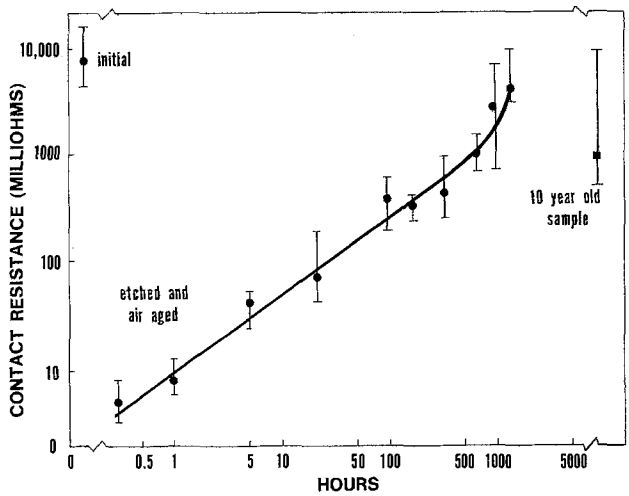


Fig. 8. ● Median contact resistance of smooth tin-nickel electrodeposit, 12 μm thick, on copper. Initial values are for electroplated sample before etching in 18% HCl. ■ Median contact resistance of 10 year old tin-nickel electrodeposit, 15 μm thick on brass. Probed at 100g with a hemispherically ended gold rod. Nine measurement at each time interval. The smallest and largest values are indicated at the ends of the vertical bars.

Figure 8 is a plot of contact resistance at 100g against time. The contact resistance of the freshly etched panel was in the range for clean metals, and increased steadily with time, approximating the value of the sample prior to etching in 1500 hr. The panel used for the contact resistance study was 3 months (*ca.* 2100 hr) old when etched.

Also shown is the contact resistance of a 10 year old sample of single phase tin-nickel 15 μm thick, plated on polished brass. Small differences in method of sample preparation probably account for its contact resistance being slightly lower than that of the 3 month old ("initial") sample of this study.

This trend of contact resistance is consistent with a mechanism of film growth which continues slowly, over a period of weeks, to some limiting value. The thickness has been estimated to be about 30Å by the electron spectroscopy for chemical analysis (ESCA) method combined with depth profiling and is believed to consist of tin oxide mixed with tin and nickel hydroxides (17). Adherent, compact films form a barrier between air and the metal, and grow at a diminishing rate with time, often following logarithmic kinetics near room temperature (18). The increase of contact resistance on aging parallels the increase in corrosion resistance of freshly plated tin-nickel, tin-nickel fracture surfaces, and tin-nickel whose passive surface oxide has been removed by mechanical wear, and occurs in the same time frame. Thus, development of full passivity to severe corrodents may take 30-60 days in air at room temperature (Table I), as long as it takes for contact resistance to reach a limiting value.

Conclusions

Tin-nickel and thin (porous) gold-plated tin-nickel electrodeposits on copper have earlier (4) been found to be corrosion resistant to a wide variety of synthetic polluted atmospheres. These findings apply to both the single phase SnNi material and to a multiphase mixture of SnNi, Ni_3Sn_4, and Ni_3Sn_2. The present work shows that this passivity is not an inherent characteristic of the material, but is due to a protective film on the tin-nickel surface which develops as the freshly plated deposit is aged in air. If this film is removed by wear or by chemical etching, it will spontaneously reform. A similar film forms on surfaces created by fracturing tin-nickel electrodeposits. In indoor environments, it may take approximately 1500 hr for the equilibrium film to be achieved. This film has the same

contact resistance characteristics as that on surfaces stored in the same environment much longer times.

The resistance to corrosion of tin-nickel and gold-plated tin-nickel increases with time of aging, but even in a few days after removing the passive film a large measure of the corrosion resistance of long aged tin-nickel is restored.

In this study wear was produced by scribing the samples with a sharply pointed diamond. This simulates the sliding action of an opposed contact of a hard material having sharp edges and possibly of loose foreign hard particles between the contacts which could contaminate the surface during handling. In conventional electrical contact applications with gold-plated tin-nickel, the mating member is a precious metal (usually gold or gold alloy) rounded contact generally having a much larger radius of curvature than the diamond. Adhesive wear with wiping contacts occurs in that case rather than the ploughing wear of these experiments. Contact lubricants can be used to reduce the severity of adhesive wear (19). The brittle fracture of tin-nickel observed in this work is not expected to occur at such conditions except at high loads with deformable substrates.

In testing for surface damage of gold-plated tin-nickel in sliding electric contact applications by exposure to corrosive gases such as HNO_3 vapor, evidence of wear-through of the gold layer to tin-nickel is dependent on the time between wear and exposure. That is, conventional "porosity tests" for wear, which are widely used for gold on corrodible substrates such as copper or nickel, can be misleading unless the self-healing characteristics of exposed tin-nickel surfaces are recognized.

Acknowledgments

The cooperation of P. T. Woodberry, E. T. Ratliff, and the Tin Research Institute, Incorporated is acknowledged for preparing some of the samples used in this study.

Manuscript submitted Nov. 23, 1976; revised manuscript received March 9, 1977.

Any discussion of this paper will appear in a Discussion Section to be published in the June 1978 JOURNAL. All discussions for the June 1978 Discussion Section should be submitted by Feb. 1, 1978.

Publication costs of this article were assisted by Bell Laboratories.

REFERENCES

1. M. Hansen, "Constitution of Binary Alloys," p. 1042, McGraw-Hill Book Co., New York (1958).
2. P. K. Dutta and M. Clarke, *Trans. Inst. Met. Finish.*, **46**, 20 (1968).
3. J. E. Bennett and H. G. Tompkins, *This Journal*, **123**, 999 (1976).
4. M. Antler, M. Feder, C. F. Horning, and J. Bohland, *Plating and Surface Finish.*, **63**, 30 (1976).
5. M. Antler, *IEEE Trans. Parts, Hybrids, Packaging*, **php-11**, 216 (1975).
6. M. Antler, in "Gold Plating Technology," F. H. Reid and W. Goldie, Editors, chap. 36, pp. 478-494, Electrochemical Publications, Ltd., Ayr, Scotland (1974).
7. T. P. Hoar, M. Talerman, and E. Trad, *Nature Phys. Sci.*, **244**, 41 (1973).
8. H. G. Tompkins and J. E. Bennett, *This Journal*, **123**, 1003 (1976).
9. V. R. Ramanathan, *Trans. Inst. Met. Finish*, **34**, 1 (1957).
10. G. C. Wilson, *ibid.*, **50**, 109 (1972).
11. ASTM B583-73, "Standard Methods of Test for Porosity in Gold Coatings on Metal Substrates" (1973).
12. "Electroplated Tin-Nickel Alloy," Tin Research Institute, Publication 235, 4th ed. (1962).
13. H. J. Noonan, *Plating*, **53**, 461 (1966).
14. E. Rabinowicz, "Friction and Wear of Materials," p. 194, John Wiley & Sons, Inc., New York (1965).
15. M. Antler, in "Gold Plating Technology," F. H. Reid and W. Goldie, Editors, chap. 26 pp. 334-344, Electrochemical Publications, Ltd., Ayr, Scotland (1974).
16. M. Antler, *Plating*, **56**, 1139 (1969).
17. J. H. Thomas, III and S. P. Sharma, *J. Vac. Sci. Technol.* Paper accepted for publication.
18. L. L. Shreir, "Corrosion," Vol. 1, pp. 1-165, John Wiley & Sons, Inc., New York (1963).
19. M. Antler, *IEEE Trans. Parts, Hybrids, Packaging*, **php-9**, 4 (1973).
20. M. Clarke and A. M. Chakrabarty, *Trans. Inst. Met. Finish*, **50**, 11 (1972).

Emission from Triplet State in Electrochemiluminescence of Pyrene at Low Temperatures

Takeshi Suminaga and Sohachiro Hayakawa

Department of Applied Physics, Tokyo Institute of Technology, Ookayama, Meguro-ku, Tokyo, Japan

ABSTRACT

The green emission from pyrene excimer has been observed usually in the electrochemiluminescence (ECL) of pyrene. The red emission, however, is observed additionally at low concentration. The ECL of pyrene at low concentration in dimethylformamide (DMF) is investigated at various temperatures between room temperature and −51°C. The red emission with a maximum about at 600 nm is observed predominantly at low temperature, and it has almost the same spectrum as the phosphorescence of pyrene. The current-potential curves and emission-potential curves are measured for these cases. The red ECL can be concluded to be the phosphorescence from the triplet state of pyrene and a probable mechanism is proposed for it.

The ECL of pyrene results mainly from the direct excimer formation via anion-cation annihilation (1-3). The ECL's of rubrene, perylene, and 9-10 diphenylanthracene are emitted from either the excited singlet state or excimer (4-5). Recently the possibility of the triplet-triplet annihilation was proposed (6) in the ECL's of the above-mentioned compounds. Nevertheless the emission from the excited triplet state to the ground state was hardly observed. Sano (7) reported that the red chemiluminescence in dimethylformamide was probably the phosphorescence of pyrene through comparison with the phosphorescence of pyrene in a rigid glass. Nakaharai (8) confirmed the

Key words: electrochemiluminescence, pyrene, triplet state.

prominence of red chemiluminescence having a maximum at 600 nm for solutions of lower concentration of pyrene. Though the emission was predicted to become stronger at lower temperatures (9), no work has been reported on the measurement of temperature effect for ECL of pyrene. The purpose of this work is to obtain some information on the mechanism of this red chemiluminescence of pyrene by measurements at low temperatures.

Experimental

Pyrene was recrystallized carefully from benzene solution. Tetra-n-butylammonium bromide (TBAB) to be used as a supporting electrolyte was recrystallized from ethyl-acetate solutions. The concentration of pyrene was 1 mM and that of TBAB was 10 mM in all experiments. The cell used for ECL measurement was made of Pyrex glass. A Pt disk (3 mm diam) was used as a working electrode and Ag wire was used as a reference electrode. The temperature of the cell was reduced by cooled N_2 gas through a Cu pipe which surrounded the cell. The temperature range for measurements was between room temperature and about −51°C and the solvent was frozen below −59°C. The emission intensity of ECL was measured with a Phillips 5-6 AVP photomultiplier through color filters, and the ECL spectrum was obtained by the use of OCLI rotational filters. The cyclic voltammograms and emission *vs.* potential curves were recorded on an X-Y recorder at various temperatures.

Results

The cyclic voltammogram of pyrene at low temperatures and the emission *vs.* potential curves from room temperature to −51°C are presented in Fig. 1. The former curves showed only slight changes as the temperature changed, and therefore only one curve is shown in the figure. As the temperature falls, the emission-potential curve separates into two parts, one of which is the emission at potentials below −2.8V (*vs.* Ag) (denoted by emission 1 hereafter) and the other of which appears at about 0V (emission 2).

As the temperature falls the emission 2 becomes stronger than that of 1, and the total emission intensity increases at first, reaches a maximum at about −30°C, and then decreases for lower temperatures. The dependence of the direction of the potential sweep is presented in Fig. 2.

No emission is observed in the case of anodic potential sweep. The emission can be observed only with the cathodic potential sweep and the emission intensity is independent of the anodic sweep before the cathodic sweep. Figure 3 shows the emission *vs.* potential curves in the case of a rectangular potential sweep. Figure 4 shows the ECL spectrum of pyrene at a low temperature. This is the spectrum of emission 1, and that of emission 2 cannot be observed.

But the shapes of emission *vs.* potential curves, measured through Toshiba glass filters VO-54 (cut off below 540 nm) and VR-60 (cut off below 600 nm), are almost the same and the intensity of the latter is about a half of the former.

This indicates that emission 2 has the same spectrum as that of the emission 1.

Discussion

The ECL of pyrene is considered mainly to result from the direct formation of excimer which gives a green emission spectrum with a maximum at about 480 nm. However, the red emission was observed at low concentration in this work and its spectrum has a maximum at about 600 nm. This emission may be concluded to be the phosphorescence from the triplet state of pyrene according to the following four reasons.

(*i*) In case the excited state is generated due to the anion-cation annihilation, the excited triplet state may be generated quite probably.

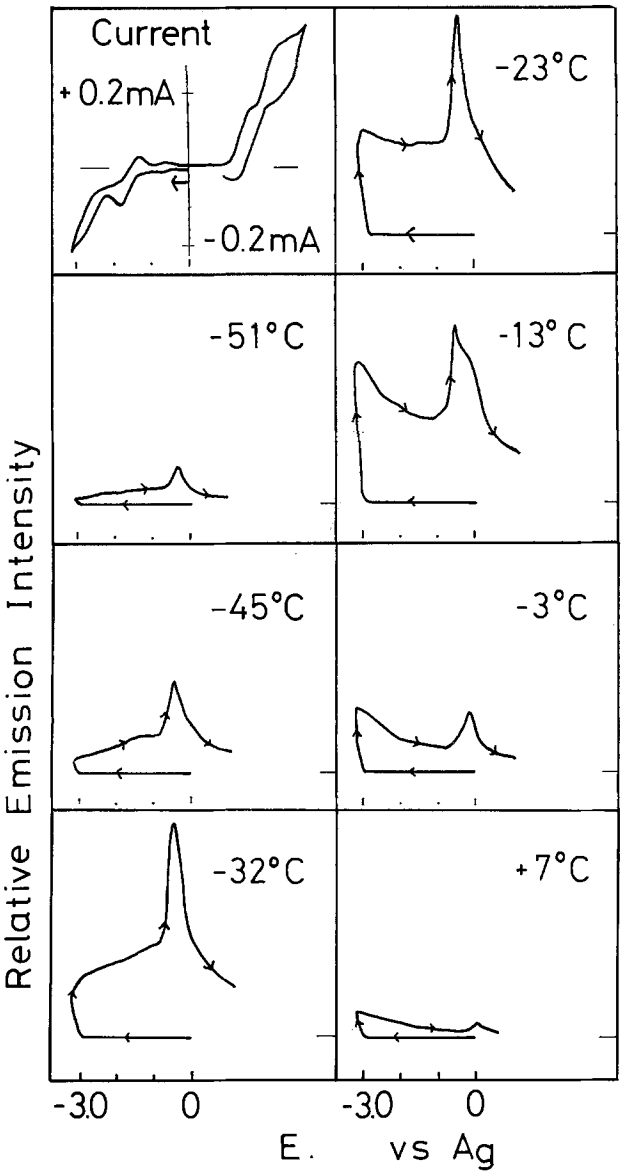


Fig. 1. Relation between the emission intensity and the applied triangular potential: pyrene 1 mM; TBAB 10 mM in DMF; scan rate 100 mV/sec.

(*ii*) The spectrum of red emission was found in the wavelength range from 570 to 660 nm with a maximum at about 600 nm which corresponded to the phosphorescence spectrum measured for pyrene in rigid glass by Hochstrasser (10).

(*iii*) No fluorescent material having a spectrum in the similar wavelength range (~600 nm) was observed after the electrolysis.

(*iv*) The strong emission observed in solutions with lower concentrations indicates that the triplet state of pyrene is not easily quenched at lower concentrations. It shows the case of pyrene to be somewhat like the case of rubrene in which both anion and cation radicals work as a quencher for the triplet state of rubrene.

Mechanism of emission.—The coexistence of anion and cation radicals of pyrene may be not necessary in the processes. Only existence of pyrene is necessary for the red emission because it can be observed only with the cathodic potential sweep.

Figure 3 shows that the relationship between the emission and the applied potential is independent of the electrolysis at −1.8V or +1.6V (in the region where anion or cation radicals of pyrene are produced) before the electrolysis at −3.0V. Then it is assumed that dianions of pyrene are produced at −3.0V. Two kinds

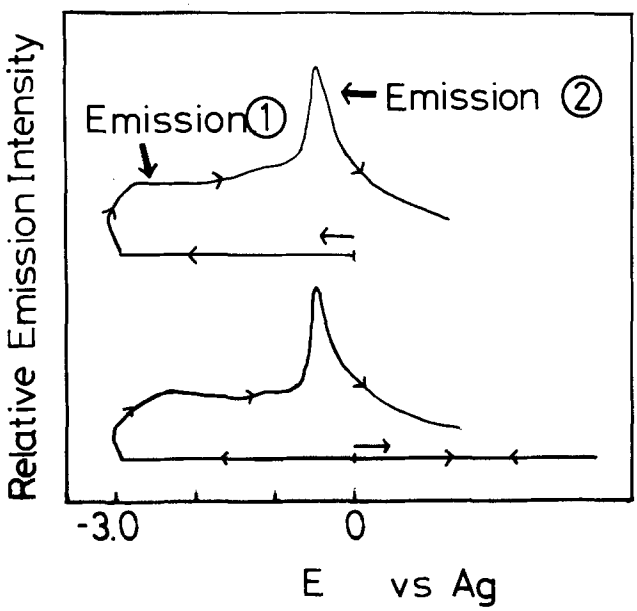


Fig. 2. Difference in the direction of potential sweep at −34°C; scan rate 100 mV/sec.

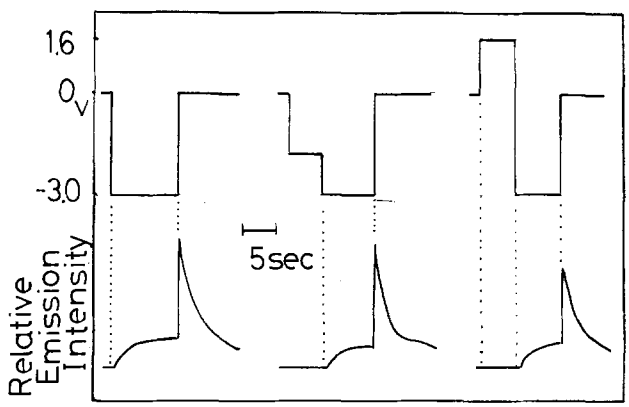


Fig. 3. Rectangular potential sweep electrolysis at −45°C

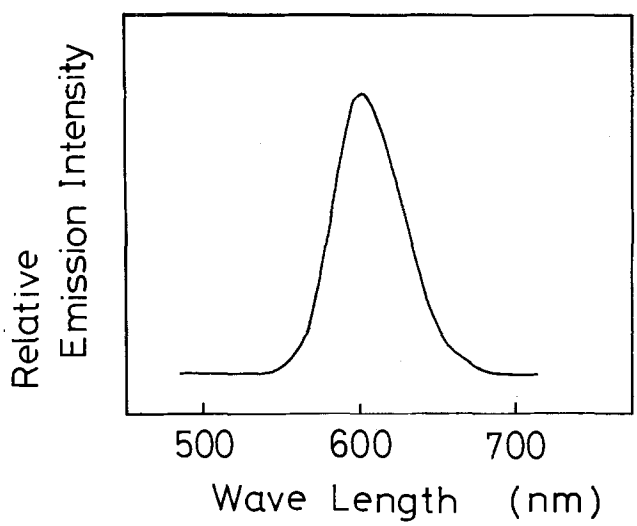


Fig. 4. ECL spectrum of pyrene in DMF at low temperature

of oxidants are proposed to exist because the cation radical of pyrene is apparently not useful as the oxidant for dianion of pyrene. One of them is produced depending on the potential and the other is not so. After the production of dianion of pyrene (P^{2-}) in the potential region near −3.0V, the following reaction occurs due to the first oxidant D

$$P + 2e^- \rightarrow P^{2-} \quad [1]$$

$$P^{2-} + 2D \xrightarrow{k_1} {}^3P^* + 2D^- \quad [2]$$

$$^3P^* \rightarrow P + h\nu \quad [3]$$

The emission in the reaction [3] is denoted by 1 in the figures. But in the region near 0V, another oxidant A reacts with the remaining P^{2-}. The reaction of [4] is estimated to be a rapid one with higher efficiency than the reaction [2]

$$P^{2-} + 2A \xrightarrow{k_2} {}^3P^* + 2A^- \quad [4]$$

$$^3P^* \rightarrow P + h\nu \quad [5]$$

The emission in the reaction [5] may correspond to emission 2 denoted in the figures.

Temperature effect.—As the temperature decreases, the peak of emission 2 becomes stronger than that of 1. This is explained in terms of increased viscosity and decreased rate constant k_1 in reaction [2]. The change of total emission intensity can be explained as follows. As the temperature becomes lower, the emission efficiency of $^3P^*$ increases but the rate constants k_1 and k_2 (reaction [4]) decrease. It, however, is acceptable that at first the former may give larger influence on the ECL than the latter but that next the latter may start to give larger influence than the former. Thus the total emission intensity may go through a maximum. Next the temperature effect of emission 2 will be considered on following reactions

$$P^{2-} + 2A \rightarrow {}^3P^* + 2A^-$$

$$^3P^* \xrightarrow{f_1} P + h\nu$$

$$^3P^* \xrightarrow{f_2\exp(-E/RT)} P \quad \text{(quenching process)}$$

$n(T)$ shows the concentration of $^3P^*$ at temperature T, the emission intensity $I(T)$ is given by

$$I(T) = \alpha n(T) \frac{f_1}{f_1 + f_2 \exp(-E/RT)}$$

$$I\infty = \alpha n\infty \quad \text{at large T}$$

$$\frac{I\infty}{I(T)} = \frac{n\infty}{n(T)} \left\{ 1 + \frac{f_2 \exp(-E/RT)}{f_1} \right\}$$

if $f_2 \exp(-E/RT) >> f_1$

$$\log I(T) = E/RT + \log n(T)/n\infty + \text{constant}$$

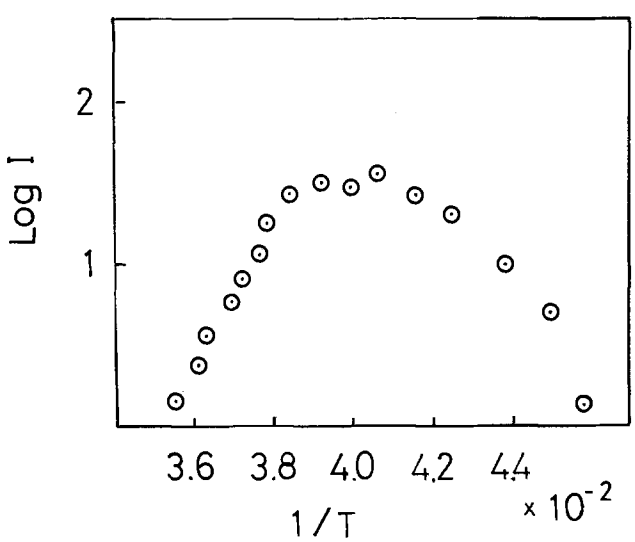


Fig. 5. Temperature effect of the emission 2

The effect of the second term of $1/T$ comes to be predominant at first and $I(T)$ increases as the temperature decreases. But that of the third logarithm term comes predominant in the lower temperature and $I(T)$ decreases through a maximum. The explanation may give temperature dependency like shown in Fig. 5.

Manuscript submitted Dec. 14, 1976; revised manuscript received March 11, 1977.

Any discussion of this paper will appear in a Discussion Section to be published in the June 1978 JOURNAL. All discussions for the June 1978 Discussion Section should be submitted by Feb. 1, 1978.

Publication costs of this article were assisted by the Tokyo Institute of Technology.

REFERENCES

1. B. Fleet, *J. Electroanal. Chem.*, **30**, 115 (1971).
2. J. T. Maloy, *J. Am. Chem. Soc.*, **93**, 5968 (1971).
3. K. Honda, *J. Electroanal. Chem.*, **47**, 116 (1973).
4. D. M. Hercules, *J. Am. Chem. Soc.*, **88**, 4578 (1966).
5. C. A. Parker, *Trans. Faraday Soc.*, **63**, 2618 (1967).
6. T. C. Werner, *J. Am. Chem. Soc.*, **92**, 763 (1970).
7. M. Sano, *Bull. Chem. Soc. Jpn.*, **41**, 1490 (1968).
8. S. Nakaharai, Private communication.
9. T. Matsumoto, *Bull. Chem. Soc. Jpn.*, **46**, 369 (1973).
10. R. M. Hochstrasser, *J. Chem. Phys.*, **40**, 1041 (1964).

Cerium and Terbium Luminescence in $ThOF_2$

A. M. J. H. Seuter and P. F. J. van den Boom

Philips Lighting Division, Eindhoven, The Netherlands

ABSTRACT

Under 254 nm excitation $ThOF_2$:Ce shows emission peaking at 313 nm with a quantum efficiency up to 70% at Ce contents of 20 a/o. On addition of Tb efficient Ce-Tb transfer is observed. The quantum efficiencies amount to 10% for Ce and 65% for Tb emission. The Ce-Tb energy transfer is discussed.

Efficient Ce and Tb luminescence has been reported in the compound CeF_3:Tb (1, 2). $ThOF_2$ crystallizes in the same hexagonal structure, the structure of tysonite (3). In this arrangement the cation has five equidistant anion neighbors and twelve cations as next nearest neighbors. In $ThOF_2$, the Th ions appear in two configurations. One has two oxygen and three fluorine neighbors, the other is surrounded by one oxygen and four fluorine ions. The present paper deals with the luminescence of Ce and Tb in $ThOF_2$.

Experimental

One mol analytical grade $Th(NO_3)_4 \cdot 5H_2O$ (Merck) and 7 mol NH_4HF (Riedel-de Haën) were fired at 650°C in an ambient atmosphere consisting of 98% nitrogen and 2% hydrogen. The procedure yielded white ThF_4 with hardly any $ThOF_2$ contamination.

The ThF_4 obtained was mixed with the amounts of ThO_2 (British Drug House), CeO_2, and Tb_4O_7 (Péchiney) required to obtain phosphors of compositions $Th_{1-x-y}Ce_xTb_yO_{1-x-y}F_{2+x+y}$. The mixtures were fired for 1 hr in an ambient of nitrogen and 1% hydrogen. The x-ray diagrams of the resulting white powders only showed the reflections of $ThOF_2$.

The optical experiments were performed as described previously (4).

Results and Discussion

Cerium activation.—Excitation, diffuse reflection, and emission spectra of $Th_{0.9}Ce_{0.1}O_{0.9}F_{2.1}$ at 300°K are shown in Fig. 1 and 2. The Ce emits with a band (48 nm) peaking at 313 nm. As long as charge compensation of Ce by F is maintained, the shape and position of the emission are hardly influenced at Ce contents between 1 and 40 atom percent (a/o). In contradistinction, a decrease in fluorine content yields both an excitation and emission shift to higher wavelengths (*e.g.*, $Th_{0.95}Ce_{0.05}OF_{1.90}$ peaks at 320 nm).

In comparison with phosphors such as LaF_3:Ce and CeF_3 (2), $ThOF_2$:Ce emits at lower energy. Apparently the influence of crystal fields on the Ce ion grows with increasing charge of the host lattice cations.

Key words: quantum efficiency, transfer mechanism, concentration quenching.

Usually Ce emission consists of a doublet due to the splitting of the ground state. In $ThOF_2$:Ce, however, only one emission band is observed, even at 77°K. Possibly the Ce ions occupy the two distinct cation sites in $ThOF_2$, thus obscuring observation of the emission-band splitting.

In Fig. 3 the quantum efficiency of $ThOF_2$:Ce is given as a function of the Ce concentration. The quantum efficiency first rises with increasing Ce concentration and is nearly constant above 20 a/o Ce. The lower quantum efficiencies at lower Ce concentrations are due to host lattice absorption. The constant value of the quantum efficiency at higher Ce concentration permits the conclusion that concentration quenching and energy transfer between Ce ions is not important. The latter conclusion is in agreement with the small overlap between emission and excitation bands.

Terbium activation sensitized by cerium.—Terbium can be excited directly into a broad band, due to a 4f-5d transition at the Tb ion (5). In $ThOF_2$ the position of this band is at high energy (>50 kK). For effective excitation at longer wavelength sensitization by Ce is required.

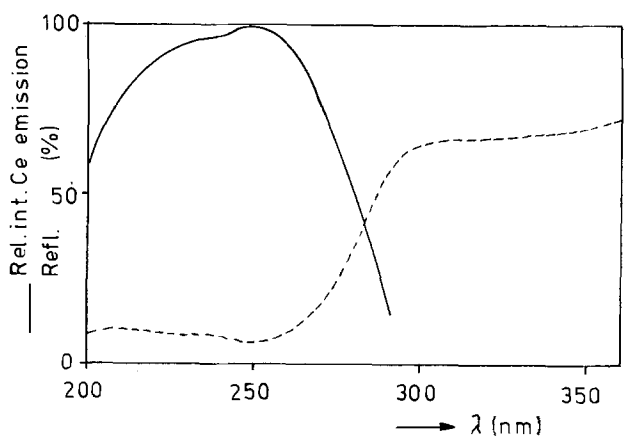


Fig. 1. Diffuse reflection (dashed) and excitation (solid) spectra of $Th_{0.9}Ce_{0.1}O_{0.9}F_{2.1}$.

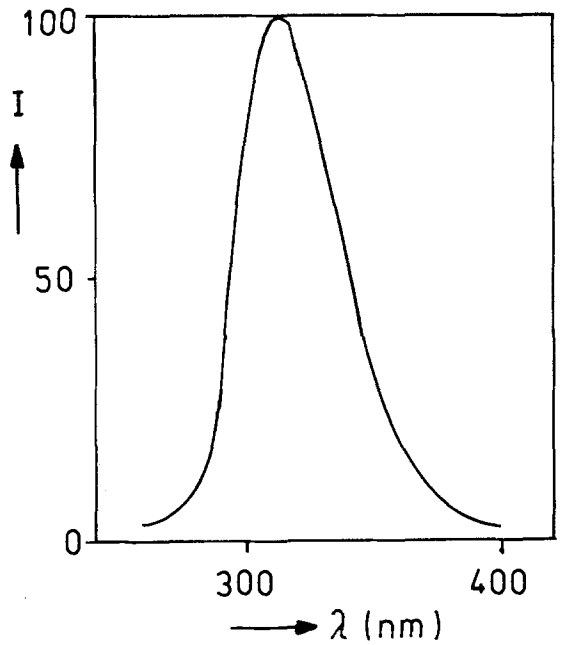


Fig. 2. Spectral energy distribution of the emission of $Th_{0.9}Ce_{0.1}O_{0.9}F_{2.1}$ under 254 nm excitation. I denotes the radiant power in arbitrary units.

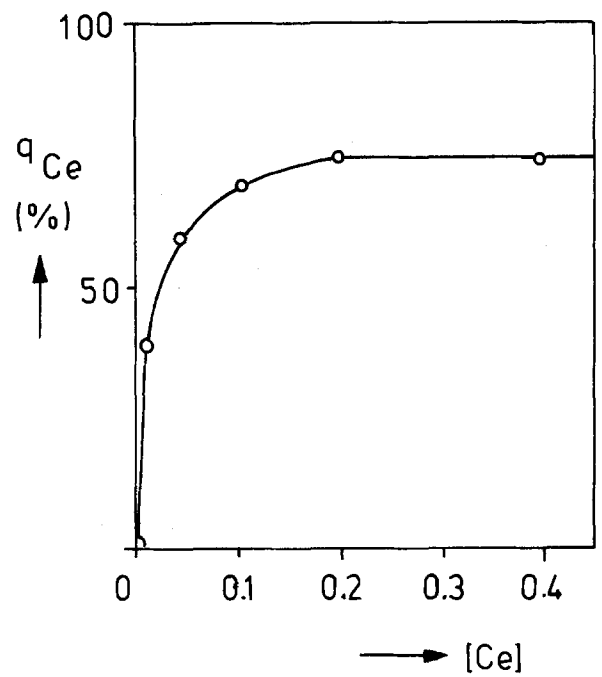


Fig. 3. Quantum efficiency of $ThOF_2$:Ce as a function of Ce concentrations.

Figures 4 and 5 show the terbium excitation spectrum and the emission spectrum of $Th_{0.7}Ce_{0.1}Tb_{0.2}O_{0.7}F_{2.3}$. There is a close similarity with the Ce excitation spectrum in $Th_{0.9}Ce_{0.1}O_{0.9}F_{2.1}$ (cf. Fig. 1), as must be expected in the case of energy transfer from Ce to Tb. The high energy part of the excitation spectrum is also observed in TbF_3 and must be ascribed to excitation in the broad band of Tb itself.

Table I gives the quantum efficiencies of Ce and Tb emission in $ThOF_2$ doped with 10 a/o Ce and various concentrations of Tb.

Mechanism of Ce-Tb transfer.—Because the Ce emission corresponds to an allowed electric dipole transition, we will only consider electric dipole-multipole interaction. To distinguish between the several possibilities (electric dipole-dipole, exchange, and electric dipole-quadrupole interaction) we will use arguments

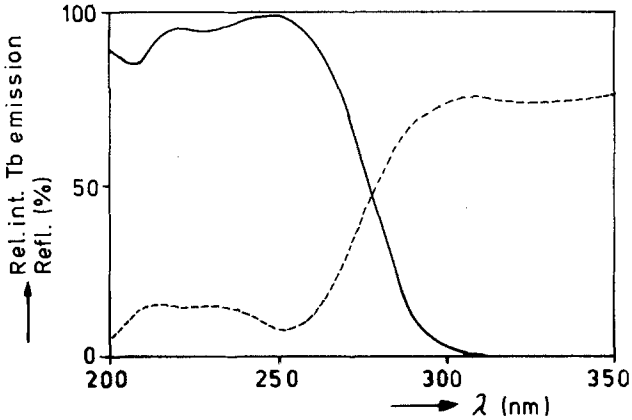


Fig. 4. Diffuse reflection (dashed) and excitation (solid) spectra of $Th_{0.7}Ce_{0.1}Tb_{0.2}O_{0.7}F_{2.3}$.

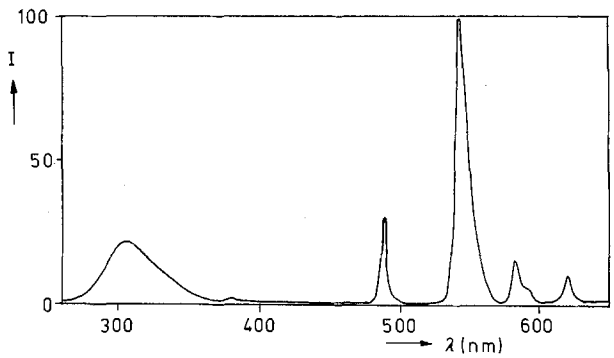


Fig. 5. Spectral energy distribution of the Ce and Tb emission in $Th_{0.7}Ce_{0.1}Tb_{0.2}O_{0.7}F_{2.3}$ under 254 nm excitation. I stands for the radiant power in arbitrary units.

similar to those considered by Verstegen *et al.* (6). Both Dy and Eu as activators in $ThOF_2$:Ce show less efficient energy transfer from Ce to the activator than Tb does. This is a strong indication that electric dipole-dipole and exchange interaction can be neglected. Therefore we assume that the energy transfer in $ThOF_2$:Ce,Tb results from an electric dipole-quadrupole interaction. Since these interactions are restricted to short distances, it may be expected that only nearest neighbor cations are involved in the energy transfer (7). Furthermore, the absence of concentration quenching in Ce-activated $ThOF_2$ led us to the conclusion that Ce-Ce transfer can be neglected. As a consequence, the energy from Ce to Tb is proportional to the fraction of Ce ions with at least one Tb ion as a nearest cation neighbor.

The fraction of Ce ions without Tb neighbors varies with the terbium concentration, (Tb), as $[1 - (Tb)]^{12}$, because every cation is surrounded by twelve cation neighbors at distances between 4.05 and 4.33Å. Hence, the fraction of Ce ions with at least one Tb ion as a nearest neighbor is $1 - [1 - (Tb)]^{12}$.

Assuming that the Tb emission varies proportionally with the fraction of Ce ions with at least one Tb ion neighbor, we obtain

$$q_{Tb} = q_{max}\,\alpha\{1 - [1 - (Tb)]^{12}\} \qquad [1]$$

where q_{Tb} stands for the quantum efficiency of the

Table I. Quantum efficiency of Ce and Tb emission (*viz.* q_{Ce} and q_{Tb})

x	q_{Ce} (%)	q_{Tb} (%)
0	70	—
0.05	39	30
0.10	27	49
0.20	12	64
0.30	8	61
0.40	9.5	60.5

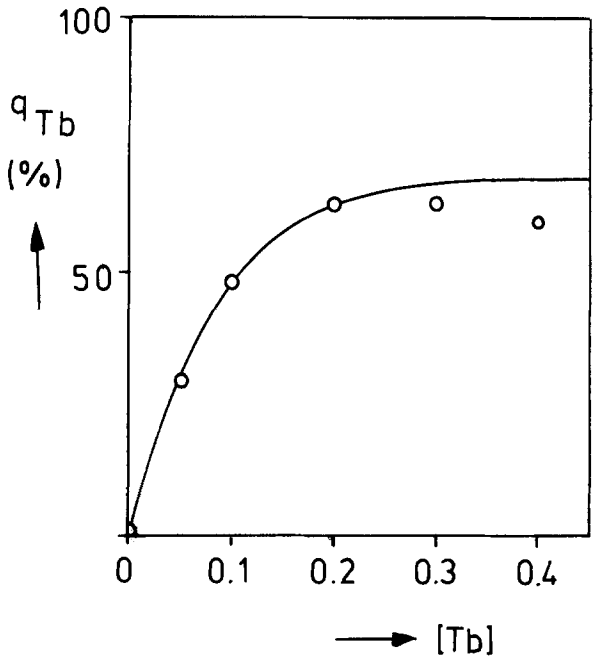


Fig. 6. Concentration dependence of the Tb quantum efficiency. The solid curve is obtained from Eq. [1]. The open data points refer to measurements.

Tb emission, q_{max} for the maximum quantum efficiency of the sum of Tb and Ce emission, and α for the probability of energy transfer from Ce to a Tb neighbor.

For a Tb concentration amounting to 0.2 the quantum efficiencies of Ce and Tb emission are 11 and 64% (cf. Table I). Hence we obtain for the probability factor

$$\alpha \approx 0.9$$

In Fig. 6 the quantum efficiency of the Tb emission, as calculated from Eq. [1], with $\alpha = 0.9$ and $q_{max} = 0.75$, is compared with the experimental results.

Manuscript received Feb. 11, 1977.

Any discussion of this paper will appear in a Discussion Section to be published in the June 1978 JOURNAL. All discussions for the June 1978 Discussion Section should be submitted by Feb. 1, 1978.

Publication costs of this article were assisted by Philips Lighting Division.

REFERENCES

1. F. A. Kröger, "Some Aspects of the Luminescence of Solids," Elsevier, Amsterdam (1948).
2. G. Blasse and A. Bril, *J. Chem. Phys.*, **51**, 3252 (1969).
3. W. H. Zachariasen, *Acta Cryst.*, **2**, 388 (1949).
4. W. L. Wanmaker, J. W. ter Vrugt, and E. P. J. de Meester, *This Journal*, **119**, 1237 (1972).
5. G. Blasse and A. Bril, *Philips Res. Rep.*, **22**, 481 (1967).
6. J. M. P. J. Verstegen, J. L. Sommerdijk, and J. G. Verriet, *J. Lumin.*, **6**, 425 (1973).
7. J. L. Sommerdijk and J. M. P. J. Verstegen, *ibid.*, **9**, 415 (1974).

Sapphire Substrate Misorientation and SOS/MOS Transistor Performance

C. E. Weitzel* and R. T. Smith

RCA Corporation, RCA Laboratories, Princeton, New Jersey 08540

ABSTRACT

Experimental data are presented which show that the crystalline perfection of silicon-on-sapphire epitaxial films as measured by x-ray diffractometry is dependent on both the magnitude and direction of misorientation of the {1$\bar{1}$02} sapphire substrate. Data obtained from SOS/MOS transistors indicate that devices fabricated in highly imperfect films have lower FET mobilities and exhibit leakage current asymmetry.

It has long been recognized that epitaxial {100} silicon films grown on {1$\bar{1}$02} sapphire substrates are subject to large stresses. This stress has been measured by various experiments to be on the order of 10^9-10^{10} dyne/cm^2 (1, 2). In all probability this stress results from both the difference in coefficient of linear expansion of the two materials (3) and the lattice mismatch between the {100} silicon and {1$\bar{1}$02} Al_2O_3 (4). The presence of this stress has a significant effect on the electrical properties of the SOS film. Carrier lifetimes in SOS films are much smaller than in bulk silicon wafers (5). The carrier mobility is somewhat smaller than that in bulk silicon and decreases the closer one gets to the silicon-substrate interface (6, 7). Moreover, a mobility anisotropy in SOS films (8) has been measured.

* Electrochemical Society Active Member.
Key words: x-ray diffractometry, θ:2θ half-width, FET mobility, leakage current.

A study of test transistor characteristics fabricated using the P+ polysilicon gate deep depletion process (9) indicated that there was considerable variation in device parameters for identically processed wafers. Assuming that the processing and epitaxial silicon growth were well enough controlled so as not to be the cause of such variations, a detailed study of the effect of substrate misorientation on SOS/MOS transistor parameters was begun. The initial results of this study are discussed in this report. The data to be presented show that the crystalline perfection of the silicon epitaxy, as measured by θ:2θ half-widths, is a function of the substrate misorientation. Moreover, there is a correlation between the crystalline perfection and SOS/MOS transistor parameters. Devices fabricated in highly imperfect epitaxial films have lower FET mobilities and exhibit source-drain leakage current asymmetry.

Experimental Techniques

The sapphire substrates used in this investigation were cut from EFG (Edge-Defined Film-Fed Growth) ribbon supplied by Tyco. The 1½ in. diam substrates were polished by Insaco, Incorporated. At the time these substrates were purchased state-of-the-art polishing techniques did not include a final Syton polish. Since a systematic investigation of substrate misorientation was planned, the misorientation of a large number of substrates was measured using x-ray Laue and diffractometry techniques.

Each wafer had a fiducial flat ground at 45° to an Al_2O_3 "a" axis lying in the plane of the wafer face. The projection of the Al_2O_3 "c" axis in the polished side of the wafer was determined relative to the ground fiducial flat by the back-reflection Laue method. Components of misorientation of the face of the wafers from the $\{1\bar{1}02\}$ were thus measured in orthogonal directions perpendicular and parallel to the projection of the c axis. The orthogonal components of misorientation were measured on a Siemens diffractometer equipped with a Siemens single crystal orienter, and using a Cu $K\alpha_1$ $\{1\bar{1}02\}$ reflection. Components of misorientation were read directly to an accuracy of ±0.02°.

From this pool of substrates groups of five substrates were selected to be processed together. In selecting the substrates for each group, care was taken to select substrates with widely varying misorientation so that any difference in transistor parameters would be obvious. Figure 1 shows the misorientation components of 25 of the substrates which were studied. The ordinate is the Al_2O_3 mirror plane and the abscissa is the a axis. A perfectly oriented wafer would be located at the origin of this graph. The solid circle gives the misorientation components of each wafer, and the arrow points in a direction perpendicular to the wafer flat. At the time the wafers were purchased, the orientation specification was 4.0° in any direction from $\{1\bar{1}02\}$. Only wafers No. 5 and 9 were outside of this specification. It is interesting to note that almost all of the substrates have an a axis component of misorientation greater than 1.0°. This is probably a result of the manner in which the ribbon was seeded.

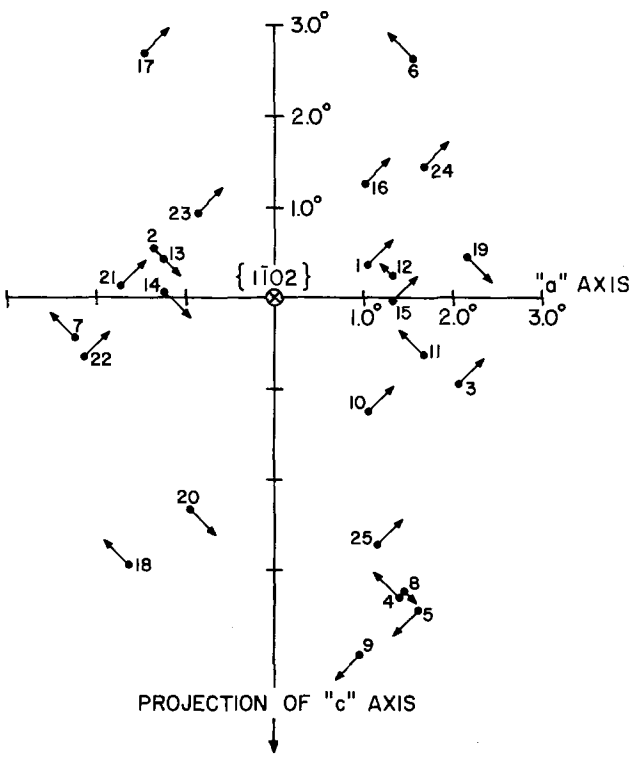


Fig. 1. Misorientation components of 25 EFG substrates. The arrow points in the direction perpendicular to the wafer flat.

Following characterization the substrates were fired in H_2 at 1200°C for 30 min. The epitaxial silicon films were grown on 5 substrates at a time in a 5 sided barrel reactor by the pyrolysis of SiH_4 at nominally 970°C. Nominally 0.6μ films were grown in 20 sec. Following epitaxial silicon growth, diffraction profiles were obtained from both the Al_2O_3 $\{2\bar{2}04\}$ and Si {400} in the rocking curve (ω scan) and θ:2θ modes. A Siemens ω drive diffractometer with Cu Kα radiation was used to record the peak profiles. The smallest entrance and receiving slits (0.125 mm; 0.05 mm) were used to minimize the instrumental broadening. Scanning speeds were ⅛°/min in the θ:2θ mode and ¼°/min in the ω mode. The crystal scanning-chart speed coupling gave a strip-chart recording sensitivity of 0.03125°/cm and 0.0625°/cm in the θ:2θ and ω modes, respectively. In the θ:2θ mode, one samples only from a set of parallel planes, and the broadening over instrumental may be caused by any crystalline defect causing nonuniformity in the d-spacing of these planes and/or small crystallite size effects. In the ω mode the detector is set at a fixed position centered within an angular range of 0.02° about the maximum diffracted intensity setting; hence any plane having a d-spacing characteristic of the angular setting of the detector may be sampled from as the crystal alone is rotated through its diffracting range. Broadening in this mode may be caused by relative misorientation of crystallites and/or sample curvature. Each sample was oriented such that its diffraction normal was in the plane of the diffractometer. This was accomplished by incrementally rotating the sample about its face normal and successively readjusting the crystal ω setting and detector 2θ setting to maximize the diffracted intensity. The correct setting is attained when ω reaches a maximum or minimum value.

Following characterization of the epitaxial silicon film, SOS/MOS transistors were fabricated using the P+ polysilicon gate deep depletion process (9). Briefly, the processing steps are; silicon island definition and etching, growth of 1200Å of channel oxide, polysilicon deposition, doping and etching, channel oxide self-aligned etch, doping of sources and drains from doped oxides, contacts, metallization, and overcoat. The process results in the fabrication of a n-channel deep depletion transistor and a p-channel enhancement mode transistor.

The FET mobility reported later in this report as the mobility for the wafer was arrived at by plotting the drain current *vs.* gate voltage with $V_D = 0.1V$. The test transistors were 12.56 mil wide with a source-drain spacing of 0.4 mil. With $V_D = 0.1V$, the device is operating in the so-called linear region of the MOS transistor characteristics. Theoretically, the drain current is related to the gate voltage by the equation

$$I_D = \frac{W}{L}\mu C_{ox}\left[(V_G - V_T)V_D - \frac{V_D^2}{2}\right] \qquad [1]$$

where I_D is the drain current, L the source-drain spacing, W the width of the transistor perpendicular to the direction of current flow, μ FET mobility, C_{ox} channel oxide capacitance, V_G gate voltage, V_T threshold voltage, and V_D drain voltage. The transconductance of the transistor is given by the slope of the I_D *vs.* V_G curve, or theoretically by

$$g_m = \frac{\delta I_D}{\delta V_G}\Bigg|_{V_D=\text{constant}} = \frac{W}{L}\mu C_{ox}V_D \qquad [2]$$

Using this equation and the experimentally determined slope, the FET mobility can be calculated. For all the data presented in this report, the transconductance was determined from the linear part of the curve where the g_m is maximum. For most devices this occurred in the 10-30 μA range, so the FET mobilities are for current

levels of about a μA/mil. The g_m decreases at large V_G because of increased surface scattering.

The threshold voltage and source-drain leakage current of test transistors across an entire wafer were measured using an automatic tester which is interfaced with a time-sharing computer system. The threshold voltage was measured by determining the voltage which when connected to the gate and drain caused 1 μA/mil to flow through the device. The leakage current was measured with the gate and source grounded with 10, 15, or 20V applied to the drain. The minimum measurable leakage current was 5 nA because of automatic tester noise.

Experimental Results

Substrate misorientation and silicon epitaxial perfection.—Of the four diffraction profiles obtained from each sample, the Si θ:2θ half-widths were found to have the greatest correlation to device performance. The Si ω scan half-widths paralleled those of the θ:2θ with some exceptions. It is thought that these exceptions are due to the dependence of the ω scan half-width on the direction of scan. Since each crystal was oriented so that it was scanned in the direction of misorientation and the orientation of each was different, a common scanning direction did not exist. Nonetheless, the θ:2θ half-widths remain a valid qualitative comparison of relative crystalline quality or perfection. In the following discussion we have chosen to compare device performance characteristics with the crystalline quality as obtained from θ:2θ scan half-widths.

Half-widths obtained from $\{22\bar{0}4\}$ θ:2θ scans of all the Al_2O_3 substrates were found to have a mean value of 0.0425° ± 0.0025°, while the {400} θ:2θ half-widths of Si deposited on these substrates ranged from 0.1170° to 0.2125°. The half-width of a {400} Cu $K\alpha_1$ reflection of bulk Si obtained with the same instrumental conditions was found to be 0.0500°. Thus it appears that the method was insensitive to any variations in the quality of the Al_2O_3 substrate, if present, while the θ:2θ half-widths of the epi Si were 2.34-4.25 times as large as those of bulk Si. Typical recorded diffraction profiles of the {400} Si reflection are shown in Fig. 2. Profiles of the least and most perfect SOS epitaxial layers are shown, Fig. 2c and 2b, respectively, and may be compared with the profile obtained from bulk Si, Fig. 2a. In the case of bulk Si, the $K\alpha_1$ and $K\alpha_2$ components are completely resolved, however, this is not true for the profiles of the SOS layers. There is enough resolution of the $K\alpha_1$ and $K\alpha_2$ components of the best layer to prevent asymmetric broadening of the $K\alpha_1$ component at half-maximum intensity. It can be seen that asymmetric broadening of the $K\alpha_1$ component of the worst layer does occur. Where asymmetric broadening was observed, only the low angle half of the $K\alpha_1$ component was measured and then doubled, thereby eliminating problems caused by asymmetrical broadening. Since the θ:2θ half-widths had the most relevance to device performance, these are plotted in Fig.

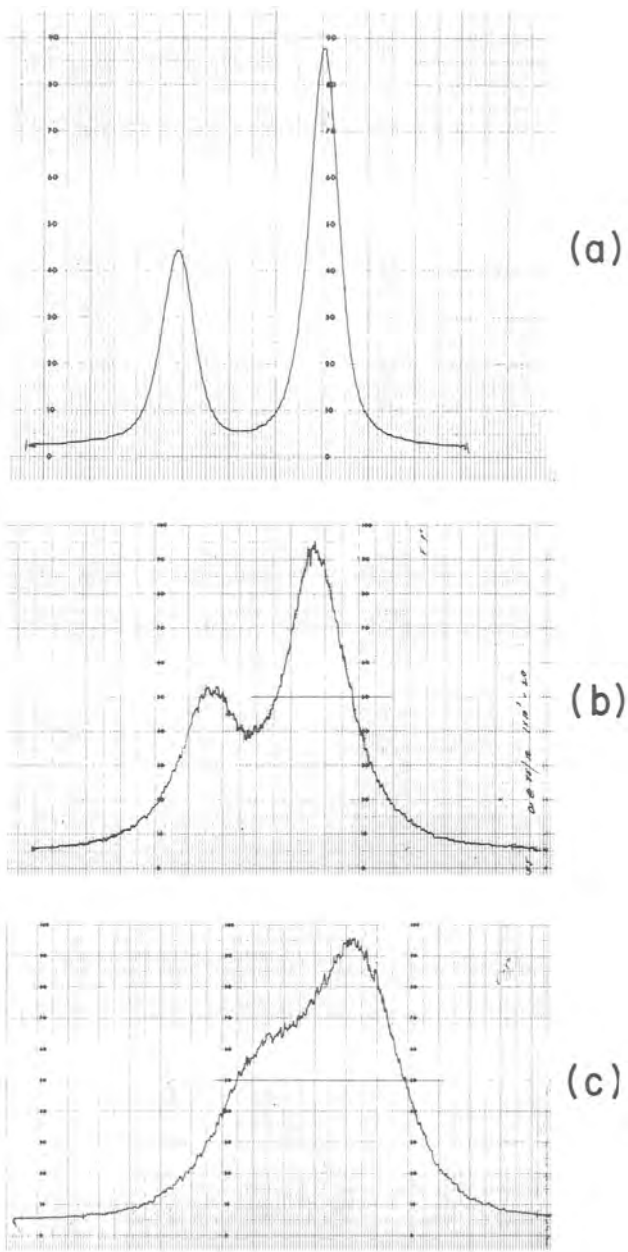


Fig. 2. Diffraction profiles of the {400} Si reflection for (a) bulk Si, (b) least imperfect SOS, and (c) highly imperfect SOS.

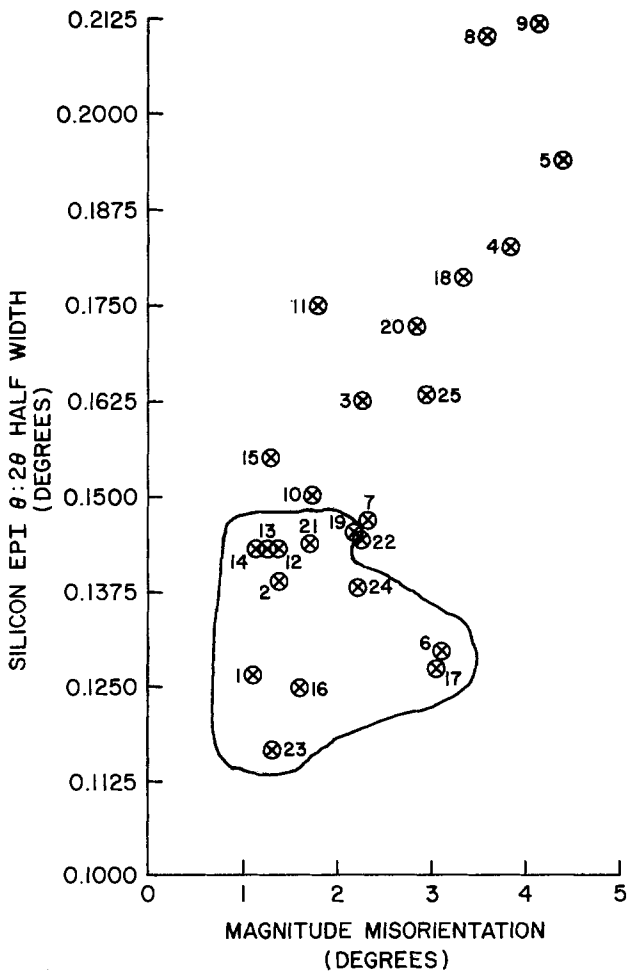


Fig. 3. θ:2θ half-width of silicon epitaxial film vs. the magnitude of misorientation of the substrate.

3 for the 25 wafers shown in Fig. 1. The $\theta:2\theta$ half-width (degrees) is plotted along the ordinate and the magnitude of misorientation (degrees) is plotted along the abscissa. The wafers are numbered the same in Fig. 1 and 3. The half-widths given for each sample are that of the $K\alpha_1$ components at half-maximum intensity corrected, when necessary, for broadening due to $K\alpha_1$-$K\alpha_2$ overlap.

After careful examination of the data presented in Fig. 1 and 3 one very interesting fact becomes obvious. Epitaxial silicon grown on wafers which are plotted in the top half plane of Fig. 1 has a lower $\theta:2\theta$ half-width than silicon grown on wafers plotted in the bottom half plane. By comparing the location of the numbered points in Fig. 1 with the data in Fig. 3, it can be seen that all of the data points in the top half plane of Fig. 1 are enclosed by the irregularly shaped solid line in Fig. 3. Therefore, with the exception of data point No. 22 every silicon film grown on a substrate misoriented in the top half plane of Fig. 1 is more perfect than every silicon film grown on a substrate misoriented in the bottom half plane. The data in Fig. 3 also show that as the magnitude of misorientation of substrates located in the bottom half plane increases so does the $\theta:2\theta$ half-width. This behavior is radically different from that of substrates located in the top half plane. For substrates removed farther and farther from the origin, half-widths do not increase. In fact, with the exception of data point No. 1, the five substrates with the smallest $\theta:2\theta$ half-width are located the farthest from the origin. These data indicate that the silicon epitaxial perfection is a function of a misorientation component which is parallel to the mirror plane. No correlation was found between the half-widths and the component of misorientation perpendicular to the mirror plane.

To examine this correlation more carefully, data from ten of these wafers are plotted, using a different format in Fig. 4. The $\theta:2\theta$ half-width is plotted on the abscissa and the component of misorientation which is parallel to the mirror plane is plotted on the ordinate. The data also show the wafers grouped together into 5 wafer lots for processing. The silicon epitaxial film was grown on these 5 wafers at the same time. The solid and dashed lines were drawn to connect data points in each lot. The data clearly show that as the component of substrate misorientation parallel to the mirror plane changes from large negative values to positive values, the $\theta:2\theta$ half-width decreases from over 0.18° to less than 0.14°. It is worth noting here that the half-width obtained from a bulk silicon wafer is typically 0.05° with the same x-ray diffraction parameters. Therefore, even the SOS films on substrates in the top half-plane have half-widths which are almost three times wider than typical bulk silicon. This larger half-width is an indication of the higher defect densities in SOS films than in bulk silicon. Some information on these defects is given by Abrahams and Buicchi (10).

Up to this point we have only established a correlation between substrate orientation and the $\theta:2\theta$ half-width of silicon-on sapphire epitaxial films thereon. If this were as far as the correlation went, this phenomenon would probably only be of scientific interest. As we shall see in the next section, however, this phenomenon significantly affects MOS transistor performance.

$\theta:2\theta$ half-width and FET mobility.—Since the $\theta:2\theta$ diffraction profile is a measure of the quality of the epitaxial film, one might intuitively feel that such a parameter would correlate with electrical parameters of the film which are also affected by film quality. This is indeed observed. The mobility of charge carriers is limited by scattering events. Therefore, the mobility of carriers in a more highly defected material would necessarily have to be smaller than in a more defect-free material.

This behavior is clearly illustrated in Fig. 5, where the FET mobility for n-channel deep depletion transistors and p-channel enhancement transistors is plotted against the $\theta:2\theta$ half-width of the silicon epitaxial film. The data show that the mobility in the accumulation layer of the n-channel device is reduced from 338 cm^2/V sec for a half-width of 0.130° to 155 cm^2/V sec for a half-width of 0.212°. The mobility in the inversion layer of the p-channel device decreases from 248 cm^2/V sec to 139 cm^2/V sec.

Threshold voltage data obtained from the automatic tester also agree with this correlation. Both n-channel and p-channel devices fabricated in highly defected epitaxial films had higher threshold voltages than devices fabricated in less imperfect SOS. Everything else being equal, devices fabricated in lower mobility material will need larger gate voltages to achieve a prespecified current level. It must be kept in mind,

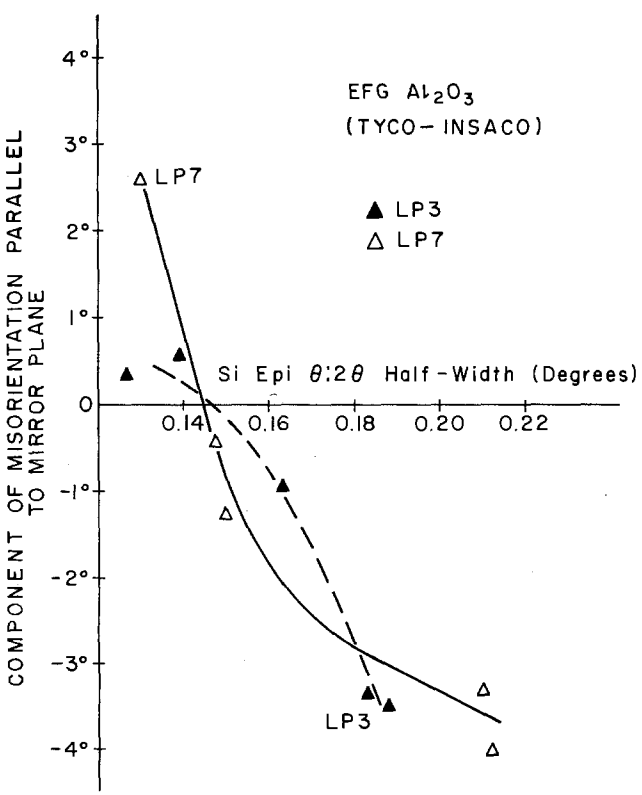


Fig. 4. Component of misorientation parallel to the mirror plane vs. $\theta:2\theta$ half-width of silicon epitaxial film.

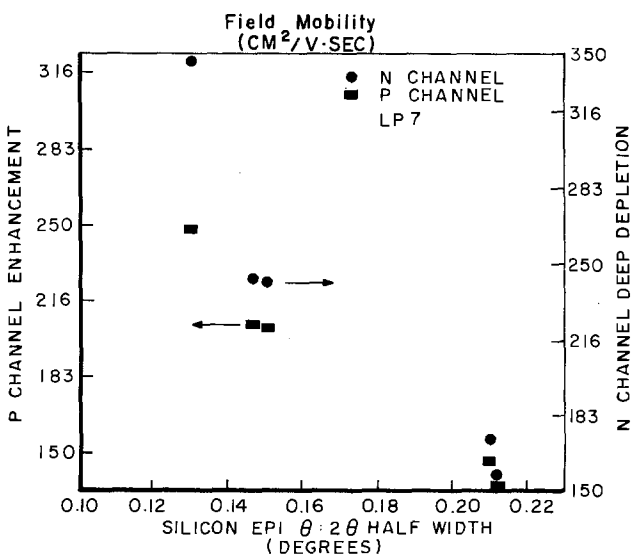


Fig. 5. FET mobility of n-channel deep depletion and p-channel enhancement transistors vs. $\theta:2\theta$ half-width of silicon epitaxial film.

however, that the threshold voltage is much more susceptable to processing variations than FET mobility. This is because the threshold voltage is strongly dependent on oxide charge and silicon film doping density. Nevertheless, the correlation between threshold voltage and substrate misorientation is observed.

Since the crystalline perfection correlates with misorientation direction and also with the FET mobility, the mobility must also correlate with misorientation direction. This is shown in Fig. 6 for processing lot LP3. In Fig. 6 the misorientation components for each substrate are plotted on a graph similar to Fig. 1. Next to each point is given the n-channel and p-channel FET mobility. Devices fabricated on substrates which are above the origin which in Fig. 3 have been shown to have lower defect concentrations have higher FET mobilities than devices fabricated on substrates which are located below the origin which have been shown to have higher defect concentrations.

A comparison of the respective device mobilities shown in Fig. 5 and 6 illustrate another phenomenon frequently observed with SOS/MOS transistors. Although the silicon epitaxial films for the two lots were grown under supposedly identical conditions and the processing of transistors was also done under identical conditions, the maximum FET mobilities are considerably different. In lot LP3 the maximum n-channel mobility is 407 cm^2/V sec, whereas the maximum p-channel mobility is 158 cm^2/V sec. On the other hand, in lot LP7 the maximum n-channel and p-channel mobility are 337 cm^2/V sec and 248 cm^2/V sec. Of course, the source of these variations could be process related, but it is also quite likely that these differences are caused by variation in the SOS film. These data have clearly shown that substrate orientation can have a significant effect on SOS film properties. However, there are probably many other unidentified parameters which also have a significant effect on the quality of silicon-on-sapphire films.

θ:2θ half-width and leakage current asymmetry.— Another anomalous phenomenon which the additional Si imperfection causes is source-drain leakage current asymmetry. Experimental data from test transistors fabricated in highly defective SOS films show that the leakage current from source to drain differs by orders of magnitude depending on which electrode is designated the source and drain. This is indeed anomalous behavior when one considers the symmetry of an MOS transistor. Figure 7 shows typical leakage current data from an n-channel deep depletion transistor fabricated in a highly imperfect SOS film. The leakage current is plotted on the ordinate using a log scale and the source-drain voltage is plotted on the abscissa also using a log scale. These data were taken from an SOS/MOS transistor 6.28 mil wide with a source-drain spacing of 0.4 mil. The gate electrode is grounded. In an MOS transistor biased in this way, the drain junction is reversed biased whereas the source junction is forward biased. The leakage current is primarily the result of the generation of carriers in the depletion region and also a result of junction breakdown. For source-drain voltages below about 2V, the leakage current through both junctions is the same. However, above this voltage the leakage current through the left-hand junction increases rapidly. 2V could, therefore, be called the threshold voltage for the change in current-voltage dependence. The threshold voltage for the right-hand junction, on the other hand, is about 8V. At $V_{SD} = 10V$ this 6V difference in threshold voltage results in over a three order of magnitude difference in leakage current through the two junctions of the same transistor. Defining the amount of junction asymmetry as the ratio of the larger current to the smaller current, the leakage current asymmetry at $V_{SD} = 10V$ is about 1750.

If this type of behavior was exhibited by only a few devices on a wafer and if on the average as many left-hand junctions as right-hand junctions had the lower threshold voltage, the cause of the asymmetry could be random defects. Data taken using the automatic tester, however, indicate that this is not the case. Data obtained from about 500 transistors of different

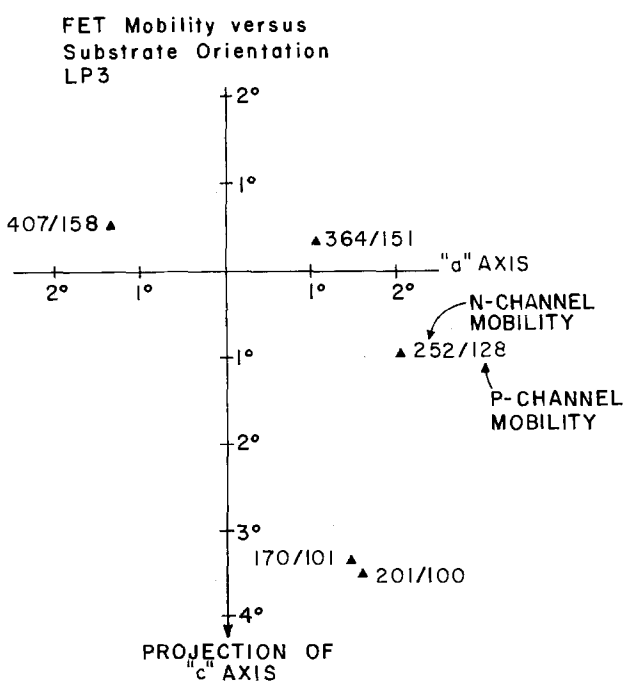


Fig. 6. FET mobility of n-channel deep depletion and p-channel enhancement transistors vs. components of substrate misorientation.

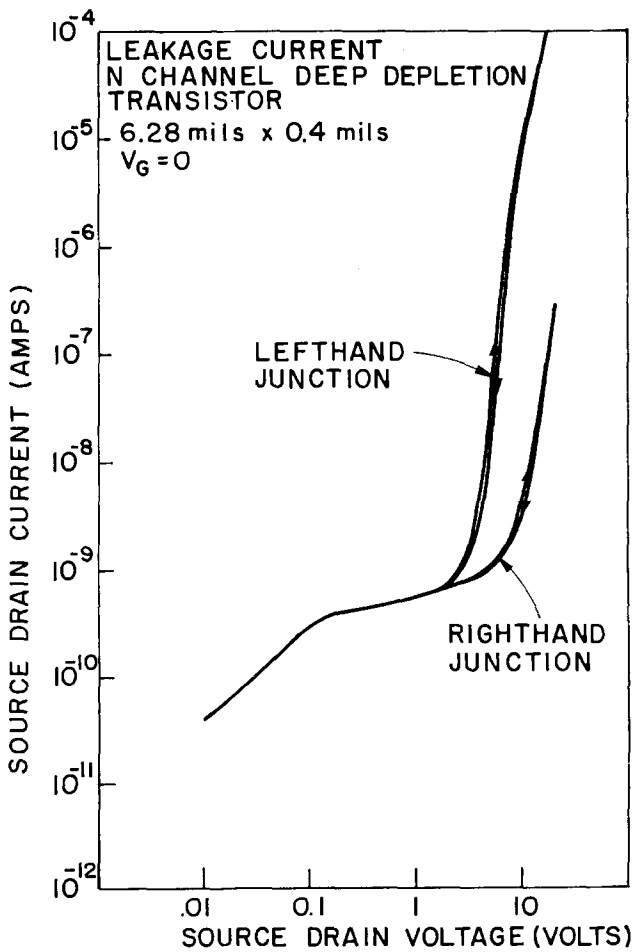


Fig. 7. Source-drain leakage current vs. source-drain voltage for both junctions of an SOS/MOS n-channel deep depletion transistor in highly imperfect SOS film.

sizes on a wafer indicate that over 95% of the devices have the same high leakage and low leakage junction. Moreover, this phenomenon has been observed on numerous wafers. It was also found that the junction which has the higher leakage current differs from wafer to wafer. A careful examination of data from devices fabricated in more and less perfect epitaxial SOS films from two 5 wafer processing lots indicated that the amount of leakage current asymmetry correlates with the $\theta:2\theta$ half-width. This correlation is shown by the data in Fig. 8. The $\theta:2\theta$ half-width is plotted along the abscissa and the junction asymmetry is plotted on the ordinate. The junction asymmetry was calculated by measuring the source-drain leakage current at 10, 15, and 20V of about 500 transistors on each wafer. The leakage current was measured through each transistor in both directions. The computer provided the geometric mean of the leakage current of all of the transistors at the three drain voltages of both possible device configurations. The asymmetry was calculated by dividing the geometric mean of the leakage current of one source-drain configuration by the geometric mean of the leakage current of the other source-drain configurations. These quotients for different size devices at different source-drain voltages were then averaged to give the junction asymmetry. The maximum asymmetry of 1000 was observed for n-channel deep depletion transistors on wafer D which also had the largest $\theta:2\theta$ half-width of 0.20°. P-channel devices on wafer D had a somewhat smaller asymmetry of 100. However, the functional dependence of asymmetry on $\theta:2\theta$ half-width was the same for p-channel transistors. As the $\theta:2\theta$ half-width decreases so does the junction asymmetry. Devices fabricated on wafers H, I, and J whose $\theta:2\theta$ half-widths are less than 0.14° exhibit essentially no asymmetry.

A large enough number of highly imperfect SOS wafers were examined to establish a correlation between the direction of the asymmetry and the direction of misorientation relative to the wafer flat. The graph in Fig. 9 shows the components of misorientation of highly imperfect SOS wafers from four proc-

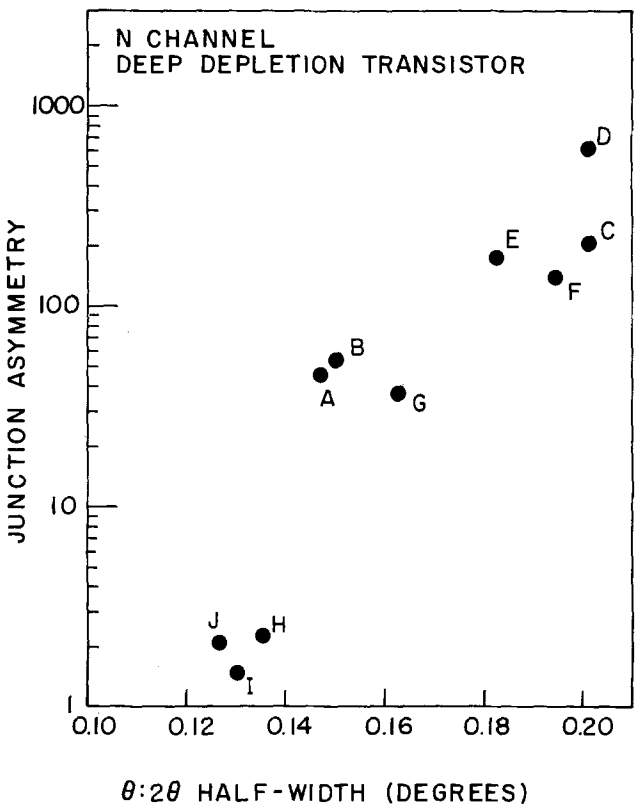
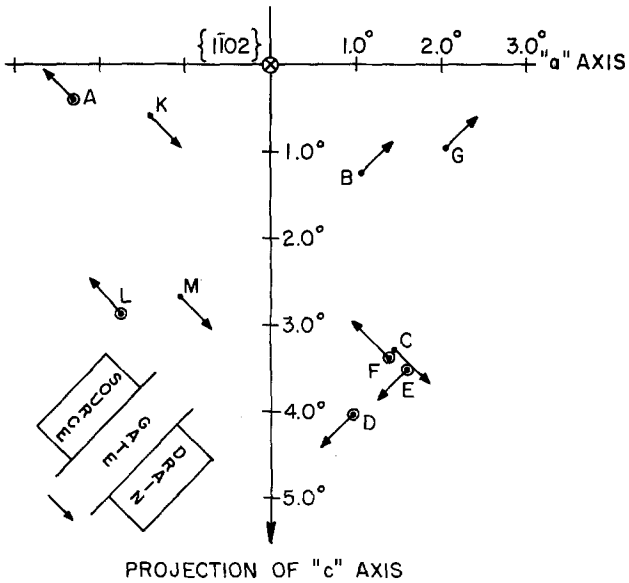


Fig. 8. MOS transistor leakage current junction asymmetry vs. $\theta:2\theta$ half-width of silicon epitaxial film.



• RIGHTHAND JUNCTION HAS HIGHER LEAKAGE CURRENT

⊛ LEFTHAND JUNCTION HAS HIGHER LEAKAGE CURRENT

Fig. 9. Misorientation components of sapphire substrates showing location of high leakage junction.

essing lots. The magnitude of the asymmetry of devices on wafers A-G is shown in Fig. 8. The arrows in Fig. 9 point in a direction perpendicular to the wafer fiducial. When the wafers were processed, the SOS/MOS devices on all the wafers were laid out the same way relative to the wafer flat. The relationship between the wafer flat and the location of the source and drain of each transistor is shown by the insert in the lower left-hand corner of Fig. 9. The source-drain current of all the devices on all of the wafers is perpendicular to the wafer flat. This is equivalent to being parallel to the arrow which is perpendicular to the wafer flat. Thus, from a crystallographic standpoint the devices on wafers A and K are rotated by 180°. The data in Fig. 9 show that the low leakage junctions are also rotated by 180°. Moreover, this relationship between low and high leakage junctions and placement of the device junction relative to the wafer flat is consistent for all 10 wafers investigated. Wafers A, L, and F all have lower leakage junctions on the same side and opposite to that of wafers C, K, and M. The same is true of wafers D and E and wafers B and G. The data suggest that some property of the silicon epitaxial layer, possibly defects, is causing the asymmetry.

Discussion

Previous experimental results have clearly shown that the structural and electrical characteristics of silicon-on-sapphire films are dramatically different from bulk silicon (1-8). All of this anomalous behavior probably results from the difference in coefficient of linear expansion of the silicon and sapphire, and also the lattice mismatch between the {100} silicon and $\{1\bar{1}02\}$ Al_2O_3. The data presented in this report are the first evidence that the quality of the SOS film is also dependent on the orientation of the substrate. It should be emphasized that we are talking about small misorientation from the $\{1\bar{1}02\}$ axis. The current specification for Czochralski substrates is 2° in any direction from the $\{1\bar{1}02\}$ axis. The data show that silicon epitaxial films grown on substrates which are misoriented at opposite extremes of this specification along the mirror plane would have significantly different $\theta:2\theta$ half-widths. As a result SOS/MOS transistors fabricated in these films would have significantly different FET mobilities. More importantly SOS-integrated cir-

cuits fabricated on substrates misoriented at these two extremes would have different maximum operating frequencies. As a result, this observation of the dependence of film quality on substrate orientation is of practical importance. The data also imply that less variability between SOS films would be observed if the substrate orientation were specified about some point in the top half-plane of Fig. 1 rather than about the origin as is presently done. The location of this optimum point in the top half-plane of Fig. 1 is presently being sought. It should be kept in mind, however, that all of these observations were made using substrates grown by the EFG process. In addition, these substrates were not polished using a final Syton step. A study of state-of-the-art Czochralski substrates is presently underway. The results of this additional study are very important because they will indicate whether this phenomenon is dependent on the source of the sapphire or the polishing technique. If the study of Czochralski substrates yields the same results, we will be forced to conclude that this phenomenon is a result of the bonding interaction between the silicon and sapphire. This being the case, these observations are relevant to sapphire from all sources and maybe even to other insulating substrates.

Regardless of the outcome of additional experiments, however, these results clearly show the utility of the θ:2θ half-width measurement for characterizing the SOS film. Few techniques have been available for measuring film quality prior to device fabrication. The data presented here are the first direct correlation between preprocessing film quality and SOS/MOS device FET mobility. In terms of integrated circuit speed, FET mobility is a very important device parameter.

When one considers the symmetry of a MOS transistor, the asymmetry of leakage current through SOS/MOS transistors fabricated in highly defective epitaxial film is a unique effect. Before developing a model to explain this effect, it is necessary to understand the conduction mechanism of the leakage current in the high conductivity region. Since the leakage current of the left-hand junction in Fig. 7 is plotted on a pendence to another, in all probability the I-V characteristic is controlled by a mechanism which was not active below the threshold voltage. If the leakage current of the left-hand junction in Fig. 7 is plotted on a logarithm scale and the source-drain voltage is plotted as the square root of voltage $(V_{SD})^{1/2}$ the data points fall along a straight line. This fact is evidence that the conduction mechanism is Frenkel-Poole emission (11). For this conduction mechanism the current density J is related to the electric field E by the equation

$$J = J_o \exp\left(\frac{q}{kT}\sqrt{qE/\pi\epsilon}\right) \quad [3]$$

where J_o is the current density before the Frenkel-Poole conduction begins, q is the electronic charge, k is Boltzmann's constant, T is the absolute temperature, and ϵ is the permittivity of the material. Having identified a likely conduction mechanism, we can now speculate as to the cause of the junction asymmetry. Since at low fields the pre-Frenkel-Poole conduction current is symmetrical, the only parameter in Eq. [3] which could be asymmetrical is the electric field. Since the electric field which determines breakdown in thin film transistors is the field between the gate electrode and drain electrode, we must conclude that this field is different depending on which electrode is designated the source and drain. This could only occur if the diffusion profiles of the source and drain are different. A defect in the SOS film which propagates from the silicon-sapphire interface to the surface of the film could cause such asymmetrical diffusion profiles if it were inclined at some angle between 0° and 90° and if the density of defects in one direction exceeded the density in other directions. Such defects have actually been observed in SOS films (10). From a scientific standpoint this possible correlation between silicon film defects and MOS transistor leakage current asymmetry is very interesting. From a practical standpoint, however, devices should be fabricated in nearly perfect films to achieve maximum mobilities and as a result, no asymmetry will be observed, as shown by the data in Fig. 8.

Summary

Using x-ray diffraction techniques, a correlation between the quality of silicon-on-sapphire films and the misorientation of the {1$\bar{1}$02} substrates was found. The data clearly show that the θ:2θ half-widths of silicon films grown on substrates whose orientation differed by only a couple of degrees were significantly different. A correlation was also established between the θ:2θ half-width and SOS/MOS device performance. Devices fabricated in highly imperfect films had lower FET mobilities and exhibited source-drain leakage current asymmetry. It is proposed that the leakage current asymmetry results from the directional nature of defects in the SOS film. These observations establish x-ray line broadening studies as a valuable tool for characterizing preprocessed SOS films and also indicate that less variability in SOS film properties would result if the substrates were cut off axis in a specified direction.

Acknowledgments

The authors wish to thank the following people for their invaluable assistance with this work: D. Capewell, T. Pawlicki, C. Tayag, and J. Petrushun.

Manuscript submitted Sept. 2, 1976; revised manuscript received March 7, 1977.

Any discussion of this paper will appear in a Discussion Section to be published in the June 1978 JOURNAL. All discussions for the June 1978 Discussion Section should be submitted by Feb. 1, 1978.

Publication costs of this article were assisted by RCA Laboratories.

REFERENCES

1. D. J. Dumin, *J. Appl. Phys.*, **36**, 2700 (1965).
2. C. Y. Ang and H. M. Manasevit, *Solid-State Electron.*, **8**, 994 (1965).
3. G. W. Cullen, *J. Cryst. Growth*, **9**, 107 (1971).
4. R. L. Nolder and I. B. Cadoff, Technical Conference on Solid State Interfaces, Boston (1964).
5. D. J. McGreivy and C. R. Viswanathan, *Appl. Phys. Lett.*, **25**, 505 (1974).
6. A. C. Ipri, *J. Appl. Phys.*, **43**, 2770 (1972).
7. S. T. Hsu and J. H. Scott, Jr., *RCA Rev.*, **36**, 240 (1975).
8. A. J. Hughes, *J. Appl. Phys.*, **46**, 2849 (1975).
9. A. C. Ipri and J. C. Sarace, *IEEE J. Solid-State Circuits*, **sc-11**, 329 (1976).
10. M. S. Abrahams and C. J. Buicchi, *Appl. Phys. Lett.*, **27**, 325 (1975).
11. J. Frenkel, *Phys. Rev.*, **54**, 647 (1938).

Nondestructive, Reverse Decoration of Defects in IC Passivation Overcoats

Robert B. Comizzoli*

RCA Laboratories, Princeton, New Jersey 08540

ABSTRACT

A new method for decoration and detection of defects in insulating films on semiconductor devices is described. The sample, which can be a wafer, chip, or opened packaged device, is first exposed to an atmospheric pressure, high voltage discharge (corona) of positive polarity. Then it is immersed in a suspension of carbon black in insulating liquid. Since the carbon black particles are negatively charged, they are attracted to and deposited on the positively charged insulating regions of the sample except at defects such as pinholes or cracks over metal. In this way a reverse decoration of defects is obtained which renders them clearly visible by microscopic observation. The sample can be cleaned and wafer probe testing shows that the procedure is not destructive. Various parameters of the process are discussed and the broad applicability of the process is indicated. The process is fast, simple, and sensitive.

The integrity of insulating passivation overcoats deposited on metallized integrated circuits (IC's) is important for device yield and reliability (1). Cracks and pinholes in the passivation overcoat can lead to various failure mechanisms (2-10). In this paper I report a new method for defect detection which is fast, simple, and nondestructive. The detection method has been principally applied to overmetal passivation layers of chemical vapor deposited (CVD) SiO_2 and phosphosilicate glass (PSG), but it is also applicable to primary insulating layers such as thermal oxide over silicon, and, indeed, to any thin insulator over a conductor.

Several techniques for the decoration of defects in insulating films on semiconductor devices have been reported. These methods, reviewed by Kern (11), include electrolytic metal decoration with copper anodes, electrophoretic decoration with copper colloidal particles from a copper anode, bubble formation by electrolysis, liquid crystal light scattering, and etching of underlying aluminum through the defects.

The bubble formation and liquid crystal techniques are "real time" methods in that the decoration exists only during the process implementation. The other methods, in contrast, result in a device or wafer which is permanently decorated and which can be examined after the decoration step. However, many of these latter techniques are destructive in that conductors are deposited which cannot be removed or device metal interconnects are removed by etching.

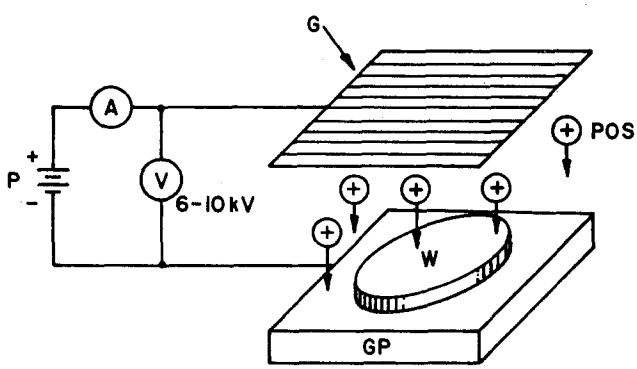
The decoration technique given in detail here was briefly described previously (12) and is one part of a larger study of new decoration methods for passivation overcoat layers (13-14). The reverse decoration technique is a two step process. In the first step, gaseous ions from an atmospheric pressure high voltage discharge (corona) are deposited on the insulating regions of the sample. Then the sample is immersed in a suspension of charged carbon black particles in an insulating liquid. The carbon black particles, of charge sign opposite to that of the ions on the insulator surfaces of the sample, are attracted to the insulator surface and deposited there, except at defects. Thus a uniform deposit of carbon is formed over the insulator surfaces except at defects such as cracks and pinholes. The defects and a halo region surrounding each defect are left bare, and their locations are easily observed microscopically. It is also possible to choose the sign of the corona ions to be the same as that of the carbon black. In this case a direct decoration (13-14) of defects is obtained which in most cases is less useful than the reverse decoration process described here. Some of the principles and methods are similar to those of electrophotography (15).

* Electrochemical Society Active Member.
Key words: passivation, defect detection, corona charging, integrated circuits, reliability.

Corona-Charging Process

The first step for the reverse decoration process is the deposition of ions on the insulating regions of the sample as shown in Fig. 1.

Equipment.—The source of ions deposited on the sample is a plane array of 40 μm diam nickel alloy wires. This wire grid consists of seven parallel wires 1.8 cm apart held in an acrylic frame in a horizontal plane. The wires are commonly connected to a high voltage d-c power supply capable of $\pm$ 10,000V and 6 mA. It is recommended that only d-c power supplies with the step-up transformer operating at radio frequency and with current limitation of no more than 10 mA be used for operator safety. A grounded plate is placed 3 cm above the wires to provide greater current uniformity and to protect the wires from mechanical damage. The sample is placed on a grounded plate 2 cm below the wire array. The power



P = POWER SUPPLY
A = AMMETER
V = VOLTMETER
G = CORONA GRID WIRE ARRAY
POS = POSITIVE IONS
W = SAMPLE WAFER
GP = GROUNDED PLATE

Fig. 1. Schematic of corona charging process

supply is operated from a foot switch. The process is carried out at relative humidity (RH) below 30% in a glove box in flowing nitrogen.

Parameter study of charging.—In order to understand the surface charge deposition process on device wafers, measurements of surface voltage of charged wafers were done as functions of sample geometry, passivating layer thickness, corona voltage, relative humidity, and corona wire-to-sample spacing. For these tests, IC wafers were not used because we wanted results to be independent of metallization patterns and bonding pad arrangements. To simulate an IC wafer, a square grid pattern was etched into thermal silicon dioxide on silicon, yielding a pattern of square islands of silicon dioxide surrounded by grid lines of bare silicon. Wafers with islands of different sizes and grid line widths were used.

Charging properties of wafers are studied by measuring the surface potential of the wafers after charging. This is done with an electrostatic voltmeter that uses a noncontacting probe with feedback to make absolute (independent of spacing) voltage measurements. The probe-to-wafer spacing is adjusted so that the geometry of the ground potential (bare silicon grid lines) and charged silicon dioxide islands is not resolved, to avoid lateral positioning errors. In this case, the probe detects an area average of the surface potential. In the following discussion the voltage values have been corrected to take into account the area ratios of charged insulator and ground potential silicon. Thus, the voltages plotted are those of the surface oxide of the square islands. All measurements were done in nitrogen ambient at RH = 25%.

The oxide surface voltage reaches a steady-state value within about 5 sec, when the corona charge is set just below sparking voltage. For lower voltages the time to steady state is greater. In the actual process used for decoration, the surface voltage reaches steady state in about 10 sec. The standard charging time used in the decoration process is set at 18 sec.

The magnitude of the oxide surface voltage at steady state depends mainly on the grid line geometry and is greater for higher ratios of oxide area to bare silicon area for a square geometry. This is shown in Fig. 2 where the oxide surface voltage, corrected for the area measurement effect, is plotted *vs.* the area of the oxide covered surface. There is little dependence on oxide thickness. This is shown in Fig. 3 for three oxide thicknesses of the same square geometry.

The observations indicate that the charging of a surface containing closely spaced insulator and conductor regions is limited mainly by the conducting areas. As the ions collect on the insulator they generate an electric field in the gas ambient which causes subsequent ions to move toward the ground potential regions before arriving at the insulator surface. Thus,

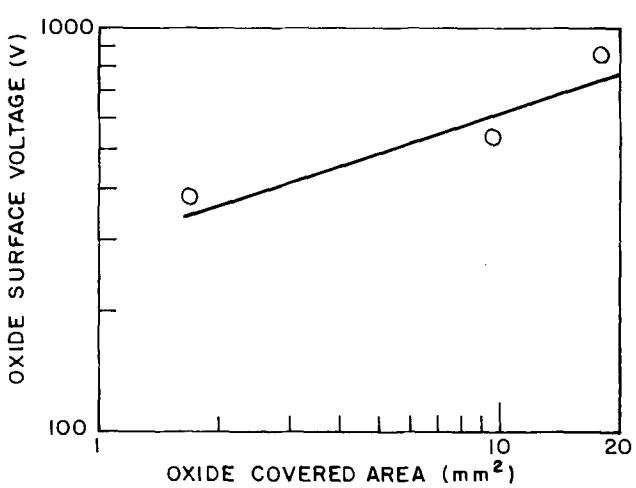


Fig. 2. Oxide surface voltage charged to saturation *vs.* area of oxide-covered surface. Oxide thickness is 10,000Å.

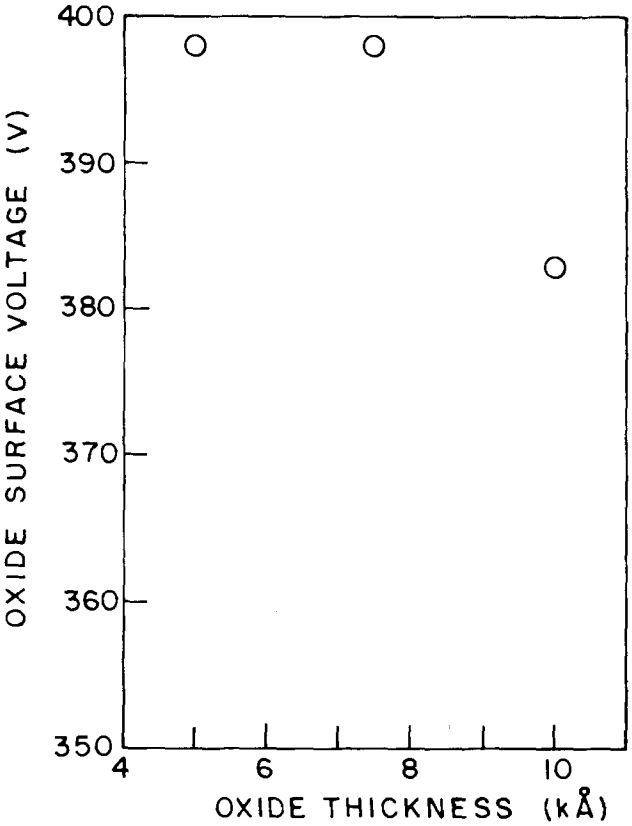


Fig. 3. Oxide surface voltage charged to saturation *vs.* oxide thickness for oxide-covered area of 1.7 mm².

for the geometries of interest, the oxide surface voltage is not determined by the oxide breakdown potential (except for very thin oxides or very large insulator areas).

Further support for the above is gained from the dependence of oxide steady-state voltage on corona voltage, shown in Fig. 4, and on corona wire-to-sample spacing, shown in Fig. 5. Based on the geometry-limited model of charging, the decrease in voltage for decreasing corona voltage or increasing spacing is related to deflection of incident ions from the charged oxide.

The ambient relative humidity must be controlled to prevent lateral current flow on the oxide surface.

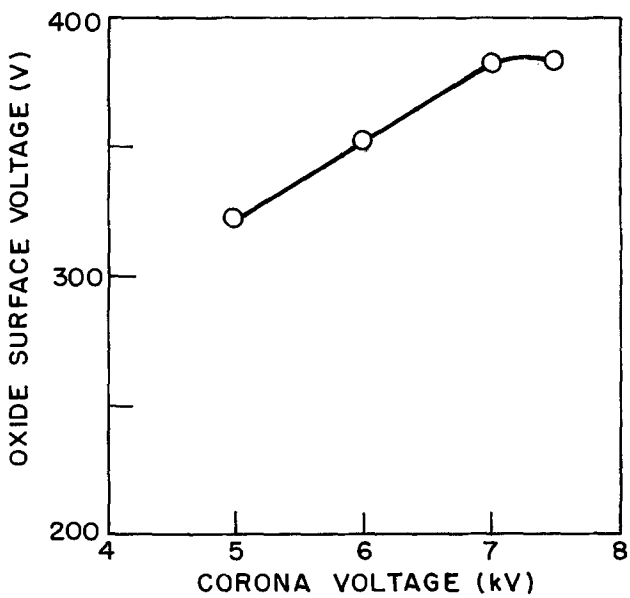


Fig. 4. Oxide surface voltage charged to saturation *vs.* voltage of corona wires for oxide 10,000Å thick and area of 1.7 mm².

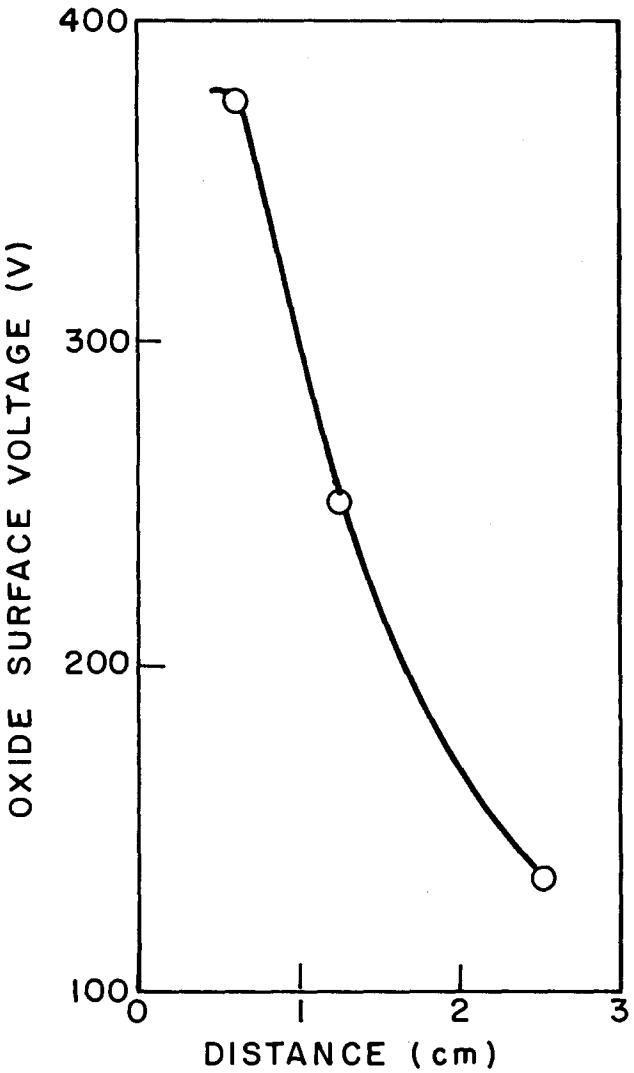


Fig. 5. Oxide surface voltage charged to saturation vs. distance from wafer to corona wires at 10 kV for oxide 10,000Å thick and area of 1.7 mm².

The oxide surface voltage decay rate after charging increases greatly above 30% RH for thermal silicon dioxide, CVD silicon dioxide, and CVD PSG, as shown in Fig. 6. The surface voltage will also decay rapidly if the bulk conductivity of the oxide is high due to the presence of moisture. Thus it is best to remove adsorbed or absorbed water before charging by heating at 200°C for 5 min in air. This has been made the first step in the standard process to ensure retention of surface charge on the sample.

The fact that the surface voltage of the sample insulator regions depends on the geometry of insulator and conductor regions is very important for the process implementation. Since the surface voltage depends on this geometry, it does not depend on the insulator thickness except for very thin insulators not used for passivation. Thus, the surface voltage is not set by insulator dielectric breakdown (except at latent or partial defects, as will be described later). If the surface voltage were set by dielectric breakdown the insulator regions over metal would have a lower voltage than those over the primary silicon oxide. In this case, a decoration conforming to the metal interconnects would result after charging and decoration. This is not normally desired for defect detection.

In the above discussion we have assumed that the sample is a chip or a wafer with the passivating layer etched open at the contact pads and at the grid lines. These etched-open regions furnish the closely spaced geometry of insulator-conductor required so that the surface voltage does not depend on whether the

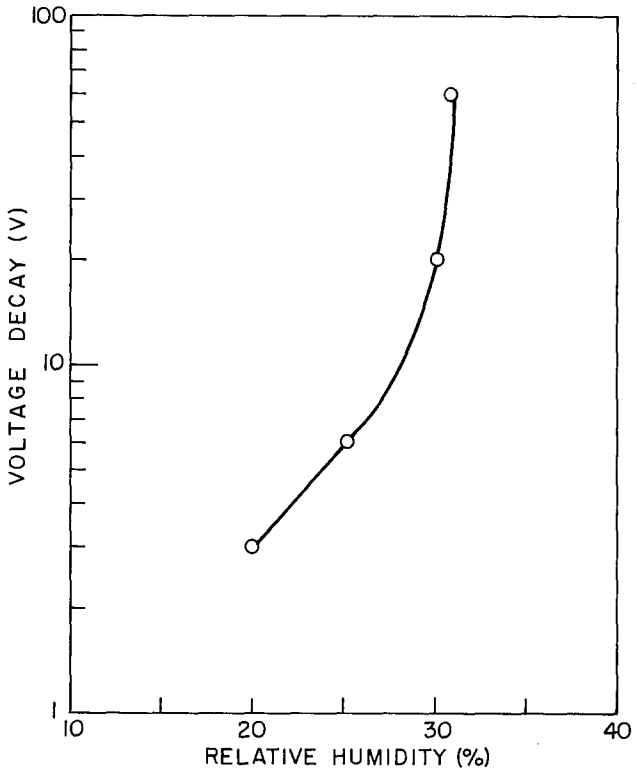


Fig. 6. Oxide surface voltage decay in first minute after charging vs. relative humidity.

passivating layer is over metal or over insulator. It is also possible to decorate wafers with a uniform insulator over metal (before the passivation layer is etched open). This can be done if a grounded conducting grid is placed over the wafer during the charging. A convenient grid consists of an aluminum sheet (0.8 mm thick) with 3.5 mm diam holes on 5.0 mm centers. This grid, placed over the wafer, furnishes the closely spaced insulator; conductor geometry required for the proper charging. When the grid is used, charge is deposited only at openings in the grid.

An important consequence of the charging properties is that the surface charge and potential around a defect decrease laterally as the defect is approached due to ion deflection during charging and to surface conduction. Thus, there is a smaller margin around a crack or pinhole of lower surface potential than around the potential in nondefect areas. This effect increases detectability since it magnifies the defects as far as charged particle deposition is concerned by providing a halo region free of carbon. The margin is of the order of 25 μm in lateral dimension.

For the process implementation it is necessary that the surface charge remain on the passivating layer for a time equal to the delay between charging and deposition plus the deposition time. This total time is about 20 sec, and it is required that the dielectric relaxation time of the passivation layer be about 20 sec or greater. Thus a bulk resistivity of about 10^{13} Ω cm or greater (at room temperature) is needed. By cooling the sample during charging and by the use of cooled particle suspensions it is possible to decorate defects on layers of lower resistivity.

Carbon Black Deposition

After the sample is charged it is immersed in a suspension of charged carbon black particles in an insulating liquid. The carbon black particles are of sign opposite to that of the surface charge and are thus deposited on the nondefect regions of the insulator, resulting in a reverse decoration, as shown in Fig. 7.

Suspension properties.—Various carbon black suspensions were tested which included commercially available electrophotographic toner concentrates and

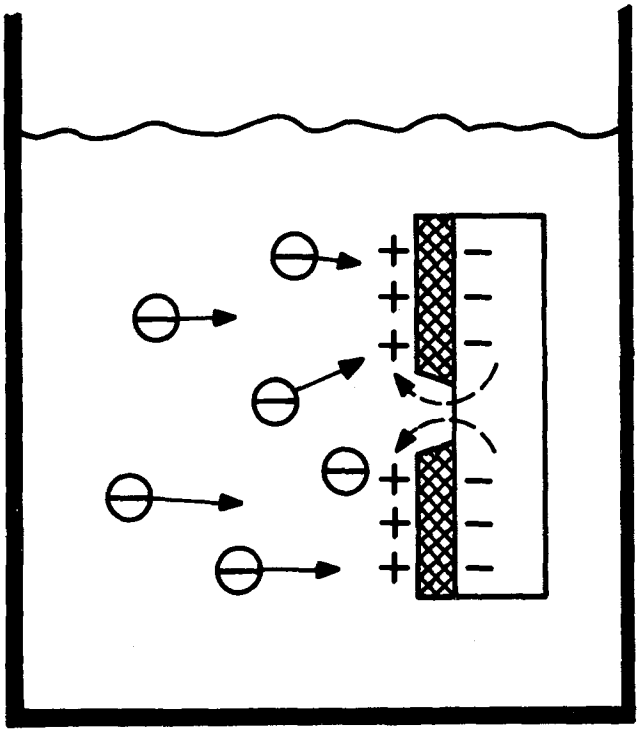


Fig. 7. Reverse decoration of defects after corona charging of insulator regions with ions of opposite sign to that of decorating particles in suspension. Dashed lines indicate forces on carbon particles at defect.

formulations prepared in our laboratory. Best results were obtained with a carbon black suspension (16) prepared in the following way. First a concentrate is made from: 17.0g Raven 1255 carbon black (Columbian Division, Cities Service Company); 100.0 ml toluene; 10.0 ml of 50g/50 ml toluene dilution of Lubrizol 894 (Lubrizol Corporation); and 10.0 ml of 50g/90 ml toluene dilution of AC Polyethylene-grade 430 (Allied Chemical). These ingredients are agitated for about 5 min with an ultrasonic probe at 100W power level to disperse the carbon black.

This concentrate is added at a proportion of 0.75 to 1.00 ml to 400 ml $C_2Cl_3F_3$ and stirred to produce the suspension. The concentrate and dilute suspension are stable for long periods (months). The carbon black in this suspension is negatively charged so that positive corona potentials are used for reverse decoration.

The materials used are readily available. The carbon black has an arithmetic mean particle diameter of 200Å and a nitrogen adsorption surface area of 130 m^2/g. The surface of the carbon black as supplied is acidic by addition of volatiles (17). Lubrizol 894 is an ashless dispersant additive for heavy-duty engine oils. Weight percent of nitrogen ranges from 1.65 to 1.95% (18). AC Polyethylene-grade 430 is a polyethylene-vinyl acetate copolymer (30% vinyl acetate). Its softening point is 60°C (19).

Measurements were conducted to characterize the electrical state of the carbon particles in the dilute suspension by depositing the carbon black on metal foils while recording the current, and then weighing the deposited carbon by difference. This was done as a function of applied voltage and time. The weight of carbon black deposited and the charge transported varied linearly with voltage and time. For electrode spacings of 1.7 cm on each side of a metal foil, an applied voltage of 100V for 4 min resulted in a deposition of 3.2×10^{-4}g carbon black per square centimeter. Tests such as these are convenient for monitoring the electrical properties of the suspension and ensuring reproducibility of these properties. Combined charge transport and weight measurements resulted in a charge per single carbon black particle of 5×10^{-2} electronic charge per particle, assuming all particles to be 200Å diam and singly dispersed. Since the minimum charge can be no less than 1 electronic charge per particle, the carbon black is not monodispersed but is aggregated at least by a factor of 20. Indeed, this aggregation is essential to obtaining dense black on the charged insulator surface since the surface charge after corona charging is only about 4×10^{11} electronic charges per square centimeter. This would result in somewhat less than monolayer coverage if the carbon were monodispersed with one electronic charge per particle. Actually, the layer deposited is many particles thick. Thick layers are an advantage since the optical density is saturated, and relatively large variations in thickness can be tolerated without affecting the percentage of light reflected.

The recommended ratio of 1 ml of the concentrate in 400 ml of $C_2Cl_3F_3$ results in a suspension containing 0.1g of carbon black; at least 10 IC wafers (75 mm diam) can be decorated with it.

Deposition Properties

The detection of cracks and pinholes is carried out quite conveniently by microscopic observation. An example is shown in Fig. 8. In this sample defects were deliberately induced by extreme heat-treatments not normally experienced in manufacturing or use. This was done with all samples shown here to generate high defect densities for purposes of illustration. Extensive comparison tests confirmed that every defect detected by etching (13,14) of the underlying aluminum through the defects was detected by the carbon black reverse decoration. This was done in two ways. Wafers and chips were decorated with carbon black, and photomicrographs were taken of crack and pinhole patterns. The carbon black was then removed and aluminum etching at 50°C for 5, 7, 10, and 15 min was done. The samples were again photomicrographed and the results compared. Hundreds of micrographs from many different sample types were compared and, in every case, all defects detected by etching were also clearly outlined by the carbon black. In the second method samples were decorated with carbon black and then aluminum etched with the carbon black in place. Again, the correlation was excellent. An example of the latter test is shown in Fig. 9, where the carbon black surrounds a pinhole defect in the passivation layer as confirmed by etching of the underlying aluminum.

Various carbon black suspensions have different voltage thresholds for deposition (20). The voltage threshold is that surface voltage on the insulator below which the carbon black will not deposit. For a given surface charge density, it is a function of the carbon black suspension and of the insulator properties. Since

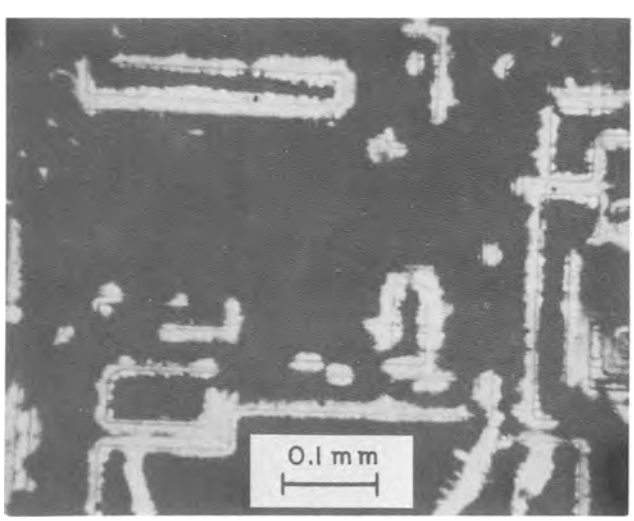


Fig. 8. Carbon black deposited on device to reverse decorate the defects. High contrast renders microscopic evaluation fast and sensitive.

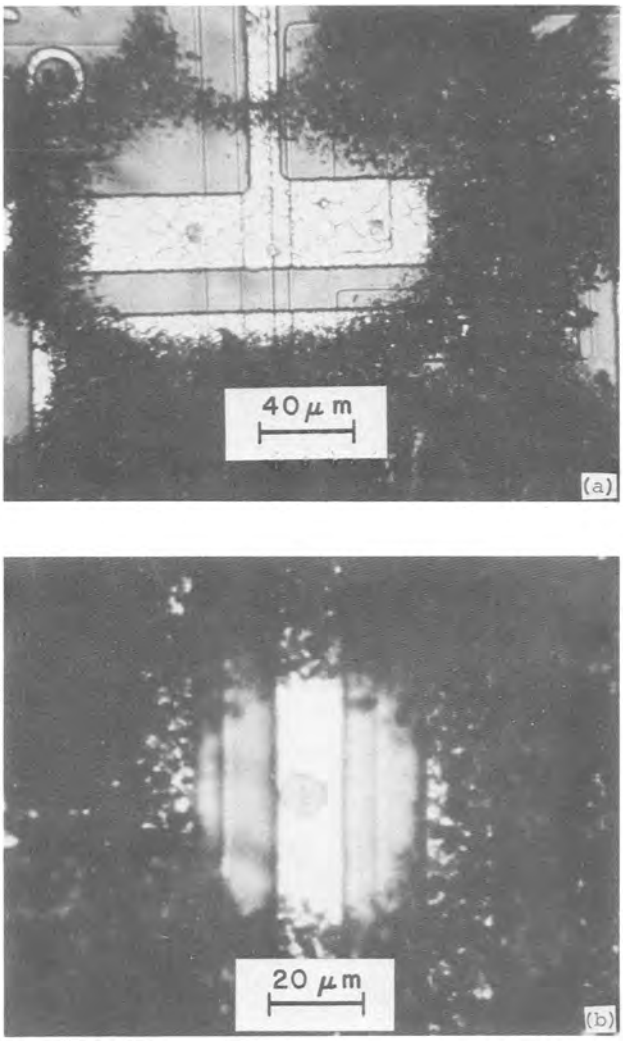


Fig. 9. Confirmation of defect detection by the reverse decoration method. Sample was aluminum etched at 50°C for 5 min without removing carbon black. Etched aluminum is seen as slightly darker circular area in the aluminum line.

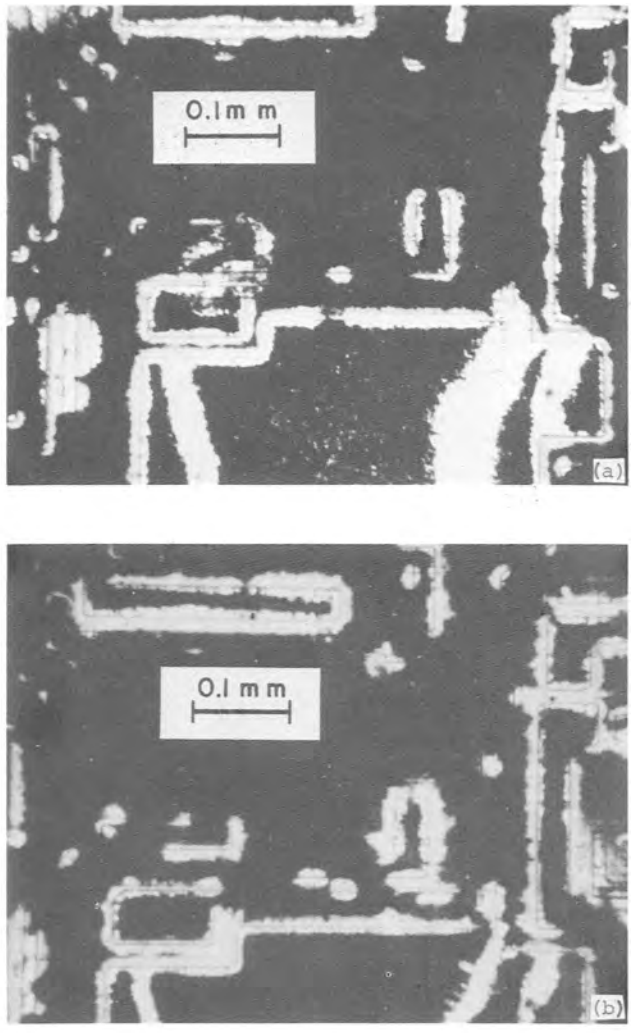


Fig. 10. Carbon black deposition with high threshold voltage in (a) compared to one with low threshold voltage in (b).

the surface voltage profile decreases to zero voltage radially around a pinhole, and laterally at a crack, a clear margin in which no carbon black is deposited is found around defects. The extent of this clear area or halo is a function of the threshold voltage for deposition and the surface conductivity. To avoid excessive width of clear areas a carbon black suspension formulated to have low threshold voltage was used, as described previously. This may be compared with a high threshold formulation in Fig. 10(a) and (b), where the differing margins are clearly evident.

As noted, the decrease in surface voltage near a defect leads to a clear margin around defects. Two effects contribute to the voltage decrease: (*i*) During charging ions are deflected to the defect area by the fringing fields; and (*ii*) finite surface conduction results in surface charge motion which modifies the charge distribution. At high corona potentials (10,000V) the ion deflection is a relatively small factor and, in this case, surface ion motion results in a nondeposited area which increases with time between charging and carbon deposition. For the lower voltage normally used (7000V) ion deflection effects are much greater, and in this case surface ion motion tends to shrink the nondeposited area for the first few seconds between charging and deposition. These effects are shown in Fig. 11(a), (b), and (c). In (a), deposited 4 sec after charging, there is a wide margin due to ion deflection during the charging. In (b), deposited 10 sec after charging, the margin has decreased due to surface ion motion. In (c), deposited 120 sec after charging, the margin has increased due to surface charge leaking off. Because of these effects a standard delay of 10 sec is used between the cessation of charging and the deposition of carbon black.

The width of clear, undeposited margin can be varied also by varying the temperature of the sample during charging and deposition. Using a thermoelectric cold plate, samples were cooled to −7°C during charging and then immersed in the carbon suspension held at −7°C. The defect margin was only about one third of that found for the same sample decorated at 23°C due to reduced surface conductivity.

Detection of partial pinholes is also possible with the reverse technique. Partial pinholes of 5000Å depth in 7000Å total thickness of thermally grown silicon oxide and 1.5 μm diam could be detected by heating the sample for 10 sec at 100°C between charging and deposition.

The reverse decoration process is very sensitive. Using this process, cracks induced by high temperatures were found in passivation glass at the edges of large aluminum areas on an IC. An example is shown in Fig. 12(a). The cracks shown by carbon black in Fig 12(a) were not seen before the heat-treatment. Thus they are not thin spots at the metal edge but are true cracks induced by heating. These cracks could not be detected by attempts to etch the underlying aluminum through the crack, nor were they detectable by scanning electron microscopy at 20,000X as shown in Fig. 12(b). Thus, carbon black reverse decoration can find defects not detectable by etching nor by SEM. When these samples were given a buffered hydrofluoric

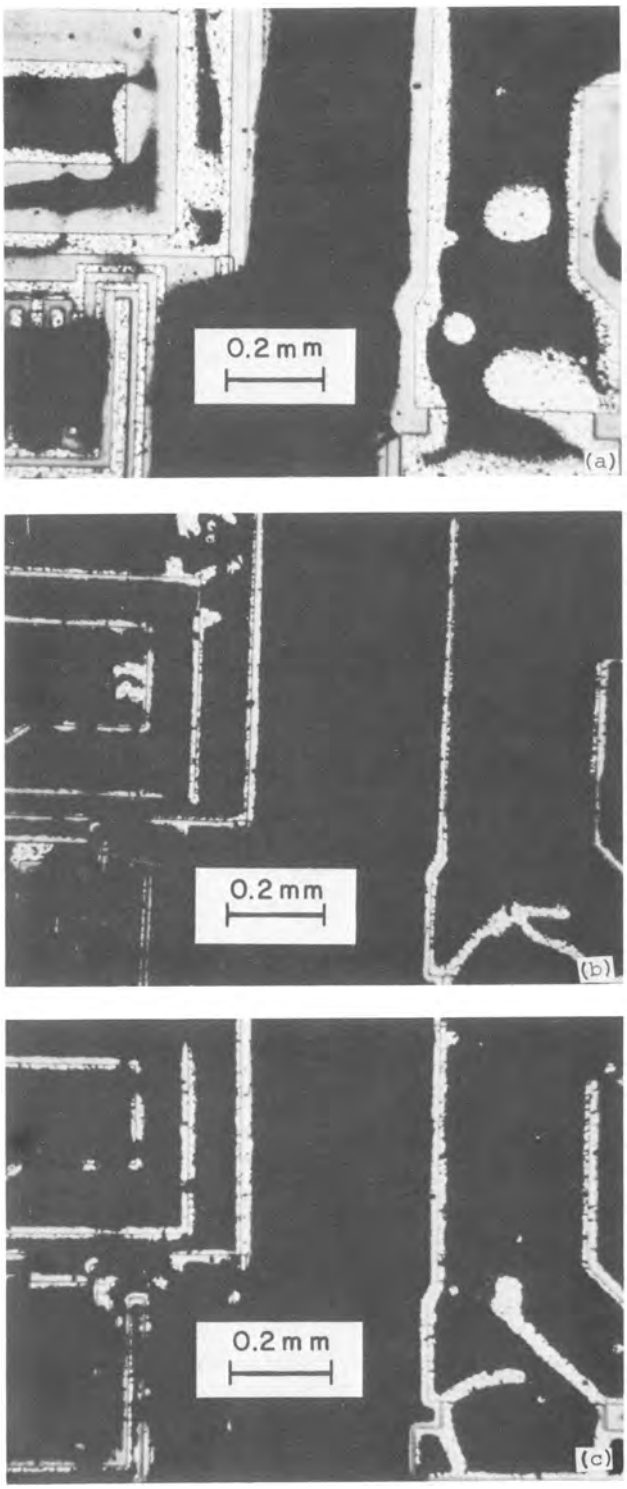


Fig. 11. Carbon black reverse decoration as function of time delay between charging and deposition. The time delays are (a) 4 sec, (b) 10 sec, (c) 120 sec.

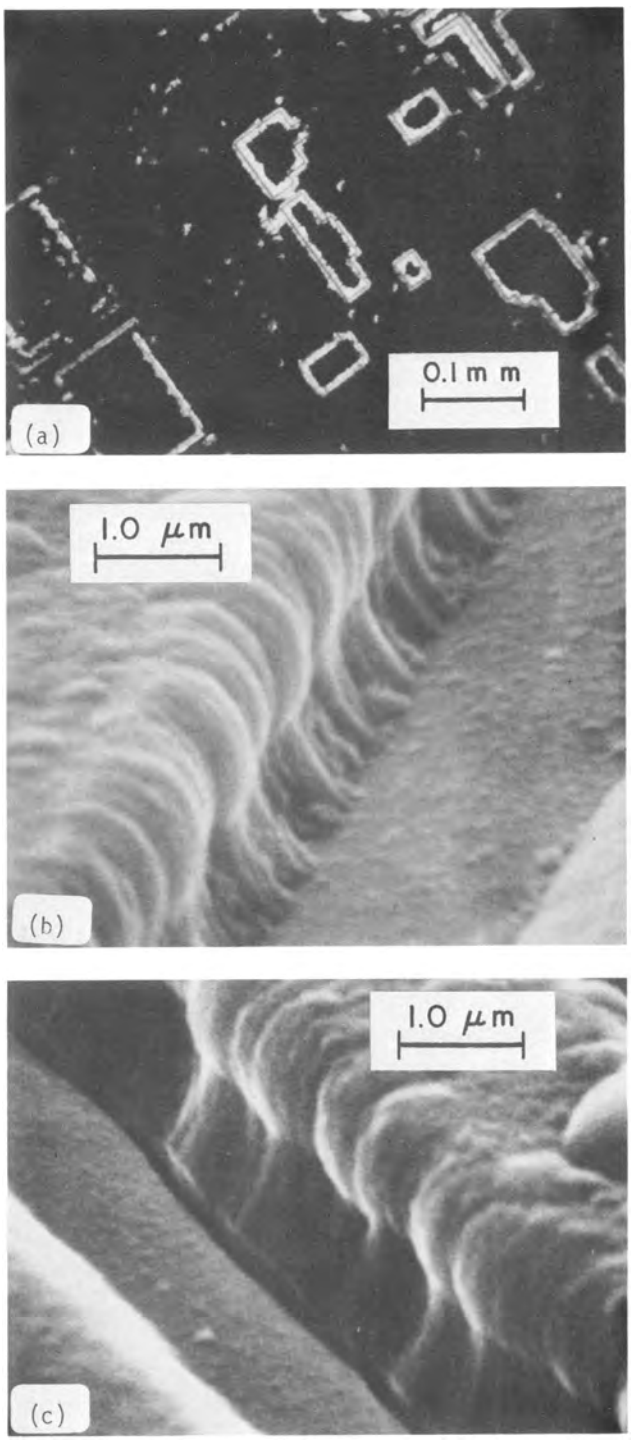


Fig. 12. Example of cracking at edges of large aluminum areas due to extreme heat-treatment. (a) Cracks outlined by carbon black; (b) SEM cannot detect cracks; (c) after 10 sec buffered hydrofluoric acid etching, the SEM does resolve the cracks.

acid etch for 10 sec, which widened the cracks to about 2000Å, it was possible to detect the cracks by aluminum etching and by SEM. The crack detected by SEM in Fig. 12(c) is at the lower edge of the passivation glass over the aluminum metal step. It should be noted that the cracking shown in Fig. 12(a) was exactly reproduced on every IC of an entire wafer. Many of these cracked regions were examined by SEM and no cracks could be detected until the sample was etched in buffered HF. After etching, the cracks as shown in Fig. 12(c) were visible at all edges of the aluminum areas as detected by the carbon black in Fig. 12(a).

Standard Process

The optimum procedure for sample decoration is summarized here: Dust and other particles should be removed from samples by blowing with clean air or by distilled water rinsing, followed by careful drying on a spinner or by rinsing in acetone and then in $C_2Cl_3F_3$.

It is required that the sample be grounded; thus, for wafers, it is sufficient to place the wafer on a grounded plate after ensuring that the reverse side is bare silicon. The normal native oxide is tolerable.

Chips are conveniently handled by fastening them to metal strips with conducting silver paste. Several can be processed at one time. For opened packaged devices,

the lead frame and wire bonds will normally act to connect the silicon to ground. If necessary, the ground connection can be made by painting conducting silver paste from the chip edge to some region of the package which can be grounded.

Samples should be baked at about 200°C for 5 min prior to corona charging. This is conveniently done on a hot plate for wafers and chips or in an oven for opened packaged devices.

The sample should be charged with positive corona for 18 sec with corona wires 2 cm from the sample at a wire potential of +7000V d-c. For wafers or wafer sections which do not have bond pads or grid lines etched open, a grounded grid must be placed over the sample during charging as described previously.

After a 10 sec delay wafers and chips are immersed for 12 sec and opened packaged devices for 6 sec in the carbon black suspension. The entire process is carried out in a glove box at RH $\lesssim$ 30%. The suspension is made from the concentrate described previously in the ratio of 1 ml concentrate to 400 ml $C_2Cl_3F_3$. After the sample is decorated and examined, the carbon black can be removed by ultrasonic agitation in toluene (13).

Nondestructiveness of Method

Several types of extensive tests were done to establish the nondestructive nature of the process. In one test, device wafers were aluminum etched to reveal pinholes. Then the wafers were exposed to the corona discharge at 10,000V d.c. for various times ranging up to 100 sec. After the corona discharge, aluminum etching revealed no new pinholes.

In a second test, a set of five device wafers was reverse decorated with carbon black, examined microscopically, and cleaned. This process was repeated five times. Only one wafer showed new defects (pinholes). These were found after the third carbon black deposition test. During cleaning, this wafer had been placed face down in the bottom of the ultrasonic tank, and it is believed that the mechanical contact caused these defects. Subsequent tests with the ultrasonic tank used in this manner did induce defects.

A third test involved automatic probe testing of CMOS wafers. These were chosen since it is known that CMOS devices are susceptible to static electrical damage. Two large (75 mm) CMOS device wafers were probed, and a map was made of good and bad devices. Then the wafers were charged, decorated, and cleaned. The wafers were probed again. One wafer showed a net loss of four devices out of about 130 good devices. The other wafer showed a net gain of five devices out of about 100 good devices. These variations are within the normal tolerance of repeated wafer probe testing.

In a fourth test, hermetically packaged CD 4007 devices were delidded and the threshold voltages and subthreshold leakage currents of the NMOS and PMOS devices were measured. The devices were then submitted to the decoration process and cleaned. Threshold voltages and leakage currents were measured again and no changes were found.

It is concluded that the process of corona charging and decoration is nondestructive. No life tests of decorated and cleaned devices were done, however. Thus, it may be possible to use decorated wafers for product, but an assessment of reliability by accelerated life testing is needed.

Feasibility Study of Automated Read-Out

A major advantage of the carbon black reverse decoration method is the high optical contrast available in reflected light microscopy. This permits a fairly simple form of automated quality assessment with a microscope-mounted photocell to measure the integrated light reflected from the defect areas. This technique is much simpler than the use of computer-implemented image analysis. The latter would provide a defect count, which the integrated reflected light method does not furnish. However, based on our feasibility study, it is believed that the simple method explored here could be used in a production facility to rank wafer quality and set a quality acceptance criterion.

A photocell microscope system was assembled to take direct readings of reflected light from decorated wafers. The arrangement used is shown schematically in Fig. 13. By placing a plano-convex lens of 57 mm focal length at the end of the camera tube, an image of the light source field stop was obtained about 6 cm from the end of the camera tube. This image, of uniform luminance, was placed on the photocell faceplate. The photocell employed an S-11 cathode and was operated at 100V. Light intensity was adjusted to give convenient current levels, and the over-all magnification was chosen so that a large portion of the circuit was visible, but bond pads and grid lines were excluded. Shielding prevented introduction of ambient light. Current readings were taken of each of 20 circuits of two wafers. For the "good" wafer, the lowest individual current was 2.9×10^{-9}A, the highest was 5.5×10^{-9}A, and the average was 3.5×10^{-9}A. For the "bad" wafer, the lowest current was 6.7×10^{-9}A, the highest was 1.5×10^{-8}A, and the average was 1.0×10^{-8}A. Pinhole counts on these wafers resulted in a difference of a factor of two in defect density. Thus, the photocell current measurement can easily detect a difference of a factor of two in pinhole density and is probably more sensitive than this.

Advantages of the Reverse Decoration-Carbon Black Method

In this section the relative advantages of the carbon black reverse decoration technique are summarized. In the discussion several unique advantages of the

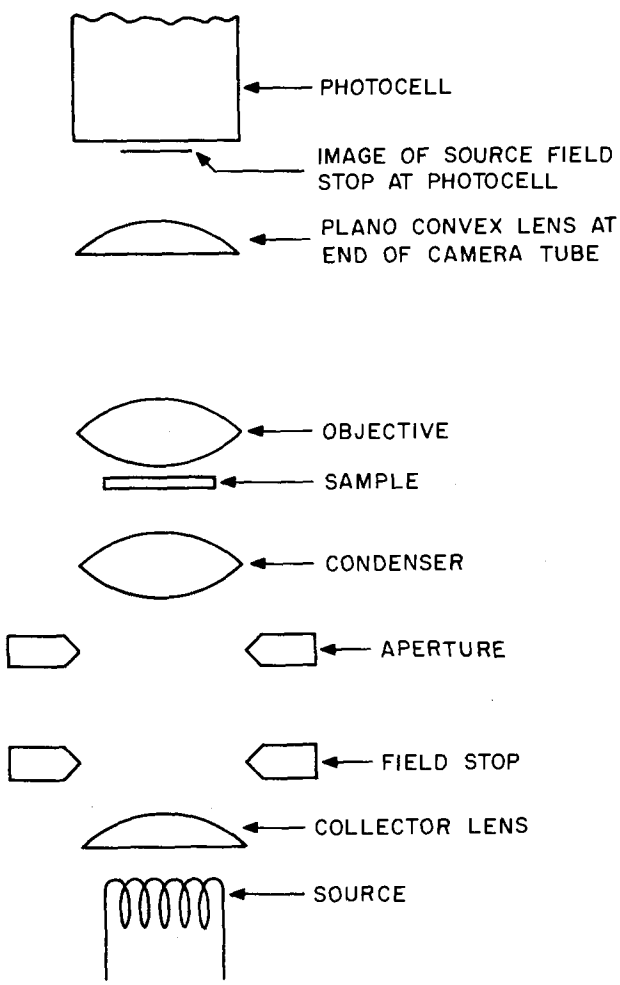


Fig. 13. Schematic of microscope use for obtaining image of source field stop at photocell for reflected light measurements.

corona-charging technique as used in the reverse decoration are pointed out. The use of the high voltage discharge, which initially appears to violate the normal rules for treatment of devices (particularly MOS type), is seen to be a definite advantage and to render the process actually nondestructive.

Speed.—In the standardized process the sample is charged for 18 sec, and after a 10 sec delay is immersed in the carbon black suspension for 6-12 sec. Thus the total decoration process time is, at most, about 40 sec. We do not include in this time the recommended 5 min, 200°C bake since this can be done in batch.

Simplicity.—The process is very simple and does not require precise positioning or delicate manipulations. The sample is placed on a platform for charging and then dipped into the carbon black suspension. The process thus shares the simplicity of chemical etching, with the added relaxation that the time of immersion in the liquid is constant for a wide range of samples, and does not depend on sample parameters.

Permanence of decoration.—Liquid crystal and bubble formation techniques (11) are real-time methods in that the decoration exists only during the process implementation. A photograph must be made for later examination. The carbon black decorated sample, however, has a permanent decoration and it may be set aside for future examination.

Nondestructive nature.—Tests by wafer probing showed no device loss after cleaning, as described previously. In methods which make use of voltages applied between electrodes and the sample in an electrolyte (11), as used in copper decoration, for example, there is the possibility of sample damage by high currents at dielectric weak spots. The corona-charging process in a dry ambient (RH $\lesssim$ 30%) is inherently nondestructive since corona potentials are well below sparking voltage and the corona has a very high impedance. Furthermore, any dielectric weak spot will discharge only the surface charge immediately surrounding it, and the stored energy is not great enough to cause any dielectric damage.

Avoidance of junction effects.—Decoration methods using electrolytes or other low resistivity liquids, such as alcohol or acetone, are limited by device junction effects. For example, a dielectric defect over a reverse-biased junction may not be detected or the deposition rate of decorating material may be slow. This effect can be overcome or moderated by illuminating the sample to induce photocurrents in reverse-biased junctions, but this may be difficult in some cases. For example, in the case of a large sample, as a wafer immersed in a decorating suspension of light-scattering particles, insufficient light may reach certain portions of the sample. On the other hand, the corona current impedance is so great that even reverse-biased junctions are sufficiently conducting that they do not interfere with charging effects.

High contrast.—The reverse decoration with carbon black provides a very high contrast when imaged in a microscope in reflection. This high contrast contributes to rapid evaluation of the relative quality of samples by the observer and, in addition, permits automated assessment by use of a photocell attachment to the microscope.

Ease of observation.—The reverse decoration process leaves the defect uncovered for easy examination by optical or electron microscopy. All other known processes result in direct decoration and the defect is covered or altered in some way.

Limitation.—The only fundamental limitation encountered thus far has been devices with regions of metal not connected to the semiconductor. This floating metal is brought to a high potential by the corona so that the metal is outlined with carbon black, but no defects can be detected over it. Thus, floating gates on some memory devices would not decorate properly if the device were examined at a stage of processing before the overlying metal is deposited. The other regions of the sample could be successfully decorated, however. After the device is completed and the second metal covers the floating gate, then it is possible, of course, to decorate the device in the standard manner.

Conclusion

A simple, nondestructive technique for detection of defects in insulating passivation layers on IC's has been described. It is useful for process research and control since it is very sensitive and results in a high contrast decorated sample. Because of the reverse nature of the decoration, the defect is left exposed for examination. Since the method is nondestructive, the carbon black can be removed and a process sequence can be evaluated at various stages with the same sample. The method holds promise as a production monitoring tool since it is nondestructive and since automated defect assessment is possible.

The principal application of this decoration process, thus far, has been that of detecting defects in and optimizing processing conditions of CVD SiO_2 and PSG passivation layers. In addition, defects in thermal SiO_2, including gate oxides, can be detected. Pinholes in photoresist and other polymer layers have been found using this method. Cracks and pinholes in protective glass coatings on steel plates also can be readily detected.

Acknowledgments

This work was one phase of a larger contract study of which Werner Kern was project scientist. For his advice and careful manuscript review I am very grateful. George L. Schnable made many important suggestions throughout this effort. Ruth Allen did most of the processing and experimental work, and C. Edward Tracy confirmed the carbon black defect detection by using etching techniques. A. Wayne Fisher, Leon Greenberg, Eugene Jordan, and Robert Vibronek supplied samples and I am grateful to them and to Gerald S. Lozier for useful discussions. Also, K. Schlesier assisted in some measurements.

The research contained in this report was partially supported by the Advanced Research Projects Agency, Order 2397, through the National Bureau of Standards Semiconductor Technology Program, Contract 5-35913, and RCA Laboratories, Princeton, New Jersey.

Manuscript submitted Dec. 2, 1976; revised manuscript received March 21, 1977. This was Paper 434 presented at the Washington, D.C., Meeting of the Society, May 2-7, 1976.

Any discussion of this paper will appear in a Discussion Section to be published in the June 1978 JOURNAL. All discussions for the June 1978 Discussion Section should be submitted by Feb. 1, 1978.

Publication costs of this article were assisted by RCA Laboratories.

REFERENCES

1. G. L. Schnable, W. Kern, and R. B. Comizzoli, *This Journal*, **122**, 1092 (1975).
2. H. Koelmans, *Ann. Proc. Reliab. Phys. (Symp.)*, **12**, 168 (1974).
3. W. M. Paulson and R. W. Kirk, *ibid.*, **12**, 172 (1974).
4. A. Shumka and R. R. Piety, *ibid.*, **13**, 93 (1975).
5. F. J. Grunthaner, T. Griswold, and H. Bright, *ibid.*, **13**, 99 (1975).
6. A. J. Gregoritsch and R. G. Berger, *ibid.*, **13**, 121 (1975).
7. J. J. Bart, *ibid.*, **13**, 128 (1975).
8. R. B. Comizzoli, *This Journal*, **123**, 386 (1976).
9. R. B. Comizzoli, *RCA Rev.*, **37**, 472 (1976).
10. R. B. Comizzoli, *ibid.*, **37**, 483 (1976).
11. W. Kern, *ibid.*, **34**, 655 (1973).
12. R. B. Comizzoli, Recent News Paper 434 presented at The Electrochemical Society Meeting, Washington, D.C., May 2-7, 1976.
13. W. Kern and R. B. Comizzoli, "Development of Techniques for Measuring the Integrity of

Passivation Overcoats on Integrated Circuits," Final Report for the period April 1975-April 1976, National Bureau of Standards Contract No. 5-35913 (to be issued as NBS Special Publication 400-31).
14. W. Kern and R. B. Comizzoli, *J. Vac. Sci. Technol.*, **40**, 32 (1977).
15. R. B. Comizzoli, G. S. Lozier, and D. A. Ross., *Proc. IEEE*, **60**, 348 (1972).
16. Originally prepared by G. S. Lozier, RCA Laboratories.
17. Data Sheet, "Industrial Carbon Blacks," Cities Service Company, Akron, Ohio (1975).
18. Data Sheet, "Lubrizol 894," Lubrizol Corporation, Cleveland (1974).
19. Data Sheet, "A-C Polyethylene," Allied Chemical Company, Morristown, New Jersey (1975).
20. G. S. Lozier, 23rd Ann. Conf. Phot. Sci. Eng., preprint of paper summaries, p. 165, New York (1970).

Morphology and Transport Rates of Mixed IV-VI Compounds in Micro-Gravity

H. Wiedemeier, H. Sadeek, F. C. Klaessig, M. Norek, and R. Santandrea

Department of Chemistry, Rensselaer Polytechnic Institute, Troy, New York 12181

ABSTRACT

The positive effects of micro-gravity on crystal growth and basic properties of the vapor transport reaction were established by analyzing the results of three transport experiments of multicomponent systems performed during the Apollo-Soyuz mission. The systems employed were $GeSe_{0.99}Te_{0.01}$-GeI_4 (A), $GeS_{0.98}Se_{0.02}$-$GeCl_4$ (B), and GeS-$GeCl_4$-Ar (C). The crystallographic analysis is based on a direct comparison of space- and earth-grown (prototype) crystals, employing x-ray diffraction, microprobe, microscopic, and chemical etching techniques. The results demonstrate a considerable improvement of the space-grown crystals in terms of chemical and crystalline homogeneity, surface morphology, and bulk perfection relative to earth specimens. The confirmation of greater mass transport rates than predicted for diffusion-controlled transport in micro-gravity suggests the existence of "thermochemically" induced convective motion in chemical vapor transport systems. The morphological observations indicate, that the presence of different convective components yields turbulence which adversely affects crystal quality as observed on earth. The internal consistency and agreement between our ASTP and Skylab results obtained for several compounds, transport agents, and temperature gradients strongly support the validity of these observations.

Present models of chemical vapor transport (1) in closed ampuls predict that mass transfer via the gas phase is diffusion controlled at lower system pressures and occurs by convection at higher pressures. Crystal growth studies on MnS, MnSe (2), and on CdSe (3) indicate the effects of tube treatment, transport rate (2), and of transport mode (3) on crystal morphology. Systematic mass transport rate studies on the systems GeTe (4) and GeSe (5) demonstrated distinct changes in growth habit as a function of transport mode and a decrease in crystalline perfection with increasing convective contribution to the transport process. Analogous studies of other IV-VI and II-VI compounds in our laboratory reveal similar results. Based on the above observations it was predicted that crystals of improved quality could be grown in the absence of convective interference in a micro-gravity environment. The results of our transport studies on GeSe and GeTe performed on Skylab (6) demonstrate a considerable improvement in crystal morphology relative to corresponding ground specimens. In addition, the mass transport rates observed in space (6) are significantly greater than expected for a diffusion-controlled transport process.

In view of the unexpected mass flux results (6), an extension of these studies to modified systems and experimental conditions was desirable. The primary objectives of the present Apollo-Soyuz space experiments were to confirm the improved crystal morphology and the flux results observed previously (6), to extend these findings to mixed systems, and to further elucidate the cause of the higher transport rates (6).

Key words: chemical vapor transport, Ge-chalcogenides, micro-gravity.

For this purpose, three transport experiments on the systems $GeSe_{0.99}Te_{0.01}$-GeI_4 (A), $GeS_{0.98}Se_{0.02}$-$GeCl_4$ (B), and GeS-$GeCl_4$-Ar (C) were performed during the Apollo-Soyuz Test Program (ASTP). The definition of experimental conditions to meet the above objectives within the technical constraints on ASTP is based on extensive ground studies on these systems. The results of the latter studies in terms of mass flux *vs.* transport agent pressure are shown in Fig. 1. The pressures are for GeI_4 and $GeCl_4$ calculated at the mean temperature of the gradient assuming the ideal gas law. The flux curves reveal the diffusion-controlled transport regime at lower pressures (decreasing flux with increasing pressure) and convection-controlled transport at higher pressures (increase in flux with increasing pressure) (5). Further details are discussed below in connection with the flux results. The analysis of the space experiments is based on a direct comparison of crystal morphology and mass transport rates obtained on earth and in space.

Experimental Procedures

Apparatus.—The transport experiments on Apollo-Soyuz were performed in the multipurpose electric furnace which has been described previously (6). The three transport ampuls enclosed in separate metal cartridges were heated simultaneously in the reaction cavities of the furnace. The temperature gradient employed was 604° → 507°C with an isothermal region of about 1.5 cm length in the hot zone followed by a nearly linear gradient toward the cold end of the ampul. The same temperature gradient and profile were used in the prototype furnace for comparative ground-based studies.

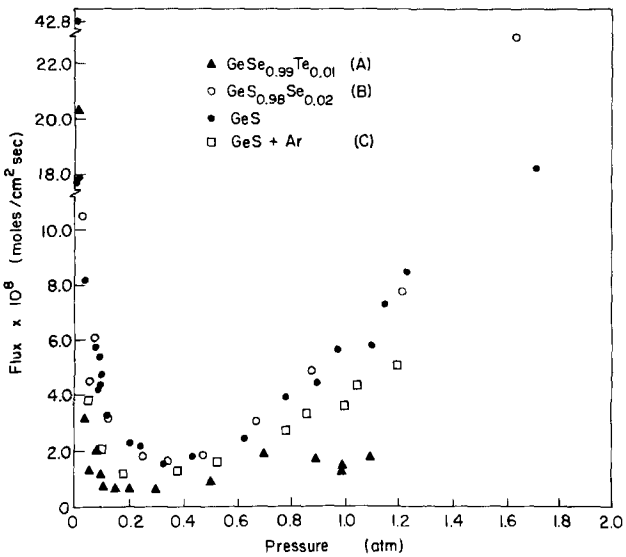


Fig. 1. Mass transport rates in terms of flux vs. pressure of transport agent for the temperature gradient 604° → 507°C determined under ground-based conditions. Transport agent for system A: GeI_4(g); for systems B, C, and GeS:$GeCl_4$(g).

Ampul and sample preparation.—The transport ampuls were made of fused silica tubing of 13.7 mm inner diameter and 150 mm in length. Close to the rounded end the ampuls contained two thin silica rods to prevent the source material from moving throughout the tube. The pretreatment, loading, and sealing procedures of the ampul have been discussed before (2). The polycrystalline starting materials were synthesized by repeated annealing at about 600°C of the appropriate stoichiometric mixtures of the binary compounds GeS, GeSe, and GeTe. The latter ones were prepared from high purity elements (99.999%) by annealing and subsequent sublimation of the products (5). Their crystallographic identity was established by x-ray diffraction techniques, and lattice parameters agreed with literature values for GeS (7), GeSe (8), and GeTe (9). Debye-Scherrer powder patterns of the two mixed compounds used in these experiments (systems A and B) confirmed the presence of a single phase with orthorhombic structure. High purity GeI_4 (99.999%) and $GeCl_4$ (99.999%) were used as transport agents. Ultrahigh purity argon was employed as an inert gas in system C. The ampul designated A in this experiment contained 1.50g of $GeSe_{0.99}Te_{0.01}$ and 123.5 mg GeI_4. Ampul B was loaded with 1.50g of $GeS_{0.98}Se_{0.02}$ and 59.1 mg of $GeCl_4$. The third ampul (C) contained 1.50g of GeS, 61.8 mg of $GeCl_4$, and 1.91 atm of Ar. The corresponding pressures of the transport agents computed for the mean temperature of the gradient in terms of GeI_4 and $GeCl_4$, respectively, and ideal conditions are 0.70 atm (A), 0.94 atm (B), and 0.96 atm (C). The argon pressure in ampul C is twice the partial pressure of $GeCl_4$, thus, yielding a total pressure of about three times the pressure employed for the closely related system B. Under the above pressure conditions, the mass transports on earth are affected by a low (A) and medium (B and C) convective contribution to the over-all transport process (Fig. 1). The ampuls of the comparative prototype (ground-based) experiments were identical with those used in space in terms of dimensions and content. The predominant chemical transport reactions of the solid solutions are analogous to those of the binary compounds (4) represented by

$$GeX(s) + GeY_4(g) = 2GeY_2(g) + \tfrac{1}{2}X_2(g) \quad [1]$$

where X = S, Se, and Te and Y = Cl and I, respectively.

Heating cycle.—The transport ampuls enclosed in hermetically sealed metal cartridges were inserted into the multipurpose furnace by the astronauts. After a heat-up period of about 2 hr the desired temperature gradient (604°C at the source and 507°C at the condensation region) was established. This gradient was maintained within ± 3°C for 16 hr, during which transport and crystal growth occurred. After termination of the experiment, cooling of the ampuls to ambient temperature took place in the furnace over a period of about 4 hr during which a helium quench of the metal cartridges was employed. The amount of transport during the heat-up and cool-down periods, which were identical for the earth and space experiments, was considered in the final flux calculations. In the returned ampuls the residual source material was firmly attached to the ampul wall of the source region. For further analysis the transport tubes were opened in a metal dry box which contained P_2O_5 as a desiccant and which was continuously flushed with purified nitrogen.

Results and Discussion

Structural and chemical homogeneity.—The crystallographic identification of crystals obtained in microgravity was established by means of Debye-Scherrer and Laue x-ray diffraction techniques, using a 114.59 mm diameter powder camera and standard Laue equipment. The lattice parameters of the space-grown crystals and the orientation of their native growth faces are in agreement with those of corresponding ground-based specimens. In view of the relative magnitude of chemical bonding and gravitational forces, the above results were entirely expected.

Laue transmission photographs of $GeSe_{0.99}Te_{0.01}$ (system A) ground and space crystals reveal considerable differences as shown in Fig. 2. The pronounced striations and multiplicity of individual diffraction spots in the Laue pattern of the ground-based crystal (Fig. 2a) indicate a high degree of strain and microstructural inhomogeneities. The x-ray pattern of the space crystal (Fig. 2b) shows the twofold symmetry of the predominant (001) oriented growth face. The considerably better defined diffraction spots indicate improved crystallographic perfection relative to the ground-based sample. Similarly striking differences in diffraction patterns are observed for the majority of randomly selected specimens of $GeS_{0.98}Se_{0.02}$ (system B) and GeS (system C) ground and space crystals.

In order to examine the chemical homogeneity of the solid solutions (systems A and B), the distribution of Te in GeSe (A) and of Se in GeS (B) was investigated using an electron microprobe analyzer (Model EPA 400S). For this purpose, cleaved faces of earth (prototype) and space-grown crystals and stoichiometric GeSe and GeTe as reference crystals were used. The relative concentration of Te (in GeSe) and of Se (in GeS) was measured along three directions approximately parallel to the a and b axes of the (001) ori-

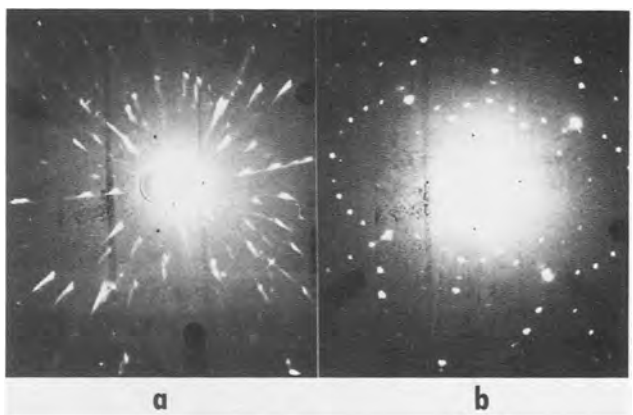


Fig. 2. Laue x-ray diffraction transmission photographs of (001) oriented $GeSe_{0.99}Te_{0.01}$ (system A) single crystal platelets: (a) ground-based (prototype), (b) space grown.

Table I. Distribution of Te (A) and Se (B) in ground-based and ASTP space-grown crystals

System	Concentration (atomic %) Average all data	Average parallel a axis	Average parallel b axis
$GeSe_{0.99}Te_{0.01}$ (ground-based, A)	1.83 ± 0.6	2.03 ± 0.5 1.71 ± 0.6 1.78 ± 0.4	1.59 ± 0.4 2.07 ± 0.3 1.81 ± 0.4
$GeSe_{0.99}Te_{0.01}$ (ASTP, A)	1.56 ± 0.1	1.59 ± 0.03 1.52 ± 0.08 1.56 ± 0.02	1.58 ± 0.04 1.57 ± 0.06 1.58 ± 0.02
$GeS_{0.98}Se_{0.02}$ (ground-based, B)	0.395 ± 0.092	0.371 ± 0.068 0.399 ± 0.061 0.399 ± 0.028	0.374 ± 0.034 0.402 ± 0.020 0.422 ± 0.015
$GeS_{0.98}Se_{0.09}$ (ASTP, B)	0.462 ± 0.048	0.470 ± 0.014 0.448 ± 0.020 0.470 ± 0.007	0.459 ± 0.046 0.471 ± 0.009 0.463 ± 0.007

ented crystal platelet. Along each direction intensity measurements were performed at several different locations. The results in columns 3 and 4 of Table I are average values for data points along a given direction. The error limits represent maximum deviations in atomic concentration of individual locations from the mean value for all points along the particular direction. The corresponding data for all points are listed in column 2. Based on the relative magnitude of the local variations in concentration, the distribution of Te in the solid solution of starting composition $GeSe_{0.99}Te_{0.01}$ is considerably more homogeneous in the space than in the ground-based crystals. Under present conditions, the uncertainty in the Te concentration of individual points is between 4 and 5% for the space and ground-based crystals. The corresponding improvement in the distribution of Se in the space crystals compared to the ground specimens for the compound of initial composition $GeS_{0.98}Se_{0.02}$ is less pronounced than for Te in system A. The uncertainty in Se concentration of individual points is about 5% for the ground and space crystals. For the space-grown materials of both systems, the local variations in the concentration of Te and Se, respectively, along different directions in the (001) plane are within the limits of uncertainty. The deviation of observed concentrations of Te and Se, respectively, in the transported crystals from the composition of the starting materials is due to slightly different transport properties of the binary compounds in the mixed systems. The inclusion of transport agent in the ground and space crystals appeared to be at the detection limits (about 10^{-2}%) of the instrument (6).

Optical microscopy of crystals.—Before a discussion of the microscopic examination of individual single crystals, a macroscopic view of the condensation pattern of the residual gas phase (primarily transport agent GeI_4) on the ampul walls of system A (Fig. 3) obtained during the cool-down period shows significant differences. The GeI_4 deposition in the ground (prototype) ampul (Fig. 3a) shows predominantly clustering and dendritic-type material with a distinct curvature of individual dendrites which have a length of up to about 8 mm. The transport agent in the space ampul (Fig. 3b) is condensed in form of well-developed, transparent single crystal platelets and a few needles. Based on the deposition patterns observed in space and on earth, the apparent presence of turbulent gas motion under ground conditions (Fig. 3a) during rapid cooling of the ampul is completely absent in micro-gravity environment.

Optical photomicrographs of representative $GeSe_{0.99}Te_{0.01}$ (system A) ground (prototype) and space crystals show qualitative differences in surface morphology (Fig. 4). The majority of prototype crystals (Fig. 4a) reveals ragged edges, twinning, and frequently stepped faces. The space crystals (Fig. 4b) have smoother surfaces and usually better defined edges. The average edge lengths of the ground specimens range from about 2-8 mm. The slightly smaller dimensions of the space

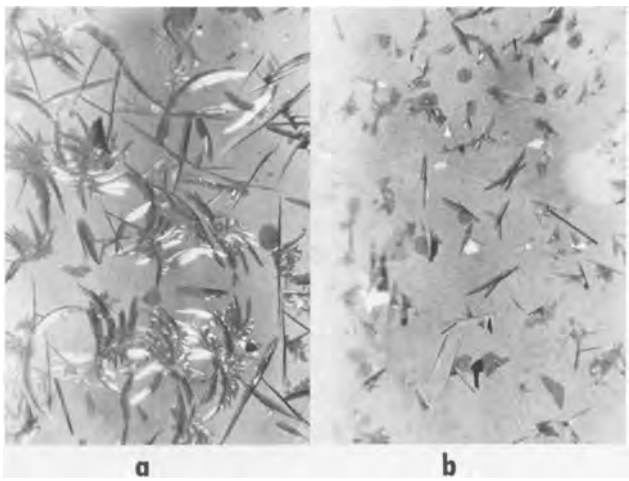


Fig. 3. Deposition pattern of transport agent GeI_4 (system A) on ampul walls: (a) obtained under ground-based (prototype) conditions, length of crystals 2-8 mm; (b) observed in micro-gravity, crystal sizes about 2-4 mm.

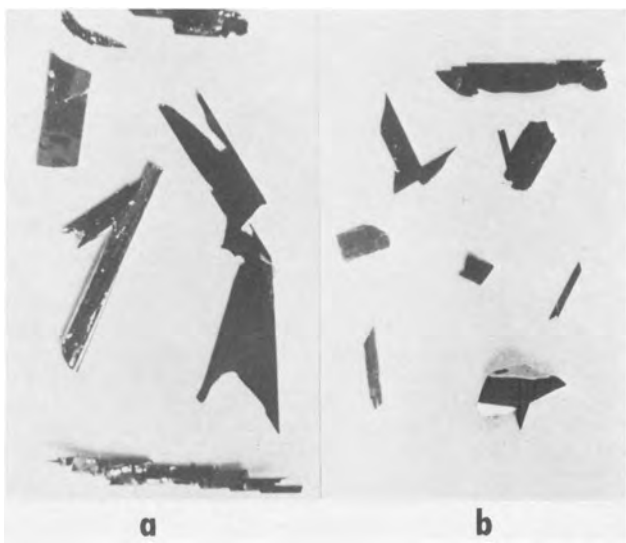


Fig. 4. Representative crystals of $GeSe_{0.99}Te_{0.01}$ (system A): (a) ground-based (prototype), (b) space grown. Edge lengths of ground (a) crystals 2-8 mm and of space (b) platelets 2-4 mm.

crystals are consistent with the lower transport rates in micro-gravity observed for this system (Table II).

Photomicrographs of typical $GeS_{0.98}Se_{0.02}$ (system B) ground (prototype) and space crystals in Fig. 5 reveal distinct morphological differences. The prototype crystals (Fig. 5a) show considerable aggregation, undefined edges, and very rough surfaces. The improved surface and edge morphology of the space crystals is evident from Fig. 5b. The average dimensions of the space material range from about 1-7 mm edge length. Since the transport rates for system B (Table II) are the same under ground and space conditions, the external morphological differences reflect the absence of grav-

Table II. Mass transport rates under ground-based (prototype) and micro-gravity conditions

System	Mass flux ((mol/cm² · sec) × 10^{-9}) Normal gravity	Micro-gravity	Extrapolated diff. mode
$GeSe_{0.99}Te_{0.01}$ (A)	7.9	4.2	1.4
$GeS_{0.98}Se_{0.02}$ (B)	22.1	22.1	6.5
GeS + Ar (C)	15.0	13.0	2.8

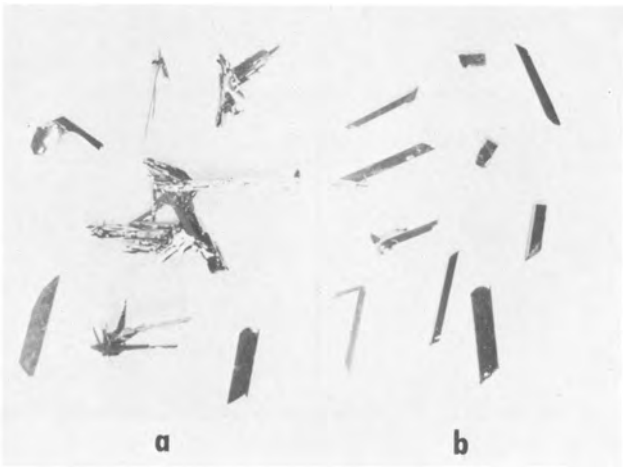


Fig. 5. Representative crystals of $GeS_{0.98}Se_{0.02}$ (system B): (a) ground-based (prototype), (b) space grown. Edge lengths of space crystals about 1-7 mm. Same magnification used for (a) and (b).

ity-driven convective interference with the transport and condensation process in micro-gravity environment. Similar differences in growth habits and surface morphology were observed for GeS crystals (system C).

Scanning electron microscopy.—Scanning electron photomicrographs (400×) of native faces and edges of $GeS_{0.98}Se_{0.02}$ (system B) ground (prototype) and space crystals in Fig. 6 reveal significant morphological differences. The surface of the ground crystal (Fig. 6a) shows extended channels and cavities penetrating into the bulk of the material. The smoother areas of the surface are nonplanar and separated by rounded edges. In addition polycrystalline deposits are visible. The surface perfection of the space crystal (Fig. 6b) is considerably improved relative to the ground specimen. The greater crystalline quality of the space material is attributed to significantly reduced convective interference and is not due to lower transport rates (Table II). Similar morphological differences between ground and space crystals were observed for the other systems. In particular, the majority of investigated ground specimens reveals nearly macroscopic imperfections for at least one edge extending into the bulk of the crystal; most space crystals have all edges well defined. These observations confirm similar results of the Skylab experiments (6).

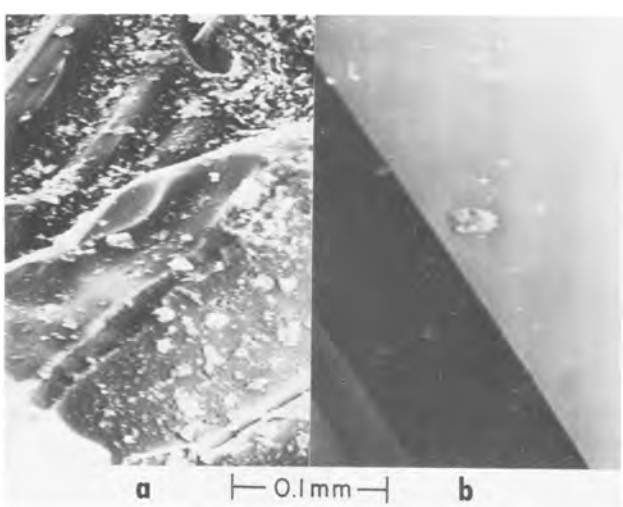


Fig. 6. Scanning electron photomicrographs (original magnification 400×) of native faces of $GeS_{0.98}Se_{0.02}$ (system B) crystals: (a) ground-based (prototype), and (b) micro-gravity grown. Crystal area shown in (a) corresponds to light face in (b) which is (001).

Chemical etching studies.—In order to determine differences in the degree of bulk crystalline perfection, freshly cleaved faces [parallel to the (001) plane] of ground and space crystals were investigated by chemical etching and optical microscopy. A warm (~60°C) solution containing 15% KOH applied for about 1 min gave reproducible results.

A representative optical photomicrograph (200×) of the cleaved (001) face of a $GeSe_{0.99}Te_{0.01}$ (system A) ground crystal (Fig. 7a) shows large cavities in the bulk of the material. Similar gross imperfections are observed on most ground specimens. Chemical etching of the same crystal area shows a high concentration of etch pits (Fig. 7b). It is interesting to note that the planar areas of the crystal which appear to be mirror smooth at this magnification (Fig. 7a) apparently have a higher etch pit density than the walls of the large cavity. The concentration of etch pits indicates a high degree of structural imperfections in the ground-based material which was observed for the majority of investigated crystals.

Application of the same cleaving and etching procedures to space-grown crystals of system A yields distinctly different results (Fig. 8). The photomicrograph (200×) of the cleaved crystal (Fig. 8a) reveals a greater structural quality than the corresponding ground specimen (Fig. 7a). This type of cleavage plane (Fig. 8a) was observed for the majority of space crystals. The photomicrograph (200×) of the cleaved and etched space crystal platelet (Fig. 8b) is nearly free

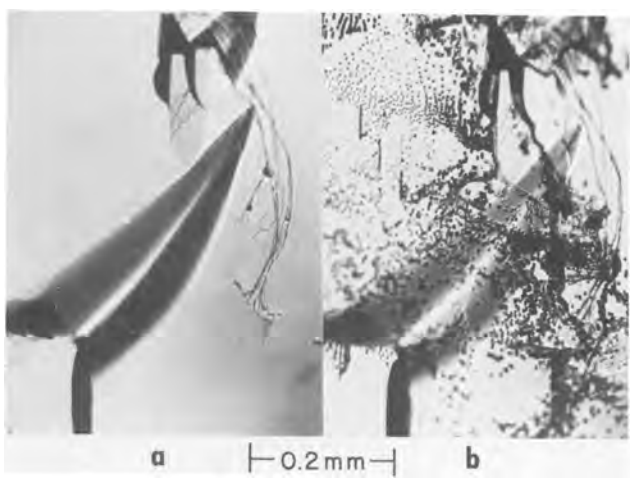


Fig. 7. Optical photomicrographs (original magnification 200×) of a cleaved and etched (001) face of a ground-based (prototype) $GeSe_{0.99}Te_{0.01}$ (system A) crystal platelet: (a) cleaved, (b) cleaved and etched.

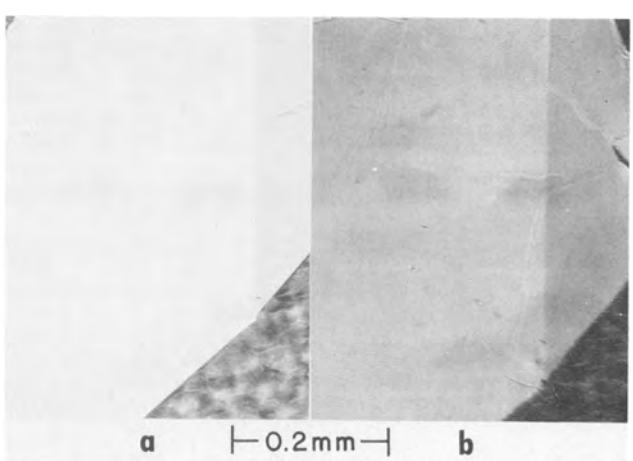


Fig. 8. Optical photomicrographs (original magnification 200×) of a cleaved and etched (001) face of a space-grown $GeSe_{0.99}Te_{0.01}$ (system A) crystal platelet: (a) cleaved, (b) cleaved and etched.

of etch pits indicating a high degree of structural microhomogeneity. The line pattern of the crystal face is due to cleavage, showing (001) planes of different depth with respect to the native surface.

Similar differences in etch patterns were observed for ground- and space-grown $GeS_{0.98}Se_{0.02}$ (system B) crystals shown in Fig. 9 and 10. For comparative purposes, the (001) cleavage plane (200×) of an above average quality ground crystal is shown in Fig. 9a. The majority of ground crystals (system B) contains cavities and elongated channels in the bulk of the material. Chemical etching of the cleaved (001) face (200×) yields large etch pits and lines (Fig. 9b) indicative of crystallographic imperfections. This is contrasted by optical photomicrographs (200×) of cleaved and etched (001) faces of average space crystals of this system (Fig. 10). The appearance of few isolated etch pits and large areas free of pits in the crystal plane (Fig. 10b) indicate the high degree of crystalline perfection of the space-grown material.

The above illustrated differences in cleavage and etch patterns are observed for the majority of investigated ground and space crystals for all systems. Considering the nonuniform distribution of etch pits in different planes of the ground specimens and their isolated appearance in the space samples, numerical values for the etch pit counts of individual crystals would not be too meaningful. The average density of etch pits is approximately one to two orders of magnitude lower in the space than in ground samples. The combined results of the morphological studies are consistent with those of x-ray diffraction techniques and show the considerably improved crystallographic perfection of crystals grown in the micro-gravity environment.

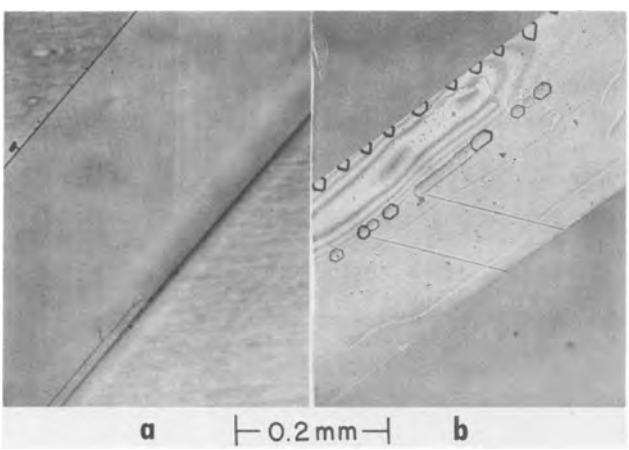


Fig. 9. Optical photomicrographs (original magnification 200×) of a cleaved and etched (001) face of a ground-based (prototype) $GeS_{0.98}Se_{0.02}$ (system B) crystal platelet: (a) cleaved, (b) cleaved and etched.

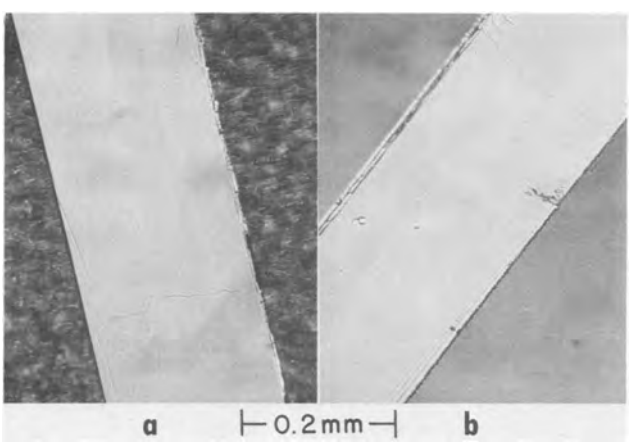


Fig. 10. Optical photomicrographs (original magnification 200×) of a cleaved and etched (001) face of a space-grown $GeS_{0.98}Se_{0.02}$ (system B) crystal platelet: (a) cleaved, (b) cleaved and etched.

Mass transport rates.—The mass transport rates observed in micro-gravity and under corresponding prototype (ground-based) conditions are calculated from the mass of the transported crystals and the mass loss of the source material. The numerical results of the ASTP experiments are listed in Table II. The experimental uncertainties associated with the recovery of crystals were combined to yield minimum values for the mass fluxes observed in micro-gravity. Under these conditions the errors of the values listed in column 3 are estimated to be about + 30%. The computation of the transport rates expected for diffusion listed in column 4 is based on a graphical extrapolation of the diffusion-controlled region of the respective ground-based experimental flux curves shown in Fig. 1. For this purpose, flux *vs.* pressure data were plotted in logarithmic scales and the resulting straight line was extended to the flux corresponding to the pressure employed in the ASTP experiments. This is shown for system B and for GeS-$GeCl_4$ in Fig. 11. A similar plot was used for the A-system. In order to maximize the predicted flux values, the data selected for the extrapolation are close to the minimum of the diffusion branch of the individual flux curves (Fig. 1) with some convective contribution. The flux curves in Fig. 1 were established in our laboratory. Due to slight differences in temperature profiles between the laboratory and prototype furnace (the latter one was used for all direct comparisons), the flux values in Fig. 1 are greater than those obtained in the prototype furnace (column 2) for the corresponding systems and pressures. This and the above extrapolation procedures yield maximum values for the extrapolated fluxes with an estimated uncertainty of about −30%. The extrapolations are based on the assumption that mass transport in micro-gravity is exclusively by diffusion and that gravity- and nongravity-caused transport effects, *e.g.*, streaming, are included in the extrapolation of experimental flux data. The predicted flux value for system C was obtained analytically from the identical extrapolated values for system B and GeS (Fig. 11) and the argon pressure in system C, considering the different molecular weights of Ar and $GeCl_4$. The transport properties of system B and GeS (Fig. 1 and 11) and the transport agent ($GeCl_4$) pressures of systems B and C are close enough to allow a direct comparison of the effect of argon on the mass flux of these systems. The flux curve for GeS with $GeCl_4$ as a transport agent (Fig. 1) is shown for comparative purposes. The difference between this and the corresponding curve for system C is the presence

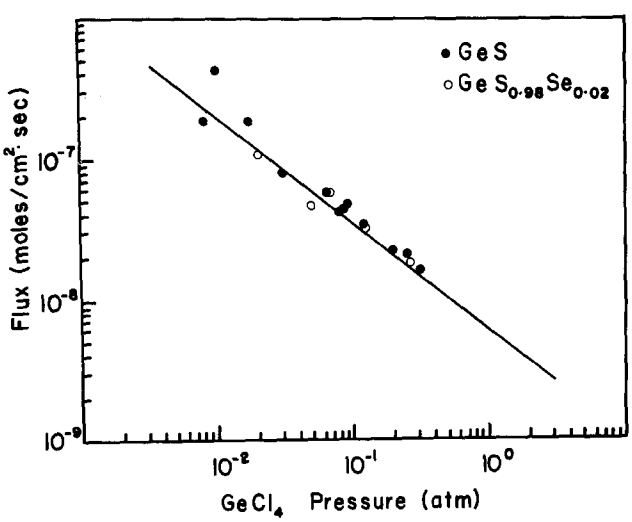


Fig. 11. Extrapolation of flux *vs.* pressure data of the diffusion-controlled region of the ground-based flux curves (Fig. 1) for systems B and GeS-$GeCl_4$.

of argon in the latter one. The argon pressure employed in the individual transport experiments of system C was approximately twice the pressure of transport agent ($GeCl_4$) given on the abscissa of the diagram. The observed reduction in transport rate upon the addition of argon to the GeS-$GeCl_4$ system was expected for the diffusion-controlled but unexpected for the convection-controlled regime of the ground-based flux curves.

The mass fluxes observed in micro-gravity (Table II) are about three to five times greater than predicted (extrapolated) for a diffusion-controlled transport process. For system A the transport rate in space is less than under prototype (ground) conditions. For system B the fluxes obtained on earth and in space are the same. These observations are consistent with the Skylab results (6) and confirm the trend in terms of the flux-pressure relationship observed in the previous space experiments (6). A comparison of the individual flux data of systems B and C obtained under prototype (ground) and space conditions leads to several important conclusions. Firstly, if vapor transport in space were exclusively by diffusion, then the mass fluxes of systems B and C in micro-gravity should be in the ratio of the diffusion coefficients. Estimated diffusion coefficients for these multicomponent systems (10) yield a minimized ratio of about 2.4 which agrees with the ratio of extrapolated fluxes but is greater than the observed ratio J_B/J_C in space. Although not conclusive by itself, the difference is consistent with other evidence and indicates that the effect of argon on the diffusion mode of system C is less important than on other properties which affect mass flux. Secondly, if the observed transport rates in space were caused by gravity fluctuations due to space craft operations, such fluctuations should affect the "diffusion mode" of systems B and C equally and the flux ratio J_B/J_C should again reflect a diffusion-type transport (11). Since that is not the case, gravity fluctuations could not be the only source of the observed higher space fluxes. Thirdly, estimates of the effects of gravity perturbations for the Skylab experiments (6) revealed that their contributions to the mass transport rates in space were negligible. This indicates that "G-jitter" is insignificant with respect to the transport rates observed in the ASTP experiments. Fourthly, a comparison of systems B and C demonstrates, that the effect of argon on the mass transport rates is the same within error limits under prototype (ground) and micro-gravity conditions. The observed decrease in flux upon addition of argon (in the "convection branch" for ground conditions) is in agreement with ground-based inert atmosphere studies indicated in Fig. 1. The combined experimental data strongly suggest that the addition of inert atmosphere affects those inherent properties of the transport systems which are the same on earth and in space and are gravity independent.

Before any further interpretation of these unconventional transport phenomena in micro-gravity, it is desirable to demonstrate independently the validity of the discrepancies between the mass fluxes observed in space and predicted (extrapolated) for a diffusion-type transport. This was accomplished by computing flux curves for diffusion-controlled vapor transport based on models proposed by Schäfer *et al.* (12), Lever (13), Mandel (14), and Faktor *et al.* (15). Computational procedures have been discussed previously (6). Emphasis was placed on the appropriate treatment of the so-called streaming effect (Stephan flow) and on the calculation of partial pressure gradients as a function of total pressure which are treated differently in the above models. The same procedures were applied to the transport systems and conditions of the ASTP and Skylab experiments. The calculations are based on reaction [1]. The required thermochemical data for the GeSe-GeI_4 system have been used previously (5). The heat of formation and absolute entropy of GeS(s) are from Ref. (16) and (17), respectively. For the heat capacity of GeS(s) the value for α-SnS(s) (18) was used. The corresponding enthalpies of formation and absolute entropies for $GeCl_4(g)$ and $GeCl_2(g)$ were derived from the heat and entropy of the reaction $Ge(s) + GeCl_4(g) = 2\,GeCl_2(g)$ (19) with the heat capacities for Ge(s) (20) and $GeCl_4(g)$ (21). The heat capacity for $GeCl_2(g)$ was estimated at 15 cal/deg · mole. The heat of formation (22), absolute entropy (22), and heat capacity (23) of $S_2(g)$ were used in these calculations. The contributions of GeTe in system A and of GeSe in system B to the pressures and mass transport rates of the major species are insignificant and have been neglected in these computations. The "theoretical" flux curves were fitted to the diffusion branch of the corresponding experimental ground-based curves [Fig. 1 for the present ASTP and accordingly for the Skylab (6) experiments] to obtain optimal agreement. This procedure yielded the numerical constants required for each model to compute the fluxes for the specific ASTP and Skylab conditions. The numerical results of these computations are listed in Table III together with the observed and extrapolated fluxes. A comparison of the data shows that the flux values obtained from the model computations agree within a factor of two with our extrapolated values. In no case are the transport rates predicted by the models greater than the observed fluxes, although, as pointed out above, the latter represent minimum values. Considering the uncertainties associated with thermodynamic calculations of partial pressures and transport effects, the agreement between the model calculations and experimental extrapolation procedures is reasonable. Because of these uncertainties our extrapolated data are considered the most reliable values for comparison. The combined data confirm that the discrepancies between predicted and observed fluxes in micro-gravity are real and that the latter cannot be explained on the basis of an exclusively diffusion-type process. This leads to the conclusion that the greater than predicted mass transport rates in the space environment are due to other nongravity-caused transport effects. The internal consistency and close agreement between the flux results of the present ASTP and earlier Skylab (6) experiments obtained for different chemical systems, eight pressures, two transport agents, and three temperature gradients strongly support the validity of the above conclusions.

The apparent failure to explain the observed transport phenomena in space on the basis of a diffusion process suggests the presence of convective gas flow in closed-tube vapor transport systems which measurably affects the mass flux in micro-gravity environment. The positive identification of the source of such convective motion requires a detailed analysis of available convection models and their application to transport conditions at normal and reduced gravity. This is beyond the scope of the present work and will be presented, together with additional ground-based experi-

Table III. Mass transport rates observed and predicted for micro-gravity conditions

System	Mass flux ((mol/cm² · sec) × 10^{-9})					
			Modeled according to			
	Observed	Extrapol.	Schäfer (12)	Lever (13)	Mandel (14)	Faktor (15)
	Apollo-Soyuz (604° → 507°C)					
$GeSe_{0.99}Te_{0.01}$ (A)	4.2	1.4	2.5	2.7	2.6	3.1
$GeSe_{0.98}Se_{0.02}$ (B)	22.1	6.5	8.9	9.1	9.1	9.5
GeS + Ar (C)	13.0	2.8	3.6	3.7	3.2	5.2
	Skylab 3 (524° → 422°C)					
GeSe (A)	5.0	0.5	0.80	0.89	0.86	1.1
GeSe (B)	10.0	2.5	3.4	3.7	3.6	4.2
GeTe (C)	3.0	0.5	0.84	0.87	0.87	0.92
	Skylab 4 (412° → 346°C)					
GeSe (A)	0.8	0.15	0.14	0.14	0.14	0.15
GeSe (B)	1.8	0.35	0.29	0.30	0.30	0.30
GeTe (C)	1.0	0.40	0.79	0.79	0.79	0.79

ments, in a forthcoming publication. Present results of this analysis are briefly summarized below. Convective flow in a horizontal, closed-ampul vapor transport system was analyzed by Klosse and Ullersma (24). The end result of their treatment (24) is a dimensionless parameter K, which is the ratio of convective to diffusive mass transfer. This flux ratio K is expressed in terms of Grashof and Schmidt numbers and two other dimensionless quantities, which are solely functions of the aspect ratio of the ampul. Computations of Klosse and Ullersma's ratio K for conditions representative of our Skylab and ASTP experiments and normal gravity ($G = 980$ cm $\cdot$ sec^{-2}) show, that on earth convection is predominant at a total pressure of about 1 atm. The convective contribution to the over-all mass transport decreases with decreasing pressure and becomes negligible at pressures of about 0.1 atm. These results are in agreement with the shape of our experimental ground-based flux curves for the ASTP (Fig. 1) and Skylab (6) experiments. Analogous computations for these systems with the above model (24) for micro-gravity conditions (10^{-4}G or less) reveal that convective mass transport is negligible at all pressures applied in these experiments.

The above results are in qualitative agreement with independent estimates of thermogravitational flow obtained from a dimensional analysis (25). This involves the calculation of Rayleigh numbers for both ground and space conditions and the comparison of these values to the critical Rayleigh number. In addition, the aspect ratio and Prandtl number of the system are important parameters. For the purpose of these calculations system A of the Skylab 3 experiments (6) (Table III) was selected which showed the largest discrepancy between observed and predicted fluxes for micro-gravity. The pressure of $GeI_4(g)$ in Skylab 3A experiment (6) was 1.50 atm for the mean temperature of the gradient (470°C) and ideal gas conditions. The analysis (25) is based on a rectangular container with cross section 15 $\times$ 1.4 cm and on a residual gravity of about 10^{-4}G. In addition to the effect of constant residual gravity, the influence of gravity perturbations on the mass transport rate was studied. Although qualitative in nature, the results of the computer model analysis (25) show that the combined effects of steady 10^{-4}G convection and G-jitter (vibration) convection could not yield more than a 20% increase in mass transport rate over pure diffusion. This is negligible compared to the magnitude of the observed fluxes in micro-gravity.

In view of the combined results, we propose the following explanation for the unexpected transport phenomena in space. Present vapor transport models for diffusive and convective flow consider only the chemical reactions at the source and seed crystal. When these heterogeneous reactions are in a steady state and the partial pressure gradients are established, the gas phase is treated as an inert fluid migrating from the source to the condensation region. However, the vapor phase of a chemical transport system consists of reactive chemical species, and homogeneous chemical reactions in the gas phase should be considered. The energies associated with such reactions can cause localized temperature changes, which, in turn, will produce local density fluctuations superimposed on the density gradient due to the over-all temperature gradient. The instabilities caused by such temperature-density fluctuations could lead to "thermochemically" induced convective motion of the gas phase. Preliminary model calculations indicate that local temperature changes of several degrees can be expected if only minute amounts of gaseous species undergo chemcial reactions. In addition, changes in the number of moles of gaseous species as a result of homogeneous reactions could lead to pressure-volume changes and subsequent flow. Actual temperature oscillations in a closed ampul containing $TeCl_4$ in a vertical temperature gradient have been reported (26) earlier. At normal gravity, "thermochemical" convection may be overshadowed by gravity convection. In micro-gravity environment, the thermochemically driven component could have a significant contribution to mass transfer. The morphological differences between ground and space crystals indicate a more turbulent type of convection on earth and a laminar-type flow in space. This model would explain the unexpected transport phenomena observed in micro-gravity and any discrepancies between ground-based convection models (1, 24) and experimental flux data (27). A more detailed treatment of the above computations and proposed model will be presented separately.

Summary and Conclusions

The original objectives of these experiments were to investigate the effects of micro-gravity on the morphology of single crystals of mixed systems and to confirm the unusual mass transport rates observed earlier (6). The analysis of these experiments based on x-ray diffraction, microscopic, and etching techniques demonstrates a measurable improvement in structural and chemical homogeneity of the space-grown crystals relative to ground specimens. This is attributed to reduced convective turbulence and interference with the transport process. In addition to the confirmation of the greater mass transport rates in micro-gravity than predicted by present transport models, the analysis of the flux results points to the existence of thermochemically induced convection in reactive solid-gas phase systems. The morphological observations suggest that the interaction between different convective components causes turbulence and negative effects on crystal quality as observed on earth. The good agreement between the results of these and previous (6) vapor transport experiments performed in space supports the validity of the above conclusions.

Acknowledgments

This work was performed during the joint U.S.-U.S.S.R. Apollo-Soyuz Test Program (ASTP). The authors are pleased to express their sincere appreciation to the National Aeronautics and Space Administration for the opportunity to participate in the Apollo-Soyuz Test Program. We would like to thank the scientific and technical staff of the George C. Marshall Space Flight Center and the Astronauts of the ASTP Mission who made the performance of these experiments possible.

Manuscript submitted Dec. 27, 1976; revised manuscript received March 8, 1977. This was Paper 232 presented at the Las Vegas, Nevada, Meeting of the Society, Oct. 17-22, 1976.

Any discussion of this paper will appear in a Discussion Section to be published in the June 1978 JOURNAL. All discussions for the June 1978 Discussion Section should be submitted by Feb. 1, 1978.

Publication costs of this article were assisted by Rensselaer Polytechnic Institute.

REFERENCES

1. H. Schäfer, "Chemical Transport Reactions," Academic Press, New York (1964).
2. H. Wiedemeier and A. G. Sigai, *J. Cryst. Growth*, **6**, 67 (1969).
3. A. G. Sigai and H. Wiedemeier, *ibid.*, **9**, 244 (1971).
4. H. Wiedemeier, E. A. Irene, and A. K. Chaudhuri, *ibid.*, **13/14**, 393 (1972).
5. H. Wiedemeier and E. A. Irene, *Z. Anorg. Allg. Chem.*, **400**, 59 (1973).
6. H. Wiedemeier, F. C. Klaessig, E. A. Irene, and S. J. Wey, *J. Cryst. Growth*, **31**, 36 (1975).
7. E. Shimazaki and T. Wada, *Bull. Chem. Soc. Jpn.*, **29**, 294 (1956).
8. S. N. Dutta and G. A. Jeffrey, *Inorg. Chem.*, **4**, 1363 (1965).
9. D. K. Hohnke, H. Holloway, and S. Kaiser, *J. Phys. Chem. Solids*, **33**, 2053 (1972).
10. J. O. Hirschfelder, C. F. Curtiss, and R. B. Bird, "Molecular Theory of Gases and Liquids," John Wiley & Sons, Inc., New York (1965).

11. B. Gebhart, *AIAA J.*, **1**, 380 (1963).
12. H. Schäfer, H. Jacob, and K. Etzel, *Z. Anorg. Allg. Chem.*, **286**, 27 (1956).
13. R. F. Lever, *J. Chem. Phys.*, **37**, 1078 (1962).
14. G. Mandel, *ibid.*, **37**, 1177 (1962).
15. M. M. Faktor, I. Garrett, and R. Heckingbottom, *J. Cryst. Growth*, **9**, 3 (1971).
16. G. P. Adams, J. L. Margrave, and P. W. Wilson, *J. Chem. Thermodyn.*, **2**, 591 (1970).
17. C. Hirayama, *J. Chem. Eng. Data*, **9**, 65 (1964).
18. K. K. Kelley, *U.S. Bur. Mines, Bull.*, **584**, 191 (1960)
19. T. O. Sedgewick, *This Journal*, **112**, 496 (1965).
20. K. K. Kelley, *U.S. Bur. Mines, Bull.*, **584**, 71 (1960).
21. K. K. Kelley, *ibid.*, **584**, 72 (1960).
22. D. R. Stull and G. C. Sinke, *Adv. Chem. Ser.*, **18**, 193 (1956).
23. K. K. Kelley, *U.S. Bur. Mines, Bull.*, **584**, 181 (1960).
24. K. Klosse and P. Ullersma, *J. Cryst. Growth*, **18**, 167 (1973).
25. S. V. Bourgeois and L. W. Spradley, NASA Final Report, LMSC-HREC TR D496534, Lockheed Missiles and Space Company, Inc., Huntsville, Alabama.
26. F. Rosenberger, M. C. Delong, and J. M. Olson, *J. Cryst. Growth*, **19**, 317 (1973).
27. H. Wiedemeier and F. C. Klaessig, Unpublished results.

Ion-Implanted Gallium-Arsenide-Phosphide Surfaces

Thomas C. Arnoldussen* and Eugene Greenstein*

General Motors Corporation, Research Laboratories, Electronics Department, Warren, Michigan 48090

ABSTRACT

Study of thermal degradation of mechanical surface perfection and surface photoluminescence (PL) of $GaAs_{0.6}P_{0.4}$ samples, some of which received high dose room temperature Zn^+ or Ar^+ ion implants and others of which were unimplanted, strongly suggests that PL degradation and thermal etch pit formation have a common origin. Thermal etch pits are believed to nucleate at dislocations reaching the surface and these same dislocations act as sources of vacancy injection into the bulk, resulting in PL degradation. Ion implants rendering the surface amorphous are found to retard formation of thermal etch pits and to retard PL degradation during high temperature anneals. The model presented may explain the unusual dish-shaped p-n junction profiles observed when Zn^+ is implanted into n-type $GaAs_{0.6}P_{0.4}$ at room temperature and annealed.

Light emitting diodes fabricated by ion implantation of Zn into n-type GaAsP have been reported previously (1, 2). While we have also made such devices with efficiencies comparable to diffused diodes, the work reported here pertains not to diode behavior as such, but to the effects of room temperature, high dose ion implants on reducing surface degradation during high temperature annealing. The samples studied were $GaAs_{0.6}P_{0.4}$ grown on GaAs substrates. The constant composition region was ~80 μm thick and doped with 1.5×10^{17} cm^{-3} Te. The orientation of the surface was (100)[1].

The results we report suggest that dislocations reaching the $GaAs_{0.6}P_{0.4}$ surface act as vacancy generators during annealing and high dose room temperature ion implants reduce the surface dislocation density and vacancy generation rate during subsequent annealing. These results are in agreement with those recently reported by Okabayashi (3) in which anneal-induced photoluminescence degradation in $GaAs_{0.62}P_{0.38}$ was related to Ga vacancy formation. Our work not only corroborates this, but further delineates the anneal degradation mechanism by correlating photoluminescence degradation with heterogeneous thermal pit nucleation.

Mechanical Surface Effects

It is well known that materials such as GaAsP suffer dissociation and severe surface deterioration when annealed at high temperatures without adequate surface passivation. A pure, dense Si_3N_4 coating provides good protection, though at high enough temperatures some degradation can still occur. SiO_2, while not as good as Si_3N_4, can provide reasonable protection provided it is dense. Si_3N_4, SiO_2, and $(Si_3N_4)_{1-x}(SiO_2)_x$ films which are insufficiently dense provide diminished protection and at high anneal temperatures surface deterioration can occur.

In the first experiment reported here six chips were cut from a single wafer. Three of these were implanted with 8×10^{15} cm^{-2} Zn^+ ions at 50 keV, room temperature, and at 7° beam incidence. The remaining three were left unimplanted. All six chips were then coated with 700Å of $(Si_3N_4)_{1-x}(SiO_2)_x$ by reactively sputtering a Si target in a N_2 atmosphere after an incomplete pumpdown. This "contaminated nitride" provided some protection but allowed slow thermal degradation to occur during the high temperature anneal. The refractive index, ellipsometrically determined, of this coating was 1.8 compared to 2.0 for pure dense nitride.

One implanted sample and one unimplanted sample were annealed together at 850°C for 1 hr. A second implanted/unimplanted pair was annealed for 2 hr, and a third pair for 3 hr. In this way the unimplanted specimens, processed identically to their paired implanted chips, served as controls in order to separate the effects of the ion implantations. These anneal times were much longer than would normally be used in LED fabrication.

Extensive surface pitting occurred on the unimplanted samples, but a relatively small number of pits formed on the implanted chips during the anneals. Figures 1-3 show micrographs of these surfaces. Figure 4 shows an enlarged view of pits on 2 hr annealed samples. For both the implanted and unimplanted samples it appears that early nucleation of pits is followed by pit growth without continuing nucleation of new pits. These pit densities were about 5.7×10^4 cm^{-2} for unimplanted samples and 1.8×10^3 cm^{-2} for implanted samples. The pit density was thus over 30 times lower on the implanted samples.

* Electrochemical Society Active Member.

Key words: photoluminescence, vacancies, dislocations, damage, anneal.

[1] $GaAs_{0.6}P_{0.4}$ material was purchased from Applied Materials Technology, Incorporated.

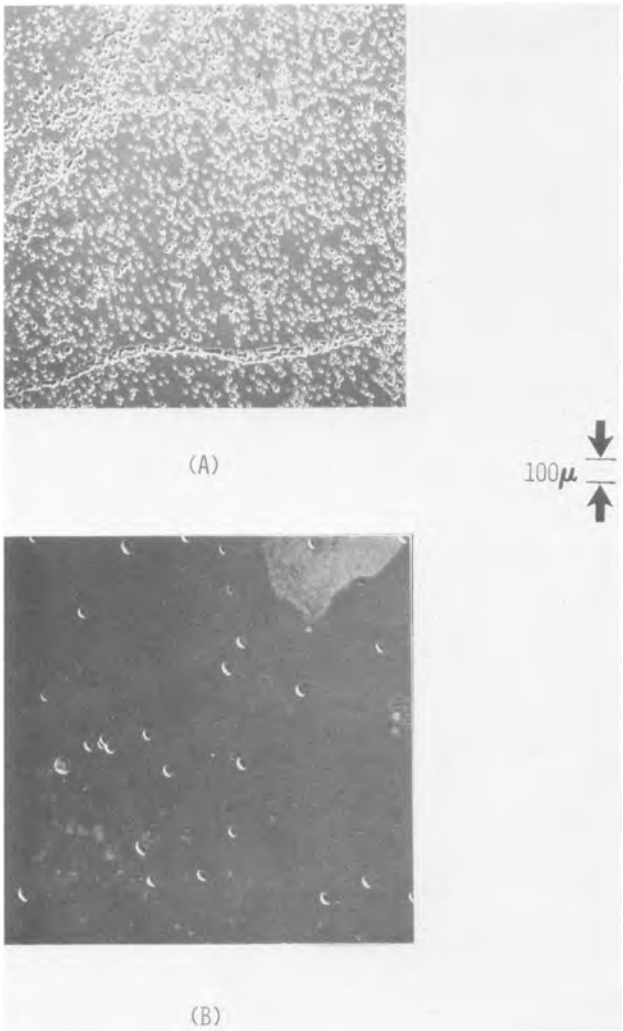


Fig. 1. Thermal etch pits seen at 30° incidence in (100) surface after 1 hr anneal at 850°C; (a) unimplanted, (b) implanted.

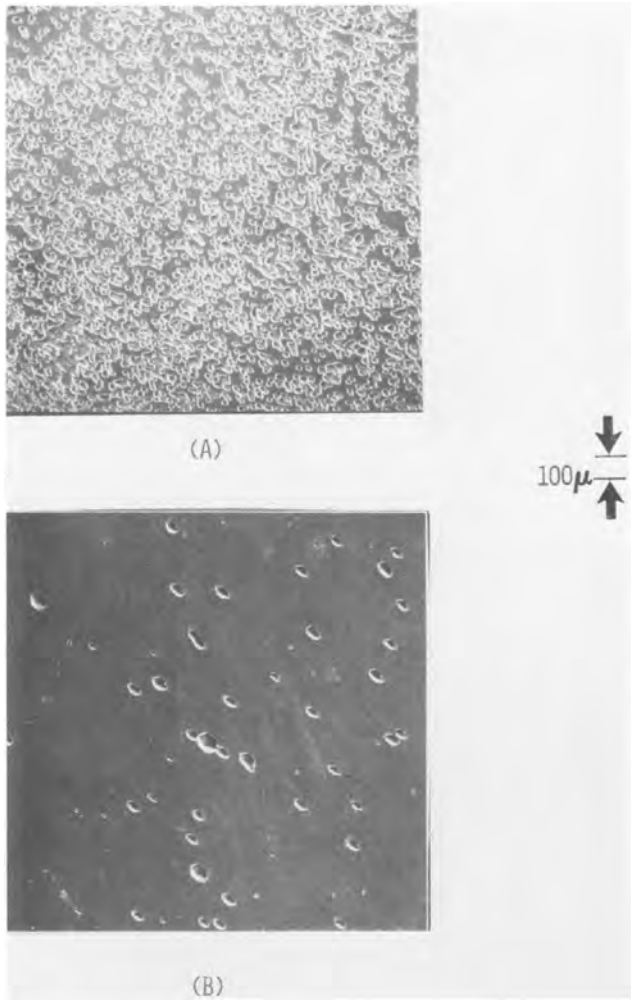


Fig. 2. Thermal etch pits seen at 30° incidence in (100) surface after 2 hr anneal at 850°C; (a) unimplanted, (b) implanted.

Photoluminescence effects.—Another set of six chips was cut from a similar wafer. Two of these were implanted with 8×10^{15} cm^{-2} Zn^+ ions, two were implanted with 8×10^{15} cm^{-2} Ar^+ ions, and the remaining two were left unimplanted. The implants were all performed at room temperature. All six samples were coated with 700Å Si_3N_4 reactively sputtered from a Si target in 4×10^{-3} Torr N_2 after an initial vacuum of $<1 \times 10^{-6}$ Torr had been achieved. Substrate temperature during sputtering was about 400°C. The Si_3N_4 sputtered under these conditions was pure and dense and had a refractive index of 2.0. The samples were then annealed at 900°C in sets for 15 and 30 min, as described in Table I. The Si_3N_4 coating was removed and no visible surface deterioration (thermal pitting) was observed, indicating the more adequate protection afforded by this pure, dense Si_3N_4.

Photoluminescence spectra were taken on each of these six samples plus a virgin sample using an argon laser (4900Å) for excitation. The optical absorption coefficient for this excitation is about 5×10^4 cm^{-1}. Figure 5 shows the magnitude of the PL photon intensity at the spectral peak for each of the samples normalized to that of virgin material (taken as unity).

Table I

Sample number	Implant	Anneal time
1a	none	
1b	Ar	15 min
1c	Zn	
2a	none	
2b	Ar	30 min
2c	Zn	

The Ar^+-implanted samples as well as the unimplanted samples [Fig. 5 (1a), (2a), (1b), and (2b)] showed a PL peak at 6620Å with a peak half-width of 140Å, compared with a virgin sample PL peak at 6600Å with a 140Å half-width. Both Zn^+-implanted samples [Fig. 5 (3a) and (3b)] showed a PL peak at 6700Å with a peak half-width 280Å. No subsidiary peaks (*e.g.*, from possible nitrogen doping) were observed for any sample.

The unimplanted samples showed a PL degradation by a factor of ~50. This is due primarily to the high anneal temperature used (900°C) and not to the quality of the coatings. Harris *et al.* (4) have reported annealing GaAs at 750°C using Si_3N_4 coatings with little PL degradation, despite having problems with Si_3N_4 adhering to the GaAs. We had no problem with nitride adherence, but the dissociation pressure (5) of GaAs (which we expect is comparable to $GaAs_{0.6}P_{0.4}$) is at least 100 times greater at 900°C, and atomic migration through the coatings is likewise enhanced.

The Ar^+ implants, which we expect are chemically and electronically inert, were found to diminish the high temperature anneal-induced PL degradation by a factor of 5-7.

The Zn^+ implants enhance the PL photon intensity by a factor of about 10 over the virgin sample. This increase is primarily a result of changing the dominant recombination mechanism from a donor-to-valence band mechanism to a conduction band-to-zinc acceptor band mechanism (6), as indicated by the PL peak shift to 6700Å and increase in peak half-width.

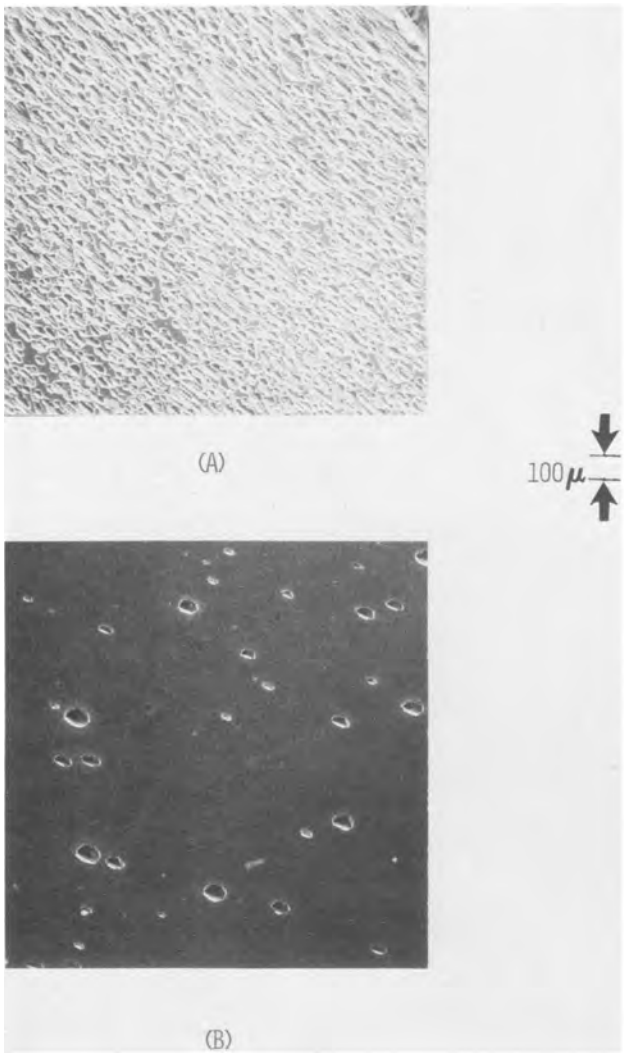


Fig. 3. Thermal etch pits seen at 30° incidence in (100) surface after 3 hr anneal at 850°C; (a) unimplanted, (b) implanted.

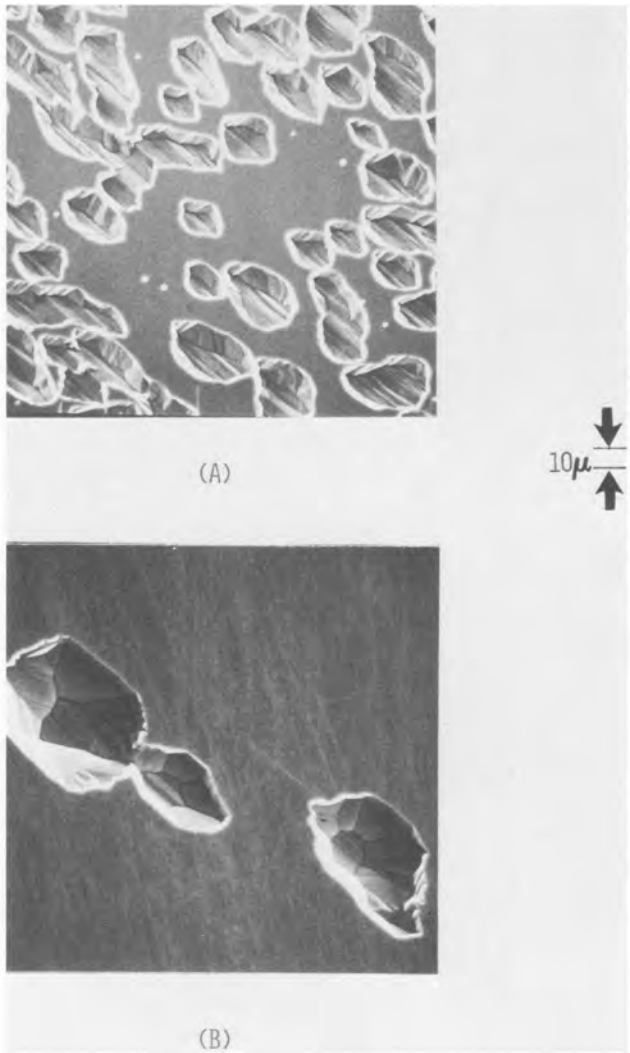


Fig. 4. Enlarged view of thermal etch pits seen at 30° incidence in (100) surface after 2 hr anneal at 850°C. The pits are estimated to be 30-40μ deep; (a) unimplanted, (b) implanted.

Discussion

From the thermal pitting experiment we may draw several conclusions. (*i*) The thermal pit density independence of anneal time indicates that pits nucleate heterogeneously. Increased anneal time causes pit growth but no additional nucleation. (*ii*) If pits nucleate heterogeneously, then we may conclude that the room temperature 8×10^{15} cm^{-2} Zn^+ implant reduces the heterogeneous pit nucleation sites, since the pit density is drastically reduced on these samples. (*iii*) It is obvious that the "contaminated nitride" is a sufficiently poor coating to allow pitting to occur, but the pit nucleation is not correlated with the nitride coating since the same "lossy" coating was simultaneously deposited on implanted and unimplanted samples with a vast difference in pit density.

The photoluminescence experiment allows us to draw the following additional conclusions. (*iv*) The good nitride coating virtually eliminates the formation of thermal pits on all samples though, at 900°C anneal, induced PL degradation still occurs. However, while PL degradation occurs in unimplanted samples the principal radiative recombination mechanism is not changed from that in virgin material; namely donor-to-valence band. Therefore, we conclude that anneal-induced PL degradation results from production of competing nonradiative recombination centers of some sort. (*v*) The 8×10^{15} cm^{-2} Ar^+ implanted samples show a 5-7 times smaller anneal-induced PL degradation while exhibiting essentially the same radiative recombination mechanism as the virgin and unimplanted annealed samples. We conclude, therefore, that the Ar^+ implant reduces the production of competing nonradiative recombination centers in the region sampled by the exciting light. (*vi*) The Zn^+ implant shifts the PL peak by 0.030 eV and doubles the PL peak half-width. By analogy with radiative recombination studies made on Te- and Zn-doped GaAs (6, 7), we would expect the Zn acceptor density in the region sampled by the exciting light to be $\sim 1 \times 10^{19}$ cm^{-3} based on the PL peak shift and half-width change observed. In GaAs the radiative efficiency of 1×10^{19} cm^{-3} Zn acceptor doped-material is about 20 times that of 1.5×10^{17} cm^{-3} Te-doped material (6). By analogy we might expect our Zn-implanted $GaAs_{0.6}P_{0.4}$ to show an increase in PL intensity by a factor of about 20 over the virgin 1.5×10^{17} cm^{-3} Te-doped material. We observe an increase by a factor of 10, very close to that expected. We conclude then that in the 2000-4000Å region sampled by the light very few anneal-induced nonradiative centers have been produced during the anneal.

Interpretation

Matthews *et al.* (8) have shown that lattice misfit strain can be used to remove threading dislocations by a horizontal glide mechanism under proper conditions. They verified this by growing epitaxial $GaAs_{(1-x)}P_x$ on GaAs substrates making appropriate changes in composition variable x during growth so that the lattice misfit strain would drive the "glide-out" of threading dislocations in the thin epitaxial layer at the growth

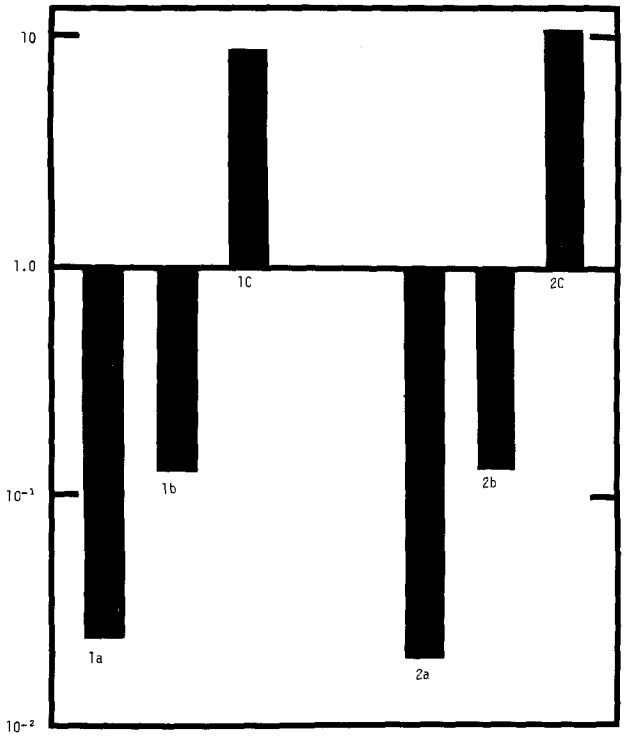


Fig. 5. Photon PL intensities of samples described in Table I relative to PL intensity of virgin (unimplanted, uncoated, unannealed) $GaAs_{0.6}P_{0.4}$ material taken as 1.0 in the figure.

temperature of 750°C. The critical (minimum) film thickness for this mechanism to occur was estimated to be ~60Å.

We propose that a similar mechanism is operating in the ion-implanted samples we studied. The 8×10^{15} cm^{-2} ion implants, of range ~200Å, severely strain the lattice near the surface of the sample and very likely drive it amorphous (9). During the activation anneal, while implant species diffusion and perhaps epitaxial recrystallization occur, the lattice strain resulting from the high dose implant drives threading dislocations laterally out of the implanted region of the sample by glide. It is also possible that vacancies produced by the implant or generated during the anneal are consumed along dislocation lines and assist dislocation removal by a climb mechanism.

We assert that the heterogeneous thermal pit nucleation sites correspond to dislocations terminating on the sample surface. The thermal pit density on unimplanted annealed samples is indeed of the same magnitude as dislocation densities in these materials (8, 10). The strain-induced glide (and perhaps climb) dislocation removal in the implanted samples therefore leads to a decrease in heterogeneous pit nucleation despite a substandard protective coating. The small number of pits which do still form may result from incomplete dislocation removal or from pinholes or other imperfections in the coating.

We propose that the reduction in anneal-induced PL degradation after the inert Ar^+ implant arises in the following way. Ga vacancies generated during the anneal are the most plausible origin of nonradiative recombination (NR) centers (3). We assert that NR center formation on the second set of samples and thermal pit formation on the first set are related and propose that dislocations reaching the surface act as primary Ga vacancy generators. When a high dose implant causes dislocations to be removed from the area implanted (at least not terminated on the implanted area surface) Ga vacancy generation is diminished accordingly, hence PL degradation diminishes.

Anomalous junction depth and curvature.—Junction depth and shape of 12 mil diam (7.3×10^{-4} cm^2) circular diodes were determined by cleaving the sample and staining to delineate the junction. These diodes were fabricated under conditions similar to the PL samples described above (room temperature 8×10^{15} cm^{-2} Zn^+ implant, 2800Å Si_3N_4 coating, 900°C anneal for 15-30 min). Figure 6 shows an electron micrograph of such a junction.

Similar to results reported by Itoh and Oana (12), the junction depth is anomalously large compared to that expected for diffused junctions formed at the same temperatures used for the implant anneal. Normal diffusion would result in 5-20 times shallower junction depths. Indeed, Itoh (11) observed that for $\lesssim 10^{15}$ cm^{-2} Zn^+ implants into $GaAs_{0.62}P_{0.38}$ anomalously large junction depths were observed for implant substrate temperatures $\lesssim$ 100°C. For implant temperatures greater than this (and fixed-anneal conditions) the junction depth decreased with increasing implant temperature to approximately the depth expected for normal diffusion.

Zelevinskaya *et al.* (12) observed similar results for Cd^+ implants into GaAs. In earlier work (13) they had shown evidence that diffusion of Zn implanted into GaAs is slowed by excess vacancies. In both cases Zelevinskaya *et al.* postulate that fast diffusion occurs by interstitial migration of atoms. Excess vacancies trap the Zn or Cd on substitutional sites resulting in slow diffusion. At implant temperatures $\gtrsim$ 100°C vacancy formation and trapping of Zn or Cd occurs during the implant. Most of the implanted atoms already reside on substitutional sites when the anneal is begun, and hence diffusion is slow. At implant temperatures $\lesssim$ 100°C, for high enough doses thermal vacancy generation is slow and most of the implanted atoms are in interstitial sites. During subsequent annealing these interstitial atoms diffuse rapidly. Forcing implanted atoms into fast diffusion interstitial sites may also be associated with recrystallization of a layer driven amorphous by a high dose, low temperature implant (12). Whether or not recrystallization is occurring, considerable stress is built up during high dose, low temperature implants and the fast diffusion is probably indicative of stress release;

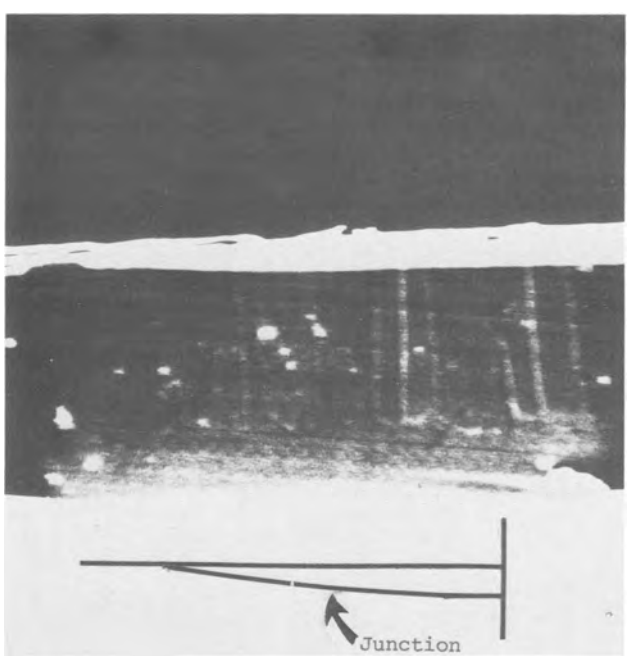


Fig. 6. SEM micrograph of a cleaved junction (white area) which had been annealed 15 min at 900°C. The maximum junction depth is 6.35μ and the curved region extends ~75μ. Magnification 1000X.

the same driving force which apparently drives dislocations out of the surface region.

In addition to anomalously large junction depths we observe a peculiar dish-shape junction for the circular diodes. There is virtually no lateral diffusion outside the implanted region as one might expect to occur in normal diffusion. Instead, the junction curves slowly over a distance of ~75 mm from the edge of the implanted region. This may be due to an anisotropic stress-enhanced diffusion. On the other hand, if vacancy generation during the anneal is higher in the unimplanted surrounding region, as we propose, not only would lateral diffusion of implanted atoms be retarded by vacancy capture, but vacancy diffusion laterally into the implanted area would retard vertical Zn diffusion. This vertical retardation would be greatest at the edge of the implanted region, where vacancy concentration is largest, and diminish toward the center, giving a dish-shaped junction profile.

Conclusion

Correlated observations of thermal pitting, photoluminescence, and anomalous junction profiles in $GaAs_{0.6}P_{0.4}$ on GaAs substrates receiving high dose, room temperature ion implants suggest that thermal pit nucleation sites (causing mechanical surface degradation) and vacancy generation sites (causing photoluminescence degradation) may both be identified with dislocations reaching the surface. Severe strain introduced by high dose, room temperature ion implants may act to remove dislocations which would otherwise terminate at the surface by a glide mechanism similar to that described by Matthews *et al.* (8). We propose that such dislocation removal decreases vacancy generation during anneal, thereby diminishing anneal-induced PL degradation. Anomalous junction depths and shapes offer additional evidence of high strain, low vacancy generation in the implanted region compared to the unimplanted region.

The mechanical and photoluminescence degradation observed here are able to occur only because the Si_3N_4 protective coatings are in varying degrees nonideal. However, the parallel processing of implanted and unimplanted control samples removes from consideration any question that the nitride quality is responsible for the degradation differences between implanted and unimplanted samples.

Acknowledgments

The authors would like to thank B. A. MacIver, D. M. Roessler, and M. C. Steele for their assistance and support of this work.

Manuscript submitted July 6, 1976; revised manuscript received Jan. 28, 1977.

Any discussion of this paper will appear in a Discussion Section to be published in the June 1978 JOURNAL. All discussions for the June 1978 Discussion Section should be submitted by Feb. 1, 1978.

Publication costs of this article were assisted by General Motors Corporation.

REFERENCES

1. C. Y. Lou and G. A. Somorjai, *J. Chem. Phys.*, **55**, 4554 (1971).
2. T. Itoh and Y. Oana, *J. Appl. Phys.*, **44**, 4982 (1973).
3. H. Okabayashi, *Appl. Phys. Lett.*, **28**, 490 (1976).
4. J. S. Harris, F. H. Eisen, B. Welch, J. D. Haskell, R. D. Pashley, and J. W. Mayer, *Appl. Phys. Lett.*, **21**, 601 (1972).
5. "Compound Semiconductors," Vol. 1, 476, R. K. Willardson and H. L. Goering, Editors, p. 476, Reinhold Publishing Corp., New York (1962).
6. D. A. Cusano, *Solid State Commun.*, **2**, 353 (1964).
7. M. I. Nathan and G. Burns, *Appl. Phys. Lett.*, **1**, 89 (1962).
8. J. W. Matthews, A. E. Blakeslee, and S. Mader, *Thin Solid Films*, **33**, 253 (1976).
9. R. G. Hunsperger and O. J. Marsh, *Metall. Trans.*, **1**, 603 (1970).
10. M. G. Craford, *Prog. Sol. State Chem.*, **8**, 127 (1973).
11. T. Itoh and Y. Oana, *Appl. Phys. Lett.*, **24**, 320, (1974).
12. V. M. Zelevinskaya, G. A. Kachurin, N. P. Bogomyakov, B. S. Azikov, and L. L. Shirokov, *Sov. Phys. Semicond.*, **8**, 164 (1974).
13. V. M. Zelevinskaya, G. A. Kachurin, N. B. Pridachin, and L. S. Smirnov, *ibid.*, **4**, 1529 (1971).

A Quantitative Model for the Diffusion of Phosphorus in Silicon and the Emitter Dip Effect

R. B. Fair* and J. C. C. Tsai

Bell Laboratories, Reading, Pennsylvania 19604

ABSTRACT

A consistent model of P diffusion in Si is presented which accounts quantitatively for the existence of electrically inactive P, the "kink" and the tail regions of the P profile, and the emitter dip effect. In this model it is shown that three intrinsic P diffusion coefficients exist, each one associated with the diffusion of P with vacancies in three different charge states. In the so-called "anomalous" high concentration region of the profile ($n \gtrsim 10^{20}$ cm^{-3}), it is shown that equilibrium concentration of $P^+V^=$ pairs dominates P diffusion and P electrical activity. At lower electron concentrations when the Fermi level is ~0.11 eV below the conduction band, the $V^=$ vacancy gives up an electron, and the 0.3 eV lower binding energy of the resulting P^+V^- pairs enhances the probability for pair dissociation by a factor of 10-35, depending on the temperature. This effect creates a steady-state excess concentration of V^- vacancies which flow away from the point of pair dissociation. The concentration of excess V^- vacancies created is proportional to the number of $P^+V^=$ pairs created at the Si surface times the enhanced probability for pair dissociation. These vacancies in the V^- charge state interact with P to create the enhanced tail diffusion. In a npn structure, the charge state of the excess vacancies becomes V^+ in the base region, thus enhancing the diffusivity of the base dopant and causing the emitter dip effect. The magnitude by which the P tail diffusivity and the base dopant diffusivity are enhanced is the same and may reach a factor of 135 for a 900°C diffusion.

At high concentrations the diffusion of phosphorus (P) into silicon (Si) produces an impurity atom distribution that differs considerably from the Gaussian or complementary error-function distributions (1-7). Numerous models have been proposed to explain this anomalous deviation from simple diffusion theory. Lawrence (8) suggested that the retardation of P diffusion was a result of the precipitation of P at moving dislocations. Dash and Joshi similarly postulated that the onset of anomalous P diffusion occurred simultaneously with the generation of dislocations in the Si lattice, at a critical integrated P concentration (9). However, the recent results of Sato *et al.* (10) disagree with this model, and Duffy *et al.* (11) found no evidence of dislocations or precipitation following the predeposition of prominently kinked P profiles. Significant numbers of dislocations and accompanying precipitation occur only after the drive-in cycle (11).

Other P diffusion models include the saturated lattice site model of Bakeman and Borrego (12), the thin surface barrier model of Makris *et al.* (13), impurity band effects on the electron activity coefficient (10, 14), the existence of a molten Si-P phase to explain the apparent flattened region of the P profile (15), and Thai's model of enhanced diffusion due to plastic deformation and subsequent generation of excess vacancies (16, 17). All of the above models have been criticized by Hu in a recent review (18), and so additional comments will not be made here.

Since Hu's review in 1972, several additional P diffusion models have evolved which support the idea that P diffuses via an intrinsic defect mechanism. Schwettmann and Kendall (19) observed that the concentration at which the kink occurs in the P profile varies with temperature with a constant activation energy. They suggested a two species mechanism with the faster diffusing species being the neutral phosphorus-vacancy pair (E center). The negative E center was proposed as the slower species, but no mechanism for excess vacancy generation was discussed. The P isoconcentration study of Makris and Masters (20) also suggests that the E center is the dominant diffusing pair.

Peart and Newman (21) have suggested that the high concentration region of the P profile is formed by a simple phosphorus-vacancy mechanism of diffusion where the vacancy is in a single negative charge state. When the Fermi level drops below the vacancy acceptor level of $E_C - 0.44$ eV in the bandgap, the P^+V^- pair breaks up and creates the nonequilibrium vacancy excess that accounts for the enhanced P diffusion in the tail region. This model suffers from the fact that a similar phenomenon is not observed during the diffusion of As in Si, since As diffuses via the As^+V^- pair (22). However, the basic concept of pair dissociation during a charge-state change of the vacancy does apply to the model to be presented in the present work.

Yoshida *et al.* (23) have shown that if at constant surface concentration 900°C P diffusion profiles obtained for different diffusion times are plotted *vs.* $x/\sqrt{t}$ (depth/$\sqrt{\text{time}}$), then the profiles practically fall on top of each other. This means that the diffusivity of P in Si is independent of position or time and depends only upon the local P concentration. This observation negates one of Hu's (18) earlier criticisms regarding the validity of using the Boltzmann-Matano analysis for extracting P diffusion coefficients from measured profiles. This also means that P diffusion in Si is not dominated by processes which involve interactions such as precipitation, generation of nonequilibrium vacancy transients by climbing dislocations, and trapping and complex formations that are far from equilibrium. This result does not rule out processes that generate steady-state concentrations of vacancies that rapidly equilibrate and which remain constant during the diffusion interval. It will be shown that such a process controls the tail region diffusion of P. Additional data supporting the important observation by Yoshida are shown in Fig. 1 for three diffusion temperatures. It can be seen that for the three diffusion temperatures chosen, the profile data plotted with $x/\sqrt{t}$ as the abscissa are independent of x and t. Experimental details will be given below.

* Electrochemical Society Active Member.

Key words: electrical activity, diffusion in silicon, vacancy diffusion.

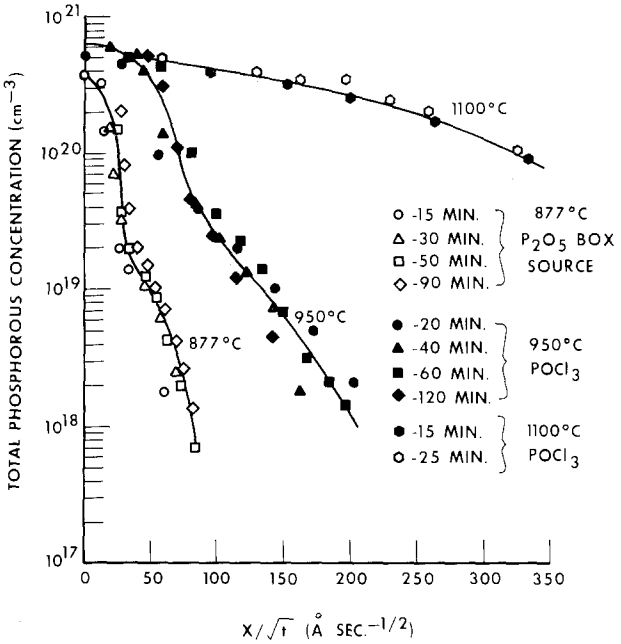


Fig. 1. Total phosphorus concentration *vs.* reduced distance for three diffusion temperatures.

Yoshida proposed that P diffuses only via the diffusion of E centers. His model says that P enters the Si surface in the form of an E center, which then flows into the bulk. Since the energetics of E center formation are more favorable at the Si surface, a supposed excess of E centers results which yields a supersaturation of vacancies due to E center dissociation. This source of vacancies causes the enhanced tail region diffusivity as some of these vacancies diffuse into the bulk. This model is useful since it contains elements which support some experimental facts, but no attempt was made to compare the theory in a quantitative way with experimental results. In addition, there was no mention of the charge state of the vacancies involved in the E center dissociation.

Most recently Shaw (24) proposed that P diffuses in the form of a P-neutral vacancy pair, $(P^+V^\times)$, and also as a P-singly ionized vacancy acceptor pair (P^+V^-). Shaw attributes the kink in the P profile to oxygen donors simultaneously diffusing with P from the surface oxide layer. The disappearance of the kink at lower P surface concentrations is attributed to a reduction of [O] in the crystal. However, the characteristic kink has been observed in ion-implanted P profiles that were diffused in an Ar ambient (25), as shown in Fig. 2. This result also refutes Yoshida's model, since the enhanced tail region can be seen to exist even though no excess E centers were formed via attachment of vacancies at the Si surface during the implantation of P. The fact that the implanted-diffused profile shows the characteristic kink also refutes the thin surface barrier model of Makris *et al.* (13).

In the following sections new experimental data on P diffusivity and P electrical activity in Si are presented, as well as a quantitative model of P diffusion which is supported by experimental measurements. It is shown that P diffuses via the E center as has been proposed earlier, but the diffusion proceeds with the vacancy in three different charge states. Dissociation of the $P^+V^=$ pair at a well-defined Fermi level position of $E_C - 0.11$ eV creates the excess V^- vacancies which enhance the tail region diffusivity. The kink region occurs where the P diffusivity becomes dominated by excess P^+V^- pair formation. For P diffusions in which the surface concentration is less than $\sim 10^{19}$ cm^{-3}, diffusion is dominated by the exchange of P with $V^\times$ neutral vacancies.

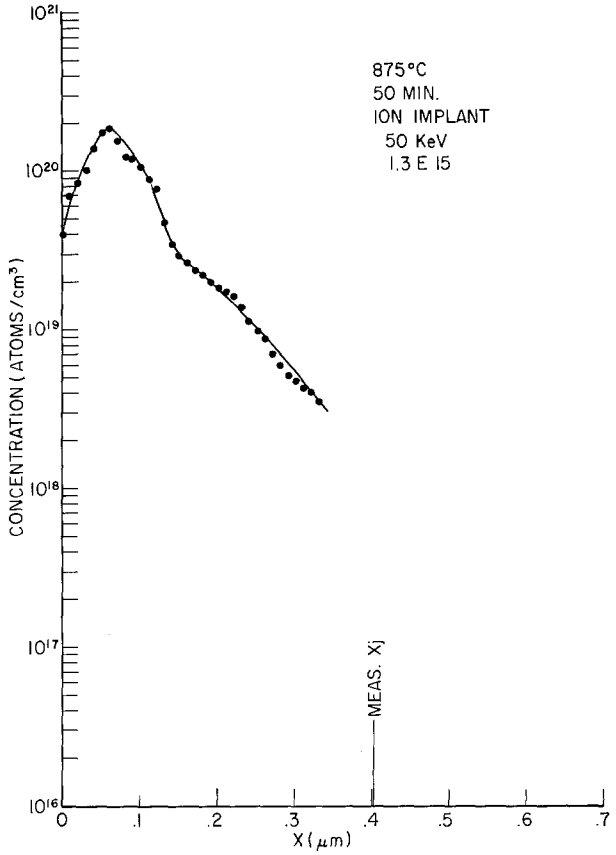


Fig. 2. Ion implanted-diffused phosphorus layer in silicon showing the presence of the kink and tail regions.

Experimental Technique and Results

Starting materials and diffusion conditions.—Diffusions were performed in p-type Si of 0.5-1 Ω/cm resistivity in both <111> and <100> orientation wafers. In most cases the front of the wafers were Syton polished and the backs were chemically polished. The wafers were degreased, cleaned, acid etched, and rinsed in DI water, and spun dry.

The diffusion source was $POCl_3$ for all diffusion temperatures except 875°C. In this case the diffusion source was P_2O_5 + CaO in a platinum box. The $POCl_3$ liquid source was transported into the diffusion furnace with either N_2 or Ar at flow rates typically set at 30 cm^3/min. Mixture with the main gas stream of N or Ar and O_2 occurred in the furnace with flow rates of 1500 and 75 cm^3/min, respectively. No differences in the diffusion profiles were observed when either N_2 or Ar carrier gases were used (25).

Profile determination.—Electron concentration vs. resistivity.—Details of the differential conductivity measurements made on the diffused samples appear in Ref. (7). In the past, Irvin's resistivity *vs.* concentration curve (26) has been used to convert differential conductivity measurements into doping density *vs.* depth. However, recent measurements by Mousty *et al.* (27) and Baccarani and Ostoja (28) indicate that Irvin's curve overestimates electron concentration for a given resistivity for $\rho \lesssim 5 \times 10^{-3}$ Ω/cm in P-doped Si. These authors have also shown that the electron mobility in P-doped Si becomes constant for P concentrations greater than $\sim 2 \times 10^{19}$ cm^{-3}. Tannenbaum (1) has also assumed a constant electron mobility for $\rho < 5 \times 10^{-3}$ Ω/cm. This means that the slope of the ρ *vs.* n curve should be constant in this range. Data from several authors (27, 29, 30) on ρ *vs.* n as determined by Hall measurements on P-doped Si samples are shown in Fig. 3. A "best fit" constant-slope ρ *vs.* n curve is drawn through the data points. It can be seen that Irvin's curve, which is based on radio-

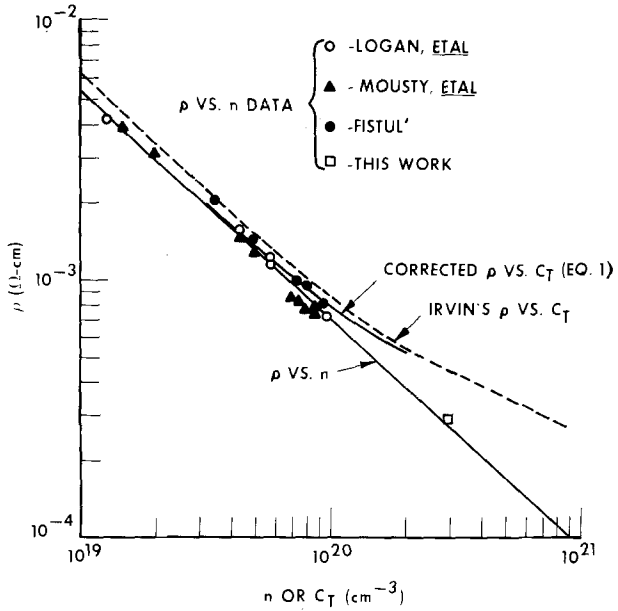


Fig. 3. Resistivity *vs.* phosphorus and electron concentrations in silicon.

tracer P data for concentrations greater than 10^{20} cm^{-3} does not represent the electrically active P^+ concentration. Also drawn in Fig. 3 is a "corrected" curve of ρ *vs.* total P concentration, C_T, based upon data obtained in this study which is discussed below. It can be seen that above $\sim 1.5 \times 10^{20}$ cm^{-3} P doping, good agreement is obtained with Irvin's ρ *vs.* C_T curve.

Total phosphorus concentration.—Secondary ion mass spectrometry was performed on some of the diffused samples in order to determine total P profiles (31). The SIMS data were calibrated using neutron activation analysis (NA) measurements of the same profiled wafers. A typical profile is shown in Fig. 4 of a 1000°C, 60 min diffusion. Also shown is the electrically active

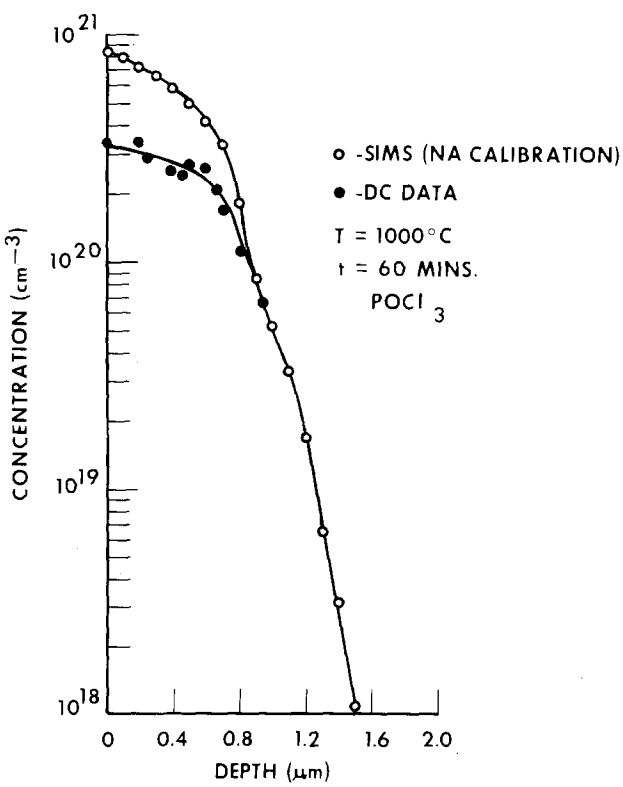


Fig. 4. Total and electrically active phosphorus diffusion profiles obtained by secondary-ion mass spectrometry (neutron-activation calibration) and by differential conductivity measurements.

P^+ profile obtained from differential conductivity (DC) measurements and the ρ *vs.* n curve of Fig. 3. The ratio of total P/cm^2 to n/cm^2 is $Q_T/Q_A = 2$, which agrees with previous results at 1000°C (32).

Additional total P and electrically active P profiles were obtained at 900° and 1050°C. These data are summarized in Fig. 5 where the corresponding n *vs.* C_T data are plotted. Included are the 1050°C data of Tannenbaum (1). These data can be described by an empirical equation relating n to C_T

$$C_T = n + 2.04 \times 10^{-41} n^3 \qquad [1]$$

This expression is plotted in Fig. 3 as the corrected resistivity *vs.* total P concentration curve previously described.

Phosphorus diffusion coefficients.—Since it has been established that the Boltzmann-Matano analysis is valid for P diffusion profiles in Si, this technique was applied to numerous profiles obtained over the temperature range of 875° to 1290°C. The results for 1000°C are displayed in Fig. 6 where D *vs.* n data are plotted. Also plotted are the isoconcentration D *vs.* n data

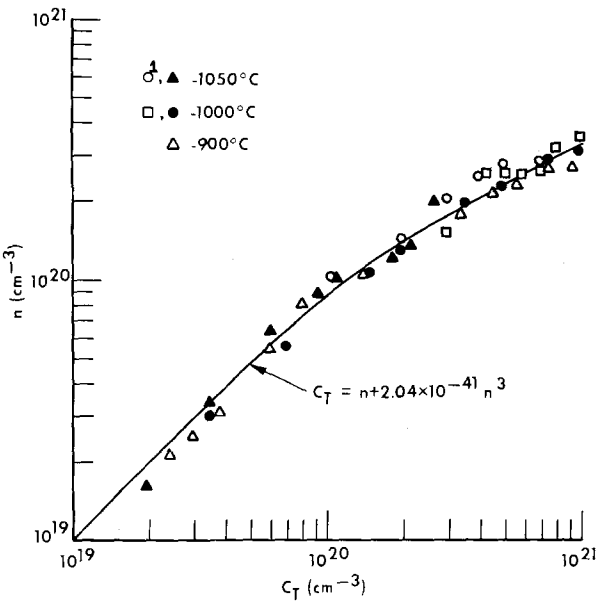


Fig. 5. Total phosphorus concentration *vs.* electron concentration in silicon.

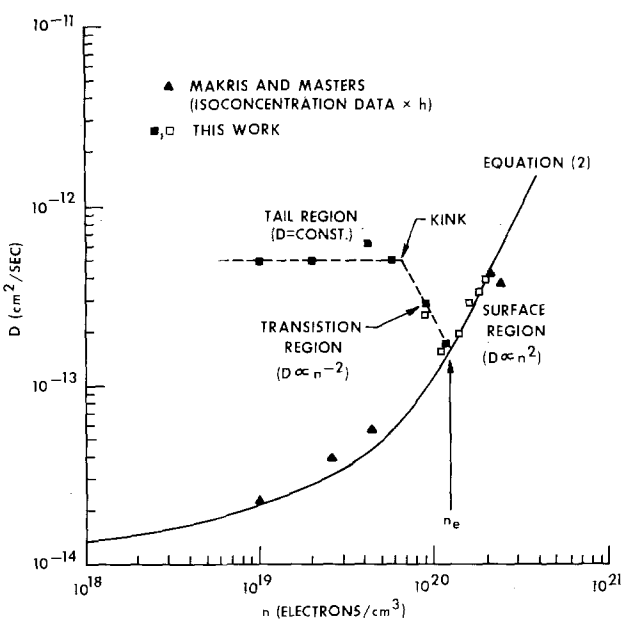


Fig. 6. 1000°C phosphorus diffusivity *vs.* electron concentration in silicon.

(▲ data) of Makris and Masters (20) for 1000°C where the D values have been multiplied by an electric-field enhancement factor (≅2) in order to be comparable with the other data in the figure. Since the data of Makris and Masters were total P data, they were converted to electron concentration *vs.* D by using Fig. 3.

There are several regions of interest in Fig. 6. In the surface region of the P profile, the D *vs.* n data show a slope of 2 when plotted on log-log scales ($D \propto n^2$). When the electron concentration drops to a critical value of $n = n_e$, an abrupt change occurs in the diffusivity by going from an n^2 dependence to a n^{-2} dependence. Finally, by the time the concentration has dropped to the well-known kink region, the diffusivity has increased and remains constant in the tail region (dashed curve). It can be seen that the isoconcentration data do not exhibit the same dependence of D on n as the data taken from profiles of P diffused into 1 Ω/cm Si. However, these data do fall on a curve extrapolated from the surface region data which has the form of

$$D = h\left[D_i^{\times} + D_i^{=}\left(\frac{n}{n_i}\right)^2\right] \qquad [2]$$

where $D_i^{\times}$ and $D_i^{=}$ are diffusion constants and h is the electric-field enhancement factor which approaches a value of 2 at high concentrations (18). D values will be discussed below, but at this point it can be said that $D_i^{\times}$ is the diffusion coefficient usually quoted in low concentration P diffusion studies (20).

The 1000°C data shown in Fig. 6 are plotted in Fig. 7 along with diffusivity data obtained from profiles diffused at 875°-1290°C. The comments applicable to Fig. 6 apply to the data in Fig. 7, except that the transition region ($D \propto n^{-2}$) disappears at 1050°C. However, the constant diffusivity tail region exists for all of the diffusions performed. The solid curves in Fig. 7 are of the form of Eq. [2].

The electron concentration corresponding to the observed abrupt change in D in going from an n^2 dependence to a n^{-2} dependence or n^0 dependence will be called n_e. These n_e data are plotted in Fig. 8 *vs.* $1/T$. Also plotted in Fig. 8 are the electron concentration values from Fig. 5 where the n *vs.* C_T data change slope from a value of 1 to a value of 1/3. It can be seen that the n_e values obtained from Fig. 7 and from Fig. 5 are approximately equal as a function of temperature. Also plotted are data from the D *vs.* n curves of Matsumoto (34). The solid curve drawn through these points corresponds to the electron concentration *vs.* $1/T$ at which the Fermi level is 0.11 eV below the conduction band. The calculation of the electron concentration corresponding to $E_C = 0.11$ eV was based on Fermi statistics with temperature-dependent effective electron mass (33), but with no impurity-band formation. Also shown in Fig. 8 are data of the electron concentration at the kink *vs.* $1/T$ (Δ data) obtained from numerous profiles (7, 19, 25, 35-37). The point to be made here is that the location of the kink, while significant, has far less significance than the concentration n_e. It is argued below that the kink occurs because of phosphorus-vacancy pair dissociations when $E_F = E_C$-0.11 (or $n = n_e$), and that the kink in the P profile exists as a result of these dissociation processes at $n = n_e$.

Sufficient diffusivity data in the tail region were available at 900° and 1100°C to plot D_{TAIL} *vs.* n_s, the electron concentration at the diffused Si surface. The tail region diffusivity at a concentration of 10^{18} cm^{-3} is plotted *vs.* n_s in Fig. 9. It can be seen that above a certain value of n_s, $D_{TAIL} \propto n_s^3$. The solid curves are calculated curves and are described below.

Finally, data representing the temperature dependence of D_{TAIL} for $n_s = 1.5$ to 2×10^{20} cm^{-3} are shown plotted in Fig. 10. These data were obtained from the present study and from other sources (24, 34), and are normalized with respect to the intrinsic P diffusivity at $n = 10^{18}$ cm^{-3}, $D_i^{\times}$. Also plotted in Fig. 10 are enhanced-base diffusivity data obtained on shallow npn structures with P emitters (emitter dip effect) (38-40). These data are normalized with respect to the intrinsic base diffusion coefficients. It can be seen that good agreement with the $D_{TAIL}/D_i^{\times}$ data is obtained, indicating similar magnitudes of enhanced diffusion. The

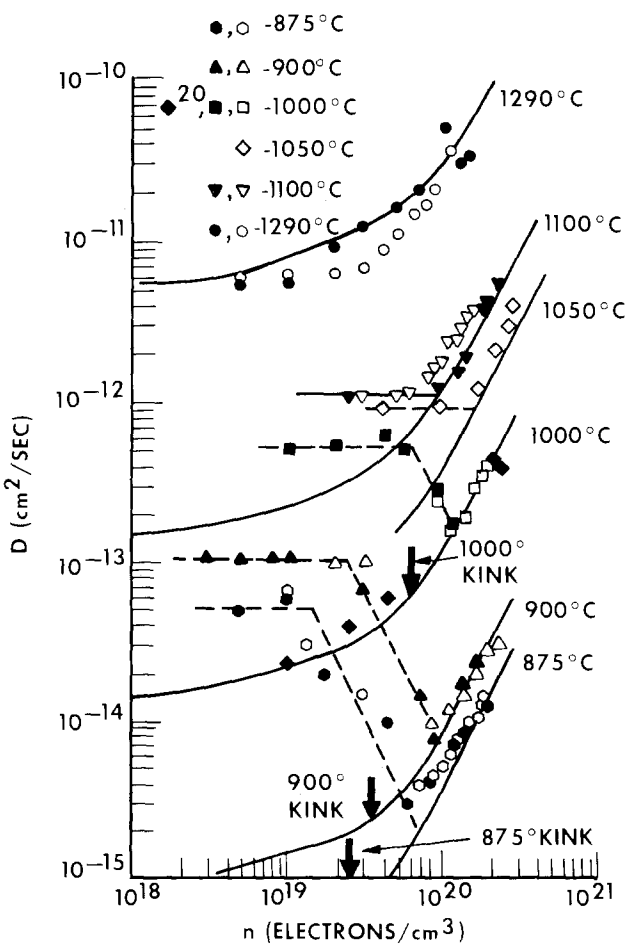


Fig. 7. Phosphorus diffusivity *vs.* electron concentration in silicon

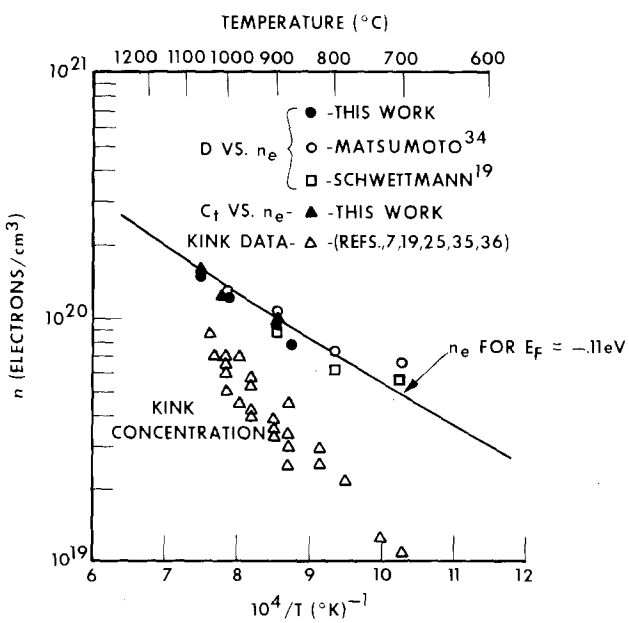


Fig. 8. Electron concentration, n_e, at which diffusivity becomes proportional to n^2 *vs.* $1/T$. Also shown is the electron concentration at which the kink occurs *vs.* $1/T$.

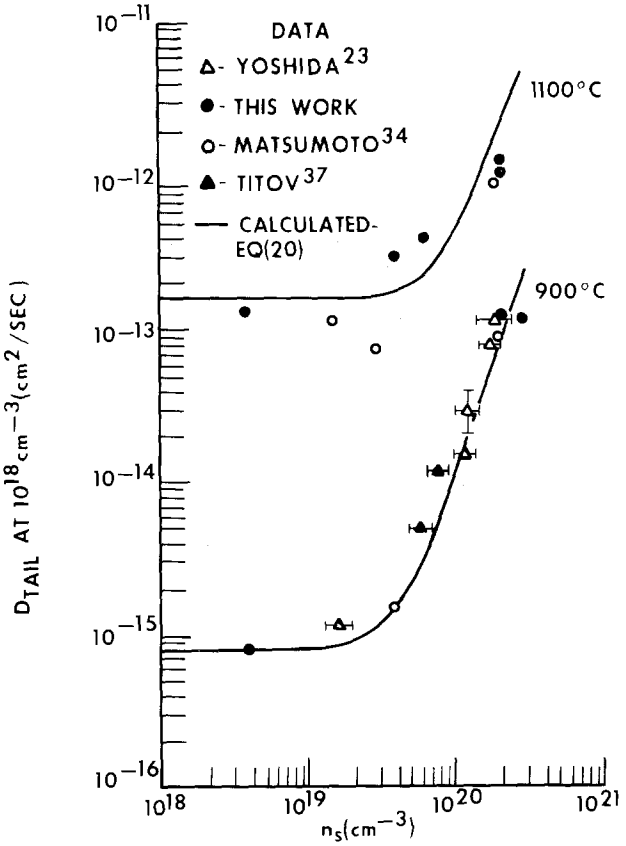


Fig. 9. Phosphorus diffusivity in the tail region at 1×10^{18} cm^{-3} vs. the surface electron concentration.

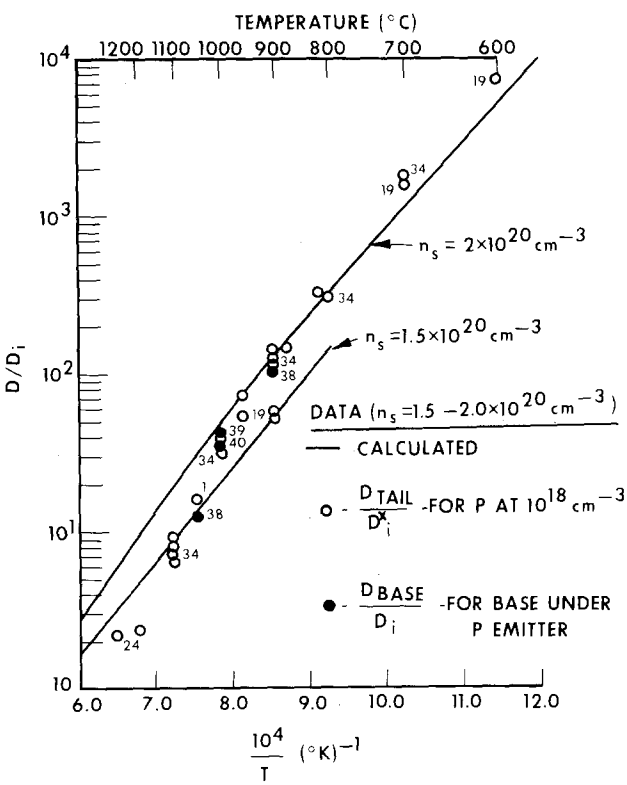


Fig. 10. Phosphorus tail diffusivity and enhanced base diffusivity due to the emitter dip effect.

solid curves in Fig. 10 are calculated and are discussed subsequently.

Analysis of Results

High concentration region.—At electron concentrations greater than n_e (see Fig. 8), the D *vs.* n data in Fig. 6 and 7 have a slope of 2 on log-log scales and the C_T *vs.* n data in Fig. 5 have a slope of 1/3. It is shown in Fig. 8 that n_e *vs.* $1/T$ corresponds to the electron concentration at which the Fermi level is 0.11 eV below the conduction band. Recently, Kimmerling has identified an energy level at $E_C = 0.11$ eV as the second-acceptor level of the Si vacancy (41). His findings are based upon observations of the annealing kinetics of radiation-induced defects in P-doped Si using deep level transient spectroscopy. Therefore, the analysis of the experimental results in this paper will assume the existence of P impurity — $V^=$ vacancy interactions in high concentration phosphorus diffusion.

C_T vs. n.—The reaction between an ionized P^+ atom located on a lattice site and a single negatively charged vacancy whose second acceptor level is unoccupied can be written as

$$V^- + P^+ + e^- \leftrightarrows P^+V^= = PV^- \qquad [3]$$

Reaction [3] is likely to proceed to the right only if the Fermi level position in the bandgap is favorable (close to $E_C = 0.11$ eV). The effect of reaction [3] has been to remove an electron from the conduction band and to bind it to the vacancy. Simultaneously, a hole is created which becomes a free carrier in the valance band. The same reaction product will occur if the P^+ ion reacts with a $V^=$ vacancy, where the second-acceptor level has already been filled.

The equilibrium constant for reaction [3] is

$$K_2(T) = \frac{C_{PV^-}}{\gamma_P \cdot \gamma_V \cdot C_{V^-} \cdot C_{P^+} \cdot \gamma_n \cdot n} \qquad [4]$$

where C_{PV^-}, C_{V^-}, and C_{P^+} are the concentrations of $P^+V^=$ pairs, V^- vacancies, and P^+ ions, respectively, and γ_V, γ_P, and γ_n are activity coefficients. The $\gamma_P \cdot \gamma_V$ product is approximately constant (33) and $\gamma_n \cong 1$ seems to occur in As-doped Si at least up to $n \cong 3 \times 10^{20}$ cm^{-3} (22). The fact that $\gamma_n \cong 1$ is observed at high concentrations supports the fact that impurity-band formation does not significantly affect the Fermi level position in Si at diffusion temperatures, at least up to concentrations of 3×10^{20}, which agrees with Hu's observation (42).

Solving for the concentration of $P^+V^=$ pairs from Eq. [3] using the law of mass action for C_{V^-} and C_{P^+} yields

$$C_{PV^-} = K_2^1(T) C^i_{V^-} \frac{n^3}{n_i^2} \qquad [5]$$

where $C^i_{V^-}$ is the intrinsic concentration of V^- vacancies. The total concentration of P atoms is

$$C_T = C_{P^+} + C_{PV^-} = n + K_3^1(T) \frac{n^3}{n_i^2} \qquad [6]$$

where all the constants in Eq. [4] and [5] are contained in $K_3^1(T)$.

Reference to Fig. 5 shows that Eq. [6] expresses the measured relationship between C_T and n with $K_3^1(T)/n_i^2 = 2.04 \times 10^{-41}$. Actually, this ratio does show a weak temperature dependence since the break in the C_T *vs.* n curve occurs at n_e whose temperature dependence is shown in Fig. 8. This result agrees well with direct calculations of the equilibrium coefficient for reaction [3] (41).

D vs. n.—The general expression for the diffusion coefficient of P in Si can be written as (43)

$$D = h\left[\sum_{r=0} D_i^{r-}\left(\frac{n}{n_i}\right)^r\right] \qquad [7]$$

where h is the self-electric-field enhancement factor, and D_i^{r-} is the intrinsic diffusivity of the P-vacancy pair in the rth charge state. For the present case, $r = 0$,

1, and 2 and $r^- = 0$, $-$, and $=$. Equation [7] arises because the concentration of vacancies in the rth charge state is (from mass action effects)

$$\frac{C_{Vr-}}{C^i_{Vr-}} = \left(\frac{n}{n_i}\right)^r \qquad [8]$$

and the diffusivity of the P^+-V^{r-} pair is proportional to C_{Vr-}. The need for including the electric-field enhancement arises from the fact that Makris and Masters' isoconcentration diffusivity data (20) at high concentrations were a factor of 2 lower than the data obtained in this study (Fig. 6) for the same temperature and doping ($h = 2$ for $n >> n_i$). It is shown in Fig. 11 that the electric-field enhancement is evident at lower concentrations when the dominant diffusing species is the $P^+V^\times$ pair. Since it has previously been shown (22) that electric-field effects are important in the diffusion of As^+V^- pairs, it can be concluded that it is necessary to consider the electric-field effect regardless of the charge state of the diffusing species.

The preceding analysis and the data in Fig. 7 for $n > n_e$ strongly support the existence of the $P^+V^=$ pair, and consequently $D \propto (n/n_i)^2$ is evident. However, the existence of the P^+V^- pair (single negatively charged vacancy) is not evident. In order to try to observe the effect of the P^+V^- pair on D, diffusivity data were obtained on profiles whose surface doping, n_s, was $< n_e$, but greater than n_i ($10^{19} \lesssim n_s \lesssim 7 \times 10^{19}$ cm^{-3}). From these data the D/D_i *vs.* n/n_i relationship was determined. Similar data were obtained for As diffusions with $n_s < 7 \times 10^{19}$ cm^{-3}. Figure 11 is a plot of these data. The recent P data of Matsumoto *et al.* (44) are also included. It can be seen that there is a distinct difference between the P data and the As data. It has been well established that As^+V^- pairs diffuse and cause the observed concentration-dependent diffusion coefficient for As in Si (22). However, in the case of phosphorus, the only concentration-dependent diffusivity observed in this range is due to the self-electric-field enhancement when $n/n_i \gtrsim 1$. Therefore, due to lack of significant enhancement of P diffusivity in this concentration range, the dominant diffusing species must be the $P^+V^\times$ pair with an intrinsic diffusion coefficient, $D_i^\times$. At high concentrations the dominant species is the $P^+V^=$ pair with intrinsic diffusivity $D_i^=$, and the effect of the P^+V^- species is either negligible or nonexistent. Thus, if the presence of the tail is ignored, the total P diffusion coefficient can be written as

$$D = h\left[D_i^\times + D_i^= \left(\frac{n}{n_i}\right)^2\right] \qquad [2]$$

with

$$h = 1 + \frac{n}{n_i}\left[\left(\frac{n}{2n_i}\right)^2 + 1\right]^{-1/2} \qquad [9]$$

The intrinsic diffusivity of the P^+V^- pair must be very small. Its value will be estimated from the tail diffusivity data in the next section.

The diffusivity data for $D_i^\times$ ($P^+V^\times$) pair has been selected from the literature in which the P profiles were directly measured on samples with $n_s << n_i$. The best sources of these data are Ghostagore (45), Makris and Masters (20), and Tsai (46). These data are plotted in Fig. 12 and can be fitted to the Arrhenius equation

$$D_i^\times = 3.85 \exp\left(\frac{-3.66\text{ eV}}{kT}\right) \qquad [10]$$

The diffusivity data for $D_i^=$ can be obtained from Eq. [2] and the data shown in Fig. 7 for $n > n_e$. These data are plotted in Fig. 12. Also, the high concentration diffusivity data of Makris and Masters (20) are plotted in Fig. 12. These results were obtained from isoconcentration studies in which the samples were doped uniformly to 4.5×10^{20}P atoms/cm^3. From Fig. 3 this P concentration corresponds to $n = 2.1 \times 10^{20}$ cm^{-3}. Setting $h = 1$ in Eq. [2] (no concentration gradient; no electric field) and solving for $D_i^=$ using Makris and Masters' measured results gives good agreement with the other $D_i^=$ data shown in Fig. 12. These results can be fitted to the Arrhenius equation

$$D_i^= = 44.2 \exp\left(\frac{-4.37\text{ eV}}{kT}\right) \qquad [11]$$

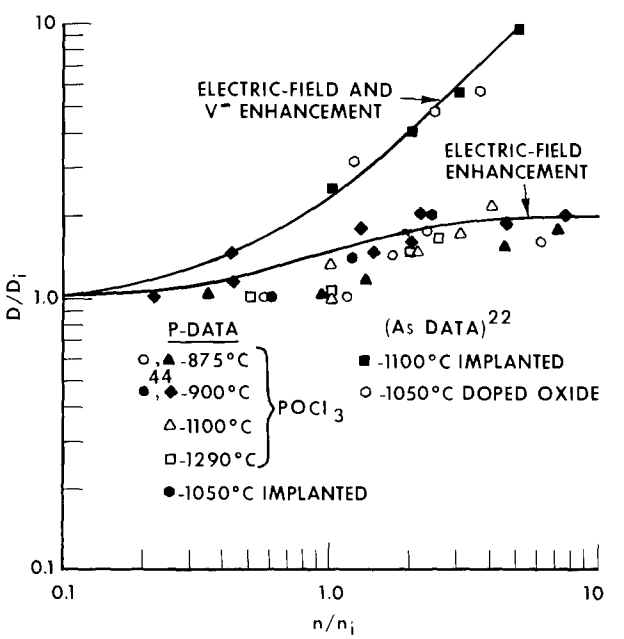


Fig. 11. A comparison between the diffusivities of arsenic and phosphorus in silicon for surface concentrations less than 7×10^{19} cm^{-3}.

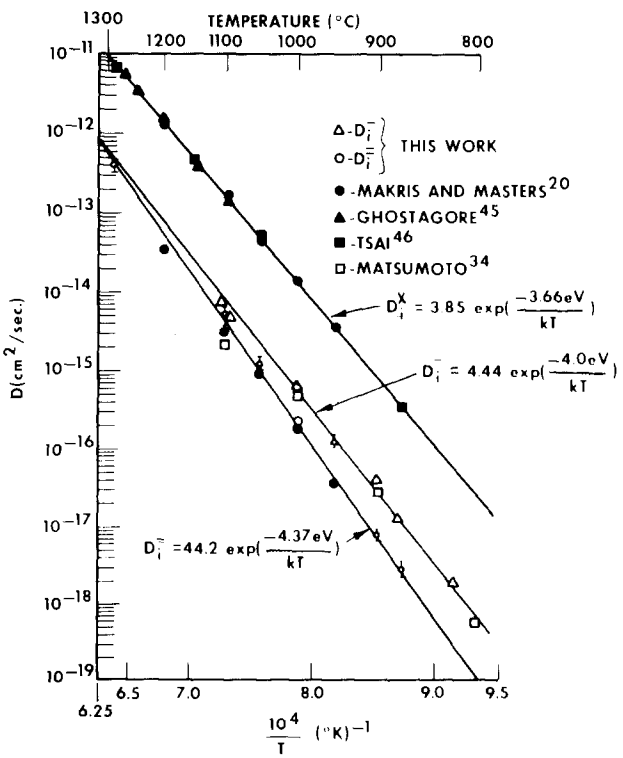


Fig. 12. The three intrinsic diffusion coefficients of phosphorus in silicon.

Equation [2] with $D_i^{\times}$ and $D_i^{=}$ given by the above expressions is plotted in Fig. 6 and 7 (solid curves) for the temperatures shown. Good agreement with the measured data is obtained.

Phosphorus tail region.—In order to understand the processes which contribute to the enhanced P tail region diffusivity, consider the idealized P profile shown in Fig. 13. When P enters the surface, some fraction will become paired with $V^{=}$ vacancies according to the reaction

$$P^{+} + V^{=} \rightleftarrows P^{+}V^{=} \qquad [12]$$

The mass action relation for Eq. [12] at the surface can be written in a similar manner to Eq. [5]

$$\frac{C_{PV^-}}{C^i_{PV^-}} = \frac{n_s^3}{n_i^3} \qquad [13]$$

where n_s is the surface electron concentration or the peak concentration (*i.e.*, for a Gaussian distribution, etc.), and $C^i_{PV^-}$ is the intrinsic concentration of $P^+V^=$ pairs. The condition expressed by Eq. [13] is assumed to hold throughout the highly doped surface region. Referring to Fig. 4 it can be seen that in the first 6000Å of the electron profile, the concentration remains at approximately $n_s = 3 \times 10^{20}$ cm^{-3} (the so-called "flat" region). Thereafter, the measured concentration drops with a doping gradient of 6×10^{24} cm^{-4} to $n_e = 1.3 \times 10^{20}$ cm^{-3}, which occurs at a depth of 8000Å from the surface.

When $P^+V^=$ pairs leave the flat region and diffuse down the steep doping gradient, it is proposed that they do not dissociate significantly until the Fermi level is ~0.11 eV below the conduction band, *i.e.*, until the concentration drops to n_e. This is reasonable in view of the fact that Hirata *et al.* (47) estimated that the phosphorus-vacancy pairs in their annealing experiments underwent $\sim 10^5$ jumps before dissociation. The observation that dissociation is more probable at $n = n_e$ can be understood by noting that the probability for pair dissociation is dependent on the pair binding energy. Thus the pair vibration frequency, γ ($\sim 10^{13}$ Hz), multiplied by exp $(-E_b/kT)$ yields the number of dissociation events/second, N_D (41). The ratio of the

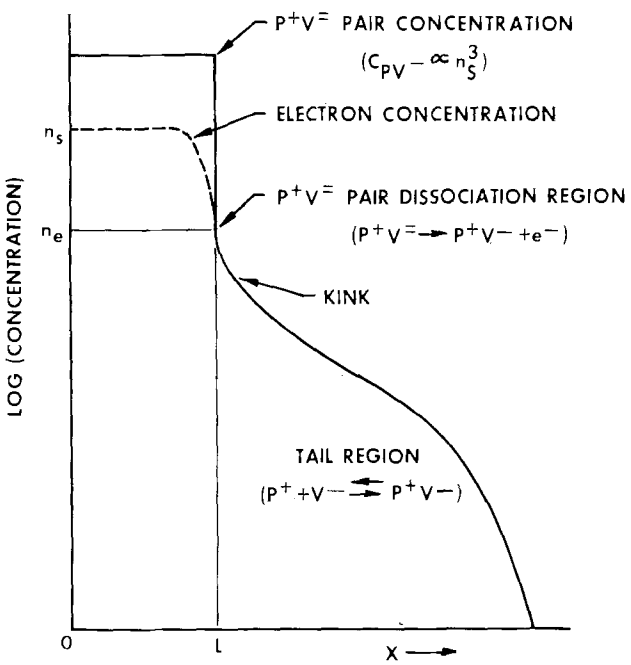


Fig. 13. Idealized phosphorus profile and vacancy generation model. $P^+V^=$ pairs formed in the surface region dissociate when the electron concentration drops to $n = n_e$. At this concentration the Fermi level coincides with the second acceptor level of $V^=$. The freed vacancies diffuse until they recombine with P^+ atoms in the tail region and form P^+V^- pairs.

dissociations/second for the P^+V^- pair to that of the $P^+V^=$ pair is

$$\frac{N_D^-}{N_D^=} = \exp\left(\frac{0.3\text{ eV}}{kT}\right) \qquad [14]$$

This follows since the binding energy, E_b, of the P^+V^- pair is ~0.3 eV lower than the binding energy of the $P^+V^=$ pair (48). Thus, when $E_F = E_C - 0.11$ eV

$$P^+V^= \rightleftarrows P^+V^- + e^- \rightleftarrows P^+ + V^- + e^- \qquad [15]$$

will be favorable as the $V^=$ vacancy loses an electron to the conduction band, and in its new charge state the P^+V^- pair is more likely to dissociate.

The mass action equation at $n = n_e$ for the reaction in Eq. [15] can be written as

$$\frac{C_{V^-}}{C^i_{V^-}} = \left(\frac{n_i}{n_e}\right)^2 \frac{C_{PV^-}}{C^i_{PV^-}} \qquad [16]$$

where C_{V^-} is the concentration of V^- vacancies, and $C_{PV^-}/C^i_{PV^-}$ is given by Eq. [13]. In order to account for the fact that reaction [12] also is generating $V^=$ vacancies which give up an electron to become V^- vacancies, and that reaction [15] is exp (0.3 eV/kT) times more probable than [12], the total concentration of generated V^- vacancies becomes

$$\frac{C_{V^-}}{C^i_{V^-}} = \frac{C_{V^=}}{C_{V^=i}}\frac{n_i}{n_e} + \frac{C_{PV^-}}{C^i_{PV^-}}\left(\frac{n_i}{n_e}\right)^2 \exp\left(\frac{0.3\text{ eV}}{kT}\right)$$
$$= \frac{n_s^3}{n_e^2 n_i}\left[1 + \exp\left(\frac{0.3\text{ eV}}{kT}\right)\right] \qquad [17]$$

Equation [17] represents the steady-state concentration of V^- vacancies referenced to $P^+V^=$ and P^+V^- pair dissociation events with the latter event being exp (0.3 eV/kT) times more probable. Values of the exponential term range from 36 at 700°C to 9 at 1300°C. It is the temperature dependence of the dissociation effect that accounts for the disappearance of the kink at higher temperatures ($T \gtrsim 1100$°C), *i.e.*, the probability for excess V^- generation decreases as temperature increases.

In the tail region the excess, steady-state V^- vacancies interact with P^+ ions to enhance phosphorus diffusion. Assuming that the P diffusivity is proportional to C_{V^-} yields

$$\frac{D^-}{D_i^-} = \frac{n_s^3}{n_e^2 n_i}\left[1 + \exp\left(\frac{0.3\text{ eV}}{kT}\right)\right] \qquad [18]$$

Equation [18] is the expression for the P tail-region diffusivity. In order to find D_i^- as a function of temperature, Eq. [18] can be solved for D_i^-, and measured profiles (known n_s) with known tail-region diffusivities, D^-, provide the required information. The results are plotted in Fig. 12 [Δ data from this work and □ data from Matsumoto, *et al.* (34)]. The Arrhenius equation that best describes these data is

$$D_i^- = 4.44 \exp\left(\frac{-4.0\text{ eV}}{kT}\right) \qquad [19]$$

It is now obvious why the data in Fig. 7 and 11 can be described by Eq. [2] without a D_i^- (n/n_i) term. At no temperature is this term more than 10% of the total P diffusivity. A discussion of this result is presented below.

The total tail-region diffusivity is

$$D_{TAIL} = D_i^{\times} + D^- \qquad [20]$$

with D^- given by Eq. [18]. Equation [20] is plotted in Fig. 9 (solid curves) for $T = 900°$ and 1100°C. Good agreement between the calculated curves and the data is obtained.

Dividing both sides of Eq. [20] by $D_i^{\times}$ gives the diffusivity enhancement factor in the tail region, $D_{TAIL}/D_i^{\times}$. This result is plotted with the data shown in Fig. 10 for $n_s = 1.5 \times 10^{20}$ cm^{-3} and 2×10^{20} cm^{-3}, which is the range of the data also plotted in the figure. Again the agreement between the calculated curves and the data is good.

Transition region.—The transition region is the portion of the D *vs.* n curves shown in Fig. 6 and 7 in which $D \propto n^{-2}$. For the profiles whose diffusivity data are shown in Fig. 7, the width of the transition region varies from 500Å at 1000°C to 1500Å at 875°C. This distance is too small to be associated with the vacancy diffusion length which is reported to be greater than 10 μm at 1050°C (49). This region is probably a result of the additional pair dissociations that occur at concentrations below $n = n_e$. Thus, the concentrations of liberated V^- vacancies and P^+V^- pairs build up with increasing depth into the crystal, but in a region where the concentration gradient is very steep.

Discussion

Vacancy concentrations.—The model presented in the preceding section predicts that a significant excess concentration of vacancies occurs in the P tail region due to $P^+V^=$ pair dissociation. It is assumed that some fraction of P atoms entering the crystal combine with $V^=$ vacancies to form $P^+V^=$ pairs which dissociate at some distance L from the surface and contribute vacancies to the steady-state vacancy distribution (see Fig. 13). It should be pointed out that the reaction which forms $P^+V^=$ pairs does not reduce the concentration of simple single vacancies. More single vacancies are generated at the surface to keep [V] in equilibrium. Thus, the flux of $P^+V^=$ pairs entering the region where dissociation occurs equals the flux of vacancies away from the point of dissociation. If it is assumed that all of the vacancies flow to the surface, then

$$\frac{D_V(C_V - C_V^{\circ})}{L} = D\frac{\partial C_{PV^-}}{\partial x} \qquad [21]$$

where $D_V = 1.4 \times 10^{-4} \exp(-0.33 \text{ eV}/kT)$ is the vacancy diffusivity, and C_V and C_V° are the excess and total equilibrium vacancy concentrations, respectively. D is the P diffusivity given by Eq. [2] and $\partial C_{PV^-}/\partial x$ is the gradient of the total P less the electrically active P distributions at $x = L$. The left-hand term represents the flux of vacancies to the surface where the vacancy concentration is pinned at C_V°. For the 1000°C diffusion shown in Fig. 4, evaluation of Eq. [21] yields

$$C_V - C_V^{\circ} = 2.3 \times 10^{13} (\text{cm}^{-3})$$

At 1000°C, $C_V^{\circ} \cong 1.2 \times 10^{15}$ cm^{-3} when $n = 2 \times 10^{20}$ cm^{-3}, and $C_V \cong 1.2 \times 10^{15}$ cm^{-3}. Therefore, the vacancies generated from $P^+V^=$ pair dissociation at $x = L$ do not significantly perturb the equilibrium vacancy concentration in the highly doped surface region. This result is consistent with the observed equilibrium dependence of C_T on n (Eq. [6]) and D on n^2 (Eq. [2]).

If the same calculation is performed to determine $C_V - C_V^{\circ}$ in the lightly doped bulk where (50, 51) $C_V^{\circ} \sim 5 \times 10^{13}$ cm^{-3} and $L_V \approx 25$ μm, then if it is assumed that all of the generated vacancies flow into the bulk

$$C_V - C_V^{\circ} \sim 8 \times 10^{14} (\text{cm}^{-3})$$

and $C_V \sim 8.5 \times 10^{14}$ cm^{-3}. Both calculations yield C_V values which are reasonably close to each other, *i.e.*, $C_V \sim 1 \times 10^{15}$ cm^{-3}. This value of vacancy concentration is also approximately equal to the $V^=$ concentration necessary to account for the observed flux of $P^+V^=$ pairs entering the Si surface during diffusion. Therefore, the model is entirely consistent with the absolute concentrations of vacancies available in the Si crystal.

In the P tail region at $n = 1 \times 10^{18}$ cm^{-3}, most of the dissociated vacancies will still be in the V^- charge state. The equilibrium concentration of neutral vacancies at 1000°C is (51)

$$C_V^{\times} = 5.5 \times 10^{22} \exp\left(\frac{-2.6 \pm 0.2 \text{ eV}}{kT}\right) \qquad [22]$$

Therefore, $C_V/C_V^{\times} \cong C_V/C_V^{\times} \cong 10$. This result can be compared with the 1000°C $D_{TAIL}/D_i^{\times}$ data shown in Fig. 10. It can be seen that the calculated magnitude of the excess vacancy concentration is of the correct magnitude to explain the observed P tail diffusion enhancement.

P-vacancy binding energy and Si self-diffusion.—The results of the previous sections indicate that P diffuses by interacting with vacancies in three different charge states. At this point it is appropriate to see if these results are consistent with the data available on the diffusion of other Group V impurities in Si and Si self-diffusion. The energy for Group V impurity diffusion is

$$Q_I^r = \Delta H_V^r + Q_E^r - E_b^r \qquad [23]$$

where Q_I^r is the impurity diffusion energy when the dopant interacts with a vacancy in the rth charge state, ($r = x, -, =$), ΔH_V^r is the vacancy formation enthalpy in the rth charge state, Q_E^r is the migration energy of the corresponding impurity-vacancy E center, and E_b^r is the E center binding energy.

From the microscopic cavity model of Phillips and Van Vechten (52), the formation enthalpy of a neutral vacancy in Si is $\Delta H_V^{\times} = 2.66$ eV. When a vacancy is ionized two new carriers of opposite charge are created. One is bound in the vicinity of the vacancy and the other is a free carrier in the valence band for acceptor-type vacancies. Thus, ΔH_V for an ionized vacancy must include the enthalpy of ionization, ΔH_I. The values of ΔH_I have been calculated (53) and yield the result that if the Fermi level is near the conduction band edge

$$\Delta H_V^- = 3.6 \text{ eV}$$

$$\Delta H_V^= = 3.93 \text{ eV}$$

A check on the correctness of these values can be obtained by calculating ΔH_V^- and $\Delta H_V^=$ from Si self-diffusion data. Thus

$$\Delta H_V^r = Q_{Si}^r - \Delta H_m^r \qquad [24]$$

where Q_{Si}^r is the activation energy for Si self-diffusion with a vacancy in the rth charge state, and ΔH_m^r is the corresponding vacancy migration enthalpy. Van Vechten (51) has reviewed the appropriate values of ΔH_m^r in Si and has argued that at high diffusion temperatures, $\Delta H_m^r \cong 1.2 \pm 0.3$ eV. The activation energy for Si self-diffusion with neutral vacancies has been consistently reported to be $\lesssim 4$ eV. Watkins and Corbett (54) reported $Q_{Si} = 3.95$ eV from low temperature annealing of E centers. The N_i precipitation in Si data of Seeger and Chik (55) show a 3.93 eV activation energy for Si diffusion below ~850°C. The recent loop annealing data of Sanders and Dobson (56) show $Q_{Si} \cong 4.1$ eV in intrinsic Si below ~1050°C. At higher temperatures the Q_{Si} energy in intrinsic Si appears to increase to 5.13 eV (57). However, it has been shown (58) that above ~1050°C the intrinsic diffusivities associated with SiV^+, SiV^-, and $SiV^=$ pairs exceed the diffusivity of the $SiV^{\times}$ pair. Thus, the Q_{Si} energy is only an apparent energy and reflects the diffusion of Si with vacancies in multiple charge states. Thus

$$Q_{Si}^{\times} \cong 3.95 \text{ eV}$$

and (58)

$$Q_{Si}^- \cong 5.0 \text{ eV}$$

for Si diffusion via V^- vacancies. Therefore, from Eq. [24] $\Delta H_V^{\times} = 2.75$ eV and $\Delta H_V^- = 3.8$ eV in agreement with the theoretical values.

For the $SiV^{=}$ pair it can be shown that $Q_{Si}^{=} \cong 5.43$ eV (58). From Eq. [24] this yields $\Delta H_V^{=} = 3.93$ eV with $\Delta H_m = 1.5$ eV, in good agreement with the calculated value.

Kimmerling *et al.* (48) have measured $Q_E^{-} = 0.95 \pm 0.03$ eV for the neutral E center migration energy. Thus, from Eq. [23]

$$E_b^{-} = 0.55 \text{ eV}$$

for the P^+V^- pair binding energy.

For the $P^+V^{=}$ pair (negative E center), $Q_E^{=} = 1.25 \pm 0.05$ eV (48). The 0.3 eV difference between Q_E^{-} and $Q_E^{=}$ can be accounted for by an increase in the coulomb energy required to produce a third-neighbor separation between P^+ and $V^{=}$. On this basis $E_b^{=} = E_b^{-} + 0.3 = 0.85$ eV. Using Eq. [23] with $Q_I^{=} = 4.37$ eV and $\Delta H_V^{=} = 3.93$ eV yields

$$E_b^{=} = 0.81 \text{ eV}$$

in excellent agreement. Likewise, the binding energy of the $P^+V^\times$ pair should be $E_b^\times \cong E_b^{-} - 0.3 = 0.25$ eV. Calculations by Swalin (59) indicate that the strain energy released when a neutral vacancy moves into a nearest neighbor position to an impurity atom is about 0.3 eV in Si. The result for $E_b^\times$ is in excellent agreement with this value.

Because the elastic interaction between an impurity and a vacancy in Si is short ranged, varying as r^{-3}-r^{-5} (see Ref. 60-62), the pair migration energy, $Q_E^\times$, is zero since no pair migration occurs. Thus, $Q_I^\times$ for an impurity in Si should be approximately

$$Q_I^\times = \Delta H_V^\times + \Delta H_m^\times - E_b^\times \qquad [25]$$

For the $P^+V^\times$ diffusion with $Q_I^\times = 3.66$ eV and the appropriate vacancy formation and migration enthalpies, $E_b^\times = 0.29$ eV. Again, good agreement is obtained with the previously calculated value.

Diffusion activation energy data obtained from low concentration doping profiles of other Group V impurities in Si are listed in Table I (63, 64) (surface concentration $<< n_i$). The $Q_I^\times$ values of the various $I^+V^\times$ diffusing species average out to 3.69 eV. Also shown is the difference between $Q_{Si}^\times$ and $Q_I^\times$ which averages ~0.32 eV. This difference is due to the impurity-vacancy binding energy which is very short ranged. Therefore, it is expected that $Q_{Si}^\times$ and $Q_I^\times$ should be very close in value, as pointed out by Hu (65).

Q_I^- values for I^+-V^- pairs in Si are also shown in Table I. These data were taken from high concentration diffusion profiles (surface concentration $>n_i$) (22, 66-68). The average Q_I^- value is 4.1 eV. The average difference between the Si self-diffusion energy Q_{Si}^- (with negatively charged vacanices) and Q_I^- is 0.79 eV. This follows since

$$\begin{aligned} Q_{Si}^- - Q_I^- &= \Delta H_m^- - Q_E^- + E_b^- \text{ (eV)} \\ &= 1.2 - 0.95 + 0.55 \\ &= 0.8 \text{ eV} \end{aligned}$$

Table I. Energetics related to diffusion of Group V impurities in silicon

Diffusing pair	Q_E (eV)	E_b (eV)	Q_I (eV)	$Q_{Si} - Q_I$ (eV)
$P^+V^\times$	— (a)	0.25	3.66	0.29
$As^+V^\times$	—	0.33	3.58	0.37
$Sb^+V^\times$	—	0.24	3.65	0.3
$Bi^+V^\times$	—	0.06	3.85	0.1
$SiV^\times$			3.95	
P^+V^-	0.95	0.55	4.0	1.0
As^+V^-	1.07	0.45	4.1	0.9
Sb^+V^-	1.28	0.35-0.57	3.98-4.2	0.9
Bi^+V^-	1.46	0.43	4.12	0.88
SiV^-			5.0	
$P^+V^{=}$	1.25	0.81	4.37	1.06
$SiV^{=}$			5.43	

(a) Short-range elastic interaction only, no pair migration

when the impurity is phosphorus. These results are far more consistent than previous attempts to construct such tables (43, 47, 65) since a proper accounting has been made of the vacancy charge state in Table I.

The P^+-V^- *anomaly.*—It is evident from Table II that the binding energies of the the P^+V^- pair and the As^+V^- pair are approximately the same, as are their activation energies for diffusion. However, it is evident from Fig. 11 that the As^+V^- pair dominates the diffusion of As at high concentrations ($n \gtrsim n_i$), but the P^+V^- pair does not contribute to the diffusion of P except as a result of the dissociation of $P^+V^{=}$ pairs.

The diffusion coefficient of As associated with As^+V^- migration is shown in Fig. 14 to be (22)

$$D_i^-|_{As} = 22.9 \exp\left(\frac{-4.1 \text{ eV}}{kT}\right) \qquad [26]$$

Comparing this result with Eq. [19] for D_i^- for P shows that the ratio of the prefactors is

$$\frac{D_o^-|_P}{D_o^-|_{As}} \cong 0.2 \qquad [27]$$

where D_o^- is the prefactor in the general expression $D_i^- = D_o^- \exp(-Q_I/kT)$. The ratio in Eq. [27] can be written as

$$\frac{D_o^-|_P}{D_o^-|_{As}} = \frac{\gamma_P^- f_P^- \exp\left(\frac{\Delta S_P^-}{k}\right)}{\gamma_{As}^- f_{As}^- \exp\left(\frac{\Delta S_{As}^-}{k}\right)} \qquad [28]$$

where γ^- is the mean vibrational frequency of the impurity atom, f^- is the correlation factor, and ΔS^- is the change in entropy associated with the diffusion process.

Hirata *et al.* (47) have shown that $\gamma^- \exp(\Delta S^-/k)/N_J = 5 \times 10^7$ Hz for P and 2×10^8 Hz for As. Assuming $f_P^- \cong f_{As}^-$ (65), and the number of jumps, N_J, of the P^+V^- pair prior to dissociation is the same for the As^+V^- pair (47), then Eq. [28] predicts

$$\frac{D_o^-|_P}{D_o^-|_{As}} = 0.25$$

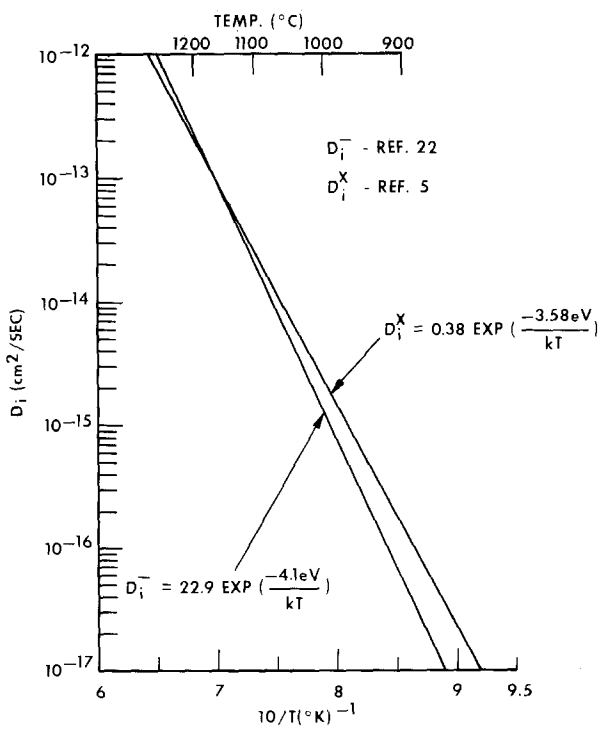


Fig. 14. Intrinsic diffusion coefficients of arsenic in silicon

in excellent agreement with the result expressed in Eq. [27]. Therefore, it can be concluded that the relatively small diffusion coefficient, $D_i^-|_P$ is a result of the lower P atom vibrational frequency and ΔS^- which appears to correlate with the relative size of P compared to As (47). This result gives support to the correctness of the prefactor of D_i^- for P, and the consistency of the 4.0 eV activation energy with the other Group V elements supports the analysis used to calculate the D_i^- data in Fig. 12.

A similar analysis for the $P^+V^\times$ and $As^+V^\times$ pairs shows that their prefactor ratio is

$$\frac{D_o^\times|_P}{D_o^\times|_{As}} \cong 10 \qquad [29]$$

This result reflects the fact that $D_i^\times|_P >> D_i^\times|_{As}$, although a satisfactory explanation is not available. Inspection of Fig. 14 shows that for As, $D_i^\times \cong D_i^-$, whereas the results of this study show that for P, $D_i^\times >> D_i^-$. This observation accounts to a significant extent for the differences in the As and P diffusion profile shapes.

Sample P profile calculation.—It is appropriate at this point to present the initial results of numerical calculations of P diffusion profiles. Detailed aspects of these calculations will be published at a later date. Essentially, the general diffusion equation was numerically integrated after it was expressed as a finite difference equation. The diffusivity of P at concentrations greater than n_e was calculated from Eq. [2], while the tail-region diffusivity was determined from Eq. [18] and [20]. The transition region diffusivity was estimated from its n^{-2} dependence. The results for a 900°C, 30 min diffusion are presented in Fig. 15. The calculation was performed with $n_s = 2 \times 10^{20}$ cm^{-3}, but what is shown in Fig. 15 is the total P concentration curve which was obtained by converting the calculated n *vs.* x curve to C_T *vs.* x from Fig. 3. The data shown were determined from differential conductivity measurements of a 900°C, 30 min $POCl_3$ diffusion. Agreement between the measured data and the calculated curve is quite good, with the calculated kink occurring at $C_T \cong 5 \times 10^{19}$ cm^{-3}.

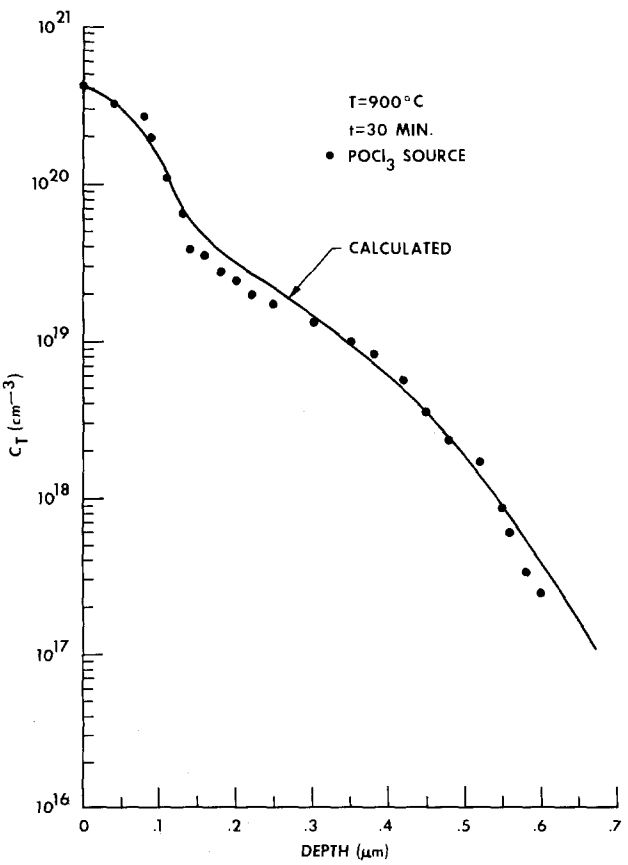


Fig. 15. Calculated and measured total phosphorus profiles in silicon.

Emitter dip effect.—It was pointed out in Fig. 10 that the enhanced base diffusivity resulting from the emitter dip effect of the P emitter diffusion is comparable with $D_{TAIL}/D_i^\times$. The emitter dip effect and the various theories proposed to describe it have been adequately reviewed by Hu (18).

The model proposed in this paper requires that the inner base diffusivity (under the emitter) be

$$D_{in}^B = D_i^B \left(\frac{D_{TAIL}}{D_i^\times} \right) \Bigg|_{phos} \qquad [30]$$

where D_i^B is the intrinsic diffusivity of the base dopant (boron or gallium) under normal diffusion conditions. This result is reasonable since the enhancement factor is measured with respect to $D_i^\times$ which is proportional to the neutral vacancy concentration which, in turn, is constant throughout the n and p regions of the emitter-base structure (indepedent of Fermi level position). Implicit in Eq. [30] is the assumption that the dominant charge state of the vacancies responds to the local Fermi level position which continuously changes with depth into the Si crystal. In the p-type base region, the dominant charge state of the vacancies is assumed to be V^+, which is the type of vacancy that dominates B and Ga diffusion. From Eq. [18] and [20]

$$D_{in}^B = D_i^B \left[\frac{n_s^3}{n_e^2 n_i} \left\{ 1 + \exp\left(\frac{0.3 \text{ eV}}{kT} \right) \right\} \right] \frac{D_i^-}{D_i^\times} \Bigg|_{phos} \qquad [31]$$

If the base is assumed to be Gaussian, then the standard deviation of the initial distribution is

$$W_o = \frac{0.4\, Q_o}{C_{po}} \qquad [32]$$

where Q_o is the integrated doping of the initial base profile and C_{po} is the peak concentration (atom/cm^3). During thermal redistribution

$$W^2(t) = W_o^2 + 2\, D^B t \qquad [33]$$

The amount of base push-out is the difference between the inner base and outer base diffusion distance

$$\delta(t) = W_{in}(t) - W_{out}(t),$$

$$= W_o \left[\sqrt{1 + \left(\frac{2\, D_{in}^B t}{W_o^2} \right)} - \sqrt{1 + \left(\frac{2\, D_{out}^B t}{W_o^2} \right)} \right] \qquad [34]$$

In order to apply Eq. [31] and [34] for the calculation of $\delta(t)$, measured profile data is required to determine n_s and W_o. Becker *et al.* (69) have generated P profile data as a function of $POCl_3$ source flow rates using differential conductivity measurements and Irvin's curve. Base push-out data was also recorded. Converting their data to n_s *vs.* δ using Fig. 3, the results are plotted in Fig. 16. A standard BN base diffusion and oxidation step was employed to establish the initial base layer. This diffusion step has been profiled by Rhoads (35). The initial base parameters are shown in Fig. 16. Substituting the appropriate numbers in Eq. [31] and [34] gives the calculated curve shown in Fig. 16. Excellent agreement with these reliable data is achieved.

At this point it is reasonable to consider the depth to which the generated steady-state flux of vacancies extends, *i.e.*, the vacancy diffusion length. Yoshida *et al.* (23) studied the outdiffusion of an epitaxial P-doped

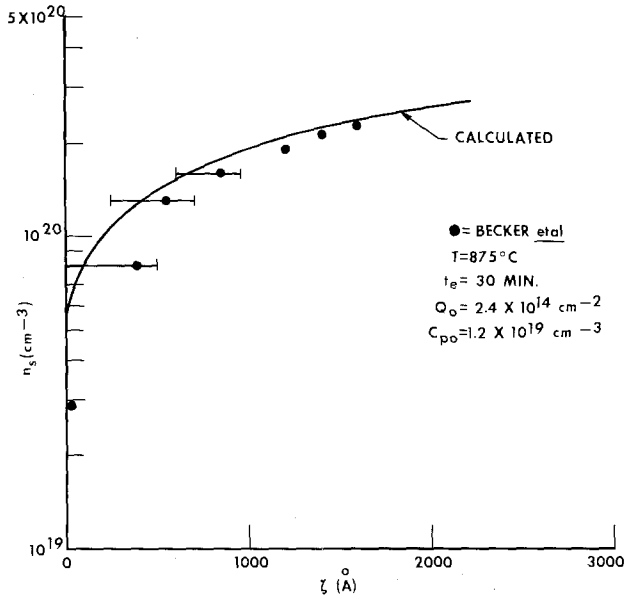


Fig. 16. Base region push-out distance vs. surface electron concentration; the emitter dip effect.

layer located 20 μm from the Si surface. A surface P diffusion was performed over part of the wafer with $n_s \cong 2 \times 10^{20}$ cm^{-3}. Following the 900°C, 1385 min diffusion the portion of the epi under the surface diffused area had itself diffused 1.9 μm. However, the junction at the epi interface in the nondiffused surface portion had not moved appreciably. The diffusion length associated with this latter region is

$$L_{epi} = 2\sqrt{D_i{}^{\times} t}$$
$$= 0.16\ \mu\text{m}$$

for 900°C and 1385 min. From the reported concentrations of the epi ($\sim 2 \times 10^{19}$ cm^{-3}) and the substrate ($\sim 2 \times 10^{16}$ cm^{-3}), the 1.9 μm enhanced diffusion is equal to approximately two diffusion lengths. Thus, the ratio of the diffusion coefficients in the two regions is

$$\frac{D}{D_i{}^{\times}} \cong 35$$

From Fig. 10 it can be seen that for shallow 900°C diffusions with $n_s = 2 \times 10^{20}$ cm^{-3}, $D/D_i \cong 135$. Therefore, in 20 μm the excess vacancy concentration has dropped to $\sim$1/4 of its original value, giving a vacancy diffusion length of $\sim$25 μm and a vacancy lifetime of $\sim$1/4 sec. These results are probably dependent upon the dislocation density of the Si.

Conclusions

A consistent model of P diffusion in Si has been presented which accounts quantitatively for the existence of electrically inactive P, the kink and the tail regions of the P diffusion profile, and the emitter-dip effect. The following points have been made:

1. Phosphorus diffuses in Si by interacting with vacancies in three different charge states: $P^+V^{\times}$, P^+V^-, and $P^+V^{=}$.

2. At high concentration ($n > n_e$) the $P^+V^{=}$ pair dominates. For example, at a total P concentration of 10^{21} cm^{-3}, $\sim$67% of the P is paired with $V^{=}$ vacancies. This pair removes an electron from the conduction band to fill the second-acceptor level of the vacancy, thus accounting for the electrically inactive P concentration.

3. At electron concentrations where the Fermi level is $\sim$0.11 eV below the conduction band ($n \cong n_e$), the $V^{=}$ vacancy has a higher probability of losing an electron to become V^-. The 0.3 eV lower binding energy of the P^+V^- pair enhances the pair dissociation probability significantly, thus creating an excess of V^- vacancies above the equilibrium value. This excess steady-state generation of vacancies accounts for the enhanced P tail diffusion as well as the emitter dip effect to depths greater than 25 μm from the Si surface.

4. When proper account is taken of the charge state of the vacancies, the activation energies for P diffusion are consistent with other Group V elements.

5. The observed differences between P and As diffusion profiles in Si are a result of the differences in the relative importance of the diffusing species. Neglecting pair dissociation, the dominant species in P-doped Si are $P^+V^{\times}$ and $P^+V^{=}$. In As-doped Si, $As^+V^{\times}$ and As^+V^- dominate up to $n \cong 3 \times 10^{20}$ cm^{-3}.

Acknowledgments

The authors would like to thank L. C. Kimmerling and G. H. Gilmer for their helpful discussions, especially regarding the pair dissociation mechanism of P.

Manuscript submitted Sept. 14, 1976; revised manuscript received Dec. 23, 1976.

Any discussion of this paper will appear in a Discussion Section to be published in the June 1978 JOURNAL. All discussions for the June 1978 Discussion Section should be submitted by Feb. 1, 1978.

Publication costs of this article were assisted by Bell Laboratories.

REFERENCES

1. E. Tannenbaum, *Solid-State Electron.*, **2**, 123 (1961).
2. V. K. Subashiev, A. P. Landsman, and A. A. Kukharskii, *Sov. Phys. Solid State*, **2**, 2406 (1961).
3. S. I. Maekawa, *J. Phys. Soc. Jpn.*, **17**, 1592 (1962).
4. P. A. Iles and B. Leibenhaut, *Solid-State Electron.*, **5**, 331 (1962).
5. E. Kooi, *This Journal*, **111**, 1383 (1964).
6. R. A. McDonald, G. G. Ehlenberger, and T. R. Huffman, *Solid-State Electron.*, **9**, 807 (1966).
7. J. C. C. Tsai, *Proc. IEEE*, **57**, 1499 (1969).
8. J. E. Lawrence, *J. Appl. Phys.*, **37**, 4106 (1966).
9. S. Dash and M. L. Joshi, in "Silicon Device Processing," C. P. Marsden, Editor, p. 202, National Bureau of Standards Special Publication 337, Gaithersburg, Maryland (1970).
10. K. Sato, A. Miyazaki, and T. Abe, Unpublished results.
11. M. C. Duffy, F. Barson, J. M. Fairfield, and G. H. Schwuttke, *This Journal*, **115**, 1291 (1968).
12. P. E. Bakeman, Jr. and J. M. Borrego, *This Journal*, **117**, 688 (1970).
13. J. Makris, A. Ferris-Prabhu, and M. L. Joshi, *IBM. J. Res. Dev.*, **15**, 132 (1971).
14. H. C. Casey, Jr., M. B. Panish, and L. L. Chang, *Phys. Rev.*, **162**, 660 (1967).
15. R. Gereth, P. G. G. Van Loon, and W. Williams, *This Journal*, **112**, 323 (1965).
16. N. D. Thai, *Solid-State Electron.*, **13**, 165 (1970).
17. N. D. Thai, *J. Appl. Phys.*, **41**, 2859 (1970).
18. S. M. Hu, in "Atomic Diffusion in Semiconductors," D. Shaw, Editor, Chap. 5, Plenum Publishing Corp., London (1972).
19. F. N. Schwettmann and D. L. Kendall, *Appl. Phys. Lett.*, **21**, 2 (1972).
20. J. S. Makris and B. J. Masters, *This Journal*, **120**, 1252 (1973).
21. R. F. Peart and R. C. Newman, in "Radiation Damage and Defects in Semiconductors," J. E. Whitehouse, Editor, p. 170, Institute of Physics, London (1973).
22. R. B. Fair and J. C. C. Tsai, *This Journal*, **122**, 1689 (1975).
23. M. Yoshida, E. Arai, H. Nakamura, and Y. Terunuma, *J. Appl. Phys.*, **45**, 1498 (1974).
24. D. Shaw, *Phys. Status Solidi A*, **30**, K139 (1975).
25. W. H. Eckton, Jr. and J. C. Tsai, Unpublished.
26. J. C. Irvin, *Bell Syst. Tech. J.*, **41**, 387 (1962).
27. F. Mousty, P. Ostoja, and L. Passari, *J. Appl. Phys.*, **45**, 4576 (1974).
28. G. Baccarani and P. Ostoja, *Solid-State Electron.*, **18**, 579 (1975).
29. R. A. Logan, J. F. Gilbert, and F. A. Trumbore, *J. Appl. Phys.*, **32**, 131 (1961).

30. V. I. Fistul', "Heavily Doped Semiconductors," p. 129 Plenum Publishing Corp., New York (1969).
31. J. C. C. Tsai, J. M. Morabito, and R. K. Lewis, in "Ion Implantation in Semiconductors and Other Materials," B. L. Crowder, Editor, p. 7, Plenum Publishing Corp., New York (1973).
32. P. Negrini, D. Nobili, and S. Solmi, *This Journal*, **122**, 1254 (1975).
33. R. K. Jain and R. J. Van Overstraeten, *IEEE Trans. Electron Dev.*, **ed-21**, 155 (1974).
34. S. Matsumoto, M. Yoshida, and T. Niimi, *Jpn. J. Appl. Phys.*, **13**, 1899 (1974).
35. A. W. Rhoads, Jr., Unpublished.
36. E. Bierdermann and A. Bohg, *Appl. Phys. Lett.*, **17**, 457 (1970).
37. V. V. Titov, *Phys. Status Solidi A*, **2**, 203 (1970).
38. C. L. Jones and A. F. W. Willoughby, *Appl. Phys. Lett.*, **25**, 114 (1974).
39. J. W. Colby and P. Miller, Paper 57 presented at The Electrochemical Society Meeting, San Francisco, California, May 12-17, 1974.
40. R. Gereth, P. G. G. Van Loon, and V. Williams, *This Journal*, **112**, 323 (1965).
41. L. C. Kimmerling, Private communication.
42. S. M. Hu, *Phys. Rev.*, **180**, 773 (1969).
43. D. Shaw, *Phys. Status Solidi B*, **72**, 11 (1975).
44. S. Matsumoto, E. Arai, H. Nakamura, and T. Niimi, *Jpn. J. Appl. Phys.*, **14**, 1665 (1975).
45. R. N. Ghoshtagore, *Solid-State Electron.*, **15**, 1113 (1972).
46. J. C. C. Tsai, Unpublished.
47. M. Hirata, M. Hirata, and H. Saito, *J. Phys. Soc. Jpn*, **27**, 405 (1969).
48. L. C. Kimmerling, H. M. DeAngelis, and J. W. Diebold, *Bull. Am. Phys. Soc.*, **19**, 210 (1974).
49. D. B. Lee and A. F. W. Willoughby, *J. Appl. Phys.*, **43**, 245 (1972).
50. L. Elstner and W. Kamprath, *Phys. Status Solidi B*, **22**, 541 (1967).
51. J. A. Van Vechten, *Phys. Rev. B*, **10**, 1482 (1974).
52. J. C. Phillips and J. A. Van Vechten, *Phys. Rev. Lett.*, **30**, 220 (1973).
53. J. A. Van Vechten and C. D. Thurmond, *Phys. Rev. B*, **14**, 3539 (1976).
54. G. D. Watkins and J. W. Corbett, *Phys. Rev. A*, **134**, 1359 (1964).
55. A. Seeger and K. P. Chik, *Phys. Status Solidi B*, **29**, 455 (1968).
56. I. R. Sanders and P. S. Dobson, *J. Mater. Sci.*, **9**, 1987 (1974).
57. J. M. Fairfield and B. J. Masters, *J. Appl. Phys.*, **38**, 3148 (1967).
58. R. B. Fair, To be published.
59. R. A. Swalin, *J. Appl. Phys.*, **29**, 670 (1958).
60. J. D. Eshelby, *Solid State Phys.*, **3**, 79 (1956).
61. J. R. Hardy and R. Bullough, *Philos. Mag.*, **15**, 237 (1967).
62. A. D. Braisford, *J. Appl. Phys.*, **40**, 3087 (1969).
63. R. N. Ghostagore, *Phys. Rev. B*, **3**, 397 (1971).
64. L. P. Adda, Unpublished.
65. S. M. Hu, *Phys. Status Solidi, B*, **60**, 595 (1973).
66. J. J. Rohan, N. E. Pickering, and J. Kennedy, *This Journal* **106**, 705 (1959).
67. D. Pommerren, *Acta Phys. Austriaca*, **20**, 338 (1965).
68. D. Drimer, P. Taranu, A. Hafner, L. Vescan, and L. Nemoda, *Acad. Rep. Pop. Rom., Fil. Iasi, Stud. Cercet., Stint., Fiz. Stiint. Teh.*, **13**, 39 (1960).
69. W. H. Becker, W. H. Eckton, Jr., and G. A. Kelley, Jr., Unpublished.

Impurity Profile Measurements of Thin Epitaxial Silicon Wafer by Multilayer Spreading Resistance Analysis

Y. Iida* **and H. Abe**

Nippon Electric Company, Limited, Central Research Laboratories, Kawasaki 213, Japan

and M. Kondo

Nippon Electric Company, Limited, Semiconductor Division, Kawasaki 211, Japan

ABSTRACT

A new algorithm for spreading resistance measurement data processing is proposed. The method, originally used for solving a thermal resistance problem of a multilayered heat sink, is applied to electrical resistance problems to give fast, exact, multilayer correction factors for converting measured spreading resistances to a profile. The correction factor is calculated by N times multiplication of (2×2) matrices instead of the inversion of a $(2N \times 2N)$ matrix, where N is an arbitrary number changing with the data points of spreading resistances (layers). The computer program, developed on the basis of this algorithm, is applied to impurity profile evaluation of thin (0.5-1.5 μm) epitaxial silicon wafers for millimeter wave IMPATT diode fabrication and affords the results agreeing with capacitance voltage profiling.

Spreading resistance measurement (SRM) is now widely accepted in the semiconductor industry as one of the most convenient methods to measure impurity profiles (1). Multilayer analysis, first proposed by Schuman and Gardner (2), is used for the evaluation of steep impurity profiles as are found in thin epitaxial layers and shallow diffusion layers. On the multilayer analysis, the correction factor C, which is required for converting measured spreading resistance to local resistivity, is expressed for two point probe configuration (3) as

$$C = \frac{4}{\pi}\int_0^\infty f(\lambda)\,\frac{\sin\lambda a}{\lambda}\left[\frac{J_1(\lambda a)}{\lambda a} - \frac{1}{2}J_0(\lambda D)\right]d\lambda$$

where, J_0 and J_1 are Bessel functions of the first kind of zeroth and first order, respectively, a is the probe contact radius, D is the probe spacing, and $f(\lambda)$ is an integration factor, which depends on both the resistivities and thickness of individual layers. In the first developed program, it was necessary to convert a $(2N \times 2N)$ matrix for obtaining an integration factor, where N is an arbitrary number changing with data points of spreading resistances (layers), and required a lengthy computation time (4). Many authors have tried to

* Electrochemical Society Active Member.
Key words: thermal spreading resistance, boundary condition problem, chemical selective etching, capacitance voltage profiling.

30. V. I. Fistul', "Heavily Doped Semiconductors," p. 129 Plenum Publishing Corp., New York (1969).
31. J. C. C. Tsai, J. M. Morabito, and R. K. Lewis, in "Ion Implantation in Semiconductors and Other Materials," B. L. Crowder, Editor, p. 7, Plenum Publishing Corp., New York (1973).
32. P. Negrini, D. Nobili, and S. Solmi, *This Journal*, **122**, 1254 (1975).
33. R. K. Jain and R. J. Van Overstraeten, *IEEE Trans. Electron Dev.*, **ed-21**, 155 (1974).
34. S. Matsumoto, M. Yoshida, and T. Niimi, *Jpn. J. Appl. Phys.*, **13**, 1899 (1974).
35. A. W. Rhoads, Jr., Unpublished.
36. E. Bierdermann and A. Bohg, *Appl. Phys. Lett.*, **17**, 457 (1970).
37. V. V. Titov, *Phys. Status Solidi A*, **2**, 203 (1970).
38. C. L. Jones and A. F. W. Willoughby, *Appl. Phys. Lett.*, **25**, 114 (1974).
39. J. W. Colby and P. Miller, Paper 57 presented at The Electrochemical Society Meeting, San Francisco, California, May 12-17, 1974.
40. R. Gereth, P. G. G. Van Loon, and V. Williams, *This Journal*, **112**, 323 (1965).
41. L. C. Kimmerling, Private communication.
42. S. M. Hu, *Phys. Rev.*, **180**, 773 (1969).
43. D. Shaw, *Phys. Status Solidi B*, **72**, 11 (1975).
44. S. Matsumoto, E. Arai, H. Nakamura, and T. Niimi, *Jpn. J. Appl. Phys.*, **14**, 1665 (1975).
45. R. N. Ghoshtagore, *Solid-State Electron.*, **15**, 1113 (1972).
46. J. C. C. Tsai, Unpublished.
47. M. Hirata, M. Hirata, and H. Saito, *J. Phys. Soc. Jpn*, **27**, 405 (1969).
48. L. C. Kimmerling, H. M. DeAngelis, and J. W. Diebold, *Bull. Am. Phys. Soc.*, **19**, 210 (1974).
49. D. B. Lee and A. F. W. Willoughby, *J. Appl. Phys.*, **43**, 245 (1972).
50. L. Elstner and W. Kamprath, *Phys. Status Solidi B*, **22**, 541 (1967).
51. J. A. Van Vechten, *Phys. Rev. B*, **10**, 1482 (1974).
52. J. C. Phillips and J. A. Van Vechten, *Phys. Rev. Lett.*, **30**, 220 (1973).
53. J. A. Van Vechten and C. D. Thurmond, *Phys. Rev. B*, **14**, 3539 (1976).
54. G. D. Watkins and J. W. Corbett, *Phys. Rev. A*, **134**, 1359 (1964).
55. A. Seeger and K. P. Chik, *Phys. Status Solidi B*, **29**, 455 (1968).
56. I. R. Sanders and P. S. Dobson, *J. Mater. Sci.*, **9**, 1987 (1974).
57. J. M. Fairfield and B. J. Masters, *J. Appl. Phys.*, **38**, 3148 (1967).
58. R. B. Fair, To be published.
59. R. A. Swalin, *J. Appl. Phys.*, **29**, 670 (1958).
60. J. D. Eshelby, *Solid State Phys.*, **3**, 79 (1956).
61. J. R. Hardy and R. Bullough, *Philos. Mag.*, **15**, 237 (1967).
62. A. D. Braisford, *J. Appl. Phys.*, **40**, 3087 (1969).
63. R. N. Ghostagore, *Phys. Rev. B*, **3**, 397 (1971).
64. L. P. Adda, Unpublished.
65. S. M. Hu, *Phys. Status Solidi, B*, **60**, 595 (1973).
66. J. J. Rohan, N. E. Pickering, and J. Kennedy, *This Journal* **106**, 705 (1959).
67. D. Pommerren, *Acta Phys. Austriaca*, **20**, 338 (1965).
68. D. Drimer, P. Taranu, A. Hafner, L. Vescan, and L. Nemoda, *Acad. Rep. Pop. Rom., Fil. Iasi, Stud. Cercet., Stint., Fiz. Stiint. Teh.*, **13**, 39 (1960).
69. W. H. Becker, W. H. Eckton, Jr., and G. A. Kelley, Jr., Unpublished.

Impurity Profile Measurements of Thin Epitaxial Silicon Wafer by Multilayer Spreading Resistance Analysis

Y. Iida* **and H. Abe**

Nippon Electric Company, Limited, Central Research Laboratories, Kawasaki 213, Japan

and M. Kondo

Nippon Electric Company, Limited, Semiconductor Division, Kawasaki 211, Japan

ABSTRACT

A new algorithm for spreading resistance measurement data processing is proposed. The method, originally used for solving a thermal resistance problem of a multilayered heat sink, is applied to electrical resistance problems to give fast, exact, multilayer correction factors for converting measured spreading resistances to a profile. The correction factor is calculated by N times multiplication of (2×2) matrices instead of the inversion of a $(2N \times 2N)$ matrix, where N is an arbitrary number changing with the data points of spreading resistances (layers). The computer program, developed on the basis of this algorithm, is applied to impurity profile evaluation of thin (0.5-1.5 μm) epitaxial silicon wafers for millimeter wave IMPATT diode fabrication and affords the results agreeing with capacitance voltage profiling.

Spreading resistance measurement (SRM) is now widely accepted in the semiconductor industry as one of the most convenient methods to measure impurity profiles (1). Multilayer analysis, first proposed by Schuman and Gardner (2), is used for the evaluation of steep impurity profiles as are found in thin epitaxial layers and shallow diffusion layers. On the multilayer analysis, the correction factor C, which is required for converting measured spreading resistance to local resistivity, is expressed for two point probe configuration (3) as

$$C = \frac{4}{\pi}\int_0^\infty f(\lambda)\,\frac{\sin\lambda a}{\lambda}\left[\frac{J_1(\lambda a)}{\lambda a} - \frac{1}{2}J_0(\lambda D)\right]d\lambda$$

where, J_0 and J_1 are Bessel functions of the first kind of zeroth and first order, respectively, a is the probe contact radius, D is the probe spacing, and $f(\lambda)$ is an integration factor, which depends on both the resistivities and thickness of individual layers. In the first developed program, it was necessary to convert a $(2N \times 2N)$ matrix for obtaining an integration factor, where N is an arbitrary number changing with data points of spreading resistances (layers), and required a lengthy computation time (4). Many authors have tried to

* Electrochemical Society Active Member.
Key words: thermal spreading resistance, boundary condition problem, chemical selective etching, capacitance voltage profiling.

shorten the computation time by various methods. The devices utilized to achieve this were (*i*) limitation of layer numbers, taken in the calculation, in a few layers near the surface to keep the matrix compact, ten layers in (3) and two layers in (5); (*ii*) adoption of an approximation for obtaining the integration factor, such as power law (3, 6), instead of using conversion of a $(2N \times 2N)$ matrix; or (*iii*) modification of a correction factor equation derived from the two layer problem, which can afford the results fitting in those measured with independent profiling methods such as capacitance voltage or incremental sheet resistance measurements (7).

In the present data processing procedure, the integration factor is calculated by N times multiplication of (2×2) matrices as a way to exactly solve the multilayer problem. This approach was applied to calculation of the thermal spreading resistance of multilayered heat sinks by one of the authors (8) and is expected to reduce computation time for SRM data processing just as the recurrence formula approach proposed by Leong *et al.* (9).

This paper describes the matrices-multiplication approach which is adopted as an exact way to solve multilayer problems. The results of applying this approach to the impurity profile evaluation of epitaxial wafers used for millimeter wave IMPATT diode manufacture are also presented.

Data Processing

The algorithm for calculating the correction factor is essentially the same as that used in the calculation of heat resistance of semiconductor devices, fabricated with the plated heat sink technology, such as Gunn and IMPATT diodes. In these devices, one or more Si or GaAs chips in a disk shape with about 50 μm diameter are placed on an electroplated metal layer with 50-200 μm thickness. This plated heat sink is then soldered on a metal block with a gold-silicon eutectic alloy layer. The heat resistance calculation of such devices has to take the multilayer effect into account, just as the SRM data processing does.

Correction factor derivation.—The mathematical basis for correction factor computation is explained as follows. As shown in Fig. 1, the potential distribution is considered when current I_0 flows from or collects into a disk electrode set on a multilayer structure, where each layer has specific resistance, ρ_1, ρ_2, -----, ρ_N, moving from top to bottom. In the figure, the sequence of boundaries is z_1, z_2, -----, z_{N_0}, and each layer thickness is h_1, h_2, -----, h_{N_0}, respectively.

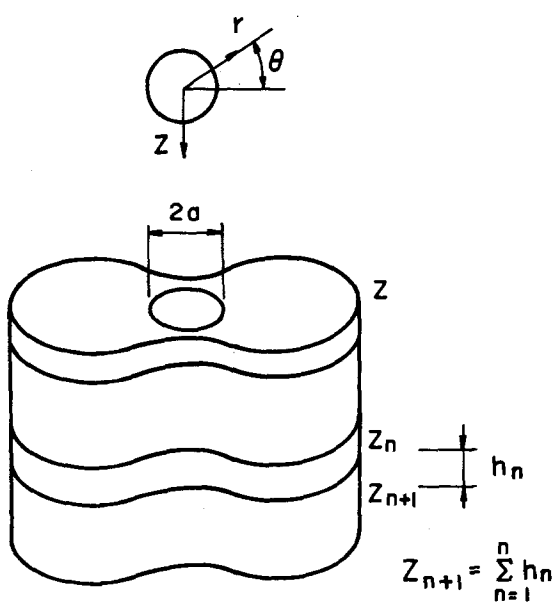


Fig. 1. Geometry for the multilayer problem

Let $V_N(r, z)$ be the potential distribution within the Nth layer. $V_N(r, z)$ is expanded as Eq. [1], using the Bessel function of the first kind of zeroth order, J_0, because $\Delta V_N(r, z) = 0$.

$$V_N(r,z) = \frac{\rho_N}{2\pi a} \cdot I \cdot \int_0^\infty [A_N(\lambda) \cdot e^{-\lambda(Z-Z_{N_0})} + B_N(\lambda) \cdot e^{\lambda(Z-Z_{N+1})}] \cdot \frac{\sin(\lambda a)}{\lambda} \cdot J_0(\lambda r)\, d\lambda \quad [1]$$

where $A_N(\lambda)$ and $B_N(\lambda)$ are functions of λ defined with boundary condition. From the conditions for continuity of potential and current, sequential matrix [2] is obtained

$$\begin{pmatrix} A_N(\lambda) \\ B_N(\lambda) \end{pmatrix} = \frac{\rho_{N+1} + \rho_N}{2\rho_N} \cdot e^{\lambda h_{N_0}} \cdot \begin{bmatrix} 1 & \frac{\rho_{N+1} - \rho_N}{\rho_{N+1} + \rho_N} e^{-\lambda h_{N+1}} \\ \frac{\rho_{N+1} - \rho_N}{\rho_{N+1} + \rho_N} e^{-\lambda h_{N_0}} & e^{-\lambda(h_{N_0} + h_{N+1})} \end{bmatrix} \cdot \begin{pmatrix} A_{N+1}(\lambda) \\ B_{N+1}(\lambda) \end{pmatrix} \quad [2]$$

The boundary condition is assumed at $z = z_1 = 0$

$$-\frac{1}{\rho_1} \cdot \frac{\partial}{\partial z} \cdot V_1(r,z) = \begin{cases} \frac{I_0}{2\pi a} \frac{1}{\sqrt{a^2 - r^2}} & r < a \\ 0 & r > a \end{cases} \quad [3]$$

On the other hand, the boundary condition at $z = z_{N+1}$, where the multilayer slab contacts an insulator, is as follows

$$-\frac{1}{\rho_1} \cdot \frac{\partial}{\partial z} \cdot V_{N_0}(r,z)\Big|_{z=z_{N_0+1}} = 0 \quad [4]$$

Boundary conditions in Eq. [3] and [4] have forms changed according to Eq. [1]

$$\int_0^\infty [A_1(\lambda) - B_1(\lambda) \cdot e^{-\lambda h_1}] \sin(\lambda a) J_0(\lambda r)\, d\lambda = \sin(\lambda a) J_0(\lambda r)\, d\lambda = \begin{cases} \frac{1}{\sqrt{a^2 - r^2}} & r < a \\ 0 & r > a \end{cases} \quad [5]$$

$$\int_0^\infty [A_{N_0}(\lambda) e^{-\lambda h_0} - B_{N_0}(\lambda)] \sin(\lambda a)\, J_0(\lambda r)\, d\lambda = 0 \quad [6]$$

Thus, $[A_1(\lambda), B_1(\lambda)]$ and $[A_{N_0}(\lambda), B_{N_0}(\lambda)]$ has the relationship

$$\left.\begin{aligned} A_1(\lambda) - B_1(\lambda) e^{-\lambda h_1} &= 1 \\ A_{N_0}(\lambda) - B_{N_0}(\lambda) e^{\lambda h_0} &= 0 \end{aligned}\right\} \quad [7]$$

If $A_1(\lambda)$ and $B_1(\lambda)$ are derived from Eq. [2] and [7], the potential distribution at $z = 0$ is

$$V_1(r, z=0) = \frac{\rho_1 \cdot I_0}{2\pi a} \int_0^\infty (A_1(\lambda) + B_1(\lambda) e^{-\lambda h_1}) \frac{\sin(\lambda a)}{\lambda} J_0(\lambda r)\, d\lambda = \frac{I_0 \cdot \rho_1}{2\pi a} \int_0^\infty (2A_1(\lambda) - 1) \frac{\sin(\lambda a)}{\lambda} J_0(\lambda r)\, d\lambda \quad [8]$$

And

$$\langle V_a \rangle - V_D = \left\{ \frac{\rho_1}{\pi a} \int_0^\infty (2A_1(\lambda) - 1) \frac{\sin(\lambda a)}{\lambda} \left(\frac{J_1(\lambda a)}{a} - \frac{1}{2} J_0(\lambda D) \right) d\lambda \right\} I_0 \quad [9]$$

where $\langle V_a \rangle$ is the potential average at $0 < r < a$, and V_D is the potential at $r = D > a$.

In two probe spreading resistance measurements, one probe emits the current I_0 and the other one emits current $-I_0$. The spreading resistance between two probes is

$$R_{SR} = 2 \cdot \frac{\langle V_a \rangle - V_D}{I_0} = \frac{2\rho_1}{\pi a} \int_0^\infty (2A_1(\lambda) - 1) \frac{\sin(\lambda a)}{\lambda} \left[\frac{J_1(\lambda a)}{\lambda a} - \frac{1}{2} J_0(\lambda D) \right] d\lambda \quad [10]$$

From Eq. [7], we can obtain the following expression

$$B_{N0}(\lambda) = A_{N0}(\lambda)\, e^{-\lambda h_{N_0}} \quad [11]$$

and define $\alpha[\lambda]$ and $[P(\lambda)/Q(\lambda)]$ as follows

$$\alpha(\lambda) = \frac{\rho_1 + \rho_2}{2\rho_2} \cdot \text{----} \cdot \frac{\rho_{N0-1} + \rho_{N0}}{2\rho_{N0-1}} \cdot e^{(h_1 + \text{----} + h_{N_0-1})} \cdot A_{N0}(\lambda)$$

$$\begin{pmatrix} P(\lambda) \\ Q(\lambda) \end{pmatrix} = \begin{Bmatrix} 1 & \frac{\rho_2 - \rho_1}{\rho_2 + \rho_1} \cdot e^{-\lambda h_2} \\ \frac{\rho_2 - \rho_1}{\rho_2 + \rho_1} e^{-\lambda h_1} & e^{-\lambda(h_1 + h_2)} \end{Bmatrix} \cdot \text{----} \cdot \begin{Bmatrix} 1 & \frac{\rho_{N0} - \rho_{N0-1}}{\rho_{N0} + \rho_{N0-1}} \cdot e^{-\lambda h_N} \\ \frac{\rho_{N0} - \rho_{N0-1}}{\rho_{N0} + \rho_{N0-1}} \cdot e^{\lambda h_{N_0-1}} & e^{-\lambda(h_{N_0} + h_{N_0-1})} \end{Bmatrix} \begin{pmatrix} 1 \\ e^{-\lambda h_{N_0}} \end{pmatrix} \quad [12]$$

From Eq. [2]

$$A_1(\lambda) = \alpha(\lambda) \cdot P(\lambda)$$
$$B_1(\lambda) = \alpha(\lambda) \cdot Q(\lambda) \quad [13]$$

combined with Eq. [7]

$$A_1(\lambda) = \frac{P(\lambda)}{P(\lambda) - Q(\lambda) e^{-\lambda h_1}}$$
$$2A_1(\lambda) - 1 = \frac{P(\lambda) + Q(\lambda) e^{-\lambda h_1}}{P(\lambda) - Q(\lambda) e^{-\lambda h_1}} \quad [14]$$

Put Eq. [14] into Eq. [10], and spreading resistance R_{SR} becomes

$$R_{SR} = \frac{\rho_1}{2a} \cdot \frac{4}{\pi} \int_0^\infty \frac{P(\lambda) + Q(\lambda) e^{-\lambda h_1}}{P(\lambda) - Q(\lambda) e^{-\lambda h_1}} \cdot \frac{\sin(\lambda a)}{\lambda} \left[\frac{J_1(\lambda a)}{\lambda a} - \frac{1}{2} \cdot J_0(\lambda D) \right] d\lambda \quad [15]$$

Then

$$\rho_1 = 2aR_{SR}/c(\rho_1; \rho_2, \text{-----}, \rho_{N0})$$

where $c(\rho_1; \rho_2, \text{-----}, \rho_{N0})$ is a correction factor, and

$$c(\rho_1; \rho_2, \text{-----}, \rho_{N0}) = \frac{4}{\pi} \int_0^\infty \frac{P(\lambda) + Q(\lambda) e^{-\lambda h_1}}{P(\lambda) - Q(\lambda) e^{-\lambda h_1}} \cdot \frac{\sin(\lambda a)}{\lambda} \cdot \left[\frac{J_1(\lambda a)}{\lambda a} - \frac{1}{2} \cdot J_0(\lambda D) \right] d\lambda \quad [16]$$

Now, the correction factor $c(\rho_1; \rho_2, \text{-----}, \rho_{N0})$ is shown to be obtained by the multiplication of N square matrices and a vector of the second order.

Programming.—In an actual system, measured resistance R_m consists of spreading resistance R_{SR} and contact resistance R_B. It can be assumed that R_B depends only upon first layer specific resistance ρ_1

$$R_B = \frac{\rho_1}{2a} \cdot [K(\rho_1) - 1]$$

Then

$$\rho_1 = 2aR_m/[K(\rho_1) - 1 + c(\rho_1; \rho_2, \text{-----}, \rho_{N0})]$$

$K(\rho)$ is deduced from the calibration line made by some measurements of thick and homogeneous samples having different specific resistances.

In computation of the correction factor [16], it is better to separate the calculation of the term connected with the boundary condition from that composed of a trigonometric function and Bessel function, because the former term changes value according to the number of layers, but the latter does not. Equation [16] is expressed as $\int (\text{DETERM}) \times (\text{JBFUNC}) d\lambda$ for the explanation. For JBFUNC, it is necessary to calculate only for the first layer. The subsequent calculation can use the memory. The derivation described in the prior paragraph makes it possible to obtain $P(\lambda)$ and $Q(\lambda)$ necessary for the term DETERM from only one multiplication of (2×2) matrix and (2×1) matrix. That is

$$\begin{pmatrix} P(\lambda) \\ Q(\lambda) \end{pmatrix} = \begin{Bmatrix} 1 & \frac{\rho_2 - \rho_1}{\rho_2 + \rho_1} \cdot e^{-\lambda h_2} \\ \frac{\rho_2 - \rho_1}{\rho_2 + \rho_1} e^{-\lambda h_1} & e^{-\lambda(h_1 + h_2)} \end{Bmatrix} \cdot \begin{pmatrix} P'(\lambda) \\ Q'(\lambda) \end{pmatrix}$$

where $P'(\lambda)$ and $Q'(\lambda)$ are those used for the $c(\rho_2; \rho_3, \text{-----}, \rho_{N0})$ calculation and are stored in the memory. The present approach requires only the first layer condition for obtaining the correction factor, different from that proposed by others (4, 10). Thus, correction factor is obtained on the flow, as shown in Fig. 2.

Thin Epitaxial Wafer Evaluation

To demonstrate the usefulness of this newly proposed correction factor computation algorithm, the de-

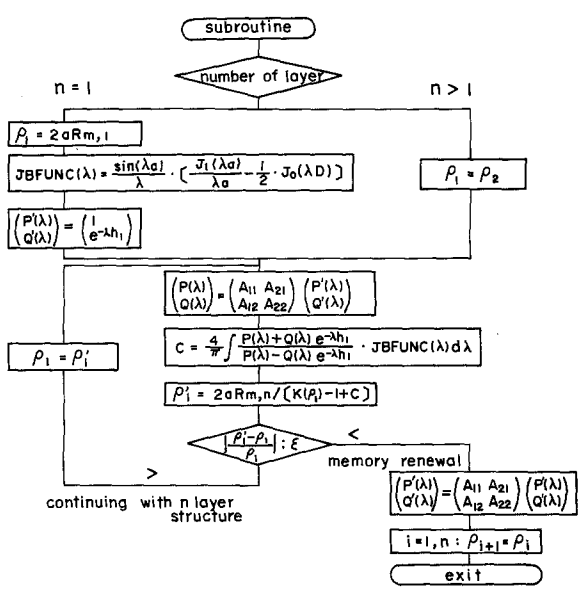


Fig. 2. Subroutine flow chart for correction factor calculation

veloped program is applied to impurity profile evaluation of thin (0.5-1.5 μm) epitaxial silicon wafers for millimeter wave IMPATT diode fabrication.

After SiO_2 deposition of around 2000Å thick, epitaxial wafers were polished with commercial diamond paste (average diameter 0.25 μm) (11) on a plastic plate (12) by a reciprocating lapping machine. The small angles on the beveled silicon wafers, typically 10 to 30 min, were measured with the laser beam reflection method (13) using photodiode as a detector. The spreading resistance equipment used is a commercial two-point probe system, ASR-100. To convert the resistivity to donor density, Irvin's curve was employed (14).

For the epitaxial wafers for IMPATT diodes, there are two important factors to be evaluated. One is the n layer thickness and the other is the n layer donor density. To examine the accuracy of the former factor in spreading resistance method, the epitaxial thickness is measured by the selective etching method. Epitaxial wafer samples lapped in angle by the above described procedures are etched by impurity concentration selective etchant to produce the gap at n layer-n^+ substrate boundary (15). As shown in Fig. 3, the intersection of extrapolation line from the substrate region and that from the epitaxial-substrate transition region, which could be defined as the n layer thickness measured by SRM, agrees well with the thickness obtained by the selective etching method, W_{sel}. The impurity concentration, where the arrow crosses, is a reasonable value, since it coincides with the transition point of etching selectivity, that is around 2×10^{-19} cm^{-3}. In Fig. 3, the results with capacitance voltage profiling method are also plotted. *C-V* characteristics are measured after boron is diffused to 0.12 μm from the surface. Because of the built-in potential and of the avalanche breakdown, the *C-V* method is only applicable to the impurity profile at the depths between about 0.3 μm to about 0.6 μm. Donor densities obtained from the *C-V* method show a good agreement within experimental error.

A few measured profiles of epitaxial wafers used for G-band (40-80 GHz) IMPATT diode fabrication are shown in Fig. 4. CPU time to obtain a complete profile from 30 points of the spreading resistances is around 23 sec by ACOS-700. In order to compare the present approach with Hu's (3), Lee's (6), and Choo's (10) methods, in terms of computation time, some data are obtained (5) or estimated (3, 10). Our computation time would be comparable with other methods, *i.e.*, 60 sec or more (Hu), 16-32 sec (Lee), and 12 sec (Choo). It should be noted that Lee's and ours are the times required for obtaining a profile, for which iteration work[1] is necessary for consistency between $K(\rho)$ and the correction factor. Hu's and Choo's, however, are the calculation times to obtain only correction factors. Additional adoption of our algorithm to Hu's and Lee's approximation analysis should reduce their computation time, since they also need to solve the matrix equations at the points selected as the standards for interpolations.

Conclusion

The spreading resistance measurement for estimating an impurity profile for semiconductors is improved on data processing. A new approach for solving the boundary condition problem is proposed. It requires N times multiplication of (2×2) matrices to obtain the correction factor, but not inversion of the $(2N \times 2N)$ matrix which appears in the computation program of Yeh *et al.* N is an arbitrary number changing with data points of spreading resistances (layers). And Schuman's multilayer structure model for precise impurity profile estimation became more realistic for computation. Average CPU time to obtain a complete profile from 30 data points of spreading resistances was around 23 sec using ACOS-700.

[1] On our data, average iteration number was 2.5.

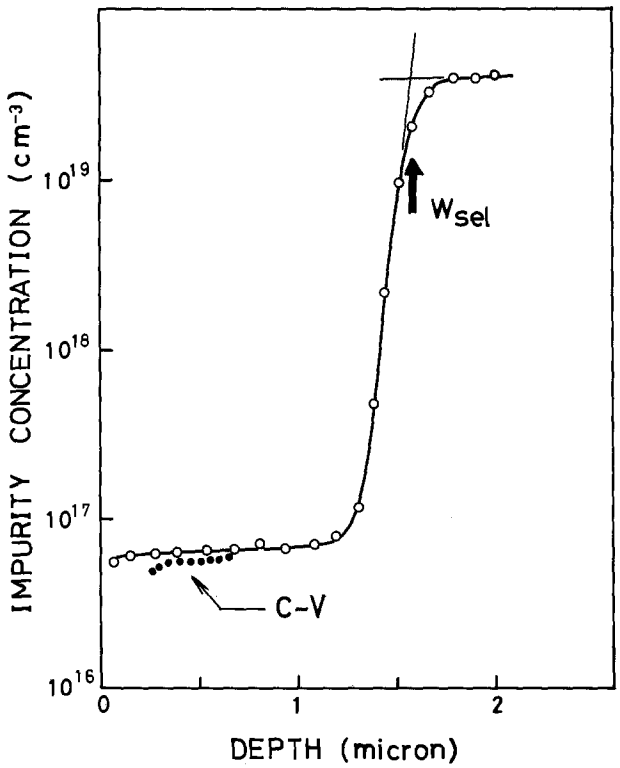


Fig. 3. Comparison between SRM and C-V methods about impurity concentration and that between SRM and selective etching methods about epitaxial thickness.

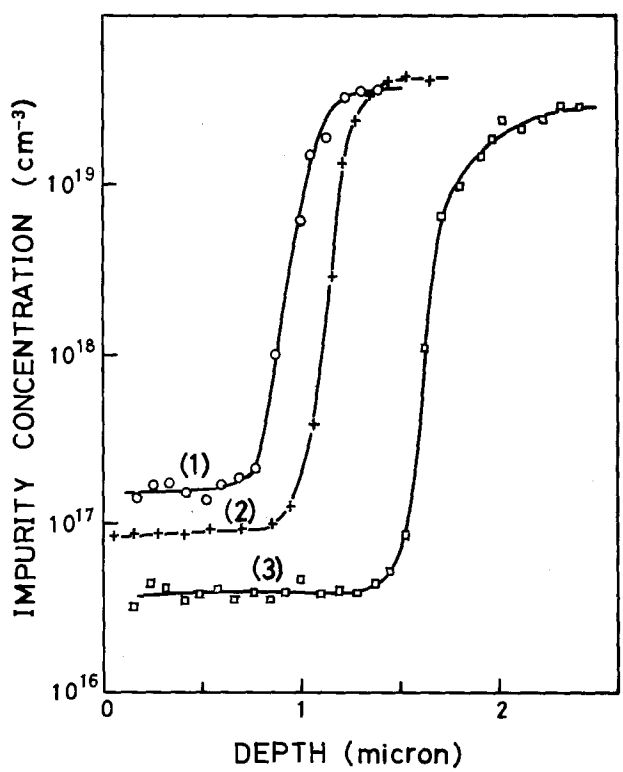


Fig. 4. n/n^+ epitaxial wafer impurity profile: (1) For 80 GHz IMPATT diode fabrication; (2) For 65 GHz; (3) For 40 GHz.

Acknowledgment

The authors wish to thank Mrs. S. Hara and Mr. T. Ishii for their technical assistance, and also thank Messrs. H. Muta and E. Nagasawa for informative discussions. They also would like to thank Drs. N. Kawamura and K. Sekido for their encouragement.

Manuscript submitted Nov. 12, 1976; revised manuscript received Feb. 28, 1977.

Any discussion of this paper will appear in a Discussion Section to be published in the June 1978 JOURNAL. All discussion for the June 1978 Discussion Section should be submitted by Feb. 1, 1978.

Publication costs of this article were assisted by Nippon Electric Company, Limited.

REFERENCES

1. B. L. Morris, *This Journal*, **121**, 422 (1974).
2. P. A. Schumann, Jr. and E. E. Gardner, *Solid-State Electron.*, **12**, 371 (1969).
3. S. M. Hu, *ibid.*, **15**, 809 (1972).
4. T. H. Yeh and K. H. Khokhani, *This Journal*, **116**, 1461 (1969).
5. T. E. Hendrickson, *ibid.*, **122**, 1539 (1975).
6. G. A. Lee, NBS/ASTM Spreading Resistance Symposium; Gaithersburg, Maryland, NBS Special Publication 400-10, 75 (1974).
7. B. L. Morris, P. H. Langer, and J. C. White, Jr., *ibid.*, 400-10, 63 (1974).
8. H. Abe, *Trans. Inst. Elect. Comm. Eng. Japan*, **J55-C**, 558 (1972).
9. M. S. Leong, S. C. Choo, and K. H. Tay, *Solid-State Electron.*, **19**, 397 (1976).
10. S. C. Choo, M. S. Leong, and K. L. Kuan, *ibid.*, **19**, 561 (1976).
11. J. L. Deines, E. F. Gorey, A. E. Michel, and M. R. Poponiak, NBS/ASTM Spreading Resistance Symposium; Gaithersburg, Maryland, NBS Special Publication 400-10, 169 (1974).
12. The operation manual for ASR-1000, Solid-State Measurements Inc., Murrysville, Pennsylvania.
13. A. Mayer and Schwartzman, NBS/ASTM Spreading Resistance Symposium; Gaithersburg, Maryland, NBS Special Publication 400-10, 123 (1974).
14. J. C. Irvin, *Bell Syst. Tech. J.*, **41**, 387 (1962).
15. M. Kondo, H. Abe, and Y. Iida, Extended Abstracts of Annual Meeting, Tokyo, Inst. Elect. Comm. Eng. Japan, 2-76 (1976).

Role of Grain Growth in the Oxidation of Nickel

Frederick N. Rhines and Richard G. Connell, Jr.

Department of Materials Science and Engineering, University of Florida, Gainesville, Florida 32611

ABSTRACT

The isothermal growth of a NiO scale upon nickel 270 at 800°-1000°C is accompanied by a coordinated growth of the grains of the oxide, wherein the mean intercept of the grains (measured parallel with the scale surface) is directly proportional to the thickness of the scale. The average grain volume of the columnar grains of the scale is directly proportional to the time of oxidation. Correspondingly, the scale thickness and the mean intercept of the grains increase in proportion to the cube root of the time. Markers maintain the same relative positions in the scale as the scale thickens, showing that the scale grows by swelling. These findings are explained by the formation of new oxide, mainly along grain boundaries, where oxygen diffusing inward upon grain boundaries meets nickel diffusing outward through the NiO grains. The sweeping of the grain boundaries that accompanies grain growth serves to distribute the new oxide uniformly throughout the volume of the scale, resulting in growth by swelling.

Although it has long been recognized that the grain size of the oxide scale that forms on metals at elevated temperature is coarser in thick than in thin scales, no importance seems to have been attributed to this fact. The present authors (1) were the first to demonstrate that there is a quantitative relationship between the grain structure and the thickness of the scale upon nickel. They accomplished this by counting the number of grain boundaries crossed by unit length of line (N_L) laid parallel with the surface of the scale, at midthickness of the scale. It was found that any NiO scale on nickel 270 having specific thickness always displays the same value of N_L, irrespective of the temperature of oxidation or of the sequence of atmospheric conditions imposed in forming the scale. It was concluded that the mechanisms of grain growth and of scale growth are interrelated.

Further studies, presented in this paper, have shown that the scale thickness (x) is directly proportional to the reciprocal of N_L, which is a measure of the mean intercept of the grains ($\overline{\lambda}$)

$$1/N_L = \overline{\lambda} \propto x \qquad [1]$$

The scale thickness is also proportional to the cube root of the average grain volume ($\overline{V}_g$), as is the mean intercept of the grains

$$\overline{V}_g^{1/3} \propto \overline{\lambda} \propto x \qquad [2]$$

Key words: oxides, diffusion, quantitative microscopy, stress effects, oxide coatings, metallography.

These relationships apply as well to the kinetics of grain growth and oxidation. The average grain volume increases in direct proportion to the time of oxidation (t)

$$\overline{V}_g \propto t \qquad [3]$$

while the scale thickness and the mean intercept of the grain increase in proportion to the cube root of the time

$$x \propto \overline{\lambda} \propto t^{1/3} \qquad [4]$$

Marker movement observations have made it clear, also, that the NiO scale grows mainly by swelling. New oxide is generated almost homogeneously throughout the volume of the scale, instead of at one of its interfaces, as has been postulated in the familiar theories of oxidation. Nickel ions diffusing outward through the NiO crystals of the scale meet oxygen ions diffusing inward upon grain boundaries of the NiO, and are delivered throughout the volume of the scale by the sweeping of the grain boundaries accompanying grain growth. Thus, both scale growth and grain growth, being limited by the rate of sweep of the grain boundaries, are mutually related in their kinetics.

Experiments and Observations

Nickel 270 (nominally 99.99+% nickel) in the form of rolled sheet specimens, 12.7 × 12.7 × 1.6 mm, was oxidized in pure oxygen at 800°, 900°, and 1000°C, for times up to 225 hr. Prior to oxidation the specimens were annealed 1 hr at 1200°C in air. They were then

ground free of oxide, using SiC grit and finishing with 600 grit in water. Before placing in the oxidizing furnace, they were further degreased with acetone, ethanol, and water and were dried. The furnace and gas-handling systems were constructed entirely of stainless steel and of nickel tubing and fittings, the hot gases being exposed to no material except nickel. During heat-up and cool-down, the furnace was maintained with flowing cold-trapped helium. Pure dry oxygen was admitted for the specified interval of oxidation. The nickel 270 specimens developed regular scales without cracking, spalling, or other physical defects. Some specimens of nickel 200 (commercial purity) that were prepared in the same fashion tended to spall slightly. All speciments were sectioned, mounted, and prepared for metallographic examination using conventional methods. The polishing medium was diamond grit; a hydrofluoric acid, acetic acid, electrolytic etch was employed. Typical microstructures of the scales on nickel 270 and nickel 200 are shown in Fig. 1-4.

Scale thickness (x) was measured directly upon the microscope using a calibrated optical system. The identification of the location of the metal-oxide interface is uncertain in photomicrographs, such as those of Fig. 1-4, because polishing leaves a step in level between the metal surface and the oxide surface. This step, being out of focus, appears wide. By making the readings directly upon the microscope, it is possible to so adjust the focus as to locate the interface with precision. There remains, however, a variation in the true thickness of the scale from point to point. To obtain reproducible readings, therefore, values of x were read at many random sites and averaged. All of the measurements of scale thickness on nickel 270 are reported in Table I. Scale thickness (x) is plotted as a function of the cube root of the time of oxidation ($t^{1/3}$) in Fig. 5. Proportionality of the scale thickness to the cube root of time has been observed by several prior investigators (2), but has yet to be explained adequately.

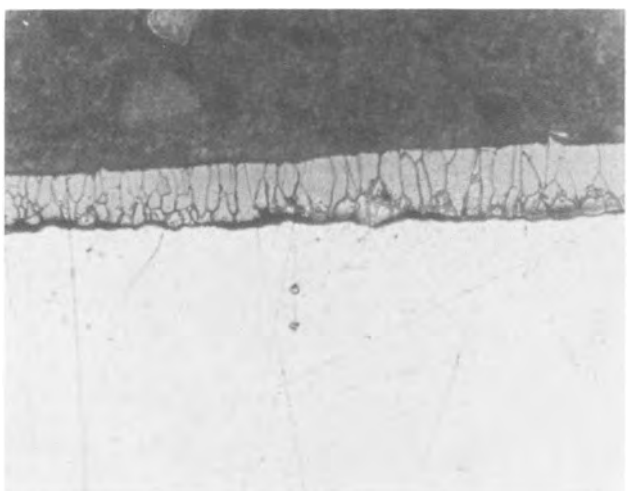


Fig. 1. Ni 270, 1000°C, 4 hr, 700×

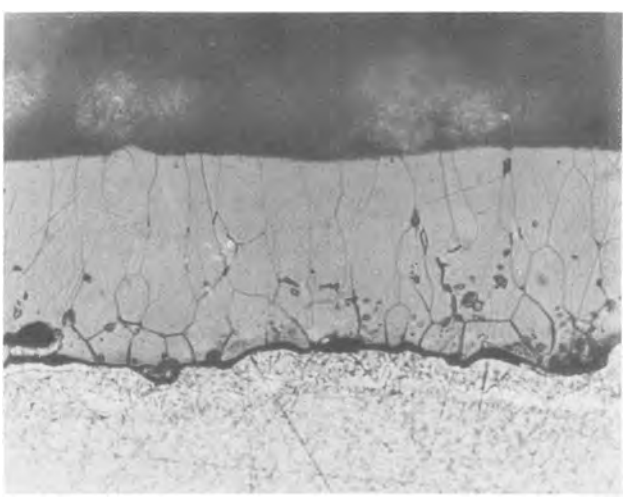


Fig. 2. Ni 270, 1000°C, 49.5 hr, 700×

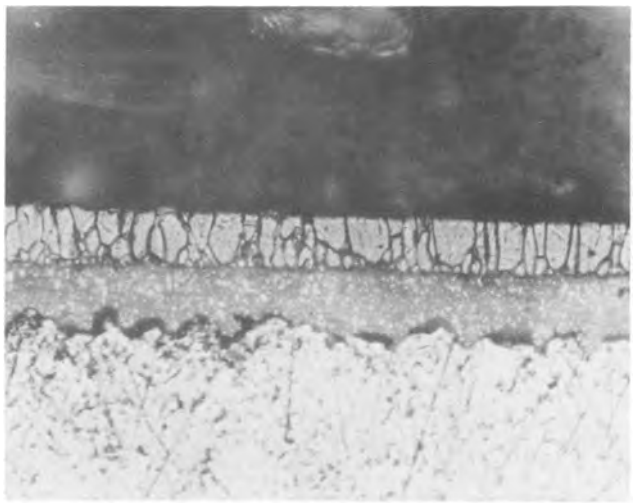


Fig. 3. Ni 200, 800°C, 64 hr, 700×

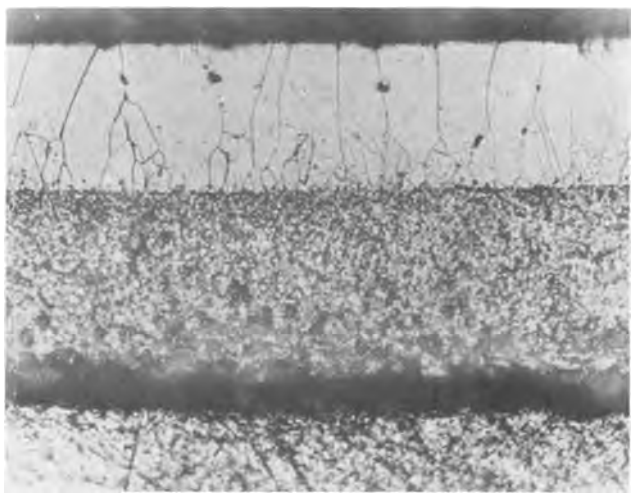


Fig. 4. Ni 200, 1000°C, 49 hr, 700×

Grain mean intercept measurements ($1/N_L = \bar{\lambda}$) were also made directly upon the microscope. As can be seen by reference to Fig. 1-4, the outer portion of the scale is always composed of columnar grains that extend to the oxide-atmosphere interface. A horizontal line drawn at midthickness passes through this columnar zone. The measurement of N_L consists in counting the number of grain boundaries crossed by unit length of such a line. Values of $\bar{\lambda}$ obtained in this way are shown for all of the nickel 270 specimens in Table I. If the grains of the oxide had been equiaxed, $2N_L$ would have been equal to the grain boundary area in unit volume of the scale. Its direct meaning in the case of columnar grains is uncertain, but its reciprocal ($1/N_L$) is equal to the mean intercept ($\bar{\lambda}$) of the columnar grains in a direction perpendicular to their long axes. Values of $\bar{\lambda}$ are plotted as a function of scale thickness (x) in Fig. 6, where it will be seen that a direct proportionality exists.

Table I. Scale thicknesses, mean grain intercepts, and average grain volumes for Ni 270 specimens oxidized at 800°, 900°, and 1000°C

Time (hours)	Scale thickness* ($\times 10^{-3}$ mm)			Mean grain intercept $\lambda = 1/N_L$ ($\times 10^{-3}$ mm)			Average grain volume ($\times 10^{-8}$ mm^3)
	800°C	900°C	1000°C	800°C	900°C	1000°C	
1.00	—	4.90	6.30	—	1.52	1.40	—
2.00	—	5.46	—	—	1.69	—	—
2.25	—	—	9.73	—	—	1.71	8.1980
4.00	—	8.62	11.27	—	1.94	2.16	18.8972
9.00	10.73	9.60	14.70	1.68	1.85	3.29	—
16.00	10.15	11.36	20.54	1.91	2.09	3.07	51.9184
25.00	11.05	14.32	22.88	1.93	2.23	3.58	—
36.00	14.43	15.69	29.18	2.16	2.63	4.17	—
49.00	14.29	19.91	—	2.31	2.75	—	—
49.50	—	—	34.17	—	—	5.00	137.7790
60.00	—	19.56	—	—	3.50	6.37	—
64.00	16.84	—	39.69	2.36	—	6.07	—
81.00	14.74	21.14	41.21	2.17	3.08	—	—
100.00	18.58	30.00	—	2.28	4.00	—	—
143.00	21.57	—	—	2.96	—	7.25	—
225.00	—	—	57.73	—	—	—	1085.7763

* The maximum error in the measurement of scale thicknesses and mean grain intercepts is in no case greater than ±7% of the mean values reported as computed at a confidence level of 95%.

The grain structure appears as though optically magnified to maintain proportionality with the scale thickness.

Average grain volume ($\overline{V}_g = 1/N_V$) is usually measured in metals by serial section analysis. This is a laborious procedure, at best, but becomes nearly impossible in application to thin scales of fragile oxides. To the extent that the grains of the scale are truly columnar, however, it is possible to determine their number in unit volume of scale (N_V) by simply counting their ends as they emerge upon the external surface. The oxide grain size is usually too fine to permit such counting by optical methods, but the scanning electron microscope provides both the magnification required and the depth of focus needed for such counts. Five nickel 270 specimens of the 1000°C series were so counted (Table I). In Fig. 7, the average grain volume ($\overline{V}_g$) is plotted as a function of the time of oxidation (t). The linear relationship exhibited by this plot is identical with that found for steady-state grain growth in aluminum (3).

The plots of Fig. 5, 6, and 7, derived as they are from three different kinds of measurements, display a remarkable self-consistency. The average grain vol-

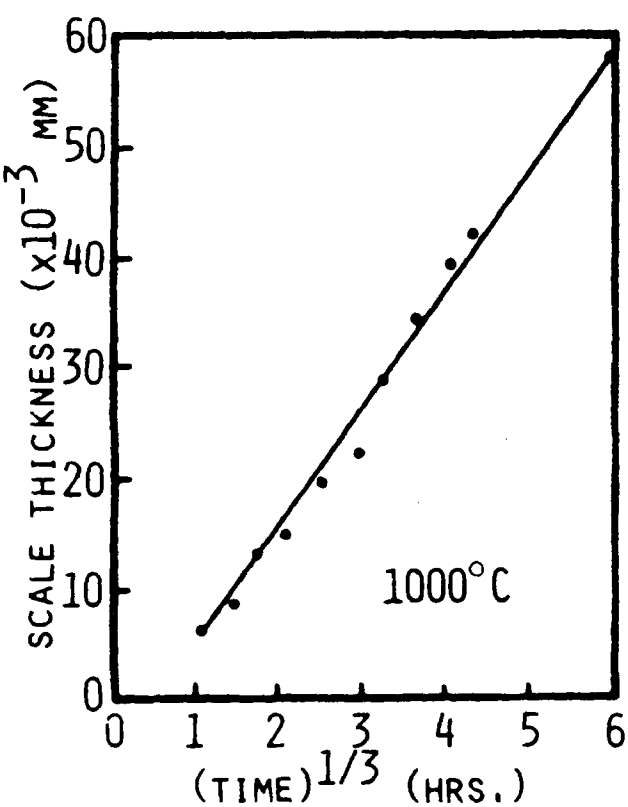


Fig. 5. Scale thickness vs. cube root of time

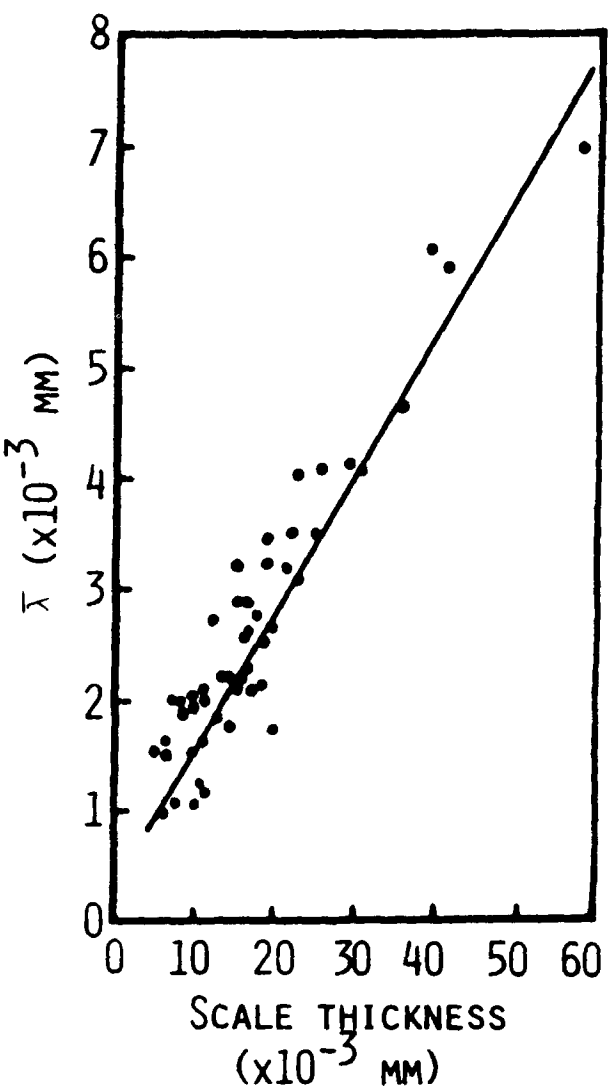


Fig. 6. Mean grain intercept vs. scale thickness

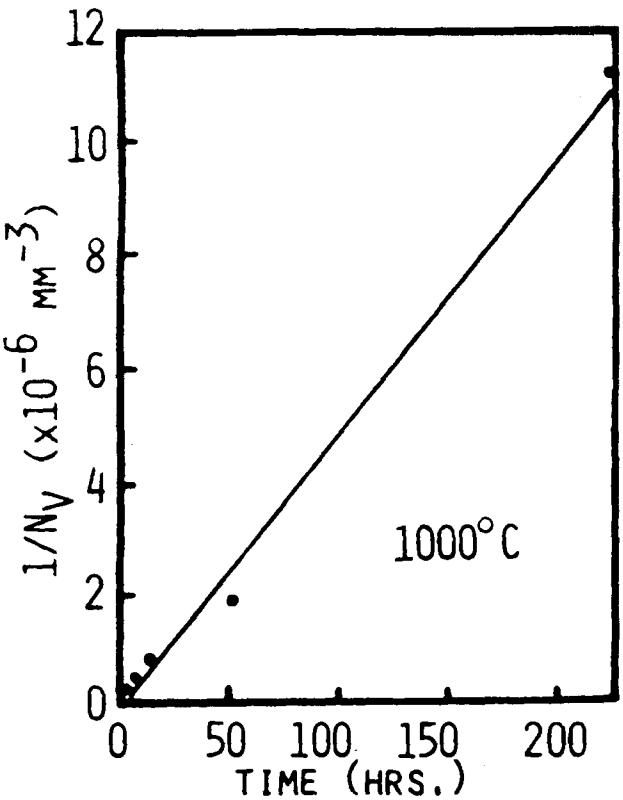


Fig. 7. Average grain volume vs. time

ume ($\overline{V}_g$), being proportional directly to the time of oxidation, implies that any lineal parameter of the grains, such as the mean intercept ($\overline{\lambda}$), should be proportional to the cube root of the time of isothermal oxidation. As anticipated, $\overline{\lambda}$ is proportional to scale thickness, which, in turn, is proportional to the cube root of the time. This leaves little room for doubt that scale and grain growth are functionally related processes.

Two layers can be distinguished in each of the scales of Fig. 1-4. The distinction is mainly one of grain size, the inner layer being finer grained. This difference is much more pronounced and the boundary between the layers is much more distinct in the scale on the less pure nickel 200 than it is in the scale on the purer nickel 270. This structural feature has been noted by almost every investigator of NiO scale microstructure. The presence of the finer grained layer demonstrates that new grains of NiO are nucleated during oxidation. Their absence from the outer layer suggests that they are generated somewhere in the inner layer, probably at the metal-oxide interface. The great refinement of the grains in the inner layer on nickel 200 suggests further that the nucleation of new grains is somehow stimulated by the presence of impurities in the nickel. One possibility is that the impurities in the nickel first form a subscale which is consumed by the growing external scale, each particle of impurity oxide in the subscale giving rise to a new grain of NiO as it enters the external scale.

Probably the most significant characteristic of the layers in the NiO scale is that they maintain a constant ratio of thickness throughout scale growth. This is true not only of the leading front of the boundary between the layers, but applies also to the location of markers within the inner layer. The fine structure of the inner layer formed on nickel 200, Fig. 3 and 4, coarsens with scale growth, so that each marker particle maintains its same relative position in the thickening scale. Such behavior is characteristic of swelling of the matrix in which the particles are embedded.

The texture of the external surface of the NiO scale varies in a regular fashion in the course of scale growth. As soon as any structure becomes visible (with the aid of the scanning electron microscope) the outlines of grains are seen. These outlines develop into ridges which are more pronounced in scales formed at 800°C than at the higher temperatures. At this stage it would be difficult to define the thickness of the scale, because it is much thicker in the neighborhood of the grain boundaries than it is in the central portions of the grains. As oxidation proceeds, the ridges broaden and merge. Thereafter, the grains continue to be distinguishable by virtue of their tendency to form crystalline facets upon their exposed surfaces. Grain growth can be observed by comparing scanning electron microscope pictures of the same locality on the scale surface after successive intervals of heating in oxygen.

Marker Movements During Scale Growth

In 1929 Pfeil (4), studying the high temperature oxidation of iron, reported that inert matter originally upon the metal surface becomes enveloped by the growing scale and is found ultimately near the center of the scale layer. He recognized that this behavior (*i*) denies formation of new oxide by the inward diffusion of oxygen reaction exclusively at the metal-oxide interface; and (*ii*) denies outward diffusion of the metal reaction with oxygen exclusively at the exterior surface. If oxygen alone were to be the mobile species the inert matter should remain upon the exterior of the scale layer. If the metal were to be oxidized only at the exterior surface, then the inert matter should remain at the metal-oxide interface. The inference that the new oxide is generated throughout the mass of the scale was resisted upon the basis that this reaction can occur only at a planar interface, where the diffusing reactants meet. No resolution of this paradox was offered at that time, nor until 1970, when Rhines and Wolf (5) pointed out that the reaction front could reside in the grain boundaries where metal diffusing through the grains meets oxygen entering along grain boundaries. In the light of the new knowledge that grain growth and scale growth are interrelated, it becomes evident that the motion of the grain boundaries that takes place in the course of grain growth also provides a sweeping reaction front that reaches the entire volume of the scale.

From the observation that the scale layer boundary maintains its relative position near the center of the scale it is apparent that almost equal volumes of new NiO are generated on the two sides of this boundary. The further observation that marker points in the inner layer of scales on nickel 200 also maintain constant relative positions with respect to the thickness of the scale means that the same amount of new oxide is being produced everywhere within the scale. Scale growth evidently occurs by swelling, rather than by accretion at the surface of the scale, as had once been supposed. The further fact that the swelling is homogeneous throughout the scale is most remarkable and resists explanation for the lack of more detailed knowledge of the structural behavior of the inner layer.

Plastic Deformation of the NiO Scale

Swelling of the scale develops a shear stress between the metal and the oxide, which was measured by Rhines and Wolf (5) and found to exceed 1500 psi in samples oxidized at 1000°C. If the nickel substrate is thin this stress is sufficient to cause it to bend, or to elongate in creep. When the nickel is too massive to yield the plastic response to the oxidation stress oc-

Table II. Kinetic parameters of NiO scale thickening for oxidation at 1000°C

Time, t (hr)	Scale thickness, x ($\times 10^{-3}$ mm)	Time interval, Δt (sec)	Thickness increase, Δx ($\times 10^{-7}$ mm)	Volume increase, ΔV_o ($\times 10^{-5}$ mm^3)	Volume increase per second, $\Delta V_o/\Delta t$ ($\times 10^{-5}$ mm^3/sec)	Volume swept per second, $V_S/\Delta t$ (mm^3/sec)	Thickness increase per second, $\Delta x/\Delta t$ ($\times 10^{-7}$ mm/sec)	Rate of scale thickening, dx/dt ($\times 10^{-7}$ mm/sec)
2.25	9.73	0.003564	0.01926	0.01979	5.55300	280.5840	5.4040	5.40860
4.00	11.27	0.011260	0.04100	0.03638	3.23100	88.8100	3.6410	3.68550
16.00	20.54	0.180200	0.25300	0.12320	0.68370	5.5500	1.4040	1.46260
49.50	34.17	1.725000	1.18800	0.34770	0.20160	0.5800	0.6887	0.68887
225.00	57.73	35.643000	8.94700	1.55000	0.04349	0.0281	0.2510	0.25102

curs mainly in the scale. At 1000°C the creep stress for NiO is nearly the same as that for nickel. Where the oxidizing surface is flat there is room for scale growth only normal to the plane of the surface. All scale growth in directions parallel with the surface must, therefore, be diverted into growth perpendicular to the surface. This means that the scale must extrude outward as its volume increases.

Although the flow pattern of the oxide cannot be analyzed upon the basis of currently available evidence, some idea of its form is suggested by the grain boundary ridges that develop during early oxidation (1, 6). These ridges represent the outward extrusion of new NiO before sweeping of the boundaries has commenced. The grain boundary contribution to the general oxidation is then limited to the vicinity of relatively static grain boundaries and thrusts outward in place. As the grain boundaries begin to sweep, it may be imagined that each carries with it a wave of extruding oxide that results in a uniform thickening of the scale.

The plastic deformation that results in extrusion of the oxide is also essential in the promotion of oxidation *per se*, because without it grain growth and the accompanying grain boundary sweeping would not occur. The present authors have reported previously that grain growth ceases when oxidation is suspended by substituting helium for oxygen in the oxidizing furnace. This is because the grain boundaries of the scale are normally anchored at the two surfaces of the scale, as well as being pinned upon any impurity particles that may be present in the scale. Only in the presence of deformation can the boundaries break free and migrate under the influence of surface tension. The uniformity of swelling of the scale suggests that plastic deformation is also uniformly distributed through the structure.

Kinetics of Grain Growth and of Scale Growth

If grain growth in the scale were to represent only the increase in the volume of the oxide the columnar grains would simply grow lengthwise, the number of grains in the system remaining constant except for new grains formed at the metal-oxide interface. The average grain volume would be proportional to the volume of the scale (*i.e.*, to its thickness). But the experimental evidence shows that the average grain volume increases as the cube of the scale thickness. In this respect grain growth in the scale is like steady-state grain growth in metals, where equiaxed grains expand three dimensionally. There are, however, the differences that: (*i*) the space into which the oxide grain growth is occurring is increasing and (*ii*) the oxide grains in the outer layer are columnar, rather than equiaxed.

Columnar grains have a minimal energy form wherein their cross sections are two-dimensionally equiaxed. Their longitudinal walls meet the external surface at right angles, a configuration which, though not constituting true pinning, offers no impetus to grain boundary migration. Neither is curvature of the walls of the columnar grains required for space filling, as is true of three-dimensionally equiaxed grains. For these reasons, there is no inevitable grain boundary curvature to promote grain growth under the driving force of surface tension. The curvature required for grain growth is provided, however, by plastic deformation which bends the grain boundaries and disengages them from pinning (7). Thereupon surface tension, tending to straighten and reduce the area of grain boundary, causes it to migrate. The result is grain growth and also growth in the volume of the scale.

It has been shown elsewhere (3) that four grains are lost from unit volume of material each time that grain boundary sweeps[1] this volume once in the elimination of these grains and in restoring the remaining grains to equiaxedness. Thus the volume swept by grain boundary can be computed from the change in the average grain volume, as measured experimentally, and can be associated with the quantity of new oxide deposited through the gain in scale thickness in the corresponding time interval. The results of these computations are shown in Table II for five samples of nickel 270 oxidized at 1000°C, the original data being given in Table I. The computative procedure follows.

From the measurements recorded in Table I, the scale thickness (x) is related to the time (t) of oxidation by

$$x = kt^{1/3} \qquad [5]$$

where $k = 0.01003$, with a correlation coefficient of 0.9978. The average grain volume ($1/N_V$) is related to the time (t) by

$$1/N_V = k't \qquad [6]$$

where $k' = 4.8891 \times 10^{-8}$, with a correlation coefficient of 0.9957. By differentiation, the rate of scale thickening is

$$dx/dt = 3.3433 \times 10^{-3}t^{-2/3} \qquad [7]$$

and the rate of change in the number of grains in unit volume (N_V) becomes

$$dN_V/dt = -2.0454 \times 10^7 t^{-2} \qquad [8]$$

If a unit volume of oxide scale is swept once by grain boundary, four grains per unit volume will disappear as a result of grain growth. Accordingly, the time interval for grain boundary to sweep unit volume of oxide scale can be computed by integrating Eq. [8] and solving for the unknown limit of integration t_2

$$\int_{N_{V1}}^{N_{V2}} dN_V = -2.0454 \times 10^7 \int_{t_1}^{t_2} t^{-2}dt \qquad [9]$$

where: $N_{V1} = 12{,}980{,}000$ grains in 1 mm^3 (unit volume); $N_{V2} = 12{,}979{,}996$ (*i.e.*, $N_{V1} - 4$) grains in 1 mm^3; and $t_1 = 2.25$ hr. Integrating and solving for t_2, $t_2 = 2.25000099$ hr. Thus, the time interval for the grain boundary to sweep one unit volume of oxide scale is $\Delta t = t_2 - t_1 = 9.9 \times 10^{-7}$ hr, or 3.564×10^{-3} sec. The average rate of grain boundary sweep ($V_S/\Delta t$) is 1 mm^3 in 3.564×10^{-3} sec, or $V_S/\Delta t = 280.584$ mm/sec at 2.25 hr.

The corresponding increase in scale thickness can be obtained by integrating Eq. [7]

[1] The term "grain boundary sweeping" refers to the three-dimensional grain boundary migration that accompanies grain growth.

$$\int_{x_1}^{x_2} dx = 3.3433 \times 10^{-3} \int_{t_1}^{t_2} t^{-2/3} dt \qquad [10]$$

where: $x_1 = 9.73 \times 10^{-3}$ mm, $t_1 = 2.25$ hr, and $t_2 = 2.25000099$ hr. Integrating and solving for x_2, $x_2 = 9.730001926 \times 10^{-3}$ mm. Thus, the scale thickness increase in the time interval of one sweep at 2.25 hr is $\Delta x = x_2 - x_1 = 1.926 \times 10^{-9}$ mm. The rate of thickness increase at 2.25 hr is, therefore, $\Delta x/\Delta t = 5.404 \times 10^{-7}$ mm/sec (Table II).

The rate of volume increase of the scale ($\Delta V_o/\Delta t$) at 2.25 hr is 5.554×10^{-5} mm³/sec. This is equivalent to a thickness increase ($\Delta x/\Delta t$) of 5.404×10^{-7} mm/sec. The observed rate of oxidation (dx/dt), obtained by evaluating Eq. [7] at 2.25 hr is 5.4086×10^{-7} mm/sec, showing that the computations are self-consistent. Similar computations were performed for oxidation times of 4, 16, 49.5, and 225 hr, and the results are given in Table II.

These results are of particular interest in the picture that they provide of the behavior of the columnar grain boundaries. Early in oxidation the grain boundary sweeps the volume of the oxide hundreds of times each second. After 225 hr the rate has decelerated to barely 1 sweep/min. At the same time, the quantity of new oxide generated with each sweep is on the increase, producing approximately 100 times as much new NiO per sweep at 225 hr as at 2.25 hr. The net result is, of course, a decelerating rate of oxide growth, because the slowing of grain boundary sweeping dominates. The fact that the grain boundary produces more new oxide per sweep the slower the sweeping rate suggests that the depth of the region about the boundary in which new oxide is being formed is greater the slower the sweeping. Indeed, the values in Table II lead to the conclusion that the rate of new oxide formation ($\Delta V_o/\Delta t$) is proportional to the square root of the rate of grain boundary sweeping ($V_S/\Delta t$)

$$\frac{\Delta V_o}{\Delta t} = 3.3672 \times 10^{-6} \left(\frac{V_S}{\Delta t} \right)^{1/2} - 4.1448 \times 10^{-7} \qquad [11]$$

Correlation coefficient = 0.9996

Some additional relationships which can be derived from Table II follow: The rate of change of the average grain volume

$$\frac{dV_o}{dt} = \frac{d\left(\frac{1}{N_V}\right)}{dt} = 4.8891 \times 10^{-8} \text{ mm}^3/\text{sec} \qquad [12]$$

The rate of sweep *vs.* time in hours

$$\frac{V_S}{\Delta t} = 4.378 \times 10^2 t^{-2} - 67.227 \text{ mm}^3/\text{sec} \qquad [13]$$

Correlation coefficient = 0.9113

The increase in the volume of NiO per sweep *vs.* time in hours

$$\Delta V_o = 6.851 \times 10^{-8} t + 8.8201 \times 10^{-8} \text{ mm}^3 \qquad [14]$$

Correlation coefficient = 0.9999

The increase in scale thickness per sweep *vs.* time in hours

$$\Delta x = 6.540 \times 10^{-10} t^{4/3} - 2.1998 \times 10^{-10} \text{ mm} \qquad [15]$$

Correlation coefficient = 0.9999

The rate of increase in scale volume per sweep *vs.* time in hours

$$\frac{\Delta V_o}{\Delta t} = 1.2695 \times 10^{-4} \left(\frac{1}{t} \right) - 4.065 \times 10^{-7} \text{ mm}^3/\text{sec} \qquad [16]$$

Correlation coefficient = 0.9996

Transport of Reactants

The premise that nickel diffuses outward through the bodies of the NiO grains and that oxygen diffuses inward along grain boundaries is derived from measurements reported in the literature. Moore and coworkers (8), as well as others, have reported diffusion rates for Ni^{++} in single crystals of NiO in the neighborhood of 10^{-3} cm²/sec. Moore (9) found the diffusion of O^{--} to be only of the order of 10^{-5} cm²/sec in NiO single crystals. Volpe and Reddy (10), however, measured the diffusion of oxygen through polycrystalline NiO and obtained a value of the order of 10^{-1}. Thus, the diffusion of oxygen upon the grain boundaries is seen to be very rapid indeed, although it is negligible through the grains.

The delivery of the two reactants throughout the scale layer requires that there be a concentration gradient of Ni^{++} from the metal-oxide interface to the external surface and a concentration gradient of O^{--} from the external surface to the metal interface. These gradients must cross each other because the grain boundary forms a closed network. Such crossing is made possible by the fact that the reaction $Ni^{++} + O^{--} = NiO$ tends to establish equilibrium with the reaction constant (K) everywhere the same

$$K = \frac{p[Ni^{++}] \cdot p[O^{--}]}{p[NiO]} \qquad [17]$$

Near the metal-oxide interface the activity of Ni^{++} is comparatively large and that of O^{--} small, while the opposite prevails near the external surface. Thus, both gradients can exist while producing new oxide all along the grain boundaries.

It should be appreciated that much of the foregoing interpretation is based upon measurements confined to the outer layer of the scale. While the uniformity of scale swelling implies that a common mechanism must prevail throughout the scale, the fact of the finer grain size of the inner layer raises questions that cannot be answered in the absence of more detailed knowledge of the structural behavior of the inner layer. It should be understood, as well, that none of the foregoing is intended to deny the existence of ranges in which oxide growth is dominated by different mechanisms. Graham, Caplan, and Cohen (11) have demonstrated clearly that the growth of NiO as a single crystal is controlled by the diffusion rate of the metal ion. The presently proposed mechanism is seen as applying to that extensive range of scale growth within which the kinetics are dominated by grain boundary oxide generation.

Acknowledgment

The authors wish to express their indebtedness to the National Science Foundation for the support of Grant Number GH-41005 under which this research was performed.

Manuscript received Oct. 27, 1976; revised manuscript received Feb. 18, 1977. This was Paper 127 presented at the Las Vegas, Nevada, Meeting of the Society, October 17-22, 1976.

Any discussion of this paper will appear in a Discussion Section to be published in the June 1978 JOURNAL. All discussions for the June 1978 Discussion Section should be submitted by Feb. 1, 1978.

Publication costs of this article were assisted by the University of Florida.

REFERENCES

1. F. N. Rhines and R. G. Connell, Jr., in "Influence of Stress upon the High Temperature Oxidation of Nickel, Stress Effects and the Oxidation of Metals," J. V. Cathcart, Editor, pp. 94-113, Fall Meeting TMS-AIME 1974, Published by The Metallurgical Society of AIME, New York (1975).
2. W. W. Smeltzer, *Acta Metall.*, **7**, 191 (1959).

3. F. N. Rhines, K. R. Craig, and R. T. DeHoff, *Metal. Trans.*, **5**, 413 (1974).
4. L. B. Pfeil, *J. Iron Steel Inst., London*, **119**, 501 (1929).
5. F. N. Rhines and J. S. Wolf, *Metal. Trans.*, **1**, 1701 (1970).
6. J. S. Wolf and J. M. Grochowski, in "The Nature of Gas-Metal Reactions under Conditions of Anisothermal Oxidation, Stress Effects and the Oxidation of Metals," J. V. Cathcart, Editor, pp. 279-299, Fall Meeting TMS-AIME 1974, Published by The Metallurgical Society of AIME, New York (1975).
7. F. N. Rhines, *Metall. Trans.*, **1**, 1105 (1970).
8. M. T. Shim and W. J. Moore, *J. Chem. Phys.*, **26**, 802 (1957); J. S. Choi and W. J. Moore, *J. Phys. Chem.*, **66**, 1308 (1962); R. Lindner, Å. Åkerstrom, *Discuss. Faraday Soc.*, **23**, 133 (1957).
9. M. O'Keefe and W. J. Moore, *J. Phys. Chem.*, **65**, 1438 (1961).
10. M. L. Volpe and J. Reddy, *J. Chem. Phys.*, **53**, 1117 (1970).
11. M. J. Graham, D. Caplan, and M. Cohen, *This Journal*, **119**, 1265 (1972).

Alternating-Current Properties of Organic Semiconductor Solid Capacitor

Yoshimasa Itoh and Susumu Yoshimura

Matsushita Research Institute Tokyo, Incorporated, Ikuta, Tama-ku, Kawasaki 214, Japan

ABSTRACT

This paper deals with the a-c properties of a new type of aluminum solid electrolytic capacitor in which organic semiconductors are employed as the counterelectrode. Both equivalent series capacitance and resistance (ESR) were measured between 90 Hz and 22 MHz frequencies and their temperature dependence was determined between −55° and +85°C. Excess series capacitance and ESR which were introduced by the use of the organic semiconductor counterelectrode were separated analytically, and the origin of the impedance connected in series of the anodic oxide is discussed. Very stable a-c properties were observed in the high frequency and low temperature regions, which permitted explanation of the a-c properties with simple models, such as a distributed circuit or dispersions owing to various interfaces. In the low frequency region, the capacitance and ESR increased with decreasing frequency and increasing temperature. It is suggested that the low frequency dissipation is dominated by the interfacial polarization due to polymer binder in contact with the anodic oxide.

The solid electrolytic capacitor has been an important passive component in both transistor and hybrid circuitry. The conventional manganese dioxide (MnO_2) counterelectrode has offered great advantage to the capacitor performance, such as a larger capacitance/volume ratio over the thin film capacitors and superior low temperature characteristics over the dry electrolytic capacitors (1). Recently, we have developed a new type of solid electrolytic capacitor in which MnO_2 was replaced by organic semiconductors (2), the ion-radical salts based on 7,7,8,8-tetracyanoquinodimethane (TCNQ) (3). The capacitor has been referred to as the organic semiconductor solid (OSS) capacitor. The organic semiconductor coating was deposited from a solution in a uniform film with polymers. This process is likely to have imposed little or no damage to the anodic oxide as compared with the thermal decomposition of MnO_2, so that the OSS capacitor can be considered to have a simpler structure and superior frequency stability (2).

The a-c properties have been used for many years as a tool for inspecting the nature of the electrolytic capacitors (4). Young (5) and Winkel and de Groot (6) have presented fundamental explanations on the a-c properties of the anodic oxide. The a-c properties of the tantalum solid electrolytic capacitor were examined originally by McLean (7) and lately by a number of workers, Goudswaard (8), for example, and several analytical methods useful for development investigations have been proposed.

Key words: solid electrolytic capacitor, solid electrolyte, tetracyanoquinodimethane (TCNQ).

In this paper, we wish to report the a-c properties of the OSS capacitor and identify the characteristic features of the new type capacitor. We will also present a phenomenological model for the solid electrolytic capacitor which will be a useful tool for the characterization of this kind of capacitor. This paper deals primarily with the equivalent series capacitance (C_s) and resistance (R_s or ESR) in the frequency range between 90 Hz and 22 MHz and also with their temperature dependence between −55° and +85°C.

Experimental

Construction of capacitor.—Foil-type solid Al capacitors were fabricated with processes described in Ref. (2). The Al foils were electrolytically etched in an aqueous sodium chloride solution to about 70 times the apparent surface area and formed to in a boric acid-borate solution to 200V at a rate of 10 V/min or at about 1 mA/cm^2 current density. The counterelectrode consisted of a TCNQ salt, quinolinium $(TCNQ)_2$, and polymers polyvinylpyrrolidone and related polymers, which were deposited from an acetonitrile-based solution. The anode assembly was covered with colloidal graphite and silver paint, and finally packaged with epoxy resin. Comparative studies were made on a conventional Al (foil-type) and solid electrolytic capacitor and a dried anodized Al capacitor with a graphite counterelectrode. The Al solid electrolytic capacitor was fabricated using the same Al anode as the OSS capacitor, so that the effect of the counterelectrode may well be compared between the two cases.

Apparatus.—No single apparatus allowed the measurements of both C_s and R_s over the entire frequency range of interest, because the capacitor studies had relatively large C_s and small R_s. A standard Wien bridge with sharply tuned detector was used between 90 Hz and 10 kHz and a Yokogawa-Hewlett-Packard (YHP) 4342A Q-meter was used between 22 kHz and 22 MHz. In the latter experiment, the Q value and the resonance frequency of a serial network of a test sample and a coil were compared with those of a circuit in which the sample terminals were shorted with a dummy sample having the same reactance as the test sample. As a check, the impedance and the phase angle of each sample were measured between 500 kHz and 100 MHz with a YHP 4815A RF vector impedance meter, and the capacitance at the frequency of resonance between the sample capacitance and the lead reactance ($\theta = 0$) was determined.

The temperature dependence of the a-c characteristics of the OSS capacitor was measured with thermostat equipment, Sigma Electric TE-307S, between −55° and +85°C for frequencies from 90 Hz to 10 kHz. In the Q-meter measurements (from 22 kHz to 22 MHz), a miniature-sized heating attachment was used to attain temperatures above 25°C.

Results

Figure 1 shows the frequency dependence of the relative capacitance and ESR of the two typical OSS capacitors, OSS-A and OSS-B. The OSS-A was chosen as a representative of those capacitors with lowest dissipation factor (about 0.5%) at 120 Hz, while the OSS-B was with higher dissipation factor (about 1.5%). The difference was due mainly to the polymer composition, and the former sample was brought about by polymers with high adhesion force to both Al_2O_3 and the organic semiconductor particles, such as copoly(vinylpyrrolidone-acetate) or polyvinylbutyrale. This figure also includes data on an Al solid capacitor and a dried anodized Al capacitor with a graphite counterelectrode. The capacitance at 120 Hz was 0.16, 0.15, 0.10, and 0.0073 μf for the OSS-A, OSS-B, Al solid, and dried anodized capacitors, respectively. The ESR of each sample was normalized by multiplying its capacitance at 120 Hz. Since the capacitance, *i.e.*, the dielectric constant ϵ, is a weak function of frequency at low frequencies, the normalized ESR, ESR*, roughly corrects for the differences in the actual surface area, S; $C = \epsilon S/d_o$ and ESR* $\propto$ ESR $\times$ S, where d_o is the oxide thickness which is nearly the same for all the capacitors.

The capacitance change and the ESR of the solid electrolytic capacitors had many common features of frequency dependence, irrespective of the kind of counterelectrode. The results are to be compared with

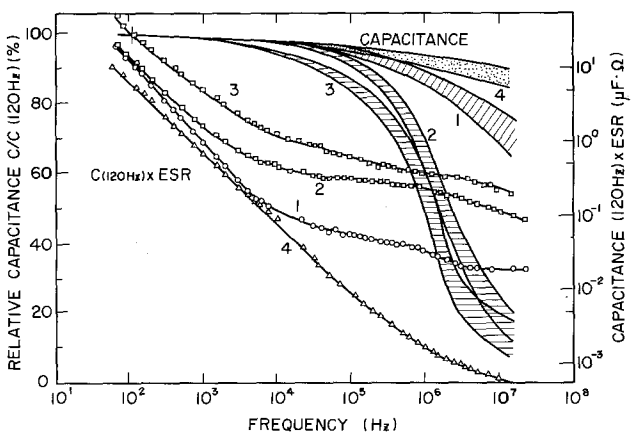


Fig. 1. Normalized equivalent series capacitance and ESR as a function of frequency at room temperature: 1, OSS-A; 2, OSS-B; 3, Al solid; and 4, dried anodized capacitors.

those of Goudswaard (8), McLean (7), and the same authors (2) on conventional tantalum solid electrolytic capacitors. The ESR had a peak or a plateau at intermediate frequencies, from 10 kHz to 1 MHz, and the relative capacitance started to fall rapidly at a frequency roughly corresponding to that of the peak of ESR. The OSS-A displayed the most excellent stability at high frequencies; the capacitance change was smallest of all the electrolytic capacitors, which correlated to a very small value of ESR. With the OSS-B is presented a less satisfactory performance in which the capacitance change and the magnitude of ESR were amplified over those of the OSS-A.

The dried anodized capacitor exhibited a frequency dependence quite different from those of the solid electrolytic capacitors; the capacitance change was smallest and the ESR decreased monotonically until the highest frequency measured. These properties seem to be those of a metal-oxide-metal capacitor and the measured frequency characteristics are thought to be inherent to the anodic oxide dielectric, for the ESR strictly follows a $1/f$ dependence over a wide range of frequency (5, 6). For the OSS-A, the slope of the ESR* was higher than 45° and the ESR* approached that of the dried anodized capacitor at 6 kHz. This result indicates that the incorporation of the organic semiconductor layer has introduced an increasing resistance with decreasing frequency at low frequencies. The comparative studies on the representative capacitors furthermore indicate that the counterelectrode has a general adverse effect of presenting a plateau at intermediate frequencies (9). Goudswaard (8) has ascribed it to the resistance of MnO_2 residing in the pores of anode. The ESR* of the OSS-A capacitor was about one-tenth of that of the MnO_2-based Al solid capacitors at the frequency of the plateau, about 1 MHz. The specific resistivity of the organic semiconductor film was about 1 Ω-cm experimentally, and published data for MnO_2 range from 0.1 to 10^3 Ω-cm (10). However the specific resistivity of the latter in a solid capacitor which is manufactured with usual procedures is estimated experimentally to be higher than 10 Ω-cm due partly to incomplete pyrolysis and partly to the formation of lower exides, so that the small ESR of the OSS-A may be explained by the low resistance of the organic semiconductor film residing in the etch tunnels of the aluminum anode. In case of the OSS-B, it appears that the organic semiconductor film has been deposited into a less dense or less conductive film.

Figure 2 shows the frequency dependence of C_s and R_s of the OSS-A capacitor at various temperatures. In the low frequency region, both C_s and R_s increased rapidly with rising temperature, which seriously affected the dissipation factor at high temperatures (2). In the high frequency region, however, the ESR changed very little with temperature as shown in Fig. 3. At frequencies higher than 22 kHz, the relative capacitance and ESR were independent of temperature within experimental error. The temperature dependence of the OSS capacitor at high frequencies was in apparent contrast to that of the MnO_2-based capacitor. Figure 4 shows the frequency dependence of C_s and R_s at various temperatures for the Al solid electrolytic capacitor. In this case, the capacitance decreased rapidly and the ESR grew very high above 1 kHz at −55°C. Several authors have reported that the conventional solid electrolytic capacitors display an increase in the high frequency ESR at low temperatures (1, 8, 11), and the semiconductive nature of MnO_2 has been thought to be responsible for it. That the OSS capacitor showed virtually no temperature variation in the relative capacitance and ESR at high frequencies may be ascribed to the very low resistivity of the electrolyte film and/or the metallic-like nature of the organic semiconductor (12). This

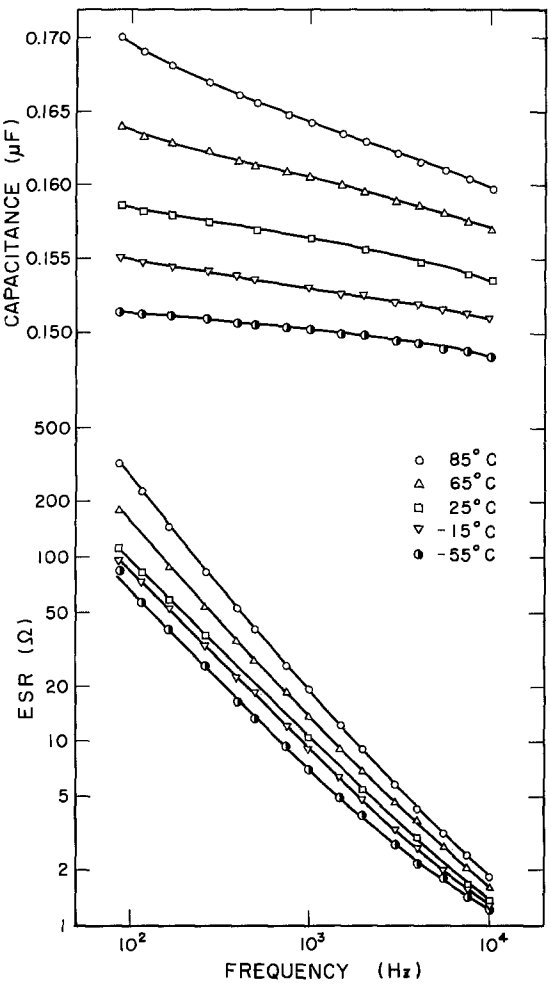


Fig. 2. Capacitance and ESR as a function of frequency for the OSS-A capacitor.

capacitor may have represented the coupled effects of the anodic oxide and the organic semiconductor counterelectrode. In order to obtain an equivalent circuit explaining the a-c properties of the capacitor, we must identify the electrode effects. Generally the impedance of the anodic oxide is explained by Winkel-de Groot theory which is based on an exponential distribution of relaxation time (6)

$$\frac{\partial(1/C_s)}{\partial(\ln f)} = 4\frac{R_s}{1/f} \qquad [1]$$

For special cases, however, each term on both sides can be equated to be a constant b or $4a$ (this is to be defined as a "linealization"), which leads to a set of equations known as the Young equation (5). We will take this approximation for the anodic oxide of the OSS capacitor. The reason for this is multifold: (*i*) the Al-oxide-graphite capacitor displays wide applicability of the linealized equations, (*ii*) the high frequency deviations in R_s and C_s are too large to be explained by [1], and (*iii*) the large oxide thickness (200V forming) and supposed absence of hydrated oxide exclude the possibility of the nonlinear equation. Accordingly, C_s and R_s are described by the following equations

$$R_s = \frac{a}{f} + \Delta R_s \qquad [2]$$

$$\frac{1}{C_s} = b \log f + \frac{1}{\Delta C_s} \qquad [3]$$

$$\frac{b}{a} = 4 \qquad [4]$$

where the extra capacitance and resistance introduced by the counterelectrode are expressed by ΔC_s and ΔR_s, respectively. The capacitance change shown in Fig. 1 was best fitted to [3] with $1/\Delta C_s$ = constant in the frequency range between 90 Hz and about 10 kHz. The constant b was determined from the linear portion of the $1/C_s$ *vs.* log f curve and a was calculated using [4]. Figure 5 shows the extra resistance for the OSS-A and OSS-B capacitors, where the constant a was 5200 and 7400 Ω Hz for the former and the latter, respectively. ΔR_s is enhanced mainly in two frequency regions; a plateau centering at 100 kHz and a rapidly growing resistance with lowering frequency in the

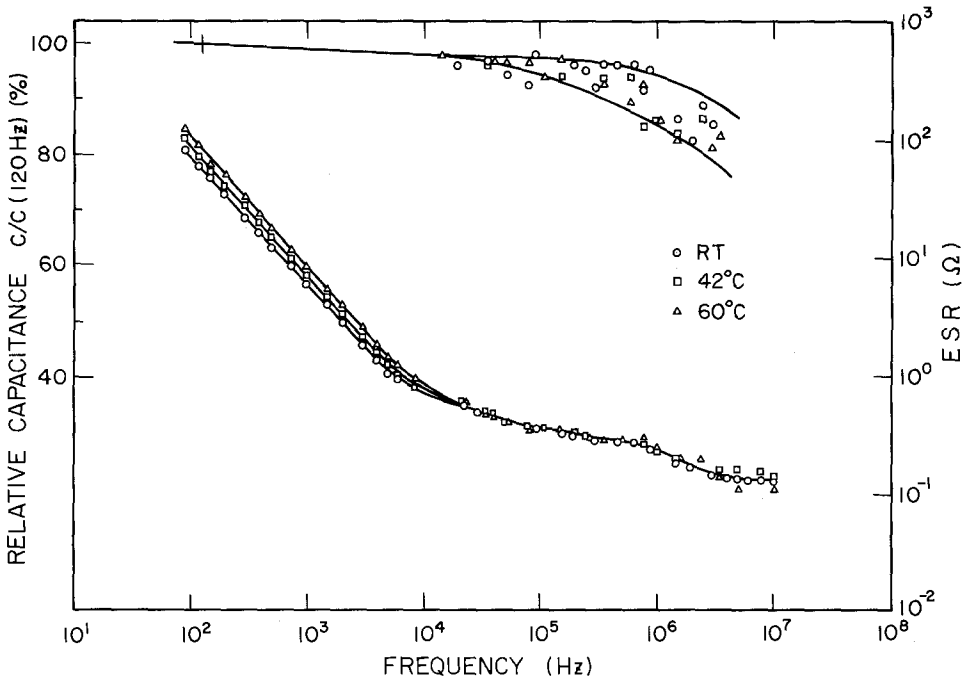


Fig. 3. Relative capacitance and ESR as a function of frequency for the OSS-A capacitor at room temperature (○), 42°C (□), and 60°C (△).

explanation is in accordance with that of Parisi (13) on the temperature dependence of a thin film capacitor with a lead dioxide counterelectrode.

Discussion

Electrolyte effects on the a-c properties.—The experimental data on the a-c properties of the OSS

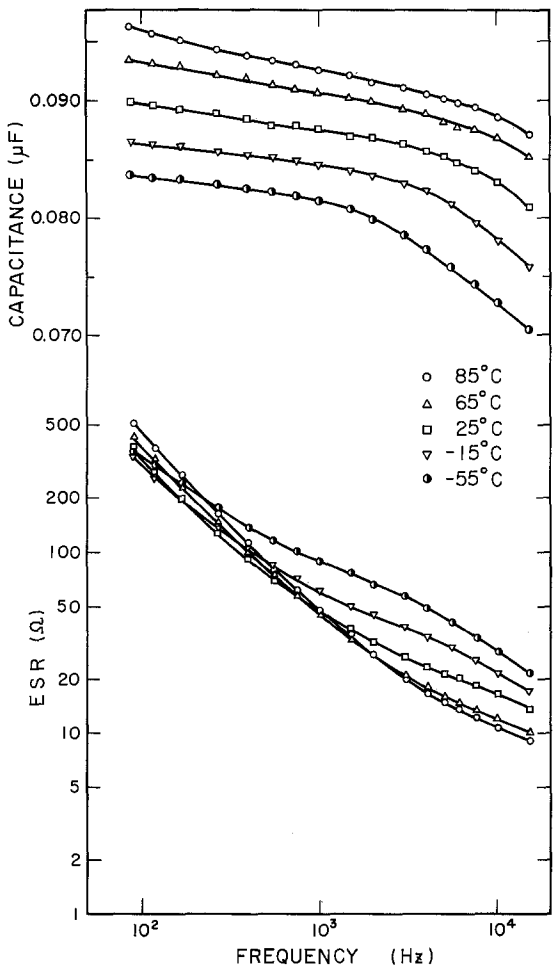


Fig. 4. Capacitance and ESR as a function of frequency for the Al solid electrolytic capacitor.

the other data suggest that the extra ESR is associated with the resistance of the counterelectrode. First we will consider the change in the extra capacitance ΔC_s. Figure 6 shows $1/\Delta C_s$ plotted against frequency for the OSS-A and OSS-B. The diagram implies that the capacitance drops of the OSS-A and OSS-B shown in Fig. 1 need to be interpreted with more than one mechanism. For the OSS-A, the following relationship held from 40 kHz to 10 MHz

$$C \propto f^{-1/2} \qquad [5]$$

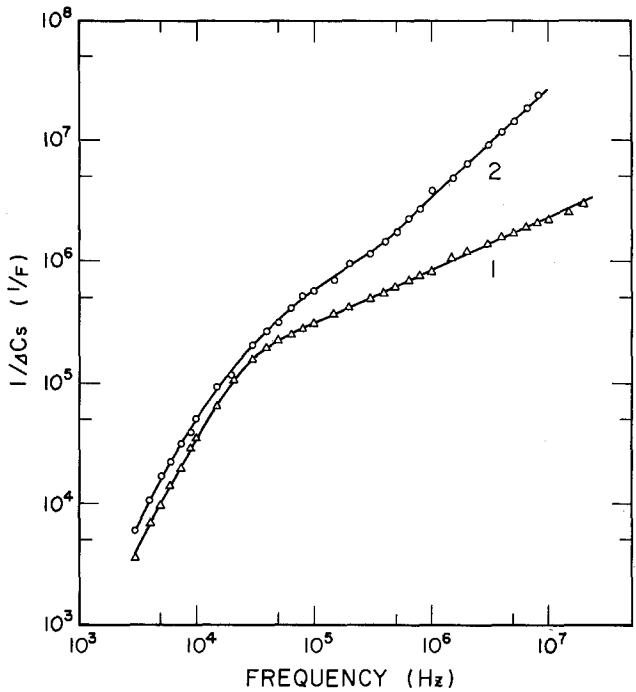


Fig. 6. Inverse extra capacitance (Eq. [2]) as a function of frequency for the OSS-A (curve 1) and OSS-B (curve 2) capacitors.

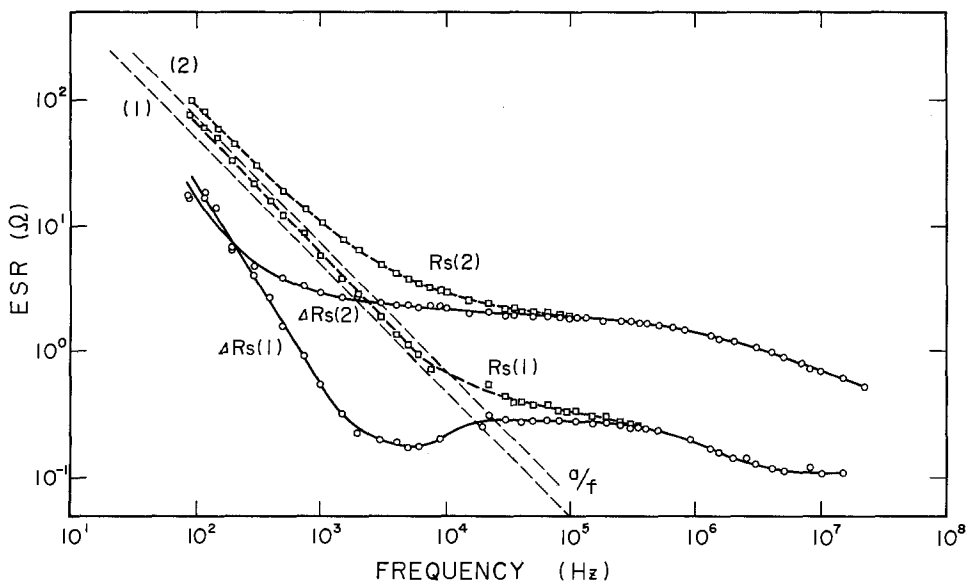


Fig. 5. ESR as a function of frequency at room temperature for the OSS-A (curve 1) and OSS-B (curve 2) capacitors; ΔR_s represents extra ESR due to the solid electrolyte (see Eq. [1]).

low frequency side. Although Fig. 1 seemed to indicate a $1/f$ law of ESR for the OSS-B capacitor, we conclude from this analysis that the $1/f$ dependence appeared accidentally owing to the plateau starting from that low frequency. The same discussion may apply to the apparent $1/f$ dependence of the ESR for the MnO_2-based capacitors.

High frequency properties.—The OSS capacitor has an ESR plateau centering at about 100 kHz, which contrary to the conventional solid electrolytic capacitors was virtually temperature independent. Our and This specific frequency dependence may be understood on the basis of a distributed circuit model. Nishikata (14) has systematically considered the effect of the distributed circuit on the a-c properties of various electrolytic and thin film capacitors and has shown that the capacitance change is generally expressed by [4] in the high frequency region. In view of the fact that ΔR_s did not decrease as $f^{-1/2}$, the model best fitted to our case seems to be that of a counter-lead-type evaporated capacitor where the circuit is distributed on account of its very thin electrode (15).

Since in the OSS-A the semiconductor was deposited in a very dense and thin layer, the distribution model is quite reasonable.

The OSS-B exhibited a complicated frequency dependence of ΔC_s, which was difficult to explain with a simple model. As the OSS-B was composed of less adhesive polymers, polyvinylpyrrolidone, for example, the extra impedance may be ascribed to the resistance of the organic semiconductor film. We will try to describe the data with a combination of several simple equivalent circuits, after which the physical meaning of each equivalent circuit will be given. Figure 7 shows the extra capacitance and resistance of the OSS-B with respect to those of the OSS-A. They were analytically fitted to an equivalent circuit consisting of three serially connected, parallel CR networks as shown in the insertion. The best fitted results were: $R_1 = 0.534\Omega$, $C_1 = 1.65\ \mu f$; $R_2 = 0.570\Omega$, $C_2 = 0.170\ \mu f$; $R_3 = 0.630\Omega$, $C_3 = 0.0158\ \mu f$; and the cutoff frequency of each CR network was 180 kHz, 1.64 MHz, and 16.0 MHz, respectively.

The a-c conductivity of pressed powders of organic semiconductors has been studied by Huggins and Sharbaugh (16). They have represented the a-c properties with two CR networks; one for the organic semiconductor particles and the other for series contacts between particles. This idea led us to measure the frequency dependence of the ESR or capacitance of the organic semiconductor in various forms and to compare the results with those of Fig. 7. Figure 8 shows the ESR as a function of frequency for quinolinium $(TCNQ)_2$ in strongly and lightly pressed pellets with and without polymer, polyvinylpyrrolidone, and also in a solution-deposited film with the polymer. It was demonstrated by the experiments with pressed

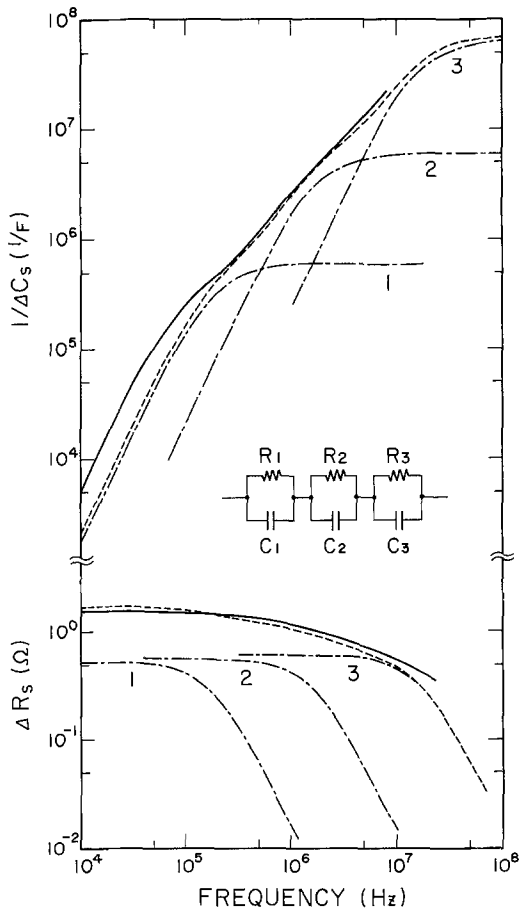


Fig. 7. $1/\Delta C_S$ and ΔR_S for the OSS-B with respect to those of the OSS-A as a function of frequency; solid lines represent experimental data and dotted lines fitted data with illustrated network.

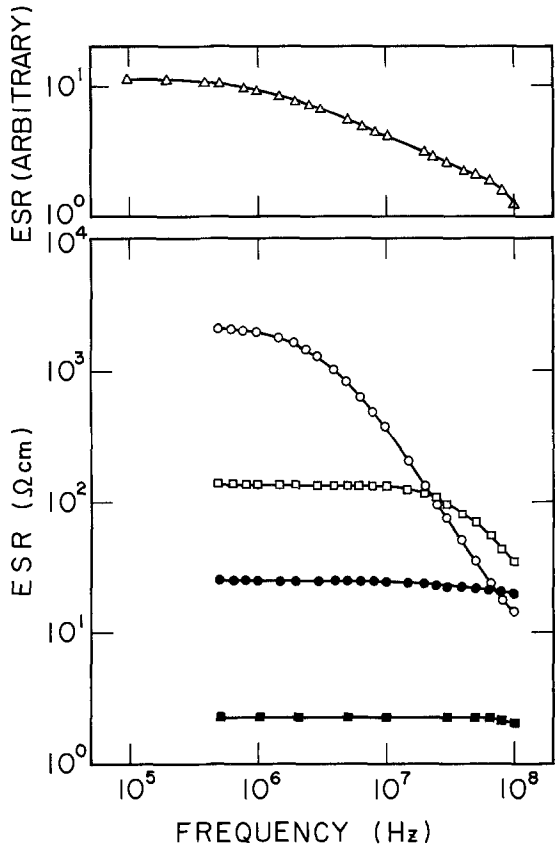


Fig. 8. ESR as a function of frequency for quinolinium $(TCNQ)_2$ at room temperature; points marked ■ refer to the strongly pressed pellet at about 620 kg/cm^2, and □ to lightly pressed pellet at about 11 kg/cm^2. Points marked ● and ○ refer to pellets containing polyvinylpyrrolidone by 10 weight percent pressed at 620 and 11 kg/cm^2, respectively. The top curve marked △ represents solution-deposited film with the polymer.

pellets that two characteristic cutoff frequencies appeared from 500 kHz to 100 MHz frequencies. The lower one (around 2 MHz) was thought to arise from organic semiconductor-polymer effect and the higher (around 50 MHz) from particle-particle effect of the organic semiconductor. The results for the dispersed film are likely to represent the coupled properties of the above two effects. Coming back to Fig. 7 with the results of Fig. 8, we note that two CR networks of the three were simulated by the model experiments. Consequently $(CR)_2$ and $(CR)_3$ are ascribed to the semiconductor-polymer and the semiconductor-semiconductor interfaces, respectively. Since the cutoff phenomena due to the semiconductor particle or more tightly bound interfaces, such as semiconductor-graphite or semiconductor-silver counterelectrodes, do not appear in Fig. 8, the lowest network may be an analog of the electrolyte-oxide interface.

Low frequency properties.—The low frequency deviation in ESR was larger for higher temperatures as shown in Fig. 2 and 3. The capacitance also displayed a slight increase with decreasing frequency at 65° and 85°C (Fig. 2). The increase in C_s and/or R_s at low frequencies has been explained by several mechanisms, but most of them may be ruled out because of their temperature dependence and their relative significance. For example, the blocking of the ionic conduction at the oxide-electrode interface (17) or the dispersion of adsorbed water at the interface has a reverse temperature dependence of R_s and C_s. The d-c leakage current, which has similar temperature dependence as R_s, does not contribute much to the ESR, because the insulation resistance is as high as $10^{13}\Omega$ at room temperature and $4 \times 10^{11}\Omega$ at 85°C. At the present time, we have no definite explanation

of the results, but we suggest that the low temperature impedance is dominated by the interfacial polarization of the polymer which is in contact with the anodic oxide. The trend in the temperature and frequency dependence of C_s and tan δ is indicative of a well-known Debye law or Cole-Cole relation as has been observed for most polymers. Although in case of OSS-A or OSS-B no peak appeared in the tan δ-T or tan δ-f curve, we frequently obtained such peaks for capacitors with much less adhesive polymers, polyacrylonitrile and polyurethane (2). The behavior of the ΔC_s and ΔR_s may be a result of mixed effects of polymers, semiconductor, and the oxide, because the frequency dependences did not entirely coincide with the intrinsic dielectric properties of the polymers.

Conclusions

Both equivalent series capacitance and resistance of the newly developed OSS capacitor were measured over a wide range of frequency and the results were compared with those of the MnO_2-based capacitors. The OSS capacitors exhibited improved a-c properties at high frequencies and low temperatures. The extra capacitance and resistance that were thought to be introduced by the organic semiconductor electrolyte were analytically separated and their origins were considered. The plateau of ESR at intermediate frequencies was ascribed various effects of the electrolyte, such as the distributed resistance and the dispersions due to particle-particle or particle-polymer interfaces.

The improved characteristics of the OSS capacitor may extend the applicability of the solid electrolytic capacitor from the ordinary low frequency use. In view of the extended breakdown voltage in both the forward and reverse directions (2) and higher capacitance density (770 pf/mm^3) of the OSS capacitor, we suggest that the OSS can compete with film capacitors, such as a polycarbonate film capacitor (about 60 pf/mm^3) and a metallized polyester film capacitor (about 150 pf/mm^3). The prominent high frequency stability of the OSS capacitor will be more effective in a leadless device. A thin film capacitor with a screened organic semiconductor counterelectrode is currently being developed, and detailed a-c properties of the capacitor will be reported elsewhere.

Acknowledgments

It is a pleasure to acknowledge Dr. Katsue Hasegawa for his valuable discussions and continual encouragement. We also wish to thank Shohzoh Takahashi and Midori Shinoda for the skill and patience with which they fabricated the OSS capacitors. Most helpful discussions have been made with Mutsuaki Murakami, Masahito Yasuda, and Reiji Sano, to whom we offer our sincere appreciation. We acknowledge various comments made by one of the reviewers, especially on interpretation of the low frequency characteristics.

Manuscript submitted Sept. 13, 1976; revised manuscript received March 10, 1977.

Any discussion of this paper will appear in a Discussion Section to be published in the June 1978 JOURNAL. All discussions for the June 1978 Discussion Section should be submitted by Feb. 1, 1978.

Publication costs of this article were assisted by Matsushita Research Institute Tokyo, Incorporated.

REFERENCES

1. D. A. McLean and F. S. Power, *Proc. IRE*, **44**, 872 (1956).
2. S. Yoshimura, Y. Itoh, M. Yasuda, M. Murakami, S. Takahashi, and K. Hasegawa, *IEEE Trans. Parts, Hybrids, Packaging*, **php-11**, 315 (1975).
3. L. R. Melby, R. J. Harder, W. Mahler, R. E. Benson, and W. E. Mochel, *J. Am. Chem. Soc.*, **84**, 3374 (1962).
4. I. F. M. Walker, *Radio Electron. Components*, **1963**, 25.
5. L. Young, *Trans. Faraday Soc.*, **51**, 1250 (1955).
6. P. Winkel and D. G. de Groot, *Philips Res. Rep.*, **13**, 489 (1958).
7. D. A. McLean, *This Journal*, **108**, 48 (1961).
8. B. Goudswaard, *Electrochem. Technol.*, **6**, 178 (1968).
9. F. E. Rosztoczy and M. H. Read, *This Journal*, **116**, 1752 (1969).
10. P. H. Klose, *ibid.*, **117**, 854 (1970).
11. S. Boone, H. Voeten, and H. Hendricks, *IEEE Trans. Component Parts*, **cp-10**, 3, (1963).
12. V. Walatka, Jr. and J. H. Perlstein, *Mol. Cryst. Liquid Cryst.*, **15**, 269 (1971).
13. G. I. Parisi, *IEEE Trans. Parts, Hybrids, Packaging*, **php-8**, 33 (1972).
14. K. Nishikata, *J. IEE Jpn.*, **89**, 1333 (1969).
15. P. S. Castro, *Electrical Eng.*, **80**, 536 (1961).
16. C. M. Huggins and A. H. Sharbaugh, *J. Chem. Phys.*, **38**, 393 (1963).
17. A. B. Lidiard, in "Handbuch der Physik," XX, S. Flugge, Editor, p. 311, Springer-Verlag, Berlin (1957).

Technical Notes

Phosphorus Concentration of Chemical Vapor Deposited Phosphosilicate Glass

Kuen Chow[1] and L. G. Garrison*

Burroughs Corporation, San Diego, California 92127

Chemical vapor deposited phosphosilicate glass serves the important functions of passivating the ionic contamination and stabilizing the silicon surface of bipolar and MOS devices. The effectiveness of this passivation function is directly related to the phosphorus concentration in the glass. Therefore a technique which can offer fast and accurate routine monitoring of the concentration of phosphosilicate glass

* Electrochemical Society Active Member.
[1] Present address: Hughes Research Laboratories, Malibu, California 90265.
Key words: silicon, sheet resistivity, neutron activation analysis, etch rate.

will be very desirable for the integrated circuit processing technology.

Many different techniques have been utilized to evaluate the phosphorus concentration in silicate glass. These include neutron activation (1-3), gravimetric (4), infrared spectrometry (5), electron microprobe (5), and etch rate (4-8) techniques. While neutron activation and electron microprobe give accurate absolute measurement of the phosphorus concentration, they are tedious and expensive. On the other hand, infrared and etch rate techniques are fast and inexpensive, but their accuracy is generally not very satisfactory. In this technical note we report the results of an investigation of the CVD phosphosilicate glass concentration using both etch rate technique and neutron activation analysis. The sheet resistivity of the silicon substrate resulting from these glasses being densified at 1100°C for 2 hr in N_2 ambient was correlated with the phosphorus concentration in the oxide obtained from etch rate technique. The etch rate determined dopant concentrations were also compared with those obtained from neutron activation analysis. From these a reliable relationship between the substrate sheet resistivity, the oxide etch rate, and the phosphorus concentration was established which can be used for fast and accurate routine phosphorus concentration evaluation.

CVD phosphosilicate glass was obtained both from the Applied Materials 2640 reactor and Unicorp Pyrox reactor. The deposition temperature was 450°C in the AMT reactor and 400°C in the Unicorp reactor and the oxygen to silane ratio was 11 and 16, respectively. Most of the runs were deposited at 4200Å (±10%) while several runs of 10,000Å were also made. The thickness of the glass before and after etching was measured with a Beckman Model DB spectrophotometer and also with a Gaertner Model 117 ellipsometer. The wafers were positioned carefully so that the area measured was the same in each and subsequent measurement.

The etch rates of as-deposited and densified phosphosilicate glasses as functions of dopant concentration have been reported by Tenney and Ghezzo (8) using infrared spectrometry. The glasses were deposited on chemically polished 10 Ω-cm, p-type 1 in. silicon wafer, by the reaction of argon-diluted mixture of O_2, SiH_4, and PH_3 at 300°-500°C. The oxide was generally 7000Å thick.

Densification at 1100°C for 2 hr was performed in an open tube furnace flushed with pure argon. The etching solutions were prepared by adding deionized water in the desired proportion to buffered HF solution (10 parts 40% NH_4F to 1 part 48% HF by volume) and all etching experiments were carried out at room temperature.

It is well known that the etch rate of as-deposited undensified CVD silicate glass is very sensitively dependent on the deposition parameters (such as flow rate, deposition temperature, growth rate, gas flow pattern, etc.) and the thermal history of the oxide. Consequently etch rates of as-deposited oxide prepared in different conditions are usually not comparable. On the other hand, it is also recognized that after densification at very high temperature, the physical properties of the oxide approach those of the thermal oxide and become uniformly comparable. We can therefore compare the physical properties of the high temperature densified glasses even though they were deposited in different environments. Based on this fact, we have subjected the deposited glasses to a similar 2 hr 1100°C densification, albeit in dry nitrogen ambient instead of argon. The etch rates of the densified glass in 25 and 50% 10:1 BHF were then measured and compared with those measured by Tenney and Ghezzo (8). From this comparison the mole percent (m/o) concentration of P_2O_5 in the densified glass was derived. The etch rate and P_2O_5 concentration results are listed in Table I. In the process of etch rate measurement it was observed that the etch rate generally increases from the surface layer down toward the oxide-silicon interface. The variation ranges from 0 to 40% with an average of 20%. This has been attributed partly to the poor wetting of fresh oxide in diluted HF (7) and partly to the evaporation loss of phosphorus from the surface layer during densification (9). As a result, the etch rate and hence the P_2O_5 concentration inferred at the midthickness of the oxide were taken to be the true average value, respectively.

Table I. Etch rate, P_2O_5 concentration of CVD phosphosilicate glasses and substrate sheet resistivity and free carrier concentration*

Wafer lot number	Mid-thickness etch rate (Å/min)	P_2O_5 concentration from etch rate (m/o)	P_2O_5 concentration from neutron activation calibrated curve (m/o)	Sheet resistivity (Ω/□)	Free carrier concentration (10^{20} cm^{-3})
1	975	3.60		10.7	
1	810	2.95		13.8	
2	400	0.90		55.1	
3	890	3.30	4.20	9.2	2.00
3	735	2.60	3.30	14.4	1.28
	720	2.55	3.15	15.8	1.15
6	1410	5.00		4.1	
7	990	3.65		13.8	
7	1070	3.90		10.8	
8	770	2.80		19.5	
8	690	2.40		24.1	
9	500	1.40		45.4	
9	445	1.10		53.1	
10	435	1.05		55.3	
10	380	0.75		72.1	
45			0.55	92.8	0.21
46			1.00	62.8	0.33
47			1.85	33.5	0.60
48			2.70	19.7	0.95
48			2.80	18.4	0.99
49			3.00	17.0	1.10
50			0.30	138.0	0.13
51	840	3.10	3.50	12.0	1.45
52	900	3.30	4.20	9.3	2.00
53	1040	3.80	4.35	8.7	2.10
54	1180	4.30	5.35	6.2	2.80
54	1170	4.25	5.45	6.0	3.00
55	1390	4.95	6.70	4.5	4.10
55	1300	4.70	6.80	4.4	4.50
57	465	1.20		30.1	
59	355	0.55	0.50	105.6	0.21
60	530	1.60	1.85	33.5	0.62
61	700	2.45	2.80	19.0	1.10
62	1100	4.00	4.80	7.4	2.60
88	470	1.25		45.0	
89	770	2.80		18.9	
90	1120	4.10		10.6	
91	1700	5.90		4.9	
93	1540	5.45		5.3	

* The etch rates were measured in 25% 10:1 BHF. Runs No. 1-10 were deposited in AMT-2640 reactor, runs No. 45-93 were deposited in Unicorp Pyrox reactors.

After the etch rates were measured, the residual oxide was stripped clean in 1:1 HF. The sheet resistivity at the point on the wafer where the etch rate and phosphorus concentration were evaluated was then measured with a four-point probe. These sheet resistivity values are listed in Table I and plotted in Fig. 1 as a function of the mole percent of P_2O_5 in the oxide. Large variation was observed in the correlation between the substrate sheet resistivity and the oxide phosphorus concentration arrived from etch rate technique. This indicates the inaccuracy involved when etch rate alone is used to determine the phosphorus concentration.

Since the phosphorus concentration was derived from Tenney and Ghezzo's etch rate data which was only indirectly calibrated with infrared spectrometry, we have also tried to calibrate our result by means of neutron activation analysis. Four 2-in. wafers with as-deposited phosphosilicate glass of varying concentrations were sent to General Activation Analysis, Inc. for neutron activation and radioactive tracing analysis (10). The samples plus comparator standards were irradiated for 30 min in a TRIGA Mark I nuclear

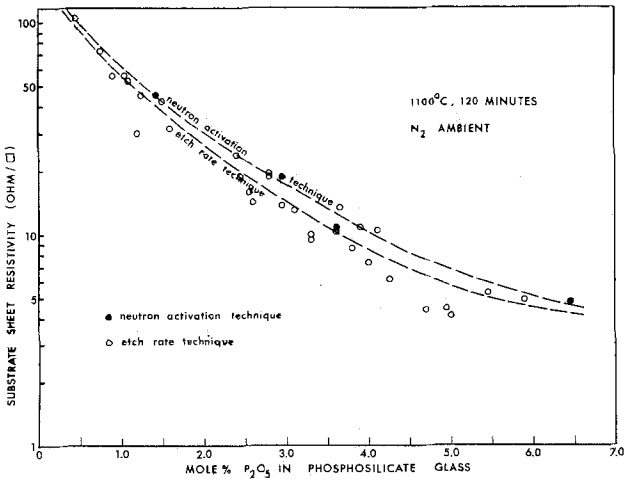


Fig. 1. Substrate sheet resistivity resulting from the 1100°C, 2 hr densification-diffusion in N_2 as a function of m/o P_2O_5 in the glass.

reactor at a flux of 1.8×10^{12} n/cm²-sec. Following the irradiation the surface of the wafer was etched in 1:1 HF. The solution was transferred to a Teflon beaker with 30 mg of phosphorus added. Phosphorus was then precipitated as molybdate. After purification steps the final precipitate was filtered, dried, and weighed to determine recovery. The precipitate was β-counted several times during the next 30 days to determine the amount of radioactive P-32. The weight of phosphorus measured from this radioactive tracing process was then compared with the total mass of the glass which was determined with an assumed density of 2.20 g/cm³ before densification. In the meantime, two other wafers of each composition which were deposited right beside the wafer activation analyzed were densified and used to determine the oxide etch rate and substrate sheet resistivity. The phosphorus concentrations of the undensified, activation-analyzed samples were then correlated with the substrate sheet resistivity obtained on the other two wafers. These four activation-analyzed points are shown as filled circles in Fig. 1. As can be seen, the activation-analyzed data generally indicate a richer P_2O_5 concentration than those arrived at from etch rate technique. Since the activation-analyzed samples have not been subjected to the high temperature densification, this discrepancy probably represents the loss of phosphorus due to evaporation into the ambient flow and diffusion into the silicon substrate. This explanation is also supported by the observation that the etch rate of densified glass usually increases from the oxide surface down toward the oxide-silicon interface.

As a further verification of the correlation between the substrate sheet resistivity and the oxide phosphorus concentration, we have also measured the junction depth of diffusion with the grooving and staining technique. The average conductivity arrived at from the sheet resistivity and junction depth measurements was then used to find the free carrier concentration at the silicon surface from Irwin's curve (11). The resulting free carrier concentrations are plotted in Fig. 2 as a function of the phosphorus concentration in the oxide which were derived from the neutron activation calibrated curve in Fig. 1. These data are compared with the theoretical model proposed by Ghoshtagore (2) which gives the surface concentration of free carrier $C_s(t)$ as

$$C_s(t) = C_{ox}\sqrt{\frac{D_1}{D_2}}\exp\left(\frac{K_{os}^2 t}{D_2}\right)\operatorname{erfc}\left(K_{os}\sqrt{\frac{t}{D_2}}\right)$$

where C_{ox} is the dopant concentration in doped oxide (cm^{-3}), t is the diffusion-densification duration (sec),

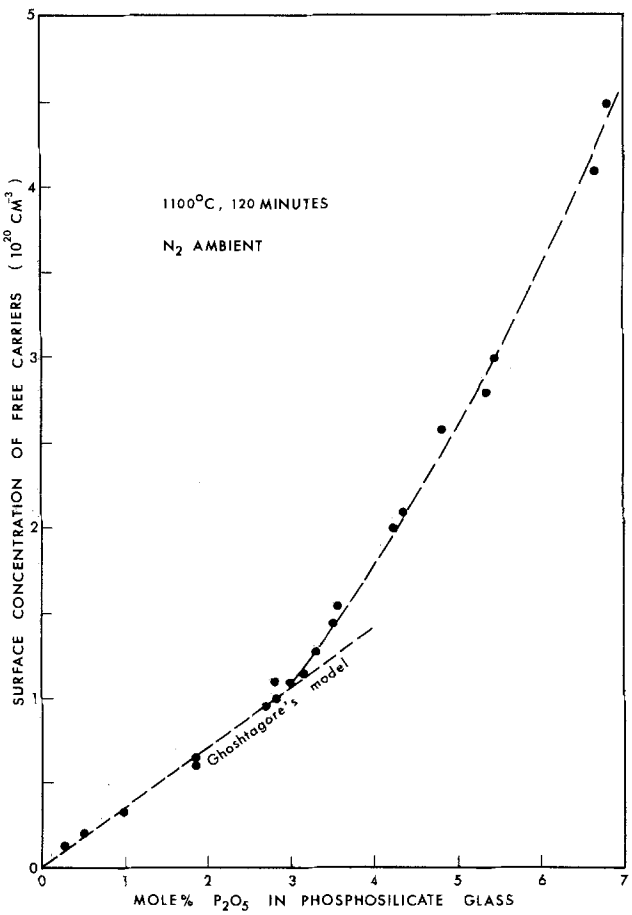


Fig. 2. Silicon surface free carrier concentration from the 1100°C, 2 hr densification-diffusion in N_2 as a function of m/o P_2O_5 in the glass.

D_1 is the diffusivity in doped oxide at concentration C_{ox} (cm²/sec), D_2 is the diffusivity in silicon (cm²/sec), and K_{os} is the surface barrier constant of phosphorus for oxide-silicon interface (cm/sec). As can be seen, with $D_1 = 4.52 \times 10^{-16}$ cm²/sec, $D_2 = 1.47 \times 10^{-13}$ cm²/sec, and $K_{os} = 1.7 \times 10^{-9}$ cm/sec at 1100°C as proposed by Ghoshtagore, the agreement between theory and experiment is very good at P_2O_5 concentrations below 3 m/o. This agreement thus seems to lend further support for the neutron activation calibrated curve presented in Fig. 1. It is however necessary to be cautioned that since Ghoshtagore's model is valid only for surface concentration levels of 1×10^{19} cm^{-3} or less, the fit at higher concentrations should be considered fortuitous.

In conclusion, we have reported in this technical note the evaluation of phosphorus concentration in CVD phosphosilicate glass by means of etch rate, diffusion, and neutron activation analysis techniques. It was shown that etch rate technique alone does not result in very accurate measurement of phosphorus concentration. When compared with data from neutron activation analysis, they are usually 0.2 to 1.5 m/o less than the absolute value. The neutron activation analysis calibration has helped to establish a more reliable correlation between substrate sheet resistivity and the phosphorus concentration in the glass. With this correlation known, it is thus possible to obtain fast and accurate routine determination of the phosphosilicate glass concentration with a 2 hr, 1100°C densification and the subsequent measurement of the substrate sheet resistivity.

Acknowledgments

The authors are indebted to L. E. Kovar for his work on the neutron activation analysis. Helpful

discussions with V. A. Bluhm, C. S. Chen, and Dr. R. N. Ghoshtagore are gratefully acknowledged.

Manuscript submitted July 7, 1975; revised manuscript received Oct. 3, 1976.

Any discussion of this paper will appear in a Discussion Section to be published in the June 1978 JOURNAL. All discussions for the June 1978 Discussion Section should be submitted by Feb. 1, 1978.

Publication costs of this article were assisted by the Burroughs Corporation.

REFERENCES

1. E. Tannenbaum, *Solid State Electron.*, **2**, 123 (1961).
2. R. N. Ghostagore, *ibid.*, **17**, 1065 (1974).
3. E. Kool, *This Journal*, **111**, 1383 (1964).
4. E. H. Snow and B. E. Deal, *ibid.*, **113**, 263 (1966).
5. A. S. Tenney and M. Ghezzo, *ibid.*, **120**, 1276 (1973).
6. W. A. Plishkin and R. P. Gnall, *ibid.*, **111**, 872 (1964).
7. J. M. Eldridge and P. Balk, *Trans. Met. Soc. AIME*, **242**, 539 (1968).
8. A. S. Tenney and M. Ghezzo, *This Journal*, **120**, 1091 (1973).
9. P. Balk and J. M. Eldridge, *Proc. IEEE*, **57**, 1558 (1969).
10. L. E. Kovar, Private communication.
11. J. C. Irwin, *Bell Syst. Tech. J.*, **41**, 387 (1962).

Cathodoluminescent Efficiency

R. C. Alig and S. Bloom

RCA Laboratories, Princeton, New Jersey 08540

Several years ago Kingsley and Ludwig examined the correlation of cathodoluminescent phosphor efficiencies with other material properties (1). In the course of this work they observed that a high plasma resonance energy in a phosphor host is correlated with a low cathodoluminescent efficiency, *i.e.*, all the efficient phosphor hosts have relatively low plasma energies. This observation is illustrated[1] in Fig. 1 where the maximum cathodoluminescent power efficiency η_m ever measured for a phosphor host is plotted *vs.* its calculated plasma resonance energy E_p. In 1970 Kingsley and Ludwig remarked that the upper right-hand region of this graph defined by the dashed lines is devoid of phosphors; only one exception (HfP_2O_7) to this remark is known today even though the number of phosphor hosts with efficiencies above 6% included in the figure has been more than doubled.

It is also quite generally accepted (2) that the efficiency of a phosphor can be expressed as

$$\eta = S E_{ph}/\epsilon \qquad [1]$$

where ϵ is the average energy needed to create an electron-hole pair in the phosphor, E_{ph} is the energy of the emitted photon, and S is the probability that electron-hole pairs are converted to photons. Since E_{ph} is largely fixed by the activator ion, it cannot be related to E_p to explain the correlation illustrated in Fig. 1. Hence this correlation must come either from a relation between ϵ and E_p or between S and E_p^{-1}.

In the early 1960's Lappe empirically found (3) a relation between the electron-hole pair creation energy ϵ and the fundamental electronic bandgap E_g of a semiconductor, *i.e.*

$$\epsilon \approx 2.8\, E_g \qquad [2]$$

This result has been verified repeatedly since then, both theoretically and experimentally, for a broad range of semiconductors (4). Hence, if ϵ and E_p are related, then E_g and E_p must be related, a result we know and expect to be generally untrue of semiconductors.

From Eq. [1] and [2] we expect the efficiency η to be related to E_g^{-1}. Therefore, in Fig. 2 we plotted η *vs.* E_g^{-1} for several phosphors. For phosphors activated by the same impurity ion there does indeed seem to be a relation between η and E_g^{-1}, *i.e.*, for Cu-, Pb-, and Eu^{3+}-activated phosphors, lines from the origin fit the data well. Using measured values[2] of the emitted photon energies E_{ph}, values of the energy transfer probabilities S were calculated from the slopes of these lines; these are listed in Fig. 2. Since S is the same for several phosphor hosts, it is hard to see how it could be related to E_p.

Thus the correlation illustrated in Fig. 1 appears to be inconsistent with Eq. [1] and [2]. The plasma energies used in the construction of Fig. 1 were calculated from the crystal structure of the phosphors, so if the correlation shown there is indeed real, it ought to improve when these calculated values of E_p are replaced by measured values of E_p. Using electron energy loss data measured by Hengehold and Pedrotti (7) for several II-VI compounds, by Yamamoto and Tonomura (8) for several of the more efficient phosphors, and by Best (9) for some alkali halides, Fig. 3 was drawn. In contrast with Fig. 1 there is no hint in Fig. 3 of a relation between maximum phosphor efficiency and plasma resonance energy.

The plasma energies used in drawing Fig. 1 were calculated from the formula $E_p = \hbar(4\pi n_v e^2/m)^{1/2}$ where e and m are the electron charge and mass and n_v is the valence electron density. More specifically, the valence electron density is defined, somewhat

Table I. The cathodoluminescent power efficiency η, the valence electron density n_v, and the fundamental bandgap E_g (at 300°K) of selected phosphors

Phosphor	η (%)	Ref.	n_v (A^{-3})	Ref.	E_g (eV)	Ref.
ZnS : Cu	23	(12)	0.202	(23)	3.9	(11)
SrS : Cu	18	(13)	0.147	(23)	4.4	(5)
CaS : Cu	18	(6)	0.174	(23)	4.8	(5)
CaS : Pb	17	(6)	—	—	—	—
CaS : Ce	22	(6)	—	—	—	—
CaO : Pb	10	(6)	0.288	(23)	7.7	(11)
Y_2O_2S : Eu	10	(14)	0.296	(23)	4.6	(27)
Y_2O_2S : Tb	18	(15)	—	—	—	—
La_2O_2S : Eu	11	(16)	0.243	(23)	4.4	(27)
La_2O_2S : Tb	12	(16)	—	—	—	—
Gd_2O_2S : Eu	10	(16)	0.280	(23)	4.5	(28)
Gd_2O_2S : Tb	15	(15)	—	—	—	—
Gd_2O_3 : Eu	12	(16)	0.304	(23)	5.3	(29)
Y_2O_3 : Eu	8	(14)	0.322	(23)	5.6	(29)
YVO_4 : Eu	6	(14)	0.401	(23)	8.0	(30)
NaI : Tl	13	(17)	0.118	(23)	5.9	(11)
CsI : Tl	11	(15)	0.084	(23)	6.4	(11)
LaOBr : Tb	20	(18)	0.254	(23)	—	—
ZnSe : Cu	14	(21)	0.176	(23)	2.7	(11)
BaFCl : Eu	13	(15)	0.231	(24)	—	—
ZnO : Zn	7	(6)	0.336	(23)	3.4	(11)
$CaGa_2S_4$: Eu	8	(19)	0.209	(19)	—	—
$ZnSiO_4$: Mn	8	(14)	0.367	(23)	—	—
$NaGdO_2$: Eu	9	(16)	0.280	(25)	—	—
$Zn_3(PO_4)_2$: Mn	6	(6)	0.397	(23)	—	—
ZnF_2 : Mn	8	(20)	0.463	(23)	—	—
$CaWO_4$: Pb	3.4	(16)	0.410	(23)	—	—
$Y_2Si_2O_7$: Ce	8	(22)	0.392	(26)	—	—
HfP_2O_7 :	10	(31)	0.405	(31)	—	—

Key words: phosphors, plasma energy, correlations.

[1] Much of the data needed for the figures is summarized in Table I of this paper.

[2] The emission energy data for Cu-activated phosphors come from Ref. (5) and (6), for Pb activation from Ref. (6) and for Eu^{3+} activation from Ref. (1).

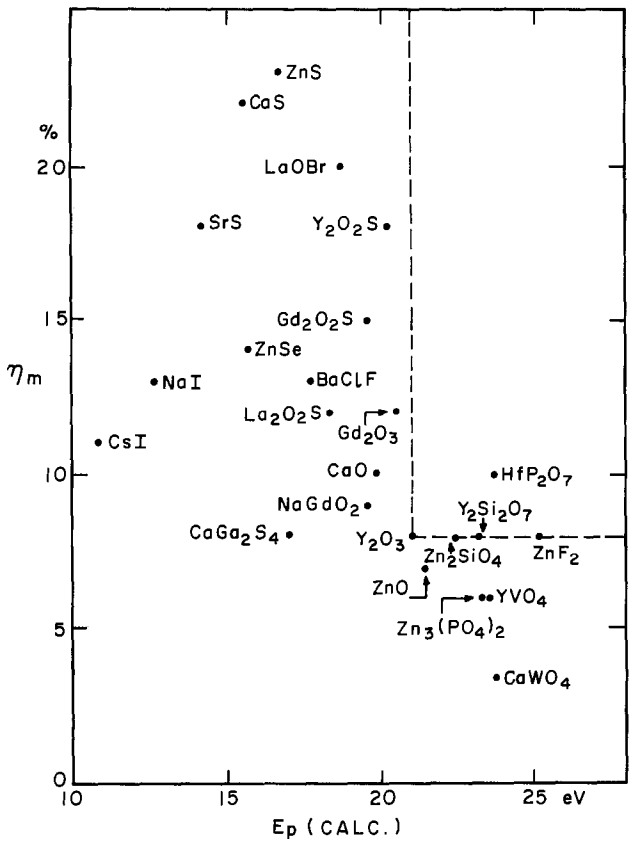


Fig. 1. The maximum cathodoluminescent energy efficiency η_m is plotted *vs.* the calculated plasma resonance energy E_p for selected phosphor hosts. The dashed lines define the region devoid of phosphors.

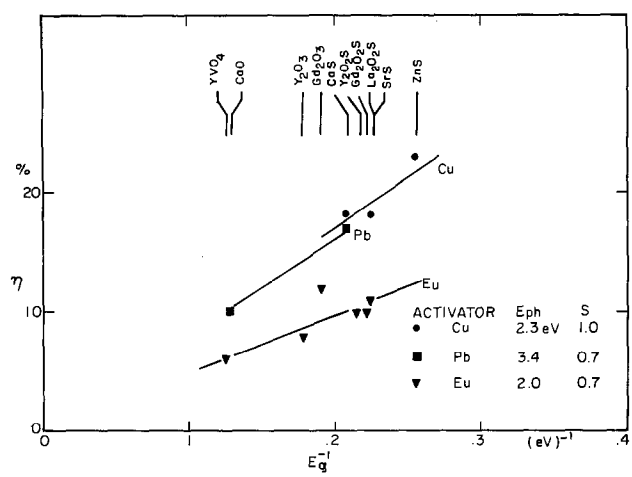


Fig. 2. The measured cathodoluminescent energy efficiencies η of several phosphors, *vs.* the reciprocal of the fundamental band-gap E_g of the phosphor host. The phosphor hosts are indicated at the top of the figure and the activators are indicated by the symbols shown at the right of the figure. Straight lines of slope parameter S, calculated using photon energy E_{ph} and Eq. [1] and [2] have been fitted to selected points associated with the same activator.

arbitrarily, as 8 times the density of halide and chalcogenide atoms in the phosphor host. To establish the existence of a relationship between η_m and n_v, as suggested by the data in Fig. 1, the efficiency η_m is plotted *vs.* n_v^{-1} in Fig. 4. From this figure the relationship does appear to exist; statistically (10) the probability of no correlation lies below 1% for the materials shown in Fig. 4.

If the relation shown in Fig. 4 does indeed exist, then from Eq. [1] and [2] we must expect to find a relation

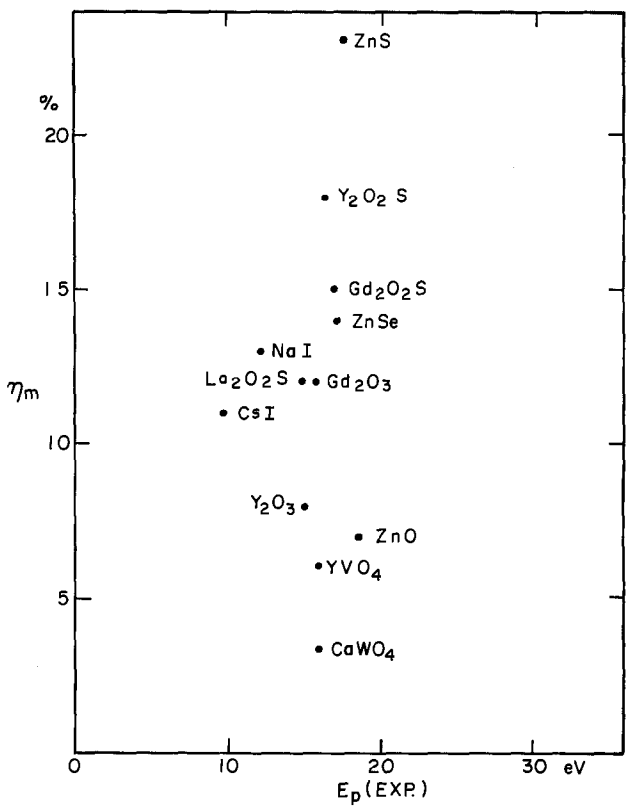


Fig. 3. The maximum efficiency η_m is plotted *vs.* the experimental plasma energy E_p for selected phosphor hosts.

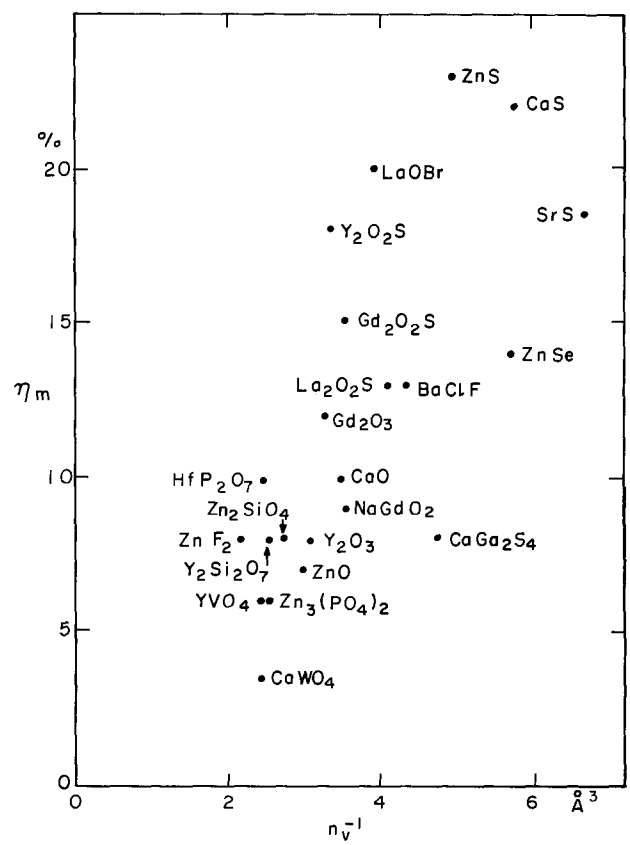


Fig. 4. The maximum efficiency η_m is plotted *vs.* the reciprocal of the valence electron density n_v for selected phosphor hosts.

between E_g and n_v for those materials which host efficient phosphors. This data is plotted in Fig. 5. Indeed there does appear to be a relation, and again the statistical probability of no correlation lies below 1% for the nonhalide materials shown. However, this relation-

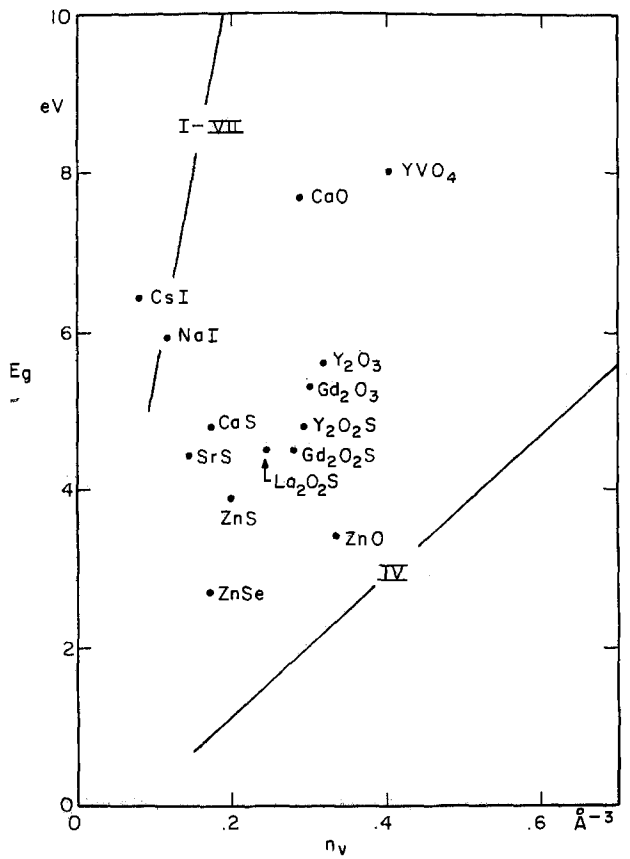


Fig. 5. The fundamental bandgap E_g is plotted vs. the valence electron density n_v for several semiconductors which host efficient phosphors. Similar data is indicated by solid lines for alkali halide and Group IV materials. The valence electron density of the Group IV materials was defined as 4 times the atomic density.

ship is restricted to the efficient phosphors. Similar data for a selection of materials for which bandgap data (11) is available is also indicated in Fig. 5; with this additional data the appearance of a correlation fades.

It can be seen from Fig. 5 that a correlation between the valence electron density and the bandgap does exist for those semiconductors having a similar ratio of ionic to covalent banding. That is, the Group IV semiconductors, which are largely bound covalently, fall on one line, while the alkali halides, which are largely bound ionically, fall on another line. Thus, if most of the popular phosphor hosts had about the same ratio of ionic to covalent bonding, the correlation discovered by Ludwig and Kingsley could be understood. Indeed the two phosphor hosts in which this ratio exhibits the greatest departure from the average, NaI and CsI, had to be excluded from Fig. 4 because they lie far to the right of the right-hand margin of this figure; they depart greatly from the correlations illustrated in Fig. 4 and 5. Therefore, we understand the correlation illustrated in Fig. 1 to be a consequence of the similar ratio of ionic to covalent bonding of the popular phosphor hosts.

Acknowledgment

Discussions with P. N. Yocom and W. M. Yim were very helpful in the development of these ideas.

Manuscript submitted Feb. 9, 1977; revised manuscript received March 21, 1977. This was Paper 154 presented at the Washington, D.C., Meeting of the Society, May 2-7, 1976.

Any discussion of this paper will appear in a Discussion Section to be published in the June 1978 JOURNAL. All discussions for the June 1978 Discussion Section should be submitted by Feb. 1, 1978.

Publication costs of this article were assisted by RCA Laboratories.

REFERENCES

1. J. D. Kingsley and G. W. Ludwig, *This Journal*, **117**, 353 (1970).
2. A. Rothwarf, *J. Appl. Phys.*, **44**, 752 (1973).
3. F. Lappe, *J. Phys. Chem. Solids*, **20**, 173 (1961).
4. R. C. Alig and S. Bloom, *Phys. Rev. Lett.*, **35**, 1522 (1975).
5. W. Lehmann, *This Journal*, **117**, 1389 (1970).
6. W. Lehmann, *ibid.*, **118**, 1164 (1971).
7. R. L. Hengehold and F. L. Pedrotti, *Phys. Rev. B.*, 2262 and 3026 (1972); *J. Appl. Phys.*, **47**, 287 (1976).
8. H. Yamamoto and A. Tonomura, *J. Lumin.*, **12**, 947 (1976); J. D. Kingsley and G. W. Ludwig, *J. Appl. Phys.*, **41**, 370 (1970).
9. P. E. Best, *Proc. Phys. Soc.*, **79**, 133 (1962).
10. J. S. Bendat and A. G. Piersol, "Random Data: Analysis and Measurement Procedures," p. 128, Interscience Pubs., Inc., John Wiley & Sons, New York (1971).
11. W. H. Strehlow and E. L. Cook, *J. Phys. Chem. Ref. Data*, **2**, 163 (1973).
12. A. Bril and H. A. Klasens, *Philips Res. Rep.*, **7**, 401 (1952).
13. J. Gerber, Private communication.
14. V. D. Meyer, *This Journal*, **119**, 920 (1972).
15. A. L. N. Stevels and F. Pingault, *Philips Res. Rep.*, **30**, 277 (1975).
16. G. W. Ludwig and J. D. Kingsley, *This Journal*, **117**, 348 (1970).
17. G. F. J. Garlick, in "Luminescence of Inorganic Solids," P. Goldberg, Editor, p. 685, Academic Press, Inc., New York (1966).
18. J. G. Rabatin, Paper 102 presented at The Electrochemical Society Meeting, San Francisco, California, May 12-17, 1974.
19. T. E. Peters and J. A. Baglio, *This Journal*, **119**, 230 (1972).
20. H. W. Leverenz, "An Introduction to Luminescence of Solids," p. 72, Dover Publications, Inc., New York (1968).
21. A. Bril and H. A. Klasens, *Philips Res. Rep.*, **10**, 305 (1955).
22. A. Bril, G. Blasse, A. H. Gomes de Mesquita, and J. A. de Poorter, *Philips Tech. Rev.*, **32**, 125 (1971).
23. R. W. G. Wyckoff, "Crystal Structures," 2nd edition, Vol. 1, 3, and 5, Interscience Pubs. Inc., John Wiley & Sons, Inc., New York (1963).
24. E. Nicklaus and F. Fischer, *J. Cryst. Growth*, **12**, 337 (1972).
25. G. Blasse, *J. Inorg. Nucl. Chem.*, **26**, 901 (1964).
26. A. H. Gomes de Mesquita and A. Bril, *Mater. Res. Bull.*, **4**, 643 (1969).
27. P. N. Yocom and R. E. Shrader, *Proc. Rare Earth Res. Conf., 7th*, Vol. II, p. 601 (1968).
28. J. Gerber, Private communication.
29. S. S. Derbeneva and S. S. Batsanov, *Dokl. Akad. Nauk. SSSR*, **175**, 1062 (1967).
30. J. D. Kingsley, Paper 86 presented at The Electrochemical Society Meeting, San Francisco, California, May 12-17, 1974.
31. I. Shidlovsky, J. Gerber, and C. W. Struck, Paper 95 presented at The Electrochemical Society Meeting, San Francisco, California, May 12-17, 1974.

Poly(vinylethers) as X-Ray Resists

Saburo Imamura, Shungo Sugawara, and Kei Murase

Nippon Telegraph and Telephone Public Corporation,
Ibaraki Electrical Communication Laboratory, Tokai, Ibaraki, 319-11, Japan

X-ray resist materials for production of microelectronic circuits have recently become subjects of renewed interest (1). In the present work, a series of poly(vinylethers) were studied as new resist materials. The effects of the chlorine-containing side chain and unsaturated groups on x-ray irradiation characteristics were investigated.

Several vinylethers listed in Table I were polymerized in absolute toluene at −70° to −60°C under a nitrogen atmosphere, using a small amount of $BF_3 \cdot OEt_2$ as the cationic polymerization initiator (2). All polymers were purified by precipitation into methylalcohol or water and by washing several times. The intrinsic viscosity of each of the polymers obtained was measured at 30°C in benzene with an Ubbelohde viscometer. Weight average molecular weight $\overline{M}w$ was calculated with Manson's viscosity equation for poly(methylvinylether) $[\eta] = 7.6 \times 10^{-4}\ \overline{M}w^{0.60}$ (3). The polymers were spincoated to about 0.5 μm thickness on silicon wafers from methylethylketone-xylene (4:1) mixed solution. After prebaking at 50°C for 30 min, the resist-coated substrates were exposed to soft x-rays ($\lambda = 5.4$Å, Mo L line). The exposure system was used for evaluation of resist sensitivity and replication of mask patterns. The system was of the two chamber type. In the high vacuum chamber (10^{-6} Torr), a rotating water-cooled Mo target was pumped with a 3.2 kW, 16 kV electron beam. X-rays emitted were passed through a 12 μm polyester window into an exposure chamber vacuum pumped down to 10^{-3} Torr. Resist-coated substrates were held on a fixture mounted 12 cm from the target.

The flux of characteristic x-ray incident on the resist-coated substrate was measured with a gas-flow proportional counter, using P-10 gas at 0.16 kW, 4 kV electron beam, which is within measurable limit of the gas-flow counter. Flux ϕ can be calculated from

$$\phi = 1/T_m \times 1/T_{Al} \times 1/\mu_g \times d_c^2/d_r^2 \times 1/S \times C \times E$$

where T_m and T_{Al} is transparency of the gas-flow counter window [5 μm Mylar (0.805) and 1 μm evaporated aluminum (0.653)], μ_g is absorption of P-10 gas (0.675/2 cm path), d_c (15 cm) and d_r are the distances from target to counter and the resist-coated substrate, S is counter window area (3.4×10^{-6} cm^2), C is photon count (1.3×10^4 counts/sec), and E is photon energy for Mo L radiation (3.8×10^{-13} mJ/photon). The flux was 0.063 mJ/cm^2/sec at 0.16 kW electron beam and was 0.21 mJ/cm^2/sec at 3.2 kW, corrected

Key words: x-ray lithography, polymer resist, negative resist.

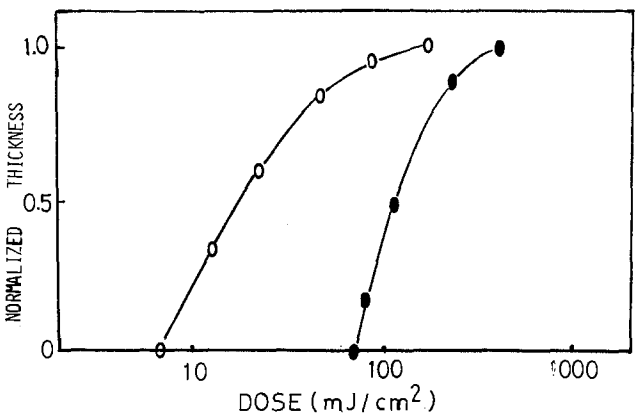


Fig. 1. Sensitivity curves for CEVE-co-VOEA 0, and CEVE-co-IBVE 0. Initial resist thickness was 0.5 μm.

with sensitivity-measured resists at 0.16 kW, such as epoxidized polybutadiene and poly(2-chloroethylvinylether-co-vinyloxyethylacrylate). The exposed films were developed by dipping into isoamylacetate for 30 sec. After heat-treatment at 120°C, the remaining film thickness was measured.

Table I shows the characteristics of the polymers studied. Mass-absorption coefficient μ_m is an additive function of the various atomic species present in the material, with consideration of weight percent (w/o) according to

$$\mu_m = \sum_i P_i \mu_{mi}$$

μ_{mi} = mass absorption coefficient of atom i
P_i = weight percent of atom i

Sensitivity is defined as the irradiation dose required to yield 50% of the initial film thickness. Contrast (γ) is defined as the slope of the extrapolated linear portion of the dose-thickness curve and may be expressed as

$$\gamma = [\log_{10}(D_0/D_g^i)]^{-1}$$

where D_g^i and D_0 are the dose of 0 to 100% film remaining (4).

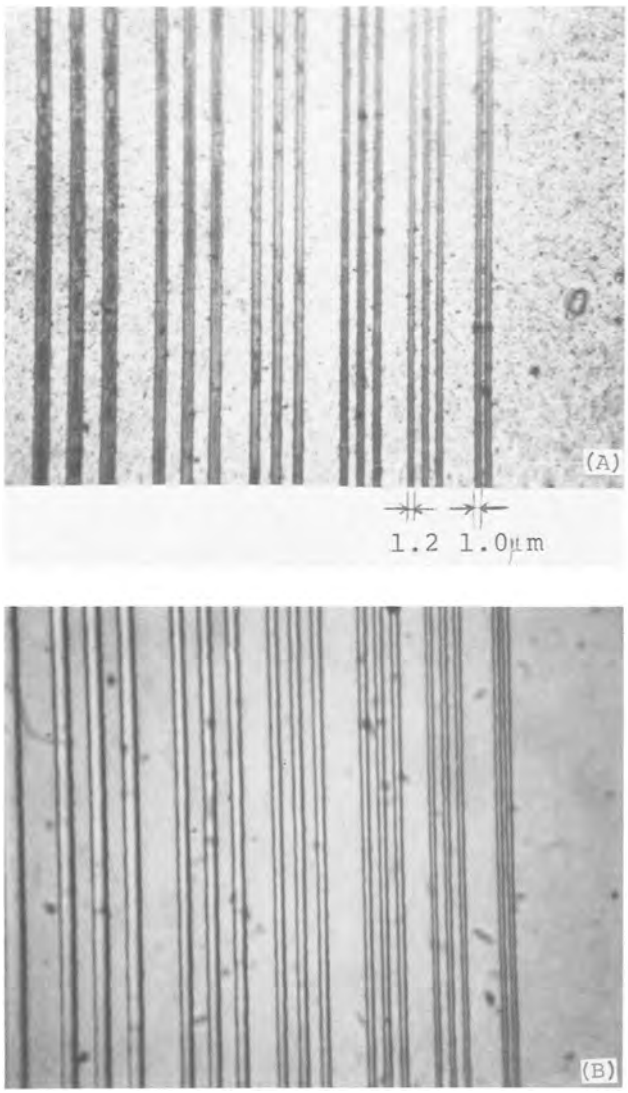
Figure 1 shows sensitivity curves for poly(2-chloroethylvinylether-co-vinyloxyethylacrylate) (CEVE-co-VOEA) and poly(2-chloroethylvinylether-co-isobutylvinylether) (CEVE-co-IBVE).

The results show that (i) The polymers containing chlorine in the side chain have relatively high sensitivities and the polymer containing 1% of vinyloxy-

Table I. Physical characteristics of a series of poly(vinylethers) and other resists

Polymer	$[\eta]$† (dl/g)	$\overline{M}w \times 10^{-3}$	μ_m†† [cm²/g]	Contrast (γ)	Sensitivity [mJ/cm²]	Remarks
Poly(2-chloroethylvinylether)	0.32	24	258	1.5	180	Rubbery
CEVE-co-VOEA*	0.23	13†††		1.1	18	Rubbery
CEVE-co-EVE**	0.37	32	243	1.1	72	Soft, slightly tacky
CEVE-co-IBVE***	0.34	27	233	2.2	120	Rubbery
Poly(ethylvinylether)	0.57	71	228	0.8	674	Soft, nontacky
Poly(isobutylvinylether)	0.43	42	210	1.1	1010	Tough, nontacky
Poly(methylmethacrylate				1.7	2475	Ref. (5)
Epoxidized poly(butadiene)				0.7	5.2	Ref. (5)

* Poly(2-chloroethylvinylether-co-vinyloxyethylacrylate); monomer ratio 100:1.
** Poly(2-chloroethylvinylether-co-ethylvinylether); monomer ratio 1:1.
*** Poly(2-chloroethylvinylether-co-isobutylvinylether); monomer ratio 1:1.
† Intrinsic viscosity, 30°C in benzene.
†† Calculated mass absorption coefficient.
††† $\overline{M}w = 5.2 \times 10^4$, $\overline{M}w/\overline{M}n = 2.8$ by gel permeation chromatography.



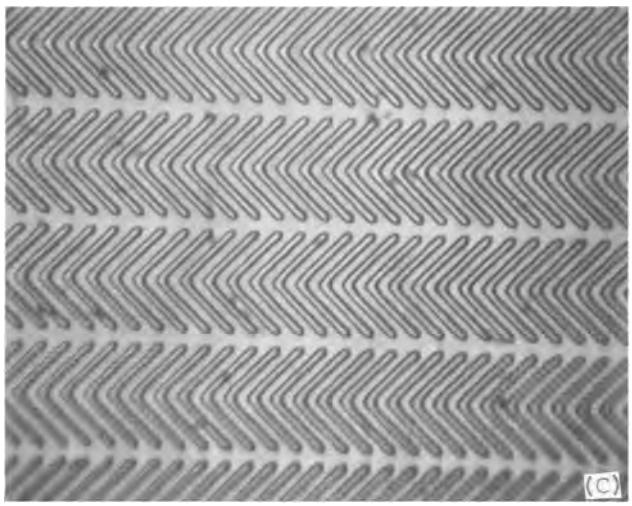


Fig. 2. (A) X-ray exposure mask patterns; (B) replicated CEVE-co-VOEA resist patterns; (C) replicated CEVE-co-VOEA resist chevron patterns.

ethylacrylate has the highest sensitivity; and (*ii*) Polymers containing chlorine also have relatively high contrast; CEVE-co-IBVE is the highest contrast ($\gamma = 2.2$) resist. This value is much higher than contrast values usually observed for negative resists, which can be as low as $\gamma = 0.7$ observed for epoxidized polybutadiene (5). The reason why polymers containing chlorine and an unsaturated group in the side chain have higher sensitivity is considered to be due to its higher reactivity, because differences in the molecular weight and mass absorption coefficient relative to the usual resist materials are small.

Figure 2(A) shows mask patterns and Fig. 2(B) and 2(C) show CEVE-co-VOEA resist patterns on a silicon wafer after pattern replication using soft Mo Lα x-rays emitted with a 1 kW, 10 kV electron beam. Resist-coated substrates were mounted on a fixture below the mask with a 12 μm gap (polyvinylidenefluoride spacer). The mask consists of Si (4 μm thick) with a gold absorber (4000Å thick). It was designed with a minimum line width of approximately 1 μm. The resist was spin coated to an initial thickness of about 0.5 μm. Exposure time was about 7 min. Patterns were developed by dipping into n-butyl acetate and successively rinsed by dipping into isopropanol. The final resist thickness in Fig. 2(A) and 2(C) was 0.25-0.3 μm. It is apparent that this resist has at least 1.0 μm resolution and it could be used successfully to wet etch into SiO_2.

Acknowledgment

The authors are grateful to K. Matsuyama, M. Kakuchi, and K. Sukegawa for their helpful discussions.

Manuscript submitted Jan. 17, 1977; revised manuscript received March 10, 1977.

Any discussion of this paper will appear in a Discussion Section to be published in the June 1978 JOURNAL. All discussions for the June 1978 Discussion Section should be submitted by Feb. 1, 1978.

Publication costs of this article were assisted by Nippon Telegraph and Telephone Public Corporation.

REFERENCES

1. D. L. Spears and H. I. Smith, *Solid State Technol.*, **15**, 21 (1972); P. V. Lenzo and E. G. Spencer, *Appl. Phys. Lett.*, **24**, 289 (1974).
2. L. Fishbein and B. F. Crowe, *Macromol. Chem.*, **48**, 221 (1961).
3. J. A. Manson and G. J. Arquette, *ibid.*, **37**, 187 (1960).
4. L. F. Thompson, *Solid State Technol.*, **27**, (1974).
5. M. Kakuchi, Unpublished.

Brief Communications

Electrical Properties of $LiFe_5O_8$

Tsuneo Matsui[1] and J. Bruce Wagner, Jr.*

Materials Research Center and Department of Materials Science and Engineering, Northwestern University, Evanston, Illinois 60201

The lithium ferrite spinel ($LiFe_5O_8$) has the inverse spinel structure $Fe^{3+}[Li_{0.5}^{+}Fe_{1.5}^{3+}]O_4$. One-eighth of the tetrahedral (A) sites are occupied by Fe^{3+} ions, and Li^+ and Fe^{3+} ions share one-half of the octahedral (B) sites within the fcc sublattice of oxygen ions (1). There has been considerable interest in lithium compounds for use as solid-state electrolytes and as electrode materials in batteries involving lithium as one reactant. Some measurements of the electrical conductivity of $LiFe_5O_8$ have been made by using d-c (2-4) and a-c methods (5), but the results obtained so far have been inconsistent. The a-c conductivity measurements have been made only at room temperature in air by Samokhvalov *et al.* (5). Accordingly, a study of the electrical properties of $LiFe_5O_8$ was undertaken to contribute to an understanding of this class of materials.

In the present paper, the a-c and d-c electrical conductivity measurements of $LiFe_5O_8$ have been carried out as a function of temperature (22°-850°C) and oxygen partial pressure (oxygen, air, and argon). The samples were polycrystalline pellets pressed from powders and having 94-96% of the theoretical density. The powders were prepared by heating a ferric oxalate ($Fe_2(C_2O_4)_3 \cdot 6H_2O$) and lithium carbonate (Li_2CO_3, 99.999%) mixture at 900°C for 0.5 hr in gold foil, then sintering at 1100°C for 0.5 hr, 1000°C for 2 hr, and finally 700°C for 14 hr in air. The argon gas was purified by passing first over heated copper turnings at 400°C and then through a tube of silica gel to remove water vapor. The oxygen partial pressure in the resulting argon gas was determined to be below 10^{-6} atm by measuring the electrical resistance of a nonstoichiometric cobaltous oxide wire (Johnson Matthey Company reactor grade cobalt) at 1000°C (6-10).

X-ray diffraction patterns of the $LiFe_5O_8$ samples (which were heated in oxygen, air, or argon at 850°C for 15 hr, annealed at 700°C for 15 hr and then cooled slowly to room temperature over a period of 24 hr) were obtained at room temperature by using a Phillips diffractometer with CuKα radiation through a Ni filter. The x-ray results are summarized in Table I. The single α-$LiFe_5O_8$ phase was observed in the samples heated in air and argon, but traces of α-Fe_2O_3 in addition to the α-$LiFe_5O_8$ phase were observed in the samples heated in oxygen. The lattice constant of the $LiFe_5O_8$ sample prepared in air in the present study is in good agreement with that ($a_o = 8.337$Å) of single crystal $LiFe_5O_8$ also prepared in air by Schieber (11).

The a-c conductivity measurements were made using a General Radio 1650A a-c bridge in the frequency range 1-20 kHz using an oscillator (Hewlett Packard Model 202D). Gold foils were used as the electrodes and electrical contact was ensured by spring-loaded quartz glass plates and lava blocks. The results of the a-c and d-c conductivity measurements at 1 kHz are shown in Fig. 1 and summarized in Table II. The a-c conductivity values of $LiFe_5O_8$ were found to vary from sample to sample below 740°C, but reproducible and consistent values (± 3% error) were obtained in all samples above 750°C (in the β-phase whose conduction was 100% electronic). However, even below 740°C the majority of the $LiFe_5O_8$ samples exhibited nearly identical values of conductivity (± 10% error). The inconsistency among the conductivity data of $LiFe_5O_8$ samples is considered to be due to the polarization between sample and electrodes (blocking gold elec-

Table I. X-ray data of lithium ferrite spinel at 22°C

Oxygen partial pressure	Lattice constant (A)	Phase
1 atm	8.346 ± 0.003	α-$LiFe_5O_8$ + trace α-Fe_2O_3
Air (0.21 atm)	8.338 ± 0.002	α-$LiFe_5O_8$
Ar (less than 10^{-6} atm)	8.330 ± 0.005	α-$LiFe_5O_8$

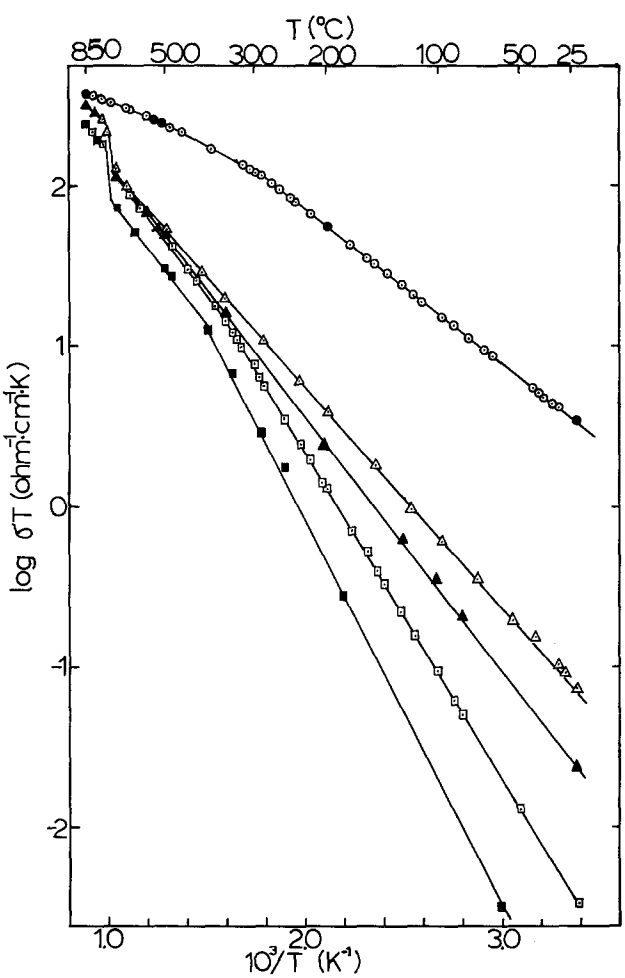


Fig. 1. The temperature dependence of the electrical conductivity of $LiFe_5O_8$ at 1 kHz: ■ d-c method, □ a-c method in O_2; ▲ d-c and △ a-c in air; ● d-c and ○ a-c in argon.

* Electrochemical Society Active Member.
[1] Present address: Center for Solid State Science, Arizona State University, Tempe, Arizona 85231.
Key words: lithium ferrite spinel, conductivity.

Table II. Conductivity data of lithium ferrite spinel

Oxygen partial pressure	Temperature range (±5°C)	Activation energy* (kcal/mole)	Approximate te**
1 atm	22° ≦ T ≦ 350°	9.33 ± 1.85	0.2 ~ 0.6
	350° ≦ T ≦ 740°	7.31 ± 1.40	0.5 ~ 0.6
	750° ≦ T ≦ 850°	6.62 ± 0.13	1
Air (0.21 atm)	22° ≦ T ≦ 620°	6.07 ± 1.21	0.35 ~ 0.95
	620° ≦ T ≦ 740°	5.04 ± 1.10	0.95
	750° ≦ T ≦ 850°	5.52 ± 0.10	1
Argon (less than 10^{-6} atm)	22° ≦ T ≦ 300°	4.42 ± 0.20	1
	300° ≦ T ≦ 550°	2.89 ± 0.09	1
	550° ≦ T ≦ 850°	1.90 ± 0.05	1

* Calculation based on the log $\sigma_{a.c.}$ T *vs.* $1/T$ plot.
** Electronic transport number based on the data of d-c polarization taken after 1 hr of current flow between "blocking electrodes" of gold, see text.

trodes in this study), and also due to the sluggish transition from the disordered β-phase to the ordered α-phase which was observed by Kato (2) and Schieber (11). To reach equilibrium values of a-c conductivity after transition from β- to α-phase, it was necessary to anneal at 700°C for 15 hr. The a-c conductivity was independent of frequency between 1 and 10 kHz, but at some temperatures a conductivity increase (5 ~ 40%) was observed between 8 and 20 kHz. The a-c conductivity value of $LiFe_5O_8$ at room temperature in the present study is in good agreement with previous data (5).

Wagner's polarization method (12, 13) was not used in the present study to determine the partial electronic conductivity because of the reactivity of reversible lithium electrode with the sample, air, and oxygen. Alternatively Vest and Tallan's method (14) was employed. The polarization potential of the cell with two blocking electrodes (both anode and cathode were gold electrodes) produced by the constant current flow from the current source (Keithley Model 225) was measured as a function of time by a Keithley 610B electrometer and/or Doric digital voltmeter. The applied current to the sample was limited to voltages below the decomposition potential of $LiFe_5O_8$. The d-c potentials used were between 0.01 and 0.60V. However, the polarization potential (i.e., electronic conductivity) still changed with time even after 1 hr. In this polarization cell there was no reversible electrode to fix the chemical potential of the sample, and thus the electronic conductivity changed with time due to the deviation of stoichiometry created by the current flow when the polarization proceeded. The electronic transference number calculated based on the data after 1 hr is summarized to estimate approximately the electronic portion of total conductivity. The difference between Wagner's polarization method and Vest and Tallan's method has been discussed in detail by Joshi and Wagner (15). In the β-phase in air and in oxygen, and both in the β- and α-phase in argon, the polarization potential did not change with time, indicating that in these phases of $LiFe_5O_8$ conduction was 100% electronic. Electrical conductivities calculated from initial transient d-c voltages were in good agreement with those obtained by a-c measurements.

Lithium ferrite spinel contains reducible iron ions (Fe^{3+}) and lithium ions, and therefore it is expected that this material exhibits both electronic and ionic conduction. As seen in Fig. 1, the electronic contribution to the total conductivity increased with decreasing partial oxygen pressure, which is due to the increase of the ferrous (Fe^{2+}) ion concentration reduced from ferric (Fe^{3+}) ions. The same tendency has been observed in potassium ferrite by Roth and Romanczuk (16). The electrical conductivity increased with decreasing partial oxygen pressure (n-type conductor), which is reasonable because p-type $LiFe_5O_8$ is not expected to exist (both Li^+ and Fe^{3+} ions are in their highest valence states). The small activation energy values for the electronic conduction and the linear relation between log σT *vs.* $1/T$ may indicate that the small polaron model of electron hopping motion between Fe^{2+} and Fe^{3+} offer the best possibility for charge-transfer mechanism for $LiFe_5O_8$, which is the same mechanism as that proposed in the potassium ferrite by Roth and Romanczuk (16) and Dudley *et al.* (17).

The phase transition of $LiFe_5O_8$ from α- to β-phase has been found at 750°C by x-ray diffraction (11, 18) and d-c conductivity measurements (2). This is the order-disorder type of transition in the distribution of the Li^+ and Fe^{3+} ions in the octahedral sites (1, 2). In the present study abrupt jumps in the conductivity curves were observed at the phase transitions both in air and oxygen, and the transition temperatures thus obtained were both 740° ± 5°C. There was no difference in the transition temperature within experimental error between samples in air and in oxygen. This is because the $LiFe_5O_8$ phase coexisted with α-Fe_2O_3 in the sample in oxygen and the difference in the composition between samples in air and oxygen was small. At the phase transition the change in conductivity of the sample in air was smaller than that of the sample in oxygen. No significant jump in the conductivity curve was observed for the sample in argon but a change of slope was observed at 550° ± 5°C. It is considered that partial disordering in the distribution of iron ions may occur even in the low temperature phase in argon because of the large concentrations of ferric ions, and thus the jump which corresponds to the change of degree of disordering at the transition was too small to be observed in this study.

Tretyakov and Rapp (19) have proposed the interstitial lithium and interstitial iron model in the lithium ferrite spinel at 1005°C by high temperature electrochemical measurements. In the present study the defect structure was estimated from the partial oxygen pressure (p_{O_2}) dependence of electrical conductivity (σ) in the high temperature β-phase (750° ≦ T ≦ 850°C) where the conduction was 100% electronic. But the dependence between air and argon ($p_{O_2} \leqq 10^{-6}$ atm) was too weak to explain by using a simple defect model (oxygen vacancy model, $\sigma \propto p_{O_2}^{-1/4}$ and $p_{O_2}^{-1/6}$; interstitial lithium model, $\sigma \propto p_{O_2}^{-1/5.5}$; and interstitial iron model, $\sigma \propto p_{O_2}^{-1/5.5}$). To explain the weak dependence, the complex defect model [for example, the clustering and decomposing model of two different types of defects which have been applied for uranium oxides (8, 20, 21)] would be more suitable. However, the detailed determination of crystal structure of $LiFe_5O_8$ in argon at high temperature is required to test such a complex defect model.

Acknowledgments

The authors wish to express their gratitude to Professor K. Naito of Nagoya University for the gift of cobalt wire used for the oxygen monitor.

This work was supported by the Advanced Research Projects Agency of the Department of Defense and was monitored by the Office of Naval Research through the Materials Research Center of Northwestern University. It was completed at the Center for Solid State Science at Arizona State University.

Manuscript submitted Jan. 26, 1977; revised manuscript received March 8, 1977.

Any discussion of this paper will appear in a Discussion Section to be published in the June 1978 JOURNAL. All discussions for the June 1978 Discussion Section should be submitted by Feb. 1, 1978.

REFERENCES

1. P. Braun, *Nature (London)*, **170**, 1123 (1952).
2. E. Kato, *Bull. Chem. Soc. Jpn.*, **31**, 113 (1958).
3. F. F. Y. Wang, R. L. Gravel, and M. Kestigian, *I.E.E.E. Trans. Magn.*, **4**, 55 (1968).

4. R. G. West and A. C. Blackenship, *J. Am. Ceram. Soc.*, **50**, 343 (1967).
5. A. A. Samokhvalov, S. A. Ismailov, and A. A. Obukhov, *Sov. Phys. Solid State*, **9**, 688 (1967).
6. K. Naito, T. Tsuji, and T. Matsui, *J. Nucl. Sci. Technol.*, **11**, 22 (1974).
7. K. Naito, T. Tsuji, and Y. Asakura, *ibid.*, **12**, 314 (1975).
8. T. Matsui and K. Naito, *J. Nucl. Mater.*, **56**, 327 (1975).
9. A. Duquesnoy and F. Marion, *C. R. Acad. Sci. (Paris)*, **256**, 2862 (1963).
10. B. Fisher and D. S. Tannhauser, *J. Chem. Phys.*, **44**, 1663 (1966).
11. M. Schieber, *J. Inorg. Nucl. Chem.*, **26**, 1363 (1964).
12. C. Wagner, "Proceedings 7th International Committee for Electrochemical Thermodynamics and Kinetics, London, 1955," Butterworths Scientific Publications, London (1957).
13. J. B. Wagner and C. Wagner, *J. Chem. Phys.*, **26**, 1597 (1957).
14. R. W. Vest and N. M. Tallan, *J. Appl. Phys.*, **36**, 543 (1965).
15. A. V. Joshi and J. B. Wagner, *J. Phys. Chem. Solids*, **33**, 205 (1972).
16. W. L. Roth and R. J. Romanczuk, *This Journal*, **116**, 975 (1969).
17. G. J. Dudley, B. C. H. Steele, and A. T. Howe, *J. Solid State Chem.*, **18**, 141 (1976).
18. J. C. Anderson and M. Schieber, *Sci. Ceram.*, **2**, 345 (1965).
19. Y. D. Tretyakov and R. A. Rapp. *Trans. Metall Soc. AIME*, **245**, 1235 (1969).
20. T. Matsui and K. Naito, *J. Nucl. Sci. Technol.*, **12**, 250 (1975).
21. T. Matsui, T. Tsuji, and K. Naito, *ibid.*, **11**, 317 (1974).

Experiments Showing the Absence of Electromigration of As and Al in Peltier LPE of GaAs and $Ga_{1-x}Al_xAs$

J. J. Daniele*

Philips Laboratories, Briarcliff Manor, New York 10510

Peltier-induced LPE is LPE in which an electric current is passed through the solid-liquid (S-L) interface and directly cools it by the Peltier effect. The resulting crystal growth takes place at constant temperature and the electric current is the sole externally applied driving force for growth. Peltier LPE has been performed on InSb, GaAs, and GaAlAs (1-5) and CW GaAs/GaAlAs DH lasers have been grown (6, 7). The growth is characterized by a growth rate (v_p) roughly proportional to the applied current. In addition, the growth rate is too large [v_p observed $\approx$ 1 μm/min, v_p calculated from a diffusion model (8) $v_p \approx 0.05$ μm/min] to be due solely to diffusion. To account for the elevated growth rate, electromigration (3-5) or convection (2-4) have been suggested as possible transport mechanisms. This communication presents recent data which show that electromigration of As and Al does not play a significant role in the Peltier LPE of GaAs and GaAlAs.

The theoretical basis for the present experiment is that electromigration is strongly dependent on (and proportional to) the applied electric field (9) and if the electric potential is reversed then the direction of electromigrative flow of species in solution must also be reversed (see Fig. 1). In order to separate the thermal and electrical effects, it is imperative that the Peltier cooling is the same for both current directions. Identical thermal conditions for opposite directions of current can be achieved in separate experiments by using p- and n-type substrates since these have roughly equal and opposite Peltier coefficients at 800°C (measured with respect to Ga and verified in a separate experiment; $\pi_n \cong -0.30$, $\pi_p \cong 0.35$V). Thus, equivalent Peltier cooling and opposite electromigration effects result when opposite electric currents are applied to p- or n-type GaAs. As a result, if Peltier LPE of GaAs or $Ga_{1-x}Al_xAs$ is performed under identical thermal conditions (except for the current direction and substrate conductivity type) and if electromigration toward the substrate is responsible for the very high growth rates, then electromigration away from the substrate should give a very slow growth or a meltback.

In the present experiments, GaAs and $Ga_{1-x}Al_xAs$ (x = 0.15 and 0.3) were grown by Peltier LPE on p- and n-type GaAs substrates ([100]GaAs, p, n $\approx 3 \times 10^{18}$/cm^3, 2 mm thick). The experiments were identical except for the conductivity type of the substrates, and the current direction. The epilayers were undoped and were thin ($\leq$50 μm) with respect to the substrate thickness so that the substrate dominates the thermal process. The growth took place at 800°C. The growth system and growth procedure have been described previously (3).

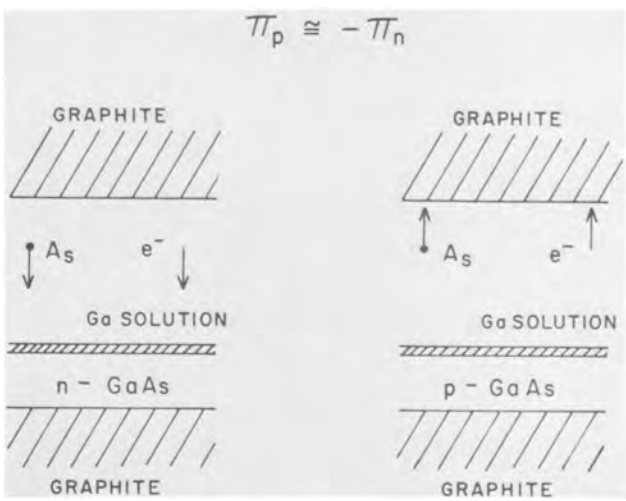


Fig. 1. Schematic of Peltier LPE growth cell showing the solution, substrate and epitaxial layer and illustrating the effects of electromigration on Peltier LPE on p- and n-type substrates. Since $\pi_p \cong -\pi_n$, opposite electric currents are required for cooling in the two cases and thus an opposite electromigration direction must result.

Table I. Experimental results

Substrate type	Normalized current, A/cm^2	X_{Al} (solid)	Average growth rate (v_p), μm/min
p	+10	0	0.5
n	−10	0	0.5
p	+10	~0.15	0.25
n	−10	~0.15	0.4
p	+10	~0.3	0.3
n	−10	~0.3	0.3

* Electrochemical Society Active Member.
Key words: LPE, Peltier effect, growth rate.

The results of these experiments are shown in Table I. From the data it is clear that regardless of current direction the Peltier-induced LPE growth rate is roughly the same for GaAs and $Ga_{1-x}Al_xAs$ ($x = 0.15$ and 0.3). The marked difference indicative of electromigration is not present. Thus, electromigration of As and Al cannot be playing a significant role in the Peltier LPE process and other mechanisms such as convection and boundary layer formation should be more closely investigated. Moreover, preliminary experiments show that the Peltier LPE growth rate of GaAs and GaAlAs decreases with diminishing melt height until a critical height of ~2 mm is reached (10). These experiments indicate that convective stirring and formation of a diffusion boundary layer may be present and can account for the observed elevated growth rate.

Acknowledgment

The author is grateful to Dr. T. S. Hurle of Royal Radar Establishment for suggesting the use of p- and n-type substrates. The author also acknowledges the excellent technical assistance of Robert Peterson.

Manuscript submitted Dec. 27, 1976.

Any discussion of this paper will appear in a Discussion Section to be published in the June 1978 JOURNAL. All discussions for the June 1978 Discussion Section should be submitted by Feb. 1, 1978.

Publication costs of this article were assisted by Philips Laboratories.

REFERENCES

1. M. Kumaguawa, A. F. Witt, M. Lichtensteiger, and G. C. Gatos, *This Journal*, **120**, 583 (1973).
2. J. J. Daniele and C. Michel, in Proc. 5th Int'l. Symposium on GaAs and Related Compounds, Deauville, France (1974), Vol. 24, p. 155, British Inst. of Physics, London (1975).
3. J. J. Daniele, *Appl. Phys. Lett.*, **27**, 373 (1975).
4. D. J. Lawrence and L. F. Eastman, *J. Cryst. Growth*, **30**, 267 (1975).
5. L. Jastrzebski, H. C. Gatos, and A. F. Witt, *This Journal*, **123**, 1121 (1976).
6. G. A. Acket, J. J. Daniele, W. Nijman, R. P. Tijburg, and P. J. De Waard, *Philips Tech. Rev.*, **36**, 198 (1976).
7. J. J. Daniele, D. A. Cammack, and P. M. Asbeck, *J. Appl. Phys.*, **48**, 914 (1977).
8. S. I. Long, J. M. Ballantyne, and L. F. Eastman, *J. Cryst. Growth*, **26**, 13 (1974).
9. J. N. Pratt and R. G. R. Sellors, "Electrotransport in Metal and Alloys," Defect and Diffusion Monograph series No. 2, Tran Tech SA/Riehen/ Switzerland (1973).
10. J. J. Daniele, To be submitted.

Investigation of the Formation of Gaseous Sodium Sulfate in a Doped Methane-Oxygen Flame

C. A. Stearns, R. A. Miller,* F. J. Kohl, and G. C. Fryburg#

National Aeronautics and Space Administration, Lewis Research Center, Cleveland, Ohio 44135

In hot corrosion research it has generally been assumed that sodium sulfate is formed in the combustion process by reaction of contaminants contained in the fuel and intake air. A commonly proposed reaction is:

$$2NaCl(g) + SO_2 + 1/2O_2 + H_2O = Na_2SO_4(g) + 2HCl$$

Our Knudsen cell study of the vaporization of sodium sulfate has lent credence to such reactions by establishing the existence of gaseous Na_2SO_4 and values for its thermodynamic properties (1).

$Na_2SO_4(g)$ formation was measured at atmospheric pressure in CH_4-O_2 flames. High pressure, free-jet expansion, mass spectrometric sampling was used to identify and measure reaction products. The flame holder and sampler are shown in Fig. 1. The flame was doped by adding SO_2 and by nebulizing aspirated solutions of $NaCl+H_2O$ into the mixing chamber. Burner surface to sampler orifice distance, z, was varied with a precision of 0.025 mm.

Fig. 2 shows measured composition profiles of reaction products for a doped 9.5 mole ratio O_2/CH_4 flame. Weight percentages of reactants were, 4.7 CH_4, 89.0 O_2, 3.5 H_2O, 2.0 SO_2 and 0.35 NaCl. Attachment of the flame to the sampling cone was at z=0.8 mm. The profiles for O_2, H_2O and CO_2 are similar to those reported for CH_4-O_2 flames (2). For the sodium- and sulfur-containing species (except Na_2SO_4) the observed profiles seem reasonable. Results could not be obtained for NaOH because of interference due to an argon peak. We speculate that the Na_2SO_4 profile may have resulted from several interrelated factors: cooling of the flame by the sampling cone at small z (stability of $Na_2SO_4(g)$ increases with decreasing temperature); actual variation of the flame temperature as a function of z; existence of a region of supersaturation for this species. The species $NaSO_2(g)$ and $NaSO_3(g)$ were positively identified and we consider these to be stable reaction intermediates because the respective ions do not appear as fragments in the Knudsen cell vaporization of sodium sulfate (1). Both of these species have been postulated for appropriately doped flame systems (3,4). The composition profiles of these species displayed peaks similar to the Na_2SO_4 at small z, but the intensities decreased to values below our detection sensitivity for z greater than 1.2 mm. The profile shapes of $NaSO_2(g)$ and $NaSO_3(g)$ may have resulted from the same factors that account for the $Na_2SO_4(g)$ profile.

To facilitate a comparison of experimental observations with equilibrium thermodynamic predictions, we calculated the mole fractions of the flame reaction products. Calculations were performed with the NASA chemical equilibrium computer program as described in Ref. 1. Calculations for $NaSO_2(g)$ and $NaSO_3(g)$ were not performed because no thermodynamic data exists for these species. In the calculations CH_4 and SO_2 were labeled 'fuel' while O_2, H_2O and NaCl were labeled 'oxidant'. Experimental results are compared to calculations by noting that according to this labeling convention the ratio of fuel to oxidant for the experimental flame was 0.072. Calculated mole fractions of products are shown on the right-hand side of Fig. 2. The calculated adiabatic flame temperature was 2032K. Considering that the experimental results were not 'calibrated' (Mach number focusing and spectrometer mass discrimination) and that the calculations are for equilibrium conditions, the agreement between experiment and prediction is good for O_2, H_2O, CO_2,

*NRC Resident Research Associate.
#Electrochemical Society Active Member.

SO_2, and SO_3. Discrepancies with most of the sodium-containing species arose because these are markedly dependent on the fuel to oxidant ratio and the experimental ratio was somewhat uncertain because of the method used to introduce NaCl. Likewise, the stability of $Na_2SO_4(g)$ is a rapidly varying function of temperature and the experimental flame temperature is expected to be significantly lower than the calculated adiabatic temperature. We calculate that for a 200K cooler flame, the predicted $Na_2SO_4(g)$ level would equal the experimentally measured value.

Residence time is a critical parameter in the formation of $Na_2SO_4(g)$. For these experiments we calculated residence times on the basis of cold gas flow velocities. The composition profiles of Fig. 2 indicate that $Na_2SO_4(g)$ was formed in less than one millisecond. This formation time is considerably less than the one reported by Hanby (5) for experimental conditions where sulfide sulfur rather than SO_2 was the reactant.

REFERENCES

1. Kohl, F.J., Stearns, C.A., and Fryburg, G.C., in "Metal Slag Gas Reactions And Processes", Ed. by Z.A. Foroulis and W.W. Smeltzer, The Electrochemical Society, p. 649 (1975).
2. Peeters, J. and Mahnen, G., Fourteenth Symp. (Int'l) on Combustion, The Combustion Institute, Pittsburgh, Pa., p. 133 (1973).
3. Fenimore, C.P., Ibid., p. 955.
4. Durie, R.A., Johnson, G.M. and Smith, M.Y., Fifteenth Symp. (Int'l) on Combustion, The Combustion Institute, Pittsburgh, Pa., p. 1123 (1975).
5. Hanby, V.I., Trans. ASME, J. Eng. Power, 96, 129 (1974).

Manuscript received March 30, 1977.

Publication costs of this article were assisted by the National Aeronautics and Space Administration.

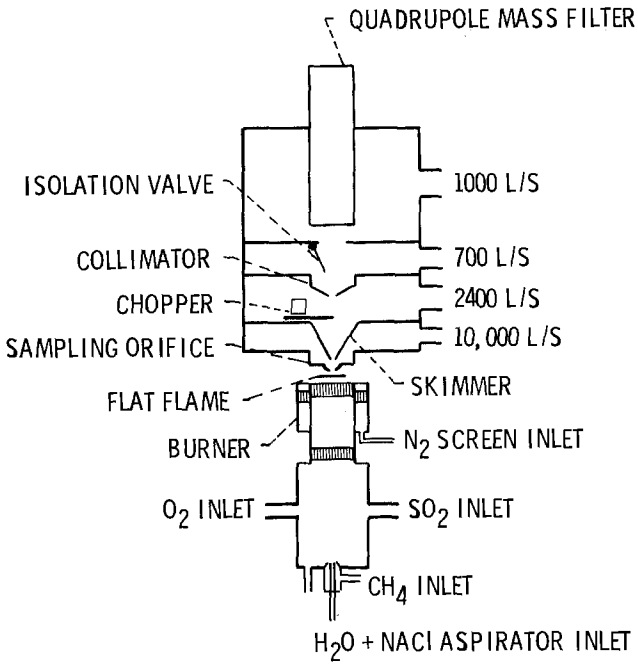


Figure 1. Schematic of high pressure mass spectrometric flame sampling apparatus.

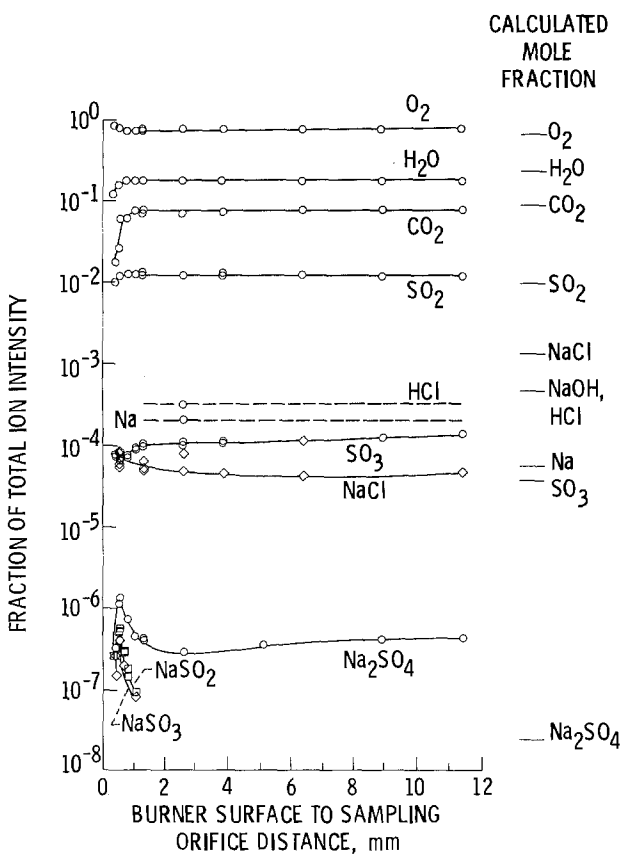


Figure 2. Composition profiles for CH_4-O_2 flame doped with $NaCl+H_2O+SO_2$.

Mechanism of Beneficial Effect of Tantalum in Hot Corrosion of Nickel-Base Superalloys

George C. Fryburg,* Carl A. Stearns, and Fred J. Kohl

National Aeronautics and Space Administration, Lewis Research Center, Cleveland, Ohio 44135

Recently, we reported (1) on a study of Na_2SO_4-induced oxidation (hot corrosion) of the four nickel-base superalloys: B-1900, NASA TRW VIA, 713C and IN738. Oxidations were performed at 900 and 1000°C in slowly flowing oxygen with two doses of Na_2SO_4: 2/3 and 3 mg cm^{-2}. It was found that all of the alloys underwent accelerated or catastrophic oxidation under some conditions. However, several samples of VIA resisted hot corrosion at 900°C when treated with the low dose: specific weight gain was only 0.4 mg cm^{-2} after 100 hr. In addition, preoxidized samples of 738 treated with the large dose resisted corrosion at 900°C for times out to 460 hr, the length of the test: specific weight gain was only 3 mg cm^{-2}.

The oxide scales formed on the samples that resisted hot corrosion were adherent and resisted spallation upon cooling to room temperature. An X-ray diffraction analysis of the scales revealed that all the samples exhibited a prominent $NaTaO_3$ pattern in addition to spinel, tapiolite, and NiO for VIA; and NiO and spinel for 738. The observation of the $NaTaO_3$ was unique and had never been observed for any specimens that underwent hot corrosion.

The specimens were examined in the electron microprobe to determine the distribution of $NaTaO_3$ in the oxide scales. Since $NaTaO_3$ is water soluble, the specimens were prepared for examination by the following procedure: coated with a heavy copper layer in a vacuum evaporator; electroplated additional copper over the layer; cross sectioned very slowly without any coolant; mounted in epoxy and polished in kerosine; polished surface shadowed with carbon.

The most striking set of micrographs were obtained from one of the 738 specimens. This sample had been preoxidized for 100 hours at 900°C prior to the 3 mg cm^{-2} Na_2SO_4-induced oxidation which was continued for 460 hours. Some of the pertinent elemental X-ray micrographs along with the back scattered electron micrograph are presented in Figure 1. The sodium and tantalum maps match up nicely showing the position of the $NaTaO_3$ in the outer layer of the oxide. None of the other elements in the oxide displayed a similar correlation. Sulfur, which appeared to be associated with titanium, occurred below the oxide scale in the alloy substrate. No sulfur was evident associated with sodium. No concentration of molybdenum was observed in the oxide scale.

The VIA samples displayed a thin oxide scale with tantalum distributed evenly throughout. Sodium appeared throughout the oxide also but was concentrated more toward the outer portion. Again, sulfur was situated below the oxide scale in the alloy substrate, and none was evident in the oxide associated with the sodium. No concentration of molybdenum was observed in the oxide. A continuous layer of Al_2O_3 was evident along the inner portion of the scale.

If one accepts the chemical mechanism of Na_2SO_4-induced corrosion of B-1900 proposed in our recent report (1), the beneficial effect of tantalum can be explained within that framework. According to the mechanism, the protective Al_2O_3 scale is dissolved by acid fluxing of MoO_3 (2) after the oxide ion concentration has been lowered by the reaction of MoO_3 with the Na_2SO_4:

$$MoO_3(\ell) + Na_2SO_4(\ell) \rightarrow Na_2MoO_4(\ell) + SO_3(g) \quad [1]$$

Once the scale is breached, the molten $Na_2MoO_4 + MoO_3$ phase undercuts the scale exposing the alloy substrate and initiating a sudden increase in the rate of oxidation. The action of the tantalum oxide is preferential reaction with the Na_2SO_4 forming solid $NaTaO_3$:

$$Ta_2O_5(s) + Na_2SO_4(\ell) \rightarrow 2NaTaO_3(s) + SO_3(g) \quad [2]$$

We estimate that the ΔG for reaction [2] is more negative than for reaction [1].

*Electrochemical Society Active Member.

The absence of MoO_3 in the elemental X-ray micrographs of our hot corrosion resistant samples arises from the fact that $MoO_3(\ell)$ has a very high vapor pressure: $\sim 10^{-1}$ atm at 1200K. In samples that undergo hot corrosion the molybdenum is generally found lying along the oxide-alloy interface. This results from the fact that $Na_2MoO_4(\ell)$ formed by reaction [1] has a much lower vapor pressure than $MoO_3(\ell)$: we estimate that it is around 10^8 less at 1200K.

In brief, the beneficial effect of tantalum with respect to hot corrosion attack arises from the ability of the Ta_2O_5 to tie-up the Na_2O and prevent the formation of a molten Na_2MoO_4 phase.

REFERENCES

1. G.C. Fryburg, F.J. Kohl, and C.A. Stearns, in "Properties of High Temperature Alloys", Z.A. Foroulis and F.S. Petit, Editors, p. 585, The Electrochemical Society, Princeton, N.J. (1977), also NASA TM X-73479 (1976); (b) NASA TN D-8461 (1977).

2. J.A. Goebel, F.S. Petit, and G.W. Goward, Met. Trans. 4, 261 (1973).

Manuscript received April 25, 1977.

Publication costs of this article were assisted by the National Aeronautics and Space Administration.

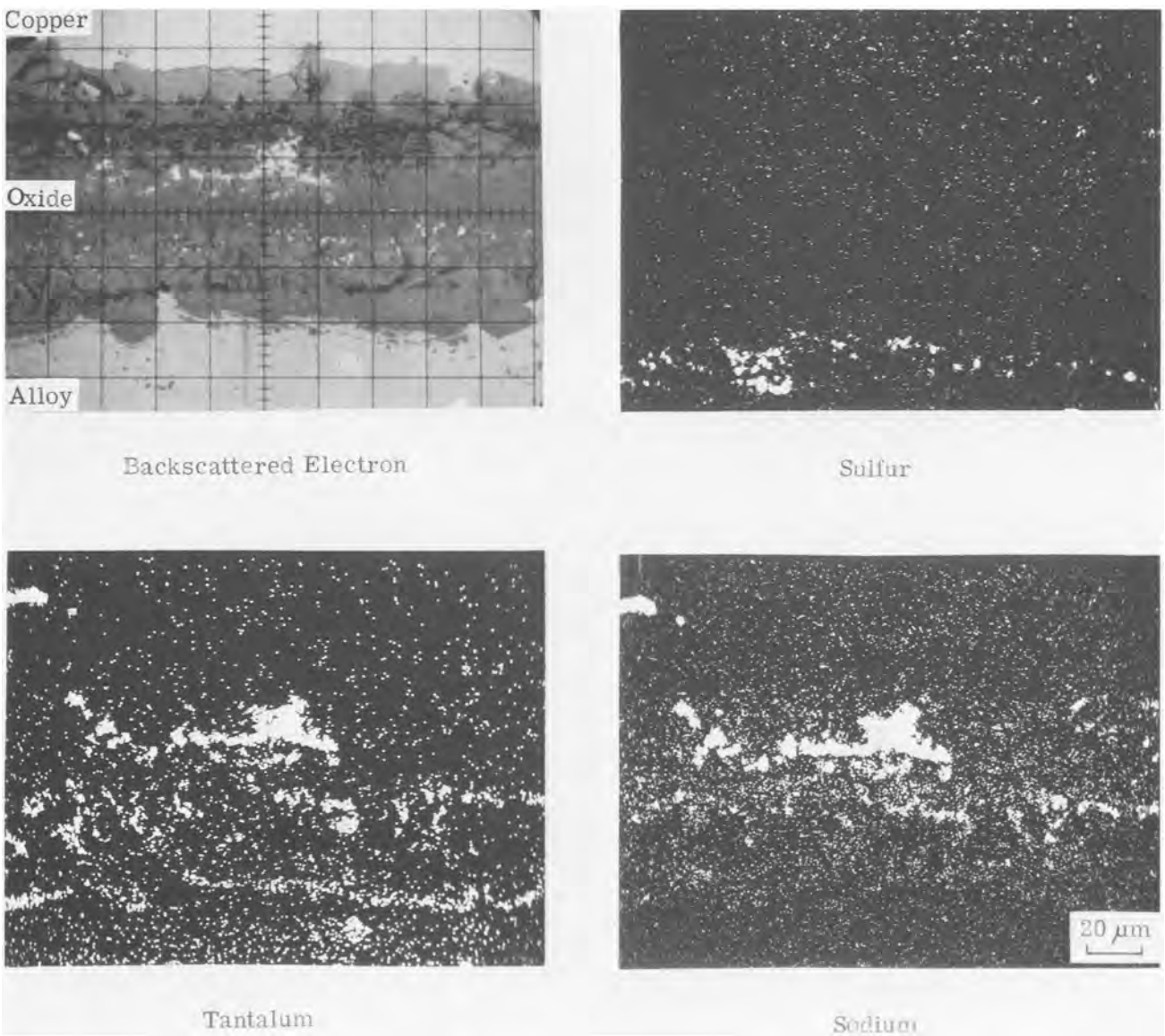


Figure 1. Electron and elemental X-ray micrographs of a cross section of oxide formed on 738 pre-oxidized 100 hr and oxidized with 3 mg cm^{-2} Na_2SO_4 for 460 hr at 900°C in slowly flowing oxygen.

JOURNAL OF THE ELECTROCHEMICAL SOCIETY

ELECTROCHEMICAL SCIENCE AND TECHNOLOGY

AUGUST 1977

Evaluation of Porous Paper and Felt Ceramics for Electrode Separators in High Temperature Li-Al/LiCl-KCl/FeS_x Cells

J. P. Mathers, T. W. Olszanski, and J. E. Battles*

Argonne National Laboratory, Argonne, Illinois 60439

ABSTRACT

Porous papers and felts fabricated from BN and Y_2O_3 fibers have been evaluated as electrode separators for Li-Al/LiCl-KCl/FeS_x cells. The physical and mechanical properties were determined, and in-cell tests exceeding 1000 hr were conducted. The papers and felts had adequate strength and flexibility for cell assembly and performed well during cell testing. Results from the property measurements are presented and the performance of these materials in the cell tests is discussed.

High temperature, molten salt Li-Al/LiCl-KCl/FeS_x ($x = 1$ or 2) cells are being developed by Argonne National Laboratory (ANL) for electric vehicle propulsion and for energy storage on electric utility systems (1). One of the requirements for the successful development of cells for commercial applications is the identification of a low cost, porous electrode separator. The primary function of the electrode separator is to prevent direct electron flow between the electrodes without unduly restricting ionic flow through the electrolyte. In addition, separators for Li-Al/LiCl-KCl/FeS_x cells must retain the Li-Al and FeS_x active materials within the electrodes. This requirement is significant because the Li-Al and FeS_x are in the form of powders, and penetration of the separator by these fine particles may lead to a loss in cell capacity or electrical short circuits between the electrodes. The optimum structure and properties desired in the electrode separator have not been fully determined; however, the following general requirements must be satisfied: (*i*) The separator must be a good electrical insulator to prevent direct electron flow between the electrodes. (*ii*) It should be <2 mm thick to permit close electrode spacing, and it must contain a large volume of open porosity, probably >50%. These factors minimize the cell weight and the resistance to ionic flow between the electrodes. (*iii*) The pore channels should be <20 μm diam to prevent penetration of the separator by the active powders in the electrodes. (*iv*) The separator must be chemically stable in the cell environment at the operating temperature (about 450°C). (*v*) The mechanical strength and flexibility must be sufficient to allow easy cell assembly, and to withstand the forces exerted on the separator by the volume changes which occur in the electrodes during cycling. (*vi*) The separator must have a potential cost of <\$22/m^2 if the cost goals for a commercial cell are to be achieved.

A flexible, fibrous ceramic appears to have the greatest potential for satisfying these requirements. At present, interest is centered on two ceramics, BN and Y_2O_3; both of these have proved to be compatible with the cell environment and are available in the form of fibers (2). Boron nitride fabric is currently being used as a separator material, and engineering test cells with BN separators have been operated for periods up to 7800 hr (1, 3, 4). However, it does not appear that the cost goal of \$22/m^2 can be achieved with this material. Also, the fabric weave presently attainable is not tight enough to prevent penetration of the separator by the active powders in the electrodes (5). The latter problem has led to the use of a layer of ZrO_2 fabric which has a much tighter weave over the faces of the electrodes to aid in particle retention. Zirconia fabric becomes electrically conductive in the cell environment, and thus cannot be used as an electrode separator; however, its conductivity does not preclude the use of zirconia as a particle retainer.

Papers and felts made from BN and Y_2O_3 fibers are being developed as alternatives for the BN fabric/ZrO_2 fabric combination. These materials are expected to be considerably less expensive than the BN fabric and to provide more effective particle retention within the electrodes. The results obtained from evaluation tests of three promising separators which appear to have the potential for reaching the cost goal of \$22/m^2 are presented.

Experimental Procedure

The first material tested was a composite paper of Y_2O_3 fibers and 10 weight percent (w/o) asbestos fibers developed at the University of Florida (6). The asbestos was used to provide the strength necessary for handling during cell assembly, however, it was not expected to be stable in the cell environment. The second material was a BN felt, developed by the Carborundum Company,[1] in which BN fibers were bonded with a BN binder. The third material was an Y_2O_3 felt developed by Zircar Products, Incorporated.[2] It was prepared by a process in which fibers of a rayon felt were impregnated with YCl_3 and then converted to fibers of Y_2O_3 by controlled pyrolysis (7, 8).

The candidate paper and felt separators were characterized by measuring the thickness, porosity, air resistance, burst strength, flexibility, and wettability. The

* Electrochemical Society Active Member.

Key words: electrode separator, boron nitride, yttrium oxide, molten salt cell.

[1] R. S. Hamilton, Research and Development Division, Niagara Falls, New York, funded by Argonne National Laboratory.

[2] Florida, New York.

thickness was measured with an AMES No. 16 Dial Comparator[3] equipped to provide a contact pressure of 763 Pa. The porosity was calculated from the thickness and weight per unit area of the separator, and from the weight fractions and densities of the component materials. The air resistance was measured with a Model 4110 Densometer.[4] This property is an indication of the volume of open porosity and the lengths of the transport paths in the material. The densometer measures the time for the flow of a standard volume of air through a standard area of the sample under a uniform pressure. The burst strength of each material was measured on a Mullen Burst Testor, Model C.[5] In this test, the material being evaluated is clamped over a rubber diaphragm, and then the diaphragm is expanded against the material by hydraulic pressure until the material ruptures; the pressure at rupture is reported as the burst strength. The flexibility of each separator was evaluated by bending it around a series of successively smaller cylindrical mandrels. The value reported for the flexibility represents the diameter of the smallest mandrel around which the separator could be bent without tearing.

The ability of each material to be wet by the electrolyte was evaluated by immersing a sample in the molten electrolyte (LiCl-KCl eutectic) at 450°C. If the sample could be impregnated by the electrolyte without the aid of a vacuum, the material was classified as having "good" wettability. When vacuum impregnation was required, the wettability was classified as "fair"; when the material could not be vacuum impregnated after 1½ hr of exposure to the molten salt, the wettability was classified as "poor". The amount of material available for determining the above properties was very limited and, as a result, only one measurement was made for each property.

Scanning electron microscope (SEM) examinations were conducted to observe the structure of each separator material and the morphology of the fibers and binders. A small sample (~5 × 5 mm) of each material was mounted on an aluminum specimen mount using a thin layer of silver paint as a glue. After the mounted sample was thoroughly dried, it was sputter coated with 10 nm of carbon followed by 10 nm of gold. This mounting procedure was sufficient to obtain micrographs with magnifications below 1000×; however, to obtain micrographs of higher magnification without electrical charging effects, a second mounting procedure was devised. An aluminum specimen mount was coated with a thin layer of silver paint and individual fibers of the paper or felt were dispersed on the wet paint. After drying, the specimen was sputter coated with 25 nm of gold. Using this procedure, high quality micrographs of individual fibers could be obtained up to 12,000×.

Functional tests of the candidate separators were performed in unsealed Li-Al/LiCl-KCl/FeS cells. The cylindrical test cell, illustrated in Fig. 1, was 7.6 cm diam and 5 cm high. The cell housing, which also served as the lower electrode housing, was made from AISI-1008, low carbon steel, and the upper electrode housing was made from Hastelloy B[6] (Ni-28Mo-5Fe-1Cr). The electrodes were assembled by vibratorily loading powdered Li-Al (48 atomic percent (a/o) Li) or powdered FeS into iron RETIMET,[7] a porous (~5% dense) iron structure which served as a current collector. In the test of the Y_2O_3-asbestos paper, the cell was constructed with FeS in the upper electrode and Li-Al in the lower electrode. The theoretical capacity of each electrode was 31.5 A-hr. In the tests of the BN and Y_2O_3 felts, however, the Li-Al electrode was uppermost, and each electrode had a theoretical capacity of 20 A-hr. Zirconia fabric[8] and 60 mesh stainless steel screens (spot welded in place) were used to retain the active materials in the electrodes. The upper electrode was electrically insulated from the lower electrode and the cell housing by the separator material being tested and by tightly packed BN or Y_2O_3 fibers, as shown in Fig. 1. One layer of the test separator was used on each side of the upper electrode, except in the cell containing the Y_2O_3-asbestos paper where two layers of the separator material were used on each side. This arrangement provided a separator thickness of ~1.8 mm for each of the test cells. The electrical lead to the upper electrode was insulated from the cell housing by a BN sleeve, which was pretreated for 6 hr at 1750°C in a N_2 atmosphere to reduce the oxygen content of the BN and thus improve its compatibility with lithium (2). The top of the cell housing was not welded to the lower portion of the housing; therefore, it was free to move if dimensional changes occurred in the electrodes during cell operation. Openings were provided in the top of the cell housing and in the top of the upper electrode to facilitate loading the cell with the molten salt electrolyte (LiCl-KCl eutectic).

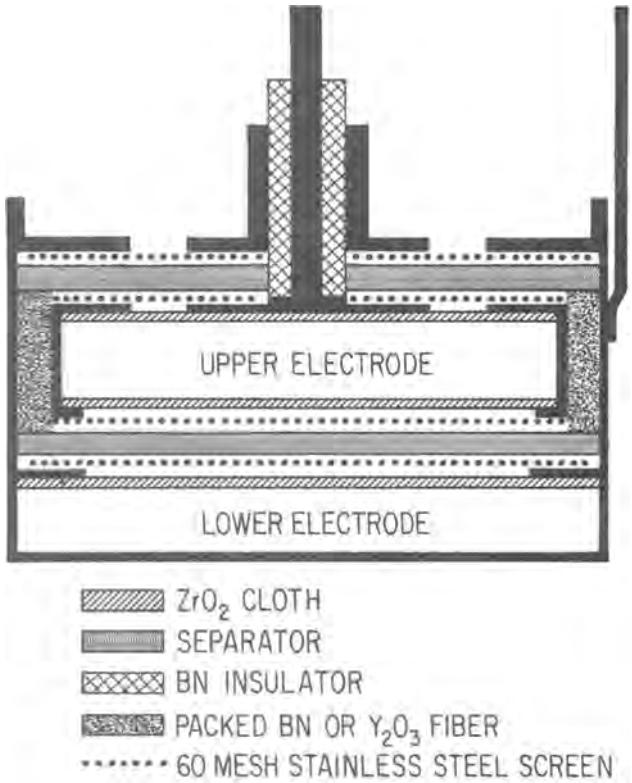


Fig. 1. Test cell design

The cells were assembled in a helium-atmosphere glove box, and were operated at 450°C in a helium-atmosphere furnace attached to the glove box. The cells were cycled continuously between a discharge cutoff potential of 0.9V and a charge cutoff potential of 1.67V (internal resistance included). The cell was placed on open circuit for 10 min after each charge and discharge. The current density was increased in steps from 20 to 76 mA/cm² during the first 200-500 hr of cell operation, and then maintained at 76 mA/cm². After 1000 hr of cycling, cell operation was terminated for post-test examination of the cells and separator materials.

The cells were sectioned in a helium-atmosphere glove box, and samples of the separators between the electrodes were removed for SEM examination and x-ray diffraction analysis. The electrolyte was removed from the separator materials by repeated washing with

[3] B. C. Ames Company, Waltham, Massachusetts.
[4] Teledyne Gurley, Troy, New York.
[5] P. F. Perkins, Chicopee, Massachusetts.
[6] Cabot Corporation, Stellite Division, Kokomo, Indiana.
[7] Manufactured by Dunlop, Limited, England. Distributed by Hydro-Jet Corporation, Rancho Sante Fe, California.
[8] Zircar Products, Incorporated, Florida, New York.

Table I. Properties of paper and felt electrode separators

Property	Y_2O_3-asbestos paper	BN felt	Y_2O_3 felt
Thickness (mm)	0.89	1.83	1.73
Porosity (%)	79.0	93.0	96.0
Air resistance (sec)	17.8	0.2	0.1
Burst strength (kPa)	5.0	4.0	10.0
Flexibility (cm)	2.5	2.5	0.5
Wettability	Good	Poor	Fair

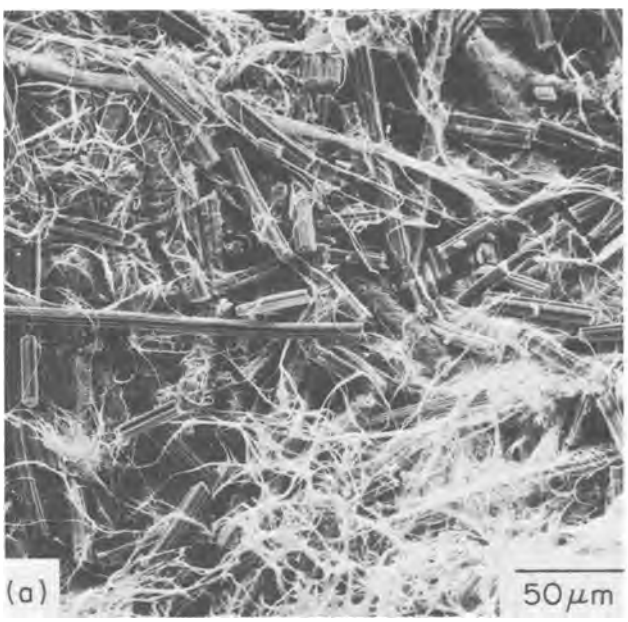
hot water. The SEM mounting techniques described earlier were also found to be suitable for post-test examination.

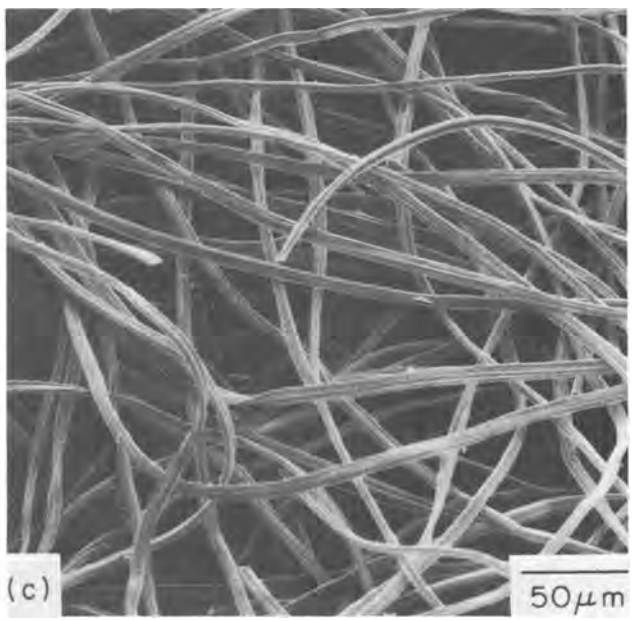
Results

The physical and mechanical properties of the three separator materials are presented in Table I. The thickness, porosity, and air resistance are useful in evaluating the resistance of the separator to ionic transport and the ability of the separator to retain the active materials of a cell within the electrodes. Thin materials with high porosity and low air resistance should have low resistance to ionic transport, whereas thick materials with low porosity and high air resistance should provide good particle retention. The results obtained for the candidate separators indicate that the BN and Y_2O_3 felts should allow the best ionic conductivity, but the Y_2O_3-asbestos paper should provide better particle retention. However, in the evaluation process, consideration must be given to the possibility that swelling of the electrodes during cell operation, and consequent compression of the separator, may alter the thickness, porosity, and air resistance of the separator.

The burst strength and flexibility are useful in evaluating the ease with which the separators can be handled during cell assembly and, also, how well the materials can maintain their integrity when dimensional changes occur in the electrodes during cell operation. The Y_2O_3 felt had the best combination of strength and flexibility, but all three materials had sufficient strength and flexibility, at least for handling during cell assembly.

The wettability of the separator by the electrolyte is a measure of how easily the separator becomes impregnated with electrolyte when the cell is filled with electrolyte. The wettability of the three separators





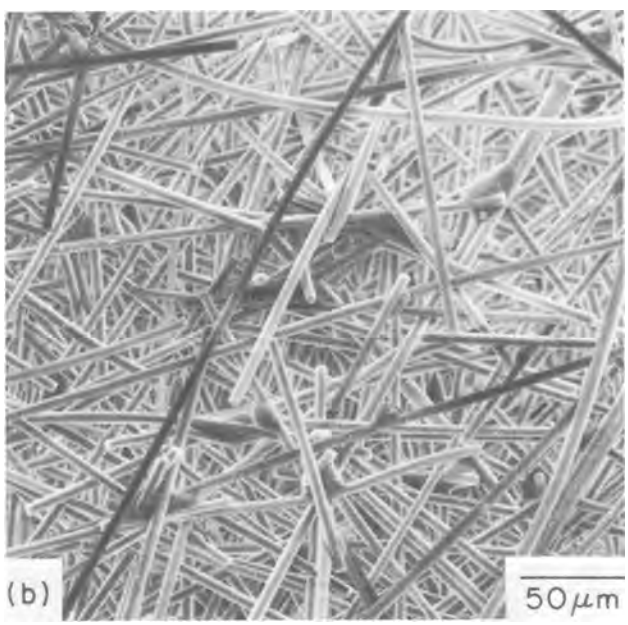


Fig. 2. Paper and felt separators: (a) Y_2O_3-10 w/o asbestos paper; (b) BN felt; (c) Y_2O_3 felt.

ranged from good (Y_2O_3-asbestos) to fair (Y_2O_3 felt) to poor (BN felt), and these evaluations were borne out when the test cells were filled with electrolyte. The cell containing the Y_2O_3-asbestos paper was easily filled with electrolyte, while some difficulty was encountered in filling the cells containing the BN and Y_2O_3 felts. The reason for the superior wettability of the Y_2O_3-asbestos paper compared with that of the Y_2O_3 felt has not been determined. It could be related to differences in the pore structure of the materials or to the presence of asbestos, which is easily wet by the molten electrolyte. The poor wettability of the BN felt is in agreement with the poor wetting characteristics of other BN materials (fabric and paper) in molten electrolyte (9).

The fibrous structure of each separator material is shown in Fig. 2. The Y_2O_3-asbestos paper consists of asbestos fibers (~0.02 μm diam) intertwined around the much larger Y_2O_3 fibers (~10 μm diam). The Y_2O_3 fibers are quite short, thereby allowing them to be closely packed. The average pore opening appears to be 15 μm or less. The BN felt has much longer fibers which are bonded at some intersections by the BN binder. The average pore opening of this material appears to be ~30 μm. The fibers of the Y_2O_3 felt are extremely long and are intertwined; as a result no binder is required to maintain the structure. The average pore opening of the Y_2O_3 felt appears to be ~30 μm. The more open structure of the BN and Y_2O_3 felts compared to that of the Y_2O_3-asbestos paper is consistent with the porosities and air resistances obtained for these materials.

A single Y_2O_3 fiber is shown in Fig. 3. The ridges along the length of the fiber result from the characteristic shape of the rayon precursor fiber. Individual fibers and the binder from the BN felt are shown in Fig. 4. Boron nitride fibers normally have a circular cross section and a very smooth surface; however, the surfaces of the fibers, and to a much lesser extent those of the binder, were covered with small crystallites. A view of these crystallites at higher magnification is shown in Fig. 5. The crystallites are flat hexagons that are insoluble in water. These characteristics suggest that the crystallites are probably BN. The crystallites are believed to have developed during a high temperature heat-treatment used to improve the compatibility of the felt with lithium.

The electrical performance of the test cells is summarized in Table II. The entries for coulombic efficiency and percent utilization represent average values obtained during the last 500 hr of operation at a current density of 76 mA/cm². For the cell that contained the Y_2O_3-asbestos paper separator, utilization after initial start-up was 33% of theoretical, with a coulombic efficiency of 100%. The utilization gradually increased to 56% during the first 700 hr of operation, while the coulombic efficiency remained near 100%. During the final 300 hr of operation the utilization slowly decreased to 41% and the coulombic efficiency to 91%. Post-test examination of the cell revealed that

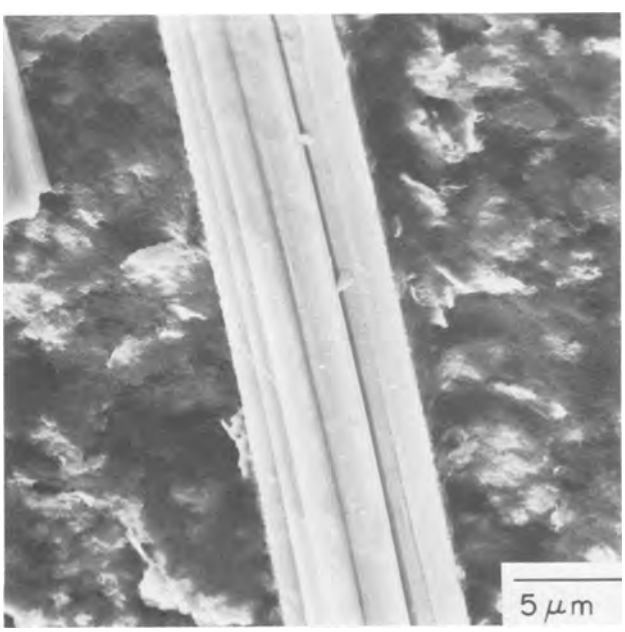


Fig. 3. Single Y_2O_3 fiber

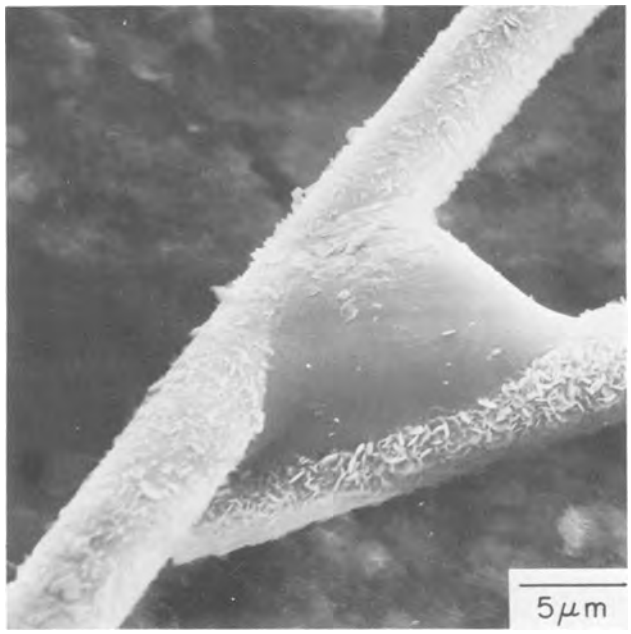


Fig. 4. BN fibers and BN binder

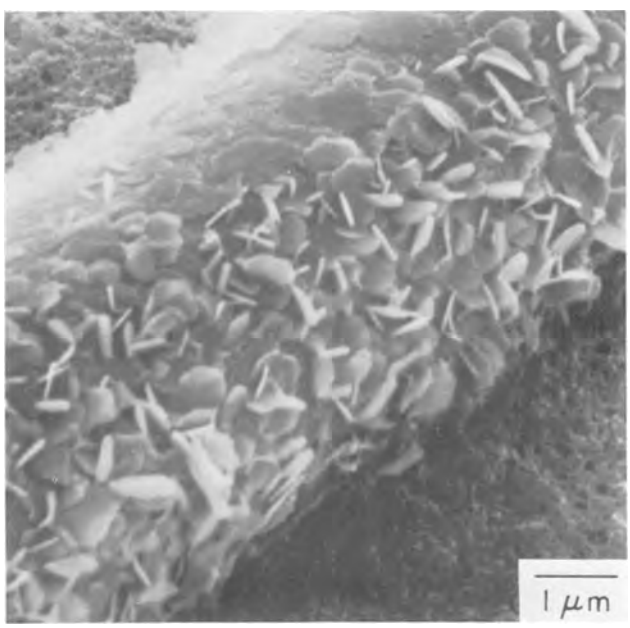


Fig. 5. Crystallites on BN fiber

Table II. Electrical performance of test cells

	Y_2O_3-asbestos paper	BN felt	Y_2O_3 felt
Operating time (hr)	1030	1056	1104
Cycles	56	115	103
Coulombic efficiency (%)	95	97	99
Utilization (%)	47	35	45

the upper electrode cup had ruptured from swelling of the FeS; this rupture may have caused the decline in cell performance. The structure of the separator had been maintained between the electrodes where it would have been in a state of compression, but the fibers had drifted away from one another in the peripheral areas of the cell. SEM examination showed no evidence of any corrosive attack on the Y_2O_3 fibers, as can be seen from a comparison of Fig. 3 and 6. No asbestos fibers were observed in the separator, but a large quantity of crystalline debris was present. X-ray diffraction analysis of the separator revealed Y_2O_3 and possibly $Mg(OH)_2$, α-Fe, and FeS. The presence of Fe or FeS from the positive electrode is another factor that may have been responsible for the decline in cell performance. It is apparent that the asbestos was destroyed in the cell environment as expected, but the structure of the separator between the electrodes was maintained by the compressive forces exerted on it by the electrodes.

In the test cells containing the BN and Y_2O_3 felts, the FeS was placed in the lower electrode and the loading of both electrodes was reduced to avoid failure of the upper electrode container. The cell containing the BN felt separator had a utilization of only 2% after initial start-up, and a coulombic efficiency of 97%. After the furnace chamber containing the cell was evacuated and repressurized several times to aid in impregnating the separator with electrolyte, the utilization began to increase steadily with a coulombic efficiency of 100%. The utilization reached 42% after 700 hr of operation and leveled off at that value for the remaining 300 hr of operation. Post-test examination of the cell revealed that the upper electrode cup had ruptured owing to expansion of the Li-Al. The separator had maintained its structure in all areas of the cell, even where it was not compressed by the cell components. No evidence of corrosive attack on the fibers or the binder was revealed by the SEM examination, as shown in Fig. 7. However, most of the small crystallites that had been present on the BN material initially were either attacked by the cell environment or removed by mechanical interaction of the fibers.

The test cell containing the Y_2O_3 felt separator had an initial utilization of 24% and a coulombic efficiency of 100%. After the furnace chamber was evacuated and repressurized, the utilization gradually improved to 51% after 800 hr of operation and remained at that level for the final 200 hr. The coulombic efficiency remained >98% during the entire operation of the cell. Post-test examination revealed that the upper electrode cup of this cell had also ruptured. The Y_2O_3 felt separator had maintained its structure in all areas of the cell, just as the BN felt had. SEM examination showed no evidence of any corrosive attack on the fibers, but many of the fibers appeared to have been fractured, probably from the pressure exerted on the separator by the swelling electrodes.

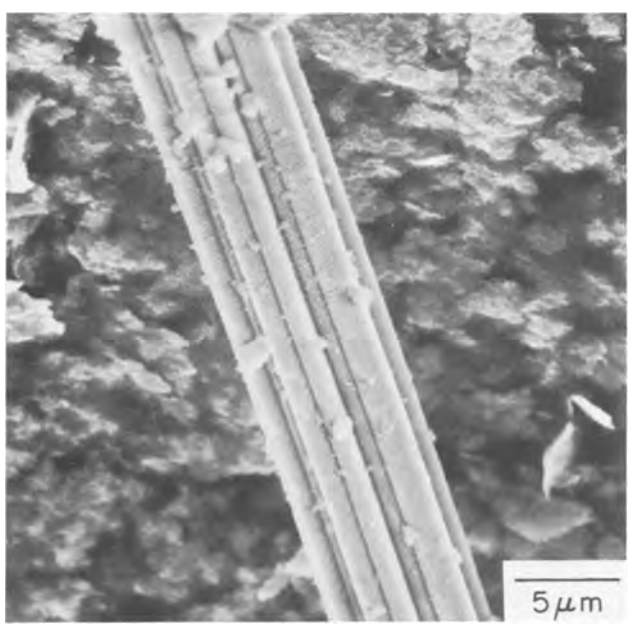


Fig. 6. Single Y_2O_3 fiber after cell test

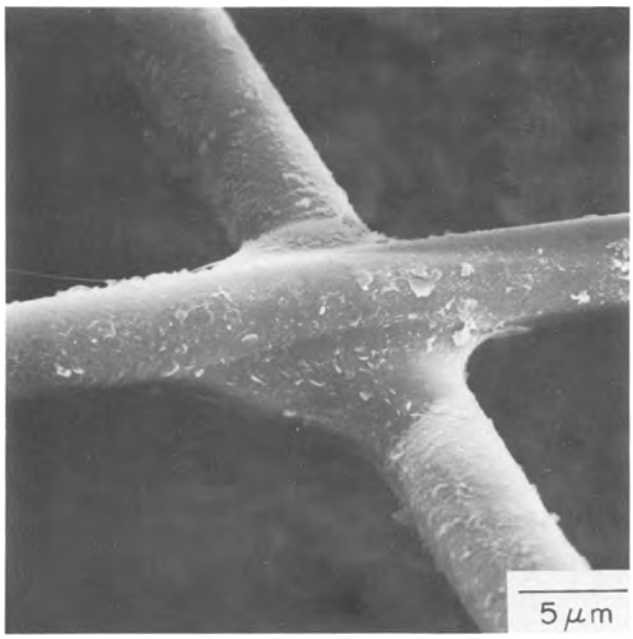


Fig. 7. BN fibers and BN binders after cell test

Conclusions

All three materials tested are good candidates for electrode separators in Li-Al/FeS_x cells. Asbestos is not stable in the cell environment; however, the Y_2O_3-asbestos paper can be used successfully in cells where the separator is maintained in a state of compression. The BN and Y_2O_3 felts have an advantage over the Y_2O_3-asbestos paper because they maintain their structure during cell operation without the need for a compressive stress; thus, a cell-design feature that ensures compression of the separator would be a less important consideration with separators of BN or Y_2O_3 felt.

In all three tests, ZrO_2 fabric was used to retain particles of active materials within the electrodes. Therefore, further testing of all three materials in the absence of ZrO_2 fabric will be necessary to establish the effectiveness of these separator materials as particle retainers. Long-term testing of these papers and felts in larger engineering-scale cells is now in progress, and these tests will provide further information on the suitability of these materials as electrode separators.

Acknowledgments

The authors wish to express their appreciation to L. Burris, D. S. Webster, and P. A. Nelson for administrative support. The separator materials evaluated in this work were supplied by R. D. Walker and C. C. Cheng, University of Florida; R. S. Hamilton, The Carborundum Company: and B. H. Hamling, Zircar Products, Incorporated. Their cooperation is gratefully acknowledged. The authors also wish to express their appreciation to G. M. Kesser for editorial assistance.

This work was performed under the auspices of the U.S. Energy Research and Development Administration.

Manuscript received Jan. 24, 1977. This was Paper 40 presented at the Las Vegas, Nevada, Meeting of the Society, Oct. 17-22, 1976.

Any discussion of this paper will appear in a Discussion Section to be published in the June 1978 JOURNAL. All discussions for the June 1978 Discussion Section should be submitted by Feb. 1, 1978.

Publication costs of this article were assisted by Argonne National Laboratory.

REFERENCES

1. P. A. Nelson, R. O. Ivins, N. P. Yao, J. E. Battles, A. A. Chilenskas, E. C. Gay, R. K. Steunenberg, and W. J. Walsh, Argonne National Laboratory Report ANL-76-45 (1976).
2. J. E. Battles, F. C. Mrazek, W. D. Tuohig, and K. M. Myles, in "Corrosion Problems in Energy Conversion and Generation," C. S. Tedman, Jr., Editor, p. 20, The Electrochemical Society, Softbound Symposium Series, Princeton, New Jersey (1974).
3. J. E. Battles and F. C. Mrazek, U.S. Pat. 3,915,742 (1975).
4. J. S. Dunning, T. G. Bradley, and E. J. Zeitner, Proceedings of the Eleventh Intersociety Energy Conversion Engineering Conference, Vol. 1, p. 491, State Line, Nevada (1976).
5. P. A. Nelson, J. E. Battles, A. A. Chilenskas, E. C. Gay, R. O. Ivins, R. K. Steunenberg, and W. J. Walsh, Argonne National Laboratory Report ANL-8109 (1975).
6. R. D. Walker, C. C. Cheng, J. E. Battles, and J. P. Mathers, Argonne National Laboratory Report ANL-76-8, p. B41 (1976).
7. B. H. Hamling, U.S. Pat. 3,385,915 (1968).
8. B. H. Hamling, Personal communication.
9. J. G. Eberhart, Argonne National Laboratory Report ANL-76-8, p. B74 (1976).

Zinc-Bromine Secondary Battery

H. S. Lim,* A. M. Lackner, and R. C. Knechtli

Hughes Research Laboratories, Malibu, California 90265

ABSTRACT

A zinc-bromine secondary battery with circulating aqueous electrolyte showed 80% over-all (round-trip) energy efficiency at a current density of 20 mA/cm^2 for 10 hr charge and 10 hr discharge cycles. The battery characteristics may be attractive for load leveling and other applications if a low cost separator is developed.

The zinc-bromine secondary battery appears to be a potentially attractive battery for energy storage, especially for load leveling applications, because of the low cost and wide availability of the active materials, high theoretical energy density, and low electrode polarizations. The Zn-Br_2 battery has been studied (1-7) for a long time. However, it is not fully developed for commercial applications yet, probably because of its high self-discharge rate (2, 6) and corrosion problems due to bromine. The high self-discharge rate is mostly due to the bromine diffusion from the positive electrode (where bromine is generated during charge) to the negative electrode where it is chemically reacted with zinc.

We have recently developed a new zinc-bromine battery which includes an electrolyte circulation system and an ion exchange membrane as a separator. An energy efficiency of 80% has been demonstrated in a 10 hr charge and 10 hr discharge experiment at a current density of 20 mA/cm^2. Efficiencies are defined throughout the paper as follows

$$\text{voltage efficiency} = \frac{\text{average charge voltage}}{\text{average discharge voltage}}$$

$$\text{coulomb efficiency} = \frac{\text{amount of charge consumed during discharge to 1.0V}}{\text{amount of charge consumed during charge}}$$

$$\text{energy efficiency} = (\text{voltage efficiency}) \times (\text{coulomb efficiency})$$

The electrode reactions in the battery can be described as follows

$$(+)\ \text{electrode:}\quad 2Br^- \underset{\text{discharge}}{\overset{\text{charge}}{\rightleftharpoons}} Br_2 + 2e$$

$$(-)\ \text{electrode:}\quad Zn^{++} + 2e \underset{\text{discharge}}{\overset{\text{charge}}{\rightleftharpoons}} Zn$$

over-all reaction:

$$Zn^{++} + 2Br^- \underset{\text{discharge}}{\overset{\text{charge}}{\rightleftharpoons}} Zn + Br_2$$

Bromine and bromide ions will probably be present in equilibrium with complex species

$$xBr_2 + Br^- = Br_{2x+1}^-$$

Experimental

A schematic diagram of the battery is shown in Fig. 1. Self-discharge due to the direct chemical reaction of zinc and bromine was minimized by using a separator such as a sulfonated Teflon ion exchange membrane (*e.g.*, Nafion 125, manufactured by E. I. du Pont de Nemours and Company) or a polypropylene microporous film (*e.g.*, Celgard 3400, manufactured by Celanese Plastics Company). The electrolyte, which was 1.0-7.7M aqueous zinc bromide ($ZnBr_2$), was circulated through the cell from two separate storage tanks for the catholyte and the anolyte. The electrolyte was either pure $ZnBr_2$ solution or $ZnBr_2$ with additives such as potassium chloride (KCl) or sodium chloride (NaCl). The catholyte initially contained about 0.05M excess bromine in order to promote complete discharge of the negative electrode. Chemicals used were Baker Analyzed Reagents, J. T. Baker Company. The electrodes

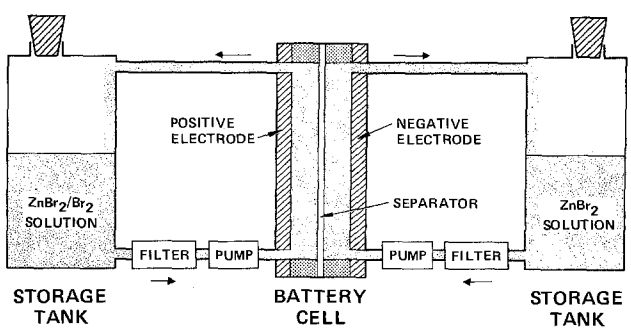


Fig. 1. Schematic drawing of zinc-bromine battery

* Electrochemical Society Active Member.

Key words: Zn-Br_2 battery, bromine electrode, conductivity of $ZnBr_2$ solution.

were carbon electrodes with an active geometrical area of 60 cm^2. The circulation rate of the electrolyte was 0.5-3.2 ml/sec. Electrode separation was about 5 mm with the separator membrane in the middle. All charge-discharge experiments were done with constant currents.

Polarizations of the electrodes and the potential drop across the separator were measured by placing reference electrodes (saturated calomel electrode) right after the cell in the circulation system. Conductivity of the electrolyte was measured with an a-c bridge with 1-10 kHz signal in a conductivity cell. Electrode separation of the conductivity cell was 11 cm and the cross-sectional area of the cell was 0.27 cm^2.

Results and Discussion

Conductivity of electrolyte.—Resistivities of aqueous $ZnBr_2$ solutions at 25° and 55°C, respectively, are shown in Fig. 2 as a function of the concentration of $ZnBr_2$. The resistivity minimum was observed at about 2M. When NaCl or KCl was added to a solution of a given concentration in $ZnBr_2$, the resistivity of the solution was reduced, as shown in Fig. 3. With the same concentration of additive, KCl was much more effective in lowering the resistivity than NaCl. When 4M KCl was added to concentrated solutions of $ZnBr_2$, the resistivity at 25°C was changed by a factor of two, *i.e.*, from 8.4 to 3.7 Ω-cm with 2M $ZnBr_2$ and from 11.4 to 6.3 Ω-cm with 4M $ZnBr_2$. The resistivity of 2M $ZnBr_2$ with 4M KCl at 55°C was as low as 2.5 Ω-cm (Fig. 3).

Polarizations.—The polarization at the bromine electrode was extremely low, *i.e.*, up to a current density of 100 mA/cm^2 the polarizations were less than 20 mV at 25° and 10 mV at 54°C in the concentration range of 1.0-7.7M in $ZnBr_2$. The polarization at zinc electrodes was also very low (see Fig. 4). The polarization stayed less than 100 mV up to the current density of 60 mA/cm^2 at 54°C, even in 1M $ZnBr_2$. Little changes in the polarizations of zinc electrode were observed when the temperature was lowered to room temperature or when KCl was added up to 4M in concentration.

The potential drop in the battery was mostly across the electrolyte and separator. The potential drop was linear with the current density. The slope depended on the conductivity of electrolyte and separator material. The potential drops at various concentrations of $ZnBr_2$ were measured at 54°C as a function of current densities (Fig. 4) when a Nafion 125 cation exchange membrane was used as the separator and the electrode separation was about 5 mm. The potential drop was 85-90 mV at 54°C when concentration of $ZnBr_2$ was 2M and current density was 15 mA/cm^2, while it was 125-130 mV at room temperatures (23°-25°C). When the electrolyte was 2M in $ZnBr_2$ and 4M in KCl, the potential drop was 70-80 mV at 54°C. The slight decrease in the potential drop by the addition of KCl appeared to indicate that the major portion of the potential drop was across the separator rather than across the electrolyte layer. The resistivity across the Celgard

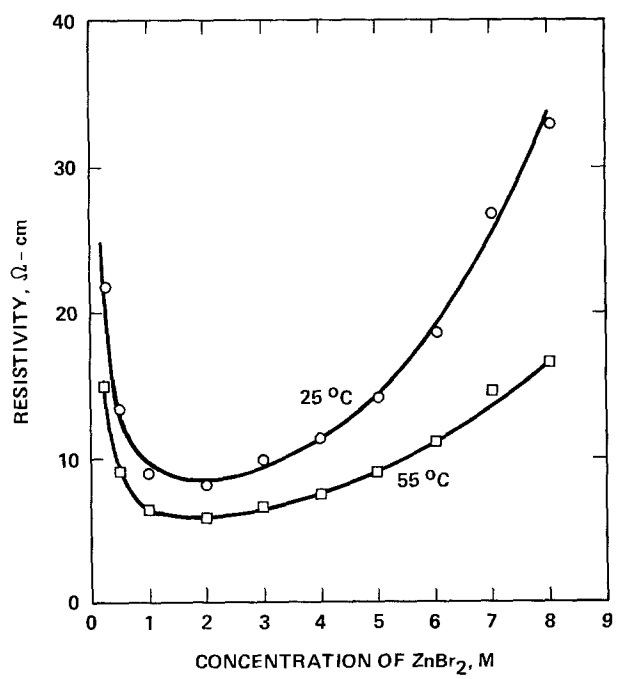


Fig. 2. Resistivity of zinc bromide solutions at various temperatures

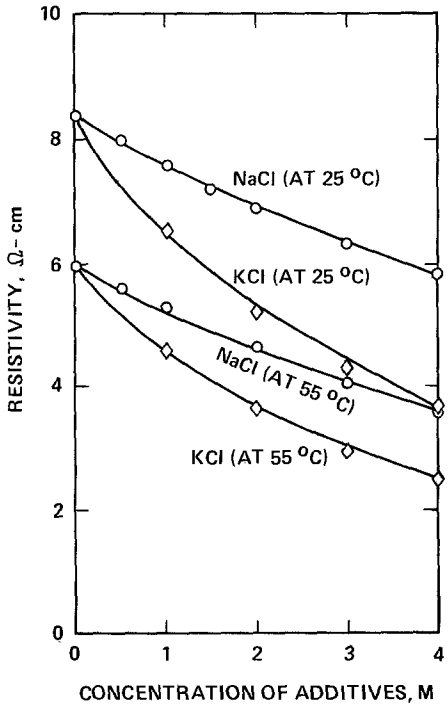


Fig. 3. Resistivity of 2M zinc bromide solution with KCl and NaCl additives.

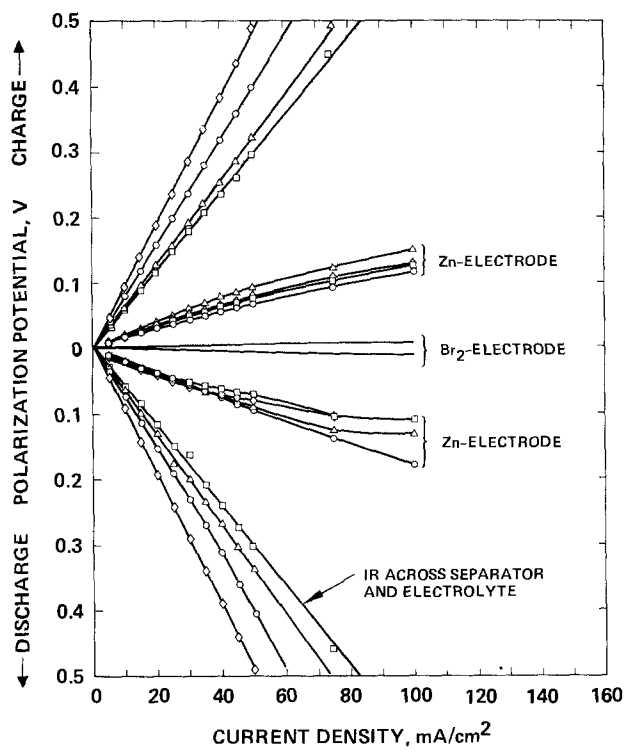


Fig. 4. Polarizations of zinc and bromine electrodes and *IR* drop across the separator and electrolyte in the battery with Nafion 125 separator at 54°C. Concentrations of zinc bromide: △, 1M; □, 2M; ○, 4M; and ◇, 6M.

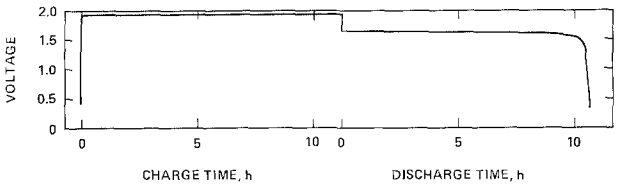


Fig. 5. A typical charge-discharge curve of zinc-bromine battery. Electrolyte: 2M $ZnBr_2$, pH = 1.4. Current density: 15 mA/cm². Temperature: ~25°C. Separator: Nafion 125.

3400 separator in the electrolyte was similar to that of Nafion 125.

Dendrites and hydrogen evolution.—Dendrites were visible on zinc electrodes when current densities were greater than 15 mA/cm². The dendrite growth, however, was cut off when it touched the separator. There was no evidence that the dendrite went through either kind of separator. Loose particles of zinc, however, were collected on the filter of the anolyte when the cell was discharged after a charge at current densities greater than 20 mA/cm². It was speculated that the bases of the dendrites were anodically dissolved during discharge before the dissolution of the main body of the dendrites, thus giving loose particles of zinc. Operating conditions showing poor coulomb efficiency of the battery were accompanied by the observation of loose zinc particles.

Hydrogen evolution at the zinc electrode was observed at low pH's (pH < 3), but it was not a severe problem unless the pH was maintained below one, which was not required.

Performance of battery.—A typical charge-discharge curve of the battery is shown in Fig. 5. The charge potential stayed almost constant during the whole charge period, while the discharge potential was decreased slightly as it was discharged at a constant current. Charge voltages, discharge voltages, and voltage efficiencies of one of the test batteries with a Nafion 125 separator at various current densities are shown in Table I. The voltage efficiency was over 80% at current densities up to 30 mA/cm². During 10 hr charge and 10 hr discharge experiments, coulomb efficiencies as high as 95% at 15 mA/cm² at room temperature and 92% at 20 mA/cm² at 54°C have been observed with over-all energy efficiency of over 80%. When current densities were increased above 20 mA/cm², the coulomb efficiency was decreased rapidly on 10 hr charge experiments. The maximum charge loading was about 200 mA-hr/cm². A similar maximum loading of zinc on negative electrodes of an aqueous zinc-chlorine battery has been reported (8, 9).

The performance characteristics of the batteries with a Celgard 3400 microporous separator were similar to those with Nafion 125 except for coulomb efficiency. Coulomb efficiency of the batteries with Celgard 3400 was usually much lower than with the other separator. This was due to a higher bromine transfer rate through the Celgard separator than through the Nafion 125. The color of the anolyte during battery operation was yellow due to the bromine transfer from the catholyte when the separator was Celgard 3400, while it was colorless when the separator was Nafion 125, indicating that very little bromine was transferred through this separator. The trade-offs between the two separators are the relative cost and possible stability problems in addition to the relative coulomb efficiency. Nafion material should be very stable, while polypropylene may or may not be stable in the battery electrolyte which contains aqueous bromine solution. The Nafion membrane, however, is presently much more expensive than the Celgard microporous film.

Table I. Operation characteristics of the zinc-bromine battery*

Current density (mA/cm²)	Voltage, charge	Voltage, discharge	Voltage efficiency (%)
0	1.785	1.784	100
10	1.854	1.715	92.5
20	1.920	1.647	85.8
30	1.986	1.580	79.8
40	2.052	1.509	73.5
50	2.118	1.438	68.0
60	2.183	1.366	65.5
70	2.249	1.302	58.0
100	2.444	1.135	46.4

* Electrolyte: 2M $ZnBr_2$, 4M KCl, pH ~ 1.5. Temperature: 54°C. Separator: Nafion 125.

The power needed for the pump of the circulation system is ignored in the discussion. It is generally believed that this power loss can be minimized to a small fraction of the total output of the battery, especially in a large battery system.

Life tests of the battery were very preliminary. No visible sign of degradation nor any change in performance was observed after six full charge-discharge cycles.

Comparison with zinc-chlorine battery.—The zinc-bromine battery was compared with a zinc-chlorine battery (10, 11) which is one of the contenders for load leveling batteries. The basic difference between the two batteries is the difference in active materials, *i.e.*, chlorine *vs.* bromine at the positive electrode. The advantages of the zinc-bromine battery over the zinc-chlorine battery are as follows:

1. Polarization of the bromine electrode is much lower than that of the chlorine electrode.
2. An electrolyte cooling system is not essential in a zinc-bromine battery. It is an essential part of a zinc-chlorine battery where chlorine is stored as chlorine hydrate which requires low temperature (~9.6°C at 1 atm) (10).
3. The electrolyte of the zinc-bromine battery can be stored above the ambient temperature while the chlorine hydrate cannot.
4. Bromine is chemically less reactive than chlorine. Therefore, the corrosion problem may be less severe with bromine than with chlorine.

The probable disadvantages of the zinc-bromine battery are as follows:

1. The zinc-bromine battery has lower emf (1.78V) than the zinc-chlorine battery (2.12V).
2. Bromine is more expensive than chlorine, although the cost of these materials is a minor part of the total battery cost.
3. Bromine is less abundant than chlorine.
4. The zinc-bromine battery needs a separator which may not be required in the zinc-chlorine battery.

An estimate of battery cost.—A complete battery cost estimate is premature at this early stage of development. As a first-order guideline, however, it is possible to estimate the contribution of the active materials and of the separator membrane to the anticipated battery cost. The active materials are zinc and bromine. The cost of either of these elements is below $0.80/kg. With full utilization of the active material and 100% energy efficiency, the energy density of the active material in the battery is 432 W-hr/kg. Our measurements showed that the battery performance was relatively insensitive to zinc bromide concentration changes over a range of from 1 to 4M (Fig. 2 and 4), indicating that the battery operation in this concentration range is reasonable. It is therefore conservative to assume at least 50% active material utilization in a practical zinc-bromine battery, leading to over 200 W-hr/kg of active material. With a cost of less than $0.80/kg, this leads to a cost of active material below $4/kW-hr, which is an attractive figure.

The effect of the separator cost on the battery cost is determined by the current density. Our experiments showed good performance up to a current density of 20 mA/cm² for a 10 hr charge rate. This corresponds to

0.2 A-hr/cm². With a battery voltage in excess of 1.5V, this is equivalent to more than 0.3 W-hr/cm² or about 3 ft² of separator per kilowatt-hour. Present cost of Navon 125 membrane in small quantity is on the order of \$30/ft². This leads to a cost of \$90/kW-hr for the battery using presently available separator material. This cost is about an order of magnitude too high for a low cost battery. If the cost of the present separator can be lowered by a factor of 10 or if another suitable separator which costs less than \$3/ft² is developed, the battery should be attractive for load leveling application. Operation at more than 20 mA/cm² can also reduce the cost of the battery. The total material cost of the battery can be lower than \$15/kW-hr (assuming electrode and other material costs to be \$2/kW-hr), provided that a separator membrane comparable in performance with Nafion 125 can be developed with a cost of less than \$3/ft².

Conclusion

The present zinc-bromine battery is demonstrated to have good performance up to a current density of 20 mA/cm². The life tests of the battery have not yet been made. However, it appears that the battery could be attractive for load leveling application, especially because of the low electrode polarization, low cost, and wide availability of the active materials and electrodes. There is no obvious life-limiting component in the battery for the short term when the Nafion separator is used, although possible slow corrosion of the graphite electrode by aqueous bromine could not be ruled out for the long-term life problem. Overcharge and overdischarge should not damage the battery. Electrolysis of water will take place during overcharge or overdischarge of the battery, changing the water content and the *p*H of the electrolyte, which can easily be compensated by addition of water and acid. The battery should not have the shape change problems of the zinc electrode because the electrode can easily be rejuvenated by complete discharge of the battery.

Acknowledgments

The authors wish to thank Dr. J. D. Margerum for many helpful discussions and Mr. K. Barnett for his help on the dendrite experiments.

Manuscript submitted Oct. 12, 1976; revised manuscript received April 22, 1977.

Any discussion of this paper will appear in a Discussion Section to be published in the June 1978 JOURNAL. All discussions for the June 1978 Discussion Section should be submitted by Feb. 1, 1978.

Publication costs of this article were assisted by Hughes Research Laboratories.

REFERENCES

1. C. S. Bradley, U.S. Pat. 312,802 (1885).
2. S. Barnartt and D. A. Forejt, *This Journal*, **111**, 1201 (1964).
3. D. R. Riffe, U.S. Pat. 3,328,202 (1967).
4. R. Zito, Jr., U.S. Pat. 3,382,102 (1968); 3,640,770 (1972); 3,640,771 (1972); 3,642,538 (1972); 3,700,-514 (1972).
5. H. B. Smith, U.S. Pat. 3,682,703 (1972).
6. M. S. Walsh, U.S. Pat. 3,816,177 (1974); M. Walsh and D. Crouse, 10th Intersociety Energy Conversion Engineering Conference, Conference Record, p. 1141 (1975).
7. J. J. Leddy and G. Gritzner, U.S. Pat. 3,929,506 (1975).
8. A. F. Sammells, in "Energy Storage," H. P. Silverman and J. B. Berkowitz, Editors, p. 121, The Electrochemical Society Softbound Symposium Series, Princeton, N.J. (1976).
9. A. F. Sammells and L. W. Eaton, Paper 13 presented at The Electrochemical Society Meeting, Washington, D.C., May 2-7, 1976.
10. P. C. Simons and P. Carr, Proceedings of 8th Intersociety Energy Conversion Engineering Conference, p. 72 (1973).
11. P. C. Simons, U.S. Pat. 3,713,888 (1973).

Structural Principles for Silver Halide Superionic Conductors

Douglas O. Raleigh*

Rockwell International, Science Center, Thousand Oaks, California 91360

ABSTRACT

The reasons why so many alkali and organic-base iodides form solid ionic conductors with AgI, while others, apparently similar, do not, are discussed in terms of geometric structural principles. It is proposed that the principal functions of the additive cation are to force the structure into a greater degree of face-sharing of the iodide coordination polyhedra than in β-AgI by coordinating more iodide ions than Ag^+, and to relieve tetrahedral distortion in the resulting structures.

There are at present well over 50 solid chemical compounds which have room temperature silver-ion conductivities in excess of 10^{-4} Ω^{-1} cm^{-1}. The reported discovery (1, 2) of the highly conductive MAg_4I_5 group (M = K, Rb, or NH_4) was soon followed by that of the QI · *n*AgI compounds (3, 4) in which Q is one of a great variety of nitrogenous organic bases (tetraalkylammonium, pyridinium, quinolinium, etc.) and in which *n* ranges 4 to 8. Since that time, conductive compounds have been reported from the addition of AgI to silver oxy-salts [phosphates (5), tungstate (6), molybdate (7), chromate (7), vanadate (8), arsenate (8)], cyanides (9), polymethonium iodides (10), sulfonium iodides (11, 12), tropyllium iodides (13), and mercuric iodochalcogenides (14). Takahashi (15) has provided an excellent review of compounds reported up to 1972. More recently, Takahashi *et al.* (16) and Sammells *et al.* (17) have reported room temperature copper ion conductivity in a variety of organic halide-copper halide addition compounds in which analogous structural considerations should apply.

To date, structures have been determined for only several of these compounds. It is clear, however, that more is involved in the AgI-based compounds than the simple addition of a minor component to stabilize the highly conductive α-AgI structure. The structures thus

* Electrochemical Society Active Member.
Key words: solid electrolyte structure, silver halide electrolytes, solid ionic conductors.

far reported are generally highly unique and unlike α-AgI. Also, several of the alkali metal iodides (LiI and NaI) and a large number of the nitrogenous-base QI compounds result either in no addition compound or a stable but nonconductive one. Geller (18) states that the common structural motif in the conductive compounds is the existence of passageways of face-shared iodide ion polyhedra. However, it has not been explained why such a variety of cationic and/or anionic groups produces such structures, while apparently similar groups do not, other than evidence that the ionic size plays a role (4, 19).

Several explanations have been proposed for the apparently unique ability of Ag^+ and Cu^+ ions to result in such structures. Armstrong *et al.* (20) have noted the near-uniqueness of Ag^+ and Cu^+ ions in forming stable 3- and 4-coordinated structures, and the role of $d\pi$ bonding by anions such as iodide in stabilizing such structures. Face-shared iodide ion tetrahedra appear to be a recurrent structural element in these compounds, and the energetics of silver ion migration through shared tetrahedral faces should be lowered if 3-coordinated complexes are stable. Quite recently, Phillips (21) has proposed that the borderline ionic-covalent character of AgI, resulting in comparable stability of Ag^+ in 4- and 6-coordination, permits a large variety of low symmetry "scaffolding" structures because of the low energetics of Ag-I bond-bending. In these structures, iodide complexes of the "minority cation" (M^+ in MAg_4I_5 and Q^+ in QI · nAgI) are said to provide a rigid skeletal framework which is "decorated" by loosely bound quasi-interstitial Ag^+ ions which supply a neutralizing charge sheath enveloping the over-all structure. Geller (22), however, maintains that there is really no crystallographic evidence for the relative rigidity of the minority cation part of the structure and "softness" of the AgI elements.

In 1975, I briefly proposed a basically geometric rationale for the existence of the conductive MAg_4I_5 and QI · nAgI structures (23). The purpose of the present communication is to expand upon this suggestion and offer additional, basically geometric, functions for the M^+ or Q^+ cation. The other categories of Ag^+ ion conductive solids and Cu^+ ion conductors will not be specifically discussed, since no detailed structures have yet been determined and because these geometric considerations are less readily visualized for, *e.g.*, the "anion-stabilized" conductors. Still, similar considerations may well apply.

How to Increase Face-Sharing

In AgI, MAg_4I_5, and the QI · nAgI compounds, it is clear that the geometric arrangement of the relatively large iodide ions determines whether a conductive structure results. The wurtzite and zinc blende structures of β- and γ-AgI, stable at room temperature, result in relatively poor conduction. The body-centered cubic structure of α-AgI, stable above 147°C, permits the highest Ag^+ ion conductivity in existence, despite being actually 5-6% denser than the β- and γ-AgI structures, so that Ag^+ ions should, in principle, have less "room" in which to migrate.

Geller and co-workers have determined the detailed structures of the room temperature Ag^+ ion conductors $RbAg_4I_5$ (24), $((CH_3)_4N)_2Ag_{13}I_{15}$ (25), and the two pyridinium iodide compounds $(C_5H_5NH)_5Ag_{18}I_{23}$ (26) and $(C_5H_5NH)Ag_5I_6$ (27). In each case, the common structural element permitting Ag^+ ion conductivity was identified as the presence of multiple-faced-shared iodide ion polyhedra, partially occupied by Ag^+ ions, which form networks of passageways for Ag^+ ion conduction through the structure. In the first three of these compounds, the polyhedra are tetrahedra; in the last, a mixture of tetrahedra and octahedra.

Figure 1 is a schematic of silver ion migration through a passageway of face-shared iodide ion tetrahedra. If these tetrahedra are only partially occupied, and if the energetics of passing through their shared triangular faces are relaxed by either facile bond-bending or the stability of 3-coordinated Ag^+ ion complexes, then conduction may result by Ag^+ ion hopping from filled to adjacent empty tetrahedra under the influence of an applied electric field. Obviously, at least two faces of each polyhedron must be shared with others to result in a network of conductive paths through the structure. In the $RbAg_4I_5$, $((CH_3)_4N)_2Ag_{13}I_{15}$, and $(C_5H_5NH)Ag_5I_6$ structures, a three-dimensional matrix of multiple-faced-shared iodide polyhedra extends throughout the structure, while in $(C_5H_5NH)_5Ag_{18}I_{23}$ the network is two-dimensional.

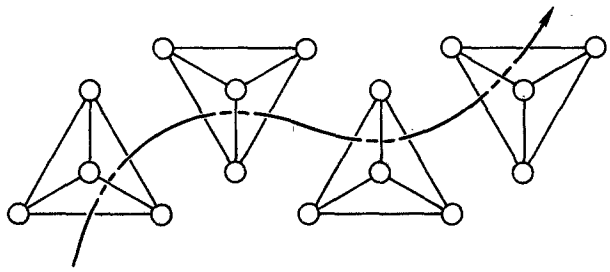


Fig. 1. Schematic of ion migration through face-shared tetrahedra. Though drawn separately for illustration, the ions on the shared faces are identical.

It is the central thesis of this section that an important function of the M^+ or Q^+ ion incorporated into a structure with AgI is to increase the degree of face-sharing by iodide ion coordination polyhedra, resulting in conductive structures, by coordinating a greater number of anions than the Ag^+ ion. To see how this is so, consider the wurtzite structure of β-AgI, from which the conductive MAg_4I_5 and QI · nAgI compounds can be considered to be formed by the addition of 10-20 mole percent (m/o) MI or QI. In this structure, shown in Fig. 2, each Ag^+ ion is coordinated by an I_4 tetrahedron. Each I^- ion "corner" is fourfold shared and each Ag^+-filled I_4 tetrahedron shares a face with one adjacent empty one. This arrangement does not in itself permit bulk conductivity, since the Ag^+ ion could at most hop back and forth between the pair of face-shared tetrahedra, and even this is energetically not permitted by the symmetry of the structure. Obviously the I_4 tetrahedron needs to share faces with at least two neighbor polyhedra, and the symmetry of the structure needs to be low enough to permit some randomness of occupancy without undue energetic "cost."

In solid crystalline compounds, corner-, edge-, and face-sharing of anion coordination polyhedra result as a necessity whenever the average coordination number of the cations is greater than the stoichiometric ratio of anions to cations (28). Only by such sharing are there enough anions to "go around." If, then, a significant mole fraction (*e.g.*, 0.1-0.2) of an iodide MI can form a solid solution with β-AgI in which the M^+ ion has a larger coordination number than the Ag^+ ion (>4), structures must result in which the degree of

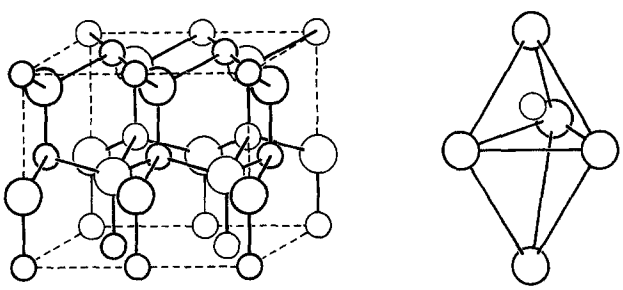


Fig. 2. The wurtzite crystal structure of β-AgI. The large circles represent I^- ions; small circles, Ag^+ ions.

face-sharing by iodide ion coordination polyhedra is considerably increased; very possibly to the point where a conductive structure results. The energetic feasibility of such structures may be argued from factors previously mentioned (polarizability of the large I^- ion, $d\pi$ bonding, low energetics of Ag-I bond-bending), but the driving force for increased face-sharing appears to be the increased coordination "demand" of the M^+ ions upon the available I^- ions.

A multiplicity of low symmetry structures seems permitted by the fact that most of the energy required for distortion from more regular geometric structures is recovered through electronic polarization. Since, in this variety of structures, a number of face-sharing arrangements are possible that greatly increase the "utilization" of the anions, structures can result where there is more anion-sharing than is required to accommodate the coordination numbers of all the cations. The result is that a number of the anion polyhedra are empty, which fulfills the additional requirement of a conductive structure besides face-sharing.

With this picture, the maximum Q^+ ion size and proportion for forming conductive $QI \cdot nAgI$ structures can be understood. For the larger Q^+ ions, the iodide ion coordination number would seem to be less a matter of specific chemical coordination than of the size of the "hole" required to accommodate the Q^+ ion; this hole being composed of the surrounding faces of the adjacent iodide ion polyhedra. If the Q^+ ion becomes too large, it will defeat its original purpose by "using up" in its coordination polyhedron the additional iodide ions made available by the more face-sharing arrangement it was employed to promote. The ultimate, and quite sudden, result is that anions are no longer available for forming empty polyhedra, and one obtains a perfectly stable structure that is an insulator. Owens (19) has reported that an abrupt transition from conductive to insulating structures occurs with few exceptions when the estimated Q^+ ion volume exceeds 85Å^3. This appears to hold for a broad variety of tetraalkylammonium and azacyclic substituted ammonium $QI \cdot nAgI$ compounds.

Owens' conductivity-composition data for the lower tetraalkylammonium compounds (3) show a maximum conductivity at 13 m/o QI for the Me_4NI-AgI system, 12½ m/o QI in the Me_2Et_2NI-AgI system, and 12 m/o QI for the Et_4NI-AgI system. Thus, as the size of the Q^+ ion increases, there is the expected decrease in the amount required to maximize the conductivity. In addition, while results were only reported at $\geq$ 5 m/o intervals for QI contents greater than 15 m/o, a rapid drop-off of conductivity was observed at higher QI contents, resulting in insulating compounds ($\sigma \sim 10^{-8}\ \Omega^{-1}\ cm^{-1}$) at $\geq$ 33.3 m/o QI. Thus, increasing the proportion of QI in compounds formed from the lower molecular weight Q^+ ions would seem to have the same effect as increasing the size of the Q^+ ion at constant mole fraction; that of "tying up" I^- ions needed for the formation of empty polyhedra.

Additional Additive Ion Functions

Another function of the M^+ or Q^+ additive ion appears to be that of reducing distortion energy in the space-filling arrangement of the iodide ions. We have already noted that in the $RbAg_4I_5$, $((CH_3)_4N)_2Ag_{13}I_{15}$, and $(C_5H_5NH)Ag_5I_6$ structures, the multiple-faced-shared iodide ion polyhedra form a three-dimensional network, extending throughout the structure to fill the space not occupied by the M^+ or Q^+ ions, while in the $(C_5H_5NH)_5Ag_{18}I_{23}$ structure, the network is two-dimensional. In all of the structures, Ag^+ ions appear to prefer 4-coordination, resulting in iodide ion tetrahedra for all Ag^+ sites except a minor fraction of those in the $(C_5H_5NH)Ag_5I_6$ structure.

From the viewpoints of coordination and conductivity, then, the "ideal" structure would be a space-filling arrangement of completely face-shared I_4 tetrahedra. Regular tetrahedra, however, cannot by themselves form space-filling arrangements without distortion. Much of this distortion may be removed by replacing an occasional tetrahedron by a higher order polyhedron. Thus, space is completely filled without distortion by a 2:1 arrangement of regular tetrahedra and octahedra of the same size faces (*i.e.*, in the fcc structure) and is filled with only modest distortion if a smaller number of octahedra is employed. The latter appears to be the arrangement in $RbAg_4I_5$, where tetrahedral distortion in an icosahedral arrangement of 56 I_4 tetrahedra per unit cell is reduced by the presence of 4 distorted RbI_6 octahedra in a cubic-symmetry arrangement.

It follows that tetrahedral distortion could likewise be reduced by the substitution of an occasional Ag^+ ion by any of a number of monovalent cationic species that would create a "hole" somewhat larger and more many-sided than an I_4 tetrahedron, or even a continuous structural element such as the hexagonal "tunnel" holes in the $(C_5H_5NH)Ag_5I_6$ structure. We have already discussed the effect of size for the organic-based cations. For the MAg_4I_5 structures, the suitable size range for the alkali cation would seem to be that which is optimal for the distortion-reducing MI_6 octahedral hole.

In the structures with the larger organic-base cations, the "determinative structural role" of the minority cation suggested by Phillips (21) becomes quite evident. Thus, it is not surprising that the pyridinium compounds have the hexagonal symmetry of the pyridinium group and the hole it occupies. In these cases, Phillips' "scaffolding" structures for the minority cation seem reasonable, and one can envision that the cation acts as a "seed site" for a particular space-filling structure of face-shared iodide ion polyhedra.

Summary

In conclusion, the minority cation, M^+ or Q^+, seems to serve several functions in creating ionically conductive structures with β- or γ-AgI. First, AgI is capable of participating in a variety of low symmetry structures because of the small energy differences associated with various Ag-I bonding geometries. Addition of an M^+ or Q^+ ion that coordinates 6 iodide ions or a Q^+ ion that requires an n-hedral iodide ion "hole" with $n > 4$ encourages the formation of structures with the much increased degree of face-sharing by I^- coordination polyhedra required for conductive structures. The increased utilization of the I^- ions in these structures also permits a stoichiometric excess of I^- polyhedra over Ag^+ and M^+ (or Q^+) ions, resulting in the second requirement of conductive structures. However, introduction of too many M^+ or Q^+ ions, or of Q^+ ions that are too large, "uses up" the excess coordination capacity that permits empty polyhedra and results in insulating structures. In addition, the M^+ or Q^+ ion helps stabilize these structures of predominantly space-filling face-shared I^- ion tetrahedra by creating holes that reduce tetrahedral distortion. Also, at least in the case of the larger Q^+ ions, the minority cation plays a determinative role in the symmetry and over-all arrangement of the structure.

Manuscript received Jan. 31, 1977.

Any discussion of this paper will appear in a Discussion Section to be published in the June 1978 JOURNAL. All discussions for the June 1978 Discussion Section should be submitted by Feb. 1, 1978.

Publication costs of this article were assisted by Rockwell International.

REFERENCES

1. J. N. Bradley and P. D. Greene, *Trans. Faraday Soc.*, **62**, 2069 (1966); *ibid.*, **63**, 424 (1967).
2. B. B. Owens and G. R. Argue, *Science*, **157**, 308 (1967).
3. B. B. Owens, *This Journal*, **117**, 1536 (1970).

4. B. B. Owens, J. H. Christie, and G. T. Tiedeman, *ibid.*, **118**, 1144 (1971).
5. T. Takahashi, S. Ikeda, and O. Yamamoto, *ibid.*, **119**, 477 (1972).
6. T. Takahashi, S. Ikeda, and O. Yamamoto, *ibid.*, **120**, 647 (1973).
7. G. Chiodelli, A. Magistris, and A. Schiraldi, *Electrochim. Acta*, **19**, 655 (1974).
8. B. Scrosati, F. Papaleo, G. Pistoia, and M. Lazzari, *This Journal*, **122**, 339 (1975).
9. G. W. Mellors and D. V. Louzos, *ibid.*, **118**, 846 (1971).
10. M. L. Berardelli, C. Biondi, M. De Rossi, G. Fonseca, and M. Giomini, *ibid.*, **119**, 114 (1972).
11. T. Takahashi, N. Wakabayashi, T. Miyazaki, and O. Yamamoto, *Nippon Kagaku Kaishi*, **1975** (2), 266.
12. R. G. Linford, J. M. Pollock, and C. F. Randell, *Nature*, **256**, 398 (1975).
13. J. H. Christie, B. B. Owens, and G. T. Tiedeman, *Inorg. Chem.*, **14**, 1423 (1975).
14. T. Takahashi, K. Kuwabara, and O. Yamamoto, *This Journal*, **120**, 1607 (1973).
15. T. Takahashi, *J. Appl. Electrochem.*, **3**, 79 (1973).
16. T. Takahashi, O. Yamamoto, and S. Ikeda, *This Journal*, **120**, 1431 (1973); T. Takahashi and O. Yamamoto, *ibid.*, **122**, 83 (1975).
17. A. F. Sammells, J. Z. Gougoutas, and B. B. Owens, *ibid.*, **122**, 1291 (1975).
18. S. Geller, in "Fast Ion Transport in Solids," W. van Gool, Editor, p. 607, North Holland, Amsterdam (1973).
19. B. B. Owens, "Advances in Electrochemistry and Electrochemical Engineering," Vol. 8, p. 57, John Wiley & Sons, Inc., New York (1971).
20. R. D. Armstrong, R. S. Bulmer, and T. Dickinson, in "Fast Ion Transport in Solids," W. van Gool, Editor, p. 269, North Holland, Amsterdam (1973).
21. J. C. Phillips, *This Journal*, **123**, 934 (1976).
22. S. Geller, Private communication.
23. D. O. Raleigh, in "Topics in Pure and Applied Electrochemistry," S. K. Rangarajan, Editor, p. 103, SAEST Commemorative Publication, Karaikudi, India (1975).
24. S. Geller, *Science*, **157**, 310 (1967).
25. S. Geller and M. D. Lind, *J. Chem. Phys.*, **52**, 5854 (1970).
26. S. Geller, P. M. Skarstad, and S. A. Wilber, *This Journal*, **122**, 332 (1975).
27. S. Geller, *Science*, **176**, 1016 (1972); S. Geller and B. B. Owens, *J. Phys. Chem. Solids*, **33**, 1241 (1972).
28. See, for instance, E. W. Gorter, *J. Solid State Chem.*, **1**, 279 (1970).

EMF Studies of Lithium-Rich Lithium-Aluminum Alloys for High-Energy Secondary Batteries

J. R. Selman,*[1] D. K. DeNuccio,[2] C. J. Sy, and R. K. Steunenberg*

Argonne National Laboratory, Chemical Engineering Division, Argonne, Illinois 60439

ABSTRACT

Emf measurements were made across the lithium-rich half of the lithium-aluminum system at temperatures from 390° to 550°C using a cell of the type Li/LiCl-KCl (or LiF-LiCl-LiBr)/Li-Al. The lithium activity increases from 0.007 to approximately 0.7 over the composition range of 48-56 atomic percent (a/o) lithium (the β-phase region). A compound, Li_3Al_2, rather than Li_2Al, as reported in standard compilations, exists at temperatures up to the peritectic decomposition at 520°C and forms a two-phase region of high lithium activity (>0.85) with the lithium-rich liquid phase. This compound has an estimated free energy of formation of −58 kJ/mole at 700°K. The emf data indicate that the lithium-rich liquidus is about 2 a/o richer in lithium than the composition shown in standard compilations of binary phase diagrams.

The present work was prompted by an interest in lithium-rich alloys as potential electrode materials. Lithium has attracted attention as a negative electrode material in the development of high-energy secondary batteries (Li/Cl_2, Li/S, Li/FeS_x). The metal, which is liquid at the operating temperatures of these batteries (400°-500°C), is usually contained in a porous nickel or stainless steel matrix. Cells containing liquid lithium electrodes pose special materials problems because of the extreme corrosivity of the metal, particularly toward ceramics. These problems are compounded by: (*i*) The solubility of lithium in the molten LiCl-KCl electrolyte (approximately 0.17 mole percent (m/o) at 700°K), and (*ii*) a gradual decrease of the capillary retention of lithium by most matrix materials upon repeated charge-discharge cycling. This "de-wetting" tendency may lead to cell shorting by lithium globules.

These problems can be avoided or alleviated by using a lithium alloy that is solid at the cell operating temperature (1). The most commonly used alloy is β-phase lithium-aluminum, of nominal composition LiAl, which melts at 718°C (991°K). During most of the charge and discharge, the electrode composition traverses a two-phase region consisting of a saturated solid solution of lithium in aluminum (α-phase) and the β-phase.

The potential of the two-phase alloy is approximately +0.3V relative to lithium metal, which corresponds to a lithium activity of 0.007 of the pure metal. This loss of emf over most of the discharge, compared with a cell containing a liquid lithium electrode, and the relatively low weight fraction of lithium, 20 weight percent (w/o) in the β-phase alloy, imply a considerable (15-20%) decrease in the specific energy of the cell. It would be desirable to use alloys having lithium concentrations higher than 50 atomic percent (a/o) to increase the specific energy of the cell, provided that the lithium activity of the alloy does not exceed a value of, say, 0.2.

The compound Li_2Al, which had been reported by earlier investigators (2, 3) and is represented in standard compilations (4), was considered as a potential candidate. Also, the compounds Li_3Al_2 and Li_9Al_4 have recently been identified at room temperature (5, 6) and would be potential candidates, if stable at 400°-500°C.

Little information is available on the lithium activity of solid lithium-aluminum alloys outside the ($\alpha + \beta$) two-phase region. Emf measurements at 300°-380°C by

* Electrochemical Society Active Member.
[1] Present address: Department of Chemical Engineering, Illinois Institute of Technology, Chicago, Illinois 60616.
[2] Present address: Southern Illinois University, Carbondale, Illinois 62901.
Key words: high temperature cell, LiAl, Li_3Al_2, Li_2Al, phase diagram.

Yao *et al.* (1) indicate an initial decrease of the emf in the β-phase, relative to the value of +0.3V *vs.* liquid lithium observed in the two-phase region. At 50 a/o lithium, the richest composition reported, the emf appears to be approximately +0.18V.

Consequently, the present work was directed first toward obtaining a lithium-activity profile for the lithium-rich half of the phase diagram at temperatures between 400° and 500°C. It was expected that this would also yield indirect information confirming or contradicting the existence of the various compounds mentioned earlier. Two rather divergent sets of data have been reported for the alloy composition at the lithium-rich liquidus. At 427°C (700°K) the liquidus composition is 84 a/o according to Shamray and Saldau (3), whose liquidus data are adopted in Hansen's standard compilation. Grube *et al.* (2) report the liquidus composition as 86 a/o at 427°C. Therefore, accurate data were sought for the alloy composition at the lithium-rich liquidus using coulometric methods.

We report here electromotive force measurements of lithium-rich alloys using the cell

$$\text{Li (l, in Feltmetal}^{3}) \;\Big|\; \begin{matrix}\text{LiCl-KCl}\\ \text{(eutectic)}\\ \text{or}\\ \text{LiF-LiCl-LiBr}\\ \text{(eutectic)}\end{matrix} \;\Big|\; \text{Li}_x\text{Al}_{1-x} \;\Big|\; \begin{matrix}\text{s}\\ \text{or}\\ \text{l}\end{matrix} \qquad [1]$$

Two types of measurements were carried out: measurements at fixed alloy composition in which the temperature was varied, and measurements at constant temperature in which the composition was varied coulometrically.

Experimental

Materials.—Lithium metal (Foote Mineral Corporation) was premelted in a tantalum cup at 200°C and drawn in droplets from the bottom through a hole stoppered by a conical tantalum spike. This operation, as well as the subsequent alloying and the emf measurements, took place in a high purity helium atmosphere glove box with continuous purification of the recirculated helium. Small drops (0.1-0.3g) of lithium were obtained, and only those which were visibly free of oxide or nitride layers (yellow hue) were used in this study.

Small lithium reference electrodes were made by absorbing lithium drops into porous stainless steel or nickel plaques (Feltmetal) at 600°C. The excess lithium was removed by contacting it with an empty plaque of porous metal at the same temperature.

Samples of the lithium-aluminum alloys were prepared by heating carefully weighed amounts of the metals together at 750°-800°C, stirring the melt, and absorbing it quickly in stainless steel or nickel Feltmetal or in tantalum frits, followed by annealing for 48 hr at 500°C. The aluminum metal (Materials Research Corporation) was of 99.99% purity. The composition of the alloy samples was checked by analysis as indicated below.

The LiCl-KCl eutectic (58.8 m/o LiCl-41.2 m/o KCl, mp 352°C) was obtained from the Anderson Physics Laboratory, Urbana, Illinois. For some of the experiments an all-lithium cation eutectic (22 m/o LiF-31 m/o LiCl-47 m/o LiBr, mp 430°C) was prepared from purified individual salts supplied by the Anderson Physics Laboratory.

Apparatus and procedure.—The cell shown in Fig. 1 was used for the emf measurements at fixed sample composition and varying temperature. This cell design was suggested by the desirability of a large area lithium reference electrode whose activity would not be affected by the inevitable slow reaction with gaseous

[3] A porous metallic material produced by the Brunswick Corporation

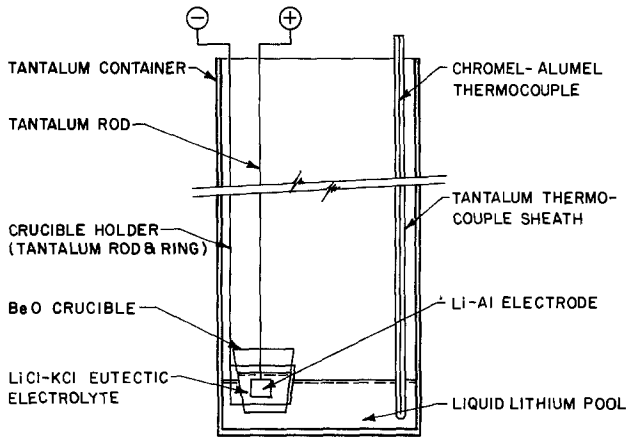


Fig. 1. Schematic diagram of cell for lithium-aluminum alloy emf measurements.

impurities in the helium atmosphere; in addition, temperature uniformity (± 1°C) was maintained in this cell by the liquid lithium pool, of approximately 10 cm diam and 1 cm depth. The lithium was skimmed from time to time to remove surface impurities.

The electrolyte and the alloy electrode were contained in a porous BeO crucible which separated the electrode from the lithium pool electrode. The crucible (National Beryllia Corporation) had a porosity of approximately 20% and was 2.5 cm in diameter and height, with a 0.2 cm wall thickness. Rapid self-discharge of the emf cell occurred in the absence of this barrier because of the high lithium activity of the electrolyte in contact with lithium metal or an alloy of high lithium activity.

Temperature equilibrium was usually attained within 20 min following a 20°C step, so that a series of traverses (390°-520°C) could be made with one sample of alloy in one or two days. Emf equilibrium appeared to follow temperature equilibrium very rapidly.

In the coulometric emf measurements, a weighed sample of liquid alloy was anodically oxidized to decrease the lithium content and the emf was recorded at regular intervals following current interruption. The current level was chosen such that the emf would reach steady state (± 1 mV) in less than 15 min.

In these measurements it was found advantageous to reverse the arrangement of Fig. 1 so that the lithium reference electrode was contained in the porous plaque and the alloy pool surrounded the BeO crucible. Therefore, the sample size of the alloy could be made fairly large (typically 4g) as compared with that contained in a porous plaque (0.1-0.4g).

This arrangement proved advantageous in spite of the longer time required to obtain a desired change in composition of the alloy while using the same current. The lithium initially contained as liquid alloy in a porous plaque electrode was removed at a rate far greater than the coulometric oxidation rate. This effect was apparently the result of appreciable solubility of lithium in the electrolyte, associated with the high lithium activity of the liquid alloy.

In the reverse arrangement of that shown in Fig. 1 the measured emf's were satisfactorily stable and reproducible. Since the ratio of the electrolyte interfacial area to the sample volume is much smaller in this cell arrangement, a likely explanation for the difference in stability is that immersed lithium alloy is oxidized more easily and continuously via impurities in the melt than in lithium alloy in direct contact with the atmosphere.

The cell temperature was measured by means of a tantalum-sheathed Chromel-Alumel thermocouple which had been calibrated against the freezing points of tin (231.9C), zinc (419.5°C,) and aluminum (659.7°C). The thermocouple emf's were read by amplifying and

recording a difference signal with respect to a L&N K-3 universal potentiometer.

The cell emf's were read with a Dana Model 5000 digital multimeter (input resistance greater than $10^{10}\Omega$) to ± 0.01 mV. The reproducibility and accuracy of emf's measured at fixed composition during fairly short periods were ± 2 mV. The uncertainty can be ascribed in part to diffusion potentials of variable magnitude caused by composition changes of the LiCl-KCl electrolyte in the pores of the BeO crucible. The electrolyte, in contact with liquid lithium, undergoes a displacement reaction

$$\mathrm{Li(l) + KCl(l) \rightarrow K(l) + LiCl(l)} \qquad [2]$$

The standard equilibrium constant of this reaction[4] at 427°C is $K = 0.046$, and at 527°C, $K = 0.084$. Since the partial pressure of potassium is appreciable at these temperatures (0.4 Torr at 427°C), reaction [2] can proceed to a considerable extent, especially at temperatures in excess of 450°C, as shown by Seefurth and Sharma (7).

The porous separator prevents rapid diffusion of excess LiCl formed at the interface (lithium/electrolyte) toward the bulk of the electrolyte, and of KCl from the bulk toward the depleted zone. Therefore, a concentration cell emf results, which declines very slowly. In accordance with this picture, a constant-sign bias potential was observed when the alloy electrode in Fig. 1 was replaced by a porous plaque electrode containing pure lithium. Whenever the bias potential was steady over several hours, the alloy emf was corrected for it; however, fluctuations of the bias potential were common, which suggests that other causes of instability were involved.

To avoid the potassium-displacement reaction [2], an all-lithium cation electrolyte was used in part of the measurements. The LiF (22 m/o)-LiCl (31 m/o)-LiBr (47 m/o) eutectic has a mp of 430°C. Stable emf's could be obtained in this electrolyte at temperatures above approximately 460°C. Attempts to use a mixture of LiF (14.7 m/o)-LiCl (35.5 m/o)-LiBr (20.0 m/o)-LiI (29.8 m/o), for which the melting range was 318°-326°C, failed because the stainless steel or nickel substrate of the porous plaque electrode was strongly attacked by the electrolyte. Therefore, measurements in the temperature range 400°-470°C were carried out with LiCl-KCl eutectic.

Chemical analyses.—Chemical analyses were performed on samples of the alloy before and after the emf measurements. The alloy was dissolved in HCl and the aluminum was separated as an oxalato complex by anion exchange (8). Lithium was determined by atomic absorption spectrometry (1-2% accuracy) or by mass spectrometry with isotopic dilution. The latter technique, using standards supplied by Oak Ridge National Laboratory, was used for small samples where a lithium-aluminum separation was impractical; its accuracy is 0.5%. Aluminum was determined by precipitation by 8-hydroxyquinoline (9).

Samples analyzed after the emf measurements contained electrolyte adhering to the alloy; the metallic lithium content was back-calculated from halide-ion or K^+-ion content by subtracting the Li^+-ion concentration corresponding to the known electrolyte composition.

The analyzed composition of the alloy in most cases agreed with the weighed composition within 1 a/o, which is assumed to be the uncertainty of the alloy compositions reported here. No signficant change in alloy composition was detected after the emf measurements (except in the coulometric sample) if the temperature did not exceed 500°C for extended periods.

Results and Discussion

The emf's of eight alloy samples were measured at various temperatures between 390° and 530°C. The analyzed compositions of the alloys, the emf's, and the lithium activities at 427°C (700°K) are listed in Table I. Also included in this table is a value for the emf in the two-phase $\alpha + \beta$ region, extrapolated to 427°C from measurements by Yao *et al.* (1) at 300°, 350°, and 380°C.

[4] Taking solid standard states for LiCl and KCl.

Table I. Emf and activity, at 427°C (700°K), and temperature coefficient of the emf (390°-470°C) of lithium-rich lithium-aluminum alloys

Atomic percent Li	Emf (mV)	Activity *vs.* Li^+/Li°	dE/dT (mV/°C)	Reference
49.3	53.0	0.415	−0.40	This work
49.8	48.5	0.448	−0.40	
50.5	57.0	0.389	−0.34	
56.8	24.0	0.672	+0.05	
59.1	21.0	0.706	+0.08	
62.8	7.5	0.883	+0.11	
69.3	10.0	0.847		
82.3	7.5	0.883		
$\alpha + \beta$	296.0*	0.007	−0.225*	(2)

* Extrapolated from measurements in the temperature range 300°-380°C.

The emf data shown in Table I and in Fig. 2 project a consistent picture of the lithium activity as a function of composition: (*i*) The steep decrease in emf as the lithium fraction exceeds 48 a/o, which was already suggested by the earlier work (1), is clearly substantiated by the present results. There appears to be no intermetallic compound with a lithium activity 0.1-0.2, except the β-phase itself over the narrow composition interval of 48-50 a/o lithium. (*ii*) No significant emf discontinuity is observed at 67 a/o Li (composition Li_2Al) or 69 a/o (Li_9Al_4), but a phase transition at 60 a/o Li (Li_3Al_2) is suggested by the data.

Attempts were made to carry out coulometric emf measurements in the range of 50-80 a/o lithium, and thereby establish the location of phase transitions. These attempts were not successful because of a high rate of self-discharge in conjunction with the low current levels necessary to avoid polarization of the wholly or partly solid electrode.

However, the present results are in good agreement with conclusions of a concurrent DTA investigation of

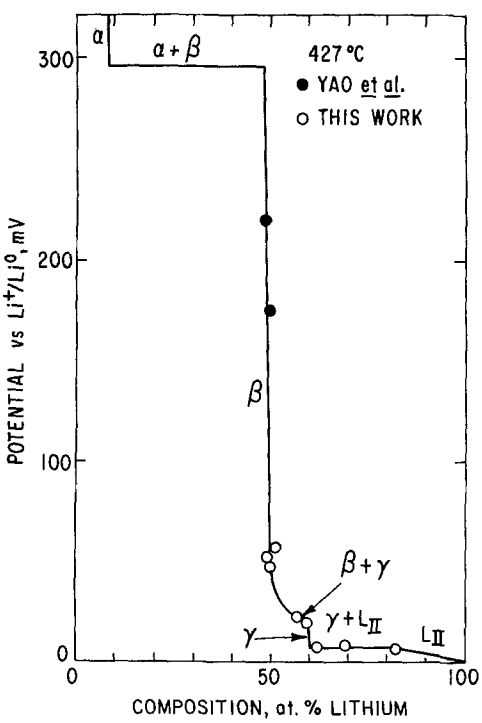


Fig. 2. Emf-composition diagram of lithium-aluminum alloy at 700°K.

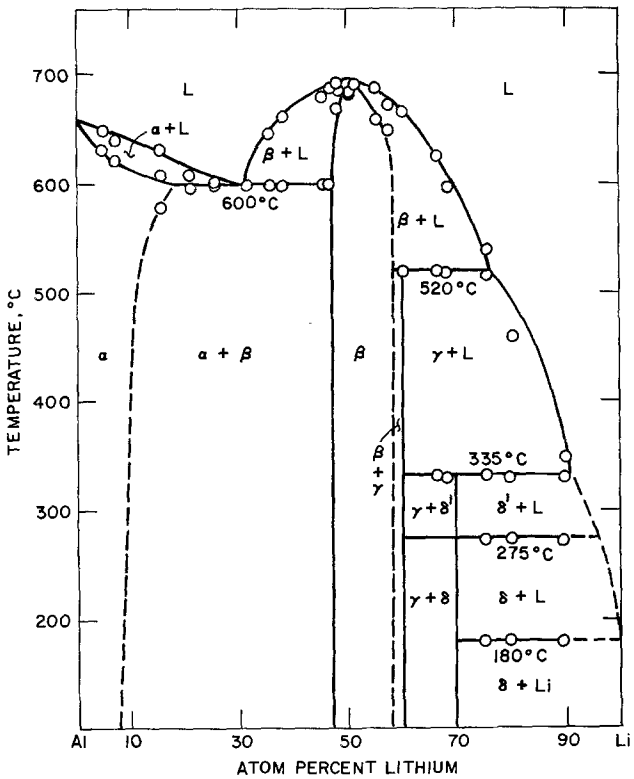


Fig. 3. Revised phase diagram of the lithium-aluminum system according to Myles and Settle (10).

the Li-Al systems by Myles and Settle of Argonne National Laboratory (10) (see Fig. 3). According to their results, the β-phase (nonstoichiometric solid LiAl) at 700°K extends from a composition between 47 and 48.3 a/o lithium to a composition in excess of 56 a/o. [The solid compound Li_3Al_2 exists, but neither Li_2Al nor Li_9Al_4 is present at 700°K. A two-phase alloy, solid Li_3Al_2 + lithium-rich liquid (L_{II}), therefore, is present at compositions in excess of 60 a/o lithium.] As shown in Fig. 3, the compound Li_3Al_2 was found to decompose peritectically at 520°C, while the compound Li_9Al_4 undergoes a peritectic decomposition at 335°C. Thus at 700°K and for compositions in excess of 60 a/o lithium, the stable phases are Li_3Al_2 and liquid lithium saturated with aluminum. The emf results are consistent with this phase diagram.

In the emf-composition diagram at 427°C (700°K), Fig. 2, the composition ranges of the phases and two-phase mixtures are taken from the phase diagram shown in Fig. 3. The lithium-rich boundary of the β-phase at 427°C was assumed to be 48 a/o lithium. A solid-solid, two-phase region, β + $Li_3Al_2(\gamma)$, is indicated in Fig. 2 although its existence and extent cannot be inferred with any certainty from the emf data. Hansen and Anderko (4) indicate 56 a/o lithium as the lithium-rich boundary of the β-phase, based on the work of Shamray (3). The recent DTA investigations do not pinpoint the boundary more accurately (Fig. 3). The lithium-rich liquidus is located at 86 a/o, in agreement with Ref. (3). Two emf data points in the β-phase region (Fig. 2) were obtained from the work of Yao *et al.* (1) by extrapolation to 700°K.

The present data, in conjunction with emf data for the two-phase α + β alloy, allow a rough estimate of the free energy of formation of Li_3Al_2, according to the reactions

$$Li + Al(\alpha) \rightarrow LiAl(\beta) \qquad [3]$$

and

$$Li + 2LiAl(\beta) \rightarrow Li_3Al_2(\gamma) \qquad [4]$$

If the presence of lithium in the α-phase is neglected, and the composition of the β-phase is considered stoichiometric, *i.e.*, LiAl, this yields, at 427°C

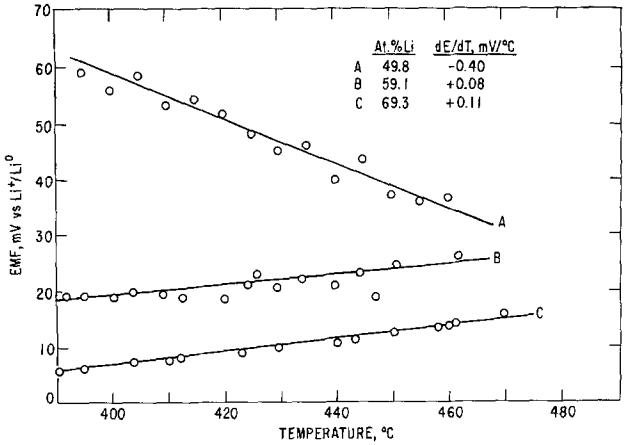


Fig. 4. Temperature dependence of the emf for alloy compositions in three different regions of the Li-Al phase diagram.

$$\Delta G_f\, LiAl(\beta) = -28.6\ kJ/mole$$

$$\Delta G_f\, Li_3Al_2(\gamma) = -58\ kJ/mole$$

The effect of temperature on the emf is illustrated in Fig. 4, for temperatures between 390° and 470°C. In the β-phase the emf temperature coefficient is negative, as is the temperature coefficient found by Yao *et al.* (1), for the two-phase α + β alloy in the temperature range of 300°-380°C (see Table I). At the lithium-rich end of the β-phase region the coefficient becomes positive. Since the temperature coefficient in the two-phase regions is directly proportional to the entropy change in lithium-addition reactions such as [3] and [4], it is apparent that β-phase formation from α-phase involves an entropy decrease, whereas further lithium addition leads to an entropy increase. This behavior appears to parallel the volume change in reactions [3] and [4] which is negative in the formation of β-phase from α-phase, and positive from β-phase to Li_3Al_2, according to room temperature density data (6).

The coulometric emf measurements to determine the lithium-rich liquidus composition started with an alloy sample containing 90.0 a/o lithium at 470°C; in these measurements the LiF-LiCl-LiBr eutectic electrolyte was used. Using the reverse cell design of Fig. 1, the sample was anodically oxidized and emf readings were taken at intervals. As shown in Fig. 5, the emf readings were sensitive to the current level; at the lower current level indicated, the emf curve in the liquid range was satisfactorily reproducible.

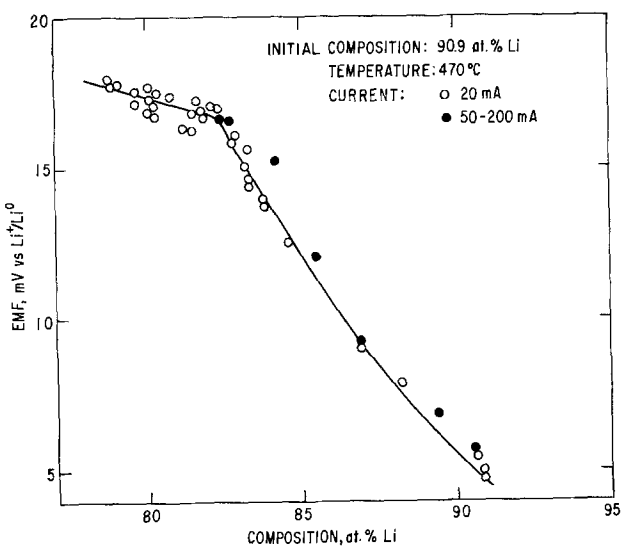


Fig. 5. Coulometric emf measurements on a liquid alloy sample at 470°C.

The discontinuity in the curve at 82.8 (±0.3) a/o corresponds to the phase transition at the liquidus composition. To the left of this point (two-phase region) the emf should be independent of composition; actually, the emf showed a slight tendency to increase but the values were rather scattered and tended to level off upon repeated cycling across the phase boundary. The large spread and the initially high values are probably caused by local formation of alloy containing less than 60 a/o lithium in the pores of the BeO separator.

The liquidus composition, 82.8 a/o at 470°C, agrees more closely with the data of Grube *et al.* (2) than with those of Shamray and Saldau (3), which were adopted by Hansen.

Figure 6 illustrates the relationship between the lithium activity and composition at the lithium-rich liquidus. The triangles are the lithium activities of a two-phase alloy sample (69.3 a/o lithium) measured with a cell as in Fig. 1. Here the emf was measured up to 550°C; the discontinuity at 522°C agrees very well with the peritectic decomposition temperature for "Li_2Al" (actually, Li_3Al_2) given by Hansen and that found by Myles *et al.* (10).

The liquidus composition at 470°C ($X_{Li} = 0.828$) is plotted in Fig. 6 as a black dot. The lithium activity coefficient at 470°C is 0.94; this is in agreement with the negative deviation from ideality recently reported (11) for the entire liquid alloy composition range between 630° and 820°C.

It is seen from Fig. 6 that the liquidus compositions reported by Shamray and Saldau (3) would lead to positive deviation from ideality below 425°C. Although this is not impossible, the evidence presented here strongly suggests that the liquidus compositions reported by Grube *et al.* (2), rather than those of Shamray and Saldau (3), are correct.

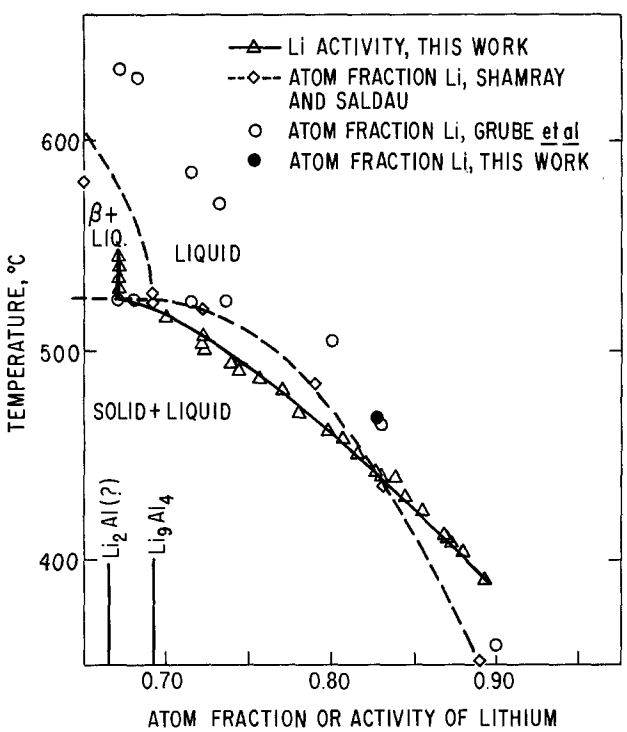


Fig. 6. Lithium activities and mole fractions at the lithium-rich liquidus as a function of temperature.

Conclusions

1. The lithium activity of β-phase lithium-aluminum alloy increases steeply, from 0.007 to approximately 0.7, as the alloy composition changes from 48 to 56 a/o lithium. In view of this high lithium activity, alloys containing more than 50 a/o lithium do not appear to be suitable as substitutes for lithium in the negative electrodes of high temperature batteries.

2. The compound Li_3Al_2, rather than Li_2Al as reported in compilations, is stable at temperatures below 520°C. With lithium-rich liquid, Li_3Al_2 forms a two-phase region of high (>0.85) lithium activity. The compound Li_3Al_2 has an estimated $\Delta G_f°$ from the elements of −58 kJ/mole at 427°C (700°K).

3. Coulometric emf measurements at 470°C and activity measurements over an extended temperature range indicate that the lithium-rich liquidus is approximately 2 a/o closer to the liquid lithium axis than is shown in standard compilations; the liquidus composition reported by Grube *et al.* (2) appears to be correct.

Acknowledgments

The analytical assistance of K. J. Jensen, R. E. Telford, and I. M. Fox is gratefully acknowledged. The authors wish to thank Drs. M. Blander, M. L. Saboungi, and J. E. Battles for their comments in the preparation of the manuscript. This work was performed under the auspices of the U.S. Energy Research and Development Administration.

Manuscript submitted Dec. 16, 1976; revised manuscript received March 14, 1977.

Any discussion of this paper will appear in a Discussion Section to be published in the June 1978 JOURNAL. All discussions for the June 1978 Discussion Section should be submitted by Feb. 1, 1978.

Publication costs of this article were assisted by Argonne National Laboratory.

REFERENCES

1. N. P. Yao, L. A. Heredy, and R. C. Saunders, *This Journal*, **118**, 1039 (1971).
2. G. Grube, L. Mohr, and L. Breuning, *Z. Elektrochem.*, **41**, 880 (1935).
3. F. I. Shamray and P. Ya. Saldau, *Izv. Akad. Nauk SSSR, Otd. Khim. Nauk*, 631 (1937).
4. M. Hansen and K. Anderko, "Constitution of Binary Alloys," McGraw-Hill Book Co. Inc., New York (1958).
5. D. A. Hansen and J. F. Smith, *Acta Crystallogr.*, **24**, 913 (1968).
6. K. F. Tebbe, H. F. v. Schnering, B. Ruter, and G. Rabeneck, *Z. Naturforsch., Teil B*, **28**, 600 (1973).
7. R. N. Seefurth and R. A. Sharma, *This Journal*, **122**, 1049 (1975).
8. F. W. E. Strelow, C. H. S. W. Weinert, and C. Eloff, *Anal. Chem.*, **44**, 2352 (1972).
9. V. N. Tikhonov, "Analytical Chemistry of Aluminum," p. 31, John Wiley & Sons, Inc., New York (1973).
10. K. M. Myles, F. C. Mrazek, J. A. Smaga, and J. L. Settle, Proceedings of Symposium and Workshop on Advanced Battery R.&D., March, 1976, U.S. ERDA Report No. ANL-76-8, p. B-50.
11. S. P. Yatsenko and E. A. Saltikova, *Russ. J. Phys. Chem.*, **48**, 1402 (1974).

On the Composition of the Passivating Films Formed on Aluminum in Chromate Solutions

Milena Koudelkova, J. Augustynski, and H. Berthou

Département de Chimie Minérale, Analytique et Appliquée, Université de Genève, Geneva, Switzerland

ABSTRACT

The chemical constitution of the passive oxide films formed on aluminum in chromate and chromate/chloride solutions under simple immersion (at open-circuit potential) and under anodic polarization has been investigated by means of x-ray photoelectron spectroscopy. It has been shown that these films, whose thickness is comparable with the mean escape depth of photoelectrons, are composed of a mixture of hydrated chromium (III) oxide, aluminum (III) oxide, and chromium (VI) species. A considerable amount of chloride species has been detected in the films formed in chromate/chloride solutions, independently whether chlorides were initially present in the solution or were added only after 18 hr immersion of the sample in chromates. The extent of chloride incorporation within the oxide film from CrO_4^{2-}/Cl^- solution was not modified by the anodic polarization of aluminum from open-circuit potential up to critical pitting potential. This situation is quite different from that observed in chloride solutions, in the absence of chromates, where the amount of chlorides in the oxide film increases appreciably between E_{st} and E_{cr}. The nature of the inhibiting effect of chromate ions on the pitting corrosion of aluminum is discussed on the basis of these results.

Although numerous studies have been devoted to clarifying the mechanism by which chromate ions inhibit the corrosion of aluminum, the exact nature of this phenomenon is still under discussion. Edeleanu and Evans (1) first attributed the inhibiting effect of chromate solutions to a redox reaction occurring between CrO_4^{2-} ions and aluminum metal to form aluminum oxide and Cr^{3+} ions. Their suggestion was further examined by Pryor (2), and by Heine and Pryor (3), who found that γ-Al_2O_3 films formed on aluminum by passivating chromate solutions exhibited lower ionic resistance and higher electronic resistance than amorphous films of comparable thickness produced by thermal oxidation. According to these authors, the inhibiting effect of chromate ions on the pitting corrosion of aluminum in chloride solutions can be explained by strong specific adsorption of divalent CrO_4^{2-} ions on the film-solution interface, preventing simultaneous adsorption of monovalent Cl^- ions and their entry into the γ-Al_2O_3 lattice. This latter theory has since received indirect support in the investigation of Böhni and Uhlig (4), who showed the existence of a linear relationship between the logarithm of the activity of Cl^- ions, and the logarithm of the activity of CrO_4^{2-} ions required to shift the critical pitting potential of aluminum to an arbitrary noble value of 0.8V *vs.* NHE. Recently, Abd Rabbo *et al.* (5) have studied the changes in the composition of anodically formed aluminum oxide films after immersion in chromate/dichromate solutions, using secondary ion mass spectrometry (SIMS). A layer of uniformly distributed Cr^+ ions[1] was detected in the outer regions of the films on immersed specimens, followed by localized Cr^+-rich areas down to the metal-oxide interface. On the basis of these results the authors have concluded that, in addition to a gradual chromate/dichromate anion entry into the film material from the oxide-solution interface, the $CrO_4^{2-}/Cr_2O_7^{2-}$ species underwent reduction to Cr_2O_3 within flaws in the film. However, the technique of ion microprobe mass spectrometry being unable to distinguish between different oxidation states of a given element, the results of Abd Rabbo *et al.* cannot be considered as direct experimental evidence for the specific incorporation of a Cr(III) species into the surface oxide film on aluminum.

Key words: x-ray photoelectron spectroscopy, inhibiting anions, chlorides.

[1] A secondary ion species produced during analysis of the sample by SIMS.

In the present study, x-ray photoelectron spectroscopy (XPS or ESCA) was used to examine the composition of the surface films formed on aluminum in chromate and chromate/chloride solutions at open circuit and under anodic polarization. The aim of this investigation was, on the one hand, to determine the extent of incorporation of different chromium species into the oxide film and, on the other hand, to clarify the effect of these species on the entry of chloride into the film.

Experimental

XPS spectra were obtained on a Varian IEE-15 photoelectron spectrometer using $MgK\alpha_{1,2}$ x-rays at 1253.6 eV. The pressure in the sample chamber of the spectrometer was in the range of 10^{-6}-10^{-7} Torr. Binding energies were referenced to the carbon 1s electron peak, at 290.0 eV, due to residual pump oil on the sample surface. The relative concentrations of the species detected in the oxide film were calculated from their XPS peak intensities using the relative photoelectron line sensitivities referenced to fluorine 1s signal (6, 7). Measured concentrations were reproducible within 15%.

All analyses were performed on cylindrical aluminum (99.99% purity) samples having a geometrical area of approximately 6.5 cm^2. Before immersion in the solution, the samples were polished with fine emery papers and washed in doubly distilled water. All solutions were made up from AR grade chemicals and doubly distilled deionized water, and were deaerated with argon. Following immersion (polarization) in the solution, the samples were carefully washed in doubly distilled water, dried in a desiccator, and transferred to the spectrometer. The potentiostatic polarization experiments were carried out with a Wenking 68 FR 0.5 potentiostat driven by a Wenking SMP 69 scanning potentiometer: the polarization rate was 3 mV/min.

Results

In order to characterize the initial state of the surface on the aluminum samples employed in this study, the XPS analysis of a freshly prepared, mechanically polished Al specimen was first performed. As expected, the presence of an 10-13Å thick oxide film having a mean composition equivalent to $Al_2O_3 \cdot 3H_2O$ (8) was determined. Exposure of this air-formed aluminum oxide film to 0.2M Na_2CrO_4 solution during 18 hr pro-

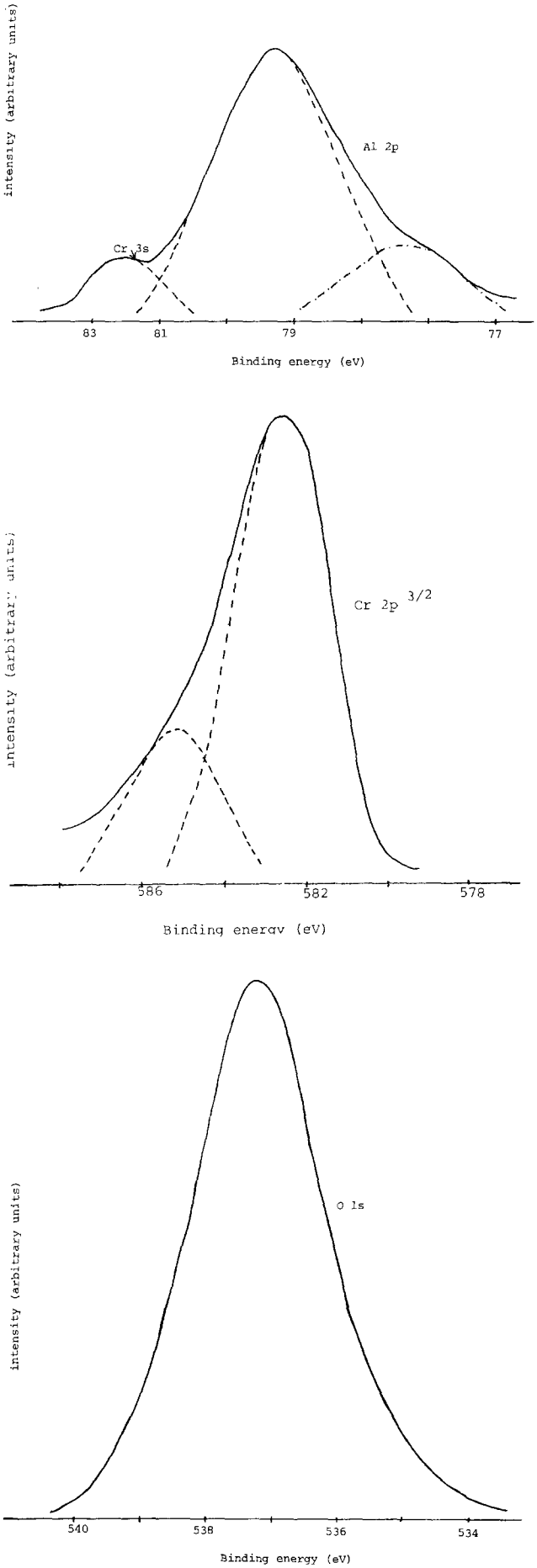


Fig. 1. Aluminum 2p, chromium $2p^{3/2}$, and oxygen 1s regions of a typical XPS spectrum for mixed oxide film formed on aluminum in 0.2M Na_2CrO_4 solution.

Table I. Relative concentrations (a/o)* of different species detected in the oxide films formed on Al samples in various solutions

	Solution composition	Al(O)	Al(III)	Cr(III)	Cr(VI)	Cl	O
1	CrO_4^{2-} 1M	Not detected	16	66	18		330
2	CrO_4^{2-} 0.2M	5	24	56	15		325
3	CrO_4^{2-} 0.2M pH = 7	8	44	38	10		310
4	CrO_4^{2-} 1M + Cl^- 0.1M	4	18	59.5	18.5	5	310
5	CrO_4^{2-} 0.2M + Cl^- 0.1M	(a) 5	22	56.5	16.5	9	320
		(b) 6	22	56.5	15.5	6	360
		(c) 5.5	23.5	55	16	6.5	340
6	CrO_4^{2-} 0.2M/Cl^- 0.1M	5	23.5	57	14.5	6.5	350
7	CrO_4^{2-} 0.2M/Cl^- 0.1M pH = 7	8	50	34	8	4	320
8	CrO_4^{2-} 0.2M + Cl^- 0.1M polarization	5	25	55	15	6	325
9	CrO_4^{2-} 0.2M/Cl^- 0.1M polarization	4	33	50	13	7	345

* The sum of concentrations of the metallic species [*i.e.*, Al(O), Al(III), Cr(III), and Cr(VI)] was taken as 100 a/o. The concentration of Cl species was referenced to the sum of Al(III) and Cr(III), and that of O species to the sum of Al(III), Cr(III), and Cr(VI).
1, 2, and 3. 18 hr immersion.
4. 18 hr immersion in 1M CrO_4^{2-}; followed by addition of 0.1M Cl^- and another 18 hr immersion.
5. 18 hr immersion in 0.2M CrO_4^{2-}; same as 4.
6. 18 hr immersion in 0.2M CrO_4^{2-}/0.1M Cl^-.
7. 18 hr immersion in 0.2M CrO_4^{2-}/0.1M Cl^- at pH = 7.
8. 18 hr immersion in 0.2M CrO_4^{2-}; followed by addition of 0.1M Cl^- and 18 hr polarization at −0.350V (NHE).
9. 18 hr immersion in 0.2M CrO_4^{2-}/0.1M Cl^-; followed by 18 hr polarization at −0.350V.

Table II. Binding energies of the $Cr2p^{3/2}$ electron for the Cr_2O_3 and CrO_4^{2-} species

Compound	Binding energy* eV ±0.2V eV
Cr_2O_3	582.0 (11)
Cr_2O_3	582.2 (12)
Cr_2O_3	582.3 (13)
Na_2CrO_4	585.2 (12)
Na_2CrO_4	584.9 (13)
Cr(III) detected in the oxide film on Al samples	582.6
Cr(VI) detected in the oxide film on Al samples	585.2

* Binding energies are given relative to the zero kinetic energy level, using 290 eV as the carbon 1s binding energy *in vacuo*.

duces a mixed oxide film[2] containing Al(III) oxide, Cr(III) oxide, and Cr(VI) species (Fig. 1 and Table I). As shown in Fig. 1a, two separate peaks were observed in the Al2p region (as in the Al2s region) of the XPS spectrum, indicating that the thickness of the surface film formed on aluminum during the immersion in sodium chromate solution is less than the mean escape depth of photoelectrons, estimated as 15-20Å (9, 10).[3] The positions of the two Al2p peaks (77.6 and 79.8 eV, respectively) were indeed those assigned normally to Al metal (first peak) and to Al(III) of aluminum oxide (second peak).

The $Cr2p^{3/2}$ electron signal (Fig. 1b), as well as the $Cr2p^{1/2}$ signal, showed significant asymmetrical character, indicating the presence of two different chromium species. On the basis of a comparison with the binding energies of various chromium compounds (Table II), the two peaks resulting from the deconvolution of the $Cr2p^{3/2}$ signal were assigned to chromium (III) of Cr_2O_3 (peak at 582.6 eV) and to chromium (VI) in CrO_4^{2-} (smaller peak at 585.2 eV). The large peak observed in the O1s region of the spectrum (Fig. 1c) was quite similar to the O1s signal for hydrated aluminum oxide (14). The abnormal width (1.2 eV) of this peak suggests the presence of at least two oxygen species but, on account of its symmetrical form, resolution was not attempted. The relative oxygen concentration, calculated from the peak intensity,

[2] A series of the XPS analyses performed on aluminum samples immersed in Na_2CrO_4 solution for different periods of time has shown that the oxide film reached its maximum thickness after 18 hr of exposure to the solution.
[3] The fact that the whole oxide film is localized in the outermost region of the aluminum surface examined by XPS, allows true mean concentration of different elements entering the film composition to be determined.

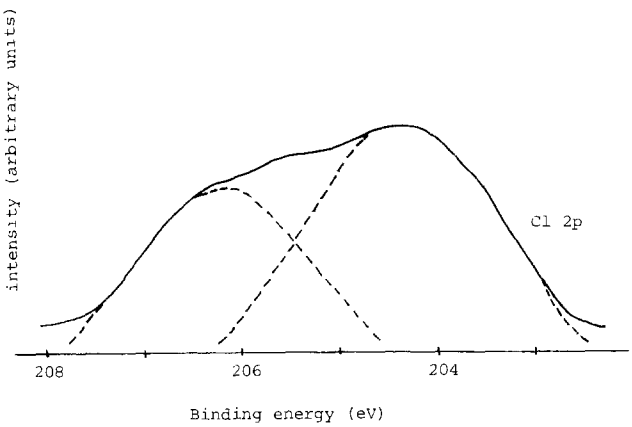


Fig. 2. Chlorine 2p photoelectron signal for the aluminum sample exposed to 0.2M Na_2CrO_4/0.1M NaCl solution.

being distinctly higher than the total amount in Al_2O_3, Cr_2O_3, and CrO_4^{2-}, this additional oxygen was assigned to hydration water. The XPS spectrum shown in Fig. 1 was quite typical of all aluminum samples pretreated in chromate and chromate/chloride solutions. For the latter, in all cases, an additional chlorine signal was detected. Figure 2 shows the Cl2p region of the spectrum obtained for an aluminum sample exposed during 18 hr to 0.2M Na_2CrO_4/0.1M NaCl solution. The position of the $Cl2p^{3/2}$ peak was in this case identical to that previously observed for chloride ions included in an aluminum oxide film, derived from sodium or aluminum chloride solution treatment (15)[4] in the absence of chromates. Another series of analyses was performed on aluminum samples immersed first during 18 hr in 0.2M Na_2CrO_4 solution and then, during a second period of 18 hr, in a solution containing both 0.2M Na_2CrO_4 and 0.1M NaCl. As shown in Table I, the composition of the oxide film formed under these conditions (and in particular the extent of chloride incorporation) was practically the same as that of the film from direct immersion in Na_2CrO_4/NaCl solution.

No significant changes in the surface film structure were observed for aluminum samples polarized anodically at −0.350V *vs.* NHE; *i.e.*, at a potential about 0.1V less noble than the critical pitting potential of aluminum in 0.2M Na_2CrO_4/0.1M NaCl solution. In these experiments, the first set of specimens was immersed directly in 0.2M Na_2CrO_4/0.1M NaCl solution for 18 hr, and then polarized anodically stepwise up to −0.350V, this potential subsequently being kept constant during another period of 18 hr. The second set of specimens was first immersed in 0.2M Na_2CrO_4 solution, and sodium chloride was added only after the initial 18 hr, at the beginning of the anodic polarization. In both cases, the extent of chloride incorporation determined by photoelectron spectrometry was about 6-7 atomic percent (a/o); *i.e.*, the same as that found for samples exposed to CrO_4^{2-}/Cl^- solution at open-circuit potential.

Discussion

The results of surface analyses performed using x-ray photoelectron spectrometry clearly confirm that chromate ions from the solution undergo reduction inside the aluminum oxide film, after being adsorbed on the oxide-solution interface. Indeed, the spectra indicate, for all samples examined, the presence of two different chromium species, which have been identified as Cr(III) in Cr_2O_3 and Cr(VI) in CrO_4^{2-}. However, one can consider rather surprising the fact that the oxide film formed on aluminum under immersion in chromate solution contains such a substantial amount of chromium (III) oxide: almost 60 a/o for 0.2M CrO_4^{2-} solution and even more than 60 a/o for 1M CrO_4^{2-} solution (Table I). Decreasing the *p*H of chromate solution from 9.5 to 7 changes the film composition in favor of an increased proportion of aluminum oxide. This observation corroborates partially the conclusions of an earlier work (2), which indicate that the dissolution rate of γ-Al_2O_3 in chromate solutions is appreciably higher at *p*H 9.5 than at *p*H 7.

[4] From a comparison of the $Cl2p^{3/2}$ binding energies of the different chlorine species it has been suggested that Cl- ions entering the aluminum oxide lattice may form an aluminum oxychloride AlOCl.

Table III. Relative concentrations of the Cl species in the oxide film on Al samples as a function of potential

Electrolyte	Potential, V *vs.* NHE	Relative concentration of Cl (a/o)
NaCl 0.1M	$E_{st} = -0.96$	5-6*
	-0.50	13*
	$E_{cr} = -0.43$	
Na_2CrO_4 0.2M/ NaCl 0.1M	$E_{st} = -0.52$	6-7**
	-0.35	6-7**
	$E_{cr} = -0.24$	6-7**

* Given with respect to Al(III).
** With respect to the sum of Al(III) and Cr(III).

The total film thickness, however, remains practically unchanged,[5] notwithstanding the *p*H modification, which means that the portion of γ-Al_2O_3 dissolved in the surface film (formed in chromate solution of *p*H 9.5) is apparently replaced by chromium (III) oxide. In this connection, it seems interesting to mention the suggestion of Pryor (2), which was based on the results of an electron optical study, and concerned the duplex nature of passive films formed on aluminum in chromate solutions. According to this author, these films would be composed of an underlying layer of amorphous γ-Al_2O_3, being overlaid by a thin layer of microcrystalline γ-Al_2O_3 having very low ionic resistance. Our XPS results strongly suggest that this outer layer consists of chromium (III) oxide, which would be responsible for the diffraction patterns attributed by Pryor to microcrystalline γ-Al_2O_3.

Another point of particular importance with regard to the mechanism by which chromates exert an inhibiting action on the corrosion of aluminum by chloride ions, is the fact that the formation of a layer of chromium (III) oxide, just as the presence of adsorbed CrO_4^{2-} ions on the film surface, has no special merit in preventing Cl^- penetration of the protective oxide film. Indeed, as shown by our XPS results (Table III) the extent of chloride incorporation within the oxide film from CrO_4^{2-}/Cl^- solution (at open-circuit potential) is quite similar to that observed for aluminum samples immersed in chloride solution not containing chromates (16).[6] It must be also emphasized that the amount of Cl^- and the over-all film composition are not visibly modified if the aluminum sample is immersed directly in CrO_4^{2-}/Cl^- solution or if chlorides are added only after the initial period of film formation in chromate solution has been achieved (Table I).

These observations are in good agreement with our previous results concerning nitrate/chloride solutions (17), which also indicate significant incorporation of Cl^- ions in the aluminum oxide film at open-circuit potential (E_{st}), in spite of the presence in solution of inhibiting NO_3^- ions.

Anodic polarization of aluminum in CrO_4^{2-}/Cl^- solution near critical pitting potential has practically no influence on the surface film composition and, in particular, the chloride content remains unchanged with respect to that at E_{st}. The situation is quite different when aluminum is polarized anodically in chloride solution not containing chromates; in this case the amount of Cl^- in the oxide film (Table III) increases

[5] This is substantiated by the presence of a comparable weak signal for metallic aluminum in the Al2p spectra of the samples pretreated in chromate solutions of *p*H 9.5 and 7.

[6] For this comparison, the relative concentrations of Cl species were referenced to the sum of Al(III) and Cr(III) in the first case and to Al(III) in the second.

from 5-6 a/o at E_{st} to about 13 a/o at E_{cr}-0.1V (16).

The above results therefore show that if chromate ions do not prevent the entry of chlorides into the protective oxide film at open-circuit potential, they largely impede their further incorporation at higher potentials. This effect is related, in our opinion, to the fact that CrO_4^{2-} ions are reduced within the oxide film, this reduction process being a film forming (and film repairing) reaction. The reduction of chromate ions[7]

$$2CrO_4^{2-} + 2Al^{3+} + 4H_3O^+ + 6e^- \rightarrow Cr_2O_3 + Al_2O_3 + 6H_2O$$

(over-all reaction)

not only produces both oxides entering the film composition (*i.e.*, Cr_2O_3 and Al_2O_3), but also consumes protons from the oxide lattice. Assuming that the preferential sites by which Cl^- and CrO_4^{2-} ions penetrate the oxide film are the same, the inhibiting action of chromates can therefore be understood in terms of shifting the potential at which a critical concentration of chlorides is established on the metal surface (at the metal-oxide interface).

On the other hand, explanation of increased stability of passive films, formed on aluminum in the presence of chromates, by a competitive adsorption effect [whereby the specifically adsorbed CrO_4^{2-} ions would displace Cl^- ions from the oxide-solution interface (3)] appears hardly compatible with the results of our work. Indeed, the fact that no difference in the extent of chloride incorporation within the protective film (at E_{st}) is observed if 0.1*N* NaCl solution contains, or does not contain, chromates, seems to exclude any significant modification of the amount of specific adsorption of Cl^- ions. This conclusion is also supported by the results of previous work of one of the authors (14), concerning interactions between sulfate ions and oxide-covered aluminum which show that, notwithstanding a large extent of incorporation in the oxide film, they exert practically no inhibiting action in the presence of chlorides. At the same time sulfates are, to our knowledge, the sole oxyanions which are not reduced within the oxide film covering aluminum metal.

[7] This reduction process must be accompanied by an anodic oxidation process occurring at the metal-oxide interface: $Al \rightarrow Al^{3+} + 3e^-$ and, at least, partial diffusion of Al^{3+} ions toward the oxide-solution interface

Manuscript submitted Feb. 16, 1977; revised manuscript received April 21, 1977.

Any discussion of this paper will appear in a Discussion Section to be published in the June 1978 JOURNAL. All discussions for the June 1978 Discussion Section should be submitted by Feb. 1, 1978.

Publication costs of this article were assisted by the University of Geneva.

REFERENCES

1. C. Edeleanu and U. R. Evans, *Trans. Faraday Soc.*, **65**, 683 (1949).
2. M. J. Pryor, *Z. Elektrochem.*, **62**, 782 (1958).
3. M. A. Heine and M. J. Pryor, *This Journal*, **114**, 1001 (1967).
4. H. Böhni and H. H. Uhlig, *ibid.*, **116**, 906 (1969).
5. M. F. Abd Rabbo, J. A. Richardson, G. C. Wood, and C. K. Jackson, *Corrosion Sci.*, **16**, 677 (1976).
6. C. D. Wagner, *Anal. Chem.*, **44**, 1050 (1972).
7. H. Berthou and C. K. Jφrgensen, *ibid.*, **47**, 487 (1975).
8. J. Augustynski, H. Berthou, and J. Painot, *Chem. Phys. Lett.*, **44**, 221 (1976).
9. A. Barrie, *ibid.*, **19**, 109 (1973).
10. M. Klasson, J. Hedman, A. Berndtsson, R. Nilsson, C. Nordling, and P. Melnik, *Phys. Scr.*, **5**, 93 (1972).
11. J. C. Carver, G. K. Schweitzer, and T. A. Carlson, *J. Chem. Phys.*, **57**, 973 (1972).
12. G. C. Allen, M. T. Curtis, A. J. Hooper, and P. M. Tucher, *J. Chem. Soc. Dalton Trans.*, 1675 (1973).
13. C. K. Jφrgensen and H. Berthou, *K. Dan. Vidensk. Selsk. Mat. Fys. Medd.*, **38**, No. 15 (1972).
14. J. Painot and J. Augustynski, *Electrochim. Acta*, **20**, 747 (1975).
15. J. Augustynski and J. Painot, *This Journal*, **123**, 841 (1976).
16. J. Augustynski, M. Koudelkova, and J. P. Coad, To be published.
17. J. Augustynski and J. Painot, Paper 136 presented at the 27th ISE Meeting, Zürich, September 6-11, 1976.

Mobility of Foreign Atoms during the Anodic Oxidation of Aluminum: As, Sb, and Bi; Se and Te

W. D. Mackintosh, F. Brown, and H. H. Plattner

Atomic Energy of Canada Limited, Chalk River Nuclear Laboratories, Solid State Science Branch, Chalk River, Ontario, Canada, K0J 1J0

ABSTRACT

Atoms of As, Sb, and Bi; Se and Te introduced into the surface layers of aluminum specimens are shown to be mobile during anodic oxidation. The direction of motion depends on whether the initial distribution of the foreign atoms is located in aluminum metal under the natural air-formed oxide or is entirely within a thin preformed surface film of anodic oxide. The rate of motion relative to aluminum was determined. This investigation complements earlier studies of the behavior of metallic and of halide foreign atoms during anodization.

In two previous papers (1, 2) we described the movement of foreign atoms during the anodic oxidation of aluminum. The metallic elements studied were K, Rb, and Cs; Ca, Sr, and Ba; Cu and Ag; Ga, In, and Tl; Hg; V; Cr; Mn, Fe, Co, and Ni. The nonmetals were Cl, Br, and I. It was shown that when these were introduced into a thin preformed oxide film which was subsequently thickened, the metallic species moved outward while the nonmetals moved inward. However, if introduced into the metal beneath the native air-formed oxide, then metallic species with oxidation potentials greater than that of Al, viz., Ag, Co, Cu, Fe, Ga, Hg,

Key words: aluminum, anodic oxidation, foreign atoms, Rutherford backscattering analysis.

In, Mn, Ni, Tl, and V retreated in whole or in part before the advancing oxide front and were found to be located in the metal after the anodic oxide film had been removed. In all cases where the final location of the foreign atoms was within a specimen (some species, under certain circumstances, were lost to the electrolyte) the distribution of the implanted atoms was largely unaltered, that is to say, the atoms moved as a group.

In this paper we extend these studies to include the Group VA elements As, Sb, and Bi; and Group VIA Se and Te. As before, ion implantation was used to introduce the foreign atoms into the specimen and Rutherford backscattering analysis to locate the ions before and after oxidation.

Experimental

The aluminum specimens were 1.2 cm in diameter and 0.4 cm thick. Surfaces were first prepared by vibratory polishing with 0.5 μm alumina. This was followed by four cycles in which the specimens were anodized then stripped of oxide with a solution of phosphoric and chromic acids at 95°C. Some samples were then exposed to the air at room temperature for a few hours, some were anodized until covered by a much thicker oxide layer.

All anodization was done in a saturated solution (approximately 5%) of ammonium pentaborate in water at 23°C. The current was kept constant at 2 mA/cm^2. The desired oxide thickness was achieved by terminating the oxidation at a voltage corresponding to the desired thickness from a previously prepared calibration curve.

After surface preparation of the specimens covered only with the air-formed oxide, As, Sb, and Bi; Se and Te were implanted at energies of 40 keV. Specimens covered with the preformed oxide were initially implanted at the same energy but the first results indicated that higher energies (300-400 keV) were preferable to avoid ambiguities. In order to ensure that the implanted ions were largely within the oxide layer it was necessary to make the preformed oxides 40-60 μg/cm^2 thick. The number of ions implanted was commensurate with the sensitivity of the Rutherford backscattering method for each species; they were in the range 10^{14}-10^{15} ions/cm^2.

The position of the implanted atoms, the thickness of the oxide films, the profile of the implant distribution, and the number of atoms implanted were then determined by Rutherford backscattering analyses. The principles of this technique for achieving these objectives and the experimental arrangements used were described in Ref. (1).

The specimens were again anodized and the analysis repeated. In many cases second and third oxidations and analysis were carried out.

Results and Discussion

Implants into preformed oxides.—Initially we implanted the foreign atoms at 40 keV into oxides approximately 10 μg/cm^2 thick. On thickening all the implanted material was found at, or very close to, the surface. Although the atoms had obviously moved outward, it was not clear whether the position they occupied was solely due to the rate of movement through the oxide or whether complicated by some surface effect. Consequently, we preformed much thicker oxides and implanted at higher energies, so that they could move a considerable distance before encountering a surface. The position of the implants in the oxide film is illustrated in Fig. 1A, using the case of Sb as an example. Here, the preformed oxide was found to be 42 μg/cm^2 thick and the center of the implant distribution was located at the depth of 25 μg/cm^2. The oxide was then thickened to 64 μg/cm^2. It is known from Ref. (1) that of the 22 μg/cm^2 of oxide grown during the second anodization 4/10 forms over the original oxide and the

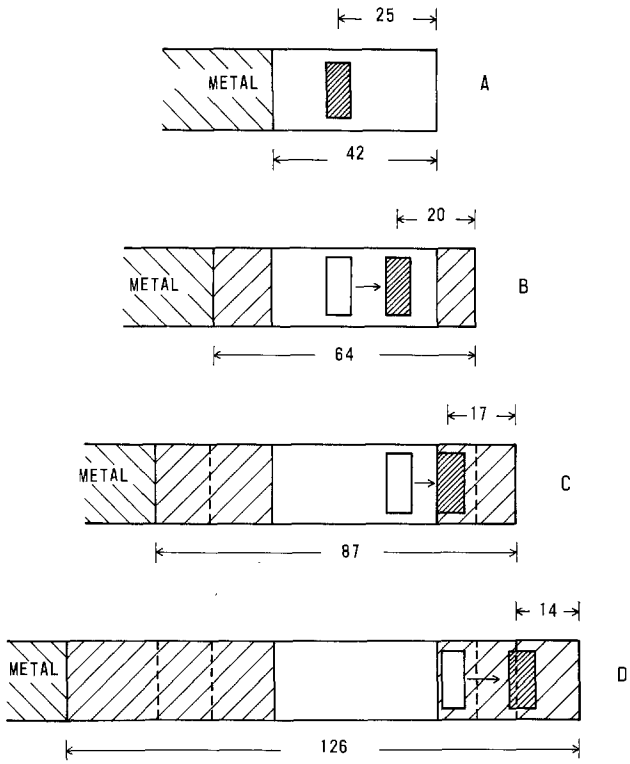


Fig. 1. The movement of Sb implanted in a preformed oxide. A, the position of the implant (solid rectangle) after implantation; B, the position of the implant (solid rectangle) and the "immobile" position (open rectangle) after thickening the oxide to 64 μg/cm^2; C, after thickening to 87 μg/cm^2; and D, after thickening to 126 μg/cm^2. Implant depths are shown in micrograms per square centimeter.

remainder under it. This is shown in Fig. 1B. The center of the implant distribution is 20 μg/cm^2 from the surface. Had the Sb atoms been immobile they would have been located at a depth of $25 + 0.4 \times 22 = 34$ μg/cm^2. This position is indicated by the open rectangle in the figure. It now follows that the Sb atoms have moved $34 - 20 = 14$ μg/cm^2. In Ref. (1) we defined a migration number as the ratio of this distance to the thickness of oxide grown. In this instance the number is 0.63. In Fig. 1C and D we show the results for further thickening. The migration numbers obtained agree with the original within the experimental precision attainable ($\pm$ 2 μg/cm^2 for depths and thicknesses). In Table I we list all these migration numbers together with the averages and the standard deviations for all species except Se. Numbers calculated from the initial experiments with low energy implants were much lower. It is therefore apparent that where the original implant is at such a depth that it can reach the surface, it will remain at the surface rather than dissolving in the electrolyte. Similar observations were made in Ref. (2) for some, although not all, species considered.

Rutherford backscattering spectra give the profiles of foreign atom distributions. The profiles of As, Sb, Bi, and Te remained virtually unchanged throughout the series of oxidations. This indicates that the foreign atoms move as a coherent group during oxidation.

In contrast, Se atoms were found dispersed throughout the preformed oxide and the new layer formed under the original. If any moved into the new layer formed over the original they were too few in number to be detectable. Because the atoms were widely dispersed no migration numbers were calculated for Se. In Ref. (1) it was shown that ions likely to be negatively charged (the halides) moved inward when implanted into an oxide layer which was subsequently thickened while those likely to be positively charged (all metals) moved outward. In this respect the metals Sb and Bi and the near metals As and Te behaved as if

Table I. Migration numbers for elements implanted into preformed oxides

Species and sample number	Thickness of oxide after thickening ($\mu g/cm^2$) 1	2	3	Migration number
As 1	111			0.39
2	108			0.56
3	108			0.51
4	109			0.41
5	108			0.52
			Avg	0.48 ± 0.07
Sb 1	64			0.64
		87		0.50
			126	0.47
2	90			0.58
		121		0.57
3	91			0.53
		121		0.66
4	102			0.53
5	102			0.49
6	115			0.60
7	110			0.60
8	109			0.50
			Avg	0.55 ± 0.06
Bi 1	117			0.74
2	118			0.65
3	118			0.70
			Avg	0.70
Te 1	92			0.48
		117		0.65
2	90			0.51
		121		0.61
3	64			0.53
4	63			0.55
5	108			0.56
6	107			0.52
7	107			0.56
			Avg	0.55 ± 0.05

positively charged. Selenium atoms, on the other hand, moved in both directions as if some atoms were of one charge, others of the opposite.

Implants into metal.—In Ref. (2) we reported that many metallic species when implanted into Al under the natural air-formed oxide behaved in a radically different manner than they did when implanted into preformed oxide films. Rather than move outward in a coherent group, some fraction was found at the metal-oxide interface while the remainder was found either in the oxide or to have passed into the electrolyte. All elements in the present study behaved similarly. A fraction of each species was found at the interface. This is illustrated for Te in Fig. 2A and B where we have plotted the backscattered yield against the depth. In A, which represents the as-implanted specimen, the highest concentration of Te is located about 5 $\mu g/cm^2$ below the surface. After anodizing to 30 $\mu g/cm^2$ of oxide the highest concentration lies at the metal/oxide interface while the remainder is distributed throughout the oxide. The profile shown in the figure is approximate only, because the finite resolution of the detector produces some distortion. Table II lists the fractions of all species found at the interface together with the corresponding oxide thickness.

The depth resolution of the Rutherford backscattering technique is not adequate to determine whether the fraction of the foreign atoms at the interface is in the metal surface layers or in the oxide layers adjacent to the substrate. However, when the oxide was stripped from a number of samples with chromic phosphoric acid, the number of foreign atoms found on subsequent analysis was identical to the number found at the interface with the oxide film intact. The foreign atoms are therefore located in the metal close to the metal/oxide interface.

When the oxide film is thickened a second and third time the amount retained in the metal decreases. Table II also lists these amounts with the corresponding oxide thicknesses. It is therefore apparent that as an oxide grows, some of the implanted atoms that were initially moved deeper into the specimen by the advancing oxide front, were transferred across the interface into the oxide.

In all specimens the fraction of the implanted material not held at the advancing oxide front was spread

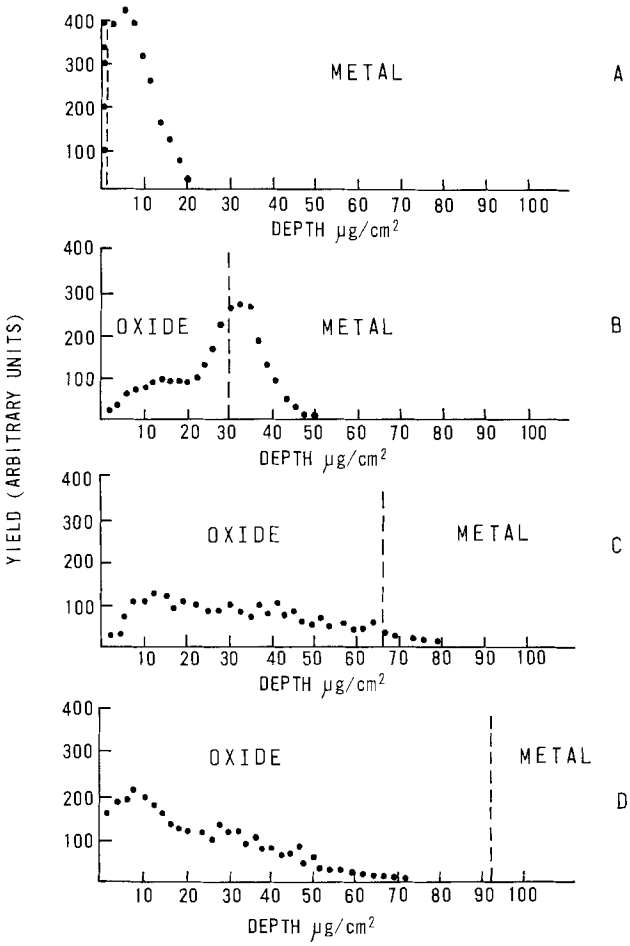


Fig. 2. The movement of Te implanted into metal under the air-formed oxide. A, the approximate profile after implanting. B, oxidized to 30 $\mu g/cm^2$; C, 66 $\mu g/cm^2$; and D, 100 $\mu g/cm^2$. The dashed vertical line represents the metal oxide interface.

throughout the oxide film; no detectable amounts were lost to the electrolyte. This is represented qualitatively in Fig. 2B, C, and D for increasing thicknesses of oxide. The change in the distribution profile is consistent with two previous observations. First, in Ref. (2) we found that the rate at which foreign atoms (specifically Tl in the work quoted) were transferred across the interface decreased as the concentration in the metal phase decreased. The dependence was first order. This accounts

Table II. Fractions located at oxide/metal interface

Species and sample number	Thickness of oxide after thickening ($\mu g/cm^2$) 1	2	3	Fraction retained in metal (%)
As 1	24.5			52
2	37			43
		69		35
			105	Nil
3	25			52
		66		22
			102	10
4	32			53
		66		22
			101	10
Sb 1	28			92
		60		84
			90	74
Bi 1	118			100
2	114			100
3	113			100
Se 1	28			60
		73.5		10
			105	5
2	31			55
		65		35
			99	12
Te 1	30			63
		66		6
			103	Nil
2	28			50
		63		6
			102	Nil

for the decreasing concentration in the oxide inward. Second, in an earlier section of this paper it was observed that the foreign atoms of all species implanted into preformed oxide moved outward during oxidation until they reached the surface where they were retained. The pile-up at the surface in Fig. 2D is evidence that the same process is occurring once an atom has been released from the metal and transferred to the oxide.

Conclusions

These experiments have shown that Groups V and VI metals and near metals, like the metals reported in Ref. (2), behave in a manner dependent on the position of the implant. When implanted in a preformed oxide all remain in the oxide but move within it. When implanted in the metal beneath the air-formed oxide all move, in whole or in part, ahead of the advancing oxide front.

The rate of movement within the oxide of As, Sb, and Bi when implanted into a preformed film which is subsequently thickened, increases with the size of the ion. The reverse was noted in the Group I metals, K, Rb, and Cs (1). However, we noted in Ref. (2) that the likely charge on the ion appears to be more significant than size, as the Group IIA metals Ca, Sr, and Ba all moved faster than Group IA. We therefore infer that the charge on Bi is greater than that of As and Sb as it moved appreciably faster.

We have shown that the direction of movement is dependent on the sign of the charge; negative ions move inward, positive ions outward (1, 2). We therefore conclude that some ions of Se are negative, some positive, as the spread of the implant throughout the oxide indicates movement in both directions.

When implanted in metal, As, Sb, and Bi; Se and Te behave in the same fashion as metals with higher oxidation potentials than Al, *i.e.*, retreat before the advancing oxide front (2). This has practical consequences. Anodic oxidation and stripping have been used as a microsectioning technique [*e.g.*, Ref. (3)] to determine range profiles and study diffusion. The present experiments show that the technique cannot be used when Group VA and VIA elements are involved as the movement of the foreign atoms during oxidation will falsify the results. In this respect these elements are similar to many others (2). Although we have not the facilities to check the entire Periodic Table it appears that the microsectioning technique is only safely used with the alkali metals, alkaline earths, halides, and noble gases.

Acknowledgments

We are grateful to O. Westcott, G. Sims, and R. Bellavance for implantation of the specimens and to J. Lori and D. Lanteigne for assistance in the Van de Graaf operations.

Manuscript received Feb. 14, 1977.

Any discussion of this paper will appear in a Discussion Section to be published in the June 1978 JOURNAL. All discussions for the June 1978 Discussion Section should be submitted by Feb. 1, 1978.

Publication costs of this article were assisted by Atomic Energy of Canada Limited.

REFERENCES

1. F. Brown and W. D. Mackintosh, *This Journal*, **120**, 1096 (1973).
2. W. D. Mackintosh, F. Brown, and H. H. Plattner, *ibid.*, **121**, 1282 (1974).
3. J. A. Davies, J. Friesen, and J. D. McIntyre, *Can. J. Chem.*, **38**, 1526 (1960).

Anodic Oxidation of Methane

S. Y. Hsieh and K. M. Chen

Department of Chemical Engineering, National Taiwan University, Taipei, Taiwan, Republic of China

ABSTRACT

The anodic oxidation of methane on a platinized platinum electrode was studied in acidic sulfate electrolytes at 80°C. Results indicate that the reaction proceeds according to $CH_4 + 2H_2O \rightarrow CO_2 + 8H^+ + 8e^-$, with ~100% current efficiency. Effects of potential, methane partial pressure, and pH on current density give the following kinetic parameters, respectively: $(\partial V/\partial \log i) \sim 2.3\ RT/\mathbf{F}$, $(\partial \log i/\partial \log p) \sim 1$, and $(\partial \log i/\partial\ pH) \sim 1$. A mechanism (up to the rate-determining step) consistent with these experimental results was suggested as

$$CH_4 \rightleftharpoons CH_3(ads) + H^+ + e^-$$

$$CH_3(ads) \xrightarrow{rds} \text{intermediates}$$

One of the key problems in fuel cell research is the achievement of high electrochemical reaction rates using cheap fuels, of which the saturated hydrocarbons represent a notable class. The electrochemical oxidation of saturated hydrocarbons has been extensively studied (1-24). Most of the previous works either emphasized the improvements of actual fuel cell performances or approached the studies of adsorption and the formation of various intermediates during oxidation. A study of electrode kinetic parameters to determine the mechanism was only approached by Bockris, Gileadi, and Stoner in the anodic oxidation of propane, n-hexane, cyclohexane, and 2,2-dimethylbutane (24). In this work, the rate and mechanism of methane oxidation on platinum in acidic sulfate solutions were studied by using the electrode-kinetic-parameter approach.

Key words: methane anodic oxidation, fuel cell methane, electrochemical oxidation methane.

Experimental

Cell and apparatus.—Electrochemical measurements were conducted in a three compartment Pyrex cell (capacity 700 ml). The anode compartment was separated from the cathode compartment by a fritted glass partition. A water-sealed stopcock and a Luggin capillary provided contact between the anode and the reference electrode. The anolyte temperature was main-

Table I. Electrode rest potentials in electrolytes bubbled with methane at 80°C

Electrolytes	pH	Rest potential, mV
1N H_2SO_4	0.35	100
1N (H_2SO_4 + KOH)	1.0	50
1N (H_2SO_4 + KOH)	1.7	0
1N (H_2SO_4 + KOH)	3.5	−110

tained at 80° ± 0.1°C except for the activation-energy determinations. Gas-flow rates through the anode compartment were maintained at 200 cm^3 (1 atm, 25°C) per minute. Both the anode and the cathode were platinized platinum gauzes, about 6 cm^2 apparent area. The platinizing procedure reported in Ref. (25) was closely followed, and the resulting anode had a roughness factor about 200. The anode was activated at the start of each run by an electrochemical pulsing technique (alternate anodic and cathodic polarization). The reference electrode was a Hg/Hg_2SO_4 (1N H_2SO_4) electrode. All anode potentials referred to are at the standard hydrogen electrode (SHE) at 80°C (26). Current-potential relations were studied by potentiostatic method. A Wenking potentiostat (Model ST72) and a Wenking scanning potentiometer (Model SMP72) were used. A Hokuto galvanostat (Model HA-104) was used for coulombic efficiency studies. All current-time and potential-time variations were recorded with a MFE 2100 series recorder. The potentials were also monitored with a Keithley 602 electrometer.

Materials.—Potassium hydroxide Baker analyzed reagent and sulfuric acid Hanawa extra pure reagent were used. Double-distilled water was used in preparation of all solutions. Methane gas was prepurified and supplied by the Chinese Petroleum Company. It was further purified by passing through an alkaline pyrogallol solution to ensure the complete removal of oxygen. Only one peak (methane) was observed in several gas-chromatographic analyses of the purified methane gas. The nitrogen used for purging and mixing with methane for partial pressure studies was at least 99.99% pure.

Results and Discussion

Rest potentials.—Table I shows the rest potentials of the platinized platinum electrode in various electrolytes saturated with methane. The electrolytes were 1.0N H_2SO_4 solutions and H_2SO_4 solutions partially neutralized with KOH to the desired pH values. The ionic strength of all electrolytes was kept the same throughout the experiments. The variation of rest potential with pH was approximately 70 mV (Fig. 1). Little effect of methane partial pressure in the range of 0.25-1 atm was noted. Similar pH and partial pressure effects were reported for other hydrocarbons (acetylene and ethylene) and maleic acid on platinum and gold electrodes (27-30), and interpretations as mixed potentials of various possible reactions were fully discussed (27). Schlatter (8) indicated that the rest potentials are probably determined largely by the concentration of hydrogen atoms resulting from dissociative adsorption of the hydrocarbons on the electrode.

Current-potential relations.—Tafel curves for methane oxidation in various electrolytes are shown in Fig. 2. The individual points represent quasi-steady-state values (current change less than 10%/hr) which were usually reached within 5 min for a potential change of 10 mV. Linear Tafel regions were observed with slopes of 70-75 mV which were close to 2.3 $RT/\mathbf{F}$. Above the linear region, mass transfer assumed significance and a limiting current region was found.

pH effects.—Figure 2 also shows that the curves shift in the negative potential direction as the pH increases. Data points taken from Fig. 2 at constant potential and constant current give $(\partial \log i/\partial \text{pH}) \sim 1$ and $(\partial V/\partial \text{pH}) \sim -70$ mV, as shown in Fig. 3 and 4.

Coulombic efficiency.—Any CO_2 contained in methane was first removed by passing the gas through concentrated potassium hydroxide solution. Then the procedure, as described in (26, 31), was slightly modified and used for the determination of the efficiency of CO_2 production. In the modified procedure, the exit gases from the anode compartment were passed through an absorption train which contained a cold trap, concentrated H_2SO_4, and two ascarite absorbers, in that order. The cold trap collected most of the water leaving the cell and the concentrated H_2SO_4 removed the remaining water from the gases before they passed through the ascarite absorbers. Ascarite absorbed CO_2 with the formation of water according to the reaction: $2NaOH + CO_2 \rightarrow Na_2CO_3 + H_2O$. Since ascarite is not a particularly good drying agent, it was therefore followed by a good desiccant $Mg(ClO_4)_2$ in the first absorber to take up any water that might escape. The second ascarite absorber was used for preventing back-diffusion of atmospheric CO_2 and moisture from getting into the first ascarite absorber. For a specified time

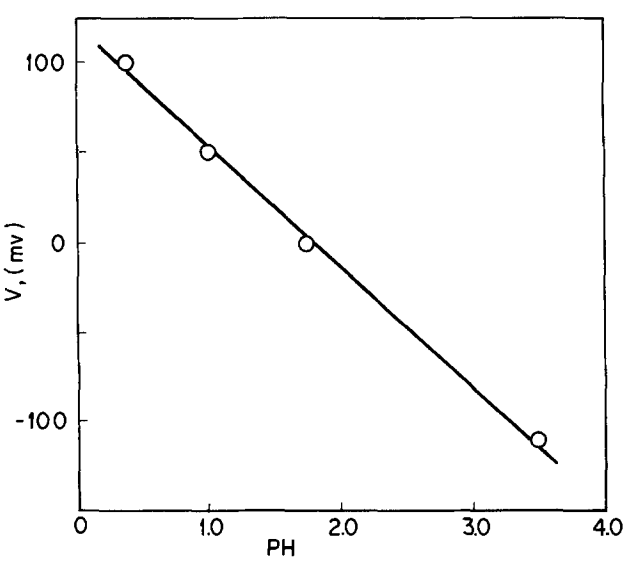


Fig. 1. Rest potential-pH relations for platinized platinum electrode in electrolytes saturated with methane.

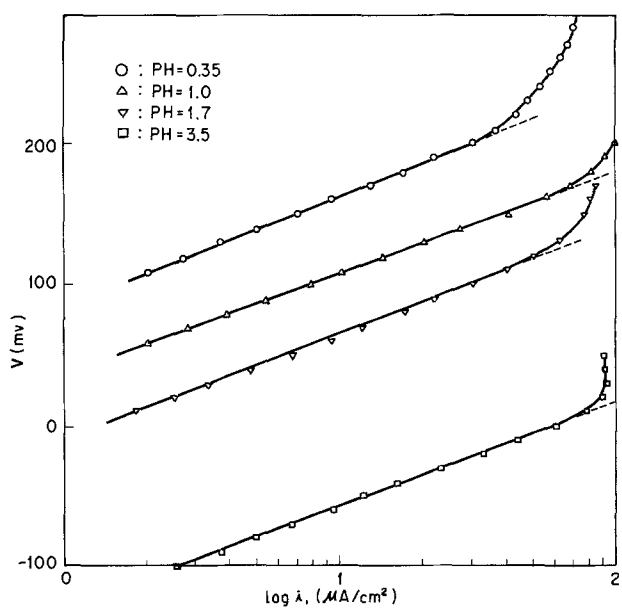


Fig. 2. Current-potential relations in electrolytes of various pH's at 80°C and $P = 1$ atm.

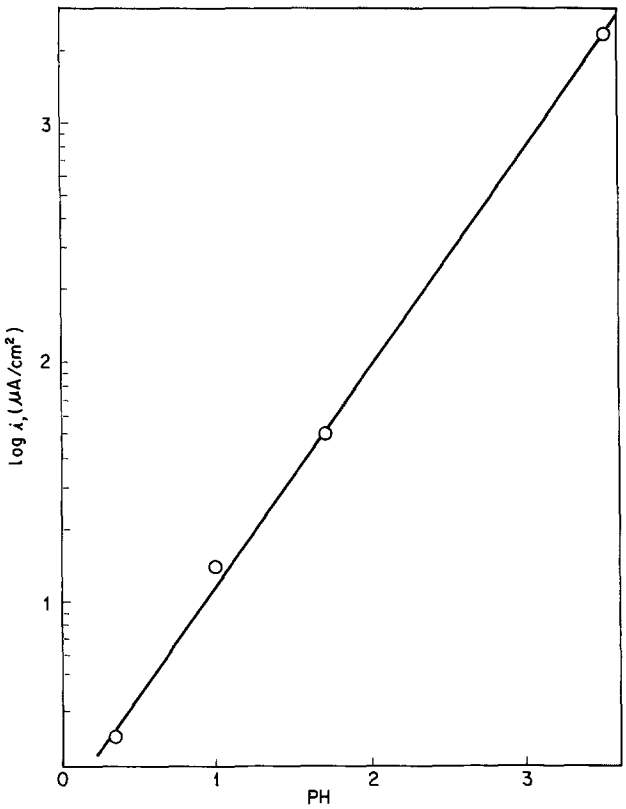


Fig. 3. Current-pH relations at constant potential (120 mV) and 80°C.

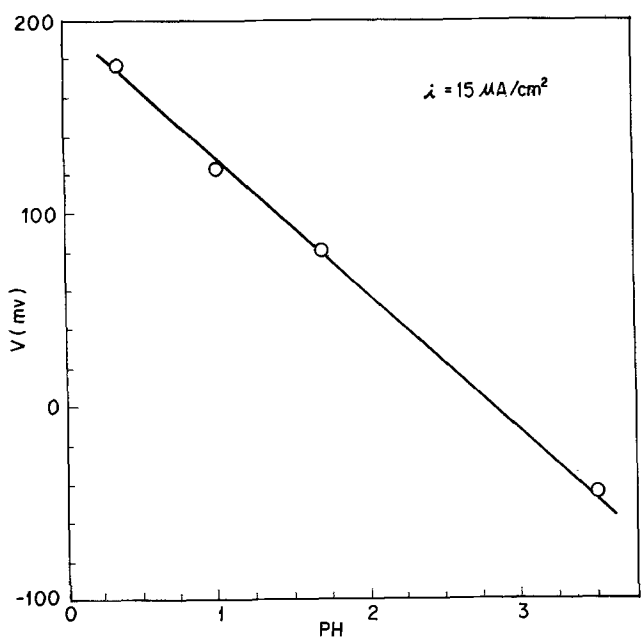


Fig. 4. Potential-pH relations at constant current density (15 μA/cm²) and 80°C.

period the CO_2 production was determined by the weight gain of the first ascarite absorber.

The coulombic efficiency for CO_2 production was determined in 1.0 H_2SO_4 electrolyte. A current density within the linear Tafel region was chosen in the study and a larger electrode was used to allow the use of a higher current. During the galvanostatic runs, anodic potentials were found to agree within 15 mV of the values read from Tafel region. Efficiencies close to 100% were obtained and results are given in Table II.

Temperature effect.—The effect of temperature on current density was measured potentiostatically at potentials within the linear Tafel region. Results are

Table II. Coulombic efficiency for anodic oxidation of methane
(1 atm, 80°C, I = 2 mA, i = 22 μA/cm², 190 ± 15 mV, 48 hr)

Run no.	Weight of CO_2 gained (grams)	CO_2 efficiency (%)
1	0.0189	96
2	0.0195	99

Table III. Activation energies for the anodic oxidation of methane on platinized platinum electrode

Electrolyte	Potential, mV	Activation energy, kcal
1*N* H_2SO_4	140	30.0
	190	28.7

shown in Fig. 5. The calculated activation energies are reported in Table III.

Pressure effect.—Methane of a given partial pressure was passed through the anode compartment while the electrode potential was held constant. After a steady-state current was reached, the methane partial pressure was changed to another value and the corresponding change of current was recorded. For methane partial pressure between 0.25 and 1 atm, $(\partial \log i/\partial P)$ ~1.0 was observed (Fig. 6).

Reaction mechanism.—In connection with the reaction mechanism, there are four results of importance. (*i*) The high efficiency of CO_2 production indicates that no branching leading to products other than CO_2 and water occurs to any appreciable extent. (*ii*) With Langmuir-type adsorption, a Tafel slope of 2.3 $RT/\mathbf{F}$ generally indicates that the rate-determining step is a chemical reaction following the first electron transfer. (*iii*) The reaction order with methane is $(\partial \log i/\partial \log P)$ ~1. (*iv*) The pH effect is $(\partial \log i/\partial \text{pH})$ ~1. A mechanism which satisfies the above kinetic parameters may be formulated as

$$CH_4 = CH_3(\text{ads}) + H^+ + e^- \qquad [1]$$

$$CH_3(\text{ads}) \xrightarrow{\text{rds}} \text{intermediates} \qquad [2]$$

The rate expression, assuming Langmuir-type adsorption and a low surface coverage of the electrode, is

$$i = n\mathbf{F}k_2K_1P{a_{H^+}}^{-1}\exp(\mathbf{F}V/RT)$$

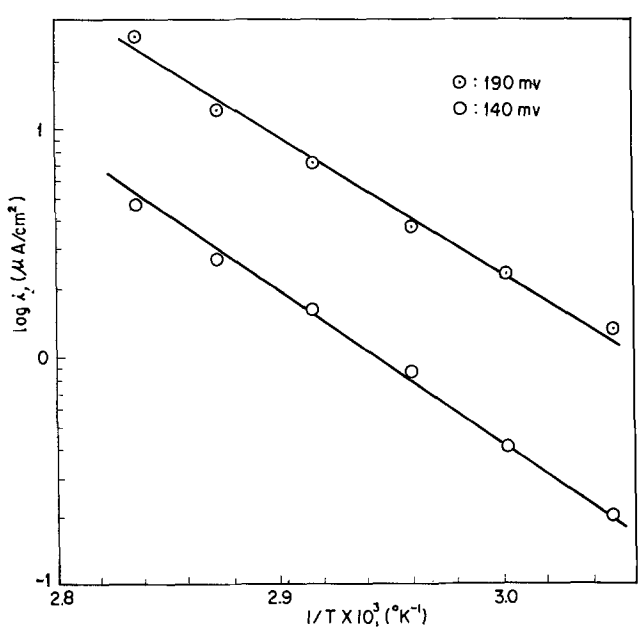


Fig. 5. Effect of temperature on current density in 1.0*N* H_2SO_4 solution, P = 1 atm.

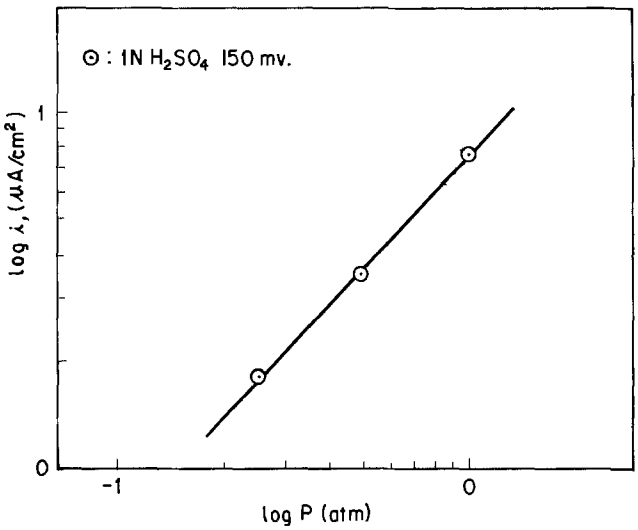


Fig. 6. Effect of methane partial pressure on current density at 80°C.

where n is the number of electrons transferred, k_2 the forward rate constant for [2], K_1 the ratio of forward and reverse rate constants for [1], a_{H+} the activity of hydrogen ion, and p the partial pressure of methane.

Table IV shows a comparison between the theoretical and experimental kinetic parameters. The proposed mechanism in this study is consistent with that described by Bockris, Gileadi, and Stoner from the investigation of other saturated hydrocarbons in phosphoric acid electrolytes (24).

Acknowledgment

The authors wish to express their thanks to the Chinese Petroleum Company, Taiwan, for the financial support and the permission to publish these results.

Manuscript submitted Dec. 22, 1976; revised manuscript received March 23, 1977.

Any discussion of this paper will appear in a Discussion Section to be published in the June 1978 JOURNAL. All discussions for the June 1978 Discussion Section should be submitted by Feb. 1, 1978.

LIST OF SYMBOLS

a_{H+} activity of hydrogen ion
$\mathbf{F}$ Faraday constant
k reaction-rate constant
K equilibrium constant
i current density
n number of electrons transferred
p partial pressure of methane
V voltage
R gas constant
T absolute temperature

Table IV. Comparison of theoretical and experimental kinetic parameters

Parameter	Theoretical value	Experimental value
$\partial V/\partial \log i$ (mV)	70	70-76
$\partial \log i/\partial$ pH	1	~1
$\partial V/\partial$ pH (mV)	−70	~−70
$\partial \log i/\partial p$	1	0.9-1.0

REFERENCES

1. W. T. Grubb and L. W. Niedrach, *This Journal*, **110**, 1086 (1963).
2. W. T. Grubb and C. J. Michalske, *Nature (London)*, **201**, 287 (1964).
3. L. W. Niedrach, *This Journal*, **109**, 1092 (1962).
4. W. T. Grubb and C. J. Michalske, *ibid.*, **111**, 1015 (1964).
5. A. A. Adams and H. J. Barger, Jr., *ibid.*, **121**, 987 (1974).
6. General Electric Research Laboratory press release, (1963).
7. W. T. Grubb, *Nature (London)*, **201**, 699 (1964).
8. M. J. Schlatter, in "Fuel Cell Systems," p. 292, American Chemical Society, Washington, D.C. (1965).
9. W. T. Grubb, *This Journal*, **111**, 1086 (1964).
10. L. W. Niedrach and H. R. Alfold, *ibid.*, **112**, 117 (1965).
11. H. Binder, A. Kohling, H. Krupp, K. Richter, and G. Sandstede, *ibid.*, **112**, 355 (1965).
12. L. W. Niedrach, *ibid.*, **111**, 1309 (1964).
13. E. J. Cairns, in "Hydrocarbon Fuel Cell Technology," p. 456, Academic Press, Inc., New York (1965).
14. R. V. Marvet and O. A. Petrii, *Elektrokhimiya*, **3**, 153 (1967).
15. S. B. Brummer and M. J. Turner, *J. Phys. Chem.*, **71**, 2825 (1967).
16. S. B. Brummer and M. J. Turner, *ibid.*, **71**, 3494 (1967).
17. A. H. Taylor and S. B. Brummer, *ibid.*, **72**, 2856 (1968).
18. A. H. Taylor and S. B. Brummer, *ibid.*, **73**, 2397 (1969).
19. S. Gilman, *Trans. Faraday Soc.*, **61**, 2546 (1965).
20. E. J. Cairns, *This Journal*, **113**, 1200 (1966).
21. L. W. Niedrach and M. Tochner, *ibid.*, **112**, 1161 (1965).
22. L. W. Niedrach, *ibid.*, **113**, 645 (1966).
23. L. W. Niedrach and M. Tochner, *ibid.*, **114**, 17 (1967).
24. J. O'M. Bockris, E. Gileadi, and G. E. Stoner, *J. Phys. Chem.*, **73**, 427 (1969).
25. M. Green, J. Weber, and V. Drazic, *This Journal*, **111**, 721 (1964).
26. J. W. Johnson, J. L. Reed, and W. J. James, *ibid.*, **114**, 572 (1967).
27. J. W. Johnson, H. Wroblowa, and J. O'M. Bockris, *ibid.*, **111**, 863 (1964).
28. J. W. Johnson, S. C. Lai, and W. J. James, *Electrochim. Acta*, **15**, 1511 (1970).
29. H. Wroblowa, B. J. Piersma, and J. O'M. Bockris, *J. Electroanal. Chem.*, **6**, 401 (1963).
30. J. W. Johnson and L. D. Gilmartin, *ibid.*, **15**, 231 (1967).
31. I. Kolthoff, E. Sandell, E. Meeham, S. Bruckenstein, in "Quantitative Chemical Analysis," Book III, p. 1106, The Macmillan Co., New York (1969).

Syntheses with Electrogenerated Halogens

Part I. Phosphorous Acid

D. A. White* and M. J. Dolan

Monsanto Company, St. Louis, Missouri 63166

ABSTRACT

A simple one step conversion of white phosphorus to phosphorous acid based on indirect electrolysis using electrogenerated halogens has been demonstrated.

Presently, the major industrial route to phosphorous acid involves the conversion of white phosphorus to the trichloride

$$1/4\ P_4 + 3/2\ Cl_2 \rightarrow PCl_3 \qquad [1]$$

followed by hydrolysis

$$PCl_3 + 3H_2O \rightarrow HPO(OH)_2 + 3HCl \qquad [2]$$

It should be noted that this route produces more hydrochloric acid than it does phosphorous acid. The disposal of large quantities of hydrochloric acid presents problems, but a closed loop can be achieved by reoxidation of the hydrochloric acid to chlorine. One of the most effective ways of doing this is via electrochemical oxidation (1)

$$3HCl \rightarrow 3/2\ H_2 + 3/2\ Cl_2 \qquad [3]$$

The over-all effect when this regeneration step is included is summarized as follows

$$1/4\ P_4 + 3H_2O \rightarrow HPO(OH)_2 + 3/2\ H_2 \qquad [4]$$

This effect is achieved in three separate steps and the objective of the present work has been to devise a one step route achieving the same results, Eq. [4], using indirect electrolysis involving electrogenerated halogens.

Experimental

Elemental phosphorus and other reagents were obtained from Fisher Scientific Company, Fairlawn, New Jersey. A sample of disodium hypophosphate, $Na_2H_2P_2O_6 \cdot 6H_2O$ was kindly supplied by M. M. Crutchfield.

Analysis.—The aqueous solutions obtained by oxidation of elemental phosphorus were analyzed by a combination of ^{31}P and ^{1}H NMR spectroscopy. For solutions in which the product concentration was less than *ca.* 1*M* (Table I, runs 1-3, 5, and 6), it was found that the ^{31}P NMR bands were broad and not suitable for measurement of the relative amounts of the various species present. However, if these solutions were made strongly basic with aqueous potassium hydroxide (50%), sharp bands were obtained. Sodium hydroxide was not suitable for this purpose, since the sodium salts of the product acids usually crystallized out of the basic solutions. The reason for the broadening in the acidic solutions is not known. After addition of a known quantity of methanol, the acidic solutions were examined by ^{1}H NMR and the quantity of phosphorous acid present was estimated from the relative areas of the $\underline{H}PO(OH)_2$ and $\underline{CH_3}OH$ resonances.

The identification of the products was by comparison of their ^{31}P NMR chemical shifts with those of authentic samples, which are shown in Table II. Because basic conditions were used for examining the reaction product mixture, the authentic samples were also made strongly basic. The doublet ^{1}H NMR resonance of phosphorous acid (7.08 ppm downfield from deuterated 3-trimethylsilylpropanesulfonic acid; $J(PH) = 684$ Hz; measured in the acidic solutions[1]) served to confirm the identity of the major product.

Apparatus.—The electrochemical cell was constructed from a 1 liter flange-jointed glass resin kettle, having a seven necked top (4 × 24/40, 3 × 10/18 standard taper joints). The necks were used for the two electrode connections, a stirrer, a water-cooled condenser, a thermometer, a nitrogen inlet, and for access to the electrolyte. The electrodes were graphite plates (grade 72C, St. Mary's Carbon Company, St. Mary's, Pennsylvania) (10 × 6 × 1.2 cm). They were maintained vertical, parallel, and 3 cm apart by 4 Teflon support rods which passed through the electrodes and fitted tightly against the inner surface of the resin kettle. The tight fit of the support rods permitted very vigorous stirring without moving the electrodes. Electrical contact with the electrodes was made via platinum wires.

A Sorenson d-c power supply, Model DCR 40-35A operating in its constant current mode, was used for the electrolyses. ^{31}P NMR spectra were measured at 40.55 MHz on a Varian Model HA-100 machine and ^{1}H NMR spectra at 60 MHz with a Varian Model A 56/60 machine.

Handling of white phosphorus.—White phosphorus is toxic and spontaneously inflammable in air. It can be safely handled under water. In the present work it was stored under water in a nitrogen-flushed glove box, washed with methanol, and dried in a stream of nitrogen before weighing. The cell was charged in the glove box and returned to it after completion of the electrolysis. Unreacted phosphorus was removed by filtration and destroyed by several weeks' contact with aqueous copper sulfate solution. The copper sulfate reacts almost instantly to form a surface coating of a copper phosphide, but prolonged contact was necessary to consume all of the phosphorus. A spray bottle of aqueous copper sulfate was used to treat accidental spills in air, and the sprayed material was then transferred to a large beaker containing other phosphorus residues. Unreacted white phosphorus tended to adhere to the electrodes. As much as possible was scraped off in the glove box. The last traces were then cautiously removed by sanding with wet emery paper, and finally by scrubbing with bleaching powder.

* Electrochemical Society Active Member.

Key words: indirect electrolysis, white phosphorus.

[1] $J(PH)$ for phosphorous acid varies considerably with *p*H [see Ref. (3)]. Thus, this value is quite different from that observed in basic solution (see Table II).

Table I. Indirect electrochemical oxidation of white phosphorus[a]

Run no.	Quantity of P_4 (g; moles)	HX[a]	Solvent[a]	Electrolysis time (hr)	Temp (°C)	Product[b,c] distribution P^3 (%)	P^4 (%)	P^5 (%)	Yield[c,d] P^3 (moles)	Current[e] efficiency (%)	Apparent conversion[f] (%)
1	41; 1.32	HBr	—	10	70-77	50	9	41	0.28	59	42
2	40; 1.29	HI	—	10	70-75	63	10	27	0.36	55	43
3	20; 0.65	HCl	$CHCl_3$	5	56	64	0	36	0.25	78	60
4[g]	104.5; 3.37	HBr	$CHCl_3$	25	56	80[g]	5[g]	15[g]	1.89	85	70
5	20.5; 0.66	HI	$CHCl_3$	5	56	80	12	8	0.39	86	74
6	20; 0.65	HI	C_6H_6	5	70	75	11	13	0.36	85	73

[a] Reactions were carried out with the concentrated acid shown (20 ml) diluted to 400 ml as the electrolyte, and with the solvent shown (200 ml) via electrolysis with a constant current of 10A for the time indicated.
[b] Via ^{31}P NMR of the basified aqueous layer.
[c] Abbreviations: $P^3 = HPO(OH)_2$; $P^4 = (HO)_2POPO(OH)_2$; $P^5 = (HO)_3PO$.
[d] Via ^1H NMR of the acidic aqueous layer to which a known quantity of methanol was added as an internal integration standard.
[e] Combined current efficiency for all three product acids.
[f] Based on quantities of acids formed and phosphorus charged.
[g] After 5 and 12 hr of electrolysis the product distributions were within experimental error, the same as that shown.

Table II. ^{31}P chemical shifts of potassium salts by phosphorus acids[a]

Conjugate acid	^{31}P chemical shift[a] Measured	Literature[b]
$HPO(OH)_2$	−3.0[c]	−4[d]
$(HO)_2POPO(OH)_2$[e]	−13.1	−9
$(HO)_3PO$	−5.1	−5.8

[a] Measured at 40.55 MHz in aqueous KOH, in ppm from external 85% $(HO)_3PO$ reference signal.
[b] From Ref. (2).
[c] Doublet, J(PH) = 564 Hz.
[d] Doublet, J(PH) = 585 Hz.
[e] Sample solution made up from $Na_2H_2P_2O_6 \cdot 6H_2O$, others made up from the acid.

Oxidation of white phosphorus.—A mixture of white phosphorus (102g; 3.29 mole) concentrated hydrobromic acid (48%; 20 ml), water (380 ml), and chloroform (200 ml) was added to the assembled nitrogen purged cell. The mixture was heated to 50° to melt the phosphorus. A constant current of 10A was then passed for 25.5 hr. Throughout the electrolysis a steady stream of nitrogen was passed over the electrolyte, and rapid stirring to mix the undissolved phosphorus and the aqueous and organic layers thoroughly was maintained. After a brief initial period the passage of the current maintained a gentle reflux and an electrolyte temperature of 56°.

In a nitrogen atmosphere, the aqueous layer of the cooled reaction mixture was separated and examined by ^1H and ^{31}P NMR spectroscopy, which showed the presence of phosphorous (1.99 mole), hypophosphoric (0.07 mole), and phosphoric (0.42 mole) acids. Unchanged phosphorus (0.65 g-atom) in the chloroform layer and around the walls of the cell was estimated by exhaustive electrooxidation to phosphoric acid, which was determined by ^{31}P NMR. Thus, the conversion of phosphorus is estimated at 80%, the combined yields of phosphorus acids at 96%, and the combined current efficiency for phosphorus acids at 91%.

Evaporation of the aqueous layer afforded a colorless viscous liquid, which was seeded with a crystal of phosphorous acid. The mixture was allowed to stand several hours at room temperature. The now mainly crystalline mass was pressure-filtered under a stream of dry nitrogen to give white crystals (111g) containing phosphorous (96% of P present), hypophosphoric, and phosphoric acids. The crystals were dissolved in water and the solution was evaporated until a mainly solid mass was obtained. Pressure filtration under dry nitrogen afforded white crystals (100g) of phosphorous acid in which no phosphorus containing impurities were detected by ^{31}P NMR. By ^1H NMR the purity was estimated at 97%, and by titration with iodine, 98%. The major impurity appears to be water. However, some hydrobromic acid was still present, since titration, using an ion-selective electrode, indicated a bromine content of 0.2%.

This experiment was similar to run 4 of Table I. That and the other experiments reported in Table I were carried out as described above to the point of determination of the product distributed and yield via ^{31}P and ^1H NMR. For those runs unreacted phosphorus was not measured and the product was not isolated as described above.

Oxidation of phosphorus acid.—Chemical.—Iodine (1.27g; 0.01 g-atom) was added to a solution of phosphorous acid (1.64g; 0.02 mole) in a mixture of water (9.5 ml) and aqueous hydriodic acid (58%; 0.5 ml). The mixture was heated to 60° and stirred at that temperature until all the iodine dissolved and a pale yellow solution was formed. About 1 hr was required. By ^{31}P NMR the phosphorus-containing species present were found to consist of phosphorous acid and phosphoric acid (24%; corresponding to a yield of 98%). No hypophosphoric acid was detected.

Electrochemical.—A solution of phosphorous acid (82g; 1.0 mole) was dissolved in aqueous hydriodic acid (58%; 40 ml diluted to 400 ml) and electrolyzed with a constant current of 10A for 1.4 hr. The solution was light brown during the electrolysis, and the passage of current maintained a temperature of 65°-70°. After switching off the current, the brown color dissipated and the solution was analyzed via ^{31}P NMR, which showed it to contain only phosphorous acid (75%) and phosphoric acid. Complete conversion to phosphoric acid was observed on passage of a current of 10A for a further 4 hr.

Results

Electrolysis of mixtures of white phosphorus and aqueous hydrobromic or hydriodic acids afforded mixtures of phosphorous, hypophosphoric, and phosphoric acids (Table I, runs 1 and 2). No attempt was made to convert all the phosphorus added, since it was considered desirable to have an excess present at all times, so that it, rather than the phosphorous acid produced, would react with the electrogenerated halogen. Nevertheless, higher oxidation state acids were produced. Another problem was the formation of a coating on the droplets of molten white phosphorus, which probably hindered contact of the halogen with the phosphorus. To alleviate the assumed further oxidation of phosphorous acid, subsequent experiments were carried out with a water-immiscible solvent present. The purpose of this was to extract the halogen from the aqueous phase in which it was generated. This should have two desirable effects: first, halogen and phosphorous acid formed would be in separate phases and this would hinder further oxidation of phosphorous acid formed; and second, the solvents used also dissolve white phosphorus, and contact between it and the halogen should be improved. The results did show a marked improvement in both selectivity to phosphorous acid and cur-

rent efficiency. Chloroform was preferred as the solvent because of its noninflammability. Benzene was also effective (Table I, run 6). Reflux of the solvent-water azeotropes (bp 56.3° for chloroform; 69.4° for benzene) provided a stable operating temperature.

Even with the solvent present, higher oxidation state acids were still formed. The presence of hypophosphoric in the product mixture suggests that further oxidation of phosphorous acid may not be entirely to blame. The oxidation of phosphorous acid by halogens is well known and is reported to give only phosphoric acid (4-6). To rule out the possibility that hypophosphoric acid may be a product at low conversions, the partial oxidation of phosphorous with iodine has been examined. At 25% conversion, phosphoric acid was detected as the only oxidation product. The hypophosphoric acid formed is evidently not formed by further oxidation of phosphorous acid. This may also be true of some of the phosphoric acid which is formed.

Discussion

Since phosphorous acid is in the middle of the range of oxidation states normally exhibited by phosphorus, selective oxidation was expected to be difficult. However, the strategy of always having unchanged white phosphorus present and using a water-immiscible solvent leads to quite high (75-80%) selectivities for phosphorous acid when the two heavier hydrohalic acids are used. When hydrochloric acid is used as the electrolyte, the lower selectivity may be due to higher reactivity of chlorine and/or its higher solubility in water. The direct electrochemical oxidation of white phosphorus has been reported (7, 8), but the selectivity to phosphorous acid was low (15-38%).

The conventional process (1, 2) for phosphorous acid achieves an essentially quantitative selectivity by distillation of the phosphorous trichloride. At that point, some pentachloride is removed and recycled to react with further phosphorus, giving more trichloride. This recycle allows quantitative conversion of phosphorus to the trichloride, which is then quantitatively hydrolyzed to phosphorous acid. Although the present process is not so selective, it has the distinct advantage of converting white phosphorus to phosphorous acid without any isolated intermediates in a single step, and without producing hydrochloric acid as a by-product.

Manuscript submitted March 7, 1977; revised manuscript received April 25, 1977.

Any discussion of this paper will appear in a Discussion Section to be published in the June 1978 JOURNAL. All discussions for the June 1978 Discussion Section should be submitted by Feb. 1, 1978.

Publication costs of this article were assisted by Monsanto Company.

REFERENCES

1. S. Payer, *Chem.-Ing.-Tech.*, **47**, 142 (1975).
2. V. Mark, C. H. Dungan, M. M. Crutchfield, and J. R. van Wazer, *Top. Phosphorus Chem.*, **5**, 227 (1967).
3. K. Moedritzer, *Inorg. Chem.*, **6**, 936 (1967).
4. I. M. Osadchenko, A. P. Tomilov, and V. V. Rublev, *Electrokhimiya*, **9**, 1492 (1973).
5. A. Hickling and D. Johnson, *J. Electroanal. Chem. Interfacial Electrochem.*, **13**, 100 (1967).
6. R. T. Jones and E. H. Swift, *Anal. Chem.*, **25**, 1272 (1953).
7. M. L. Barry and C. W. Tobias, *Electrochem. Technol.*, **4**, 502 (1966).
8. M. L. Barry, AEC Accession no. 5589, report no. NCRL-11573; *Chem. Abstr.*, **63**, 3894 (1965).

Syntheses with Electrogenerated Halogens

Part II. Oxidation of Malonate Esters

Donald A. White*

Monsanto Company, Corporate Research Department, St. Louis, Missouri 63166

ABSTRACT

The indirect electrochemical oxidation of malonate esters (I) to ethane-1,1,2,2-tetracarboxylate esters (II) has been investigated in greater detail than previously reported. With acetonitrile or an alcohol as the solvent, ethenetetracarboxylate (III), propane-1,1,2,2,3,3-hexacarboxylate (IV), and ethane-1,1,2-tricarboxylate (V) esters were also formed. If the conversion of (I) was limited to 70%, by-product formation was low and 98% yields of (II) were obtained. In acetonitrile, current efficiency was comparable with the chemical yield, but with alcoholic solvents it was lower (70-80%) due to competing indirect oxidation of the alcohol to the corresponding alkyl formate (VI). The similar coupling of monosubstituted malonate esters (VII; giving VIII) shows a marked steric effect similar to that observed in some cyanoethylation reactions, suggesting that the coupling occurs via a nucleophilic displacement reaction. The steric effect rationalizes the absence of tetrameric and higher products. The similar cyclization of some bismalonate esters (IX; giving X) is also reported.

The electrochemical conversion (Eq. [1]) of malonate esters (I) to ethane-1,1,2,2-tetracarboxylate esters (II) has been achieved via direct oxidation of the malonate carbanion (1-3) or via indirect oxidation in systems containing a halide (usually iodide) electrolyte (4, 5). This conversion was of interest as a route to tetrasodium ethane-1,1,2,2-tetracarboxylate, which has useful detergent-builder properties (6, 7). The direct oxidation gives a mixture of products (2, 3) in addition to low current efficiencies. At the time this work was initiated, it appeared that current efficiencies were also low for the indirect reaction [24% (ethanol solvent); 35% (acetonitrile solvent)] (4). However, the corresponding chemical oxidations of the malonate carbanion by iodine (8, 9) or bromine (10) have been reported to give ethanetetracarboxylate esters (II) in high yield (9, 10). This suggested that it should be possible to obtain a high efficiency, indirect electrochemical conversion

* Electrochemical Society Active Member.
Key words: indirect electrolysis, carbanion oxidation, alcohol oxidation, cyanoethylation.

and, indeed, during the course of this work Osa and co-workers (5) reported current efficiencies of up to 82% when the solvent was acetonitrile. The present work is concerned mainly with the use of alcoholic solvents, but some experiments [which show even higher current efficiencies than those reported by Osa and co-workers (5)] with acetonitrile as the solvent are reported for comparison with the use of alcoholic solvents. Other work in this laboratory on this conversion (Eq. [1]) has been concerned with a paired system in which acrylate esters are simultaneously converted to adipate esters (11).

$$2CH_2X_2 \xrightarrow{2F} CHX_2CHX_2 + H_2 \quad [1]$$

Ia, X = $COOCH_3$ IIa, X = $COOCH_3$

b, X = $COOC_2H_5$ b, X = $COOC_2H_5$

$$CHX_2CHX_2 \xrightarrow{2F} CX_2 = CX_2 + H_2 \quad [2]$$

IIIa, X = $COOCH_3$

b, X = $COOC_2H_5$

$$CH_2X_2 + CX_2 = CX_2 \xrightarrow{\text{base}} CHX_2CX_2CHX_2 \quad [3]$$

IVa, X = $COOCH_3$

b, X = $COOC_2H_5$

$$CH_2X_2 + CHX_2CHX_2 \xrightarrow{2F} CHX_2CX_2CHX_2 + H_2 \quad [4]$$

$$(II) + I^- \rightarrow RI + CO_2 + CH(COOR)_2CHCOOR \quad [5]$$

$$\rightarrow CH(COOR)_2CH_2COOR$$

Va, R = CH_3

b, R = C_2H_5

HCOOR $RCH(COOC_2H_5)_2$ $[RC(COOC_2H_5)_2]_2$

VIa, R = CH_3 VIIa, R = CH_3 VIIIa, R = CH_3

b, R = C_2H_5 b, R = C_2H_5 b, R = C_2H_5

$X_2CH(CH_2)_nCHX_2$ $CX_2(CH_2)_nCX_2$

IXa, X = $COOCH_3$, $n = 1$ Xa, X = $COOCH_3$, $n = 1$

b, X = $COOC_2H_5$, $n = 1$ b, X = $COOC_2H_5$, $n = 1$

c, X = $COOCH_3$, $n = 2$ c, X = $COOCH_3$, $n = 2$

Experimental

Solvents, electrolytes, reagents, the majority of the starting materials (dimethyl and diethyl malonate and diethyl methyl and ethyl malonate) and some authentic samples of products (triethyl ethane-1,1,2-tricarboxylate and the formate esters and other products formed by oxidation of methanol and ethanol) were obtained from Fisher Scientific Company, Fairlawn, New Jersey. Sodium bromide and iodide were dried *in vacuo* at 80°. Tetrabutylammonium iodide was recrystallized from tetrahydrofuran and then dried *in vacuo*. The substituted malonate esters were purified by distillation. The remaining compounds were used as supplied. Other starting materials [tetramethyl (12) and tetraethyl (13) propane-1,1,3,3-tetracarboxylate, tetramethyl butane-1,1,4,4-tetracarboxylate (14) and tetramethyl 3-phenylpropane-1,1,2,2-tetracarboxylate (15)] and some authentic product samples [hexaethyl propane-1,1,2,2,3,3-hexacarboxylate (16), trimethyl ethane-1,1,2-tricarboxylate (17), and diethyl bis (2-cyanoethyl) malonate (18)] were prepared by literature methods. Hexamethyl propane-1,1,2,2,3,3-hexacarboxylate was a sample prepared according to a procedure published for the hexaethyl ester (19). For ethanetetracarboxylate esters the present procedures were found to be the most convenient and economical synthetic route. Authentic samples of ethenetetracarboxylate esters were synthesized via a procedure described below.

GLC analyses of the malonate and substituted malonate ester oxidation products were carried out with a 6 ft × ⅛ in. stainless steel column packed with 5% OV-17 on Gas Chrom Q (100° programmed at 10°/min to 300°). For methanol or ethanol oxidation products a similarly sized column packed with Porapak Q (80° programmed at 10°/min to 200°) was used. A Hewlett-Packard F and M Model 5750 machine was used for the GLC analyses. Hexamethyl propane-1,1,2,2,3,3,-hexacarboxylate sometimes underwent decomposition via the reverse Michael reaction (reverse of reaction [3]) in the GLC injection port. The GLC analysis was supplemented by an NMR determination of this compound based on the area of its methine proton resonance. The similar resonance of the hexaethyl ester was obscured (at 60 MHz) by that of the ethyl group methylene protons, and it was not reliably determined. NMR spectra at 60 MHz were obtained using a Varian Model T-60 or A-56/60 machine. Elemental analyses, solution molecular weight measurements, and mass spectra were determined in this department.

For the preparative electrochemical reactions, a Sorenson Model DCR 80-6B power supply operating in its constant current mode was used. Small-scale preparative electrochemical reactions were carried out in the cell (Fig. 1) with platinum electrodes (as shown) or graphite electrodes. The graphite electrodes were 12 × ¼ in. graphite rods (Laboratory Supply and Equipment Company, Chevy Chase, Maryland), and were discarded after both ends had been used. The platinum electrodes were washed with acetone, followed by washing with water, and then heated to red heat in a flame before reuse. For larger scale preparative experiments the electrode assembly used in the small cell was transferred to a commercial 3 necked flask having a central 34/45 standard taper joint. The remaining necks in both small and large cells were used to attach a water-cooled condenser and a thermometer. For runs performed under reflux, the heating effect of current passage was used to maintain reflux. In other cases, the temperature was kept down by placing the cell in a bath of flowing cold water. Analytical data and NMR spectra are shown in Tables I and II, respectively.

Ethenetetracarboxylate esters.—Authentic samples of these compounds were obtained by the following procedure, which was found to be more convenient than that reported in the literature (20). Diethyl bromomalonate (120g; 0.5 mole) (21) was dissolved in dimethylformamide (250 ml). Potassium carbonate (69g; 0.5 mole) was added and the mixture was stirred magnetically for 18 hr (this was convenient, but the temperature behavior of the mixture—a rise to 52° after 45 min followed by a fall back to ambient—suggests that a shorter time period might be used). The mixture was filtered and dimethylformamide was used to wash the white residue. Evaporation *in vacuo* of the combined filtrate and washings yielded an oily residue which was taken up in ether. The ether solution was freed of traces of salts by filtration and then evaporated. The oil obtained crystallized on standing. It was recrystallized from ethanol (30 ml) to give tetraethyl ethenetetracarboxylate (IIIb; 52g; 67%), mp 55°-56° [Ref. (8) mp 56°].[1] Analytical data are shown in Table I.

A similar reaction using dimethyl bromomalonate (106g; 0.5 mole), instead of the diethyl ester, was worked up by addition of water (*ca.* 1 liter) to the filtered dimethylformamide solution. The product, which crystallized out as long needles, was removed by

[1] This value is more typical than the rather low figure in the reference already cited (20).

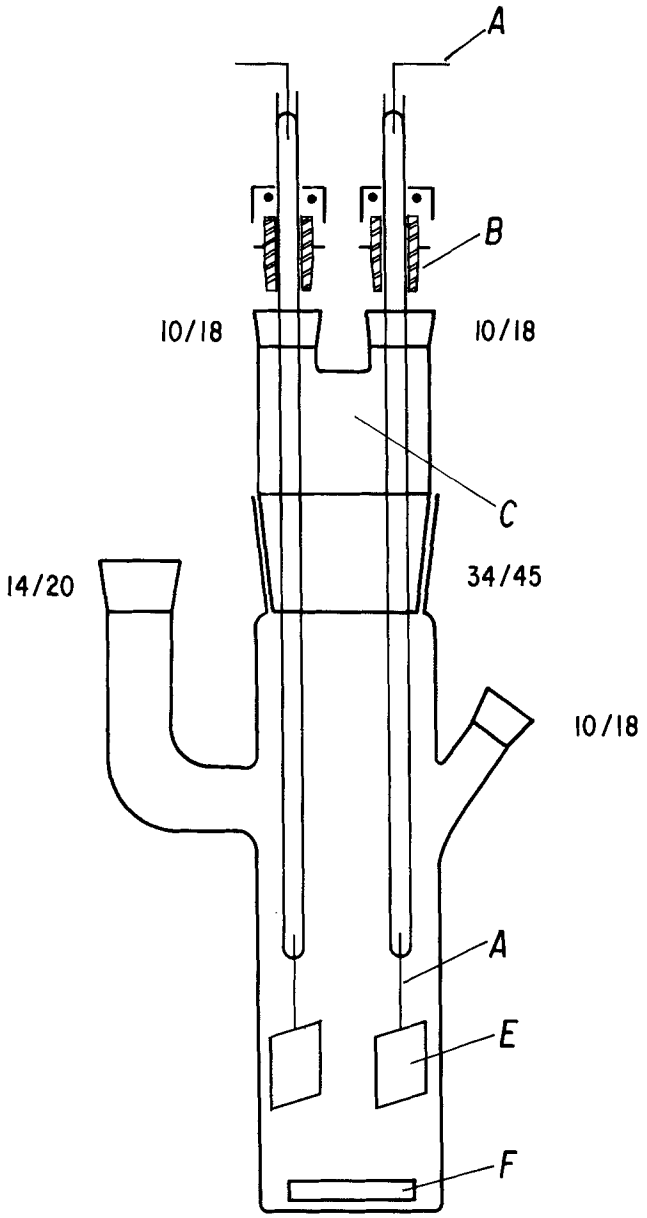


Fig. 1. Electrochemical cell. Component parts are: A, platinum wire connection; B, "thermometer" adaptor, Teflon 10/18 joint; C, electrode adaptor; D, Hg-filled 6 mm OD glass tubing; E, platinum electrodes 25 × 30 × 0.13 mm; F, Teflon-coated magnetic stirring bar. Standard taper joint sizes are shown.

filtration, washed with water, washed with methanol, and recrystallized from methanol. In this way tetramethyl ethenetetracarboxylate was obtained (IIIa; 56g; 88%), mp 119°-120° [Ref. (22) mp 121°]. Analytical data are shown in Table I.

Oxidation of malonate esters.—Dimethyl malonate.— A 1 liter flask was equipped with graphite rod electrodes inserted in the electrode adaptor shown in Fig. 1. The flask was charged with dimethyl malonate (264g; 2.00 mole), sodium iodide (30g; 0.20 mole), and methanol (500 ml). This mixture was stirred magnetically until homogeneous, and was then heated to 60°. A water-cooled reflux condenser was attached and the remaining neck was stoppered. A constant current of 3A was passed for 19 hr ($2.13F \equiv 1.06$ F/mole of ester). Throughout this reaction time the electrolyte was pale yellow and was maintained at a gentle reflux by the passage of the current. Toward the end of the electrolysis, white crystals separated out. The mixture was allowed to cool to room temperature. More crystals separated and the liquid became brown. The crystals were removed by filtration and washed with methanol, which was chilled to 5°. The crystals

Table I. Analytical data

Compound	Formula	Found C, %	Found H, %	Found N, %	Found M	Calculated C, %	Calculated H, %	Calculated N, %	Calculated M
IIa	$C_{10}H_{14}O_8$	45.9 45.8	5.5 5.4		263	45.8	5.4		262
IIb	$C_{14}H_{22}O_8$	52.6 52.7	7.1 7.1		312	52.8	7.0		318
IIIa	$C_{10}H_{12}O_8$	46.0 46.1	4.8 4.9		265	46.2	4.7		260
IIIb	$C_{14}H_{20}O_8$	53.2 53.5	6.4 6.2		314	53.2	6.4		316
VIIIa	$C_{16}H_{20}O_8$	55.0 55.1	7.2 7.4			55.5	7.6		
Xa	$C_{11}H_{14}O_8$	48.4 48.4	5.1 5.3		263	48.2	5.2		274
Xb	$C_{15}H_{22}O_8$	55.0 54.8	7.2 7.0		319	54.5	6.7		330
Xc*	$C_{12}H_{16}O_8$	50.2 50.2	5.8 5.8		274	50.0	5.6		288
XIIIa*	$C_{16}H_{20}N_2O_8$	52.2 52.4	5.5 5.6	7.6 7.8	370	52.2	5.5	7.6	368
XIIIb*	$C_{20}H_{28}NO_8$	58.9 59.0	5.6 5.6	3.1 3.3		59.3	5.7	3.5	

* New compound.

Table II. NMR Spectra[a]

Compound	NMR resonance positions[a] COOR protons CH2	COOR protons CH3	Other protons CH	Other protons CH2	Other protons CH3	Other protons C6H5
IIa		3.76	4.15			
IIb	4.20[q]	1.27[t]				
IIIa		3.88				
IIIb	4.30[q]	1.37[t]				
IVa		3.78[b] 3.80[c]	4.27			
IVb	4.22[b,q] 4.25[c,q]	1.27[t]				
VIIIa	4.20[q]	1.27[t]			1.63	
Xa		3.77		2.17		
Xb	4.13[q]	1.27[t]		2.02		
Xc		3.77		2.60		
XIIIa		3.82		2.50		
XIIIb		3.78 3.60		2.57[d] 3.60[e]		7.27

[a] Measured at 60 MHz in $CDCl_3$ in ppm downfield from internal tetramethylsilane reference; undesignated resonances are singlets.
[b] $CHX_2CX_2CHX_2$.
[c] $CHX_2CX_2CHX_2$.
[d] $C_6H_5CH_2CX_2CX_2CH_2CH_2CN$.
[e] $C_6H_5CH_2CX_2CX_2CH_2CH_2CN$.
[q] Quartet, J = *ca.* 7 Hz.
[t] Triplet, J = *ca.* 7 Hz.

were washed with chilled methanol with agitation in a blender to break up the large crystals. Filtration and air drying afforded a white solid, identified by its NMR spectrum as tetramethyl ethanetetracarboxylate (IIa; 210g; 0.80 mole). A small sample was recrystallized from methanol and had the mp 135.5°-137° [Ref. (2) mp 136°-137°)]. Analytical data are shown in Table I.

The filtrates and washings were combined after separation of this product, and the solvent was removed *in vacuo*. The residue was taken up in chloroform, washed with water, washed with aqueous sodium bisulfite, and water again. The chloroform solution was then dried ($CaSO_4$), filtered, and evaporated *in vacuo*. The solid-liquid mixture (51g) was made homogeneous by heating to 100°, and a sample was removed for analysis by NMR and GLC. The mixture was found to contain unchanged dimethyl malonate (26g; 0.20 mole), tetramethyl ethanetetracarboxylate (IIa; 4.8g; 0.018 mole), tetramethyl ethenetetracarboxylate (IIIa; 6.6g; 0.025 mole), and hexamethyl propanehexacarboxylate (IVa; 13.6g; 0.035 mole). Combining this analytical data with the quantity of isolated product shown above gives the conversion yield, and current efficiency figures shown in Table III, run 1.

Other reactions shown in Table III (runs 2-4, 12) were carried out similarly. In run 12 the material which crystallized out from the cooled electrolyte was a mixture of ethanetetracarboxylate and propanehexacarboxylate esters.

Table III. Indirect electrochemical oxidation of malonate esters[a]

Run[a]	Ester	Solvent	Electrolyte	Electrodes	Electricity passed (F/mole)	Conversion (%)	Yields II (%)	Yields III (%)	Yields IV (%)	Yields V (%)	Current efficiency II (%)	Current efficiency Total[b] (%)
1	Ia	CH_3OH	NaI	C	1.06	90	91	3	6	nd	77	88
2	Ia	CH_3OH	NaI	C	0.80	69	98	<1	2	nd	85	87
3	Ia	CH_3OH	NaI	C	0.60	51	98	<1	<1	nd	83	83
4	Ia	CH_3CN	NaI	Pt	0.70	71	98	<1	nd	<1	99	100
5	Ib	C_2H_5OH	NaI	C	1.02	70	99	<1	nm	<1	69	69
6	Ib	C_2H_5OH	NaI	Pt	0.96	71	98	<1	nm	<1	73	73
7	Ib	CH_3CN	NaI	Pt	0.97	96	91	5	nm	2	90	"102"
8	Ib	CH_3CN	NaI	Pt	0.70	69	98	<1	nm	1	97	98
9	Ib	Me_2NCHO	NaI	C	1.0	57	37	<1	nm	13	21	28
10	Ib	Me_2NCHO	$[Bu_4N]I$	Pt	2.0	95	75	<1	nm	<1	36	36
11	Ib	CH_3CN	$[Bu_4N]I$	Pt	1.0	92	91	2	nm	8	84	95
12	Ia	CH_3OH	NaBr	Pt	1.1	77	45	<1	54	<1	31	82

[a] Reactions under reflux except runs 10 (120°) and 11 (55°-60°). Considerable cathode corrosion occurred in run 10. Abbreviations: nd = not detected, nm = not measured.
[b] Combined current efficiencies for all malonate ester oxidation products (II + III + IV + V).

Diethyl malonate.—This reaction was carried out using a 500 ml, 3 necked flask containing diethyl malonate (160g; 1.00 mole), sodium iodide (30g; 0.2 mole), and ethanol (200 ml) as described above for the dimethyl ester. A current of 2.2A was passed for 12.3 hr (1.02 *F*/mole), after which the cell and contents were cooled to 5°. Filtration afforded a crude product (106g), which was recrystallized from ethanol (110 ml) to give pure tetraethyl ethanetetracarboxylate (IIb; 99g; 0.31 mole) mp 74°-75° [Ref. (1) mp 74°-75°]. Analytical data are shown in Table I.

The filtrates and washings from both the original filtration of the reaction mixture and from the recrystallization were combined and analyzed by GLC. Unchanged diethyl malonate (48g; 0.30 mole), tetraethyl ethanetetracarboxylate (IIb; 11g; 0.035 mole), and traces of tetraethyl ethenetetracarboxylate (IIIb) and triethyl ethane-1,1,2-tricarboxylate (Vb) were found. These data are summarized in Table III, run 5.

The reactions shown in Table III, runs 5-10 were carried out similarly, except that in run 9 no product crystallized out from the cooled electrolyte. Triethyl ethane-1,1,2-tricarboxylate was obtained via work up and fractional distillation of run 9, confirming the presence of this unexpected product. Tetrabutylammonium iodide was recovered unchanged from runs 9 and 10. After recrystallization from tetrahydrofuran, the "yield" of recovered material was in both cases *ca.* 90%. It had the mp of 143°-145° [Ref. (22) mp 146°].

Oxidation of alcohols.—Methanol.—The cell shown (Fig. 1) was charged with methanol (64g; 2.0 moles) and sodium iodide (3.0g; 0.02 mole). A water-cooled condenser, solid carbon dioxide cooled trap, and drying tube ($CaSO_4$) were attached in series via one neck, and the remaining unused neck was stoppered. A constant current of 1.8A was passed for 32 hr (2.0*F*). After a few minutes, the electrolyte reached reflux temperature and the cell voltage settled out at 12V. At the end of the electrolysis the cell voltage had increased very slightly to 13.5V. The liquid (15g) in the trap was identified by GLC and NMR as a mixture of methyl formate (13g) and methanol (2.0g). Small traces of methylal and methyl iodide were also detected by GLC. The liquid (47g) remaining in the cell contained methyl formate (6.6g) and methanol (36g). The yield of methyl formate based on methanol consumed is 81%, and the current efficiency is 65% (requires 4 *F*/mole of ester produced).

Ethanol.—In the apparatus used for methanol oxidation, a solution of sodium iodide (60g; 0.04 mole) in ethanol (46g; 1.0 mole) was electrolyzed. The initial current (2.0A), which produced reflux of the electrolyte, could not be maintained due to cell voltage increase (from 10 to 15V after 1 hr). The current was gradually reduced and the reaction terminated after passage of 0.50*F*. Along with the cell voltage increase, precipitation of a gelatinous solid was also observed. The trap liquid (3.05g) contained ethyl formate (2.0g; 27 mmoles), ethanol (0.67g; 15 mmoles) ethyl methyl ether (0.15g; 2.5 mmoles), methyl iodide (0.23g; 1.6 mmoles), and a trace of acetaldehyde. Further ethyl formate (0.35g; 4.8 mmoles) was found in the liquid in the cell. The current efficiency for ethyl formate is, thus, 51% (requires 8 *F*/mole of ester produced). The solid (0.26g) formed was removed by filtration. It was white, water-soluble and evolved carbon dioxide (detected with a drop of saturated calcium hydroxide suspended from a glass rod), on addition of dilute acid.

Chemical oxidation of methanol.—A solution of sodium methoxide (0.83*M*, 100 ml) was "titrated" with a solution of iodine (1.00 g-atom/liter) in methanol until a permanent yellow color developed. This required only 5 ml of the iodine solution (*i.e.*, 0.06 g-atom/mole of sodium methoxide). The experiment was repeated with a refluxing solution of sodium methoxide (0.83*M*, 100 ml) contained in a 3 necked flask equipped with a reflux condenser and burette. In this case, much more iodine solution (73 ml; 0.88 g-atom/mole of sodium methoxide) was required to produce a permanent yellow color. Methyl formate was detected as the product of this latter experiment via GLC.

Oxidation of monosubstituted malonate esters.—Diethyl methylmalonate.—A mixture of diethyl methylmalonate (VIIa; 17.4g; 0.1 mole), sodium iodide (1.5g; 0.01 mole) and ethanol (20 ml) was electrolyzed with a constant current of 1.5A for 4 hr in the cell shown (Fig. 1). The electrolyte quickly reached reflux temperature. After *ca.* 15 min of electrolysis, a solid began to precipitate and the cell voltage to increase (*cf.*, "oxidation of ethanol" above). From that point on, the polarity of the electrodes was reversed every 30 sec, which prevented the cell voltage from getting too high. The cooled, filtered electrolyte was evaporated and the oil obtained was taken up in ether. Washing of the ether solution with aqueous sodium thiosulfate decolorized the ether solution, but, on exposure to air, it became brown again. Consequently, the solution was alternately purged with air and shaken with aqueous sodium thiosulfate until it was permanently decolorized [evidently, a compound liberating iodine on exposure to air was present, perhaps diethyl iodo(methyl)malonate, the formation of which has been observed when the carbanion is treated with iodine (23) or when the ester is electrolyzed in acetonitrile containing potassium iodide (24)]. The ether solution was then washed with water, dried ($CaSO_4$), filtered, and evaporated. The oil obtained was distilled and three fractions [(*i*) 3.2g, bp 45°-50° (0.1 mmole); (*ii*) 3.9g, bp 50°-118° (0.1 mmole); and (*iii*) 8.3g, bp 118°-120° (0.1 mmole)] were collected. Fraction (*iii*) was identified as tetraethyl butane-2,2,3,3-tetracarboxylate (VIIIa) via its NMR spectrum (Table II). It was

redistilled and a center cut was taken for analysis (data in Table I).

Two minor products were tentatively identified by GLC/mass spectroscopic examination of fraction (*ii*) as diethyl ethoxy(methyl)malonate and triethyl butane-2,2,3-tricarboxylate [*cf.* (V), formed in oxidation of unsubstituted malonate esters]. Fraction (*i*) appeared to be a mixture (*ca.* 2:1M) of the starting material and the ethoxy compound, and showed a quartet NMR resonance due to the ethoxy group at 3.60 ppm downfield from internal tetramethylsilane. In a repeat experiment, the current efficiency, after passage of 1.0 *F*/mole, was estimated at 47% using the isolated compound (VIIIa) as a standard.

In a similar oxidation of diethyl ethylmalonate (VIIb), a very small quantity of the expected product appeared to be formed and was tentatively identified via GLC/mass spectroscopy. The current efficiency was crudely estimated by assuming a GLC response factor similar to that of (VIIIa). In this way the current efficiency, after passage of 1.0 *F*/mole, appeared to be *ca.* 0.3%.

Cyclization reactions.—Oxidation of the compounds (IX) was carried out in a manner similar to the oxidation of diethyl methylmalonate described above except graphite electrodes were used, without polarity reversal, and the products were isolated after passage of 1.0 *F*/mole (IXa and b) or 1.5 *F*/mole (IXc). The products isolated were tetramethyl cyclopropane-1,1,2,2-tetracarboxylate [Xa, mp 70°-71° (from methanol), Ref. (25) mp 71.5°-72°], tetraethyl cyclopropane-1,1,2,2-tetracarboxylate [Xb, mp 44°-45° (from ethanol), Ref. (26) mp 43°], and tetramethyl cyclobutane-1,1,2,2-tetracarboxylate [Xc, mp 80.5°-81° (from cyclohexane/benzene, 70%/30%)]. Analytical data are shown in Table I. All three compounds gave mass spectra consistent with their structures. Current efficiencies, after passage of 1.0 *F*/mole, shown in Table III were estimated via GLC using these isolated samples.

Hexamethyl propane-1,1,2,2,3,3-hexacarboxylate.—A mixture of the ester (11.8g; 30 mmoles), sodium iodide (1.5g; 10 mmoles), and methanol (40 ml) was placed in a cell similar to that shown (Fig. 1), but with graphite electrodes. A constant current of 1.8A was passed for 12 hr (27 *F*/mole). Within a few minutes, the electrolyte reached reflux temperature and the solid ester dissolved. After electrolysis, the electrolyte was evaporated to dryness and the residue was taken up in chloroform. The solution was washed (water, aqueous sodium thiosulfate, water again), dried ($CaSO_4$), filtered, and evaporated. The semisolid residue (11.3g) was analyzed by NMR and GLC and was found to contain unchanged starting material (6.3g; 16 mmoles), tetramethyl ethenetetracarboxylate (IIIa; 3.1g; 12 mmoles), dimethyl malonate (Ia; 1.2g; 9.0 mmoles), and tetramethyl ethanetetracarboxylate (0.3g; 1.1 mmoles).

Cyanoethylation reactions.—Tetramethyl ethane-1,1,2,2-tetracarboxylate.—The ester was cyanoethylated by the method of Koelsch and Sjolander (15). A mixture of tetramethyl ethanetetracarboxylate (78.6g; 0.3 mole), acrylonitrile (150 ml), and *t*-butanol (450 ml) saturated with potassium hydroxide was stirred under reflux for 20 hr. The mixture was cooled and the residue partitioned between ether and water. A white solid which dissolved in neither phase was removed by filtration. It was washed with methanol and dried to give tetramethyl 1,6-dicyanohexane-3,3,4,4-tetracarboxylate (XIIIa; 23g; 21%). This material appeared to be pure by NMR, but was recrystallized from methanol (1200 ml) before analysis (data in Table I). The recrystallized sample had mp 169°-170.5°.

After removal of this compound, the ether layer of the filtrate was separated and washed with water until the washings were neutral. Drying ($CaSO_4$), filtration, and evaporation yielded crude tetramethyl 4-cyanobutane-1,1,2,2-tetracarboxylate (XIIa; 65g; 69%). It was recrystallized from methanol (50 ml), giving the pure product (23g), mp 83°-84.5° [Ref. (15) mp 84°-86°].

Similar treatment of tetramethyl 3-phenylpropane-1,1,2,2-tetracarboxylate (XIIb) led to a 25% conversion to tetramethyl 5-cyano-1-phenylpentane-2,2,3,3-tetracarboxylate (XIIIb). A small amount of the latter was separated by 6 fractional crystallizations from methanol, and it had the mp 101°-102°. Analytical data are shown in Table I. The conversion reported was estimated by NMR, using the isolated product as a reference sample.

Hexaethyl propane-1,1,2,2,3,3-hexacarboxylate.—A mixture of the ester (4.76g; 0.01 mole), acrylonitrile (5 ml), and *t*-butanol (20 ml) saturated with potassium hydroxide was refluxed for 20 hr. The cooled solution was acidified with acetic acid and filtered (the solid residue appeared to be acrylonitrile polymer). The filtrate was evaporated to dryness, and the oil (5.7g) obtained was examined by NMR and GLC, which showed it to be an approximately equimolar mixture of tetraethyl ethenetetracarboxylate (IIIb) and diethyl bis(2-cyanoethyl)malonate (XI). The oil was taken up in ethanol (25 ml) and the solution was cooled to −78°. The crystals formed were removed by filtration and identified as the latter compound (XI; 0.5g), mp 61°-62° [Ref. (18), mp 62°]. This isolation of a small amount of one of the products confirms the analytical results, and quantitative separation of the products was not attempted.

Results

Oxidation of malonate esters.—Some typical results, using sodium iodide as the electrolyte and acetonitrile or the alcohol corresponding to the ester (to avoid ester interchange) as the solvent, are shown in Table III, runs 1-8. Ethanetetracarboxylate esters (II) were obtained in excellent (98-99%) yield when the conversion of the malonate ester was limited to *ca.* 70% (*cf.*, runs 1, 2, 7, and 8). Even at conversions up to 90%, yields were still *ca.* 90%. By-products were ethenetetracarboxylate (III), propanehexacarboxylate (IV), and ethane-1,1,2-tricarboxylate (V) esters. Compounds (III) and (IV) have been previously observed as by-products of the oxidation of malonate esters (2, 3, 5). They presumably arise via further oxidation of the major product (Eq. [2]) and via the Michael reaction (Eq. [3]), or cross-coupling of product and starting material (Eq. [4]). Compounds (V) may be formed by attack of iodide ion on (II), as shown (Eq. [5]) [*cf.* similar reactions of other esters (27)].

The conditions of these experiments were similar to those of Okubo and Tsutsumi (4), except that the more soluble sodium iodide was used in place of the potassium salt, and the reactions were carried out at reflux temperature (*vs.* 10°) (4). The effect of temperature is significant, since below 50° iodine generated at the anode [see reaction mechanism [6-10]; note this neglects equilibria involving I_2 and I_3^- and (in alcohol solutions) RO^- and $\overline{C}H(COOR)_2$] accumulated in the solution.

Cathode: $2M^+ + 2e^- \rightarrow 2M$ [6]

Solution:

$2M + 2CH_2X_2 \rightarrow 2M^+ + 2\overline{C}HX_2 + H_2$ [7]

$\overline{C}HX_2 + I_2 \rightarrow ICHX_2 + I^-$ [8]

$\overline{C}HX_2 + ICHX_2 \rightarrow CHX_2CHX_2 + I^-$ [9]

Anode: $2I^- \rightarrow I_2 + 2e^-$ [10]

Over-all: $2CH_2X_2 \rightarrow CHX_2CHX_2 + H_2$ [1]

$$RCHX_2 + e^- \rightarrow R\dot{C}X_2 + \tfrac{1}{2} H_2 \quad [11]$$

Cathodic reduction of dissolved iodine would, of course, lead to reduced current efficiencies. At reflux temperatures the solutions were a very pale yellow. The essentially quantitative usage of current in forming malonate ester oxidation products, when the solvent is acetonitrile (Table III, last column, runs 4, 7, and 8), suggests that this recycling has been minimized. The lower values observed when the solvent is methanol (85-90%) or ethanol (70-75%) appear to be due to competing solvent oxidation, and this is discussed below.

Even though acetonitrile gives the best current efficiencies, the use of methanol has some potential advantages. Inexpensive graphite electrodes may be used; these were considerably corroded when used in acetonitrile solutions. Another feature is that the product (Ia) is not very soluble in methanol and, in fact, crystallizes out from the refluxing methanol solution during the electrolysis, this would lend itself to a means of continuously removing product in a continuous industrial process.

Dimethylformamide was a poor solvent for the present reaction (Table III, run 9), though this may be due partially to poor choice of conditions (rather high temperature, graphite electrodes which were corroded). Ethanetricarboxylate ester (V) was positively identified as a product by isolation from this reaction. Tetrabutylammonium iodide was also effective as the electrolyte in this solvent (Table III, run 10). This was unexpected, since indirect cathodic formation of the malonate carbanion via alkali metal ion reduction (Eq. [6], [7]) had been assumed. With tetraalkylammonium salts as the electrolyte malonate esters, they undergo direct cathodic reduction (11), as postulated by Osa *et al.* (5). This phenomenon will be discussed elsewhere, but it should be noted that direct reduction of other carbon acids has been observed by other workers (28).

Use of tetrabutylammonium iodide in acetonitrile for the oxidation of malonate esters gave results (Table III, run 11) almost as good as those observed with sodium iodide. This reaction presumably involves generation of the carbanion via direct reduction. Sodium bromide was briefly investigated as a possible electrolyte (Table III, run 12), but it gave very large amounts of propanehexacarboxylate ester (IV). The reason for this is not known, but a different mechanism may operate in this case. It was observed in a divided cell experiment that the malonate esters (Ia and Ib) were readily brominated by anodically generated bromine, whereas they did not react with iodine generated in the same way. Considerable quantities of the dibromomalonate ester were formed even at low conversions, which would give rise to large amounts of either (III) or (IV) in the undivided cell, even at low conversions, as is observed

Oxidation of methanol and ethanol.—Electrolysis of refluxing methanol containing sodium iodide in an undivided cell with either graphite or platinum electrodes led to a smooth reaction giving methyl formate in *ca.* 65% current efficiency. Presumably, it is formed via formaldehyde (Eq. [10], [12]-[14]), which is further oxidized via the hemiacetal (Eq. [10], [12], [15]-[17]). The net effect is as shown (Eq. [18]). This reaction shows a temperature effect similar to that observed in the malonate ester oxidation, but more pronounced. In this case there was essentially no reaction of the electrogenerated iodine at room temperature, whereas in the malonate oxidation, the problem was rather that the reaction did not consume all of the iodine formed. The same temperature effect was observed in the chemical oxidation of sodium methoxide in methanol by iodine. There was very little consumption of iodine at room temperature (0.05 g-atom/mole CH_3ONa), but in refluxing methanol the consumption (0.88 g-atom/mole) approached that expected (Eq. [19]). In this latter experiment methyl formate was

$$4CH_3ONa + 2I_2 \rightarrow HCOOCH_3 + 4NaI + 2CH_3OH \quad [19]$$

detected by GLC/mass spectroscopy.

The ethanol oxidation was less smooth than that of its lower homolog; the cell voltage continually increased and a solid precipitated during the electrolysis (in the methanol oxidation the cell voltage was constant once reflux temperature had been attained and the electrolyte was clear throughout). In addition to ethyl formate, other products detected were ethyl methyl ether and methyl iodide. A trace of acetaldehyde was also found. Although the quantities of ethyl methyl ether and methyl iodide were less than would be expected, their presence and that of acetaldehyde suggests the mechanism shown, Eq. [20]-[24], involving oxidation to the aldehyde (Eq. [20]), iodination of the α-carbon atom (Eq. [21]), nucleophilic displacement of CI_3 by ethoxide ion (Eq. [22]), reduction of the iodoform also formed in (Eq. [22]) to methyl iodide (Eq. [23]), and reaction of methyl iodide in a Williamson ether synthesis-type reaction (Eq. [24]). An additional reduction of ethanol (Eq. [25]) is necessary to balance the electron count, and the net effect of Eq. [20]-[25] is summarized by Eq. [26]. As noted, the current efficiency for ethyl formate was low, but the reason for this has not been examined. However the solid which precipitated during the electrolysis liberates carbon dioxide on treatment with acid, and this suggests that oxidation of ethanol to carbon dioxide may also occur.

Cathode	$2CH_3OH + 2e^- \rightarrow$	$2CH_3O^- + H_2$	[12]
Solution	$CH_3O^- + I_2 \rightarrow$	$CH_3OI + I^-$	[13]
	$CH_3O^- + H{-}CH_2OI \rightarrow$	$CH_3OH + CH_2O + I^-$	[14]
Anode	$2I^- \rightarrow$	$I_2 + 2e^-$	[10]
Cathode	$2CH_3OH + 2e^- \rightarrow$	$2CH_3O^- + H_2$	[12]
Solution	$CH_3O^- + CH_2O \rightarrow$	$CH_3OCH_2O^-$	[15]
	$CH_3OCH_2O^- + I_2 \rightarrow$	CH_3OCH_2OI	[16]
	$CH_3O^- + CH_3OCHOI \rightarrow$	$CH_3OH + CH_3OCHO + I^-$	[17]
Anode	$2I^- \rightarrow$	$I_2 + 2e^-$	[10]
Over-all	$2CH_3OH \xrightarrow{4F}$	$HCOOCH_3 + 2H_2$	[18]

Electrooxidation of methanol

$$C_2H_5OH \xrightarrow{M^+I^-,\ 2F} CH_3CHO + H_2 \quad [20]$$

$$CH_3CHO + 3I^- \rightarrow CI_3CHO + 3H^+ + 6e^- \quad [21]$$

$$C_2H_5OH + CI_3CHO \xrightarrow{base} C_2H_5OCHO + HCI_3 \quad [22]$$

$$2C_2H_5OH + CHI_3 + 4e^- \rightarrow CH_3I + 2I^- + 2C_2H_5O^- \quad [23]$$

$$C_2H_5O^- + CH_3I \rightarrow CH_3OC_2H_5 + I^- \quad [24]$$

$$2C_2H_5OH + 2e^- \rightarrow 2C_2H_5O^- + H_2 \quad [25]$$

$$3C_2H_5OH \xrightarrow{M^+I^-,\ 8F} HCOOC_2H_5 + C_2H_5OCH_3 + 2H_2 \quad [26]$$

Electrooxidation of ethanol

The formate esters, which are rather volatile, were collected by passing the cell gas effluent (mainly hydrogen) through a trap at −78°. When a similar trap was attached to a cell in which (Ia) was being oxidized in methanol solution, methyl formate was again found in the trap liquid, suggesting that solvent oxidation may be a source of current efficiency losses when malonate esters are oxidized in alcoholic solvents.

$$2RCH(COOC_2H_5)_2 \rightarrow RC(COOC_2H_5)_2CR(COOC_2H_5)_2 + H_2 \quad [27]$$

VIIa; R = CH_3; b; R = C_2H_5 — VIIIa; R = CH_3; b; R = C_2H_5

$$CHX_2(CH_2)_nCHX_2 \rightarrow CX_2(CH_2)_nCX_2 + H_2 \quad [28]$$

IXa; X = $COOCH_3$; $n = 1$; b; X = $COOC_2H_5$; $n = 1$; c; X = $COOCH_3$; $n = 2$ — Xa; X = $COOCH_3$; $n = 1$; b; X = $COOC_2H_5$; $n = 1$; c; X = $COOCH_3$; $n = 2$

Oxidation of monosubstituted malonate esters.—Oxidation of the simple alkyl substituted compounds (VII) and the cyclization of the bismalonate esters (IX) has been investigated, and the results are summarized in Table IV. Oxidation of diethyl methylmalonate (VIIa) proceeds as expected, Eq. [27], but the current efficiency is low (47%) compared to that of the similar oxidation of diethyl malonate (73%; Table III, run 6). For diethyl ethylmalonate there is almost no reaction; a small amount of the expected product was detected by GLC/mass spectroscopy.

In contrast, the intramolecular reactions (Eq. [28]) proceeded with current efficiencies comparable with (IXa and b) or just less than (IXc) those observed for the corresponding unsubstituted malonate esters.

Since hexaethyl cyclopropanehexacarboxylate has been obtained (29) by treatment of compound (IVb) with base followed by bromine, a similar cyclization of the esters (IV) was expected on electrolysis with sodium iodide as the electrolyte. In fact, what was observed was simply the reverse Michael reaction (reverse of reaction [3]). Some of the malonate ester formed was oxidized to ethanetetracarboxylate ester and perhaps further to ethenetetracarboxylate ester.

Discussion

$$CH_2(COOC_2H_5)_2 + 2CH_2{=}CHCN \rightarrow (NCCH_2CH_2)_2C(COOC_2H_5)_2 \quad [29]$$

Ib — XI

$$CH(COOCH_3)_2CH(COOCH_3)_2 + CH_2{=}CHCN \rightarrow NCCH_2CH_2C(COOCH_3)_2CH(COOCH_3)_2 \quad [30]$$

IIa — XIIa

$$RC(COOCH_3)_2CH(COOCH_3)_2 + CH_2{=}CHCN \rightarrow RC(COOCH_3)_2C(COOCH_3)_2CH_2CH_2CN \quad [31]$$

XIIa; R = $NCCH_2CH_2$; b; R = $C_6H_5CH_2$ — XIIIa; R = $NCCH_2CH_2$; b; R = $C_6H_5CH_2$

$$CH(COOC_2H_5)_2C(COOC_2H_5)_2CH(COOC_2H_5)_2 + 2CH_2{=}CHCN \rightarrow (XI) + (IIIb) \quad [32]$$

IVb

The indirect electrochemical oxidation of malonate esters (Eq. [1]) emerges from this study as a useful high yield synthetic reaction. In addition to the facility with which ethanetetracarboxylate esters are formed, the pronounced detrimental effect of substituents (Table IV, runs 1, 2) serves to minimize further oxidation of the product. This steric effect is consistent with mechanism suggested (Eq. [6]-[10]), which involves a nucleophilic displacement reaction (Eq. [9]) as the actual coupling process. At high conversions the intermediates shown in Table V may be present and available for similar coupling reactions. For the nucleophiles, the relative reactivity indicated is based on their reaction with acrylonitrile reported here and in the literature. Diethyl malonate is very easily biscyanoethylated (Eq. [29]) (18, 30), indicating the high reactivity of the monomeric anion (XIV) toward acrylonitrile. Much more vigorous conditions are necessary for monocyanoethylation of tetramethyl ethanetetracarboxylate (Eq. [30]) (15), indicating the lower nucleophilicity of the dimeric anion (XV). The trimeric anion can be regarded as a compound of the general type (XII). Such compounds have been reported (15) not to undergo cyanoethylation. This is not strictly true since (XIIIa) has been obtained in the present work as a by-product in the literature (15) preparation of (XIIa). Also, (XIIb) has been observed to undergo a 25% conversion to (XIIIb) under similar conditions. The low conversions of (XIIa) and (XIIb) indicate very low reactivity of the carbanions toward acrylonitrile. For the trimeric anion (XVI), itself, the reverse Michael reaction occurs rather than cyanoethylation (Eq. [32]). The parallel between cyanoethylation and the electrochemical coupling reactions is emphasized by occurrence of the reverse Michael reaction on attempted cyclization of propanehexacarboxylate esters, also reported here. Thus, there is no evidence to suggest that the trimeric anion has any nucleophilic activity at all, even toward a very active

Table IV. Indirect electrochemical oxidation of monosubstituted malonate esters[a]

Run	Substrate	Solvent[a]	Electrodes	Product	Current efficiency,[b] %
1	VIIa	C_2H_5OH	Pt	VIIIa	47
2	VIIb	C_2H_5OH	Pt	VIIIb	<1
3	IXb	C_2H_5OH	C	Xb	74
4	IXa	CH_3OH	C	Xa	82
5	IXc	CH_3OH	C	Xc	69

[a] The electrolyte was sodium iodide.
[b] After passage of 1.0 F/mole by GLC.

Table V. Possible reactive intermediates in malonate ester oxidation reaction mixtures at high conversions

Nucleophile	Relative reactivity	Electrophile	Relative Reactivity
$\bar{C}HX_2$ XIV	Good	$ICHX_2$ XVII	Good
$\bar{C}X_2CHX_2$ XV	Poor	ICX_2CHX_2 XVIII	?
$\bar{C}X_2CX_2CHX_2$ XVI	?	$ICX_2CX_2CHX_2$ XIX	?

electrophile such as acrylonitrile. For the electrophiles (Table V), nothing is known of their reactivity. However, the malonate carbanion reacts with both chloro- and bromo-malonate esters (31, 32), to give (II), and it seems likely that iodomalonate esters would react readily with the same carbanion. Except in special situations (33) tertiary halides are poor electrophiles and the dimeric and trimeric species should be, at best, poor electrophiles. It is noteworthy that observed coupling products (II) and (IV) can be explained by the interactions of (XIV) + (XVII) and of (XV) + (XVII). Compound (IV) could also arise from the interaction of (XIV) and (XVIII), but it seems more likely that this interaction is a source of the olefin (III) [although a poor electrophile, (XVIII) should still function effectively as a carbon acid]. The absence of higher molecular weight products, such as tetramers, is evidently due to the unfavorable nucleophile-electrophile interactions required for their formation.

The noninvolvement of radical coupling in the present reaction is evident from comparison with the reported (2) direct electrochemical oxidation of the carbanion derived from diethyl methylmalonate. Radical coupling appears to be involved in that reaction and a radical disproportionation prior to coupling leads to an additional product not observed in the present indirect oxidation. Also, it has been observed that the present reactions are unaffected by the presence of butadiene, which would be expected to trap any radicals formed.

Acknowledgments

Some preliminary chemical experiments were carried out by D. M. Hemmerly, whose help is gratefully acknowledged.

Manuscript submitted March 8, 1977.

Any discussion of this paper will appear in a Discussion Section to be published in the June 1978 JOURNAL. All discussions for the June 1978 Discussion Section should be submitted by Feb. 1, 1978.

Publication costs of this article were assisted by Monsanto Company.

REFERENCES

1. T. Okubo and S. Tsutsumi, *Tec. Rep. Osaka Univ.*, **13**, 495 (1963).
2. R. Brettle and J. G. Parkin, *J. Chem. Soc.* (C), 1352 (1967).
3. R. Brettle and D. Seddon, *J. Chem. Soc.* (C), 1153 (1970).
4. T. Okubo and S. Tsutsumi, *Bull. Chem. Soc. Jpn.* **37**, 1794 (1964).
5. T. Osa, Y. Okhatsu, and M. Tezuka, Paper 307 presented at The Electrochemical Society Meeting, Washington, D.C., May 2-7, 1976.
6. M. M. Crutchfield and R. D. Harken, U.S. Pat. 3,829,384.
7. J. N. Rapko and M. M. Crutchfield, U.S. Pat. 3,929,875.
8. C. A. Bischoff and C. Rach, *Ber. Dtsch. Chem. Ges.*, **17**, 2781 (1884).
9. W. J. Bailey and W. R. Sorenson, *J. Am. Chem. Soc.*, **78**, 2287 (1956).
10. J. Walker and J. R. Appleyard, *J. Chem. Soc.*, **67**, 768 (1895).
11. M. M. Baizer and R. C. Hallcher, *This Journal*, **123**, 809 (1976).
12. E. Knoevenagel, *Ber. Dtsch. Chem. Ges.* **27**, 2345 (1894).
13. H. Meerwein and W. Schurmann, *Liebigs Ann. Chem.*, **398**, 196 (1913).
14. C. S. Marvel and R. D. Vest, *J. Am. Chem. Soc.*, **81**, 984 (1959).
15. C. F. Koelsch and J. R. Sjolander, *J. Org. Chem.*, **25**, 1479 (1960).
16. S. Ruhemann and A. V. Cunnington, *J. Chem. Soc.*, **73**, 1006 (1898).
17. C. A. Bischoff, *Ber. Dtsch. Chem. Ges.* **29**, 966 (1896).
18. H. A. Bruson and T. W. Reiner, *J. Am. Chem. Soc.*, **65**, 23 (1943).
19. M. M. Baizer, J. L. Chruma, and D. A. White, *Tetrahedron Lett.*, 5209 (1973).
20. B. B. Corson and W. L. Benson, *Org. Synth.*, Vol. II, 273 (1943).
21. C. S. Palmer and P. W. McWherter, *Org. Synth.*, Vol. I, 145 (1941).
22. C. K. Mann, *Electroanal. Chem.*, **3**, 132 (1969).
23. C. A. Bischoff and C. Rach, *Liebigs Ann. Chem.*, **234**, 54 (1969).
24. T. Okubo and S. Tsutsumi, *Denki Kagaku*, **33**, 637 (1965).
25. F. Stohmann and Cl. Kleber, *J. Prakt. Chem.*, [2], **45**, 476 (1892).
26. M. Guthzeit and O. Dressel, *Liebigs Ann. Chem.*, **256**, 171 (1890).
27. J. E. McMurry and G. B. Wong, *Synth. Commun.*, **2**, 389 (1972).
28. Y. Takahashi, M. Tokuda, M. Itoh, and A. Susuki, *Chem. Lett.*, 523 (1975); *Synthesis*, 616 (1976).
29. A. Kötz and G. Stalmann, *J. Prakt. Chem.*, [2], **68**, 156 (1903).
30. H. A. Bruson, *Org. React.*, **5**, 79 (1949).
31. M. Conrad and C. A. Bischoff, *Leibigs Ann. Chem.*, **214**, 68 (1882).
32. R. C. Hallcher, Unpublished observations.
33. N. Kornblum, *Angew. Chem.*, **14**, 734 (1975).

Breakdown of Oxide Films on Nickel

B. MacDougall* and M. Cohen*

National Research Council of Canada, Division of Chemistry, Ottawa, Ontario, Canada K1A 0R9

ABSTRACT

Oxide films have been formed on nickel by either electropolishing in H_2SO_4 or anodizing at different potentials and times in *p*H 2.8 Na_2SO_4. The 6-8Å film of NiO on electropolished nickel breaks down rapidly on open circuit at *p*H 2.8 with a poorly defined potential arrest structure. In contrast, several distinct potential arrests are observed during open-circuit breakdown of the oxide films on anodized nickel, the number of arrests and their duration being dependent on the condition of film formation and indicative of film stability. The results are interpreted in terms of the anodic formation of a nickel oxide film $\approx$ 12Å thick with a small area (<5%) covered by defective oxide. Breakdown begins at the defect sites by chemical dissolution of the oxide. Oxide undermining is responsible for removal of most of the oxide and starts when the underlying nickel metal at the defect sites has been exposed. Large variations in oxide film stability are associated with very small changes in the over-all character of the film since the small coverage with defective oxide plays the major role in film breakdown.

Thin, protective films of NiO are formed on nickel electrodes either by electropolishing with subsequent air exposure or anodic oxidation in sulfate solutions of various *p*H's (1-4). The thickness of the NiO film after electropolishing and air exposure is 6-8Å, while that formed by steady-state anodic oxidation is 9-12Å. The stability of these films toward cathodic reduction is dependent on the *p*H of the solutions; at a *p*H of 8.4, the film on electropolished nickel can be cathodically reduced but not that on anodized nickel. All the films can, however, be cathodically reduced at *p*H 2.8 and this *p*H was subsequently chosen for studying the mechanism of the anodic oxidation of nickel (2, 3).

Chemisorbed oxygen is formed during the early stages of nickel anodization and is converted to nickel oxide with continued oxidation. The stability of the different oxygen species on anodized nickel was characterized in relation to their cathodic reduction behavior. At oxygen coverages approaching a monolayer, the chemisorbed oxygen can be galvanostatically reduced with almost 100% current efficiency, giving a distinct cathodic arrest structure. Conversion of the chemisorbed oxygen to NiO gives rise to a decrease in the reduction current efficiency, *i.e.*, an increase in the film stability toward cathodic reduction. At the same time, the charge associated with the well-defined cathodic arrest diminishes and the arrest completely disappears when oxide covers the entire surface. For these reasons, the cathodic charging technique did not provide a direct method of determining the stability of oxide films (*i.e.*, NiO) formed under different conditions of anodization.

The open-circuit breakdown behavior of the oxide has also been used in studying film stability. The chemisorbed oxygen is less resistant to open-circuit breakdown than NiO, a result similar to that obtained in the cathodic reduction study. However, unlike the cathodic charging profiles for the oxide, the open-circuit decay profiles for NiO display a distinct arrest structure which varies with condition of anodization. In the present investigation, the open-circuit decay technique is used in studying the films prepared under various conditions. The experimental results are analyzed in relation to the corresponding x-ray emission and anodic coulometry data for anodically polarized nickel electrodes. The structure of the oxide film is discussed in terms of its breakdown characteristics.

Experimental

Polycrystalline specimens, 1 × 2.5 cm, were prepared from zone-refined nickel sheet of 99.996% purity as described elsewhere (1). They were degreased with benzene, chemically polished (1), electropolished for 2 min at 23°C in a 57 volume percent (v/o) sulfuric acid solution at 0.5 A cm^{-2}, and then annealed at 800°C in a vacuum of 10^{-8} Torr. The specimens were electropolished again immediately before use in an experiment. As for the reference electrode, potentials quoted in this paper are referred to the Hg_2SO_4 electrode in 0.15*N* Na_2SO_4 (+0.665V with respect to the standard reversible hydrogen electrode). Deaerated solutions of 0.15*N* Na_2SO_4 had their *p*H's adjusted to 2.8. Experiments were conducted at 25°C. A Wenking fast-rise potentiostat was used to anodize specimens. The galvanostatic cathodic charging curves and open-circuit decay profiles were recorded on a Hewlett-Packard Model 7004B X-Y recorder. A high speed Brush recorder was used to follow the initial rapid decrease of current after an anodic potential step treatment. After electropolishing, the electrodes were immersed in deaerated Na_2SO_4 solutions of *p*H 2.8 under cathodic polarization sufficient to remove the prior 6-8Å film of NiO. The oxide-free electrodes were then anodized using the potential step method. Experiments were also performed where the electropolished specimens were anodized without prior reduction of the NiO film. The anodized electrodes were discharged either on open circuit or with galvanostatic reduction. Surface activities were measured by switching the potential back to the potential of anodization and measuring the anodic charge passed during the first 2 sec. The anodic current fell by about three orders of magnitude during this time, indicating that the measured anodic charge is related to that required to recover passivity. The surface activity is the ratio of this charge to the corresponding change obtained with an oxide-free starting surface. The effect of air exposure, drying, and vacuum pumping in a stainless steel chamber to 10^{-4} Torr on the steady-state oxide films was investigated by comparing the open-circuit potential-time profiles for anodized nickel with and without this treatment.

Results

Figure 1 shows the behavior of electropolished nickel during cathodic reduction at various current densities as well as on open-circuit exposure. The charges associated with the oxide reduction arrests at 20 μA cm^{-2} and 100 μA cm^{-2} are the same and equivalent to the coulombs required to reduce $\approx$ 6Å of NiO. This is in agreement with the thickness as determined by x-ray analysis (1, 2). The film is also removed on open circuit, with a complete activation of the surface occurring within 3 min. The open-circuit potential of the oxide-free surface was −0.85V.

* Electrochemical Society Active Member.

Key words: nickel oxide, open-circuit breakdown, defective oxide, passive films.

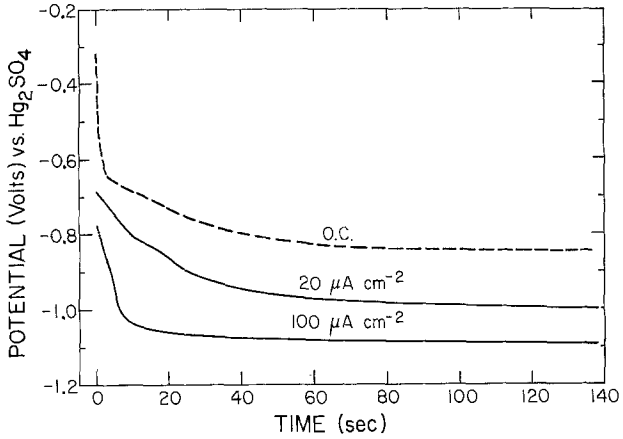


Fig. 1. Cathodic galvanostatic charging curves and open-circuit decay profile for electropolished nickel electrodes in pH 2.8 Na_2SO_4.

Figure 2a shows the cathodic charging and open-circuit results obtained with a nickel electrode which has been anodized at −0.3V for 90 sec. The arrest charges obtained during cathodic reduction at different current densities are roughly the same and correspond to a

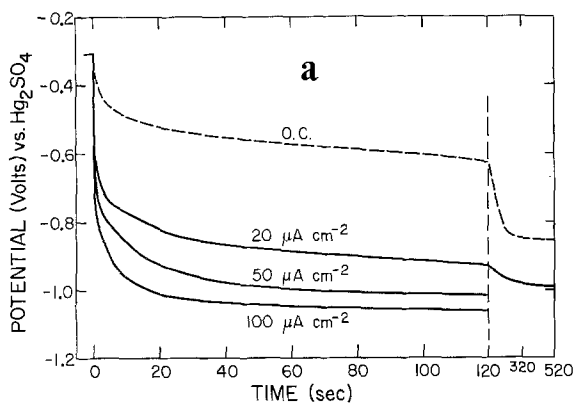


Fig. 2a. Cathodic galvanostatic charging curves and open-circuit decay profile, at pH 2.8, for nickel electrodes anodized at −0.3V for 90 sec. The oxide film on electropolished nickel was cathodically removed before anodization.

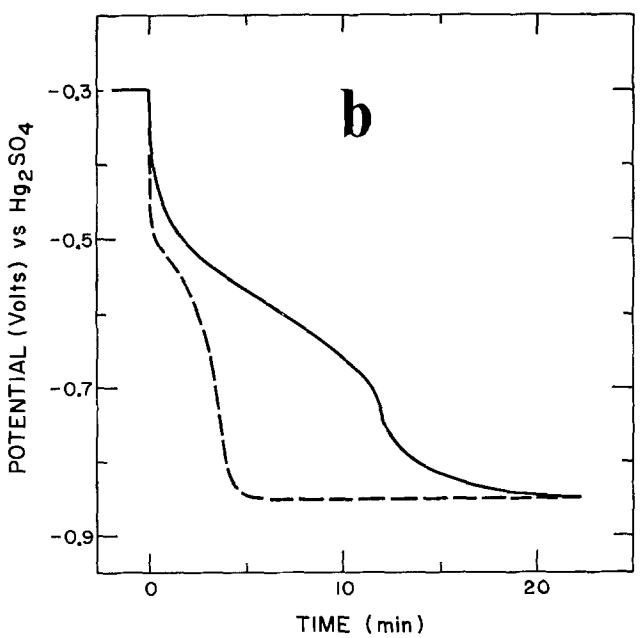


Fig. 2b. Open-circuit decay profiles, as in Fig. 2a, for nickel electrodes anodized at −0.3V for 90 sec (– – –) and 1 hr (—).

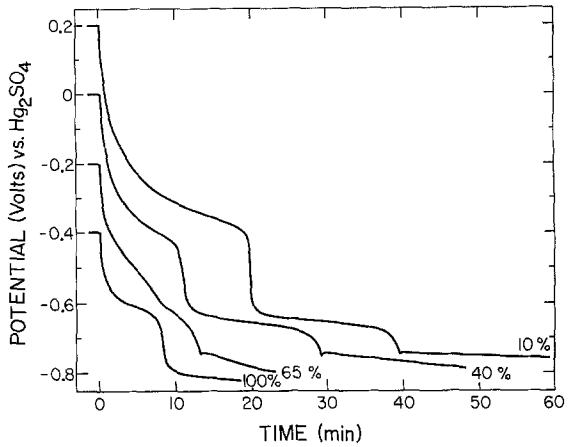


Fig. 3. Open-circuit decay profiles, at pH 2.8, of previously oxide-free nickel electrodes which had been anodized for 1 hr at various potentials. The surface activity after various times on open circuit is also given.

monolayer of chemisorbed oxygen on nickel. The surface activity at the end of the arrest is <100% due to the blocking of active sites by unreduced nickel oxide. Breakdown on open circuit is substantially slower for this film, in comparison with that on electropolished nickel, with *ca.* 7 min required for complete reactivation as indicated by the electrode potential and surface activity measurements. Figure 2b shows that the stability of the film formed at −0.3V is greatly enhanced by increasing the time of anodization to 1 hr. This is in agreement with the fact that 1 hr at −0.3V is sufficient to form a steady-state oxide film on the surface (3).

The open-circuit breakdown behavior of oxide films formed after 1 hr anodizations at different potentials is shown in Fig. 3 and 4. The number of distinct arrests increases from two to three with increasing anodic potential. Also given are measured surface activities. During open-circuit decay, the surface activity does not begin to increase significantly until the sharp potential decrease to −0.75V, this decrease generally giving rise to a potential spike. The open-circuit decay time up to the potential spike will hereafter be referred to as the induction time. In all cases, the surface activity just prior to the sharp potential decrease to −0.75V, *i.e.*, within the induction time, is <5%. For this reason, the surface activities were determined for specific times after the spike, this time being 10 min after anodizations at −0.4 and −0.2V and 20 min for all other anodization potentials (Fig. 3-6). At $V_a \leq +$ 0.2V the rate of potential decay and surface reactivation decreases with increasing anodic potential; however, at $V_a > +$ 0.2V the reverse is true. The same trends are observed after 15 hr anodizations (Fig. 5). Table I gives the corresponding anodic current densities, measured at the end of the various 1 and 15 hr anodizations, as a function of V_a.

The development of the open-circuit decay structure was also studied as a function of time of anodization at 0.0 and −0.4V (Fig. 6 and 7). The variation of the anodic current density with time of anodization at 0.0V is given in Table II. The difference between the 15 and 90 hr anodizations is not significant since the experimental precision is ± 0.01 μA cm^{-2}. At 0.0V, the stability of the oxide film toward open-circuit breakdown continues to increase with time of anodic treatment even after many hours of anodizing (Fig. 6). This increased film stability is manifested by both an increase in the induction time for significant film breakdown and a decrease in the rate of surface reactivation after the potential spike. With an increase in the anodization time from 15 min to 90 hr at 0.0V, the induction time increases by a factor of five while the surface activity recovered during a standard 20 min decay time after

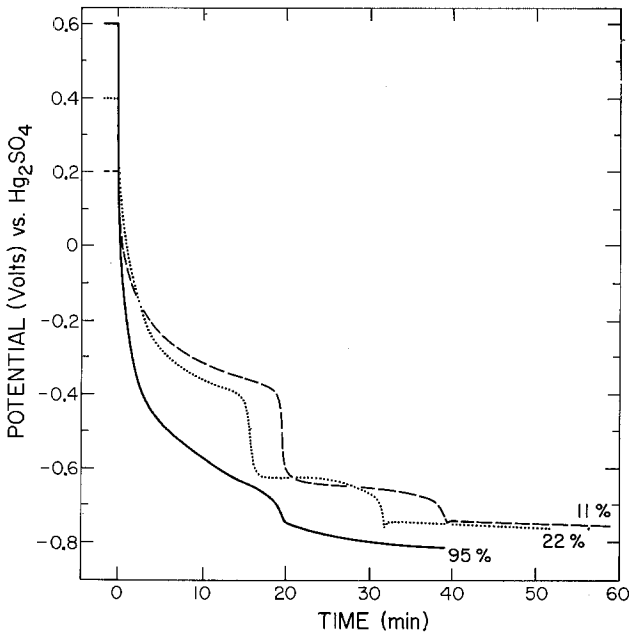


Fig. 4. As in Fig. 3 but with different 1 hr anodization potentials

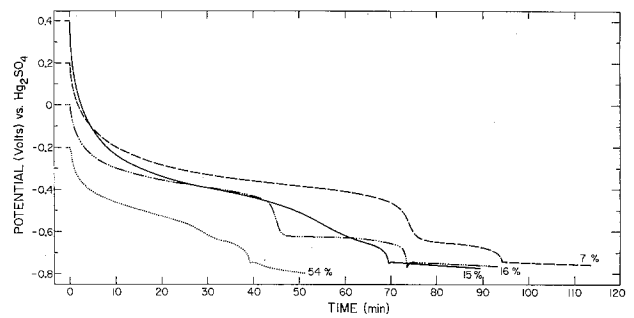


Fig. 5. As in Fig. 3 but with an anodization time of 15 hr

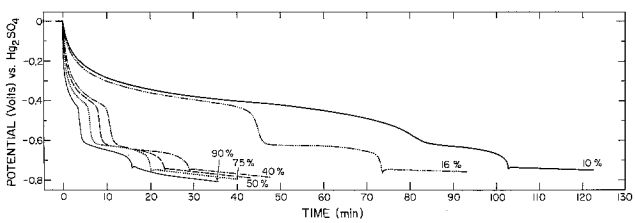


Fig. 6. Open-circuit decay profiles, as in Fig. 3, after vorious times of anodization at 0.0V: (—) 15 min; (· · ·) 30 min; (– – –) 45 min; (– · –) 1 hr; (– · · · –) 15 hr; (—) 90 hr.

the potential spike decreases by a factor of nine (Fig. 6). Clearly, for anodizations at 0.0V, the recovery rate after the potential spike is strongly influenced by the induction time to the potential spike. Although no potential spike is evident after anodizations at −0.4V (Fig. 7), the sharp potential fall to −0.75V indicates the point at which recovery of surface activity commences. In this case, however, the rate of recovery of

Table I. Current density at end of anodization

Anodization treatment	Anodic current density, μA cm^{-2}
1 hr at −0.4V	0.40
1 hr at −0.2V	0.27
1 hr at 0.0V	0.22
1 hr at +0.2V	0.35
1 hr at +0.4V	13.1
1 hr at +0.6V	28.0
15 hr at −0.2V	0.11
15 hr at 0.0V	0.06
15 hr at +0.2V	0.15
15 hr at +0.4V	5.8

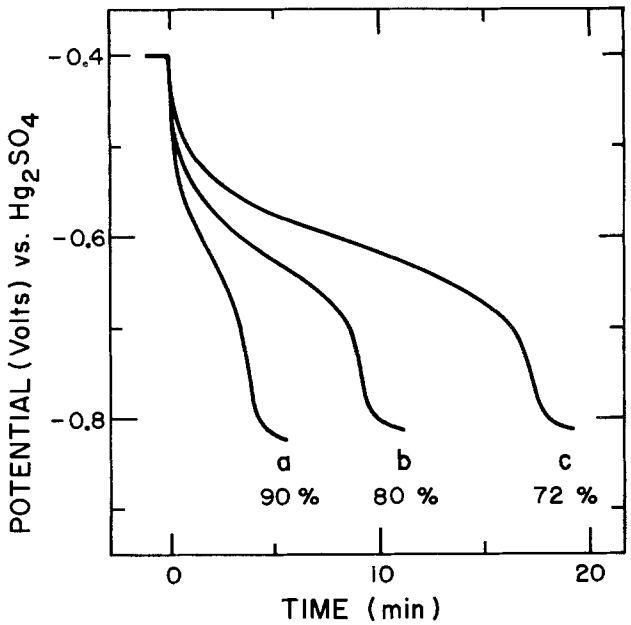


Fig. 7. As in Fig. 6 but with an anodization potential of −0.4V: (a) 15 min; (b) 1 hr; (c) 15 hr.

surface activity after the sharp potential fall is much less influenced by changes in the induction time. Also, the more anodic open-circuit arrest is not observed after the anodizations at −0.4V.

Cathodic galvanostatic charging profiles, at currents from 0.3 to 20 μA cm^{-2}, were obtained on electrodes which had been anodized under conditions known to give rise to significant open-circuit arrests at −0.4 and −0.65V, *e.g.*, 15 hr at 0.0V. In all cases, the potential decreased rapidly to *ca.* −0.75V, *i.e.*, in the region of the most cathodic open-circuit arrest, and no multiple cathodic arrest structure was observed. The sensitivity for oxygen was *ca.* 0.02 monolayer of NiO during galvanostatic cathodic reduction. Experiments were also performed where the system was switched to open circuit soon after initiating the cathodic pulse on the anodized specimen. After 15 hr at 0.0V and subsequent passage of a cathodic charge corresponding to 0.02 monolayer of NiO, the open-circuit potential was *ca.* −0.6V, *i.e.*, the arrest at −0.4V was not observed after passage of this small amount of cathodic charge.

Open-circuit decay profiles were obtained for nickel electrodes anodized at 0.0V for 1 hr both with and without prior reduction of the 6Å of NiO on the electropolished nickel, *i.e.*, the starting surface. The decay profiles were the same in both cases even though the presence of the oxide film on electropolished nickel resulted in a 10-fold decrease in the initial anodic charge which passed after potential-step anodization to 0.0V. The oxide film on electropolished nickel obviously inhibits nickel dissolution but has no substantial influence on the stability of the anodically formed steady-state oxide film.

The open-circuit decay structures obtained after 1 hr at −0.4 and 0.0V were not influenced by air exposure, compressed-air drying, and vacuum pumping of the anodized specimens. The stability of these oxides toward air exposure permitted the use of x-ray

Table II. Effect of time of anodization on final current density

Time of anodization at 0.0V	Anodic current density, μA cm^{-2}
15 min	0.60
30 min	0.36
45 min	0.28
60 min	0.22
15 hr	0.06
90 hr	0.05

emission spectroscopy in determining oxide thicknesses. Samples were analyzed by the x-ray technique after 1 hr anodizations at −0.4, 0.0, and +0.2V and 15 hr treatments at 0.0 and +0.2V. In all cases, the measured NiO thicknesses were basically the same at 9-12Å.

Discussion

Oxide films on nickel can be removed by electrochemical reduction, chemical dissolution, or undermining. The present paper is mainly concerned with the latter two topics, cathodic reduction of oxide films having been covered in previous papers (1-3). Open-circuit decay profiles, in conjunction with surface activity measurements, are shown to provide an accurate measure of oxide film stability. The results indicate that the rate of breakdown of NiO films is highly dependent on the condition of film formation. From the x-ray emission results, the large differences in film stability observed after various anodization treatments do not appear to be related to changes in oxide film thickness.

The 6Å film of NiO on electropolished nickel breaks down very rapidly on open circuit at pH 2.8 (Fig. 1). However, the arrest charge associated with its galvanostatic reduction is constant at widely varying cathodic charging currents and, hence, times of exposure to the solution. This indicates that on open circuit, undermining of the film by metal dissolution from film-free areas (2), rather than chemical dissolution of the oxide, is playing the major role in film breakdown. The polarized corrosion couple, $Ni \rightarrow Ni^{2+} + 2e$ and $2H^+ + 2e \rightarrow H_2$, is responsible for the steady-state open-circuit potential of −0.85V on oxide-free nickel. During galvanostatic charging, the applied cathodic current protects any exposed metal from dissolution by corrosion and allows the "electropolish film" to be reduced with a current efficiency close to 100%. The oxide-free regions could have already existed on the surface before immersion into the solution (*e.g.*, as pores) or could have resulted from localized chemical dissolution at weak points in the oxide film after immersion. The film on electropolished nickel has a high overvoltage for hydrogen evolution, in contrast with the anodically formed oxide which actually facilitates the reaction, and is mostly reduced at potentials which are more positive than those for hydrogen evolution on oxide-free nickel.[1]

The films on anodically oxidized nickel break down much more slowly on open circuit than the film on electropolished nickel. This is true even when the anodically formed film is thinner than the film on electropolished nickel, *e.g.*, the 1 monolayer film of chemisorbed oxygen with a very small additional coverage by oxide nuclei (3) formed after 90 sec at −0.3V (Fig. 2). This means that the approximately 50% increase in thickness of the steady-state film on anodized nickel over that on electropolished nickel is not the only factor responsible for the relative increase in stability of the former. A difference in oxide composition between electropolished and anodized nickel, indicated by the small change in oxide lattice parameter previously measured by high energy electron diffraction (2), is another possible explanation for the large stability variation. The more stable oxide, *i.e.*, that on anodized nickel, has a lattice parameter which is much closer to that of stoichiometric NiO.

The stability of the oxide films on anodized nickel toward open-circuit breakdown increases with film thickness up to the steady-state value of 9-12Å [Ref. (3) and Fig. 2b]. However, this stability continues to increase substantially with longer times and higher potentials of anodization without a corresponding increase in oxide film thickness (Fig. 3-6). The variation of "steady-state" oxide film stability with condition of anodization can be understood in terms of the detailed structure of the open-circuit decay profiles.

It has previously been shown (2) that two distinct regions of potential decay are present as characterized by the recovered surface activity. The first region is from the beginning of potential decay up to the sharp potential decrease to −0.75V (often accompanied by a potential spike as in Fig. 3) in which no significant increase in surface activity is observed and which can be viewed as an induction period before general film breakdown begins. The second region occurs after this sharp potential fall and is distinguished by an increase in the surface activity with time on open circuit. In the first region, chemical dissolution of a defective oxide ($NiO + 2H^+ \rightarrow Ni^{2+} + H_2O$) occurs at specific defect sites in the film [*cf.*, Ref. (5)].[2] The subsequent exposure of localized areas of the underlying nickel surface causes the potential to rapidly shift from that of a completely oxide-covered surface ($V \geq -0.65V$) to that associated with the galvanic corrosion couple $Ni \rightarrow Ni^{2+} + 2e$; $2H^+ + 2e \rightarrow H_2$ ($V \leq -0.75V$). The resulting nickel dissolution gives rise to undermining of the oxide film (2, 6, 7) with a corresponding increase in surface activity. Obviously the surface coverage with defect sites is small since very little surface activity (<5%) has been recovered up to the end of the first region (*i.e.*, up to the potential spike).

The stability of the steady-state oxide films toward open-circuit breakdown can thus be analyzed in terms of both chemical attack at defect sites and general film breakdown by undermining. With increasing anodic treatment, the time required for chemical dissolution of the oxide at the defect sites increases and, correspondingly, the induction time for commencement of general film breakdown (*i.e.*, undermining) increases. This can be explained by either a small increase in oxide thickness or small changes in the oxide stoichiometry and/or structure at the defect sites. Even large changes in either the thickness or stoichiometry of the oxide at defect sites would probably not be observed experimentally since their surface coverage is extremely small. The rate of reactivation by undermining (*i.e.*, after the potential jump to −0.75V) also decreases with increasing anodic treatment. This can be explained in terms of fewer defect sites breaking down during the previous induction period and correspondingly fewer sites from which undermining can occur, at least initially. If the defect sites are viewed as being nucleation centers (in this case sites for breakdown rather than formation of oxide), the equations for lateral growth of such nuclei (8) in terms of expanding circles suggest that the rate of surface reactivation is dependent on the density of nuclei. The results thus indicate that increased anodic treatment diminishes the number of sites which break down during the induction period and increases the induction time for breakdown of these active defect sites.

The over-all stability of the oxide film does not continue to increase indefinitely with increasing potential of anodization (Fig. 4). The decrease in stability at $V_a \geq +0.4V$ can be directly related to the increased anodic current at the end of the anodization (Table I) which corresponds mainly to oxygen evolution at these potentials. Oxygen evolution disrupts the perfection of the oxide, causing a rapid breakdown at the defect sites and a corresponding rapid surface reactivation by undermining. It may be that the oxide on the outer surface participates in oxygen evolution (9) and may therefore not be present on the surface long enough for the important aging effects (Fig. 6) to occur. At $V_a < +0.4V$, the anodic currents are much smaller because little or no oxygen is evolved (Table I). The general rule that a decreased anodic current is associated with a more stable oxide film (10) is only com-

[1] Although there is some overlap between these two reactions at the latter stages of oxide reduction (Fig. 1), extrapolation of the tangent lines for the two processes seems to resolve the oxide reduction charge component.

[2] It will be shown in a future paper that a general thinning of the oxide film does not occur prior to the spike, *i.e.*, significant chemical dissolution is occurring only at the defect sites.

pletely true at any one particular potential. Thus, after 1 hr at +0.2V the anodic current is actually higher than after 1 hr at 0.0V, even though the stability of the oxide film has increased substantially (Fig. 3). The extra driving force for oxide formation and/or perfection at +0.2V more than compensates for any small amount of oxygen evolution which may occur at this potential. Even at one particular potential, the anodic current at the end of the anodization will only give a direct indication of the oxide stability if it is simply due to oxide chemical dissolution and subsequent anodic reformation of the oxide. Other anodic reactions, *e.g.*, slow oxide thickening over a part of the surface or nickel dissolution through the oxide film, may contribute to the measured i_a and make it difficult to establish a definite quantitative correlation between induction time for oxide dissolution at defect sites and the anodic current density. However, there is a fairly good correlation between change in i_a and induction time with changing times of anodization at specific potentials up to +0.2V which allows the prediction of relative stabilities at one potential from measured i_a's. This is shown for 0.0V in Fig. 6 and Table II.

Increasing anodic treatment leads to the development of an additional open-circuit potential arrest during the induction period prior to general film breakdown. The potential arrest at −0.65V is evident for all anodization treatments but the arrest at −0.40V only occurs after anodization at potentials more positive than this. The absence of corresponding multiple arrests during cathodic reduction of the oxides on anodized nickel probably means that any change in oxide character is only occurring at the defect sites and hence very small reduction charges would be involved. Other workers have observed multiple arrests during the open-circuit breakdown of oxide films on anodized nickel in acid solutions and have postulated the existence of other oxides of nickel besides NiO, *e.g.*, Ni_3O_4 and/or Ni_2O_3 (11-16). Such a higher oxide may possibly explain the stabilization of the oxide defect sites with increasing anodic treatment, the higher oxide forming at and essentially deactivating certain defect sites with respect to breakdown during the induction period. The fact that one has well-resolved arrests would seem to favor such an explanation. However, the reversible potential for formation of the next higher stoichiometric oxide, Ni_3O_4, is +0.08V in the present system, and the arrest at −0.4V is present even after anodizations at −0.2V (Fig. 5).

The two potential arrests during the induction period can also be explained by assuming that the arrest at −0.65V is due to a defective oxide at the breakdown sites and not to the NiO which covers most of the electrode surface. The defective oxide may be noncrystalline NiO or a slightly nonstoichiometric NiO, *e.g.*, cation-deficient NiO, or even $Ni(OH)_2$. The defect sites could be areas of oxide located over metal grain boundaries and/or the regions where the expanding oxide nuclei meet. Although such an oxide species covers only a small area of the surface, *i.e.*, the defect sites, it could control the open-circuit potential if its exchange current were sufficiently high. With increasing extent of anodization, this oxide at the defect sites can be converted to almost stoichiometric NiO, *i.e.*, the same type of species which covers the rest of the electrode surface. This can arise from the injection of Ni^{2+} into the oxide to annihilate the cation vacancies or the expulsion of H^+ from the $Ni(OH)_2$ species, the field being in the correct direction in both cases. When stoichiometric NiO covers the entire surface, the open-circuit arrest occurs at −0.4V. This does not necessarily mean that all the defective oxide has been converted to stoichiometric NiO since the steady-state oxide is 3-4 atomic layers thick and defective oxide may still exist beneath the outer layer at the defect sites. Although the stoichiometry of this oxide is similar to that covering the rest of the surface, *i.e.*, the non-defect site area, it is still probable that the NiO at these defect sites is more reactive toward chemical dissolution. When some of this stoichiometric NiO at the defect sites has chemically dissolved, defective oxide is again exposed and the potential shifts accordingly to −0.65V. This defective oxide then breaks down and the undermining of the entire oxide begins.

To explain the decrease in the number of active defect sites, with time and potential of anodization, it can be postulated that the conversion of defective to stoichiometric oxide occurs to different extents at the various defect sites. During the induction period, those sites at which extensive conversion to stoichiometric NiO has occurred may not break down because of their increased stability. Those sites with the smallest extent of conversion to stoichiometric NiO will break down first and will thus be the ones from which undermining will eventually begin. This would explain the substantial decrease in the number of active defect sites with increasing time of anodization at 0.0V (Fig. 6).

The defective oxide can also be stabilized toward open-circuit breakdown without being completely converted to stoichiometric NiO, *i.e.*, without the involvement of the arrest at −0.4V. This is the situation for anodizations at −0.4V (Fig. 7). In that case, almost all of the defect sites are stabilized to the same extent and therefore the rate of surface reactivation after the potential spike is nearly independent of the induction time. The small changes in rate of recovery of activity can be explained in terms of the deactivation of a very small number of defect sites through the formation of some stoichiometric NiO as discussed above.

The general conclusions are therefore that oxide defect sites play the most important role in film breakdown and that only such defect sites need be stabilized by the increased anodic treatment in order to diminish the rate of over-all film breakdown. These conclusions are in agreement with the x-ray emission, cathodic reduction, and electron diffraction results which indicate that the character of the over-all oxide film does not change substantially with increasing anodic treatment, especially after a steady state has been achieved.

Summary

The results on the breakdown of anodic films formed at various stages of anodization can best be summarized by the use of the composite diagram in Fig. 8. Film formation is shown from the initial stages of oxygen chemisorption, (A), to coverage by a "monolayer" of chemisorbed oxygen, (B), with blocking of active sites by oxide nuclei in both cases. This is followed by lateral growth of the oxide nuclei to give a "flawed film" ≈ 12Å thick with <5% of the surface covered by a defective oxide, such as $Ni(OH)_2$ or nonstoichiometric NiO, in pores (C). Finally, the defective oxide in the pores is repaired, *e.g.*, by dehydration to NiO and possibly slight thickening (D). In (D) it is postulated that conversion to NiO starts at the film-solution interface and proceeds inward.

The breakdown of the film is dependent on the stage reached in the formation process. At condition A the partial chemisorbed film disappears rapidly on open circuit, probably by dissolution, leaving the nuclei at the active areas. These nuclei, although covering only a small area of the surface, can account for 50% of the surface activity. With further exposure the nuclei are removed, probably by undermining, and the surface activity increases to 100%.

The monolayer film shown in (B) takes a slightly longer time to break down and probably does so by dissolution of the chemisorbed layer. The open-circuit decay curves show a single wave and cathodic reduction takes place with high current efficiency and gives a good measure of the total chemisorbed oxygen. After the removal of the chemisorbed layer by either short cathodic reduction or dissolution, the nuclei remain on

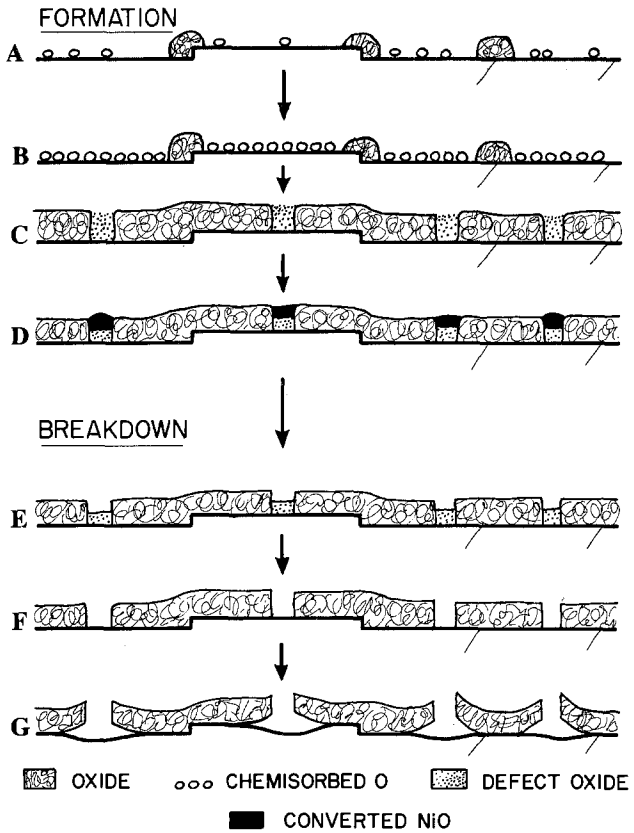


Fig. 8. Schematic diagram of the proposed mechanism of nickel oxide formation (A-D) and breakdown (E-G).

the "active sites" and, on open circuit, are again removed by undermining.

Further anodization leads to the conversion of the chemisorbed layer to oxide. This may take place by expansion of the already present nuclei to cover the whole surface with the formation of nonuniform areas or pores where the expanding nuclei meet. These areas are depicted in C and may consist of $Ni(OH)_2$ or a nonstoichiometric NiO. At this stage the breakdown occurs by dissolution of the material in the pores, as shown in F, followed by undermining of the oxide from the exposed metal side in the pores as shown in G. During open-circuit breakdown only one wave is obtained and this corresponds to the potential of a film of "defective hydrated oxide." The final potential is the nickel corrosion potential, and activity of the surface is increased by the removal of the film by undermining (as shown in G).

In the final stages of anodization shown in D the material in the pores is altered without further thickening of the main layer of oxide. The "defective hydrated oxide" is converted from the outside (film-solution interface) inward, to the metal, to NiO possibly by outward migration of H^+ assisted by the anodic field. The oxide so formed would be less dense than the bulk film oxide and hence probably more readily soluble in the slightly acid sulfate. The NiO in the main body of the film is very resistant to dissolution. The degree of conversion will depend on both the potential and time of anodization; on open circuit, breakdown is slower the longer the anodization time at any potential up to +0.2V. Two potential plateaus are observed, one for the potential of NiO and, as before, one for the defect oxide. Breakdown occurs first by dissolution of the NiO in the pores, and then by dissolution of the remaining defect oxide in the pore to the metal surface, and finally by undermining. In all cases where a full oxide film is formed during anodization, the initial opening of the pores exposes <5% of the metal surface to the solution, as indicated by the low surface activity at the spike in the potential curves. Removal of the film by undermining leads to gradually increasing surface activity until the whole surface becomes reactive.

Manuscript submitted Dec. 27, 1976; revised manuscript received March 21, 1977.

Any discussion of this paper will appear in a Discussion Section to be published in the June 1978 JOURNAL. All discussions for the June 1978 Discussion Section should be submitted by Feb. 1, 1978.

Publication costs of this article were assisted by the National Research Council of Canada.

REFERENCES

1. B. MacDougall and M. Cohen, *This Journal*, **121**, 1152 (1974).
2. B. MacDougall and M. Cohen, *ibid.*, **123**, 191 (1976).
3. B. MacDougall and M. Cohen, *ibid.*, **123**, 1783 (1976).
4. P. B. Sewell, D. F. Mitchell, B. MacDougall, and M. Cohen, *Proc. Int. Congr. Met. Corros.*, 5th, Sydney, Australia, In press.
5. H. W. Pickering and R. P. Frankenthal, *This Journal*, **112**, 761 (1965).
6. U. R. Evans, *Nature (London)*, **126**, 130 (1930); also "Metallic Corrosion Passivity and Protection," 2nd ed., Edward Arnold and Company, London (1948).
7. T. P. Hoar, *Corros. Sci.*, **7**, 341 (1967).
8. U. R. Evans, *Trans. Faraday Soc.*, **41**, 365 (1945).
9. L. A. Khanova, E. V. Kasatkin, and V. I. Veselovskii, *Elektrokhimiya*, **10**, 800, 1098 (1974).
10. R. R. Sayano and K. Nobe, *Proc. Int. Congr. Met. Corros., 3rd*, **1**, 382, Moscow (1966).
11. R. R. Sayano and K. Nobe, *Corrosion (Houston)*, **23**, 27 (1967).
12. F. Zucchi and G. Trabanelli, *Electrochim. Met.*, **4**, 313 (1969).
13. G. Okamoto and N. Sato, *Trans. Jpn. Inst. Met.*, **1**, 16 (1960).
14. G. Okamoto and N. Sato, *This Journal*, **110**, 605 (1963).
15. L. F. Trueb, G. Trumpler, and N. Ibl, *Helv. Chim. Acta*, **44**, 960 (1961).
16. T. S. de Gromoboy and L. L. Shrier, *Electrochim. Acta*, **11**, 895 (1966).

Low Potential Oxidation of Hydrogen Sulfide on a Rotating Tripolar Wiper-Blade Electrode via Continuous Anode Reactivation

M. Farooque and T. Z. Fahidy

Department of Chemical Engineering, University of Waterloo, Waterloo, Ontario, Canada N2L 3G1

ABSTRACT

The mechanism of anodic oxidation of hydrogen sulfide in an aqueous electrolyte solution was studied by means of a rotating tripolar wiped electrode system; a statistically most likely model taken from six contending models is proposed via likelihood approach. The cell can efficiently be used for the continuous reactivation of the anode surface.

The oxidation of sulfide ions in aqueous solutions is a problem of increasing importance in process metallurgy and pollution control. Although a number of electrochemical studies have been devoted to the understanding of this reaction, passivation and related problems have hindered the development of an electrochemical oxidation process of technological potential. The purpose of this paper is to present the results of a recent study in which the oxidation mechanism has been established and the anode regenerated to warrant possible industrial usefulness of the electrochemical cell employed.

A number of studies involving a wide range of potentials, current densities, and smooth platinum and other metallic anodes (1-4) indicate that, depending on the experimental conditions, elemental sulfur, polysulfides, sulfates, dithionate, and thiosulfate species may be produced during anodic oxidation of sulfide ions. The influence of dissolved H_2S on the oxidation of hydrogen and reduction of H^+ in H_2SO_4 solutions on Pt (5) has also been investigated; the presence of H_2S was found specifically (6) to suppress the reaction of chemisorbed oxygen and hydrogen. Loučka (7) studied the behavior of atomic sulfur bound to the Pt anode surface and found that at a potential of 0.4V, the nonstationary anodic oxidation current drops quickly, indicating rapid buildup of passivation of the apparently two-electron oxidation process. In all experiments, H_2 evolution at the cathode was also observed.

The current investigation began by a preliminary set of experiments in which Loučka's observations at low potentials were quantitatively confirmed via exponential decay of the nonstationary anodic current. In further experiments the mechanism of the oxidation was investigated and a continuous sulfur removal technique was developed.

The Mechanism of Anodic Oxidation of H_2S on Platinum

Experimental.—The experimental apparatus has recently been described in detail (8-10). In this part of the study, the cell was operated in a monopolar fashion without wiping action. The electrolyte was prepared by bubbling technical grade H_2S (O_2, 0.03%; CO_2, 0.25%; N_2, 0.06%; H_2S, 99.6%) through a 0.5 mole/dm^3, analytical grade H_2SO_4 solution made up with doubly deionized water; the impurities in the H_2S gas had previously been found to have no measurable influence on the reaction to be studied. The anode was prepared over a 20 min period in the following fashion, in order to produce a reproducible surface: periodic potential sweep from 0.04 to 1.5V (NHE) at a sweep rate of 0.15 V/sec in the electrolyte solution, interrupted at 0.45V anodic potential. After this sequence the cell was washed and filled with the experimental electrolyte. The concentration of H_2S in the electrolyte was determined by a standard iodometric method (11). After preparation the anode potential was raised to the desired value and the current *vs.* time variation was observed on an oscillograph during the potentiostatically controlled experiment.

Key words: anodic oxidation, rotating tripolar electrode, hydrogen sulfide, likelihood theory.

Typical variations of the anode current with time are illustrated in Fig. 1, obtained at 0.51V anode potential and at 22°C. Rapid passivation occurs during the initial period and is essentially complete within 30 sec. This observation agrees with Loučka's Fig. 1 (7) except at the very start. This apparent disagreement is probably due to a different step at the preparation stage: in his work H_2S was added to the acid solution after the oxidation potential had been raised to the desired value, not before.

More significant for the objectives of this research is Loučka's observation about anode surface reactivation: According to his findings, the anode could be reactivated by successive potential impulses in order to remove the adsorbed "poison" from the Pt surface. In order to identify the nature of this poison, the following experiments were performed: (*i*) The anode potential was raised to 0.51V in the prepared electrolyte and when the transient current had vanished the anode was removed from the cell and washed with doubly deionized water. (*ii*) The anode was put back in the cell and its potential was again raised to 0.51V in the same electrolyte. No current flow was observed; therefore, the surface poison is not a loose layer which would easily be removed by the above treatment. (*iii*) Next,

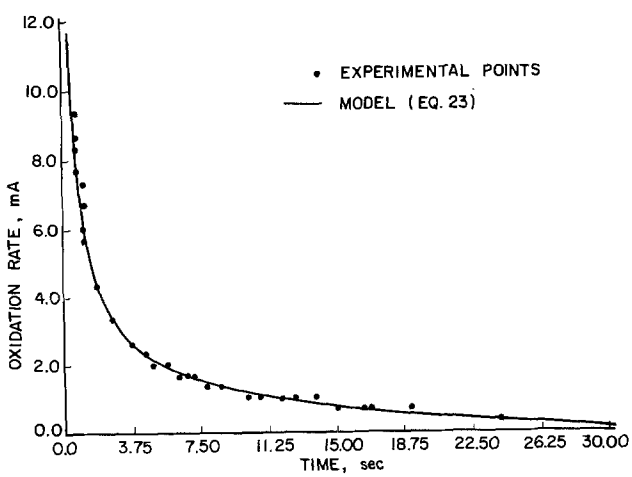


Fig. 1. Comparison of the experimental anodic oxidation rate with prediction via Eq. [23]. Anode potential 0.51V; electrolyte: 0.5 mole/dm^3 aqueous H_2SO_4 solution containing 6.73 mmole/dm^3 H_2S.

the anode was washed with deionized water, then with piperidine (a compound which is a selective solvent for sulfur) and again with deionized water. When the anode was put back in the experimental cell and its potential was raised again to 0.51V, the same transient current as in step (*i*) was observed. This test appears to confirm Loucka's proposition that the poisoning species is chemisorbed sulfur on the Pt surface.

Finally, a small set of experiments was carried out to confirm the proposition that the anodic oxidation of H_2S is a two-electron process, by repeating Loucka's procedure: The results are in agreement with previous findings (7).

It is of interest to examine, before further analysis, the origin of the anode current. It has previously been noted (6) that in a 0.5 mole/dm^3 H_2SO_4 solution saturated with H_2S the electrode reaches a rest potential of 0.165 ± 0.010V (NHE) which depends on the partial pressure of H_2S as -40 ± 15 mV/log$_{10}$ p_{H_2S}. It is also known that elemental (surface-adsorbed) sulfur is not oxidized at potentials below 1.5V (NHE) to a noticeable extent. In our test experiments no significant change in the *I-t* behavior has been observed during the 2-20 min time period in which the electrodes were dipped in the same H_2S solution before the start of the oxidation reaction. Upon introduction of H_2S into the experimental system the potential drifts toward the rest potential and the electrode is finally covered by adsorbed H_2S and possibly some (elemental?) sulfur. As soon as the potential is raised to 0.51V (NHE) or so, the adsorbed H_2S is oxidized to S_{ads} and H^+, the latter being the current source. At this low potential, sulfur on the surface does not take part in any further reaction. Its effect will be to reduce the available active area on the electrode, hence the numerical values of the experimental parameters in the forthcoming analysis will be effected in the same manner. On this basis the anode current observed in the experiments is fully attributed to the electrochemical oxidation of hydrogen sulfide.

Analysis.—In electrochemical studies, mechanistic models describing rate expressions are mainly nonlinear in both independent variables and parameters. There are two powerful statistical approaches available to establish the most likely mechanism: the likelihood approach and the Bayesian approach (12). This analysis was based on a statistical likelihood approach (12-14) whose preferability to the traditional "diagnostic criteria" method (15), in which neglect of the error structure of experimental data, simplifying assumptions, and linearization of the model equation may lead to less reliable conclusions (16), can be demonstrated (17) in electrochemical mechanism studies; the power of the statistical approach has drawn attention in a broad area of chemical kinetics (*e.g.*, 18, 19). The gist of the likelihood discrimination method is to compare the individual probability distribution functions of different competing models for the experimental observations, maximized with respect to their parameters

$$\lambda_{ij} = \frac{\max_{(\underline{a}_i)} F_i(\underline{y}, \underline{a}_i)}{\max_{(\underline{a}_j)} F_j(\underline{y}, \underline{a}_j)} = \frac{\max_{(\underline{a}_i)} L_i(\underline{a}_i)}{\max_{(\underline{a}_j)} L_j(\underline{a}_j)} \qquad [1]$$

where λ_{ij} is the likelihood ratio of model i to model j. The models are generally of the form

$$\begin{aligned} y_i &= f_1(\underline{a}_1, x_i) + \epsilon_i \\ y_i &= f_2(\underline{a}_2, x_i) + \epsilon_i \\ &\cdots\cdots\cdots \\ y_i &= f_j(\underline{a}_j, x_i) + \epsilon_i \end{aligned} \qquad [2a]$$

The error ϵ_i is defined to have zero expectation, constant variance, and a normal distribution. This is usually so, but if not in a given case, proper transformation of the data may make the error, associated with a given model, possess zero expectation, constant variance, and a normal distribution (20). Moreover, methods based on the Bayesian approach, which do not depend on any specific form of the error distribution, are also available (21).

Now, the maximum likelihood function of the jth model may be written as (12)

$$\max_{(\underline{a}_j)} L_j(\underline{a}_j) = \max_{(\underline{a}_j)} \exp\left\{ -\frac{1}{2\sigma^2} \sum_{i=1}^{n} [y_i - f_j(\underline{a}_j, x_i)]^2 \right\} \qquad [2b]$$

$$= \exp\left\{ -\frac{1}{2\sigma^2} R_j \right\} \qquad [2c]$$

in terms of the residual sum of squares, after the parameters have been estimated, and the error variance. It follows, therefore, that the model with its maximum likelihood function closest to unity is the "best" among the contenders considered (*i.e.*, not necessarily the true model in the absolute sense), and its likelihood ratios are measures of its relative preferability to all other models: the larger this ratio, the better. A $\lambda_{ij} \geq 10$ may usually be accepted for preferring model i to model j, when both have the same number of parameters; however, there is no *a priori* assurance that even the most likely model is statistically adequate to test adequacy, a goodness-of-fit analysis is required (22). The power of this approach in electrochemical mechanism studies is in yielding not only point-estimates of the reaction order, transfer coefficient, stoichiometric number, and rate constant(s), but also their probability distributions. Moreover, if deemed necessary, the estimation of parameters may be refined once the preferred model has been established. The number of experimental points required for statistical analysis may be minimized by a careful design of the experiments. Design criteria by different methods, *e.g.*, the criteria of Roth (23), Hill (24), Reilly (12), are also available. It must be emphasized that the above analysis does not decide between "right" and "wrong" mechanisms; it simply finds one (or at worst several) mechanism which is closest to the true one.

On the basis of experimental information hitherto available, the following six mechanisms were considered and subjected to likelihood analysis.

Model 1

$$H_2S \rightleftharpoons HS^- + H^+ \qquad [3]$$

$$HS^- + Pt \rightarrow Pt - SH_{ads} + e^- \qquad [4]$$

$$Pt - SH_{ads} \rightarrow Pt - S_{ads} + H^+ + e^- \qquad [5]$$

If the rate of destruction of the active electrode area by the adsorbed sulfur is a first-order process, and Eq. [4] is a diffusion-controlled process whose kinetics is much slower than that of Eq. [5], one obtains for the anodic current, the relationship

$$I = a\epsilon^{-bt}/\sqrt{t} \qquad [6a]$$

where

$$a = 2z\mathbf{F}C_{SH} - A_o\sqrt{\frac{D}{\pi}} \qquad [6b]$$

and b is the rate coefficient of the destruction of anode process. Nonlinear regression analysis of the experimental current-time data yields $a = 7.8676$ mA sec$^{1/2}$ and $b = 0.084056$ sec^{-1} at 0.51V anode potential in a 6.7 mmole/dm^3 H_2S-0.5 mole/dm^3 H_2SO_4 electrolyte solution. Twenty nine experimental points within the 0.4-32 sec range were employed in the analysis.

Model 2

$$Pt + H_2S \rightleftharpoons Pt - H_2S_{ads} \qquad [7]$$

$$Pt - H_2S_{ads} \xrightarrow{k_1} Pt - SH_{ads} + H^+ + \epsilon^- \qquad [8]$$

$$\mathrm{Pt - SH_{ads} \xrightarrow{k_2} Pt - S_{ads} + H^+ + \epsilon^-} \quad [9]$$

This mechanism corresponds to a typical consecutive reaction scheme in chemical kinetics; the current flow may be expressed as

$$I = a\left[\left(k_1 - \frac{k_1k_2}{k_1 - k_2}\right)\epsilon^{-k_1t} + \frac{k_1k_2}{k_1 - k_2}\epsilon^{-k_2t}\right] \quad [10]$$

Regression analysis yields $a = 2.7528$ mA sec, $k_1 = 0.61109$ sec^{-1}, and $k_2 = 0.079348$ sec^{-1}.

Model 3

$$\mathrm{Pt + H_2S \rightleftharpoons Pt - H_2S_{ads}} \quad [11]$$

$$\mathrm{Pt - H_2S_{ads} \xrightarrow{k_1} Pt - SH_{ads} + H^+ + e^-} \quad [12]$$

$$\mathrm{2Pt - SH_{ads} \xrightarrow{k_2} Pt - H_2S_{ads} + Pt - S_{ads} + H^+ + \epsilon^-} \quad [13]$$

Here the current equation is

$$I = AFk_1(C_{H_2S})_{ads} + \frac{1}{2}AFk_2(C_{SH})^2_{ads} \quad [14]$$

Values of $(C_{H_2S})_{ads}$ and $(C_{SH})_{ads}$ are calculated from the numerical solution of two first-order nonlinear, simultaneous differential equations. This complexity does not hinder the statistical treatment whereas the traditional "diagnostic criteria" approach would be extremely difficult to apply.

Model 4

$$\mathrm{Pt + H_2S \rightleftharpoons Pt - H_2S_{ads}} \quad [15]$$

$$\mathrm{Pt - H_2S_{ads} \xrightarrow{k_1} Pt\text{-}S + 2H^+ + 2e^-} \quad [16]$$

According to Bockris and Reddy (25) the simultaneous two-electron tunneling in Eq. [16] is very unlikely. Regression analysis yields $a = 10.457$ mA and $k_1 = 0.31972$ sec^{-1} for the expression

$$I = a\epsilon^{-k_1t}; \quad a = AzF(C_{H_2S})^{\circ}_{ads}k_1 \quad [17]$$

Model 5

In accordance with Armstrong and Harrison (26), one could visualize instantaneous or progressive two-dimensional nucleation of the $S^=$ species with diffusion control, assuming that the current stops after a poison monolayer has been formed. A somewhat involved derivation yields the current expressions and associated regression parameters

$$I = a\epsilon^{-kt}; \quad a = 10.452\,\mathrm{mA}; \quad k = 0.31972\,\mathrm{sec^{-1}} \quad [18a]$$

(instantaneous nucleation; model 5a)

and

$$I = at\epsilon^{-kt^2}; \quad a = 15.324\,\mathrm{mA\,sec^{-1}}; \quad k = 0.60084\,\mathrm{sec^{-2}}$$

(progressive nucleation; model 5b) [18b]

Model 6

$$\mathrm{Pt + H_2S \rightleftharpoons Pt - H_2S_{ads}} \quad [19]$$

fast

$$\mathrm{Pt + SH^- \rightleftharpoons Pt - SH_{ads}} \quad [20]$$

$$\mathrm{Pt - H_2S_{ads} \xrightarrow{k_1} Pt - SH_{ads} + H^+ + e^-} \quad [21]$$

$$\mathrm{Pt - SH_{ads} \xrightarrow{k_2} Pt - S_{ads} + H^+ + e^-} \quad [22]$$

It is assumed that reactions [19] and [20] occur almost instantaneously as the potential is raised at the experimental value and that current flow is due to reactions [21] and [22]. The current flow in this case may be written as

$$I = a\epsilon^{-k_1t} + b\epsilon^{-k_2t} \quad [23]$$

with regression parameter values of $a = 13.576$ mA, $b = 3.473$ mA, $k_1 = 1.191$ sec^{-1}, and $k_2 = 0.0999$ sec^{-1}.

The likelihood analysis of the six models is summarized in Table I: it is seen that the sixth model is far superior to all others considered here and may, in face of statistical evidence, be considered as the best candidate for subsequent goodness-of-fit analysis. It is instructive to point out that the first mechanism can independently be rejected by computing the apparent diffusivity coefficient from Eq. [6b]: using the numerical values (27) $K_1 = 10^{-7}$ and $K_2 = 1.2 \cdot 10^{-13}$ for the H_2S dissociation steps, $C_{SH} \cong 1.9 \cdot 10^{-9}$ mole/dm^3, and since $A_o = 93.3$ cm^2 under experimental conditions, D is computed to be about $3.7 \cdot 10^4$ cm^2/sec which is a patently absurd value.

The statistical acceptability of the sixth model is further confirmed by subsequent analysis of residues and goodness of fit whose details are described in the Appendix. Equations [19]-[22] constitute, therefore, the most likely mechanism of the anodic oxidation of H_2S in aqueous solutions on the basis of hitherto known experimental inhibition data. Figure 1 compares experimental and predicted oxidation rates, using the sixth model.

Some comments are in order with respect to the question of possible surface adsorption and/or diffusion control. In preliminary experiments, performed in the first stage of the current experimental study, it was found that the oxidation of dissolved H_2S becomes diffusion controlled only at potentials larger than 1.3V (NHE), where experimental current flows were found to be more than tenfold of the highest current flows observed at the low potentials at a given concentration. This finding is, of course, in full agreement with electrochemical theory and practice: Mass transfer becomes the rate-controlling mechanism for an electrochemical process in the neighborhood of its limiting current, *i.e.*, at relatively high potentials. Had additional models been considered (including those based on mass transfer control) the same conclusions would have nevertheless been found because the respective likelihood ratios would have been very high. The foregoing analysis was, therefore, confined to a limited number of models in order to illustrate the approach by means of a manageable number of model "candidates."

Continuous Reactivation of the Anode Surface

The electrolytic cell was operated in a typical tripolar fashion (9) where the anode rotating between three wiper blades forms three separate compartments of the cell. In the first compartment the anode surface was continuously washed with pure piperidine trickling downward along the anode and removed at the bottom of the compartment. In the second compartment the anode was washed in a similar fashion with deionized

Table I. Summary of the likelihood analysis* of various mechanisms of the electrochemical oxidation of H_2S

Anode potential, 0.51V; H_2S concentration, 6.73 mmole/dm^3; H_2SO_4 concentration, 0.5 mole/dm^3; temperature, 22°C; experimental error variance, $\sigma^2 = 0.01338$.

Mechanism index, j	Model equation	R_j	$L_j(a_j) = \exp\left(-\frac{R_j}{2\sigma^2}\right)$	$\lambda_{6j} = L_6/L_j$
1	6	1.09031	2.019×10^{-18}	5.052×10^{11}
2	10	4.07400	7.622×10^{-67}	1.338×10^{60}
3	14	217.540	3.097×10^{-3531}	3.293×10^{3524}
4	17	14.77100	1.896×10^{-240}	5.380×10^{233}
5a	18a	14.77100	1.896×10^{-240}	5.380×10^{233}
5b	18b	62.29500	9.987×10^{-1012}	1.021×10^{1005}
6	23	0.36917	1.020×10^{-6}	1.0

* The regression analysis, from which R_j and the parameter values were found, was carried out on an IBM 360 Model 75 computer using Powell's algorithmic procedure (27).

water in order to remove traces of piperidine which might remain adhered to the anode surface. The third compartment was employed as the oxidizing cell where the anode potential was varied between 0.4 and 0.5V. Blank experiments were also carried out with the third compartment containing no dissolved H_2S in the aqueous sulfuric acid electrolyte, in order to establish a (residual) reference current in the absence of H_2S oxidation. The anode rotation rate and the residence time of the anode in the active compartment (*i.e.*, the time for H_2S oxidation at the anode at each pass) are related as

$$\omega = \frac{1.5498}{T} \text{ rad/sec} \qquad [24]$$

Figure 2 shows the dependence of the continuous oxidation rate on anode potential at the anode rotation rate of 0.104 rad/sec ($T \cong 15$ sec), at low potentials, while in Fig. 3 experimentally observed rates are compared at several rotation rates with the model-based predictor equation (see Eq. [23])

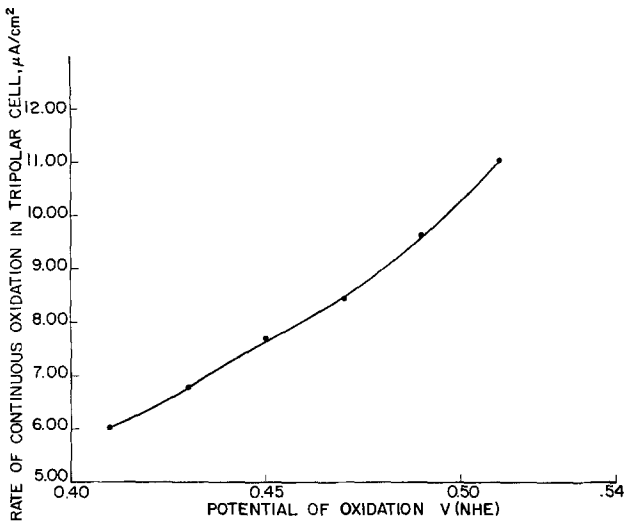


Fig. 2. The effect of oxidation potential on the continuous oxidation rate in tripolar operation (experimental conditions as in Fig. 1).

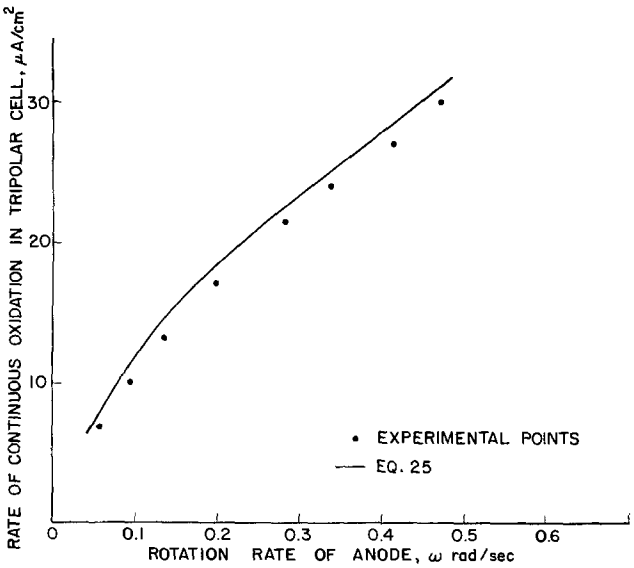


Fig. 3. The effect of the anode rotation rate on the continuous oxidation rate in tripolar operation (experimental conditions as in Fig. 1). The numerical values of parameters in Eq. [25] are: $a = 13.516$ mA, $b = 3.473$ mA, $k_1 = 1.191$ sec^{-1}, $k_2 = 0.09996$ sec^{-1}, $A = 210$ cm^2.

$$\bar{i} = \frac{1}{AT}\int_0^T (ae^{-k_1 t} + be^{-k_2 t})\,dt$$

$$= \frac{1}{AT}\left[\frac{a}{k_1}(1 - e^{-k_1 t}) + \frac{b}{k_2}(1 - e^{-k_2 t})\right] \qquad [25]$$

The theoretical prediction rate is consistently higher than the experimental rate but the two curves are almost exactly parallel, the discrepancy being about 1.15 μA/cm^2, corresponding to a maximum of 16.4% relative error at very low rotation rates and to a minimum of 3.8% relative error at higher rotation rates.

Conclusions

Hydrogen sulfide dissolved in an aqueous electrolyte solution can continuously be oxidized at a rotating platinum anode in a rotating tripolar cell employing wiper blades. The most likely oxidation mechanism involves two first-order consecutive electrochemical reactions with the SH-adsorbate as intermediate product. The oxidation rate can be predicted at an acceptable accuracy via a model equation based on statistical likelihood theory. The approach is applicable to all electrochemical mechanism studies.

Acknowledgment

This research has been supported by a National Research Council of Canada Grant and a Commonwealth Scholarship Award.

Manuscript submitted Dec. 28, 1976; revised manuscript received March 28, 1977.

Any discussion of this paper will appear in a Discussion Section to be published in the June 1978 JOURNAL. All discussions for the June 1978 Discussion Section should be submitted by Feb. 1, 1978.

Publication costs of this article were assisted by the University of Waterloo.

APPENDIX

Analysis of Residuals and Goodness of Fit of Mechanism 6

The residual pertinent to the jth model is computed as

$$R_j = \sum_{k=1}^{N} r_j^2(k) = \sum_{k=1}^{N} [I(k) - I_j^*(k)]^2 \qquad [A\text{-}1]$$

where $I(k)$, $k = 1, \ldots, N$ are the experimentally observed values of the anodic current, and $I_j^*(k)$, $k = 1, \ldots, N$ are the corresponding values computed via the jth model. The plots of $r_6(k)$ against the dependent variable of the model $[I(k)]$ and the independent variable (t) show no distinguishable tendency and this finding indicates that the normal distribution of the discrepancy between $I(k)$ and $I_6^*(k)$ may be assumed. In terms of the covariance matrix (28) of the parameter vector $\underline{\alpha}$ (containing the vector elements a, b, k_1, k_2), the likelihood distribution of the parameters is given as

$$\underline{\alpha} : N(\hat{\underline{\alpha}}, (\underline{X}'\underline{X})^{-1}\underline{I}\,\sigma^2) \qquad [A\text{-}2]$$

where $(\underline{X}'\underline{X})^{-1}\underline{I}\,\sigma^2$ is the covariance matrix of the parameters, I is the identity matrix, and $\hat{\underline{\alpha}}$ is the mean value of the likelihood distribution, *i.e.*, the statistically best estimate of the parameters. Pertinent computations give the following numerical distributions: $a = N(13.576;\ 0.20498)$, $b = N(3.473;\ 0.028178)$, $k_1 = N(1.191;\ 3.259 \cdot 10^{-3})$, and $k_2 = N(0.09996;\ 3.5992 \cdot 10^{-5})$.

The goodness of fit of the model was established via the conventional F-test

$$F_{m-p,\,n-m} = \frac{E - s^2(n-m)}{s^2(m-p)} \qquad [A\text{-}3]$$

where E is the sum of all squared residuals $r_6^2(k)$, n is the total number of observations, m is number of replica groups, p is the number of estimated param-

eters in the model tested, and s^2 is the variance estimate computed as

$$s^2 = \frac{1}{n-m} \sum_{i=1}^{m} \sum_{k=1}^{n} (I_{ik} - \bar{I}_i)^2 \qquad [A\text{-}4]$$

$\bar{I}_i$ is the mean in the ith replica group. In the given case, $E = 1.906$, $n = 145$, $m = 5$, $p = 4$, and $s^2 = 0.01338$, thus Eq. [A-3] yields the test statistical value of $F_{11,40} = 2.451$ which is less than any critical value $F_{11,40}^{*}(\alpha)$ for $\alpha \geq 0.90$. It may be concluded that the model shows no lack of fit at any confidence level of 90% and lower.

LIST OF SYMBOLS

a	model parameter; $\underline{a}$ vector of model parameters
A_o	initial active anode area in oxidizing compartment
b	model parameter
C_{SH^-}	concentration of the SH^- ion in the bulk electrolyte
D	diffusivity
$f_j(\underline{\alpha}_j, \underline{x}_i)$	predicted value via model j at the ith observation
$\mathbf{F}$	Faraday's constant (96,487 C mole^{-1})
F_i	probability distribution of model i
I	current flow
k_1, k_2	rate coefficients at a fixed potential
L_i	likelihood function of model i
n	number of observations
p	number of parameters
R_j	residual sum of squares of the jth model after estimating the parameters
T	time spent by an arbitrary point on the electrode surface in oxidizing compartment
t	time
y	dependent variable
y_i	dependent variable at the ith observation
z	valency
e_i	experimental error associated with the ith observation
λ_{ij}	likelihood ratios of model i with respect to model j
σ^2	error variance
ω	rotation speed of the anode

REFERENCES

1. W. Böhnholtzer and F. Heinrich, *Ber. Bunsenges. Phys. Chem.*, **39**, 939 (1933).
2. H. Gerischer, *Z. Anorg. Allg. Chem.*, **259**, 220 (1949).
3. H. Gerischer, *Ber. Bunsenges. Phys. Chem.*, **54**, 540 (1950).
4. A. J. Bard, "Encyclopedia of Electrochemistry of the Elements," Vol. IV, pp. 274-275, Dekka, New York.
5. A. B. Ijzermann, *Rec. Trav. Chim.*, **88**, 173 (1969).
6. A. B. Ijzermann, *ibid.*, **88**, 334 (1969).
7. T. Loučka, *Electroanal. Chem.*, **31**, 319 (1971).
8. P. R. Nadebaum, Ph.D. Thesis, University of Waterloo (1974).
9. P. R. Nadebaum and T. Z. Fahidy, *This Journal*, **122**, 1035 (1975).
10. M. Farooque and T. Z. Fahidy, Paper 370, 58th Canadian Chemical Conference, Toronto, Ontario, May 1975.
11. A. I. Vogel, "A Textbook of Quantitative Inorganic Analysis," pp. 370-371, Longmans (1961).
12. P. M. Reilly, *Can. J. Chem. Eng.*, **48**, 168 (1970).
13. G. A. Barnard, G. M. Jenkins, and C. B. Winsten, *J. Royal Stat. Soc., Ser. A*, **125**, 321 (1962).
14. G. M. Jenkins and D. G. Watts, "Spectral Analysis," Holden-Day, Inc., San Francisco, Calif. (1968).
15. J. O'M. Bockris and A. K. N. Reddy, "Modern Electrochemistry," Vol. 2, Sections 9.4, 9.5, Plenum Press, New York (1970).
16. P. M. Reilly and G. E. Blau, *Can. J. Chem. Eng.*, **52**, 289 (1974).
17. M. Farooque, Ph.D. Thesis Project, in progress, University of Waterloo.
18. J. R. Kittrel, R. Mezaki, and C. C. Watson, *Br. Chem. Engrg.*, **11**, 15 (1966).
19. V. N. Sarylov, Yn. P. Adler, and V. V. Gorskii, *J. Appl. Chem. (USSR)*, **49**, 735 (1976).
20. G. E. P. Box and D. R. Cox, *J. Royal Statist. Soc., Ser. B*, **26**, 211 (1964).
21. T. Hsiang and P. M. Reilly, *Can. J. Chem. Eng.* **49**, (1971).
22. N. R. Draper and H. Smith, "Applied Regression Analysis," pp. 86-100, John Wiley & Sons, Inc., New York (1966).
23. P. M. Roth, Ph.D. Thesis, Princeton University (1965).
24. W. J. Hill, Ph.D. Thesis, University of Wisconsin (1966).
25. J. O'M. Bockris and A. K. N. Reddy, "Modern Electrochemistry, II," p. 1082, Plenum Press, New York (1973).
26. R. D. Armstrong and J. A. Harrison, *This Journal*, **116**, 328 (1969).
27. M. J. D. Powell, *Comp. J.*, **7**, 303 (1965).
28. N. R. Draper and H. Smith, "Applied Regression Analysis," pp. 55, 81, John Wiley & Sons, Inc., New York (1966).

Effect of Orientation, Composition, and Electronic Factors in the Reduction of O_2 on Single Crystal Electrodes of the Conducting Oxides of Molybdenum and Tungsten

Jean Horkans* and M. W. Shafer

IBM Thomas J. Watson Research Center, Yorktown Heights, New York 10598

ABSTRACT

Cyclic voltammetry and steady-state techniques have been used to investigate the electrochemical behavior of single crystals of four conducting oxides of molybdenum, MoO_2, Mo_4O_{11}, Mo_8O_{23}, and Mo_9O_{26}, and one conducting oxide of tungsten, WO_2, in 1*N* H_2SO_4, and the ability of these oxides to serve as O_2-reduction catalysts in H_2SO_4 solution. The behavior of the four oxides of molybdenum was found to be similar due to the formation of a surface layer, the composition of which is more highly dependent on the past history of the electrode potential than on the composition of the bulk of the crystal. Oxygen reduction on all of these oxides occurs, for a given current density, at overpotentials which are high compared to the more common O_2-reduction catalysts such as Pt. The activity of WO_2 toward O_2 reduction is lower than that of MoO_2 because of the greater stability of the less conductive higher oxide on the WO_2 surface. Crystal orientation was found to have a substantial effect on the rate of O_2 reduction. The rate was found to be higher on surfaces which do not include short metal-metal distances. The measurement of the kinetics and mechanism of O_2 reduction is prevented by reactions of the electrode surface which occur in the same potential range.

The interest in finding new materials for fuel cell electrocatalysts has led to recent investigation of the electrochemical properties of a number of conducting transition metal oxides. One of the most extensively studied of these is the tungsten bronze electrode [*e.g.*, (1-5)]. Others include such materials as RuO_2 (6), NiO (7), and some mixed oxides (8-10). Although none of these compounds is competitive with Pt in electrocatalytic activity, these investigations have raised important questions about what electronic and physical factors are important in a good electrocatalyst. Because transition metal oxides exist with such a wide range of chemical and electronic properties, they are an interesting system for the study of these factors.

At least seven different oxides of molybdenum and five of tungsten have been prepared and characterized (11-14). These compounds are fairly stable in acid solutions and many are highly conductive. In addition, most of them can be grown as single crystals of large enough size to investigate the effects of orientation. We have studied MoO_2, Mo_4O_{11}, Mo_8O_{23}, and Mo_9O_{26} in the molybdenum-oxygen system and have investigated the effects of crystal orientation and chemical composition on their electrochemistry and catalytic activity. The oxide WO_2 of the tungsten-oxygen system has also been investigated for comparison between the molybdenum and tungsten oxides, with the aim of elucidating the role of electronic factors in electrocatalysis.

Experimental

Single crystals of the five oxides studied were grown by vapor transport techniques using the metal M and the trioxide MO_3 as starting materials and I_2 as the transporting agent (15). The desired compositions were obtained by varying the M/MO_3 ratio and the growth temperature (which was between 790° and 950°C). The crystals were typically 0.1 cm^2 on the largest faces and differed in morphology with composition. Only natural crystal faces were examined. The best crystals had 4-6 faces which were sufficiently large to allow electrochemical measurements. The crystals were identified and oriented using x-ray diffraction methods.

Contact was made to the oxide crystals by attaching a Au wire with Ag-filled epoxy (Acme Conductive Adhesives). This wire was threaded through a glass capillary, and the wire, the epoxy contact, and all of the crystal except the face of interest were masked off with a polyvinyl ketone which is used as a plater's mask (Miccrostop, Michigan Chrome and Chemical Company). The inertness of this material under the conditions of the investigation was established by partially masking off Au and Pt wires and determining their cyclic voltammetry in 1*N* H_2SO_4. No anomalous features attributable to contamination were observed. There was also no evidence that the solution was able to undercut the mask and come into contact with either the Ag in the epoxy or the Au wire.

All solutions were 1*N* H_2SO_4 prepared from deionized H_2O and reagent grade acid. A three compartment cell was used with a Pt counterelectrode and a Hg, Hg_2SO_4 reference electrode. All potentials will be quoted against the normal hydrogen electrode (NHE). During the measurements, He, N_2, or O_2 was bubbled through the solution from a bubbler slightly above the level of the working electrode. Measurements were made at room temperature.

Both potentiodynamic linear sweep and steady-state measurements were obtained. The surface electrochemical reactions of these oxides are slow, and thus the linear sweep measurements were done at a low sweep speed, 10 mV/sec. Since these oxides typically take long times to reach steady state, each steady-state measurement involved 10-15 min. The background currents, in the absence of O_2, are approximately an order of magnitude lower than the currents in the O_2-saturated solution. The steady-state results given here are the difference between the measured currents in the presence and absence of O_2. The cathodic limit of the measurements was the potential at which the steady-state current in O_2-free solution began to increase markedly. This subtraction procedure results in a small correction to the total current and does not significantly change the shape of the steady-state curves. It has been made in an effort to separate the currents due to reactions of the electrode surface from those due to O_2 reduction.

* Electrochemical Society Active Member.

Key words: molybdenum oxides, tungsten oxides, oxygen reduction, orientational effects, electrocatalysis.

Results and Discussion

The molybdenum-oxygen system contains five distinct phases, the Magneli phases, with compositions between MoO_2 and MoO_3 (11-14). Magneli phases also exist in the tungsten-oxygen system (14). The dioxides MoO_2 and WO_2 have a rutile-type structure in which MO_6 octahedra share corners and edges. The high electronic conductivity of these materials is essentially due to the short metal-metal bond distance along the direction of edge sharing. The other oxides studied, Mo_4O_{11}, Mo_8O_{23}, and Mo_9O_{26}, have a basic structure of the ReO_3 type, in which the MO_6 octahedra are joined at corners. The oxygen-deficient stoichiometry is accounted for by some of the MO_6 octahedra being joined in other ways or by different metal coordination. In Mo_8O_{23} and Mo_9O_{26} the appropriate fraction share edges; in Mo_4O_{11} there are MO_4 tetrahedra joining the basic ReO_3-type slabs. These oxides are also electronic conductors. A detailed description of these structures is given by Kihlborg (13). The pertinent structural data and the resistivities of these compounds are summarized in Table I.

Although the oxides of molybdenum are relatively stable in acid solution, they can undergo both oxidation and reduction reactions in the region of stability of H_2O. The cyclic voltammetry of five molybdenum oxides in a limited potential region is shown in Fig. 1. Each is the second sweep after the beginning of the potential scan. The shape of the cyclic voltammograms of these oxides will undergo some change with continuous sweeping. The potential region is one in which the observed currents are due to oxidation and anodic dissolution. These samples have never been at potentials more negative than 0.4V. Under these conditions, the two higher oxides, Mo_8O_{23} and Mo_9O_{26} (which were single crystal samples but which were not oriented to determine the identity of the face being examined) do not undergo further oxidation and do not exhibit anodic dissolution.

The anodic behavior of Mo_4O_{11} is highly dependent on orientation. The structure of Mo_4O_{11}, which consists of alternating slabs of MO_6 octahedra and MO_4 tetrahedra, is layered. The [111] direction is parallel to the layers and the [100] direction is perpendicular. The current densities in this potential range are substantially higher for the (111) face than for the (100) face. Both anodic and cathodic currents are observed on the (111) face, but the (100) face sustains little cathodic current in this region. In addition, the dissolution of the (100) face of Mo_4O_{11} results in a number of current peaks which Peekema and Shafer (19) have attributed to the sequential removal of single layers of the Mo_4O_{11} structure.

Table I. Structural data and resistivities of some molybdenum and tungsten oxides

Compound	Symmetry	Lattice parameter	Resistivity 300°K (Ω cm)
MoO_2	Monoclinic[a]	a = 5.61Å b = 4.85Å c = 5.62Å β = 120.95°	1.2×10^{-4}[d]
Mo_4O_{11}	Orthorhombic[b]	a = 24.49Å b = 5.45Å c = 6.75Å	2×10^{-4}[e]
Mo_8O_{23}	Monoclinic[b]	a = 16.88Å b = 4.05Å c = 13.39Å β = 106.19°	6×10^{-1}[e]
Mo_9O_{26}	Monoclinic[c]	a = 16.74Å b = 4.09Å c = 14.53Å β = 95.45°	4×10^{1}[e]
MoO_3	Orthorhombic[b]	a = 3.96Å b = 13.86Å c = 3.70Å	High
WO_2	Monoclinic[c]	a = 5.65Å b = 4.89Å c = 5.50Å β = 120 42°	2.9×10^{-3}[d]
WO_3	Triclinic[c]	a = 7.28Å b = 7.52Å c = 3.84Å β = 90.90°	High

[a] Ref. (16).
[b] Ref. (13).
[c] Ref. (14).
[d] Ref. (17).
[e] Ref. (18).

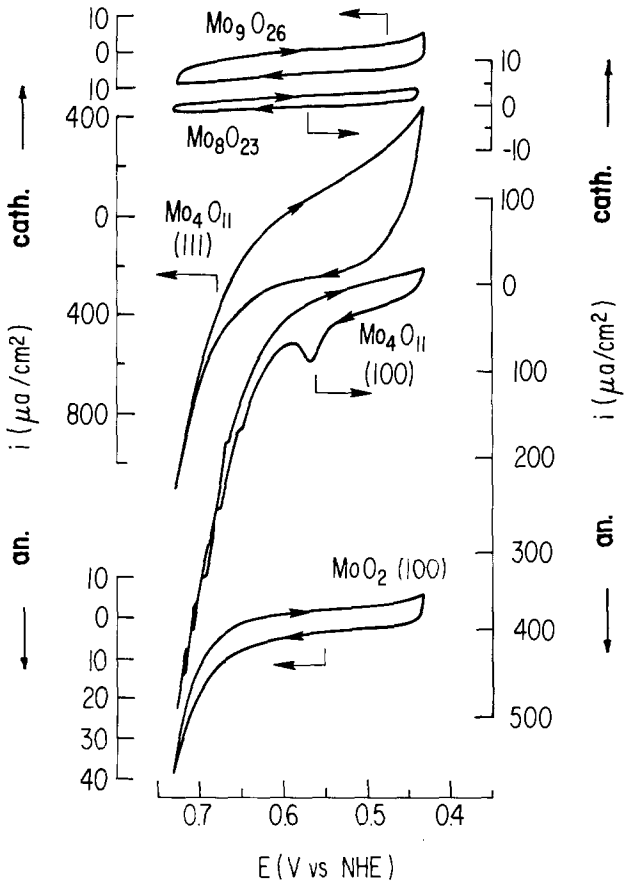


Fig. 1. Dissolution of the molybdenum oxides. Cyclic voltammetry of MoO_2, Mo_4O_{11}, Mo_8O_{23}, and Mo_9O_{26} samples which have not been subjected to potentials more negative than 0.4V. Solution is He-saturated 1N H_2SO_4. Sweep speed is 10 mV/sec.

The lowest of the oxides, MoO_2, also shows some anodic dissolution above ~0.65V. The magnitude of the dissolution current density is dependent on crystal orientation [being low for the (100) face] but the shape is similar for all orientations examined.

The differences in anodic behavior observed in Fig. 1 are thought to be related to the ability of an epitaxial layer of a higher oxide (with composition approaching MoO_3) to form on a given single crystal face. This can vary from oxide to oxide and with orientation on a single oxide. In Mo_8O_{23} and Mo_9O_{26}, most of the molybdenum is already in its highest oxidation state, and further oxidation does not occur in this potential range. However, Mo_4O_{11} and MoO_2 are further removed from MoO_3 in stoichiometry and are much more easily oxidized. Whether oxidation of a given surface results in dissolution or the formation of a stable surface layer may depend on whether the molybdenum in its higher oxidation state finds itself in a stable lattice. On the evidence of Fig. 1, it appears that the higher oxide formed on MoO_2 and on the (100) face of Mo_4O_{11} is not stable and these materials are dissolved anodically. In the case of the (111) face of Mo_4O_{11}, however, a species forms on the surface which does not entirely dissolve, and some of this is reduced during the cathodic sweep.

Very different results are obtained when the potential is swept to a more cathodic potential limit, as illustrated in Fig. 2-4. (These curves were recorded after several sweeps; changes with further cycling are not rapid.) In the potential range 0.0-0.8V, the cyclic voltammetry in He-saturated solutions of all of these molybdenum oxides except the (100) face of Mo_4O_{11} is

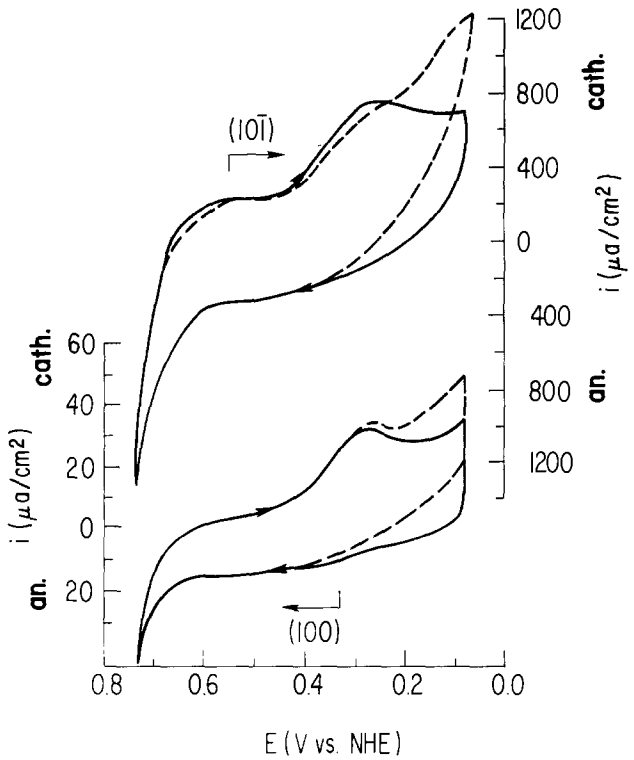


Fig. 2. Cyclic voltammetry of two single crystal faces of MoO_2 in 1N H_2SO_4. The solid curve was obtained in He-saturated solution, the dashed curve in O_2. Sweep speed 10 mV/sec.

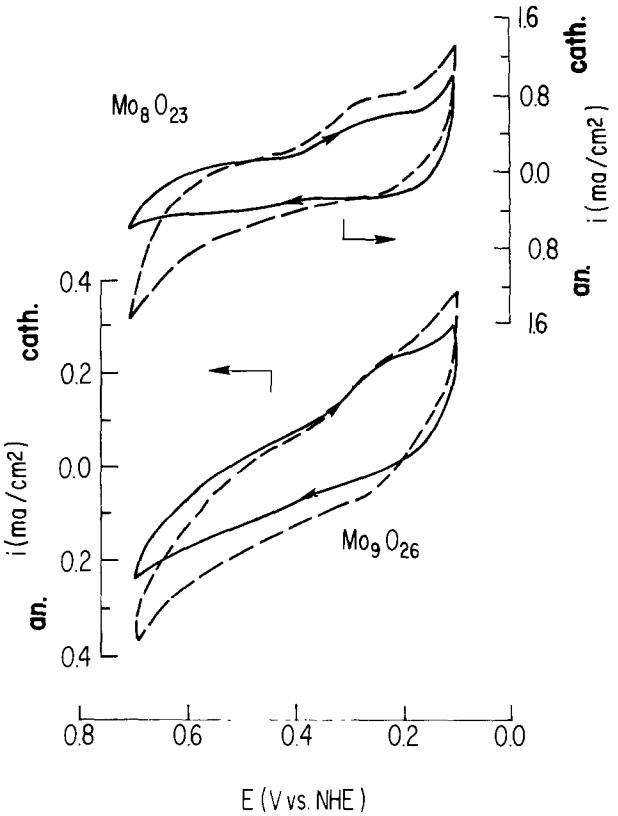


Fig. 4. Same as Fig. 2 for unoriented single crystals of Mo_8O_{23} and Mo_9O_{26}.

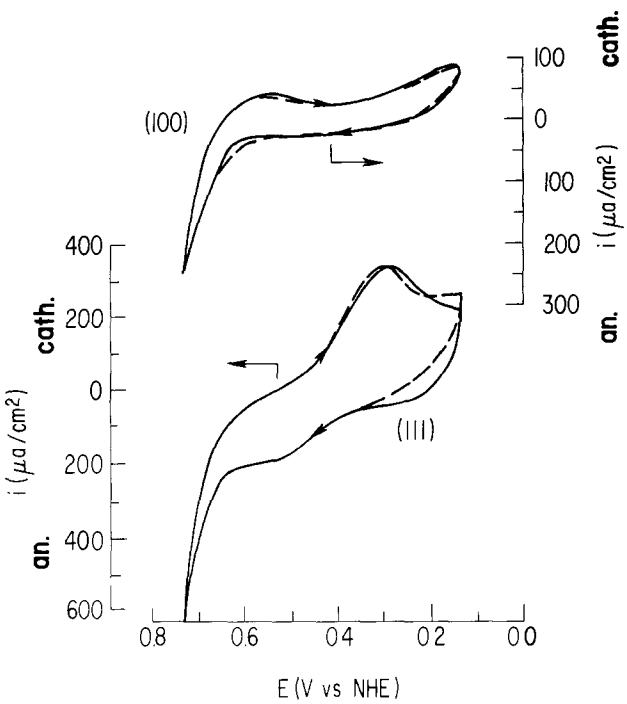


Fig. 3. Same as Fig. 2 for Mo_4O_{11}

similar, showing a broad cathodic peak at ~0.3V, which may be due to Mo(VI) + $2e^-$ → Mo(IV) (20). This behavior is due to the fact that all of these oxides undergo either oxidation or reduction in this potential range and after repeated cycling have a surface composition that is more dependent on the potential and the past history of the electrode than on the composition of the bulk oxide.

The identification of the 0.3V peak with a particular change in oxidation state of molybdenum, based on the available data, remains uncertain. The dangers of using thermodynamic data (20) to assign potential regions of stability in real systems must be kept in mind. More positive assignment of peaks cannot be made without additional, nonelectrochemical evidence. The formation of Mo(V) during anodic processes has been detected using ESR when dissolution rates were high, but it is felt that Mo(V) only occurs in the solution phase. ESCA studies of molybdenum oxide electrodes showed only Mo(VI) and Mo(IV). The solid-state reaction of the 0.3V cathodic peak is thus thought to involve direct conversion of Mo(VI) to Mo(IV).

The behavior of the (100) face of Mo_4O_{11} is somewhat different from that of any of the other crystal faces studied. This is due to the unique crystal structure of Mo_4O_{11} and the fact that the (100) face is parallel to the layers in the Mo_4O_{11} structure. The surface structure may be one with no exposed molybdenum atoms in the +6 oxidation state and thus the peak at 0.3V is not observed. The (111) face has both Mo(VI) and Mo(IV) exposed and exhibits the 0.3V peak. The 0.3V peak appears on the (100) surface after extensive cycling into the region of anodic current, which may roughen the electrode surface.

Figure 2 shows the cyclic voltammetry of two representative faces of MoO_2 scanned between ~0.0 and 0.8V. Cycling in this range results in a broad, somewhat featureless curve. In O_2-free solution, this curve apparently represents the repeated formation and reduction of a higher oxide on the MoO_2 surface. These processes occur over a wide range of potentials and do not result in sharp peaks in the cyclic voltammetry. Since the anodic and cathodic currents are not usually equal, long term changes in the cyclic voltammetry can be observed. Although the general shape of the voltammetry curves for MoO_2 is not very dependent on crystal orientation, the current density can vary by more than an order of magnitude, as illustrated in Fig. 2. The current densities for processes occurring on the (100) face of MoO_2 are much smaller than for those on the (10$\bar{1}$) face. The other faces examined fell between these extremes. The roughness factor of these mirrorlike single crystal faces is expected to be low. The differences in currents between the faces are too

large to be attributable to differences in surface roughness.

When the solution is saturated with O_2 gas, a small increase in the cathodic current on MoO_2 is observed below ~0.3V. Little change is seen at more anodic potentials in Fig. 2. At these high overpotentials, O_2 reduction currents are low on MoO_2 electrodes. The cyclic voltammetry of the (100) and (111) faces of Mo_4O_{11} over this wider potential range is shown in Fig. 3. The characteristic periodic peaks shown in Fig. 1 for the layer-by-layer dissolution of the (100) face of Mo_4O_{11} are no longer observed after continued cycling in this region. The reason for this, discussed by Peekema and Shafer (19), is a surface roughening which exposes other crystal orientations. The addition of O_2 has little effect on the cyclic voltammetry. [The comparison for the (100) face is somewhat obscured by long-term nonreproducibility of the curve.] In general, the behavior is similar to that observed on MoO_2.

Comparable curves for Mo_8O_{23} and Mo_9O_{26} are shown in Fig. 4. These measurements were made on single crystal faces, but due to the fact that crystals of a size and morphology suitable for the examination of several faces were not obtained, no effort was made to orient these crystals. When the potential is swept below ~0.3V for either Mo_8O_{23} or Mo_9O_{26}, the surface is reduced to a lower oxide which is then reoxidized in the anodic sweep to ~0.7V. After repeated cycling, the linear sweep voltammetry in He-saturated solutions is similar to that observed for the lower oxides. The curve for Mo_9O_{26} shows a marked skew with respect to the zero of current, which is probably due to *IR* effects caused by the low supply of carriers in this more highly resistive material. In the presence of O_2, somewhat higher currents are observed at both the cathodic and anodic ends of the sweep. The availability of molecular O_2 apparently promotes the oxidation or dissolution of the oxides above ~0.3V while O_2 itself is reduced at lower potentials.

Oxygen reduction on these oxide electrodes has also been studied using steady-state measurements. Figures 5 and 6 show the steady-state data for MoO_2 and Mo_4O_{11}; these curves represent the difference between the current in O_2-saturated and O_2-free solution, as discussed above. In the case of O_2 reduction on the

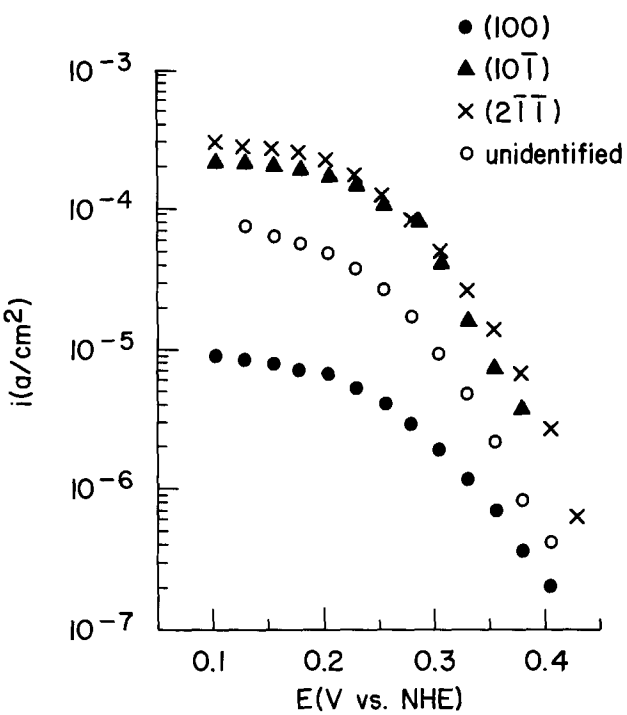


Fig. 5. Steady-state measurements of O_2 reduction on several faces of a single crystal of MoO_2. Electrolyte is 1*N* H_2SO_4.

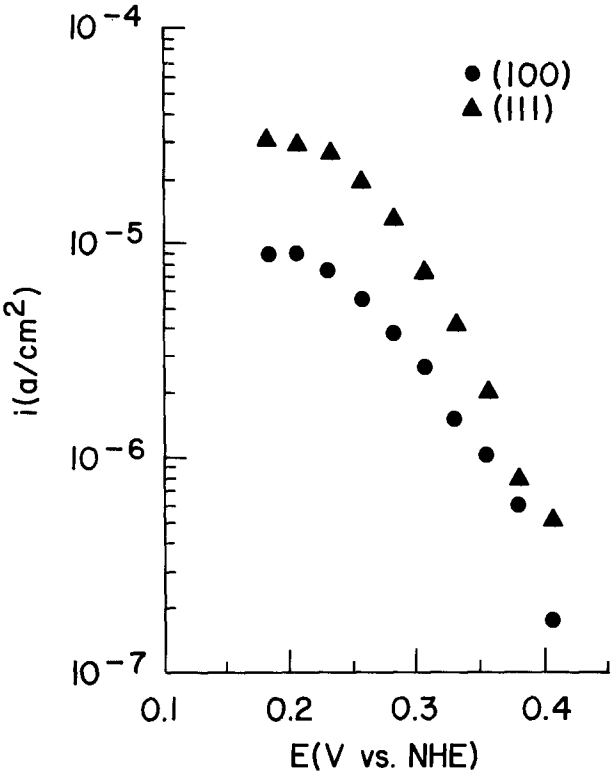


Fig. 6. Steady-state measurements for O_2 reduction on the (100) and (111) faces of Mo_4O_{11} in 1*N* H_2SO_4.

molybdenum oxides, considerable hysteresis in the measurements is observed. The data of Fig. 5 and 6 are taken in the direction of more negative potentials. If the measurements are repeated changing the potential in the anodic direction, the currents are lower than the initial measurements. The initial cathodic-going measurements can be reproduced if the pretreatment of the electrode (*i.e.*, a few cycles of the potential) is repeated. If this cycling is omitted, anomalous anodic currents due to oxidation of the electrode surface are observed at the more positive potentials in subsequent steady-state measurements.

The steady-state data for O_2 reduction on several crystal faces of MoO_2 are shown in Fig. 5. At potentials anodic to ~0.45V the measured currents are anodic and are due to oxidation of the electrode surface. Below 0.4V small O_2 reduction currents are measured. The logarithm of the current shows linear dependence on potential over a relatively narrow range between 0.3 and 0.4V. At lower potentials, the current due to O_2 reduction becomes almost independent of potential. It is difficult to measure the O_2 reduction current below ~0.2V because currents due to surface changes of the molybdenum oxide crystal are of the same magnitude as those due to O_2 reduction; the accuracy of the data in this region is low. The interference of the currents due to reduction of the surface, rather than a limit in the mass transport of species from solution, is thought to cause the change of slope at ~0.25V in Fig. 5.

The data of Fig. 5 show a large dependence of O_2 reduction current on crystal orientation. At a given potential, the current due to O_2 reduction is more than an order of magnitude higher on the (10$\bar{1}$) face of MoO_2 than on the (100) face. This is the same order of dependence of current density on orientation as was measured in the cyclic voltammetry (Fig. 2). This is believed to be a real property of the crystal face and not an artifact, such as the influence of mass transport to the crystal surface. No dependence of the measured O_2-reduction current for a given crystal face on surface area was observed, as would be expected if mass transport accounted for differences in current densities.

Oxygen reduction on MoO_2 occurs at high overpotentials with low measured current densities; the catalytic activity of MoO_2 (Fig. 5) is comparable to that measured by Randin on Pt-free Na_xWO_3 (3). The determination of the mechanism of O_2 reduction is severely complicated by simultaneous changes of the oxidation state of the electrode surface.

The extraction of kinetic parameters from the data of Fig. 5 does not appear justified due to the limited range of linearity, if any, and the extremely long extrapolation that would be required to obtain i_o. Such plots do, however, give useful information in comparing the rate and mechanism of O_2 reduction on electrodes of different composition or on different faces of the same oxide.

Figure 6 shows the steady-state measurements of O_2 reduction on the (100) and (111) faces of Mo_4O_{11}. A behavior similar to that of MoO_2 is observed; at these overpotentials the currents lie in the same range as for MoO_2 and the change of slope at low potentials is again observed. The O_2 reduction currents are lower on the (100) face of Mo_4O_{11} than on the (111) face, the same order observed in the currents in the cyclic voltammetry of Fig. 3. Rest potential measurements in O_2-free and O_2-saturated solutions were found to be not very reproducible. The presence of O_2 results in only a small (~25 mV) change in rest potential, indicating that O_2 is not involved in a reversible couple at the electrode surface. The potential is mainly determined by the composition of the electrode surface. Steady-state measurements of O_2 reduction on the higher oxides Mo_8O_{23} and Mo_9O_{26} also show behavior similar to that in Fig. 5 and 6. The small dependence of the cyclic voltammetry and the steady-state O_2 reduction measurements on the stoichiometry of the crystal is not thought to imply that the electronic properties of the oxide are not important to its electrochemical behavior. Instead, it appears that with pretreatment that includes cycling of the electrode potential over a fairly wide range, all of these materials tend to form similar surface layers. The composition of the surface in contact with the solution is more dependent on potential than on the bulk composition of the crystal.

The results obtained for the molybdenum oxides have been compared with measurements on single crystals of WO_2, which has a rutile-type structure similar to that of MoO_2, with the aim of relating the differences in behavior of these two materials toward O_2 reduction to differences in their electronic properties. However, it was found that the electrochemistry of these materials is dominated by chemical factors, specifically by the stability of their higher oxides in contact with acid solution. In this respect, WO_2 differs substantially from MoO_2.

This difference is illustrated by a comparison of Fig. 7, which shows the cyclic voltammetry of WO_2 in a potential region where mainly anodic currents flow, with Fig. 1, which includes similar data for MoO_2. The curve of Fig. 7 was obtained on an unidentified face of a WO_2 crystal. Similar curves were obtained for other orientations, although the magnitude of the current density was found to depend on orientation. Anodic currents are observed above ~0.4V (a lower potential than that for MoO_2, which does not show significant anodic currents below ~0.65V).

At least two broad current peaks are observed in this range. The WO_2 electrode undoubtedly already has a surface film as a result of storage in air, and this film is thickened during the anodic sweep of Fig. 7 without any significant reduction taking place in the cathodic sweep. This film has a defect structure, allowing charge transfer, but it becomes more highly insulating at higher potentials as its composition approaches WO_3. Further, the thicker oxide films are less likely to form epitaxial layers on the WO_2 crystal. The changes in film stoichiometry and structure probably cause the two broad peaks observed in Fig. 7.

The "WO_3" film which is formed at 1.1V is not significantly reduced above −0.17V. In addition, there is no evidence of formation of a hydrogen tungsten bronze by injection of hydrogen into the surface of the "WO_3" layer. Hydrogen tungsten bronzes are usually formed from amorphous WO_3 [*e.g.*, (22, 23)], and their formation may be energetically less favorable in the highly crystalline film of the higher oxide formed on a WO_2 single crystal in this range. Even at much more anodic potentials than shown here, a large rise in current, indicating active dissolution, does not appear. Repeated cycling shows lower current densities on each subsequent sweep. These results indicate that WO_2 does not dissolve anodically but instead forms a

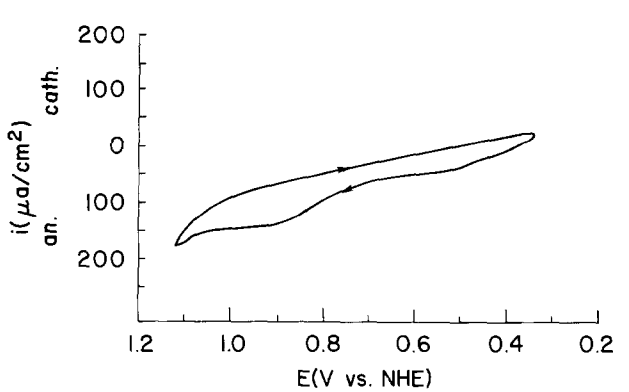


Fig. 7. Oxidation of the surface of WO_2. Cyclic voltammetry of WO_2 anodic to 0.3V. Solution is N_2-saturated 1*N* H_2SO_4. Sweep speed is 10 mV/sec.

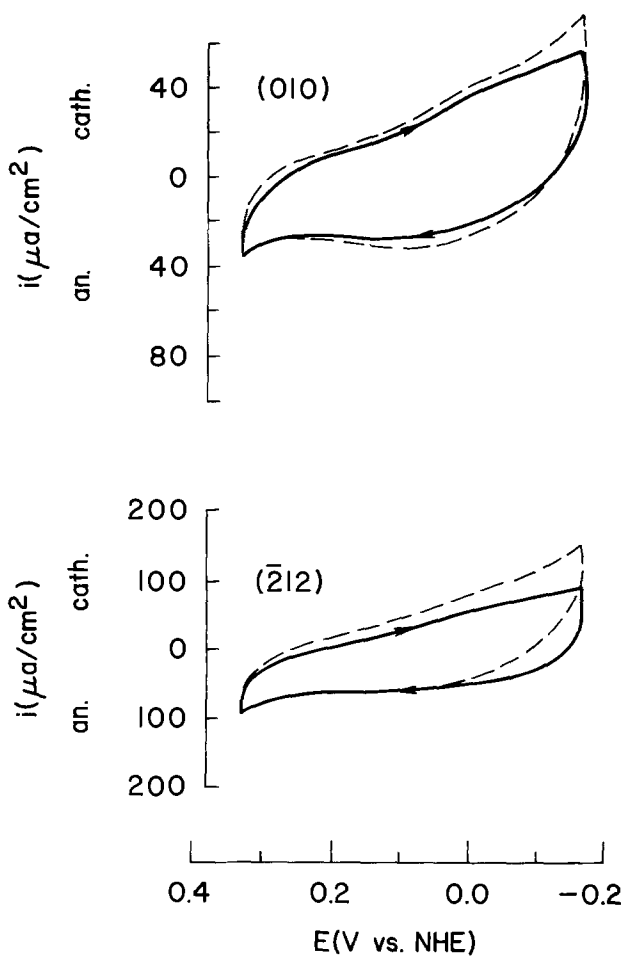


Fig. 8. Cyclic voltammetry of WO_2 cathodic to 0.33V. The solid curve was obtained in N_2-saturated 1*N* H_2SO_4, the dashed curve in O_2-saturated solution. Sweep speed 10 mV/sec.

stable WO_3 layer on its surface. The wide potential range of stability of WO_3 is indicated by Pourbaix (21).

The cyclic voltammetry of WO_2 if the potential range of formation of a higher oxide is avoided is shown in Fig. 8. Results are given for two representative crystal faces in the potential range between −0.17 and 0.33V. An almost featureless current-potential curve is observed in this region. The small hump which is barely distinguishable at ~0.0V can probably be attributed to $W(VI) + 2e^- \rightarrow W(IV)$ (21). If the solution is saturated with O_2, slightly higher cathodic currents are observed.

The steady-state measurements of O_2 reduction on WO_2 are shown for several orientations in Fig. 9. Each point represents the difference between the current density in O_2-saturated solution and that in N_2-saturated solution. The measurements were taken in the direction of more cathodic potentials. As was found to be the case for MoO_2, the measured currents were lower if the direction of measurement was reversed.

The current density due to O_2 reduction is highly dependent on crystal orientation. A given O_2-reduction current occurs at substantially higher overpotentials on WO_2 than on MoO_2. The data of Fig. 9 seem to fall into two groups. For the $(\bar{2}12)$, (010), and (121) faces, the logarithm of current is fairly linear with potential in the range examined. These three curves are approximately parallel with slopes of ~250 mV/decade. The data on the (100) and $(01\bar{1})$ faces, on the other hand, are quite nonlinear, showing a plateau at ~0.2V. The reason for these differences is not clear.

Conclusions

The cyclic voltammetry of the electronically conducting oxides of molybdenum, MoO_2, Mo_4O_{11}, Mo_8O_{23}, and Mo_9O_{26}, and of the tungsten oxide WO_2 in 1*N* H_2SO_4 exhibits broad irreversible current peaks. This implies that multiple oxide phases with compositions intermediate to MO_2 and MO_3 can be formed. A mixture of these oxide phases may exist simultaneously on the surface. If crystals of molybdenum oxides with different bulk compositions are given similar treatment, the surfaces all tend to have the same composition at a given potential. This results in a small dependence of the electrochemical behavior on composition.

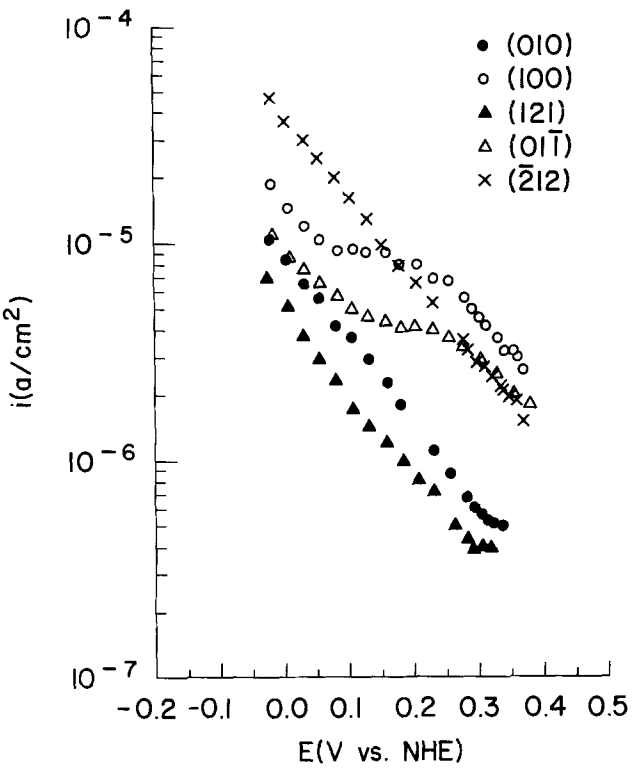


Fig. 9. Steady-state measurements of O_2 reduction on several faces of a WO_2 single crystal. Electrolyte is 1*N* H_2SO_4.

The differences between the electrochemistry of MoO_2 and WO_2 are largely explained by the differences in the stability of the higher oxides MoO_3 and WO_3 in aqueous solutions. The MoO_3 is formed at higher potentials than WO_3 and is much more soluble in acid solution (20, 21). Thus, the MoO_2 surface is more stable in solution than WO_2. The higher overvoltage for a given O_2-reduction current on WO_2 than on MoO_2 can be explained by the inhibiting nature of a less conducting higher oxide on the surface. Since both WO_2 and MoO_2 are excellent metals, *IR* effects in the crystals would not result in the observed behavior. The differences in the potential range of stability of MoO_2 and WO_2 tend to mask any comparisons which could give information about the role of electronic factors in electrochemical reactions, since their surface composition at a given potential is generally quite different.

Reactions of the electrode surface occurring in the potential range of interest interfere with the measurement of O_2 reduction kinetics and the determination of a mechanism for this reaction. Nonetheless, it is clear that the rate of the reaction can vary markedly with crystal orientation.

The feature of these rutile-type oxides which gives them their high conductivity is the small metal-metal bond length in the cathode direction. In some crystal orientations, this small metal-metal bond distance (which is about twice the O_2 bond length) appears in the plane of the surface. Of the crystal faces examined (Fig. 5 and 9), the (100), (010), and (011) have small metal-metal distances in the plane of the surface. These orientations tend to support smaller O_2 reduction currents than the other orientations. The only exception to this order is the (121) face of WO_2 which also gives low current densities without a small metal-metal distance. Thus the absence of the short metal-metal bond appears to be associated with higher rates of O_2 reduction.

Comparison of these data with results on a larger number of MO_2 electrodes with rutile structure are made in the following paper (24).

Acknowledgments

The authors would like to thank R. Figat for assistance in crystal growth, J. Angilello for orienting the crystals, T. Penney for conductivity measurements, R. Title for ESR measurements, R. Pollak for ESCA measurements, and R. Peekema for useful discussions.

Manuscript submitted Jan. 31, 1977; revised manuscript received April 11, 1977.

Any discussion of this paper will appear in a Discussion Section to be published in the June 1978 JOURNAL. All discussions for the June 1978 Discussion Section should be submitted by Feb. 1, 1978.

Publication costs of this article were assisted by IBM Corporation.

REFERENCES

1. D. B. Sepa, A. Damjanovic, and J. O'M. Bockris, *Electrochim. Acta.*, **12**, 746 (1967).
2. J. McHardy and J. O'M. Bockris, *This Journal*, **120**, 53 (1973).
3. J.-P. Randin. *ibid.*, **121**, 1029 (1974).
4. J.-P. Randin, *J. Electroanal. Chem. Interfacial Electrochem.*, **51**, 471 (1974).
5. A. J. Appleby and C. Van Drunen, *This Journal*, **123**, 200 (1976).
6. W. O'Grady, C. Iwakura, J. Huang, and E. Yeager, in "Proceedings of the Symposium on Electrocatalysis," M. W. Breiter, Editor, p. 286, The Electrochemical Society Softbound Symposium Series, Princeton, N.J. (1974).
7. H. Yoneyama, T. Fujimoto, and H. Tamura, *J. Electroanal. Chem. Interfacial Electrochem.*, **58**, 422 (1975).

8. A. C. C. Tseung and H. L. Bevan, *ibid.*, **45**, 429 (1973).
9. U. Bertocci, M. I. Cohen, J. L. Mullen, and T. Negas, Paper presented at the Workshop on Electrocatalysis on Nonmetallic Surfaces, National Bureau of Standards, December, 1975.
10. J. Brenet, Paper presented at the 27th Meeting of the International Society of Electrochemistry, Zurich, September, 1976.
11. A. Magneli, *Acta Chem. Scand.*, 2, 501 (1948).
12. A. Magneli, *ibid.*, 2, 861 (1948).
13. L. Kihlborg, *Ark. Kemi*, **21**, 471 (1963).
14. A. Magneli, G. Andersson, B. Blomberg, and L. Kihlborg, *Anal. Chem.*, **24**, 1998 (1952).
15. M. W. Shafer, R. A. Figat, and T. Penney, Unpublished results.
16. B. G. Brandt and A. C. Skapski, *Acta Chem. Scand.*, **21**, 661 (1967).
17. D. B. Rogers, R. D. Shannon, A. W. Sleight, and J. L. Gillson, *Inorg. Chem.*, **8**, 841 (1969).
18. T. Penney, Unpublished data.
19. R. M. Peekema and M. W. Shafer, *This Journal*, **123**, 1779 (1976).
20. M. Pourbaix, "Atlas of Electrochemical Equilibria," p. 275, Pergamon Press, Inc., Oxford (1966).
21. M. Pourbaix, *ibid.*, p. 282.
22. R. S. Crandall, P. J. Wojtowicz, and B. W. Faughnan, *Solid State Commun.* **18**, 1409 (1976).
23. H. N. Hersch, W. E. Kramer, and J. H. McGee, *Appl. Phys. Lett.*, **27**, 646 (1975).
24. J. Horkans and M. W. Shafer, *This Journal*, **124**, 1202 (1977).

An Investigation of the Electrochemistry of a Series of Metal Dioxides with Rutile-Type Structure: MoO_2, WO_2, ReO_2, RuO_2, OsO_2, and IrO_2

Jean Horkans* and M. W. Shafer

IBM Thomas J. Watson Research Center, Yorktown Heights, New York 10598

ABSTRACT

Six transition metal dioxides, MoO_2, WO_2, ReO_2, RuO_2, OsO_2, and IrO_2, have been examined as electrodes in H_2SO_4 solution. The oxides MoO_2, WO_2, ReO_2, and RuO_2 have broad current-potential profiles, indicating the formation of a surface layer which can exist over a range of compositions. Steady-state measurements of O_2 reduction showed catalytic activities which were low compared to common O_2 catalysts such as Pt, but of the same order as other oxide catalysts. Activities were lowest for WO_2 and ReO_2, which form resistive surface layers of a higher oxide. The only material studied which was sufficiently stable to allow measurement of both O_2 evolution and O_2 reduction was RuO_2. The current-potential profiles of OsO_2 and IrO_2 are characterized by distinct changes of oxidation state. These two oxides were not sufficiently stable to allow the measurement of O_2 reduction.

A number of transition metal dioxides which have crystal structures related to that of rutile, TiO_2, are as highly conductive as many metals. In spite of the high conductivity of these compounds and their relative stability in aqueous solution, only a few of them have been investigated as electrode materials. A notable exception is RuO_2, which, since its success as an anode in Cl_2 production, has also been studied as a catalyst for other electrode reactions (1-3). The RuO_2 electrodes studied in the past were films prepared by oxidation of Ru(III) salts, supported on another metal, often Ti, and were likely to be nonstoichiometric. Such RuO_2 films were found to be much more stable against dissolution than anodized Ru (1). Oxygen gas can be evolved for extended periods without apparent damage to the electrode; O_2 is reduced on RuO_2 by a different mechanism than that by which it is evolved (3). The O_2 evolution overpotential on RuO_2 is lower than that on Pt but the overpotential for O_2 reduction is higher.

We have examined the electrochemistry of unsupported RuO_2 crystals and compared this with the previously reported data for Ti-supported RuO_2 films. In addition, similar measurements have been made on crystals of MoO_2, WO_2, ReO_2, OsO_2, and IrO_2, all of which are highly conducting oxides with rutile-type structures. The object of examining a series of oxides with the rutile structure was to obtain more definitive information about the role of electronic factors in electrode processes and electrocatalysis. These oxides have a range of d-level occupations without major changes in the environment of the ions in the crystal. The electrode reaction which was chosen to compare these materials was the reduction of O_2, a reaction for which various other transition metal oxides have been examined as catalysts [*e.g.*, (4-7)].

* Electrochemical Society Active Member.

Key words: MoO_2, WO_2, ReO_2, RuO_2, OsO_2, IrO_2, rutile-related oxides, oxygen reduction, oxygen evolution, electrocatalysis.

Experimental

The metal dioxide crystals were grown by a variety of techniques (8) which differ somewhat from the previously published methods (9). The MoO_2 and WO_2 were grown by vapor transport using the appropriate ratio of metal powder and metal trioxide as starting materials, I_2 as the transporting agent, and a growth temperature of 850°-925°C. The best RuO_2 crystals were obtained by heating Ru metal at 1150°C in converging streams of N_2 and O_2. The RuO_2 was transported to a cooler part of the furnace where crystal growth occurred (8). The IrO_2 was prepared in a similar manner using Ir powder heated to 1250°C, the IrO_2 being transported by pure O_2 to a cooler area (~900°C), where crystal growth occurred. A prereacted powder of OsO_2 was transported in a sealed silica tube with a temperature gradient of 1050°-1000°C; no transporting agent was used. The ReO_2 crystals were obtained by transporting ReO_2 powder with I_2 in a sealed tube at 1100°-960°C.

Of the materials studied, only MoO_2 and WO_2 to date have been obtained as crystals large enough to allow

investigation of individual natural faces. Contact was made to these single crystals by attaching an Au wire with Ag-filled epoxy as described in the preceding paper (10). All of the other oxides were examined as clusters of smaller crystals as they had nucleated and grown on the container walls. The Au wire was attached to one end of such a cluster and the contact area masked off. The roughness factors of these samples vary with the size of the crystallites formed. The crystallites were quite small in the case of OsO_2 and IrO_2, fairly large (~0.1 mm on a side) for RuO_2, and even larger for ReO_2. Standard electrochemical techniques were used, which have been described in detail elsewhere (10). The current-potential profiles were recorded after an initial sweep or two. Since surface reactions on some of the oxides are slow, the relatively low sweep rate of 10 mV/sec was used in the potential sweep measurements. The solution in all cases was 1*N* H_2SO_4 prepared from reagent-grade acid and deionized H_2O. All potentials are quoted with reference to the normal hydrogen electrode (NHE).

Results and Discussion

The oxides studied in this investigation, MoO_2, WO_2, ReO_2, RuO_2, OsO_2, and IrO_2, are among the most conductive members of a larger group of transition metal dioxides which have crystal structures related to that of rutile, TiO_2 (9). The main structural units of rutile are TiO_6 octahedra, which share corners and edges in the crystal (9). The dioxides RuO_2, OsO_2, and IrO_2 are isomorphic with tetragonal TiO_2. The other dioxides, MoO_2, WO_2, and ReO_2, are made up of distorted MO_6 octahedra and have lower symmetry than tetragonal. A summary of the crystallographic data of these dioxides is given in Table I. The oxides considered here exhibit high metallic-type conductivity; the room temperature resistivities are given in Table I. This section will discuss in turn the stability of each of these oxides in sulfuric acid solution and the measurement of O_2 reduction on electrodes of these materials.

MoO_2.—The cyclic voltammetry of several crystal faces of MoO_2 and WO_2 electrodes and steady-state O_2 reduction data are given in the preceding paper (10). A broad, featureless current-potential profile is observed, Fig. 2 of (10), the shape being similar on all faces, but the magnitude of the current density varying with orientation. Anodic dissolution of MoO_2 begins at ~0.65V. The broad reduction peak observed at ~0.3V is probably associated with the process Mo(VI) + $2e^-$ → Mo(IV) (15).

Assigning peaks in the cyclic voltammograms of these rutile electrodes to changes in oxidation state of the surface is tenuous based on electrochemical evidence alone. Corroborative nonelectrochemical investigations, such as ESCA measurements, would greatly increase the understanding of these systems. Since such nonelectrochemical evidence is largely unavailable, tentative identification of the oxidation state changes of the surfaces of the rutile-related oxides has been based on the thermodynamic data of Pourbaix (15). However, thermodynamic data may not give direct information about potential regions of stability in real systems. In addition, the Pourbaix diagrams may not consider all the possible species which can form. These considerations should be kept in mind when interpreting the cyclic voltammetry of these oxides.

The broadness of the features in the cyclic voltammetry of MoO_2 indicates that the composition of the surface layer of the crystal can exist over a range of stoichiometries with different Mo(VI)/Mo(IV) ratios. The stable oxides (16) may coexist in discrete layers or patches on the surface to give a virtually continuous variation of composition with potential. The dependence of the current density on crystal orientation is explicable in terms of compatibility of the crystal structures of MoO_2 and the higher oxide forming on the surface. An epitaxial layer of the higher oxide will form much more readily on certain crystal faces than others, resulting in a higher observed current density on those faces.

The cyclic voltammetry in O_2-saturated solution shows small O_2 reduction currents cathodic to ~0.3V. The steady-state O_2 reduction data, Fig. 5 of (10), show a plateau below ~0.2V which is not thought to be due to a mass transport limitation of any species in solution. Below 0.2V, currents due to changes in oxidation state of the electrode surface are nearly as large as those due to O_2 reduction. This illustrates the difficulty of measuring O_2 reduction kinetics on MoO_2, since the composition of the electrode surface is changing in the same potential region in which O_2 reduction occurs. The effect of orientation on O_2 reduction on MoO_2 electrodes is discussed (10).

WO_2.—The chemistries of molybdenum and tungsten compounds show many similarities. The differences in the electrochemistries of MoO_2 and WO_2 can be largely explained in terms of the fact that WO_3 has a much wider potential range of stability than MoO_3, and thus WO_2 is less stable in aqueous solution than MoO_2 (15). The cyclic voltammetry of a WO_2 electrode (Fig. 8 in (10)), is also nearly featureless. A broad peak, probably attributable to W(VI) + $2e^-$ → W(IV) (15), is observed at ~0.0V. A range of possible compositions of the surface layer is likely, similar to the case of a MoO_2 electrode. Anodic currents flow at more cathodic potentials on WO_2 than on MoO_2. The WO_3 layer that forms is expected to exhibit some nonstoichiometry, does not dissolve to a significant extent, and is not reduced above −0.17V. At a given overpotential, O_2 reduction currents are lower on WO_2 than MoO_2, as shown in Fig. 9 of the preceding paper (10). Large dependences of current density on orientation are observed (10).

RuO_2.—All single crystals of RuO_2 which have been grown to date have been slightly too small to allow electrochemical measurements on individual natural faces. The RuO_2 electrodes which have been used consist of small crystallites adhering to a small piece of fused silica. Thus many crystal orientations are simultaneously exposed to the solution. X-ray diffraction analysis of the electrode surface shows an absence of reflections from low index planes. The predominant orientations are (211), (310), (301), and (321). The roughness factor is significantly greater than unity and has been estimated to be on the order of 10.

The cyclic voltammetry of a multicrystalline electrode of RuO_2 in 1*N* H_2SO_4 is shown in Fig. 1. The broad current-potential profile resembles that observed by Galizzioli *et al.* (1) and by O'Grady *et al.* (3) for

Table I. Crystallographic data and resistivities of rutile-type metal dioxides

Oxide	Symmetry	Lattice constants	Resistivity at 300°K (Ω cm)
MoO_2	Monoclinic[a]	a = 5.61Å b = 4.85Å c = 5.62Å β = 120.95°	1.2×10^{-4}[d]
WO_2	Monoclinic[b]	a = 5.65Å b = 4.89Å c = 5.50Å β = 120.42°	2.9×10^{-3}[d]
β-ReO_2	Orthorhombic[c]	a = 4.81Å b = 5.64Å c = 4.60Å	8×10^{-5}[e]
RuO_2	Tetragonal[d]	a = 4.49Å c = 3.11Å	5×10^{-5}[d]
OsO_2	Tetragonal[d]	a = 4.50Å c = 3.18Å	6×10^{-5}[d]
IrO_2	Tetragonal[d]	a = 4.50Å c = 3.15Å	6×10^{-5}[d]

[a] Ref. (11).
[b] Ref. (12).
[c] Ref. (13).
[d] Ref. (9).
[e] Ref. (14).

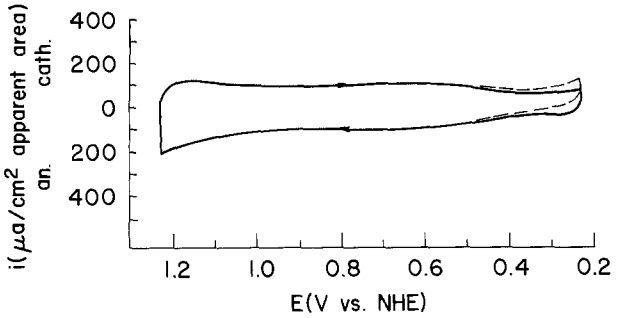


Fig. 1. Cyclic voltammetry of a group of crystallites of RuO_2 in N_2-saturated (—) and O_2-saturated (— —) 1N H_2SO_4. Sweep speed is 10 mV/sec.

RuO_x films on Ti. However, curves with such broad features would not be expected to be very sensitive to differences in the state of the electrode. The current-potential profile of Fig. 1 differs little from that obtained by continuous cycling of a Ru electrode in the same potential range (1, 17).

Figure 1 indicates that oxidation and reduction of the electrode surface occur over a wide range of electrode potentials. Two broad features are indicated, a nearly reversible peak at ~0.65V and a widening of the curve which indicates another peak above the anodic limit of 1.23V. The more anodic of these peaks has been attributed by Galizzioli *et al.* (1) to $2RuO_2 + 2H^+ + 2e^- \rightleftharpoons Ru_2O_3 + H_2O$ and the more cathodic peak to $Ru_2O_3 + 6H^+ + 6e^- \rightleftharpoons 2Ru + 3H_2O$. These reactions are limited to the surface layers of the electrode. The magnitude of the current density is the same on these crystals of RuO_2 as on the RuO_x films of O'Grady *et al.* (3) if an order of magnitude difference in roughness factor is assumed. The dashed line in Fig. 1 shows somewhat increased cathodic currents below 0.5V due to O_2 reduction when the solution is saturated with O_2 gas. Oxygen evolution is observed if the anodic limit of the sweep is higher than ~1.35V.

Ruthenium dioxide is the only rutile studied which is sufficiently stable to allow investigation of both O_2 reduction and O_2 evolution. Steady-state data for O_2 reduction on RuO_2 are shown in Fig. 2. Each point of Fig. 2 is the difference between the measured steady-state current density in O_2-saturated solution and that in N_2-saturated solution. This correction is very small in the case of RuO_2, where the background currents are smaller than the O_2 reduction currents by nearly two orders of magnitude. The hysteresis observed with reversal of the direction of potential change is small, in contrast to MoO_2 and WO_2. A considerable time is required to reach steady state; each measurement represents ~15 min.

Significant O_2 reduction currents are not observed above 0.6V. Below 0.6V, the plot of ln i *vs.* E is not linear. The extraction of kinetic parameters from Fig. 2 is not justified because of the nonlinearity and the long extrapolation to E_{rev}, as discussed in (10). The bend-over at the lowest potentials may be due to formation of a lower oxidation state of ruthenium. Galizzioli *et al.* (1) suggest penetration of hydrogen into the lattice in this potential range. The potential range of significant O_2 reduction on RuO_2 is comparable to that observed on MoO_2 electrodes.

The data of Fig. 2 are different from those obtained by O'Grady *et al.* (3) in basic solutions. These authors observe cathodic currents at lower overvoltages than those in Fig. 2 and a distinct change of slope in the E-ln i plot. Some of the differences between these two sets of data may be due to a difference in the mechanism of O_2 reduction in acidic and basic solution, to a different surface state of the electrode in acid and base, and to the fact that the present data were obtained using RuO_2 crystal electrodes while those of O'Grady *et al.* involved Ti-supported RuO_2 films. In addition,

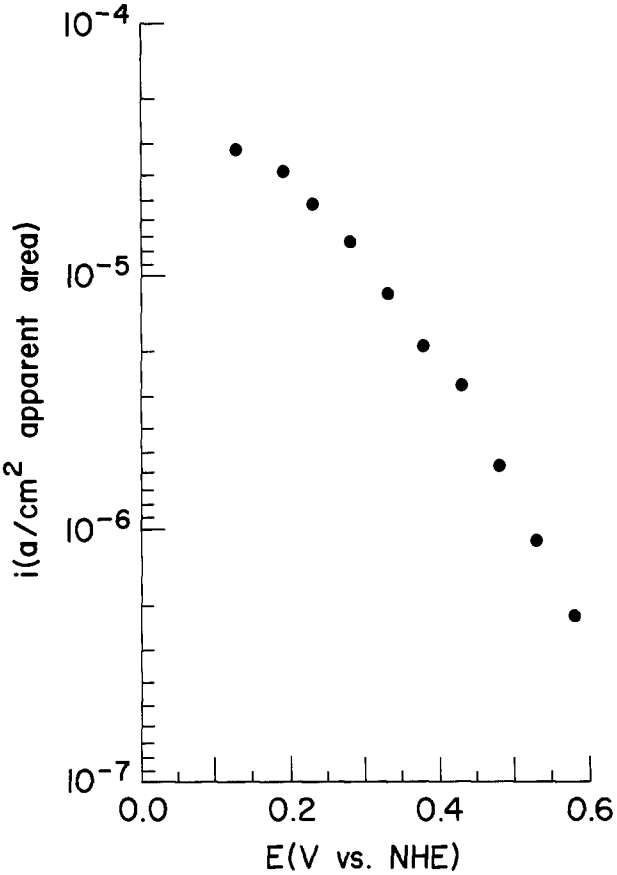


Fig. 2. Steady-state measurement of O_2 reduction on a group of crystallites of RuO_2 in 1N H_2SO_4.

our studies indicate that the 2 mV/sec sweep rate used by O'Grady *et al.* is probably not sufficiently slow to allow steady state to be attained on RuO_x films.

The steady-state data for O_2 evolution on RuO_2 crystals are shown in Fig. 3. Insignificant hysteresis is observed when the direction of measurement is reversed and less time is required to reach steady state than is required for O_2 reduction on the same electrode. The data of Fig. 3 show significant O_2 evolution anodic to 1.33V. The plot of ln i *vs.* E is linear over an order of magnitude in current. The deviation from linearity at low currents may be due to solution impurities, and the deviation at higher currents occurs because neither forced mass transport nor IR correction was used in these experiments. The linear portion of Fig. 3 has a slope of 65 mV/decade and extrapolates to an i_o of 1.4×10^{-6} A/cm² apparent area. O'Grady *et al.* (3) have measured O_2 evolution in 4M KOH on Ti-supported RuO_x and have found linearity over three orders of magnitude of current with a slope of 40 mV/decade. Differences between measurements in acid and base may again be explained by differences in the surface state of the oxide in the two solutions. The RuO_x films would also be expected to have a greater number of defects than the RuO_2 crystals, possibly resulting in a greater number of active sites and increased activity.

If the cyclic voltammetry (Fig. 1) is repeated after extensive O_2 evolution, an apparent increase in surface area is indicated by increased currents. Galizzioli *et al.* (1) report no change in Ti-supported RuO_x electrodes upon O_2 evolution except when gas bubbles do mechanical damage in micropores. However, the crystals used in this work are not expected to be microporous.

The fact that the data of Fig. 2 and 3 do not intersect at E_{rev} shows that O_2 reduction and O_2 evolution occur by completely different mechanisms on RuO_2, as is expected since the electrode surface is in a lower oxidation state in the potential region of O_2 reduction than in the potential region of O_2 evolution. Future

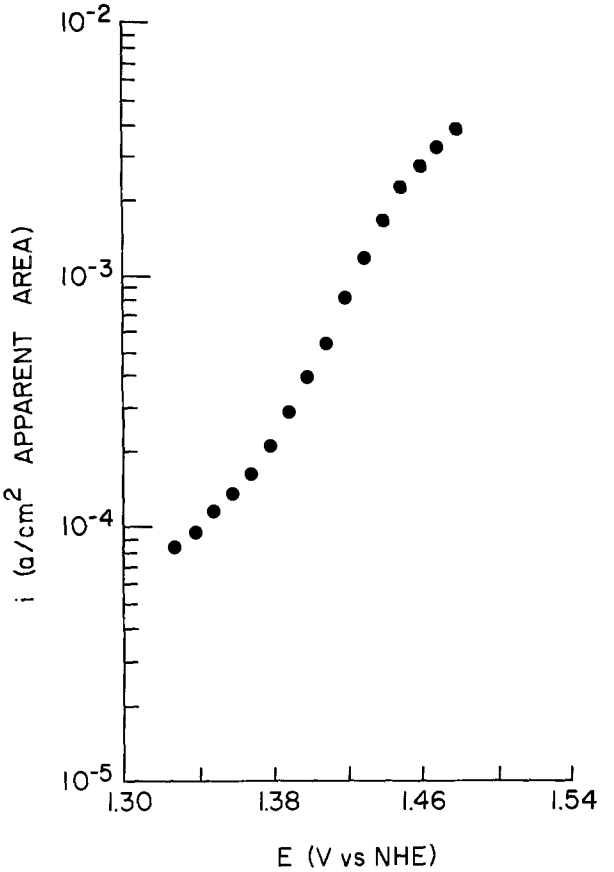


Fig. 3. Steady-state measurement of O_2 evolution on a group of crystallites of RuO_2 in 1N H_2SO_4.

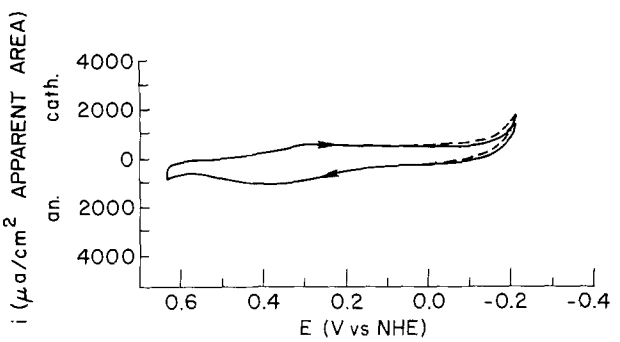


Fig. 4. Cyclic voltammetry of a group of crystallites of ReO_2 in N_2-saturated (—) and O_2-saturated (— —) 1N H_2SO_4. Sweep speed is 10 mV/sec.

work is planned to determine the dependence of O_2 evolution and O_2 reduction on crystal orientation.

ReO_2.—The Pourbaix diagram (15) for the Re-H_2O system indicates that ReO_2 has a very narrow potential range of stability in acid solution and is unstable in base. The data of Fig. 4, however, indicate that an electrode of ReO_2 in 1N H_2SO_4 undergoes neither major oxidation nor reduction in the potential range between −0.17 and 0.63V. The changes in oxidation state of the surface observed in Fig. 4 result in a relatively stable electrode surface. The large size of the ReO_2 crystallites leads to a surface roughness of the multicrystalline ReO_2 electrode significantly greater than that of the RuO_2 electrode of Fig. 1, accounting for the high apparent current densities observed in Fig. 4.

The cyclic voltammetry of ReO_2 is similar to that of the other rutiles, in that changes of oxidation state occur over broad potential regions. A broad peak centered at ~0.35V is observed, which is probably attributable to a reduction of Re(IV) to Re(III) below this potential.

Figure 4 shows that in O_2-saturated solution small O_2 reduction currents are observed below 0.0V. The steady-state data for O_2 reduction on an electrode of ReO_2 are shown in Fig. 5. These data are quite reproducible and exhibit little hysteresis. The behavior is highly nonlinear and probably reflects the fact that the electrode surface is changing over the potential range in which O_2 reduction is being measured. (A parallel reaction, such as H_2 evolution, occurring on an electrode surface of constant composition, should not lead to a slower rate of change of current with potential at more negative potentials.) The O_2-reduction current densities for a given overvoltage are comparable on ReO_2 and WO_2.

OsO_2.—The electrochemical behavior of OsO_2 is quite different from that of the other rutiles discussed so far. The cyclic voltammetry of a multicrystalline OsO_2 electrode in 1N H_2SO_4, shown in Fig. 6, is not featureless, but exhibits two broad and nearly reversible peaks, centered at ~0.95 and ~1.15V. The oxidation state of the surface changes markedly between 0.8 and

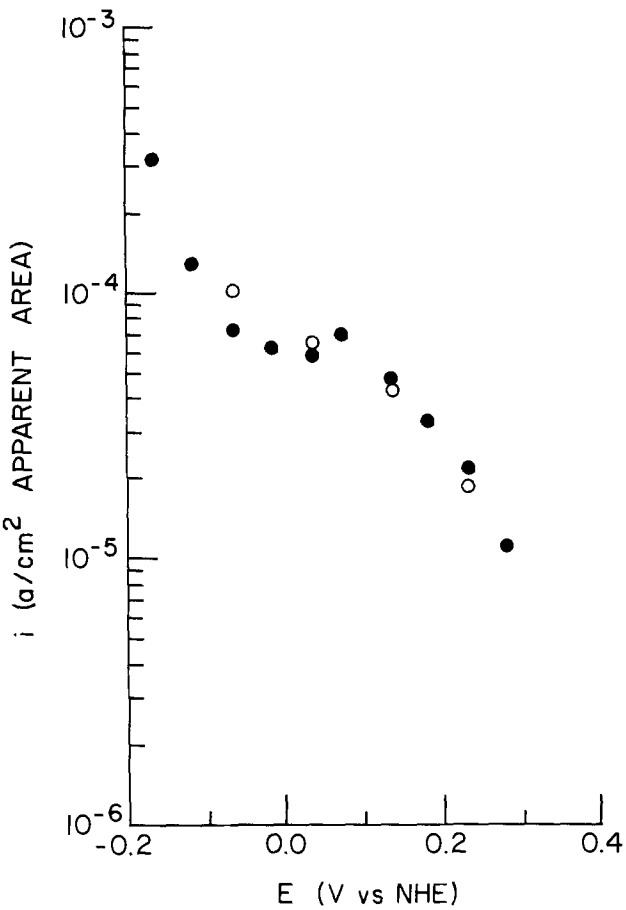


Fig. 5. Steady-state measurement of O_2 reduction on a group of crystallites of ReO_2 in 1N H_2SO_4. The closed and open points represent two sets of measurements made on consecutive days.

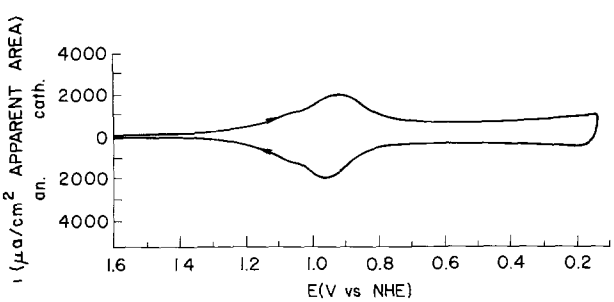


Fig. 6. Cyclic voltammetry of a group of crystallites of OsO_2 in N_2-saturated 1N H_2SO_4. Sweep speed is 10 mV/sec.

1.2V, but above and below this range only small currents are observed. As discussed above, the electrochemical and thermodynamic data do not give sufficient information for the unambiguous assignment of the oxidation state of the surface. Only hypothetical assignments can be made. The higher oxide, stable above 1.2V, is probably not OsO_4, since this compound reacts with H_2O. The surface at potentials more anodic than ~1.2V is postulated to be OsO_2. The composition of the surface at low potentials is more difficult to postulate. The Pourbaix diagram for Os (15) indicates that the surface below ~0.7V should consist of Os metal but does not indicate that two current peaks should be observed on reducing OsO_2. A lower osmium oxide, *i.e.*, an Os(II) or Os(III) species, not considered by Pourbaix, is probably formed in the intermediate potential region. When cyclic voltammetry was run in O_2-saturated solution, no evidence of O_2 reduction was observed. Repeated cycling resulted in an increase in current density, indicating an apparent increase in surface area. The electrode was not sufficiently stable to allow steady-state measurements.

IrO_2.—The cyclic voltammetry of a multicrystalline electrode of IrO_2 (Fig. 7) resembles that of OsO_2, rather than the other rutiles studied, in that it exhibits distinct current peaks. A peak occurs in the anodic sweep at ~0.8V; the cathodic sweep exhibits peaks at 0.55 and 0.6V. The total anodic and cathodic charges passed in Fig. 7 are approximately equal. The limit of the anodic sweep determines the amount of charge. As the anodic limit of the scan is made more positive, further anodic currents flow and the amount of cathodic charge consumed in the retrace becomes commensurately larger.

The Pourbaix diagram (15) for the Ir-H_2O system indicates that IrO_2 is stable in solutions of *p*H 0 from ~0.9V to potentials well above those necessary for O_2 evolution, that Ir metal is stable below 0.9V, and that an Ir(III) oxide is not stable. The observations in the preceding paragraph indicate that a considerable depth of the IrO_2 surface is reduced when the electrode is immersed in H_2SO_4 solution. This reduced surface is reoxidized to Ir(IV) above ~0.7V. The reduction in the cathodic sweep takes place in two steps, as indicated by the two cathodic peaks. The large peak at 0.6V is due to the formation of an Ir(III) species from the reduction of Ir(IV). The broad shoulder like peak at about 0.5V is a further reduction to a lower oxidation state, *e.g.*, Ir(II) or Ir(0).

The cyclic voltammetry of IrO_2, shown in Fig. 7, is quite different from that of Ir metal (18). The current-potential profile of Ir metal shows a fairly reversible peak at ~0.9V, with no major details at lower potentials which would indicate the formation of Ir(III). When the cyclic voltammetry of IrO_2 is run in O_2-saturated solution, some differences are observed. However, the stability of the IrO_2 surface in solution is not adequate to allow measurements of O_2 reduction currents. Large apparent changes in surface area occur upon cycling of the potential.

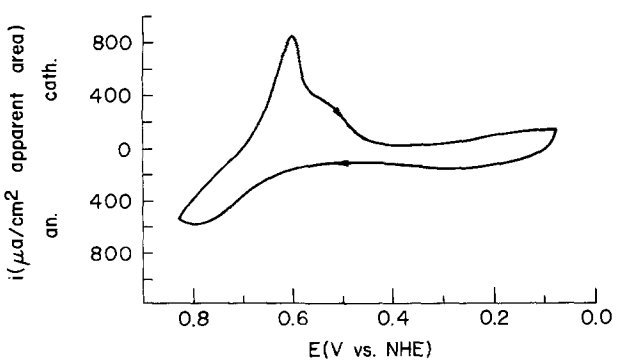


Fig. 7. Cyclic voltammetry of a group of crystallites of IrO_2 in N_2-saturated 1*N* H_2SO_4. Sweep speed is 10 mV/sec.

Conclusions

Six transition metal dioxides with rutile-related structures, MoO_2, WO_2, ReO_2, RuO_2, OsO_2, and IrO_2, were examined as electrodes in 1*N* H_2SO_4 solution. All of these compounds undergo changes in composition of their surface layers as a function of potential. However, the metal dioxides are substantially more stable in acid solution than is indicated by the equilibrium diagrams of Pourbaix (15) and caution should be used in applying these diagrams to such materials.

These oxides appear to show two types of behavior. The cyclic voltammetry of MoO_2, WO_2, RuO_2, and ReO_2 is characterized by broad, featureless current-potential profiles. Such broad profiles indicate that changes of oxidation state of the surface can occur over a range of potentials and that the composition of the surface oxide layer can vary substantially. In contrast, the current-potential profiles for OsO_2 and IrO_2 showed distinct peaks which can be associated with a fairly sharp change in the composition of the surface layer.

The rutiles on which O_2 reduction could be measured showed lower catalytic activity for this reaction than Pt but had activities of the same order as tungsten bronzes. The reaction is least favorable on the dioxides of tungsten and rhenium. This can be correlated with the fact that, of the metals studied, tungsten and rhenium have the most stable higher oxides. Thus, the coverage or partial coverage of the surfaces of WO_2 and ReO_2 by the less conducting higher oxides WO_3 and ReO_3 probably inhibits the O_2 reduction reaction.

The measurement of the kinetics and mechanism of O_2 reduction on these rutile electrodes is prevented by reactions of the electrode surface occurring in the same potential region as O_2 reduction. Only RuO_2 is stable over a sufficiently wide potential range to allow the measurement of the rates of both O_2 reduction and O_2 evolution. These two reactions proceed on surfaces of different compositions and have distinctly different kinetics.

It has been found that a direct evaluation of the role of electronic factors in electrochemistry and electrocatalysis through the examination of a series of metal dioxide electrodes with similar crystal structures but differing electronic properties is precluded by the formation of a surface layer which differs in composition from the bulk oxide. The composition of this surface layer is highly dependent on electrode potential and differs from oxide to oxide, preventing the measurement of a given reaction on several materials under the same conditions. It is this kind of consideration which makes electrocatalysis the empirical science it remains.

Acknowledgments

The authors would like to thank R. Figat for crystal growth, T. Penney for conductivity measurements, J. Angillelo for crystal orientation, and R. Peekema for useful discussions.

Manscript submitted Jan. 31, 1977; revised manuscript received April 11, 1977. This was Paper 298 presented at the Philadelphia, Pennsylvania, Meeting of the Society, May 8-13, 1977.

Any discussion of this paper will appear in a Discussion Section to be published in the June 1978 JOURNAL. All discussions for the June 1978 Discussion Section should be submitted by Feb. 1, 1978.

Publication costs of this article were assisted by IBM Corporation.

REFERENCES

1. D. Galizzioli, F. Tantardini, and S. Trasatti, *J. Appl. Electrochem.*, **4**, 57 (1974).
2. D. Galizzioli, F. Tantardini, and S. Trasatti. *ibid.*, **4**, 203 (1975).
3. W. O'Grady, C. Iwakura, J. Huang, and E. Yeager, in "Proceedings of the Symposium on Electro-

catalysis," M. W. Breiter, Editor, p. 286, The Electrochemical Society Softbound Symposium Series, Princeton, N.J. (1974).
4. J. McHardy and J. O'M. Bockris, *This Journal*, **120**, 53 (1973).
5. J.-P. Randin, *ibid.*, **121**, 1029 (1974).
6. A. C. C. Tseung and H. L. Bevan, *J. Electroanal. Chem. Interfacial Electrochem.*, **45**, 429 (1973).
7. J. Brenet, Paper presented at the 27th Meeting of the International Society of Electrochemistry, Zurich, September, 1976.
8. M. W. Shafer and R. A. Figat, To be published.
9. D. B. Rogers, R. D. Shannon, A. W. Sleight, and J. L. Gillson, *Inorg. Chem.*, **8**, 841 (1969).
10. J. Horkans and M. W. Shafer, *This Journal*, **124**, 1196 (1977).
11. B. G. Brandt and A. C. Skapski, *Acta Chem. Scand.*, **21**, 661 (1967).
12. L. Kihlborg, *Ark. Kemi*, **21**, 471 (1963).
13. A. Magneli, *Acta Chem. Scand.*, **11**, 28 (1957).
14. J. Penney, Unpublished data.
15. M. Pourbaix, "Atlas of Electrochemical Equilibria," Pergamon Press, Oxford (1966).
16. A. Magneli, G. Andersson, B. Blomberg, and L. Kihlborg, *Anal. Chem.*, **24**, 1998 (1952).
17. S. Hadzi-Jordanov, H. Angerstein-Kozlowska, and B. E. Conway, *J. Electroanal. Chem. Interfacial Electrochem.*, **60**, 359 (1975).
18. P. Stonehart, H. A. Kozlowska, and B. E. Conway, *Proc. Roy. Soc. London, Ser. A.*, **310**, 541 (1969).

Investigation of Lithium Utilization from A Lithium-Silicon Electrode

Randall N. Seefurth* and Ram A. Sharma*

General Motors Corporation, Electrochemistry Department, Research Laboratories, Warren, Michigan 48090

ABSTRACT

A half-cell of the type

Li | in solid Li_2Si or $Li_{21}Si_8$, or $Li_{15}Si_4$ || LiCl-KCl eutectic or LiF-LiCl-KCl melt or LiF-LiCl-LiBr melt | Li | in solid Li_2Si in equilibrium with Si

was used to investigate lithium utilizations (to a 0.5V cutoff *vs.* 40 atomic percent Li-Al) from Li_2Si, $Li_{21}Si_8$, and $Li_{15}Si_4$ at current densities between 20 and 1000 mA/cm^2 and at temperatures between 675° and 750°K. The lithium utilizations from these compounds did not appear to be greatly influenced by current density or temperature variations. For example, 60-80% of the lithium from the Li_2Si-Si plateau, >90% of the lithium from the $Li_{21}Si_8$-Li_2Si plateau, and 80-90% of the lithium from the $Li_{15}Si_4$-$Li_{21}Si_8$ plateau were utilized at current densities between 50 and 400 mA/cm^2. The polarization at current densities up to 500 mA/cm^2 appeared to be mostly ohmic.

In recent years, increasing effort has been devoted to the development of Li/FeS_2 cells for secondary batteries of high specific energy and high specific power (1, 2). Generally, these cells consist of FeS_2 with a current collector of expanded molybdenum or carbon foam as the positive electrode, LiCl-KCl eutectic as the electrolyte, and either lithium entrapped in a metallic matrix (stainless steel or nickel), or Li-Al alloy "β"-phase (3) as the negative electrode.

The liquid lithium electrode, although capable of the highest specific energy and current density, has a problem retaining lithium for a period greater than 1000 hr during repeated charge-discharge cycles. In addition, lithium also severely attacks many insulators and separators of the cells.

The Li-Al alloy electrode with its lower lithium activity is less likely to attack the ceramic components of the cell than is pure Li. In this case, the lithium retention problem is also avoided, but the theoretical specific energy is reduced because of the additional inert weight of aluminum and the lower cell voltage in comparison to a cell using a pure lithium electrode. Current densities are also limited, probably because of the difficulty of lithium transport through the solid alloy electrode.

Lithium-silicon compounds with high lithium content [(*i.e.*, $Li_{22}Si_5$,$Li_{15}Si_4$, $Li_{21}Si_8$, and Li_2Si (4)], seem promising for use as negative electrodes in Li/FeS_2 cells, and work is in progress to develop these electrodes (5, 6). Solid Li-Si alloy electrodes, like those of Li-Al alloy, should not have a retention problem and also may not severely attack ceramic components of the cell, such as separators and feed throughs. However, they have a definite potential for producing a higher specific energy than the Li-Al alloy electrode because of their higher lithium content. In addition, the Li-Si alloy electrode may also be capable of giving higher current densities than those of Li-Al as diffusion of lithium in silicon [$D = 3.0 \times 10^{-8}$ cm^2/sec at 723°K (7)] is faster than that of lithium in aluminum [$D = 1.2\text{-}1.7 \times 10^{-10}$ cm^2/sec at 690°K (8)].

Therefore, a systematic study was initiated to develop a Li-Si negative electrode for Li/FeS_2 cells. In an earlier work (4) results were communicated indicating the reversibility of the Li-Si electrode with respect to lithium at 680°K, the different Li-Si compounds with their respective nonstoichiometry ranges, and the electromotive forces in the temperature range between 650° and 750°K. The activities and the relative partial molar properties of lithium and silicon in the Li-Si system as well as the standard free energies of formation for Li_2Si, $Li_{21}Si_8$, $Li_{15}Si_4$, and $Li_{22}Si_5$ were also reported in this publication.

Our present investigation was carried out to determine the utilization of lithium from three Li-Si compounds ($Li_{15}Si_4$, $Li_{21}Si_8$, and Li_2Si) at different current densities and temperatures. In the case of $Li_{15}Si_4$ (2.95 A · hr/g), three voltage plateaus are observed during charge-discharge cycles; one between $Li_{15}Si_4$ and

* Electrochemical Society Active Member.

Key words: lithium-silicon electrode, high specific capacity, high current density, molten salt battery.

$Li_{21}Si_8$, one between $Li_{21}Si_8$ and Li_2Si, and one between Li_2Si and Si. In the case of $Li_{21}Si_8$ (1.52 A · hr/g), the $Li_{21}Si_8$-Li_2Si and Li_2Si-Si plateaus are observed; while in the case of Li_2Si (1.28 A · hr/g), only the Li_2S-Si plateau is seen.

Experimental

The experiments, including the preparatory work, were carried out in a helium atmosphere dry box. The electrodes were studied using cells of the type

Li { in solid Li_2Si, or $Li_{21}Si_8$, or $Li_{15}Si_4$ } | LiCl-KCl eutectic or LiF-LiCl-KCl melt or LiF-LiCl-LiBr melt | Li { in solid Li_2Si in equilibrium with Si }

in conjunction with 40 atomic percent (a/o) Li-Al reference electrodes.

A schematic diagram of the cell is shown in Fig. 1. The typical cell assembly consisted of a quartz enclosure (70 mm diam, 300 mm high) fitted with a cap which served to position the electrodes and a thermocouple, and a stainless steel cup (50 mm diam, 100 mm deep) to hold the electrolyte.

Electrode preparation.—For the Li-Si test electrode, a chamber was made by heliarc-welding a 304 stainless steel nut onto the side of a 5 mm long piece of 304 stainless steel tubing (25 mm ID, 28 mm OD). A 304 stainless steel rod (3 mm diam, 450 mm long) was threaded into the nut to serve as a current-voltage lead. After cleaning this compartment (vapor-blasting followed by acetone and deionized water rinses in an ultrasonic cleaner), the electrode was completed by inserting a 98% porous nickel current collector into the chamber and vibration-loading it with 60/100 mesh particles of Li_2Si (Appendix A). The chamber was then enclosed by spot-welding a double layer of 304 stainless steel screen (400 mesh followed by 150 mesh) over the open sides. Before assembly into the test cell, the electrode was electrochemically stripped of its lithium in a separate cell using a 80% porous nickel counterelectrode. When recharged to a composition of $Li_{15}Si_4$, these 5 cm^2 working electrodes had a theoretical capacity density of 0.75 A · hr/cm^2.

The Li-Si counterelectrode was prepared in the same manner as the test electrode, except a larger electrode chamber (12.5 mm thick, 25 mm ID, 28 mm OD) was used to increase its capacity and thus prevent it from limiting the test cycles. These 5 cm^2 counterelectrodes had a theoretical capacity density of 1.0 A · hr/cm^2 at a composition of Li_2Si.

The reference electrode also consisted of a cylindrical chamber (5 mm long, 12 mm ID, 16 mm OD) which was completed by inserting a few pieces of 40 a/o Li-Al alloy (4/20 mesh) and spot-welding 150 mesh 304 stainless steel screen disks over the open sides.

Electrolyte preparation.—Three types of electrolyte, 57 mole percent (m/o) LiCl-43 m/o KCl eutectic (9-10), 16.5 m/o LiF-67.5 m/o LiCl-16 m/o KCl [melting point = 723°K-(10)], and 23 m/o LiF-28 m/o LiCl-49 m/o LiBr [melting point = 703°K (11)] were used. They were prepared using 99.6% pure LiCl, 99.9% pure KCl, 99.0% pure LiBr, and a high purity optical grade LiF. The LiCl-KCl mixtures used for making the eutectic and ternary melt with LiF were purified by bubbling chlorine through them at 750°K for 7 ksec, and subsequently scavenging the chlorine by bubbling helium for approximately 3.5 ksec (12). The LiCl-LiBr melt used for making the ternary melt with LiF was also purified by bubbling chlorine through it at 850°K for 3.5 ksec, and subsequently removing the resultant bromine by bubbling helium for an additional 3.5 ksec.

Apparatus.—A tubular furnace (150 mm high, 75 mm diam) was used in conjunction with a proportional band temperature controller to heat the cell. Chromel-Alumel thermocouples and a millivolt potentiometer were used for temperature measurements. The other electrical instruments included a d-c power supply, together with the necessary logic and switching circuitry to cycle the cell automatically according to a preset charge-discharge program, and dual-channel recorders for measuring current and potentials between electrodes.

Procedure.—About 0.2 liter of the electrolyte was placed in the stainless steel container which, in turn, was placed inside the quartz enclosure in the furnace. The electrolyte was heated to a particular temperature and the electrodes were positioned in the melt. After thermal equilibrium was attained, charge-discharge cycles were carried out between the Li-Si working electrode composed of Li_2Si, $Li_{21}Si_8$, or $Li_{15}Si_4$ and a counterelectrode of Li_2Si in three different electrolytes. The cycles were carried out at current densities ranging from 20 to 1000 mA/cm^2 [1] at different temperatures and under conditions where no liquid Li-Si alloy was formed. During the cycles, the working electrode voltages were monitored with a 40 a/o Li-Al alloy reference electrode.[2] A cutoff voltage of 0.5V with respect to the reference electrode was used to terminate discharges, while a cutoff voltage value dictated by the current density and the Li-Si compound under study was used to terminate charge. Voltages with respect to lithium may be obtained by including the 40 a/o Li-Al alloy *vs.* lithium potential obtained from the equation $V_{(mV)} = 464.438\text{-}0.2488T$ (4).

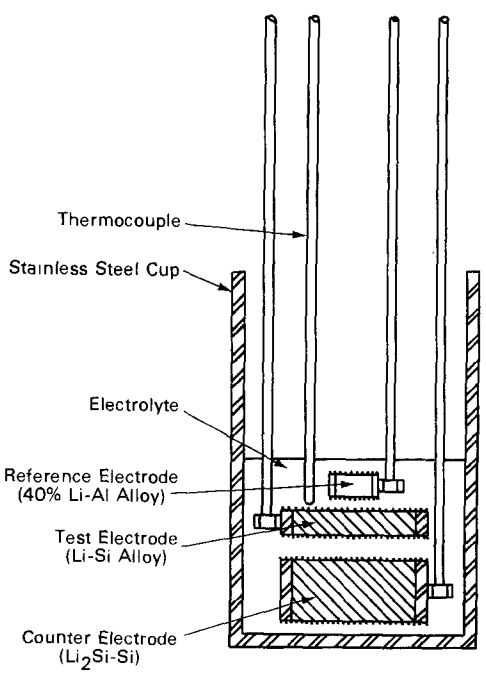


Fig. 1. Schematic representation of the lithium-silicon test cell

Results and Discussion

The results of experiments showing the effects of current density and temperature on lithium utilization (Appendix B) from the Li-Si compounds are presented in Table I and Fig. 2 for the LiCl-KCl electrolyte, Table II and Fig. 3 for the LiF-LiCl-KCl electro-

[1] The reported current densities were calculated using only the facial area of the test electrode opposite the counterelectrode. The contribution by the other face is assumed to be negligible.

[2] The placement of the reference electrode behind the working electrode (Fig. 1) is likely to cause an error in the working electrode voltages. However, voltage measurements using a liquid lithium electrode as both a reference and counterelectrode in subsequent studies indicated that the voltages measured in the present studies differed only by about 50 mV at a current density up to 300 mA/cm^2.

Table I. Electrode performance data in LiCl-KCl electrolyte at different current densities and temperatures*

Cell	Cycles	T (°K)	i_C (mA/cm²)	i_D (mA/cm²)	η_E (%)	U_1 (%)	U_2 (%)	U_3 (%)	U_T (%)	Comments
1	1-5	675	20	20	100.5	74			74	Variation of current density appears to have little effect
	6-11	675	50	50	99.7	69			69	
	12-22	675	100	100	99.8	70			70	
	23-27	675	200	200	100.1	74			74	
	28	700	200	200	102.1	77			77	Increase in temperature increases the yield
	29	725	200	200	100.8	80			80	
	30-32	725	100	200	100.3	80			80	Lower charge current does not improve utilization
	33	675	100	200	93.0	70			70	
	34-39	675	100	200	100.6	64			64	
	40-42	675	20	20	102.2	82	94		85	
	43-49	675	50	50	99.3	82	93		84	Increase in current density appears to decrease the lithium utilization
	50-54	675	100	100	99.7	75	90		79	
	55-60	675	200	200	100.5	75	93		79	
	61-64	725	200	200	99.0	72	97		78	Temperature has little effect
	65-66	675	200	200	100.1	72	100		78	Lower charge current also has little effect on utilization
	67-76	675	100	200	100.0	73	99		79	
	77-80	675	50	50	100.2	82	95	83	84	
	81-92	675	100	100	98.7	78	96	83	84	
	93-103	675	200	200	99.2	71	97	85	80	
	104-106	675	200	200	90.9	62	100	85	81	
	107-109	675	200	200	93.3	60	100	86	75	Increase in current density appears to decrease the lithium utilization
2	1-6	675	50	50	100.5	80	98	84	85	
	7-12	675	100	100	100.3	80	97	79	83	
	13-24	675	200	200	100.0	78	99	82	83	
	25-28	700	200	200	100.2	80	100	84	85	Increase in temperature did not increase lithium utilization
	29-35	725	200	200	100.4	80	100	84	84	
	36-51	700	100	400	99.6	60	(100)	85	78	
	52-59	700	400	400	100.9	70	(100)	84	80	Lower charge current has little effect on utilization
	60-68	700	200	400	99.6	65	(100)	85	80	
	69-78	700	200	600	100.7	43	(100)	90	71	
	79-86	700	200	600	95.7	52	(100)	90	72	

* Electrode area = 5 cm²; electrode thickness = 0.5 cm; electrode capacity = 0.75 A · hr/cm² (as $Li_{15}Si_4$); and discharge cutoff voltage = 0.5V *vs.* 40 a/o Li-Al reference electrode. i_C = charge current density; i_D = discharge current density; η_E = coulombic efficiency = $I_D t_D / I_C t_C$; U_1 = lithium utilization from Li_2Si to Si; U_2 = lithium utilization from $Li_{21}Si_8$ to Li_2Si; U_3 = lithium utilization from $Li_{15}Si_4$ to $Li_{21}Si_8$; and U_T = total lithium utilization from the Li-Si compound to Si.

Table II. Electrode performance data in LiF-LiCl-KCl electrolyte at different current densities*

Cycles	T (°K)	i_C (mA/cm²)	i_D (mA/cm²)	η_E (%)	U_1 (%)	U_2 (%)	U_3 (%)	U_T (%)	Comments
1-5	750	20	20	101.3	84			84	Increase in current density causes a decrease in the lithium utilization
6-11	750	50	50	100.1	79			79	
12-22	750	100	100	99.5	72			72	
23-30	750	200	200	100.1	63			63	
31-34	750	400	400	99.4	68			68	Lowering the charge current has little effect on utilization
35-39	750	100	400	100.0	68			68	
40-45	750	100	200	101.2	71			71	
46-48	750	20	200	99.9	76	85		78	Increasing the current density decreased the lithium utilization
49-56	750	50	50	100.2	76	84		77	
57-61	750	100	100	99.1	71	82		74	
62-69	750	200	200	99.9	67	81		70	
70-78	750	400	400	99.8	63	89		69	Lowering the charge current reduces the utilization
79-95	750	100	400	100.6	58	72		61	
96-99	750	50	50	100.0	72	81	74	74	Increases in current density do not affect lithium utilization
100-105	750	100	100	99.6	71	80	74	73	
106-114	750	200	200	100.0	70	79	76	73	
115-122	750	400	400	100.2	67	86	78	73	
123-132	750	50	400	99.3	59	90	74	69	
133-140	750	400	400	101.6	64	90	77	72	Further increases in current density cause a slight decrease in utilization
141-150	750	500	500	100.1	57	98	77	70	
151-154	750	700	700	100.6	(53)	(95)	78	68	
155-157	750	200	200	100.1	66	84	74	71	
158-161	750	1000	1000	94.1	(69)	(100)	30	72	Lowering the charge current reduces lithium utilization
162-176	750	100	1000	99.5				51	
177-179	750	100	100	99.9	67	75	72	70	
180-183	750	200	200	100.0	64	79	72	69	
184-189	750	200	500	99.3	58	70	75	65	
190-199	750	200	1000	95.3				50	
200-204	750	1000	1000	100.0				72	
205-213	750	1000	200	100.3	87	(100)	40	82	

* Notations shown on Table I also apply to Table II.

lyte, and Table III and Fig. 4 for the LiF-LiCl-LiBr electrolyte. In these results, the current efficiency, η_E, was calculated from the equation

$$\eta_E = \frac{I_D t_D}{I_C t_C}$$

where I_D and t_D are current and time during discharge, and I_C and t_C are current and time during charge. The current efficiency was observed to be >95% in all cases (tables).

As may be seen from Table I and Fig. 2a, it is possible to obtain a total lithium utilization of approximately 70% from Li_2Si at 675°K in LiCl-KCl eutectic using current densities between 20 and 200 mA/cm². The lithium utilization from this compound appears to remain constant in the above range of current densities, but is found to increase slightly with increase in temperature from 675° to 725°K and decrease again when the temperature is decreased (cell no. 1, cycles 23-33). Charging at lower rates (100 mA/cm²) while maintaining a discharge rate of 200 mA/cm² did not increase the

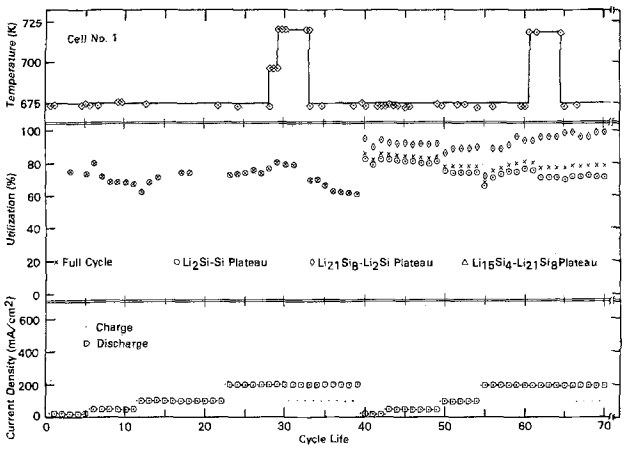


Fig. 2a. Li-Si alloy electrode performance data in LiCl-KCl electrolyte at different current densities and temperatures. Cell no. 1, cycles 1-70.

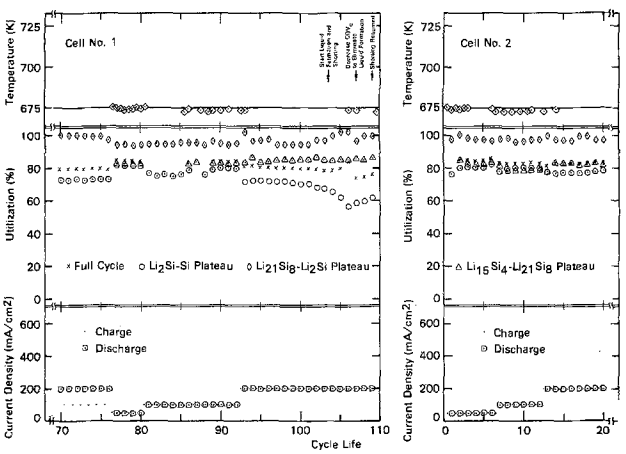


Fig. 2b. Li-Si alloy electrode performance data in LiCl-KCl electrolyte at different current densities and temperatures. Cell no. 1, cycles 70-110; cell no. 2, cycles 1-20.

lithium utilization (cycles 34-39).

It was possible to achieve a total lithium utilization of about 80% from $Li_{21}Si_8$ in LiCl-KCl eutectic at current densities between 20 and 200 mA/cm² and temperatures from 675° to 725°K (cell no. 1, cycles 40-76). The utilization from the $Li_{21}Si_8$-Li_2Si plateau was found to range between 90 and 100% while that from the Li_2Si-Si plateau was found to be between 72 and 80%. The utilization from the $Li_{21}Si_8$-Li_2Si plateau was observed to be unaffected by changes in current density between 20 and 200 mA/cm²; however, the utilization

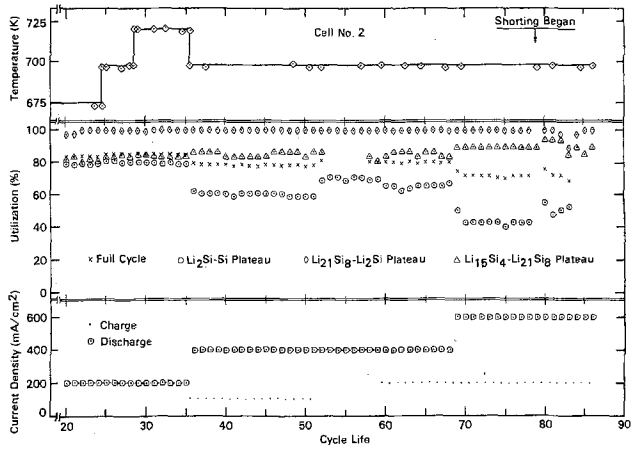


Fig. 2c. Li-Si alloy electrode performance data in LiCl-KCl electrolyte at different current densities and temperatures. Cell no. 2, cycles 20-86.

of the total $Li_{21}Si_8$ cycle and that of the Li_2Si-Si plateau were observed to decrease slightly with increasing current density (cell no. 1, cycles 40-60).

The lithium utilization of the total $Li_{21}Si_8$ cycle at 200 mA/cm² was unaffected by changes in temperature between 675° and 725°K (cell no. 1, cycles 55-66). However, a slight increase in utilization from the $Li_{21}Si_8$-Li_2Si plateau and a slight decrease in utilization from the Li_2Si-Si plateau were noted during these cycles. In addition, charging at lower rates (100 mA/cm²) while maintaining the 200 mA/cm² discharge rate did not affect the utilization (cell no. 1, cycles 65-76).

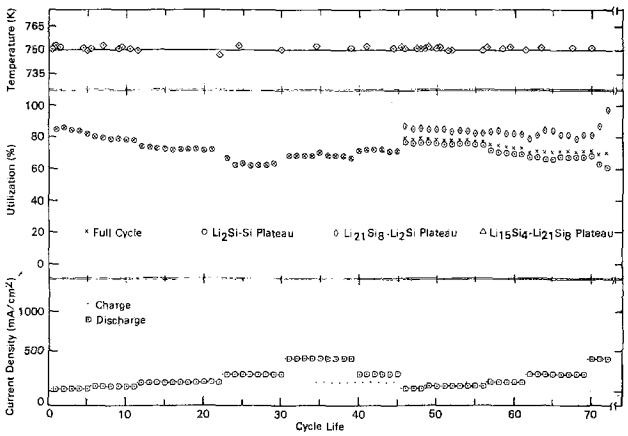


Fig. 3a. Li-Si alloy electrode performance data in LiF-LiCl-KCl electrolyte at different current densities. Cycles 1-72.

Table III. Electrode performance data in LiF-LiCl-LiBr electrolyte at different current densities*

Cycles	T (°K)	i_C (mA/cm²)	i_D (mA/cm²)	η_E (%)	U_1 (%)	U_2 (%)	U_3 (%)	U_T (%)	Comments
1-13	750	50	50	99.9	73			73	Increasing the current density decreased the lithium utilization
14-27	750	200	200	100.1	65			65	
28-41	750	400	400	101.0	58			58	
42-48	750	50	50	100.0	65	71		66	Increasing the current density decreased the lithium utilization
49-56	750	200	200	99.8	60	72		63	
57-66	750	400	400	100.5	55	76		60	
67-72	750	50	50	99.9	62	69	64	63	Increasing the current density decreased the lithium utilization
73-79	750	200	200	99.6	57	67	62	60	
80-86	750	400	400	99.1	53	68	62	58	
87-91	750	100	400	99.7	49	65	60	55	Reducing the charge current causes a reduction in lithium utilization
92-102	750	100	200	100.1	51	60	57	55	
103-106	750	500	500	99.2	43	66	57	51	
107-112	750	200	500	99.6	40	65	54	48	
113-118	750	700	700	99.2	37	66	56	48	
119-125	750	200	700	99.8	34	66	55	46	
126-131	750	200	200	100.4	47	58	51	50	

* Notations shown on Table I also apply to Table III.

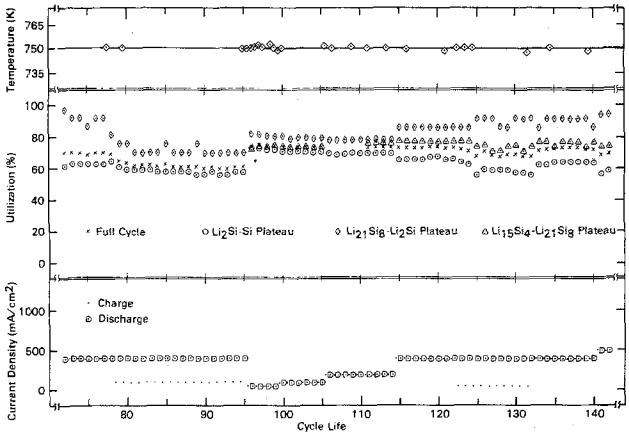


Fig. 3b. Li-Si alloy electrode performance data in LiF-LiCl-KCl electrolyte at different current densities. Cycles 72-142.

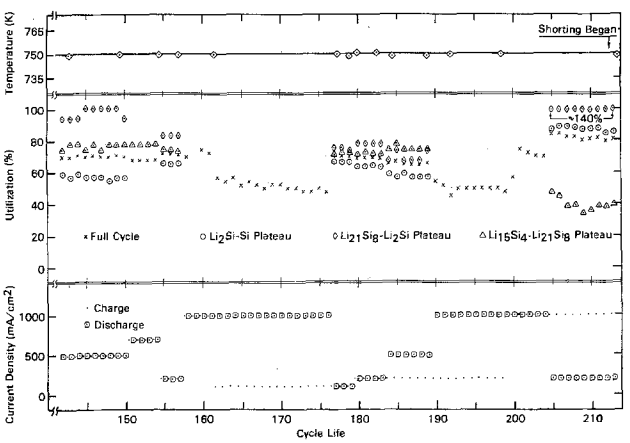


Fig. 3c. Li-Si alloy electrode performance data in LiF-LiCl-KCl electrolyte at different current densities. Cycles 142-213.

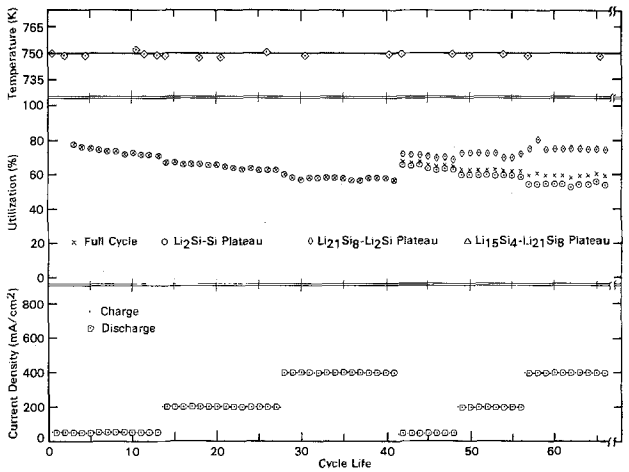


Fig. 4a. Li-Si alloy electrode performance data in LiF-LiCl-LiBr electrolyte at different current densities. Cycles 1-66.

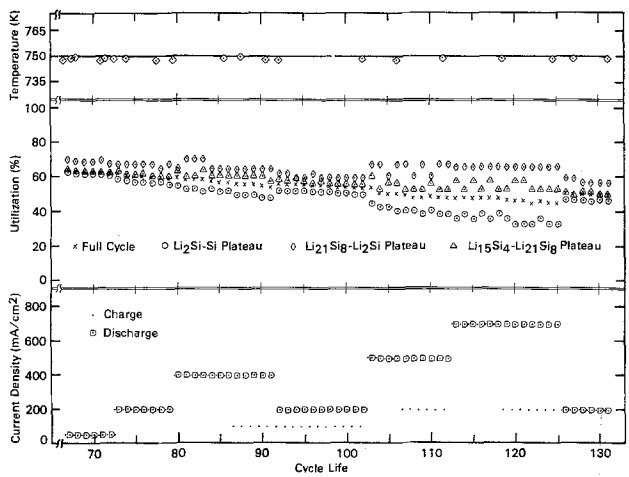


Fig. 4b. Li-Si alloy electrode performance data in LiF-LiCl-LiBr electrolyte at different current densities. Cycles 66-132.

The results presented in Table I and Fig. 2b and 2c indicate that it is possible to achieve a total lithium utilization of about 82% from $Li_{15}Si_4$ in LiCl-KCl eutectic at 675°K using current densities between 20 and 200 mA/cm² (cell no. 1, cycles 77-109; cell no. 2, cycles 1-24). The lithium utilizations from the individual plateaus were found to be approximately 83% for the $Li_{15}Si_4$-$Li_{21}Si_8$ plateau, 98% for the $Li_{21}Si_8$-Li_2Si plateau, and 75% for the Li_2Si-Si plateau during this period. Although current densities below 200 mA/cm² had little effect on the lithium utilization from any plateau, a further increase in discharge current density to 600 mA/cm² caused a decrease in utilization from the Li_2Si-Si plateau, but apparently did not affect the other plateaus (cell no. 2, cycles 69-78).

The lithium utilizations of all the plateaus at 200 mA/cm² increased slightly when temperature was increased from 675° to 700°K, but no further increase was noted when temperature was raised to 725°K (cell no. 2, cycles 13-35). Once again, lowering the charge rate while maintaining a higher discharge rate did not influence lithium utilization (cell no. 2, cycles 36-68).

The data presented in Table II and Fig. 3, which were obtained using the LiF-LiCl-KCl electrolyte at 750°K, indicate that a lithium utilization of 84-68% can be obtained from the Li_2Si-Si plateau in the range of current density between 20 and 400 mA/cm² (cycles 1-34). The utilizations decreased with increasing current density, and charging at lower rates (100 mA/cm²) while discharging at rates of 200 or 400 mA/cm² did not improve the utilization.

The total lithium utilization from the $Li_{21}Si_8$ cycle decreased from 78 to 69% when the current density was raised from 20 to 400 mA/cm² at 750°K in this electrolyte (cycles 46-78). During this current density excursion, the utilization of lithium from the $Li_{21}Si_8$-Li_2Si plateau decreased from 85 to 80% and that from the Li_2Si-Si plateau decreased from 76 to 63%.

The lithium utilization from the total $Li_{15}Si_4$ cycle was found to be about 72% at current densities between 50 and 1000 mA/cm² in this melt at 750°K (cycles 96-161). The utilizations from the $Li_{15}Si_4$-$Li_{21}Si_8$ and $Li_{21}Si_8$-Li_2Si plateaus did not decrease with increasing current density up to 500 mA/cm², but the former was lower than the latter (cycles 96-150). The utilization of lithium from the Li_2Si-Si plateau was found to decrease with increasing current density (cycles 96-154). When the current density was raised above 500 mA/cm², the total utilization was found to decrease, but the different voltage plateaus of the Li-Si compounds could not be readily distinguished. As in all previous cases, lowering the charging rate while maintaining a constant discharge rate did not improve the lithium utilizations. In fact, they appeared to decrease (cycles 158-176, 180-189, and 190-204).

The data presented in Table III and Fig. 4 were obtained using LiF-LiCl-LiBr electrolyte at 750°K. In this case also, the lithium utilization from Li_2Si was observed to decrease from 73 to 58% when current density was increased from 50 to 400 mA/cm² (cycles 1-41).

The total utilization from $Li_{21}Si_8$ and the utilization of the Li_2Si-Si plateau decreased while the utilization of the $Li_{21}Si_8$-Li_2Si plateau increased with an increase in current density from 50 to 400 mA/cm². The total lithium utilization from this compound was between 60 and 66% over the described current density range.

The total lithium utilization from $Li_{15}Si_4$ varied from 63 to 48% with an increase in current density from 50 to 700 mA/cm² (cycles 67-86, 103-106, and 113-118). The utilizations from the $Li_{15}Si_4$-$Li_{21}Si_8$, and Li_2Si-Si plateaus decreased while that from the $Li_{21}Si_8$-Li_2Si plateau remained nearly constant over the above-mentioned increase in current density. Once again, lowering charge rates while maintaining a higher discharge rate did not increase the lithium utilizations (cycles 80-91 and 103-125).

In summary, the lithium utilizations from Li_2Si, $Li_{21}Si_8$, and $Li_{15}Si_4$ showing the effects of temperature, current density, electrolyte, and different charge and discharge rates are given in Table IV.

Selected charge-discharge cycles are also plotted in Fig. 5 as terminal voltage *vs.* capacity density at different current densities in LiCl-KCl eutectic electrolyte. Since the working electrode starting material for these tests was Li_2Si, the voltage-capacity density curves are plotted to coincide at this composition. In this figure, the charge curves are folded back, and the variation of equilibrium voltage with theoretical capacity is shown by the thick solid line. Examination of these curves shows that only a limited amount of the theoretical lithium content of Li_2Si can be removed during discharge and replaced during charge. This incomplete discharge of Li_2Si to Si might be due to difficulty in transport of lithium through silicon once enough silicon is present on the electrode surface area to block diffusion. It was also found that Li_2Si could apparently be charged entirely to $Li_{21}Si_8$ and discharged back to Li_2Si with nearly total lithium utilization. On the other hand, $Li_{21}Si_8$ could not be charged completely to $Li_{15}Si_4$, presumably due to difficulty in transport of lithium through $Li_{15}Si_4$ once the electrode surface area is blocked. However, the amount of lithium charged into $Li_{15}Si_4$ could be completely recovered during discharge.

Terminal voltages *vs.* current densities are plotted in Fig. 6 for the three voltage plateaus at capacity densities of 1.6, 1.05, and 0.6 kC/cm² shown in Fig. 5 by the lines A, B, and C, respectively. As indicated by the slopes of the plots in Fig. 6, the potential shifts from equilibrium values observed in Fig. 5 appear to be mostly ohmic for current densities up to 500 mA/cm².

The results of selected charge-discharge cycles at 750°K using LiF-LiCl-KCl electrolyte are plotted in Fig. 7 as terminal voltage *vs.* capacity density at different current densities. Total lithium utilization from each of the compounds, $Li_{15}Si_4$, $Li_{21}Si_8$, and Li_2Si, as well as individual plateau utilizations are observed to be smaller than the corresponding utilizations obtained when using LiCl-KCl electrolyte at 675°K. However, the polarization during these cycles appears to be less than those observed in the case of LiCl-KCl. The decreases in utilization as well as the reduced polarization may be due to some of the silicon from the Li-Si active material alloying with the nickel current collector at this higher temperature (750°K). Thus,

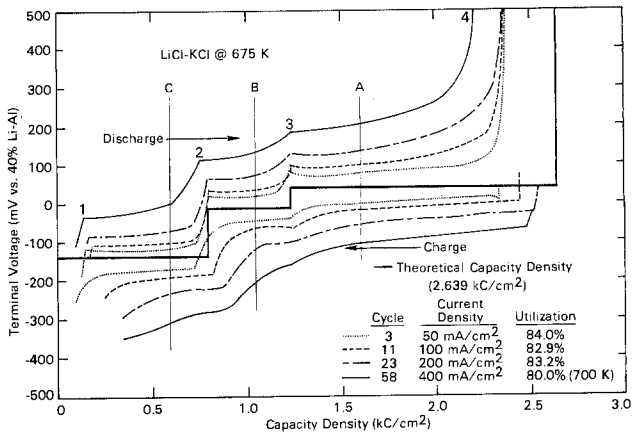


Fig. 5. Voltage-capacity density curves for a Li-Si electrode in LiCl-KCl electrolyte at different current densities.

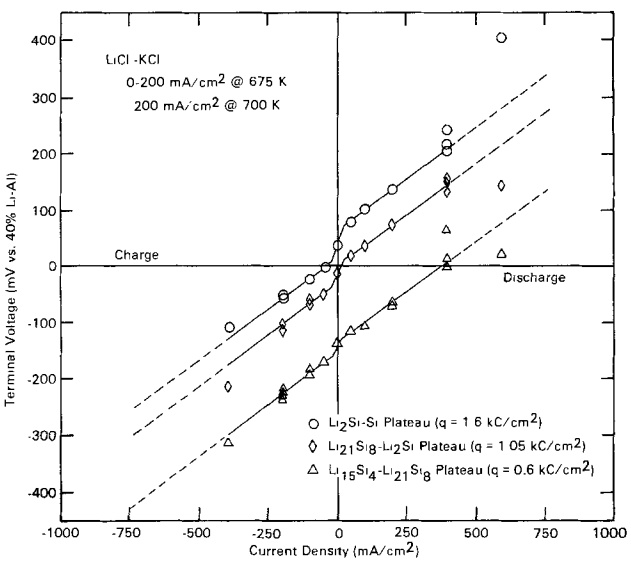


Fig. 6. Voltage-current density relationship for a Li-Si electrode in LiCl-KCl electrolyte.

the silicon would become unavailable for the electrode reaction (lower utilization), but the Ni-Si alloy might lead to better current collection (lower polarization).

In Fig. 8, terminal voltages are plotted *vs.* current density for the Li_2Si-Si, $Li_{21}Si_8$-Li_2Si, and $Li_{15}Si_4$-$Li_{21}Si_8$ plateaus at capacity densities of 1.6, 1.05, and 0.6 kC/cm² as shown in Fig. 7 by the lines D, E, and F, respectively. Once again, the slopes of the plots (Fig. 8) indicate that the potential shifts from equilibrium shown in Fig. 7 are largely ohmic for the current densities studied.

Selected results of charge-discharge cycles in LiF-LiCl-LiBr electrolyte at 750°K are plotted in Fig. 9 as

Table IV. Summary of lithium utilizations from Li-Si compounds under various conditions

Electrolytes	Temperatures (°K)	Current densities (mA/cm²)	Reducing charge current densities	Lithium utilizations (%) Li_2Si-Si	$Li_{21}Si_8$-Li_2Si	$Li_{15}Si_4$-$Li_{21}Si_8$	$Li_{15}Si_4$-Si
LiCl-KCl	675-725 Slight increase in utilization with increase in temperature	20-200 No effect	No effect	69-82	90-100	83-86	80-84
LiF-LiCl-KCl	750	20-400 Slight decrease in utilization with increase in current density	No effect	63-84	79-90	74-78	72-74
LiF-LiCl-LiBr	750	50-400 Slight decrease in utilization with increase in current density	No effect	53-73	67-76	60-64	55-63

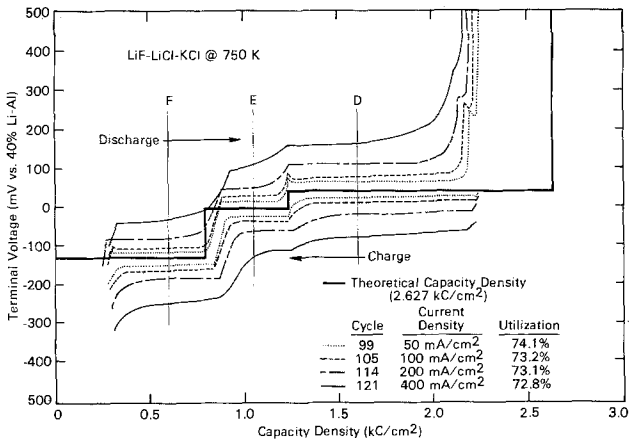


Fig. 7. Voltage-capacity density curves for a Li-Si electrode in LiF-LiCl-KCl electrolyte at different current densities.

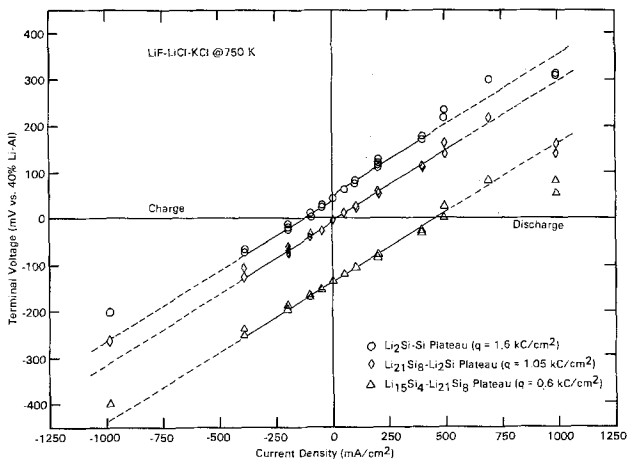


Fig. 8. Voltage-current density curves for a Li-Si electrode in LiF-LiCl-KCl electrolyte.

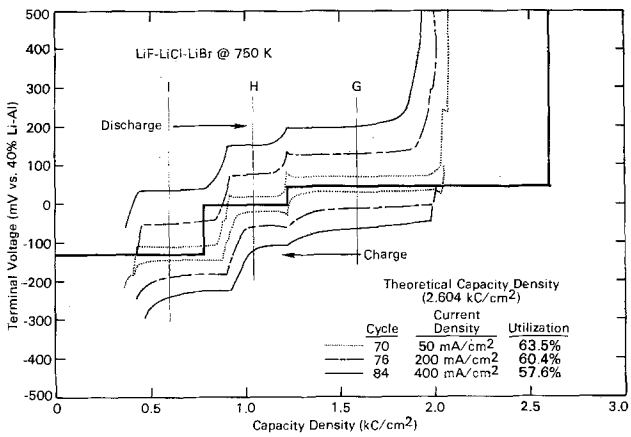


Fig. 9. Voltage-capacity density curves for a Li-Si electrode in LiF-LiCl-LiBr electrolyte at different current densities.

terminal voltage *vs.* capacity density at different current densities. At all current densities, the utilizations are smaller than those obtained under similar conditions with the other two electrolytes. This might have happened because some of the silicon from the Li-Si active material alloyed with the nickel current collector or because some of the active material was pushed out of contact with the current collector by this heavier electrolyte. In either case, some of the active material became unavailable for the electrode reaction leading to the lower lithium utilizations.

The slope of terminal voltage *vs.* current density plots (Fig. 10) for the three voltage plateaus at capacity densities shown by lines G, H, and I in Fig. 9 again show the overpotential at these compositions to

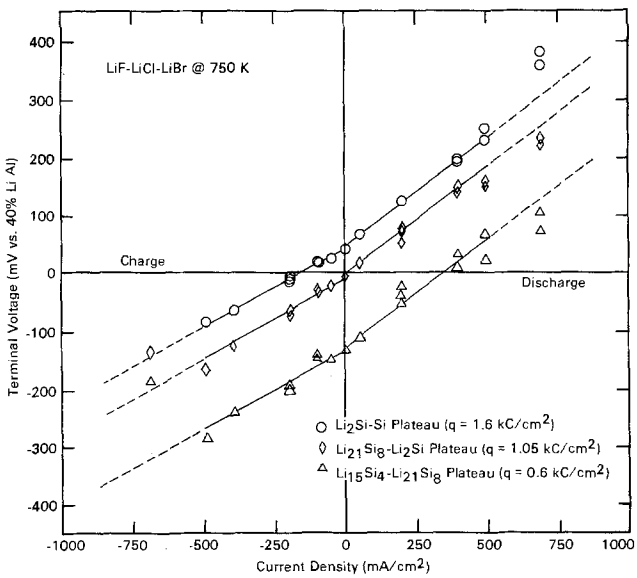


Fig. 10. Voltage-current density curves for a Li-Si electrode in LiF-LiCl-LiBr electrolyte.

be largely ohmic. However, in this case, the potential shifts during discharge are greater than those during charge (*i.e.*, the resistance is greater during discharge than charge). Since lower density Li-Si alloys form during charge, alloy volume increases and may help to develop better contact with the current collector resulting in the lower resistance. The reverse process occurs during discharge, which could increase the resistance.

Summary

Charge-discharge cycles beween electrodes of either Li_2Si, $Li_{21}Si_8$, or $Li_{15}Si_4$ and a Li_2Si counterelectrode at current densities between 20 and 1000 mA/cm² and temperatures from 675° to 750°K indicate:

1. An electrode made of any of the above compounds is promising for use as a negative electrode in Li/FeS_2 cells.
2. Current efficiencies of greater than 95% can be obtained.
3. A lithium utilization of 80-60% can be obtained from a Li_2Si electrode at current densities between 50 and 400 mA/cm².
4. A lithium utilization of 85-70% can be obtained from a $Li_{21}Si_8$ electrode under the same conditions.
5. A lithium utilization of 80-70% can be obtained from a $Li_{15}Si_4$ electrode under the same conditions.
6. The lithium utilizations were not greatly influenced by change in temperature or current density up to 200 mA/cm².
7. The lithium utilizations were observed to decrease with change of electrolyte from LiCl-KCl to LiF-LiCl-KCl to LiF-LiCl-LiBr.
8. Primarily ohmic polarizations were observed in the range of current density between 20 and 500 mA/cm² for electrodes having compositions in the plateaus.

Acknowledgments

The authors are thankful to Mr. Ernest J. Verrier for assistance with the experimental work, and Drs. Elton J. Cairns and John S. Dunning of the Electrochemistry Department for useful suggestions and discussions.

Manuscript submitted Jan. 20, 1977; revised manuscript received April 4, 1977. This was Paper 385 presented at the Philadelphia Meeting of the Society, May 8-13, 1977.

Any discussion of this paper will appear in a Discussion Section to be published in the June 1978 JOURNAL. All discussions for the June 1978 Discussion Section should be submitted by Feb. 1, 1978.

Publication costs of this article were assisted by General Motors Corporation.

APPENDIX A

Preparation of the Li_2Si Alloy

All preparatory procedures were carried out in a helium atmosphere dry box. Approximately 50g of lithium was melted in a clean, preweighed nickel cup at a temperature of 575°K. Impurity scum was scooped off with a nickel screen scoop and the lithium was recooled to room temperature. Remaining impurities at the surface of the solidified lithium were further removed by scraping with a sharp-edged scraper. The lithium was then weighed, remelted, and had its temperature raised to approximately 775°K. A calculated amount of coarse silicon powder was slowly added to the molten lithium. The silicon powder did not sink into the molten lithium, rather it floated on the surface. The molten lithium soaked into the silicon powder, an exothermic reaction was observed, and a solid mass formed at the surface of the melt. The temperature was slowly raised to 1075°K, and the solid mass sank into the melt and dissolved. The melt was then stirred with a nickel rod to insure homogeneity, cooled to room temperature, and powdered.

APPENDIX B

Lithium Utilization

The lithium utilizations were calculated on the basis of the following reactions

$$Si + 2Li \rightarrow Li_2Si \qquad [B\text{-}1]$$

$$Li_2Si + 5/8\ Li \rightarrow 1/8\ Li_{21}Si_8 \qquad [B\text{-}2]$$

$$1/8\ Li_{21}Si_8 + 9/8\ Li \rightarrow 1/4\ Li_{15}Si_4 \qquad [B\text{-}3]$$

The lithium utilization designated as U_1 was calculated by dividing the capacity obtained during the voltage plateau between Li_2Si and Si (reaction [B-1] by the theoretical capacity of that plateau.

The lithium utilization designated as U_2 was calculated by dividing the capacity obtained during the voltage plateau between $Li_{21}Si_8$ and Li_2Si (reaction [B-2] by 5/8 × 96,487 for each gram mole of Li_2Si in the electrode.

The lithium utilization designated as U_3 was calculated by dividing the capacity obtained during the voltage plateau between $Li_{15}Si_4$ and $Li_{21}Si_8$ (reaction [3]) by 9/8 × 96,487 for each gram mole of Li_2Si in the electrode.

The total lithium utilization designated as U_T was calculated by dividing the total capacity obtained for all of the plateaus under consideration by the total theoretical capacity of the electrode.

In the experiments carried out here, the onset of a plateau was marked by a sharp change of slope in the voltage *vs.* time curve. The capacity obtained between two sharp changes of slope at the beginning and end of the plateau was divided by the theoretical capacity of that plateau to obtain the lithium utilization. For example, the lithium utilization, U_3 was calculated by dividing the capacity between points 1 and 2 (Fig. 5) by the theoretical capacity of the plateau between $Li_{15}Si_4$ and $Li_{21}Si_8$. Similarly, U_2 was calculated by dividing the capacity between points 2 and 3 by the theoretical capacity of the plateau between $Li_{21}Si_8$ and Li_2Si, and U_1 by dividing the capacity between points 3 and 4 by the theoretical capacity of the plateau between Li_2Si and Si. U_T was then obtained by dividing the capacity obtained between 1 and 4 by the theoretical capacities of all of the plateaus from $Li_{15}Si_4$ to Si.

REFERENCES

1. P. A. Nelson *et al.*, Report ANL-76-45, Argonne National Laboratory, Argonne, Illinois (April 1976).
2. E. J. Cairns and J. S. Dunning, Report ANL-76-8, A-81, Argonne National Laboratory, Argonne, Illinois (1976).
3. J. L. Settle and K. M. Myles, Report ANL-76-9, p. 43, Argonne National Laboratory, Argonne, Illinois (1976).
4. R. A. Sharma and R. N. Seefurth, *This Journal*, **123**, 1763 (1976).
5. L. R. McCoy and S. Lai, Report ANL-76-8, B-167, Argonne National Laboratory, Argonne, Illinois (1976).
6. D. R. Vissers, W. R. Frost, and K. E. Anderson, Report ANL-76-35, p. 50, Argonne National Laboratory, Argonne, Illinois (1976).
7. C. S. Fuller and J. A. Ditzenberger, *Phys. Rev.*, **91**, 193 (1953).
8. L. P. Costas, TID-16676, USAEC Contract AT(07-2)-1, E. I. du Pont de Nemours & Co., Inc., Aiken, South Carolina (1963).
9. E. Elchardus and P. Laffit, *Bull. Soc. Chim. Fr.*, **51**, 1572 (1932).
10. S. I. Berezina, A. G. Bergman, and E. L. Bakumskoya, *Russ. J. Inorg. Chem.*, (*Engl. Transl.*), 1120 (1963).
11. A. G. Bergman and A. S. Arabadzhan, *ibid.*, 637 (1963).
12. R. N. Seefurth and R. A. Sharma, *This Journal*, **122**, 1049 (1975).

Current Distribution in a Tubular Electrode under Laminar Flow: Two Electrode Reactions

Richard Alkire* and Ali Asghar Mirarefi*

Department of Chemical Engineering, University of Illinois, Urbana, Illinois 61801

ABSTRACT

A computational method has been developed for calculating the current distribution along a tubular electrode when two electrode reactions occur simultaneously. The model is valid for all operating conditions between the secondary current distribution and the limiting current distribution. The model includes the Lévêque equation of convective diffusion, a one-dimensional potential distribution, and Butler-Volmer charge-transfer kinetics for each electrode reaction. Experiments on copper deposition in the presence of a Fe(III)/Fe(II) redox couple were carried out with a sectioned tubular electrode. Current distribution data were compared with theoretical expectations and good agreement was found.

Relatively few electrochemical reactions are carried out with 100% current efficiency. There are several reasons why more than one electrode reaction might occur. For example, the applied current might exceed the limiting current of the most reactive species, or the potential variation along the surface may exceed the rest potential difference between two possible reactions. That is, both mass transport and potential dis-

* Electrochemical Society Active Member.

Key words: tubular electrode, sectioned electrode, mathematical model, multiple reaction, laminar flow

tribution effects can be important in determining what reactions occur as well as where they occur along the electrode surface. Therefore in order to determine the current distribution in the presence of multiple reactions it is usually necessary to take simultaneous account of both the concentration field and the potential field.

Theoretical procedures for predicting current distributions have to date been almost entirely confined to consideration of a single reacting species in the electrolyte. In this study, the role of multiple electrode reactions was investigated with use of a tubular electrode. Theoretical predictions were compared with experimental data obtained with a system which involved copper deposition in the presence of a Fe(III)/Fe(II) redox couple. The investigation reported here (1) extends previous theoretical (2) and experimental (3) work on single electrode reactions in tubular electrode configurations. The purpose of this investigation is to provide experimental data for testing whether current distributions can be predicted accurately at currents below but at an appreciable fraction of the limiting current.

Until recently, current distribution calculations were made with consideration of either the potential field or the concentration field, but not both. For example, Masuda (4) analyzed the mass transfer current distribution at a number of electrode configurations for a variety of multiple reaction sequences, but did not include consideration of the potential field. Klatt and Blaedel (5) studied a mass transfer limited electrode reaction in a tubular electrode followed by a first-order catalytic reaction for which it was not necessary to include potential field considerations. Oesterling and Olson (6) investigated mass transfer controlled deposition of two metals in a tubular electrode.

Procedures for calculating the current distribution with simultaneous consideration of concentration and potential fields in porous electrodes have been applied to multiple reaction systems by Alkire and Gould (7). Similar procedures have been used by Alkire and Nicolaides (8, 9) in the analysis of localized differential aeration corrosion. These one-dimensional analyses are simpler than two-dimensional analyses for which more complex procedures have only recently been developed (10, 11) and applied to tubular electrode systems (2).

Experimental Apparatus and Procedures

The experiment consisted of measuring the current distribution along a sectioned tubular electrode through which electrolyte passed in steady laminar flow. Current distributions were measured at various fractions of the limiting current upon systematic variation of electrode geometry, flow rate, reactant concentration, and counterelectrode placement. The apparatus used in the experimental study was, as described previously (3), designed so that: (*i*) Laminar flow was maintained by limiting the flow rate according to the conditions $Q < 3300R_0$; (*ii*) mass transfer behavior was constrained to the entrance (Lévêque) region by requiring that $Q > 1570LD_1$; and (*iii*) potential distribution was approximately one dimensional by choosing judiciously the tube radius/length ratio.

The electrolytic solution consisted of $CuSO_4$, $Fe_2(SO_4)_3$, and $FeSO_4$ in 1.5M H_2SO_4. Acidified solutions of the copper salt and of the redox salts were prepared and analyzed separately, then combined to give the desired mixed electrolytic solution. The procedure for conducting experiments was the same as described previously (3). A mercury/mercurous sulfate reference electrode was used. Before presentation of experimental results, the theory for multiple reaction systems is described.

Theory

The mathematical model described in this study extends our earlier theoretical work (2) by including the possibility of multiple electrode reactions in a tubular electrode. The enthusiastic reader should examine the earlier papers for a more thorough discussion of the model. Figure 1 illustrates the geometry of the tubular electrode. The electrode, of radius R_0 and length L, is positioned between two long pipe sections made of insulating material. Two coordinate systems were used: one based on the pipe axis (x,r) and the other based along the electrode surface beginning at the upstream edge (z,y). The counterelectrode is placed at a distance L_1 from the tubular electrode either downstream as in Fig. 1 or upstream (not shown).

The theoretical model is based on the assumption that concentration variations are confined to a thin region near the electrode surface so that the electrolyte can be treated as two different regions: (*a*) The diffusion layer region close to the electrode surface in which the concentration of species vary, and (*b*) the bulk region which fills the remainder of the region of the cell.

Transport equations for the two regions are coupled through their boundary conditions and are therefore solved simultaneously. The electrolytic solution moves in steady laminar flow and is assumed to contain a large quantity of supporting electrolyte so that migration of reacting species is negligible.

In the electrolytic solution there are i reactive solute species which take part in j electrode reactions having the stoichiometry

$$\sum_i s_{ij} M_i^{+z_i} = n_j e^- \qquad [1]$$

The rate of arrival of reactive solute species at the electrode surface corresponds to the rate of electrode reaction by Fick's law

$$\left.\frac{\partial c_i}{\partial y}\right|_{y=0} = \frac{s_{ij}}{n_j F D_i} j_j \qquad [2]$$

For the experimental system under study, we denote

$$Fe(II) = Fe(III) + e^-$$

as reaction [1] involving species 1 [Fe(II)] and species 2 [Fe(III)], and

$$Cu(II) = Cu^o + 2e^-$$

as reaction [2] involving species 3 [Cu(II)] and species 4 (Cu^o). With this notation and in conformance with Ref. (5), the reversible reaction rate expression for the redox reaction has the general form

$$j_1 = i_{o,1}\left[\left\{\prod_{i=1,2}\left(\frac{c_{i,s}}{c_{i,\infty}}\right)^{(\delta_i+\alpha_1 s_{i1})}\right\} e^{\frac{\alpha_1 n_1 F}{R_g T}\phi} - \left\{\prod_{i=1,2}\left(\frac{c_{i,s}}{c_{i,\infty}}\right)^{(\delta_i-\beta_1 s_{i1})}\right\} e^{-\frac{\beta_1 n_1 F}{R_g T}\phi}\right] \qquad [3]$$

and the rate expression for the metal deposition reaction has the form

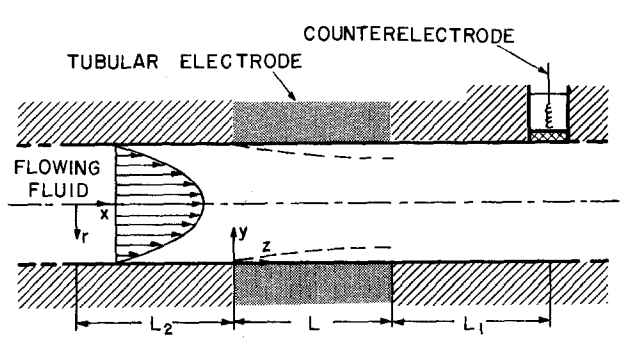


Fig. 1. Schematic diagram of tubular electrode system geometry, with downstream counterelectrode.

$$j_2 = i_{o,2}\left[\left\{\prod_{i=3,4}\left(\frac{c_{i,s}}{c_{i,\infty}}\right)^{(\delta_1+\alpha_2 s_1)}\right\} e^{\frac{\alpha_2 n_2 F}{R_g T}(\phi+\phi_r)} - \left\{\prod_{i=3,4}\left(\frac{c_{i,s}}{c_{i,\infty}}\right)^{(\delta_1-\beta_2 s_1)}\right\} e^{-\frac{\beta_2 n_2 F}{R_g T}(\phi+\phi_r)}\right] \quad [4]$$

with $s_4 = 0$ since the deposited metal does not exist in the solution phase. The potential ϕ is defined as the potential of a Fe(II)/Fe(III) reference electrode placed in the solution, adjacent to the working electrode surface, with respect to the potential of the working electrode. Cathodic processes correspond to negative values of both ϕ and j_j.

Under the assumptions of the model, the surface concentrations appearing in Eq. [3] and [4] were found from the equation of convective diffusion according to the Lévêque approximation (12)

$$\frac{4Q}{\pi R_0^3} y \frac{\partial c_i}{\partial z} = D_i \frac{\partial^2 c_i}{\partial y^2} \quad [5]$$

with the boundary conditions

$$c_i = c_{i,\infty} \text{ at } z \leq 0$$

$$c_i = c_{i,\infty} \text{ at } y = \infty,\ z > 0$$

$$\frac{\partial c_i}{\partial y} = \frac{s_i j_j}{n_j F D_i} \text{ at } y = 0,\ z > 0$$

The reaction rate distribution corresponding to Eq. [5] was determined with Laplace transform methods (1) to be

$$j_j = \frac{n_j F}{s_i R_0 \Gamma(1/3)}\left(\frac{12QD_i^2}{\pi}\right)^{1/3} \int_0^z \frac{dc_{i,s}(z')}{dz'}\frac{dz'}{(z-z')^{1/3}} \quad [6]$$

For the experimental system under study, the ratio of tube radius to tube length was sufficiently small that the potential distribution within the tube was essentially one dimensional (3). Consequently the electrode reaction rates appear as pseudohomogeneous source terms in the charge balance equation

$$j_1 + j_2 = \frac{R_0\kappa}{2}\frac{d^2\phi}{dz^2} \quad [7]$$

The boundary conditions on Eq. [7] depend on placement of the counterelectrode. For example, a downstream counterelectrode would correspond to

$$\frac{d\phi}{dz}(0) = 0$$

$$\phi(L) = \phi_m \quad \text{or} \quad \phi(L + L_1) = \phi_A$$

The applied potential ϕ_m, or ϕ_A, corresponds to the potential of a Fe(II)/Fe(III) reference electrode placed in the solution outside the tubular electrode at $y = L$, or $y = L + L_1$, respectively. The applied potential is negative in all calculations in this study, indicating that the redox reaction proceeds in the cathodic direction. The total cell voltage would be obtained by adding to ϕ_m or ϕ_A the sum of all other voltage losses which arise between the reference electrode and the counterelectrode.

Equations [3], [4], [6], and [7] constitute a set of relationships between the concentration distributions for each reacting species, the reaction rate distributions for each electrode reaction, and the potential distribution. The dimensionless ratios which are convenient for this system are

$$Z = \frac{z}{L} \qquad \rho = \frac{r}{R_0} \qquad \gamma_0 = \frac{R_0}{L}$$

$$\gamma_1 = \frac{L_1}{L} \qquad \gamma_2 = \frac{L_2}{L} \qquad \Phi = \frac{n_r F}{R_g T}\phi$$

$$j_j^* = \frac{2n_r F L^2}{R_g T R_0 \kappa} j_j \qquad \bar{\beta}_j = \frac{2n_r F L^2}{R_g T R_0 \kappa} \langle j_j \rangle \qquad C_i = \frac{c_i}{c_{i,\infty}}$$

$$C_{i,s} = \frac{c_{i,s}}{c_{i,\infty}}$$

The dimensionless model equations are

$$j_1^* = \xi_1\left[\left\{\prod_{i=1,2} C_{i,s}^{(\delta_1+\alpha_1 s_1)}\right\} e^{\frac{\alpha_1 n_1}{n_r}\Phi} - \left\{\prod_{i=1,2} C_{i,s}^{(\delta_1-\beta_1 s_1)}\right\} e^{-\frac{\beta_1 n_1}{n_r}\Phi}\right] \quad [8]$$

$$j_2^* = \xi_2\left[\left\{\prod_{i=3,4} C_{i,s}^{(\delta_1+\alpha_2 s_1)}\right\} e^{\frac{\alpha_2 n_2}{n_r}(\Phi+\Phi_r)} - \left\{\prod_{i=3,4} C_{i,s}^{(\delta_1-\beta_2 s_1)}\right\} e^{-\frac{\beta_2 n_2}{n_r}(\Phi+\Phi_r)}\right] \quad [9]$$

$$j_1^* = \frac{2n_1}{3n_r} N_{1,i} \int_0^Z \frac{dC_{i,s}(Z')}{dZ'}\frac{dZ'}{(Z-Z')^{1/3}} \quad (i = 1 \text{ or } 2) \quad [10]$$

$$j_2^* = \frac{2n_2}{3n_r} N_{2,i} \int_0^Z \frac{dC_{i,s}(Z')}{dZ'}\frac{dZ'}{(Z-Z')^{1/3}} \quad (i = 3 \text{ or } 4) \quad [11]$$

$$j_1^* + j_2^* = \frac{d^2\Phi}{dZ^2} \quad [12]$$

where

$$N_{j,i} = \frac{n_r^2 F^2 L^2 c_{i,\infty}}{-s_i \Gamma(4/3) R_g T R_0^2 \kappa}\left(\frac{12QD_i^2}{\pi L}\right)^{1/3} \quad [13]$$

$$\xi_j = \frac{2n_r F L^2}{R_g T R_0 \kappa} i_{0,j} \quad [14]$$

The parameter $N_{j,i}$ is related to the dimensionless average limiting current density by

$$\bar{\beta}_{lim,j} = -N_{j,i}\frac{n_j}{n_r} \quad [15]$$

while ξ_j is a linear polarization parameter. The physical significance of these parameters has been described in detail elsewhere (2, 3, 13, 14) and will be mentioned again upon presentation of experimental results below. The quantity n_r is introduced only to preserve dimensional consistency, and may be assigned the value of unity.

The model equations were solved by the following numerical procedure in which the potential ϕ is the independent variable. In order to begin the iterative sequence, the potential distribution was assumed to vary linearly between the value 0 (at $Y = 0$) and the value Φ_m (at $Y = 1$).

1. With the trial potential distribution in hand, Eq. [8], [9], [10], and [11] were solved to obtain the surface concentration distribution of all species. That is, Eq. [8] and [10] were combined to eliminate j_1^*, and the resulting integral sums were evaluated by the method of Acrivos and Chambré (15) beginning at the upstream edge and using Newton's method of con-

vergence as outlined previously (2). Thus at each integration point, the trial potential distribution was used to determine the trial surface concentrations of species 1 and 2. Similarly, Eq. [9] and [11] were combined and integrated to obtain the trial surface concentration of species 3.

2. The trial current distributions for each partial reaction were added together and then integrated twice over the surface, in accord with Eq. [12], to provide a new guess for the potential distribution.

3. Steps 1 and 2 were repeated until two successive distributions agreed with each other within 0.1% over the entire surface region.

Because it was found necessary to average new and previous distributions during the iterative procedure in order to achieve convergence, the speed of convergence therefore depended on the skill of the operator.

Comparison of Experimental Data with Theoretical Calculations

In order to compare data with calculated behavior, it is necessary to determine the properties of the electrochemical system. Table I contains the values used in this investigation. Because the reactant concentrations were very low, the mixed electrolyte system was assumed to exhibit no interaction effects; that is, the diffusion coefficients, etc., of the individual solutes were used. Conductivity data were measured by us (3). The exchange current density for the copper deposition reaction has been variously reported and would, following Newman (16), have the value 0.38 mA/cm^2 in the 0.01M $CuSO_4$ solution used in this study (with $\alpha = 0.75$ and $\beta = 0.25$). The presence of sulfuric acid affects the exchange current as has been analyzed by Cabán and Chapman (17) whose model IV would indicate the value 0.041 mA/cm^2 in the 0.01M $CuSO_4$ + 1.5M H_2SO_4 solution used in this study (with $\alpha = 0.54$ and $\beta = 0.19$). In this study, we compared tubular electrode polarization curves (in 0.01M $CuSO_4$ + 1.5M H_2SO_4, no $FeSO_4$) with theoretical calculations (with $\alpha = 0.75$ and $\beta = 0.25$) and found that the value of 0.16 mA/cm^2 gave good comparison for all experimental results (3); we have therefore used the value 0.16 mA/cm^2 in the calculations reported below. That is, we assumed that the copper reaction was not affected by the presence of the Fe(II)/Fe(III) couple. The exchange current density of the redox couple on copper is not reported in the literature and was difficult to measure since the copper surface corrodes except when cathodically protected by current in excess of the limiting current for ferric reduction. With the expectation that the redox exchange current density was high, a value was assigned to it which was one order of magnitude above the copper exchange current density. By this arbitrary procedure, the charge-transfer resistance of the redox couple was forced to be negligible so that errors in the precise value of i_0 were therefore unimportant.

Polarization curves and current distributions were measured over a range of applied potential, solution velocity and electrode aspect ratio as indicated in Table II.

Table I. Properties of mixed reaction system

Property	Value	Reference
ν, cm^2/sec	1.035×10^{-2}	(18)
κ, $(\Omega\text{-cm})^{-1}$	0.41	*

	Cu system value	Reference	Fe system value	Reference
α	0.75	(16)	0.5	—
β	0.25	(16)	0.5	—
i_0, A/cm^2	1.6×10^{-4}	*	—	—
D_j, cm^2/sec	5.0×10^{-6}	(19)	4.5×10^{-6}	(20)
n_j	2		1	

* Measured in our laboratory.

Table II. Experimental conditions

Q range, ml/sec: 0.18 to 10.75
ϕ_m range, mV: 0 to −700 with respect to the rest potential of the mixed system
$c_{H_2SO_4}$, M: 1.5

Run	$c_{Cu^{+2}}$ (M)	$c_{Fe^{+3}}$ (M)	$c_{Fe^{+2}}$ (M)	No. of sections	L (cm)	R_0 (cm)
174	0.01	0.01	0.01	12	5.4	0.476
217	0.01	0.02	0.02	12	5.4	0.476
220	0.01	0.02	0.02	9	4.1	0.476
227	0.01	0.02	0.02	9	4.3	0.635
232	0.01	0.02	0.02	11	5.5	0.3175

As reported elsewhere (3), experiments on single reaction systems were also carried out in the same apparatus, both at the limiting current and below the limiting current. In the multiple reaction system studied here, it is clear that one partial reaction may proceed at its partial limiting current while the less reactive species may be below its partial limiting current. When all possible reactants are simultaneously at their partial limiting currents, then (*a*) the total current is equal to the sum of the partial limiting currents, and (*b*) all partial reactions proceed with the same current distributions. Experimental data are provided below.

Figures 2 through 5 contain current distribution data which have been normalized in one of two fashions in order to compare them with theoretical calculations. By the first method, the current density from each electrode section is divided by the average total current density over the entire electrode surface

$$J = \frac{\sum_j j_j}{\sum_j \langle j_j \rangle} = \frac{\sum_j j_j^*}{\sum_j \bar{\beta}_j} \qquad [16]$$

By the second method, the current density from each electrode section is divided by the average total current density which would be obtained if both reactions were at their respective limiting currents

$$J_N = \frac{\sum_j j_j^*}{\sum_j \bar{\beta}_{\lim,j}} = \frac{\sum_j \bar{\beta}_j}{\sum_j N_{j,1}} J = fJ \qquad [17]$$

The two methods differ in that $\int_0^1 J dZ = 1$, while $\int_0^1 J_N dZ = f$, where f is the fraction of combined limiting current for both reactions.

Figure 2 provides information determined on a single reaction system (copper deposition) at various applied potentials. The counterelectrode is downstream; electrolyte flows from left to right. On the left side of the figure, the experimentally measured current distributions are given for several applied potentials. The current distributions have been normalized by division by the average current, as in Eq. [16]; as a consequence, the area under each current distribution curve is the same, as indicated in the previous paragraph. It is seen that at low potentials, the electrode is most reactive in the downstream regions, close to the counterelectrode. At intermediate potentials, mass transfer processes become more influential and the current distributions become more uniform since the upstream electrode regions become reactive. At high potentials, at the limiting current, the electrode is most

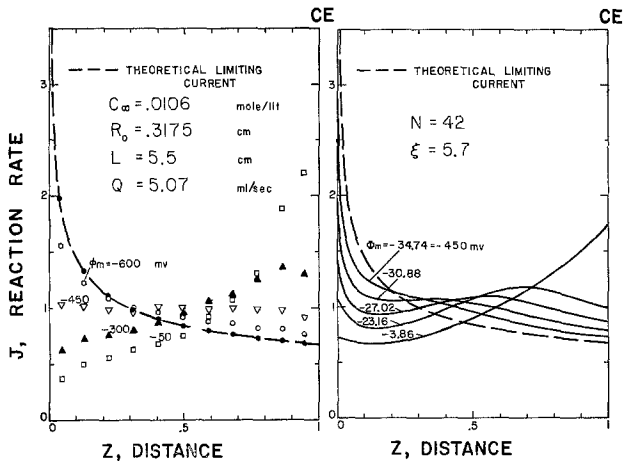


Fig. 2. Current distributions along a tubular electrode surface during copper deposition from 1.5M H_2SO_4. Left side: experimental data. Right side: theoretical calculations.

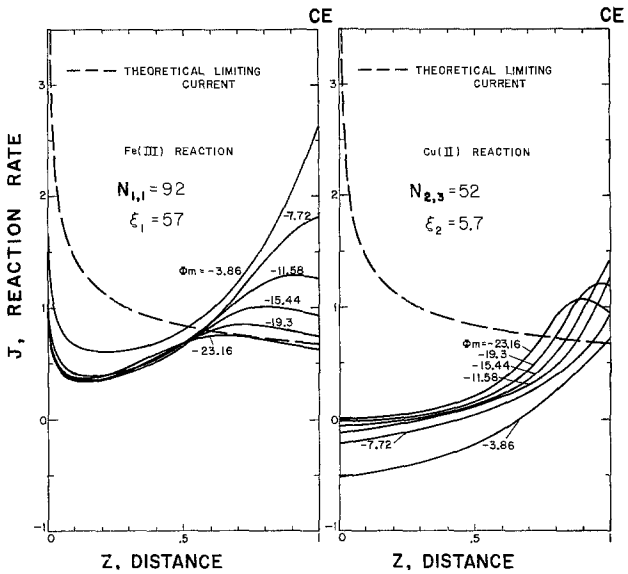


Fig. 4. Calculated current distributions for the individual reactions under the same conditions as Fig. 3. Left side: ferric reduction reaction rate distribution. Right side: copper reaction rate distribution.

reactive at the upstream region, where the diffusion boundary layer is thinnest. For this system, model calculations have been carried out with use of the system parameters given in Table II. The right-hand side of Fig. 2 gives results calculated without any artificial adjustment of parameters to "fit" the data. It is seen that the predicted current distributions agree to within roughly 20% of the data over most of the range measured. The single reaction data of Fig. 2 will now be compared with two-reaction data in the same electrode and at the same flow rate.

Figure 3 shows, on the left side, experimental current distributions for several applied potentials for the mixed cupric/ferric system. At low potentials, both the upstream and the downstream regions of the electrode are more reactive than the center. At intermediate potentials, the current distribution becomes more uniform, exhibiting both a minimum and maximum value. At high potentials, both reactions proceed at the limiting current, and the current distribution is the same as for the single reaction case previously given by Fig. 2. The right-hand side of Fig. 3 provides theoretical calculations for the multiple reaction system at hand.

A more detailed breakdown of the current distribution for each partial reaction is given in Fig. 4. On the left-hand side of Fig. 4 are the calculated results for the ferric reduction reaction; on the right-hand side are results for copper reaction. The current distributions for each reaction are normalized by the total current passing to the electrode. Therefore the area under a current distribution curve for one of the reactions gives the current efficiency of that reaction, the maximum possible area being equal to unity. The ferric partial reaction rate is large on both the upstream surface (thin diffusion layer) and the downstream surface (near the counterelectrode). As the applied potential is increased, the downstream surface becomes less reactive since the ferric ion becomes depleted. The cupric partial reaction rate is anodic on the upstream surface and cathodic on the downstream surface. That is, the ferric ion attacks the copper electrode and dissolves it; the downstream counterelectrode is too far away to provide cathodic protection to the upstream surfaces of the copper electrode. Further downstream, copper is plated onto the electrode. At the higher potentials, the copper current distribution passes through a maximum owing to depletion of copper ions at the electrode surface.

On the basis of these results it is recognized that when one of the two electrode reactions is below its own limiting current, then the multiple reaction system behavior cannot be predicted by simple combination of single reaction behavior. The over-all polarization curve is not the same as the sum of the polarization curves of the single reaction systems because the current distribution is different. In a like manner the over-all (two-reaction) current distribution is not the

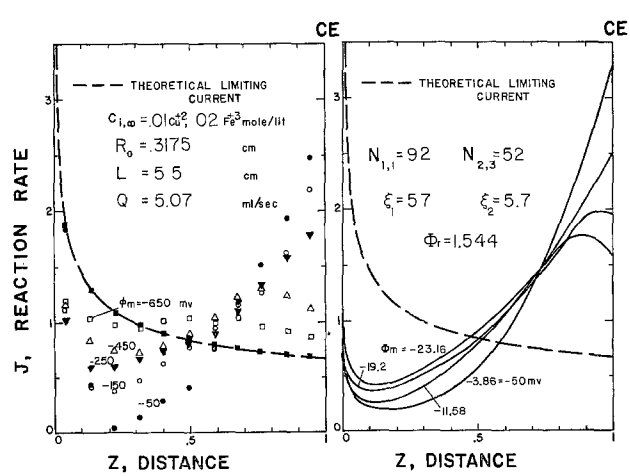


Fig. 3. Current distributions during copper deposition in the presence of ferric ions in 1.5M H_2SO_4. Left side: experimental data. Right side: theoretical calculations.

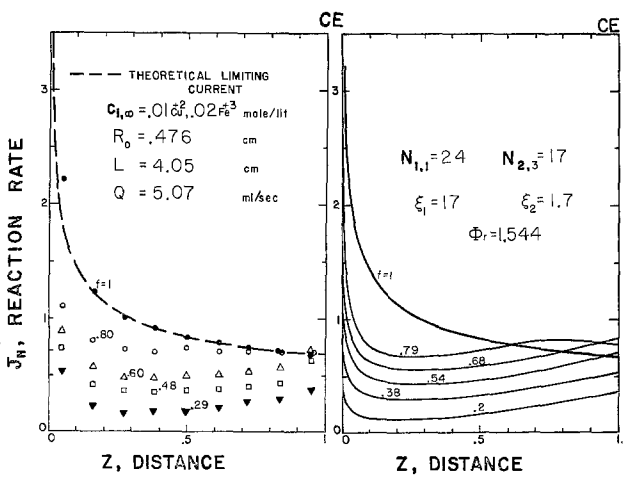


Fig. 5. Current distribution during copper deposition in the presence of ferric ions in 1.5M H_2SO_4. Left side: experimental data. Right side: theoretical calculations.

sum of the single reaction current distributions because the potential distribution is different.

A less dramatic set of data is shown in Fig. 5. The counterelectrode is downstream, and the electrolyte flow is from left to right. Whereas the flow rate is the same as in the preceding figures, the tubular electrode is shorter in length and larger in radius. For these reasons, the current can penetrate further into the electrode so that the far upstream regions are cathodically protected; corrosion of the copper electrode does not occur. On the left side of Fig. 5 are current distribution data, reported on the basis of the fraction of limiting current for both reactions. On the right-hand side are theoretical calculations for various corresponding fractions of over-all limiting current. The theory underestimates somewhat the upstream reaction rate (ferric reaction), although the over-all comparison is in agreement within less than 10%.

Additional comparisons of experiment with theory (1) have also indicated in each case that the theory underestimated the upstream reaction rate but that the agreement was very good in the downstream surfaces. It seems appropriate to observe that the comparison indicated in Fig. 3 and 5 illustrates that the model can be used to predict behavior to within reasonable engineering tolerances.

Conclusions

Experimental measurements of the over-all reaction rate distribution have been carried out for metal deposition in the presence of a redox reaction. It would be of interest to carry out similar experiments with sectioned platinum electrodes in which case postelectrolysis back-titration of the copper deposition distribution would provide direct measurement of the partial reaction distributions. Other reaction sequences could be studied experimentally, including multiple metal deposition, and coupled homogeneous-heterogeneous reactions.

A theoretical basis has been established for predicting the current distribution in multiple electrode reaction systems. The procedure is sufficiently powerful that simple alterations would permit application to a wide variety of electrode geometries, flow fields, and electrode reactions. The method of calculation may be used to calculate reaction efficiencies as a function of system parameters such as electrode length and fraction of limiting current. It seems likely that the pursuit of such engineering aspects would lead eventually to the establishment of design criteria. The theory can be used to predict behavior in corrosion systems, and could be extended with ease to the prediction of cathodic protection in pipe systems, even to the extent of including a third reaction such as hydrogen evolution.

The electrodeposition of alloys is often constrained to a relatively narrow window of operating conditions. The theory and experimental methods used here could be applied to improve understanding of the complex relation between electrode geometry, fluid flow, current density, and alloy composition.

Although gassing at electrodes involves phase changes and other complications not included in the present theory, it seems clear that detailed pursuit of such effects could be made by extension of the basic framework outlined here.

Acknowledgments

This study was supported by the National Science Foundation Grant ENG 72-04168.

Manuscript submitted Aug. 26, 1976; revised manuscript received Feb. 1, 1977.

Any discussion of this paper will appear in a Discussion Section to be published in the June 1978 JOURNAL. All discussions for the June 1978 Discussion Section should be submitted by Feb. 1, 1978.

Publication costs of this article were assisted by the University of Illinois.

LIST OF SYMBOLS

English characters

c_i	concentration of species i, g-mole/cm^3
$c_{i,s}$	concentration of species i at electrode surface, g-mole/cm^3
$c_{i,\infty}$	concentration of species i in entering stream, g-mole/cm^3
C_i	concentration of species i, dimensionless
$C_{i,s}$	concentration of species i at electrode surface, dimensionless
D_i	diffusion coefficient of species i, cm^2/sec
f	fraction of limiting current, dimensionless
$\mathbf{F}$	Faraday's constant
$i_{o,j}$	exchange current density for reaction j, A/cm^2
j_j	local reaction rate of electrode reaction j, A/cm^2
$\langle j_j \rangle$	average reaction rate on entire electrode surface of reaction j, A/cm^2
j_j^*	local reaction rate of electrode reaction j, dimensionless
J	normalized reaction rate, dimensionless
J_N	normalized reaction rate, dimensionless
L	electrode length, cm
L_1	distance between counterelectrode and tubular electrode, cm
L_2	distance indicated in Fig. 1, cm
M_i	symbol of chemical formula of species i
n_j	number of electrons taking part in reaction j
n_r	arbitrary reference value
$N_{j,i}$	velocity parameter for species i and reaction j, dimensionless
Q	volumetric flow rate, cm^3/sec
r	spatial variable in radial direction, cm
R_g	universal gas constant
R_o	tubular electrode radius, cm
s_i	stoichiometric coefficient of species i
T	temperature, deg
y	$R_o - r$, normal distance from the electrode surface
z	spatial variable in axial direction, cm
z_i	charge number of species i
Z	spatial variable in axial direction, dimensionless

Greek characters

α_j	anodic transfer coefficient of reaction j
β_j	cathodic transfer coefficient of reaction j
β_j	average current density of reaction j, dimensionless
γ_0	aspect ratio, dimensionless
γ_1	dimensionless length ratio
γ_2	dimensionless length ratio
$\Gamma(x)$	complete gamma function of argument x
δ_i	dependence of exchange current density upon composition of species i
κ	electrolyte conductivity, liter/(ohm-cm)$^{-1}$
ν	kinematic viscosity, cm^2/sec
ξ_j	kinetic parameter of reaction j, dimensionless
ρ	spatial variable in radial direction, dimensionless
ϕ	potential in the electrolyte, V
ϕ_m	potential at the tubular electrode entrance nearest the counterelectrode, V
ϕ_r	difference in rest potentials of two electrode reactions, measured at entrance concentration conditions, V
Φ	dimensionless potential

REFERENCES

1. A. A. Mirarefi, Ph.D. Thesis, Department of Chemical Engineering, University of Illinois, Urbana, (1976).
2. R. Alkire and A. A. Mirarefi, *This Journal*, **120**, 1507 (1973).
3. R. Alkire and A. A. Mirarefi, *ibid.*, **124**, 1043 (1977).
4. H. Matsuda, *J. Electroanal. Chem.*, **15**, 109, 325 (1967); *ibid.*, **21**, 433 (1969); *ibid.*, **22**, 413 (1969); *ibid.*, **25**, 461 (1970); *ibid.*, **35**, 77 (1972); *ibid.*, **38**, 159 (1972); *ibid.*, **44**, 199 (1973).
5. L. N. Klatt and W. J. Blaedel, *Anal. Chem.*, **40**, 512 (1968).
6. T. O. Oesterling and C. L. Olson, *ibid.*, **39**, 1543 (1967); *ibid.*, **39**, 1546 (1967).
7. R. Alkire and R. Gould, *This Journal*, **123**, 1842 (1976).
8. R. Alkire and G. Nicolaides, *ibid.*, **121**, 183 (1974).

9. R. Alkire and G. Nicolaides, *ibid.*, **122**, 25 (1975).
10. J. S. Newman, "Electrochemical Systems," chap. 21, Prentice-Hall, Englewood Cliffs, N.J. (1973).
11. R. Cabán and T. W. Chapman, *This Journal*, **123**, 1036 (1976).
12. R. B. Bird, W. E. Stewart, and E. N. Lightfoot, "Transport Phenomena," p. 551, John Wiley & Sons, Inc., New York (1960).
13. T. J. Kessler and R. Alkire, *This Journal*, **123**, 990 (1976).
14. T. Kessler and R. Alkire, *Plating and Surface Finishing*, 22 (September 1976).
15. A. Acrivos and P. L. Chambré, *Ind. Eng. Chem.*, **49**, 1025 (1957).
16. J. S. Newman, "Electrochemical Systems," p. 316, Prentice-Hall, Inc., Englewood Cliffs, N.J. (1973).
17. R. Caban and T. W. Chapman, *This Journal*, To be published.
18. D. C. Carbin and D. R. Gabe, *Electrochim. Acta*, **19**, 645 (1974).
19. J. Sinkovic and D. Leskovsek, *ibid.*, **16**, 2125 (1971).
20. A. M. Baticle, F. Perdu, and P. Vennereau, *C. R. Acad. Sci. (Paris)*, **264**, 12 (1967).

Studies on Flow-By Porous Electrodes Having Perpendicular Directions of Current and Electrolyte Flow

Richard Alkire* and Patrick K. Ng*,[1]

Department of Chemical Engineering, University of Illinois, Urbana, Illinois 61801

ABSTRACT

An engineering analysis was carried out on a packed-bed electrochemical reactor in which the electrolyte flowed in the axial direction and current flowed in the radial direction. Experimental measurements with a sectioned porous electrode were conducted to measure the axial current distribution both at and below the limiting current. The experiments involved deposition of copper onto stacks of copper screens with acidified copper sulfate electrolyte. Although the presence of flow channeling caused the mass transfer coefficient to be less than the value reported in the literature, an empirical correlation was established for estimating the mass transfer coefficient. The reactor system gave polarization curves which indicated that the exchange current density was 0.067 mA/cm^2 in 0.001M $CuSO_4$ + 1.5M H_2SO_4. Comparison between axial current distribution data and theory was made with respect to collection efficiency, axial current distribution, electrode polarization, and total current. Agreement was found for a range of reactors having various geometric dimensions, porosities, flow rates, and reactant concentrations. The theory was used to generate criteria for estimating the volumetric reaction rate, as well as for estimating conditions under which the perpendicular configuration reactor gives higher volumetric reaction rates than when the current and electrolyte flow in parallel directions.

By flowing reactants through porous electrodes, it is possible to achieve both high mass transfer rates and large surface areas for electrochemical reaction. Because of limitations on electrolyte conductivity, however, electrical current may not be able to penetrate deep into the porous bed, so that much of the porous electrode may thereby be inactive and, depending upon the potential distribution, reaction selectivity may be poor. That is, the porous electrode may not be effective if it is too thick when viewed from the direction of the counterelectrode.

In many applications of flow-through porous electrodes it is also necessary to provide an adequate residence time by matching the flow rate to the bed length in the direction of flow. Any locally nonuniform flow, or channeling, would be detrimental to the attainment of the desired residence time and would also affect the desired high mass transfer rate. Channeling effects are usually minimized by using uniformly porous beds which are thick when viewed along the direction of fluid flow.

When the direction of fluid flow and electrical current are parallel, then a dilemma can arise in choosing an electrode thickness which balances the need for a uniform potential distribution against the need to avoid channeling. Indeed, in the case of dilute systems of low electrolyte conductivity, there may be no acceptable middle ground whatsoever. Alternatively, when the directions of electrical current and electrolyte flow are perpendicular, then the electrode can often be designed to obtain simultaneously a uniform potential distribution and an adequate residence time. That is, the electrode can be fabricated so that it is thin, as seen by the counterelectrode, and long, as seen by the flowing fluid. The distribution of potential in the "perpendicular" configuration is inherently more complex than in the "parallel" configuration.

The purpose of this investigation was to develop a better understanding of the perpendicular configuration which would assist in engineering design and scale-up. Experiments on direct measurement of the current distribution were performed under a wide range of controlled conditions. A theoretical model was developed for comparison with experimental data, and was used to determine conditions under which the perpendicular configuration should provide a higher volumetric reaction rate than the parallel configuration.

Literature Review

The different concepts and techniques currently used for enhancing mass transport in electrochemical systems have been reviewed recently (1, 2), and porous electrodes in both parallel and perpendicular field orientations were included. A summary of porous electrode studies applicable to battery systems is also available (3). In addition to the publications cited in these review articles, several other studies have been reported on flow-by porous electrodes having the perpendicular field configuration. A fuel cell system of flowing redox solution is under development for pro-

* Electrochemical Society Active Member.
[1] Present address: Allied Chemical, Industrial Chemical Division, Solvay, New York 13209.
Key words: current distribution, copper removal, porous electrode, channeling, flow cell.

viding electrical power storage (4). Electroanalytical applications have been reported for the separation and analysis of halide ions (5), and for the analysis of free cyanide ions (6). Industrial cells involving flow-by porous electrodes include the Nalco process for tetraethyl lead (7) and the Phillips process for hydrocarbon fluorination (8). A du Pont patent utilizes a series of flow-by electrodes to accomplish removal of heavy metals from effluent streams, and the system has been demonstrated in pilot plant studies (9). A similar cell configuration has been used for electroorganic synthesis reactions and for reduction of hexavalent chromium (10). Experimental studies to date have clarified the over-all behavior of flow-by porous electrode systems. In view of the range of possible industrial applications, a detailed experimental program involving current distribution studies was carried out in order to develop an improved basis for modeling flow-by electrodes (11).

Methods for theoretical prediction of porous electrode behavior were reviewed thoroughly [see Ref. (3)]. There is only one fundamental analysis known for the flow-by perpendicular configuration (12). That model assumes plug flow of electrolyte so that conditions experienced by a fluid packet moving through the porous bed were similar to those experienced during unsteady-state operation of a stagnant porous electrode (13). The model (12) did not include a local mass transfer resistance within the packed bed and was therefore not applicable to limiting current conditions. As reported in what follows, the model has been expanded upon in order to incorporate mass transfer processes which occur under the limiting current condition (11).

Apparatus

The cylindrical electrolysis cell was fabricated from Plexiglas components as shown schematically in Fig. 1. The electrode under study, the cathode, was located in the annular region between the cylindrical anode and the insulating outer wall. The sectioned cathode was constructed from copper screens which were precisely punched out and stacked in the annular region. Electrode sections of equal size were made by insulating groups of screens from each other with a single layer each of filter paper and nylon scarf. Electrical connection to each section was made through small holes drilled through the outer cell wall and fitted with compression gaskets. A 30 gauge copper contact wire was woven into one of the screens in each section. A porous glass annulus was placed downstream from the sectioned electrode to reduce channeling effects. When the cell collar was screwed down, the cathode was compressed by action of the thin-walled piston. Additional holes in the outer wall were drilled to accommodate a reference electrode capillary and a plastic syringe for withdrawing electrolyte samples.

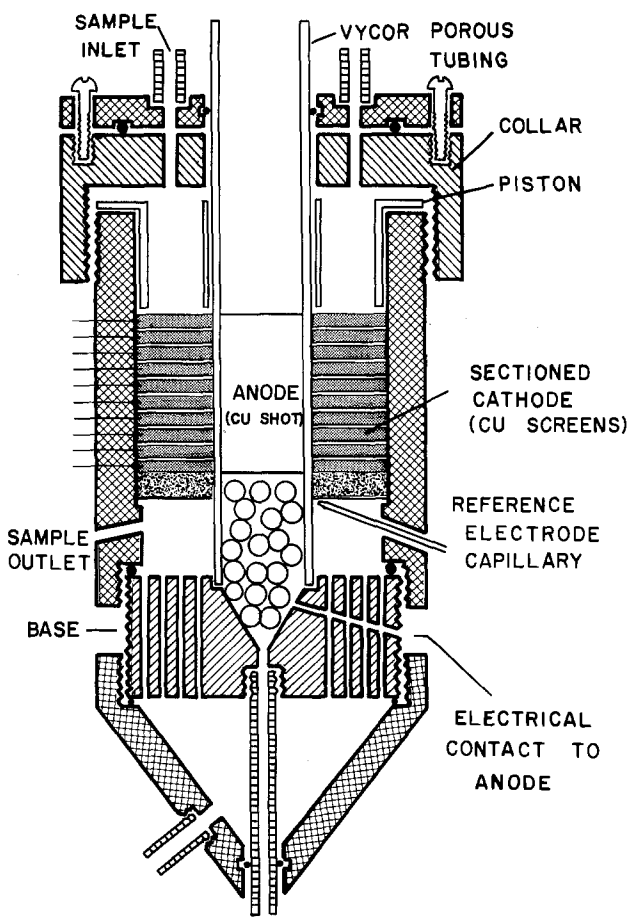


Fig. 1. Segmented porous electrode flow cell, cross-sectional view.

A porous Vycor® tube (Corning No. 7930) separated the cathode and anode compartments. The conductivity of the Vycor® tube filled with electrolytic solution was measured with a four point system and was found to be 0.04 $(\Omega cm)^{-1}$. Because the reference electrode was positioned at the outer periphery of the cell separator, the low conductivity of the separator had no effect on the performance of the sectioned cathode under investigation.

The cylindrical anode was a dumped bed of copper shot (average particle diam 0.05 cm) held between two copper screens and supported on a bed of glass spheres. Electrical contact was made with a copper wire which passed through the solution outlet tube. Auxiliary polarization measurements on the individual electrodes indicated that when the cathode operated at the limiting current, the anode polarization was negligible in comparison with the cathode polarization.

The separate gravity-driven circuits used for anolyte and catholyte flow were constructed from glass components with Tygon connections which had been leached prior to use. The anolyte flow rate was maintained at a sufficiently high level that it did not affect the current distribution in the cathode. The catholyte flow rate was measured with precision rotameters (Gilmont no. 2-5). The overhead catholyte reservoir was fitted within a vacuum device which maintained a constant head independent of the solution level in the reservoir. By this method, the catholyte flow rate remained steady to within 1% during the course of any given experiment.

A potentiostatic power supply (Wenking no. 68TS-3 or 70TS-1) was used to control the cathode potential with respect to a $Hg/Hg_2SO_4/1.5M\ H_2SO_4$ reference electrode. The cell current was monitored with a potentiostatic recorder (Sargent-Welch SRG). Individual section currents were detected with a multichannel zero-resistance operational amplifier device (built in-house) and displayed on a multipoint potentiostatic recorder (Leeds and Northrup Speedomax X). When polarization curves were measured, the potentiostat was driven with a linear ramp generator (built in-house) with display on a X-Y recorder (Houston Instruments no. 2000).

Experimental Procedures

The electrolytic solution used in this study was copper sulfate in sulfuric acid solution, prepared from reagent grade chemicals. Deionized water was distilled once in a tin-lined still and had a conductivity of 4×10^{-6} $(\Omega cm)^{-1}$. Fresh electrolytic solution was placed over clean copper shot to achieve equilibration with Cu(I), and was then deaerated under nitrogen prior to use. Above 0.003M the copper concentration was determined with a spectrophotometer (Beckman Model B); below 0.003M, the neocuproine method was used (14).

The copper screens (Unique Wire Weaving Company) were scrubbed in trichloroethylene, soaked in a hot phosphate/metasilicate solution, pickled in warm acidified ferric sulfate, etched in a mixture of nitric and sulfuric acid, and rinsed in distilled water. The electrolysis cell was assembled under water to avoid

trapped bubbles, placed in the flow circuit, and flushed with copious quantities of deaerated electrolytic solution.

The flow rate was adjusted and the electrical circuit was energized to the desired applied potential. After reaching steady state (usually in 3-4 residence times) the cell current, applied potential, and individual section currents were recorded. The applied potential was then increased and the process repeated. The exit solution concentration was determined from a 5 ml sample of electrolyte which was slowly withdrawn through the downstream syringe while keeping the flow rate constant. The flow rate was then adjusted to a new value and the entire procedure was repeated.

In this fashion, 150 experiments were carried out to refine the cell design and to obtain data under controlled conditions for comparison with theoretical calculations. After several such runs, the cell was disassembled and new electrodes were prepared. It was found that plugging of the porous cathode occurred, for example, upon passing 3500C through twelve 100 mesh screens having an annular flow cross-sectional area of 8.21 cm^2. The life of an electrode assembly was therefore purposefully restricted so as to avoid effects of changing electrode structure.

Theoretical

The mathematical model outlined in this study extends our earlier work by including a mass transfer coefficient to account for behavior at limiting current conditions. Figure 2 illustrates the geometry of the electrolysis cell under consideration. The porous flow-by electrode of interest is annular in shape, bounded on the outside by an insulating wall and on the inside by a separator and cylindrical counterelectrode. In the macroscopic model given below, the discrete structure of the porous bed is not taken into account except through average properties, and the heterogeneous electrode reaction is written as though it were a homogeneous reaction in the species conservation equation. Whereas the average electrolyte flow is in the z direction, it is clear that the microscopic flow field around particles is actually three dimensional. In a similar manner, the flow of current is nominally in the radial direction, although, at a microscopic level, the potential field is actually three dimensional. A theoretical analysis of the microscopic (three-dimensional) variations in potential and solution flow is not necessary for an engineering analysis. The model given below characterizes only the macroscopic nature of the current and velocity flows, which are approximately perpendicular, so that the differential equation can be solved by a numerical analog of the separation of variables technique. Several assumptions have been made concerning electrode operation in order to simplify mathematical treatment: (*i*) the porous electrode is highly conductive and has a uniform porosity and specific surface area which do not change during electrolysis; (*ii*) electrolysis proceeds under isothermal steady-state conditions, with steady plug flow of electrolyte in the z direction; (*iii*) a single reversible electrode reaction occurs; (*iv*) a supporting electrolyte is present which suppresses migration of reacting species, and axial diffusion is negligible; (*v*) current flows in the solution phase solely in the r direction.

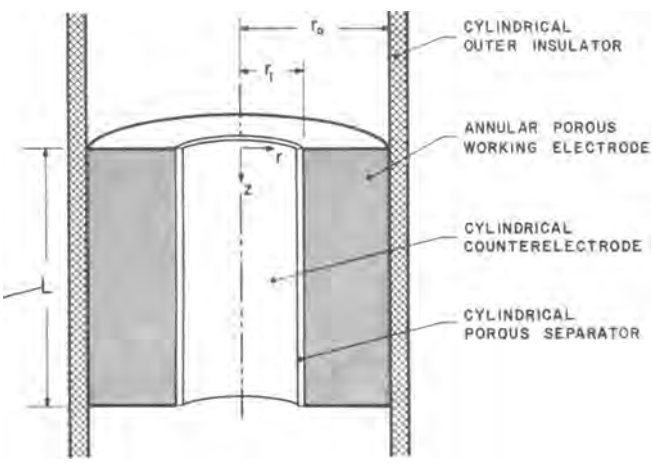


Fig. 2. Geometry and coordinate system used in the theoretical analysis.

The stoichiometry of the electrochemical reaction is defined by

$$\sum_i s_i M_i^{z_i} = ne \qquad [1]$$

In this study, the electrochemical reaction is copper deposition from divalent cupric. Under steady-state conditions, the species conservation equation for copper ion is

$$\nabla \cdot (D\nabla c - vc) = \frac{a\nu_r}{n\mathbf{F}} j \qquad [2]$$

where the source term corresponds to the electrochemical reaction rate which, for the metal deposition system studied here, is

$$j = i_o \left\{ e^{\frac{\alpha_a n\mathbf{F}}{RT}\phi} - \left(\frac{c^s}{c^b}\right) e^{-\frac{\alpha_c n\mathbf{F}}{RT}\phi} \right\} \qquad [3]$$

$\phi(y)$ is the potential difference between a reference electrode and the working electrode that would be measured by placing a Cu/Cu(II) reference electrode in an electrolyte having the composition of the inlet solution and connecting that reference electrode by a capillary to the solution adjacent to the working electrode surface at position y. Because of internal mass transfer limitations, the reactant concentration at the electrode surface, c^s, may be different from the concentration in the core of the flowing electrolyte, c. The two concentrations are related by the mass transfer coefficient

$$j = \frac{n\mathbf{F}k}{\nu_r}(c - c^s) \qquad [4]$$

In the electrolyte phase, the potential field obeys Ohm's law so that the conservation of charge equation is

$$\nabla^2\phi = \frac{a}{\kappa} j \qquad [5]$$

The boundary conditions used in the model are chosen to correspond closely to the experimental conditions described in following sections. At the inlet to the porous electrode, the reactant concentration is uniform. At the inner boundary of the annular electrode, the potential is held constant and the separator membrane is impermeable to the reactant species. The outer boundary of the electrode is an insulator. The equations corresponding to these boundary conditions are given below in dimensionless form in Eq. [12].

The equations of the model were made dimensionless by defining the following quantities

$$C = \frac{c}{c_r} \qquad C^s = \frac{c^s}{c_r}$$

$$R = \frac{r - r_i}{r_o - r_i} \qquad Z = \frac{z}{r_o - r_i}$$

$$\Phi = \frac{n\mathbf{F}\phi}{RT} \qquad J = \frac{(r_o - r_i)aj}{i(z)} \qquad [6]$$

where

$$i(z) = \frac{a}{r_i}\int_{r_i}^{r_o} rj\,dr \qquad [7]$$

As a consequence, the following dimensionless parameters were found

$$\xi = \frac{nFa(r_o - r_i)^2 i_o}{\kappa RT} \qquad \chi = \frac{a(r_o - r_i)^2 i_o}{nFc_r D}$$

$$\zeta = \frac{v_z(r_o - r_i)}{D} \qquad \Gamma = \frac{n^2F^2kc_r a(r_o - r_i)^2}{\kappa RT}$$

$$\beta(Z) = \frac{inF(r_o - r_i)}{\kappa RT} \qquad L = \frac{r_i}{r_o - r_i} \qquad [8]$$

$$\gamma = \frac{c^b}{c_r}$$

The dimensionless equations which describe the model are

$$\zeta \frac{\partial C}{\partial Z} = \frac{\partial^2 C}{\partial R^2} + \frac{1}{R + L}\frac{\partial C}{\partial R} - \frac{\chi\Gamma}{\xi}(C - C^s) \qquad [9]$$

$$\frac{d^2\Phi}{dR^2} + \frac{1}{R + L}\frac{d\Phi}{dR} = \frac{\Gamma}{\nu_r}(C - C^s) \qquad [10]$$

$$\Gamma(C - C^s) = \nu_r\xi\left\{ e^{\alpha_a\Phi} - \frac{C^s}{\gamma}e^{-\alpha_c\Phi} \right\} \qquad [11]$$

with boundary conditions

$$\text{at } Z = 0 \qquad C = \gamma$$

$$\text{at } R = 0 \qquad \frac{\partial C}{\partial R} = 0, \quad \Phi = \Phi_a$$

$$\text{at } r = 1 \qquad \frac{\partial C}{\partial R} = \frac{\partial \Phi}{\partial R} = 0 \qquad [12]$$

The coupled nonlinear model equations were solved by a numerical technique. Integration was carried out in a step-wise fashion along the axial direction beginning at the upstream surface. At each axial step, linearized finite difference equations were written in the Crank-Nicolson symmetric form. The trial matrix was inverted (15) with successive iterative correction until convergence was gained. Complete details may be found in Ref. (11).

The physical significance of the dimensionless parameters in Eq. [8] has been discussed in previous publications (12, 16). ξ contains the ratio i_o/κ and thereby indicates the relative importance of electrolyte resistance and charge-transfer resistances. In the absence of mass transport limitations, ξ is the parameter that controls electrode behavior; ξ can be regarded as a linear polarization parameter. When $\xi < 1$, the conductivity is sufficiently high that the secondary current distribution is uniform. The parameter χ indicates the relative importance of diffusion and charge-transfer resistances insofar as it contains the ratio i_o/D. In the absence of convection or internal mass transfer effects, a large value of χ indicates that slow diffusional transport will lead to nonuniform current distributions in the radial direction. The relative importance of convective transport to diffusive transport of reactants is embodied by the parameter ζ. If ζ is large, the current distribution along the axial direction will be uniform since the supply of reactants will be sufficient to insure against depletion. For lower values of ζ, axial distributions will be nonuniform owing to reactant depletion.

The parameter Γ is a dimensionless mass transfer coefficient, and did not appear in our earlier flow-by analysis in which internal mass transfer limitations were not taken into account. If Γ has a small value, then the surface concentration can be much less than the concentration in the core of the fluid "fingers" which flow through the porous electrode. Equation [11] can be used to estimate conditions under which internal mass transfer effects are appreciable. For high cathodic potentials where the back-reaction is negligible, rearrangement gives

$$C^s = \frac{\gamma}{1 - \frac{\nu_r\xi}{\gamma\Gamma}e^{-\alpha_c\Phi}} \qquad [13]$$

Equation [13] indicates that if

$$\left| \frac{\nu_r\xi}{\gamma\Gamma}e^{-\alpha_c\Phi} \right| << 1 \qquad [14]$$

then $C^s \simeq \gamma$ and our earlier analysis may be used. On the other hand, if

$$\left| \frac{\nu_r\xi}{\gamma\Gamma}e^{-\alpha_c\Phi} \right| >> 1 \qquad [15]$$

then $C^s < \gamma$ and internal mass transfer limitations must be taken into account.

Comparison of Theory with Experiment

The physical properties of the acid copper system are listed in Table I along with the geometrical properties of the porous cathodes. The wire diameters and thickness of stacked screens were measured with a micrometer. The porosity and specific surface area of the screens was calculated by the method of Armour and Cannon (17); the porosity was also measured by weighing. The value of n was determined from the copper concentration difference caused by passage of current, and was found to be 2.0 to within experimental accuracy of 2%. The electrolyte conductivity was measured with a bridge (Leeds and Northrup, no. 4959). Experiments included variation of mesh size of the electrode screen (100, 150, and 200 mesh), electrode length (0.156-2.1 cm), electrode width (0.5-1.1 cm), solute concentration (0.007-0.019M), solution flow rate (0.3-51.0 ml/min), and applied potential (20-800 mV).

Polarization curves for a typical experiment are given in Fig. 3. At low flow rates, the limiting current plateau covered a potential span of about 300 mV in this example. Under conditions of high flow rates, the limiting current plateau was not observed.

Behavior at limiting current.—The dependence of limiting current upon velocity is shown in Fig. 4 for electrodes having the same lengths and mesh size but three different annular widths. At low flow rates, all reactants which enter the reactor are consumed; the straight line on Fig. 4 corresponds to the equation

$$i_{max} = nFc^b v \qquad [16]$$

The collection effectiveness at the limiting current density, defined as

$$\text{collection effectiveness} = CE = \frac{i_{lim}}{nFc^b v} = \frac{c^b - c^l}{c^b} \qquad [17]$$

has the value of unity for the low flow rate (<3 ml/min) range in Fig. 4. At higher flow rates, the collection effectiveness is less than unity at the limiting current owing to restricted mass transport within the porous electrode. Experimental measurement of the limiting current density and the exit concentration

Table I. System properties

Electrodes Mesh no.	Wire diameter (cm)	Screen thickness (cm)	Porosity	Specific surface area (cm^{-1})
100	0.0109	0.0206	0.61	143.0
150	0.0066	0.0140	0.69	188.3
200	0.00533	0.0117	0.67	245.0

Other system parameters
n = 2 g-eq/g-mole
κ = 0.51 $(\Omega\ cm)^{-1}$
D = 5.0 × 10^{-6} cm^2/sec (23)
ν = 1.035 × 10^{-2} cm^2/sec (23)
i_o = 6.7 × 10^{-5} A/cm^2
α_a = 0.75
α_c = 0.25

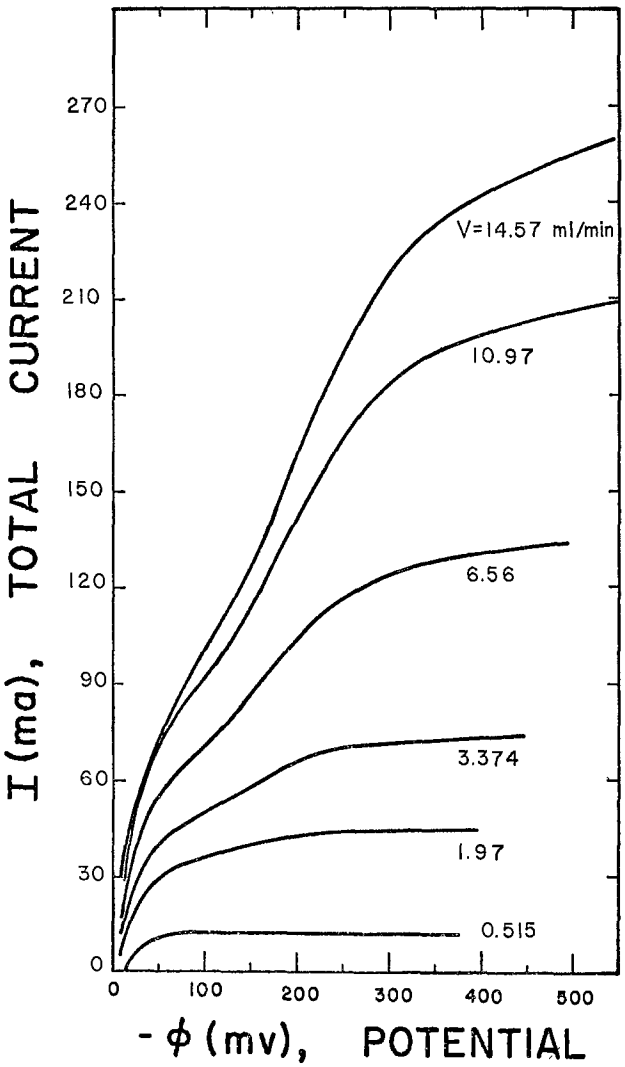


Fig. 3. Effect of catholyte flow rate on cathode polarization. (100-mesh screens, $c^b = 0.0072M$, $r_o - r_i = 0.496$ cm, $l = 0.246$ cm.)

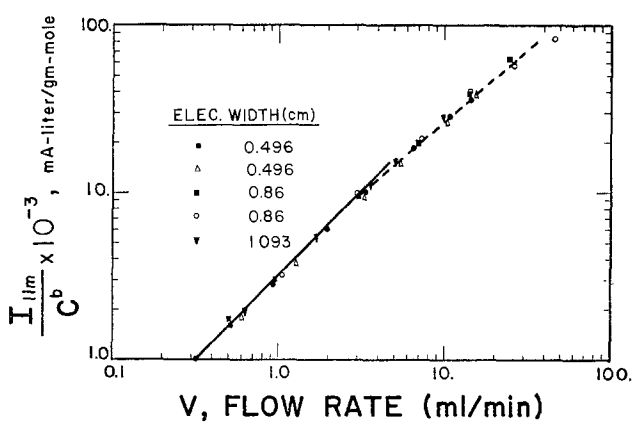


Fig. 4. Effect of catholyte flow rate on cathode limiting current. (100-mesh screens, $l = 0.246$ cm.)

were found by Eq. [17] to be in agreement to within 5%. These data indicate that internal mass transfer limitations are present within the porous electrode. Because the electrode reaction occurs under the limiting current condition without side reactions, the current distribution is controlled solely by the mass transfer characteristics of the packed bed. That is, variation of limiting current with system parameters in this study is qualitatively the same as that observed previously in packed bed reactor systems of different geometric configuration. Therefore, in this study, the mass transfer correlation of Wilson and Geankoplis (18) was used since it had been successful in the parallel flow configuration studied by Alkire and Gracon (16).

Preliminary experiments were conducted in order to demonstrate whether channeling occurred with the porous cathode. For these, prior to cell assembly, the copper screens were silver coated by immersion in a silver cyanide plating solution. After cell assembly, the cathode was operated at the limiting current, the cathode screens were later removed, and the copper deposit was examined. Without the downstream porous glass plate, severe channeling was observed. With the plate in place channeling occurred to a lesser extent. Nevertheless, the screens were more heavily coated with copper along the inner and outer perimeters. Although the channeling effect could perhaps have been further reduced by redesign of the system configuration and reaction chemistry, it was found that the over-all behavior of alternative systems was less amenable to the goal of conducting controlled experiments with known system parameters. As is discussed in detail below, the channeling effect was more pronounced at low than at high flow rates.

Current distribution data for a typical series of experiments are shown in Fig. 5. It is seen that the upstream regions are more reactive to an extent which depends upon the flow rate. At low flow rates, the downstream region of the electrode is unreactive (there being no copper left in the solution) and a collection efficiency of unity is achieved. At high flow rates, the downstream regions are much more reactive, and the collection effectiveness is less than unity. As the flow rate increases the reaction distribution becomes more uniform. Upon comparison of these data with theoretical calculations, two types of discrepancies were observed; at low flow rates the experimental distributions were more uniform than those predicted by the model,

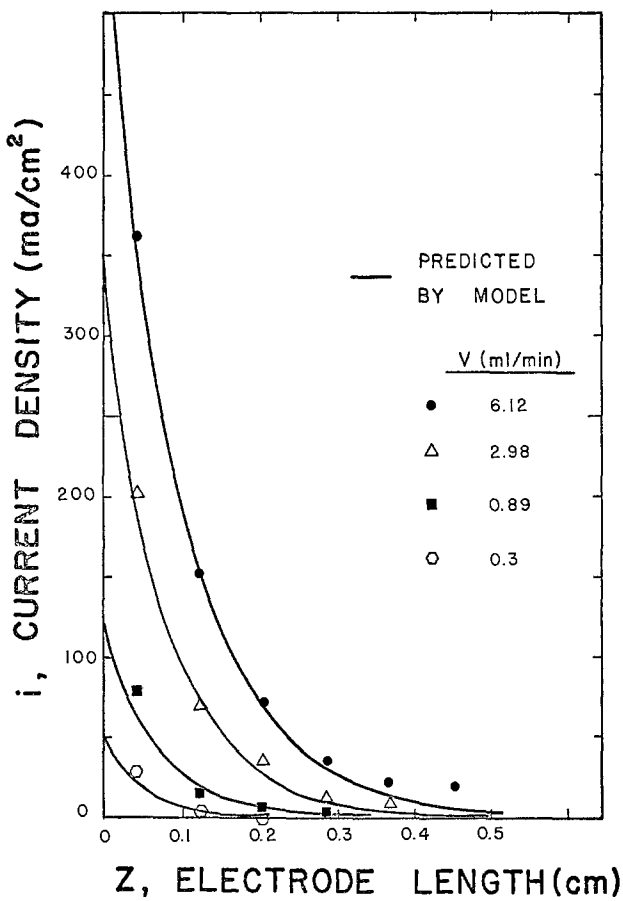


Fig. 5. Axial current distribution measured with segmented porous electrode. (100-mesh screens, $c^b = 0.0188M$, $r_o = r_i = 0.86$ cm, $l = 0.492$ cm.)

while at high flow rates the experimental limiting current was less than that predicted by the model. These discrepancies were attributed to the channeling effect observed in the preliminary experiments mentioned above. Channeling serves to decrease the internal mass transfer coefficient, or effective surface area. Adams *et al.* (19) reported similar circumstances under which channeling apparently served to decrease the effective surface area or mass transfer coefficient.

An empirical method was therefore employed to fit the theoretical model to a single set of limiting current distribution data. Figure 6 shows the correction factor by which the specific surface area in Ref. [18] needed to be multiplied in order that the model fit the predicted limiting current distribution for one electrode. The correction factor depends upon flow velocity and bed porosity as shown. It was found that this single correction was able to fit all limiting current and current distribution data measured for all mesh sizes, electrode widths, electrode lengths, concentrations, and flow velocities studied. For example, the solid lines in Fig. 5 correspond to theoretical results predicted with use of the correction factor. (The data given in Fig. 5 are not the same as those used to obtain the correction factor.) In the same manner, the dashed lines in Fig. 4 correspond to theoretical results predicted with use of the correction factor. The comparisons shown in Fig. 4 and 5 indicate that the correction factor enables one to predict total current and current distribution behavior over the entire range of parameter space studied. At still higher flow rates than those investigated, the data in Fig. 4 would be expected to increase with the cube root of solution velocity.

Electrode behavior under limiting current conditions can depend upon the rate of reactant supply or upon the rate of internal mass transfer. At low velocities, Eq. [16] shows that the limiting current is linearly proportional to the velocity and is independent of the electrode length. Under such conditions, all the entering reactants are consumed within the electrode and the collection efficiency is 100%. The flow rate above which internal mass transfer becomes appreciable may be expressed in dimensionless form as

$$\mathrm{Re}_{cr} = \left[\frac{\Gamma^* d_p \chi^Z}{\mathrm{Sc}(r_o - r_i)} \right]^{3/2} \qquad [19]$$

When the entire porous bed operates under limiting current conditions, the surface concentration of the reactant will be essentially zero throughout the electrode; therefore the radial concentration distribution will be uniform at every axial position in the reactor. For flow rates in excess of Re_{cr}, the axial distributions of concentration and reaction rate are

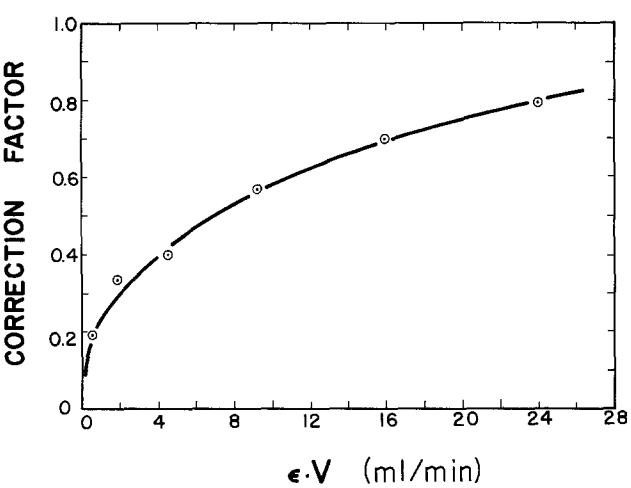


Fig. 6. Factor used in modifying mass transfer coefficient to account for channeling in porous cathode.

$$\frac{\beta(z)}{\Gamma\gamma} \frac{2L\nu_r}{(2L+1)} = C = \gamma e^{-\frac{\chi\Gamma}{\xi} z} = \frac{c^b}{c_r} e^{-\frac{akz}{v}} \qquad [20]$$

In view of the agreement between experiment and theory demonstrated in Fig. 4, it should be recognized that Eq. [20] may be used with confidence in predicting the collection efficiency, provided that the correction factor is used in determining the specific surface area.

Behavior below limiting current.—Current distribution data are given in Fig. 7 for several electrodes having different configurations but having the same values of ξ, χ, and applied potential (50 mV). The four sets of experimental data correspond to different residence times, as obtained by using different electrode lengths and solution flow rates. The data show that the current distribution becomes more nonuniform as the residence time increases. The four sets of data converge at the upstream (left-hand) side of the electrode.

In order to compare data with theoretical calculations, it was necessary to choose the values of ξ and χ which represent the system. The exchange current density for the copper deposition reaction has been variously reported and would, following Newman (20), have the value 0.36 mA/cm² in the 0.009M $CuSO_4$ solution used in this study (with $\alpha_a = 0.75$ and $\alpha_c = 0.25$). The presence of sulfuric acid reduces the exchange current density, as has been found by Cabán and Chapman (21), whose model IV correlation would

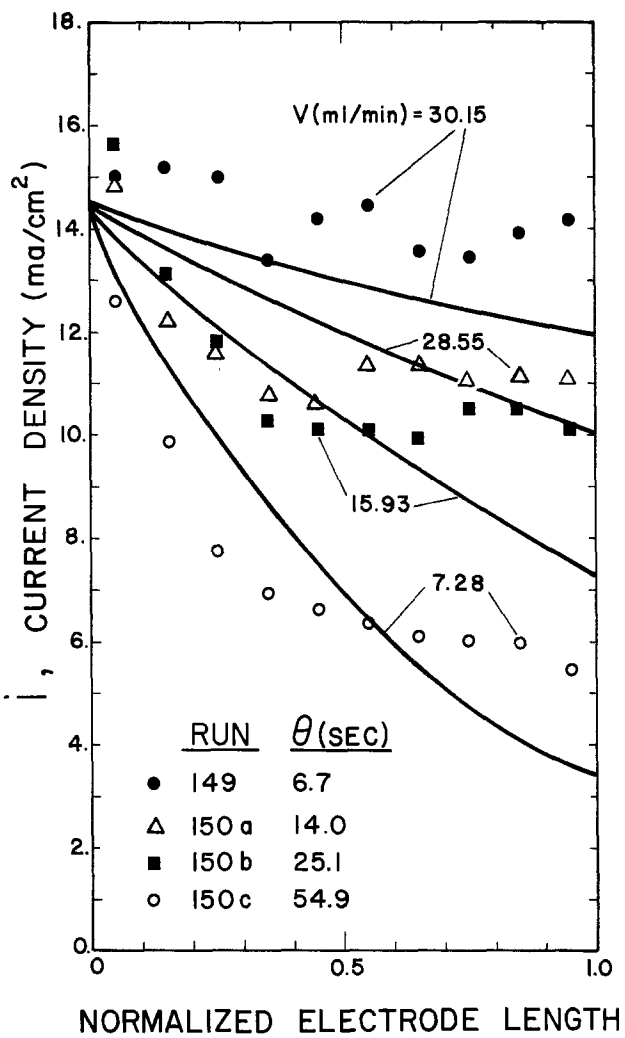


Fig. 7. Axial current distributions measured with segment electrodes under various catholyte flow rates. (100-mesh screens, 50 mV applied, $c^b = 0.0088$M, run 149: $r_o - r_i = 0.496$ cm and $l = 1.04$ cm; run 150: $r_o - r_i = 0.958$ and $l = 2.06$.)

Table II. Comparison of measured cell current with theoretical predictions

Run	Measured (mA)	Predicted (mA)	Deviation (%)
149	135	124	−4.5
150 a	220	226	+2.7
150 b	211	196	−7.1
150 c	139	140	+0.7

indicate the value 0.042 mA/cm² in the 1.5M H_2SO_4 solution (with $\alpha_a = 0.54$ and $\alpha_c = 0.19$). In this study we compared ten sets of packed-bed polarization curves with theoretical calculations made with the values $\alpha_a = 0.75$ and $\alpha_c = 0.25$, and found that the exchange current density of 0.067 mA/cm² gave a good comparison for all packed-bed experimental results. The effect of channeling was not taken into consideration while determining i_0 since the currents were only small fractions of the limiting current, so that mass transport effects were negligible.

Having thus specified ξ and χ on the basis of current-voltage data, calculations were then carried out for determining the current distribution. In these calculations, no adjustment of the mass transfer coefficient was made concerning channeling effects. The results are given by the solid lines in Fig. 7. Comparison between experimental data and theoretical calculations demonstrates agreement to within 15% over the range of cases studied. Table II contains the measured and predicted values of total current for the four cases shown in Fig. 7. It is seen that the model predicts the over-all current to within about 4%.

For the data given in Fig. 7, we compute for the left-hand side of Eq. [14] a value of 0.03, which indicates that the results of our earlier study (12) could be used to predict detailed current distribution behavior. Although the geometry of that earlier work was slightly different from the present study, it seems reasonable to suggest that curvature effects would be relatively unimportant for values of ξ less than 0.5 for which the radial current distribution is relatively uniform. Figure 8 illustrates how the total current passing to the reactor varies with residence time for eight experiments below the limiting current. These experimental data are to be compared with the solid line which was determined in the same manner as had been Fig. 5 of our earlier work. The agreement indicates clearly that the perpendicular configuration model succeeds in predicting experimental behavior to within reasonable engineering tolerances.

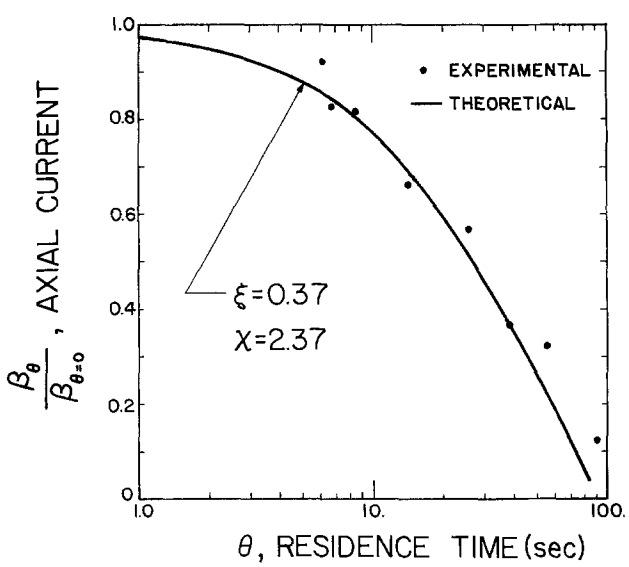


Fig. 8. Dependence of volumetric reaction rate upon residence time. (100-mesh screens, 50 mV applied, $c^b = 0.0088$-0.0096M, $V = 3$-33 ml/min, $l = 1.04$-2.06 cm, $r_o - r_i = 0.496$ cm.)

Discussion

Several aspects of behavior at the limiting current seem worthy of discussion. Consider first the case of operation at high flow rates ($Re > Re_{cr}$) where behavior is controlled by internal mass transfer. In view of the uniform radial current distribution which prevails under limiting current conditions, Eq. [10] may be simplified to

$$\frac{1}{R}\frac{d}{dR}\left(R\frac{d\Phi}{dR}\right) = \frac{\Gamma}{\nu_i}C \qquad [21]$$

Integration between $R = 0$ and $R = 1$ gives the potential drop across the annular width of the electrode

$$\Delta\Phi = \Phi|_{R=1} - \Phi|_{R=0} = \frac{\Gamma\gamma}{4\nu_i}e^{-\frac{\Gamma\chi Z}{\xi\zeta}}\left[(1+2L) - 2(1+L)^2\ln\frac{r_o}{r_i}\right] \qquad [22]$$

By neglecting the curvature terms which give Eq. [22] a complicated appearance, one has

$$\Delta\phi = \frac{n\mathbf{F}kc^b a(r_o - r_i)^2}{\kappa}e^{-\frac{akz}{v}} \qquad [23]$$

This result illustrates that the potential drop across the width of the electrode is largest at the upstream portion and decreases with axial distance downstream since the reaction rate decreases. The radial potential drop across the electrode is only weakly dependent upon the velocity insofar as the mass transfer coefficient varies with the cube root of velocity. Equation [23] may be regarded as the product of a superficial current density ($n\mathbf{F}vc$), with the reciprocal effective conductivity ($1/\kappa$), and an effective penetration depth in the radial direction [$ka(\Delta r)^2/v$)].

Now let us turn to a comparison between the parallel and perpendicular configurations in order to assess the conditions under which one might be preferable to another. As a basis for comparison, we will use the volumetric current density (A/cm³). The reactive regions of the two types of electrodes are confined to the effective depth of penetration as given above for the perpendicular configuration, and by the comments following Eq. [88] of Ref. (3). The volumetric current density over the reactive region is, for the perpendicular configuration

$$\frac{n\mathbf{F}vc^b}{l}e^{-\frac{akl}{v}} \qquad [24]$$

and, for the parallel configuration

$$n\mathbf{F}akc^b e^{-\frac{akl}{v}} \qquad [25]$$

By taking the ratio of Eq. [24] and [25], one finds that the perpendicular configuration gives the greater volumetric reaction rate under the criterion

$$\frac{v}{akl} > 1 \qquad [26]$$

which is a ratio of residence times. By the criterion of Eq. [26] it is seen that the perpendicular field is the preferred choice when design considerations call for high velocities and coarse packing (low specific surface area and low mass transfer coefficients). Equation [26] also indicates a basis for choosing the length of a perpendicular field which cannot be exceeded if the volumetric reaction rate is to remain advantageous. Other bases for comparison could be chosen, such as pumping costs, etc., and it would seem worthwhile to pursue these in future studies.

Conclusions

An advantage often claimed for electrochemical processes is their high degree of selectivity for a particular reaction product. Although high reaction rates are possible with porous electrode reactors, substantial potential variations may occur within the reactor which adversely affect the desired selectivity. The principal advantage of the perpendicular configuration is that it permits large residence times under conditions where channeling effects can be substantially reduced, while simultaneously permitting a uniform potential distribution. The type of systems where its use would be particularly advantageous would be ones in which the reactants are dilute and the conductivity is low, so that not only mass transport is important, but the potential distribution is also important for maintaining reaction selectivity.

Whereas the behavior of reactors with perpendicular flow of current and electrolyte is inherently more complex than the parallel configuration, a mathematical model has been shown to be capable of correlating experimental data at and below the limiting current for systems of various electrode lengths and widths, solution velocities, concentrations, and specific surface areas. In order to account for the presence of channeling effects, it was necessary to develop a correlation for the mass transfer coefficient. Whereas that channeling correlation was adequate over the range of variables investigated here, it is unlikely that it could be used in flow cells of different design or scale.

Should the need arise, the model could be formulated to account for other reaction rate behavior, including multiple electrode reactions and sequences involving simultaneous homogeneous chemical reactions (22). The approximate method of solution, by separation of variables, provides an accurate representation of the reactor provided that axial dispersion or channeling effects are absent (12). The model could not, however, be easily extended to account for axial dispersion or channeling effects in any fundamental manner; a more correct two-dimensional analysis would be exceedingly difficult. The approximate procedure, used here for handling channeling effects by modification of the mass transfer coefficient, provides a simple yet accurate procedure for pursuing engineering aspects of the reactor analysis problem.

Acknowledgments

This study constituted partial fulfillment of requirements for a Doctor of Philosophy degree in the Department of Chemical Engineering, University of Illinois, Urbana-Champaign, Illinois. Research costs were supported by a National Science Foundation Grant ENG 72-04168.

Manuscript submitted Aug. 30, 1976; revised manuscript received Feb. 1, 1977.

Any discussion of this paper will appear in a Discussion Section to be published in the June 1978 JOURNAL. All discussions for the June 1978 Discussion Section should be submitted by Feb. 1, 1978.

Publication costs of this article were assisted by the University of Illinois.

LIST OF SYMBOLS

English characters

a	specific surface area, cm^2/cm^3
c	concentration of copper ions, g-mole/cm^3
c^b	inlet concentration of copper ions, g-mole/cm^3
c^l	concentration at exit, g-mole/cm^3
c_r	arbitrary reference concentration, 10^{-3} g-mole/cm^3
C	concentration of copper ions, defined in Eq. [6], dimensionless
D	diffusion coefficient, cm^2/sec
d_p	characteristic diameter of screen electrode, cm
F	Faraday's constant
i	current density, A/cm^2
i_o	exchange current density under inlet concentration conditions, A/cm^2
I	total current, A
j	local reaction rate, A/cm^2
J	local reaction rate, defined in Eq. [6], dimensionless
k	mass transfer coefficient, cm/sec
l	electrode length, cm
L	ratio defined in Eq. [8]
M_i	chemical symbol for species i
n	number of electrons taking part in reaction
Q	mass flow rate, g/cm^2-sec
r	spatial variable in radial direction
r_i	inner radius of annular electrode, cm
r_o	outer radius of annular electrode, cm
Re	Reynolds number
Sc	Schmidt number
T	temperature, °K
v_z	electrolyte velocity within porous electrode, cm/sec
z	spatial variable in axial direction, cm
Z	spatial variable in axial direction, defined in Eq. [6], dimensionless

Greek characters

α_a	anodic transfer coefficient
α_c	cathodic transfer coefficient
$\beta(Z)$	current density, defined in Eq. [8], dimensionless
γ	inlet concentration of copper ions, defined in Eq. [8], dimensionless
Γ	mass transfer coefficient, defined in Eq. [8], dimensionless
Γ^*	value of Γ when Re $= 1.0$
ϵ	void fraction of packed-bed electrode
ζ	flow rate, defined in Eq. [8], dimensionless
θ	residence time, $\epsilon l/V$, sec
κ	electrolyte conductivity, $(\Omega\text{cm})^{-1}$
μ	electrolyte viscosity, g/cm-sec
ν_i	stoichiometric coefficient of species i
ξ	reaction rate constant, defined in Eq. [8], dimensionless
ϕ	potential in electrolyte, V
Φ	potential in electrolyte, defined in Eq. [6], dimensionless
χ	diffusion parameter, defined in Eq. [8], dimensionless

REFERENCES

1. R. B. MacMullin, *This Journal*, **120**, 135C (1973).
2. R. W. Houghton and A. T. Kuhn, *J. Appl. Electrochem.*, **4**, 173 (1973).
3. J. Newman and W. Tiedemann, *AIChE J.*, **21**, 25 (1975).
4. L. H. Thaller, Paper presented at the 90th Intersociety Energy Conversion Engineering Conference, San Francisco, California, August, 1974.
5. R. E. Meyer and F. A. Posey, *J. Electroanal. Chem.*, **49**, 377 (1974).
6. R. E. Meyer and P. M. Lantz, *ibid.*, **61**, 155 (1975).
7. D. G. Braithwaite, U.S. Pat. 3,391,067 (1968).
8. H. M. Fox, F. N. Ruehlen, and W. V. Childs, *This Journal*, **118**, 1246 (1971).
9. J. M. Williams and K. B. Keating, *DuPont Innovation*, **6**, 6 (1975); J. M. Williams, U.S. Pat. 3,859,195 (1975).
10. P. M. Robertson, P. Cettou, F. Schwager, and N. Ibl, Private communication.
11. P. K. Ng, Ph.D. Dissertation, University of Illinois at Urbana-Champaign, Ill. (1976).
12. R. Alkire and P. K. Ng, *This Journal*, **121**, 95 (1974).
13. E. A. Grens and C. W. Tobias, *Ber. Bunsenges Phys. Chem.*, **68**, 236 (1964).
14. A. R. Gahler, *Anal. Chem.*, **26**, 577 (1954).
15. J. Newman, *Ind. Eng. Chem. Fundam.*, **7**, 514 (1968).
16. R. Alkire and B. Gracon, *This Journal*, **122**, 1594 (1975).
17. J. C. Armour and J. N. Cannon, *AIChE J.*, **14**, 415 (1968).
18. E. J. Wilson and C. J. Geankoplis, *Ind. Eng. Chem. Fundam.*, **5**, 9 (1966).
19. G. B. Adams, R. P. Hollandsworth, and D. N. Bennion, *This Journal*, **122**, 1043 (1975).
20. J. S. Newman, "Electrochemical Systems," p. 316, Prentice-Hall, Inc., Englewood Cliffs, New Jersey (1973).
21. R. Caban and T. W. Chapman, *This Journal*, To be published.
22. R. Alkire and R. Gould, *ibid.*, **123**, 1842 (1976).
23. D. C. Carbin and D. R. Gabe, *Electrochim. Acta*, **19**, 645 (1974).

The Electroreduction of Air in Trifluoromethanesulfonic Acid Monohydrate

A. A. Adams[1] and R. T. Foley*

Department of Chemistry, The American University, Washington, D.C. 20016

and H. J. Barger, Jr.*

U.S. Army Mobility Equipment Research and Development Center, Fort Belvoir, Virginia 22060

ABSTRACT

The electroreduction of air on a platinum electrode has been investigated in trifluoromethanesulfonic acid monohydrate as part of a study involving the hydrocarbon-air fuel cell. At 135°C, the open-circuit potential of the air electrode was 1.135V (*vs.* the dynamic hydrogen electrode) and the limiting current density was higher than that observed in phosphoric acid under the same conditions. Current density-potential diagrams were constructed over the temperature range of 95°-135°C. The activation energy for the process is low; 1500-4000 cal mole^{-1}.

It has been observed that electrooxidation and electroreduction reactions in direct or indirect hydrocarbon-air fuel cells are influenced by the electrolyte (1, 2). Phosphoric acid has become the accepted acid electrolyte for most fuel cell systems developed in this country for terrestrial applications because of its stability at elevated temperatures and the ease of removal of heat and water. However, when used in direct oxidation hydrocarbon-air fuel cells, phosphoric acid has several undesirable characteristics which are demonstrated by short life and low performance. These shortcomings have been attributed to adsorption of the acid anion and low solubility of air and hydrocarbons.

The investigation of trifluoromethanesulfonic acid monohydrate was based on a consideration of the properties of the material and on the characteristics considered desirable for a hydrocarbon-air fuel cell electrolyte (3). Trifluoromethanesulfonic acid monohydrate has a high conductivity and low vapor pressure in the temperature range of 100°-150°C. The compound melts at 33°C and distills without decomposition at 217°-218°C (4). Trifluoromethanesulfonic acid itself is stable to a least 350°C and its aqueous solution is stable to at least 275°C (5). In the work in our laboratory, individual volumes of the monohydrate have been exposed to temperature cycling, potential cycling, and/or current pulsing, at 135°C, for several months without deteriorating. After several weeks at 135°C some darkening of the monohydrate is observed, but the crystallization temperature is not lowered, suggesting that any decomposition that does occur must be very slight.

The electrochemical oxidation of propane and of hydrogen was found to be significantly enhanced in trifluoromethanesulfonic acid monohydrate when compared with results obtained in 85% phosphoric acid. In the development of hydrocarbon-air and hydrogen-air fuel cells the performance of the air electrode obviously is of as much importance as the performance of the anode. The objective of this research was to investigate the electrochemical reduction of air in trifluoromethanesulfonic acid monohydrate and compare the results with those obtained for the reduction of air in 85% phosphoric acid.

Experimental

Apparatus.—The electrochemical cell and electronic apparatus have been described previously (3).

Materials.—Trifluoromethanesulfonic acid monohydrate was prepared from trifluoromethanesulfonic acid (obtained from 3M Company, Minneapolis, Minnesota), and triply distilled water by the method described by Gramstad and Hazeldine (5). Fisher reagent-grade phosphoric acid was purified and diluted to 85% volume by the technique previously described (3). Water-pumped air was obtained from Air Products, Incorporated. High purity helium (99.995%), obtained from the Matheson Company, was deoxygenated by passing through a bed of copper turnings at 400°C. The gases were humidified to maintain H_3PO_4 concentration at 85% for all cell operating temperatures; the gases were not humidified in those experiments wherein $CF_3SO_3H \cdot H_2O$ was used as the electrolyte.

Experimental technique.—In the development of the current-potential curves, a platinum mesh electrode (99.9%) of approximately 4 cm^2 "real" surface area was utilized. The "real" surface area of the electrode was determined electrochemically by the method used by Brummer (6), and the current density values reported are based on this real surface area. Current density potential diagrams were constructed for the reduction of air at several temperatures from 23° to 135°C, with most of the work from 95°-135°C. In the electrochemical experiments helium was used as a background or nonreactive gas. In performing the current *vs.* potential runs, a potential value was set and the system allowed to equilibrate for 5 min before the current value was recorded.

In conducting an experiment, the air which was previously brought to temperature was bubbled over the electrode. The system used a freely flowing gas which allowed the air to saturate the solution at any flow rate. Due to the design of the electrochemical cell there was no pressure increase at the air electrode. A flow rate of 50 ml/min was arbitrarily selected for the polarization experiments following preliminary experiments wherein the open-circuit potential and the current density were measured as a function of flow rate. This dependency for the trifluoromethanesulfonic acid monohydrate electrolyte is shown at 135°C in Fig. 1. Above a flow rate of 20 ml/min the open-circuit potential attained a steady value of 1.13V; below this flow rate the potential was lower and erratic. The current density was not greatly altered by a change in flow rate, varying only 6 μA/cm^2 from a flow rate of 3 to 40 ml/min.

Results and Discussion

The results for the electroreduction of air on a smooth platinum electrode at 95°, 115°, and 135°C are

* Electrochemical Society Active Member.
[1] Present address: U.S. Army Mobility Equipment Research and Development Center, Fort Belvoir, Virginia 22060.
Key words: fuel cell, electrolyte, hydrocarbon-air fuel cell, hydrogen-oxygen fuel cell.

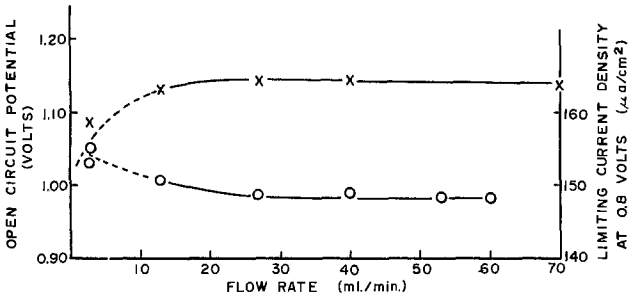


Fig. 1. Influence of air flow rate on the open-circuit potential and limiting current density of the air electrode in trifluoromethanesulfonic acid monohydrate. X = open-circuit potential (volts); O = limiting current density at 0.8V (μA/cm^2).

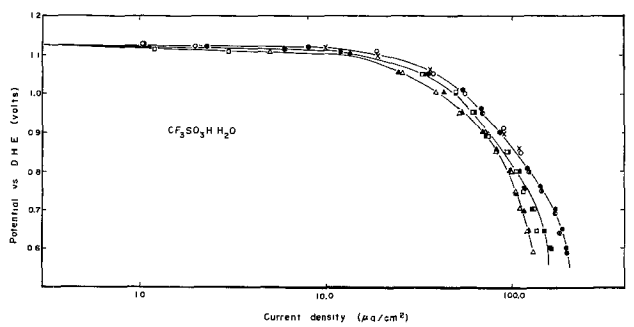


Fig. 2. Electroreduction of air on a smooth platinum electrode in trifluoromethanesulfonic acid monohydrate; at 95°C, △, ▲; at 115°C, □, ■; at 135°C, O, X, ●.

summarized in Fig. 2. These data are also indicative of the precision of the polarization runs, as experiments conducted on three different days at 135°C, on two different days at 115°C, and on two different days at 95°C are given. The curves presented in Fig. 2 represent a minimum of 10 individual polarization runs at any temperature. The potentials reported are on the "dynamic hydrogen electrode" scale (7). The current density values at a set potential increased with temperature as would be expected. Table I gives the open-circuit potentials and the limiting current densities for four temperatures.

The polarization curves of Fig. 2 are characterized by an extended range of reversibility and a short Tafel region, *i.e.*, the current density range in which the overpotential-log current density plot is linear. From the polarization curve an exchange current density of 1×10^{-5} A cm^{-2} may be extrapolated. The activation energy for the temperature range was measured at different potentials from the open-circuit potential (Fig. 3). As the potential moves from the open-circuit potential the activation energy decreases, reaches an extremely low value, and then increases. These energies are given in Table II. Over the whole range the activation energy is low, suggesting a diffusion-controlled reaction.

In Fig. 4 the electroreduction of air in trifluoromethanesulfonic acid monohydrate is compared with that in 85% phosphoric acid at 135°C. Also plotted are some recent results reported by Srinivasen (8) at 80°C for the oxygen electrode in the two electrolytes. The two

Table I. Open-circuit potentials and limiting current densities for the air electrode in trifluoromethanesulfonic acid monohydrate

Temperature (°C)	Open-circuit potential (*vs.* dynamic hydrogen electrode) (Volts)	Limiting current density (μA)
23	1.130	5
95	1.123	135
115	1.130	170
135	1.135	190

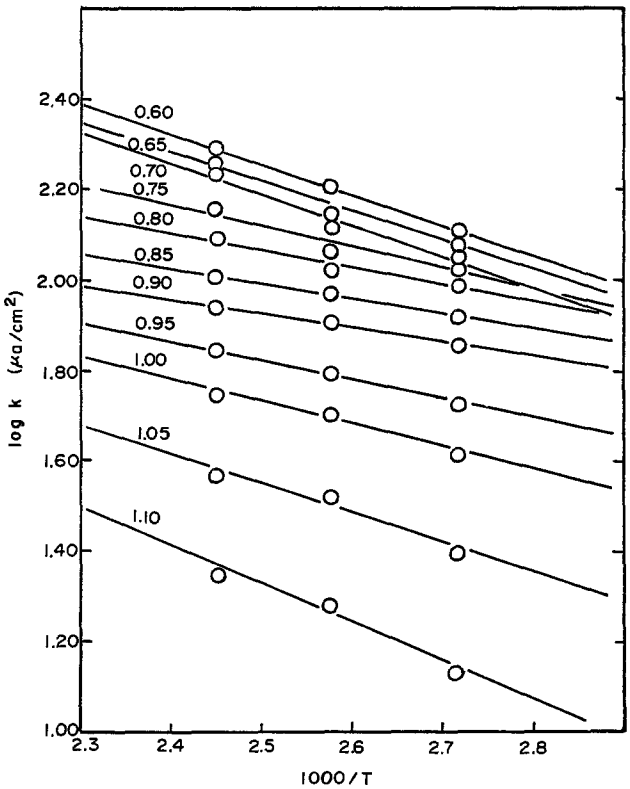


Fig. 3. Temperature dependence of the limiting current for the electroreduction of air on a smooth platinum electrode in trifluoromethanesulfonic acid monohydrate.

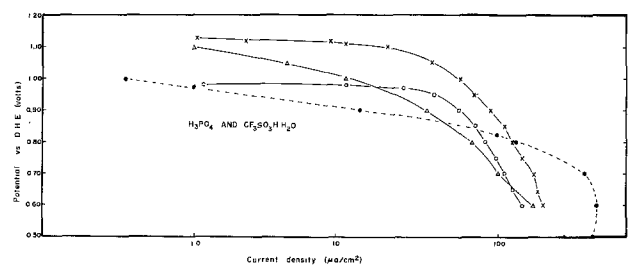


Fig. 4. Comparison of the electroreduction of oxygen and air in $CF_3SO_3H \cdot H_2O$ and H_3PO_4. △, O_2 at 80°C in $CF_3SO_3H \cdot H_2O$ (Ref. 8); X, air at 135°C in $CF_3SO_3H \cdot H_2O$; O, at 80°C in H_3PO_4 (Ref. 8); ●, air at 135°C in H_3PO_4.

studies are in agreement with respect to the higher open-circuit voltage in the sulfonic acid monohydrate of about 150 mV. However, at 135°C the crossover of the polarization curves observed at 0.86V at 80°C is not observed.

The higher current densities observed in the electroreduction of air in $CF_3SO_3H \cdot H_2O$, as compared with those observed in 85% H_3PO_4, following similar observations on the oxidation of propane and H_2, are of vital interest, not only from the practical fuel cell

Table II. Activation energy for the electroreduction of air at various potentials

Potential (*vs.* DHE, V)	ΔV from OCP (mV)	Activation energy (cal mole^{-1})
1.10	35	3885
1.05	85	2933
1.00	135	2283
0.95	185	1862
0.90	235	1373
0.85	285	1510
0.80	335	1693
0.75	385	2119
0.70	435	3125
0.65	485	2974
0.60	535	3157

viewpoint, but also from basic theoretical consideration. Several explanations seem possible, including changes in diffusion coefficients, concentration gradients, and those other factors that are incorporated in the customary limiting current density equation. However, the magnitude of the increase in current density values suggests other effects. It is our present contention that the real explanation lies in the increase in the electroactive area of the electrode in the acid monohydrate electrolyte. It is well accepted that in the adsorption process, which is a necessary preliminary step in the electrode reaction, anions and water molecules compete with the reactant species (propane, H_2, or O_2), for active sites on the electrode surface. It is believed that in the trifluoromethanesulfonic acid monohydrate electrolyte both the acid anion and the molecular "free" water adsorption is less than that in H_3PO_4.

Conclusions

The open-circuit potential for the air electrode in $CF_3SO_3H \cdot H_2O$ is approximately 150 mV closer to the thermodynamic reversible potential than the potential observed in phosphoric acid. At all potentials, at a given temperature, the current density is higher for the air reduction reaction in $CF_3SO_3H \cdot H_2O$ than in H_3PO_4. It is concluded from this and preceding work (4) that the performance of a direct hydrocarbon-air or hydrogen-air fuel cell utilizing this electrolyte would be substantially greater than that of the corresponding cell utilizing phosphoric acid.

In connection with the employment of trifluoromethanesulfonic acid monohydrate as a fuel cell electrolyte, other physical properties such as vapor pressure, the conductivity of H_2O-solutions, and the corrosion of materials that would be used for fuel cell construction, are being measured. It has been observed that the monohydrate wets Teflon, which would create a problem in the employment of Teflon-bonded electrodes in this electrolyte.

Acknowledgment

This work was supported by the U.S. Army Mobility Equipment Research and Development Center, Fort Belvoir, Virginia, under Contract DAAK02-72-C-0084.

Manuscript submitted Nov. 8, 1976; revised manuscript received April 2, 1977.

Any discussion of this paper will appear in a Discussion Section to be published in the June 1978 JOURNAL. All discussions for the June 1978 Discussion Section should be submitted by Feb. 1, 1978.

Publication costs of this article were assisted by The American University.

REFERENCES

1. E. J. Cairns, in "Hydrocarbon Fuel Cell Technology," B. S. Baker, Editor, p. 465, Academic Press, Inc., New York (1965).
2. E. J. Cairns, in "Advances in Electrochemistry and Electrochemical Engineering," Vol. 8, Charles W. Tobias, Editor, p. 337, Wiley-Interscience, New York (1971).
3. A. A. Adams and H. J. Barger, Jr., *This Journal*, **121**, 987 (1974).
4. A. A. Adams and R. T. Foley, Interim Technical Report no. 5, Contract no. DAAK02-72-C-0084, U.S. Army MERDC, Fort Belvoir, Virginia, (1974).
5. T. Gramstad and R. N. Haszeldine, *J. Chem. Soc.*, **1957**, 4069.
6. S. B. Brummer, *J. Phys. Chem.*, **69**, 562 (1965).
7. J. Giner, *This Journal*, **111**, 376 (1964).
8. S. Srinivasen and F. J. Salzano, Paper presented at the ERDA-EPRI Fuel Cell Seminar, Palo Alto, California, June 29-July 1, 1976.

Technical Notes

Source of Oscillations in the Anode Current during the Potentiostatic Pitting of Aluminum

C. B. Bargeron and R. B. Givens

Applied Physics Laboratory, The Johns Hopkins University, Laurel, Maryland 20810

Oscillations or pulsations in the anode current during the pitting corrosion of aluminum have been observed by several investigators (1-4). Included in the discussion of this observation has been speculation as to the source of such oscillations. Wood, Sutton, Richardson, Riley, and Malherbe (1) speculated that, among other possibilities, bubble evolution might sometimes be a source of current fluctuations. Videm (2) devoted considerable attention to the current fluctuations and used patterns of pulse generation to distinguish between pit growth and other breakdown events. He discussed several sources of pulse generation including that of gas egress from pits, however, it was finally concluded that the pulsing current was a result of a cyclic oxidation process rather than that the cycles observed were caused by gas evolution. Galvele, De Micheli, Muller, de Wexler, and Alanis (3) mention current oscillations also and note that they are diminished by the presence of a surface active agent. Hübner and Wranglen (4) felt the oscillations were due to the formation and blockage of pits. Current oscillations have also been reported for other metals, for example, high purity zinc (5) and stainless steels (6). Although not mentioning current pulses, numerous other workers have noted gas egress from pits in Al. Using gas chromatography, Hübner and Wranglen (4) identified the gas as H_2.

In this communication we report observations which positively correlate current pulses with gas egress through the oxide cover over a single active pit in aluminum. Earlier work by Masing and Altenpohl (7) on a specimen with more than one active pit reached a similar conclusion regarding the origin of such oscillations. Because there was only one pit in our investiga-

Key words: aluminum, pitting, corrosion, current oscillations, gas egress.

tion, a direct relationship between current fluctuations and gas bubble activity was firmly established.

The aluminum used in this investigation had a purity of 99.999% and was obtained from the Alfa Products Division of the Ventron Corporation. A typical impurity analysis supplied with the 0.25 mm foil was 3 ppm Si, 2 ppm Fe, 1 ppm Cu, and others less than 1 ppm. An annealed disk of this foil was electropolished in a 10% perchloric acid-ethanol mixture for 2 min at +20V at about 24°C. After a thorough rinse with deionized water it was anodized galvanostatically at 1 mA/cm² in 3% ammonium tartrate solution to +60V, which provides an oxide film about 800Å thick according to capacitance measurements and previous literature (8). The counterelectrode was Type 304 stainless steel. The aluminum disk was again washed abundantly in deionized H_2O and placed in a Teflon holder with exposed area of about 0.30 cm². The electrode was then mounted face up in a stainless steel beaker filled with 1M KCl. The beaker served as the auxiliary electrode. A saturated calomel electrode (SCE) was employed as the reference electrode. Using a water-immersible objective, a light microscope was focused on the specimen.

The pitting was performed potentiostatically at −0.1V SCE. Effort was expended in minimizing the noise in the potentiostat circuitry. The anode current was amplified, then both recorded and made audible via a loudspeaker system. After the pitting process the specimen was investigated in a scanning electron microscope (SEM) with an energy dispersive x-ray analysis accessory system.

After several attempts, a specimen was obtained on which there was only one pit for a period of 15-20 min. The presence of the pit was indicated by an abrupt increase in the anode current. The pit location was characterized by vigorous bubble evolution. The nature of the bubbling changed spontaneously from time to time. At times the bubbles were small and escaped through the oxide film in rapid succession. Infrequently, for this specimen, a bubble would adhere to the oxide over the pit near the center and grow quite large. Regardless of bubble rate and size, motion of the bubbles was directly correlated with the audible current noise. At one point the bubble rate slowed to about one per second. The current record during this interval is reproduced partially in Fig. 1a. This string of oscillations continued at about this rate for 328 pulses, which were both seen as bubbles and heard over the speaker as amplitude oscillations. The leading edge of each pulse correlated with a bubble breaking loose from the surface and the trailing edge corresponded to the formation and growth of a bubble at the oxide exit. For comparison, a part of the current record during a period when smaller bubbles were escaping from the pit at a higher rate is shown in Fig. 1b. The entire observation was a convincing display of the one-to-one relationship of gas egress to current oscillations.

After the potentiostat was disconnected, a pumping device was used to direct a jet of electrolyte at the specimen surface. Based on transient light reflections, it appeared that the oxide film was floating perhaps in a torn condition over the pit. After the sample was dried as described above, it was examined in the SEM. A stereo pair[1] of micrographs taken at 20 keV beam voltage is presented in Fig. 2. Although not shown completely in this stereo pair, most, if not all, of the oxide is still present. During pit growth the oxide substantially occluded the pit from the bulk electrolyte. Thus it also impeded the bubbles from leaving the pit immediately. Hence the bubble grows under the oxide until it can escape. In so doing it reduces the area available for ionic conductivity noticeably. This explains the relatively large amplitude of the current oscillations. The above discussion is confined to current pulses observed during pit growth. Shortly before the large increase of current, rather regular oscillations of a much smaller magnitude were also recorded. No source of these pulses was observed.

[1] The pit can be viewed in stereo by placing an opaque sheet of material perpendicular to the page along the line dividing the two micrographs and allowing the eyes to merge the two images. With some luck the sheet is not necessary. However, a stereoscopic viewer is best, if available.

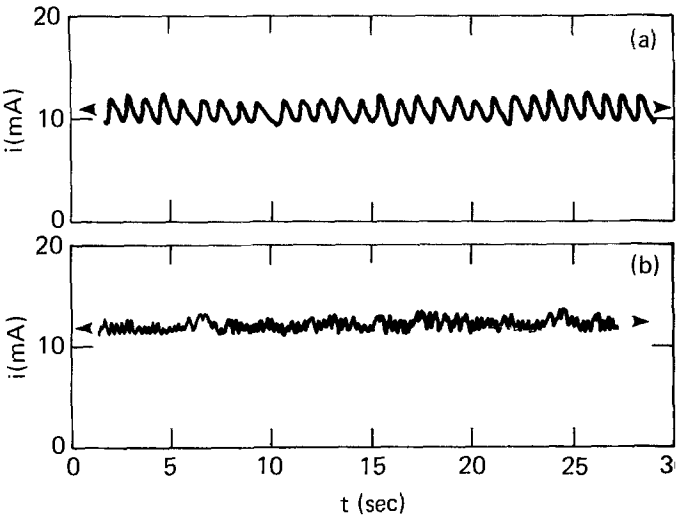


Fig. 1. Partial reproductions of the current vs. time record: (a) a portion of the record during which bubble egress was relatively slow but very uniform, 328 pulses of the type shown were recorded during this interval; (b) a portion of the record during which the bubbles were smaller but escaped at a higher rate.

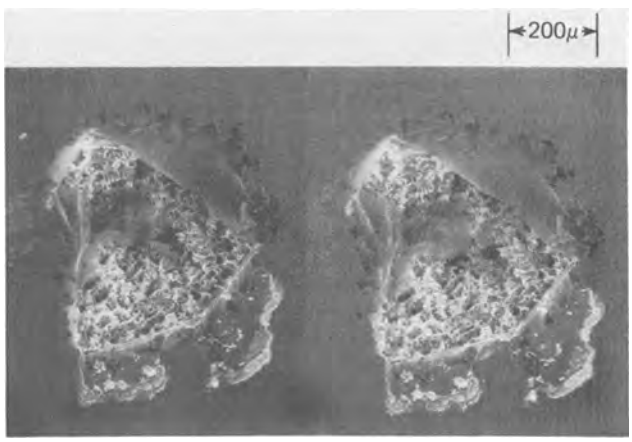


Fig. 2. A stereo pair of micrographs of the pit. The left-hand member was taken at a tilt angle of 37°, and the right-hand at 30°. The beam voltage was 20 keV.

Acknowledgments

The authors acknowledge useful discussions with R. L. Hudson during the course of the experiments.

This work was supported by the Naval Sea Systems Command, U.S. Department of the Navy under Contract N00017-72-C-4401.

Manuscript submitted Feb. 24, 1977; revised manuscript received March 21, 1977.

Any discussion of this paper will appear in a Discussion Section to be published in the June 1978 JOURNAL. All discussions for the June 1978 Discussion Section should be submitted by Feb. 1, 1978.

Publication costs of this article were assisted by The Johns Hopkins University.

REFERENCES

1. G. C. Wood, W. H. Sutton, J. A. Richardson, T. N. K. Riley, and A. G. Malherbe, in "Localized Corrosion," B. F. Brown, J. Kruger, and R. W. Staehle, Editors, p. 526, NACE-3, Houston (1974).
2. K. Videm, Kjeller Report, KR-149, 67 (1974).
3. J. R. Galvele, S. M. De Micheli, I. L. Muller, S. D. de Wexler, and I. L. Alanis, in "Localized Corrosion," B. F. Brown, J. Kruger, R. W. Staehle, Editors, p. 580, NACE-3, Houston (1974).

4. W. Hübner and G. Wranglen, *Scand. Corros. Congr.*, Bulletin no. 35 (1964).
5. M. M. Lotlikar and D. E. Davies, Proceedings of the Third International Congress on Metallic Corrosion, p. 167, Moscow (1966).
6. Z. Szklarska-Smialowska and M. Janik-Czachor, *Br. Corros. J.*, **4**, 138 (1969).
7. G. Masing and D. Altenpohl, *Z. Metallkd.*, **43**, 433 (1952).
8. G. Hass, *J. Opt. Soc. Am.*, **39**, 532 (1949).

Brief Communications

The Response of an Electrochromic Display with Viologens on a Potential Step

J. Bruinink and P. van Zanten

Philips Research Laboratories, Eindhoven, The Netherlands

The response of an electrochemical process on a potentiostatic voltage pulse is known from literature, *e.g.*, (1). There the current was expected to be proportional to $t^{-1/2}$, a diffusion-limited process. However, in a recent paper (5) it was concluded that convection predominates this diffusion limitation already after 100 msec. Since it could be expected that the display resistance might also play some role, the current-time response of an electrochromic device on a voltage step was investigated.

The electrochromic material we used was an aqueous solution of 10^{-2}M diheptyl viologen dibromide (ABr_2) and 0.3M potassium bromide. The reduction reaction is schematically given by $A^{2+} + e \rightleftarrows A^{+\cdot}$, followed by the chemical reaction $A^{+\cdot} + Br^- \rightleftarrows ABr\downarrow$ where a violet colored layer is deposited (2, 3). The electrochemical cell used had a vertically positioned transparent SnO_2 electrode (10 Ω/□, 0.4 cm²) as a working electrode, a standard Ag/AgCl electrode with a Luggin capillary as a reference electrode, and a large Pt foil separated from the cell solution by a glass frit as a counterelectrode. This three electrode system was driven by a potentiostat (Wenking St 72), and the voltage pulse was delivered by a single shot pulse generator. The response of the current to a voltage step was recorded with a storage oscilloscope.

The current-time response measured with several potential steps is shown in Fig. 1. The observed current-time transient can be divided into three regions. First is the time region directly after $t = 0$. In this region a peak current is observed which is mainly due to double layer charging. This time interval, which varies from 10 to 40 msec depending on the overpotential, was omitted in Fig. 1. The observed charging phenomena are beyond the scope of this paper and, therefore, are not to be discussed here.

In the second region the current is nearly constant, especially at lower voltages. In the third and last region the electrode process becomes diffusion limited and the current shows the familiar $t^{-1/2}$ behavior. This observed current-time response can be explained by considering the current-time relationship for a diffusion-limited electrode process (1) for the reaction $M^+ + e \rightleftarrows M\downarrow$. In this approximation, the coupled chemical reaction is assumed to be reversible

$$I = nAFC^* \left(\frac{D}{\pi t}\right)^{1/2} \left\{1 - \exp\left(\frac{nF}{RT}\eta\right)\right\} \quad [1]$$

Key words: resistance, convection, current-time response.

where I is the current; n, the number of electrons; A, the surface area; F, the Faraday constant; C^*, the bulk concentration of A^{2+}; D, the diffusion coefficient; t, the time; R, the gas constant; T, the absolute temperature; and η, the overpotential. In the absence of ohmic drop, the overpotential η is given by $\eta = E - E_e$, in which E is the applied potential and E_e is the equilibrium potential of the deposited layer in contact with the electrolyte ($\eta < 0$). In our case $E_e = -0.435$V (Ag/AgCl). If an appreciable ohmic drop R_Ω is present, the overvoltage η is given by $\eta = E - E_e + IR_\Omega$ ($I > 0$). Now η has become a function of the current I and Eq. [1] is no longer an explicit relation for I. At small values of η the exponent of Eq. [1] can be expanded in a series, and after neglecting the terms of higher order the following expression for the current is obtained

$$I = \frac{E - E_e}{P\sqrt{t} - R_\Omega} \quad \text{with} \quad P = -\frac{RT\pi^{1/2}}{n^2F^2AC^*D^{1/2}} \quad [2]$$

At short times, where $R_\Omega >> P\sqrt{t}$, the current in this constant current region ($I = I_0$) is approximately given by $I_0 = -(E - E_e)/R_\Omega$. So R_Ω can be determined from this region. The values of R_Ω obtained in this way are in good agreement with values from chronopotentiometric measurements. In our case with transparent SnO_2 electrodes, a representative value for R_Ω

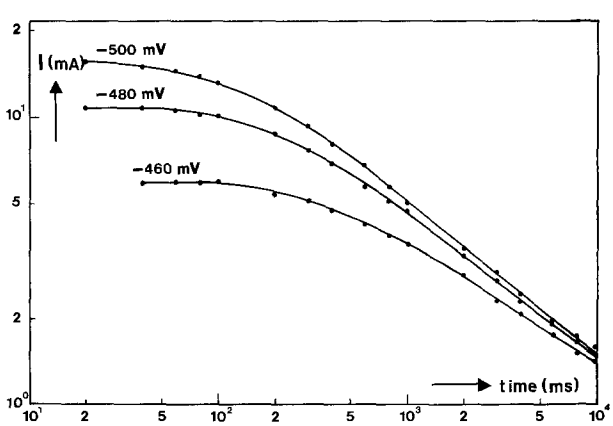


Fig. 1. Current-time behavior at several values of E (vs. Ag/AgCl). 10^{-2}M diheptyl viologen dibromide and 0.3M potassium bromide. SnO_2 electrodes, $R_\Omega = 40\Omega$.

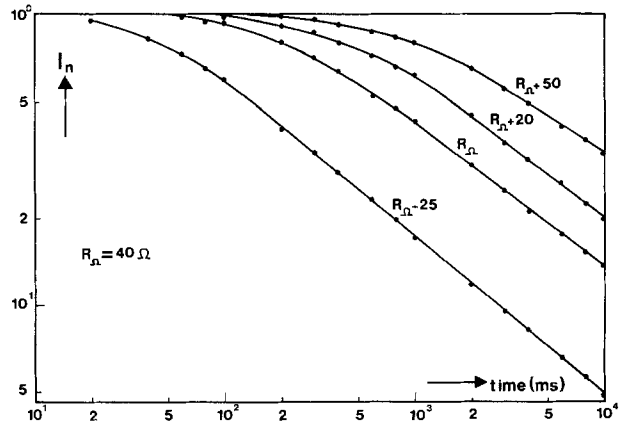


Fig. 2. Normalized current-time behavior with $E = -480$ mV (Ag/AgCl) at several values of R_Ω. 10^{-2}M diheptyl viologen dibromide and 0.3M potassium bromide. SnO_2 electrodes.

is 40Ω. The time during which the current remains nearly constant is, among other factors, determined by the value of the ohmic resistance R_Ω. This is clearly demonstrated in Fig. 2, where the dimensionless parameter $I_N = I/I_o$ is introduced. R_Ω, as given in Fig. 2, is the internal resistance between the reference and working electrode, which is due mostly to the electrode resistance, but also to the electrolyte resistance.

In further experiments, the resistance was increased by inserting an external resistance at the working electrode; decrease of the resistance was obtained by positive feedback. From Eq. [2] it is clear that at longer times ($P\sqrt{t} >> R_\Omega$) the current is diffusion limited: $I = (E - E_e)/P\sqrt{t}$. This behavior is illustrated in Fig. 1 and 2. The value of D can now be determined and is found to be about 7×10^{-6} cm^2 sec^{-1}. This is in good agreement with values obtained from chronopotentiometric measurements. Furthermore, it appears that no distortion by convection takes place up to 10 sec. This is in good agreement with theory (4), which states that the time t_c after which convection distorts the diffusion process is given by $t_c = \delta_N^2/\pi^2 D$, where δ_N is the thickness of the diffusion layer caused by natural convection.

In previous work by Chang and Howard (5, 6) diffusion limitation and convection were indicated as predominant processes in determining the current-time behavior in their electrochromic cells. From the present paper it may be concluded, however, that the current-time response of an electrochromic display due to a voltage step is governed by a combination of resistance limitation and diffusion limitation.

In a practical application, *e.g.*, displays with SnO_2 electrodes, the resistance R_Ω is rather high, varying between 50 and 100Ω. As a result a constant current is observed after a potentiostatic voltage step, especially at higher concentrations of the electroactive species. As a consequence, potentiostatic driving during writing can be more simply replaced by constant current driving. The contrast that can be obtained in a certain time interval in which resistance limitation plays a role, however, is lower than in the case of diffusion limitation only. Enhancement of the maximum attainable contrast can be achieved by means of current driving where the applied current varies proportional to $t^{-1/2}$. In this way the same contrast as with potentiostatic driving without ohmic drop can be obtained in the same time interval.

Manuscript submitted Oct. 4, 1976; revised manuscript received Dec. 18, 1976.

Any discussion of this paper will appear in a Discussion Section to be published in the June 1978 JOURNAL. All discussions for the June 1978 Discussion Section should be submitted by Feb. 1, 1978.

Publication costs of this article were assisted by Philips Research Laboratories.

REFERENCES

1. H. R. Thirsk and J. A. Harrison, "A Guide to the Study of Electrode Kinetics," Academic Press, Inc., New York (1972).
2. C. J. Schoot, P. T. Bolwijn, H. T. van Dam, R. A. van Doorn, J. J. Ponjeé, and S. van Houten, *SID J.*, 4, 146 1973).
3. H. T. van Dam and J. J. Ponjeé, *This Journal*, **121**, 1555 (1974).
4. K. J. Vetter, "Electrochemical Kinetics," p. 216, Academic Press, Inc., New York (1967).
5. I. F. Chang and W. E. Howard, *IEEE Trans. Electron Devices*, **ed-22**, 1749 (1975).
6. I. F. Chang and W. E. Howard, *This Journal*, **122**, 956 (1975).

The Potential of the Gold Overlayer on n-GaP Photoelectrodes

R. H. Wilson,* L. A. Harris, and M. E. Gerstner

General Electric Corporate Research and Development, Schenectady, New York 12301

In recent publications, Nakato *et al.* (1, 2) reported that overlayers of Au on n-GaP photoanodes allowed the photodecomposition of water to proceed while suppressing the corrosion of the GaP. These authors described two different types of behavior; type A obtained with slowly evaporated Au, and type B when the Au was evaporated rapidly.

We have reproduced the I-V curves shown by Nakato *et al.* and have extended their results to include direct measurement of the potential of the Au overlayer during the current-voltage scan. Each GaP electrode was prepared as described by Nakato *et al.* and then coated on its front face by an insulating lacquer (Hunt Waycoat negative photoresist) except for a window area about 3 mm diam. After gold was deposited over the entire surface, the sample was pressed onto a layer of silicone rubber surrounding a small (4 mm) aperture in the side of the electrolytic cell. A fine wire between the silicone and the inactive part of the gold overlayer allowed us to connect a high impedance (10^7Ω) voltmeter between the gold and the saturated calomel reference electrode.

The results shown in Fig. 1 are representative of type A behavior obtained with sputtered Au overlayers about 400Å thick. Figure 2 shows typical type B behavior obtained with rapidly evaporated Au films about 300Å thick. Illumination was provided by a 150W high pressure xenon lamp through a neutral filter which reduced the intensity to about that of the sun (roughly 100 MW/cm^2).

The type A behavior is entirely consistent with the interpretation of Nakato *et al.* (2), who postulated an

* Electrochemical Society Active Member.

Key words: photoelectrochemistry, semiconductor electrodes, photoelectrolysis.

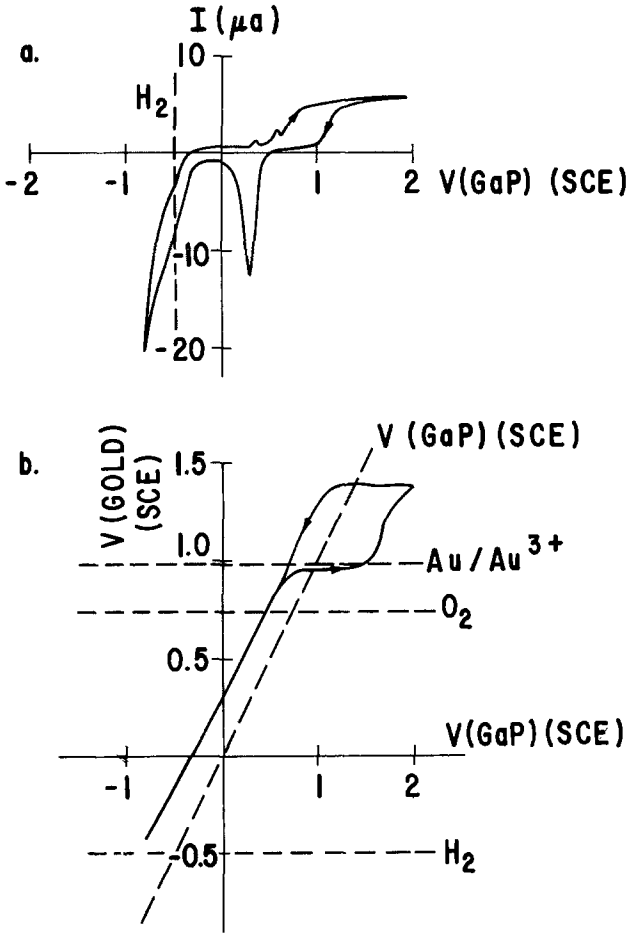


Fig. 1. Type A behavior of 400Å Au film sputtered on n-GaP. Electrolyte is 0.5M K_2SO_4 buffered to pH 4.3. (a) Current-voltage characteristic showing oxidation and reduction waves typical of Au electrodes; (b) potential of Au film with respect to SCE.

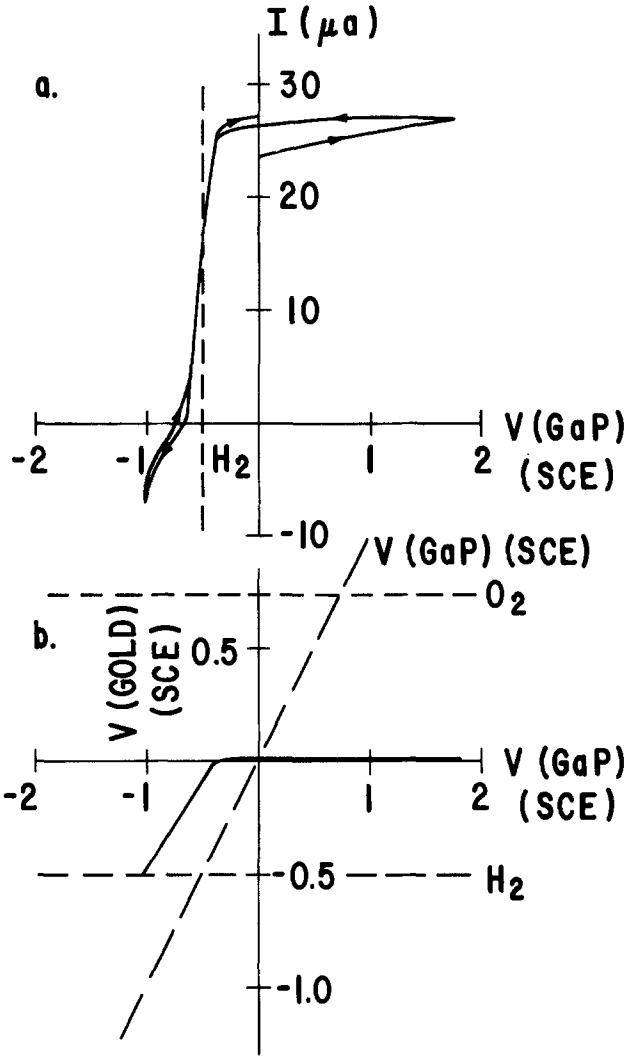


Fig. 2. Type B behavior of 300Å rapidly evaporated Au film on n-GaP. Same electrolyte as for Fig. 1. (a) Current-voltage characteristic; (b) potential of Au film with respect to SCE.

impervious Au layer between the electrolyte and the GaP. The metal-semiconductor interface forms a Schottky photodiode which is in series with a normal gold electrode. As shown in Fig. 1, the Au potential differs from that of the GaP by a constant amount until it becomes limited by an oxidation reaction with the electrolyte (either the decomposition of water or the oxidation of Au).

The above interpretation is confirmed by a second experiment in which such a sample was mounted in a cell, without electrolyte, where it could be exposed to light. The connection from the Au film was brought to a plain metallic gold electrode in contact with the electrolyte of a second cell, thus reproducing the postulated arrangement of a Schottky diode (dry) in series with a conventional electrolytic cell. The I-V curves and measurements of Au potential reproduced the type A results of Fig. 1 in all essential respects.

The type B behavior shown in Fig. 2 duplicates the I-V curves of Nakato *et al.* (2), but we failed to observe any gas evolution except for the blisters formed under the gold film as noted by those workers. It is apparent from Fig. 2 that the Au potential never reaches a value at which water can be decomposed. Indeed, it is difficult to see how at this low potential the Au can be involved in the reaction responsible for the current flow.

The observed type B current is most probably due to a corrosion reaction of the GaP with the electrolyte. This view is consistent with the blister formation, the porous nature of rapidly evaporated metal films, and the tendency of type A behavior to switch to type B after some period of time in contact with the electrolyte.

Further confirmation of this view is afforded by an experiment in which bare GaP is made to exhibit I-V curves resembling those of type B behavior. This is done by reducing the pH of the 0.5M K_2SO_4 electrolyte from about 4.3 to about 3.5 and reducing the light intensity by a factor of 2 or more. At higher intensities, the current is actually decreased after formation of a blocking layer. There is an apparent balance between the rate of formation of a blocking layer governed by light intensity and its dissolution, governed by the pH of the electrolyte.

It has been suggested (3) that if H_3O^+ ions are formed at the GaP surface, their diffusion away from the surface is retarded by the porous gold film, and then the pH near the surface is decreased. Thus the gold film promotes type B behavior by reducing the light intensity and by preventing the formation of a barrier layer through an increase in local acidity.

A more detailed exposition of these observations will follow in a later paper.

Manuscript received Feb. 4, 1977.

Any discussion of this paper will appear in a Discussion Section to be published in the June 1978 JOURNAL. All discussions for the June 1978 Discussion Section should be submitted by Feb. 1, 1978.

Publication costs of this article were assisted by General Electric Company.

REFERENCES

1. Y. Nakato, T. Ohnishi, and H. Tsubomura, *Chem. Lett.*, 883 (1975).
2. Y. Nakato, K. Abe, and H. Tsubomura, *Ber. Bunsenges. Phys. Chem.*, **80**, 1002 (1976).
3. F. Will, Private communication.

JOURNAL OF THE ELECTROCHEMICAL SOCIETY

SOLID-STATE SCIENCE AND TECHNOLOGY

AUGUST 1977

Thermodynamics of the Nonstoichiometric β_1-PtZn Phase Exhibiting the $L1_0$ Structure

Yu-Jen Hsiao, Y. Austin Chang, and Herbert Ipser[1]

Materials Department, College of Engineering and Applied Science, University of Wisconsin-Milwaukee, Milwaukee, Wisconsin 53201

ABSTRACT

Thermodynamic activities of zinc in the β_1-PtZn and the α-PtZn phases were determined at 1273°K using an isopiestic method. The theoretical thermodynamic equations by Chang and co-workers for the nonstoichiometric Ll_0 phases were modified to include the different interactions between the first nearest neighbor and the second nearest neighbor atoms. An analysis of the activity data for the β_1-PtZn phase at 1273°K in terms of the modified theoretical equation yields the following values: $\alpha = 3 \times 10^{-4}$, $\eta = 1.0$, and $\ln a_{Zn,o} = -4.65$. The thermodynamic data of the α-phase were evaluated in terms of the subregular solution model. The partial quantities of platinum and the integral quantities for the α- and β_1-phases were obtained by means of the Gibbs-Duhem relationship. A theoretical relationship between the enthalpy of formation and the model parameters for the Ll_0 phases was derived and correlated with the β_1-PtZn data and other data available in the literature.

The three group VIII transition metals, nickel, palladium, and platinum, react with the group II metal zinc to form ordered intermetallic phases with the Ll_0 structure at the equiatomic composition. This structure may be viewed either in terms of a body-centered tetragonal or a face-centered tetragonal lattice. At the stoichiometric composition, in terms of the body-centered lattice, all the A atoms occupy the body-centered positions and the B atoms the corner positions for a perfectly ordered structure. However, at any finite temperature, some degree of lattice disorder prevails. At nonstoichiometric compositions, constitutionally induced lattice disorder occurs in the lattice, in addition to that due to thermal vibration. This lattice disorder contributes to the thermodynamic properties of the intermetallic phases. Chang and co-workers (1, 2) derived theoretical equations to describe the compositional dependences of the activity and the partial molar enthalpy of the Ll_0 phases. The validity of the theoretical equations was verified using the extensive data for β_1-NiZn and β_1-PdZn (3-5). Like these phases, the β_1-PtZn[2] phase also exists over a wide range of homogeneity. The exact range of homogeneity is discussed later in this paper. The objective of the present investigation is to determine the thermodynamic properties of the β_1-PtZn phase using an isopiestic technique and to further test the validity of the theoretical equations of Chang and co-workers. Moreover, these theoretical equations are slightly modified in order to consider the possible difference between the interactions of first and second nearest neighbor atoms, which were assumed to be identical in the original development of the theoretical model (1, 2). Lastly, a relationship between the parameters of the theoretical model and the enthalpy of formation is derived. The validity of this relationship is examined using the data obtained in the present paper for the β_1-PtZn phase, as well as data available in the literature for other Ll_0 phases.

Experimental Method and Results

The isopiestic technique employed in the present study has been described previously (6). Platinum samples of approximately 1g were prepared from a 0.025 mm foil (99.99%; Engelhard, New Jersey). Zinc samples were prepared from a rod (99.999%; United Mineral and Chemical Corporation, New York). Platinum samples were cleaned with aqua regia, while the zinc samples with a solution of 15% HCl, 15% HNO_3, and 70% H_2O. The quartz tubes which contained the samples were evacuated at 5×10^{-2} Pa for 24 hr, sealed, and then placed in the furnace at ~ 1000°C for 10-12 days. The experiments were terminated by quenching the quartz tube in cold water. The composition of each sample was computed from its weight change. During the course of each experiment, the sample temperature T_S was kept constant within ± ¾°K, while the temperature of the zinc reservoir T_R within ± ¼°K. Knowing T_S, T_R, and the vapor pressures of zinc at these temperatures, the activity of zinc in each alloy was computed using Eq. [1] of Ref. (6). The vapor pressure values of zinc used are those selected by Hultgren *et al.* (3, 7). The experimental results expressed in terms of the activity of zinc a_{Zn}, are summarized in Table I. Based on the activity data at 1000°C as shown in Fig. 1, the α-phase boundary of the $\alpha + \beta_1$ two phase field is determined to be 27.5 (± 1) atomic percent (a/o) Zn, while the β_1-phase boundary to be 42 (± 1) a/o Zn. The phase boundaries

[1] Present address: Institut of Inorganic Chemistry, University of Vienna, Vienna, Austria.

Key words: thermodynamic data, platinum-zinc alloys, nonstoichometric β_1-PtZn.

[2] Following the nomenclature in the systems Ni-Zn and Pd-Zn, the Ll_0-phase in the system Pt-Zn is also designated as "β_1".

Table I. Experimental results—standard states: Pt(s) and Zn(l)

No.	a/o Zn	Phase	T_S, K	T_R, K	ln $a_{Zn,1273}$
1	19.95	α	1274	670	−10.10
2	26.23	α	1274	700	−9.14
3	44.33	β_1	1273	726	−8.38
4	46.07	β_1	1271	751	−7.71
5	49.33	β_1	1273	801	−6.54
6	49.96	β_1	1274	881	−4.92
7	50.01	β_1	1273	900	−4.56
8	50.07	β_1	1274	951	−3.73
9	51.03	β_1	1275	1018	−2.75
10	51.61	β_1	1274	1040	−2.46

were estimated by Nowotny *et al.* (8) based on x-ray analysis, microexamination, and magnetic susceptibility measurements of alloys quenched from 750° and 400°C. Extrapolating their estimated values to 1000°C yields the value of ~ 25 and ~ 32 a/o Zn, respectively. While the value of ~ 25 a/o Zn is in reasonable accord with the value of 27.5 a/o Zn determined in the present study, the value of ~ 32 a/o Zn is too low.

All samples in the β_1-phase were examined by x-rays (9) using CrKα radiation in a Debye-Scherrer camera with a diameter of 57.5 mm. The lattice parameters calculated from the photographs were found to be in general agreement with the results of Nowotny and co-workers (8, 10).

Data Evaluation and Discussion

Thermodynamic equations for the nonstoichiometric β_1-PtZn phase.—Chang and co-workers (1, 2) derived theoretical thermodynamic equations to account for the compositional dependence of the activity and the partial enthalpy in nonstoichiometric Ll_0 phases. In this model, Chang and co-workers assumed that the interaction enthalpy between an atom and its eight first nearest neighbors is the same as that between the same atom and its four second nearest neighbors, neglecting all interactions of higher order. Recently, Ipser, Neumann, and Chang (11) found that the influence of second nearest neighbor interactions is also important for some antistructure B2 phases. For this purpose, they introduced a new parameter η into the equations originally derived (2, 12, 13). Theoretical equations are presented for the Ll_0 phases, which now also take into account this new parameter η. In view of the findings for the antistructure B2 phases, it is anticipated that the value of η may deviate from a singular value for the Ll_0 phases. Furthermore, the ratio of the lattice parameters (c/a), which determines the relative distances between first and second nearest neighbors, may also influence the value of η.

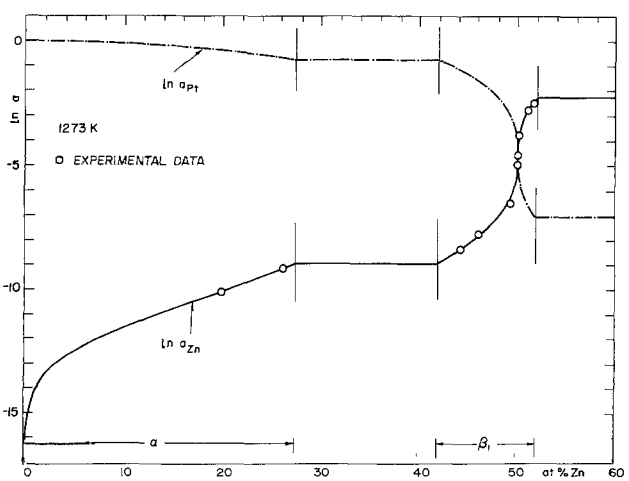


Fig. 1. Activities of zinc and platinum at 1273°K. The standard states are Pt(s) and Zn(l). The smoothed curve for the α-phase was calculated from Eq. [7] with $\epsilon^\alpha = -317.3$ kJ/g-atom and $\eta^\alpha = -209.9$ kJ/g-atom, and that for the β_1-phase from Eq. [5] with $\alpha = 3 \times 10^{-4}$, $\eta = 1.0$, and ln $a_{Zn,0} = -4.65$.

The parameter η is defined as the ratio of the interchange enthalpies between the second nearest and first nearest neighbor atoms

$$\eta \equiv \frac{V'_{AB}}{V_{AB}} \qquad [1]$$

where $V_{AB} = H_{AB} - \frac{1}{2}(H_{AA} + H_{BB})$ and $V'_{AB} = H'_{AB} - \frac{1}{2}(H'_{AA} + H'_{BB})$. The term H_{ij} is the interaction enthalpy for a pair of first nearest neighbors i-j, and H'_{ij} that for a pair of second nearest neighbors i-j. The other basic parameter of the model is the degree of lattice disorder at stoichiometry, α, which is defined as

$$\alpha \equiv \left(\frac{N_A^\beta}{N}\right)_{\chi=0} \equiv \left(\frac{N_B^\alpha}{N}\right)_{\chi=0} \qquad [2]$$

where N_A^β is the number of A atoms on the β-sublattice sites (the wrong sites), N_B^α is that of B atoms on the α-sublattice sites, and N is the total number of atoms; χ is the deviation from stoichiometry in terms of the atomic fraction and is defined as $\chi \equiv x_2 - 0.5$, with x_2 being the atomic fraction of component 2. The degree of lattice disorder at any composition χ is

$$z \equiv \left(\frac{N_A^\beta}{N}\right)_\chi \qquad [3]$$

It reduces to α when $\chi = 0$. Values of z may be computed from the following relationship expressing z as a function of χ and α

$$z = \frac{-\chi + \sqrt{\chi^2 + 4\alpha^2}}{2} \qquad [4]$$

which is Eq. [51] in Ref. (2). Using these parameters and employing the method presented in Ref. (11), the following theoretical equations for the compositional dependences of the activities and partial molar enthalpies can be derived for Ll_0 phases with antistructure defects

$$\ln \frac{a_i}{a_{i,o}} = \epsilon_i \ln \frac{z(1-2\alpha)}{\alpha(1-2z)} + \left(\frac{\frac{1}{2}\eta}{1-\frac{1}{2}\eta}\right)(2\ln 2\alpha)(2\epsilon_i + \chi)\chi \qquad [5]$$

$$\frac{\Delta\bar{H}_i - \Delta\bar{H}_{i,o}}{RT} = \left(2\alpha + \frac{\epsilon_i\chi - 4\alpha^2}{2z+\chi} + \left(\frac{\frac{1}{2}\eta}{1-\frac{1}{2}\eta}\right)2(2\epsilon_i + \chi)\chi\right)\ln 2\alpha \qquad [6]$$

where $a_{i,o}$ and $\Delta\bar{H}_{i,o}$ are the activity and the partial molar enthalpy of the component i at the stoichiometric composition, $\epsilon_i = +\frac{1}{2}$ for $i = 1$ and $\epsilon_i = -\frac{1}{2}$ for $i = 2$, and R is the gas constant.

A comparison of the above two expressions with Eq. [19] and [21] of Ref. (11) shows that the only difference is the coefficient ½ for the quantity η. For the antistructure B2 phases, the coefficient is ¾ if the expression $[3\eta/(4 - 3\eta)]$ in Eq. [19] and [21] of Ref. (11) is written as $(3\eta/4)/(1 - 3\eta/4)$. The coefficients ½ and ¾ represent the ratio of the number of the second and first nearest neighbor atoms in the Ll_0 and B2 structures, respectively. With $\eta = 1$, which is the original assumption made by Chang and co-workers (1, 2), Eq. [5] and [6] reduce to their expressions for the "one-and-half approximation," if the term β in Chang's equation is substituted by its simplified form 2 ln 2α (compare Eq. [105] and [110] in Ref. (2)).

Evaluation of experimental data.—The activity data of zinc in the β_1-phase were analyzed in terms of Eq. [5]. As can be seen from Fig. 2, excellent agreement was obtained between the experimental data and the theoretical curve with $\alpha = 3 \times 10^{-4}$, $\eta = 1.0$, and ln

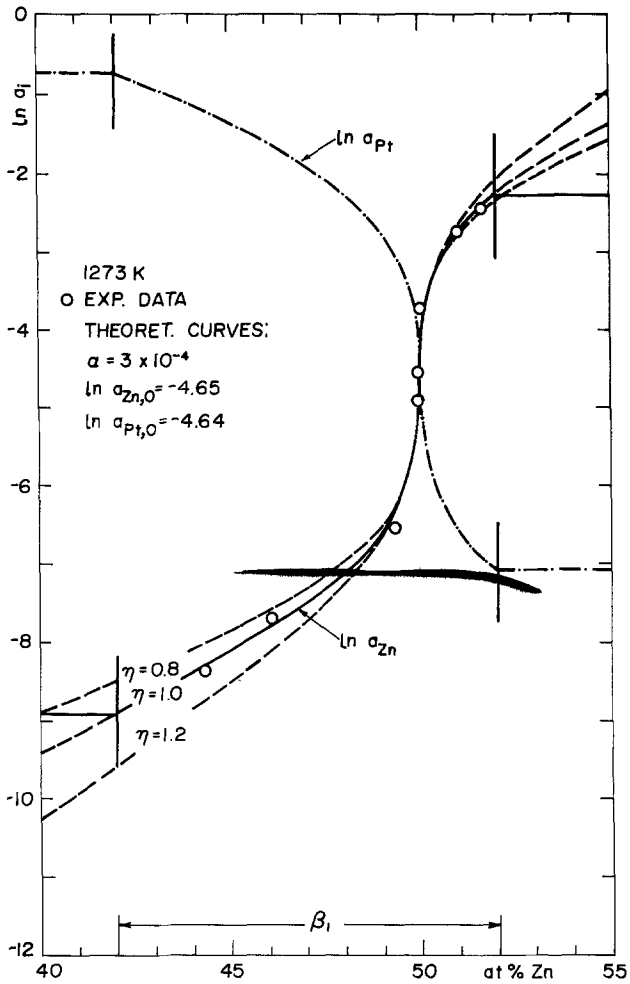


Fig. 2. Activities of zinc and platinum in the β_1-phase at 1273°K with the experimental data points for zinc. The standard states are Pt(s) and Zn(l).

$a_{Zn,O} = -4.65$. For comparison, the curves with $\eta = 0.8$ and $\eta = 1.2$ are also shown in Fig. 2 in the form of dashed lines. It is obvious that a value of $\eta = 1.0$ gives the best fit, which is in agreement with previous findings of Chang and co-workers for several Ll_o phases (2-5). As presented in the previous section, their original model assumes *a priori* that $\eta = 1.0$. Although the agreement between the theoretical predictions with $\eta = 1.0$ and the experimental data was quite good in most cases, an exception was the β_1-NiZn phase, where some deviations were noticed.

In order to obtain the partial molar quantities of platinum in the β_1-phase and the integral quantities of this phase, it is necessary to know the activities of zinc in the α-phase. The subregular solution model (14), which has been used successfully in describing the thermodynamic properties of several terminal solid solutions (3, 6, 15), is used to represent the thermodynamic properties of the α-PtZn phase. The pertinent equation for the activity coefficient of Zn, γ_{Zn}, is

$$RT \ln \gamma_{Zn} = -\Delta G_{Zn}^{\alpha \to l} + [(\epsilon^\alpha - \eta^\alpha) + \eta^\alpha x_{Zn}](1 - x_{Zn})^2 \quad [7]$$

where x_{Zn} is the atom fraction of Zn, and ϵ^α and η^α are parameters which must be obtained from experimental data. The standard states used in the present study are Pt(s) and Zn(l). Using the Gibbs energy of melting of fcc Zn according to Kaufman and Bernstein (16) and the experimental data, values of $\epsilon^\alpha = -317.3$ kJ/g-atom and $\eta^\alpha = -209.9$ kJ/g-atom are obtained. The calculated activity curve for Zn according to Eq. [7] is shown in Fig. 1. The corresponding activity curves for Pt are computed from the appropriate equations and are also shown in Fig. 1 with ln $a_{Pt,O} = -4.64$. The

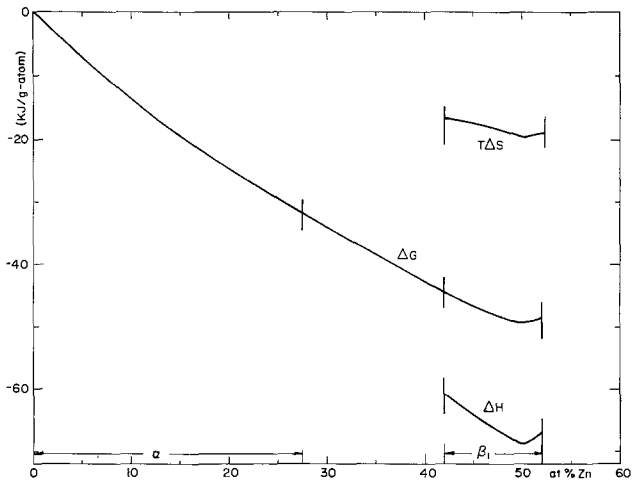


Fig. 3. Integral thermodynamic properties in the platinum-zinc system. The standard states are Pt(s) and Zn(l).

smoothed ΔG values are presented in Fig. 3. These values as well as those of a_{Pt} and a_{Zn} are given in Table II.

In order to obtain an approximate ΔH value for the β_1-phase at the stoichiometric composition, Kubaschewski's empirical correlation was used to estimate the entropy term (17). From the ΔG value given in Table II after converting to Zn(s) as standard state and the known boiling points of Pt and Zn (7), values of $\Delta S^{xs} = -15.8$ J/K g-atom and $\Delta H = -65.0$ kJ/g-atom [referred to Zn(s)] are obtained. When converted to Zn(l) as the standard state, $\Delta H = -68.7$ kJ/g-atom is obtained. The uncertainty in the ΔH value is believed to be less than ±10 kJ/g-atom.

Since the thermodynamic activities of the component elements have practically the same value at the stoichiometric composition (50 a/o Zn), it was assumed that the partial enthalpies are equal referring to Pt(s) and Zn(s). This is to be expected for nonstoichiometric phases with substantially ordered structure. For such phases the enthalpy tends toward a minimum value at the stoichiometric composition. With this assumption, the compositional dependences of the partial molar enthalpies in the β_1-phase are computed from Eq. [6] and presented in Fig. 4. The resulting ΔH values as a function of composition as well as the $T\Delta S$ values are shown in Fig. 3 in addition to the ΔG values. The thermodynamic properties of PtZn alloys at selected compositions between 0 and 52 a/o Zn are summarized in Table II, with the data derived from the estimated value for the enthalpy of formation set in parentheses.

For comparison, a value of ΔH was also computed by means of the theoretical equation derived by Miedema and co-workers (18, 19). Their theoretical model takes into account the following contributions to the enthalpy of formation; the difference in electronegativity,

Table II. Thermodynamic properties of Pt-Zn alloys at 1273°K—standard states; Pt(s) and Zn(l)

a/o Zn	Phase	ln a_{Zn}	ln a_{Pt}	ΔG, kJ(g-atom)$^{-1}$	ΔH, kJ(g-atom)$^{-1}$	$T\Delta S$, kJ(g-atom)$^{-1}$
0	α	$-\infty$	0	0		
1.0	α	−14.20	−0.01	−1.6		
5.0	α	−12.50	−0.05	−7.1		
10.0	α	−11.58	−0.13	−13.5		
15.0	α	−10.83	−0.23	−19.3		
20.0	α	−10.09	−0.39	−24.7		
25.0	α	−9.33	−0.61	−29.5		
27.5	$\alpha/(\alpha + \beta_1)$	−8.94	−0.75	−31.8		
42.0	$(\alpha + \beta_1)/\beta_1$	−8.94	−0.75	−44.4	(−60.8)	(−16.4)
45.0	β_1	−8.10	−1.37	−46.6	(−64.1)	(−17.5)
48.0	β_1	−7.10	−2.24	−48.4	(−66.9)	(−18.5)
49.0	β_1	−6.58	−2.73	−48.9	(−67.9)	(−19.0)
50.0	β_1	−4.65	−4.64	−49.2	(−68.7)	(−19.5)
		(±0.12)	(±0.20)	(±2.0)	(±10.0)	(±10.0)
51.0	β_1	−2.74	−6.57	−48.9	(−68.1)	(−19.2)
52.0	$\beta_1/(\beta_1 + \xi)$	−2.25	−7.09	−48.4	(−67.2)	(−18.8)

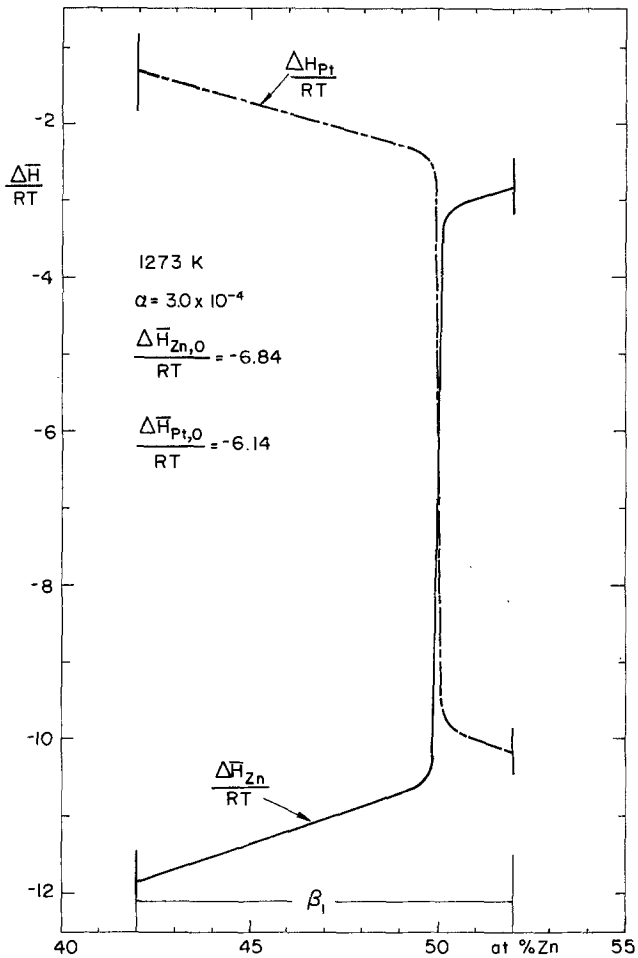


Fig. 4. Partial molar enthalpies of platinum and zinc in the β_1-phase at 1273°K. The standard states are Pt(s) and Zn(l).

the difference in the electron density at the boundary between dissimilar atoms, and, additionally, a certain hybridization energy for alloys of transition metals with nontransition metals. A value of $\Delta H = -60.3$ kJ/g-atom [referred to Zn(s)] was obtained, which is in reasonable agreement with the value obtained in the present study.

Relationship between the model parameters and the enthalpy of formation of the Ll_0-phases.—In two recent publications, Neumann *et al.* (20, 21) discussed the relationship between the disorder parameter α and the enthalpy of formation in ordered intermetallic phases with the B2 structure, and Ipser *et al.* (11) investigated the influence of the second nearest neighbor interactions on this relationship. Following the method outlined in Ref. (11) and (21), a corresponding relationship can be derived for intermetallic phases exhibiting the Ll_0 structure

$$\frac{\Delta H}{RT}(1 - \tfrac{1}{2}\eta) = \tfrac{1}{2}\ln 2 + \tfrac{1}{2}\ln \alpha \qquad [8a]$$

For the case $\eta = 1.0$, as was originally assumed by Chang and co-workers (1, 2) in the development of their theoretical equations, Eq. [8a] reduces to

$$\frac{\Delta H}{RT} = \ln 2 + \ln \alpha \qquad [8b]$$

This expression, however, can also be obtained by simplification of Eq. [98b] of Ref. 2 for $\alpha << 1$, if the term $4NV_{AB}$ (where N is Avogadro's number) is identified with ΔH.

The experimental data needed to establish the relationship between ΔH and the model parameters are summarized for convenience in Table III. Of the enthalpy of formation data (which are referred to the solid elements as standard states) listed in the table, the values for α_1''-AuCu and β_1-PdCd were determined calorimetrically, and the value for β_1-NiZn was obtained from the temperature dependence of the Gibbs energy. On the other hand, the values for β_1-PdZn and β_1-PtZn were obtained from the Gibbs energies and the estimated entropies of formation using Kubaschewski's empirical correlation (17).

Table III. Enthalpy of formation ΔH (referred to the solid elements as standard states) and disorder parameter α for Ll_0-phases

Phase	T, °K	α	ΔH, kJ(g-atom)$^{-1}$
α_1''-AuCu	653	3.75×10^{-2} (2)	−8.0 (7)
β_1-PdCd	1350	2.25×10^{-2} (2)	~−40* (22)
β_1-NiZn	905	2.5×10^{-3} (4)	−19.7 (4)
β_1-PdZn	1273	4×10^{-4} (3, 5)	−73.9 (3, 17)
β_1-PtZn	1273	3×10^{-4} (this paper)	−65.0 (this paper, 17)

* This value is the average for the β_1-PdCd phase, since Darby *et al.* (22) indicate a minimum in ΔH at 39 a/o Cd, although one would expect it at or near 50 a/o.

Figure 5 shows the comparison between the theoretical prediction according to Eq. [8b] and the available experimental data. As has been discussed in an earlier section, all of the Ll_0 phases except β_1-PtZn had been analyzed previously in terms of the original model by Chang and co-workers (1, 2), implying an η value of 1.0. However, for the β_1-PtZn phase it has been demonstrated (as shown in Fig. 2) that this particular value of η gives the best agreement between theory and experimental data.

Except for β_1-NiZn, the data points in Fig. 5 fall more or less on the straight line predicted by Eq. [8b]. However, deviations of the experimental data from the theoretical predictions may be reduced if values of η less than 1.0 are used for some of the Ll_0 phases, notably the β_1-NiZn. This is in agreement with the fact that, in the analysis of the thermodynamic data of β_1-NiZn by Lau *et al.* (4), some deviations of the experimental points from the theoretical curves were observed. A reevaluation of these data in terms of Eq.

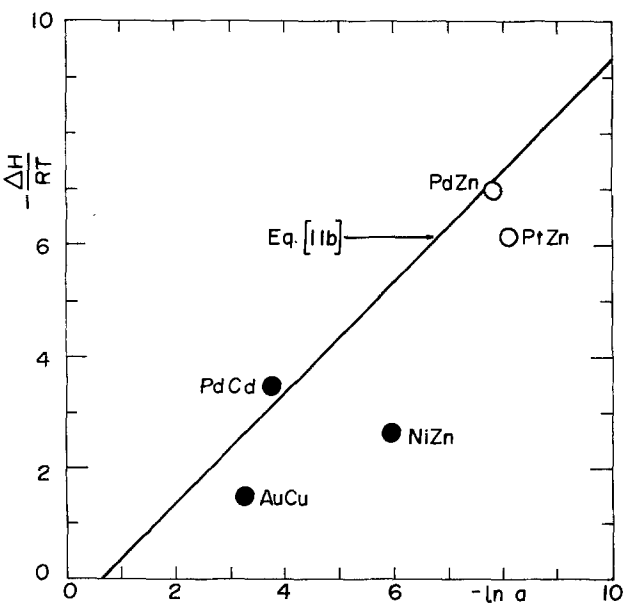


Fig. 5. A relationship between the enthalpy of formation and the degree of lattice disorder at the stoichiometric composition for the Ll_0 phases. The solid circles indicate values determined experimentally, while the open circles indicate those obtained from the experimental Gibbs energy value and the entropy value estimated from Kubaschewski's empirical correlation.

[4] and [5] might help to resolve the discrepancy in Fig. 5.

Acknowledgments

The authors wish to thank Dr. J. P. Neumann for reviewing this manuscript, and the National Science Foundation for the financial support of this work (Grant No. GH-36123).

Manuscript submitted Oct. 20, 1976; revised manuscript received March 9, 1977.

Any discussion of this paper will appear in a Discussion Section to be published in the June 1978 JOURNAL. All discussions for the June 1978 Discussion Section should be submitted by Feb. 1, 1978.

LIST OF SYMBOLS

a_i thermodynamic activity of component i in an alloy such as a_{Zn} and a_{Pt}

$\Delta\overline{G}_i$ relative partial molar Gibbs energy of component i, kJ/g-atom; superscript xs refers to the excess quantity

$\Delta G_{Zn}^{\alpha\to l}$ Gibbs energy of melting of α-Zn (fcc), kJ/g-atom

H_{ij} interaction enthalpy for a pair of first nearest neighbor atoms $i - j$, kJ; i and j stand for either the pure A or the pure B atoms

H'_{ij} interaction enthalpy for a pair of second nearest neighbor atoms $i - j$, kJ; i and j stand for either the pure A or the pure B atoms

ΔH, ΔG integral enthalpy and Gibbs energy of formation, kJ/g-atom; superscript xs refers to the excess quantity

$\Delta\overline{H}_i$ relative partial molar enthalpy of component i, kJ/g-atom

ln natural logarithm, *i.e.*, to the base e

N $N_A + N_B$ is the total number of atoms, the Avogadros' number; superscripts for N_A and N_B indicate the sublattices where the atoms are

ΔS integral entropy of formation, J/K g-atom; superscript xs refers to the excess quantity

T absolute temperature, °K; subscripts R and S refer to the reservoir and the sample

V_{AB} interchange enthalpy between the first nearest neighbor atoms, kJ

V_{AB}' interchange enthalpy between the second nearest neighbor atoms, kJ

x_i atom fraction of component i

$z = \left(\frac{N_A^\beta}{N}\right)_x$ number of A atoms on the β-sublattice

Greek symbols

α $\left(\frac{N_A^\beta}{N}\right)_{x=0} = \left(\frac{N_B^\alpha}{N}\right)_{x=0}$

$\gamma_i = \frac{a_i}{x_i}$ activity coefficient of component i such as γ_{Zn}

$\epsilon_i = +\frac{1}{2}$ for $i = 1$; $\epsilon_1 = -\frac{1}{2}$ for $i = 2$

$\epsilon^\alpha, \eta^\alpha$ parameters of the subregular α-PtZn solution, kJ/g-atom

$\eta = \frac{V_{AB}'}{V_{AB}}$

$\chi = x_2 - 0.5$

REFERENCES

1. W. W. Liang, Y. A. Chang. S. Lau, and I. Gyuk, *Acta Metall*, **21**, 629 (1973).
2. Y. A. Chang, in "Treatise on Materials Science and Technology," Vol. 4, H. Herman, Editor, p. 173, Academic Press, Inc., New York (1974).
3. T. Chiang, H. Ipser, and Y. A. Chang, *Z. Metallkd.* **68**, 141, (1977).
4. S. Lau, Y. A. Chang, and S. Kou, *Metall. Trans.*, **5**, 1979 (1974).
5. S. Kou and Y. A. Chang, *Acta Metall.*, **23**, 1185 (1975); *ibid.*, **24**, 881 (1976).
6. Y. A. Chang, G. Henning, and D. Naujock, *ibid.*, **22**, 7 (1974); *ibid.*, **22**, 1319 (1974).
7. R. Hultgren, P. D. Desai, D. T. Hawkins, M. Gleiser, K. K. Kelley, and D. D. Wagman, "Selected Values of the Thermodynamic Properties of the Elements," American Society for Metals, Metals Park, Ohio (1973).
8. H. Nowotny. E. Bauer, A. Stempfl, and H. Bittner, *Monatsh. Chem.*, **83**, 221 (1952).
9. Y. Hsiao, M.S. thesis, University of Wisconsin-Milwaukee, Milwaukee (1975).
10. H. Nowotny, E. Bauer, and A. Stempfl, *Monatsh. Chem.*, **81**, 1164 (1950).
11. H. Ipser, J. P. Neumann, and Y. A. Chang, *ibid.*, **107**, 1471 (1976).
12. Y. A. Chang, I. Gyuk, and J. Franks, *Acta Metall.*, **19**, 939 (1971).
13. I. Gyuk and Y. A. Chang, *Scr. Metall.*, **6**, 267 (1972).
14. H. K. Hardy, *Acta Metall.*, **1**, 202 (1953).
15. S. Kou and Y. A. Chang, *Metall. Trans.*, **6A**, 39 (1975).
16. L. Kaufman and R. Bernstein, "Computer Calculations of Phase Diagrams," pp. 37-46, Academic Press, Inc., New York (1970).
17. O. Kubaschewski and W. Slough, in "Progress in Materials Science," Vol. 14, B. Chalmers and W. Hume-Rothery, Editor, p. 1, Pergamon Press, Oxford (1971).
18. A. R. Miedema, R. Boom, and F. R. DeBoer, *J. Less-Common Met.*, **41**, 283 (1975).
19. A. R. Miedema, *ibid.*, **46**, 67 (1976).
20. J. P. Neumann, Y. A. Chang, and C. M. Lee, *Acta Metall.*, **24**, 593 (1976).
21. J. P. Neumann, Y. A. Chang, and H. Ipser, *Scr. Metall.*, **10**, 917 (1976).
22. J. B. Darby, Jr., K. M. Myles, and J. N. Pratt, *Acta Metall.*, **19**, 7 (1971).

Ionic Conductivity of Lithium Orthosilicate—Lithium Phosphate Solid Solutions

Y-W. Hu, I. D. Raistrick, and R. A. Huggins*

Center for Materials Research, Stanford University, Stanford, California 94305

ABSTRACT

Lithium ion conductivity in solid solutions formed between Li_4SiO_4 and Li_3PO_4 has been measured as a function of temperature and composition using a-c techniques. Highest conductivities were found at 50 and 60 mole percent (m/o) phosphate. Empirical conductivity parameters are presented and qualitatively analyzed in terms of structural and compositional effects. Unit cell parameters have been determined across the entire range of solid solution by x-ray powder diffraction.

High lithium ion conductivity in solid solutions between lithium orthosilicate (Li_4SiO_4) and lithium phosphate (Li_3PO_4) has been previously reported (1). At that time measurements had been made on compounds varying in composition between pure Li_4SiO_4 and $Li_{3.5}Si_{0.5}P_{0.5}O_4$ (50 m/o phosphate). The highest conductivity, found in $Li_{3.6}Si_{0.6}P_{0.4}O_4$, was several orders of magnitude greater than that of pure Li_4SiO_4 (2-5) at 100°C. Measurements have now been extended to include the entire range from Li_4SiO_4 to Li_3PO_4.

Sample Preparation

Lithium orthosilicate was prepared by solid-state reaction between Li_2CO_3 (Johnson-Matthey Puratronic Grade II) and SiO_2 (Johnson-Matthey Puratronic Grade I or II) at 800°C as previously described (1). Lithium phosphate was purchased from Alfa Inorganics (99+% purity). Intermediate compositions were prepared by hot pressing appropriate mixtures of Li_4SiO_4 and Li_3PO_4 in ⅜ in. diam graphite dies in an argon flow system at 1000°C and 5000 psi pressure. Pressing times varied between 30 and 60 min after reaching the maximum temperature. Carbon was removed from the surface of the disk-shaped samples by heating in air to about 400°C. All starting materials and preparations were routinely checked for completeness of reaction by x-ray powder diffraction.

Conductivity Measurements

Experimental aspects.—Samples were prepared for conductivity measurements by grinding their parallel surfaces on 600 mesh silicon carbide paper, followed by fine polishing. A layer of platinum about 1000Å thick was then sputtered onto each face of the disks. Measurements were made in air using small signal a-c measurements over the frequency range 5-100 kHz, using a General Radio 1615 bridge and a Princeton Applied Research two phase/vector lock-in amplifier. Complex plane methods were used to extract the frequency-independent bulk ionic conductivity, as has been previously described (5, 6).

Results.—Conductivity data for the entire composition range are shown plotted as log (σT) *vs.* reciprocal absolute temperature in Fig. 1 and 2. The data are a good fit to the Arrhenius equation

$$\sigma T = A \exp(-\Delta H/RT) \qquad [1]$$

ΔH is the activation enthalpy, A is a preexponential factor (obtained by extrapolation to infinite temperature T), R is the gas constant. ΔH and A are composition-dependent and their values are listed in Table I. Estimated precision is better than 5% for ΔH and within a factor of 2 for A. Most measurements were repeated on several samples of the same composition; the absolute conductivity values thus obtained were reproducible within a factor of 2. At several compositions it was found that conductivity decreased with decreasing sample density, a sample of only 70% theoretical density having a conductivity up to one order of magnitude less than a 96% dense sample. All results reported here were made on samples of 95% density or better. No corrections for residual density effects have been attempted.

X-Ray Powder Diffraction Results

Lattice parameters were determined by least squares fitting of 10-15 of the strongest reflections for each composition studied. An internal calibrant was included. Consistency of better than 0.1% between observed and calculated d values was achieved. Parameters for Li_4SiO_4 and Li_3PO_4 were within 0.1% of pre-

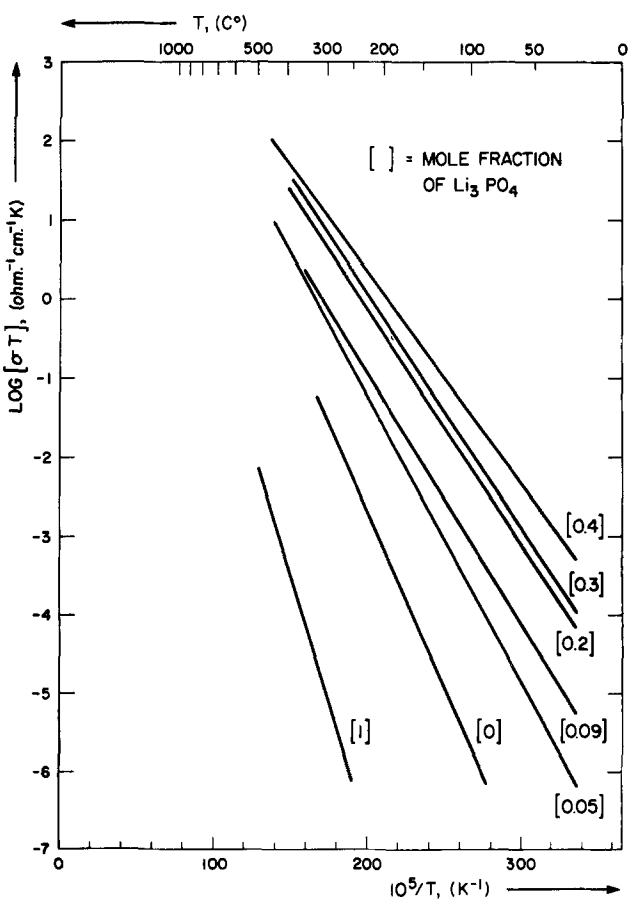


Fig. 1. Ionic conductivity of Li_4SiO_4 — Li_3PO_4 solid solutions in the composition range 0-0.4 mole fraction Li_3PO_4.

* Electrochemical Society Active Member.

Key words: ionic conductivity, lithium solid electrolytes, lithium orthosilicate, lithium phosphate.

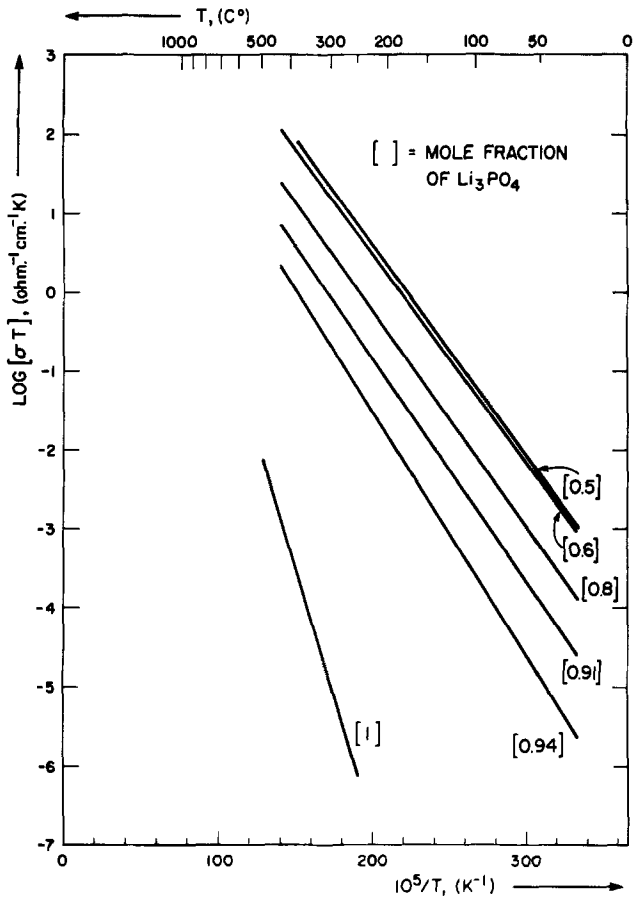


Fig. 2. Ionic conductivity of Li_4SiO_4 — Li_3PO_4 solid solutions in the composition range 0.5-1.0 mole fraction Li_3PO_4.

viously published data (7, 8). Lattice parameters are given as a function of composition in Table II. As Li_4SiO_4 and Li_3PO_4 have different, but rather closely related structures, the coordinate system for Li_3PO_4 was chosen differently from that used in Ref. (8) so that a consistent set of indexes could be compared across the entire range of composition. Over this composition range the structure changes smoothly from the Li_4SiO_4 type to that of Li_3PO_4. The value of c, the only parameter which changes appreciably, is plotted against mole fraction of phosphate in Fig. 3. The largest change in c (and hence in cell volume) occurs between 30 and 50 m/o phosphate. Beyond 50 m/o, the x-ray powder pattern bears more resemblance to Li_3PO_4 than to Li_4SiO_4. The continuous change in lattice parameter is convincing evidence for a complete range of solid solutions between the end members. Li_3PO_4 has two crystallographic forms (9). Powder diffraction showed that although the original material was of the low (monoclinic) form, after hot pressing it transformed to the high (orthorhombic) form. This change has been reported to be monotropic (9), which is consistent with present observations.

Table I. Experimental conductivity parameters A and ΔH

Composition (mole fraction Li_3PO_4)	A (Ω^{-1} cm^{-1} °K)	ΔH (kcal/mole^{-1})
0.0	1.2×10^6	20.1
0.05	1.3×10^6	16.7
0.09	6.3×10^5	14.6
0.2	8.3×10^5	13.7
0.3	1.1×10^6	13.6
0.4	5.8×10^5	12.3
0.5	6.3×10^5	11.9
0.6	4.2×10^5	11.7
0.8	1.3×10^5	12.2
0.91	5.0×10^4	12.6
0.94	3.7×10^4	13.8
1.0	2.5×10^5	30.0

Table II. Lattice parameters of Li_4SiO_4 — Li_3PO_4 solid solutions

Composition (mole fraction Li_3PO_4)	a (A)	b (A)	c (A)	β (degrees)
0.0	5.300	6.100	5.149	90.26
0.2	5.292	6.105	5.142	90.25
0.4	5.298	6.111	5.083	90.38
0.5	10.588*	6.114	5.008	90.0
0.6	10.570*	6.114	4.992	90.0
0.8	10.520*	6.110	4.959	90.0
1.0	10.476*	6.112	4.920	90.0

* Due to the orientation of the PO_4 tetrahedra, the unit cell of Li_3PO_4 is doubled with respect to that of Li_4SiO_4.

Discussion

The relative importance of the two empirical parameters A and ΔH in determining the magnitude of the conductivity changes as the composition is varied. This is illustrated in Fig. 4. From pure Li_4SiO_4 to about 40 m/o phosphate the conductivity shows a strong dependence on the activation enthalpy. Over this range the preexponential factor remains constant within experimental error. Beyond 50 m/o phosphate the change

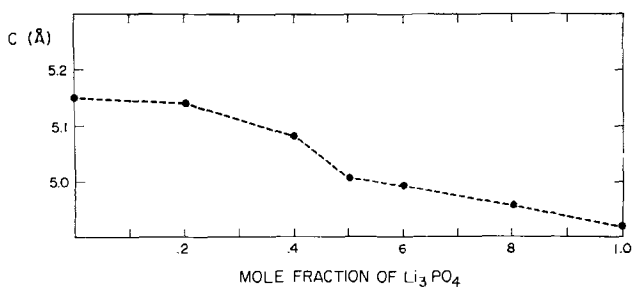


Fig. 3. Variation of c lattice parameter with composition of solid solution.

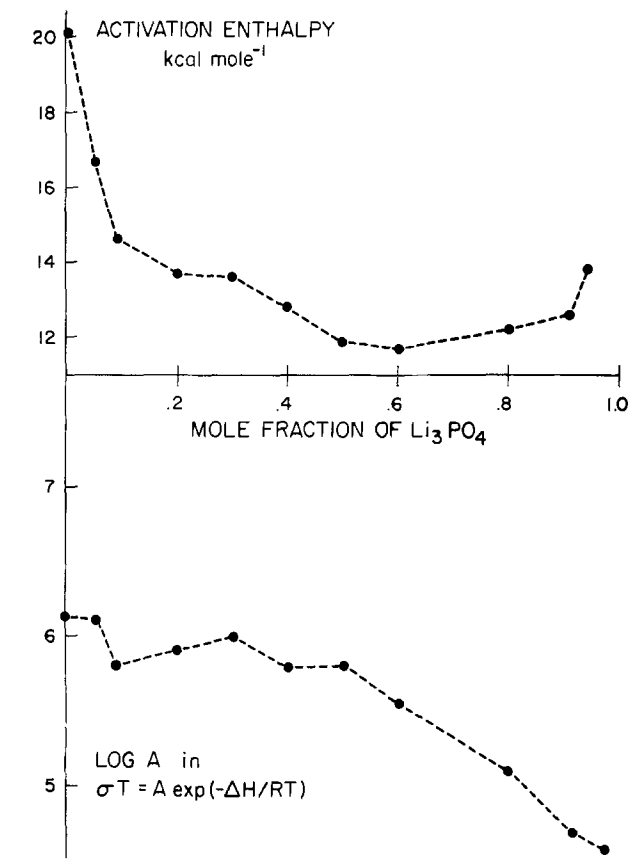


Fig. 4. Variation of experimental conductivity parameters ΔH (activation enthalpy) and A (preexponential factor) with composition of solid solutions.

in preexponential factor dominates the conductivity change; the relative change in activation enthalpy is apparently less important. Following the random walk formulation for a hopping mechanism of conductivity the preexponential factor A can be expanded

$$A = \nu_0 C \alpha d^2 \left(\frac{\mathbf{F}^2}{R}\right) z^2 \exp\left(\frac{\Delta S}{R}\right) \qquad [2]$$

Where C and z are the concentration and charge number of the mobile species, d is the jump distance, α is a geometric factor which depends on the number of available jump directions in the crystal lattice, ν_0 is the attempt frequency, taken to be the vibrational frequency of the mobile species in its potential well, ΔS is the total activation entropy for conduction, and $\mathbf{F}$ and R are the Faraday and gas constant, respectively. The experimentally obtained quantity, ΔH, can be divided into two terms; ΔH_f, which is the heat of formation of the defects necessary for conduction, and ΔH_m, which is the activation enthalpy for motion.

In materials in which there is an excess of lattice sites over ions of the conducting species [in Li_4SiO_4 there are 8 Li ions distributed over 18 sites (7)], the concentration of moving species, $C = C_0 \exp(-\Delta G_f/RT)$, where ΔG_f is the free energy of formation of the defects, is expected to be only very weakly temperature dependent, if at all. C_0 is the total concentration of both static and moving ions of the conducting species. This is because the "defects" necessary for conduction are already present as statistically empty lattice sites. If the mobile species are distributed over several different kinds of lattice sites, ΔG_f becomes equal to the difference in free energy of these sites, and may be assumed to be very small (< 1 kcal/mole) if a distribution over these same sites is crystallographically observable at room temperature. In pure Li_4SiO_4, therefore, it is probably correct to assume that all (or a large fraction of) the lithium ions are contributing to the conduction process, and that the experimentally observed enthalpy ΔH corresponds to the activation enthalpy of motion, ΔH_m, in this structure. In Li_3PO_4, however, this is not true. Two kinds of tetrahedral lithium sites are present, and they are both fully occupied at room temperature (8). Thermal energy is then necessary to create defects before conduction can take place. This presumably accounts for the much higher activation enthalpy observed for this composition. As soon as Li_4SiO_4 is added to the Li_3PO_4, however, interstitial Li ions are introduced, which can contribute to the conductivity. Thus ΔH remains almost constant at 12-13 kcal/mole over a considerable concentration range, and conductivity increases are principally due to changes in A caused by the increase in C_0. Below 50 m/o phosphate, however, A is essentially constant, and conductivity changes are presumably due to structural changes which influence the potential energy contribution to ΔH_m. Parameters contributing to A in Eq. [2], such as ΔS, ν_0, α, and d, are expected to be rather insensitive to small structural changes. ΔH_m, however, will be highly structure sensitive due to rapid changes in such terms as overlap repulsion energy with interionic distance (10, 11).

Without detailed structural information, which would include a knowledge of lithium site occupancies and energies, and a knowledge of how the silicate structure changes into the phosphate structure across the composition range, further interpretation of the data available at present would be speculative.

Acknowledgments

This research was supported by the Defense Advanced Research Projects Agency and was monitored by the Office of Naval Research under contract No. N00014-76-C-0940.

Manuscript received Feb. 28, 1977.

Any discussion of this paper will appear in a Discussion Section to be published in the June 1978 JOURNAL. All discussions for the June 1978 Discussion Section should be submitted by Feb. 1, 1978.

Publication costs of this article were assisted by Stanford University.

REFERENCES

1. Y-W. Hu, I. D. Raistrick, and R. A. Huggins, *Mater. Res. Bull.*, **11**, 1227 (1976).
2. W. Gratzer, H. Bittner, H. Nowotny, and K. Seifert, *Z. Kristallogr.*, **133**, 260 (1971).
3. A. R. West, *J. Appl. Electrochem.*, **3**, 327 (1973).
4. I. M. Hodge, M. D. Ingram, and A. R. West, *J. Am. Ceram. Soc.*, **59**, 360 (1976).
5. I. D. Raistrick, C. Ho, and R. A. Huggins, *This Journal*, **123**, 1469 (1976).
6. I. D. Raistrick, C. Ho, Y-W. Hu, and R. A. Huggins, *J. Electroanal. Chem.*, **77**, 319 (1977).
7. H. Völlenkle, A. Wittmann, and H. Nowotny, *Monatsh. Chem.*, **99**, 1360 (1968).
8. J. Zemann, *Acta Crystallogr.* Sect. B, **13**, 863 (1960).
9. A. R. West and F. P. Glasser, National Bureau of Standards Special Publication 364, p. 457 (1972).
10. W. H. Flygare and R. A. Huggins, *J. Phys. Chem. Solids*, **34**, 1199 (1973).
11. O. B. Ajayi, L. E. Nagel, I. D. Raistrick, and R. A. Huggins, *J. Phys. Chem. Solids*, **37**, 167 (1976).

Electrochemical Properties and Discharge Kinetics of Thin Layer Hydrous Molybdenum Oxide

David Elliott[1]

Department of Chemistry, University of Queensland, St. Lucia, Queensland 4067, Australia

ABSTRACT

Thin layer hydrated molybdenum oxide (oxidation state IV or V) has been deposited electrochemically on a variety of substrates, *e.g.*, polycrystalline tin oxide coated glass. It is capable of existing in an oxidized or reduced form and its equilibrium properties are described by a Nernst-like relationship. Experimentally the activities of the two forms are found to depend on a power function of their concentrations. The equilibrium position is also a function of *p*H. The rate of oxidation is described by a kinetic rate law of at least second order. Slow self-oxidation also occurs over a period of hours possibly due to the reduction of H^+.

Some of the basic properties of hydrous molybdenum oxide have recently been described (1). It is of interest as a solid redox system, as a material capable of receiving and storing charge as a thin layer battery or capacitor, and capable of accepting light-induced charges from a semiconductor and coupling the latter to redox processes in solution. Its composition and oxidation state are at present unknown but it may be identical with some compounds described much earlier by others, *e.g.*, $MoO_2 \cdot 2H_2O$ (2) or $Mo_2O_5 \cdot 3H_2O$ (3). It is here designated "Mo Ox" and the present work describes further basic properties of the material including the charge potential characteristics and the kinetics of the discharge process.

Experimental Technique

Current/potential curves were determined using a three electrode, solid-state potentiostat of conventional design assembled using the Heath ADD system. The integrator and the log amplifier used in the kinetics studies used a single operational amplifier (LM316). A Houston Omnigraphic 2000 X-Y recorder was used to record linear sweep voltammograms. The tin oxide electrodes were cut from commercial infrared reflecting glass and mounted as described earlier (4). The temperature for the experiments described was not controlled and was in the range 22°-23°C.

Preparation of Mo Ox

The material can be generated electrochemically from dilute solutions of ammonium molybdate (10^{-5}-10^{-3}M Mo) in the *p*H range 1-4. Any electrode having sufficient H_2 overvoltage may be used, *e.g.*, mercury, amalgamated silver, doped polycrystalline tin oxide, copper, etc. The observed properties on the first three are identical, whereas the properties on Cu are modified by the limited positive range of the metal (Cu corrosion sets in at about −0.25V *vs.* SCE in 1M NaCl, 0.01M HCl).

The material can also be generated on semiconductor electrodes, *e.g.*, GaAs and Si. In these cases the observed behavior depends much on the particular properties of the substrate, *e.g.*, doping level, carrier type, flatband potential, degree of illumination, etc. There is every reason to suppose, nevertheless, that the intrinsic properties of Mo Ox are not dependent on the substrate except in so far as the latter may affect the precise conditions of its generation.

Figure 1 shows the growth of the material as a thin layer on SnO_2 under the particular conditions shown. Cyclic sweep conditions seem essential for the generation of layers having near reversible properties (oxidation and reduction peaks at similar potentials) and having substantial thickness. Electrolysis at a fixed potential results in a layer of poor reversibility and low charge holding capability. During the process of growth under cyclic sweep conditions there is evidence of a two-stage process both in the oxidation and reduction phases. Eventually the more negative stage becomes dominant resulting in sharper peaks. When transferred to a fresh electrolyte solution containing no molybdenum further refinement of the shape takes place, Fig. 2 (the ultimate shape of this particular scan cycle is shown in Fig. 3a).

Thin layers adhere quite tenaciously but if growth is attempted beyond a certain thickness, the material becomes detached from the substrate and electrical contact is lost. The maximum thickness before this

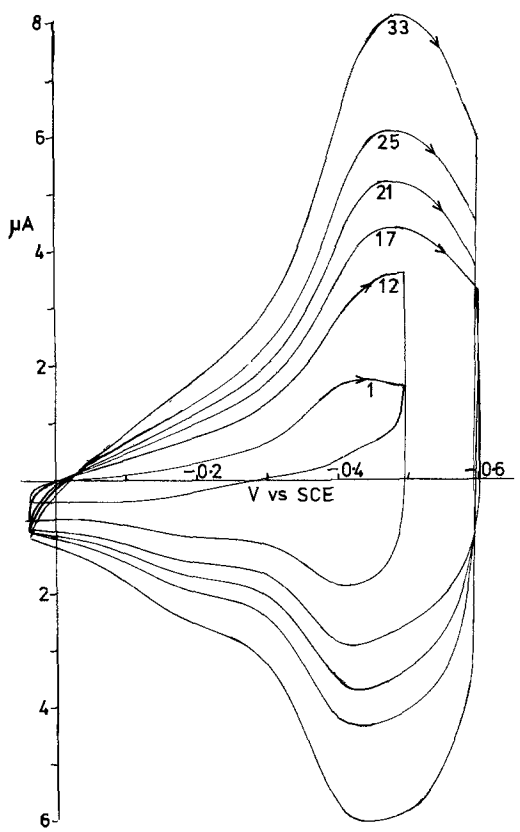


Fig. 1. Growth of molybdenum oxide layer with cyclic potential scan. Area 0.1236 cm^2; scan 0.5 V/min; solution 1M NaCl, 0.01M HCl, 10^{-4}M Mo. For clarity only some of the cycles are shown as indicated by the numbers on the graphs.

[1] Present address: Systems Research and Development Branch, Ministry of Transportation and Communications, Downsview, Ontario, Canada M3M 1J8.

Key words: thin layer battery, thin layer capacitor, solid redox system, tin oxide.

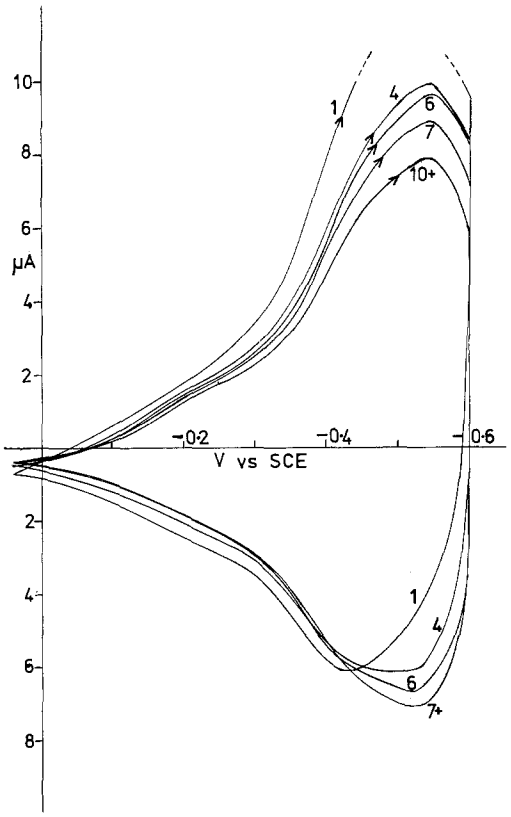


Fig. 2. Maturation of layer when transferred to and cycled in a Mo-free solution. Conditions same as Fig. 1 but molybdenum omitted. Cycles shown indicated by number.

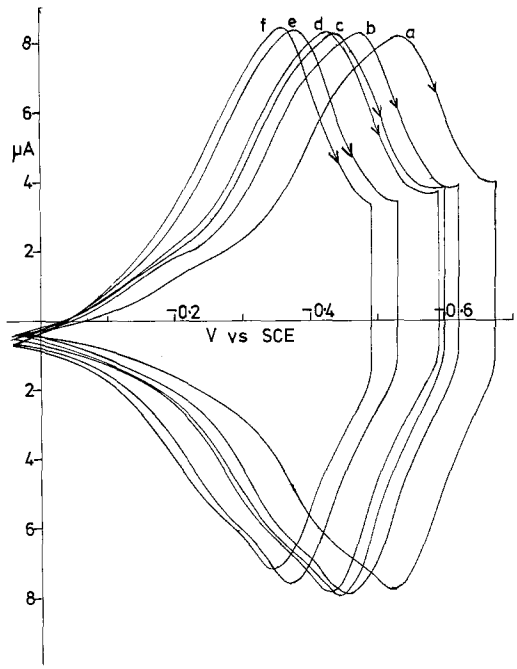


Fig. 3. Variation of scan cycle with acid strength. Conditions same as Fig. 2 but acid added as shown. (a) 10^{-2}M, (b) 6×10^{-2}M, (c) 1.08×10^{-1}M, (d) 1.58×10^{-1}M, (e) 6.2×10^{-1}M, (f) 1.04M.

event varies with the conditions of generation, particularly Mo concentration, stirring conditions, etc. On one occasion, for example, a layer was grown to about 40 mC/cm^2 total charge capacity over 25 hr of continuous cycling at 0.5 V/min before eventually becoming detached. The current/voltage curves obtained with layers as thick as this are rather poorly shaped with a pronounced overvoltage. Layers of up to about 20 mC/cm^2 total charge capacity[2] can be prepared, however, which when matured as shown in Fig. 2 have a peak separation of no more than 30 mV at 0.5 V/min. This separation is a function of the finite charge/discharge kinetic rate; *i.e.*, the degree of reduction of the layer lags behind its equilibrium value on the negative scan and the degree of reoxidation lags behind on the positive scan. At slower scan rates the peaks can be brought more nearly into coincidence.

Basic Properties

The variation of the scan of a matured layer with acid concentration is shown in Fig. 3. Though the layer behaves in a regular way beyond 1.0M acid, it is not stable at this concentration and the current slowly declines. The variation of E_0[3] with acid concentration is 0.095 V/decade (*i.e.*, approximately 0.095 V/pH unit).

The layer is stable indefinitely in solutions of pH 2 and may be dried in an air oven with no apparent change observable when returned to the solution. Heating to 220°C in air for 1 hr, however, degrades the performance of the layer causing a large reduction in the charge capacity and distortion of the I/V characteristics.

Thickness has been measured using multiple beam interferometry. A layer of 20.6 mC/cm^2 had an estimated average thickness of 0.15λ for Na-D, equivalent to 90 nm. This is consistent with layer of composition $MoO_2 \cdot 2H_2O$, density 4.0, and $n = 1$ (equivalent to 87.5 nm). This result is very tentative since the composition and density are no more than guesses based on the very meager information available on the hydrated lower oxides of molydenum. It may be sufficient to suggest, however, that the material probably has a compact rather than an open porous structure and that the charge/discharge phenomenon is a solid-state reaction of a novel type rather than a typical interfacial electrochemical reaction.

Charge/Potential Characteristic

This has been estimated in three ways.

Method (*i*): By graphical integration of the area under the linear sweep I/V curves,[4] up to the potential considered This can only give an approximate result because the curves are distorted by the finite charge/discharge rate This can be partly overcome by taking the total area, both reduction and oxidation, within the cyclic scan up to a given potential and dividing by two. The lag in equilibrium is to some extent then canceled out since it is of opposite sign for the reduction and the oxidation.

Method (*ii*): By charging the layer at a series of fixed potentials, allowing to come to equilibrium, and then scanning positively. The integrated area then represents the total charge absorbed at equilibrium at the potentials chosen, cf. Fig. 4. Since the current does not decline to zero but to a small constant value beyond about +0.1V, the choice of integration limit is somewhat arbitrary.

Method (*iii*): By charging up to a selected potential and reversing back to zero; the charge is taken as equivalent to half the total area.

The data was analyzed according to the Nernst equation

$$E - E_0 = -\frac{RT}{n\mathbf{F}} \ln\left(\frac{\gamma_R}{\gamma_O}\right)$$

where γ_R, γ_O are the activities of the reduced and oxidized forms at the potential E, and E_0 is the "standard potential" (taken as the midpoint of the reduction and oxidation peaks) Clearly the reduced and oxidized forms cannot be separate solid phases for which γ

[2] This is estimated from the charging characteristic as described in the following section.
[3] Defined in the following section.
[4] The charge is independent of scan rate between 0.5 and 0.1 V/min within the limits of experimental error.

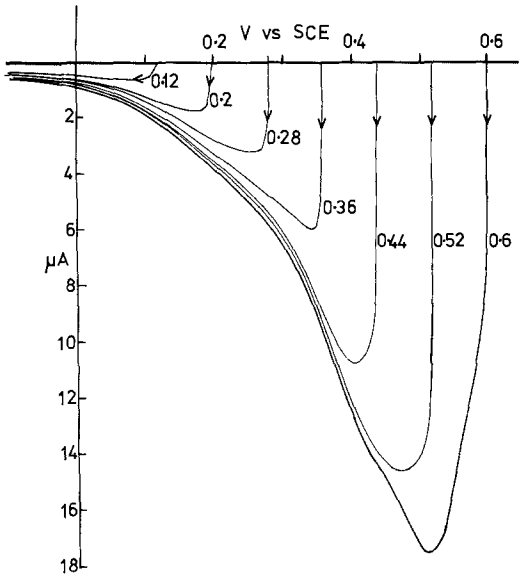


Fig. 4. Discharge current of matured layer. Charging potential indicated on curves (not the same layer as in Fig. 1 and 2). Conditions same as Fig. 2.

would be 1 or 0, otherwise the I/V curve would be a sharp pulse at the potential E_0. The assumption is first made that

$$\gamma \propto q_E$$

where q_E is the charge at potential E

$$\therefore E_0 - E = \frac{RT}{n\mathbf{F}} \ln (q_E/(Q - q_E))$$

where Q = total charge capacity. The value of Q cannot be determined directly since H_2 evolution sets in before reduction is complete. It is therefore assumed that the I/V curve is symmetrical about E_0 and that $Q = 2q_{E_0}$.

Figure 5 shows log $(q_E/(Q - q_E))$ plotted against E for a number of layer samples. The relationship is linear over most of the range with an average slope equal to 0.212 V/decade. This leads to the empirical relation

$$\gamma_R \propto q_E^{3.6} \text{ for } n = 1$$

or

$$\gamma_R \propto q_E^{7.2} \text{for } n = 2$$

Discharge Kinetics

The determination of the discharge rate is attendant with some difficulties.

The most direct method is to observe the discharge current as a function of time, but the dynamic range of this variable is so large (a few milliamperes down to a few microamperes in a few seconds) that a linear display is not sufficiently accurate. A further disadvantage of current measurements is that the current is relatively insensitive to reaction order (row 1, Table I).

Table I.

$\alpha = q/Q$ = fraction of discharge, where q = charge at time t, and Q = total charge capacity of layer.
$\alpha_0 = q_E/Q$, where q_E = initial charge at potential E.
$\alpha_\infty = q_\infty/Q = 0$ for 0.0V *vs.* SCE.
Rate expression $= -d\alpha/dt = K\alpha^n = I/Q$, where K = rate constant, n = "order," I = current at time t.

$n \neq 1$	$n = 2$	$n = 3$	$n = 4$
Current/time $I^{\frac{1-n}{n}} = (n-1)K(KQ)^{\frac{1-n}{n}} \cdot t + I_0^{\frac{1-n}{n}}$	$I^{-1/2} \propto t$	$I^{-2/3} \propto t$	$I^{-3/4} \propto t$
Concentration/time $\alpha^{1-n} = (n-1)Kt + \alpha_0^{1-n}$	$\alpha^{-1} \propto t$	$\alpha^{-2} \propto t$	$\alpha^{-3} \propto t$
Current/concentration $I = (QK)\,\alpha^n$	$I \propto \alpha^2$	$I \propto \alpha^3$	$I \propto \alpha^4$

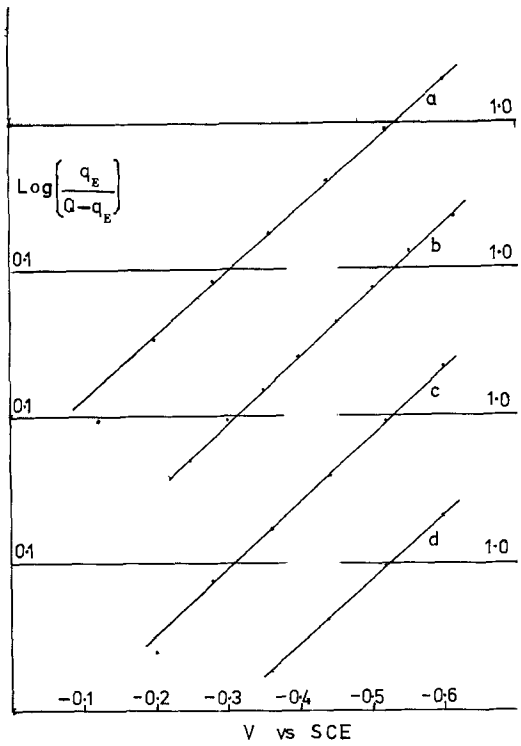


Fig. 5. Variation of log $q_E/(Q - q_E)$ with potential. Vertical axis calibrated in units of $q_E/(Q - q_E)$; successive graphs displaced by 1.0 log units. Solution and area as in Fig. 2. Total charge capacity and method of calculation: (a) 0.826 mC. Data for layer shown in Fig. 4, method (*ii*). (b) 1.45 mC, method (*i*). (c) 2.53 mC, method (*ii*). (d) 0.834 mC, method (*iii*).

An alternative technique is to record the charge flowing as a function of time. This has the advantage of a satisfactory dynamic range and a strong dependence on reaction order (row 2, Table I).

The instantaneous charge, q is now equal to $q_E - \int Idt$ and q_E can in principle be determined from the relationship

$$q_E = \int_0^\infty Idt$$

In practice, however, there is a residual current at zero volts as shown in Fig. 4 and the decline of current is very slow at long times so that the limiting value of $\int Idt$ is difficult to determine. The term q_E has therefore to be determined separately by the procedure described above [method (*ii*)], with the result that the value of q at long times becomes rather uncertain.

Layers were generated under standard conditions (1M NaCl, 0.01M HCl, 10^{-4}M Mo; 0.5 V/min) and then aged by cycling in Mo-free solution. They were then charged at fixed potentials with the potentiostat and switched suddenly to 0.0V. The current was either passed to a logarithmic amplifier or integrated electrically and the output in either case displayed on an oscilloscope.

Figure 6 and 7 show some examples of functions of charge and current, respectively, plotted against time; the assumption is made that $n = 3$ and the appropriate functions are selected from Table I. Although this value of n gives a fair fit for many such measurements, other data have been obtained in which the most appropriate value of n has varied from 2 to greater than 4. Therefore, it is not clear whether n should be an integer or indeed even a constant for different layers. A first-order reaction, which would be expected for a primary electrochemical process, seems ruled out, however. Neither is the charge (or current)/time characteristic obviously dependent on the diffusion of H^+ ions since a tenfold change (10^{-2}–10^{-1}M) has little effect on the observed rate. The rate is however some-

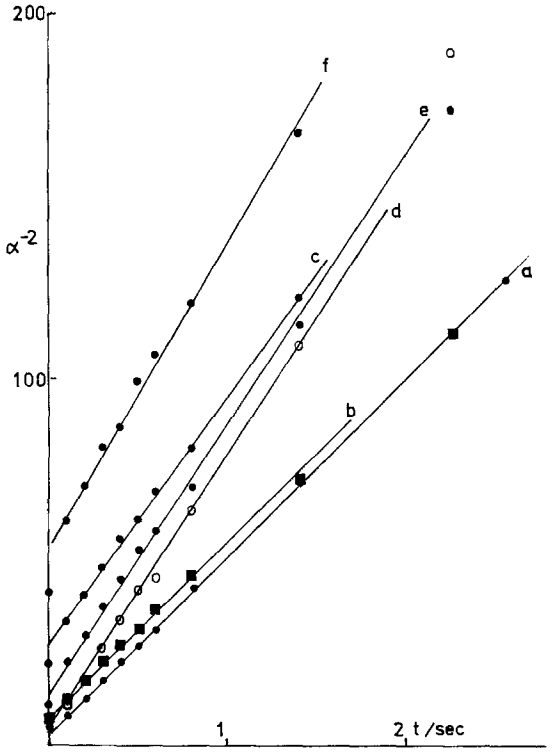


Fig. 6. Variation of α^{-2} with time for discharge from the potentials indicated below to 0.0V. Solution and area same as Fig. 2.

Total charge capacity (mC)	Potential (V) and charge (mC)					
3.08	(a) 0.52	1.46	(b) 0.48	1.18	(c) 0.40	0.653
0.834	(d) 0.52	0.406	(e) 0.44	0.246	(f) 0.36	0.129

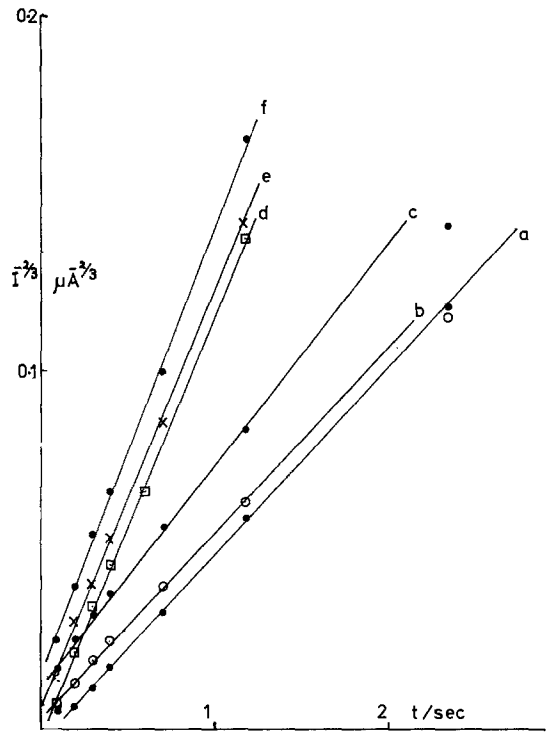


Fig. 7. Variation of $I^{-2/3}$ with time for discharge from the potentials indicated below to 0.0V. Solution and area same as Fig. 2.

Total charge capacity (mC)	Potential (V) and charge (mC)					
2.14	(a) 0.52	1.01	(b) 0.44	0.604	(c) 0.36	0.318
0.915	(d) 0.52	0.448	(e) 0.44	0.293	(f) 0.36	0.129

what decreased with increasing thickness (actually charge capacity Q).

Summary

The hydrous molybdenum oxide produced electrolytically under cyclic sweep conditions is an apparently solid and coherent layer of up to approximately 100 nm thickness. It undergoes reversible oxidation and reduction as a whole with a Nernst-like characteristic without any particular evidence of any diffusion of components in or out of it. The discharge rate is of second order or greater but the data is not sufficiently certain as yet to enable a model to be devised.

Manuscript submitted Feb. 1, 1977; revised manuscript received March 30, 1977.

Any discussion of this paper will appear in a Discussion Section to be published in the June 1978 JOURNAL. All discussions for the June 1978 Discussion Section should be submitted by Feb. 1, 1978.

REFERENCES

1. S. Gourgaud and D. Elliott, *This Journal*, **124**, 102 (1977).
2. E. Pechard, *Ann. Chim. Phys.* **28**, (6) 537 (1893); *Compt. Rend.*, **118**, 804 (1894); *Compt. Rend*, **148**, 744 (1907).
   H. Freundlich and W. Learhardt, *Koll. Beihefte.*, **7**, 172 (1915).
   P. Lagrange and J. P. Schwinge, *C. R. Acad. Sci. (Paris)*, **263**, 848 (1966).
3. C. F. Rammelsberg, *Pogg. Ann.*, **127**, 290 (1866).
   P. Klason, *Ber.*, **34**, 148 (1901).
4. D. Elliott, D. L. Zellmer, and H. A. Laitinen, *This Journal*, **117**, 1343 (1970).

The Corrosion of Steels in Molten Sodium Hydroxide

R. N. Newman, C. A. Smith, and R. J. Smith

Central Electricity Generating Board, Berkeley Nuclear Laboratories, Berkeley, Gloucestershire, United Kingdom

ABSTRACT

The role of sodium hydroxide corrosion is discussed in relation to the wastage of materials observed in fast reactor boilers under fault conditions in the vicinity of a water leak into sodium. An experimental technique to study the corrosion under varying conditions is described. The results presented are for 2¼ Cr-1Mo obtained in static sodium hydroxide in a closed volume over the temperature range 1033°-1273°K. It is found that the corrosion rate can be followed by monitoring the hydrogen produced by the reaction, which can be written as

$$Fe + 2NaOH = NaFeO_2 + NaH + \tfrac{1}{2} H_2$$

After an initial acceleration period the rate law is parabolic. The effect on the corrosion rate of melt and cover gas composition has been in part investigated, and the relevance of mass flow of reactant is discussed.

The importance of material damage in the vicinity of sodium-water leaks in sodium-cooled fast reactor boilers is well recognized. In order properly to quantify the enlargement of parent tube leaks and the wastage rate of secondary target tubes an understanding of the rate-determining steps in the process is required. A considerable amount of research effort has been applied throughout the world to investigate this phenomenon, of which most has been in the form of small and large scale modeling of the heat exchanger situation, and has provided a considerable amount of empirical data (1-3). This approach, however, has not led to a basic understanding of the processes involved, thus making the interpretation and extrapolation of the data obtained a difficult task.

It has been established that at the boundary of water/steam jets high temperatures are generated by the mixing of sodium and water and their rapid exothermic chemical reaction (1). Sodium droplets entrained from the jet envelope react as they are carried in the jet, thus creating on an adjacent tube a hot corrosive film of sodium and/or sodium-water reaction products (4, 5). It is, therefore, reasonable to assume that the wastage mechanism is integrally connected with the heat generated within this region, the hot products of the chemical reaction, or the flow of the reactants or product droplets over the metal surfaces.

Experiments to measure the relative magnitudes of the corrosive and erosive components of the wastage have been performed. Pure erosion studies have revealed that erosion of the parent material is the least likely mechanism (1, 6). Corrosion tests of boiler materials in sodium hydroxide at 973°-1473°K have been concluded to give lower wastage than found in sodium-water leak tests (1). More recently static corrosion measurements in molten sodium hydroxide were found not to account satisfactorily for wastage rates observed on steel specimens exposed to an inert gas jet containing entrained sodium hydroxide droplets, and an interaction between corrosion and erosion was postulated (6). Corrosion allows erosion to proceed by presenting a continuously weakened surface structure of solid-state corrosion products and/or parent metal whose structure has been weakened by corrosion (6, 7).

A reexamination of previous work shows that even pure corrosion studies can produce wastage rates within a factor of ~3 of that expected at leak sites (1). Modeling studies have given good correlation between extrapolated corrosion rates of steels in molten sodium hydroxide/water vapor and wastage rates of steels exposed in a bench-scale sodium vapor/water vapor jet flame (7). Corroded samples from these studies also show the same surface appearance, *i.e.*, smooth with little or no intergranular penetration, as those from real wastage tests (1). It is therefore apparent that a greater understanding of the corrosion process itself is required in order to comment upon its role in the sodium-water boiler wastage process.

Key words: iron, chromium, sodium, water, caustic melts.

To date, few studies have been made on the reaction of molten sodium hydroxide and iron or iron-based alloys. It has been found that iron, chromium, and ferrous alloys react to form metal oxides or sodium ternary oxides and hydrogen (8). Later studies have shown the enhancing effect of introducing water vapor and the very marked intergranular nature of the corrosion at the metal surface (7). The reaction has not, however, been studied in detail by a kinetic approach under controlled conditions.

This present study is mainly concerned with the corrosion rate of 2¼ Cr-1Mo samples in static molten sodium hydroxide in closed systems, and the kinetic results are presented. Additional work involving the role of water vapor, sodium, sodium oxide, and cover gas flow is at an early stage, but some preliminary findings are presented.

Experimental

Apparatus.—The apparatus for measuring the corrosion rate of metal samples is shown in Fig. 1 and consists of a stainless steel furnace tube, 27 mm internal diameter and 440 mm long, which has a manifold for evacuation and admittance of argon or hydrogen and a removable lid containing a sliding vacuum seal. The sodium hydroxide was held in this tube in a nickel beaker of 20 mm internal diameter and 280 mm long. The sample, of approximate dimensions 24 × 12 × 0.625 mm and containing a 3 mm hole, was tied to a ring on the plunger by a thin ribbon of nickel foil. The lower 130 mm of the plunger was 3 mm diameter nickel wire.

A Bell and Howell 0-3 × 10^5 nm^{-2}, 0-50 mV transducer was used for the pressure measurements. The transducer output was monitored with a Keithley 615 digital voltmeter coupled with a simple potentiometric backing off circuit so that the pressure changes could be traced on a 10 mV recorder, thus resolving a pressure change of ~3 × 10^1 nm^{-2}.

Modification of the system so that the atmosphere over the hydroxide could be continuously purged with purified argon, or other gas mixtures was made by replacing the lid with one having the appropriate inlet line. The hydrogen content of the argon leaving the apparatus was measured with either a mass spectrometer or katharometer. Water vapor can be added to the

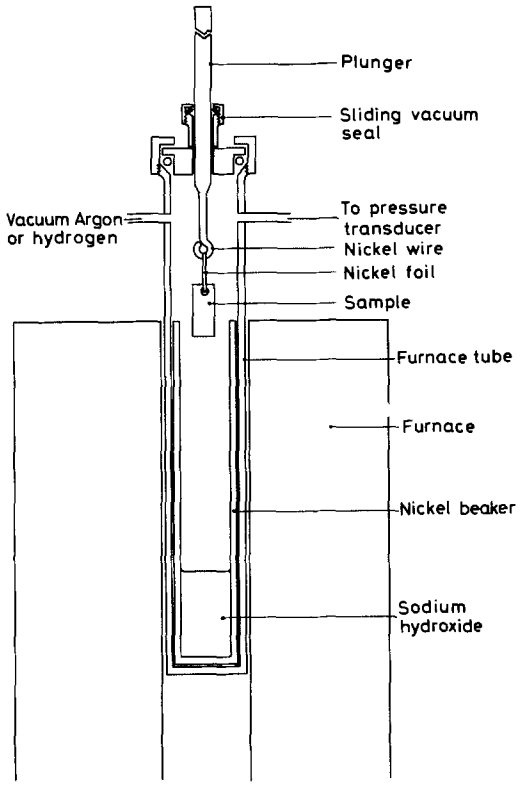


Fig. 1. Apparatus

argon by means of a water bubbler and by heating the appropriate gas lines to prevent condensation.

Experimental procedure.—Forty grams of sodium hydroxide (purity > 98% containing less than 1% sodium carbonate) was placed in the nickel beaker and heated at ~773°K under argon for a few minutes to remove traces of water. The beaker was placed in the furnace tube and the lid and plunger were replaced so that the sample was situated just above the nickel beaker.

The furnace temperature was monitored with a thermocouple placed between the furnace tube and the alumina liner of the furnace at a level near the midpoint of the sodium hydroxide. Independent tests confirmed that the temperature difference between this point and the sodium hydroxide was negligible (<5°K).

The furnace tube was evacuated while being warmed slowly to 523°-573°K before filling with hydrogen to ~1 × 10^5 nm^{-2}. The furnace was heated to the temperature of the experiment and, before immersion of the corrosion sample, the rate of hydrogen diffusion through the furnace tube walls was measured over the pressure range to be covered. This enabled a diffusion correction to be applied to the hydrogen pressures measured in the corrosion experiment. One reason for adopting this procedure was to inhibit the corrosion of the nickel beaker by the hydroxide by having a hydrogen pressure greater than the equilibrium pressure reported for this reaction by Williams *et al.* (8).

To initiate an experiment the plunger was depressed until the sample was immersed in the hydroxide and the increase in hydrogen pressure with time was recorded. At the end of the experiment, the sample was removed from the hydroxide to above the nickel beaker and allowed to cool.

Samples removed from the furnace were washed with excess water to remove sodium hydroxide and dried with acetone before weighing The adherent corrosion products were removed from the metal by etching with 50:50 phosphoric acid:water mixture at room temperature. Etching uncorroded metal samples in phosphoric acid for the same period of time showed that there was negligible attack on the parent metal under these conditions.

To determine the stoichiometry of the reaction, a correction must be applied to the measured gas pressure at the temperature of the experiment to enable its value at 273°K to be calculated. This correction was determined experimentally by filling the apparatus with argon at room temperature, heating to the required temperature, and measuring the gas pressure. A small correction was also required for the small increase in pressure produced by inserting the plunger into the furnace tube. This was measured at the temperature of each run and used to adjust each corrosion pressure trace.

Results

A typical experimental pressure recording is shown in Fig. 2 for a measurement at 1203°K. Part of the hydrogen decay curve from which the diffusion corrections were estimated is shown in the first part of the trace. The sharp trough and peak at the beginning and end of the sample exposure period was found from blank experiments to be due to the sudden cooling and heating of the gas volume, caused by the introduction and exit of the sample plunger.

Using an adaptation of the apparatus shown in Fig. 1, in which up to six small samples could be introduced consecutively to the melt and weight loss and hydrogen release measurements taken, the over-all stoichiometry of the reaction was examined over the time period of the main experiments. Figure 3 shows the consistency of the stoichiometry over the 90 min period. The mass loss is approximated to a loss in gram · atoms of iron, [≈Fe], due to the low percentage of

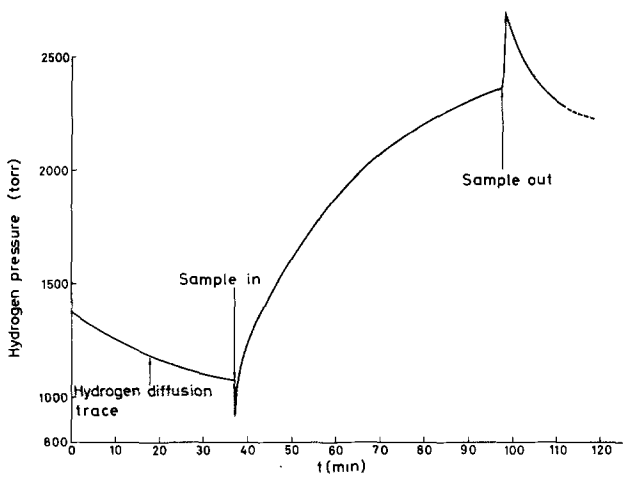


Fig. 2. Experimental pressure recording of corrosion process for 2¼ Cr-1Mo at 1203°K.

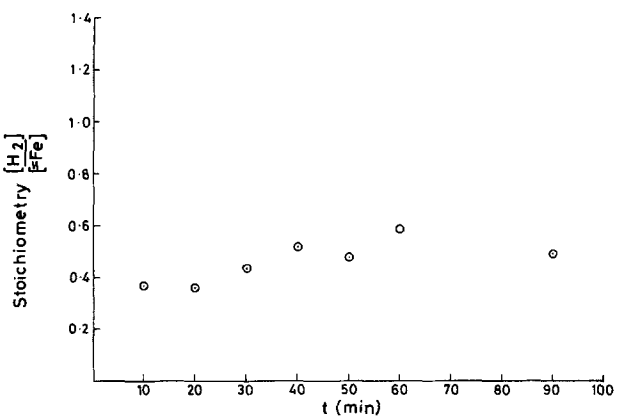


Fig. 3. Ratio of hydrogen produced to metal loss [≈Fe] with time of corrosion for 2¼ Cr-1Mo at 1203°K.

chromium in the steel and the small difference in atomic weights of chromium and iron (52:55.9).

The relationship between the corrected hydrogen pressure p_{H_2} and time was examined by plots of log p_{H_2} *vs.* log t. Beyond an initial period of 10-20 min, the value of d log p_{H_2}/d log t is near to 0.5, *i.e.*, there is a parabolic rate law. The actual values of d log p_{H_2}/d log t are shown in Fig. 4 over the temperature range 1033°-1273°K. Also shown are the values of the over-all stoichiometry after 90 min exposure to the hydroxide.

The parabolic nature of the rate dependence and initial period are illustrated in Fig. 5, where two typical plots of $(p_{H_2})^2/t$ against t at 1203° and 1153°K are shown. The close approximation to the parabolic relationship over the majority of the time period is clearly demonstrated.

Discussion

Static sodium hydroxide corrosion.—Previous work by the authors has shown that the major product of the reaction is a ternary oxide (7) and hydrogen. Williams *et al.* found that the reaction between iron and sodium hydroxide gave a stoichiometric ratio $\{H_2\}/\{\approx Fe\}$ of 3/2 and have interpreted the reaction in terms of the production of Fe_2O_3 and Na_2O or a sodium metalite (8). From examination of the stability of the $Na/H_2/NaOH$ system and identification of the corrosion products ($NaFeO_2$ and $NaCrO_2$) by x-ray powder crystallography (9), the stoichiometric ratio found in these experiments can be accounted for by writing the over-all reaction as

$$2Fe + 4NaOH = 2NaFeO_2 + H_2 + 2NaH \quad [1]$$

Chromium in the steel will react similarly.

The consistency of the parabolic region allows the calculation of a rate constant for the reaction expressed by the relationship

$$[H_2]^2 = kt \quad [2]$$

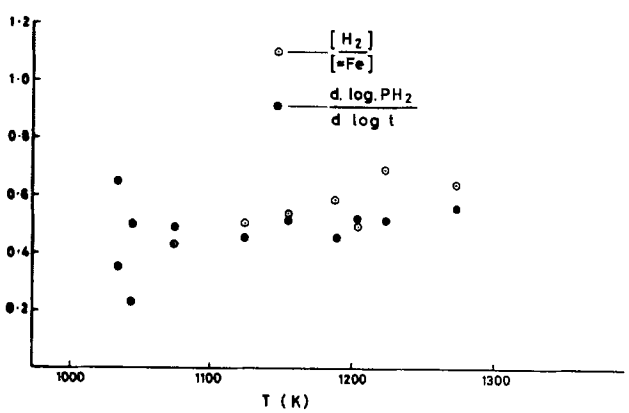


Fig. 4. Variation of stoichiometry of reaction products and d log p_{H_2}/d log t with temperature for 2¼ Cr-1Mo after 90 min exposure to $NaOH_{(l)}$.

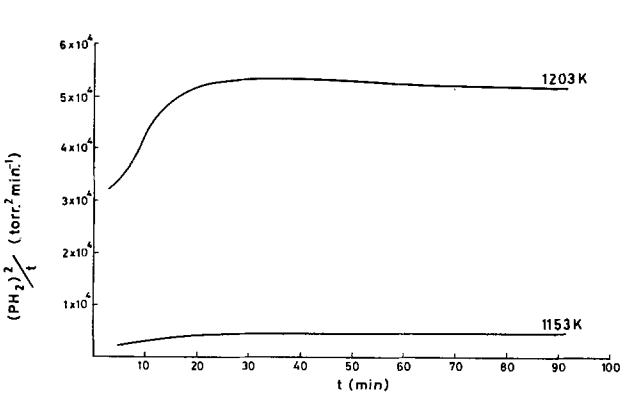


Fig. 5. Typical variation of $(p_{H_2})^2$ with time

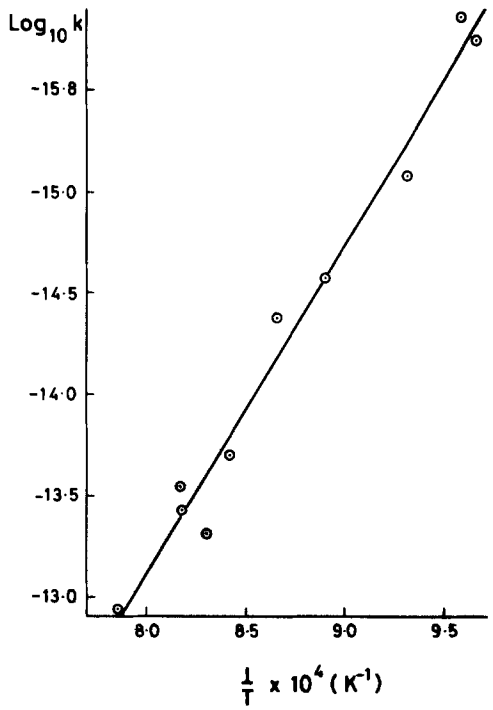


Fig. 6. The temperature dependence of rate constant K

where k has units of (moles of hydrogen $mm^{-2})^2 sec^{-1}$. The calculated values of k are displayed against temperature in an Arrhenius plot (Fig. 6) and show a straight line relationship from which k is derived as

$$k = 0.604e^{-37,000/T} \quad [3]$$

The induction period before the establishment of the parabolic rate law may in part be due to the heating of the sample to the melt temperature and the kinetics of hydrogen release from the melt.

Comparison of the present data with results reported previously (7) in which 2¼ Cr-1Mo samples were exposed to molten sodium hydroxide for periods of 5 min indicates that, in spite of the observed induction period, extrapolation of the parabolic expression to short time intervals gives good agreement with observed corrosion rates.

Hydrolysis of sodium hydroxide melts following the corrosion runs has confirmed the presence of sodium hydride through hydrogen evolution. Measurements of the amount of hydrogen released were consistent with the presence of approximately 1 mole of sodium hydride produced per gram · atom of iron/chromium consumed in the experiment. The stability of sodium hydride in sodium hydroxide was demonstrated by heating a 4 mole percent (m/o) solution of the hydride in the evacuated corrosion apparatus. The hydrogen pressure measured at 1073°K was constant at 1.41×10^5 nm^{-2} for the duration of the experiment, ~1½ hr, and indicated ~12% of the hydride had decomposed according to the reaction

$$NaH + NaOH = Na_2O + H_2 \quad [4]$$

The hydride is therefore apparently more stable than predicted from thermodynamic considerations based on JANAF (10) data with the assumption that the activities of dissolved oxide and hydride can be represented by mole fractions.

The rate of decomposition of the hydride was studied by bubbling argon through a corrosion melt and measuring the hydrogen content of the effluent gas with a katharometer. At 1203°K the process was found to be first order with a half-life of approximately 27 min when the argon flow was 2 ml sec^{-1} which is sufficiently large to give vigorous stirring of the solution. The observed stability of the hydride in the corrosion

runs is consequently a result of either solution interactions or kinetic limitations on its dissociation induced by the small area of gas-liquid interface of the sodium hydroxide and the limited stirring of the melt by convection. Figure 4 indicates that the stoichiometry of the corrosion reaction [1], $[H_2]/[\approx Fe]$ increases gradually with temperature and can be explained by the lower stability of the hydride and its greater rate of decomposition at the higher temperatures.

For reaction [1] to take place the free energy change must be a small positive to a negative value. Summation of thermodynamic data for sodium hydride and sodium hydroxide (10) indicates that the free energy of formation of sodium ferrite is given by the inequality

$$\Delta G(NaFeO_2) \lesssim -181{,}600 + 41T \text{ (cal mole}^{-1}\text{)} \quad [5]$$

The free energy of formation of sodium ferrite can be calculated from data given by Gross and Wilson (11) and Wu (12) to be

$$\Delta G(NaFeO_2) = -168{,}200 + 48T \quad \text{(from Gross and Wilson)} \quad [6]$$

$$\Delta G(NaFeO_2) = -181{,}350 + 47.5T \quad \text{(from Wu)} \quad [7]$$

Both expressions predict a free energy of formation which is less negative than required by Eq. [5], although Wu's data is more closely aligned with our experimental observations and those of Williams *et al.* (8) in which the corrosion reaction was interpreted as

$$6NaOH + 2Fe = Fe_2O_3 + 3Na_2O + 3H_2 \quad [8]$$

The results from other corrosion tests of 2¼ Cr-1Mo steel using sodium hydroxide under argon atmospheres have been reported (1). Maximum penetration was observed to occur mainly at the gas-liquid interface. The mean penetration cannot be derived accurately from the data since the surface area is not known, but estimates indicate that the mean is within a factor of four of the maximum. The maximum penetrations at 1300°K are in good agreement with our extrapolated data, while at 980°K Eq. [2] and [3] predict a penetration which is lower by a factor of ~65. The experimental conditions in the two experiments are dissimilar in the composition of the cover gas and the concentrations of reaction products and these factors may have some bearing on the different activation energies found for the corrosion process. Chamberlain (1) expressed the corrosion reaction as

$$3Fe + 8NaOH \rightarrow Fe_3O_4 + 4Na_2O + H_2 \quad [9]$$

The latter predicts an iron to sodium ratio of 0.91 when the reaction is complete. Reactions [1] and [8] would give ratios of 1.2 and 0.81, respectively, and if the sodium hydride were to distill from the reaction system following reaction [1] the ratio would increase to 2.4. Ratios of 1.3 to 1.9 were observed by Chamberlain at 1480°K, the larger value occurring at longer reaction times. At 1300°K a ratio of 1.1 was found which was virtually independent of time, but rationalization through Eq. [1] is unlikely since sodium hydride would be expected to dissociate and the sodium to distill at this temperature with long reaction times.

It was concluded by Chamberlain *et al.* (13) that as the primary reaction [9] or more generally

$$Fe + NaOH \rightarrow Fe_xO_y + Na_2O + H_2 \quad [10]$$

progressed to the right, a second corroding agent was formed, presumably Na_2O, which then reacted further with the iron according to

$$Fe + Na_2O \rightarrow Fe_xO_y + Na \quad [11]$$

with the evolution of free sodium. Secondary reactions may also take place as the evolved hydrogen reacts with and reduces the iron oxide to a lower oxide or iron

$$Fe_xO_y + H_2 \rightarrow Fe + H_2O \quad [12]$$

The difference in the experimental observations indicates that species produced in the reaction apart from determining the final product composition are also affecting the rate of the corrosion process. The presence of water vapor had previously been shown to increase the rate of corrosion of 2¼ Cr-1Mo by sodium hydroxide (7). Consequently a series of scoping experiments were performed to obtain comparative data of the influence of possible products and water vapor on the corrosion rate.

Further experiments varying the melt and gas composition.—Initial scoping experiments were to investigate the effect of sodium ferrite and sodium hydride on the corrosion rate. Sodium ferrite was added to the melts prior to corrosion runs at 1200°K. The results were somewhat inconclusive but indicated that at low concentrations (<3 m/o) there was no effect on the corrosion rate as determined from the weight loss compared with that predicted from Eq. [2] and [3] and the known stoichiometry of the reaction. At higher concentrations there was a small reduction in the corrosion rate which was accompanied by a reduction in the hydrogen released by the process. This effect was also observed by successively corroding samples in the same sodium hydroxide so that the ferrite concentration was allowed to rise. Samples removed from corrosion runs normally had a surface layer of adherent sodium ferrite which corresponded to up to 50% of the metal weight loss.

Addition of sodium (~4 m/o) to the hydroxide, followed by its conversion to the hydride by the addition of hydrogen prior to the corrosion run, produced a slight increase in the corrosion at 1200°K over that predicted.

Prior to studying the effect of passing gas mixtures through the hydroxide at 1200°K, control experiments were performed in which hydrogen was bubbled through the melt at ~2.5 ml sec^{-1}. The results obtained were identical with those found in the static system. Passing argon through the melt at the same temperature and flow rate approximately doubled the amount of corrosion. The stoichiometry of the reaction, $[H_2]/[\approx Fe]$ was found to be > 0.5 but <1 when the sample was removed, and hydrogen release from the solution was observed for some time afterward. The increased rate with argon flow may result from the presence of sodium oxide produced by the decomposition of sodium hydride as in reaction [4].

Hydrogen/water vapor mixtures were also found to increase the corrosion rate. The variation with water vapor pressure was difficult to quantify with the design of the water injection system used since raising the water vapor pressure produced a larger gas flow which cooled the sodium hydroxide. However raising the water vapor pressure initially increased the corrosion rate and an increase of a factor of two was observed with a water vapor pressure 8×10^4 nm^{-2} at 1200°K.

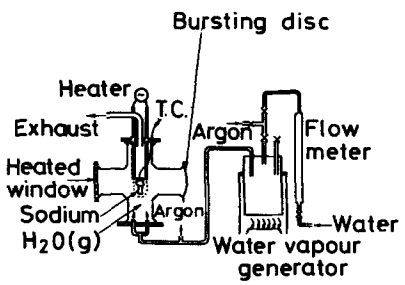
The addition of 30 m/o of sodium oxide to the melt resulted in a 5-fold increase in the corrosion rate at 1070°K. Consequently, changing the hydrogen cover gas to argon, the presence of water vapor and sodium oxide produce more rapid corrosion. High concentrations of sodium oxide would appear to be necessary to give larger effects on the corrosion rate.

In these experiments some nickel transfer was observed producing a porous deposit over the corrosion sample. To eliminate the possibility of a reduction in corrosion rate by this effect experiments were performed in alumina, silver, and 2¼ Cr-1Mo crucibles. Results in all cases were identical with those observed in nickel beakers.

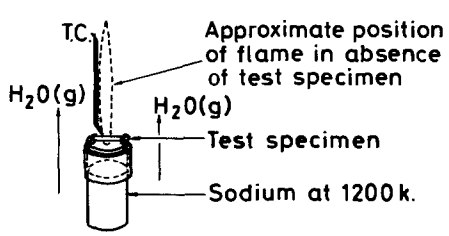
Experimental results in other systems have some bearing on the corrosion by sodium oxide. Sodium water flame studies were carried out using the apparatus shown in Fig. 7 in which sodium was boiled into water vapor at 1 atm pressure (7). Five grams of sodium boiled through the burner nozzle in 90 sec and produced a white-yellow laminar diffusion flame some 120 mm long and up to 7 mm in diameter. In wastage tests samples of candidate boiler materials were held ~2 mm above the burner nozzle which was constructed of 316 stainless steel. Thermocouples positioned on the side of the sample remote from the flame indicated temperatures of 1470°K during tests. Wastage of the nozzle was found to be seven times greater than the maximum wastage found on the 316 stainless steel samples. The temperature of the nozzle would be within the range of 1156°K (the boiling point of sodium) to 1470°K and the atmosphere in the nozzle would be sodium rich. If molten sodium hydroxide from the sodium-water reactor were present in this region calculations based on JANAF data (10) indicate that the equilibrium activity ratio for sodium oxide to sodium hydroxide would be >0.6 to >0.1 at the respective temperatures and suggests that the increased corrosion rate of the nozzle may result from the presence of sodium oxide.

Burning sodium in the above apparatus when the water vapor atmosphere had been replaced by air gave laminar sodium-oxygen flames where the product of the reaction was liquid monoxide (14). Wastage damage observed on 2¼ Cr-1Mo specimens exposed to these flames was found to be an order of magnitude smaller, from weight losses, than observed with sodium-water flames. The temperature of the specimens would be expected to be higher than those in the sodium-water flames tests. Sodium oxygen and sodium-water flame temperatures have been measured to be ~1700° and 1570°K, respectively (7, 14). It is possible that as the temperature is raised above the boiling point of sodium, sodium oxide has less effect on the corrosion process.

Rate-determining steps in wastage processes.—The parabolic rate expression implies the rate-controlling step in the sodium hydroxide corrosion of 2¼ Cr-1Mo is limited by diffusion through surface layers and the high activation energy is within the range of values quoted by Kubaschewski and Hopkins for the diffusion of metal or oxygen ions through double oxides (15). Detailed examination has not been made of the corrosion specimen surfaces but preliminary results indicate the strongly adherent corrosion product is chromium rich. Previous studies had shown the flame wastage of steels to vary linearly with their chromium content (7).



(i) General scheme showing containment and supply of water vapour.



(ii) Enlarged view of burner assembly and specimen mounting.

Fig. 7. Sodium-water flame apparatus

The majority of corrosion rates, as found by others (1, 6), are considerably lower than observed in water leak tests in sodium systems unless high temperatures are postulated for the target tubes. The influence of gas atmosphere and reaction products on the corrosion rate in static systems is relatively small in view of the above discrepancy. Consequently the flow of entrained material and sodium-water reaction products plays the major part in increasing the wastage rate observed in fast reactor boilers as modeled by Tregonning *et al.* (6). The detailed mechanism however has not been resolved. It has been suggested by Tregonning that the corrosion rates must be appreciably higher than is implied by the results of static corrosion tests and at least as high as the measured wastage rates, since the sensitivity of the wastage to the velocity of the hydroxide droplets entrained in the jet is low. The results from the present and previous experiments indicate two probable mechanisms for wastage at leak sites.

The surface of the corrosion specimens exposed to sodium-water flames exhibited little intergranular penetration in the region of maximum wastage (7). The surrounding metal showed considerable intergranular corrosion (7, 16) and suggests the enhanced corrosion may be the result of a process where the corrosion loosened metal grains in the maximum wastage area are removed by the erosive action of sodium hydroxide droplets produced in the flame.

The purely chemical aspect of this mechanism was exhibited in the sodium vapor-water vapor jet flames (16) when 316 stainless steel samples were exposed briefly to the flame some 70 mm from the nozzle where any erosive action of the smoke droplets formed would be expected to be minimal (6). During a 20 sec exposure to the flame at a temperature approaching 1473°K marked grain boundary penetrations of up to 5×10^{-3} mm sec^{-1} were observed without a measurable mass loss. It would be reasonable to assume that the grain boundary penetration rate would be dependent on the path length through the metal, thus removal of the overlying grains would shorten the path length and increase the rate.

This process would be more favored in the sodium-water leak jet where the larger entrained droplets would have a greater erosive effect than the smaller ($\lesssim 1$ μm) smoke droplets formed in the sodium vapor-water vapor flame. It would also be expected to occur at high jet temperatures where the proportion of entrained reactants was close to that of reaction [13]

$$Na_{(l)} + H_2O_{(g)} \rightarrow NaOH_{(l)} + \tfrac{1}{2} H_2 \qquad [13]$$

Secondly, corrosion in static systems where erosive forces are negligible has also produced surfaces with little intergranular penetration in the region of maximum wastage at the hydroxide cover gas interface (1, 7). The corrosion rates may be enhanced here by the thinning of the rate-restricting surface layers by solution or chemical processes to produce a transgranular reaction as rapid as the intergranular reaction. In the sodium-water leak jet this thinning would be related to mass flow effects, possibly the flux of entrained material on the target. Using the rate expression in Eq. [3] mass flow or secondary chemical effects

would need to reduce the surface layer to a steady-state thickness of $\simeq 5 \times 10^{-8}$m to maintain a wastage rate of $\simeq 4 \times 10^{-2}$ mm sec^{-1} at 1173°K. At lower temperatures near 973°K much lower thicknesses of $< 5 \times 10^{-9}$m would be required, and the extrapolation of the parabolic rate constant is probably invalid at this level. If the rate of reaction, however, is increased by the presence of sodium oxide, this mechanism becomes more feasible. A reaction between sodium oxide and the rate-restricting layers may produce a compound which is more soluble in sodium hydroxide. Consequently in the sodium-water jet, this mechanism would be favored at temperatures below the maximum jet temperatures when the jet temperature and product composition are controlled by the presence of excess sodium, reaction [14], following the complete reaction of the water

$$NaOH_{(l)} + Na_{(l)} \rightarrow Na_2O_{(s/l)} + \tfrac{1}{2} H_2 \qquad [14]$$

Until the water is completely consumed the amount of oxide present in the jet will be low since the reaction

$$Na_2O_{(s/l)} + H_2O_{(g)} \rightarrow 2NaOH_{(l)} \qquad [15]$$

is balanced appreciably in favor of sodium hydroxide at the temperatures of interest.

Conclusions

The corrosion of 2¼ Cr-1Mo in sodium hydroxide has been studied between 1033° and 1273°K by monitoring the hydrogen produced in the process. The observed chemical reaction in the closed reaction system with a hydrogen cover gas was

$$2Fe + 4NaOH = 2NaFeO_2 + H_2 + 2NaH$$

The rate law after an initial acceleration period was parabolic with

$$[H_2]^2 = kt$$

where the rate constant k has the units (moles of hydrogen mm^{-2})^2 sec^{-1}. The rate constant was found to vary with the temperature according to the expression

$$k = 0.604\, e^{-37{,}000/T}$$

The influence of water vapor, sodium hydride, sodium ferrite, and sodium oxide on the corrosion rate was found to be relatively small when compared with the difference between wastage rates observed in the static corrosion experiments and those in water injection tests. The most likely wastage mechanisms seem to involve both chemical and mass flow components but not necessarily erosion processes.

Acknowledgment

This paper is published by permission of the Central Electricity Generating Board.

Manuscript submitted Jan. 21, 1977; revised manuscript received March 30, 1977.

Any discussion of this paper will appear in a Discussion Section to be published in the June 1978 JOURNAL. All discussions for the June 1978 Discussion Section should be submitted by Feb. 1, 1978.

Publication costs of this article were assisted by the Central Electricity Generating Board.

REFERENCES

1. H. V. Chamberlain, Atomic Power Development Associates, Inc., APDA Report 257 (1970).
2. H. Nei, K. Ujhara, I. Ohshima, and M. Hori, Paper 2-4, Proceedings of Fast Reactor Safety Meeting, American Nuclear Society, Beverly Hills, California (April 1974).
3. D. A. Greene, *Nucl. Technol.*, **18**, 267 (1973).
4. R. Bell, B. E. Boyce, and J. G. Collier, *J. Br. Nucl. Energy Soc.*, **11** (2), 183 (1972).
5. T. D. A. Kennedy and J. D. Collier, Paper 83, Multiphase Flow Symposium, Institute of Chemical Engineering, Strathclyde (April 1974).
6. K. Tregonning, A. Mackay, and K. Buxton, *J. Br. Nucl. Energy Soc.*, **14** (1), 77 (1975).
7. R. N. Newman and C. A. Smith, *J. Nucl. Mater.*, **52**, 173 (1974).
8. D. D. Williams, J. A. Grand, and R. R. Miller, *J. Am. Chem. Soc.*, **78**, 5150 (1956).
9. A. J. Hooper, R. N. Newman, and C. A. Smith, Unpublished work.
10. JANAF Thermochemical Tables, Dow Chemical Co., Midland, Michigan (1970).
11. P. Gross and G. L. Wilson, *J. Chem. Soc., A*, 1913 (1970).
12. P. C. S. Wu, *Corrosion*, **31** (5), 168 (1975).
13. H. V. Chamberlain, J. H. Coleman, E. C. Kovacic, and A. A. Shondy, ANL 7520, Part 1, pp. 384-409 (1968).
14. R. N. Newman, CEGB Report RD/B/N2965 (1974).
15. O. Kubaschewski and B. E. Hopkins, "Oxidation of Metals and Alloys," Butterworths, London (1962).
16. P. Marshall, R. N. Newman, and C. A. Smith, *J. Nucl. Mater.*, **54**, 346 (1974).

The Effect of Trivalent Cations on the Conduction Characteristics of PbF_2

A. V. Joshi and C. C. Liang

P. R. Mallory & Company Incorporated, Laboratory for Physical Science, Burlington, Massachusetts 01803

ABSTRACT

The conduction characteristics of PbF_2 containing large amounts of AlF_3 were investigated in the temperature range between −50° and 300°C. It was found that the inclusion of high concentrations of AlF_3 stabilizes the cubic structure of PbF_2 and the application of a high pressure and/or mechanical stress on the PbF_2-AlF_3 sample does not result in a conversion from the cubic form to the orthorhombic form at ambient temperatures. Furthermore, the conductivity of PbF_2 was substantially increased by the incorporation of AlF_3. PbF_2 containing 12 mole percent (m/o) AlF_3 exhibited a room temperature conductivity of 1.1×10^{-4} $(\Omega\text{-cm})^{-1}$ and an activation energy for conduction of 8.2 ± 0.2 kcal/mole in the temperature range of −50°-70°C. However, the conductivity of this solid decreased substantially after annealing at a temperature above 100°C. Furthermore, the activation energy for conduction was found to be higher after annealing. The rate at which the conductivity decreases and the activation energy increases appeared to depend upon the temperature and duration of the annealing process. Inasmuch as the conductivity of the annealed sample could be increased to some extent by prolonged grinding, and the presence of an orthorhombic phase together with the predominate cubic phase was noted in the x-ray diffraction patterns of the annealed samples, we concluded that the decrease in conductivity by the annealing process may be attributed to (*i*) stress relief at the grain boundary or in the lattice upon annealing, (*ii*) partial structure conversion from the more conductive cubic form to the less conductive orthorhombic form upon annealing, and/or (*iii*) precipitation of AlF_3 or AlF_3-rich PbF_2-AlF_3 complexes from the supersaturated PbF_2-AlF_3 solid solution.

The conduction characteristics of lead fluoride in the orthorhombic form (α-PbF_2) and/or cubic form (β-PbF_2) have been studied by various investigators under a variety of conditions (1-5). It was noted from these studies that lead fluoride is virtually a pure ionic conductor and that the ionic conductivity of lead fluoride can be increased by both the monovalent and trivalent cation dopants indicating an anti-Frenkel defect structure. In view of these interesting conduction characteristics which suggest that lead fluoride may be a solid electrolyte material for solid electrolyte cells, we have widened our scope of investigation to study the effect of high concentrations of aluminum fluoride on the ionic conductivity and crystal structure of lead fluoride. The results of these investigations are discussed in this article.

Experimental

Material preparation.—Alfa Inorganics PbF_2 (99.9+% pure) and Cerac AlF_3 (99.5% pure) were used in this study without further purification. These materials were dried before use by heating in an evacuated flask at about 130°C for a minimum of 3 hr, and then transferred to a Vacuum Atmospheres dry box under argon atmosphere. The oxygen and moisture content of the box was always maintained below 15 ppm. All the sample preparations and some measurements were conducted in the dry box.

The solid solutions of PbF_2 and AlF_3 were prepared by melting in the argon atmosphere well-blended mixtures of appropriate amounts of PbF_2 and AlF_3. The resulting clear melts were quenched to ambient temperature and pulverized using a Fisher mechanical grinder. PbF_2-AlF_3 solid solutions containing 5-25 m/o AlF_3 were prepared.

Total conductivity measurements.—The total conductivities were measured at various temperatures. Graphite electrodes were used in the conductivity cells. The graphite/PbF_2-AlF_3/graphite conductivity cells were fabricated according to the following procedures.

A weighed amount of powder of the PbF_2-AlF_3 solid solution was prepressed at 4000 psi in a 0.6 in. diam steel die. While the prepressed pellet remained in the steel die, the electrode powder (graphite) was placed on both sides of the pellet, and the total assembly was pressed at 100,000 psi to form the conductivity cell. The geometric area of the pellet was calculated from the diameter, and the thickness of the pellet was determined by measuring a pellet of the same weight formed under similar conditions but without the graphite electrodes. The conductivity of the pellet was determined from the resistance of the conductivity cell which was held in a lava cell holder and measured by means of a General Radio Type 1650-B impedance bridge at 1000 Hz. Resistance measurements were also made with square wave excitation from 1000 to 10,000 Hz of a bridge constructed from Helipot precision potentiometers. A Tektronix Type E differential preamplifier made possible the application of only 3 mV peak to peak to the sample. The same results were obtained using both techniques.

A Blue M Model M10A resistance furnace was used to maintain the temperature of the conductivity cell above ambient. For the measurements at temperatures below ambient the conductivity cells were sealed in steel containers using glass-to-metal seals. A Blue M Versa-Range test chamber was used to maintain the temperature of the sealed conductivity cells below ambient.

Electronic conductivity measurements.—A Pb/PbF_2-12 m/o AlF_3/graphite cell was used for electronic conductivity measurements. The cell was constructed in the dry box according to the following procedures. A weighed amount of PbF_2-12 m/o AlF_3 powder was prepressed at 4000 psi in a 1 in. diam steel die. A well-blended mixture of Pb and PbF_2-12 m/o AlF_3 solid-solution powder was placed on one side while graphite powder was placed on the other side of the prepressed

Key words: lead fluoride, ionic conductivity, solid electrolyte, aluminum fluoride, solid solution.

pellet. The assembly was then pressed under a final pressure of 100,000 psi to form the Pb/PbF_2-12 m/o AlF_3/graphite cell. A mercury battery with a voltage divider was used as a constant potential source to furnish the polarization potentials for the Pb/PbF_2-12 m/o AlF_3/graphite cell. The polarization potential was measured by a Keithley 610B electrometer, and the current in response to the polarization potential was monitored across a precision resistor using a Dana Model 5500 digital voltmeter.

X-ray diffraction analysis.—Debye-Scherrer powder patterns of the PbF_2-AlF_3 solid solutions containing various amounts of AlF_3 were obtained at room temperature with CuKα radiation. The lattice parameter of each solid solution was obtained by the Nelson-Riley extrapolation based on the x-ray patterns. The uncertainty in the results was about ±0.01Å.

Results

Lead fluoride can exist at room temperature in either orthorhombic form (α-PbF_2) or cubic form (β-PbF_2) (1, 2). The cubic form of PbF_2 can be converted to the orthorhombic form at room temperature upon the application of pressure or stress. For example, Kennedy *et al.* (2) found that β-PbF_2 was converted to α-PbF_2 at pressures above 30,000 psi, while Liang and Joshi (1) found that the β-PbF_2 powder was converted to α-PbF_2 completely upon grinding in a mechanical grinder for about 2 hr. These characteristics were also observed in PbF_2 containing small amounts of aliovalent cation dopants. It was noted from the x-ray analysis that the PbF_2-AlF_3 (5-15 m/o) solid solutions were in the cubic form. Unlike the pure PbF_2 or PbF_2 doped with small amounts of aliovalent impurities (1, 2), the PbF_2-AlF_3 solid solutions retained the cubic structure of PbF_2 even after grinding for 2 hr and/or pressing the powder in a steel die at 100,000 psi at room temperature.

The lattice parameters of the PbF_2-AlF_3 solid solutions are given in Fig. 1. It was noted that the uncertainty of the measurements made the exact determination of the lattice parameter rather difficult. Nevertheless, the results indicated strongly that within the solubility limit of AlF_3 in PbF_2 the lattice parameter decreased linearly with the concentration of AlF_3.

The incorporation of aluminum fluoride caused a nonlinear increase in the conductivity of the polycrystalline PbF_2. Figure 2 shows the conductivity of PbF_2-AlF_3 solid solution as a function of aluminum fluoride content at 27° ± 2°C. It was noted that the maximum conductivity of about 10^{-4} $(\Omega\text{-cm})^{-1}$ was attained at 12 m/o AlF_3. Furthermore, the conductivity

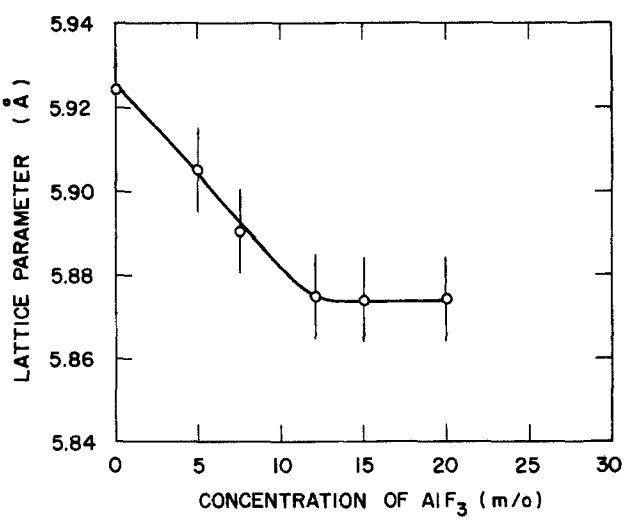


Fig. 1. Lattice parameter of the cubic PbF_2 as a function of AlF_3 content.

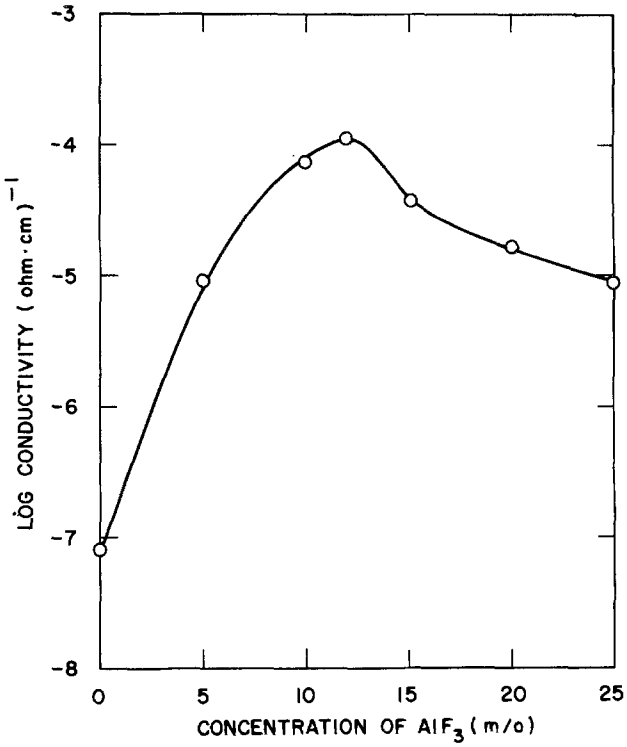


Fig. 2. Effect of AlF_3 content on the conductivity of β-PbF_2 at 27° ± 2°C.

did not change with time on storage at room temperature.

The d-c polarization measurements were carried out on a Pb/PbF_2-12 m/o AlF_3/graphite cell to deduce the partial electronic conductivity of the PbF_2-12 m/o AlF_3 solid solution. Wagner (6) showed that the total electronic current I_T can be related to the polarization potential by the following expression

$$I_T = I_e + I_h = \frac{RTA}{LF}\{\sigma_e^\circ[1 - \exp(-EF/RT)] + \sigma_h^\circ[\exp(EF/RT) + 1]\} \quad [1]$$

where I_e and I_h denote the electronic current due to electrons and electron holes, respectively; A represents the geometric area of the interface between the graphite electrode and the PbF_2-AlF_3 pellet; L represents the thickness of PbF_2-AlF_3 pellet; σ_e° and σ_h° are, respectively, the conductivities due to electrons and electron holes in PbF_2-AlF_3 equilibrated with Pb; and the other symbols have their usual meanings. Figure 3 shows the log I *vs.* E characteristics of the Pb/PbF_2-12 m/o AlF_3/graphite cell. In view of Eq. [1], the present results indicate a predominance of electrons as carriers for the electronic conductivities. Therefore, Eq. [1] can be reduced to

$$I_T = I_e = \frac{RTA}{LF}(\sigma_e^\circ); \text{ for } \exp(-EF/RT) \ll 1 \quad [2]$$

The electronic conductivity was obtained by using Eq. [2]. The value of I_e in Eq. [2] was estimated from Fig. 3 as the average value corresponding to the plateau. Based on these results, it was estimated that the electronic conductivity of the PbF_2-12 m/o AlF_3 solid equilibrated with Pb is 1.1×10^{-9} $(\Omega\text{-cm})^{-1}$ at room temperature. Consequently, the PbF_2-AlF_3 solutions are virtually pure ionic conductors and the value of the total conductivity of the solid solution is to be regarded as that of the ionic conductivity.

The fact that the PbF_2-AlF_3 solid solutions are virtually pure ionic conductors was further demonstrated by the open-circuit voltages of the Pb/PbF_2-AlF_3/AgF, Ag electrochemical cells. In these cells PbF_2-5 m/o AlF_3, PbF_2-10 m/o AlF_3, and PbF_2-12 m/o AlF_3

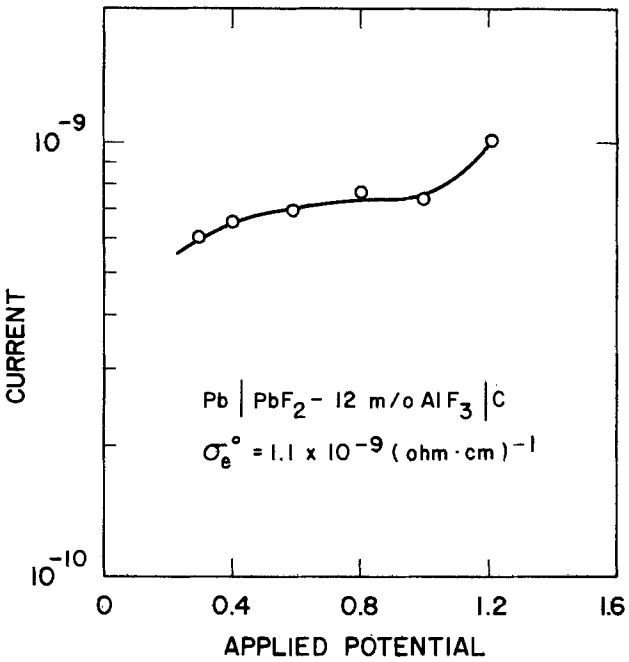


Fig. 3. Electronic current as a function of polarization potential on the Pb/PbF_2-12 m/o AlF_3/graphite cell.

were used as the solid electrolytes; a well-blended powder mixture of Pb and electrolyte was used as the anode material and a well-blended powder mixture of AgF, Ag, and electrolyte was used as the cathode material. The cells were fabricated by pressing the powders in a 0.6 in. diam steel die in a similar manner as the conductivity cells. The open-circuit voltages of the Pb/PbF_2-AlF_3/AgF, Ag cells, measured by a Keithley 610B electrometer, were 1.28 ± 0.01V at 26 ± 3°C. In view of the fact that the measured open-circuit voltage agreed well with the emf value of 1.284V calculated from the thermodynamic data (9) based on the cell reaction Pb + 2AgF → PbF_2 + Ag, we concluded that the PbF_2-AlF_3 solid solutions are virtually pure ionic conductors, and are suitable as solid electrolyte materials.

The conductivities of various PbF_2-AlF_3 solid solutions at temperatures ranging between −50° and +70°C are shown by the log σ *vs.* $1/T$ plots in Fig. 4. From these plots the activation energy for the conduction process in the temperature range between −50° and +70°C was determined to be 8.2 ± 0.2 kcal/mole. Both the log σ *vs.* $1/T$ plot and the value of the conductivity at a given temperature in this temperature range were found to be reproducible and did not depend on the direction of temperature change (descending or ascending temperature). In fact, we found that the value of conductivity at a given temperature was stable at temperatures as high as 100°C. However, when the temperature ascended beyond 100°C we noted that the conductivity decreased with time. Furthermore, the log σ *vs.* $1/T$ plot obtained in the direction of descending temperatures had a higher slope than that in the ascending direction, indicating a higher activation energy as shown by the log σ *vs.* $1/T$ plots in the temperature range between 27° and 150°C (Fig. 5).

It was also observed that the rate of conductivity change in the PbF_2-AlF_3 solid solutions at a given temperature above 100°C depended on the temperature. As a result, the conductivity values in the descending conductivity *vs.* temperature curve in Fig. 5 may not be those at equilibrium. Therefore, the solid solutions were annealed at 400°C for various periods of time and their conductivities were measured at room temperature to determine the required annealing time to reach equilibrium. It was found that the equilibrium

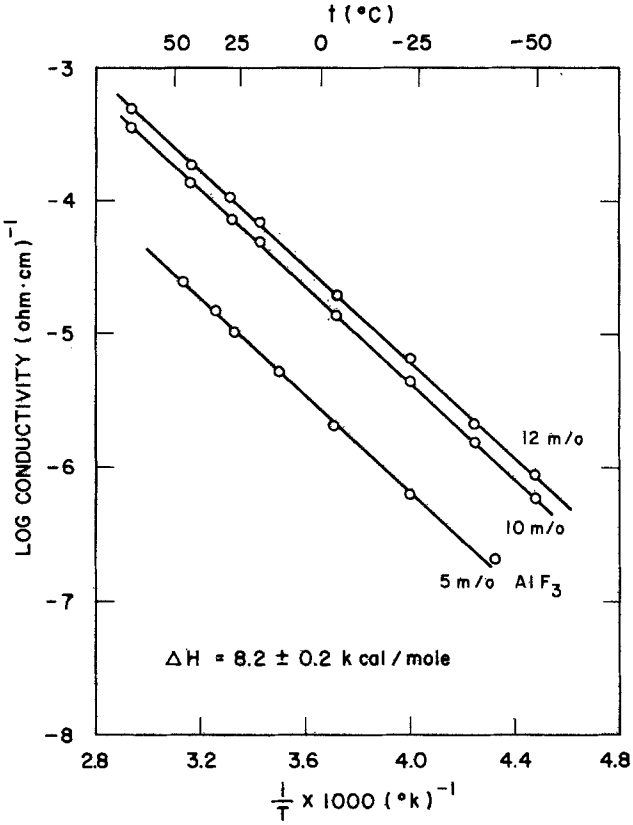


Fig. 4. Conductivity of the PbF_2-AlF_3 solid solution as a function of temperature.

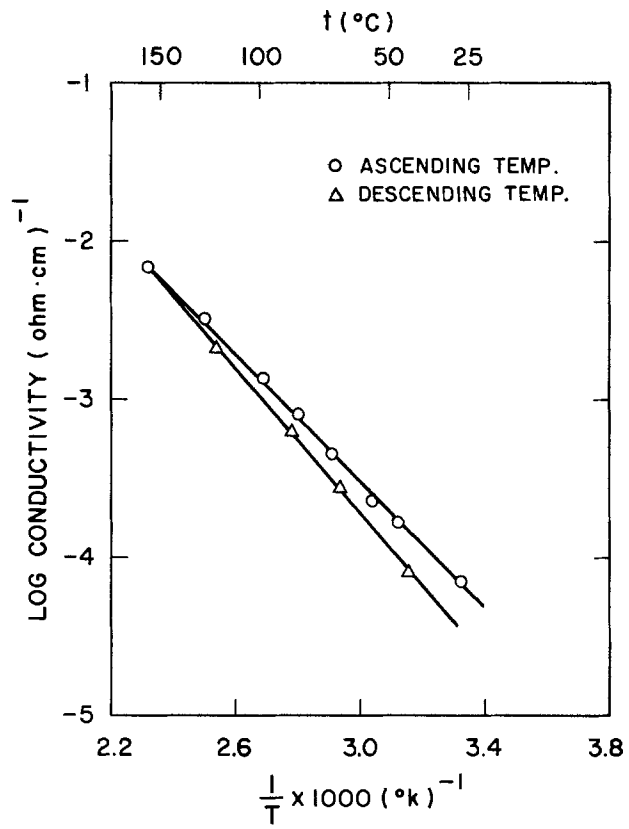


Fig. 5. Effect of the direction of temperature change on the conduction behavior of the PbF_2-10 m/o AlF_3 solid solution.

conditions were attained after a 20 hr annealing treatment. The log σ *vs.* $1/T$ plots for the PbF_2-AlF_3 solid solutions after the 400°C annealing treatment are shown in Fig. 6. It is noted from Fig. 6 that in the temperature range of 27°-125°C the activation energy

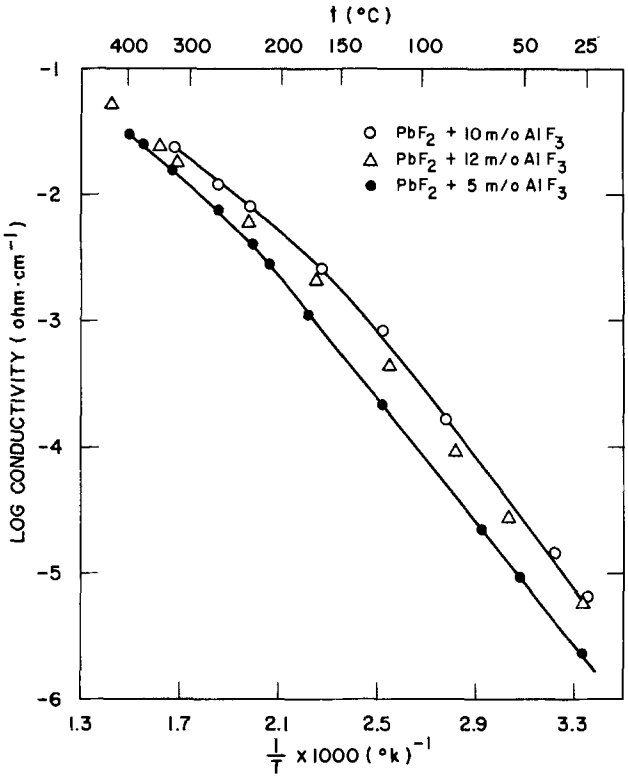


Fig. 6. Conductivity as a function of temperature for PbF_2 containing various concentrations of AlF_3 after annealing at 400°C.

for the conduction process, 12 kcal/mole, agreed well with that of the nominally pure PbF_2 and PbF_2 containing a small amount of YF_3 dopant (1). On the other hand, a decrease in activation energy is clearly noted at higher temperatures. The activation energy in the temperature range of 230°-400°C was found to be 7 kcal/mole.

In order to examine whether or not a phase transition had taken place during the 400°C annealing treatment, we obtained x-ray diffraction patterns on the annealed powder samples. It was noted that the cubic phase was still predominant. However, the patterns did show that some orthorhombic phase was present as a result of the annealing treatment.

It was further noted that the conductivity of the PbF_2-AlF_3 solid could be increased substantially by the application of mechanical stress such as prolonged grinding. For example, the room temperature conductivity of the 400°C annealed PbF_2-12 m/o AlF_3 was increased from 5.1×10^{-6} $(\Omega\text{-cm})^{-1}$ to 4.8×10^{-5} $(\Omega\text{-cm})^{-1}$ by grinding the sample in a mechanical grinder for 3 hr. Table I shows the comparison of the conductivity of the PbF_2-12 m/o AlF_3 solid solution before annealing, after annealing, and after annealing followed by the grinding treatment.

Discussion

In a recent study, Lucat *et al.* (4) found that β-PbF_2 and BiF_3 form solid solutions. Furthermore, these investigators found that the lattice parameters of β-PbF_2 decrease linearly with an increasing BiF_3 concentration in the solid solution. Inasmuch as the ionic radius of Bi^{3+} (0.96Å) is smaller than that of Pb^{2+} (1.20Å), the decrease in the lattice parameter indicates a substitutional dissolution of BiF_3 in β-PbF_2. The experimental results in the present study showed a similar behavior in the β-PbF_2-AlF_3 system. Figure 1 shows that the lattice parameter of the cubic lead fluoride decreases linearly with an increasing aluminum fluoride concentration in accordance with the Vegard law up to 12 m/o AlF_3. The fact that an AlF_3 concentration higher than 12 m/o does not result in a further decrease in the lattice parameter (Fig. 1) suggests that the solubility of aluminum fluoride in cubic lead fluoride is about 12 m/o under the experimental conditions. This conclusion is supported by the fact that the maximum conductivity of PbF_2 containing AlF_3 at room temperature was attained at PbF_2-12 m/o AlF_3, as shown in Fig. 2.

Table I. Effect of thermal and/or mechanical treatment on the conductivity of PbF_2-12 m/o AlF_3

	Treatment	Conductivity at 27° ± 2°C $(\Omega\text{-cm})^{-1}$
A.	Quenched from clear melt to room temperature and ground for about 3 hr	1.1×10^{-4}
B.	(A) followed by annealing at 400°C for 20 hr	5.1×10^{-6}
C.	(B) followed by grinding for 3 hr	4.8×10^{-5}

The cubic β-PbF_2 (both pure or containing small amount of aliovalent cation impurities) can be converted to α-PbF_2 by pressing at a pressure of 30,000 psi or higher (1, 2) or by prolonged grinding in a mechanical grinder (1). In other words, the cubic lead fluoride is not stable under pressure and/or stress. We have found, however, when a large amount of AlF_3 is dissolved in PbF_2, the cubic form is quite stable. Indeed, x-ray diffraction patterns showed that PbF_2-5 m/o AlF_3, PbF_2-10 m/o AlF_3, PbF_2-12 m/o AlF_3, and PbF_2-15 m/o AlF_3 were in the cubic form even after these powders had been ground in a mechanical grinder for more than 3 hr and/or pressed under a pressure as high as 100,000 psi. These results showed that the dissolution of relatively large amounts (5-15 m/o) of AlF_3 stabilizes the cubic structure of PbF_2.

The stability of the cubic form of lead fluoride containing a relatively large amount of AlF_3 enabled us to fabricate the β-PbF_2 conductivity cells by a simple powder pressing process. In previous studies (1) we found that it was necessary to sinter the pressed pellet, followed by a slow cooling process to room temperature to fabricate the β-PbF_2 conductivity cells. These postpressing sintering and cooling processes were no longer necessary in fabricating the β-PbF_2 (AlF_3) conductivity cells at room temperature. It is noted in Fig. 2 that a conductivity as high as 10^{-4} $(\Omega\text{-cm})^{-1}$ at room temperature is attainable at an AlF_3 concentration of 12 m/o. Figure 3 shows that the electronic conductivity of the PbF_2-AlF_3 solid solution is as low as 10^{-9} $(\Omega\text{-cm})^{-1}$ at room temperature, which means that the electronic transference number of the PbF_2-AlF_3 solid solutions is as low as 10^{-5}. Furthermore, the open-circuit voltage value of 1.28 ±0.01V for the Pb/PbF_2-AlF_3/AgF, Ag cell agrees well with the emf value of 1.284V calculated from the thermodynamic data. Therefore, the solid solutions are virtually pure ionic conductors suitable as solid electrolyte materials.

An interesting anomaly is also noted in Fig. 2. The conductivity of the β-PbF_2-AlF_3 solids does not increase linearly with the AlF_3 concentration. In fact, we have plotted in Fig. 2 the log σ *vs.* AlF_3 concentration to show that the conductivity increases at a much higher rate than predicted by the classical defect formation model with respect to the AlF_3 concentration. These characteristics are discussed in detail as follows. It has been shown (1) that β-PbF_2 has a Frenkel-type defect structure and the intrinsic point defects are interstitial fluoride ions and fluoride ion vacancies. Accordingly, upon the incorporation of AlF_3 in the β-PbF_2 lattice, the interstitial fluoride ions are induced according to the following equation

$$AlF_3 \rightarrow Al^{\cdot}_{Pb} + 2F_F^{x} + F_i' \qquad [3]$$

where $Al^{\cdot}_{Pb}$ denotes the aluminum ion at a lead ion site with an effective charge of +1, F_F^{x} and F_i' represent, respectively, the fluoride ion at a fluoride ion site and the interstitial fluoride ion with an effective charge

of −1. Based on Eq. [3] it is reasonable to assume that the concentration of the interstitial fluoride ions is much higher than that of the fluoride ion vacancies in the AlF_3-doped β-PbF_2, and the conductivity, σ, should be a linear function of the AlF_3 concentration in view of the following equation

$$\sigma = n_{F_i'} e \mu_{F_i'} \quad [4]$$

where $n_{F_i'}$ and $\mu_{F_i'}$ denote the concentration and the mobility of the interstitial fluoride ion and e represents the electronic charge. The experimental fact was that upon dissolution of AlF_3 the conductivity of β-PbF_2 increased substantially more than predicted by Eq. [3] and [4]. A similar observation was made by Kennedy and Miles (3), who studied the effect of monovalent cation dopants in PbF_2 and found that at higher doping levels the conductivities of PbF_2 were higher than predicted by the linear increase in the defect concentration. They attributed this behavior to the decrease in activation energy at higher doping levels. This explanation, however, cannot be applied to the present case inasmuch as we have found that the activation energy for the conduction process is constant for all the PbF_2-AlF_3 solid solutions as shown in Fig. 4.

The defect structure of the fluorite solid solutions of CaF_2 and YF_3 was investigated by Cheetham *et al.* (7). Based on the results of the Bragg neutron diffraction studies, these investigators concluded that the dissolution of YF_3 in CaF_2 resulted in the formation of two types of fluoride interstitials (F_I' located along the <110> direction and F_{II}' located along the <111> direction from the cubic position), and a fluoride ion vacancy. Furthermore, based on the observed occupation numbers, Cheetham *et al.* proposed that these defects appeared in various types of defect clusters in the solid solutions. It is possible, according to the cluster model, that in heavily doped crystals the number of vacancies would increase more rapidly with respect to the dopant concentration than predicted by the classical substitutional model Lucat *et al.* (4) applied this model to describe the conduction characteristics of the PbF_2-BiF_3 solid solutions. They attributed the high conductivity of the solid solution to the high mobility of the vacancies.

The conduction mechanism based on the defect clusters cannot be confirmed or denied by the present investigation. Nonetheless, it is unlikely that a straightforward fluoride ion vacancy mechanism prevails in the PbF_2-AlF_3 solid solutions, as shown in the following discussion. It has been shown in a previous investigation (1) that the activation energy for the mobility of fluoride ion vacancies is 4.1 kcal/mole in β-PbF_2. We have observed in the present studies that the activation energy for the conduction process of the PbF_2-AlF_3 solids is 8.2 ± 0.2 kcal/mole. Consequently, the fluoride ion vacancy mechanism cannot be applied to the PbF_2-AlF_3 solid solutions. On the other hand, it has been shown (1) that the activation energy for the mobility of interstitial fluoride ions is 14 kcal/mole in β-PbF_2, which is also considerably different from the 8.2 kcal/mole obtained for the PbF_2-AlF_3 solids. Furthermore, the nonlinearity of the conductivity *vs.* AlF_3 concentration plot (Fig. 1) shows that a simple fluoride ion interstitial mechanism cannot be applied to the present case. Although a detailed conduction mechanism cannot be elucidated for the PbF_2-AlF_3 solid solutions from the available data, it can be concluded that it is a complex one involving both vacancies and interstitials, and possibly even defect clusters.

As we discussed in the previous section, the conductivities of the PbF_2-AlF_3 solid solutions are stable at relatively low temperatures. No change in the values of conductivities is observed even after a prolonged storage period at room temperature. However, it has been observed that annealing the solid solution at a temperature above 100°C results in a substantial decrease in the conductivity and a substantial increase in activation energy (Fig. 5 and 6). On the other hand, the room temperature conductivity of the high temperature annealed sample can be increased, though not to the level of the preannealing sample, by grinding the powder in a mechanical grinder. These characteristics may be due to one or more of the following factors:

1. *Stress factors.*—The solid solution was prepared by heating the PbF_2-AlF_3 powder mixture to 1000°C to form a clear melt then quenched to room temperature. The quenching process may result in a great deal of stress to the solid solution. Another way of looking at this situation would be that a large number of line defects would be frozen in the solid solution. The stress or line defects may contribute to the conduction process, resulting in a higher conductivity. The annealing process would relieve the stress or annihilate the line defects created by quenching. Consequently, a decrease in conductivity was observed after annealing. The annealed sample can be restressed or the line defects in the sample can be reformed by the application of mechanical stress such as grinding in a mechanical grinder for a long period of time. Indeed, after grinding the conductivity was again increased, as shown in Table I. It should be noted that the positions of the lines in the x-ray diffraction patterns of the annealed samples are identical to those of the ground samples. However, the lines in the patterns of the ground samples are broader and less intense, indicating a more glassy or amorphous nature of the solid solutions.

2. *Orthorhombic phase.*—It is possible that a conversion of the cubic phase to the less conductive orthorhombic phase (1) takes place upon annealing. We noted from the x-ray diffraction patterns that indeed some orthorhombic phase along with a prominate cubic phase was present in samples which were annealed at 400°C for about 20 hr. Consequently, a partial conversion upon annealing may also be one of the causes for the decrease in conductivity.

3. *Precipitation of AlF_3.*—It is conceivable that the quenched PbF_2-AlF_3 solid solutions are supersaturated with AlF_3. Upon annealing, AlF_3 may precipitate from the solid solution as AlF_3 or as low conductivity AlF_3-rich PbF_2-AlF_3 complexes (8). As a result, the annealing process decreased the conductivity of the PbF_2-AlF_3 solid solutions. It should be noted, however, that in the x-ray diffraction patterns of the annealed PbF_2-AlF_3 sample we did not observe any lines which may be attributed to a separate phase of AlF_3. Nonetheless, we would not rule out the precipitation of AlF_3 as being a possible cause for the decrease in conductivity upon annealing the PbF_2-AlF_3 solids, in view of the fact that detection of small amount of impurities from x-ray diffraction patterns may be difficult.

Manuscript submitted Jan. 5, 1977; revised manuscript received March 22, 1977. This was Paper 69 presented at the Washington, D.C., Meeting of the Society, May 2-7, 1976.

Any discussion of this paper will appear in a Discussion Section to be published in the June 1978 JOURNAL. All discussions for the June 1978 Discussion Section should be submitted by Feb. 1, 1978.

Publication costs of this article were assisted by P. R. Mallory & Company Incorporated.

REFERENCES

1. C. C. Liang and A. V. Joshi, *This Journal*, **122**, 466 (1975).
2. J. H. Kennedy, R. Miles, and J. Hunter, *ibid.*, **120**, 1441 (1973).
3. J. H. Kennedy and R. C. Miles, *ibid.*, **123**, 47 (1976).
4. C. Lucat, G. Campet, J. Claverie, J. Portier, J. M. Reau, and P. Hagenmuller, *Mater. Res. Bull.*, **11**, 167 (1976).
5. J. Schoonman, G. J. Dirksen, and G. Blasse, *J. Solid State Chem.*, **7**, 245 (1973).
6. C. Wagner, in 7th Proceedings of the International Committee of Electrochemical Thermodynamics

and Kinetics (1955), p. 363, Butterworths, London (1957).
7. A. K. Cheetham, B. E. F. Fender, and M. J. Cooper, *J. Phys. C*, **4**, 3107 (1971).
8. R. G. Shore and B. M. Wanklyn, *J. Am. Ceram. Soc.*, 52, 79 (1969).
9. C. E. Wicks and F. E. Block, "Thermodynamic Properties of 65 Elements—Their Oxides, Halides, Carbides and Nitrides," Bulletin 605, Bureau of Mines (1963).

Etching Characteristics of Silicate Glass Films in CF_4 Plasma

Kiyokatsu Jinno, Hiroshi Kinoshita, and Yasuo Matsumoto

Toshiba Research and Development Center, Saiwai-ku, Kawasaki, Japan 210

ABSTRACT

In order to delineate doped silicate glass layers, gas plasma etching has been found to be useful. Compared with conventional wet chemical processes, the etching characteristics with gas plasma processes are less dependent on deposition temperature and are more dependent on the dopant concentrations. These results can be explained by the volatility of dopant-fluorine compounds.

The uses of doped silicate glasses as dielectric materials, passivation layers, diffusion sources, etc., have become increasingly important in semiconductor device fabrication.

Conventional wet chemical etching techniques have been used to delineate silicate glass films. The conventional techniques, however, require complicated compositions of chemicals, precise control of etching bath temperature, and sometimes ultrasonic agitation. Further, the conventional chemical etching techniques have inherent disadvantages, such as undercutting caused by poor photoresist adhesion, which reduces the yield and reliability of the devices, and the etching controllability. The etching solutions may also contain harmful dust particles. The refuse chemicals must be treated carefully in order to minimize water pollution. Clean and safe operation environments must be maintained.

Recently, gas plasma techniques for stripping photoresist films in O_2 and etching silicon and silicon nitride films in CF_4 have been extensively developed (1-9). These new gas plasma techniques are found to be very useful for simplifying the wafer process without reducing the resolution capability, and for overcoming the disadvantages inherent in the conventional wet chemical etching techniques.

A freon gas plasma may also be used to etch silicate glass films. It is the purpose of this report to clarify the etching characteristics of the silicate glass films in the CF_4 plasma.

Experimental

The silicate glass films were deposited on chemically polished 20 Ω-cm p-type 2 in. silicon wafers by the reaction of SiH_4 with O_2 in an Ar ambient at 440°-550°C. The silicate glass films were doped respectively with B_2H_6, PH_3, AsH_3, or mixtures of these gases. The films were about 5000Å thick.

The positive photoresist (OFPR-2 manufactured by Tokyo Ohka) was used as an etching mask.

Resolution test patterns were exposed by a projection aligner (Canon FPA-120) and developed in a choline solution. Plasma etching was carried out in the IPC 2005-1813 SC plasma etcher with an 8 in. diam quartz reactor with an aluminum plasma shield. The etching gases were CF_4 and the mixtures of CF_4 and O_2. During the series of experiments the pressure in the reactor was maintained at 0.6 Torr, and the rf power was typically kept at 150W.

Key words: dopant effect, temperature dependency, volatility.

Film thicknesses were determined with Talystep, and the etch rate was defined as the decrement of film thickness per unit time. As the reference, wet chemical etching was performed at 25°C using NH_4F solution.

Results

Effect of silicate glass deposition temperature on the etch rate.—In Fig. 1, the etch rates of undoped silicate glass films in the CF_4 plasma and the NH_4F solution are shown as a function of silicate glass deposition temperature. As can be seen in Fig. 1, the etch rate in the NH_4F solution slightly decreases as the deposition temperature increases, while the etch rate in the CF_4 plasma is nearly constant. The etch rate of the undoped silicate glass films deposited at 550°C was 110 Å/min in the plasma and 3100 Å/min in the solution.

This result indicates that the etch rate in the CF_4 plasma is almost independent of the deposition temperature.

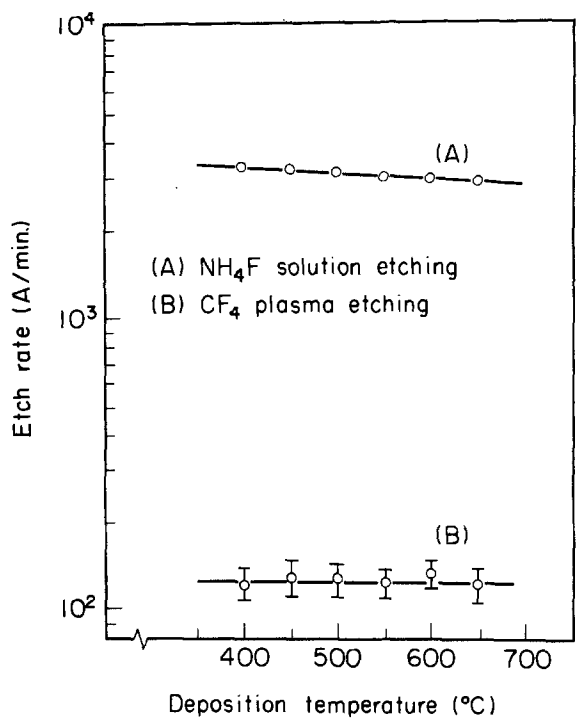


Fig. 1. Etch rate of silicate glass films vs. deposition temperature.

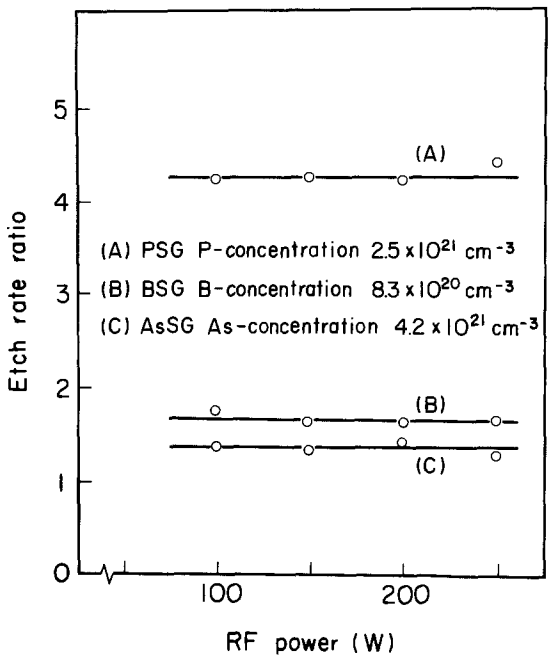


Fig. 2. Etch rate ratio vs. rf power

Effect of rf power on the etch rate.—The etch rate ratios, defined as the ratio of the etch rate of the doped silicate glass films to that of the undoped silicate glass films, are shown in Fig. 2 as a function of rf power.

It is apparent that the etch rate ratio does not depend on the power examined, so that the etch rate ratio can be used for compact representation of our etch rate results.

Effect of heat-treatment after deposition of silicate glass films.—The etch rate in the CF_4 plasma and NH_4F solution of undoped silicate glass films deposited at 500°C was examined after heat-treatment for 10 min in the temperature range 800°-1100°C. The result is shown in Fig. 3. Both in CF_4 plasma and in NH_4F solution etching, the etch rates of undoped silicate glass films decrease as the heat-treatment temperature increases. Therefore, it is concluded that the plasma etch rate depends on the material density.

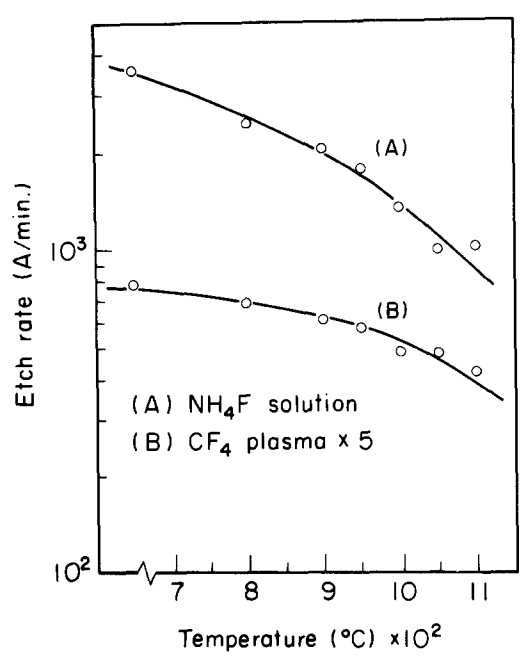


Fig. 3. Etch rate ratio vs. heat-treatment temperature after deposition of silicate glass films.

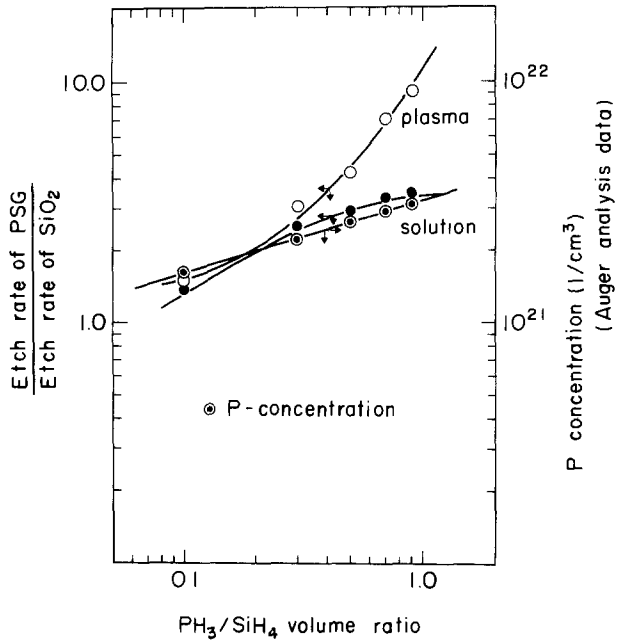


Fig. 4. Etch rate ratio of phosphosilicate glass films vs. PH_3/SiH_4 volume ratio.

Etching characteristics of phosphosilicate glass films.—The etch rate ratios of phosphosilicate glass films in CF_4 plasma and NH_4F solution etching were determined.

In Fig. 4, the results are shown as a function of the flow volume ratio of PH_3 to SiH_4 into the deposition chamber. It is clear that the etch rate ratio of phosphosilicate glass films increases with increasing phosphorus concentration in the glass films. This phenomenon is particularly remarkable in CF_4 plasma etching.

Etching characteristics of borosilicate glass films.—The etch rate ratios of borosilicate glass films in plasma and solution etching were determined as shown in Fig. 5. In NH_4F solution etching, the minimum in the etch rate ratio was reproducibly obtained at a boron concentration of about $7 \times 10^{20}/cm^3$.

In CF_4 plasma etching, the etch rate ratio increases with boron concentration over the entire range examined.

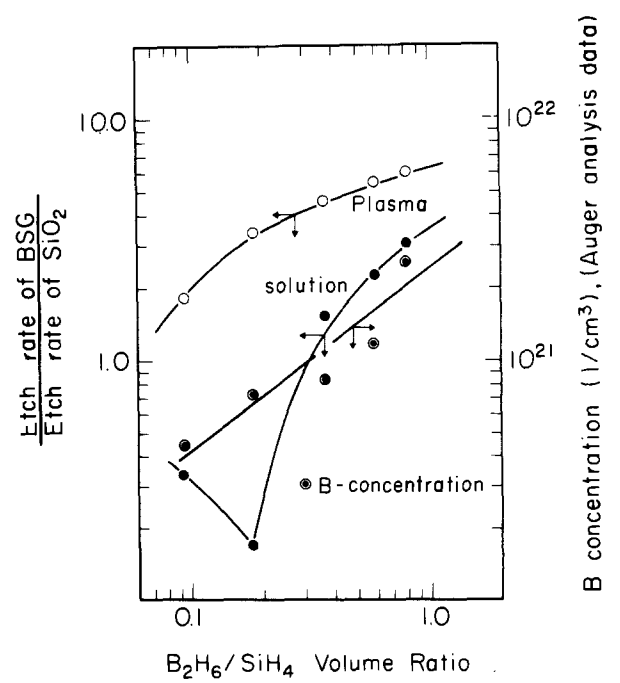


Fig. 5. Etch rate ratio of borosilicate glass films vs. B_2H_6/SiH_4 volume ratio.

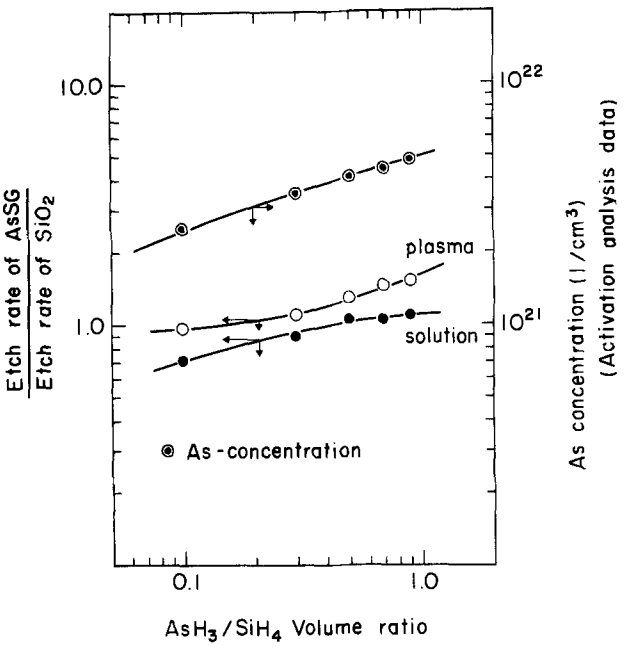
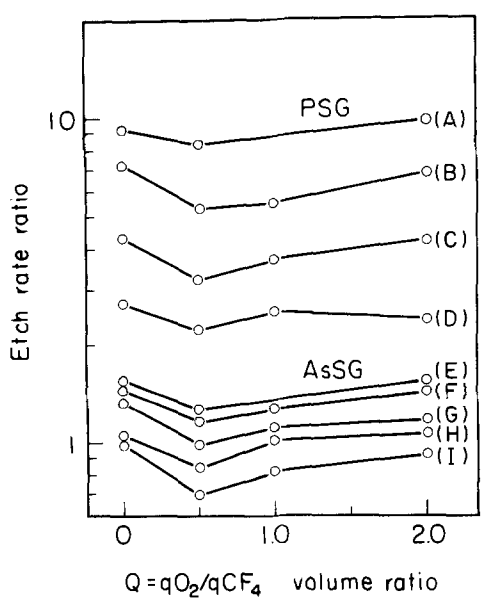


Fig. 6. Etch rate ratio of arsenosilicate glass films vs. AsH_3/SiH_4 volume ratio.

Etching characteristics of arsenosilicate glass films.—The etch rate ratios of arsenosilicate glass films were determined as shown in Fig. 6. The etch rates of arsenosilicate glass films are nearly the same as those of undoped glass films, and increase slightly with arsenic concentration.

Effect of additive oxygen in the CF_4 plasma.—The etch rate ratios of phosphosilicate glass and arsenosilicate glass films were examined as a function Q, the flow volume ratios of O_2 to CF_4, with dopant concentration as a parameter.



(A)	P-concentration	3.1×10^{21}	cm^{-3}
(B)	"	2.9×10^{21}	cm^{-3}
(C)	"	2.7×10^{21}	cm^{-3}
(D)	"	2.2×10^{21}	cm^{-3}
(E)	As-concentration	4.8×10^{21}	cm^{-3}
(F)	"	4.4×10^{21}	cm^{-3}
(G)	"	4.1×10^{21}	cm^{-3}
(H)	"	3.5×10^{21}	cm^{-3}
(I)	"	2.5×10^{21}	cm^{-3}

Fig. 7. Etch rate ratios vs. volume ratio (Q) of O_2 to CF_4

As shown in Fig. 7, the plasma etch rate of both silicate glass films are dependent on the additive O_2 concentration. At the range above $Q = 1.0$, the etch rate ratios for these silicate glass films increase with Q value. Each curve has a minimum at $Q = 0.5$.

Effect of plasma etching temperature.—Figures 8, 9, and 10 show the Arrhenius plots for plasma etching of phosphosilicate, borosilicate, and arsenosilicate glass films in the temperature range from 25° to 180°C, respectively. During etching, wafers were heat-controlled by a heating stage in contact with the back-side of each wafer. The activation energies for the etching reaction of phosphosilicate glass, borosilicate glass, and

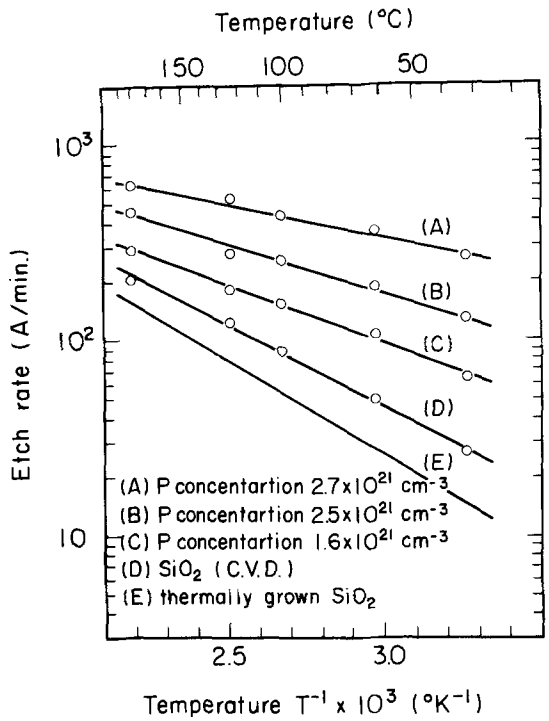


Fig. 8. Etch rate vs. temperature T for various phosphosilicate glass films.

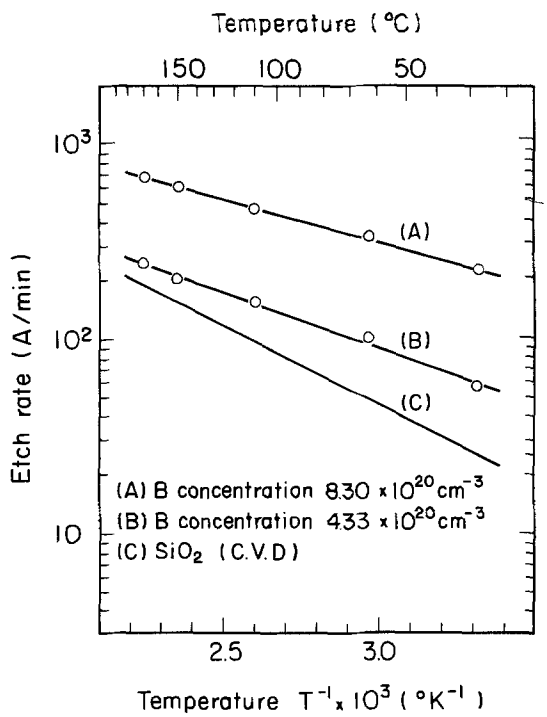


Fig. 9. Etch rate vs. temperature T for various arsenosilicate glass films.

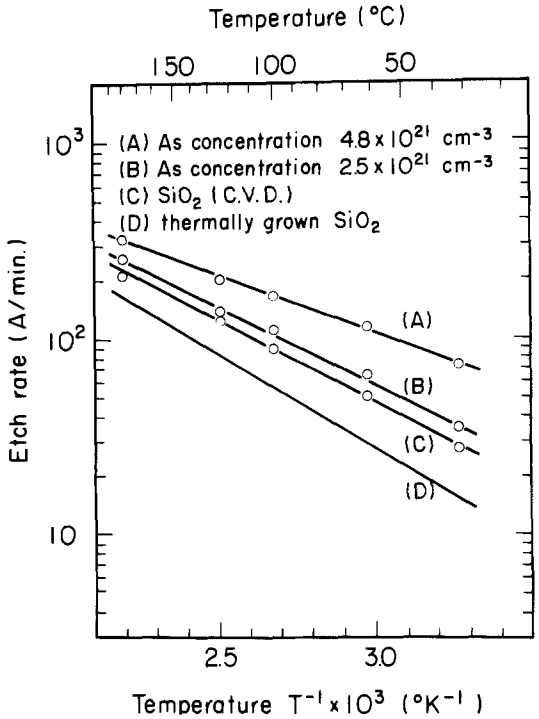


Fig. 10. Etch rate *vs.* temperature *T* for various borosilicate glass films.

arsenosilicate glass films obtained from the above results are summarized in Table I.

The activation energies may be due to differences in the reactions of SiO_2-F*, P_2O_5-F*, B_2O_3-F*, and As_2O_5-F*, etc.

Discussion

From the experimental results shown in Fig. 4-6 it is clear that the etch rate of silicate glass films in a CF_4 plasma is dependent on the dopant concentration in a range from $10^{21}/cm^3$ to $10^{22}/cm^3$, as observed also for NH_4F solution etching.

In solution etching, the effect of dopant concentration is interpreted as follows (10).

The monotonic increase in the etch rates with dopant concentration observed for doped silicate glass films except boron concentration below $10^{21}/cm^3$ suggests that the etch rate is controlled primarily by the dissolution of the SiO_2 in the doped silicate glass, and adding dopant oxide facilitates dissolution.

Thus the etching process can be explained as a combination of the dissolution of the SiO_2 by NH_4F originated species such as F^- in the NH_4F solution, and that of the dopant oxide in water. The etch rates of phosphosilicate glass films increase much more rapidly with dopant concentration than those of borosilicate and arsenosilicate glass films, which apparently are related to the relative solubilities of P_2O_5, B_2O_3, and As_2O_3 in water, respectively. But the relationship between etching characteristics and dopant oxide solubility does not extend to borosilicate glass films with boron concentration below $1 \times 10^{21}/cm^3$. Then the etching is complicated by formation of insoluble boron compounds, for example.

Meanwhile in CF_4 plasma etching, effects were observed for phosphosilicate, borosilicate, and arsenosilicate glass films that were similar to those observed for solution etching. The etch rate of phosphosilicate glass films increases much more rapidly with dopant concentration than those of borosilicate and arsenosilicate glass films. But, a significant difference was observed in the etching of borophosphosilicate glass films. The etch rate ratio of borophosphosilicate glass films in the CF_4 plasma etching was determined to be 3.05 and that in the NH_4F solution, 0.55.

In CF_4 plasma etching, the gas plasma is generated in the chamber by rf power, then silicon compound films begin to react with activated fluorine in the CF_4 plasma.

What seems to happen in the plasma etching process is that fluorine atoms from the plasma are chemisorbed on the silicon surface to form silicon fluoride compounds which are volatile even below room temperature; hence silicon is removed.

From the previous discussion, it is assumed that a large plasma etch rate is obtained for elements which produce fluorides with high volatility.

If we assume that doped silicate glasses are binary mixtures as follow; phosphosilicate glass: P_2O_5-SiO_2, borosilicate glass: B_2O_3-SiO_2, arsenosilicate glass: As_2O_3-SiO_2, the expected fluorides produced in CF_4 plasma are PF_3, PF_5, BF_3, AsF_3, and AsF_5. The vapor pressure of these fluorides are shown in Table II (11).

From this discussion, it is apparent that the plasma etch rate is dependent on volatility of the reaction products, and dopant effect in plasma etching is interpreted to originate in the difference of volatility of the dopant fluorides, *i.e.*, PF_3, BF_3, and AsF_5.

Table I. Activation energy of plasma etching reactions

Substrates	*E*, activation energy (kcal/mole)
Phosphosilicate glass	
p-concentration	
1.7×10^{21} cm^{-3}	2.78
2.5×10^{21} cm^{-3}	2.05
2.8×10^{21} cm^{-3}	1.61
Borosilicate glass	
B-concentration	
4.4×10^{20} cm^{-3}	3.51
8.2×10^{20} cm^{-3}	2.85
Arsenosilicate glass	
As-concentration	
2.5×10^{21} cm^{-3}	3.65
4.8×10^{21} cm^{-3}	2.57
Silicate glass deposited CVD	4.09
Thermally grown SiO_2	4.31

Conclusion

The etching characteristics of silicate glass films in the CF_4 plasma were studied. As a conclusion:

1. The plasma etch rate is almost independent of the silicate glass deposition temperature.
2. The etch rates of undoped silicate glass films decrease as the temperature of the heat-treatment after deposition increases. Therefore, the plasma etch rate depends on the density of materials.
3. The plasma etch rate of silicate glass films is dependent on the dopant concentrations. This characteristic can be explained by the volatility of fluorides such as PF_3, BF_3, and AsF_5, similar to solubility of dopant oxides, P_2O_5, B_2O_3, and As_2O_3 in water in solution etching.

Acknowledgment

The authors express their sincere thanks to Dr. Y. Nishi, Dr. S. Horiuchi, and T. Shinozaki for their useful discussions. They are also grateful to T. Moriya, K. Kirita, Y. Tsuji, M. Yamanaka, and T. Matsuo for their valuable support in the sample preparation, and to T. Inoue for auger spectrometric analysis.

Table II. Vapor pressure data of fluorides

Fluorides	Temperature (°C) 760 mm Hg	1 mm Hg
PF_3	−101.5	—
PF_5	−75	—
BF_3	−99.9	−154.6
AsF_3	−63	s
AsF_5	−53	−117.9
SiF_4	−94.8	−144.0

Manuscript submitted Dec. 28, 1976; revised manuscript received Feb. 23, 1977. This was Paper 292 presented at the Las Vegas, Nevada, Meeting of the Society, Oct. 17-22, 1976.

Any discussion of this paper will appear in a Discussion Section to be published in the June 1978 JOURNAL. All discussions for the June 1978 Discussion Section should be submitted by Feb. 1, 1978.

Publication costs of this article were assisted by the Toshiba Research and Development Center.

REFERENCES

1. H. Abe, in Proceedings of 6th Conference, Solid State Devices, Tokyo (1974); O. Buturi, *J. Jpn. Soc. Appl. Phys.*, **44**, Supplement 287 (1975).
2. R. A. H. Heinecke, *Solid State Electron.*, **18**, 1146 (1975).
3. Y. Horiike and M. Shibagaki, in Proceedings of 7th Conference, Solid State Devices, Tokyo (1975); Supplement, *Jpn. J. Appl. Phys.*, **15**, 13 (1976).
4. K. Jinno, Y. Matsumoto, and S. Inomata, *J. Electrochem. Soc. Jpn.*, **44**, 204 (1976).
5. L. Zielinski and G. C. Schwarz, Abstract 75-1, p. 117, The Electrochemical Society Extended Abstracts, Spring Meeting, Toronto, Canada, May 11-16, 1975.
6. H. A. Clark, *Solid State Technol.*, **19**, 51 (1976).
7. A. R. Reinberg, in "Etching," H. G. Hughes and M. J. Rand, Editors, The Electrochemical Society Softbound Symposium Series, Princeton, New Jersey (1976).
8. M. Brochu and R. G. Poulsen, *ibid.*, p. 111.
9. A. Jacob, *Solid State Technol.*, **70**, 1919 (1976).
10. A. S. Tenney and M. Ghezzo, *This Journal*, **120**, 1091 (1973).
11. Handbook of Chemistry and Physics, WEAST 56th, CRC Press (1975-1976).

The Loading Effect in Plasma Etching

C. J. Mogab

Bell Laboratories, Murray Hill, New Jersey 07974

ABSTRACT

The dependence of etch rate on the quantity of material being etched, often referred to as the loading effect, for plasma etching is analyzed quantitatively with the aid of some simplifying assumptions. The etch rate is related to the quantity of material being etched through three phenomenological parameters β, τ, and G, which are related to the affinity of the etching material for the active species created in the plasma, the lifetime of the active species, and the volume generation rate of the active species, respectively. It is shown analytically that the reciprocal of the etch rate, when N identical wafers are etching simultaneously, is directly proportional to N. Data are presented for the plasma etching of Si in a CF_4-O_2 plasma which confirm the analytical prediction. The significance of loading with respect to the measurement of etch rate, end-point detection, and the interpretation of the temperature dependence of etch rate is discussed. A brief discussion of the physical meaning of the phenomenological parameters and their relation to process parameters subject to control such as power, pressure, and temperature is also included.

Plasma etching refers to the selective removal of a solid by the formation of a volatile compound upon chemical reaction of the solid with an active species created in a low pressure gas discharge. Silicon and its compounds of importance in silicon integrated circuit (SIC) fabrication can be etched, for example, in a low pressure (~0.2-1.0 Torr) rf discharge of CF_4 by virtue of the formation of volatile products such as SiF_4.

The so-called "loading effect" is familiar to anyone who has utilized plasma etching in a batch-type operation where the quantity of material being etched may vary from run to run. In SIC processing, for example, the number of wafers in a batch may vary from a few to as many as 20 or more. The loading effect is characterized by a decrease in etch rate as the quantity of material to be etched is increased, for a given set of etching conditions. The etching conditions subject to control include gas pressure, gas flow rate, rf power density, and the temperature of the solid being etched.

The loading effect is most evident with a rapidly etching material such as polycrystalline silicon. If the etch rate as determined from measurements on a single wafer is utilized to predict the time needed for complete etching of a batch of several wafers, it is invariably found that this time is insufficient to clear all wafers. Obviously, this leads to problems in maintaining dimensional tolerances when fine line patterns are being etched in a material which is partially masked. The etching will be incomplete if the etch time is too short, whereas undercutting of the mask and loss of pattern fidelity will result if the etch time is too long. Moreover, an incorrect etch time may also produce undesirable consequences with respect to the etch profile, that is, the shape of the edge of an etched feature.

If the variation of etch rate with load cannot be predicted, then a time consuming, trial and error process must be used to determine an appropriate etch time for each particular load or some means of end-point detection must be employed. For example, frequency-selective monitoring of the optical emission from the plasma has been suggested and used to determine the end point of certain plasma etching operations (1-3).

The objective of this paper is to analyze the loading effect with particular reference to a plasma reactor employing radial flow as depicted in Fig. 1 (4). We show that by making some reasonable, simplifying assumptions, a phenomenological equation can be developed which predicts the loading effect; that is, the dependence of etch rate on the amount of material being etched. Experimental verification of the predicted effect is given for plasma etching of single crystal silicon wafers in a CF_4-O_2 plasma. A discussion of some of the implications of loading with respect to end-point detection and interpretation of the temperature dependence of etch rates is also included, as is a brief consideration of the physical significance of

Key words: silicon, silicon dioxide, CF_4-O_2, reactor, etch rate, etching end point detection.

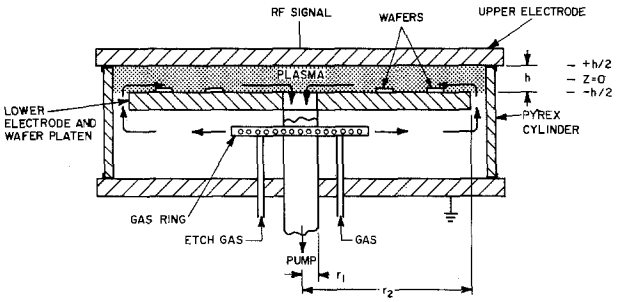


Fig. 1. Schematic illustration of a radial flow reactor

the phenomenological parameters appearing in the expression relating etch rate to the quantity of material being etched.

Theory

It is recognized that plasma etching, while conceptually simple, encompasses several rather complex processes which are, at best, poorly understood. The etching process depends not only on the complicated phenomena occurring in the discharge itself, *e.g.*, the production of ions and radicals, but also on the kinetic details of the interaction of the solid with one or more active species (reactants) adsorbed at the solid surface. One can anticipate that the production of active species in the plasma is dependent on power, pressure, flow rate, and reactor geometry, while the surface processes are sensitive to temperature. A detailed analytical description which could account for the influence of all these variables, however, would obviously be difficult to formulate. Alternatively, by making some reasonable assumptions, a phenomenological treatment is possible. Thus one can introduce certain parameters which, presumably, are related to the aforementioned variables, in order to characterize the process.

We assume that a single species, B, generated in the plasma is actively etching solid A according to the over-all reaction

$$aA + bB = A_aB_b\uparrow \qquad [1]$$

where A_aB_b is a volatile compound (*e.g.*, $Si + 4F \rightarrow SiF_4\uparrow$). Let the concentration of species B in the plasma be C_N. The subscript N refers to the number of identical wafers (substrates, films, etc.) being etched ($N = 0, 1, 2, \ldots$). The rate at which the active species are generated in the plasma, *e.g.*, by collisions between gas molecules and energetic electrons is designated G (the volume generation rate). It is assumed that, when no etchable material, A, is present in the reactor, the lifetime of an active species, B, is determined by adsorption, recombination, and flow processes in a way that can be described by a mean lifetime, τ. Then, if R_N is the etch rate of material A when N identical wafers are etching, the equation of continuity for the concentration of active species B is

$$\frac{\partial C_N}{\partial t} = D\nabla^2 C_N + G - \frac{df}{h}R_N - \frac{C_N}{\tau} - \nabla \cdot (C_N v) \qquad [2]$$

where

$$d = \frac{b\rho N_o}{M}$$

is a constant with b = coefficient in reaction equation [1]; ρ = density of solid A; N_o = Avogadro's number; M = molecular weight of A; h = interelectrode spacing; f = fraction of the wafer platen area occupied by etchable material (Fig. 1); v = gas flow velocity vector; and D = diffusion coefficient of B in the plasma. In general, C_N, G, R_N, and v must be considered to be functions of time and position. However, it is possible to simplify Eq. [2] considerably as follows.

In a reactor of the type under consideration here, the radial flow velocity of the gas is inversely proportional to radial position (5). It can also be shown (6) that the electron density in the plasma takes the form of a zero-order Bessel function with respect to radial position; thus it is maximum at the center of the reactor and drops to zero at the periphery.[1] Consequently, in this type of system the average gas molecule spends most of its transit time where the electron density is low and much less time where it is high. The significance of this fact is that the concentration of active species, created by collisions of gas molecules and energetic electrons, can be made uniform across the wafer platen. That is, the gas velocity and electron density profiles offset each other in such a way that the probability of producing an active species by collision is roughly independent of position. Accordingly, it is assumed that both C_N and G are uniform throughout the plasma volume.[2]

The last term on the right-hand side of Eq. [2] relates to flow effects and vanishes if C_N is uniform (independent of position) since the flow velocity $\vec{v}$ is divergenceless. Thus, for steady-state etching ($\partial C_N/\partial t = 0$) Eq. [2] becomes

$$R_N = \frac{h}{df}\left[G - \frac{C_N}{\tau}\right] \qquad [3]$$

The area fraction, f, is given by

$$f = \frac{A_W}{A}N \qquad [4]$$

where A_W = area of etchable material per wafer and A = total wafer platen area.

Substitution of Eq. [4] into Eq. [3] gives

$$R_N = \frac{hA}{dA_WN}\left[G - \frac{C_N}{\tau}\right] \qquad [5]$$

In order that R_N remain finite as $A_WN \rightarrow 0$ it must be true that

$$G = \frac{C_o}{\tau} \qquad [6]$$

Where C_o is the concentration of B in the absence of etchable material ($A_W \underset{\text{LIM}}{N} \rightarrow 0^{C_N = C_o}$). Thus, substituting Eq. [6] into Eq. [5]

$$R_N = \frac{hA}{dA_WN\tau}[C_o - C_N] \qquad [7]$$

It is reasonable to suppose that the etch rate is directly proportional to the concentration of active species B for a given set of etching conditions, that is

$$R_N = \beta C_N \qquad [8]$$

where β is a proportionality factor whose magnitude depends on the affinity of the material being etched for the active species B. Substituting Eq. [8] into Eq. [7] and combining terms yields

$$\beta^{-1}R_N = C_N = \frac{C_o}{1 + \frac{dA_W}{V}\beta\tau N} \qquad [9]$$

where $V = hA$ is the plasma volume. Finally, using Eq. [6] and [9], we obtain

$$R_N = \frac{\beta\tau G}{1 + \beta\tau\frac{dA_W}{V}N} \qquad [10]$$

From Eq. [10] it is apparent that the etch rate for N

[1] The zero-order Bessel function can be viewed, for qualitative considerations, as similar in form to the cosine function from 0 to $\pi/2$.

[2] This assumption is probably valid, to a first approximation, for other types of reactors, too, since the low viscosity gases employed in plasma etching discourage the formation of sizable concentration gradients in the bulk of the plasma.

wafers is a function of N, that is, Eq. [10] predicts a loading effect. Equation [10] also contains three phenomenological parameters (β, τ, G) which are discussed further on. First, it is shown that Eq. [10] is obeyed for the etching of Si wafers.

Experimental

Single crystal wafers of silicon with both 2 and 3 in. diameters were used in this study. The crystals had a [111] orientation and were polished on the side exposed to the plasma. Etch rate was measured by weight change, with a measurement precision of 0.1 mg. The etch time was selected so that weight changes were of the order of tens of milligrams. Etching was carried out in a 92% CF_4-8% O_2 plasma. The wafers were unmasked.

Relative etch rates were also measured by an optical technique which requires some explanation. The active species for etching Si in a CF_4 plasma is atomic fluorine, and the etch product is SiF_4. This has been ascertained from several observations. First, the reactor effluent was monitored with a quadrupole mass spectrometer during etching. Peaks consistent with the mass spectrum of SiF_4 appear when Si is actively etching. The intensity of the major peak (at measured etch rate = 85) compares favorably with the quantity of SiF_4 expected from the measured etch rate, assuming SiF_4 to be the only etch product. Secondly, a correlation between the intensity of optical emission from electronically excited states of F and the etch rate has been noted in two separate experiments. In the work of Harshbarger *et al.* (3), the etch rate of Si and the intensity of emission from excited F at 703.7 nm were measured as a function of the O_2 content of CF_4-O_2 mixtures. It was found that oxygen enhances the intensity of optical emission from excited states of F in the same proportion that etch rate is enhanced by the addition of oxygen.

Figure 2 illustrates that the emission intensity from the 703.7 nm F line tracks the etch rate of Si, measured by weight change for a single 2 in. diam wafer, as a function of rf power. (Optical emission was measured with a 0.3m Ebert polychromator and a Princeton Applied Research optical multichannel analyzer.) The emission points were measured with the reactor empty ($N = 0$). If one assumes that the intensity of emission for the empty chamber, I_o, is proportional to C_o according to $I_o = \alpha^{-1} C_o$, where α is independent of rf power, then Eq. [9] can be written

$$R_N = \frac{C_o \beta}{1 + \dfrac{\beta \tau d A_W N}{V}} = \frac{\alpha I_o \beta}{1 + \dfrac{\beta \tau d A_W N}{V}}$$

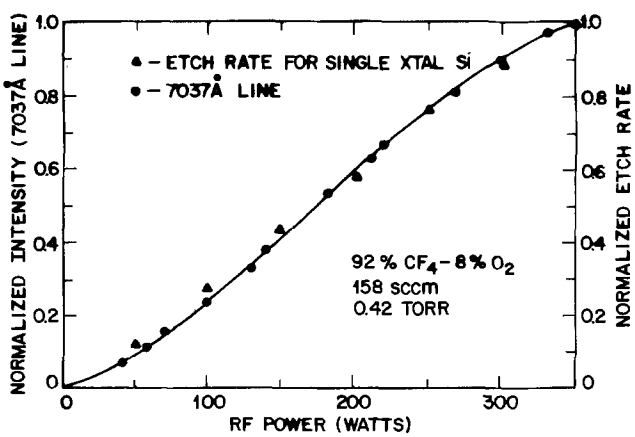


Fig. 2. Variation of etch rate for a 2 in. Si wafer and intensity of emission from electronically excited F as a function of rf power in a CF_4-8%O_2 plasma. The data are normalized to the highest power level.

Therefore the variation of etch rate with power, for a given load, can be determined by measuring the variation of emission intensity with power for an empty reactor. The data of Fig. 2 are normalized to the maximum values of intensity and etch rate to emphasize the strong correlation between etch rate and F concentration. These data confirm the validity of Eq. [8] for this case. Thus, available evidence indicates that F is the active species for etching Si.

It follows from Eq. [8], therefore, that the etch rate of Si is reflected in the intensity of emission from excited states of F. That is

$$R_N = \gamma I_N \qquad [11]$$

where γ is a constant at fixed temperature and pressure.[3] The main advantage in using optical monitoring in this manner is that it is far less time consuming than direct measurement of etch rate. All of the optical emission data reported subsequently, refer to the 703.7 nm F line. Other F lines can be used, however, this one has the maximum intensity for plasma conditions employed in these studies.

Inverting Eq. [10] gives

$$R_N^{-1} = (\beta \tau G)^{-1} + \left(\frac{dA_W}{GV} \right) N \qquad [12]$$

Therefore, the reciprocal of etch rate is linear in N. Moreover, using Eq. [10] and [11]

$$\frac{R_o}{R_N} = \frac{I_o}{I_N} = 1 + \beta \tau \frac{dA_W}{V} N \qquad [13]$$

In order to test the validity of Eq. [12], several runs were made in which only the number of 3 in. diam, bare Si wafers was varied. The wafers were weighed, etched for 15 min, and then reweighed. A fresh batch of wafers was used in each run and the wafers were placed immediately adjacent to one another so that their centers were on a circle concentric with the inner and outer edges of the wafer platen. The circle of centers was chosen such that 10 wafers could just be placed on it with no overlap. The results of this experiment are shown in Table I. The weight changes listed in the second column of Table I are arranged to reflect the position of the wafers on the circle of placement. (The first and last figures are for the wafers on the "ends" of a partial ring; with 10 wafers present the ring is continuous.)

Two observations can be made concerning the data of Table I. First, as the number of wafers increases, the standard deviation, which reflects the nonuniformity of etching from wafer to wafer, increases to a near maximum for a half-full ring, and then decreases again as the ring of wafer sites is filled beyond the halfway point. Second, for runs with an unfilled ring, the "end" wafers ($N \geq 3$) consistently show more etching than inner wafers. These two facts suggest that the concentration of active species is not exactly uniform, except when the etchable material is symmetrically distributed. The concentration of active species is somewhat higher near a wafer which is not surrounded by other wafers. This is not surprising since it is simply a manifestation of loading, *i.e.*, a competition for active species. This same competitive effect can presumably lead to an etch rate dependence on feature size, with small isolated features etching more rapidly than large, less isolated features on a wafer. From a practical viewpoint, it is clear that loads should be distributed symmetrically in order to obtain a maximum uniformity of etching.

The measured weight changes given in Table I were converted to average etch rates across each wafer and then the reciprocal of the average of these values for

[3] The parameter γ must be assumed to be pressure dependent unless it can be demonstrated that the plasma is optically thin at all pressures of interest. This means that the variation of emission intensity with pressure cannot be used to predict the variation of R_N with pressure, other conditions being held constant.

Table I. Dependence of etch rate on loading conditions: 92%CF_4-8%O_2, 300W, 0.3 Torr, 150 SCCM, 100°C, 15 min of etching

No. of wafers etched	Measured weight change (mg)	Average weight change (mg)	Standard deviation (mg)
1	69.3	69.3	0
2	48.8 51.5	50.2	1.91
3	39.9 34.7 42.0	38.9	3.76
4	34.4 29.3 29.3 35.4	32.1	3.26
5	31.0 24.9 24.4 25.8 32.1	27.6	3.62
6	27.2 22.5 20.4 20.0 23.0 28.6	23.6	3.54
8	23.3 20.5 18.2 17.2 19.7 20.5 20.1 24.0	20.4	2.30
10	18.7 16.5 16.6 15.1 16.9 15.9 17.3 16.0 17.4 17.7	16.8	1.03

each run was plotted against the number of wafers in the run, as shown in Fig. 3. It is evident that Eq. [12] is obeyed.

Similar experiments in which the intensity of emission from excited F was measured as a function of N have been run with both 2 and 3 in. diam wafers. Figure 4 illustrates results typical of these experiments.

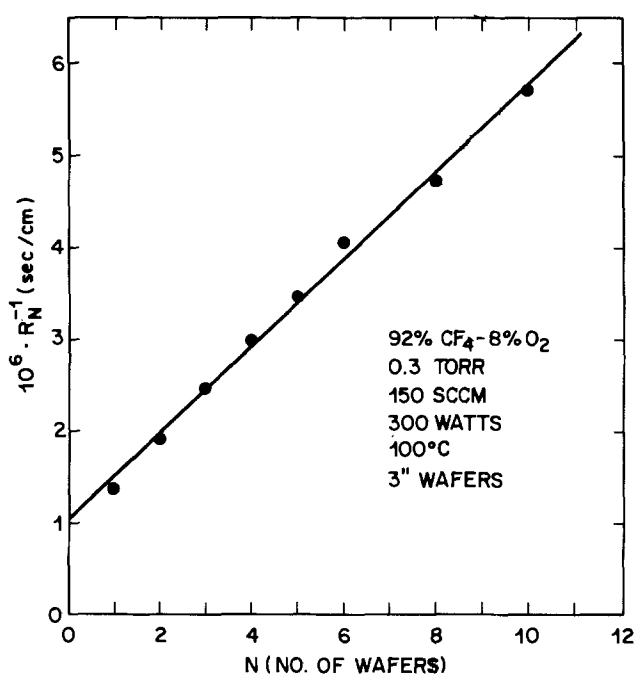


Fig. 3. Reciprocal of average etch rate vs. number of wafers for the data of Table I.

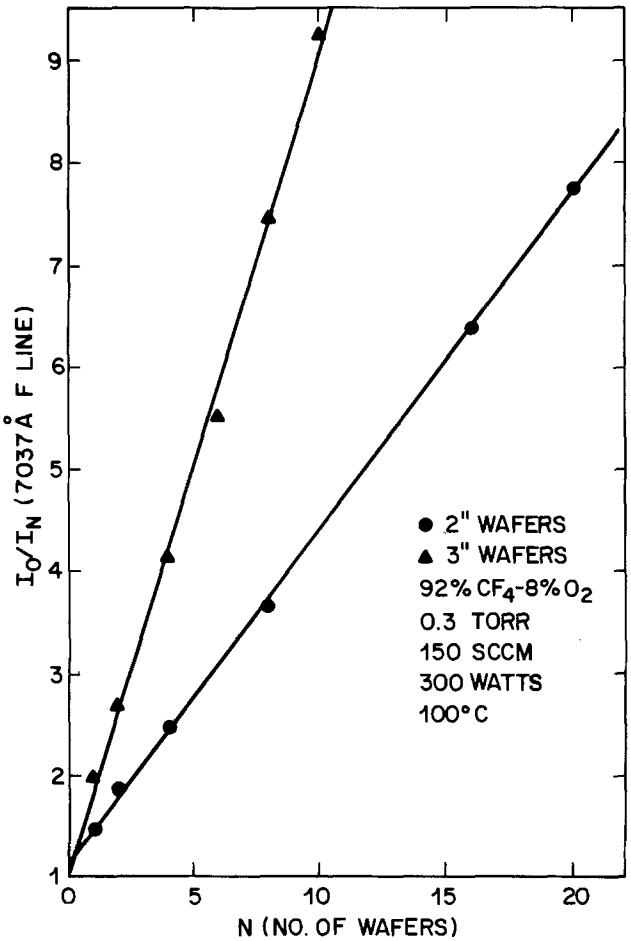


Fig. 4. The ratio of emission intensity of excited F for an empty reactor to the intensity when N wafers are etching plotted vs. N.

The data are plotted in the form suggested by Eq. [13]. Intensities were measured after 5 min of etching to ensure steady-state readings. The lines drawn through the data points are least squares fits. Note that the lines have a unit intercept (within experimental error), as predicted by Eq. [13]. According to Eq. [13], the ratio of the slopes of the lines in Fig. 4 (3 *vs.* 2 in. wafers) should be proportional to the ratio of wafer areas which is $3^2/2^2 = 2.25$. The measured ratio of slopes for the least squares lines is 2.4, which is in reasonable agreement considering that the wafer surfaces roughen somewhat during etching. This has the effect of increasing the surface area in proportion to the geometric area, which would tend to make the ratio of slopes greater than 2.25 as observed.

Discussion

Loading effects.—According to Eq. [10], loading effects can be expected whenever

$$\beta\tau \frac{dA_W}{V} N \sim 1 \qquad [14]$$

whereas no loading will occur when

$$\beta\tau \frac{dA_W}{V} N << 1 \qquad [15]$$

It follows that, for a given load and mask pattern, loading can be suppressed only by increasing the plasma volume V. Of course, there are physical limitations to the extent to which this alternative can be pursued. It can also be seen that, for a given amount of exposed material per wafer (A_W), loading will be more prevalent for faster etching materials (large β) and for species with a long lifetime (large τ). This simply reflects the fact that the active species will be

used up more quickly when the higher etch rate material is present. Loading is, of course, a natural consequence of competition for the etchant in what amounts to a very "dilute solution." The plasmas used in plasma etching are rather weak (electron density $\sim 10^9/cm^3$).

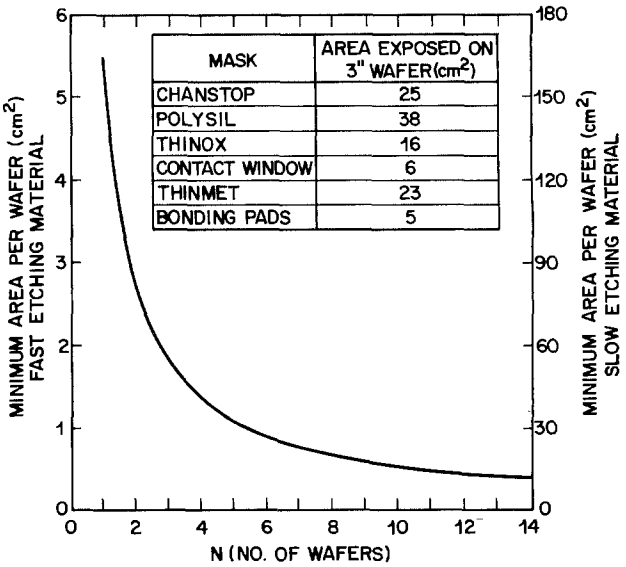
When loading effects are present, specification of etch rate should be made with reference to the amount of material being etched. Alternatively, the etch rate for a small quantity of material ($A_W N \to 0$) should be measured and reported as R_o. If the etch rate can be measured for two different loads, the linear relation given by Eq. [12] can be used to predict etch rates for other load sizes by extrapolation or interpolation. This is easily done by plotting R_N^{-1} *vs.* N for two points, and drawing a straight line between them.

Obviously, if there is more than one material etching on a wafer, the material with a maximum βA_W product will dominate loading. Thus when masked wafers with exposed Si backs are etched in a vertical position, typical of some reactor designs, the back of the wafer will cause loading even if the front side contains only a small area of slowly etching material, which by itself, would produce no loading.

End-point detection.—Two means of determining the end point of etching, both based on frequency-selective detection of optical emission from the plasma, have been suggested (1-3). In the first method, emission from an etching product is detected. It is apparent that when a reaction product, unique to the material being etched, can be detected by some means, the end point can be determined with a sensitivity equivalent to that of the detector employed. Alternatively, when the etch-active species generated in the plasma can be identified and detected, changes in the concentration of this reactant can be used as an end-point indicator. In this case, however, the sensitivity of the technique is dependent both on the capability of the detector and the extent to which a loading effect is present. This follows immediately from Eq. [13] and [14], since this method depends on detecting an increase in the intensity of a signal proportional to the reactant concentration at the completion of etching.

It is instructive to estimate the sensitivity of the latter technique for a rapidly etching material such as Si and a more slowly etching material such as SiO_2, assuming that the over-all sensitivity is limited by the extent of loading rather than by the detector. From the slopes of the lines in Fig. 4 we find $\beta\tau \simeq 5 \times 10^{-23}$ cm^4 (at 100°C). For Si, $d \cong 2 \times 10^{23}/cm^3$ and for the present reactor $V \simeq 550$ cm^3. It follows that for loading to be detectable, requiring say a 10% change in intensity, we must have $A_W N \gtrsim 0.1V/\beta\tau d \cong 5.5$ cm^2 for Si.

Atomic fluorine is also the major active species for etching SiO_2 in a CF_4 plasma. For conditions equivalent to those used in etching Si (Fig. 3 and 4), the etch rate of thermally grown SiO_2 is approximately 30 times less than R_o for Si. Thus, to a first approximation, $\beta\tau$ for SiO_2 is 1/30 of that for Si. Accordingly, for SiO_2 etching, $A_W N \gtrsim 165$ cm^2 is required. These conditions are expressed graphically in Fig. 5, which shows the minimum area of etchable material per wafer needed to make end-point detection, by monitoring a reactant, feasible for "fast" (left-hand ordinate) and "slow" (right-hand ordinate) etching materials, as a function of N. Also shown in Fig. 5 is a table listing the approximate area of etchable material per wafer exposed by various masks typical of an SIC fabrication process, using a CMOS technology, for 3 in. diam wafers. These values were obtained from densitometer measurements on working masks. It is evident from Fig. 5 that even a single 3 in. wafer will permit detection with a rapidly etching material such as polysilicon. On the other hand, plasma etching of contact windows through a slowly etching dielectric



MASK	AREA EXPOSED ON 3" WAFER(cm^2)
CHANSTOP	25
POLYSIL	38
THINOX	16
CONTACT WINDOW	6
THINMET	23
BONDING PADS	5

Fig. 5. A plot of the minimum area of etchable material per wafer which must be exposed in order to detect the end point of etching, by a change in the concentration of the active species in the plasma, as a function of the number of wafers being etched. It is assumed that a 10% change in signal is the minimum that can be sensed. The table gives typical values of total exposed area for various mask levels representative of CMOS integrated circuit fabrication for 3 in. diam wafers.

will be difficult to monitor for typical, maximum batch sizes, whereas etching of SiO_2 at the Thinox level would require a minimum load of $\approx$ 10, 3 in. wafers.

In the event that the exposed area is insufficient to allow end-point detection, one might consider including a "monitor wafer" covered with a sufficient area of the material to be etched. This would require that the monitor and device wafers etch at the same rate, despite the absence of masking on the monitor.

The factors β, τ, and G.—The factor β was introduced in Eq. [7] to relate the etch rate to the concentration of etch-active species formed in the plasma. β thus has the form of a kinetic rate constant for the reaction which produces etching. Accordingly, one can anticipate that β will be temperature dependent and, in particular, if the reaction occurs via some thermally activated process, that this temperature dependence will have an Arrhenius form ($\beta = \beta_o e^{-Q/kT}$, where Q is the activation energy, k is Boltzmann's constant, T is the absolute temperature of the etching surface, and β_o is a pre-exponential constant). On the other hand, since β mainly reflects processes occurring on the solid surface, it is likely to be independent of plasma parameters such as power and pressure, provided that the reaction mechanism and the etch-active species do not change with power and pressure. Of course, in reactors where wafer temperature control cannot be maintained, an increase in power will cause wafer heating and thereby indirectly influence β.

The lifetime, τ, will depend on the various processes, exclusive of etching, which consume active species (*e.g.*, bulk and surface recombination, adsorption, and removal by convection). It is likely then that τ will depend on system geometry, materials of construction, reactor temperature, vacuum integrity, and probably other less obvious factors. In any case, one can reasonably expect that τ will vary from reactor to reactor for a particular active species. With respect to flow processes it seems plausible that τ will take the form

$$\frac{1}{\tau} = \frac{1}{\tau_r} + \frac{1}{\tau_f} \qquad [16]$$

where τ_f is the flow-limited lifetime, and τ_r is the lifetime due to all other consumption processes. Thus,

when flow rates become high enough so that $\tau_f << \tau_r$, the etch rate will become flow limited. In this limiting case, active species will be swept through the system too rapidly to accomplish etching. The residence time ($\sim\tau_f$) for the average molecule flowing through the system illustrated in Fig. 1 is of the order of a few tenths of a second at an input flow rate of 200 SCCM. This time is large compared to the expected range for τ_r (7). This implies that, at the maximum flow rates which can be sustained with the pumping speeds normally employed with plasma reactors, an etch rate controlled by convective losses is unlikely. We note, however, that a report on plasma stripping of photoresists indicates a stripping rate inversely proportional to flow rate, at high flow rates (8). [Note that $\tau_f \propto$ (flow rate)$^{-1}$.] In the system used in the present work the etch rate of Si is essentially independent of flow rate up to the maximum flow rate attainable (~300 SCCM) at a pressure of 0.4 Torr.

It is difficult to estimate the effect of parameters such as power, pressure, and temperature on τ except to say that recombination and adsorption processes are likely to show a strong pressure dependence.

It is evident from Eq. [10] that β and τ cannot be determined individually from etch rate data since only the product $\beta\tau$ appears. Experimentally, we have found that while Eq. [12] and [13] are consistently obeyed for plasma etching of Si wafers, the empirically determined values of $\beta\tau$ vary from day to day for experiments made under nominally identical conditions. The variation can be as much as a factor of two. Thus, for example, from the slope and intercept of the least squares fitted line in Fig. 3, $\beta\tau \simeq 3 \times 10^{-23}$ cm^4, while the slopes of the lines in Fig. 4 give $\beta\tau \simeq 5 \times 10^{-23}$ cm^4. It is believed that this may reflect the dependence of τ on the history of the reactor; for instance, on the surface condition of the Pyrex chamber which contains the plasma and is itself etched slowly and roughened.

The generation rate of active species (G) will depend on pressure and power. In order to determine this dependence one must first know the particular mechanism by which the active species are generated. For example, if the active species are generated by collisions of parent gas molecules with free electrons, the rate of generation will depend on the electron density and the frequency of collisions of a type which produce the active species. These parameters, in turn, will depend on the electron energy distribution and the variation of collision cross section with electron energy. A detailed discussion of these factors is beyond the scope of this paper. It suffices to say that if the electron energy distribution and the appropriate collision cross sections were known as a function of power and pressure, one could relate G directly to power and pressure. However, this is not a simple problem even in the limiting case where the plasma is assumed to be in equilibrium.

An empirical value of G can be derived from Eq. [12] and the slope of the line in Fig. 3. Thus, at 0.3 Torr, 300W in a CF_4-8%O_2 plasma, the empirical rate of generation of fluorine atoms is $\sim 10^{16}$ cm^{-3} sec^{-1}. Since the electron density in a plasma of this type is of the order of 10^9-10^{10} cm^{-3} and the collision frequency is of the order of 10^9 sec^{-1}, this implies that about one collision in every 10^2 or 10^3 is effective in producing a fluorine atom.[4]

Determination of activation energy.—Recent results in this laboratory and elsewhere have indicated that the plasma etch rates of several materials exhibit an Arrhenius type of temperature dependence (8-10). Generally, the empirical activation energies are low, being no more than a few tenths of an electron volt per molecule. As regards experimental determination of activation energy, it is important to note that, for materials which exhibit a loading effect, a plot of the logarithm of etch rate *vs.* reciprocal absolute temperature, even if strictly linear, will not necessarily yield the proper activation energy. This is most easily seen by example.

Suppose the temperature dependence of etch rate is determined by etching a single wafer at several temperatures while holding all other conditions fixed. According to Eq. [10] for this case ($N = 1$)

$$R_1 = \frac{\beta\tau G}{1 + \beta\tau d\dfrac{A_W}{V}}$$

It is apparent that if the temperature dependence resides in the parameter β according to $\beta = \beta_0 e^{-Q/kT}$, and if loading is not negligible (*i.e.*, if $\beta\tau d\ A_W/V$ is not $<<1$), then the logarithm of R_1 is not linear in T^{-1}. Nevertheless, the data are likely to produce a reasonable fit to a straight line because of the small activation energies and the characteristics of logarithmic scaling. The activation energy so determined will be in error.

As an illustration of the magnitude of the error, we have measured the etch rates for a single 3 in. Si wafer as a function of temperature and plotted them on a logarithmic scale against reciprocal temperature in Fig. 6. We have also derived values of $\beta\tau$ from the slopes of plots such as shown in Fig. 4 (see Eq. [13]) where the intensity data were measured at several different temperatures. These values are also plotted in Fig. 6.

The activation energy derived from the $\beta\tau$ values is $\simeq$0.1 eV/molecule, whereas the etch rate data when plotted directly yield $\simeq$0.04 eV/molecule. Two conclusions can be drawn from this. First, when loading is present, the magnitude of the apparent activation energy, derived from an Arrhenius plot of each rate, will depend on the size of the load. Second, the parameter β (or at least the product $\beta\tau$) contains the temperature dependence of etch rate as hypothesized previously.

The simplest way to determine the activation energy is to measure the etch rate on a quantity of etchable material small enough to preclude loading. That is, A_W should be reduced to the point where Eq. [15] holds at all temperatures of interest. In that case an Arrhenius plot of R_N will yield the correct value of activation energy.

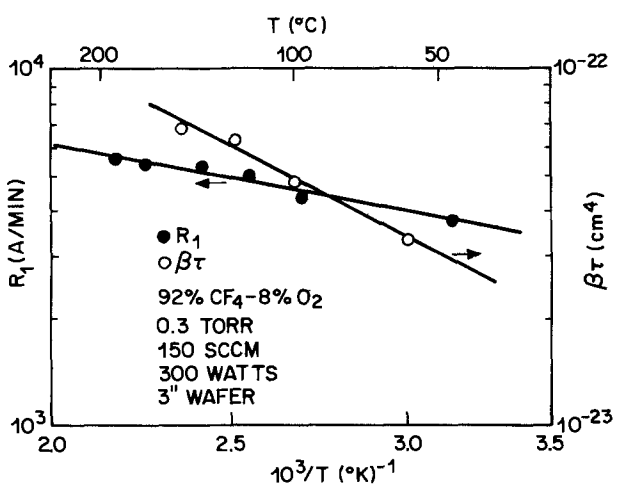


Fig. 6. Variation of the etch rate for a 3 in. diam Si wafer as a function of temperature, displayed on an Arrhenius plot. On the same plot is shown the experimentally determined variation of $\beta\tau$ with temperature. The activation energy, determined from the etch rate plot, is less than the true value, determined from the $\beta\tau$ plot, because of loading.

[4] The mechanism for F atom production in the CF_4-O_2 plasma is not known; however, electron-molecule collisions presumably are an essential part of the production process.

Conclusions

A phenomenological equation has been derived which correctly predicts the loading effect observed in a horizontal, radial flow, plasma etching reactor. This equation relates the observed etch rate to the quantity of material being etched. The loading effect is dependent upon: (*i*) the affinity of the material being etched for the active species created in the plasma; (*ii*) the area of exposed material; (*iii*) the plasma volume; and (*iv*) the lifetime of the active species. Specifically, the reciprocal of etch rate has been shown to be a linear function of the quantity of material being etched. Consequently, linear extrapolation or interpolation can be used to predict the variation of etch rate with load if the etch rates for two different loads are measured for a particular reactor and set of etching conditions (gas composition, power, pressure, temperature, etc.).

Detection of the end point of plasma etching by monitoring the concentration of etch-active species in the plasma is useful only when sufficient loading occurs. In particular, for SIC fabrication, the applicability of this method depends, in part, on the amount of etchable material exposed by a given mask.

In principle, etch rate can be related to the experimental variables, power, pressure, and temperature through three phenomenological parameters β, τ, and G. However, to arrive at the analytical dependence of each of these parameters on the experimental variables would require a detailed mechanistic picture of plasma etching which is presently unavailable. Nevertheless, some reasonable inferences regarding the qualitative dependences of these parameters on power, pressure, and temperature can be drawn.

Finally, it was pointed out that simple Arrhenius plots of etch rate can yield erroneous values for the activation energy of plasma etching when loading occurs.

Acknowledgments

The author is grateful to H. J. Levinstein for encouragement, to J. McNulty for technical assistance, and to M. J. Cowan for advice on the densitometer measurements of masks.

Manuscript submitted Jan. 17, 1977; revised manuscript received April 15, 1977.

Any discussion of this paper will appear in a Discussion Section to be published in the June 1978 JOURNAL. All discussions for the June 1978 Discussion Section should be submitted by Feb. 1, 1978.

Publication costs of this article were assisted by Bell Laboratories.

REFERENCES

1. E. O. Degenkolb, C. J. Mogab, M. R. Goldrick, and J. E. Griffiths, *Appl. Spectrosc.*, **30**, 520 (1976).
2. E. O. Degenkolb and J. E. Griffiths, *ibid.*, To be published.
3. W. R. Harshbarger, T. A. Miller, P. Norton, and R. A. Porter, Paper presented at Interface '76—Kodak Microelectronics Seminar, Monterrey, California, October 4, 1976.
4. A. R. Reinberg, Paper 6 presented at The Electrochemical Society Meeting, San Francisco, California, May 12-17, 1974; U.S. Pat. 3,757,733.
5. R. B. Bird, W. E. Stewart, and E. N. Lightfoot, "Transport Phenomena," p. 114, John Wiley & Sons, Inc., New York (1960).
6. E. Nasser, "Fundamentals of Gaseous Ionization and Plasma Electronics," pp. 415-416, Wiley-Interscience, New York (1971).
7. F. K. McTaggart, "Plasma Chemistry in Electrical Discharges," American Elsevier Publishing Co., Inc., New York (1967).
8. E. P. G. T. Van deVen and H. Kalter, Paper 124 presented at The Electrochemical Society Meeting, Washington, D.C., May 2-7 (1976).
9. Y. Horiike and M. Shibagaki, Proceedings of the 7th Conference on Solid State Devices, Tokyo (1975). Supplement to *Jpn. J. Appl. Phys.*, **15**, 13 (1976).
10. W. R. Harshbarger and R. A. Porter, Private communication.

Superionic Conduction in $AgCrS_2$ and $AgCrSe_2$

D. W. Murphy* and H. S. Chen

Bell Laboratories, Murray Hill, New Jersey 07974

and B. Tell

Bell Laboratories, Holmdel, New Jersey 07733

ABSTRACT

Ionic and electronic conductivity has been measured in $AgCrS_2$ and $AgCrSe_2$. Ionic conductivity was measured by using $RbAg_4I_5$ as a blocking electrode for electronic conduction. Transference numbers were confirmed by cells of the type $Ag/AgCrX_2/X,C$. Ionic conductivities were 3×10^{-4} and $\sim 1\ (\Omega\text{-cm})^{-1}$ for $AgCrS_2$ and $AgCrSe_2$, respectively, at room temperature. The conductivity of $AgCrS_2$ increases abruptly at $\sim 170°C$ to $\sim 1\ (\Omega\text{-cm})^{-1}$. A transition at this temperature was observed by DSC.

A large number of compounds of the general formula AMX_2 (*e.g.*, A = Ag, Cu, Li, Na; M = Cr, Ti, Zr, Ta, Nb; X = S, Se) exhibit structures containing two-dimensional layers of A and M (1). That ionic mobility of A is high in a number of these compounds is evidenced by the formation of a number of them from the MX_2 at ambient temperature. Lithium NMR also indicates rapid Li ion motion in a number of these compounds with A = Li (2). Since many of these compounds form a continuous phase from MX_2 to AMX_2, they are interesting as cathodic electrodes in batteries, especially for A = Li (3). Direct measurement of the ionic conductivity in these compounds has been lacking because of their high electronic conductivity (4).

As a starting point in determining ionic conductivity in AMX_2, we chose to investigate $AgCrS_2$ and $AgCrSe_2$. The electronic conductivity is less than many of the others, and techniques to separate ionic and electronic

* Electrochemical Society Active Member.

Key words: silver, chalcogenide, ionic conductivity.

conductivity exist for Ag ion conductors. Engelsman *et al.* (5) reported that the structure of $AgCrS_2$ and $AgCrSe_2$ contained CrX_2^- sandwiches with the Ag^+ in half of the tetrahedral holes. The structure of the Ag-S layers is shown in Fig. 1. The Ag ions exhibited anomalously large and anisotropic thermal parameters at room temperature, and at higher temperatures (202°C for $AgCrSe_2$ and 397°C for $AgCrS_2$) a reversible phase transition occurred involving a random distribution of the Ag^+ over all tetrahedral sites between the CrX_2^- layers. Thus, it was expected that the ionic conductivity might be large at room temperature and might increase sharply at the phase transition.

The α-phases of Ag_2S and Ag_2Se are known to be superionic Ag ion conductors. The electronic conductivity is appreciably larger than the ionic conductivity (6). The $\beta \rightarrow \alpha$ transitions occur at 180°C (Ag_2S) and 132°C (Ag_2Se), respectively, and a second transition occurs in Ag_2S at 350°C.

Experimental

The $AgCrS_2$ and $AgCrSe_2$ powders were prepared from stoichiometric mixtures of the binary chalcogenides. The mixtures were heated to 700°C for 1 week, then cooled to room temperature over several hours. X-ray powder patterns agreed well with the literature values, and care was taken that no unreacted Ag_2S or Ag_2Se was present.

The conductivity and electromotive cells were formed by pressing the $AgCrS_2$ or $AgCrSe_2$ powder into 2 mm inner diameter thick walled Pyrex tubes of ~4 cm length. Graphite rods were press fit into the tubes for external electrical contact. The powder thickness varied from a few millimeters to greater than 1 cm. The tubes were subsequently annealed for 1-2 hr in N_2 or Ar to 450°C for $AgCrS_2$ and 350°C for $AgCrSe_2$ prior to making electrical measurements. For total conductivity measurements (*i.e.*, cells of the type $Ag/AgCrS_2/Ag$), powdered Ag electrodes were pressed into the Pyrex tubes. For measurements of ionic conductivity (cells of the type $Ag/RbAg_4I_5/AgCrS_2/Ag$) an ~1-2 mm thick layer of $RbAg_4I_5$ was pressed into contact with the sulfide or selenide and was in turn contacted by the Ag. The technique of blocking the electronic component of the conductivity by interposing a layer of AgI or $RbAg_4I_5$ is well documented, and is confirmed in our experiments as discussed below. The Pyrex tubes were then placed in a cylindrical bore aluminum block on which was mounted a Fe-constantan thermocouple, and placed inside a box furnace. Sufficient time was allowed between measurements for the system to equilibrate, and for annealed samples, no hysteresis occurred between measurements made on the up and down heating cycles.

Two point resistance measurements were made with a Hewlett Packard Type 4800 A vector impedance meter, in which the measuring frequency could be varied from 0.5 Hz to 0.5 MHz. For cases in which the resistance was frequency dependent, the resistance was extrapolated to infinite frequency. The frequency-dependent part was attributed to contact capacitance (7), the effects of which disappeared within the frequency range of the instrument. The reproducibility in the electrical measurements between different cells was ~30% for conductivities less than ~1 $(\Omega\text{-cm})^{-1}$ and approximately a factor of 2 or 3 for conductivity greater than ~1 $(\Omega\text{-cm})^{-1}$. This reduced reproducibility was partly due to the error in subtracting lead resistance and the $RbAg_4I_5$ resistance which became a significant fraction of the total resistance.

For measurement of the electromotive force, cells of the type $Ag/AgCrS_2/S,C$ and $Ag/RbAg_4I_5/AgCrSe_2/Se,C$ were formed (8). Twenty-five percent graphite mixed with the sulfur or selenium served to make the electrode both electronically and ionically conducting. The resulting emf (open-circuit voltage) was measured with a Keithley Model 610C electrometer.

Specific heat measurements were performed with a Perkin Elmer differential scanning calorimeter. Several scans were made for each compound under various quenching and annealing treatments.

Results

The total and ionic conductivities of $AgCrS_2$ and $AgCrSe_2$ were measured from room temperature to ~200°C in cells of the type $Ag/AgCrS_2/Ag$ and $Ag/RbAg_4I/AgCrS_2/Ag$. At room temperature, the ionic conductivity of $AgCrS_2$ is moderately high [$\sim 3 \times 10^{-4}$ $(\Omega\text{-cm})^{-1}$] with the total conductivity being about twice the ionic conductivity as seen in Fig. 2. The ionic conductivity increased exponentially with an activation energy of 0.4 eV until ~150°C, where a transition to a highly conducting state begins with a leveling of the conductivity near 170°C. The ionic conductivity above 170°C is of the same magnitude as those for α-AgI and $RbAg_4I_5$. However, the total conductivity above the transition is several times larger than the ionic.

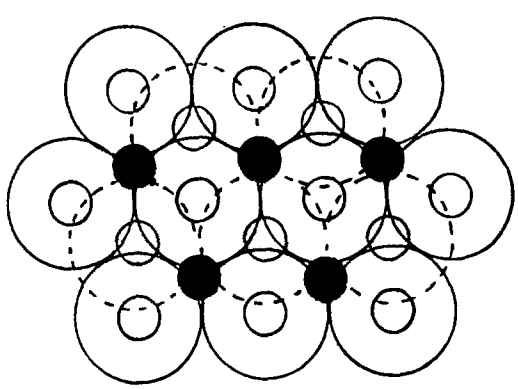


Fig. 1. The two dimensional sites available to Ag. Also shown are X in adjacent layers and alternative octahedral sites occupied by Li in $LiCrS_2$. ●, Octahedral, M directly above and below metal slabs; ○, tetrahedral sites (2 per M).

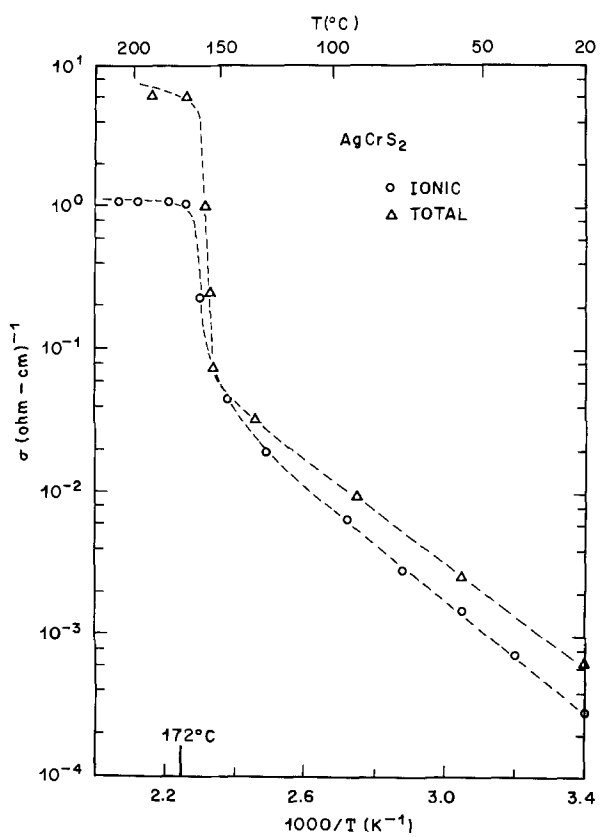


Fig. 2. The ionic and total conductivity of $AgCrS_2$ as a function of reciprocal temperature.

The electrical evidence of a phase transition in $AgCrSe_2$ is not so dramatic, since $AgCrSe_2$ is already highly conducting at room temperature as seen in Fig. 3. The ionic conductivity at room temperature is comparable to that of Ag_4RbI_5, but the electronic component is several times larger than the ionic component. The ionic conductivity increases with an activation energy of 0.11 eV, comparable to those measured for other Ag superionic conductors (9).

Electromotive force measurements serve as a useful complement to conductivity measurements. They confirm the presence of ionic conductivity and can determine the ratio of ionic to total conductivity. The open-circuit voltage of cells of the type $Ag/AgCrS_2/S,C$ and $Ag/AgCrSe_2/Se,C$ were measured from room temperature to ~200°C. The voltage E depends on the ionic transference number t_i by the relationship (8)

$$E = t_i E_0$$

where E_0 is the thermodynamic equilibrium potential and $t_i = \sigma_i/\sigma_t$ is the ratio of ionic conductivity to total conductivity. At room temperature, E_0 equals 0.21V for Ag_2S and 0.26V for Ag_2Se. The room temperature open-circuit voltage for the sulfide cell was in the range of 0.12-0.18V (depending on thermal treatment). This reflects the fact that the magnitude of the ionic and electronic conductivity are comparable. Above room temperature, the voltage decreases slowly until a sudden drop occurs in the same temperature vicinity where the conductivity transition occurs. This is illustrated in Fig 4. The drop is presumably due to the more rapid increase in the electronic conductivity compared to the ionic conductivity at the transition.

For cells of $Ag/AgCrSe_2/Se,C$, the open-circuit voltage was in the millivolt range, reflecting the fact that the electronic conductivity is significantly higher than the ionic conductivity. Cells of the type $Ag/Ag_4RbI_5/AgCrSe_2/Se,C$ were also formed, and the full expected open-circuit voltages (0.26V at 20°C and 0.285V at 200°C) were obtained. This result confirms that the

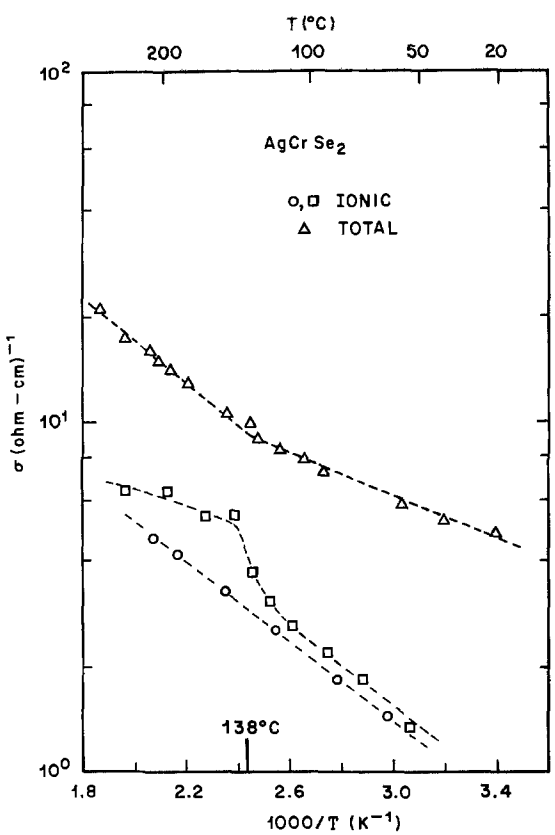


Fig. 3. The ionic and total conductivity of $AgCrSe_2$ as a function of reciprocal temperature. The ionic conductivity is shown for two samples.

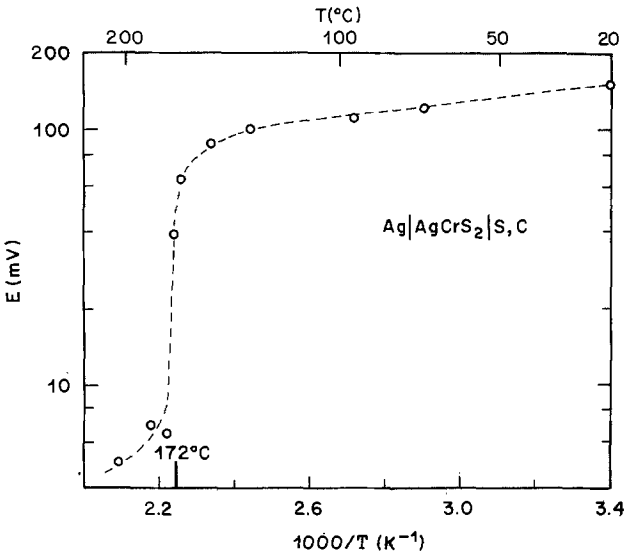


Fig. 4. Open-circuit voltage for the cell $Ag/AgCrS_2/S,C$

Ag_4RbI_5 effectively blocks the electronic component of the conductivity.

The occurrence in $AgCrS_2$ of the rapid increase in conductivity and the rapid decrease in cell potential near 170°C led us to suspect the presence of a phase transition. However, previous neutron diffraction and DTA work did not indicate any anomalies near 170°C in $AgCrS_2$ (5). However, our measurement of the specific heat of $AgCrS_2$ revealed transitions at 172° and 400°C. The 400°C transition corresponds closely to the transition previously attributed to a Ag ion disorder. The latent heat is ~100 cal/mole at 172°C and ~250 cal/mole at 400°C. This is illustrated in Fig. 5a. The specific heat of $AgCrSe_2$ was also measured. Again, as illustrated in Fig. 5b, two anomalies are observed, at 138° and 205°C. The 205°C transition corresponds closely to that previously observed by neutron diffraction and DTA and ascribed to the Ag ion disorder. The total heat involved is around 250 cal/mole, with ap-

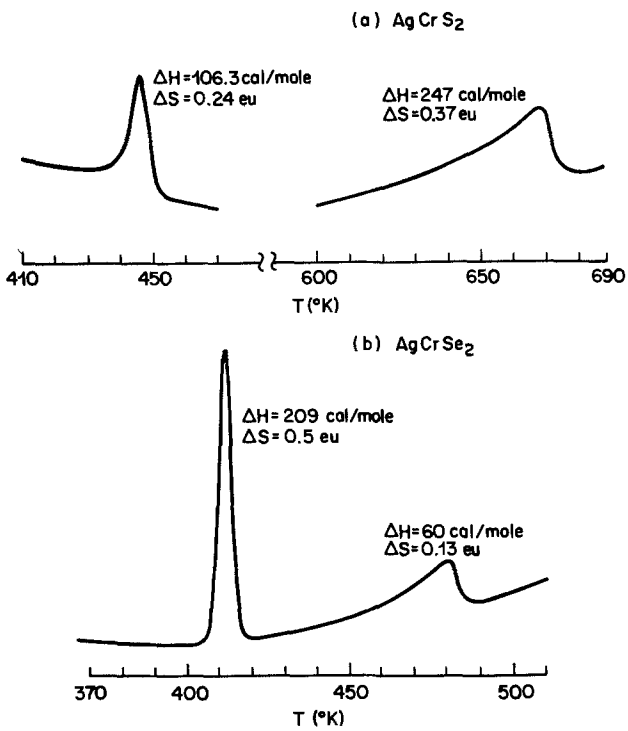


Fig. 5. Differential scanning calorimeter spectra for (a) $AgCrS_2$ and (b) $AgCrSe_2$. The latent heat and entropy of each transition are noted.

proximately 200 cal/mole in the transition at 138°C. The distribution is opposite to the case for $AgCrS_2$ where most of the latent heat is in the high temperature transition.

Discussion

Similar to Ag_2S and Ag_2Se (6), $AgCrS_2$ and $AgCrSe_2$ exhibit both high ionic and electronic conductivity at moderate temperatures. However, the ionic conductivity of $AgCrSe_2$ is high at room temperature as well, in contrast to Ag_2Se. The transformation temperatures as determined by DSC are comparable, but the latent heats are quite different. The low temperature transitions in AgI (9) and Ag_2S (9) (the $\beta \rightarrow \alpha$ transformations) involve significant changes in crystallographic structure, whereas the change in Ag_4RbI_5 (9, 10) is more subtle. These transformations make available equivalent sites for the Ag ions resulting in a large increase in the ionic mobility and consequently the conductivity. As previously mentioned, neutron diffraction data on $AgCrS_2$ and $AgCrSe_2$ did not reveal any structure changes below the complete disordering transformation, but small subtle changes might go undetected.

It is interesting to compare the latent heats for the low temperature transformations which involve crystallographic symmetry changes as given in Table I. For significant changes (AgI from hexagonal to bcc and Ag_2S from monoclinic to bcc) in crystal structure, the latent heat is large, being approximately 1 kcal/mole for both materials. For $RbAg_4I_5$, $AgCrS_2$, and $AgCrSe_2$ the latent heat is less by a factor of 5, indicative of a smaller change in structure. There is also a trend in the conductivity change at the transition temperature. The larger structural changes in AgI and Ag_2S result in larger conductivity changes. These results are also given in Table I.

Table I. The transition temperatures, latent heats, and conductivity increases at the lower temperature transition in several Ag compounds

Compound	T (°K)	Ref.	Latent heat (kcal/mole)	Ref.	Conductivity increase	Ref.
AgI	421	(11)	1.5	(11)	10^4	(12)
Ag_2S	450	(13)	0.95	(13)	10^2-10^3	(6)
Ag_4RbI_5	122	(14)	0.19	(14)	10^2	(15)
$AgCrS_2$	445	*	0.11	*	25	*
$AgCrSe_2$	405	*	0.21	*	1.2	*

* This work.

Conclusion

The ionic conductivity in $AgCrS_2$ and $AgCrSe_2$ is quite similar to that in Ag_2S and Ag_2Se, even though the structure is more open. It is dangerous to extrapolate data for Ag ion mobility in these compounds to Li or Na ion mobility since the sites occupied are different (tetrahedral *vs.* octahedral) and the types of transition states the ions may accommodate are different.

Acknowledgment

We appreciate stimulating discussions with J. C. Phillips.

Manuscript submitted Feb. 22, 1977; revised manuscript received April 14, 1977.

Any discussion of this paper will appear in a Discussion Section to be published in the June 1978 JOURNAL. All discussions for the June 1978 Discussion Section should be submitted by Feb. 1, 1978.

Publication costs of this article were assisted by Bell Laboratories.

REFERENCES

1. See, for example, J. M. Vandenberg, in "Physics and Chemistry of Materials with Layered Structures," Vol. IV, P. A. Lee, Editor, p. 423, D. Reidel/Dordrecht, Holland.
2. B. G. Silbernagel, *Solid State Commun.*, **17**, 361 (1975).
3. M. S. Whittingham, *This Journal*, **123**, 315 (1976).
4. D. W. Murphy, F. J. Di Salvo, G. W. Hull, and J. V. Waszczak, *Inorg. Chem.*, **15**, 17 (1976).
5. F. M. R. Engelsman, G. A. Wiegers, F. Jellinek, and B. Ban Laar, *J. Solid State Chem.*, **6**, 574 (1973).
6. S. Miyatani, *J. Phys. Soc. Jpn.*, **14**, 996 (1959).
7. A. D. Franklin, *J. Am. Ceram. Soc.*, **58**, 465 (1975).
8. K. Kiukkola and C. Wagner, *This Journal*, **104**, 379 (1957).
9. H. Wiedersich and S. Geller, in "The Chemistry of Extended Defects in Non-Metallic Solids," L. Eyring and M. O'Keeffe, Editors, pp. 629 ff, North Holland Publishing, Amsterdam (1970).
10. S. Geller, *Science*, **157**, 310 (1967).
11. C. M. Perrott and N. H. Fletcher, *J. Chem. Phys.*, **48**, 2144 (1968).
12. K. H. Lieser, *Z. Phys. Chem. (N.F.)*, **9**, 302 (1956).
13. C. M. Perrott and N. H. Fletcher, *J. Chem. Phys.*, **50**, 2344 (1969).
14. W. V. Johnston, H. Wiedersich, and G. W. Lindberg, *J. Chem. Phys.*, **51**, 3739 (1969).
15. B. B. Owens and G. R. Argue, *Science*, **157**, 308 (1967).

The Thermoluminescence Characteristics of Binary Sulfate Phosphors

M. Sakaguchi, M. Ohta, K. Nakazato, and T. Kondoh

Department of Applied Chemistry, Faculty of Engineering, Niigata University, Nagaoka, Niigata, Japan

ABSTRACT

The effect of the physicochemical structure of the matrices used on the thermoluminescence (TL) characteristics of TL phosphors [$(K_{1-x}Na_x)_2SO_4$:Tl^+, $Ba_{1-y}Mg_ySO_4$:Eu^{3+}, and $K_{2(1-z)}Ca_zSO_4$:Tl^+], has been investigated by using TL analytical, x-ray powder diffraction, and radioactive (^3H-H_2O) methods. All kinds of phosphors exhibited the brightest TL at such matrix compositions as $K_3Na(SO_4)_2$, $BaMg(SO_4)_2$, and $K_2Ca_2(SO_4)_3$ which were thermally stable compounds. On $(K_{1-x}Na_x)_2SO_4$:Tl^+ phosphors, the solubility of the larger Tl^+ ion in the matrix was enhanced due to the presence of smaller Na^+ ions (volume compensation); therefore, the TL intensity increased relative to the K_2SO_4:Tl^+ phosphor. The TL center was destroyed by the escape of bound water released mostly near the temperature at which the rotation of SO_4^{2-} radical becomes activated, and the TL intensity decreased simultaneously. On $Ba_{1-y}Mg_ySO_4$:Eu^{3+} and $K_{2(1-z)}Ca_zSO_4$:Tl^+ phosphors, each TL intensity increased abruptly in the initial stage of firing due to the crystallization of the compounds [$BaMg(SO_4)_2$ and $K_2Ca_2(SO_4)_3$].

One-component crystals of alkali or alkaline earth sulfates have been extensively utilized as a matrix in thermoluminescence (TL) phosphors, however, few binary sulfate crystals have been done yet. Sakaguchi *et al.* (1) have previously reported that β-ray irradiated K_2SO_4:Tl^+ phosphors emitted TL, and in the binary sulfate phosphor [$K_3Na(SO_4)_2$:Tl^+], which was prepared by using as a matrix the crystals obtained by reacting K_2SO_4 with Na_2SO_4, the TL intensified remarkably. Ryan *et al.* (2) and Blasse *et al.* (3, 4) reported that the activated $BaMg(SO_4)_2$ phosphors exhibited optical spectra characterized by sharp fluorescence. Also, Soudagar and Narayana (5) reported that (Ba:Sr)SO_4:Ce^{3+} and (Ba:Cd)SO_4:Ce^{3+} phosphors exhibited an extremely bright TL following x-ray irradiation. These results have suggested that the binary sulfate crystals could have interesting properties as phosphor hosts. In this paper, the TL character of the binary sulfate phosphors such as $(K_{1-x}Na_x)_2SO_4$:Tl^+, $Ba_{1-y}Mg_ySO_4$:Eu^{3+}, and $K_{2(1-z)}Ca_zSO_4$:Tl^+ is studied in connection with the crystal growth of these matrices.

Experimental

The phosphors used, $(K_{1-x}Na_x)_2SO_4$:Tl^+, $Ba_{1-y}Mg_ySO_4$:Eu^{3+}, and $K_{2(1-z)}Ca_zSO_4$:Tl^+, were prepared as follows. In $(K_{1-x}Na_x)_2SO_4$:Tl^+ phosphors, one set of samples was prepared by evaporation to dryness of a mixed aqueous solution of K_2SO_4, Na_2SO_4, and Tl_2SO_4 with various molar ratios followed by vacuum drying at 130°C for 2 hr (unfired phosphors); the other samples were prepared by firing the unfired phosphors at 250°-1000°C for 1 hr in He (fired phosphors). Unfired and fired phosphors which were used to determine the amount of bound water were prepared by the above-mentioned method using ^3H-labeled water as a tracer. Different compositions involving mixtures of $BaSO_4$, $MgSO_4$, and $Eu_2(SO_4)_3$ were prepared by careful blending with methanol followed by vacuum drying at 130°C for 1 hr, then $Ba_{1-y}Mg_ySO_4$:Eu^{3+} phosphors were prepared by firing the mixtures at 600°-1200°C for 0-6 hr in air. $K_{2(1-z)}Ca_zSO_4$:Tl^+ phosphors were prepared by firing mixtures of K_2SO_4, $CaSO_4$, and Tl_2SO_4 (blended by a similar procedure) at 500°-1000°C for 0-8 hr in He, O_2, or air. The time interval required to reach the firing temperature was adjusted to be 30 min in all cases, and the firing time denoted as zero means that the firing was stopped instantly at the given temperature.

He and O_2 used for the firing atmosphere were obtained by further purifying cylinder He or O_2 by passage through a glass tube containing molecular sieve 5A at −196°C for He or at 0°C for O_2.

The static apparatus used for preparing phosphors in He or O_2 was constructed of borosilicate glass tubing except for a reaction tube made of quartz, and a sample vessel was made of quartz for $(K_{1-x}Na_x)_2SO_4$:Tl^+ phosphors or of platinum for $K_{2(1-z)}Ca_zSO_4$:Tl^+ phosphors. Alumina crucibles were used for preparing phosphors in air.

Glow curves were measured using a TL analyzing system composed of the thermoluminescence dosimetry (TLD) (Aloka Company, Limited, Type TLR-101B), electrometer (Takeda Riken Industry Company, Limited, Type TR-8651), and X-Y recorder (Riken Denshi Company, Limited, Type F-3C). Thirty milligrams of phosphor were uniformly spread on the tray (14.5 mmϕ × 2 mm) made of silver, and the glow curve was immediately recorded after the phosphor was exposed to the β-ray source (^{90}Sr, 100 μCi) at a distance of 2 mm at 25°C for 10-180 sec. Furthermore, in order to eliminate the effect of cosmic and other external radiation on TL, all phosphors were preheated up to 260°C prior to the β-ray irradiation.

The crystal structure of the phosphors was examined by x-ray powder diffraction method using nickel-filtered Cu radiation.

The amount of bound water in $(K_{1-x}Na_x)_2SO_4$:Tl^+ phosphors prepared by using ^3H-labeled water was determined by the liquid scintillation countermethod with PCS scintillant (supplied by Amersham/Searle Company).

Results and Discussion

$(K_{1-x}Na_x)_2SO_4$:Tl^+ phosphors.—These phosphors exhibited similar glow curves with two glow peaks at 100° and 160°C. The height of the 100°C peak was selected to compare with that of K_2SO_4:Tl^+ phosphor reported previously (1).

X-ray powder diffraction traces on unfired phosphors showed formation of $K_3Na(SO_4)_2$ (glaserite) (6). Figure 1 shows the relation between the amount of $K_3Na(SO_4)_2$ crystals produced and the TL intensity in these phosphors. The TL intensity increased with the diffraction peak intensity of glaserite, and it indicated a maximum for the phosphor prepared with the matrix composition at x near 0.3. A similar exami-

Key words: thermoluminescence, phosphor, binary sulfate, glaserite, calcium langbeinite.

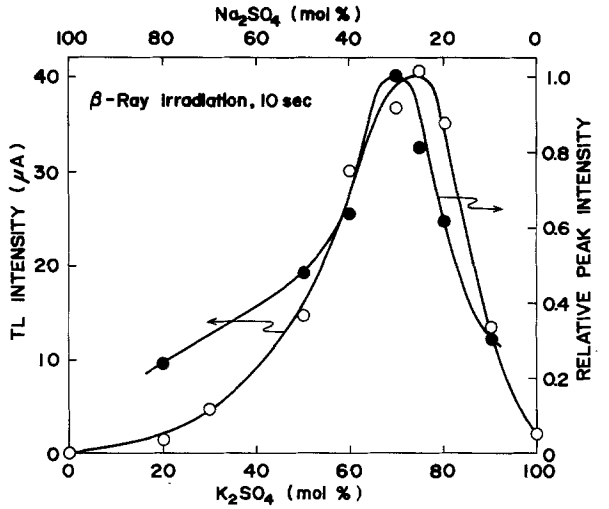


Fig. 1. Relation between the TL intensity and the (110) diffraction peak intensity of $K_3Na(SO_4)_2$ crystals in unfired $(K_{1-x}Na_x)_2SO_4$:Tl^+ (2.5 m/o) phosphors.

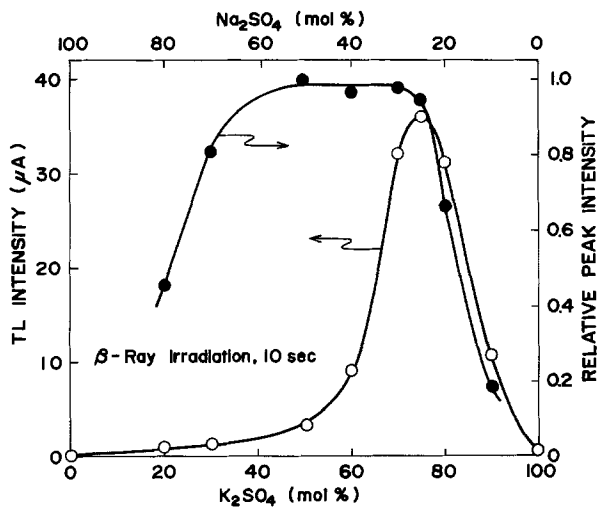


Fig. 2. Relation between the TL intensity and the (110) diffraction peak intensity of $K_3Na(SO_4)_2$ crystals in $(K_{1-x}Na_x)_2SO_4$:Tl^+ (2.5 m/o) phosphors fired at 750°C for 1 hr in He.

nation was carried out on fired phosphors (Fig. 2). A higher yield of glaserite structure was obtained over a wide range of composition, in contrast to the fixed composition in unfired phosphors. Nevertheless, the higher TL intensity was limited to the phosphor prepared at the calculated composition, *i.e.*, $K_3Na(SO_4)_2$. Hence the TL character on both unfired and fired phosphors, which were prepared with $K_3Na(SO_4)_2$ crystals as a matrix, was subsequently investigated.

The phosphors had a maximum in TL intensity at Tl^+ concentration of 2.5 mole percent (m/o). This increase of a factor of 2.5 in the Tl^+ concentration as compared with K_2SO_4:Tl^+ (1.0 m/o) phosphor,[1] is attributed to the increase of Tl^+ solubility where the larger radius of Tl^+ (1.57Å) was compensated by the smaller Na^+ (0.97Å) than K^+ (1.33Å) (volume compensation).

It could be assumed that the unfired phosphor prepared as mentioned above occluded bound water at such active sites in crystals as subgrain boundaries, cracks, and so on, during the crystallization (7, 8). It should be remarked how bound water affects the crystal structure during firing. To investigate this feature, the amount of bound water in unfired phosphor was determined by using water labeled with ^3H as a tracer;

[1] K_2SO_4:Tl^+ phosphor had a maximum in TL intensity at Tl^+ concentration of 1.0 m/o (1).

Table I. Amount of bound water in unfired phosphors

Phosphor	Amount of bound water (mole/mole-phosphor)
K_2SO_4:Tl^+ (1.0 m/o)	3.94×10^{-3}
$K_3Na(SO_4)_2$: Tl^+ (2.5 m/o)	1.46×10^{-3}

the water persisted in the phosphor after vacuum drying at 130°C for 2 hr; this water was defined as bound water.

The data given in Table I show bound water to be clearly present in the unfired phosphors, and the amount of bound water occluded in $K_3Na(SO_4)_2$:Tl^+ phosphor was much less than that in K_2SO_4:Tl^+ phosphor. The decrease of the active sites for occlusion of bound water in $K_3Na(SO_4)_2$:Tl^+ phosphor may result from the release of the strain in the crystal lattice due to the solution of a larger Tl^+ ion in K_2SO_4 crystals in the presence of a smaller Na^+ ion.

The behavior of bound water during firing was investigated by using the unfired phosphors of both K_2SO_4:Tl^+ and $K_3Na(SO_4)_2$:Tl^+ (Fig. 3 and 4), where the 25°C value corresponded to the unfired phosphor. In the case of K_2SO_4:Tl^+ phosphor (Fig. 3), bound water diminished abruptly near 400°C, then could not be detected after firing at 750°C, and the TL intensity decreased obviously with diminution of bound water. On the other hand, bound water in $K_3Na(SO_4)_2$:Tl^+ phosphor was no longer detectable at 400°C, and the TL intensity jumped after removal

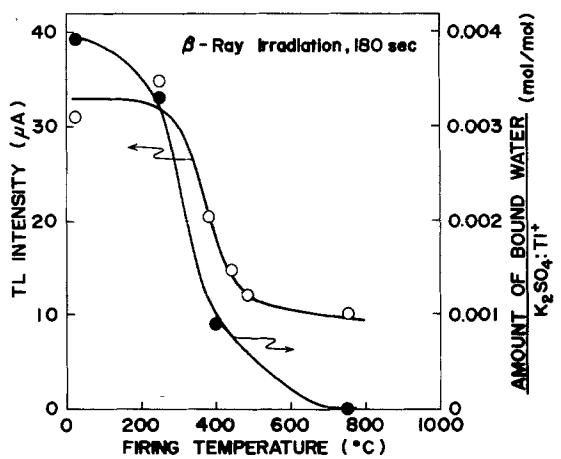


Fig. 3. Relation between the TL intensity and the amount of bound water in K_2SO_4:Tl^+ (1.0 m/o) phosphor fired at various temperatures for 1 hr in He.

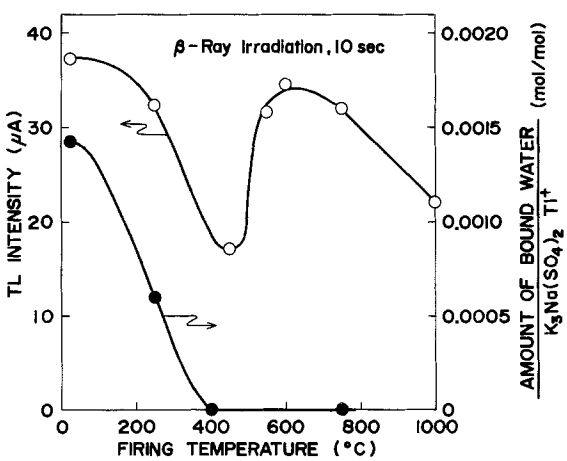


Fig. 4. Relation between the TL intensity and the amount of bound water in $K_3Na(SO_4)_2$:Tl^+ (2.5 m/o) phosphor fired at various temperatures for 1 hr in He.

of bound water (near 550°C) then declined again above 750°C. These facts suggest that bound water in $K_3Na(SO_4)_2$ crystals was more easily desorbed.

It has been already reported that the rotation of SO_4^{2-} radical in K_2SO_4 crystals was initiated at 375°C (9); then bound water must desorb easily when the rotation of SO_4^{2-} becomes activated. Scanning electron micrographs of fired phosphor indicated the existence of many micropores and cracks resulting from a destructive process, which was caused by the escape of both bound water and gases produced by the thermal decomposition of blended Tl_2SO_4 (decomposition point: 632°C). Consequently, the TL center would be damaged during the destructive process. The restoration of the TL intensity on $K_3Na(SO_4)_2:Tl^+$ phosphor which dropped near 400°C (Fig. 4) could be ascribed to the recrystallization of a matrix after desorbing bound water, and the drop in TL intensity above 750°C was caused by the thermal decomposition of Tl_2SO_4. On the other hand, the restoration of TL intensity on $K_2SO_4:Tl^+$ phosphor (Fig. 3) would be impossible due to the presence of residual bound water under the experimental conditions.

$Ba_{1-y}Mg_ySO_4:Eu^{3+}$ phosphors.—These phosphors exhibited similar glow curves with three glow peaks at 100°, 150°, and 230°C. The 230°C peak (main peak) was selected for the investigation of the TL character.

X-ray powder diffraction traces on $Ba_{1-y}Mg_ySO_4:Eu^{3+}$ phosphors showed formation of $BaMg(SO_4)_2$ as found by Ryan *et al.* (2). Figure 5 shows the relation between the amount of $BaMg(SO_4)_2$ crystals produced and the TL intensity in these phosphors. The TL intensity increased with the diffraction peak intensity of $BaMg(SO_4)_2$ crystals, and it indicated a maximum for the phosphor prepared with the matrix composition at $y \simeq 0.5$. The TL intensity in $BaMg(SO_4)_2:Eu^{3+}$ phosphor had a maximum at 10^{-2} m/o Eu^{3+}. From Fig. 6, the degree of crystallization of $BaMg(SO_4)_2$ indicated a maximum on firing at 1000°C for 1 hr. However, the crystals decomposed rapidly for a longer firing interval at 1000°C.

$K_{2(1-z)}Ca_zSO_4:Tl^+$ phosphors.—These phosphors exhibited similar glow curves with two glow peaks; main at 90°C and shoulder at 130°C. The 90°C peak was selected for the investigation of the TL character.

X-ray powder diffraction traces on $K_{2(1-z)}Ca_zSO_4:Tl^+$ phosphors showed formation of $K_2Ca_2(SO_4)_3$ (calcium langbeinite) (10). Figure 7 shows the relation between the amount of $K_2Ca_2(SO_4)_3$ crystals produced and the TL intensity in these phosphors. The TL intensity increased with the diffraction peak intensity of calcium langbeinite, and it indicated a maximum for the phosphor prepared with the matrix composition at z near 0.7. The TL intensity in $K_2Ca_2(SO_4)_3:Tl^+$ phosphor had a maximum at 1.0 m/o Tl^+. From Fig. 8, the degree of crystallization of $K_2Ca_2(SO_4)_3$ increased with

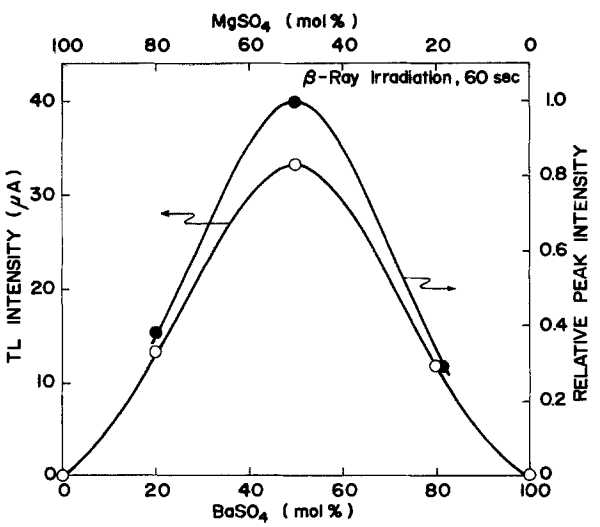


Fig. 5. Relation between the TL intensity and the diffraction peak intensity at $2\theta = 23.6°$ of $BaMg(SO_4)_2$ crystals in $Ba_{1-y}Mg_ySO_4:Eu^{3+}$ (10^{-2} m/o) phosphors fired at 1000°C for 1 hr in air.

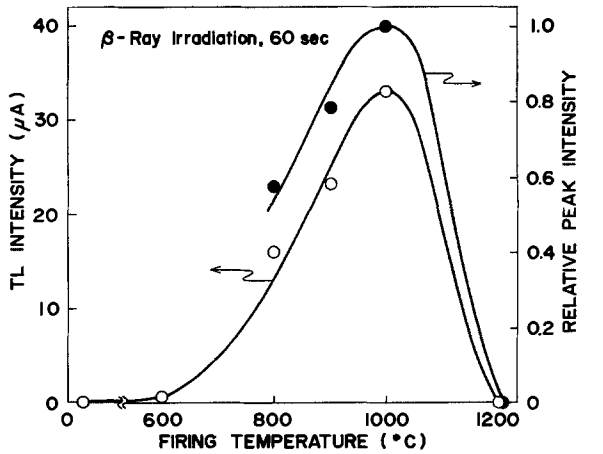


Fig. 6. Effects of firing temperature on the TL intensity and the diffraction peak intensity at $2\theta = 23.6°$ of $BaMg(SO_4)_2$ crystals in $BaMg(SO_4)_2:Eu^{3+}$ (10^{-2} m/o) phosphors fired for 1 hr in air.

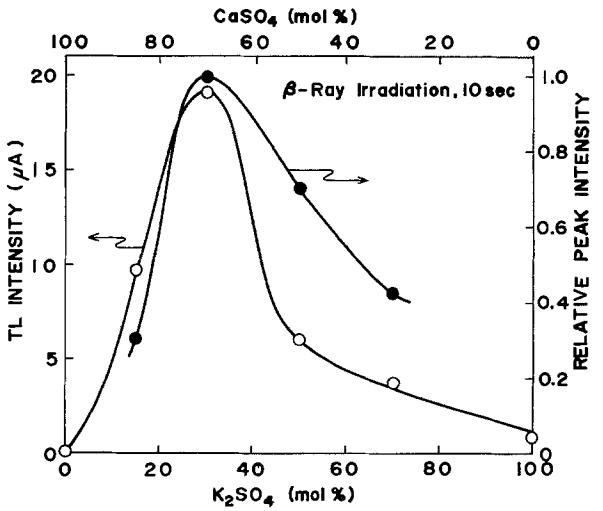


Fig. 7. Effects of matrix composition on the TL intensity and the (132) diffraction peak intensity of $K_2Ca_2(SO_4)_3$ crystals in $K_{2(1-z)}Ca_zSO_4:Tl^+$ (1.0 m/o) phosphors fired at 900°C for 1 hr in air.

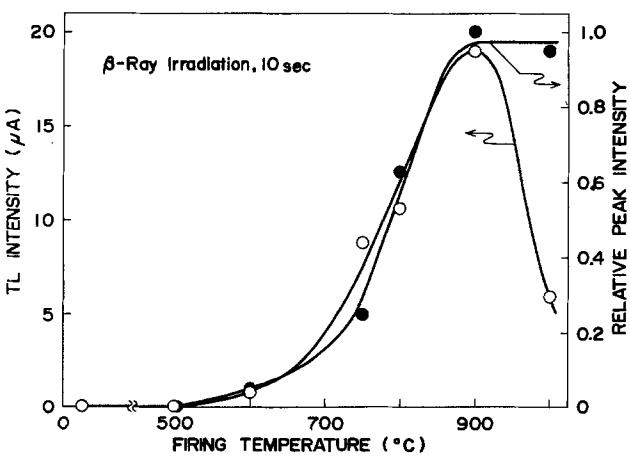


Fig. 8. Effects of firing temperature on the TL intensity and the (132) diffraction peak intensity of $K_2Ca_2(SO_4)_3$ crystals in $K_2Ca_2(SO_4)_3:Tl^+$ (1.0 m/o) phosphor fired for 1 hr in air.

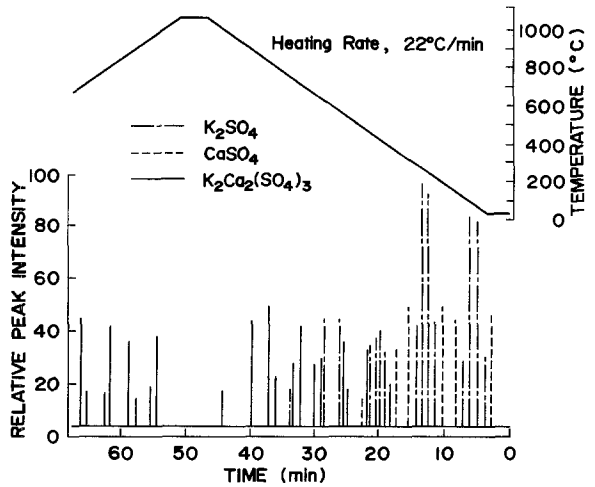


Fig. 9. High temperature x-ray diffraction trace of $K_2Ca_2(SO_4)_3:Tl^+$ (1.0 m/o) phosphor.

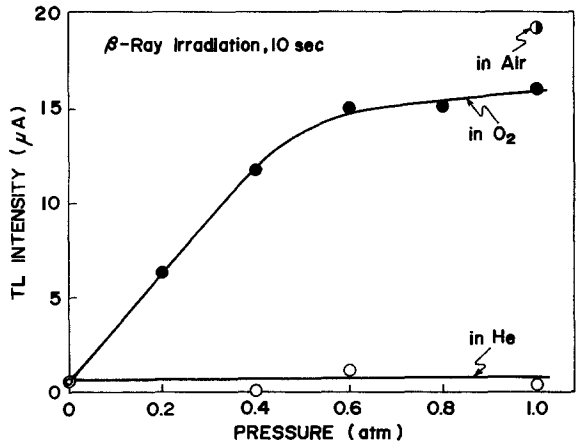


Fig. 10. Gas pressure dependence of firing atmosphere on the TL intensity of $K_2Ca_2(SO_4)_3:Tl^+$ (1.0 m/o) phosphor fired at 900°C for 1 hr.

the firing temperature, then it did not change above 900°C; however, the TL intensity decreased abruptly. Also, the crystals decomposed gradually for a longer firing interval at 900°C.

Further details on the formation reaction of $K_2Ca_2(SO_4)_3:Tl^+$ phosphor in the mixture of the molar ratio $K_2SO_4:CaSO_4:Tl_2SO_4 = 3:7:0.1$ were investigated by using a high temperature x-ray diffractometer. The result obtained in the 2θ region of 29.0°-33.0° [2] is shown in Fig. 9. On elevating temperature, the diffraction peak intensities of both K_2SO_4 and $CaSO_4$ starting materials diminished near 400°C while the peak of $K_2Ca_2(SO_4)_3$ crystals emerged; the peak intensity reached a maximum near 900°C, then it disappeared above 900°C; this fact suggests melting of $K_2Ca_2(SO_4)_3$ crystals. On cooling, a peak of the crystals emerged again near 900°C.

These facts are explained by referring to Fig. 8 as follows. The diffusion rate of Tl^+ dopant into the $K_2Ca_2(SO_4)_3$ crystals can increase during the noticeable change in crystal structure near 900°C; the phosphor fired at 900°C exhibited extremely bright TL. On the other hand, during cooling, most of Tl^+ dopant in the crystals produced by the recrystallization from the molten salt would be segregated on the grain boundaries, thus the amount of available Tl^+ for the TL center must decrease. Therefore, the TL intensity of the phosphor fired at 1000°C decreased remarkably.

The effect of firing atmosphere on the TL intensity of $K_2Ca_2(SO_4)_3:Tl^+$ phosphor is shown in Fig. 10. The phosphor fired in O_2 was much stronger in TL intensity than that fired in He. This fact may be due to the stabilization of Tl^+ dopant in the crystals by the presence of oxygen.

Conclusion

The phosphors prepared by using binary sulfate crystals as a matrix exhibited a much brighter TL than those prepared by using each crystal which constituted binary sulfate crystals, and the TL intensity of $K_2Ca_2(SO_4)_3:Tl^+$ phosphor prepared by recrystallization from molten salt decreased remarkably. The TL center in $K_3Na(SO_4)_2:Tl^+$ phosphor was destroyed by the escape of bound water.

[2] X-ray diffraction peaks of K_2SO_4, $CaSO_4$, and $K_2Ca_2(SO_4)_3$ crystals are detected in this 2θ region.

Acknowledgment

We wish to thank Mr. K. Uematsu for his assistance with the experimental work.

Manuscript submitted Aug. 11, 1976; revised manuscript received March 28, 1977.

Any discussion of this paper will appear in a Discussion Section to be published in the June 1978 JOURNAL. All discussions for the June 1978 Discussion Section should be submitted by Feb. 1, 1978.

Publication costs of this article were assisted by Niigata University.

REFERENCES

1. M. Sakaguchi, T. Hirabayashi, M. Mochizuki, and H. Sakurai, *Nippon Kagaku Kaishi*, **1975**, 1458.
2. F. M. Ryan, W. Lehmann, D. W. Feldman, and J. Murphy, *This Journal*, **121**, 1475 (1974).
3. G. Blasse and G. P. M. van den Heuvel, *J. Inorg. Nucl. Chem.*, **38**, 876 (1976).
4. G. Blasse, G. P. M. van den Heuvel, and J. Stegenga, *J. Solid State Chem.*, **17**, 439 (1976).
5. M. K. Soudagar and K. L. Narayana, in Proceedings of National Symposium on Thermoluminescence: Its Application, 1975, p. 119.
6. H. Winchell and R. J. Benoit, *Am. Mineral.*, **36**, 590 (1951).
7. R. Brooks, A. T. Horton, and J. L. Torgesen, *J. Cryst. Growth*, **2**, 279 (1968).
8. T. Fujie, *Hyomen*, **8**, 578 (1970).
9. T. Watanabe, K. Sakai, and S. Iwai, *Acta Crystallogr., Sect. A*, **28**, Supplement, 187 (1972).
10. National Bureau of Standards, Monograph 25, Sect. 7, 39 (1969).

The Luminescence of Eu^{3+} and Bi^{3+} in the Two Modifications of $CaLaGaO_4$

H. Ronde, D. M. Krol, and G. Blasse

Physical Laboratory, State University, Sorbonnelaan 4, Utrecht, The Netherlands

ABSTRACT

The luminescence of Eu^{3+} and Bi^{3+} in the two modifications of $CaLaGaO_4$ is reported. The Eu^{3+}-activated α-phase (with olivine structure) shows a bright red luminescence at room temperature, whereas the Eu^{3+}-activated β-phase (with K_2NiF_4 structure) shows a red luminescence of much lower intensity at room temperature. This difference in efficiency is discussed and correlated with the dramatic shift of the charge-transfer band of the Eu^{3+} ion to lower energies in going from the α- to the β-phase. Furthermore, additional information on the crystal structure of α-$CaLaGaO_4$ can be deduced from this emission, *viz.*, the Ca^{2+} and La^{3+} ions are ordered with the Ca^{2+} ions on the (4a) and the La^{3+} ions on the (4c) sites. The Bi^{3+}-activated α-phase shows a bright blue luminescence at room temperature. The activated β-phase, however, shows only a very weak blue luminescence at temperatures below room temperature. This difference in efficiency is discussed and correlated with the stiffness of the surroundings of the luminescent centers in the different host lattices. The activated α-phase shows two emission bands peaking at about 420 and 480 nm. The bands are ascribed to electronic transitions on two crystallographically different Bi^{3+} centers, *viz.*, Bi_{La}^{x} and $Bi_{Ca}^{\cdot}$, respectively. The decay time of the two emissions at different temperatures is reported; the temperature dependence of the decay time is described in terms of a three level scheme.

During the course of our investigations we came upon an interesting class of compounds, *viz.*, the gallates $CaLnGaO_4$ (Ln = Y, lanthanide) (1). The normal temperature and pressure modification (denoted by α) of these compounds has an olivine-type crystal structure. At high temperatures (Ln = La, Pr, Nd, Sm) or pressures (Ln = Eu, Gd, Tb, Dy) a β-modification appears with the K_2NiF_4 or a distorted K_2NiF_4 structure. The $\alpha \rightarrow \beta$ transition is irreversible. It seemed interesting to dope one of these compounds with luminescent activators (*e.g.*, Eu^{3+} or Bi^{3+}) to investigate the influence of the crystal structure of the two modifications on the luminescence properties of the activated compounds. Since the high pressure induced phase transitions are far beyond the working range of our piston-cylinder apparatus, we had to choose a substance which shows a temperature-induced transition. Within this class of compounds only $CaLaGaO_4$ has no optical transitions at wavelengths longer than 240 nm, so that we selected $CaLaGaO_4$ as a host lattice. An additional advantage of this choice is the fact that of all compounds which show a temperature-induced transition, only $CaLaGaO_4$ has the regular K_2NiF_4 structure in the β-phase.

The red luminescence of the Eu^{3+} ion has found wide technical application. It has been suggested that the efficiency of this luminescence is determined by the spectral position of the Eu^{3+} charge-transfer band in the u.v. region (2, 3). Hoefdraad (4) has proposed a model which shows that the coordination of the Eu^{3+} ion in oxides is one of the important factors determining the position of the charge-transfer band. In this paper we give further experimental evidence supporting Hoefdraad's model.

The luminescence of phosphors activated with ions with ns^2 configuration is well known (5). Blasse *et al.* have recently shown that the thermal quenching temperature of the luminescence of the Bi^{3+} and Pb^{2+} ion depends strongly on the stiffness of the host lattice (6). In this paper we report another example supporting this general rule.

Experimental

Starting materials were $CaCO_3$ (Merck p.a.), La_2O_3 (Koch Light 99.9%), Gd_2O_3 (Fluka A.G. 99.9%), Ga_2O_3 (Alusuisse 99.99%), $Al(OH)_3$ (UCB), Eu_2O_3 (Fluka A.G. Puriss), and Bi_2O_3 (Baker 99.7%). Samples α-$CaLa_{0.99}Eu_{0.01}GaO_4$ were prepared by firing an intimate mixture of the starting materials for about 50 hr at 1250°C in air. The irreversible phase change occurs at 1310°C, whereas the melting point is at about 1350°C. The temperature range in which we could transform the α-phase into the β-phase is, therefore, rather small. In addition, the phase transition is sluggish. As a consequence we were not able to prepare a completely α-free β-modification. From the x-ray powder diagram the amount of α-phase in our β-phase samples is estimated to be 10% at maximum.

Samples α-$CaLa_{1-x}Bi_xGaO_4$ (x = 0.001, 0.005, 0.03) were prepared by firing intimate mixtures of the starting materials for about 15 hr at 1150°C in air. In view of the difficulties met in the preparation of the pure β-modification in the Eu^{3+} case and the volatility of bismuth oxide, we decided to simulate the β-phase by doping $CaGdAlO_4$ with Bi^{3+}. This compound has the K_2NiF_4 structure (7) and shows some similarity with $CaLaGaO_4$. $CaGd_{0.99}Bi_{0.01}AlO_4$ was prepared by firing the starting materials for about 50 hr at 1300°C in air. Samples were checked by x-ray analysis on a Philips diffractometer using Cu-Kα radiation. The performance of the optical experiments has been described elsewhere (8).

Results and Discussion of the Eu^{3+}-Doped Samples

A careful inspection of the unactivated samples $CaLaGaO_4$ revealed that these samples show a very weak blue luminescence at and below room temperature. Since this very weak luminescence does not disturb our measurements, we will not consider it further.

At 77°K and at room temperature

$$\alpha\text{-}CaLa_{0.99}Eu_{0.01}GaO_4$$

shows a bright red luminescence under u.v. excitation. In Fig. 1 we present the emission spectrum of α-$CaLa_{0.99}Eu_{0.01}GaO_4$ recorded at room temperature. We notice that this spectrum consists of a large number of sharp lines. The $^5D_0 \rightarrow {}^7F_2$ transition is the most intense one. Furthermore, the number of lines resulting from the transition from the $^5D_0$ level is restricted (4-5 for the $^5D_0 \rightarrow {}^7F_2$ transition, 3 for the $^5D_0 \rightarrow {}^7F_1$

Key words: luminescence Eu^{3+}, Bi^{3+}, $CaLaGaO_4$.

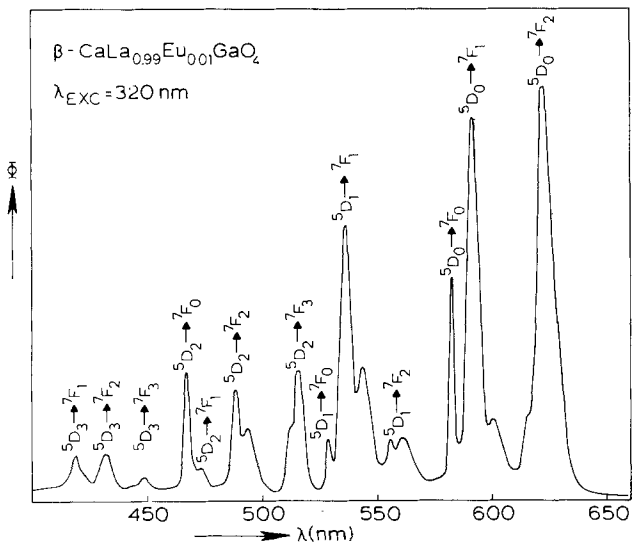


Fig. 1. Spectral energy distribution of α-$CaLa_{0.99}Eu_{0.01}GaO_4$ at room temperature under 254 nm excitation. Φ denotes the spectral radiant power per constant wavelength interval in arbitrary units. Note change in scale at the right-hand side.

transition). In addition, we also observe emission from the $^5D_3$, $^5D_2$, and $^5D_1$ levels.

At 77°K and at room temperature

$$\beta\text{-}CaLa_{0.99}Eu_{0.01}GaO_4$$

shows a red luminescence of much lower intensity under u.v. excitation. The emission spectrum of β-$CaLa_{0.99}Eu_{0.01}GaO_4$ recorded at room temperature is presented in Fig. 2. We notice that this spectrum consists of a large number of lines which are less sharp than the corresponding lines in the α-modification. Also in this case emissions from the $^5D_3$, $^5D_2$, and $^5D_1$ levels are observed. Furthermore, the intensity of the emission from the $^5D_3$ level relative to the intensities of the emissions from the $^5D_2$ and $^5D_1$ levels is much lower in the β-phase than in the α-phase.

In Fig. 3 the excitation spectra of the Eu^{3+} emission (610 nm) recorded at room temperature are given for both the α- and the β-phase. We want to emphasize the fact that we can excite the β-phase selectively at 320 nm, so that the emission spectrum given in Fig. 2 can

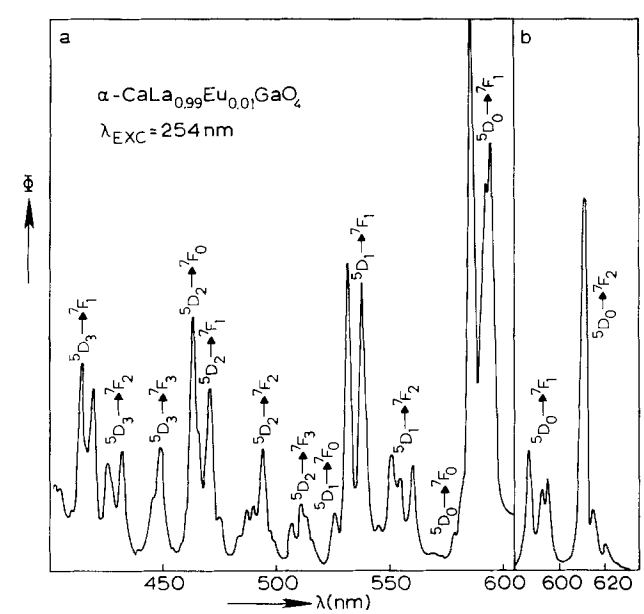


Fig. 2. Spectral energy distribution of β-$CaLa_{0.99}Eu_{0.01}GaO_4$ at room temperature under 320 nm excitation. The slit width in Fig. 1 and 2 is the same.

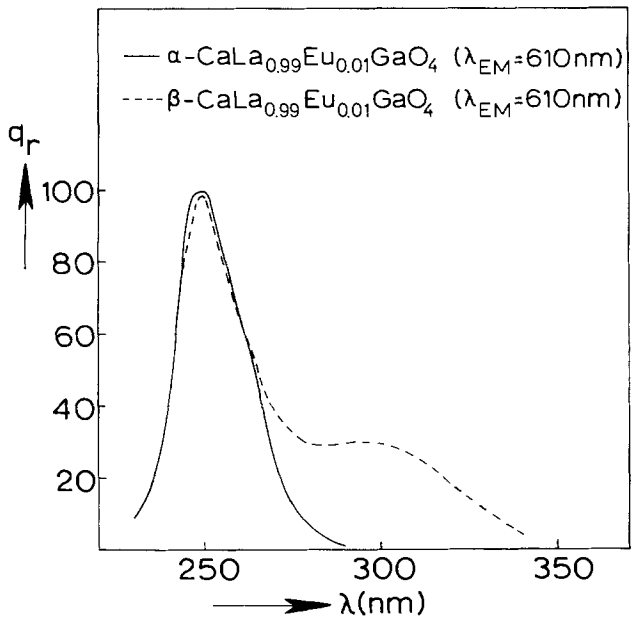


Fig. 3. Relative excitation spectra of the Eu^{3+} 610 nm emission of α-$CaLa_{0.99}Eu_{0.01}GaO_4$ and β-$CaLa_{0.99}Eu_{0.01}GaO_4$ at room temperature. q_r denotes the relative quantum output.

be regarded as the emission spectrum of the pure β-phase. Furthermore, we observed that when we excite the activated β-phase with 360 nm radiation, the $^5D_3$ emission has the same intensity as in the α-phase where the $^5D_3$ emission intensity does not depend upon the excitation wavelength.

In the olivine phase the coordination number of the cations, denoted by roman figures, is as follows: α-$^{VI}Ca^{VI}La^{IV}GaO_4$. There are two crystallographically different octahedral sites, one being centrosymmetric (site symmetry C_i), whereas the other is not (site symmetry C_s). The distribution of the Ca^{2+} and La^{3+} ions among these sites has not been described in the previous paper (1). The sharpness of the lines in the emission spectrum of Fig. 1 indicates a unique crystal field at the Eu^{3+} ion, so that there must be a long-range ordering of the Ca^{2+} and La^{3+} ions among the octahedral sites. The high intensity of the $^5D_0 \rightarrow {}^7F_2$ forced electric-dipole transition relative to the intensity of the $^5D_0 \rightarrow {}^7F_1$ magnetic-dipole transition indicates that the Eu^{3+} ion occupies the noncentrosymmetric site (9). Moreover, the number of lines observed for the $^5D_0 \rightarrow {}^7F_1$ and $^5D_0 \rightarrow {}^7F_2$ transitions is in agreement with the number expected for C_s symmetry. In this way we have obtained additional information on the crystal structure of α-$CaLaGaO_4$, *viz.*, the Ca^{2+} and La^{3+} ions are ordered with the Ca^{2+} ions on the (4a) and La^{3+} ions on the (4c) sites. This ordering is in agreement with an empirical rule given by one of us before (10), *viz.*, in the superstructure of olivine the (4a) sites are preferred by the lower charged octahedral cations.

If we compare the emission spectra of

$$\alpha\text{-}CaLa_{0.99}Eu_{0.01}GaO_4$$

with that of the isomorphous $LiY_{0.99}Eu_{0.01}SiO_4$ (10), a striking difference is noted; the silicate does not show emission from the $^5D_3$, $^5D_2$, and $^5D_1$ levels of the Eu^{3+} ion, whereas the gallate has a considerable amount of emission from these levels. This can be explained as follows. Relaxation from the above-mentioned levels to the $^5D_0$ level occurs via phonon emission. The energy differences between the levels within the ^5D manifold amount to 1750 cm^{-1} or more. In the case of $LiY_{0.99}Eu_{0.01}SiO_4$ this energy can be dissipated by a two phonon relaxation process due to the presence of the silicate group with its high energy phonons. In α-$CaLa_{0.99}Eu_{0.01}GaO_4$ this relaxation can only be achieved by at least a three phonon process, because

the phonon cutoff frequency is about 600 cm^{-1}, as found by us from the infrared spectrum.

The excitation band of the α-modification presented in Fig. 3 corresponds to the optical absorption caused by a charge-transfer transition within the Eu^{3+}-oxygen complex (9). The position of the maximum of this band (40 kK at 300°K, 41.5 kK at 77°K) is in agreement with a model by Hoefdraad (4). For Eu^{3+} in octahedral coordination he predicts this charge-transfer band to be situated at about 42 kK independent of the host lattice. Since oxides containing octahedrally coordinated La^{3+} ions are rare, Hoefdraad could find only one example of Eu^{3+} on an octahedrally coordinated La^{3+} site, *viz.*, $NaLaO_2$:Eu. This substance did not obey the prediction, the charge-transfer band being situated at only 36 kK. We reinvestigated $NaLa_{0.97}Eu_{0.03}O_2$ at room temperature and measured a value of about 38.5 kK for the position of the maximum of the charge-transfer band; furthermore we found a value of 36 kK for this position in the case of Eu^{3+}-activated La_2O_3 at room temperature. We therefore conclude that the value of 36 kK reported earlier (11) is probably due to Eu^{3+}-activated La_2O_3, which originates from hydrolysis of the hygroscopic $NaLaO_2$. The value of 38.5 kK cannot be considered as a serious deviation from the model of Hoefdraad, so that there is now evidence that this model can be extended to Eu^{3+} on an octahedrally coordinated La^{3+} site.

In the K_2NiF_4 structure the cations are coordinated as follows; β-$^{IX}Ca^{IX}La^{VI}GaO_4$. The IX-coordinated sites are crystallographically equivalent (site symmetry C_{4V}), the Ca^{2+} and La^{3+} ions being distributed at random among these sites.

We assign the maximum in the excitation spectrum of the β-modification at 33.3 kK (cf. Fig. 3) to a charge-transfer transition within the Eu^{3+}-oxygen complex. This dramatic shift of the first charge-transfer band of the β-phase with respect to the α-phase can be explained as follows: In the first place the number of ligands increases from six to nine in going from the α- to the β-phase, leading to a lowering of the energetic position of the first charge-transfer state (12). In addition, the position of the charge-transfer band of nine coordinated Eu^{3+} does depend on the host lattice, in such a way that the charge-transfer band shifts to higher energy for smaller lanthanide host lattice ions. This was shown by one of us for the series of compounds $NaLn_{0.98}Eu_{0.02}TiO_4$ (Ln = La, Gd, Y, and Lu) which also have the K_2NiF_4 structure (13). In the case of $NaLa_{0.98}Eu_{0.02}TiO_4$ this charge-transfer band was reported to be situated at about 31 kK. In the case of the smaller Ln^{3+} ions this charge-transfer transition is hidden under the first optical absorption band of the TiO_6 octahedra at about 35 kK. Hoefdraad showed that the variation of the charge-transfer band of the Eu^{3+} ion in VIII and XII coordination is proportional with the Eu-O distance, with increasing bond length the band shifts to lower energies. We conclude that Hoefdraad's reasoning can be extended to Eu^{3+} in nine coordination.

The lower intensity of the emission of the β-modification in comparison with the α-modification is compatible with the above-mentioned shift of the charge-transfer band. From a simple configurational-coordinate diagram it follows immediately that the Mott-Seitz activation energy decreases with a decrement of the energetic position of the parabola for the excited state (9).

Another consequence of a charge-transfer band at low energies is an increase of the relaxation rates of the ^5D_J levels as shown by Struck and Fonger (14) for Eu^{3+} in the oxysulfides. This is due to the fact that a ^5D_J level can be emptied via the charge-transfer state to the $^5D_{J-1}$ level. This is indeed observed here; the $^5D_3$ emission is more intense in the α-phase than in the β-phase upon charge-transfer excitation. If, however, excitation is into the $^5D_3$ level of Eu^{3+} in β-$CaLaGaO_4$ (λ_{exc} = 360 nm), the $^5D_3$ emission has the same intensity as in the α-phase where the $^5D_3$ emission intensity does not depend upon the excitation wavelength.

As mentioned before, the Ca^{2+} and La^{3+} ions are distributed at random among the C_{4V} sites in the β-modification. This is fully confirmed by the emission spectrum of β-$CaLa_{0.99}Eu_{0.01}GaO_4$, the broadness of the bands indicating all sorts of crystallographically different Eu^{3+} ions.

Results and Discussion of the Bi^{3+}-Doped Samples

At 77°K and at room temperature, samples with composition α-$CaLa_{1-x}Bi_xGaO_4$ (x = 0.001, 0.005, 0.03) show a bright blue luminescence under u.v. excitation. We present the emission and excitation spectra of α-$CaLa_{0.995}Bi_{0.005}GaO_4$ recorded at 4°K in Fig. 4. We note that there are two emission and excitation bands. Apparently, the long wavelength excitation band corresponds to the long wavelength emission band and, similarly, the short wavelength excitation band corresponds to the short wavelength emission band. Furthermore, the long wavelength excitation band contains two overlapping subbands. These general features are also observed in the spectra of the 0.1 and 3% Bi^{3+} samples.

In the case of the 0.5 and 3% Bi^{3+}-doped samples, the two emissions are of about equal intensity at all temperatures (4°, 77°, and 300°K) when excited in the maximum of their corresponding excitation bands. The 0.1% Bi^{3+}-doped sample showed considerably more short wavelength than long wavelength emission. Upon exciting the samples with 320 nm radiation, we did not observe any increase in the intensity of the long wavelength side of the short wavelength emission in the sequence x = 0.001, x = 0.005, x = 0.03; this seems to exclude efficient energy transfer processes between the two band systems.

For the sample α-$CaLa_{0.995}Bi_{0.005}GaO_4$ we measured the decay time τ of the emission around 450 nm under excitation with a broad spectrum of u.v. radiation (240-360 nm). Figure 5 presents τ as a function of temperature. Within the experimental error the intensity *vs.* time relations were single exponentials. We emphasize the fact that in the temperature range from 4° to 400°K the total intensity of the emissions remains constant. Therefore the sudden decrease of τ in the region between 40° and 80°K cannot be the result of temperature quenching of the emission.

$CaGd_{0.99}Bi_{0.01}AlO_4$ shows a weak blue luminescence at 77°K under u.v. excitation; at room temperature this luminescence is quenched. At 4°K the emission spectrum of $CaGd_{0.99}Bi_{0.01}AlO_4$ consists of a very broad band peaking at about 400 nm, with a shoulder at about 450 nm. The corresponding excitation spectrum consists of one band peaking at about 290 nm. Because of the low efficiency of this luminescence, we did not perform detailed measurements on this composition.

For the interpretation of the experimental results we will use the atomic energy level diagram of the Bi^{3+}

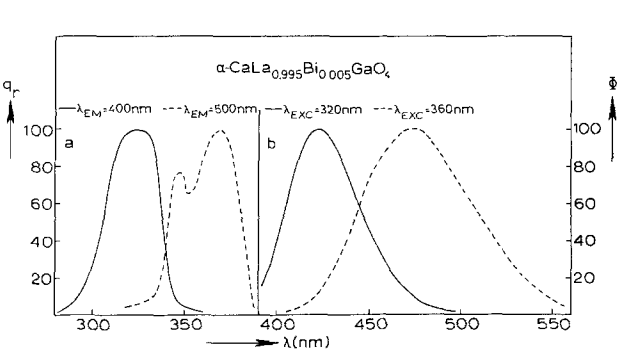


Fig. 4. a. LHeT excitation spectra of α-$CaLa_{0.995}Bi_{0.005}GaO_4$. b. LHeT emission spectra of α-$CaLa_{0.995}Bi_{0.005}GaO_4$.

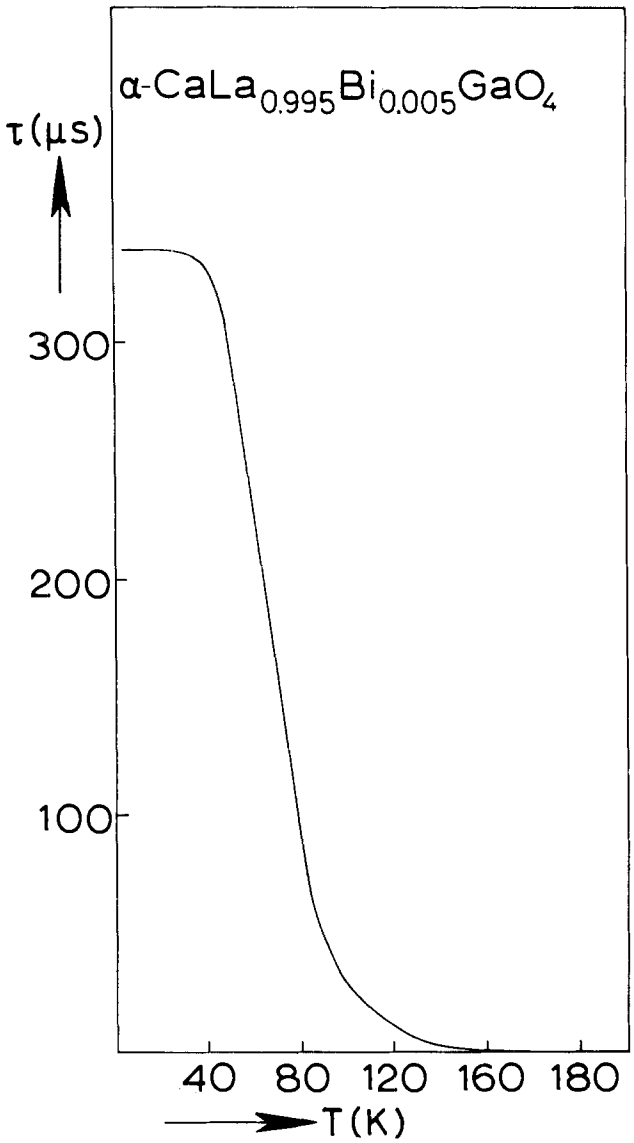


Fig. 5. Temperature dependence of the decay time of the 450 nm emission of α-$CaLa_{0.995}Bi_{0.005}GaO_4$ under a broad spectrum of u.v. radiation (240-360 nm). Above 160°K the decay time amounts to 1 μsec (measurements up to 300°K).

ion. The $6s^2$ configuration of the Bi^{3+} ion gives rise to a $^1S_0$ ground state. The first excited configuration 6s6p gives rise to four states, *viz.*, $^3P_0 < {}^3P_1 < {}^3P_2 << {}^1P_1$ (15). The allowed transitions within this energy level diagram are $^1S_0 \rightarrow {}^3P_1$ and $^1S_0 \rightarrow {}^1P_1$ (15). The distance between the excitation bands of Fig. 4 is about 3.6 kK, which is considerably less than the energy difference between the $^3P_1$ and $^1P_1$ levels. Blasse reports the following values for the distance between the $^1S_0 \rightarrow {}^3P_1$ and $^1S_0 \rightarrow {}^1P_1$ transitions of Bi^{3+} in Y_2O_3, YOCl, and LaOCl; 8, 9, and 7 kK, respectively (5). Moreover, Jørgensen reports this distance to amount to 12 kK and even 15 kK in the case of Bi^{3+} in bromide and chloride complexes, respectively (16). We therefore conclude that the excitation bands of Fig. 4 are lying too close together to correspond to the $^1S_0 \rightarrow {}^3P_1$ and $^1S_0 \rightarrow {}^1P_1$ transitions of one and the same Bi^{3+} ion. We assign these bands to $^1S_0 \rightarrow {}^3P_1$ transitions on two crystallographically different Bi^{3+} centers. An obvious possibility is Bi^{3+} on La^{3+} sites (Bi_{La}^{x}) and Bi^{3+} on Ca^{2+} sites ($Bi_{Ca}^{\cdot}$). In the case of $LiYSiO_4$-Bi, which has the ordered olivine structure, only one emission and excitation band has been reported, the maxima of which lie at about 28.6°K and 35.7 kK, respectively (5). These bands correspond with transitions on the Bi_Y^x center. Comparing these values with those for α-$CaLa_{1-x}Bi_xGaO_4$, the short wavelength excitation and emission bands (maxima at about 31 and 24 kK, respectively) are most likely to correspond with transitions within the Bi_{La}^{x} center. The long wavelength excitation and emission bands (maxima at about 27 and 21 kK, respectively) are then ascribed to transitions on the $Bi_{Ca}^{\cdot}$ center. The position of these latter bands is at rather low energy in comparison with values found for other Bi^{3+}-doped oxides (5). This may be due to the fact that a Bi^{3+} ion on a Ca^{2+} site is effectively positive, so that the Bi-O bond will be relatively covalent and the electronic transitions will lie at low energy (16). Thus accepting the interpretation given above as the simplest model that elucidates the major part of our experimental observations, we assign the emission bands to $^3P_{1,0} \rightarrow {}^1S_0$ transitions on two different Bi^{3+} centers. The lower $^3P_0$ level plays only a role in the luminescence process at low temperatures. This follows from the decay measurements as is now shown.

The experimental conditions for the decay measurements had to be taken so that we excited predominantly in the short wavelength excitation band and measured mainly the decay of the short wavelength emission band. However, since the intensities of the emissions do not differ very much, and in view of the fact that we excited partly also in the long wavelength excitation band and detected for a part also the long wavelength emission band, we certainly would have noticed any significant difference in the decay times of the two centers, if such a difference would have been present. As mentioned before, we measured single exponentials at all temperatures. We, therefore, conclude that the decay times of the two centers are approximately equal. This is in agreement with the fact that the decay time of the Bi^{3+} activator does not depend strongly on the host lattice (17). The temperature dependence of the decay time can be described with a three level scheme; the ground state $^1S_0$ and two excited levels ($^3P_0$, $^3P_1$), the lower of which is metastable ($^3P_0$).

Using the formulas of Boulon (17) for the case that the intensity of the emission is temperature independent in the region in which τ varies, we arrive at the following values for the radiative transition probabilities $P_{^3P_0} \rightarrow {}^1S_0$, $P_{^3P_1} \rightarrow {}^1S_0$ and the energy separation

$$\Delta E = E(^3P_1) - E(^3P_0)$$

$$P_{^3P_0} \rightarrow {}^1S_0 = 3 \times 10^3\ \text{sec}^{-1}$$

$$P_{^3P_0} \rightarrow {}^1S_0 = 10^7\ \text{sec}^{-1}$$

$$\Delta E = 0.05\ \text{eV}$$

These values are in fair agreement with the values found by Boulon (17) for the Bi^{3+} activator in all sorts of compounds.

The broadness of the emission band of $CaGd_{0.99}Bi_{0.01}AlO_4$ indicates that there are several crystallographically different Bi^{3+} centers in agreement with the crystal structure. As in the α-modification, the emission is assigned to the $^3P_{1,0} \rightarrow {}^1S_0$ transitions. Again the lower $^3P_0$ level will only play a role in the luminescence process at low temperatures. The excitation band is likewise ascribed to the $^1S_0 \rightarrow {}^3P_1$ transition.

The efficiency of the Bi^{3+} emission in $CaGd_{0.99}Bi_{0.01}AlO_4$ is low in comparison with that of Bi^{3+} in the olivine phase. Blasse *et al.* (6) have also reported a very low luminescence efficiency for Pb^{2+} in Ba_2ZrO_4 with K_2NiF_4 structure. These authors argued that the stiffness of the surroundings of the PbO_n-center influences strongly the thermal quenching temperature T_q and the efficiency of the Pb^{2+} luminescence.

Here we have found another example supporting this simple model. The increase of the Stokes shift in going from the α- to the β-phase ($\Delta^\alpha E_s = 0.9$ eV; $\Delta^\beta E_s = 1.2$ eV) and the decrease of T_q ($T_q^\alpha > 300$°K; $T_q^\beta << 300$°K) is ascribed to the fact that the lattice of the β-phase is less stiff than that of the α-modification. This

can be easily seen as follows: the K_2NiF_4 structure can be regarded to exist of relatively stiff perovskite layers separated by relatively soft (Ca, La)-O layers; along the c-axis the stiffness of the lattice is low, and this will result in a relatively large value of Δr. The olivine structure, however, is based upon a hexagonal close packing of oxygen ions. The Ga^{3+} ions occupy tetrahedral sites in such a way that a three dimensional framework of GaO_4 tetrahedra is formed. These tetrahedra are bound together by the Ca^{2+} and La^{3+} ions. Further, the lower coordination numbers in the olivine phase will also promote a higher stiffness. We, therefore, expect a small value of Δr.

Manuscript submitted Dec. 28, 1976; revised manuscript received March 21, 1977. This was Paper 136 presented at the Philadelphia, Pennsylvania, Meeting of the Society, May 8-13, 1977.

Any discussion of this paper will appear in a Discussion Section to be published in the June 1978 JOURNAL. All discussions for the June 1978 Discussion Section should be submitted by Feb. 1, 1978.

Publication costs of this article were assisted by the State University at Utrecht.

REFERENCES

1. A. Daoudi, G. Demazeau, and G. Le Flem, *Rev. Chim. Miner.*, **11**, 327 (1974).
2. G. Blasse and A. Bril, *This Journal*, **115**, 1067 (1968).
3. G. Blasse, A. Bril, and J. A. de Poorter, *J. Chem. Phys.*, **53**, 4450 (1970).
4. H. E. Hoefdraad, *J. Solid State Chem.*, **15**, 175 (1975).
5. G. Blasse and A. Bril, *J. Chem. Phys.*, **48**, 217 (1968).
6. G. Blasse, A. W. M. Braam, and M. Heerschop, submitted to *J. Solid State Chem.*
7. J. P. Oudalov, A. Daoudi, J. Joubert, G. Le Flem, and P. Hagenmuller, *Bull. Soc. Chim. Fr.*, **10**, 3408 (1970).
8. H. Ronde and G. Blasse, *J. Solid State Chem.*, **17**, 339 (1976), and references therein.
9. G. Blasse and A. Bril, *Philips Tech. Rev.*, **31**, 304 (1970).
10. G. Blasse and A. Bril, *J. Inorg. Nucl. Chem.*, **29**, 2231 (1967).
11. G. Blasse and A. Bril, *J. Chem. Phys.*, **45**, 3327 (1969).
12. J. C. Baines and H. Pincott, *J. Chem. Soc.*, **111**, 1363 (1964).
13. G. Blasse and A. Bril, *J. Chem. Phys.*, **48**, 3652 (1968).
14. C. W. Struck and W. H. Fonger, *J. Lumin.*, **10**, 1 (1975); *J. Chem. Phys.*, **52**, 6364 (1970); *J. Lumin.*, **1,2**, 456 (1970).
15. See *e.g.*, C. Kittel, "Introduction to Solid State Physics," John Wiley & Sons, Inc., New York.
16. C. K. Jørgensen, "Absorption Spectra and Chemical Bonding in Complexes," p. 186, Pergamon Press, Inc., Elmsford, N.Y. (1962).
17. G. Boulon, *J. Phys.*, **32**, 333 (1971).

The Structure Sensitivity of the U^{6+} Ion Luminescence in Oxides

G. Blasse

Physical Laboratory, State University, Sorbonnelaan 4, Utrecht, The Netherlands

ABSTRACT

This paper discusses how the luminescence of the U^{6+} ion in oxides is influenced by the crystal structure and the chemical composition of the host lattice. The vibrational fine structure of the emission band, the decay time, and the thermal quenching temperature of the luminescence are the properties which we concentrate on. Starting point of the discussion is the perfectly cubic UO_6^{6-} group, the emission of which corresponds to a zero-phonon magnetic-dipole transition followed by mainly one-photon vibronics. The influence of symmetry lowering on this emission is described. This influence becomes of striking importance if the U^{6+} ion is introduced in host lattices containing edge-sharing MO_6^{6-} (M = Te, W) groups. Finally some general aspects of the vibrational fine structure, in particular the length of the progression in ν_1, are discussed. The strong dependence of the thermal quenching temperature of the U^{6+} luminescence on the host lattice can be explained using a configurational-coordinate diagram with three parabolas.

The luminescence of the hexavalent uranium ion in oxides is well known and has been studied for many years. A main issue in the discussion has been the nature of the emitting center which has been proposed to be UO_2^{2+} (uranyl), UO_6^{6-} (octahedral uranate), or UO_4^{2-} (tetrahedral uranate) (1). This paper describes the dependence of the hexavalent uranium luminescence characteristics on the symmetry of the uranium site and the chemical composition of the host lattice. In contradiction with the majority of the work up to 1970 the measurements have been extended down to liquid helium temperatures and the decay time of the emission has been measured. This is essential in our interpretation. Because we want to describe a number of luminescence properties and their dependence on the crystallographic surroundings of the emitting center, the approach is of a qualitative nature only. We hope to extend the present ideas in the near future.

Key words: uranium luminescence, uranium activated phosphors, lithium tungstate.

Experimental

All samples were prepared according to the usual methods described earlier in the literature for the appropriate host lattice Firing was performed in an oxygen atmosphere The uranium concentration amounts to 0.3 atomic percent (a/o) relative to the hexavalent metal ion of the host lattice (tellurium or tungsten). All samples were checked by x-ray analysis.

All optical measurements were performed as described in detail previously (2).

Results

The luminescence of the hexavalent uranium ion has been studied in a large number of host lattices.

Part of the results have been published before. The host lattices relevant for the present discussion are:

1. The ordered perovskite structure. In this structure the $[M^{6+}O_6]^{6-}$ octahedra are isolated from each other, *i.e.*, they do not have oxygen ions in common, and the M^{6+} ion occupies a site with cubic symmetry. The results of the study of the uranium emission in this lattice are the basis for the present approach. They have been published elsewhere (2-4) and are summarized below.

2. A number of lattices containing isolated $[M^{6+}O_6]^{6-}$ octahedra, but with lower than cubic symmetry, viz., Mg_3TeO_6 and Y_6WO_{12} (5), $Y_3Li_3Te_2O_{12}$ (6), and finally Li_6WO_6. The crystal structure of the latter compound seems to be a short-range ordered variant of the rock-salt structure but details are still lacking (7, 8). Uranium-doped Li_6WO_6 appears to be a very efficient, green-emitting phosphor at room temperature. At lower temperatures the green emission band shows fine structure and, in addition, a blue band appears (see Fig. 1). The blue band, which is due to the tungstate octahedron in Li_6WO_6, can be excited in an excitation band with a maximum at about 280 nm; the green uranium emission can be excited in a broad excitation band with a maximum at about 340 nm (direct excitation) or in the tungstate excitation band (see Fig. 1). Although energy transfer from the tungstate to the uranate group definitely occurs in Li_6WO_6-U, it is not as efficient as in some ordered perovskites where no tungstate emission is observed for a uranium concentration of 0.3 a/o (9). The reason for this is undoubtedly the very small spectral overlap between the tungstate emission band and the uranium excitation band at 340 nm, so that transfer from the tungstate group to the uranate group occurs straight into the parity-forbidden energy levels of the latter (9).

Table I gives more details on the fine structure of the green emission band at liquid helium temperature. The assignment is discussed below.

The thermal quenching temperature of the emission under 340 nm excitation is high: The luminescence intensity remains temperature independent up to 400°K, above which temperature thermal quenching occurs ($T_{1/2}$ = 450°K).

Table I. The vibrational fine structure in the emission spectrum of Li_6WO_6-U at LHeT (except for the first two lines). All values in cm^{-1}. The vibronics are counted from the zero-phonon transition. The intensity is given between brackets ((very) weak, medium, strong)

Position	Assignment	Remarks
+240 (vw)	ν_3	Only at LNT, not at LHeT
+130 (m)	$\nu_{lat.}$	Only at LNT, not at LHeT
19.970 (w)	0-0	Zero-phonon transition
−150 (s)	$\nu_{lat.}$	
−280 (m)	ν_6	
−410 (m, br)	ν_4	Broad line; shoulder contains probably ν_3
−800 (vw)	ν_1	
−(800 + 160) (m)	$\nu_1 + \nu_{lat.}$	
−(800 + 260) (w)	$\nu_1 + \nu_6$	
−(800 + 400) (w)	$\nu_1 + \nu_4$	

Figure 2 presents the temperature dependence of the decay time of the uranium emission of Li_6WO_6-U. Note that the luminescence intensity is not temperature dependent in the temperature range of this figure, so that we are dealing with a temperature-dependent radiative transition probability (4).

3. The compound Li_4WO_5; this compound has an ordered rock-salt structure where the tungstate octahedra occur presumably in edge-sharing pairs (10). The luminescence characteristics of Li_4WO_5-U differ markedly from those of the phosphors mentioned under 1 and 2, above, and have been given elsewhere (11).

4. $MgWO_4$ with strings of zig-zag edge-sharing WO_6^{6-} octahedra and in relation with this compound some compounds with WO_4^{2-} tetrahedra (scheelites) (12).

Finally we remeasured the uranium luminescence in Y_2TeO_6 and La_2TeO_6 (13) and $LaAlTeO_6$ (14). It has been suggested in the literature that the efficient uranium luminescence from these lattices would originate from the uranyl group (13) This point is discussed below. Table II shows the vibrational fine structure of the emission of Y_2TeO_6-U and La_2TeO_6-U at LHeT, whereas Fig. 3 gives an over-all view of the emission of La_2TeO_6-U. The fine structure in the case of

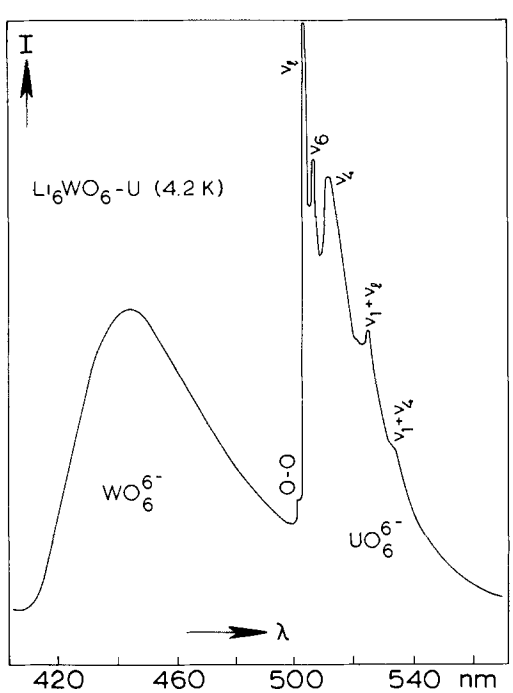


Fig. 1. Spectral energy distribution of the emission of $Li_6W_{0.997}U_{0.003}O_6$ at 4.2°K under 280 nm excitation. Uncorrected recorder curve. The photomultiplier correction would increase the long wavelength emission relative to the short wavelength emission.

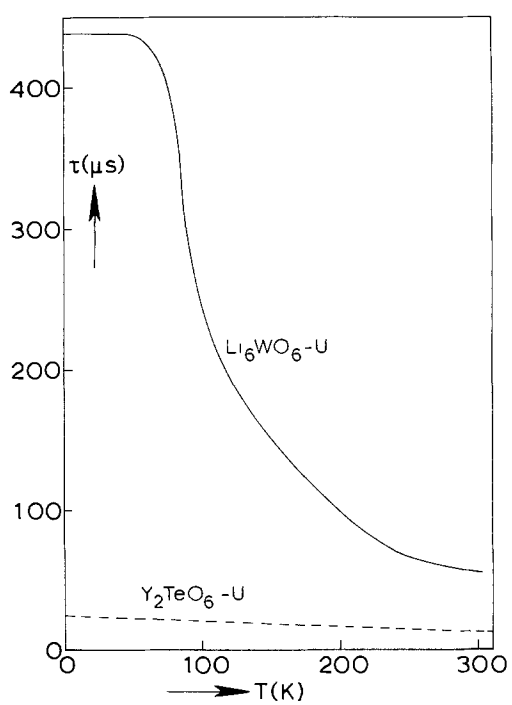


Fig. 2. Decay time of the uranium emission as a function of temperature for $Li_6W_{0.997}U_{0.003}O_6$ (full curve) and $Y_2Te_{0.997}U_{0.003}O_6$ (broken curve). The intensity-time curves for a given temperature were pure exponentials.

Table II. The vibrational fine structure in the emission spectrum of Y_2TeO_6-U and La_2TeO_6-U at LHeT. All values in cm^{-1}. See Table I

Y_2TeO_6		La_2TeO_6
Position	Assignment	Position
19,630 (s)	0-0	19,870 (s)
−110 (m)	$\nu_{lat.}$	−60 (m)
−200 (m)		−165 (m)
−280 (m)		−225 (m)
−455 (w)		
−790 (m)	ν_1	−730 (m)
−(790 + 80) (w)	$\nu_1 + \nu_{lat.}$	−(730 + 60) (w)
−(790 + 260) (w)		−(730 + 180) (w)
		−(730 + 240) (w)
−1540 (vw)	$2\nu_1$	−1470 (vw)
−(1540 + 70) (vw)	$2\nu_1 + \nu_{lat.}$	−(1470 + 70) (vw)
−(1540 + 250) (vw)		
−2310 (vvw)	$3\nu_1$	−2170 (vvw)

$LaAlTeO_6$-U is similar to that of La_2TeO_6 and, therefore, not given in more detail.

The thermal quenching temperature of the uranium emission of Y_2TeO_6-U and La_2TeO_6-U is again high. The $T_{1/2}$ value is about 400°K. The temperature dependence of the decay time is given in Fig. 2 and is less pronounced than in the case of Li_6WO_6-U.

Discussion of the Emission Spectra

The luminescence of the U^{6+} ion in ordered perovskites (2, 3) is easy to interpret and is used as a starting point. At low enough temperatures the fine structure in the emission band consists of a zero-phonon line [relatively low intensity; magnetic-dipole emission (15)], a number of one-phonon lines due to coupling with the ungerade internal modes of the UO_6^{6-} octahedron (ν_6, ν_4, ν_3) and a relatively weak progression of these lines in ν_1 (the symmetrical UO_6 stretching frequency). The radiative decay time is long (about 350 μsec) and temperature dependent. All this shows that the emission transition of the cubic UO_6^{6-} group consists of a parity-forbidden electric-dipole transition. In view of the high intensity of the one-phonon lines the coupling between the electronic and vibrational states must be weak, *i.e.*, weaker than in the case of the uranyl group in the emission of which the more-phonon lines dominate (16).

Figure 4 presents a schematic overview of some emission spectral of oxides doped with hexavalent uranium. Those of the ordered perovskite Ba_2CdWO_6-U and of $SrZnP_2O_7$-U, a compound in which uranium has been proposed to be present as uranyl (17), illustrate the remarks made above

The emission pattern and the low temperature value of the decay time of the uranium emission do not change very much upon symmetry lowering if a center of symmetry remains present. The one-phonon lines still dominate, although their number increases. This is illustrated in Fig. 4 by the case of Mg_3TeO_6-U (5). The site symmetry of the hexavalent ions in this crystal structure is S_6 (18). As a consequence the threefold-degenerate ν_3, ν_4, and ν_6 split resulting in a larger number of one-phonon lines.

The luminescence characteristics of Li_6WO_6-U can be explained in an analogous way. The decay time is long and temperature dependent as required for a parity-forbidden electric-dipole transition. The fine structure in the emission spectrum (Table I) contains a weak zero-phonon line, strong one-phonon lines due to coupling with a lattice mode and ν_6 and ν_4, and a weak progression in ν_1. The one-phonon lines are not split, but somewhat broadened.

Unfortunately the crystal structure of Li_6WO_6 is not known in detail. Hauck (7) has proposed that tungsten occupies 50% of the 2a sites of space group Immm (D_{2h}^{25}) in a short-range ordered way; further the position of two of the six lithium ions is unknown. The symmetry of this 2a site is D_{2h}. Inversion symmetry at the hexavalent ion sites seems, therefore, to be a good first-order approach, but it should be realized that the crystal field at these ions varies from site to site as a consequence of the short-range order. This may explain why the threefold-degenerate vibronics do not split and are a little broad. Note that the progression in ν_1 is as weak as in the perovskites.

In the crystal structure of Li_4WO_5 we have edge-sharing between two WO_6^{6-} octahedra (10). Introduction of uranium into this lattice yields an emission with different characteristics. The low temperature value of the decay time is lower (viz., 160 μsec) than in the systems mentioned above. The fine structure of the emission band is quite simple (Fig. 4). The zero-phonon line dominates in this case. Together with the

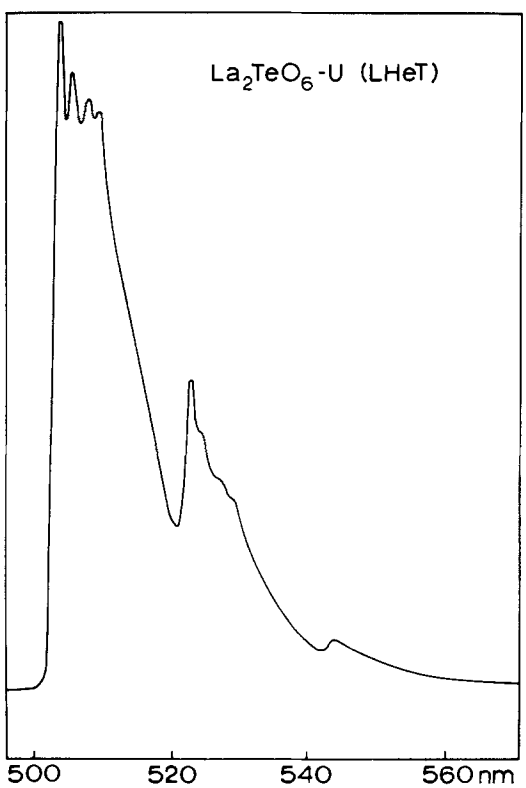


Fig. 3. Emission spectrum of $La_2Te_{0.997}U_{0.003}O_6$ at 4.2°K under 320 nm excitation. See Fig. 1.

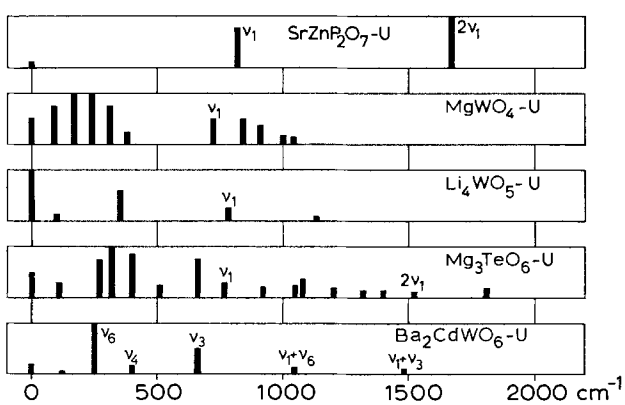


Fig. 4. Schematical representation of the vibrational fine structure of a number of U-activated oxides at 4.2°K. The position of the zero-phonon line is at 0 cm^{-1} and is the origin of the wave number scale. The height of the blocks indicates the peak intensity of the vibronic lines and is, therefore, not a reliable measure for the integrated intensity. Data for $SrZnP_2O_7$-U were obtained at 4.2°K in this laboratory and are not essentially different from the room temperature values reported in Ref. (17). The emission line in the $SrZnP_2O_7$-U spectrum marked $2\nu_1$ is the most intense line in this spectrum. The intensity of $n\nu_1$ ($n > 2$), not shown here, is lower.

shorter decay time this indicates a considerably higher transition probability for this line. This must be connected with the absence of inversion symmetry at the uranium center in a complex like $[WUO_{10}]^{8-}$. Vibronic emission lines are due to coupling with a lattice vibration, with a U-O deformation and with a U-O stretching vibration. Since these vibrational modes have not been studied in detail, we refrain from further discussion.

In $MgWO_4$ the lattice contains strings of edge-sharing WO_6 octahedra. The decay time of uranium in this lattice is much shorter (viz., 35 μsec at 4.2°K) and the vibrational fine structure in the emission band is apparently different (Fig. 4). The latter fact is due to stronger coupling with lattice modes. Similar characteristics have been reported for uranium in the scheelites MWO_4 (M = Ca, Sr, Ba) (19) and Y_2WO_6 (12). The emission band in all these compounds has shifted from the green to the red part of the spectrum, which is not essential for the present discussion. In these compounds inversion symmetry is definitely lacking. As a consequence the number of selection rules on the vibronic lines decreases, so that the decay time becomes shorter and the fine-structure pattern more complicated.

We also investigated some efficient uranium-activated phosphors reported before, viz, Y_2TeO_6-U and La_2TeO_6-U. Their emission characteristics are very much like those of $MgWO_4$-U, *i.e.*, relatively short decay time and high intensity for the zero-phonon and one-phonon lines. Unfortunately, their crystal structures have not been solved up till now. The structure of $LaAlTeO_6$ is an ordered variant of the $PbSb_2O_6$ structure containing isolated TeO_6^{6-} groups (14). The luminescence of U^{6+} in this lattice is similar to that observed for Y_2TeO_6-U and La_2TeO_6-U. This seems to indicate that the U^{6+} ion is in six-coordination in all these tellurates. From the high intensity of the zero-phonon transition and the short decay time of the emission (which in addition shows only a weak temperature dependence in comparison with, *e.g.*, Li_6WO_6-U, see Fig. 2), we conclude that the uranium ion does not occupy a site with inversion symmetry in these compounds. A detailed analysis of these crystal structures would be of great help for the discussion of the uranium luminescence.

All these results together lead to the conclusion that the emission spectra of $U^{6+}(O^{2-})_n$ complexes show fine structure and radiative transition probabilities that depend strongly upon the site symmetry of the uranium. We feel that a detailed discussion of the luminescence characteristics of the U^{6+} ion in oxides should start from these experimental data and not from a discussion on the value of n of the emitting center as has been done many times in the years before.

Two clear phenomena in these emission spectra ask for a further treatment, viz., the pronounced host lattice dependence of the length of the progression in ν_1 and the host lattice dependence of the ratio of the coupling strengths with lattice modes and with internal uranate modes (see Fig. 4).

The latter is not discussed here because we feel that a detailed analysis of the vibrational modes in the relevant host lattices is necessary. Nevertheless we remark that the vibronics due to coupling with lattice modes seem to have higher intensity, if the separation between external and internal modes becomes less meaningful. This is not unexpected.

As far as the progressions are concerned a rough model can be proposed to account for the dependence of the progression length on the host lattice. The exact nature of the emission transition in the uranate group is not known. It is often assumed to be a charge-transfer transition between oxygen 2p and uranium 5f levels (20). Recent Xα-calculations on UF_6 have shown that the uppermost filled orbital of this molecule is the $t_{1u}\sigma$ orbital, made up of U 6d, U 5f, and F 2p functions, whereas the lowest unoccupied orbitals are all predominantly U 5f in character (21, 22). For the moment we assume that the same orbital scheme is valid in principle for the UO_6^{6-} octahedron (and probably also for the other $U^{6+}(O^{2-})_n$ complexes). This implies that the emission transition is in fact a charge-transfer transition from a predominantly nonbonding orbital to a σ-bonding orbital. It also means that the difference between the equilibrium distance in the emitting state and that in the ground state, Δr, must be positive. Using an approximation suggested by Ballhausen (23) it is possible to estimate Δr from the relative intensities of the lines in the progression in ν_1. Taking Ba_2MgWO_6-U with UO_6^{6-} octahedra as a representative sample (2, 3) we arrive at $\Delta r \cong 0.02$Å. The longer the progression in ν_1, the larger the value of Δr will be. In view of the nonbonding character of the emitting state we assume that the host-lattice dependence of the progression length arises mainly from the lattice dependence of the ground state. It is obvious that a relatively short U-O distance (high degree of covalency) in the ground state will involve a relatively large Δr and, therefore, a long progression in ν_1. Taking $\nu_1 = 750$ cm^{-1}, it is an easy task to calculate that Δr should be about 0.04Å in in order to attain that the second repetition in ν_1 has the maximum intensity in the emission spectrum of the UO_6^{6-} octahedron (this is the situation in the emission spectrum of $SrZnP_2O_7$-U, see Fig. 4, where probably the uranyl group is the emitting center). This illustrates that variations of less than 0.01Å in Δr are enough to explain our observations, since the case of $SrZnP_2O_7$-U is an extreme. The observations are the following:

1. The progression is longer in U-activated tellurates than in tungstates (see, *e.g.*, Fig. 4); this becomes especially clear, if isomorphous tungstates and tellurates are compared [*e.g.*, $Ba_2MgM^{6+}O_6$-U (24)]. The most reliable ionic radii for Te^{6+}, W^{6+}, and U^{6+} in six-coordination are 0.56, 0.60, and 0.73Å, respectively (25). As a consequence the U-O distance in the uranate center in the ground state will be smaller in tellurates than in tungstates resulting in a longer progression.

2. The cations surrounding the uranate center have a marked influence on the progression length: The progression becomes more intense and longer if the surrounding cations are smaller and/or higher charged. This follows immediately from our simple model. If the U^{6+} ion is substituted for the Te^{6+} or W^{6+} ion, the surroundings have to expand in view of the larger radius of the U^{6+} ion. If the surroundings are relatively stiff (small and/or highly charged cations), the expansion will be relatively small and the U-O distance, therefore, relatively short. This results in a longer progression. There is experimental evidence for this reasoning. In the series MWO_4-U (M = Ca, Sr, Ba) the progression becomes the more intense, the smaller the M^{2+} ion (19). In the series Ba_2MTeO_6-U (M = Mg, Ca, Sr) the progression becomes more intense, the smaller the M^{2+} ion (3, 24). A stiff lattice like Mg_3TeO_6 yields U^{6+} emission with a long progression if it is activated with uranium (see Fig. 4). Still stiffer seems to be the trirutile Al_2TeO_6 (26, 27). At the moment we are studying the uranium luminescence in this compound. Provisional measurements indicate that in the emission of Al_2TeO_6-U the first repetition of the one-phonon lines is more intense than the one-phonon lines themselves in striking agreement with our expectation (28)

3. Since the U-O distance in a molecule is much shorter than in a solid, we expect longer progressions for molecules or "molecule-like" configurations than for solid solutions. This has been observed: for the molecule UF_6 (29) and for the UO_6^{6-} center in fluorides (30).

We realize the shortcomings of this approach, but we believe that at the moment this is the best that can be done. Quantitative calculations yielding such

Table III. The differences Δ between the position of the excitation and emission bands at room temperature for some U^{6+}-activated host lattices (all values in 10^3 cm^{-1}) vs. the thermal quenching temperature of the emission $T_{1/2}$ (temperature at which the luminescence intensity has decreased to 50% of the low temperature value). Spectral data for the lower two cases are at liquid nitrogen temperature

Host lattice	Excitation	Emission	Δ	$T_{1/2}$ (°K)	Ref.
$Y_3Li_3Te_2O_{12}$	31	17.5	13.5	540	(6)
Mg_3TeO_6	31.5	18.7	12.8	500	*
Li_6WO_6	30	19.5	10.5	450	*
Li_4WO_5	29.5	19.2	10.5	440	(11)
La_2TeO_6	29.5	19.8	9.5	400	*
$BaLi_{0.4}W_{0.6}O_3$	~26	17.5	8.5	375	(31)
Ba_2MgWO_6	27	19.5	7.5	350	(2)
$MgWO_4$	24	17.5	6.5	150	(12)
$BaNa_{0.4}W_{0.6}O_3$	24	19.2	5	<100	(32)

* This work.

small variations in the value of Δr are probably not worth the trouble and cost.

Discussion of the Temperature Quenching

The thermal quenching temperature of the emission of U^{6+}-activated oxides depends also markedly on the host lattice. This can be seen in Table III where some of the compounds investigated have been tabulated. As pointed out before (6) it is also clear that this quenching temperature seems to be related to the difference in energy between the position of the intense ultraviolet excitation band and that of the emission band of the U^{6+} luminescence (see Table III).

In view of the small value of Δr between the ground state and the emitting state (see discussion above) it is rather improbable that the process of temperature quenching occurs between the two parabolas for these two states in the configurational-coordinate diagram. The data of Table III rather suggest that a higher excited state plays an important role. Since the optical transition corresponding to the ultraviolet excitation band of the uranium luminescence is an allowed one and its broad band character with only scarce fine structure indicates a relatively large value of Δr between this state and the ground state, a schematic configuration coordinate diagram as drawn schematically in Fig. 5 seems to explain the relation of Fig. 4 reasonably. The emitting state is represented by the parabola BCF, whereas the parabola EFG represents the state to which the system is promoted by excitation into the near-ultraviolet absorption band (AE). At low temperatures the system relaxes from E to C via F followed by emission (CD). At high enough temperatures a radiationless transition via the crossover G is possible, resulting in temperature quenching of the emission CD. It will be clear that the difference Δ in Table III is the difference in energy between AE and CD in Fig. 5, The larger the value of Δ, the higher will be the crossover G resulting in a high value $T_{1/2}$. We aim to make this model more quantitative in the near future.

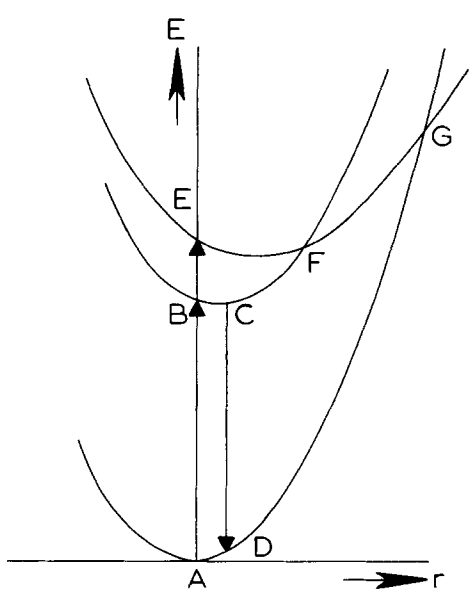


Fig. 5. Configurational-coordinate diagram of the luminescent uranate center. Thermal quenching of the emission CD is proposed to occur via the crossover G. See text.

In closing we remark that the model of Fig. 5 shows a clear resemblance to the model for temperature quenching of the Eu^{3+} luminescence in oxysulfides proposed by Struck and Fonger (33). Here the two lower parabolas relate to the $4f^6$ configuration of the Eu^{3+} ion and the higher one to the charge-transfer state.

Acknowledgment

Mr. G. P. M. van den Heuvel assisted in the experimental part of the investigations.

Manuscript submitted Feb. 10, 1977; revised manuscript received April 20, 1977. This was Paper 135 presented at the Philadelphia, Pennsylvania, Meeting of the Society, May 8-13, 1977.

Any discussion of this paper will appear in a Discussion Section to be published in the June 1978 JOURNAL. All discussions for the June 1978 Discussion Section should be submitted by Feb. 1, 1978.

Publication costs of this article were assisted by the State University at Utrecht.

REFERENCES

1. See, *e.g.*, G. Blasse, *This Journal*, **115**, 738 (1968).
2. J. Th.W. de Hair and G. Blasse, *J. Lumin.*, **14**, 307 (1976).
3. J. Th.W. de Hair and G. Blasse, *J. Solid State Chem.*, **19**, 263 (1976).
4. J. Th.W. de Hair and G. Blasse, *Chem. Phys. Lett.*, **36**, 111 (1975).
5. G. Blasse, *ibid.*, **41**, 210 (1976).
6. R. H. Alberda and G. Blasse, *J. Lumin.*, **12/13**, 687 (1976).
7. J. Hauck, *Z. Naturforsch., Teil B*, **24**, 251 (1969).
8. J. Hauck, *J. Inorg. Nucl. Chem.*, **36**, 2291 (1974).
9. A. C. van der Steen, J. Th.W. de Hair, and G. Blasse, *J. Lumin.*, **11**, 265 (1976/6).
10. G. Blasse and G. P. M. van den Heuvel, *J. Inorg. Nucl. Chem.*, **39**, 548 (1977).
11. G. Blasse, *Chem. Phys. Lett.*, **44**, 61 (1976).
12. G. Blasse, G. P. M. van den Heuvel, and J. J. A. van Hesteren, *J. Solid State Chem.*, **21**, 99 (1977).
13. S. Natansohn, *This Journal*, **116**, 1250 (1969).
14. G. Blasse and A. D. M. de Pauw, *J. Inorg. Nucl. Chem.*, **32**, 2533 (1970).
15. N. B. Manson, G. A. Shah, and W. A. Runciman, *Solid State Commun.*, **16**, 645 (1975).
16. See, *e.g.*, H. D. Burrows and T. J. Kemp. *Chem. Soc. Rev.*, **1974**, 139.
17. M. V. Hoffman, *This Journal*, **117**, 227 (1970).
18. H. Schulz and G. Bayer, *Acta Crystallogr., Sect. B*, **27**, 815 (1971).
19. A. M. Morozov, L. G. Morozova, and P. P. Feofilov, *Opt. Spectrosc. (USSR) (Engl. Transl.)*, **32**, 50 (1972).
20. See, *e.g.*, g. K. Jφrgensen, *Acta Chem. Scand.*, **11**, 166 (1957); C. K. Jφrgensen and R. Reisfeld, *Chem. Phys. Lett.*, **35**, 441 (1975); G. Blasse, *Struct. Bonding*, **26**, 43 (1976).
21. M. Boring, J. H. Wood, and J. W. Moskowitz, *J. Chem. Phys.*, **61**, 3800 (1974).
22. D. H. Maylotte, R. L. St. Peters, and R. P. Messmer, *Chem. Phys. Lett.*, **38**, 181 (1976).
23. C. J. Ballhausen, *Theor. Chim. Acta*, **1**, 285 (1963).
24. J. Th.W. de Hair and G. Blasse, Unpublished.
25. R. D. Shannon, *Acta Crystallogr., Sect. A*, **32**, 751 (1976).
26. A. Bystrom, B. Hok, and B. Mason, *Akiv Kemi, Min. Geol.*, **15B**, no. 4 (1941).
27. G. Bayer, Thesis, Zürich (1962).

28. J. P. M. van den Dungen and G. Blasse, Unpublished.
29. W. B. Lewis, L. B. Asprey, L. H. Jones, R. S. McDowell, S. W. Rabideau, A. H. Zeltmann, and R. T. Paine, *J. Chem. Phys.*, **65**, 2707 (1976).
30. W. A. Runciman, *Proc. R. Soc. London, Ser. A*, **237**, 39 (1956).
31. G. Blasse, *J. Solid State Chem.*, **14**, 366 (1975).
32. K. C. Bleijenberg and G. Blasse, Unpublished.
33. C. W. Struck and W. H. Fonger, *J. Lumin.*, **1,2**, 456 (1970); *J. Chem. Phys.*, **52**, 6364 (1970).

GaP Red Light Emitting Diodes Produced by a Rotating Boat System of Liquid Phase Epitaxial Growth

Tatsuhiko Niina

Sanyo Electric Company, Limited, Research Center, Hirakata, Osaka, Japan

ABSTRACT

An improved rotating boat system for liquid phase epitaxial growth has been developed. With this system GaP red light emitting diodes can be mass produced. Its features are that substrates can be fixed by the remarkably simple method of attaching a small volume of melted gallium to the substrate holding plate and pressing the substrate closely against it. It is also suitable for mass production in that the construction of the boat for liquid phase epitaxial growth simplifies the operation for crystal growth; large quantities of substrates of large diameter (30-50 mm) can be treated in one processing batch; the consumption of the Ga melt is small. The growing surface is mirrorlike. A double step process, in which n- and p-type layers are grown in two separate steps is used in the diode fabrication. Another feature is that the same Ga melt is used ten times for the growth of n- and p-type layers, respectively. Encapsulated mesa diodes with efficiencies of 6% (current density = 2 A/cm^2) are routinely obtained from the sequential use up to ten times of the Ga melt and also, the average electroluminescence time decay is 500 nsec. The maximum efficiency is 10% (current density = 2 A/cm^2).

To manufacture low cost GaP light emitting diodes (LED's), it is necessary to develop a p-n junction formation technique using a liquid phase epitaxial (LPE) growth system and a single crystal growth technique suitable for mass production. For the single crystal growth technique, the liquid encapsulated Czochralski (LEC) method was developed in 1968 (1). Improvements in single crystal growth have progressed rapidly, until now it is possible to obtain substrate crystals of large diameter (30-50 mm) on an industrial scale. In the p-n junction formation by LPE (used to obtain LED's of high efficiency) it is necessary to precisely control the concentration of impurities in the neighborhood of the p-n junction and to improve crystallinity. At present, the maximum efficiency of the red LED is 12.6% (2), and in the case of mass production, efficiencies of 6% (3) have been achieved. The major task for the future is to obtain LED's with high efficiencies using an LPE growth system suitable for mass production.

In the rotating boat LPE growth systems suitable for mass production hitherto reported (3-6), the crystal growth is, in most cases, that of the open-flow system (4-6) with a large melt consumption. In the closed type system (3), suspension of the substrate is rather complicated.

This paper describes the process of manufacturing red LED's using the rotating boat LPE growth system. Features of this method are: (*i*) The substrates can be fixed by the simple method of attaching a small volume of molten gallium to the substrate holding plate and pressing the substrate closely against it. (*ii*) It is suitable for mass production in that the construction of the boat for LPE growth makes operation easy. (*iii*) Repeated use of a (Ga + GaP + impurities) melt for the growth of the n- and p-layers minimizes the consumption of gallium. (*iv*) As the boat is sealed, the loss of volatile dopant from the melt is small. Even when the melt is used repeatedly, there is no change in the doped quantity of impurities; thus, it is possible to control the concentration of impurities accurately.

Key words: light emitting diode, crystal growth, junction formation.

This paper first explains the rotating boat LPE crystal growth system, then the doping system of controlling impurities. It also describes changes in the carrier concentration in the neighborhood of the p-n junction due to the frequency of the use of the melt when LED's are made, changes in efficiencies, the growth surface after crystal growth, and various characteristics of the red LED's.

Explanation of the Rotating Boat LPE Growth System

In a method suitable for the mass production of red LED's by an LPE growth method, it is necessary: (*i*) to treat many substrates in one processing batch, (*ii*) for optical characteristics in the same lot to be uniform, (*iii*) to use gallium metal efficiently as it is costly and used in large quantities as a medium of crystal growth, (*iv*) for the substrates to be fixed by a simple method and to simplify the operation for crystal growth. The above (*i*), (*ii*), and (*iii*) have been discussed in Ref. (3). The improved rotating boat system is in principle identical to Ref. (3) but the main features of the improved rotating boat system are (*iii*) and (*iv*), above. As concerning (*iii*), the substrates are held erect by a suitable support, then put into the boat and arranged in a transverse direction. This arrangement of the substrates is a major feature of the rotating LPE growth. If the substrates are arranged vertically, and the melt is run into the space between the substrates, the thickness of the melt will automatically be determined. This is particularly important when making a melt of small thickness. Furthermore, the repeated use of the melt reduces the consumption of the melt per substrate. As concerning the above (*iv*), in the usual system, since the substrates are set in a longitudinal direction, the method of fixing them is difficult. In the existing rotating boat

LPE growth (3), the substrate is fixed by spacer clamps made of quartz. Two substrates are fixed by sticking them together back-to-back with spacer clamps, or quartz plates are put between the two substrates and then fixed with spacer clamps. This method, however, complicates the suspension of the substrate. On the other hand, in the system used here a small volume of melted gallium is placed on the back of the substrate and pressed closely against the quartz plate. One hundred lots were made by this method and there has been no case where the substrate has ever fallen off.

The operation is as follows: Fig. 1a shows the condition before crystal growth. If the boat is turned clockwise from this position, the melt flows out toward the substrates (Fig. 1b). If, after the melt has flowed out sufficiently, the boat is turned counterclockwise, the substrates dip into the melt (Fig. 1c). If the boat is turned counterclockwise after LPE growth, the melt begins to flow out of the substrate portions (Fig. 1d). If the boat is turned clockwise when the melt has fully flowed out, it returns to its original position, and the substrates and the melt are completely separated (Fig. 1a). The above operation is performed either by fixing the boat to a horizontally positioned reaction tube and turning the tube or by turning the boat itself by some outside means.

Figure 2 shows the lid of the boat, the square-shaped vessel, and the screws and nuts for clamping the lid and the square-shaped vessel together. The portion on the bottom of the lid and the portion on the top of the vessel form the joint between the lid and the vessel. This edge is 10-15 mm wide. It is constructed this way so that it can be completely fixed by firmly bonding this portion and clamping it with screws and nuts, thus shutting it off from the outside. The parts are all made of quartz. Figures 3 and 4 show the substrate holders. These are also made of quartz. Two methods of holding the substrate can be used. Figure 3 shows the system wherein quartz columns (1-3 mm in diameter) are welded by fusion in the shape of a (/\) in the lower position on the quartz plate. On this the substrates are installed, parallel to the quartz plate. With this method, by changing the angle of the (/\), it is possible to hold substrates of any size. (By welding 5-10 sheets of these quartz plates together, laid one upon another by fusion, a casette-type substrate holder can be made.) The thickness of the melt is

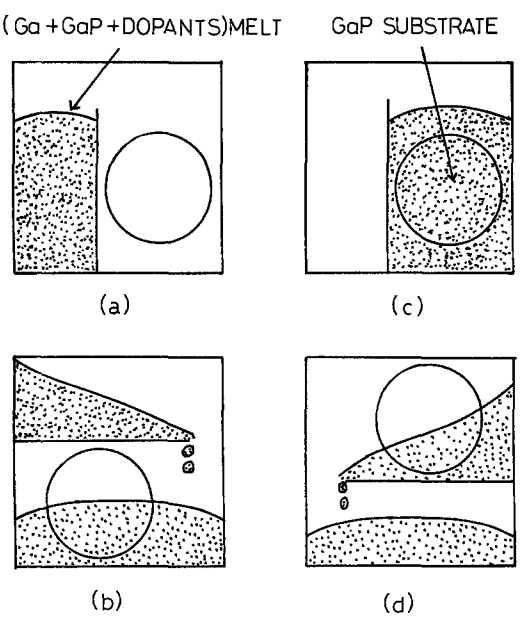


Fig. 1. The schematic representation of the rotating boat system and operation procedure: (a) the condition before crystal growth; (b) the melt flows out toward the substrates; (c) the substrates dip into the melt; (d) after LPE growth, the melt begins to flow out of the substrate portions.

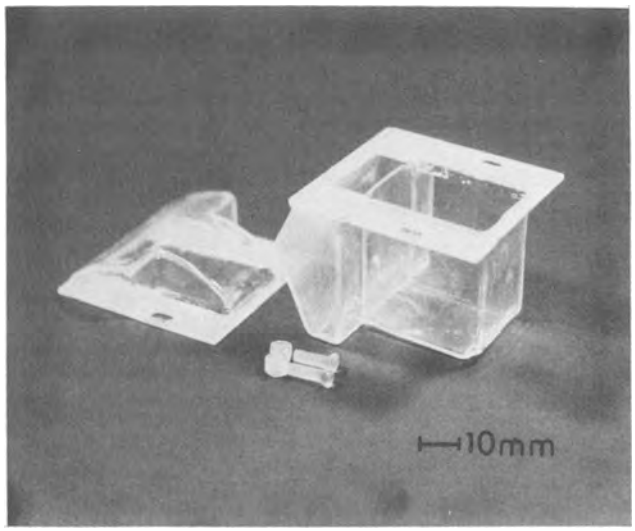


Fig. 2. The lid of the boat, the square-shaped vessel, and the screws and nuts for clamping the lid and the square-shaped vessel together.

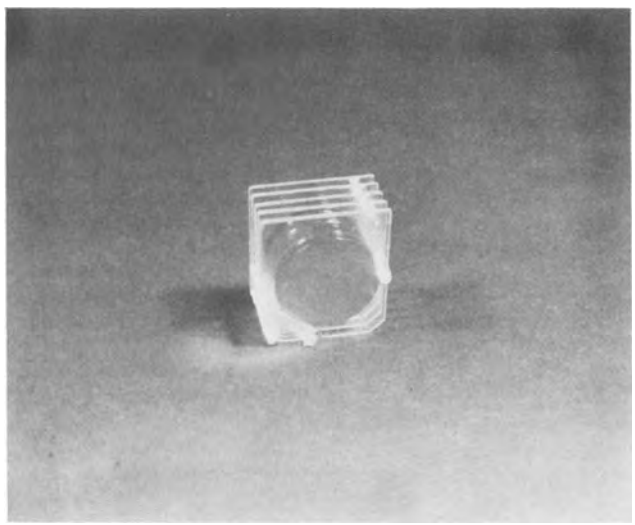


Fig. 3. The substrate holder on which the substrates are fixed

controlled by changing the diameter of the quartz columns. In this experiment, 2 and 3 mm quartz columns are used, and the thickness of the melt is 2 and 3 mm. Figure 4 shows another method for holding the substrates. In this method, a small amount of melted gallium metal is made to adhere to the substrate holding plate and by letting the substrates adhere closely to it, they are fixed. The thickness of the melt is controlled by the height of the quartz column (1-2 mm diam) attached to three corners of the quartz plate.

This experiment is conducted on two kinds of melt, 2 and 3 mm thick. In this method, quartz plates, to which the substrates are fixed on both surfaces, are put successively into the right-hand portion of the square-shaped vessel. It is also possible to use 5-10 quartz plates and to process 10-20 substrates at a time. Either of the substrate fixing methods makes it possible to fix a substrate with up to a 50 mm diameter. Figure 5 shows how the boat is set with the melt and substrate.

Experiment

The electric furnace in this experiment is a horizontal-type resistance heating furnace. Boats are made of quartz of high purity with no copper. These boats can each simultaneously process 10-20 substrates of a 30-50 mm diameter.

First, in order to test the variation of the carrier concentration in an LPE layer for the melt reuse with

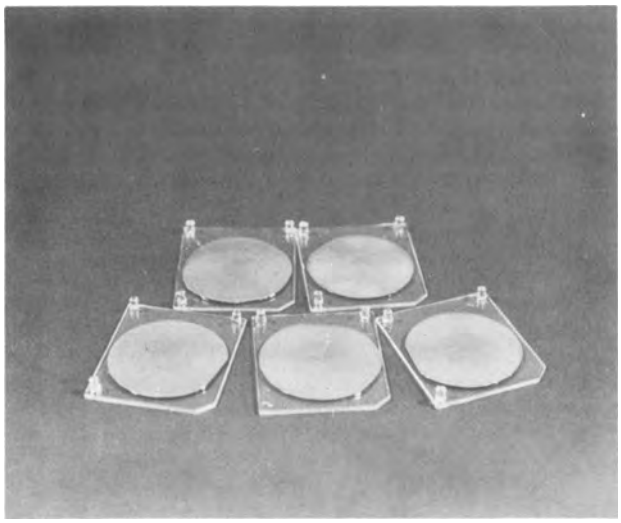


Fig. 4. Another type of substrate holder on which the substrates are fixed.

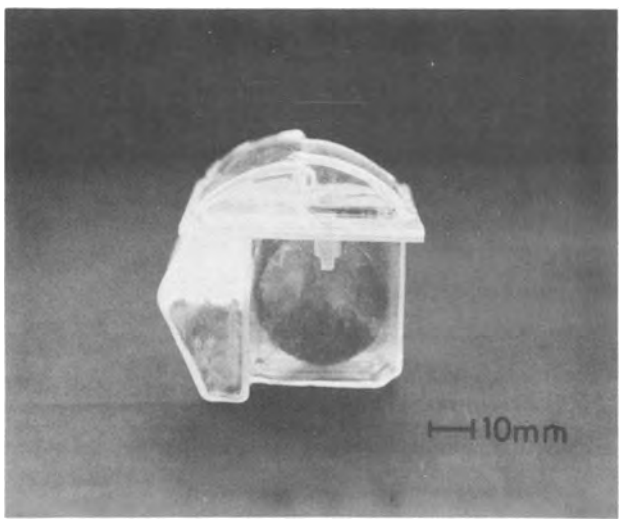


Fig. 5. The boat completely loaded with the melt and the substrates

no added impurities, the same melt is used in the 1st to 10th crystal growth. In the 2nd to 10th growths, only a small amount of GaP polycrystal is added. The procedures are as follows: (*i*) The well-washed boat is heated with nothing in it at 1200°C for about 60 min. The atmosphere is Ar gas, as for crystal growth. (*ii*) In its preparation, Ga metal and GaP polycrystal are first put in the left portion of the boat, and in the right side are put the substrates previously fixed to the substrate holder. The cover is then placed over the boat, which is next inserted in the reaction pipe to bring it to a uniform temperature region. (*iii*) The starting temperature of the LPE layer growth is 1040°C. The cooling speed is 1-3°C/min. The temperature is cooled to 980°C. The substrate used is the n-type (of three kinds) whose carrier concentrations are about $5 \times 10^{16}/cm^3$, $2 \times 10^{17}/cm^3$, and $8 \times 10^{17}/cm^3$. Samples for measuring the carrier concentration are cut equally (5×5 mm) from the wafer in 5 places. Sample surfaces lap by a small angle and Schottky barriers are formed by evaporating Au to the lapped surfaces.

Second, in order to test the variation of the carrier concentration in the case of the addition of impurities, n- and p-layers are grown separately on the substrate. The conditions for the starting temperature, the cooling speed, and the stopping temperature for the n- and p-layer growth are the same as for the undoped layer growth. The dopant is Te for the n-type layer growth and is Zn for the p-layer growth. The quantity of Te added to the melt is 1.6×10^{-2} to 3.3×10^{-1} atomic percent (a/o) and the quantity of Zn added to the melt is 2.8×10^{-3} to 5.4×10^{-2} a/o. The carrier concentration of the n-layer is measured on the grown surface at 980°C and the carrier concentration of the p-layer is measured in the neighborhood of the grown layer at 1040°C.

Finally, to make LED's, the n- and p-layers are continually grown on an n-type LEC substrate with a separate melt. That is, for both the n- and p-layer growth, the first growth is made by adding impurities to the melt beforehand. In the 2nd to 10th growths, the melt used in the first growth is used with no addition of impurities, only a small amount of GaP polycrystal is added. As for O, which is necessary for the formation of the Zn-O complex (the radiative recombination center) O is added to the p-melt in the form of Ga_2O_3. The condition for the n- and p-layer growth is the same as mentioned above. After the crystal growth is finished, the wafers are heat-treated at 550°-600°C for 8-16 hr. After the mesa-type etching is made on the surface of the growth layer, the contacts (small sized dot Zn-Au contacts on the p-side and middle sized dot Sn-Au contacts on the n-side) are evaporated. The contacts are alloyed, then scribing these wafers to the size of $400 \times 400\mu$, the LED pellets are mounted on white ceramic headers, coated with the transparent epoxy resin, and various electrical and optical characteristics are measured. The carrier concentration is found from the C-V measurement. The efficiency is measured with a calibrated integrating sphere. The electroluminescence time decay (τ_D) is measured by a photomultiplier (7102) with a 50Ω load and 1 mA current pulses with 1 μsec width are applied.

Results and Discussion

Carrier concentration in crystals with no added impurities.—LPE crystals are grown using a quartz boat. With a quartz boat, pollution by Si that melts from the boat and pollution of the melt resulting from other impurities gained by moving the holder in and out when replacing the substrate should be considered. A reduction in the efficiency due to these remaining impurities is a problem, especially during the crystal growth of the n- and p-layers with a quartz boat, when using the melt as many as 10 times. There is a fear of the melt being polluted. Without adding impurities, which become carriers, the melt for crystal growth could be used as often as 10 times running as it is at the same growth temperature as when the LED's are prepared. When a quartz boat is used, the growth layer is of the n-type and the carrier concentration is about $5 \times 10^{16}/cm^3$ in the neighborhood of the growth interface and $6 \times 10^{16}/cm^3$ on the growth surface, for the first use of the melt, with a concentration gradient. With the 10th use, this concentration becomes about $8 \times 10^{16}/cm^3$ for the interface and about $10 \times 10^{16}/cm^3$ for the surface. Thus, the carrier concentration tends to successively increase little by little with the number of times the melt is used. No difference in the substrate due to a difference in the carrier concentration is observed. The increase in the carrier concentration toward growth is the same as previously reported (7), and is considered to be due to a gradual increase of Si. The increase in the carrier concentration due to the frequency of the use of the melt is also thought to be due to Si. As seen from the above, the quartz boat is slightly polluted by Si, but because the Ga_2O_3, which becomes the radiative recombination center, is reduced with the use of a graphite boat, and this reduces the quantity of O added to the crystal, a quartz boat is used for red LED preparation.

Control of the concentration of impurities.—In the LED, the carrier concentration of the n- and p-layers affects the efficiency. Therefore, let us consider the

controllability of the concentration of the impurities in the rotating boat LPE growth system.

For LED preparation, Te and Zn are first added to the melt for the growth of the n- and p-layers. Figure 6 shows the relationship between the quantity of Te added to the melt and the carrier concentration of the grown surface at 980°C. For quantities under 4.4×10^{-2} a/o, the gradient is $m = 1$, and for quantities exceeding 4.4×10^{-2} a/o, the gradient is $m = ½$; thus, 4.4×10^{-2} a/o is the fork point. These results show the tendency previously reported (8, 9). Figure 6 also shows the relationship between the quantity of Zn added to the melt and the carrier concentration of the grown layer at 1040°C. In this case, the fork point is 10^{-2} a/o and the gradient (m) is ½ and 1, respectively. These results also show the tendency previously reported (8, 9). Thus, fairly accurate control of the concentration of impurities is possible.

The relationship between carrier concentration and the frequency of the use of the melt.—N- and p-type impurities are added only when the melt is first used; not in the 2nd to 10th uses. Therefore, since the melt is used repeatedly, if the carrier concentration in the n- and p-layers changes, it ought to greatly affect the efficiency.

Figure 7 shows the change in the carrier concentration according to the frequency of the use of the melt when the optimum quantity of Te and Zn (3.28×10^{-2} and 5.38×10^{-3} a/o, respectively) is added. The carrier concentration of the p-layer in the neighborhood of the p-n junction is about $2 \times 10^{17}/cm^3$. This value is nearly constant until the melt is used for the 10th time which, as the quartz boat is sealed, shows that the quantity of evaporated Zn is small. The carrier concentration of the n-layer in the neighborhood of the p-n junction is almost constant ($8 \times 10^{17}/cm^3$) from the 1st to the 10th use of the melt.

Emission wavelength and the frequency of the use of the melt.—The emission spectrum of the red LED has a peak wavelength of 7000Å and a half-value width of 1000Å; neither this peak wavelength nor the half-value width change with the frequency of the use of the melt.

The relationship between efficiency, electroluminescence time decay, and the frequency of the use of the melt.—Figure 8 shows the change in efficiencies based on the frequency of the use of the melt. No change in efficiencies occurs due to the frequency of the use of the melt from the 1st to the 10th use. An average efficiency of 6% (current density = 2 A/cm²) is obtained with good reproducibility at the time of mass production, and the maximum efficiency (current density = 2 A/cm²) of 10% is obtained.

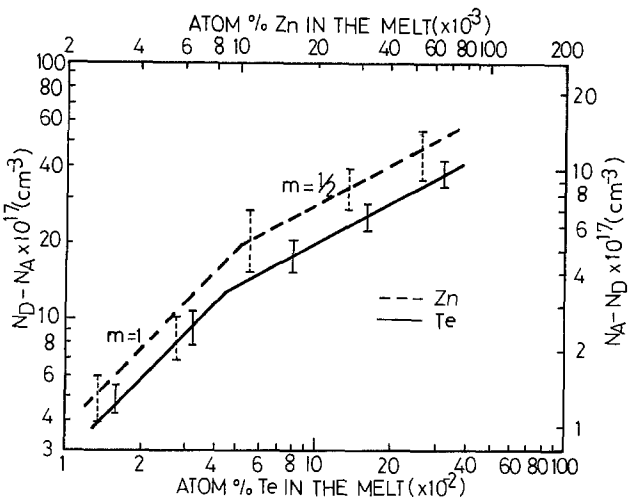


Fig. 6. The relationship between the quantity of added Te and Zn in the melt and the carrier concentration of the grown surface at 980°C and the grown layer at 1040°C.

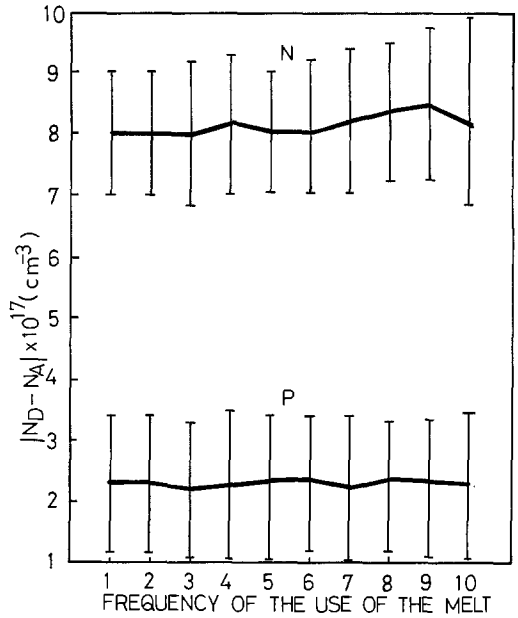


Fig. 7. The carrier concentration with the sequential use of the melt.

Figure 8 also shows the change in the electroluminescence time decay due to the frequency of the use of the melt. In using the n- and p-melts for the 1st to the 10th, the average electroluminescence time decay is about 500 nsec. This also shows that the various contaminations during the LPE procedure are small.

Relationship between efficiency and current.—In the red LED's, at a current density of 2-3 A/cm², the saturation of the efficiency occurs. When the current density becomes higher, the efficiency is linearly reduced. However, the degree of reduction varies with the type of LED; one group having high efficiency and another group having low efficiency. Reduction of the efficiency with the former group is greater. The photoluminescence of the p-layer of these wafers is measured before assembling the LED, and shows no difference in emission intensity.

The difference in the carrier concentration in the neighborhood of the p-n junction is constant. These facts indicate that it is the difference in crystallinity in the neighborhood of the p-n junction that causes

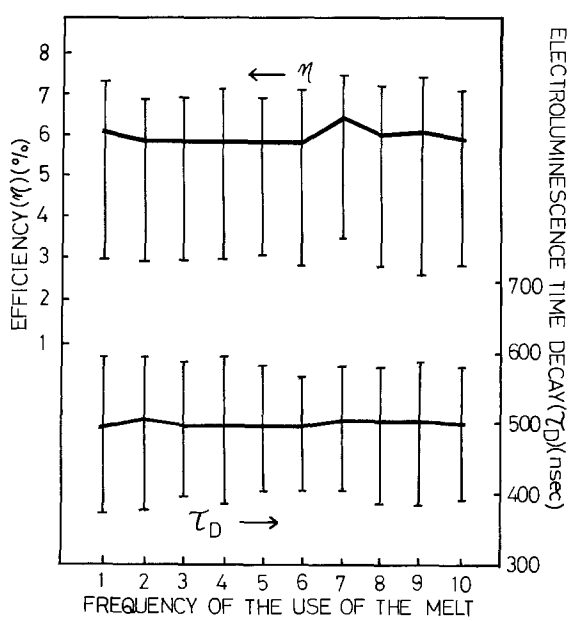


Fig. 8. The relationship between the efficiency (η) of LED's, the electroluminescence decay time, and the frequency of the use of the melt.

the difference in the ratio of the reduction in the efficiency. It is believed that in the LED's with low efficiency, the recombination generation current via the deep levels which exist in the depletion layer becomes predominant with low current. The electron concentration which contributes to radiative recombination is restricted; and the change in the efficiency to the current becomes smaller.

The condition of the surface after LPE crystal growth.—Figure 9 shows the interference microphotograph of the surface of the wafer after the LPE growth. In the rotating boat LPE growth system, the melt is completely removed from the surface of the substrate at the termination of growth, so that a very smooth surface is obtained. This does not change even if the melt is used repeatedly. The surface of the growth layer is mirrorlike, even after the 10th use of the melt.

Conclusion

To lower the production costs of GaP LED's, LPE growth, which is the most important of the production processes, has been considered and a rotating boat LPE growth system has been studied. Results are as follows: (*i*) In the rotating boat LPE growth system, 10-20 substrates can be treated at a time, and the carrier concentration necessary for manufacturing LED's can be controlled quite accurately. In addition, there is little change in the optical characteristics of the same lot and between separate lots. (*ii*) For the red LED, a double step system, which makes the n- and p-layers grow separately, is used. This reduces the consumption of Ga by using the same melt in both n- and p-layer growth up to 10 times. It makes it possible to remove the melt completely after growth is finished, and a mirrorlike growth surface can be obtained up to the 10th use. (*iii*) Red LED's with high efficiencies (average, 6%; maximum, 10%) are obtained with good reproducibility.

Thus, the rotating boat LPE growth system is excellent as a mass production system.

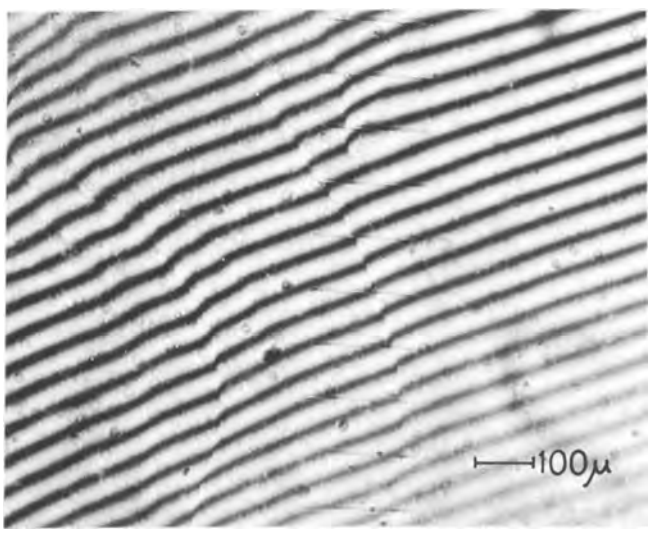


Fig. 9. The interference microphotograph of the surface of the wafer after the LPE growth.

Acknowledgment

I wish to thank Dr. M. Yamano and Mr. H. Takesada for their guidance and encouragement and am also greatly indebted to Mr. Y. Hosomi for helpful discussion.

Manuscript submitted Aug. 8, 1975; revised manuscript received April 16, 1977.

Any discussion of this paper will appear in a Discussion Section to be published in the June 1978 JOURNAL. All discussions for the June 1978 Discussion Section should be submitted by Feb. 1, 1978.

Publication costs of this article were assisted by Sanyo Electric Company, Limited.

REFERENCES

1. S. G. Brass, D. E. Oliver, and F. E. Birbeck, *J. Cryst. Growth*, **2**, 169 (1968).
2. Nikkei Electronics 8-27, 45 (1973).
3. O. G. Lorimor, R. H. Saul, L. R. Dawson, and C. R. Poola, *Solid State Electron.*, **16**, 1289 (1973).
4. A. A. Bergh, R. H. Saul, R. C. Vehse, and C. R. Poola, 367 RNP, *This Journal*, **119**, 303C (1972).
5. J. A. Donahue and H. T. Minden, *J. Cryst. Growth*, **7**, 221 (1970).
6. J. Vilms and J. P. Garrett, *Solid State Electron.*, **12**, 337 (1972).
7. R. H. Saul, J. Armstrong, and W. H. Hackett, Jr., *Appl. Phys. Lett.*, **15**, 2229 (1969).
8. A. S. Jordan, *This Journal*, **118**, 781 (1971).
9. F. A. Trumbore, H. G. White, M. Kowalchik, R. A. Logan, and C. L. Luke, *ibid.*, **112**, 782 (1965).

Device Quality GaAs Grown at Low Temperature by the Halide Process

J. Hallais,* D. Boccon-Gibod, J. P. Chané, J. M. Durand, and L. Hollan

Laboratories d'Electronique et de Physique Appliquée, 94450 Limeil-Brévannes, France

ABSTRACT

A study of the parameters which must be controlled to enable the vapor growth of GaAs at low temperature (LT.VPE) using the $AsCl_3/GaAs/H_2$ system has led to routine growth of MESFET layers at 630°C. The source temperature was determined from transport efficiency measurements and set in the range 670°-680°C. The growth rate dependence on temperatures and the $AsCl_3$ mole fraction were determined. The morphology of the layer was optimized as a function of the $AsCl_3$ mole fraction and the misorientation of the substrate. The best value of misorientation is about 6° off (001). These growth conditions were applied to submicron layer growth, and MESFET devices were fabricated. A comparison of the device performances obtained on layers deposited at high (750°C) and low (630°C) temperature shows an improvement on unbuffered layers grown at low temperature. Furthermore, the growth of an n^- buffer layer at low temperature improves the noise figure still further. Typical results without buffer layers, at 10 GHz, are 4 dB NF, 7.5 dB associated gain, and 11 dB maximum gain.

The $AsCl_3/Ga/H_2$ and $AsCl_3/GaAs/H_2$ chemical vapor transport systems, first described by Knight *et al.* (1), are widely used for the epitaxial growth of device-quality GaAs. Most of the work is performed using deposition temperatures T_D in the range 770°-705°C (2-4), but for several reasons it becomes attractive to lower the source and deposition temperatures ($T_D < 700$°C): Firstly, according to Weiner's calculation (5) and Di Lorenzo's data (6), silicon contamination is minimized at low temperatures; the second aspect is related to the thermal stability of GaAs (7). This last factor is of particular interest for MESFET devices for which submicron layers are deposited on semi-insulating substrates and whose rf performances and static characteristics are strongly dependent on the material and interface quality (8).

Several workers (9, 10) have reported on new methods for low temperature epitaxy (< 700°C), but most of their experimental conditions were based on out-of-equilibrium or out-of-steady-state conditions. Their results suggest that undecomposed $AsCl_3$ molecules cause supplementary reactions which allow larger supersaturation.

The aim of this work is: first, to define what can be expected for transport conditions in the temperature range 600°-700°C, and more particularly at 630°C, which is near the congruent evaporation point of GaAs (11); and second, to define an optimum set of conditions for epitaxial growth and to apply it to the MESFET layers.

Experimental Conditions

Both transport efficiency measurements and epitaxial growths are carried out in a classical $AsCl_3/GaAs$ (or $Ga)/H_2$ system described elsewhere (12). Most of the experiments were performed using solid GaAs sources in order to avoid the difficulties associated with Ga melt saturation with As (13). Undoped polycrystalline GaAs was used as the starting material. The transport rate was measured by the weight-loss method (14). The Ga/Cl ratio was calculated from the weight decrease of the source and the mole number of introduced $AsCl_3$.

Semi-insulating chromium-doped GaAs substrates were (001) oriented, a few degrees off, toward the (110) plane. Lens-shaped substrates were also used to study the influence of the misorientation following the technique described by Hollan *et al.* (15). Optical micrographs were used to observe the morphology on the surface plane and to determine the growth rates on stained cleavage surfaces. Electrical assessment was based on C-V measurements using the double mercury Schottky diode (16). Hall data were obtained by the classical Van der Pauw technique (17). A Hall pattern was also incorporated in the masks used for the FET technology. An aluminum layer is evaporated on the Hall sample, which enables measurements to be made at several biases and gives the mobility *vs.* the thickness of the undepleted layer. MESFET devices were fabricated using a previously described technique (18); two geometries of devices are labeled A and B types in Table I.

Experimental Results

Temperature dependence of the Ga/Cl ratio.—According to Watanabe (10) an "anomalous" transport reaction of GaAs by $AsCl_3$ is observed at low temperatures. Figure 1 shows the theoretical variation of the Ga/Cl ratio *vs.* temperature for the H_2 and neutral carrier gas (10, 14) and the experimental data obtained for the H_2 carrier gas. The Ga/Cl ratio dependence on the gas flow rate shows that there is a non-equilibrium phenomenon attributed to the reaction of the GaAs source with both undecomposed $AsCl_3$ and free HCl (10). At 630°C equilibrium is reached in the case of low flow rate values, but a deviation is observed for the high flow rates for temperatures up to 700°C. As the aim is to work at the lowest deposition temperature and with $T_S > T_D$, the flow rates were chosen in the range 30-130 cm^3/min, the source temperature was set in the range 670°-680°C and the source geometry was kept constant. The Ga/Cl ratio variation for a given $\Delta T = T_S - T_D$ is smaller in the low temperature range (680°-630°C) than in the classical temperature range (850°-750°C) and thus should lead to smaller growth rates. An influence of the $AsCl_3$ mole fraction (MF) on the Ga/Cl ratio is also expected

Table I

FET type	Gate width, μm	Gate length, μm	Drain-source length, μm
A	200	0.8	2.5
B	150	0.6	1.5

* Electrochemical Society Active Member.

Key words: $AsCl_3/GaAs/H_2$ process, vapor growth epitaxy, low noise MESFET.

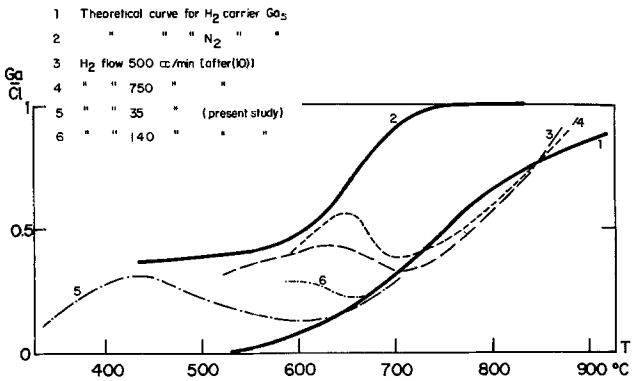


Fig. 1. Chemical transport of GaAs, variation of Ga/Cl vs. temperature. Full lines, theoretical curves; dotted lines, experimental data. Respective H_2 flows are: curve 5, 35 c^3/min; curve 6, 140 cm^3/min; curve 3, 500 cm^3/min; curve 4, 750 cm^3/min.

from theoretical calculations (19), but this effect was negligible in these experimental conditions ($10^{-4} \leq$ MF $\leq 10^{-2}$).

Temperature dependence of the growth rate.—Figure 2 shows the experimental results. As expected, a decrease of the growth rate is observed when the deposition temperature decreases for constant values of ΔT (50°C) and of the $AsCl_3$ mole fraction ($1.4\ 10^{-3}$). As previously mentioned (20), it is obvious that no linear dependence can be deduced from the data. It is worth noting that these growth conditions gave a good surface quality (no pyramids) over the whole of the investigated temperature range. Very small growth rates ($\sim$ 2 μm/hr) are interesting in practice for the fabrication of the submicron layers (0.2-0.3 μm) which are required for MESFET devices.

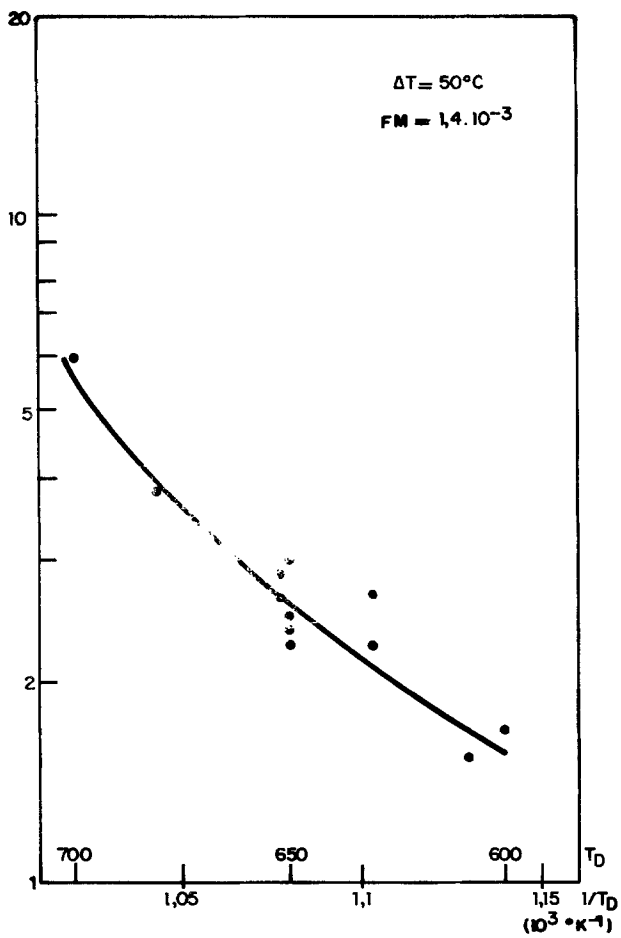


Fig. 2. Growth rate dependence on deposition temperature for constant ΔT and $AsCl_3$ mole fraction.

Growth rate and morphology dependence on the $AsCl_3$ mole fraction.—A large range of $AsCl_3$ MF was investigated for substrate and source temperatures of 630° and 670°C, respectively. The growth rate increased rapidly with the $AsCl_3$ MF (Fig. 3). The same effect has been previously reported (2, 3) for a higher deposition temperature and higher supersaturation. A rough comparison of the data (Fig. 3) shows that the growth rate is almost an order of magnitude higher at 750°C and rather similar at 705°C, but further conclusions cannot be deduced because the growth rate is highly sensitive to several parameters which are quite different for all these experiments (supersaturation, flow rates, misorientation). Surface morphology also depends on the $AsCl_3$ MF (Fig. 4). In practice, mirror-smooth layers are only obtained for $AsCl_3$ MF in the range 1-4 10^{-3}. At lower mole fractions the surface is pitted; at higher mole fractions macroscopic defects appear (pyramids). This effect was mentioned in a study of localized epitaxy (21) and more detailed work on growth anisotropy at low temperatures and high $AsCl_3$ MF's will be published later (22).

Growth rate and morphology dependence on substrate misorientation near (001) plane.—The influence of the misorientation of the deposition surface is conveniently investigated using lens-shaped substrates. The basic plane is (001) and the radius of curvature of 59.25 mm allows a misorientation angle α of about 9°. The other parameters are: $AsCl_3$ MF = $3\ 10^{-3}$, T_D = 630°C, T_S = 670°C. Figure 5 shows the growth anisotropy corresponding to the <110> and <1$\bar{1}$0> directions, and the same phenomenon is mentioned by Hollan (15) at 750°C.

The relative variation of τ, the growth rate, with α seems practically independent of the deposition temperature. The morphologies observed on the lens-shaped substrates are presented in Fig. 6. The two main directions of misorientation were <110> Ga and

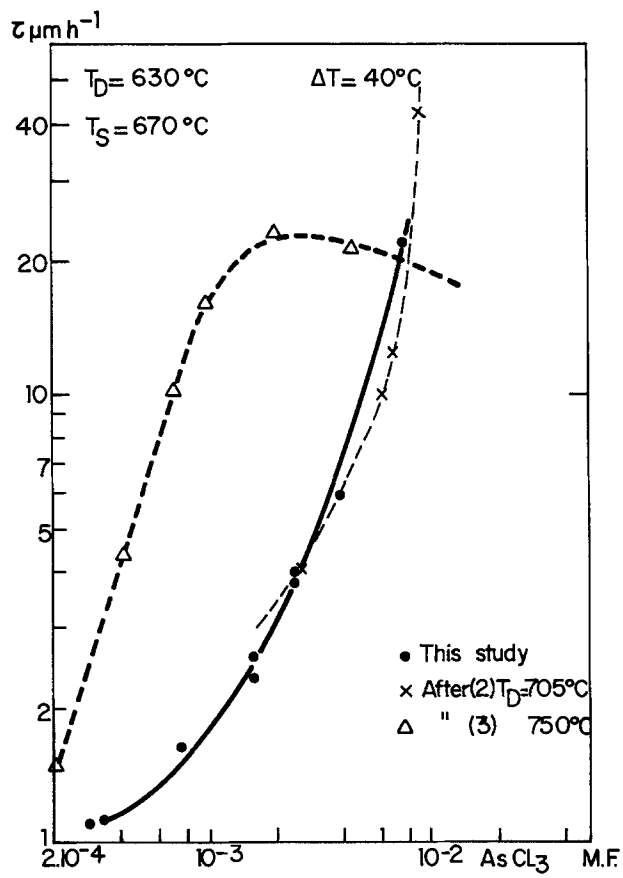


Fig. 3. Growth rate dependence on $AsCl_3$ mole fraction for constant source and deposition temperature. ● This study; x after (2) T_D = 705°C; △ after (3) T_D = 750°C.

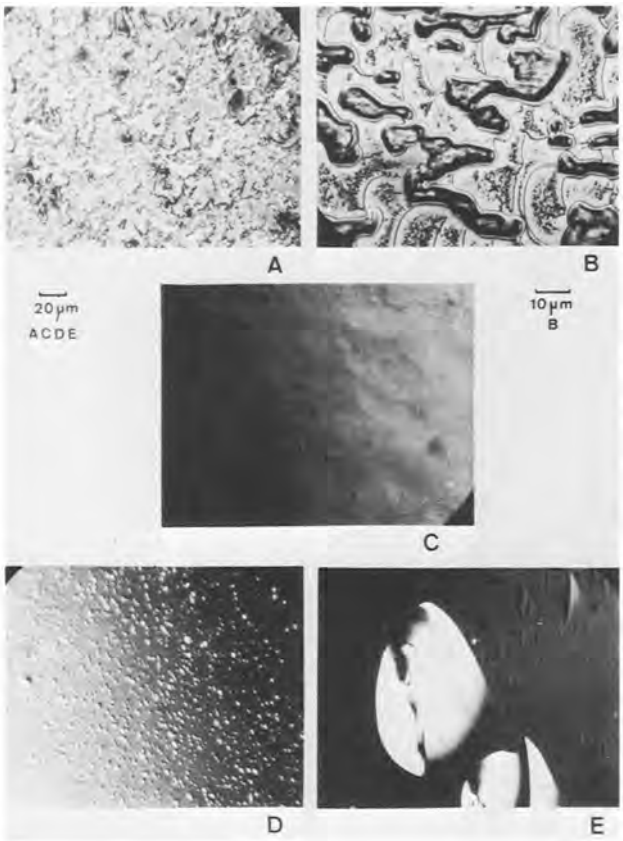


Fig. 4. Typical surface morphologies of layers deposited at 630°C. A and B, $AsCl_3$ MF = 10^{-3}; C, $AsCl_3$ MF = 3 10^{-3}; D and E, $AsCl_3$ MF = 5 10^{-3}.

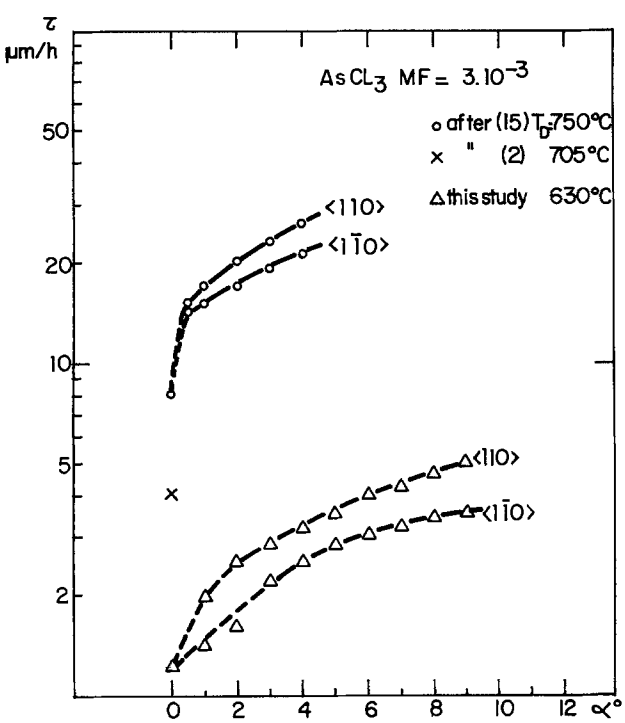


Fig. 5. Growth rate dependence on misorientation angle α. $AsCl_3$ MF = 3 10^{-3}; △ this study, T_D = 630°C, ● after (15); T_D = 750°C, x after (2) T_D = 705°C.

<1$\bar{1}$0> As. The exact (001) plane exhibits a high density of pyramids but the density and the dimensions of the defects decrease rapidly with increasing misorientation. For each direction, a misorientation

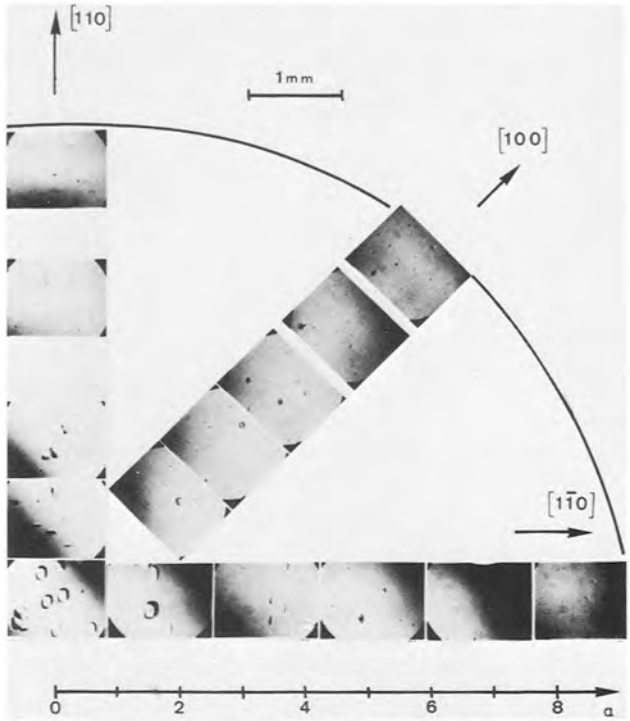


Fig. 6. Morphologies on a lens-shaped substrate for the three main misorientation directions.

angle α of 6°-7° gives a smooth, defect-free surface. This value is two times larger than is usual in high temperature VPE.

Electrical properties.—The residual doping level is n-type and depends on the $AsCl_3$ MF, (Table II). The variation of n is drastic as the $AsCl_3$ MF increases and the low concentration material becomes rather compensated.

Applications of Low Temperature Growth to Devices

Device-oriented epitaxy.— The main results of the last section were applied to the fabrication of practical layers. The experimental conditions are listed in Table III.

The semi-insulating GaAs substrate was cleaned in a dust-free room and directly inserted into the epitaxy reactor. The required layer thickness is in the range 0.2-0.3 μm. Mirror-smooth and macroscopic defect-free layers are routinely obtained. Deliberate sulfur doping is used to achieve the required n^+ level (1-2 10^{17} cm^{-3}). The sulfur mole fraction is about 7 10^{-10}, which is nearly 30 times less than at the high deposition temperature (750°C). Mobility profiles measured on a sample are presented in Fig. 7. By comparison with a high temperature (750°C) layer it appears that there is

Table II

$AsCl_3$ MF $\times 10^3$	$N_D - N_A$, cm^{-3}	$\mu_{300°K}$, cm^2 V^{-1} sec^{-1}
3	3 10^{15}	7500
3, 5	2 10^{14}*	5500
4	About 10^{13}*	6000
5	Semi-insulating	—

* The layer is photosensitive.

Table III

Temperatures	Source 670°C	Substrate 630°C
$AsCl_3$ MF	3-4 10^{-3}	
Substrate orientation	(001) 6° off toward (110) Ga	
Growth rate	2-5 μm/hr	

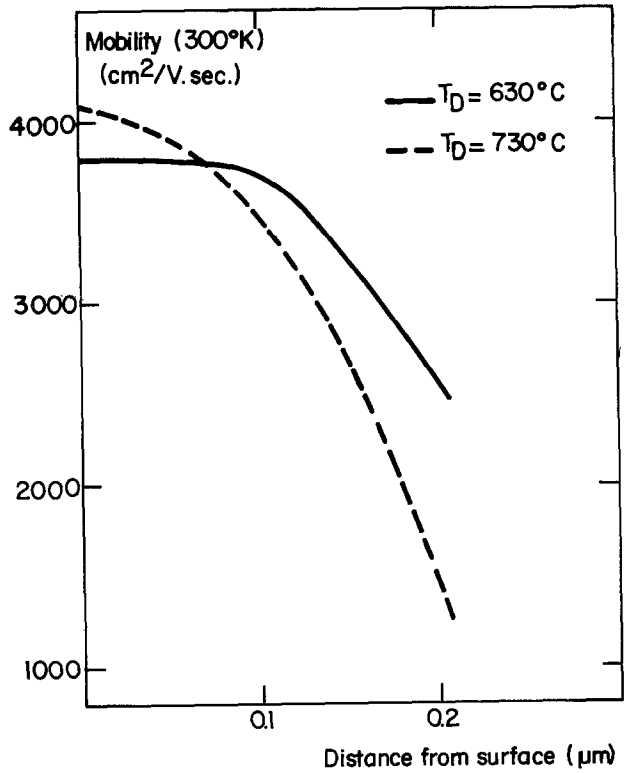


Fig. 7. Mobility vs. depth of unbuffered FET layers. Solid line, $T_D = 630°C$; dotted line, $T_D = 750°C$.

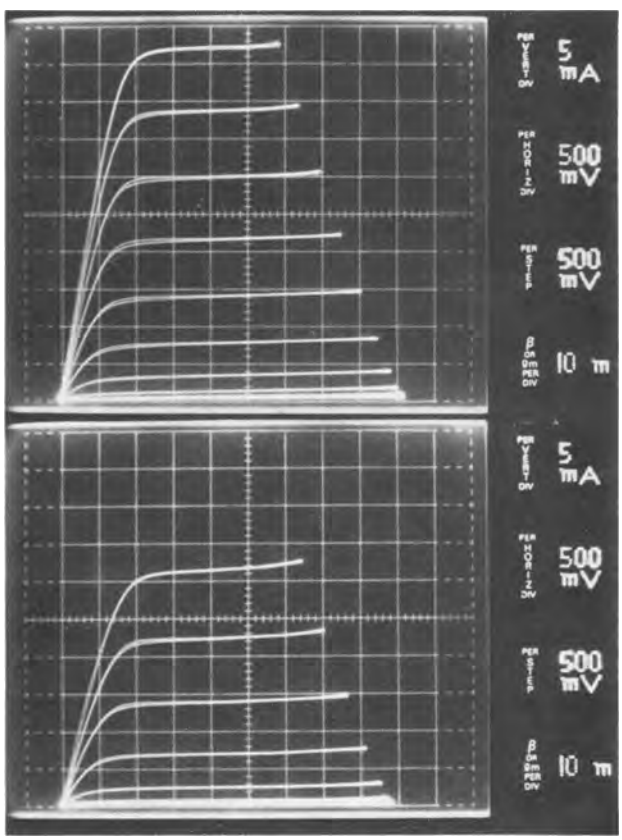


Fig. 8. Static characteristics of the FET devices

an improvement in the mobility at the interface for the low temperature layer. By changing the $AsCl_3$ MF during the growth (see Table II), an $n^+/n^-/SI$ multilayered structure can also be obtained, but the n^- buffer layer, a few microns thick, is rather compensated.

MESFET results.—Defects of the static characteristics such as bumping or looping, which are often related to the interface quality (8), do not appear at all on the present devices (Fig. 8). Table IV shows typical results for several devices. The figure of merit M is defined by the relation $M = \frac{NF - 1}{1 - \frac{1}{G_{NF}}}$ where NF is the noise figure and G_{NF} the associated gain, both expressed with a linear scale. It can be noticed that the performances at 10 GHz for unbuffered layers LT.VPE give a better figure of merit than for the unbuffered HT VPE or MBE layers.[1] Moreover, the results for the $n^+/n^-/SI$ structure are close to the best published data (23).

Table IV

Growth characteristics		MESFET technology	Performances at 10 GHz (10 dB)			Figure of merit, M
Method	Buffer layer		NF	G_{NF}	G_{max}	
VPE	—	A	4.8	5	10.5	3
	—	A	4	6.1	8.5	2
LT.VPE	—	B	4	7.5	11	1.8
	—	A	4.6	7.1	9.4	2
MBE*	—	B	4.7	9	9.2	2
VPE	x	A	4.2	6.6	9.8	2.5
LT.VPE	x	A	3.3	5.1	8.9	1.6

Doping levels of the active layer in the range 1-3 10^{17} cm^{-3}.
* Grown at MRL.

Conclusions

It is shown that the $AsCl_3/GaAs/H_2$ epitaxy process can be used at deposition temperatures as low as 630°C. The necessary conditions to grow defect-free layers are an $AsCl_3$ mole fraction of 3-4 10^{-3} and a substrate orientation of 6° off (001) toward <110> Ga. The small growth rates in the range 1-2 μm/hr are very useful for the submicron layers (0.2-0.3 μm) required for MESFET devices.

Until now, on VPE devices the only convenient way to reduce the noise figure was to grow an n^- buffer layer between the SI substrate and the active layer. The present process appears to give an alternative method, which, like the MBE, uses also a low deposition temperature, and could lead to the same results without a buffer layer. The process seems then well adapted to an industrial development.

Acknowledgments

The authors would like to acknowledge the assistance of Mrs. Baelde and M. Bellaiche for technical help. Sincere thanks are also due to C. Schiller, Mrs. A. Gallais, C. Binet and P. Baudet for helpful discussions, and to J. Magarshack for critical review.

This work is supported by the D.G.R.S.T.

Manuscript submitted Oct. 27, 1976; revisions made by divisional editor. This was Paper 240 presented at the Las Vegas, Nevada, Meeting of the Society, Oct. 17-22, 1976.

Any discussion of this paper will appear in a Discussion Section to be published in the June 1978 JOURNAL. All discussions for the June 1978 Discussion Section should be submitted by Feb. 1, 1978.

Publication costs of this article were assisted by Laboratories d'Electronique et de Physique Appliquée.

[1] Layers grown at Mullard Research Laboratories, Redhill, Surrey, England by B. A. Joyce, C. E. C. Wood, and G. Laurence.

REFERENCES

1. J. R. Knight, D. Effer, and P. R. Evans, *Solid-State Electron.*, **8**, 178 (1965).
2. J. V. Di Lorenzo, *J. Cryst. Growth*, **17**, 189 (1972).
3. L. Hollan, in "Gallium Arsenide and Related Compounds 1974," p. 22, Institute of Physics, London (1975).
4. T. Aoki, *Jpn. J. Appl. Phys.*, **14**, 1267 (1975).
5. M. E. Weiner, *This Journal*, **119**, 496 (1972).
6. J. V. Di Lorenzo and G. E. Moore, Jr. *ibid.*, **118**, 1823 (1971).
7. J. Hallais, A. Mircea-Roussel, J. P. Farges, and G. Poiblaud, To be published.
8. T. Nozaki, M. Ogawa, H. Terao, and H. Watanabe, in "Gallium Arsenide and Related Compounds, 1974," p. 46, Institute of Physics, London (1975).
9. H. Seki, A. Kookitu, K. Ohta, and M. Fujimoto, *Jpn. J. Appl. Phys.*, **15**, 11 (1976).
10. H. Watanabe, *ibid.*, **14**, 1451 (1975).
11. C. T. Foxon, J. A. Harvey, and B. A. Joyce, *J. Phys. Chem. Solids*, **34**, 1693 (1973).
12. L. Hollan and A. Mircea, Proceedings of the 4th International Symposium on Gallium Arsenide and Related Compounds, 1972, Institute of Physics, p. 217, London (1973).
13. D. W. Shaw, *J. Cryst. Growth*, **8**, 117 (1971).
14. A. Boucher and L. Hollan, *This Journal*, **117**, 932 (1970).
15. L. Hollan and C. Schiller, *J. Cryst. Growth*, **13/14**, 319 (1972).
16. M. Binet, *Electron. Lett.*, **24**, 11 (1975).
17. L. J. Van der Pauw, *Philips Res. Rep.*, **13**, 1 (1958).
18. P. Baudet, M. Binet, and D. Boccon-Gibod, *IEEE Trans. Microwave Theory Tech.*, **24**, 372 (1976).
19. A. Gallais, Private communication.
20. L. Hollan, J. M. Durand, and R. Cadoret, To be published in *J. Cryst. Growth*.
21. J. P. Chane, L. Hollan, and E. Schiller, *J. Cryst. Growth*, **13/14**, 325 (1972).
22. L. Hollan and J. M. Durand, To be published.
23. B. S. Hewitt, H. M. Cox, H. Fukuri, J. V. Di Lorenzo, W. O. Schlosser, and D. E. Iglesias, *Electron. Lett.*, **12**, 309 (1976).

Kinetics of Titanium Oxidation in Water Vapor Argon Ambient Mixtures

Fradelle G. Fuhrman[1] and Frank C. Collins[2]

Department of Chemistry, Polytechnic Institute of New York, Brooklyn, New York 11201

ABSTRACT

Kinetic studies of the thermal oxidation of polycrystalline and single crystal titanium in ambient mixtures containing water vapor and argon were carried out at atmospheric pressure in the temperature range 400°-500°C. An analytical method was developed utilizing reflectance interference measurements in the u.v.-VIS-*IR* range, which allowed precision of about 2-5% of film thickness, in the range of 5-200 nm of film. In all cases, the kinetics followed a modified parabolic form which implied an initial surface-controlled reaction followed by a diffusion-controlled process complying with a parabolic growth law. Arrhenius plots were made for the growth rates, leading to calculated activation energy of 168.4 ± 0.2 kJ/mole (1.75 ± 0.005 eV) for the parabolic process on both the polycrystalline and single crystal material. No effect on the reaction was observed by either varying the water vapor pressure (above 4.6 Torr) or adding oxygen to the water vapor argon system. This observed zero-order dependence is consistent with the model of a water vapor saturated outer surface which has been observed for rutile in the presence of trace amounts of water vapor. No conclusive evidence has been obtained which would positively identify any single species as the only one migrating.

Oxidation of metals at temperatures below about 300°C usually follows a direct or inverse logarithmic law, and in many cases, ceases with the formation of a protective oxide film. These films are not protective at higher temperatures, and the oxidation then usually proceeds by a diffusion-controlled process which follows parabolic kinetics. At still higher temperatures, depending on the metal involved, other kinetics are obtained.

Oxidation of titanium at temperatures above 350°C has produced growth curves which are generally parabolic (1-6), sometimes indicating the presence of a second process, possibly linear, occurring simultaneously with the parabolic one. However, Hurlen (5) and Kučírek (6) report logarithmic growth below 650°C, while Jenkins (3) and Davies and Birchenall (7) find linear kinetics above 650°C. Tikomirov and Dyach'kov (8, 9) investigated the high temperature (750°-1050°C) oxidation of titanium with dry oxygen and found compliance with a linear parabolic growth equation first proposed by Evans (10)

$$X^2 + (k_p/k_l)X = k_p t$$

where X is the thickness of the oxide film, k_p and k_l the parabolic and linear rate constants, respectively, and t the time. They were able to distinguish for two different temperature regions the separate rate constants for the two processes and to determine activation energies for each. A similar linear parabolic law for the high temperature (850°-1000°C) oxidation of silicon in wet oxygen was analyzed by Nakayama and Collins (11) to give linear and parabolic rate constants and activation energies which they assigned to the separate surface and diffusion processes. Subsequently, Chen (12) showed that the medium temperature (600°-850°C) oxidation of chromium in wet ambients followed a similar linear-parabolic law. In view of the ambiguous results in the literature for titanium oxidation, a precise study seemed necessary to clarify and perhaps more closely define the processes occurring.

Since the study of titanium oxidation in oxygen involves an uptake of dissolved oxygen which is large

[1] Present address: Cooperative College Center, State University of New York, Purchase, Mt. Vernon, New York 10555.
[2] Present address: Washington, D.C. 20036.
Key words: reflectance, interference, spectrophotometry, activation energies.

and difficult to measure (5, 8, 9), particularly with volumetric or gravimetric methods of analysis, and since "dry" oxygen systems may contain small but catalytically active amounts of water vapor (11), particularly in quartz furnace systems, it was of interest to determine the kinetics of oxidation of titanium by water vapor alone, and in the absence of oxygen from the reaction system. Also, since the possible solution of water vapor by the titanium system could not be ruled out, it appeared desirable to use an analytical method directly related to the actual film thickness. A method utilizing reflectance interference was therefore developed for this purpose.

The effect of the state of crystallinity of the surface has not been studied in the case of titanium oxidation. For this investigation, therefore, both single crystal and polycrystalline samples of research grade titanium were used.

The titanium samples for this study were sliced, polished manually and by wheel, and oxidized in a furnace under varying mixtures of water vapor and argon at atmospheric pressure. The samples were removed at intervals, cooled, and analyzed for film thickness in the optical setup described below. After measurements, the samples were replaced in the furnace system for further oxidation. Five to nine measurements were made for each sample, covering an oxidation period of several hours, for the temperature range 397°-549°C. The thickness of the measured films ranged from about 3 nm (the "native" oxide thickness which appears almost instantaneously on the freshly polished titanium) (2, 6) to several micrometers after thermal oxidation.

The data obtained were plotted on straight parabolic plots to give determinations of the parabolic rate constants. From these rate constants at different temperatures activation energies were determined for the process.

Experimental

Preparation of samples.—For the main oxidation studies two types of titanium were used. The polycrystalline material was obtained as a 2 in. long, ½ in. diam bar. The single crystal sample, obtained from Materials Research Corporation as a cylinder 1 in. long and ¼ in. diam, was oriented and sliced by the manufacturer along the long axis parallel to the 0001 plane. An x-ray diffraction image confirmed the single crystal structure, alpha (hexagonal) form, and the 0001 orientation. X-ray diffraction studies on the polycrystalline material showed no preferred orientation.

Since both the oxidation process and the optical analysis required as perfect a surface as possible, attention was focused sharply on the slicing and polishing of samples. Titanium in the pure state is a soft malleable metal, and exhibits a high degree of surface flow under strain. This characteristic led to difficulties in both slicing and polishing. The most successful cut was achieved with a diamond dust wire cutter operating at a very slow speed. The single crystal block was cut into three pieces, each with the 0001 face exposed. The polycrystalline bar was cross cut into slices about 1/8-1/16 in. thick. For the polishing, a relatively simple, although not altogether satisfactory, procedure was developed for both the polycrystalline and single crystal slices which involved the usual hand grinding down to 600 grit silicon carbide paper, wheel polishing with 0.3 and 0.05 micron alumina powder using Gamal cloth, with ultrasonic cleaning in warm acetone between steps to remove adherent grit particles which might cause pitting during wheel polishing. Heavy hand pressure seemed effective, with rapid wheel rotation. Significantly better results were achieved using an aluminum sample holder than either stainless steel or lucite of the same type, the abraded aluminum possibly providing an effective additional abrasive. A number of samples were polished using only abraded aluminum with apparently superior results.

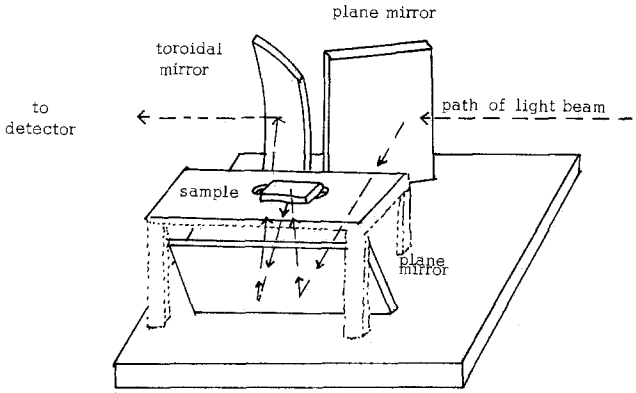


Fig. 1. Sketch of Barnes 134 reflectance attachment (schematic)

All of the holders received polishes far superior to those of the slices they were servicing. Specularity of the sample was judged adequate when the image of a human hair could be distinguished at a distance of about 6 in. Under the low power microscope all polished samples showed many small pits.

Oxidation of samples.—The oxidation system consisted of a gas (argon or argon and oxygen) carrier inlet, several humidiostats to provide water vapor at the proper partial pressures, and a furnace in which the oxidation took place. Analysis was carried out on a Carey 14 spectrophotometer[3] using a specular reflectance accessory in the sample chamber (Fig. 1).

The polished titanium specimens were cleaned ultrasonically with warm acetone for 5-10 min and allowed to stand in air for 1-3 days. The native oxide growth, which begins to form immediately on freshly polished samples except under very high vacuum, seems to be self-limiting, and becomes protective at about 3 nm of film, preventing any additional growth at room temperature.

The oxidation reaction was carried out in a 3 zone single control diffusion furnace which was heated by three helically wound metal rods, with a 10 in. long center section within which control could be maintained to within 1°C. Temperature was determined by a Chromel-Alumel thermocouple placed in the sample position and checked after each run. A calibration of furnace setting number *vs.* temperature gave a straight line with no apparent dependence upon whether the temperature was being lowered or raised. This was a check upon subsequent thermocouple readings.

The furnace tube and all connections were of fused quartz, the tube itself of single wall 2 in. internal diam., and 45 in. in length. All quartz components were connected by 12/5 ball joints with spring clamps. The outlet of the furnace tube was stuffed with glass wool to prevent dust or other solid contaminants from entering the furnace system. The ambient flow during the oxidation runs prevented the entrance of laboratory air into the system. Any absorption of water vapor by the quartz system or diffusion into the interior of the furnace tube was masked by the ambient flow of the water vapor oxidant into the furnace tube.

The quartz boat holding the sample was removed and replaced each time by a fused quartz rod with a hooked end, marked to indicate the position of the sample in the center zone of the furnace. The sample was removed from the boat with forceps and cooled in a glass petri dish before being placed in the sample chamber of the analyzing spectrophotometer.

The ambient argon gas (Matheson, high purity)[4] was controlled by a dual float flowmeter and set for 500 ml/min, corresponding to a linear flow rate of 4.97 cm/sec inside the furnace tube, previous studies having shown that increasing the flow rate beyond this magnitude had no effect on the reaction rates. Water vapor was introduced by first passing the argon through a

[3] Varian Instrument Division, Palo Alto, California.
[4] Matheson Gas Products, East Rutherford, New Jersey.

quartz humidiostat maintained at the required temperature for the desired vapor pressure. For the 0°C water vapor equilibrium (4.6 Torr) an ice bath was employed, with a precooling of the ambient gases in an ice-chilled column. For the higher vapor pressure of 55 Torr a heating unit was used, with a 40W long form light bulb as the heater and a thermistor-controlled regulator which provided temperature control of the bath to within 0.1°C. An infrared heater aimed at the exit tube of the humidiostat prevented water vapor condensation prior to its entering the tube of the furnace.

The furnace temperature was set at least one day in advance, and the ambient gases allowed to flow for 10 min prior to introduction of the sample. The titanium slices, either singly or in duplicate, were placed in the quartz boat and introduced into the furnace. The sample was removed at intervals, cooled, and placed on the sample platform of the reflectance unit inside the spectrophotometer for analysis. The sample was then replaced in the furnace for further oxidation. Three to nine measurements were made during each run, the average being about five, at intervals of 2 min to 2 hr. Readings at given oxidation times did not seem to depend upon whether the sample had been previously removed from the furnace or not.

For the run containing oxygen as one of the ambient gases, a second flowmeter set for 100 ml/min controlled the oxygen flow, which joined the 500 ml/min of argon prior to entering the humidiostat. Mixing was accomplished by turbulent flow through the inlet coils. This yielded an effective pressure of 120 Torr of oxygen within the system. The oxygen was Matheson, ultradry (99.6%).

Prior to the series of oxidation runs, the entire quartz system was cleaned in a dilute hydrofluoric acid-nitric acid mixture, and maintained thereafter as free as possible of contamination.

Analytical Procedure

The quantitative nature of interference phenomena resulting from reflectance at two surfaces is known exactly only for perfect reflectors, where the phase change at the interface is either 0 or pi, depending on the relative index of refraction of the two media. For the case of a real transparent film on an opaque surface, the absorptivity of both the film and the substrate will result in phase changes different from those where perfect reflectors are involved (13, 14). These phase differences will effectively add an apparent optical path to the reflected rays, giving an apparent film thickness greater than the actual value. Although the phase change difference is a function of wavelength, as is the real index of refraction, within a small range of wavelengths we may treat them as effectively constant to a first approximation, particularly if only zero order reflectance minima are used. The thickness of the real film may then be expressed as

$$X_r = \frac{\lambda}{4n} - \delta$$

where X_r is the film thickness, λ the wavelength at which zero order reflectance minimum occurs, n the real film index of refraction, and δ the apparent additional thickness due to the phase change. When the thickness of the real film is zero, then λ will have a positive value equal to $4\,n\delta$, although this is not a measurable value, as there is no interference without a reflecting film. However, the thickness of the real film is never zero, as the native oxide forms immediately on the freshly polished surface. The thickness (X_o) at zero time will therefore be that of the native oxide, and the wavelength zero (λ_o) extrapolated to zero time will consist of two terms, one being due to the native oxide, and the other being due to the phase change difference. The equation may be expressed as

$$\lambda_o = 4\,nX_o + 4\,n\delta$$

We can then write the thermally grown thickness of the oxide film as

$$X = X_r - X_o = \frac{\lambda}{4n} - \frac{\lambda_o}{4n} \text{ or } \frac{\lambda - \lambda_o}{4n}$$

where X_r is the real thickness at time of measurement, and X the thermally grown thickness.

Instrumentation

For the measurement of reflected intensity a Barnes Model 134 reflectance accessory[5] was modified for use in the Cary 14 spectrophotometer. An aluminum platform in the sample chamber of the Cary replaced the usual Cary sample holder, and the reflectance accessory was placed on the platform, after which the mirrors were adjusted to give maximum reflectance (Fig. 1). About 70% of full-scale intensity could be received by the detector with the unit in place and a front surface aluminized mirror in the sample position. Actual reflected intensities were much lower with the sample in place, but since most of the minima went completely off scale there was no real problem in locating them, even with the low light levels present at certain thicknesses. The thin oxide films showed brilliant interference colors, some of which, such as the deep indigo, reflected little visible light. The extended range of the Cary made this instrument extremely useful, as wavelengths from 280 nm to 2.6 μm could be scanned in one reading (three source lamps were available). This covered thicknesses from about 2.5 to about 250 nm. An attempt was made to measure thicker films by use of the reflectance attachment in the Perkin Elmer 21 spectrophotometer in the 2.5-12 μm range, but the reflectance spectra at these wavelengths showed excessive electrical noise, the spectral trace consisting of very jagged lines in which the minima were not readable with any reasonable precision. Beyond about 6 μm absorption bands appear and blank out any interference effects. These absorption bands could be used for the measurement of thicker films, but the method was not developed here.

Precision and Reproducibility

The forms of some spectrophotometric curves are shown in Fig. 2. Although in most cases the actual minimum was off scale, estimation of the minimum wavelength could easily be made to less than 5 nm for the narrower bands, and 50-100 nm for the widest ones. Since 5 nm of λ represents about 0.5 nm of film, it is seen that the precision is on the order of 2-5% of total film thickness, except for perhaps some very early points. The reproducibility of the measurements is better than this. When duplicate runs were made on the same sample area using both visible and u.v. sources within the same low wavelength range, the two curves were usually very closely coincident.

Although separate samples oxidized together under the same conditions varied between themselves as much as 10% of actual film thickness, the measured slopes for the parabolic portion agreed very closely for duplicate samples, indicating that the thickness difference was a function of the initial portion of the oxidation process. Repeat optical measurement of each sample always gave results within the readable precision. It is clear that the analytical method itself is capable of greater precision than the system requires, and shows less variability than the oxidation process itself.

Experimental Results

Computation of growth rates from optical data.— The raw data generated by the interference spectra consists of wavelength readings (λ) at which deep reflectance minima occur, each minimum being a characteristic of a particular oxide film on a particular sample substrate. These minima occur at higher and higher wavelengths as the oxide film increases in thickness (Fig. 3).

[5] Barnes Engineering Company, Stamford, Connecticut.

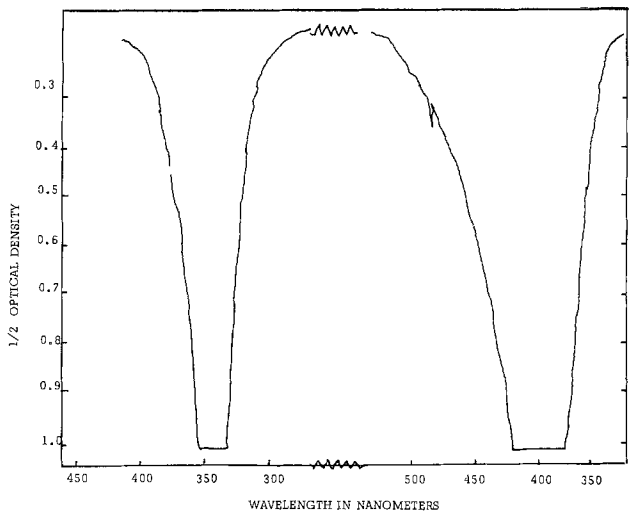


Fig. 2. Spectral curves showing interference minima on two successive samplings, Left; sample 53, $t = 3.2$ min, $\lambda_{min} = 343$ nm: Right sample 53, $t = 8.8$ min, $\lambda_{min} = 400$ nm.

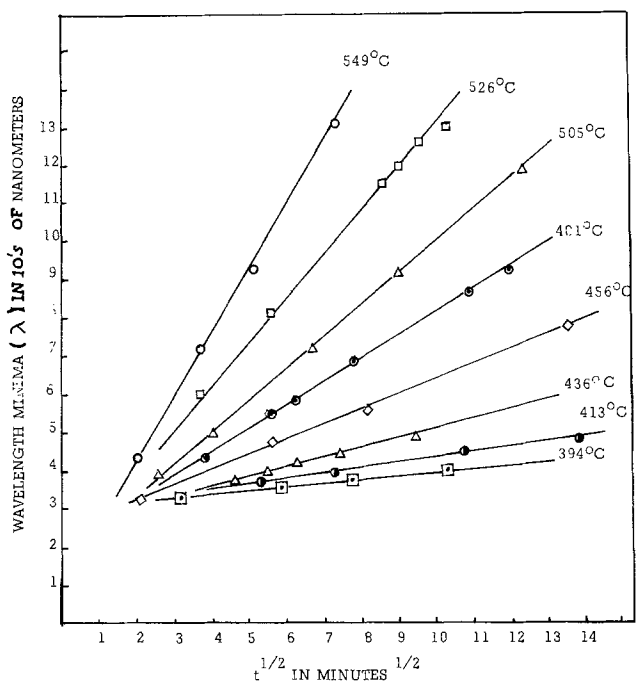


Fig. 3. Typical growth curves of oxide films on titanium in water vapor argon ambient mixtures.

At oxidation temperatures below about 570°C the plot of wavelength minima *vs.* time for any single sample shows a parabolic form with the wavelengths seeming to originate from some λ_o at zero time. Plots of λ *vs.* $t^{1/2}$ show straight lines which intersect not at zero time but at some later t, the form of the curve indicating that an initial term is involved relating to the initial growth process which is probably surface, rather than diffusion, controlled. A parabolic rate constant k_p, may be read directly from the parabolic portion of the curve, with

$$k_p = (dx/dt^{1/2})^2$$

Preliminary runs carried out at oxidation temperatures of 572°C and above showed a breakdown of this parabolic form (Fig. 4) and it was decided to concentrate on the lower temperature range where the simpler and probably more basic kinetics were obtained.

Arrhenius plots of the rate constants *vs.* the reciprocal of the absolute temperature were made on semilog graph paper, and the activation energies were calculated from the slopes. Single crystal runs were indis-

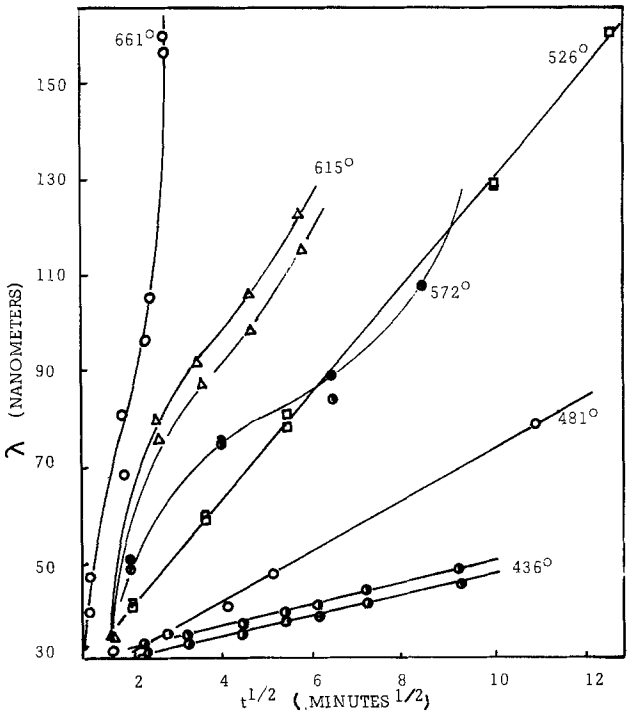


Fig. 4. Plot of preliminary runs showing breakdown of parabolic kinetics at temperatures of 572°C and above.

tinguishable from polycrystalline runs in the parabolic region of the kinetics, although in all cases the initial rates for the single crystal material were lower. The activation energy for the diffusion-controlled region was determined to be 168.4 ± 0.2 kJ/mole (40.3 kcal/mole, or 1.75 eV) (Fig. 5).

Addition of oxygen to the system (about 120 Torr) and the increase of water vapor partial pressure from 4.6 to 55 Torr had no noticeable effect on either the initial or parabolic region of the kinetics. The rate constants fell smoothly on the same Arrhenius plots as those runs with no oxygen, or with lower vapor pressure.

Discussion of Results

The modified parabolic form of the rate curves within the time range of 0-2 hr and at temperatures of 394°-549°C fits a rate law of the form

$$f(X) + BX^2 = t$$

where $f(X)$ represents the initial process, possibly of limited duration, occurring during the first few minutes of reaction, and either ceasing or being dominated thereafter by the parabolic process normally associated with diffusion control as the film builds up to the point where the oxidant species no longer has full free access to the metal surface.

The theoretical basis of the rate law has been investigated by Collins and Nakayama (15). Their results were applied to the data of Nakayama and Collins (11) on the oxidation of silicon, and to that of Chen (12) on the oxidation of chromium. The results of the present study on titanium oxidation may be attributed to the same electrochemical model.

In this model, the oxide layer, which is a semiconductor at oxidation temperatures, separates the substrate from the adsorbed gas. The Fermi potential difference between the energy levels of the electrons in the metal and the adsorbed gas causes a movement of electrons and/or holes through the film. The electrostatic potential difference ΔV set up by this movement of charge causes a drift of ions, the resulting ionic current balancing the mobile carrier current to conserve charge. The growth rate of the oxide layer is proportional to the ionic current which supplies the active species to the reaction systems. Thus

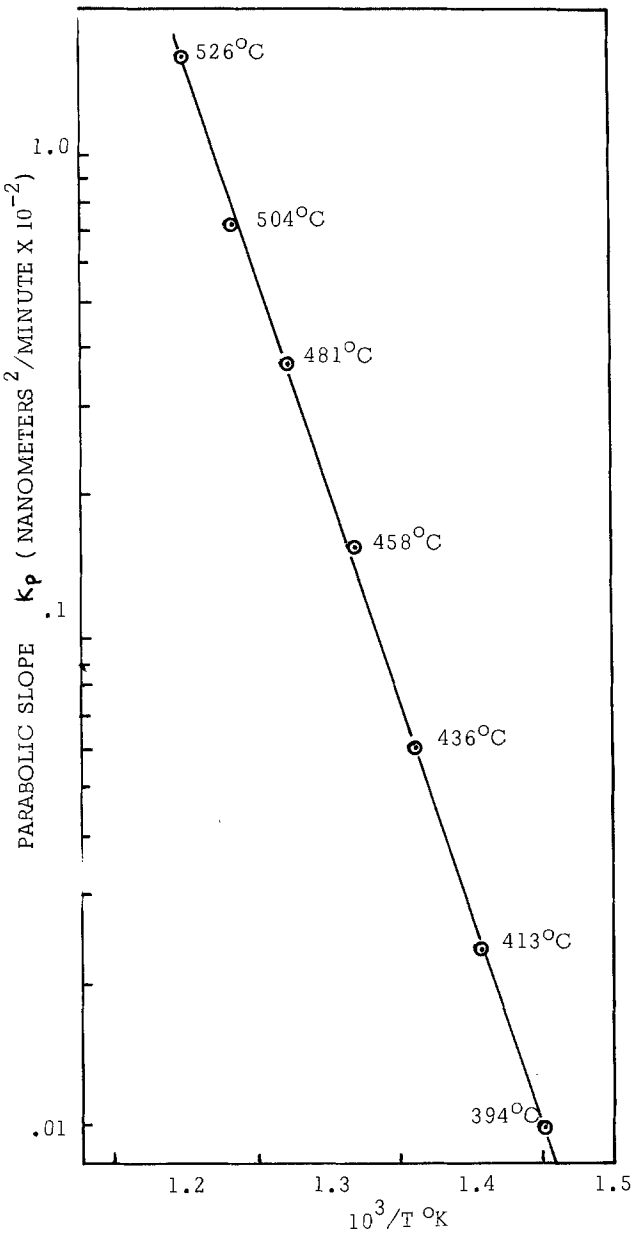


Fig. 5. Arrhenius plot of parabolic slopes k_p read directly from data. All runs on polycrystalline Ti samples with 4.6 Torr H_2O, with argon to 1 atm. E_a = 168.4 ± 0.2 kJ/mole.

$$I = 4q(N/V_m)(dX/dt)$$

where I is the current density, q the electronic charge, N Avogadro's number, V_m the molar volume of the oxide, and dX/DT the rate of increase of thickness of the growing oxide film.

In the absence of space charge, the ionic flux, in terms of numbers of ions per unit area per unit time, may be put into the form

$$J = -\frac{Dq\Delta V}{kTX}\frac{c(X)e^{-q\Delta V/kT} - c(O)}{e^{-q\Delta V/kT} - 1}$$

where D is the coefficient of ionic diffusion, X the thickness of the film, and $c(X)$ and $c(O)$ the concentrations of active species at the two surfaces of the film. It can be seen that in the steady states where $c(X)$ and $c(O)$ are constant, parabolic growth will be observed, assuming ΔV to be constant. Since ΔV depends on the electronic conductivity and the electrochemical cell potential $E°$, this constancy is obtained here at least in the early stages of the reaction (15).

Where an additional term appears in the rate law, the surface concentrations $c(X)$ must be examined for their role in rate control. Nakayama and Collins have applied an adsorption-desorption equilibrium to the system, and derive the rate law

$$\tfrac{1}{2}\left(\frac{k_aP}{k'} + \frac{k_d}{k'}\right)(X_r^2 - X_o^2) + (X_r - X_o) = k_aC_oPt$$

where the k's refer to the process of adsorption, desorption, and diffusion, respectively, with P the partial pressure of the oxidizing species, and C_o the concentration of active sites on the adsorbing surface.

It is seen that the linear rate constant here appears as

$$k_l = k_aC_oP$$

corresponding to adsorption rate control of the growth process at small values of X.

In this study of titanium oxidation no dependence of either initial or parabolic rates on water vapor partial pressure was observed in any of the runs. If, as Hollabaugh (16) has suggested, the rutile surface is saturated with chemisorbed water molecules at all except "trace" ambient pressures, this zero order dependence suggests that both the processes involved in the rate law are supplied with a surplus of oxidant species, even at very low pressures. The adsorption rate control described by Nakayama and Collins for silicon oxidation would be replaced here by some surface process control, the nature of which is not immediately apparent from the data. It could be the surface dissociation of adsorbed water to produce OH^- ions, or perhaps the freeing of Ti^{+4} ions from the substrate metal.

The fact, however, that the initial rates, although not subject to any systematic effect of ambient pressures, did show relatively large variability from sample to sample, indicates great sensitivity of the initial process to the state of the individual surface. These effects could be caused by surface contamination, surface discontinuities, exposure of particular crystal faces, etc. The lower initial rates shown by single crystal samples confirm the role of the surface form in the initial process.

The parabolic rate constants showed no effect of either changing oxidant pressure or crystal form, mono- and poly-crystals showing identical parabolic rate constants and activation energies. The diffusion-controlled process, then, which is involved in the parabolic rate constants, is not affected by surface form or structure, and we may say that the bulk properties of the oxide films are uniform and not dependent upon the surface details, at least for reasonably smooth, polished surfaces. When nonspecular surfaces are involved, however, this may not necessarily hold, and this fact may be responsible for the great variation shown in the literature values of activation energies for these processes.

The lack of response of the reaction system to the addition of oxygen to the wet ambients is consistent with the picture of a water-saturated outer surface of rutile. It also may suggest that the reaction of Ti with water vapor is faster than that with oxygen, which is consistent with Kučírek's (6) suggestion that this may account for his finding that Ti reacts more quickly, under otherwise identical conditions, with air than with dry oxygen.

Acknowledgment

This paper is taken from the dissertation of one of the authors (Fradelle G. Fuhrman), submitted in partial fulfillment of the requirements for the Ph.D. (chemistry) to the Faculty of the Polytechnic Institute of Brooklyn (currently known as the Polytechnic Institute of New York) 1973.

Manuscript submitted April 9, 1976; revised manuscript received Feb. 25, 1977.

Any discussion of this paper will appear in a Discussion Section to be published in the June 1978 JOURNAL. All discussions for the June 1978 Discussion Section should be submitted by Feb. 1, 1978.

REFERENCES

1. E. A. Gulbransen and K. F. Andrew, *Metall. Trans.*, **185**, 741 (1949).
2. R. C. Menard, *J. Opt. Soc. Am.*, **52**, 427 (1952).
3. A. E. Jenkins, *J. Inst. Met.*, **82**, 213 (1953-1954).
4. L. S. Richardson and N. J. Grant, *Trans. Am. Inst. Min. Met. Eng.*, **200**, 69 (1954).
5. T. Hurlen, *J. Inst. Met.*, **89**, 128 (1960-1961).
6. J. Kučírek, *Czech J. Phys.*, **23**, 1382 (1973).
7. M. H. Davies and C. E. Birchenall, *Trans. Am. Inst. Min. Met. Eng.*, **191**, 877 (1951).
8. V. I. Tikhomirov and V. I. Dyach'kov, *Vestn. Leningr. Univ. Fiz. Khim.*, **22**, 155 (1966); *Zh. Prikl. Khim. (Leningrad)*, **40**, 2405 (1967).
9. V. I. Dyach'kov and V. I. Tikhomirov, *Vestn. Leningr. Univ. Fiz. Khim.*, **24**, 158 (1968).
10. U. Evans, *Trans. Electrochem. Soc.*, **48**, 247 (1924).
11. T. Nakayama and F. C. Collins, *This Journal*, **13**, 706 (1966).
12. L. C. Chen, Thesis (Ph.D.) Polytechnic Institute of Brooklyn (1971).
13. A. B. Winterbottom, *Trans. Faraday Soc.*, **42**, 487 (1946).
14. A. Charlesby and J. J. Polling, *Proc. R. Soc. London, Ser. A*, **227**, 434 (1955).
15. F. C. Collins and T. Nakayama, *This Journal*, **114**, 167 (1967).
16. C. M. Hollabaugh, Thesis (Ph.D.) Lehigh University (1959).

Brief Communication

Three-Dimensional Distribution of Twins in Epitaxial Silicon on Sapphire

J. Trilhe

Nuclear Studies Center of Grenoble, 38041 Grenoble Cedex, France

Silicon layers in the 0.5μ thickness range are quite interesting for planox technology. We report here transmission electron microscopy observations of 0.4μ epitaxial layers deposited on a sapphire substrate. The silicon, the interface, and part of the sapphire are thin enough to be transparent to 200 keV electrons. Milling of the extra sapphire has been performed from one side, with an argon ion gun at grazing incidence.

Figure 1 is the diffraction diagram of the sample. The interface has been imaged (Fig. 2) in a dark field on a (110) plane of sapphire (spot I). One family of twins is evident (Fig. 3) in a dark field image using twin spot (II) of the same area of the crystal. The edge of the beveled sample is on the left-hand side.

Figure 4 is a schematic of the sample assuming a uniform bevel. The position of the interface is given by the dark field of the sapphire. Twins can be tridimensionally represented, having one (110) direction with no deformation and assuming that twins lie in (111) planes. This classical technique for twin observation in epitaxial silicon layers is shown to be as powerful for this application as the cross-section technique which has been developed elsewhere (1). But it is easier and allows the study of numerous samples.

In the figures of this work we showed a high density of little twins in the first 500Å of the silicon deposit; these twins disappear in the left side of the picture when the interfacial silicon has been removed by ion milling. There is also a random distribution of twins, less numerous, which get through the silicon deposit.

It is interesting to note that these first 500Å in thickness of the silicon deposit are of the same order of magnitude as the thickness needed to reach coalescence of a silicon deposit on a sapphire substrate in the usual conditions for chemical vapor deposition. A possible explanation for twin formation is the outgassing of impurity from the substrate. When the substrate is completely covered, the outgassing comes only from the back side, so the twin density decreases considerably.

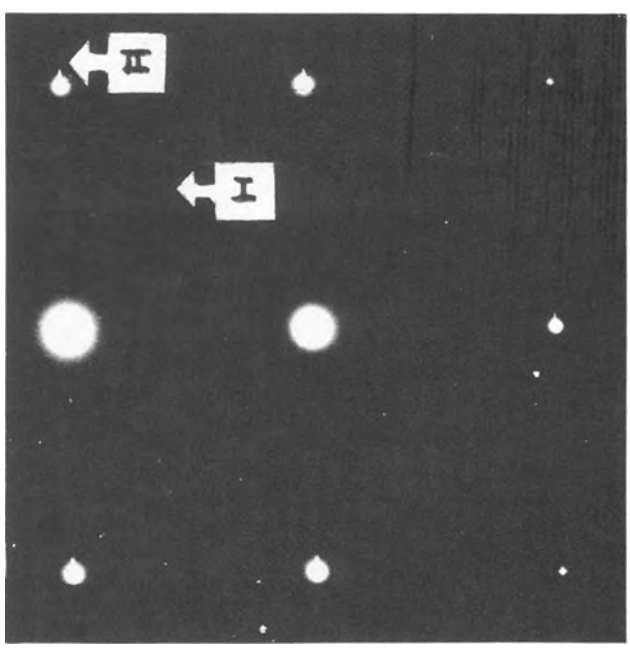


Fig. 1. Diffraction diagram

Key words: electron microscopy, twin, silicon on sapphire.

Acknowledgment

We acknowledge M. Dupuy, who performed the transmission electron microscopy observations.

Manuscript submitted Jan. 26, 1977; revised manuscript received March 30, 1977. This was Paper 176



Fig. 2. Dark field on sapphire, spot I



Fig. 3. Dark field on a twin, spot II

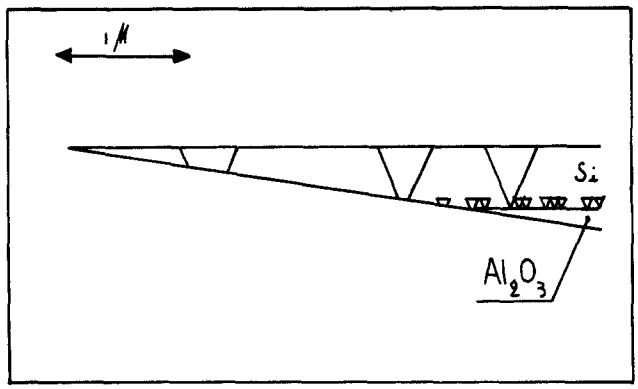


Fig. 4. Schematic cross section of the twin distribution in the silicon.

presented at the Las Vegas, Nevada, Meeting of the Society, Oct. 17-22, 1976.

Any discussion of this paper will appear in a Discussion Section to be published in the June 1978 JOURNAL. All discussions for the June 1978 Discussion Section should be submitted by Feb. 1, 1978.

Publication costs of this article were assisted by the Center of Nuclear Studies of Grenoble.

REFERENCE

1. W. E. Ham, Paper 172 presented at The Electrochemical Society Meeting Las Vegas, Nevada, Oct. 17-22, 1976.

JOURNAL OF THE ELECTROCHEMICAL SOCIETY

ACCELERATED BRIEF COMMUNICATIONS

AUGUST 1977

Galvanic Corrosion of Al Alloys Monitored by Acoustic Emission

F. Mansfeld* and P. J. Stocker

Science Center, Rockwell International, Thousand Oaks, California 91360

Rettig and Felsen (1) have recently shown that acoustic emission has some promise in monitoring corrosion reactions of unstressed, freely corroding materials and galvanic couples. The data presented were typically taken over a 10 to 30 min. period with emphasis on Al alloys. We have started a program to evaluate the acoustic emission method in more detail, determine the source of the signal monitored and obtain correlations between electrochemical and acoustic data.

The results presented here involve the Al alloys 1100-0 and Al 2024-T851 coupled to Cu (OFHC), 4130 steel, Cd (99.97%) and Zn (99.9%) in aerated 3.5% NaCl. The corrosion behavior of the galvanic couples has been studied in detail earlier (2). The acoustic emission from the sample is detected by a piezoelectric transducer (PZT) which has a peak frequency response in the 150-200 KHz range. Details of the method of counting the individual sound bursts will be described elsewhere (3). The Al alloys were deoxidized in AMCHEM-deoxidizer for 10 min. at 21°C and then immersed in deionized water for one hour. The sample was then immersed in 3.5% NaCl for one hour and the accumulated counts and the corrosion potential ϕ_{corr} monitored on a two-pen strip chart recorder. After one hour the Al alloy was coupled to one of the dissimilar metals and the accumulated counts, the galvanic current measured as described earlier (2) and the potential of the couple ϕ_g monitored for 30 min., after which time the sample was decoupled and acoustic emission and ϕ_{corr} were monitored for an additional 30 min.

Fig. 1 and Table I show the results obtained for Al 2024. The corrosion rates for uncoupled (r_o) and coupled (r_A) Al alloys are from Mansfeld et al (2) for 24 hour tests. The reproducibility of the acoustic emission data was quite satisfactory for the uncoupled alloy with an average rate of 41 ± 5 counts per min. When the Al alloy was coupled to 4130 steel or Cu a sharp rise occurred. The count rate decreased somewhat after about 5 min. and became constant for the rest of the 30 min. When the dissimilar metal was disconnected, the acoustic emission rate increased for a short time and then decreased again to low values. The data in Table I are average values for the 60 min. or 30 min. time periods. For Al 2024 coupled to Cd acoustic emission was very much reduced with a rate of 0.5 counts/min. When contact to Cd was disconnected, the count rate first increased and then decreased again. This phenomenon was much more pronounced when Al 2024 was coupled to zinc. In this case the count rate decreased somewhat when the zinc was disconnected. The potential of the Al alloy became more positive (Fig. 2) and when it reached a maximum of about -0.61V vs SCE the count rate increased sharply. Presumably, at this potential pitting occurs again. About 10 min. after decoupling the count rate decreased again.

Table I. Acoustic Emission from Al Alloys in 3.5% NaCl, 21 ± 1°C

	Uncoupled 60 min.		Coupled 30 min.		Uncoupled 30 min.
	Counts/ Min.	r_o (mdd)	Counts/ Min	r_A (mdd)	Counts/ Min.
Al 2024/Cu	41	5.25	497	68.4	85
Al 2024/Steel	50	5.25	730	43.4	117
Al 2024/Cd	32	5.25	0.5	11.2	97
Al 2024/Zn	42	5.25	50	24.6	385
Al 1100/Cu	1.5	0.24	5200	40.6	1.6
Al 1100/Steel	3.0	0.24	4550	30.4	1.3
Al 1100/Cd	1.1	0.24	1.0	1.5	0.9
Al 1100/Zn	5.0	0.24	3.3	8.8	12

Note: Corrosion rate data r_o, r_A are from Ref. 2.

Al 1100, which is much more corrosion resistant than Al 2024 in 3.5% NaCl (2), produces only very few counts when freely corroding (3 ± 2 counts/min., Table I). When

*Electrochemical Society Active Member

coupled to Cu or steel the count rate increases tremendously (Table I) reflecting the pronounced increase in dissolution rates due to coupling reported earlier. When coupled to Cd or Zn, on the other hand, the count rate did not increase. When Cu or steel are disconnected from Al 1100, the count rate decreases almost immediately returning to the value found initially for the freely corroding Al 1100.

The origin of the acoustic emission is not clear yet. Our observations on steel and stainless steel in acid media suggest, however, that hydrogen gas generated within the pits in the Al alloy is contributing significantly to the acoustic emission. The present preliminary results suggest that acoustic emission can become a valuable tool for corrosion research and monitoring of corrosion reactions. A comparison of the acoustic emission and corrosion rate data in Table I shows that the acoustic measurements reflect accurately the effect of the dissimilar metal and the different corrosion behavior of the two Al alloys. The results of Fig. 2 seem to give information about the pitting process which could not be followed with electrochemical techniques in the same manner.

ACKNOWLEDGEMENT

The authors acknowledge helpful discusions with Lloyd Graham and Dr. Otto Buck. The project was funded by the Science Center IR&D project "Corrosion and Electrodeposition".

REFERENCES

1. T. W. Rettig and M. J. Felsen, Corrosion, 32, 121 (1976).
2. F. Mansfeld, D. H. Hengstenberg and J. V. Kenkel, Corrosion, 30, 343 (1974).
3. F. Mansfeld and P. J. Stocker, "Corrosion Monitoring with Acoustic Emission", to be submitted to Corrosion Science.

Key words: galvanic corrosion, Al alloys, localized corrosion, pitting, acoustic emission.

Manuscript received May 11, 1977.

Publication costs of this article were assisted by Rockwell International.

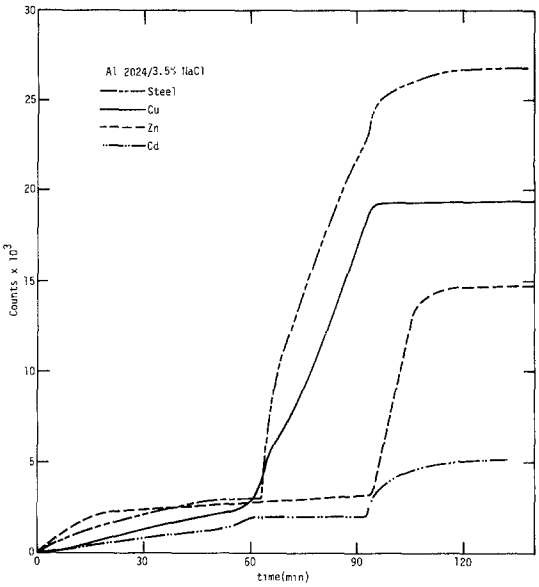


Fig. 1. Acoustic emission from Al 2024 in 3.5% NaCl. One hour uncoupled, 30 min. coupled, 30 min. uncoupled.

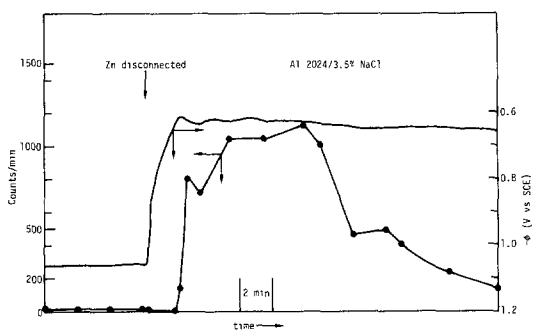


Fig. 2. Count rate and potential of Al 2024 coupled to Zn and uncoupled in 3.5% NaCl.

Specular Reflectance of Mirrors

R. W. Revie*

Department of Engineering Physics, Research School of Physical Sciences, The Australian National University, Canberra, A.C.T. 2600, Australia

This note describes an experimental method and some preliminary results thereby obtained in an investigation of mirror materials for a solar power station that will employ a distributed array of concentrators (1,2). The mirrors ultimately used in this application must specularly reflect a high percentage of the incident solar radiation and either the reflectance must not irreversibly deteriorate excessively over the lifetime of the power station or the mirror surface must be replaceable.

The apparatus used to evaluate specular reflectance is shown in Figure 1. The light used in the present studies, obtained from a helium-neon laser, has a wavelength of 6328 Å.** Using this apparatus, the scattering of light about the angle of reflection may be evaluated, and the angle of incidence may also be varied. The photomultiplier light detector, with a 0.3 mm slit, has an acceptance angle of 0.55 milliradians. For calibration of the apparatus, the photomultiplier arm is rotated to align with the laser beam directly.

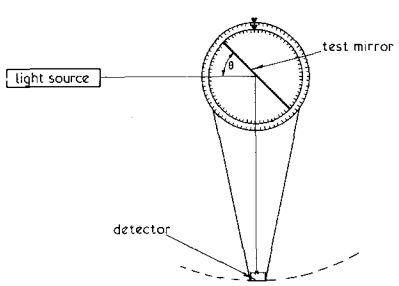


Figure 1. Apparatus for studying specular reflectance and light scattering.

Figure 2 illustrates the data obtained using no mirror (calibration position)

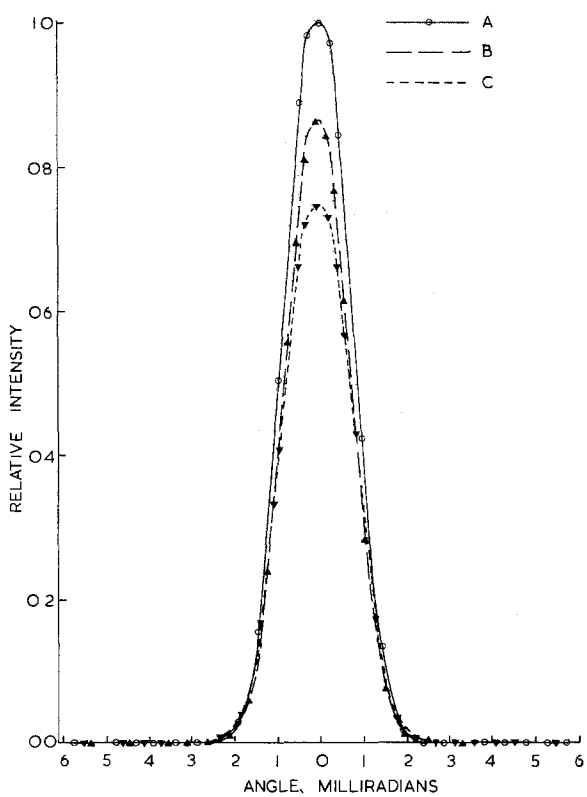


Figure 2. Intensity vs. Angle.
A. No Mirror - Calibration Position
B. Evaporated Aluminium - Quartz Overcoat, Not Weathered
C. As in B - Weathered 31 Days

*Electrochemical Society Active Member
**Additional experiments using monochromatic light at wavelengths over the solar spectrum are in progress.

Key words: solar energy, reflectance, specularity, mirror.

and using a front-surface mirror (45° incident angle) of evaporated aluminium (600 Å thick) with a quartz overcoat (1/20 wave thick).* The degradation of reflectance after natural weathering at an inclined angle of 10°, facing north, in the Canberra, Australia environment for 31 summer days is evident - the specular reflectance (measured by the peak intensity) decreases from 86% to 75%.

To determine the effect of cleaning the surface on increasing the specular reflectance, cleaning was attempted by directing a jet of distilled water and also of a 3% potassium oleate solution from a squeeze-bottle. The effects were negligible. On the other hand, scrubbing with cotton wool soaked in the soap solution, followed by rinsing with distilled water, caused the specular reflectance to increase to 85%. These experiments tend to indicate that cleaning methods - to be effective - will require mechanical action, which may be obtained either by liquid spray operating at high pressure or by wipers similar to those used in window cleaning procedures.

REFERENCES

(1) P.O.Carden, Solar Energy, in press.
(2) P.O.Carden, A large Scale Solar Plant Based on the Dissociation and Synthesis of Ammonia, Energy Conversion Tech. Rep. No.8, Research School of Physical Sciences, The Australian National University, Canberra, Australia, November, (1974).

Manuscript received May 2, 1977.

*Obtained from Libbey-Owens-Ford Company, Toledo, Ohio.

JOURNAL OF THE ELECTROCHEMICAL SOCIETY

REVIEWS AND NEWS

MAY 1977

Reports on Electrochemical Society Summer Fellowship Awards

During the summer of 1976 the following graduate students received $1000 each, representing the three Summer Fellowship Awards of The Electrochemical Society.

Mr. Robert J. Nowak, University of Cincinnati, Cincinnati, Ohio, was awarded the Edward Weston Fellowship.

Mr. John S. Hammond, Purdue University, West Lafayette, Indiana, was designated as the recipient of the Colin Garfield Fink Fellowship.

Mr. Donald L. Feke, Case Western Reserve University, Cleveland, Ohio, received the Joseph W. Richards Fellowship.

The Summer Fellowship Awards are made "without regard to sex, citizenship, race, or financial need, to a fellow or teaching assistant pursuing work between the degrees of B.S. and Ph.D. on a subject in a field of interest to The Electrochemical Society. They are intended to cover a period during which the recipient has no financial support for the continuance of his work.

The Edward Weston Summer Fellowship Report

Mr. Nowak's report is given below.

Anisotropic Highly Conductive Inorganic Polymer as Electrode Material

Recently the characteristics of fully oriented epitaxially grown thin films and crystals of polymeric sulfur nitride [polythiazyl or $(SN)_x$] have been reported (1, 2). An ordered array of parallel fibers makes up the $(SN)_x$ crystal whose d-c electrical conductivity is highly anisotropic with the highest conductivity, about 3.7×10^3 $(\Omega\text{-cm})^{-1}$ at room temperature, along the chain of the polymer (3). The conductivity perpendicular to the chain axis is somewhat less. Thus, the material is classified as a metal.

Studies of the electrode behavior of crystals of $(SN)_x$ in aqueous media were undertaken with the ultimate goal of producing specific surface-modified electrodes. Linear sweep cyclic voltammetry and chronoamperometry were employed for evaluation of $(SN)_x$ with respect to the criteria presented by Mueller and Adams (4).

As $(SN)_x$ is chemically and electrically anisotropic, studies were performed with either parallel (sides of fibers exposed to the solution) or perpendicular (ends of fiber bundles exposed) electrodes. The electrochemical behavior of these two surfaces was found to be quite different in studies using different supporting electrolytes with and without electroactive species present.

Without electroactive species present there was evidence of irreversibly coupled surface redox processes on both parallel and perpendicular $(SN)_x$. Changing the cation from cesium to lithium had a dramatic effect on the anodic and cathodic breakdown limits and surface redox current magnitudes for parallel but not perpendicular $(SN)_x$. Lithium extends the cathodic breakdown current by *ca.* 300 mV and eliminates the hysteresis observed on the reverse (positive) scan for the former.

As the geometric features of the crystals employed for electrochemical studies were quite varied, the ferri/ferrocyanide couple was used in chronoamperometric experiments to determine areas. This system behaved nearly reversibly on both parallel and perpendicular $(SN)_x$ when compared to similar studies at platinum-disk electrodes. The data adhered well to the theoretical equations for the methods employed.

Electrodeposition of lead was also studied on both parallel and perpendicular $(SN)_x$ (5). Voltammograms obtained with perpendicular electrodes appeared much like those obtained on platinum-disk electrodes except they lacked underpotential peaks often seen on the latter. Parallel electrodes yielded more irreversible voltammograms with a marked hysteresis on the reverse (positive) scan. This hysteresis can be totally eliminated by brief pretreatment of the $(SN)_x$ electrode with mercuric ion. These results along with the supporting electrolyte studies seem to indicate that cations with high positive charge densities interact more strongly with parallel than perpendicular $(SN)_x$.

Currently, several irreversible redox couples are being used as probes to investigate the structure of the electrical double layer at $(SN)_x$ electrodes. The results of these studies will be submitted to *This Journal* and will be presented at the 173rd National Meeting of the American Chemical Society in New Orleans.

Acknowledgments

The author wishes to thank Dr. Harry B. Mark, Jr., Dr. Alan G. MacDiarmid, and Dr. Wlodzimierz Kutner for their valuable assistance. and The Electrochemical Society for its financial support through the Edward Weston Fellowship.

REFERENCES

1. C. M. Mikulski, P. J. Russo, M. S. Saran, A. G. MacDiarmid, A. F. Garito, and A. J. Heeger, *J. Am. Chem. Soc.*, **97**, 6358 (1975).
2. E. J. Louis, A. G. MacDiarmid, A. F. Garito, and A. J. Heeger, *J. Chem. Soc., Chem. Commun.*, **12**, 426 (1976).
3. A. G. MacDiarmid, C. M. Mikulski, M. S. Saran, P. J. Russo, M. J. Cohen, A. A. Bright, A. F. Garito, and A. J. Heeger, in "Inorganic Compounds with Unusual Properties," R. Bruce King, Editor, American Chemical Society, Washington, D.C. (1974).
4. T. R. Mueller and R. N. Adams, *Anal. Chim. Acta*, **23**, 467 (1960).

5. R. J. Nowak, H. B. Mark, Jr., A. G. MacDiarmid, and D. Weber, *J. Chem. Soc., Chem. Commun.*, In press; Presented at the 172nd National Meeting of the American Chemical Society, San Francisco, California, August 29-September 3, 1976.

The Colin Garfield Fink Summer Fellowship Report

Mr. Hammond's report is given below.

ESCA Analysis of Electrochemical Underpotential Deposition

X-ray photoelectron spectroscopy (XPS or ESCA) has recently become a valuable spectroscopic tool for the investigation of electrode surface states (1). The surface specificity of XPS analysis (10-50Å), coupled with the ability to examine the electronic environment of surface atoms through the use of binding energy chemical shifts, permits elemental and molecular analysis of electrochemically prepared surface states. The initiation of electrochemical metal atom deposition on foreign solid metal electrodes produces electrode surface states which have long held the curiosity of electrochemists. In particular, the deposition of metal ions at potentials more positive than that predicted by bulk Nernstian thermodynamics, *i.e.*, underpotential deposition (UPD), has not been fully elucidated by classical electrochemical techniques. The objective of this study was, therefore, to apply XPS to the study of underpotential deposition. The results of this study (*i*) provide valuable spectroscopic information on the nature of the metal adatom-metal substrate bond involved in underpotential deposition, (*ii*) demonstrate the use of unique electrode samples for the testing of the present theories of XPS binding energy chemical shifts, and (*iii*) broaden the scope of XPS analysis of electrode surface states in general.

The underpotential deposition of copper and silver on platinum electrodes was investigated. The clean Pt electrode surfaces were first characterized by cyclic voltammetry. Silver or copper underpotential metal films on the Pt electrodes were then prepared under potentiostatic control. The electrolyte was then removed under potentiostatic control and XPS analysis was performed on the electrode surface. To complement the electrochemical deposition studies, thin metal films on copper and silver were vapor deposited on clean platinum foils in the spectrometer. Details of electrode construction, sample preparation, and XPS analysis have been recently published (2-4).

The results of the XPS analysis have conclusively demonstrated that the silver and copper thin films produced during underpotential electrochemical deposition in H_2SO_4 media are not found as metal oxides or chemisorbed copper sulfate or silver sulfate complexes. Rather, the XPS results indicate that in the absence of an applied electrochemical potential, binding energy shifts are observed in the core photoelectron spectra which are indicative of the copper and silver UPD adatom surface states. The XPS binding energy shift is insensitive to the parameters responsible for the multiple UPD anodic stripping peaks and remains constant with coverage, up to one monolayer.

The *in situ* vapor deposition does, however, produce geometric effects in the XPS binding energy shifts. At very low average coverages (less than 20% of one monolayer thickness), the vapor deposition XPS binding energy shift is equivalent to the electrochemical deposition binding energy shifts. Higher coverages produce XPS results intermediate between UPD and bulk metal deposits. The results, therefore, indicate the metallic nature of the UPD deposits and the capabilities of electrochemical deposition for producing unique samples for surface science investigation.

The interpretation of the observed binding energy shifts is presently not without ambiguity. The binding energy shifts in XPS core level spectra generally correlate with the charge density of the observed atom. However, to provide an interpretation of changes in charge density, the core level binding energy must be referenced to the vacuum level. The XPS experimental binding energies are referenced to the Fermi level, with an unknown work function relating the Fermi level and vacuum level.

One possible approach for dealing with this problem is through the use of the Auger parameter. The kinetic energy for a *kll* Auger transition can be approximated

$$E^V(kll) = E_B^V(k) - 2E_B^V(l) - F + 2E_R + R_e \quad [1]$$

where $E^V(kll)$ is the vacuum level referenced kinetic energy of the *kll* transition, $E_B^V(k)$ and $E_B^V(l)$ are the vacuum level referenced one electron binding energies of the k and l orbitals, F is the hole-hole interaction term due to the double ionization of the final state, $2E_R$ is the intra-atomic "static" relaxation contribution to the second $E_R^V(l)$ binding energy due to the previous creation of a l hole state, and R_e is the extra-atomic relaxation. The binding energy equivalent to the $E^V(kll)$ kinetic energy is $E_B^V(kll)$ where

$$E_B^V(kll) = h\nu - E^V(kll) \quad [2]$$

and $h\nu$ is the x-ray photon energy.

The Auger parameter α is then defined as

$$\alpha = E_B^V(k) - E_B^V(kll) \quad [3a]$$

$$= E_B^F(k) - E_B^F(kll) \quad [3b]$$

$$= 2E_B^F(k) - 2E_B^F(l) - F + 2E_R + R_e - h\nu \quad [3c]$$

The Auger parameter is in fact independent of the sample work function and either E_B^F or E_B^V values can be used. The difference in the Auger parameter $\Delta\alpha$ can then be defined as

$$\Delta\alpha = \alpha_{metal} - \alpha_{UPD} \quad [4]$$

where α_{metal} is the Auger parameter for the bulk metal of the UPD species and α_{UPD} is the Auger parameter for the UPD adsorbate species. For the Ag UPD system, $\Delta\alpha$ is +0.65 eV and for the Cu UPD system $\Delta\alpha$ is +0.95 eV.

These $\Delta\alpha$ terms are not inconsistent with an increase in the cohesive energy of the UPD adatom-metal substrate bonds relative to the respective bulk copper or silver cohesive energies (4). To provide an unambiguous interpretation of Eq. [3c], the $E_B^F(l)$ terms should be spectroscopically measured. This is not possible at present. In addition, the theoretical understanding of extra-atomic relaxation is still in its infancy. Further experimentation and theoretical advances are needed to more fully elucidate the underpotential deposition phenomena.

REFERENCES

1. J. S. Hammond and N. Winograd, in "Comprehensive Treatise on Electrochemistry," Vol. 5, J. O'M. Bockris, B. E. Conway, and E. Yeager, Editors, chap 5, Plenum Press, New York (in press).
2. J. S. Hammond and N. Winograd, *J. Electroanal. Chem.*, In press.
3. J. S. Hammond and N. Winograd, *ibid.*, In press.
4. J. S. Hammond and N. Winograd, Submitted to *ibid.*

The Joseph W. Richards Fellowship

Mr. Feke's report is given below.

Electrochemical Disposal of H_2S

During the period of the fellowship, significant progress was made in determining the feasibility of electrochemically disposing hydrogen sulfide. The purpose of the research was to determine whether H_2S could be made to decompose by electrolysis to elemental sulfur and hydrogen. A process utilizing this technology could have several applications.

5. R. J. Nowak, H. B. Mark, Jr., A. G. MacDiarmid, and D. Weber, *J. Chem. Soc., Chem. Commun.*, In press; Presented at the 172nd National Meeting of the American Chemical Society, San Francisco, California, August 29-September 3, 1976.

The Colin Garfield Fink Summer Fellowship Report

Mr. Hammond's report is given below.

ESCA Analysis of Electrochemical Underpotential Deposition

X-ray photoelectron spectroscopy (XPS or ESCA) has recently become a valuable spectroscopic tool for the investigation of electrode surface states (1). The surface specificity of XPS analysis (10-50Å), coupled with the ability to examine the electronic environment of surface atoms through the use of binding energy chemical shifts, permits elemental and molecular analysis of electrochemically prepared surface states. The initiation of electrochemical metal atom deposition on foreign solid metal electrodes produces electrode surface states which have long held the curiosity of electrochemists. In particular, the deposition of metal ions at potentials more positive than that predicted by bulk Nernstian thermodynamics, *i.e.*, underpotential deposition (UPD), has not been fully elucidated by classical electrochemical techniques. The objective of this study was, therefore, to apply XPS to the study of underpotential deposition. The results of this study (*i*) provide valuable spectroscopic information on the nature of the metal adatom-metal substrate bond involved in underpotential deposition, (*ii*) demonstrate the use of unique electrode samples for the testing of the present theories of XPS binding energy chemical shifts, and (*iii*) broaden the scope of XPS analysis of electrode surface states in general.

The underpotential deposition of copper and silver on platinum electrodes was investigated. The clean Pt electrode surfaces were first characterized by cyclic voltammetry. Silver or copper underpotential metal films on the Pt electrodes were then prepared under potentiostatic control. The electrolyte was then removed under potentiostatic control and XPS analysis was performed on the electrode surface. To complement the electrochemical deposition studies, thin metal films on copper and silver were vapor deposited on clean platinum foils in the spectrometer. Details of electrode construction, sample preparation, and XPS analysis have been recently published (2-4).

The results of the XPS analysis have conclusively demonstrated that the silver and copper thin films produced during underpotential electrochemical deposition in H_2SO_4 media are not found as metal oxides or chemisorbed copper sulfate or silver sulfate complexes. Rather, the XPS results indicate that in the absence of an applied electrochemical potential, binding energy shifts are observed in the core photoelectron spectra which are indicative of the copper and silver UPD adatom surface states. The XPS binding energy shift is insensitive to the parameters responsible for the multiple UPD anodic stripping peaks and remains constant with coverage, up to one monolayer.

The *in situ* vapor deposition does, however, produce geometric effects in the XPS binding energy shifts. At very low average coverages (less than 20% of one monolayer thickness), the vapor deposition XPS binding energy shift is equivalent to the electrochemical deposition binding energy shifts. Higher coverages produce XPS results intermediate between UPD and bulk metal deposits. The results, therefore, indicate the metallic nature of the UPD deposits and the capabilities of electrochemical deposition for producing unique samples for surface science investigation.

The interpretation of the observed binding energy shifts is presently not without ambiguity. The binding energy shifts in XPS core level spectra generally correlate with the charge density of the observed atom. However, to provide an interpretation of changes in charge density, the core level binding energy must be referenced to the vacuum level. The XPS experimental binding energies are referenced to the Fermi level, with an unknown work function relating the Fermi level and vacuum level.

One possible approach for dealing with this problem is through the use of the Auger parameter. The kinetic energy for a *kll* Auger transition can be approximated

$$E^V(kll) = E_B^V(k) - 2E_B^V(l) - F + 2E_R + R_e \quad [1]$$

where $E^V(kll)$ is the vacuum level referenced kinetic energy of the *kll* transition, $E_B^V(k)$ and $E_B^V(l)$ are the vacuum level referenced one electron binding energies of the k and l orbitals, F is the hole-hole interaction term due to the double ionization of the final state, $2E_R$ is the intra-atomic "static" relaxation contribution to the second $E_R^V(l)$ binding energy due to the previous creation of a l hole state, and R_e is the extra-atomic relaxation. The binding energy equivalent to the $E^V(kll)$ kinetic energy is $E_B^V(kll)$ where

$$E_B^V(kll) = h\nu - E^V(kll) \quad [2]$$

and $h\nu$ is the x-ray photon energy.

The Auger parameter α is then defined as

$$\alpha = E_B^V(k) - E_B^V(kll) \quad [3a]$$

$$= E_B^F(k) - E_B^F(kll) \quad [3b]$$

$$= 2E_B^F(k) - 2E_B^F(l) - F + 2E_R + R_e - h\nu \quad [3c]$$

The Auger parameter is in fact independent of the sample work function and either E_B^F or E_B^V values can be used. The difference in the Auger parameter $\Delta\alpha$ can then be defined as

$$\Delta\alpha = \alpha_{metal} - \alpha_{UPD} \quad [4]$$

where α_{metal} is the Auger parameter for the bulk metal of the UPD species and α_{UPD} is the Auger parameter for the UPD adsorbate species. For the Ag UPD system, $\Delta\alpha$ is +0.65 eV and for the Cu UPD system $\Delta\alpha$ is +0.95 eV.

These $\Delta\alpha$ terms are not inconsistent with an increase in the cohesive energy of the UPD adatom-metal substrate bonds relative to the respective bulk copper or silver cohesive energies (4). To provide an unambiguous interpretation of Eq. [3c], the $E_B^F(l)$ terms should be spectroscopically measured. This is not possible at present. In addition, the theoretical understanding of extra-atomic relaxation is still in its infancy. Further experimentation and theoretical advances are needed to more fully elucidate the underpotential deposition phenomena.

REFERENCES

1. J. S. Hammond and N. Winograd, in "Comprehensive Treatise on Electrochemistry," Vol. 5, J. O'M. Bockris, B. E. Conway, and E. Yeager, Editors, chap 5, Plenum Press, New York (in press).
2. J. S. Hammond and N. Winograd, *J. Electroanal. Chem.*, In press.
3. J. S. Hammond and N. Winograd, *ibid.*, In press.
4. J. S. Hammond and N. Winograd, Submitted to *ibid.*

The Joseph W. Richards Fellowship

Mr. Feke's report is given below.

Electrochemical Disposal of H_2S

During the period of the fellowship, significant progress was made in determining the feasibility of electrochemically disposing hydrogen sulfide. The purpose of the research was to determine whether H_2S could be made to decompose by electrolysis to elemental sulfur and hydrogen. A process utilizing this technology could have several applications.

Specifically, work during the fellowship term included the design and construction of an electrolysis cell. This cell withstands pressures up to 2000 psi and enables the experiments to be performed on the condensed phase of H_2S at temperatures up to the critical temperature of 100°C.

Products of the electrolysis reactions were identified. The anodic product was elemental sulfur, which precipitates from solution as crystalline α-sulfur (rhombohedral) when the H_2S is evaporated. The cathodic reaction product was gaseous elemental hydrogen. In these experiments pyridine was used as the electrolyte.

Transient electrodic measurements were taken to determine cell time constants as well as voltage drops across the double layer at the electrodes. Preliminary analysis of these measurements indicates that the total overvoltages depend strongly on electrode material. Of the electrode materials tested to date, nickel appears to have the lowest overvoltages.

Present research is concerned with the measurement of the faradaic current efficiency. Work during the summer also led to the design of a new cell configuration that reduces solution resistance and allows for better product separation. Further experiments will be made using this improved cell design.

Progress in Organic Electrochemistry–1952-1977

Manuel M. Baizer*

Monsanto Company, Corporate Research Department, St. Louis, Missouri 63166

The 1952 review and overview of progress in this field (1), presented when The Electrochemical Society, Inc. was celebrating its fiftieth anniversary, surveyed a fifty-year period. The present article examines progress in the last quarter century. If the number of review papers published in this last decade alone (2-24), repetitious though some of them may be, is any indication of interest or need or activity, the next survey should encompass no more than an eighth century.

The newcomer entering the field today may not be aware of the gap that existed in the presentation of the subject as a whole between 1956 (67) or 1958 (35) and 1969 (34), for in the last few years a number of books both comprehensive and on selected pertinent topics have been published (25-44). In-depth reviews of individual aspects have abounded (47-66). Stimulating new books on general electrochemistry have appeared (39-44) and several series volumes have become established (45-47). Electrochemical engineering has reawakened (69-72). Awareness of organic electrochemistry by undergraduate and graduate students of organic chemistry is also being sponsored by detailed descriptions of experiments (73-74) and by peripatetic "short courses" (75-76). The practitioner of organic electrochemistry has had, in addition to societies within his own country, an abundance of forums at which to present, discuss, and learn of new work (77-97). New research groups in organic electrochemistry have been installed in industry and university. Although the extent of introduction of courses in the subject into the regular curriculum (at least in terms of an option) is still spotty, particularly in the U.S., electrochemical engineering is well established in at least the universities of California (Berkeley), Michigan, Illinois, Newcastle upon Tyne, and the E.T.H. in Zürich. "Working parties" in France and the U.K., the second successive one in the latter country, have recommended programs of research and education to their respective national research councils.

Key Developments

This tremendous upsurge in activity in the last twenty-five years, which has brought with it advances on many fronts, is truly impressive. What influences have brought this about? What components does ghost chromatographic analysis of the Zeitgeist reveal? Organic electrochemists selected at random might draw up similar lists of components but each would probably consider the weighted contributions of his own subdiscipline to be high. (The very existence of so many subdisciplines attests to the fertility of the field.) The following citation listing attempts to exclude conscious bias; no ranking is to be inferred from the order of discussion.

1. *Advances in the science, art, and theory of organic chemistry.*—Particularly germane have been the developing areas of ion radical chemistry, homogeneous electron-transfer reactions, regio- and stereocontrolled synthesis, general acid-base reactions, and derivative work in polymerization (*e.g.*, "living" anionic systems) and homogeneous catalysis by transition metal complexes. Many of these developments have had their counterparts and perhaps their predecessors in organic electrochemistry (*e.g.*, the generation, detection, and reactions of ion radicals).

2. *Instrumental methods.*—The invention, development, and universal acceptance of a host of instrumental methods, particularly chromatographic and spectroscopic, for the rapid detection and quantification of small quantities of organic components has immensely accelerated the pace at which the results of electrolytic experiments can be evaluated and judgment can be made concerning the future direction of a project.

3. *Electrochemical techniques.*—The invention or development and application with increasing degree of sophistication of a variety of electrochemical techniques [polarography, cyclic volummetry, chronopotentiometry and coulometry, pulsing (≡potential step), rotating ring-disk electrodes, electrolysis-cum-spectroscopy, and others] has also been significant. This has had major impact on rational planning of syntheses, characterization of "intermediates," and elucidation of organic electrode processes, particularly the unraveling of sequential electrochemical (E) and chemical (C) steps and the determination of relevant rate constants.

4. *Potentiostats.*—The universal availability and use of potentiostats, now purchasable at moderate cost, could hardly have been imagined a few decades ago. This has been a prerequisite for the development of most of the techniques cited above; in addition, it has facilitated the duplication of results, mechanistic or synthetic, from laboratory to laboratory.

5. *The application of computer science and technology to data processing.*

6. *Electrolyte solvent systems.*—Refinement of the understanding of the role of solvents/supporting electrolytes (particularly salts) has made it increasingly clear that the supporting electrolyte/solvent system serves not only as a means of passing current through a solution containing a nonconducting organic com-

* Electrochemical Society Active Member.

pound; the discharge potentials for the cation and anion, respectively, define the electrochemical domain (electroactivity) range within which an organic compound may be reduced or oxidized. Beyond this, the size, solvation, "softness/hardness," and degree of pairing of (98) the supporting ion may have a determining effect upon the nature of the electrolysis products. With proper choice of solvent and cation, it is now possible to carry out direct reductions to about −3.0V (*vs.* SCE) or, at a less negative potential, to discharge solvated electrons (99) which in solution can "indirectly" reduce substances (*e.g.,* benzene) not directly reducible at a cathode (equivalent of the Birch reduction). At the other extreme, the use of very difficultly oxidizable anions (*e.g.,* BF_4^-, ClO_4^-, $SF_6^=$) permits the oxidation of relatively inert substrates not previously accessible. Likewise, prior protonation (by superacids) (100) or deprotonation (by electrogenerated bases) (101) many produce electroactive species from precursors that have very little, if any, electroactivity as neutral molecules. The greater attention to electrolyses in "aprotic" organic media, in which proton transfers do not intervene as "coupled" reactions in the first electron transfer steps, has greatly expanded our ability to elucidate the mechanisms of organic electrochemical reactions. It has also called to our notice the frequent ability of the organic substrates themselves to act as acids and bases (102).

7. *Large-scale industrial electro-organic processes.*—Announcement was made in the mid-1960's that two industrial organic electrochemical processes had come on stream, Nalco's for tetraalkyllead and Monsanto's for adiponitrile. The former was impressive because it achieved very high yields of R_4Pb and demonstrated that large-scale electrolysis in a nonaqueous medium (of a Grignard reagent) was viable. An alternative electrochemical process for Et_4Pb (103), although not commercialized, using tetraethylaluminates as electrolytes was likewise shown to be technically and economically feasible. The Monsanto electrohydrodimerization (EHD) process not only has been the largest scale organic electrochemical synthesis thus far achieved but has demonstrated that even relatively low cost materials could be economically processed electrochemically. With this impetus (new) industrial groups were encouraged to examine or reexamine the potentialities of organic electrochemistry; utilization of some of the important factors leading to the success of EHD led to great improvements in the sodium amalgam reduction of activated olefins; variants of the Monsanto process, which right from the start (107) described the use of divided and undivided cells and a variety of suitable electrolytes, have demonstrated the presumed successes of electrolyzing emulsions (108) and the utility of a new type of cell, the capillary gap cell (109). The wide scope of EHD, involving as it does olefins $R_1R_2C{=}CCR_3R_4$ in which at least R_1 but also R_1 and R_3 are electron-withdrawing groups, presented mechanistic problems (particularly elucidation of EC *vs.* ECE sequences) which have been brilliantly attacked by academic scientists (104) and have led to increasingly sophisticated use of a battery of techniques for elucidating the mechanisms of organic electrode reactions and to the invention of new techniques (105).

Several other processes, albeit on a smaller scale, have reached actual or near commercialization stage and have served to further arouse the interest of industrial chemists: the reduction of phthalic to dihydrophthalic acid (106); the oxidation (100) of benzene to quinone (with optional further chemical or electrochemical reduction of the intermediate products to hydroquinone); the Crum Brown-Walker oxidation of monoalkyl adipates to dialkyl sebacates (111); the reductive coupling of acetone to pinacol (112).

8. *Catalytic chemistry.*—The explosive pace of development of catalytic chemistry, particularly homogeneous catalysis using dissolved complexes or complexes on supports or more recently complexes bound to polymer backbones, together with the development in the world-wide fuel cell program of electrodes in which catalytic materials were incorporated into conducting matrices is also remarkable.

Selected Bibliographic Items

The bibliography provided with this article offers a fairly complete guide to the developments of the last twenty-five years. The specialist is already familiar with them but may find it convenient to have the items assembled in one place. Those for whom this banquet of information is too lavish may find their appetites whetted by the following limited offering of hors d'oeuvres, limited by the space of this groaning board:

1. The development of the theory and technique of cyclic voltammetry (113) and the wealth of information it provides has led to its universal adoption as one of the major means used early in a study of the mechanism of an electrode reaction. Concurrently, the capabilities of single sweep voltammetry have been expanded (114).

2. Polarography (40a-40d, 65, 68), adopted by only a few for use in organic electrochemistry by 1952 (1), has grown at a fantastic rate (49). Its development in scope and depth has not only led to its universal adoption in analysis but has provided great insight into the mechanisms of organic electrode reactions (34). Coupled with macroelectrolyses, sometimes on a very small scale (115), it has guided immensely useful syntheses and led to correlations and predictions (116). The newest variant of this technique, differential pulse polarography, has become an extremely sensitive analytical method, particularly for the determination of drugs in biological fluids (117).

3. The technique for carrying out an electrolysis in the cavity of an ESR spectrometer (118) has been widely used to observe and record the spectra of anion radicals, particularly those derived from the one-electron reduction of nitro compounds.

4. The presently emerging techniques for attaching chiral reagents to electrode surfaces (119) is opening up new possibilities for preparing chiral products.

5. The discovery that porous carbon under certain conditions may be used as anodes instead of the "classical" nickel for fluorination has opened new prospects for the moderated preparation of a variety of organofluorine compounds (120).

6. A very striking example of how the course of organic electrochemical reactions may be changed by control of concentration, electrode potential, and mass transfer rates was provided in the electrolysis of cyclohexene plus chloride in acetonitrile (121): either 1-chlorocyclohexene or the 1-chlorocyclohexyl carbonium ion can be made the principal initial product.

7. Oxidative couplings with "electron-rich" olefins, undertaken initially to provide the complement to EHD, has, like EHD, been expanded to provide a synthetic method of wide scope (122). More generally, the study of anodic reactions, long relegated to a minor role, has been greatly expanded (52).

8. The demonstration (123) that anodic oxidation of aliphatic carboxylates at carbon leads preferentially to carbonium ion-derived rather than the radical-derived products of the classical Kolbe (and Crum Brown-Walker) reactions at platinum has added considerably to our understanding of the not yet completely resolved mechanism(s) of the Kolbe reaction and has produced, among other results, an electrochemical equivalent of the Ritter reaction (124).

9. The Nalco process mentioned above uses a fixed bed, in this case consumable, lead shot anode. Slurried (125) and, more prominently, fluidized bed electrodes (126) achieve much higher space-time yields than do planar electrodes but their utilization in organic electrochemical synthesis has not yet been as promising as originally anticipated.

10. The electrochemical equivalent of the Birch reduction of aromatic nuclei, using alkali metal salts in amines (127) and, more strikingly, in HMPT plus alcohol (128), has developed entirely since 1963.

11. Electrochemiluminescence (ECL), in which electrogenerated anion and cation radicals undergo mutual annihilation with emission of light, has yielded much interesting theoretical information (129); the present prospects for the fabrication of devices built upon these principles are poor.

12. After uncertain starts in the previous quarter-century, electropolymerization has made firm progress from about 1960 on. The well-known types of initiators have been made electrochemically (130) and used inside or outside a cell (131). Fine control of molecular weights and molecular weight distributions, long predicted, has been realized. Few claims for the superiority of this technique over the conventional one have been made. Electrosustained polymerization, as in the formation of polyesters by reducing of xylylene dihalides in the presence of CO_2, awaits study in depth (132).

13. Imagination and daring are being shown in the design and optimization of new cells and systems (133).

Prospects for the Future

We have been privileged in 1952-1977 to stand upon the shoulders of our illustrious predecessors and get an overview of their era and ours; our lofty perch also allows us to peer into the near future. Excessive empiricism has given way to increasing rationalism; because many of the theories and means for doing so are now at hand, we can look forward to a rapid acceleration of this process. Many of the broad challenges enunciated in 1952 (1) have not yet been very well met (*e.g.*, influence of the nature, structure, and history of an electrode upon the specificity of the electrode reaction; invention of a variety of viable paired organic syntheses). Even so, new ones are upon us, particularly since the emergence of new technological constraints in the last decade: increasing cost and eventual decreasing supply of petroleum-based raw materials; need for synthetic systems which minimize energy requirements and environmental burdens. The newer optimistic assessment of the economics of electrochemical processes in this context augurs well for the future (134).

Progress in the following areas, among others, is virtually mandatory:

1. Further work to bring space-time yields in electrochemical reactors on a par with those in catalytic processes.

2. Characterization of the first intermediate formed after an electron transfer and following its "evolution" to the final product(s).

3. Defining the potentialities of combined photo- and electrochemical techniques.

4. Organic syntheses from nonpetroleum-derived materials (135).

5. Improvement of membranes for use in aprotic systems.

6. Paired syntheses yielding one or two useful products without sacrificial by-products (136).

7. Replacement of many chemical processes which use stoichiometric quantities of redox reagents by electrochemical processes which regenerate these reagents used in catalytic amounts (137).

8. Reexamination in undivided cells of many reductions which have dogmatically been carried out in divided cells.

9. Further exploitation of electroinitiated homogeneous electrotransfers for difficult reductions, initiation of polymerization, etc. (138).

10. More vigorous development of the electrochemistry of transition metal complexes for the preparation of new and old catalysts.

Progress and challenge evolve together and propel us toward an "endless frontier." We are now in a better position than in 1952 to control our direction. The best is yet to be. Professor E. B. Yeager has referred to organic electrochemistry as a "sleeping giant." Those who have been active in this field this past quarter-century will agree with the noun but not with the adjective.

Manuscript received Feb. 7, 1977.

Any discussion of this paper will appear in a Discussion Section to be published in the December 1977 JOURNAL. All discussions for the December 1977 Discussion Section should be submitted by Aug. 1, 1977.

Publication costs of this article were assisted by the Monsanto Company.

REFERENCES

1. S. Swann, Jr., *This Journal* **99**, 125C (1952); H. J. Creighton, *ibid.*, **99**, 127C (1952).
1a. K. A. Korinek, *Chem. Ind. (London)*, **21**, 931 (1976).
2. C. Lanarre and H. K. Vijh, *Chem. Can.*, **27**, 15 (1975).
3. M. M. Baizer, in "Topics in Pure and Applied Electrochemistry," S. K. Rangarajan, Editor, pp. 185-199, SAEST, Karaikudi, India (1975).
4. L. Eberson, *Sven. Naturvetensk.*, **1974**, 43.
5. N. Weinberg, *Chem. Technol.*, **1974**, 184 (March).
6. F. Beck, *Ber. Bunsenges. Phys. Chem.*, **77**, 810 (1973).
7. H. Behret and H. Binder, *Chem.-Ztg.*, **97**, 378 (1973).
8. J. H. P. Utley, *Chem. Ind. (London)*, **17**, 22 (1972).
9. U. R. Mehta, *Indian Chem. Manuf.*, **9**, 12 (1971).
10. P. E. Iversen, *Dan. Kemi*, **52**, 173 (1971).
11. E. Barendrecht, *Chem. Weekbl.*, **67**, 14 (1971).
12. L. Eberson and N. Weinberg, *Chem. Eng. News*, **40**, (Jan. 1971).
13. G. Faita, *Chim. Ind. (Milan)*, **53**, 472 (1971).
14. S. Wawzonek, *Synthesis*, **1971**, 285.
15. H. Fischer, *Chem.-Ing.-Tech.*, **42**, 1293 (1970).
16. A. P. Kotlobay and A. A. Cherkasova, *Soviet Chem. Ind. (Engl. Transl.)*, **1970**, 83.
17. F. Beck, *Chem.-Ing.-Tech.*, **42**, 153 (1970); F. Beck, *Elektrowaerme Int.*, **31**, B118 (1973).
18. T. Sekine, *Chem. Abstr.*, **72**, 2731z (1970).
19. M. Ya. Fioshin and A. P. Tomilov, *Int. Chem. Eng.*, **9**, 375 (1969).
20. M. M. Baizer, *Naturwissenschaften*, **58**, 405 (1969).
21. S. Wawzonek, *Science*, **155**, 39 (1967).
22. M. E. Peover, *The Chemical Engineer*, **CE192** (1967).
23. K. Sugino, *Chem. Abstr.*, **66**, 51572h (1967).
24. G. Cauquis, *Bull. Soc. Chim. Fr.*, **1966**, 459.
25. S. Ross, M. Finkelstein, and E. F. Budd, "Anodic Oxidation," Academic Press, New York (1975).
26. M. R. Rifi and F. H. Covitz, "Introduction to Organic Electrochemistry," Marcel Dekker, New York (1974).
27. N. L. Weinberg, Editor "Technique of Electroorganic Synthesis," Part I and Part II, Wiley-Interscience, New York (1974 and 1975).
28. F. Beck, "Elektroorganische Chemie," Verlag Chemie, Weinheim, Germany (1974).
29. M. M. Baizer, Editor "Organic Electrochemistry," Marcel Dekker, New York (1973).
30. A. P. Tomilov *et al.*, Editors, "The Electrochemistry of Organic Compounds," Halsted Press, New York (1972). Translation of 1968 book.
31. A. J. Fry, "Synthetic Organic Electrochemistry," Harper and Row, New York (1972).
32. L. Eberson and H. Schäfer, *Fortschr. Chem. Forsch.*, **21** (1971). In English.
33. G. K. Mann and K. K. Barnes, "Electrochemical Reactions in Nonaqueous Systems," Marcel Dekker, New York (1970).
34. P. Zuman, "The Elucidation of Organic Electrode Processes," Academic Press, New York-London (1969).
35. M. J. Allen, "Organic Electrode Processes," Reinhold Publishing Co., New York (1958).
36. P. Delahay, "Double Layer and Electrode Kinetics," Wiley-Interscience, New York (1965).
37. P. Delahay, "New Instrumental Methods in Electrochemistry," Wiley-Interscience, New York (1954).
38. B. B. Damaskin, D. A. Petrii, and V. V. Batrakov, "Adsorption of Organic Compounds on Electrodes," Plenum Press, New York-London (1971).
39. D. T. Sawyer and J. L. Roberts, Jr., "Experimental Electrochemistry for Chemists," Wiley-Interscience, New York (1974).
40. K. J. Vetter, "Electrochemical Kinetics," Academic Press, New York-London (1967).
40a. L. Meites, "Polarographic Techniques," 2nd ed.,

Interscience, New York (1965).
40b. R. Kalvoda, "Techniques of Oscillographic Polarography," 2nd ed., Elsevier, Amsterdam (1965).
40c. S. G. Mairanovskii, Ya. P. Stradyn, and V. D. Bezuglyi, "Polarography in Organic Chemistry," Khimiya, Leningrad (1975).
40d. P. Zuman, *Fortschr. Chem. Forsch.*, **12**, 1-76 (1969).
41. A. J. Bard, Editor, "Encyclopedia of Electrochemistry of the Elements," Vol. 3, Marcel Dekker, New York (1975).
42. N. S. Hush, Editor, "Reactions of Molecules at Electrodes," John Wiley & Sons, New York (1972).
43. J. O'M. Bockris and A. N. Reddy, "Modern Electrochemistry," Vol. I and II, Plenum Press, New York (1970).
44. R. N. Adams, "Electrochemistry at Solid Electrodes," Marcel Dekker, New York (1969).
45. A. J. Bard, Editor, "Electroanalytical Chemistry," Vol. 1-8, Marcel Dekker, New York (1966-1975).
46. P. Delahay, C. W. Tobias, *et al.*, Editors, "Advances in Electrochemistry and Electrochemical Engineering," Vol. 1 and 9, Wiley-Interscience, New York (1961 and 1973).
47. A. Bewick and D. Pletcher, *Electrochemistry*, **1**, 98 (1970); A. Bewick and D. Pletcher, *ibid.*, **2**, 1 (1972); P. M. Robertson, *ibid.*, **3**, 120 (1973); P. M. Robertson, *ibid.*, **4**, 277 (1974); O. R. Brown, *ibid.*, **5**, 220 (1975).
48. N. L. Weinberg and H. R. Weinberg, *Chem. Rev.*, **68**, 449 (1968).
49. D. J. Pietrzyk (formerly S. Wawzonek), *Anal. Chem.*, annual reviews on polarographic literature. Discontinued after 1974.
50. A. J. Fry, *Top. Curr. Chem.*, **34**, 1 (1972); G. Dryhurst, *ibid.*, **34**, 47 (1972).
51. M. M. Baizer and J. P. Petrovich, in "Progress in Physical Organic Chemistry," Vol. 7, A. Streitwieser, Jr. and R. W. Taft, Editors, pp. 189-227, Interscience, New York (1970).
52. L. Eberson and K. Nyberg, *Tetrahedron*, **32**, 2185 (1976).
53. L. Eberson and K. Nyberg, in "Advances in Physical Organic Chemistry," Vol. 12, V. Gold and D. Bethell, Editors, pp. 1-129, Academic Press, New York (1976).
54. J. D. Anderson, J. P. Petrovich, and M. M. Baizer, in "Advances in Organic Chemistry," Vol. 6, E. C. Taylor and H. Wynbert, Editors, pp. 25-283, Interscience, New York (1969).
55. M. Fleischmann and D. Pletcher, in "Advances in Physical Organic Chemistry." Vol. 10 V. Gold, Editor, pp. 155-225, Academic Press, New York (1973).
56. A. A. Humffray, in "Modern Aspects of Electrochemistry," Vol. 8, J. O'M. Bockris and B. Conway, Editors, pp. 121-238 Plenum Press, New York (1972).
57. M. Ya Fioshin, A. P. Tomilov, and L. G. Feoktistov, *Elektrosint. Mekh. Org. Reakts.*, **1973**, 7.
58. G. J. Hoytink, in "*Advances* in *Electrochemistry and Electrochemical Engineering*," Vol. 7, P. Delahay, Editor, p. 221 ff, Interscience, New York (1970).
59. H. Lund, in "Advances in Heterocyclic Chemistry," Vol. 12, A. R. Katritzky and A. J. Boulton, Editors, pp. 213-316, Academic Press, New York (1970).
60. L. Eberson, in "The Chemistry of Carboxylic Acids and Esters," S. Patai, Editor, pp. 53-101, Interscience, New York (1969).
61. H. G. Gilde, in "Methods in Free Radical Chemistry," Vol. 3, E. S. Huyser, Editor, pp. 1-82, Marcel Dekker, New York (1972).
62. L. Meites, in "Physical Methods of Chemistry," Part II, A. Weissberger and B. W. Rossiter, Editors, Interscience, New York (1971).
63. J. Chang, R. F. Large, and G. Popp, in "Techniques of Chemistry," Vol. 1, Part II B, A. Weissberger and B. W. Rossiter, Editors, Wiley-Interscience, New York (1971).
64. D. M. Hercules, in *ibid.*, pp. 257-344.
65. C. L. Perrin, in "Progress in Physical Organic Chemistry," Vol. 3, S. G. Cohen, A. Streitwieser, Jr., and R. W. Taft, Editors, pp. 210-219, Wiley-Interscience, New York (1965).
66. T. Kuwana and N. Winograd, in "Electroanalytical Chemistry," Vol. 7, A. J. Bard, Editor, pp. 1-78, Marcel Dekker, New York (1974).
67. S. Swann, Jr., in "Technique of Organic Chemistry," Vol. II, 2nd ed., A. Weissberger, Editor, Interscience, New York (1956).
68. S. Wawzonek (collaborator), in "Polarography," 2nd ed., I. M. Kolthoff and J. J. Lingone, Editors, Interscience, New York (1952).
69. A. T. Kuhn, Editor, "Industrial Electrochemical Processes," Elsevier, Amsterdam-New York (1971).
70. P. Gallone, "Treatise on Electrochemical Engineering," Tamburini, Milan (1973).
71. J. Newman, "Electrochemical Systems," Prentice-Hall, Englewood Cliffs, New Jersey (1973).
72. C. L. Mantell, "Electro-Organic Chemical Processing," Noyes Development Corp., Park Ridge, New Jersey (1968).
73. *e.g.*, L. Eberson, K. Nyberg, and H. Sternerup, *Chem. Scr.*, **3**, 12 (1973); R. Sioda, *Electrochim. Acta*, **19**, 57 (1974); J. Hanzlik, *Chem. Listy*, **66**, 313 (1972); G. Cauquis and B. Haemmerle, *Bull. Soc. Chim. Fr.*, **1970**, 2000; H. Lund, in "Organic Electrochemistry," M. M. Baizer, Editor, pp. 169-194, Marcel Dekker, New York (1973).
74. *e.g.*, P. E. Iversen, *J. Chem. Educ.*, **51**, 489 (1974); P. E. Iversen, *ibid.*, **48**, 136 (1971); M. R. Rifi, *Org. Synth.*, **52**, 22 (1972).
75. *e.g.*, N. L. Weinberg, Short Course in Electroorganic Synthesis, American Chemical Society, New Jersey, New York, Illinois, and Pennsylvania 1972-1974; Total attendance about 350.
76. Short Course in Advanced Instrumental Methods for Electrochemical Kinetics, American Chemical Society alternately at the Universities of Southampton and Newcastle, England; *ibid.*, Columbus, Ohio, 1974.
77. USSR Conferences on Electrochemistry of Organic Compounds, every 2-3 years since 1958, All-Union since 1969. Four books, edited by A. N. Frumkin and several coeditors, containing the plenary lectures presented at these conferences have been published;
78. Gordon Conference on Electrochemistry, Santa Barbara, California, annually January/February.
79. Gordon Conference on Organic Reactions and Processes, New Hampshire, July 1975. Five of thirteen papers were on organic electrochemistry.
80. Electrochemical Reaction Engineering, 78th Meeting, AIChE., Salt Lake City, Utah, August 18-21, 1974.
81. Heyrovsky Discussion, Czechoslovakia, 1967-present. Almost all relevant to organic electrochemistry.
82. EUCHEM Conference on Organic Electrochemistry, Schloss Elmau, Germany, April 1-4, 1974; Pitlochry, Scotland, May 1977.
83. Intermediates in Electrochemical Reactions, Faraday Society Discussion, Oxford, England, September 18-20, 1973.
84. XXIVth IUPAC Congress, Hamburg, Germany, September 3-8, 1973.
85. Symposium on Organic Electrochemistry, 166th National Meeting, American Chemical Society, Chicago, Illinois, August 26-31, 1973.
86. Technical Electrochemistry, Electrochemical Processes, Dechema, Frankfurt, Germany, June 25, 1973.
87. EUCHEM Conference on Organic Electrochemical Synthesis, Ronneby Brunn, Sweden, June 6-11, 1971.
88. Advances in Organic Electrochemistry, Leeton College of Technology, England, March 11-12, 1971.
89. Electrochemical Conversion of Hydrocarbon-Based Raw Materials, 160th National Meeting, American Chemical Society, Chicago, Illinois, September 14-18, 1970.
90. Symposium on Nonaqueous Electrochemistry, Paris, France, July 8-10, 1970.
91. Journées d'Electrochimie Organique, Clermont-Ferrand, France, May 28-29, 1970.
92. Organic Electrosynthesis, G.D.Ch., Bonn, Germany, October 6-8, 1969.
93. Society for Electrochemistry, Thornton Research Centre, Chester, England, April 15-16, 1969.

94. Synthetic and Mechanistic Aspects of Electroorganic Chemistry, U.S. Army Research Office, Durham, North Carolina, October 14-16, 1968.
95. Electrode Reactions of Organic Compounds, Faraday Society, Newcastle upon Tyne, England, April 2-4, 1968.
96. Symposium on Electrochemical Processes, Division of Fuel Chemistry, 153rd National Meeting, American Chemical Society, Miami, Florida, April 9-14, 1967.
97. C.I.T.C.E. Meeting, Tokyo, Japan, September 5-9, 1966.
98. B. B. Damaskin, D. A. Petrii, and V. V. Batrakov, "Adsorption of Organic Compounds on Electrodes," pp. 194 ff, Plenum Press, New York-London (1971).
99. H. Lund, in "Organic Electrochemistry," M. M. Baizer, Editor, p. 839 ff, Marcel Dekker, New York (1973).
100. *e.g.*, D. Pletcher and C. Z. Smith, *Chem. Ind. (London)*, **21**, 371 (1976).
101. P. E. Iversen, *Tetrahedron Lett.*, **1971**, 55; R. C. Hallcher and M. M. Baizer, *Justus Liebigs Ann. Chem.*, **1977**.
102. *e.g.*, R. C. Buchta and D. H. Evans, *This Journal*, **117**, 1494 (1970).
103. K. Ziegler and H. Lehmkuhl, U.S. Pat. 3,372,097 (1968).
104. J-M. Nigretto and A. J. Bard, *This Journal*, **123**, 1303 (1976); L. Nadio and J.-Saveant, *J. Electroanal. Chem.*, **44**, 327 (1973).
105. J. M. Savéant and D. Tessier, *ibid.*, **61**, 251 (1975).
106. H. Suter, H. Nohe, F. Beck, and A. Hrubesch, U.S. Pat. 3,471,381 (1969).
107. M. M. Baizer, *This Journal*, **111**, 215 (1964).
108. M. Seko, *Chem. Econ. Eng. Rev.*, **7**, 20 (1975).
109. F. Beck and H. Gutke, *Chem.-Ing.-Tech.*, **41**, 943 (1969); L. Cedheim, L. Eberson, B. Helgee, K. Nyberg, R. Servin, and H. Sternerup, *Acta Chem. Scand.*, **B29**, 617 (1975).
110. J. P. Millington, Brit. Pat. 1,377,681 (1974); *Chem. Abstr.*, **82**, 125099p (1975).
111. E. P. Kovsman *et al.*, *Sov. Chem. Ind.*, **5**, 13 (1973) and many, many others from USSR, B.R.D., U.K., Japan, and U.S.
112. N. Shuster, K. J. O'Leary, and A. D. Babinsky, Abstract 276, p. 694, The Electrochemical Society Extended Abstracts, Spring Meeting, Washington, D.C., May 2-7, 1976.
113. R. S. Nicholson and L. Shain, *Anal. Chem.*, **36**, 706 (1964); *ibid.*, **37**, 178 (1965); R. S. Nicholson, *ibid.*, **37**, 667 (1965).
114. J.-M. Savéant, *Electrochim. Acta*, **12**, 753 (1967).
115. P. Zuman, in "Organic Electrochemistry," M. M. Baizer, Editor, p. 160, Marcel Dekker, New York (1973).
116. An extensive series of papers by S. Wawzonek and co-workers, *e.g.*, S. Wawzonek and A. Gundersen, *This Journal*, **111**, 324 (1964); S. Wawzonek and S. M. Heilmann, *ibid.*, **121**, 516 (1974).
117. M. A. Brooks, J. A. F. de Silva, and M. R. Hackman, *Am. Lab.*, **5**, 23 (1973).
118. D. H. Geske and A. H. Maki, *J. Am. Chem. Soc.*, **82**, 2671 (1959).
119. Anon., *Chem. Eng. News*, **54**, 23 (1976); P. R. Moser and R. W. Murray, *J. Am. Chem. Soc.*, **98**, 7435 (1976); B. F. Watkins, J. R. Behling, E. Kariv, and L. L. Miller, *ibid.*, **97**, 3549 (1975).
120. H. M. Fox, F. N. Ruehlen, and W. V. Childs, *This Journal*, **118**, 1246 (1971).
121. M. Fleischmann, G. Faita, and D. Pletcher, *J. Electroanal. Chem.*, **25**, 455 (1969).
122. H. Schäfer, *Chem.-Ing.-Tech.*, **42**, 164 (1970); H. Schäfer and E. Steckhan, *Tetrahedron Lett.*, **1970**, 3835; O. Palmquist, A. Nilsson, V. C. Parker, and A. Ronlan, *J. Am. Chem. Soc.*, **98**, 2571 (1976).
123. E. J. Corey, N. L. Bould, R. T. LaLonde, J. Casanova, Jr., and E. T. Kaiser, *ibid.*, **82**, 2645 (1960); W. J. Koehl, Jr., *ibid.*, **86**, 4686 (1964); W. J. Koehl, Jr., *J. Org. Chem.*, **32**, 614 (1967).
124. L. Eberson and K. Nyberg, *Acta Chem. Scand.*, **18**, 1567 (1964).
125. H. Gerischer, *Ber. Bunsenges. Phys. Chem.*, **67**, 164 (1964); H. Gerischer, Auslegeschrift 1,162,-433 (1964); Shell International Research, Brit. Pat. 1,098,837 (1968).
126. J. R. Backhurst, J. M. Coulson, M. Fleischmann, F. Goodridge, and R. E. Plimley, *This Journal*, **116**, 1600 (1969).
127. *e.g.*, R. A. Benkeser, H. Watanabe, S. J. Mels, and M. A. Sobol, *J. Org. Chem.*, **35**, 1210 (1970).
128. H. W. Sternberg, R. E. Markby, I. Wender, and D. M. Mohilner, *J. Am. Chem. Soc.*, **91**, 4191 (1969).
129. D. M. Hercules, in "Techniques of Chemistry," Vol. 1, Part II B, A. Weissburger and B. W. Rossiter, Editors, Wiley-Interscience New York (1971); C. P. Keszthelyi and A. J. Bard, *J. Org. Chem.*, **39**, 2936 (1974).
130. B. L. Funt and J. Tanner, in "Technique of Electroorganic Synthesis," Part II, N. L. Weinberg, Editor, pp. 559 ff, Wiley-Interscience, New York (1975); G. Parravano, in "Organic Electrochemistry," M. M. Baizer, Editor, pp. 947 ff, Marcel Dekker, New York (1973).
131. M. R. Rifi, U.S. Pat. 3,645,986 (1972).
132. D. A. Tyssee, J. H. Wagenknecht, M. M. Baizer, and J. L. Chruma, *Tetrahedron Lett.*, **1972**, 4811.
133. A. T. Kuhn and R. W. Houghton, in "Topics in Pure and Applied Electrochemistry," S. K. Rangarajan, Editor, pp. 133-166, SAEST, Karaikudi, India (1975).
134. J. L. Fitzjohn, *Chem. Eng. Prog.*, **7**, 85 (1975).
135. R. Ercoli, M. Guainazzi, G. Silvestri, S. Gambino, G. Filardo, B. Giannici, and M. Galluzzo, *Chim. Ind. (Milan)*, **55**, 156 (1973); D. Pletcher and C. Z. Smith, *Chem. Ind. (London)*, **21**, 371 (1976); D. A. Tyssee, J. H. Wagenknecht, M. M. Baizer, and J. L. Chruma, *Tetrahedron Lett.*, **1972**, 4811; F. Goodridge and K. Lister, Brit. Pat. 1,411,371 (1975); *Chem. Abstr.*, **84**, 66955f (1976).
136. M. Ya. Fioshin, *Khim. Promst. (Moscow)*, **44**, 882 (1968); *Chem. Abstr.*, **70**, 63434k (1969); M. M. Baizer and R. C. Hallcher, *This Journal*, **123**, 809 (1976).
137. R. Clarke, A. Kuhn, and E. Okoh, *Chem. Br.*, **11**, 59 (1975).
138. J. Pinson and J.-M. Savéant, *J. Chem. Soc., Chem. Commun.*, **1974**, 933; V. Mairanovskii *et al.*, *Dokl. Akad. Nauk. SSSR*, **223**, 643 (1975); *Chem. Abstr.*, **83**, 177754p (1975); J. Simonet, M.-A. Michel, and H. Lund., *Acta Chem. Scand.*, **29B**, 489 (1975); G. Kreysa and E. Heitz, *Chem.-Ing.-Tech.*, **48**, 852 (1976).

JOURNAL OF THE ELECTROCHEMICAL SOCIETY

REVIEWS AND NEWS

JUNE 1977

Correlations Between the Structure and Reactivity at Solid-Gas and Solid-Liquid Interfaces[1]

G. A. Somorjai

Materials and Molecular Research Division, Lawrence Berkeley Laboratory and Department of Chemistry, University of California, Berkeley, California 94720

I am greatly honored to be the Lecturer for the 150th Meeting of this distinguished and successful Society. I would like to start by making a prediction: I assert that *the new developments in the fundamental understanding of electrode processes and of chemical phenomena that take place at the solid-liquid interface will come from correlations with studies of equivalent processes at the solid-gas interface.*

Now let me explain why I believe this to be the case.

Over the past decade there has been a dramatic improvement of our knowledge of surface phenomena on the atomic and molecular scale at the solid-vacuum and solid-gas interfaces. Techniques that use the surface scattering of electrons, ions, and molecules have become available that determine the atomic and electronic structure of the surface monolayer, its composition and valency of surface atoms. Some of the more widely used techniques are listed in Table I. Low energy electron diffraction (LEED) is utilized to determine the structure of the clean surface and of the monolayer of ordered adsorbates (1). Auger electron spectroscopy (AES) (2), and photoelectron spectroscopy (XPS) (3), are used to determine the chemical composition and valency of surface atoms; while ion scattering spectrometry (ISS) (4), and secondary ion mass spectrometry (SIMS) (5), are utilized to determine the composition in the submonolayer region. Although all of these techniques, except LEED, can be used to study surfaces, regardless of their atomic structure (polycrystalline foils, evaporated films, liquids, or powders), many of the major advances in our understanding of the chemistry of surface atoms has come from studies of well-ordered crystal faces of single crystals. Using crystals, we can vary the concentration of different surface sites that are distinguishable by the number of nearest neighbors. The three types of surfaces that exhibit the various surface sites which are important in studies of chemisorption and surface chemical reactions are shown in Fig. 1 (6). Figure 1a shows a low Miller index (111) surface in which most of the surface atoms are in locations where they are surrounded by six nearest neighbors in the surface plane. Although the low Miller index surface may be rough on a macroscopic scale, full of defects that are induced by the presence of dislocations in the bulk, the surface can be prepared in such a way that most of its atoms are in their equilibrium, high symmetry sites. Figure 1b shows a surface with a high density of steps of atomic height. In such a surface there are large concentrations of surface sites of two types: step atoms and atoms in terraces. The former has less number of nearest neighbors. Many high Miller index surfaces exhibit this surface structure (7). Finally, Fig. 1c shows another type of high Miller index surface that has three types of surface sites in high concentrations: terrace and step atoms and atoms at kinks in the steps. Crystal surfaces can be cut and prepared in which every third atom in the step is a kink atom. One example of this is shown in Fig. 1c.

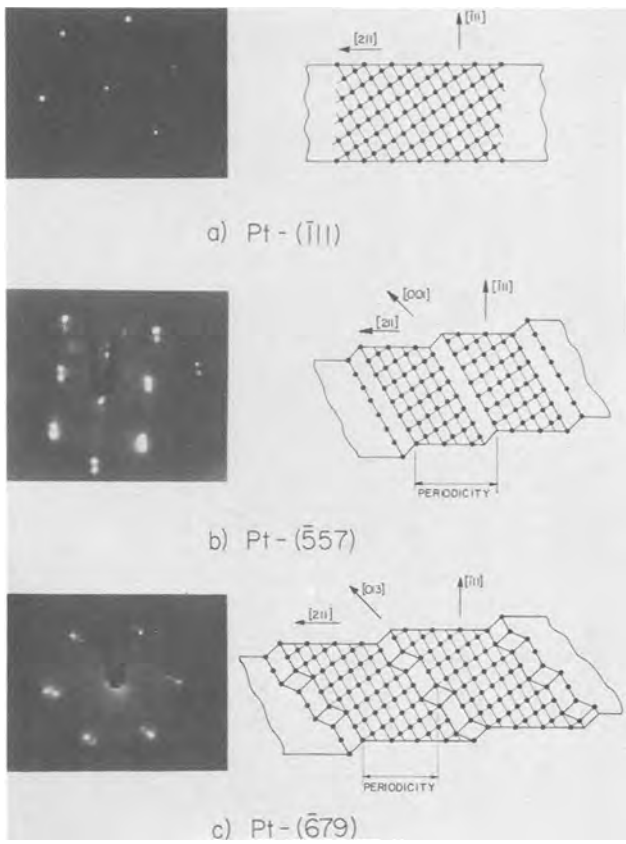


Fig. 1. Diffraction pattern and schematic of mean surface configurations for platinum crystal surfaces exhibiting (a) low defect density, (b) regular step arrays with an average spacing between steps of 6 atoms, and (c) regular step arrays with kink sites along the steps. Note the spot splittings in (b) and (c) indicative of the periodic step arrays.

There is a great deal of experimental evidence accumulating in recent years that indicates that the chemical activity of these various surface sites (kinks, steps, and terrace atoms) is different (8, 9). They form chemical bonds that differ in strength by about ±5 kcal/mole (10) or carry out surface reactions on transition metal surfaces with different rates and selectivity (11). Of course, when a polycrystalline surface (wire or foil

[1] The Electrochemical Society Lecture delivered at the Las Vegas, Nevada, Meeting of the Society, October 1976

Table I. Techniques of surface analysis that are most frequently employed at present

Technique	Probe	Main output information	Sensitivity (monolayer)	Depth sampled	Commercially available	Depth profile
AES Auger electron spectroscopy	Electrons ~2 keV ~50 μA	Surface composition qualitative & quantitative	$\sim 10^{-2}$-10^{-3}	1-7 layers	Yes	Yes
LEED Low energy electron spectroscopy	Electrons ~100 eV ~10 μA	Surface structure	$\sim 10^{-1}$-10^{-2}	1-7 layers	Yes	No
XPS X-ray photoelectron spectroscopy	X-rays ~1 keV	Oxidation state & composition	$\sim 10^{1}$-10^{-2}	1-7 layers	Yes	Yes
ISS Ion scattering spectroscopy	Ions He, Ne ~1 keV ~10^{-8}A	Surface composition	$\sim 10^{-3}$-10^{-4}	1 layer	Yes	Yes
SIMS Secondary ion-mass spectroscopy	Ions Ne, Ar, O_2 ~1 keV ~10^{-8}A	Surface composition	$\sim 10^{-6}$	1 layer	Yes	Yes

or thin film) is studied, one detects a chemical behavior (heat of chemisorption, reaction rate, and product distribution) that is integrated over all these surface atoms. Thus, identification of the various reactive surface sites cannot be made in this circumstance.

At the same time the surface diagnostic techniques were developing that are listed in Table I that, by and large, scrutinize the surface in static, low pressure conditions, several techniques were developing in my laboratory for kinetic studies of surface reactions under low pressure and high pressure conditions (12, 13). Using suitable apparatus, one can measure the rate and product distribution in surface reactions while also monitoring the structure and composition of the surface using small surface area (approximately 1 cm^2) single crystal samples. This way the relationships between the reactivity of the surface and the structure and composition can be determined.

The apparatus that is used to study high pressure gas reactions and is also suitable to study surface reactions at the solid-liquid interface is shown in Fig. 2 (13). The sample (polycrystalline foil or single crystal) is located at the center of the axis of the ultrahigh vacuum chamber and it is accessible to the LEED, AES, ion bombardment, and mass spectrometry facilities. It is spot-welded to two heating rods which are attached to copper conducting bars in a quartz insulating tube. This is attached to a Teflon compression-sealed stainless steel shaft which allows 180° rotation of the sample at any pressure (10^{-9}-10^{5} Torr). The rotary motion is necessary to clean the sample with the ion gun, then rotate it for LEED, AES, and thermal desorption measurements. The sample may be enclosed by a small high pressure cell which is operated by hydraulic pressure from above and engages a copper sealing gasket below the sample. The internal volume of this isolation chamber is small, about 30 cm^3. Access to the central chamber is made via inlet ports running down the axis of the tube. The sample is heated resistively via the feed-throughs in the lower portion of the manipulator and the temperature is measured with a thermocouple

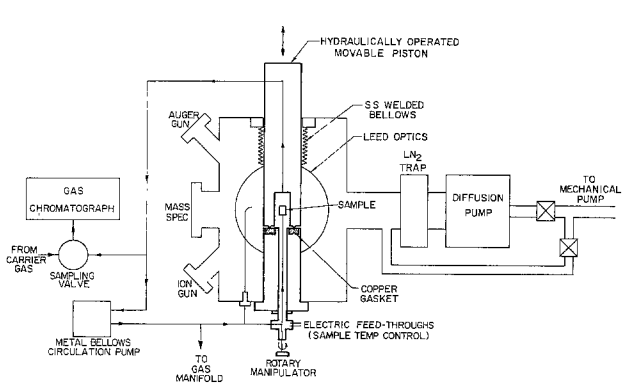


Fig. 2. Surface analysis apparatus for catalytic studies and for studies of the solid-liquid interface at high pressures (0.1-100 atm) with a small volume isolation cell.

spot-welded to the sample. Gases are admitted to the circulation loop and reaction cell from a suction-pumped manifold and a small metal bellows diaphragm pump is used to circulate gases around the loop. The gases pass through a low-internal-volume gas-sampling valve which extracts 0.1 mm of gas for gas chromatographic analysis.

At present this apparatus is being used to study the hydrogenation of carbon monoxide at both low and high pressures (as high as 100 atm) on small surface area metal surfaces (14). There is no reason why an apparatus of this type could not be adapted for studies of the solid-liquid interface. The liquid could readily be introduced and then pumped out after the studies and the surface can be studied by the various surface diagnostic techniques that are listed in Table I. *This apparatus or similar types will be the instruments, I believe, that will permit us to develop the correlations between surface phenomena that occur at the solid-liquid and solid-gas interfaces.*

Below, I briefly review our present view of the atomic and electronic structure of surfaces and adsorbates, and the surface composition of binary alloy systems as it emerges from modern studies of the solid-vacuum and solid-gas interfaces. Then I shall review some of the surface reaction studies that have been carried out recently to correlate the reactivity of the surface with its structure and composition. Finally, I shall propose various research projects that would be of importance in order to begin to correlate surface phenomena at solid-liquid and solid-gas interfaces.

Atomic Structure of Clean Solid Surfaces as Determined by LEED

The atoms at the surface are in an asymmetric environment. They are surrounded by atoms in the surface layer and from beneath but there are no atoms above them. This surface environment also has lower symmetry than that provided for atoms in the bulk. The structural asymmetry experienced by atoms at the surface has a major effect that leads to surface reconstruction: atoms in the surface may move into new equilibrium positions that provide higher symmetry or greater overlay of available positions.

Surface reconstruction.—There are several types of surface reconstruction observed for clean solid surfaces. Many surfaces have atomic structures that are different from that expected from the projection of the x-ray bulk unit cell. The surface atoms assume new equilibrium positions by out-of-plane buckling or by relaxing inward (contraction) that often results in entirely different-ordered surface structures. An example of this is shown in Fig. 3. The diffraction pattern and schematic representation shown here are characteristic of the surface structure of the (100) crystal face of platinum. This surface exhibits the so-called (5 × 1) surface structure (15). There are two perpendicular domains of this structure and there are 1/5, 2/5, 3/5, and 4/5 order spots between the (00) and (10) diffraction beams. The surface structure appears to be stable

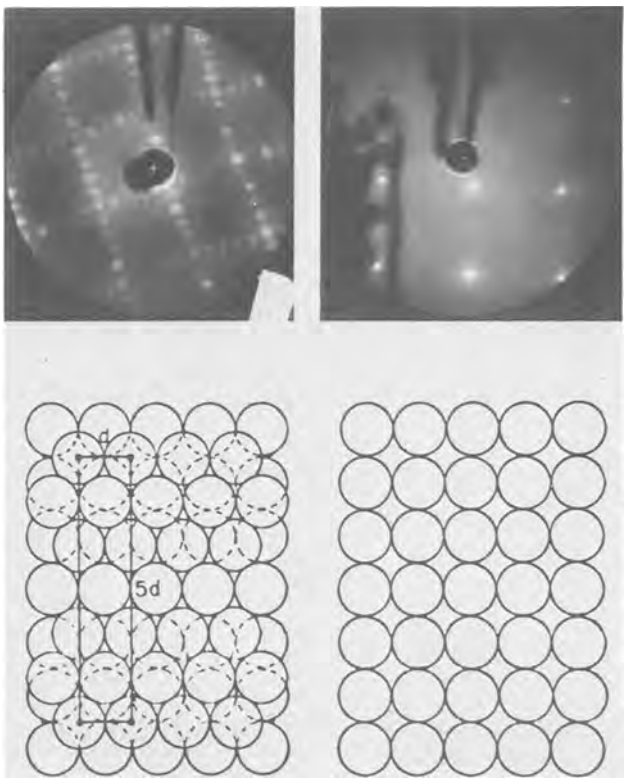


Fig. 3. (a, upper left) Diffraction pattern from the Pt(100)-(5 × 1) structure. (b, lower left) Schematic representation of the (100) surface with hexagonal overlayer. (c, upper right) Diffraction pattern from the Pt(100)-(1 × 1) structure. (d, lower right) Schematic representation of the (100) surface.

at all temperatures from 25°C to the melting point, although at elevated temperatures impurities from the bulk can come to the surface and cause a transformation of the structure to the impurity stabilized (1 × 1) surface structure. Preliminary calculations by Clark *et al.* (16) and in this laboratory indicate that a model for Pt(100) in which the surface atoms assume a distorted hexagonal configuration by out-of-plane buckling is favored. The apparent (5 × 1) unit cell is then the result of the coincidence of the atomic positions of atoms in the surface, *i.e.*, in the distorted hexagonal layer, with atoms of the undistorted second layer below. The (100) crystal faces of gold (17) and iridium (18) that are neighbors of platinum in the Periodic Table exhibit the same surface reconstruction and the same surface structure as that of platinum that is shown in Fig. 3. The (110) crystal faces of these three elements are also restructured (19) and exhibit different unit cells than that expected from the bulk x-ray structure. On the other hand, the (111) crystal face of these three metals appears to have the same surface structure as that indicated by the bulk unit cell.

For semiconductors, most crystal planes that have been studied show reconstruction (20). Monatomic and diatomic semiconductor surfaces have been investigated in large numbers and surface reordering has been observed for most of them. Frequently there are changes of surface structure with temperature that are often irreversible.

For many metal surfaces, the distance between the uppermost two layers, *i.e.*, the z-spacing, is equal to that of the bulk value to within the estimated accuracy of about 5%. However, the Al(110) (21), Mo(100) (22), and W(100) (23) surfaces seem to show substantial contraction in the upper layer z-spacing with respect to the bulk while retaining the (1 × 1) surface unit cell. A simple contraction or expansion of the interplanar z-spacing of this kind is usually termed a "relaxation."

For many diatomic solids there is nonstoichiometry in the surface layer, that is, the surface composition may be different from that in the bulk (20). Nonstoichiometry is apparently a major factor in the observed reconstruction of the polar faces of the III-V semiconductors such as gallium arsenide, GaAs. The (111) face, for example, would ideally have all gallium atoms at the surface bonded to arsenic atoms immediately beneath the surface while the reverse would be true of the $(\bar{1}\bar{1}\bar{1})$ face. However, the $(\bar{1}\bar{1}\bar{1})$ surface has been found to lose arsenic at elevated temperatures and this is associated with the appearance of a new surface structure, while at low temperature another surface structure is arsenic stabilized (24). Similarly, phosphorus is found to preferentially desorb at high temperatures from the gallium phosphide $(\bar{1}\bar{1}\bar{1})$ surface (25). On the other hand, the gallium arsenide (110) surface, which has an equal number of gallium and arsenic surface atoms, does not exhibit reconstruction. A number of studies have pointed to possible nonstoichiometry in alkali-halide crystal surfaces also upon cleavage (26). On oxide surfaces, such as aluminum oxide (27) and vanadium pentoxide (28), changes in chemical composition and valency of surface atoms have been related to the formation of new surface unit cells.

Molecular crystals constitute a large and important group of materials that include most organic solids, but only very recently have the surface structures of some of these materials been investigated on an atomic scale by low energy electron diffraction. Ice and naphthalene have been grown by vapor deposition (29) and ordered surface structures of crystals of many other organic solids such as benzene, trioxene, n-octane, cyclohexene, and methanol have been grown on metal substrates at low temperatures (30). Phthalocyanine crystals have been vapor grown on ordered metal surfaces (31). These large molecular weight, large-size organic crystals exhibit a different kind of surface reconstruction. When copper phthalocyanine was grown on the copper (111) surface, the surface structure of the growing organic crystal layer did not resemble the structure of any of the simpler crystal planes in the bulk structure of the organic crystal. It appears that the ordered metal substrate predetermined the orientation and packing of the phthalocyanine monolayer, which in turn controlled the orientation and packing of the organic layer deposited on top of it. For large molecules, such as phthalocyanine, restructuring into a more stable crystallographic arrangement requires molecular rotation and diffusion processes that are too slow under conditions of crystal growth. Thus the molecules are frozen into a surface structure that is predetermined by the structure of the substrate and the first adsorbed organic monolayer.

Surface irregularities.—The surfaces of real solids are atomically heterogeneous and not smooth as shown schematically in Fig. 4. There are several atomic sites present simultaneously that are distinguishable by their number of nearest neighbors. The symmetry of these low coordination number sites and their charge density are different from that of the sites on the smooth surface and are different from each other. As a result, large variation in chemical bonding of adsorbates at these different sites could occur. Indeed, there is an increasing body of experimental evidence that indi-

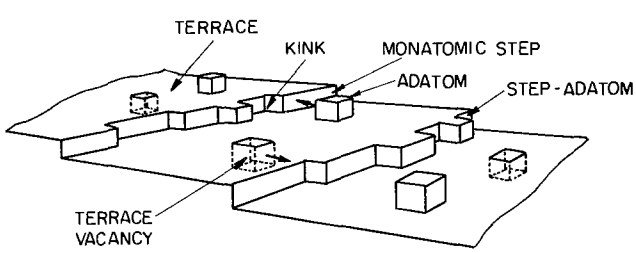


Fig. 4. Model of heterogeneous solid surface depicting different surface sites. These sites are distinguishable by their number of nearest neighbors.

cates that atomic steps and kinks behave as different chemical entities at transition metal (32, 33) and semiconductor surfaces (34), forming chemical bonds of different strengths as compared to that of the atoms on the terraces.

Preparation of surfaces with a large concentration of stable and ordered irregularities (steps and kinks) can be carried out by cutting crystal faces along high Miller index directions. Stepped surfaces of several metals (35), semiconductors (36), and oxide surfaces (37) were prepared this way.

Charge Density at Clean Solid Surfaces

Let us consider an atomically smooth surface where each atom is in the same structural environment. The surface atoms have less nearest neighbors as compared to atoms in the bulk. As a result, electronic orbitals that are used for bonding of bulk atoms are available at the surface, giving rise to increased charge density. These localized unsaturated bonding orbitals are frequently called dangling bonds and the angular distribution of their charge density largely depends on the structural arrangement (packing of atoms, orientation) at the surface. There is excess free electron density at metal surfaces that is not localized at a given atom that gives rise to an induced surface dipole. The presence of this dipole is responsible for changes of the work function of metals from crystal face to crystal face. The formation of the surface dipole can be rationalized and demonstrated using the so-called jellium model. There are strong exchange correlation forces which act on the electrons in the solid due to their many-body coulomb interactions. In the metal interior each electron lowers its energy by pushing others away to form the exchange-correlation "hole." This attractive interaction is lost when the electron leaves the solid so there is a sharp potential barrier at the surface. In the jellium model the positive charge density from the ion cores is smeared out over the atomic volume and the conduction electrons are free to respond to the surface barrier potential. At the surface, however, the electrons are not totally trapped and there is a small probability to leak out in the vacuum. This charge leakage creates a dipole effect which modifies the self-consistent surface barrier potential. This dipole creates an additional electrostatic barrier for the electrons in the solid, V_{dipole}, so that the total barrier, $V_{total} = V_{exchange} + V_{dipole}$. This gives the work function, $\phi = V_{exchange} + V_{dipole} - E_F$, where E_F is the energy at the Fermi level. Variations of the work function from crystal face to crystal face are well documented.

Surface irregularities, like atomic height steps at the surface, exhibit different work functions as determined by Wagner and Besocke recently (38). Recent theoretical studies provide firm foundation of the effect of surface heterogeneity and irregularities on the density of states at the Fermi level (39) and on the angular distribution of charge densities (40) at these low coordination number surface sites. The structural heterogeneity at the surface leads to the chemical heterogeneity, *i.e.*, the ability of the surface to carry out complex chemical rearrangements involving the simultaneous forming and breaking of surface bonds of varied strength at the various atomic surface sites.

The Surface Crystallography of Adsorbed Monolayers of Atoms

The structural asymmetry and excess charge experienced by atoms at the surface have an important effect on the structure of the adsorbate substrate system. In the presence of adsorbates, bonds are formed that make optimum use of the available bonding orbitals. For small adsorbed atoms and molecules this often leads to the formation of a close-packed adsorbate structure in which the adsorbate occupies the high symmetry atomic sites that correspond to the continuation of the bulk structure. We shall review several examples of chemisorbed structures of these types below.

For most of the over 200 surface structures of adsorbed monolayers that have been studied so far, only the two-dimensional symmetry of the diffraction pattern has been determined (41). Thus, only the size and shape of the two-dimensional surface unit cell is known. Determination of the actual positions of the adsorbed atoms requires analysis of the intensity of the diffraction beam and has been performed only on a small number of systems, almost all for atomic adsorption and low Miller index surfaces of face-centered cubic metals. The first of these analyses was carried out by Anderson and Pendry (42), who examined sodium adsorption on the nickel (100) crystal face and reported that the sodium atoms occupy four-coordinated sites at a distance of 0.87Å above the topmost nickel layer. Demuth *et al.* (43) have examined the overlayer structures of oxygen, sulfur, selenium, and tellurium on nickel (100). On this surface they find the adsorbed atom to occupy four-coordinated bonding sites at displacements of 0.9, 1.3, 1.45, and 1.9Å, respectively, from the center of the top nickel layer. Results are also given for nickel (111) and nickel (110). Forstmann *et al.* (44) reported iodine adsorbed on Ag(111) to occupy the threefold sites at a distance of 2.5Å above the topmost layer. Oxygen adsorption on tungsten (45) and nitrogen on tungsten (46) and other body-centered cubic metals has also been studied.

Several general observations appear to be emerging from this work. Chemisorbed atoms seek an adsorption site which allows them to maximize their coordination. The substrate-adsorbate bond length, at least for the strongly chemisorbed systems studied thus far, can be reproduced rather well by adding the metallic radius of the substrate and the single bond covalent radius of the adsorbate. This is shown in Table II which lists the experimentally determined bond length and the predicted bond length obtained by summing the covalent radii. In most cases, the difference is within the 0.1Å accuracy claimed for the experimental determination and in no case is the discrepancy greater than 10%. This result suggests that the chemisorption bond of the small adsorbate atoms studied so far is basically covalent in character, which means that theoretical treatment in terms of localized surface complexes and clusters should be applicable to their chemisorption.

The small adsorbate atoms that are listed in Table II occupy sites of the highest symmetry. These sites would also be the location of the next layer of metal atoms if we were to continue building up the solid layer by layer. The adsorbate-metal atom bond distance is equal, within the experimental accuracy, to the sum of the covalent radii of the two atoms. There are other types of surface bonding, however, that are neither simple nor readily rationalized using simple chemical arguments. For example, when oxygen adsorbs on nickel (110), the best agreement with experiment is obtained assuming that oxygen atoms are lying in a twofold bridge site between 1.41 and 1.51Å above the nickel layer (47). This is clearly not the highest coordination site on the surface. The fact that bridge bonding is preferred suggests that atomic oxygen bonds to two adjacent nickel atoms via the oxygen p_x and p_y atomic orbitals. The bond angles and atomic distances are very

Table II. Adsorbate-substrate bond lengths determined by LEED

Substrate	Adsorbate	Bond length (experimental, Å)	Bond length (predicted, Å)
Ni(001)	O	1.97	1.90
	S	218	2.28
	Se	2.27	2.41
	Te	2.58	2.61
	Na	3.37	3.10
Ni(110)	O	1.91	1.90
	S	2.17	2.28
Ni(111)	S	2.02	2.28
Ag(001)	Se	2.80	2.61
Ag(111)	I	2.75	2.77
Al(100)	Na	3.52	3.32
Mo(001)	N	2.02	2.03
W(110)	O	2.08	2.05

close to what one expects from X_2O compounds, where X is the metal atom.

Another example of unusual bonding has been recently detected in studies of hydrogen adsorption to the nickel (110) surface. A new surface structure forms and surface crystallography studies indicated that this unit cell is a consequence of the restructuring of the nickel (110) surface as a result of hydrogen chemisorption and not due to ordering of the hydrogen adsorbate (48). The surface structure model that gave best fit to the experimental data consists of distorting the nickel surface atoms so as to produce the new (1×2) periodicity. This is carried out by simple depression or raising of every alternate row of nickel atoms in one direction, or a pairwise distortion of every alternate row of nickel atoms in the plane of the surface. The optimal agreement with experimental curves is obtained by a 0.1Å compression of the surface layer and a 0.1Å alternate displacement of the rows of nickel atoms in the $[\bar{1}10]$ direction.

Another example of unusual structure comes from studies of the titanium-oxygen system. It has been reported recently (49) that upon chemisorption, oxygen atoms are located *below* the first layer of titanium atoms in the (0001) surface. There is little doubt that future studies will reveal the richness and complexity of surface bonding and will yield many unexpected bonding configurations.

Studies of Hydrocarbon Bonding to Metal Surfaces

The surface crystallography of acetylene on Pt-(111).—Acetylene, C_2H_2, forms a (2×2) overlayer on the platinum (111) crystal surface. In recent experimental studies, Stair and Somorjai (50), and Kesmodel *et al.* (51) have reported the LEED *I-V* profiles for the acetylene-platinum system. In particular, two different (2×2) structures of adsorbed acetylene were identified, which we refer to briefly as stable and metastable state and which have been interpreted as involving different chemical bonding. The metastable (2×2) structure is observed to form initially at low exposure (one langmuir $= 10^{-6}$ Torr-sec) of C_2H_2 at room temperature but transforms in 1 hr to the stable (2×2) structure upon gentle heating to 100°C. Both structures are characterized by the same (2×2) surface unit cell and involve the same carbon coverage as determined by Auger electron spectroscopic analysis. However, they are readily distinguishable by their different *I-V* characteristics.

Let us examine the various modes of bonding of acetylene to platinum in the context of high symmetry bonding sites available on the (111) face of fcc crystal. As illustrated in Fig. 5, we distinguish four sites designated as: (a) one-coordinate π, (b) di-σ, (c) bridging (sometimes referred to as μ-bridging), and (d) triangular complexes. We have indicated for each site only those surface metal atoms expected to have significant metal-carbon interaction. It is natural to discuss these surface geometries in terms of structural analogies of organometallic complexes. In these terms, the one-coordinate π-complex, (a), involves the interaction of one or both sets of π-orbitals of the acetylene molecule with a single metal surface atom. The bridging site, (c), utilizes both sets of π-orbitals to bond with two surface atoms; both (a) and (c) in principle entail little rehybridization of the molecule since essentially undistorted π-orbitals would be involved. However, the di-σ bond, (b), implies $sp \rightarrow sp^2$ rehybridization and the formation of two carbon metal σ-bonds accompanied by large hydrogen *cis* bending (CCH angle $\simeq 120°$). This possibility has received serious consideration in the catalysis literature. Finally, the triangular structure, (d), commonly found in trinuclear metal alkyne

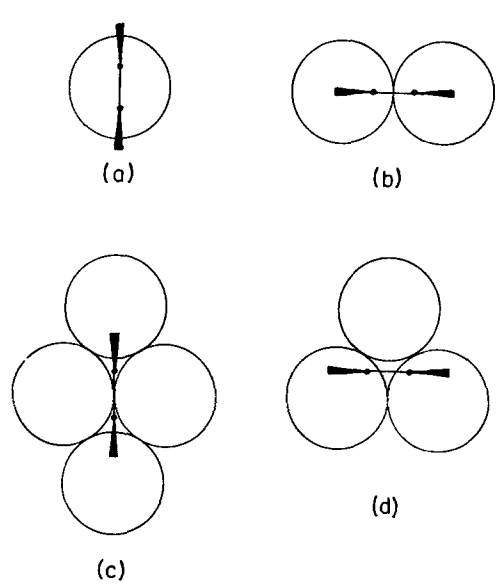


Fig. 5. Schematic indicating various high symmetry local bonding sites for acetylene on the (111) face of a fcc crystal: (a) one-coordinate π, (b) di-σ, (c) bridging, and (d) triangular.

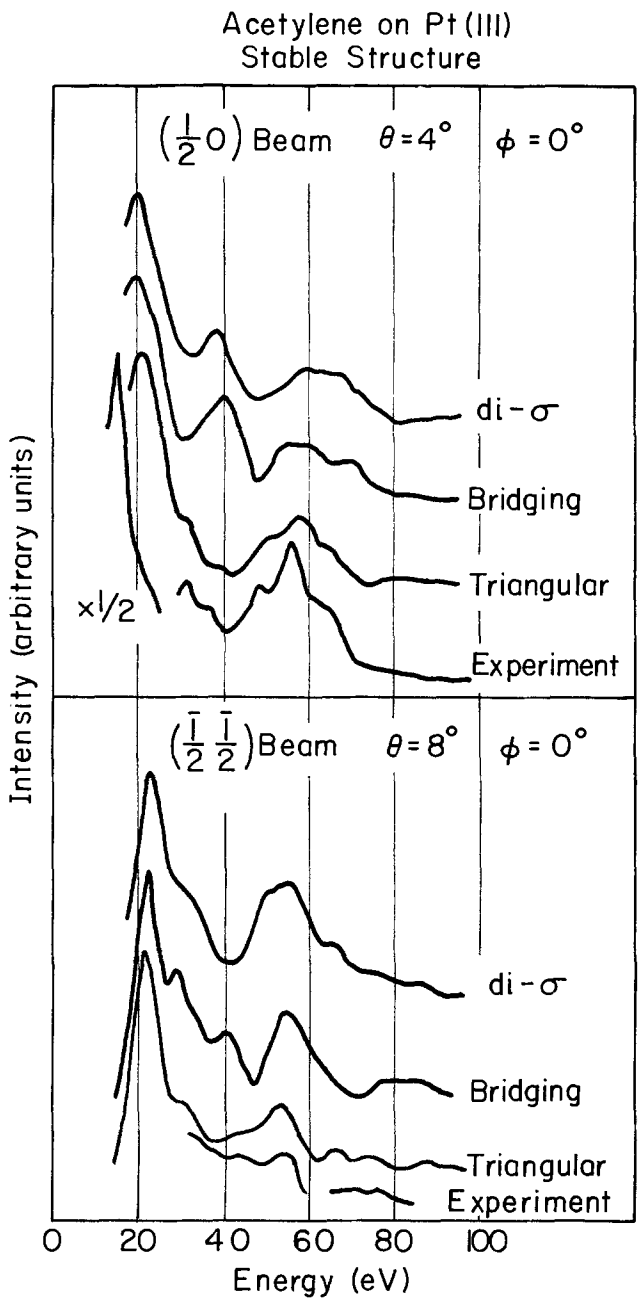


Fig. 6. Comparison of calculated *I-V* profiles for various model geometries ($\zeta = 1.9$Å) to experiment (stable acetylene overlayer) for two fractional order beams.

complexes illustrates a mode of bonding loosely referred to in terms of both σ- and μ-bonds. This triangular geometry is found to be the favored arrangement in the stable structure. Analysis of Fig. 6 and 7 and other data similarly obtained shows that the triangular geometry gives consistently better agreement than either the bridging or di-σ geometries. The metastable C_2H_2 structure exhibits bonding similar to the one-coordinate π complex. The stable C_2H_2 has a z-distance of 1.9Å, and C-Pt distances of 2.2Å for C_2H_2 centered on the triangular site. This value is very close to the predicted covalent bond distance of 2.16Å.

It has been possible to distinguish among various proposed bonding models for acetylene adsorption on the Pt(111) surface using dynamical analysis of low energy electron diffraction intensity profiles. It was found that bonding of acetylene in a triangular site on the Pt(111) surface is the stable and preferred configuration. It is interesting to note that this same bonding geometry is exhibited in trinuclear metal alkyne clusters; moreover, the average C-Pt distance found for C_2H_2 adsorbed on Pt(111) is similar to that determined for the osmium trinuclear cluster, the osmium covalent radius being only 0.04Å shorter than that of platinum. Although one cannot detect a small C-C bond length change, we do anticipate a C-C bond stretch of about 0.1Å to occur for acetylene adsorption judging from the C-C length found in x-ray crystal structure determinations of the metal alkyne clusters.

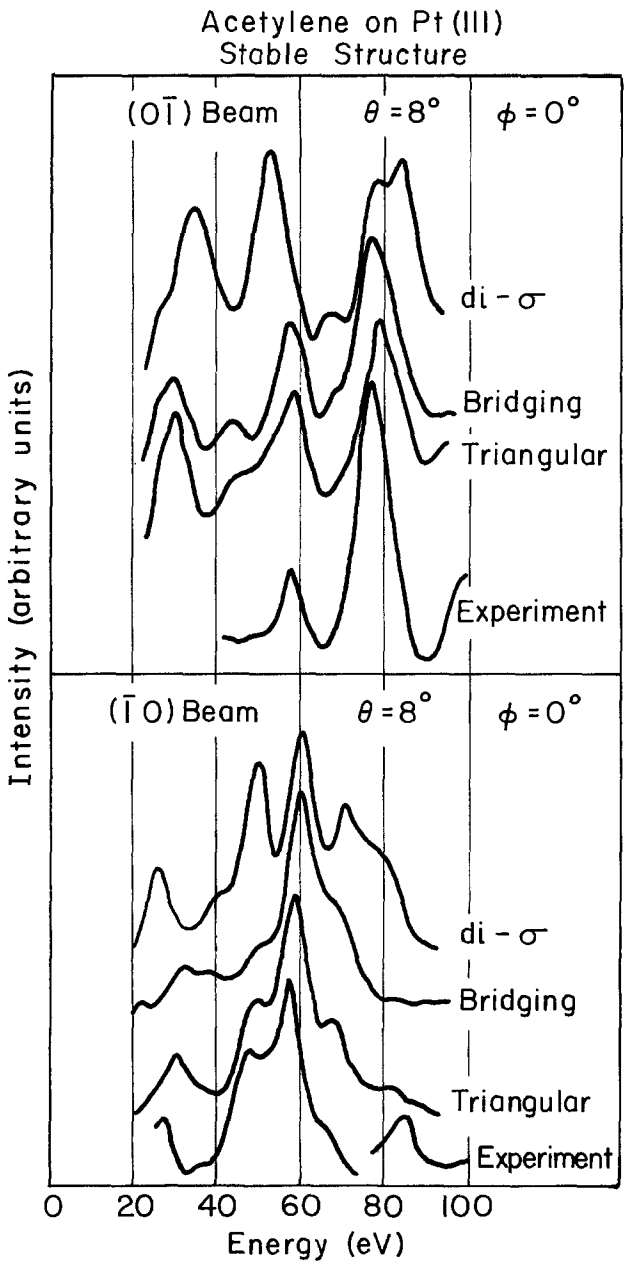


Fig. 7. Comparison of calculated *I-V* profiles for various model geometries (ζ = 1.9Å) to experiment (stable acetylene overlayer) for two integral order beams.

Studies of other hydrocarbons by electron spectroscopy.—The bonding and the composition of C_2H_4 was studied on the nickel (111) crystal face by UPS (52). At 100°K, the organic molecule adsorbs by bonding via its π-orbitals to the metal surface. On heating to 230°K, C_2H_4 dehydrogenates to form C_2H_2 that is bound with even stronger π-bonds to the nickel surface. UPS could monitor changes in bonding caused by the activated dehydrogenation that occurs as a function of temperature. Chemisorption involved predominantly π-d bonding, thus rehybridization of the adsorbed molecule does not seem to occur.

Similar studies were carried out with C_2H_4 adsorbed on the W(110) crystal face (53). At 300°K, the molecule dehydrogenates upon adsorption to form C_2H_2 that π-bonds to the metal. As the surface temperature is increased to 500°K, breaking of the carbon-hydrogen bond occurs and the C_2 fragments are identified by UPS by the presence of C-C and C-W bonds. Upon heating to 1100°K, the C-C bond breaks and carbon atoms remain on the surface in a disordered state.

One of the striking features of the adsorption process is the existence of small (of the order of kT) activation energy barriers in the path of various bond-breaking reactions. As a result an organic molecule may be adsorbed intact even on the most reactive metal surface at sufficiently low surface temperatures. As the temperature is increased, electron spectroscopy can be used to identify the different bond-breaking processes that seem to occur in readily distinguishable steps.

Studies of CO Bonding

The chemisorption of CO was studied on several metal surfaces by electron spectroscopy. Using synchrotron radiation, Shirley *et al.* have found that CO adsorbed in a bridge structure bound through the carbon to the metal on the platinum (111) crystal face, while the oxygen end of the molecule is pointing away from the surface (54). Using the high Miller index (775) surface that has a large concentration of kink atoms of low coordination number, Mason *et al.* (55) found that the CO dissociates at the kink sites, while the carbon monoxide does not dissociate on atoms in terrace sites. These studies were carried out using UPS and XPS techniques. The concentration of carbidic carbon was equal to the kink concentration and was produced at the initial stages of CO chemisorption on this kinked, high Miller index, platinum surface. Thus, the adsorption of CO takes place first at kink sites where the molecule dissociates. Once the kinks are blocked by carbon, CO further chemisorbed in the molecular state on the other atomic sites of the heterogeneous platinum surface. CO adsorbed in several bonding sites, some of them molecular, some of them dissociated on tungsten crystal surfaces (56).

The Surface Composition of Binary Alloys

The composition of alloys in the topmost monolayer is likely to be very different from the bulk composition for several reasons and we shall review briefly each one of them.

1. For systems that exhibit regular solution behavior, the surface free energy (which is always positive) is minimized by the segregation of that constituent with the lower surface tension. For metals that have high tensions as compared to organic surfaces or most oxide surfaces, such surface enrichment is likely to be very marked indeed. For a system obeying regular solution theory, it has been shown (57, 58) that the composition of the surface monolayer is given by

$$\frac{x_l^A}{x_l^B} = \frac{x_b^A}{x_b^B} \exp\left(\frac{(\sigma^B - \sigma^A)a}{RT}\right) \exp\left[\frac{\Omega(l+m)}{RT}((x_b^B)^2 - (x_b^A)^2) + \frac{\Omega l}{RT}((x_l^A)^2 - (x_l^B)^2)\right] \quad [1]$$

Where x_l and x_b are the atom fractions in the surface monolayer and bulk, respectively. In this expression σ is the surface energy, a is the molar surface area, T is the absolute temperature, R is the ideal gas constant, Ω is the regular solution parameter which is given from the heat of mixing ΔH_m by

$$\Omega = \Delta H_m / x_b^B x_b^A \quad [2]$$

The packing parameter l gives the fraction of an atom's nearest neighbors which are in the same plane parallel to the surface as the atom. Similarly m is the fraction of nearest neighbors which are in an adjacent parallel plane. For instance, in a fcc lattice, an atom has twelve nearest neighbors so a (111) plane has six nearest neighbors in the plane of an atom and three nearest neighbors in the plane below the atom. Thus in this case $l = 6/12$ and $m = 3/12$.

Electron spectroscopy techniques, especially Auger electron spectroscopy and photoelectron spectroscopy, have been eminently successful in determining the surface phase diagrams, *i.e.*, the surface composition as a function of bulk composition and temperature, for several binary metal systems. A typical Auger spectrum of an alloy system, that of palladium-gold, is shown in Fig. 8 (59). From the Auger peak intensities one may determine surface composition for a series of bulk compositions and from this data the surface phase diagram is deduced. The most serious experimental difficulty in converting the Auger peak intensities to surface concentrations lies in estimating the depth near the surface from which the Auger electrons of different kinetic energy are emitted and the relative scattering power of the two types of atoms in this volume sampled by the electrons. Since part of the Auger signal is due to atoms below the surface, it is essential to subtract this part from the signal intensities in order to extract the surface contribution. Much of the discrepancy between results reported from different laboratories on the same alloy system can be attributed to difficulties in estimating relative contributions of surface atoms to the various Auger peak intensities.

2. Adsorbed gases or impurities segregating at the surface can markedly change the surface composition. If one of the constituents forms strong chemical bonds with the adsorbate (oxygen, CO, carbon, sulfur, or calcium, most commonly) it will be accumulating on the surface even though it may not be at the surface in the absence of the absorbate. CO, for example, which forms strong bonds with many transition metal atoms, may aid the segregation of these atoms at the surface at the expense of other constituents that form weak CO bonds. In essence an adsorbate converts a two-component system to a three-component system, thereby altering the surface composition at equilibrium.

3. Solute atoms with large or small radii with respect to the size of the solvent (majority) atoms may be "excluded" from the bulk because they introduce excessive strain in the crystal lattice. As a result, surface segregation of one component that is misfit in the crystal lattice can be observed. The strain energy contribution may enhance the surface concentration of that component that would segregate on the surface on account of its effect of decreasing the total surface free energy. Conversely, this strain energy contribution may oppose the effect of surface segregation of one constituent in some cases.

4. There are complex phase diagrams that exhibit the formation of stable compounds of high lattice energy. In this circumstance the energy necessary to exchange the two atoms, A and B, by removing them from their equilibrium lattice site is so large that it overrides the influence of surface forces that would induce surface segregation. Thus the bulk composition pins the surface composition, *i.e.*, the surface and bulk compositions remain identical. We have found in studying the complex gold-tin phase diagram that this phenomenon occurs at the bulk composition of AuSn that forms a compound with high cohesive energy.

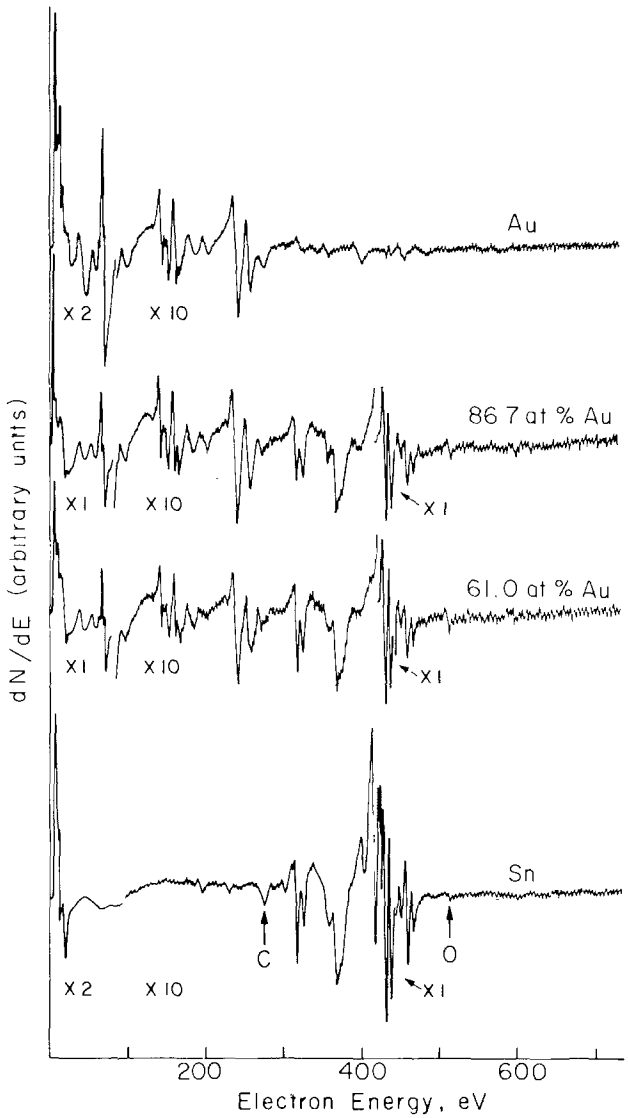


Fig. 8. Derivative Auger spectra for pure gold, pure tin, and two representational alloys.

In Table III we list those metal systems that have been studied by electron spectroscopy and indicate which element is found in excess at the surface. The surface composition is determined by the interplay of three physical parameters: (*i*) the surface free energy difference of the two components, (*ii*) the relative sizes of the two types of atoms in the alloy, and (*iii*) the magnitude of the bond energy between unlike atoms when a compound forms. For regular solutions, *i* and *ii* determine the surface composition. For substitution-

Table III. Surface enrichment of binary metal alloys

System	Excess on surface
Ag-Au (28)	Ag
Ag-Pd (31)	Ag
Al-Cu (32)	Al
Au-Cu (33)	Au
Au-In (34)	In
Au-Ni (35)	Au
Cu-Ni (36, 37)	Cu
In-Pb (38)	Pb
Ni-Pd (39)	Pd
Fe-Cr (40)	Cr
Pt-Sn (41)	Sn

ally ordered compounds of high binding energy, *iii* may override the effects of *i* and *ii*.

Studies of Catalytic Reactions

The purpose of these investigations is to understand the mechanism of catalyzed surface reactions on the atomic scale. We have recently developed new instruments for *in situ* studies of the reactivity of crystal surfaces at both low and high pressures. The scheme of one of these apparatus is shown in Fig. 2. At low pressures (10^{-7}-10^{-4} Torr), the reaction rate and product distributions are monitored by a quadrupole mass spectrometer while the surface structure and composition are determined by low energy electron diffraction and Auger electron spectroscopy, respectively. Then a small cup (total volume approximately 10 cm^3) can be placed around the crystal sample that isolates it from the rest of the chamber that can be pressurized to over 100 atm, if desired, using the mixture of gaseous reactants. The high pressure reaction chamber is connected to a gas chromatograph that serves to monitor both rate and product distributions in this circumstance. The structure and composition can be determined *in situ* by LEED and Auger before and after the high pressure experiment once the cup is removed.

Catalysis of Hydrocarbon Reactions by Platinum

Dehydrogenation of cyclohexane or cyclohexene to benzene occurs only on stepped platinum surfaces at an appreciable rate at low pressures. Figure 9 shows the step and kink density dependence of the rate of cyclohexene dehydrogenation to benzene to demonstrate this effect. While the rate increases markedly with increasing step density (Fig. 9a), it is relatively unaffected by changes of kink density (Fig. 9b).

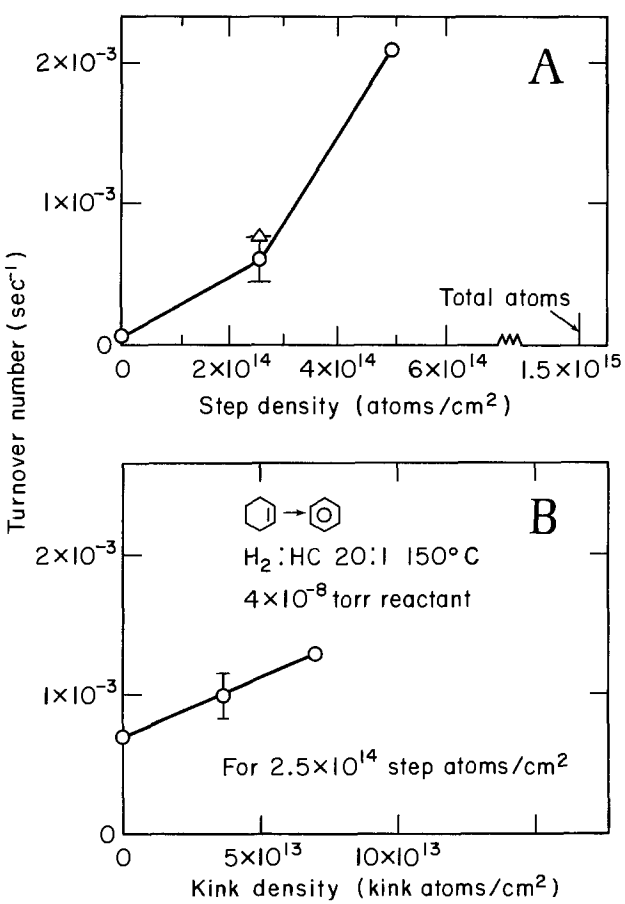


Fig. 9. Initial rate of cyclohexene dehydrogenation to benzene on platinum single crystal catalysts as a function of (a) increasing step density and (b) increasing kink density at constant step density. The reaction conditions are 5 × 10^{-8} Torr of cyclohexene, 1.0 × 10^{-6} Torr of hydrogen, and 423°K catalyst temperature.

The rate of cyclohexane dehydrogenation to benzene is constant as long as there are steps on the catalyst surface, but it is almost an order of magnitude lower on the Pt(111) surface, as seen in Fig. 10a. Thus atomic steps appear to be preferred surface sites for breaking H-H and C-H bonds (H-H bond breaking has been studied by the H_2-D_2 exchange).

Cyclohexane undergoes both dehydrogenation and hydrogenolysis on the stepped Pt surfaces. The relative rates of these two reactions can best be monitored by the ratio of benzene to n-hexane in the reaction product. As is demonstrated in Fig. 10, the rate of benzene production is independent of step and kink density while n-hexane production increases slowly with step density and rapidly with kink density. Rates of cyclohexane hydrogenolysis to n-hexane per kink site is determined by the slope of the line in Fig. 7b representing hydrogenolysis and is 3 × 10^{-28} moles of n-hexane/kink atom/sec. This is almost an order of magnitude higher than the slope in Fig. 8a which is 4 × 10^{-29} moles of n-hexane/step atom/sec. The observed low hydrogenolysis activity on the type of

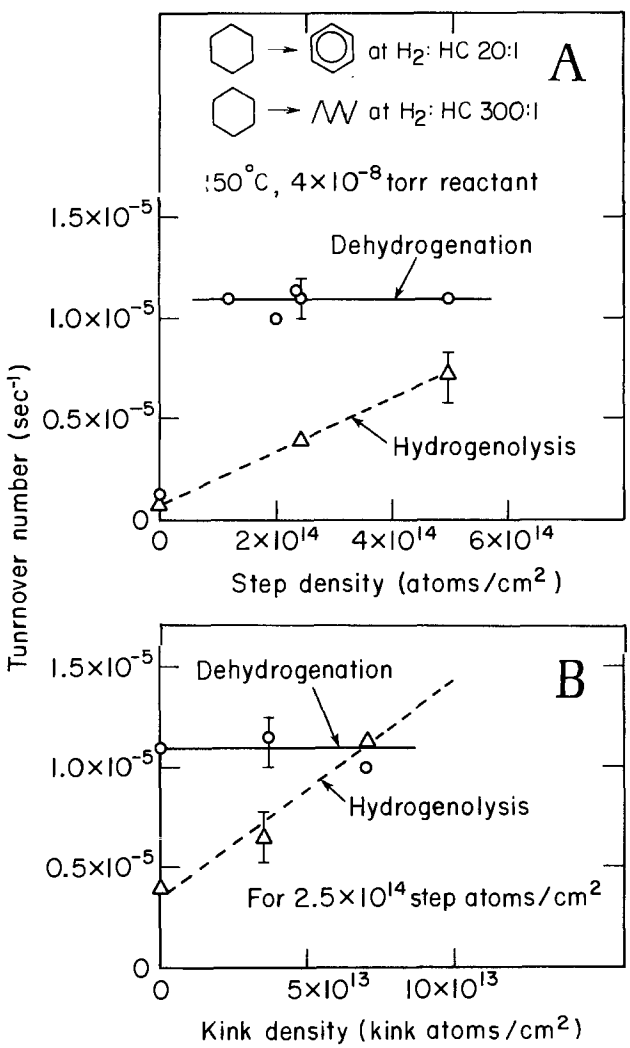


Fig. 10. Initial steady-state rates of cyclohexane dehydrogenation to benezene (o) and hydrogenolysis to n-hexane (Δ) on platinum single crystal catalysts as a function of (a) increasing step density and (b) increasing kink density at constant step density of 2.4 × 10^{14} step atoms/cm^2. The reaction conditions are 5 × 10^{-8} Torr of cyclohexane, 1.0 × 10^{-6} Torr of hydrogen, and 423°K catalyst temperature. The rate of dehydrogenation is constant at 2.8 × 10^{-14} mole cm^{-2} sec^{-1} with steps present but is less (0.3 × 10^{-14} mole cm^{-2} sec^{-1}) one the (111) surface (near zero step density). The rates of hydrogenolysis per surface sites are the slope of the lines representing hydrogenolysis and are 3 × 10^{-28} mole (kink atom)$^{-1}$ sec^{-1} and 4 × 10^{-29} mole (step atom)$^{-1}$ sec^{-1}.

stepped surfaces represented by Fig. 10a may be caused by some thermally regenerated kinks in the steps. n-Hexane formation and the formation of other hydrogenolysis products must be the result of C-C bond scissions. It appears that kinks are very effective in breaking C-C bonds in addition to C-H and H-H bonds. Thus we have been able to identify two active sites of lower coordination number of platinum surfaces: steps with C-H and H-H and kinks in steps with C-C, C-H, and H-H bond-breaking activity.

The Hydrogenation of CO and CO_2 over Polycrystalline Rhodium at 1 Atm (14)

The formation of hydrocarbons from CO-H_2 mixtures is thermodynamically favorable, although higher pressures (in excess of 1 atm) are necessary to facilitate the formation of higher molecular weight products.

The rates of formation of products by this reaction are very low as compared to other hydrocarbon reactions (dehydrogenation or hydrogenolysis). Thermodynamic equilibrium between reactants and the many possible products is not established even at the high pressures commonly employed.

We have studied the reaction of CO and H_2, and CO_2 and H_2 to form hydrocarbons, using polycrystalline rhodium as a catalyst. The kinetics of methanation on this metal foil of about ~1 cm^2 area is in excellent agreement with the results obtained on dispersed and supported rhodium catalysts.

There is evidence for the presence of both molecular and dissociated CO on the surface, during the synthesis. The active rhodium surface develops a carbonaceous deposit, while chemisorbed oxygen is rapidly removed from the surface layer by CO and H_2. Oxygen also appears to be located below the metal surface. By changing the composition and/or structure of the rhodium-carbon surface complex by pretreatment (with acetylene or oxygen), both the reaction rate and the product distribution can be markedly altered. The CO_2-H_2 reaction yielded methane predominantly, in contrast with the much broader distribution obtained from CO-H_2 reactions under the same conditions.

Variation of methanation activity and product distribution on clean and pretreated rhodium surfaces is shown in Table IV.

The high pressure apparatus has been a great asset to correlate the reactivity of the surface with the catalyst surface structure and composition for the important CO-H_2 and CO_2-H_2 reactions. As a result a better physical picture of heterogeneous catalysis emerges. It is my hope that using similar apparatus the reactivity, the structure, and the composition at solid-liquid interfaces will also be explored.

Table IV. Variation in methanation activity and product distributions for the CO-H_2 and CO_2-H_2 reactions on clean and pretreated rhodium surfaces. (Reaction conditions 1:3 ratio, 700 Torr, 300°C.)

Reaction gases	Surface pretreatment*	Methanation rate (300°C) (turnover number)	Product distribution (%)
CO-H_2	None	0.15 ± 0.05	88 C_1 9 C_2 3 C_3
CO_2-H_2	None	0.33 ± 0.05	100 C_1
CO-H_2	O_2	0.33 ± 0.05	87 C_1 10 C_2 3 C_3
CO_2-H_2	O_2	1.7 ± 0.2	98 C_1 2 C_2
CO-H_2	CO	0.15 ± 0.05	88 C_1 9 C_2 3 C_3
CO_2-H_2	CO	0.33 ± 0.05	100 C_1
CO-H_2	C_2H_2	0.07 ± 0.02	78 C_1 18 C_2 4 C_3
CO_2-H_2	C_2H_2	0.07 ± 0.02	96 C_1 3 C_2 1 C_3

* Heated for 15 min in 700 Torr of the particular gas, then thermally desorbed to 1000°C *in vacuo* before reaction.

Correlations of Structure, Composition, and Reactivity at Solid-Gas and Solid-Liquid Interfaces

The same questions that are asked in studies of solid-gas interfaces are also important to answer in studies of solid-liquid interface phenomena. What is the atomic and electronic structure and composition of the solid surface at the liquid interface in the presence of an external electric field and in the absence of such an electrochemical potential? How does this structure and composition correlate with reactivity during an electrochemical reaction or for surface reactions at the liquid interface? Since the solid surface structure and composition cannot be studied in the presence of a liquid with our surface-sensitive techniques that are presently available, just as in the case of high pressure, solid gas studies, the surface structure and composition will have to be determined before and after the solid-liquid interface reaction.

The simplest question that one may ask is whether stable surface structure of adsorbates and the bonding of these adsorbates are the same when adsorption occurs from the liquid face as compared to that from the vapor of the same molecule. Water or organic solvents (n-heptane, benzene, etc.) and ionic substances (sulfates, chlorates, halogens, and alkali metals) may come to mind as likely candidates for these studies. The high pressure apparatus that has been described above is most suitable to carry out these investigations. One may wish to investigate the surface structure of a single crystal face as the external electrochemical potential is changed. Simultaneously, one would wish to determine how the surface composition varies as oxidation or reducing surface conditions are established using an external potential. For example, what is the coverage and bonding of oxygen and hydrogen on the surface as a function of variation of the external electric field. The aim of these early studies should be to discover patterns of similarity and change with studies of the same type at the solid-liquid and solid-gas interface. Once these correlations of changes of surface structure and composition are established, electrochemical and other solid-liquid interface studies can draw on the wealth of information that is available from studies of the solid-gas interface. Then patterns of similarity may emerge for surface reaction studies as well, such as electrocatalysis and heterogeneous catalysis.

Admittedly, during the transient period while the liquid phase or high pressure gas phase is removed from the vicinity of the solid surface to be studied, many of the weakly bound surface intermediates may change their bonding or desorb altogether. Thus, studies of the surface structure and composition before and after the surface reaction may not always yield a complete physical picture of the working surface under reaction conditions. It is feasible, however, to remove or reintroduce a liquid or high pressure gas within milliseconds thereby increasing the probability to detect even weakly bound, short residence time surface species. [The surface residence time (τ) is commonly given as $\tau = \tau_0 \exp(\Delta H/RT)$ where τ_0 is often equated with vibrational times approximately 10^{-12} sec and ΔH is the heat of adsorption.] Such rapid pumping techniques will be developed in the near future no doubt.

Modern surface science developed on account of the atomic and molecular level information that has become available by applications of the new surface diagnostic techniques. Determination of the structure and composition of the working metal catalyst or the corroding surface also presented the opportunity to develop new catalysts and to passivate the surface against corrosion. There are several innovations of commercial significance that owe their birth to modern surface science. It is likely that studies of the solid-liquid interface will yield major advances in the field of elec-

trochemistry and perhaps establish new areas of electrochemical science.

Acknowledgment

This work was carried out under the auspices of the U.S. Energy Research and Development Administration.

REFERENCES

1. L. L. Kesmodel and G. A. Somorjai, *Phys. Chem. Ser. Two*, **7**, 1 (1975).
2. C. C. Chang, *Surf. Sci.*, **25**, 53 (1971).
3. W. M. Riggs and M. J. Parker, in "Methods of Surface Analysis," A. W. Czanderna, Editor, Elsevier, Amsterdam (1975).
4. E. P. Brongersma and P. M. Mul, *Surf. Sci.*, **35**, 393 (1973).
5. A. Benninghoven, *ibid.*, **53**, 596 (1975).
6. G. A. Somorjai, *Acc. Chem. Res.*, **9**, 248 (1976).
7. D. W. Blakely and G. A. Somorjai, *Surf. Sci.*, To be published.
8. D. W. Blakely and G. A. Somorjai, *J. Catal.*, **42**, 181 (1976).
9. S. L. Bernasek and G. A. Somorjai, *J. Chem. Phys.*, **62**, 3149 (1975).
10. L. D. Schmidt and R. W. McCabe, *Surf. Sci.*, **60**, 85 (1976).
11. D. W. Blakely and G. A. Somorjai, *Nature*, **258**, 580 (1975).
12. L. A. West, E. I. Kozak, and G. A. Somorjai, *J. Vac. Sci. Technol.*, **8**, 430 (1971).
13. D. W. Blakely, E. Kozak, B. A. Sexton, and G. A. Somorjai, *ibid.*, **13**, 1091 (1976).
14. B. A. Sexton and G. A. Somorjai, *J. Catal.*, To be published.
15. L. L. Kesmodel and G. A. Somorjai, *Acc. Chem. Res.*, **9**, 392 (1976).
16. T. A. Clarke, R. Mason, and M. Tescari, *Surf. Sci.*, **30**, 553 (1972).
17. P. W. Palmberg and T. N. Rhodin, *Phys. Rev.*, **161**, 586 (1967).
18. J. T. Grant, *Surf. Sci.*, **18**, 228 (1969).
19. M. A. Chesters and G. A. Somorjai, *Annu. Rev. Mater. Sci.*, **5**, 99 (1975).
20. E. G. McRae and C. W. Caldwell, Jr., *Surf. Sci.*, **2**, 509 (1964).
21. J. A. Strozier, Jr., D. W. Jepsen, and F. Jona, in "Surface Physics of Materials," Vol. I, J. M. Blakely, Editor, Academic Press, New York (1975).
22. M. A. Van Hove and S. Y. Tong, *Surf. Sci.*, **54**, 91 (1976).
23. See, for example, the series of three papers by T. E. Gallon, I. G. Higginbotham, M. Prutton, and H. Tokutaka, *Surf. Sci.*, **21**, 224 (1970) and references therein.
24. J. R. Arthur, *ibid.*, **43**, 449 (1974).
25. H. H. Brongersma and P. M. Mul, *ibid.*, **35**, 393 (1973).
26. P. D. Townsend and J. C. Kelly, *Phys. Lett. A*, **26**, 138 (1968).
27. T. M. French and G. A. Somorjai, *J. Phys. Chem.*, **74**, 2489 (1970).
28. L. Fiermans and J. Vennik, *Surf. Sci.*, **18**, 317 (1969).
29. L. E. Firment and G. A. Somorjai, *J. Chem. Phys.*, **63**, 1037 (1975); *Surf. Sci.*, **55**, 413 (1976).
30. L. E. Firment and G. A. Somorjai, *J. Chem. Phys.*, To be published.
31. J. C. Buchholz and G. A. Somorjai, *ibid.*, To be published.
32. S. L. Bernasek, W. J. Siekhaus, and G. A. Somorjai, *Phys. Rev. Lett.*, **30**, 1202 (1973).
33. B. Lang, R. W. Joyner, and G. A. Somorjai, *Surf. Sci.*, **30**, 440 (1972).
34. H. Ibach, K. Horn, R. Dorn, and H. Luth, *ibid.*, **38**, 433 (1973).
35. D. I. Hagen, B. E. Nieuwenhuys, G. Rovida, and G. A. Somorjai, *ibid.*, **57**, 632 (1976).
36. J. E. Rowe, S. B. Christman, and H. Ibach, *Phys. Rev. Lett.*, **34**, 874 (1975).
37. W. P. Ellis and R. L. Schwoebel, *Surf. Sci.*, **11**, 82 (1968).
38. H. Wagner and K. Besocke, *Surf. Sci.*, **52**, 653 (1975).
39. L. L. Kesmodel and L. M. Falicov, *Solid State Commun*, **16**, 1201 (1975).
40. Y. W. Tsang and L. M. Falicov, *J. Phys. C*, **9**, 51 (1976).
41. J. C. Buchholz and G. A. Somorjai, *Acc. Chem. Res.*, **9**, 333 (1976).
42. S. Andersson and J. B. Pendry, *J. Phys. C*, **5**, L41 (1972).
43. J. E. Demuth, D. W. Jepsen, and P. M. Marcus, *Phys. Rev. Lett.*, **31**, 540 (1973).
44. F. Forstmann, W. Berndt, and P. Buttner, *ibid.*, **30**, 17 (1973).
45. M. Van Hove and S. Y. Tong, *ibid.*, **35**, 1092 (1975).
46. A. Ignatiev, F. Jona, D. W. Jepsen, and P. M. Marcus, *Surf. Sci.*, **49**, 189 (1975).
47. J. E. Demuth, *Prog. Colloid Surf. Sci.*, To be published.
48. H. D. Shih, F. Jona, D. W. Jepsen, and P. M. Marcus, *Phys. Rev. Lett.*, **36**, 14 (1976).
49. L. L. Kesmodel, P. C. Stair, R. C. Baetzold, and G. A. Somorjai, *ibid.*, **36**, 1316 (1976).
50. P. C. Stair and G. A. Somorjai, *Chem. Phys. Lett.*, **41**, 391 (1976).
51. L. L. Kesmodel and G. A. Somorjai, *Surf. Sci.*, to be published.
52. J. E. Demuth and D. E. Eastman, *Phys. Rev. B*, **11**, 1523 (1976).
53. E. W. Plummer, B. J. Waclawski, and T. V. Vorburger, *Chem. Phys. Lett.*, **28**, 510 (1974).
54. D. A. Shirley *et al.*, *Phys. Rev. Lett.*, **37**, 1497 (1976).
55. R. Mason and G. A. Somorjai, *Chem. Phys. Lett.*, **44**, 468 (1976).
56. T. Yates, N. E. Erickson, S. D. Worley, and T. E. Madey, in "The Physical Basis for Heterogeneous Catalysis," E. Drauglis and R. Jaffee, Editors, p. 75, Plenum, New York (1975).
57. S. H. Overbury, P. A. Bertrand, and G. A. Somorjai, *Chem. Rev.*, **75**, 547 (1975).
58. S. H. Overbury and G. A. Somorjai, *Faraday Discuss. Chem. Soc.*, **60**, 279 (1975).
59. S. H. Overbury and G. A. Somorjai, *J. Chem. Phys.*, To be published.

PEOPLE



David G. Thomas has been elected to the grade of Fellow by the Institute of Electrical and Electronics Engineers (IEEE). The honor, conferred upon 133 chosen from nine countries, is given to people with "demonstrated outstanding and extraordinary qualifications and experience" who have made important contributions to their profession. Dr. Thomas, Executive Director of the Transmission Systems at Bell Laboratories in Holmdel, has been selected in particular "for contributions to the understanding of luminescense in semiconductors, and to the development of light-emitting diodes." His studies led to the development of gallium-phosphide light-emitting diodes (LED's), which consume less power and last longer than tungsten lamps. LED's are used extensively in the Bell System as indicator lights on maintenance equipment, central-office control panels, and some new multiline telephones and business telephone consoles.

Dr. Thomas has been an Active Member of the Society since 1968.

Robert Baboian has been honored as a "TI Fellow" by Texas Instruments Incorporated. He was presented with a plaque designating him as such in special recognition of his contributions to Texas Instruments in science and technology during his ten year career with the company. He is the sixth person to receive the award.

Dr. Baboian received his B.S. degree in chemistry from Suffolk University, Boston, and his Ph.D. in physical chemistry from Rensselaer Polytechnic Institute in Troy, N.Y. He did postdoctoral research as a Ford Foundation Fellow at the University of Toronto. He is presently working in the Materials and Electrical Products Group in Attleboro, Vermont, and is Texas Instruments' leading expert on corrosion resistant materials. Some of his earliest work at TI involved the investigation of the use of stainless-steel-clad aluminum trim materials on automobiles. He has developed fundamental principles for galvanic corrosion, established test methods and design criteria for clad metal systems, and has established electrochemical techniques for investigation of corrosion reactions. His work on impressed current cathodic protection has led to wide use of platinum-clad columbium anodes for corrosion protection. Since joining TI in 1956, he has been issued five U.S. patents and 27 international patents.

Dr. Baboian has been an Active Member of the Society since 1934.

Section News cont.

Metropolitan New York Section

On March 16, 1977, the Metropolitan New York Local Section held a joint meeting with the Newark Branch of the American Electroplaters Society. The meeting was attended by 49 ECS and AES members, guests, and students. Professor Rolf Weil, Chairman of this Local Section, presented a talk entitled "The Structure of the Early Stages of Nickel Electrodeposition." Dr. Weil showed how brighteners have not only an effect on the formation of multiple layers of electrodeposited metal, but also have substantial effect on the formation of the initial layer of metal. Under ideal conditions, electrodeposition should initiate at kink sites and spread two dimensionally to form a monolayer. This typically does not occur. Both clumps and pyramids grow from nucleation sites and coverage occurs by coalescence of these islands of atoms. Addition agents such as saccharin reduce the clumping tendency and also decrease mismatch stress caused by the difference between the atomic spacing of nickel and substrate.

The last meeting of the season, Ladies Night, was held on April 27, 1977, at the Stevens Institute of Technology, Hoboken, New Jersey. After a business meeting at which new officers were elected (results to be published in a later issue of **This Journal**) a social evening was held at which there were door prizes, entertainment, and a featured speaker.

John Broadhead
Vice-Chairman

NEW MEMBERS

It is a pleasure to announce the following new members of The Electrochemical Society as recommended by the Admissions Committee and approved by the Board of Directors in April 1977.

Active Members

Askew, B. A., Washington, D.C.
Bahl, S. K., Dayton, Oh.
Battey, J. F., Los Altos, Ca.
Besson, J., St. Martin D'Heres, France
Drake, M. P., Harlow Essex, England
Ekern, R. J., Rolling Meadows, Il.
Hall, D. E. Suffern, N.Y.
Hibbert, D. B., London, England
Hong, I., Seoul, Korea
Locke, C. E., Norman, Ok.
Minh, N. Q., Cambridge, Ma.
Niazy, N. N., Devon, Pa.
Papatheodorou, G., Argonne, Il.
Pierini, P. E., Berkeley, Ca.
Reagor, B. T., Ocean, N.J.
Rosler, R. S., Santa Clara, Ca.
Salama, A. M., Los Angeles, Ca.
Schmidt, N. O., Soeborg, Denmark
Senoo, T., Osaka, Japan
Sugimoto, K., Montreal, Canada
Tapping, R. L., Kingston, Ont., Canada
Yamaoka, H., Kobe, Japan
Yoo, J. H., Columbus, Ms.

Student Members

Hammerschmidt, R. F., Lincoln, Ne.
Hema, A. S., Cleveland, Oh.
Hsu, Y.-S., Troy, N.Y.
Lassow, E. S., Cambridge, Ma.
Nelson, N. K., Jr., Seattle, Wa.

Reinstatement

Masi, J. A., Wilmington, De.
Prado, F. G., Lakeland, Fl.

Transfer

Cahen, G. L., Jr., Charlottesville, Va.
Dallek, S., Adelphi, Md.
Huang, M., Groton, Ct.

BOOK REVIEWS

"Silicon Carbide—1973," edited by R. C. Marshall, J. W. Faust, Jr., and C. E. Ryan. Published by the University of South Carolina Press, Columbia, South Carolina (1974). 692 pages.

This volume is a compilation of 75 papers delivered at the Third Silicon Carbide Conference held September 17-20, 1973, sponsored by AFCRL. The papers stress the "glamour" areas of SiC research such as fundamental physical properties, new methods of crystal growth, and electronic devices (especially LED's), but also cover more practical nonelectronic research including, for example, a paper on the production of SiC from rice hulls.

For over twenty years SiC has been a promising material for LED's and other electronic applications because of its wide bandgap, ease of being doped either n- or p-type, and high thermal conductivity and stability. However, the field is still severely impeded by the tremendous difficulty of growing single crystals and diffusing the material to form useful devices, processes which must be carried out at temperatures between 1800° and 2300°C. Because of this, nearly a third of the papers in this volume deal with crystal growth, including liquid and vapor phase epitaxial growth.

The degree of sophistication of SiC crystal growth is seen to parallel that of the more widely used, commercially

Continued on p. 219C

Abstracts of "Recent News" Papers—Philadelphia Meeting 215C-216C
Changes in Spring Meeting 216C
News Item 216C
Section News 216C-217C
People 217C
New Members 217C
Book Reviews 217C-220C
Vittorio de Nora and Diamond Shamrock Award 218C
1977 Becket Award Winner 218C
Positions Available 222C
Positions Wanted 222C

Continued from p. 217C

successful III-V compounds. An example of perhaps the most sophisticated crystal growth technique is presented in a paper by Rutz and Cuomo of IBM, who grew single crystals of SiC by close-spaced vapor deposition at 1860°C on single crystalline AlN layers grown by reactive sputtering on single crystal tungsten layers deposited on sapphire substrates.

Another very interesting paper is a review of the status of SiC LED's, including a comparison with GaP, a competing material for which an advanced LED technology has been developed. The paper is by two Russian authors, Kholuyanov and Vodakov, who are well qualified because of their heavy involvement in LED research and by the fact that most SiC LED work has been carried out in the Soviet Union. They conclude that at very low current densities (< 0.1 A/cm^2) the best SiC diodes are superior to either Zn, O-doped red, or N-doped green emitting diodes. However, it should be understood that at normal operating current the situation is reversed. For example, at 10 A/cm^2, the GaP:N LED's are a factor of ~ 20 brighter.

In spite of the good and original research presented in this volume, one has the feeling that SiC for electronic applications still remains "subthreshold," as characterized by R. C. Marshall in the opening comments, and is falling further and further behind the rapidly advancing III/V and elemental semiconductors.

This book will be indispensible to workers in the area of SiC. It is also an excellent source for researchers involved in electronic materials research who want a compact compilation of the recent work in SiC and its present status.

G. B. Stringfellow
Hewlett-Packard
Palo Alto, California

"Progress in Solid State Chemistry," Vol. 10, edited by J. O. McCaldin and G. Somorjai. Published by Pergamon Press, Inc., Elmsford, New York (1976). 284 pages; $37.50.

The well-known series on "Solid State Chemistry" has added a new edition, the tenth, which starts a new mode of publication. Camera-ready manuscripts are printed so that faster publication is assured and several volumes per year may be issued. With nine papers covering a wide range of topics, Volume 10 is a welcome addition to this series, as it treats a group of important projects.

Carl Wagner contributes a paper on the transport equations in solid oxides and sulfides of transition metals. As these materials are of technical importance in metallurgical processes, amorphous structures, thin films, electrolytic cells, and semiconductor electronics, the solutions of the transport equations (basically of the Onsager-type) for different cases (ratio between ion and electron conduction, composition gradient, rate of oxidation, defect density) are essential. This paper written by a recognized authority will be of great interest for those working in this field.

A second paper on the oxides of transition metals (W. W. Smeltzer and D. J. Young) contributes to the chemical and structural features of these compounds. Major aspects of the oxide formation are discussed: thermodynamics (metal-oxide equilibria); lattice defect structures (point defects vs. electron concentration); diffusion (self, tracer, defect, and chemical diffusivities); boundary conditions and interfacial processes including defects; and oxidation rate equations and rate control by electron injection and transport. On the experimental side, the authors develop detail of oxide film growth in the case of nickel, copper, and zinc, and discuss conducting oxide films.

Finally, high temperature scale formation is described in the context of the experimental facts (phase diagrams, diffusion coefficients, parabolic kinetics) for the above metals and cobalt, chromium and manganese. There is an intimate connection between scale growth and growth of dislocation networks. (See also: "International Colloquium on Grain Boundaries in Metals," Journal de Physique, Colloque C-4 supplement No. 10, October 1975.)

J. H. Sinfelt contributes an article on heterogeneous catalysis by metals. The great importance of the catalytic potential of the group VIII metals (iron, cobalt, nickel) and copper is emphasized from the outset. Heterogeneous catalysis is discussed qualitatively as a large surface area chemical interaction with specificity for the chemical reaction induced. Particular features or classes of reactions on metals are discussed: hydrogenation, hydrogenolysis, isomerization, oxidation.

A. Rothwarf and K. W. Boer summarize the status in the field of solar cells in their contribution on direct conversion of solar energy through photovoltaic cells. The article is an in-depth review of the field starting with the basic equations for the state density, statistics, band scheme, junction behavior, and diode forms (homojunctions and metal-semiconductor junctions). The more complex cases of heterostructures (Cu_2S-CdS) are discussed and a few practical questions concerning solar cell efficiency (reflection, absorption losses) and the basic set of transport equations are given. Boundary conditions, drift field effects, diffusion length, mobility, and lifetime are part of the general topics leading to a consideration of the solar cell efficiency. After discussion of the important Schottky diode cells (with a practical list of observed barrier heights), some experimental results are given and future forms are discussed. In this fast moving field, it is difficult to stay abreast of the latest development. Thus numbers given and materials quoted are partially outdated already, but the in-depth survey conveys an excellent picture of the technologies involved.

Ivan Haller gives a description of the thermodynamic and static properties of liquid crystals. The review is limited to thermotropic liquid crystals with emphasis on nematic materials, and it pursues the ideas concerning the nature of liquid crystalline phase transitions. Particular topics treated are molecular structure and phase transitions, eutectic compositions, surface chemistry and alignment, refractive index, and the order parameter. The industrial importance of the liquid crystals (displays) and their biological significance (membranes) has resulted in numerous other reviews quoted by the author.

The paper by A. D. Pelton and W. T. Thompson on phase diagrams correlates graphical representations with analytical thermodynamic expressions. The integral molar-free energy of a phase is combined with the expression for the chemical potential. The shape of the isotherms is expressed via the temperature dependence of the integral molar Gibbs free energy of mixing. Numerous binary and ternary systems are calculated and the result compared to experimental phase diagrams. The authors have made great strides to further the understanding of the many parameters influencing phase equilibria.

A. Y. Cho and J. R. Arthur contribute a paper on molecular beam epitaxy. This is the ultimate in localized definition of epitaxial growth; different from CVD (Chemical Vapor Deposition) and LPE (Liquid Phase Epitaxy), individual molecular species are deposited under ultrahigh vacuum conditions. The method allows a submicron control of deposition and so-called superlattices are feasible by subsequent layer deposition. The authors show how the difficulties of monocrystallization can be overcome. Clean deposition conditions plus annealing steps yield very perfect monocrystallinity. Also the doping problem can be solved in most cases. The authors show as proof a number of devices and their performance data.

A paper on surface physics of silver halides (Yen T. Tan) adds interesting information on the structure of AgBr and AgCl. The ionic space-charge model of halide surfaces is addressed specifically and the theory underlying this phenomenon is reviewed. As the vacancy gradient and uncompensated surface charges give rise to a rearrangement of ions near the surface, a type of Boltzmann distribution of excess subsurface charges is postulated. Experimental conductivity vs. thickness results and potentials plotted by the Kelvin probe are discussed. The presence of these space-charge layers is also postulated in emulsions and microcrystals with the additional feature of an even higher conductivity due to interstitial silver

Continued over

Electrocapillary Curves for Gold

K. F. Lin and T. R. Beck*

Department of Chemical Engineering, University of Washington, Seattle, Washington 98195

Electrocapillary curves have been determinded for gold by measuring the elongation of a thin gold ribbon as a function of potential. Elongation is measured by an extensometer instrument previously described (1,2). Change in surface stress, $\Delta\sigma_s$, of the ribbon is measured which with this instrument is approximately equal to change in surface tension, $\Delta\gamma$.

The gold ribbons had the dimensions 12.5 μm thickness x 0.32 cm wide with about 50 cm length immersed in the electrolyte. The ribbons were rolled from 99.99% gold. The counterelectrode was a ribbon of the same material to minimize contamination to the system. A saturated calomel reference electrode was connected to the measuring cell through a salt bridge containing the electrolyte under study. Electrolyte was prepared from reverse-osmosis purified water and ACS-reagent grade chemicals. Initial experiments were with nondearted solutions. A new purification system has been assembled which continuously deaerates with purified nitrogen, absorbs with activated carbon and preelectrolyzes with ribbons of the same metal as under study.

An electrocapillary curve for gold in 0.1*N* KCl solution was previously shown (1). Similar parabolic-shape curves are also obtained in other solutions. The potential of the surface stress maximum for gold was found to be independent of *p*H in 0.1*N* potassium sulfate and perchlorate solutions. Gold has a high hydrogen overvoltage and a high oxidation potential so that it has a wide electrical double layer region like mercury.

Surface active anions shift the surface stress maximum in the negative direction as shown in Fig. 1. (These curves were moved on the surface-stress scale to bring them tangent on the negative branch.) The order of adsorption of the anions on gold is the same as for mercury (3) but the magnitude of the shift is greater. A similar larger magnitude shift in the point of zero charge of gold measured by double layer capacitance minima and integration of capacitance for dilure halide solutions was observed by Clavilier and Van Huong (4). These data are compared in Table I. The bias between the two sets of data hopefully can be resolved upon more rigorous purification.

Table I. Potential of surface stress maximum and point of zero charge for gold

	ϕ (σ_s max) (V_{SCE})	ϕ_z (V_{SCE})	$\Delta\phi$ (V)
Cl^-	-0.4	-0.18	0.22
Br^-	-0.70	-0.42	0.28
I^-	-0.98	-0.70	0.28

Order of magnitude checks have been obtained between surface stress and double layer capacitance using the Lippmann equation.

ACKNOWLEDGMENT

This work was supported by National Science Foundation Grant GK33934

REFERENCES

1. T. R. Beck, J. Phys. Chem., 73, 466 (1969).
2. T. R. Beck and K. W. Beach, in "Electrocatalysis," M. Breiter, Editor, p. 357, The Electrochemical Society, Inc., Princeton, N.J. (1974).
3. D. C. Graham, Chem. Rev., 41, 441 (1947).
4. J. Clavilier and N. Van Huong, Electroanalytical Chemistry and Interfacial Chemistry, 41, 193 (1973).

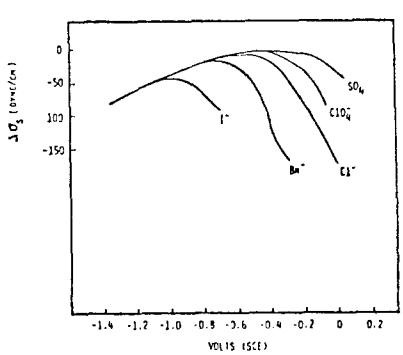


Fig. 1. Electrocapillary curves for gold in 0.1*N* solutions.

*Electrochemical Society Active Member.

JOURNAL OF THE ELECTROCHEMICAL SOCIETY

ELECTROCHEMICAL SCIENCE AND TECHNOLOGY

SEPTEMBER 1977

The Hydrogen Electrode in Molten Carbonate

W. M. Vogel* and C. D. Iacovangelo*,[1]

United Technologies Corporation, Advanced Fuel Cell Research Laboratory, Power Systems Division, Middletown, Connecticut 06457

ABSTRACT

Open-circuit potentials are reported for the hydrogen (Au) electrode in molten carbonate at 650°C. The data, with few exceptions, agree with thermodynamic values calculated assuming simultaneous equilibrium of the shift and the methane reactions. The exceptions are those instances where methane has to be oxidized almost completely to reach equilibrium, and those where carbon can form during preheating of the gas.

The anodic activation polarization of the hydrogen electrode in alkali carbonate melts should be small because of the required high temperatures. This is evidently true because the nature of the electrode metal has no effect on the polarization (1). Ohmic losses can be estimated from the conductance of the electrolyte and should be generally small even in a porous gas diffusion electrode except when poorly conducting surface oxides are formed on the electrode metal. Thus, with negligible activation polarization and ohmic losses the anode polarization should consist, at potentials below the metal oxidation potential, of concentration overvoltages plus, possibly, some contribution from liquid junction potentials between anode and cathode.

Broers *et al.* (2) have found that the polarization of such anodes results primarily from the accumulation of reaction products (CO_2, H_2O) rather than from a lack of hydrogen. The anode reaction

$$H_2 + CO_3^{=} = H_2O + CO_2 + 2e^- \qquad [1]$$

produces CO_2 and H_2O both of which are acids in molten carbonates. Both enter into acid-base equilibria (3, 4) with the strongly basic $O^=$ ion

$$CO_2 + O^{=} = CO_3^{=} \qquad [2]$$

$$H_2O + O^{=} = 2\,OH^- \qquad [3]$$

The acidity constants, *i.e.*, the equilibrium constants of reactions [2] and [3] are of similar magnitude. Busson *et al.* (5) reported the values $K_{CO_2} = 10^{7.5}$ and $K_{H_2O} = 10^6$ for 600°C. The alkalinity of the melt, expressed as $pO \equiv -\log[O^=]$ in analogy to the pH of aqueous solutions (6), is therefore not determined by the CO_2 pressure alone but by both the pressures of H_2O and CO_2. Because of this simultaneous dependency of the oxygen ion concentration on both pressures, it appears more suitable to use the pO as the measure for acidity rather than the $PCO_2 \equiv -\log p_{CO_2}$ which was suggested by Janz *et al.* (7) for hydrogen-free systems.

A given melt can then be considered acidic if the pO is larger than a certain neutrality value, and alkaline if the reverse is true. Busson *et al.* (5) reported for the solubility of CO_2 the relationship $(CO_2) = 0.1\,P_{CO_2}$ (P_{CO_2} in atmospheres, (CO_2) in mole/liter). Together with the acidity constant of CO_2 we have, at 600°C

$$(CO_2)\,(O^=) = 10^{-8.5} \qquad [4]$$

We consider a melt to be neutral when $(CO_2) = (O^=)$, *i.e.*, at $pO = 4.25$. As long as the water pressure is not extremely high, the OH^- ions can be assumed to be dissolved in molten carbonate and we can use the same pO value for a neutral melt containing both acids, H_2O and CO_2. An equilibrium oxygen electrode can then be used as a pO indicator with the potential

$$E = E_o + \frac{RT}{4F} \ln P_{O_2} + \frac{2.3RT}{2F} \cdot pO \qquad [5]$$

The results of Broers *et al.* (2) indicate, in this terminology, a lack of buffer capacity of the electrolyte (8) as a main cause for the polarization of a hydrogen anode. This explanation assumes that the electrode reaction is, at all current densities, close to equilibrium, *i.e.*, the iR-free electrode potential is nearly identical with the equilibrium potential calculated with the activities of the reactants as they prevail at the metal/liquid interface. However, this explanation is in apparent contradiction to data in Ref. (5) which describes deviations from equilibrium even at open circuit. The discrepancies were as large as 100 mV with the largest differences observed in acidic and alkaline melts, *i.e.*, just where polarized molten carbonate electrodes are assumed to operate.

A number of factors can cause real or apparent discrepancies between calculated thermodynamic potentials and observed open-circuit potentials (ocp). The equilibrium potential of reaction [1] is given by

$$E = E^\circ + \frac{RT}{2F} \ln \frac{P_{H_2O} P_{CO_2}}{P_{H_2}} \qquad [6]$$

If arbitrary mixtures of H_2, CH_4, CO, and CO_2 are used we can calculate the equilibrium pressures of H_2O, CO_2, and H_2 provided that carbon is not formed.

* Electrochemical Society Active Member.
[1] Present address: General Electric Company, Research and Development Center, Schenectady, New York 12301.
Key words: molten carbonates, hydrogen electrode, open-circuit potentials.

However, the actual pressures at the electrode may be different, resulting in discrepancies between calculated and observed potentials.

It is also possible that observed differences are due to fundamental uncertainties which are introduced by the type of reference electrode used in previous studies. The H_2O and CO_2 pressures at a molten carbonate electrode cannot be changed without simultaneously changing the electrolyte composition (Eq. [2], [3]). As written, Eq. [6] assumes that E is measured against a reference in the same medium, and that the reference potential varies with the carbonate ion activity in the same way as that of the hydrogen electrode. An example is an oxygen reference electrode with the same H_2O and CO_2 pressures as the hydrogen electrode. In this case, E is simply the cell voltage for the water reaction and $E°$ can be calculated very accurately. Differences between such calculated values for E and observed ocp have to be due to nonequilibrium conditions of the working electrode. Such experiments are thermodynamically well defined but they are also cumbersome, requiring changes in the gas composition at the reference in concert with those at the working electrode.

It is more common to use a constant reference electrode. Such experiments are simpler to do but they are thermodynamically less well defined, *i.e.*, observed potentials cannot be compared with calculated values without additional assumptions. Assume that an oxygen electrode in a carbonate melt of fixed acidity (CO_2 pressure) is used as reference. Equation [6] can then be applied provided that liquid junction potentials and differences in the carbonate ion activities at the two electrodes are negligible. These conditions should be fulfilled except for very alkaline conditions at the working electrode. Similar restrictions apply to potentials referred to a metal/metal ion electrode such as that of Danner and Rey (9). With such a reference, furthermore, the standard potential $E°$ cannot be calculated from thermodynamic data but has to be determined empirically.

The present study was undertaken in an attempt to identify the reasons for previously reported deviations of ocp from thermodynamic values, and to determine how and under what circumstances the ocp can be calculated.

Experimental

The apparatus used in measuring the ocp is illustrated in Fig. 1. The electrolyte, which was a fused binary eutectic of 62 mole percent (m/o) Li_2CO_3 and 38 m/o K_2CO_3, was contained in a tapered crucible made of Degussit AL-23 (99.5% Al_2O_3, dense).

The working electrode (WE) was a 0.020 in. diam gold wire inside a 0.50 in. diam AL-23 tube with a 1 mm opening to the melt at the bottom. The tube was vented to the atmosphere through a 0.125 in. diam alumina tube.

The initial partial pressures of H_2 and CO_2 in the feed gas to the WE were regulated by flowing each gas through Gilmont Flowmeters (no. 1) connected by a tee to 0.25 in. diam tubing, 2 ft in length, where they were allowed to mix prior to entering the water saturator. The initial water pressure was established by flowing the gas mixture through a saturator maintained at the required temperature. The saturator efficiency was checked by absorbing the H_2O with Dri-Rite. The feed gas was subsequently preheated to 650°C by flowing at 200 ml/min through 0.25 in. diam 316 stainless steel tubing 7 ft in length. The latter was wrapped around the outside of the cell crucible.

The apparatus was heated in a Lindberg furnace. All experiments were done at 650° ± 0.5°C. The temperature was measured inside the cell with a thermocouple contained within an alumina tube.

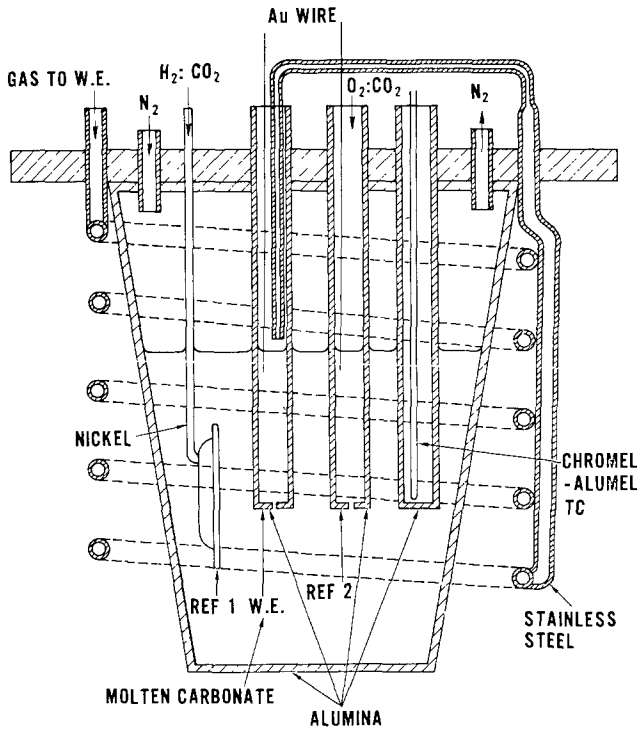


Fig. 1. Cell assembly

Cell voltages were measured with a Newport digital voltmeter having an input resistance of $10^9\Omega$.

For the present study a constant oxygen reference electrode was used [O_2, CO_2 (Au) with $P_{O_2} = 1/3$ and $P_{CO_2} = 2/3$ atm]. This choice of reference introduces fundamental inaccuracies which were described in the introduction. Significant errors of this nature should produce deviations of the ocp from theoretical values. As will be shown later, good agreement was observed which indicates that such errors were small for the range of compositions studied. The reference was checked against a CO/CO_2 electrode of similar melt composition ($P_{CO} = 0.382$ and $P_{CO_2} = 0.618$ atm). The difference between the observed and the calculated voltage of this cell [using data from Ref. (10)] was 2 mV which demonstrates the usefulness of our reference. Similar reliability in a ternary melt of alkali metal carbonates has been reported by Borucka *et al.* (11, 12).

Results and Discussion

The observed open-circuit potentials for initially dry mixtures of H_2 and CO_2 are listed in Table I. Included in this table are the pressures of H_2, H_2O, and CO_2 which were calculated assuming shift equilibrium ($K_p = 1.96$), and also simultaneous equilibrium of the shift and the methane reactions ($K_p = 2.68$). The data are plotted in Fig. 2. We see that neither assumption explains the experimental results.

One likely cause for the differences is carbon formation. If the gases are heated instantaneously to 650°C, carbon cannot form since the potential of the C/CO_2 reaction would be negative relative to the hydrogen potential if either shift or complete equilibrium is assumed. However, in our experiments the gas was heated gradually as it passed through the preheater tubing. At temperatures below 650°C the C/CO_2 potential becomes increasingly more anodic to the hydrogen potential assuming, *e.g.*, shift equilibrium, and carbon formation is likely.

The experiments were repeated with an addition of 14% H_2O vapor to the H_2-CO_2 mixtures. The re-

Table I. Initial (index°) and calculated pressures assuming equilibrium for the shift reaction only

Initially		Shift equilibrium				Shift and methane equilibrium					
$P_{H_2}°$	$P_{CO_2}°$	P_{H_2}	P_{CO_2}	P_{H_2O}	$E_{theor.}$	P_{H_2}	P_{CO_2}	P_{H_2O}	P_{CH_4}	$E_{theor.}$	$E_{expt.}$
0.05	0.95	0.005	0.905	0.045	−899	0.0045	0.905	0.045	3.4×10^{-8}	−894	−916
0.1	0.9	0.017	0.817	0.083	−927	0.017	0.817	0.083	1.7×10^{-6}	−926	−945
0.2	0.8	0.059	0.659	0.141	−964	0.059	0.659	0.141	7.7×10^{-5}	−964	−975
0.3	0.7	0.121	0.521	0.179	−993	0.120	0.523	0.179	6.4×10^{-4}	−992	−985
0.4	0.6	0.199	0.399	0.201	−1018	0.195	0.404	0.202	0.0027	−1017	−1000
0.5	0.5	0.292	0.292	0.208	−1045	0.279	0.301	0.214	0.0075	−1041	−1010
0.6	0.4	0.399	0.199	0.201	−1074	0.370	0.212	0.217	0.016	−1065	−1025
0.7	0.3	0.521	0.121	0.179	−1109	0.472	0.135	0.211	0.029	−1094	−1045
0.8	0.2	0.659	0.059	0.141	−1156	0.591	0.068	0.192	0.043	−1138	−1070
0.9	0.1	0.817	0.017	0.083	−1235	0.748	0.017	0.142	0.049	−1212	−1105

Table II. Initial (index°) and calculated pressures assuming equilibrium for shift reaction only, and assuming complete equilibrium

Initially			Shift equilibrium				Shift and methane equilibrium					
$P_{H_2}°$	$P_{CO_2}°$	$P_{H_2O}°$	P_{H_2}	P_{CO_2}	P_{H_2O}	$E_{theor.}$	P_{H_2}	P_{CO_2}	P_{H_2O}	P_{CH_4}	$E_{theor.}$	$E_{expt.}$
0.043	0.817	0.14	0.013	0.787	0.170	−890	0.013	0.787	0.170	1.4×10^{-7}	−890	−895
0.086	0.774	0.14	0.030	0.718	0.196	−921	0.030	0.718	0.196	2.7×10^{-6}	−921	−925
0.172	0.688	0.14	0.076	0.592	0.236	−958	0.076	0.592	0.236	6.4×10^{-5}	−958	−960
0.258	0.602	0.14	0.134	0.478	0.264	−985	0.133	0.479	0.264	3.9×10^{-4}	−984	−982
0.344	0.516	0.14	0.204	0.376	0.280	−1009	0.201	0.378	0.281	0.0014	−1008	−1010
0.430	0.430	0.14	0.285	0.285	0.285	−1032	0.277	0.289	0.289	0.0037	−1030	−1030
0.516	0.344	0.14	0.376	0.204	0.280	−1057	0.360	0.209	0.290	0.0076	−1053	−1050
0.602	0.258	0.14	0.478	0.134	0.264	−1086	0.451	0.139	0.284	0.0129	−1079	−1078
0.688	0.172	0.14	0.592	0.076	0.236	−1121	0.555	0.077	0.267	0.0185	−1113	−1112

sults are given in Table II, together with the pressures of H_2, H_2O, and CO_2 again calculated with the assumption that only the shift reaction is in equilibrium. The ocp and the thermodynamic potentials E, derived from these calculated pressures, are plotted in Fig. 3a against the activity term in Eq. [6]. The agreement is better than in Table I. However, at low potentials the experimental data still are more positive than the calculated values. The ocp appears to be a mixed potential with the hydrogen reaction being anodically polarized and some other reaction proceeding cathodically. This electrochemical description is being used because any of the possible chemical reactions (shift, Boudouard, etc.) can be considered as the neutral sum of electrochemical partial reactions. It does not matter, for the present purpose of determining equilibrium potentials, where these reactions occur, *i.e.*, at the metal/liquid interface or somewhere upstream from the electrode.

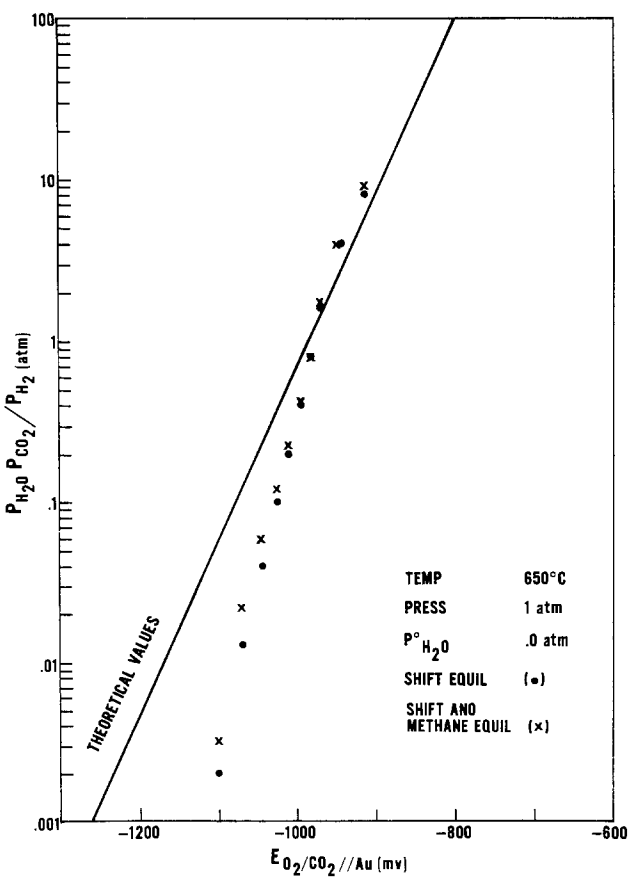


Fig. 2. Open-circuit potentials for dry mixtures of H_2 and CO_2. Partial pressures of H_2, CO_2, and H_2O calculated assuming equilibrium for the shift reaction only.

We have the following four reactions, combinations of which yield all other possible reactions (chemical or electrochemical)

$$H_2 + CO_3^= = CO_2 + H_2O + 2e^- \quad [7]$$

$$CO + CO_3^= = 2CO_2 + 2e^- \quad [8]$$

$$C + 2CO_3^= = 3CO_2 + 4e^- \quad [9]$$

$$CH_4 + 4CO_3^= = 5CO_2 + 2H_2O + 8e^- \quad [10]$$

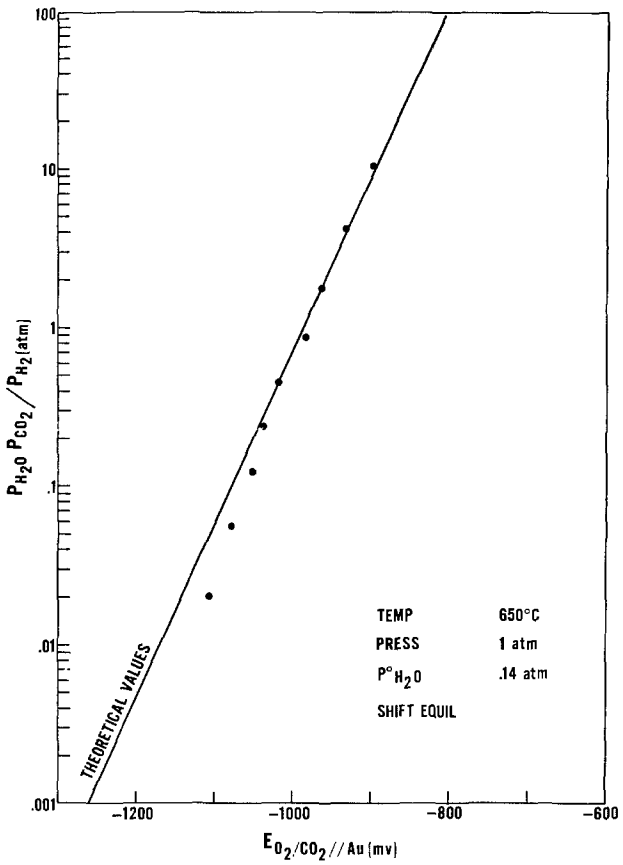
Since, by adding 14% H_2O, we had raised the value of E for reaction [7] above that for reaction [9] no carbon formation was possible. Reaction [8] was accounted for by assuming equilibrium for the shift reaction which is the (electrically neutral) sum of reactions [7] and [8]. It was indicated, therefore, that the cathodic branch of reaction [10] was responsible for the remaining differences in Fig. 3a.

The equilibrium pressures for the gas mixtures in Table II were recalculated assuming that reactions [7], [8], and [10] were in equilibrium. Thus, in addition to the shift reaction, the methane formation, which results from a combination of reactions [10] and either [7] or [8], was assumed to be in equilibrium. The value

$$K = \frac{P_{CO} P_{H_2}^3}{P_{CH_4} P_{H_2O}} = 2.68 \quad [11]$$

was used. The results are given in Table II and Fig. 3b. Agreement between observed and theoretical potentials appears satisfactory.

In Fig. 4 and Table III the results are given for gas mixtures containing a constant initial amount of methane. The experimental and theoretical potentials agree with each other except for those gases for which complete equilibrium requires nearly complete oxidation of methane, *i.e.*, to pressures below approximately 0.0006 atm.



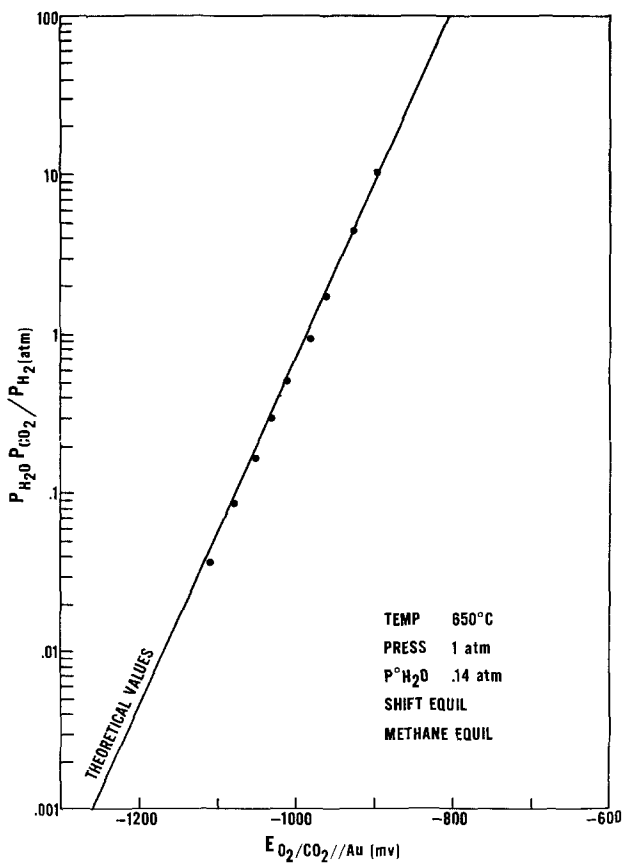


Fig. 3 (a, top; b, bottom) The ocp for humidified mixtures of H_2 and CO_2. Partial pressures of H_2, CO_2, and H_2O calculated assuming equilibrium for shift reaction only (a), and complete equilibrium (b).

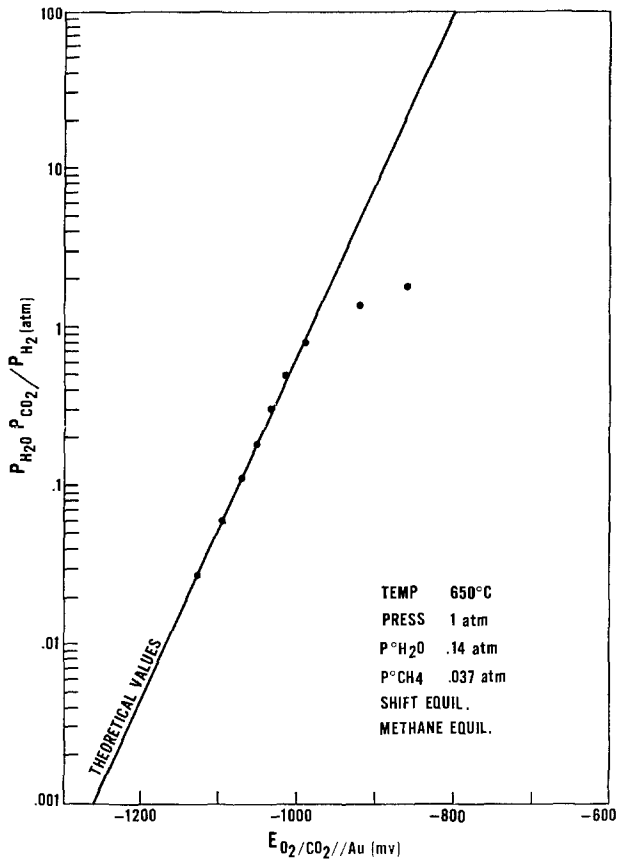


Fig. 4. The ocp for mixtures of H_2, CH_4, H_2O, and CO_2. Partial pressures calculated assuming complete equilibrium.

Conclusions

We conclude that, in calculating the ocp of a hydrogen electrode from the composition of the (initially cold) feed gas, the entire experimental setup has to be considered including the device used to preheat the gas. Large errors can result if complete equilibrium is not achieved. This is particularly true if the initial gas contains insufficient water to prevent carbon formation at lower temperatures encountered by the gas during heating. If, on the other hand, an equilibrium gas mixture is supplied, the ocp in most instances agrees accurately with the thermodynamic value. Exceptions are experiments in which equilibrium can be obtained only by nearly complete oxidation of excess methane in the feed gas.

Manuscript submitted Nov. 8, 1976; revised manuscript received April 21, 1977.

Any discussion of this paper will appear in a Discussion Section to be published in the June 1978 JOURNAL. All discussions for the June 1978 Discussion Section should be submitted by Feb. 1, 1978.

Publication costs of this article were assisted by United Technologies Corporation.

REFERENCES

1. L. P. Klevtsov, G. G. Arkhipov, and G. K. Stepanov, *Elektrokhimia*, **3**, 785 (1967).
2. G. H. J. Broers and M. Schenke, in "Hydrocarbon Fuel Cell Technology," B. S. Baker, Editor, Academic Press, New York (1965).
3. H. Lux, *Z. Elektrochem.*, **45**, 303 (1939).
4. H. Flood and T. Forland, *Acta Chim. Scand.*, **1**, 592 (1947); *ibid.*, **1**, 781 (1947); *ibid.*, **1**, 790 (1947).
5. N. Busson, S. Palous, J. Millet, and R. Buvet, *Electrochim. Acta*, **12**, 1609 (1967).
6. R. Littlewood, *This Journal*, **109**, 525 (1962).
7. M. D. Ingram and G. J. Janz, *Electrochim. Acta*, **10**, 783 (1965).
8. J. T. Lundquist and W. M. Vogel, *This Journal*, **116**, 1066 (1969).

Table III. Initial (index°) and calculated pressures assuming complete equilibrium

Initially				Shift equilibrium					Shift and methane equilibrium					
$P_{H_2}°$	$P_{CO_2}°$	$P_{H_2O}°$	$P_{CH_4}°$	P_{H_2}	P_{H_2O}	P_{CO_2}	P_{CH_4}	$E_{theor.}$	P_{H_2}	P_{H_2O}	P_{CO_2}	P_{CH_4}	$E_{theor.}$	$E_{expt.}$
0.0411	0.782	0.14	0.037	0.0125	0.169	0.753	0.037	−890	0.061	0.176	0.648	0.00005	−957	−860
0.082	0.741	0.14	0.037	0.029	0.193	0.688	0.037	−922	0.083	0.192	0.594	0.00014	−970	−920
0.165	0.658	0.14	0.037	0.073	0.231	0.567	0.037	−959	0.134	0.218	0.493	0.00061	−991	−991
0.247	0.576	0.14	0.037	0.129	0.258	0.459	0.037	−986	0.193	0.234	0.403	0.0018	−1011	−1015
0.329	0.494	0.14	0.037	0.196	0.273	0.361	0.037	−1010	0.258	0.244	0.321	0.0043	−1030	−1035
0.412	0.412	0.14	0.037	0.274	0.278	0.274	0.037	−1033	0.327	0.248	0.249	0.0084	−1049	−1050
0.494	0.329	0.14	0.037	0.361	0.273	0.196	0.037	−1058	0.403	0.246	0.183	0.0144	−1070	−1070
0.576	0.247	0.14	0.037	0.458	0.258	0.129	0.037	−1087	0.485	0.239	0.125	0.0220	−1093	−1096
0.658	0.165	0.14	0.037	0.567	0.231	0.073	0.037	−1122	0.578	0.223	0.073	0.0296	−1124	−1127
0.741	0.082	0.14	0.037	0.688	0.193	0.029	0.037	−1173	0.691	0.190	0.029	0.0331	−1174	−1175

9. G. Danner and M. Rey, *Electrochim. Acta*, 4, 274 (1961).
10. JANAF Thermodynamic Tables, 2nd ed., U.S. Dept. of Commerce, NSRDS-NBS 37 (1971).
11. A. Borucka and C. M. Sugiyama, *Electrochim. Acta*, 13, 1887 (1968).
12. A. Borucka and C. M. Sugiyama, *ibid.*, 14, 871 (1969).

Equilibrium Properties of Lithium/Niobium Selenide, Nonaqueous Secondary Cells

J. N. Carides and D. W. Murphy*

Bell Laboratories, Murray Hill, New Jersey 07974

ABSTRACT

Equilibrium-open-circuit potentials of Li/$LiClO_4$, PC/$NbSe_x$ (x = 2, 3, 4, 4.5) cells were measured as a function of the state of charge of these cells. For $NbSe_2$ the emf decreased monotonically from ~2.3 to 1.65V at full discharge (1 Li/Nb) and was independent of prior history. With $NbSe_3$ two distinct types of emf curves were found: (*i*) a constant emf of ~1.7V from 0-2Li/Nb followed by a monotonic decrease in emf to ~1.5V at 3Li/Nb, and (*ii*) a "stepped" form with breaks at 1 and 2Li/Nb. Neither type of curve was reproduced on cycling. The emf of $NbSe_4$ and $NbSe_{4.5}$ was nearly constant at 1.83V to ~4Li/Nb. The $NbSe_4$ exhibits a monotonic decrease in emf to ~1.6V at 5Li/Nb. The emf curves obtained on the first charge and subsequent cycles were higher in value. The implications of this data on the chemistry of cell discharge is discussed.

Interest in nonaqueous reversible cells of lithium with metal chalcogenides prompted a study on the equilibrium properties of these cells with the series of niobium selenides $NbSe_2$, $NbSe_3$, and $NbSe_{4+x}$ to determine equilibrium properties, and to better understand the chemistry in this series. The selenides of niobium were chosen because they exhibit a wide range of stoichiometries. Dynamic electrochemical results have been reported for $NbSe_3$ (1) and for $NbSe_{4+x}$ (x = 0-0.5) (2). The class of metal dichalcogenides has been suggested to form reversible cathodes with Li (3, 4), prompting the examination of $NbSe_2$.

Experimental

Materials.—Niobium powder (30 μm, 99.95% purity), selenium shot (5*N* purity), graphite powder (325 mesh), lithium foil (Foote Mineral Company), and polyethylene powder (Microthene 500, U. S. Industrial Chemicals) were used as received. Propylene carbonate (PC) and tetraglyme (TTG) were vacuum distilled from lithium. Lithium hexafluorophosphate (Ventron) and lithium perchlorate (Ventron) were vacuum dried at ~ 150°C. The selenides of niobium were prepared by direct reaction of the elements in sealed vitreous silica ampuls at 750°, 680°, and 450°C for $NbSe_2$, $NbSe_3$, and $NbSe_{4+x}$, respectively. X-ray diffraction patterns agree with those previously reported for these phases.

Construction of Test Cells

Except for $NbSe_3$, cathodes were prepared by hot pressing a mixture of 65-70% active powder (150 mesh), 30-25% graphite, and the balance polyethylene (PE). Pressing was done at ~123°C and 3.5 × 10^4 psi yielding samples of ~ 7 mil thickness that were cut to convenient sizes. The natural growth habit of $NbSe_3$ resulted in a conducting, feltlike material of interwoven fibers, which was cut into sections and used directly. All samples were sandwiched between nickel screen to provide support and external connection.

The cathodes were placed horizontally in a crystallizing dish together with a lithium electrode, separation provided by glass filter paper or glass wool.

With one exception, the electrolyte was 1.0*M* $LiClO_4$ in PC. One cell, using $NbSe_4$, was constructed with 0.1*M* $LiPF_6$ in TTG to determine the significance of the electrolyte.

Cells were constructed in an inert atmosphere box under argon, and were mounted in air-tight Mason jars fitted with electrical feed throughs.

Test Procedure

Voltages were measured using a Keithley 160B digital multimeter. Cells were discharged at low current densities for periods of 8-24 hr, representing a suitable fraction of the theoretical capacity. Typical current densities were of the order of 50 μA/cm^2. Following

* Electrochemical Society Active Member.
Key words: batteries, intercalation, chalcogenides.

discharge the cell was disconnected and allowed to equilibrate for periods of 16-48 hr. Approach to equilibrium was determined by periodic potentiometric readings during the time interval. When voltage readings indicated a change of 0.010V or less over an 8 hr sampling period, the cell was regarded as having attained equilibrium and the voltage at that point recorded; discharge to the next point was then resumed. The same procedure was followed on charging. All voltage readings were made at 24° ± 2°C.

Several cells of each type were tested and the curves derived were the best fit for all points.

At least one representative of each cathode material was cycled several times. Some cells were cycled within a range that represented only a fraction of the theoretical capacity.

After the tests were completed, each cell was dismantled and the cell components visually inspected. None of the electrodes showed any deterioration or other abnormalities.

Results and Discussions

$NbSe_2$.—Lithium is introduced into $NbSe_2$ according to $xLi + NbSe_2 \rightarrow Li_xNbSe_2$ ($0 \leq x \leq 1$) (5, 6). Figure 1 shows a gradual decrease in emf indicating that Li_xNbSe_2 is single phase over the entire composition range. The shape may be understood to arise from a gradual filling of the metallic d band in $NbSe_2$, lithium inserting between Se layers in which only Van der Waals bonding exists. This result is similar to that previously discussed for TiS_2 (3, 7), whose equilibrium emf is compared in the same figure. Upon recharging $NbSe_2$ cells, the equilibrium voltage curve tracks the discharge curve within 3%, confirming that the same composition is obtained from charge or discharge.

These results were reproduced in several test cells and in each case the cells could be discharged to at least 95% of theoretical capacity (1 lithium) while still permitting recovery of at least 90% of the amount discharged.

Previous work (8) on $NbSe_2$ in Li cells containing I_2 suggested that $NbSe_2$ acted as a "host" for I. Reexamination of that cell data shows a substantial capacity in the voltage range observed here for lithium intercalation.

$NbSe_3$.—Results for $NbSe_3$ (Fig. 2) are ambiguous. In some cases the equilibrium emf was similar to that found for slow discharge (9), and OCV data for TiS_3 (3). Other cells behaved quite differently, sometimes even for material taken from the same sample preparation and with identical x-ray powder patterns. After cycling, all the $NbSe_3$ cells exhibited a gradual sloped emf. These differences in various $NbSe_3$ electrodes and the changes in emf on cycling imply that the structure is changing on cycling. Inspection of the structure of $NbSe_3$ (Fig. 3) (10) suggests the possibility that the complex arrangement of chains in the structure may not be unique. Such polytypism has been noted for a number of two-dimensional compounds involving coordination geometry and registry of the layers. The polytype formed at 680°C may not be the most stable at room temperature and also might change via lithiation and delithiation. We have been unable to detect

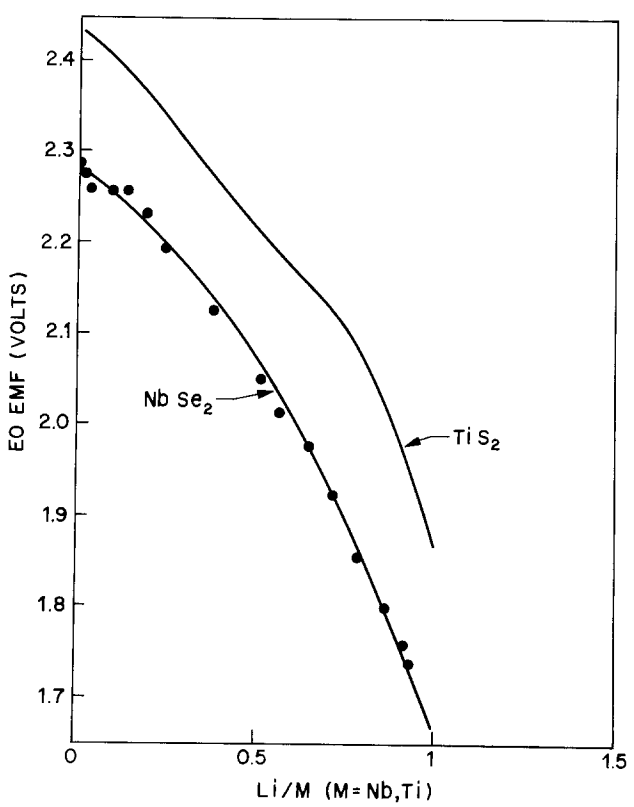


Fig. 1. Equilibrium voltage of $NbSe_2$ as a function of Li composition, compared with results given for TiS_2 (3).

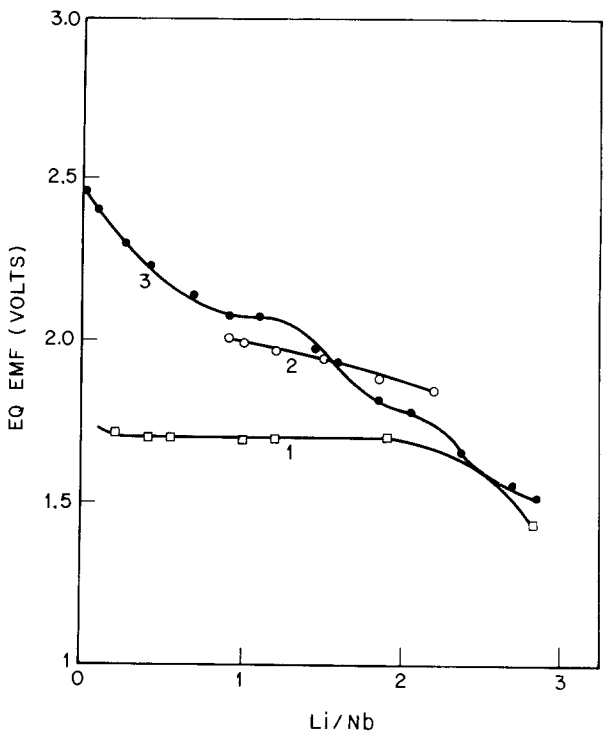


Fig. 2. Equilibrium voltage curves for $NbSe_3$ as a function of Li content. Curve 1 is first discharge curve for one type of behavior; curve 2 is the equilibrium curve for the same type on second discharge. Some $NbSe_3$ cells yielded a "stepped" voltage on first discharge, as shown by curve 3.

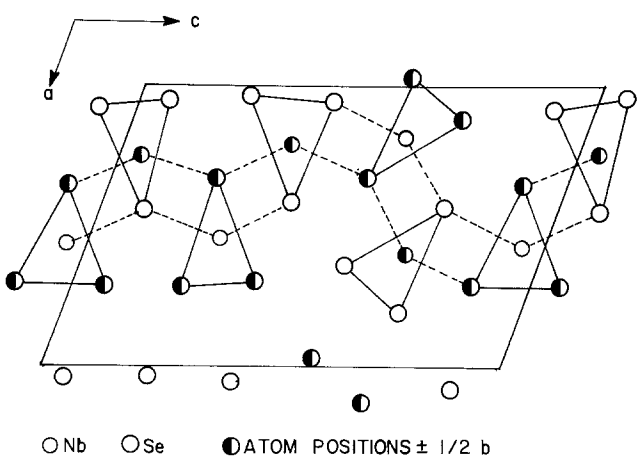


Fig. 3. Structure of $NbSe_3$ (10)

these changes by x-ray powder patterns, the patterns being quite complex, weak, and diffuse.

$NbSe_4$.—Cells were cycled to 2Li/Nb, 4Li/Nb, and 5Li/Nb. The equilibrium emf's are shown in Fig. 4. The curve is almost flat (slightly negative slope) from 1-3Li at about 1.83 ± 0.02V. This curve differs from that reported (2) under dynamic conditions in that a break appears beginning at about 3.5Li, with the voltage remaining above 1.5V at 5Li, as opposed to a sharp drop in voltage at 4Li in the dynamic study. This particular cell was recharged to ~ 84% of amount discharged.

Cells limited to 2 or 4Li showed better rechargeability, ~93% of amount discharged. In the initial part of the first recharge, the 0-4Li emf levels off at ~ 2.07V, and the 0-2Li emf merges with the 0-4Li emf near 1.5Li; therefore, these charge curves tracked each other. When both these types of cells were subsequently discharged (second discharge), they continued tracking each other closely, although at a higher but still flat emf (1.92 ± 0.02V) over the range 1.5-3.8Li. The second discharge curve for the 0-5Li cell started at higher voltages than the first discharge, but ultimately converged with the others in the range ~ 2.8-4Li. This phenomenon of different discharge curves converging to the same emf, and the relative flatness of the composite second discharge curve was true of the $NbSe_{4.5}$ series as well.

Another $NbSe_4$ cell using 0.1*M* $LiPF_6$ in TTG yielded a curve similar to that using $LiClO_4$/PC, but approximately 3% lower in emf, indicating any role played by the electrolyte is minimal.

$NbSe_{4.5}$.—Cells were cycled from 0 to 2Li, and 0 to 4Li. Recoverability was about 90% for all these cells. One cell was discharged to 4.3Li/Nb, but further discharge was not possible without a precipitous drop in the cell voltage below ~ 1.2V (recoverability for the cell was about 87%). The emf remained at 1.83 ± 0.01V to 4.3Li, thus there was no gradual decrease in emf as with $NbSe_4$. The initial equilibrium curve was nearly flat (1.83 ± 0.01V) over most of the range as shown in Fig. 4.

Except for the cell that was discharged beyond 4Li, the various initial charge and second discharge curves

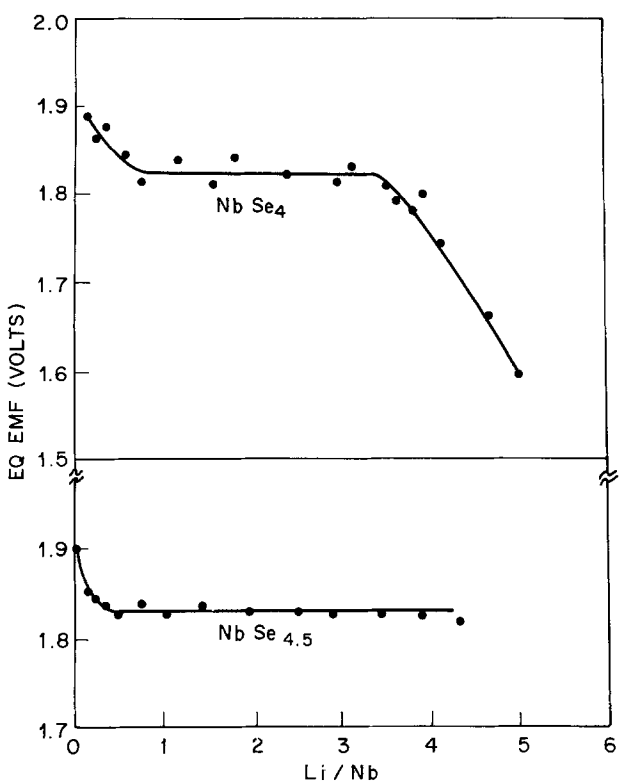


Fig. 4. Composite results for equilibrium voltages of $NbSe_4$ and $NbSe_{4.5}$, as a function of Li content; first discharge.

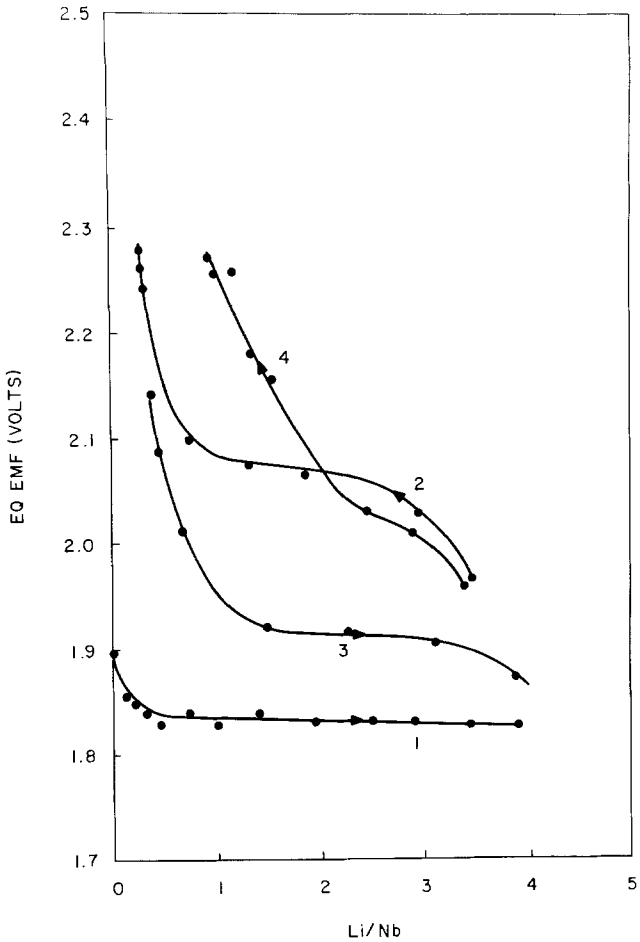


Fig. 5. Equilibrium voltages for two complete cycles of an $NbSe_{4.5}$ cell, as a function of lithium content.

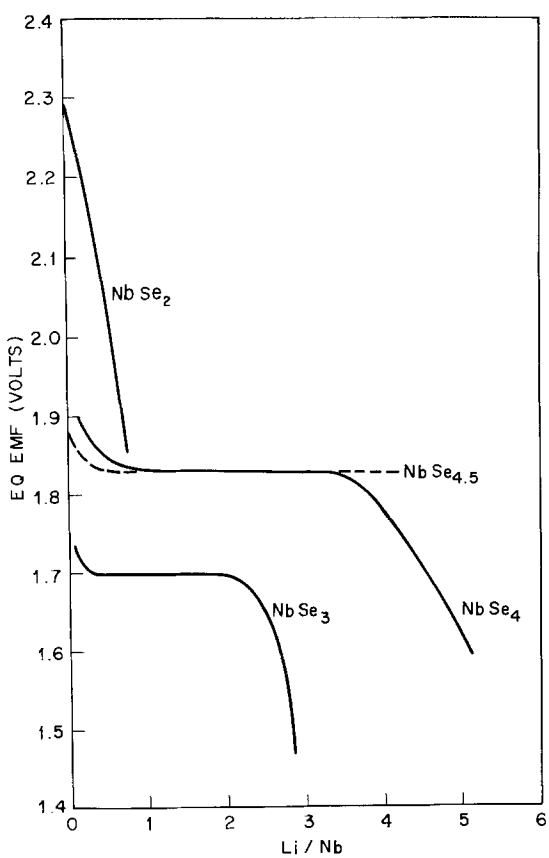


Fig. 6. Composite showing equilibrium voltages for cell $NbSe_x$ compounds studied in this series.

converged in a manner similar to that described for $NbSe_4$. The second discharge curve is flat at about 1.93 ± 0.02V over the range 1-3Li. Typical emf curves for 2 full cycles are shown in Fig. 5.

Discussion

All the initial discharge data are compared and summarized in Fig. 6. For $NbSe_3$ we observed varying initial discharge curves on samples giving identical x-ray patterns. We have included in Fig. 6 the curve resembling that previously published (9).

$NbSe_2$ is essentially fully reversible by the mechanism of lithium intercalation involving virtually no irreversible chemical changes, similar to TiS_2 (3). The shape of the equilibrium emf *vs.* composition curves confirm that a single phase is involved during cycling. The higher selenides of niobium were reversible in varying degrees, but the charge curves were significantly different than the discharge curves. Indeed, the equilibrium charge voltage exceeded the initial discharge voltages by at least 15%. In these cases, the chemistry is obviously more complex and significant changes take place within the first cycle. The very low current densities and long equilibration times minimized effects due to solvent incorporation. The test with 0.1*M* $LiPF_6$ in TTG supports this conclusion.

For $NbSe_3$ (curve 1, Fig. 2) the flat portion of the discharge curve is lost after the first cycle, while in $NbSe_4$ and $NbSe_{4.5}$ level, although higher than original, emf's persist and data points from cells having different cycle history tend to converge during some overlapping parts of the cycle span. This behavior is best reproduced when a composition of Li_4NbSe_{4+x} ($x = 0, 0.5$) is not exceeded.

The changing OCV curves on cycling the higher selenides $NbSe_3$ and $NbSe_{4+x}$ ($x = 0, 0.5$) seems to indicate a multiphase system or a gradual structure change in these cases. Further studies are needed to confirm and elucidate such changes.

Manuscript submitted March 7, 1977; revised manuscript received April 14, 1977.

Any discussion of this paper will appear in a Discussion Section to be published in the June 1978 JOURNAL. All discussions for the June 1978 Discussion Section should be submitted by Feb. 1, 1978.

Publication costs of this article were assisted by Bell Laboratories.

REFERENCES

1. J. Broadhead and F. A. Trumbore, Paper 178 presented at The Electrochemical Society Meeting, Chicago, Illinois, May 13-18, 1973.
2. D. W. Murphy, F. A. Trumbore, and J. N. Carides, *This Journal*, **124**, 325 (1977).
3. M. S. Whittingham, *ibid.*, **123**, 315 (1976).
4. G. L. Holleck, F. S. Shuker, and S. B. Brummer, Paper No. 759070, 10th International Energy Conversion Engineering Conference, 1975.
5. M. B. Dines, *Mater. Res. Bull.*, **10**, 287 (1975).
6. D. W. Murphy, F. J. Di Salvo, G. W. Hull, Jr., and J. V. Waszczak, *Inorg. Chem.*, **15**, 17 (1976).
7. M. S. Whittingham, *Science*, **192**, 1126 (1976).
8. J. Broadhead, in "Power Sources 4," D. H. Collins, Editor, p. 469, Oriole Press, Newcastle Upon Tyne, England (1973).
9. D. W. Murphy and F. A. Trumbore, *This Journal*, **123**, 960 (1976).
10. A. Meerschaut and J. Rouxel, *J. Less Common Metals*, **39**, 197 (1975).

The Allotropes of Dibasic Lead Oxide: A Quantitative X-Ray Diffraction Analysis

J. R. Dafler*,[1]

ESB Incorporated, Technology Center, Yardley, Pennsylvania 19067

ABSTRACT

The allotropes of PbO are important in the formulation of positive and negative elements for lead-acid, SLI-battery systems. Recently, there has been renewed interest in making plates rich in tetrabasic lead sulfate [$(PbO)_4PbSO_4$] or tribasic lead sulfate [$(PbO)_3PbSO_4(H_2O)$], with special attention to which species predominates in the fully conditioned plate. The form is, characteristically, related to whether the starting oxide for paste formulation is rich in orthorhombic or tetragonal PbO. A quantitative technique, using x-ray diffractometry, to determine the amount of one allotrope in mixtures of both is given here, with a discussion of sources of probable error and the character of analyses based on linear calibration curves.

Dibasic lead oxide (PbO) occurs in two polymorphic forms: the tetragonal, t-PbO; and the orthorhombic, o-PbO; oxides. Both oxides are important in the lead-acid battery industry, and t-PbO is a major component of most commercial oxides used to make porous, pasted electrodes for storage batteries. The two oxides have slightly different densities and, according to Clark and Kern (1) and others (2-4), differing reactivities. Some battery manufacturers prefer to formulate pastes for electrode manufacture with oxide mixtures that contain no o-PbO. These oxides, the very low yellow (VLY) oxides, are considered by some to be superior for paste production and battery element fabrication. The presence of o-PbO is now considered desirable or undesirable only according to the crystal form sought in cured, pasted, unformed plates. If $(PbO)_4PbSO_4$ [tetrabase] is desired (5, 6), o-PbO rich oxides are selected, while the formation of $(PbO)_3PbSO_4(H_2O)$ [tribase] appears favored by the presence of t-PbO. Pavlov and Papazov (7) have recently summarized the results of a large amount of careful experimental work concerning the interplay of the divalent oxides in yielding the final form of battery plates. Their conclusions with respect to the morphologies of cured plate species disagree with ours, but their summaries of pasting and paste manufacturing do not.

* Electrochemical Society Active Member.
[1] Present address: Institute of Gas Technology, Chicago, Illinois 60616.
Key words: basic lead sulfates; lead oxides, dibasic; x-ray diffractometry.

Considerable battery practice has been devoted to developing cured plates rich in $(PbO)_3PbSO_4(H_2O)$, and Mrgudich (8), using VLY oxides found a modified or activated PbO that apparently was a distorted t-PbO. Moreover, in his work, mixing and pasting techniques that produced $(PbO)_4PbSO_4$ yielded little of the distorted species, suggesting a special propensity to incorporate into the tetrabase lattice. Clark and Tyler (3) had systematically studied the Pb(II) oxides and found an "active" PbO that had unusual properties which could be indexed by catalytically decomposing hydrogen peroxide, though some of their o-PbO:t-PbO mixtures also had unusual activity for H_2O_2 decomposition. Later Clark and Rowan (9) found that o-PbO could be converted to a distorted t-PbO by grinding. They attributed this to transformations taking place in imperfectly crystallized regions that were undergoing natural o-PbO → t-PbO transitions. Petersen (10) summarized much of the early effort devoted to preparation and identification of the allotropes of PbO.

In agreement with long standing experience, Pavlov and Iliev (11) established that $(PbO)_3PbSO_4(H_2O)$ is the preponderant phase in pastes made at temperatures below 80°C. They suggested that $(PbO)_4PbSO_4$ was formed at higher temperatures by reacting $(PbO)_3PbSO_4(H_2O)$ with t-PbO, but only if o-PbO was present. Pavlov and Papazov contend the necessary o-PbO will be generated by processes in paste mixing, and by oxidizing the metallic lead in commercial oxides when H_2SO_4 is present.

For reasons of older battery practice and craft, and evaluation of treated ores and commercial oxides for purchase, it was necessary to have a fast and reasonably simple technique to quantitatively determine o-PbO in a given oxide sample.

X-ray diffraction of Pb(II) oxides.—Orthorhombic and tetragonal PbO possess distinct, sharply defined x-ray diffraction spectra (12) and, moreover, their most intense diffraction maxima (I_{100}) occur quite close to one another in a spectrum of mixtures, making quantitative diffractometry appear a very promising method of analysis (13, 14). Mixtures of t-PbO and o-PbO, and commercial oxides for lead-acid battery manufacture represent quasi two-component systems in which the mass absorption coefficients, μ_{xi}, are the same, obviating the need to make absorption corrections to the measured intensities (15). Alexander and Klug have shown that the measured intensity, I_i, of a line in a mixture where $\mu_{xi} = \mu_{xj}$, is a linear function of the fraction of the ith component in an i-j mixture (14). Ores and commercial oxides sometimes contain metallic lead in quantities up to 30%, however, this component represents no difficulty, except as a relatively constant matrix diluent.

The method of standard additions is frequently used in atomic absorption spectrophotometry (16) and stripping voltammetry (17), and can be applied to any analytical problem in which matrix interference effects need to be minimized (18, 19). Klug and Alexander adumbrated the use of this method for quantitative diffraction analysis of very small samples (20).

Quantitative diffractometry by the method of standard additions is one depending on linear calibration curves, and the difficulties inherent in such analyses is discussed by Mandel and Linnig (21). The method and treatment of data derived using linear calibrations is treated in detail by Larsen, Hartmann, and Wagner (22). Basically what is done is the unknown matrix is scanned carefully and the ratio of the analyzed, I_{100}-line intensities is determined, preferably in a statistical fashion from several separate, discrete scans. The sample is then "spiked" or diluted with carefully measured amounts of the subject polymorph (in this case o-PbO) to produce two or three calibrating samples. These are mixed with extreme care and the x-ray intensity ratios, R_i, measured.

The standard addition samples are used to generate an analysis, or calibration curve, produced by plotting the appropriate R-values as a function of percent added o-PbO. Since linear regression analysis is available so casually through the use of hand-held calculators, a least squares line can usually be determined within minutes. The line will have a positive slope and a negative intercept on the abscissa. The absolute value of the x-intercept (percent added o-PbO concentration) will be the determined value of the unknown quantity. If the line is translated so that it includes the origin, a recalculation of all points must lie on a straight line parallel the original calibration curve.

The analytical possibilities inherent in the x-ray diffraction spectrum, apparently were first listed by Hull (23). The first practical analysis appears to be that of Clark and Reynolds (19), and since the work of Klug and Alexander and colleagues (14, 15, 20, 24) quantitative diffractometry has found widespread application.

Experimental Procedures

A commercial lead oxide was used for this study. It is a standard "leady" oxide used to prepare $(PbO)_3PbSO_4(H_2O)$-rich elements for positive plate manufacture. It contained 17.6% metallic lead, the rest being t-PbO. This was VLY oxide and contained no o-PbO. The o-PbO was a high purity litharge supplied by Johnson, Matthey and Company, Limited of London. An x-ray diffraction spectrum of a "nonleady" commercial oxide is shown in Fig. 1. The diffraction maxima useful in this analysis are noted.

Portions of the VLY oxide were carefully diluted with small amounts of o-PbO, the additions to represent, approximately 5, 10, 15, and 20%. The carefully measured chemicals were then mixed thoroughly in a SPEX shaker mill with a single alumina ball.

A Philips Electronics, Incorporated x-ray diffractometer, using Cu radiation was used for all intensity measurements. This unit has a curved crystal monochromator (LiF). For analytical measurements the scanning rate was 0.25°/min, with a 0.2° receiving slit, and beam settings of 42 kV:22 mA. These instrument settings yield a natural linewidth of ~0.2°.

Four spectra of the interesting regions were made for each sample. After each scan, the sample was discarded and the storage bottle once more shaken in the SPEX mill. Samples were back-filled into the holders to minimize possible orientation effects.

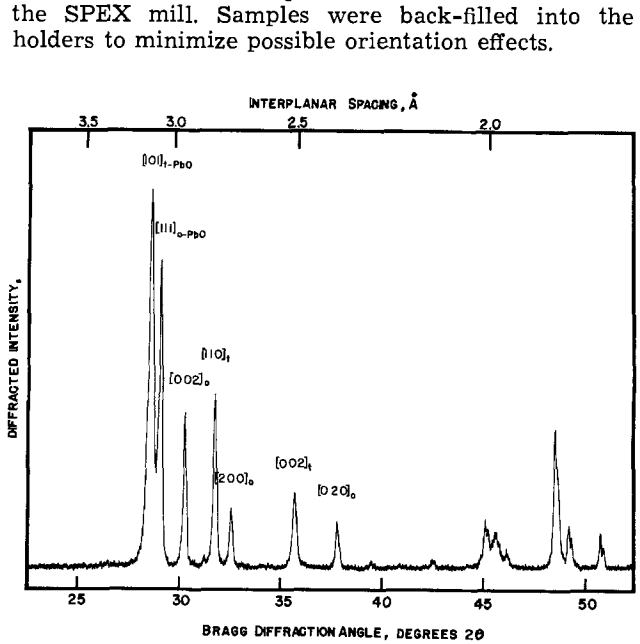


Fig. 1. X-ray diffraction spectrum of a "nonleady" commercial oxide. The principal x-ray diffraction maxima of t-PbO and o-PbO are indicated.

Commercial oxides for lead-acid battery plate manufacturing are generally very fine, and all but a very small fraction of the material used did not pass a 325 mesh ASTM sieve. Crystallite size and particle size in these oxides are so small, generally, that some line broadening is seen. This enhances the practicability of the analysis: Alexander, Klug, and Kummer (24) have shown that reproducibility of intensity measurements is highest if the average particle size is less than $\sim 5\mu$. Wilchinsky has correlated the effects due to crystal, grain, and particle size on diffracted beam power (25).

To simulate unknown analysis and visually establish the linearity of the intensity ratio: percent added o-PbO calibration, all samples were scanned in serial order, After the initial remixing of the samples, each was scanned three more times in random order. The pooled data were then subjected to multiple linear regression analysis using a digital computer to establish the over-all "goodness" of the calibration line, and to obtain a statistically derived standard error of estimate, *Sr*. The data were also processed with a hand calculator that featured linear regression analysis (Texas Instruments SR-51A). The simulated analyses that follow were processed using the hand calculator.

Results and Discussion

The two x-ray diffraction maxima used in this determination are: o-PbO, the [111] line; 3.07Å at a Bragg angle of 29.06°; and t-PbO, the [101] line; 3.12Å at a Bragg angle of 28.58°. The base line for the intensity measurements was established between the steady background at 26.5° and the diffraction minimum at 29.8°. The relative intensity ratio, $R = I(\text{o-PbO[111]})/I(\text{t-PbO[101]})$, is obtained from the uncorrected peak height measurements. The method is illustrated in Fig. 2, which shows two typical scans for samples containing differing amounts of o-PbO.

The values of R calculated from four different "spiked" samples of the commercial oxide are summarized in Table I. The initial, serially obtained values are denoted with asterisks. They are discussed in another section as a simulated unknown analysis. The data in the table are listed in order of increase in R-value to facilitate initial statistical treatment. The line "added o-PbO" is used in a later section to discuss regular analysis of an unknown (in this case the first sample, 6.875% o-PbO, is the simulated unknown).

The sixteen data were subjected to linear regression analysis after examination for gross error. Of the two data that are questionable and do not fit their populations well (underlined in Table I) only the second, the 0.2595, point can be rejected by the ratio test of Crow *et al.* (26).

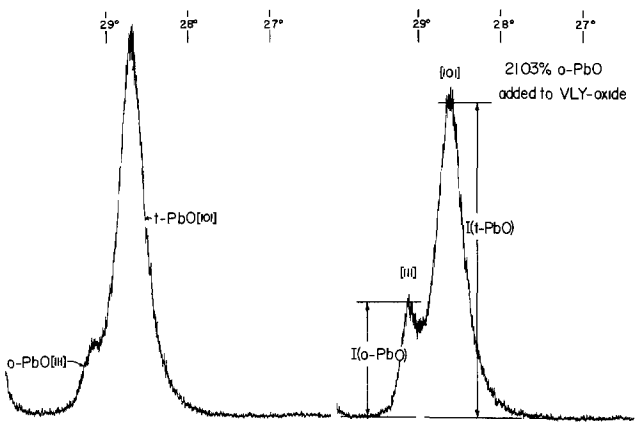


Fig. 2. Two analytical scans of the t-PbO/o-PbO region. The method of measuring line intensities is indicated on the right. The left-hand spectrum represents the simulated unknown.

Table I. Summary of intensity data for "spiked" oxides

Percent o-PbO (%)	6.876	9.128	14.58	21.03
Added o-PbO (%)	0.00	2.253	7.705	14.16
R-values	0.1341	0.1656	0.2595*	0.4003
	0.1365*	0.1729	0.2805	0.4012*
	0.1405	0.1764*	0.2812	0.4072
	0.1410	0.1794	0.2820	0.4097
Average *R*-values	0.1380	0.1736	0.2812	0.4046
Standard deviation	0.00330	0.00594	0.00075	0.00458
Range of *R*	0.0064	0.0138	0.0015	0.0094
Relative error	0.0239	0.0342	0.00267	0.0113

* Initial datum for each mixture.

Linearization: digital computer.—The program used yields a multiple linear regression analysis line that is weighed according to the density and distribution of observations about their mean value. The line obtained gave the percent o-PbO, *Y*, as a function of the intensity ratio, *X*. The *F*-value for the line was ~7000 with a sum of squares, attributable to the regression, of ~480. Statistically, this is a very good calibration curve, and indicates data linearization to be appropriate. The correlation coefficient was 0.9991. The equation is

$$Y = -0.10902 + 52.56X \qquad [1]$$

and the standard error of estimate, *Sr*, is 0.259, which indicates, or suggests that using this calibration will produce determinations, o-PbO = (Y ± 0.259)%, 64% of the time, and o-PbO = (Y ± 0.518)%, 90% of the time, etc.

Linearization: hand calculator.—To analyze the pooled data using the hand calculator, the averaged *R*-values were used, because multiple linear regression is not available on the instrument. The expression for percent o-PbO was

$$Y = -0.19620 + 52.53X \qquad [2]$$

The standard error of estimate calculated for this regression line for the four averaged values was 0.192. When calculated for all fifteen data, the value for *Sr* was 0.257. As expected, the linearization was very good, the correlation coefficient being 0.9997.

The error of estimate for both treatments is quite low but, of course, for low o-PbO contents (1-10%) would represent a fairly large relative error in the determination. For commercial ores and oxides that contain o-PbO this is a sufficiently precise and sensitive analysis.

As Klug (27) and others (28) have pointed out the sufficiency conditions for quantitative diffractometry (linearity in the analytical relationship) is met very well. The necessary conditions that the analytically interesting diffraction maxima intercept the same region of analyzing radiation (29) is, clearly, well met (cf. Fig. 2).

The analysis of an unknown.—To analyze an unknown, the *R*-values for the unknown and the "spiked" samples are plotted on any convenient axis; such as intensity ratio, *R*, *vs.* concentration added o-PbO. The unknown's *R*-value is plotted as 0.0% added o-PbO. To simulate analysis we plotted the values from Table I under the "added o-PbO" heading, on just such an axis. Since we know the correct, measured value of percent o-PbO in the simulated unknown we can discuss the precision and accuracy of this analytical method for the PbO allotropes.

To further simulate laboratory practice we will use the four initial readings only, then analyze the one-time analysis situation compared to the replicated analysis, using the pooled data. In the unknown determination, the *R*-values are treated as the dependent variables, functions of the percent of added o-PbO, *P*.

The data from Table I marked with asterisks were plotted on analysis axes, as shown in Fig. 3. One of the lines is a casual fit made by visually averaging the point splits, and may closely approximate real practice in the laboratory. The other line is the result of linear regression analysis by the hand calculator. The equation of the line is

$$R_{initial} = 0.1320 + 0.01847P \quad [3]$$

with a P-intercept of -7.146 added o-PbO. We can generate a table of residuals and calculate Sr for this line. The standard error of estimate for this determination is 0.671, worse than for the replicated data (0.259 and 0.257). The analysis for o-PbO is in error by 3.94%, nearly twice the error of the answers derived using pooled data (2.20% for the computer linearization and 2.97% for the SR-51A linearization). It is interesting to note the casual, visual linearization led to a determination of 6.55% o-PbO, an error of 4.73%, not much worse than the answer calculated from Eq. [3].

The ordinary expectation is that precision and, presumably, the accuracy will be no worse than the error reflected in the distribution of the replicated data (Table I). The answer obtained in simulated analysis has a larger error than the replicated data, and the answers from pooled data indicate the relative error in the determination is larger than the error in the pooled data. The fact the computer linearization was outstanding (correlation coefficient = 0.9991) appears to offer us a paradox. The data are far better than the answer. This appears to be a property of the calibration line and its relationship to the data (21).

The solution lies in the fact that linear calibration lines are "best fits" of data that randomly fluctuate in the neighborhood of the line. It is, in fact, data scatter about the calibration curve that determines and defines the measure of precision and therefore the accuracy of this analysis (30) and it is always larger than the error in the replicated data. That is so, because, superimposed onto the replication error, as a source of scatter, are the ordinary experimental errors: in this case powder sample packing and mixing, peak height measurement, etc.

The reliability of the calibration line is a two-dimensional problem, and as Mandel and Linnig (21) and Lark (31) have shown, a complex one. The uncertainty in the slope and intercept of the least squares calibration line defines a two-dimensional confidence region, centered on the fitted (slope, intercept)-data pair (21, 26, 32). The area of the confidence region depends on the magnitude of the experimental errors that yielded the raw data, and the width of the confidence band, superimposed onto the linear calibration curve, defines the limits of precision and accuracy of such a method.

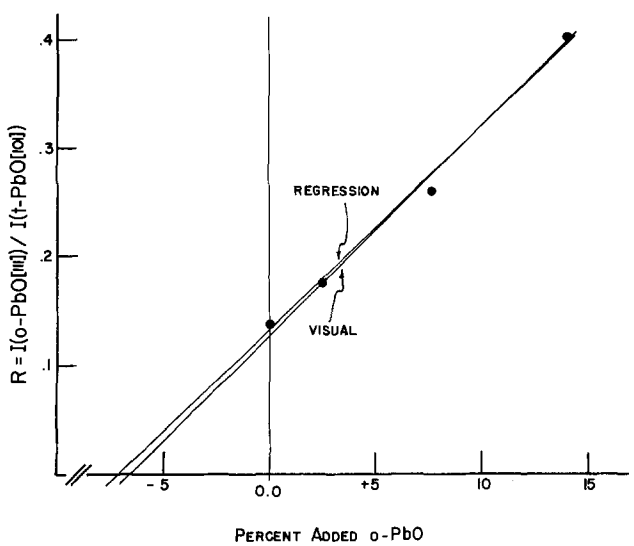


Fig. 3. Analysis plot for o-PbO determination. A casual, visual averaging of the initial points is shown compared to the least squares line.

A deeper analysis would yield the confidence band for any given selected confidence interval (σ, 2σ, 3σ . . .). That is unnecessary at this point, but it has been necessary to indicate how normal distribution of data can lead to unexpectedly large errors in analyses dependent on linear calibrations. This technique for the allotropes of PbO is a sound and useful method, providing normal care in preparation and experimental procedure is taken. The simulated analysis has shown that determinations without replication of observations leads to a less precise answer, with the decision whether or not to do data replication most likely to depend on the need to adjust formulated oxide mixtures for the presence or absence of one of the allotropes. The required degree of preciseness will depend on the required preciseness in the o-PbO analysis.

Acknowledgments

The author wishes to thank ESB Incorporated for support of this work, and thanks to Ted Blickwedel for computer analysis of data. Barbara Campbell assisted with x-ray diffraction measurements.

Manuscript submitted March 21, 1977; revised manuscript received April 28, 1977.

Any discussion of this paper will appear in a Discussion Section to be published in the June 1978 JOURNAL. All discussions for the June 1978 Discussion Section should be submitted by Feb. 1, 1978.

Publication costs of this article were assisted by ESB Incorporated.

APPENDIX

To investigate the expectation for accurate analyses from any set of four data we randomized the data pool with the 0.2595 point omitted, then wrote fifteen regressions using data sets made up by randomly selecting four R-values from the data pool. In each case we calculated the percent o-PbO of the "unknown," generated tables of residuals, and calculated the Sr-value for each of the fifteen lines (there are 192 possible combinations of data). These data are shown in Table II. The range in percent error in o-PbO and Sr are 11.44% and 0.435, respectively.

It is instructive to plot the signed percent error in o-PbO analysis as a function of the standard error of estimate of the fifteen lines. This can be seen as Fig. 4. The points from the computer and hand calculator analyses of the pooled data are also plotted. The distribution of the points in Fig. 4 appears strongly to indicate the presence of a systematic error that yields high values for o-PbO, giving regression lines that more frequently yield answers with a positive error. The source is probably a tendency to overestimate the intensity of the o-PbO[101] line, leading to high R-values.

Table II. Analysis of random data set linearization

Index	Intercept	Slope	o-PbO (%)	Sr	Error (%)	C_t
1	0.1333	0.01931	6.905	0.051	0.436	0.9999
2	0.1380	0.01852	7.452	0.160	8.39	0.9998
3	0.1371	0.01870	7.333	0.123	6.65	0.9999
4	0.1349	0.01927	7.004	0.331	1.88	0.9992
5	0.1319	0.01943	6.789	0.130	−1.25	0.9998
6	0.1315	0.01960	6.710	0.141	−2.41	0.9998
7	0.1372	0.01863	7.346	0.059	7.05	0.9999
8	0.1381	0.01848	7.475	0.171	8.73	0.9997
9	0.1369	0.01914	7.151	0.231	4.01	0.9995
10	0.1368	0.01898	7.207	0.214	4.83	0.9995
11	0.1380	0.01859	7.422	0.166	7.96	0.9958
12	0.1335	0.01890	7.061	0.494	2.70	0.9979
13	0.1367	0.01867	7.320	0.281	6.47	0.9993
14	0.1295	0.01917	6.758	0.335	−1.70	0.9990
15	0.1364	0.01863	7.325	0.264	6.54	0.9994

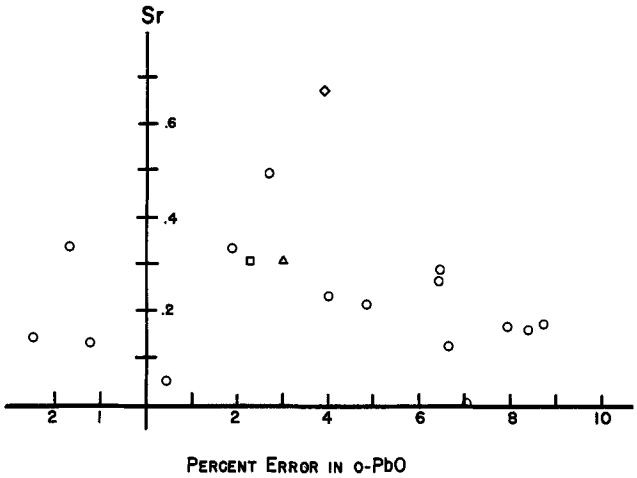


Fig. 4. Scatter diagram for standard error of estimate and signed error in o-PbO determination. The fifteen randomly generated regressions are shown as open circles: ◇ represents the visual averaging, while □ and △ are the computer and hand calculator values for the pooled data.

Figure 4 indicates the occurrence of very large error is coupled to small *Sr*-values, so that empirically the expectation of very large error is small. If we assume $Sr > 0.257$, the smallest value found for the treated, replicated data, then large errors correspond to *Sr*-values that are unrealistically small (outside the confidence band). The largest error in o-PbO analysis seen in this sampling, for $Sr > 0.26$ is ~6.65%.

REFERENCES

1. G. L. Clark and S. F. Kern, *J. Am. Chem. Soc.*, **64**, 1637 (1942).
2. H. Bode and E. Voss, *Electrochim. Acta*, **1**, 318 (1959).
3. G. L. Clark and W. P. Tyler, *J. Am. Chem. Soc.*, **61**, 58 (1939).
4. S. Ikari, S. Yoshizawa, and S. Okada, *J. Electrochem. Soc. Jpn.* (overseas ed.), **27**, E167 (1959).
5. R. V. Biagetti and M. C. Weeks, *Bell Syst. Tech. J.*, **49**, 1305 (1970).
6. C. W. Fleischmann and W. J. Schlotter, *This Journal*, **123**, 969 (1975).
7. D. Pavlov and G. Papazov, *J. Appl. Electrochem.*, **6**, 339 (1976).
8. J. M. Mrgudich, *Trans. Electrochem. Soc.*, **81**, 165 (1942).
9. G. L. Clark and R. Rowan, *J. Am. Chem. Soc.*, **63**, 1302 (1941).
10. M. Petersen, *ibid.*, **63**, 2617 (1941).
11. D. Pavlov and V. Iliev, *Elektrokhimiya*, **11**, 1735 (1975).
12. Joint Committee for Powder Diffraction Standards, Index to the Powder Diffraction File. No. 5-561 and 5-570.
13. U. W. Arndt, in "X-Ray Diffraction of Polycrystalline Materials," H. S. Peiser, H. P. Rooksby, and A. J. C. Wilson, Editors, chap. 7, p. 229, Chapman and Hall, London (1960).
14. H. P. Klug, L. E. Alexander, and E. Kummer, *Anal. Chem.*, **20**, 607 (1948).
15. L. Alexander and H. P. Klug, *ibid.*, **20**, 886 (1948).
16. R. Kunkel and S. E. Manhan, *ibid.*, **45**, 1465 (1973).
17. O. P. Bhargava, *Am. Lab.*, **7** (7), 11 (1975).
18. S. Sherken and E. J. Friedman, *Anal. Chem.*, **45**, 2399 (1973).
19. G. L. Clark and D. H. Reynolds, *Ind. Eng. Chem., Anal. Ed.*, **8**, 36 (1936).
20. H. P. Klug and L. E. Alexander, "X-ray Diffraction Procedures," Second ed., p. 553, John Wiley & Sons, Inc., New York (1974).
21. J. Mandel and F. J. Linnig, *Anal. Chem.*, **29**, 743 (1957).
22. I. L. Larsen, N. A. Hartmann, and J. J. Wagner, *ibid.*, **45**, 1511 (1973).
23. A. W. Hull, *J. Am. Chem. Soc.*, **41**, 1168 (1919).
24. L. Alexander, H. P. Klug, and E. Kummer, *J. Appl. Phys.*, **19**, 742 (1948).
25. Z. W. Wilchinsky, *Acta Cryst.*, **4**, 1 (1951).
26. E. L. Crow, F. A. Davis, and M. W. Maxfield, "Statistics Manual," pp. 102ff, 252, Dover Publications, Inc., New York (1960).
27. H. P. Klug, *Anal. Chem.*, **25**, 704 (1953).
28. R. A. Spurr and H. Myers, *Anal. Chem.*, **29**, 760 (1957).
29. L. E. Copeland and R. H. Bragg, *ibid.*, **30**, 196 (1958).
30. F. J. Linnig and J. Mandel, *ibid.*, **36** (13), 25A (1964).
31. P. D. Lark, *ibid.*, **26**, 1712 (1954).
32. M. G. Natrella, "Experimental Statistics," NBS Handbook No. 91, pp. 5-1ff, U.S. Government Printing Office, Washington, D.C. (1963).

Study by Auger Spectrometry and Cathodic Reduction of Passive Films Formed on Ferritic Stainless Steels

M. da Cunha Belo, B. Rondot, F. Pons, J. Le Héricy, and J. P. Langeron

National Center of Scientific Research, 94400 Vitry sur Seine, France

ABSTRACT

This paper deals with the passivation of ferritic stainless steels (26% Cr) in a 3.5% NaCl solution. The passive state was examined by Auger electron spectrometry and electrochemical reduction techniques. From the chemical composition profiles it appears that the passivation of these alloys is characterized by the formation of a thin oxide film and the development of a chromium-depleted zone in the metallic substrate near the metal-oxide interface. The composition of the passive film changes continuously with the depth. The number of atoms within a given layer of the film is lower than in the layers of the metallic matrix. The thickness and chemical composition of passive films change with the temperature of the corrosive medium. The study by cathodic reduction shows that molybdenum additions especially affect the properties of the inner layers of the passive film.

The great interest in the development of the passive state on iron-chromium steels is due both to the complexity of this phenomenon and to its practical importance. Despite numerous studies on this subject, there are still no definite conclusions relative to the nature and structure of the passive film formed on the surface of the alloys. There is some experimental evidence that the thickness of the oxide film varies from monolayer dimensions near the active-passive transition, up to dimensions of 10-50Å in the passive potential region. However, at present, it is not possible to identify the oxide phase as a single oxide, a duplex oxide, or an oxide not related to any known oxide.

It is obvious that an accurate and extended knowledge of the passivity phenomenon requires further experimentation, especially in connection with the factors affecting the ionic and electronic processes, the local electric potential, and the spatial variation of these through the film. In addition, more quantitative data must be obtained concerning chemical composition and structure.

Further investigation should take advantage of promising new techniques of surface analysis such as electron spectroscopy for chemical analysis (ESCA), low energy ion-scattering spectrometry (ISS), secondary ion mass spectroscopy (SIMS), Mössbauer spectroscopy, nuclear microanalysis, and activation analysis.

This work consists of a study by Auger electron spectrometry and coulometric techniques of passive films formed on very pure ferritic stainless steels exposed to a 3.5% NaCl (*p*H 2.5) solution. The influence of the passivation potential, alloy composition, and temperature of the corrosive medium were examined.

We have developed in a previous paper (1) some quantitative aspects of Auger electron spectrometry, and a general formalism has been given elsewhere (2). Up to now, determinations of surface concentrations have been carried out by resorting to standards. However, studies that have been published in the last 5 years (3-6) indicate the possibility of doing absolute measurements by taking an element of the matrix as a reference element. It is the purpose of this article to demonstrate the use of quantitative Auger analysis in the study of passivating films.

Experimental

Materials.—The alloys investigated were very high purity ferritic stainless steels prepared by plasma furnace melting (7). In these alloys the total content of metallic impurities is less than or equal to about 10 ppm by weight, and that of the nonmetallic impurities is also very low (typically: 10 ppm C, 7 ppm N, 10 ppm O).

The specimens were polished through 600 grade carborundum paper and then vacuum annealed for 1 hr at 900°C. Before introduction into the electrolytic cell the specimens were electropolished in a glacial acetic acid/perchloric acid mixture (3.2:1, by volume).

Electrochemical procedure.—Passivation experiments were carried out in 3.5% NaCl (*p*H 2.5) solution completely deaerated with pure nitrogen. Potentials are reported *vs.* the saturated calomel electrode (SCE). The specimen was polarized in the cathodic region at −700 mV/SCE for 2 min, and then submitted to a slight anodic dissolution: The specimen was put on open circuit for several seconds and then brought to the desired potential in the passive region. According to Frankenthal, this procedure gives the most reliable results (8). After passivation treatment, each specimen was rinsed in distilled water and dried in a stream of dry air.

The passivating films are formed at constant potential in the passive potential range. Passivation treatments correspond to a film growth stage where the log/log plots of the current *vs.* time give a straight line for periods of several hours. This stage occurs after about 30 sec of film growth. The study of the earlier stage of film formation during which the anodic current density decreases abruptly has not been considered here. Furthermore, it must be pointed out that the analytical and cathodic reduction study deals with films formed electrochemically with intermediate exposure to the atmosphere.

Passivation experiments were followed by analytical or coulometric measurements. The study of the cathodic reduction curve was conducted in 18*N* H_2SO_4 solutions deaerated with pure nitrogen (9). The passive film was cathodically reduced at a constant current of 5 $\mu A/cm^2$.

Analytical procedure.—The samples are introduced into the chamber of the Auger spectrometer a few minutes after formation of the passive film. The surface is bombarded under a vacuum of a few times 10^{-9} Torr with a beam of primary electrons having a kinetic energy of 2500 eV. The target current is 200 μA.

The Auger spectrometer operates with a conventional cylindrical mirror analyzer (CMA), *i.e.*, with a coaxial

Key words: passive films, Auger spectrometry, coulometry.

electron gun which bombards the surface of the sample at normal incidence. The emitted secondary electrons enter the CMA with an emission angle θ of 42°18′ with respect to the normal, and an angular aperture of the beam limited to ± 3°. Our spectrometer yields the differential energy distribution curve $dN(E)/dE$ of the secondary electrons emitted from the surface. We assume that the peak-to-peak amplitude of the Auger transition is due to the contribution of the atomic layers in the vicinity of the surface and proportional to the corresponding Auger current. From this hypothesis the peak-to-peak amplitude of the Auger signal due to an element I given by all the i layers, is

$$H_I = \sum_{i=0}^{\infty} h_I^{(i)} = \sum_{i=0}^{\infty} \alpha_I K_I^{(i)} N_I^{(i)}$$

where $N_I^{(i)}$ is the number of atoms I in the layer i, α_I is a sensitivity coefficient (characteristic of the element I), and $K_I^{(i)}$ is the contribution coefficient of the layer i to the total signal given by the whole specimen. (See the Appendix for the formalism leading to a quantization of Auger spectrometry and for more complete information relative to the physical meaning of the various factors.)

In the choice of the appropriate Auger peak for the assessment of the concentration of the various elements, the following conditions have been taken into account: The Auger peak should not involve valence electrons and should not be superimposed on another peak. In the case of iron, we chose the peak at 598 eV, and we converted it to an apparent peak at 703 eV by multiplying the measured height by a coefficient equal to the ratio of the peak heights at 598 and 703 eV, respectively, as determined on a pure iron matrix.

An approximate value of the sensitivity coefficients of iron, chromium, and molybdenum can be obtained from the study of the metallic matrix when the passive film has been completely removed by ion etching. This way the Auger signals are only related to the base elements of the alloy, the concentrations of which are well known. This assumes that sputtering is not selective, which seems to be verified by the constancy of the total number of atoms in every layer. By taking iron as a reference material, we obtain the sensitivity coefficients of the other elements I (I = A, B, C . . .), by satisfying the following relationship

$$\sum_{I=A}^{c} H^* = \sum_{I=A}^{c} \frac{H_I}{\alpha_I} = \text{constant}$$

where H^* is the corrected peak height.

The contribution coefficient K of iron has been calculated from Eq. [2] in the Appendix for different kinds of matrixes (metal or oxides). For the other elements the values of K are obtained by the same procedure (Table I).

Though a statistical approach enables one to show theoretically that the sputtering of atoms does not leave an atomically planar surface, we have nevertheless supposed for the sake of convenience that etching strips a complete layer before attack on the subsequent one. This approximation is more accurate when the number of layers removed is low. The focus of the ion beam is such that the irradiated area is much larger than the one sampled by the primary electrons.

To obtain the depth profile for the various elements, argon ions accelerated by a potential of 600V were used with the ionic current between the limits of 0.3×10^{12}-3×10^{12} ions cm^{-2} sec^{-1}. It has been derived (10) that the number n of argon ions impinging on a 1 cm^2 area of surface is proportional to the sputtering rate, *i.e.*, $n = \gamma(p \cdot t)$, in which p is the argon pressure in Torr, t is the sputtering time t in minutes, and the constant γ is equal to 4.1×10^{18} cm^{-2} $Torr^{-1}$ min^{-1}. If the sputtering rate of one Torr · min is taken as unity, and supposing that the atom density of a surface layer is nearly 10^{15} cm^{-2}, we obtain a sputtering rate of one monolayer for $p \cdot t \sim 0.2 \times 10^{-3}$ Torr · min. This is approximately the case for iron and chromium in the present study, the sputtering yields of which are, respectively, 1.25 and 1.26. This value for $p \cdot t$ is also compatible with the sputtering of monolayers obtained by thermal segregation.

Table I

Elements	Fe	Cr	Mo	O	Cl
Energy, eV	598	529	186	510	181
α	1	0.9	3.1	2.1	1.9
K	0.73	0.70	0.57	0.70	0.57

Our method of quantifying the Auger spectra entails the measurement of the peak amplitude H_I of the characteristic Auger signals chosen for the various elements. The change of H_I as a function of the sputtering rate is plotted and this curve is cut by vertical and parallel lines corresponding to a separation equal to 0.2 $\times 10^{-3}$ Torr · min; this regular interval is consistent with the removal of a monolayer from the surface. The relevant abscissas of the points of intersection H_A^i and H_A^{i+1} permit the determination of the concentration of the element A in the layer i (*c.f.*, Eq. [4] in Appendix).

By applying Eq. [3] in the Appendix to each couple of successive vertical lines, we obtain, knowing the contribution coefficient k, the number of atoms of an element in the monolayer bounded by these lines.

From Table I it is seen that the carbon peak has not been taken into account. That element is only observed during the first sputtering period, and its concentration is considerably reduced in the second atomic layer. Nevertheless it represents the major constituent in the overlayer as the sample is taken from the electrolytic cell and is introduced into the spectrometer. Due to some difficulty in assigning an accurate sensitivity coefficient to carbon, it was decided to ignore that element, which has the drawback of leading to concentration values without physical meaning in the outermost layer of the sample, but does not significantly perturb the concentration profiles of the other elements in subsequent layers.

In addition to Auger electron technique, activation analysis was used to obtain in a quantitative manner the oxygen contained in the passive film; specimens are irradiated in a beam of tritons accelerated in a Van de Graaf generator. The following nuclear reaction has been used: $^{16}_{8}O(t,n)^{18}_{9}F^*$ (T = 110 min). A detection limit of 0.004 $\mu g \cdot cm^{-2}$ may be obtained for a 10 min irradiation with 0.2 μA of tritons at 2 MeV (11, 12).

Results

Passive film formed electrochemically.—Figure 1 shows the composition profiles of the passive film on a ferritic 26% Cr-1% Mo steel that was passivated for 6 hr at a potential of + 650 mV/SCE in a 3.5% NaCl (pH 2.5) solution. Passivation of the ferritic steels is characterized by the formation of an oxide film 8-9 atomic layers in thickness, and by the development of a chromium-depleted zone inside of the matrix at the oxide-metal interface.

The diagram shows that the overlayer of the passive film is principally carbon, the concentration of which decreases abruptly and completely disappears beyond the fourth layer. Chlorine is also found in the first layers of the oxide. The depth of penetration of carbon and chlorine are similar.

From the depth profiles it can be seen that each atomic layer of the passive film has a particular composition. The internal layers of the oxide are richer in chromium than the matrix, while the iron concentration in the same layers is lower. There exist steep gradients of concentration near the metal-oxide and oxide-solution interfaces.

For the 26% Cr-1% Mo steel, the molybdenum concentration in the passive film is very low (Fig. 1 and 2). Nevertheless, the presence of that element in the

steel slightly modifies the depth profiles. Particularly, it appears that the maximum chromium content in passive films on the alloys without molybdenum (Fig. 3) is higher than that in films on alloys containing molybdenum (Fig. 2).

The thicknesses of passive films vary very slightly with potential and with the length of passivation (at least for times greater than 30 min). However, the depth of the chromium-depleted zone increases linearly with passivation time at all passivation potentials (Fig. 4).

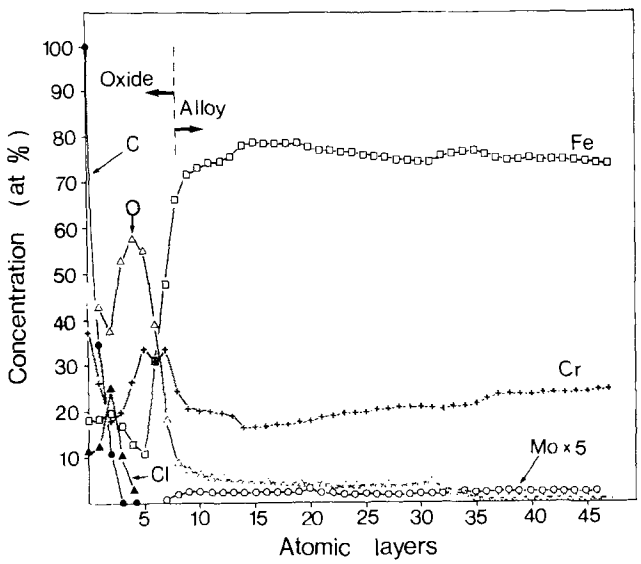


Fig. 1. Composition profiles of the principal elements in the passive film and in the alloy. (26% Cr-1% Mo steel) passivated for 6 hr at a potential of +650 mV/SCE in a 3.5% NaCl (pH 2.5) solution at 5°C.

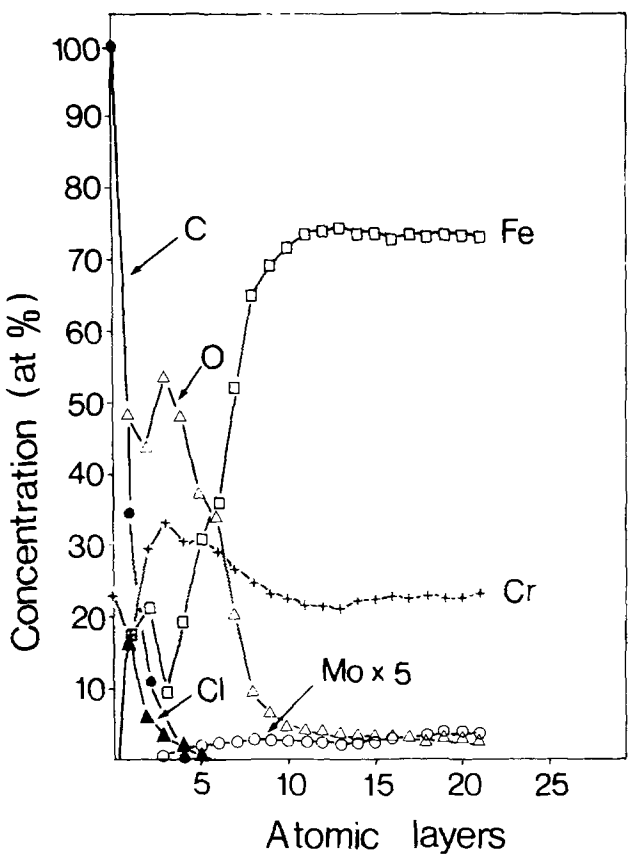


Fig. 2. Composition profiles of the principal elements in the passive film and in the alloy. (26% Cr-1% Mo steel) passivated for 6 hr at a potential of −250 mV/SCE in a 3.5% NaCl (pH 2.5) solution at 5°C.

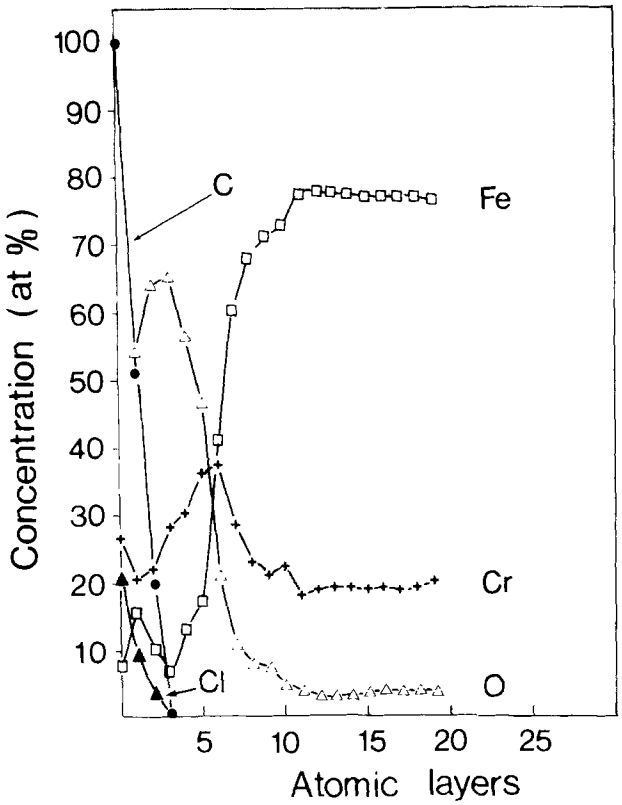


Fig. 3. Composition profiles of the main elements in the passive film and in the alloy. (26% Cr steel) passivated 6 hr at a potential of −250 mV/SCE in a 3.5% NaCl (pH 2.5) solution at 5°C.

The chromium concentration at the minimum of the composition profile is low for short passivation times (30 min), but rises progressively to a constant value as the time is increased. It appears that changes in alloy composition at the film-matrix interface can proceed long after the passive film has been formed.

Figures 5 and 6 show the influence of the temperature of the corrosive medium on the depth profiles of passive films. In the first example (Fig. 5), the potential of the sample was kept at −250 mV/SCE and the chloride solution was held at 98°C. In the second one (Fig. 6), the same alloy was passivated at a potential of +650 mV/SCE and removed from the solution when its temperature reached the critical pitting temperature, *i.e.*, the temperature beyond which localized attack is likely to occur. It can be seen that the films formed under these conditions are generally thicker. It also appears that the penetration of carbon and chlorine is more extensive. Both elements are detected in the film near the oxide-metal interface. In comparison with the experiments carried out at 5°C, the following differences are also noticed: the dip in the iron profile inside the passivating film is not as deep or broad and can hardly be seen for the experiment at 98°C; and the enrichment in chromium affects a much wider zone and is observed as a large hump in the concentration profile.

The curves giving the number of the atoms N_I^i of each element and those giving the total number of the atoms ΣN_I^i in each layer of the passive film are plotted in Fig. 7 as a percentage of the number of the atoms in a layer of the matrix. The number of atoms in each layer of the passive film is generally lower than in the layers of the matrix. This number is relatively low in the layers close to the oxide-solution interface, increases in the first layers, and then decreases at the oxide-metal interface. It also seems that the layers located in the chromium-depleted zone of the metallic matrix have a slightly smaller number of atoms than

in the deeper layers where the alloy reaches its true composition.

Hydrogen atoms are not detected by the Auger effect. This element could be present in the film in the form

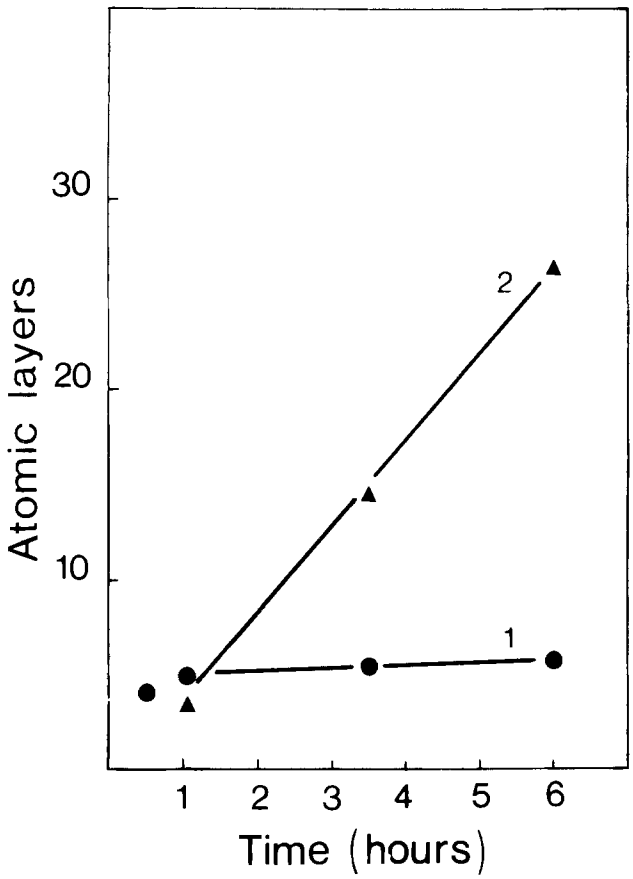


Fig. 4. Number of atomic layers in the passive film (curve 1) and in the chromium-depleted zone (curve 2) vs. the time of passivation. (26% Cr-1% Mo) steel passivated at a potential of +650 mV/SCE, in a 3.5% NaCl (pH 2.5) solution at 5°C.

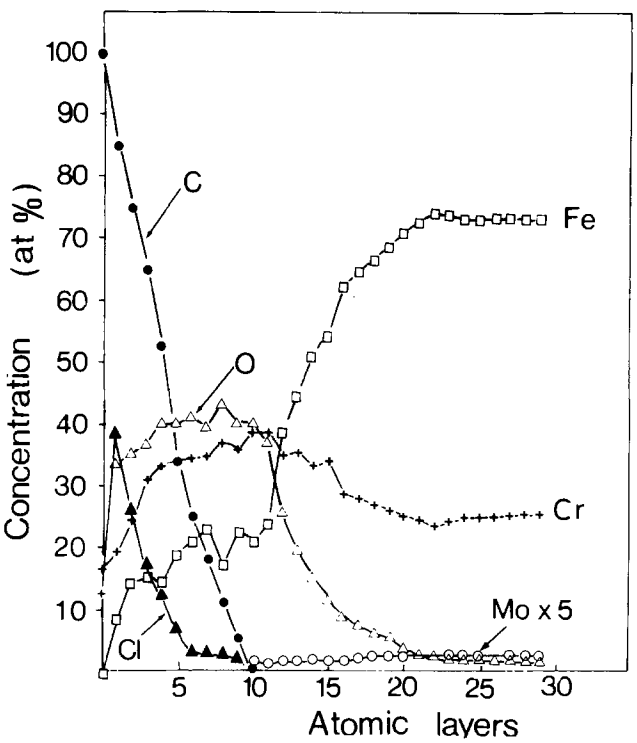


Fig. 5. Composition profiles of the principal elements in the passive film and in the alloy. (26% Cr-1% Mo) steel passivated for 1 hr at a potential of −250 mV/SCE in a 3.5% NaCl (pH 2.5) solution at 98°C.

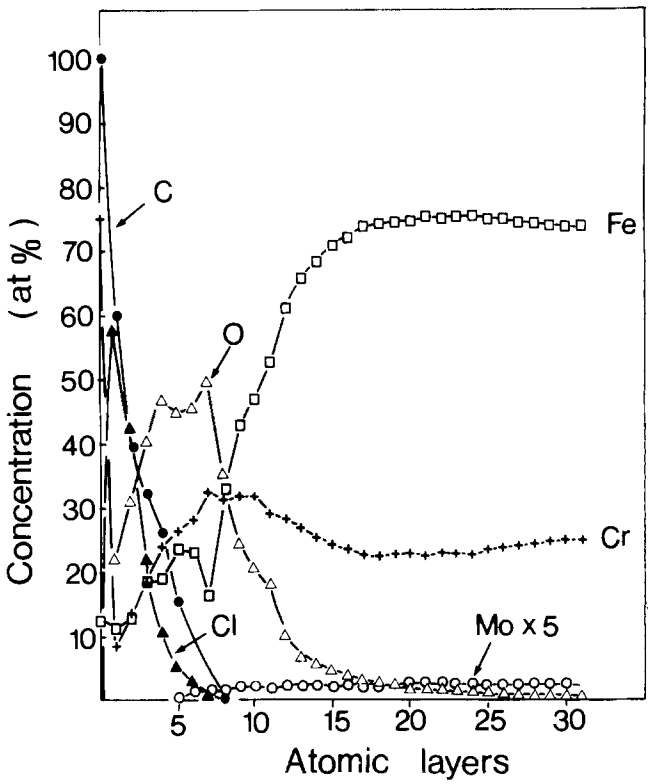


Fig. 6. Composition profiles of the principal elements in the passive film and in the alloy. (26% Cr-1% Mo) steel passivated for 1 hr at a potential of +650 mV/SCE, in a 3.5% NaCl (pH 2.5) solution at 34°C.

of water molecules, as has been suggested for the passive films formed on pure iron (13) and on stainless steels exposed to different solutions (14). Obviously, the presence of hydrogen can affect the total number of the atoms in each layer, and particularly near the oxide-solution interface.

The influence of the temperature of the corrosive environment upon the number of atoms of each element in an atomic layer appears very clearly: The films formed in a chloride solution heated at a temperature of 98°C (Fig. 7b) accommodate fewer atoms in a layer (lower ΣN_i^i) than those growing in the same medium at a temperature of 5°C (Fig. 7a).

Passive films formed in the air.—Passivation in air of a ferritic steel maintained for a fortnight in a desiccator at 25°C (Fig. 8) presents some analogies with that obtained in a chloride solution. The depth profiles show the presence of carbon and chlorine in the first layers of the film, chromium enrichment in the internal layers, and strong gradients of composition at the interfaces. In comparison with the passive films formed in an aqueous solution it appears that for the iron profile the minimum is much wider and its value is much higher. The external ridge of the well is also at a higher level. The concentration gradient for chromium is decreasing towards the surface. The molybdenum in the film is very low as in the films formed in aqueous solution. It is also observed that the number of atoms within a given layer of the film is lower than in the metallic matrix. Nevertheless, in the air-formed films the cations originating from the steel substrate tend to accumulate in the outer layers of the film, as a result of the absence of a dissolution process.

Activation analysis.—Activation analysis shows that oxygen content in the film varies only very slightly with the potential. For the 26% Cr-1% Mo steel passivated 1 hr in a 3.5% NaCl solution, the quantity of oxygen contained in the oxide varies from 0.40 to 0.45 $\mu g/cm^2$ when the potential is changed from −250 to +650 mV/SCE. However the oxygen content increases with the temperature of the solution (0.6 $\mu g/cm^2$ after

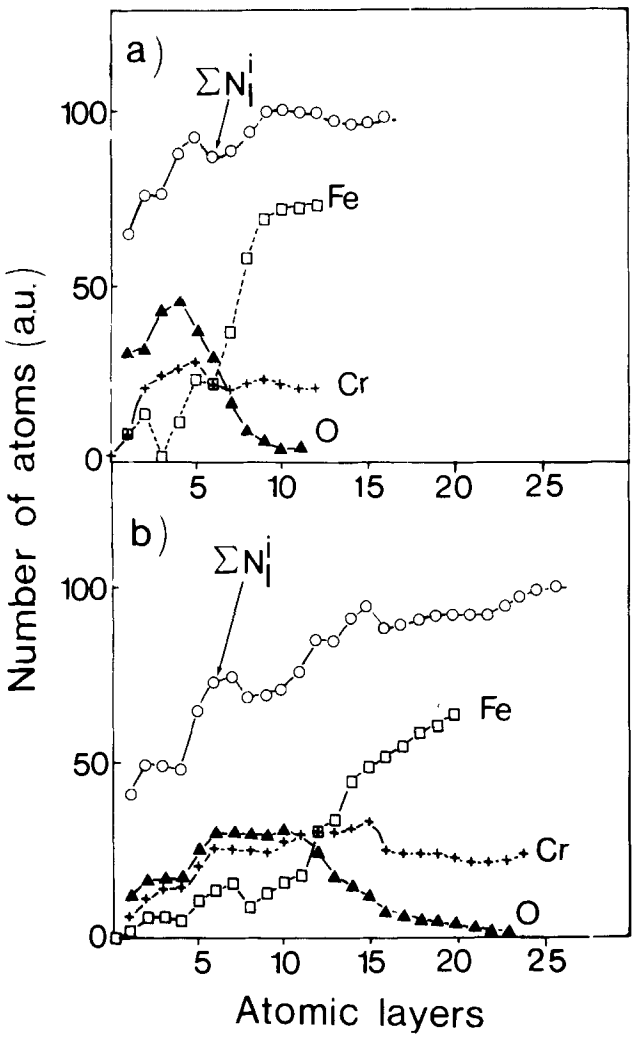


Fig. 7. Composition profiles giving the number of atoms of the principal elements within each layer of the passivated film and in the alloy. (26% Cr-1% Mo) steel passivated for 1 hr at a potential of +650 mV/SCE in a 3.5% NaCl (pH 2.5) solution. a. solution temperature 5°C; b. solution temperature 98°C.

passivation at −250 mV/SCE, when the solution is at 98°C).

Coulometric measurements.—The apparent coulombic thickness of the passivating films has been measured. Further, coulometric measurements have been made to learn more about the influence of molybdenum on the properties of the passive film.

Figure 9 shows the coulometric reduction results obtained with two different alloys (26% Cr and 26% Cr-1% Mo ferritic steels) for 1 hr polarization at a given potential. It appears that the quantity of charge used in the film reduction process increases with the passivation potential. Two different potential regions are indicated: the first is located at lower potentials and the second extends to the higher values. This behavior has been reported by many workers for the passivation of iron (15, 16) and stainless steel (14).

The efficiency of the cathodic process, measured as the quantity of charge required for reduction of the film decreases with molybdenum additions (Fig. 9 and 10). More precisely, the molybdenum content of the alloy has little influence on the reduction of the outer layer of the film (Fig. 9 and 10, curves a). However, the alloys with molybdenum require more charge for the reduction of the inner layers, particularly the layer next to the oxide-metal interface (Fig. 9 and 10, curves c). The quantity of charge for the reduction process increases with the temperature of the corrosive medium. It is also important to observe that the plateau in the potential-time curve disappears at the high temperature (Fig. 11).

Discussion

The analytical study by Auger electron spectrometry indicates that the composition of the passive film changes continuously with depth. This information supports recent ion-scattering spectrometry work for air-formed oxide film on a series of iron chromium alloys (17).

Previous ESCA studies (18) of films formed on chromium steels have shown that chromium is in a trivalent state in all zones of the passivating film, while iron is trivalent in the outer layers with a gradual transition to divalent state in the layers near the metal-oxide interface. These results can be correlated with the iron profile obtained by Auger-spectrometry. The minimum which can be observed in the concentration profile for iron (Fig. 1-3) leads us to consider two zones in the passive film: an inner nonporous oxide which exhibits good electronic conduction and in which cation transport could be expected, and an outer porous oxide in which anions can migrate. A difference between our results and those given by ESCA is worth noting: The

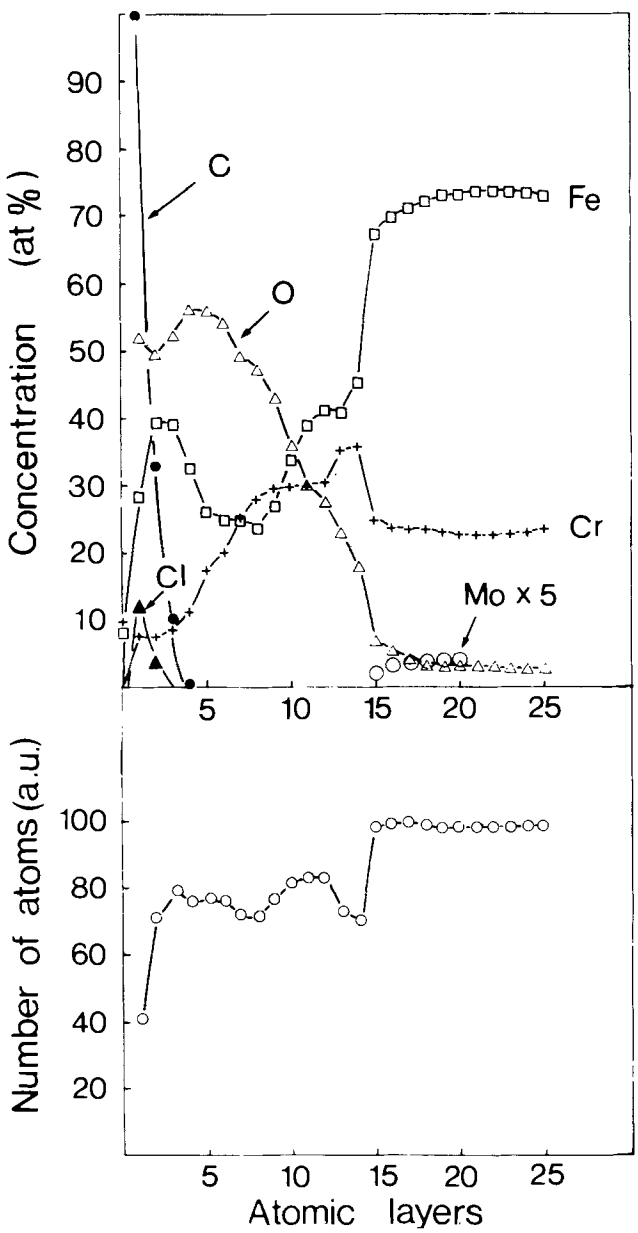


Fig. 8. Composition profile and number of atoms detected in the passive film. Ferritic 26% Cr-1% Mo steel maintained 15 days in a desiccator at 25°C.

chromium concentration gradient in the passive film formed on steels with 4-30% Cr at 25°C in oxygenated water is the inverse of that observed by Auger spectrometry in this work (except for the very first layers, where the sign of the slope is the same). Analytical results show that the thickness of the film does not depend directly on the electrode potential. However it must be recognized that changes in the defect structure probably occur with potential variations (15, 16).

The passive film formed on iron-chromium alloys appears to be a duplex oxide similar to that suggested for passivation of iron (19-23) and austenitic stainless steel (23a). Chlorine penetrates into the outer layers of the film at all potentials. Aggressive ions are stopped only by the inner layers of the film at all potentials. Aggressive ions are stopped only by the inner layers of the film, even when the temperature of the corrosive medium is increased.

In previous papers, the properties of films formed on stainless steels have been associated with an amorphous structure (14, 25). This gel-like structure may be more protective, because it offers a higher resistance to cation transport than crystalline structures (26). In our opinion the amorphous state is characteristic of the outer layers of the passive film. In this zone channels may be formed, and large ions can move (27-30). Further, if we assume that the outer layer forms a poor conductor, anion transfer may be assisted by a high field (16). The less dense matter of the outer zone implies a porous structure, and the presence of Cl^- in the outer layer is consistent with this model.

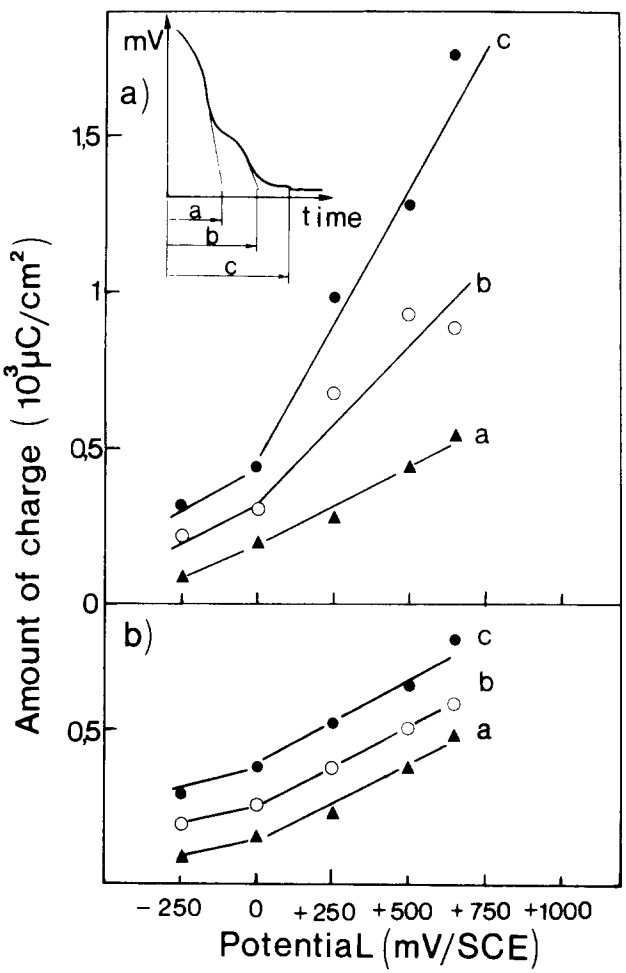


Fig. 9. Quantity of charge associated with the cathodic reduction process for each zone of the passivating film. Films were formed during polarization for 1 hr at different potentials in a 3.5% NaCl (pH 2.5) solution at 5°C. Curves a, b, and are related to the reduction of the outer, transition, and inner layer zones. Coulometric measurements were carried out in 18N H_2SO_4 solutions. a. Ferritic 26% Cr-1% Mo steel; b. ferritic 26% Cr steel.

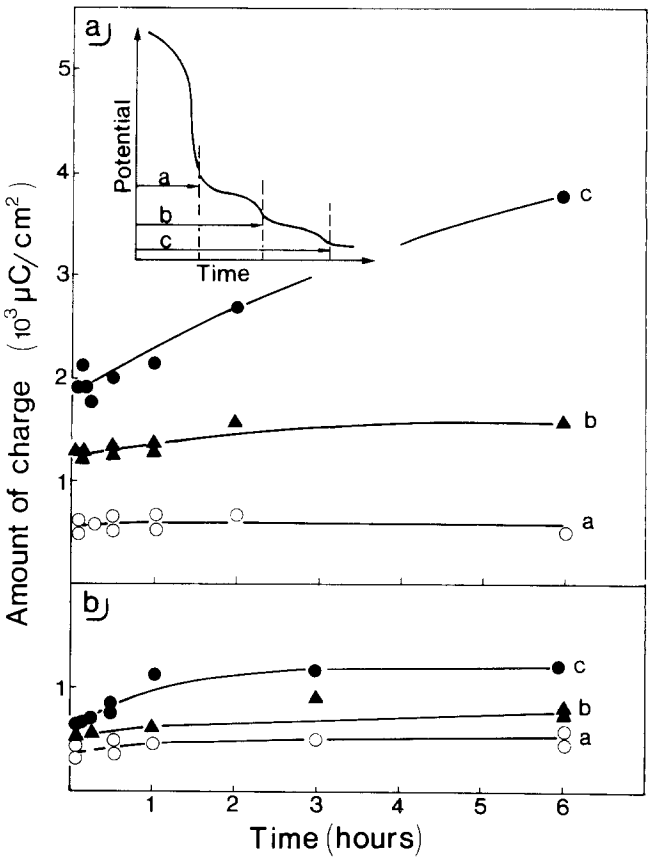


Fig. 10. Quantity of charge associated with each zone of the passivating film formed at +650 mV/SCE for different times of passivation (experimental conditions are the same as in Fig. 9). a. Ferritic 26% Cr-1% Mo steel; b. ferritic 26% steel.

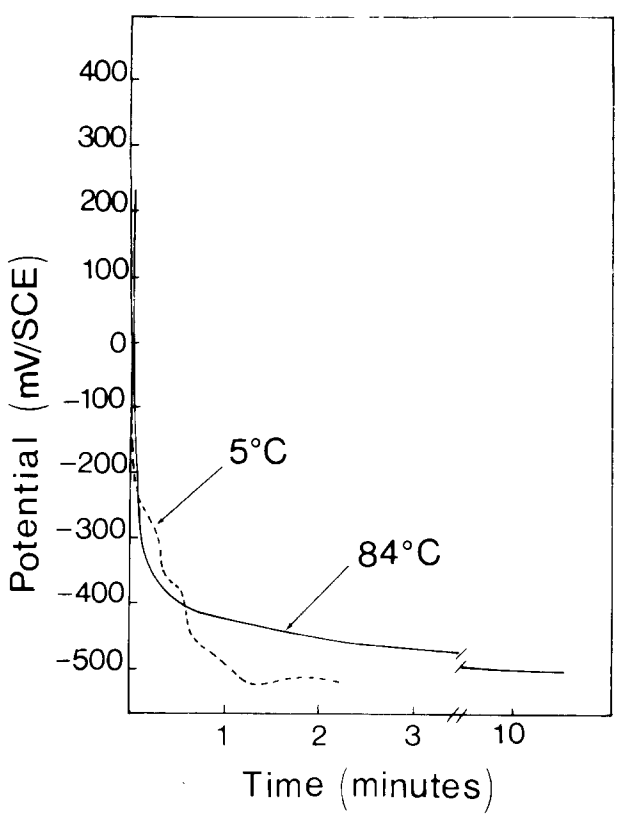


Fig. 11. Potential-time curves obtained during cathodic reduction. Films formed at —250 mV/SCE in a 3.5% NaCl (pH 2.5) solution at different temperatures (Ferritic 26% Cr-1% Mo steel).

The compositional analysis is in agreement with recent results (31), and shows that the molybdenum concentration in the passive films formed on ferritic stainless steels is very low (even in the case of an alloy with 3% Mo) and is only detectable in the inner part of the films. However, coulometric measurements indicate that the passive films formed on Fe-Cr-Mo alloys require a much greater quantity of charge for reduction than do the films formed on Fe-Cr alloys. This electrochemical behavior of the Mo alloys may be associated with their greater corrosion resistance (32-37). It should be pointed out that molybdenum additions have little effect on chromium depletion. This phenomenon, which occurs in high temperature oxidation of iron-chromium alloys (38-41), has not been mentioned as a possible process at low temperatures.

Conclusions

The passive film formed on iron-chromium alloys in NaCl solution is approximately 10 atomic layers thick. The film is enriched in chromium relative to iron. The composition profile of iron in the film shows a deep minimum with a value near to zero in the middle of the film, and a marked increase near the oxide-solution interface. There is a narrow zone inside the film which is only a chromium oxide, behind which molybdenum rises to a level equal to its concentration in the alloy. Further, we observe in the alloy chromium depletion at the oxide-metal interface. On the whole, the total number of atoms per layer is not the same in the oxide film as in the matrix. The less dense matter in the passive film implies a porous structure. Chlorine is always present in the outer zone of the film but does not penetrate into the inner zone. It appears that molybdenum additions increase the stability of the inner layers of the film near the oxide-metal interface.

Manuscript submitted Oct. 26, 1976; revised manuscript received May 11, 1977.

Any discussion of this paper will appear in a Discussion Section to be published in the June 1978 JOURNAL. All discussions for the June 1978 Discussion Section should be submitted by Feb. 1, 1978.

Publication costs of this article were assisted by the National Center of Scientific Research.

APPENDIX

Contribution of Each Atomic Layer to the Total Auger Signal: A Quantitative Approach

If we study a heterogeneous sample, the composition of which is a function of the depth in a direction normal to the surface but homogeneous within each atomic layer parallel to the surface, we may consider that the Auger current due to element A given by the whole specimen represents the sum of the contributions of each atomic plane. The peak-to-peak amplitude of the signal $h_A^{(i)}$ corresponding to the Auger current due to the layer i is expressed by the following relationship

$$h_A^{(i)} = \alpha_A k_A^{(i)} N_A^{(i)} \qquad [A\text{-}1]$$

where $N_A^{(i)}$ is the number of the atoms A in the layer i, a fraction of which are excited by the incident electron beam and yield Auger electrons. This proportion is taken into account in the α term. α_A is a sensitivity coefficient, characteristic of the element A, which includes the ionization cross-section, the probability of the Auger transition, as well as many constants of the spectrometer such as the intensity of the incident beam and the collection factor of the analyzer. This term has a fixed value provided the intensity of the beam and the energy of the primaries are well determined. Therefore, it is independent of the matrix insofar as there is no chemical binding resulting in a change of the Auger transition probability. $k_A^{(i)}$ is the contribution coefficient of the layer i to the total signal given by the whole specimen. It takes into account the escape depth of the Auger electrons in the layers before they reach the level i and the backscattering within the matrix.

Owing to these effects, it can be shown that the contribution coefficients are in geometrical progression: 1, K, K^2 ..., with the expression of K given by

$$K = \exp - \left(\frac{d}{D_x \cos\theta} + \frac{d}{D_p} \right) \qquad [A\text{-}2]$$

where d is the thickness of a monolayer, D_s the escape depth of the Auger electrons, D_p the depth of penetration of the primary electrons, and θ, the angle of acceptance of the Auger electrons in the cylindrical mirror analyzer.

If we designate by $H_I^{(0)}$ the initial Auger signal relative to the element I (I = A, B, C ...), when the zero layer is present we may write

$$H_A^{(0)} = \alpha_A (N_A^{(0)} + K_A N_A^{(1)} + K_A^2 N_A^{(2)} + \ldots + K_A^i N_A^{(i)} + \ldots)$$

$$H_B^{(0)} = \alpha_B (N_A^{(0)} + K_B N_B^{(1)} + K_B^2 N_A^{(2)} + \ldots + K_B^i N_B^{(i)} + \ldots)$$

$$H_I^{(0)} = \alpha_I (N_I^{(0)} + K_I N_I^{(1)} + K_I^2 N_I^{(2)} + \ldots + K_I^i N_I^{(i)} + \ldots)$$

and after removal of the zero layer, when layer one becomes the outermost layer, we may write

$$H_A^{(1)} = \alpha_A (N_A^{(1)} + K_A N_A^{(2)} + \ldots + K_A^{i-1} N_A^{(i)} + \ldots)$$

$$H_B^{(1)} = \alpha_B (N_B^{(1)} + K_B N_B^{(2)} + \ldots + K_B^{i-1} N_B^{(i)} + \ldots)$$

$$H_I^{(1)} = \alpha_I (N_I^{(1)} + K_I N_I^{(2)} + \ldots + K_I^{i-1} N_I^{(i)} + \ldots)$$

Hence, if we suppose a layer-by-layer ion etching, the number of the atoms of the element A in the "zero" layer can be deduced

$$N_A^{(0)} = \frac{H_A^{(0)} - k_A H_A^{(1)}}{\alpha_A} \qquad [A\text{-}3]$$

and those contained in layer "one" can be computed from the peak heights $H_A^{(1)}$ and $H_A^{(2)}$. More generally, for any element I (I = A, B, C ...), the number of atoms in the layer i is given by

$$N_I^{(i)} = \frac{H_I^{(i)} - k_I H_I^{(i+1)}}{\alpha_I}$$

The total number of the atoms present in layer i obviously is

$$\sum_{I=A}^{C} N_I^{(i)} = N_A^{(i)} + N_B^{(i)} + N_C^{(i)}$$

If it is certain that this quantity is the same in every layer, its value must be constant. It is therefore possible to choose the sensitivity coefficients α_A, α_B, α_C ... to verify that $\sum_{I=A}^{C} \frac{H_I^{(i)}}{\alpha_I}$ = constant. Inversely, if the values of α_A, α_B, α_C are known, the number of the atoms in each atomic layer can be deduced. The atomic fraction of the element A in layer i is given by

$$C_A^{(i)} = \frac{N_A^{(i)}}{\sum_{I=A}^{C} N_I^{(i)}} = \frac{\frac{H_A^{(i)} - k_A H_A^{(i+1)}}{\alpha_A}}{\sum_{I=A}^{C} \frac{H_I^{(i)} - k_I H_I^{(i+1)}}{\alpha_I}} \qquad [A\text{-}4]$$

REFERENCES

1. B. Rondot, F. Pons, J. Le Héricy, M. da Cunha Belo, and J. P. Langeron, Paper presented at the Second Colloquium of the Physics and Chemistry of Surfaces, France, May 27-30, 1975.
2. F. Pons, J. Le Héricy, and J. P. Langeron, *Surf. Sci.*, To be published.
3. P. W. Palmberg, *Anal. Chem.*, **45**, 549A (1973).
4. C. C. Chang, in "Characterization of Solid Surfaces," P. F. Kane and G. R. Larrabee, Editors, p. 509, Plenum Press, New York (1974).
5. R. Bouwman, L. H. Toneman, and A. A. Holscher, *Vacuum*, **23**, 163 (1973).

6. J. P. Coad and J. G. Cunningham, *J. Electron Spectrosc. Relat. Phenom.*, **3**, 435 (1974).
7. J. C. Durand, B. Rondot, and J. Montuelle, *Mem. Sci. Rev. Metall.*, **68**, 639 (1971).
8. R. P. Frankenthal, *This Journal*, **114**, 542 (1967); *ibid.*, **116**, 580 (1969).
9. P. Berge, *C. R. Acad. Sci.*, **245**, 1239 (1957).
10. F. Pons, Thesis, Paris XI (1976).
11. J. N. Barrandon and P. Albert, *Rev. Phys. Appl.*, **3**, 111 (1968).
12. G. Revel, M. da Cunha Belo, J. P. Mériaux, C. Schneider, M. Hilleret, and R. Bourguillot, *J. Radioanal. Chem.*, **17**, 101 (1973).
13. R. W. Revie, B. G. Baker, and J. O'M. Bockris, *This Journal*, **122**, 1460 (1975).
14. G. Okamoto, *Corros. Sci.*, **13**, 471 (1973).
15. N. Nagayama and M. Cohen, *This Journal*, **110**, 670 (1963).
16. J. Kruger and J. P. Calvert, *ibid.*, **114**, 43 (1967).
17. R. P. Frankenthal and D. L. Malm, *ibid.*, **123**, 186 (1976).
18. I. Olefjord, *Corros. Sci.*, **15**, 687 and 697 (1975).
19. K. G. Weil and K. F. Bonhoefer, *Z. Phys. Chem.*, **4**, 175 (1955).
20. H. Göhr and E. Lange, *Naturwissenschaften*, **43**, 12 (1956); *Z. Electrochem.*, **61**, 1291 (1957).
21. M. J. Pryor, *This Journal*, **106**, 557 (1959).
22. K. Hauffe, *Werkst. Korros.* **6**, 117 (1955).
23. K. H. Vetter, *This Journal*, **110**, 597 (1963).
23a. G. M. Bolman and A. C. C. Tseung, *Corros. Sci.*, **13**, 531 (1973).
24. C. L. Mc Bee and J. Kruger, *Electrochim. Acta*, **17**, 1337 (1972).
25. T. N. Rhodin, *Corrosion (NACE)*, **12**, 465t (1956).
26. T. P. Hoar, *This Journal*, **117**, 17C (1970).
27. H. Rawson, "Inorganic Glass Forming Systems," Academic Press, London (1967).
28. F. Ordway, *Science*, **143**, 800 (1964).
29. W. H. Zachariasen, *J. Am. Chem. Soc.*, **54**, 3841 (1932).
30. B. E. Warren, *J. Am. Ceram. Soc.*, **21**, 259 (1938).
31. J. B. Lumsden and R. W. Staehle, *Scr. Metall.*, **6**, 1205 (1972).
32. L. Colombier and J. Hochmann, "Aciers Inoxydables, Aciers Refractaires," 2nd ed., Dunod, Paris (1965).
33. E. A. Lizlovs and A. P. Bond, *This Journal*, **118**, 72 (1971).
34. A. P. Bond, *ibid.*, **120**, 630 (1973).
35. R. J. Brigham and E .W. Tozer, *Corrosion (NACE)*, **29**, 33 (1973).
36. R. Mayoud, *Bull. Cercle Etud. Met.*, **12**, 643 (1974).
37. M. B. Rockel, *Corrosion (NACE)*, **29**, 393 (1973).
38. D. P. Whittle, D. J. Evans, J. C. Scully, and G. C. Wood, *Acta Metall.*, **15**, 1421 (1967).
39. G. C. Wood, *Oxid. Met.*, **2**, 11 (1970).
40. G. C. Wood, M. G. Hobby and B. Vaszko, *J. Iron Steel Inst. (London)*, **202**, 685 (1964).
41. T. Heumann and H. Boehmer, *Arch. Eisenhuettenwes*, **31**, 749 (1960).

The Pb/Pb^{+2} Exchange Reaction in Perchlorate Acidic Solutions

A. S. Gioda, M. C. Giordano, and V. A. Macagno

Department of Physical Chemistry, National University of Córdoba, 5000 Córdoba, Argentina

ABSTRACT

The Pb/Pb^{+2} exchange reaction mechanism in acidic perchlorate solutions has been investigated. Tafel slopes of about 30 mV are found for both Pb dissolution and deposition under steady-state and nonsteady-state conditions, respectively. Empirical rate equations for electrodissolution and electrodeposition are

$$i_a = k_a \mathbf{F} \exp \frac{2\mathbf{F}E}{RT}$$

and

$$i_c = k_c \mathbf{F}\, C^2_{Pb^{+2}} \exp - \frac{2\mathbf{F}E}{RT}$$

respectively. A mechanism with a chemical step as the rds is proposed to explain the experimental results. Although there has been special interest in the study of lead electrodes as anode energy producers in acid and alkali media (1, 2), less is known about the anodic behavior of lead electrodes in acidic solutions without film formation.

The anodic dissolution of lead has been studied (3) in KNO_3, $Pb(Ac)_2$, and NH_4Ac solutions, and a mechanism involving Pb^+ ions was postulated. On the other hand, results of impedance and double impulse measurements (4) have shown that at low Pb^{+2} concentrations the exchange process was controlled by lattice growth and dissolution. A full account of kinetic parameters for the Pb/Pb^{+2} exchange reaction in the presence of different types of electrolyte solutions is compiled elsewhere (2). In $HClO_4$ acid solutions in particular (5) only the passivation time of polycrystalline lead anodes was studied as a function of current density. The authors concluded that the process of anodic passivation is controlled by mass transport in solution.

Recently (6) the anodic oxidation of solid Pb in H_2SO_4 has been investigated and compared with measurements on solid Pb in $HClO_4$ solutions. Although some interesting features are shown, a full account of kinetic parameters are missing. Nevertheless, they concluded that the slow step for surface area changes with $HClO_4$ solutions is located in the surface since the curves do not depend on rotation speed.

This paper reports the results of kinetic studies of the exchange reaction at polycrystalline lead electrodes in acidic perchlorate solutions containing different amounts of Pb^{+2} ions, using several electrochemical techniques under a wide range of experimental conditions.

Key words: electrodeposition, dissolution mechanism, adions.

Experimental

A common three-electrode Pyrex glass cell was used for this investigation. The electrolyte solutions were deareated with purified nitrogen before each run. Temperature was maintained at 25° ± 0.1°C.

Polarization curves were obtained with a fast rise time potentiostat. Linear potential sweep experiments were performed with a specially designed triangular pulse generator (7) provided with electronic ohmic compensation. Potential current curves were recorded with a X-Y EAI Variplotter or with a 545 B Tektronix oscilloscope. Potential/time curves were obtained with a specially constructed power supply of ±0.1% stability. Transients were recorded either with a Sargent MR register or with the oscilloscope. Rotating-disk electrode assembly was previously described (8).

A saturated calomel electrode was used as the reference electrode. It was conveniently isolated from the working solution by an agar plug and glass joint. The reference compartment was in contact with the electrolyte through a Haber-Luggin capillary.

Lead electrodes were prepared from a bar stock of 99.999% Koch-Light Limited. A Teflon electrode assembly was used (9) to support the piece of Pb bar. The seal is produced using the principle of a drill chuck. The collet was made in Teflon, while the truck and the chuck were made in Teflon charged with fiber glass to make it harder. The surface exposed to the solution was a disk of either 4×10^{-3} or 6.1×10^{-2} cm^2. The exposed surface was ground with carborundum paper 600A with distilled water, as the lubricant, washed with distilled water, and then placed immediately in the cell. The same procedure was repeated before each run. Although mechanical polishing for soft metals has been criticized (10), we found that the several electropolished electrodes tested were unable to give reproducible results. The auxiliary electrode was a Pt foil of about 6 cm^2.

Solutions were prepared from $NaClO_4$, Koch-Light crystallized from distilled water, and $HClO_4$ acid Merck pA. $Pb(ClO_4)_2$ was obtained from lead electrolytic dissolution in $HClO_4$-$NaClO_4$ solutions and standardized with EDTA. Concentration range was between 2×10^{-3} and 1.64M for ClO_4^- ions, from 10^{-5} to 10^{-1}M for H^+, and between 2.3×10^{-5} and 1.34×10^{-2}M for Pb^{+2}.

The steady-state rest potential was taken at open circuit until the drift in potential was 5 mV/hr or less, and it was measured with a pH Meter 4 Radiometer potentiometer. The time elapsed to reach the steady state depends on the type of solution and concentration.

Current efficiency for an exchange of two Faradays per mole was verified through quantitative determination of Pb^{+2}. Unless indicated otherwise, all potentials are quoted against the saturated calomel electrode.

Results

Potentiostatic polarization curves.—Two types of solution composition were studied: a mixture of $NaClO_4$-$HClO_4$, and the same mixture with addition of $Pb(ClO_4)_2$. The dependence of the steady-state rest potential with the different species involved are compiled in Fig. 1. It can be seen that E_r appears almost independent of ClO_4^- and H^+ species concentration. On the other hand, in the Pb^{+2} concentration range studied, a plot of E_r *vs.* log $C_{Pb^{+2}}$ shows a slope

$$\frac{\delta E_r}{\delta \log C_{Pb^{+2}}} = 0.03\text{V} \qquad [1]$$

and with an intersect at log $C_{Pb^{+2}} \simeq 0$ very close to $E°_{Pb/Pb^{+2}}$ electrode, indicating that a Nernst's equation for the process

$$Pb \rightleftharpoons Pb^{+2} + 2e \qquad [2]$$

is followed.

Figure 2 shows some of the anodic polarization behavior of Pb electrodes in the two types of solutions. A linear dependence of E *vs.* log i_a is observed over at least two decades of logarithm even for the most dilute solutions. The addition of different amounts of Pb^{+2} produces an increase on the exchange current, but it has no appreciable effect on Pb dissolution. The polarization data obtained with stationary and rotating-disk electrodes were similar except for the region near the rest potential where the effect for the backward reaction becomes important and at high overpotentials where mass transport interferes. Anodic Tafel slopes in both types of solutions are around 30 mV/decade. A similar value was also reported previously (6).

The experimental dependence of anodic dissolution current densities on ClO_4^-, H^+, and Pb^{+2} concentration gives the following results

$$\left(\frac{\delta \log i_a}{\delta \log C_{ClO_4^-}}\right)_{E,H^+,Pb^{+2}} = \left(\frac{\delta \log i_a}{\delta \log C_{H^+}}\right)_{E,ClO_4^-,Pb^{+2}} = \left(\frac{\delta \log i_a}{\delta \log C_{Pb^{+2}}}\right)_{E,ClO_4^-,H^+} = 0 \qquad [3]$$

Although ionic strength was not constant for the first relationship, the effect of ϕ_2 potential on i is minimal when the reaction is independent of the ion concentration, as it seems to be in this case.

The variation of exchange current density with Pb^{+2} concentration obtained by extrapolating the Tafel line to the rest potential is

$$\frac{\delta \log i_o}{\delta \log C_{Pb^{+2}}} = 1 \qquad [4]$$

as shown in Fig. 3. Also, from the dependence of the rest potential on Pb^{+2} concentration, a value of Pb^{+2} concentration at the surface could be calculated in the type solutions. This average exchange current is also included in Fig. 3.

On the other hand, i_o appears as almost independent on H^+ and ClO_4^- ions concentrations as it is shown in Table I. Thus

$$\left(\frac{\delta \log i_o}{\delta \log C_{H^+}}\right)_{Pb^{+2}} = \left(\frac{\delta \log i_o}{\delta \log C_{ClO_4^-}}\right)_{Pb^{+2}} = 0 \qquad [5]$$

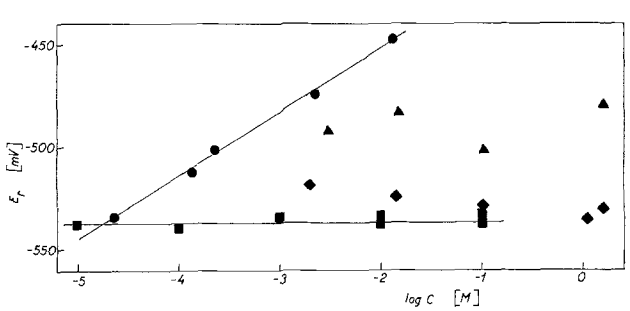


Fig. 1. Dependence of the steady-state rest potential with different species. ● *vs.* $C_{Pb^{++}} - C_{ClO_4^-} = 1.11$M, $C_{H^+} = 0.1$M; ■ *vs.* $C_{H^+} - C_{ClO_4^-} = 1.06$M; ▲ *vs.* $C_{ClO_4^-} - C_{Pb^{+2}} = 0.001$M, $C_{H^+} = 0.001$M; ♦ *vs.* $C_{ClO_4^-} - C_{H^+} = 0.001$M.

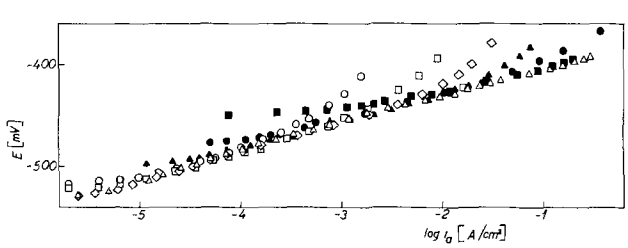


Fig. 2. Polarization curves for Pb electrodissolution. ○, □, ◇, △ $C_{H^+} = 0.001$M and $C_{ClO_4^-} = 0.002$, 0.014, 0.1, and 1.64M, respectively. ■ $C_{ClO_4^-} = 1.13$M, $C_{H^+} = 0.001$M, $C_{Pb^{+2}} = 0.013$M; ● $C_{ClO_4^-} = 1.64$M, $C_{H^+} = 0.001$M, $C_{Pb^{+2}} = 0.001$M; ▲ $C_{ClO_4^-} = 1.13$M, $C_{H^+} = 0.1$M, $C_{Pb^{+2}} = 0.0002$M.

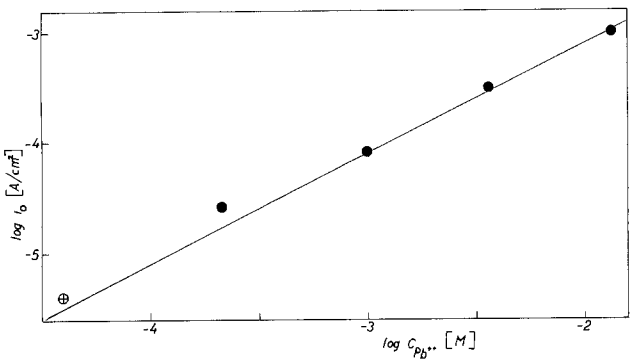


Fig. 3. Dependence of the exchange current density on log $C_{Pb}{}^{+2}$. ⊕ Concentration calculated as is indicated in the text.

Stoichiometric numbers (11) were experimentally obtained from current densities values at low overpotentials, as

$$\nu = \frac{i_o n\mathbf{F}}{RT}\left(\frac{\delta\eta}{\delta i_a}\right)_{\eta\to 0} \qquad [6]$$

Figure 4 gives typical η *vs.* i_a plots. The ν values obtained for the different types of solutions are compiled in Table I, and the average result is 0.5. In order to obtain reproducible results for the cathodic reaction, the electrode was rotated and the potential scanned at a constant rate of 5 mV/sec. Under this condition it is supposed that a quasisteady state is reached since no appreciable change in the E/i curves was found with potential sweep rates up to 20 mV/sec.

Figure 5 shows representative polarization curves for Pb deposition. Limiting currents are obtained which depend linearly on the square root of electrode rotation speed and Pb^{+2} concentration. Taking into account the Levich's equation (12)

$$i_L = 0.62\, n\mathbf{F}D^{2/3}\nu^{1-1/6}\omega^{1/2}C_b \qquad [7]$$

the diffusion coefficient can be evaluated. The average $D_{Pb^{+2}}$ is 4.8×10^{-6} cm² sec^{-1}.

The half-wave potential does not depend on rotation speed, this being an indication that the reaction behaves in a reversible way (13). On the other hand, a plot of η *vs.* log $[(i_L - i_c)/i_L]$ (12) gave a straight line with a slope of about 30 mV/decade.

Galvanostatic potential-time curves.—Representative potential-time curves for Pb^{+2} electrodeposition are shown in Fig. 6. Only one transition time is observed at all current densities studied. Nevertheless, an increase in the transition time was observed in repetitive runs performed at low current densities. This effect together with the increase of the $i_c\tau^{1/2}/C$ ratio as i_c is decreased, Fig. 7, could be attributed to an appreciable increase in the electrode area due to deposition. At moderate and high current densities a linear dependence of $i_c\tau^{1/2}/C$ *vs.* i_c is found.

By applying Sand's equation (14) to the linear region, the diffusion coefficient can be evaluated as

$$\frac{i_c\tau^{1/2}}{C_b} = \frac{n\mathbf{F}\pi^{1/2}D^{1/2}}{2} \qquad [8]$$

Table I. Kinetic parameters for Pb electrodissolution

$C_{ClO_4}{}^-$ (M)	C_{H^+} (M)	$C_{Pb^{+2}}$ (M)	b_a (V)	log i_o (A/cm²)	ν
			0.030	−5.48	—
		—	0.026	−5.32	—
			0.027	−5.44	0.40
			0.029	−5.44	0.54
1.64	0.001		0.028	−3.88	0.40
		0.001	0.027	−4.00	0.73
			0.027	−3.72	0.59
			0.029	−5.24	—
		—	0.030	−5.40	0.38
0.1	0.001		0.029	−3.88	0.46
		0.001	0.032	−3.92	—
			0.033	−5.72	0.54
		—	0.030	−5.27	—
			0.031	−5.60	—
0.014	0.001	0.001	0.030	−3.83	0.67
			0.028	−5.88	—
0.002	0.001	—	0.028	−5.20	0.49
0.003	0.001	0 001	0.029	−4.10	0.46
		0.002	0 025	−3.68	—
1.13	0.001	0.013	0.030	−2 36	—
		0.0002	0.026	−4.48	—

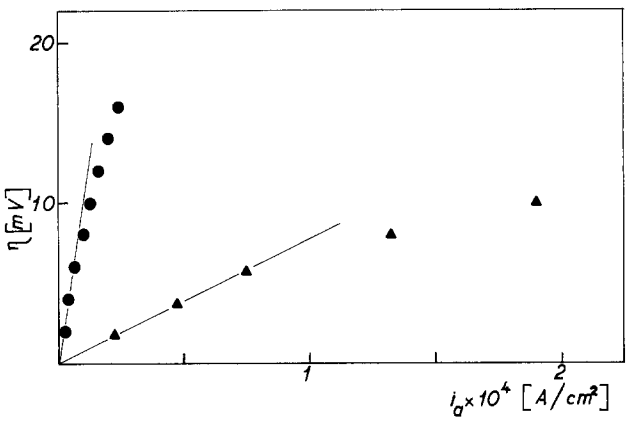


Fig. 4. Plots of overpotential *vs.* current density. $C_{ClO_4}{}^- = 1.64$M, $C_{H^+} = 0.001$M. ● Without Pb^{+2}; ▲ $C_{Pb^{+2}} = 0.001$M.

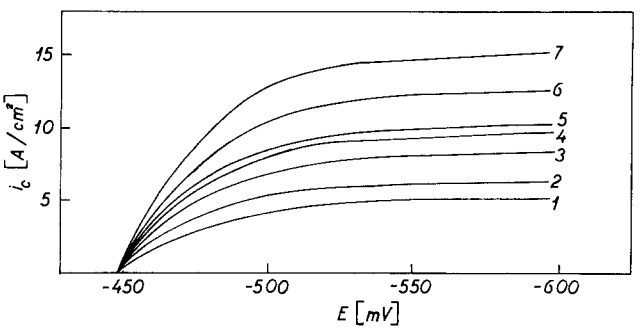


Fig. 5. Polarization curves for electrodeposition obtained at the RDE. $C_{Pb^{+2}} = 0.013$M, $C_{ClO_4}{}^- = 1.64$M, $C_{H^+} = 0.1$M. ω (rad/sec): 1 = 19.8; 2 = 40.2; 3 = 58.2; 4 = 77.4; 5 = 96.9; 6 = 128; 7 = 187.

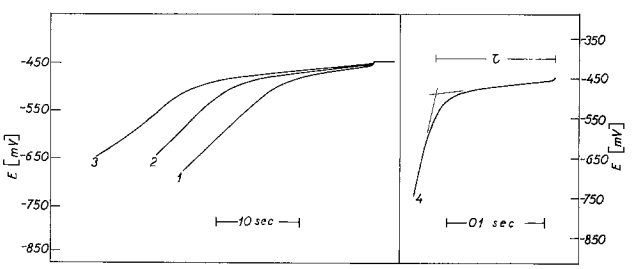


Fig. 6. Galvanostatic potential-time curves. $C_{ClO_4}{}^- = 1.13$M, $C_{H^+} = 0.1$M. 1, 2, and 3 repetitive runs, $C_{Pb^{+2}} = 1.34 \times 10^{-2}$M, $i_c = 2.05 \times 10^{-3}$ A/cm², 4, $C_{Pb^{+2}} = 0.0036$M, $i_c = 4.60 \times 10^{-3}$ A/cm².

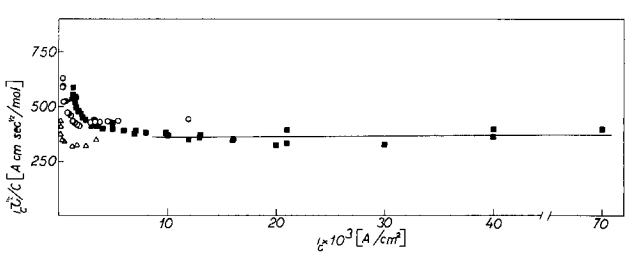


Fig. 7. Dependence of the chronopotentiometric constant on current density. $C_{ClO_4}{}^- = 1.13$M, $C_{H^+} = 0.1$M; ○, ■, △ $C_{Pb^{+2}} = 0.0036$, 0.013, and 0.0009M, respectively.

giving an average value of 4.5×10^{-6} cm^2 sec^{-1}. A plot of E *vs.* log ($\tau^{1/2} - t^{1/2}$) (14) gives a good straight line with a slope of 30 mV/decade.

Linear sweep voltammetry.—The dissolution curve appears as a typical process without film formation with a continuous increase in current as the potential is increased. On the reverse sweep a cathodic current appears near the rest potential. Voltammograms for Pb deposition are shown in Fig. 8. The cathodic i/E curves show a peak current that depends on sweep rate.

A plot of i_p *vs.* $v^{1/2}$, Fig. 9, shows a complex behavior. At low v there is a straight line dependence of i_p with $v^{1/2}$. As sweep rate is increased there is a transition to a lower slope. From the highest slope, the diffusion coefficient for a two electrons reversible process was calculated. The average value results 4.3×10^{-6} cm^2 sec^{-1}.

In Fig. 10, the behavior of E_p *vs.* log v is analyzed. Two different zones are observed depending on sweep rate. At low sweep rates, E_p remains constant independent of v, while after a certain v value the variation of E_p *vs.* log $v^{1/2}$ takes a slope of

$$\frac{\delta E_p}{\delta \log v^{1/2}} = 30 \text{ mV} \qquad [9]$$

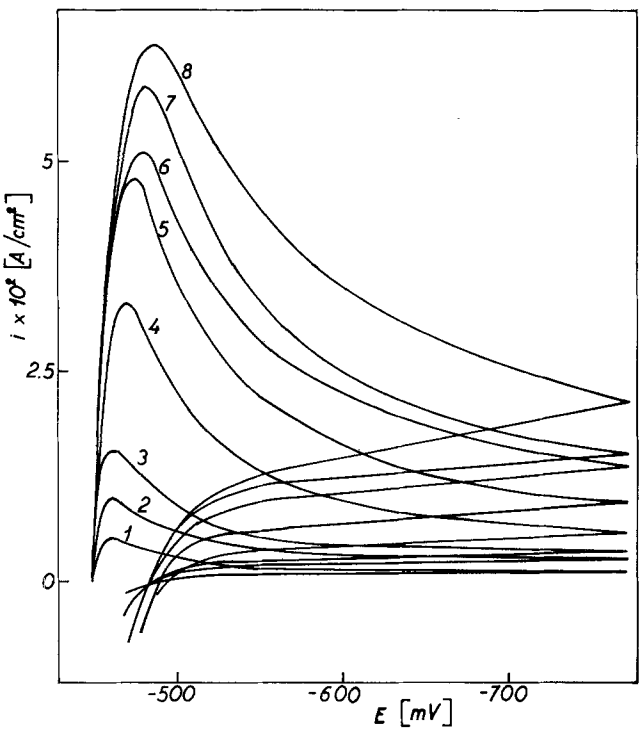


Fig. 8. Voltammograms for Pb^{+2} deposition. $C_{Pb^{+2}} = 0.013$M, $C_{ClO_4^-} = 1.13$M, $C_{H^+} = 0.1$M. Sweep rate (V/sec): 1 = 0.02; 2 = 0.1; 3 = 0.2; 4 = 0.8; 5 = 2; 6 = 4; 7 = 6; and 8 = 10.

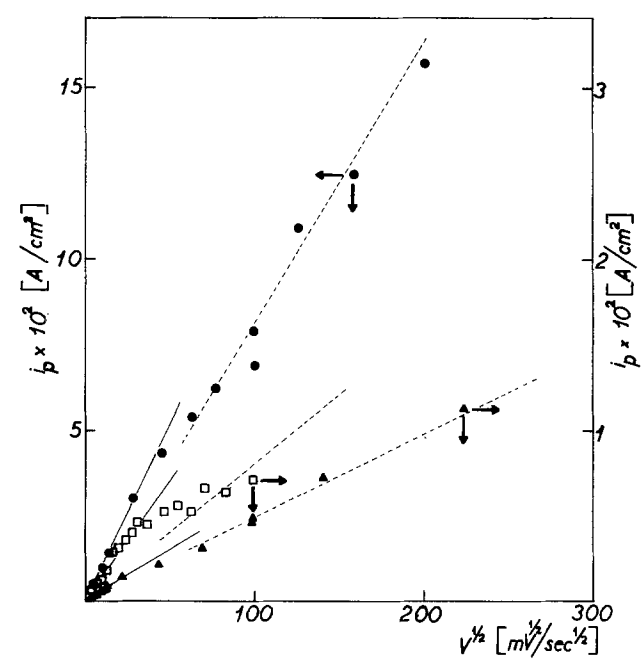


Fig. 9. Dependence of the peak current density on sweep rate for Pb^{+2} deposition. $C_{ClO_4^-} = 1.13$M, $C_{H^+} = 0.1$M. ●, □, ▲ $C_{Pb^{+2}} = 0.013$, 0.0036, and 0.0009M, respectively.

Discussion

From the experimental results given above, the rate for the anodic reaction can be derived from the theoretical expression (15)

$$i_a = \mathbf{F}k_a(\pi_s C_s Z_{a,s}) \exp(\alpha_a \mathbf{F}E/RT) \qquad [10]$$

With the experimental values of $\alpha_a = 2$ and Z_a for all species as zero, the empirical rate equation for the anodic reaction is obtained

$$i_a = \mathbf{F}k_a \exp \frac{2\mathbf{F}E}{RT} \qquad [11]$$

Introducing the overpotential in Eq. [10] as $\eta = E - E_r$, the theoretical rate equation is rewritten as

$$i_a = \mathbf{F}k_a(\pi_s C_s^{Z_{a,s}}) \exp[\alpha_a \mathbf{F}(\eta + E_r)/RT] \qquad [12]$$

when $\eta = 0$, $i_a = i_c = i_o$ and the exchange current results

$$i_o = \mathbf{F}k_a(\pi_s C_s^{Z_{a,s}}) \exp(\alpha_a \mathbf{F}E_r/RT)$$
$$= \mathbf{F}k_c(\pi_s C_s^{Z_{o,s}}) \exp(-\alpha_c \mathbf{F}E_r/RT) \qquad [13]$$

On the other hand, the Nernst equation can be written as

$$E_r = E_o - \frac{RT}{n\mathbf{F}} \ln \pi_s C_s^{m_s} \qquad [14]$$

which according to Eq. [2] takes the form

$$E_r = E_o + \frac{RT}{2\mathbf{F}} \ln C_{Pb^{+2}} \qquad [15]$$

Furthermore, the equilibrium constant of the total electrochemical reaction is related to the anodic and cathodic rate constants (15) as follows

$$\frac{k_a}{k_c} = K^{1/\nu} \qquad [16]$$

Taking into account the above equations, the following relations between kinetics parameters are found

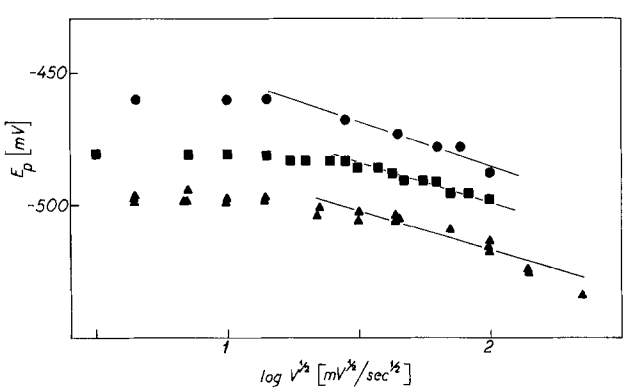


Fig. 10. Dependence of the peak potential on log $v^{1/2}$ for Pb^{+2} deposition. $C_{ClO_4^-} = 1.13$M, $C_{H^+} = 0.1$M. ●, ■, ▲ $C_{Pb^{+2}} = 0.013$, 0.0036, and 0.0009M, respectively.

$$n = \nu(\alpha_a + \alpha_c) \quad [17]$$

and

$$m_s = \nu(Z_a - Z_c) \quad [18]$$

Thus Eq. [13] for the exchange current can be transformed to

$$i_o = (k_c K^{1/\nu})\mathbf{F}\left[\pi_s C_s\left(\frac{m_s}{\nu} + Z_c\right)\right]\exp(\alpha_a \mathbf{F} E_r/RT) \quad [19]$$

Equation [19] shows that from a plot of ln i_o *vs.* ln $C_{Pb^{+2}}$ the cathodic reaction order can be found. Experimentally

$$\frac{\delta \ln i_o}{\delta \ln C_{Pb^{+2}}} = \left(\frac{m_s}{\nu} + Z_c\right) - m_s = 1 \quad [20]$$

hence, as $m_s = -1$ and $\nu = 0.5$, results are $Z_c = 2$. Also, according with Eq. [17], $(\alpha_a + \alpha_c) = n/\nu = 4$ and $\alpha_c = 2$; thus the rate equation for the cathodic reaction results in

$$i_c = \mathbf{F} k_c C^2_{Pb^{++}} \exp -\frac{2\mathbf{F}E}{RT} \quad [21]$$

Deposition of Pb^{+2} behaves as a rather reversible reaction under steady-state conditions. Nevertheless under linear sweep voltammetry a certain degree of irreversibility can be inferred from i_p *vs.* $v^{1/2}$ dependence, Fig. 9, and also from E_p *vs.* log $v^{1/2}$, Fig. 10, at high sweep rates giving a Tafel slope of about 30 mV/decade in agreement with the theoretical $\alpha_c = 2$.

By combining data represented in Fig. 9 and 10 the cathodic reaction order was obtained from log i_p *vs.* log $C_{Pb^{+2}}$ at constant E_p, Fig. 11. The experimental value is in agreement with the kinetic Eq. [21]. In a general case of a multistep reaction (16) the transfer coefficients α are denoted as

$$\alpha_a = \left(\frac{\gamma_a}{\nu} - \beta_r\right) \quad [22]$$

and

$$\alpha_c = \left(\frac{n - \gamma_a}{\nu} + \beta_r\right) \quad [23]$$

where γ's and r are the number of electrons transferred before and during the rds, respectively. β is usually taken as 0.5. On the bases of the kinetic parameters obtained, only one set of numbers of electrons transferred before and during the rds are possible. Thus,

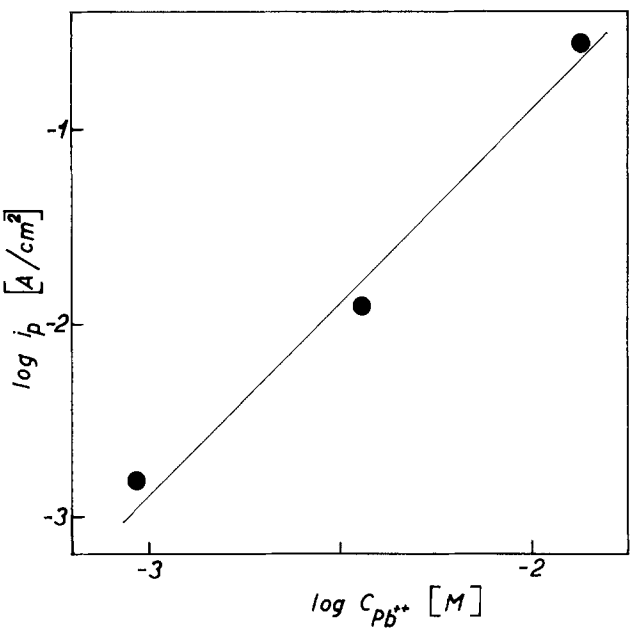


Fig. 11. Reaction order for electrodeposition with respect to Pb^{+2}. $C_{ClO_4^-} = 1.13M$, $C_{H^+} = 0.1M$, $E_p = -500$ mV.

for $\alpha_a = 2$ and $\nu = 0.5$, with $\beta = 0.5$ results $\gamma_a = 1$ and $r = 0$.

Accordingly a mechanism with a charge transfer in quasiequilibrium followed by a chemical step as the rate-determining step could be postulated as the most probable pathway for Pb/Pb^{+2} exchange reaction in acidic perchlorate solutions. Taking into account that Pb^{+2} concentration does not affect the anodic reaction rate, a loop-containing mechanism could be discarded in principle (17). On the other hand, the stoichiometric number of ½ experimentally obtained is an indication that for each occurrence of the rds the total reaction goes twice to completion. Hence, a quasiequilibrium one-electron charge transfer step to form species Pb(I) adion could be postulated for the first step (11). It is more difficult to assign a formal equation for the rds. Nevertheless, a chemical interaction between two Pb(I) adions to form a more suitable specie for the second charge transfer could be a plausible explanation for the $\nu = 0.5$ found experimentally. Formally, a sequence of steps

$$Pb \rightleftharpoons Pb(I) + 1e \quad [24]$$

$$2\,Pb(I) \xrightarrow{rds} [Pb(I)]_2 \quad [25]$$

$$[Pb(I)]_2 \rightleftharpoons 2Pb^{+2} + 2e \quad [26]$$

would be in agreement with the experimental data correlated by the empirical Eq. [11] and [21]. Much work is indicated in order to clarify the complex nature of the rds, but this investigation has shown that the behavior of the Pb/Pb^{+2} exchange reaction agrees with a series of previous results obtained with *sp* metals (18).

Acknowledgment

A. S. Gioda is grateful to the Consejo Nacional de Investigaciones of Argentina for the award of an Initiation Research Fellowship. This work was also supported in part by CONICET and CUI of Córdoba University.

Manuscript submitted Dec. 21, 1976; revised manuscript received May 16, 1977.

Any discussion of this paper will appear in a Discussion Section to be published in the June 1978 JOURNAL. All discussions for the June 1978 Discussion Section should be submitted by Feb. 1, 1978.

LIST OF SYMBOLS

A	amperes
b_a	anodic Tafel slope
C_b	concentration of diffusing specie in the bulk
C_s	concentration of *s* specie
D	diffusion coefficient
E	electrode potential
$E_{1/2}$	half-wave potential
E_o	standard potential
E_p	peak potential
E_r	steady-state rest potential
$\mathbf{F}$	Faraday's constant
i	current density
i_a	anodic net current density
i_c	cathodic net current density
i_L	limiting current density
i_p	peak current density
i_o	exchange current density
k_a	anodic specific rate constant
k_c	cathodic specific rate constant
K	equilibrium constant
m_s	stoichiometric coefficient of *s* specie in the overall reaction
n	number of electrochemical equivalents per mole
r	number of electrons transferred in the rds
R	gas constant
t	time
T	absolute temperature (°K)
v	sweep rate
V	volts
$Z_{a,s}$	anodic reaction order for the *s* specie
$Z_{c,s}$	cathodic reaction order for the *s* specie

α_a anodic transfer coefficient
α_c cathodic transfer coefficient
β symmetry factor
γ_a number of electrons transferred before the rds
η overpotential
ν stoichiometric number
ν^1 kinematic viscosity
π_s productory over s
τ transition time
ϕ_2 potential at the outer Helmholtz plane
ω electrode rotation speed (radians/sec)

REFERENCES

1. G. Archdale and J. A. Harrison, *J. Electroanal. Chem. Interfacial Electrochem.*, **47**, 93 (1973).
2. T. F. Sharpe, "Encyclopedia of Electrochemical Elements," Vol. 1, Chap. 1-5 (1973).
3. J. W. Johnson, C. K. Wu, and W. J. James, *Corros. Sci.*, **8**, 309 (1968).
4. N. A. Hampson and D. Larkin, *Trans. Faraday Soc.*, **65**, 1660 (1969).
5. C. J. Bushrod and N. A. Hampson, *Br. Corros. J.*, **6**, 87 (1971).
6. A. N. Fleming and J. A. Harrison, *Electrochim. Acta*, **21**, 905 (1976).
7. G. Paus, A. J. Calandra, and A. J. Arvía, *Annales de la Soc. Cient. (Argentina)*, **192**, 35 (1971).
8. L. Sereno, V. A. Macagno, and M. C. Giordano, *Electrochim. Acta*, **17**, 561 (1972).
9. A. Capon and R. Parsons, *J. Electroanal. Chem. Interfacial Chem.*, **39**, 275 (1972).
10. C. V. D'alkaine, S. B. Estevez, and D. J. Schiffrin, *Metallurgical Journal No. 6*, Argentine Society of Metals, Buenos Aires, Argentina (1974).
11. J. O'M. Bockris, in "Modern Aspects of Electrochemistry," No. 1, J. O'M. Bockris, Editor, Chap. 4 Butterworths, London (1954).
12. A. C. Riddiford, in "Advances in Electrochemistry and Electrochemical Engineering," Vol. 4, P. Delahay and C. W. Tobias, Editors, Interscience, New York (1966).
13. G. Charlot, J. Badoz-Lambling, and B. Trémillon, Les Reactions Electrochimiques, Masson and Cie., Paris (1959).
14. P. Delahay, "New Instrumental Methods in Electrochemistry," Interscience, New York (1954).
15. T. Kodera, H. Kita, and M. Honda, *Electrochim. Acta*, **17**, 1361 (1972).
16. J. O'M. Bockris and A. K. N. Reddy, "Modern Electrochemistry," Vol. 2, Plenum Press, New York (1970).
17. A. R. Despić, Dj. Jovanović, and T. Rakić, *Electrochim. Acta*, **21**, 63 (1976).
18. T. Hurlen, *Acta Chem. Scand.*, **16**, 1337 (1962).

The Electrochemical Reduction of Carbon Dioxide, Formic Acid, and Formaldehyde

P. G. Russell,[1] N. Kovac,* S. Srinivasan, and M. Steinberg**

Brookhaven National Laboratory, Department of Applied Science, Upton, New York 11973

ABSTRACT

The prospects for the electrochemical reduction of carbon dioxide to methanol were examined by investigating the intermediate reactions. The reduction of carbon dioxide was carried out in a neutral electrolyte at a mercury electrode. The high overvoltage observed for carbon dioxide reduction to the formate anion reflects a low value for the efficiency of electric energy utilization for this process. Formic acid can be reduced to methanol in a perchloric acid electrolyte (at a lead electrode) or in a buffered formic acid electrolyte (at a tin electrode). The faradaic efficiency for methanol formation is close to 100% at the tin electrode in a narrow potential region corresponding to a low current density. The potential dependence of formic acid reduction to methanol suggests that the adsorption of formic acid on the electrode, near the pzc, may be the rate-controlling step in the over-all reaction. The reduction of formaldehyde to methanol occurs with a faradaic efficiency exceeding 90% in a basic solution. The Tafel slope decreases when either the formaldehyde concentration is increased (at constant pH) or when the pH of the solution is increased (at constant concentration). The polyoxymethylene glycols present as impurities in formaldehyde solutions may influence the mechanism of the electrode process through interaction with formaldehyde molecules and/or other adsorbed species resulting in small changes of the Tafel slope.

The prospects for electrochemical production of methanol from carbon dioxide.—With the increasing possibility of the unavailability of oil in 20-30 years, methanol will probably be the substitute liquid fuel (or fuel intermediate) in the future. New methods for the production of methanol should be economically competitive with existing technology. One approach for the production of methanol from nonfossil sources is by the electrochemical reduction of carbon dioxide. This will be feasible only with a potentially cheap source (*e.g.*, controlled thermonuclear generation) of electrical energy. Methanol may also be considered as a medium for the storage of hydrogen.

The purpose of this work is to evaluate the optimum conditions (electrode, electrolyte, pH, etc.) for the conversion of carbon dioxide to methanol. The high overpotentials observed for the reduction of carbon dioxide and its intermediates result in an over-all low energy efficiency. The reduction of carbon dioxide to formic acid has been studied extensively. However, few studies describe the further reduction of formic acid to methanol.

Previous studies on the electrochemical reduction of carbon dioxide.—The electrolytic reduction of carbon dioxide in aqueous solutions has been the subject of many investigations. According to the earlier papers (1-5) formic acid (or the formate ion) was found to be the principal product with the highest current efficiency being obtained at amalgamated electrodes (see Table I). The electrolyte, containing the alkali salt (bicarbonate, carbonate, or sulfate) was usually saturated with carbon dioxide gas [pressures of up to 50 atm were used in some experiments (4)]. High cur-

* Electrochemical Society Student Member.
** Electrochemical Society Active Member.
[1] Present address: Sprague Electric Company, Research and Development Laboratories, North Adams, Massachusetts 01247.

Table I. Results of some previous studies on carbon dioxide reduction in aqueous solution

Cathode	Anode	Separator	Electrolyte	Pressure of CO_2	Products other than HCOOH. Final conc. of HCOOH, g/liter	Percent faradaic efficiency for $HCOO^-$ production	Ref.
Zn electrodeposited on Cu, then amalgamated	Pb	Porous cell	Sat'd K_2SO_4	5 atm	—	98.6	(4)
Cu electrodeposited on Cu	Pb	Porous cell	Sat'd K_2SO_4	50 atm	—	86.4	
Zn (Hg)	Pb	Porous cell	Sat'd K_2SO_4	50 atm	96.4	49	
Rotating amalgamated Cu rod	Pb	Porous diaphragm	10% Na_2SO_4	Sat'd CO_2	1.8 as HCOONa	81.3	(12)
		Cation exchange membrane			From 190 to 200	80	
Hg						93 to 100	(13)
Ga(s)		3				34	
Ga(l)	Pt	Compartment	0.5M $NaHCO_3$	Sat'd CO_2		34.9	
Cerrolow 136(s)		Cell				24.3	
Cerrolow 136(l)						36	
In							
Pb			1M Me_4NHCO_3			<80	(14)
Pb			1M $NaHCO_3$	Sat'd CO_2	Only H_2		
Hg							
Cd							
Carbon			1M ET_4NHCO_3	Sat'd CO_2	Some H_2 glycolic acid results from oxidation of carbon electrode		
Pt			pH = 8 in these solutions				
WC			1Me_4NHCO_3	Sat'd CO_2	Only H_2		
Pb				1 atm		80	(15)

rent efficiencies for formate production (~ 99%) were obtained in short-term electrolysis experiments where the diffusion of the formate anion was negligible.

After long-term contact of a solution of sodium bicarbonate with sodium amalgam, appreciable concentrations of formate ion were detected (6). This result led some workers to believe that the bicarbonate and carbonate anions were electroactive species and that the reduction of carbon dioxide occurred on electrodes having high hydrogen overpotentials (2, 3). Polarographic waves observed in solutions containing carbon dioxide were interpreted as being due to the reduction of carbon dioxide (7-9). Later studies (10, 11) confirmed the above interpretation and showed that carbon dioxide, and not the bicarbonate or carbonate anion, is the electroactive species.

Intermediates are formed during the reduction of carbon dioxide. A number of studies have dealt with the properties of a "reduced carbon dioxide" species, $(CO_2)_r$, formed when carbon dioxide is reduced to formic acid in aqueous solution. The results of one study (16) carried out in acid solution show that carbon dioxide reacts with chemisorbed hydrogen (electrochemically formed) on bright platinum in the potential region 0 to +250 mV *vs.* the RHE to form $(CO_2)_r$. The rate of reaction is slow at room temperature, but increases rapidly with temperature. On platinized platinum at 90°C, chemisorbed hydrogen reacts rapidly with carbon dioxide. In another study (17), this reaction intermediate was produced at a platinum electrode and then oxidized at a constant current. The amount of carbon dioxide formed was determined by gas liquid chromatography. The results showed that two electrons are transferred during oxidation of each $(CO_2)_r$ species. In comparison with the results of similar experiments carried out using carbon monoxide, it was suggested that $(CO_2)_r$ is carbon monoxide, chemisorbed in the first layer on platinum.

Previous studies on the electrochemical reduction of formic acid.—The reduction of formic acid is more difficult and thus fewer studies have appeared in the literature. In one study, on the reduction of carboxylic acid esters (18), an ester of formic acid was found to be reduced with difficulty. In 1907, a patent was granted for an electrochemical method of reducing monobasic fatty acids to aldehydes and alcohols (19). Specific mention is made of formic acid reduction. In a 10% sulfuric acid electrolyte solution formic acid was reduced preferentially to formaldehyde at low current densities and to methanol at high current densities. In general, low current densities were recommended for carrying out the reduction. A number of metals were suggested for use as cathodes (lead, spongy nickel, iron, cobalt, and platinized platinum) but the coulombic efficiency for methanol production on the individual metals was not presented. In a recent two-part study (20, 13) tin was found to be a good electrocatalyst for formic acid reduction. In part I (20) formic acid was reported to be reduced to methanol with a 100% current efficiency at low current densities. A selective oxidation and titration scheme of the formic acid, formaldehyde, and methanol present was the analytical method used in the product analysis. However, in part II (13) of this work, significant analytical results showed that the current efficiency is quite low; polished tin (7%), electroplated tin (13%), and Cerrolow 136 (solid phase ~7.4%, liquid phase ~13.7%). The best results (for longer run tests) were obtained with the molten Cerrolow 136 (low melting point alloy containing tin) where the maximum effective current density was only 140 $\mu A/cm^2$.

Previous studies on the electrochemical reduction of formaldehyde.—The reduction of formaldehyde has been studied extensively in classical polarography [see Ref. (21) for a review of the earlier work]. The polarographic wave increases rapidly with the *p*H and temperature of the solution. The low kinetic current is attributed to the fact that formaldehyde is present predominantly in the electroinactive hydrated form, methylene glycol. The limiting current for reduction is governed by the reaction rate for methylene glycol dehydration to formaldehyde, which is the electroactive species. This dehydration appears to be a base catalyzed reaction. In solutions with a *p*H value greater than 12, the limiting current decreases with increase in the *p*H. This decrease probably results from the formation of an anion of methylene glycol, $H_2C(OH)O^-$, in high *p*H solutions which is the intermediate for formaldehyde formation. In a recent study (21) the presence of $H_2C(OH)O^-$ was observed through its u.v. absorption peak at 215 nm. The following mechanism (21, 22) has been proposed for formaldehyde formation in solution at a *p*H between 12 and 13

$$CH_2(OH)_2 + OH^- \underset{k_{-1}}{\overset{k_1}{\rightleftarrows}} CH_2(OH)^- + H_2O \qquad [1]$$

$$CH_2(OH)O^- \underset{k_{-2}}{\overset{k_2}{\rightleftarrows}} H_2C{=}O + OH^- \qquad [2]$$

Measurement of these rate constants using pulse polarography (22) can explain the sharp decrease ob-

served in the limiting current with an increase in *p*H above a value of 13.2. With lower *p*H values the rate of methylene glycol dehydration determines the available amount of formaldehyde.

In a previous study (23) on formaldehyde reduction evidence was found for a CECE mechanism in the *p*H region of 9 and below while a CEEC mechanism was suggested for the *p*H region of 13 and above. In cyclic voltammetry experiments with 5×10^{-2}M formaldehyde solutions an anodic peak (considered to be the oxidation of the radical anion intermediate resulting from the first electron transfer step) was obtained in a borate buffer (*p*H of 9) at a sweep rate of 100 V/sec. This peak was not observed in a solution of lower *p*H (phosphate buffer, *p*H = 6.8) and it disappeared at a *p*H above 9.5. These results, along with other evidence, suggested that in a neutral solution the chemical reaction following the first electron transfer step is fast enough so that no peak occurs. As the *p*H of the solution increases, this reaction becomes slower and an anodic peak occurs at fast sweep rates. In the absence of any appreciable dimerization of the adsorbed radical anion, the disappearance of this peak with a further increase of *p*H (greater than 9.5) indicated that a second electron transfer step, favored by the increase in the negative potential at the electrode surface due to the higher solution *p*H, occurs prior to the chemical step.

In addition to methylene glycol and a small amount of formaldehyde [$K \sim 10^{-4}$ for $H_2C(OH)_2 \rightleftarrows H_2CO + H_2O$], there are small amounts of polyoxymethylene glycols [$HO(CH_2O)_nH$ where $n \geq 2$], the concentrations of which depend on formaldehyde concentration (24). The amount (mole percent) of methylene glycol decreases while the amount of the polyoxymethylene glycols increases with increasing formaldehyde concentration. A number of equilibria can be written among the different species present in solution (the equilibria involving the anion of methylene glycol discussed above are not included here)

$$\begin{array}{ccc} H_2C(OH)_2 + HO(CH_2O)_nH & \rightleftarrows & HO(CH_2O)_{n+1}H + H_2O \\ \downarrow\uparrow & & \downarrow\uparrow \\ H_2CO + H_2O & & HO(CH_2O)_nH + H_2CO \end{array} \quad [3]$$

Previous studies (25) indicate that with increase in the *p*H of the solution, the amount of methylene glycol increases. Any mechanism study of formaldehyde reduction is complicated by the presence of these species.

Experimental

Types of studies.—Three types of experimental studies (carried out at 25° ± 3°C) were conducted: (*i*) current-potential relations obtained from steady-state potentiostatic experiments at a mercury electrode in electrolyte solutions containing either carbon dioxide or formaldehyde; (*ii*) current-potential relations obtained from nonsteady-state (cyclic voltammetric) experiments in electrolyte solutions at a hanging mercury drop electrode containing formaldehyde; and (*iii*) products formed in long-term electrolysis experiments with formic acid (carried out at both lead and tin electrodes) and formaldehyde (carried out at a mercury pool) as reactants were identified quantitatively, using gas chromatographic techniques.

Electrochemical instrumentation.—A PAR potentiostat (Model 173) and digital coulometer (Model 179) were used for the long-term electrolysis experiments on formic acid and formaldehyde. For the steady-state potentiostatic experiments a PAR potentiostat (Model 173) and a Keithley 160B digital multimeter were employed. The electronic instrumentation for the cyclic voltammetric studies consisted of the PAR potentiostat (Model 173), PAR universal programmer (Model 175), and a Hewlett Packard X-Y recorder (7047A) or Tektronix storage scope (702BA). The cyclic voltammograms obtained at a 10 mV/sec scan rate were displayed on the X-Y recorder while those obtained at faster sweep rates were recorded on the storage scope. The *IR* corrections (for the steady-state polarization curves) were made by the current interruptor method using a mercury relay switch and the storage scope.

Electrochemical cells.—The long-term electrolysis experiments with formaldehyde and the steady-state polarization measurements on formaldehyde and carbon dioxide were carried out in a Pyrex cell having a fine glass frit separating the working and counterelectrode compartments. The counterelectrode was platinized platinum. In these experiments the reference electrode (SCE) was placed 4-6 mm above (and in the center of) the 1 in. diam (5.06 cm^2) mercury pool. The reduction of formic acid was carried out in an enclosed glass cell in order to minimize the loss of any volatile products formed during electrolysis. The three anode compartments were symmetrically arranged and separated from the large cathode compartment (containing an electrode with geometric surface area of 50 cm^2) by fine glass frits each of which is covered with a layer of agar (containing either sodium or tetraethyl ammonium perchlorate). The sealed cell containing a nitrogen atmosphere above the oxygen-free electrolyte, is further isolated in a desiccator, (also containing a nitrogen atmosphere) during the electrolysis which lasted 40 hr or more.

Solutions and materials.—All solutions were made from reagent grade chemicals and distilled water which was redistilled in a Corning apparatus (Model AG-2). The buffer solutions were made in the following way: (*i*) *p*H 6.8, 0.05M KH_2PO_4 + 0.05M K_2HPO_4; (*ii*) *p*H 9.0, 0.1M $NaHCO_3$ + NaOH; (*iii*) *p*H 11.1, 0.1M Na_2CO_3 + NaOH; (*iv*) *p*H 13.0, 0.055M KCl + 0.145M NaOH. The stock formaldehyde solutions were prepared by bubbling the formaldehyde gas (obtained by heating paraformaldehyde) through water. The concentration was determined by the sulfite method (24). In the steady-state polarization experiments with carbon dioxide, good results were obtained with a commercial grade carbon dioxide gas. Reagent grade lead and tin and triply distilled mercury were used for the electrodes.

Gas chromatographic analysis of products.—A Carle analytical gas chromatograph with flame ionization detection modified with a catalytic converter (for reducing small molecules to methane) was used for the analysis of the products in the electrolyte solution. Matheson zero gas grade helium and hydrogen and ultra zero grade air were necessary for maximum sensitivity. A glass column (to minimize adsorption of formic acid) packed with Porapak QS was found to be best for the separation of formaldehyde, methanol, and formic acid in the presence of large amounts of water. Typical chromatograms run on a formaldehyde solution before and after electrolysis are shown in Fig. 1. The initial small amounts of methanol observed in the chromatograms are produced during preparation of the formaldehyde solution. A calibration curve to determine the quantity of methanol obtained during electrolysis is shown in Fig. 2. A similar calibration procedure was used to determine the quantity of methanol produced during the reduction of formic acid solutions.

Results and Discussion

Electrochemical reduction of carbon dioxide.—Detailed kinetic studies have been carried out on the reduction of carbon dioxide at a Hg-pool electrode by Eyring and co-workers (26, 27). Figure 3 shows the polarization curve for the reduction of carbon dioxide to the formate anion in a neutral solution where the faradaic efficiency is 100% (in acid solution the efficiency for formate production is much less because of a

parallel electrode reaction leading to the formation of molecular hydrogen). These results are in good agreement with previously published data (26). The galvanostatic charging curve experiments indicated that the coverage by an adsorbed intermediate is large ($\theta \rightarrow 1$) in region I (low overvoltage region with a Tafel slope of ~91 mV) and is small ($\theta \rightarrow 0$) in region II (with a Tafel slope of ~240 mV). The adsorbed intermediate was suggested to be the formate radical, HCO_{2ads}. In addition the reaction order for the concentration of carbon dioxide was found to approach a value of zero and one in region I and II, respectively. The following mechanism best represents the experimental results (27)

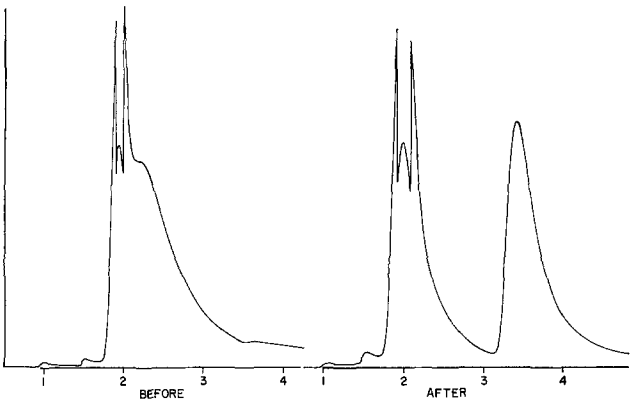


Fig. 1. Chromatograms of 0.1M formaldehyde and 0.1M sodium carbonate solution before and after electrolysis. The concentration of methanol in the solution is obtained from the area under the methanol peak and the calibration curve (Fig. 2).

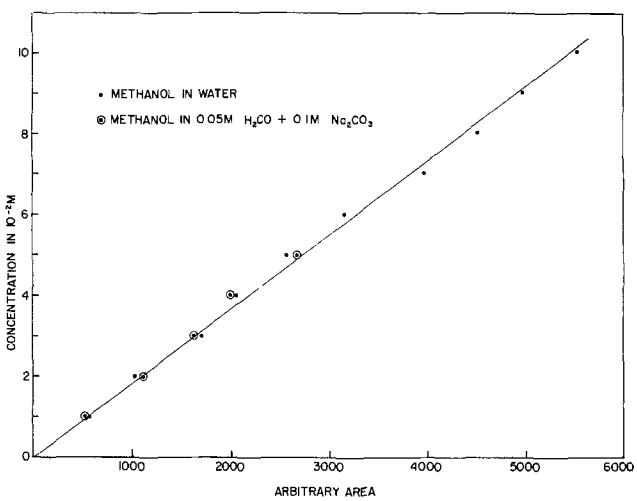


Fig. 2. Calibration curve for methanol detection in the electrolysis of formaldehyde solutions.

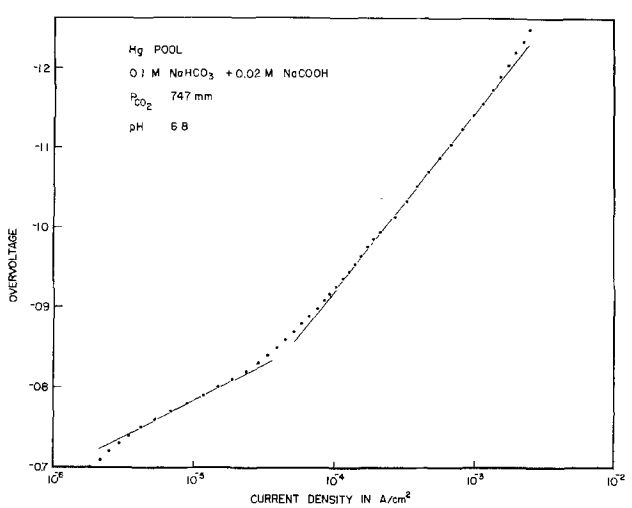


Fig. 3. Polarization curve for the reduction of carbon dioxide to the formate anion in a neutral solution. The overvoltage for the reduction of carbon dioxide is obtained by subtracting out the reversible potential which exists for the conditions of the experiment (26). The curve has been corrected for *IR* effects.

$$CO_2 + e^- \rightarrow CO_{2\cdot ads}^- \quad [4]$$

$$CO_{2\cdot ads}^- + H_2O \xrightarrow{\text{fast}} HCO_{2ads} + OH^- \quad [5]$$

$$HCO_{2ads} + e^- \rightarrow HCO_2^- \quad [6]$$

In region I of the polarization curve, the step represented by Eq. [6] is considered to be rate determining while in region II the first step (Eq. [4]) is the rds. Water may be a reactant in the first step which then leads to the formation of HCO_{2ads}. The variation of the reduction potential of carbon dioxide in DMSO with water content supports this hypothesis (28). For this case, the first step was proposed as the combination of Eq. [4] and Eq. [5] into a single step (26). When a more detailed analysis (which includes adsorption characteristics of the intermediate) is made, it is found that the experimental results (Tafel slope and reaction orders of carbon dioxide) are best explained when the intermediate is assumed to undergo activated adsorption according to the Temkin isotherm (26).

The intermediate may, however, not always be an adsorbed species with a large coverage. In another study (29) the intermediate (generated by a modulated cathode potential at a lead electrode) was found to be the carbon dioxide anion radical, CO_2^-. The technique of modulated specular reflectance spectroscopy was used to detect the presence of this radical by its optical absorption. The optical response of this radical indicated that it undergoes a rapid chemical reaction and that the amount calculated to be present would only form 2% of a monolayer.

The energy efficiency, ϵ, for the reduction of carbon dioxide to formic acid can be expressed in the following manner

$$\epsilon = \frac{\Delta H \times (\text{percent faradaic efficiency})}{n\mathbf{F}\{E_{rev} + \eta_c + \eta_a + \eta_{IR}\}} \quad [7]$$

where $\Delta H = 64.4$ kcal/mole and E_{rev} is 1.43V for the reaction $CO_2(g) + H_2O(l) \rightarrow HCOOH(aq) + \frac{1}{2} O_2(g)$. In a neutral solution (100% faradaic efficiency for formate production) a current density of 1 mA/cm² on mercury requires an overpotential, η_c, of 1.15V (see Fig. 3). Using a value of 0.5V for the value of the overpotential for oxygen evolution at the anode and neglecting all *IR* losses a value of 45% is obtained for ϵ. In a practical cell (with *IR* losses), the value of ϵ would be much less. The efficiency has been found to decrease with current density for a given electrode (12, 14, 30). In one series of experiments (12), a cell potential of 3.5V gave the highest coulombic efficiency (81.5%), at the lowest current density of 20 mA/cm². This yielded an energy efficiency of ~33%.

In order to improve the energy efficiency, it is necessary to test other electrode materials. Recently a number of sp metals (Zn, Pb, Sn, In, and Cd) have been tested as electrocatalysts for the reduction of carbon dioxide (30). The highest faradaic efficiency (92%) for formic acid production was obtained using an In electrode at a current density of 2.9 mA/cm² in 0.1*N* Li_2CO_3 electrolyte. On In, the overpotential is 400 mV lower than on a Hg electrode at the same current density.

Electrochemical reduction of formic acid.—The reduction of formic acid to methanol was carried out at both lead and tin electrodes. Product analysis revealed no detectable amounts of formaldehyde. Table II shows

Table II. Faradaic efficiency for formic acid reduction to methanol on lead (area of electrode, 50 cm^2) in 0.1*N* $HClO_4$ at 25°C

Experiment number	Range of working electrode potential, mV	Range of current, mA (average current density, $\mu A/cm^2$)	Time, hr	Charge, C	Number of moles, methanol		Percent faradaic efficiency
					Maximum	Expt.	
1	−900 to −1000	20 to 5 (155)	68	1900	0.00492	0.00059	11.9
2	−900 to −1000	20 to 6 (185)	42	1403	0.00364	0.00001	0.28
3	−1320 to 1260	10 (200)	68	2440	0.00632	None	0
4	−900 to −1000	14-2 (151)	44	1245	0.00323	0.00007125	2.2
5	−900 to −1000	30-5 (346)	23	1435	0.00372	0.0000195	0.53

the results of the experiments at a lead electrode using 0.1M formic acid in 0.1M perchloric acid electrolyte. The current efficiency varied from zero to a maximum value of 12% for methanol production. In the potentiostatically controlled experiments, a low current density (for maximum efficiency) was maintained by making periodic adjustments to the working potential (*vs.* SCE) in the range −900 and −1000 mV. In a number of galvanostatic experiments (experiment 3 is an example) carried out at higher current densities, the working potential was always below −1000 mV and no methanol was produced during the electrolysis. The results on lead are not very reproducible. This may be due in part to variations in the chemical polishing procedure of the electrode surface prior to each experiment. In some experiments, an anodic potential was applied in a preelectrolysis step, but this procedure did not appear to stabilize the electrode surface in a way that would lead to consistent results.

Higher efficiencies and stable currents were obtained when the lead electrode was replaced with an electroetched tin electrode (Table III). The electrolyte (0.25M HCOOH + 0.1M $NaHCO_3$) is a formic acid/sodium formate solution buffered to a *p*H of about 3.8. In this case, good results (up to ~100% efficiency) are obtained only in a narrow potential region (with a lower limit of about −720 mV) where the average current density is less than 4.0 $\mu A/cm^2$ (experiments 5, 6, 7, and 9). In some of these potentiostatically controlled experiments, it was necessary to lower the potential occasionally in order to maintain a small electrolytic current density. In galvanostatic experiments (experiments 2, 3, and 4), where the working potential remained below −720 mV throughout most of the electrolysis (the initial potential is given in parentheses), no methanol was produced. In previous work (20), the 100% efficiency reported initially was obtained at a current density of 5 $\mu A/cm^2$, corresponding to a potential of −990 mV *vs.* SCE. In the present experiments, the lower end of the potential region for a high efficiency is more positive by about 270 mV. This discrepancy may be due in part to differences in the surface preparation of the electrodes (higher surface area).

The energy efficiency in an electrolysis cell for formic acid reduction to methanol will be low because of the large overvoltage required at a low current density. The overvoltage has been estimated for the conditions found in experiment 7 (Table III) assuming that $HCOOH_{aq} + 4H^+ + 4e^- \rightleftarrows CH_3OH_{aq} + H_2Ol$ is the half-cell reaction. The equilibrium potential (*vs.* SCE) obtained for this half-cell reaction after 31.4C has passed through a cell containing 20 ml of solution (*p*H ~3.8) is ~ − 0.3V. This corresponds to an overvoltage of ~420 mV at a current density of 3.6 $\mu A/cm^2$.

The present results on both lead and tin electrodes, along with previous results on tin, indicate that the reduction of formic acid occurs in a narrow potential region. On the other hand, the reduction of carbon dioxide and formaldehyde (see following section) occurs over wide potential regions (on a mercury electrode) and are activation-controlled processes. It may be only a coincidence that the reduction of formic acid occurs near the pzc which for lead and tin (*vs.* NHE) are −0.69 and −0.35V, respectively (31). Although these values change somewhat with the electrolyte composition, the maximum efficiency for formic acid reduction occurs at a potential slightly below the pzc (~ 0.1V) on both lead and tin. In this case, the adsorption of formic acid molecules (assuming these are the electroactive species) would appear to be a necessary and potential-dependent step in the reduction mechanism. Further studies (measurement of pseudocapacitance using impedance techniques, etc.) will be required before the role of adsorption in formic acid reduction can be determined.

A number of suggestions have been made (20) for increasing the current density of formic acid reduction: (*i*) increase in the real surface area; (*ii*) increase in the temperature of the reaction; (*iii*) increase in the reaction rate by using metals with lower pzc (a good choice here is cadmium); and (*iv*) application of a pulsed potential profile by which the molecules adsorbed at a potential near the pzc are reduced much faster at a more negative applied potential.

Electrochemical reduction of formaldehyde.—The electrolytic reduction of formaldehyde to methanol occurs, with a better than 90% faradaic efficiency, in a basic solution (*p*H ~11). In each experiment, a 100 ml sample containing 0.1M H_2CO in 0.1M Na_2CO_3 was electrolyzed (~1000C passed through the cell) in the limiting current region (current density ~10 mA/cm^2, see Fig. 10). Product analysis showed that the efficiency

Table III. Faradaic efficiency for formic acid reduction to methanol on tin (area of electrode, 50 cm^2) in 0.1*N* $NaHCO_3$

Experiment number	Range of working electrode potential, mV	Range of current, mA (average current density, $\mu A/cm^2$)	Time, hr	Charge, C	Number of moles, CH_3OH		Percent faradaic efficiency
					Maximum	Expt.	
1	−620 to −870	0.8 (16)	19.8	57	0.000148	0.00006	40.5
			67.7	195	0.0005062	0.00008	15.8
2	(600) −900 to −1000	1 (20)	23.6	85		None	0
3	(600) −800 to −730	0.9 (18)	17.9	56.6		None	0
4	(620) −860 to −920	0.8 (16)	27	60.5		None	0
5	−680 to −700	(2.96)	46	24.4	0.0000632	0.0000608	96.2
6	−700	(1.6)	45	13.5	0.0000349	0.0000314	90
7	−680 to −720	(3.6)	48.5	31.4	0.000081	0.0000808	99.6
8	−690	(3.0)	90	48.8		None	0
9	−700	(3.2)	30.5	17.4	0.0000451	0.0000416	92.2

for methanol production was 103 ± 10%. This value includes a correction for the small amount of methanol produced in the initial formaldehyde solution (Fig. 1). No indication was found for the formation of a dimerization-type product such as ethylene glycol.

The energy efficiency in an electrolysis cell for formaldehyde reduction to methanol is low because of the large overvoltage at a moderate current density. The overvoltage was estimated for the conditions found in one electrolysis experiment assuming that $H_2CO_{aq} + 2H^+ + 2e^- \rightleftarrows CH_3OH_{aq}$ is the half-cell reaction. The equilibrium potential (*vs.* SCE) for this half-cell reaction, after 965C were passed through a cell operated in the limiting current region ($E_w = -1.8$V *vs.* SCE), is ~ −0.6V. This gives an overvoltage at the cathode of 1200 mV for a current density of ~10 mA/cm^2.

Cyclic voltammetry experiments have been carried out in 0.11M formaldehyde solutions buffered at different *p*H values (6.8, 9.0, 11.1, and 13.0) at sweep rates from 10 mV/sec to 1000 V/sec. The results of these experiments are in basic agreement with those in a previous study (23). A small anodic peak appears in each solution at sweep rates higher than a threshold value. In contrast to the previous results, however, this anodic peak is found in a solution having a *p*H of 6.8. In this solution it is more easily observed at lower sweep rates where the double layer charging current is less. In addition the anodic peak does not disappear in a solution having a *p*H value greater than 9.5 for fast sweep rates.

The *p*H dependence of this peak is shown in Fig. 4 for a sweep rate of 50 V/sec. It is observed in a solution with a *p*H of 6.8 and 9.0 but not in a solution with a *p*H of 13.0. The threshold sweep rates (in volts/second) are approximately 2, 10, 50, and 100 for solutions having *p*H values of 6.8, 9.0, 11.1, and 13.0, respectively. This peak, which has a longer lifetime in the neutral solution, is most likely due to the oxidation of the radical intermediate and/or its anion. Any methanol formed during the cathodic sweep will not be oxidized at the potential of the anodic peak. A log-log plot of the anodic peak current, I_{PA}, *vs.* the sweep rate, v (volts/second), (Fig. 5), shows that $I_{PA} \propto v^{1/2}$ and the reaction is, thus, diffusion controlled at a *p*H of 9 and below. For *p*H 11 and above, the slope is greater than 0.5 and the amount of intermediate available for oxidation appears to be no longer entirely diffusion controlled. The cathodic peak current appears to be diffusion controlled in a solution buffered at a *p*H of 6.8. The dehydration rate of methylene glycol is relatively slow at this *p*H and the amount of formaldehyde available for reduction can be considered to be fixed during the time interval of an experiment carried out at fast sweep rates (5-500 V/sec). The transfer of formaldehyde molecules across the interphase region to the electrode surface results in a diffusion-controlled current. In a solution of higher *p*H, where the reaction rate for the formation of formaldehyde (either from methylene glycol or its anion) is increased, the amount of formaldehyde available for reduction can no longer be considered constant throughout the lifetime of the cyclic sweep. Instead, it appears that the current is limited by the reaction kinetics of the reduction process at fast sweep rates (100-1000 V/sec). This results in a decrease of the slope (for log I_{PC} *vs.* log v) with increase in *p*H to a value approaching zero in a solution with a *p*H of 13.

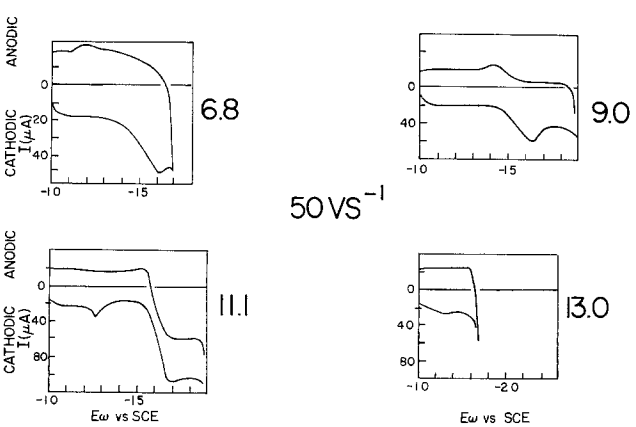


Fig. 4. Cyclic voltammograms obtained at a hanging mercury drop electrode (area ~0.22 cm^2) in 0.11M formaldehyde showing the *p*H dependence of the anodic peak. (An impurity cathodic peak appears in the solutions having a *p*H value of 11.1 and 13.0 in the −1.2 to −1.3V region). In order to observe whether an anodic peak is present in the high *p*H (13.0) solution, the current sensitivity is the same as in two of the other buffer solutions. At this amplification only the current trace in the −1.0 to −1.6V region is shown.

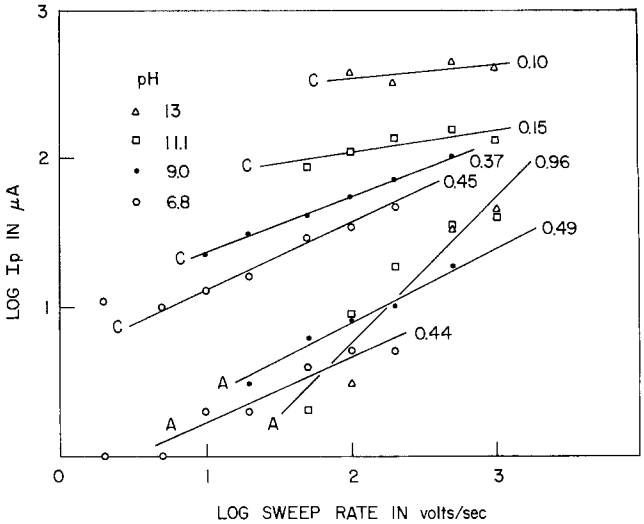


Fig. 5. Log-log plot of cathodic peak current, I_{PC}, and anodic peak current, I_{PA}, *vs.* sweep rate. The value of the slope is given to the right of each anodic line, A, and cathodic line, C. Any value of I_{PA} is one-tenth or less than the corresponding value of I_{PC} and is much less than the double layer charging current at higher sweep rates. As a result, there is more scatter in the data used for the anodic plots. For a *p*H of 11.1 and 13 a line with a slope of 0.96 is shown, whereas a lower value is probably more realistic.

The Tafel slope is observed to decrease with an increase in the *p*H of the solution (Fig. 6). In addition, it can be seen that the limiting current is not a simple function of the solution *p*H over the range of values examined here. In one solution (*p*H 13.0) the limiting current peaks and then it decreases somewhat at higher potentials. This observation may be explained by the mechanism (Eq. [1] and [2]) which accounts for the high *p*H behavior of the limiting current. The rapid generation of hydroxyl ions as the current density increases would momentarily increase the *p*H value in the double layer region. This causes a decrease in the amount of formaldehyde available for reduction (Eq. [2]).

The effect of *p*H on the Tafel slope, along with the cyclic voltammetry results, may be explained in terms of a mechanism change for formaldehyde reduction. The observed Tafel slopes fall in the range of 66-36 mV. The first electron transfer step is therefore not rate determining. A value of 60 mV is expected for the Tafel slope (under conditions of Langmuir adsorption) in the CECE mechanism (Fig. 7) if step 3 is rate determining. A value of 66 mV was observed for the Tafel slope in a neutral solution (*p*H = 6.8). However, step 4 may be the rds. In this case, the radical intermediate and its anion must be stabilized in order for the quasi-equilibrium condition to hold for all except the rds. A fast protonation reaction would produce an intermediate that is more easily stabilized than the

radical anion. Under these conditions, step 4 (with a 40 mV Tafel slope) would be the rds. Temkin adsorption could then account for the increase in Tafel slope observed here. The oxidation of the radical intermediate and/or its anion is controlled by the rate of diffusion of the radical species away from the electrode surface in solutions with a *p*H of 6.8 and 9.0. With increase in *p*H, a second charge transfer step, prior to the chemical reaction is favored due to the decrease in the hydrogen ion concentration and to an increase in the negative electrode potential. A charge transfer to the radical anion should occur at a slower rate since the radical already has a negative charge. However, the experimental results indicate that this electron transfer occurs at a relatively fast reaction rate. The anodic peak is more stable in a neutral solution, since it is observed at a slower sweep rate. The absence of this peak at the slow sweep rates (in the higher *p*H solutions) indicate that a second electron transfer can compete with the protonation reaction to produce a dianion

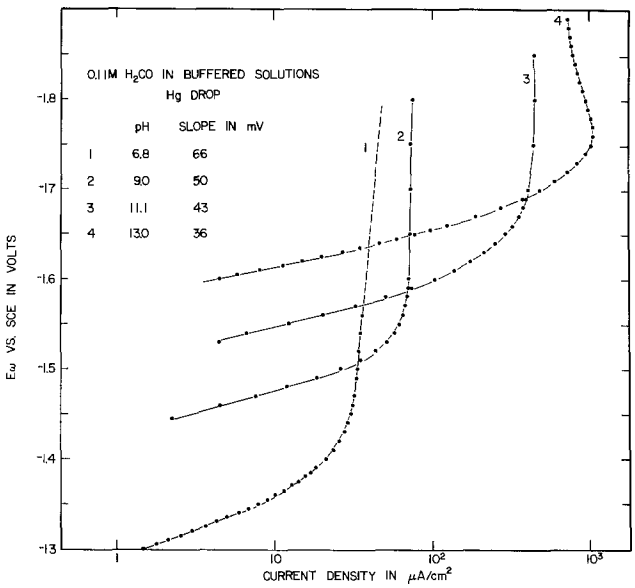


Fig. 6. Effect of *p*H on the Tafel slope. These polarization curves were obtained from the cyclic voltammetry experiments carried out at a 10 mV/sec sweep rate at a hanging mercury drop electrode where the hysteresis is small.

of methanol. Although this species is not expected to be adsorbed at the electrode surface, it may be partially stabilized by one of the adsorbed species. This is necessary if the quasi-equilibrium condition is to hold for step 3 of the CEEC mechanism. In this case, the following chemical reaction (step 4 of the CEEC mechanism, Fig. 8) is the rds with a Tafel slope of 30 mV expected under conditions of Langmuir adsorption. A Tafel slope of 36 mV was observed in a solution with a *p*H of 13.0. The anodic peak current should then result from a diffusion-controlled process. The experimental results (Fig. 5) are not clear in the high *p*H solutions. If the reduction current is limited at fast sweep rates by the reaction kinetics, then a change in the slope, from a value of 0.5 of the I_{PA} *vs.* v plot would be expected. Interactions of the methanol dianion with adsorbed species and/or its repulsion from the double layer region could also affect the slope. In addition to the possibility that changes in the solution *p*H modify the reaction kinetics causing a change in mechanism, an indirect effect may result from a change in the composition of adsorbed species with *p*H. This can influence the Tafel slope through interactions with the electroactive species. The observed values of the Tafel slope are somewhat larger than the values expected under conditions of Langmuir adsorption. Evidence for Temkin adsorption, which could account for the larger values, was found in the steady-state measurements as discussed below.

Steady-state polarization curves were obtained with solutions containing different formaldehyde concentrations (*p*H ~11.3). Some variation of the Tafel slope was observed in different runs on a given sample (Fig. 9). In the first run, the current stabilized quickly above −1.56V but at points below this potential, the current increased slowly for some time before reaching a steady value. Current readings obtained before steady-state conditions gave a low value for the Tafel slope. A 2-3 hr preelectrolysis, carried out prior to the first run, may have conditioned the electrode surface with various adsorbed species. Steady current values were obtained over the entire potential range in the second and third run. In these experiments, a 10% error can be expected in measuring the value of the Tafel slope under steady current conditions. The effect of concentration on the Tafel slope is shown in Fig. 10. Good agreement is obtained for the value of the Tafel slope in the 0.11M solution (47 mV) with the previous result (43 mV) near the same *p*H value at the mercury drop

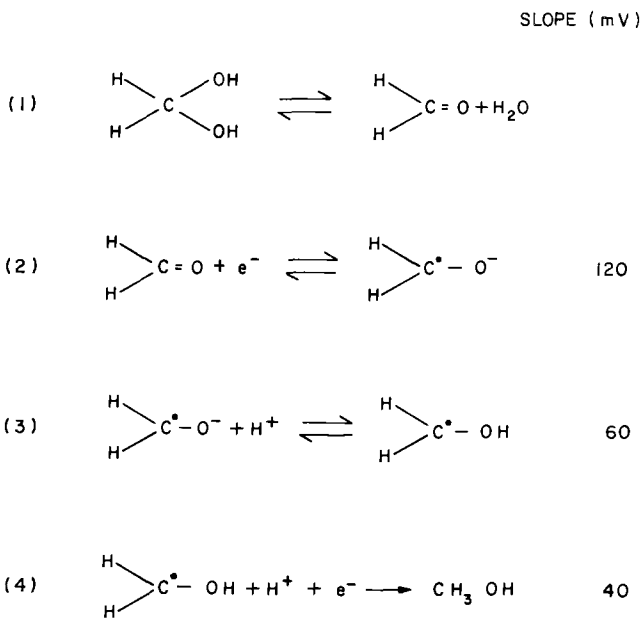


Fig. 7. Proposed mechanism for formaldehyde reduction in the *p*H region 6.8-9.

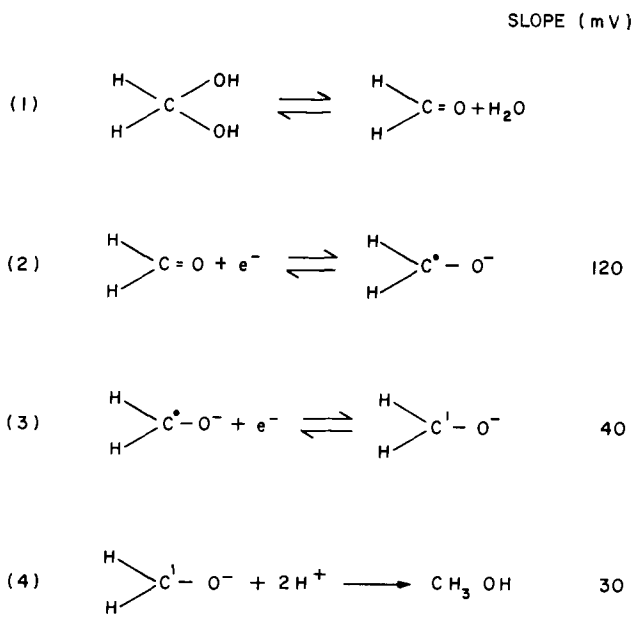


Fig. 8. Proposed mechanism for formaldehyde reduction in the *p*H region 11.1-13.0.

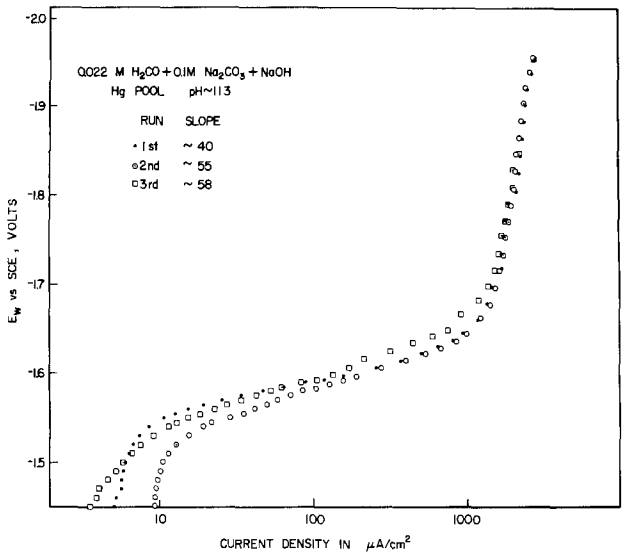


Fig. 9. Steady-state polarization curves for three runs made on a 0.022M formaldehyde solution. The limiting current is almost the same in each of the three runs. The curves have been corrected for *IR* effects.

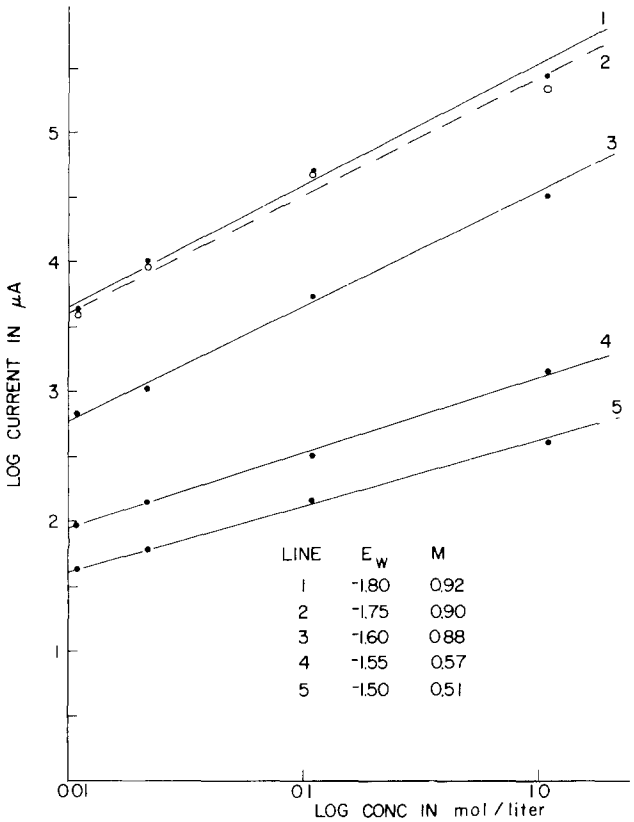


Fig. 11. Reaction order for formaldehyde reduction in the Tafel and limiting current regions obtained from steady-state polarization curves (Fig. 10).

electrode (Fig. 6). The value of the Tafel slope was found to decrease from 60 to 37 mV when the concentration of formaldehyde was increased by a factor of one hundred (0.011-1.09M). Adsorption effects may be partly responsible for this large decrease. A similar though smaller decrease in slope (9 mV) was observed in the reduction of acetophenone (32) at a mercury electrode in a methanol + sulfuric acid solution, containing a small amount of water when the concentration of acetophenone was increased by a factor of 10 (0.045-0.46M). The change in Tafel slope is attributed to adsorption effects.

The reaction order for formaldehyde reduction (Fig. 11) over the above concentration range is close to the expected value of one (0.92) in the limiting current region, but it aproaches a value of one-half in the Tafel region. A fractional reaction order indicates that the coverage, θ, by formaldehyde or an intermediate species is controlled by Temkin adsorption. The reaction order in the limiting current region should be independent of the reaction mechanism. It might be argued, however, that the decrease observed in the Tafel slope indicates a change in the reaction mechanism or a change in the rds (of a given mechanism) when the concentration is increased. Thus, it may not be valid to determine the reaction order over the entire concentration range. However the reaction order remains fractional and constant for a given working potential so that regardless of any mechanism change that might occur with increase of concentration the experimental results most likely indicate conditions for Temkin adsorption over the entire concentration range examined at a pH of 11.3. Temkin adsorption should occur over a wide range of pH values. Some evidence for this was given above.

Coverage by the adsorbed species, formaldehyde, and/or an intermediate, increases with the logarithm

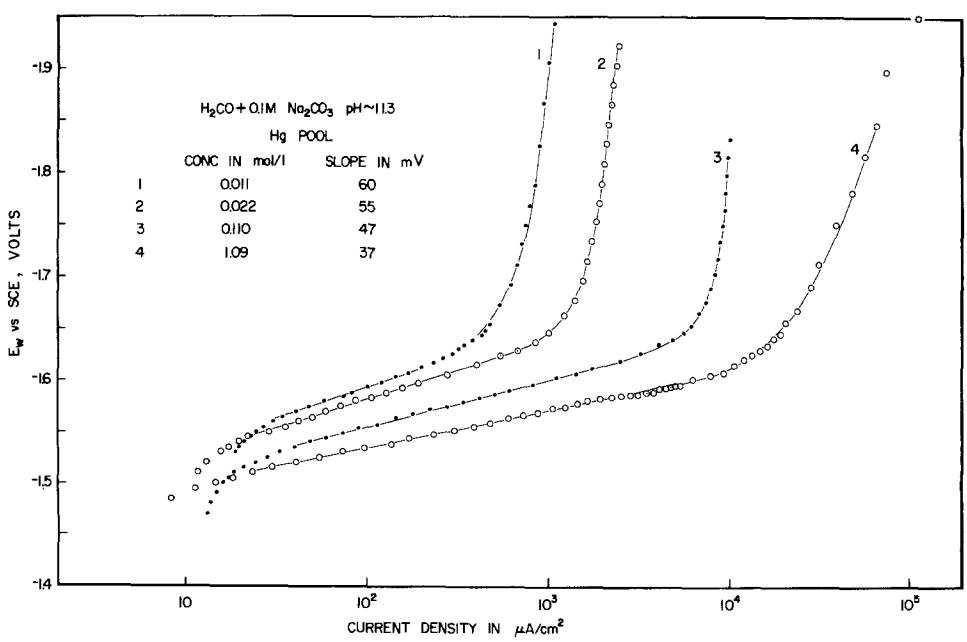


Fig. 10. Steady-state polarization curves for formaldehyde reduction showing the effect of formaldehyde concentration on the Tafel slope for solutions with a pH of 11.3. The curves have been corrected for *IR* effects.

of the concentration under conditions for Temkin adsorption. In addition, coverage by the much smaller amounts (mole percent) of the large species (polyoxymethylene glycols) present in solution may be increased at higher formaldehyde concentrations by preferential adsorption under Langmuir conditions, where the coverage is proportional to the concentration. Coverage by the adsorbed species will increase substantially as the formaldehyde concentration increases by a factor of 100. Normally, the Tafel slope would not be expected to change if this change in coverage remains within the Temkin region. The Tafel slope decreases almost linearly with the logarithm of the concentration (Fig. 12). If the coverage by formaldehyde molecules is predominant, then the decrease in the Tafel slope indicates an attraction between a formaldehyde molecule and nearby adsorbed species. However, the fractional reaction order, the presence of an anodic peak in cyclic voltammetry experiments, and the relatively low Tafel slope values suggest that coverage in the Temkin region is primarily due to an intermediate.

A change in coverage can affect the Tafel slope in a number of ways: (*i*) The adsorption kinetics may change with the increased coverage in such a way that a different step in the reaction mechanism becomes rate determining, and results in a lower value of the Tafel slope. (*ii*) A change in the energy of adsorption may accompany the increase in coverage. The standard free energy (for a coverage equal to θ) when an interaction occurs among the adsorbed species is given by

$$\Delta G^\circ_\theta = G^\circ_{\theta=0} + \alpha r\theta \qquad [8]$$

where r is the interaction parameter and $\alpha < 1$ for activated adsorption and $\alpha = 1$ for nonactivated adsorption (33). A decrease in Tafel slope, with an increase in coverage, requires that a change from activated to nonactivated adsorption occurs. (*iii*) A change in the number of water molecules displaced during the adsorption of the electroactive species will affect the Tafel slope (34). A decrease in Tafel slope requires that the number of water molecules displaced during the adsorption process decreases with increase in concentration (coverage). Small amounts of polyoxymethylene glycols adsorbed on the electrode surface could influence the adsorption process and hence the Tafel slope through interactions with formaldehyde and/or its intermediates. Measurement of double layer and adsorption capacitance will help determine the role of adsorption in the mechanism for formaldehyde reduction.

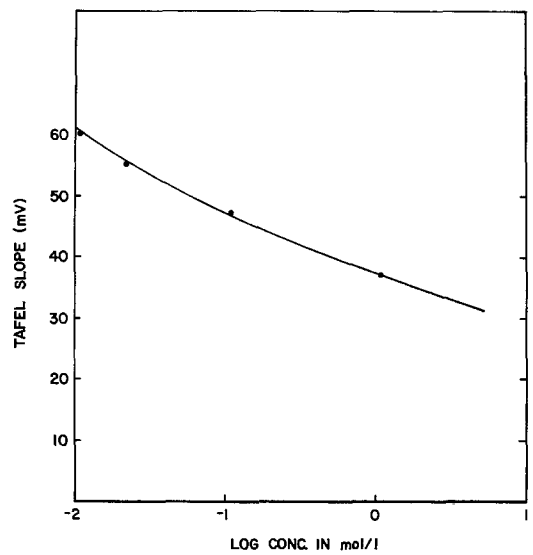


Fig. 12. Change in Tafel slope with formaldehyde concentration

Conclusions

Some conclusions can be made based on the results of this study: (*i*) It is difficult to find conditions for the direct electrochemical reduction of carbon dioxide to methanol. The reduction of carbon dioxide and formaldehyde occur readily in neutral and basic solutions, respectively, while formic acid reduction (assuming the molecule to be the electroactive species) requires an acid or buffered acid solution. (*ii*) The reduction of carbon dioxide to formic acid can be carried out quantitatively on sp-metals having high overpotential for hydrogen evolution at an estimated maximum energy efficiency of ~45% (on Hg). (*iii*) The reduction of formic acid to methanol is difficult to carry out simultaneously at a high faradaic efficiency and high current densities due to the limited potential region for formic acid reduction. (*iv*) The reduction of formaldehyde to methanol was carried out quantitatively on Hg at a current density of ~10 mA/cm^2. The Tafel slope was observed to decrease with an increase in concentration (at constant pH) and with an increase in pH (at constant concentration). The adsorption of polyoxymethylene glycols, which is both concentration and pH dependent, may cause changes to occur in the Tafel slope through interactions with formaldehyde and/or intermediate species.

Acknowledgments

The authors acknowledge the assistance of Mr. George Kissel in the solution of a number of experimental problems that occurred during this work. We would like to thank Drs. Stephen Feldberg and Shimshon Gottesfeld for a number of suggestions that were useful in the interpretation of our results. We would also like to express our gratitude to Professor Brian Conway for a number of stimulating discussions and for his continued interest throughout the course of this work. The authors are grateful to the referees of the original manuscript. Their critical comments were valuable in the preparation of the revised version. This work was performed under the auspices of the U.S. Energy Research and Development Administration.

Manuscript submitted Dec. 27, 1976; revised manuscript received May 2, 1977. This was Paper 286 presented at the Washington, D.C., Meeting of the Society, May 2-7, 1976.

Any discussion of this paper will appear in a Discussion Section to be published in the June 1978 JOURNAL. All discussions for the June 1978 Discussion Section should be submitted by Feb. 1, 1978.

Publication costs of this article were assisted by Brookhaven National Laboratory.

REFERENCES

1. M. E. Royer, *C. R. Hebd Seances Acad. Sci.*, **70**, 731 (1870).
2. A. Cohen and S. Jahn, *Ber. Dtsch. Chem. Ges.*, **37**, 2836 (1904).
3. R. Ehrenfeld, *ibid.*, **38**, 4138 (1905).
4. F. Fischer and O. Prziza, *ibid.*, **47**, 256 (1914).
5. M. Rabinowitsch and A. Maschowetz, *Z. Elektrochem.*, **36**, 846 (1930).
6. A. Lieben, *Monatsh.*, **16**, 211 (1895).
7. P. Van Rysselberghe, *J. Am. Chem. Soc.*, **68**, 2047 (1946).
8. P. Van Rysselberghe and G. J. Alkire, *ibid.*, **66**, 1801 (1944).
9. P. Van Rysselberghe, G. J. Alkire, and J. M. McGee, *ibid.*, **68**, 2050 (1946).
10. T. E. Teeter and P. Van Rysselberghe, *J. Chem. Phys.*, **22**, 759 (1954).
11. T. E. Teeter and P. Van Rysselberghe, Proceedings of the 6th Meeting of the International Committee on Electrochemical Thermodynamics and Kinetics, p. 538 (1955).
12. K. S. Udupa, G. S. Subramanian, and H. V. K. Udupa, *Electrochim. Acta*, **16**, 1593 (1971).
13. F. H. Meller, Final Report (Phase II), Contract no. NOOO14-66-CO139 (1968).

14. V. Kaiser and E. Heitz, *Br. dB. Gesellschaft*, **77**, 818 (1973).
15. T. N. Andersen, B. A. Miner, E. Bibble, and H. Eyring, *Stud. Trop. Oceanogr.*, **5**, 229 (1965).
16. J. Giner, *Electrochim. Acta*, **8**, 857 (1963).
17. M. W. Breiter, *ibid.*, **12**, 1213 (1967).
18. J. Tafel and G. Friedrichs, *Ber. Bunsenges. Phys. Chem.*, **37**, 3187 (1904).
19. C. Ellis and K. P. McElroy, U.S. Pat. 867,575 (1907).
20. F. B. Leitz and H. I. Viklund, Final Report (Phase I), Contract no. NOOO14-66-CO139 (1967).
21. D. Barnes and P. Zuman, *J. Electroanal. Chem.*, **46**, 323 (1973).
22. J. M. Los, A. A. A. Brinkman, and B. J. C. Wetsema, *ibid.*, **56**, 187 (1974).
23. S. Clarke and J. A. Harrison, *ibid.*, **36**, 109 (1972).
24. J. F. Walker, "Formaldehyde," Van Nostrand-Reinhold, New York (1974).
25. R. Sauterey, *Ann. Chim. (Paris)*, **12**, 7, 1 (1952).
26. J. Ryu, T. N. Andersen, and H. Eyring, *J. Phys. Chem.*, **76**, 3278 (1972).
27. W. Paik, T. N. Andersen, and H. Eyring, *Electrochim. Acta*, **14**, 1217 (1969).
28. L. V. Haynes and D. T. Sawyer, *Anal. Chem.*, **39**, 332 (1967).
29. A. W. B. Aylmer-Kelly, A. Bewick, P. R. Cantrill, and A. M. Tuxford, *Discuss. Faraday Soc.*, **56**, 96 (1973).
30. K. Ito, T. Murata, and S. Ikeda, *Bull. Nagoya Inst. Technol.*, **27**, 369 (1975).
31. E. Gileadi, Editor, "Electrosorption," Plenum Press, New York (1967).
32. E. J. Rudd and B. E. Conway, *Trans. Faraday Soc.*, **67**, 440 (1971).
33. B. E. Conway, "Theory and Principles of Electrode Processes," The Ronald Press Co., New York (1965).
34. T. Bejerano, Ch. Forgacs, and E. Gileadi, *J. Electroanal. Chem.*, **27**, 69 (1970).

The Application of Concentration Jump and Impedance Measurements to the Mechanistic Study of the Fluoride Solid-State Electrode

P. Van den Winkel and J. Mertens

Farmaceutisch Instituut, Vrije Universiteit Brussel, Paardenstraat 67, B-1640 St. Genesius-Rode, Belgium

T. Boel

Hoger Rijksinstituut voor Technisch Onderwijs, Welvaarstraat, B-9300 Aalst, Belgium

and J. Vereecken*

Laboratorium voor Metallurgie en Electrochemie, Vrije Universiteit Brussel, Campus Oefenplein, Gebouw G, B-1050 Brussel, Belgium

ABSTRACT

This study describes the combined use of a-c impedance and fast flow techniques to elucidate the mechanism of the fluoride solid-state electrode. By describing fast flow data in the complex frequency Laplace plane and correlating it with a-c impedance data, it has been possible to separate interfacial and mass transport contributions to over-all electrode behavior; and describe the manner in which the electroactive species modifies individual reaction steps. Using this, a preliminary mechanism for the fluoride solid-state electrode involving heterogeneous F^- exchange reactions at two types of sites, one involving electronic and the other ionic conduction, is presented.

Various experimental methods are described for the study of electrode processes of ion-sensitive electrodes. These methods may be classified according to the type of input function applied to an electrochemical cell built up from the electrode of interest and a suitable nonpolarizable reference electrode immersed in an appropriate test solution.

As shown in Table I, two types of experiments may be used. One type of experiment deals with the study of the response signal measured as a function of time when a well-known electrical signal (the driving force or excitation function) is applied to the cell. For example, phase and impedance measurements using small sinusoidal input voltages were employed in this study. The system frequency response is usually represented in a Cole-Cole diagram in the complex plane. From experimental data in a frequency range from 10^{-3} up to 10^5 Hz for various concentrations of the electroactive species an equivalent circuit for the test electrode is obtained. The transfer impedance for this equivalent circuit can be calculated and so the behavior of the system with regard to a specified input is characterized. Physicochemical phenomena associated with the electrode processes are then interpreted in terms of diffusion, double layer, and space charge impedances (1-6).

The second type of experiment deals with the measurement of the transient signal caused by a rapid concentration change of the electroactive species around the sensor surface using fast flow techniques. From these experiments a dynamic response equation for the sensor is obtained. Based on experimental data, rate-limiting processes, as for instance solvation-desolvation (7), adsorption (8), and diffusion (9), were proposed. However, it should be pointed out that the mathematical form of the semiempirical response equation may lead to an erroneous interpretation of the rate-limiting process (10).

As the electrochemical behavior of a sensor is characterized by its transfer function, both types of experiments must supply information about the rate-limiting

* Electrochemical Society Active Member.
Key words: selective electrode, impedance measurements, fluoride.

Table I. Study of electrode processes: mechanistic studies

Method	Driving force	Example	Result
1	Electrical signals of small amplitude excursion	Phase-impedance measurements (10^{-3}-10^{5} Hz)	Linearized electrical equivalent model and transfer impedance
2	Concentration gradients of the electroactive species	Dynamic response studies (fast flow injection experiments)	Transfer function and transfer impedance

process. Nevertheless, fast flow experiments should supply information only about the interfacial process. Indeed, due to the high linear flow rates, the thickness of the hydrodynamic layer is reduced to a minimum (11). Therefore little or no data concerning a Warburg-type process are available from kinetic measurements under these conditions. Moreover, time constants associated with macroscopic electrode kinetics are large compared with those obtained from impedance measurements in a higher frequency range and which are related mainly to space charge impedances. Therefore, a comparison and/or correlation of the results of both kinetic and impedance measurements is valid only in the time constant range obtained in fast flow experiments.

The present paper deals with the equivalent model and rate-limiting processes of the ORION 94-09A electrode. Fast flow studies (11) and impedance measurements (12) were performed. By conversion of the dynamic response equation from fast flow studies into the Laplace domain, the transfer function for this sensor will be calculated. As the transfer function arising from linear networks must be rational, a rational approximation of the experimental and irrational transfer function will be made so that a reasonable comparison of fast flow and impedance data can be made. Making then simple assumptions about the excitation function applied in fast flow studies allows the transfer impedance for the intermediate frequency range to be calculated.

Both transfer impedances or equivalent circuits, one obtained from impedance measurements, the other from fast flow kinetics, contribute to the physicochemical interpretation of the interfacial sensor process.

Experimental Results from Fast Flow Kinetics and Impedance Measurements

The results of kinetic fast flow experiments were reported in a previous paper (11). They revealed that the dynamic response of new fluoride electrodes with an internal reference system of the wick type can be represented by a hyperbol

$$E_t = \frac{t}{a + bt} \qquad [1]$$

where a and b are constants and $t_{50} = a/b$ (*i.e.*, the time required to reach 50% of the steady-state potential); E_t = potential as function of time; $E_{t=0} = 0$, $E_{t=\infty} = 1/b = S \log a_2/a_1$; S = slope of the indicator electrode; and a_1 and a_2 = initial and final concentration of the jump.

The striking discrepancy in rate of response between fast flow and continuous auto analyzer systems (11) is attributed to a rate-limiting film diffusion process in the hydrodynamic layer when the sensor is mounted in a sample processor. In fast flow experiments this layer is reduced to a minimum and hence the response is fast.

From impedance measurements in a range 10^{-3} up to 10^5 Hz, the locus for the same electrode was obtained (12). It is shown in Fig. 1. Three parts can be distinguished. The high frequency and perfect semicircle is due to space charge and to geometrical and wiring impedances. The lowered semicircle is attributed to a slow interfacial charge transfer represented by a time constant related to an apparent transfer resistance and a double layer capacitance. The influence of the concentration of the potential-determining ion on this part of the complex plane plot is obvious. Egorov and Novell'skii (13) proved that a depressed semicircle is also obtained for a series of two parallel networks with R and C of the same order of magnitude.

The very low frequency part of the complex plane plot is characteristic for a film diffusion process. If the slope equals one, it can be interpreted as a Warburg impedance. Deviations from unity slope are attributed to adsorption of intermediate species or to a nonlinear diffusion path at the interface. The latter is related to the surface structure of the membrane, which is far from ideal as was shown by microscopic examination.

Mathematical Treatment of the Dynamic Response Equation

Laplace transform of the dynamic response $r(t)$ of an electrical network to a known excitation function $x(t)$ yields

$$R(s) = G(s) \cdot X(s) \qquad [2]$$

where $R(s)$ = response in the s-domain, s = Laplace variable; $G(s)$ = transfer function of the network; and $X(s)$ = excitation in the s-domain.

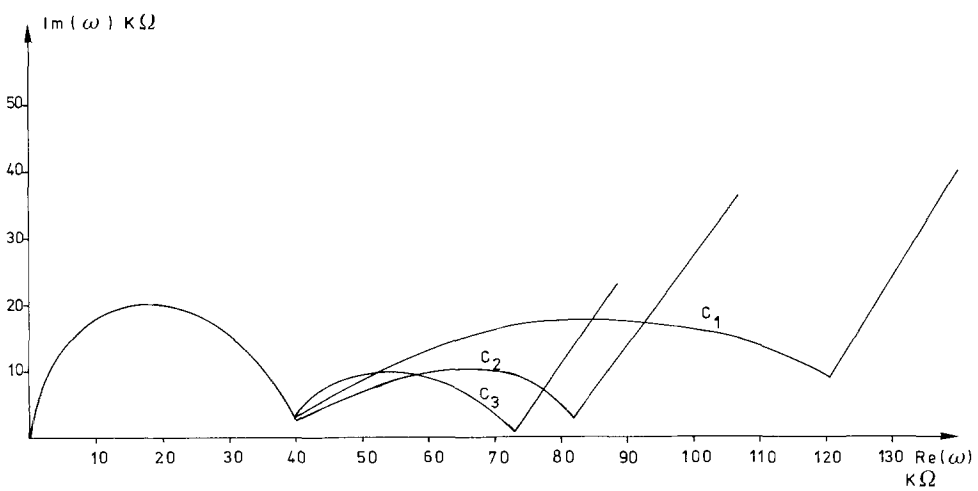


Fig. 1. Indication of the fluoride electrode (Orion 94-09A), influence of the concentration.

With Eq. [1], one obtains

$$R(s) = \mathcal{L}\left\{\frac{t}{a+bt}\right\} = \frac{1}{bs}\cdot\left\{1-\frac{as}{b}\cdot e^{as/b}\cdot E_1\left(\frac{as}{b}\right)\right\} \quad [3]$$

where $E_1(as/b)$ is the exponential integral.

As $1/bs$ represents a step input excitation with amplitude $1/b$, one may put

$$X(s) = \frac{1}{bs} \quad [4]$$

and

$$G(s) = 1-\frac{as}{b}\cdot e^{as/b}\cdot E_1\left(\frac{as}{b}\right) \quad [5]$$

As the transfer function must be rational, an appropriate rational approximation of Eq. [5] must be applied. According to Hastings (14) and with $x = as/b$

$$x\cdot e^x\cdot E_1(x) = \frac{x^2+a_1x+a_2}{x^2+b_1x+b_2}+\epsilon(x) \quad [6]$$

where $|\epsilon(x)| < 5\cdot 10^{-5}$; $a_1 = 2.334733$; $a_2 = 0.250621$; $b_1 = 3.330657$; and $b_2 = 1.681534$.

Neglecting the correction term $\epsilon(x)$ and introducing the numerical values for a_1, a_2, b_1, and b_2 yields

$$G(s) \cong K\cdot\frac{(s+\alpha)}{(s+\beta)(s+\gamma)} \quad [7]$$

with $K = b/a$, $\alpha = 1.43\ b/a$, $\beta = 0.63\ b/a$, and $\gamma = 2.71\ b/a$.

As β and γ are positive, $G(s)$ is the transfer function of a stable network. $G(s)$ is a function of a/b, the half-time potential, *i.e.*, the time required to reach 50% of the steady-state potential $1/b$, and which is an experimental datum. In Fig. 2 the relation between the irrational transfer function and its rational approximation is represented. The agreement is excellent.

Equation [7] may be used either to evaluate an exponential form of the hyperbolic response (Eq. [1]) or to calculate the frequency response of the sensor. The first is accomplished by multiplying Eq. [7] by $1/bs$ (for a step input excitation) and applying an inverse Laplace transform

$$E_t = \frac{t}{a+bt} \cong \mathcal{L}^{-1}\left\{\frac{1}{bs}\left(\frac{K(s+\alpha)}{(s+\beta)(s+\gamma)}\right)\right\} \quad [8]$$

$$= K_0 - K_1e^{-\beta t} - K_2e^{-\gamma t} \quad [9]$$

and $K_0 = 0.851$, $K_1 = 0.226$, $K_2 = 0.625$, $1/\beta = 0.369\ a/b$, and $1/\gamma = 1.613\ a/b$.

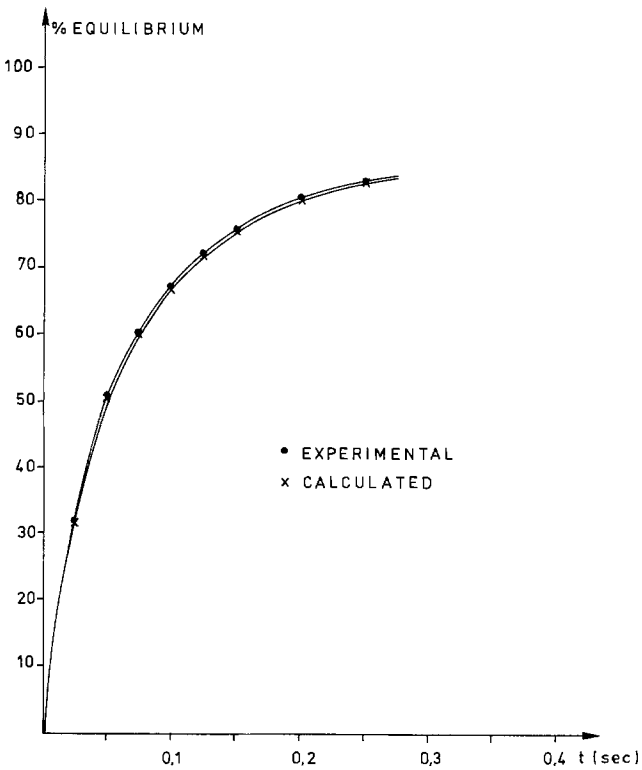


Fig. 3. Concentration jump $10^{-5} \rightarrow 10^{-3}$M F^- in 1/3 TISAB

In Fig. 3 the experimental hyperbolic dynamic response and its calculated exponential approximation for a concentration jump 10^{-5}-10^{-3}M NaF in 1/3 TISAB (total ionic strength adjustment buffer) is shown. As the thickness of the hydrodynamic layer is practically zero in the experimental conditions, the existence of two time constants $1/\beta$ and $1/\gamma$ of the same order of magnitude are most likely associated with interfacial processes. The transfer function $G(s)$ (Eq. [7]) suggests two parallel first-order processes as rate-limiting phenomena. These could be, for instance, exchange reactions of F^- anions at the interface at two types of exchange sites. For LaF_3 crystals doped with Eu(II), these might be

1. $(EuF_2)_c + F^-{}_s \rightarrow (EuF_3)_c + e^-$ (electronic conduction) [10]
2. $(LaF_3)_c + [\,] \rightarrow (LaF_2)^+{}_c + [F^-]$ (ionic conduction) [11]

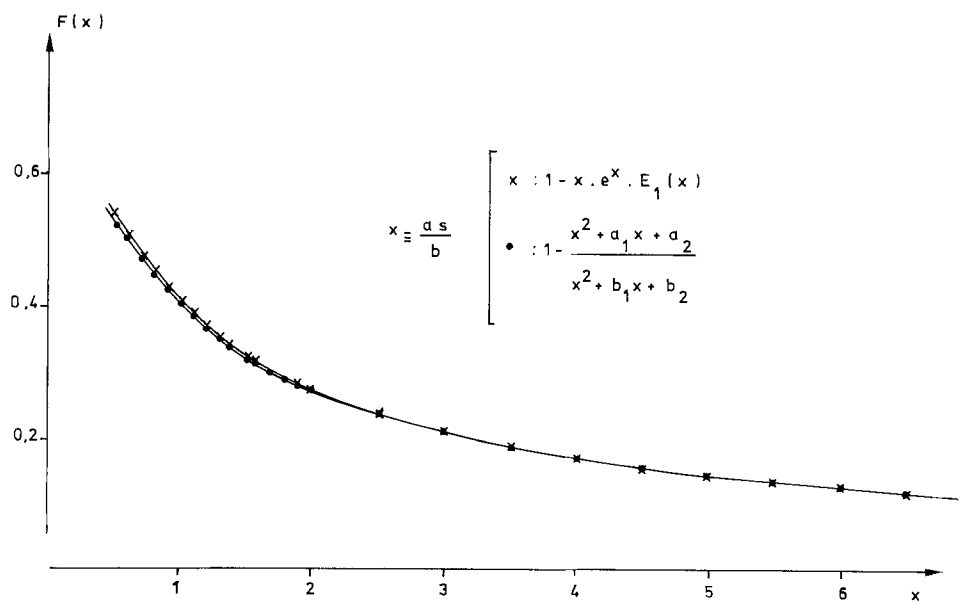


Fig. 2. Rational approximation of the transfer function.

$$(LaF_2)^+_c + F^-_s \rightarrow (LaF_3)_c \quad [12]$$

where c = crystal, s = solution, and [ ] = lattice vacancy.

The first can be interpreted as a semiconductor behavior with a deep donor level of Eu(II), *i.e.*, 0.41 eV energy gap between donor and conduction levels (12). The second reaction involves a crystal F^- anion to jump into a lattice vacancy near the crystal surface followed by the exchange of a F^- with the solution. The fluoride initially trapped in the vacancy then contributes to the ionic conduction of the crystal. To the credit of this mechanism is the remarkable coincidence that the hyperbolic response also holds for other electrodes, *i.e.*, the Ag_2S electrode (15), which exhibit both ionic and electronic conduction (16). Resistance measurements as a function of increasing temperature show increasing conductance in both cases. Therefore the contribution of both types of conduction can be possibly evaluated by Hall effect measurements as a function of frequency or by the square wave method applied by Koebel *et al.* (16).

The calculation of the frequency response of the electrode at lower frequencies can also be done by means of the transfer function $G(s)$ (Eq. [7]), obtained from kinetic fast flow experiments.

Writing the excitation function $1/bs$ as

$$\frac{1}{bs} = \frac{i}{s} \cdot R \quad [13]$$

i.e., the step input voltage excitation is formally treated as the product of a step input current i/s multiplied by a resistor R. Therefore

$$R(s) = \frac{i}{s} \cdot \frac{K \cdot R \cdot (s+\alpha)}{(s+\beta)(s+\gamma)} \quad [14]$$

and the transfer impedance $Z(s)$ is given by

$$Z(s) = \frac{K \cdot R \cdot (s+\alpha)}{(s+\beta)(s+\gamma)} \quad [15]$$

which means that the response in the s-domain is given by the product of a step input current i/s and the transfer impedance $Z(s)$. For low frequencies $s = j\omega \cong 0$. Therefore, neglecting the influence of the concentration change on the transfer resistance

$$Z(o) = \frac{K \cdot R \cdot \alpha}{\beta \cdot \gamma} = R_t \quad [16]$$

with R_t the total transfer resistance. As $K\alpha/\beta \cdot \gamma \simeq 1$, R equals the total transfer resistance as obtained from impedance measurements (see Fig. 1). As a lowered semicircle is the result of two parallel RC networks in series, the components of these networks can be evaluated by identifying the corresponding terms in the expressions [15] and [17]

$$Z(s) = \frac{C_A + C_B}{C_A \cdot C_B} \cdot \left\{ \frac{S + \dfrac{R_A + R_B}{R_A \cdot R_B (C_A + C_B)}}{\left(S + \dfrac{1}{R_A C_A}\right)\left(S + \dfrac{1}{R_B C_B}\right)} \right\} \quad [17]$$

For the given example, the result is represented in Fig. 4. Moreover, the dynamic response to a current step input is a hyperbola and in addition, the values of R_t, K, α, β, and γ allow the complex plane response to be calculated by means of the well-known formulas for phase angle $\phi(j\omega)$ and magnitude $|Z(j\omega)|$

$$\phi(j\omega) = \tan^{-1}\left(\frac{\omega}{\alpha}\right) - \left[\tan^{-1}\left(\frac{\omega}{\beta}\right) + \tan^{-1}\left(\frac{\omega}{\gamma}\right)\right] \quad [18]$$

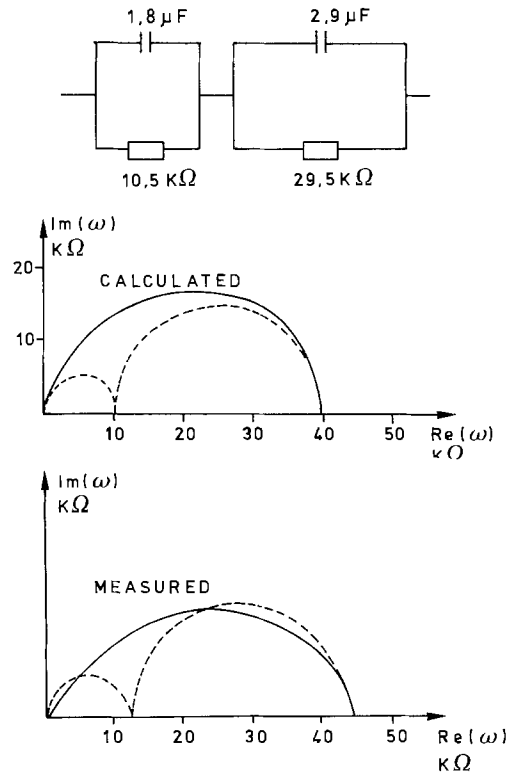


Fig. 4. (a, top) Equivalent circuit. (b, center) (c, bottom).

$$|Z(j\omega)| = R_t \cdot K \cdot \frac{\sqrt{\omega^2 + \alpha^2}}{\sqrt{\omega^2 + \beta^2} \cdot \sqrt{\omega^2 + \gamma^2}} \quad [19]$$

The result is a lowered semicircle which is known to be the result of two perfect semicircles.

Conclusion

From impedance measurements (12) in a frequency range 10^{-3}-10^5 Hz we concluded that the equivalent circuit of the 94-09A fluoride electrode involves: (*i*) a parallel RC network representing space charge and geometrical impedances (R = 100 kΩ, C = 100 pf), (*ii*) a diffusion impedance which is not a pure Warburg impedance due to complex diffusion at the surface, and (*iii*) a series of two parallel RC networks representing double layer capacitance and transfer resistance at both sides of the membrane.

From the present discussion it is obvious that both kinetic fast flow studies and a-c impedance measurements do inform about the rate-limiting process at the electrode-solution interface as evidenced by the lowered semicircle of the complex plane response. Mathematical treatment of kinetic fast flow data allows the evaluation of double layer capacitance and charge transfer resistors and hence allows the elucidation of the electrode process to a greater extent.

Manuscript submitted Dec. 27, 1976; revised manuscript received April 21, 1977.

Any discussion of this paper will appear in a Discussion Section to be published in the June 1978 JOURNAL. All discussions for the June 1978 Discussion Section should be submitted by Feb. 1, 1978.

Publication costs of this article were assisted by Vrije Universiteit Brussel.

REFERENCES

1. R. P. Buck, *Electroanal. Chem. Interfacial Electrochem.*, **18**, 363 (1968).
2. R. P. Buck and I. Krull, *ibid.*, **18**, 387 (1968).
3. J. R. Sandifer and R. P. Buck, *ibid.*, **56**, 385 (1974).
4. M. J. D. Brand and G. A. Rechnitz, *Anal. Chem.*, **10**, 1185 (1969).
5. M. J. D. Brand and G. A. Rechnitz, *ibid.*, **41**, 1788 (1969).

6. M. J. D. Brand and G. A. Rechnitz, *ibid.*, **42**, 478 (1970).
7. K. Toth and E. Pungor, *Anal. Chim. Acta*, **64**, 417 (1973).
8. R. P. Buck, *Anal. Chem.*, **48**, 23R (1976).
9. W. E. Morf, E. Lindner, and W. Simon, *ibid.*, **47**, 1596 (1975).
10. J. Mertens, Ph.D. Thesis, University of Brussels (V.U.B.) (1976).
11. J. Mertens, P. Van den Winkel, and D. L. Massart, *Anal. Chem.*, **48**, 272 (1976).
12. J. Mertens, P. Van den Winkel, and J. Vereecken, To be published.
13. L. Ya Egorov and I. M. Novosel'skii, *Electrokhimiya*, **5** (3), 274 (1969); (U.D.C. 541.138: 621.3.0218).
14. C. Hastings Jr., "Approximations for Digital Computers," Princeton University Press, Princeton N.J. (1955).
15. R. H. Müller, *Anal. Chem.*, **41** (12), 113A (1969).
16. M. Koebel, N. Ibl., and A. M. Frei, *Electrochim. Acta*, **19**, 287 (1974).

An Electrochemical Study of Flavin Adenine Dinucleotide

Robert D. Braun*[1]

Department of Chemistry, Vassar College, Poughkeepsie, New York 12601

ABSTRACT

Flavin adenine dinucleotide (FAD) is examined using polarography, cyclic voltammetry, and controlled potential coulometry. At *p*H less than 6.5 and at *p*H greater than 10, the reaction proceeds in two single electron steps through the semiquinone. At intermediate *p*H the reaction consists of a preceding hydrogen ion addition followed by a two-electron transfer which in turn is followed by a second hydrogen ion addition.

The flavins are an important class of biochemical compounds which are found in both plants and animals. Due to their importance, most of the flavins have been the subject of many studies. In particular isoalloxazine, lumichrome, lumiflavin, riboflavin, and flavin mononucleotide (FMN) have been thoroughly investigated and excellent reviews of these studies are available (1, 2). Although flavin adenine dinucleotide (FAD) occupies a key position in the respiratory transport chain (2), relatively few electrochemical studies of this compound are available (3, 4). These electrochemical studies consisted entirely of polarographic examinations at the dropping mercury electrode (DME). No successful attempt has been made to unravel the electrochemical reaction mechanism or to examine the kinetics of the reaction. In the present study polarography, controlled potential coulometry, cyclic voltammetry, and voltammetry at a rotating platinum disk electrode have been used to study the electrochemical reaction mechanism of FAD throughout a broad *p*H range in aqueous solution.

Experimental

Chemicals.—FAD was obtained from the Sigma Chemical Company and used without further purification. The manufacturer's assay listed the purity of the FAD as 95%. Spectrophotometric analysis at 450 nm assuming a molar absorptivity of 1.13×10^4 l mole^{-1} cm^{-1} (5) resulted in a calculated purity of 92% (14 trials). Any impurity in the FAD was not electroactive within the potential region used in this study. All other chemicals were reagent grade.

Buffer solutions were prepared to be 0.1*M* in their minor constituent except for the *p*H 2.1 HCl solution and the *p*H 11 or greater sodium hydroxide solutions. The ionic strength of each buffer solution was adjusted to 0.5M with KCl except for the *p*H 7.5 Tris buffer and the *p*H 10.0 and 10.2 carbonate buffers which had ionic strengths of 0.8, 0.8, and 1.3*M*, respectively. The buffer solution components were HCl at *p*H 2.1, acetic acid and sodium acetate at *p*H 4-5.1, potassium hydrogen phthalate and sodium hydroxide at *p*H 5.9, potassium dihydrogen phosphate and dipotassium hydrogen phosphate at *p*H 6-8, tris (hydroxymethyl) aminomethane (Tris) and HCl between *p*H 7.5 and 9.2, potassium hydrogen carbonate and potassium carbonate between *p*H 8 and 10.2, and NaOH at *p*H greater than 11.

Apparatus.—Experiments were performed using a Beckman electroscan 30 in its controlled potential mode equipped with an electroscan 30P integrator which was used to integrate the area under controlled potential coulometry current-time curves. The output pulses from the integrator were counted with a Heathkit IM-4100 counter.

Rotating platinum disk electrode (RPDE) studies were performed at 1800 rpm (Sargent synchronous rotator). Cyclic voltammetry experiments were carried out at a hanging mercury drop electrode (HMDE). Polarographic studies were carried out at a conventional dropping mercury electrode (DME). The reference electrode was a saturated calomel electrode (SCE). The auxiliary electrode was made of platinum foil.

All experiments were carried out at 25° ± 0.5° in either a water-jacketed, three-compartment cell, or in a commercially available water-jacketed cell with accompanying cell top (Princeton Applied Research 9300 and 9350). In either case separation between the compartments was effected by medium porosity glass frits and salt bridges containing saturated KCl in agar gels.

Solutions were deaerated prior to examination with Linde high purity dry grade nitrogen which was passed through two wash towers containing acidic ammonium metavanadate and amalgamated zinc, and a final wash tower containing distilled water (6a). All *p*H measurements were made with a Radiometer PHM62 *p*H meter.

Results and Discussion

A cursory polarographic examination of FAD shows a single cathodic wave throughout the *p*H range 2-13. A plot of $E_{1/2}$ *vs.* *p*H yields three straight-line portions corresponding to Eq. [1], [2], and [3] for the acidic, neutral, and basic regions, respectively. The two inflection points in the

* Electrochemical Society Active Member.
[1] Present address: Department of Chemistry, University of Southwestern Louisiana, Lafayette, Louisiana 70504.
Key words: polarography, cyclic voltammetry, coulometry.

$$E_{1/2} = -0.010\text{-}0.0646\,pH \quad [1]$$

$$E_{1/2} = -0.205\text{-}0.0342\,pH \quad [2]$$

$$E_{1/2} = 0.056\text{-}0.0604\,pH \quad [3]$$

plot occurred at pH of 6.4 and 10.0 in fair agreement with previously reported values (3, 4). The first inflection point in the $E_{1/2}$-pH curve has been attributed to the acid dissociation constant of the reduced form of FAD and the second inflection point to the dissociation constant of the oxidized form (1, 3). In the acidic region the slope of the $E_{1/2}$-pH curve was found to be −0.065 V/pH unit. Between the two inflection points in the curve the slope was −0.034 V/pH unit, and at pH greater than 10.1 the slope was −0.060. These values compare to slopes of −0.06, −0.03, and −0.06 reported earlier (3).

Controlled potential coulometry was carried out at several pH's and the results are shown in Table I. In each case the potential was adjusted to a position on the plateau of the polarographic wave and the electrolysis carried out to completion. Throughout the entire pH range a coulometrically calculated value of $n_{\text{redn.}}$ of 2 was obtained. The resulting reduction products were examined polarographically and in a few instances the potential was adjusted on the plateau of the reduced FAD anodic wave and exhaustive electrolysis carried out. The coulometrically calculated values of $n_{\text{oxdn.}}$ obtained in these oxidations are also listed in Table I. After each oxidation the products were examined polarographically and found to have exactly the same $E_{1/2}$ and i_d as did the original FAD sample, *i.e.*, the original FAD was regenerated with no loss to other possible products.

The values of $n_{\text{oxdn.}}$ obtained in basic solutions varied from 0.7 at pH 9.25 to a high value of 1.7 at pH 8.18. These values are all less than the expected coulometric value of 2.0, apparently as a result of air oxidation of the FAD reduction products. Even with nitrogen flowing through the cell it was found that in basic solution the reduced FAD reverts to FAD at a rate that is significant with respect to the relatively long times (about 1 hr) used for the controlled potential oxidations. The pseudo first-order rate constant for the conversion of the reduction products to FAD under the experimental conditions at pH 8.18 was estimated by measuring the increase in the diffusion current of the FAD wave with time and found to be 1.1×10^{-4} sec^{-1}. Consequently after 1 hr about 40% of the reduced substance reverts to FAD.

Table I. Controlled potential coulometry data obtained on FAD and reduced FAD samples

Initial FAD conc, mmole	pH	Working electrode	Reduction potential, −V	$n_{\text{redn.}}$	Oxidation potential, −V	$n_{\text{oxdn.}}$
1.20	4.1	Hg	0.60	1.82		
0.46	4.1	Hg	0.40	2.3	0.20	2.04
0.57	4.1	Hg	0.40	1.74		
0.52	8.2	Pt	0.60	1.98		
0.84	8.2	Pt	0.60	1.92		
1.11	8.2	Pt	0.60	1.98		
0.40	8.2	Hg	0.60	2.16		
0.66	8.2	Hg	1.00	2.04		
1.17	8.2	Hg	1.00	2.02		
0.45	8.2	Hg	1.00	1.99		
0.55	8.2	Hg	0.80	2.03	0.20	1.0*
0.59	8.2	Hg	0.80	1.92	0.30	1.4*
1.54	8.2	Pt	0.80	1.96	0	1.7*
0.68	9.3	Hg	0.60	1.97		
0.21	9.3	Hg	0.60	2.13		
0.42	9.3	Hg	0.60	2.02	0.20	0.72*
0.51	10.2	Hg	0.90	2.09		
0.97	10.2	Hg	0.90	2.05		
			Average	2.01		

* The low $n_{\text{oxdn.}}$ values reported here are apparently due to relatively rapid air oxidation of the reduced FAD in alkaline solutions.

Rapid air oxidation of reduced FAD was not observed in solutions of pH 4.08. For convenience the remainder of this report is divided into sections corresponding to the pH range throughout which a particular reaction mechanism takes place

pH 6.6-8.6.—Careful polarographic examination (DME) of the FAD wave in this pH range revealed only a single cathodic wave. The "anomalous" wave at a potential more negative than the main wave observed by Ke (3) was not observed in this study.

A requirement of a reversible electrode reaction is that the half-wave potential of the oxidized species must be identical to that of the reduced species (6b). Half-wave potentials were obtained for the FAD reduction waves from plots of E *vs.* log $(i/i_d - i)$ at the point where the log term was zero. Half-wave potentials for the oxidation of reduced FAD were similarly obtained from plots of E *vs.* log $(i_d - i/i)$. Throughout the remainder of this paper these plots are referred to as log plots. In each case in this pH region the log plots were linear. The average difference between the half-wave potentials of FAD and reduced FAD at the pH's in this range was 0.012 ± 0.006V for five trials at differing pH. The uncertainty is expressed as the standard deviation. A "t" test for significance indicated that at the 90% probability level the confidence limit was identical to the standard deviation. Since the oxidized and reduced forms of FAD do not have identical $E_{1/2}$'s, this system cannot be classified as reversible in this pH range as has been done previously (3). The cathodic FAD wave does overlap with the anodic reduced FAD wave however and consequently this system is best described as quasireversible. A typical FAD cathodic wave and the corresponding reduced FAD anodic wave are shown in Fig. 1.

Slopes of log plots for reversible systems at 25° are given by Eq. [4]. The slopes of log plots obtained

$$\text{slope} = -0.059/n \text{ V/decade} \quad [4]$$

with FAD solutions are listed in Table II. The average

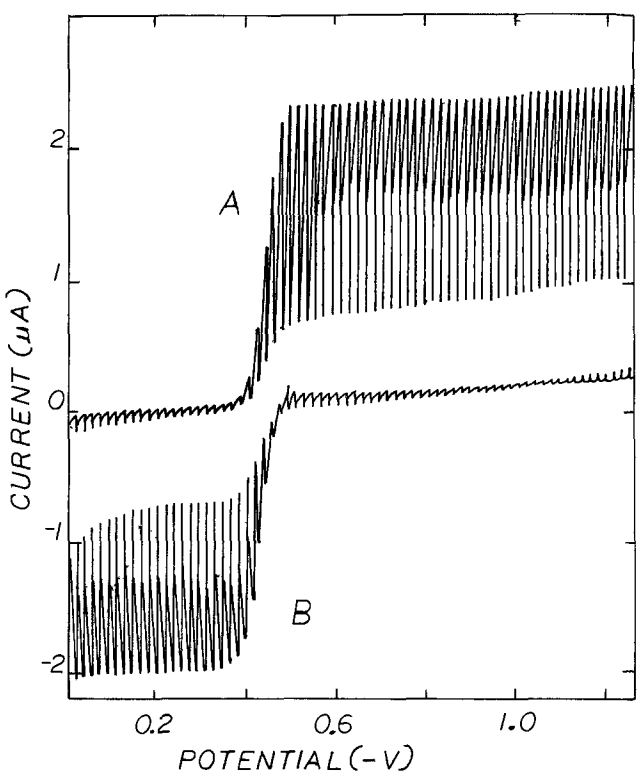


Fig. 1. Polarograms obtained in pH 8.2 Tris buffer. A, 0.41 mmole FAD; B, 0.41 mmole reduced FAD.

Table II. Slopes obtained from log plots* of various FAD solutions at differing pH values

FAD conc, mmole	pH	Slope, −V/decade
0.208	6.82	0.036
0.208	6.96	0.037
0.208	7.92	0.039
0.208	8.09	0.037
0.208	8.13	0.038
0.59	8.18	0.039
0.78	8.18	0.035
0.59	8.18	0.037
0.208	8.59	0.034
0.51	9.13	0.040
0.42	9.25	0.043
0.68	9.25	0.034
0.208	9.25	0.034
0.51	9.26	0.034
0.51	9.28	0.035

* Log plots are defined as plots of E *vs.* log $(i/i_d - i)$ on the rising portion of the cathodic wave.

slope throughout this pH range was −0.037. This value is closer to the value expected for a two-electron reversible process (−0.030) than to the value for a one-electron reversible process (−0.059). It should be noted that the values of the log plot slopes obtained in this study differ significantly from the value of 0.06 obtained at pH 7.4 by Ke (3). A similar examination of the anodic wave of reduced FAD at pH 8.2 revealed the slope to be 0.030 ± 0.003 (four trials) where the uncertainty is expressed as the standard deviation.

At pH 8.2, i increased linearly with increasing $h^{1/2}_{corr.}$, and $i_d/h^{1/2}_{corr.}$ decreased slightlly with increasing $h^{1/2}_{corr.}$ for solutions of FAD and reduced FAD thereby apparently indicating diffusion control of both the cathodic and anodic FAD reactions (6c). A plot of i_d as a function of FAD concentration was linear and when extrapolated passed through the origin. From the slope of the plot, the diffusion current constant ($I = i_d/Cm^{2/3}t^{1/6}$) was found to be 3.0. The values of m and t used in this calculation were measured in the supporting electrolyte-buffer solution on the plateau of the wave at −0.8V and the diffusion current was measured as the maximum drop current using no recorder damping. This same data was used to calculate the FAD diffusion coefficient from Eq. [5]. The terms in parentheses in Eq. [5] were set equal

$$i_d = (708nD^{1/2}m^{2/3}t^{1/6})C \qquad [5]$$

to the slope of the $i_d - C$ plot and the coulometric value of n of 2.0 used to obtain a value of D of 4.5×10^{-6} cm^2 sec^{-1}. As expected this value is slightly less than the average D of 6.5×10^{-6} which has been calculated for the lighter riboflavin at pH 7.4 (7). Between pH 6.8 and 13, the ratio of diffusion current to concentration never varied by more than 5% (solutions at 10 different pH's examined) and consequently the value of D given above may be assumed to be approximately constant throughout this entire pH range. There was no noticeable variation in $E_{1/2}$ with FAD concentration at the pH's examined.

Similar behavior was observed at the RPDE. A single wave was observed throughout the pH range from 2 to 10. The $E_{1/2}$ of the wave varied with pH in a manner similar to that observed at the DME. The RPDE wave occurred about 0.11V negative of the corresponding DME wave. At pH 8.2 the limiting current increased linearly with increasing FAD concentration. Since the RPDE wave was not as well formed as the DME wave, accurate potential measurements at the RPDE were impossible. Consequently the RPDE offered no particular advantage in studying the FAD system and its use was abandoned after the pH study and an examination of the variation of limiting current with concentration.

Cyclic voltammetry studies were carried out at both the HMDE and at a platinum disk. In order to remove the platinum oxide coating on the platinum disk it was necessary to pretreat the electrode by dipping it in concentrated nitric acid, rinsing with distilled water, and reducing the oxide coating by controlled potential electrolysis at a potential on the platinum oxide peak. Even this procedure was not always adequate at the relatively high current sensitivities used in this study, however, and as a result, after the studies in this pH region, the use of the platinum disk was abandoned.

Between pH 6.8 and 8.6, a single cathodic-anodic peak couple was observed at both the platinum disk and the HMDE (Fig. 2). Application of the diagnostic criteria of Nicholson and Shain (8) to the cathodic peaks resulted in plotted curves (Fig. 3) with shapes characteristic of an electrochemical mechanism consisting of a reversible first-order or pseudo first-order preceding reaction followed by a reversible electron transfer. Since the equilibrium constant for the preceding reaction is not known, it is not possible to use the method of Nicholson and Shain to obtain the rate constant for the preceding chemical reaction.

Reduced FAD in the pH 6.8-8.6 region had a single cyclic voltammetry anodic-cathodic peak pair. Application of the diagnostic criteria to the anodic peak resulted in curves similar in shape to those shown in Fig. 3 for the cathodic peak. This appears to indicate that the oxidation of reduced FAD also follows an electrochemical mechanism consisting of a first-order reaction followed by a reversible electron transfer.

All of the studied flavin compounds have been shown to undergo an over-all reduction to the dihydroflavin compounds (1, 2) as shown in Eq. [6]. As has been previously suggested by Ke (3)

$$F + 2H^+ + 2e = FH_2 \qquad [6]$$

this apparently is also the case for FAD. Between pH 6.8 and 8.6 the cyclic voltammetry data indicate a chemical reaction prior to the electron transfer. For a fast acid-base reaction prior to the electron transfer (Eq. [7] and [8]), if the unprotonated species, O, predominates in this pH range, then the slope of the

$$O + pH^+ = H_pO^{p+} \qquad [7]$$

$$H_pO^{p+} + ne = RH_p \qquad [8]$$

polarographic $E_{1/2}$ − pH curve is given by $-0.059p/n$ (6d). Since n has been shown by both controlled-potential coulometry and by the slope of the log plots to be 2 in this region, and the slope of the $E_{1/2}$ − pH

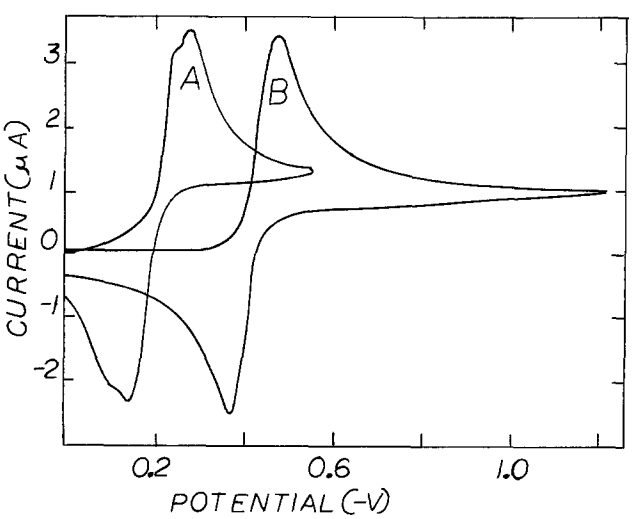


Fig. 2. Cyclic voltammograms obtained at a HMDE. A, 0.53 mmole FAD in pH 4.08 acetate buffer at 0.2 V sec^{-1}; B, 0.72 mmole FAD in pH 8.2 Tris buffer at 0.10 V sec^{-1}.

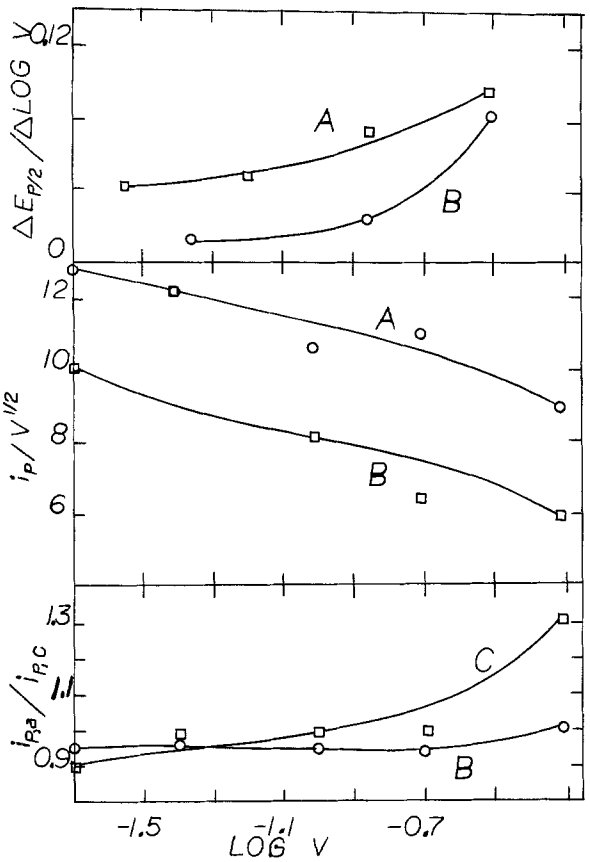


Fig. 3. Application of the diagnostic criteria of Nicholson and Shain (8) to cyclic voltammograms of FAD in pH 8.2 Tris buffer. A, 0.55 mmole at the HMDE; B, 0.87 mmole at the Pt disk; C, 0.87 mmole at the HMDE.

curve was −0.034, then p must be equal to 1. Cyclic voltammetry data also indicates a chemical step prior to oxidation of reduced FAD. The electrochemical mechanism which appears to best explain all of these observations is the three-step mechanism shown in Eq. [9], [10] and [11] where Eq. [9] is the rate-determining step for FAD reduction and Eq. [11] is the rate-determining step for FADH oxidation. In this pH range the present study contains no evidence for semiquinone formation. Semiquinone formation is clearly indicated, however

$$FAD + H^+ = FADH^+ \quad [9]$$

$$FADH^+ + 2e = FADH^- \quad [10]$$

$$FADH^- + H^+ = FADH_2 \quad [11]$$

in other pH ranges (see the following discussion). It should be noted that Eq. [9], [10], and [11] are not meant to imply a specific acidity state of FAD. The K_a values of various flavin compounds are listed elsewhere (1, 9).

Although the reaction apparently does not proceed in the single step indicated by Eq. [6], it is informative to calculate the rate constant for this over-all reaction. The rate constant can be calculated from cyclic voltammery data at the HMDE (10) by assuming n is the coulometrically determined value of 2 and D of FAD is the polarographically calculated value of 4.5×10^{-6} cm^2 sec^{-1}. Several calculated values of the rate constant (k_s) for a 0.21 mmole FAD solution are listed in Table III. The rate of the reaction decreases with increasing pH as would be expected if Eq. [9] were the rate-determining step for FAD reduction.

pH 2.1-6.5.—Polarographic examination at the DME of FAD in this pH region revealed a single cathodic

Table III. Calculated values of the pseudo first-order rate constant (k_s) for the over-all electrochemical reduction of 0.21 mmole FAD

pH	Scan rate, V sec^{-1}	ΔE_p*xn, mV	k_s, cm sec^{-1} × 10^{-3}
6.96	0.020	84	4.7
6.96	0.040	100	3.8
8.09	0.040	104	3.4
8.13	0.020	100	2.7
8.59	0.040	110	3.0

* $\Delta E_p = E_{p,\text{anodic}} - E_{p,\text{cathodic}}$.

wave at pH above about 6 which split into two overlapping waves of equal height (Fig. 4) at lower pH's. If a slow scan rate is not employed while recording the polarogram, the split into two waves can be easily overlooked, as was apparently done in the earlier study (3). In this instance a scan rate of 0.5 mV sec^{-1} was used. At pH 2.2 the proximity of the adsorption prewave (11) to the main FAD wave made it impossible to determine whether one or two waves were present.

Log plots at pH 4.08 yielded straight lines from which the half-wave potentials of the two waves could be determined. In drawing the lines through the log plot points it was necessary to neglect those points at potentials on wave I_c which were more than one-fourth of the way up the wave and those points on wave II_c which were less than three-fourths of the way up the wave. The overlapping of the waves in the intermediate region caused the log plots to curve away from the straight line. Using this method the $E_{1/2}$ of wave I_c was found to be 8 mV less negative than the $E_{1/2}$ of wave II_c. The average slopes (three trials) of the log plots were −0.055 V/decade for wave I_c and −0.052 V/decade for wave II_c. Both of these values are only slightly less than the −0.059 V/decade expected for a reversible one-electron process.

At pH's of 6.43, 6.20, and 6.04 the single cathodic FAD waves yielded log plots which were linear but which had two segments of slightly differing slope (Fig. 5). This can be interpreted to mean that two cathodic waves were present which overlapped to an extent which made separate wave identification impossible.

FAD which had been reduced by electrolysis showed only a single anodic wave in the acidic pH region unlike the behavior of FAD prior to reduction. Apparently two waves were not observed since the $E_{1/2}$'s of the waves were too close to each other to allow differentiation. Log plots of reduced FAD at pH 4.08 were linear with a slope of −0.041 V/decade. The

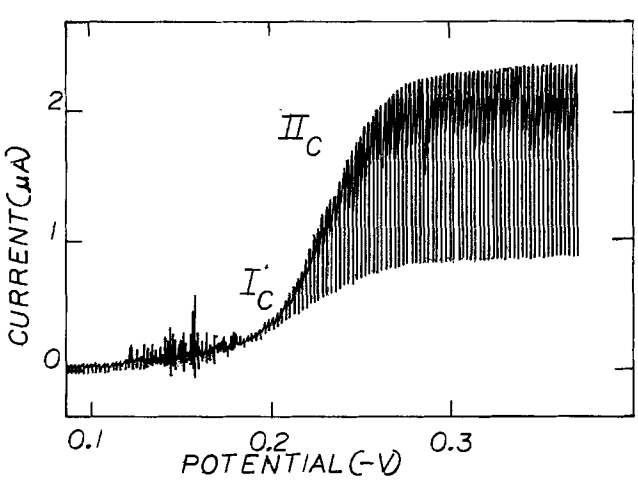


Fig. 4. A polarogram of 0.53 mmole FAD in pH 4.08 acetate buffer. I_c, the first cathodic wave; II_c, the second cathodic wave.

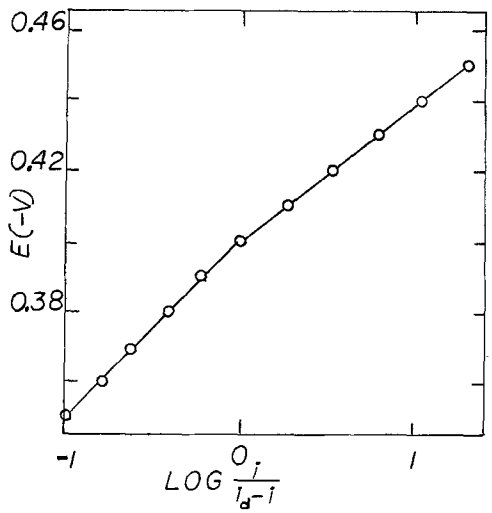


Fig. 5. A log plot of 0.19 mmole FAD in pH 6.04 phosphate buffer

average $E_{1/2}$ of the anodic wave (three trials) was −0.232V. In each case the diffusion current of the reduced FAD anodic wave equaled the total diffusion current of the two cathodic waves of the FAD starting material.

At pH 4.08 the total diffusion current ($i_{d,tot.}$) for the two FAD waves increased linearly with increasing $h^{1/2}_{corr.}$ and $i_{d,tot.}/h^{1/2}_{corr.}$ decreased slightly with increasing $h^{1/2}_{corr.}$ apparently indicating diffusion control of the electrode process. The diffusion current for the reduced FAD anodic wave behaved similarly.

A plot of $i_{d,tot.}$ as a function of FAD concentration at pH 4.08 was linear with a slope of 3.78 μA mmole^{-1}. The single reduced FAD wave behaved identically. From the slope of these straight lines and the measured values of m and t on the plateaus of the cathodic and anodic waves, the diffusion current constants (maximum drop currents used throughout) for FAD and reduced FAD at pH 4.08 were found to be 2.35 and 2.32, respectively. The diffusion coefficients were calculated from Eq. [5] using the coulometrically determined n of 2 and found to be 2.75×10^{-6} cm^2 sec^{-1} and 2.68×10^{-6} cm^2 sec^{-1}, respectively.

Cyclic voltammetry experiments were performed at the HMDE. At slower scan rates in the acidic pH range two overlapping cathodic peaks and two overlapping anodic peaks were observed (Fig. 2). At scan rates above about 0.25 V sec^{-1} the two cathodic and the two anodic peaks merged into a single cathodic-anodic peak pair. Cyclic voltammograms of reduced FAD showed two overlapping anodic peaks which did not completely merge even at 0.50 V sec^{-1}. Scan reversal at potentials cathodic of the anodic peak revealed two overlapping cathodic peaks at scan rates up to 0.05 V sec^{-1} and a single cathodic peak at higher scan rates. Since the cathodic peaks (and the anodic peaks) overlap each other it is impossible to apply the diagnostic criteria used earlier in the neutral pH range.

Controlled potential coulometry data has shown the total n for the over-all reduction of FAD to be 2. Since the polarograms of FAD in acidic solutions exhibit two waves of equal height, FAD must be reduced in two, one-electron steps. The slope of the $E_{1/2}$-pH curve in this pH range has been shown to be −0.065. For a fast acid-base reaction prior to the electron transfer (if the unprotonated FAD species predominates) or for a simultaneous addition of hydrogen ion and an electron, the slope of the polarographic $E_{1/2}$-pH curve is given by $-0.059p/n$ (see earlier discussion). Since n for each individual step is 1, then for each cathodic FAD wave the number of hydrogen ions added (p) is also 1. The electrochemical reaction mechanism which appears to best explain these results as well as the two cathodic cyclic voltammetry peaks is the stepwise reduction of FAD first to the semiquinone and finally to $FADH_2$ (Eq. [12] and [13]). It is not possible from the present data to determine when the hydrogen ions

$$FAD + H^+ + e = FADH^\cdot \quad [12]$$

$$FADH^\cdot + H^+ + e = FADH_2 \quad [13]$$

are added. The data may be interpreted to indicate either H^+ addition prior to or simultaneous with the addition of each electron.

pH 9-13.—Between pH 9.13 and 9.28 a single FAD cathodic wave was observed at the DME which yielded a linear log plot with an average slope of −0.037 V/decade (Table II). Between pH 9.34 and 9.89 the single polarographic wave resulted in a log plot with two linear portions of slightly differing slopes (similar to Fig. 5). Both portions had slopes of about −0.035 V/decade. The more cathodic portion always had the slightly greater negative slope. At pH's of 10.0 or greater two close polarographic waves were observed. By using the log plot method discussed earlier the separation between the $E_{1/2}$'s of the two waves at pH 10.2 (0.97 mmole solution) was found to be 24 mV.

At pH 10.2, 0.51 mmole FAD which had been exhaustively reduced by electrolysis showed two overlapping anodic waves of equal height. The difference in $E_{1/2}$ of the waves was 26 mV. The $E_{1/2}$ of the more positive anodic wave was 6 mV more positive than the $E_{1/2}$ of the more positive cathodic wave of the original FAD. Likewise the $E_{1/2}$ of the more negative anodic wave was 5 mV more positive than the $E_{1/2}$ of the more negative cathodic wave of the FAD starting material. This appears to indicate the presence of two quasireversible electrode reactions. The total diffusion current of the two anodic reduced FAD waves equaled the total diffusion current of the two cathodic waves of the original FAD.

At pH 9.25 i_d increased linearly with increasing $h^{1/2}_{corr.}$ and $i_d/h^{1/2}_{corr.}$ decreased slightly with increasing $h^{1/2}_{corr.}$ for solutions of FAD and reduced FAD. This is normally considered to be evidence of diffusion control of the electrode process.

At pH 12.3 the polarogram of FAD revealed two small waves at −1.1 and −1.4V and two small maxima at about −1.6 and −1.7V in addition to the main FAD wave (Fig. 6). With time the main FAD wave was observed to decrease in height while the wave at about −1.1V grew. The waves at −1.4 and −1.7V also became slightly more prominent (Fig. 6). Apparently the small waves observed in the original FAD polarogram in basic solution were due to FAD decomposition products. The identity of the decomposition products is presently unknown. The "anomalous" postwave observed by Ke (3) may have been due to one of these decomposition products.

Throughout the entire pH 9-13 range, cyclic voltammograms of FAD obtained at the HMDE revealed two overlapping cathodic peaks (*i.e.*, a major peak with a shoulder) and, upon scan reversal, two overlapping anodic peaks (similar to Fig. 2, curve A). In some cases the two cathodic peaks and the two anodic peaks merged to give a single cathodic-anodic peak pair at a scan rate of 0.5 V sec^{-1}. At scan rates of 0.02 and 0.04 V sec^{-1} the cyclic voltammetry traces were erratic making meaningful observations at these scan rates impossible. The overlapping of the peaks made it impossible to apply the diagnostic criteria of Nicholson and Shain to either of the cathodic peaks. Cyclic voltammograms obtained on solutions of reduced FAD showed two overlapping anodic peaks and, after scan reversal, two overlapping cathodic

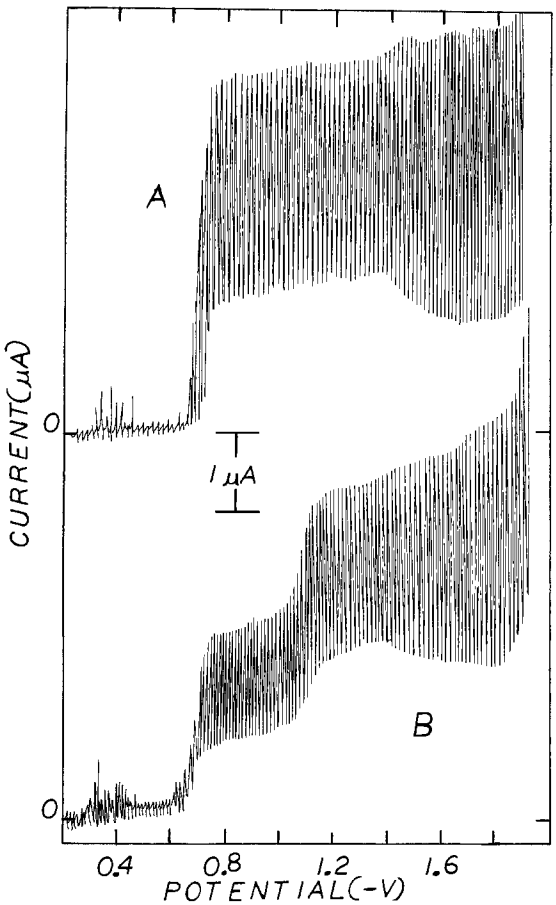


Fig. 6. Polarograms of 0.92 mmole FAD at pH 12.3. A, Immediately after solution preparation; B, 43 hr after solution preparation.

peaks. As with FAD, these peaks often merged into a single anodic-cathodic pair at a scan rate of 0.5 V sec^{-1}.

In the *p*H 10-13 range, reasoning completely analogous to that used in the acidic *p*H region leads to the conclusion that FAD is reduced in two single-electron steps first to the semiquinone and finally to $FADH_2$ (Eq. [12] and [13]). Information concerning the order in which the hydrogen ions are added is not available. In the *p*H region between 9 and 10, the two cyclic voltammetry cathodic peaks indicate two single-electron transfers, however, the single polarographic wave and the slope of the log plots indicate a single two-electron transfer. It appears likely that in the *p*H 9-10 region the actual electrochemical reaction mechanism is a combination of that given by Eq. [9], [10], and [11] and that given by Eq. [12] and [13], *i.e.*, in this *p*H region the reaction mechanism is switching from the mechanism observed at neutral *p*H to the one observed in basic solution.

Acknowledgments

The author gratefully acknowledges the assistance of Professor Philip J. Elving in providing the three-compartment water-jacketed cell and of the Society of Sigma Xi for a Grant-In-Aid-of-Research which was used to partially support this study.

Manuscript submitted Feb. 2, 1977; revised manuscript received *ca.* May 1, 1977.

Any discussion of this paper will appear in a Discussion Section to be published in the June 1978 JOURNAL. All discussions for the June 1978 Discussion Section should be submitted by Feb. 1, 1978.

Publication costs of this article were assisted by Vassar College.

REFERENCES

1. B. Janik and P. J. Elving, *Chem. Rev.*, **68**, 295 (1968).
2. A. L. Underwood and R. W. Burnett, "Electroanalytical Chemistry," A. J. Bard, Editor, p. 60, Marcel Dekker, New York (1973).
3. B. Ke, *Arch. Biochem. Biophys.*, **68**, 330 (1957).
4. Y. Asahi, *J. Pharm. Soc. Jpn.*, **76**, 378 (1956).
5. L. G. Whitby, *Biochem. J.*, **54**, 437 (1953).
6. L. Meites, "Polarographic Techniques," 2nd ed., Interscience, New York (1965): a, p. 89; b, p. 218; c, pp. 132-133; d, p. 282.
7. R. Brdicka, *Z. Elektrochem.*, **48**, 686 (1942).
8. R. S. Nicholson and I. Shain, *Anal. Chem.*, **36**, 706 (1964).
9. L. Michaelis, M. P. Schubert, and C. V. Smythe, *J. Biol. Chem.*, **116**, 587 (1936).
10. R. S. Nicholson, *Anal. Chem.*, **37**, 1351 (1965).
11. A. M. Hartley and G. S. Wilson, *ibid.*, **38**, 681 (1966).

The Rate of the Photoelectrochemical Generation of Hydrogen at p-Type Semiconductors

J. O'M. Bockris* and K. Uosaki[1]

School of Physical Sciences, Flinders University, Adelaide, Australia 5042

ABSTRACT

The current-potential relations with and without illumination, quantum efficiency-wavelength relations at several potentials, the flatband potentials, the transient behavior, and the stability of seven p-type semiconductors, *i.e.*, ZnTe, CdTe, GaAs, InP, GaP, SiC, and Si, have been measured in 1*N* NaOH and 1*N* H_2SO_4. The position of the photocurrent-potential relations are related to the flatband potential and the energy gap of the semiconductor. The existence of the maximum in quantum efficiency-wavelength relation is analyzed by considering surface recombination. The stability and the transient behavior are analyzed.

Photoelectrochemical production of hydrogen was envisaged by Fujishima and Honda in 1972 (1). To obtain hydrogen, either a *p*H gradient or an external power source in the cell was required (2-4). However, homogenization of the solution would inevitably occur on prolonged functioning in such an arrangement.

The lack of need for single crystals in the photoelectrochemical approach to energy conversion (5, 6) gives the prospect of favorable economics in purely photoelectrochemical hydrogen production from water. The primary aim is the development of a suitable cathode, so that light may be directed both onto the cathode and anode, with the objective of obtaining stable photoelectrolysis in a cell with a uniform *p*H. A previously reported photocathode is unstable (7). We report investigations concerning the stability and efficiency of certain new photocathodes.

Experimental

Apparatus.—The photoelectrochemical cell is shown in Fig. 1. Stopcocks and taps were Teflon. To avoid contact of the metal used to form an ohmic contact with the solution, the back face and side of the electrode were covered with epoxy resin. To minimize contact of this with the solution, a Teflon electrode holder was used. The absence of a leak was verified by the small magnitude of the dark current. All photoelectrode areas were 0.125 cm^2.

A PAR Model 173 potentiostat/galvanostat, with a Model 176 current-potential converter, was used to control the potential. The electrode potential was swept by a Wenking SMP 69 potential stepping motor control. The current-potential relationship was recorded by a Hewlett-Packard Model 7004B X-Y recorder. The time dependence of the photocurrent was recorded by means of a Hitachi QD25 recorder.

A 900W xenon lamp (Canrad-Hanovia 538C1) was used as a light source and a Jarrell-Ash quarter-meter grating monochrometer (Cat. no. 82-410) was employed to obtain monochromatic light. An *IR* absorbing filter (Oriel G-776-7100) was placed between the cell and the light house, when current-potential measurements were carried out without the monochrometer. However, a quartz lens (d = 5 cm, f = 5 cm) was employed to concentrate the light on the electrode surface when the photocurrent was measured under monochromatic light. In this case, two long pass filters (Oriel G-772-3900 and Oriel G-772-5400) were used with an *IR* absorbing filter to eliminate second-order diffraction. The conditions used in this respect were: 3000 ~ 5000Å, *IR* absorbing filter only; 5000 ~ 7000Å, *IR* absorbing filter + G-772-3900 filter; 7000 ~ 7500Å, *IR* absorbing filter + G-772-5400 filter; 7500Å, G-772-5400 filter only.

The intensity of light was measured by means of a Hewlett-Packard Model 8334 radiant flux meter with either a 8334A radian flux detector or a Carl Zeiss vacuum thermocouple (VT Q3/A) with a Keithley 149 millimicrovoltmeter. The error in relative intensity measurement was < 5%. However, absolute intensity measurements had an uncertainty of ± 20% error.

The electrochemical cell and the optical system were set up on an optical bench.

Impedance measurement.—The cell for impedance measurements had a working electrode surrounded by a cylindrical platinized platinum counterelectrode, apparent area 60 cm^2. Hydrogen gas was passed into the solution before and during measurement.

The direct method was employed (8, 9). The circuit contained a dry cell (6V) as a d-c source and the potential was controlled by a ten-turn variable resistor

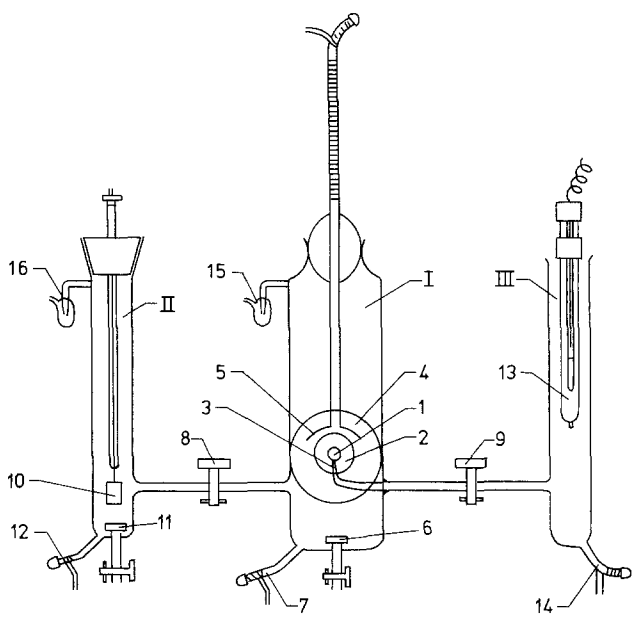


Fig. 1. The photoelectrochemical cell (front view). I, Working electrode compartment (*d* = 50 mm); II, counterelectrode compartment (*d* = 25 mm); III, reference electrode compartment (*d* = 20 mm). 1, Working (semiconductor) electrode; 2, Teflon electrode holder; 3, Luggin capillary; 4, quartz optical flat; 5, gas collector; 6, 11, frits (gas inlets); 7, 12, 14, drains; 8, 9, Teflon stopcocks; 10, Pt counterelectrode; 13, reference electrode (SCE); 15, 16, gas bubbler.

* Electrochemical Society Active Member.

[1] Present address: Mitsubishi Petrochemical Company, Limited, Ami, Ibaraki, Japan.

Key words: hydrogen production, photoelectrochemical reaction, p-type semiconductors, photocathodes.

while being monitored by means of a Keithley 616 digital electrometer. The a-c source was a Mini-Lab Model 603A (B.W.D. Electronics). A capacitor (10 μf) and a choke coil (35 H) were in the circuit. The resistor, the value of which was several hundred times larger than the cell impedance, Z_{cell}, was connected in series to the cell so that the alternating current, I, became constant, and independent of the cell voltage. The impedance of the choke was at least one hundred times larger than that of the cell.

Signals taken from two points in the circuit and applied to the X and Y inputs of a cathode ray oscilloscope (Tetronix 5103N with 5A20N and 5A2IN differential amplifiers) displayed Lissajou's figures. Since the X and Y inputs showed I ($Z_{cell} + R$) and IZ_{cell}, respectively, and $R >> Z_{cell}$, the absolute value of the cell impedance, and phase difference due to the cell, could be ascertained. Assuming a series equivalent circuit (measurements were carried out under nearly ideally polarized conditions), the cell capacitance, which is effectively the space charge capacitance of the semiconductor electrode, can be obtained.

The accuracy of the direct method is low compared with that of the bridge method (8, 9). At metal electrodes the phase difference is small, and hence determination of C is inaccurate by this method.

However, at semiconductor electrodes, capacitance is low so that the phase difference can be measured accurately.

Semiconductors chosen.—Cathodes were selected on the basis of sufficiently low values of energy gap (2.574 $E_G < 1.3$ eV) and electron affinity ($E_a < 4.0$ eV) (28).

Zinc telluride (ZnTe).—A ZnTe single crystal (Ag doped), grown by the Bridgeman method, was cut parallel to the cleaved face (100). After being etched in $K_2Cr_2O_7$-HNO_3 aqueous solution, the specimen was dipped in $HAuCl_4$ solution to make an ohmic contact (10). It was masked with paraffin, later removed in trichloroethylene. The contact was ohmic and the specific resistance was 0.2 Ω · cm. The face of the specimen was polished by means of emery paper to 600 grade. The electrode was etched in HF-HNO_3 (11) solution.

Cadmium telluride (CdTe).—A CdTe single crystal (undoped) grown by the Bridgeman method was cut parallel to the cleaved face (100). The specimen was heated in Te vapor at 500°C for 8 hr to increase nonstoichiometry. Thereafter, the crystal was etched in $K_2Cr_2O_7$-HNO_3 (12), dipped into $AgNO_3$ solution, and heated at 200°C for 30 min. Finally, a gold film was grown on the crystal by dipping it into aqueous $HAuCl_4$ (13). During the processes of etching and dipping into $AgNO_3$ and $HAuCl_4$ solutions, the crystal was covered with paraffin except for the spots where it was intended to make a contact. The specific resistance was 10^3 Ω · cm and the ohmic character of the contact good. The face to be used was polished by emery paper, 400 to 600 grade, and the surface etched in HF-HNO_3 solution.

Gallium arsenide (GaAs).—The GaAs was a single crystal in wafer form, (100) face; Zn doped; carrier density = 2×10^{19} cm^{-3}; 0.5 mm thick. It was etched (12) by dipping into CH_3OH-Br_2 (5%) solution, for 1 min before an ohmic contact was made by soldering with indium (14). The I-V relation was ohmic. The specific resistance was 0.2 Ω · cm.

Indium phosphide (InP).—The InP was a single crystal wafer (100) face, Zn doped; carrier density 5.6×10^{18} cm^{-3}; 0.8 mm thick. Treatment was as for GaAs except that the ohmic contact was by means of an In-Zn alloy (15). The specific resistance was 0.21 Ω · cm.

Gallium phosphide (GaP).—The GaP was a single crystal wafer, Zn doped; carrier density 6.7×10^{17} cm^{-3}; (111) face; 0.4 mm thick. A HNO_3-HCl mixture was used for etching (12). An ohmic contact was obtained by the use of an In-Zn alloy (7). The specific resistance was 2.0 Ω · cm.

Silicon carbide (SiC).—The silicon carbide was a single crystal; (000$\bar{1}$) face; Al doped; carrier density 4×10^{18} cm^{-3}; 0.2 mm thick. "Acme" conductive adhesive gave an ohmic contact if heated in hydrogen at 300°C for 2 hr. The specific resistance was 0.31 Ω · cm. The electrode was dipped in HF for 1 min before each experiment.

Silicon (Si).—The silicon was a single crystal wafer, (100) face; B doped; 0.2 mm thick. An In-Zn alloy was used to obtain an ohmic contact. The specific resistance was 1.2 Ω · cm. The crystal was etched in HF solution before each experiment.

Results

The current-potential relations.—The current-potential relations with and without illumination by means of a 900W Xe lamp were measured in 1*N* NaOH and in 1*N* H_2SO_4. The relations found can be divided into two groups. Results typical of the first group (ZnTe, CdTe, GaP,[2] SiC, and Si) are exemplified in Fig. 2 (ZnTe). Dark curents are low. Typical results of the second group (GaAs and InP) are in Fig. 3 (GaAs).[2] The degree of displacement of the current-potential

[2] In the measurements of Gerischer *et al.* (16), GaAs showed saturation photocurrents at −1.0V, but such saturation was not observed in our work, probably due to a lower intensity of illumination. The current-potential curves observed for GaP were similar to those reported earlier by other workers (17-19).

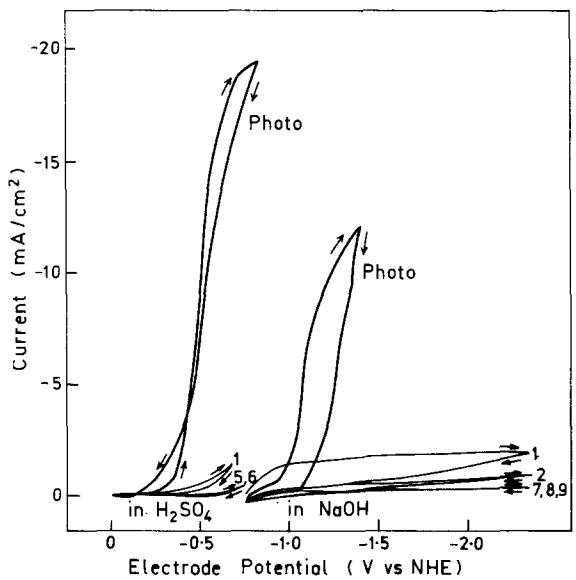


Fig. 2. The current-potential relations of ZnTe in 1*N* NaOH and 1N H_2SO_4 with and without illumination by a 900W Xe lamp. Sweep rate: 1.5 V/min. Intensity of light 0.08 W/cm². Arrows show the direction of the polarization. 1, 1st sweep in dark; 2, 2nd sweep in dark. 5, 6, 7, 8, 9, 5th, 6th, 7th, 8th, and 9th sweeps in dark.

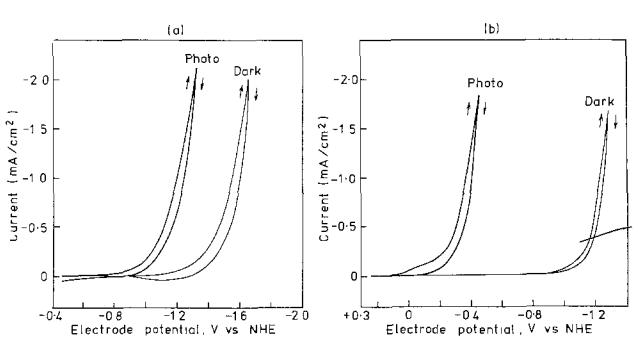


Fig. 3. The current-potential relations of GaAs with and without illumination by a 900 Xe lamp in 1*N* NaOH (a) and 1*N* H_2SO_4 (b). Sweep rate: 1.5 V/min. Intensity of light: 0.08 W/cm².

curves in H_2SO_4 and NaOH respectively is shown in Table I.

At CdTe in NaOH no photocurrent was observed at a potential more positive than −0.75V, when the oxygen concentration in the solution had been sufficiently diminished.

A white film was observed on the InP electrode after measurements in 1*N* H_2SO_4. Mayumi *et al.* (20) observed such white films: Irreproducibility due to them may account for the fact that the critical potential observed by Mayumi was 0.5V more negative than that reported here. No films were observed in 1*N* NaOH.

Photocurrents at SiC electrodes were < 10 μA cm^{-2}.

Quantum efficiency-wavelength relations at several potentials.—Photocurrents were measured under monochromatic light at several potentials. Quantum efficiencies were calculated by using measured values of the photocurrents and the light intensity. Typical results are shown in Fig. 4 (GaP).[3] The spectral response of the quantum efficiency in 1*N* NaOH of the semiconductors examined in this work except for GaP and SiC are shown in Fig. 5. Those in 1*N* H_2SO_4 are as in 1*N* NaOH. Quantum efficiencies at SiC in 1*N* NaOH (Fig. 6) are low.

The flatband potential.—The flatband potentials were determined by using Mott-Schottky plots. A typical plot is shown in Fig. 7 (SiC). Table II shows the flatband potential of the semiconductors in 1*N* NaOH and 1*N* H_2SO_4 and the slopes of the corresponding Mott-Schottky plot. The flatband potentials of InP in 1*N* H_2SO_4 and Si in 1*N* NaOH and 1*N* H_2SO_4 could not be measured due to the instability of these materials in solution.

Gleria and Memming reported (22) difficulties in respect to the Mott-Schottky plot on SiC but none were noted here.

Transient measurement.—Current-time relations at fixed potentials following illumination and interruption of light were measured in 1*N* NaOH and 1*N* H_2SO_4. Typical results are in Fig. 8. When the potential is relatively negative, the current becomes stable just after the light was on or off, but when the electrode potential became relatively positive, it took time to attain a steady state (Fig. 8d).

Stability.—The photocurrents at fixed potentials were measured as a function of time (1-20 hr) at all semiconductors mentioned above in 1*N* NaOH and 1*N* H_2SO_4. Results are listed in Table III in terms of $(1/i)$ (di/dt), which is a measure of the instability.

Discussion

By analogy to well-known behavior at the metal-vacuum interface, the electrode potential corresponding to the commencement of electron emission ("the critical potential") would have been expected to vary with change of the frequency of the exciting source. That the critical potential is not thus dependent for the semiconductor-solution interface is demonstrated in Fig. 9 (ZnTe). An interpretation is that electron-phonon collisions in the semiconductor cause the electrons photogenerated within the semiconductors at various energies (depending on the wavelength of the incident light) to fall to the bottom of the conduction band before they have reached the electrode surface.

The i_{photo}-V relations are Tafel-like (Table IV), whereas, at metals, $i^{0.4}$ is linear with V. Thus, in metals, nearly all the photoactivated electrons decay before the surface is reached. The small fraction ($< 10^{-2}$%) of photoactivated electrons which reach the surface and emit have an energy distribution which is a function of the energy of the exciting source. In the semiconductor, a greater fraction ($\sim$ 1%) of the photogenerated electrons reaches the surface but the energy of nearly all of them is that of the conduction band, Fig. 10. (See above). The variation of the electrochemical photocurrent with potential then becomes subject to the reasoning [*e.g.*, Ref. (23)] which relates the thermal current to potential at metals.

The saturation part of the photocurrent-potential relation can be understood from Fig. 11. When the electrode potential is such that the energy of the emitting electrons is equal to that of the ground state of the acceptor levels in H_3O^+, no further increase in the availability of acceptor levels in solution occurs as the potential is made more negative (24).

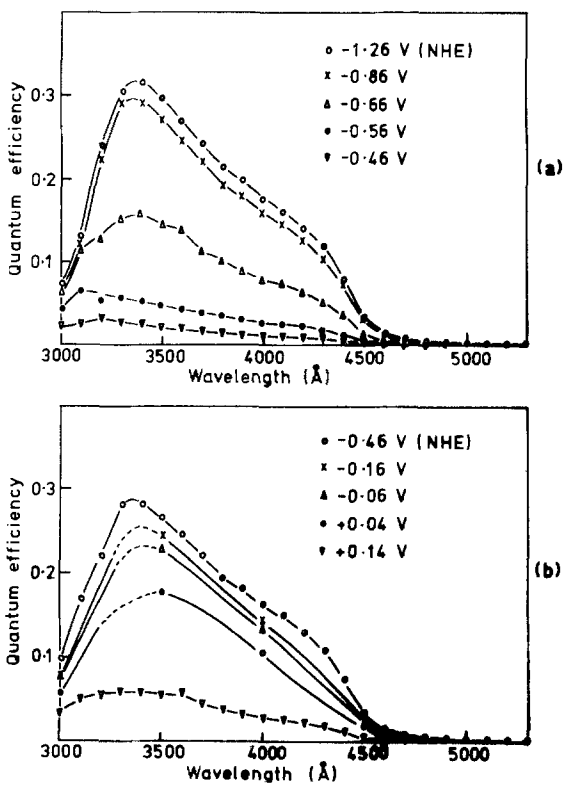


Fig. 4. The quantum efficiency-wavelength relations of GaP in 1*N* NaOH (a) and 1*N* H_2SO_4 (b) at several electrode potentials.

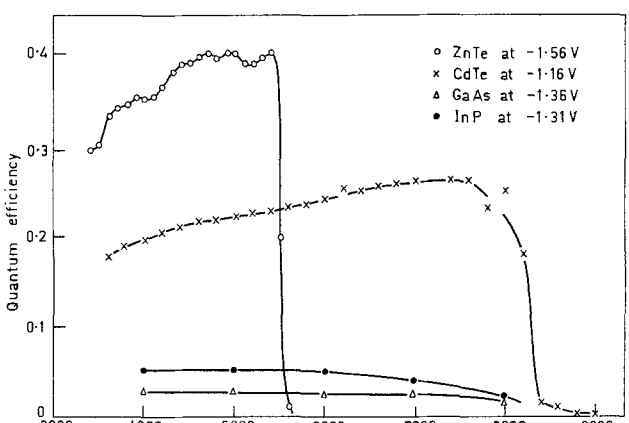


Fig. 5. The quantum efficiency wavelength relations for ZnTe, CdTe, GaAs, and InP in 1*N* NaOH.

[3] Reasonable agreement was observed with the results of Yoneyama *et al.* (21), but the maximum in the quantum efficiency-wavelength relation was at 4500Å in their measurement and at 3500Å in ours. In the Yoneyama work, published data on xenon lamps (instead of calibration) was used.

Table I. The difference in the range of potentials (volts) for photocurrent-voltage relations in NaOH and H_2SO_4

ZnTe	0.6
CdTe	0.5
GaAs	0.8
InP	0.5
GaP	0.6
SiC	Not applicable
Si	0.5

The "critical potential".—$\Delta H'(e)$ (Fig. 12) at the flatband potential is given by (23)

$$\Delta H'(e) = -L_o + E_a - J + A + R + ({}^{S.C}\Delta^{S}\phi)_{fbp} \quad [1]$$

where L_o, E_a, J, A, R, and $({}^{S.C}\Delta^{S}\phi)_{fbp}$ are the hydration energy of the proton, electron-affinity of the semiconductor, ionization energy of hydrogen, adsorption energy of hydrogen, H-H_2O repulsive force, and the potential drop in the electric double layer at the flatband potential.

$({}^{S.C}\Delta^{S}\phi)_{fbp}$ can be estimated as follows.

The flatband potential, V_{fbp}, with respect to normal hydrogen electrode (NHE) is given by

$$V_{fbp} = {}^{Pt}\Delta^{S.C}\phi + ({}^{S.C}\Delta^{S}\phi)_{fbp} + ({}^{S}\Delta^{Pt}\phi)_{\substack{p_{H_2}=1 \\ C_{H^+}=1}} \quad [2]$$

where ${}^{Pt}\Delta^{S.C}\phi$ is the potential difference between the semiconductor and the Pt wire, $({}^{S}\Delta^{Pt}\phi)_{\substack{p_{H_2}=1 \\ C_{H^+}=1}}$ is the potential drop in the electric double layer of the semiconductor at the flatband potential and $({}^{S}\Delta^{Pt}\phi)_{\substack{p_{H_2}=1 \\ C_{H^+}=1}}$ is the potential drop in the electric double layer at the Pt electrode in the presence of 1 atm of hydrogen gas and with $C_{H^+} = 1$. (See Fig. 12).

Since

$$\mu_e{}^{-Pt} = \mu_e{}^{-S.C} \quad [3]$$

where $\mu_e{}^{-Pt}$ and $\mu_e{}^{-S.C}$ are the electrochemical potentials of electrons in Pt and the semiconductor, respectively. Hence

$${}^{Pt}\Delta^{S.C}\phi = (\mu_e{}^{Pt} - \mu_e{}^{S.C})/F \quad [4]$$

where $\mu_e{}^{Pt}$ and $\mu_e{}^{S.C}$ are the chemical potentials of Pt and the semiconductor, respectively. Therefore

$$V_{fbp} = \{({}^{S.C}\Delta^{S}\phi)_{fbp} - \mu_e{}^{S.C}/F\} - [({}^{Pt}\Delta^{S}\phi)_{\substack{p_{H_2}=1 \\ C_{H^+}=1}} - \mu_e{}^{Pt}/F] \quad [5]$$

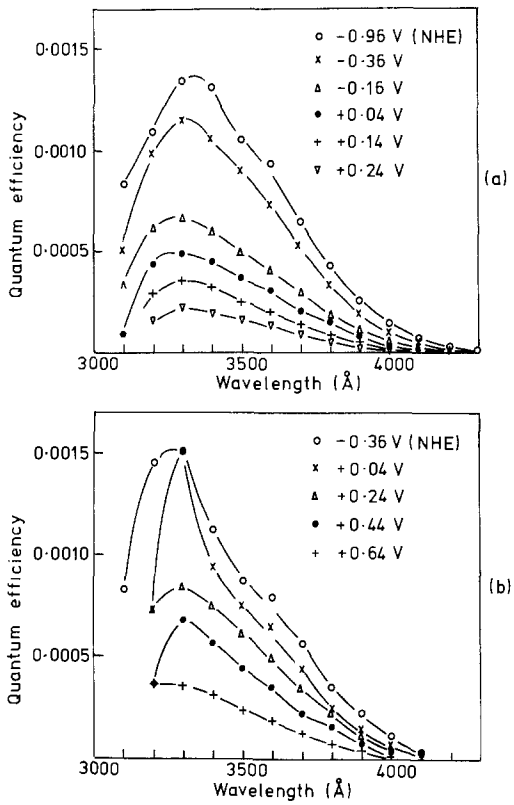


Fig. 6. The quantum efficiency-wavelength relations of SiC in 1*N* NaOH (a) and 1*N* H_2SO_4 (b).

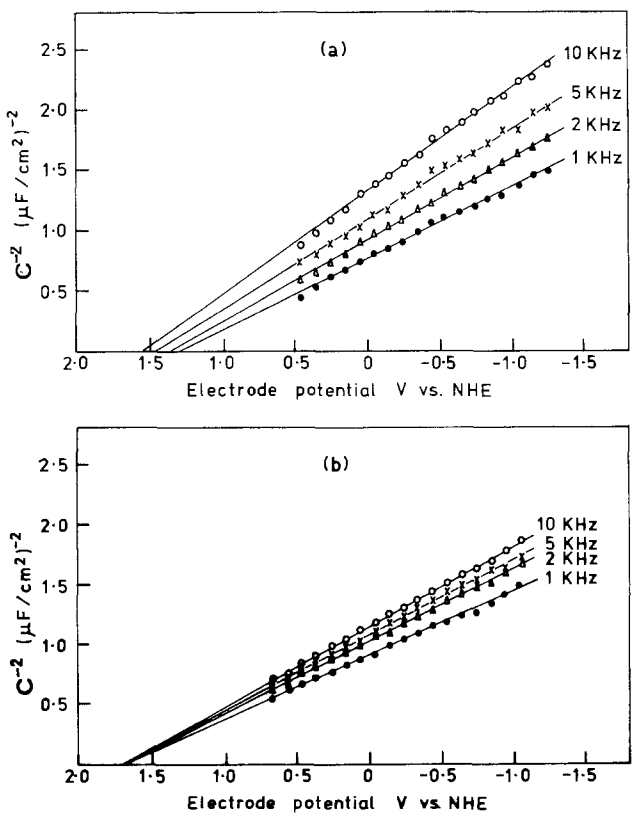


Fig. 7. The Mott-Schottky plots of SiC in 1*N* NaOH (a) and 1*N* H_2SO_4 (b) at several frequencies.

Table II. The flatband potential and slope of Mott-Schottky plots of semiconductors

Semiconductors	1*N* NaOH Flatband potential, V, NHE	1*N* NaOH Slope ($\mu f/cm^2)^{-2}$/V	1*N* H_2SO_4 Flatband potential, V, NHE	1*N* H_2SO_4 Slope ($\mu f/cm^2)^{-2}$/V
ZnTe	−0.79	28	0.04	150
CdTe	0.21	6000	−0.35	2200
GaAs	−0.04	0.12	0.43	0.22
InP	−0.07	0.48	—	—
GaP	0.18	6.0	1.13	4.6
SiC	1.38	0.86	1.68	0.7

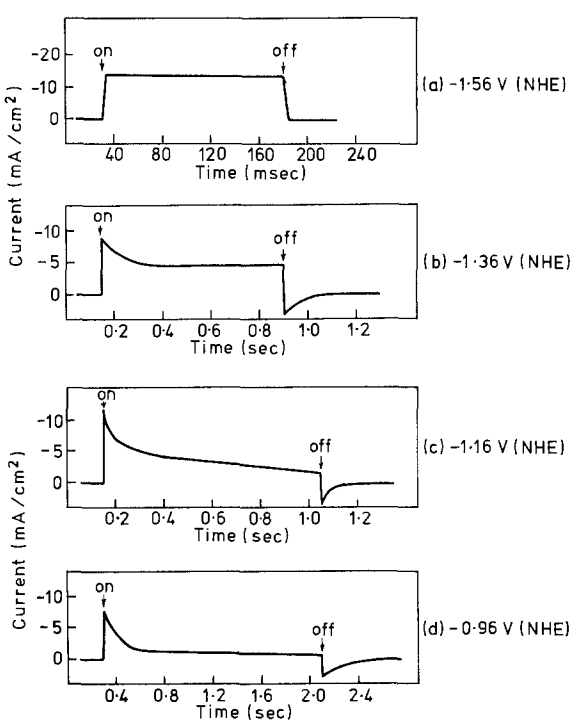


Fig. 8. The transient behavior of the current of ZnTe after illumination and interruption of light in 1*N* NaOH at several potentials. The current before illumination is taken as zero. Intensity of light: 0.08 W/cm².

Table III. The stability of photocathodes, as measured by their change with time at various potentials (given)

Semiconductor	Value of $\frac{1}{i}\frac{di}{dt}$ (sec^{-1}) 1N NaOH	1N H_2SO_4
ZnTe	6×10^{-4} (−1.26V)	5×10^{-5} (−0.56V)
CdTe	2.5×10^{-6} (−1.16V)	1×10^{-6} (−0.76V)
GaAs	2×10^{-4} (−1.36V)	3×10^{-4} (−0.76V)
InP	2×10^{-5} (−1.36V)	2×10^{-4} (−0.46V)
GaP	5×10^{-5} (−0.76V)	5×10^{-5} (−0.26V)
SiC	0* (−1.16V)	0* (−0.76V)
Si	5×10^{-6}** (−1.06V)	1.7×10^{-4}** (−0.41V)

* Current is very small 9 μA/cm² in 1N NaOH and 3 μA/cm² in 1N H_2SO_4.
** After 10 hr in dark, almost no photocurrent was observed.

Thus, the potential drop in the electric double layer of the semiconductor at the flatband potential is given by

$$({}^{S.C}\Delta^{S}\phi)_{fbp} = V_{fbp} + [\,({}^{Pt}\Delta^{S}\phi)_{\substack{p_{H_2}=1 \\ C_{H^+}=1}} - \mu_e{}^{Pt}/F] + \mu_e{}^{S.C}/F$$
$$= V_{fbp} + [\,({}^{Pt}\Delta^{S}\phi)_{\substack{p_{H_2}=1 \\ C_{H^+}=1}} - \mu_e{}^{Pt}/F] - (\Phi/F - \chi^{S.C}) \quad [6]$$

where Φ is the work function of the semiconductor and $\chi^{S.C}$ is potential drop in the semiconductor.

$$[({}^{Pt}\Delta^{S}\phi)_{\substack{p_{H_2}=1 \\ C_{H^+}=1}} - \mu_e{}^{Pt}/F]$$

was calculated by Trasatti (25) using a method suggested by Bockris and Argade (26), as 4.3V. Therefore

$$({}^{S.C}\Delta^{S}\phi)_{fbp} = 4.3/F + V_{fbp} - (\Phi/F - \chi^{S.C}) \quad [7]$$

A schematic of the energy levels of a semiconductor which has surface states in a vacuum is shown in Fig. 13. From this figure, $\chi^{S.C}$ is given by

$$F\chi^{S.C} = \Phi + \Delta E - E_a - E_g \quad [8]$$

where ΔE is the energy difference between the Fermi level and the top of the valence band in the bulk. Hence, Eq. [7] becomes

$$({}^{S.C}\Delta^{S}\phi)_{fbp} = 4.3/F + V_{fbp} - (E_a + E_g - \Delta E)/F \quad [9]$$

As a first approximation, ΔE is assumed to be zero for all p-type semiconductors concerned.

The values of $({}^{S.C}\Delta^{S}\phi)_{fbp}$ were calculated from Eq. [9] for semiconductors listed in Table V. $({}^{S.C}\Delta^{S}\phi)_{fbp}$ is negative in all cases, ${}^{S.C}\Delta^{S}\phi$ in NaOH is more negative than that in H_2SO_4 for most electrodes except CdTe.

From Eq. [1] and [9]

$$\Delta H(e) = -L_o + E_a - J + A + R + 4.3/F + V_{fbp} - (E_a + E_g - \Delta E)/F$$
$$\simeq -L_o - J + A + R + 4.3/F + V_{fbp} - E_g/F + \Delta E/F \quad [10]$$

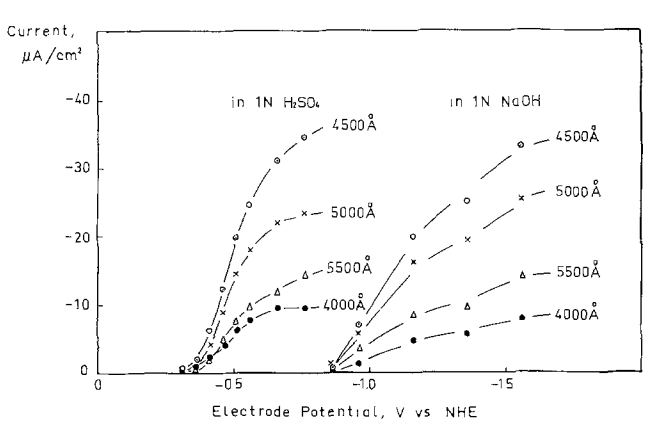


Fig. 9. The photocurrent-potential relations of ZnTe in 1N NaOH and in 1N H_2SO_4 for light of several wavelengths.

Table IV. Slope of log i_p-V relations

	1N NaOH	1N H_2SO_4
ZnTe	0.165	0.13
GaAs	0.3	0.25
GaP	0.1	0.18
CdTt	Not available because of high resistance	
Si	0.17	0.21

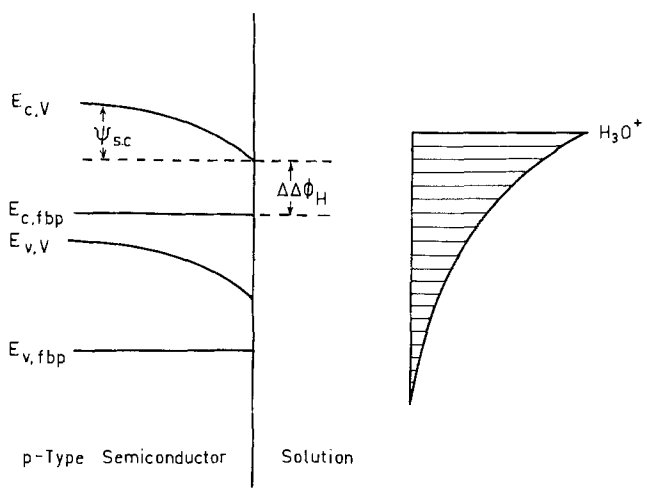
where L_o, J, and R do not depend on semiconductor and the dependence of A on the semiconductor is less than 0.1 eV (27), Therefore, $\Delta H(e)$ is given by

$$\Delta H(e) \simeq \text{const.} + V_{fbp} - E_g/F \quad [11]$$

The probability of the existence of acceptors at energy E, $G(E)$, is given by

$$G(E) = \exp(H(e) - E_v)/kT \quad [12]$$

where E is the energy of the electrons at the surface at a potential V.



$$\begin{cases} V - V_{fbp} = \psi_{s.c} + \Delta\Delta\phi_H \\ \Delta\Delta\phi_H = ({}^{S.C}\Delta^{S}\phi)_V - ({}^{S.C}\Delta^{S}\phi)_{fbp} \end{cases}$$

Fig. 10. The schematic diagram of energy levels of the valence band and conduction band of a semiconductor and of an acceptor.

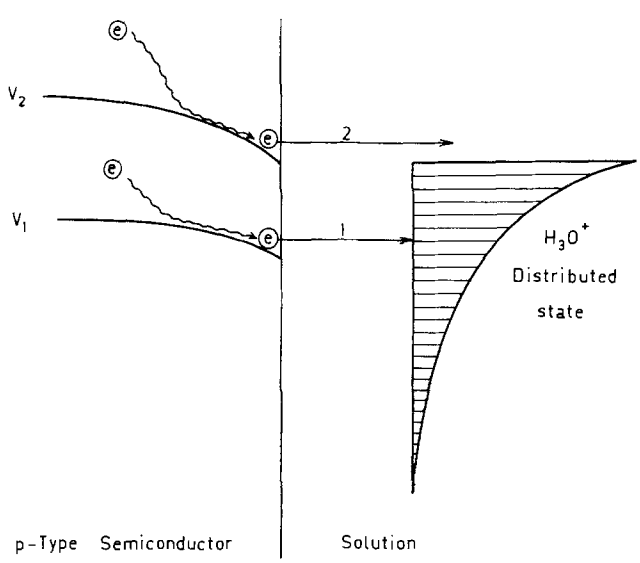


Fig. 11. Schematic illustration of the model proposed to describe the observed photocurrent behavior of semiconductor electrodes.

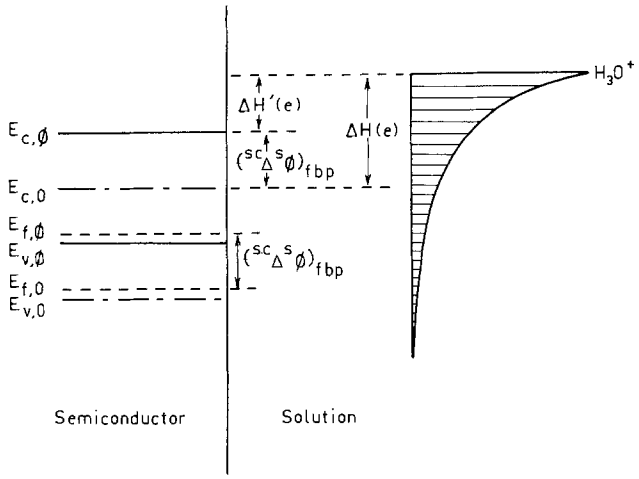


Fig. 12. The energy levels at a semiconductor solution interface

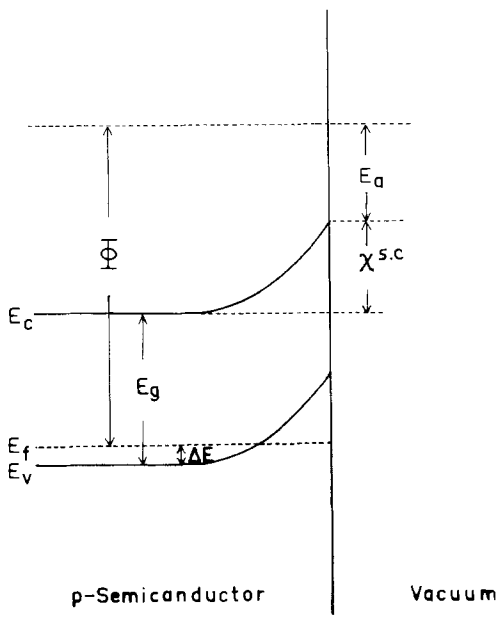


Fig. 13. Schematic diagram of the energy levels of a semiconductor with surface states in a vacuum.

E_v is given by

$$E_v = -F(V - V_{fbp}) \qquad [13]$$

where each of these potentials is on (*e.g.*) the N.H. scale. Therefore, E_v at the critical potential E_{crit} is given by

$$E_{crit} = -F(V_{crit} - V_{fbp})$$

At the critical potential, it can be assumed that $G(E)$ corresponds to an energy value of 0.1-0.2 eV from the ground state of H_3O^+.

Therefore

$$\Delta H(e) \simeq -F(V_{crit} - V_{fbp}) \qquad [14]$$

From Eq. [12] and [14], a linear relation between $(V_{fbp} - E_g/F)$ and $(V_{crit} - V_{fbp})$ is expected. Figure 14 shows this relation. The relation shows the importance of any energy gap in respect to the critical potential. Although a small energy gap is required from the point of solar energy absorption, the smaller the energy gap, the more negative the critical potential (with respect to the flatband potential) and, therefore, the smaller the efficiency of the hydrogen production.

Table V. Calculated values of the potential drop (volts) in the electric double layer at the flatband potential (see Eq. [10])

Semiconductor	1*N* NaOH $^{s.c}\Delta^{s}\phi$, V	1*N* H_2SO_4 $^{s.c}\Delta^{s}\phi$, V
ZnTe	−2.25	−1.42
CdTe	−1.27	−1.83
GaAs	−1.20	−0.77
InP	−1.42	—
GaP	−2.07	−1.12

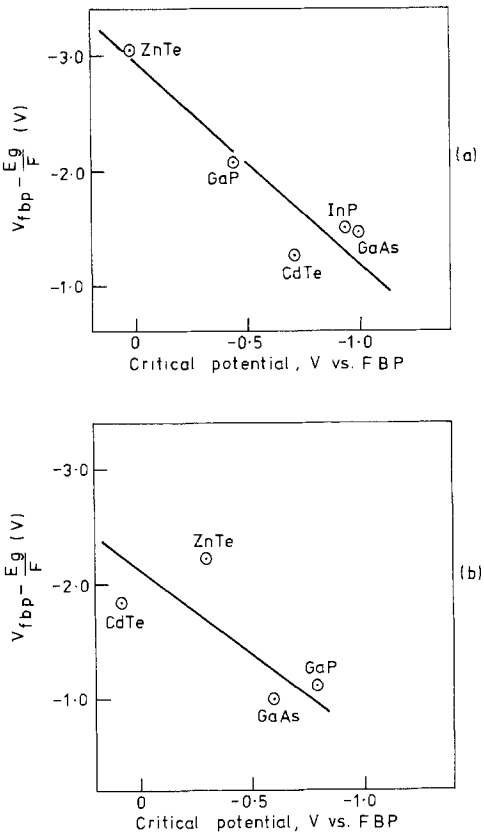


Fig. 14. The relations between $V_{fbp} - E_g/F$, and the critical potential with respect to the flatband potential in 1*N* NaOH (a) and 1*N* H_2SO_4 (b).

The quantum efficiency-wavelength relation.—Quantum efficiency-wavelength relation shown in Fig. 4-6 exhibit two features. (*i*) The quantum efficiency wavelength relation passes through a maximum. (*ii*) The height of the maximum decreases as the potential becomes more positive and therefore nearer to the flatband potential.

The position of the maximum can be interpreted by considering the photocurrent (i_p) as a function of the surface recombination.

Thus, i_p is given by

$$i_p = f(i_{\text{electron arriving at surface}}) - f(v_{\text{surface recombination}}) \qquad [15]$$

As the wavelength decreases, the photon absorption increases and the number of electrons created per average photon increases and therefore the quantum efficiency. At sufficiently small wavelengths, the position of the average absorption of photons gets nearer to the surface. Hence, the effect of surface recombination will become more important and decrease the net current or quantum efficiency.

Stability.—The most outstanding differences in stability (Table III) are for ZnTe and CdTe.

Figures 15 and 16 (drawn for us by Dr. T. Ohashi) show the equilibrium potentials for several reactions relevant to ZnTe and CdTe. For CdTe, the equilibrium potential of hydrogen evolution at pH = 14 is more negative than that of the decomposition of CdTe. Hence, CdTe will not decompose in the potential range of hydrogen evolution. For ZnTe, the equilibrium potential of hydrogen evolution is close to that of ZnTe decomposition.

Transient behavior.—Surface recombination.—The transient behavior may be due to either a process in the semiconductor or a process in the surface of the electrode, or a process in solution.

In the former case, the behavior would be due to time dependence of the electron concentration at the surface. The time constant is 10^{-3} sec and could arise from the recombination process. Then, the number of excess electrons t sec after illumination, $N(t)$, is

$$N(t) = N(1 - e^{-t/\tau}) \quad [16]$$

where N represents excess electrons at the steady state and τ is the lifetime of the excited electron. The number of electrons t sec after illumination is turned off, $N'(t)$, is

$$N'(t) = Ne^{-t/\tau} \quad [17]$$

The time constant of diffusion is less than that of recombination process, so that

$$N_o(t) = N_o(1 - e^{t/\tau}) \quad [18]$$

when the light is on and

$$N'_o(t) = N_o e^{-t/\tau} \quad [19]$$

when the light is off, where N_o is the steady-state concentration of excess electrons at the surface.

Since the photocurrent, $i_p(t)$ is

$$i_p(t) \alpha N_o(t) \quad [20]$$

the time dependence of the photocurrent is

$$i_p(t) = i_{st.}(1 - e^{-t/\tau}) \quad [21]$$

with illumination on, where $i_{st.}$ is the steady-state photocurrent. Also

$$i_p(t) = i_{st.}e^{-t/\tau} \quad [22]$$

when the light is off.

The photocurrent according to Eq. [21] and [22] is shown in Fig. 17. The result of the behavior found in the present work was quite different from these predictions, especially when the electrode potential was near to the flatband potential (Fig. 17).

Hence, since the lifetime of excited electrons is $<10^{-3}$ sec, the transient behavior observed is due to surface electrochemical processes, such as the reduction of oxygen. Thus

$$i_p = i_{p,H_2} + i_{p,red} = k_{H_2}C_{H_3O^+} + k_{red}C_{red} \quad [23]$$

where k_{H_2} and k_{red} are the rate constant for hydrogen evolution reaction and for some other reduction reaction, respectively.

Using Faraday's laws

$$i_p(t) = i_{p,H_2}C_{H_3O^+} + k_{red}C_{o,red} \exp\left(-\frac{M}{\mathbf{F}}k_{red}t\right) \quad [24]$$

where $C_{o,red}$ is the concentration of the species to be reduced at time zero.

From Eq. [24], $\log \dfrac{i(t) - i(\infty)}{i(o)}$ should be proportional to time, as shown in Fig. 18 [see also Ref. (28)].

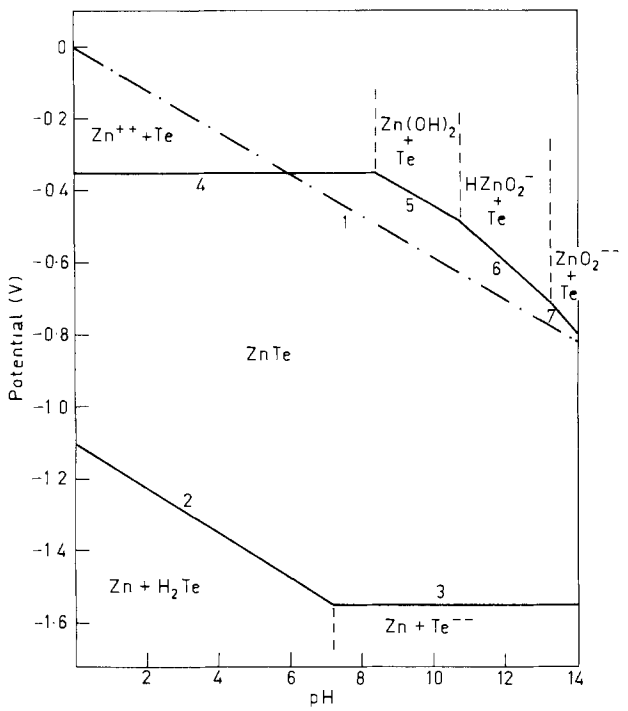


Fig. 15. Potential-pH equilibrium diagram for the system ZnTe-water at 25°C.

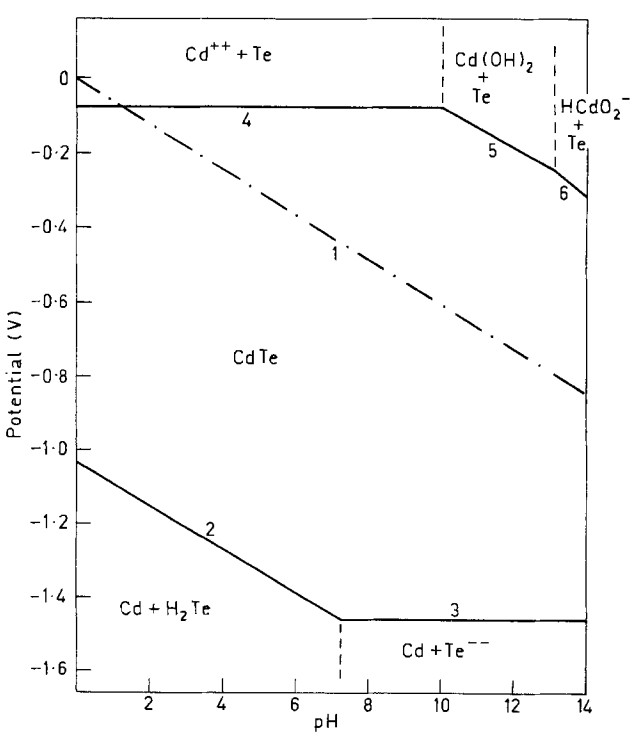


Fig. 16. Potential-pH equilibrium diagram for the system CdTe-water at 25°C.

Acknowledgments

We thang Mr. H. Kimura of Mitsubishi Electric Company Limited, Dr. O. Mizuno of Nippon Electric Company Limited, Dr. K. Akita of Fujitsu Laboratory

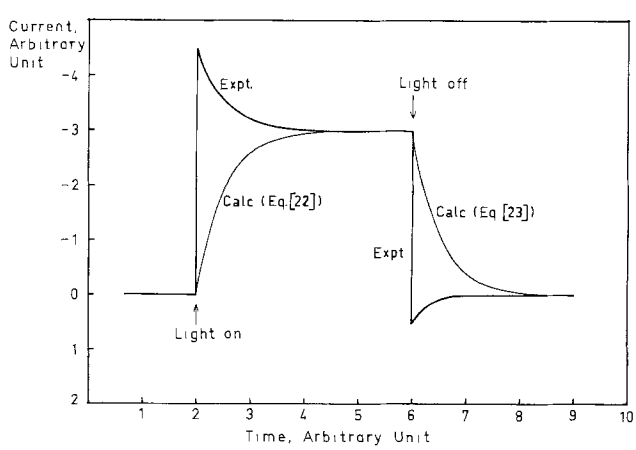


Fig. 17. Schematic diagram of the transient behavior of the current after illumination and interruption of light. 1, Equations [21] and [22]; 2, experimental.

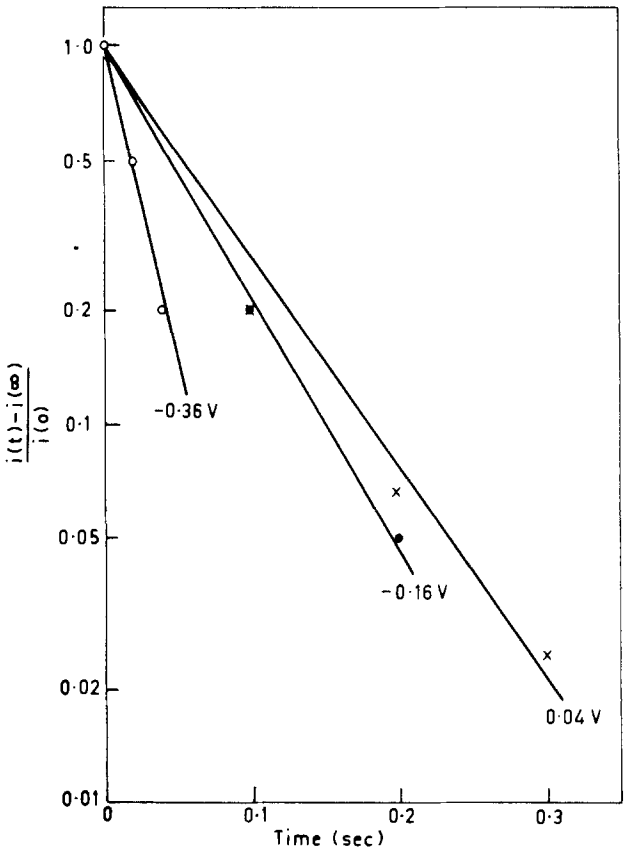


Fig. 18. The relation between $\frac{i(t) - i(\infty)}{i(0)}$ and time for GaP in 1N H_2SO_4.

Limited, Professor von Munch of Technical University of Hannover, and Toyo Silicon Company Limited for their donation of semiconductor single crystals. Thanks are due to Dr. K. Ohashi for discussion. One of us (K.U.) thanks Flinders University for its Flinders University Research Scholarship.

Manuscript submitted Dec. 13, 1976; revised manuscript received April 1, 1977.

Any discussion of this paper will appear in a Discussion Section to be published in the June 1978 JOURNAL. All discussions for the June 1978 Discussion Section should be submitted by Feb. 1, 1978.

Publication costs of this article were assisted by Flinders University of South Australia.

REFERENCES

1. A. Fujishima and K. Honda, *Nature (London)*, **238**, 37 (1972).
2. W. Gissler, P. L. Lensi, and S. Pizzini, *J. Appl. Electrochem.*, **6**, 9 (1976).
3. A. J. Nozik, *Nature (London)*, **257**, 383 (1975).
4. M. S. Wrighton, D. S. Ginsley, P. T. Wolczauski, A. B. Ellis, D. L. Morse, and A. Lind, *Proc. Natl. Acad. Sci., U.S.A.*, **72**, 1518 (1975).
5. K. L. Hardee and A. J. Bard, *This Journal*, **122**, 75 (1975).
6. A. Fujishima, K. Kohayakawa, and K. Honda, *ibid.*, **122**, 1487 (1975).
7. H. Yoneyama, H. Sakamoto, and H. Tamura, *Electrochim. Acta*, **20**, 341 (1975).
8. H. Gerischer, *Z. Elektrochem.*, **59**, 9 (1954).
9. M. Sluyters-Rehbach and J. H. Sluyters, "Electroanalytical Chemistry: A Series of Advance," Vol. 4, A. J. Bond, Editor, chap. 1, Marcel Dekker, Inc., New York (1970).
10. W. D. Baker and A. G. Milnes, *This Journal*, **119**, 1269 (1972).
11. V. I. Sapritskii and N. G. Bardina, *Elektrokhimiya*, **18**, 655 (1972).
12. H. C. Gatos and M. C. Lavine, *Prog. Semiconductors*, **9**, 1 (1965).
13. M. Aven and W. Garwacki, *This Journal*, **114**, 1063 (1967).
14. J. Lowen and R. H. Rediker, *ibid.*, **107**, 26 (1960).
15. O. Mizuno, Private communication.
16. H. Gerischer and I. Mattes, *Z. Phys. Chem. (N.F.)*, **49**, 112 (1966).
17. K. H. Beckmann and R. Memming, *This Journal*, **116**, 368 (1969).
18. R. Memming and G. Schwandt, *Electrochim. Acta*, **13**, 1299 (1968).
19. R. Memming, *This Journal*, **116**, 785 (1969).
20. S. Mayumi, C. Iwakura, H. Yoneyama, and H. Tamura, *Denki Kagaku*, **44**, 339 (1976).
21. H. Yoneyama, H. Sakamoto, and H. Tamura, *Electrochim. Acta*, **20**, 341 (1975).
22. M. Gleria and R. Memming, *J. Electroanal. Chem.*, **65**, 163 (1975).
23. J. O'M. Bockris and A. K. N. Reddy, "Modern Electrochemistry," Vol. 2, chap. VII, Plenum Press, New York (1970).
24. A. R. Despic and J. O'M. Bockris, *J. Chem. Phys.*, **32**, 389 (1960).
25. S. Trasatti, *J. Electroanal. Chem.*, **52**, 313 (1974).
26. J. O'M. Bockris and S. O. Argade, *J. Chem. Phys.*, **49**, 5133 (1968).
27. J. O'M. Bockris and K. Uosaki, *Adv. Chem. Ser.*, Am. Chem. Soc., In press (1976).
28. K. Uosaki, Ph.D. Thesis, The Flinders University of South Australia (1976).

Chemical Action of Glow Discharge Electrolysis on Ethanol in Aqueous Solution

M. A. Almubarak and A. Wood

Chemistry Department, Liverpool Polytechnic, Liverpool L3 3AF, United Kingdom

ABSTRACT

The action of anodic glow discharge electrolysis (gde) on ethanol in neutral aqueous phosphate buffer gave acetaldehyde, butan-2,3-diol, hydrogen peroxide, and acid. The yields of these products were found to vary substantially with the presence or absence of oxygen and in particular with oxygen flow rate and substrate concentration. A mechanism has been proposed for the reaction of substrate in both the presence and absence of oxygen.

Ethanol vapor and water vapor, over aqueous ethanol solutions, were subjected to glow discharge electrolysis (gde) by Klemenc (1), who examined the gaseous products only. Gde has been performed also on pure methanol (2), with a variety of supporting electrolytes; products were a complex mixture of simple breakdown species. Scholes and co-workers (3) studied the effects of x-rays (200 kV) on ethanol in aqueous solution and found that in the presence of oxygen the products were hydrogen peroxide and acetaldehyde alone. Using deaerated solutions they found acetaldehyde and butan-2, 3-diol, with traces of hydrogen peroxide (under acid conditions). Seddon and Allen (4) studied the hydrogen yields arising from the γ-radiolysis of neutral aqueous solutions of ethanol both in the presence and in the absence of oxygen. Recently Schultze and Schulte-Frohlinde (5) studied the effects of the γ-irradiation of dilute aqueous ethanol under a gaseous mixture of oxygen and nitrous oxide. The products were acetaldehyde, acetic acid, glycolaldehyde, ethylene glycol, and hydrogen peroxide.

A careful study was made of the total yields in the present work to determine the ultimate fates of all the radicals generated by gde: As will be seen, we have accounted for G(OH) in terms of our products. We also studied carefully the proportion of acetaldehyde and hydrogen peroxide since this gives valuable evidence about the reaction possibilities, and we were able to show that in gde under oxygen flow rates high enough to scavenge all the 1-hydroxyethyl radicals (CH_3CHOH) and at ethanol concentrations high enough to scavenge all the hydroxyl radicals, there is a particularly straightforward interaction between the 1-hydroxyethylperoxyl radicals ($CH_3\underset{\displaystyle O_2}{\underset{|}{C}}HOH$) yielding acetaldehyde and hydrogen peroxide in 2:1 proportions.

Experimental

The ethanol solutions were prepared by dissolving the correct amounts of pure absolute ethanol in neutral phosphate buffer solution, except for runs on acid determination under oxygen where very dilute alkali was used. The solutions after gde were analyzed for hydrogen peroxide (6), acetaldehyde (7), butan-2, 3-diol, and acid since these compounds were the products of x-irradiation of phosphate buffer/ethanol solutions (3). Other species sought by the workers who used x-irradiation were acetic acid, ethylene glycol, glycolaldehyde, ethyl hydroperoxide, diethyl peroxide, peracetic acid, and ethyl acetate, but no evidence was found for any of these. The acetaldehyde determination is essentially colorimetric: the absorbance, which declined rapidly, was recorded as a function of time and extrapolated backward to the point of preparation of the final solution. Butanediol was determined by reaction with potassium periodate at about pH 9 (bicarbonate); the unreacted periodate was determined, as I_3^-, by addition of excess potassium iodide.

The acid produced in gde was measured in separate experiments using very dilute alkali to carry the current and also to measure the acid formed as a fall in the pH of the solution during the gde.

The equipment required for rectification and control at the high currents and high voltages required was constructed specially and has been described elsewhere (8). The gde cell and vacuum line were of conventional design (9). The quantity of electricity was obtained by using a sampling digital voltmeter together with the electric clock. Typical run conditions used a current of 30 mA, a vacuum main pressure of 10 cm Hg, a stirring rate of "9" (ideally about 1500 rpm), and an oxygen flow rate of 900 $cm^3\ min^{-1}$. Run times varied from 30 to 300 sec, typically, the quantities of electricity passed being of the order of 10-100 μf. Substrate solutions were degassed with argon or saturated with oxygen, as required. When using argon it was usual to close the system so as to have no gas flow, since the argon flow did not affect the processes (argon not being involved chemically) except at very high flow rates where some arc instability occurred. Manostat gas flow regulation (9) was not always satisfactory and in later runs manual control was used.

Results

Gde on ethanol in neutral aqueous solution produces acetaldehyde, hydrogen peroxide, butan-2, 3-diol, and acid. The yields (in moles per faraday) of these products were found to vary substantially with the presence or absence of oxygen and with its flow rate and with ethanol concentration. Other factors which would affect the yields of the above products are the stirring rate, the gas pressure, the current, and the quantity of electricity.

The original work on the oxygen flow rate effect was reported by Almubarak (10). It was found from preliminary results here that the hydrogen peroxide yield increased with increasing oxygen flow rate. Hence oxygen is involved in the reaction and in the formation of hydrogen peroxide, and the hydrogen peroxide yield was used, therefore, as a convenient measure of the degree of mass transfer of oxygen from gas phase to liquid phase and as an indication of solution-oxygen content. (It was later shown that the hydrogen peroxide comes from two sources: ethanol, involving reactions, and preliminary processes, the first of these being the major source at sufficiently high ethanol concentrations.) This measure of oxygen availability in the solution was confirmed by measurements of

Key words: glow discharge electrolysis, ethanol, mechanism.

the butanediol yield which decreased to zero at very high oxygen flow rates (indicating total scavenging by oxygen of reaction intermediate CH_3CHOH).

Flow rate experiments were repeated, using argon, but no change in hydrogen peroxide yield was observed except at high flow rate values where some discharge instability may be expected.

Increasing the current at a given oxygen flow rate caused the hydrogen peroxide yield to fall (suggesting that the oxygen flow rate was not sufficient to scavenge all the 1-hydroxyethyl radicals): However, the yield could be restored to its original value by increasing the oxygen flow rate. In gde, increases in the discharge current cause increases in the glow spot area; the current density and the radical concentration tend to remain constant. Hence an increase in current at constant hydrogen peroxide yield increases the demand for oxygen. There was a limit, however, to the extent to which the hydrogen peroxide yield could be maintained at its high value by increases in oxygen flow rate; this limit arose from the instability of the discharge at very high gas flow rates. In practice, therefore, a low current (30 mA) was used, together with an oxygen flow rate which was high enough to scavenge most of the 1-hydroxyethyl radicals but not high enough to introduce discharge instability.

Hydrogen peroxide yields varied a little with stirring rate, a fairly rapid rate appearing to be the most suitable. Pressure changes did not affect the peroxide yield significantly at high oxygen flow rates, though it is possible that sufficiently high pressures would improve the mass transfer of oxygen from the gaseous to the solution phases at low oxygen flow rates.

Gde on aqueous ethanol in neutral phosphate buffer at the oxygen flow rate selected produced hydrogen peroxide, acetaldehyde, some diol (none at the highest oxygen flow rates where, however, some arc instability occurs), and acid. The yields of hydrogen peroxide related linearly to the quantity of electricity, showing that there were no peroxide-destruction reactions under the conditions used in this work. Linearity of butanediol yield with quantity of electricity was assumed, when required, since this product is nonvolatile. Acid appeared only in the combined presence of oxygen and substrate.

Under argon, low or zero flow rates were used and the products were acetaldehyde, hydrogen peroxide, and butan-2, 3-diol. It was verified that the yields of the nonvolatiles were linear functions of the quantity of electricity.

The graphs of yield *vs.* quantity of electricity and the results of the acetaldehyde work, whether under oxygen or argon, showed a tendency of the acetaldehyde yield to show a possible stationary state. The effect may arise from chemical decomposition of the acetaldehyde (*e.g.*, reaction with the aqueous electron) but it seems more likely to arise from vaporization because of the high temperature of the arc and the low boiling point of the acetaldehyde. A mathematical analysis, in essence, obtained the initial slopes of the plots of number of moles of acetaldehyde *vs.* quantity of electricity.

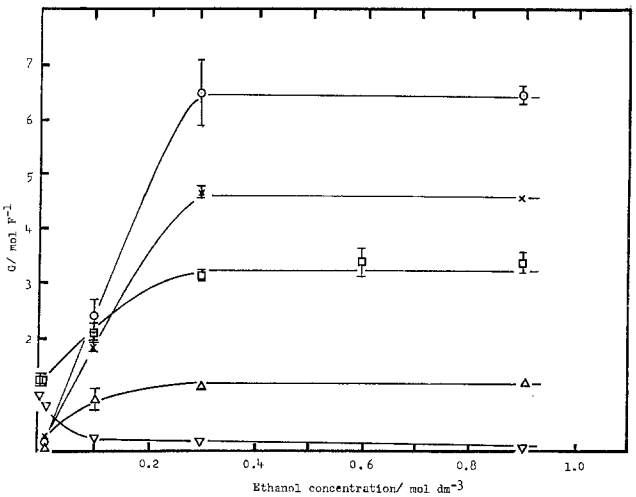


Fig. 1. G *vs.* ethanol concentration: ○, G(CH_3CHO, O_2); ×, G(CH_3CHO, Ar); □, G(H_2O_2, O_2); △, G($C_4H_{10}O_2$, Ar); ▽, G(H_2O_2, Ar).

Discussion

Plots of G-values *vs.* substrate concentration for each of the products are given in Fig. 1 and Table I.

Taking the argon runs first, G(H_2O_2) falls as the ethanol concentration increases, becoming very small. It is possible that at least some of this residual hydrogen peroxide corresponds to the generation of hydroxyl radicals at a rate (represented by 30 mA) slightly too high to permit total scavenging by ethanol within the concentration range used here. G(CH_3CHO) increases sharply, eventually leveling off. G($C_4H_{10}O_2$) increases in a like manner, the plateau value being about 1.16 mole F^{-1}.

In general gde of aqueous solutions may be regarded as producing the following species from the primary reaction zone (9, 11, 12)

$$H_2O \rightsquigarrow e_{aq}^-, H, OH, H^+, OH^-, H_2O_2, H_2, H_2O \quad [1]$$

In the absence of oxygen and in the presence of sufficient ethanol, the initial main reaction was OH + C_2H_5OH. Other radicals, H and e_{aq}^-, undergo slower reactions, under our conditions. The reactions of hydrogen and hydroxyl radicals with ethanol are well known. The hydroxyl radicals abstract hydrogen atoms from ethanol to form CH_3CH_3O (2.5%), CH_2CHOH (84.3%), and CH_2CH_2OH (13.2%) (13). The hydrogen radical abstracts a hydrogen atom primarily from the CH_2 group (14). The rate of reaction of the hydrogen radicals is about 1% of the rate of reaction of the hydroxyl radicals and may be neglected. In the same way reactions between hydrogen radicals and other substrates here are likely to be much slower than reactions between hydroxyl radicals and the same substrates. The CH_3CH_2O radicals pick up hydrogen atoms from ethanol molecules. The CH_2CH_2OH radicals may undergo a similar reaction, so improving the conversion of the hydroxyl radicals to 1-hydroxyethyl radicals, since separate measurements of G(OH, ferrocyanide) agree well with a G(OH) calculated from

Table I. Variation of G-values for acetaldehyde, butan-2,3-diol, and hydrogen peroxide with ethanol concentration and gas

[C_2H_5OH]/ mole dm^{-3}	G(H_2O_2)/mole F^{-1}		G(CH_3CHO) mole F^{-1}		G($C_4H_{10}O_2$)/mole F^{-1}
	Oxygen	Argon	Oxygen	Argon	Argon
0	1.24 ± 0.08	0.89 ± 0 03	0		0
0.01	1.25 ± 0.08	0.79 ± 0.04	0.18 ± 0.02	0.25 ± 0 01	0.05 ± 0.09
0.1	2.11 ± 0.17	0.21 ± 0.05	2.39 ± 0 29	1.83 ± 0 08	0.90 ± 0.19
0.3	3.12 ± 0 08	0.17 ± 0.02	6.47 ± 0.60	4.67 ± 0.11	1.14 ± 0.07
0.6	3.38 ± 0 26	—	—	—	—
0.9	3.39 ± 0.16	0.10 ± 0.01	6.44 ± 0.13	4.56 ± 0.04	1.20 ± 0.05

the product yields discussed here, under both argon and oxygen. Thus the main species formed from ethanol in the secondary reaction zone are 1-hydroxyethyl radicals. We assumed that the reactions of hydroxyl radicals with butan-2, 3-diol [$k = 8.1 \times 10^8$ dm^3 mole^{-1} sec^{-1} (15)] and acetaldehyde (possibly of similar rate constant) do not affect the yields of these two products significantly: The ethanol concentration was much higher than the concentration of these two products, there was no deviation from linearity in the plots of yields of nonvolatile products *vs.* quantity of electricity (suggesting therefore insignificant destruction reactions) and G(OH), ferrocyanide (see below) agrees well with G(OH) calculated from product yields. The reaction of hydrogen atoms with ethanol constitutes the fastest process involving these radicals, but it is still much slower than the rate of reaction of hydroxyl radicals with ethanol.

The products of the gde of aqueous ethanol in neutral phosphate buffer, under argon, are hydrogen peroxide, butanediol, and acetaldehyde, formed according to the following proposed reactions.

$$OH + OH \rightarrow H_2O_2 \quad [2]$$

$$2CH_3CHOH \rightarrow C_4H_{10}O_2 \quad [3]$$

$$2CH_3CHOH \rightarrow CH_3CHO + CH_2OH \quad [4]$$

Formation of acetaldehyde by additional radical/1-hydroxyethyl radical reactions seems unlikely. However, we do know that two 1-hydroxyethyl radicals interact to form butan-2, 3-diol, so we propose that under argon this interaction can yield acetaldehyde also, by disproportionation (reaction [4]).

Of the possible reactions of the aqueous electrons, those with peroxide and acetaldehyde (16) are the most probable

$$e_{aq}^- + CH_3CHO \rightarrow CH_3CHO^- \quad [5]$$

$$CH_3CHO^- + H_2O \rightleftharpoons CH_3CHOH + OH^- \quad [6]$$

$$e_{aq}^- + H_2O_2 \rightarrow OH + OH^- \quad [7]$$

Under oxygen, G(H_2O_2) and G(CH_3CHO) increase with increasing ethanol concentration and level off. G(CH_3CHO, O_2) was always greater than G(CH_3CHO, Ar). No butanediol is detectable at sufficiently high oxygen flow rates. These two facts point to a change of mechanism. Under oxygen G(CH_3CHO) is almost exactly double G(H_2O_2). The actual peroxide:acetaldehyde ratio under oxygen is 3.39:6.46. In the absence of oxygen, and persisting even at the highest ethanol concentrations, there is a small residue of hydrogen peroxide; if we assume that this residue also occurs in the runs under oxygen we can subtract it from G(H_2O_2, O_2), leaving 3.25 mole F^{-1}. The hydrogen peroxide:acetaldehyde ratio is then 3.25:6.46, which is very close to 1:2. Reactions of the 1-hydroxyethyl radicals other than those giving acetaldehyde and hydrogen peroxide in the correct proportions can be neglected. We assume that the 1-hydroxyethyl radicals are scavenged completely by oxygen, under the high gas flow rate

$$CH_3CHOH + O_2 \rightarrow \underset{\displaystyle O_2}{\overset{\displaystyle |}{CH_3CHOH}} \quad [8]$$

and this accounts for the disappearance of the butanediol. The 1:2 hydrogen peroxide:acetaldehyde ratio can be accounted for by

$$\underset{\displaystyle O_2}{\overset{\displaystyle |}{2CH_3CHOH}} \rightarrow 2CH_3CHO + H_2O_2 + O_2 \quad [9]$$

Because of the 1:2 hydrogen peroxide:acetaldehyde ratio we can assume also that the aqueous electron does not react significantly with products (reactions [5]-[7]). However, it could be argued that reactions [5] and [6] regenerate the 1-hydroxyethyl radical and hence, regenerate acetaldehyde. Nevertheless any cyclic process involves losses and the total hydroxyl radical yield, as estimated from the reaction products, would be less than G(OH, ferrocyanide). Reaction [7] would constitute clear loss of hydrogen peroxide also, since the hydrogen peroxide/hydroxyl radical scheme would mean loss of at least half a molecule of hydrogen peroxide at each cycle.

The peroxyl radical, HO_2, is of importance in radiation chemistry

$$H + O_2 \rightarrow HO_2 \quad [10]$$

$$e_{aq}^- + O_2 \rightarrow O_2^- \quad [11]$$

O_2^- is in equilibrium with HO_2. The peroxyl radical could take part in the main acetaldehyde-hydrogen peroxide-generating processes by reactions such as the following

$$2HO_2 \rightarrow O_2 + H_2O_2 \quad [12]$$

$$HO_2 + \underset{\displaystyle O_2}{\overset{\displaystyle |}{CH_3CHOH}} \rightarrow CH_3CHO + H_2O_2 + O_2 \quad [13]$$

Both these reactions would upset the 1:2 hydrogen peroxide:acetaldehyde ratio and therefore are not important here.

An alternative reaction scheme for the 1-hydroxyethylperoxyl radicals is as follows and involves formation of ethanol hydroperoxide (1-hydroxyethyl hydroperoxide) (15)

$$\underset{\displaystyle O_2}{\overset{\displaystyle |}{2CH_3CHOH}} \rightarrow \underset{\displaystyle H}{\overset{\displaystyle OH\ |}{CH_3COOH}} + CH_3CHO + O_2 \quad [14]$$

Ethanol hydroperoxide undergoes various possible reactions, in particular a rapid base-catalyzed decomposition to acetaldehyde and hydrogen peroxide (17)

$$\underset{\displaystyle H}{\overset{\displaystyle CH_3\ |}{CH_3COOH}} \xrightarrow[\text{Heat}]{OH^-} CH_3CHO + H_2O_2 \quad [15]$$

This reaction requires an elevated temperature, as is found under the glow spot (18). Reactions [14] and [15], therefore, are alternatives to reaction [9].

Ethanol hydroperoxide also tends to convert to the di-peroxide in aqueous systems (19). No evidence could be found (3) for this di-peroxide in x-irradiation studies.

The exactness of the hydrogen peroxide:acetaldehyde ratio shows that little, if any, of the product is locked up in the form of organic peroxides. It is possible, on the other hand, that the organic peroxides reacted as mixtures of hydrogen peroxide and acetaldehyde, since time was always allowed for the analytical processes to reach completeness, but the balance of the evidence is against significant organic peroxide formation.

A further possibility is the elimination of the hydroperoxyl radical from the 1-hydroxyethylperoxyl radical, followed by disproportionation of the former species

$$\underset{\displaystyle O_2}{\overset{\displaystyle |}{CH_3CHOH}} \rightarrow CH_3CHO + HO_2 \quad [16]$$

$$2HO_2 \rightarrow O_2 + H_2O_2 \quad [12]$$

This gives the correct product ratio but the possibility of side reactions of peroxyl radicals makes the above scheme less probable. Reaction [12] was investigated

in the absence of ethanol and using dilute aqueous alkali: No change in pH was observed after gde, so no hydrogen peroxide formation was inferred.

Reactions such as

$$CH_3CHOH + HO_2 \rightarrow CH_3CHO + H_2O_2 \quad [17]$$

or

$$CH_3CHOH + HO_2 \rightarrow CH_3\overset{\overset{OH}{|}}{C}HOOH \quad [18]$$

followed by

$$CH_3\overset{\overset{OH}{|}}{C}HOOH \xrightarrow[\text{Heat}]{OH} CH_3CHO + H_2O_2 \quad [15]$$

can be discounted, since they give an unambiguously incorrect product ratio.

If the oxygen flow rate is not high enough the 1-hydroxyethyl radicals are incompletely scavenged and some butanediol appears, possibly with some disproportionation also. The ethanol scavenges most, but not all, of the OH radicals as deduced from our G(OH, ferrocyanide) work and from the small residual peroxide in the argon runs. It was found that the total nonacid yield corresponded very closely to G(OH, ferrocyanide): see Table II. The gde work on neutral and also on alkaline ferrocyanide gave closely similar ferricyanide yields, and no hydrogen peroxide, indicating total scavenging of the hydroxyl radicals by ferrocyanide.

Schultze and Schulte-Frohlinde (5) also postulated the decomposition of ethanol hydroperoxide to acetic acid and water

$$CH_3-\overset{\overset{OH}{|}}{C}HOOH \xrightarrow{H^+} CH_3COOH + H_2O \quad [19]$$

The reaction is acid-catalyzed. Our G-values for acid were very high (of the order of 9 mole F^{-1}). Acid formation as proposed above must involve a chain process, starting from ethanol, since G(acid) is so large: Such a process might involve acetaldehyde, as an intermediate or by-product, and this would upset the 1:2 hydrogen peroxide:acetaldehyde ratio and also the correlation between G(OH, ferrocyanide) and total yields. If acetaldehyde were the source of the acid, then, in order to preserve the acetaldehyde yield, another chain process would be required, consuming ethanol. The gain in acid does not correlate with the loss in acetaldehyde. Further, the acid yield *vs.* quantity of electricity curve flattens off with increasing run time, suggesting some kind of saturation. Acid was found also in gde studies on aqueous isopropanol, involving either a combustion process (yielding carbon dioxide) or C-C bond fission. Acid formation involves the simultaneous presence of oxygen and substrate. The observed hydrogen peroxide:acetaldehyde ratio is consistent with the mechanism proposed above but does not account for the acid. If other reactions occur they must somehow produce acid and the proper product ratio. It is concluded tentatively that the acid arises from combustion processes.

Table II. Total yields under oxygen

	G/mole F^{-1}
G(OH, ferrocyanide)	7.19 ± 0.66
$G(CH_3CHO, O_2)$	6.44 ± 0.13
$2G(C_4H_{10}O_2, O_2)$ (trace)	0.45 ± 0.05
$2G(H_2O_2, Ar)$ (trace)	0.19 ± 0.02
	7.08 ± 0.14

The total yield calculation was repeated for the argon runs, G(OH) being estimated to be 7.145 ± 0.149 mole F^{-1}. It seems we have accounted for all the hydroxyl radicals. Other species may compete, but at a much lower level. We did not find any need to assume loss of products (except for acetaldehyde): Decomposition of products is a main feature of Seddon and Allen's radiolysis work (4).

In the absence of ethanol and in the absence of oxygen, under established conditions, the product-destroying reactions

$$H + H_2O_2 \rightarrow OH + H_2O \quad [20]$$

and

$$OH + H_2O_2 \rightarrow HO_2 + H_2O \quad [21]$$

might occur, but the extent is not clear. The main product under argon and in the absence of ethanol is hydrogen peroxide and possible reactions are

$$H + H \rightarrow H_2 \quad [22]$$

$$H + OH \rightarrow H_2O \quad [23]$$

$$OH + OH \rightarrow H_2O_2 \quad [2]$$

In the presence of oxygen and in the absence of ethanol oxygen/radical or oxygen/aqueous electron reactions compete with radical/radical processes. Perhydroxyl radical formation may be possible, giving some additional peroxide by self-reaction.

It is possible that some or all of the aqueous electrons which may be generated in gde may react with hydrogen ions also generated or with those from water. There seems to be no need to include this species in the yield analyses: For example, under oxygen the aqueous electron has an opportunity to partake via reaction [11] but there is no evidence for this.

The radiation and gde chemistry of aqueous ferrocyanide has been reviewed by Denaro and Owens (20) and further work carried out by others, especially Almubarak and Wood (21). It was found (21) that G(ferricyanide) was independent of pH (from pH 7 upward). In alkali, inorganic peroxide is expected to reduce ferricyanide, *i.e.*, reducing G(ferricyanide); it was concluded that at sufficiently high ferrocyanide concentrations no peroxide occurs and all the hydroxyl radicals are scavenged by the substrate. The absence of any oxygen flow rate effect suggests that reactions involving the hydroperoxyl radical or its anion can be neglected here also. For similar reasons contributions by hydrogen radicals and by aqueous electrons to the reaction system were discounted also. It was concluded that G(ferricyanide) represented G(OH). It is hoped to publish details of this work shortly.

Further work on the gde of aqueous ethanol in selected buffers is proposed in order to investigate the mechanism at various pH values and also to examine the possibility that ethanol itself is decomposed directly by the bombardment processes. This latter may be achieved by analysis for other products, such as ethylene glycol and 1,3-propanediol, arising from C-C fission. The ultimate fate of the hydrogen radicals and the aqueous electrons requires further study also, and substrates likely to show improved reactivities toward these species have been selected.

Manuscript submitted Jan. 20, 1977; revised manuscript received April 23, 1977.

Any discussion of this paper will appear in a Discussion Section to be published in the June 1978 JOURNAL. All discussions for the June 1978 Discussion Section should be submitted by Feb. 1, 1978.

REFERENCES

1. A. Klemenc, *Z. Electrochem.*, **53**, 694 (1953).
2. G.-A. Mazzochin, G. Bontempelli, and F. Magno, *Electroanal. Chem. Interfacial Electrochem.*, **42**, 243 (1973).

3. G. G. Jayson, G. Scholes, and J. Weiss, *J. Chem. Soc.*, **1957**, 1358.
4. W. A. Seddon and A. O. Allen, *J. Phys. Chem.*, **71**, 1914 (1967).
5. H. Schultze and D. Schulte-Frohlinde, *J. Chem. Soc. Faraday Trans. 1*, **71**, 1099 (1975).
6. J. Brode, *Z. Phys. Chem.*, **37**, 257 (1901).
7. G. R. A. Johnson and G. Scholes, *Analyst*, **79**, 217 (1954).
8. N. J. Davies, A. R. Denaro, A. Wood, and M. A. Almubarak, *J. Appl. Chem. Biotechnol.*, **26**, 715 (1976).
9. A. Hickling, in "Modern Aspects of Electrochemistry," Vol. VI, J. O'M. Bockris, Editor (1971).
10. M. A. Almubarak, M.Sc. Thesis, University of Aberdeen (1972).
11. G. Hughes, "Radiation Chemistry," (1973).
12. A. R. Denaro and G. G. Jayson, "Fundamentals of Radiation Chemistry," (1972).
13. K.-D. Asmus, H. Möckel, and A. Henglein, *J. Phys. Chem.*, **77**, 1218 (1973).
14. A. Appleby, G. Scholes, and M. Simic, *J. Am. Chem. Soc.*, **85**, 3891 (1963).
15. M. Anbar and P. Neta, *Int. J. Appl. Rad. Isotopes*, **18**, 493 (1967).
16. D. W. Johnson and G. A. Salmon, *J. Chem. Soc. Faraday Trans. 1*, **71**, 583 (1975); K.-D. Asmus, A. Henglein, A. Wigger, and G. Beck, *Ber. Bunsenges. Phys. Chem.*, **70**, 756 (1966); M. Simic, P. Neta, and E. Hayon, *J. Phys. Chem.*, **73**, 3794 (1969).
17. D. Swern, "Organic Peroxides," (1970).
18. A. Reiche and R. Meister, *Ber. Dtsch. Chem. Ges.*, **68**, 1465 (1935); A. Reiche, *Angew. Chem.*, **70**, 251 (1958).
19. A. Rieche, *Ber. Dtsch. Chem. Ges.*, **64**, 2328 (1931); P. L. Kooijman and W. L. Ghijsen, *Rec. Trav. Chim.*, **66**, 205 (1947).
20. A. R. Denaro and P. A. Owens, *Electrochim. Acta*, **13**, 157 (1968).
21. M. A. Almubarak and A. Wood, To be published.

X-Ray Photoelectron Spectroscopic Studies of Tin Electrodes after Polarization in Sodium Hydroxide Solution

R. O. Ansell, T. Dickinson,* A. F. Povey,[1] and P. M. A. Sherwood

School of Chemistry, The University, Newcastle upon Tyne, NE1 7RU, United Kingdom

ABSTRACT

The surface of tin electrodes after potentiostatic polarization in 0.50 mole dm^{-3} sodium hydroxide solution has been examined by x-ray photoelectron spectroscopy. Stannous oxide and hydroxide are shown to be present in the prepassive region. At higher potentials stannic oxide and hydroxide are formed. The thickness of the layer is evaluated over the potential range −0.95 to +0.40V using various models and is in the range 30-86Å.

X-ray photoelectron spectroscopy (XPS) has been shown to be a valuable tool in the study of electrode surfaces (1-6). Information on the species present and quantitative information on thickness of layers and their distribution may be established. These may lead to proposed mechanisms being disproved or substantiated (7).

In this study tin electrodes have been examined after potentiostatic polarization in 0.5 mole dm^{-3} sodium hydroxide solution. Much of the previous electrochemical work on this system involved galvanostatic methods (8-13) but some workers have adopted a potentiostatic approach (14-18). The anodic polarization curve shows two peaks in the active-passive region. The occurrence of the first passivation has been attributed to the formation of a layer of SnO or $Sn(OH)_2$ by a dissolution precipitation mechanism (13, 15). The second region of passivity has been attributed to the presence of SnO_2 (13, 15).

In this study we have investigated the effect of potentiostatic polarization over a wide potential range. The existence of Sn II and Sn VI species is confirmed.

Experimental

All the spectra were run on an AEI ES200B spectrometer using Mg $K\alpha_{1\alpha_2}$ radiation. Both the analyzer entrance and exit slits were set at their minimum values to give maximum resolution conditions. The electron gun was operated at 120W power for all the studies to give a relatively low x-ray flux [and thus minimize any x-ray reduction (19)] and to enable the intensities of the photoelectron peaks to be compared. No time dependence of the spectra was observed. The spectrometer was operated in the fixed retardation ratio mode for the recording of all the photoelectron peaks. The scan speed used was either 0.05 or 0.02V sec^{-1} depending on the absolute intensity of the peaks. The binding energies are calibrated with respect to the C1s electron peak at 284.6 eV due to residual pump oil on the sample surface. This gave a value of 484.1 eV for the Sn(metal) 3d5/2 electron peak. This was subsequently used to calibrate the spectra where such a peak was clearly observed. The pressure in the sample chamber was, typically, 10^{-8} Torr. This was achieved rapidly after the insertion of the sample probe with the aid of a titanium sublimation pump. The temperature of the samples was maintained at 10°C.

Curve resolution was carried out on a du Pont Model 310 curve resolver using a 50:50 Gaussian-Lorentzian shape fit. For both the tin and oxygen spectra curves were fitted to be within ±0.3 eV of the binding energy quoted and ±0.2 eV of the separation from the tin metal 3d5/2 electron peak where this is observed. In the case of the tin spectra the separation of the 3d5/2 electron peaks due to Sn II and Sn IV from that due to tin metal (when this was observed) was within ±0.2 eV of the difference between their quoted binding energies.

A current-voltage curve was recorded (Fig. 1a), using a triangular voltage sweep at a sweep rate of 10 mV sec^{-1} before any other measurements were made to ensure the system was behaving satisfactorily.

* Electrochemical Society Active Member.
[1] Present address: Central Electricity Research Laboratories, Leatherhead, Surrey, KT22 7SE, United Kingdom.
Key words: photoelectron, tin, oxide, passivation.

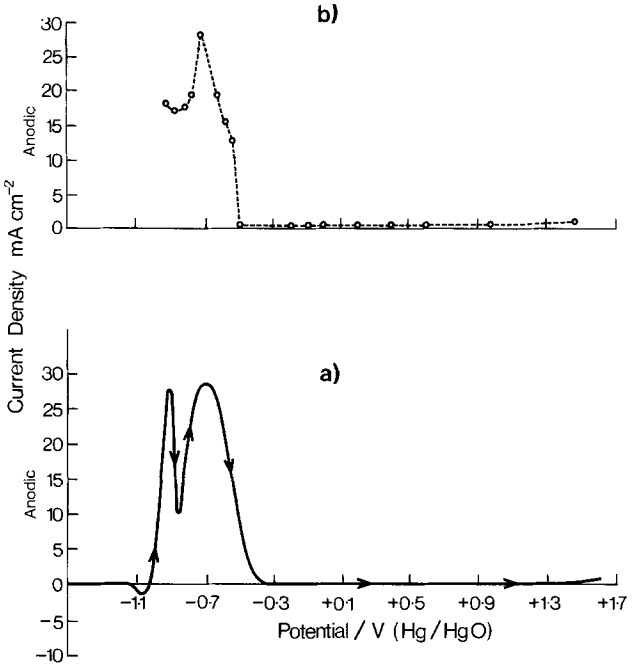


Fig. 1. (a) A current-voltage curve for the tin electrode in 0.50 mole dm^{-3} sodium hydroxide solution at a sweep rate of 10 mV sec^{-1}. Ordinate: Current density mA cm^{-2}. Abscissa: Potential/V (Hg/HgO). (b) The steady-state current-voltage curve for tin electrodes polarized in 0.50 mole dm^{-3} sodium hydroxide solution and subsequently examined by XPS. Ordinate: Anodic current density mA cm^{-2}. Abscissa: Potential/V (Hg/HgO).

Fresh electrodes were used for each measurement to eliminate the possibility of inadequate removal of the electrochemically formed oxide. Ventron (Alpha Products) tin foil (m5N) was used for the electrode studies. The electrodes were degreased in acetone and rinsed copiously before introduction into the cell. They were prepolarized initially for 10 min at −2.00V, the potential was slowly turned to −1.50V, and allowed to rest there for 1 min to allow the hydrogen gas bubbles to disperse. The potential was then either pulsed to the required value or adjusted to the required potential over a few seconds. The electrodes were polarized for 10 min at each potential studied; the current having become steady within this time. These steady-state currents are shown in Fig. 1b.

The electrochemical cell has been described before (7). In this case the electrode was carefully positioned next to the Luggin capillary tip to minimize effects of *iR* drop in the solution. The cell was housed in a nitrogen-filled glove box to enable anaerobic transfer of the electrode to the spectrometer as described previously (5).

All potentials in these experiments were measured and are quoted with respect to the mercury-mercuric oxide electrode in 0.5 mole dm^{-3} sodium hydroxide solution.

Table I

	Binding energy (eV)*		
	Sn 3d5/2	O1s	Na2s
SnO	485.8	529.8	—
SnO_2	486.3	530.4	—
Sn (foil) (21) "as received"	485.8	531.2	—
Sn(m) (metal) (21)	484.1	—	—
NaOH	—	531.5	63.7
Na_2SnO_3	487.0	531.3	63.9

* With respect to C1s = 284.6 eV.
— Not present.

Results

The tin 3d5/2, oxygen 1s and sodium 2s electron peaks were studied for the treated electrodes, and were compared with spectra obtained from tin compounds (Table I). The tin 3d5/2 electron peak observed with treated electrodes could be resolved in all cases into two or three peaks at binding energies of 484.1, 485.8, and 486.3 eV corresponding to tin metal, stannous oxide and/or hydroxide, and stannic oxide and/or hydroxide, respectively (Table II). Representative spectra are shown in Fig. 2.

The oxygen 1s electron peak could be resolved into two or three peaks at binding energies of 532.3, 531.4, and 529.9 eV (Table II, Fig. 3). The peak at 532.3 eV is present on all samples introduced into the spectrometer and may be shown to be due to a surface species by angular variation experiments (21). This peak is therefore assigned to adsorbed oxygen or water. In those cases in which the proportion of the total peak area assignable to these species is <5% this peak has not been shown in Fig. 3. The peak at 529.9 eV may be assigned to oxide oxygen by comparison with the tin oxides studied (Table I). A hydroxyl oxygen species would, on a simple basis of charge, be expected to have a higher binding energy and this has been the case for many hydroxide species studied [Table I and previous work (3-7)]; thus the peak at 531.4 eV is assigned to hydroxyl oxygen.

Table II

	Proportions of photoelectron peaks assigned to each species						Absolute intensity of sodium 2s electron peak
Potential	Tin 3d5/2 electron region			Oxygen 1s electron region			
vs. Hg/HgO	SnO_2/ $Sn(OH)_4$	SnO/ $Sn(OH)_2$	Sn(metal)	O_2 ads/ H_2O	OH^-	O^{2-}	Na2s
−0.95	—	65	35	25	59	16	0.15
−0.90	—	60	40	21	52	29	—
−0.85	—	57	43	19	63	19	—
−0.80	—	67	33	—	>95	—	—
−0.75	~10	58	32	—	76	24	0.09
−0.70	16	50	34	—	61	39	0.46
−0.60	21	44	35	—	64	36	—
−0.55	30	38	32	—	62	38	—
−0.50	75	~10	15	—	64	37	—
−0.20	80	—	20	—	58	42	0.18
−0.10	83	—	17	—	57	43	0.05
0.00	84	—	16	—	66	34	0.28
+0.20	92	—	8	—	45	55	0.08
+0.40	~95	—	~5	—	48	52	—
+0.60	>95	—	—	—	47	53	0.13
+1.00	>95	—	—	—	35	65	—
+1.50	>95	—	—	—	30	70	0.10
+2.40	>95	—	—	—	28	72	—

— Not detectable.

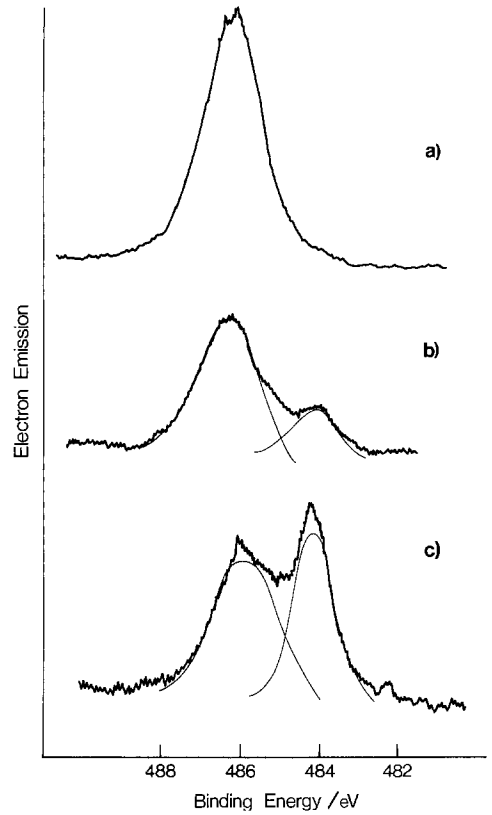


Fig. 2. Representative spectra of the tin 3d5/2 electron region of the tin electrodes after polarization at a potential of (a) —0.90V, (b) —0.10V, (c) +1.50V. Ordinate: Electron emission. Abscissa: Binding energy/eV.

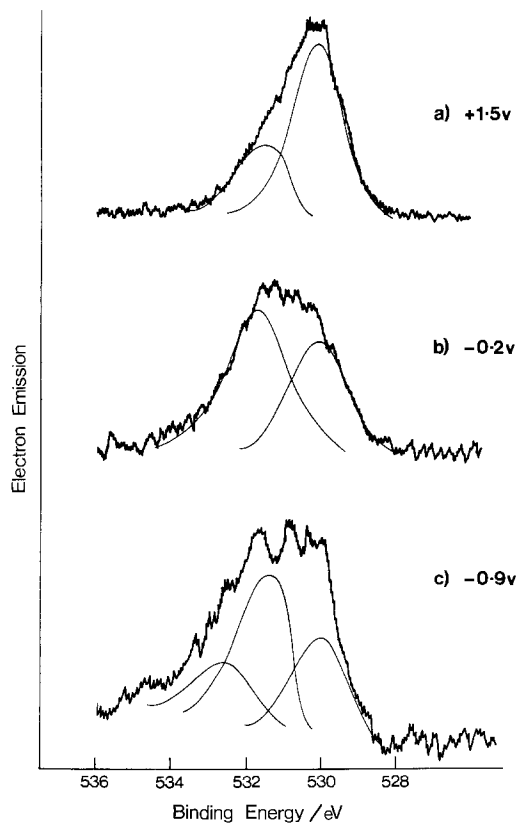


Fig. 3. Representative spectra of the oxygen 1s electron region of the tin electrodes after polarization at a potential of (a) —0.90V, (b) —0.10V, (c) +1.50V. Ordinate: Electron emission. Abscissa: Binding energy/eV.

A single peak at 63.5 eV could be detected at many potentials due to sodium incorporation in the layer. The absolute intensity of this peak in the spectrum of the treated electrodes is given in Table II.

In spite of the precaution taken in transferring the electrode to the spectrometer, even after pretreatment at —2.00V for 10 min the presence of some stannous hydroxide could be detected. Since similar results were obtained after polarizing in the active region no useful information could be deduced from them. At more positive potentials, however, significant differences were observed in the spectra.

Characterization of the layer.—It has been demonstrated previously how the relative intensities of the photoelectron peaks from the surface oxide and substrate metal may be used to derive the thickness of the layer (3-5, 7). When two oxides/hydroxides possibly of different valence states are present a more comprehensive study may reveal how the species are distributed over the surface and thus explain more fully the nature of the passivation process (20).

In this case in order to analyze the intensity data it is convenient to divide the potential range into four sections. The region from —0.95 to 0.80V in which Sn II species are present, from —0.75 to —0.50V in which both Sn II and Sn IV species are present, and —0.20 to +0.40V in which Sn IV species are present. In these three regions the metal substrate is also detectable. In the fourth region, +0.60 to +2.40V the substrate is no longer detectable; this implies the layer is greater than *ca.* 90Å thick (see Table III).

The first and third regions have been analyzed assuming the electrode is completely covered by an oxide/hydroxide layer. The relevant equation is then

$$\frac{I_{ox}}{I_m} = K\frac{(1 - \exp(-x\sigma_{ox}))}{\exp(-x\sigma_{ox})} \qquad [1]$$

where the symbols have the same meaning as before (4, 5, 7). Taking values of 1.81 and 27.7Å for K and $1/\sigma_{ox}$, respectively, arising from our previous angular variation study (21) the thickness of the layer can be evaluated (Table III).

In the second region where two different valency states of tin are present in the surface layer the data may be analyzed in various ways. The results are given in Table IV and discussed below.

Discussion

Assignment of the photoelectron peaks.—The spectra show that oxide/hydroxide species are present on the electrode over the total potential range studied. Assignment of the tin species is based partly on a comparison with the spectra of stannous oxide and stannic oxide. The total Sn 3d5/2 electron peak envelope can be satisfactorily resolved into peaks due to these two species and tin metal. There is no evidence for a chemical shift between stannous oxide and hydroxide in the Sn 3d5/2 electron peak. Thus for the tin foil as received the tin 3d5/2 electron peak is at the same bind-

Table III

Potential *vs.* Hg/HgO	Thickness,* A
−0.95	35
−0.90	32
−0.85	30
−0.80	37
−0.20	51
−0.10	56
0.00	57
+0.20	75
+0.40	86

The thickness of the layer in the regions where only one oxide is present.

* Assuming $\lambda_{SnO} = \lambda_{SnO_2} = 27.7$Å, and D_{SnO} and D_{SnO_2} are the atom densities of the bulk species.

Table IV

Model	A patchy layer, Substrate covered but detectable under both oxides		Homogeneous mixture. Substrate covered but detectable		Two distinct layers. Substrate covered but detectable			
					$\lambda_1 = \lambda_2$, $D_1 = D_{SnO}$, $D_2 = D_{SnO_2}$			
Assumptions made*	Thickness of patches is same $\lambda_1 = \lambda_2$ $D_1 = D_{SnO}$, $D_2 = D_{SnO_2}$		$\lambda_1 = \lambda_2$, $D_1 = D_{SnO}$, $D_2 = D_{SnO_2}$		Sn IV on top of Sn II		Sn II on top of Sn IV	
					Thickness, A		Thickness, A	
Potential vs. Hg/HgO	Thickness, A	Coverage of surface by Sn II	Thickness, A	Fraction of atoms as Sn II	Sn IV layer	Sn II layer	Sn IV layer	Sn II layer
−0.75	38	0.85	38	0.85	3.1	35	11	27
−0.70	36	0.75	36	0.75	5.2	31	15	21
−0.60	36	0.68	36	0.67	7.1	29	18	18
−0.55	38	0.55	38	0.55	11	28	24	14
−0.50	59	0.11	59	0.11	40	19	56	2.6

* Subscript 1 refers to Sn II species. Subscript 2 refers to Sn IV species.

ing energy as that for SnO although the oxygen peaks are shifted. Similarly the spectra of the electrode after polarization at −0.80V show only hydroxide oxygen species and the Sn 3d5/2 peak can be readily resolved into peaks at 485.8 and 484.1 eV. Neither is there any evidence for a chemical shift of the Sn 3d5/2 electron peak between stannic oxide and hydroxide. At very high potentials where there is a high proportion of oxide the tin 3d5/2 electron peak is virtually identical to that at lower potentials where a considerably higher proportion of hydroxide is present.

The assignment of the oxygen 1s electron peak at 531.4 eV to hydroxyl species is based on previous work (5, 7). There is no doubt that there are at least two different oxygen-containing species present in the layer and it seems reasonable to assign one to oxide and one to hydroxide.

The amount of sodium present shows no correlation with potential or with any of the other species present. This is probably due to a small amount of sodium incorporation in the layer and/or some residual NaOH being left on the surface after washing.

Characterization of the layer.—The analysis of the positions and intensities of the photoelectron peaks suggest that in the prepassive region only Sn II species are present.

Both oxide and hydroxide are present in this region and the total thickness is in the range 20-26Å. We have found, previously, that metal dissolution may proceed at a high rate even when the electrode surface is covered by thick layers of oxide/hydroxide (5).

Both Sn II and Sn IV species are present in the region −0.25 to −0.50V. The oxygen 1s electron spectra show only hydroxide is present at −0.80V but at all higher potentials both oxide and hydroxide are present. The total layer thickness is in the range 38-59Å for each of the models chosen for the analysis (Table IV).

In the region −0.20 to +0.40V there is a steady increase in the thickness of the layer which is composed solely of Sn IV species. The oxide/hydroxide ratio also shows an increasing trend with increasing potential (Tables II and III). This trend continues at higher potentials where the substrate is no longer detectable. The film becomes visible at very high potentials suggesting the thickness has increased further.

Correlation with the electrochemical data.—It is important to see if the species identified, the layer thickness, and the distribution of the species can be correlated with the electrochemical data; in particular the current-potential curve (Fig. 1b). In the prepassive region only stannous oxide and hydroxide are present. The current is $\geq$ 15 mA cm^{-2} throughout this region indicating that this layer is not strongly passivating.

The fall in current between −0.95 and −0.90V is probably due to the increased proportion of oxide in the surface layer (Table II). The subsequent increase in current may be tentatively correlated with the decrease in proportion of stannous oxide and of course the more positive potentials.

The true passivation correlates with an increasing proportion of the tin 3d5/2 electron envelope being due to Sn IV species. The intensities have been analyzed using four different models (Table IV). A satisfactory model must explain a slowly decreasing current from −0.75 to −0.55V, followed by a very abrupt decrease at −0.50V to a value of 0.05 mA cm^{-2}. The model must also give a total thickness of about 35Å from −0.75 to −0.55V, since the proportion of the tin 3d5/2 electron envelope due to the metal is approximately constant from −0.80 to −0.55V. A considerably thicker layer (*ca.* 50Å) must be present at −0.50V because, at this potential, the proportion of the tin peak due to the metal falls to a value similar to that observed in the potential range −0.20 to 0.00V.

All models give values for the total thickness which satisfy the requirements described above. This is, indeed, to be expected since, lacking the appropriate data, it has been necessary to assume that $\lambda_1 = \lambda_2$. The slow decrease in current could be explained, by the patchy layer model, as due to an increasing coverage by Sn IV species; as discussed above the Sn II species are not strongly passivating. A fivefold increase in the coverage by Sn IV species (from −0.55 to −0.50V) does not, however, seem a sufficient change to account for the very large fall in the current.

It is difficult to decide whether a homogeneous layer is physically realistic, what properties it would have, and how changes in its composition would affect the degree to which it passivated the electrode.

Both the models involving two distinct layers predict an increase in the thickness of the Sn IV layer with potential, as seems to be necessary to account for the decreasing current. If the lower layer is composed of Sn IV species, it appears that this would have a thickness corresponding to that of at least two unit cells, even at −0.75V (SnO_2 has a tetragonal structure with unit cell dimensions of a = 4.74Å and c = 3.19Å). Since the electrode undergoes rapid dissolution at this potential, whereas Sn IV species appear to be strongly passivating, it seems unlikely that such a relatively thick film would be present. If the upper layer consists of Sn IV species, the thicknesses involved are more acceptable and the fourfold increase in the thickness of this layer between −0.55 and −0.50V would account for the dramatic fall in the current which accompanies this change in potential.

So far as it is possible to analyze this situation, therefore, the balance of evidence suggests that, in the potential range between −0.75 and −0.50V, two distinct layers are present on the electrode surface. It also appears, as is to be expected on thermodynamic

grounds, that the layer nearest the electrode is that of lowest oxidation state.

When the electrode is fully passivated, there is very little dependence of the current on potential (between −0.5 to +0.60V). This can be explained in terms of both the increasing thickness of the layer (22) (Table III) and its progressive dehydration; the oxide/ hydroxide ratio shows a generally increasing trend as the potential is made more positive (Table II). At still more positive potentials the thickness continues to increase but the current rises somewhat. This may be due to the onset of oxygen evolution or to imperfections in the layer.

Acknowledgments

A.F.P. would like to thank I.C.I. for the award of a fellowship and R.O.A. would like to thank the Science Research Council for the award of a research associateship.

Manuscript submitted Jan. 21, 1977; revised manuscript received April 28, 1977.

Any discussion of this paper will appear in a Discussion Section to be published in the June 1978 JOURNAL. All discussions for the June 1978 Discussion Section should be submitted by Feb. 1, 1978.

REFERENCES

1. K. S. Kim, A. F. Gossman, and N. Winograd, *Anal. Chem.*, **46**, 197 (1974).
2. G. C. Allen, P. M. Tucker, A. Capon, and R. Parsons, *J. Electroanal. Chem.*, **50**, 335 (1974).
3. A. F. Povey, Ph.D. Thesis, University of Newcastle-upon-Tyne (1975).
4. T. Dickinson, A. F. Povey, and P. M. A. Sherwood, *J. Chem. Soc., Faraday Trans. 1*, **71**, 298 (1975).
5. T. Dickinson, A. F. Povey, and P. M. A. Sherwood, *ibid.*, **73**, 327 (1977).
6. R. O. Ansell, T. Dickinson, and A. F. Povey, *Corros. Sci.*, In press.
7. T. Dickinson, A. F. Povey, and P. M. A. Sherwood, *J. Chem. Soc. Faraday Trans. 1*, **72**, 686 (1976).
8. A. W. Hothersall, S. G. Clarke, and D. J. Macnaughton, *J. Electrodep. Tech. Soc.*, **9**, 101 (1934).
9. F. F. Oplinger and C. J. Wernlund, U.S. Pat. 1,919,000 (1933).
10. R. Kerr, *J. Soc. Chem. Ind.*, **57**, 405 (1938).
11. H. Barbre, C. Bagger, and E. Maahn, *Electrochim. Acta*, **16**, 559 (1971).
12. D. Eurof Davies and S. N. Shah, *ibid.*, **8**, 663 (1963); *ibid.*, **8**, 703 (1963).
13. N. A. Hampson and N. E. Spencer, *Br. Corros. J.*, **3**, 1 (1968).
14. M. N. Anwar, *U.A.R.J. Chem.*, **13**, 109 (1970).
15. B. N. Stirrup and N. A. Hampson, *J. Electroanal. Chem.*, **67**, 45 (1976).
16. B. N. Stirrup and N. A. Hampson, *ibid.*, **67**, 57 (1976).
17. D. R. Gabe and P. Sripatr, *Trans. Inst. Met. Finish.*, **51**, 141 (1973).
18. T. Dickinson and S. Lotfi, In preparation.
19. A. F. Povey and P. M. A. Sherwood, *J. Chem. Soc., Faraday Trans. 2*, **70**, 1240 (1974).
20. A. F. Povey, Submitted to *J. Electron Spectrosc. Rlat. Phenom.*
21. R. O. Ansell, T. Dickinson, A. F. Povey, and P. M. A. Sherwood, *ibid.*, **11**, 301 (1977).
22. K. J. Vetter, *Electrochim. Acta*, **16**, 1923 (1971).

Diffusion and Charge Transfer Parameters for the Ag/AgCl Electrode

Hiram Gu* and Douglas N. Bennion*

Energy and Kinetics Department, School of Engineering and Applied Science, University of California, Los Angeles, California 90024

ABSTRACT

Galvanostatic formation and potentiostatic reduction of silver chloride on silver have been studied. Experiments were conducted in 0.5, 1.0, 1.5, 2.0, and 3.0*N* KCl solutions. The effective mass transfer coefficient, k_m^o, for the transport of complex silver ions from AgCl crystals to reaction sites on the silver surface was found to depend on KCl concentrations in the form

$$k_m^o = 1.808 \times 10^3 [\exp(-1.519 \times 10^3 c_e)] \text{ cm/sec}$$

with c_e in mole per cubic centimeter. The apparent cathodic charge transfer coefficient, α_c, was determined to be 0.30, and the exchange current density

$$i_o = 0.15 (c_R^{sat}/10.1 \times 10^{-8})^{0.70} \text{ A/cm}^2$$

with c_R^{sat} (mole per cubic centimeter) being the saturated concentration of complexed silver ions in the KCl solution.

In addition to being used as reference electrodes, silver/silver chloride electrodes have found use as porous electrode plates in batteries such as the seawater battery. Previous studies on porous Ag/AgCl electrodes (1, 2) have indicated that the electrode may be used successfully in secondary storage batteries.

The silver/silver chloride electrode is an electrode with a sparingly soluble reactant, AgCl. Numerous studies have been conducted on the thermodynamics of Ag/AgCl electrodes (3) and the mechanism of AgCl formation and reduction at silver electrodes (4-11). The studies of Kurtz (4) and Lal *et al.* (5) suggested that electrolytically formed AgCl films are porous in nature. Briggs and Thirsk (6) studied the galvanostatic reduction of silver chloride films on silver at different current densities and KCl concentrations. They found that an increase in the initial AgCl layer thickness reduces the number of reduction centers visible at a given percentage reduction. Jaenicke *et al.* (7) found that if a pore-free AgCl layer is reduced by a cathodic current, pores soon appear. Fleishmann and Thirsk (8) studied the growth of AgCl on Ag and concluded that the growth of AgCl is two dimensional. Giles (9), however, believed that the formation of AgCl is by progressive nucleation and growth of three-dimensional centers and that the diffusion of $AgCl_{n+1}^{-n}$ may

* Electrochemical Society Active Member.
Key words: porous electrodes, batteries, exchange current.

be rate determining. The value of n for the complex may be 0, 1, 2, or 3. Katan *et al.* (10) studied the reduction of silver ions from potassium chloride solutions saturated with AgCl. A rotating disk silver electrode was used. Their results also indicate that the formation and reduction of silver chloride involves the solution diffusion of $AgCl_{n+1}^{-n}$. Aleskovskii *et al.* (11) studied the structure of silver deposits with respect to electrode potentials at which the reduction of AgCl takes place. They also suggested that the reduction is via a solution diffusion path.

No information regarding the charge transfer overvoltage of Ag/AgCl electrodes was found in the literature. The absence of charge transfer studies on Ag/AgCl electrodes is probably due to two reasons. First, the overvoltage in the case of solid silver electrodes consists mainly of crystallization and diffusion overvoltage with large exchange current density according to Gerischer and Tischer (12, 13) and Bockris *et al.* (14, 15). Second, the coverage of silver surface by silver chloride adds complexity to the analysis of experimental data.

The present study was conducted with the intention of determining apparent diffusion and charge transfer parameters for the Ag/AgCl system. These parameters are to be used in the mathematical modeling of Ag/AgCl porous electrodes.

The potentiostatic reduction of porous silver chloride films on silver was analyzed. As the silver chloride is being converted to silver, the silver area available for charge transfer increases. The cathodic current increases to a maximum and decreases as the silver chloride is being depleted. The maximum current density reached during potentiostatic reduction was used to construct the current-overpotential curves. From the i-η curves, values of four parameters were deduced. They are: the cathodic charge transfer coefficient, α_c; the mass transfer coefficient of complexed silver ions, k_m^o, for solution phase transport between Ag surface and AgCl surface; the exchange current density, i_o; and the order of dependence of i_o on silver ion concentration, γ.

Qualitative results observed on the galvanostatic formation of AgCl are also presented.

Experimental

The experimental arrangement is shown in Fig. 1. The electrode studied was a circular silver disk 1/8 in. in diameter embedded in Lucite. Another Lucite piece that consisted of the counterelectrode compartment, a 1/8 in. diam tunnel, and a small branch tunnel approximately 1/32 in. diam was spring pressed against the working electrode piece. The 1/8 in. tunnel was aligned with the silver disk allowing uniform primary current distribution on the electrode surface. A thin film of electrolytic solution approximately 10 μm thick existed between the two Lucite pieces which provided a solution connection between the main cell and the reference electrode compartment. The reference electrode was a Ag/AgCl electrode. The same KCl concentration as the main cell was used in the reference electrode compartment. A tube pump was used to circulate the electrolyte so as to maintain a constant electrolyte concentration near the electrode surface. The electrolyte flow rate used during experimental runs was 3.5 cm^3/sec.

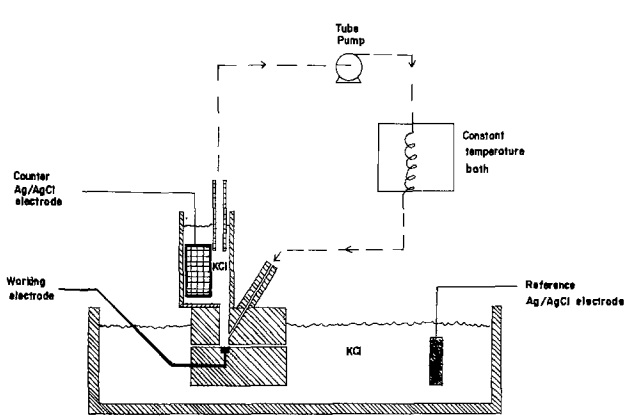


Fig. 1. Experimental arrangement

The KCl solutions used were prepared from doubly distilled water and reagent grade KCl. The initial silver surface was mechanically finished with 4/0 emery polishing paper purchased from Buehler Limited.

The experiments were conducted at 25° ± 1°C in 0.5, 1.0, 1.5, 2.0, and 3.0N KCl solutions. The electrode was galvanostatically charged at 5 mA/cm^2 and subsequently reduced potentiostatically. A PAR Model 173 potentiostat/galvanostat was used to impose the experimental current or voltage.

The overpotential, η, reported in this communication is the potential measured or imposed between the working electrode and the Ag/AgCl reference electrode.

Results

Galvanostatic formation of AgCl.—Typical η-t (overpotential-time) curves for the galvanostatic charging (passage of constant anodic current) of silver electrodes in KCl solutions are shown in Fig. 2. Curve a was obtained when silver chloride was formed on an electrode with a freshly polished silver surface. The curve shows a close to linear rise in potential with time. After the electrolytically formed silver chloride was totally reduced back to silver (either galvanostatically or potentiostatically), galvanostatic recharging of the electrode exhibited a different η-t curve (curve b). The η-t curve has a rather flat portion at the beginning followed by a rapid rise. Additional cycling (charged and discharged) did not seem to have further effect on the η-t curves for galvanostatic charging nor was there any observable dependence (based on scanning electron microscope observation) of the electrode surface roughness on the number of cycles. However, it was observed that the flat portion of the η-t curve was usually lower and the rapid rise in potential was usually earlier (shorter t_p as defined in Fig. 2) when higher concentrations of KCl solutions were used. Figure 3 shows the equivalent amount of charge, Q^* (equal to it_p), at t_p with respect to KCl concentrations. The time t_p is time at which rapid rise in potential begins as defined in Fig. 2. Galvanostatic charging in 1N KCl with current densities from 2.5 to 100 mA/cm^2 indicated that the value of Q^* is independent of the charging current in the range studied.

Scanning electron microscope pictures of the electrode surfaces at positions 1, 2, and 3 as indicated in

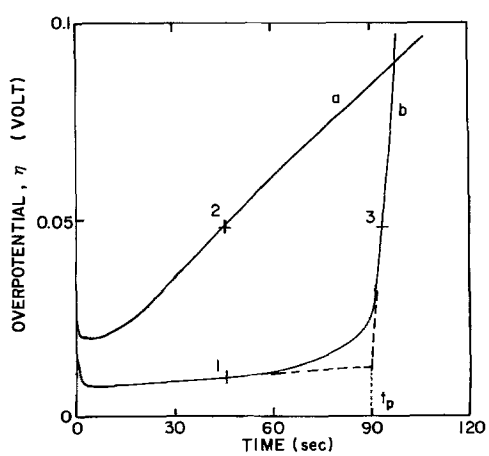


Fig. 2. Overpotential vs. time curves for the galvanostatic formation of silver chloride at 5 mA/cm^2 in 1.5N KCl solution. Curve a, initial freshly polished silver surface; curve b, cycled silver surface.

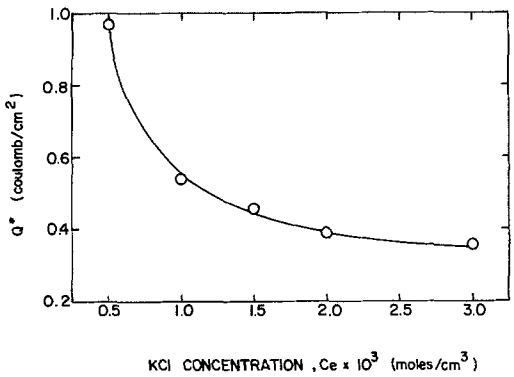


Fig. 3. Dependence of Q* on KCl concentrations. Anodic charging current was 5 mA/cm².

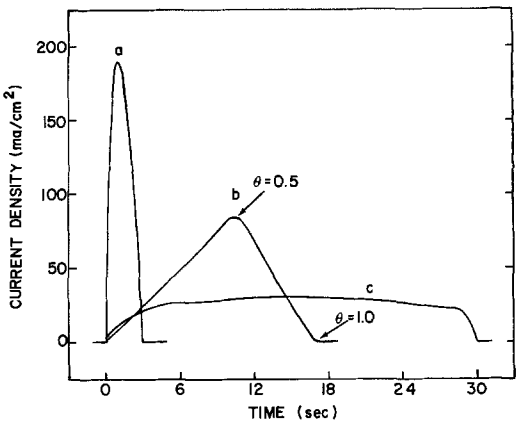


Fig. 5. Current-time curves for the potentiostatic reduction of AgCl at −100 mV in 1N KCl solution. Curve a, initial porous coverage of AgCl; curve b, heavy initial coverage of AgCl; and curve c, nonporous initial coverage of AgCl with few reduction centers.

Fig. 2 are shown in Fig. 4. Figures 4a and 4b give comparison of the surfaces (fresh and cycled) at the same state of charge while Fig. 4b and 4c give comparison of the surfaces at the same electrode potential. The small particles between the AgCl crystallites in Fig. 4c are silver.

Potentiostatic reduction of AgCl.—The current flow during the reduction of AgCl depends on the rate of diffusion of complexed silver ions from the silver chloride surface to the silver surface. As an approximation, one can say that the silver area is θA and the silver chloride area is $(1 - \theta)A$. Here A is the total electrode area and θ is the fraction of silver area exposed. By assuming a linear concentration profile between the AgCl area and Ag area, the reaction rate, based on the area A, can be written as (16)

$$i = n\mathbf{F}k_m^{o}(\theta)^{1/2}(1-\theta)^{1/2}(c_R^{s} - c_R^{sat}) \qquad [1]$$

where c_R^s is the concentration of complexed silver ions at the silver surface where charge transfer reaction takes place and c_R^{sat} is the saturation concentration of complexed silver ions which prevails at the AgCl surface. **F** is the Faraday constant and n is the number of electrons involved in the charge transfer reaction. The mass transfer coefficient, k_m^o, is equal to D/δ where D is the complexed ions diffusion coefficient and δ is the average diffusion length. One can also define an over-all mass transfer coefficient, k_m, such that

$$k_m = k_m^{o}(\theta)^{1/2}(1-\theta)^{1/2} \qquad [2]$$

The over-all mass transfer coefficient thus varies with the amount of surface coverage by AgCl.

The maximum current density reached during potentiostatic reduction was found to depend on the initial coverage of silver surface by AgCl. If the initial coverage, $1 - \theta$, was above 0.5 and below about 0.8 (state of charge in the flat portion of curve b in Fig. 2), the maximum current remained the same over a wide range of initial charge. However, if the electrode was initially heavily covered by AgCl (state of charge corresponding to rising portion of curve b in Fig. 2), lower maximum currents were obtained. Typical i-t curves are shown in Fig. 5. Curve a was obtained with an initially porous silver chloride film. Curves b and c were obtained from initially heavily charged electrodes. Curve c had a more dense coverage of AgCl compared to curve b.

Surface morphology of the electrode at the cathodic current maximum for the cases corresponding to curves a and c in Fig. 5 are shown in Fig. 6. For the case with initial heavy coverage, there were few reduction centers, and the boundaries of the centers expanded in a circular manner as AgCl was being reduced (Fig. 6 d and e). For the case where the initial AgCl film was quite porous, there were many more reduction centers dispersed among the silver chloride crystallites (Fig. 6 a, b, and c). Figure 6c shows the structure of reduced silver after the remaining silver chloride had been removed by sodium thiosulfate. Similar surface morphology was also reported by Briggs and Thirsk (6).

Cathodic i-η curves obtained for KCl concentrations of 0.5, 1.0, 1.5, 2.0, and 3.0N are shown in Fig. 7. Experiments were performed on a cycled electrode with the surface undisturbed between runs. Before each potentiostatic reduction run, the electrode was charged galvanostatically at 5 mA/cm² to approximately 85% of t_b (see Fig. 2). This assured that the AgCl film was porous and the surface coverage was approximately the same for each run. Data points in Fig. 7 correspond to maximum currents reached during potentiostatic reductions. At the maximum current, the fraction of ex-

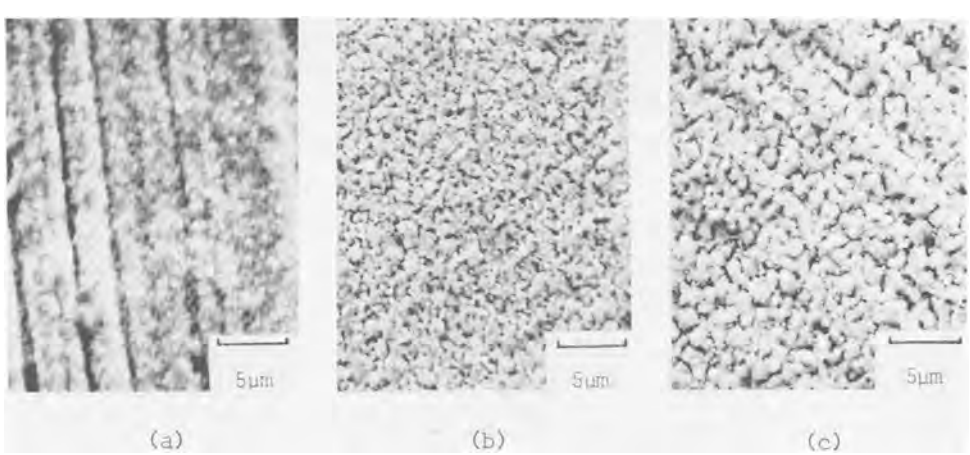


Fig. 4. Scanning electron microscope pictures of the electrode surface during galvanostatic formation of AgCl. Pictures a, b, and c correspond to positions 2, 1, and 3 in Fig. 2, respectively.

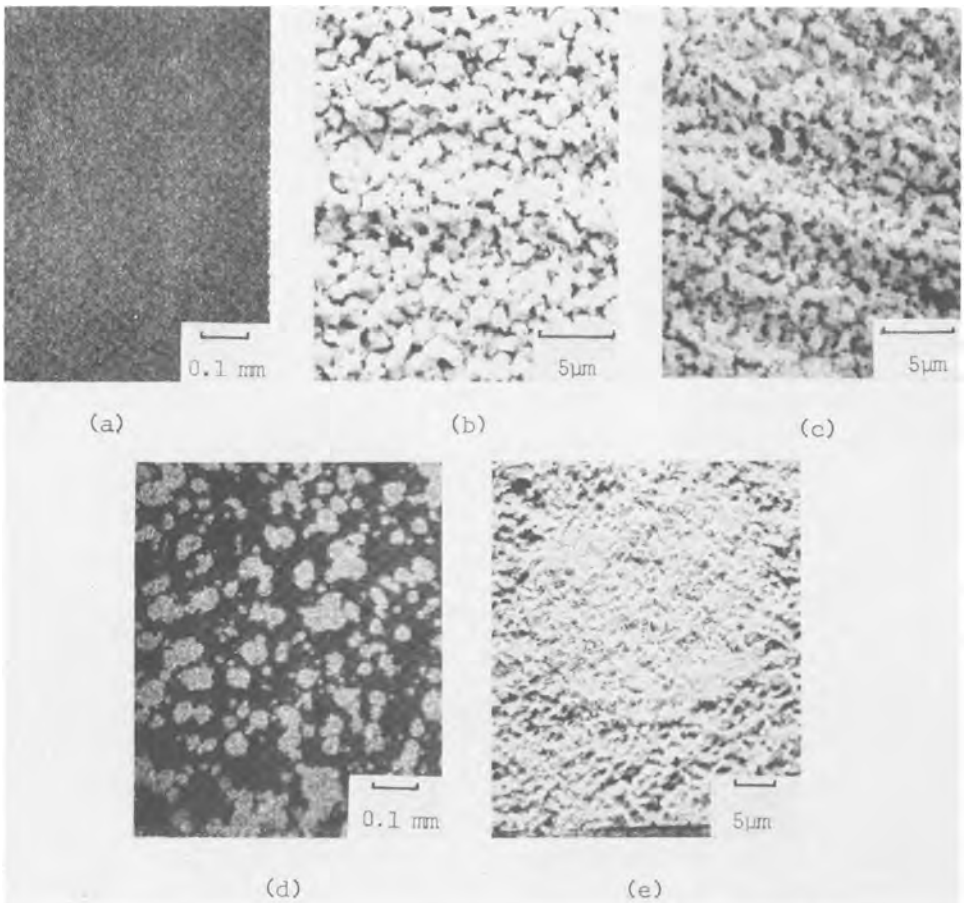


Fig. 6. Pictures showing electrode morphology at the maximum cathodic current. a, b, and c correspond to curve a in Fig. 5. a, Optical microscope picture of the surface; b, SEM picture of the surface; c, SEM picture of the surface after the remaining AgCl has been removed by sodium thiosulfate; d, e, correspond to curve c in Fig. 5 with d, optical microscope picture showing large reduction centers, and e, SEM picture showing circular growth of the reduction center.

posed silver area, θ, was 0.5 as determined from microscope pictures.

No limiting current plateau was observed in the 0.5N KCl solution. From the limiting current plateaus in 1.0, 1.5, 2.0, and 3.0N KCl solutions, the over-all mass transfer coefficients for the transport of $AgCl_{n+1}^{-n}$ (at $\theta = 0.5$) were calculated using the following equation

$$\kappa_m = \frac{-i_{lim}}{\mathbf{F} c_R^{sat}} \qquad [3]$$

Values of c_R^{sat} were obtained from experimental results (17). The mass transfer coefficient, k_m^o, was then calculated from Eq. [2] where k_m^o is $2k_m$ at $\theta = 0.5$.

The mass transfer coefficient was found to depend on KCl concentrations (Fig. 8). Examination of Fig. 8 shows that the dependence follows the relationship

$$k_m^o = B \exp(Ec_e) \qquad [4]$$

with $B = 1.808 \times 10^3$ cm/sec and $E = -1.519 \times 10^3$ cm^3/mole.

The kinetic rate expression applied to the present system can be written as

$$i = \theta i_o \left[\left(\frac{c_R^s}{c_R^{sat}} \right)^{\gamma - \alpha_a} \exp\left(\frac{\alpha_a \mathbf{F} \eta}{RT} \right) - \left(\frac{c_R^s}{c_R^{sat}} \right)^{\gamma - \alpha_c} \exp\left(\frac{-\alpha_c \mathbf{F} \eta}{RT} \right) \right] \qquad [5]$$

where γ is the order of dependence of i_o on the complexed silver ion concentration; α_a and α_c are the anodic and cathodic charge transfer coefficients, respectively; R is the gas constant; and T is the absolute temperature. The exchange current density i_o can be written as

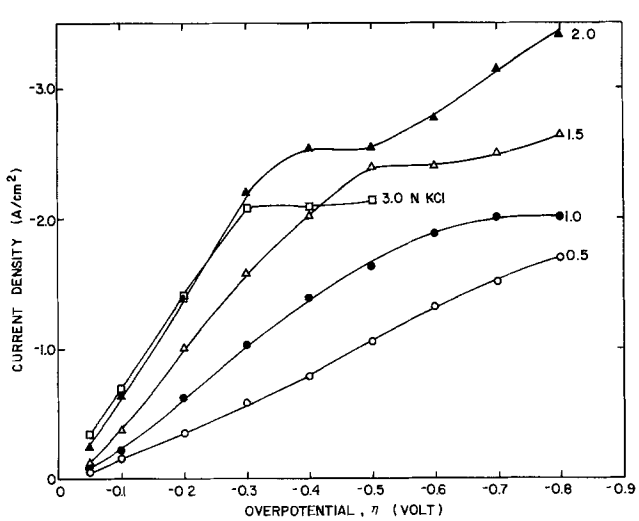


Fig. 7. Current-overpotential curves for the reduction of silver chloride. The current is the maximum current from the i-t curves.

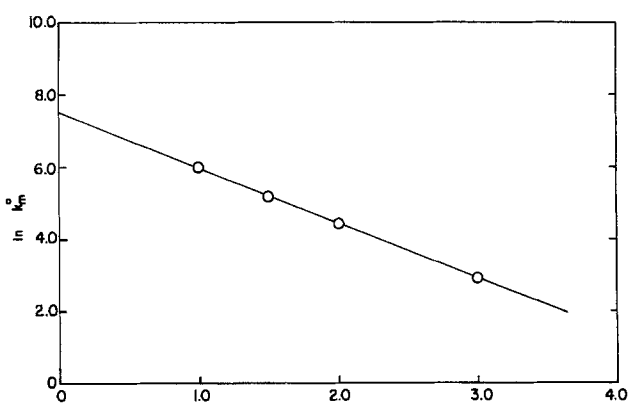


Fig. 8. Dependence of the mass transfer coefficient on KCl concentrations.

$$i_o = i_o^o \left(\frac{c_R^{sat}}{c_R^*} \right)^{\gamma} \quad [6]$$

where i_o^o is the exchange current density corresponding to the concentration of complexed silver ions, c_R^*. In the present investigation, c_R^* was selected as the saturated concentration of $AgCl_{n+1}^{-n}$ in 1N KCl solution, *i.e.*, $c_R^* = c_R^{sat}$ in 1N KCl.

It is believed that the silver dissolution and deposition involves a one-electron transfer elementary step. Therefore, Eq. [5] can be rearranged, with $\gamma = \alpha_a$ and $\alpha_a + \alpha_c = 1.0$, to read

$$\ln \frac{i}{\left[\left(\frac{c_R^{sat}}{c_R^s} \right) \exp \left(\frac{F\eta}{RT} \right) - 1 \right]} - \ln \left(\frac{c_R^s}{c_R^*} \right) = \ln \theta i_o^o - \alpha_c \left[\frac{F\eta}{RT} + \ln \left(\frac{c_R^{sat}}{c_R^*} \right) \right] \quad [7]$$

Using the results from Fig. 7 and 8, values of c_R^s were first calculated from Eq. [1]. The left-hand side of Eq. [7] was then plotted against the terms in the bracket on the right-hand side as shown in Fig. 9. The slope of the plot allowed the detemination of α_c and the intercept gives the value of θi_o^o with $\theta = 0.5$ (since the peak current was used). The values of α_c and i_o^o were determined to be 0.3 and 0.15 A/cm^2, respectively.

The current density, i, can be calculated with respect to θ at a fixed η by solving Eq. [1] and [7] simultaneously. Calculations of i *vs.* θ for several different η indicate that the maximum currents occur at θ around 0.75 instead of 0.5 as was experimentally observed. The solubility of AgCl is quite low and thus the distance from silver chloride sites where $AgCl_{n+1}^{-n}$ ions are reduced is probably quite small. It is possible that the effective charge transfer silver area for the reduction of $AgCl_{n+1}^{-n}$ was actually less than the total exposed silver area when the electrode surface was less than 50% covered by AgCl.

A model was developed to calculate the effective silver reacting area. The model assumes that the effective silver area per silver chloride center is a ring extending a fixed distance from the perimeter of the silver chloride-silver interface. The effective width of the ring is calculated by assuming that all the exposed Ag is effective at θ equals 0.5. At $\theta \leq 0.5$

$$\theta_{eff} = \theta \quad [8a]$$

and at $\theta \geq 0.5$

$$\theta_{eff} = (1 - \sqrt{0.5})\,[2\sqrt{(1 - \theta)} + (1 - \sqrt{0.5})] \quad [8b]$$

An effective silver chloride area was also assumed for the supply of complexed silver ions at $\theta < 0.5$. Similar to the treatment in obtaining effective silver area at $\theta < 0.5$, the effective silver chloride area per center at $\theta < 0.5$ was also assumed to be a ring extending a fixed distance from the silver chloride-silver interface; the distance being calculated by assuming that all the silver chloride area is effective at $\theta = 0.5$. Therefore, at $\theta \leq 0.5$

$$(1 - \theta)_{eff} = 2\sqrt{1 - \theta}\sqrt{0.5} - 0.5 \quad [9a]$$

and at $\theta \geq 0.5$

$$(1 - \theta)_{eff} = 1 - \theta \quad [9b]$$

According to the model, θ and $(1 - \theta)$ in Eq. [1], [2], [5], and [7] should now be replaced by θ_{eff}, and $(1 - \theta)_{eff}$, respectively. The k_m in Eq. [2] is thus in the form, at $\theta \leq 0.5$

$$k_m = k_m^o\,[2\sqrt{1 - \theta}\sqrt{0.5} - 0.5]^{1/2}[\theta]^{1/2} \quad [10a]$$

and at $\theta \geq 0.5$

$$k_m = k_m^o\,[1 - \theta]^{1/2}[2\sqrt{1 - \theta}\,(1 - \sqrt{0.5}) + (1 - \sqrt{0.5})^2]^{1/2} \quad [10b]$$

Applying this revised form of the model, a maximum in current was obtained mathematically at $\theta = 0.5$.

To obtain the variation of θ with respect to Q (accumulated charge) for application in porous battery electrode modeling, the i-θ profiles were first calculated at various η using revised Eq. [1] and [5] for KCl concentration of 1.0N. From the experimental potentiostatic i-t curves at the corresponding η, a set of i-Q curves were then obtained approximately by graphical integration. Comparison of the calculated i-θ curves with the corresponding i-Q curves gave the variation of θ with respect to Q. It was found that the best fitted relationship is of the form

$$\theta = (0.25)^{Q/Q^*} \quad [11]$$

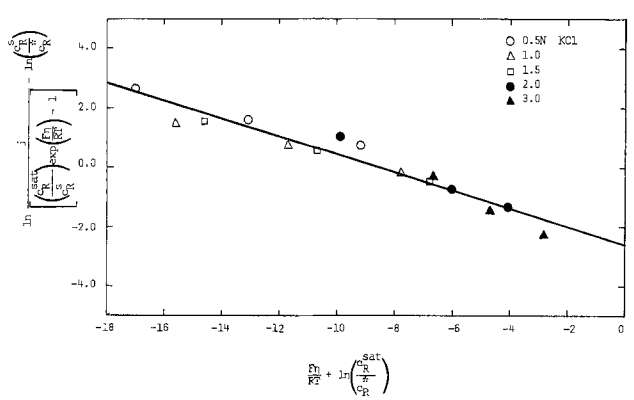


Fig. 9. Plot corresponding to Eq. [7]

Discussion

The two differently shaped η-t curves obtained on two different silver surfaces have also been observed separately by previous investigators. Briggs and Thirsk (6) obtained curves similar to curve a in Fig. 2 on their freshly polished silver surface while Katan *et al* (10) obtained curves similar to curve b on their cycled silver surface. The exchange current densities on a freshly polished silver surface and a cycled silver surface are probably different. The growth of AgCl on the two different surfaces is also different as can be seen from Fig. 4. On a freshly polished silver surface, there are a large number of AgCl nucleation centers formed at the beginning. As more charge is passed, the porous AgCl film thickens with a slow decrease in porosity. On a cycled surface, there are less nucleation centers and more crystal growth of silver chloride (Fig. 4 b and c). In addition, the true silver surface area of a cycled electrode is larger, as has been reported by Giles (9), and can be seen from Fig. 4 b and c. As a result, there is more silver surface available for charge transfer to occur for a longer duration and the overpotential is smaller. Finally, as anodic charging continues on the cycled Ag electrode, the AgCl crystallites begin to grow together, blocking off the silver surfaces, and the rapid rise in overpotential results. These observations support the fact that the formation of AgCl is mainly via solution phase diffusion of $AgCl_{n+1}^{-n}$ followed by crystal growth from a supersaturated solution.

For cycled surfaces, higher KCl concentrations produced lower overpotentials. This is attributed to higher $AgCl_{n+1}^{-n}$ solubility and resulting smaller concentration overpotentials. The shorter time to surface coverage, t_p, at higher KCl concentrations seems to indicate earlier coverage of the silver surface by AgCl in solutions of higher Cl^- content. The earlier coverage can be due to the increase in nucleation sites. Briggs and Thirsk (6) have also observed the earlier surface coverage in higher KCl concentrations. From their η-t curves (which are similar to curve a of Fig. 2), one

can see that the slopes of the curves are steeper in higher KCl concentrations.

The initial higher overpotential of the galvanostatic η-t curves of Fig. 2 are probably due to slow nucleation leading to a "nucleation overpotential" (18).

An electrolyte flow rate of 3.5 cm²/sec was used to keep the KCl concentration near the electrode surface constant. No dependence of current densities on the flow rate was observed during potentiostatic reduction within the flow rate range of 2.0-7.4 cm³/sec. With no circulation of the electrolyte, the measured current densities were higher as a result of the increase in KCl concentrations near the electrode surface as the AgCl was being converted to silver, the increase in KCl concentrations increases the solubility of the silver chloride.

The fact that no limiting current was observed during potentiostatic reduction in 0.5N KCl solution can be explained by nonuniform secondary current distributions and nonuniform concentration distributions of complexed silver ions at the silver surface. The experimental arrangement was designed for uniform macroscopic primary current distribution. However, due to the roughness of the electrode surface and because the reactants are supplied from the silver chloride crystallites, the secondary current distribution and the reactant concentration on a micro scale on the order of 1 μm at the silver surface are not uniform with respect to distance from AgCl crystals. This is especially true in 0.5N KCl, where the solubility of AgCl is lower and the microscale nonuniformity becomes more pronounced. As a result, the diffusion limiting current of silver deposition was not separable from the onset of another reaction (possibly hydrogen evolution) for the 0.5N KCl run.

An increase in silver chloride coverage reduces the number of reduction centers. The lesser number of reduction centers resulted in larger area per reduction center at $\theta = 0.5$ during discharging. For the case with heavy initial coverage of silver chloride, i-η curves similar to those reported by Katan *et al.* [Fig. 7 of Ref. (10)] were obtained. As can be expected, no limiting currents were observed due to the large area per reduction center at $\theta = 0.5$ (see Fig. 6 d and e), which resulted in very nonuniform microscale distribution of complexed silver ions and secondary reaction current across the exposed silver surface. The total effective silver area (boundaries of reduction centers) for the reduction of complexed silver ions was very small as compared to the total exposed silver area. Again, the limiting diffusion current was obscured by the onset of another reaction. The total effective area for the case with a large area per reduction center is also smaller than that for the case with a large number of reduction centers, and resulted in lower currents at $\theta = 0.5$ during potentiostatic reduction (Fig. 5, curve c).

The almost order of magnitude difference in maximum currents between curve a and curve c in Fig. 5 supports the solution diffusion mechanism in the electrochemical formation and reduction of silver chloride. If significant solid phase transport had occurred, there should have been less differences in the magnitude of the maximum currents.

The decrease in k_m^o at higher concentrations of KCl is due to the increased portion of $AgCl_4^{-3}$ present as can be shown from calculations using stability constants (19). The complexed $AgCl_4^{-3}$ has a larger ionic radius and thus a smaller diffusion coefficient than the other complexes. The measured k_m^o which includes all $AgCl_{n+1}^{-n}$, is therfore smaller at higher concentrations of KCl. Katan *et al.* (10), from their rotating disk experiments, also obtained a smaller effective diffusion coefficient for complexed silver ions in 4N KCl compared to that obtained in the 2N KCl solution.

The overpotential η, as measured, includes concentration overpotential, η_c as well as the charge transfer overpotential, η_s. At high overpotentials, η_c becomes important. The terms involving c_R^s/c_R^{sat} were introduced in Eq. [5] to correct for the concentration overpotential. At low overpotentials (less than -60 mV), surface diffusion of adions may become rate determining as was indicated by Bockris *et al.* (14, 15) in their studies of the dissolution and deposition of silver from solutions of silver perchlorate in aqueous perchloride acid. The effect of adion surface diffusion was not included in Eq. [5]. Therefore, in obtaining the slopes and intercepts according to Eq. [7], only data points above cathodic overpotential of 100 mV were used. In addition, since kinetic parameters were to be determined, data in the range where reaction rates might be predominantly solution phase mass transfer limiting were also excluded when constructing Fig. 9. The data excluded were $|\eta| > 0.4$V in 0.5, 1.0, and 1.5N KCl, $|\eta| > 0.3$V in 2.0N KCl, and $|\eta| > 0.25$V in 3.0N KCl.

It might be emphasized that the data in Fig. 7 and 9 are the same with the exceptions noted. The combination of Eq. [1] and [5] correlate the data as shown in Fig. 9. Since Fig. 7 presents the same data, it follows that these same equations yield approximately the curves shown in Fig. 7. The curves in Fig. 7 can be seen to be S shaped, the lower portions being near the inflection point of the S. The data at low η are in the region of exponential dependence of i on η shown in Eq. [5]. However, at larger η the curve in Fig. 7 bends downward due to a decrease in c_R^s as described by Eq. [1].

The overpotential as measured by the reference electrode also contained a small IR or ohmic resistance contribution which was considered negligible. The KCl solutions served as supporting electrolytes with high conductivity. Calculations showed, for example, at a current density of 2.0 A/cm², in 1N KCl, the maximum IR drop was about 20 mV, approximately 3% of the total observed overpotential, η.

Current densities as reported in this communication are based on the apparent electrode area. As mentioned earlier, the true surface area increases after the electrode has been cycled in KCl solutions. To account for the surface roughness based only on scanning electron microscope observations would not be very accurate. It was decided, therefore, that the results should be reported based on the apparent electrode area, keeping in mind that the experiment was performed on cycled electrode surfaces.

The true surface area also varied slightly between runs. Random checks showed that the current densities reported are reproducible to within $\pm 10\%$.

It must also be pointed out that the variation of θ with accumulated charge shown in Eq. [11] is quite approximate. The variation of θ is actually potential dependent. This is because the growth of silver deposits is potential dependent as has been indicated by Aleskovskii *et al.* (11). The result also varied somewhat with the KCl concentration. However, the results shown in Eq. [11] appear to be suitable for purposes of mathematical modeling of porous Ag/AgCl battery electrodes.

Conclusions

The electrochemical behavior of a Ag/AgCl electrode is highly dependent on the surface coverage by AgCl during galvanostatic charging. The η-t (overpotential-time) curves differ widely in shape depending on whether the silver surface is freshly polished or previously cycled.

The number of silver chloride nucleation centers increases with increasing KCl concentrations during galvanostatic charging.

Experimental observations support previous conclusions that the formation and dissolution of AgCl on silver is via solution diffusion of complexed silver ions, $AgCl_{n+1}^{-n}$, with $n = 0$, 1, 2, or 3.

The maximum current density during potentiostatic discharge depends highly on the number of reduction centers. The number of reduction centers in turn depends on the degree of initial coverage by silver chloride. A heavier initial coverage gives lesser number of reduction centers during discharge. A larger number of small reaction sites leads to lower overpotentials at comparable current densities.

The mass transfer coefficient, k_m^o, for the diffusion of $AgCl_{n+1}^{-n}$ was found to depend on KCl concentrations in the form

$$k_m^o = B \exp(Ec_e)$$

with $B = 1.808 \times 10^3$ cm/sec and $E = -1.519 \times 10^3$ cm^3/mole.

The exchange current density was determined to be

$$i_o = 0.15 \left(\frac{c_R^{sat}}{10.1 \times 10^{-8}} \right)^{0.70} \text{A/cm}^2$$

The units of c_R^{sat} are mole per cubic centimeter.

The cathodic charge transfer coefficient, α_c was determined to be 0.30.

Acknowledgment

This work was supported by the Office of Naval Research under Contract no. N0014-75-C-0794 and the University of California, Los Angeles, California.

Manuscript submitted Oct. 18, 1976; revised manuscript received April 23, 1977.

Any discussion of this paper will appear in a Discussion Section to be published in the June 1978 JOURNAL. All discussions for the June 1978 Discussion Section should be submitted by Feb. 1, 1978.

Publication costs of this article were assisted by the University of California.

LIST OF SYMBOLS

- A electrode surface area, cm^2
- c_e electrolyte concentration, mole/cm^3
- c_R^s complexed silver ions concentration at the silver surface mole/ cm^3
- c_R^{sat} saturated concentration of complexed silver ions in the KCl solution mole/cm^3
- c_R^* saturated concentration of complexed ions in 1N KCl solution, mole/cm^3
- D effective diffusion coefficient of complexed silver ions, cm^2/sec
- $\mathbf{F}$ Faraday constant, 96,487 C/equiv.
- i current density, A/cm^2
- i_o exchange current density, A/cm^2
- i_o^o exchange current density based on saturated concentrations of complexed ions in 1N KCl solution, A/cm^2
- k_m surface coverage dependent mass transfer coefficient, cm/sec
- k_m^o effective mass transfer coefficient of complexed silver ions (equal to $2k_m$ at $\theta = 0.5$), cm/sec
- n number of electrons transferred in electrode reaction; or number of charge on complexed silver ions
- Q charge, C/cm^2
- Q^* charge parameter, equal to it_p, C/cm^2
- RT gas constant multiplied by absolute temperature, J/mole
- α_a, α_c anodic and cathodic charge transfer coefficients
- γ exponent in composition dependence of the exchange current density
- δ effective diffusion path, cm
- η overpotential, $\eta = \eta_c + \eta_s$, V
- η_c concentration overpotential, V
- η_s charge transfer overpotential, V
- θ fraction of silver surface not covered by silver chloride

REFERENCES

1. H. Gu, D. N. Bennion, and J. Newman, *This Journal*, **123**, 1364 (1976).
2. T. Katan, H. Gu, and D. N. Bennion, *ibid.*, **123**, 1370 (1976).
3. G. J. Janz, in "Reference Electrodes," D. J. G. Ives and G. J. Janz, Editors, chap. 4, Academic Press, New York (1961).
4. L. J. Kurtz, *C. R.* URSS, **11**, 283 (1935).
5. H. Lal, H. R. Thirsk, and W. F. K. Wynne-Jones, *Trans. Faraday Soc.*, **47**, 70 (1951).
6. G. W. D. Briggs and H. R. Thirsk, *ibid.*, **48**, 1171 (1952).
7. W. Jaenicke, R. P. Tischer, and H. Gerischer, *Z. Elektrochem.*, **59**, 448 (1955).
8. M. Fleischmann and H. R. Thirsk, *Electrochim. Acta*, **1**, 146 (1959).
9. R. D. Giles, *J. Electroanal. Chem.*, **27**, 11 (1970).
10. T. Katan, S. Szpak, and D. N. Bennion, *This Journal*, **120**, 883 (1973).
11. V. B. Aleskovskii, E. V. Bairashnyi, E. G. Ivanov, and V. A. Nikoshii, *Sb. Rab. Khim. Istochnikam*, **4**, 241 (1969).
12. H. Gerischer and R. P. Tischer, *Z. Electrochem.*, **61**, 1159 (1957).
13. H. Gerischer, *ibid.*, **62**, 256 (1958).
14. W. Mehl and J. O'M Bockris, *J. Chem. Phys.*, **27**, 818 (1957).
15. A. R. Despic and J. O'M Bockris, *ibid.*, **32**, 389 (1960).
16. H. Gu, Ph.D. Thesis, School of Engineering, University of California, Los Angeles (1977).
17. W. F. Kinke, "Solubilities (Seidell)," 4th ed., Vol. I, p. 67, D. Van Nostrand Co., Inc., New York (1958).
18. M. Fleischmann and H. R. Thirsk, in "Advances in Electrochemistry and Electrochemical Engineering, III," P. Delahay, Editor, p. 168, Interscience Publishers (1963).
19. L. G. Sillen and A. E. Martell, "Stability Constants," Spec. Pub. No. 17, The Chemical Society, London (1964).

Statistical Analysis of Electrode Kinetics Measurements–Copper Deposition from $CuSO_4$-H_2SO_4 Solutions

Reinaldo Cabán[1] and Thomas W. Chapman*

Department of Chemical Engineering, University of Wisconsin, Madison, Wisconsin 53706

ABSTRACT

The kinetics of electrochemical copper deposition from copper sulfate-sulfuric acid solutions have been studied by measuring polarization curves with a rotating-disk electrode. Kinetics models are evaluated and their parameters determined by nonlinear regression analysis of 87 data points. The data are fit within experimental error by a five-parameter model which includes the effects of both copper sulfate and sulfuric acid concentrations. The statistical analysis is made feasible by the rapid simulation of the experimental system by orthogonal collocation. The simulation involves computation of current distribution below limiting current at a specified applied potential for a given kinetics model.

The determination of quantitative electrode kinetics expressions is difficult because of the large number of variables and parameters involved and because of the complicated nonlinear form of the electrochemical kinetics relationships. As a result most kinetic studies focus on only a subset of parameters such as the exchange current density or a reaction order, and do not attempt often to cover a wide range of experimental conditions. For engineering calculations, however, it is necessary to have a fairly complete kinetics expression which can predict local current density over a range of composition and potential.

It is risky to construct a kinetics expression for a given reaction by taking an exchange current density from one experiment and a Tafel slope from another experiment, etc., because there is no guarantee that such parameters are truly independent and that the composite expression will represent properly the behavior of a particular experimental system. For example, the metal surface formed in copper electrowinning probably has quite different catalytic properties from one prepared in the laboratory for a basic mechanistic study. It would be preferable for engineering purposes to determine a complete, empirical kinetics expression with all of its parameters estimated simultaneously from a set of experimental data which cover the ranges of variables to be encountered in a system of practical interest.

Statistical Treatment of Complex Systems

The problem of estimating multiple parameters of nonlinear models from data has been studied in some detail by statisticians (1-3), and methods have been developed for treating many complex phenomena, for example, heterogeneous catalysis (4). The appropriate statistical procedures are indicated in Fig. 1. The form of a kinetics model is postulated and incorporated in a simulation of the experimental system behavior. The parameters of the model are adjusted to make the simulation match the experimental data within experimental accuracy. Figure 1 indicates that least squares fitting of the data yields not only a set of parameters for a given kinetics model but also quantitative measures of goodness of fit and a parameter-estimate correlation matrix. The former may be compared with experimental error as determined by experimental replication to inspect whether or not a postulated kinetics model is adequate to fit the data. The latter indicates whether various parameters characterize independent effects or whether some are superfluous.

In most electrochemical experiments the data are some sort of current-potential relationship, and the simulation of the system behavior requires consideration of mass transfer and potential distribution effects in addition to the specific kinetics model. The major difficulty in applying nonlinear least squares regression analysis to fitting such electrochemical polarization data with a set of parameters is that the data analysis is an iterative procedure in which trial values of the parameters are repeatedly revised until the variance between the observed and predicted data is minimized. At each iteration one must generate not only a simulation or prediction of the experimental system output for each data point but also derivatives of the predicted output with respect to each parameter value, which are used in revising the parameter estimates.

Because electrochemical systems are so complicated these requirements imply a large and expensive computational effort. Recently we have described an approximate procedure for simulating electrochemical cell polarization which is significantly faster in computation time than alternative methods (5). The method known as orthogonal collocation is well suited to the repetitive calculations of nonlinear least squares analysis of electrochemical kinetics data. In this paper we demonstrate the combination of system simulation by collocation with nonlinear least squares estimation of electrochemical kinetics parameters by analyzing

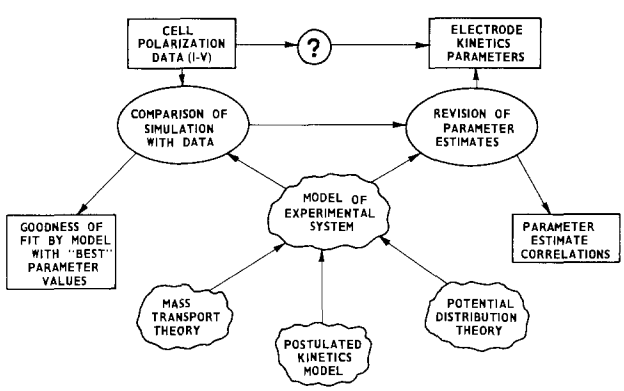


Fig. 1. Schematic representation of information flow in the global least squares fitting of an electrode kinetics model to cell polarization data.

* Electrochemical Society Active Member.

[1] Present address: Department of Chemical Engineering, University of Puerto Rico, Mayaguez, Puerto Rico 00708.

Key words: copper sulfate, sulfuric acid, rotating disk, current distribution, orthogonal collocation.

steady-state polarization measurements on a rotating-disk electrode. Measurements have been made with copper sulfate in sulfuric acid, and the kinetics parameters determined here are compared with earlier results.

Simulation of the Rotating-Disk Electrode

The problem of current distribution on a rotating-disk electrode below limiting current was first solved by Newman (6) in one of the earliest analyses of moderately complicated electrochemical transport problems. The problem was made tractable by a thin diffusion-layer approximation so that potential distribution and mass transfer effects could be treated separately (7). Since the solution to Laplace's equation for the potential in this geometry can be expressed as a series of Legendre functions, a summation of Legendre polynomials was used to describe the current distribution on the electrode. A second series was postulated for the concentration, and the two were matched by relating the current density to the flux of reactant at the surface. It was not recognized at the time that a formal solution for the concentration can be obtained as a superposition integral over the current density, but a later communication clarifies the point (8). Ten approximating functions were required to describe a metal deposition reaction, and a solution to the system of algebraic equations was obtained by repetitive substitution. Numerous convergence and precision difficulties were reported.

It is our purpose to show here how the incorporation of orthogonal collocation concepts in the solution of this problem can result in a faster and more stable computational algorithm. It is important to recognize that we are more interested in computing total current rather than computing detailed current distributions. Since the method of orthogonal collocation renders the solution at Gaussian quadrature points, estimates of the average current density can be obtained with considerably more accuracy than the detailed current distribution at any given order of approximation. Consequently, fewer approximating functions are required, and precision difficulties are minimized. Furthermore, it will be seen that the numerous integrals needed in the nonlinear regression calculations can be evaluated easily by Gaussian quadrature.

Mathematical formulation of the problem.—Newman (7) has presented the mathematical formulation for the current distribution problem for a disk electrode of radius r_0 embedded on an infinite rotating disk with a counterelectrode placed at infinity. According to the usual boundary layer arguments, concentration gradients can be neglected in the bulk of the solution such that Laplace's equation for the potential holds. A solution to the Laplace equation in rotational elliptical coordinates is (7, 9)

$$\phi(\xi,\rho) = \frac{RT}{|n|\mathbf{F}} \sum_{k=0}^{\infty} D_k P_{2k}(\rho) M_{2k}(\xi) \qquad [1]$$

where $y = r_0\xi\rho$, $r = r_0\sqrt{(1+\xi^2)(1-\rho^2)}$, y is the normal distance from the electrode, r is the radial distance, P_{2k} is a Legendre polynomial $[-1, 1]$ of degree $2k$, and M_{2k} is a Legendre function of imaginary argument, zeroeth order, and degree $2k$ (10). The latter is subject to the condition $M_{2k}(0) = 1$ and can be expressed formally as

$$M_{2k}(\xi) = \frac{(-1)^k(k!)^2 i}{(2k)!\pi} \int_{-1}^{+1} \frac{(1-t^2)}{(i\xi - t)^{2k+1}}\, dt \qquad [2]$$

The multiplicative constant in Eq. [1] is included for convenience. For large ξ, far from the disk, the first term in a series solution of Eq. [2] provides a useful approximation

$$M_{2k}(\xi) = \frac{(k!)^2}{\pi(2k)!\xi^{2k+1}} \frac{\Gamma(2k+1)\Gamma(1/2)}{\Gamma(2k+3/2)} \qquad [3]$$

The potential in the solution extrapolated to the surface of the electrode is given by

$$\phi_0(\rho) = \phi(0,\rho) = \frac{RT}{|n|\mathbf{F}} \sum_{k=0}^{\infty} D_k P_{2k}(\rho) \qquad [4]$$

Thus, the normal current density at the electrode is given by

$$\frac{i}{\kappa_\infty} = -\left.\frac{\partial\phi}{\partial y}\right|_{y=0} = \left.\frac{-1}{r_0\rho}\frac{\partial\phi}{\partial\xi}\right|_{\xi=0}$$

$$= \frac{-RT}{r_0\rho|n|\mathbf{F}} \sum_{k=0}^{\infty} D_k P_{2k}(\rho) M_{2k}'(0) \qquad [5]$$

where

$$M_{2k}'(0) = -\frac{2}{\pi}\frac{\{2^k k!\}^4}{\{(2k)!\}^2} \qquad [6]$$

We restrict our discussion to systems with an excess of supporting electrolyte so that the effect of ionic migration may be neglected. The equation of convective diffusion for every minor species in solution reads

$$v_r\frac{\partial c_i}{\partial r} + v_y\frac{\partial c_i}{\partial y} = \mathcal{D}_i\frac{\partial^2 c_i}{\partial y^2} \qquad [7]$$

in cylindrical coordinates, where $\mathcal{D}_i$ is the pseudobinary diffusion coefficient. An analytical solution to Eq. [7] may be obtained for the thin diffusion layer case where the first terms in the small y expansions of Von Kármán's velocity profiles may be used (11, 12). The appropriate approximations for the radial and axial velocity components are

$$\left.\begin{aligned} v_r &= a r y \Omega\sqrt{\Omega/\nu} \\ \text{and} \qquad v_y &= -a y^2 \Omega\sqrt{\Omega/\nu} \end{aligned}\right\} \qquad [8]$$

with $a = 0.51023$ (13). The solution to Eq. [7] corresponding to the limiting current ($c_R(0,r) = 0$) is

$$i_{\lim} = \frac{n\mathbf{F}\mathcal{D}_R c_\infty}{s_R\Gamma(4/3)}\left(\frac{a\nu}{3\mathcal{D}_R}\right)^{1/3}\left(\frac{\Omega}{\nu}\right)^{1/2} \qquad [9]$$

Below limiting current we find it convenient to express the surface concentration as a superposition integral over the prevailing current density which is to be determined. For each reacting species

$$c_i(0,r) = c_{i0}(r) = c_{i\infty} + \frac{n\mathbf{F}\mathcal{D}_i}{s_i\Gamma(2/3)}$$

$$\left(\frac{3\mathcal{D}_i}{a\nu}\right)^{1/3}\left(\frac{\nu}{\Omega}\right)^{1/2}\int_0^r \frac{i_y(\zeta)\zeta d\zeta}{[r^3-\zeta^3]^{2/3}} \qquad [10]$$

which can be obtained as shown in Section 58 of Levich (11) or, more easily, by applying Eq. [40] in a paper by Stewart (13).

Equations [5] and [10] relate the potential and concentration distributions on the electrode to the current distribution function. Another relationship among these quantities is needed, specifically a kinetics expression. Let us consider an electrode reaction

$$\sum_i s_i M_i^{z_i} \rightleftharpoons ne^- \qquad [11]$$

which follows kinetics of, say, the Butler-Volmer type. Many reactions have been shown to follow such a rate expression, which in general can be written as

$$i(r) = {}^0i_0\left[\prod_i c^{\gamma_i}{}_{i0}(r)\right]\left[e^{\alpha_a\frac{\mathbf{F}\eta_s(r)}{RT}} - e^{-\alpha_c\frac{\mathbf{F}\eta_s(r)}{RT}}\right] \qquad [12]$$

where ${}^0i_0$ is the standard exchange current density ($c_{i0} = 1M$, all i), η_s is the surface overpotential, and α_a and α_c are the anodic and cathodic transfer coefficients, respectively. According to the simplified activated complex analysis from which Eq. [12] follows, one should have for a single step redox reaction ($0 + e^- \rightleftharpoons R$) following first-order kinetics, $\alpha_a = \alpha_c = \gamma_0 = \gamma_R = 1/2$.

The surface overpotential in Eq. [12] is related to other contributions to the cell potential by

$$V = U(c_\infty) + \phi_0(r) + \eta_s(r) + \eta_c(r) \qquad [13]$$

where V is the potential applied to the working electrode, $U(c_\infty)$ is the equilibrium cell potential for the conditions prevailing in the bulk of the solution, and η_c is the concentration overpotential given by

$$\eta_c = \frac{-RT}{n\mathbf{F}} \sum_i s_i \ln \frac{c_{i0}}{c_{i\infty}} \qquad [14]$$

In order to reduce the number of independent parameters we define the following dimensionless variables

$$E^* = E\frac{|n|\mathbf{F}}{RT} \qquad E = (V, \eta_s, \eta_c, U, \phi) \qquad [15]$$

$$i^* = \frac{i}{|i_{\lim}|} \qquad [16]$$

$$c_i^* = c_{i0}/c_{1\infty} \qquad [17]$$

$$x = r/r_0 \qquad [18]$$

$$\alpha = \alpha_a/|n| \qquad [19]$$

$$\beta = \alpha_c/|n| \qquad [20]$$

and

$$\mathrm{T} = \frac{|i_{\lim} n| r_0 \mathbf{F}}{\kappa_\infty RT} \qquad [21]$$

Consequently, the basic equations [4], [5], [10], and [12-14] become

$$\phi_0^*(x) = \sum_{k=0}^{\infty} D_k P_{2k}(\rho) \qquad [22]$$

$$i^*(x) = -\frac{1}{\mathrm{T}_\rho} \sum_{k=0}^{\infty} D_k P_{2k}(\rho) M'_{2k}(0) \qquad [23]$$

$$c_i^*(x) = c_{i\infty}^* + \left(\frac{\mathcal{D}_1}{\mathcal{D}_i}\right)^{2/3} \frac{3\sqrt{3}}{2\pi} \left(\frac{s_i}{s_1}\right) \int_0^x \frac{i^*(\xi)\xi d\xi}{[x^3 - \xi^3]^{2/3}} \qquad [24]$$

$$i^* = {}^0i_0^* \left[\Pi(c_i^*(x)/c_{i\infty}^*)^{\gamma_i}\right]\left[e^{\alpha\eta_s^*(x)} - e^{-\beta\eta_s^*(x)}\right] \qquad [25]$$

$$V^* = U_\infty^* + \phi_0^*(x) + \eta_c^*(x) + \eta_s^*(x) \qquad [26]$$

and

$$\eta_c^* = \sum_i s_i \ln \frac{c_i^*}{c_{i\infty}^*} \qquad [27]$$

where $\rho^2 = 1 - x^2$. Simulation of polarization of a rotating-disk electrode requires solution of these equations for the current distribution for given values of V^* and system parameters.

Solution by orthogonal collocation.—We implement the orthogonal collocation procedure by postulating a trial solution as a finite summation of orthogonal polynomials $Q(x)$; that is

$$\overset{(N)}{i^*}(x) = \sum_{k=0}^{N-1} A_k Q_{2k}(x) \qquad [28]$$

for the Nth approximation. The polynomials Q_{2k} are orthogonal over $[-1, 1]$; since $i^*(x)$ is an even function only even polynomials of order 0, 2, . . . , $2N$-2 are included. At this stage the selection of particular polynomials need not be specified. If Eq. [22] and [23] are truncated to the first N terms, and Eq. [28] is substituted into Eq. [24], yielding a finite series of integrals which can be evaluated, the problem is reduced to solving a set of algebraic equations with N unknown coefficients A_k. We obtain a solution by requiring Eq. [22-27] to be satisfied exactly at N discrete points x_i which are selected as the roots of Q_{2N}. The rationale for this choice is that the error contributed by the first neglected term in the truncated series [28] is made identically zero. Also, because such a choice of collocation points corresponds to Gaussian quadrature abscissas, the average error in the approximation is minimized, and the evaluation of integrals involving any of the functions arising in the basic equations can be made with considerable accuracy by quadrature, even with small N. For example, it will be necessary to compute the total current, which is given by an integral. In this problem we take Q_{2k} to be a Legendre polynomial, P_{2k}, defined as (14)

$$\left.\begin{aligned} P_{2k} &= \sum_{m=0}^{k} a_{km} x^{2k-2m} \\ \text{where} \quad a_{km} &= \frac{(-1)^m}{2^{2k}} \binom{2k}{2m} \binom{4k-2m}{2k} \end{aligned}\right\} \qquad [29]$$

This choice is natural because these functions have already arisen in solving the Laplace equation. The total current can now be computed by

$$I = 2\pi r_0^2 \int_0^1 i(x)x\,dx \doteq 2\pi r_0^2 \sum_{k=0}^{N-1} w_i x_i i(x_i) \qquad [30]$$

where x_i and w_i are the points and the weights, respectively, of Gaussian Legendre quadrature (14). The quadrature in Eq. [30] will be exact for current distributions which can be represented by polynomials of degree $4N$-2 or less. The choice of a different quadrature formula may result in a more accurate approximation. For example, Tchebychev quadrature would be more accurate for highly nonuniform current distributions because it would give more weight to the function values near the edge of the disk than does the Legendre quadrature. Depending on the choice of quadrature formula, the polynomials $Q_k(x)$, the points x_i, and the weights w_i are chosen accordingly.

If we consider the reaction $O + e \rightleftharpoons R$ and take O as the reference species, substitution of Eq. [28] into [24] gives

$$\left.\begin{aligned} c_O^*(x) &= 1 + \frac{3\sqrt{3}}{2\pi} \sum_{k=0}^{N-1} A_k E_k(x) \\ \text{and} \quad c_R^*(x) &= c_{R\infty}^* - \frac{3\sqrt{3}}{2\pi} \left(\frac{\mathcal{D}_R}{\mathcal{D}_O}\right)^{2/3} \sum_{k=0}^{N-1} A_k E_k(x) \end{aligned}\right\} \qquad [31]$$

where

$$E_k(x) = \int_0^x \frac{P_{2k}(\xi)\xi d\xi}{[x^3 - \xi^3]^{2/3}}$$

$$= \Gamma(4/3) \sum_{m=0}^{k} a_{km} \frac{\Gamma\left(\frac{2k-2m+2}{3}\right)}{\Gamma\left(\frac{2k-2m+3}{3}\right)} x^{2k-2m} \qquad [32]$$

The coefficients in the potential distribution can be related to those in the trial function in the manner suggested by Newman (7), that is, by requiring Eq. [28] and [23] to be equal, multiplying both sides of the equality by $\rho P_{2s}(\rho)$, and integrating with respect to ρ

$$\sum_{k=0}^{N-1} A_k \int_0^1 \rho P_{2k}(x) P_{2s}(\rho)\, d\rho = \frac{-1}{T} \sum_{k=0}^{N-1} D_k M'_{2k}(0) \int_0^1 P_{2s}(\rho) P_{2k}(\rho)\, d\rho \quad [33]$$

By virtue of the orthogonality condition Eq. [33] becomes

$$D_k = \frac{-T(4k+1)}{M'_{2k}(0)} \sum_{l=0}^{N-1} A_l G_{lk} \quad [34]$$

where

$$G_{kl} = G_{lk} = \int_0^1 \rho P_{2k}(x) P_{2l}(\rho)\, d\rho$$

$$= \sum_{m=0}^{l} a_{lm} \sum_{p=0}^{k} a_{kp} \sum_{q=0}^{l-m} \left\{ \frac{(-1)^q \binom{l-m}{q}}{2q+2k-2p+2} \right\} \quad [35]$$

These coefficients need be calculated only once for a given order of approximation.

Computational procedure and results.—The unknown coefficients A can be obtained by requiring the trial current distribution function to match the current density as given by the kinetic rate expression. That is

$$f(x_i) \equiv \sum_{k=0}^{N-1} A_k P_{2k}(x_i) - {}^0i_0{}^* \left[\frac{c_O{}^*(x_i)}{c_{O\infty}{}^*} \right]^{\gamma_1} \cdot \left[\frac{c_R{}^*(x_i)}{c_{R\infty}{}^*} \right]^{\gamma_2} \cdot \{ e^{\alpha \eta_s{}^*(x_i)} - e^{-\beta \eta_s{}^*(x_i)} \} = 0 \quad [36]$$

at all x_i ($i = 1, 2, \ldots, N$) which are the positive roots of $P_{2N}(x)$. The values of A may be obtained by a Newton-Raphson iteration about an appropriate initial guess. The following order of computation is convenient:

1. Given T, V^* and all kinetic parameters adopt an initial guess for A. For example, obtain the leading coefficient A_0 from the zeroeth order solution (constant current distribution) and set the remaining coefficients to some small number.

2. Calculate $c_O{}^*(x)$ and $c_R{}^*(x)$ from Eq. [31], where x represents the set of N points x_i.
3. Calculate $\eta_c{}^*(x)$ from Eq. [27].
4. Calculate $\phi_0{}^*(x)$ from Eq. [22].
5. Calculate $\eta_s{}^*(x)$ from Eq. [26].
6. Calculate the residuals $f(x)$ from Eq. [36] and the Jacobian matrix of elements $\partial f(x_i)/\partial A_k$. New coefficient values are obtained as

$$A^{(n+1)} = A^{(n)} - [J^{(n)}]^{-1} f^{(n)} \quad [39]$$

where the superscript is an iteration index.

7. Return to step two with the $A^{(n+1)}$ if the rms of the normalized residuals is not less than some specified tolerance, that is, if

$$\left\{ \frac{1}{(N-1)} \sum_{i=1}^{N} \left(\frac{f(x_i)}{i^*(x_i)} \right)^2 \right\}^{1/2} \leqq \epsilon$$

is not satisfied. We have used $\epsilon = 10^{-3}$.

In principle, the procedure outlined above must be repeated for increasing values of N until a characteristic quantity, say $\langle i^* \rangle = I^*/\pi r_0{}^2$, converges to a stationary value. A value of $N = 6$ has been found to be sufficient here to achieve not only a stationary $\langle i^* \rangle$ but also a satisfactory distribution $i^*(x)$. This small number of terms alleviates the numerical precision problems encountered by Newman (7) in dealing with Legendre polynomials of degree 20. The results of our calculations appear to be comparable to those presented by Newman (7). The principle difference in the two computational procedures is that our method exploits the accuracy of Gaussian quadrature in evaluating the integrals involved and allows us to work with fewer unknown coefficients and a small number of discrete points x_i on the electrode.

The complete solution of the current distribution problem for a given set of parameters at $N = 6$ required from 3 to 7 iterations and less than 0.25 sec of computing time on a Univac 1110 computer. Complete polarization curves could be generated economically, and extensive simulations made to study the sensitivity of the polarization curve to the kinetic parameters in the Butler-Volmer kinetics, Eq. [12]. As an example, Fig. 2 shows cathodic polarization curves computed for a redox reaction at various values of $i_0{}^*$ and α_c. It is apparent that the experimental discrimination of ${}^0i_0$ and α_c from experimental polarization curves of this sort requires analysis of data at values of $\langle i^* \rangle$ where variations in the surface concentrations become significant and must be accounted for in the data treatment. With the collocation simulation of the experimental system written for any postulated kinetics model and provided as a computer subroutine, nonlinear least squares regression routines can be used to determine kinetic parameters from a set of cell polarization data.

Statistical Analysis of Polarization Data

A common practice in the study of electrode kinetics is to postulate Butler-Volmer kinetics (Eq. [12]) with a symmetry factor $\beta = 1 - \alpha = 1 - \gamma_1 = \gamma_2$. The two parameters ${}^0i_0$ and β are obtained by comparing data at different degrees of polarization with limiting forms of the model, corresponding to linear and Tafel kinetics, respectively (15). It is also common to fix the value of β at 0.5, thus leaving ${}^0i_0$, or the rate constant, as the only independent parameter. A more reliable approach, at least for engineering purposes, will be to start with a rate expression of the form of Eq. [12] including the possibility that all the parameters are independent. A complete statistical analysis will involve the simultaneous estimation of all parameter values for a postulated kinetic model and an assessment of how well the model describes the data. Investigation of the parameter correlations and the variations of residuals in the experimental space guides one in revising the kinetic model to obtain a better fit of the data.

Consider a set of experimental data consisting of an array of observable quantities y and an array of independent or state variables ζ. A mathematical model is proposed to relate the two in terms of some system parameters θ, namely

$$\hat{y} = g(\zeta; \theta) \quad [40]$$

where $\hat{y}$ is the array of predicted responses. The statistical problem is to obtain estimates of the param-

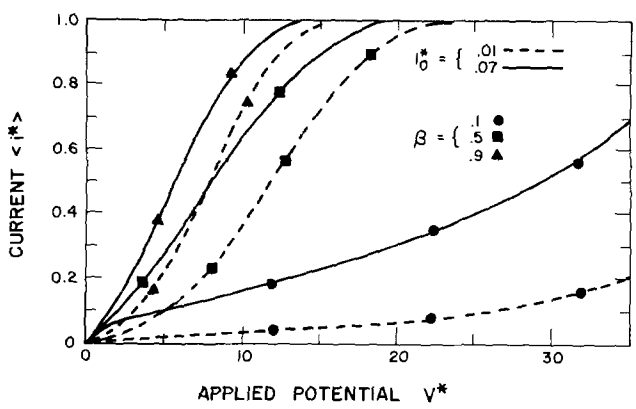


Fig. 2. Simulated cathodic polarization curves for a redox reaction on a rotating-disk electrode for $T = 7$ and various values of ${}^0i^*_0$ and β. $\gamma_O = \gamma_R = \frac{1}{2}$; $\alpha = 1 - \beta$; $n = 1$ (see Eq. [25]).

eters θ such that the best predictions of the observable quantity are obtained according to some optimality criterion. A common approach is to minimize the sum of squares of the errors. That is, values of θ are determined which minimize the quantity

$$\text{SSQ} \equiv \left\{ \sum_{\text{observations}} u_i (y_i - \hat{y}_i)^2 \right\} \qquad [41]$$

where u_i is some suitable weighting function which reflects the distribution of experimental accuracy (4). In polarization experiments, the total current is the observable quantity, and Eq. [40] may be written as

$$\hat{y} = \int_0^1 i^*(x, \Upsilon, V^*; \theta)\, x dx \qquad [42]$$

where the kinetic model for i^* might be of the form of Eq. [12], so that $\theta = (\alpha, \beta, i_0, \gamma_1, \gamma_2)$.

In the least squares fitting of such a model to a set of data, one starts with initial guesses for the parameters θ and computes from the simulation procedure a prediction $\hat{y}_i$ for each experimental point. Then SSQ can be computed according to Eq. [41], and some standard computer algorithm, such as Marquardt's method (16), can be used to find the values of θ which minimize SSQ. Such minimization programs require evaluation of a Jacobian or covariance matrix of partial derivatives of $\hat{y}$ with respect to each of the parameters. It is clear from the form of Eq. [42] that the elements of such a matrix will contain integrals. For example, we would have from Eq. [25] and [42]

$$\frac{\partial \hat{y}}{\partial \gamma_1} = {}^0i_0^* \int_0^1 c_O^{*\gamma_1} \ln (c_O^*)\, c_R^{*\gamma_2} [e^{\alpha\eta_s^*} - e^{-\beta\eta_s^*}] x dx \qquad [43]$$

and

$$\frac{\partial \hat{y}}{\partial \beta} = {}^0i_0^* \int_0^1 c_O^{*\gamma_1} c_R^{*\gamma_2} \eta_s^* e^{-\beta\eta_s^*} x dx \qquad [44]$$

Now, since the collocation simulation generates the value of every term in these integrands at Gaussian quadrature points, the integrals can be evaluated quite rapidly and accurately. An alternative procedure, computing the derivatives by finite differences, would require the complete solution of the current distribution problem at perturbed values of the parameters, and would increase the computation time considerably.

Experimental Measurements and Data Analysis

To demonstrate the application of these methods to electrochemical kinetics, we have studied copper deposition from aqueous $CuSO_4$-H_2SO_4 solutions onto a rotating-disk electrode. This system was chosen because of its industrial importance and because published results (15, 17-19) provide a good basis for comparison.

In order to discriminate the effects of the various parameters in Eq. [12], operation at high overpotentials, and hence at appreciable fractions of the limiting current, is necessary. The collocation method allows the appropriate interpretation of polarization curves in that region by expedient solution of the complete current distribution problem.

Experimental.—Potentiostatic measurements were made on an ESB Research Depak rotating-disk electrode assembly by means of a Princeton Applied Research Model 170 electrochemistry system. Although the ESB Depak indicates rotation speed on a digital meter, more accurate measurement of rotation speed was made by use of a stroboscope.

The working electrode was a 0.1 cm^2 platinum disk embedded in the end of a 1.6 cm diam Teflon shaft. The platinum electrode was covered with copper by deposition from the solution A (see Table I) at 0.2 mA for 2 min.

The cell was made of glass and had a cylindrical shape, 6.4 cm diam and 7.4 cm deep, and was blanketed with nitrogen. The reference electrode was a copper wire placed at 4.5 cm from the disk on the axis. The counterelectrode was a loop of copper wire, 6 cm diam, placed at the bottom of the cell. The reference and the counterelectrodes were covered with fresh deposits of copper from solution A. The solutions were prepared by weight from twice distilled water and reagent grade copper sulfate and sulfuric acid. The temperature was 21° ± 0.5°C. The solutions were thoroughly deaerated with nitrogen before each experiment.

Measurements were made for different levels of metal and acid concentration, the applied potential and disk rotation speeds were varied to obtain currents between 0.45 and −4.25 mA/cm^2, and concentrations were chosen to avoid complications due to varying physical properties and ionic migration. Table I shows the concentrations of the 6 solutions studied and the rotation speeds used. Limiting currents shown are those measured experimentally. Copper diffusivities were estimated from the compilation given by Selman (20). Using the latter, we verified the linear dependance of i_{lim} on $\Omega^{1/2}$ (21). Conductivities were calculated from the correlation given by Hsueh (22)

$$\kappa_\infty = 0.011163 + 0.030798\ (CuSO_4) + 0.423553\ (H_2SO_4) - 0.045224\ (H_2SO_4)^2 - 0.135359\ (H_2SO_4)\,(CuSO_4) \qquad [45]$$

where molar analytical concentrations are used.

Smooth traces of current *vs.* potential were obtained for each of the 16 cases indicated in Table I by scanning the potential from anodic to cathodic at 5 mV/sec. Repeated scans on the same surface provided reproducible traces. The maximum noise was observed at limiting current, where fluctuations were less than 5% of the measured current. Replicate experiments, in which complete cell preparation was repeated, were conducted with solution A. Reproducibility of the current measurements between replicates was within 10%.

Sampled data points from the 16 polarization curves are given in Table II, where the observed currents have been divided by the measured limiting current.

Data analysis.—It has been verified (19) that the copper (II) deposition-dissolution reaction in acid sulfate systems takes place in two steps

Table I. Experimental conditions for Cu(II) deposition studies*

Concentration of $CuSO_4$ (M) \ Concentration of H_2SO_4 (M)	2.0	0.70	0.20
0.100	A 64 (911) 45 (400) 40 (295) 39 (300) $\mathcal{D}_{Cu^{+2}} = 3.82$	x	x
0.0316	B 27.5 (1757) 18.0 (596) $\mathcal{D}_{Cu^{+2}} = 4.41$	D 28.0 (1462) 17.5 (443) $\mathcal{D}_{Cu^{+2}} = 5.24$	x
0.0100	C 11.6 (2340) 9.4 (1592) 4.8 (430) $\mathcal{D}_{Cu^{+2}} = 4.67$	E 8.0 (995) 5.0 (313) $\mathcal{D}_{Cu^{+2}} = 5.35$	F 11.7 (1815) 8.0 (834) 6.8 (466) $\mathcal{D}_{Cu^{+2}} = 6.0$

* Entries are limiting current densities in mA/cm^2 and corresponding rotation speeds Ω (rpm). Copper diffusivities are in cm^2/sec × 10^6.

$$\left.\begin{aligned} Cu^{2+} + e^- &\rightleftharpoons Cu^+ \quad \text{(slow)} \\ Cu^+ + e^- &\rightleftharpoons Cu \quad \text{(fast)} \end{aligned}\right\} \quad [46]$$

The assumption of Butler-Volmer kinetics with a symmetry factor $\alpha_c = 1/2$ for the slow reaction and of equilibrium for the fast reaction yields

$$i = {}^0i_0(CuSO_4)^\gamma \left[e^{\alpha_a \frac{F\eta_s}{RT}} - e^{-\alpha_c \frac{F\eta_s}{RT}} \right] \quad [47]$$

Table II. Summary of experimental results

Solution identification	Limiting current (mA/cm²)	Applied potential (V)	Observed current $\langle i^* \rangle_{OBS}$	Predicted current $\langle i^* \rangle_{PRED}$	Error $\frac{\langle i^* \rangle_{PRED} - \langle i^* \rangle_{OBS}}{\langle i^* \rangle_{OBS}}$
A	4.65	0.025	0.097	0.073	0.244
		−0.100	−0.118	−0.136	−0.153
		−0.200	−0.473	−0.420	0.111
		−0.300	−0.549	−0.785	0.076
A	3.25	−0.100	−0.154	−0.186	−0.207
		−0.200	−0.554	−0.519	0.063
		−0.300	−0.8.2	−0.852	0.045
		−0.040	−0.068	−0.076	−0.120
A	2.35	−0.100	−0.208	−0.242	0.098
		−0.150	−0.481	−0.411	0.146
		−0.200	−0.702	−0.609	0.133
		−0.250	−0.851	−0.783	0.080
		−0.025	−0.055	−0.070	−0.273
A	4.50	−0.100	−0.167	−0.140	0.158
		−0.200	−0.489	−0.429	0.122
		−0.300	−0.800	−0.792	0.010
		−0.400	−0.944	−0.962	−0.019
A	3.90	−0.100	−0.141	−0.159	−0.127
		−0.200	−0.410	−0.468	−0.141
		−0.300	−0.756	−0.820	−0.085
		−0.400	−0.936	−0.970	−0.037
B	1.80	0.030	0.133	0.119	0.109
		−0.010	−0.022	−0.020	0.085
		−0.020	−0.039	−0.037	0.056
		−0.050	−0.083	−0.078	0.070
		−0.100	−0.172	−0.160	0.069
		−0.150	−0.275	−0.293	−0.054
		−0.200	−0.472	−0.476	−0.009
		−0.250	−0.733	−0.673	0.082
		−0.300	−0.861	−0.829	0.037
B	3.00	−0.050	−0.067	−0.048	0.282
		−0.100	−0.133	−0.102	0.236
		−0.150	−0.240	−0.196	0.185
		−0.200	−0.433	−0.344	0.206
		−0.300	−0.750	−0.724	0.035
		−0.400	−0.873	−0.942	−0.078
C	0.48	−0.050	−0.135	−0.128	0.056
		−0.100	−0.223	−0.252	−0.101
		−0.150	−0.396	−0.427	−0.080
		−0.200	−0.625	−0.628	−0.005
		−0.250	−0.813	−0.799	0.016
		−0.300	−0.953	−0.908	0.052
C	0.94	0.030	0.106	0.106	0.000
		−0.050	−0.069	−0.069	−0.001
		−0.100	−0.128	−0.145	−0.132
		−0.150	−0.245	−0.268	−0.097
		−0.200	−0.415	−0.447	−0.077
		−0.250	−0.628	−0.647	−0.030
		−0.300	−0.798	−0.812	−0.017
		−0.350	−0.894	−0.915	−0.024
D	1.75	−0.050	−0.114	−0.121	−0.056
		−0.100	−0.234	−0.238	−0.016
		−0.150	−0.400	−0.403	−0.008
		−0.200	−0.611	−0.538	0.022
		−0.300	−0.886	−0.892	−0.007
		−0.350	−0.943	−0.957	−0.015
D	2.80	0.030	0.096	0.115	−0.188
		−0.010	−0.018	−0.021	−0.149
		−0.020	−0.029	−0.037	−0.301
		−0.050	−0.068	−0.079	−0.158
		−0.100	−0.168	−0.161	0.041
		−0.150	−0.296	−0.290	0.023
		−0.200	−0.500	−0.466	0.069
		−0.300	−0.857	−0.814	0.050
		−0.350	−0.936	−0.915	0.022
E	0.50	−0.050	−0.200	−0.184	0.079
		−0.100	−0.340	−0.344	−0.013
		−0.200	−0.700	−0.730	−0.042
		−0.300	−0.900	−0.944	−0.049
E	0.80	0.020	0.094	0.105	−0.121
		−0.010	−0.044	−0.033	0.249
		−0.020	−0.069	−0.059	0.140
		−0.030	−0.086	−0.082	0.067
		−0.040	−0.106	−0.102	0.036
		−0.050	−0.125	−0.123	0.018
		−0.150	−0.363	−0.413	−0.138
		−0.250	−0.700	−0.785	−0.122
		−0.350	−0.888	−0.961	−0.083
F	0.62	−0.020	−0.097	−0.086	0.111
		−0.030	−0.145	−0.118	0.185
		−0.070	−0.242	−0.233	0.038
		−0.100	−0.355	−0.329	0.074
		−0.200	−0.758	−0.706	0.069
F	1.17	0.020	0.162	0.143	0.117
		−0.100	−0.231	−0.201	0.131
		−0.200	−0.573	−0.530	0.074
		−0.300	−0.872	−0.852	0.023

with $\gamma = (2 - \alpha_c/2) = 0.75$ and $\alpha_a = 2 - \alpha_c = 1.5$. Equation [47] may not apply very precisely to the dissolution process because it does not account for diffusion of Cu(I) away from the electrode (23).

Statistical regression analyses of our data with Eq. [47] and several other models were performed with 87 discrete points selected from the 16 polarization curves. Simulation was accomplished by using the algorithm described above with two collocation points ($N = 4$). For lack of a better criterion, these were selected at potential intervals of 0.05 or 0.10V to get about 4 or 5 points from each curve as indicated in Table II. Some observations on the anodic side were necessary for the independent estimation of the anodic transfer coefficient, but these were taken only at currents small compared to the cathodic limiting current. The variable used in the statistical analysis was dimensionless average current density $\langle i^* \rangle = \langle i \rangle / i_{lim}$, and a weighting factor u_i of $1/\langle i^* \rangle^2_{obs}$ was used. This renders the residuals on a percentage basis which is representative of the error distribution in the instrument.

Table III summarizes the parameters estimated from the data for four kinetics models which were tested and their respective sums of squares. Models I and II correspond to those used by the investigators cited earlier. Model II, in which the two transfer coefficients are estimated independently, gives a better fit. However, neither model fits the data within experimental accuracy, and an investigation of their residuals reveals a correlation with sulfuric acid concentration.

To account for the acid concentration effect, we devised semiempirical models III and IV. Because of the precautions taken in selecting the relative concentrations of acid and metal, we can safely neglect the effect of the acid on copper migration. On the other hand, the scant data available on activity coefficients for aqueous $CuSO_4$-H_2SO_4 solutions point to a strong dependence of copper sulfate activity on the concentration of sulfuric acid (24, 25). In view of the large excess of sulfuric acid present, a first-order approximation of the activity coefficient variation should be obtained with an expression of the form $e^{-\delta(H_2SO_4)}$ (26). It is apparent from the results in Table III that the inclusion of such a term reduces the sum of squares considerably, with the model which allows the independent estimation of transfer coefficients, Model IV, being the more likely. Note that the term $\theta_1 e^{-\delta(H_2SO_4)}$ represents the standard exchange current densities for Models III and IV.

In Table II we have listed with the data the residuals corresponding to Model IV. It is seen that the largest percentage deviations occur for very small potentials and that there is no apparent correlation of errors between runs at different concentrations.

The standard deviation obtained for Model IV, about 11%, is roughly equal to that obtained from the replicate runs with solution A, so that within the limits of experimental reproducibility, Model IV describes our experimental observations adequately.

Figure 3 compares two representative experimental curves with the results of the simulation with Model IV shown as discrete points. The results shown here are typical of those obtained for all 16 experimental curves. Although the largest relative error occurs at small currents, the largest absolute discrepancy in the current appears in the intermediate range. In all cases, however, the error is less than 0.3 mA, which should be satisfactory for most practical purposes.

Discussion of Results

It has been found that Model IV in Table III describes our data within the accuracy of the experimental measurements, that is, with a standard deviation of about 11%. On the other hand, Model I with the parameters listed in Table III exhibits a standard deviation of 22% and is not considered to be a satisfactory model for reproducing the data. It appears that sulfuric acid

Table III. Models for Cu (II) deposition and dissolution kinetics

	Model*	Parameters					SSQ (87 observations)
		${}^{c}i_0$ or θ_1 (mA/cm²)	γ	α_A	α_c	δ (M^{-1})	
I	$i = {}^{c}i_0(\mathrm{Cu})^{\gamma}\left[e^{(2-\alpha_c)\eta\frac{F}{RT}} - e^{-\alpha_c\eta\frac{F}{RT}}\right]$	5.51	0.62	—	0.42	—	4.231
II	$i = {}^{c}i_0(\mathrm{Cu})^{\gamma}\left[e^{\alpha_A\eta\frac{F}{RT}} - e^{-\alpha_c\eta\frac{F}{RT}}\right]$	6.78	0.58	1.09	0.36	—	3.051
III	$i = \theta_1(\mathrm{Cu})^{\gamma}e^{-\delta(\mathrm{H_2SO_4})}\left[e^{(2-\alpha_c)\eta\frac{F}{RT}} - e^{\alpha_c\eta\frac{F}{RT}}\right]$	14.5	0.72	—	0.43	0.40	2.117
IV	$i = \theta_1(\mathrm{Cu})^{\gamma}e^{-\delta(\mathrm{H_2SO_4})}\left[e^{\alpha_A\eta\frac{F}{RT}} - e^{-\alpha_c\eta\frac{F}{RT}}\right]$	15.6	0.67	1.08	0.39	0.37	1.123

* Concentrations are analytical concentrations in moles/liter.

concentration has a measurable effect on copper deposition kinetics.

The principal purpose of this work has been to develop a systematic methodology for obtaining kinetic data for practical engineering purposes. Thus, we were content to take our example data at room temperature (21°C) rather than at 25.0°C, and to prepare electrode surfaces in a rather arbitrary way. Nevertheless, it is interesting to compare our experimental results with those of earlier workers.

For the description of kinetic behavior in a solution of fixed composition, the kinetics expression may be written

$$i = i_0\left[e^{\alpha_a\eta F/RT} - e^{-\alpha_c\eta F/RT}\right] \qquad [48]$$

where the preexponential factor is called simply the exchange current density. By comparison with Model IV, the exchange current density i_0 should be

$$i_0 = 1.58(\mathrm{Cu})^{0.67}e^{-0.36(\mathrm{H_2SO_4})}\mathrm{mA/cm^2} \qquad [49]$$

where the concentrations are expressed in moles/liter. Table IV compares kinetic parameters i_0, γ, α_a, and α_c indicated by this work with results reported by earlier workers. Specific concentrations have been chosen in each case to make the i_0 comparison possible. It is gratifying that the i_0 values predicted from Eq. [49] agree so well with the results of the earlier workers, particularly considering the wide ranges of composition involved. Better agreement could hardly be expected among workers who prepared electrodes differently

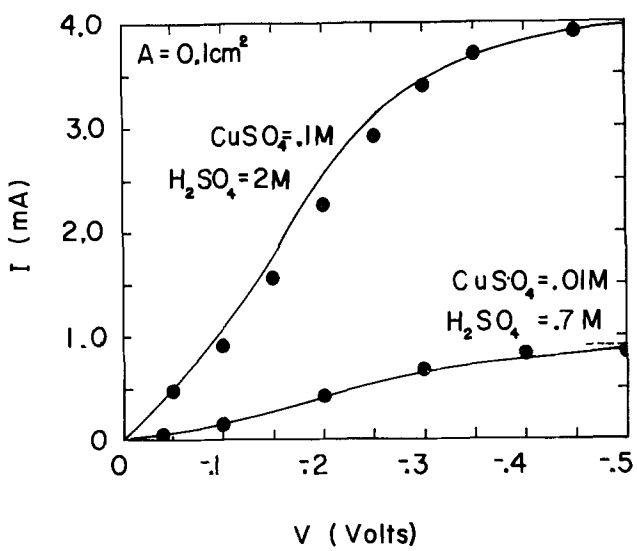


Fig. 3. Comparison of two experimental polarization curves with point values predicted by Model IV and the collocation simulation.

and made different types of measurements. Also, the temperature differences should affect i_0.

The reaction order γ is also in good agreement with earlier work. On the other hand, it is somewhat distressing that our transfer coefficients are significantly lower than those obtained previously. We see no obvious explanation of this discrepancy, but we note that in Models I and III, where $\alpha_a = 2 - \alpha_c$, the statistical analysis yields a larger value for α_c.

Table V shows the correlation matrix for the parameters of Model IV. It is seen that the correlation coefficients are generally small, which means that each parameter is characterizing a different aspect of the kinetics law. The largest correlation, 0.843, is between θ_1 and γ. This probably means that the model is not accounting as well as it might for the dependence of the rate on the copper concentration. Clearly, the use of γ is not redundant as shown by the range of i_0 in Table IV, but the assumed form of the copper dependence may not be satisfactory. For example, a factor for the copper dependence of the activity coefficient might be appropriate.

It should not be surprising that the best empirical parameters for the models tested do not agree with the theoretical values of Eq. [47]. Copper sulfate-sulfuric acid solutions are quite nonideal with $CuSO_4$ ion pair formation likely (24). For engineering purposes it is necessary to obtain experimental kinetics data measured under conditions similar to those where the data will be applied. Measurement on a rotating disk with proper analysis of transport effects satisfies this requirement in the sense that the boundary layer phenomena on the disk should be similar to those in electrolysis cells (27).

It should be noted that the data analysis presented here can be simplified by using a one-point approximation ($N = 1$). In that case, $i^* = A_0$, $c_0^* = 1 + A_0$, $c_R^* = 1 - A_0$, $\phi_0 = \Upsilon\pi A_0/4$, etc., and the statistical parameter determination can be done quite easily. An important point, however, is that this first approximation of the complete model does not correspond to the simple one-dimensional model commonly used.

Summary

Nonlinear regression analysis can be used to determine empirical parameters for a postulated electrode kinetics expression. All parameters are estimated simultaneously from a set of polarization data to obtain an optimal fit of the data. Accordingly, the resulting kinetics model should be useful for engineering analysis of experimental systems where the same range of conditions is encountered.

Practical implementation of the regression analysis requires rapid simulation of the experimental system. Approximate computation of current distribution by orthogonal collocation fulfills this requirement and

Table IV. Comparison of Model IV parameter estimates with published results for copper electrode kinetics in acidic sulfate solutions

Source	$CuSO_4$ (M)	H_2SO_4 (M)	i_o (mA/cm²)	i_o predicted by Eq. [49] (mA/cm²)	γ	α_a	α_c
Mattsson and Bockris (15)	0.075	0.5	2.2-3.7	2.3	0.6	1.3	0.49
Hurlen (17) (extrapolated)	1	0.05	23.6	15.5	0.73	1.5	0.50
Karasky and Linford (18)	0.75	0.25	11.4	11.9	—	—	0.59
This work					0.672	1.07	0.38

Table V. Parameter estimate correlation matrix for Model IV

	θ_1	α_c	α_A	γ	δ
θ_1	1				
α_c	0.29	1			
α_A	−0.18	0.52	1		
γ	0.84	0.64	0.15	1	
δ	−0.70	−0.42	−0.04	−0.51	1

facilitates the iterative calculations which yield the parameter values.

We have demonstrated the application of these methods to the rotating-disk system. Because of the flexibility and efficiency of the collocation method it can be applied to other geometries and extended to multiple reaction cases as well (21).

Acknowledgments

Reinaldo Cabán has been supported by the University of Puerto Rico at Mayaguez. This work has been funded in part by the National Oceanic and Atmospheric Administration's Office of Sea Grant, Department of Commerce, through an institutional grant to the University of Wisconsin.

Manuscript submitted Aug. 16, 1976; revised manuscript received May 17, 1977.

Any discussion of this paper will appear in a Discussion Section to be published in the June 1978 JOURNAL. All discussions for the June 1978 Discussion Section should be submitted by Feb. 1, 1978.

LIST OF SYMBOLS

A_k coefficients defined by Eq. [28]
a coefficient in Eq. [8]
a_{km} coefficients defined by Eq. [29]
c^* dimensionless concentration
c concentration, mole/m³
D_k coefficients defined by Eq. [1]
$\mathcal{D}_i$ pseudobinary diffusion coefficient of species i in solution, m²/sec
E_k functions defined by Eq. [32]
$\mathbf{F}$ Faraday's constant, 96,487 C/equiv.
f residual defined by Eq. [36]
G_{kl} coefficients defined by Eq. [35]
I total current, A
i current density, A/m² or mA/cm² in numerical results
$\langle i \rangle$ average current density, A/m²
i_o exchange current density, A/m²
$^0i_0$ standard exchange current density, A/m²
i_{lim} limiting current density, A/m²
i^* dimensionless current density, normal component at electrode
M_i chemical species i
M_{2k} Legendre function defined by Eq. [2]
N number of collocation points
n number of electrons produced by electrode reaction
P_i Legendre polynomial of degree i
Q_{2k} polynomial of order $2k$, members of an orthogonal set
R universal gas constant, 8.3143 J/mole-°K
r radial position, m
r_0 radius of disk electrode, m
s_i stoichiometric coefficient of species i
SSQ sum of squares, defined by Eq. [41]
T temperature, °K
u_i weight factor in Eq. [41]
U equilibrium cell potential, V
v velocity, m/sec
w_i quadrature weights
x_i collocation abscissas
x dimensionless radial position on electrode surface, r/r_0
y normal distance from electrode, m
$\hat{y}$ predicted experimental response
z_i charge number of species i

Greek letters

α_a anodic transfer coefficient
α scaled anodic transfer coefficient, $\alpha_a/|n|$
α_c cathodic transfer coefficient
β scaled cathodic transfer coefficient, $\alpha_c/|n|$
β_0 derivative of axial velocity at the wall, sec⁻¹
γ a kinetic parameter, reaction order
$\Gamma(x)$ Gamma function of x
δ parameter in kinetics model, (mole/liter)⁻¹
ϵ error tolerance
ζ dummy integration variable
η_s, η surface overpotential, V
η_c concentration overpotential, V
θ kinetic parameters
κ conductivity, $\Omega^{-1}m^{-1}$
ν kinematic viscosity, m²/sec
ξ a rotational elliptical coordinate defined below Eq. [1]
ρ a rotational elliptical coordinate defined below Eq. [1]
Υ dimensionless parameter defined by Eq. [21]
ϕ potential in the solution, V
Ω rotation speed, rad/sec

Common subscripts

i of species i or evaluated at collocation point x_i
0 evaluated at the surface of the electrode
∞ evaluated in the bulk of the solution
R reactant or reduced species
O oxidized species

Common superscripts

$*$ dimensionless variable
(N) refers to the Nth approximation
(n) refers to nth iteration

REFERENCES

1. G. E. P. Box and W. G. Hunter, *Technometrics*, **4**, 301 (1962).
2. G. E. P. Box and W. J. Hill, *ibid.*, **9**, 57 (1967).
3. N. R. Draper and H. Smith, "Applied Regression Analysis," John Wiley & Sons, New York (1966).
4. J. R. Kitrell, W. G. Hunter, and C. C. Watson, *AIChE J.*, **12**, 5 (1966).
5. R. Cabán and T. W. Chapman, *This Journal*, **123**, 1036 (1976).
6. J. Newman, *This Journal*, **13**, 1236 (1966).
7. J. Newman, "Electrochemical Systems," Prentice-Hall, Inc., Englewood Cliffs, New Jersey (1973).
8. J. Newman, *This Journal*, **114**, 239 (1967).
9. J. Newman, "The Fundamental Principles of Current Distribution and Mass Transfer in Electrochemical Cells," *UCRL-20547*, University of California, Berkeley (1971).
10. P. M. Morse and H. Feshbach, "Methods of Theoretical Physics," McGraw-Hill Book Co., New York (1953).
11. V. G. Levich, "Physicochemical Hydrodynamics," Prentice Hall, Inc., Englewood Cliffs, New Jersey (1962).
12. G. K. Batchelor, "An Introduction to Fluid Dynamics," Cambridge University Press, Great Britian (1970).
13. W. E. Stewart, *AIChE J.*, **9**, 528 (1963).

14. "Handbook of Mathematical Functions," M. Abramowitz and I. Stegun, Editors, National Bureau of Standards, Washington, D.C. (1964).
15. E. Mattsson and J. O'M. Bockris *Trans. Faraday Soc.*, **55**, 1586 (1959).
16. D. L. Marquardt, *J. Soc. Ind. Appl. Math.*, **2**, 431 (1963).
17. T. Hurlen, *Acta Chem. Scand.*, **15**, 630 (1961).
18. L. Karasyk and H. B. Linford, *This Journal*, **110**, 895 (1963).
19. O. R. Brown and H. R. Thirsk, *Electrochim. Acta*, **19**, 383 (1965).
20. J. R. Selman, Ph.D. Dissertation, University of California, Berkeley (UCRL-20557) (1971).
21. Reinaldo Cabán, Ph.D. Thesis, University of Wisconsin, Madison (1976).
22. L. Hsueh, Dissertation, UCRL-18597, University of California, Berkeley, California (1968).
23. C. Wagner, *Electrochim. Acta*, **14**, 971 (1969).
24. R. A. Robinson and R. H. Stokes, "Electrolyte Solutions," 2nd ed., Butterworths Publications Ltd., London (1959).
25. T. W. Chapman, Unpublished research.
26. E. A. Guggenheim, "Thermodynamics," 5th ed., North-Holland Publishing Co., Amsterdam (1967).
27. J. Newman, *Int. J. Heat Mass Transfer*, **10**, 983 (1967).

Double Layer Capacitance and Charging Rate of Ultramicroporous Carbon Electrodes

J. Koresh and A. Soffer

Atomic Energy Commission, Nuclear Research Centre-Negev, Beer-Sheva, Israel

ABSTRACT

Adsorption of ions from aqueous solutions into pores, as narrow as 3.7Å was observed, using linear sweep cyclic voltametry. The conductivity of the solution in pores of less than 7Å diameter is several orders of magnitude lower than that of a free 0.1*N* NaCl solution in contact with the carbon electrode. It seems negligibly slow in pores of less than 3.7Å diameter, which are still completely filled with water. Highly oxidized ultramicroporous carbons show much lower double layer capacitance at positive potentials than nonporous carbon surfaces. This is interpreted as repulsive ion-dipole interaction of the anion with the dipole of the chemisorbed oxygen. Ions can penetrate the tiny pores after depletion of the hydration sheath. The double layer charging rate is therefore much slower if 0.1*N* NaCl is replaced by 0.1*N* LiCl. A brief discussion is presented in order to confirm that the electroactive surface groups can be treated in terms of (capacitative) double layer charging.

One of the fundamental requirements of electrochemical power sources are low overvoltage electrodes. Optimization of the physical design of the electrode is partially achieved by increasing the ratio of internal, S_i, to geometrical, S_g, surface area; this lowers the real current density. The S_i/S_g can be increased by using a thicker electrode and/or by increasing the porosity of the electrode. However, since the porous matrix serves as sink for the electrical charge, and due to the resistivity of the solution in the pores, the current decays rapidly on moving away from the counterelectrode. This imposes a limit for the thickness of a practical electrode. The question now is whether the increased active surface area of the porous electrode has also theoretical limitations. Ion mobility in the narrow pores of high internal surface area electrodes may rule out the availability of this surface for the electrode process.

Extensive studies were published on the transport properties of porous electrodes (1, 2), where models of continuous electrode media were used, but the role of pore structure was mostly neglected Only recently has the simplest of these models been satisfactorily matched with experiment (3, 4).

Another property of high surface porous electrodes is their probable usefulness as high capacity electroadsorbent. This idea, which was first put forward by Garten and Weiss (5), was examined experimentally by Murphy *et al.* (6). Much later, the electrosorptive properties were attributed to the electric double layer (7, 8), but again the influence of the fine structure was still disregarded. The pore structure which is characterized by a solid-gas system is being investigated, and several techniques for the characterization of mean pore diameter and pore diameter distribution have been developed (9). The kinetics of adsorption of neutral molecules from solution into porous solids have also been studied (10).

Key words: double layer charging, ultramicropores, carbon electrode.

In the present work pore structure of various carbons and graphites are characterized by means of the well-established methods of gas adsorption, and then the double layer capacitance (C_d) and ion transport through the pore are examined.

An ultramicroporous carbon, with pore size comparable to that of small molecules, is studied. Because of their electrical charge, the rate of transport and adsorbability of ions into narrow pores may have some special features which are encountered neither in solid-gas adsorption systems nor in solid-nonelectrolytic liquid interfaces. As carbon and graphite have polar oxygen surface groups (11), short range ion-dipole interactions influence the behavior of ions in ultramicroporous carbon, unlike flat or wide pore carbon electrodes.

Experimental

The porous carbon electrode was TCM 128 carbon cloth and TGM 389 served as nonporous reference carbon, both supplied by Le Carbonne Loraine, France. Both electrode materials are composed of fibers of cylindrical cross sections of approximately 3 μm for TGM 389, and 6-10 μm for TCM 128 (Fig. 1 and 2). A special feature of TCM 128 and of some other nonactivated fibrous carbons is the complete absence of pores larger than ultramicropores. The diameter of the pores was less than 3.7Å (12). This is the reason that almost all of the surface area results from ultramicropores and only a very small part from the outer surface area of the fibers. The geometrical surface area, S_g, of TGM 389, calculated from an average diameter of 3.2 μm, is

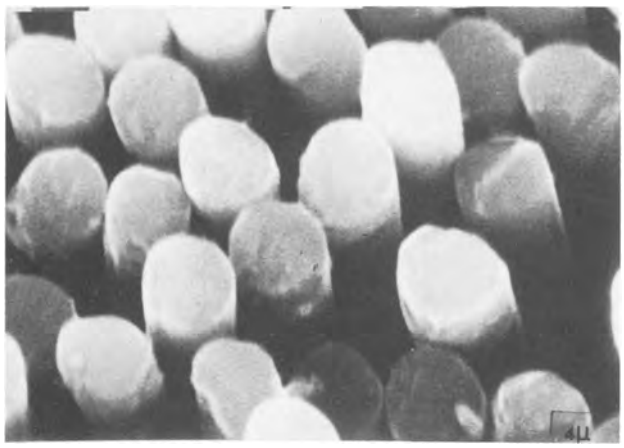


Fig. 1. SEM micrograph of the graphitized carbon fibers TGM 389.

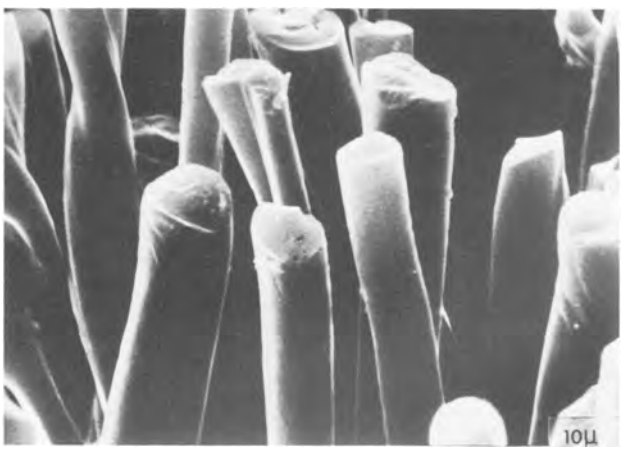


Fig. 2. SEM micrograph of the ultramicroporous carbon fibers TCM 128.

approximately 0.3 m^2/g. The BET surface area (S_{BET}) of TGM 389, measured on a 3g sample, was 1.2 m^2/g. This corresponds to a roughness factor of $S_{BET}/S_g = 4$.

The ultramicropores of the as-received TCM 128 carbon were too narrow to accommodate N_2 molecules (12), therefore the BET surface area obtained from nitrogen adsorption isotherms gave the outer surface area (as for TGM 389) 0.95 m^2/g. From an average diameter of 8 μm we have approximately 0.12 m^2/g for the geometrical surface. This corresponds to a roughness factor of 8. These rough outer surface areas are negligible compared to the much larger (> 250 m^2/g) area of the ultramicropores of TCM 128 (12).[1] Some of the manufacturers' specifications of the carbons are given in Table I.

The electrolytes were sodium chloride and lithium chloride, analar grade. Water was triply distilled.

The electrochemical cell.—Through the openings in the cover of a standard Metrohm cell, three electrodes, deaeration tubes, and a gas outlet were introduced. The reference electrode was a 0.1*N* NaCl calomel electrode half-cell. The auxiliary electrode was a platinum and later a silver rod, enclosed in a glass tube with a sintered base containing the solution. The carbon cloth, working electrode ($\sim 3 \times 3$ cm^2) was stretched across the opening of another glass tube and tightened with gold wire which also served as current collector. The reference electrode was mostly introduced into this tube so that the *IR* drop was screened off by the carbon cloth. At currents below 50 μA the reference electrode was transferred to the main compartment of the cell, since otherwise its complete freedom from *IR* drop at the first mode resulted in an oscillatory response of the potentiostat. This is because the *R*-*C* impedance of the working electrode in the double layer range produces a delay in the potential response at the solution compartment opposite the counterelectrode (4). The electrolytic solution used mostly was sodium chloride 0.1*N*. The maximum value of the *IR* drop was evaluated by interrupting the charging current and measuring the sudden change in potential. It was never above the millivolt range and had thence been neglected.

Instrumentation.—An electromechanical ramp generator, driven by a synchronous motor, was used to obtain very slow voltage sweep rates for following the slow charging rates of the ultramicroporous carbons. For fast voltage sweep a Hewlett Packard function generator, Model 3300 A, was used, and the voltammogram was recorded on a Tektronix, Type 549, storage oscilloscope. A Kepco bipolar operational amplifier power supply was used as potentiostat. Figure 3 is a diagram of the circuitry.

Methods of measurement.—Evaluation of pore diameters and pore surface.—The treatment of the carbon cloth, TCM 128, and the estimation of pore diameters by probe molecules are described elsewhere (12). The probe molecules were H_2 ($d = 3.7$Å), N_2 ($d = 4.3$Å), and SF_6 ($d = 5.6$Å). The molecular diameter was calculated by the equation $d = 2^{1/6}V_L$, where V_L is the molecular volume of a single molecule in the liquid phase, assuming hexagonal packing of spherical molecules. It is well known that pores, almost impermeable to a given molecule at a certain temperature, can become permeable at higher temperatures (13). This was taken into consideration when the various pore diameter ranges were estimated. The amount of chemisorbed oxygen was changed to a certain extent by high temperature, stepwise, evacuation (12) or by limited O_2 chemisorption on oxygen depleted samples.

The internal surface area of TCM 128 was estimated as needed, by BET, Langmuir, and Polanyi-Dubinin models (14).

Evaluation of double layer capacitance (C_d) and kinetic parameter.—Considering the porous electrode as an *R*-*C* network, it can be easily deduced that the application of a constant potential sweep dv/dt starting at time $t = 0$, results in a current transient which decays to the pure capacitor behavior

$$i_\infty = C_d\, dv/dt \qquad [1]$$

where C_d is the total capacitance of the *R*-*C* network. A current transient should similarly occur after the inversion of the linear potential sweep at each end of

[1] A discrimination between roughness and porosity has to be made. Roughness is a property of the outer geometrical surface. It results from shallow pores of a depth not much greater than the diameter. Porosity is a property of the entire solid where the pore length is several orders of magnitude more than their diameter.

Table I. General characteristics of carbon and graphite textiles

Characteristics	Unit	TCM 128	TGM 389
Diameter of thread	mm	0.2-0.4	—
Thickness	mm	0.25	0.2-0.25
Weight per m^2	g	60	120
Electrical resistance of a square	ohm	1-1.5	0.8-0.9
Carbon content	%	92-96	99-100
Ashes	%	0.3-1	<0.1
Volatile material	%	4-7	<1

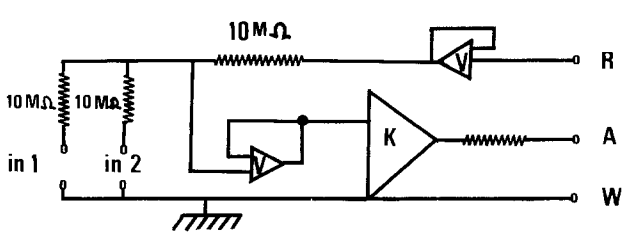


Fig. 3. The potentiostat circuitry. K, Kepco operational power supply amplifier; V, voltage follower (bias current < 10^{-11}A).

the cyclic voltametry half-cycle. This should result in distortion of the symmetry of the voltamogram *vs.* the potential axis (Fig. 4). The distortion is more pronounced by the edges of the voltamogram when the former transient is well relaxed as compared to the new one produced after the potential inversion. This transient behavior has been thoroughly studied by Austin and Gagnon (15) for the specific model of undimensional distribution of capacitance and resistivity. It can, however, be easily recognized that the same behavior holds qualitatively for any ideally polarized electrode model with resistive restrictions.

Cyclic voltametry on a wide potential range, appeared to be a fast and sensitive method of measuring C_d and for evaluating the double layer relaxation time. It is, however, quite complex for quantitative analysis unless C_d and/or the charging relaxation time are independent of potential, as was the system studied by Austin and Gagnon (15). The slower and less convenient measurements of current transients resulting from small potential steps, are easier to interpret quantitatively, since the C_d and the relaxation time can be assumed to be constant.

The experimental results of cyclic voltametry are given in this work in terms of apparent differential capacitance, C_d via Eq. [1], rather than in terms of the directly measured current. This was found more informative since C_d is the fundamental property which rules the current. One should, however, keep in mind that Eq. [1] is valid only after the decay of the transient, *i.e.*, at the symmetrical portions of the voltamogram. The various plots of C_d are given in two scales: farad per gram (f/g) and microfarad per square centimeter (μf/cm^2) of total surface area. The first unit (f/g) does not take into account the surface area measurements while the second enables comparison of ultramicroporous (3-10Å), with microporous (10-30Å) (8) or nonporous carbon electrodes and also with the classical mercury electrode interface.

Results and Discussion

Nonporous graphitized carbon TGM 389 was investigated in order to have a reference for nonporous carbon surface behavior. The apparent differential capacity obtained from cyclic voltametry is given in Fig. 5 for two very different sweep rates, 1000 and 1 mV/sec. It can be seen that the inversion of the linear sweep produces a very fast current reversal. A slight asymmetry, corresponding to a contribution of slowly charging sites, can be observed at the slower sweep rate. These slow sites are attributed (16) to "slow" electronic surface states which are isolated from the bulk conduction band of graphite by a potential barrier.

The roles of pore diameter and of concentration of oxygen surface groups have been examined in TCM 128 carbon, using thermal treatments under vacuum and in the presence of oxygen or air. The various samples used are given in Fig. 6. The C_d *vs.* potential plot is given in Fig. 7 for carbon I. This sample was activated for 2 hr in air at 450°C in order to obtain relatively large ultramicropores. The slow current inversion indicates a considerably low charging rate com-

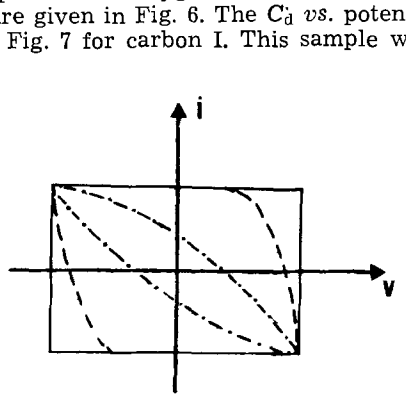


Fig. 4. Illustration of the response of the current to the reversal of potential linear sweep for a constant ideally polarized electrode. a, "Fast" electrode; b, "slow" electrode; relaxation during half-cycle time; c, "very slow" electrode, relaxation time greater than the half-cycle time.

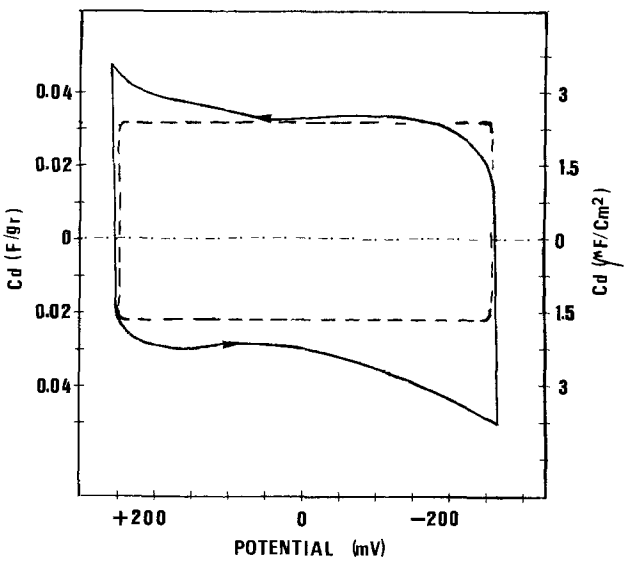


Fig. 5. C_d *vs.* *V* curve of TGM 389, ----, 1000 mV/sec; ——, 1 mV/sec. Potential *vs.* 0.1*N* NaCl C.E. The μf/cm^2 scale stands for the outer surface area of the fiber.

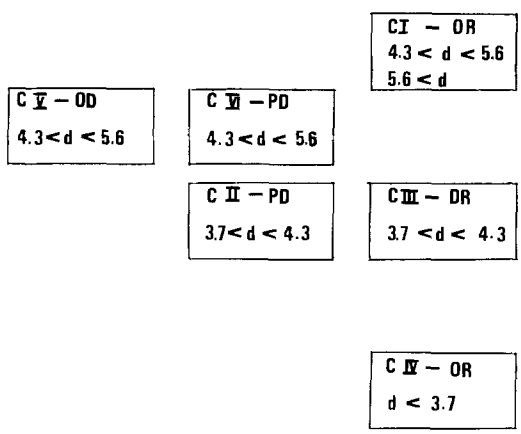


Fig. 6. Diagram of the various carbons according to their pore diameter and surface oxidation state. Moving to the right: samples with higher surface oxygen concentration. Moving to the bottom: samples with lower pore diameter. OD, oxygen depleted; OR, oxygen rich; PD, partly oxygen depleted.

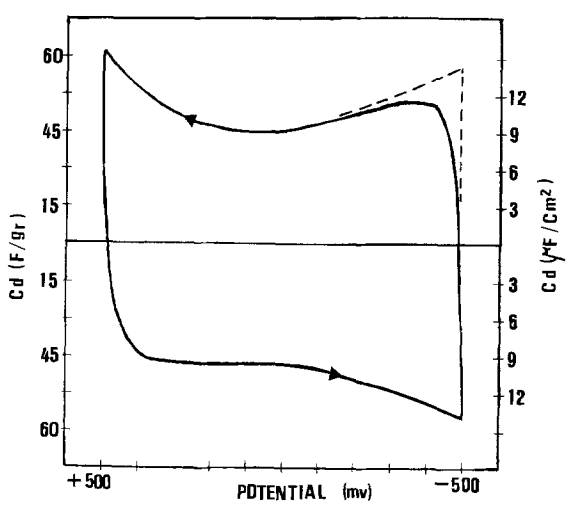


Fig. 7. C_d *vs.* *V* curve of carbon CI-OR in 0.1*N* NaCl; potential *vs.* 0.1*N* NaCl C.E.; 0.5 mV/sec. Dotted line is the symmetrical image of the lower curve for calculating the relaxation time.

pared to the nonporous TGM 389 (Fig. 5), but it is three orders of magnitude higher in capacitance per gram, thereby indicating that the high surface ultramicropores take part in double layer charging and in ion transport.

The carbon II samples were prepared by evacuation at 200°C during 2 days. This caused a slight depletion of chemisorbed oxygen which was removed as CO_2 (18). The lower pore diameter range resulted in a great decrease of C_d. No potential range could be found at which C_d from the increasing voltage sweep is equal to C_d of the decreasing sweep, because the charging rate slowed to such an extent that the C_d-V curve (Fig. 8) was completely distorted. This implies that the relaxation time of double layer charging is considerably greater than the half-cycle time of the cyclic voltamogram. The higher capacitance at negative potentials is connected with chemisorbed oxygen. The role of chemisorbed oxygen is well demonstrated by carbon III in Fig. 9. The pore diameter range of this carbon is much the same as the slightly oxygen depleted carbon II; it was obtained by widening the pores of the original TCM 128 by oxidation in air at 450°C for 1 hr, rather than by prolonged evacuation at 200°C. This is known to result in a highly oxidized surface (19). The C_d retains the high values of carbon I at negative potentials. It corresponds also to the C_d values of microporous (10-30Å) carbons (8). However, unlike these examples, where C_d changes only slightly with potential, it gradually decreases in carbon III by two orders of magnitude at +500 mV (Fig. 10).[2]

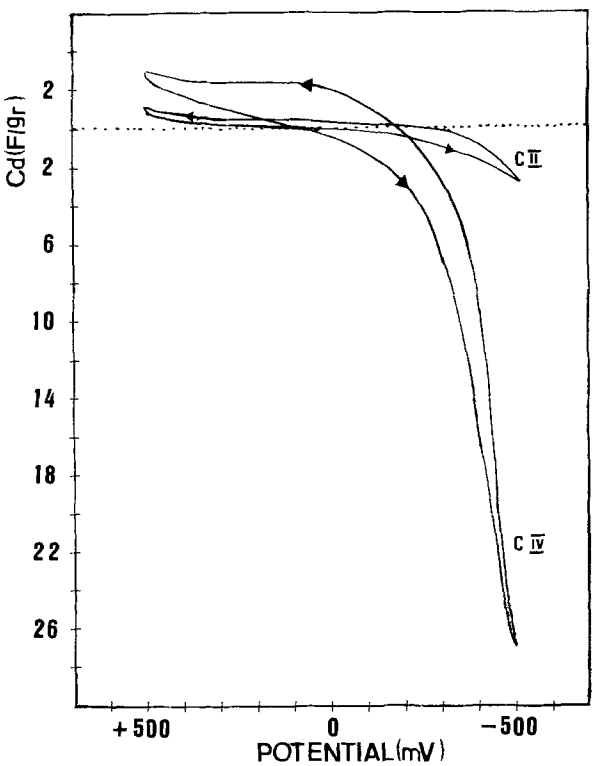


Fig. 8. C_d *vs. V* curve of the carbons C II-PD and C IV-OR in 0.1*N* NaCl; potential *vs.* 0.1*N* NaCl C.E.; 0.5 mV/sec.

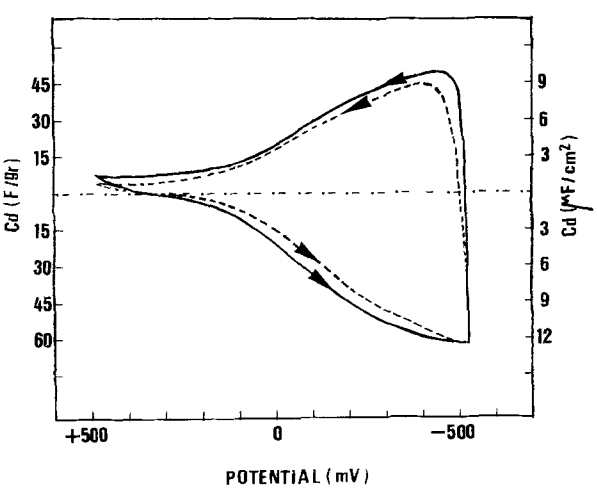


Fig. 9. C_d *vs. V* curve of carbon C III-OR in 0.1*N* NaCl. – – – –, 0.5 mV/sec; ——, 0.166 mM/sec; potential *vs.* 0.1 NaCl C.E.

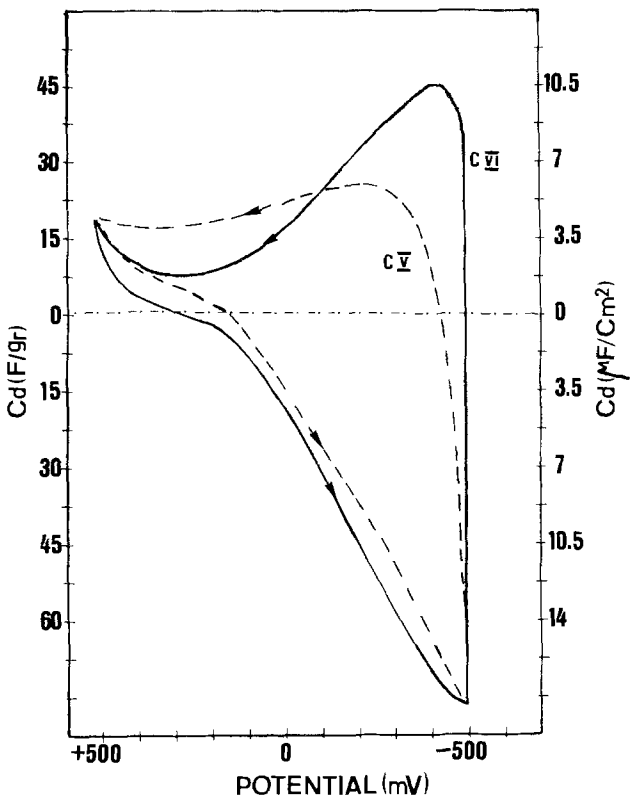


Fig. 10. C_d *vs. V* curve of the carbons C V-OD and C VI-PD in 0.1*N* NaCl; potential *vs.* 0.1*N* NaCl C.E., which shows the influence of reoxidation on double layer behavior; 0.5 mV/sec.

To our knowledge no such extreme change in C_d has been found, with the exception of peaks in C_d for some organic molecules (20). Moreover, the negative branch is almost symmetrical with respect to the potential axis, showing equilibration of the double layer during the half-cycle time, while at positive potentials the C_d-V curve resembles the extremely slow charging rate of carbon II. The fact that the C_d-V curve at a sweep rate of 0.5 mV/sec (Fig. 9) is very similar to that of the threefold slower sweep rate, indicates that the difference in C_d between the positive and negative potentials is due to equilibrium properties and not to different charging rates. A previous study (8) shows that at potentials greater than −190 mV *vs.* 0.1 NCE, cations are repelled from the interface of an oxidized microporous carbon electrode, resulting in a negative cation surface excess. At more negative potentials, anions are repelled similarly. This behavior can be explained by elementary electrostatic considerations, provided there is no specific ion adsorption (21).

Assuming that the oxidized carbon III has a pzc close to that found in a previous work (8), we deduce that the very low capacity at positive potentials originates from repulsive interaction of the anions with the negative dipoles of the surface oxides which, up to +500 mV, is not compensated by the attractive positive electronic charge. The opposite is obviously deduced for cations which penetrate and adsorb into the 3.7-4.4Å pores of the oxidized surface of carbon III. The adsorp-

[2] The capacitance which corresponds to the sweep rates of Fig. 10 is taken to be half the distance between the upper and lower curve.

tion is virtually nonexistent at the slightly less oxidized surface of carbon II, which has the same pore diameter range. The fact that anions are "normally" adsorbed at the carbon I oxidized surface (Fig. 7) is attributed to the larger pores which allow greater ion-interface distance. Here anion adsorption becomes possible again, since the repulsive ion-dipole potential decreases quicker than the attractive ion point charge or the ion-distributed surface charge of the carbon electrode.

The effect of surface oxides can be further demonstrated by starting from the oxygen depleted carbon V and inducing oxygen chemisorption at 300°C which will result in carbon VI, while the pore diameters remain essentially unchanged. The C_d-V curves for these two samples are given in Fig. 10. It can be seen that the charging rate and, to a lesser extent, the C_d increases at negative potentials for the oxidized carbon VI and decreases at positive potentials. This shows that the direct chemisorption of oxygen is the cause of the different double layer behavior. It also shows that the oxidized electrodes favor cation adsorption at the larger diameter (4.3-5.6Å) as well.

A further reduced pore diameter was studied in the original TCM 128 fiber (designated carbon IV). The narrow pores of this carbon could still accommodate water up to 16% w/w. This enabled a minute penetration and adsorption of solvated ions (Fig. 8), resembling the behavior of carbon II. The higher capacitance as compared to carbon II, especially at negative potentials, is due to the slightly larger amount of chemisorbed oxygen. Here again the charging rate is much slower than the potential sweep rate.

The role of the hydration sheath.—The experimental results lead to the conclusion that when the pore diameter is reduced to less than 5.6Å, slowing down of charging rate and dependence of C_d on the amount of surface oxides becomes significant. Since below 5.6Å and especially below 4.7Å (carbons II, III, and IV) ions can penetrate the pores only after partial depletion or distortion of the hydration sheath (22) different behavior could be expected from the various ions. Preliminary results are given in Fig. 11 which shows the effect of exchanging Na^+ by Li^+ on a carbon III ($3.7 < d < 4.3$) electrode. The charging rate of the extensively hydrated Li^+ ion is considerably slower at negative potentials. This is seen by comparing Fig. 9 and 11. Upon a tenfold reduction of the sweep rate, the shape of the C_d curve of LiCl (Fig. 11b) retains the C_d-V curve of NaCl (Fig. 9). This indicates that the equilibrium behavior of Li^+ on carbon III is similar to that of Na^+, but their charging rates differ considerably. This is unlike the difference in equilibrium behavior of cation and anion (negative and positive branches), demonstrated by the two curves in Fig. 9. The apparent selectivity, when accommodating the less hydrated cations, is common to other systems which have molecular size cages, *i.e.*, crown-ether complexes (23), and to highly cross-linked cation exchanger resins (24). In the first case the cation is held by ion-dipole forces, while in the second, interaction with the resin's negative charge takes place. The negatively charged ultramicroporous carbon comprises both types of interaction.

Influence of concentration and voltage sweep rate.—The higher concentration of the electrolyte seems to increase both the charging kinetics and C_d, as is shown in Fig. 12. The effect of the very high 5*N* NaCl concentration needs more study, as there is evidence of pore enlargement during slow charging cycles.

The above porous carbons have at least two different surface areas, that of the ultramicropores which is very large and always charged slowly, and that of the outer surface of the fibers, which should be compared to the nonporous graphite TGM 389 (Fig. 5), concerning C_d and charging rate. Figure 13 shows that the increase of the sweep rate excludes contribution of the micropores to C_d. The remaining much lower capacitance at the

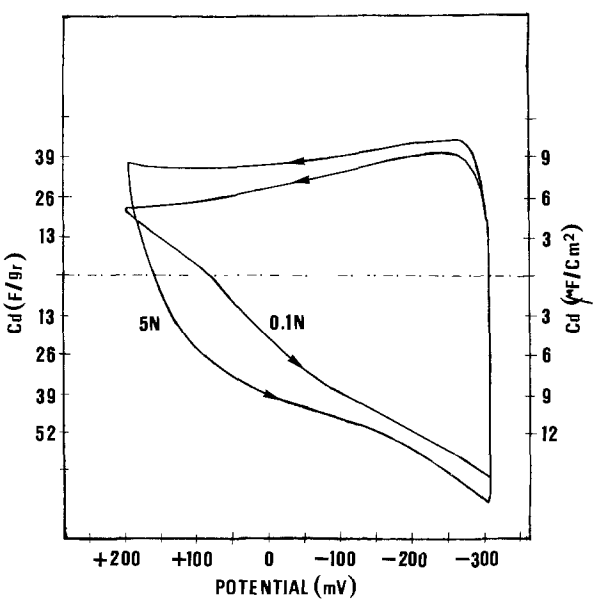


Fig. 12. The influence of increasing concentration on kinetics and C_d of carbon C V-OD in 0.1*N* NaCl and 5*N* NaCl. Potential *vs.* 0.1*N* NaCl C.E.; 0.15 mV/sec.

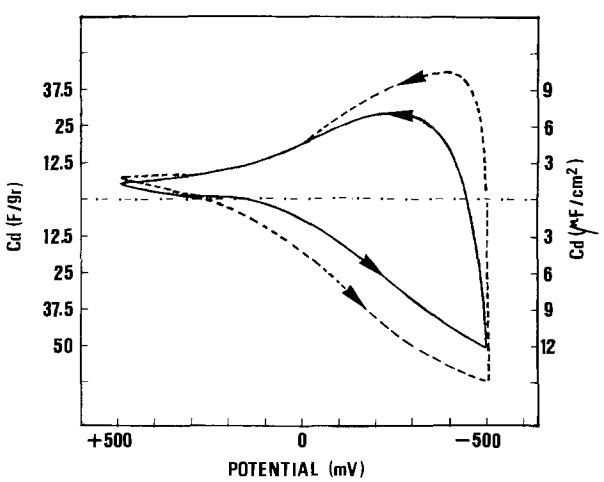


Fig. 11. C_d *vs.* V curve of carbon C III-OR in LiCl 0.1*N*. ----, 0.05 mV/sec; ——, 0.5 mV/sec; potential *vs.* 0.1*N* NaCl C.E.

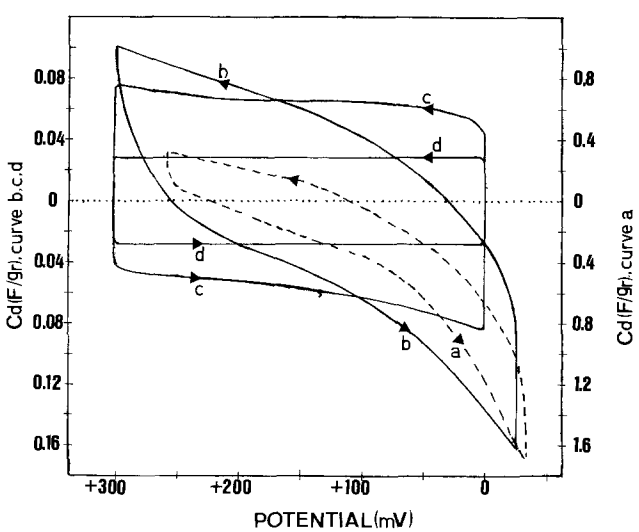


Fig. 13. The influence of potential sweep rate on C_d of carbon C IV-OR in 0.1*N* NaCl, potential *vs.* 0.1*N* NaCl C.E. a, 0.5 mV/sec; b, 10 mV/sec; c, 60 mV/sec; d, 600 mV/sec.

sweep rate of 600 mV/sec (Fig. 13d) corresponds to $2.8 \cdot 10^{-2}$ f/g. A doubled value of C_d, observed at 60 mV/sec (Fig. 13c), and a third charging process was observed (Fig. 13b) at an intermediate sweep rate of 10 mV/sec. All three curves were symmetrical and the current changes sign very fast by inversion of the voltage sweep. They are clearly distinct from the much slower and unsymmetrical ultramicropore charging process (Fig. 13a). The difference in C_d for Fig. 13(d, c, and b) is probably due to the difference between the geometrical and the BET surface area of the fibers. The same shallow micropores which cause the roughness factor might also be responsible for the intermediate rate charging process exhibited by Fig. 13b.

Estimation of ionic conductivity into the pores.—The delay of the current inversion after reversal of the sweep rate may be considered as a measure of restricted transport of ions into the pores. A characteristic relaxation time, τ, of the system could thus be the retention time of the symmetry between the upper and lower C_d-V curves. This value is deduced from Fig. 7 and 9. It could not be obtained from other curves, where no symmetry was achieved, with respect to the potential axis, during the voltametric cycle time. Regarding the porous electrode impedance as an R-C combination, we can write

$$\tau = RC_d \quad [2]$$

from which the order of magnitude of the specific resistivity ρ_P of the solution into the pores can be derived. Considering the radial symmetry of the current flow, the porous fiber is viewed as a solution conductor of a cross-sectional area A and length l. The area A is given by

$$A = A'P \quad [3]$$

where A' is the geometric surface area per gram of the fibrous material and P is the porosity in volume percent, which is about 30% for carbon I and III (12). The approximate length (l) of the ion pathway is expressed by

$$l = \frac{r}{2} \cdot T \quad [4]$$

where r is the average fiber radius and T is tortuosity factor of the conductance path, taken as 2 (4), thus $l \simeq r$. The cylindrical geometry of the fiber is thus approximated to be linear by means of Eq. [4]; therefore

$$R = \frac{\rho_R l}{A} \quad [5]$$

Substituting Eq. [4] and [2] in [5] and substituting the corresponding C_d values from the C_d-V curves at the negative inversion potentials of Fig. 7 and 9, we obtain $\rho_P^{I} = 1.1 \cdot 10^{11}$ Ω-cm and $\rho_P^{III} = 10^{11}$ Ω-cm for carbon I and III, respectively. This is several orders of magnitude larger than the resistivity of the bulk of 0.1N NaCl solution ($\rho \simeq 100$ Ω-cm).

The rough approximation applied renders ρ_P accurately only within the order of magnitude. It is still of value because of the great deviation of ρ_P from ρ. Extension of such studies over wider pore diameter ranges and to solutions used in practical porous electrode systems could provide information about the availability of the tiny pores for electrochemical reactions.

Faradaic and double layer currents.—On studying the electrochemical properties of carbon surfaces, discrimination between faradaic and double layer processes has to be made regarding the various surface groups existing on carbon. Recognizing that electrochemical reactions of surface groups involve the adsorption or desorption (in the thermodynamic, Gibbsian sense of surface excesses) of "aqueous components" (17) such as H^+, OH^-, H_2O_2 as well as electronic charge, we consequently deduce that surface groups fall within the generalized double layer concept. This concept has been put forward by Frumkin and coworkers (25) and later by Soffer (17). It is valid for both ideally polarized and reversible electrodes and makes no fundamental discrimination between them. The surface groups are simply considered as part of the components of the interface or the generalized double layer.

Putting the above argument into more experimental terms: The capacitor behavior of the double layer will not be imparted by the presence of the surface group in the sense that the interface should still acquire, for a finite potential change, a finite electronic charge which corresponds quantitatively with surface coverage constraints. This is unlike true faradaic processes which require an amount of charge according to the concentration and amount of redox components in the solution, regardless of surface coverage constraints.

The differential capacitance C_d (or the current) *vs.* potential function may, however, exhibit certain peaks due to specific surface groups if they are electroactive in a sufficiently narrow potential range. We have not encountered this behavior in sodium chloride solutions here and elsewhere (8, 16), nor in H_2SO_4 solution (26) in the range 0-650 mV *vs.* NHE. Peak-shaped voltamograms have been observed, however, in hot concentrated phosphoric acid (27) and in dilute HCl (28) and it may obviously depend on the type of carbon and surface treatment. In light of the above considerations, however, peak behavior is not necessarily an indication of faradaic response. It may simply be a hump in the C_d-V function.

In this work the electrode potential was always kept far from the thermodynamic potential of water decomposition. The pH was frequently monitored in order to assure, as has been done in a former work (8), that pH changes, if they occur at all, are too small to account for the charge delivered. We found, in fact, that the ultramicroporous electrodes were more immune to capacitance increase and pH changes at extreme potentials, than open structure electrodes.

Last but not least, no conceivable amounts of redox impurities could account for the delivered charges. On the other hand, these charge densities did correspond always to reasonable double layer charge values.

Conclusion

This work is restricted to ultramicropores of dimensions from close to those of water molecules up to 6Å. Qualitative evaluation, using constant sweep cyclic voltametry, showed that the mobility of ions into ultramicropores is several orders of magnitude smaller than in the free solution outside the pores. The surface dipoles have a stronger effect on adsorption and mobility into ultramicroporous carbons than on flat surfaces.

Manuscript submitted Jan. 11, 1977; revised manuscript received April 25, 1977.

Any discussion of this paper will appear in a Discussion Section to be published in the June 1978 JOURNAL. All discussions for the June 1978 Discussion Section should be submitted by Feb. 1, 1978.

REFERENCES

1. R. De Levie, in "Advances in Electro hemistry and Electrochemical Engineering," Vol. 6, P. Delahay and C. W. Tobias, Editors, Intersci nce Publishers, London, New York (1966).
2. See Ref. 3-10, 16, 17 in Ref. (4).
3. E. C. Gagnon, *This Journal*, **121**, 512 (1974).
4. M. Yaniv and A. Soffer, *ibid.*, **123**, 506 (1976).
5. G. W. Garten and D. E. Weiss, *Rev. Pure Appl. Chem.*, **7**, 69 (1957).
6. G. W. Murphy *et al.*, Demineralization of Saline Water by Electrically Induced Adsorption on Porous Carbon Electrodes, Annual Rep. U.S. Dept. of the Interior (1958).
7. J. Newman, *This Journal*, **118**, 510 (1971).
8. A. Soffer and M. Folman, *J. Electroanal. Chem.*, **38**, 25 (1972).
9. C. Orr and J. M. Dallavalle, "Fine Particle Measurement" MacMillan, New York (1960).

10. J. J. Kipling, "Adsorption from Solutions of Non-Electrolytes," chap. 13, Academic Press, London and New York (1965).
11. B. R. Puri, in "Chemistry and Physics of Carbon," Vol. 6, P. L. Walker Jr., Editor, p. 191, Marcel Dekker, Inc., New York (1970).
12. J. Koresh and A. Soffer, To be published.
13. S. J. Gregg and K. S. Sing, "Adsorption, Surface Area and Porosity," p. 214, Academic Press, London and New York (1967).
14. S. J. Gregg and K. S. Sing, *ibid.*, p. 223
15. L. G. Austin and E. G. Gagnon, *This Journal*, **120**, 251 (1973).
16. M. Yaniv, M.Sc. Thesis, Weizman Institute of Science, Rehovot, Israel (1974).
17. A. Soffer, *J. Electroanal. Chem.*, **40**, 153 (1972).
18. S. S. Barton and B. H. Harrison, *Carbon*, **10**, 245 (1972).
19. B. G. Linsen, "Physical and Chemical Aspect of Adsorbent and Catalyst," p. 458, Academic Press, London and New York (1970).
20. P. Delahay, "Double Layer and Electrode Kinetics," chap. 5, Interscience Publishers, London and New York (1956).
21. D. C. Graham and B. A. Soderberg, *J. Chem. Phys.*, **22**, 449 (1954).
22. E. Glueckauf, in "The Structure of Electrolyte Solution," W. J. Hamer, Editor, John Wiley & Sons, Inc. New York (1959).
23. H. K. Frensdorff, *J. Am. Chem. Soc.*, **93**, 600 (1971).
24. E. Riand, in "Physics of Electrolytes," Vol. 1, J. Hladik, Editor, Academic Press, London and New York (1972).
25. A. N. Frumkin, O. S. Petrii, and B. B. Damaskin, *Elektrokhimiya*, **6**, 614 (1970).
26. E. Keren and A. Soffer, *J. Electroanal. Chem.*, **44**, 53 (1973).
27. K. Kinoshita and J. A. S. Bett, *Carbon*, **11**, 403 (1973).
28. C. Tobias and A. Soffer, Unpublished results.

Technical Note

A Method for Direct, Real-Time Display of Q-$t^{1/2}$ Chronocoulometric Data

K. Keiji Kanazawa and R. K. Galwey

IBM Research Laboratory, San Jose, California 95193

In single step chronocoulometry, the time dependence of the charge Q passing through the working electrode in an electrochemical cell due to a step function of applied potential is recorded and studied. This technique was introduced many years ago (1). Even then, the utility of a Q *vs.* $t^{1/2}$ plot was recognized and discussed. The variety of information which can be obtained using this and related techniques has been reviewed by Murray (2).

A linear Q-$t^{1/2}$ dependence is a limiting case of a more general time dependence. To examine the generalized time dependence of charge, the data should be processed using digital computation. This can be done on line, and such systems have been described (3). For less demanding applications however, the necessary time and money investment required for laboratory automation is not warranted. This is particularly true when the functional time dependence is specified and only that dependence is examined. This note describes the technique which we have used to implement a real-time display of Q-$t^{1/2}$ data, permitting a quick assessment of the experimental conditions and eliminating the time, tedium, and possible error involved in manual plotting.

A block diagram of the experimental arrangement is shown in Fig. 1. An analog current-follower potentiostat was used for these measurements. Such instruments have been discussed in detail by Harrar (4). The output of the current follower in the potentiostat is a voltage e_I which is proportional to the cell current. Analog integration of this voltage yields a voltage e_Q which is proportional to the charge Q. Such circuitry is common (5), although special care must be taken in certain coulometric applications (6). Essentially, we want to plot e_Q against a voltage e_T which varies as the square root of time. One could conceivably have used analog techniques to generate this particular function of time. However, to provide maximum flexibility a stored waveform digital generator was used to produce e_T (7). The block diagram for this generator is shown in Fig. 2.

Key words: chronocoulometry, digital function generation, instrumentation.

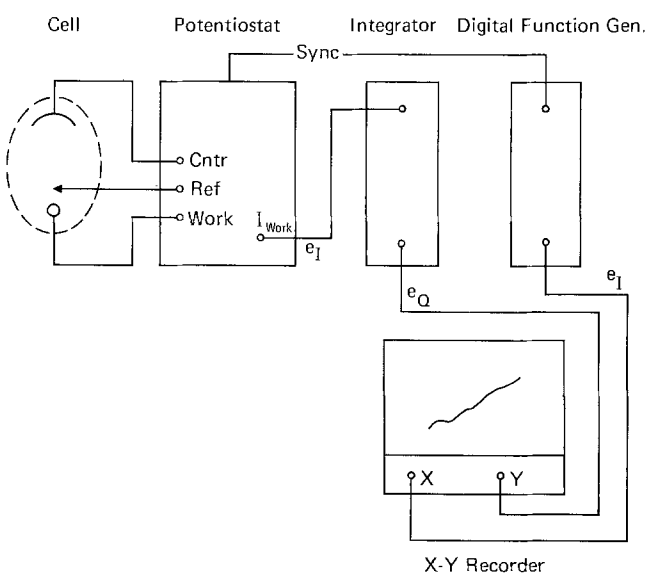


Fig. 1. A block diagram, showing the arrangement of the basic modules.

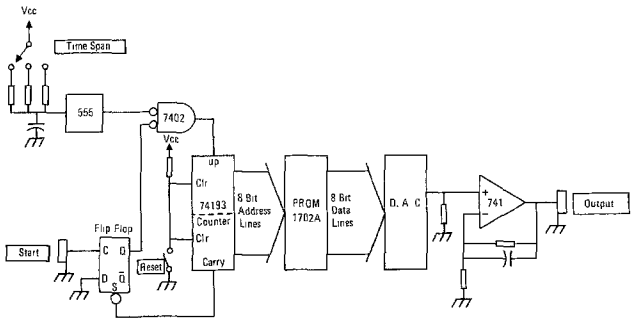


Fig. 2. A functional schematic diagram of the digital function generator.

The requirement on the circuitry is to produce an analog, time-dependent waveform which is digitally derived. The fundamental concepts for this circuit are described below. The digital equivalent of the waveform is stored in an erasable programmable read-only memory (Intel 1702A, 8×256 PROM). By sequentially addressing the PROM, the contents are sensed by the digital to analog converter (Hybrid Systems 371-8, DAC), and converted to the appropriate analog value. The amplifier provides proper scaling and filtering of the DAC output. The filtering is chosen commensurate with the instrument used for recording. In our particular case, where an X-Y recorder was used, the amplifier had a gain of 5 and was rolled off at 40 Hz. The PROM addresses are derived by incrementing an 8 bit binary counter. A clock provides the periodic pulses which increment the counter. We used an NE 555 timer because of ease of operation, simplicity, and cost. Depending on the specific application's needs, different timers may be selected.

Application of the clock signal is controlled by the NAND and the D flip-flop. The intent of these logical elements is to cause the counter to first be reset to address zero (or count zero) when the reset button is momentarily depressed. Simultaneous with the application of the step function voltage to the potentiostat, a "start" pulse must be received by the clock (C) input of the flip-flop. Its "Q" output will then go to a zero state. This zero state is NANDed by the negative-going clock pulses, resulting in positive-going pulses being sent to the counter. The counter will then begin incrementing, causing updated values to be sent to the DAC at the clock rate. When 256 clock pulses (the capacity of the PROM) have been received by the counter, a carry pulse will be generated by the counter. This pulse is received by the flip-flop, causing the "Q" output of the flip-flop to go to a "1" state. This "1" state inhibits any further pulses from incrementing the counter. Thus the cycle is complete.

There are two principal sources of error from the digital function generator. The 8 bit resolution introduces a digitization error. The maximum percentage error is 2% occurring near the beginning of the scan. After the first five points, this error is less than 1%. Since data reduction involves slope and/or intercept determination using a sizable fraction of the sweep data, the error introduced by this is much less than 1%. When the clock is an R-C controlled timer, as in this circuit, a larger uncertainty exists in the clock rate. Use of trimming techniques allows this error source to be reduced to less than 1%. This error is acceptable, being smaller than the 5-10% uncertainties introduced by other sources, such as cell geometry, incomplete IR compensation, and instrument and recorder calibration.

An example of a Q-$t^{1/2}$ plot obtained by us is shown in Fig. 3. This is an actual recording of the signal obtained in a cell using a 0.2 cm^2 Pt button working electrode in a solution containing 0.1M tetraethylammonium fluoborate in acetonitrile. The active species was methoxy pyrazoline, present at 0.001M concentration.

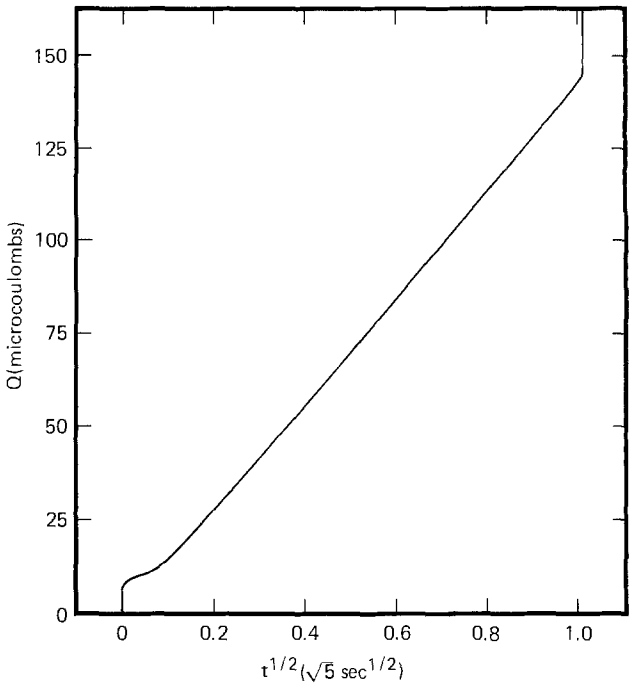


Fig. 3. An example of a direct display of Q-$t^{1/2}$ coulometric data.

For detailed work, the effective electrode area should be evaluated using a known electrochemical system, as was done, for example, by Bacon and Adams (8). The data were plotted using a Hewlett-Packard 7040A X-Y recorder. The hump at the beginning of the plot is due to overshoot in the potentiostat-cell system.

It is clear that this same technique could be used to examine other time dependencies. In fact, any waveform which can be stored with sufficient accuracy in the PROM can be used to drive the recorder X axis. For example, we have generated a $t^{-1/2}$ voltage function to compare these coulometric studies with a direct display of current *vs.* $t^{-1/2}$. We found the Q-$t^{1/2}$ technique to be superior, primarily because it was much less demanding of the recorder response time. We are finding this technique increasingly useful and feel that the versatility of this technique will permit the study of other interesting time behaviors.

Acknowledgments

The authors thank J. Gordon and A. Diaz for their insights and expertise. We are indebted to H. Seki for his support and encouragement.

Manuscript submitted March 2, 1977; revised manuscript received April 20, 1977.

Any discussion of this paper will appear in a Discussion Section to be published in the June 1978 JOURNAL. All discussions for the June 1978 Discussion Section should be submitted by Feb. 1, 1978.

Publication costs of this article were assisted by IBM Corporation.

REFERENCES

1. J. H. Christie, G. Lauer, R. A. Osteryoung, and F. C. Anson, *Anal. Chem.*, **35**, 1979 (1963).
2. Royce R. Murray, in "Physical Methods of Chemistry," Vol. I., Part IIA, Chapter VII, A. Weissberger and B. W. Rossiter, Editors, Wiley Interscience, New York (1971).
3. G. Lauer, R. Abel, and F. C. Anson, *Anal. Chem.*, **39**, 765 (1967).
4. J. E. Harrar, in "Electroanalytical Chemistry," Vol. 8, p. 43, A. J. Bard, Editor, Marcel Dekker, Inc., New York (1973).

5. "Operational Amplifiers, Design and Applications," pp. 213-218, J. G. Graeme, G. E. Toby, and L. P. Huelsman, Editors, McGraw-Hill Book Co., New York (1971).
6. W. S. Woodward, T. H. Ridgway, and C. N. Reilley, *Anal. Chem.*, **46**, 1151 (1974).
7. "Analog-Digital Conversion Handbook," pp. I-(68-79), D. H. Sheingold, Editor, Analog Devices, Inc., Norwood, Massachusetts (1972).
8. J. Bacon and R. N. Adams, *Anal. Chem.*, **42**, 524 (1970).

Brief Communication

n-Butyllithium–An Effective, General Cathode Screening Agent

M. Stanley Whittingham* and Martin B. Dines

Exxon Research and Engineering Company, Linden, New Jersey 07036

Currently, high energy density lithium storage systems are the focus of intense interest and expectation (1,2). In order to scan and characterize oxidants as potential cathodes, it would be very useful to have a reliable chemical reagent which could, in effect, mimic the half-cell reaction under consideration. Although reagents formed by dissolving alkali metals in ammonia, polyamines, polynuclear aromatic solutions in ethers, or hexamethyl phosphoramide (3) might be used, they have a number of shortcomings. Their reactions are difficult to run, since they involve extremely reactive materials, very dark opaque media, their polar solvents can also partake in the reaction, and it is difficult to separate the product from residual reagent. It would be preferable to have instead an agent whose lithium activity is more on the order of a volt or so below the alkali itself. We report that n-butyl lithium serves as such an agent.

The use of butyllithium to chemically mimic an electrochemical reaction was first mentioned by Armand (4) in connection with work on chromium oxide/graphite compositions. Dines (5, 6) then discovered that the lithium intercalates of the lamellar transition metal dichalcogenides were readily afforded without any of the degradation of their crystalline form previously seen, for instance, with lithium naphthalide (7) or lithium in ammonia, for which it is necessary to subsequently remove, by heating to 250°C, the coincorporated solvent (8). This latter effect, the coinsertion of solvating neutral molecules, has even been observed during electrochemical discharge in organic electrolytes (1). No such complications accompany the inclusion of lithium from butyllithium-hydrocarbon solutions. Because the solution is light and clear, the effect of the reagent on the oxidant can be visually [even microscopically (9)] observed during the process of lithiation.

n-butyl lithium, previously extensively used as an alkylating agent (3), is commercially available as a 1.5-2.0 molarity solution in hexane. In a typical experiment, a known quantity (~100 mg) of the candidate solid oxidant (Ox) was placed in contact with an excess of butyl lithium solution in a dry box and allowed to react for several days at room temperature, after which the solid was filtered, washed with hexane, and examined by x-ray diffraction. The reaction, which is shown schematically (10)

$$C_4H_9Li + (Ox) \rightarrow Li^+ (Ox)^- + (C_4H_9) \rightarrow \tfrac{1}{2}\, C_8H_{18}$$

was followed by acid-base titration of the unreacted butyl lithium and by monitoring the octane formed using gas chromatography. The latter is less reliable because of the possible formation of butene and butane from the butyl radicals. The results are summarized in Table I. A number of materials were found not to react at all, including graphite, aluminum, and antimony.

These results indicate that the reaction is indeed a general one, and that where battery discharge capacity data are available, excellent agreement is obtained. Thus, the carbon fluorides react with the stoichiometric quantity of lithium (11), and cupric sulfide takes up almost two equivalents as expected for formation of lithium sulfide and copper. Tetracyanoquinodimethane (TCNQ) reacts with one lithium to form $TCNQ^-$, in agreement with previous cell data (12). The oxides of vanadium and molybdenum reacted with about 2, and 1.5 equivalent of lithium, respectively, as previously reported (13, 14), and in both cases x-ray analysis indicated that two new phases were being formed. With TiO_2 (anatase form), butyllithium reacted vigorously forming first a blue, then a black compound. The degree of reaction was much higher than that reported by Johnson (19) for rutile, however, preliminary NMR results suggest that the lithium atoms are mobile just as he found them to be. The observed low level of reaction of CuF_2 could be related to the presence of a

Table I. Summary of results

Oxidant	Equivalent BuLi consumed	Oxidant	Equivalent BuLi consumed
$CF_{1.1}$	1.10	TiS_2(Se)	1.0
CuF_2	0.17	ZrS_2(Se)	1.0
CuS	1.72	HfS_2(Se)	1.0
TCNQ	1.00	NbS_2(Se)	0.8 (1)
$Ni(CN)_2$	2.00	TaS_2(Se)	1.0
FeS_2 (natural)	1.70	MoS_2(Se)	>1.5
SnO_2	0.09	WS_2(Se)	0.3 (>1.5)
Bi_2Te_3	1.26	VSe_2	>1.5
GaS	0.30	TiS_3	3.0
TiO_2	0.60	ZrS_3(Se)	3.0
Cr_2O_3	0.12	HfS_3(Se)	2.8
Ta_2O_5	3.70	NbS_3(Se)	3.0
V_2O_5	2.00	VS_4	~2.0
MoO_3	1.55	SnS_2	0.25
WO_3	0.00		

* Electrochemical Society Active Member.

Key words: cathode chemistry, n-butyllithium, screening agent, redox reactions, chalcogenides, oxides, titanium disulfide, lithium cells.

product film of LiF which prevented further reaction. The trichalcogenides, first studied in cells by Broadhead *et al.* (16), all reacted with about 3 moles of butyllithium, and have recently been extensively studied (17, 18). The reactivity of materials such as WO_3 might be enhanced by going to elevated temperatures to overcome kinetic barriers.

The use of butyllithium solutions also allows the rate of the process to be derived. This can be accomplished either by titrating aliquots of the supernatant reagent at appropriate time intervals, thereby following its consumption by the oxidant, or, as depicted in Fig. 1, by measuring the temperature rise of a reaction of the solid on addition to an excess of a molar solution of the reagent. The more rapid the temperature rise, the greater the reaction rate (and the potential discharge current density). As the figure shows, of TiS_2, MoO_3, and V_2O_5, the sulfide holds the greatest rate capability; this is consistent with our finding that current densities of 10 mA/cm^2 and greater can be attained in practical cell configurations (19, 20). In principle, the area under such curves can give a relative measure of the potential energy densities; strictly speaking it is the heat of the reaction which is measured, rather than the free energy. Thus, in the example given in the figure, V_2O_5 would promise the highest energy density. By carrying out the reactions in a calorimeter, a quantitative determination of the heat of reaction could be obtained for those cases where the reaction is rapid (such as TiS_2 and V_2O_5). However, in these qualitative studies, care must be taken in drawing conclusions of comparative behavior, since properties such as particle size obviously influence the results.

A problem in the discharge of cells is that conductive diluents, or other binding agents such as Teflon, must often be utilized in order to allow for the function of the cathode, but these additives are not necessary with the chemical reaction. Thus the butyllithium technique has allowed for the formation of the discharge product of a cell in a form readily amenable to x-ray analysis (21) and other physical measurements (22-24) without the complications of any possible side reactions or additional phases as might be present after disassembly of a battery. X-rays showed that these products were the same as those formed in cells.

That the effective cutoff of the voltage of butyllithium is on the order of *ca.* 1.4V below lithium itself is gathered from the behavior of $NbSe_3$. It has been found that on discharge the triselenide takes up 3 lithiums, with a final open-circuit voltage of above 1.4V (18). This sets an upper limit to the difference in activity between lithium and butyllithium, since the latter also yields Li_3NbSe_3. An approximate lower limit to the activity difference can be inferred from the observation that antimony does not react with butyllithium, and has a voltage relative to lithium of about 1V (25). Therefore, we can say that butyllithium is less active than lithium by 1-1.4V. Since the free energy of formation of octane is +4 kcal/mole (26), one infers a value for the free energy of formation of butyllithium of about 25 kcal/mole (±5 kcal/mole).

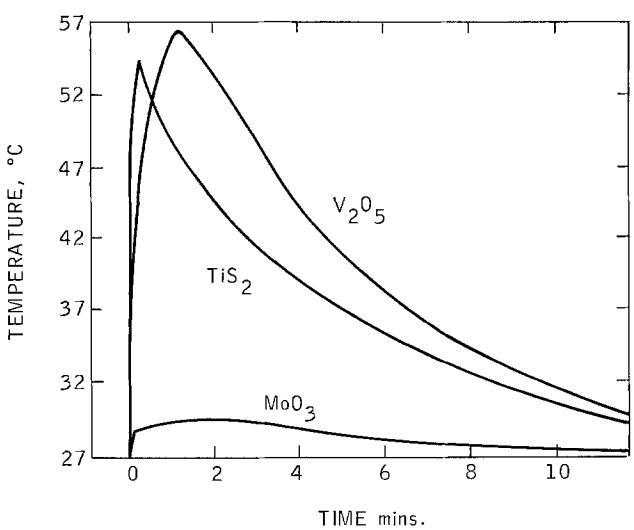


Fig. 1. Effect of the addition of excess butyllithium to equivalent slurries of V_2O_5, TiS_2, and MoO_3.

Manuscript submitted March 21, 1977; revised manuscript received April 11, 1977. This was Paper 31 presented at the Dallas, Texas, Meeting of the Society, Oct. 5-9, 1975.

Any discussion of this paper will appear in a Discussion Section to be published in the June 1978 JOURNAL All discussions for the June 1978 Discussion Section should be submitted by Feb. 1, 1978.

Publication costs of this article were assisted by Exxon Research and Engineering Company.

REFERENCES

1. M. S. Whittingham, *This Journal*, **123**, 315 (1976).
2. J. O. Besenhard and G. Eisenger, *J. Electroanal. Chem. Interfacial Chem.*, **77**, 1 (1976).
3. E. Bayer and W. Rudorff, *Z. Naturforsch.*, **27b**, 1336 (1972).
4. M. B. Armand, in "Fast Ion Transport in Solids," W. Van Gool, Editor, North-Holland (1973).
5. M. B. Dines, U.S. Pat. 3,933,688 (1976).
6. M. B. Dines, *Mater. Res. Bull.*, **10**, 287 (1975).
7. W. Rudorff, *Chimia*, **19**, 489 (1965).
8. A. Leblanc-Soreau, M. Danot, L. Trichet, and J. Rouxel, *Mater. Res. Bull.*, **9**, 191 (1974).
9. R. R. Chianelli, *J. Cryst. Growth*, **34**, 239 (1976).
10. B. J. Wakefield, "The Chemistry of Organolithium Compounds," Pergamon Press, Inc., New York (1974).
11. M. S. Whittingham, *This Journal*, **122**, 526 (1975).
12. F. Gutmann, A. M. Hermann, and A. Rembaum, *ibid.*, **114**, 323 (1967).
13. C. R. Walk and J. S. Gore, Paper 27 presented at The Electrochemical Society Meeting, Toronto, Canada, May 11-16, 1975.
14. F. W. Dampier, *This Journal*, **121**, 656 (1974).
15. O. W. Johnson, *Phys. Rev.*, **A136**, 284 (1964).
16. J. Broadhead and F. Trumbore, Paper 178 presented at The Electrochemical Society Meeting, Chicago, Illinois, May 13-18, 1973; U.S. Pat., 3,864,167.
17. R. R. Chianelli and M. B. Dines, *Inorg. Chem.*, **14**, 2417 (1975).
18. Papers 443 RNP and 26 presented at The Electrochemical Society Meeting, Toronto, Canada, May 11-16, 1975; Paper 31 presented at The Electrochemical Society Meeting, Dallas, Texas, October 5-9, 1975. To be published by Chianelli *et al.* and Murphy *et al.*
19. M. S. Whittingham, *Science*, **192**, 1126 (1976); U.S. Pat. 4,009,052.
20. L. H. Gaines, R. W. Francis, G. H. Newman, and B. M. L. Rao, Proceedings of the 11th Intersociety Energy Conversion, p. 418 (1976).
21. M. S. Whittingham and F. R. Gamble, *Mater. Res. Bull.*, **10**, 363 (1975).
22. B. G. Silbernagel, *Solid State Communications*, **13**, 1911 (1975).
23. B. G. Silbernagel and M. S. Whittingham, *J. Chem. Phys.*, **64**, 3670 (1976).
24. D. W. Murphy, F. J. DiSalvo, G. W. Hull, and J. V. Waszczak, *Inorg. Chem.*, **15**, 17 (1976).
25. H. P. Fritz and J. Besenhard, U.S. Pat. 3,960,594 (1976).
26. N. A. Lange, "Handbook of Chemistry," Revised 10th ed., p. 1655, McGraw-Hill Book Co., New York (1967).

JOURNAL OF THE ELECTROCHEMICAL SOCIETY

SOLID-STATE SCIENCE AND TECHNOLOGY

SEPTEMBER 1977

Electrochemical Properties of Dopants and the D-C Dynamic Scattering of a Nematic Liquid Crystal

H. S. Lim,* J. D. Margerum, and A. Graube

Hughes Research Laboratories, Malibu, California 90265

ABSTRACT

Flow of liquid crystal from one electrode to the other was observed during dynamic scattering of a phenyl benzoate nematic liquid crystal. The direction of the flow depended upon the electrochemical properties of dopants. The flow was from cathode to anode when the dopant was an electron acceptor, and vice versa when the dopant was a donor. A redox dopant gave distinctively different d-c dynamic scattering patterns from a salt dopant, and did not give the Williams domain pattern which was observed with a salt dopant. Charge conduction mechanisms through the liquid crystal are discussed in terms of the electrode reactions of the liquid crystal components and the dopants.

Dopants are commonly used to improve the properties of nematic liquid crystals (LC) for dynamic scattering (DS) displays (1). The conductivity anisotropy (2-4) of a LC depends very much on the dopants which are used. The a-c dynamic scattering characteristics depend strongly on the conductivity anisotropy. Lower threshold voltages (3, 4) and higher scattering levels (4) were observed as the value of the anisotropy was increased. The conductivity anisotropy depends on the structure of the dopant as well as on the liquid crystal material itself (4). The d-c-DS characteristics also depend on the electrochemical properties of the dopant; redox dopants consisting of electron acceptors, donors, or a combination of both, give a low threshold voltage (5, 6) and a high scattering level (6). A combination of an electron acceptor and a donor gives good electrochemical stability (6-8) for long-term d-c-DS of liquid crystals. Redox dopants which can be reduced and oxidized much more easily than the LC compounds minimize the participation of the LC compounds in the electrode reactions which are responsible for their decomposition (6, 9).

In a recent preliminary report (9), we showed that the charge injection and LC flow direction as well as the scattering patterns in a d-c activated LC depended upon the dopants that were used. Earlier, Heilmeier *et al.* (10) reported that in anisylidene-*p*-aminophenylacetate the DS was initiated from the negative electrode and was propagated to the positive electrode. However, they used geometrically dissimilar electrodes and they did not specify the dopants responsible for the observed conductivity and DS of their Schiff base. Lacroix and Tobazeon (11) carried out studies on N-(*p*-methoxybenzylidene)-*p*-*n*-butylaniline (MBBA) in a special cell in which the electrodes were coated with anion-permeable membranes. They observed that the LC motion started at the negative (anion-injecting) electrode and spread toward the positive (collector) electrode, giving a "finger"-type flow pattern followed by a turbulent region spreading toward the collector.

In the present paper we first report studies on the electrode reactions of various dopants and of 4 ester liquid crystal components in solutions of acetonitrile or dimethyl formamide. Then we report studies of the hydrodynamic flow patterns and dynamic scattering effects of these dopants dissolved in the nematic ester liquid crystal mixture when d-c voltages are applied.

Experimental

The LC used was a phenyl benzoate mixture designated as HRL-2N10. It was a four-component mixture of *p*-butylphenyl *p*-toluate, *p*-butoxyphenyl *p*-butoxybenzoate, *p*-butoxyphenyl *p*-hexyloxybenzoate, and *p*-butoxyphenyl *p*-octyloxybenzoate in a weight ratio of 15:5:9:9, respectively. It had a nematic range of about 20°-55°, a dielectric anisotropy of $\Delta\epsilon = -0.12$ (25°C, 500 Hz), and a birefringence of $\Delta n = 0.14$ (25°C, 545 nm). Before dopants were added, the resistivity of the LC at 25°C was greater than 10^{11} Ω-cm at 100 Hz. The resistivity of the LC after doping ranged from 4×10^8 to 1×10^{10} Ω-cm. The individual components of the LC were prepared by the reactions of the corresponding substituted benzoyl chloride and the substituted phenol in pyridine. The reaction products were recrystallized several times. Three types of dopants were used: (*i*) electrochemically inactive salts, tetrabutylammonium perchlorate (TBAP), and tetrabutylammonium trifluoromethanesulfonate (TBATMS); (*ii*) electron acceptors, 7,7',8,8'-tetracyanoquinodimethane (TCNQ), and (2,4,7-trinitro-9-fluoroenylidene)malononitrile (TFM); and (*iii*) electron donors, di-*n*-butylferrocene (DBF) and tetrathiofulvalene (TTF). The acceptor and donor dopants are called "redox" dopants throughout this paper. TBATMS was prepared (12) by reaction of trifluoromethanesulfonic acid and

* Electrochemical Society Active Member.

Key words: redox dopant, salt dopant, liquid crystal, electrohydrodynamic motion, dynamic scattering.

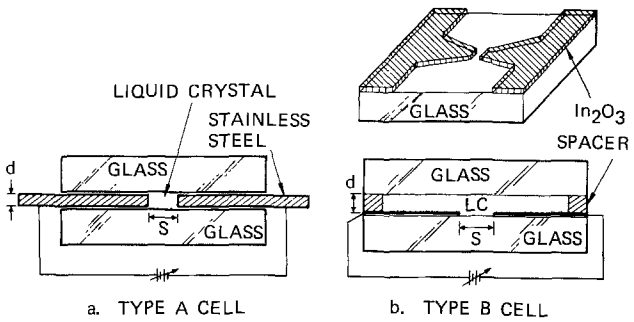


Fig. 1. Schematic drawings of test cells

tetrabutylammonium bromide. The crude product was recrystallized from water and dried. TBAP was the polarographic grade from Southwestern Analytical Chemicals, Incorporated. It was vacuum dried at 50°C before use. TCNQ (from either Aldrich Chemical Company or Eastman Organic Chemicals) was recrystallized more than twice from acetonitrile (AN). TFM (Aldrich Chemical Company) was recrystallized from AN. DBF (Research Organic Chemical Company) was purified by vacuum distillation. The TTF sample was donated by Dr. Fred G. Yamagishi.[1] The solvents AN (Burdick and Jackson Laboratories Incorporated) and spectrophotometric grade dimethyl-formamide (DMF) (J. T. Baker Chemical Company) were used as purchased for electrochemical studies.

The electronic apparatus employed for the cyclic voltammetry was similar to that described earlier (13). The cyclic voltammograms were recorded on an Omnigraphic Model 2000 X-Y recorder (Houston Instrument) using a conventional two-compartment cell. The electrodes used for cyclic voltammetry were either commercially available hanging mercury drop electrodes or a platinum ball attached to a fine platinum wire sealed in glass. Potentials were measured against a saturated calomel electrode (SCE), and solution resistance was not compensated. All experiments were carried out at room temperature.

Two different types of test cells for liquid crystals were used for the microscopic study. Schematic diagrams of type A and B cells are shown in Fig. 1. The LC was restricted to a small interelectrode space in the type A cell. The purpose of the type B cell was to allow enough space so that the liquid crystal could move from one electrode to the other without generating a compensating flow in the area under observation. The electrode separations (S) were varied from 180 to 600 μm, and the thickness of the liquid crystal layer (d) from 25 to 200 μm. The liquid crystal was aligned either perpendicular or parallel to the electric field and parallel to the surface of the glass substrates by manually rubbing the substrate with Kimwipes. The perpendicular alignment was obtained by bonding long alkyl chains onto the surface of the substrates. The microstructure of the DS was observed from a direction perpendicular to the direction of the applied electric field using a Zeiss standard WL polarizing microscope.

Results and Discussion

Electrode reactions in solvents.—The electrode reactions of the liquid crystal components were studied by cyclic voltammetry using platinum and mercury electrodes. The cyclic voltammograms of the LC components in AN are shown in Fig. 2. Anodic oxidations of the compounds occurred at potentials more positive

[1] Preparation of TTF: 1,3-dithiole-2-thione (Strem Chemicals Incorporated) was oxidized with peracetic acid [E. Klingsberg, *J. Am. Chem. Soc.*, 26, 5240 (1964)], and the resulting salt was converted to 1,3-dithialium perchlorate with perchloric acid [D. Leaver *et al.*, *J. Chem. Soc.*, 5104 (1962)]. Deprotonation of this compound with triethylamine [D. L. Coffen *et al.*, *J. Am. Chem. Soc.*, 93, 2258 (1971)] gave TTF in quantitative yield. After recrystallization from hexane, the product was gradient-sublimed (75°C, 10^{-5} Torr) [A. R. McGhie *et al.*, *J. Cryst. Growth*, 22, 295 (1974)] to give orange prisms, mp 118°-119.5°C.

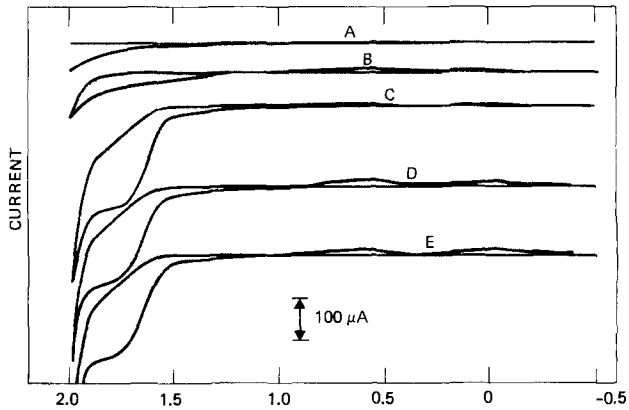


Fig. 2. Cyclic voltammograms of the LC components in 0.1M TBAP solution of AN. Electrode, platinum ball; voltage scan rate, 100 mV/sec; (A) blank solution; (B) 2 mM *p*-butylphenyl toluate; (C) 2 mM *p*-butoxyphenyl *p*-butoxybenzoate; (D) 2 mM *p*-butoxyphenyl *p*-hexyloxybenzoate; and (E) 2 mM *p*-butoxyphenyl *p*-octyloxybenzoate.

than 1.5V *vs.* SCE. A coupled reduction peak of the anodic peak (Fig. 2) of the compounds was not observed, indicating that the oxidation products were not readily rereduced in the experimental conditions. Typical cyclic voltammograms are shown in Fig. 3 of one of the LC components in DMF for the cathodic process. A cathodic reduction of *p*-butylphenyl *p*-toluate (not shown in Fig. 3) occurred at more negative potentials than −2.0V *vs.* SCE, while the reduction of the other three compounds occurred at more negative potentials than −2.1V *vs.* SCE, as in Fig. 3. No coupled oxidation peaks to the reduction peaks were observed at low voltage scan rates [Fig. 3(A)]. As the scan rates were increased above a certain value (*e.g.*, about 100 mV/sec for *p*-butoxyphenyl *p*-hexyloxybenzoate), an oxidation peak which appeared to be coupled with the reduction peak was observed [Fig. 3(B) and (C)]. This observation indicated that a chemical reaction of the primary reduction product might be followed by the cathode reaction to give a reaction product which was not easily oxidizable at the electrode. Primary reaction products of both cathodic and anodic processes would probably be radical ions (14, 15) of the LC esters, which would be unstable in the experimental conditions.

The cyclic voltammograms of the dopants in 0.1M TBAP solution of AN using the platinum electrode are shown in Fig. 4. The cathodic and anodic peaks of all the redox couples in Fig. 4 were separated by about 70-100 mV. The separation of the cathodic and anodic peaks (70 or 80 mV) of the two one-electron reduction steps of TFM appeared to indicate that the electrode reactions were reversible. The values of the peak potential separation (slightly larger than the theoretical

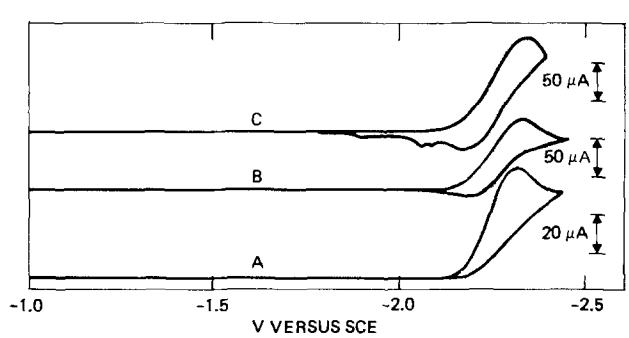


Fig. 3. Cyclic voltammograms of 1 mM *p*-butoxyphenyl *p*-hexyloxybenzoate in 0.1M TBAP solutions of DMF. Hanging drop mercury electrode. Voltage scan rates: (A) 20 mV/sec; (B) 100 mV/sec; and (C) 200 mV/sec.

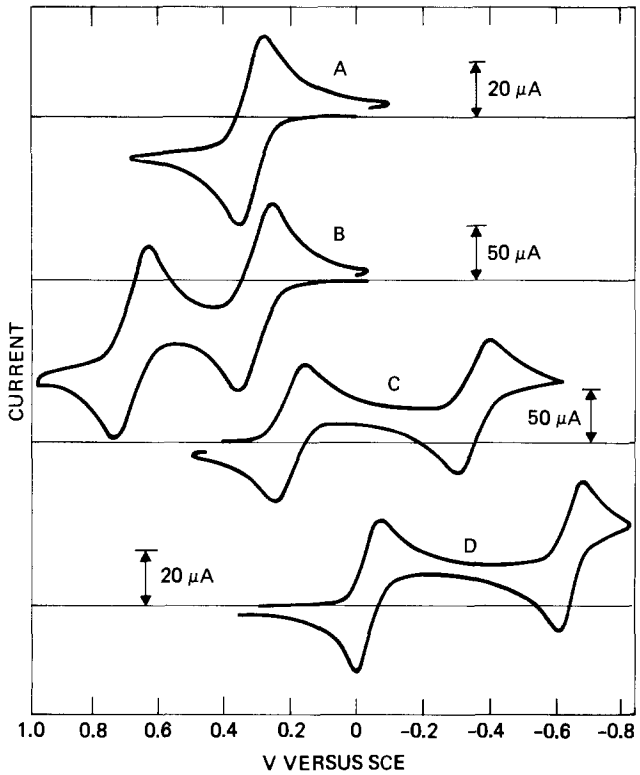


Fig. 4. Cyclic voltammograms of the redox dopants in 0.1M TBAP solution of AN. Electrode, platinum ball; voltage scan rate, 100 mV/sec; (A) 1.0 mM DBF; (B) 3 mM TTF; (C) 2.5 mM TCNQ; and (D) 1.1 mM TFM.

value of 58 mV) might be due to the uncompensated resistance of the electrolyte in the test cell.

Reversible electrode reactions in AN have been reported for the two one-electron oxidations of TTF (16) and also for the first one-electron reduction step of the two one-electron reduction steps of TCNQ (17, 18). Such reversibility has not been reported for TFM and DBF, but in the latter case a similar structure [1,1'-diethylferrocene (19)] was reported to show a reversible one-electron oxidation step.

The redox potentials of the dopants indicate that the electron acceptors such as TFM and TCNQ and donors such as DBF and TTF are expected to dominate cathodic and anodic processes, respectively, in the LC if they are present in sufficient concentrations.

Liquid crystal studies.—The dominating effects of the electrode reactions of dopants on the electrohydrodynamics of the LC have been observed during the microscopic study of DS with applied d-c fields. The characteristic microscopic patterns of DS with various types of dopants are shown in Fig. 5 and 6. Salt dopants [Fig. 5(B) and 6(A)] and redox dopants [Fig. 5(B-D) and 6(B-F)] showed distinctly different DS patterns. When the dopant was salt type and the liquid crystal alignment was perpendicular to the electric field and parallel to the glass substrate, the scattering pattern had a line or channel structure [Fig. 5(A) and 6(A)] which was asymmetric with respect to the polarity of the field but otherwise similar to that previously observed by Chang (20) with MBBA subjected to an a-c signal. (When the alignment was parallel to the electric field, the line structure was spatially very irregular; otherwise, the appearance was similar to the perpendicular case.) Thin flow lines of liquid crystal [Fig. 5(A)] were initiated from both electrodes visibly at the same time and propagated toward the opposite electrodes. The initiation of these flow lines alternated regularly from one electrode to the other. Dust particles moved in one direction along the flow lines originating at one electrode, and in the opposite direction along the flow lines originating at the other electrode, indicating that the lines were caused by LC flow. These particles moved back and forth along the flow channels. This observation is consistent with earlier observations on Williams domain patterns (21). There appeared to be little or no net flow of liquid crystal from one electrode to the other, even with type B cells in which room for net flow was provided.

When the dopant was a redox-type, *i.e.*, an electron acceptor or an electron donor, the general appearance of the scattering pattern was quite different from that observed with the salt dopants. Turbulent motions of liquid crystal were observed at lower voltages, without formation of the regular line or channel structure discussed above. The turbulence was initiated from one electrode and propagated to the other at a visible rate. Except at very high voltages, the turbulence did not reach the opposite electrode and remained localized near the electrode where it was initiated [Fig. 5(B-D) and 6(B-E)]. A surprising observation was that the turbulence was initiated from the cathode when the dopant was an electron donor and from the positive when the dopant was an electron acceptor, *i.e.*, the turbulence was observed at the opposite electrode of

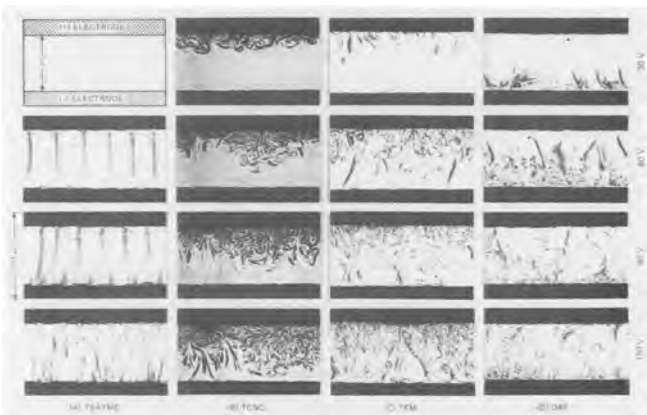


Fig. 5. Photographs of the microscopic patterns of DS using type A cells. A single polarizer parallel to the direction of LC alignment was used. The alignment of LC was perpendicular to the electric field and parallel to the surface of the glass substrate. d = 51 μm. (A) 0.03%, $\rho \sim 4 \times 10^8$ Ω-cm; (B) saturated, $\rho \sim 10^{10}$ Ω-cm; (C) 0.5%, $\rho \sim 10^{10}$ Ω-cm; and (D) 1%, $\rho \sim 10^{10}$ Ω-cm.

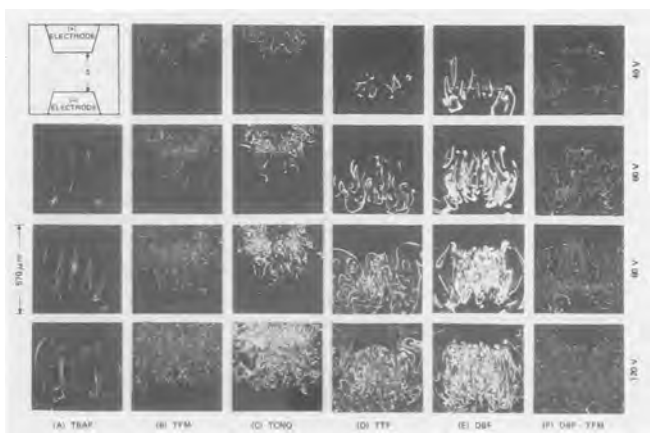


Fig. 6. Photographs of the microscopic patterns of DS using type B cells. Crossed polarizers are used with one polarizer parallel to the direction of LC alignment. The alignment of LC was perpendicular to the electric field and parallel to the surface of the glass substrate. d = 51 μm. (A) 0.02% TBAP, $\rho \sim 2 \times 10^9$ Ω-cm; (B) 0.2% TFM, $\rho \sim 10^{10}$ Ω-cm; (C) saturated TCNQ, $\rho \sim 10^{10}$ Ω-cm; (D) 0.5% TTF, $\rho \sim 9 \times 10^{10}$ Ω-cm; (E) 0.2% DBF, $\rho \sim 10^{10}$ Ω-cm; and (F) 0.1% DBF-TFM, $\rho \sim 10^{10}$ Ω-cm.

the electrode from which the charge injection was expected through the faradaic reaction of the dopant.

The flow of LC under the influence of the applied d-c field was also observed with the redox dopants. A unidirectional flow from one electrode to the other was observed with these dopants, unlike the case of salt dopants. The direction of the flow was always from the anode to the cathode when the dopant was a donor, and from the cathode to the anode when the dopant was an acceptor. Figure 7 shows an example of microscopic flow patterns with a donor dopant (DBF). As indicated by arrows in the figure, average dust particles moved from the back side of the electrode from which charge injection is expected through the faradaic reaction of the dopants toward the opposite electrode, traveled across the electrode boundary and came back to the starting point by the periphery of the electrodes where the electrical field was weak. The dopant-dependent flow of LC was confirmed by another independent method using a test cell which is shown schematically in Fig. 8. The field was applied across two metal screen electrodes and a net liquid flow in a given direction introduced a pressure which changed the height of the liquid crystal in the capillaries. When voltage was applied to the cell, the LC column was displaced from the anode side to the cathode side when the dopant was an electron donor, and vice versa when the dopant was an acceptor. When the dopant was



Fig. 7. Flow pattern of LC in a type B cell. Alignment of LC was perpendicular to the surface of the glass substrate. Photographs were taken with crossed polarizers. Dopant: 0.2% DBF. Applied voltage: 120V.

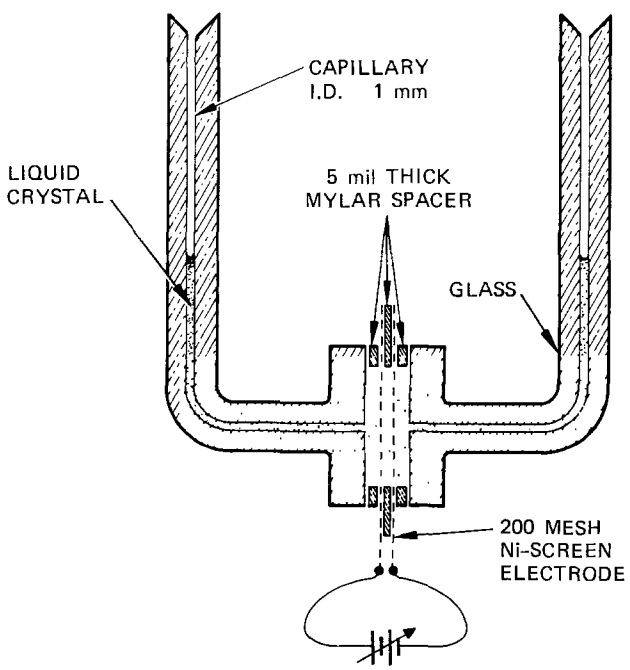


Fig. 8. Liquid crystal flow detection cell.

either a salt or an equimolar mixture of the donor (DBF) and the acceptor (TFM), the displacement was much smaller than previous cases.

The dopant-dependent flow of LC under the influence of the d-c field clearly indicated that the electrode reactions of the dopants played the dominant role in the electrohydrodynamics of the LC. The observation with the redox dopants appears to be consistent with the charge conduction mechanisms, as shown in Fig. 9(a) and (b), which involve a unipolar charge injection through the faradaic reaction of the dopant at our electrode followed by space charge (11) migration to the opposite electrode where the charge is neutralized by the reverse electrode reaction. The space charge should be associated with the radical ions of the dopants. When the dopant is an electron acceptor [Fig. 9(a)], negative charge injection occurs at the cathode ($A + e \rightarrow A^-$), the charge migrates to the anode in the form of a space charge to be neutralized at the anode ($A^- \rightarrow A + e$), and vice versa when the dopant is a donor [Fig. 9(b)]. The LC flow is caused by the migration of ions through it. The alternative mechanisms shown in Fig. 9(c-f) which do not require space charge formation do not explain the unidirectional flow of the LC.

When the redox dopant was a mixture of an electron acceptor and a donor, the direction of the net flow of LC depended on relative amounts of each component. Microscopic studies showed that the over-all flow pattern of the LC was a mixture of regions which were similar to the pattern with an acceptor dopant and those with donor dopant rather than those of a salt dopant with a flow line structure. The patterns contained regions of turbulence which were similar to those with an acceptor dopant and regions which were similar to those with a donor dopant [Fig. 6(F)]. This observation was also supported by the motion of dust particles which moved from one electrode to the other in one region and in the opposite direction in the adjacent region. The charge conduction mechanism appears to involve regions where the mechanism shown in Fig. 9(a) operates, and other regions where the mechanism shown in Fig. 9(b) operates. These two

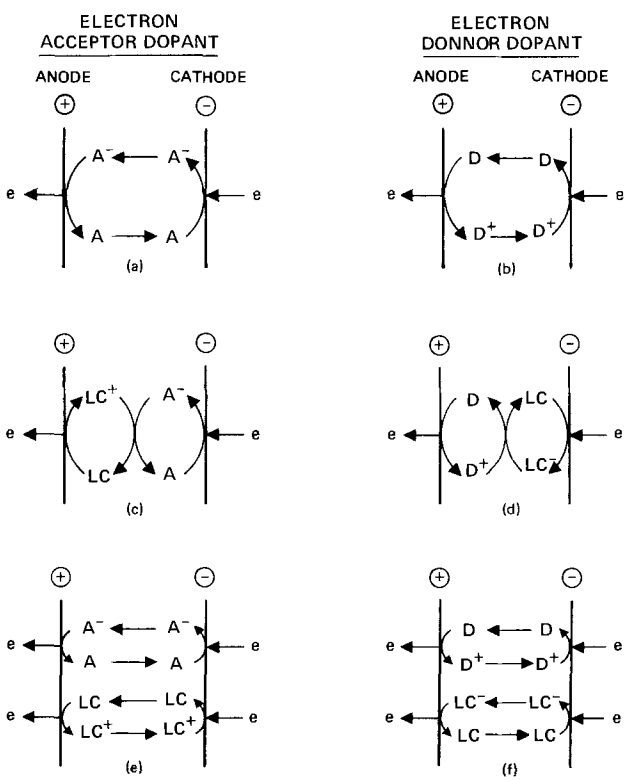


Fig. 9. Charge conduction mechanisms through LC when the dopant is a redox type.

different regions are randomly distributed throughout the conduction area.

When the dopant is a salt, the charge conduction mechanism is probably as shown in Fig. 10(a). The LC components are reduced at the cathode to give a radical anion ($LC + e \rightarrow LC^-$), and oxidized at the anode to give a radical cation ($LC \rightarrow LC^+ + e$). At the same time, channels of cation and anion space charge regions are formed during the charge migrations to the opposite electrodes, and the charge is neutralized at the opposite electrodes by reverse reactions. An alternate mechanism (22) [Fig. 10(b)] which includes a reaction of the cation and anion in the bulk of LC does not explain the alternating flow channels of LC which are observed with the salt dopant.

The hydrodynamic instability of LC with the salt dopants to form the flow channel structure has been theoretically analyzed previously (23). However the reason, why the turbulence pattern is formed during dynamic scattering of LC when the dopant is a redox type and why the turbulence is localized at one particular electrode are not known presently. The reason why two different turbulence regions are formed when the dopant is a mixture of an electron acceptor and a donor, instead of giving the flow channel structure, remains also to be explained.

The turbulent LC flow patterns observed in Fig. 5 and 6 correspond to the dynamic scattering (DS) effects observed in display cells. The DS threshold voltage is considerably higher in the present test cells than in conventional sandwich-type display cells because of the surface boundary conditions. Comparison of the microscopic patterns of salt-doped LC in Fig. 5(A) and 6(A) (no DS was observed at 30 and 40V, respectively) with those of redox-doped LC in Fig. 5(B-D) and 6(B-F) showed that the redox dopants gave lower DS threshold voltage than the salt dopants. Threshold voltages of 2.0-2.1V for a redox dopant and 3-5V for a salt dopant were observed (6) in a comparable resistivity range of the LC in conventional 13 μm thick display cells in which the LC was sandwiched between 2 flat transparent electrodes. The comparison of the microscopic patterns also indicated that the LC doped with a redox dopant would give a higher DS level than the LC with a salt dopant. The scattering levels in a given voltage in the display cells were always higher with the redox dopants than the salt dopants (6).

Our observations (6) of long d-c operational lifetimes of LC with redox dopants as compared to short lifetimes with salt dopants are consistent with the present charge conduction mechanism. In 13 μm thick display cells an operational lifetime of more than 18,000 hr with continuous 20V d-c operation has been achieved when the LC was doped with 0.5% DBF and 0.5% TFM, while the lifetime was shorter by more than two orders of magnitude when the LC was doped with a salt dopant. The shorter lifetime with a salt dopant was probably due to the formation of LC radical ions which are unstable, while in the presence of redox dopants such LC radical ions were not formed.

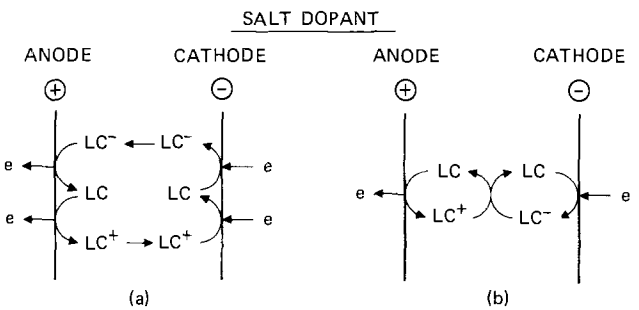


Fig. 10. Charge conduction mechanisms through LC when the dopant is a salt.

Conclusions

1. Discretely different d-c-activated hydrodynamic instabiltities were observed with a redox dopant than with a salt dopant in the same ester liquid crystal. At voltages just above the threshold the liquid crystal with salt dopants showed a flow pattern with periodically arrayed flow channels, while the liquid crystal with redox dopants showed turbulence motion.

2. A unidirectional flow of LC from one electrode to the other has been observed during the DS of the LC which was doped with either an electron acceptor or a donor. The direction of the flow depended on the dopants. The flow was from the positive electrode to the negative when the dopant was an electron donor and vice versa when the dopant was an acceptor.

3. The observations of the flow appeared to be consistent with the charge transport mechanisms which involved a unipolar injection of charge at the anode when the dopant was a donor and at the cathode when the dopant was an acceptor through the faradaic reaction of the dopants and migration of the injected space charge toward the opposite electrode to be neutralized by the reverse electrode reactions.

4. When the dopant was a redox type, dynamic scattering appeared to be initiated and localized (at lower voltages) at the opposite electrode of charge injection.

5. The higher d-c scattering levels (6) of the present liquid crystal with redox dopants rather than with salt dopants appeared to be due to the distinctively different hydrodynamic instability patterns.

Acknowledgment

We are indebted to the Directorate of Chemical Sciences, Air Force Office of Scientific Research, Contract F44620-72-C-0075 for partial financial support of this research. We also wish to thank Mrs. Anna M. Lackner for her help in cyclic voltammetric experiments, Mr. Michael J. Little for helpful discussions on the experimental setup, and Dr. Leroy J. Miller and Mr. John E. Jensen for the synthesis of the liquid crystal materials.

Manuscript submitted Nov. 5, 1976; revised manuscript received May 20, 1977.

Any discussion of this paper will appear in a Discussion Section to be published in the June 1978 JOURNAL. All discussions for the June 1978 Discussion Section should be submitted by Feb. 1, 1978.

Publication costs of this article were assisted by Hughes Research Laboratories.

REFERENCES

1. G. H. Heilmeier, L. A. Zanoni, and L. A. Barton, *IEEE Trans. Electron Devices*, **17**, 22 (1970).
2. R. Chang, in "Liquid Crystals and Ordered Fluids," Vol. 2, J. F. Johnson and R. S. Porter, Edtors, p. 367, Plenum Publishing Corp., New York (1974).
3. M. I. Barnik, L. M. Blinov, M. F. Grebenkin, S. A. Pikin, and V. G. Chigrinov, *Phys. Lett.*, **51A**, 175 (1975); *Zh. Eksp. Teor. Fiz.*, **69**, 1080 (1975).
4. J. D. Margerum, H. S. Lim, P. O. Braatz, and A. M. Lackner, *Mol. Cryst. Liq. Cryst.*, **38**, 219 (1977).
5. A. I. Baise, J. Teucher, and M. M. Labes, *Appl. Phys. Lett.*, **21**, 142 (1972).
6. H. S. Lim and J. D. Margerum, *ibid.*, **28**, 478 (1976).
7. Y. Ohnishi and M. Ozutsumi, *ibid.*, **24**, 213 (1974).
8. S. Barret, F. Gaspard, R. Hernio, and F. Mondon, *J. Appl. Phys.*, **47**, 2375 (1976).
9. H. S. Lim and J. D. Margerum, *This Journal*, **123**, 837 (1976).
10. G. H. Heilmeier, L. A. Zanoni, and L. A. Barton, *Proc. IEEE*, **56**, 1162 (1968).
11. J. C. Lacroix and R. Tobazeon, *Appl. Phys. Lett.*, **20**, 251 (1972).
12. K. Rousseau, G. C. Farrington, and D. Dolphin, *J. Org. Chem.*, **37**, 3968 (1972).
13. G. Lauer, Ph.D. Thesis, California Institute of Technology (1967).
14. A. Lomax, R. Hirasawa, and A. J. Bard, *This Journal*, **119**, 1679 (1972).

15. A. Denat and B. Gosse, *Chem. Phys. Lett.*, **22**, 91 (1973).
16. S. Hünig, G. Kiesslich, H. Quast, and D. Scheutzow, *Justus Liebigs Ann. Chem.*, **1973**, 310.
17. D. S. Acker and W. R. Hertler, *J. Am. Chem. Soc.*, **84**, 3370 (1962).
18. L. R. Melby, R. J. Harder, W. R. Hertler, W. Mahler, R. E. Benson, and W. E. Mochel, *ibid.*, **84**, 3374 (1962).
19. T. Kuwana, D. E. Bublitz, and G. Hoh, *J. Am. Chem. Soc.*, **82**, 5811 (1960).
20. R. Chang, *J. Appl. Phys.*, **44**, 1885 (1973).
21. P. A. Penz, *Phys. Rev. Lett.*, **24**, 1405 (1970); *Phys. Rev. A*, **10**, 1300 (1974).
22. M. Voinov and J. S. Dunnett, *This Journal*, **120**, 922 (1973).
23. W. Helfrich, *J. Chem. Phys.*, **51**, 4092 (1969).

Chemical Mechanisms in Photoresist Systems

I. Photochemical Cleavage of a Bisazide System

Shigeki Shimizu[1] and George R. Bird

School of Chemistry, Rutgers University, New Brunswick, New Jersey 08903

ABSTRACT

We have investigated the familiar photoresist system of cyclized polyisoprene + bis(4-azidobenzal)cyclohexanone by the methods of infrared and u.v. spectroscopy, solvent extraction, and thin layer chromatography. The principal photoreaction is the simultaneous cleavage of both azido groups on a single molecule by absorption of a single photon with 43% quantum yield. The observed traces of monoazides and or other materials are insufficient to justify a biphotonic mechanism. The reacted bisazide (bisamine and/or by-products) acts as a quencher for neighbor bisazide molecules, producing a complicated kinetic behavior which may simulate a second-order (biphotonic) reaction.

Among the practical photoresist systems used to fabricate printed microcircuits or lithographic plates, symmetrical bisazides have been widely used as the photoactive, cross-link-forming element.[2] It is obvious from the wide acceptance of this class of materials that the quantum yield for formation of cross-links must be high. In describing these systems, Kosar (1) makes repeated mention of the thermal stability of the azide group, a stability which may be contrasted with the relative thermal instability of most photochemical initiators and cross-linking agents (2). Since single-cross-links suffice to bind and immobilize large polymer molecules, a photoresist system must be considered as a chemical image amplifier with a gain roughly proportional to the degree of polymerization of the parent polymer. This amplification applies equally to the desired image of actinic photons and to the undesired thermal initiation of cross-linking reactions.

The high sensitivity of bisazide photoresist systems was called to our attention by John Weigl (3), who indicated that the system described by Clecak, Cox, and Moreau (4) was "a extraordinary fast system described in the literature." This system involves partially cyclized polyisoprene as the starting polymer and 2,6-bis(4-azidocinnamylidene)cyclohexanone as the cross-linking agent (I). Related initiators involving cyclopentanone and methyl substituted cyclic ketones have been described (5). We were initially interested in the question of thermal instability of the cinnamylidene bisazide, but soon discovered that the question of instability could not be approached without a satisfactory understanding of the mechanism of the primary photoreactions of these systems. Conversations with Dr. Moreau indicated that a commercially available material, 2,6-bis(4-azidobenzal)cyclohexanone (II), would be a much more suitable material for investigation, so we began a mechanistic investigation on this compound as a photo-cross-linking agent for partially cyclized polyisoprene.

The scientific literature is ambiguous as to the initial step in the photoreaction of a variety of bisazides. It is clear that N_2 is split off and nitrene formed as a highly reactive intermediate, but it is not at all clear whether absorption of a single photon results in the cleavage of one or both of the azido groups. Reiser *et al.* (6, 7) have analyzed the photoreactions of a number of bisazides in frozen matrixes at 70°K, and reported quantum yields for 2 separate steps in the formation of the bisnitrene (stable only in the frozen matrix). One very notable exception in this investigation is the listing of the compound p,p'-diazidobenzophenone at the end of the table of the quantum yields with the single entry $\Phi = 1.00$ and no indication as to whether this refers to the quantum yields of 2 discrete steps or to the simultaneous cleavage of both azido groups by absorption of a single photon. Trozollo *et al.* (8) have reported on the ESR spectra of some bisnitrenes in frozen matrixes, and suggested in the text that these may be formed by simultaneous single photon cleavage in some cases.

In an attempt to settle the distinction between simultaneous, monophotonic cleavage and stepwise two-photon cleavage, we examined the details of light sensitivities reported by Clecak *et al.* (4). Although these workers write an explicit biphotonic equation, their system sensitivity suggests simultaneous cleavage. Thus, the absorption of some 5.0×10^{14} photons/cm^2 suffices to insolubilize over 90% of a film of polymer containing 8.7×10^{14} molecules/cm^2. One could appeal to thermal reactions to make up the difference to at least one reacted azido group per bisnitrene molecule, but such extensive thermal reaction would imply instability on storage, which is not observed.

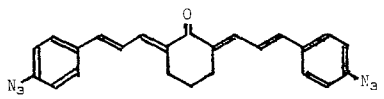
[1] Present address: Mitsubishi Chemical Industries, Research Laboratory, Midori-ku, Yokohama, Japan.

Key words: cross-linking, energy transfer, infrared spectrometry.

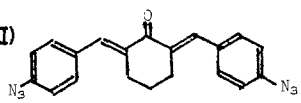
[2] Since the bisazide systems form cross-links and become resistant to solution in exposed areas, they are described as "negative photoresists" by analogy to a photographic negative.

We observed the photoreaction of bisazide (II), monitoring azido group absorption at room temperature in the polyisoprene matrix by infrared spectrometry. This observation was made directly on the actual photoresist composition as coated on high resistivity Si wafers, which allowed us to take advantage of the infrared transparency of pure Si. Photoreaction of quinone diazide (III) which makes a positive[3] photoresist system was also observed by infrared spectroscopy to illustrate the difference of the photoreaction mechanisms between these positive and negative photoresists. In particular, the quinone diazide is a monofunctional reagent, in contrast to the bisazide crosslinking agent. It forms no quenchers in the course of photoreaction, and thus gives uncomplicated kinetic behavior.

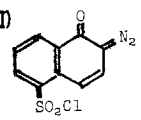
(I)



(II)



(III)



Results and Discussion

Photoreaction characteristic of positive and negative resists.—Figures 1 and 2 show the plot of logarithms of infrared absorbance *vs.* photodosing time at constant intensity. In the case of the positive photoresist (Fig. 1), the logarithmic plot is linear, indicating that the photoreaction is a simple first-order reaction in terms of unreacted quinone diazide (9, 15).[4] No quenching by reaction products is observed, nor was any expected.

In the case of the bisazide photoresist (Fig. 2), the decrease of azide absorbance shows a sharp retardation as the photoreaction proceeds. The reaction curve is more complicated than a simple second-order reaction. We first tried to explain this phenomena by a sequential two-photon process, as proposed by Reiser *et al.* (6). As will be seen, this proved to be impossible to do.

Simulation of photoreaction of bisazide by a sequential two-photon process.—If the bisnitrene is formed through a sequential two-photon process, the decrease of bisazide and increase of intermediate azidoamine can be expressed in Eq. [1] and Eq. [2]. Also, their concentrations (A and B) can be expressed by Eq. [3] and Eq. [4], where K_1 and K_2 are the first-order reaction rate constants for the first and second step, respectively, and are given by products of quantum yields and rates of absorption of photons.

[3] In this system, exposure forms solubilizing groups, so the polymer is removed in exposed areas. Such a system is described as a "positive photoresist".

[4] First-order kinetics are observed when a reaction proceeds at constant quantum yield in an optically dilute sample.

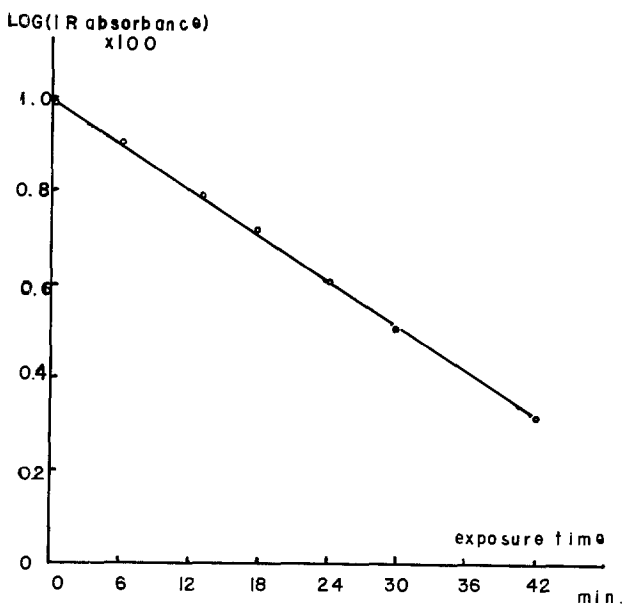


Fig. 1. Disappearance of diazo absorption of positive photoresist (quinone diazide-novolac). Dosing condition, 365 nm, 6.1 mJ/cm² min; photoresist coating, 0.96 μm on Si.

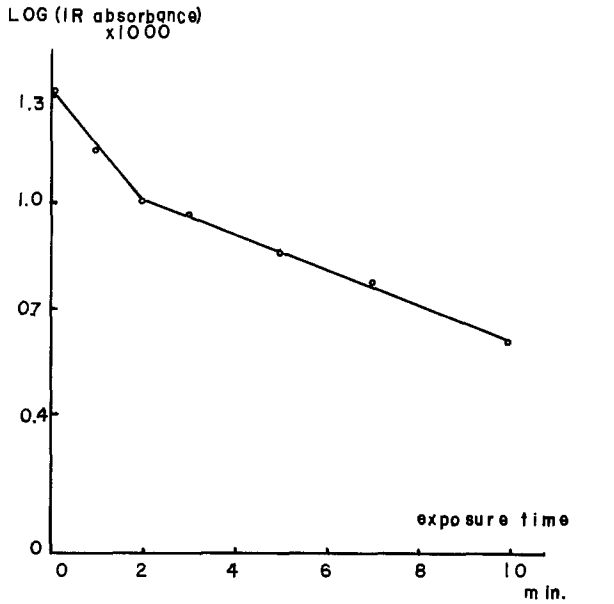


Fig. 2. Disappearance of azido absorption of negative photoresist (bisazide-polyisoprene). Dosing condition, 365 nm, 5.8 mJ/cm² min; photoresist 3 w/o bisazide based on polymer, 1.2 μm coating on Si.

Sequential two-photon mechanism

bisazide (A) $\xrightarrow{h\nu \downarrow K_1}$ $\frac{dA}{dt} = -K_1A$ [1]

azido amine (B) $\xrightarrow{h\nu \downarrow K_2}$ $\frac{dB}{dt} = K_1A - K_2B$ [2]

bisamine $A = e^{-K_1t}$ [3]

$$B = \frac{K_1}{K_2 - K_1}(e^{-K_1t} - e^{-K_2t}) \quad [4]$$

By assuming that the infrared azido absorption coefficient of azidoamine is half of that of bisazide, we can plot the expected azido absorbance ($2A + B$) *vs.* photodosing time at different K_2 values. The dotted line in Fig. 3 shows the experimental data from a 3% wt. bisazide (II) photoresist coated on NaCl. Other solid lines represent simulated data from Eq. [3] and Eq. [4] in which K_1 was determined to be 0.48 min^{-1} from the observed decrease during the first 1 min, and from the assumption that the initial reaction rate involves only cleavage of a single azido group. Figure 4 shows the simulated concentration of the intermediate azidoamine under the same conditions as Fig. 3.

We had searched carefully with a high resolution infrared spectrometer (PE 521) for the expected shift of the infrared band shape and position upon formation of increasing monoazide, and observed none (Fig. 5). The experimental conditions for Fig. 5 are completely the same as Fig. 3.

Extraction of azide from photoresist films.—When it became clear that the observations could not be fitted to a sequential two-photon mechanism, we made a careful analysis of the reaction products in photoresist films. Several mixtures of methanol and benzene were tested to find the conditions for extracting only starting bisazide and low molecular weight reaction products from the photoresist film without removing appreciable

polymer. After extracting the photoresist for 3 min, we analyzed the remaining azide and polyisoprene by the infrared N_3 band and CH band absorbances, respectively. As shown in Fig. 6, an equal volume mixture of methanol and benzene will extract only low molecular weight materials from the polymer layer. All of the uncross-linked polyisoprene is found to dissolve in benzene, so pure benzene can be used for "development" of the exposed photoresist.

We performed extractions from photoresists coated on silicon wafers after different exposure times. The azide remaining in the film was observed by infrared spectrometry. The extracts were separated by TLC (E. Merck, Silica Gel 60 F-254, $CHCl_3$ solvent) and starting bisazide ($R_f = 0.6$) and other colored products ($R_f = 0.0$-0.2) were detected. The R_f (0.6) and u.v. spectrum of the principal extracted material matched the unreacted bisazide (II).

The low mobility colored products were difficult to characterize. They are proved not to be azidoamine (azidonitrene-polyisoprene adducts), but rather by-products of nitrene-bisazide coupling side-reaction from the following observations:

1. The TLC spots of these products can be moved to the solvent front ($R_f = 1.0$) by using polar solvents ($MeOH/CHCl_3 = 5/2$), while cyclized polyisoprene (not cross-linked) does not move at all ($R_f = 0.0$).

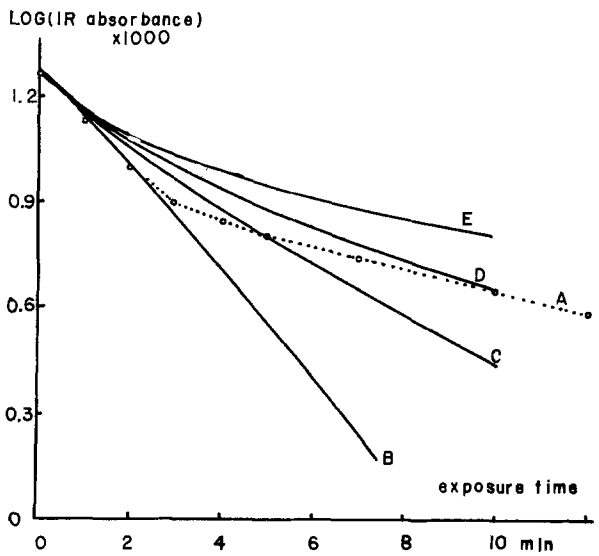


Fig. 3. Simulation of total azido absorbance by sequential two-photon process. Dosing condition, 365 nm, 5.8 mJ/cm² min. A, observed from 3% bisazide photoresist, coated 1.2 μm thick on NaCl; B, simulated from $K_1 = 0.48$ min^{-1}; $K_2 = 0.48$ min^{-1}; C, simulated from $K_1 = 0.48$ min^{-1}, $K_2 = 0.16$ min^{-1}; D, simulated from $K_1 = 0.48$ min^{-1}, $K_2 = 0.096$ min^{-1}; E, simulated from $K_1 = 0.48$ min^{-1}, $K_2 = 0.048$ min^{-1}. K_1 is fixed by observation.

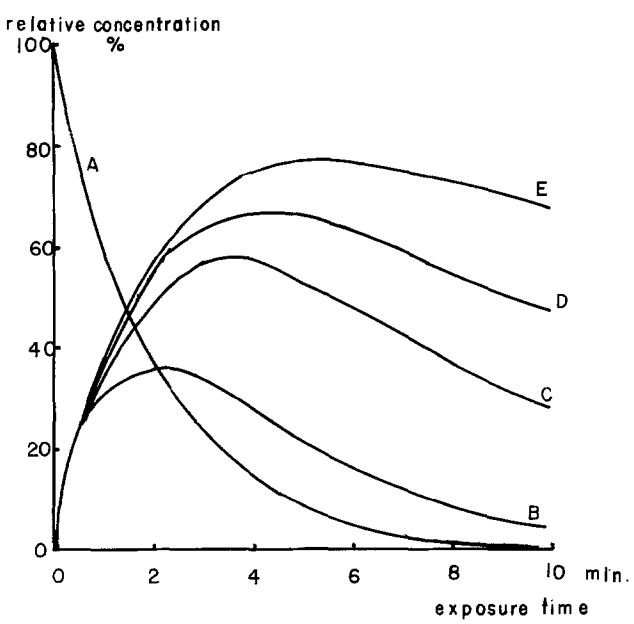


Fig. 4. Simulation of azidoamine and bisazide concentration by sequential two-photon process. A, bisazide simulated from $K_1 = 0.48$ min^{-1}; B, azidoamine simulated from $K_1 = 0.48$ min^{-1}, $K_2 = 0.48$ min^{-1}; C, azidoamine simulated from $K_1 = 0.48$ min^{-1}, $K_2 = 0.16$ min^{-1}; D, azidoamine simulated from $K_1 = 0.48$ min^{-1}, $K_2 = 0.096$ min^{-1}; E, azidoamine simulated from $K_1 = 0.48$ min^{-1}, $K_2 = 0.048$ min^{-1}. K_1 is fixed by observation.

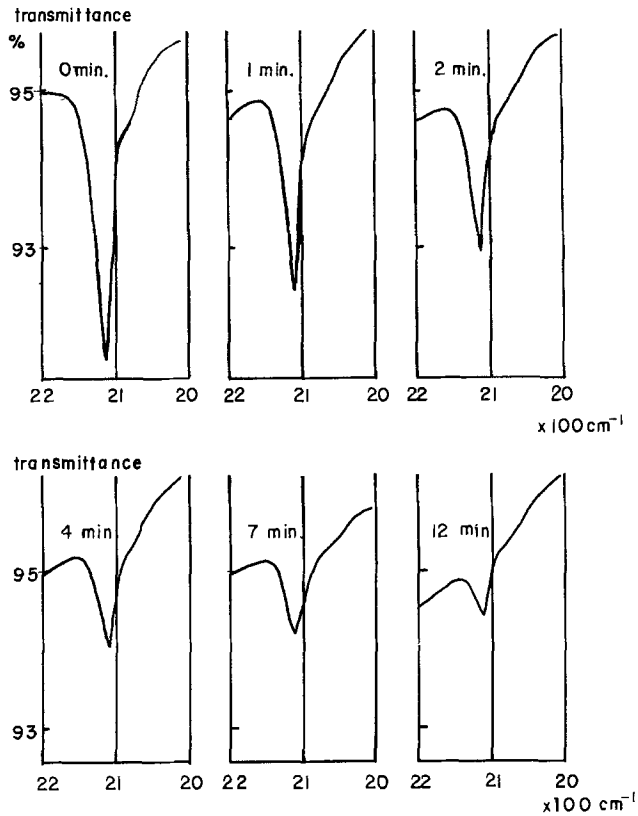


Fig. 5. Infrared spectra (expansion times 10) of photoresist at different photodosing times. Dosing condition, 365 nm, 5.8 mJ/cm² min; photoresist, 3% bisazide, 1.2 μm coating on NaCl.

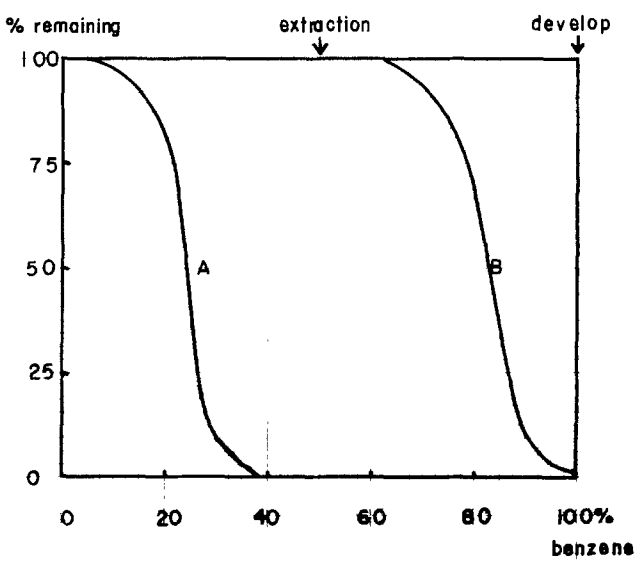


Fig. 6. Extractability of unexposed bisazide and cyclized polyisoprene by methanol-benzene acting for 3 min on a 1.2 μm film containing 3% bisazide. A, bisazide; B, cyclized polyisoprene.

2. The shape, frequency, and especially the relative strength of infrared CH-stretching absorptions are very different from those of cyclized polyisoprene. The ratio of total CH to N_3 absorptions is very low.

3. The low mobility colored spots increased with photodosing time, and never decreased, precluding monoazide intermediates.

4. The infrared spectrum of the mixture of colored products extracted from the low mobility TLC spots by methanol/benzene (1/1) showed a weak azido absorption.

The bisazide spots ($R_f = 0.6$, $CHCl_3$) were scraped from the TLC plate, extracted again by methanol/benzene (1/1), and analyzed by u.v. spectrometer. The results of the extractions are summarized in Table I. In every case almost all the azido compound can be extracted from the polymer layer, as shown by the disappearance of the infrared azido absorption after extraction.

Discussion on the simultaneous single photon mechanism and the sequential two-photon mechanism.— Azidonitrene, which is supposed to be the intermediate product of the two-photon mechanism, is expected to react almost instantaneously with polyisoprene to form polymer adducts (azidoamine) which cannot then be extracted by polar solvent (methanol/benzene = 1/1). These adducts should show an infrared azido absorption, which we have not observed. We can compare the absence of observed azido absorption after extraction with the calculated minimum absorption required to support a sequential two-photon mechanism. The relation between any first-order photochemical reaction rate constant K (min^{-1}) and quantum yield (Φ) and fraction of incident light absorbed (A) can be expressed as follows

$$K = \frac{\Phi \times \text{photon flux for 1 min} \times A}{\text{starting bisazide molecular concentration}}$$

The parameters for a hypothetical biphotonic decomposition (Φ, A) can be approximated from observed infrared and u.v. data which are summarized in Table II.

Φ_1, which is the quantum yield of the hypothetical first process, can be calculated by assuming equal infrared absorbance for all azido groups. Table II shows an infrared absorbance decrease from 0.0179 to 0.0136 for the first 1 min, which would have to mean that 2.46×10^{15} bisazide molecules/cm^2 were decomposed to monoazide. U.V. absorbance shows that the average absorbance is 0.306 at 365 nm for the first 1 min, so the fraction of light absorbed (A_1) is 50.6%, which means that 5.3×10^{15} photons/cm^2 were absorbed in the first 1 min. Therefore the quantum yield (Φ_1) can be calculated at 46.4% in this particular 3% film.

The fraction of light absorbed by half-reacted bisazide existing as monoazide-monoamine (A_2) can be calculated by taking the mean of initial and final u.v. absorption coefficient of bisazide upon exposure. Table II shows that the absorbance of photoresist at 365 nm decreased to 54% of the initial value when almost all the azido groups are decomposed after a massive 50 min dosing. By taking the mean of 100% and 54%, the average absorbance of the photoresist film can be estimated as $0.306 \times 0.77 = 0.236$, which would mean that A_2 is 41.8%.

When the quantum yield of the hypothetical second step (Φ_2) is assumed to be high, smaller amounts of azidonitrene adducts are to be expected in the photoresist after extraction. In the limiting case with $\Phi_2 = 100\%$, K_2 can be estimated as follows

$$K_2 \approx \frac{1.00(\Phi_2) \times 0.418\,(A_2) \times 0.48\,(K_1)}{0.464\,(\Phi_1) \times 0.506\,(A_1)} = 0.85\ \text{min}^{-1}$$

Figure 7 shows the minimum azido absorbance required to agree with a two-photon mechanism in which the infrared absorption coefficient of azidoamine is half that of bisazide. This is a conservative approximation because it has been reported that the infrared absorption coefficient of the azido group increases when conjugated electron-accepting groups are replaced by electron-donating groups, as would be the case if one azido group were converted to a secondary or tertiary amine (10). An azidonitrene would react with polymer to form azidoamine, which can thus be expected to increase the absorption coefficient per azido group.

Figure 8 shows the infrared azido band before and after extraction. The minimum amount of absorbance allowable for a sequential two-photon process is shown aside. The observed absorbance in the polymer after

Table I. Analysis of extracted photoresist and extracts after different amount of photodosing (365 nm)

Photoresist; 3% bisazide, 1.2 μm coating on Si
Extraction; dissolving in methanol-benzene(1/1) solvent for 3 min

Remaining N_3 absorbance after exposure (%)	Remaining N_3 absorbance after extraction (%)	Recovered bisazide from TLC spot of extracts (%)
78	≦4.0	61
67	≦5.5	
65	≦5.0	54
61	8 ± 3	45
51	6 ± 3	
47		28
46		24
40	10 ± 4	19
38	6 ± 4	
32	10 ± 3	22

* The notation ≦ indicates that there appears to be a trace of azide absorption, but the quantity present could range from zero to the stated upper value.

Table II. Observed infrared and u.v. absorbance of bisazide and photoresist

Photoresist; 3% bisazide, 1.2 μm coating on NaCl
Dosing condition; 365 nm, 1.04×10^{16} photon/cm^2 min

	Infrared (2110 cm^{-1})	U.V. (365 nm)
Molar absorption coefficient of bisazide (II)	2.1×10^3 $mole^{-1} \cdot l \cdot cm^{-1}$	3.73×10^4 $mole^{-1} \cdot l \cdot cm^{-1}$
Absorbance of photoresist upon exposure		
$t = 0$	1.79×10^{-2}	3.32×10^{-1}
$t = 1$ min	1.36×10^{-2}	2.80×10^{-1}
$t = 50$ min	$\leq 0.15 \times 10^{-2}$	1.80×10^{-1}

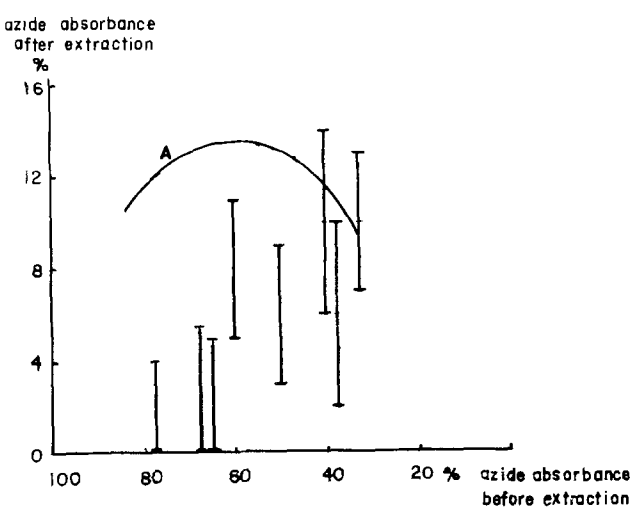


Fig. 7. Comparison of azido absorbance between observed and calculated (two-photon process). A, calculated minimum absorbance for sequential two-photon process, $\Phi_2 = 100\%$; I, observed data of photoresist, 3% bisazide based on polymer, 1.2 μm coating on Si, methanol-benzene (1/1) extraction for 3 min.

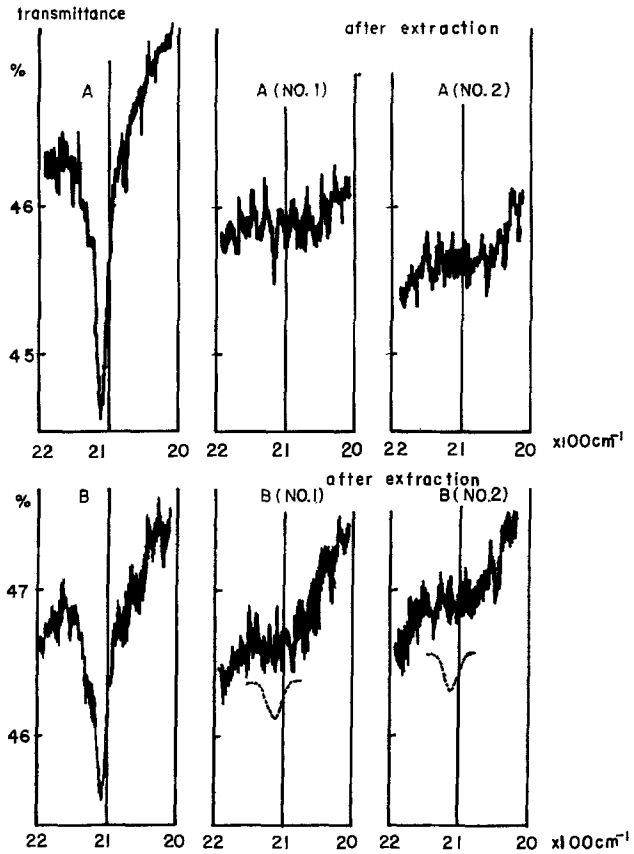


Fig. 8. Infrared spectra (times 20 expansion) of photoresist before and after extraction. A, no exposure, 3% bisazide, 1.2 μm coating on Si; B, partial exposure (remaining azido absorbance is 66%), 3% bisazide, 1.2 μm coating on Si, no. 1 and 2 refer to repeated observations. Note that much of the fine structure (as seen especially clearly in spectrum A-1), is the interference pattern imposed by the high refractive index of the Si wafer (n = 3.4). Fortunately, the azide absorption band is considerably broader than the repeat period of this pattern.

extraction is considerably less than the calculated absorbance.

Thus the two-photon mechanism is inadequate to explain the results and products above mentioned; instead, the simultaneous one-photon mechanism seems much more reasonable. The small amount of azido absorption detected after extraction in Fig. 8 can be attributed in part to unextracted bisazide, because repeated extraction further lowers the intensity of the azido absorption in the polymer while the intensity of the CH absorption is unchanged. Perhaps the over-all cross-linking makes the extraction of bisazide more difficult. The increase in the retained azide with photodosing time (Fig. 7) is thus assigned to cross-linking and reduced swelling of the polymer in the methanol/benzene (1/1) extraction.

The one-photon mechanism also suggests that effective cross-linking occurs at the early stages of photodosing. By measuring the film thickness after development (dissolve in benzene for 3 min), we can estimate the extent of the cross-linking. The results, shown in Table III, give a satisfactory fit for a one-photon mechanism.

Energy transfer.—If we accept a simple one-photon mechanism, the reduced photodecomposition rate of bisazide after *ca.* 50% of photoreaction is still to be explained. We made several coatings with different azide concentration, and observed their azido absorbance decrease upon photodosing. The results are shown in Fig. 9. The decrease of rate with increasing concentration suggests some inhibition of the primary photoreaction by its products. At highest concentration (7% bisazide based on polymer), quenching is observed from the

Table III. Fraction of cross-linked polymer after different amount of photodosing

Photoresist; 3% bisazide, 1.2 μm coating on Si
Exposure; 365 nm
Development; dissolve in benzene for 3 min

Decreased amount of N_3 absorbance upon exposure (%)	Remaining polyisoprene after development (%)
43	43
47	49
55	67
71	82

earliest stages and reaction is completely quenched after about 50% of completion. On the other hand, low concentration photoresist layers (1% bisazide based on polymer) show higher initial rate and only slight quenching.

Figure 10 shows the u.v. absorption of negative photoresist before exposure, after complete photodosing, and after development. During photo exposure, a new long-wavelength absorption around 410 nm appears

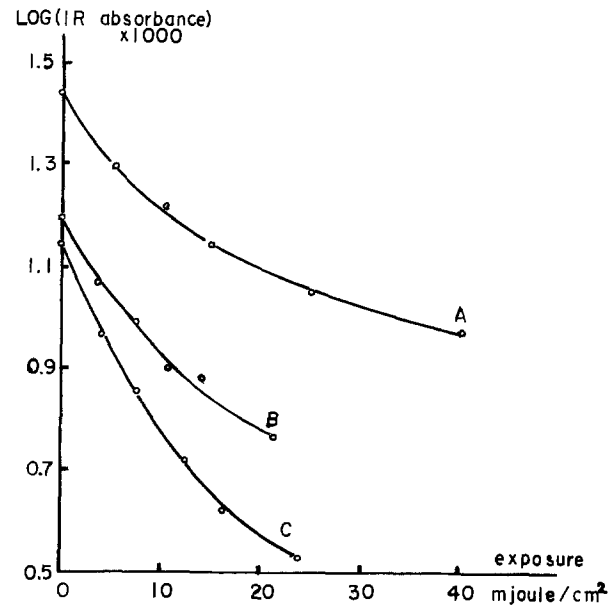


Fig. 9. Rate of disappearance of azido absorbance. Dosing, 365 nm, photoresist A, 7% bisazide, 0.8 μm coating on Si; photoresist B, 3% bisazide, 1.0 μm coating on Si; photoresist C, 1% bisazide, 2.3 μm coating on Si.

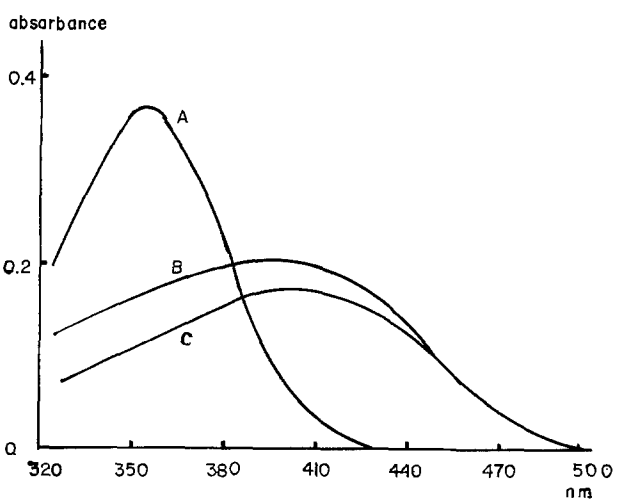


Fig. 10. U.V. spectra of negative photoresist. Photoresist, 3% bisazide, 1.2 μm coating on NaCl, dosing condition, 365 nm, 5.8 mJ/cm² min. A, before exposure; B, after 50 min exposure; C, after development of exposed film.

and remains fixed in the cross-linked polymer after development. We assign this absorption to reacted bisnitrene, presumably bisamine,[5] which forms the actual cross-links. The absorption decrease (curves B and C in Fig. 10) around 350 nm is due to extractable low molecular weight by-products which have been discussed (the low mobility spots).

For the moment we can only note that both of the absorption spectra (bisamine and byproducts) lie at longer wavelength than the spectrum of the starting material. Thus, direct singlet-singlet intermolecular energy transfer can occur. Further, this is a very concentrated system, and the potential donors and acceptors are nearly in contact. Triplet-triplet transfer may also occur (11), but we have no indication supporting or disproving it. The bisamine appears to be inert to direct photoreaction and to reaction by energy transfer. Thus the retardation of decomposition in this system is explicable in terms of energy transfer to the reaction product.

The u.v. absorption of the positive photoresist shows no long-wavelength absorption in the course of photodosing. The absorbance of every peak decreases according to simple first-order reaction kinetics and no quenching is observed (15). The contrast between the complicated concentration dependence shown by the bisazide system and the single first-order dependence of the quinone diazide system can be examined to emphasize the importance of energy transfer in the bisazide system.

The highest quantum yield of bisazide decomposition observed was 43% (one-photon process). The conditions were as follows: bisazide concentration, 0.56% based on polymer; film coating, 3.5 μm on NaCl; photon flux, 8.22×10^{15} photon/cm^2 min; fraction of light absorbed, 29.7%; decomposed bisazide after 1 min dosing, 1.06×10^{15} molecule/cm^2. An even higher quantum yield is to be expected from shorter exposure times and lower azide concentrations, but these conditions lie beyond the accuracy of the infrared observations.

Experimental

The negative-type photoresist was made by dissolving bis(4-azidobenzal)-cyclohexanone(II) and cyclized polyisoprene in Kodak KTFR Thinner.[6] Cyclized polyisoprene was prepared by refluxing a solution of toluene, cis-1,4-polyisoprene (MW 110,000-150,000, Goodyear NATSYN-200) and p-toluenesulfonic acid for 6 hr (12). Cyclicity (1.7-2.3) and uncyclized isoprene unit (4-6%) were characterized by NMR (Varian T-60). Cyclized rubber was dissolved to 10-15 weight percent (w/o) in KTFR Thinner, and bisazide(II) was added 1-7 w/o based on polymer.

The positive-type photopolymer was prepared by condensing pheno-formaldehyde polymer (Union Carbide, NOVOLAC BRN-5834) with 50 w/o of o-naphthoquinone diazide sulfonyl chloride (III) in the presence of sodium carbonate (13). About 20% of the hydroxyl groups were substituted by the quinone diazide sulfonyl group. The photoresist was made by dissolving this photopolymer to 25 w/o in Shipley AZ-1350 Thinner.[7]

The photoresist films were spincoated on silicon wafers and prebaked at 80°C for 20 min in an oven before use. The film thickness was calculated from the interference pattern obtained by measurement of specular reflectance, using the Model 1413 reflectance attachment of a Cary 14 spectrophotometer.

A medium pressure mercury lamp (100W, GE 100A4/T) was used as the u.v. light source. Specific wavelengths were selected using interference filters (365 nm, 405 nm). During photodosing, light intensity was monitored with an EMI S-10 photomultiplier, which was calibrated by a potassium ferrioxalate actinometer (14). Nitrogen gas was flushed through the photoreaction box during photodosing.

The reactions of bisazide and quinone diazide were monitored by observing the infrared absorption of the azido (2110 cm^{-1}) and diazo (2120 cm^{-1}) group using the scale expansion attachment of the Perkin Elmer 521 spectrophotometer (Fig. 11).

P-doped silicon wafers with a high infrared transmittancy of 45-55% at 2100 cm^{-1}, resistance of 300Ω cm^{-1}, diam of 2 in., thickness of 0.27 mm were obtained from Monsanto Chemical Company, and they were used without further heating. A silver bromide window (blue and u.v. absorbing) was placed in front of the photoresist to protect the bisazide and quinone diazide from any actinic light emitted by the infrared light source. When both infrared and u.v. information was needed, the photoresist layers were coated on sodium chloride plates instead of the silicon wafers.

Conclusions

From the infrared study of azido absorption of photoresist upon exposure, and from the analysis of low molecular weight compounds extracted from exposed photoresists, we obtained the following conclusions:

1. The cleavage of both azido groups of the starting bisazide is brought about by absorption of a single photon. This is established by the following observations: (*i*) Azidoamine, which is considered to be the intermediate of the two-photon process, is not observed in partially exposed photoresists; and (*ii*) bisazide is the principal azido compound still existing after any amount of photodosing.

2. The photodecomposition rate of bisazide is reduced as cross-linking proceeds. This is probably due to energy transfer from unreacted bisazide to reacted bisazide (bisamine cross-link and/or byproducts).

Acknowledgments

The authors gratefully thank Dr. W. M. Saltman of Goodyear Corporation for supplying cis-polyisoprene, Mr. B. Herbert of Monsanto Company for supplying Si

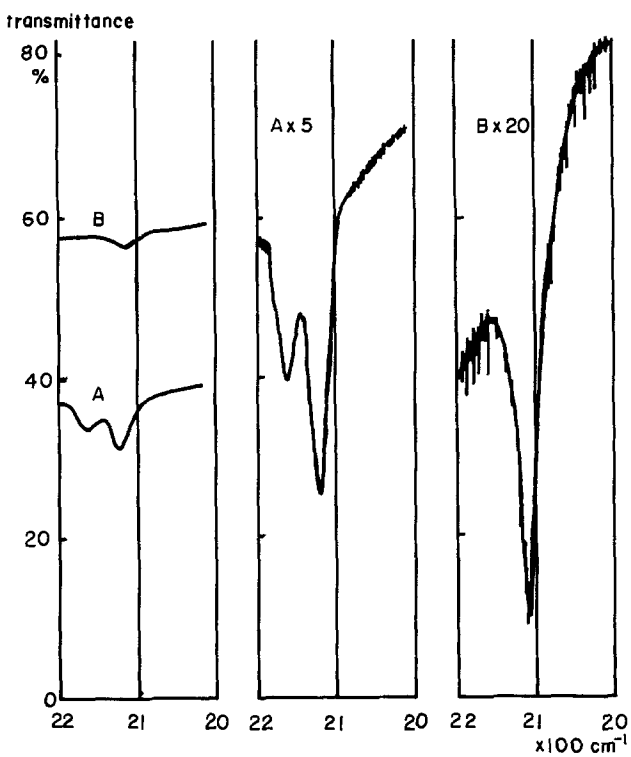


Fig. 11. Infrared spectra of photoresists and their expansion. A, positive-type resist, 0.96 μm coating on Si; B, negative-type resist, 3% bisazide, 1.2 μm coating on Si.

[5] This assignment was confirmed by the absorption spectrum of a related bisamine, bis(4-dimethylaminobenzal)-cyclohexanone, which showed an almost identical absorption band (425 nm) to reacted bisazide (Fig. 10C).

[6] This material is observed by infrared and NMR to be substantially o-xylene.

[7] This material is analyzed by GC to be cellosolve acetate (90%), butyl acetate (5%), and xylene (5%).

wafers, Mr. Harding of Union Carbide Corporation for supplying Novolac, and Dr. F. Hessert of Fairmount Chemical Company for supplying bisazides. Stimulating discussions with Dr. W. Moreau of IBM Corporation and Dr. J. Weigl of Xerox Corporation are gratefully acknowledged.

Manuscript submitted Feb. 22, 1977; revised manuscript received April 15, 1977. This was Paper 75 presented at the Philadelphia, Pennsylvania, Meeting of the Society, May 8-13, 1977.

Any discussion of this paper will appear in a Discussion Section to be published in the June 1978 JOURNAL. All discussions for the June 1978 Discussion Section should be submitted by Feb. 1, 1978.

REFERENCES

1. J. Kosar, "Light Sensitive Systems," p. 336, John Wiley & Sons, Inc., New York (1965).
2. W. D. Pandolfe and G. R. Bird, "Unconventional Photographic Systems Symposium," p. 19, SPSE (1975).
3. Private communication, Xerox Corp.
4. N. J. Clecak, R. J. Cox, and W. M. Moreau, *Polym. Eng. Sci.*, **14**, 491 (1974).
5. H. F. Mark and N. M. Bikales, "Encyclopedia of Polymer Science and Technology," Supplement Vol. 1, p. 401, Wiley-Interscience, New York (1976).
6. A. Reiser, H. M. Wagner, R. Marley, and G. Bowes, *Trans. Faraday Soc.*, **63**, 2403 (1967).
7. A. Reiser and R. Marley, *Trans. Faraday Soc.*, **64** 1806 (1968).
8. A. M. Trozzolo, R. W. Murray, G. Smolinsky, W. A. Yager, and E. Wasserman, *J. Am. Chem. Soc.*, **85**, 2526 (1963).
9. J. Kosar, "Light Sensitive Systems," p. 342, John Wiley & Sons, Inc., New York (1965).
10. Y. N. Sheinker and L. B. Senyania, *Izv. Akad. Nauk SSSR, Ser. Khim. Nauk*, 2113 (1964).
11. T. Tsunoda, T. Yamaoka, and G. Nagamatsu, *Photogr. Sci. Eng.*, **17**, 390 (1973).
12. R. K. Agnihotri, D. L. Falcon, F. P. Hood, L. G. Lesoine, C. D. Needham, and J. A. Offenbach, *Photogr. Sci. Eng.*, **16**, 443 (1972).
13. S. Amakawa, Japan Pat. SHO-459610.
14. J. G. Calvert and J. N. Pitts, "Photochemistry," p. 780, John Wiley & Sons, Inc., New York (1966).
15. D. Ilten and R. J. Sutton, *This Journal*, **119**, 539 (1972).

On the Use of X-Ray Screens in Mammography

A. L. N. Stevels

Philips Research Laboratories, Eindhoven, The Netherlands

and F. Pingault

Massiot-Philips, 80690 Ailly-Le-Haut-Clocher, France

ABSTRACT

Measurements on $CaWO_4$ screen/film combinations show that in mammography significant speed gains compared with the no-screen film technique can be realized. However, the resolution of such high speed systems is poor. Calculations on recently developed powder phosphors like $BaFCl:Eu^{2+}$, $LaOBr:Tb^{3+}$, $Y_2O_2S:Tb^{3+}$, and $Gd_2O_2S:Tb^{3+}$ show that there are prospects of even faster mammography screens, but the resolution obtained with thinner layers of such new phosphors is expected to be only marginally better. Measurements of the sharpness of imaging phantoms indicate that indeed the resolution is hardly improved by employing new phosphors. The speed gains with respect to $CaWO_4$ are about a factor 2 lower than the calculated ones. New screen technologies have to be found to eliminate the resolution bottleneck. It is found that vapor-deposited CsI:Na and CsI:Tl layers would be very promising candidates for use in mammography. However, hygroscopy is at present a serious obstacle to their application, especially in the CsI:Na case.

The use of x-ray intensifying screens in film radiography is always in the nature of a compromise. On the one hand the speed of the system is increased, so that x-ray exposure can be reduced. On the other hand the quality of the image obtained is reduced by insertion of such an intensification device in the x-ray system.

The choice of an optimum trade-off between speed and image quality depends in the first instance on the type of radiological examination involved. From a technical point of view, not only do all these trade-off points have to be covered by the availability of the corresponding screen-film systems, but also a continuous effort is needed to extend the limits of the system.

As far as the last aspect is concerned, encouraging progress has been made in the last decade. Basically these improvements originate from the availability of new x-ray phosphors (1) which have the potential to replace traditional phosphors like $CaWO_4$ in certain radiological techniques. CsI:Na, CsI:Tl have largely replaced (Zn,Cd)S:Ag in the input screens of image intensifier tubes. For some of the new phosphors (CsI:Na, CsI:Tl) new screenmaking technologies can be applied. Vapor-deposited layers of these materials give rise to less image blurring than comparable ones prepared by the usual powder sedimentation techniques (1-4).

Meanwhile, mainly theoretically (1, 5, 6) and mainly practically oriented (2-4, 7-11) studies have been devoted to the use of new phosphors in x-ray intensifying screens. Almost all of them pertain to the "normal" radiological range, that is to x-rays with energies between 30 and 100 keV.

The present paper pays attention to the use of screens in mammography. Usually in these examinations x-ray films with high silver content are directly exposed to "soft" x-rays with energies between 6 and 30 keV. The main purposes of employing intensifying screens are x-ray dose reduction and economizing on the use of silver in the x-ray film.

First, we compare the properties of $CaWO_4$ screen-film combinations with those of "no-screen" films. After that we calculate what improvements can be

expected from the use of new phosphors and discuss some practical realizations. The results obtained here for soft x-rays are compared with those for the harder x-rays of the 30-100 keV range.

Experimental

The x-ray source used in this investigation was a Rotalix type with W-anode operated at 30 kV. The focus was 0.3 × 0.3 mm², the focus-film distance 1m. No radiation filter was used.

When a double-coated x-ray film is employed, the screen/film combination consists of a front and a back screen with the film in between. With a single-coated film, the screen is placed (with respect to the x-ray source) at the back.

The screens investigated were prepared at our own laboratories or commercially obtained from various sources. For their characterization we use plots of relative speed against resolution. The relative speed is defined as the exposure needed to obtain unit film density above the fog, the mammography no-screen film Kodak PE 4006 being the standard of comparison. All films used in this investigation were processed for 90 sec. The resolution of the system is characterized by the frequency in line pairs per centimeter at which the amplitude of the square wave response of a test grid, consisting of lead strips at varying distances apart, had dropped to 30% of its value at zero frequency. Again the PE 4006 film was used as a standard.

Some Properties of $CaWO_4$ Screen-Film Combinations

In Fig. 1 we have plotted relative speed against resolution for $CaWO_4$ screen/film combinations. The upper curve refers to screens used in combination with double-coated film, type Agfa-Geveart RP3, the lower curve to combinations with a single-coated film, type du Pont "Lo-dose." The points labeled by the subscript 1 represent a standard $CaWO_4$ screen, the Philips Universal type. It is seen that under mammography

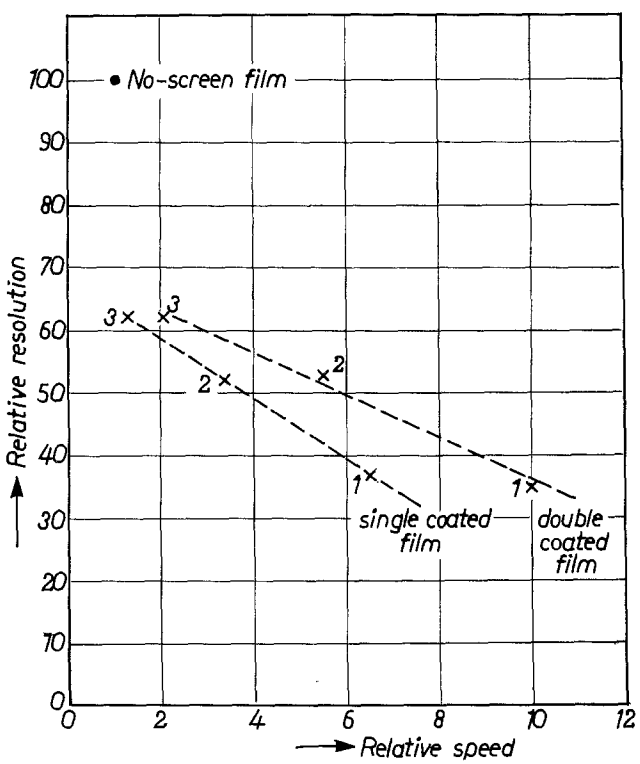


Fig. 1. Relative resolution against relative speed for various screen/film combinations. The no-screen film has a speed equal to unity and a resolution equal to 100. The x-ray source (W-anode) was operated at 30 kV. 1 = $CaWO_4$ standard screen, 2 = $CaWO_4$ high resolution screen, 3 = $CaWO_4$ very high resolution screen (see text also).

conditions its speed is 6.5 (single-coated film) or 10 times (double-coated film) higher than a no-screen film system. The resolution, however, has dropped to about 35% of that of the last-named system. In the literature (12-15) such a deterioration of image quality is stated to be completely unacceptable in mammography. Hence we conclude that with $CaWO_4$ screens maximal speed gains can be achieved which, while preserving a resolution acceptable for mammography, are definitely lower than 6.5× for single-coated film systems and 10× for double-coated film systems.

When a Philips "Micro" screen (points indicated by 2) is used instead of a Universal one the speed is reduced by a factor of about 2, whereas the resolution gain is only a factor of 1.5. It should be noted here that the thickness of the phosphor layer and its packing density are equal to that of a Universal one (≈120 μm and ≈55%). The different properties of the Micro screen have been achieved by adding to the binder some paint which absorbs laterally spread light more than directly escaping light. This method to increase the resolution is more attractive than making the phosphor layer thinner, because in the last-named case the intrinsic x-ray quantum noise of the system increases.

Returning now to Fig. 1, we conclude that also a further reduction of the speed of the system does not result in a compensating increase in resolution: the very high resolution MCD screen (laboratory-made, more heavily colored than Micro), labeled by 3, shows a speed reduction of about 2.5× with respect to the Micro screen, whereas the gain in resolution is only some 20%. Figure 1 suggests that for both types of film there is a limit in resolution of about 65% compared to no-screen film. There are several reasons for this "resolution gap":

1. To a limited extent this gap is due to the fact that the RP3 and the "Lo-dose" films used in combination with the screens contain less silver than the no-screen PE 4006 one. The resolution of the three films is found to be essentially identical. This implies that in Fig. 1 the reference point might shift a bit to the left. In connection with this we note that the speed and the resolution of PE 4006/screen combinations are found to be about equal to those of the RP3/screen combination. Apparently the screen is the limiting factor of the system. This conclusion is also supported by the observation (see Fig. 1) that systems with double-coated films have a speed which is approximately 1.5× that of the ones with single-coated films, whereas the resolution is about equal.

2. A large contribution to the resolution gap is due to geometrical reasons. If, for instance, measurements are made on screens without a plastic protective layer in between the phosphor and the film, the resolution figures are about a factor of 1.2 higher than those given in Fig. 1. If the focus-film distance is increased the resolution gain is small, however.

3. The above-mentioned factors do not bridge the resolution gap indicated in Fig. 1. It is obvious to think that the remaining part is due to the very fact that the $CaWO_4$ phosphor considered is used in the form of a light scattering powder.

On basis of the foregoing section we now formulate several conclusions regarding the use of x-ray screens in mammography:

1. Whatever speed increases can be realized, a resolution drop has to be accepted. Among other things this drop is due to geometrical factors, such as the presence of a protective layer between phosphor and film and the fact that the focus-film distance is not infinite.

2. The use of light scattering powder phosphors gives rise to an additional resolution drop. This makes the image quality marginal in cases where substan-

tial speed gains can be achieved. The impact of laterally scattered light of powder phosphors might be reduced by decreasing the mean grain size of the phosphor and by making the phosphor layer thinner. Regarding the first suggestion we note that in the $CaWO_4$ screens discussed the mean grain size is already low (2.3 μm). Further reduction would entail serious technological problems as well as substantial losses in light output. Thinner phosphor layers would give rise to less x-ray absorption in the screens and hence to increased quantum mottle ("noise") on the film.

3. Screen/single-coated film combinations are disadvantageous from a speed point of view. At present there are no indications that such systems would give a substantially better resolution than those with double-coated films.

4. The use of new powder phosphors instead of $CaWO_4$ gives additional degrees of freedom regarding the realization of screens. Whether this only implies increases of speed or whether it also reduces the resolution drop is a question to be studied. For instance, if a phosphor has higher x-ray absorption per unit length than $CaWO_4$ the phosphor layer thickness can be diminished without increasing the quantum noise above the $CaWO_4$ level.

Calculated Properties of New Phosphors in the Mammography (6-30 keV) Energy Range

A few years ago we studied extensively the properties of new x-ray phosphors in the 30-100 keV energy range (1). We now extend the calculations made in Ref. (1) to the 6-30 keV "mammography" energy range. In order to link up as closely as possible to practical conditions we give data for 100 μm thick powder phosphors screens in contact with u.v./blue sensitive "standard" film or with green sensitive film. We consider 100 μm thick vapor-deposited screens only for CsI:Na (or Tl).

We now discuss the following new materials: $Gd_2O_2S:Tb^{3+}$, CsI:Na (or Tl), $LaOBr:Tb^{3+}$, $Y_2O_2S:Tb^{3+}$, $BaFCl:Eu^{2+}$, and (Zn,Cd)S:Ag. Brief particulars of these phosphors and references to original literature are given in Ref. (1). For $BaFCl:Eu^{2+}$ see also Ref. (8).

The inclusion of $LaOBr:Tb^{3+}$ deserves some special comment. Some two years ago it seemed that this phosphor was not practical because of its hygroscopy and afterglow properties. However, these obstacles to its application now seem to have been eliminated. It should further be noted that the $Gd_2O_2S:Tb^{3+}$, CsI:Tl, and (Zn,Cd)S:Ag phosphors cannot be used in combination with standard x-ray film; green-sensitive films have to be employed instead.

In Fig. 2 we present data on the calculated relative x-ray absorption of the new phosphors, taking a 100 μm thick $CaWO_4$ powder layer as a reference.[1]

Data from tables published by Storm and Israel (16) were used. For the 100 μm powder layers a packing density of 50% was assumed, for the CsI evaporated layers the density was taken to be 100%.

It is seen in Fig. 2 that in the complete 6-30 keV range the x-ray absorption of all the new phosphors considered does not much exceed that of $CaWO_4$. In the case of some well-known candidates for application in standard intensifying screen like $BaFCl:Eu^{2+}$ and $Y_2O_2S:Tb^{3+}$ the absorption in the main part of the mammography range is even substantially lower than that of $CaWO_4$. It is also noted that CsI evaporated layers, which show a superior x-ray absorption in the 40-100 keV range due to their high packing density, need this high density here to have a performance comparable to that of the tungstate.

The fact that, at equal screen thicknesses, the x-ray absorption of the new phosphors is not better than

[1] For reasons of simplicity we have smoothed the curves between 10.2 and 12.1 keV. They would otherwise show small jumps due to L transitions in W at 10.2, 11.5, and 12.1 keV.

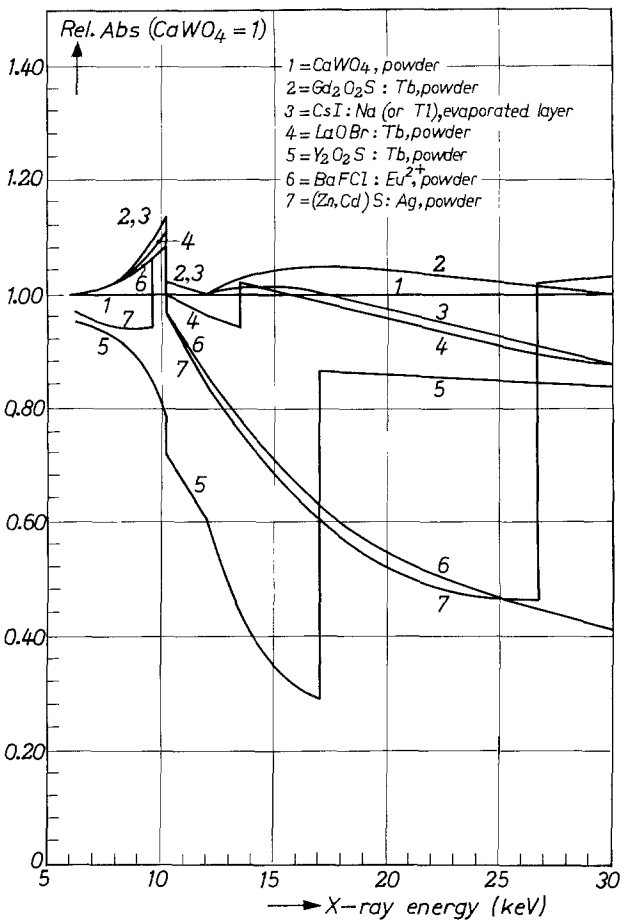


Fig. 2. Calculated relative x-ray absorption ($CaWO_4$ = 1) of various phosphors in the 6-30 keV range. The curves between 10.2 and 12.1 keV have been smoothed (see text).

that of $CaWO_4$ make us conclude that it is probably not possible to improve the resolution of mammography powder screens by decreasing their thickness. The main reason behind this is that the absorption-related [see Ref. (1)] noise properties of the new phosphors are not better and in some cases even inferior to those of $CaWO_4$. At present, the only candidates for mammography screens with improved resolution seem to be those phosphors for which screen technology can be changed, as for instance CsI:Na or CsI:Tl. However, as will be discussed in more detail below, these phosphors have the serious drawback of being hygroscopic, especially in the CsI:Na case.

The speed gains to be expected are shown in Fig. 3, where the relative quantum detection efficiency *QDE* is plotted against x-ray energy. As in Ref. (1) and (6) *QDE* is defined as

$$QDE_E = A_E \cdot \eta \cdot \lambda_{Em} \cdot C_E \cdot D_\lambda$$

where A_E is the x-ray absorption of the screen (as a percentage), η is the luminescence radiant efficiency under cathode-ray excitation of the phosphor[2] (as a percentage), λ_{Em} is the mean wavelength of the detected emission, C_E is a factor representing the energy losses in the screen, and D_λ is the efficiency for detection of the screen luminescence, I_λ, by a detector with response R_λ. D_λ is defined as $\int I_\lambda R_\lambda d\lambda / \int I_\lambda d\lambda$. Details of the calculations are given in Ref. (1).

In Fig. 3, the *QDE* curves of CsI:Na with standard film and of CsI:Tl with green emitting film happen to coincide within 5%. We have drawn data for these two combinations as one curve. As in Fig. 1, the curves have been smoothed between 10.2 and 12.1 keV.

[2] In contrast to efficiencies under x-ray excitation, these are fairly accurately known.

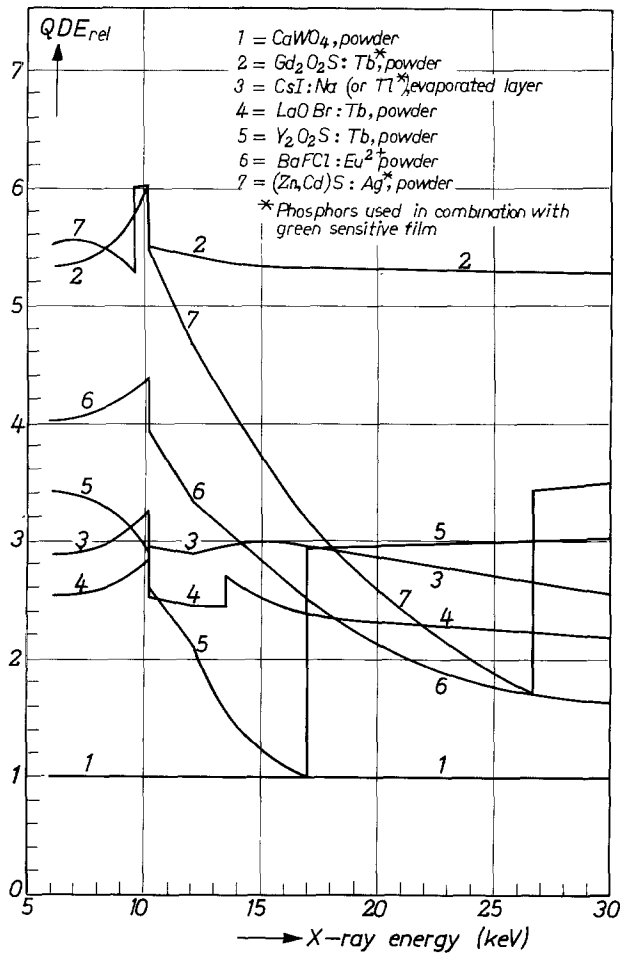


Fig. 3. Calculated relative quantum detection efficiency ($CaWO_4$ = 1) of various phosphors in the 6-30 keV range. The curves between 10.2 and 12.1 keV have been smoothed (see text).

It is concluded from Fig. 3 that the highest *QDE* figures are found at low x-ray energies. In this region the differences in x-ray absorption are small (see Fig. 2) so that the suggested gains almost completely originate from differences in luminescence conversion efficiency and in the match between the spectral distribution of the generated light and spectral sensitivity of the film. Green-emitting phosphors perform especially well in this region, the main reason being that these materials yield more quanta per percent energy efficiency than blue-emitting materials.

The drop in *QDE* above 10 keV is due to the absorption properties of the phosphors. In the most important region for mammography, 15-20 keV (17), the *QDE* lies between 1 and 3 for blue emitting phosphors and between 2.5 and 5.5 for materials to be used in combination with green-sensitive film. In the blue, evaporated layers of CsI:Na are considered to be the best proposal, followed by BaFCl:Eu^{2+} and LaOBr:Tb^{3+} powders. Y_2O_2S:Tb^{3+} performs well above 17 keV but not below that energy. The best phosphor in the green seems to be Gd_2O_2S:Tb^{3+} powder, whereas the promising candidate from a resolution point of view, (see introduction) seems to be CsI:Tl. However, these calculated speed gains with respect to $CaWO_4$ are not as impressive for mammography screens as for screens used at higher x-ray energies. Table I lists some QDE_{rel} data at 15 and 20 keV (100 μm thick screens) and at 60 keV [200 μm thick screen, see Ref. (1)]. It is seen that in most cases the ratio $QDE_{15\ keV}/QDE_{60\ keV}$ or $QDE_{20\ keV}/QDE_{60\ keV}$ is below 1. The more promising candidates even score ratios below 0.5.

Application of the New Phosphors; Measured Properties of Some New Mammography Screens

As concluded in the section on properties of $CaWO_4$ screen-film combinations, an inprovement of the resolution of mammography screens is more urgently needed than a further increase of speed. Therefore CsI:Na and CsI:Tl vapor-deposited screens seem to be the most obvious candidates to replace $CaWO_4$ screens. Impressive resolution gains have in fact been realized for CsI:Na screens used as input screens in an image intensifier tube (1, 3, 4). Good agreement between calculated and measured *QDE* has also been found (6). However, this material can only be used in vacuum devices like the image intensifier tube. Up to now no plastic covers have been found that protect CsI:Na screens sufficiently against moisture, which makes this material unattractive for mammography application.

CsI:Tl is much less hygroscopic than the Na-activated material. A drawback of such screens is, however, that a special green sensitized film should be used in combination with the screen to realize substantial speed gains. In many cases this requires adaptation of existing "dark room" lighting. The strong afterglow of CsI:Tl (1) observed for x-rays with energies of the usual radiological range, might also be a serious application disadvantage. We have found, however, that the soft x-rays used in mammography give rise to a negligible amount of afterglow.

It is concluded that vapor-deposited CsI:Tl layers are candidates for application in mammography screens. We hope to report more details on their properties in the near future.

Regarding powder phosphors, Fig. 4 shows some results of measurements on BaFCl:Eu^{2+} (Philips "Bfc") and LaOBr:Tb^{3+} (Agfa "MR") screens. These screens have thicknesses comparable to those of $CaWO_4$ Universal or Micro screens discussed above. Gd_2O_2S:Tb^{3+} screens, which have to be used with green sensitive films have not yet been considered by us. It is seen in Fig. 4 that, at equal resolution, the speed gains with respect to $CaWO_4$ are only marginal, namely about a factor of 1.2 or 1.3 for use in combination with double-coated film and 1.1 or 1.2 for use in combination with single-coated film. These gain factors are about half of the calculated ones. This result corroborates our conclusion (6) that the screen technology for these new powder phosphors still lags behind the well-established technology for $CaWO_4$.

Table I. Relative x-ray quantum efficiencies (*QDE*) of x-ray screen/film combinations

Screen phosphor	Film	*QDE* at x-ray energies of: (100 μm thick layers) 15 keV	(100 μm thick layers) 20 keV	(200 μm thick layer) 60 keV	ratio $\frac{QDE_{15\ keV}}{QDE_{60\ keV}}$	ratio $\frac{QDE_{20\ keV}}{QDE_{60\ keV}}$
$CaWO_4$	standard (u.v./blue sensitive)	1.0	1.0	1.0	1.00	1.00
Gd_2O_2S:Tb^{3+}	green sensitive	5.3	5.3	12.0	0.44	0.44
CsI:Na	standard	3.0	2.9	14.6	0.21	0.20
CsI:Tl	green	2.9	2.8	14.0	0.20	0.19
LaOBr:Tb^{3+}	standard	2.4	2.3	5.2	0.46	0.44
Y_2O_2S:Tb^{3+}	standard	1.2	3.0	3.5	0.34	0.86
BaFCl:Eu^{2+}	standard	2.8	2.1	5.2	0.54	0.40
(Zn,Cd)S:Ag	green	3.9	2.8	3.2	1.21	0.87

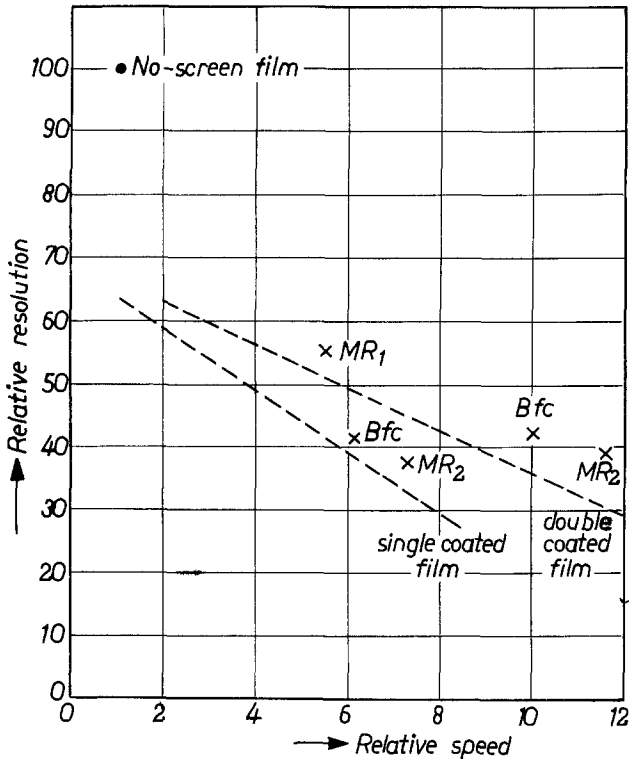


Fig. 4. Relative resolution against relative speed for BaFCl:Eu^{2+} (Bfc) and LaOBr:Tb^{3+} (MR) screen/film combinations. The no-screen film has a speed equal to unity and a resolution equal to 100. The dashed line represents results for $CaWO_4$ screen/film systems, taken from Fig. 1. The x-ray source (W-anode) was operated at 30 kV.

Conclusions

The use of x-ray screens in mammography can give rise to substantial speed gains and hence to x-ray dose reduction. The simultaneously occurring deterioration of the image quality as established by physical measurements, makes the benefits rather questionable. Whether this also holds true from a clinical point of view needs further investigation. Replacement of $CaWO_4$ by more recently developed x-ray powder phosphors like BaFCl:Eu^{2+} or LaOBr:Tb^{3+} does not drastically change these conclusions.

New screen technologies have to be found to give mammography screens better properties. Improvement of the screen resolution is a primary prerequisite, although the resulting improvement of the system may be limited by geometrical factors.

Manuscript submitted March 2, 1977; revised manuscript received May 13, 1977. This was Paper 150 presented at the Philadelphia, Pennsylvania, Meeting of the Society, May 8-13, 1977.

Any discussion of this paper will appear in a Discussion Section to be published in the June 1978 JOURNAL. All discussions for the June 1978 Discussion Section should be submitted by Feb. 1, 1978.

Publication costs of this article were assisted by Philips Research Laboratories.

REFERENCES

1. A. L. N. Stevels, *Med. Mundi*, **20**, 12 (1975).
2. C. Bates, *Adv. Electron. Electron Phys.*, **28A**, 451 (1969).
3. A. L. N. Stevels and A. D. M. Schrama-de Pauw, *Philips Res. Rep.*, **29**, 353 (1974).
4. A. L. N. Stevels and W. Kühl, *Med. Mundi*, **19**, 3 (1974).
5. G. W. Ludwig, *This Journal*, **118**, 1152 (1971).
6. A. L. N. Stevels and A. D. M. Schrama-de Pauw, *ibid.*, **123**, 887 (1976).
7. J. G. Rabatin, Abstract 102, p. 250, The Electrochemical Society Extended Abstracts, Spring Meeting, San Fransisco, Calif., Vol. 74-2 (1974).
8. A. L. N. Stevels and F. Pingault, *Philips Res. Rep.*, **30**, 277 (1975).
9. R. V. Alves and R. A. Buchanan, *IEEE Trans. Nucl. Sci.*, **19**, 415 (1972).
10. R. A. Buchanan, S. I. Finkelstein, and K. A. Wickersheim, *Radiology*, **105**, 187 (1972).
11. G. W. Ludwig and J. S. Prener, *IEEE Trans. Nucl. Sci.*, **19**, 3 (1972).
12. J. C. Price and P. D. Butler, *Br. J. Radiol.*, **43**, 251 (1970).
13. O. Camby and W. Gordenn, *J. Belge. Radiol.*, **56**, 237 (1973).
14. E. Deichgräber, S. Reichmann, and M. Burén, *Acta Radiol. Diagn.*, **15**, 93 (1974).
15. J. L. Lamarque, *J. Radiol. Electrol.*, **52**, 797 (1971).
16. E. Storm and H. I. Israel, U.S. Nat. Techn. Information Service Rep. La 3753 (1967).
17. K. Kyser, *Fortschr. Röntgenstr.*, **116**, 818 (1972).

Auger Analysis of Thermally Oxidized GaAs Surfaces

Ikuo Shiota, Nobuo Miyamoto, and Jun-ichi Nishizawa*

Research Institute of Electrical Communication, Tohoku University, Sendai, Japan 980

ABSTRACT

We have investigated in-depth composition profiles of the GaAs crystals with thermally oxidized (100) and (111) surfaces by Auger electron spectroscopy during Ar sputter etching. The Ga depletion is found at two different positions when the oxide thickness is less than about 250 and about 140Å for the closed- and the open-tube oxidation, respectively. One of the positions is within the oxide layer and is always accompanied by the increase in As concentration, while the other is at the oxide-GaAs interface and appears upon the formation of Ga_2O_3 thicker than ~50Å. It is found that the oxide growth rate, the transition layer width, and the composition ratio between As and Ga near the interface strongly depend upon the surface orientation. It turns out that there are three different oxidation kinetics as functions of oxide thickness: the reaction of oxygen with GaAs at the interface, and in- and out-diffusions of oxidizing species and Ga.

GaAs is an important semiconducting material for various optoelectronic and high frequency devices. At the present stage, however, it is still difficult to control the surface properties of GaAs. The difficulty lies in the fact that the surface composition of GaAs easily deviates from its stoichiometry by heating even at lower temperatures and by any chemical treatments. This is due to the high equilibrium vapor pressure of As (1) and the different reactivities of Ga and As with the oxidizing species and chemical reagents (2). This situation does correspond to the thermal oxidation of GaAs surfaces.

The detailed mechanism of thermal oxidation of binary semiconductors (3) such as GaAs (4-9), particularly in relation to the role of As atoms in the oxide, has not been accounted for. In this work, we have investigated the in-depth profiles of thermally oxidized GaAs (100) and (111) surfaces by Auger electron spectroscopy during Ar sputter etching. It has turned out that As plays an important part in the formation of oxide films and exhibits a peculiar compositional distribution in the case of the lower temperature oxidation.

Experimental

Undoped GaAs (100) and (111) wafers were cut from the same boatgrown ingot with a carrier concentration of 1×10^{16} cm^{-3} and an etch pit density of 5000 cm^{-2}. After mechanical polishing, the surfaces were thoroughly degreased using trichlorethylene and methanol cycles in an ultrasonic bath, and then the damaged surface layer was etched off in a solution of 4 parts H_2SO_4, 1 part H_2O_2, and 1 part H_2O, followed by dipping in a concentrated HF solution for 5 min after rinsing with deionized water. The wafers were finally rinsed with doubly distilled methanol.

In the open-tube oxidation system, the flow rate of oxygen gas was about 500 cm^3/min, while in the closed-tube system with the closed inlet and outlet valves of the quartz reaction tube, oxidation took place in a stationary oxidizing atmosphere. The wafers oriented to (100) and (111) were simultaneously oxidized in a resistance heating furnace under identical experimental conditions.

The Auger transitions used for in-depth profiling of the oxide-GaAs system are those in the higher energy states of 1087 and 1228 eV $L_3M_{4,5}M_{4,5}$ for Ga and As, respectively, in order to avoid peak overlapping as observed in the lower energy range (< 100 eV) and also to obtain precise peak-to-peak values of their Auger signals. A 510 eV $KL_{2,3}L_{2,3}$ transition was monitored for oxygen profiling. An accelerating voltage of 4 kV was employed as the primary electron beam to excite the higher energy Auger electrons, the beam current used being 1 μA. The modulation amplitude of the phase-sensitive detector was set at 5 eV, the time constant at 1 sec, and the scanning rate at 6 eV/sec. The peak-to-peak Auger signals were monitored automatically by a physical electronics multiplex control system.

In taking the lower energy part of the Auger spectrum, an excitation voltage of 2 kV was used to avoid sample charging. Furthermore a modulation amplitude of 2 eV, a time constant of 1 sec, and a scanning rate of 1 eV/sec were employed to increase the resolution of the spectrum.

Simultaneous sputter etching was made at a sputtering voltage V_{sp} of 1 or 2 kV, and an emission current of 30 mA under a 5×10^{-5} mm Hg Ar atmosphere. The sputtering rate of the Ga oxide formed in a series of experiments was determined to be 20 and 55 Å/min for $V_{sp} = 1$ and 2 kV, respectively. In this evaluation the oxide thickness measured by a multiple-beam interferometer was divided by the sputtering time when the Auger peak ratio, O/Ga, started to decrease from the value of 1.75 for the bulk oxide. Once the sputtering rate was calibrated, the oxide thickness was determined from the sputtering time defined above. This method was also applied to the oxide in which the interface with the GaAs substrate was not clearly defined and which contained a considerable amount of As.

Results and Discussion

A characteristic compositional distribution in which the amount of Ga is depleted at two different positions has been found in the thermal oxide-GaAs system for the oxides, less than about 250 and 140Å in thickness, formed in the closed- and the open-tube system, respectively. Typical examples are shown in Fig. 1 and 2. Figure 1 shows the GaAs (100) surface oxidized at 500°C for 20 min in the closed-tube system, and Fig. 2 shows the same surface oxidized at 450°C for 60 min in the open-tube system. Two Ga valleys, *i.e.*, the two Ga depletion regions, were observed not only in the (100) surfaces but also in the (111) A and B surfaces. One valley was within the oxide layer 50Å off from the oxide surface [hereafter called the outer (Ga) valley], and the other at the oxide-GaAs interface [hereafter called the inner (Ga) valley]. At the outer valley the amount of As took a peak value and O acted like Ga; that is, the Ga and O distributions showed a tendency opposite to that of the As distribution. It should be further noted that the amounts of Ga and O in the region between the outer and the inner valley are

* Electrochemical Society Active Member.
Key words: composition profile, inner and outer Ga depletion, oxidation kinetics.

smaller than those of the surface layer of the oxide, and that the coexistence of a considerable amount of As is observed between the two valleys. These observations suggest that the total amount of Ga oxide and As remains constant throughout the oxide, and that the close packing of Ga oxide up to its maximum density is impeded by the presence of As. The oxide with the two Ga valleys was more easily created in the closed-tube oxidation than in the open-tube one. For instance, the two valleys were formed by oxidation at 600°C for 10 min or 500°C for 30 min in the closed-tube system, while the outer valley disappeared even by oxidation at 550°C for 10 min in the open-tube system. The inner valley was always observed when the oxide thickness became more than 50Å, as is the case with the oxide formed by violent chemical etching of GaAs surfaces (8, 10). This would mean that the occurrence of Ga depletion at the oxide-GaAs interface is a fundamental phenomenon in the formation of a native Ga oxide on the GaAs substrate by thermal oxidation.

The Auger spectra corresponding to the points indicated by the numbered arrows in Fig. 1 are shown in Fig. 3. The Ga $M_2M_4M_4$ peak and the Ga M_2M_4V peak made chemical shifts of 5 and 5.5 eV toward the lower energy side from their original energies of 54 and 81 eV for the clean GaAs surface. It is obvious that the spectrum at point 1 has a closer resemblance to that at point 3 than the spectrum at point 2. It is evident that at the outer valley (at point 1), a weak but unchemically shifted Ga peak was observed, and the chemical shift of the As Auger peak is much smaller (< 1 eV) throughout the oxide layer compared with that of Ga. These facts indicate the presence of a small amount of the unoxidized Ga at the outer valley, and the presence of the unoxidized As throughout the oxide layer except the uppermost surface layer.

As the oxidation proceeded, the outer valley became shallower, flattened out, and finally disappeared. Thus, only the inner valley remained. With further oxidation, the amounts of Ga and O gradually increased inward from the oxide surface, accompanied by a decrease of the As content in the oxide. Finally the oxide became homogeneous Ga_2O_3. In the single valley oxide formed above 700°C the unchemically shifted Ga Auger peak was observed.

The Auger peak ratio, O/Ga, showed a constant value of 1.75 ± 0.05 throughout the oxide regardless of whether the oxide system had one or both of the Ga valleys, although in the latter case a considerable amount of As was present between the two Ga valleys. It can be inferred from this result that the O atoms around a Ga atom are identical in coordination throughout the oxide layer and only the Ga oxide density varies in it, and that the O atoms are preferentially bound with Ga atoms rather than As atoms. This

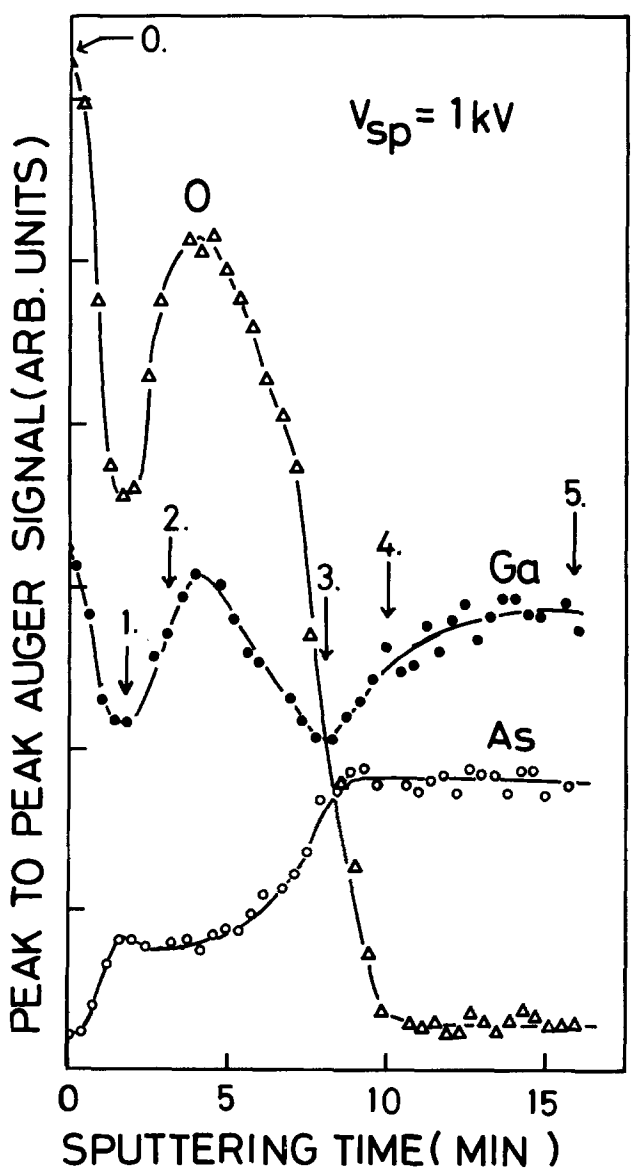


Fig. 1. Composition profile of a thermally oxidized GaAs (100) surface in the closed-tube system at 500°C for 20 min.

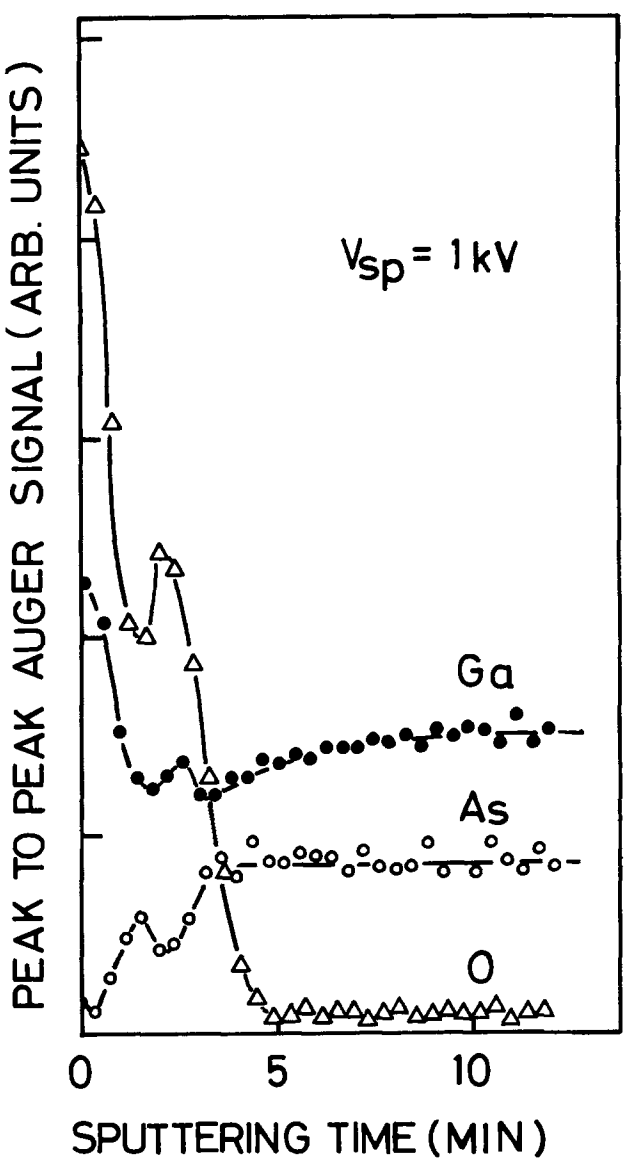


Fig. 2. Composition profile of a thermally oxidized GaAs (100) surface in the open-tube system at 450°C for 60 min.

conception can well explain the previously described result that the chemical shift of the As Auger peak is negligibly small.

The composition profile at the interface shows a large dependence on the crystal orientation and the oxidation condition. Typical examples for the orientation dependence of composition profiles of the (100), (111) B, and (111) A surfaces are shown in Fig. 4, 5, and 6, respectively. Each surface was oxidized at 700°C for 10 min in the open tube. In these figures, the ratios of O and As to Ga Auger peaks are also shown. In the (111) B surface the O penetrated very deeply into the GaAs bulk and the interface was elongated, while in the (100) and (111) A surfaces the interfaces were clearly defined. A remarkable As accumulation appeared only at the (100) interface and increased up to approximately 700°C, beyond which it disappeared. There occurred a weaker As accumulation in the closed-tube oxidation at the (100) interface.

Figures 7 and 8 show the dependence of oxide thickness and Δt on the reciprocal oxidation temperature, where the oxidation was performed for 10 min at each temperature. The quantity Δt is the duration of sputtering time for a half recovery of the Ga Auger peak to the value of the bulk GaAs as indicated in the insert of Fig. 8, and gives a measure of the thickness of the transition layer at the interface. The oxide growth rate is equal between the (100) and the (111) faces below 500°C, but it is greater for the (111) face than that for

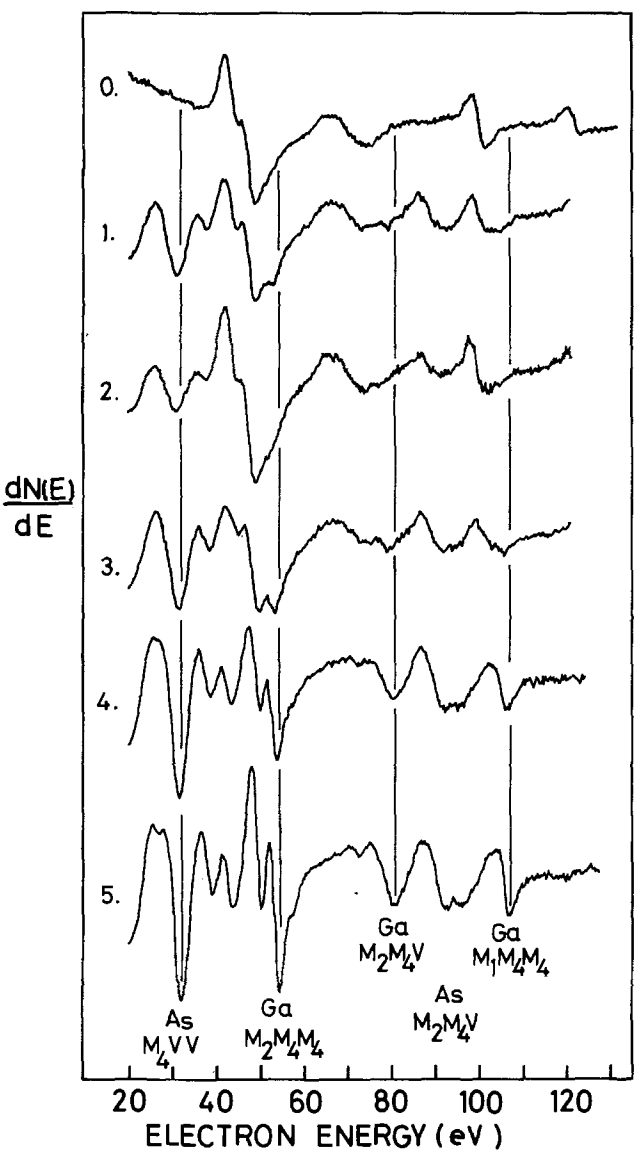


Fig. 3. Auger spectra corresponding to the points indicated by the numbered arrows in Fig. 1.

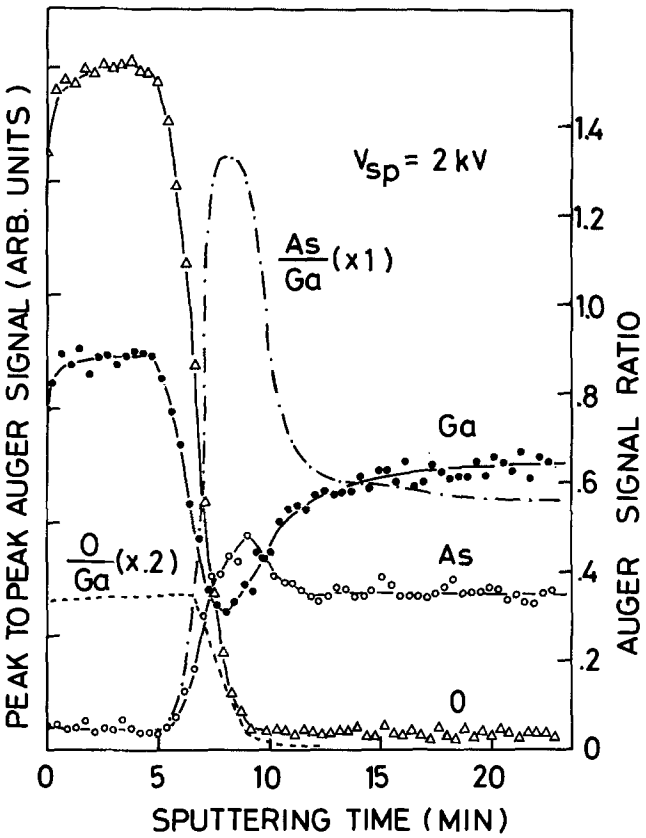


Fig. 4. Composition profile of a thermally oxidized GaAs (100) surface in the open-tube system at 700°C for 10 min.

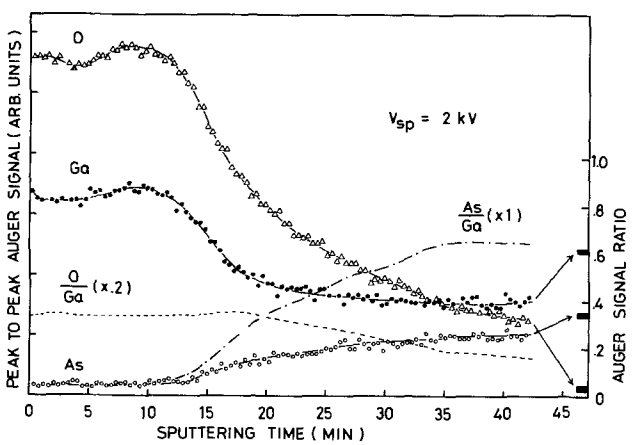


Fig. 5. Composition profile of a thermally oxidized GaAs (111) A surface. Other conditions are the same as used in Fig. 4.

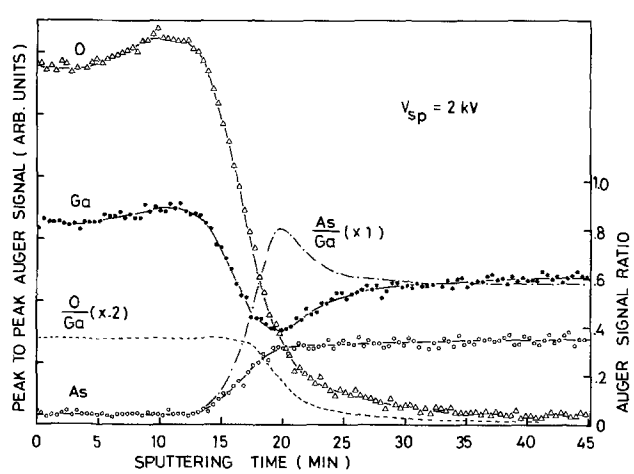


Fig. 6. Composition profile of a thermally oxidized GaAs (111) A surface. Other conditions are the same as used in Fig. 4.

the (100) face above 500°C. From Fig. 7 and 8, it is obvious that the thermal oxidation has three different rate-limiting processes, depending on the values of activation energy E_a. For the (100) faces, E_a is approximately 0.4 eV between 500° and 700°C, and E_a = 1.3 ~ 1.4 eV at both sides out of that temperature range. For the (111) faces, the temperature range with E_a = 0.4 eV starts from about 550°C.

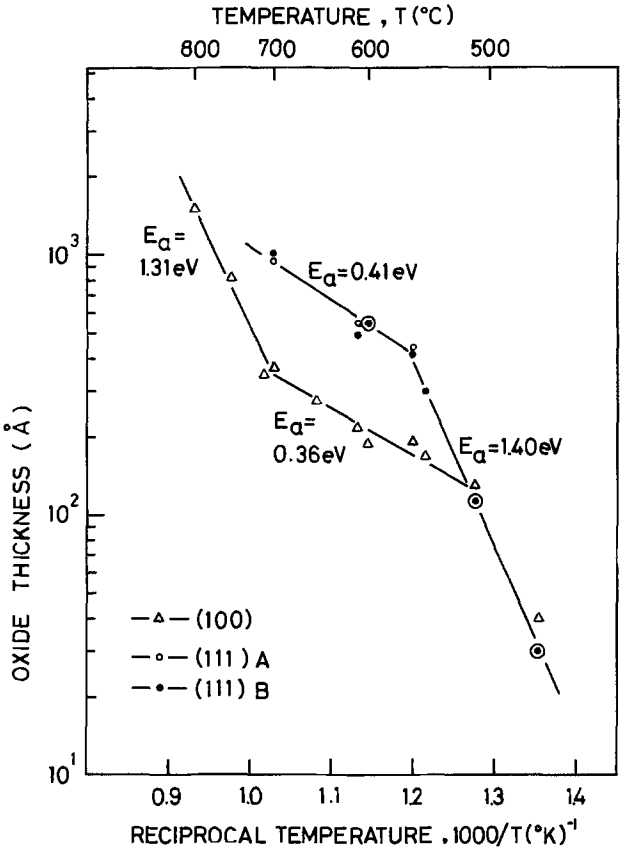


Fig. 7. Oxide thickness as a function of reciprocal temperature. Oxidation was made for 10 min at the specified temperatures.

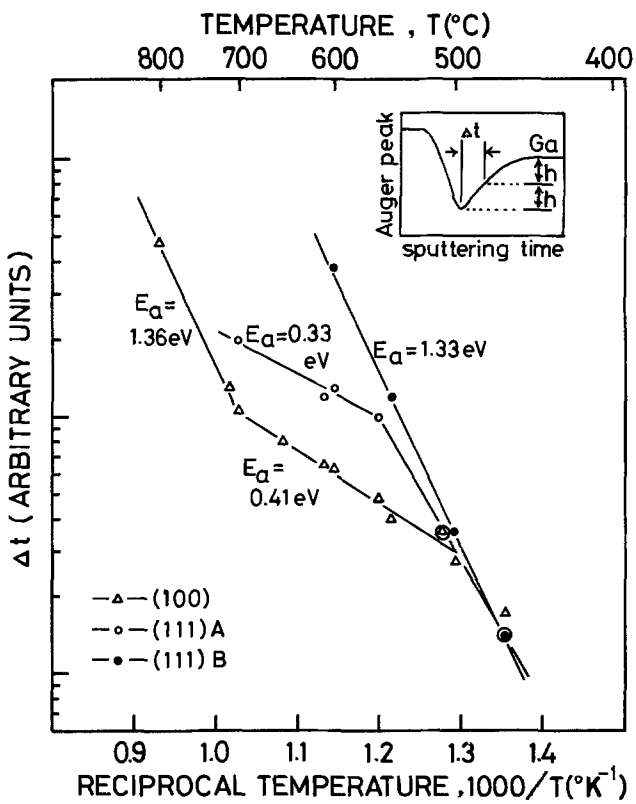


Fig. 8. Δt, the duration of sputtering time for a half recovery of the Ga Auger peak to the value of the bulk GaAs, as a function of reciprocal temperature for the same samples as used in Fig. 7.

In the oxidation at 510°C where E_a falls on 1.3 ~ 1.4 eV for the (111) and 0.4 eV for the (100) face, the relation between oxide thickness and oxidation time is linear for the (111) A and B faces and is parabolic for the (100) face. However, the oxidations at 600° and 730°C with E_a = 0.4 and 1.3 ~ 1.4 eV, respectively, obey an identical parabolic law for both (100) and (111) faces. These results lead to the conclusion that the oxidation in the temperature range where a linear law holds, and E_a = 1.3 ~ 1.4 eV is controlled by the reaction of O with GaAs at the interface. Thus, the remaining As will be distributed in the oxide and near the interface. In the other temperature ranges the oxidation will be controlled by the in- and outdiffusion of oxidizing species such as water and Ga with E_a = 0.4 and 1.3 ~ 1.4 eV, respectively. The diffusion of water is inferred from the analogy with the thermal oxidation of Si in an atmosphere containing water vapor (11). The Δt data plotted in Fig. 8 also show a similar behavior to the oxide thickness for the reciprocal temperature; above 500°C the transition layer at the interface is wider in the (111) surface than in the (100) one. It should be noted here that the width of the transition layer in the (100) surface is narrower than in the (111) surface, but the inner valley is deeper in the (100) than in the (111) surface.

From Fig. 7 and 8, it is apparent that for the same oxide thickness in the range of less than approximately 300Å, the value of Δt is nearly the same regardless of the difference in surface orientation. This suggests that Δt depends solely on the oxide thickness in such a thickness range, and hence the orientation dependence of sputtering may safely be ignored. In the oxide thickness range of more than 300Å, however, Δt becomes dependent not only on the oxide thickness, but on the surface orientation; that is, in the (111) B face Δt is greater than that of the (100) and (111) A faces when the oxide thickness is the same. It is very difficult to understand these results only in terms of such artifacts as selective sputtering and the implantation effect, because the former seems to give the same effect on Δt regardless of the difference in surface orientation when the oxide thickness is the same, and the latter should give an equivalent effect on Δt for the identical surface orientation regardless of the difference in oxidation temperature. Therefore, some other fundamental explanation is indispensable to the understanding of the observed phenomena at the interface. The occurrence of the inner Ga depletion cannot be related to the oxidation kinetics because the inner Ga valley appears inevitably whenever the oxide thickness is in excess of 50Å. Therefore, the cause of the depletion should be sought from the oxide formation itself. A possible explanation may be given as follows. As described above, Ga is preferentially oxidized and consequently As atoms accumulate around the interface, resulting in a relative decrease of the Ga to As ratio in that region. That is to say, the inner Ga depletion is caused by a selective oxidation of Ga and the resulting As accumulation at the interface.

Conclusions

We have obtained new results on the thermal oxidation of GaAs surfaces by measuring in-depth profiles of the compositional distribution by Auger electron spectroscopy during Ar sputter etching. The thermal oxide films can be classified in two groups. One is the oxide with two Ga valleys and the other is the oxide with a single Ga valley. The Ga depletion at the oxide-GaAs interface appears inevitably upon the formation of the oxide layer thicker than ~ 50Å. The Ga depletion in the oxide near the outer surface is always accompanied by the increase in As. The close packing of the Ga oxide up to its maximum density is hindered

by the presence of As. It has been made clear for the first time that the behavior of As plays an important role in the formation of the Ga oxide by thermal oxidation of GaAs surfaces.

Three different oxidation kinetics have been proposed: The first is the reaction of O with GaAs at the interface and dominates the formation of thin oxide films characterized by the two Ga valleys; the second and the third correspond to the indiffusion of oxidizing species, such as water, and to the outdiffusion of Ga. For the (100) surfaces, the second mechanism holds for the temperature range between 500° and 700°C, and the third does above 700°C. In these temperature ranges, the growth rate, the transition layer width, and the composition ratio strongly depend on the crystal orientation.

Manuscript submitted Aug. 31, 1976; revised manuscript received May 1, 1977.

Any discussion of this paper will appear in a Discussion Section to be published in the June 1978 JOURNAL. All discussions for the June 1978 Discussion Section should be submitted by Feb. 1, 1978.

Publication costs of this article were assisted by Tohoku University.

REFERENCES

1. J. Nishizawa, H. Ohtsuka, S. Yamakoshi, and K. Ishida, *Jpn. J. Appl. Phys.*, **13**, 46 (1974).
2. D. R. Wood and D. V. Morgan, *This Journal*, **122**, 773 (1975).
3. A. J. Rosenberg, *J. Phys. Chem.*, **64**, 1135, 1143 (1960).
4. H. T. Minden, *This Journal*, **109**, 733 (1962).
5. M. Rubenstein, *ibid.*, **113**, 540 (1966).
6. K. Navrátil, *Czech. J. Phys.*, **B18**, 266 (1968).
7. S. P. Murarka, *Appl. Phys. Lett.*, **26**, 180 (1975).
8. I. Shiota, S. Yamakoshi, N. Miyamoto, and J. Nishizawa, Paper presented at the second research meeting Surface Electronics, Ministry of Education of Japan, Sendai, Japan, October 13, 1975.
9. T. Sugano *et al.*, Technical Digest of the Meeting of Japan Society of Applied Physics, Fukuoka, Japan, November 23, 1975.
10. I. Shiota, K. Motoya, T. Ohmi, N. Miyamoto, and J. Nishizawa, *This Journal*, **124**, 155 (1977).
11. G. L. Holmberg, A. B. Kuper, and F. D. Miraldi, *ibid.*, **117**, 677 (1970).

The Properties of Silica Diffusion Sources under Oxidizing Ambient Conditions and Their Application to Solar Cell Fabrication

T. C. Chandler, Jr.,[1] R. B. Hilborn, Jr., and J. W. Faust, Jr.*

College of Engineering, University of South Carolina, Columbia, South Carolina 29208

ABSTRACT

In this paper a technique for the design and fabrication of silicon solar cells using spin-on silica doping sources is discussed. This technique involves the use of an oxidizing ambient during diffusion which limits the diffusion flux and yields lower surface concentrations of impurities and shallow p-n junctions. It is shown that the uniformity of the film thickness is an important factor in maintaining a uniform surface concentration of impurities in a diffused substrate. Data are given to demonstrate the effects of such silica film thickness variations on solar cell performance.

During the past four years industry and government interest in silica films as diffusion sources in electronic device applications has grown immensely (1, 2). The silica film itself has been in small scale use for some time, but the recent interest in developing inexpensive solar cells has renewed interest in this technology. Doped silica diffusion sources may reduce the cost of solar cell processing and have the advantage of better over-all process control (3).

Silica sources (or doped SiO_2) exist in a variety of forms. Owen and Schmidt (4) have reported on the use of thin anodic silicon dioxide films as diffusions sources, but their analysis is hampered by experimental conditions which are difficult to control. Reactive sputtering has also been investigated (5) but results have not been consistent enough for applications in photovoltaics. A more recent development is the paint-on or spin-on silica film. These films when applied properly, yield excellent p-n junction uniformity, surface concentration of impurities, and minimal surface damage. The silica solutions consist of organic silicates and the appropriate dopant elements dissolved in an alcohol solution. These types of solutions have a typical room temperature viscosity of 25 cp making them well suited for standard photoresist spinning apparatus. Herein lies a primary advantage of the spin-on silica film. The simplicity of the technique and equipment makes this an inherently cheaper process than the anodized or sputtered films mentioned above.

In this paper we describe the diffusion theory and technique used to fabricate p-n junction silicon solar cells using doped, spin-on films. Experimental data are presented to demonstrate the controllability obtained from spin-on silica films.

Diffusion Theory

In a recent paper Barry (3) has demonstrated that in a nonoxidizing ambient, diffusions from doped silicon dioxide films agree with the solutions to Fick's second law to within experimental error and that the surface concentrations of impurities resulting from such diffusions are functions of the silica dopant concentration. It was shown that the surface concentration was independent of diffusion time and temperature for surface concentrations less than or equal to 1.0×10^{20} cm^{-3}. This limitation in Barry's model is an important point. Other studies (6-8) show that for surface concentrations greater than 1.0×20^{20} anomalous diffusion profiles result, leading to regions near the surface of constant impurity concentration having

* Electrochemical Society Active Member.
[1] Present address: U.S. Air Force Materials Laboratory, Electromagnetic Materials Division (LPO), WPAFB, Ohio 45433.
Key words: silicon dioxide, diffusion flux, phosphorus.

a very high diffusion-induced density of dislocations and consequently low minority carrier lifetimes. These are the regions described in the literature as "dead layers" (9). Hence, if one wishes to manufacture silicon solar cells with the highest obtainable efficiencies one must limit the surface concentration to values less than 2×10^{20} cm^{-3} so that the dead layer is eliminated.

Flux limiting.—A method of maintaining a surface concentration at the proper level is to introduce oxygen into the ambient during diffusion (6). The presence of sufficient quantities of oxygen allows oxidation to take place at the silicon surface thus limiting diffusion at the oxide-silicon interface. By proper control of the thermal oxidation rate, one can control the diffusion-limiting process and consequently, the surface concentration. The use of an oxidizing ambient causes deviations from Fick's laws of diffusion resulting in shallow p-n junction depths and, unlike Barry's model, surface concentrations that are functions of the diffusion temperature.

Intuitively, one sees that diffusion in the presence of a retarding mechanism (diffusion limiting due to oxidation) requires changing the boundary conditions of the diffusion model, since the physical boundary (oxide-oxide interface) is in motion.

This moving boundary can be described by two coordinate axes (Fig. 1) X and X'. X is fixed with its origin at the oxide-silicon interface. X' has its origin at the oxide-oxide interface. X and X' are related by

$$X' = X - \frac{R\sqrt{t}}{N} \qquad [1]$$

Where R is the oxidation rate constant in cm/sec$^{1/2}$ and N is the volume ratio of silicon dioxide to silicon (equal to 2.30). (Notice that this formulation of the moving boundary condition is relative in nature. It is just as correct to assume that the oxide-oxide interface is fixed and to allow the oxide-silicon interface to move.) It can be demonstrated by Eq. [1] that in the oxidizing ambient, diffusion is a function of the oxidation rate and not the oxide thickness. It was assumed in this study that the oxide growth followed the parabolic law[2] (5)

$$\alpha = (\alpha_0^2 + R^2 t)^{1/2} \qquad [2]$$

where α is the total oxide thickness, and in practice α_0, the initial oxide thickness, is zero.

Fick's second law can be written for region B and C of Fig. 1 yielding

$$\frac{\partial C_B}{\partial t} = D_B \frac{\partial^2 C_B}{\partial X'^2} \qquad [3]$$

[2] This is a good approximation for temperatures falling in the range 950°C $\leq T \leq$ 1250°C) (5).

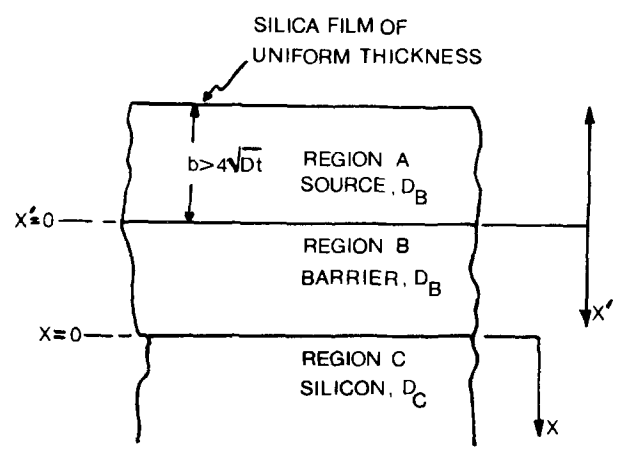


Fig. 1. The three layer diffusion system showing the origin of the X and X' axis.

and

$$\frac{\partial C_c}{\partial t} = D_C \frac{\partial^2 C_c}{\partial X^2} \qquad [4]$$

The solution (10) to Eq. [4] is

$$C_c(X, t) = \gamma C_0 \operatorname{erfc} \frac{X + \dfrac{R\sqrt{t}}{N}}{2\sqrt{D_c t}} \qquad [5]$$

where

$$\gamma \simeq \frac{1}{1 + \sqrt{\dfrac{D_c}{D_B}}} \qquad [6]$$

and C_0 is the concentration of dopant (atoms/cm^3) in the source material. Evaluating Eq. [5] at $X = 0$ the surface concentration is found to be

$$C_s = \gamma C_0 \operatorname{erfc} \frac{R}{2N\sqrt{D_c}} \qquad [7]$$

These equations show that unlike Barry's fixed boundary model, C_s is a function of temperature and also the junction depth is shallower by the quantity $R\sqrt{t}/N$.

Theoretical limitations.—The theory given above is dependent on two basic assumptions. The first assumption is that the oxidation rate constant, R, is independent of time and is only a function of temperature. This assumption is only valid when the silica film is of uniform thickness. Experiments show that oxidation constants for localized regions of thin silica film ($<<$200Å) have somewhat higher values of R and oxidation in these regions is not independent of time. Figure 2 shows a plot of R *vs.* temperature for two different silica layers. Notice that the thin SiO_2 film has a slightly higher R value. This behavior is not completely understood but from microscopic examina-

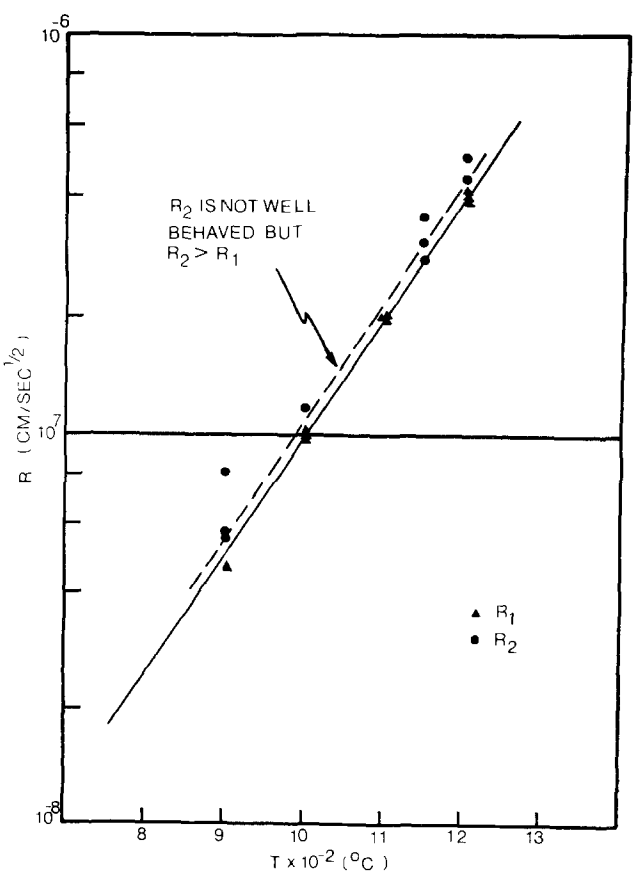


Fig. 2. Plot of R *vs.* temperature. R_1 is measured for thin silica regions and R_2 is measured for thick regions.

tion of such thin regions it is felt that the film has poor oxide integrity, *i.e.*, there are regions which are cracked and porous so that the migration of oxygen ions necessary for the oxidation is somewhat enhanced, unlike the regions of thick SiO_2 coverage (see Fig. 3) which display a reasonably constant R.

The problem of thin regions in the silica film is inseparably linked with the second limitation of the foregoing theory. To maintain the constant source condition of a silica (or deposited SiO_2) film, its thickness must equal or exceed the diffusion length of a dopant atom in the oxide (3, 10), *i.e.*, the silica thickness b must obey the inequality

$$b^2 > 4D_B t \qquad [8]$$

When inequality [8] is not satisfied, the film is quickly depleted of dopant; and, over the extended period during which an ideal erfc profile would have resulted, the profile for such a nonconstant source would be gaussian with a reduced value of C_s. Figure 4 shows the source thickness necessary for a given temperature. Satisfying conditions [8] might seem like a formidable problem, but fortunately the thickness of a spin-on source can be easily controlled by the spin speed and duration.

Solar Cell Processing

Given below is the general procedure for fabricating a silicon solar cell using silica films. The process can be divided into four major segments, prediffusion cleaning, application and examination, diffusion, and metallization. Both prediffusion cleaning and metallization are covered adequately in the literature (1, 5). Application and diffusion are discussed here because they involve implicitly the silica film.

Application.—It has been found by trial and error that silica films, utilizing an alcohol carrier liquid, spin on best at temperatures from 20°C up to 25°C. Spin speeds can vary but the best range is between 2500 and 3500 rpm. Best results are obtained when the substrate is the same temperature as the source liquid; however it cannot have a temperature above the source liquid temperature.

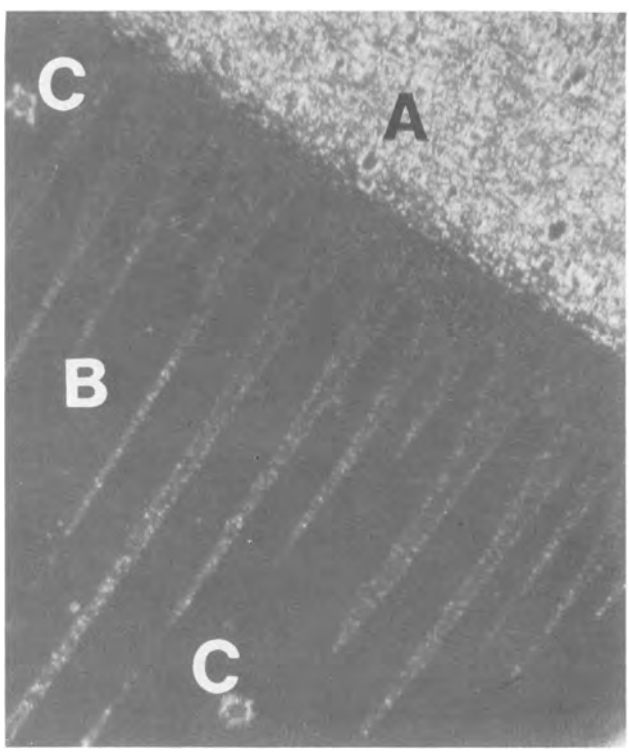


Fig. 3. Purposely induced thin regions of a spun-on silica film. Notice that the thin regions (A) provide poor coverage as opposed to the thick regions (B). C is due to bubble damage. (Magnification 160X.)

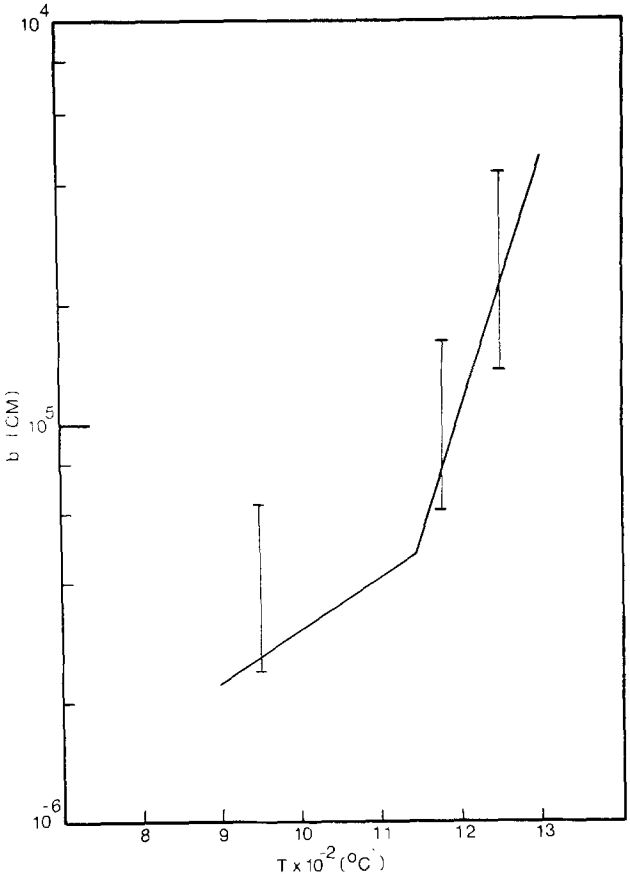


Fig. 4. Plot of source thickness necessary for maintaining constant source conditions as a function of temperature.

To prepare a liquid solution for application, it should be placed in a container so that it fills it completely, with no empty space, and allowed to come slowly to some temperature less than 25°C. If the source liquid is stored for this period in a large partially filled container, evaporation of the alcohol will generate bubbles which can degrade the uniformity of the film, see Fig. 3 and 6.

After the film has been spun on the substrate, it should be examined to see if the source layer is uniform, or if it has thickness variations (12) similar to Fig. 3. (This step is necessary because the properties of commercially available films differ from type to type, batch to batch, etc. Once satisfied that these guidelines are adequate, this step may be deleted.) These variations in thickness can yield thin spots on the order of 200Å or less. The cause is improper film application as described by Chandler *et al.* (12). Similar bad results occur when particles of dust or debris touch the silica film. It has been observed in this laboratory that a particle 1μ in diameter can result in poor silica coverage for a distance of 50μ around the particle. Elimination of these thin areas is essential in view of the theoretical limitation described previously. The silicon beneath a thin area oxidizes faster and the forming oxide, in effect, dilutes the source diffusion. More importantly, one can see from Fig. 4 that a silica thickness of 200Å is far from satisfying inequality [8] for common diffusion temperatures. The cumulative effect is the dilution of a source which itself is growing smaller with time. It has been experimentally confirmed that extremely shallow junctions, if present at all, will form under these thin layers.

If the deposited films have thickness variations, holes, or striation (12), the poor results discussed above will occur; hence the application procedure,

however different from the recommended process, must be altered to insure a uniform silica film. Figure 5 illustrates a ripple formation of the type encountered. During the bakeout cycle the organic compounds are driven off, the film becomes rigid, and the variations are frozen into the silica layer. Hence one means of reducing the thickness variations is to delay the bakeout until the wet film can flow to a more uniform layer. This technique works best below 25°C where evaporation of the alcohol is slow. Delaying the bakeout cycle will not eliminate thickness variations but it will allow thin areas to change sufficiently to satisfy the inequality [8].

Once the film integrity has been established, the substrate should be baked in dry nitrogen at 200°C for 4 hr. This step drives off the organic carrier liquids, leaving a doped silica film on the wafer.

Diffusion.—Diffusion of the substrate was carried out in an ambient mixture of 50% nitrogen and 50% oxygen at a temperature of 1000°C. The doping element was phosphorus at a concentration, C_o, of 4×10^{20}. The values of the oxidation constant R were determined experimentally. These conditions were chosen because they yield a uniform shallow junction.

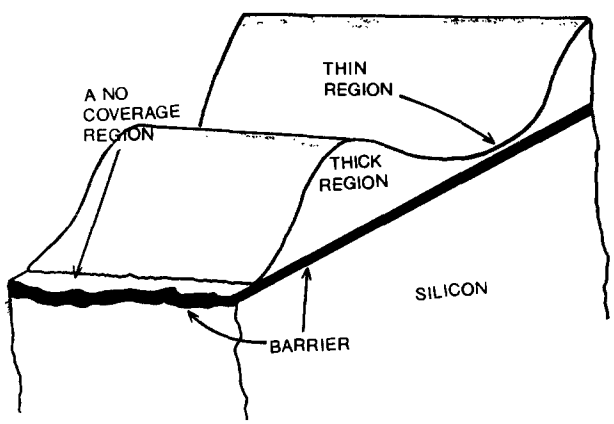


Fig. 5. Artist's conception of a ripple formation in a silica film. The thin regions of the film produce poor p-n junction characteristics.



Fig. 6. Photograph of a silica film with bubbles trapped in the film. If these bubbles remain in the film when it is drying, the damage shown in Fig. 3 results. (Magnification 100X.)

Results

Four series of solar cells were fabricated. Table I gives some data on each series. Each substrate had a background resistivity of 1 Ω cm and a thickness of 200μ. The contact pattern utilized is a common type having a center bar with six fingers. The contact metal was aluminum and the contacts were sintered in an N_2 ambient at 450°C for 10 min. No antireflection coatings were applied. The light source was the sun and the incident solar power was determined by pyranometer measurements.

The first two series were done with no control of the silica film uniformity. The third run utilized the simple temperature/spin guideline given above, and the fourth series was fabricated making sure that the silica film was more uniform by delaying the bakeout. Difference in cell performance is obvious from Table I. Runs 1 and 2 are not encouraging.

The nonuniformity of the film allowed diffusion to take place in a nonuniform fashion so that some regions of the cell display extremely high sheet resistances. In some areas where doping levels were not degenerate, the p-type contact on the n-type diffused region formed p-n junctions. It was found that the level of photon-generated current in the poorly diffused region was low also. Steps were taken to minimize these flaws so run 3 showed that when the uniformity of the silica film improved so did the characteristics of the solar cells.

Series 3 cells were moderately efficient, having fill factors averaging 0.60, but this was greatly improved in series 4.

The solar cells of series 4 were designed using the theory presented in this paper. The diffusion model defined by Eq. [1] through [7] allows the diffusion to take place at a higher temperature and achieve the same surface concentration and junction depth as for the low temperature diffusion. It has been found that diffusion from silica sources is more uniform for temperatures of 1000°C. The results were significant. By eliminating the diffusion inhomogeneities, the series resistance was reduced to tolerable levels. The results of junction depth and surface concentration measurements show good agreement between the theory and the diffused region of the cells.

Figure 7 shows the theoretical junction depth for a surface concentration of 1.2×10^{20} cm^{-3}, and a background concentration of 1×10^{16} cm^{-3}, at various diffusion times. The experimental points show that agreement with theory is good except at very short intervals (less than 5 min). This is probably due to the presence of an unavoidable oxide on the substrate before the source application, such that there is an initial oxide layer which has to be penetrated in a finite amount of time.

In Fig. 8 is an evaluation of the surface concentration for various diffusion times. This figure demonstrates that C_s is not time dependent for periods longer than 5 min and less than 60 min. Inside this time interval the curve of Fig. 8 is in agreement with Eq. [7]. The deviation from simple theory seen here can be explained. The low C_s seen for short diffusion times can be attributed to the residual oxide layer that was evidenced in the junction depth data. Deviations seen for

Table I. $X_j = 4000$Å

Series	I_{SC} (mA)	V_{OC} (V)	R-sheet (Ω/□)	R_S (Ω)	Fill factor (avg)
1	50	0.44	750	3	0.30
2	51	0.45	710	2.8	0.31
3	110	0.56	120	0.5	0.60
4	140	0.57	85.0	0.3	0.70

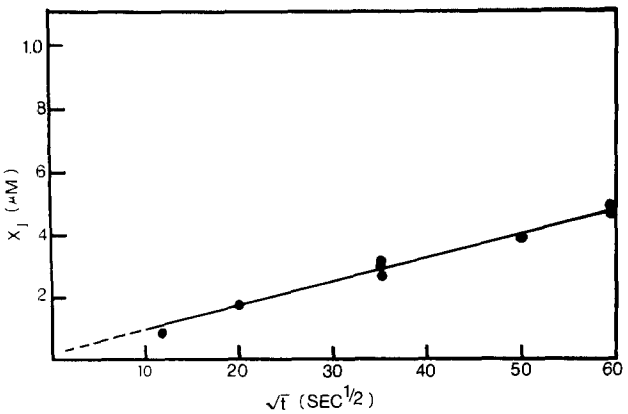


Fig. 7. Plot of junction depth *vs.* $\sqrt{t}$ for diffusion at 1000°C in an atmosphere of 50% O_2 and 50% N_2.

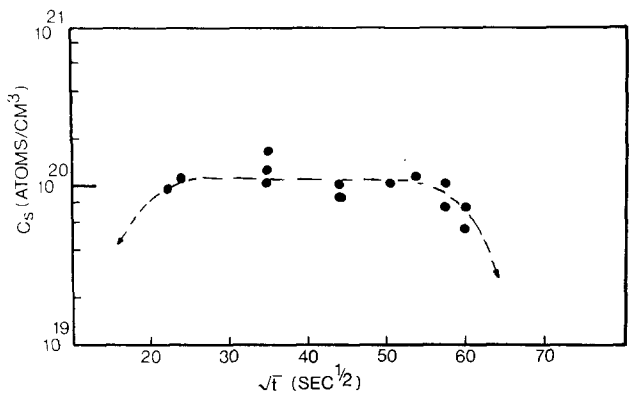


Fig. 8. Plot of surface concentration *vs.* $\sqrt{t}$ for 1000°C and an atmosphere of 50% O_2 and 50% N_2. $C_0 \simeq 4 \times 10^{20}$ cm^{-3}.

periods greater than 60 min indicate that the source material is becoming depleted of its dopant.

Solar cells processed by this technique and described here have better characteristics than those previously reported (12); their series resistances are comparable to standard, commercially diffused cells. These improvements are due to the uniformity of the silica film which results in a homogeneous surface concentration approximately equal to 1×10^{20} cm^{-3} and a shallow, uniform junction.

The uniformity of the degenerate surface concentration is the most important factor. To test qualitatively for uniformity of surface concentration a staining etchant which turns n^+ regions dark (5) was applied. Results show that when the film is uniform the surface concentration of impurities is uniform.

The junction depth was also established by the standard method involving angle lapping and staining (5, 11). The results were consistent with theory.

Conclusions

A model and general technique for fabricating solar cells using silica films is presented. This technique yields predictable, uniform shallow junctions, and acceptable surface concentrations for most diffusion cycle times. Calculations show also that for a given value of C_0 and temperatures between 950° and 1250°C, C_s varies little with the diffusion temperature. This technique is further simplified by the fact that excellent process control can be achieved by varying C_0 and the percent of oxygen in the ambient. It is obvious from the test data that moderately efficient solar cells can be fabricated using spin-on silica sources, and, when care is taken to insure proper film thickness and uniformity, cells comparable to those produced by standard, more expensive diffusion techniques can be manufactured.

The most important feature of this technique is that by introducing an oxidizing ambient, the resulting diffusion retardation allows the diffusion of impurities to be carried out at temperatures exceeding 1000°C while maintaining junction depths which are less than 0.5μ. This is significant because spin-on silica films yield more uniform junctions for temperatures greater than or equal to 1000°C. Although this uniformity could be obtained by using a nonoxidizing ambient, without the benefit of the diffusion retardation, deeper (>0.5 μm) p-n junctions would result. Because this technique also yields degenerate surface concentrations with no dead layer, the resulting solar cells have low series resistance and high blue response.

In view of the data presented in this paper, it seems that there is only one problem related to the full scale use of doped silica films, the rather long bake-out times required for these films. It is felt that the advantages of using silica films probably outweigh this minor difficulty. The original wafer diameters utilized in this research range from less than 2 cm to over 5 cm. No variation in film quality due to wafer size was observed, indicating that the silica films might be applied economically to larger diameter slices. It was also found that once the proper procedure was established for applying these films, the analytical procedures given in this paper could be eliminated. This reduced the somewhat tedious procedures outlined here to mere routine.

Manuscript submitted Dec. 16, 1976; revised manuscript received April 18, 1977.

Any discussion of this paper will appear in a Discussion Section to be published in the June 1978 JOURNAL. All discussions for the June 1978 Discussion Section should be submitted by Feb. 1, 1978.

Publication costs of this article were assisted by the University of South Carolina.

REFERENCES

1. R. H. Hopkins, J. R. Davis, P. Rai-Choudhury, and P. D. Blais, First Quarterly Report, Silicon Materials Task of the Low Cost Solar Array Project (Part 2), October-December 1975, NAS-100.
2. J. A. Becker, Solid-State Electron., **17**, 87 (1974).
3. M. L. Barry and P. Olofsen, **116**, 854 (1969).
4. A. E. Owen and P. F. Schmidt, *This Journal*, **116**, 548 (1969).
5. R. M. Burger and R. P. Donovan, "Fundamentals of Silicon Integrated Device Technology," pp.36-105, p. 175, Prentice Hall, Englewood Cliffs, N.J. (1967).
6. R. A. McDonald, G. G. Ehlenberger, and T. R. Huffman, *Solid-State Electron.*, **9**, 807 (1966).
7. P. A. Iles and B. Leibenhaut, *ibid.*, **5**, 331 (1962).
8. E. Tannenbaum, *ibid.*, **2**, 123 (1961).
9. J. Lindmayer, *Comsat Tech. Rev.*, **2**, 105 (1972).
10. D. Kahng, Ph.D. Dissertation, Ohio State University (1959).
11. C. S. Fuller and J. A. Ditzenberger, *J. Appl. Phys.*, **27**, 544 (1956).
12. T. C. Chandler, R. B. Hilborn, Jr., and J. W. Faust, Jr., Presented at IEEE/ERDA 12th Photovoltaics Specialists Conference, Baton Rouge, La. (Nov. 1976).

The Effect of Growth Rate and Temperature on the Incorporation of Sn in GaAs during LPE

Ulf König[1]

Institüt für Halbleitertechnik Sonderforschungsbereich 56, Technische Hochschule, Aachen, Germany

ABSTRACT

A growth rate dependence of the impurity incorporation has been measured for the first time: average carrier $\bar{n}$, donor $\bar{N}_D$, and acceptor $\bar{N}_A$ concentrations of heavily Sn-doped GaAs layers grown by liquid phase epitaxy (LPE) increase in the range $0.2 < \bar{V}/\mu m/min < 6$. At faster growth rates, the concentrations tend to be constant ($1.4 \cdot 10^{19}$ cm^{-3} for donors, $3.5 \cdot 10^{18}$ cm^3 for acceptors). Growth rates between 0.2 and 35 μm/min have been adjusted by varying the cooling rates of the epitaxial processes between 0.04° and 100°C/min. It can be reported that the relation between $\bar{N}_{D/A}$ and $\bar{V}$ corresponds to the theoretical predictions under surface equilibrium conditions. The most important parameter is the barrier height of the system melt and semiconductor, modified by a concentration-dependent barrier lowering in the case of heavy doping. Based on the same assumptions, the temperature dependence of the measured incorporation $\bar{N}_{D/A}$ (T) is explained. This results from a comparison of the possiole incorporation theories surface and bulk equilibrium.

During epitaxial growth from the liquid phase, the interface between melt and semiconductor can be regarded as a metal semiconductor contact because of the great density of conduction electrons in the melt. The Schottky model is then applicable to the surface. Merten and Hatcher (1) have pointed this out. Later on Zschauer and Vogel (2) and Casey *et al.* (3) used this model. As a consequence of such an electrical model, the thermodynamic equation for the impurity incorporation will have electrical properties like the Fermi level or the barrier height (3, 4).

According to the growth conditions, two aspects have to be distinguished: the bulk equilibrium and the surface equilibrium. If the growth rates of the crystal are slow compared with the impurity diffusion in the semiconductor, there exists a thermal equilibrium between the two phases, melt and semiconductor bulk (bulk equilibrium). This model explains the impurity incorporation of Zn (5, 6) and Cu (7) in GaAs. Where the ratio of the growth rate to the solid diffusion constant is large, the melt is in equilibrium with the surface of the growing crystal only. The important parameter of the surface equilibrium theory is represented by the height of the Schottky barrier. The validity of this theory has been shown for the incorporation of Te (8) and for the Sn donor (4, 9). Panish has found that the incorporation of Sn in GaAs can be better explained if one also assumes a Sn acceptor complex $Sn_{As}2V_{Ga}$ using the surface equilibrium theory again (4). The concentration in the case of bulk equilibrium is almost proportional to the square root of the atomic fraction of tin X_{Sn} in the melt, while in the case of surface equilibrium it is directly proportional to X_{Sn}. In spite of the principal agreement Panish obtained with the surface equilibrium theory, for high Sn concentrations above $4 \cdot 10^{17}$ cm^{-3} there exists a discrepancy between theory and experiment: Experimentally evaluated concentrations indicate a weaker slope with higher X_{Sn} data than expected (4). This can probably be interpreted as a concentration dependence of the barrier height, resulting in a lowering of the barrier (10).

Some authors (11, 12) suspect an additional manifestation of the barrier height or the Fermi level in a cooling rate dependence of the Sn segregation coefficient during liquid phase epitaxy (LPE). As the cooling rate influences the growth rate, this amounts to a growth rate dependence of the impurity concentration. Panish (4), however, did not detect such a dependence of the Sn doping when slightly varying the cooling rate. There is no record of systematic experiments. Zschauer and Vogel (2) predicted a quantitative dependence of the impurity incorporation on the growth rate. Experimental proof has not yet been obtained, partly because the cooling rates, or growth rates, respectively, have not been varied over an extended range large enough to observe this effect. Such a variation is possible, using the epitaxial apparatus and the experimental procedure described in this paper.

Experimental

Crystal growth process.—The heavily tin-doped GaAs layers are grown in a horizontal crucible of high purity graphite, with a fixed chamber for the GaAs-Sn melt and a movable graphite slider for the substrate (13). A radiation heating furnace is used. For the desired experiments, the low heat capacity of the furnace, the small crucible (length 6 cm, diam 2.2 cm), and the small melt (2.5g) in addition, are preferable to allow fast heating and cooling rates. For the rest, this setup corresponds to conventional equipment.

During heating at a constant temperature the GaAs pieces dissolve in the liquid tin. This forms a saturated solution with the liquidus composition of the binary Sn-GaAs cut of the ternary system for the respective saturation temperature. The boat is cooled down to room temperature. The substrate is then positioned in the boat. After a few minutes at saturation temperature, the system is cooled at a constant rate R between 0.04° and 100°C/min. The cooling rate is established by actual measurement of the boat temperature. 2°-10°C below the saturation temperature, the substrate is brought into contact with the melt. As there occurs no spontaneous crystallization during this initial cooling, the result is a supercooled melt of 2°-10°C, or according to the solution diagram of GaAs in Sn, a supersaturation of approximately 2-10%. The cooling continues during the growth period. The growth is terminated by removing the graphite with the substrate from the melt. To avoid strong annealing effects on the average electron concentration during the epitaxial process, the growth times of the examined layers do not exceed 20 min (14).

Two kinds of experiments have been carried out: variation of the cooling rate at an initial process temperature of 650°C, and variation of the initial process

[1] Present address: Forschunginstitut AEG Telefunken, D7900 Ulm, Germany.

Key words: liquid phase epitaxy, impurity concentration, growth rate, gallium arsenide.

temperature from 570° to 710°C. For the later experiments, the cooling rates have to be varied between 0.7° and 1.7°C/min to make sure that the temperature dependence of the growth rate is compensated. The average growth rates of the layers are then approximately 0.6 μm/min for each process temperature.

Growth rate and doping measurements.—The (100) orientated crystals are cleaved in (110) directions, and the cross-sections are etched under illumination with a $HF-H_2O_2-H_2O$ solution. The thickness L of the epitaxial layer grown during the time t is measured optically. An average growth rate of the epitaxial layer is defined as $\overline{V} = L/t$. As it is preferable to grow the layers at an initial supersaturation, actual and average growth rates (V and $\overline{V}$) of a layer decrease with time of growth. $\overline{V}$ is varied over an extended range for the experiments reported here. In a small range, this is attained by varying the growth time at constant cooling rate, in an extended range, however, by varying the cooling rate. [$\overline{V}$ increases approximately linearly with cooling rate R and is a function of temperature (15).] Although it would be better to describe the doping studies in terms of the actual growth rate V, the average growth rate $\overline{V}$, when combined with average doping parameters, is also informative.

The doping data for the epitaxial layers are measured by the Van Der Pauw method. The thicker edges of the layers are removed to avoid errors in the measurements. Ohmic contacts are made by alloying Sn in forming gas at about 400°C. Even the layers grown at 100°C/min are smooth enough to guarantee an accurate measurement of the doping properties.

As the GaAs layers are grown out of a Sn-rich GaAs solution, the expected electron concentration will be in the range of 10^{18} cm^{-3}. Where the materials are heavily doped, the donor and acceptor concentrations can be estimated by the equations of Kressel and Nelson (16), using the measured $\overline{n}$ and $\overline{\mu}$ data at room temperature, and the mobility μ_u of uncompensated material. For μ_u, the highest reported values, extrapolated to carrier concentrations of 10^{19} cm^{-3}, are used (16). To consider the geometrical effects of a nonideal Van Der Pauw structure, a systematic error of +5% for μ and −5% for n was taken into account (17).

Results and Discussion

Growth rate dependence of the Sn concentration.—The average values of carrier concentration $\overline{n}$ (300°K) and mobility $\overline{\mu}$ (300°K) *vs.* the cooling rate R of layers grown at an initial process temperature of 650°C are shown in Fig. 1. The cooling rate varies from 0.04° to 100°C/min. $\overline{n}$ and $\overline{\mu}$ are constant for cooling rates greater than 10°C/min, and decrease or increase, for lower cooling rates. Mobility values of 1200-1400 cm²/Vsec are typical of heavily tin-doped GaAs (4, 18) grown at cooling rates less than 1°C/min. For the higher cooling rate range, no comparable data are available in print. The increase of $\overline{\mu}$ with decreasing $\overline{n}$ is similar to that given by Sze (19), but weaker than that found by Panish (4) with various liquidus compositions of Sn. This can be attributed to a decreasing compensation ratio with $\overline{n}$ or the growth rate, as shown in Fig. 2.

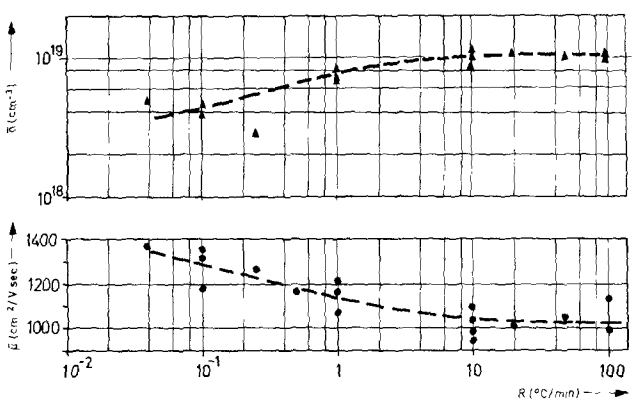


Fig. 1. Average carrier concentration $\overline{n}$ and average carrier mobility at room temperature of several heavily Sn-doped GaAs layers, grown at different cooling rates R.

With the Van Der Pauw data of Fig. 1, the average donor and acceptor concentrations are calculated. As the cooling rate is a process specific parameter only, it is better to use the growth-specific parameter; the average growth rate $\overline{V}$. $\overline{N}_D$, $\overline{N}_A$, and $\overline{N}_A/\overline{N}_D$ are drawn *vs.* the average growth rate $\overline{V}$ in Fig. 2, now showing the uncertainty of the measurements. In spite of a scatter in the experimental data, a significantly steeper increase of $\overline{N}_D$ than $\overline{N}_A$ is observed at slow growth rates. This results in a decreasing compensation ratio with increasing growth rate.

A growth rate dependence can be caused by the redistribution of dissolved Sn in the melt in front of the growing interface because of its small segregation coefficient ($\approx 10^{-4}$). To avoid this effect, $V \cdot L/D_{Sn(m)} < 10^{-1}$ has to be fulfilled (2). This is best guaranteed by the self-diffusion of tin $D_{Sn(m)} \geq 10^{-4}$ cm²/sec (20), the measured epitaxial layers $L < 20$ μm, and growth rates $\overline{V} < 40$ μm/min.

Another possible way of describing a growth rate dependence follows from the surface equilibrium theory. It can be explained qualitatively with the scheme in Fig. 3: in case of surface equilibrium the donor concentration is a function of the electron concentration n_S in the thin surface layer. According to the Schottky theory, n_S depends on the barrier height Φ_{Bn} and the temperature T. It amounts to a varying donor concentration with the parameter Φ_{Bn}/kT at fast growth rates or high ratios of growth rate and diffusion constant (see Fig. 3). For slow rates,

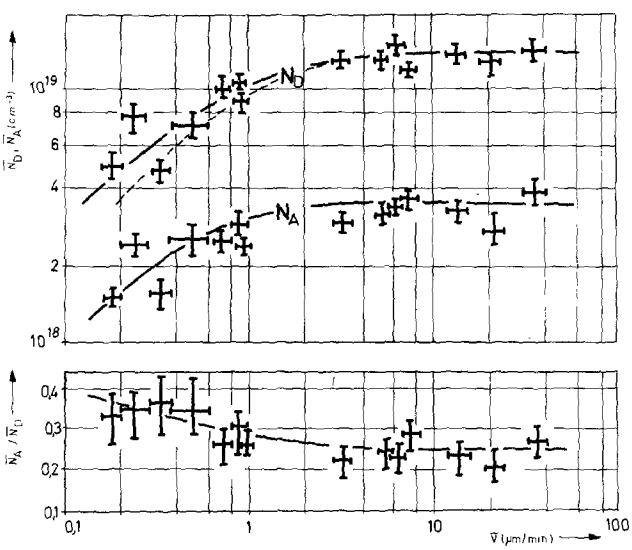


Fig. 2. + Experimental average data $\overline{N}_D$ or $\overline{N}_A$ or $\overline{N}_A/\overline{N}_D$ vs. average growth rate $\overline{V}$. —— Theoretical curves N_D or N_A or N_A/N_D vs. constant growth rate V. Parameter $\Phi_{Bn}(650°C) = 0.51$ eV for donors and $\Phi_{Bp}(650°C) = 0.61$ eV for acceptors at low concentrations. A concentration-dependent barrier lowering is taken into account (*cf.* Table I). Fitting parameter; $\overline{N}_{D/A}$ ($\overline{V} > 6$ μm/min) and $D_{Sn\,D/A} = 3 \cdot 10^{-14}$ cm²/sec. – – – – Theoretical curve $N_D(V)$, to demonstrate the sensitivity of the theory for a larger barrier height $\Phi_{Bn}(650°C) = 0.61$ eV or a 0.1 eV smaller barrier lowering.

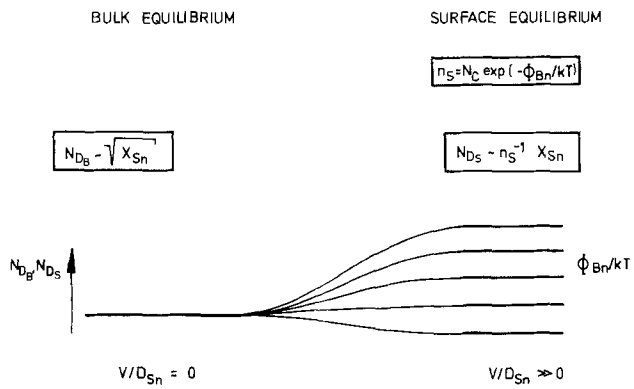


Fig. 3. Scheme for qualitative explanation of the growth rate dependence of the concentration using bulk equilibrium ($V/D_{Sn} \approx 0$) and surface equilibrium ($V/D_{Sn} >> 0$).

on the other hand, in the case of bulk equilibrium such dependence does not exist. Then such transitions as drawn for intermediate V/D_{Sn} values will certainly be possible. Zschauer and Vogel (2) have formulated the corresponding theoretical relationship between impurity concentration N_D, N_A, or in the case of an amphoteric impurity ($N_D + N_A$) and a temporal constant growth rate, on the premises of an intrinsic semiconductor at the epitaxial process temperature. These equations have been derived by Zschauer for donors on Ga and acceptors on As vacancies. In the case of Sn it is not considered that the Sn acceptor is likely to have the more complex structure $Sn_{As}2V_{Ga}$.

For Sn, Zschauer's equation of ($N_D + N_A$) ought to be applicable. Nevertheless, it would be better to regard the growth rate dependence of N_D and N_A separately; by this it is avoided that a characteristic slope of N_A (*cf.* Fig. 2) disappears in the experimental uncertainties of the slope of ($N_D + N_A$). In this case, no mutual influence of donors and acceptors during the incorporation process is assumed. The theory, originally valid for low doping, is modified for heavy doping studied here. The concentration dependence of some properties has to be taken into account (*cf.* Appendix I).

The computation with the equations of Zschauer and Vogel modified with respect to heavy doping, details of which are described in Appendix I, results in the growth rate dependence of donors and acceptors plotted in Fig. 2. (solid and dashed curves). The different slopes of the experimental $\overline{N_D}$ and $\overline{N_A}$ can be fitted by the theoretical curves for N_D and N_A. Consequently, the theory agrees with the increasing compensation ratio at decreasing growth rate (Fig. 2). Satisfactory explanation of the experimental $\overline{N_D}$ and $\overline{N_A}$ by independent theoretical equations points to a separate incorporation of donors and acceptors during the epitaxial growth process.

The fitting parameters for the calculated growth rate dependence are the solid diffusion constants D_{SnD} and D_{SnA} for the Sn donor and the Sn acceptor (see Eq. [1] in Appendix I). The same value for D_{SnD} and D_{SnA} has been found by the fitting. With $3 \cdot 10^{-14}$ cm²/sec, the diffusion constants are relatively large compared with data at 650°C in older literature (21). But new measurements by Peart (22) yield a Sn solid diffusion constant between 10^{-13} and 10^{-14} cm²/sec in the temperature range of 650°-750°C. This confirms the validity of the fitting.

The established growth rate dependence of the concentration does not indicate the transition to constant concentration at slow growth rates (compare Fig. 2 and 3). The bulk equilibrium in this case is not reached before approximately 0.02 μm/min, as it is calculated theoretically. Strictly speaking, the surface equilibrium ($N_{D/A}$ = constant at fast growth rates) is valid only for growth rates above 6 μm/min (Fig. 2), but because of the extended transition region up to bulk equilibrium, it is approximately applicable for some slower growth rates, too.

The transition region is changed at lower doped layers. The equations of Zschauer and Vogel can then be used in their unmodified form. As Zschauer stated, the surface equilibrium theory ought to be applicable for growth rates which fulfil $V/D_{SnD/A} \cdot \lambda_i > 10$ (λ_i intrinsic reciprocal Debye length). Using the fitting parameter D_{SnD} of this work, it is estimated that in the case of low doping the Sn incorporation ought to follow from the surface equilibrium theory already for growth rates above 0.7 μm/min. A possible concentration dependence of the diffusion constant has not been considered. The decrease of the concentration in the transition between surface equilibrium and bulk equilibrium is also much weaker in the case of intrinsic-doped layers. Probably this is the reason why the growth rate influence established for heavily Sn-doped layers has not yet been observed in the case of low-doped layers.

It should be emphasized that the theoretical relationship between temporal constant growth rate V (presumption of Zschauer's equations) and the concentrations $N_{D/A}$ has been compared with the corresponding experimental relationship $\overline{N}_{D/A}(\overline{V})$ for average properties. Strictly speaking this is correct for completely constant doping and mobility within the layer. But this is not valid here because of the established growth rate dependence of concentration and mobility (Fig. 1, 2) and a temporal varying growth rate during the LPE process with a supersaturated melt. In the ideal case of constant profiles, the experiments would have yielded a similar structure, but shifted to faster growth rates and higher concentrations. In addition, the concentration profiles are slightly influenced by the respective process temperature during extended cooling periods, especially at fast cooling rates. To eliminate this effect a constant growth temperature has to be assumed. It is estimated that for this ideal case the expected concentration at fast cooling rates would only be 15% above the experimental value established. For these reasons, the comparison between theory and experiment may be regarded as a first approximation only.

Temperature dependence of the Sn concentration.— The relation between N_D, N_A, and the atomic fraction of tin in the melt X_{Sn} can be described using the surface equilibrium theory at different temperatures above 700°C (4). In this section, however, the temperature dependence $N_{D/A}(T)$ at large X_{Sn} data is deduced. The respective working points for each temperature considered are then positioned on the quasi-binary Sn-GaAs cut of the ternary phase diagram. Experimental data $\overline{N_D}$, $\overline{N_A}$ are compared with the ones expected at surface and bulk equilibrium to examine the validity of the surface equilibrium theory for the heavily Sn-doped layers reported here. All the temperature-dependent values have to be considered, partly computed and partly from literature, while in the case of the $N_{D/A}(X_{Sn})$ dependence, most of the temperature-dependent properties can be comprehended in a normalization constant at each temperature considered (4).

For both possible incorporation theories, surface and bulk equilibrium (S.EQ. and B.EQ.), the theoretically expected concentrations for the Sn donor on Ga vacancies and the Sn acceptor [which is possibly the complex Sn_{As} $2V_{Ga}$ (4)] are plotted in Fig. 4. The essential steps for its calculation are presented in Appendix II. N_D and N_A are normalized on the established concentrations $\overline{N_D}$ or $\overline{N_A}$ at the lowest experimental temperature T_i = 843°K. In the case of surface equilibrium (S.EQ.), an increase in N_D of about 70% is expected. In the case of bulk equilibrium (B.EQ.) a more distinct temperature dependence between 843° and 983°K with an increase of about 400% is estimated.

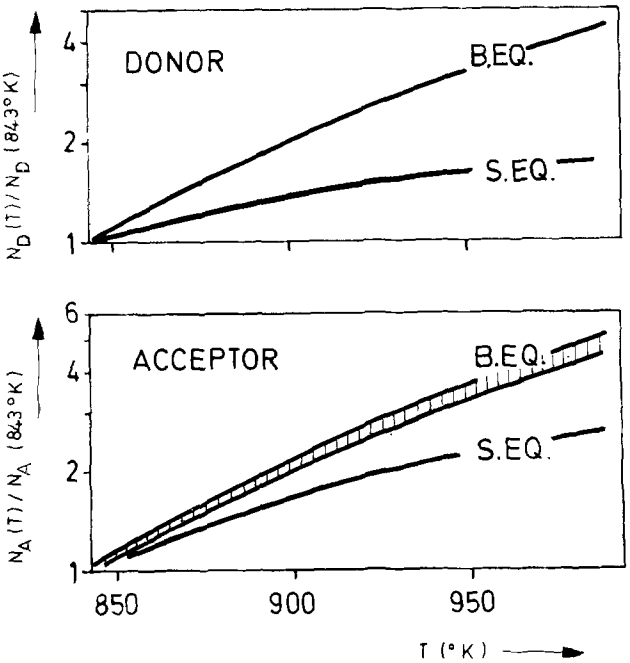


Fig. 4. Semiquantitative computation of the temperature dependence for the Sn donor and the Sn acceptor, normalized at the lowest experimental concentration $\bar{N}_{D/A}$(843°K). B.EQ.: curve for bulk equilibrium; S.EQ.: curve for surface equilibrium.

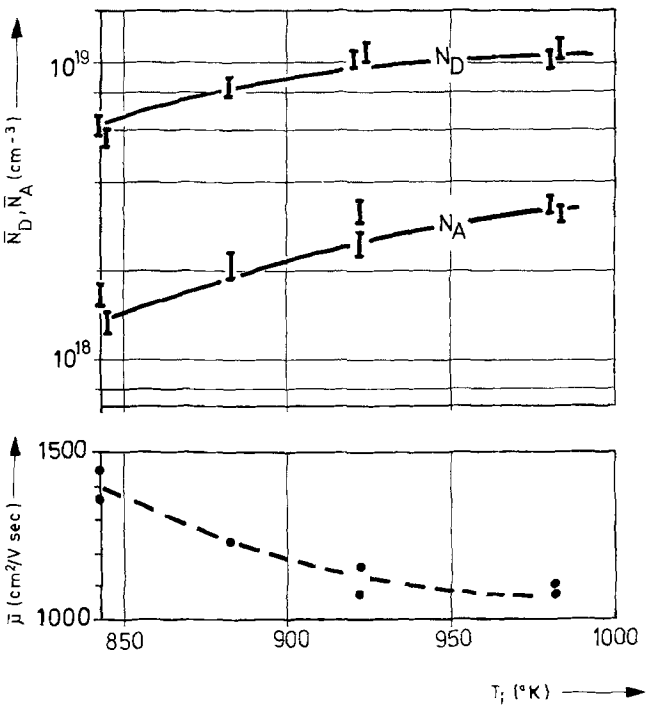


Fig. 5. I Experimental average concentrations $\bar{N}_D$ and $\bar{N}_A$, and ● experimental average mobility vs. process temperature T_i. —— Theoretical curves for N_D and N_A in the case of surface equilibrium.

For the acceptor concentrations calculated with bulk equilibrium, the shaded area has to be plotted in Fig. 4 because of an uncertainty in the transition of the hole activity coefficient between unity and the calculated values at high concentrations (*cf.* Table II in Appendix II). Comparing the curves S.EQ. and B.EQ., a steeper slope was found for the bulk equilibrium both for the donor and for the acceptor.

Experiments at several process temperatures T_i for high Sn contents in melt and solid, for which the calculations are made, are carried out. The layers have been grown at approximately the same growth rate to avoid the influence of different growth rates on the concentrations (see Experimental section). The average donor and acceptor concentration $\bar{N}_D$, $\bar{N}_A$, and the average mobility $\bar{\mu}$ in the range 843°-983°K are shown in Fig. 5. The experimental concentrations are compared with the respectively calculated concentrations in the case of surface equilibrium, as shown in Fig. 4 (solid curves in Fig. 5). Considerable agreement with the temperature behavior expected can then be established. The curves B.EQ. of Fig. 4 instead would be too steep to fit the experiments. According to these experiments at several temperatures, it can be concluded that the bulk equilibrium cannot be responsible for the incorporation of Sn. This conclusion is consistent with the results of $N_{D/A}$ (X_{Sn}) experiments by Panish (4).

As the experimental compensation ratio $\bar{N}_A/\bar{N}_D$ increases, the average Hall mobility decreases with temperature. The measured value of $\bar{N}_A/\bar{N}_D = 0.32$ at 983°K agrees with the one Panish applied to his $N_A(X_{Sn})$ calculations at 973° and 1073°K. According to the increase of the compensation ratio with temperature dealt with in this paper, however, at 1073°K a larger compensation ratio ought to be better. The above values for the compensation ratio may be used for cooling rates of approximately 1°C/min. Otherwise, the cooling rate or growth rate dependence, shown in Fig. 2, has to be considered. The above statements of the compensation ratio reported at high atomic fractions of Sn in the melt should be approximately valid for lower doping, too, if one considers the theoretical results of thermodynamic calculations that the X_{Sn} dependence of N_A is similar to that of N_D and therefore the compensation ratio is independent of X_{Sn}. This is only approximately correct. Regarding the donor and acceptor concentrations found at large X_{Sn} values, different barrier lowerings for donors and acceptors are to be expected which result in different slopes of $N_D(X_{Sn})$ and $N_A(X_{Sn})$ (10). Therefore, the experimental compensation ratio can change slightly in the upper X_{Sn} range.

Summary

The behavior of the concentrations $\bar{N}_D$ and $\bar{N}_A$ for heavily Sn-doped layers indicates the transition region between surface equilibrium and bulk equilibrium, *i.e.*, between fast and slow growth rates of the LPE layers. Donor and acceptor seem not to interact. The increase of the experimental concentrations with the epitaxial process temperature could be explained by surface equilibrium only, in spite of relatively slow average growth rates $\bar{V} \approx 0.6$ μm/min in this kind of experiment. Surface equilibrium, consequently, ought to be applicable for most of the reported epitaxial layers. The barrier height of the system melt-solid is an important property. Attention is drawn to an additional influence of barrier lowering in the high concentration range.

Acknowledgments

I am indebted to Dr. K. Heime for many valuable discussions. I am grateful to Dr. K. H. Zschauer (Siemens, Munic) for suggesting that his calculations might be applicable and for stimulating discussions. I wish to thank A. Dierick for computer programming. Financial support provided by the Deutsche Forschungsgemeinschaft, Sonderforschungsbereich Festkörperelektronik is gratefully acknowledged.

Manuscript submitted May 28, 1976; revised manuscript received March 25, 1977. This was Paper 263 RNP presented at the New York, New York, Meeting of the Society, Oct. 13-17, 1974.

Any discussion of this paper will appear in a Discussion Section to be published in the June 1978 JOURNAL. All discussions for the June 1978 Discussion Section should be submitted by Feb. 1, 1978.

Publication costs of this article were assisted by Sonderforschungsbereich 56.

APPENDIX I

Details of the semiquantitative computation process for the growth rate dependence with heavy Sn doping and the important parameters tabulated are presented. No interdependence of donors and acceptors during the incorporation process is presumed. This allows the separate consideration of the carriers in the solid.

The growth rate dependence of donors and acceptors $N_{D/A}(V)$ normalized at very slow growth rates $N_{D/A}(V \approx 0)$ were formulated by Zschauer and Vogel for an intrinsic semiconductor

$$\frac{N_{D/A}(V)}{N_{D/A}(V \approx 0)} = \frac{D_{Sn\,D/A}}{V}\left[\int_0^\infty \exp(\mp \psi_{D/A}[l]) \exp\left(-\frac{V}{D_{Sn\,D/A}}\right) dl\right]^{-1} \quad [A\text{-}1]$$

The minus sign stands for donors and the plus sign for acceptors ($l = 0$ the moving interface between melt and semiconductor; dl, differential layer increase; $D_{Sn\,D/A}$, solid diffusion of the donor and acceptor Sn). $\psi_{D/A}[l]$ represents the normalized potentials of the Schottky barrier, only temperature dependent. It contains the intrinsic reciprocal Debye length and the built-in potential.

In heavy doping, however, the concentration dependence of some properties has to be taken into account; the "quadratic" approximation for the Schottky barrier potential

$$\psi_{D/A}(l) = \pm 0.5([2\psi_{D/A}(l=0)]^{1/2} - \lambda_{D/A} l)^2 \quad [A\text{-}2]$$

and the built-in potentials

$$kT\,\psi_{oD} = kT\,\psi_D(l=0) = (\Phi_{Bn} - \Delta\Phi_n) - (E_G - E_{FD})$$
$$kT\,\psi_{oA} = kT\,\psi_A(l=0) = E_{FA} - (\Phi_{Bp} - \Delta\Phi_p) \quad [A\text{-}3]$$

have to be used now (E_G, bandgap), with the concentration-dependent reciprocal Debye lengths $\lambda_{D/A}$ and the Fermi levels E_{FD} (N_D) and E_{FA} (N_A.) The important parameters are the barrier heights Φ_{Bn}, Φ_{Bp} of donors and acceptors. The currently available room temperature barrier height $\Phi_{Bn} = 0.83$ eV for Sn on GaAs (19, 23) seems to be a satisfactory approach for the experimental situation of a Sn-GaAs melt containing 92 atomic percent (a/o) of Sn. The respective barrier heights at the process temperature $T = 923$°K are evaluated with (18, 24)

$$E_G(T) = \Phi_{Bn}(T) + \Phi_{Bp}(T) \quad \text{and}$$
$$E_G(T) - \Phi_{Bn}(T) = \text{constant} \quad [A\text{-}4]$$

i.e., the position of the Fermi level at the surface remains at a fixed energy above the valence band as the temperature varies. The above assumptions that the barrier heights are only metal and temperature dependent is correct for low solid concentrations. In the concentration range of this work, a barrier lowering probably due to a dipole layer at the interface between metal and semiconductor ought to be considered as well for donors ($\Delta\Phi_n$) as for acceptors ($\Delta\Phi_p$). Calculations of Crowell *et al.* (25) for n-Si Schottky diodes lead to a constant barrier height up to a doping level of approximately 10^{16} cm^{-3}, and a decrease of 0.23 eV at $N_D = 10^{18}$ cm^{-3} or 0.33 eV at $N_D = 10^{19}$ cm^{-3}. But these authors also feel that the calculated falling off at large N_D is too rapid. For GaAs Schottky diodes, however, such a distinct concentration dependence is not expected because of a larger density of surface states compared with Si. There are some hints for quantitative values of the Sn barrier heights (10), as already mentioned in the introductory section of this work.

Due to the $N_{D/A}$ dependence of $\lambda_{D/A}$, $E_{F\,D/A}$ and $\Delta\Phi_{n/p}$ at heavy doping, a semiquantitative calculation is performed. According to Eq. [1], [2], and [3], the growth rate dependence is computed for a lot of values of N_D or N_A, respectively (for several concentrations the values used in the calculation are presented in Table I). The highest concentrations, the computations of which are made, are the characteristic experimental data at fast growth rates $N_{D/A}(V > 6\ \mu$m/min) (see Fig. 2). Each curve of the calculated family is presumed to be approximately valid in a small concentration range around the respective values of $N_{D/A}$. A graphical approximation follows. This procedure results in the solid and dashed curves of Fig. 2, evaluated now having taken into account the concentration dependence of all parameters.

APPENDIX II

The important equations for calculating the temperature dependence of the donor and the acceptor concentration with heavy Sn doping (N_D and N_A) and the temperature dependent properties tabulated are shown. The donor on Ga vacancies can be calculated in the case of surface equilibrium with

$$N_{DS} = A_{DS}\,X_{Sn}\,n_S^{-1}\,\gamma_n^{-1} \quad [A\text{-}5]$$

and in the case of bulk equilibrium with

$$N_{DB} = \left(\gamma_n^{-1}\left(1 + \frac{n_i^2}{A_{DB}\,X_{Sn}}\right) A_{DB}\,X_{Sn}\right)^{1/2} \quad [A\text{-}6]$$

Each property depends on the temperature (see Table II). A_{DS} and A_{DB} are the product of the mass-action constant K, the As activity $\gamma_{As}X_{As}$, the activity constant γ_{Sn}, as well as the normalization constants K_{DS} and K_{DB} for surface and bulk equilibrium. K_{DS} and K_{DB} contain a factor, usually temperature dependent, between the atomic fraction of the liquid and the concentration of the solid, that is essentially the segregation coefficient. But in the case of high Sn concentrations in melt and semiconductor the segregation coefficient was found to be approximately independent of the process temperature in the low temperature range (15). This corresponds to theoretical calculations of the segregation coefficient by Stringfellow (26). The normalization constant is evaluated with the lowest experimental concentration $\overline{N_D}$ (843°K). The temperature-dependent properties γ_{As}, γ_{Sn}, X_{As}, and X_{Sn} are determined by the working points on the quasibinary Sn-GaAs cut of the ternary phase diagram (27), where heavily Sn-doped solids are concerned. The other temperature-dependent data, the Schottky barrier concentration

Table I. Parameters for calculating $N_D(V)$ and $N_A(V)$ at the process temperature 923°K

Temperature T (°K)	Carrier type	Bulk concentration $\overline{N_D}$ / $\overline{N_A}$ (10^{18} cm^{-3})	Reciprocal Debye length λ_D / λ_A (10^5 cm^{-1})	Barrier height $\Phi_{Bn}(300)$ / $\Phi_{Bp}(300)$ (eV)	Barrier height $\Phi_{Bn}(T)$ / $\Phi_{Bp}(T)$ (eV)	Barrier lowering $\Delta\Phi_n(\overline{N_D})$ / $\Delta\Phi_p(\overline{N_A})$ (eV)	Fermi level $E_F(\overline{N_D})$ / $E_F(\overline{N_A})$ (eV)	Built in potential $\psi_{oD}(T,\overline{N_D})$ / $\psi_{oA}(T,\overline{N_A})$	Solid diffusion constant $D_{Sn\,D}$ / $D_{Sn\,A}$ (10^{-14} cm^2/sec)
923	D	14	5.05	0.83	0.51	0.220	1.29	5.8	3
		10	4.27			0.190	1.26	5.8	
		6	3.31			0.155	1.21	5.6	
		4	2.70			0.130	1.14	5.4	
		2	1.91			0.085	1.11	5.2	
		1	1.35			0.050	1.04	4.8	
	A	3.5	2.53	0.61	0.61	0.115	0.23	−3.3	
		2.0	1.91			0.085	0.27	−3.2	
		1.0	1.35			0.050	0.33	−2.9	
		0.6	1.05			0.035	0.38	−2.5	
		0.4	0.85			0.025	0.41	−2.2	
		0.1	0.43			0.005	0.53	−0.9	

Table II. Parameters for calculating $N_D(T)$ and $N_A(T)$ in the case of surface (S.EQ.) and bulk (B.EQ.) equilibrium

Temperature T (°K)	Mass-action constant K (10^{-4})	Activity product $\gamma_{As}\gamma_{Sn}X_{As}X_{Sn}$ (atomic fraction^2)	Equilibrium type	Carrier type	Normalization concentration $\overline{N}_D$(843°K) $\overline{N}_A$(843°K) (10^{18} cm^{-3})	Barrier height Φ_{Bn}(300) Φ_{Bp}(300) (eV)	Barrier height $\Phi_{Bn}(T)$ $\Phi_{Bp}(T)$ (eV)	Barrier lowering $\Delta\Phi_n(N_D)$ $\Delta\Phi_p(N_A)$ (eV)	Schottky barrier concentration $n_S(T,N_D)$ $p_S(T,N_A)$ (10^{16} cm^{-3})	Activity constant $\gamma_n(n_s$ resp. $N_D)$ $\gamma_p(p_s$ resp. $N_A)$
843	1.67	0.038	S.EQ.	D	6.0	0.83	0.55	0.155	0.89	1.00
				A	1.5	0.61	0.61	0.055	2.02	1.00
			B.EQ.	D	6.0					0.2
				A	1.5					0.7-1.0
883	3.03	0.05	S.EQ.	D	6.0	0.83	0.53	0.165	1.76	0.98
				A	1.5	0.61	0.61	0.075	3.96	1.00
			B.EQ.	D	6.0					0.19
				A	1.5					0.6-1.0
923	5.18	0.07	S.EQ.	D	6.0	0.83	0.51	0.175	3.51	0.97
				A	1.5	0.61	0.61	0.095	7.42	1.00
			B.EQ.	D	6.0					0.18
				A	1.5					0.52-0.95
983	9.98	0.095	S.EQ.	D	6.0	0.83	0.48	0.192	8.75	0.89
				A	1.5	0.61	0.61	0.110	14.3	1.00
			B.EQ.	D	6.0					0.17
				A	1.5					0.47-0.8

$$n_S = N_C \exp\left[(\Phi_{Bn} - \Delta\Phi_n)/kT\right] \quad [7]$$

including the conduction band concentration N_C and the barrier height Φ_{Bn}, the intrinsic concentration n_i, and the activity coefficient of the electrons γ_n (which is a function of n_S/N_C with surface, or N_{DB}/N_V with bulk, equilibrium), have been computed using published data (19, 23, 28, 29). (As to the concentration dependent barrier lowering $\Delta\Phi_n$, see Appendix 1 and Table II.)

Equations similar to [5], [6], and [7] are used for the Sn acceptor, which is possibly the complex Sn_{As} $2V_{Ga}$. As Panish stated (4), both equations for the donor can be used for the respective acceptor concentrations N_{AS} and N_{AB}; only N_C is substituted by N_V, Φ_{Bn} by Φ_{Bp}, γ_n by γ_p, besides the normalization constants $K_{DS/B}$ by $K_{AS/B}$. Taking into account Eq. [4] of Appendix I, the barrier height for the acceptor in GaAs is found to be independent of temperature. A small barrier lowering $\Delta\Phi_p$, the value of which depends on the respective acceptor concentration N_A in the bulk of the solid, is used. There are some suggestions of a barrier lowering for acceptors with the same value as the one for donors at corresponding concentrations (10).

The properties $\Delta\Phi_n$, $\Delta\Phi_p$, and γ_n, γ_p on the right side of Eq. [5], [6], and [7], and the respective ones for the acceptor depend on the bulk concentrations $N_{DS/B}$ or $N_{AS/B}$. This allows a semiquantitative calculation only. Starting from the properties obtained with the experimentally established bulk concentrations at the normalization temperature 843°K, an iterative calculation for the temperatures considered yields to the parameters listed in Table II and the theoretical concentrations plotted in Fig. 4.

LIST OF SYMBOLS

A_{DS}, A_{DB} constants in the case of surface, bulk equilibrium incorporation
D, A symbols for donors, acceptors
$D_{Sn}, D_{Sn\ D/A}, D_{Sn\ D}, D_{Sn\ A}$ diffusion constants of Sn in the solid (cm^2/sec)
$D_{Sn(m)}$ diffusion constant of Sn in the melt (cm^2/sec)
$E_{F\ D/A}, E_{FD}, E_{FA}, E_F(N_D), E_F(N_A)$ Fermi level of donors, acceptors (eV)
E_G bandgap energy (eV)
k Boltzmann constant
K mass-action constant
$K_{D\ S/B}, K_{DS}, K_{DB}, K_{A\ S/B}$ normalization constants of surface, bulk equilibrium for donors, acceptors
l direction into substrate or LPE layer (μm)
L total epitaxial layer thickness (μm)
$\overline{n}$ experimental average carrier concentration of a layer (cm^{-3})
n_i intrinsic concentration (cm^{-3})
n_S electron concentration in the Schottky surface (cm^{-3})
$N_{D/A}, N_D, N_A$ theoretical donor, acceptor concentrations (cm^{-3})
$N_{D\ S/B}, N_{DS}, N_{DB}, N_{A\ S/B}, N_{AS}, N_{AB}$ theoretical donor, acceptor concentrations in the case of surface, bulk equilibrium (cm^{-3})
$\overline{N}_{D/A}, \overline{N}_D, \overline{N}_A$ experimental average donor, acceptor concentrations (cm^{-3})
N_C, N_V effective concentration of states in conduction, valence band (cm^{-3})
p_S hole concentration in the Schottky surface (cm^{-3})
R cooling rate of the LPE process (°C/min)
t growth time of a LPE layer (min)
T, T_i temperature, initial process temperature (°K)
V momentary growth rate (μm/min)
$\overline{V}$ average growth rate of a LPE layer (μm/min)
X_{As}, X_{Sn} atomic fraction of arsen, tin in the melt (at. fr.)
γ_{As}, γ_{Sn} activity coefficients of arsen, tin
γ_n, γ_p activity coefficients of electrons, holes
$\Delta\Phi_n, \Delta\Phi_p$ barrier lowering of Φ_{Bn}, Φ_{Bp} (eV)
$\lambda_{D/A}, \lambda_D, \lambda_A$ reciprocal Debye length of donors, acceptors (cm^{-1})
λ_i intrinsic reciprocal Debye length (cm^{-1})
$\overline{\mu}$ average mobility of a LPE layer (cm^2/V sec)
μ_u mobility of uncompensated GaAs (cm^2/V sec)
$\Phi_{Bn/p}, \Phi_{Bn}, \Phi_{Bp}$ barrier height of donors, acceptors (eV)
$\psi_{D/A}, \psi_D, \psi_A$ normalized Schottky barrier potential of donors, acceptors (eV)
ψ_{oD}, ψ_{oA} normalized built-in potential of donors, acceptors (eV)

REFERENCES

1. U. Merten and A. P. Hatcher, *J. Phys. Chem. Solids*, **23**, 533 (1962).
2. K. H. Zschauer and A. Vogel, Gallium Arsenide and Related Compounds, Proceedings of the Third International Symposium, Institute of Physics and the Physics Society, p. 100, London (1971).
3. H. C. Casey Jr., M. B. Panish, and K. B. Wolfstirn, *J. Phys. Chem. Solids*, **32**, 571 (1971).
4. M. B. Panish, *J. Appl. Phys.*, **44**, 2659 (1973).
5. M. B. Panish and M. C. Casey Jr., *J. Phys. Chem. Solids*, **29**, 1719 (1968).
6. A. S. Jordan, *This Journal*, **118**, 781 (1971).
7. Y. Furikawa and C. D. Thurmond, *J. Phys. Chem. Solids*, **26**, 1535 (1965).
8. M. C. Casey and M. B. Panish, *J. Cryst. Growth*, **13/14**, 818 (1972).
9. U. König, Paper presented at the DGKK Meeting, Freiburg, Germany (1972).
10. U. König and F. Schwocula, To be published.
11. R. H. Saul and W. H. Hackett Jr., *This Journal*, **117**, 921 (1970).
12. F. E. Rosztoczy, This was Paper 526 presented at The Electrochemical Society Meeting, Montreal, Quebec, Canada, Oct. 6-11, 1968.
13. H. Beneking, P. Mischel, and G. Schul, *Electron. Lett.*, **8**, 16, (1972).

14. E. Falkenberg, U. König and K. Heime, Paper presented at the DPG Meeting, Münster, Germany (1975).
15. U. König, Ph.D. Thesis, Technische Hochschule Aachen, Germany (1973).
16. H. Kressel and H. Nelson, *J. Appl. Phys.*, **40**, 3720 (1969).
17. R. Ehret, FTZ, 18, TBr 6, Darmstadt, Germany (1974).
18. E. Grobe and H. Salow, FTZ, A65, TBr. 2, Darmstadt, Germany (1969).
19. S. M. Sze, "Physics of Semiconductor Devices," Wiley-Interscience, New York, (1969).
20. "Gmelins Handbuch der anorganischen Chemie," Zinn, Teil B, 152 Gmelin Institut der MPG, Springer Verlag, Berlin (1971).
21. D. L. Kendall, in "Semiconductor and Semimetals IV," p. 163, Willardson, Beer, Academic Press, New York (1968).
22. R. F. Peart, Paper presented at the Meeting of the Institute of Physics, London (1974).
23. G. B. Seiranyan and Yu. A. Tkhorik, *Phys. Status Solidi A*, **13**, K115 (1972).
24. Y. Nannichi and G. L. Pearson, *Solid-State Electron.*, **12**, 341 (1969).
25. C. R. Crowell and G. J. Roberts, *J. Appl. Phys.*, **40**, 3726 (1969).
26. G. B. Stringfellow, *J. Phys. Chem. Solids*, **35**, 775 (1974).
27. M. B. Panish, *J. Less-Common Met.*, **10**, 416 (1966).
28. A. Dierick, Wahlarbeit, Technische Hochschule Aachen, Institut für Halbleitertechnik (1974).
29. C. J. Hwang and J. R. Brews, *J. Phys. Chem. Solids*, **32**, 837 (1971).

Silicon Nitride Coatings on Molybdenum by RF Reactive Ion Plating

Masao Fukutomi, Masahiro Kitajima, Masatoshi Okada, and Ryoji Watanabe

National Research Institute for Metals, 2-3-12, Nakameguro, Meguroku, Tokyo, Japan

ABSTRACT

Rf reactive ion plating technique has been applied to the preparation of protective silicon nitride coating on molybdenum. All the deposits prepared at deposition temperature of less than 1000°C were amorphous. Silicon in deposits was found to be present as nitride by Auger electron spectroscopic, infrared absorption spectroscopic, and x-ray diffraction analyses. Nearly stoichiometric silicon nitride deposits were obtained at a deposition rate of as high as 1 μm/min. Several factors affecting the stoichiometry of the silicon nitride were discussed. Oxidation test of the coated specimens showed that the silicon nitride layer obtained under optimum conditions protected the molybdenum substrate from oxidation in Ar-1% O_2 gas mixtures up to approximately 1200°C. Typical pitting corrosion was observed in the coating film at the higher temperatures.

Silicon nitride films have received much attention especially for applications in the semiconductor industry because of their excellent chemical stability and resistance to diffusion of impurities. Many authors have studied the preparation of silicon nitride films and their structural and electrical properties. Most of the existing studies are, however, mainly concerned with thin films formed by sputtering (1-4) or chemical vapor deposition (5, 6). Little work on the ion-plated silicon nitride film has been reported in the literature except by Chin *et al.* (7), who dealt with the silicon nitride coatings for thermoelectric couples. On the other hand, the applications of molybdenum as a high temperature material are limited by its severe oxidation at temperatures above 800°C. Considerable effort, therefore, has been made to develop various high temperature protective coatings for molybdenum such as metallic, disilicide-based diffusion, and ceramic overlay coatings (8). The present paper describes a preparation technique of silicon nitride by reactive ion-plating, and the structural and compositional characteristics of the film obtained. An attempt to apply this silicon nitride film to the high temperature oxidation resistant coating for molybdenum is also described.

Experimental

Apparatus.—The apparatus shown in Fig. 1 is specially designed for the rf reactive ion plating of silicon nitride. The rf ion-plating technique was basically the same as that described by Murayama (9). The rf coil electrode (7 turns and 10 cm in spiral coil diam) was placed directly above the evaporation source and connected to a 13.56 MHz, 300-VA rf power supply to make a glow discharge region for the ionization and activation of the reactants. The 6 kW electron beam gun has a 180° bent beam whose spot was swept over the entire source surface for the uniform melt and evaporation rate. The vacuum chamber is separated by the conductance baffle to maintain pressures of less than 10^{-3} Torr around the EB gun, while pressures are as high as 2×10^{-2} Torr in the deposition side. The substrate holder was constructed such that a bias from 0 to −3 kV d.c. could be applied to the substrate for the acceleration of ionized particles toward it. The source-to-substrate distance was approximately 14 cm for all experiments. The substrate was heated by radiation from a tantalum resistance heater to a desired temperature between 400° and 1000°C. The temperature was measured with a Chromel-Alumel thermocouple placed in contact with the back side of the substrate. Gas pressure was measured with a Schulz-Phelps and a Bayard-Alpert ionization gauge and controlled to a desired level by a high vacuum leak valve.

Evaporation source, substrate, and reactive gas.—Semiconductor-grade silicon was used as the evaporation source. Substrate for deposition was prepared from sintered molybdenum sheet and electrochemically polished prior to mounting on the substrate holder. The source for nitrogen was ammonia, supplied by Mathieson Gas Products with a purity of 99.99%. The ultrahigh purity argon was also used for the sputter cleaning of substrate.

Coating procedures.—In a typical coating experiment, the vacuum chamber was evacuated to approximately 5×10^{-6} Torr or lower. Prior to each deposi-

* Key words: silicon nitride, ion plating, protective coating, molybdenum.

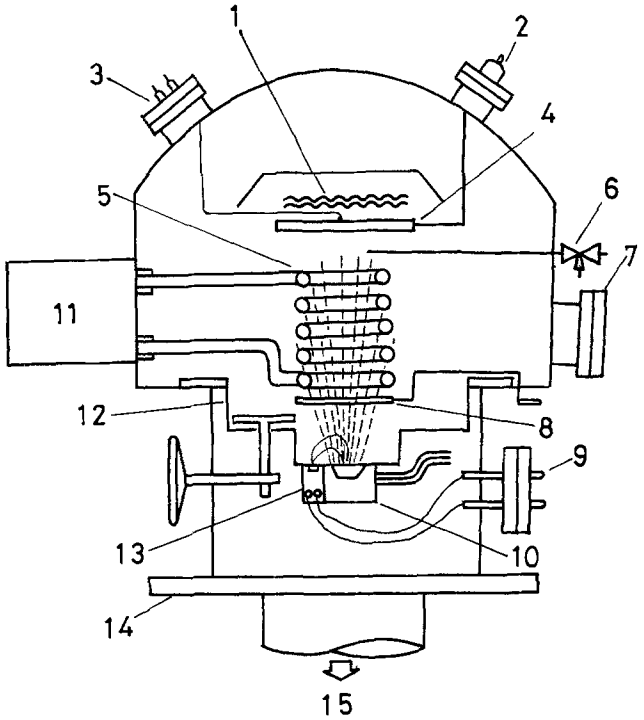


Fig. 1. Ion plating apparatus: 1, substrate heater; 2, high voltage feedthrough (—d.c. power); 3, thermocouples; 4, substrate holder; 5, rf coil; 6, variable leak valve; 7, view port; 8, shutter; 9, electrical feedthrough (EB power); 10, water-cooled copper hearth; 11, impedance matching box; 12, conductance baffle; 13, sweep, focus coils, and EB gun; 14, base plate; 15, pumping system.

tion, the substrate was sputter cleaned for about 10 min under argon pressure of 2×10^{-2} Torr. As for the evaporation of silicon, uncontrolled splatting of the silicon frequently occurred during melting even after the electron beam power inputs were limited to a low enough level. The same trouble was already reported by Chin *et al.* (7). After examining the vaporization technique, we found that silicon was vaporized significantly without any splatting when it was melted together with several pieces of tantalum sheet. Emission spectroscopic analysis of the deposits obtained by this technique showed traces of tantalum in the film deposited around the crucible but not in the deposited film on the substrate. This is probably due to the very low vapor pressure of tantalum compared with that of silicon. After initiating the evaporation of silicon, the ammonia gas was introduced into a chamber and the rf power supply was increased until a steady glow was observed in the chamber. No apparent changes in the deposited film were observed depending upon the distance between the outlet of ammonia gas feed pipe and the substrate. The shutter was then opened to begin the deposition of nitride under various conditions as given in Table 1. The coating was 7-10 min for most experiments.

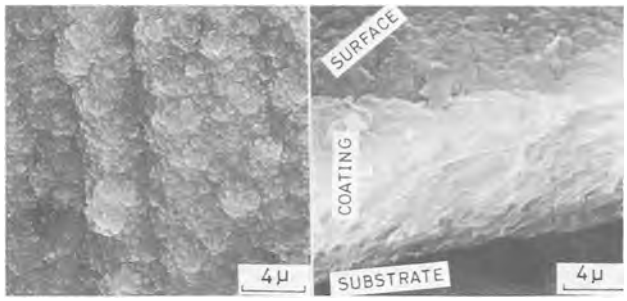


Fig. 2. Scanning electron micrograph of silicon nitride coating (left; coating surface, right; fracture cross section for the same deposit). Deposition rate was 1 μm/min at a substrate temperature of 950°C.

Results

Analysis of ion-plated silicon nitride.—Visual and scanning electron microscopic observations.—The silicon nitride deposits were obtained at a deposition rate of from 0.1 to 1.2 μm/min depending upon the coating conditions. Most deposits showed a dark green color, but some were gray and/or red brown. Figure 2 shows typical scanning electron microphotographs of silicon nitride coatings. Although large primary grains composed of many small grains were observed in the coating surface, no clear grain boundaries in cross-sectional structure were visible. This vitreous structure seems to be characteristic of the deposits obtained in the present work.

Auger electron spectroscopic analysis.—The chemical compositions of the deposited silicon nitride films were determined by means of Auger spectroscopic analysis (Cylindrical Mirror Analyzer, PHI Incorporated). Concentrations were calculated from the peak-to-peak Auger signal height by using relative elemental sensitivity factors given in the literature (10). Table I summarizes the chemical composition representative of the various deposits together with their coating conditions. For comparison, electron probe microanalysis (EMX-SM Shimazu Seisakusho, Limited) was also carried out by using BN as the standard sample for nitrogen. The results are also shown in parentheses in Table I. In certain cases, the results show considerable discrepancy between the two. This can be considered due to the difficulty of quantitative analysis of nitrogen in thin film by electron probe microanalyzer. As for the effect of the deposition temperature, no apparent composition changes in the film were observed in the temperature range from 400° to 1000°C. Nitrogen contents in the film varied over a wide range depending upon the deposition conditions. It should be noted that nearly stoichiometric deposits were obtained in runs 73, 76, and 78, in which silicon was vaporized with EB gun power of about 2 kW under reactant gas pressure of as high as 10^{-2} Torr. Further discussions on this point are made later. Oxygen and carbon were prominent con-

Table I. Deposition conditions and chemical analyses of silicon nitride films formed on molybdenum

Run no.	Reactant gas pressure (Torr)	Electron beam gun power (kW)	RF power (W)	Substrate voltage (−kV)	Substrate temperature (°C)	Composition (weight percent)			
						Si	N	O	C
18	9.0×10^{-3}	1.0	190	0.5	—[b]	49	45	0	5.9
39	5.5×10^{-3}	1.0	200	0.3	—	61	37	0.8	1.2
69	5.0×10^{-3}	1.2	150	0.3	800	97	2.6	0	—[c]
72	5.0×10^{-3}	1.5	150	0.3	—	68 (58)[a]	29 (42)	1.0 (0)	2.0 (—)
73	1.5×10^{-2}	2.0	210	0.3	700	51 (51)	42 (49)	3.0 (0)	4.0 (—)
76	1.0×10^{-2}	1.8	200	0.4	950	62 (42)	35 (56)	1.0 (2.0)	2.0 (—)
78	8.0×10^{-3}	1.8	220	0.4	—	59	39	1.0	2.0

[a] Value obtained by EPMA analysis is in parenthesis.
[b] Not heated but the temperature rises to ~400°C because of ion bombardment.
[c] Not analyzed.

taminants in these deposits. Presumably, they come from the impurities in the reactant gas. As the formation of nearly stoichiometric silicon nitride has been so far ascertained by the compositional data in Table I, the chemical state of silicon in deposits is hereafter examined in some detail. Figure 3 shows an example of Auger spectra for the silicon nitride coatings obtained in this study. After 3 min Ar-sputtering (removing ~300Å), AES signals from silicon and nitrogen increased in intensity, while those from oxygen and carbon became very weak, with an additional peak from argon atoms implanted during sputter cleaning. A detailed comparison of our Auger electron spectra with published data (10-12) revealed that the chemical shift and Auger electron peak shape from silicon in the spectra given in Fig. 3 are completely different from those of elemental Si and SiO_2, but showed a significant agreement with those from silicon in Si_3N_4 and in $Si_{0.54}N_{0.46}$ (10, 12).

Infrared spectroscopic analysis.—Infrared absorption of the deposits was measured by using a double-beam spectrophotometer (JASCO A-3, Japan Spectroscopic Company Limited). The silicon nitride layer removed from the molybdenum substrate was ground to micro-size with potassium bromide and the mixture was pressed into a pellet. In a typical infrared absorption profile shown in Fig. 4, a strong, broad band with its center at 830 cm^{-1} was observed and was identical with the Si-N stretching band reported by many other investigators (1-3, 5). The very weak absorption peaks for N-H and Si-H also were discernible. This hydrogen contamination seems to come from ammonia gas used.

X-ray analysis.—In the as-coated condition, all the coatings obtained in this study proved to be amorphous because no peaks except for the molybdenum substrate were obtained. For further confirmation of the formation of silicon nitride, the coating layer removed mechanically from the substrate was heat-treated at 1400° and 1500°C for about 2 min under 10^{-6} Torr. This caused the crystallization of amorphous deposits. Figure 5 shows the x-ray diffraction profile obtained with Ni-filtered CuKα radiation. All peaks corresponded to those of silicon and Si_xN reported in the ASTM powder diffraction data. The latter substance was originally obtained by Decker (13) together with free silicon when commercial silicon nitride was arc melted. It is obvious from this and previous studies already described that silicon in ion-plated films is present as the nitride. In addition, the deposits were nearly stoichiometric compounds.

Oxidation test of silicon nitride coated molybdenum.—The oxidation resistance of coated specimens was examined by thermogravimeter. Coated specimens of about 1 × 0.5 × 0.07 cm were heated at a rate of 20°C/min in the Ar 1% O_2 gas mixtures with a flow rate of ~200 ml/min. Figure 6 shows the results of oxidation tests for typical coated specimens. Uncoated specimens which were oxidized under the same conditions show a drastic weight decrease at about 790°C. This is because the MoO_3 formed begins to melt at this temperature and has a high vapor pressure. In this test, the edges of the specimens were painted with Al_2O_3 slurry to protect the cut edges and the film defect in the vicinity of edges in specimens. Observation of specimens after oxidation test, however, showed that film failure ascribed to the unprotected cut edges still existed. The oxidation test profiles shown in Fig. 6, therefore, give a rough estimation for the oxidation resistance of silicon nitride coatings. In the coated specimens which showed a marked decrease in weight at relatively low temperature, typical pitting corrosion shown in Fig. 7 was observed. On the other hand, the film adherence to the substrate generally plays an important role in

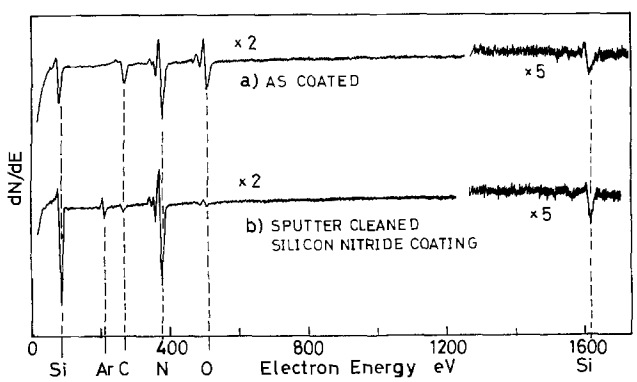


Fig. 3. Auger spectra from a) as coated surface; b) sputter-cleaned surface of silicon nitride coating (Run no. 76).

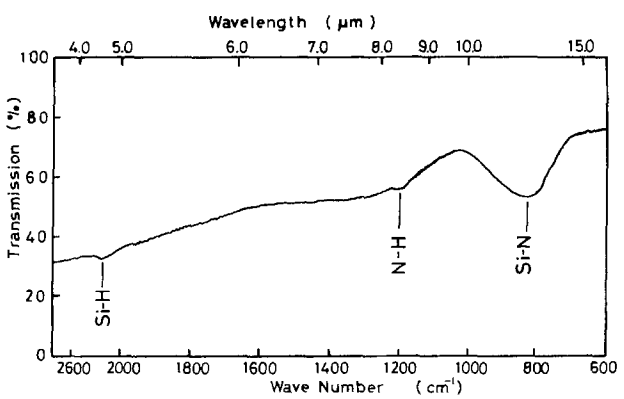


Fig. 4. Typical infrared spectrum of ion-plated silicon nitride film. (Run no. 72), the decrease of transmission in shorter wavelengths is ascribed to the difference in particle size between the sample and KBr reference.

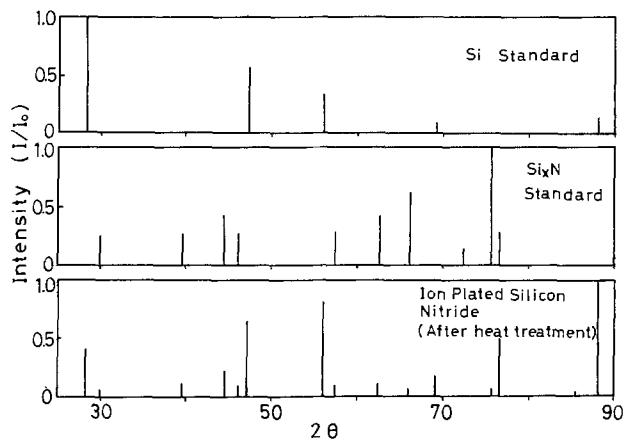


Fig. 5. X-ray diffraction pattern of the silicon nitride deposit (heat-treated at 1400°C for 2 min under 10^{-6} Torr).

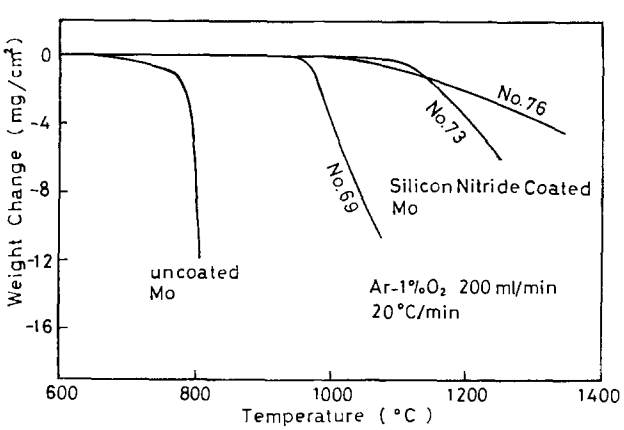


Fig. 6. Weight change vs. temperature of uncoated and silicon nitride coated molybdenum.

Table II. Variation of Si/N (atomic ratio) in deposit with EB power and the deposition site

Run no.	Electron beam gun power (kW)	Evaporation rate of Si (g/min)	A		B		C	
			Si/N	μ	Si/N	μ	Si/N	μ
51	1.2	0.07	0.9	2.5	1.0	~1	1.6	~1
53	1.1	0.1	1.4	3.5	1.9	~1.5	3.9	~1
78	1.8	0.3	0.7	9.9	0.6	6.8	1.3	2.3

protective coating technology. On this point, silicon nitride layer obtained in this study showed comparatively poor adherence to molybdenum substrate. The bonding was improved to some extent when the substrate was heated during coating. It can still, however, be removed by bending the specimens, even though not as easily as in specimens obtained without the substrate heating. Further investigations concerning the pitting corrosion and the film adherence are needed to obtain more protective silicon nitride coatings for molybdenum.

Discussion

Table I indicates that the ion-plated films vary considerably in their chemical composition, depending upon the coating conditions. For the purpose of examining the several factors affecting the stoichiometry of deposits, another ion-plating experiment was undertaken using a long strip-shaped molybdenum substrate. As shown schematically in Fig. 8, the substrate length is large enough compared with the diameter of rf coil. Evaporation rates of silicon were varied from 0.07 to 0.3 g/min. After the coating experiment, silicon nitride deposits from three different places on the substrate were analyzed by Auger electron spectroscopy. The atomic ratio between silicon and nitrogen in the deposits and the coating thickness measured by scanning electron microscopy are summarized in Table II. A, B, and C in Table II correspond to the three places on the substrate, *i.e.*, directly above the center, close to, and outside of the rf coil, respectively. In each run, as the deposition site was moved closer to the center of the rf coil, namely site A, a smaller value of Si/N was obtained and the deposit became nearly stoichiometric. This is probably because the concentration of ionized reactants is largest in the center of rf coil. On the other hand, when the EB gun power input was increased to as high as 1.8 kW, the deposition rate noticeably increased. Furthermore, the film became close to stoichiometric silicon nitride. This result is consistent with those of run 73 and 76 in Table I. This high rate deposition of nearly stoichiometric silicon nitride can be attributed to the fact that the power of EB gun as well as that of rf discharge is highly effective for the ionization or activation of reactants. The advantage of the use of electron beam evaporation technique for ion plating which was introduced by Chambers and Carmichael (14) has been pointed out by other investigators too (15, 16). From the fact mentioned above, it is concluded that nearly stoichiometric silicon nitride can be ion plated with a rather high speed, as long as the reactants are sufficiently ionized or activated.

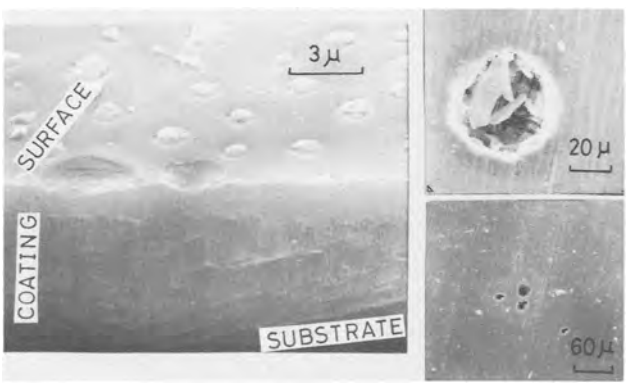


Fig. 7. Scanning electron microphotograph of typical film failure after oxidation test.

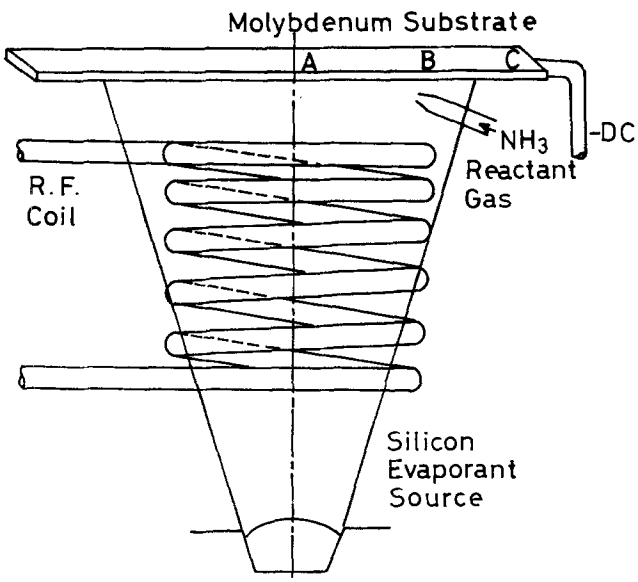


Fig. 8. Schematic illustration of ion-plating experiment using a long strip-shaped substrate.

Conclusions

Nearly stoichiometric silicon nitride coatings on molybdenum can be prepared by rf reactive ion plating from Si and NH_3. The most important factors affecting the stoichiometry of the deposit seemed to be an electron beam power into the Si evaporation source and the condition of rf glow discharge region, where most of the ionized or activated species of the reactants might be produced. The oxidation tests performed on coated specimens showed that the silicon nitride layer restrained the oxidation of molybdenum up to approximately 1200°C, but typical pitting-like failure in the deposited film occurred at the higher temperature.

Acknowledgments

The authors would like to express their appreciation to Dr. K. Yoshiwara and Dr. M. Kurahashi for the Auger electron spectroscopy measurements. The cooperation of the Physical and Chemical Analysis Departments of the National Research Institute for Metals is gratefully acknowledged.

Manuscript received March 18, 1977.

Any discussion of this paper will appear in a Discussion Section to be published in the June 1978 JOURNAL. All discussions for the June 1978 Discussion Section should be submitted by Feb. 1, 1978.

Publication costs of this article were assisted by the National Research Institute for Metals.

REFERENCES

1. G. J. Kominiak, *This Journal*, **122**, 1271 (1975).
2. S. M. Hu and L. V. Greger, *ibid.*, **114**, 826 (1967).
3. C. J. Mogab, P. M. Petroff, and T. T. Sheng, *ibid.*, **122**, 815 (1975).
4. S. I. Raider, R. Flitsch, J. A. Aboaf, and W. A. Pliskin, *ibid.*, **123**, 560 (1976).
5. J. A. Aboaf, *ibid.*, **116**, 1736 (1969).

6. R. C. G. Swann, R. R. Mehta, and T. P. Cauge, *ibid.*, **114**, 713 (1967).
7. J. Chin and N. B. Elsner, *J. Vac. Sci. Technol.*, **12**, 821 (1975).
8. High Temperature Oxidation-Resistant Coatings, Committee on Coatings, National Research Council, National Academy of Sciences, Washington D.C., p. 99 (1970).
9. Y. Murayama, *J. Vac. Sci. Technol.*, **12**, 818 (1975).
10. L. E. Davis, N. C. MacDonald, P. W. Palmberg, G. E. Riach, and R. E. Weber, "Handbook of Auger Electron Spectroscopy," 2nd ed., Physical Electronics Industries, Inc. (1976).
11. P. H. Holloway and H. J. Stein, *This Journal*, **123**, 723 (1976).
12. P. H. Holloway, *Surf. Sci.*, **54**, 506 (1976).
13. Index to the X-ray Powder Data File (1962).
14. D. L. Chambers and D. C. Carmichael, *Research/Development Magazine*, **22**, 32 (1971).
15. L. B. Leder, *Met. Finish.*, **72**, 41 (1974).
16. R. F. Bunshah and A. C. Raghuram, *J. Vac. Sci. Technol.*, **9**, 1385 (1972).

Precipitation-Induced Currents and Generation-Recombination Currents in Intentionally Contaminated Silicon P^+N Junctions

H. H. Busta[1] and H. A. Waggener

Teletype Corporation, Skokie, Illinois 60076

ABSTRACT

The effects of impurities such as gold, iron, copper, nickel, tantalum, and tungsten on junction reverse *I-V* characteristics were investigated using DLTS (deep level transient spectroscopy), TSCAP (thermally stimulated capacitance), *I-V*, *C-V*, and *I-T* measurements. In almost all cases, the reverse *I-V* characteristics consisted of two components; a normal Shockley-Read-Hall (SRH) generation component and a soft leakage component which dominates the SRH component above a given onset voltage. Only the SRH component can be detected with the DLTS and TSCAP methods. The soft leakage currents were ascribed to the presence of impurity precipitates lying near the metallurgical junction of the devices. Soft leakage currents measured at 80°K were fitted to a Fowler-Nordheim field-emission model. Localized electric field values near the precipitates of the order of 10^6-10^7 V/cm were obtained by this analysis. These values could be correlated with the possible shape of the precipitates. The distribution of the SRH generation centers within the active regions of the devices and the activation energies of the emission rates of above-mentioned impurities were measured using the DLTS technique. The following results were obtained: Au 0.55 eV (c), Fe 0.57 eV (c); Cu 0.2 eV (c), 0.49 eV (*v*), 0.41 eV (*v*); Ni 0.19 eV (c), 0.36 eV (c); Ta 0.21 eV (c); and W 0.25 eV (c), 0.28 eV (c), respectively. Here c and *v* represent measurements from the conduction band and valence band, respectively.

It is well known that point defects distributed in the bulk or at the surface of pn junctions can act as generation centers for electron-hole pairs and thus cause diode leakage. These defects can be process-induced defects, dislocations, radiation-induced defects, or impurities such as gold, iron, copper, manganese, nickel, sulfur, etc. They are characterized by activation energies which lie within the forbidden bandgap of the semiconductor, and by their thermal capture and emission rates for minority and majority carriers, respectively. Their contribution toward diode leakage is governed by the Shockley-Read-Hall generation-recombination theory (1). The most effective centers, in terms of the generation component, lie near the midgap of the semiconductor.

Detection of these defects can be achieved, for instance, by using thermally stimulated current (TSC) (2, 3) measurements. Identification of a given generation center with the above techniques can be achieved in certain cases. Complications arise due to the fact that for some impurities such as gold, iron, copper, sulfur, manganese, etc., the near midgap energy levels are separated by only a few millielectronvolts, which in terms of temperatures, corresponds to only a few degrees difference in the position of the measurement signals. When using the TSC and TSCAP methods, the position of the signals is strongly dependent on heating rates. Therefore, for identification purposes, these rates have to be known precisely. Lang has recently published a paper on deep level transient spectroscopy (DLTS) measurements (4). The advantage of this method is that it is heating rate independent. For a given fixed emission rate window, the position of the signals occurs at the same temperature. Another advantage of the DLTS method is that it is spectroscopic in nature, which means that it has a zero base line. However, this can also be achieved by using the differential TSCAP method (5)

The intention of this work was to identify leakage mechanisms of some diodes fabricated in our facilities using DLTS, TSCAP, *I-V*, *C-V*, and *I-T* measurements. These measurements were performed on planar diodes, gate-controlled diodes, and MOS capacitors. In the course of this work, some devices with known characteristics (6) were intentionally contaminated with gold, iron, copper, nickel, tantalum, and tungsten. It was found that for gold- and tungsten-doped diodes the generation components increased by three orders of magnitude as compared to the precontamination level. This gave rise to large DLTS signals ($N_t \simeq 10^{14}$ cm^{-3}). The reverse *I-V* characteristics of these diodes were almost ideal over the entire voltage range, with *I* varying as $V^{1/2}$. For all the other elements, the generation components increased only moderately, giving rise to weak DLTS signals ($N_t \simeq 10^{11}$-10^{13} cm^{-3}). However,

[1] Present address: Gould Laboratories, Rolling Meadows, Illinois 60008.

Key words: junction leakage, defects in pn junctions, field emission, tunneling, deep level transient spectroscopy.

these diodes showed soft characteristics. In some extreme cases, the onset of the soft current component occurred at voltages as low as 1V. Goetzberger and Shockley (7) attributed this softness to the formation of metallic precipitates, and conjectured that Zener tunneling at localized high field points was responsible for the observed soft leakage currents. They reported leakage currents proportional to V^n, with n ranging from 3 to 7. However, no attempts were made to explain the exponent n in terms of a physical model.

In this paper, the soft component of leakage current is modeled in two ways and experimental results are compared to these models. First, a tunnel or field-emission model is considered. From analysis of the data, values of the electric field at localized high field spots, information about the shape of the precipitates, and estimates of the local extension of the emission sites are obtained. The information gained from this analysis has to be considered more qualitatively than quantitatively, since the expression used for the tunneling current density is only applicable to direct gap tunneling. In the indirect case, such as silicon, effects due to momentum conservation and multiple band effective masses should be included. Second, the possibility that these currents arise from SRH centers is presented. There are other mechanisms which might explain soft leakage currents. Charge multiplication due to impact ionization at localized areas of high electric fields might be one possibility. The reason why a tunneling approach is chosen in this work is due to the experimentally observed fact that leakage currents have a negative temperature coefficient, *i.e.*, at a given voltage the current increases with increasing temperature. Also, in all cases, a temperature-independent component was observed at liquid nitrogen temperatures. Impact ionization has a positive temperature coefficient, *i.e.*, at a given voltage the ionization rate increases with decreasing temperature (8).

Device Fabrication

The diodes were fabricated using Czochralski-grown n-type (111) wafers having an uncompensated phosphorus concentration of approximately 1×10^{15} cm^{-3}. BN disks were used for the p^+ diffusion. Diodes from different stages during the common p-channel MOS process were used for this experimentation. Before testing, all devices were either nitrogen annealed or forming gas annealed at 450°C in order to reduce the surface component of the leakage.

Before the devices were subjected to the impurity diffusion, reverse I-V control measurements were performed. After appropriate cleaning of the slices, the elements under investigation were either filament or electron beam evaporated on the back of the wafers, and diffused in a nitrogen atmosphere. In most cases, a new quartz furnace tube was used for each element. Diffusion temperatures ranged from 800° to 1150°C.

Experimental Results

Leakage mechanisms.—Figure 1 shows the current-reverse voltage characteristics of two diodes. The measurements of Fig. 1 were taken at room temperature and 80°K, respectively. The room temperature plots consist of two distinct regions: a region where the current varies approximately as $V^{1/2}$, followed by a region of very strong voltage dependence. For both junctions, the leakage currents below the onset of the soft knees are governed by Shockley-Read-Hall generation centers. At low temperatures, these currents decrease, due to the exponential temperature dependence of the electron-emission and hole-emission rates (1, 2). The soft component of diode A is almost temperature independent in the range from 80° to 300°K. Diode B does show some temperature dependence of its soft characteristics, however, measurements showed that from 80° to 130°K this component is also temperature independent. Experimentally, it was observed that for a given impurity, both type A and B behavior were present for

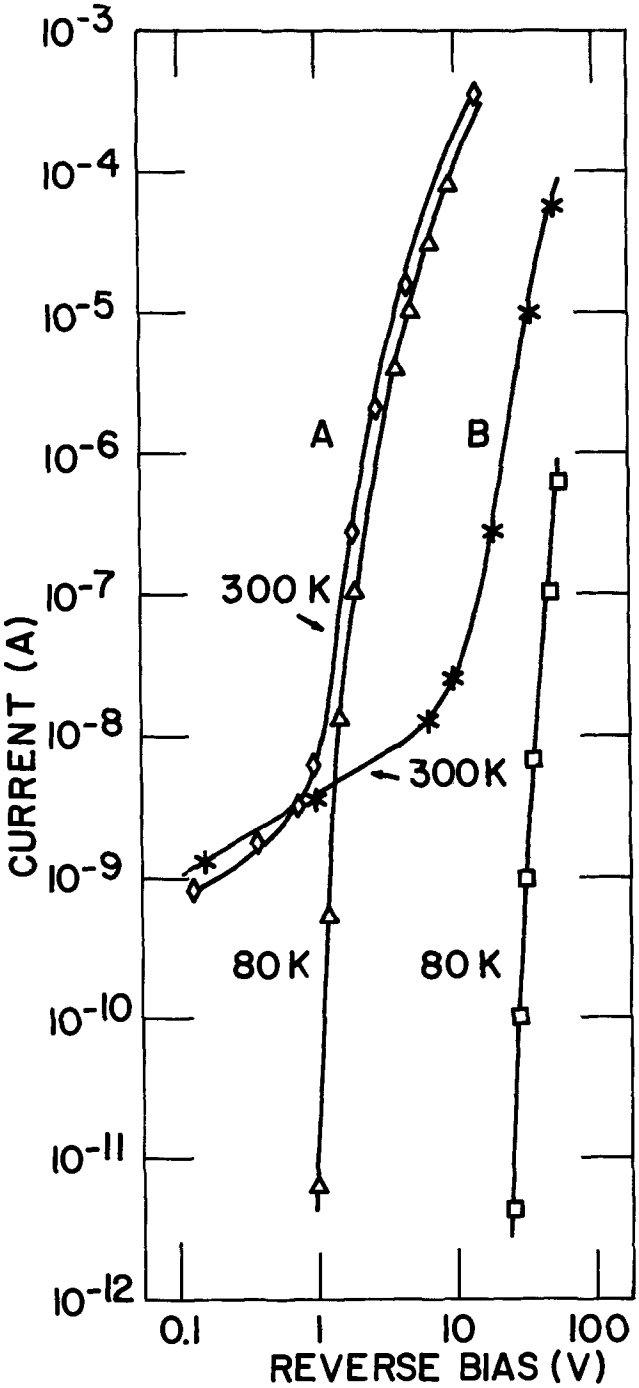


Fig. 1. A: I-V_R characteristics of the tantalum-doped diode C-4 of lot 4521, W-8, chip J-7 measured at 300° and at 80°K, respectively. B: I-V_R characteristics of the tungsten-doped diode C-4 of lot 4521, W-7, chip G-13 measured at 300° and at 80°K, respectively.

a given wafer. Also, the onset voltages of the soft knees varied over wide ranges. In some cases values ranging from 1 to 40V were observed. Due to these reasons, no attempt was made to rank order the influence of the individual impurities upon diode leakage. However, based upon the limited sample size which was investigated, some general comments can be made. Iron, nickel, copper, and tantalum gave rise to the formation of soft diodes with low SRH generation components. The concentrations of generation centers ranged from 10^{11} to 10^{13} cm^{-3}. Tungsten-doped diodes showed softness occurring at voltages of larger than 20V. A large generation component was observed with a concentration of generation centers larger than 10^{14} cm^{-3}. No softness was observed for gold-doped diodes. Their concentration of SRH centers was approximately 10^{14} cm^{-3}. As mentioned, the existence of a temperature-

independent soft leakage component and of a negative-temperature coefficient led to the consideration of a tunnel or field-emission mechanism.,

Tunnel or field emission.—Before discussion of the data, some of the expressions which are used in the analysis of the data are summarized. In this work, only the temperature-independent components of soft leakage currents are analyzed.

The basic law governing field emission is given by the Fowler-Nordheim equation. The current density at temperature $T = 0$ is given by (9)

$$J = \frac{q^3E^2}{16\pi^2\hbar\, q\, \Phi_B t^2(y)} \exp\left(-\frac{4(2m^*)^{1/2}(q\Phi_B)^{3/2}\, v(y)}{3\hbar\, qE}\right) \quad [1a]$$

with t and v being tabulated functions of the argument y, which is given by

$$y = (q^3E)^{1/2}/q\Phi_B \quad [1b]$$

Here E is the applied electric field, $q\Phi_B$ is the barrier height, and m^* is the tunneling effective mass. The function $t(y)$ in Eq. [1a] is almost independent of y. It monotonically increases from 1.00 to 1.11 as y varies from 0 to 1. The barrier-lowering factor $v(y)$ decreases monotonically from 1 to 0 as y varies from 0 to 1. To test if a field-emission process can be used to describe soft leakage currents, the data is plotted in the form $\ln J/E^2$ *vs.* E^{-1} (Fowler-Nordheim plot). A straight line should be obtained, the slope of which is given by

$$-\frac{4(2m^*)^{1/2}\,(q\Phi_B)^{3/2}\, v(y)}{3\hbar\, q}. \quad [2]$$

Near a precipitate it is assumed that the electric field E is enhanced by a factor of β above the unperturbed background field of the junction. A similar assumption was made in Ref. (10), where Fowler-Nordheim field emission from protruding whiskers on nickel cathodes was considered. The electric field is then given by

$$E = \beta E_{\text{unperturbed}} \quad [3]$$

Using the abrupt junction approximation (11)

$$E_{\text{unperturbed}} = E_{\max} = \left(\frac{2qN_D}{\epsilon_s}\right)^{1/2} (V_{bi} + V_R)^{1/2} \quad [4]$$

Here N_D is the donor-doping concentration, ϵ_s is the dielectric constant of the semiconductor, V_{bi} is the built-in voltage, and V_R is the reverse bias voltage. Two further conditions are invoked. It is assumed that one end of the precipitate is located near the maximum field, while the other end of the precipitate extends into the heavily doped region. Therefore, only a small voltage drop can exist between the precipitate and the heavily doped region. With these conditions, the unperturbed field at the tip of the precipitate is the maximum field in the junction, $E_{\max}$. Since under these conditions E is proportional to $(V_{bi} + V_R)^{1/2}$, a Fowler-Nordheim plot should be of the form $\ln J/(V_{bi} + V_R)$ *vs.* $(V_{bi} + V_R)^{-1/2}$ with a slope of

$$-\frac{4(2m^*)^{1/2}\,(q\Phi_B)^{3/2}}{3\hbar\, q\left(\frac{2qN_D}{\epsilon_s}\right)^{1/2}}\,\frac{v(y)}{\beta} \quad [5]$$

By using Eq. [5], it is possible to obtain estimates of the field-enhancement factors at the precipitates. From these values, information about the shape of the precipitates can be deduced.

Since the devices were contaminated with metals, it is assumed that the precipitates are either metallic or in the form of conductive silicides such as CuSi, Ni_2Si, FeSi, $TaSi_2$, WSi_2, etc. Assuming a spherical precipitate imbedded in a dielectric medium, the field inside the sphere is zero; the field outside the sphere is given by (12)

$$\hat{E}(r, \theta) = E(1 + 2a^3/r^3)\cos\theta\hat{r} - E(1 - a^3/r^3)\sin\theta\hat{\theta} \quad [6]$$

Here E is the uniform background field, a is the radius of the sphere, r and θ are the polar coordinates, and $\hat{r}$ and $\hat{\theta}$ are the unit vectors. For $r = a$ and $\theta = 0$, $\hat{E}(a, 0) = 3E$. This means that the field-enhancement factor at the precipitate has a value of 3. As can be seen from Eq. [6] the field-enhancement factor has a strong spatial dependence. In the case of a conducting prolate spheroidal-shaped precipitate, the field-enhancement factor depends strongly on the c/b ratio (10). Here c is the extension of the precipitate in the direction of the field, and b is the diameter. For $c/b = 1$, β reduces to 3, the value of the field-enhancement factor for a sphere. It should be mentioned that field enhancement also occurs for noncontacting precipitates. For instance, the field enhancement for a spherical SiO_2 precipitate is approximately 1.5 (12).

Fowler-Nordheim plots of the temperature-independent components of the two diodes shown in Fig. 1, as well as of one other diode, are shown in Fig. 2 where $V_R^{-1/2}$ is used as the abscissa. From the slopes corresponding to large reverse voltages, (*i.e.*, $V_R + V_{bi} \simeq V_R$), values of $\beta' = (m_e/m^*)^{1/2}v^{-1}\,\beta$ can be obtained. Here m_e is the free electron mass. Using Eq. [5] and taking for $q\Phi_B = 0.5$ eV and for $N_D = 1 \times 10^{15}$ cm^{-3}, these values ranged from 9.4 to 114 for the diodes shown in Fig. 2. Similar values were obtained for iron-, nickel-, and copper-doped diodes. Using Eq. [3] and [4] and assuming that $m^* \simeq m_e$, and $v(y) \simeq 1$, values of the electric field at the precipitates of 0.82×10^6 V/cm for $-V_R = 25$V and of 1.33×10^6 V/cm for $-V_R = 65$V were obtained for diode B of Fig. 1 and 2. This is close to the reported value of 10^6 V/cm for silicon where currents due to tunneling become significant (13). Taking $\beta \simeq 114$ for diode A, values of the electric fields of 2×10^6 V/cm for $-V_R = 1$V and of 6.32×10^6 V/cm for $-V_R = 10$V were obtained. The actual field values are reduced somewhat since $v(y) \leq 1$, and since it is expected that $m^* < m_e$. Since these field values are one to two orders of magnitude larger than the avalanche breakdown field in a junction of approximately 5×10^5 V/cm, they have to be restricted within a small volume, otherwise localized charge multiplication due to impact ionization would take place giving rise to a discontinuous slope in the current-voltage characteristics whenever the multiplication factor reaches the value of one. Using the conditions invoked above, a field-enhancement factor of 9.4 corresponds to a c/b ratio of 3. For $\beta = 114$, the c/b ratio is approximately 20. Again, due to the unknown values of m^*, $q\Phi_B$, and $v(y)$, the c/b ratios have to be viewed more qualitatively than quantitatively. However, by comparing the c/b ratios of diodes A and B of Fig. 1 and 2, it can be concluded that the current contributing precipitates in diode A are more needle-like than the precipitates in diode B. Bearing in mind that the enhanced field at a precipitate can only occur over a small fraction of the junction area, Eq. [1] was used to check if the calculated current densities are consistent with this assumption. The emission area can be estimated from

$$I(V_R) = J(T = 0, V_R)A_p \quad [7]$$

where I is the measured temperature-independent current at a given reverse bias voltage, J is the current density given in Eq. [1], and A_p is the emission area at a precipitate. The results are: $A_p \simeq 10^{-10}A_j$ for diode A, and $A_p \simeq 10^{-3}A_j$ for diode B. Here A_j is the junction area. The value for diode B seems quite large, but since these junctions were intentionally contaminated, it is conceivable that in some cases quite a few precipitates of similar emissivity formed during the cooling cycle.

From Fig. 2 it can be seen that for diode A deviations from a straight line occur at voltages below 3V. This is expected since according to Eq. [4] the electric field is only proportional to $V_R^{1/2}$ for $V_R > V_{bi}$. Incorporating V_{bi} and plotting $\ln I/(V_{bi} + V_R)^{3/2}$ *vs.* (V_{bi}

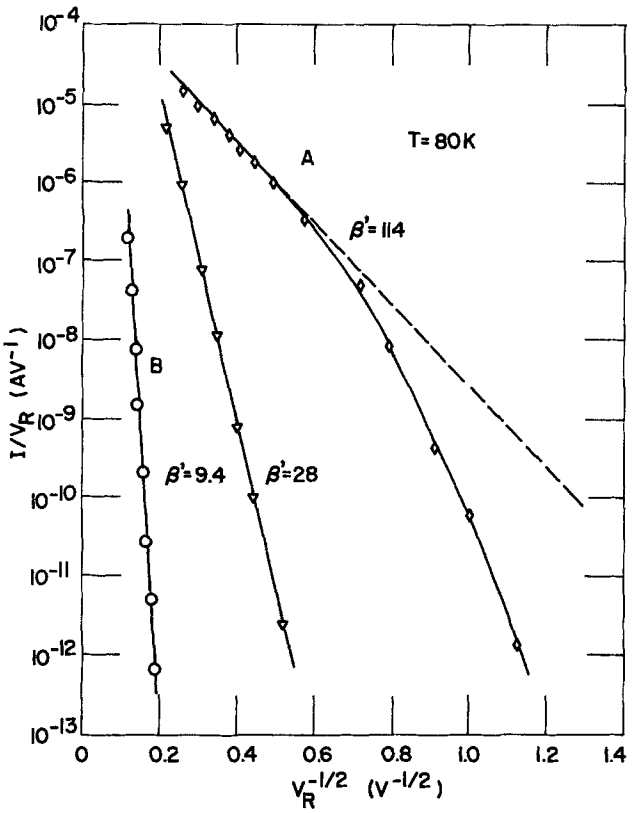


Fig. 2. Log I/V_R vs. $V_R^{-1/2}$ plots of the temperature-independent soft leakage component of several diodes.

$+ V_R)^{-1/2}$, however, did not result in a straight line fit at voltages below 3V.

Detection and distribution of SRH generation centers.—During the early stages of this work, the possibility was considered that the soft leakage component might be due to nonuniform distribution of generation centers or due to field-enhanced emission rates. To investigate this, DLTS measurements were taken at different voltage ranges. Examples of such measurements are given in Fig. 3 and 4. Figure 3 shows the *I-V* characteristics of a soft diode which was contaminated with tantalum. DLTS 1 was obtained for a quiescent reverse bias of −3V which was momentarily reduced to 0V. DLTS 2 was obtained for a quiescent reverse bias of −10V which was momentarily reduced to −6V. The width of the bias reduction pulse was 400 μsec. These two spectra are shown in Fig. 4. From the analysis of the data, the concentration of the near midgap levels were N_t(DLTS 1) $\simeq 1.2 \times 10^{13}$ cm^{-2} and N_t(DLTS 2) $\simeq 1.5 \times 10^{13}$ cm^{-3}, respectively. This moderate increase in N_t from DLTS 1 to DLTS 2 cannot be the cause of the sharp increase in the leakage current from −3 to −10V. From Fig. 4 it can be seen that the maxima of the near midgap peaks of the two spectra occur at the same temperature. This means that the emission rate in the two cases is the same. Therefore the observed large leakage current cannot be explained by a field-enhanced emission rate. The soft leakage component measured at 80°K was subsequently fitted to the precipitation model. From the analysis, a field-enhancement factor of 28 was obtained. It should be mentioned that the near midgap peak in Fig. 4 is due to gold contamination. This was established from control measurements. Therefore only the low temperature peak (0.21 eV, Table I) is associated with tantalum.

DLTS measurements were also used to measure the lateral distribution of generation centers. For this purpose, gate-controlled diodes and in some cases MOS capacitor structures, were employed. In some cases it was observed that up to 40 times more impurities in the form of generation centers were present in the depletion region of the field-induced junction of a gate-

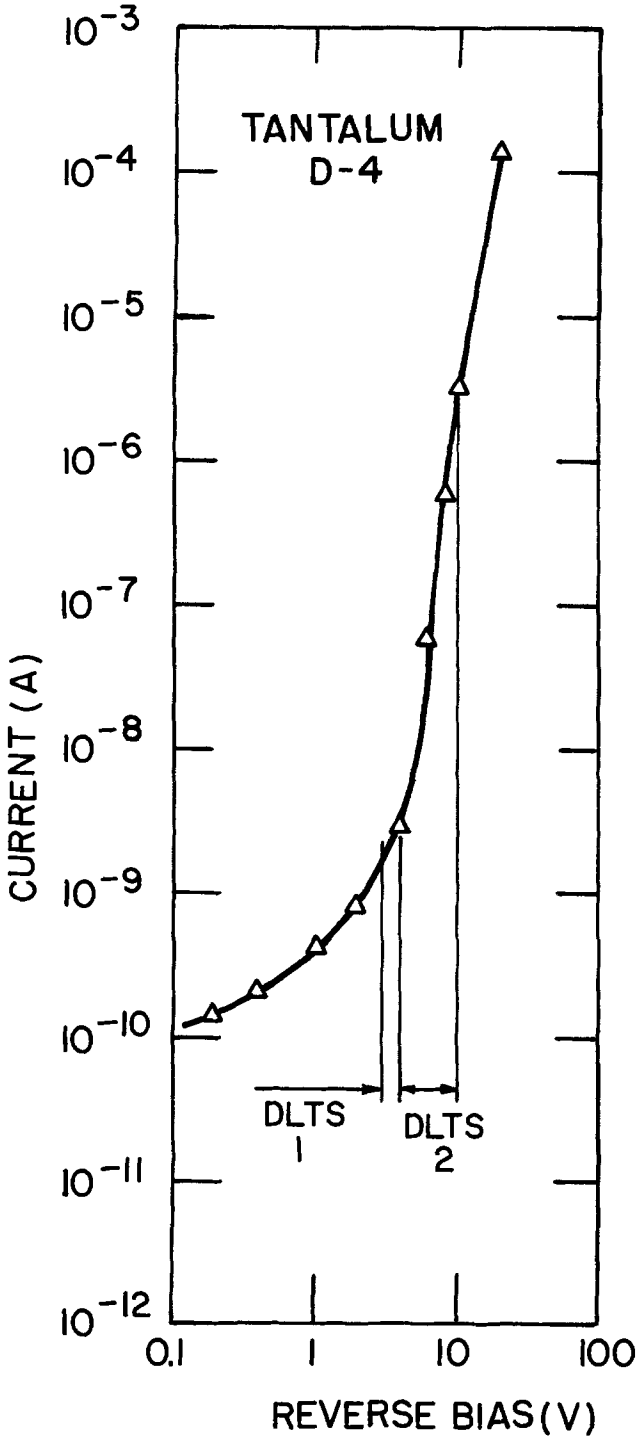


Fig. 3. I-V_R characteristics of the tantalum-doped diode C-4 of lot 4321, W-8, chip D-4, measured at room temperature. Indicated by DLTS 1 and DLTS 2 are the two voltage ranges for which DLTS spectra were obtained in order to measure possible nonuniform impurity distributions and/or field-enhanced emission rates.

controlled diode as compared to the depletion region associated with the metallurgical junction. This was seen for iron- and tantalum-doped diodes, both of which showed soft *I-V* characteristics. Either gettering effects in the p^+ region or formation of precipitates near the metallurgical junction might be responsible for the depletion of generation centers near the metallurgical junction. In the case of the tungsten-doped diodes, an almost uniform distribution of the near midgap impurities in those two regions was observed. An example of such a measurement is given in Fig. 5. It shows the I-V_R characteristics of the metallurgical junction and of the field-induced junction of a tungsten-doped gate-controlled diode. Over most of the

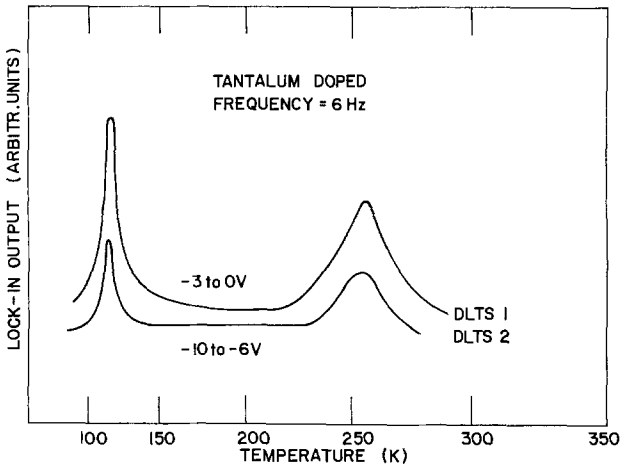


Fig. 4. DLTS spectra of the tantalum-doped diode C-4 of lot 4321, W-8, chip D-4. The spectra were measured at different reverse bias voltages and at different pulse heights.

voltage range the current of the metallurgical junction and of the field-induced junction varies as $V_R^{1/2}$. The current of the metallurgical junction was measured at a gate voltage $V_G = 0$. The current of the field-induced junction was obtained by taking the difference of the currents measured at strong inversion and at $V_G = 0$ (or for weak accumulation). V_R was held at a constant value. The measured current change $I_{FIJ}/(I_{FIJ} + I_{MJ})$ at $V_R = -1V$ is 23.2%. Assuming that the leakage is caused by the near midgap center, a similar change in the height of the DLTS peak should be expected. The DLTS spectra are shown in the insert of Fig. 5. The observed change in the amplitude of the signals is 22.2%. This is in excellent agreement with the above value. It should be mentioned that none of the observed soft leakage currents of gate-controlled diodes could be accounted for by surface generation-recombination centers. The surface recombination velocity s_0 of the diodes investigated ranged from 5 to 100 cm/sec.

In the usual treatment of junction leakage it is assumed that the entire contribution of SRH leakage comes from the depletion region which is associated with the lighter doped side of a junction. In practical cases, however, there is a nonzero depletion width which extends into the more heavily doped side of a junction. An indication that SRH centers lying in the p^+ regions contribute to diode leakage was obtained for copper-doped diodes. Figure 6 shows the DLTS spectra of a copper-doped diode and of a MOS capacitor lying adjacent to the diode. (Copper was filament

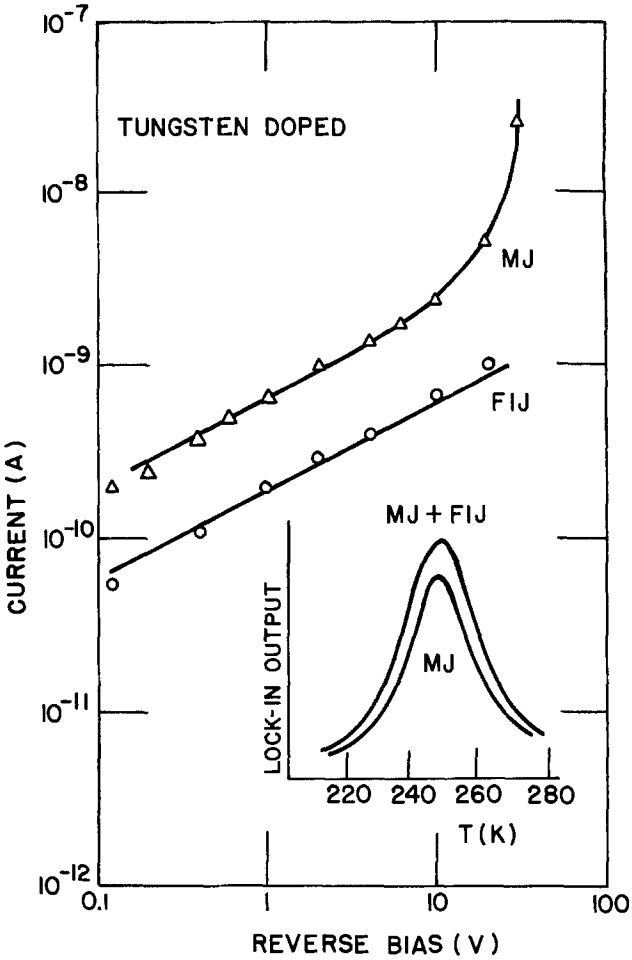


Fig. 5. I-V_R characteristics of the tungsten-doped diode D-1 of lot 4521, W-7, chip G-17. The insert shows the near midgap DLTS spectra for gate voltages $V_G = 0$ (designated as MJ) and for $V_G = -100V$ (designated as MJ + FIJ), respectively.

evaporated on the backs of the wafers and diffused at 1050°C in N_2 for 2 hr. The wafers were then fast pulled to room temperature.) Three peaks are discernible for the p^+n junction. Only one peak is obtained for the MOS capacitor. The increase of the signal of the MOS capacitor spectrum above 200°K is due to the fact that at the temperature where reemission of the trapped electrons would occur, thermal bulk and/or surface generation of minority carriers can invalidate the deep

Table I. Deep energy levels in silicon

Impurity	This work* (DLTS)		A. G. Milnes (15)**		
Au	0.55(c)	0.54(c)	0.54(c)	0.30(c)	
		0.35(v)	0.35(v)	0.83(v)	
Fe				0.14(c)	
	0.57(c)		0.55(c)	0.51(c)	
		0.40(v)	0.40(v)	0.40(v)	
Cu	0.20(c)			0.26(c)	
	0.49(v) } or process in-	0.52(v)	0.52(v)	0.53(v)	
	0.41(v) } duced, (c)?	0.37(v)	0.37(v)	0.40(v)	
		0.24(v)	0.24(v)		
Ni	0.19(c)				
	0.36(c)	0.35(c)	0.35(c)		
		0.23(v)	0.22(v)		
Ta	0.21(c)	<0.14(c)			
		0.43(c)			
W	0.25(c)	0.22(c)			
	0.28(c)	0.30(c)			
		0.37(c)			
		0.34(v)			
		0.31(v)			

* Measurements by DLTS methods.
** Conventional techniques and surface capacitance studies.
(c) Measured from the conduction bandedge.
(v) Measured from the valence bandedge.

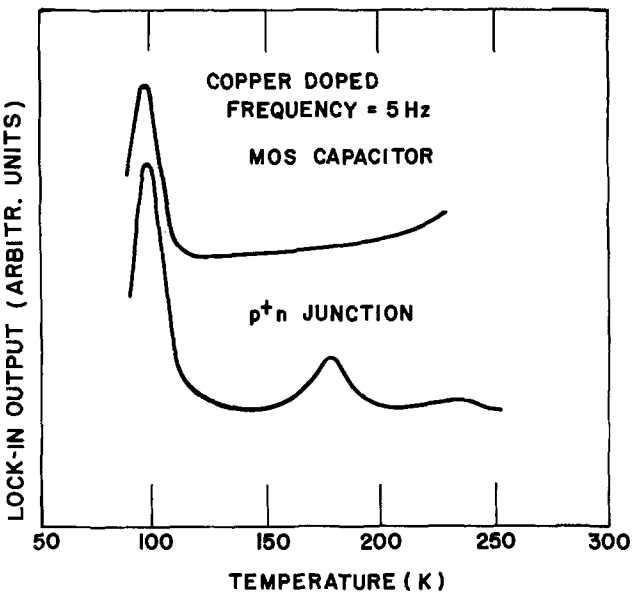


Fig. 6. DLTS spectra of the MOS capacitor C-3 and p+n junction C-4 of lot 5173, chip M-15. The wafer was doped with copper.

depletion condition by forming an inversion layer near the insulator-semiconductor interface. The two extra signals in the diode spectrum could also be process-induced defects (3, 14), but since the measured energy values are close to the published values for copper (see Table I), it is believed that these signals come from generation centers which are located in the more heavily doped p region. In principle, soft leakage currents could be explained by assuming a highly nonuniform distribution of SRH centers in the p^+ region. However, the experimentally observed temperature-independent current component does not agree with the exponentially dependent temperature dependence of the emission rates of SRH centers. It should be mentioned that for the chosen biasing conditions of the DLTS measurements (no minority carrier injection), only traps lying in the upper half of the bandgap can be observed with p^+n junction structures, assuming that the signals come from the more lightly doped side of the junction. For n^+p diodes and the same assumptions, only traps lying in the lower half of the bandgap can be detected. Therefore, the energy values of the additional signals coming from the p region of the p^+n diodes have to be measured from the valence band. Table I summarizes the energy values obtained by the DLTS method and compares them to published values (15).

Summary

The effects of impurities such as gold, iron, copper, nickel, tantalum, and tungsten on junction reverse *I-V* characteristics were investigated. In all cases, excluding gold, the reverse *I-V* characteristics consisted of two components; a normal Shockley-Read-Hall (SRH) generation component and a soft leakage component which dominates the SRH component above a given onset voltage. Only the SRH component can be detected with the DLTS and TSCAP methods. In many cases, when the soft leakage component dominated over almost the entire voltage range, only weak DLTS signals were observed ($N_t \simeq 10^{11}$-10^{13} cm^{-3}). In none of the cases investigated could soft leakage currents be associated with SRH centers. They were ascribed to the presence of impurity precipitates lying near the metallurgical junction of the devices. These currents, measured at 80°K, were fitted to a tunneling or field-emission model. It was found that the onset voltage of the soft leakage current depends on the magnitude of the field-enhancement factors and on the magnitude of the SRH component. Assuming that the precipitates are in the form of prolate spheroids and other conditions with regard to their position within a junction, information about the geometry (sphere-like to needle-like) could be obtained from the field-enhancement factors. Local electric fields of the order of 10^6-10^7 V/cm were obtained by this analysis.

DLTS measurements were used to obtain the distribution of the SRH centers within the active region of the devices by employing gate-controlled diode structures and MOS-capacitor structures. Activation energies of the emission rates of electrons and, in some cases, of holes, were measured. Hole emission was observed from impurities lying in the heavily doped p regions of the junctions.

It is expected that soft leakage currents will arise whenever conditions exist in fabrication where impurities are introduced in quantities exceeding the solid solubility at temperatures where sufficient impurity mobility permits precipitation. Clearly, the nature of impurity introduction, stresses, kinetics of precipitation, density, and location of nucleation sites will influence the effects of a given precipitate on junction leakage. For these reasons it has not been possible to systematically determine the relative effects of various contaminants with respect to precipitate-induced leakage.

Acknowledgments

Certain individuals and institutions contributed to the completion of this work. Numerous discussions pertaining to the DLTS and TSCAP measurements with D. V. Lang, L. C. Kimerling (both of Bell Laboratories, Murray Hill, New Jersey) and M. G. Buehler (National Bureau of Standards, Gaithersburg, Maryland) are sincerely appreciated. Thanks go to the staff members of Department 9133 and to the personnel of the Microelectronic Model Shop and the production MOS facility. Thanks are also due to C. Allen, S. Ostrowski, and V. Kosmas for their special packaging efforts.

Manuscript submitted July 13, 1976; revised manuscript received May 16, 1977. This was Paper 127 presented at the Washington, D.C., Meeting of the Society, May 2-7, 1976.

Any discussion of this paper will appear in a Discussion Section to be published in the June 1978 JOURNAL. All discussions for the June 1978 Discussion Section should be submitted by Feb. 1, 1978.

Publication costs of this article were assisted by Teletype Corporation.

REFERENCES

1. R. N. Hall, *Phys. Rev.*, **83**, 228 (1951), **87**, 387 (1952). W. Shockley and W. T. Read, Jr.; *ibid.*, **87**, 835 (1952).
2. M. G. Buehler, *Solid-State Electron.*, **15**, 69 (1972).
3. C. T. Sah and C. T. Wang, *J. Appl. Phys.*, **46**, 1767 (1975).
4. D. V. Lang, *ibid.*, **45**, 3014, 3023 (1974).
5. L. D. Yau and C. T. Sah, *Solid-State Electron.*, **17**, 193 (1974).
6. H. Sue and H. A. Waggener, Paper 108 presented at The Electrochemical Society Meeting, Washington, D.C., May 2-7, 1976.
7. A. Goetzberger and W. Shockley, *J. Appl. Phys.*, **31**, 1821 (1960).
8. S. M. Sze, "Physics of Semiconductor Devices," Chapter 2, Wiley-Interscience (1969).
9. R. H. Good and E. W. Müller, "Handbuch der Physik," 21, 176 (1956).
10. I. Brodie, *J. Appl. Phys.*, **35**, 2324 (1964).
11. A. S. Grove, "Physics and Technology of Semiconductor Devices," Chapter 6, John Wiley & Sons, Inc., New York (1967).
12. Oleg D. Jefimenko, "Electricity and Magnetism," Chapter VIII, Appleton-Century-Crofts, New York (1966).
13. J. L. Moll, "Physics of Semiconductors," p. 253, McGraw-Hill Book Co., New York (1964).
14. M. G. Buehler, in "Semiconductor Silicon 1973," H. R. Huff and R. R. Burgess, Editors, p. 549, The Electrochemical Society Softbound Symposium Series, Princeton, N.J. (1973).
15. A. G. Milnes, "Deep Impurities in Silicon," p. 14, John Wiley & Sons, New York (1973)

Properties of CdS Films Prepared by Spray Pyrolysis

Yale Y. Ma[1] and Richard H. Bube*

Department of Materials Science and Engineering, Stanford University, Stanford, California 94305

ABSTRACT

A detailed investigation has been made of the properties of CdS films deposited on amorphous glass substrates by the technique of spray pyrolysis. The variation of the electrical transport properties of these films as a function of substrate temperature has been correlated with variations in orientation, cubic/hexagonal phase ratio, and morphology. Additional effects of cooling rate, spraying rate, heat-treatment in hydrogen, and variations in substrate are also considered. By heat-treatment in hydrogen it is possible to produce films on amorphous glass substrates with an electron density in excess of 10^{18} cm^{-3} and an electron mobility of 90 cm^2/V-sec at 300°K.

The method of spray pyrolysis (or solution spraying) is a convenient and economical method for the deposition of materials suitable for this technique. The production of CdS films by spraying a solution of $CdCl_2$ and thiourea was described by Chamberlin and Skarman (1) following a patent by Hill and Chamberlin (2). The electrical properties of films produced by spray pyrolysis (SP) have been investigated by Micheletti and Mark (3), and by Wu and Bube (4). Solar cells have been produced by the deposition of n-CdS films by SP on p-CdTe single crystal substrates with a solar efficiency of over 6% (5), and SP films of n-CdS are also being used in p-Cu_2S/n-CdS heterojunctions for solar energy conversion (6). The SP technique is convenient for the deposition of ternaries involving sulfides and selenides, and the properties of CdS_xSe_{1-x} and $Zn_xCd_{1-x}S$ films prepared by this method have been described (7).

There is therefore ample motivation to understand the deposition of CdS films by the SP technique. We report here the results of a detailed investigation of the preparation and properties of such films as a function of substrate temperature, cooling rate, spraying rate, postdeposition heat-treatment in hydrogen, and choice of a substrate. By combining measurements of film orientation, cubic/hexagonal phase ratio, morphology, and optical transmission with analysis of electrical transport through thermoelectric and photothermoelectric measurements, it is possible to define some of the correlations between structure and electrical properties of these films.

Preparation of Films

All the films prepared in this paper were prepared by spraying an equimolar (0.1M) solution of $CdCl_2$ and thiourea onto a heated substrate. The solution was sprayed by an atomizer spray nozzle and the liquid spray rate was controlled by a flow meter and the air pressure applied to the nozzle. After the solution is sprayed onto the substrate, thermal decomposition of the complex ion $Cd(CN_2H_4S)_2Cl_2$ takes place, and uniform CdS films are grown on the substrate.

For most of the experiments described in this paper, amorphous glass substrates were used. In order to have a systematic investigation of the effect of substrate temperature on the properties of the films, a series of CdS films was prepared with all the parameters fixed except the substrate temperature. The spray rate used was fixed at 4.2 cm^3/min, and the films were removed from the substrate heater immediately after deposition of a 2 μm thick film. Subsequent portions of the investigation involved using crystalline substrates, changing the spraying rate, or allowing the films to cool slowly on the substrate heater. All spraying was done under air pressure and in an air environment.

It is well known that the electrical properties of CdS films prepared by SP can be affected by chemisorbed oxygen (3, 4). Our previous work, however, has shown that heat-treatment in air lowers the conductivity compared to an as-deposited film, and that subsequent heat-treatment in vacuum restores the conductivity to approximately the same as the as-deposited condition (4). Measurements reported here are primarily on as-deposited films, rapidly cooled and without subsequent heat-treatment in air, and measured by thermoelectric power in 10^{-5} Torr vacuum. For such films oxygen adsorption effects should be minimized.

Effect of Substrate Temperature

A series of films was deposited for substrate temperatures between 320° and 570°C. The room temperature electrical conductivity of these films is shown in Fig. 1a. The dark conductivity is a striking function of substrate temperature, exhibiting fluctuations by three orders of magnitude for differences in substrate temperature of 20°-30°C. Although this conductivity is so strongly temperature dependent, it is still possible to

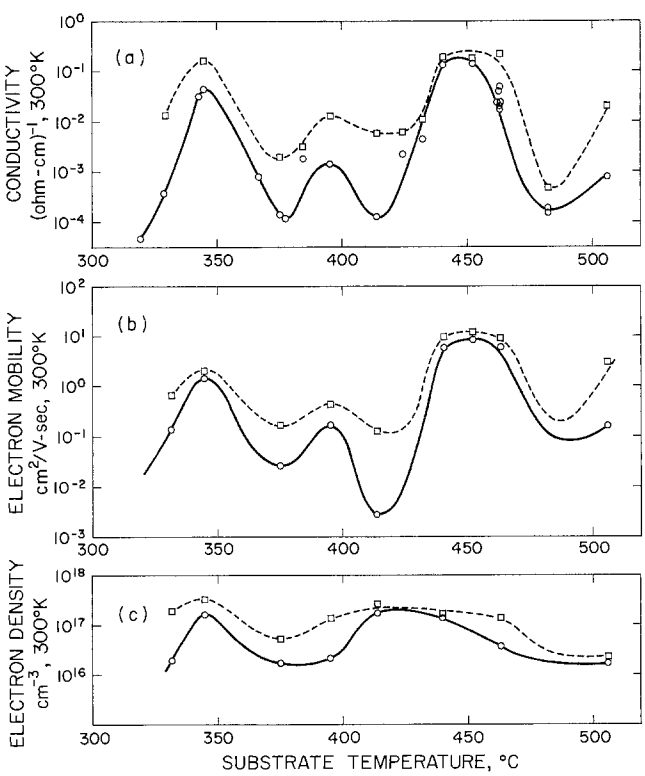


Fig. 1. Dependence of electrical conductivity, electron density, and electron mobility at 300°K on the substrate temperature during CdS film deposition. Solid curves are in dark; dashed curves are under illumination.

* Electrochemical Society Active Member.

[1] Present address: Optical Coating Laboratory, Inc., Santa Rosa, California 95400.

Key words: cadmium sulfide, films, spray pyrolysis, solution spraying, transport in films, thermoelectric power of films.

prepare highly reproducible films by carefully controlling substrate temperature, spraying rate, film thickness, cooling rate, etc. Most of the maximum and minimum conductivity points of Fig. 1a have been repeated several times in order to establish that the variations shown are not the consequence of uncontrolled preparation variables. Films prepared at 461°C, for example, have been repeated many times under the same spraying conditions; the reproducibility in conductivity in these films is within a factor of two.

In order to determine the relative contributions to these conductivity variations by changes in electron density and electron mobility, thermoelectric power measurements were made as a function of temperature in the dark and under photoexcitation. Samples subjected to this measurement were mounted on a sample holder, which consisted of two aluminum strips with heaters inserted into each strip. The heaters were used not only to heat the sample above room temperature, but also to establish a temperature gradient across the sample. Cooling of the sample below room temperature was controlled by a Joule-Thomson cryotip system. The temperature gradient and the thermoelectric voltage were measured by thermocouples and electrical leads mounted at the ends of the sample. The electron density n and the electron mobility μ of the CdS films were calculated from the equations

$$\alpha = -\frac{k}{e}[A + \ln(N_c/n)] \qquad [1]$$

$$\mu = \sigma/ne \qquad [2]$$

where α is the thermoelectric power obtained from the slope of the thermoelectric voltage *vs.* temperature gradient curve at each sample temperature, A is a constant taken equal to 2.5 for CdS (4), N_c is the effective density of states in the conduction band, and σ is the measured conductivity of the film.

The variation of the measured electron mobility at 300°K as a function of substrate temperature during deposition is given in Fig. 1b, and the variation of the electron density at 300°K in Fig. 1c. It is evident that the dependence of the electron mobility on substrate temperature is the determining factor in the dependence of the electrical conductivity on substrate temperature. All of the films have relatively high electron densities because of chlorine donors incorporated during preparation from the $CdCl_2$.

Typical light and dark electron density and mobility values as a function of temperature are shown in Fig. 2 as calculated from thermoelectric power measurements for the 441° and the 507°C samples. For both samples the electron density is relatively independent of temperature in both dark and light, as would be expected for totally ionized chlorine donors. The dark electron mobility for both samples is thermally activated with a larger activation energy in the higher temperature range than in the lower, and the activation energies are larger for the lower conductivity 507°C film than for the 441°C film. Under photoexcitation the electron mobility for the 507°C sample ceases to be temperature dependent.

These measured mobility variations can be described at least formally by the fairly universal expression (3 ,4)

$$\mu = \mu_0 \exp(-\phi/kT) \qquad [3]$$

where ϕ can be physically interpreted as the barrier height to electron transport between grains of the film. A summary of values of ϕ as a function of substrate temperature is given in Fig. 3a, and a summary of values of μ_0 in Fig. 3b. Comparison of Fig. 1b with Fig. 3a shows that large values of mobility are in general associated with small values of barrier height ϕ. The major conductivity maxima near 350° and 450°C are associated with values of ϕ approaching zero.

The higher temperature portion of the mobility curves of Fig. 2 can be interpreted as resulting from thermal excitation over the intergrain barriers, and the lower temperature portion of these curves can be

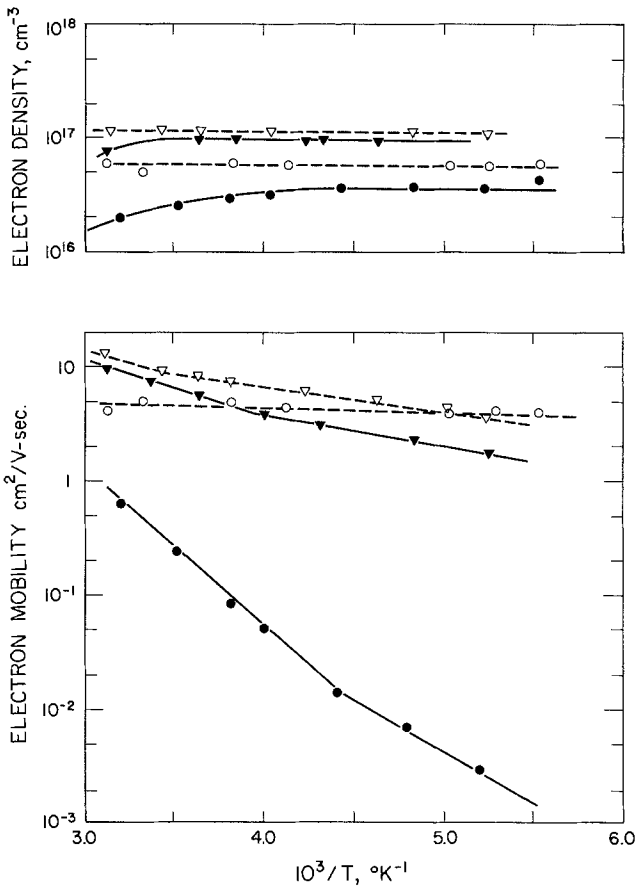


Fig. 2. Temperature dependence of the electron density and electron mobility in CdS films sprayed at 441°C (▼, ▽) and 507°C (●, ○). Solid curves are in dark; dashed curves are under illumination.

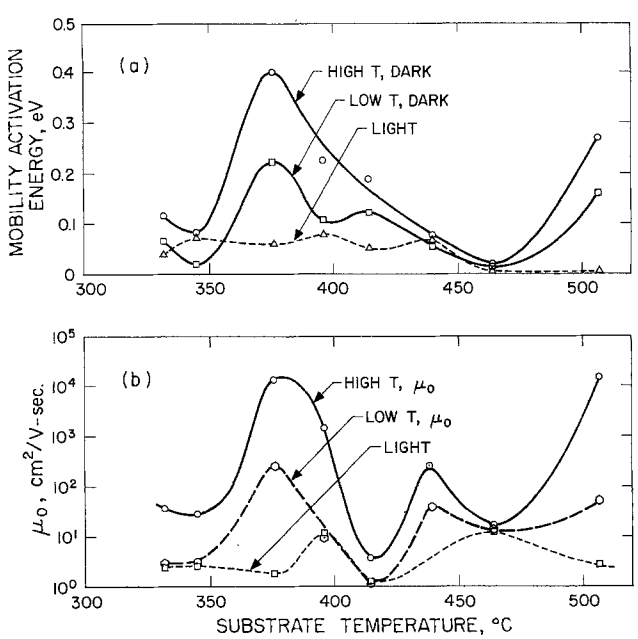


Fig. 3. Values of mobility activation energy ϕ and preexponential term μ_0 as a function of substrate temperature during deposition of CdS films, assuming $\mu = \mu_0 \exp(-\phi/kT)$. Where different values are found at high and low temperatures, both are indicated. Solid curves are in dark; dashed curves are under illumination.

interpreted as caused by thermally assisted tunneling through these intergrain barriers. Under photoexcitation, tunneling without thermal activation dominates in the 507°C film of Fig. 2.

The effect of photoexcitation is to make the variation with substrate temperature less pronounced, in every case causing variations that tend to equalize differences in conductivity, electron density, electron mobility, mobility activation energy, and μ_0 over the whole substrate temperature range explored. Such behavior is consistent with the effect of photoexcitation being both to decrease the barrier height and to enhance tunneling through the barrier, as previously reported (3, 4).

A correlation between the physical properties of the various films produced at different substrate temperatures and these electrical transport properties has been sought with results described as follows.

Orientation effects.—The structure of these films was analyzed by x-ray diffraction techniques. The preferred orientation of the films was determined by using the modified Debye-Scherrer x-ray camera (8) for qualitative analysis, to be compared with the quantitative data obtained from diffractometer patterns. These diffractometer patterns indicate that for substrate temperatures between 322° and 414°C, (11,2) and (10,1) reflections increase in intensity with substrate temperature, whereas (00,2) reflections decrease. Above 441°C the reverse trend is seen with (00,2) reflections increasing and (11,2) and (10,1) decreasing. The Debye-Scherrer patterns of films prepared below 350°C show uniform intensity in (00,2), (11,2), and (10,1) reflections, indicating that the crystallites in the films are randomly oriented. Preferred orientation occurs in the films deposited above 350°C, the degree of preferred orientation depending on the substrate temperature during deposition.

The intensities of the major x-ray reflections, I(10,1), I(00,2), and I(11,2), measured from diffractometer patterns, are plotted as a function of substrate temperature, and are compared with the electrical conductivity of the films, in Fig. 4. It is convenient to divide the temperature range into four regions as indicated. Orientation effects appear to be strongly correlated with conductivity variations in regions II, III, and IV. Between 400° and 483°C, the variation of the conductivity is similar to the variation of the I(10,1), and almost exactly inverse to the variation of I(11,2). In region II between 346° and 376°C, it can be speculated that the inverse variation of conductivity according to I(11,2) dominates over the direct variation according to I (10,1) because of the larger variation of the former with substrate temperature. In region IV, only the (00,2) orientation remains at 507°C; in this range the presence of the cubic phase also affects the conductivity, as described in the following section.

Cubic-hexagonal phase ratio.—CdS can exist in an hexagonal (wurtzite) structure or in either zincblende or rocksalt cubic structures. Cubic phases may be expected in films produced by SP for two reasons: The cubic phase is stable below about 400°C, and may therefore be expected in the films prepared with lower substrate temperatures; and the fast-cooling process can induce stacking faults with cubic structure because of the difference in thermal expansion coefficients of the CdS and the substrate. Such stress-induced stacking faults have been found in the films by observation of the (220) rocksalt cubic reflection in the x-ray diffractometer patterns for films prepared at 397°, 414°, 483°, and 490°C. These rocksalt reflections can also be observed in the modified Debye-Scherrer patterns. The probability of finding the zincblende structure reflections in the diffraction patterns is small since most of the zincblende reflections are superimposed on reflections of the hexagonal hcp phase.

The proportionality of hexagonal hcp phase in the films, called "hexagonality" H, can be calculated from the intensity ratio R of (10,1) to (00,2) reflections in the x-ray pattern, according to

$$H(\%) = \frac{15.9R - 8.1}{13.5R + 25.1} + \frac{33.2 - 2.5R}{32.5 + 71.2R} \qquad [4]$$

This equation was derived by following the suggestions of Smith (9) and Short and Steward (10) in their derivations of the proportion of cubic phase in ZnS and CdS powders. The constants in Eq. [4] are calculated by using the x-ray diffractometer patterns of the SP

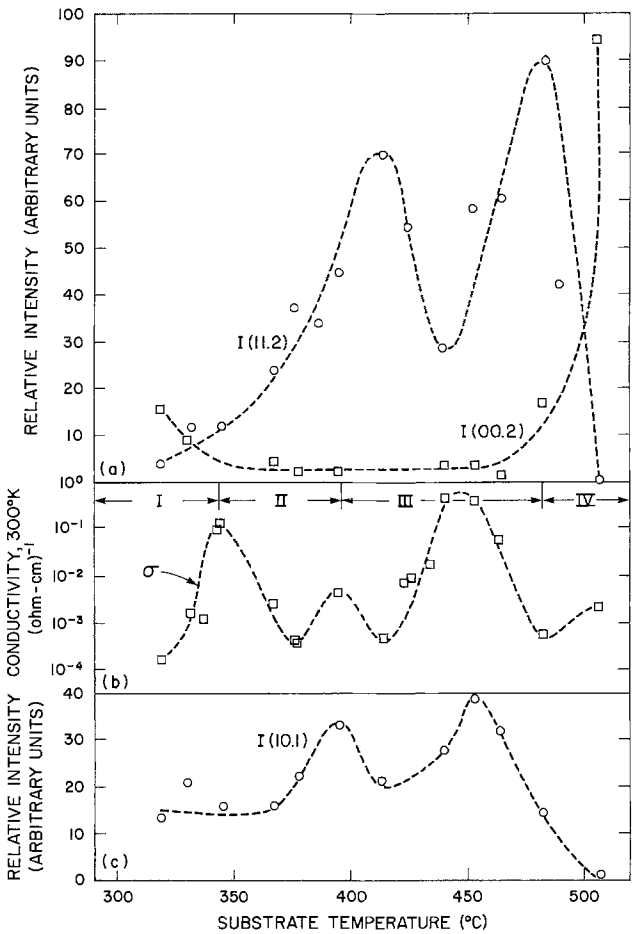


Fig. 4. Relative intensity of (11,2), (10,1), and (00,2) reflections in films of CdS as a function of the substrate temperature during deposition, compared with the electrical conductivity variation with substrate temperature.

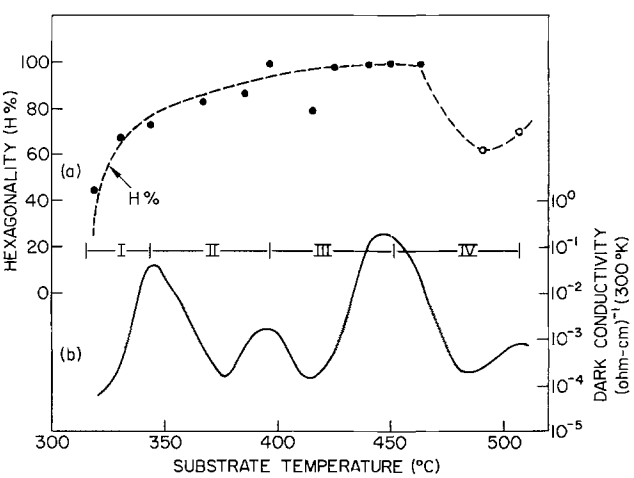


Fig. 5. Hexagonality (as defined in Eq. [4]) as a function of substrate temperature during deposition of CdS films, compared with the electrical conductivity variation with substrate temperature.

films prepared from 322° to 507°C. Detailed derivation of the equation is given elsewhere (11).

Values of H from Eq. [4] are plotted in Fig. 5 as a function of the substrate temperature. In the range of substrate temperatures between 322° and 346°C, H increases from 46 to 71%. Since there is no large change in crystallite orientation in this region the increase of conductivity appears to be associated with this change in phase composition. In region IV, the decrease of conductivity is again associated with an increase in cubic phase. Since the 507°C films are highly oriented in the (00,2) direction, the energy required to generate stacking faults in the close-packed (00,2) plane is small, and thermal or internal stress in the film can generate large proportions of cubic phase.

Surface morphology.—The surface morphology of films prepared at different substrate temperatures was investigated by TEM replica techniques. Figure 6 shows photographs of the surface microreliefs of films prepared at four different substrate temperatures, with different values of H. For the films prepared at 397° and 441°C, for which $H \sim 100\%$, the microreliefs show distinct grains with uniform size. For the films prepared at 332° and 507°C, however, with appreciable proportions of the cubic phase, the microreliefs show a range of grain sizes from less than 0.1 μm to 0.5-0.9 μm. By comparing the electron diffraction patterns of evaporated CdS films to x-ray diffraction patterns of the same samples, Shalimova *et al.* (12) and Galkin *et al.* (13) discovered that the larger grains were hexagonal, while the smaller grains were a mixture of cubic and hexagonal phases. The microreliefs of Fig. 6 are consistent, therefore, with the conclusion that relatively high proportions of the cubic phase are present even at the higher substrate temperature of 507°C.

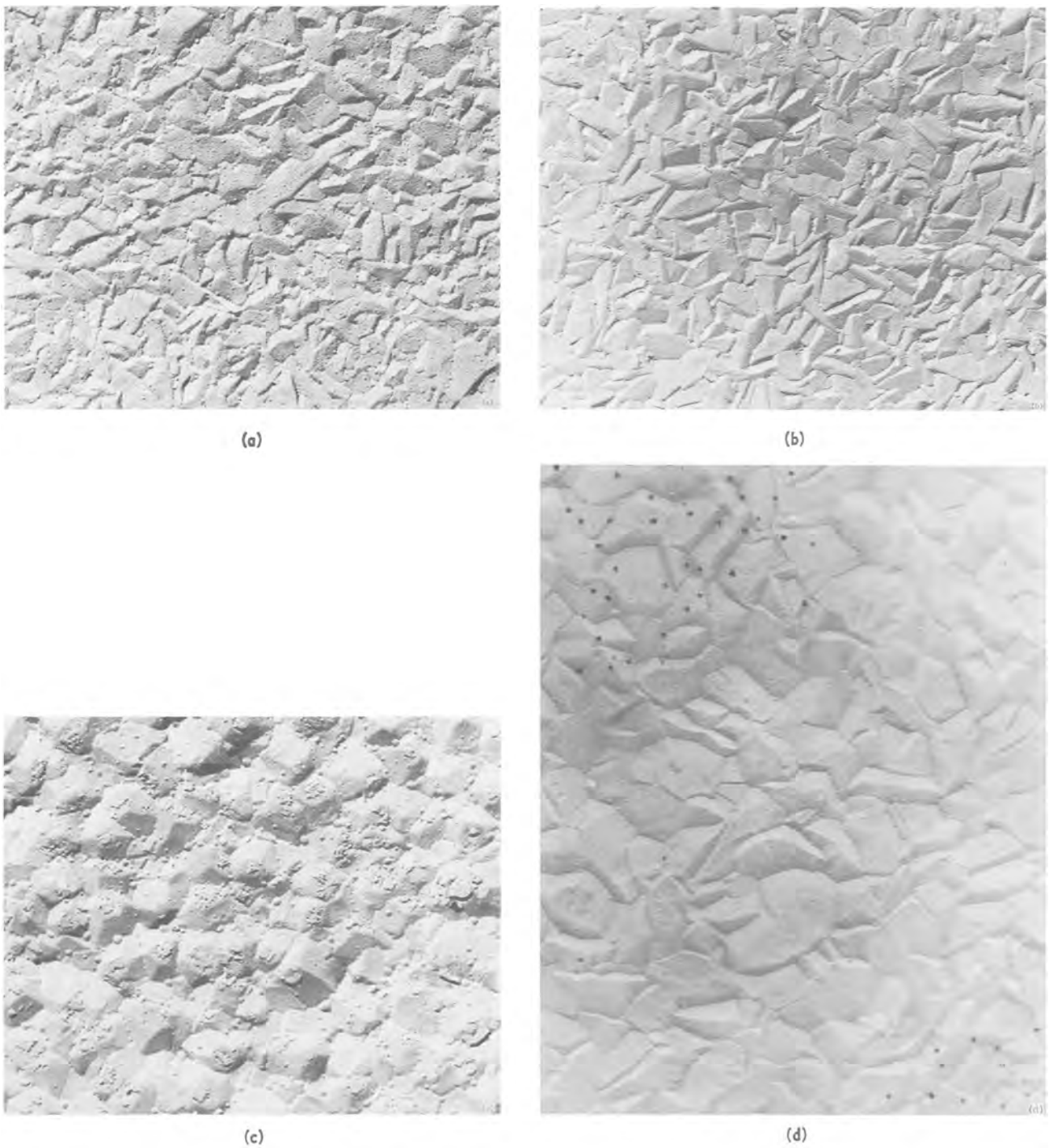


Fig. 6. TEM microreliefs showing surface morphology of CdS films deposited on substrates at (a) 332°C, (b) 397°C, (c) 507°C, and (d) 441°C. Magnification: X44,000.

Optical transmission.—Optical transmission measurements as a function of substrate temperature are summarized in Fig. 7. The film prepared at 332°C has the lowest optical transmittance as well as the lowest electrical conductviity. Auger analysis (14) of this film shows a high concentration of chlorine inside the film, which may contribute to the low optical transmission. Alisoukas *et al.* (15) have also reported that the spectral distribution of photoconducting CdS sintered layers depends on the concentration of $CdCl_2$ used in the sintering and on the sintering temperature. The highest values of optical transmission are for the films prepared at 441° and 451°C, which also exhibit the highest values of electrical conductivity.

Effect of Cooling Rate

The effect of cooling rate was investigated for films prepared at 461°C. One sample was fast-cooled as described above, a second sample was cooled slowly from 461° to 100°C in 80 min, and a third was cooled slowly from 461° to 100°C in 115 min.

Figure 8 compares the electron density and mobility as a function of temperature for these three samples. The slower cooling decreases both the electron density and the mobility compared to the faster cooling, and increases the intergrain barrier height as determined from the mobility activation energy.

X-ray diffraction patterns indicate that the slow-cooled films have a reduced intensity for the (11,2) and (10,1) reflection, and an increase in the intensity of (00,2) reflections, indicating growth of (00,2) crystallites at the expense of others during slow cooling. Since the slow-cooled samples were exposed to air during the long period of cooling, it is likely that the slow-cooling procedure is equivalent to an air bake, causing the chemisorption of oxygen as discussed in the previous section on preparation of films, with related decrease in electron density and increase in intergrain barrier heights.

Effect of Spray Rate

Sensitivity of film properties to the spray rate appears to vary critically with substrate temperature. At

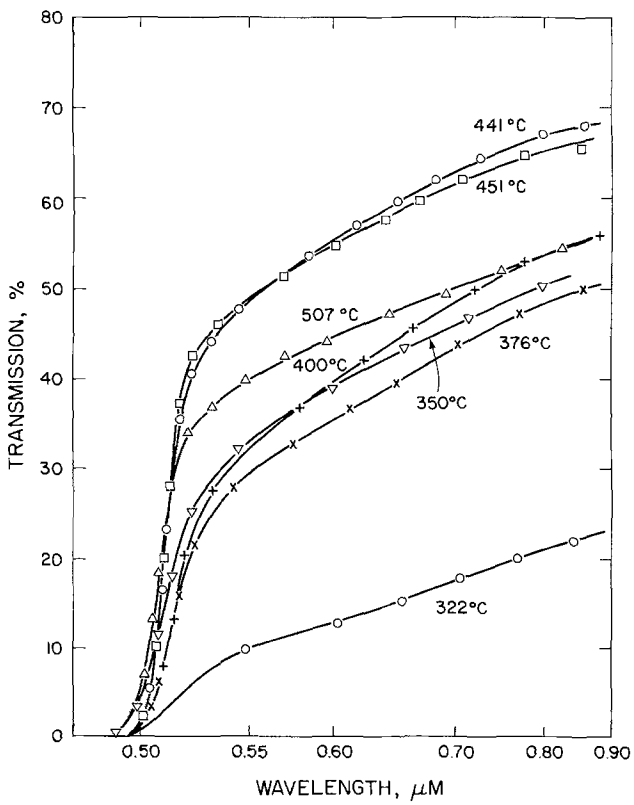


Fig. 7. Optical transmission of CdS films for various substrate temperatures during deposition.

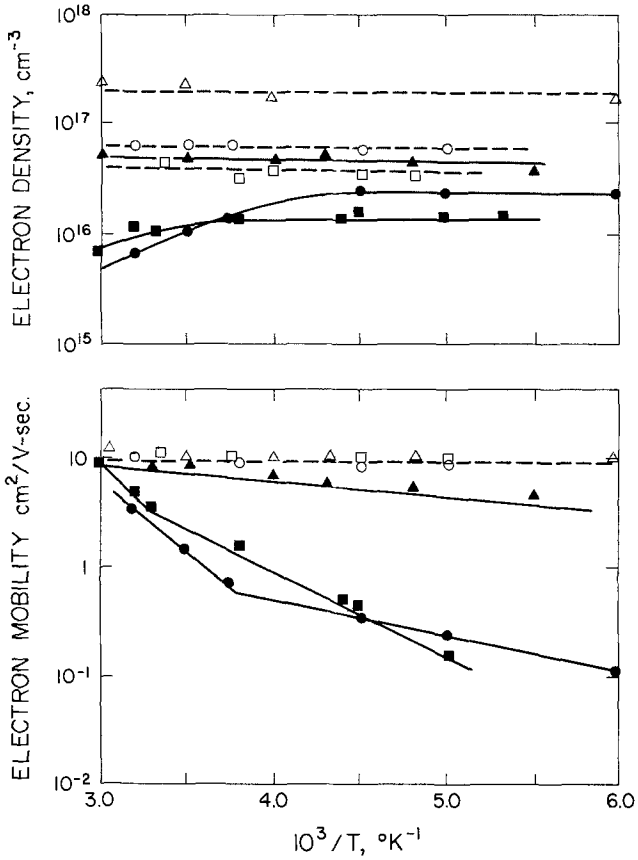


Fig. 8. Temperature dependence of the electron density and the electron mobility of CdS films deposited at a substrate temperature of 461°C for a fast-cooled sample (▲, △), and two slow-cooled samples (●, ○) and (■, □). Solid curves are in the dark; dashed curves are under illumination.

322°C, for example, the conductivity is relatively independent of changes in spray rate from 1.6 to 8.4 cm³/min. At 464°C, the effect is small but detectable; a variation in the spray rate from 4.2 to 10.3 cm³/min produced a decrease in conductivity by a factor of four, attributable to a decrease in mobility by a factor of four because of an increase in the barrier height between grains from 0.016 to 0.049 eV. At 346°C, however, the effect of spraying rate is very strong; the conductivity increases from 5.8×10^{-5} to 6×10^{-2} $(\Omega\text{-cm})^{-1}$ as the spray rate is increased from 1.6 to 4.0 cm³/min, and then decreases again to 4.7×10^{-6} $(\Omega\text{-cm})^{-1}$ as the spray rate is increased further to 8.3 cm³/min.

The major effect of a fast spraying rate is to introduce defects, such as stacking faults, dislocations, and vacancies into the films. Since 350°C is reported to be the phase transition temperature from cubic CdS to hcp (16), these defects generated by the fast spraying rate may increase the internal stress in the films and hence affect the phase transformation, particularly for films deposited at 346°C, close to this critical temperature. The hexagonality for these films shows a dramatic decrease from 83 to 43% as the spray rate is increased from 4.0 to 8.3 cm³/min. Increased spray rate also causes a decrease in grain size observed in TEM micrographs, and a slight peak broadening in x-ray diffraction patterns indicating decreased crystallinity.

Effect of Heat-Treatment in Hydrogen

Heat-treatment of SP CdS films after deposition can increase their conductivity by as much as three orders of magnitude. The results of thermoelectric power measurements on films prepared under the same conditions with and without heat-treatment are given in Fig. 9. After 5 min heat-treatment in H_2 at 400°C, the films become partially degenerate with an electron

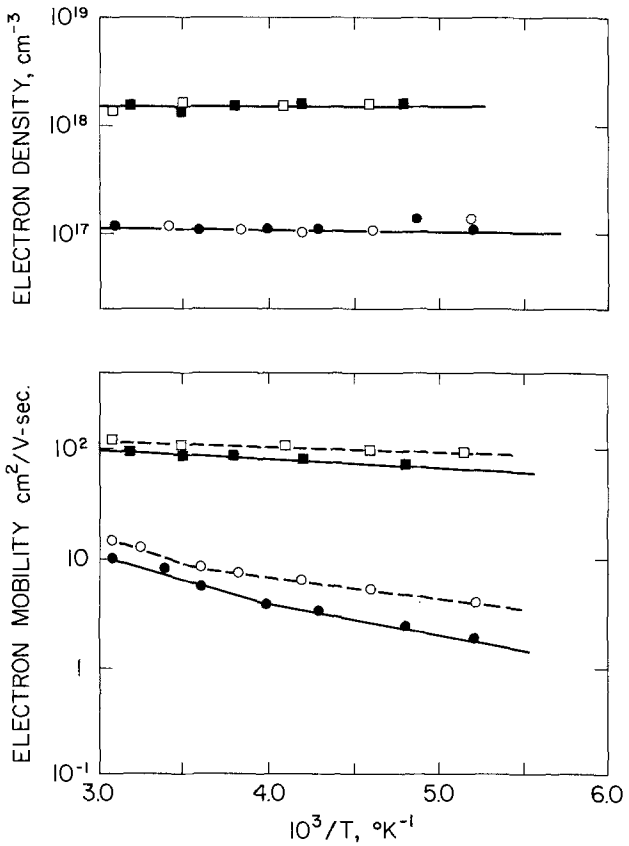


Fig. 9. Temperature dependence of the electron density and the electron mobility of CdS films before and after heat-treatment in H_2 for 5 min at 400°C. Before heat-treatment (●, ○), and after heat-treatment (■, □). Solid curves are in the dark; dashed curves are under illumination. No effects of illumination on the electron density are observed in these films.

density of 1.5×10^{18} cm^{-3}. The electron mobility is also increased by about an order of magnitude to a value of 90 cm^2/V-sec in the dark at 300°K. The dark mobility activation energy decreases from 0.083 eV to 0.015 eV as a consequence of the H_2 heat-treatment. X-ray diffraction patterns indicate both a growth in crystallites with the same orientation as in the non-heated film, and a growth of certain orientations at the expense of others. Heat-treatment in hydrogen is also expected to increase the nonstoichiometry of the film, producing excess cadmium donors, increasing the free electron density in the grains, and reducing intergrain barrier heights. Heat-treatment in H_2 should also remove any vestige of chemisorbed oxygen with similar consequences.

Effect of Substrates

A very limited survey was made of the electrical properties of CdS films deposited on a variety of crystalline substrates, to compare with those prepared on amorphous substrates and described at some length above. In this comparison a single deposition temperature of 461°C was used, together with a fixed spraying rate, cooling rate, etc. Substrates chosen included single crystal CdTe with (110) and (111) orientations, single crystal sapphire with (0001) and (1102) orientations, single crystal quartz, and a (100) oriented polycrystalline film of indium-tin oxide.

All of these films deposited on single crystal substrates have a strong (00,2) orientation, indicating that the c-axis of the film is perpendicular to the substrate, regardless of the specific orientation of the substrate. In spite of this difference, the measured 300°K conductivity of the films sprayed at 461°C was about the same on the crystalline substrates as on the amorphous substrates.

The only additional investigation carried out to date has been the preparation of n-CdS/p-CdTe heterojunctions by the SP deposition of CdS films on single crystalline p-CdTe substrates. As described more fully elsewhere (5), SP-deposited CdS films on substrates at 450°C had an as-deposited conductivity of about 10^{-2} $(\Omega\text{-cm})^{-1}$: This conductivity could be increased to 10^2 $(\Omega\text{-cm})^{-1}$ by heating for 5 min in H_2 at 420°C.

Conclusions

The method of spray pyrolysis for the deposition of thin films of materials like CdS is attractive for its technological ease and economy. This investigation shows that the optical and electrical properties of these films can be strongly influenced by substrate temperature, cooling rate, spraying rate, and postdeposition heat-treatments. It is therefore essential to have carefully controlled preparation conditions in order to achieve reproducible high quality films. With such care it is possible to prepare a wide variety of films with 300°K conductivity between 10^{-4} and 10^2 $(\Omega\text{-cm})^{-1}$, corresponding to electron mobilities between 10^{-3} and 10^2 cm^2/V-sec.

Acknowledgment

This research was supported by the National Science Foundation.

Manuscript submitted Feb. 8, 1977; revised manuscript received April 29, 1977.

Any discussion of this paper will appear in a Discussion Section to be published in the June 1978 JOURNAL. All discussions for the June 1978 Discussion Section should be submitted by Feb. 1, 1978.

Publication costs of this article were assisted by Stanford University.

REFERENCES

1. R. R. Chamberlin and J. S. Skarman, *This Journal*, **113**, 86 (1966).
2. J. E. Hill and R. R. Chamberlin, U.S. Pat. 3,148,084 (1964).
3. F. B. Micheletti and P. Mark, *Appl. Phys. Lett.*, **10**, 136 (1967).
4. C. Wu and R. H. Bube, *J. Appl. Phys.*, **45**, 648 (1974).
5. Y. Y. Ma, A. L. Fahrenbruch, and R. H. Bube, *Appl. Phys. Lett.*, **30**, 423 (1977).
6. J. F. Jordan and G. A. Samara, Proceedings of the 2nd ERDA Semiannual Solar Photovoltaic Conversion Program Review, 299 (1976).
7. R. S. Feigelson, A. N'Diaye, S.-Y. Yin, and R. H. Bube, *J. Appl. Phys.*, **48**, 3162 (1977).
8. M. H. Read and C. Altman, *Appl. Phys. Lett.*, **7**, 51 (1965).
9. F. G. Smith, *Am. Mineral.*, **40**, 658 (1955).
10. M. A. Short and E. G. Steward, *Phys. Chem.* **13**, 298 (1957).
11. Y. Y. Ma, Ph.D. dissertation, Stanford University (1977).
12. K. V. Shalimova, A. F. Andrushko, and V. A. Dmitriev, *Sov. Phys. Crystallogr.*, **8**, 618 (1964).
13. B. D. Galkin. N. V. Troitskaya, and R. D. Ivanov, *ibid.*, **12**, 766 (1968).
14. Y. Y. Ma and R. H. Bube, Unpublished.
15. A. Alisoukas, J. Jakimouicius, B. Alksiejunas, and A. Sirvoitis, *Liet. Fiz. Rin. Kimys.*, **13**, 427 (1973).
16. H. Holloway and E. Wilkes, *J. Appl. Phys.*, **39**, 5087 (1968).

Photoelectrolysis of Water with Semiconductor Materials

Micha Tomkiewicz and Jerry M. Woodall*

IBM Thomas J. Watson Research Center, Yorktown Heights, New York 10598

ABSTRACT

In an effort to find a semiconductor electrode with a bandgap in the visible part of the spectrum that can serve in the catalytic photodecomposition of water, different systems were explored. The first was sputtered thin films of wide bandgap semiconductor materials such as TiO_2, SnO_2, Nb_2O_3, Al_2O_3, and Si_3N_4 on low bandgap, n-type semiconductors such as GaAs and GaAlAs. Scanning electron micrographs showed that corrosion is greatly reduced but continues by diffusion of the electrolyte through the film, undermining the film by pit formation in the low bandgap semiconductor. There was no evidence for hole conduction through the film. The second system employed p-type GaP as the cathode and Pt as the anode. It was observed that this cell catalytically photoelectrolyzes water with conversion efficiency of 0.1%. The efficiency of the device is a strong function of crystal orientation, surface treatment, and purity of the crystal. The results are explained in terms of an energy diagram of the entire system. Areas for possible improvement are mentioned.

Photoassisted electrolysis of water using illuminated semiconductor electrodes has been demonstrated recently in several systems (1-14). In order for such devices to make significant contributions in the conversion and storage of solar energy they must meet two criteria. First, it is essential that a significant fraction of the solar radiation be absorbed by the semiconductor and efficiently converted to electrical energy in the form of charge separation. Second, this electrical energy must be converted into chemical energy that can be stored and then used in any required mode. The first reported photoassisted electrolysis by Fujishima and Honda (1) employed n-type TiO_2 as the anode and Pt as the cathode using either a two-compartment or single compartment device. Since then, many other n-type materials have been tried as anodes.

Two other basic configurations have also been studied. In the first one, a p-type semiconductor is used as the cathode and Pt as the anode (15). This is discussed in the last part of this paper. The other configuration employs n-type semiconductor anode and p-type semiconductor cathode (6, 14, 16) with light being absorbed by both semiconductor electrodes. This last configuration seems very attractive at first glance, since it avoids the highly restrictive condition of matching the flatband potential and the bandgap energies with the potentials of both the hydrogen and the oxygen electrodes. However, it appears that the efficiency of such a device is going to be limited to the lower efficiency of the separate electrodes. This is due to a charge imbalance and, hence, a loss which occurs as a result of the different efficiencies of the two electrodes.

In this paper, we describe some experiments in which we attempted to identify semiconductor systems which absorb visible light, photoelectrolyze water, and will not photocorrode. Our experiments involved both n- and p-type semiconductors. We discuss separately devices based on each kind of semiconductor.

n-type materials.—It has been observed that most small bandgap n-type materials (smaller than 3 eV) tend to corrode in a photoelectrolytic cell, whereas some large bandgap n-type semiconductors will photoelectrolyze water and remain stable. Recently, Fe_2O_3 (9) and WO_3 (13), both with bandgaps smaller than 3 eV, have been shown not to photocorrode. A natural consequence of this is to try to coat the low bandgap semiconductor with a thin protecting film to prevent direct contact between the semiconductor and the electrolyte, and thus prevent corrosion (7). At the same time, it was hoped that such a film would not prevent holes from reaching the aqueous interface.

One choice for such a film is a thin, inert, semitransparent metal film. This approach was tried, (17) and the main conclusion was that light was converted to electrical energy by providing a "negative overpotential" (18) to various electrochemical reactions including water electrolysis. The stability of this electrode system was vaguely mentioned and details about testing this aspect were not given. In our opinion the main drawback in this solution is that it does not appear to offer any advantage over the combination of two already well-established techniques, namely, a standard electrolytic cell connected to Schottky diode photovoltaic device. The reported (17) negative overvoltage is well within the capacity of the direct voltage delivery of metal/semiconductor junctions.

Another choice and the device we investigated will be called the semiconductor insulator electrolyte (SIE) device. This device employs a thin film of photoelectrolytically stable insulator or wide bandgap semiconductor on an efficiently solar absorbing material, with the hope that photogenerated holes, created by illuminating the solar absorbing material, can be transported to the electrode-electrolyte interface.

p-type materials.—Photoinduced hydrogen evolution on p-type semiconductor electrodes has been previously observed (19). However, the potential of this phenomenon in solar energy utilization was realized only recently (14-16). In solar-absorbing n-type materials, photogenerated holes are expected to migrate through the interface to interact with water. Instead they usually break up the crystal structure and form the thermodynamically very stable oxygen-metal bonds that will eventually cause dissolution in the electrolyte and corrosion of the surface. If a chemical change is to take place on p-type materials it will be through reduction of the surface by the minority carriers generated in the conduction band. Those reduction products are in most cases less stable than the parent semiconductor, and the electrons have a greater probability of interacting on the semiconductor electrolyte interface without permanent damage to the crystal lattice.

Experimental

A standard three-electrode electrochemical cell was used with a switch to monitor separately the current-potential and the current-voltage curves. The samples, which were usually in the form of thin wafers, were etched and cleaned. An ohmic contact was then applied. Au-In alloy was used for the n-type materials

* Electrochemical Society Active Member.

Key words: photoelectrolysis, semiconductor electrolyte, interface, photocorrosion.

and Zn-Au was used for the p-type samples. The contacts were alloyed at ~400°C under a forming gas atmosphere. A copper wire was attached to the ohmic contact with silver epoxy. All the nonilluminated areas were masked with polyvinyl ketone. This mask proved to be resistant to both chemical attack and photochemical degradation. This material maintained also constant density even after prolonged exposure to highly basic or acidic solutions. The sample thus prepared was mounted on a Teflon holder and placed in the cell. A 4 cm^2 platinum sheet was used as the counterelectrode, and calomel electrode was used as reference. The light source was a water filtered 75W xenon lamp. Calibrated neutral density filters were used to change the light intensity. Corning, 300Å bandpass intereference filters were used for the spectral measurements. After each measurement, an Eppley thermopile was placed at the same position as the working electrode to monitor the light intensity.

The SIE devices were prepared by either sputtering the insulator (or the high bandgap semiconductor) on the low bandgap material (TiO_2, Al_2O_3, and Si_3N_4 on GaAs and GaAlAs) or by anodic deposition (SnO_2 and Nb_2O_5 on GaAs). The ohmic contact was made to the low bandgap material. The samples were washed with ethanol and distilled water prior to use.

The bulk GaP wafers used throughout this work were prepared by the liquid encapsulation method (20), cleaned with $HF:HNO_3:H_2O$ in the ratio of 1:3:4, and polish etched by mechanical polish in Br_2-methanol solution. The epitaxial GaP was grown on n-type GaP by liquid phase epitaxy. Orientations were determined by x-ray and doping levels by Hall measurements.

Results and Discussion

SIE devices.—The small bandgap, solar absorbing semiconductors that were studied were n-type GaAs and GaAlAs, and the wide bandgap semiconducting films were SnO_2, Nb_2O_5, Al_2O_3, TiO_2, or Si_3N_4. In all cases except TiO_2, the corrosion, as measured by photocurrent of the low bandgap semiconductors (a few $\mu A/cm^2$ for 500 mW/cm^2 xenon lamp illumination), was reduced by a few orders of magnitude compared with unprotected samples. For TiO_2, the photocurrent was about 100-200 $\mu A/cm^2$. However, corrosion was never completely eliminated. At first we believed that the corrosion was initiated by pinholes in the film which enabled the electrolyte to diffuse through localized spots. Corrosion could then continue through lateral diffusion of the electrolyte. However, optical microscopy revealed that the corrosion sites were not localized around presumed pinholes but were scattered uniformly all across the semiconductor surface. In order to reduce the contribution of pinholes to the corrosion, we took special care to prepare films which were pinhole free. This was done by sputtering multilayers of the films and checking them by SEM at magnifications up to 20,000 times.

After determination that within a 300Å resolution, there were no pinholes, the sample was put in the electrolytic cell and the current-voltage characteristics measured. If oxygen and hydrogen were observed, the system was kept electrolyzing water for a short time. Then the electrode was taken out, washed with distilled water, and examined with SEM. The results at two different magnifications are shown in Fig. 1. These pictures suggest that the corrosion can be explained by a mechanism involving diffusion of some species in the electrolyte through the intact film, which then corrodes the surface underneath the film by forming pits in the low bandgap semiconductor. This occurs while the film above the pit is still intact. Eventually the film forms a bubble above the pit which collapses due to surface pressure with the collapsed film hanging toward the interior of the pit. This finding indicates that more care and sophistication in the deposition of the film are not likely to eliminate this problem. Next, it was determined whether or not photogenerated holes were actually being transported to the electrolyte from the small bandgap material. This was done by comparing the photoinduced electrolytic current, using light with photon energies higher than the bandgap of the insulator film with that produced by photon energies less than the bandgap of the film. Specifically, for a 400Å TiO_2 film on GaAs and GaAlAs a cutoff filter of 480 nm was used to distinguish between direct absorption by the film and charge transport due to absorption of light by the low bandgap semiconductor. We found that except for a small corrosion photocurrent, all the observed photocurrent is produced by direct absorption of light by the film. This does not preclude the possibility that a pair might be found with band matching that will allow minority carriers to diffuse through much thicker films than 400Å.

p-type materials.—Current-potential and current-voltage curves were studied on a number of p-type

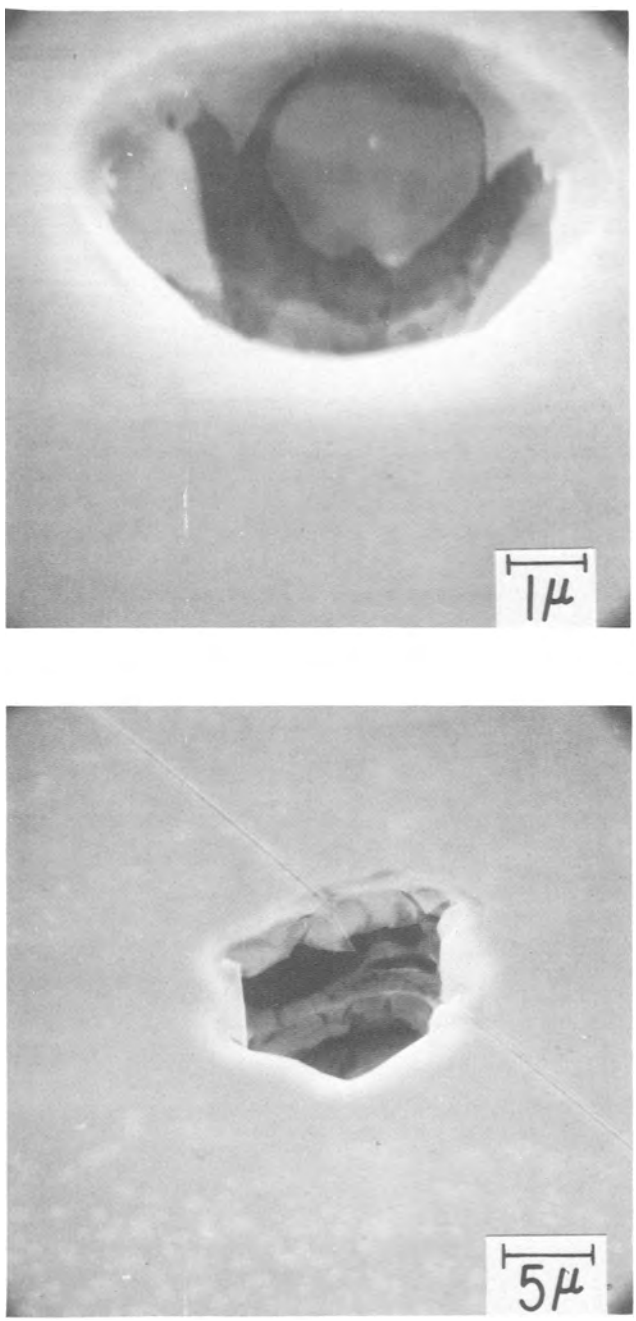


Fig. 1. SEM photomicrograph at two different magnifications of a 400Å TiO_2 film, sputtered on n-type GaAs, after 3 hr of photoelectrolysis in 0.33M phosphate buffer at pH = 7 at an average current density of 0.1 mA/cm^2.

semiconductors which included GaAs, GaAsP, GaP, and InP. It was found that in all cases except GaP the external bias which was needed to start photoelectrolysis exceeded the 'thermoneutral potential" (21), thus making the energy conversion efficiency negative regardless of the generated photocurrent. Only in the case of GaP did we find positive energy conversion efficiency. Thus, this discussion is limited to this semiconductor.

The current voltage behavior of a cell with a p-type $(\bar{1}\bar{1}\bar{1})$ GaP wafer as the cathode and platinum foil as anode in cell with 0.5M Na_2SO_4 + 10^{-2}M NaOH is shown in Fig. 2. When current is flowing through the cell, hydrogen and oxygen could be seen bubbling from the electrode/electrolyte interface for a light intensity as low as 50 mW/cm^2. Figure 2 also shows the conversion efficiency of such a cell when the conversion efficiency is defined as (15)

$$\eta = \frac{I_c \times (1.48 - V) \times 100}{I_a} \quad [1]$$

where I_c is the current flowing in the system, expressed in mA/cm^2, V is the cathodic bias on the GaP electrode, 1.48 is the "thermoneutral potential" (21), and I_a is the intensity of the light incident on the sample, expressed in mW/cm^2.

The current voltage behavior of a GaP (111) wafer from the same crystal is shown in Fig. 3. In this case,

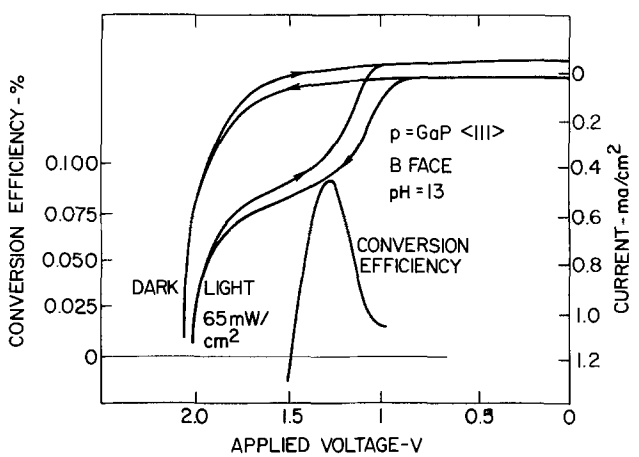


Fig. 2. Current-voltage and conversion-efficiency-voltage diagram for a cell made of Zn-doped GaP $(\bar{1}\bar{1}\bar{1})$ as cathode and Pt foil as the anode. The electrolyte was 10^{-2}M NaOH + 0.5M Na_2SO_4.

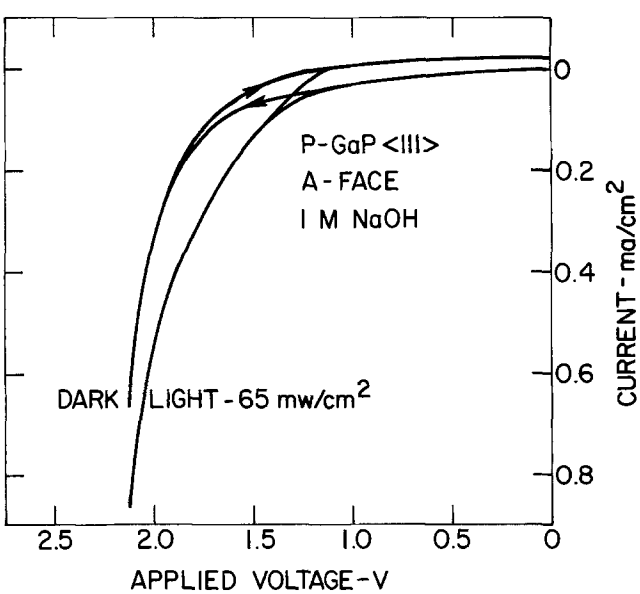


Fig. 3. The same as Fig. 2 except that the (111) surface was exposed. The electrolyte is 1M NaOH.

the bias voltage needed to produce current under illumination is somewhat higher than that needed for $(\bar{1}\bar{1}\bar{1})$ wafers, and, hence, according to Eq. [1], the efficiency will be lower.

The dependence of the light-induced current with light intensity at two different bias conditions is shown in Fig. 4. Above the saturation voltage the current is proportional to the light intensity, while at lower bias the current tends to saturate with light intensity.

Figure 5 shows the spectral response of the quantum efficiency of the photocurrent. The quantum efficiency peaks near 40% at a wavelength which is ~150 nm shorter than the bandgap. We have normalized this spectrum to the condition where only those photons that are absorbed within the first 0.2 μm from the electrolyte interface will lead to charge separation. Any photon that will be absorbed deeper than that will be lost, presumably due to charge recombination. This behavior is not an inherent property of GaP but a very strong function of the particular crystal that is being used.

Figure 6 shows normalized spectrum of two different samples of GaP, one grown by the liquid encapsulation technique and the other epitaxially on GaP. There is a shift of 70 nm in the action spectrum in those two samples. The decline in efficiency at shorter wavelengths is probably caused by increased surface recombination of carriers generated near the surface. If this is so, then the action spectrum should be time dependent, because hydrogen diffusion through the surface is known to have strong effects on the surface recombination rate in semiconductor electrodes (26).

Stability.—The stability of the electrode was checked by passing 100C of electricity through a 1 cm^2 sample

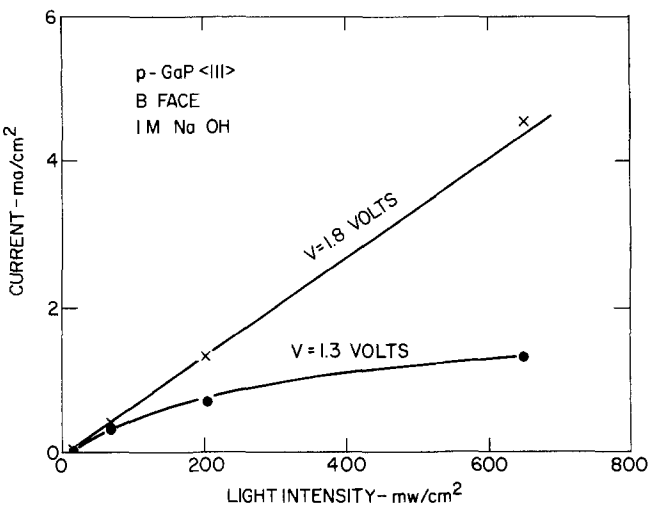


Fig. 4. Dependence of the photocurrent on the light intensity under two different bias conditions.

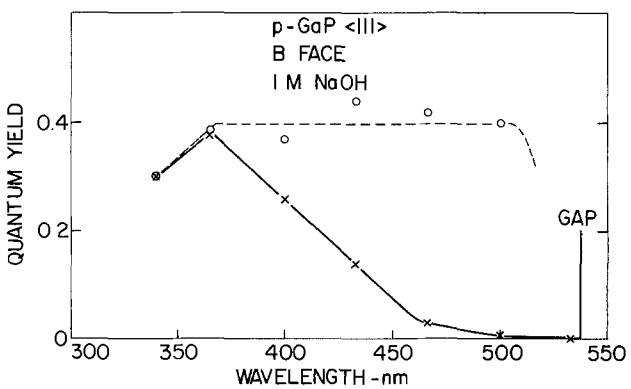


Fig. 5. Solid-line, the spectral response of the quantum yield of the photocurrent; dashed line, calculated spectral response, assuming charge separation in the first 0.2 μm from the electrolyte interface.

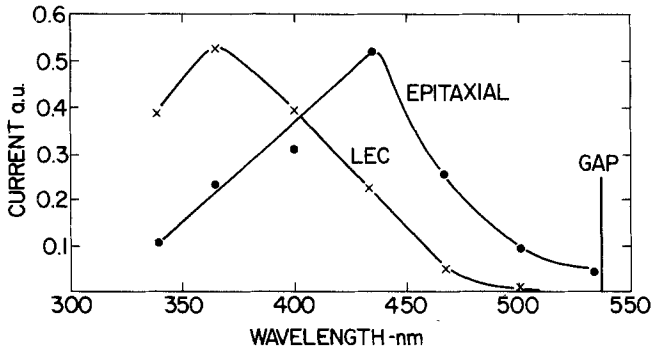


Fig. 6. Normalized spectral response of the photocurrent for two different GaP crystals. One was grown epitaxially on GaP and the other is a liquid encapsulation grown (LEC) wafer.

at an average current density of 5 mA/cm^2 in 0.5M H_2SO_4. Under these conditions the sample did not show any signs of dissolution or corrosion. Optical microscopy did not show any visual change in the surface, and atomic absorption spectroscopy of the electrolyte did not detect any presence of gallium with sensitivity better than 1.5×10^{-7} moles. One additional criterion for the stability of the semiconductor electrode is the stability of the photocurrent with time (14). Figure 7 shows the variation of the photocurrent with time of illumination, under potentiostatic conditions, and under constant bias conditions. It can be seen that under potentiostatic conditions the current is stable, at least for the time period shown here. We found some irregular variations with time over longer periods of illumination. These variations were caused mainly by accumulation of hydrogen bubbles on the electrode. The situation is different when we work under constant bias conditions. The time variation is evident there, but the current could be restored to its original value by turning the light off for a short period of time and then on again. Surface conditions and surface treatment have strong influence on this time behavior. The reversibility of the process indicates that it is not due to any permanent damage to the electrode. The probable cause is formation of surface states due to the hydrogen or metal impurities (22, 23). More studies are needed to explore this important aspect in the performance of the cell.

Energy diagram.—The current potential curve of GaP was measured against standard calomel electrode and agrees with results published earlier (24, 25). The current potential of the platinum electrode was measured and found to be independent of the light. The value of the flatband potential was taken from the work of Memming (24) after correction for the pH. Based on this information, a simplified energy diagram of the cell, under short-circuit conditions and under cathodic bias at the maximum conversion efficiency, was drawn and is shown in Fig. 8. From an examination of Fig. 8,

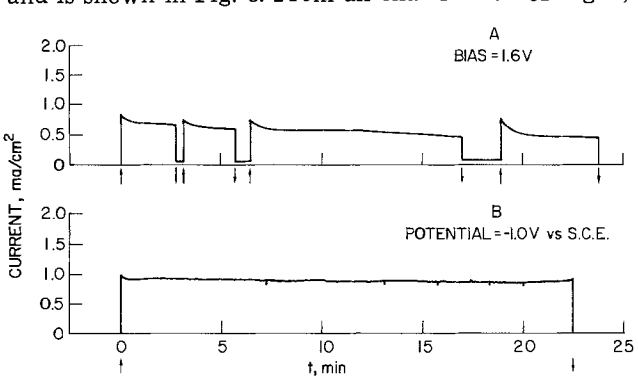


Fig. 7. Variation of the photocurrent with time, at a standard calomel electrode potential of 1.0V. A. under constant bias; B. under potentiostatic conditions. Conditions similar to Fig. 2: ↑ indicates light on; ↓ indicates light off.

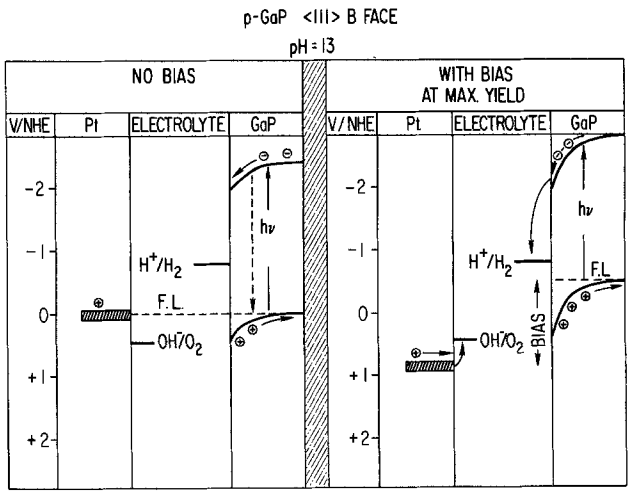


Fig. 8. Energy diagram of the combined cell. All energies are with respect to a standard hydrogen electrode. F.L. is the GaP Fermi Level. 1) under no bias and no photoelectrolysis conditions; 2) under conditions for which the maximum conversion efficiency was obtained.

it appears that the bias which is needed to get the maximum conversion efficiency is divided between the need to raise the potential of the platinum electrode from rest around 0.0V *vs.* a standard hydrogen electrode (SHE) to +0.9V *vs.* SHE. The position of the reversible oxygen electrode is ~ +0.5V *vs.* SHE and the difference is the overvoltage which is required for the evolution of oxygen. This overvoltage could be reduced by platinizing the platinum. The rest of the bias is being applied to increase the band bending of GaP from ~ 0.5V at zero bias to 1V when the light limiting quantum conversion is observed. This relatively high band bending is required to ensure efficient charge separation. A considerable increase in efficiency should be realized if efficient charge separation would occur with smaller band bending.

Conclusions

Two photoelectrolytic devices were discussed in this paper. The first one employed n-type semiconductors as anodes which were embodied in a structure that involved a thin film of insulator or a large bandgap semiconductor, deposited on a solar absorbing n-type wafer. It was shown that in this configuration, even intact films as thick as 400Å could not prevent corrosion of the semiconductor. Furthermore, it was found that these films did not transport charges which were created by absorption of light in the lower bandgap material. It was also shown that p-type semiconductors can serve as stable photocathodes in a photoelectrolytic device. However, among the materials that were studied only p-type GaP showed a positive energy conversion efficiency. The maximum yield that was found was 0.1%. The yield is limited largely by the minority carriers diffusion length and the quality of the crystals used, and by the large overvoltage on the oxygen electrode.

Manuscript submitted Oct. 5, 1976; revised manuscript received May 2, 1977.

Any discussion of this paper will appear in a Discussion Section to be published in the June 1978 JOURNAL. All discussions for the June 1978 Discussion Section should be submitted by Feb. 1, 1978.

Publication costs of this article were assisted by IBM Corporation.

REFERENCES

1. A. Fujishima and K. Honda, *Nature (London)* **238**, 37 (1972).
2. A. Fujishima, K. Kohayakawa, and K. Honda, *This Journal*, **122**, 1437 (1975).

3. M. S. Wrighton, D. S. Ginley, P. T. Wolczanski, A. B. Ellis. D. L. Morse, and A. Linz, *Proc. Nat'l. Acad. Sci. U.S.A.*, **72**, 1518 (1975).
4. M. S. Wrighton, D. L. Morse, A. B. Ellis, D. S. Ginely, and H. B. Abrahamson, *J. Am. Chem. Sco.*, **98**, 44 (1976).
5. A. J. Nozik, *Nature (London)*, **257**, 383 (1975).
6. J. G. Mavroides, D. I. Tchernev, J. A. Kafalas, and D. F. Kolesar, *Mater. Res. Bull.*, **10**, 1023 (1975).
7. P. A. Kohl, S. N. Frank, and A. J. Bard, Submitted to *This Journal*.
8. K. L. Hardee and A. J. Bard, *ibid.*, **122**, 139 (1975).
9. K. L. Hardee and A. J. Bard, *ibid.*, **123**, 1024 (1976).
10. J. Keeney, D. H. Weinstein, and G. M. Haas, *Nature (London)*, **253**, 719 (1975).
11. J. G. Mavroides, J. A. Kafales, and D. F. Kolesar, *Appl. Phys. Lett.*, **28**, 241 (1976).
12. J. H. Carey and B. G. Oliver, *Nature (London)*, **259**, 554 (1976).
13. G. Hodes, D. Cahen, and J. Manassen, *ibid.*, **260**, 312 (1976).
14. H. Yoneyama, H. Sakamoto, and H. Tamura, *Electrochim. Acta*, **20**, 341 (1975).
15. M. Tomkiewicz and J. M. Woodall, 443RNP, *This Journal*, **123**, 189C (1976); To be published.
16. A. J. Nozik, To be published.
17. Y. Nakato, T. Ohnishi, and H. Tsubomura, *Chem. Lett.*, 883-886 (1975).
18. D. Laser and J. Bard, *Chem. Phys. Lett.*, **34**, 605 (1975).
19. A. K. Vijh, "Electrochemistry of Metals and Semiconductors," Chapters 3 and 4, Marcel Dekker Inc., New York (1973).
20. S. E. Blum, R. J. Chicotka, and B. K. Bischoff, *This Journal*, **115**, 324 (1968).
21. D. Gregory, in "The Hydrogen Energy System," p. III-4, prepared for American Gas Association by I.G.T. (1973).
22. P. J. Boddy and W. H. Brattain, *This Journal*, **109**, 812 (1962).
23. A. Many, Y. Goldstein, and N. B. Grover, "Semiconductor Surfaces," North Holland, Amsterdam (1965).
24. R. Memming, *This Journal*, **116**, 785 (1969).
25. R. Memming and H. Tributsch, *J. Phys. Chem.*, **75**, 562 (1971).

Variation of GaAs Epitaxial Growth Rate with Distance along Substrate within a Constant Temperature Zone

J. Komeno, S. Ohkawa, A. Miura, K. Dazai, and O. Ryuzan

Fujitsu Laboratories, Limited, Kamikodanaka 1015, Nakahara, Kawasaki, Japan

ABSTRACT

On the basis of a model which assumes a laminar boundary layer, a rate equation is derived for the vapor phase epitaxial growth of GaAs within a constant temperature zone. The equation can be used to predict the variation of growth rate with distance along the substrate. The predictions of the equation are shown to be in excellent agreement with the experimental results obtained with the open-tube $AsCl_3$-Ga-N_2 system. It is also shown both theoretically and experimentally that the variation of growth rate decreases with increasing gas velocity and also with decreasing substrate temperature, whereas the initial $AsCl_3$ mole fraction has no effect on the growth rate variation.

One of the requirements for many GaAs devices is to prepare epitaxial layers uniform in thickness. Since a vapor phase epitaxial (VPE) growth method for GaAs was first proposed by Effer (1), many investigations have been reported on VPE growth of GaAs (2-6). However, very little has been published on the variation of growth rate with distance along the substrate. It is of considerable importance for preparing uniform thickness epitaxial layers to understand the growth rate at various positions on the substrate. In order to understand this in the case of growth in a graded temperature zone, which is usually employed in the VPE growth of GaAs, it is convenient to investigate the growth rate variation on the substrate in the gas flow direction in a constant temperature zone.

In the present study, a rate equation for epitaxial growth is obtained from a model based on a laminar boundary layer, and is applied to the calculation of the rate of GaAs epitaxial growth. The epitaxial growth within a constant temperature zone was carried out in the diffusion-limited region using the $AsCl_3$-Ga-N_2 system (7). Good agreement between calculated and experimental values is obtained.

Theory

In the VPE growth of a binary semiconductor, the growth rate, R, can be written as (8, 9)

Key words: VPE, binary semiconductor, reacting species, boundary layer, diffusion coefficient.

$$R = [k_s h_g/(k_s + h_g)](C_t/N_1)nM_f \quad [1]$$

where k_s is the surface-reaction rate constant, h_g is the mass transfer coefficient, n is the number of crystal component atoms in a molecule of the rate-limiting reacting species, M_f is the mole fraction of the rate-limiting species, C_t is the total number of molecules per cubic centimeter in the gas, and N_1 is the number of gallium or arsenic atoms incorporated into unit volume of the epitaxial layer. The value of N_1 for GaAs is 2.22×10^{22} cm^{-3}.

The mass transfer coefficient h_g is defined as

$$h_g = D/\delta \quad [2]$$

where D is the diffusion coefficient of the reacting species and δ is the thickness of the boundary layer (9, 10).

Substitution of Eq. [2] into Eq. [1] leads to

$$R = k_s D C_t n M_f/(k_s\delta + D)N_1 \quad [3]$$

Figure 1 shows a schematic diagram of a horizontal reactor with a boundary layer. According to Schlichting (11), the thickness of the boundary layer along a thin flat plate, $\delta(x)$, is given by

$$\delta(x) = 5.0\ (\mu x/\rho V)^{1/2} \quad [4]$$

where x is the distance from the leading edge of the substrate, μ and ρ are the viscosity and density of the

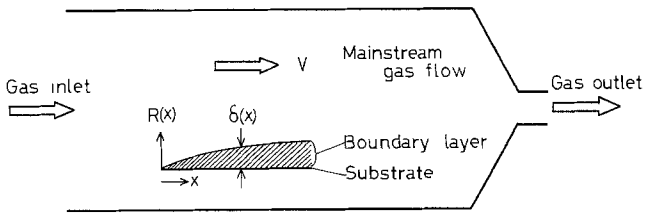


Fig. 1. Schematic diagram of a horizontal reactor with a boundary layer.

gas, respectively, and V is the velocity of the gas outside the boundary layer.

Substitution of Eq. [4] into Eq. [3] yields

$$R(x) = k_s D C_t n M_f / [5.0\, k_s N_1 (\mu x/\rho V)^{1/2} + N_1 D] \quad [5]$$

In order to apply this equation to the actual growth, it is necessary to obtain the temperature dependences of D and k_s.

The temperature dependence of the gaseous diffusion coefficient can be expressed as

$$D_s = D_0 (T_s/T_0)^m \quad [6]$$

where T_s and T_0 are the substrate temperatures (°K) and 273°K, respectively, D_s and D_0 are the diffusion coefficients of the reacting species in nitrogen at T_s and T_0, respectively, and m has a value between 1.75 and 2 (12). In the present study, a value of $m = 2$ is used because most gases diffuse in nitrogen with this m value (13, 14). Thus, Eq. [6] is expressed by

$$D_s = D_0 (T_s/T_0)^2 \quad [7]$$

In the low temperature region, the growth rate increases with increasing substrate temperature. This region is identified as a kinetically or surface-reaction limited region where the over-all epitaxial growth rate is limited by some slow surface process (15). In the case of present system, the apparent activation energy measured in the kinetically limited region is about 1.2 eV. Therefore, the surface-reaction rate constant k_s can be written as

$$k_s = A \exp(-1.2\ \text{eV}/kT_s) \quad [8]$$

where A is a frequency factor and k is the Boltzmann constant (9).

Using Eq. [7] and [8], Eq. [5] can be rewritten as

$$R(x) = nM_f K_1 / [(x/V)^{1/2} + K_2] \quad [9]$$

where

$$K_1 = C_t D_0 (T_s/T_0)^2 \rho^{1/2} / 5.0\, N_1 \mu^{1/2} \quad [10]$$

and

$$K_2 = D_0 (T_s/T_0)^2 \rho^{1/2} / 5.0\, \mu^{1/2} A \exp(-1.2\ \text{eV}/kT_s) \quad [11]$$

Normalizing $R(x)$ by dividing by the growth rate at the point $x = L$ cm, it follows that

$$R(x)/R(L) = [(L/V)^{1/2} + K_2]/[(x/V)^{1/2} + K_2 \quad [12]$$

Experimental

Figure 2 shows the growth apparatus and the temperature profile used for this series of experiments. The apparatus consists of a quartz reactor tube, a Ga source boat, an $AsCl_3$ bubbler, a substrate holder, and a doping tube. The reactor tube had an inside diameter of 44 mm. The purity of Ga and $AsCl_3$ was seven nines and six nines, respectively. The nitrogen gas was purified by a USD nitrogen purifier.

The temperature of the $AsCl_3$ bubbler was varied from 293° to 303°K. The Ga source temperature was held at 1123°K. Constant temperature growth zones of 973°, 987°, and 998°K were employed in the study. The flow rate of nitrogen through the $AsCl_3$ bubbler was kept to 300 cm³/min, and that of nitrogen through the bypass tube was varied from 300 to 1500 cm³/min. It was confirmed that the nitrogen carrier gas was saturated with $AsCl_3$ for the flow rate of 300 cm³/min.

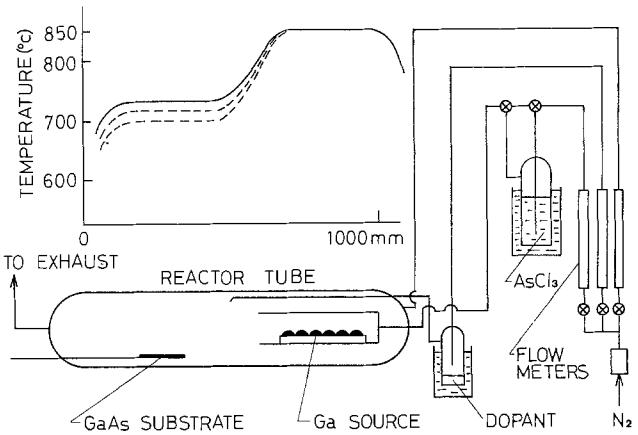


Fig. 2. Schematic diagram of the apparatus and the temperature profile for the epitaxial growth of GaAs.

The substrates used were tellurium-doped GaAs with a resistivity of approximately 2×10^{-3} Ω-cm. Their surfaces were oriented 2° off (100) toward <110>, and the area was 20 × 30 mm. The substrate was placed on a substrate holder in a direction parallel to the gas flow, with a distance between the source and substrate of 20 cm.

The thickness of the grown layer was measured by the infrared interference method (16, 17). The infrared spectrophotometer used was a Beckman IR-18 with a wavelength range of 2.5-16 μm.

Results and Discussion

Diffusion coefficient of reacting species.—In the case of epitaxial growth of GaAs, both gallium- and arsenic-bearing reacting species must arrive at the GaAs surface before the reaction can take place. In the present study, it is assumed that the reacting species bearing both components diffuse through the boundary layer and react at the surface. If, however, one is transported to the surface at a significantly slower rate, it will control the over-all growth rate. Since As_4 is the principal arsenic species and is the largest molecular species in the present GaAs epitaxial growth system, it is reasonable to assume that its diffusion through the boundary layer will be the rate-limiting process. In the present system, GaCl, As_2, and As_4 are considered as the principal reacting species. However, the fluxes of these molecules are in the order

$$F_{GaCl} > F_{As_4} > F_{As_2} \quad [13]$$

over the entire range of growth conditions (18, 19). It is apparent that the process is limited principally by arsenic transport. Thermodynamic considerations (20), however, indicate that F_{As_4} is approximately fifty times as great as F_{As_2} over the range of temperatures employed. Thus, it is reasonable to assume that the over-all growth rate is limited by the process of As_4 diffusion through the boundary layer. Therefore, in order to apply Eq. [9] to the actual growth, the mole fraction of As_4 in the reaction tube must be calculated. The As_4 mole fraction can be calculated from the initial $AsCl_3$ mole fraction; assuming that above approximately 970°K complete reduction of $AsCl_3$ occurs according to the following reaction (20, 21)

$$2AsCl_3 = \tfrac{1}{2}\, As_4 + 3Cl_2 \quad [14]$$

A typical plot of growth rate *vs.* distance along the substrate under a diffusion-limited growth condition is shown in Fig. 3. Values of K_1 and K_2 in Eq. [9] are calculated, by least squares analysis of this plot, to be 7.441×10^{-5} cm/sec$^{1/2}$ and 1.535 sec$^{1/2}$, respectively. The gas viscosity μ and its density ρ at 973°K are taken to be 3.19×10^{-4} g/cm sec and 3.51×10^{-4} g/cm³, respectively (13). Using these values, the diffusion coefficient D_0 and the frequency factor A are calculated as follows

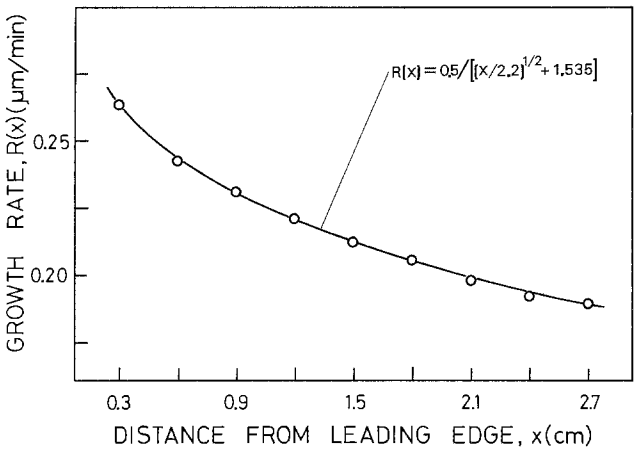


Fig. 3. Growth rate as a function of distance from the leading edge of the substrate. Initial $AsCl_3$ mole fraction 11.20 × 10^{-3}, growth temperature 973°K, gas velocity 2.2 cm/sec.

$$D_0 = 0.083\ \text{cm}^2/\text{sec} \quad \text{and} \quad A = 2.34 \times 10^5\ \text{cm/sec}$$

It is evident that the value of D_0 obtained approximately represents the diffusion coefficient of As_4 in nitrogen. On the basis of the molecular weight of As_4, this value of D_0 seems reasonable (13, 22).

Effect of initial $AsCl_3$ mole fraction.—Figure 4 shows the experimental and the calculated results of $R(x)/R(0.3)$ *vs.* distance x for different initial $AsCl_3$ mole fractions (M_f) at fixed substrate temperature and gas velocity. Variations in the initial $AsCl_3$ mole fraction were obtained by varying the $AsCl_3$ temperature. As can be seen in the figure, there is good agreement between the experimental results and the curve calculated from Eq. [12].

Figure 4 also shows that the variation of growth rate with distance along the substrate is independent of the initial $AsCl_3$ mole fraction M_f. This is because both mass transfer coefficient h_g and surface-reaction rate constant k_s are independent of M_f, since the thickness of the boundary layer is insensitive to variations in M_f, as is evident from Eq. [4]. However, it should be noted here that according to Eq. [9], the growth rate is proportional to the initial $AsCl_3$ mole fraction.

Effect of gas velocity.—The experimental and the calculated results of $R(x)/R(0.3)$ *vs.* x for different gas velocities (V) at a fixed substrate temperature are shown in Fig. 5. The gas velocity was varied by changing the bypass flow so that the efficiency of source

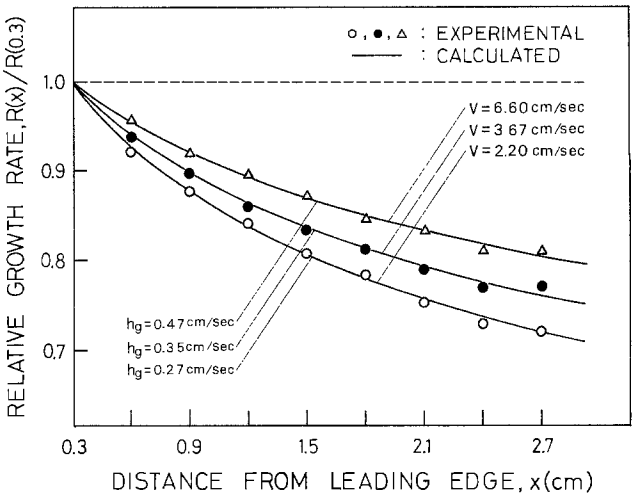


Fig. 5. Comparison of calculated and experimental results of $R(x)/R(0.3)$ as a function of distance from the leading edge of the substrate for different gas velocities (V). Growth temperature 973°K.

reaction did not change. Also given in the figure are the values of h_g at $x = 1.5$ cm for each gas velocity and, as can be clearly seen, there is good agreement between the experimental results and the predictions of Eq. [12].

Figure 5 also reveals that the variation of growth rate along the substrate decreases as the gas velocity is increased. This can be explained by the fact that the mass transfer coefficient h_g increases in proportion to the square root of the gas velocity, which is evident from Eq. [2] and [4], while the surface-reaction rate constant k_s is independent of the gas velocity. It is also evident that further increase in h_g would lead to the kinetically limited region where the growth rate is limited by some relatively slow surface process (adsorption, surface reaction, or desorption). In the kinetic region the growth rate is independent of distance x, as shown by the broken line in Fig. 5. It should also be noted here that the growth rate at each distance x increases as the gas velocity is increased, due to a reduction in the thickness of the boundary layer, provided that the initial $AsCl_3$ mole fraction is held constant.

Effect of substrate temperature.—In Fig. 6 the experimental and the calculated results of $R(x)/R(0.3)$ *vs.* x for different substrate temperatures (T_s) at fixed initial $AsCl_3$ mole fraction and gas velocity are shown. As is evident from the figure, the agreement between

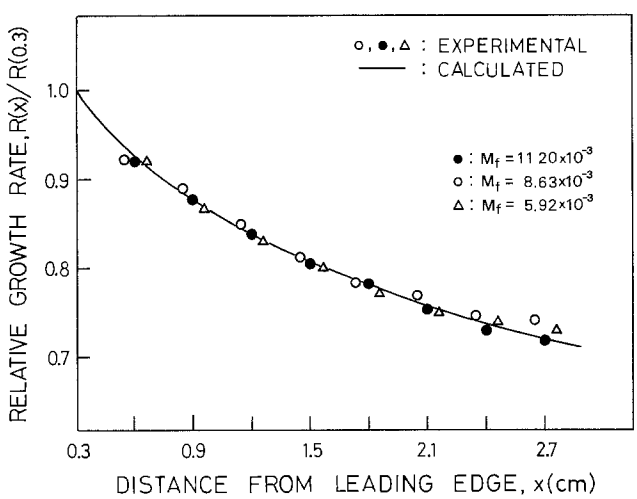


Fig. 4. Comparison of calculated and experimental results of $R(x)/R(0.3)$ as a function of distance from the leading edge of the substrate for different initial $AsCl_3$ mole fractions (M_f). Growth temperature 973°K, gas velocity 2.2 cm/sec.

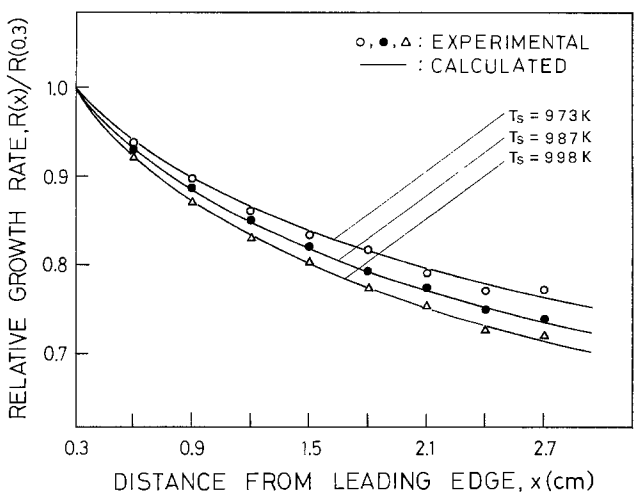


Fig. 6. Comparison of calculated and experimental results of $R(x)/R(0.3)$ as a function of distance from the leading edge of the substrate for different substrate temperatures (T_s). Initial $AsCl_3$ mole fraction 6.71 × 10^{-3}, gas velocity 3.67 cm/sec.

the experimental and the calculated values is very good.

In the figure the variation of growth rate along the substrate is observed to decrease as the substrate temperature is decreased. This tendency is due to the fact that, according to Eq. [8], the surface-reaction rate constant k_s rapidly decreases with decreasing substrate temperature while the mass transfer coefficient h_g is nearly independent of the substrate temperature. Further decrease in k_s would also lead to the kinetically limited region where the growth rate is independent of distance x.

Conclusions

The present investigation has resulted in the following:

1. A rate equation for the epitaxial growth of GaAs has been derived from a model based on a laminar boundary layer. Use of this equation permits the description of the variation of growth rate with distance along the substrate in a constant temperature growth zone. The validity of this equation has been demonstrated by comparison of the calculated growth rate variation with that obtained experimentally.

2. The effects of the initial $AsCl_3$ mole fraction, gas velocity, and substrate temperature on the variation of growth rate with distance along the substrate, in a constant temperature growth zone, have been determined. The variation of growth rate is dependent on the gas velocity and on the substrate temperature, but not on the initial $AsCl_3$ mole fraction.

Acknowledgment

The authors would like to thank Messrs. A. Shibatomi, K. Nakai, and K. Ogasawara for their helpful comments and suggestions.

Manuscript submitted Nov. 3, 1976; revised manuscript received April 29, 1977.

Any discussion of this paper will appear in a Discussion Section to be published in the June 1978 JOURNAL. All discussions for the June 1978 Discussion Section should be submitted by Feb. 1, 1978.

Publication costs of this article were assisted by Fujitsu Laboratories, Limited.

REFERENCES

1. D. Effer, *This Journal*, **112**, 1020 (1965).
2. M. Rubenstein and E. Myers, *ibid.*, **113**, 365 (1966).
3. R. C. Taylor, *ibid.*, **114**, 410 (1967).
4. D. W. Shaw, *J. Cryst. Growth*, **8**, 117 (1970).
5. P. Rai-Choudhury, *ibid.*, **11**, 113 (1971).
6. H. Seki, H. Eguchi, and H. Kobayashi, *ibid.*, **24/25**, 225 (1974).
7. M. Ihara, K. Dazai, and O. Ryuzan, *J. Appl. Phys.*, **45**, 528 (1974).
8. A. S. Grove, *Ind. Eng. Chem.*, **58**, 48 (1966).
9. A. S. Grove, "Physics and Technology of Semiconductor Devices," John Wiley & Sons, Inc., New York (1967).
10. R. E. Treybal, "Mass-Transfer Operations," McGraw-Hill Book Co., New York (1955).
11. H. Schlichting, "Boundary Layer Theory," 4th ed., chap. 7, McGraw-Hill Book Co., New York (1960).
12. W. Jost, "Diffusion in Solids, Liquids and Gases," Academic Press, New York (1960).
13. "Amercian Institute of Physics Handbook," 3rd ed., McGraw-Hill Book Co., New York (1972).
14. P. C. Rundle, *J. Cryst. Growth*, **11**, 6 (1971).
15. D. W. Shaw, *This Journal*, **115**, 405 (1968).
16. M. P. Albert and J. F. Combs, *ibid.*, **109**, 709 (1963).
17. P. A. Schumann, Jr., R. P. Phillips, and P. J. Olshefski, *ibid.*, **113**, 368 (1966).
18. B. G. Secrest, W. W. Boyd, and D. W. Shaw, *J. Cryst. Growth*, **10**, 251 (1971).
19. A. Boucher and L. Hollan, *This Journal*, **117**, 932 (1970).
20. D. J. Kirwan, *ibid.*, **117**, 1572 (1970).
21. R. R. Fergusson and T. Gabor, *ibid.*, **111**, 585 (1964).
22. W. H. Shepherd, *ibid.*, **112**, 988 (1965).

Oxygen Sensing with $Co_{1-x}Mg_xO$ Ceramics

Kwansuh Park and E. M. Logothetis

Ford Motor Company, Dearborn, Michigan 48121

ABSTRACT

Use of $Co_{1-x}Mg_xO$ ceramics for fabrication of oxygen sensors is reported. The phase stability, electrical conductivity, and thermoelectric power of these solid solutions with $x < 0.85$ have been investigated in the range 700°-1100°C and for oxygen partial pressures in the range $1\text{-}10^{-20}$ atm. The nonstoichiometric defects appear to be singly and doubly ionized cobalt vacancies and give rise to a p-type conductivity. These materials have properties, including stability over a wide range of oxygen pressures and temperatures, that make the $Co_{1-x}Mg_xO$ oxygen sensors particularly suited for monitoring and control of combustion processes. Some results on sensor performance in an internal combustion engine are presented.

In recent years there has been an increased interest in oxygen sensors, particularly those that can be used for the monitoring and control of the combustion process in an internal combustion (IC) engine or a furnace (1-4). The objective of this control is the optimization of the combustion process with respect to fuel economy, emissions, and system performance. Monitoring of the combustion process by means of oxygen sensing is possible because there is a direct relationship between the equilibrium oxygen partial pressure in the exhaust from an engine or furnace and the air-to-fuel ratio (A/F)[1] of the burned mixture. Sensor characteristics that are necessary or desirable for these applications, especially the control of IC engines, include fast response time (generally 1 sec or less), the ability to operate at high temperatures, and the ability to withstand corrosive or contaminating environments. For most furnaces and several IC engine systems, optimization of the combustion process is achieved with air-to-fuel mixtures corresponding to "lean-burn" combustion, *i.e.*, there is more than enough oxygen in the mixtures to convert all the hydrocarbons of the fuel to

Key words: oxygen sensing, combustion process control, ceramics, electrical properties, oxide solid solutions.

[1] A/F is defined as the ratio of the mass of air to the mass of fuel that make up the mixture before combustion.

water and carbon dioxide. Under these conditions, the oxygen partial pressure (P_{O_2}) of the exhaust gas from an engine or furnace is generally in the range of 10^{-3} to 10^{-1} atm.

In a previous publication (5) we reported the use of CoO ceramics as oxygen sensors for lean-burn applications. Pure, stoichiometric CoO is a wide-gap semiconductor with very high resistivity. However, deviations from stoichiometry result in structural defects (cobalt vacancies) that strongly influence electronic conductivity. These properties make the conductivity of CoO at high temperatures depend on the ambient P_{O_2} (5-8). Although CoO ceramic sensors heated at temperatures 900°-1000°C were shown (5) to possess characteristics that make them well suited for lean-burn applications, their usefulness is limited by the fact that CoO decomposes to metallic Co at low P_{O_2}; for example, at 1000°C, the CoO/Co phase boundary occurs at $P_{O_2} \approx 10^{-12}$ atm (Fig. 1); this corresponds to an equivalent air-to-fuel ratio (A/F) of about 14, *i.e.*, a value slightly rich of the stoichiometric A/F ratio. The CoO decomposition does not allow the prolonged exposure of the sensors to very low P_{O_2} such as those corresponding to very rich air-to-fuel mixtures. In the present paper we report the use of solid solutions of CoO with MgO to obtain oxygen sensors with characteristics similar to CoO but without the rich-mixtures-exposure limitation. Since systems operating at high P_{O_2} (lean A/F mixtures) may experience prolonged exposures to very low P_{O_2} (*e.g.*, those corresponding to very rich A/F mixtures) either accidentally or as the result of a certain normal operating mode, the use of $Co_{1-x}Mg_xO$ materials greatly increases the usefulness of these oxygen sensors. Furthermore, the $Co_{1-x}Mg_xO$ sensors can be operated at temperatures lower than CoO.

Properties of $Co_{1-x}Mg_xO$ Materials

The $Co_{1-x}Mg_xO$ materials have been prepared by high temperature reaction of CoO and MgO. Powders of the two oxides were milled together and then fired at temperatures in the range 1400°-1600°C for a few hours. This process was repeated several times until x-ray diffraction measurements indicated that a single phase material was obtained. Ceramic specimens of $Co_{1-x}Mg_xO$ were prepared by standard ceramic techniques involving cold pressing, with or without binder and subsequent sintering.

Figure 1 shows a portion of the P_{O_2}-T phase diagram for the Co-Mg-O system (9). This diagram is

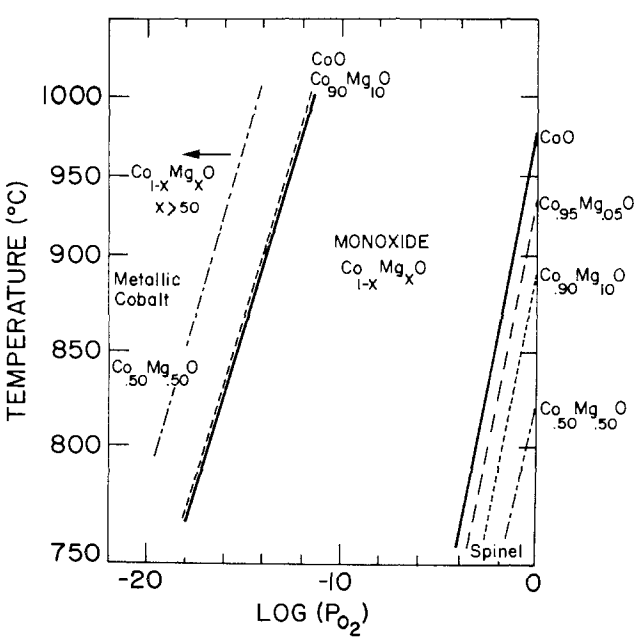


Fig. 1. Approximate P_{O_2}-T phase diagram for the Co-Mg-O system.

only approximate because of difficulties arising from hysteresis phenomena at each phase change; for example, at a given P_{O_2}, the temperature of the phase change from monoxide to spinel is lower than the temperature for the reverse change. The hystereses become more pronounced at lower temperatures and higher rates of change of T (or P_{O_2}). The transition temperature (or P_{O_2}) from one phase to another was determined by monitoring the electrical resistance; this is possible because all three phases (metallic, monoxide, and spinel) have very different resistivities. As Fig. 1 shows, the addition of small amounts of MgO (*e.g.*, $x < 0.10$) into CoO increases the stability range of the monoxide phase by a corresponding suppression of the spinel phase without a noticeable shift in the CoO/Co phase boundary; this boundary, however, shifts substantially to lower P_{O_2} (at a given temperature) for large MgO content (*e.g.*, $x > 0.50$). The wider stability range of the $Co_{1-x}Mg_xO$ materials allows safe exposure of those with $x > 0.5$ to P_{O_2} considerably lower than that for which CoO is decomposed; in addition, at high P_{O_2} (*e.g.*, 0.1 atm) these materials can be maintained at lower temperatures than CoO without transforming to spinel. The spinel composition derived from pure CoO is Co_3O_4; however, when MgO is added, the spinel phase appears to be generally a two phase region consisting of $Co_{1-y}Mg_yO$ and $(Co_{1-z}Mg_z)_3O_4$ (spinel).

The high temperature electrical properties of $Co_{1-x}Mg_xO$ were investigated in the 700°-1100°C temperature range and at P_{O_2} between 1 and 10^{-20} atm. Electrical connections to the ceramic specimens were made by attaching Pt wires with Pt paste. The specimens were mounted inside a quartz vessel that was placed in a furnace. The oxygen partial pressure was established by a continuous flow through the vessel of gas mixtures at a total pressure of 1 atm, O_2 in CO_2 or O_2 in N_2 for high P_{O_2} and CO in CO_2 for low P_{O_2}. At high temperatures, nonohmic behavior and polarization phenomena were absent and 2-probe and 4-probe measurements gave the same results. Figure 2 shows some results on the dependence of the electrical resistivity of the $Co_{1-x}Mg_xO$ ceramics on P_{O_2} at 1000°C. On the high P_{O_2} side the data terminate at approximately the monoxide-to-spinel phase boundary, whereas on the low P_{O_2} side the data terminate at the metal-to-monoxide phase boundary; (for materials with $x > 0.40$, the latter phase boundary extends beyond 10^{-14} atm; see Fig. 1). Complete results on the dependence of the electrical conductivity and the thermoelectric power of $Co_{1-x}Mg_xO$ materials on P_{O_2} and temperature (700°-1100°C) for $0 \leq x < 1$ will be published elsewhere (10).

The behavior of the electrical resistivity of the $Co_{1-x}Mg_xO$ materials appears to be generally the same as that of CoO. In the temperature range of 700°-1100°C, the resistivity is approximately proportional to $P_{O_2}^{-1/4}$ at high P_{O_2} and tends toward a $P_{O_2}^{-1/6}$ dependence for the lower P_{O_2}. These dependences are consistent with a simple model of point defects (most likely Co vacancies) that are predominantly singly ionized at high P_{O_2} and predominantly doubly ionized at low P_{O_2} (6-8, 10). The P_{O_2} range with a $P_{O_2}^{-1/6}$ dependence (doubly ionized defects) widens as the Mg content in the materials increases. At very low P_{O_2}, the resistivity of the materials with $x > 0.5$ tends to saturate. The saturation becomes more pronounced at the lower temperatures and is probably due to donor impurities in the specimens (10). The absolute value of the resistivity increases slowly with x for small x, becoming a strong function of x for large x. The activation energy for the conductivity remains close to that of CoO ($\approx$ 0.5 eV) for $x < 0.20$ and increases strongly for larger x, attaining a value of 1.2 eV for $x = 0.85$. These results in the range 700°-1000°C appear to be generally consistent with the results of thermogravimetric and conductivity studies by Von G. Schwier *et al.* (11, 12)

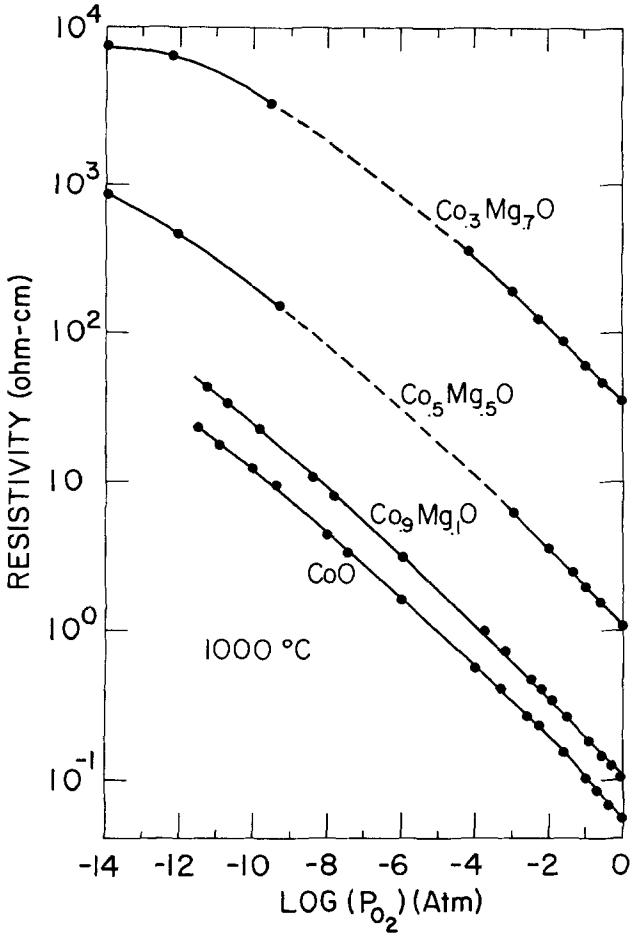


Fig. 2. Dependence of the resistivity of $Co_{1-x}Mg_xO$ alloys on the oxygen partial pressure at 1000°C.

at higher temperatures (900°-1300°C) and at P_{O_2} in the range $1\text{-}10^{-4}$ atm.

For the thermoelectric power measurements, temperature differences ΔT between the two ends of a $Co_{1-x}Mg_xO$ ceramic were established with a small platinum heater near one end of the specimen. Values of ΔT were measured with two Pt/Rh thermocouples, attached to the two ends of the ceramic specimen with platinum paste. The thermoelectric voltage was measured with the platinum legs of the two thermocouples. The sign of the thermoelectric power S shows that the conductivity in all $Co_{1-x}Mg_xO$ solid solutions studied here ($x \leq 0.85$) is p-type, *i.e.*, the charge carriers are holes; this is consistent with the interpretation that the intrinsic defects in these materials are Co vacancies. Furthermore, for materials with $x < 0.5\text{-}0.7$, a plot of S *vs.* $1/T$ gives a straight line having a slope E_S that is equal to the activation energy E_C of the conductivity. This suggests that the exponential increase in the conductivity with temperature results from a similar increase in the carrier concentrations and not from an activated mobility. It thus appears that, as for CoO, the holes in $Co_{1-x}Mg_xO$ with $x < 0.5\text{-}0.7$ are not small polarons but rather itinerant carriers. For $x > 0.5\text{-}0.7$, it was found that $E_C > E_S$ which suggests that the mobility becomes activated. A change from band conduction to hopping conduction is thus indicated at high Mg content. These preliminary results are in disagreement with those of Von G. Schwier *et al.* (11, 12); from combination of mass loss and conductivity measurements these authors concluded that the mobility is activated for all x. It is pointed out that similar discrepancy on the nature of the carrier mobility deduced from mass/loss conductivity and thermoelectric power/conductivity data exists for pure CoO (6-8, 10-13). Experimental uncertainties do not appear to be the source for this discrepancy, since such results for CoO have been obtained consistently by many investigators (6-8, 10-13).

Oxygen Sensor Characteristics

Experimental $Co_{1-x}Mg_xO$ sensors have been fabricated with a configuration similar to that of CoO sensors (5). The ceramic sensing element is in the form of a small bar or disk with two imbedded platinum wires as resistance sensing electrodes. The temperature of the sensor is maintained at some approximately constant value in the range 700°-1000°C by means of a small furnace surrounding the ceramic element.

Figure 3 shows some results on the performance of these oxygen sensors from the specific application of sensing the air-to-fuel ratio of an IC engine. Several sensors were inserted into the exhaust from an 8-cylinder 351 CID (cubic inch displacement) engine and the dependence of the d-c resistance of the $Co_{1-x}Mg_xO$ elements on A/F ratio was investigated. The A/F ratio was determined by conventional gas analysis techniques (14). Figure 3 shows the resistance of the ceramic element of a sensor with composition $Co_{0.3}Mg_{0.7}O$ as a function of the A/F ratio in the range A/F $\simeq$ 15-18 (lean region). The temperature of the sensor was 900°C. The approximate P_{O_2} of the exhaust is also shown at the top of the figure.

Figure 3 shows an approximate two-to-one change in resistance over the range of A/F measured. This change is large enough to be useful in practical applications, provided the materials properties are stable and extraneous changes in resistance (*e.g.*, those due to temperature fluctuations) are small. The resistance *vs.* P_{O_2} relationship and the activation energy of the $Co_{1-x}Mg_xO$ ceramics were found to be very reproducible at least for $T > 800$°C and $P_{O_2} > 10^{-6}$ atm. In addition, they were independent of the porosity of the ceramics in the range 0-50%. These characteristics as well as the absolute value of the resistance remained unchanged after more than 1000 hr of operation at temperatures in the range 800°-1000°C. The tempera-

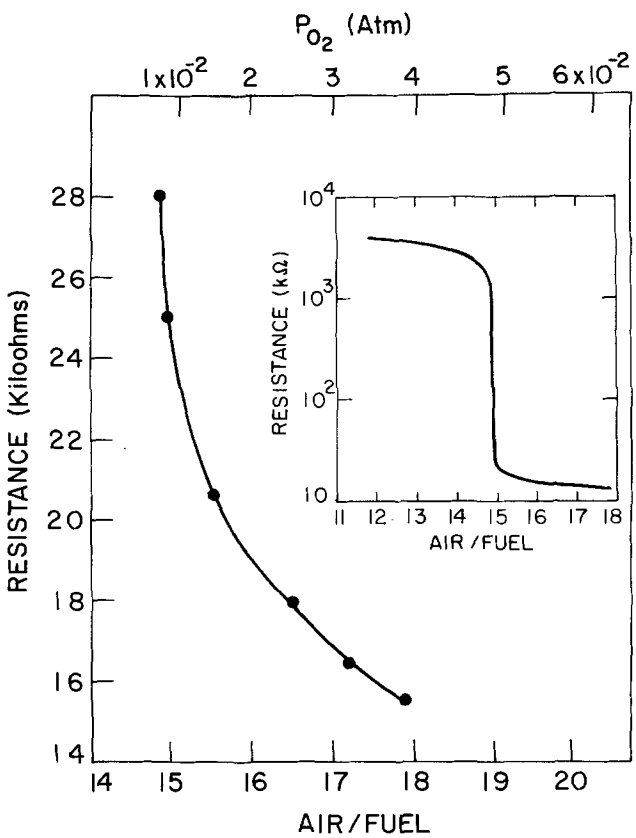


Fig. 3. Dependence of the resistance of a $Co_{0.3}Mg_{0.7}O$ sensor on air-to-fuel ratio (A/F) of an IC engine for A/F > $(A/F)_{stoichiometric}$, and on oxygen partial pressure P_{O_2}. The temperature of the sensor was 900°C. The inset shows the behavior of the sensor resistance for an extended A/F range including the stoichiometric A/F ratio.

ture coefficient of resistance increases with x from 0.3% per °C for CoO to 0.6% per °C for $Co_{0.3}Mg_{0.7}O$ in the neighborhood of 1000°C. These coefficients become about 0.4% and 0.7% per °C respectively in the neighborhood of 800°C.

An important characteristic of an oxygen sensor is its response time. The requirements on response time depend on the application. Sensors made from porous $Co_{1-x}Mg_xO$ ceramics have shown response times similar to the CoO sensors, *i.e.*, of the order of 1 sec or less (5). Shorter response times are expected by optimization of the ceramic structure. It appears that for $P_{O_2} > 10^{-6}$ atm, the response time of the $Co_{1-x}Mg_xO$ sensors is determined by a combination of gas transport through the pores (gas exchange) and the equilibration kinetics (diffusion) within the individual grains.

Since $Co_{1-x}Mg_xO$ materials with $x > 0.5$ do not decompose at very low P_{O_2} (*e.g.*, very rich air-fuel mixtures such as those with A/F = 11), oxygen sensors made from these compositions can be used not only for sensing lean A/F mixtures but also for sensing passage through the stoichiometric A/F mixture. Such "stoichiometric" A/F sensors are presently of considerable interest for the control of engine systems that use a 3-way catalytic converter for the simultaneous removal of all three pollutants (hydrocarbons, CO, NO_x) from the exhaust. Figure 3 (inset) shows the dependence of the resistance of a $Co_{0.3}Mg_{0.7}O$ sensor on A/F ratio for a wide range of A/F ratios, from very rich (A/F = 11) to very lean (A/F = 18). The large step-wise change in the resistance at A/F $\approx$ 14.8 signifies the passage through the stoichiometric A/F mixture and arises from a corresponding large change in the P_{O_2} of the exhaust gas. When the $Co_{1-x}Mg_xO$ is used as an indicator of passage through stoichiometry, the requirements for temperature control are greatly reduced.

Conclusions

Our initial laboratory measurements indicate that oxygen sensors made from $Co_{1-x}Mg_xO$ have electrical properties as well as materials stability over a wide range of P_{O_2} and temperatures, that make them attractive for a variety of applications. The reproducibility and stability of the resistance *vs.* P_{O_2} (or A/F) relationship, the absence of drifts and polarization effects, the relatively small temperature coefficient of resistance, and the fast speed of response, all combine to give a sensor with good performance at high P_{O_2} (lean air-fuel mixtures). More complete evaluation of these sensors for the application of monitoring and control of combustion processes is in progress.

Acknowledgment

We thank G. Beaudoin for the assistance in the fabrication and testing of the oxygen sensors.

Manuscript submitted March 1, 1977; revised manuscript received May 5, 1977.

Any discussion of this paper will appear in a Discussion Section to be published in the June 1978 JOURNAL. All discussions for the June 1978 Discussion Section should be submitted by Feb. 1, 1978.

Publication costs of this article were assisted by the Ford Motor Company.

REFERENCES

1. R. Zechnall, G. Baumann, and H. Eisele, Paper No. 730566, SAE National Automotive Engineering Meeting, Detroit, May 1973.
2. T. Y. Tien, H. L. Stadler, E. F. Gibbons, and P. J. Zacmanidis, *J. Am. Ceram. Soc.*, **54**, 280 (1975).
3. E. M. Logothetis, Proceedings of the International Conference on Electronic Properties of Oxides, Purdue University, May 1974; *J. Solid State Chem.*, **12**, 331 (1975).
4. H. E. Hendler, *Chem. Eng. Prog.*, **71**, 39 (1975).
5. E. M. Logothetis, K. Park, A. H. Meitzler, and K. R. Laud, *Appl. Phys. Lett.*, **26**. 209 (1975).
6. B. Fisher and D. S. Tannhauser, *J. Chem. Phys.*, **44**, 1663 (1965).
7. N. G. Eror and J. B. Wagner, *J. Phys. Chem. Solids*, **29**, 1597 (1968).
8. I. Bransky and J. M. Wimmer, *ibid.*, **33**, 801 (1972).
9. See also, "Phase Diagrams for Ceramicists." E. M. Levin, C. R. Robbins, and H. F. McMurdie, The American Ceramic Society (1964).
10. Some results have already been reported: E. M. Logothetis and K. Park, *Bull. Am. Phys. Soc.*, **20**, 469 (1975); K. Park and E. M. Logothetis, *Am. Ceram. Soc. Bull.*, **55**, 416 (1976).
11. Von G. Schwier, R. Dieckmann, and H. Schmalzried, *Ber. Bunsenges. Physik. Chem.*. **77**, 402 (1973).
12. Von G. Schwier and H. Schmalzried, *ibid.*, **77**, 721 (1973).
13. A. J. Bosman and C. Crevecoeur, *J. Phys. Chem. Solids*, **30**, 1151 (1969).
14. N. A. Henein and D. J. Patterson, "Emission from Combustion Engines and Their Control," Chap. 9, Ann Arbor Science Pub., Inc., Ann Arbor, Mich.

Vapor-Phase Etching and Polishing of GaAs Using Arsenic Trichloride

Rajaram Bhat*,[1] and Sorab K. Ghandhi*

Electrical and Systems Engineering Department, Rensselaer Polytechnic Institute, Troy, New York 12181

A study of the vapor-phase etching and polishing of GaAs substrates using hydrogen chloride gas was presented in a previous paper (1). In that study, it was observed that the etching process critically depended on the purity of the etchant. Arsenic trichloride is readily available in purities better than six nines, and is less expensive compared to HCl gas on the basis of the number of moles of available chlorine. It is, therefore, an attractive alternative for *in situ* etching of GaAs substrates. Knight, Effer, and Evans (2), Hirao and Nakashima (3), and Nozaki and Saito (4) have investigated the etching of gallium arsenide substrates in a $Ga/AsCl_3/H_2$ vapor deposition reactor. Further, DiLorenzo (5) has studied the etching of GaAs substrates with $AsCl_3$ in a helium ambient. However, a detailed information on the effect of temperature, substrate orientation, and $AsCl_3$ mole fraction on the etching and polishing of GaAs substrates, in a H_2 atmosphere, is not available. In this paper, we present results obtained for $AsCl_3$ etching of GaAs substrates in a cold-wall reactor, and compare them with those obtained using HCl gas in the same system. Throughout these etching experiments, a flow of arsine gas was maintained to prevent decomposition of the GaAs. The apparatus and experimental procedure were similar to those used in (1), and the etch rate was defined and determined as in (1).

Experimental Results

Temperature.—The effect of temperature on etch rate was determined for (100) and $(\bar{1}\bar{1}\bar{1})$ oriented, Te-doped GaAs substrates[2] using a flow of 5 liters/min of hydrogen, 30 ml/min of arsine, and 70 ml/min of hydrogen through the $AsCl_3$ bubbler, which was kept at 25°C. Under these conditions, as seen in Fig. 1, the activation energies of the etching reaction and the temperatures at which the etching reaction became mass-transport (type II) limited (6) and independent of crystallographic orientation, were found to be the same as those reported for HCl gas (1). Again, as in (1), GaAs substrate surfaces of both (100) and $(\bar{1}\bar{1}\bar{1})$ orientation were featureless when etched above 870°C, and were faceted with the simultaneous formation of etch pits or hillocks when etched below this temperature. Further, etching experiments with $AsCl_3$ and HCl gas conducted under otherwise identical conditions resulted in equal etch rates for an HCl gas mole fraction which was three times that of $AsCl_3$ in the input gas stream. This indicates that $AsCl_3$ completely dissociates within the reactor before reaching the substrate. The dissociation of $AsCl_3$ produces HCl gas since chlorine is unstable in an atmosphere of hydrogen at the etching temperature (7).

$AsCl_3$ concentration.—Figure 2 shows the etch rate of (100) Te-doped GaAs substrates as a function of the hydrogen flow through the $AsCl_3$ bubbler. These experiments were conducted at a temperature of 900°C, using a total hydrogen flow of 5 liters/min and an arsine flow of 30 ml/min in a reactor tube of 50 mm ID. The etch rate was found to vary superlinearly with HCl concentration. Similar nonlinear dependence of the etch rate on etchant gas flow, under mass-transport (type II) limited conditions, was observed in the etching of Si (8, 9), Ge (10), and GaAs (1). This result differs from the findings of Hirao and Nakashima (3), who observed a linear variation of etch rate with $AsCl_3$ concentration during experiments performed in a hot wall reactor.

Arsine flow.—The effect of arsine flow on etch rate and surface quality under mass-transport (type II)

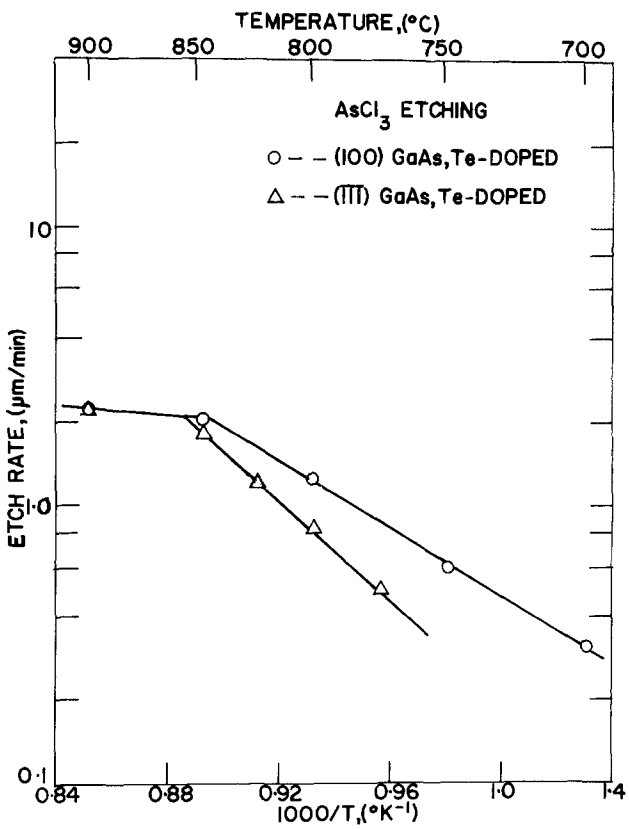


Fig. 1. Variation of etch rate with temperature

* Electrochemical Society Active Member.

[1] Present address: General Electric Company, Advanced Technology Group, Semiconductor Products Department, Syracuse, New York 13201.

Key words: gallium arsenide, arsenic trichloride, etching, polishing.

[2] All (100) substrates mentioned in this paper were misoriented 2° from (100) towards (110).

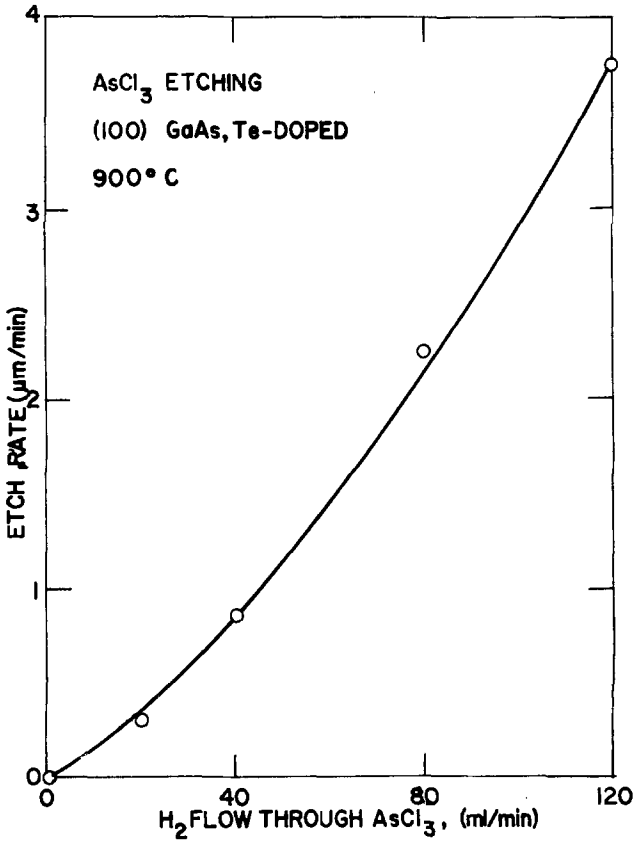


Fig. 2. Variation of etch rate with $AsCl_3$ concentration

limited conditions was investigated at 900°C using a hydrogen flow of 5 liters/min. It was found that at least 15 ml/min of arsine were required to prevent decomposition of the substrate. There was no appreciable change in surface quality for arsine flows between 15 and 30 ml/min, and the etch rate did not change within experimental error. These results are in agreement with those obtained with HCl gas (1).

Orientation and dopant type.—Investigations of the etch rate under mass-transport (type II) limited and kinetically controlled conditions for (100) Cr- and Zn-doped GaAs indicated that it was the same as for their Te-doped counterparts. Therefore, as in (1), the etch rate for $AsCl_3$ etching of GaAs substrates is also independent of dopant type.

It was possible under mass-transport (type II) limited conditions to obtain specular surfaces for (100) Cr- and Zn-doped and $(\bar{1}\bar{1}\bar{1})$ Cr-, Si-, and Zn-doped substrates. In agreement with results obtained in (1), the quality of $(\bar{1}\bar{1}\bar{1})$ Cr- and Si-doped substrates was inferior to that obtained with Te- and Zn-doped GaAs substrates. However, unlike the HCl gas etching study (1), no difference was observed in the quality of (100) oriented Te- and Cr-doped substrates etched with $AsCl_3$. This result is in contrast to that obtained by Hirao and Nakashima (3), who failed to obtain specular etched surfaces for Cr-doped GaAs.

It was noted during the etching of GaAs using HCl gas that the use of a less pure etchant resulted in nonspecular surfaces. Since the $AsCl_3$ was considerably purer than the HCl gas used, we conclude that the difference in the quality of Cr-doped GaAs substrate surfaces etched with HCl gas or $AsCl_3$ was mainly due to the difference in purity of the etchant.

Dopant segregation.—Auger spectra taken on etched and unetched Te-, Si-, and Cr-doped GaAs substrates showed no segregation of dopants on the surface within the limits of detectability.[3] This is in agreement with the results obtained by Moon and James (11) for Te- and Si-doped substrates.

Conclusion

The etching reaction of $AsCl_3$ with GaAs in a hydrogen ambient at temperatures above 700°C has been shown to be identical to that of HCl gas. The ability to obtain equally good specular etched surfaces for both Te- and Cr-doped GaAs substrates makes $AsCl_3$ more attractive than HCl gas in the choice of an etchant.

Acknowledgment

The authors would like to thank R. Rafun for assistance in manuscript preparation. This work was supported by Grant No. DAAG29-76-G-0127 from the U.S. Army Research Office, Durham, North Carolina.

Manuscript submitted Feb. 24, 1977; revised manuscript received May 6, 1977.

Any discussion of this paper will appear in a Discussion Section to be published in the June 1978 JOURNAL. All discussions for the June 1978 Discussion Section should be submitted by Feb. 1, 1978.

Publication costs of this article were assisted by Rensselaer Polytechnic Institute.

[3] 0.1% of the atoms in the first monolayer.

REFERENCES

1. R. Bhat, B. J. Baliga, and S. K. Ghandhi, *This Journal*, **122**, 1378 (1975).
2. J. R. Knight, D. Effer, and P. R. Evans, *Solid-State Electron.*, **8**, 178 (1965).
3. M. Hirao and H. Nakashima, *J. Jpn. Soc. Appl. Phys., Suppl.*, **40**, 46 (1971).
4. T. Nozaki and T. Saito, *Jpn. J. Appl. Phys.*, **11**, 110 (1972).
5. J. V. DiLorenzo, Proceedings of the 5th International Symposium on GaAs and GaAs Related Compounds. p. 362, Institute of Physics, Deauville, France (1976).
6. D. W. Shaw, in "Crystal Growth Theory and Techniques," Vol. 1, C. H. L. Goodman, Editor, Chapter 1, Plenum Press, New York (1974).
7. D. J. Kirwan, *This Journal*, **117**, 1573 (1970).
8. G. A. Lang and T. Slavish, *RCA Rev.*, **24**, 488 (1963).
9. W. H. Shepherd, *This Journal*, **112**, 988 (1965).
10. J. A. Amick, E. A. Roth, and H. Gossenberger, *RCA Rev.*, **24**, 473 (1963).
11. R. L. Moon and L. W. James, *This Journal*, **120**, 581 (1973).

Lifetime Degradation in Silicon by Emitter Diffusion

R. N. Ghoshtagore*

Westinghouse Research Laboratories, Pittsburgh, Pennsylvania 15235

The electrical characteristics of silicon devices are critically dependent on wafer processing parameters. Most of these device characteristics are directly derived both from such high temperature process-induced gross internal changes in silicon as resistivity type and level, resistivity gradients and thicknesses of different layers, and such subtle changes in the bulk as heavy metal, vacancy, and oxygen precipitations, minority carrier lifetimes in each doped layer, etc. In this work, the effects of different techniques of one such processing step, namely, $POCl_3$ emitter diffusion, on the minority carrier recombination lifetime of the starting material was investigated.

The starting material in all these experiments was (111) ± 1° orientation, boron-doped, 20-30 Ω-cm, 1-1/4 in. diam, 8 ± 1 mil thick, one-side chem-mechanically polished, < 500/cm² dislocation density, p-silicon, with photoconductivity lifetime of ~225 μsec. The wafers were cleaned by standard techniques with the peroxide process used just before diffusion. They were blown dry with nitrogen before loading into the diffusion furnace. All $POCl_3$ diffusions were done with 4 wafer batches at 1200°C in a 50 mm ID quartz tube for 1-59-1 m (1 preheat time; 59 deposition time; 1 flush time). $POCl_3$ bubbler temperature was controlled to 20° ± 0.5°C by a thermocooler. The carrier gas flow was uniformly N_2 at 2 liters/m. N_2 flow through the bubbler and oxygen flow into the furnace were controlled directly as percentages of the main-line nitrogen carrier gas flow rates. After the emitter diffusion cycle the wafers were cooled by either quenching (by pulling the boat out of the furnace) or slow cooling the furnace (with a programmer) at fixed rates to 600°C and then pulling the boat out of the furnace.

After diffusion, the phosphosilicate glass thicknesses were measured as SiO_2 equivalents, glass stripped in HF, and sheet resistivity and junction depths (angle lap and stain) recorded. The n layer was then lapped off the polished side, and 1/16 in. diam mesa n^+p diodes (1/4 in. apart) fabricated (on the lapped side). Evaporated Al contacts were used on both sides. Open-circuit voltage decay (OCD) lifetime was measured for corresponding diodes under low injection conditions (1 mA forward current) using the relationship (1)

$$\tau = \frac{kT}{q}\left(\frac{dv}{dt}\right)^{-1}$$

All the OCD measurements were made in the dark at room temperature under flowing nitrogen ambients with no further surface passivation of the mesa diodes (1). Surface leakage currents were not a problem in these measurements.

For any particular type of cooling cycle, the phosphosilicate glass thickness on the wafers increased more than linearly with increasing $POCl_3$ concentration in the gas stream, the thicknesses being higher with slower cooling rates. In the entire range of experiments reported here no "bubbles" were observed in the glass. For the experiments where the wafers were pulled out of the furnace after diffusion (quench), junction depths were 6.9 ± 0.8μ. In the slow cool runs, junction depths increased uniformly with decreasing rates of cooling with a 90 ± 5% increase of x_j (over quench) for 0.5°C/min cool rate. Gas phase reactant concentrations (in the range used) had no detectable effect on x_j. Similarly, measured sheet resistivities were primary functions of $POCl_3$ gas phase concentration. Variation of oxygen concentration produced second-order effect that was almost masked by experimental perturbation. All the sheet resistivities were in the range of 0.70-1.33 Ω/□ in. Surface concentrations, calculated from spreading resistance profiles, were also the direct function of only $POCl_3$ gas phase concentration. They ranged from 1×10^{20} to 1.9×10^{20} cm^{-3} in all these experiments. From the spreading resistance profiles, the run conditions with >3.25% $POCl_3$ were difficult to distinguish mainly due to wafer-to-wafer and run-to-run variations.

As we present the OCD lifetime data in Fig. 1-3, the following processing questions will be specifically addressed: (*i*) What is the best $POCl_3$ gas phase concentration for the maximum lifetime preservation? (*ii*) Is there a corresponding O_2:$POCl_3$ ratio? (*iii*) From the same point of view, what is the best range of cooling rates? (*iv*) What deleterious effect, if any, does the thermal preoxidation of wafers have? For a direct basis of comparison of the measured OCD lifetimes, some of the same wafers were used to fabricate 750°C Sb-Au alloyed-in 1/8 in. diam n^+p diodes. The OCD lifetime of such diodes averaged about 60 μsec. The diode size has never been found to have any effect on such measurements.

Minority carrier lifetimes measured by the low injection OCD technique were plotted as a histogram

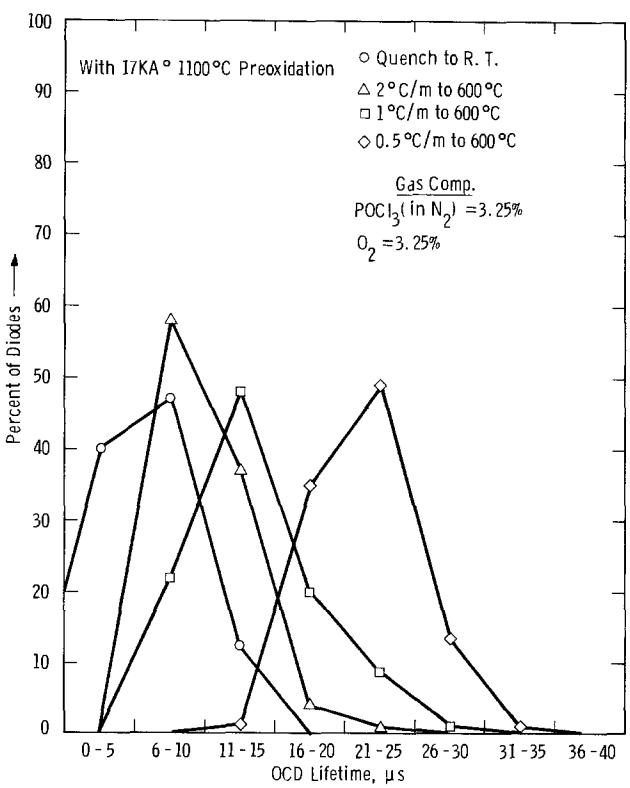


Fig. 1(a). OCD lifetime spectra of 1100°C 17 kÅ preoxidized wafers after the medium concentration emitter diffusion at different slow cooling rates (diffusions at 1200°C).

* Electrochemical Society Active Member.

Key words: silicon, lifetimes, phosphorus, diffusion, degradation, slow cooling.

of the percent of the measured diodes (~100 in each run) as a function of the lifetime divided into 5 μsec groups. Examination of the statistical data in such a form is expected to indicate only the trend of the effect of processing variables experimented. Emitter diffusions were performed for $POCl_3$ gas phase concentrations of 1-10%; O_2:$POCl_3$ ratios of 0.5-3.0 at each $POCl_3$ concentration, and at four primary slow cool rates under any fixed O_2 plus $POCl_3$ concentration condition. Figure 1(a) shows one such set of OCD data illustrating the deleterious effect of wafer preoxidation on the peak OCD lifetime value. Similar effects were observed with unoxidized wafers [Fig. 1(b)]. It should be noted that the maximum programmed slow cool rate of 2°C/min is about equivalent to furnace shut-off condition. Figure 2 shows the peak OCD lifetime data as a function of $POCl_3$ gas phase concentration under two primary O_2:$POCl_3$ ratios. From the trend curves drawn through the data points, it is clear that for the maximum possible lifetime preservation at $\leq$ 2°C/min, cooling rates emitter diffusion must be performed at ~6% $POCl_3$ concentration condition. Under these conditions, peak OCD lifetime initially increases with increasing $POCl_3$ gas phase concentration up to ~6.5%, probably due to heavy metal gettering. But the subsequent drop in each τ value with further increase of gas phase phosphorus concentration must be due to defect generation in the undiffused bulk (2). Both of these gettering and bulk defect generation phenomena become neutralized by the opposing kinetics at low cooling rates (*i.e.*, < 1° C/min). Although Fig. 2 shows that the effect of O_2:$POCl_3$ ratio on the peak τ_{OCD} is very minor, a detailed examination of all the data indicate that the optimum emitter processing should be done at O_2:$POCl_3$ = 2.5-3.0:1.

The topic of the effect of slow cool rate on peak τ_{OCD} is the most controversial one. It has been generally considered to provide considerable time (at different temperatures) for gettering of heavy metals, dissolution of appropriate precipitate centers, annihilation of planar and line-type lattice defects, etc., and thus enhance minority carrier recombination lifetime in heat-treated silicon. As shown in the typical data sets of Fig. 1, all the results obtained in this study

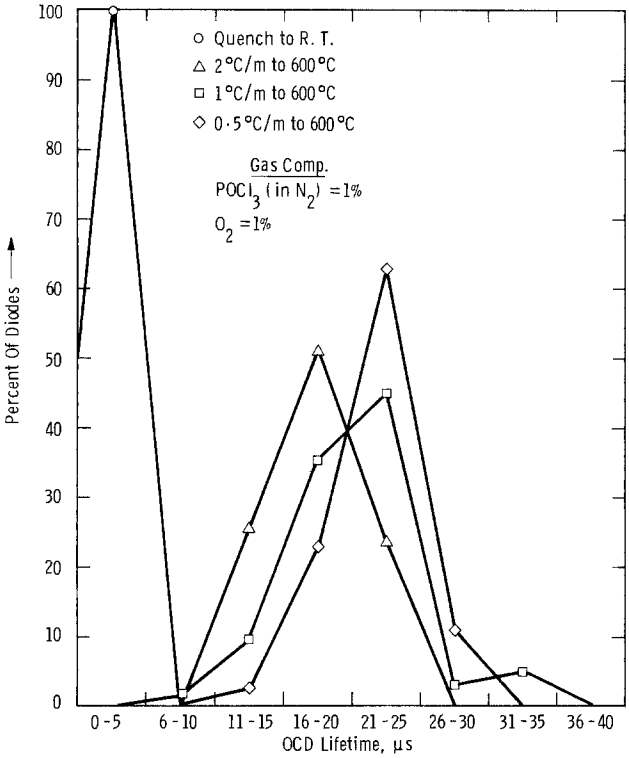


Fig. 1(b). OCD lifetime spectra after low concentration emitter diffusion at 1200°C for different slow cooling rates (no preoxidation).

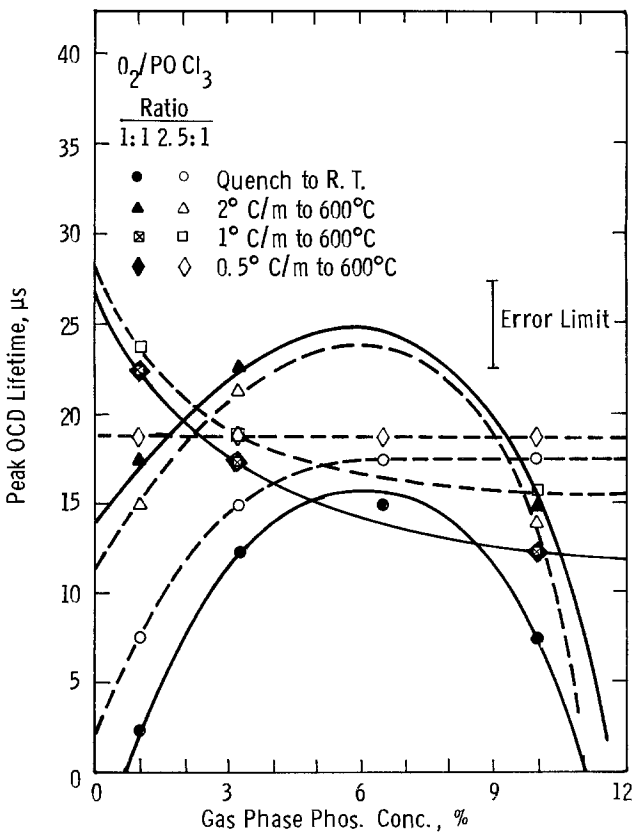


Fig. 2. The dependence of peak τ_{OCD} on the gas phase diffusion conditions at different postdiffusion cooling rates from 1200°C (no preoxidation).

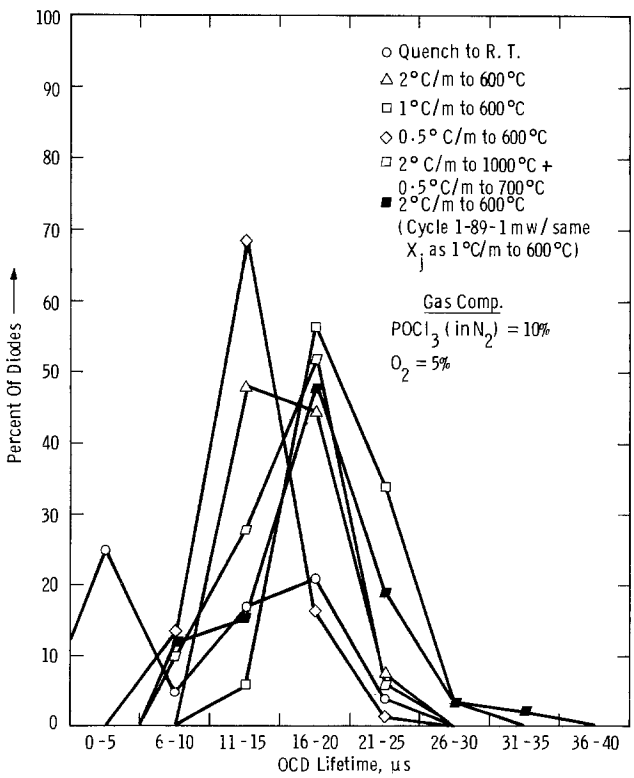


Fig. 3. The effects of low oxygen concentration, junction depth, and different cooling rates at different temperatures on the OCD lifetime spectra of 1200°C emitter diffusion (no preoxidation).

unequivocally indicate longer lifetimes under slow cool conditions, within the aforementioned constraints of gas phase reactant concentrations. As can be seen from Fig. 2, in the case of bare silicon under increasing gas phase phosphorus concentrations, the effects of different slow cool rates on peak τ_{OCD} become minimal. Emitter diffusions under different slow cool rates also drastically alter the distribution of τ_{OCD} values obtainable in any one run. It should be pointed out that in all the data obtained in this study, the trends of the maximum lifetime as a function of slow cooling rates are not monotonically varying. However, with oxidized wafers, the slower the cooling rate the higher is the peak τ_{OCD} [Fig. 1(a)]. Lifetime degradation in preoxidized wafers, being the most relevant to device processing, should determine the best cooling rate (*i.e.*, 0.5°C/min). Slowest cooling rate being equivalent to the maximum x_j immediately raises the question of x_j dependence on τ_{OCD}. Figure 3 attempts to answer that question for an O_2:$POCl_3$ ratio of 0.5:1.0. The set of data with 2°C/min cooling rate (to 600°C) with a 1-89-1 min diffusion cycle is equivalent to that with 1°C/min cooling rate (to 600°C) with a 1-59-1 min diffusion cycle insofar as x_j is concerned (11.0μ). Their lifetime spectra are also nearly identical. This is also approximately the case with that set of data where the slow cool rate was changed from 2° to 0.5°C/min at 1000°C. This latter set of data indicate the importance of the slowest possible cooling rate under 1000°C (0.5°C/min data being anomalous). It has also been observed that the x_j dependence on peak τ_{OCD} ceases to exist after $\sim x_j$ = 12-14μ. Finally, it should be mentioned that all the lifetime data were highly reproducible in the general shape of the spectra. Over 50% of the runs were repeated twice at different times, with some 5-10% being repeated several times.

It is probably appropriate at this point to speculate on the possible mechanisms operating to degrade minority carrier lifetime by emitter diffusion alone. From the clear trend of the data presented, it is not unreasonable to assume that heavy metal contamination is not involved in general, and the wafer cleaning procedure was consistent enough. The presence of optimum $POCl_3$ and O_2 gas phase concentrations probably is consistent with that of least SiP-type precipitation center density production (2). Such incoherent precipitation within the diffused layer is normally associated with dislocation-type recombination centers extending well into the base material. Slow cooling quite possibly could anneal out a fraction of such centers (sessile dislocations). The major effects of slow cooling must, however, be either vacancy annealing (3) and/or oxygen evolution in the silicon lattice as SiO_4-polyhedra. To obtain a clearer idea of the type of thermally induced centers introduced, their densities and locations in the bandgap should be established. Other methods of lifetime determinations could also be usefully employed.

Manuscript submitted Feb. 22, 1977; revised manuscript received May 16, 1977. This was Paper 338 presented at the Las Vegas, Nevada, Meeting of the Society, Oct. 17-22, 1976.

Any discussion of this paper will appear in a Discussion Section to be published in the June 1978 JOURNAL. All discussions for the June 1978 Discussion Section should be submitted by Feb. 1, 1978.

Publication costs of this article were assisted by Westinghouse Research Laboratories.

REFERENCES

1. Y. C. Kao and J. R. Davis, *IEEE Trans. Electron Devices*, **ed-17**, 652 (1970).
2. P. Negrini, D. Nobili, and S. Solmi, *This Journal*, **122**, 1254 (1975).
3. C. T. Sah and C. T. Wang, *J. Appl. Phys.*, **46**, 1767 (1975).

Electrolytic Etching of Aluminum from an Al-Al_3Ni Two-Phase Matrix in Aluminum Chloride Containing Molten Salts

C. L. Hussey,* J. C. Nardi, L. A. King,* and J. K. Erbacher

The Frank J. Seiler Research Laboratory (AFSC), United States Air Force Academy, Colorado 80840

The growth of an aligned microstructure of a controlled eutectic alloy trialuminum nickelide (Al_3Ni) has been investigated by several workers as a means of providing tensile strength enhancement in aluminum (1, 2). A practical method of producing Al_3Ni whiskers in an aluminum matrix utilizes a unidirectional solidification technique (1, 2). In order to properly evaluate the quality of the filament network that has been produced with this growth procedure, it is necessary to remove the solid aluminum phase without causing damage to the filaments. Small diameter fibers composed of Al_3Ni are also expected to find useful application in industrial and military microelectronics if they can be removed undamaged from the aluminum matrix in which they are imbedded. Thus, a practical means of removing aluminum from a two-phase Al-Al_3Ni matrix without damage to the Al_3Ni fibers would be useful to investigators studying the two-phase Al-Al_3Ni system.

Previous attempts using aqueous electrolytes or acid etches for removing or dissolving aluminum from an Al-Al_3Ni matrix have almost always been accompanied by gas evolution, resulting in disordering of the fiber bundles as they are exposed (3). A problem also encountered with aqueous acid etches is low selectivity of attack; *i.e.*, the Al_3Ni fibers are dissolved as well as the bulk aluminum. An electrolyte that would sustain aluminum electrolysis without gas evolution while permitting selective attack on the bulk aluminum phase would be a potential way to circumvent these problems.

Aluminum has been anodized in aprotic media (4, 5), but generally the rate of removal of aluminum is limited by the low electrical conductivity of these media. Application of molten salt media, particularly those containing aluminum chloride, to the anodization of

* Electrochemical Society Active Member.
Key words: aluminum chloride, 1-ethylpyridinium, thin filaments, electrolytic etching, anodization.

aluminum has been demonstrated in both alkali chloride-aluminum chloride (6, 7) and organic salt-aluminum chloride (8, 9) mixtures. Separation procedures using these types of materials provide a number of advantages. Foremost, the method is electrolytic in nature, and therefore provides a great deal of control in the attack. Secondly, the process is not accompanied by gas evolution provided the electrode is not made so anodic as to decompose the melt. Finally, because the electrolyte used is a molten salt the conductivity is high, allowing a rapid removal of material.

King, Brown, and Frayer (6) showed that the anodic dissolution of aluminum proceeds at 100% efficiency at 175°C in a 3:2 molar ratio $AlCl_3$-NaCl melt over the current range 63-500 mA/cm^2. Recently, Gale and Osteryoung (7) found similar results in a 1:1 molar ratio $AlCl_3$-NaCl melt over the current range 0.03-6.30 mA/cm^2 at 175°C. Anodization of aluminum in an organic room temperature molten salt such as 2:1 molar ratio $AlCl_3$-1-ethylpyridinium bromide was also reported to occur with 100% current efficiency (8, 9).

This investigation was undertaken to examine the practicability of using these types of electrolytes to remove the bulk aluminum from a two-phase Al-Al_3Ni matrix.

Experimental

Melts were prepared and maintained and experiments were conducted in a nitrogen filled glove box (Vacuum/Atmospheres Corporation, Model HE 43-6 DRI-LAB). The moisture content was maintained below 10 ppm.

1-ethyl pyridinium bromide (EPB) was prepared by refluxing ethyl bromide (Baker A.R. Grade) with 10% excess pyridine (Baker A.R. Grade) in acetone (Eastman). The resulting white hygroscopic crystals were washed with anhydrous diethyl ether (Baker A.R. Grade) and vacuum dried at 34°C. The melting point of the dried EPB was 121°C and compared favorably with published values of 120°-121°C (10).

A 2:1 molar ratio room temperature melt of $AlCl_3$-EPB was prepared by adding aluminum chloride (Fluka, A.G., iron free) to the EPB. A melt of $AlCl_3$-NaCl saturated with NaCl [49.75 mole percent (m/o) $AlCl_3$] was prepared by fusing aluminum chloride with excess sodium chloride (Baker A.R. Grade) at 175°C. Both melts were purified utilizing a constant current electrolysis procedure (7), and after at least 10 days of electrolysis were clear. They exhibited no evidence of impurities with cyclic voltammetry at a glassy carbon electrode (Fig. 1). The importance of removing impurities from the melt was demonstrated by Gale and Osteryoung (7), who reported that a black deposit forms on aluminum anodes during electrolysis in impure aluminum chloride containing melts.

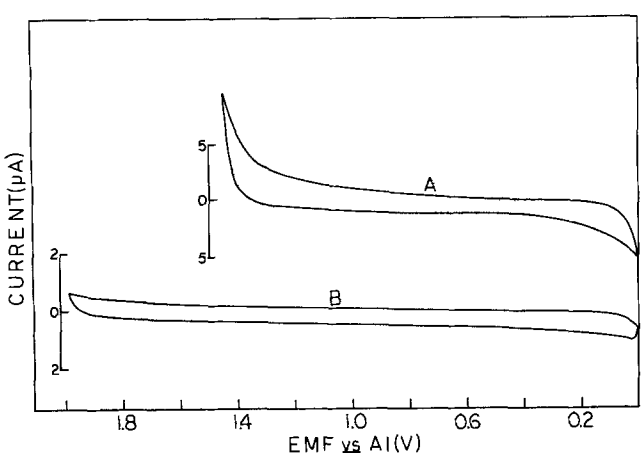


Fig. 1. Cyclic voltammograms at a glassy carbon electrode (A ~ 0.2 cm^2). A is the $AlCl_3$-EPB melt at 23°C and B is the $AlCl_3$-NaCl melt at 175°C. Sweep rate was 100 mV/sec.

Samples of the Al-Al_3Ni matrix were obtained as 3.20 by 0.32 cm diam rods. In addition, a pure sample of Al_3Ni alloy was furnished which had been produced by fusing stoichiometric quantities of aluminum and nickel. This was shaped into a rod of similar dimensions.

Electrodes were fashioned from the samples by wrapping aluminum wire around the ends of the specimens that were not immersed in the melt to provide electrical contact. The immersed area of the Al-Al_3Ni specimen was determined from geometry to be 0.6 cm^2. The Al_3Ni electrode was quite porous, resembling felt metal. A geometrical area, 1 cm^2, was estimated.

Constant current and controlled potential electrolyses were accomplished with a potentiostat/galvanostat (Princeton Applied Research Corporation, Model 173). A voltage programmer (Princeton Applied Research Corporation, Model 175) was coupled to the potentiostat/galvanostat for linear sweep or cyclic voltammetry.

For voltammetry experiments, either a glassy carbon electrode, a pure aluminum wire, or the Al_3Ni electrode was used as the working electrode in a three-electrode cell. The Al_3Ni rod was the working electrode in selective etching experiments. The counter-electrode was a cup-shaped piece of aluminum foil (Research Organic/Inorganic Company, m5n purity), and the reference electrode was a spiral aluminum wire (Alfa-Ventron, m5n purity) isolated from the melt by a 10 mm fine porosity Pyrex frit. The composition of melt in the reference compartment was identical to that of the bulk melt. All potentials described during this investigation were measured against this electrode, *i.e.*, the Al(III)/Al couple.

Cell temperature was maintained at 175°C with a platinum resistance element controlled furnace for experiments with the $AlCl_3$-NaCl melt. Experiments with the $AlCl_3$-EPB melt were conducted at 23°C.

Cyclic voltammograms to determine the melt purity and the $AlCl_3$-EPB anodic limit were constructed by sweeping the glassy carbon electrode between the anodic limit of the melt and the point at which aluminum deposition occurs, *i.e.*, 0.0V at a sweep rate of 100 mV/sec. Linear sweep voltammograms with Al_3Ni or aluminum electrodes were accomplished by sweeping the electrode from 0.0V to the desired anodic potential at a sweep rate of 20 mV/sec.

Results and Discussion

The anodic potential limit of $AlCl_3$-NaCl molten mixtures has been established at *ca.* 2.2V *vs.* Al (11), and was attributed to the oxidation of chloride-containing species to chlorine gas. For the 2:1 $AlCl_3$-EPB melt the limit was determined in this study to be about 1.50V (Fig. 1). Repeated anodization of a glassy carbon electrode in this melt at potentials exceeding 1.50V imparted an orange coloration, suggesting the formation of bromine.

In order that the best electrolysis conditions might be determined, *i.e.*, maximum rate of aluminum removal with minimum fiber attack, it was necessary to know the approximate potential at which significant electrolysis of Al_3Ni took place. For this reason anodic linear sweep voltammograms of aluminum and Al_3Ni were run in both melts. The open-circuit potential of Al_3N was about 0.35V *vs.* Al in both melts.

Linear sweep voltammograms of aluminum and Al_3Ni in the $AlCl_3$-NaCl melt at 175°C (Fig. 2) show that aluminum anodization begins approximately 0.5V before appreciable anodization occurs at the Al_3Ni sample. Therefore, aluminum can be removed in this melt without appreciable attack at the Al_3Ni whiskers, providing the potential of the matrix rod sample is kept below 0.9V. Since this potential is considerably more cathodic than the melt limit, no gas evolution was observed.

The onset of aluminum anodization in this melt is preceded by a reproducible 0.3V overpotential. This

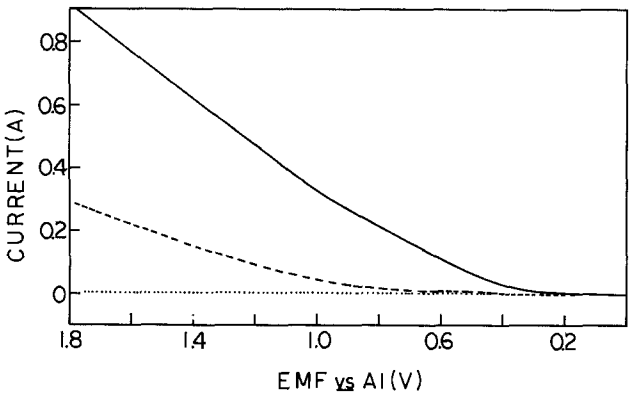


Fig. 2. Anodic linear sweep voltammograms for aluminum and Al_3Ni electrolysis in the $AlCl_3$-NaCl melt at 175°C. Sweep rate was 20 mV/sec. Initial potential was 0.0V vs. Al. —— pure aluminum wire ($A \sim 1$ cm^2); ---- Al_3Ni electrode ($A \sim 1$ cm^2); .... glassy carbon electrode ($A \sim 0.2$ cm^2).

overpotential was not affected by pretreatment of the aluminum electrode. An overpotential of similar magnitude was also observed during steady-state current-potential experiments made in this laboratory. This phenomena is in contrast to the behavior of aluminum in $AlCl_3$ rich $AlCl_3$-KCl-NaCl reported in the literature (12) and in $AlCl_3$ rich $AlCl_3$-NaCl melts observed in this laboratory. Unfortunately a detailed discussion of this phenomena is outside the scope of the present investigation.

A similar experiment in the $AlCl_3$-EPB melt at 23°C (Fig. 3) revealed different behavior for the aluminum electrode than in the previous case. Anodization begins almost immediately and a linear rise in current with increasing potential is evident to about 1.1V. At this point the current fell to a constant value, suggesting the formation of a partially insulating film of $AlCl_3$ (12). Attack of the Al_3Ni electrode was negligible until a potential of about 1.0V was attained. Thus, at potentials below 1.0V aluminum can be removed without significant attack on the Al_3Ni fibers. All electrolysis experiments demonstrating the selective removal of aluminum from the Al-Al_3Ni matrix in $AlCl_3$-EPB were carried out in a stirred melt in an attempt to limit the formation of the passivating film at the electrode. The results of these experiments are given below.

Photomicrographs of a portion of an Al-Al_3Ni rod prior to its electrolysis revealed no discernible exposed fibers (Fig. 4). Examination of the rod end surface at greater magnification (Fig. 5) showed Al_3Ni rods which protrude slightly from the Al-Al_3Ni matrix surface where the rod was saw cut. After electrolysis for 1 hr at a potential of 0.9V in an unstirred solution of $AlCl_3$-NaCl at 175°C, a photomicrograph (Fig. 6) revealed myriad-exposed Al_3Ni fibers. During electrolysis the current progressed from an initial value of 0.3 A/cm^2 to a final value of 0.02 A/cm^2. Similar results were obtained after 2 and 5 mA/cm^2 (Fig. 7) constant current electrolysis in the stirred $AlCl_3$-EPB melt at 23°C. During this experiment the potential did not exceed 0.5V.

There appeared to be no discernible difference in the appearance of Al_3Ni fibers exposed by electrolysis in the $AlCl_3$-NaCl melt and those produced in the $AlCl_3$-EPB melt. This was true in spite of the significant differences in the media used for anodizing the Al-Al_3Ni matrix. However, more extensive studies will be required before the extent of damage to the Al_3Ni fibers can be fully assessed. The fibers do appear to be suffi-

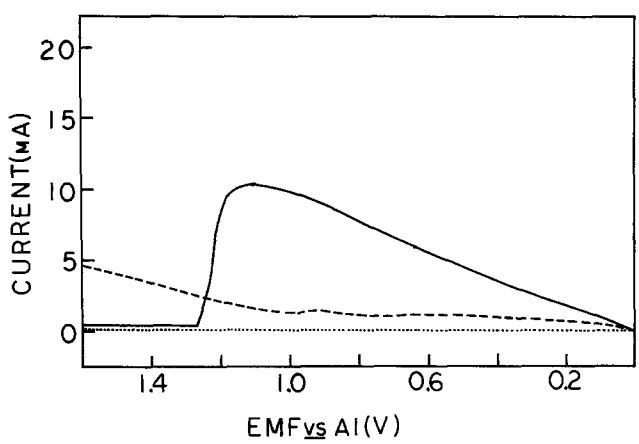


Fig. 3. Anodic linear sweep voltammograms for aluminum and Al_3Ni electrolysis in the $AlCl_3$-EPB melt at 23°C. Sweep rate was 20 mV/sec. Initial potential was 0.0V vs. Al. —— pure aluminum wire ($A \sim 1$ cm^2); ---- Al_3Ni electrode ($A \sim 1$ cm^2); .... glassy carbon electrode ($A \sim 0.2$ cm^2).

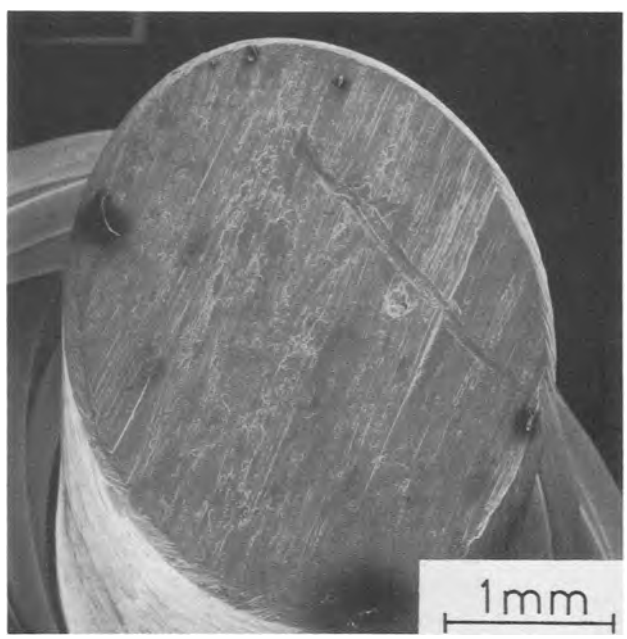


Fig. 4. End-on view of two-phase Al-Al_3Ni matrix rod prior to electrolysis.

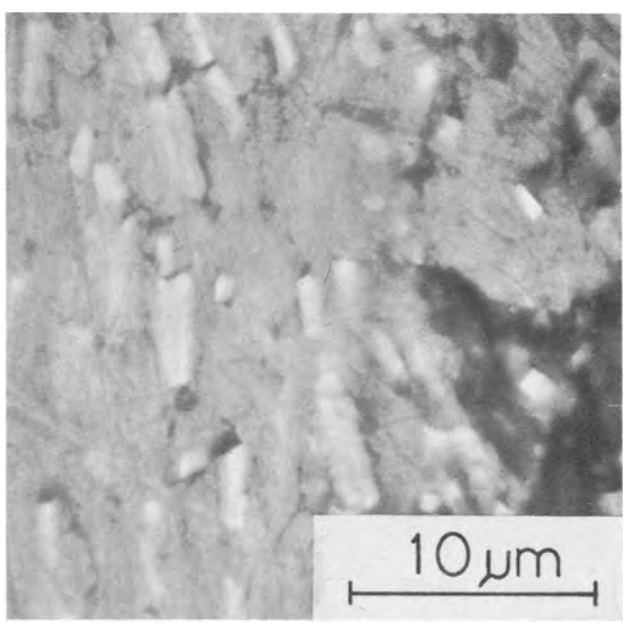


Fig. 5. Al-Al_3Ni matrix rod surface prior to electrolysis

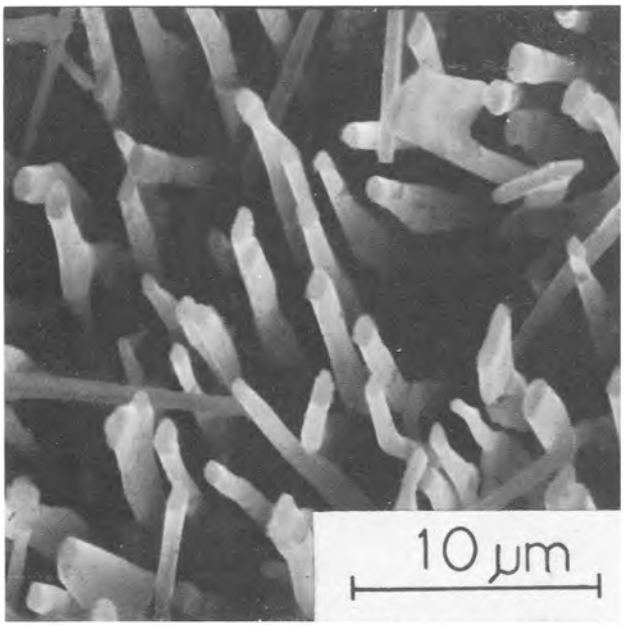


Fig. 6. Al_3Ni filaments exposed with controlled potential electrolysis in $AlCl_3$-NaCl at 175°C. Electrolysis potential was 0.9V.

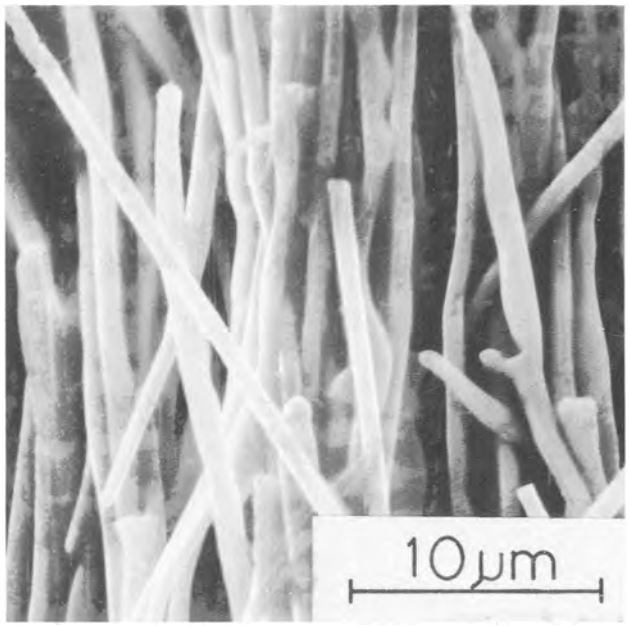


Fig. 7. Al_3Ni filaments exposed with constant current electrolysis in $AlCl_3$-EPB at 23°C. Current density was 5 mA/cm^2.

ciently intact to provide information about the quality of growth techniques used to produce them.

Conclusion

The selective electrolytic etching of aluminum from a two-phase Al-Al_3Ni matrix has been shown to be feasible in aluminum chloride containing molten salts. The molten salts chosen for this study, NaCl saturated $AlCl_3$-NaCl and 2:1M ratio $AlCl_3$-1-ethylpyridinium bromide represent wide extremes in conductivity and liquidus temperature available in aluminum chloride containing molten salts. It should be possible to employ almost any aluminum chloride containing molten salt whose properties lie within these extremes for the selective electrolytic etching of aluminum from an Al-Al_3Ni matrix providing the selectivity constraints are predetermined. In addition, the procedure demonstrated in this study appears promising for scale-up separation operations in which it is desired to produce free, intact, Al_3Ni filaments.

Acknowledgments

Financial assistance in this investigation was provided by the Rome Air Development Center (AFSC), Hanscom AFB, Massachusetts. We would like to thank Dr. J. Hutta and Dr. N. Klausutis of that organization for furnishing samples and for their helpful discussions of the work. We wish to express our appreciation to Dr. J. Clifford and Dr. R. Swedenburg of the Department of Physics, United States Air Force Academy, Colorado, for SEM photographs, and to Dr. J. Robinson and Dr. R. A. Osteryoung, Colorado State University for the gift of a glassy carbon electrode.

Manuscript submitted Jan. 1, 1977; revised manuscript received April 25, 1977.

Any discussion of this paper will appear in a Discussion Section to be published in the June 1978 JOURNAL. All discussions for the June 1978 Discussion Section should be submitted by Feb. 1, 1978.

Publication costs of this article were assisted by the U.S. Air Force Systems Command.

REFERENCES

1. B. J. Bayles, J. A. Ford, and M. J. Salkind, *Trans. Metall. Soc. AIME*, **239**, 844 (1967).
2. F. D. Lemkey, R. W. Hertzberg, and J. A. Ford, *ibid.*, **233**, 334 (1965).
3. J. Hutta, Personal communication.
4. A. W. Davidson and F. Jirik, *J. Am. Chem. Soc.*, **72**, 1700 (1950).
5. W. E. Bennett, A. W. Davidson, and J. Kleinberg, *ibid.*, **74**, 732 (1952).
6. L. A. King. A. D. Brown, and F. H. Frayer, Proc. OAR Res. Appl. Conf., 21 March 1968, p. J-1.
7. R. J. Gale and R. A. Osteryoung, *This Journal*, **121**, 983 (1974).
8. F. H. Hurley and T. P. Wier, *ibid.*, **98**, 203 (1951).
9. W. H. Safranek, W. C. Schickner, and C. L. Faust, *ibid.*, **99**, 53 (1952).
10. J. Willems and J. Nys, *Bull. Soc. Chim. Belg.*, **66**, 502 (1957).
11. Iu K. Delimarskii and B. F. Markov, "Electrochemistry of Fused Salts," p. 145, The Sigma Press, Publishers, Washington D.C. (1961).
12. G. L. Holleck and J. Giner, *This Journal*, **119**, 1161 (1972).

Sputter Deposition of a Metastable Equiatomic Tin-Nickel Alloy

J. A. Augis and J. E. Bennett

Bell Laboratories, Columbus, Ohio 43213

The equiatomic metastable tin-nickel alloy, "Sn-Ni", used for protective and decorative purposes and in electronic components, shows a remarkable resistance to most corrosive agents (1). It is a metastable single phase alloy which has been made only by electrodeposition (2, 3).

Thin film deposition (including electrodeposition) of metals and alloys often leads to phases which cannot be obtained by standard metallurgical techniques. Due to the different rates of nucleation and growth encountered in thin film deposition, it is possible to "quench-in" microstructures (4) which would evolve toward different equilibrium structures during typical metallurgical processing. Two important parameters ruling the microstructures and the kinetics of transformation during film deposition are the flux of impinging atoms and the temperature of the substrate.

While the impinging flux is more easily controlled during electrodeposition, the substrate temperature is more easily controlled during vacuum deposition. It seems reasonable then to expect that a metastable phase could also be produced by sputtering methods. The motivation behind sputtering tin-nickel is twofold: firstly, can certain undesirable properties of the electrodeposited alloy (*e.g.*, brittleness) be improved by the sputtering process; secondly, can the comparisons in physical properties of the two kinds of deposits (sputtered and plated) help to elucidate the nature of the metastable phase? This paper will simply confirm that a metastable tin-nickel alloy can be prepared by sputtering.

Experimental

The equiatomic "Sn-Ni" alloy was deposited using a MRC sputtering head mounted on a Veeco oil-diffusion pumping system. The sputtering gas was argon.

The deposition was made on a substrate of either molybdenum or copper placed on a platen assembly which could be either water cooled or heated and kept at a predetermined temperature. The temperature of the upper face of the substrate was monitored by a compensated thermocouple.

A target having a composition close to equiatomicity was needed. The mixture of equilibrium phases corresponding to the equiatomic composition (Ni_3Sn_4 and Ni_3Sn_2) is extremely brittle, and this precluded the manufacturing of a 5 in. thin disk by melting, forming, and homogenizing nickel and tin. Consequently, the target was prepared by electroplating 10 ml of the metastable phase from the bath previously described in Ref. (3) on a 254 μm thick layer of the 12.7 cm diam copper plate.

Sputter depositions were made under various conditions: the d-c voltage was kept at 3800V; the argon pressure was varied from 10 to 40 mTorr, corresponding to deposition rates ranging from 100 to 325 Å/min; and the substrate temperatures were fixed at values from 40° to 220°C.

Results

The metastable phase can be identified by x-ray diffraction and thermal analysis (3). The equilibrium system (5) corresponding to equiatomicity is a mixture of Ni_3Sn_4 and Ni_3Sn_2. The tin-rich phase Ni_3Sn_4 crystallizes in the monoclinic system; the phase Ni_3Sn_2 crystallizes in the hexagonal system and has the NiAs ($B8_2$) structure. The $B8_2$ structure was also assigned to the electroplated metastable phase by Rooksby (6). However, the x-ray diffraction patterns for two of the three phases are quite similar, suggesting analogous atomic arrangements. In particular, both "Sn-Ni" and Ni_3Sn_2 structures can be described by hexagonal cells with dimensions which are almost equal. The main difference between the two cells concerns the lattice spacings of the (110) and (102) planes. While in Ni_3Sn_2, the spacings are sufficiently different to give two resolvable diffraction peaks for this region of 2θ; the x-ray diffraction pattern shows only one peak for both the 110 and 102 reflections in the case of the electroplated metastable phase. Ni_3Sn_4 shows a somewhat different x-ray pattern in the same region of 2θ where 3 peaks can be resolved. Because only the x-ray pattern of Ni_3Sn_4 is sufficiently distinctive, we checked primarily for the presence of Ni_3Sn_4 diffraction lines in the sputtered deposit.

Table I shows the various sputtering conditions that were used, along with the nature of the film obtained. The compositions of the films were determined with energy-dispersive x-ray analysis (EDAX) using ingot Ni_3Sn_2, ingot Ni_3Sn_4, and electroplated "Sn-Ni" as standards. The latter sample had been previously analyzed by a wet chemistry method (3). It is generally observed during sputtering of alloys that the composition of the deposit is close to the composition of the target. Within the limits of the compositional analysis technique (EDAX), the sputtered films show Ni to Sn ratios comparable to that observed in typical electroplated films. In the two cases where copper substrates were used and sputtering was made at high temperatures (190° and 220°), the lower concentration of tin in the deposit is probably the result of its interdiffusion with the substrate. An evolved gas analysis (EGA) was run on a few samples. The plated samples evolved some water, oxygen, and chlorine. The sputtered samples showed mostly water and argon.

The next to last column of Table I indicates either the absence or the presence of x-ray lines characteristic of Ni_3Sn_4. The equilibrium equiatomic alloy should contain approximately 50% of the Ni_3Sn_4 phase. Only for the three cases where the substrate temperature was at 180°, 190°, or 220°C were any Ni_3Sn_4 x-ray lines observed. It was concluded that for all the runs where the substrate temperature was 100°C or below, a metastable deposit similar to the electroplated alloy was obtained.

Upon heating, the electroplated metastable phase reverts exothermically (3) to the equilibrium mixture presumably by the following reaction

$$6\ \text{"Sn-Ni"} \rightarrow Ni_3Sn_4 + Ni_3Sn_2 + \text{heat}$$

As in Ref. 3, a heat-treatment was given to some of the sputtered films. Substrates were etched away and the films (10 μm thick) were ground to a fine powder. Figure 1a shows the x-ray pattern obtained from unheated powder, and it is similar to the pattern of the as-plated "Sn-Ni" (ASTM x-ray diffraction file card 7-256). In Fig. 1b, which is the pattern given by the heat-treated powder (500°C, 1 hr), lines corresponding to Ni_3Sn_4 and Ni_3Sn_2 can be observed (ASTM

Key words: alloy surfaces, sputtering films, phase transformation stoichiometry.

Table I. Occurrence of the metastable "Sn-Ni" phase under varied sputtering conditions

Identification	Type of substrate	Substrate temperature (°C)	Deposition rate (Å/min)	Composition, atomic percent	Ni_3Sn_4 x-ray lines	Structure
Mo I	Mo unpolished	36	100	53Ni, 47Sn	none	metastable
Mo II	Mo unpolished	100	180	53Ni, 47Sn	none	metastable
Mo III	Mo unpolished	180	220	51.5Ni, 48.5Sn	yes	stable
Cu V	Cu unpolished	50	160	52Ni, 48Sn	none	metastable
Cu VI	Cu polished	190	150	55.25Ni, 44.75Sn	yes	stable
Cu VII	Cu polished	220	370	55.25Ni, 44.75Sn	yes	stable
Cu VIII	Cu polished	84	380	52.25Ni, 47.75Sn	none	metastable
Cu X	Cu polished	80	330	53Ni, 47Sn	none	metastable
Cu XI	Cu polished	80	330	52Ni, 48Sn	none	metastable

cards 4-0845 and 6-0141), showing that transformation to the equilibrium structures takes place during heat-treatment of the sputtered deposit also. These results were confirmed using the technique of differential thermal analysis (DTA) [see Ref. (3)]. Similar to the as-plated alloy, the sputtered material exhibits a broad exothermic peak. In Fig. 2, three DTA traces are shown. It is apparent that the exothermic peaks for the sputtered samples occur at a substantially higher temperature and are much larger than was observed for the plated sample. This indicates somewhat different kinetics of transformation, possibly linked to a different microstructure.

Discussion

From both the x-ray and thermal analyses results we can conclude that sputtering, just as electroplating, produces films of "Sn-Ni" having a different phase structure than equilibrium alloys of the same composition. Both types of films (plated and sputtered) are close to being equiatomic and, following heat-treatment, both have x-ray diffraction patterns corresponding to a mixture of the equilibrium phases Ni_3Sn_4 and Ni_3Sn_2. We have already mentioned in the preceding paragraph that the DTA results for the sputtered films indicate somewhat different kinetics of transformation. The x-ray data, besides showing strong similarities between the two types of films, also reveal some differences.

As explained in the results section, the main difference between the x-ray patterns of Ni_3Sn_2 and "Sn-Ni" is that the 110 and 102 reflections coalesce into a single broad peak in electroplated "Sn-Ni", while they are easily resolved in Ni_3Sn_2. The corresponding 2θ regions of the x-ray patterns for the sputtered samples were carefully examined. For the as-deposited sputtered films, which were believed to be the metastable phase, a small shoulder was always present on the lower 2θ side of the main peak when the sample was actually in film form. Sputtered and electroplated films often show strong preferred orientation. The main reflection which was enhanced by the preferred orientation in the as-sputtered films was found to be 110 using the Laue transmission pinhole technique, and the small shoulder corresponded to the 102 reflection. Effects of preferred orientations were minimized by using powder samples, and there is evidence of peak splitting (102, 110) in Fig. 1a. The x-ray spectra for powder smears of sputtered "SnNi", plated "SnNi", and Ni_3Sn_2 are shown in Fig. 3 with an extended 2θ scale. Note that for the sputtered sample in powder form the 102 peak is now more intense than the 110 peak which is the reverse of that observed for the film samples.

Table II shows the calculated d_{110} and d_{102} values for some of the films. Even when metastable character is attributed to the sputtered films, d_{102} is separated

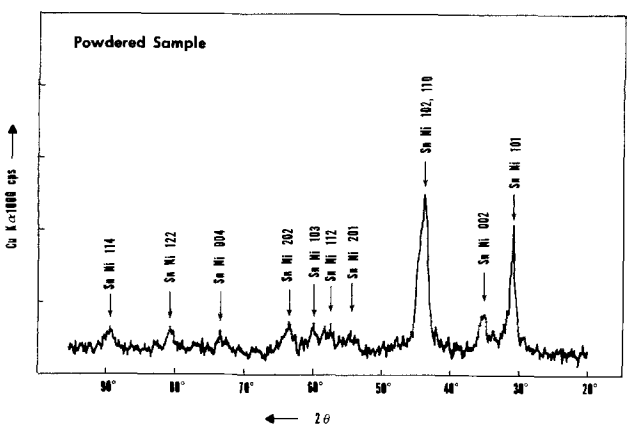


Fig. 1a. Full x-ray diffraction pattern of sputtered tin-nickel in powder form, (sample Cu X) before heat-treatment. Filtered copper radiation 50 kV, 30 mA.

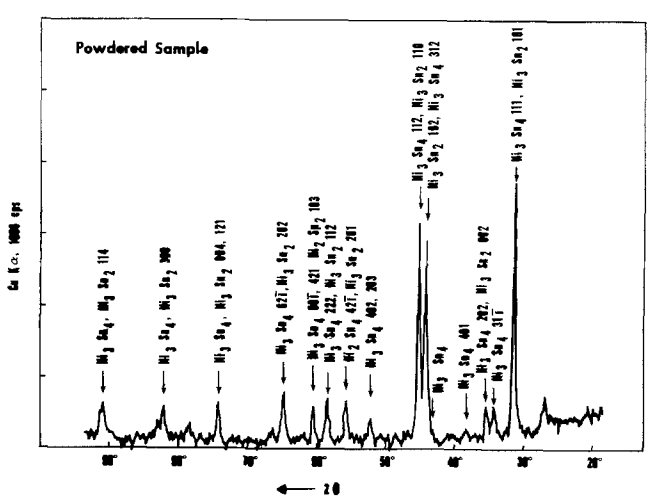


Fig. 1b. Same as above, after 1 hr-500°C heat-treatment of the sample Cu X.

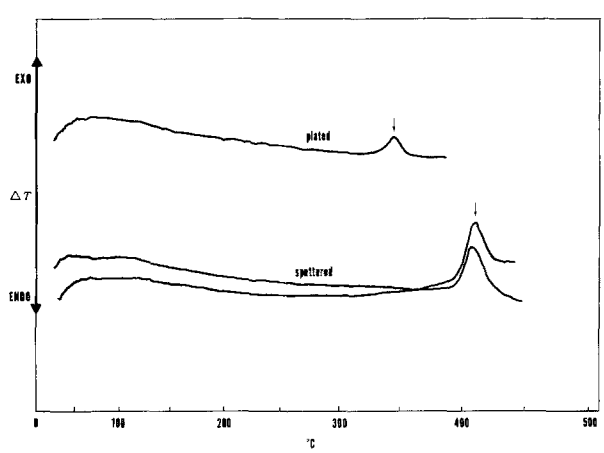


Fig. 2. DTA curves for heating of plated and sputtered tin-nickel alloy. Atmosphere, flowing Ar (0.035 liter/min); heating rate, 5°C/min; reference, α Al_2O_3; sample weight = reference weight = 0.007g.

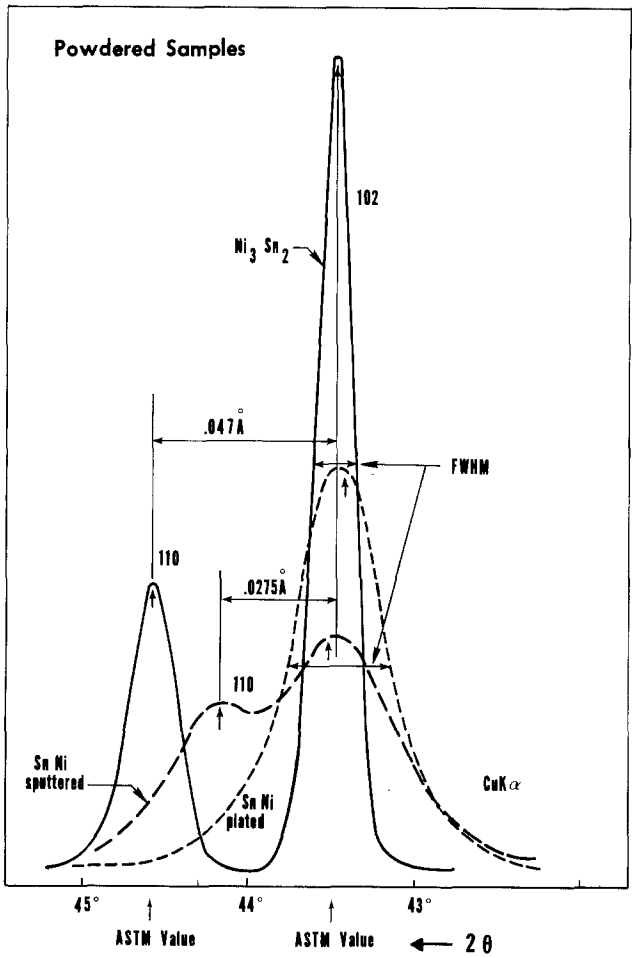


Fig. 3. X-ray diffractometer peaks 110 and 102 for powder samples of plated "Sn-Ni," sputtered "Sn-Ni," and ingot Ni_3Sn_2. The peaks have been normalized to unit area. Filtered Cu radiation 50 kV, 30 mA.

from d_{110} by a Δd ranging from 0.02 to 0.033Å. It should be noted that with increasing substrate temperature, Δd tends toward the value observed for Ni_3Sn_2 of 0.041Å. The last four entries of Table II show the data on powder samples in which preferred orientation did not exist. The results for powders are also illustrated by Fig. 3. In this figure the x-ray traces for the 110 and 102 peaks (normalized to unit area) are shown for equilibrium Ni_3Sn_2, electroplated "Sn-Ni", and sputtered "Sn-Ni". The 102 peaks have been arbitrarily centered at the ASTM value for better illustration. In spite of a rather large broadening effect, two separate peaks can be resolved for the sputtered sample, while no such separation is observed for the plated sample. The extent of the peak broadening is also recorded in Table II as the corrected full width at half-maximum (FWHM). The correction was made by using the gaussian approximation and taking as instrument broadening the width observed for the equilibrium Ni_3Sn_2 sample. X-ray line broadening is known to be due to small grain size, internal microstresses, and/or lattice defects. While it is not possible in the present case to separate these three factors, the line breadth is still a semiquantitative measure of the lattice "irregularities." Results in Table II indicate that the amount of "irregularities" observed in the sputtered sample was comparable to that observed in the plated sample. It is also significant that the line breadth decreased with increasing substrate temperature, and increased with deposition rate. If the line breadth was due only to small crystallite size, the Scherrer formula (7) predicts crystallite main dimensions of roughly 100-150Å for the samples showing the most line broadening.

From these results we can reasonably conclude that both electroplating and sputtering deposit a seemingly homogeneous and equiatomic phase of tin-nickel, the lattice cell of which bears strong resemblance to the cell of the equilibrium phase Ni_3Sn_2. Both methods of deposition, due to the slow rates of growth and migration at low substrate temperature, lead to fine-grained and highly distorted structures. On the other hand, the NiAs-Ni_2In structure, in which both Ni_3Sn_2 and the metastable phase crystallize, is known to accommodate defects and a wide range of composition (8). It is possible then that the metastable "Sn-Ni" is not a new phase as thought by Clarke (9), but the result of a distorted Ni_3Sn_2 lattice as suggested originally by Rooksby (6). In this light, the differences exhibited by plating and sputtering can be attributed to differences in the levels of microstress and deformation produced in the two processes or minor differences in microstructure.

In the first approximation, the microstructure of thin films is primarily fixed by the substrate temperature, but the flux of impinging species in electroplating was almost two orders of magnitude greater than the rate observed in sputtering. Also, plating is a charged process while sputtering is neutral. These differences can lead to a greater "quenching" effect in plating than in sputtering. Also there is the possibility that the difference in impurity levels and impurity species stabilizes differently the plated and sputtered structures. As a consequence, plating may deposit a film with the Ni_3Sn_2 lattice having enough anisotropic deformation and microstresses to make d_{110} and d_{102} equal. Sputtering, however, may allow enough relaxation to produce a lattice in which deformation is not as severe, and thus d_{110} and d_{102} are different. This difference is not as much as in the equilibrium Ni_3Sn_2 compound.

Unfortunately, the dissimilarity in the DTA results, *i.e.*, the apparent shift in the transformation temperature and larger heat of reaction, do not lend themselves to a ready explanation. The DTA results in-

Table II. Differences in lattice spacing and line broadening for the (110) and (102) planes in "Sn-Ni" and Ni_3Sn_2

Sample	State of sample	d_{110} (Å)	d_{102} (Å)	Δd (Å)	Corrected FWHM (degrees)	Structure
Mo I	film	2 070	2.090	0.02	0.38	metastable
Mo II	film	2.060	2 09	0.03	0.38	metastable
Mo III	film	2 066	2.093	0.033	0.22	stable
Cu V	film	2.057	2 085	0.028	0.75	metastable
Cu VI	film	2.044	2.085	0.041	0.19	stable
Cu VII	film	2.047	2.088	0.041	0.22	stable
Cu VIII	film	2.055	2.088	0.033	1.16	metastable
Cu X	powder	2.056	2.089	0.033	0.80	metastable
Cu XI	powder	2.058	2.083	0.025	0.85	metastable
Electroplated	powder	2.076*	2.076*	0	0.69-1.10	metastable
Ingot Ni_3Sn_2	powder	2.036*	2.077*	0.041	0	stable

* ASTM values.

dicate that the sputtered films are stable to a higher temperature and release more energy upon decomposition. Both a thermal kinetic study and an electron microscope study are in progress to clarify these observations and ascertain the causes for these differences.

Conclusion

By using sputtering, we have been able to deposit a metastable equiatomic tin-nickel alloy which is in many ways similar to that which previously has been obtainable only by electrodeposition. Results show that the sputtered alloy has the same basic crystal structure and composition as the electroplated alloy and undergoes the same transformation to equilibrium compounds upon heating. The observed minor differences in x-ray results and stability of the two types of deposits are possibly linked to differences in microstructures and/or microstresses.

Acknowledgments

The authors extend their sincere appreciation to G. V. McIlhargie for his special expertise and effort in preparation of the electroplated sputtering target, T. M. Paskowski for his diligence in obtaining the DTA data, and P. K. Gallager who conducted the E.G.A. study.

Manuscript submitted April 4. 1977; revised manuscript received May 26, 1977.

Any discussion of this paper will appear in a Discussion Section to be published in the June 1978 JOURNAL. All discussions for the June 1978 Discussion Section should be submitted by Feb. 1, 1978.

Publication costs of this article were assisted by Bell Laboratories.

REFERENCES

1. M. Antler, *IEEE Trans. Parts, Hybrids, Packag.*, **php-11**, 216 (1975).
2. N. Parkinson, *J. Electrodepositors Tech. Soc.*, **27**, 129 (1951).
3. J. E. Bennett and H. G. Tompkins, *This Journal*, **123**, 999 (1976).
4. K. L. Chopra, "Thin Film Phenomena," Chapter IV, McGraw-Hill Book Co., New York (1969).
5. M. Hansen, "Constitution of Binary Alloys," p. 1042, McGraw-Hill Book Co., New York (1958).
6. H. P. Rooksby, *J. Electrodepositors Tech. Soc.*, **27**, 153 (1951).
7. H. Klug and L. Alexander, "X-Ray Diffraction Procedures." p. 491, John Wiley & Sons, New York (1967).
8. A. Kjekshus and W. B. Pearson, "Progress in Solid State Chemistry," Vol. 1, Chapter 3, Pergamon Press, New York (1964).
9. M. Clarke and P. K. Dutta, *J. Phys. D*, **4**, 1652 (1971).

Brief Communication

Passivation of Silicon p-n Junctions by Slightly Conductive Chalcogenide Films

E. T. J. M. Smeets, J. Dieleman, F. H. M. Sanders, and D. de Nobel

Philips Research Laboratories, Eindhoven, The Netherlands

Edge breakdown and excessive surface leakage are two well-known hazards of reverse-biased p-n junctions. As a result of numerous studies about the properties of thermal SiO_2 and its interface with silicon, the semiconductor technologist has learned how to avoid these hazards in most cases. Nevertheless, edge breakdown and excessive leakage remain a problem in devices with features that make them prone to these failures. Such features are, for instance, high internal fields, a shallow p-n junction (sharp edges), or a technology that precludes the use of high-temperature oxidation to passivate the critical region where the p-n junction intersects the surface.

The present contribution gives some results of an investigation aimed at exploring the merits of passivation by means of slightly conducting films directly applied to the silicon at a low temperature. With a proper conductivity such a film will cause a gradual voltage drop at the surface of the silicon and thus extend the depletion layer parallel to the surface, thereby reducing the curvature of the depletion layer at the edge of the p-n junction. It is shown that thin chalcogenide films can effectively suppress edge breakdown. Although this goes at the expense of some increase in reverse current because of the additional leakage path created by the chalcogenide film, it has nevertheless proved possible to keep reverse currents in the low nanoampere range and, what is also important, the currents were observed to stay in this range during operation.

Key words: passivation, chalcogenide films, p-n junctions.

The semiplanar mesa-type avalanche photodiode sketched in Fig. 1 was chosen as a vehicle for this study. This device is hard to passivate (1), and it shows all the awkward features mentioned above. The n^+ layer is a shallow ion-implanted layer (0.5 μm), and therefore the critical edges (A and A' in Fig. 1) are sharp and for this reason prone to edge breakdown. The device is designed for operation slightly below the intrinsic breakdown voltage of the active central part. $V_{BD}{}^{i} = 135$V, which is rather high. Moreover, the use of oxidation at high temperature and the use of a diffused guard ring is impracticable because of the risk of spoiling the critical doping profile at the interface between the p- and the π-layer, which was grown epitaxially in an earlier processing step. Attempts to passivate this device by thermal oxidation at or below 900°C or by applying oxide films with low temperature CVD or sputtering met with no success. Edge breakdown remained or the dark current was high and/or increased with time.

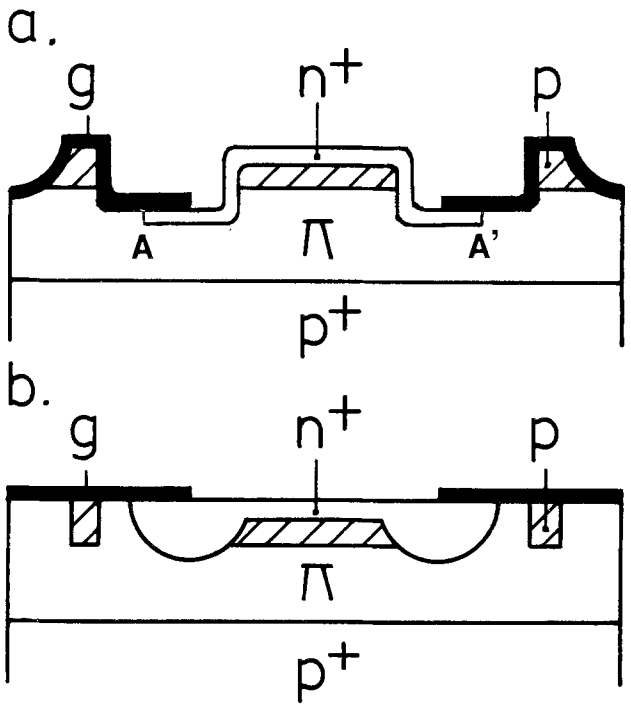


Fig. 1. Main Si APD structures: a. semiplanar mesa type; b. planar type. Both types have the $n^+pp^-p^+$ structure with the circular, active n^+p region surrounded by a concentric annular p-type channel stopper. The planar APD contains an additional n^+ guard ring at the edge of the active n^+p region. The film indicated by "g" is the chalcogenide film applied for edge breakdown suppression and/or passivation.

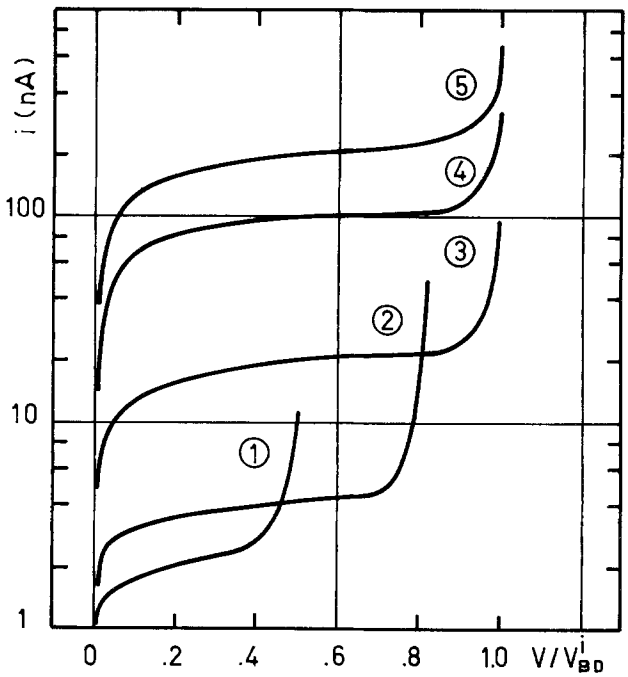


Fig. 2. I-V characteristics of the mesa-type APD for various conductivities of the chalcogenide film g. Curve 1 for a 0.1μ thick GaSe film; curve 2 for $GaSe_{1-x1}Te_{x1}$ with x_1 a few percent; curve 3 for $GaSe_{1-x2}Te_{x2}$ with $x_2 > x_1$ and just sufficient to suppress edge breakdown; curve 4 for a 0.5μ thick CdTe film heat-treated for 2 hr at 150°C in air; curve 5 for the as-deposited CdTe film.

Subsequently, chalcogenide films were examined, with particular emphasis on glassy films based on GaSe. These films are inert against corrosion in air and have high crystallization temperature of up to 450°C. Moreover, GaSe-based films, for instance, can be made over a large range of conductivities. The conductivity of these films increases with increasing substitution of Te for Se or of In for Ga (2, 3).

Figure 2 shows the reverse characteristics for such semiplanar mesa diodes (diameter n^+ region 400 μm) passivated with thin chalcogenide films. The conductivity of the films increases in the sequence 1-5. Curves 4 and 5 refer to diodes with a polycrystalline CdTe film, whereas curves 1, 2, and 3 give results for the glassy chalcogenide films.

The curves show that with increasing conductivity of the passivating film the breakdown voltage quickly rises up to the intrinsic breakdown voltage $V_{BD}{}^i$ (135V); apparently the passivation works satisfactorily. As expected, the reverse current increases with increasing conductivity of the film. This might suggest that the increased reverse current of the diodes is simply due to a resistive parallel leakage path. If this were the case, however, one would expect incomplete saturation of the reverse current with rising conductivity of the passivating film, which is not observed in Fig. 2. Apparently the assumption of simple parallel leakage is an oversimplification of the actual situation.

In Fig. 2 the switch towards intrinsic breakdown occurs somewhere between curves 2 and 3, *i.e.*, between diodes with leakage currents with, say, 4 and 20 nA. By proper adjustment of the Te content, films were deposited which gave diodes with intrinsic breakdown (135V) and a leakage current of only 5 nA at $V = 0.9\ V_{BD}{}^i$.

Another test was made on planar devices [see Fig. 1b and Ref. (1)], where, owing to the presence of a diffused guard ring, edge breakdown was no problem. Here films with even lower conductivities could be used satisfactorily. After stripping the oxide passivation of planar devices and deposition of a glassy GaSe film instead, good planar APD's (diam 450 μm) were obtained with stable dark currents as low as 2 nA at $V = 0.9\ V_{BD}{}^i$ ($V_{BD}{}^i = 250$V), *i.e.*, only about a factor of two higher than that of the original devices with standard high temperature thermal-oxide passivation. In summary, the present work shows that in cases where the well-established passivation with high temperature thermal oxide cannot be used, chalcogenide films of the kind described offer interesting possibilities.

Manuscript submitted April 19, 1977.

Any discussion of this paper will appear in a Discussion Section to be published in the June 1978 JOURNAL. All discussions for the June 1978 Discussion Section should be submitted by Feb. 1, 1978.

Publication costs of this article were assisted by Philips Research Laboratories.

REFERENCES

1. L. J. M. Bollen, J. J. Goedbloed, and E. T. J. M. Smeets, *Philips Tech. Rev.*, **36**, 205-210 (1976).
2. J. Dieleman and A. M. E. Hoeberechts, U.S. Pat. 3,982,149.
3. C. Wood, L. R. Gilbert, C. M. Garner, and J. C. Shaffer, "Proceedings of the 5th International Conference on Amorphous and Liquid Semiconductors," J. Stuke and W. Brenig, Editors, p. 285, Taylor and Francis, London (1974).

Comparison of the Erosion of Vitreous Carbon and High Density Graphite in Molten Silicon

R. E. Chaney*

Motorola Incorporated, Semiconductor Group, Phoenix, Arizona 85008

Materials compatibilty problems have seriously affected the development of new silicon ribbon crystal growth technologies. One of the most notable problems has been the degradation of forming dies used for the edge-defined film-fed growth (EFG) process (1), the capillary action shaping technique (CAST) (2), and the inverted Stepanov technique (3). In an effort to understand the materials interaction phenomena, an investigation was undertaken to study the erosion processes of several materials in molten silicon (4, 5). In the previously reported work the materials studied were chosen because of possibly very low erosion, negligible contamination effects, and low porosity. Vitreous carbon[1] was selected as the most promising candidate of the various carbon products. However, many investigators use high density graphite for die fabrication. The purpose of this note is to compare the erosion characteristics of the two carbon products.

The experimental procedure was to immerse rods of the test materials in molten silicon. The rod was either withdrawn or immersed, in stages, to yield a sample with several segments which had been exposed to the melt for various lengths of time. At the top of each section, at the liquid-solid-ambient interface, a groove was produced by the combined effects of surface erosion and surface tension driven flow (6). That this effect is at least partially responsible for severe degradation of the edges of forming dies is a reasonable assumption. The radius change of the lower portion of the segment gives a measure of the surface erosion rate of the test material in silicon. The ambient was one atmosphere of helium while the temperature was maintained at the melting point plus 5°C.

Figure 1 graphically shows the surface erosion *vs.* exposure time for high density graphite.[2] Sample 1 gave very poor results. Several of the zones were so badly pitted that radius measurements were not possible. Sample 2 shows an offset from the axis indicating that the initial melt temperature was too close to the melting point, allowing a protective coating of silicon to be frozen onto the sample initially. Samples 3 and 4 gave reproducible results. All samples were polished prior to testing. The erosion rates for the surface of the rod and for the groove (near the liquid-solid-ambient interface) are tabulated in Table I for high density graphite and vitreous carbon. Fused silica is given as a reference.

* Electrochemical Society Active Member.

Key words: silicon, crystal growth, vitreous carbon, graphite, erosion.

[1] Beckwith Carbon Corporation.

[2] DFP-2, Poco Graphite.

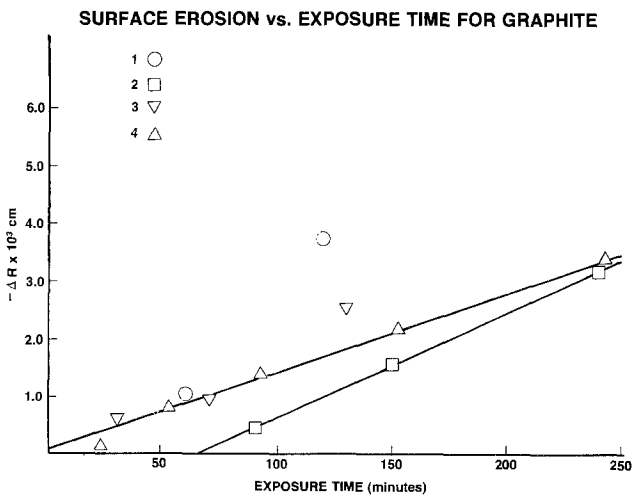


Fig. 1

The plot of groove depth *vs.* exposure time yields the erosion rate (groove) listed in Table I. Samples 1 and 3 were eroded severely, consequently the results were nonuseable. Samples 2 and 4 did yield a linear relationship similar to that for erosion of the rod surface.

Based only on the data in Table I it is not apparent that there is much difference in the behavior of the two carbon materials in molten silicon. However, investigation of cross sections of the interface between the test rods and the silicon adhering to the rod tip gives an insight into the erosion process. Results for vitreous carbon are given elsewhere (5). The nonporous material erodes by a simple dissolution mechanism involving the formation of a continuous and uniform SiC boundary layer. The presence and effects of this layer are discussed by Swartz *et al* (7).

Figure 2 shows the interface between the high density graphite and silicon. The boundary layer is thin but apparent. The broad light colored band, indicated by the arrow, between the interface and the bulk material is the region of penetration of the graphite by the melt after a 4 hr exposure. It consists of graphite, Si, and SiC in the pores of the bulk material. It is approximately 0.5 mm thick, and contrasts with the absence of penetration of vitreous carbon by the melt (5).

A closer view of the boundary layer is shown in Fig. 3. The layer is irregular and noncontinuous. The arrows indicate particles of SiC which appear to have been released from the layer and frozen into the melt at the termination of the experiment. During ribbon crystal growth such particles which are swept to the crystal growth interface cause twinning and polycrystalline ribbons (2, 3).

It is apparent that high density graphite undergoes erosion by a complex mechanism involving the formation and dissolution of a second phase compound (SiC) and intergranular corrosion.

From these results and those of previously reported work, it can be concluded that while the two carbon materials erode at approximately the same rate, the mechanism is more complex for high density graphite. Intergranular attack appears to result in SiC particles in the melt which affect the ribbon crystallinity and will produce irregular die surface geometry. Thus, forming dies fabricated from vitreous carbon, where

Table I. Erosion results

Sample	Erosion rate (surface)	Erosion rate (groove)
Graphite		
1	—	—
2	1.8×10^{-5} cm/min	11.3×10^{-5} cm/min
3	1.4	—
4	1.4	3.3
Vitreous carbon (5)	1.7	0 to 44
SiO_2 (4)	1.15	3.4

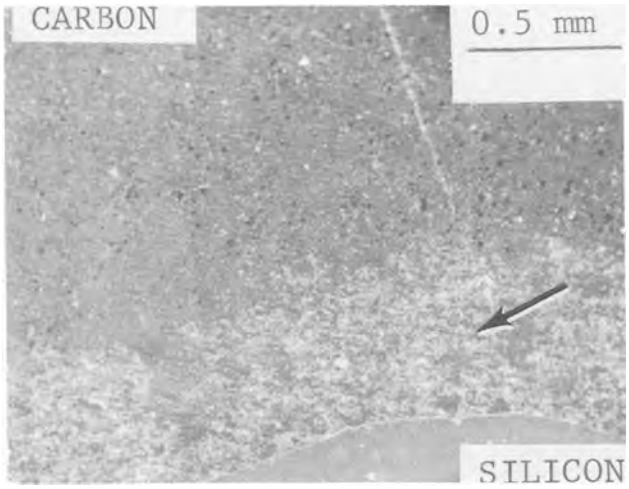


Fig. 2. Photomicrograph of a cross section of the silicon-graphite interface. The SiC boundary layer is apparent between the carbon and silicon. The arrow indicates the penetration region of silicon into the bulk graphite.

intergranular corrosion is not a factor, should yield a superior crystal product.

Acknowledgments

The author would like to thank C. J. Varker for many valuable discussions and for the SEM photographs, and F. R. Garcia for technical assistance.

Manuscript submitted April 13, 1977; revised manuscript received June 6, 1977.

Any discussion of this paper will appear in a Discussion Section to be published in the June 1978 JOURNAL. All discussions for the June 1978 Discussion Section should be submitted by Feb. 1, 1978.

Publication costs were assisted by Motorola Incorporated.

REFERENCES

1. A. D. Morrison, K. V. Ravi, C. V. Hari Rao, T. Surek, D. F. Bliss, L. C. Garone, and R. W. Hogencamp, "Large Area Silicon Sheet by EFG," Fourth Quarterly Report, ERDA/JPL 954355 (1976).

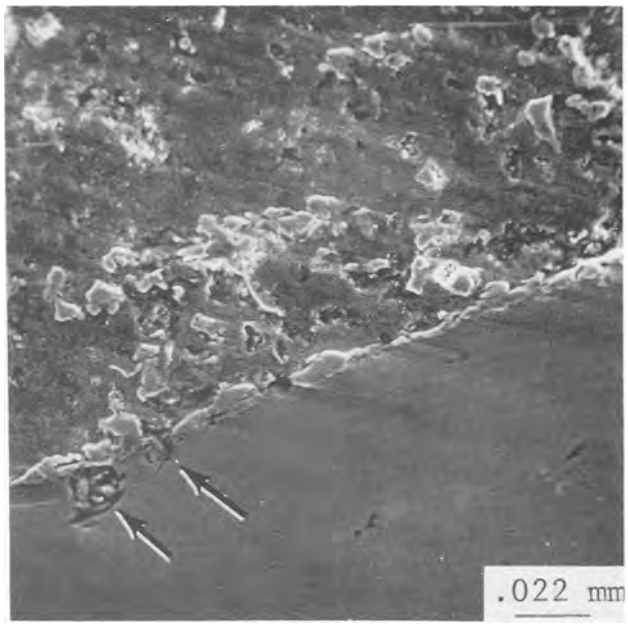


Fig. 3. A closer view of the SiC boundary layer. The arrows indicate particles which have broken away from the boundary layer into the melt. Note the SiC particles formed in the bulk due to penetration of the graphite by the melt.

2. G. H. Schwuttke, T. F. Ciszek, and A. Kran, "Silicon Ribbon Growth by a Capillary Action Shaping Technique," Sixth Quarterly Report, ERDA/JPL 954144 (1976).
3. K. M. Kim, G. W. Cullen, S. Berkman, and A. E. Bell, "Silicon Sheet Growth by the Inverted Stepanov Technique," Third Quarterly Report, ERDA/JPL 954465 (1976).
4. R. E. Chaney and C. J. Varker, *J. Cryst. Growth*, **33**, 188 (1976).
5. R. E. Chaney and C. J. Varker, *This Journal*, **123**, 846 (1976).
6. R. A. Laudise, "The Growth of Single Crystals," p. 187, Prentice-Hall, Inc., Englewood Cliffs, N.J. (1970).
7. J. C. Swartz, T. Surek, and B. Chalmers, *J. Electron. Mater.*, **4**, 255 (1975).

A Technique for Fabricating Oxide Passivated BARITT Diodes

B. M. Armstrong, R. A. Moore, H. S. Gamble, and J. Wakefield

Department of Electrical and Electronic Engineering,
The Queen's University of Belfast, Belfast, BT7 1NN, Northern Ireland

It is well known that oxide passivation as used in the "Planar" process greatly improves the reliability, life and yield of semiconductor devices. However, mesa diodes as used in microwave devices such as IMPATTs and BARITTs are not normally oxide passivated. It has been observed with such devices, particularly when Schottky barriers are employed, that degradation of the d.c. characteristic can occur leading to premature failure of the device.

This note reports on a fabrication technique for producing oxide passivated silicon BARITT mesa diodes. These may have either platinum silicide Schottky injecting contacts (M-N-P^+ BARITT) or diffused P^+ injecting contacts (P^+-N-P^+ BARITT). Particular features of this process are the method of production of the self-aligned contacts and the simple method of chip separation.

Experimental Procedure.-- Silicon nitride, because of its slow rate of oxidation (1) and resistance to silicon etch is ideally suited to the processes described below. Following an initial boron diffusion the wafers are coated with C.V.D. silicon nitride and silicon dioxide layers. These layers are then patterned with a scribe-line type network using standard photolithographic techniques, the silicon dioxide layer acting as a mask during etching of the nitride in hot orthophosphoric acid. The line network is then chemically etched into the silicon to a depth of about 10μm forming a matrix of squares which define the individual chips and aid device separation.

The remaining layers of silicon dioxide and nitride are re-patterned into an array of dots and 10μm tall mesas are formed by chemical etching. After removal of the masking oxide the wafers are thermally oxidised in water vapor at 1000°c for 20 minutes giving approximately 0.2μm of oxide on the mesa sides. The remaining nitride is easily removed in hot orthophosphoric acid leaving oxide passivated mesas with exposed silicon on

Keywords: transit-time devices, passivation, silicon nitride, Schottky barrier.

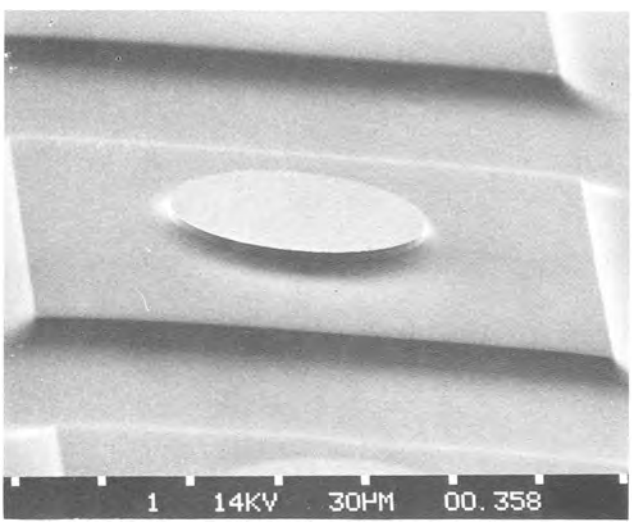


Fig. 1. Scanning electron micrograph of a mesa prior to thinning and separation X500.

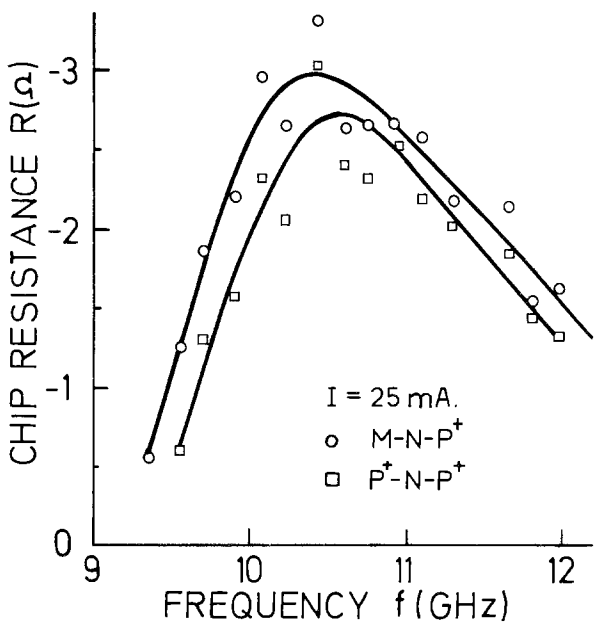


Fig. 2. Small signal chip resistance versus frequency.

top.

Platinum is sputtered over the whole wafer and annealed in nitrogen at 600°c to form platinum silicide on the mesa tops only. For bonding purposes the platinum is covered with evaporated layers of chromium and gold. The unalloyed platinum over the oxide is removed in an ultrasonic bath and this lifts off the chromium-gold leaving self-aligned contacts on the mesa tops. Fig. 1 shows a scanning electron micrograph of a typical mesa, with self-aligned contact, surrounded by etched channels.

The wafers are thinned from the back by mounting them face down on a float which is placed in a chemical bath (2). The process is stopped once the wafers have been thinned down to the scribe lines giving an overall device thickness of about 20μm. The individual chips remain fixed on the float and are coated with evaporated layers of chromium and gold. This chromium-gold layer is then copper plated to a reasonable thickness for handling. At this stage the copper plated chips are removed from the float as a unit and fine lines are scribed in the chromium-gold exposing the underlying copper which is then etched through in dilute nitric acid to produce isolated chips.

In the fabrication of M-N-P^+ BARITT diodes the initial diffusion is omitted and the platinum silicide layer becomes a rectifying Schottky barrier contact to the N-layer.

Results.-- Diodes manufactured using this technique exhibit excellent current-voltage characteristics. Schottky barrier and diffused BARITTs were fabricated from the same wafer to operate at approximately 10.5GHz. The N layer doping was $3 \times 10^{15} cm^{-3}$ and the respective active lengths were 4.4μm and 4.1μm giving punch-through voltages of 40.5V and 35.5V which are in good agreement with theoretical predictions.

The small signal r.f. impedance of these diodes was measured using a Hewlett Packard network analyser. Both types of diode, of area $1.8 \times 10^{-4} cm^2$, produced about 3 ohms of chip negative resistance at 10.5GHz as shown in Fig. 3. When operated in a triple slug-tuned coaxial circuit the P^+-N-P^+ diode produced a maximum power of 8mW and 0.82% efficiency while the M-N-P^+ diodes produced 13mW with 1% efficiency. These results were in good agreement with a computer analysis (3) assuming a diode series resistance of 0.5 ohms indicating that the oxide passivation does not appear to degrade the microwave performance of these diodes.

Conclusions.-- We have found with our oxide-passivated structures that failure due to metal contamination deposited on the mesa sides during top-cap welding is no longer a problem, and in general, oxide passivation reduces the loss of devices during handling and packaging. It has also been found that the technology outlined above produces high yields of good operating devices. Some devices have been operated for several months without a top-cap (i.e. exposed to the room atmosphere) and have shown no degradation, making them suitable for unpackaged insertion into microstrip. In conclusion these BARITT diodes have the advantages associated with semiconductor devices made by the "Planar" process.

Acknowledgements.-- Thanks are due to E. Duffin and J.A.C. Stewart for carrying out the microwave measurements. The financial support of the Science Research Council is gratefully acknowledged.

REFERENCES

1. J.A. Appels, E. Kooi, M. Paffen, J.H. Schatorje, and W. Verkuylen, Philips Res. Repts., 25, 118 (1970)
2. S. Opresko, R.F. Speers and A.I. Stoller, RCA Review, 30, 265 (1970)
3. J.A.C. Stewart, Electron Lett., 9, 345 (1975)

Manuscript received May 17, 1977.

Publication costs of this article were assisted by The Queen's University of Belfast.

JOURNAL OF THE ELECTROCHEMICAL SOCIETY

ELECTROCHEMICAL SCIENCE AND TECHNOLOGY

OCTOBER 1977

Aspects of Molybdenum Chemistry in the Basic NaCl/$AlCl_3$ Melt at 175°C

J. Phillips[1] and R. A. Osteryoung*

Department of Chemistry, Colorado State University, Fort Collins, Colorado 80523

ABSTRACT

A number of molybdenum chlorides and oxychlorides have been investigated in the sodium tetrachloroaluminate melt. The three- and five-oxidation states were stable in the melt, but the six-oxidation state, added as MoO_3, MoO_2Cl_2, and $MoOCl_4$, oxidized the melt and was itself reduced to Mo(V). The behavior of this Mo(V) was indistinguishable from that of Mo(V) added directly to the melt as the pentachloride. Mechanisms have been proposed to rationalize the electrochemical oxidation of Mo(III) and reduction of Mo(V), although in the latter case layer formation on the electrode surface prevented a dennitive characterization. A disproportionation mechanism is believed to be operative in the oxidation of Mo(III), and by cyclic voltammetry and rotating ring-disk techniques it has been possible to detect an intermediate Mo(IV) species.

Investigations involving molybdenum salts in fused salt media have been largely confined to the molten alkali halides (1-6). Popov (6) has defined the electrochemistry of MoO_3 in a LiCl/NaCl melt at 450°C in terms of the species MoO_2Cl_2, $Mo_2O_7^=$, and $MoO_4^=$. Reduction of these species results in a surface film of lower oxidation state molybdenum oxides. A study of the deposition of Mo from Mo(III) chloride at 600°C resulted in the postulation of a stable polymeric ion in equilibria with an electrochemically active monomer (3).

More limited investigations have been undertaken in alkali tetrachloroaluminate melts (7-8). Because of their low liquidus temperature, these melts provide excellent electrolytes for high energy battery and fuel cell systems. In this context, both $MoCl_5$ and MoO_3 have been investigated (9) and found to be eminently suitable as cathode materials in pelletized thermal batteries. In an investigation of both MoO_3 and K_3MoCl_6 in a ternary alkali tetrachloroaluminate melt, Marshall and Yntema (7) determined the deposition and decomposition potentials of a "black spongy deposit," and obtained values of 0.3 and 1.85V (*vs.* an Al reference electrode), respectively. This was assumed to be the deposition potential of molybdenum, the last reduction step being identical in the cases of MoO_3 and K_3MoCl_6. Senderoff (1) questioned the validity of these results, contending that air contamination of K_3MoCl_6 resulted in the production of higher valence oxygenated molybdenum compounds, which upon reduction deposit a mixture of molybdenum and molybdenum oxides. More recently, MoO_3 has found application as a cathode material in a nonaqueous secondary battery based on the solvent butyrolacetone (10-12).

The present investigation examines the electrochemical behavior of MoO_3, $MoCl_5$, MoO_2Cl_2, $MoOCl_4$, and K_3MoCl_6 in the sodium tetrachloroaluminate melt. The techniques employed included cyclic voltammetry, normal pulse voltammetry, and the rotating-disk electrode, as well as the newly developed rotating ring-disk electrode (13).

Molten NaCl:$AlCl_3$ (1:1) may be considered to consist of Na^+ and $AlCl_4^-$ ions. By a variation of the mole fractions of the component salts, it is possible to control the acidity of the melt. The dominant acid-base property is determined by the equilibrium (22) $2\,AlCl_4^- = Al_2Cl_7^- + Cl^-$, $K_M = 1.06 \times 10^{-7}$. The potential of an aluminum electrode immersed in the melt, *vs.* an aluminum electrode in a sodium chloride saturated reference compartment functions as a chloride ion indicator, and the pCl^- may be altered by anodizing or cathodizing this electrode.

Experimental

The cyclic voltammetric and rotating-disk studies were carried out using a potentiostat developed in these laboratories. Normal pulse voltammetry was achieved using a PAR 174 instrument. The independent control of the disk and ring potentials of the rotating ring-disk electrode (RRDE) was undertaken using a bipotentiostat based on the circuitry of Bruckenstein *et al.* (15). An ASR servocontrolled motor-tachometer (as supplied by the Pine Instrument Company) served to rotate the electrodes. Current voltage traces were recorded on a Housten Model 2000 X-Y recorder and a Techtronix storage oscilloscope.

The experimental work was carried out under a purified argon atmosphere in a Vacuum Atmospheres Company dry box equipped with a Model HE-493 Dri-Train for constant recirculation of the argon gas through a column of activated copper and molecular sieves. As an additional precaution, P_2O_5 was exposed to the dry box atmosphere. The criteria used to assess the purity of the atmosphere in the dry box was the duration of lifetime of a 25W light bulb filament run

* Electrochemical Society Active Member.
[1] Present address: Department of Chemistry, Carleton University, Ottawa, Ontario, Canada.
Key words: sodium tetrachloroaluminate, fused salts, molybdenum.

from the line voltage (16). A five-day period was associated with an atmosphere of acceptable purity.

The basic sodium tetrachloroaluminate melt was prepared by the addition of aluminum chloride (Fluka A.G.) to a molar excess of sodium chloride (Fischer certified A.S.C. grade), and their subsequent fusion at 175°C. Purification of the melt was accomplished by preelectrolysis, using an aluminum rod anode (Johnson Matthey Specpure grade) and a coiled aluminum wire cathode (Alfa Inorganics m5N) (14). After 10 days of preelectrolysis at a current density of 1 mA cm^{-2}, the resultant melt was clear and colorless. Prior to use, the melt was filtered through a medium porosity glass-sintered frit in order to remove suspended aluminum particles.

The current-voltage curves were obtained with a Pyrex glass cell with a Teflon top. To allow free rotation of the rotating-disk electrodes, the hole for the RDE was made slightly larger than the diameter of the electrode. The cell was thus "open" to the dry box atmosphere.

Coulometry experiments were carried out in a glassy carbon crucible, also used as the working electrode.

Auxiliary and reference electrodes were isolated from the bulk melt by fine glass frits. Both electrodes consisted of aluminum wires. The reference electrode was allowed to equilibrate in the sodium chloride-saturated reference compartment for several hours before use. All working electrodes were G.C. 20 grade glassy carbon (as supplied by the Tokai Electrode Manufacturing Company Limited) sealed in Pyrex glass.

The u.v. spectra were recorded with a Carey Model 17 Spectrophotometer, using 1 cm pathlength Suprasil cells fitted with a ground glass joint. The sample compartment of the spectrophotometer was spacious enough to accommodate an aluminum block furnace (10 × 10 × 10 cm) which was heated by 4 Chromalox cartridge heaters.

Results

$MoCl_5$ in the sodium chloride-saturated melt.—Figure 1 illustrates the rotation speed dependence of the current voltage curve on a glassy carbon rotating-disk electrode (area 0.2 cm^2) for $MoCl_5$ in the melt. It is convenient to consider the cathodic going sweep in three distinct regions, *i.e.*: (*i*) a rotation speed-dependent wave at approximately 1.2V; (*ii*) a more cathodic wave at 0.5V; and (*iii*) a reduction peak prior to the potential associated with aluminum deposition. The anodic going sweep shows additional peaks at 340, 1600, and 1850 mV. At the rotating-disk electrode, these must be associated with the oxidation of material deposited on the electrode surface.

A coulometry experiment was carried out at successively more cathodic potentials, *i.e.*, 1.1, 0.5, and 0.1V. The number of electrons involved in each case was 1.95, 1.03, and 2.3, respectively, indicating that the three regions corresponded to the production of molybdenum three, two, and molybdenum species of low oxidation state, possibly molybdenum zero. The accuracy of the last coulometry experiment is of course limited by background currents close to aluminum deposition.

The reduction plateau at 1.0V was shown to be diffusion limited by its adherence to the Levich relationship. The data were derived from a steady-state determination. The slopes of the lines were proportional to the concentration of Mo(V) in solution, and a diffusion coefficient was calculated as 3.2×10^{-6} cm^2 sec^{-1}. An order plot, *i.e.*, log i *vs.* log $(i_d - i/w^{1/2})$ for the reduction [obtained from the rotation speed dependence of the current (17)], showed strict first-order kinetics with respect to Mo(V) throughout the potential and concentration range investigated. Tafel plots, corrected for first-order kinetics, were linear (Fig. 2) with a slope of 160 mV, which corresponded to an αn value of 0.6 at 175°C; α refers to the symmetry factor and n to the number of electrons in the rate-determining step.

Figure 3 illustrates the effect of the variation of the cathodic sweep limit upon the system. No oxidation wave in the voltage range 2.0-1.5V is associated with the diffusion-limited reaction at 1.0V: The products of this reaction wave would therefore appear soluble. Extending the sweep limit to encompass the second reduction wave results in a small oxidation current at 1600 mV. Further extension of the cathodic limit into the steeply rising current region results in the appearance of an oxidation wave at 1800 mV. These peaks are enhanced by increased cathodic limit or polarization

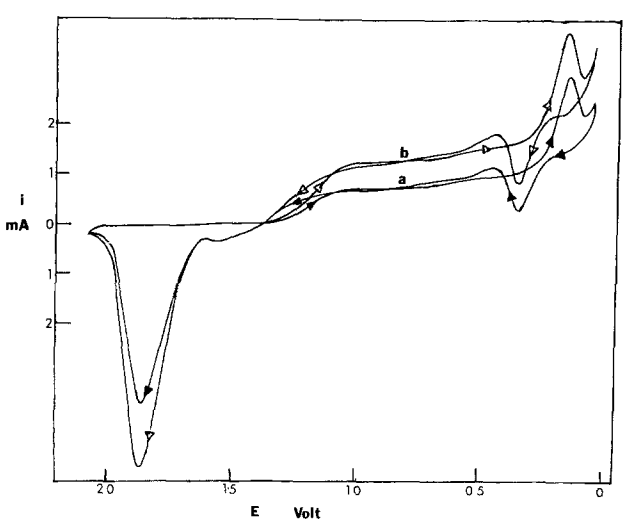


Fig. 1. Current voltage curves for $MoCl_5$ on a glassy carbon rotating disk in a basic tetrachloroaluminate melt. Curve a, 600 rpm; curve b, 2000 rpm; sweep rate, 18 mV sec^{-1}; concentration of $MoCl_5 = 4.5 \times 10^{-3}$M.

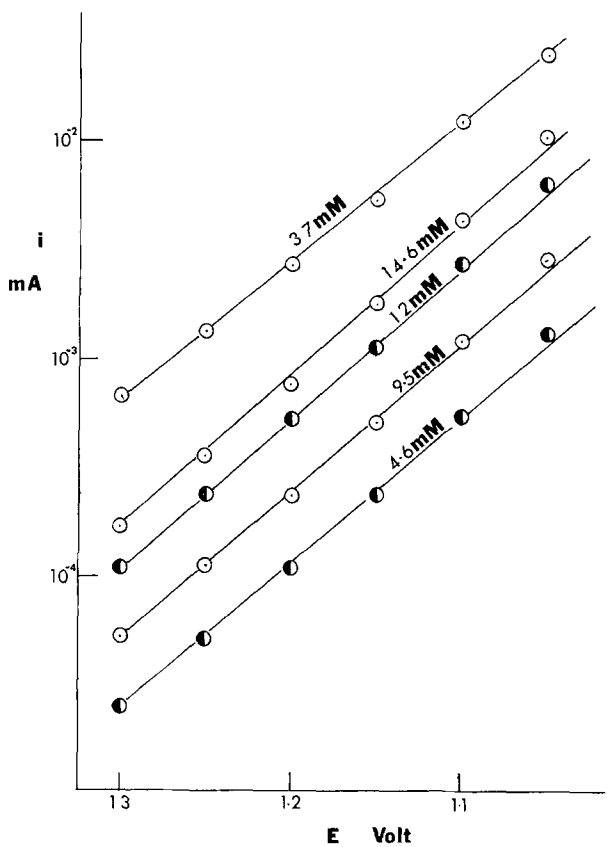


Fig. 2. Tafel plot for the first reduction wave for $MoCl_5$ at various concentrations, i, as plotted $i_{(observed)E} \times i_d/i_d - i(E)$.

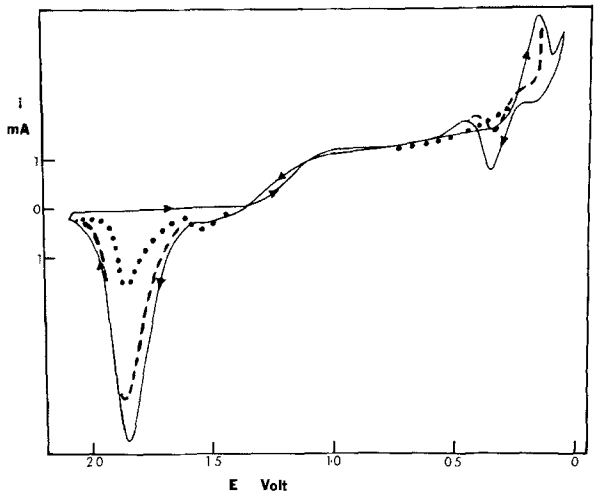


Fig. 3. Effect of varying the cathodic sweep limit upon the current-voltage curve for $MoCl_5$ in the basic melt. Rotation speed 2000 rpm; concentration 4.5 × 10^{-3}M. ------- Sweep reversed at 0.2V, . . . sweep reversed at 0.3V.

time at these cathodic potentials. From the rotation rate dependence, it is concluded that the peaks correspond to the oxidation of surface films, and are only rotation-speed dependent as a result of the deposition being influenced by rotation speed. Potential excursions beyond the reduction peak at approximately 0.1V results in an additional oxidation peak at 340 mV.

It can be seen (Fig. 4) by varying the anodic sweep limit that the reduction processes at more negative potentials involve surface species, which when not oxidized at more positive potentials, *i.e.*, 1.5-1.8V, increase in surface concentration by further reduction, hence the enhanced oxidation peaks at 340 and 1800 mV. The appearance of an additional anodic shoulder on the oxidation peak at 1800 mV subsequent to this more prolonged cathodic treatment suggests a progressive modification of the low oxidation state molybdenum surface species.

A significant feature of the current-voltage curves obtained with the rotating disk was the rotation speed dependence of the ratio of the heights of the two waves at 1.2 and 0.5V (see Table I). The coulometric experiment would indicate an expected value of 0.5; however, the decreasing values obtained as the rotation speed increased would be characteristic of a product of the first reduction undergoing a chemical reaction prior to the second reduction.

Table I. The dependence of the ratio of the limiting current at 0.5V to the limiting current at 1.0V as a function of rotation speed in the basic melt. 5 mM $MoCl_5$

W (rpm)	i_1/i_2
500	0.44
1000	0.38
2000	0.33
4000	0.30
6000	0.28

The rotating ring-disk electrode was utilized to detect solution products of the reduction and oxidation processes observed on the rotating-disk electrode. Adjusting the ring electrode potential to 1.9V, just cathodic of chlorine evolution, enabled the ring to oxidize Mo(III) reaching it from the disk. Figure 5 shows the ring response at this potential as the disk potential is swept. As the disk potential proceeds more cathodically, the ring oxidation current increases, and a current plateau is obtained at a disk potential of 800 mV.

The collection efficiency of the ring was calculated as 38%, and has been measured on known systems and found to be 40% (13). When the ring current is corrected by a factor of 2.5, the ring current does not correspond to 100% of the disk plateau current at 0.8V, but lies between 50 and 70% of that expected in the range of rotation speeds used. As the rotation speed of the electrode was increased to 6000 rpm, the proportion collected was 50% of that expected, and this percentage increased monotonically as the rotation speed was decreased. This rotation speed dependence of the collection efficiency implies the interference of chemical steps either during the transit time of a species between the disk and ring electrodes, or in the electrochemical oxidation process occurring at the ring. The former alternative would imply the generation of an electrochemically inactive species, as the product of the first reduction wave at 1.0V. This would then be expected to interconvert to a more electrochemically active species.

The second wave at 0.5V on the disk electrode is characterized by a decrease in the current response on the ring electrode. This indicates the further reduction of Mo(III) at the disk to an insoluble Mo(II) species. It is significant that this second reduction wave on the disk does not reduce all of the Mo(III) to an insoluble species, as indicated by the fact that the ring current is not reduced to zero. The depletion of the ring current when the disk is more negative than 0.5V is greatest at low rotation speeds (50% at 500 rpm), and

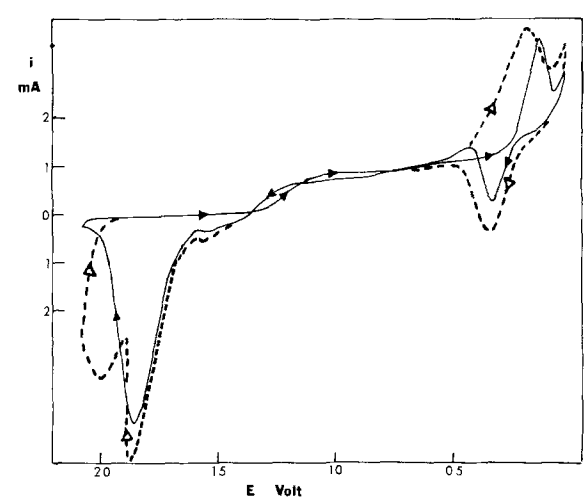


Fig. 4. Effect of varying the anodic sweep limit upon the current-voltage curve for $MoCl_5$ in the basic melt. – – – Sweep reversed at 0.5V. Rotation speed 1000 rpm; concentration 4.5 mM.

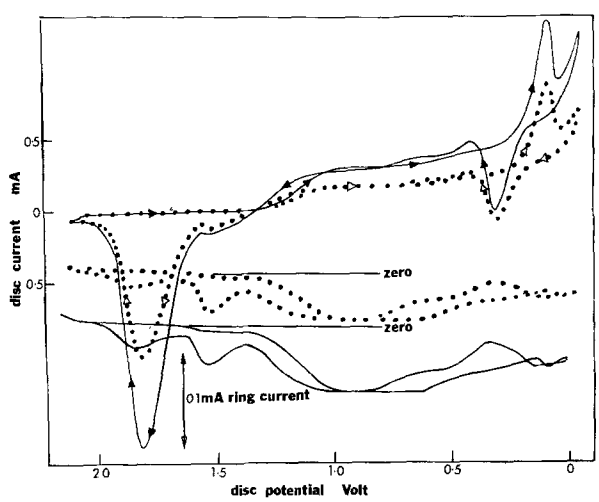


Fig. 5. Current-voltage curves obtained with the rotating ring-disk electrode. Concentration $MoCl_5$ 4.5 mM. Potential of ring electrode = 1.9V. Sweep rate on disk, 18 mV/sec; ——— rotation speed 2000 rpm; . . . rotation speed, 600 rpm.

is progressively lower as the rotation speed increases, *i.e.*, 40% at 1000 rpm and 30% at 3000 rpm. This reflects the existence of a chemical step occurring prior to the second electrochemical reduction at the disk electrode. A longer residence time (low rotation speeds) in the vicinity of the disk electrode allows the product of the first electrochemical reduction to undergo chemical change.

The potential region on the disk, corresponding to the more steeply rising current, is characterized on the ring by a further depletion of ring current. This is probably a result of the reduction of a small amount of soluble Mo(II) to a surface molybdenum species of low oxidation state. The prominent depletion of the ring current associated with the oxidation peak at 0.3V on the disk suggests that a reaction is occurring between the oxidized surface molybdenum species and the product of the first reduction wave on the disk, prior to its chemical reaction. As the disk electrode surface undergoes oxidation at 1.8V, the ring electrode detects two peaks corresponding to the liberation from the disk of oxidizable soluble species.

The surface electrochemistry involved here is certainly complex; however, the evidence of the ring-disk and disk electrodes indicates that the deposition of molybdenum species on the surface of the disk can be correlated somewhat to a chemical step subsequent to the first reduction wave.

The peak current at 0.1V on the disk electrode must be associated with a passivation phenomena. At higher Mo(V) concentrations (20 mM), the second reduction wave at 0.5V on the disk becomes peak-like, and upon potential reversal at 0.4V, the limiting currents for the Mo(V) reduction wave are significantly reduced, and exhibit a rotation speed dependence normally associated with a blocked electrode (18).

Upon adjusting the potential of the ring electrode to 800 mV [the diffusion-limited potential for Mo(V) reduction] the current response manifested two current values with and without the shielding effect of the disk electrode, *i.e.*, as the Mo(V) is reduced at the disk electrode, the amount reaching the ring decreases. A reduction peak was observed for the ring current as the disk was oxidized at 1800 mV. This indicated the retrieval of Mo(V). Normal pulse voltammetry was carried out upon $MoCl_5$ in the melt. The starting potential was 1600 mV, and a scan rate of 5 mV/sec was employed. Current-voltage curves resembling those obtained with the rotating-disk electrode resulted. The diffusion coefficient of the species was 3×10^{-6} cm^2 sec^{-1}, in good agreement with the RDE data. An αn value of 0.63 was obtained from a linear plot based on the analysis of Oldham and Parry (19). Again, a first-order dependence of the current upon the molybdenum concentration was indicated.

The reduction wave at 1.0V was further investigated by cyclic voltammetry at a stationary electrode. Figure 6 illustrates a typical voltammogram obtained at a sweep rate of 8 V/sec, where two reduction and one oxidation peak are observed. The more anodic reduction peak at 1600 mV was only observed after the first sweep and at lower sweep rates, *i.e.*, at less than 1 V/sec it could not be observed at all. The inability to observe this peak at low scan rates must be associated with the removal of the species involved by a chemical step.

The value of the quotient $i_p/\nu^{1/2}$ (between 0.2 and 8 V/sec) as a function of sweep rate for the reduction peak at 1.0V was constant, and substantiated the diffusion-limited nature of the reduction peak. An αn value of 0.53 is obtained from a plot of E_p *vs.* log ν, in good agreement with RDE work. The diffusion coefficient obtained from this data was 2.5×10^{-6} cm^2 sec^{-1}, a value slightly lower than the values obtained from the RDE and NPP. Figure 7 shows the ratio of the peak current for the reduction of Mo(V) at 1.0V to the peak current for the oxidation of Mo(III) as a function of

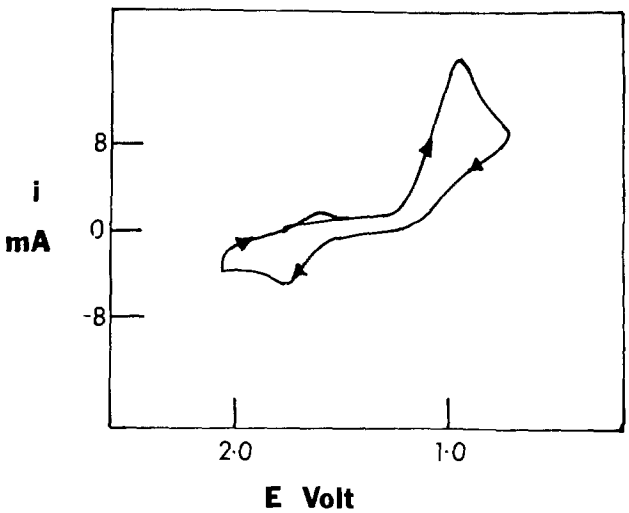


Fig. 6. Cyclic voltammogram for $MoCl_5$ in a basic melt over a limited voltage range. Concentration 37 mM; sweep rate 8V/sec; initial potential 1780 mV; initial scan cathodic.

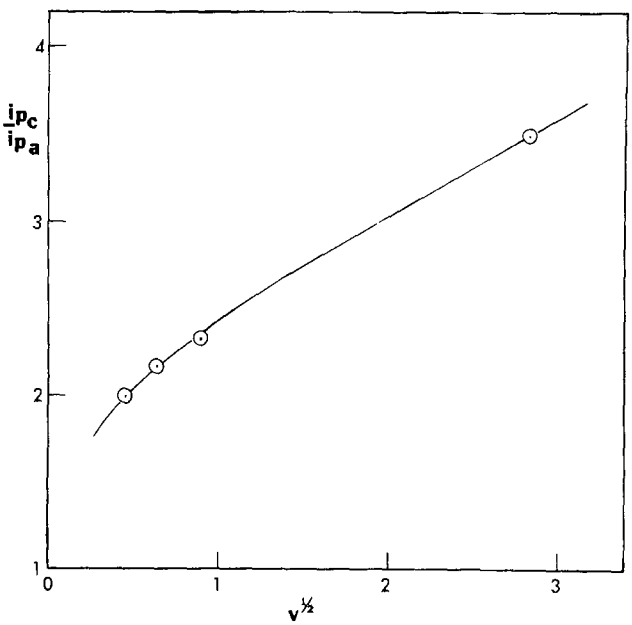


Fig. 7. The ratio of the peak current for Mo(V) reduction (at 1.0V) to the peak current for Mo(III) oxidation as a function of sweep rate.

sweep rate. At higher sweep rates, the value increases, supporting the conclusions arrived at with the RRDE.

The behavior of K_3MoCl_6 in the sodium chloride saturated melt.—This substance was introduced directly into the melt to yield an orange coloration. Some difficulty was encountered in dissolving the solid, particularly as the concentration rose above 3 mM.

The current-voltage curve obtained on the RRDE is illustrated in Fig. 8. On the disk electrode, the relief of the current-voltage is characterized by a double layer region in the midvoltage range. At anodic potentials lies a rotation speed-dependent limiting current which is superimposed upon the current, resulting from the reduction process occurring at cathodic potentials. An initial anodic going sweep from the rest potential at 1.0V reveals only the limiting current phenomena. The superimposed surface oxidation currents behave in an analogous manner to those of $MoCl_5$, in relation to the cathodic deposition potentials.

Coulometry on a K_3MoCl_6 solution indicated that the oxidation of Mo(III) at 1700 mV produced Mo(V). The

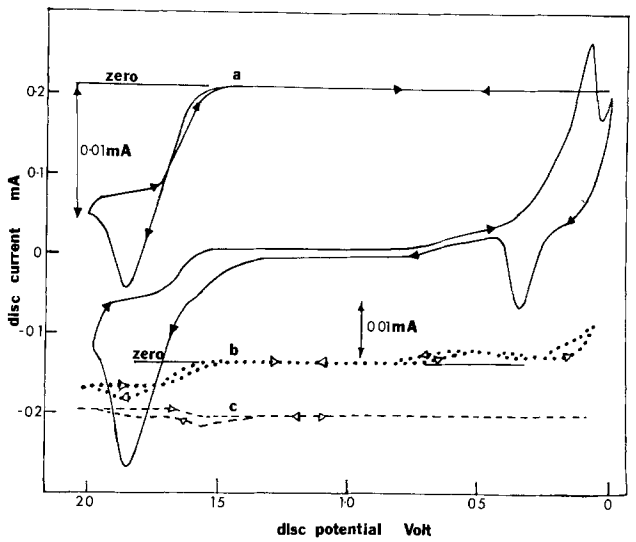


Fig. 8. Current voltage curves obtained on a rotating (2000 rpm) ring-disk electrode for K_3MoCl_6 in a basic melt. Concentration 3.2 mM; sweep rate 18 mV/sec; ring electrode potentials; curve a, 0.8V; curve b, 1.3V, curve c, 2.0V.

latter product could then be quantitatively reduced to Mo(III) again. Reduction of a Mo(III) solution at +0.1V gave a n value of 2.75. Holding the ring potential at 0.8V (Fig. 8) resulted in the detection of Mo(V). As the disk was scanned over the anodic potentials corresponding to the oxidation of Mo(III) to Mo(V), the current on the ring was 40% of that obtained on the disk, and was invariant with rotation speed. Figure 8 also shows the effect of holding the ring at 1300 mV and sweeping the voltage on the disk. This is the more cathodic potential of the reduction wave seen in Fig. 6. In this case, two processes are observed. As oxidation of Mo(III) occurs at anodic disk potential a ring reduction current is observed, which as a percentage of the disk plateau current, increases with rotation speed. Secondly, at cathodic potentials an oxidation current is observed which corresponds to the oxidation of any soluble Mo(II) species. The third ring response in this figure is obtained with a ring potential of 2.0V, where a shielding effect as well as the liberation of Mo(III) from the surface of the disk is shown.

An examination of the concentration dependence of the limiting current for Mo((III) oxidation at fixed rotation speed exhibited a positive deviation from linearity at higher concentrations. Investigations at higher concentrations encountered solubility problems. The rotation speed dependence of the limiting current is illustrated in Fig. 9. The relief of this series of curves is indicative of chemical reactions preceding charge transfer. At high rotation speeds, the reactive entity has been swept from the surface of the disk almost before the chemical reaction has occurred; hence the almost diffusion-limited behaviors.

Cyclic voltammograms illustrating the oxidation of Mo(III) are shown in Fig. 10. All scans were initially anodic going from the rest potential. At lower sweep rates, *i.e.*, less than 1 V/sec, the reduction peak at 1600 mV was not observed. In this range of sweep speeds, significant differences in the two peak heights were observed, with the peak height for the oxidation process being approximately two times that for the reduction process. The reduction peak at 1600 mV which appears at faster scan rates is identical with that observed in the case of Mo(V) solutions.

It is clear from the varying relative magnitudes of the two reduction peaks as a function of scan rate that one of two things occur. There could be an interconversion between two Mo(V) species, the more active, *i.e.*, that species which is reduced more anodically, being produced directly as a result of the Mo(III) oxi-

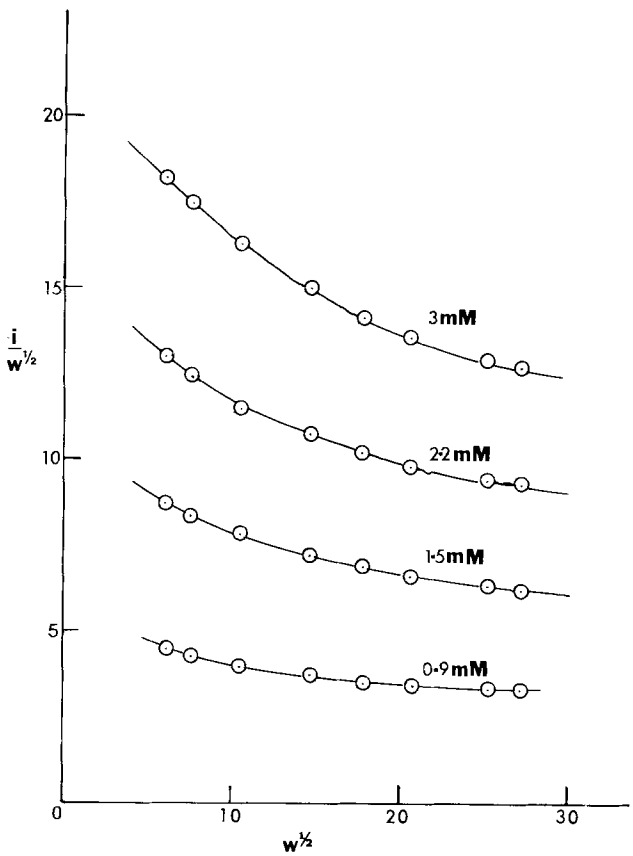


Fig. 9. The rotation speed dependence of the limiting current for the oxidation of Mo(III) at several concentrations.

dation, and then undergoing an interconversion to the less active state. Necessarily the equilibrium constant for the two species must favor the less active species, as this is the only species observed at lower sweep rates. The other possibility is that an ECE-type mechanism for the oxidation of Mo(III) is operative. In this case, the two one-electron transfer steps are linked by a chemical step. Under these conditions the more anodic reduction peak, observed at fast scan rates, will correspond to the reduction of an intermediate, while the more cathodic reduction wave corresponds to the normal reduction of Mo(V), the final oxidation product after the passage of two electrons.

Two schemes are capable of explaining the behavior of the Mo(III) and Mo(V) in the cyclic voltammetric and RRDE experiments. These are designated Scheme A and Scheme B.

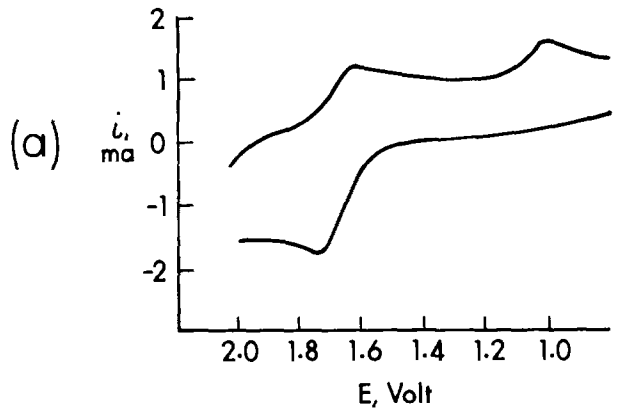
Scheme A

$Mo(III) \rightleftarrows Mo'(III)$	C
$Mo'(III) \rightleftarrows Mo(V) + 2e$	E
$Mo(V) \rightleftarrows Mo'(V)$	C

Scheme B

$Mo(III) \rightleftarrows Mo(IV) + e$	E
$Mo(IV) \rightleftarrows Mo'(IV)$	C
$Mo'(IV) \rightleftarrows Mo(V) + e$	E

Scheme A necessitates the inclusion of a preceding chemical step between two forms of Mo(III), an electrochemically active form, Mo(III), and an electrochemically inactive form, Mo'(III). The inactive form, *i.e.*, the product of Mo(V) reduction and the interconversion of these two molybdenum three states, would explain the nature of the rotating ring-disk response as the rotation speed varies. In addition, the rotation speed and sweep speed dependence of the current for the oxidation of Mo(III) may be rationalized in terms of an equilibrium constant defining almost



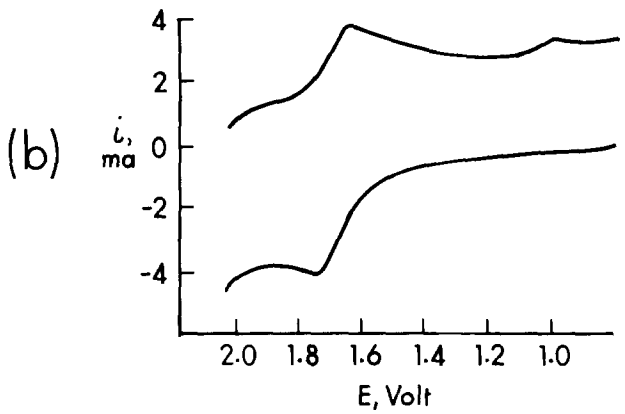


Fig. 10. Cyclic voltammograms for the oxidation of Mo(III). Concentration 1.5 mM; starting potential 1.0V; curve a sweep rate 2 V/sec; current 1 mA per division, curve b sweep rate 8 V/sec; current 0.2 mA per division; horizontal axis 1 division = 0.2V.

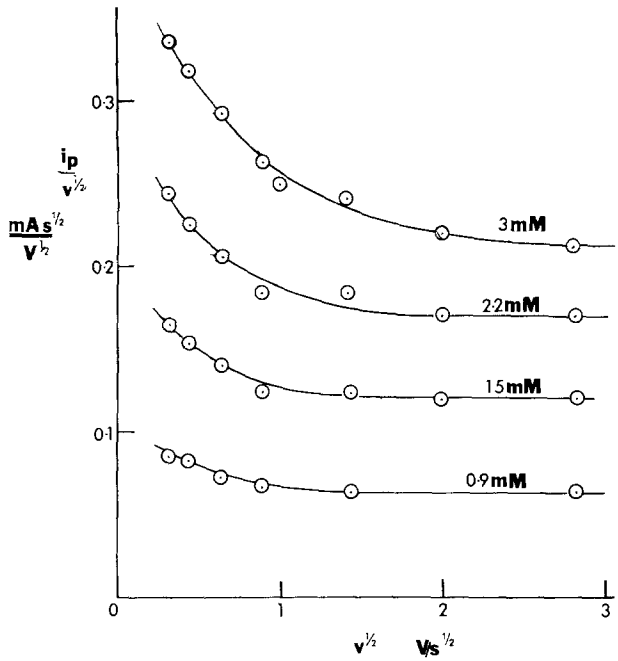


Fig. 11. The dependence of the peak current for the oxidation of Mo(III) upon sweep rate, at various concentrations of glassy carbon stationary electrode.

equal amounts of the two forms in the basic melt. Hence at higher sweep and rotation rates, the current becomes diffusion limited owing to a finite concentration of the active Mo(III) species in solution.

In Scheme B, the observed phenomena may be explained in terms of the reaction occurring at the electrode surface. An additional feature is the stability of Mo(IV) and its apparent chemical reaction. Although the rotating disk results from the reduction of Mo(V) also suggest the existence of two molybdenum three states, a fact that would support Scheme A, the observed phenomena are more readily interpreted in terms of a Scheme B-type mechanism.

The extreme values of $i_p/\nu^{1/2}$ and $i_d/\omega^{1/2}$ (*i.e.*, at low and high sweep and rotation rates) are very close to a 2:1 ratio (Fig. 9 and 11). A value of 1 for the equilibrium constant for the two postulated Mo(III) species would be very fortuitous. In addition, at high sweep rates in the cyclic voltammetry experiments, the peak for the oxidation of Mo(III) does not appear to move along the potential axis as the sweep rate is changed, suggesting that the electrochemical oxidation process occurring in the absence of the chemical step is reversible. The separation of the peaks of this anodic redox couple is 120 mV, a value closest to that expected for a reversible one-electron transfer (89 mV). Thus, the 2:1 ratio of the peak heights for the oxidation of Mo(III) to the reduction of Mo(V) can be ascribed to the reversible and irreversible nature of the charge transfer processes. Furthermore, evidence from the ring-disk examination of the Mo(V) reduction indicated that the percentage of Mo(III) retrieved on the ring as a function of $\omega^{1/2}$ varied in a manner analogous to that in Fig. 9 and 11; *i.e.*, at low rotation speeds the collection efficiency tended to 100% of that expected, and at higher rotation speeds it appeared to limit at approximately 50% of the expected value. The Mo(V)/Mo(IV) couple of Scheme B would meet these criteria.

The rest potential of the Mo(III)/Mo(V) system was linearly dependent upon the logarithm of the ratio of their two concentrations, and exhibited a slope of 42 mV decade.$^{-1}$. This is in good agreement with the theoretical slope of 44 mV decade^{-1} for a two-electron process at 175°C (Fig. 12). Scheme A could only accommodate this result if the inactive and active species of Mo(V) and Mo(III) were both monomers, in which case the active potential determining species would be linearly related to the total concentration.

The electrochemical behavior of the molydenum three and the molybdenum five states were further investigated by varying the acidity of the melt. The melt composition was varied over the range 49.78-49.98 mole percent (m/o) of $AlCl_3$. This range of composition was effective in changing the chloride concentration by a factor of 30. More acidic conditions radically affected the behavior of the species. At the mole fraction for chloride of $10^{-3.5}$, the Mo(III) appeared to precipitate from solution, and the wave corresponding to Mo(V) reduction underwent noticeable modification. Under even more acidic conditions, no wave was observed for the Mo(III) oxidation, and the Mo(V) reduction occurred as a kinetically controlled process on the surface of the electrode.

In the workable pCl^- range, *i.e.*, less than 50 m/o $AlCl_3$, the limiting currents on the rotating-disk electrode for the oxidation of Mo(III) showed no noticeable effect as the chloride ion concentration was systematically varied. However, the peak potentials at fast scan rates, *i.e.*, where the chemical step was minimal (>1 V/sec), showed a 90 mV anodic shift as the chloride concentration was altered by a factor of 10. This indicated that in the absence of the participation of the chemical step in the Mo(III) oxidation, the number of electrons involved was equal to the number of chloride ions.

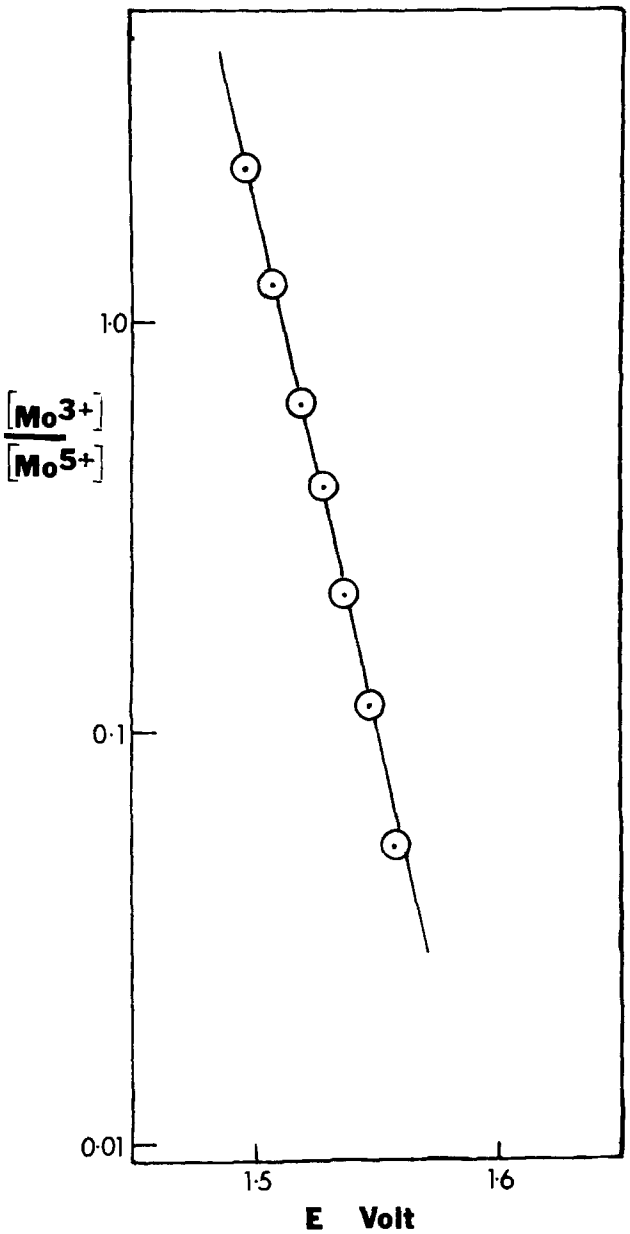


Fig. 12. The rest potential dependence upon the ratio of the total Mo(III) concentration of the total Mo(V) concentration.

The dependence of the rest potential of a fixed ratio of Mo(III)/Mo(V) upon the chloride ion concentration enabled the authors to estimate the ratio of chloride ions to electrons in the over-all reaction. As indicated by Fig. 13, a tenfold change in the chloride ion concentration resulted in a 78 mV potential change. This is close to the value of 89 mV expected for a ratio of 1 for the number of chloride ions to electrons.The acidity independence of the value of limiting current for Mo(III) oxidation at high rotation speeds renders Scheme A untenable on the basis that an equilibrium between two monomer Mo(III) species would be expected to show a chloride ion dependence.

A mechanism for the oxidation of Mo(III) is therefore proposed based on the ECE type reaction. The first electrochemical step has been proven to involve one chloride ion; however, the nature of the chemical step has not been established. Two types of chemical step are feasible: (*i*) the classical second-order disproportionation reaction as $2Mo(IV) \rightleftarrows Mo(III) + Mo(V)$, or (*ii*) a first-order interconversion between two Mo(IV) states, possibly involving an adsorbed species.

The first alternative is supported by evidence from the cyclic voltammograms (Fig. 10) as the concentration is varied. Table II shows the ratio of the anodic

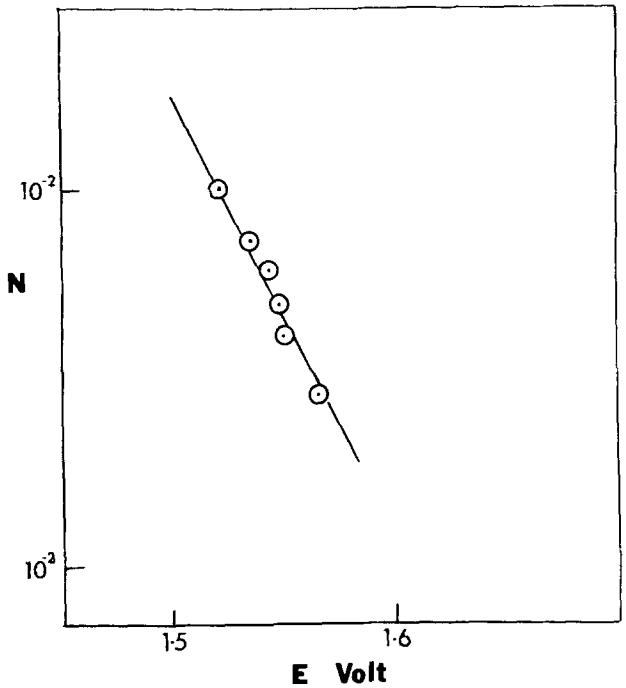


Fig. 13. The dependence of the rest potential upon the mole fraction of chloride ion at a fixed Mo(V)/Mo(III) concentration, using a GC indicator electrode.

peak current for Mo(III) oxidation to the cathodic peak current for the reduction of Mo(V) at a constant sweep rate as the concentration of Mo(III) is varied. The decreased ratio, indicating an increasing percentage of product at higher concentrations, indicates a second-order reaction. The nonlinearity of limiting current with concentration referred to earlier also supports this.

The data (from Fig. 9) was treated as suggested by Feldberg (20), and apparent n values were calculated for the currents at low rotation speeds, assuming the current at high rotation speeds for the 0.9 mM case to be diffusion limited. Figure 14 shows the requisite dependence of n apparent upon the logarithm of C/W. The rate constant for the disproportionation reaction was calculated from the working curve of Feldberg (20) and is given as

$$1.0 \pm 0.3 \times 10^3 \text{ liters mole}^{-1} \text{ sec}^{-1}$$

A mechanism was sought for the reduction of Mo(V); however, the difficulty encountered in maintaining an electrode surface of constant activity undermined an accurate determination of the order of the reaction with respect to the chloride ion. The over-all stoichiometry has been established, and the rotating-disk behavior suggested a following chemical reaction involving two Mo(III) states. On the basis of this information and the Tafel slope value of 0.6, as well as the concentration and potential independent first-order dependence upon Mo(V) a probable mechanism is

Table II. The ratios of the anodic peak current for the oxidation of Mo(III) to the cathodic peak current for the reduction of Mo(V) at concentrations $a = 0.85$ mM, $b = 1.5$ mM, $c = 2.2$ mM, and $d = 3$ mM at various sweep rates

Sweep rate, V/sec	*a*	*b*	*c*	*d*
0.8	—	2.0	2.05	1.96
2	2.9	2.3	2.08	2.06
4	—	2.75	2.8	2.3
8	5.5	4.125	4	2.64
16	—	—	4.86	4

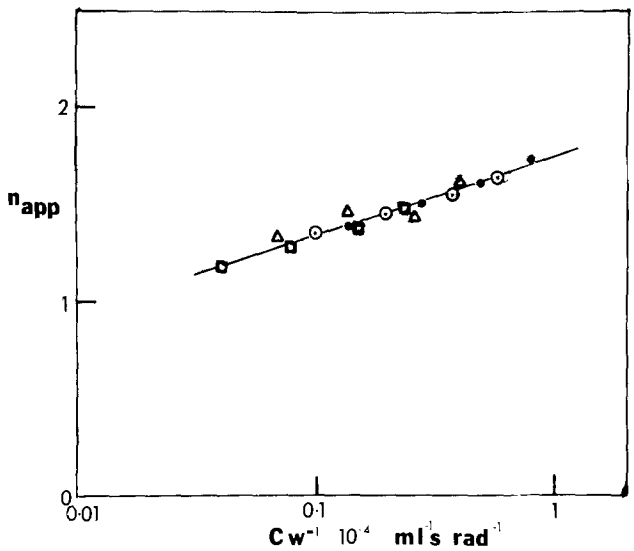


Fig. 14. The dependence of the number of apparent electrons upon the ratio of the concentration to rotation speed.

$$\text{Mo(V)} + e \xrightarrow{\text{RDS}} \text{Mo(IV)}$$

$$\text{Mo(IV)} + e \rightarrow \text{Mo'(III)}$$

$$\text{Mo'(III)} \rightleftharpoons \text{Mo(III)}$$

The latter equilibrium is assumed to greatly favor Mo'(III) in order to explain the results for the oxidation of molybdenum III.

The electrochemistry of the Mo(VI) states.—A variety of Mo(VI) compounds were added to the melt. They included MoO_3, MoO_2Cl_2, and $MoOCl_4$. Each compound exhibited a behavior similar to $MoCl_5$ in both the RRDE and cyclic voltammetric behaviors. Upon the addition of each of the three Mo(VI) compounds, there appeared at approximately 2.0V an additional reduction wave which disappeared with time. All data acquisition was carried out subsequent to the disappearance of this reduction wave. The reduction wave at 1.0V was diffusion limited, and the order of the reduction was one with respect to the active species. In each case the Tafel slope was linear, exhibiting a slope of 140 mV/decade.

Coulometry yielded an n value of 2 on the reduction wave at 1.0V, carried out upon solutions of MoO_3, and after the disappearance of the reduction wave at 2.0V. A rotating-disk electrode current-voltage curve run on the resultant melt indicated that the product of the coulometric reduction was Mo(III). Addition of a further vial of MoO_3 resulted in the immediate reduction of the wave height for Mo(III) oxidation, and the number of electrons involved in a second reduction was approximately three.

The presence of chlorine above the melt to which MoO_3 had been added was confirmed qualitatively with potassium iodide paper. The three electrons involved in the second coulometric experiment can thus be explained on the basis that either the chlorine evolved from the second addition reoxidizes the Mo(III) state present in the solution to Mo(V), or the MoO_3 oxidizes the Mo(III) state directly. Hence, the similarity in the current-voltage behavior between the Mo(V) and Mo(VI) can be ascribed to an equilibrium in the nature of $2Cl^- + 2Mo(VI) = 2Mo(V) + Cl_2$. Although this equilbrium appears to favor the formation of Mo(VI), it will, of course, be driven totally to the RHS as a result of the chlorine being able to escape from the cell. The diffusion coefficient for the Mo(V) generated from the Mo(VI) species was found to be $2.5 \pm 0.5 \times 10^{-6}$ cm^2 sec^{-1}.

Discussion

The electrochemically indistinguishable behavior of $MoCl_5$ and the molybdenum five complex derived from the oxygenated six states would suggest that $AlCl_4^-$ is instrumental in abstracting the oxygen ligands from the six state to render it unstable, particularly in view of the fact that Mo(VI) is apparently stable in the LiCl/KCl melt. These references would seem to contradict the contention of Kühn (21) that in the equimolar melt, MoO_3 "yields either MoO_2Cl_2 or a complex mixture of volatile Mo(VI) and Mo(V) oxide chlorides containing some $AlCl_3$." Certainly the latter alternative in a sealed system cannot be discounted. In an attempt to resolve the problem, the u.v. spectra of MoO_3, MoO_2Cl_2, and $MoCl_5$ were examined in a sodium chloride-saturated melt. All three compounds gave identical spectra, exhibiting a strong absorption at 305 nm and a shoulder at approximately 365 nm, suggesting that the species present was a Mo(V) complex involving no oxygen. It does remain a possibility, however, that AlOCl impurity in the melt could provide a reservoir of oxygen capable of "raising" the common denominator species to a singly oxygenated species. We believe this to be unlikely based on additional work (23). The results presented here have not directly suggested the participation of a dimeric molybdenum (III) series. Equilibrium potential measurements for the Mo(V)/Mo(III) system suggest that any equilibrium in the nature of $2MoCl_6^{3-} \rightleftarrows Mo_2Cl_9^{3-} + 3Cl^-$ lies in favor of the monomeric species. This is not entirely unexpected in view of the low molybdenum (III) concentrations and relatively basic melt conditions employed in this work. The possibility of dimer participation cannot be entirely discounted in view of the fact that two molybdenum three species are suggested by the rotation speed dependence of the second reduction wave for $MoCl_5$ at 0.5V. The kinetic nature of these currents could accommodate a dimer-monomer equilibrium favoring the monomer complex. Polymeric species certainly offer a plausible explanation for the marked changes in Mo(III) electrochemistry as the acidity of the melt is increased. Polymeric Mo species have been prepared in chloroaluminate melts (24).

Further work is necessary to unambiguously determine the final oxidation state of the molybdenum species formed on the surface of the electrode at potentials close to aluminum deposition. Coulometry experiments suggest that the oxidation state is very close to zero, and for the purpose of the mechanistic scheme this is assumed to be the final oxidation state. A scheme is proposed to account for the reduction of Mo(V), although by the very nature of the ill-defined surface chemistry it may be considered incomplete.

$$2e + \text{Mo(V)} \rightleftarrows \text{Mo(III)'}$$

$$\text{Mo(III)'} \rightleftarrows \text{Mo(III)}$$

$$e + \text{Mo(III)} \rightleftarrows \text{Mo(II)}$$

$$e + \text{Mo(III)} \rightleftarrows \text{Mo(II)}_{\text{Ads}}$$

$$\text{Mo(II)}_{\text{Ads}} + \text{Mo(III)'} \rightleftarrows \text{Mo}_x\text{(Y)}_{\text{Ads}}$$

$$Ye + \text{Mo}_x\text{(Y)}_{\text{Ads}} \rightleftarrows \text{Mo(0)}_{\text{Ads}}$$

$$2e + \text{Mo'(II)} \rightleftarrows \text{Mo(0)}_{\text{Ads}}$$

$$2e + \text{Mo(II)'}_{\text{Ads}} \rightleftarrows \text{Mo(0)}_{\text{Ads}}$$

Acknowledgments

Support from the Air Force Office of Scientific Research (AFOSR-76-2978) is gratefully acknowledged; a grant-in-aid from the Alcoa Foundation also is appreciated.

We would particularly like to thank Lieutenant Colonel Lowell King and Captain Charles Hussey of the Frank J. Seiler Research Laboratory, United States Air Force Academy, for helpful discussions.

Manuscript submitted Jan. 4, 1976; revised manuscript received June 10, 1977.

Any discussion of this paper will appear in a Discussion Section to be published in the June 1978 JOURNAL. All discussions for the June 1978 Discussion Section should be submitted by Feb. 1, 1978.

Publication costs of this article were assisted by Colorado State University.

REFERENCES

1. L. Senderoff and A. Brenner, *This Journal*, **101**, 16 (1954).
2. L. M. Sellis, *ibid.*, **113**, 37 (1966).
3. L. Senderoff and G. W. Mellors, *ibid.*, **114**, 556 (1967).
4. T. Suzuki, *Electrochim. Acta*, **15**, 127 (1970).
5. D. Inman, R. S. Sethi, and R. Spencer, *Electroanal. Chem.*, **29**, 187 (1971).
6. B. N. Popov, Ph.D. Thesis, University of Zagreb, Zagreb, Yugoslavia (1972).
7. E. E. Marshall and L. F. Yntema, *J. Phys. Chem.*, **46**, 353 (1942).
8. W. Dorman, M.S. Thesis, Iowa State University, Ames, Iowa (1972).
9. C. L. Hussey, J. K. Erbacher, and L. A. King, Final Technical Report FJSRL-TR-76-0003.
10. L. Campanella and G. Pistoia, *This Journal*, **118**, 1905 (1971).
11. L. Campanella and G. Pistoia, *ibid.*, **120**, 383 (1973).
12. F. Dampier, *ibid.*, **121**, 656 (1974).
13. J. Phillips, R. J. Gale, R. G. Wier, and R. A. Osteryoung, *Anal. Chem.*, **48**, 1266 (1976).
14. L. G. Boxall, H. L. Jones, and R. A. Osteryoung, *This Journal*, **121**, 212 (1974).
15. S. Bruckenstein, D. T. Napp, and D. C. Johnson, *Anal. Chem.*, **39**, 481 (1967).
16. I. D. Eubanks and F. J. Abbot, *ibid.*, **41**, 1708 (1969).
17. A. C. Riddiford, in "Advances in Electrochemistry and Electrochemical Engineering," Vol. 4, P. Delahay, Editor, Interscience Publishers, New York (1966).
18. R. Landsberg and R. Thiele, *Electrochim. Acta*, **11**, 1243 (1966).
19. K. B. Oldham and E. P. Parry, *Anal. Chem.*, **40**, 65 (1968).
20. L. S. Marcoux, R. N. Adams, and S. W. Feldberg, *J. Phys. Chem.*, **73**, 2611 (1969).
21. H. Kuhnl, *Angew. Chem. Internat. Ed. Engl.*, **6**, 641 (1967).
22. L. G. Boxall, H. L. Jones, and R. A. Osteryoung, *This Journal*, **120**, 223 (1973).
23. B. Gilbert and R. A. Osteryoung, To be published in *J. Am. Chem. Soc.*
24. W. C. Dorman and R. E. McCarley, *Inorg. Chem.*, **13**, 491 (1974).

The Kinetics of a Chlorine Graphite Electrode in the Zinc-Chlorine Battery

Jung Taek Kim* and Jacob Jorné**

Department of Chemical and Metallurgical Engineering, Wayne State University, Detroit, Michigan 48202

ABSTRACT

The cathodic and anodic reactions for chlorine on a graphite electrode were investigated in concentrated $ZnCl_2$ solution using a rotating-disk electrode. The diffusion coefficient, Tafel kinetic parameters, rate constants, and reaction order were obtained. A likely cathodic reaction mechanism and rate-determining step is postulated.

The Zn-Cl_2 battery has been under intensive investigation and development during recent years for vehicular application and as a load leveling device (1). This secondary battery consists of a Zn electrode, Cl_2 graphite electrode, and $ZnCl_2$ aqueous solution. During charge Zn is deposited on the cathode and Cl_2 evolves at the graphite electrode. During discharge Zn and Cl_2 react to give aqueous $ZnCl_2$.

The Cl_2 graphite electrode represents a major limitation to the Zn-Cl_2 cell performance. In order to reach a stage where the design and performance of a flow-through porous graphite Cl_2 electrode is fully understood, the kinetics and the mass transfer of the Cl_2 electrode should be investigated on a nonporous graphite electrode under well-defined conditions.

In the present investigation, the kinetics of the Cl_2 electrode reaction is studied in a $ZnCl_2$ aqueous solution using a dense graphite rotating-disk electrode (RDE) under various Cl_2 concentrations. Limiting currents were detected at various Cl_2 concentrations and rotational speeds, from which the Cl_2 diffusion coefficient was determined. The kinetic parameters: exchange current density, reaction order, transfer coefficients, Tafel slopes, and apparent rate constants were determined. The mechanism of the Cl_2 electrode reaction is proposed and discussed in light of the present results.

The cathodic over-all reaction for Cl_2/Cl^- on a graphite electrode is $Cl_2 + 2e \rightleftarrows 2Cl^-$ $E^\circ = 1.36$V. The mechanism of this reaction and its kinetics have not been studied in concentrated $ZnCl_2$ aqueous solution. Most of the work in the past covered the anodic reaction in NaCl solution, and little attention was given to the cathodic reduction of Cl_2 (2-5). Frumkin and Tedoradze (2) studied the reduction of Cl_2 using a Pt rotating-disk electrode, and suggested the mechanism

$$Cl_2 + e \rightleftarrows Cl_{ads} + Cl^-$$

and

$$Cl_{ads} + e \rightleftarrows Cl^-$$

however, the mechanism is not fully substantiated. Sureno, Macagno, and Giordano (3) investigated the Cl_2 reaction in nonaqueous solvents using Pt RDE. Hine and Yasuda (6) studied the mechanism of the anodic oxidation of Cl^- on graphite RDE in NaCl solution, and found that the rate-determining step is

$$Cl_{ads} + Cl^- \rightarrow Cl_2 + e$$

Experimental

The graphite rotating-disk electrode consists of a Teflon support rod and a central dense graphite elec-

* Electrochemical Society Student Member.
** Electrochemical Society Active Member.
Key words: chlorine, graphite, zinc chloride, kinetics, zinc-chlorine battery.

trode ATJ Union Carbide. The central graphite electrode was embedded in the Teflon rod. The diameter of the graphite electrode was 0.95 cm, and the diameter of the Teflon rod was 1.9 cm. The rotator was a Pine Instrument ASR rotator with a rotational speed of 0-10,000 rpm. The surface of the electrode was polished with waterproof Al_2O_3 paper and a fine paper using the rotator (ω = 4000 rpm).

A 1000 ml Pyrex vessel fitted with a Teflon cover was used as the cell container. It was equipped with a 2.25 cm^2 platinum counterelectrode compartment connected to the cell by a small glass tube. A saturated calomel electrode (SCE) served as a reference electrode, and was placed in a separate reference electrode compartment connected to the main cell by a capillary extending to the side of the rotating-disk electrode. The tip of the Luggin capillary was located at a distance of 3.5 cm from the center of the disk. The ohmic drops were calculated according to Newman (7).

The potential of the graphite disk electrode was controlled by a Wenking LT 73 potentiostat. A wave form generator TWG 500 was used in conjunction with the potentiostat in order to sweep the potential of the disk electrode. The sweep rate was 10 mV/sec. The potential-current data was recorded on a Houston Instrument 2000X-Y Recorder.

The $ZnCl_2$ solution was obtained from EDA, Incorporated, where it was prepared by direct recombination of Cl_2 gas and pure Zn rods (99.999%, New Jersey). The $ZnCl_2$ concentration was measured by hydrometer. Cl_2-N_2 gas mixtures were fed into the cell by a gas expenser, and the dissolved Cl_2 concentration was maintained by measuring the Cl_2 and N_2 flow rates. The dissolved Cl_2 concentration was measured by standard titration using 1/100 normal $Na_2S_2O_3 \cdot 5H_2O$. Dissolved oxygen was removed by bubbling N_2 prior to the experiments, and the Cl_2-N_2 gas mixture was bubbled throughout the experiments. The *p*H of the solution was measured with a Beckman *p*H meter. The temperature was 25° ± 1°C, and the kinematic viscosities were corrected for temperature variations.

Results and Discussion

Cl_2 diffusion coefficient.—Cathodic polarizations of dissolved Cl_2 on a graphite rotating-disk electrode are shown in Fig. 1 and 2. The observed limiting currents depend on the rotational speed and the dissolved chlorine concentration. The cathodic reaction, $Cl_2 + 2e \rightarrow 2Cl^-$, is therefore mass transfer limited, and the diffusion coefficient of dissolved Cl_2 in $ZnCl_2$ solution can be determined from the Levich equation for convective diffusion near the rotating-disk electrode

$$i_l = 0.62nFD^{2/3}\nu^{-1/6}c_b\omega^{1/2} \qquad [1]$$

The kinematic viscosity of 37% $ZnCl_2$ solution at 25°C is 1.53 × 10^{-2} cm^2/sec (11).

Figure 3 shows the plot of the limiting current *vs.* $\omega^{1/2}$, and the average diffusion coefficient obtained from the slope is D_{Cl_2} = 0.664 × 10^{-5} cm^2/sec, and is in good agreement with the value of D_{Cl_2} = 0.633 × 10^{-5} cm^2/sec obtained in our laboratory from weight loss

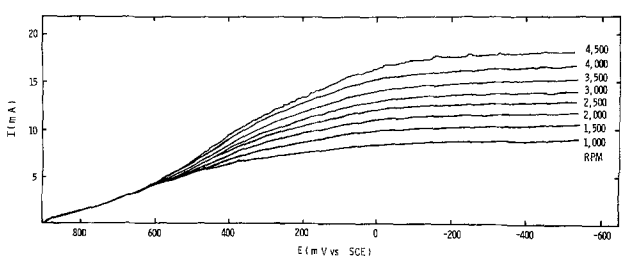


Fig. 1. Cathodic polarization of graphite electrode in 37% weight $ZnCl_2$ solution at different rotational speeds. $[Cl_2]$ = 0.95 g/l; area = 0.713 cm^2; *p*H = 3.29.

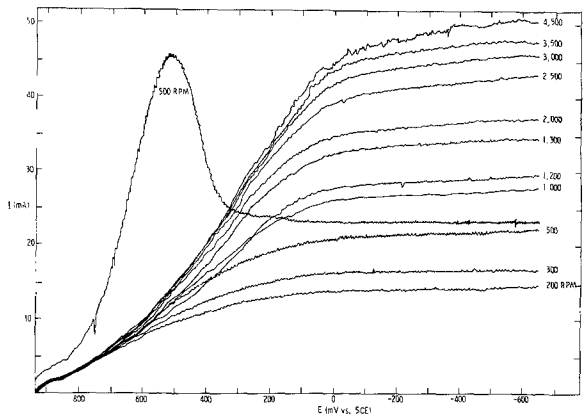


Fig. 2. Cathodic polarization of graphite electrode in 37% weight $ZnCl_2$ solution at different rotational speeds. $[Cl_2]$ = 3.02 g/l; area = 0.713 cm^2; *p*H = 3.15.

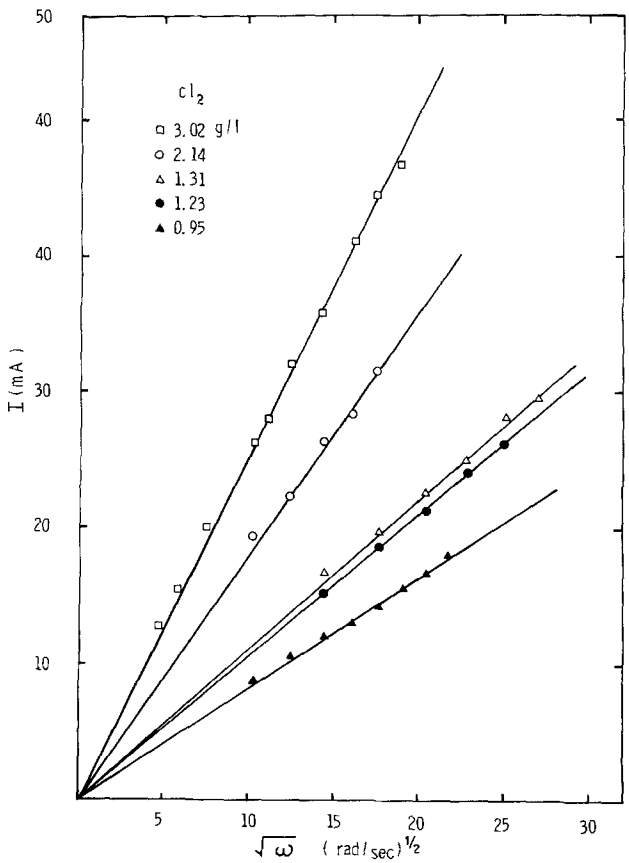


Fig. 3. The cathodic limiting current *vs.* the square root of the rotational speed at different Cl_2 concentrations.

measurements of a rotating Zn hemisphere in chlorinated $ZnCl_2$ solution (8). These values are in general agreement with the diffusion coefficient of Cl_2 in water (9), D_{Cl_2} = 1.22 × 10^{-5} cm^2/sec, after correction for different viscosities.

When the potential was scanned cathodically beyond the Cl_2 limiting current, a steep rise in the current was observed at about −1.0V *vs.* SCE, and is attributed to Zn deposition and H_2 evolution. A cathodic peak can be observed in Fig. 2 at 500 rpm during the cathodic scanning of the graphite-chlorine electrode. This current peak is due to unsteady-state effects, and was reproducible after the electrode was pretreated anodically or after leaving the graphite electrode overnight in chlorinated solution. The explanation for this peak is as follows. During anodization, Cl_2 is evolved and accumulated within the graphite porous structure.

Upon cathodic polarization, more Cl_2 is available and the current exceeds the apparent limiting current which is limited by the transport of dissolved Cl_2 to the projected apparent surface of the graphite electrode. After Cl_2 is depleted from the pores the current drops to the steady-state limiting value at the same rotational speed.

Cl_2 reaction order and rate constant.—Figure 4 shows the cathodic current as a function of the square root of the rotational speed for three fixed potentials. At $E = -390$ mV (*vs.* SCE) the potential is well within the limiting current region. The reaction is totally mass transfer limited, and a through-the-origin straight line is obtained according to the Levich convective diffusion equation. When the potential is fixed below the limiting current region ($E = 310$ or 410 mV *vs.* SCE) the reaction is partially controlled by mass transfer and surface reaction, and the I *vs.* $\omega^{1/2}$ plots are not linear (Fig. 4). Using the graphical method of Riddiford (10), the Cl_2 reaction order Z_{Cl_2} can be obtained by plotting arbitrary vertical lines ABC, DEF in Fig. 4, and Z_{Cl_2} is given by

$$Z_{Cl_2} = \frac{\log FE/CB}{\log CA/BA - \log FD/ED} = \frac{\log i_k - \log i}{\log i_l - \log (i_l - i)} \quad [2]$$

The reaction order was found to be $Z_{Cl_2} = 0.6$ in $1.75 \times 10^{-2}M$ Cl_2 in 37.6% $ZnCl_2$ solution. The reaction order was also obtained by the conventional method of varying the Cl_2 bulk concentration, as shown in Fig. 5

$$Z_{Cl_2} = \frac{\partial \log i}{\partial \log [Cl_2]} = 0.74$$

According to the present values, $Z_{Cl_2} = 0.6$ or 0.74, the reaction order can be half-order or first order. The polarization data were tested according to these two possibilities:

(*i*) If the reaction is assumed to be half-order, then the current is given by (10)

$$i^2 = i_k^2 - (i_k^2/B)(i/\omega^{1/2}) \quad [3]$$

where B is a constant ($0.62\, n\mathbf{F}D^{2/3}\nu^{-1/6}C_b$) and $i_k = n\mathbf{F}kC_b^{1/2}$ (surface reaction rate). A plot of i^2 *vs.* $i/\omega^{1/2}$ should give a straight line for a half-order reaction. As shown in Fig. 6, the behavior is not linear and the half-order assumption is incorrect.

(*ii*) If the reaction is assumed to be first order, the current is given by (10)

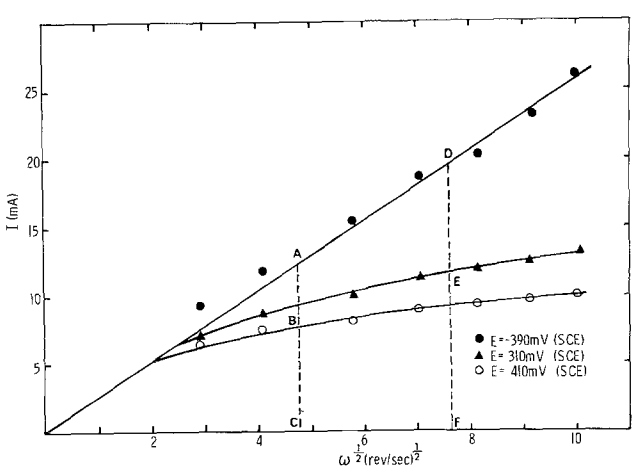


Fig. 4. The cathodic current *vs.* the square root of the rotational speed at three cathodic potentials. $[Cl_2] = 1.23$ g/l; area = 0.713 cm²; pH = 3.29.

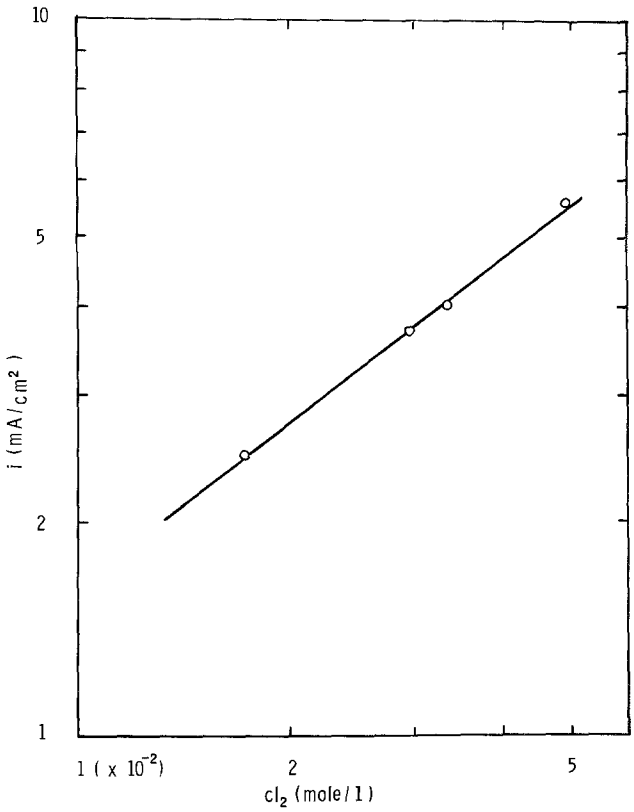


Fig. 5. The Cl_2 reaction order determination: $Z_{Cl_2} = 0.74$

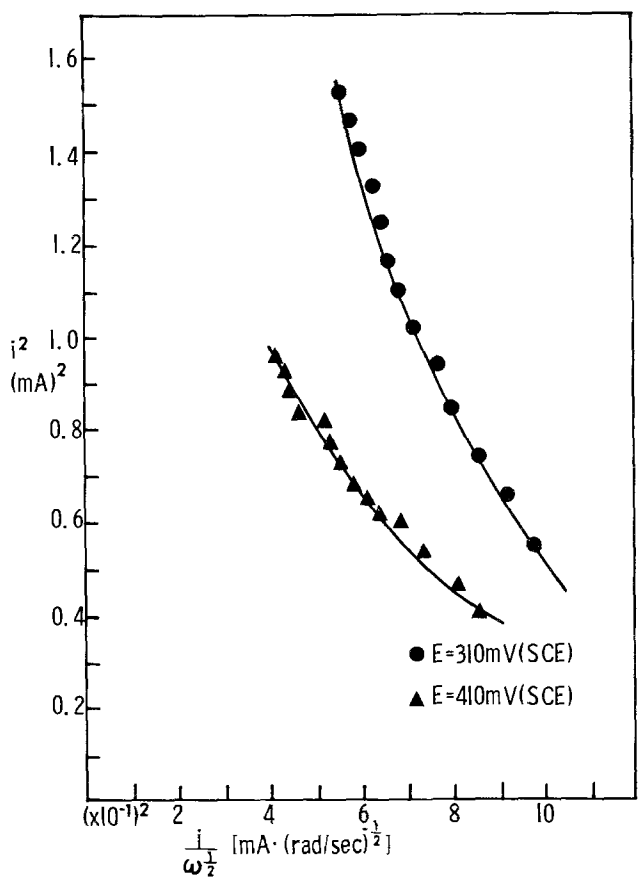


Fig. 6. The test for half-order reaction at different potentials. $[Cl_2] = 1.23$ g/l; area = 0.713 cm²; pH = 3.29.

$$1/i = 1/i_k + 1/i_l \quad [4]$$

where the limiting current is $i_l = 0.62\, n\mathbf{F}D^{2/3}\nu^{-1/6}C_b\omega^{1/2}$ and $i_k = n\mathbf{F}kC_b$. Rewriting Eq. [4] gives

$$1/i = 1/n\mathbf{F}kC_b + (1.61\nu^{1/6}/n\mathbf{F}D^{2/3}C_b)\,\omega^{-1/2} \quad [5]$$

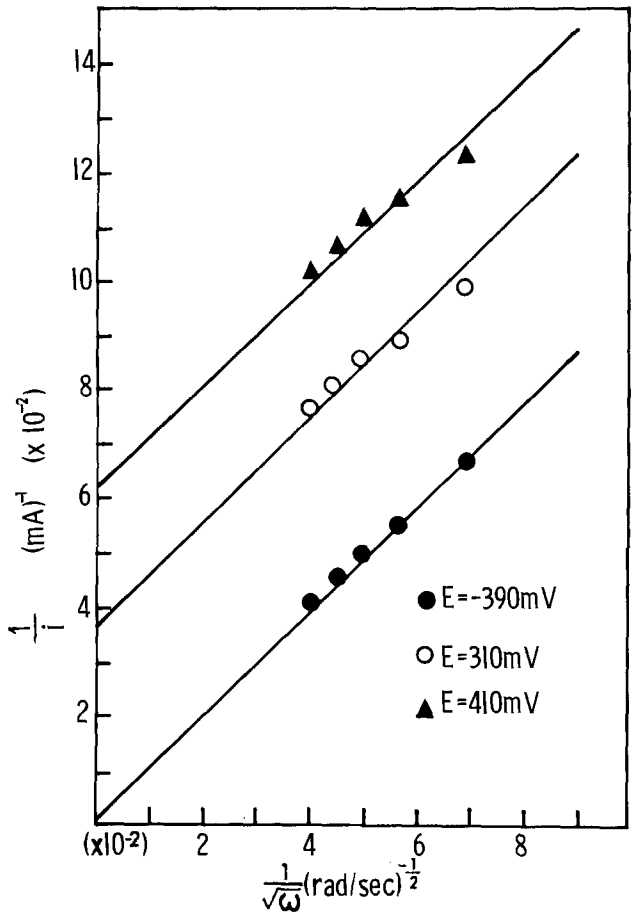


Fig. 7. The test for first-order reaction at different potentials. $[Cl_2]$ = 1.23 g/l; area = 0.713 cm^2; pH = 3.29.

Figure 7 shows the plot of $1/i$ *vs.* $\omega^{-1/2}$. The behavior is linear in accordance with Eq. [5], and the reaction is believed to be first order.

Extrapolating to $\omega^{-1/2} \rightarrow 0$ (or $\omega \rightarrow \infty$) permits the determination of the rate constant k. The obtained rate constants are 1.16×10^{-2} and 6.76×10^{-3} cm/sec for E = 310 and 410 mV *vs.* SCE, respectively. The rate constant k is a function of the potential, and increases as the potential becomes more negative (more cathodic). At the far cathodic potential, E = −390 mV *vs.* SCE, the reaction rate is very fast and can be neglected. The reaction is totally mass transfer limited, and a through-the-origin straight line is obtained according to the Levich convective diffusion equation.

Tafel's kinetic parameters.—The Tafel polarization plot for Cl_2/Cl^- on a dense graphite electrode is shown in Fig. 8. The data was corrected for ohmic drop using Newman's method (7). The apparent exchange current density, i_o = 1.11 mA/cm^2, is obtained from the intercept of the cathodic and anodic polarization branches. The anodic and cathodic Tafel slopes are b_a = 124 and b_c = −120 mV/decade, respectively. The present parameters are in agreement with the results of Hine (6) for NaCl solution (i_o = 1.2 mA/cm^2, $b_a = -b_c$ = 120 mV/decade). The deviation from linearity at the far cathodic potential range $E < 0.75$V *vs.* SCE in Fig. 8 is due to mass transfer overpotential.

The cathodic Tafel slope at a low cathodic overpotential $E > 0.810$V *vs.* SCE is b_c = −39.7 mV/decade, as can be seen in Fig. 9. In this region it is assumed that the fractional coverage is very small, $\theta_{Cl} \simeq 0$. The fractional coverage changes from θ = 0 at low current density to θ = 1 at high current density below the limiting current. The fractional coverage is assumed to follow the Langmuir isotherm form. The stoichiometric coefficient was obtained from the slope at low overpotential

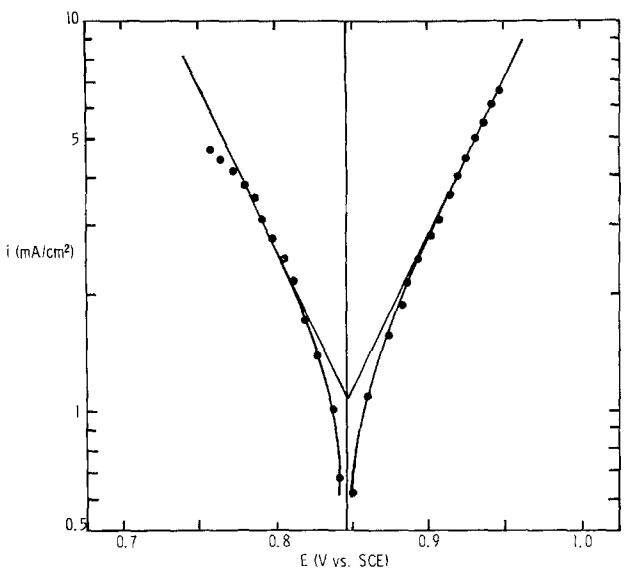


Fig. 8. Anodic and cathodic Tafel polarizations of graphite electrode in 37% weight $ZnCl_2$ solution. $[Cl_2]$ = 1.17 g/l; area = 0.713 cm^2; pH = 3.29.

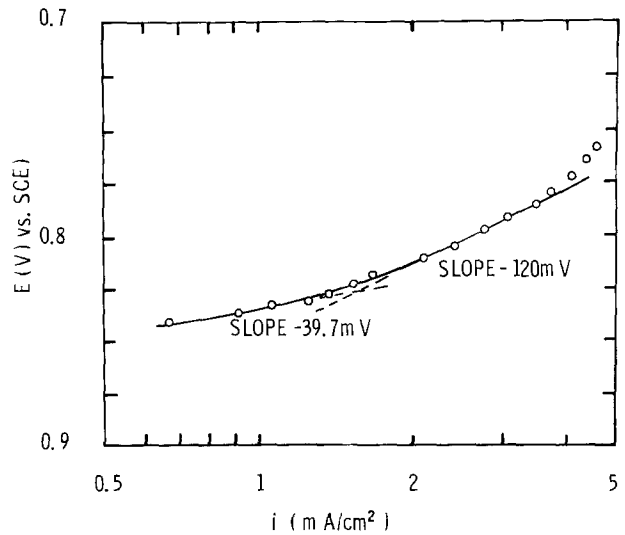


Fig. 9. Cathodic Tafel polarization of graphite electrode in 37% weight $ZnCl_2$ solution. $[Cl_2]$ = 1.17 g/l; area = 0.713 cm^2; pH = 3.29; $E > 0.810$V, b_c = −39.7 mV/decade; $E < 0.810$V, b_c = −120 mV/decade.

$$\mu = \frac{2F}{RT} i_o \left(\frac{\partial E}{\partial i} \right)_{\eta=0} = 1.2$$

The reaction mechansim.—The over-all cathodic Cl_2/Cl^- reaction is given by

$$Cl_2 + 2e \rightleftarrows 2Cl^-$$

The possible hypothetical reaction mechanisms are mechanism A

$$Cl_2 + e \leftrightarrows Cl_{ads} + Cl^- \quad [6]$$

$$Cl_{ads} + e \leftrightarrows Cl^- \quad [7]$$

mechanism B

$$Cl_2 \rightleftarrows 2Cl_{ads} \quad [8]$$

$$Cl_{ads} + e \rightleftarrows Cl^- \quad [9]$$

The theoretical parameters for the two mechanisms are shown in Table I, and were obtained from the Butler-Volmer rate equations including fractional coverage under steady-state assumption. If it is assumed that reaction [6] is the rate-determining step (rds), then the theoretical Tafel slope for reaction [6]

Table I. Parameters for cathodic Cl_2 reaction (theoretical)

Rate determining step	μ	Tafel slope $\theta \to 0$	Tafel slope $\theta \to 1$	Z_{Cl_2} $\theta \to 0$	Z_{Cl_2} $\theta \to 1$
Mechanism A					
(1) $Cl_2 + e \rightleftarrows Cl_{ads} + Cl^-$	1	$-2RT/F$	—	1	—
(2) $Cl_{ads} + e \rightleftarrows Cl^-$	1	$-2RT/3F$	$-2RT/F$	1	0
Mechanism B					
(3) $Cl_2 \rightleftarrows 2Cl_{ads}$	1	$-\infty$	—	1	—
(4) $Cl_{ads} + e \rightleftarrows Cl^-$	2	$-2RT/F$	$-2RT/F$	½	0

is $b_c = -120$ mV/decade under the assumption of $\theta_{Cl} \to 0$ at low current density (Table I). The experimental slope of −39.4 mV/decade in Fig. 9 indicates that reaction [6] is not the rds.

Assuming reaction [7] is the rds, the theoretical Tafel slopes are (Table I) $b_c = -40$ mV/decade for $\theta \to 0$, and $b_c = -120$ mV/decade for $\theta = 1$, in excellent agreement with the experimental values of −39.7 and 120 mV/decade, respectively. Thus, mechanism A appears to be correct, and reaction [7] is the rds. The experimental results are in disagreement with the theoretical parameters for mechanism B, as shown in Table I.

Although the $ZnCl_2$ solutions in the present work are acidic (pH = 3.2), and the molecular Cl_2 is the predominant species, the concentrations of hypochlorous acid HOCl and trichloride ion Cl_3^- are not negligible (8). The dissociation constant of hypochlorous acid to hypochlorite is very small $K = 4\ 10^{-8}$ (12), and in the present acidic solution hypochlorite is not present. However the transport and kinetic parameters obtained in the present work represent average values for the predominant molecular Cl_2, and minute concentrations of HOCl and Cl_3^-.

Conclusions

The cathodic reaction for Cl_2/Cl^- on a dense graphite electrode in $ZnCl_2$ solution has been investigated. Cathodic limiting currents were obtained at various rotational speeds and dissolved Cl_2 concentrations, and the Cl_2 diffusion coefficient was obtained. The reaction is first order with respect to the Cl_2 concentration.

The Tafel parameters were obtained for the anodic and cathodic polarizations. The following mechanism was established

$$Cl_2 + e \rightleftarrows Cl_{ads} + Cl^-$$

and

$$Cl_{ads} + e \overset{rds}{\rightarrow} Cl^-$$

and the second reaction is the rate-determining step.

The cathodic reaction rate constants were evaluated at several potentials. The cathodic reduction of Cl_2 was found to be partially mass transfer and kinetics limited.

The kinetics and transport parameters obtained in the present work are necessary in the design and optimization of a practical Cl_2 electrode in the Zn-Cl_2 battery. It is clear that a flow-through porous electrode is needed in order to maintain high currents.

Acknowledgments

This work was supported by Energy Development Associates, Madison Heights, Michigan, and Electric Power Research Institute, Palo Alto, California. The stimulating discussions with Drs. Philip Symons and Charles Ward are gratefully acknowledged.

Manuscript submitted April 29, 1977; revised manuscript received June 7, 1977.

Any discussion of this paper will appear in a Discussion Section to be published in the June 1978 JOURNAL. All discussions for the June 1978 Discussion Section should be submitted by Feb. 1, 1978.

Publication costs of this article were assisted by Wayne State University.

LIST OF SYMBOLS

A	electrode area, cm^2
b_a	anodic Tafel slope, V/decade
b_c	cathodic Tafel slope, V/decade
c_b	bulk concentration, $mole/cm^3$
D	diffusion coefficient, cm^2/sec
E	potential, V
$\mathbf{F}$	Faraday's constant, 96,487 C/equiv.
I	current, A
i	current density, A/cm^2
i_k	kinetic current density, A/cm^2
i_l	limiting current density, A/cm^2
i_o	exchange current density, A/cm^2
k	rate constant, cm/sec
n	number of electrons transferred in electrode reaction
R	universal gas constant, 8.3143 J/mole°K
Z	the reaction order
η	overpotential, V
θ	fractional coverage
μ	stoichiometric coefficient
ν	kinematic viscosity, cm^2/sec
ω	rotational speed, rad/sec

REFERENCES

1. P. C. Symons and P. Carr, in Proceedings of the 8th Inter-Society Energy Conversion Engineering Conference, pp. 72-77 (1973).
2. A. N. Frumkin and G. A. Tedoradze, *Dokl. Acad. Nauk, SSSR.*, **118**, 530 (1958).
3. L. Sereno, V. A. Macagno, and M. C. Giordano, *Electrochim. Acta*, **17**, 561 (1972).
4. T. Dickinson, R. Greef, and L. Wynne-Jones, *ibid.*, **17**, 561 (1972).
5. G. Faita, G. Fiori, and J. W. Augustynski, *This Journal*, **116**, 928 (1969).
6. F. Hine and M. Yasuda, *ibid.*, **121**, 1289 (1974).
7. J. Newman, *ibid.*, **113**, 501 (1966).
8. J. T. Kim and J. Jorné, *ibid.*, In press (1977).
9. J. Arnold, *J. Am. Chem. Soc.*, **52**, 3937 (1930).
10. A. C. Riddiford, in "Advances in Electrochemistry and Electrochemical Engineering," Vol. 4, P. Delahay, Editor, Wiley-Interscience, New York (1966).
11. J. Mellor, "Comprehensive Treatise on Inorganic and Theoretical Chemistry," Vol. 2, Longmans, Green and Co., London (1974).
12. M. S. Chao, *This Journal*, **115**, 1172 (1968).

The Effect of Phosphoric Acid on the Positive Electrode in the Lead Acid Battery

Kathryn R. Bullock*[1] and Donald H. McClelland*

The Gates Rubber Company, Denver, Colorado 80217

ABSTRACT

The effect of phosphoric acid on the positive electrode reaction in a lead-acid battery is studied by cyclic voltammetry. It is proposed that phosphate reversibly adsorbs on the PbO_2 during charge, and modifies the crystal growth of PbO_2 on the lead grid. The form of PbO_2 produced in the presence of phosphate is not easily reduced to lead sulfate and, therefore, the positive grid does not become insulated from the active material. The limit of this effect is reached at a low concentration of phosphoric acid.

Phosphoric acid and various phosphate compounds have been used as additives to lead-acid batteries since 1900 (1, 2). A number of patents have been issued since that time in which phosphates are claimed to improve battery performance (3-10). In particular, they are reported to increase cycle life by reducing the shedding and irreversible sulfation of the positive-plate active material. Eberts (11) has shown that phosphoric acid improves the cycle life of a battery with a lead-calcium grid.

Adverse effects of phosphoric acid which have been reported include capacity loss in the initial cycles, excessive mossing (7), and poor low temperature performance (12).

More recently, phosphates have been used in gelled electrolytes (13-17). In spite of their widespread use, very little is understood about the mechanisms by which phosphates affect the performance of lead-acid batteries. Tudor, Weisstuch, and Davang (18-20) used an autoradiographic technique to study the effect of phosphoric acid on the performance of thin-plate, lead-calcium grid batteries. They showed that phosphoric acid reduces the amount of sulfate on the grid of the positive electrode during float charging and cycling, and that the phosphate enters the positive plate during charge and leaves during discharge.

Several authors have found lead(IV) complexes with phosphate which can be produced both chemically and electrochemically (21-24). Amlie and Berger (25) have noted that a soluble lead(IV) species can be detected polarographically in sulfuric acid only if phosphoric acid is present.

In a previous publication (26), we have shown that phosphoric acid in the electrolyte of a sealed lead-acid cell inhibits the rate of the self-discharge reaction. The rate-determining step in that reaction is probably

$$PbO_2 + H_2SO_4 \rightarrow PbSO_4 + H_2O + \tfrac{1}{2} O_2$$

Several investigators have published voltammograms of lead in sulfuric acid (27-37). Of these papers, three have discussed the $PbO_2/PbSO_4$ electrode reaction in some detail. Panesar (29) has investigated the reaction on electrodes made from α- and β-PbO_2, as well as anodized lead at room temperature. Valeriote and Gallop (32) and Chang, Wright, and Valeriote (33) have studied the reaction in the 25° to −40°C temperature range on anodized pure lead and antimonial lead.

Experimental

Pure lead electrodes were cycled in 34 and 43% by weight sulfuric acid in the 25° to −40°C temperature range at slow scan rates. The working and counterelectrodes were made from pure lead rods set in epoxy or dental acrylic and cut off to obtain a flat, circular lead electrode with an area of approximately 0.32 cm^2. Immediately prior to cycling, the lead was polished with 600 Grit Carborundum paper and shined with a clean tissue. A $Hg/Hg_2SO_4/H_2SO_4$ electrode containing the same concentration of sulfuric acid as the experimental solution served as the reference electrode.

Reagent-grade sulfuric and phosphoric acids and doubly distilled water were used to prepare the electrolyte. Before the voltammograms were recorded, the electrodes were cycled at a scan rate of 1 mV/sec for at least 24 hr under the conditions of interest. This served to develop the PbO_2 coating on the working electrode, and to allow the electrode reactions to reach a steady state.

The temperature was controlled by a stirred water bath regulated by a Sargent Model T thermonitor. The instruments used in the study were a Princeton Applied Research Model 371 potentiostat and Model 175/99 signal source, and a Hewlett Packard Model 7035 X-Y recorder.

Results

Some typical voltammograms of lead in 43% H_2SO_4 are shown in Fig. 1 at four different temperatures. The scan is begun at 1.05V *vs.* a $Hg/Hg_2SO_4/43\%$ H_2SO_4 reference electrode, and is reversed at 1.53V. The scan rate is 1 mV/sec. On the anodic scan, the wave corresponding to the oxidation of $PbSO_4$ to PbO_2 can be seen, followed by oxygen evolution. On the return scan, the wave corresponding to the reduction of PbO_2 to $PbSO_4$ is apparent.

A comparison of the waves at the four different temperatures reveals that the separation between the anodic and cathodic peaks decreases with increasing temperature. Thus, the reaction is becoming more nearly reversible as the temperature increases. Furthermore, better resolution is obtained between the anodic peak and the oxygen evolution wave. Finally, the cathodic peak becomes sharper, and more fine structure is seen in the reduction wave. At 40°C at least three different reduction waves can be distinguished.

A similar effect can be obtained by decreasing the scan rate, as is shown in Fig. 2. The voltammogram in this figure at the 1 mV/sec scan rate is identical to that shown for 40°C in Fig. 1. As the scan rate is decreased from 5 to 0.1 mV/sec, the voltammogram continues to become more nearly reversible. Again, the most positive reduction peak becomes sharper, and the resolution between the anodic wave and the region of oxygen evolution improves.

On the basis of these results, we decided to study the wave at the lowest scan rate (0.1 mV/sec) and the highest temperature (40°C) which could consistently be obtained with our equipment. Under these conditions, the reaction became fast enough and the experimental observation became slow enough, so that the reaction appeared to be reasonably reversible, and the

* Electrochemical Society Active Member.
[1] Present address: Globe-Union, Incorporated, Milwaukee, Wisconsin 53201.
Key words: lead-acid battery, phosphoric acid, lead dioxide, lead sulfate, cyclic voltammetry.

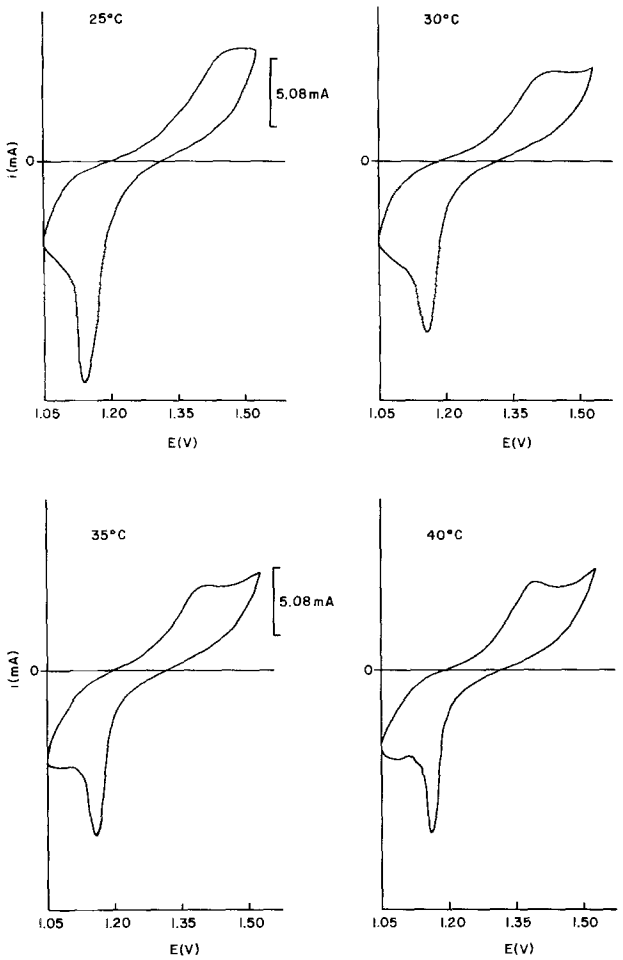


Fig. 1. Cyclic voltammograms of lead in 43% H_2SO_4. Scan rate = 1 mV/sec.

reactions being studied had rates comparable to those observed when cycling an actual lead-acid battery at a moderate rate (approximately 1.3 hr charge or discharge at 40°C).

The voltammograms in Fig. 1 and 2 were run on solutions containing very small traces of phosphoric acid. We subsequently found that care had to be taken to prevent phosphoric acid from leaking out of cracks at the interface between the lead and the epoxy surrounding it if the electrode had previously been cycled in an electrolyte containing phosphoric acid. This problem was overcome by trimming the end of the electrode before each set of experiments to insure that the electrode surface was fresh.

In Fig. 3, the voltammograms of lead cycled in 34% sulfuric acid with and without phosphoric acid are shown. It is not practical to exclude phosphate entirely from the electrolyte, since even Ultrex grade sulfuric acid contains approximately 50 ppb phosphate. Thus, the differences between the two voltammograms are those of degree rather than kind. Nevertheless, the differences are striking. The most positive reduction peak shifts to a more positive potential in the presence of phosphoric acid. At the same time, the two more negative reduction peaks, which were just barely discernible in the pure electrolyte, have grown considerably in the presence of phosphate. Furthermore, the area of the wave in the solution containing 0.1% phosphoric acid is over twice that of the wave in the pure electrolyte. Although the areas are slightly dependent on the length of time the electrode has cycled, the magnitude of this effect is too large to be explained on that basis.

Similar results were obtained in 43% sulfuric acid. In Fig. 4, the voltammograms taken in electrolyte containing 0.1% phosphoric acid are compared for 34 and

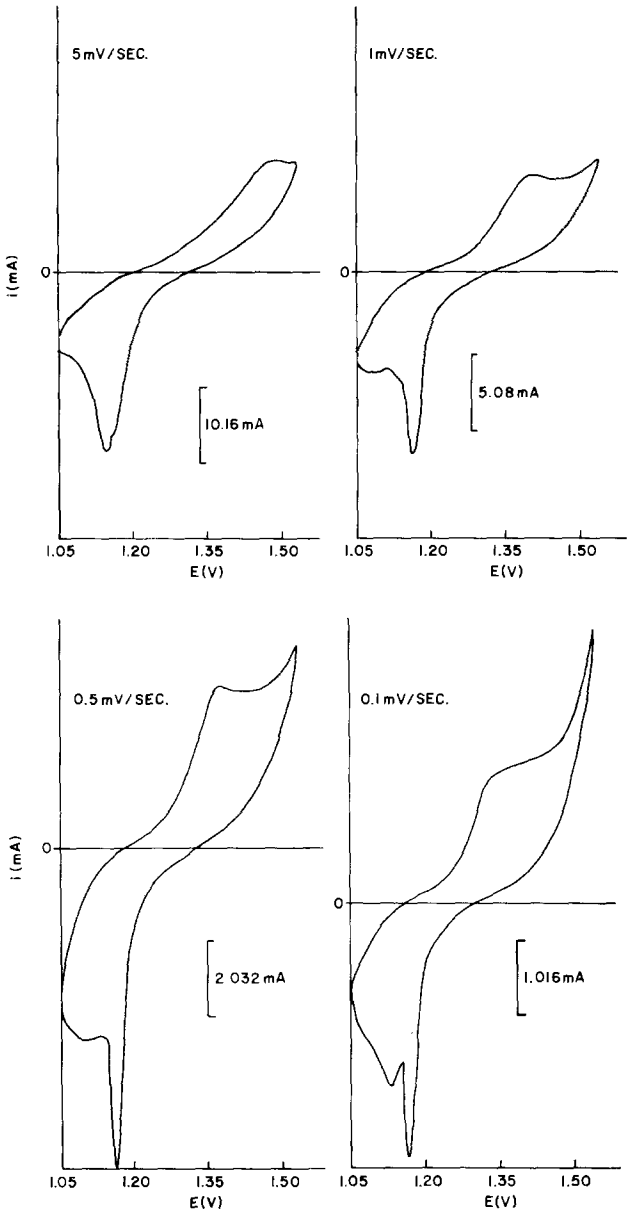


Fig. 2. Cyclic voltammograms of lead in 43% H_2SO_4 at 40°C

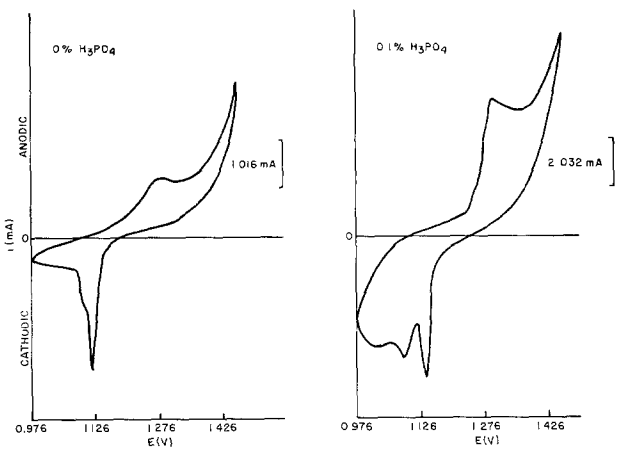


Fig. 3. Cyclic voltammograms of lead at 40°C in 34% H_2SO_4. Scan rate = 0.1 mV/sec.

43% sulfuric acid. The reversible potential of the $PbO_2/PbSO_4$ electrode at 40°C is 1.188V in 43% sulfuric acid, and 1.117V in 34% acid (38) *vs.* the $Hg/Hg_2SO_4/H_2SO_4$ reference electrode of the same acid concentration. The voltage range is adjusted accordingly for this change in electrode potential with electrolyte concentration.

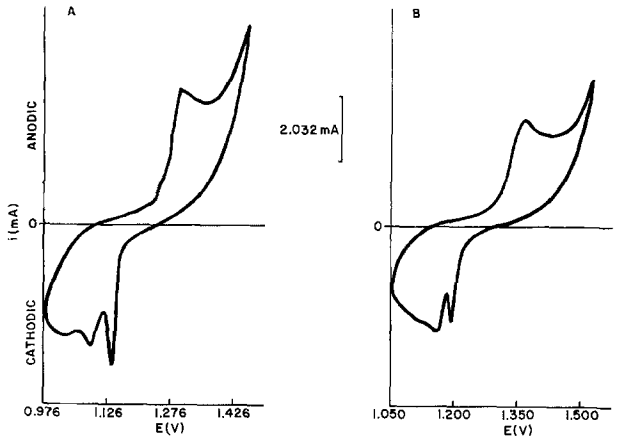


Fig. 4. Cyclic voltammograms of lead at 40°C in 34% (curve A) and 43% (curve B) H_2SO_4 containing 0.1% H_3PO_4. Scan rate = 0.1 mV/sec.

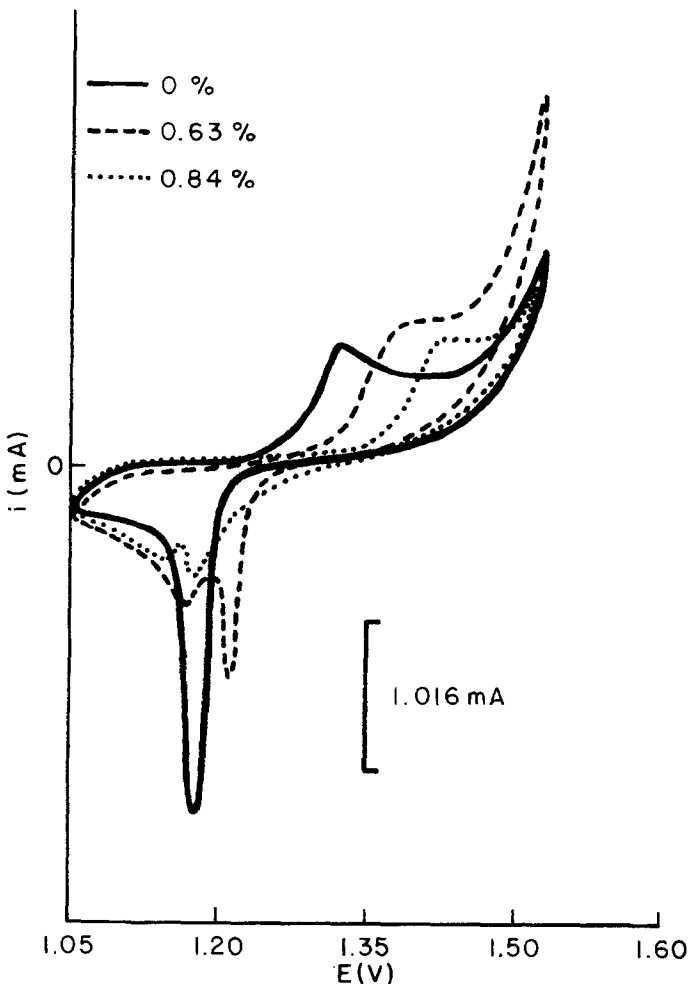


Fig. 5. Effect of H_3PO_4 additions to 43% H_2SO_4. T = 40°C. Scan rate = 0.1 mV/sec.

Figure 5 illustrates the results of an experiment in which a solution of 43% sulfuric acid was titrated with phosphoric acid in approximately 0.2% increments, and the change in the voltammogram after each addition was observed. The solid line shows the voltammogram in the pure electrolyte. With each addition of phosphoric acid, the reduction peak shifted in the positive direction and simultaneously decreased in height. As this peak shifted, the more negative peak appeared and grew in height. The dashed curve shows the voltammogram taken after 0.63% phosphoric acid had been added.

When 0.84% phosphoric acid had been added, the more positive reduction peak disappeared altogether and the more negative peak split into two peaks. This can be seen in the dotted curve in Fig. 5. It was apparent that this change did not represent a mere shift in the two peak potentials for two reasons. First, the solution was not stirred after each addition of phosphate in order to avoid disturbing the electrode surface and to observe the change in the waves as the phosphate diffused into the solution. Thus, the disappearance of the more positive wave and the splitting of the negative wave could be observed from one cycle to the next as the phosphate was mixed into the solution. Secondly, all three waves can be observed in the same voltammogram under some conditions (see Fig. 4).

Comparable changes occurred in the anodic wave, although these are more difficult to observe because of the interference of the oxygen evolution current. Nevertheless, it is apparent that the peak of the anodic wave is shifting to a more positive potential as the phosphate concentration is increased.

Further additions of phosphate caused no further changes in the voltammogram. Nor did the wave change significantly when the electrode was cycled for several days after the last addition of phosphate. Reducing the phosphate concentration by adding more electrolyte reversed the effect.

Similar results were obtained at several higher scan rates. However, since at higher scan rates the reduction waves are not as well resolved and are less reversible, the exact effect of phosphate addition on the three waves is more difficult to observe. A plot of the peak current of the most positive reduction wave as a function of the concentration of phosphoric acid added is shown in Fig. 6. The relationship is linear until the addition of 0.84% H_3PO_4 causes the peak to disappear completely.

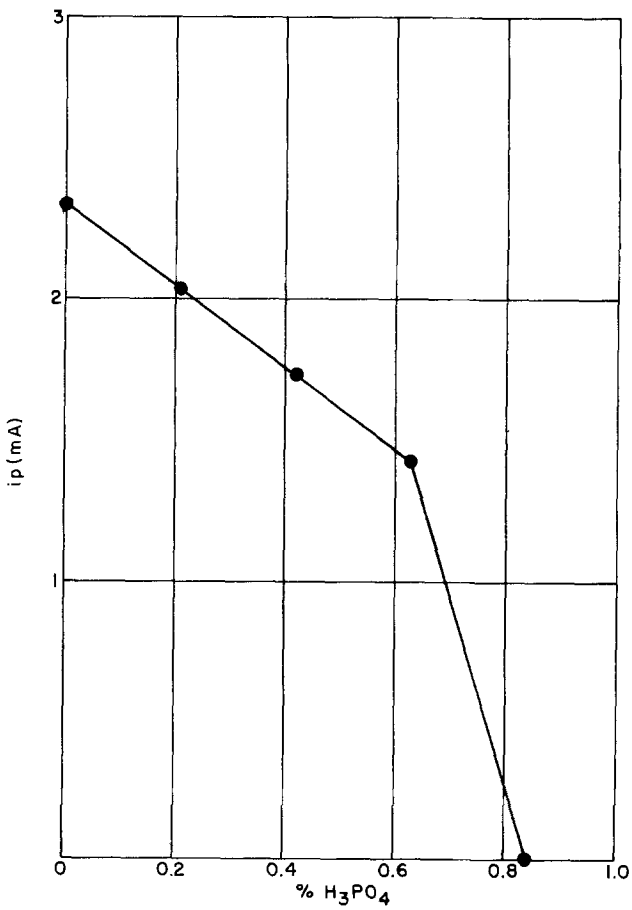


Fig. 6. Plot of current of positive reduction peak as a function of phosphoric acid concentration.

Discussion

Laitinen and Watkins have recently published similar results (23, 39) in their study of the analysis of lead in nitric acid by cathodic stripping voltammetry. In their work, Pb(II) in HNO_3 solution is electrodeposited as PbO_2 on tin oxide, and the reduction waves of the PbO_2 deposit are then observed. As the voltage is scanned in the negative direction, a single, sharp reduction wave is observed, followed by a broad, irreversible wave. Addition of phosphate to the solution causes the height of the first reduction wave to decrease and the peak potential to shift in the positive direction. Simultaneously, the second broad reduction peak increases in height. When multiple layers of PbO_2 are deposited in the presence of phosphate, three or more reduction waves are observed (23), in agreement with our results.

Kinard and Propst (40) have observed nearly identical reduction peaks in the cathodic stripping analysis of Pb(II) in dilute sulfuric acid using a conducting glass electrode. They did not, however, study the effect of phosphate on these waves. The shapes of the peaks indicate that the more positive reduction wave is reversible, while the more negative wave is irreversible. Laitinen and Watkins have substantiated this by comparing the peak potentials of the waves at stationary and rotating electrodes (39).

The same authors have studied the electrodeposition of PbO_2 on tin oxide in more detail by potentiostatic current-time curves, scanning electron microscopy, and electron spectroscopy (ESCA). They have concluded that the phosphate adsorbs on the lead dioxide monolayer and inhibits the three-dimensional growth of PbO_2 crystals in favor of two-dimensional growth of nuclei. The PbO_2 formed by two-dimensional growth is less easily reduced than that formed by three-dimensional growth. In the absence of phosphate about 3% of the surface is covered by the irreversible PbO_2 species, whereas in the presence of phosphate, a continuous monolayer of the irreversible PbO_2 species is formed. Furthermore, no phosphorus is observed on the surface of the deposit by ESCA. Apparently, the phosphate is incorporated into the bulk phase as a solid solution (41).

Carr and Hampson (42) have shown that phosphate is reversibly adsorbed on lead dioxide. This is in agreement with our observation that the magnitude of the effect of phosphate on the reactions at the positive electrode can be reduced by reducing the concentration of the phosphate.

A comparison of our results with those of other investigators (23, 39, 40, 42) leads us to propose the following model for the effect of phosphate on the positive electrode of a lead-acid battery. The phosphate adsorbs on the PbO_2 and modifies its crystal growth. The PbO_2 formed in the presence of phosphate is less easily reduced than the species formed when phosphate is absent. Thus, during reduction, the insulating sulfate layer between the positive grid and the active material is not formed. This is in agreement with Tudor, Weisstuch, and Davang (18-20), who have observed by an autoradiographic technique that the sulfate layer is not formed in cells containing phosphoric acid.

The beneficial effect of phosphoric acid limits at approximately 0.8%, as was shown in Fig. 5. This is in agreement with the patent literature, in which the recommended amount of the additive has always been a low percentage (4, 7-10). Apparently, the surface becomes saturated once phosphate has adsorbed on the active sites of the PbO_2. Higher concentrations can be detrimental to battery performance. For example, excessive "mossing" is seen at higher phosphate concentrations (7), and this may be related to the increased solubility of lead(IV) under these conditions.

Finally, the cyclic voltammograms shown in Fig. 5 give some support to the observation that phosphoric acid reduces the low temperature performance of lead-acid batteries (12). In the presence of phosphate, the potential required to oxidize the lead sulfate to lead dioxide is higher than in the absence of phosphate. At this higher voltage, the oxygen evolution reaction rate is also higher and, therefore, the charging efficiency is lower. Decreasing the temperature has a similar effect on the charging efficiency, as can be seen in Fig. 1. Thus, it appears that the presence of phosphoric acid intensifies the problems already present in low temperature charging.

Acknowledgments

The authors are indebted to Robert Amlie for calling Ref. (23) to their attention and to Will Bundy and Everett Ritchie for helpful discussions.

Manuscript received Feb. 15, 1977. This was Paper 14 presented at the Las Vegas, Nevada, Meeting of the Society, Oct. 17-22, 1976.

Any discussion of this paper will appear in a Discussion Section to be published in the June 1978 JOURNAL. All discussions for the June 1978 Discussion Section should be submitted by Feb. 1, 1978.

Publication costs of this article were assisted by The Gates Rubber Company.

REFERENCES

1. C. Brault, U.S. Pat. 625,287 (1900).
2. E. A. Sperry, U.S. Pat. 660,228 (1901).
3. F. D. Cheney, U.S. Pat. 1,385,305 (1921).
4. M. Kugel, German Pat. 480,149 (1926).
5. K. Neumann, French Pat. 690,409 (1930).
6. H. R. Harner and M. F. Chubb, U.S. Pat. 2,035,315 (1935).
7. D. Evers, U.S. Pat. 3,011,077 (1961).
8. E. A. Willihnganz, French Pat. 1,517,629 (1968).
9. S. Tudor, A. Weisstuch, and S. H. Davang, U.S. Pat. 3,447,969 (1969).
10. K. Yonetsu *et al.*, Japanese Pat. 48-5175 (1973).
11. K. Eberts, in "Power Sources 2," D. H. Collins, Editor, p. 69, Pergamon Press, Inc., Elmsford, New York (1968).
12. Annual Report on ILZRO Combined Research Projects LE-82 and LE-84, No. 2 (1967).
13. M. H. Little, U.S. Pat. 3,530,002 (1970).
14. R. F. Amlie, U.S. Pat. 3,556,860 (1971).
15. O. Jache, U.S. Pat. 3,765,942 (1973).
16. R. F. Amlie, E. Y. Weissman, and N. M. Qureshi, in Proceedings of the 25th Power Sources Symposium, p. 67, (1972).
17. R. F. Amlie, E. Y. Weissman, C. K. Morehouse, and N. M. Qureshi, *This Journal*, **119**, 568 (1972).
18. S. Tudor, A. Weisstuch, and S. H. Davang, *Electrochem. Technol.*, **3**, 90 (1965).
19. S. Tudor, A. Weisstuch, and S. H. Davang, *ibid.*, **4**, 406 (1966).
20. S. Tudor, A. Weisstuch, and S. H. Davang, *ibid.*, **5**, 21 (1967).
21. H. Bode and E. Voss, *Electrochim. Acta*, **6**, 11 (1962).
22. V. F. Huber and M. S. A. El-Meligy, *Z. Anorg. Allg. Chem.*, **367**, 154 (1969).
23. H. A. Laitinen and N. H. Watkins, *Anal. Chem.*, **47**, 1352 (1975).
24. M. Fleischmann, J. R. Mansfield, H. R. Thirsk, H. G. E. Wilson, and L. Wynne Jones, *Electrochim. Acta*, **12**, 967 (1967).
25. R. F. Amlie and T. A. Berger, *J. Electroanal. Chem. Interfacial Electrochem.*, **36**, 427 (1972).
26. K. R. Bullock and D. H. McClelland, *This Journal*, **123**, 327 (1976).
27. M. P. J. Brennan, B. N. Stirrup, and N. A. Hampson, *J. Appl. Electrochem.*, **4**, 49 (1974).
28. J. P. Carr, N. A. Hampson, and R. Taylor, *J. Electroanal. Chem. Interfacial Electrochem.*, **33**, 109 (1971).
29. H. S. Panesar, in "Power Sources 3," D. H. Collins, Editor, p. 79, Oriel Press, Newcastle upon Tyne, England (1971).
30. T. F. Sharpe, *This Journal*, **122**, 845 (1975).
31. J. L. Urrutia, *Rev. Metal (Madrid)*, **10**, 241 (1974).
32. E. M. L. Valeriote and L. D. Gallop, in "Power Sources 5," D. H. Collins, Editor, p. 55, Academic Press, Inc., New York (1975).
33. T. G. Chang, M. M. Wright, and E. M. L. Valeriote, Paper presented at Power Sources Conference, Brighton, England, September 1976.
34. T. F. Sharpe, *This Journal*, **124**, 158 (1977).

35. J. L. Weininger, Paper 6 presented at The Electrochemical Society Meeting, Las Vegas, Nevada, October 17-22, 1976.
36. J. G. Sunderland, *J. Electroanal. Chem. Interfacial Electrochem.*, **71**, 341 (1976).
37. S. E. Afifi, W. H. Edwards, and N. A. Hampson, *Surf. Technol.*, **4**, 173 (1976).
38. H. S. Harned and W. J. Hamer, *J. Am. Chem. Soc.*, **57**, 27 (1935).
39. H. A. Laitinen and N. H. Watkins, *This Journal*, **123**, 804 (1976).
40. J. T. Kinard and R. C. Propst, *Anal. Chem.*, **46**, 1106 (1974).
41. H. A. Laitinen, Private communication.
42. J. P. Carr and N. A. Hampson, *J. Electroanal. Chem. Interfacial Electrochem.*, **28**, 65 (1970).

Changes in Alkaline Electrolyte Concentration and Its Effect on the Open-Circuit Potentials in the Nickel-Cadmium Cell

Gerald Halpert*

NASA/Goddard Space Flight Center, Greenbelt, Maryland 20771

and Leopold May[1]

Department of Chemistry, The Catholic University of America, Washington, D.C. 20064

ABSTRACT

In the electrode reactions of the nickel cadmium cell there is an interchange of H_2O and OH^- at the electrodes, depending on whether the cell has been charged or discharged. The calculations described below are based on a reaction involving KOH adsorption/desorption. The results from experimental cells are found to be consistent with this model. Electrolyte concentrations are calculated for different states of charge of a cell where the effect of precharge is considered. The open-circuit potentials (negative, positive, and cell) are calculated for various KOH concentrations (10.3-45.2%) and temperatures (0°-40°C). The calculated temperature coefficient for the cell potential is found to be −0.45 mV/deg, which is comparable to that found in previous experiments.

The concentration and distribution of aqueous potassium hydroxide (KOH) electrolyte in a sealed nickel cadmium cell has been the subject of considerable discussion. The reactions at both electrodes during charge and discharge involve the production or utilization of hydroxyl ion (OH^-) or water (H_2O), which directly affects concentration. The potential developed between the cadmium hydroxide (negative) electrode and the nickel hydroxide (positive) electrode depends upon the concentration of the potassium hydroxide electrolyte. The open-circuit potentials for the cell and each half-cell varies with the concentrations of the hydroxide and temperature. In addition to the changes at each electrode, there is a net change in concentration of the electrolyte in the cell as a whole. During charge there is an increase in water; during discharge, a decrease in water. If we consider a more correct reaction equation, there is also a decrease in OH^- on charge associated with KOH adsorption at the positive electrode and increase during discharge. The net effect is a significant decrease in concentration from beginning to end of charge, and an increase during discharge. The extent of precharge must also be considered in that during this process OH^- is converted to water that also dilutes the electrolyte.

The Basic Cell Reaction

The sealed nickel-cadmium cell consists of electrodes containing cadmium and nickel hydroxides as the active materials, and aqueous potassium hydroxide as the electrolyte. The open-circuit potential of the cell is determined in part by the concentration of the hydroxide, as can be seen by the equations for the half-cell potentials involving the cadmium and nickel hydroxide electrodes and the composite equation for the potential of the cell. The reaction at the positive electrode is

$$2NiOOH + 2H_2O + 2e \rightleftharpoons 2Ni(OH)_2 + 2\,OH^- \quad [1]$$

and for the negative electrode

$$Cd(OH)_2 + 2e \rightleftharpoons Cd + 2\,OH^- \quad [2]$$

The over-all reaction for the cell is therefore the difference of the two half-cell reactions

$$2NiOOH + 2H_2O + Cd \underset{\text{charge}}{\overset{\text{discharge}}{\rightleftharpoons}} 2Ni(OH)_2 + Cd(OH)_2 \quad [3]$$

Changes in Electrolyte Concentration During Cell Operation

During charge at the positive electrode, 1 mole of OH^- is consumed and 1 mole of H_2O is produced for every mole of electrons produced. Based on the Faraday constant, this is equivalent to 26.8 A-hr. Therefore, the loss of OH^- (0.63 g/A-hr) and gain of water (0.67 g/A-hr) play a significant role in electrolyte dilution at the positive electrode. The depletion of OH^- at the electrode is compensated for by OH^- migrating and diffusing from the negative electrode. At the negative electrode 1 mole of OH^- is produced for every 26.8 A-hr. Thus, an increase in 0.67 g/A-hr significantly increases the concentration at the negative electrode. The net cell reaction identifies the production of 1 mole of water for every 26.8 A-hr or 0.67 g/A-hr. The result is not only a net decrease in electrolyte concentration during the charge process, but also a changing concentration as the state of charge is increased from the discharged condition to the fully charged condition. The calculations for typical 6, 12, and 20 A-hr cell sizes appear in Table I,

* Electrochemical Society Active Member.
[1] ASEE/NASA Faculty Fellow.
Key words: nickel-cadmium, alkaline electrolyte, open-circuit potentials and activities.

Table I. Electrolyte concentration change after charge

A Cell capacity (A-hr)	B 31% electrolyte (ml)	C Weight of electrolyte (g) (SG = 1.300)	D Weight KOH (g)	E Weight H_2O (g)	F Estimated cell capacity (1.2 × nominal)	G Increase in water (g)	H Total weight after charge (g) C + G	I % KOH after charge D/H
6	18	23.40	7.25	16.15	7.20	4.82	28.22	25.7
12	36	46.80	14.51	32.29	14.40	9.65	56.45	25.7
20	68	88.40	27.40	61.00	24.00	16.08	104.48	26.2

which illustrates a change in concentration from 31% added initially to 26% KOH for a cell fully charged without considering the effect of precharge.

The following reactions are given for the overcharge process in sealed cells

electrode	reaction	
+	$4\,OH^- \rightarrow O_2 + 2H_2O + 4e^-$	
−	$2Cd(OH)_2 + 4e \rightarrow 2Cd + 4\,OH^-$	[4]
	$O_2 + 2Cd + 2H_2O \rightarrow 2Cd(OH)_2$	
	net reaction = 0	

During overcharge there is no net change in over-all cell with regard to electrolyte concentration. However, as indicated above, at the positive electrode the concentration diminishes and at the negative electrode the concentration increases.

In order to achieve a desirable electrode balance in a cell, additional charge is given to the cadmium hydroxide electrode over and above that given the nickel hydroxide electrode. This excess charge referred to as precharge is required for adequate oxygen recombination during overcharge, and to assure that the positive electrode is the limiting electrode on discharge. There are several methods used for this. The most common is to vent oxygen gas from a temporary sealed cell during overcharge. In this manner the negative electrode is given the excess charge, while the positive electrode is unaffected. The reactions given below describe the process and also illustrate that as oxygen is produced and eliminated, water is also produced

electrode	reaction	
+	$4\,OH^- \rightarrow O_2 + 2H_2O + 4e$	
−	$Cd(OH)_2 + 4e \rightarrow 2Cd + 4\,OH^-$	[5]
	$2Cd(OH)_2 \underset{\text{discharge}}{\overset{\text{charge}}{\rightleftharpoons}} O_2 + 2Cd + 2H_2O$	

The net reaction involves an increase in 0.5 mole of H_2O for every 26.8 A-hr, or a gain of 0.34g H_2O/A-hr. The effect is seen in Table II, which is a continuation of Table I. The level of precharge for the 6, 12, and 20 A-hr size cell is generally 2.60, 5.20, and 9.80 A-hr, respectively.

The result of increasing the amount of water during precharge is a decrease in over-all cell electrolyte concentration to 25%. The new weight of electrolyte (L) and percent KOH final (M) represents the effect of charge and precharge. Percent KOH of the electrolyte after precharge only is found to be 29.9%.

The reverse of that described above occurs during discharge of the cell. However, the precharge is fixed, and thus, even though a cell is in the discharged and shorted condition the concentration of electrolyte in the cell is lower than the initial concentration by approximately 1%.

Table II. Effect of charge and precharge on electrolyte concentration

A Capacity (A-hr)	I % KOH after charge	J Suggested precharge (A-hr)	K Additional water (g) (0.34 g/A-hr)	L New weight of electrolyte H + K	M % KOH final D/L
6	25.7	2.60	0.88	29.10	24.9
12	25.7	5.20	1.77	58.22	24.9
20	26.2	9.80	3.33	107.81	25.4

A more correct cell reaction.—The complex reaction at the nickel hydroxide electrode is not described in the cell reactions above. Several authors (1, 2) have discussed the absorption of water and KOH at the nickel hydroxide electrode. An equation given by Falk and Salkind (3) is considered more correct than the general one given in Eq. [3]

$$2Ni(OH)_2{}^* + Cd(OH)_2 + \sim 0.1KOH_{(aq)} \underset{\text{discharge}}{\overset{\text{charge}}{\rightleftharpoons}} 2NiOOH^* \cdot (\sim 0.1KOH_{ads}) + Cd + 2H_2O \quad [6]$$

where the asterisk represents an unknown quantity of adsorbed water. Considering this reaction in place of the general one will provide information if there is a more severe drop in electrolyte concentration during cell operation than predicted by Eq. [3].

During charge the net change is a loss of 0.05 mole of KOH from aqueous solution to the bound adsorbed state for every 26.8 A-hr (0.104 g/A-hr). This is in addition to an increase in 1 mole of water during the charge for every 26.8 A-hr (0.67 g/A-hr). The effect of using the corrected equation is given in Table III. This table is similar to Table I for the uncorrected equation. Note that the electrolyte concentration (column R) is lower by almost 2% when compared with the concentration calculated using Eq. [3] (column I, Table I). The addition of precharge to the electrode balance has the same effect of decreasing concentration during charge as in the uncorrected equation. The reason is that the corrected positive electrode reaction need not be considered during overcharge. The results (a continuation of Table III) are given in Table IV. The concentration has changed by less than 1% due to precharge, comparing column R (Table III) and column T (Table IV). Note the 2% difference in final electrolyte concentration using the uncorrected equation (column M, Table III) and using the corrected equation (column T, Table IV).

Concentration and depth of discharge (DOD).—As described above, there is an increase in water (decrease in concentration) on charge and decrease in water (increase in concentration) on discharge. The concentrations have been calculated for 25, 50, 75, and 100% (DOD), and full discharge for each of the 6, 12, and 20 A-hr size cells, and are plotted in Fig. 1 for the precharge values given in column J of Table IV. The concentration of KOH in the fully discharged cell containing precharge is found from the following equation

$$\%\ KOH(\text{discharged}) = \frac{g_{KOH}}{g_{soln}} 100 \quad [7]$$

where

$$g_{KOH} = (\%\ KOH)_i v_i d_i / 100$$

and

$$g_{soln} = v_i d_1 + 0.34\ \text{A-hr}_p$$

$(\%\ KOH)_i$ refers to the concentration of KOH in the initial volume, v_i, of the electrolyte whose density is d_i. A-hr$_p$ is the quantity of negative electrode precharge in ampere hour, d_i is the density of the initial KOH, and 0.34 is the conversion factor relating A-hr to equivalent weight of the negative electrode. The electrolyte concentration can be estimated for any condition of charge or discharge from the following equation

Table III. Change in electrolyte concentration during charge—corrected equation

A Cell capacity (A-hr)	D Weight of KOH (g)	E Weight of H_2O (g)	G Increase in H_2O (g)	N Decrease in KOH (g)	P Net KOH weight D − N	Q Weight of solution E + G + P	R Percent KOH P/Q	Δ Column R-column I (%)
6	7.25	16.15	4.82	(0.76)	6.41	27.49	23.6	−2.1
12	14.50	32 29	9.68	(1.51)	13.00	54.98	23.7	−2.0
20	27.40	61.00	16.08	(2.52)	24.88	101.96	24.4	−1.8

Table IV. Effect of charge and precharge electrolyte concentration—corrected equation

A Cell capacity (A-hr)	J Suggested precharge (A-hr)	K Additional water (g)	S Total solution weight K + Q (g)	T Percent KOH P/S	Δ′ Column T-column R	Δ″ Column T-column M
6	2.60	0.88	28.34	22.9	−0.7	−2.0
12	5.20	1.77	56.71	22.9	−0.8	−2.0
20	9.80	3.33	105.29	23.6	−0.8	−1.8

$$\% \text{ KOH} = \frac{g_{KOH} - \text{A-hr}_{NC}(1.2)(0.104)(CHG)}{\text{A-hr}_{NC}(1.2)(0.670 - 0.104)(CHG) + g_{soln}} \quad [8]$$

where A-hr_{NC} is the nominal capacity of the cell, 1.2 is the factor that accounts for the capacity in excess of the nominal cell capacity, 0.104 is the equivalent weight of KOH removed from electrolyte during charge, and 0.670 is the equivalent weight of water produced during charge. CHG is the fractional charge related to the cell capacity by CHG = 1.00 − DOD, where DOD is the fractional depth of discharge.

The validity of these equations was confirmed by measurements on 6 A-hr hermetically sealed, aerospace nickel-cadmium cells. These cells which are included in an accelerated test program contained varying concentrations (22-38%), volumes (17.5-21.5 ml) of electrolyte, and amounts of precharge (2.2-3.3 A-hr). As part of the program, the cells were opened and analyzed by the accepted procedure (5). The results are given in Table V. These cells had been subjected to manufacturer's electrical tests and preliminary electrical evaluation tests before electrolyte analysis. All cells were analyzed in the discharged condition. The differences between observed and calculated results are relatively consistent (2-5%) and may be related to the error introduced by the assumption that all the electrochemical reactions are completely reversible. Equation [6] is correct as written and the initial changes that occur during the cell activation processes are insignificant.

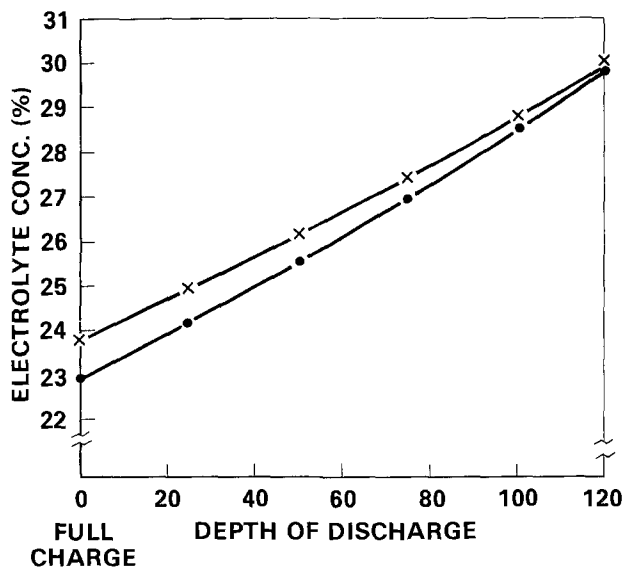


Fig. 1. Electrolyte concentration as a function of depth of discharge. 6 and 12 A-hr cell, × 20 alternating cell.

Table V. Verification of corrected Eq. [6]

Cell	Initial Percent KOH	Initial KOH ml	A-hr pre-charge	Final Total g KOH Found*	Final Total g KOH Calculated	Percent difference**
38	30	21.5	2.8	8.02	8.34	4
67	34	18.5	2.5	8.23	8.37	2
1	22	19.5	2.8	5.08	5.17	2
13	30	19.5	2.2	7.25	7.54	4
23	30	17.5	2.8	6.55	6.27	3
230	38	19.5	2.8	9.84	10.20	4
56	30	19.5	3.3	7.22	7.54	4
213	30	19.5	2.8	7.18	7.54	5

* Corrected for carbonate content.
** Percent difference = $\frac{\text{g KOH (calculated)} - \text{g KOH (found)}}{\text{g KOH (found}} \times 100.$

Open-circuit potentials.—The equilibrium potentials of the half-cells and the over-all cell depend upon the concentrations of the electrolyte and the temperature. The Nernst equations for the half-cell reactions can be written at any temperature (t) using the standard equilibrium reduction potentials

$$E_{pos}(t) = E^\circ_{pos}(t) - \frac{RT}{2F}\ln\frac{a_{OH^-}}{a_w^2} = E^\circ_{pos}(t) - \frac{RT}{F}\ln\frac{a_{OH^-}}{a_w} \quad [9]$$

$$E_{neg}(t) = E^\circ_{neg}(t) - \frac{RT}{2F}\ln a_{OH^-}{}^2 = E^\circ_{neg}(t) - \frac{RT}{F}\ln a_{OH^-} \quad [10]$$

where R is the gas constant, T is the absolute temperature in °K, $\mathbf{F}$ is the Faraday, and a_w and a_{OH^-} are the activities of the water and hydroxyl ion, respectively. $E^\circ_{pos}(t)$ is $E^\circ_{pos}(25°C) + (dE/dT)(t - 25)$ or $+0.518V - 0.0004$ V/deg $(t - 25)$ (6), and $E^\circ_{neg}(t)$ is $-0.809V - 0.000143$ V/deg $(t - 25)$ (7). $R/\mathbf{F}$ is equal to 8.619×10^{-5}. For the composite cell reaction at any temperature

$$E_{cell}(t) = E_{pos}(t) - E_{neg}(t) = E^\circ_{cell}(t) + 8.619 \times 10^{-9} \ln a_w$$

where

$$E^\circ_{cell}(t) = E^\circ_{pos}(t) - E^\circ_{neg}(t)$$

Variation of Potential with Hydroxide Concentration and Temperature

In order to calculate the variation of the cell potential with the concentration of the hydroxide in the electrolyte and the temperature of the cell, the activities of the water at various concentrations of the hydroxide must be known. These activities can be

found from the vapor pressure lowering of various hydroxide solutions. Then, Eq. [11] becomes

$$E_{cell}(t) = E°_{cell}(t) + 8.619 \times 10^{-5} + \ln (p/p°) \quad [12]$$

where p is the vapor pressure of the water over the hydroxide solution, and $p°$ is the vapor pressure of pure water at the same temperature. Bro and Kang (8) have measured the vapor pressures of hydroxide solutions at various temperatures. They found that the variation of the vapor pressure with temperature for a given hydroxide concentration can be expressed as

$$p = A \exp (-B/T) \text{ or } \ln p = \ln A - (B/T)$$

where A and B are constants for each hydroxide concentration. The values for these constants are given in Table VI for the six concentrations used in these calculations. Substituting this equation into Eq. [12], the cell potential becomes

$$E_{cell}(t) = E°_{cell}(t) + 8.619 \times 10^{-5}T(\ln A - (B/T) - \ln p°)$$

or

$$E_{cell}(t) = E°_{cell}(t) + 8.619 \times 10^{-5} [T(\ln A - \ln p°) - B] \quad [13]$$

The potentials for the whole cell at six concentrations of KOH (10.3-45.2%) whose vapor pressures were measured are given in Table VII at various temperatures (0°-40°C). The cell potentials are plotted in Fig. 2.

The calculation of the individual half-cell potentials (Eq. [9] and [10]) require the activities of the hydroxide ions as well as the activity of water. Akerlof and Bender (9) have made the electromotive force measurements that allow the calculation of the mean activity coefficient of KOH at various temperatures and at concentrations of as high as 18M. The activity of the hydroxide ion is related to the mean activity coefficient of KOH, $\gamma_\pm$ by $a_{OH^-} = \sqrt{\gamma_\pm M}$, where M is the molality of the hydroxide solution. The half-cell potentials for both the positive and negative electrodes using the activities calculated in this manner are given in Table VII at various concentrations of the hydroxide and at various temperatures. The potentials are also plotted in Fig. 3a and 3b.

Table VI. Constants for equation $\ln p = \ln A - (B/T)$ for KOH*

Percent KOH	Molality	ln A	B
10.3	2.04	21.67	5546
14.8	3.08	21.34	5457
23.0	5.32	21.52	5564
30.3	7.75	21.29	5572
37.0	10.5	20.36	5423
45.2	14.7	22.29	6330

* From Bro and Kang (8).

Table VII. Cell potentials at various KOH concentrations and temperatures, V

Percent KOH	E_{cell}	E_{pos}	E_{neg}	Percent KOH	E_{cell}	E_{pos}	E_{neg}
	t = 0°C				t = 25°C		
10.3	1.335	0.517	−0.812	10.3	1.324	0.507	−0.816
14.8	1.334	0.508	−0.820	14.8	1.321	0.496	−0.825
23.0	1.328	0.488	−0.833	23.0	1.316	0.478	−0.839
30.3	1.320	0.468	−0.846	30.3	1.308	0.457	−0.851
37.0	1.310	0.445	−0.859	37.0	1.296	0.431	−0.864
45.2	1.287	0.406	−0.876	45.2	1.278	0.397	−0.882
	t = 10°C				t = 30°C		
10.3	1.330	0.513	−0.814	10.3	1.321	0.505	−0.817
14.8	1.329	0.504	−0.822	14.8	1.320	0.495	−0.825
23.0	1.323	0.484	−0.836	23.0	1.314	0.475	−0.839
30.3	1.316	0.464	−0.848	30.3	1.306	0.454	−0.852
37.0	1.304	0.439	−0.861	37.0	1.293	0.428	−0.866
45.2	1.284	0.402	−0.878	45.2	1.277	0.396	−0.882
	t = 20°C				t = 40°C		
10.3	1.326	0.509	−0.816	10.3	1.317	0.502	−0.819
14.8	1.324	0.499	−0.824	14.8	1.315	0.492	−0.827
23.0	1.318	0.480	−0.838	23.0	1.309	0.472	−0.841
30.3	1.310	0.459	−0.850	30 3	1.301	0.451	−0.854
37.0	1.298	0.434	−0.863	37.0	1.288	0.424	−0.867
45.2	1.280	0.399	−0.880	45.2	1.273	0.393	−0.884

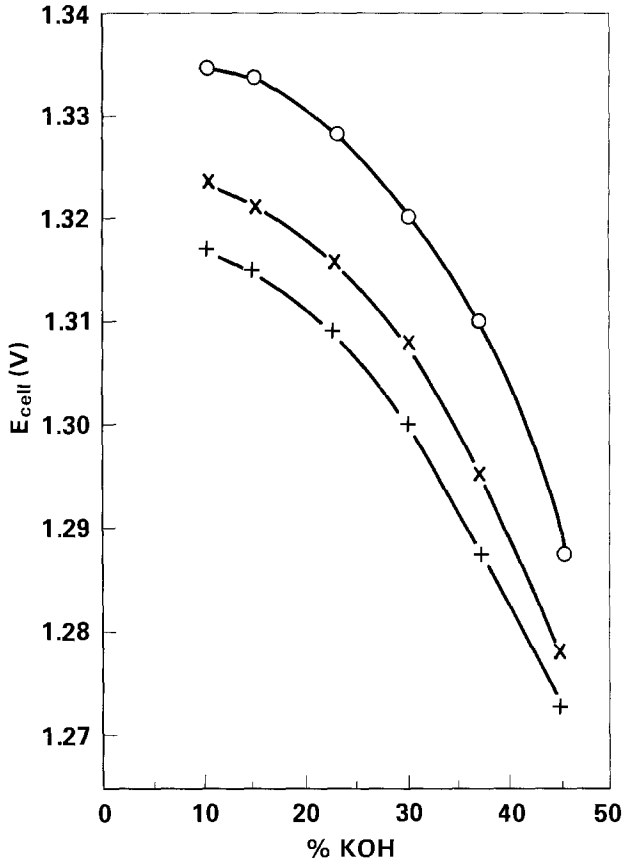


Fig. 2. Variation of cell open-circuit potential with electrolyte concentrations. ○, 0°; ×, 25°; +, 40°C.

The potential change of the negative electrode over the 20-30% KOH range at 25°C is 12 mV. The positive electrode changes by 21 mV over the same range. Although the half-cell potentials differ by 12 and 21 mV, respectively, over the 10% KOH range, the cell potential which is the difference between these half-cells changes by only 9 mV.

The average temperature coefficient for the cell potential is −0.45 mV/deg in this range of KOH concentrations. Values found experimentally vary with the type of construction of the cells (10). Pocket-plate or tubular-plate electrodes give values of −0.3 to −0.4 mV/deg, depending upon the capacity of the cell. The range with pressed-plate electrodes is −0.16 to −0.25 mV/deg, and with sintered-plate electrodes the range is −0.16 to −0.5 mV/deg.

The average temperature coefficient for the positive electrode is similar to that of the cell potential, 0.41 mV/deg. The average coefficient for the negative electrode is smaller than the others, −0.19 mV/deg. The temperature coefficient for all cases is greatest with the concentration of KOH of 37.0%.

Early in this century, Zedner (11) found that a change from 40 to 24% KOH led to a change in the calculated voltage of 0.04V, which is comparable in magnitude to the voltage changes in Table VII. Falk (12) measured the cell voltage at three concentrations of KOH, and found that the potential decreased about 0.07V as the concentration increased from 5 to 45% KOH. He also found that the experimental and theoretical variation of the negative electrode's potential

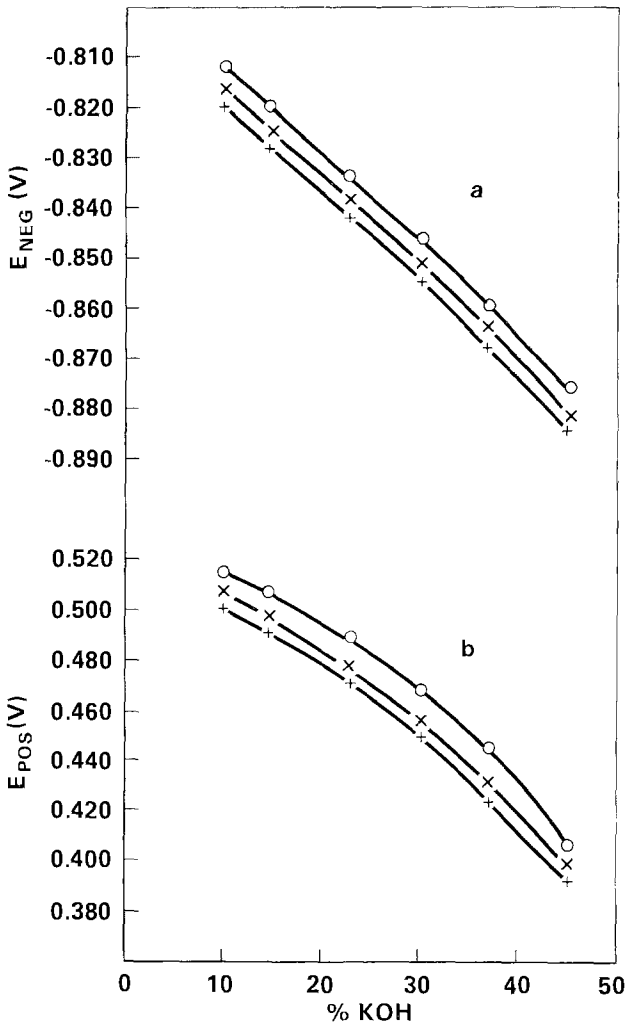


Fig. 3. Variation of open-circuit potentials of negative electrode (a) and positive electrode (b). ○, 0°; ×, 25°; +, 40°C.

with the concentration was in agreement. As can be seen from the plot in Fig. 3a, there is not quite a linear relationship, particularly at concentrations below 10%. Falk (12) also observed that the potential at the positive electrode varied in a manner similar to that shown in Fig. 3b. The experimental values differed from those calculated from the Nernst equation for the positive electrode.

Variation of Cell Potential with Depth of Discharge

Figure 1 gives the variation of the electrolyte concentration with depth of discharge. The open-circuit potential can then be evaluated from Fig. 1 and 2. The variation of the cell potential with DOD is shown in Table VIII. The variation in the cell open-circuit potential from full charge to complete discharge is in the order of 8 mV, and does not vary to any extent with the capacity of the cell.

Table VIII. Cell potentials at various depths of discharge*

Capacity Percent DOD	6 A-hr Percent KOH	E_{cell}	12 A-hr Percent KOH	E_{cell}	20 A-hr Percent KOH	E_{cell}
Full charge	22.9	1.316	22.9	1.316	23.6	1.315
25	24.2	1.315	24.2	1.315	24.8	1.314
50	25.5	1.314	25.9	1.314	26.0	1.313
75	27.0	1.311	27.0	1.311	27.3	1.311
100	28.5	1.309	28.5	1.309	28.9	1.309
120	29.8	1.308	29.9	1.308	29.9	1.308

* Percent KOH from Fig. 1, and E_{cell} from Fig. 2 at 25°C.

Manuscript submitted Dec. 13, 1976; revised manuscript received May 5, 1977.

Any discussion of this paper will appear in a Discussion Section to be published in the June 1978 JOURNAL. All discussions for the June 1978 Discussion Section should be submitted by Feb. 1, 1978.

Publication costs of this article were assisted by Goddard Space Flight Center.

REFERENCES

1. B. C. Bradshaw, *Proc. Ann. Power Sources Conf.*, **12**, (1958); B. V. Ershler, G. S. Tyurikov, and A. S. Smirhova, *J. Phys. Chem. (Moscow)*, **14**, 985 (1940); F. Kornfeil, *Proc. Ann. Power Sources Conf.*, **12**, 1 (1958).
2. P. L. Bourgault and B. E. Conway, *Can. J. Chem.*, **38**, 1557 (1960).
3. S. U. Falk and A. J. Salkind, "Alkaline Batteries," p. 54, John Wiley & Sons, Inc., New York (1969).
4. "Accelerated Test Program for Sealed Nickel Cadmium Spacecraft Batteries/Cells", Rept. Contract WQEC/C 76-B (Feb. 13, 1976).
5. G. Halpert, O. Ogunyankin, and C. Jones, Procedure for Analysis of Nickel-Cadmium Cell Materials, GSFC X-761-73-314 (1973).
6. A. J. Salkind and P. F. Bruins, *This Journal*, **109**, 356 (1962).
7. A. J. deBethune, T. S. Licht, and N. Svendeman, *ibid.*, **106**, 616 (1959).
8. P. Bro and H. Y. Kang, *ibid.*, **118**, 1430 (1971).
9. G. C. Akerlof and P. Bender, *J. Am. Chem Soc.*, **70**, 2366 (1948).
10. E. W. Broomman, "An Annotated Bibliography of the Thermal Properties of Primary and Secondary Cells," Rept. AFAPL-TR-70-34 (June 1970).
11. J. Zedner, *Z. Elektrochem.*, **22**, 463 (1906); quoted in J. T. Crennell and F. M. Lea, "Alkaline Accumulators," p. 96, Longman, Greens and Co., London (1928).
12. S. U. Falk, *This Journal*, **107**, 661 (1960).

Pore Volumes and Densities of Unformed Pastes of Lead Acid Battery Plates

II: Tetrabasic Lead Sulfate Pastes

W. J. Schlotter and C. W. Fleischmann*

Eltra Corporation, C&D Batteries Division, Plymouth Meeting, Pennsylvania 19462

ABSTRACT

The values of specific pore volume, v, and the solids' density, d, were determined for unformed lead-acid battery pastes prepared from $4PbO \cdot PbSO_4$. v varied with D, the apparent density of the dry paste according to $v = 0.398 - 0.0698D$. The parameters d and D were related by $d = D(0.0698D^2 - 0.398D + 1)^{-1}$. By that relationship, however, d is variant with D, an unexpected result. It is proposed that the variance results because the crystals of $4PbO \cdot PbSO_4$ tend to orient in tight bundles, especially for the pastes with the highest values of D. Such bundles entrap open pits on the crystal surfaces, and the measured values of d are then reduced.

A previous report (1) dealt with the pore volumes and densities of dry pastes of acidified lead oxides when these were used to prepare the active material of electrodes for the lead-acid battery. The methods for making such electrodes are well known (2, 3). This report presents data for pastes prepared from tetrabasic lead sulfate rather than lead oxide.

Biagetti and Weeks (4) and Yarnell (5, 6) have described the use of tetrabasic lead sulfate, $4PbO \cdot PbSO_4$, for the manufacture of electrodes for the lead-acid battery. Pastes using $4PbO \cdot PbSO_4$ are prepared from water rather than acid. In contrast to the traditional mixtures (2, 3), no chemical reactions occur (6). Positive electrodes prepared from tetrabasic lead sulfate pastes were reported to provide (4, 5) improved cycling characteristics compared to electrodes from traditional pastes. Cycle life increased with the apparent density of the active material (4).

Pastes prepared from $4PbO \cdot PbSO_4$ are characterized, in this report, in terms of the relationship between the specific void volume, v (cm^3/g), the density of the solids, d (g/cm^3), and the apparent density, D (g/cm^3).

Experimental

Tetrabasic lead sulfate was obtained from both Eagle-Picher Industries and Halstab Incorporated. Several lots from each supplier were employed. Density measurements of the starting materials were by means of gas pycnometry and were a purchased service from Micromeritics Instrument Corporation, Norcross, Georgia.

Values of the wet paste density, the dry paste density, and the pore volume of the pastes were determined by techniques described earlier (1). As for conventional pastes (1), the wet and dry paste densities were found to be linearly related for a fixed grid thickness and mode of pasting. Using such relationships, any preselected dry paste density could be obtained.

Different wet paste densities were obtained by changing the amounts of water (4, 6) added to the solids and by varying the mixing time (6). The pastes were applied by hand to conventional, flat, industrial-type battery grids (2) of thicknesses 4.1, 6.8, and 7.9 mm. Grids of 6.4 mm thickness of the design used for the new cylindrical batteries for telephone exchanges (7) were loaded with paste by a special factory technique (10).

The scanning electron micrographs were obtained as a purchased service from SKF Industries, King of Prussia, Pennsylvania. Prior to examination, the samples, were gold-coated to make them conductive.

The linear regressions and simple linear correlations were calculated using the programs in the Texas Instruments Calculator, Model SR-51A.

Results and Discussions

Starting materials.—The density of the commercial tetrabasic lead sulfate was measured to be 7.94 ± 0.03 g/cm^3 by helium pycnometry. This value is 2.6% lower than the theoretical value, 8.15 g/cm^3 (8). The lower density of the commercial product is attributed to occluded voids. Numerous gross imperfections in the crystals, especially the tendency to develop hollow cores, may be seen in the scanning electron micrographs (Fig. 1-5). The crystals of $4PbO \cdot PbSO_4$ are the large prismatic masses that appear in the scanning electron micrographs. Occasionally fine filaments are visible in addition to the prisms, as in Fig. 1. These filaments develop if moist $4PbO \cdot PbSO_4$ is exposed to air. They are taken to be slight carbonation (6).

It is instructive to compare the surfaces of the crystals before and after preparation into a pasted

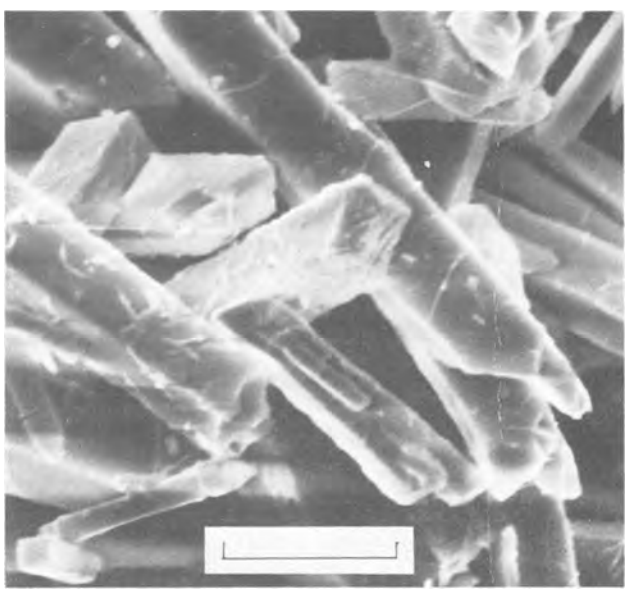


Fig. 1. $4PbO \cdot PbSO_4$ crystals prior to plate preparation. Marker equals 5μ.

* Electrochemical Society Active Member.

Key words: accumulator, electrode porosity, electrode density.

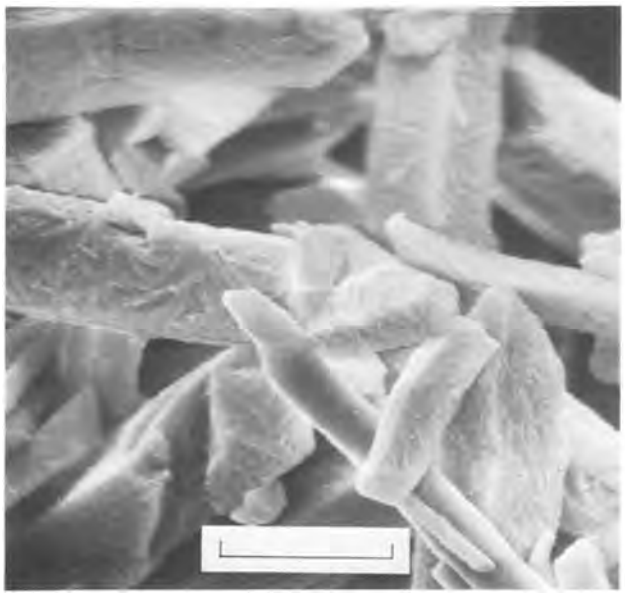


Fig. 2. $4PbO \cdot PbSO_4$ crystals of the same lot as shown in Fig. 1, but after preparation in a pasted plate with a dry paste density of 3.49 g/cm^3. Marker equals 5μ.

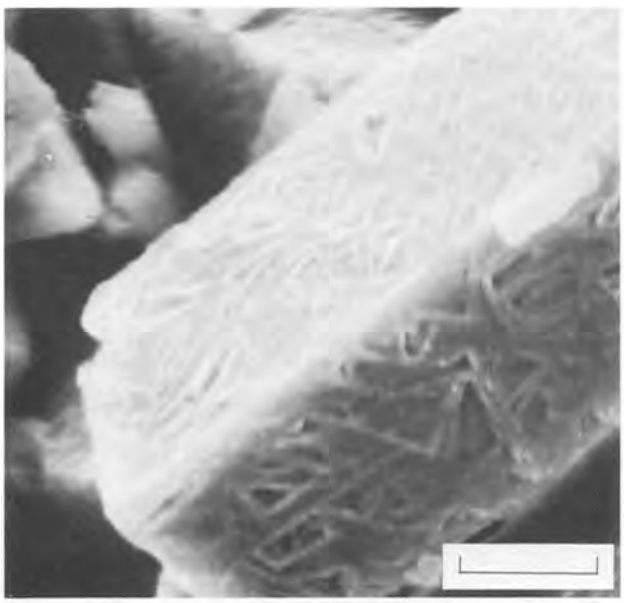


Fig. 3. Single $4PbO \cdot PbSO_4$ crystals in a pasted plate with a dry paste density of 4.52 g/cm^3. Note the surface imperfections and holes. Marker equals 2μ.

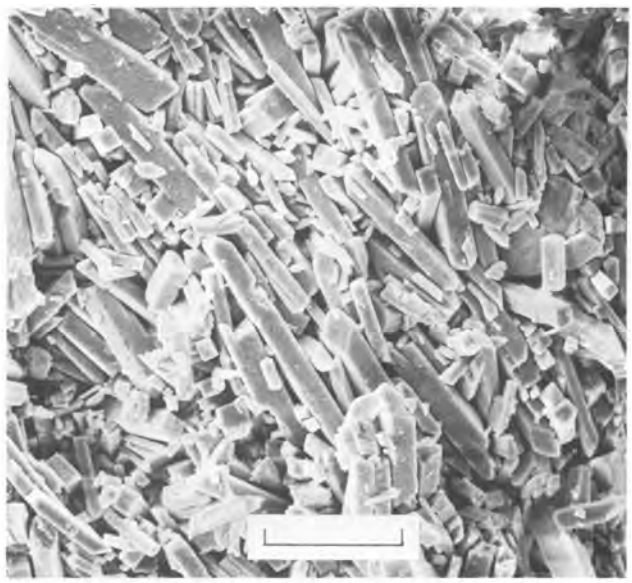


Fig. 4. Cross section of pasted plate prepared from $4PbO \cdot PbSO_4$ at a dry paste density of 4.52 g/cm^3. The random size of the crystals and the close packing in a high density paste are shown. Marker equals 20μ.

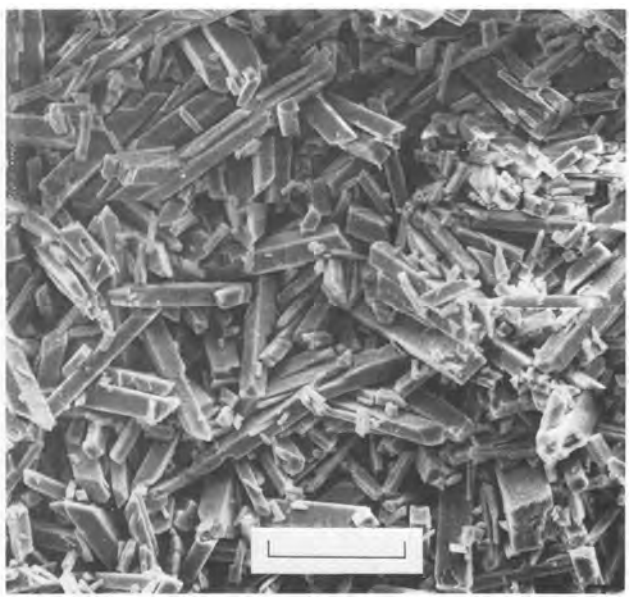


Fig. 5. Cross section of pasted plate prepared from $4PbO \cdot PbSO_4$ at a dry paste density of 3.49 g/cm^3. The random size of the crystals and the loose packing in a low density paste are shown. Marker equals 20μ.

plate, Fig. 1 and 2, respectively. The surfaces of the $4PbO \cdot PbSO_4$ crystals appear to have become rougher as a result of pasting and curing. It is assumed that the roughing is due to abrasion caused by the mixing action, and is not the result of dissolution, since the crystals do not react with the water (6). Scanning electron microscopic examination of the crystals before and after aqueous washes also confirmed no changes of the surface.

Specific void volume vs. dry paste density.—The specific pore volumes of the pastes are plotted against the dry paste densities in Fig. 6. Data are not distinguished according to plate thickness nor method of pasting because no systematic correlations were observed. The data obey the straight line given by Eq. [1] with a correlation coefficient of 0.966. In Fig. 6, Eq. [1] is described by the solid line through the data points. The meaning of the broken line is discussed below.

The relationship given in Eq. [1] is similar to that given in Eq. [R1], previously determined for conventional pastes in which $4PbO \cdot PbSO_4$ was developed *in situ* by means of a special curing process (1)

$$v = 0.398 - 0.0698D \quad [1]$$

$$v = 0.356 - 0.0569D \quad [R1]$$

$$v = 0.271 - 0.0415D \quad [R2]$$

Both Eq. [1] and [R1] are different from the line defined by Eq. [R2]. The latter was obtained from data for conventional pastes, in which the curing

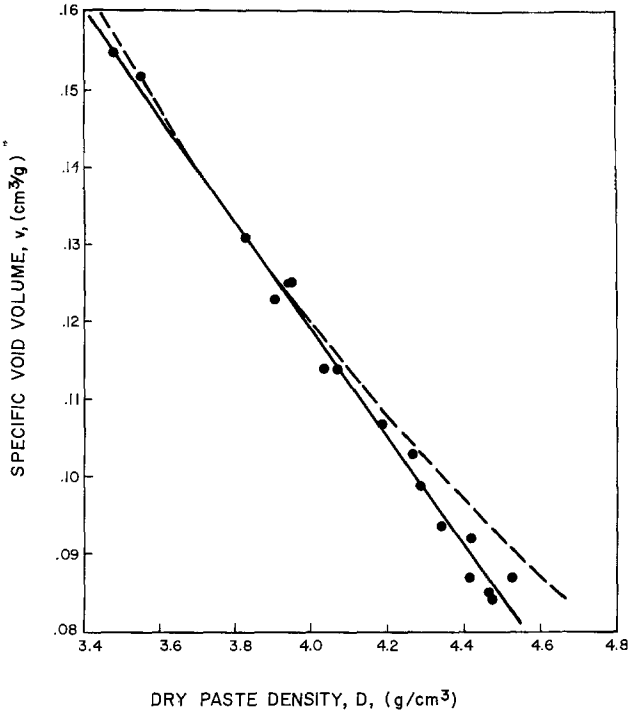


Fig. 6. Specific void volumes of dry pastes of 4PbO · $PbSO_4$ plotted against the corresponding dry paste densities (points and solid line). The broken line is calculated for the specific void volumes corresponding to pastes with solids of constant density at 3.79 g/cm³ (the maximum value in Fig. 7).

process did not develop $4PbO \cdot PbSO_4$ (1). According to Eq. [1] and [R1], both the paste that contained $4PbO \cdot PbSO_4$ crystals as the starting material and that in which $4PbO \cdot PbSO_4$ was formed *in situ* have more void volume at a given dry paste density than pastes not treated to develop $4PbO \cdot PbSO_4$. It has been previously reported (9) that pastes of $4PbO \cdot PbSO_4$ are more porous than conventional pastes, but, because of the different relationships that exist between v and D, it is misleading to compare porosities without specifying a fixed dry paste density.

The volume density, D^{-1}, occupied by a unit weight of paste must be the sum of the void volume, v, and the volume d^{-1}, occupied by the solids portion of the paste, as given in Eq. [2]

$$D^{-1} = d^{-1} + v \qquad [2]$$

From Eq. [1] and [2]

$$d = D(0.0698D^2 - 0.398D + 1)^{-1} \qquad [3]$$

The function given by Eq. [3] is plotted in Fig. 7. At D = 3.79 g/cm³, d goes through a maximum value of 7.67 g/cm³. Since pastes of $4PbO \cdot PbSO_4$ are unreactive, it was unexpected that d should be variant with D. In Fig. 6, the dashed line corresponds to an invariant value of d. That value was arbitrarily selected at 7.67 g/cm³ for comparison purposes. Observing the fit to the data of that line compared to the solid line, it is apparent that d is variant.

Yarnell (6) presented scanning electron micrographs to illustrate how the crystals of $4PbO \cdot PbSO_4$ tend to fagot. Figures 4 and 5 represent an observation, from the present study, that the fagoting increased with dry paste density. There is little adhesion between the individual crystals. Crystals which are not held in place or trapped by other crystals are often displaced by the force of the electron beam when examining the samples by scanning electron microscopy. This displacement results in loss of part of the gold coating, and an incomplete picture, as may be seen in Fig. 5 where several lines cross the photograph and the crystals appear to be sheared off.

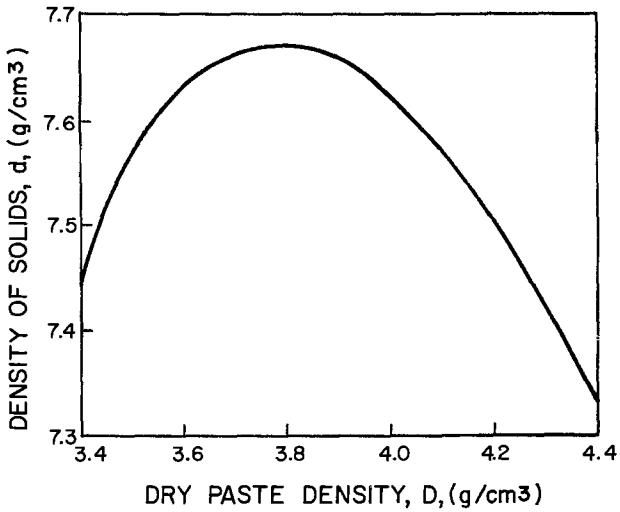


Fig. 7. Calculated density of the solids in the dry pastes as a function of the dry paste density for pastes of 4PbO · $PbSO_4$.

As the contiguous surfaces of the crystals become more tightly packed, open-surface voids become occluded voids, and the measured solids' density decreases. By that interpretation, however, a minimum of fagoting occurred when the dry paste density was 3.79 g/cm³ (Eq. [3] or Fig. 7), rather than at the lowest dry paste density. The points at the low values of D, however, could be fitted to either the variant or invariant relationships. Therefore, the decrease in d for values of D less than 3.79 g/cm³, may be an artifact due to assuming the linear relationship over the entire range of the data. On the other hand, the act of abrasion on the crystals, discussed above, may significantly contribute to the surface voids, and the abrasion may be a complex function of the variables used to adjust the paste density.

Conclusions

A linear relationship was found between specific void volume and dry paste density for battery pastes prepared from $4PbO \cdot PbSO_4$. This relationship is similar to that for conventional pastes in which the $4PbO \cdot PbSO_4$ crystals were formed *in situ*. The specific void volumes of pastes containing $4PbO \cdot PbSO_4$, regardless of origin, were greater than for pastes which did not contain $4PbO \cdot PbSO_4$. Unexpectedly, the density of the solids in the pastes made from $4PbO \cdot PbSO_4$ varied with the dry paste density. This variance may result from the dominant alignment of the faces of the $4PbO \cdot PbSO_4$ crystals in the pastes of highest densities because voids on the surface become trapped and occluded.

Acknowledgments

This work was supported, in part, by Eltra Corporation's Prestolite Battery Division. The authors thank Mr. D. Kemble Bauman, who conducted much of the experimental work, and Mr. Joe Gunder of the C&D Batteries plant in Leola, Pennsylvania, who supplied the factory-loaded plates.

Manuscript received May 17, 1977.

Any discussion of this paper will appear in a Discussion Section to be published in the June 1978 JOURNAL. All discussions for the June 1978 Discussion Section should be submitted by Feb. 1, 1978.

Publication costs of this article were assisted by Eltra Corporation.

LIST OF SYMBOLS

- D density of the dry paste, the apparent density, g/cm^3
- d density of the solids' portion of the dry paste, g/cm^3
- v specific void volume of the dry paste, cm^3/g

REFERENCES

1. C. W. Fleischmann and W. J. Schlotter, *This Journal*, **123**, 969 (1976).
2. G. W. Vinal, "Storage Batteries," 4th ed., John Wiley & Sons, Inc., New York (1967).
3. J. F. Dittman and H. R. Harner, "Paste Preparation and Plate Control, Starting and Lighting Batteries," No. 7, Eagle-Picher Company, Cincinnati (1956).
4. R. V. Biagetti and M. C. Weeks, *Bell Syst. Tech. J.*, **49**, 1305 (1970).
5. C. F. Yarnell, Paper 31 presented at The Electrochemical Society Meeting, New York, New York, October 13-17, 1974.
6. C. F. Yarnell, Paper 32 presented at The Electrochemical Society Meeting, New York, New York, October 13-17, 1974.
7. D. E. Koontz, D. O. Feder, D. Babusci, and H. J. Luer, *Bell Syst. Tech. J.*, **49**, 1253 (1970).
8. J. Burbank, *This Journal*, **113**, 10 (1966).
9. E. Skoluda, B. Szczesniak, and S. Tabat, *Przem. Chem.*, **54**, 648 (1975).
10. A. H. Haller, J. J. Larkin, and R. P. Walters, U.S. Pat. 3,782,595 (1974) and 3,841,362 (1974).

Lithium-Aluminum Electrode

B. M. L. Rao,* R. W. Francis,* and H. A. Christopher

Exxon Research and Engineering Company, Linden, New Jersey 07036

ABSTRACT

Lithium-aluminum anodes were investigated as a possible approach to minimizing the lithium dendrite problem in organic electrolyte secondary cells. Electroformation and pyrometallurgical techniques were used in the preparation of the electrodes. The equilibrium emf composition relationship and the cycling behavior were evaluated. This paper reports that under certain conditions Li-Al compositions approaching lithium potentials may be used, reducing the voltage penalty required to minimize the dendrite problem.

Dendritic deposition of lithium appears to be an adverse phenomenon encountered in the development of high energy density rechargeable lithium organic electrolyte cells. This has been discussed in a recent review (1). It is hypothesized that freshly deposited lithium is highly active, and it reacts with most solvents and/or associated impurities in the cells resulting in dendritic plating. Use of purified solvents that do not have any intrinsic reactivity to lithium is one other solution to the problem. Yet another approach is to reduce the activity of the deposited lithium by alloying or by using lithium intermetallics so that the anode material will not react with the purified solvent. This paper reports the behavior of lithium-aluminum electrodes studied in context with the latter approach.

Lithium alloys/intermetallics of aluminum, magnesium, silicon, and boron have been studied for application in high temperature cells. Electroformation of a large number of lithium alloys/intermetallics in organic electrolytes was demonstrated by Dey (2). Detailed investigations of the lithium-magnesium electrodes in propylene carbonate have been reported by Nicholson (3). Galvanostatic polarization of lithium alloys containing 5 atomic percent (a/o) aluminum and magnesium has been measured by Sam and Ambrus (4). Cyclic voltametric investigations of the cathodic reduction of lithium on microcrystalline silicon have been studied by Antula and Becker (5). Investigations on electrochemical behavior of Li-Al alloy intermetallics in an organic electrolyte are presented in this paper.

Experimental

Both commercial powders and foils of Li-Al and electroformed samples were used in the experiments. The commercial alloys were procured from Foote Mineral Company, and the electroformed samples were prepared in the laboratory. The investigation covered 5-80 a/o lithium in Li-Al. All the measurements were carried out at room temperature (~25°C).

Porous Li-Al electrodes were fabricated in a helium dry box by pressure ($4.1 \times 10^4 - 6.9 \times 10^4$ kPa) sintering of Li-Al powder ($\leq 150\mu$) on nickel grids at 315°-360°C for ½ hr. The resultant electrodes were 35-45% porous and contained ~60 mA-hr/cm^2 lithium. The composition of starting material for the porous electrodes ranged from 50-67 a/o lithium.

Specific experiments.—Electroformation of Li-Al and the measurement of emf composition relationship.— Electroformation of Li-Al electrodes was carried out by coulometric cathodic charging of lithium into ($2.54 \times 2.54 \times 0.013$) cm^3 aluminum foil (99.999%) with nickel foil backing in a 2M $LiClO_4$ solution in a mixed solvent of tetrahydrofuran [70 volume percent (v/o)] and dimethoxyethane (30 v/o) using solvents distilled over Na-K alloy and anhydrous salt (H_2O in solution < 10 ppm). The working electrode was held in a parallel plate configuration with a lithium counterelectrode and a layer of microporous polypropylene (Celanese Celgard 2400 and fiberglass paper (65% porous) separator using a spring clamp. The assembly was held in a limited electrolyte configuration with a stack pressure of 70 kPa. The electroformation of Li-Al was carried out at 3.8 mA/cm^2 in a successive sequence of 30 min charging and 15 min open-circuit periods. Using a lithium reference electrode in the cell, the polarization voltage as well as the open-circuit emf of the aluminum half-cell, was measured. Upon attainment of a lithium-rich composition (~75 a/o) the procedure was reversed, and the working electrode was anodically stripped of lithium. Emf measurements were taken during the process. The composition of the electroformed Li-Al electrode was derived from a comparison of the total coulometric charge passed, and the lithium-aluminum phase diagram. This was based on the fact that the faradaic efficiency was 100% for charge-discharge.

* Electrochemical Society Active Member.

Key words: lithium cell, lithium-aluminum electrode, organic electrolyte cell.

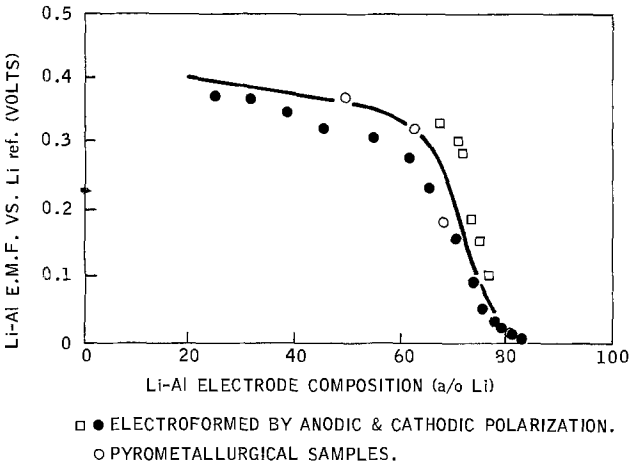


Fig. 1. Emf composition data

Data on the variation of equilibrium emf for porous Li-Al electrodes as a function of lithium content are given in Fig. 1 for both commercial and electroformed samples. Sharp variations expected in the Li-Al electrode potentials at and across phase boundaries is not delineated in the data of Fig. 1. This is not unreasonable, however, since the kinetics for complete solid-state equilibration would be more favorable at higher temperatures.

Cycling behavior of Li-Al electrodes.—In order to follow the cycling behavior of Li-Al electrodes, limited electrolyte cells containing 6.45 cm^2 Li-Al anodes (50 a/o Li) and 6.45 cm^2 pressed powder TiS_2 (6-9) cathodes were fabricated using the separators and stack pressure described earlier. The cell had suitable Li reference electrodes to monitor the anode and the cathode half-cells. The cells possessed capacity densities of 30 and 60 mA-hr/cm^2 for the TiS_2 cathode and Li-Al anode, respectively.

The Li/TiS_2 cells were cycled at 10 mA/cm^2 discharge and 2.5 mA/cm^2 charge in a continuous sequence, to 2.6 and 1.5V cut-off potentials *vs.* Li for the charging and discharging, respectively, using automatic cycling equipment. The selection of the cycling conditions adopted in the experiments was based on requirements for electric vehicle battery design (11) that would meet EPA urban cycle. The voltage-time behavior of the Li-Al anodes was followed during the process, and is presented in Fig. 2.

X-ray diffraction studies on spent anodes.—X-ray diffraction analysis of the commercial samples of Li-Al

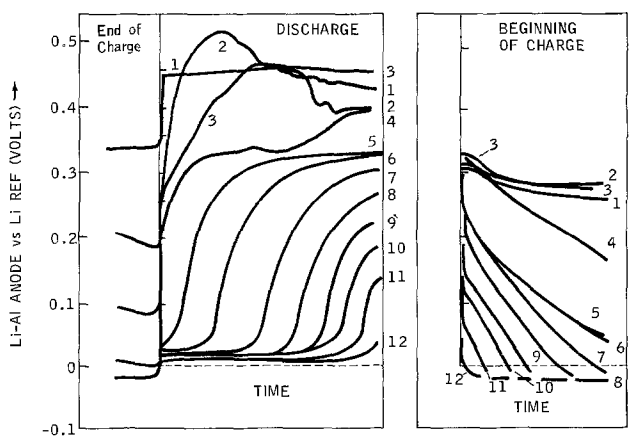


Fig. 2. Cycling data on β-LiAl in LiAl/TiS_2 cell

of composition 20, 30, and 34 weight percent (w/o) lithium was carried out to generate standards and for comparison with measurements made on cycled electrodes. A Phillips diffractometer generating CuK_α radiation was used in the analysis. Lattice spacing data obtained on spent electrodes are presented, and the composition is identified in Table I.

Results and Discussion

The equilibrium emf values of the electroformed Li-Al electrodes and those observed for commercial samples of Li-Al are given in Table II. It is noted that there is general agreement in the emf values observed during the electroformation for both charge and discharge, and these values agree with the measurements made on the electrodes from commercial samples of Li-Al at similar compositions. The former attests to the reversible behavior of Li-Al electrodes in the organic electrolyte. Based on the recent phase diagram of Settle, Myles, and Battles (10), the equilibrium emf values correspond to the compositions in Table II.

Extensive cycling of the electroformed Li-Al anodes could not be carried out because of the dendritic problem associated with the lithium counterelectrode. Examination of the electrode indicated a structural degradation of the aluminum foil with the formation of loosely adherent powder. Another difficulty associated with the electroformation was that the procedure followed was inapplicable for the formation of thick electrodes (40-60 mA-hr/cm^2) of homogeneous composition. The electrodes exhibited high overpotentials for discharge at high current densities, *i.e.*, $\eta = 0.25V$ at 10 mA/cm^2 at 50 a/o lithium. To circumvent these difficulties encountered in the case of the electroformed anodes, investigations were carried out on porous electrodes fabricated by the pyrometallurgical technique.

From a thermodynamic point of view, it is anticipated that β-LiAl may provide adequate protection as the equilibrium emf at this composition (50 a/o Li) is 0.375V more noble to the lithium potential in the same solution. Based on this, cycling of β-LiAl/TiS_2 cells was carried out. The open-circuit voltage of LiAl/TiS_2 cells was 2.175V, as expected. Data on the initial cycling behavior of the cells in a 10 mA/cm^2 discharge and 2.5 mA/cm^2 recharge is presented in Fig. 2. The

Table I. X-ray diffraction data on cycled β-LiAl electrodes

Lattice spacings observed on cycled LiAl electrode d(A)	Identification of possible phases of Li-Al from a comparison with the standard*
10.155	Li_9Al_4
8.750	Li_9Al_4, Li_3Al_2
7.2782	Li_9Al_4
4.1678	Li_9Al_4 or Li_3Al_2
3.6896	β-LiAl
2.3540	Li_9Al_4 (701)
2.2766	Li_9Al_4 or LiAl
2.3042	Li_3Al_2
1.9278	β-LiAl
1.6040	Li_9Al_4
1.4679	β-LiAl
1.4378	Li_9Al_4 or β-LiAl
1.3089	Li_9Al_4, Li_3Al_2 or β-LiAl
1.2239	β-LiAl

* Standard generated by lattice spacing measurements on 20, 30, and 34 w/o Li in Li-Al alloys.

Table II. Emf and composition relationship of Li-Al electrodes

Composition of phase	Lithium content (a/o)	Emf of Li-Al *vs.* Li (ref.) volts
(α + β)-LiAl	15-50	0.4-0.37
β-LiAl	46-56	0.37-0.365
β-LiAl + Li_3Al_2	56-60	0.365-0.350
Li_3Al_2 + Li_9Al_4	60-67	0.350-0.275
Li_9Al_4 + Li	>67	<0.275
Li	100	0.0

following behavior was observed during cycling: (*i*) The cells operated with a primary discharge of 64% cathode capacity, resulting in a change in anode composition from 50 to 35 a/o lithium, changing from β-LiAl to the ($\alpha + \beta$) Li-Al phases; (*ii*) the anode voltage exhibited a noisy discharge ± 0.005V during the first three cycles; (*iii*) there was an initial overshoot in the primary discharge of the β-LiAl half-cell. The magnitude of the overpotential gradually decreased as discharge progressed; (*iv*) the Li-Al half-cell potential gradually drifted toward the lithium electrode potential during successive recharge and discharge, and stabilized in about 12 cycles. The coulombic efficiency of the anode was 100%. The discharge behavior was similar to that observed on the 12th cycle during the next 150 cycles.

Examination of the spent anodes from extensively cycled β-LiAl/TiS_2 cells indicated active material delamination at the nickel grid, and loss of structural integrity similar to that observed on electroformed samples. The unsteady voltage behavior was attributed to these causes. It was noted that as long as the assembly was under a stack pressure, the delamination and structural degradation did not seem to interfere with the cycling capability of the electrodes. The initial overshoot is attributed to oxide film on the surface.

The change in emf of the Li-Al electrode with cycling is interesting. It appears from the data in Fig. 2 that the charging current is distributed between the reformation of the starting material, *i.e.*, β-LiAl and the formation of new phases that are rich in lithium content, *i.e.*, $Li_3Al_2 + Li_9Al_4$, $Li_9Al_4 + Li$, and the like. The formation of these lithium-rich phases was confirmed from x-ray diffraction analysis of the cycled Li-Al electrodes, and this is illustrated in Table I.

Based on the discharge-recharge potentials observed during cycling of β-LiAl electrodes in Fig. 2 and the x-ray diffraction data on the cycled half-cells, the following explanation may be hypothesized for the origin of the behavior, as illustrated in Fig. 3.

On the first discharge, lithium is removed from the initial LiAl β-phase to produce a two-phase alloy of α and β. Based on the high discharge rate and the low overpotentials, the lithium diffusion in the β-phase is apparently quite fast. According to the phase diagram (10), regions highly deficient in lithium from the α-phase, whereas adjacent regions consist of the less lithium-rich β-phase, *i.e.*, β_-. Thus, a certain ratio of β_- to α is established to account for the over-all change of lithium content from 50 to 35 a/o during discharge.

If one assumes a lithium diffusion coefficient in the β-phase which is greater than that in the α-phase, as suggested above, complete phase equilibration according to the phase diagram will not be attained on the subsequent recharge. The result is to shift the β_--phase to the lithium-rich side of the β-phase, *i.e.*, β_+. Due to the assumed lower lithium diffusion in α, this phase does not readily revert to β. As a result, the β-phase is driven on charge continuously through the β_+ boundary into the lithium-rich two-phase regions, $\beta + Li_3Al_2$ and $Li_3Al_2 + Li_9Al_4$. Successive cycling transforms the dynamic coexistence of these phases to more stable lithium-rich intermetallics, as evidenced by the lithium potential after the 12th cycle.

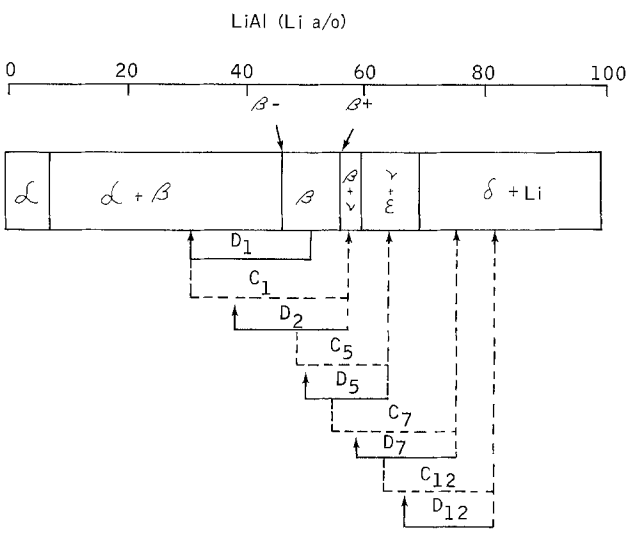


Fig. 3. Mechanism of voltage drift during cycling

It is of interest to note that no problems of cell shorting due to lithium dendrite were experienced after the 12th cycle, in spite of the negative electrode potential approaching 0V *vs.* Li^+/Li. This indicated that the chemical gradient due to the diffusion of lithium in the composition range of 60-80 a/o lithium is sufficient to absorb the deposited metal into the solid phase, thus preventing the dendritic growth. It is to be noted that problems due to dendritic growth may be encountered either by overcharging or by plating lithium at higher current densities.

The shift in lithium concentration at the Li-Al/electrolyte interface to a lithium-rich composition is time dependent, and reflects the relative lithium diffusion coefficients in the various Li-Al phases. Complete equilibration is therefore dependent on the experimental as well as any steady-state, cyclical changes in the morphology of the various phases that occur during cycling. It was observed that the electrode potential does not revert back to the initial value of 0.375V on open-circuit standing over a period of several days. Thus, it appears that the lithium-rich phases formed are stable, with the unexpected result that it has been possible to reduce the voltage penalty required to inhibit the dendrite growth by employing β-Li-Al electrodes.

Acknowledgments

The authors wish to thank Dr. J. A. Shropshire for helpful discussions, and M. T. Vidnansky for laboratory assistance.

Manuscript submitted March 4, 1977; revised manuscript received June 7, 1977. This was Paper 68 presented at the Las Vegas, Nevada, Meeting of the Society, Oct. 17-22, 1976.

Any discussion of this paper will appear in a Discussion Section to be published in the June 1978 JOURNAL. All discussions for the June 1978 Discussion Section should be submitted by Feb. 1, 1978.

Publication costs of this article were assisted by Exxon Research and Engineering Company.

REFERENCES

1. J. O. Besenhard and G. Eichinger, *J. Electroanal. Chem. Interfacial Electrochem.*, **68**, 1 (1976).
2. A. N. Dey, *This Journal*, **118**, 1547 (1971).
3. M. M. Nicholson, *ibid.*, **121**, 736 (1974).
4. D. Sam and J. H. Ambrus, Paper 22 presented at The Electrochemical Society Meeting, New York, New York, October 13-17, 1974.
5. J. Antula and B. F. Becker, *J. Phys. Chem.*, **79**, 2470 (1975).
6. M. S. Whittingham, Belgium Pat. 819,672 (1973).
7. M. S. Whittingham, *This Journal*, **123**, 315 (1976).
8. G. L. Holleck, F. S. Shuker, and S. B. Brummer, in Proceedings of the 10th Intersociety Energy Conversion Conference, Delaware (1975).
9. G. H. Newman and L. H. Gaines, To be published.
10. J. L. Settle, K. M. Myles, and J. E. Battles, AEC, Pat. application 481-285, June 20, 1974.
11. L. H. Gaines, R. W. Francis, G. H. Newman, and B. M. L. Rao, in Proceedings of the 11th IECEC (1976).

Some Aspects of the Anodic Oxidation of V, Mo, and W

M. R. Arora*,[1] and Roger Kelly*

Institute for Materials Research, McMaster University, Hamilton, Ontario, L8S 4M1 Canada

ABSTRACT

V, Mo, and W can be readily anodized in an electrolyte consisting of acetic acid, 0.02M $Na_2B_4O_7 \cdot 10H_2O$, and 1.0M additional water as proposed orginally by Keil and Salomon for V. The resulting films, when formed in the presence of air, are duplex, being crystalline and of lower stoichiometry near the metal-film interface but having stoichiometries near V_2O_5, MoO_3, and WO_3 beyond the metal-film interface. The films formed on V and Mo are subject to significant dissolution such that time-independent dissolution currents (i_3) of 0.11 and 0.04 mA/cm^2 can be inferred; with W, by contrast, the dissolution current was only ~0.001 mA/cm^2. The electronic currents (i_2) are estimated to be 0.09 mA/cm^2 for V, 0.12 mA/cm^2 for Mo, and 0.03 mA/cm^2 for W, and the constant-current efficiency follows as being given by the relation $\eta = (I - i_2 - i_3)/I$, where I is the total applied current. The efficiencies for V and Mo thus lie in the interval 0.60-0.92 for $0.5 \leq I \leq 2.0$ mA/cm^2, whereas W shows essentially unit current efficiency. Efficiencies are also deduced for conditions of mixed constant current and constant voltage. That of V is unusually low, as is to be expected for such conditions, whereas that of Mo is unusually high, suggesting that the average stoichiometry of the film is measurably less than MoO_3. Again W shows essentially unit efficiency.

The pioneer work of Güntherschulze and Betz (1) initiated much of the present day interest in the formation of anodic oxide films. They fitted their data on the kinetics of anodization to an empirical relation of the type

$$i_1 = A \exp(B\mathcal{E}_d) \quad [1]$$

where i_1 is the ionic current and $\mathcal{E}_d$ is the field across the film during formation, *i.e.* the differential field. Elementary considerations relate A and B to more fundamental parameters, in particular $B \propto 1/kT$, but such elaboration will not be required in what follows. Anodic films are of considerable technological importance, for example, in corrosion protection, metal finishing, batteries, electrolytic capacitors, and semiconductor processing. Recently, major indirect uses have been developed for anodic films in the study of diffusion profiles at low temperatures (2, 3) and in the study of depth distributions of implanted ions (4, 5). In these cases, use is made of the fact that, if anodic oxidation is carried out at a constant voltage, then within a few minutes the film thickness approaches an approximately constant value and the resulting film may be assumed to be extremely uniform. If such films can be removed without affecting the substrate, then it becomes possible to remove successive layers of metal as thin as 1-5 nm and one speaks of "anodic sectioning." By contrast, a technique such as H^+ or He^+ backscattering, though having the important advantage of being nondestructive, has a resolving power of roughly 10-15 nm (6).

The purpose of the present study was to complete a project on the anodic sectioning of V, Mo, and W (5, 7, 8) by presenting a brief study of the kinetics of the formation of the relevant anodic films. The main difference from related studies, for example, the work of Ammar and Salim (9, 10), will be the use of a combination of gravimetric and electrochemical information. A further study on film structure and stoichiometry is published elsewhere (11).

Vanadium is of particular interest because of the repeated failures [*e.g.*, Ref. (12, 13)] in attempts to grow macroscopic films. The first successful results date from 1965-1968, when Keil and Salomon (14, 15) devised an electrolyte based on acetic acid, and 1974, when Pelleg (16) found a second successful electrolyte based on acetone. In summarizing the results we will distinguish between those cases where air was excluded and those where it was not. Concerning work done in the absence of air, voltages up to 110V were achieved (15), the current efficiency was close to 100% (15), no dissolution could be detected after an initial induction period (15), Eq. [1] was obeyed (17), and, most significantly, the film had the unexpected composition ~VO_2 (15). Work done in the presence of air succeeded in showing thick films to be amorphous (11) and to have a stoichiometry $V_2O_{5\pm0.3}$ (18), and thin films to be crystalline and almost certainly of lower stoichiometry than V_2O_5 (11). The average stoichiometry is thus somewhat less than that of V_2O_5. The anodic sectioning of V is described in Ref. (7, 16).

Molydenum, when polarized anodically in most electrolytes, fails to develop a macroscopic film (13, 19, 20). Lavrenko and Pen'kov (21) claim to have anodized Mo in saturated boric acid at up to 200V. We could not reproduce their results, while Ikonopisov (22) suggests that the high voltage drop observed by Lavrenko and Pen'kov may have been due to the high resistance diaphragm between the electrodes. The first successful results are accordingly those of the present authors with an acetic acid-based electrolyte (5) and of Ikonopisov with a glycol-borate electrolyte (22). The films supported up to 200-300V and were suited for anodic sectioning (5). More recently, film formation in the acetic acid-based electrolyte has been shown (23) to follow Eq. [1], thick films have been shown to be amorphous (9) and to have an average stoichiometry $MoO_{2.75}$ (23), and thin films have been shown to be crystalline and with a diffraction pattern resembling that of $MoO_2 \cdot H_2O$ (11). The tentative identification of $MoO_2 \cdot H_2O$ helps to explain why the average stoichiometry should be less than that of MoO_3.

Tungsten has, relatively speaking, been studied in great detail, including from the point of view of anodic sectioning (8, 24), and presents few problems. The only unacceptable electrolytes appear to be those based on alkaline solutions, since they cause W to go into solution rather than into a macroscopic film (9). Examples of successful electrolytes include an aqueous solution of KNO_3 (0.4M) and HNO_3 (0.04M), with which voltages as high as 75V can be achieved (24), various dilute acids, leading to voltages as high as 85V (10), and the acetic acid-based electrolyte to be used here, leading to voltages as high as 140V (8). Film growth kinetics appear (10), in general, to follow Eq. [1],

* Electrochemical Society Active Member.
[1] Present address: Unican Electrochemical Products Limited, Montreal, Quebec, Canada.
Key words: vanadium, molybdenum, tungsten, anodization, stoichiometry, differential field, current efficiency.

thick films have been shown to be amorphous (11) and to crystallize to a mixture of WO_2 and disordered $WO_{2.90}$ (25), and thin films have been shown to consist of crystalline WO_2 (11). The average stoichiometry is thus somewhat less than that of WO_3.

Experimental

Polycrystalline metal foils, with dimensions of 20 × 15 × 0.1 mm and with purities claimed to be at least 99.8%, were used as specimens. The surface preparation and other preanodizing treatment have been described previously (5, 7, 8), while the electrolyte was similar to the acetic acid-based mixture proposed by Keil and Salomon for V (15). It consisted of acetic acid, 0.02M $Na_2B_4O_7 \cdot 10H_2O$, and 1.0M additional water, and thus had roughly half the water content as in Ref. (15). The water content is to some extent an optimum, in that less than 1.0M reduces the conductivity to an inconvenient extent and more than 2.0M leads to films on V and Mo which are excessively unstable. We would emphasize that the present results are probably particular to the electrolyte used as well as to the anodizing conditions, and as evidence for this would cite the significantly different stoichiometry found here ($\sim V_2O_5$) and by Keil and Salomon ($\sim VO_2$) for the anodic film on V. As far as we can see, the origin of the difference lies simply in whether or not air was present.

The anodic films formed on V and Mo were rather unstable in that they would change interference colors and eventually disappear when exposed to air. They could be stabilized either by dipping them in glacial acetic acid followed by drying them with filter paper or by using a jet of compressed air immediately after their withdrawal from the electrolyte. Once stabilized, they could be stored in a desiccator almost indefinitely. In all anodizations, a cylindical platinum cathode 25 mm in diameter was used, the specimens were placed along the axis, the temperature was 25° ± 1°C, and air was present.

It was observed, during the course of constant-current experiments, that stirring the electrolyte affected the rate of film formation with V and Mo but not W. The curves of V *vs.* t were lowered, especially for currents of $\leq$0.5 mA/cm² (Fig. 1), and, since this may be taken as indicative of enhanced film dissolution, the present experiments were carried out with neither stirring nor gas bubbling.

Results and Discussion

Gravimetric information.—Experiments relating to the weights of anodic films on V, Mo, and W are described in detail in Ref. (5, 7, 8, 26). They were based, in the case of thick films, on direct weighing and, in the case of thin films, on techniques linked to the depth distributions of implanted ^{85}Kr. The main results are summarized in Table I. They are in all cases valid for the acetic acid-based electrolyte, for the presence of air, and for conditions of mixed constant current and constant voltage, such that the current was preset at 2.0 mA/cm², the voltage was preset at whatever value was desired, and the total anodizing time was 6 min.

Additional experiments were undertaken to determine the extent of film dissolution. Specimens were prepared with a preset current of 2.0 mA/cm², a preset voltage of 50V, and were then anodized with times of 6-60 min. If the film weights are re-expressed in terms of the metal present in the films, then the loss by dissolution is given by (metal-removal weight) minus (metal present in film). The results are shown in Fig. 2 and can also be represented by formulas based on a least squares analysis, as follows

dissolution loss of V $= -0.4 \pm 0.2$

$+ (0.0117 \pm 0.0002) \times t$ μg/cm² of metal

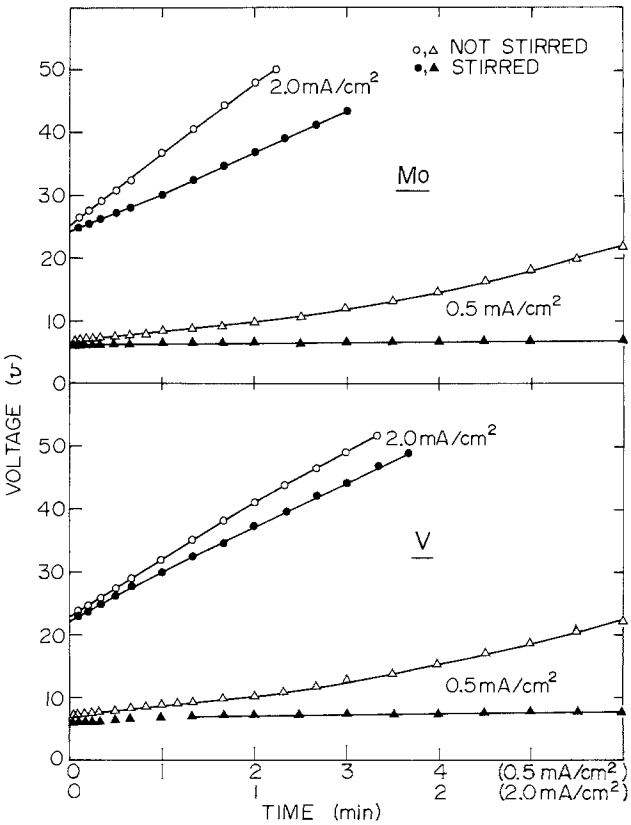


Fig. 1. Effect of stirring on film growth at constant current as revealed in voltage-time curves. The growth rates on V and Mo but not W are significantly reduced by stirring, this being a qualitative indication that film dissolution is a problem.

dissolution loss of Mo $= -2 \pm 1$

$+ (0.0069 \pm 0.0006) \times t$ μg/cm² of metal

dissolution loss of W = undetectable gravimetrically.

Here t stands for time in seconds. The main uncertainty in the approach used lies in the assumption of the stoichiometries V_2O_5 and MoO_3; if the real stoichiometries were lower, the calculated dissolution losses would also be lower.

The problem of dissolution was further investigated, in the case of W, by the following more sensitive method. Specimens were labeled with 10 keV ^{85}Kr to a dose of 5×10^{15} ions/cm² and it was shown by means of anodic sectioning (8) that the Kr had an integral concentration profile given approximately by

$$\text{integral concentration} = \exp(-x \ln 2/R_m)$$

with R_m equal to 13 μg/cm². The distribution curves,

Table I. Film and metal-removal weights for V, Mo, and W when anodized in the acetic-acid based electrolyte*

Metal	Film weight (μg/cm²)	Metal-removal weight† (μg/cm²)	Region of validity (V)
V	$2 \pm 2 + (1.15 \pm 0.04) \times V$	$6 \pm 1 + (0.63 \pm 0.01) \times V$	7.5 or 4 to 110
Mo	$1 \pm 1 + (1.58 \pm 0.02) \times V$	$5 \pm 2 + (1.05 \pm 0.03) \times V$	10 or 7.5 to 110
W	$10 \pm 3 + (1.38 \pm 0.05) \times V$	$6.5 \pm 2 + (1.09 \pm 0.03) \times V$	10 or 7 to 100‡

* The weights are taken from Ref. (26), where they are based on a least squares analysis, rather than Ref. (5, 7, 8), where the analysis was simpler.

† A metal-removal weight can also be described as the metal removed from a specimen during a full anodizing-stripping sequence.

‡ Valid to 140V if the current is present at 10.0 mA/cm² instead of 2.0 mA/cm² beyond 100V.

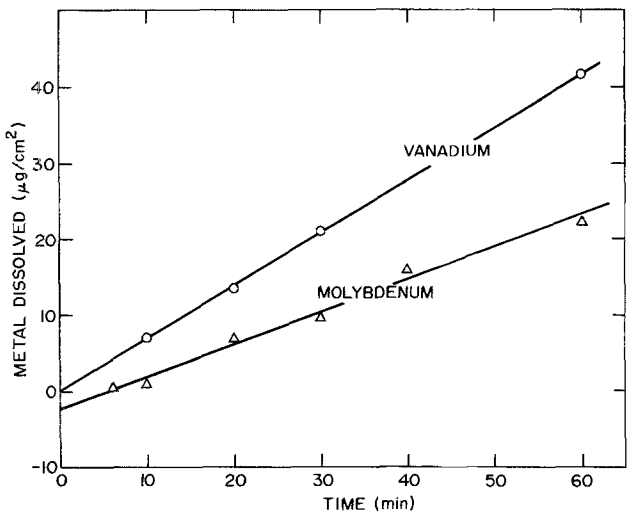


Fig. 2. Dissolution loss for V and Mo as a function of the total anodizing time. The experimental points are based on the stoichiometries V_2O_5 and MoO_3, and would have lower values if the stoichiometries were lower.

which resemble those for Kr → Mo (5), are discussed in Ref. (26). The specimens were next anodized for 6 min, with the current preset at 2.0 mA/cm² and the voltage preset at 10 or 25V, and were counted to determine the residual activity with the films still present. The normalized value was 0.992 ± 0.010, indicating a dissolution loss of about 4×10^{-4} μg/cm² sec. Loss thus occurs at about 3-6% the rate found with V or Mo.

Analysis of gravimetric information.—The first step in any discussion of anodizing transition metals is to estimate the film stoichiometry. One of the least controversial approaches is based on thickness information as in Table I, where the thicknesses will be noted to have the general form

$$\text{thickness} = C + D \times V$$

The constant terms, C, will include contributions from interfacial potentials, from pre-existing films, as well as, in the case of metal removal, from dissolution, whereas the slopes, D, will be largely unaffected by these. We have therefore deduced the stoichiometries from the slopes as detailed in Table II. The conclusion is that the stoichiometries, valid beyond the region at the metal-film interface, lie near V_2O_5, MoO_3, and WO_3 as distinct from VO_2, MoO_2, and WO_2. We would recall that the main result of Ref. (11) was to demonstrate the thinnest anodic films on V, Mo, and W to be crystalline and of known (W) or suspected (V, Mo) low stoichiometry. The over-all films are thus duplex, as in fact they must be thermodynamically, and have average stoichiometries which are somewhat low. The results of the present work together with Ref. (11) can be summarized schematically as follows

Table II. Stoichiometries of anodic films on V, Mo, and W

Metal	Slope of experimental metal-removal weight (μg/cm² · V)	Slope of inferred film weight (μg/cm² · V)	Slope of experimental film weight (μg/cm² · V)	Conclusion regarding stoichiometry
V	0.63 ± 0.01	1.03 ± 0.02 if VO_2 1.13 ± 0.02 if V_2O_5	1.15 ± 0.04	~V_2O_5
Mo	1.05 ± 0.03	1.40 ± 0.04 if MoO_2 1.58 ± 0.05 if MoO_3	1.58 ± 0.02	~MoO_3
W	1.07 ± 0.03	1.28 ± 0.04 if WO_2 1.37 ± 0.04 if WO_3	1.38 ± 0.05	~WO_3

Table III. Resistivities of oxides of V, Mo, and W

Oxide	Resistivity (Ω-cm)	Ref.
V_2O_5 (amorphous)	10^6	(27)
V_6O_{13}	10^3	(28)
VO_2 (crystalline)	10-100	(29, 30)
VO_2 (amorphous)	10^{-2}	(30)
MoO_3	$>10^{10}$	(31, 32)
$MoO_{2.88}$	~250	(33)
MoO_2	10^{-4}	(34)
WO_3	10^5-10^6	(32)
$WO_{2.90}$	Metallic	(35)
WO_2	10^{-3}	(34)

Table IV. Values of $\mathcal{E}_d$ and i_3 as obtained from gravimetric information

Metal	Differential field, $\mathcal{E}_d$* (V/cm)	Dissolution current, i_3 (mA/cm²)
V	$(2.9 \pm 0.1) \times 10^6$	0.111 ± 0.002
Mo	$(2.95 \pm 0.05) \times 10^6$	0.042 ± 0.004
W	$(5.2 \pm 0.2) \times 10^6$	~0.001

* As discussed in the text, the real uncertainties are greater than those shown.

$$V|<V_2O_5|\sim V_2O_5$$

$$Mo|MoO_2\cdot H_2O(?)|\sim MoO_3$$

$$W|WO_2|\sim WO_3$$

More subtle distinctions, as between WO_3 and $WO_{2.90}$, cannot be made with gravimetric information. Electron diffraction is often a useful alternative, but it fails in the present case owing to the amorphicity of the films formed on V, Mo, and W (11). It is more helpful to note that slightly reduced forms of transition-metal oxides tend to have metallic or near-metallic resistivities (Table III). Bearing in mind that, for an anodizing current of 2.0 mA/cm² and a differential field near $(3\text{-}5) \times 10^6$ V/cm (to be shown below), the implied resistivity is ~10^9 Ω-cm, it is clear that the films formed on V, Mo, and W must be fully oxidized.[2]

The film weights enable estimates to be made of the differential field, which is, ideally, the same field $\mathcal{E}_d$ as appears in Eq. [1]. We again use the slopes and obtain results as in Table IV, provided the densities can be taken as for crystalline V_2O_5, MoO_3, and WO_3. These values of $\mathcal{E}_d$ are subject to two conflicting errors. They will tend to be high owing to the use of crystalline densities. They will tend to be low owing to the film thicknesses being based on anodizing cycles which involve first a constant-current segment and then a constant-voltage segment rather than (as in the following sections) constant current alone. The real uncertainties are therefore greater than shown in Table IV.

Finally, the dissolution losses can be used to evaluate i_3, the current associated with film dissolution. If the dissolution losses are written in the form

$$\text{loss} = E + F \times t \quad \mu g/cm^2$$

then a time-independent i_3 follows as

$$i_3 = (FzF/M) \times 10^{-3} \quad mA/cm^2$$

where z is the cation valence, F is Faraday's constant, and M is the cation molecular weight. The results are included in Table IV.

Constant-current film growth.—Curves of V *vs.* t, obtained with a potentiometric recorder at various current densities, are shown in Fig. 3-5. The voltage first rose sharply due to the ohmic drop across the

[2] Keil and Salomon's (15) basic result that the film on V anodized in the absence of air is ~VO_2, while well-substantiated experimentally, causes some concern in view of the low resistivity of VO_2 (Table III).

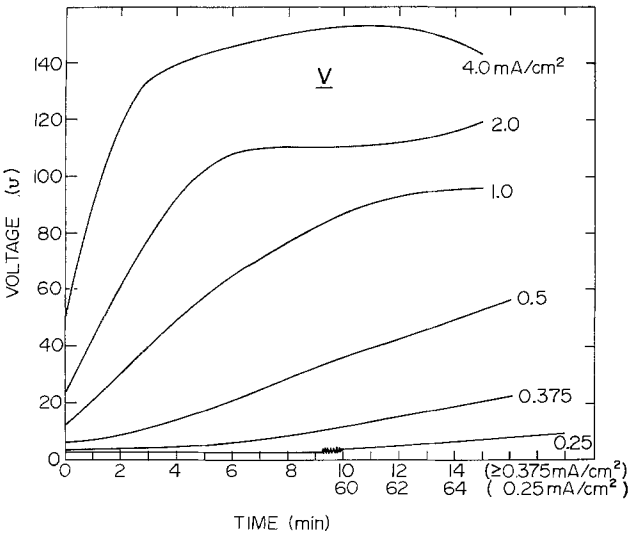


Fig. 3. Typical voltage-time curves for the anodization of V at the indicated current densities.

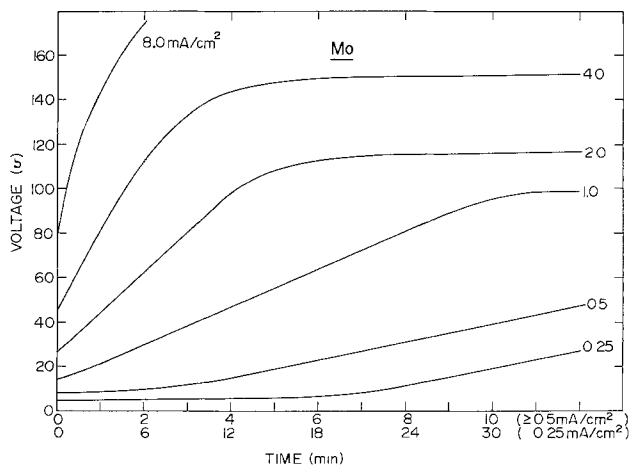


Fig. 4. Typical voltage-time curves for the anodization of Mo at the indicated current densities.

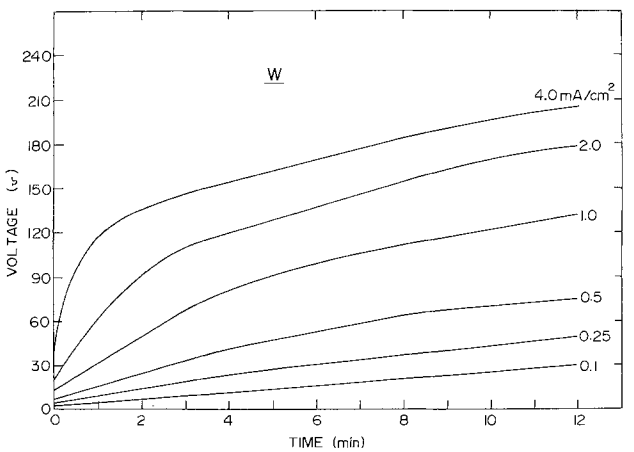


Fig. 5. Typical voltage-time curves for the anodization of W at the indicated current densities.

electrolyte and then increased linearly with time as the films grew. With V and Mo an induction period is evident for current densities of $\leq$0.5 mA/cm², such that the linear voltage rise was delayed for 4-60 min. We do not regard the induction periods as due to the formation of slightly reduced phases such as those inferred by Ikonopisov (22) using a glycol-borate electrolyte, as there was no darkening; rather we attribute them to film dissolution such as that suggested by Fig. 1 and demonstrated explicitly in the preceding section. In most cases there was a critical region of voltage beyond which breakdown can be inferred, *i.e.*, beyond which the voltage ceased to rise linearly, there was an accompanying evolution of gas, and occasional sparks appeared. Specimens anodized into the breakdown region lost their interference colors and gradually became grayish. By correcting the observed breakdown voltages for the ohmic drop one obtains true breakdown voltages of 80-100V for all three metals.

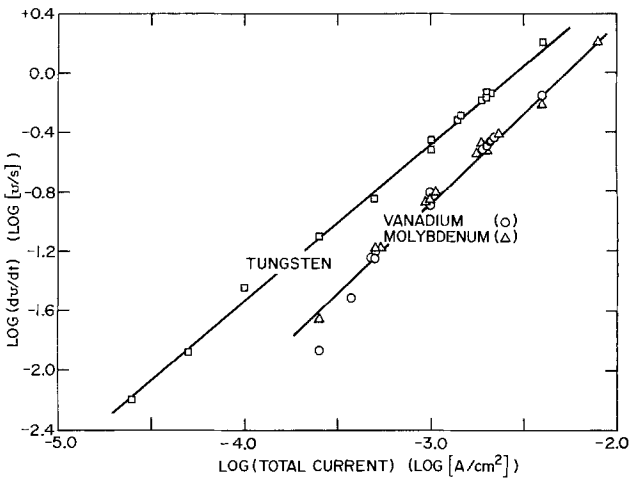


Fig. 6. Curves of log (dV/dt) vs. log I as based on material like that of Fig. 3-5. The slopes and intercepts yield the parameters a and b of Eq. [2].

Analysis of constant-current film growth.—Van Ryselberghe *et al.* (12, 36) analyze curves of V *vs.* t with an empirical relation of the form

$$dV/dt = aI^b \qquad [2]$$

where I is the total applied current and a, b are constants. That this relation applies to the present results follows from Fig. 6, with values of a and b as given in Table V.

In general, an analysis based on Eq. [2] must be regarded as unproductive as it is difficult to relate a and b to more fundamental parameters. The main exception concerns b, in that if b is observed to exceed unity so the current efficiency (η) can be inferred to be an increasing function of I and theretfore less than unity. We thus anticipate V and Mo to anodize with low efficiency but W with near unit efficiency.

More explicit information on current efficiency, together with new estimates for $\mathcal{G}_d$, follows from the conservation relation

$$dV/dt = \eta IM\mathcal{G}_d/z\mathbf{F}\rho \equiv \eta Ir\mathcal{G}_d \qquad [3]$$

where ρ is the film density and where we neglect any consideration of surface roughness. The total applied current I has three possible components, namely, ionic current leading to persistent film (i_1), electronic current (i_2), and current associated with film dissolution (i_3). As such, the efficiency is just

$$\eta = (I - i_2 - i_3)/I \qquad [4]$$

Table V. Values of the constants a and b in Eq. [2]

Metal	a* (V/sec)	b
V	480	1.20
Mo	480	1.20
W	470	1.05

* The numerical values of a are such as arise when I is in A/cm².

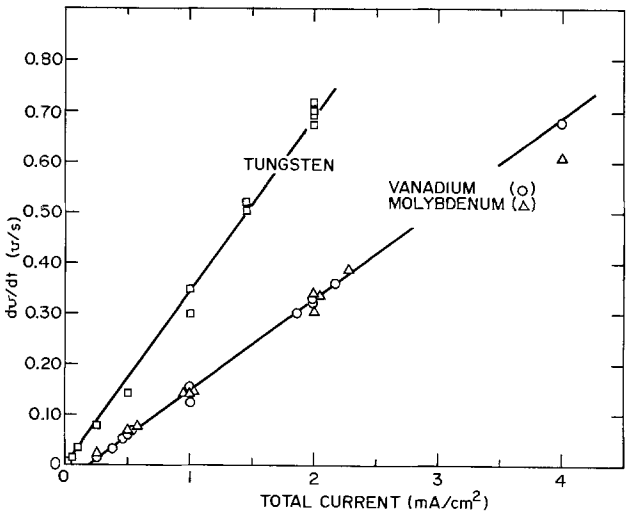


Fig. 7. Curves of dV/dt vs. I as based on material like that of Fig. 3-5. The slopes and intercepts yield approximations to the parameters $r\mathcal{E}_d$ and $(i_2 + i_3)$ of Eq. [6a] and [6b].

Also, since Eq. [1] is obeyed by V, Mo, and W (17, 23, 10), $\mathcal{E}_d$ can be written as

$$\mathcal{E}_d = (1/B) \ln [(I - i_2 - i_3)/A] \qquad [5]$$

and this enables one to conclude that a plot of dV/dt vs. I will have a slope

$$\text{slope} = r\mathcal{E}_d(1 + \{\ln [(I - i_2 - i_3)/A]\}^{-1}) \approx r\mathcal{E}_d \qquad [6a]$$

and an intercept

$$\text{intercept} = i_2 + i_3 + A \approx i_2 + i_3 \qquad [6b]$$

The slope will be a sort of average, valid for the experimental current interval.

We have assumed, in arriving at Eq. [6a], that i_2 and i_3 were both independent of I. Thus i_2 should depend only on $\mathcal{E}_d$ and the latter is, according to Eq. [1] or [5], related to I logarithmically; the dependence is thus weak. Likewise i_3 is naturally constant for a film with fixed stoichiometry, a constancy which is explicitly confirmed for those anodizing voltages for which the film weights can (as in Table I) be written in the form $C + D \times V$. The approximations indicated with Eq. [6a] and [6b] require that A be small, as it in fact often (12, 37) but not always (9, 10) appears to be.

Figure 7 shows a plot of dV/dt vs. I, while Table VI summarizes the relevant values of $r\mathcal{E}_d$ (from the slopes using a least squares analysis), $\mathcal{E}_d$ (deduced with ρ as for crystalline V_2O_5, MoO_3, and WO_3), $i_2 + i_3$ (from the intercepts using a least squares analysis), i_2 (deduced with the help of i_3 from Table IV), and η (deduced according to Eq. [4]). The values of $\mathcal{E}_d$ are subject to errors both of which make them high. These are the use of crystalline densities and the approximation in Eq. [6a], and as such the real uncertainties are greater than shown in Table VI.

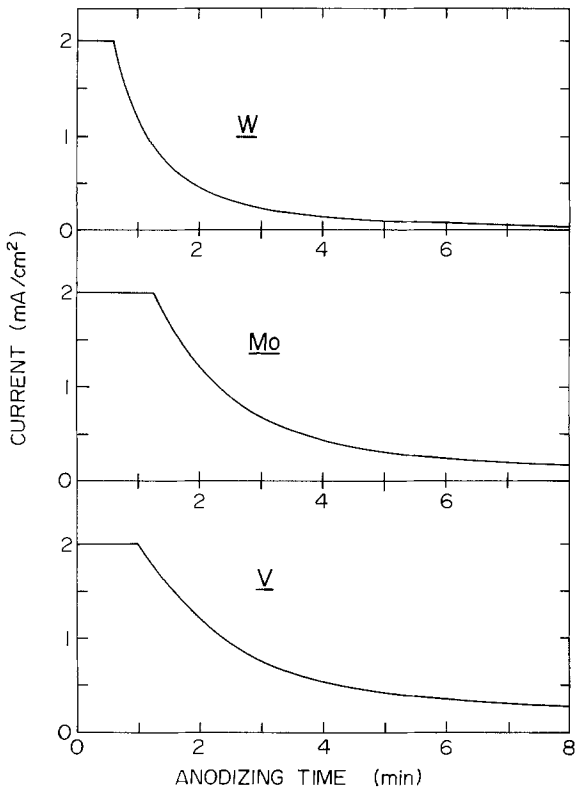


Fig. 8. Typical current-time curves for the anodization of V, Mo, and W when the current is preset at 2.0 mA/cm² and the voltage at 50V. The areas of these curves infer film weights according to Eq. [7], thence modified current efficiencies ($\eta' = \eta z\langle M\rangle / \langle z\rangle M$) by comparison with the explicit film weights of Table I.

Three indications of the self-consistency of the results are (*i*) that $\mathcal{E}_d$ of Tables IV and VI are similar, (*ii*) that $i_2 + i_3$ of Table VI exceeds i_3 of Table IV, and (*iii*) that η is less than unity with V and Mo, corresponding to b in Eq. [2] exceeding unity to a significant extent.

Film growth with mixed constant current and constant voltage.—Curves of I vs. t relevant to mixed constant current and constant voltage were obtained with V, Mo, and W by anodizing for a total time of 6 min with the current preset at 2.0 mA/cm² and the voltage preset at 50V. Typical examples are shown in Fig. 8 and are seen to be characterized by a constant-current portion during which the voltage rose to the preset value, a rapid fall in current qualitatively in accordance with Eq. [1], and an approach to what is in principle $i_2 + i_3$. They will be here used to make new estimates of current efficiency.

Analysis for mixed constant current and constant voltage.—Curves of I vs. t as in Fig. 8 infer film weights according to the conservation relation

$$\text{weight} = (\eta z\langle M\rangle/\langle z\rangle M)\,(\textstyle\int I dt)\,(M/z\mathbf{F})\,(10^6) \quad \mu g/cm^2 \qquad [7]$$

where z is the ideal valence of cations in the film (*e.g.*, 6 for Mo), $\langle z\rangle$ is the actual average valence [*e.g.*, <6

Table VI. Values of $\mathcal{E}_d$, $i_2 + i_3$, i_2, and η as obtained from information on constant-current film growth

Metal	$r\mathcal{E}_d$ (V · cm²/sec · A)	$\mathcal{E}_d$* (V/cm)	$i_2 + i_3$ (mA/cm²)	i_2 (mA/cm²)	η at 0.5 (mA/cm²)	η at 2.0 (mA/cm²)
V	180 ± 6	(3.2 ± 0.1) × 10^6	0.20 ± 0.05	~0.09	0.60	0.90
Mo	180 ± 8	(3.4 ± 0.2) × 10^6	0.16 ± 0.05	~0.12	0.68	0.92
W	350 ± 20	(6.3 ± 0.4) × 10^6	0.03 ± 0.05	~0.03	0.94	0.99

* As discussed in the text, the real uncertainties are greater than those shown.

Table VII. Efficiencies for mixed constant current and constant voltage as obtained from information as in Fig. 8

Metal	Film weights as calculated from Eq. [7] ($\mu g/cm^2$)	Experimental film weights for 50V from Table I ($\mu g/cm^2$)	Modified current efficiency η'
V	73.5 ± 2	59.5 ± 3	0.81 ± 0.05
Mo	82.5 ± 2	80.0 ± 1.5	0.97 ± 0.03
W	79.2 ± 2	79.0 ± 4	1.00 ± 0.06

for Mo (11, 23)], and M and $\langle M \rangle$ are the analogous molecular weights. Accordingly, by comparing film weights inferred from Eq. [7] with explicit weights as in Table I, one obtains a modified current efficiency, $\eta' = (\eta z \langle M \rangle / \langle z \rangle M)$. The results are summarized in Table VII.

A detailed interpretation of the current efficiencies of Table VII is difficult for two reasons. One is that the observed quantity is η' rather than η. The other is that an efficiency measured when the current is initially constant but then falls, as here, is inherently lower than one based on constant-current data, as in Table VI. Nevertheless, certain conclusions can be derived as follows:

(*i*) V shows the expected reduced current efficiency for an anodizing cycle in which current is first constant and then falls. This is consistent with V having a high value of $i_2 + i_3$ (Table VI), although it also requires that the average stoichiometry be close to V_2O_5.

(*ii*) Mo shows a higher efficiency in Table VII (0.97) than in Table VI (0.92), a result which is possible only if $z/\langle z \rangle$ is greater than unity, as when the average stoichiometry of the film is measurably low. In fact, the observed results are understandable with an average stoichiometry similar to $MoO_{2.75}$ (23), whence $z\langle M \rangle / \langle z \rangle M = 1.06$.

(*iii*) W anodizes with essentially 100% efficiency under all circumstances, as in fact it must if $i_2 + i_3$ is close to zero (Table VI) and the average stoichiometry is close to WO_3.

Conclusions

V, Mo, and W have been anodized in an electrolyte consisting of acetic acid, 0.02M $Na_2B_4O_7 \cdot 10\ H_2O$, and 1.0M additional water as proposed originally by Keil and Salomon for V (14,15). The resulting films, when formed in the presence of air, have weights as summarized in Table I and from these weights the stoichiometries, valid beyond the region at the metal-film interface, follow as being near V_2O_5, MoO_3, and WO_3 (Table II). More subtle distinctions, as between WO_3 and $WO_{2.90}$, cannot be made with gravimetric information; nevertheless, slightly reduced phases can be excluded on the grounds that, in so far as they have been studied, they tend to have metallic or near-metallic resistivities (Table III). We note in particular that the stoichiometry of the film on V appears to depend critically on air, as $\sim VO_2$ is obtained in the absence of air (15) but $\sim V_2O_5$ in the presence [here and Ref. (18)].

The film-weight information of Table I also permits $\mathcal{E}_d$, the differential field, to be estimated (Table IV). Additional weight measurements, obtained as a function of anodizing time, enable i_3, the time-independent current associated with film dissolution, to be evaluated (Table IV).

When films are grown at constant current, curves of V *vs.* t are readily obtained. Those for V, Mo, and W were in most cases characterized by segments showing an ohmic voltage drop, a linear rise as the films grew, and evidence for breakdown, although when V and Mo were anodized at ≤ 0.5 mA/cm^2 induction periods lasting 4-60 min could also be identified. The induction periods were attributed to film dissolution.

The analysis of V-t curves according to Eq. [2], *i.e.*, $dV/dt = aI^b$, is regarded as unproductive except to demonstrate that, since b exceeds unity with V and Mo (Table V), these two metals anodize with low efficiency. Equation [3], *i.e.*, $dV/dt = \eta I r \mathcal{E}_d$, is far more useful and leads to explicit estimates of the differential field ($\mathcal{E}_d$), the nonfilm forming current ($i_2 + i_3$), and the current efficiency (η) (Table VI).

When films are grown with mixed constant current and constant voltage, curves of I *vs.* t become of interest. Those for V, Mo, and W had segments showing a constant current, a rapid fall of current qualitatively in accordance with Eq. [1], *i.e.*, $i_1 = A \exp(B\mathcal{E}_d)$, and an approach to what is in principle $i_2 + i_3$. Such curves infer film weights in accordance with Eq. [7] and when these are compared with explicit film weights, as in Table I, a modified current efficiency η' is obtained (Table VII). The numerical value of η' for V is low, 0.81, as can be expected whenever films are grown with an anodizing cycle in which current is first constant and then falls. More significantly, the numerical value for Mo is high, 0.97, this being possible only if $z/\langle z \rangle$ is greater than unity, as when the average stoichiometry of the film is measurably low.

Manuscript submitted March 1, 1977; revised manuscript received June 3, 1977.

Any discussion of this paper will appear in a Discussion Section to be published in the June 1978 JOURNAL. All discussions for the June 1978 Discussion Section should be submitted by Feb. 1, 1978.

REFERENCES

1. A. Güntherschulze and H. Betz, "Elektrolyt-Kondensatoren," 2nd ed., Cram, Berlin (1952).
2. R. E. Pawel and T. S. Lundy, *J. Appl. Phys.*, **35**, 435 (1964).
3. J. L. Whitton and G. V. Kidson, *Can. J. Phys.*, **46**, 2589 (1968).
4. J. A. Davies, J. Friesen, and J. D. McIntyre, *ibid.*, **38**, 1526 (1960).
5. M. R. Arora and R. Kelly, *This Journal*, **119**, 270 (1972).
6. E. Bøgh, *Can. J. Phys.*, **46**, 653 (1968).
7. M. R. Arora and R. Kelly, *This Journal*, **120**, 128 (1973).
8. M. R. Arora and R. Kelly, *Electrochim. Acta*, **19**, 413 (1974).
9. I. A. Ammar and R. Salim, *Werkst. Korros.*, **23**, 161 (1972).
10. I. A. Ammar and R. Salim, *Corros. Sci.*, **11**, 591 (1971).
11. M. R. Arora and R. Kelly, *J. Mater. Sci.*, **12**, 1673 (1977).
12. H. A. Johansen, G. B. Adams, and P. van Ryssel-berghe, *This Journal*, **104**, 339 (1957).
13. G. C. Wood and C. Pearson, *Corros. Sci.*, **7**, 119 (1967).
14. R. G. Keil and R. E. Salomon, *This Journal*, **112**, 643 (1965).
15. R. G. Keil and R. E. Salomon, *ibid.*, **115**, 628 (1968).
16. J. Pelleg, *J. Less-Common Met.*, **35**, 299 (1974).
17. B. H. Ellis, M. A. Hopper, and D. J. DeSmet, *This Journal*, **118**, 860 (1971).
18. W. D. Mackintosh and H. H. Plattner, *ibid.*, **123**, 523 (1976).
19. G. Masing and G. Röth, *Werkst. Korros.*, **3**, 176 (1952).
20. M. N. Hull, *J. Electroanal. Chem.*, **30**, App. **1-3** (1971).
21. V. A. Lavrenko and A. A. Pen'kov, *Russ. J. Phys. Chem. (Engl. Transl.)*, **37**, 551 (1963).
22. S. Ikonopisov, *Electrodeposition Surf. Treat.*, **1**, 305 (1972/1973).
23. C. M. Daly and R. G. Keil, *This Journal*, **122**, 350 (1975).
24. M. McCargo, J. A. Davies, and F. Brown, *Can. J. Phys.*, **41**, 1231 (1963).
25. D. G. Brandon, J. Zahavi, A. Aladjem, and J. Yahalom, *J. Vac. Sci. Technol.*, **6**, 783 (1969).
26. M. R. Arora, Ph.D. Thesis, McMaster University (1974).
27. T. N. Kennedy, R. Hakim, and J. D. Mackenzie, *Mater. Res. Bull.*, **2**, 193 (1967).
28. S. Kachi, T. Takada, and K. Kosuge, *J. Phys. Soc. Jpn.*, **18**, 1839 (1963).
29. C. R. Everhart and J. B. MacChesney, *J. Appl. Phys.*, **39**, 2872 (1968).
30. T. N. Kennedy and J. D. Mackenzie, *J. Non-Cryst.*

Solids, **1**, 326 (1969).
31. S. K. Deb and J. A. Chopoorian, *J. Appl. Phys.*, **37**, 4818 (1966).
32. J. Rudolph, *Tech. Wiss. Abh. Osram-Ges.*, **8**, 86 (1963).
33. L. Kihlborg, *Acta Chem. Scand.*, **13**, 954 (1959).
34. D. B. Rogers, R. D. Shannon, A. W. Sleight, and J. L. Gilson, *Inorg. Chem.*, **8**, 841 (1969).
35. J. M. Berak and M. J. Sienko, *J. Solid State Chem.*, **2**, 109 (1970).
36. M. Maraghini, G. B. Adams, and P. van Ryssselberghe, *This Journal*, **101**, 400 (1954).
37. G. B. Adams, P. van Rysselberghe, and M. Maraghini, *ibid.*, **102**, 502 (1955).

Pulsed Potentiostatic Deposition of Gold from Solutions of the Au(I) Sulfite Complex

Jean Horkans* and L. T. Romankiw*

IBM Thomas J. Watson Research Center, Yorktown Heights, New York 10592

ABSTRACT

The kinetics of Au deposition from Au(I) sulfite solutions in the pH range 8.5-13 has been studied using cyclic voltammetry and single potential step methods. At potentials more positive than −0.8V *vs.* NHE, the potential step data can be explained by a C.E. mechanism, probably dissociation of the gold complex followed by charge transfer. At more cathodic potentials the mechanism may involve direct electron transfer to the complexed gold ion. The effect of pulsed potentiostatic deposition on the properties of Au films deposited from sulfite solutions was investigated. Although variation of the frequency of the potential pulse was shown to affect the distribution of Au deposited through a photoresist pattern, the stress, grain size, purity, and resistivity of gold deposited pulsed potentiostatically showed no clear dependence on frequency. This can be explained in terms of irreversibility of the Au/Au(I) couple in sulfite solution.

A number of investigators, *e.g.*, (1-12), report that the physical properties of electrodeposits can be improved when deposition is carried out under pulsed potential or pulsed current conditions rather than under the usual potentiostatic or galvanostatic conditions. The reason for this improvement is assumed to lie in the time-dependent variation of the diffusion layer thickness at the electrode surface. The period between pulses, during which no deposition takes place, allows the concentration of the metal ion or metal complex in the diffusion layer near the cathode to relax from its depleted value to a value approaching the concentration in the bulk solution. Based on this reasoning, the time-averaged diffusion layer under pulsed conditions is thinner than that prevailing under galvanostatic or potentiostatic conditions. This thinner diffusion layer more closely follows the contours of the surface and results in a deposit of more uniform thickness. In addition, Popov *et al.* (5-7) have shown that pulsed potentiostatic deposition decreases deposit porosity.

A model of pulsed potentiostatic deposition has been developed by Despic and Popov (1, 2). Their solution of Fick's second law, with the appropriate boundary conditions, for an ideally reversible electrode shows that under conditions of pulsating potential a stable, time-independent diffusion layer is established. The dependence of the diffusion layer thickness δ_N on frequency ν is $\delta_N \propto \nu^{-1/2}$. Thus the deposits with greatest thickness uniformity and lowest porosity should be attained at the highest frequency. According to this model, the criterion which must be met in order that surface roughness not be amplified is that δ_N should be less than the radius of curvature of the irregularities. Despic and Popov (1) found experimentally that the growth of dendrites of Cu and Zn was inhibited by pulsing the electrode potential.

In the case of a nonreversible electrode, the concentration of ions at the electrode surface is not able to follow the changing electrode potential. When the Despic and Popov model is applied to a nonreversible system (2), the result is a time-dependent diffusion layer thickness and the amplification of surface roughness.

The use of pulsed current to affect mass transport during metal deposition has been discussed by Braun and Ibl (4, 5). Although Despic and Popov (1, 2) claim that pulsed current should give the same results as direct current at high frequencies, Braun and Ibl report very smooth deposits of Cu using high frequency pulses at high current densities.

We have chosen to investigate the pulsed potentiostatic deposition of Au from solutions of its sulfite complex. The Au(I) sulfite complex is thought to have the composition $[Au(SO_3)_2]^{3-}$ (13, 14). Because sulfite is not toxic and is the basis of a commericial gold plating bath, this complex is becoming increasingly important in Au plating for electronic applications (15, 16). However, the electrochemistry of the gold sulfite complex is much more poorly understood than that of the gold cyanide complex, which has been more widely studied. We have studied Au deposition from unstirred sulfite solutions using cyclic voltammetry and potential step methods, and have determined the effects of pulsed potentiostatic deposition on the deposit properties.

Experimental

All solutions used in this investigation were 0.15M in the Au(I) sulfite complex, contained a total Na_2SO_3 concentration of 0.5M, and were saturated (a few tenths molar) in $Na_4P_2O_7$. No brightening or leveling agents were added. Solutions were prepared with deionized H_2O, and were deaerated by bubbling N_2 gas. The bubbler was raised above solution level during the measurements. (The presence of the reducing SO_3^{2-} eliminates O_2 from the solution. However, O_2 was excluded to maintain a constant SO_3^{2-} concentration.)

A three-electrode system under potentiostatic control was used. The cell, shown in Fig. 1, was designed to give a highly uniform primary current distribution at the surface of the working electrode in the absence

* Electrochemical Society Active Member.

Key words: pulsed plating, gold sulfite baths, gold deposition, plating through a mask.

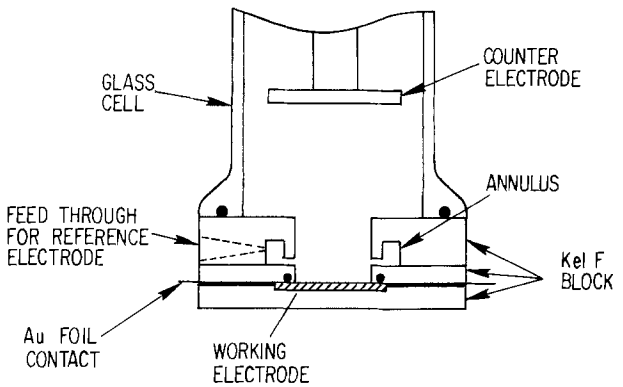


Fig. 1. Cell design

of convection. This is achieved by mounting the working electrode at the bottom of a cylindrical opening in a Kel F block, and placing the reference electrode, in a manner similar to that used by Cahan *et al.* (17), in an annulus in this block which is connected to the solution by a 0.10 in. slit just above the electrode surface. This gives a potential reference which does not block the lines of current flow. Potential control was maintained by a Tacussel-type PIT 20-2X potentiostat used in conjunction with a PAR Model 175 waveform generator.

The working electrode was an evaporated Au film on a 1¼ in. wafer of Corning 0211 glass. The thickness of the Au was 200Å for all samples studied by x-ray diffraction, and 2000Å otherwise. A 200Å film of evaporated Nb was deposited on the glass under the evaporated Au to improve adhesion. According to Adzic *et al.* (18), Nb interferes less with electrochemical measurements than other commonly used adhesion layers.

The reference electrode was Hg-Hg_2SO_4. All potentials here are quoted with reference to the normal hydrogen electrode NHE. In the potential step measurements, the short-time current response was stored in a multipurpose signal averager, Type AA1, manufactured by Hi-Tek Instruments (England), then plotted on a X-Y recorder. The thicknesses of the sheet Au deposits were determined by masking a narrow line with photoresist, etching using a KI, I_2 etch, and determining the depth of the line with a Clevite Surfanalyzer 1200 profilometer. Impurity levels in the deposits were obtained from electron microprobe measurements. Resistivities were determined using a four-point probe. In addition to the sheet films, some deposits were made through masks of Shipley AZ 1350J photoresist. The thickness of these deposits was also measured with a surface profilometer.

Results and Discussion

Kinetic measurements.—Cyclic voltammograms of a Au electrode in the Au(I) sulfite solution at three different *p*H values are shown in Fig. 2. The potential range of Fig. 2 is that in which Au deposition is expected to be the only significant electrode reaction. Comparison of cyclic voltammetry curves obtained in solutions containing no pyrophosphate with those of Fig. 2 showed that the pyrophosphate ion does not contribute to any of the electrode processes in this potential range. The current begins to rise rapidly at ~ -0.4 and peaks at ~ -0.8V. At the two extremes of the *p*H range studied, this -0.8V peak is the dominant feature of the cyclic voltammetry, although a small shoulder at more cathodic potentials is apparent, particularly in the measurement at *p*H 12.5. A second peak occurs at ~ -1.0V in the *p*H range from 9.5 to 11.5 in unstirred solutions.

The dependence on sweep speed of the two peaks observed at *p*H 10.5 is shown in Fig. 3. As the sweep speed is reduced, little change in the more anodic peak is observed. The more cathodic peak is highly dependent on sweep speed. The size of the peak decreases as the sweep speed is reduced, becoming a current plateau without evidence of a peak at 10 mV/sec. In the anodic-going portion of the scan, two plateaus are observed which correspond to the two peaks in the cathodic scan.

The current-potential profile for the measurement at *p*H 12.5 can be changed by altering the conditions of

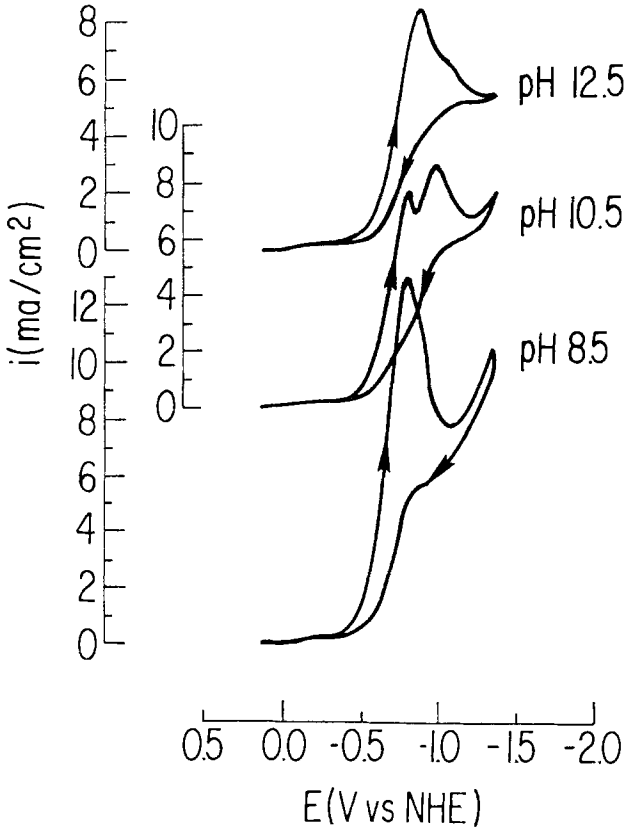


Fig. 2. *p*H dependence of the cyclic voltammetry of an Au electrode in a ~0.15M Au(I) sulfite solution containing 0.5M Na_2SO_3, and saturated with $Na_4P_2O_7$. Sweep speed 50 mV/sec.

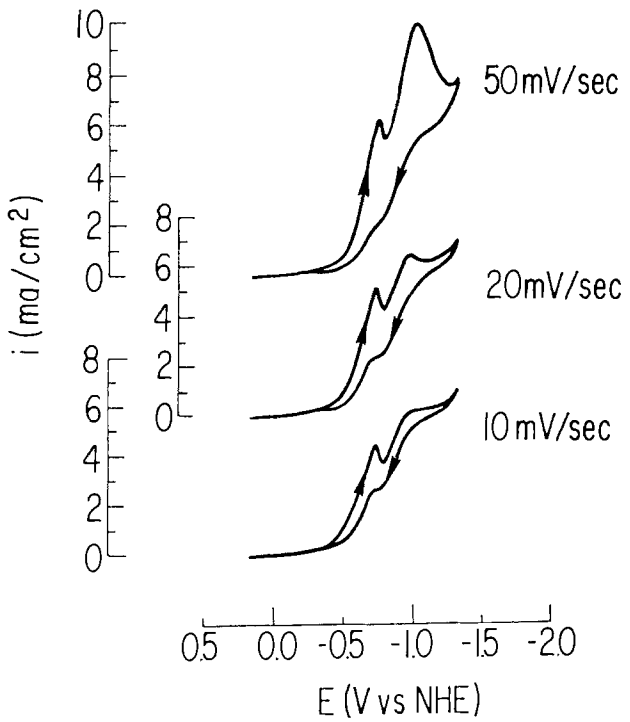


Fig. 3. Dependence on sweep speed of the cyclic voltammetry of an Au electrode in a solution with the same composition as that for Fig. 2, *p*H 10.5.

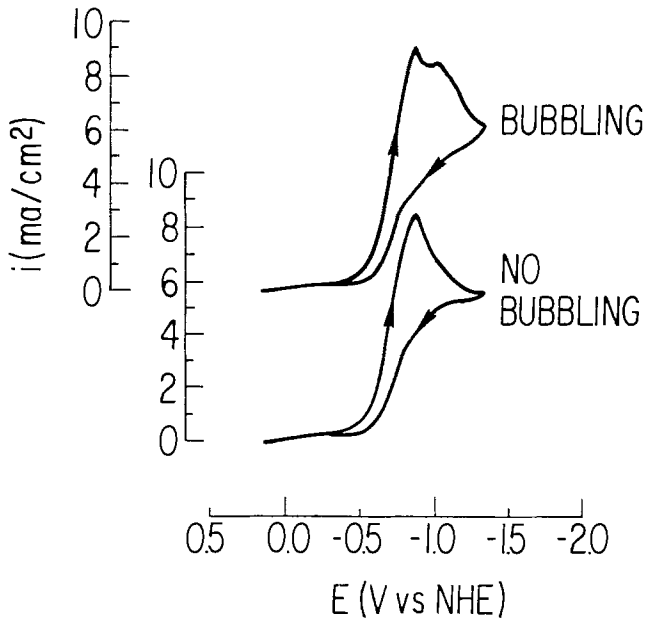


Fig. 4. Dependence on mass transport of the cyclic voltammetry of an Au electrode in a solution with the same composition as that for Fig. 2, pH 12.5. Sweep speed 50 mV/sec.

mass transport, as illustrated in Fig. 4. The lower curve was obtained in the same manner as the pH 12.5 curve in Fig. 2. The upper curve shows the current potential behavior when the N_2 bubbler remained in the solution during the measurement, thereby increasing the mass transport. In this case, the peak appearing at more negative potentials is much more distinct. This second peak is increased in size by increased mass transport at all pH values studied except pH 8.5, where it is not clearly observed.

An experiment was carried out in which the electrode potential was swept at 50 mV/sec from 0.2V to the potential of the peak, and then held at the peak potential. When the potential is swept only to the first peak (that at less negative potentials) and held there, the current decays in a uniform fashion. The current decay is much more complex when the potential is swept to the second peak and held. After an initial decay, a small increase in current is observed, followed by further slow decay.

The existence of two peaks in the cyclic voltammetry indicates that the one-electron reduction of the gold sulfite complex to metallic Au is taking place via two different mechanisms. The kinetics and mechanism of this process have been further investigated using the potential step method. The potential of the working electrode was stepped from 0.2V, where no Au deposition occurs, to a potential of active Au deposition, and the time dependence of the current was monitored. The results of a potential step from −0.2 to −0.51V, a potential (Fig. 2) well on the positive side of the first current peak, are shown in Fig. 5. (A change in the time scale occurs at the center of the abscissa in order to allow a wider range of times to be displayed conveniently in the same graph.) At this potential, the current decays in a smooth, monotonic fashion.

These data have been analyzed using the method of Gerischer (19) for study of an electron transfer preceded by a chemical reaction. This method assumes a mechanism in which the complex first loses the ligand X

$$A \underset{+\gamma X}{\overset{-\gamma X}{\rightleftarrows}} B \qquad [1]$$

and then the charge transfer occurs

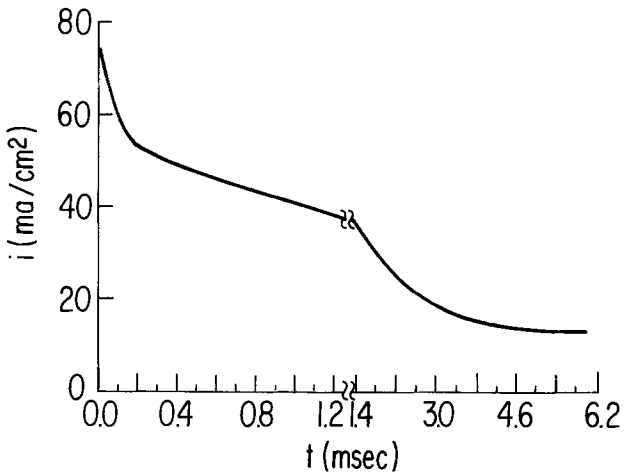


Fig. 5. Time dependence of current decay after a potential step from 0V to −0.51V for a Au electrode in a solution with the same composition as that for Fig. 2, pH 10.5.

$$B \underset{-ne^-}{\overset{+ne^-}{\rightleftarrows}} C \qquad [2]$$

For this over-all reaction [1]-[2], Gerischer (19) determined that

$$i = -2i_A(t/\pi\tau)^{1/2} \text{ when } t << \tau \qquad [3a]$$

$$i = i_A(\tau/\pi t)^{1/2} \text{ when } t >> \tau \qquad [3b]$$

where

$$i_A = n\mathbf{F}(C_A^\circ + C_B^\circ)\sqrt{D/\tau}$$

C_A° and C_B° are bulk concentrations, D is the diffusion coefficient (assumed equal for A and B)

$$\tau = k_B/k_A^2$$

and k_A and k_B are, respectively, the forward and reverse rate constants of Eq. [1]. The current in the time region where Eq. [3a] is applicable is determined by reaction rate, while [3b] describes the current under diffusion control. At times that are short compared to τ, i is a linear function of $t^{1/2}$ with a slope s_1 of $-2i_A(\pi\tau)^{-1/2}$; at times that are long compared to τ, i is a linear function of $t^{-1/2}$ with a slope s_2 of $i_A(\tau/\pi)^{1/2}$. From these two values, i_A and τ can be determined.

The analysis outlined here, which uses data at both short and long times in the determination of i_A and τ, differs slightly from that described by Gerischer (19). He describes how to determine these two parameters using data only from regions where $t << \tau$, $t >> \tau$, or t is on the order of τ. Consistency of the measured parameters in the different time regions provides a test of the mechanism. Comparison of values of i_A and τ by this method with those obtained by Gerischer's method in the range $t << \tau$ shows good agreement.

The data of Fig. 5 can be fit by the Gerischer mechanism, as shown in Fig. 6, in which the data of Fig. 5

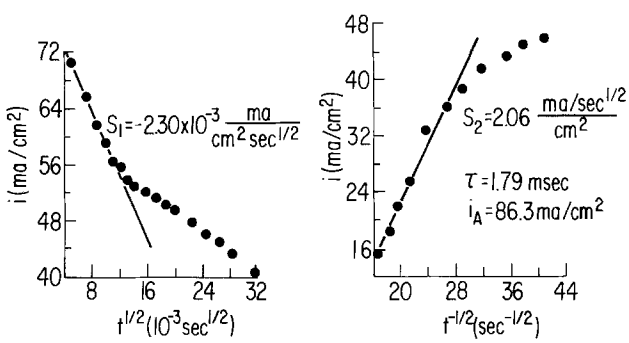


Fig. 6. The data of Fig. 5 plotted as a function of $t^{1/2}$ and $t^{-1/2}$

have been plotted as a function of $t^{1/2}$ and $t^{-1/2}$. From the linear portions of the two curves in Fig. 6, τ and i_A are determined to be 1.8 msec and 86 mA/cm^2, respectively. Since the equilibrium constant K is not known for the gold sulfite complex, k_A and k_B cannot be determined.

It was found at all pH values studied that the Au deposition process could be adequately described by Eq. [1] and [2] as long as the final potential of the step was anodic to ~ -0.8V. For larger potential steps, the current no longer decays in a monotonic fashion, and plots of i *vs.* $t^{1/2}$ and $t^{-1/2}$ do not have linear portions. These results are consistent with the results of the cyclic voltammetry shown in Fig. 2. The first current peak occurs at ~ -0.8V, and the mechanism of Au deposition becomes more complicated at potentials more negative than this.

Below the potential of the first current peak, both i_A and τ were found to increase with increasing potential of the pulse. The scatter in the data was found to be of the same order of magnitude as the variation of these parameters with pH. The results of the measurements are shown in Table I.

On the basis of the cyclic voltammetry and the potential step results, we propose that, at potentials less negative than ~ -0.8V, the deposition of Au from its sulfite complex can be described by the two-step mechanism consisting of the dissociation of the complex followed by electron transfer. This is postulated to be the following.

$$[Au(SO_3)_2]^{3-} \rightleftarrows Au^+_{ads} + 2SO_3^{2-} \quad [4]$$

$$Au^+_{ads} + e^- \rightarrow Au \quad [5]$$

At more negative potentials, a second mechanism is possible. This is thought to be a direct electron transfer to the undissociated $[Au(SO_3)_2]^{3-}$ complex. This mechanism apparently does not involve a strongly adsorbed intermediate and has a stronger dependence on mass transport than the mechanism of Eq. [4] and [5]. Increasing the rate of mass transport therefore increases the size of the second peak relative to the first peak.

The observed pH dependence is complex. The proposed direct electron transfer to the sulfite complex is unfavorable at pH 8.5. It occurs at all higher pH values but is most rapid at pH 10.5, and is again less favorable at high pH. This behavior cannot be readily interpreted in terms of the dissociation constants of the species believed to exist in solution. The $[Au(SO_3)_2]^{3-}$ complex becomes unstable at pH values lower than 8. The decreased stability of the complex at low pH may make the mechanism involving the dissociation of the complex more favorable than the direct electron transfer to the complex.

Effects of pulsed potentiostatic deposition on deposit properties.—In order to examine the effects of pulsed potentiostatic deposition on the properties of Au films deposited from the sulfite solution, a series of Au films of approximately 1 μm thickness was deposited on a substrate which had a 200Å thickness of evaporated Au on an adhesion layer of 200Å evaporated Nb. Frequencies from constant potential to 1 kHz were used with solutions of pH 8.5 and 13. The potential was pulsed from -0.19V, a potential at which no deposition occurs, to a potential E_2, at which deposition takes place. The duration of the pulse to the potential E_2 was chosen to be 10% of the total cycle in order to allow the diffusion layer to relax back as close as practical to the bulk concentration.

Table I. Kinetic parameters τ and i_A obtained from potential step measurements

pH	Final potential (V *vs.* NHE)	i_A (mA/cm^2)	τ (msec)
8.5	0.31	56	2.6
8.5	0.51	73	2.9
8.5	0.71	85	2.7
10.5	0.31	47	1.1
10.5	0 51	86	1.8
10.5	0.71	96	2.2
13.0	0.31	47	1.2
13.0	0.51	70	2.1
13.0	0.71	91	2.1

Table II. Rate of deposition and resistivity of films deposited pulse potentiostatically from Au(I) sulfite solutions

f (Hz)	E_2 (V *vs.* NHE)	pH	Over-all deposition rate (Å/min)	ρ ($\mu\Omega$ cm)
Constant E	−0.56	8.5	1465	2.98
Constant E	−0.56	13.0	1865	3.98
1	−0.56	8.5	150	2.67
5	−0.56	8.5	120	3.12
5	−0.56	13.0	180	2.99
10	−0.56	8.5	75	2.59
10	−1.31	8.5	2190	4.12
50	−1.31	8.5	625	3.02
50	−1.31	13.0	1110	2.81
100	−1.31	8.5	105	2.57
100	−1.81	8.5	695	2.95
500	−1.81	8.5	65	4.26
500	−1.81	13.0	75	3.89
1000	−1.81	8.5	40	3.74

Gold is deposited at a constant potential of -0.56V from the additive-free gold sulfite solution at $\sim$1500 Å/min in the form of a large-grained deposit of a dull, brownish color. The potential of -0.56V was chosen because deposition at this potential from the additive-free gold sulfite solution occurs at a steady-state current of the order recommended for galvanostatic plating from commercial sulfite baths[1] (1-3 mA/cm^2). When deposition takes place under pulsed potentiostatic conditions, the appearance of the films changes somewhat with frequency and potential E_2. However, none of the conditions investigated results in bright deposits.

The over-all rate of deposition shown in Table II, falls off rapidly with increasing frequency, since at higher frequencies a larger fraction of the time at E_2 is necessary for double layer charging. (The rates given in Table II are over-all rates. Since the actual time of deposition in the pulsed mode is 10% of the total time, the instantaneous rate is about 10 times greater. This means the instantaneous deposition rates at constant potential and 5 Hz are approximately the same.) Within limits, the rate can be increased by making E_2 more cathodic, but the drop-off in rate is so rapid that for frequencies greater than 100 Hz, even for pulses to -1.81V, several hours are necessary to obtain 1 μm films. The disparity in rates also makes it difficult to compare directly films obtained at low and high frequencies, since at E_2 values which are sufficiently low to avoid gassing at low frequencies, deposition rates at high frequencies are negligible. Under any given set of conditions, the rate of Au deposition from the pH 13 solution is substantially higher than that from the pH 8.5 solution.

Table II also shows the resistivities of these films. These values were obtained from a four-point probe determination of resistance and a profilometer thickness measurement of a step etched in the film. The resistivities of these films (uncorrected for thin film effects) are low, in most cases approaching that of bulk Au (2.44 $\mu\Omega$ cm at 20°C). The resistivity appears to have no clear dependence on frequency of deposition or pH.

The main factor contributing to the low resistivities of these films is believed to be their high purity. Electron microprobe analysis showed that S, P, and Cl, the most likely contaminants, were below the limits of detection of the method (i.e., <200 ppm by weight for S and P, and <300 ppm by weight for Cl).

Information about the surface topology of these deposits has been obtained using scanning electron mi-

[1] Sel-Rex BDT 510 Au bath. Sel-Rex Corporation, Nutley, New Jersey.

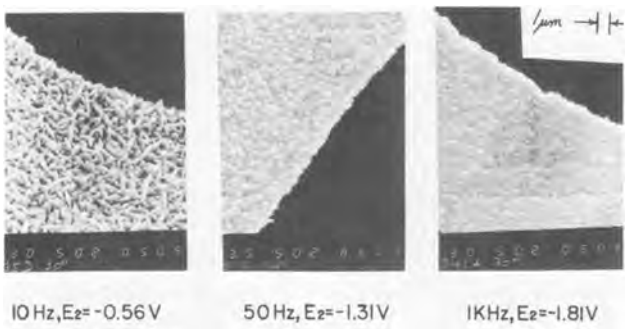


Fig. 7. SEM's of Au deposits from the sulfite solution at pH 8.5 at three different frequencies.

croscopy. Figure 7 shows SEM's of Au films deposited at three frequencies from the pH 8.5 solution. The surface morphology is found to vary with the conditions of deposition. At low frequencies the Au is deposited in the form of crystallites with clearly developed shapes and faces. As the frequency of deposition increases, the crystallites become smaller and partly rounded. Similar trends were observed for deposits from the pH 13 solution, which have somewhat larger surface features than deposits from the pH 8.5 solution.

These deposits have also been examined using x-ray diffraction methods. The defect structure of the pulsed potentiostatically deposited Au films has been investigated using a single peak variation of the multiple order Warren-Averbach analysis. The Warren-Averbach analysis is described by Warren (20); the single peak thin film variation is described by Gangulee (21). Such analyses give information about texture, macro- and microstresses, average grain size, the probability of stacking faults and twinning, and dislocation density in the Au films. These data are summarized in Table III. The values tabulated are σ_{xx}, the macrostress; D^{hkl}, the average grain size in the [hkl] direction; $\langle E_{50}^2 \rangle^{1/2}$, the root mean square microstrain averaged over a 50Å region; and N_d, the dislocation density. The negative sign of σ_{xx} indicates tensile stress. Other values which were measured but not tabulated are the probabilities of intrinsic and extrinsic stacking faults, which were approximately zero in all cases, and the probability of twinning, which was in the range 0.003-0.005.

Of the properties summarized in Table III, only the texture of the deposit shows a marked dependence on the conditions of deposition. Comparison of Tables II and III shows that the primary texture can differ from (111) when the deposition rate is high. At high rates of deposition the preferred texture becomes (110). Although Table III indicates that the primary texture of the constant potential sample varies with pH, the pole figures for these two films are similar; the film deposited from the pH 13 solution has only slightly more (100) texture.

Both the macrostresses and microstrains of these deposits are small and show no clear dependence on frequency. The macrostresses are slightly larger in the deposits from the higher pH solution. The grain size is large and not significantly decreased by the use of higher frequencies. The grain size measured by x-ray diffraction is not the same as the crystallite size which is seen in the SEM photographs of Fig. 7. The SEM indicates surface morphology, and may not reveal individual grains without etching. The quantity measured by x-ray diffraction is the grain size perpendicular to the surface.

The observed result that the use of pulsed potentiostatic deposition does not cause distinct changes in the properties of Au deposited from sulfite solutions is apparently due to the irreversibility of the Au/Au(I) couple in sulfite solution. A Au electrode immersed in the gold sulfite solution does not establish a stable reversible potential. The results in the nonreversible sulfite solution can be contrasted with the studies of the pulsed galvanostatic deposition of Au from a cyanide citrate bath by Reed and Safranek (11). The effectiveness of pulsed methods in improving the properties of Au deposited from its cyanide complex can be explained by the greater reversibility of the electron transfer in this system.

Pulsed potentiostatic deposition through a mask.— Gold was deposited pulsed potentiostatically from the pH 8.5 gold sulfite solution through a photoresist test mask. The test mask consisted of an area of lines 50 μm wide at variable spacings, a similar area consisting of 25 μm wide lines, an area of 50 μm squares at variable spacings, and a similar area of 25 μm squares. The closest spacing was 6.25 μm; the largest was about ten times the line width. A second test mask consisted of a 10 times reduction of this pattern; in the smaller pattern, the narrowest spacing, 0.625 μm, was not resolved during exposure of the photoresist. Gold was deposited through these masks at several frequencies, with the pulse to E_2 being 10% of the cycle.

Figure 8 shows the profile of Au deposited by a 100 Hz pulse to −1.81V through the portion of the mask consisting of nominally 50 μm lines. Under these conditions, the deposit was found to be substantially thicker at the edge of the line than in the center. This effect became more pronounced as the spacing between lines increased. The lines also became thicker with larger spacing, Both of these effects are explained by the crowding of lines of current flow at the edges of lines as spacing between them is increased. The thickness of the Au deposit in the squares on the same wafer was found to be 2-4 times that in the lines of the same width, a result which can also be explained by crowding of the lines of current flow at the edges, since the squares have a greater edge/area ratio than the lines.

When a 500 Hz pulse to −1.81V is used, the uniformity of the deposit in the same pattern is greatly improved, as shown in Fig. 9. Under these conditions, there is less variation in deposit thickness across a given line. A nonuniformity in line thickness with spacing still exists, but it is quite different than that observed at the lower frequency.

Table III. Summary of x-ray diffraction data for Au films deposited pulsed potentiostatically

f (Hz)	E (V vs. NHE)	pH	Primary texture	σ_{xx} (10^8 d/cm²)	D_{eff}^{200} (Å)	D_{eff}^{111} (Å)	D_{true}^{111} (Å)	$\langle E_{50}^2 \rangle^{1/2}$ (10^4)	N_d (10^{10} cm/cm³)
Constant E	−0.56	8.5	111	−6	—	650	820	6	1.1
Constant E	−0.56	13.0	100	−13	540	690	880	7	1.2
1	−0.56	8.5	111	−3	—	690	970	6	0.9
5	−0.56	8.5	111	−4	—	690	880	8	1.3
5	−0.56	13.0	111	−3	—	750	980	7	1.0
10	−0.56	8.5	111	−2	—	720	920	6	1.0
10	−1.31	8.5	110	−13	—	510	600	8	2.0
50	−1.31	8.5	110	~0	480	720	1160	6	0.8
50	−1.31	13.0	110	−24	—	570	750	4	0.8
100	−1.31	8.5	111	−14	420	550	720	7	1.4
100	−1.81	8.5	111	−9	—	590	780	8	1.5
500	−1.81	8.5	111	−12	—	480	610	9	2.2
500	−1.81	13.0	111	−25	—	440	540	9	2.4
1000	−1.81	8.5	111	~0	340	450	590	9	2.2
				±2	±5%	±5%		±2	

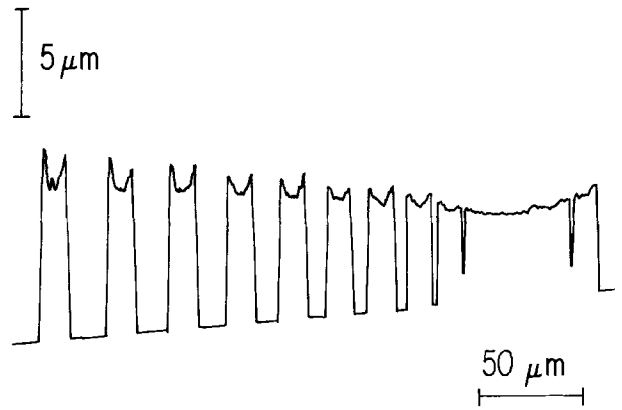


Fig. 8. Profile of Au deposited through a mask consisting of nominally 50 μm lines using a 100 Hz pulse to −1.81V. pH is 8.5.

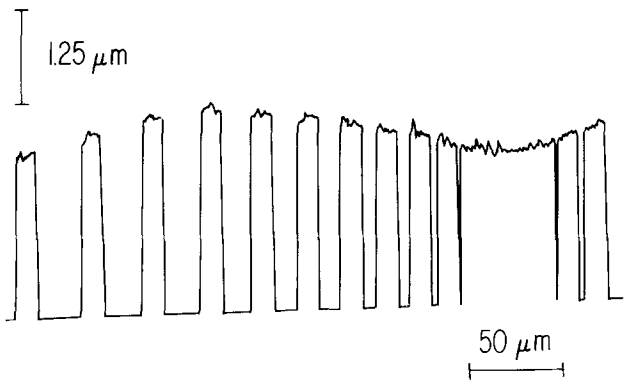


Fig. 9. Profile of Au deposited through a mask consisting of nominally 50 μm lines using a 500 Hz pulse to −1.81V. pH is 8.5.

The result of deposition at 500 Hz through the nominally 5 μm lines is shown in Fig. 10. In this case, uniformity both across the line and across the pattern is good. The total area sampled in Fig. 10 is only about 10% of that sampled in Fig. 8 and 9, and the size of the features is small compared to the distances over which nonuniformities are apparent in Fig. 8 and 9.

Rates of Au deposition through the mask are much greater than the rate of deposition of unpatterned films, due to the inceased edge to area ratio. Representative deposition rates for sheet films and patterns are given in Table IV.

Conclusions

Investigation of Au films deposited from sulfite solutions at pH 8.5-13 showed no apparent dependence of the purity, resistivity, grain size measured by x-ray diffraction, microstrain, or macrostress on the frequency of deposition. This result is consistent with the model of Despic and Popov (2) for pulse potentiostatic deposition in nonreversible systems. Those properties which were influenced by the conditions of deposition were the thickness distribution of Au deposited through a mask, the crystallographic texture, and surface morphology. The Au deposited from solutions of the Au(I) sulfite complex is a soft, low stress film with a large grain size. It has high purity and low resistivity.

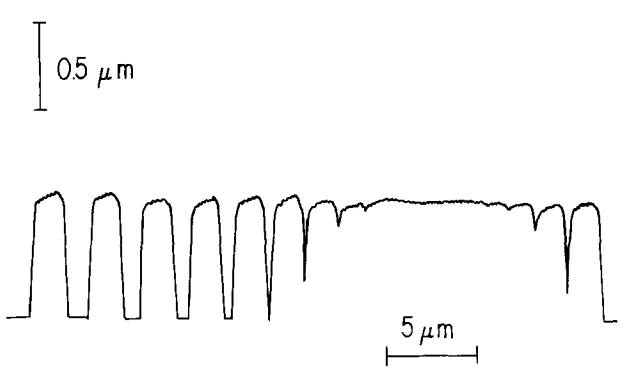


Fig. 10. Profile of Au deposited through a mask consisting of nominally 5 μm lines using a 500 Hz pulse to −1.81V. pH is 8.5.

Table IV. Comparison of deposition rates on sheet substrates and through a mask for the pH 8.5 gold sulfite solution

f (Hz)	E_2 (V vs. NHE)	Deposition rate sheet film (Å/min)	Deposition rate 50 μm lines (Å/min)	Deposition rate 5 μm lines (Å/min)
50	−1.31	625	~2800	~2500
100	−1.81	695	~3100	~1300
500	−1.81	65	~290	~350

The mechanism of deposition of Au from solutions of its sulfite complex at potentials less negative than ~ −0.8V can be interpreted as a dissociation of the complex to form Au(I) adsorbed on the electrode surface, followed by a single electron transfer. At more cathodic potentials, a second reduction mechanism occurs which is thought to be direct electron transfer to the complexed gold ion. This second process is mass transfer controlled, and exhibits a pH dependence. It becomes less favorable at low pH.

Gold deposited through a photoresist mask from solutions of its sulfite complex show large thickness variations both across any given line and from line to line across the pattern. These thickness variations can be influenced by pulsed potentiostatic deposition. Use of high frequencies is effective in eliminating nonuniformity in the thickness of a given line. Line to line variations are more difficult to eliminate.

Acknowledgments

The authors would like to thank A. Gangulee for the x-ray diffraction measurements and their interpretation. The experimental help of C. Aliotta, M. Blakeslee, S. Ellmann, V. Maniscalco, P. McCaffrey, J. Olsen, and A. Pfeiffer is gratefully acknowledged. The authors have profited from discussion of this work with R. Acosta, V. Brusic, and A. Tuxford.

Manuscript submitted March 21. 1977; revised manuscript received June 13, 1977. This was Paper 335 presented at the Washington, D.C., Meeting of the Society, May 2-7, 1976.

Any discussion of this paper will appear in a Discussion Section to be published in the June 1978 JOURNAL. All discussions for the June 1978 Discussion Section should be submitted by Feb. 1, 1978.

Publication costs of this article were assisted by IBM Corporation.

REFERENCES

1. A. R. Despic and K. I. Popov, *J. Appl. Electrochem.*, **1**, 275 (1971).
2. A. R. Despic and K. I. Popov, in "Modern Aspects of Electrochemistry," Vol. 7, B. E. Conway and J. O'M. Bockris, Editors, p. 199, Plenum Press, New York (1972).
3. G. Savic-Maglic and A. R. Despic, *Electrodeposition Surf. Treat.*, **1**, 429 (1973).
4. K. I. Popov, B. J. Lazarevic, and M. Kostic, *J. Appl. Electrochem.*, **3**, 161 (1976).
5. K. I. Popov, D. N. Keca, D. A. Draskovic, and B. I. Vuksanovic, *ibid.*, **6**, 155 (1976).
6. K. I. Popov, D. N. Keca, S. I. Vidojkovic, B. J. Lazarevic, and V. B. Milojkovic, *ibid.*, **6**, 365 (1976).
7. K. I. Popov, D. N. Keca, and G. R. Ostojic, *ibid.*, **6**, 425 (1976).
8. H. Y. Cheh, *This Journal*, **118**, 551 (1971).
9. M. Braun and N. Ibl, *Oberflaeche*, **14**. 49 (1973).
10. M. Braun, Doctoral dissertation, Eidgenossischen Technische Hochschule, Zurich (1973).
11. A. H. Reed and W. H. Safranek, Battelle Columbus

Laboratories Report to the Chamber of Mines of South Africa, March, 1973.
12. V. J. Marchese, *This Journal*, **99**, 39 (1952).
13. P. T. Smith, U. S. Pat. 3,057,789 (1962).
14. R. T. Page, "A Review of Gold Electroplating Systems," p. 25, Fuel and Metallurgical Journals, Ltd., Redhill, England (1974).
15. A. M. Tuxford and L. T. Romankiw, Paper 223 presented at The Electrochemical Society Meeting, New York, New York, Oct. 13-17, 1974.
16. E. Spiller, R. Feder, J. Topalian, E. Castellani, L. T. Romankiw, and M. Heritage, *Solid State Technol.*, **19**, 62 (1976).
17. B. D. Cahan, Z. Nagy, and M. A. Genshaw, *This Journal*, **119**, 64 (1972).
18. R. Adzic, J. Horkans, B. D. Cahan, and E. Yeager, *This Journal*, **120**, 1219 (1973).
19. H. Gerischer, *Z. Elektrochem.*, **64**, 29 (1960).
20. B. E. Warren, "X-Ray Diffraction," p. 251-313, Addison-Wesley, Reading, Mass. (1969).
21. A. Gangulee, *J. Appl. Crystallogr.*, **7**, 434 (1974).

Electro-Optic Investigations of Thin, Electrodeposited Germanium Layers

W. Paatsch

Bundesanstalt für Materialprüfung, Berlin, Germany

ABSTRACT

50Å to 30 μm thick germanium layers were electrodeposited on copper, silver, and gold substrates using organic nonaqueous electrolytes. X-ray, electrochemical, and electro-optic investigations were carried out to characterize the layers. X-ray studies show that the layers are of amorphous structure. The electrochemical properties of the thick electroplated germanium are not significantly different from the behavior of the crystalline material. From photopotential measurements it is concluded that the layers are of n-type conductivity. Electroreflectance spectra are characteristic for an amorphous semiconductor.

In spite of numerous investigations on the physical properties of germanium only a little work exists about electrodeposited thin germanium layers. Because of the potential distribution at the solid-state/electrolyte interface, using this technique for sample preparation, nucleation and the growth of crystallites takes place far away from equilibrium conditions. Therefore amorphous or at least strong disordered structures will be expected, which are of great interest.

Experimental Details

Germanium films were prepared from organic nonaqueous solutions of 7% $GeCl_4$ in ethylene glycol, $C_3H_6(OH)_2$ (1). The electrolyte temperature during electrodeposition was 59°C, the current density 400 mA cm^{-2}. Because of the codeposition of hydrogen the current efficiency was about 1%, the rate of deposition 20 Å sec^{-1}. The layer thickness was varied from 50Å to 30 μm. As substrates electroplated copper, gold, and silver were used, which were mechanically polished by diamond pastes of various sizes down to 0.25 μm and cleaned in the usual manner.

To characterize the morphology of the layers scanning electron microscope, microanalyzer, and x-ray diffraction experiments were carried out. In addition the electrochemical and optical properties of the layers were studied. The experimental equipment was previously described in detail (2, 3).

Experimental Results

The surface morphology of the copper substrate and a 10 μm thick electroplated germanium layer studied by scanning electron microscopy is shown in Fig. 1. With germanium electroplating, surface roughness and flaws of the substrate are leveled and a very smooth and mirrorlike appearance is obtained.

X-ray diffraction pattern of the germanium layers consisted only of a few broad rings; that means the thin films were amorphous as was also expected from etching experiments (4). Annealing for some hours beyond the amorphous-crystalline transition temperature of 235°C (5) (16 hr at 400°C in a protective gas atmosphere consisting of 95% nitrogen and 5% hydrogen) gives distinct 111-reflections and a lattice parameter which agrees fairly well with the value 3.27Å of crys-

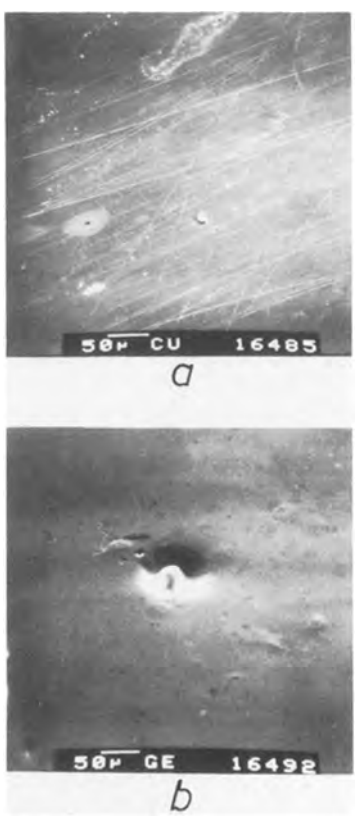


Fig. 1. Scanning electron micrograph of the copper substrate (a) and a 10 μm thick electrodeposited germanium layer (b).

Key words: amorphous semiconductors, semiconductor-electrolyte interface, photovoltage, electroreflectance.

talline material. From the diffraction experiments the crystal size can be estimated as less than 50Å.

Microprobe analysis of unannealed, approximately 500Å thick germanium layers showed that a homogeneous surface coverage of the copper substrate was formed by electroplating. For very thin layers, however, this was not always obtained because of crystal defects of the substrate in connection with an inhomogeneous field strength at the interface.

Further, the electrochemical properties of the germanium layers, as, *e.g.*, hydrogen evolution, in acid solutions were studied. It is well known that the hydrogen overvoltage is very sensitive to the energetic surface state as it was studied for the crystal orientation in the case of germanium single crystal electrodes (6). Figure 2 shows the connection between the hydrogen overvoltage and the layer thickness related to the value of the copper substrate. (Using the current density of $i = 125\ \mu A\ cm^{-2}$ the absolute values related to the potential of the saturated calomel electrode, SCE, for the copper substrate and crystalline compact germanium were −60 mV and −700 mV). The shape of the curve clearly shows that for thickness values greater than 1 μm the electrode behavior is only influenced by the germanium which proves that the layers were compact. With decreasing layer thickness, in agreement with the results of the microprobe experiments, the germanium coverages become porous and below a limiting value of about 40Å the hydrogen overvoltage is given only by the copper substrate.

Further information concerning the electrode behavior can be obtained by the measurements of the differential capacity of the interface. Figure 3 gives the relation between the current density as well as the capacity and the electrode potential for an n-doped germanium single crystal electrode. In the experiment the electrode potential was modulated by a sine wave of 5 kHz frequency and 10 mV peak-to-peak amplitude and the capacity was analyzed using a lock-in amplifier and the conventional equivalent-circuit diagram of the solid-state/electrolyte interface. Studying a semiconductor electrode it is important to remember that the space charge capacity and the Helmholtz capacity of the electrochemical double layer form a series connection. It follows that only the space charge capacity is measured because of being an order of magnitude lower than the double layer capacity. In contrast to the current density which is very low and nearly constant, the capacity changes characteristically in the potential region between the anodic dissolution of germanium and the cathodic hydrogen evolution. Changing the electrode potential in the anodic-cathodic direction near $V_E = -100$ mV a minimum is obtained which appears near $V_E = -400$ mV in the opposite polarization direction. It was shown by Gobrecht and co-workers (7) that these capacity minima belong to

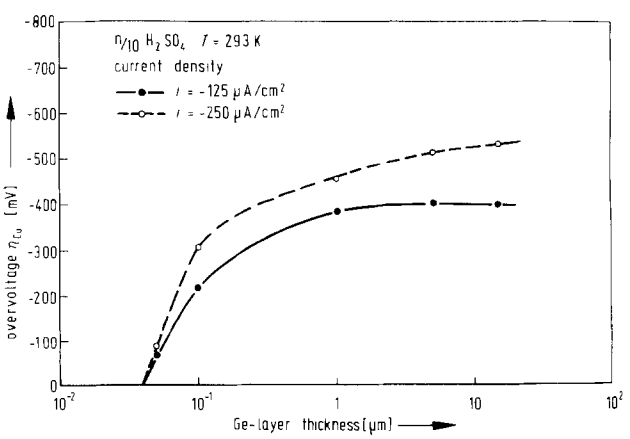


Fig. 2. Relative hydrogen overvoltage as a function of the germanium layer thickness.

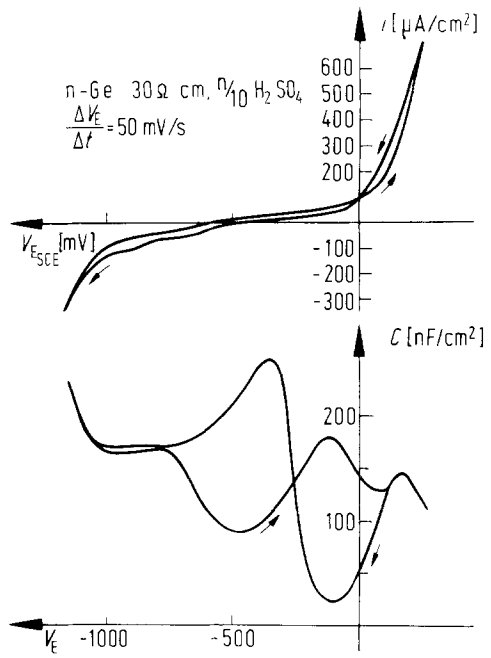


Fig. 3. Current and capacity potential characteristic of a germanium single crystal electrode.

the stable surface coverages Ge-OH and Ge-H. The transition in acid solutions is given by the following equation

$$Ge - OH + 2H^+ + 2e^- \rightleftarrows Ge - H + H_2O$$

As the potential decay in the Helmholtz layer remains constantly in the potential region between the two capacity minima every change of the electrode potential affects the space charge of the semiconductor and therefore the surface field strength. In this region investigation of the electroreflectance are possible and are discussed later.

The behavior of the current density and the capacity of 1 μm thick electrodeposited germanium are shown in Fig. 4. Very little differences are obtained between thick amorphous layers and compact crystalline material: For electroplated germanium the absolute values of the current density are lower and in this connection

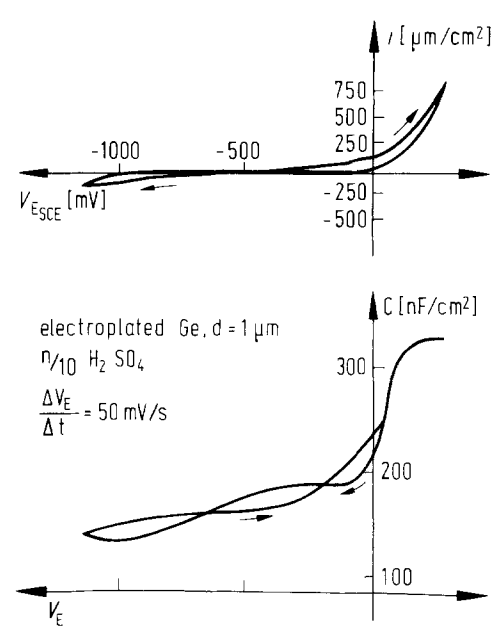


Fig. 4. Current and capacity potential characteristic of a 1 μm thick electrodeposited germanium layer.

the capacity minima are not so distinct. But obviously the same electrochemical processes and a comparable potential distribution at the interface take place. The influence of the layer thickness for values lower than 1 μm is given in Fig. 5. For clarity only the capacity for the first cycle, starting in the anodic potential region, is shown. As can be expected from the results of the hydrogen evolution studies with decreasing thickness of the germanium layer the capacity is affected by the copper-base metal. Especially the order of magnitude of the capacity changes from some nF cm^{-2} in the case of thicker layers to some μF cm^{-2} for thicknesses less than 0.1 μm, which is characteristic for metal electrodes. The capacity minimum and maximum for the copper electrode in the anodic-cathodic direction are caused by the hydrogen adsorption, which is discussed elsewhere (8).

The electro-optical properties of the electroplated germanium layers were studied by photopotential and electroreflectance measurements. In order to avoid electrochemical reactions and to obtain in agreement with the Dewald theory (9) a constant charge density at the surface, the potential region between −800 and 0 mV was studied and the electrode was illuminated with light flashes of 10^{-4}-10^{-3} sec. The photopotential V_{ph} was measured between the galvanostatically polarized germanium electrode and a second, not illuminated and nonpolarized platinum electrode using a signal averaging system (3). Figure 6 shows the dependence of the photopotential on the electrode potential for different germanium layer thickness values. The graph is characteristic for n-doped germanium; the influence of the layer thickness seems not to be very unique. It is however remarkable that the sign of the photopotential changes always at the electrode potential $V_E = -350$ mV and does not depend on the layer thickness. This value is the flatband potential if no fast surface states are present and if a correction for the Dember potential is done. The influence of fast surface states cannot be excluded *a priori* in the experiments with the thin layers on germanium on a copper substrate. Figure 6 shows, however, that the sign reversal of the photovoltage does not depend on the thickness of the germanium layers in the range between 0.6 and 15 μm. This hints at a negligible influence of fast surface states on the flatband potential. Assuming approximately the same mobility for electrons and holes

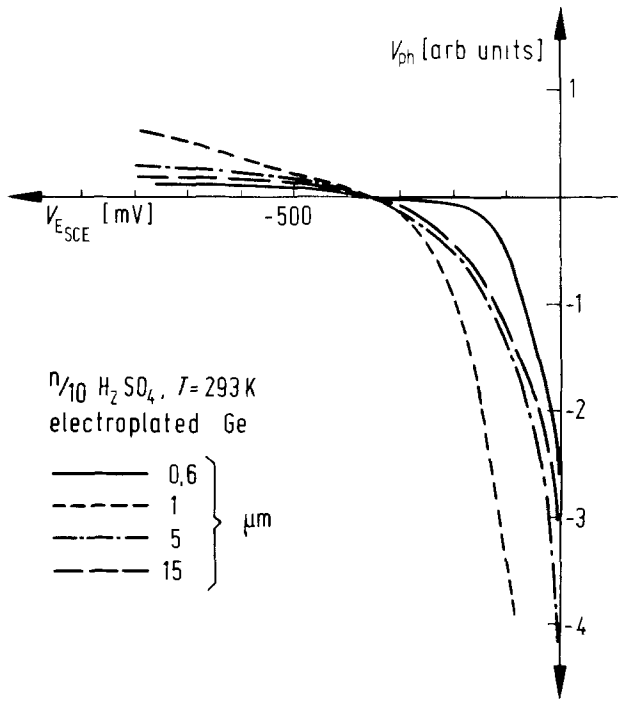


Fig. 6. Photopotential of electrodeposited germanium as a function of the electrode potential.

in the germanium layers it follows that all studied electroplated germanium layers with a thickness greater than 1 μm have the same composition and show n-type conductivity. Comparing the measured flatband potential with values on doped bulk germanium under the same experimental conditions (10) the layers have a specific conductivity of about 10 Ω cm. The reason for the doping effect is not absolutely clear. No influence of the substrate exists: Normally copper diffuses very easily into germanium and forms three valent acceptors, which give p-type conductivity (11). On the other hand, the photopotential behavior shown in Fig. 6 was obtained without any difference using silver and gold substrates, metals with lower diffusion coefficients for germanium. Doping effects are possible, however, by the incorporation of hydrogen or hydrolysis products (12) caused by the hydrogen codeposition during the germanium electrodeposition and the increase of the pH in the surface cathode film.

The electroreflectance spectrum for a germanium single crystal electrode and electrodeposited germanium for the Λ_3-Λ_1 electron transition in the 111-direction of the Brillouin zone is shown in Fig. 7. Analysis for the surface field strength value zero gives transi-

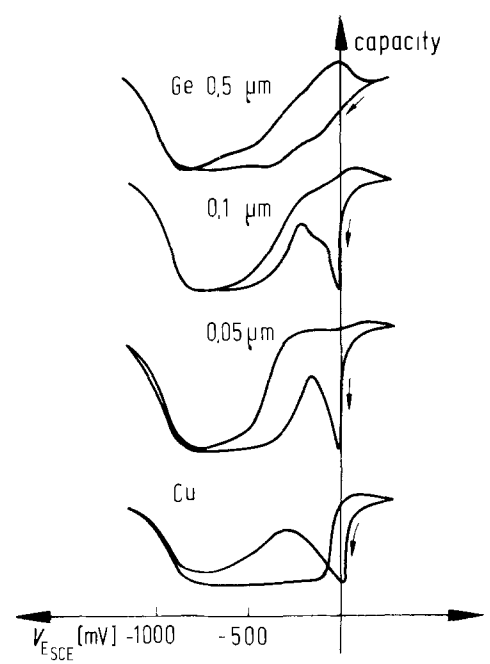


Fig. 5. Relation between the capacity potential characteristic and the thickness of electrodeposited germanium.

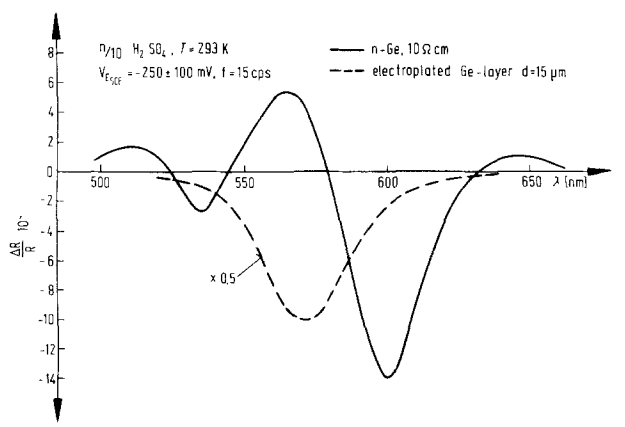


Fig. 7. Electroreflectance spectrum of a single crystal electrode and electrodeposited germanium.

tion energy values of 2.1 and 2.3 eV which belong to the Λ_3-Λ_1 transition and the corresponding split valence band term. In the case of the amorphous electrodeposited germanium layers only a broad, "unstructured" minimum of the modulated reflectance appears at lower wavelength values. This is in agreement with the investigation of the reflectance and electroreflectance of amorphous germanium layers which were prepared by other techniques (13, 14) as well as other amorphous semiconductors (15).

Summary

Germanium layers which were prepared by electrodeposition from organic nonaqueous solutions on copper, silver, and gold substrates are amorphous. Electrochemical experiments show that layers thicker than 1 μm are compact with an electrode behavior not significantly different from that of crystalline electrodes. According to photopotential measurements electroplated germanium has an n-type conductivity which does not depend on the layer thickness. The electroreflectance spectra are characteristic for amorphous semiconductors.

Acknowledgments

This work was supported by the Deutsche Forschungsgemeinschaft (DFG) which is gratefully acknowledged. For their assistance I thank Mr. W. Winkelmann and G. Blum.

Manuscript submitted Dec. 17, 1976; revised manuscript received April 20, 1977.

Any discussion of this paper will appear in a Discussion Section to be published in the June 1978 JOURNAL. All discussions for the June 1978 Discussion Section should be submitted by Feb. 1, 1978.

REFERENCES

1. G. J. Szekely, *Electroch. Soc.*, **98**, 318 (1951).
2. W. Paatsch, *Ber. Bunsenges. Phys. Chem.*, **77**, 895 (1973).
3. W. Paatsch, *ibid.*, **79**, 922 (1975).
4. T. Papa, D. Sette, and L. Stagni, *J. Phys. D*, **7**, 2024 (1974).
5. J. S. Johanessen, *Phys. Status Solidi*, **26**, 571 (1974).
6. I. A. Kazantsev and I. V. Kudryaskov, *Zh. Fiz. Khim.*, **50**, 566 (1976).
7. H. Gobrecht, M. Schaldach, F. Hein, R. Blaser, and H. G. Wagemann, *Ber. Bunsenges. Phys. Chem.*, **69**, 338 (1965).
8. W. Paatsch, *ibid.*, **81**, 645 (1977).
9. J. F. Dewald, in "Semiconductors." ACS Monograph No. 104, Vol. 2, N. B. Hannay, Editor, p. 343, Butterworths, London (1959).
10. V. A. Myamlin and Yu. V. Pleskov, "Electrochemistry of Semiconductors," Plenum Press, New York (1967).
11. C. S. Fuller and J. A. Ditzenberger, *J. Appl. Phys.*, **28**, 40 (1957).
12. A. J. Lewis, G. A. N. Connel, W. Paul, J. R. Pawlik, and R. J. Temkin, NSF-Report (USA), Grants No. GH 33576 and GH 38830 X.
13. H. Piller and R. C. Whited, *J. Phys. Chem. Solids*, **34**, 1449 (1973).
14. N. Shevchik, G. A. Neville Connell, W. Paul, J. Tejeda, and D. L. Camphansen, in Proceedings of the 2nd International Conference on Conduction in Low-Mobility Materials, pp. 207-210.
15. G. Weiser and J. Stuke, *Phys. Status Solidi*, **35**, 747 (1969).

Kinetics of the Deposition of Alumina Particles from Copper Sulfate Plating Baths

J. P. Celis and J. R. Roos

Departement Metaalkunde, Katholieke Universiteit Leuven, de Croylaan 2, B-3030 Heverlee, Belgium

ABSTRACT

In 1972 Guglielmi proposed a physical model describing the codeposition mechanism of inert particles from electrolytic baths. The proposed mechanism was based on two successive adsorption steps. The present authors demonstrated the validity of that mechanism for the codeposition of alumina and copper from acidified copper sulfate plating baths. From an experimentally derived relationship between electrolytic conditions and codeposition, the importance of the reduction of copper ions adsorbed onto Al_2O_3 is shown. The influence of monovalent cations like thallium is discussed based on the mechanism proposed by Guglielmi.

In recent years the interest in electrodeposited composite coatings rapidly increased. This was mainly due to their expected new engineering applications. Such coatings are produced by codeposition of fine inert particles and a metal matrix from electrolytic baths. Industrial applications of composite coatings with a nickel (1) or a cobalt (2) matrix have already been developed. The codeposition of inert particles and copper seemed, however, to be more difficult to realize. Sautter (3) stated that the codeposition of alumina or silicon carbide and copper from acidified copper sulfate baths was not possible. According to Williams and Martin (4) the codeposition of alumina, silicon carbide, or boron carbide and copper from a copper cyanide plating bath could readily be obtained. Chen (5) pointed out the influence of the structure of the inert particles on the codeposition. α-alumina with a hexagonal structure could be codeposited from an acidified copper sulfate bath; while γ-alumina with a spinel-type cubic structure could not be codeposited from an analogous plating bath. Tomaszewski (6) claimed that the addition of monovalent cations to the copper sulfate plating baths promoted the codeposition.

The mechansism of electrocodeposition of inert particles and metals is far from being well understood. Three mechanisms, namely, mechanical inclusion, electrophoresis, and adsorption of inert particles onto the cathode, are generally proposed in order to explain the observed codeposition. The relative importance of these three processes cannot be deduced from published experimental work. Some of those results are even contradictory. Guglielmi (7) is the only one who proposed a mathematical model for the electrocodep-

Key words: dispersion coatings, electrodeposition mechanism, copper electrolysis.

osition of inert particles. His model is based on two successive adsorption steps. In the first step the inert particles are loosely adsorbed on the cathode and they are in equilibrium with the particles in suspension. The particles are still surrounded by aosorbed ions and solvent molecules. In the second step this screen is broken through so that a strong electrochemical adsorption of the particles on the cathode takes place. The inert particles are now permanently bound to the cathode and are consequently embedded in the deposit. For this model Guglielmi derived the following equation

$$\frac{C}{\alpha} = \frac{Wi_o}{n\mathbf{F}dv_o} \cdot e^{(A-B)\eta} \cdot \left(\frac{1}{k} + C\right) \qquad [1]$$

where C is the concentration of suspended particles, α the volume fraction of particles in the deposit, W the atomic weight of the electrodeposited metal, d the density of the same, n the valence, and $\mathbf{F}$ the Faraday constant. The parameters i_o and A are related to the metal deposition and are the constants in the Tafel equation which gives a relation between the current density (i) and the overpotential (η)

$$i = i_o \cdot e^{A\eta} \qquad [2]$$

The parameters v_o and B play a symmetrical role with the parameters i_o and A but are related to the inert particle deposition. k is derived from the Langmuir adsorption isotherm and depends essentially on the intensity of the interaction between particles and cathode. Guglielmi verified the validity of his model for the codeposition of titania and silicon carbide with nickel from a nickel sulfamate bath. The present authors investigated the validity of Guglielmi's model for the codeposition of α-alumina and copper from copper sulfate plating baths. Based on experimental evidence the codeposition mechanism is further explained.

Experimental

A plate pumping process was used as the plating cell with a stainless steel cathode and a copper anode. The plating solution was an acidified copper sulfate bath and had the following composition: $CuSO_4 \cdot 5H_2O$ 118 g/liter, H_2SO_4 120 g/liter, pH 0.3. The tests were conducted at room temperature. The following products were added to this plating solution: (i) α-Al_2O_3, mean size 0.3 μm, density 3.98 g/cm^3 (Linde A, Buehler Limited); (ii) thallium (I) sulfate, "highest purity" grade (U.C.B.). All deposits were obtained at constant current density. The quantitative determination of alumina embedded in the copper matrix was performed by chemical analysis (8).

Results

Thalliumless plating baths.—The codeposition of α-alumina and copper from thalliumless plating baths was studied at different current densities. The volume percentage of embedded alumina is plotted in Fig. 1 *vs.* the volume percentage of alumina in suspension. It can be seen that maximum codeposition is attained at 2 A/dm^2 and that the curves look like a Langmuir isotherm. Such a maximum was also determined by Kariapper and Foster (9) for the codeposition of titania and nickel from nickel sulfamate baths. If the results in Fig. 1 fulfill Eq. [1] a sheaf of straight lines must be obtained when C/α is plotted *vs.* C for different values of η. The slope of those lines is then given by

$$\tan\psi = \frac{Wi_o}{n\mathbf{F}dv_o} \cdot e^{(A-B)\eta} \qquad [3]$$

In Fig. 2 the results of Fig. 1 are plotted according to Eq. [1]. The results at 0.75 A/dm^2 are mean values of three experiments. Some other results do not fit exactly and those could not be weighted since for these electrolysis conditions it was difficult to obtain a smooth adherent deposit. If these points are thrown out a good agreement is found for current densities from 0.5 to 3.5 A/dm^2.

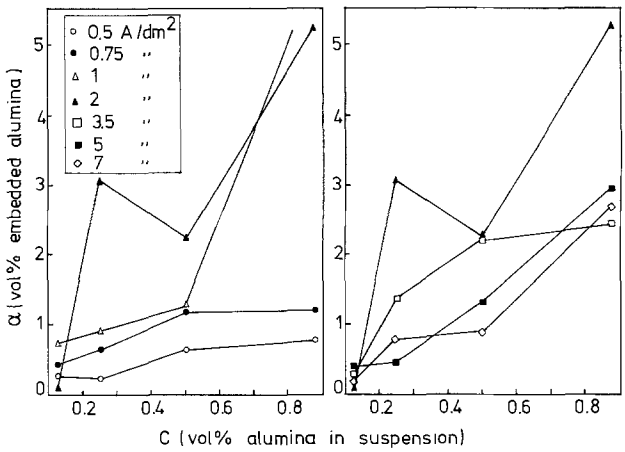


Fig. 1. Codeposition of α-alumina and copper from a copper sulfate bath.

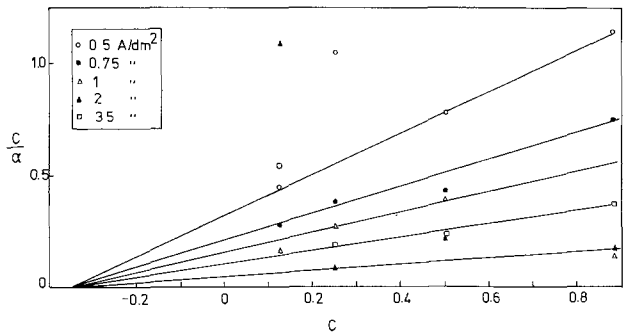


Fig. 2. Codeposition of α-alumina and copper from a copper sulfate bath, according to Eq. [1].

Plating baths containing thallium.—The results of codeposition of α-alumina and copper from copper sulfate baths containing 1 g/liter Tl_2SO_4 are plotted in Fig. 3. In the presence of monovalent thallium ions the volume percentage of embedded alumina is practically independent of the current density for values below 2 A/dm^2. For such plating baths the plots C/α *vs.* C are in accord with Eq. [1] for current density values between 0.5 and 3.5 A/dm^2. At $C/\alpha = 0$ the common intersection of the sheaf of straight lines ($1/k$) is equal to 0.35. The same value is obtained in thalliumless plating baths (Fig. 1). From this it can be seen that the interaction between the particles and the cathode,

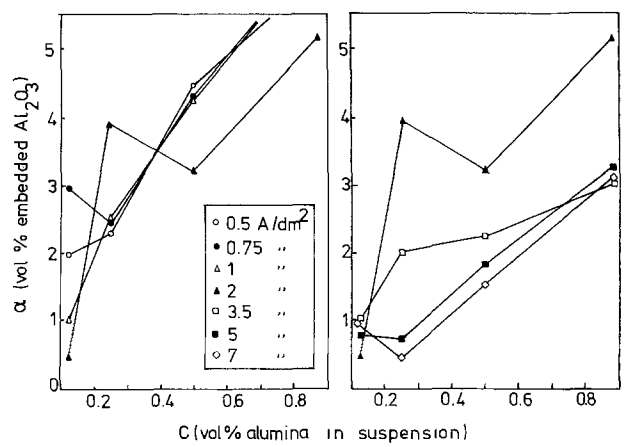


Fig. 3. Codeposition of α-alumina and copper from a copper sulfate bath containing 1 g/l Tl_2SO_4.

represented by the parameter k, seems to be unaltered by the addition of thallium to the plating baths.

Discussion

From Eq. [2] and [3] Guglielmi deduced

$$\log \tan \psi = \log \frac{Wi_0 B/A}{n\mathbf{F}dv_0} + \left(1 - \frac{B}{A}\right) \log i \quad [4]$$

which shows a linear dependence of log tan ψ on log i. The slopes of the straight lines in Fig. 2 and 4 are plotted in a log tan ψ/log i diagram (Fig. 5). For thalliumless copper sulfate baths a straight line with a negative slope is obtained for current densities below 2 A/dm^2. According to Eq. [4] B can be expressed in

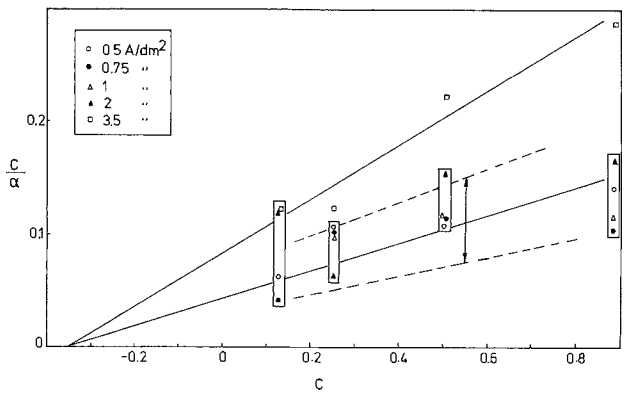


Fig. 4. Codeposition of α-alumina and copper from a copper sulfate bath containing 1 g/liter Tl_2SO_4, according to Eq. [1].

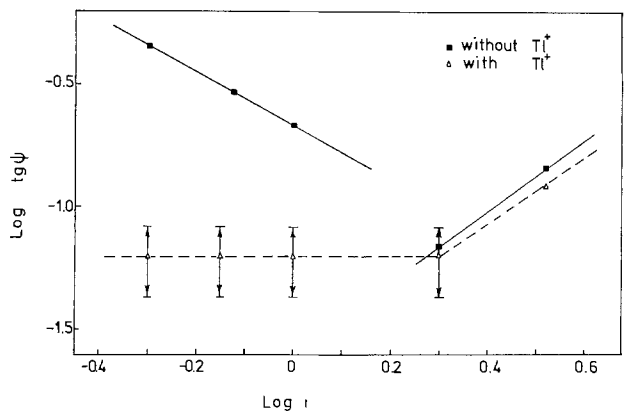


Fig. 5. Codeposition of α-alumina and copper from a copper sulfate bath, according to Eq. [4].

terms of A. For current densities below 2 A/dm^2 B is found to be equal to 1.53A. For current densities above 2 A/dm^2 the slope is positive and B is equal to 0.26A. From this it can be seen that when the current density increases the slope in Fig. 5 must change from negative to positive. This means that at a certain current density the parameter B must be equal to A. From Fig. 5 we see that this case happens at low current densities when monovalent thallium ions are added to the sulfate plating baths. Eq. [1] then reduces to

$$\frac{C}{\alpha} = \frac{Wi_0}{n\mathbf{F}dv_0} \cdot \left(\frac{1}{k} + C\right) \quad [5]$$

This fits well with the conclusions gathered from Fig. 3. The parameters W, i_0, n, $\mathbf{F}$, and d in Eq. [5] are related to the metal deposition, in this case copper, so that α is dependent on the parameters v_0 and k. As the value of k is unaltered by the presence of thallium in the plating bath, the value of α is determined by the value of v_0.

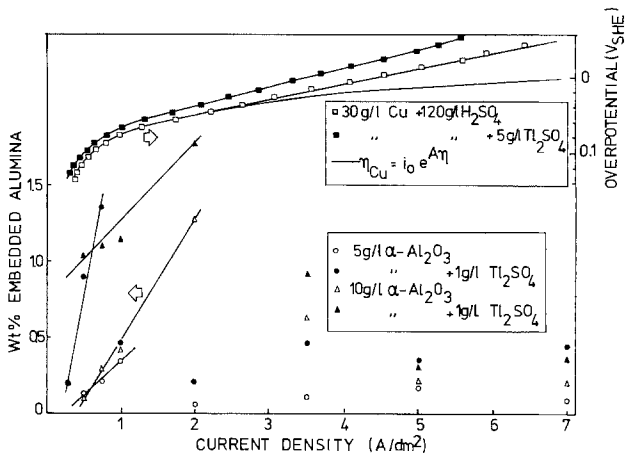


Fig. 6. Weight percentage of embedded alumina and overvoltage vs. current density.

Meaning of the parameter v_0.—The meaning of the dependence of α on v_0 can be deduced from Fig. 6. In this figure the overvoltage and the weight percentage of embedded particles are plotted *vs.* the current density for copper sulfate baths with and without thallium (I) sulfate addition. From the log i-η curves the Tafel constants i_0' and A were calculated and put in Eq. [2] which is also represented in Fig. 6. We note that in area I (below 2 A/dm^2) the experimental polarization curves and the Tafel equation curve fall together. The reduction of the copper ions is then under charge-transfer overvoltage control. In area II the experimental curves and the Tafel equation curve are divergent. Concentration overvoltage then determines the reduction rate of copper ions. In area I we find an increasing weight percentage of embedded particles with increasing current densities. Thus when the current density increases, or, in other words, when the rate of reduction of copper ions increases, the rate of embedding of alumina particles increases more than proportionally. The increase of the current density results from an increasing overvoltage. So we can say that a higher overvoltage produces an increased rate of embedding. We can conclude that in area I: (*i*) the reduction of copper ions is under charge-transfer overvoltage control, and (*ii*) an increasing weight percentage of embedded particles is formed with an increasing overvoltage. From this it seems that the codeposition rate of alumina with copper is determined by the reduction rate of copper ions which are adsorbed onto the alumina particles. Different investigators (9, 10) determined the adsorption of copper ions on alumina in diluted copper sulfate solutions. We determined colorimetrically an adsorption of 0.20 mg Cu^{++} per gram of alumina in an acidified copper sulfate bath with pH 0.3 (11).

From Fig. 6 we can also conclude that in area I the addition of monovalent thallium ions to the baths produces a shift to higher weight percentages of embedded alumina. Thallium ions have a standard potential of −0.338V SHE and are not reduced during electrolysis at the applied overvoltage. Even at 7 A/dm^2 we found, from chemical analyses of coatings, that no thallium was present in the deposits. From conductivity measurements in dilute solutions we also found no thallium ions to be adsorbed onto the alumina particles (11). We established that only small quantities of monovalent thallium ions were needed in order to obtain an increased codeposition of alumina and copper (Table I). The effect of thallium on the weight percentage of embedded alumina can be explained if thallium is considered as a catalyst for the embedding of the alumina particles by increasing the rate of reduction of adsorbed ions on alumina and thus facilitating the second adsorption step.

Table I. Effect of the addition of thallium to a copper sulfate bath on the weight percentage of embedded alumina at 1 A/dm^2 and for 10 g/l alumina in suspension

Tl_2SO_4 (mg/l)	α-Al_2O_3 (weight percent)
0	0.415
1	1.015
	1.147
10	0.949
	1.065
50	1.461
	1.361
100	1.003
	0.945
1000	1.148

We can thus conclude that the parameter v_o is related to the rate of reduction of ions adsorbed on the alumina particles. Through this reduction a permanent contact can be realized between the alumina particles and the cathode.

Conclusions

The physical model proposed by Guglielmi was shown to be valid for the codeposition of α-alumina and copper from a copper sulfate plating bath. The hypothesis of a codeposition mechanism based on a two-step adsorption process agreed well with our experimental results. From our results on the codeposition of alumina and copper from sulfate plating baths with and without addition of monovalent thallium ions we conclude that the second adsorption step is rate determining. In that adsorption step a real contact is realized between alumina particles and the cathode by the breakthrough of the layer of ions adsorbed on the alumina particles. So we found that when the reduction of the copper ions is under charge-transfer overvoltage control a considerable increase of the amount of embedded alumina particles is obtained with increasing current densities. The monovalent thallium ions promote the codeposition. We consider thallium as a catalyst for the codeposition of alumina in copper sulfate baths. Further research on the catalytic action of thallium and other monovalent cations should provide more information on the codeposition mechanism.

Manuscript submitted Feb. 10, 1977; revised manuscript received May 27, 1977.

Any discussion of this paper will appear in a Discussion Section to be published in the June 1978 JOURNAL. All discussions for the June 1978 Discussion Section should be submitted by Feb. 1, 1978.

REFERENCES

1. N.S.U. Neckarsulm, Br. Pat., 1,200,410 (July 1970).
2. E. C. Kedward, K. W. Wright, and A. A. B. Tennett, *Tribol. Int.*, **7**, 221 (1974).
3. F. K. Sautter, *This Journal*, **110**, 557 (1963).
4. R. V. Williams and P. W. Martin, Proceedings 6th International Conference on Electrodeposition and Metal Finishing, p. 182 (1964).
5. E. S. Chen, G. R. Lakshminarayanan, and F. K. Sautter, *Met. Trans.*, **2**, 937 (1971).
6. T. W. Tomaszewski, L. C. Tomaszewski, and H. Brown, *Plating*, **56**, 1234 (1969).
7. N. Guglielmi, *This Journal*, **119**, 1009 (1972).
8. J. P. Celis, J. Helsen, P. Hermans, and J. Roos, To be published in *Anal. Chim. Acta.*
9. A. M. J. Kariapper and J. Foster, *Trans. Inst. Metal Finishing*, **52**, 87 (1974).
10. D. W. Snaith and P. D. Groves, *ibid.*, **50**, 95 (1972).
11. J. P. Celis, Ph.D. Thesis, Katholieke Universiteit Leuven (1976).

The Role of Metal Overlayers on Gallium Phosphide Photoelectrodes

L. A. Harris, M. E. Gerstner, and R. H. Wilson*

General Electric Company, Corporate Research and Development Center, Schenectady, New York 12301

ABSTRACT

A recent publication by Nakato *et al.*, suggested that thin gold overlayers could be made to protect GaP photoelectrodes from corrosion. Repetition of their experiments, including simultaneous measurement of the gold potential, duplicates the volt-ampere characteristics reported in that paper. Gas evolution was not observed, and the gold potential remains too low to decompose water at its surface. An alternative interpretation of the action of the Au overlayer is suggested.

In a recent paper, Nakato *et al.* (1) described two classes of behavior of gallium phosphide photoelectrodes with thin overlayers of metal on their surfaces. Type A behavior was characterized by the oxidation and reduction peaks of the metal (gold) overlayer with the onset of photocurrent more than 1V anodic of the hydrogen potential. Type B behavior exhibited an onset of photocurrent slightly cathodic of the hydrogen potential with the current rising to high well-defined plateaus resembling the volt-ampere curves reported for other semiconductor electrodes like TiO_2 (2). They reported that the type B electrodes could photoelectrolyze water without corroding. These findings appeared significant enough to warrant experimental verification and clarification.

We have been able to duplicate both types of *I-V* curves, but could not reproduce the oxygen evolution and corrosion-free operation that they described for type B electrodes. We can confirm their interpretation regarding type A behavior, but direct measurement of the metal film potential and other experiments lead us to a quite different interpretation of the type B operation, as reported briefly in an earlier communication (3). It is the purpose of the present paper to describe these experiments in greater detail and to present the basis for this alternative view of the role of the overlayer in determining the nature of the *I-V* characteristic.

Experimental

Slices of n-GaP with one side polished had contacts of gallium-silver paste applied on the unpolished face. The wafers were baked in dry N_2 at 400°C for about

* Electrochemical Society Active Member.
Key words: photoelectrochemistry, semiconductor electrodes, photoelectrolysis.

5 min to ensure ohmic contacts. After the contact sides were protected with a coat of lacquer, the polished faces were etched in aqua regia for 1 min, rinsed, and dried. The wafers were then cut into individual samples and recleaned, preparatory to overlayer deposition. Most of the experiments were done with the (100) face of GaP, but some tests with the (111) and $(\bar{1}\bar{1}\bar{1})$ faces gave essentially the same results.

Those samples to be coated with metal had their surfaces covered, except for a window about 3 mm in diam, with an ~ 25 to 100 μm thick layer of insulating photoresist lacquer (Hunt Waycoat Negative Photoresist). The resist was painted on by hand, oven dried, and polymerized by exposure to u.v. light. Metal overlayers were then applied over the entire sample, window, and lacquer.

Metal films were deposited by sputtering about 400Å of gold, or by evaporating various thicknesses (300, 50, or 10Å) of gold, silver, or palladium. The thickness of the evaporated film was calculated from the known weight of metal completely evaporated from a tungsten filament at a known distance from the sample (4).

Prior to testing in the electrochemical cell, the samples were screened for short circuits or nonohmic contacts by measuring the diode characteristics of the GaP-metal junctions. Only those specimens that exhibited the rectification characteristic of a good Schottky barrier were used (5).

The samples were tested in a previously described electrochemical cell (6). The sample was pressed against a silicone rubber gasket surrounding a small (4 mm diam) opening in the side of the cell. A quartz window facing this opening provided for illumination of the portion of the electrode in contact with the electrolyte. To measure the potential of the metal film, a fine platinum wire was placed between the gasket and the portion of the sample protected by the lacquer ring, as shown in Fig. 1. This arrangement worked well with metal films 300Å or more in thickness, but the 50 and 10Å films were not continuous enough to provide the necessary surface conductivity. The measurements of film potential to be presented later were thus made only with the thicker metal overlayers.

Current (I) dependence on half-cell potential (V_1) was measured using a potentiostat (Princeton Applied Research Model 173) controlled by a programmer (PAR Model 175) to sweep at rates of 10 or 20 mV/sec. The potential V_1 of the back contact of the GaP was measured with respect to a saturated calomel reference electrode (SCE). The metal film potential with respect to the SCE was read, point by point, from a battery-operated digital voltmeter (Danameter Model 2000), and recorded as the I-V_1 curve was swept. Curves were taken first in the dark and then with increasing intensities of full-spectrum illumination from a 150W xenon lamp (Oriel Corporation Model 7292). Full light intensity at the sample was about 620 mW cm^{-2} (measured by a Hewlett-Packard HP 8330A Radiant Flux Meter), and was reduced by inserting neutral density filters in the light path.

The electrolyte for all experiments was 0.5F K_2SO_4 adjusted to various pH values either by the addition of buffers or additional H_2SO_4. At pH = 4.3, where most experiments were done, the H^+/H_2 potential was −0.5V (SCE), and it was verified that buffered and unbuffered solutions behaved similarly. The cathode was a large area platinized Pt sheet for all experiments.

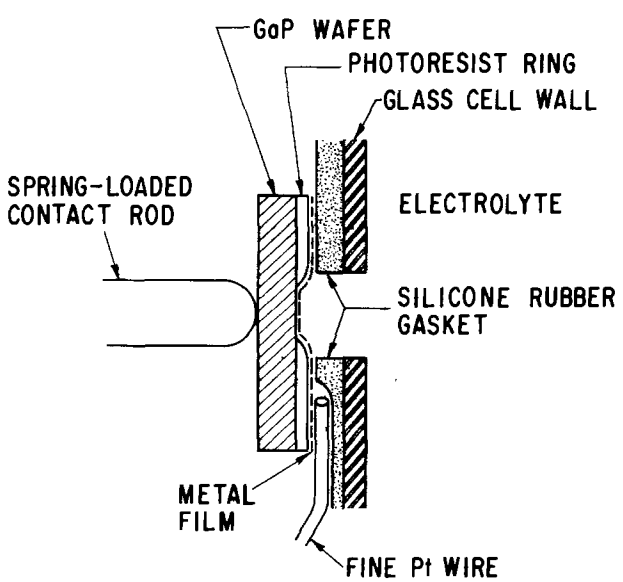


Fig. 1. A cross-sectional view of the sample loaded in the test cell. Thicknesses are exaggerated.

Results and Discussion

Type A.—Only when gold was sputtered on the GaP in a layer about 400Å thick did we reliably obtain type A behavior. No attempts were made to use other metals to obtain this mode of operation. Even when gold was slowly evaporated, type B was more likely to result, but when type A did occur it changed to B after brief operation.

As Nakato *et al.* have suggested, type A operation occurs when the metal overlayer is continuous enough to prevent effective contact of the electrolyte with the semiconductor. Such an impermeable but partially transparent layer on the GaP is equivalent to a gold electrode in series with a Schottky photodiode, which is really external to the electrochemical cell. This view is supported by the I-V_1 curves of Fig. 2 which were obtained from: (a) the gold overlayer on GaP, (b) a composite cell consisting of an illuminated Schottky diode, physically external to the electrochemical cell and consisting of an evaporated gold overlayer on GaP, connected to a metallic gold electrode in the cell, and (c) the plain gold electrode. The circuit for the composite cell (b) is illustrated in Fig. 3. Note that the independent variable, V_1 (SCE), is the potential of the GaP of the dry Schottky diode.

It is apparent from Fig. 2 that the sputtered Au overlayer on GaP when used as a photoelectrode is qualitatively equivalent to the composite cell of Fig. 3. The shift of the reduction peak of curves a and b by 0.3-0.5V in the cathodic direction relative to the peak of

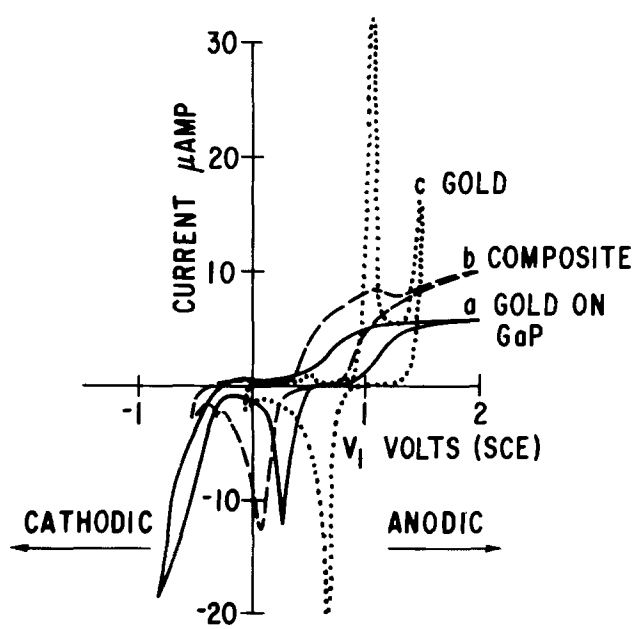


Fig. 2. The current-voltage characteristics showing type A behavior of (a) an n-GaP electrode with Au overlayer, (b) the composite cell shown in Fig. 3, (c) a plain gold electrode, all run in 0.5F K_2SO_4, pH = 4.3.

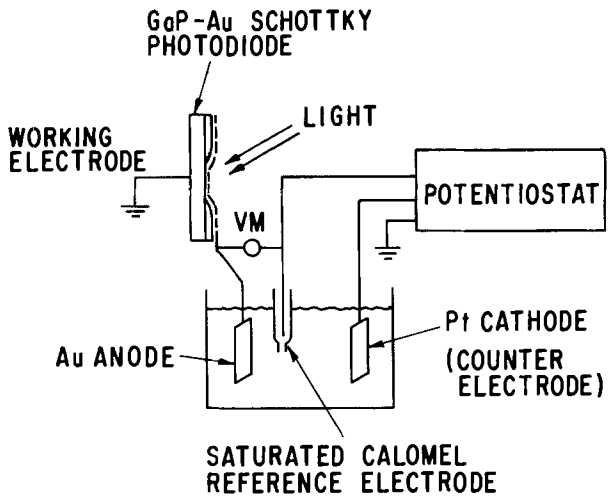


Fig. 3. The circuit diagram for the composite cell

curve c is due to the photovoltage of the Schottky diodes. The sharp peaks in the anodic region are missing from curves 2a and 2b because the GaP in each case limits the current to a value determined by the light intensity.

The measured gold potentials in cases a and b bear out this interpretation. These potentials, shown in Fig. 4, follow the GaP potential, but are displaced cathodically by the same 0.3 to 0.5V observed in Fig. 2. Ultimately the potential of the gold is limited by its own oxidation or by the liberation of O_2, the overpotential for the latter being determined by the current density, which in turn is governed by the intensity of light reaching the GaP. Figure 4 provides further evidence of the equivalence of a type A electrode and the composite arrangement of Fig. 3.

Type B.—Figure 5 shows the type B behavior of a 300Å thick film of silver on GaP, operated at pH = 4.3. Films of palladium and of gold acted similarly. The features of I-V_1 curves characteristic of this mode of operation that lead us to equate it with the type B behavior of Nakato *et al.* are the rather high, flat saturation regions with various levels of illumination, the sharp onset of current, and the open-circuit voltage (where $I = 0$) cathodic of the hydrogen potential for that electrolyte. Even at the highest light intensities we found no clear evidence of gas evolution at the

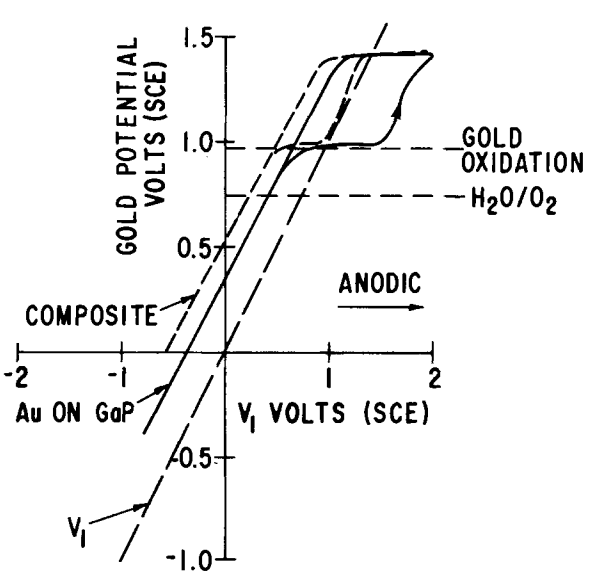


Fig. 4. The Au film potentials (SCE) in type A behavior for the gold overlayer on n-GaP and the composite cell, described as (a) and (b) in Fig. 2.

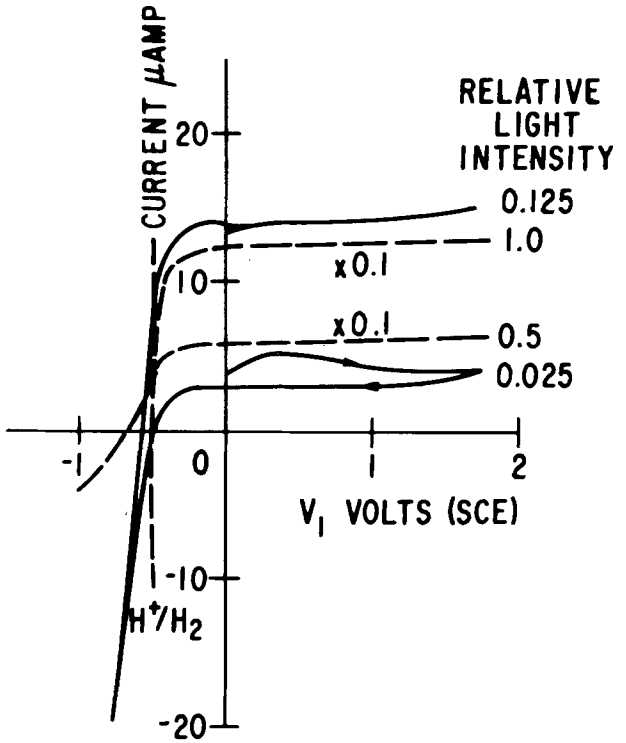


Fig. 5. Type B behavior of a 300Å rapidly evaporated Ag film on n-GaP shown for different light intensities. Full light intensity corresponds to 620 mW cm^2. The electrolyte is 0.5*F* K_2SO_4, adjusted to pH = 4.3.

semiconductor electrode, although we did observe the blister formation reported by Nakato *et al.* (1). Electrodes that had been run with full illumination for an hour or so had badly blistered or peeling overlayers, and showed clear evidence of corrosion in the form of surface roughening of the GaP.

The absence of gas evolution in type B behavior is consistent with the observed potential of the silver overlayer shown in Fig. 6. These potential measurements were made at the same time as the current mea-

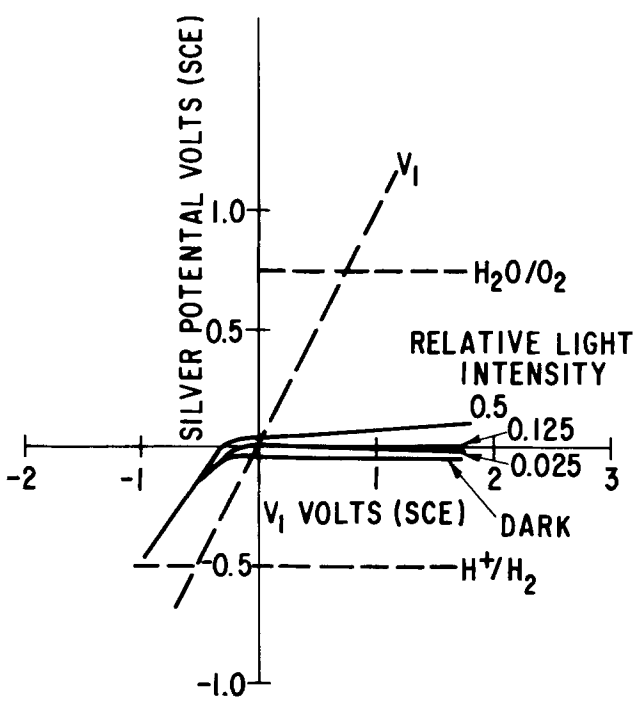


Fig. 6. The potential of the 300Å thick Ag film on n-GaP shown for various light intensities. Potential values were measured simultaneously with the data in Fig. 5.

surements in Fig. 5. The potential of the silver remains well below the oxygen potential throughout the voltage sweep. Measurements on gold and palladium films showed similar behavior. From this evidence we conclude that reactions at the metal films do not contribute to the observed current.

To understand the process responsible for the current, it is instructive to compare the curves of Fig. 5 with those obtained on bare GaP in an electrolyte of the same pH, as shown in Fig. 7. These curves show the same open-circuit voltage, but a much more gradual onset of current and a less clearly defined saturation region. At $V_1 = 0$, upon the first exposure to light, it was typical for bare GaP to produce an appreciable initial current which decayed within a few minutes to a much lower steady value. This process was often repeated each time the light intensity was increased. (The curves of Fig. 7 were recorded after this initial adjustment was completed.) As can be seen by comparing Fig. 5 and 7, the current levels are much lower for bare GaP, even though there is no metal film present to absorb the light. This current decay is similar to that observed when anodizing metals such as aluminum or tantalum, and is strongly suggestive of the formation of a surface layer which blocks the flow of current.

The open-circuit voltage from Fig. 5 coincides with that from Fig. 7 for bare GaP, suggesting that with type B electrodes the electrolyte is effectively in contact with the GaP substrate. This idea is consistent with the model of Nakato *et al.*, postulating penetration of the rapidly evaporated film by the electrolyte (1). It is also consistent with the observed changes from type A to type B with use, or even with prolonged contact with the electrolyte, and the absence of changes from B to A.

The low metal potentials preclude the metal's participation in any significant electrochemical reaction, yet its presence has clearly increased the current markedly and altered its dependence on V_1, the half-cell voltage. In order to define the role of the metal film, some additional experiments were performed. One of these was to measure the I-V_1 characteristic of bare GaP for different light intensities as in Fig. 7, but for different pH values of the electrolyte.

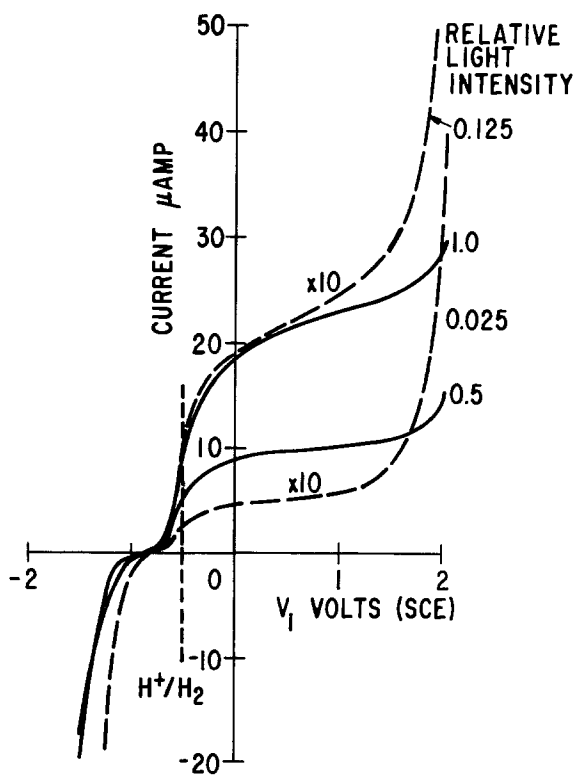


Fig. 7. The current voltage characteristics of bare n-GaP run in 0.5F K_2SO_4, pH = 4.3, for various light intensities.

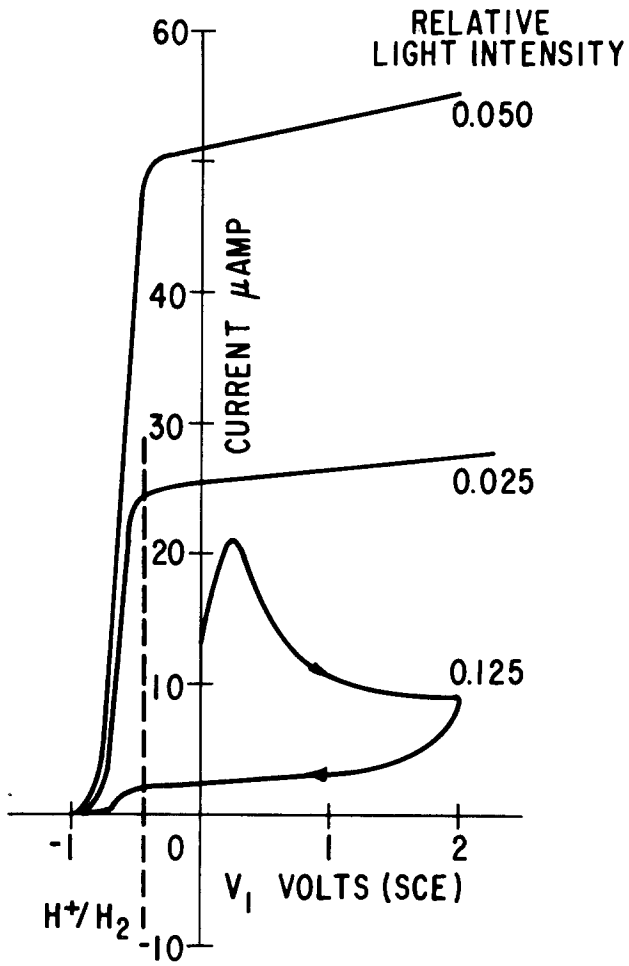


Fig. 8. The current-voltage characteristic for the same test as Fig. 7, but with electrolyte pH = 3.7.

Figure 8 shows that a remarkable change occurs in the nature of the I-V_1 characteristic's dependence on light intensity when the acidity is increased. With low illumination levels, at pH 3.7, the I-V_1 curve has all the characteristics of the type B response shown in Fig. 5 for the semiconductor with metal overlayer. When the light intensity is increased beyond a certain point, the current reverts to a smaller value, and its dependence on voltage is more like that of bare GaP at the higher pH value. Even in this regime, however, the current for a constant light intensity increases with acidity, as Fig. 9 shows.

This behavior is consistent with the notion of a blocking layer, formed on the surface of the GaP by the photostimulated anodic current flow, and removed or dissolved by the electrolyte at a rate depending on the acidity. If the rate of formation of this layer (possibly Ga_2O_3, though its nature is uncertain) is less than the rate of its removal, the surface remains clear and the current high (type B); but if the formation rate exceeds the removal rate (high light intensity, low acidity) then the blocking layer grows until it limits the current to a value where the rates are balanced.

This view of the behavior of bare GaP can be reconciled with the type B behavior of electrodes with a thin metal overlayer. Since the metal plays no electrochemical part in the electron transfer process at the interface, it must play some physical role. It acts as a diffusion barrier between the bulk of the electrolyte and the electrolyte that has penetrated to the active surface of the GaP. At the same time, the metal film attenuates the light reaching the semiconductor. If the electrochemical reaction responsible for current flow produces H^+ ions, the local acidity at the interface increases. Thus the metal film reproduces the conditions

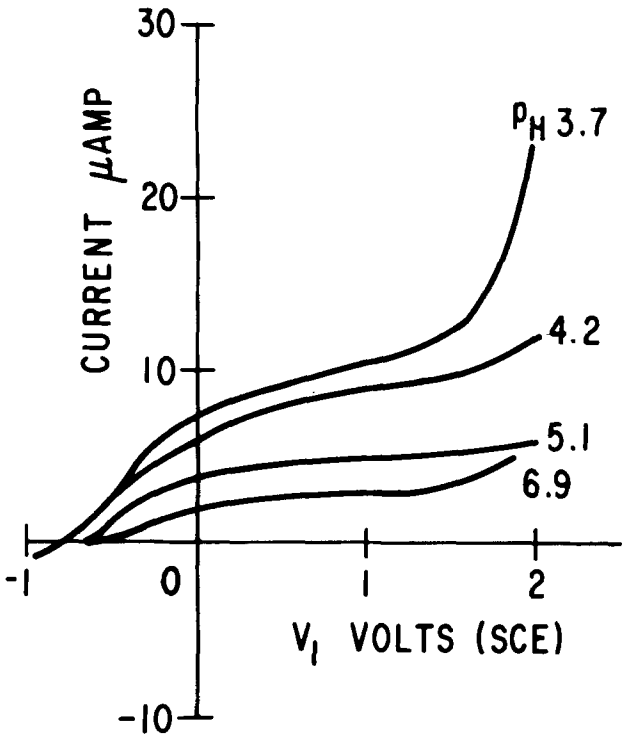


Fig. 9. The current-voltage characteristics for bare n-GaP run in 0.5*F* K_2SO_4 electrolytes adjusted to different *p*H's at a constant light intensity using a 25% transmission filter.

of low illumination and high acidity that gave us the type B curves shown in Fig. 8 for bare GaP.

To support this view of the overlayer as a simple diffusion barrier, we can demonstrate that some other chemically inactive diffusion barrier brings about the same behavior. Samples of GaP were prepared as usual and their front surfaces were covered with a very thin layer of stop-off lacquer or of photoresist lacquer, judged to be only a few microns thick from their interference patterns. These specimens, tested in electrolyte of *p*H = 4.3, resulted in very high current levels with the type B characteristic. After the tests, when the samples were removed from the cell, we could see that electrolyte was trapped under the blistered lacquer in the area that had contacted the electrolyte. These lacquer films could serve only to limit diffusion; they were too thin to attenuate the light appreciably, so the current levels were even higher than with metal films.

Figure 10 summarizes the currents observed in a number of cases of interest. Results for 10Å metal films are omitted because they were the same as those for bare GaP. In most cases the current, measured at $V_1 = 0$ (SCE), is essentially the saturation current, and is proportional to light intensity; the higher currents for 50Å films are consistent with their greater light transmission. The increase of current from bare GaP to type B metal-coated electrodes is strikingly evident; the further increase obtained with a nonopaque diffusion barrier is equally striking.

Conclusions

The experiments reported here verify the view of Nakato *et al.* that type A behavior of n-GaP electrode with a metal overlayer is obtained when the metal film is partially translucent but impermeable to the electrolyte. The electrode then acts as a Schottky photodiode in series with a simple metal electrode contacting the electrolyte.

Type B behavior occurs when the electrolyte permeates the metal overlayer. The current onset is at a potential cathodic to the hydrogen potential and is equal to that seen on bare GaP, and it rises rapidly to a high, well-defined plateau determined by light intensity.

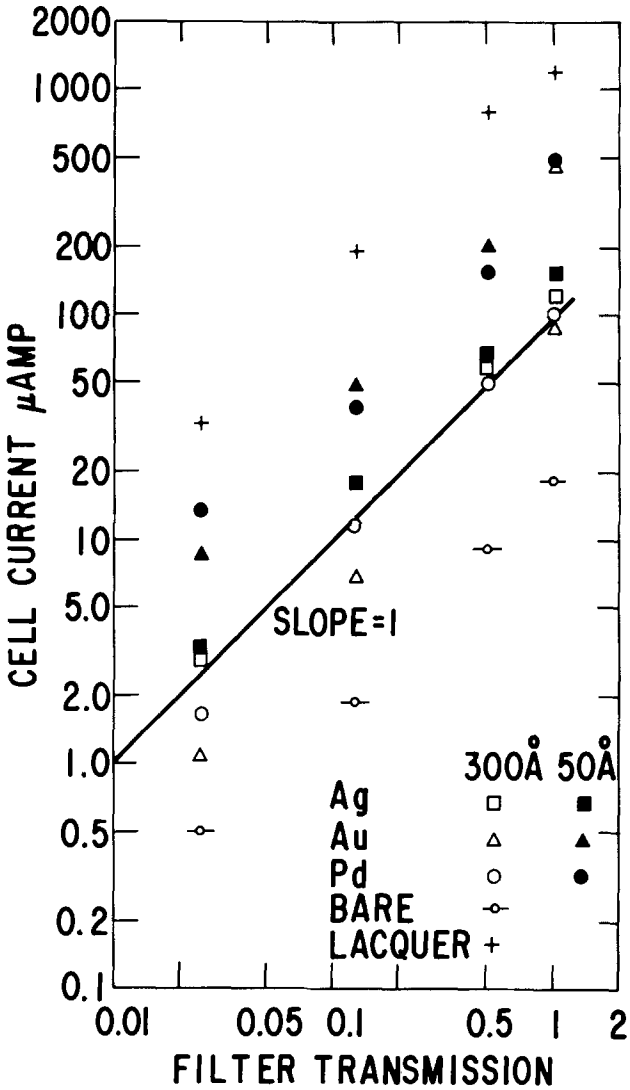


Fig. 10. The current of different samples measured at $V_1 = 0$ (SCE) as a function of filter transmission. The electrolyte in all cases is 0.5*F* K_2SO_4, *p*H = 4.3.

In our observations this behavior is independent of whether the overlayer is Ag, Au, or Pd. In each case the metal potential is too low for it to take part in the electrochemical reaction responsible for current flow.

Type B behavior can be produced on bare GaP by reducing the *p*H of the electrolyte and the illumination intensity, or by coating the electrode with a thin layer of insulating but permeable lacquer. These results suggest that the metal overlayer acts as a light attenuator and a diffusion barrier, thus changing the balance between rates of growth and removal of a surface-insulating layer. There is no evidence of water splitting, and used samples do show signs of corrosion. The current flow we observe is probably related to a corrosion reaction of the electrolyte with GaP, and the overlayers likely enhance, rather than suppress, this corrosion process.

Acknowledgments

The authors are grateful to Dr. F. Will for useful discussions, and to I. Mullin and A. Golab for depositing the evaporated and sputtered films.

Manuscript submitted April 11, 1977; revised manuscript received June 15, 1977.

Any discussion of this paper will appear in a Discussion Section to appear in the June 1978 JOURNAL. All discussions for the June 1978 Discussion Section should be submitted by Feb. 1, 1978.

Publication costs of this article were assisted by General Electric Company.

REFERENCES
1. Y. Nakato, K. Abe, and H. Tsubomura, *Ber. Bunsenges. Phys. Chem.*, **80**, 1002 (1976).
2. A. Fujishima and K. Honda, *Nature (London)*, **238**, 37 (1972).
3. R. H. Wilson, L. A. Harris, and M. E. Gerstner, *This Journal*, **124**, 1233 (1977).
4. L. Holland, "Vacuum Deposition of Thin Films," p. 143, J. Wiley and Sons, Inc., New York (1960).
5. C. R. Crowell, *J. Vac. Sci. Technol.*, **11**, 951 (1974).
6. L. A. Harris, D. R. Cross, and M. E. Gerstner, *This Journal*, **124**, 839 (1977).

Photoelectrolysis of Water in Sunlight with Sensitized Semiconductor Electrodes

Amal K. Ghosh and H. Paul Maruska*

Exxon Research and Engineering Company, Solar Energy Conversion Unit, Linden, New Jersey 07036

ABSTRACT

In all previous studies of the photoelectrolysis of water, very little attention has been paid to the carrier generation and transport properties of the optically active semiconductor electrode. To gather such information the present work theoretically analyzes the spectral response of TiO_2 photoelectrolysis cells. Comparison with experimental results allows us to determine the diffusion length of minority carriers in TiO_2 for the first time. It is the hole transport that governs the spectral response curve, not the electron transport. The quantum efficiency of carrier generation in TiO_2 electrodes in the photolysis mode can be increased to 80% by doping the crystals with Al. The sunlight conversion efficiency has been raised to 1.3% from 0.4% reported earlier by others. The spectral response of the device has been extended into the visible portion of the spectrum through sensitization of the TiO_2 with Cr dopant impurities, allowing hydrogen generation with visible light. The photoelectrolytic processes associated with the impurity doped crystals are discussed.

During the last few years, there has been an extensive study of the photoelectrolysis of water by the action of light on a semiconductor immersed in an electrolyte. Many semiconductor materials, such as TiO_2 (1-7), $SrTiO_3$ (8, 9), $KTaO_3$ (10), $BaTiO_3$ (11), SnO_2 (12), CdS (13-15), GaP (17, 18), and Si (19), have been used in such photoelectrolysis cells. By far the most popular materials have been TiO_2 and $SrTiO_3$, because even though they are transparent to visible light and, hence, relatively poor absorbers of sunlight, they remain chemically stable under anodic polarization (1, 4, 8), while many other smaller bandgap materials dissolve (20). The present work reports on techniques for improving the response of TiO_2 which have led to cells with the highest sunlight conversion efficiency demonstrated to date.

In this paper we present some theoretical studies showing how the response of an illuminated TiO_2 electrode can be expected to behave as a function of the wavelength of the incident light (absorption constant or penetration depth), carrier diffusion length (carrier lifetime and mobility), and barrier width. By using this analysis of the system, we have been able to measure important parameters, such as the minority carrier diffusion length, and to modify the TiO_2 electrodes so as to improve these parameters and hence, increase the cell efficiency. The major improvement in the response of TiO_2 in its fundamental absorption region ($\lambda < 420$ nm) has been accomplished by sensitization with the addition of aluminum impurities. Such Al-doped TiO_2 electrodes have exhibited quantum efficiencies as high as 80%, and engineering conversion efficiencies in actual sunlight (defined as the ratio of the energy content of the hydrogen produced to the energy of the incident solar flux) of 1.3%. Results are presented to show that contrary to normal beliefs, a cell with a small applied bias can actually be more efficient than one which requires no biasing.

The most important problem inherent in utilizing the wide bandgap oxides TiO_2 and $SrTiO_3$ in solar-driven water photoelectrolysis cells is that less than 10% of the solar radiation incident on the earth at AM1 is contained in the u.v. spectral region below 400 nm, where TiO_2 and $SrTiO_3$ strongly absorb (21). Since the greatest portion of the solar flux lies in the visible portion of the spectrum, the maximum sunlight conversion efficiency of cells based on these materials is severely limited, even under the best conditions. However, we will show that it is possible to extend the spectral response of TiO_2 well into the visible portion of the spectrum by sensitizing the crystals with another appropriate dopant, chromium. Doping TiO_2 with chromium has allowed us to generate hydrogen in a photoelectrolysis cell illuminated with only visible light ($\lambda > 400$ nm).

Experimental

The photoelectrolysis cell.—Two types of photoelectrolysis cells were used in this study; a homogeneous cell and a differential cell. The homogeneous cell consisted of a single compartment, 80 mm diam, quartz dish filled with an electrolyte solution into which were inserted the active semiconductor electrode, the reference saturated calomel electrode, and the platinum-black counterelectrode. The differential cell had two separate compartments connected together by a salt bridge, with electrolytes of different *p*H in each compartment. With the active electrode in a solution of *p*H = 14 (5M KOH) and the platinum-black counterelectrode in *p*H = 1 (1M H_2SO_4), a dark potential of 0.8V appears across the cell. An equivalent situation can be maintained in a homogeneous cell by applying the bias with an external power source.

Sample preparation.—Single crystal boules of TiO_2 and $SrTiO_3$ were obtained from NL Industries. TiO_2

* Electrochemical Society Active Member.
Key words: hydrogen generation, water decomposition, TiO_2, impurity dopants, sunlight conversion efficiency.

crystals were either undoped, Al doped [0.05 weight percent (w/o)], or Cr doped (from 0.0004 to 0.4 w/o), while $SrTiO_3$ crystals were not intentionally doped. These boules were 15-25 mm in diam, and slices 1 mm thick were sawed from them, exposing the (0001) surface. The slices were heated in flowing hydrogen for an hour each to make them conducting, TiO_2 at 600°C, and $SrTiO_3$ at 900°C. All of the samples then had measured resistivities of 0.1-1 Ω-cm.

Indium solder was used to make ohmic contact to the back of samples. Copper wires were electroplated with indium before bonding to the indium solder. The entire back and edges of the wafers were then coated with epoxy, followed by RTV-3140 silicone rubber, to insure the insulation of these areas from the electrolyte. The front surfaces were cleaned before use with nitric acid, but were not polished, since polishing was found to degrade performance.

Equipment.—Electrochemical measurements were made with a Princeton Applied Research PAR-170 electrochemistry system. Cell potentials were monitored with a Keithley 610C electrometer. Either of two light sources, a Bausch and Lomb 150W xenon lamp and a Schoeffel 200W mercury lamp, was used for illuminating the cells. The intensity of sunlight was measured with an Eppley pyranometer. When visible light was required, a 4 mm thick polished slab of stoichiometric TiO_2 was used as a filter to remove the u.v. component of the light output of these sources. This TiO_2 filter was placed between the lamp and the cell. Undoped or Al-doped TiO_2 electrodes exhibited no detectable photocurrents upon illumination when the filter was in place. Therefore, we are confident that the filter was sufficiently thick to entirely remove that portion of the lamp (or sunlight) spectrum containing any photons capable of exciting transitions from the valence band to the conduction band in TiO_2. The remaining photons from the visible portion of the spectrum only have enough energy to generate a photocurrent by exciting carriers from the Cr centers into the conduction band.

The Spectral Response of TiO_2 at Bandgap and Higher Energies

The short-circuit photocurrent action spectra of TiO_2 and other photocatalysts have been reported by many [see, for example, Ref. (4, 5, 7-9)]. Some of these spectra are for crystals, while others are for thin films or pressed pellets. Most spectra are for cells operating in the photoelectrolysis mode, where chemical products are created at the electrodes (specifically, hydrogen and oxygen), while some are for what are termed photogalvanic cells,[1] where a chemical couple is oxidized and reduced at the electrodes, producing electrical power but generating no net chemical products. Some of the reported spectra have been corrected for the spectral response of the measuring instruments; others have not. The spectra we are going to discuss are for a photoelectrolysis cell, *i.e.*, one in which oxygen and hydrogen are being evolved. These spectra are most conveniently presented as quantum efficiency *vs.* wavelength, where the quantum efficiency is the ratio of the number of charge carriers collected (current flowing in the external circuit) to photons incident. The spectra that we have observed are similar in shape to those presented by Wrighton *et al.* (4). The most efficient cells that we tested had Al-doped TiO_2 anodes, and such devices had quantum efficiencies as high as 80% at wavelengths less than 360 nm. Cells with undoped TiO_2 electrodes generally exhibited quantum efficiencies which were lower by a factor of 10 than the values for Al-doped material in the flat response region below 350 nm, and we attribute the high response to the effects of the Al-doping, as is discussed in the present paper. No response was found at wavelengths greater than about 420 nm, where the fundamental absorption edge of TiO_2 is located, with either undoped or Al-doped TiO_2 anodes. Quantum efficiencies as high as 0.6 have been reported by Ohnishi *et al.* (22) and by Laser and Bard (23), but the impurity content of their TiO_2 electrodes was not discussed.

Rutile (TiO_2) used in an electrolytic cell is expected to behave like a conventional Schottky barrier, and many authors have stressed the importance of this barrier region (carrier depletion region) at the TiO_2-electrolyte interface in the process of carrier generation by light absorbed in this region (2, 7, 9, 11, 17, 22-24). However, no suitable theory has been presented so far to explain the variation in spectral response that can be encountered with different samples. Even though extensive work has been done with rutile, little attention has been paid to the kinetics of photoinduced carrier generation and transport. For example, the spectral curves for TiO_2 in an electrolyte do not agree with the photoconductivity spectral response curves for rutile reported in entirely solid-state measurements (*i.e.*, both metal contacts) (25), because in the solid-state measurements the photoconductivity peaks between 375 and 410 nm. This may simply be related to the difference in experimental conditions, but it is also possible that in the case of metallic contacts the measured photocurrent may be due to majority carriers (electrons), while in a photoelectrolysis cell the dominant process will be hole transport. In highly n-type (strongly reduced) TiO_2 samples used in photoelectrolysis cells, the light-generated electrons are fewer in number than those present due to thermal ionization of the donor centers. Therefore, the excess carriers generated by the light have little effect on the electron Fermi level; on the other had, the hole quasi-Fermi level is shifted substantially. Although previous discussions of photoelectrolysis results have emphasized the electron transport in the photoconductor, we will show that the process is limited by hole transport, and that the hole diffusion length (which depends on the hole mobility and lifetime) is an important parameter. It should be noted that since TiO_2 is a n-type semiconductor, the electron lifetime in the bulk material is infinite.

In general, we can describe the spectral response of a Schottky barrier device as a function of absorption constant (and hence, wavelength of incident light) by a relationship derived in Ref. (26), as long as surface recombination is not an important factor. Since the Schottky barrier devices of interest to us can be expected to differ in several unknown parameters, we will modify the expression in Ref. (26) by a factor G to account for these differences between samples. The factor G is expected to be related to the photoconductive gain in the barrier region, as well as to the process governing the transport of the holes across the TiO_2-solution interface to ions in the electrolyte. Thus, the factor G may be controlled by transport within the Schottky barrier or by the rate of electrochemical reaction after the holes reach the interface. With this modification then, the expression becomes

$$J = qNG\left[\,[1 - \exp(-\alpha l_b)] + \frac{\alpha}{\alpha + \beta}\exp(\beta l_b)\,\{(\exp -(\alpha + \beta)l_b) - (\exp -(\alpha + \beta)l)\}\right] \quad [1]$$

where J = photocurrent/cm², α = absorption constant, q = electronic charge, N = number of photons incident/cm²-sec, l = sample thickness, l_b = barrier

[1] Usually a photogalvanic cell is considered to be one in which the light is absorbed by the solution, resulting in oxidation and reduction of species in the solution and a current in the external circuit. The type of cell we are mentioning above in which the light is absorbed by the electrode and no net chemical products are produced is an electrochemical photocell.

width, $\beta = 1/L$, and L = minority carrier diffusion length. The first part of the equation gives the charge due to carriers generated within the barrier region, and the second part accounts for carriers generated in the bulk (field-free) region of the sample. A computer program was written to generate spectral response curves predicted by the equation for a variety of combinations of barrier width and diffusion length, always using a 1 mm sample thickness. For example, the expected barrier and bulk components of the response for a diffusion length of 10^{-4} cm and a barrier width of 10^{-6} cm are shown in Fig. 1. We have determined from such plots that the total response is rather insensitive to the barrier width: The narrower the barrier, the larger the diffusion component from the bulk, so that the sum is always about the same. However, the response is strongly affected by the diffusion length, as shown in Fig. 2. In these curves we have taken the factor qNG to be unity.

In order to apply the expression above (Eq. [1]) to our experimentally determined photoelectrolysis cell response, it was necessary for us to obtain an accurate optical absorption spectrum for TiO_2. The best absorption spectrum for TiO_2 appears to be the one given by Eagles (27), which is in rough agreement with most experimental data, including ours. This spectrum is presented in Fig. 3. Using this absorption spectrum in conjunction with Eq. [1], we have determined the best fit to our experimental data for undoped and Al-doped TiO_2, as shown in Fig. 4. The ordinate axis in this plot is given in units of J/qN, which is the quantum efficiency, and the value of G for each sample has been taken so as to normalize the maximum efficiencies to unity for convenience of comparison. There is excellent agreement between the experimental data points and the calculated curves over 4-5 orders of magnitude of change in absorption constant. Although the response is not very sensitive to barrier width, we have been able to distinguish a better fit for a 10^{-6} cm width than for a 10^{-5} cm width for all samples studied. Significantly, the barrier widths determined by our C-V measurements are also of the order of 100Å. From the data presented in Fig. 4 we have determined that the diffusion length is 4.5μ for Al-doped TiO_2, and 1.2μ for undoped TiO_2.

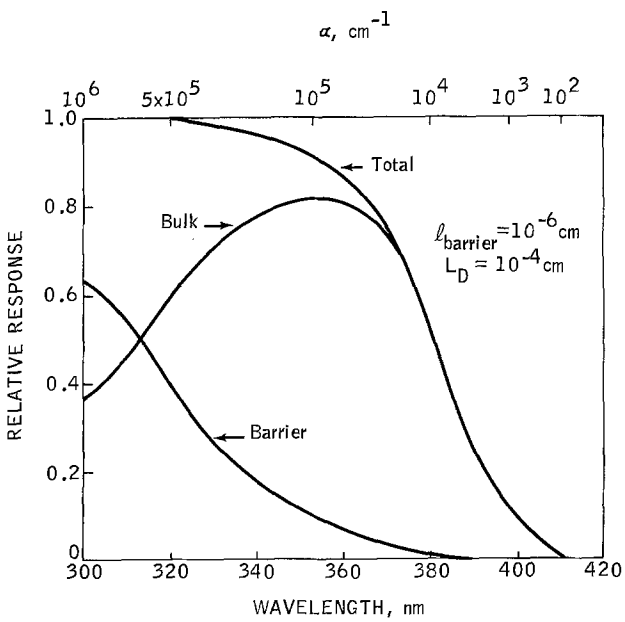


Fig. 1. Illustration of the barrier and bulk contributions to the spectral response of a Schottky barrier device having barrier width $l_b = 10^{-6}$ cm, diffusion length $L_D = 10^{-4}$ cm, and absorption constant as shown.

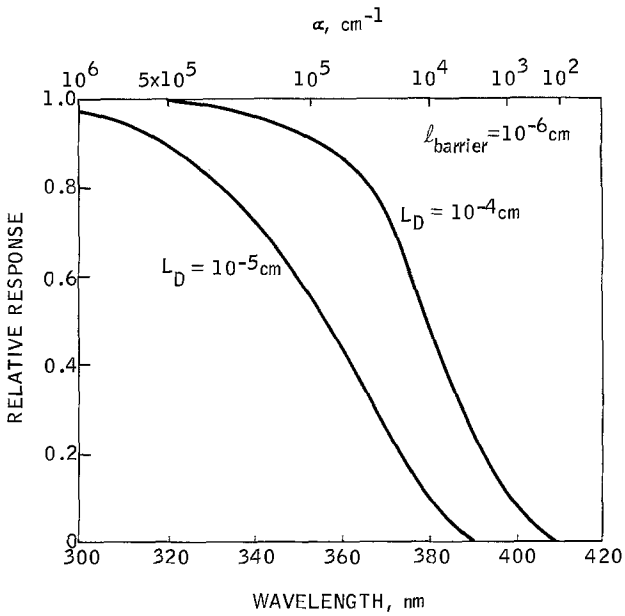


Fig. 2. Effect of an order of magnitude change in diffusion length L_D on the spectral response of a Schottky barrier device having a barrier width $l_b = 10^{-6}$ cm, and absorption constant as shown.

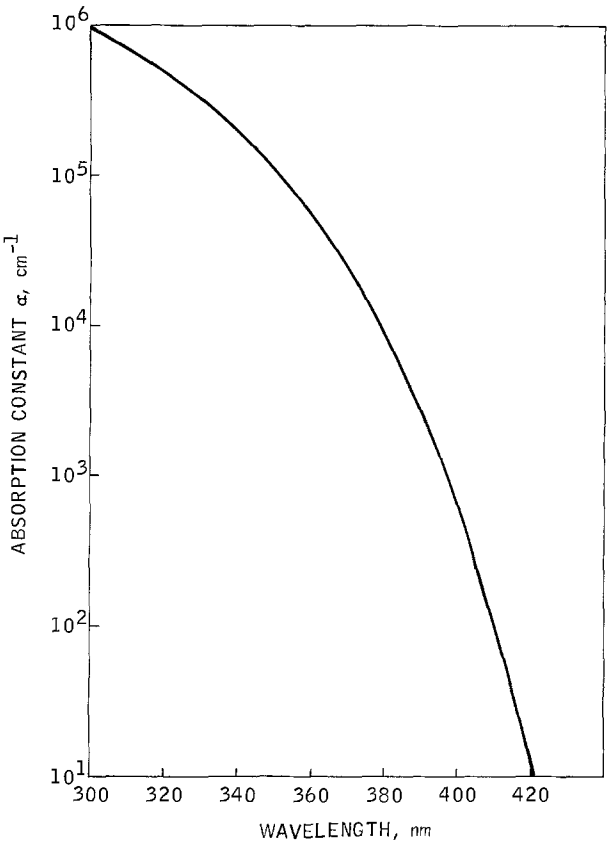


Fig. 3. Absorption constant of TiO_2

It now becomes quite apparent that surface recombination is indeed not important, because there is no reduction in response at short wavelengths; *i.e.*, the efficiency of carrier generation is not affected by how close to the surface the generation occurs.

Plots of the actual (not normalized) quantum efficiency data for two representative samples of Al-doped and undoped TiO_2 are presented in Fig. 5. For various samples the maximum plateau region quantum efficiency can vary between 0.1 and 0.3 for undoped TiO_2, and 0.8-1.0 for Al-doped material, although in

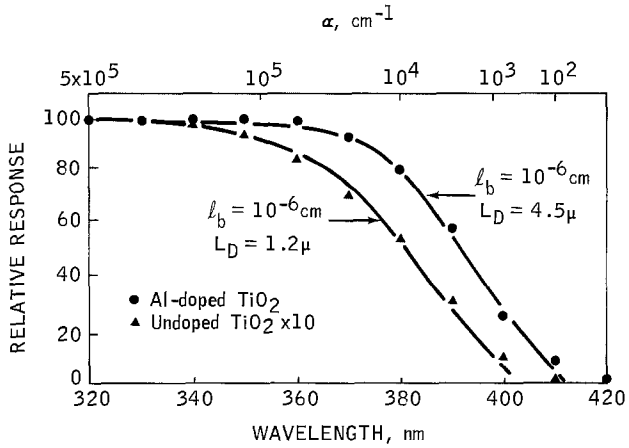


Fig. 4. Best fit of the theoretically derived Schottky barrier response curves to the experimentally determined response of undoped and Al-doped TiO_2 devices.

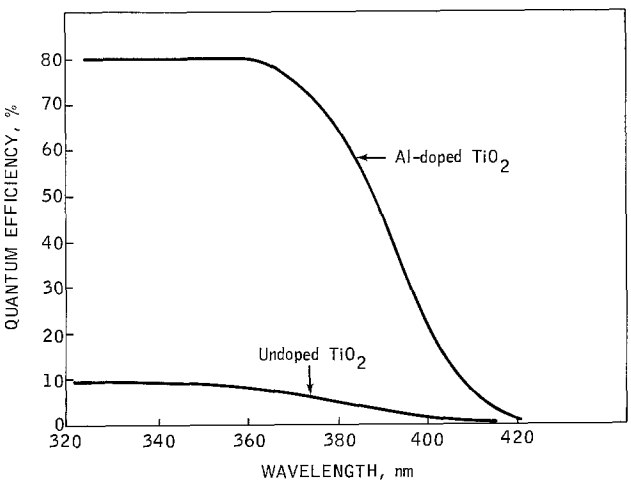


Fig. 5. Measured quantum efficiencies for undoped and Al-doped TiO_2 devices (corrected for instrument factors).

most cases the ratio of plateau quantum efficiencies for Al-doped and undoped samples is about 10:1. We attribute this difference to differences in the value of G. There are two possible processes, described above, which can determine G. Let us consider the photoconductive gain, g, in the barrier region. By definition

$$g = \frac{\tau}{T} \qquad [2]$$

where τ is the carrier lifetime and T is the transit time across the electric field region. Now

$$T = \frac{l_b^2}{V\mu} \qquad [3]$$

where l_b = barrier width, V = height of potential barrier, and μ = mobility, while

$$\tau = \frac{q}{kT}\frac{L_D^2}{\mu} \qquad [4]$$

where L_D = diffusion length. We have shown that for all of our samples, $L_D >> l_b$, so as long as L_D and μ have the same values in the barrier region as in the bulk, then $g \approx 1$ for short wavelength light absorbed entirely within the barrier region. Thus, we may conclude that for both undoped and Al-doped TiO_2 electrodes illuminated with short wavelength ($\lambda < 340$ nm) light, all of the photogenerated holes should reach the semiconductor-electrolyte interface. For light with $340 < \lambda < 420$ nm, a larger proportion of carriers are collected in Al-doped TiO_2 due to improved diffusion from the bulk.

It is possible that the hole lifetime and mobility are different from the bulk values in the barrier region, and then differences in these barrier region values from sample to sample could explain the observed variation in G. However, we feel that it is more likely that the rate-limiting step is the process of hole transfer to the electrolyte. This process may either involve the transition of the holes from the valence band to surface states in contact with the ions in the solution, or else the actual transfer of charge from the surface into the solution. The possible importance of surface states in electrochemistry at TiO_2 electrodes has been described by Frank and Bard (28). In a strongly alkaline solution, the hole transfer to the solution is usually written as

$$2p^+ + 2\,OH^- \rightarrow H_2O + \tfrac{1}{2}\,O_2 \qquad [5]$$

The surface states may in fact be introduced by absorbed OH^-, since it has been shown by photoemission studies that an absolutely clean TiO_2 (or $SrTiO_3$) surface has no filled surface states (29). The critical importance of the TiO_2 surface was further illustrated by a polishing experiment. A single crystal slice (1 mm thick) was cut from a boule, and reduced in hydrogen. When it was first tested in a photoelectrolysis cell, both sides of the wafer showed exactly equivalent photoelectrical properties. However, when one side was then polished to a mirror finish, the photocurrent from that side decreased by an order of magnitude, while the photocurrent from the unpolished side remained the same as before.

We also feel that it is possible that Al doping not only improves the carrier diffusion length, but also may introduce or modify surface states that are essential in the oxidation of OH^-. Aluminum is reported (30) to enter the rutile lattice at both substitutional and interstitial sites in a 3:1 ratio, and an EPR study (31) has shown that the substitutional and interstitial Al^{3+} will reside in reduced TiO_2 on adjacent sites in conjunction with one or two Ti^{3+} on next adjacent sites. Al^{3+} will form acceptor states which may be more properly aligned energetically at the surface (where they are assumed to be filled) with the position of the OH^-/O_2 redox level. The role of Al in enhancing the photoelectrolysis current in TiO_2 will require further study.

Sunlight Conversion Efficiency of TiO_2

There are a number of different ways to define the optical conversion efficiency of a photoelectrolysis cell. The simplest and most popular definition has been

$$\eta_1 = \frac{\text{energy output}}{\text{energy input}} \qquad [6]$$

For a cell generating hydrogen, the energy output is taken as the heat of combustion of the hydrogen that is produced under illumination (68,000 cal/mole), and the energy input is the intensity of the light source. Since this type of cell is intended for use as a solar energy device, the only appropriate light source is the sun. A number of publications have given efficiencies based on various "solar simulator" lamps (such as a xenon lamp), but such sources do not have the same spectral content as sunlight and therefore do not allow comparison. Honda (3) has measured a TiO_2 cell in sunlight and reported $\eta_1 = 0.4\%$. Another recent report (32) of this efficiency assumed the solar intensity to be only 40 mW/cm², which is considerably lower than the average value of about 100 mW/cm² expected on a clear day. All of our sunlight measurements were made on a particularly clear day when we measured a solar intensity of 105 mW/cm². For cells using Al-doped TiO_2, we found $\eta_1 = 1.3\%$, while

with undoped TiO_2, η_1 was at most 0.4%. (5M KOH electrolyte, Pt counterelectrode, and an external bias were supplied.)

It has been argued (33) that if a photoelectrolysis cell is being biased by maintaining different pH's in the anode and cathode compartments, then the heat of neutralization of H^+ by OH^- ought to be considered in the efficiency calculation. The cell reactions are

$$\text{cathode} \quad 2H^+ + 2e^- = H_2 \qquad [7]$$

$$\text{anode} \quad 2\,OH^- = 1/2\,O_2 + H_2O + 2e^- \qquad [8]$$

$$\text{neutralization} \quad 2H_2O = 2H^+ + 2\,OH^- \qquad [9]$$

$$\text{total reaction} \quad H_2O = H_2 + 1/2\,O_2 \qquad [10]$$

Thus, two charges are transferred through the circuit per mole of hydrogen produced. The heat of combustion of 1 mole of hydrogen is 68,000 cal, while the heat of neutralization of 2 moles of H^+ is 28,000 cal. We may define

$$\eta_2 = \frac{\frac{I}{nF}(68{,}000\text{-}28{,}000)}{W_L} \qquad [11]$$

where I is the cell current (A/cm^2), $n = 2$, $F = 23{,}050$ coulomb-cal/J-mole, and W_L is the energy content of the incident light (W/cm^2). For our Al-doped TiO_2 cells with 1M H_2SO_4 and 5M KOH (ΔpH = 13), $\eta_2 = 0.8\%$, while for undoped TiO_2, $\eta_2 = 0.28\%$.

Furthermore, it is possible to calculate the efficiency on the basis of free energies involved. If the hydroyen produced is to be used in a fuel cell, then it will generate a potential of 1.23V. The cell bias is now supplied by a variable voltage source, V_b, so that

$$\eta_3 = \frac{1.23I - V_bI}{W_L} \qquad [12]$$

This efficiency is strongly dependent on the magnitude of the bias voltage, as our experimental results in Fig. 6 show. Our maximum value, $\eta_3 = 0.6\%$, was found with a bias of 0.4V in an Al-doped TiO_2 cell.

It can be argued that it would probably be most beneficial to supply the bias energy chemically, because the acid and base could be generated with cheaper offpeak power at night and stored for use in the cell during the day. Furthermore, the hydrogen is most likely to be used for heating purposes, and therefore the second definition of efficiency is the most useful one for these purposes. However, the efficiency values which are reported for commercially available silicon solar cells are free energy efficiencies, and in order to allow a direct comparison of photoelectrolysis cells with silicon cells one must use the free energy efficiency η_3.

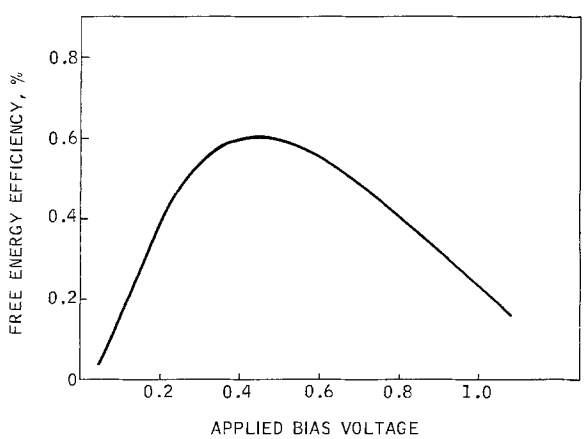


Fig. 6. Effect of applied bias voltage on the sunlight conversion free energy efficiency of a TiO_2:Al photoelectrolysis cell.

Photoelectrolysis with Cr-Doped TiO_2 and Visible Light

One of the most promising techniques that we have applied to extend the response of TiO_2 into the visible portion of the spectrum is impurity doping. The dopant that we have studied for this effect is chromium, and the absorption spectrum of chromium-doped TiO_2 is shown in Fig. 7. The presence of chromium in the rutile lattice was found to give rise to optical absorption extending from the fundamental bandedge of TiO_2 at 415 nm to well past 550 nm, a wavelength region containing a major portion of the solar radiation. Such chromium-doped TiO_2 crystals were reduced in hydrogen (which renders them equally as conducting as undoped samples), and then employed as anodes in our photoelectrolysis cells. Photocurrents were measured in these cells with light of wavelengths ranging from the u.v. up through 550 nm. The short-circuit photocurrent spectra for undoped and Cr-doped TiO_2 electrodes are compared in Fig. 8. It will be seen that the photocurrent spectrum for Cr-doped TiO_2 is substantially equivalent to the optical absorption spectrum for this material. The magnitude of the photoresponse depends upon the concentration of chromium impurity; no extended response was measured at concentrations of 0.0004 w/o (10^{17} Cr atoms/cm^3) or less, while the maximum response was obtained with a concentration of 0.4 w/o (10^{20} Cr atoms/cm^3). Higher Cr doping levels in TiO_2 are impossible because of solubility problems (34).

We have successfully generated hydrogen gas with visible light in a photoelectrolysis cell using Cr-doped TiO_2. As described in the experimental section, the visible light was obtained by using a filter of undoped

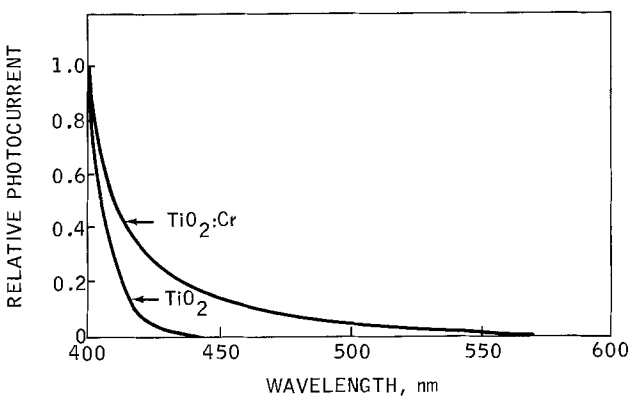


Fig. 7. Optical absorption of undoped and Cr-doped TiO_2

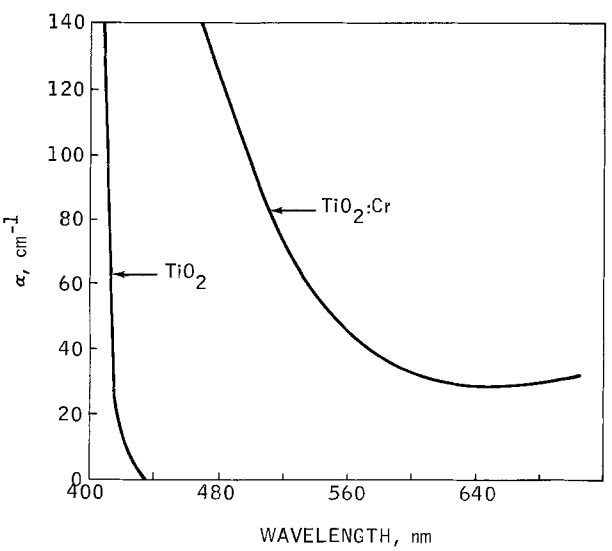


Fig. 8. Short-circuit photocurrent spectra of TiO_2 and TiO_2:Cr

TiO_2 with a 150W xenon lamp. It should be stressed that no photocurrents are measured with undoped (or Al-doped) TiO_2 electrodes when this filter is in place. The hydrogen collected at the Pt electrode was analyzed by a mass spectrometer. The quantity of gas collected corresponded exactly to the electrical current flowing in the cell. Oxygen was generated at the TiO_2:Cr anode. The maximum open-circuit photovoltage found with Xe lamp visible light excitation was 0.44V (*i.e.*, this is the shift in the electron quasi-Fermi level with illumination). No degradation in sample performance was noted, in any case, even after weeks of exposure to visible light. The electrolyte used in these cells was 5M KOH solution, and once again, just as in the case of u.v. excitation, it was determined that an external bias was necessary to allow the generation of hydrogen. The minimum bias for hydrogen generation with Cr-doped TiO_2 and visible ($\lambda > 415$ nm) light is 0.6V. It is significant that since conventional electrolysis of water requires at least 1.2V, the results with our visible light photoelectrolysis cell indicate that a savings of at least 50% in applied potential is possible in sunlight.

The measured quantum efficiency of Cr-doped TiO_2 cells in the region of 400-560 nm is shown in Fig. 9, where the response of undoped TiO_2 is also shown for comparison. For example, a quantum efficiency of 0.35% is obtained at 500 nm (where the solar irradiance is at maximum). However, when we recalculate this visible light response on the basis of carriers absorbed in the active region rather than per carrier incident, we find that the devices approach 100% collection efficiency. Measurements on cells in bright sunlight (105 mW/cm^2) showed that the Cr dopant adds 10% to the total current collection. This factor was once again determined by inserting the undoped TiO_2 filter between the sun and the sample. The expected increase in current due to the Cr dopant is readily calculated from a knowledge of the experimental quantum efficiency (Fig. 9) and the wavelength distribution of the solar flux [see, for example, Ref. (21)]. By integrating the product of these two functions over the wavelength region of interest. we have confirmed that the increase in current for Cr doping should indeed be 10%. Thus, we have effectively demonstrated the principle that adding a dopant impurity

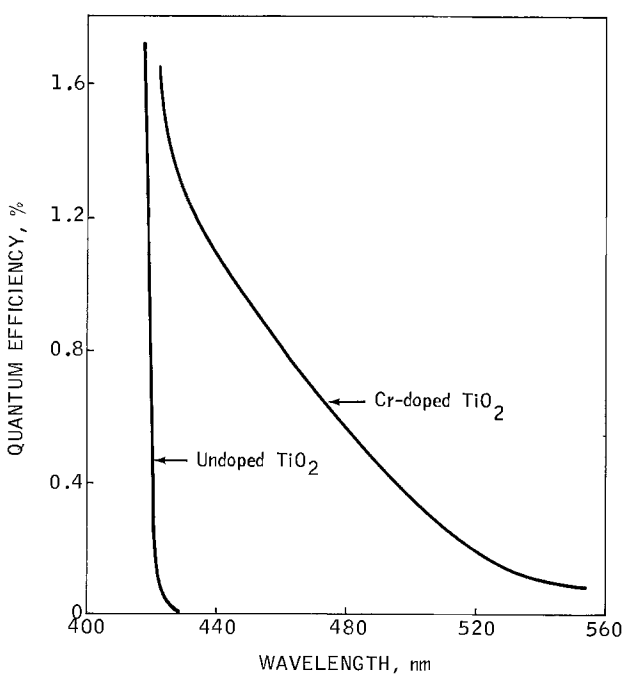


Fig. 9. Comparison of the quantum efficiencies of undoped and Cr-doped TiO_2 anodes in a differential cell.

such as Cr to TiO_2 does extend the response into the visible portion of the spectrum, from 400 to 560 nm. Our results show that the electronic holes created by the visible light excitation of the formerly filled Cr acceptor levels (which are about 0.5 eV above the top of the valence band) are in fact transported to the TiO_2 surface, where they can oxidize water. The mechanism for this hole transport has not yet been elucidated, but heating the solution as high as 90°C did not significantly increase the magnitude of the photocurrent. As we see it, a much larger increase in visible light efficiency should be possible with more suitable dopant impurities. Chromium does not give a strong enough absorption; the oscillator strength for substitutional Cr in TiO_2 is reported to be only 10^{-4} (35). Clearly, since most of the solar insolation is in the visible rather than the u.v. portion of the spectrum, a relatively small increase in visible light absorption (*i.e.*, quantum efficiency) will result in a large increase in the ratio of visible to u.v. response.

Conclusion

Impurity doping is an important technique for improving the response of TiO_2 photoelectrolysis cells. Aluminum doping increases the minority carrier diffusion length, which therefore permits an increase in collection of photogenerated carriers. In addition, Al doping may be responsible for providing surface states essential in the oxidation of OH^-. The combination of these effects has led to an improved sunlight engineering efficiency of 1.3%. Chromium doping extends the spectral response of TiO_2 into the visible portion of the spectrum, and has allowed us to generate hydrogen and oxygen using only visible light. The additional response of Cr-doped TiO_2 results in an increase by 10% in the sunlight conversion efficiency over undoped TiO_2. However, Cr centers in TiO_2 have a low oscillator strength. Therefore we must look for other dopants and combinations of dopants (such as Al + Cr), which will give still greater improvements.

Acknowledgment

The authors would like to thank NSF for supporting the early phases of this research and the work reported in Ref. (36) under Grant EPR75-13901. Thanks are due to Dr. John A. Eckert and Dr. Dale E. Hall for helpful discussions during the course of the work, and Mr. Charles Fishman for writing the computer programs.

Manuscript submitted March 14, 1977; revised manuscript received June 15, 1977.

Any discussion of this paper will appear in a Discussion Section to be published in the June 1978 JOURNAL. All discussions for the June 1978 Discussion Section should be submitted by Feb. 1, 1978.

Publication costs of this article were assisted by Exxon Research and Engineering Company.

REFERENCES

1. A. Fujishima and K. Honda, *Nature (London)*, **238**, 37 (1972).
2. A. Fujishima, K. Kohayakawa, and K. Honda, *Bull. Chem. Soc. Jpn.*, **48**, 1041 (1975).
3. A. Fujishima, K. Kohayahawa, and K. Honda, *This Journal*, **122**, 1487 (1975).
4. M. S. Wrighton, D. S. Ginley, P. T. Wolczanski, A. B. Ellis, D. L. Morse, and A. Linz, *Proc. Natl. Acad. Sci. U.S.A.*, **72**, 1518 (1975).
5. K. L. Hardee and A. J. Bard, *This Journal*, **122**, 739 (1975).
6. A. J. Nozik, *Nature (London)*, **257**, 383 (1975).
7. J. G. Mavroides, D. I. Tchernev, J. A. Kafalas, and D. F. Kolesar, *Mater. Res. Bull.*, **10**, 1023 (1975).
8. M. S. Wrighton, A. B. Ellis, P. T. Wolczanski, D. L. Morse, H. B. Abrahamson, and D. S. Ginley, *J. Am. Chem. Soc.*, **98**, 2774 (1976).
9. J. G. Mavroides, J. A. Kafalas, and D. F. Kolesar, *Appl. Phys. Lett.*, **28**, 241 (1976).

10. A. B. Ellis, S. W. Kaiser, and M. S. Wrighton, *J. Phys. Chem.*, **80**, 1325 (1976).
11. J. H. Kennedy and K. W. Frese, Jr., *This Journal*, **123**, 1683 (1976).
12. M. S. Wrighton, D. L. Morse, A. B. Ellis, D. S. Ginley, and H. B. Abrahamson, *J. Am. Chem. Soc.*, **98**, 44 (1976).
13. R. Williams, *J. Chem. Phys.*, **32**, 1505 (1960).
14. A. B. Ellis, S. W. Kaiser, and M. S. Wrighton, *J. Am. Chem. Soc.*, **98**, 1635 (1976).
15. W. W. Anderson and Y. G. Chai, *Energy Convers.* **15**, 85 (1976).
16. R. A. L. Vanden Berghe and W. P. Gomes, *Ber. Bunsenges. Phys. Chem.*, **76**, 481 (1972).
17. H. Yoneyama, H. Sakamoto, and H. Tamura, *Electrochim. Acta*, **20**, 341 (1975).
18. A. J. Nozik, *Appl. Phys. Lett.*, **29**, 150 (1976).
19. R. M. Candea, M. Kastner, R. Goodman, and N. Hickok, *J. Appl. Phys.*, **47**, 2724 (1976).
20. R. Williams, *J. Vac. Sci. Technol.*, **13**, 12 (1976).
21. M. P. Thekaekara, *Sol. Energy*, **18**, 308 (1976).
22. T. Ohnishi, Y. Nakato, and H. Tsubomura, *Ber. Bunsenges. Phys. Chem.*, **79**, 523 (1975).
23. D. Laser and A. J. Bard, *This Journal*, **123**, 1828 (1976).
24. T. Watanabe, A. Fujishima, and K. Honda, *Chem. Lett.*, **3**, 897 (1974).
25. A. K. Ghosh, F. G. Wakim, and R. R. Addiss, Jr., *Phys. Rev.*, **184**, 979 (1969).
26. A. K. Ghosh, D. L. Morel, T. Feng, R. F. Shaw, and C. A. Rowe, Jr., *J. Appl. Phys.*, **45**, 230 (1974).
27. D. M. Eagles, Jr., *Phys. Chem. Solids*, **25**, 1243 (1964).
28. S. N. Frank and A. J. Bard, *J. Am. Chem. Soc.*, **97**, 7427 (1975).
29. G. F. Derbenwick, Ph.D. Thesis, Stanford University, Stanford, California (1970); R. A. Powell and W. E. Spicer, *Phys. Rev. B*, **13**, 2601 (1976).
30. R. A. Slepetys and P. A. Vaughan, *J. Phys. Chem.*, **73**, 2157 (1969).
31. J. Kerssen and J. Vogler, *Physica (Utrecht)*, **69**, 535 (1973).
32. J. F. Houlihan and D. Madacsi, *Mater. Res. Bull.*, **11**, 1191 (1976).
33. R. Bezman, *This Journal*, **123**, 842 (1976).
34. H. M. Dess, Private communication, NL Industries.
35. A. K. Ghosh, R. B. Lauer, and R. R. Addis, Jr., *Phys. Rev. B.*, **8**, 4842 (1973).
36. A. K. Ghosh and H. P. Maruska, in "Proceedings of the International Symposium on Solar Energy," J. B. Berkowitz and I. A. Lesk, Editors, p. 29, The Electrochemical Society Softbound Symposium Series, Princeton, N.J. (1976).

Photoelectrochemical Properties of the Lead Electrode during Anodic Oxidation in Sulfuric Acid Solution

D. Pavlov, S. Zanova, and G. Papazov

Central Laboratory of Electrochemical Power Sources, Bulgarian Academy of Sciences, Sofia 1000, Bulgaria

ABSTRACT

During oxidation of a lead electrode in a H_2SO_4 solution at potentials between −200 and +900 mV (*vs.* Hg/Hg_2SO_4 electrode) an anodic layer containing tet-PbO and $PbSO_4$ is formed. When oxidation is conducted in the dark, PbO does not display photoelectrochemical properties. In order to constitute a photoelectrochemical system the electrode has to be photoactivated by illumination with a given quantity of light at potentials more positive than 0 mV. In this case the PbO layer converts into a PbO_n layer with $1 < n < 2$. When a photoactivated electrode is illuminated three types of photoelectrochemical processes occur. The first type leads to photoionization of lead oxide and OH_{ad} and O_{ad} are evolved at the PbO_n/solution interface. These processes take place at potentials between −400 and 0 mV. The second kind occurs at potentials more positive than 0 mV and leads to the formation of PbO_n and photoactivation of the oxide. The mechanism according to which these processes take place includes the formation of Pb^{4+} ions in the oxide via photochemical reactions, reconstruction of the unit cell of PbO into that of PbO_2 containing oxygen vacancies, and reactions of these vacancies with water with the subsequent formation of PbO_n. The third kind of photoprocesses leads to photolysis of water at the surface of the PbO_n layer with formation of O_2.

It was found (1-4) that during anodic oxidation of a lead electrode in sulfuric acid an anodic layer with a variable phase composition originates. In our work (3, 4) the potential range between the equilibrium potential of the $Pb/PbSO_4$ electrode (−970 mV *vs.* Hg/Hg_2SO_4, in the present work all potentials are given with respect to this electrode) and the evolution potential of oxygen (about +1250 mV) was divided into three regions: (*i*) lead sulfate region, from −970 mV to about −200 mV. The anodic layer consists only of $PbSO_4$ crystals; (*ii*) lead oxide region, from about −200 mV to about +900 mV. The anodic layer is built up by a porous layer of $PbSO_4$ crystals and a layer of tet-PbO; and (*iii*) lead dioxide region, above +900 mV. The anodic layer contains the two polymorphs of PbO_2.

Key words: lead electrode—anodic oxidation, photoelectrochemical properties, photoelectrochemical oxidation; lead oxide electrode—photoelectrochemical activation, mechanism of the photoelectrochemical processes.

It appeared of interest to establish if in the PbO potential region the properties of the lead electrode are determined by PbO. The electrochemical methods do not offer many possibilities in this respect since the electrode is passivated. Therefore, other techniques were sought which could make it possible to reveal the properties of the anodic layer in the PbO potential region.

PbO is a semiconductor with a bandgap energy of 2.6-2.8 eV. Tet-PbO has a level in the bandgap with an energy of 1.9 eV (5). It displays a clearly expressed photoconductivity in the visible region of the spectrum (6-15). This property of PbO may be used in the study of the properties of the lead electrode between −200 and +900 mV.

The influence of light on the O_2 evolution at the PbO_2 electrode was investigated by Izidinov (16). A careful survey of the literature failed to reveal any

study of the photoelectrochemical properties of the lead electrode during oxidation in the PbO potential region in a H_2SO_4 solution.

The present work aims at determining the photoelectrochemical properties of the lead electrode during oxidation in the PbO potential region.

Experimental

During anodic polarization of the electrode in the PbO region an anodic deposit consisting of a porous crystalline layer of $PbSO_4$ and of a dense layer of PbO located between Pb and $PbSO_4$ is formed (4). The determination of the properties of this lead electrode upon illumination with polychromatic light was performed under potentiostatic conditions of oxidation. The lead electrode was a cylinder introduced in a Teflon holder so that only the base of the cylinder with an area of 0.5 cm^2 is in contact with 1*N* H_2SO_4 solution and is illuminated. Pb of 99.9999% purity was used. The illumination of the lead electrode was performed by means of a 100 W bulb with a tungsten filament. The infrared region of the spectrum was filtered by means of a cell containing a 2% solution of $CuSO_4$.

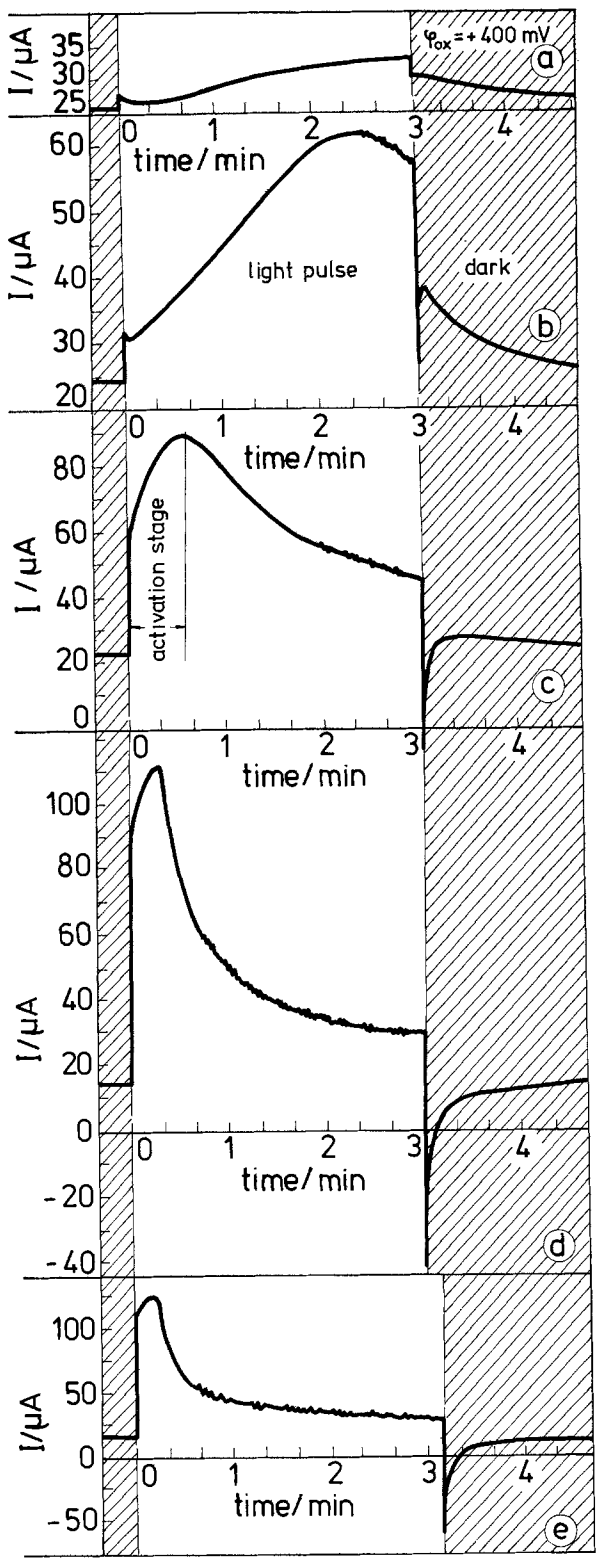


Fig. 1. Change of the current during the first five light pulses in the initial photoactivation period. Oxidation potential +400 mV. Interval between two light pulses 30 min.

Results

Photoactivation of the electrode.—The formation of tet-PbO takes place after the electrode has been covered by a $PbSO_4$ layer. The electrode was oxidized in the dark for 1 hr at a potential +400 mV. Subsequently it was illuminated by a series of light pulses with a duration of 3 min separated by 30 min intervals. Figure 1 represents the change of the current with time during the first five successive pulses.

From Fig. 1a it is seen that during the oxidation in the dark the PbO formed in the anodic layer is photoinactive. When a given amount of light energy falls on the electrode the latter transforms into a photoactive system Fig. 1e. This process may be denoted as photoactivation of the electrode. It ends when after several successive light cycles the photocurrent changes reproducibly in the dark and upon illumination. Photoactivation of the PbO layer occurs at potentials more positive than 0 mV.

The photoactivation of PbO represents, in fact, an increase of its photoconductivity. This takes place if, as a result of the photoreactions, the composition of the lead oxide is modified. It can be assumed that the compounds formed are nonstoichiometric lead oxides with a valency higher than 2. Let us denote these oxides with PbO_n with $1 < n < 2$. A method was tried to make visible the phase PbO_n formed during illumination. To this effect a slit was placed in front of the electrode. After illumination, the projection of the slit on the electrode surface turned brown. This indicates that PbO_n has a composition with $n > 1$. The electrode is shown in Fig. 2.

Influence of the oxidation potential on the nature of the photoeffect.—After an initial photoactivation at +400 mV the electrode potential was changed to the desired value. The electrode was oxidized in the dark

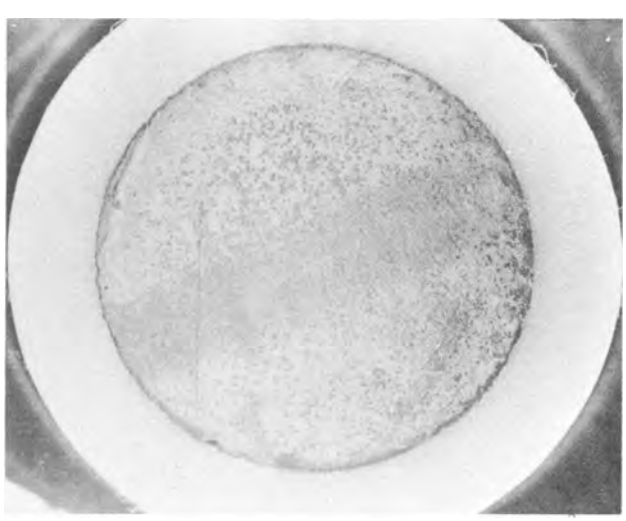


Fig. 2. Photograph of the electrode surface after dissolution of the divalent lead compounds in NH_4COOCH_3 solution. The electrode is oxidized at +400 mV for 4 hr and illuminated through a slit for 40 min. The dark portion of the electrode surface is a light brown PbO_n deposit obtained upon illumination.

for 20 min and was illuminated for 3 min after which it was left for 5 min at the same potential in the dark. In order to restore the initial state, the electrode was oxidized for 20 min at +400 mV. A 3 min light pulse was applied, and after 5 min oxidation in darkness the potential was changed once again.

Figure 3 illustrates the change in the photocurrent at potentials 0, +50, +100, and +400 mV and Fig. 4 at potentials −200, −400, and −600 mV. These results make it possible to differentiate the following three kinds of processes:

(*i*) Processes of the first kind. They proceed individually at potentials between −400 and 0 mV (Fig. 3d,

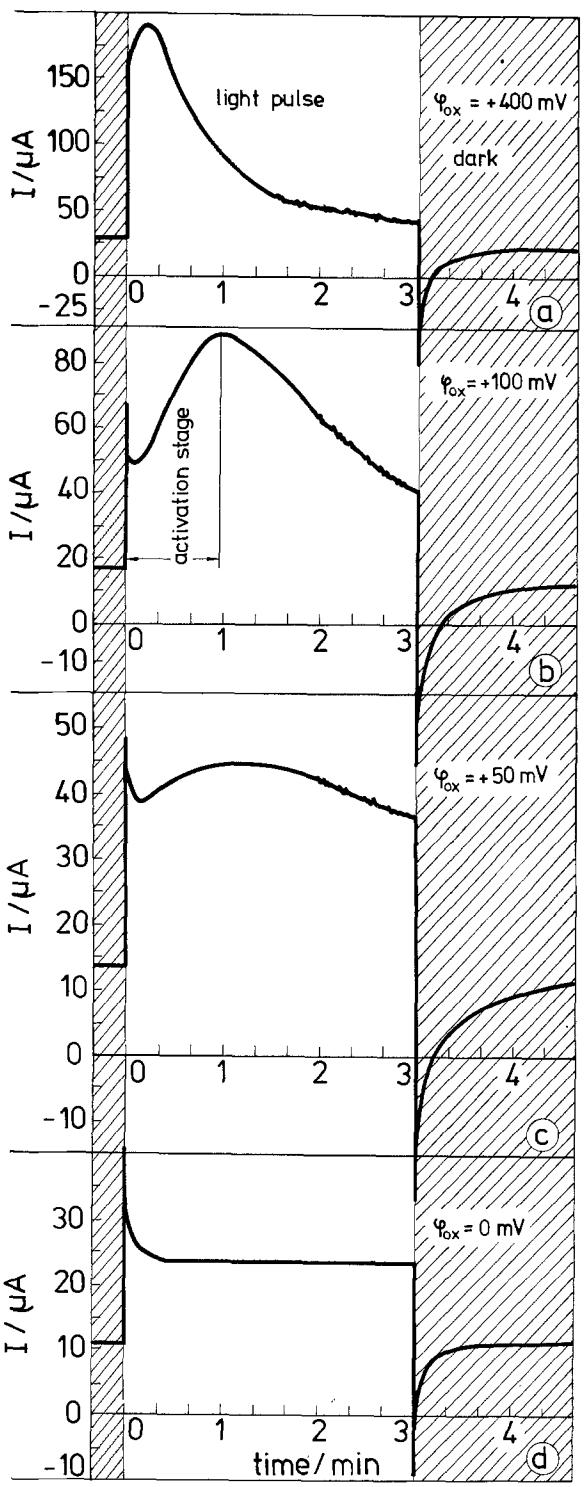


Fig. 3. Change of the current upon illumination of an initially photoactivated electrode during oxidation at potentials +400, +100, +50, and 0 mV.

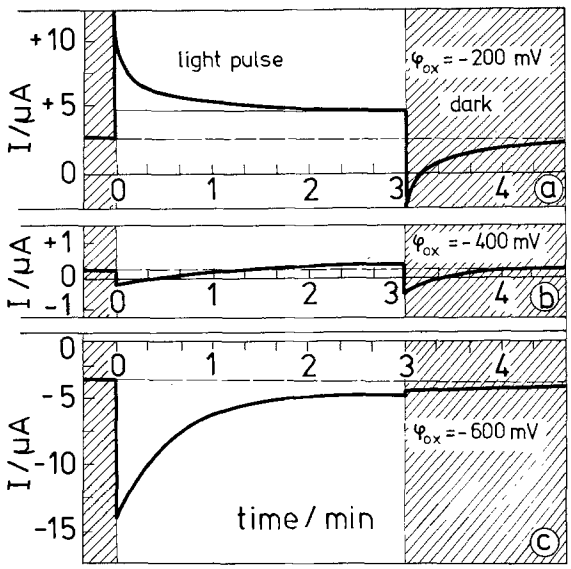


Fig. 4. Change of the current upon illumination of an initially photoactivated electrode during polarization of the electrode at −200, −400, and −600 mV.

4a). Upon illumination of the electrode a photocurrent appears which exponentially decreases down to a constant value. When light is switched off a cathodic current passes during a given interval of time. It can be assumed that as a result of the photoelectrochemical processes of the first kind positive charges are formed in PbO_n as well as products which are reduced when light is switched off. This leads to the appearance of the cathodic current.

(*ii*) Processes of the second kind. They proceed at potentials more positive than 0 mV (Fig. 3a, b, c). The photocurrent increases as a result of these processes. The appearance of a minimum in the curve of the photocurrent (Fig. 3b, c) indicates that the processes of the second kind follow these of the first kind. It was established that precisely as a result of the reactions of the second kind nonstoichiometric PbO_n originates. This means that these processes involve the transfer of oxygen ions from the solution (the water) into the crystal lattice of PbO. This reaction proceeds until n reaches a certain value in PbO_n for each determined potential and intensity of light.

(*iii*) Processes of the third kind. They follow the processes of the second kind and proceed when the current begins to decrease. Figure 5 illustrates the change of the current over various periods of time during which the processes of the third kind take place. After the 3 and 5 sec light pulses, cathodic current does not flow when light is switched off. This shows that the PbO_n phase formed is not rapidly reduced. In the case of the pulses longer than 5 sec, processes of the third kind proceed and the cathodic component of the current appears when light is switched off. This indicates that the products formed during the third kind of the photoelectrochemical processes are readily reduced in the dark. It can be assumed that these are oxygen evolution processes. The reaction of oxygen evolution proceeds in several stages in which OH radicals, O atoms, and O_2 are formed. The irregular oscillations of the current during the processes of the third kind are due precisely to the evolution of O_2. Upon switching off the light the adsorbed OH radicals and O atoms are reduced and a cathodic current begins to flow. This is observed in the case of pulses longer than 5 sec (Fig. 5).

From Fig. 4 it is seen that the photocurrent disappears at −400 mV and becomes cathodic at potentials more negative than −400 mV. A series of experiments

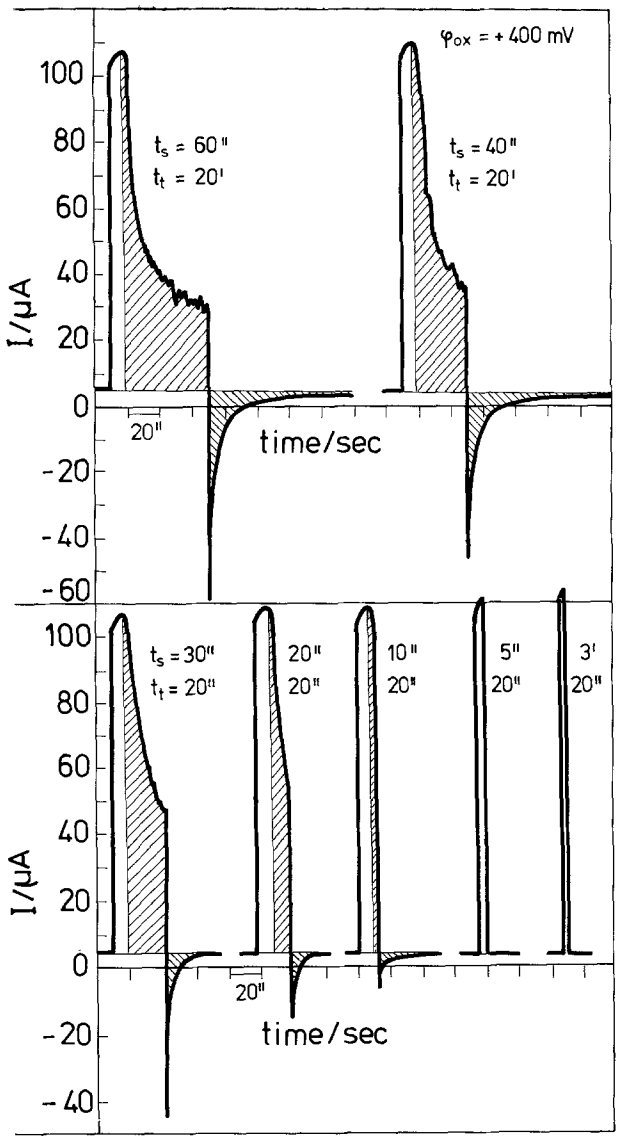


Fig. 5. Change of the current upon illumination of an initially photooctivated electrode with light pulses of decreasing duration. Oxidation potential +400 mV. t_t = interval between two light pulses 20 min, t_s = period of light pulse in seconds.

showed that the change in the sign of the photocurrent takes place in the range −400 ± 50 mV. Obviously, the zero charge potential is located in this potential range. Above this potential the potential of lead is more positive than that of PbO_n. Experiments showed that at −600 mV the photocurrent decreases with time and disappears after a given period of time. This process is connected with the decrease in photoactivity and consequently with the reduction of the PbO_n layer. When PbO_n is reduced to PbO the electrode loses its photoactivity.

It was found that the initial photocurrent which is determined by the processes of the first kind is controlled by the intensity of the white light and that the straight lines of the function photocurrent-light intensity pass through the origin of the coordinate system. This shows that to every incident photon there is a corresponding act of the photochemical process.

It was established that the electrode shows a photoreaction when it is illuminated with light with a wavelength shorter than 650 nm which corresponds to the bandgap energy (1.9 eV). This is in agreement with the results obtained for tet-PbO (5).

Photopotential at open circuit.—Figure 6 illustrates the potential change of a photoactivated electrode oxidized at +400 mV after opening the circuit. A photopotential appears upon illumination. Its magnitude

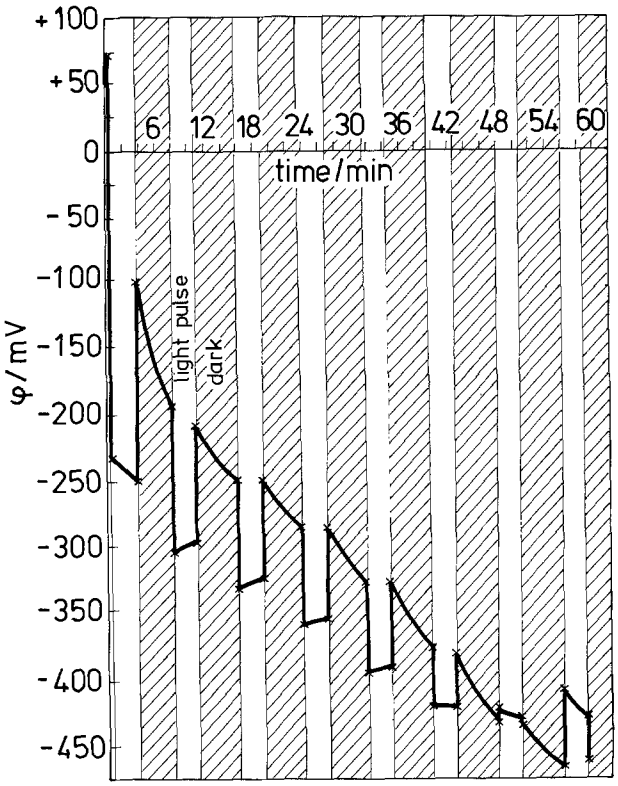


Fig. 6. Change of the electrode potential of an initially photoactivated electrode at open circuit in the dark and upon a series of the light pulses.

and sign depend on the potential in the dark. At about −400 ± 50 mV the sign of the photopotential changes due to the passage through the zero charge potential (Fig. 6). At potentials more negative than −450 mV after a certain period of polarization, the electrode loses its photoactivity. This is connected with the processes of reduction of PbO_n to PbO.

Discussion of the Results

Structure of the anodic layer in the lead oxide potential region.—As has been found (3, 4) the anodic deposit consists of two layers: a layer of $PbSO_4$ crystals and a dense layer of tet-PbO. The $PbSO_4$ layer possesses the properties of a semipermeable membrane (17-18). The current flows through it via H^+ and OH^- ions. Through the PbO layer the current flows in the solid phase. It is limited by the conductivity of the layer and by the processes which take place at the Pb/PbO and PbO/solution interfaces.

Upon oxidation of the lead electrode in the dark tet-PbO is only an ionic conductor. The thermal activation energy is 0.3-0.5 eV (19). This low value indicates that the flow of current through the PbO layer takes place via oxygen vacancies. The latter are formed at the Pb/PbO interface, Pb being oxidized to PbO. The oxygen vacancies move through the PbO layer and at the PbO/solution interface react with water which gives once again PbO. The H^+ ions obtained in this reaction migrate from the $PbSO_4$ layer toward the bulk of the solution. This is the mechanism of the reactions which determine the dark current.

When the electrode potential is more positive than 0 mV and the anodic layer is illuminated with a given amount of light the electrode is photoactivated and PbO transforms into PbO_n. The latter is an n-type semiconductor. As a result the lead electrode acquires the following structure:

metal Pb	n-type semiconductor PbO_n	semipermeable $PbSO_4$ membrane containing electrolyte	H_2SO_4 solution

$PbSO_4$ single crystals in the $PbSO_4$ layer are optically transparent and the light penetrates into the PbO layer.

Elementary reactions in the first kind of photoelectrochemical processes.—For clarity let us assume that the crystal lattice of PbO consists of individual molecules of PbO. The photoelectrochemical reactions in the first kind of processes as a result of which current flows through the anodic layer may be represented by the model given on Fig. 7.

When a $h\nu$ photon falls on a PbO "molecule" of the bulk of the PbO layer, the following photochemical reaction will take place

$$PbO + h\nu \rightarrow PbOh^+ + e^- \quad [1]$$

which results in the creation of the pair: electron e^--hole h^+. The electron jumps over the bandgap and passes into the conduction band of the oxide (Fig. 7a).

Under the action of the electric field the holes move within the layer. However, the PbO layer contains a high concentration of structural defects, traps PbOd. The holes interact with these traps

$$PbOd + h^+ \rightarrow PbOd^+ \quad [2]$$

and charged centers $PbOd^+$ are formed. Such a center contains a Pb^{3+} ion. It is unstable. By taking up a second hole it transforms into a double charged center

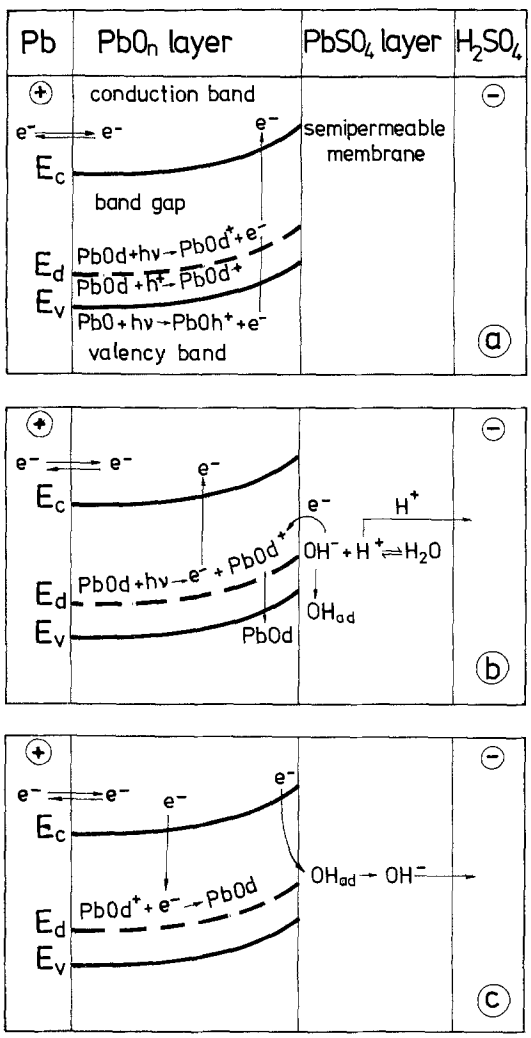


Fig. 7. a,b. Diagram of the model of the reactions of the first kind which proceed in the anodic layer of a photoactivated electrode upon illumination during polarization of the electrode at potentials between —400 and 0 mV. c. Diagram of the reactions which take place after switching off light during polarization of the electrode at potentials between —400 and 0 mV.

$$PbOd^+ + h^+ \rightarrow PbOd^{2+} \quad [3]$$

the lead ion being of fourth valency.

The traps may also accept a photon (Fig. 7a) and the next photoreaction proceeds

$$PbOd + h\nu \rightarrow PbOd^+ + e^- \quad [4]$$

Since there is an electronic equilibrium between the metal and the conduction band of the PbO_n layer the increase in the electron concentration in the conduction band brought about by reactions [1] and [4] leads to an electron transfer in the metal, *i.e.*, to the appearance of a photocurrent.

As a result of reactions [1], [2], [3], and [4] the concentration of $PbOd^+$ and $PbOd^{2+}$ in the PbO_n layer increases. This creates a bulk positive charge in the layer. The electrode potential at the PbO_n/solution interface changes in the positive direction. At this interface $PbOh^+$, $PbOd^+$, and $PbOd^{2+}$ interact with the OH^- ions of the solution and the following electrochemical reactions take place (Fig. 7b)

$$PbOh^+ + OH^- \rightarrow PbO + OH_{ad} \quad [5]$$

$$PbOd^+ + OH^- \rightarrow PbOd + OH_{ad} \quad [5']$$

$$PbOd^{2+} + 2\,OH^- \rightarrow PbOd + 2\,OH_{ad} \quad [5'']$$

$$2\,OH_{ad} \rightarrow O + H_2O \quad [6]$$

As a result of these reactions OH radicals and O atoms are obtained at the PbO_n interface.

Reactions [1]-[5"] involve the motion and transfer of electrons and holes. This is why they are rapid ones. They determine the current in the first kind of photoprocesses. The shape of the current curve of Fig. 3d and 4a can be described in terms of the above reactions. Upon illumination reactions [1], [2], [3], and [4] take place. The PbO_n layer acquires a positive space charge. Reactions [5]-[5"] proceed at the PbO_n/solution interface. The photocurrent increases with a jump.

As a result of processes [5]-[5"] and [6] on the PbO surface OH_{ad} radicals and O_{ad} atoms are obtained. They partially passivate the electrochemical reactions and the photocurrent goes down to a steady-state value (Fig. 3d and 4a).

Upon switching off the illumination OH radicals and O atoms adsorbed at the PbO_n surface accept electrons from the conducting band and the reactions

$$OH_{ad} + e^- \rightarrow OH^- \quad [7]$$

$$O_{ad} + 2e^- + H_2O \rightarrow 2\,OH^- \quad [8]$$

take place (Fig. 7c). The cathodic current flows through the electrode. Since the amount of OH_{ad} and O_{ad} decreases with time the dark current goes up to the steady-state value in the dark (Fig. 3d and 4a).

Elementary reactions in the second kind of photoelectrochemical processes.—As shown in the previous section double charged positive centers are formed during the photoprocesses of the first kind. Since the structural changes are small they may transform into $O^{2+}_{\square}$ vacancies

$$PbOd^{2+} \rightarrow PbO \cdot O^{2+}_{\square} \quad [9]$$

This process may be easily understood by using the idealized model suggested by Bode and Voss (20) and represented on Fig. 8. Under some assumptions and with certain approximations these authors showed that the structures of Pb, tet-PbO, and α-PbO_2 are closely related to one another. The unit cells contain four molecules. They are built up of a lead sublattice consisting of four lead ions. When the lead ions are divalent the oxygen sublattice contains four O^{2-} ions and is only half-filled. Tet-PbO is formed. When the lead ions are tetravalent the oxygen sublattice consists of eight oxygen ions and is completely filled.

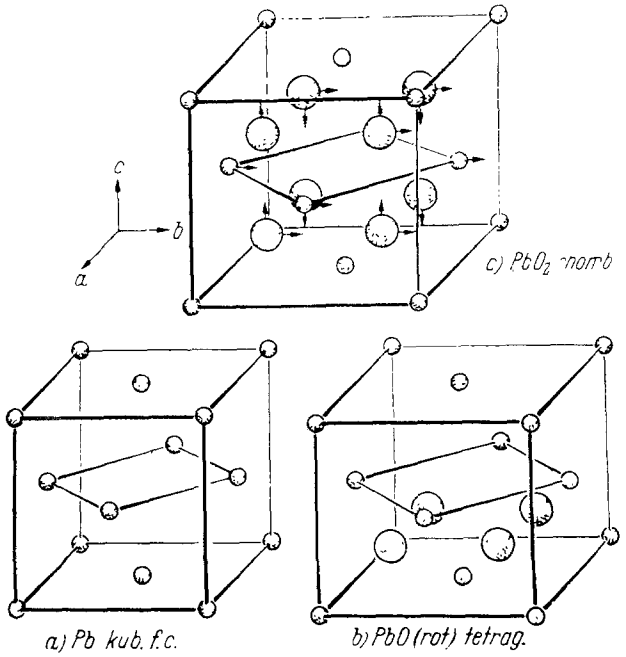


Fig. 8. Model of the unit cells of Pb, tet-PbO, α-PbO_2 according to Bode and Voss (20). The structures are represented so that the lead is located at (000). o = Lead atom, O = oxygen atom.

α-PbO_2 is formed. The O^{2-} ions are arranged in two planes.

The transformation of the unit cell of tet-PbO into that of α-PbO_2 leads to a volume increase of only 4% (21). This process does not involve any volume hindrances.

A model of the reactions by means of which current flows through the anodic layer is given on Fig. 9. The photochemical reaction is a generalization of reactions [1] and [4]. When the $O^{2+}_{\square}$ vacancies reach the PbO/solution interface the reaction

$$Pb \cdot O^{2+}_{\square} + H_2O \rightarrow PbO_2 + 2H^{2+} \qquad [10]$$

proceeds. Since the unit cell consists of four "molecules" and not all of the ions of the lead sublattice have reached the tetravalent state simultaneously, PbO_n forms

$$mPbO + kPbO_2 \rightarrow PbO_n \qquad [11]$$

where m and k are fractional numbers.

According to the experimental data given in Fig. 3 reaction [10] proceeds only if the electrode potential is more positive than 0.0V.

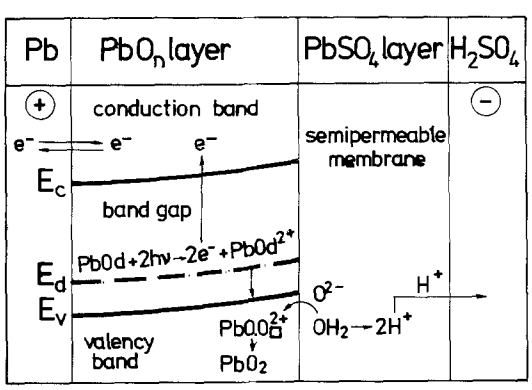


Fig. 9. Diagram of the model of the reactions of the second kind which take place in the anodic layer of a photoactivated electrode during illumination and lead to the formation of PbO_n.

When reaction [10] proceeds "PbO_2 molecules" are formed at the interface. The $O^{2+}_{\square}$ vacancy concentration at this interface goes down. This brings about the formation of a flow of $O^{2+}_{\square}$ vacancies from the bulk of the PbO_n layer. During this process n in PbO_n rises. The growth of the PbO_2 concentration in the PbO_n layer raises the mobility of the electrons in the layer (22). The ohmic drop decreases. Since upon potentiostatic oxidation the lead potential at the Pb/PbO_n interface is a support one, the decrease in the ohmic drop in the layer increases the potential at the PbO_n/solution interface in the positive direction. This accelerates the rate of reaction [10]. The concentration of $O^{2+}_{\square}$ vacancies in the layer goes down with time. This decreases the rate of reaction [10]. These processes indicate that during the photoactivation stage on illumination the rate of the processes of the second kind must pass through a maximum. Such a change of the photocurrent is indeed experimentally observed in Fig. 1 and 3.

Consequently, the processes of photo-oxidation of PbO to PbO_2 reduce to an electronic process, which leads to an increase of the valency of the ions of the lead sublattice and to an ionic process connected with the filling of the second half of the oxygen sublattice. In these processes the highest energy barrier which must be overcome is the passage of the electrons through the bandgap. The penetration of the photoelectrons into the metal creates uncompensated positive charges in the lead sublattice. The energy in the lead sublattice increases. This leads to structural rearrangements in the lattice which give rise to oxygen vacancies in the unit cell of PbO_n. They create conditions favorable for an ionic process of introduction of O^{2-} ions into the PbO_n layer through the PbO_n/solution interface. The oxygen ions are provided by water. When the potential is more positive than 0 mV, reaction [10] proceeds. The O^{2-} ions within the PbO_n layer move by a vacancy mechanism. This ensures them a good ionic conductivity. The filling of the second half of the oxygen sublattice takes place gradually which makes it possible to consider the PbO_n layer as a solid electrolyte.

Elementary reactions of the third kind of photoelectrochemical processes.—As a result of the reactions of the second kind the concentration of "PbO molecules" at the PbO_n/solution interface has become negligible and the potential has become more positive. This raises the adsorption of OH^- ions on the PbO_n surface. Since PbO_n is an n-type semiconductor it has a determined bandgap. The adsorbed OH^- ions may be considered as surface states in this band. In this case when a photon falls on the chemisorbed OH^- ion one electron may enter the conduction band and the following reactions take place

$$OH^- + h\nu \rightarrow OH_{ad} + e^- \qquad [12]$$

$$2\,OH_{ad} \rightarrow 1/2\,O_2 + H_2O \qquad [13]$$

When "PbO molecules" are present at the PbO_n/solution interface reactions [1] to [5] are also possible.

Processes in the dark.—When light is switched off the oxide layer consists of PbO_n and at the oxide/solution interface are absorbed OH_{ad} and O_{ad}. The concentrations of all products which have formed upon illumination become nonsteady state. In the PbO_n layer and at its surface processes occur which lead to a new steady state in the dark. Two types of processes proceed in the dark. The first one is relatively rapid and is connected with the reduction of OH_{ad} and O_{ad}

$$OH_{ad} + e^- \rightarrow OH^- \qquad [14]$$

$$O_{ad} + H_2O + 2e^- \rightarrow 2\,OH^- \qquad [15]$$

These processes take place immediately after light has

been switched off. They determine the current during the nonsteady-state stage in the dark (Fig. 1, 3, and 5).

The second kind of processes in the dark is connected with the reduction of "PbO_2 molecules"

$$PbO_2 + H_2O + 2e^- \rightarrow PbO + 2\,OH^- \qquad [16]$$

This reaction brings about a change in the composition of the PbO_n layer. When the electrode is left in the dark for a short time the reduction of the PbO_n is negligible. The boundary value of n in PbO_n (for the oxidation potential and light intensity of the preceding pulse) is retained. This is why upon renewed illumination the processes of the third kind begin immediately. When an electrode is left in the dark for a long period, upon renewed illumination a photoactivation period is observed. As a result of reaction [16] in the dark the concentration of "PbO_2 molecules" in the PbO_n layer decreases. Upon renewed illumination n in PbO_n will reach once again its boundary value if reactions of the second kind take place. This happens in a photoactivation period.

Reaction [16] proceeds more rapidly at open circuit and when the oxidation potential is more negative than −400 mV.

From the present investigations it becomes obvious that in the lead oxide potential region the electrochemical properties of the electrode are determined by lead oxide. By means of illumination and electrode potential the elementary physicochemical processes were differentiated. This made it possible to reveal the mechanism of the elementary processes of the oxidation of PbO to PbO_2. It can give an insight into the elementary processes which take place during formation of positive lead-acid battery plates.

Acknowledgments

Thanks are due to Prof. E. Budewski and Prof. J. Malinowski for fruitful discussion of the manuscript and to Mrs. J. Eneva for technical assistance.

Manuscript submitted March 14, 1977; revised manuscript received June 2, 1977.

Any discussion of this paper will appear in a Discussion Section to be published in the June 1978 JOURNAL. All discussions for the June 1978 Discussion Section should be submitted by Feb. 1, 1978.

REFERENCES

1. J. J. Lander, *This Journal*, **98**, 213 (1951).
2. J. Burbank, *ibid.*, **103**, 87 (1956).
3. D. Pavlov, C. N. Poulieff, E. Klaja, and N. Iordanov, *ibid.*, **116**, 316 (1969).
4. D. Pavlov and N. Iordanov, *ibid.*, **117**, 1103 (1970).
5. V. A. Izvozchikov and G. A. Bordovski, *Dokl. Akad. Nauk. SSSR*, **145**, 1253 (1962).
6. H. Kazi, *J. Appl. Phys.*, **33**, 2606 (1962).
7. J. R. Anderson and V. B. Tare, *J. Phys. Chem.*, **68**, 1482 (1964).
8. V. I. Veselovskii, Treatise, Institute "L. Karpova," Moscow (1949).
9. E. K. Puzeiko, *Izv. Akad. Nauk. SSSR, Ser. Fiz.*, **16**, 34 (1952)
10. L. Heyne, *Acta Electron.*, **2**, 124 (1957-1958).
11. M. Wada, T. Takahaschi, and T. Seki, *J. Appl. Phys. Jpn.*, **28**, 216 (1959).
12. P. P. Konorov and A. N. Sokolov, *Phys. Status Solidi*, **2**, 2240 (1960).
13. M. S. Kosmar and V. A. Izvozchikov, *ibid.*, **3**, 119 (1961).
14. V. A. Izvozchikov, *ibid.*, **3**, 2060 (1961); *ibid.*, **3**, 3229 (1961).
15. F. Lappe, *Phys. Chem. Solids*, **20**, 175 (1961).
16. S. O. Izidinov, *Electrochemistry*, **4**, 647 (1968).
17. D. Pavlov, *Electrochim. Acta*, **13**, 2051 (1968).
18. D. Pavlov and R. Popova, *ibid.*, **15**, 1483 (1970).
19. D. Pavlov and St. Ruevski, *Commun. Dept. Chem. Bulg. Acad. Sci.*, In press.
20. H. Bode and E. Voss, *Ber. Bunsenges. Phys. Chem.*, **60**, 1053 (1953).
21. J. Burbank, NRL Report 6345 (1965).
22. W. Mindt, *This Journal*, **116**, 1076 (1969).

A Flow-Through Porous Electrode Model: Application to Metal-Ion Removal from Dilute Streams

James A. Trainham* and John Newman*

Materials and Molecular Research Division, Lawrence Berkeley Laboratory and Department of Chemical Engineering, University of California, Berkeley, California 94720

ABSTRACT

A one-dimensional model for flow-through porous electrodes operating above and below the limiting current of a metal deposition reaction has been developed. The model assumes that there is one primary reactant species in an excess of supporting electrolyte, and that a simultaneous side reaction may occur. The model predicts nonuniform reaction rates due to ohmic, mass-transfer, and heterogeneous kinetic limitations; the effects of axial diffusion and dispersion are included. Results are compared with the experimental data observed by various authors for the deposition of copper from sulfate solutions with the simultaneous generation of dissolved hydrogen. Satisfactory agreement between model predictions and experimental data on over-all reactor performance and deposit distributions has been accomplished. For an upstream counterelectrode, distributions of reaction rate (for both single and multiple reactions), concentration, and potential describe the detailed system behavior.

Recent publications (1-8) show that flow-through porous electrodes can remove heavy metals from dilute streams, and direct comparisons with other electrode systems (fluidized bed electrodes and parallel plate electrodes) (9-11) show that flow-through porous electrodes can perform better. However, before they are used commercially it must be demonstrated that they can compete successfully with other established processes (*e.g.*, foam fractionation, ion exchange, pre-

* Electrochemical Society Active Member.

Key words: current distribution, potential distribution, mass transfer, axial dispersion, side reaction.

cipitation, and cementation). To help design better flow-through porous electrodes so they can compete with these other processes, more sophisticated models are required.

In previous work (1, 12-15), a flow-through porous electrode operating at the limiting current was treated. Sioda (16) gave an analysis for a flow-through porous electrode operating below the limiting current for a reversible reaction described by the Nernst equation, which also includes treatment of the interfacial mass-transfer resistance. Alkire and Gracon (13) included a very general analysis of a single electrode reaction below the limiting current, including the effects of axial diffusion; results are given for an upstream counterelectrode. Recently, Alkire and Gould (17) have extended this work to multiple reaction sequences, which includes: deposition of several metals, deposition of a metal in the presence of a redox system, and an ECE sequence applicable to electroorganic synthesis; results are given for a downstream counterelectrode. Ateya and Austin (18) give an analysis similar to Sioda (16) for a single electrode reaction described by the Nernst equation, and they study the effects of axial diffusion and dispersion under conditions when the interfacial mass-transfer resistance appears to be negligible.

The present analysis complements previous work by predicting nonuniform reaction rates due to ohmic, mass-transfer, and heterogeneous kinetic limitations in the presence of a side reaction. Also included are the effects of axial diffusion and dispersion without simplification of the Danckwerts (19), Wehner-Wilhelm (20) boundary conditions, as was done in previous work (13, 17). Simplifications made possible in the treatment of the side reaction due to the small reactant concentration and the desire to operate at high current efficiencies should make this analysis attractive for design purposes.

Model

The case of metal-ion removal from dilute streams using a flow-through porous electrode with parallel current and fluid flow can be modeled with the following restrictions: (*i*) The model is one-dimensional; (*ii*) The porous cathode is of length L and has an isotropic porosity ϵ and specific surface area a which remain constant in time; (*iii*) The hydrodynamics are characterized by the superficial velocity v and an average mass-transfer coefficient k_m, where axial diffusion and dispersion account for deviations from plug-flow; (*iv*) There is one reactant species in excess supporting electrolyte; (*v*) A simultaneous side reaction may occur which is characterized by its rate at the half-wave potential of the primary reaction. Also, if the side reaction involves generation of a gas, it is assumed that the gas will remain in solution so that the velocity profile will not be disturbed; (*vi*) The conductivity of both the matrix and pore solution phases is uniform.

Assumptions (*i-iii*) simplify the calculational procedure, and are necessary due to the lack of a better description of the complex porous geometry. The validity of assumptions (*iv-vi*) rests on the small reactant concentration. As a consequence of assumptions (*iv*) and (*v*), the current efficiency should be high, which further simplifies the model by removing the need to follow any reactant species concentration which participates in the side reaction. This approach emphasizes the salient features of the interaction between the unwanted side reaction and the metal deposition reaction.

Analysis

The equations which describe the behavior of porous electrodes have been reviewed recently by Newman and Tiedemann (12).

Only one material balance is required—that for the metal-ion reactant. At steady state, this may be expressed as

$$\frac{dN_R}{dx} = aj_{Rn} \qquad [1]$$

where in the absence of migration effects the superficial flux N_R of the metal-ion reactant in the direction of the fluid flow is given by

$$N_R = -\epsilon(D_R + D_a)\frac{dc_R}{dx} + c_R v \qquad [2]$$

and the local pore-wall flux to the flowing solution is related to the average mass-transfer coefficient k_m [corrected for axial diffusion and dispersion (14)] by

$$j_{Rn} = k_m(c_{Rw} - c_R) \qquad [3]$$

The quantities c_{Rw} and c_R are the wall concentration and the pore solution concentration of the metal-ion reactant averaged over the volume of the pores. In Eq. [2], D_R is the effective diffusion coefficient of the metal-ion reactant within the pore solution, and represents a correction to the molecular diffusion coefficient D_o for tortuosity ($D_R = D_o/\tau^2$, where τ is the tortuosity factor). D_a is the axial dispersion coefficient taken to be (14)

$$D_a = \frac{3v}{a\epsilon}(1 - \epsilon) \qquad [4]$$

which is a fit of a large number of data correlated by Sherwood *et al.* (21) [see also Ref. (12)].

In the matrix phase, the transport of electrons is governed by Ohm's law

$$i_1 = -\sigma\, d\Phi_1/dx \qquad [5]$$

Since it has been assumed that the concentration of the limiting reactant is small compared to the supporting electrolyte concentration, the diffusion potential is neglected; consequently, the current density i_2 in the solution phase is governed by Ohm's law

$$i_2 = -\kappa\, d\Phi_2/dx \qquad [6]$$

where κ is the effective conductivity of the solution within the pores, related to the bulk conductivity κ_o as follows (22)

$$\kappa = \kappa_o\epsilon^{1.5} \qquad [7]$$

A consequence of electroneutrality is that charge is conserved between the matrix and pore-solution phases. Mathematically this means the divergence of the total current is zero

$$\frac{di_1}{dx} + \frac{di_2}{dx} = 0 \qquad [8]$$

The transfer current is due to the sum of the individual electrode reactions

$$\frac{di_2}{dx} = \sum_j ai_{nj} \qquad [9]$$

where i_{nj} is the average transfer current density (from the matrix phase to the pore solution phase) due to reaction j in an electrode reaction of the form

$$\sum_i s_{ij}M_i^{z_i} \rightarrow n_j e^- \qquad [10]$$

With the assumption that the principal reactant R participates only in the primary reaction, we can write

$$i_{nR} = -\frac{n\mathbf{F}}{s_R}j_{Rn} = \frac{n\mathbf{F}}{s_R}k_m(c_R - c_{Rw}) \qquad [11]$$

For the case under consideration, the mass-transfer

resistance is unimportant for the side reaction, and substitution of Eq. [11] into Eq. [9] yields

$$\frac{di_2}{dx} = -\frac{anF}{s_R} j_{Rn} + a i_{nS} \quad [12]$$

where the subscript S refers to the side reaction.

In general, the average transfer current density due to reaction j may be approximated by the Butler-Volmer equation

$$i_{nj} = i_{oj}\left[\exp\left(\frac{\alpha_{aj}F}{RT}\eta_{sj} \right) - \exp\left(-\frac{\alpha_{cj}F}{RT}\eta_{sj} \right) \right] \quad [13]$$

where i_{oj} is the exchange current density which is assumed to have a composition dependence of the form

$$i_{oj} = i_{oj,\mathrm{ref}} \prod_i \left(\frac{c_{iw}}{c_{i,\mathrm{ref}}} \right)^{\gamma_{ij}} \quad [14]$$

where $i_{oj,\mathrm{ref}}$ is the value of the exchange current density for reaction j at a reference composition $c_{i,\mathrm{ref}}$. It was further assumed that the transfer coefficients α_{aj} and α_{cj} sum to n_j (a positive number, see Eq. [10]) and that the exponents γ_{ij} have the form

$$\gamma_{ij} = q_{ij} + \frac{\alpha_{ij}}{n_j} s_{ij} \quad [15]$$

such that $q_{ij} = -s_{ij}$ for a cathodic reactant and zero otherwise.

In Eq. [13], the surface overpotential for reaction j is given by

$$\eta_{sj} = \Phi_1 - \Phi_2 - U_{jw} \quad [16]$$

where

$$U_{jw} = U_j^{\theta} - U_r^{\theta} - \frac{RT}{n_jF} \sum_i s_{ij} \ln \frac{c_{iw}}{\rho_o} + \frac{RT}{n_rF} \sum_i s_{ir} \ln \frac{c_{ir}}{\rho_o} \quad [17]$$

which is the theoretical open-circuit potential for reaction j at the local wall composition relative to a reference electrode of a given kind, where the subscript r refers to the reference electrode compartment. (The pure-solvent density ρ_o should be expressed in kg/cm³ if the concentrations are given in mole/cm³.)

For the case of metal-ion removal from dilute streams, Eq. [13]-[17] can be simplified greatly. Let the reference electrode be of the same kind as the metal deposition reaction, where the concentration of the primary reactant in the reference electrode compartment c_{Rr} and the reference concentration in Eq. [14] $c_{R,\mathrm{ref}}$ are set equal to c_{Rf} (the upstream feed concentration of the metal-ion reactant). Also assume that the stoichiometric coefficient $s_R = -1$. Then Eq. [13] for a metal deposition reaction reduces to

$$i_{nR} = i_{oR,\mathrm{ref}} \left\{ \exp\left[\frac{\alpha_{aR}F}{RT} (\Phi_1 - \Phi_2) \right] - \frac{c_{Rw}}{c_{Rf}} \exp\left[-\frac{\alpha_{cR}F}{RT} (\Phi_1 - \Phi_2) \right] \right\} \quad [18]$$

For a simultaneous side reaction, such as the decomposition of the solvent, Eq. [13] reduces to an even simpler form

$$i_{nS} = i_{oS,\mathrm{ref}} \left\{ \exp\left[\frac{\alpha_{aS}F}{RT} (\Phi_1 - \Phi_2 - \Delta U) \right] - \exp\left[-\frac{\alpha_{cS}F}{RT} (\Phi_1 - \Phi_2 - \Delta U) \right] \right\} \quad [19]$$

where ΔU is the difference in the theoretical open-circuit potentials of the side reaction and the primary reaction ($\Delta U = U_S - U_R$) at the reference concentrations, which in this case are at the upstream feed composition. Note that any explicit dependence of the rate of the side reaction on the composition has been ignored. This assumption is justified if the current efficiency is high and the ratio of the metal-ion reactant to the reactant species involved in the side reaction (*e.g.*, the hydrogen ion) is small.

Let $\eta = \Phi_1 - \Phi_2$ be defined as the local overpotential, and combine Eq. [5] and [6]

$$d\eta/dx = d(\Phi_1 - \Phi_2)/dx = -i_1/\sigma + i_2/\kappa \quad [20]$$

The elimination of c_{Rw} between Eq. [3] and [18] yields

$$j_{Rn} = -\frac{\dfrac{c_R}{c_{Rf}} - \exp\left[(\alpha_{aR} + \alpha_{cR})F\eta/RT\right]}{\dfrac{1}{c_{Rf}k_m} - \dfrac{nF}{s_R i_{oR,\mathrm{ref}}} \exp\left[\alpha_{cR}F\eta/RT\right]} \quad [21]$$

Next combine Eq. [1], [2], and [21] to eliminate N_R and j_{Rn}, which results in a material balance equation for the limiting reactant with unknowns c_R and η

$$v\frac{dc_R}{dx} = (D_R + D_a)\frac{d^2c_R}{dx^2} - a\frac{\dfrac{c_R}{c_{Rf}} - \exp\left[(\alpha_{aR} + \alpha_{cR})F\eta/RT\right]}{\dfrac{1}{c_{Rf}k_m} - \dfrac{nF}{s_R i_{oR,\mathrm{ref}}} \exp\left[\alpha_{cR}F\eta/RT\right]} \quad [22]$$

An equation for the potential distribution results from elimination of i_1, i_2, and i_{nS}, between Eq. [8], [12], and [19]-[21] by differentiating Eq. [20]

$$\frac{d^2\eta}{dx^2} = \left(\frac{1}{\kappa} + \frac{1}{\sigma}\right) a \left\{ i_{oS,\mathrm{ref}} \left[\exp\left(\frac{\alpha_{aS}F}{RT} (\eta - \Delta U) \right) - \exp\left(-\frac{\alpha_{cS}F}{RT} (\eta - \Delta U) \right) \right] - \left(-\frac{nF}{s_R} \right) \frac{\dfrac{c_R}{c_{Rf}} - \exp\left[(\alpha_{aR} + \alpha_{cR})F\eta/RT\right]}{\dfrac{1}{c_{Rf}k_m} - \dfrac{nF}{s_R i_{oR,\mathrm{ref}}} \exp\left[\alpha_{cR}F\eta/RT\right]} \right\} \quad [23]$$

Before Eq. [22] and [23] can be solved simultaneously for c_R and η, four boundary conditions are required. For c_R the following conditions were used

$$c_{Rf}v = c_R v - \epsilon(D_R + D_a)\frac{dc_R}{dx} \text{ at } x = 0 \quad [24]$$

where c_{Rf} is the upstream feed concentration, and

$$\frac{dc_R}{dx} = 0 \text{ at } x = L \quad [25]$$

—the Danckwerts (19), Wehner-Wilhelm (20) conditions when axial diffusion and dispersion are included. The conditions on η depend on the placement of the counterelectrode. For an upstream counterelectrode, the current density is zero in the matrix phase at the cathode inlet and equal to $-i$ (the total current density to the electrode) in the pore solution phase; the opposite is true at the cathode outlet. Application of these conditions to Eq. [20] yields appropriate conditions on η

$$\frac{d\eta}{dx} = -\frac{i}{\kappa} \text{ at } x = 0 \quad [26]$$

and

$$\frac{d\eta}{dx} = \frac{i}{\sigma} \text{ at } x = L \quad [27]$$

To reduce the large number of parameters, Eq. [22]-[27] may be expressed in dimensionless form: Material balance

$$\frac{d\theta}{dy} = D' \frac{d^2\theta}{dy^2} - \frac{\theta - P_1 \exp\left[(\alpha_{aR}/\alpha_{cR} + 1)\eta'\right]}{1 + \exp(\eta')} \quad [28]$$

Potential distribution

$$\frac{d^2\eta'}{dy^2} = P_2 \left\{ P_3 \exp(-\alpha_{cS}\eta'/\alpha_{cR}) \left[1 - P_4 \exp\left(\frac{\alpha_{aS} + \alpha_{cS}}{\alpha_{cR}} \eta' \right) \right] + \frac{\theta - P_1 \exp\left[(\alpha_{aR}/\alpha_{cR} + 1)\eta'\right]}{1 + \exp(\eta')} \right\} \quad [29]$$

Boundary conditions

$$\theta - D' \frac{d\theta}{dy} = 1 \text{ and } \frac{d\eta'}{dy} = P_5 I^* \text{ at } y = 0 \quad [30]$$

and

$$\frac{d\theta}{dy} = 0 \text{ and } \frac{d\eta'}{dy} = -P_6 I^* \text{ at } y = aL \quad [31]$$

where θ is the reactant concentration divided by its value upstream in the feed. Here the distance and the overpotential were made dimensionless in such a manner as to emphasize the pertinent physical phenomena. The dimensionless coordinate y, as suggested by the limiting current analysis (1), is the physical distance x divided by the quantity $1/a = v/a\, k_m$, representing the effective depth of penetration of the reaction into the electrode at the limiting current. In this way, the parameter

$$D' = (D_R + D_a)\, a\, k_m / v^2 \quad [32]$$

relates to the effect of axial diffusion and dispersion. For flow-through reactors, effects of convection, reaction, and mass transfer to the wall are dominant, while axial diffusion and dispersion are secondary. Thus, it it appropriate to have these latter effects included in only one parameter, D', and to have the dimensionless coordinate y determined by the dominant effects. However, at low Péclet numbers, $v/a\, D_o < 100$, axial diffusion and dispersion effects are not small (14), and the inclusion of the corresponding terms in Eq. [28] and in the boundary condition (Eq. [30]) is necessary.

The local overpotential η was made dimensionless by the relation

$$\exp(\eta') = -\frac{n\mathbf{F}k_m c_{Rf}}{s_R i_{oR,\text{ref}}} \exp(\alpha_{cR}\mathbf{F}\eta/RT) \quad [33]$$

which also shifts the overpotential by an additive amount based on the exchange current density $i_{oR,\text{ref}}$ of the main reaction and the feed concentration c_{Rf} of the reactant. This shift is in recognition of the fact that the electrode will be run with a relatively high electric driving force, so that the main reaction can be carried to a high degree of completion. The backward term of the main reaction is then characterized by the parameter

$$P_1 = \left(-\frac{s_R i_{oR,\text{ref}}}{n\mathbf{F}k_m c_{Rf}} \right)^{1 + \alpha_{aR}/\alpha_{cR}} \quad [34]$$

which will be insignificant when the reaction exhibits Tafel behavior.

Under these conditions, the relative importance of the ohmic potential drop within the porous electrode is characterized by the parameter

$$P_2 = \frac{\alpha_{cR} n\mathbf{F}^2 v^2 c_{Rf}}{s_R a\, k_m RT} \left(\frac{1}{\kappa} + \frac{1}{\sigma} \right) \quad [35]$$

and the side reaction is characterized by

$$P_3 = -\frac{s_R i_{oS,\text{ref}}}{n\mathbf{F}k_m c_{Rf}} e^{\alpha_{cS}\mathbf{F}\Delta U/RT} \left(-\frac{n\mathbf{F}k_m c_{Rf}}{s_R i_{oR,\text{ref}}} \right)^{\alpha_{cS}/\alpha_{cR}} \quad [36]$$

at the half-wave potential of the main reaction. The half-wave potential may be calculated from Eq. [33] by setting η' equal to zero. This is seen from the second term on the right side of Eq. [28], which represents the dimensionless transfer current of the primary reaction—setting η' equal to zero yields a value in the denominator of two. The backward term of the side reaction is characterized by the magnitude of the parameter

$$P_4 = \left(-\frac{s_R i_{oR,\text{ref}}}{n\mathbf{F}k_m c_{Rf}} \right)^{\frac{\alpha_{aS} + \alpha_{cS}}{\alpha_{cR}}} \exp\left[-\mathbf{F}(\alpha_{aS} + \alpha_{cS})\Delta U/RT\right] \quad [37]$$

The parameters P_5 and P_6 represent the relative importance of the ohmic potential drop in the pore solution phase and the matrix phase, respectively, and are related to the parameter P_2

$$P_5 = -\frac{\sigma P_2}{\sigma + \kappa} \quad [38]$$

and

$$P_6 = -\frac{\kappa P_2}{\sigma + \kappa} \quad [39]$$

so that

$$-P_2 = P_5 + P_6 \quad [40]$$

The total current density i to the reactor was made dimensionless with the limiting current density that would exist if all the reactant in the feed were completely reacted

$$I^* = \frac{s_R i}{n\mathbf{F}v c_{Rf}} \quad [41]$$

Numerical Solution

The governing Eq. [28] and [29] were first linearized about a trial solution, and then, along with the boundary conditions (Eq. [30] and [31]), cast in finite-difference form accurate to order h^2, where h is the dimensionless distance between the mesh points, and solved by a numerical technique developed by Newman (23).

Unfortunately, it was found that the standard central-difference approximations of the derivatives were not sufficiently accurate to approach the limiting-current result, which can be calculated analytically. This anomalous behavior was primarily due to the high degree of nonuniformity in the current and concentration distributions near the front of the electrode. Therefore, to obtain accurate results, new finite-difference approximations to the derivatives were developed (see Appendix).

Results

Comparisons between model predictions and experiments.—For the calculations to be presented, the counterelectrode is upstream, the primary reaction is the deposition of copper, and the side reaction is the generation of dissolved hydrogen. Two types of data on copper removal (1, 13) are utilized to demonstrate the effectiveness of the model. In the first data set (1), predictions of the over-all reactor performance are tested. This includes predicting the current-potential behavior of the porous cathode and the effluent concentration of the reactant species. The remaining data set (13) is used to test model calculations of the current distribution within the porous cathode.

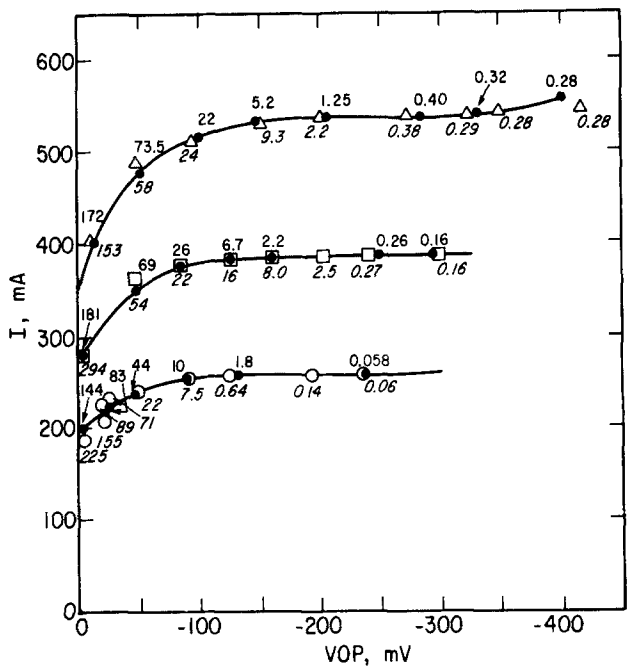


Fig. 1. Current-potential curves for an electrode 10.1 cm in diam and 6 cm deep (1), packed with porous carbon flakes and chips. Open symbols are experimental data points; closed symbols are calculated. Calculated effluent concentrations (in milligrams/liter) are indicated above the corresponding points in upright type; experimental values are given in italic type below the corresponding data points. The flow rate was 8 cm³/min for the circles, 12 cm³/min for the squares, and 16 cm³/min for the triangles.

Figure 1 displays the model fit to the data of Bennion and Newman (1) for copper removal using a porous carbon electrode. The quantities I and VOP are the total current to the reactor and the potential of the cathode current collector relative to a saturated calomel reference electrode placed in the effluent stream, respectively. The experimental effluent copper concentrations (in mg/liter) are shown as the numbers below each curve corresponding to the open triangles △, squares □, and circles ○. The numbers above each curve correspond to the solid circles ●, and are the calculated values of the effluent copper concentration. Values of the parameters used to fit the data shown in Fig. 1 are given in Table I.

Five parameters were adjusted to obtain agreement between the calculated and experimental values in Fig. 1: one value of the exchange current density for copper deposition was determined by fitting the data at the left side of the top curve; one value of the exchange current density for hydrogen evolution attempts to fit the rise in the current due to the observed onset of hydrogen evolution at the right side of the top curve; and three values of the mass-transfer coefficient k_m corresponding to the three different flow rates were determined mainly by the effluent concentration at the right side of each experimental curve.

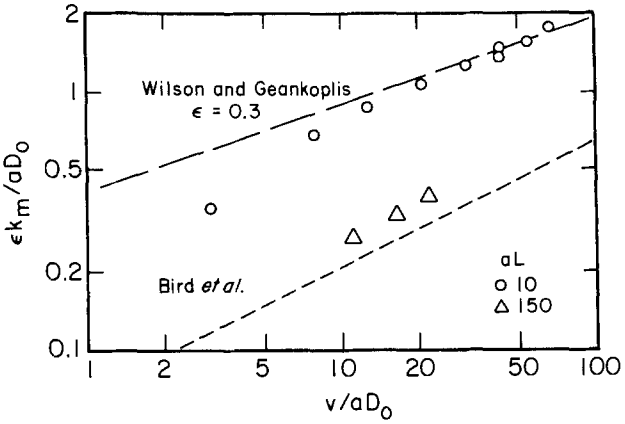


Fig. 2. Correlation of the Sherwood number as a function of Péclet number and dimensionless electrode thickness aL. Open triangles come from a fit of the data of Fig. 1; open circles are the result of Appel and Newman (26). Two correlations from the literature are also shown.

In Fig. 2, the fitted values of k_m (shown by the open triangles △) have been plotted in terms of the dimensionless Sherwood number $\epsilon k_m/aD_o$ as a function of the dimensionless Péclet number v/aD_o. The upper dashed line is the Wilson and Geankoplis correlation (24)

$$\frac{\epsilon k_m}{aD_o} = \frac{1.09}{[6(1-\epsilon)]^{2/3}} \left(\frac{v}{aD_o}\right)^{1/3} \qquad [42]$$

and the lower dashed line is a correlation suggested by Bird *et al.* (25)

$$\frac{\epsilon k_m}{aD_o} = 0.91\,\epsilon \left(\frac{v}{a\nu\psi}\right)^{0.49} \psi^2 \left(\frac{\nu}{D_o}\right)^{1/3} \qquad [43]$$

where a value of $\epsilon = 0.3$ has been used in calculating each line. Also shown in Fig. 2 by means of the open circles ○ are the data of Appel and Newman (26) where $\epsilon = 0.372$. It should be noted that it has been assumed that the dimensionless correlations for k_m (given by Eq. [42] and [43]) have been corrected for dispersion. Appel's results have not, and therefore k_m in this case is fundamentally a different quantity [see Ref. (14) for this correction and a discussion of different definitions of k_m].

Table I. Values of the parameters used in fitting the data in Fig. 1 and in generating the curves in Fig. 5-11

$\alpha = 25$ cm^{-1}	$\epsilon = 0.3$	$D_o = 6 \times 10^{-6}$ cm²/sec
$\kappa_o = 0.17$ mho/cm	$\sigma = 10^4$ mho/cm	$s_R = -1$
$n = 2$	$T = 298.15$°K	$\alpha_{aR} = 1.5$
$\alpha_{cR} = 0.5$	$\gamma = 0.75$	$\alpha_{aS} = 0.5$
$\alpha_{cS} = 0.5$	$U_S - U_R = 0.281$V	$L = 6$ cm

$k_m \times 10^4$, cm/sec	$v \times 10^3$, cm/sec
1.922	3.328
1.620	2.496
1.315	1.664

$i_{oR} = 3.8 \times 10^{-5}$ A/cm² at $c_R = 0.1$ mole/liter
$i_{oS} = 7 \times 10^{-6}$ A/cm² at $c_S = 1$ mole/liter, $p_S = 1$ atm
$i_{oS,ref} = 3.717 \times 10^{-12}$ A/cm²

dimensionless parameters as a function of c_{Rf} and v

$c_{Rf} \times 10^5$, moles/cm³	1.050	1.050	1.050	1.011	1.003	0.1003	0.01003
$v \times 10^3$, cm/sec	9.984	6.656	3.328	2.496	1.664	1.664	1.664
$P_1 \times 10^9$	9.461	22 99	104.9	215 9	501.3	5013.0	50130.0
P_2	−16.05	−8.905	−3.254	−2 091	−1.136	−0.1136	−0.01136
$P_3 \times 10^5$	1.247	1.247	1.247	1.295	1.305	13.05	130.5
$P_4 \times 10^9$	1.761	2.745	5.863	8.253	12.53	12.53	12.53
P_5	16.05	8.905	3.254	2.091	1.136	0.1136	0.01136
$P_6 \times 10^6$	44.83	24.87	9.089	5.842	3.173	0.3173	0.03173
$D' \times 10^2$	7.385	8.877	12.17	13.68	16.70	16.70	16.70

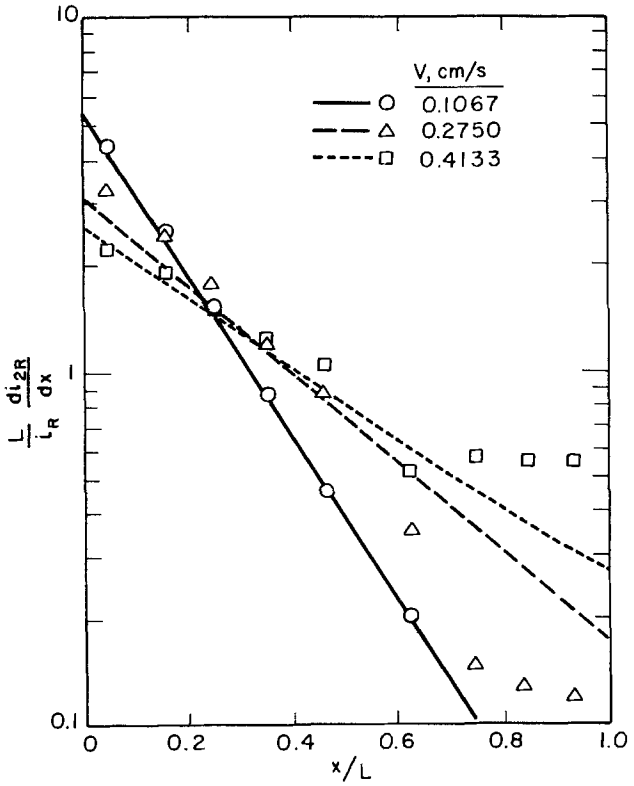


Fig. 3. Normalized distribution of copper deposition. Experimental data (13) and calculations are for deposition from a 2 mM cupric solution onto a bed 0.4 cm thick with a porosity of 0.64 and a specific surface area of 260 cm^{-1}, constructed of layers of Pt screens.

The model fit of the limiting current-distribution data of Alkire and Gracon (13) for copper deposition on platinum screen electrodes is shown in Fig. 3. The transfer current density for the main reaction di_{2R}/dx has been normalized by the total current density i_R due to the primary reaction and the electrode length L. A uniform current distribution would correspond to a horizontal line at an ordinate value of 1. Values of the parameters used to fit these data are given in Table II.

The data for the smallest flow rate (v = 0.1067 cm/sec) were fitted first by using literature values of the exchange current densities for copper deposition and hydrogen evolution on copper (23, 27) (any i_o values would work, however, since the data (13) were obtained at the limiting current), and adjusting the value of the mass-transfer coefficient k_m to obtain reasonable agreement between the calculated and experimental values. This value for the mass-transfer coefficient was then used to change the coefficient in the Wilson-Geankoplis correlation (24) (given by Eq. [42]) to 0.85

Table II. Values of the parameters used in fitting the data in Fig. 3

a = 260 cm^{-1}	ϵ = 0.64	D_o = 7.6 × 10^{-6} cm^2/sec
κ_o = 0.55 mho/cm	σ = 10^4 mho/cm	s_R = −1
n = 2	T = 298.15°K	α_{aR} = 1.5
α_{cR} = 0.5	γ = 0.75	α_{aS} = 0.5
α_{cS} = 0.5	$U_S - U_R$ = 0.481V	L = 0.4 cm

i_{oR} = 10^{-3} A/cm^2 at c_R = 0.1 mole/liter
i_{oS} = 10^{-7} A/cm^2 at c_S = 1 mole/liter, p_S = 1 atm
$i_{oS,ref}$ = 1.732 × 10^{-12} A/cm^2

dimensionless parameters as a function of v (c_{Rf} = 2 × 10^{-6} mole/cm^3)

v, cm/sec	0.1067	0.2750	0.4133
P_1 × 10^9	290.3	82.17	47.73
P_2	−0.1968	−0.9532	−1.880
P_3 × 10^5	3.779	3.779	3.779
P_4 × 10^{12}	4.001	2.128	1.622
P_5	0.1967	0.9532	1.880
P_6 × 10^6	5.540	26.84	52.93
D' × 10^2	6.040	3.203	2.439

$$\frac{ek_m}{aD_o} = \frac{0.85}{[6(1-\epsilon)]^{2/3}}\left(\frac{v}{aD_o}\right)^{1/3} \quad [44]$$

The remaining lines in Fig. 3 for the higher flow rates were then calculated using this expression for the mass-transfer coefficient and no additional adjustment of parameters.

It may be noted that Alkire and Gracon (13) proposed that the estimated specific interfacial area be reduced by a multiplier of 0.81 to yield an adjusted value. When used in the Wilson-Geankoplis correlation (24), this effectively reduces the coefficient to 0.947 if one continues to use the estimated value. In this case, the value of ak_m (which is the quantity which enters into the model equations) is reduced by a multiplier of 0.704 from the value which would be predicted by the Wilson-Geankoplis correlation and the estimated area. By our reducing the coefficient from 1.09 to 0.85, we have effectively reduced the value of ak_m by a multiplier of 0.78. Alkire and Gracon's choice of the multiplier of 0.81 was evidently based on the values of the total limiting current, not on a fit of the distribution data as in Fig. 3.

Theoretical predictions.—Again the results presented are divided into two categories, microscopic distributions and over-all reactor performance. For the calculations which follow, the counterelectrode is upstream, the primary reaction is again the deposition of copper, and the side reaction is the generation of dissolved hydrogen.

Figure 4 shows the reaction rate distributions for the primary electrode reaction only, at and below the limiting current, for the physical parameters and dimensionless parameters (corresponding to v = 3.328 × 10^{-3} cm/sec) in Table I, but with P_3 and P_4 equal to zero (*i.e.*, a single electrode reaction). The limiting

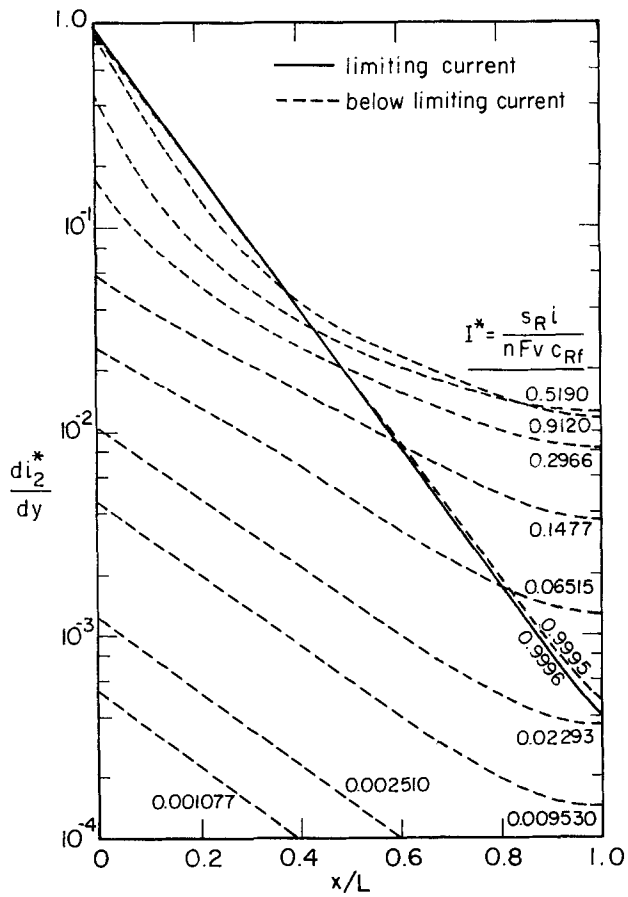


Fig. 4. Reaction distribution for copper deposition in the absence of a side reaction, calculated for αL = 8.663, D' = 0.1217, and P_2 = −3.254.

current distribution includes the effect of axial diffusion, and dispersion and was determined from the analysis of Newman and Tiedemann (14)

$$\frac{di_2^*}{dy} = \frac{Be^{-y/B} + (B-1)\,e^{By/D'} \exp\left[-\alpha L\left(\frac{1}{B}+\frac{B}{D'}\right)\right]}{B^2 - \frac{D'}{B}(B-1)\exp\left[-\alpha L\left(\frac{1}{B}+\frac{B}{D'}\right)\right]} \quad [45]$$

where

$$i_2^* = \frac{s_R i_2}{n\mathbf{F}vc_{Rf}} \quad [46]$$

and

$$B = \frac{1+\sqrt{1+4D'}}{2} \quad [47]$$

Integration of Eq. [45] from $y = 0$ to $y = \alpha L$ yields an expression for the total dimensionless limiting current density to the electrode

$$-i_2^*(0) = I^* = \frac{1 - e^{-\alpha L/B} + \frac{D'(B-1)}{B^3}\exp\left[-\alpha L\frac{1}{B}+\frac{B}{D'}\right](e^{B\alpha L/D'}-1)}{1-\frac{D'}{B^3}(B-1)\exp\left[-\alpha L\frac{1}{B}+\frac{B}{D'}\right]} \quad [48]$$

Figures 5-8 show current, potential, current efficiency, and concentration distributions within a reactor operating at conditions which correspond to the point on the upper curve of Fig. 1 where VOP = −403 mV and the outlet concentration is 0.28 mg/liter.

In Fig. 9 the solution-phase ohmic potential drop $\Delta\Phi_2$ across a reactor has been plotted as a function of the electrical driving force at the back of the reactor $(\Phi_1 - \Phi_2)_{\alpha L}$ for two cases: (*i*) the primary reaction only and (*ii*) when the side reaction is included, for values of the physical parameters and dimensionless parameters (corresponding to $v = 3.328 \times 10^{-3}$ cm/sec) in Table I. The ohmic potential drop has been made dimensionless with the quantity

$$\Delta\Phi_2' = \frac{n\mathbf{F}vc_{Rf}}{s_{R\kappa}}\frac{v}{ak_m} \quad [49]$$

which is an estimate of the ohmic potential drop across a reactor operating at the limiting current (1) when the effluent concentration is zero and the effects of axial diffusion and dispersion are negligible. The potential $(\Phi_1 - \Phi_2)_{\alpha L}$ is the potential of the cathode current collector relative to a copper reference electrode (with a concentration of c_{Rf} in the reference electrode compartment) placed at the back of the reactor.

At large negative values of $(\Phi_1 - \Phi_2)_{\alpha L}$ when only the primary reaction is considered, the ordinate approaches the value predicted by the limiting-current analysis of Newman and Tiedemann (14)

$$\frac{\Delta\Phi_2}{\Delta\Phi_2'} = \frac{\left(1+\frac{D'}{B^2}\right)[B^2 - (\alpha L + 1 + D')e^{-\alpha L/B}]}{B + \frac{D'}{B^2}(1-B)\exp\left[-\alpha L\frac{1}{B}+\frac{B}{D'}\right]} - \frac{D'}{B} \quad [50]$$

and has a value of 1.1057 in this case.

Figures 10 and 11 show that the effect on the current-potential curve if the fluid velocity is increased

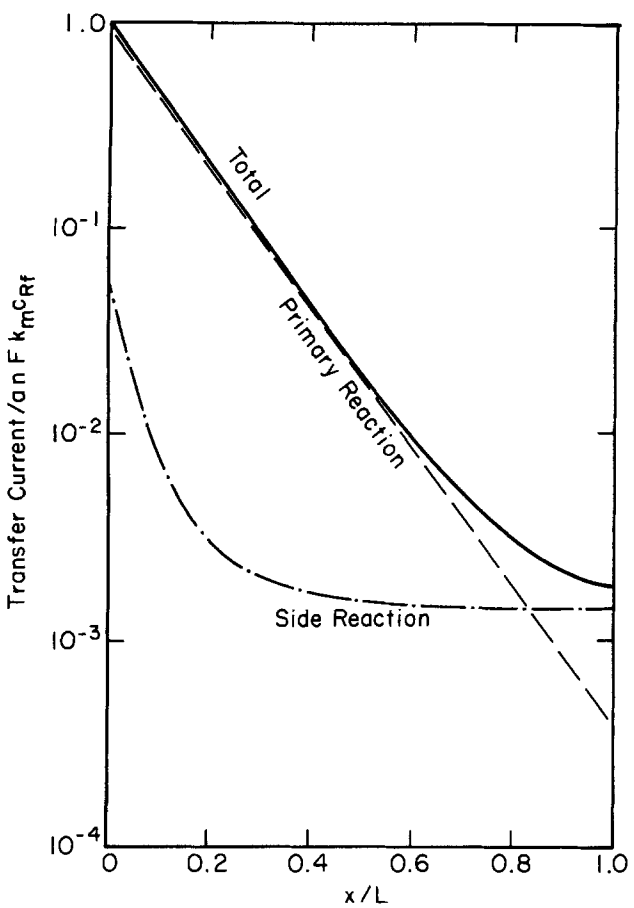


Fig. 5. Current distributions for deposition of copper and generation of dissolved hydrogen within a porous electrode with fluid flow from left to right, calculated for $v = 0.003328$ cm/sec, $a = 25$ cm^{-1}, $\epsilon = 0.3$, $L = 6$ cm, $c_{Rf} = 0.0105$ mole/liter, and VOP = −0.403V relative to a calomel reference electrode in the dilute-product stream.

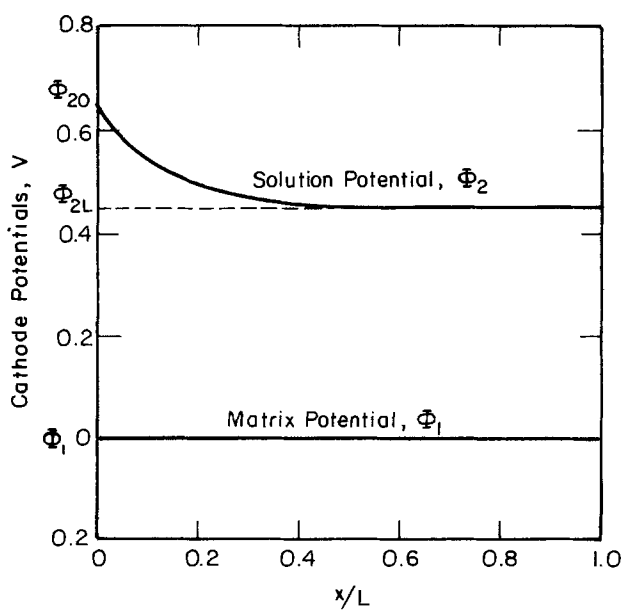


Fig. 6. Solution-phase and solid-matrix-phase potentials, as functions of cathode position, for the conditions of Fig. 5.

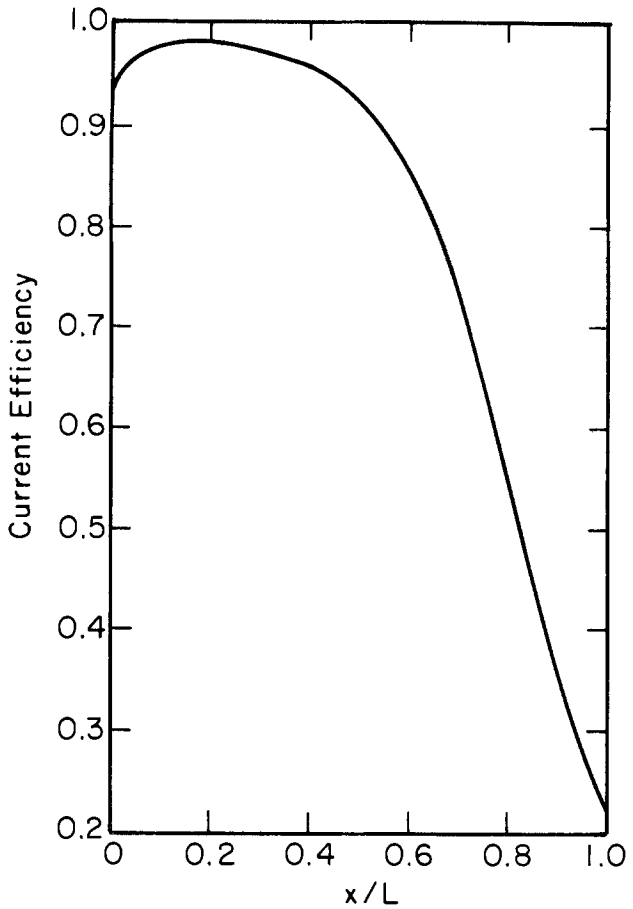


Fig. 7. Local current efficiency as a function of cathode position, for the conditions of Fig. 5. The over-all current efficiency is 0.962.

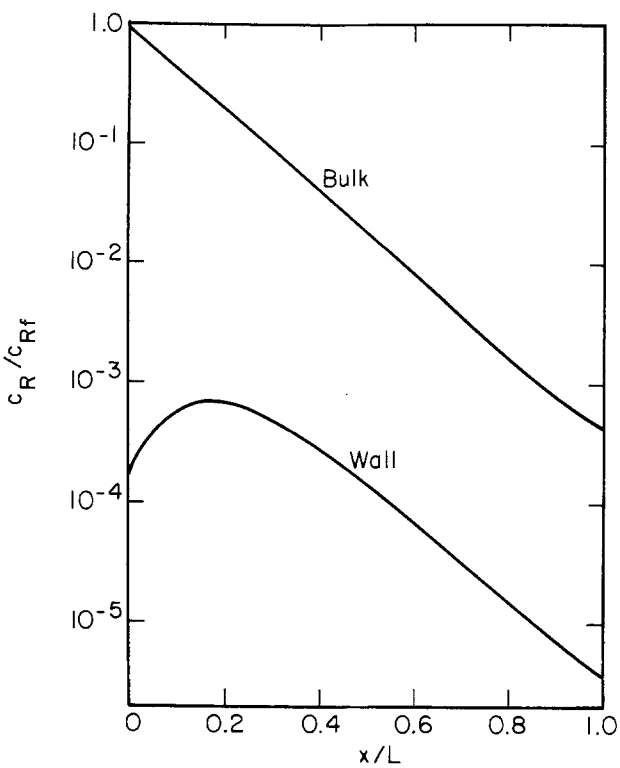


Fig. 8. Distribution of copper concentration in the flowing stream and along the pore wall, for the conditions of Fig. 5.

or the feed concentration decreased. The curve labeled with a v in Fig. 10 corresponds to the upper curve in Fig. 1, and the curve labeled $10^{-2}M$ in Fig. 11 corresponds to the lower curve in Fig. 1. (See also Table I.)

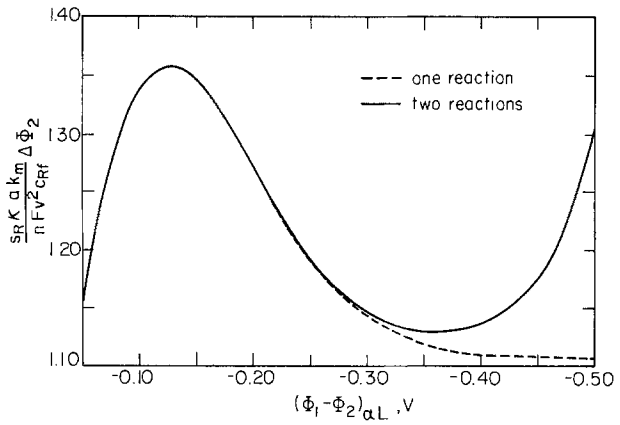


Fig. 9. Ohmic potential drop across the solution within the porous electrode—under the conditions of Fig. 4 and also with simultaneous generation of dissolved hydrogen.

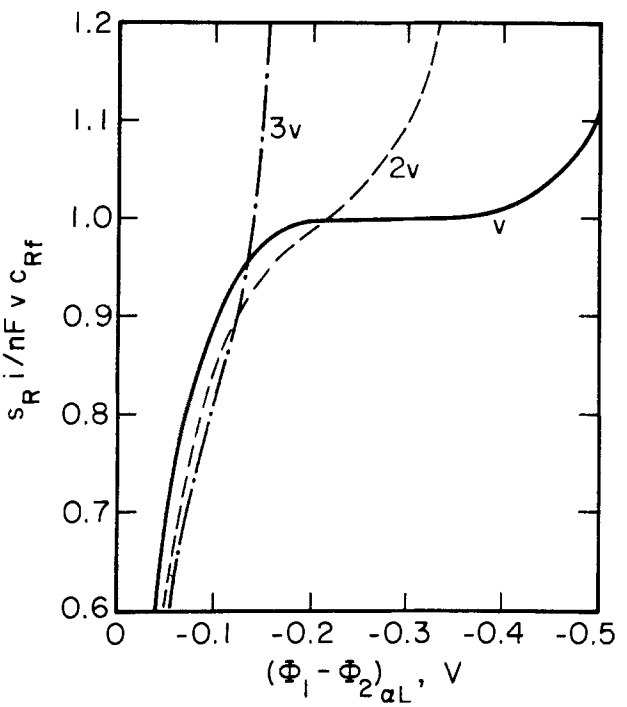


Fig. 10. Effect of flow rate on the current-potential curve. Operation at flow rates substantially above the design value (1) (here v = 0.003328 cm/sec) obscures the limiting-current plateau because of the high ohmic potential drop in the solution phase. For parameter values, see Table I.

Discussion

Agreement between model calculations and the experimental data of Bennion and Newman (1) shown in Fig. 1 should be considered satisfactory. However, the values of the parameters found by fitting the data need some clarification.

The fitted values of the exchange current densities for copper deposition and hydrogen evolution on carbon (see Table I) are 0.035 and 70 times the reported literature values ($i_{o,Cu} = 10^{-3}$ A/cm^2 (23) and $i_{o,H_2} = 10^{-7}$ A/cm^2 (27)) for these reactions on copper, respectively. However, it should not be interpreted that there is anything fundamental about these fitted values since the data are insufficient at the extreme values of the current to provide for their accurate evaluation. We also wish to emphasize that we do not suggest this as a method for determining fundamental kinetic parameters, since the bed is operating with a highly

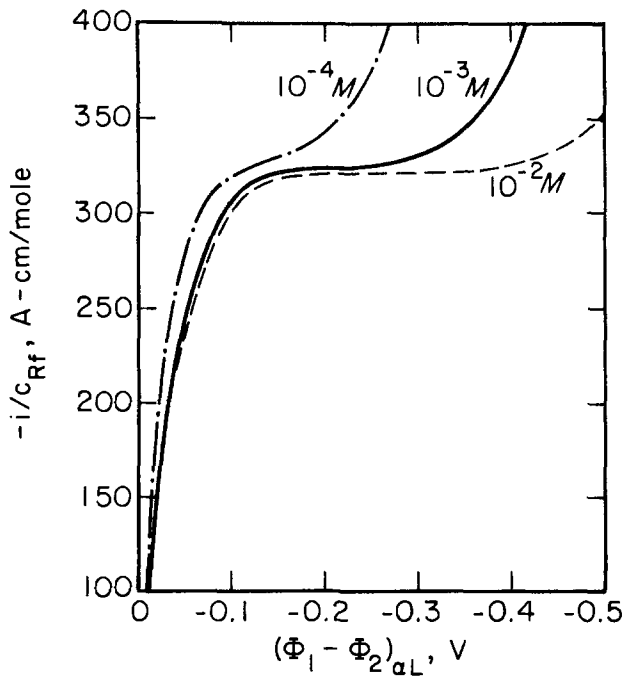


Fig. 11. Effect of feed concentration on the current-potential curve. Low concentrations correspond to low currents for the primary reaction, and these are easily obscured by the side reaction even in the absence of a significant ohmic potential drop within the reactor. For parameter values, see Table I.

nonuniform current density and mass-transport limitations dominate the data in certain regions.

The fitted values of k_m (given in Table I), determined mainly by the effluent concentration at the right on the experimental curves of Fig. 1 and plotted in Fig. 2, show a clear dependence on the velocity as follows

$$\frac{\epsilon k_m}{aD_o} = 0.07054\left(\frac{v}{aD_o}\right)^{0.5454} \qquad [51]$$

Data obtained in this manner (1) yield fundamental information about k_m [*e.g.*, Appel and Newman (26)]. Unfortunately, the value used for the specific interfacial area a of 25 cm^{-1} is an effective value and may be low by a factor of 4 to 12 (28). If larger values of a are used, the value of k_m will decrease, and the triangles plotted in Fig. 2 would move down and to the left toward lower values of the Sherwood and Péclet numbers.

The purpose of Fig. 2 is to call attention to the fact that the behavior of k_m is not well established in this flow region. Newman and Tiedemann (14) have suggested, for a restricted range of flow rates: $1 \leq Pe < 10^4$ and $Re < 10$, where Pe is the Péclet number v/aD_o and Re is the Reynolds number $v/a\nu$, there should exist an entry region such that the local mass-transfer coefficient is larger than the asymptotic value for deep bed electrodes, and that the average value of the mass-transfer coefficient will be dependent on the quantity aL. Since most measurements for k_m involve short electrodes, small aL (*e.g.*, Eq. [42] of Wilson and Geankoplis (24), where $1.8 \leq aL \leq 27$), the entire electrode may be within the entry region and will therefore predict too large a value for k_m when aL is large (deep beds), as is the case for Bennion and Newman's data (1).

Also in Fig. 2, a correlation found in Bird *et al.* (25) (Eq. [43]) has been extrapolated by at least an order of magnitude in Reynolds number below the range for which the correlation has been tested. However, this equation appears to give a conservative estimate for k_m, and may be useful for design purposes until better correlations are developed for this region of flow.

In Fig. 3 agreement between model calculations and the experimental data of Alkire and Gracon (13) for the smallest flow rate (0.1067 cm/sec) is good. The almost linear behavior on the semilog plot for the predicted limiting current distribution is expected based on the analysis of Bennion and Newman (1) for the special case of mass-transfer control. As expected, the value of k_m which best fits the data (given by Eq. [44]) is less than that predicted by Eq. [42] of Wilson and Geankoplis (24) due to the large value of $aL = 104$. The reason for using Eq. [44] at the two higher flow rates is to have some basis for changing k_m with the velocity since no data on the effluent concentration are given in Ref. (13) to enable an estimation of k_m as was done with the data of Bennion and Newman (1) in Fig. 1. (A graph of the total limiting current is presented by Alkire and Gracon (13), from which one could infer the effluent concentration if side reactions are negligible. However, values from this graph cannot be obtained with great precision, and, as pointed out by Appel and Newman (26), the total current is an inherently inaccurate method of measuring the mass-transfer coefficient when the overall conversion is close to 100%.)

In Fig. 3, at least two reasons are responsible for the discrepancies between the model calculations and the experimental data at the higher flow rates. First, the data are a replot of data taken from an arithmetic plot and are subject to error. Second, k_m may not be a constant throughout the electrode as assumed in the model. However, the discrepancies in Fig. 3 are considerably less than those between Alkire and Gracon's Fig. 6 and 9, where the lack of explanation has already been noted in the literature (18). One may speculate as to why the agreement between the model of Alkire and Gracon and their data is poor. This is perhaps due to the inadequate representation of the derivatives in the governing equations at the limiting current by standard central-difference approximations. New finite-difference approximations to the derivatives (developed in the Appendix) are required as discussed earlier.

The reaction rate distribution when only the metal deposition reaction is considered is plotted in Fig. 4 for various fractions of the limiting current. The effect of axial diffusion and dispersion is apparent in the limiting current distribution as di_2^*/dy is less than one at x/L equal to zero. The fact that I^* is not equal to one for the limiting current distribution is because mass-transfer limitations exist within the electrode, and therefore a small fraction of the feed concentration will escape unreacted.

For an appreciable fraction of the limiting current ($I^* > 0.9$), the reaction rate near the front of the electrode is high and decreases almost exponentially, similar to the behavior of the limiting current distribution (see Eq. [45]). Near the back of the electrode, the rate of reaction for the limiting current distribution is small because most of the copper is removed near the front of the electrode. Therefore, the reaction rates below the limiting current are greater at the back of the electrode (for values of $I^* > 0.03$), and are more uniform than the limiting current distribution. Actually, the reaction rate at the back of the electrode ($di_2^*/dy|_{y=aL}$) increases as the value of I^* decreases from 0.9996 to 0.7273, passes through a maximum at $I^* = 0.7273$, and then decreases monotonically with I^*. Thus, the effective depth of penetration of the reaction into the electrode also has a maximum near $I^* = 0.7273$.

For small values of the current ($I^* < 0.03$), the reaction rate distributions take on the same shape and can be described by a model with linear electrode

kinetics and no concentration variations [see Euler and Nonnenmacher (29) and Newman and Tobias (30)].

Figure 5 shows the relative rates of reaction for the primary reaction and the side reaction as they are distributed throughout the porous electrode. The total current density to the electrode was chosen close to the limiting current ($I^* = 1.038$) for the deposition of copper. Consequently, the reaction rate for the primary reaction decreases almost exponentially with distance (see Eq. [45]), as the solution is depleted with copper while flowing through the electrode. The side reaction, generation of dissolved hydrogen, responds mainly to the electric driving force between the solid matrix and the electrolytic solution. Its rate is high near the entrance to the porous electrode, and drops to a nearly constant value near the rear. The reason for this can be seen in Fig. 6, which represents the variation in the solution-phase potential Φ_2 for a counterelectrode placed upstream of the working electrode. The matrix conductivity is high, and therefore its potential Φ_1 is nearly a constant. The solution potential Φ_2 varies little near the rear because the current carried in the solution is small in this region. Because the driving force $(\Phi_1 - \Phi_2)$ is essentially uniform for some distance at the back of the electrode, measurement of $(\Phi_1 - \Phi_2)_{\alpha L}$ can lead to a lower bound thermodynamic estimate of the minimum concentration attainable in a flow-through porous electrode [see Trainham and Newman (31) for details].

In Fig. 7, the local current efficiency actually goes through a slight maximum near $x/L = 0.18$. The current efficiency is low at the entrance because the high electric driving force leads to a relatively high rate for the side reaction. For somewhat larger values of x, the rate of the side reaction decreases more rapidly than the primary reaction, and the local current efficiency rises. However, the primary reaction rate continues to decrease with distance because of the depletion of copper ions, and consequently the local current efficiency eventually drops to about 23% at the rear of the electrode. One might well ask, "Why not eliminate the last 40% of the thickness of the electrode?"

Figure 8 shows the concentration of copper ions through the thickness of the electrode. The high electric driving force at the entrance results in a very low wall concentration there. As the electric driving force decreases with x, the wall concentration rises toward the bulk value. With the diminishing reaction rate through the next part of the electrode, the wall concentration is able to decrease also, despite the smaller electric driving force in this region. We can also see from this figure that the bulk concentration is depleted by an additional factor of 20 in the last 40% of the electrode, despite the lowered current efficiency in this region. This additional metal ion removal can be achieved with relatively little additional expense for the added electrode thickness, and virtually no added cost due to added ohmic potential drop.

In Fig. 9, the ohmic potential drop across the solution within the reactor exhibits a maximum and then a minimum as the driving force increases at the back of the reactor. The maximum occurs at $I^* = 0.95$, and is due to a combination of effects: (*i*) the driving force is high, and the current is only increasing slowly, (*ii*) the reaction rate at the back of the electrode goes through a maximum at a value of $I^* = 0.7273$ as discussed previously in Fig. 4, and (*iii*) the driving force, though high, is not large enough for the side reaction to contribute substantially to the ohmic potential drop. For larger values of $(\Phi_1 - \Phi_2)_{\alpha L}$, the ohmic potential drop decreases due to a decreasing rate of reaction at the back of the electrode. Thus, the depth of penetration of the reaction is decreasing at $I^* = 0.95$. This was shown clearly in Fig. 4 as the primary reaction approaches the limiting current distribution.

The minimum in the ohmic potential occurs simultaneously with the minimum in the total reaction rate at the back of the electrode $(di_2^*/dy)|_{\alpha L}$. At this point the rate of the side reaction becomes significant, and the ohmic drop increases accordingly.

We wish to emphasize that the existence of a local maximum and local minimum is dependent on the physical parameters and operating conditions. For example, if the exchange current density for the side reaction were significantly larger relative to the primary reaction, the driving force required to make the side reaction occur to a significant extent would be much less. Thus instead of the ohmic potential drop exhibiting a local maximum due mainly to the effects of the primary reaction (or lack of effect of the side reaction), the side reaction becomes the controlling factor and $\Delta\Phi_2$ increases monotonically with increasing $(\Phi_1 - \Phi_2)_{\alpha L}$.

Another way to achieve a similar result (using the same physical parameters) is to increase the ohmic potential drop by increasing the superficial velocity as shown in Fig. 10. The reactor cannot be operated at even twice the superficial velocity without loss of the limiting current-plateau and a lack of a local maximum and a local minimum in the ohmic potential drop, which is due to extensive interference by the side reaction. In harmony with the quantitative design principles (1), these calculations show that an increase in the superficial velocity increases the ohmic potential drop in the solution so that there is either excessive side reaction at the entrance to the porous electrode or a failure to maintain the limiting-current condition near the exit. A decrease in the feed concentration as shown in Fig. 11 will also increase the side reaction relative to the primary reaction and cause the limiting-current plateau to become less distinct. The ability to calculate the current distributions below the limiting current and in the presence of a side reaction permits one to determine the economically optimum operating conditions and even permissible operating conditions when the side reaction accounts for a substantial fraction of the total current, and there is a penalty for making the electrode thicker because the side reaction does not necessarily decrease with increasing distance through the electrode.

Conclusion and Summary

A theoretical model for flow-through porous electrodes has been described for the specific application to metal-ion removal from dilute streams. A new set of dimensionless parameters has been suggested from the analysis, which characterize the relative importance of the following physical phenomena within a flow-through porous electrode: axial diffusion and dispersion (D'), backward rate of the primary reaction (P_1), ohmic potential drop (P_2), and forward (P_3) and backward (P_4) rates of the side reaction. Satisfactory agreement between model predictions and experimental data on over-all reactor performance and deposit distributions has been achieved.

The knowledge of distributions of current, potential, and concentration in the presence of a side reaction above and below the limiting current of the primary reaction makes it possible to design and optimize an electrode system for the most economical removal of metal ions, but this design may only be accomplished if there are sufficient experimental data. Most important are values for the specific interfacial area a, the mass-transfer coefficient k_m, and the exchange current densities for the primary reaction and the side reaction.

Acknowledgment

This work was supported by the U.S. Energy Research and Development Administration.

Manuscript submitted Feb. 14, 1977; revised manuscript received June 13, 1977.

Any discussion of this paper will appear in a Discussion Section to be published in the June 1978 JOURNAL. All discussions for the June 1978 Discussion Section should be submitted by Feb. 1, 1978.

Publication costs of this article were assisted by the University of California at Berkeley.

APPENDIX

To obtain a more accurate representation of the derivatives in Eq. [28]-[31] more of the physics needed to be incorporated in their dependence. This was done by considering the concentration distribution at the limiting current, which decreases exponentially with electrode thickness (1, 14). With this in mind, a new variable was defined

$$\theta = e^C \qquad [A\text{-}1]$$

Now apply this equation to the upstream boundary condition on the concentration (Eq. [30]) to obtain

$$e^C\left(1 - D'\frac{dC}{dy}\right) = 1 \qquad [A\text{-}2]$$

Next introduce the central-difference approximations at the first real mesh point ($j = 2$, mesn point 1 is an image point)

$$\theta_2\left(1 - D'\frac{C_3 - C_1}{2h}\right) = 1 \qquad [A\text{-}3]$$

or

$$\theta_2\left(1 - \frac{D'}{2h}\ln\frac{\theta_3}{\theta_1}\right) = 1 \qquad [A\text{-}4]$$

If θ is approximately exponential in distance, then C will be approximately linear, and less error will be introduced when the derivative is approximated by a finite-difference form in the variable C.

Similarly, a central-difference approximation for the axial diffusion and axial dispersion term in Eq. [28] can be derived for any interior mesh point j

$$D'\frac{d^2\theta}{dy^2} = \frac{D'\theta_j}{h^2}\left[\frac{1}{4}\left(\ln\frac{\theta_{j+1}}{\theta_{j-1}}\right)^2 + \ln\left(\frac{\theta_{j+1}\theta_{j-1}}{\theta_j^2}\right)\right] \qquad [A\text{-}5]$$

The resulting material balance equation at any interior mesh point j now becomes

$$\frac{\theta_j}{2h}\ln\frac{\theta_{j+1}}{\theta_{j-1}} = \frac{D'\theta_j}{h^2}\left[\frac{1}{4}\left(\ln\frac{\theta_{j+1}}{\theta_{j-1}}\right)^2 + \ln\left(\frac{\theta_{j+1}\theta_{j-1}}{\theta_j^2}\right)\right] - J_{Rj} \qquad [A\text{-}6]$$

where

$$J_{Rj} = \frac{\theta_j - P_1 e^{(\alpha_{aR}/\alpha_{cR}+1)\eta'_j}}{1 + e^{\eta'_j}} \qquad [A\text{-}7]$$

To check *a posteriori* the over-all application of Faraday's law, whereby the integral of the transfer current J_R for the principal reaction should be related to the difference between the inlet and outlet concentrations of the principal reactant, one should use an integration formula J_R which also takes account of the approximately exponential dependence of J_R on distance.

So that the integrated current is also correct for the side reaction, combine Eq. [28] and [29] by eliminating J_R from both equations to yield

$$\frac{d}{dy}\left(\frac{1}{P_2}\frac{d\eta'}{dy} + \theta - D'\frac{d\theta}{dy}\right) = J_S \qquad [A\text{-}8]$$

where

$$J_S = P_3 \exp\left(-\alpha_{cS}\eta'/\alpha_{cR}\right)\left[1 - P_4\exp\left(\frac{\alpha_{aS} + \alpha_{cS}}{\alpha_{cR}}\eta'\right)\right] \qquad [A\text{-}9]$$

Next express the outer derivative in Eq. [A-8] as a central difference written between points halfway between mesh points

$$\frac{1}{h}\left[\left(\frac{1}{P_2}\frac{d\eta'}{dy} + \theta - D'\frac{d\theta}{dy}\right)_{j+1/2} - \left(\frac{1}{P_2}\frac{d\eta'}{dy} + \theta - D'\frac{d\theta}{dy}\right)_{j-1/2}\right] = J_S \qquad [A\text{-}10]$$

Now express the terms $\theta - D'd\theta/dy$ halfway between two mesh points using Eq. [A-1] and the values of θ at the adjacent mesh points (see also Eq. [A-2])

$$\left(\theta - D'\frac{d\theta}{dy}\right)_{j+1/2} = \sqrt{\theta_j\theta_{j+1}}\left(1 - \frac{D'}{h}\ln\frac{\theta_{j+1}}{\theta_j}\right) \qquad [A\text{-}11]$$

and

$$\left(\theta - D'\frac{d\theta}{dy}\right)_{j-1/2} = \sqrt{\theta_j\theta_{j-1}}\left(1 - \frac{D'}{h}\ln\frac{\theta_j}{\theta_{j-1}}\right) \qquad [A\text{-}12]$$

With these approximations and a central-difference expression for the derivative of η', the resulting equation for the potential at any interior mesh point j becomes

$$\frac{1}{P_2}\frac{\eta'_{j+1} + \eta'_{j-1} - 2\eta'_j}{h^2} + \frac{\sqrt{\theta_j\theta_{j+1}}}{h}\left(1 - \frac{D'}{h}\ln\frac{\theta_{j+1}}{\theta_j}\right) - \frac{\sqrt{\theta_j\theta_{j-1}}}{h}\left(1 - \frac{D'}{h}\ln\frac{\theta_j}{\theta_{j-1}}\right) = J_{Sj} \qquad [A\text{-}13]$$

Similarly, to treat the upstream boundary condition for the potential, integrate Eq. [A-8] from zero to $h/2$ to yield

$$\left(\frac{1}{P_2}\frac{d\eta'}{dy} + \theta - D'\frac{d\theta}{dy}\right)_{h/2} - \left(\frac{1}{P_2}\frac{d\eta'}{dy} + \theta - D'\frac{d\theta}{dy}\right)_0 = \frac{h}{2}J_{Sj} \qquad [A\text{-}14]$$

Use the same approximations as above for $y = h/2$, and use the boundary conditions in Eq. [30] to obtain (for $j = 2$)

$$\frac{2}{h}\frac{1}{P_2}\frac{\eta'_{j+1} - \eta'_j}{h} + \frac{2}{h}\sqrt{\theta_j\theta_{j+1}}\left(1 - \frac{D'}{h}\ln\frac{\theta_{j+1}}{\theta_j}\right) - \frac{2}{h}\left(\frac{P_5}{P_2}I^* + 1\right) = J_{Sj} \qquad [A\text{-}15]$$

With Eq. [A-13] at the interior mesh points, this corresponds then to a trapezoidal integration of the transfer current J_S over the thickness of the porous electrode.

The governing finite-difference Eq. [A-6] and [A-13], along with the upstream boundary conditions [A-4] and [A-15] were then linearized about a trial solution and solved simultaneously with the downstream boundary condition for θ and η' using Newman's technique (23). The new approximations to the derivatives in concentration provided accurate values for θ and η' at the mesh points without introducing anomalous values for the integrated current.

LIST OF SYMBOLS

a	specific interfacial area, cm^{-1}
B	see Eq. [47]
C	$\ln\theta$
c_R	concentration of metal-ion reactant, mole/cm^3
c_{Rf}	upstream feed concentration of metal-ion reactant, mole/cm^3
c_{Rw}	wall concentration of metal-ion reactant
c_S	hydrogen ion concentration, mole/cm^3
D_a	axial dispersion coefficient of metal-ion reactant, cm^2/sec

D_o molecular diffusion coefficient of metal-ion reactant, cm²/sec
D_R effective diffusion coefficient of metal ion reactant, cm²/sec
D' dimensionless parameter describing the relative importance of axial diffusion and dispersion, see Eq. [32]
$\mathbf{F}$ Faraday's constant, 96,487 C/equivalent
h dimensionless distance between mesh points
i superficial current density to an electrode, A/cm²
i_{oj} exchange current density for reaction j, A/cm²
$i_{oj,\mathrm{ref}}$ exchange current density for reaction j at a reference composition $c_{i,\mathrm{ref}}$, see Eq. [14], A/cm²
i_1 superficial current density in the matrix, A/cm²
i_2 superficial current density in pore-solution phase, A/cm²
i_{nj} transfer current for reaction j per unit interfacial area, A/cm²
I^* dimensionless superficial current density to an electrode, see Eq. [41]
i_2^* dimensionless current density in pore-solution phase, see Eq. [61]
$i_2^*(o) = -I^*$ total dimensionless current density in pore-solution phase, see Eq. [48]
i_R total current density to an electrode due to metal-deposition reaction, A/cm²
I total current to an electrode, A
j_{in} pore-wall flux of species i, mole/cm²-sec
J_R dimensionless transfer current of metal deposition reaction, see Eq. [A-6]
J_S dimensionless transfer current of side reaction, see Eq. [A-9]
k_m average mass-transfer coefficient between flowing solution and electrode surface, cm/sec
L thickness of porous electrode, cm
M_i symbol for the chemical formula of species i
n number of electrons transferred in metal deposition reaction
n_j number of electrons transferred in reaction j
N_R superficial flux of metal-ion reactant, mole/cm²-sec
p_S hydrogen partial pressure, atm
Pe Péclet number v/aD_o
P_1 dimensionless parameter describing the relative importance of the backward term in the metal deposition reaction, see Eq. [34]
P_2 dimensionless parameter describing the relative importance of the ohmic potential drop, see Eq. [35]
P_3 dimensionless parameter describing the relative importance of the forward term in the side reaction, see Eq. [36]
P_4 dimensionless parameter describing the relative rate of the backward term in the side reaction, see Eq. [37]
P_5 dimensionless parameter which characterizes the ohmic potential drop in the pore-solution phase, see Eq. [38]
P_6 dimensionless parameter which characterizes the ohmic potential drop in the matrix phase, see Eq. [39]
q_{ij} cathodic reaction order
R universal gas constant, 8.3143 J/mole-°K
s_{ij} stoichiometric coefficient of species i in electrode reaction j
s_R stoichiometric coefficient of metal-ion reactant
T absolute temperature, °K
U_{jw} open-circuit potential for reaction j at local wall composition relative to a reference electrode of a given kind, V, see Eq. [17]
U_j^θ standard electrode potential for reaction j, V
U_r^θ standard electrode potential of reference electrode, V
$\Delta U = U_S - U_R$ difference in open-circuit cell potentials of the side reaction and primary reaction at the reference composition, V
v superficial fluid velocity, cm/sec
VOP potential of the cathode current collector relative to a saturated calomel reference electrode placed in the dilute product stream, V
x distance through porous electrode, cm
y $x\,ak_m/v$ dimensionless distance through porous electrode
z_i valance or charge number of species i

Greek Letters

$\alpha = ak_m/v$, reciprocal of penetration depth at the limiting current, cm⁻¹
α_{aj} anodic transfer coefficient for reaction j
α_{cj} cathodic transfer coefficient for reaction j
γ_{ij} exponent in composition dependence of exchange current density
porosity or void volume
$\eta_{sj} = \Phi_1 - \Phi_2 - U_{jw}$ surface overpotential for reaction j, V
$\eta = \Phi_1 - \Phi_2$ local overpotential, V
η' dimensionless local overpotential, see Eq. [33]
κ effective conductivity of solution, mho/cm
κ_o intrinsic conductivity of solution, mho/cm
ν kinematic viscosity of solution, cm²/sec
ρ_o density of pure solvent, kg/cm³
σ effective conductivity of solid matrix, mho/cm
ψ dimensionless particle shape factor (0.86 for flakes)
Φ_1 electrostatic potential in matrix phase, V
Φ_2 quasielectrostatic potential in the pore solution phase, V
$\Delta\Phi_2$ ohmic potential drop across porous electrode, V
$\Delta\Phi_2'$ estimate of ohmic potential across porous electrode at the limiting current, V, see Eq. [49]
τ tortuosity factor
$\theta = c_R/c_{Rf}$, dimensionless concentration of metal-ion reactant

Subscripts

r reference electrode compartment
R metal-ion reactant or primary reaction
ref reference composition
S side reactant or side reaction
w wall or electrode surface

REFERENCES

1. D. N. Bennion and J. Newman, *J. Appl. Electrochem.*, **2**, 113 (1972).
2. R. S. Wenger, D. N. Bennion, and J. Newman, Paper 236 presented at The Electrochemical Society Meeting, Chicago, Illinois, May 13-18, 1973; *This Journal*, **120**, 1096 (1973).
3. Robert S. Wenger, M.S. Thesis, University of California, 1974.
4. F. A. Posey, Report ORNL-TM-4112, Oak Ridge National Laboratory, Oak Ridge, Tennessee.
5. A. T. Kuhn and R. W. Houghton, *J. Appl. Electrochem.*, **4**, 69 (1974).
6. J. M. Williams and K. B. Keating, *DuPont Innovation*, **6**, 6 (1975).
7. A. K. P. Chu, M. Fleischmann, and G. J. Hills, *J. Appl. Electrochem.*, **4**, 323 (1974).
8. J. Van Zee and J. Newman, *This Journal*, **124**, 706 (1977).
9. R. D. Armstrong, O. R. Brown, R. D. Giles, and J. A. Harrison, *Nature (London)*, **219**, 94 (1968).
10. G. Kreysa, S. Piontech, and E. Heitz, *J. Appl. Electrochem.*, **5**, 305 (1975).
11. A. T. Kuhn and R. W. Houghton, *Electrochim. Acta*, **19**, 733 (1974).
12. J. Newman and W. Tiedemann, *AIChE J.*, **21**, 25 (1975).
13. R. Alkire and B. Gracon, *This Journal*, **122**, 1594 (1975).
14. J. Newman and W. Tiedemann, Paper submitted to *Adv. Electrochem. Electrochem. Eng.*
15. R. E. Sioda, *Electrochim. Acta*, **20**, 457 (1975).
16. R. E. Sioda, *J. Electroanal. Chem. Interfacial Electrochem.*, **34**, 399 (1972).
17. R. Alkire and R. Gould, *This Journal*, **123**, 1842 (1976).
18. B. G. Ateya and L. G. Austin, *ibid.*, **124**, 83 (1977).
19. P. V. Danckwerts, *Chem. Eng. Sci.*, **2**, 1 (1953).
20. J. F. Wehner and R. H. Wilhelm, *ibid.*, **6**, 89 (1956).
21. T. K. Sherwood, R. L. Pigford, and C. R. Wilke, "Mass Transfer," p. 136, McGraw-Hill, Inc., New York (1975).
22. R. E. de la Rue and C. W. Tobias, *This Journal*, **106**, 827 (1959).
23. J. Newman, "Electrochemical Systems," p. 177, Appendix C, Prentice-Hall, Englewood Cliffs, New Jersey (1973).

24. E. J. Wilson and C. J. Geankoplis, *Ind. Eng. Chem. Fundam.*, **5**, 9 (1966).
25. R. Byron Bird, W. E. Stewart, and E. N. Lightfoot, "Transport Phenomena," pp. 411-412, John Wiley & Sons, New York (1960).
26. P. W. Appel and J. Newman, *AIChE J.*, **22**, 979 (1976).
27. T. Erdez-Gruz, "Kinetics of Electrode Processes," p. 165, Wiley-Interscience, New York (1972).
28. D. N. Bennion, Paper 69 presented at The International Society of Electrochemistry meeting, Zurich (1976).
29. J. Euler and W. Nonnenmacher, *Electrochim. Acta*, **2**, 268 (1960).
30. J. S. Newman and C. W. Tobias, *This Journal*, **109**, 1183 (1962).
31. J. A. Trainham and J. Newman, *J. Appl. Electrochem.*, **7**, 287 (1977).

Steady-State Polarization at Porous, Flow-Through Electrodes with Small Pore Diameter

II. Irreversible Kinetics for One-Electron and Consecutive Two-Electron Transfer Reactions

B. G. Ateya*,[1] and L. G. Austin*

Fuel Science Section, Department of Material Sciences, The Pennsylvania State University, University Park, Pennsylvania 16802

ABSTRACT

In this paper a model is proposed for the performance of a porous flow-through electrode working on a redox couple, for one-dimensional systems with fine pores. The model includes the combined effects of mass transfer by forced convection and axial diffusion, ohmic potential drop in the pore electrolyte, and activation polarization, on the over-all current-polarization relations. The cases of front and rear reactant supply are treated. The treatment is extended to the case of a consecutive two-electron transfer reaction where the rate equation is rather complicated. Experimental results are presented to test several aspects of the model. The agreement between theory and experiment is generally good for moderate ohmic effects.

Porous flow-through electrodes have several advantages over porous diffusion electrodes mainly because of the high mass transfer rates and high limiting currents possible. It is, therefore, desirable to be able to describe quantitatively the dependence of the over-all rate of reaction in such an electrode on the physical and catalytic properties of the electrode matrix and the properties of reactant-product system and supporting electrolyte.

This system is currently attracting considerable attention. It has been suggested for removing dissolved copper (1-3) and antimony ions (4) and for converting ferrous into ferric ions in industrial waters (5). The original work on this system is due to Perskaya and Zaidenman (6) and was subsequently extended simultaneously by Gurevich and Bagotsky (7) and Austin *et al.* (8). There are several other treatments, some of which are concerned with mass transfer and ohmic effects, neglecting activation polarization (1, 3), or with activation and ohmic polarizations in the near reversible region and neglecting concentration polarization (9, 10). Wroblowa *et al.* (11, 12) have also presented theoretical treatments of this system and experimental results using the I_2/I^- reversible system (11). They recently (12) treated the effects of a pre-electrode diffusional boundary layer and of axial diffusion on the limiting current and on concentration, current, and potential distributions under conditions of very low flow speeds, $u \simeq 10^{-5}$-10^{-3} cm/sec. Only the case of rear reactant supply was considered and no experimental testing was offered.

There is a large body of semiempirical treatments presented by Sioda (13) essentially for packed and folded (80 mesh) screen electrodes operating on reversible reactions. Alkire *et al.* (14), using packed (100 mesh) screen electrodes, found that the limiting current is critically dependent on flow rate and electrode thickness. They presented a mathematical model to explain the lower efficiency (obtainable at high flow rates and/or thin electrodes) in terms of internal mass transfer limitations.

The experimental results presented in the above works were obtained on reversible electrode reactions and mostly at electrodes of very low specific surface area (large pore diameter). Such electrodes are of limited importance because of their low reactive surface area and the loss of their efficiency (poor reactant utilization) due to radial diffusion limitations (15-18).

This paper deals with the case of irreversible, one-electron transfer kinetics where activation polarization is needed to support large reaction rates, and it considers rear and front reactant supply over the entire current-polarization range. The treatment is extended to the case of a consecutive two-electron transfer kinetics where the rate equation is considerably more complicated. The theoretical predictions are tested experimentally by using the Sn^{2+}/Sn^{4+} redox couple which is highly irreversible, and has reasonably well-understood kinetics (19-21). The corresponding model for reversible kinetics has been presented and tested in part I (22).

Theoretical Steady-State Treatments

The system is assumed to be one dimensional such that radial diffusion is fast and velocity and concentration entrance effects are negligible. The electrode has narrow (~1 μm radius) and highly interlinked pores such that velocity, current, concentration, and potential are uniform at any depth inside the electrode. The electrical resistivity of the electrode material is very low compared to that of the electrolyte which is assumed to be constant and independent of reactant concentration. The latter is achieved by using a supporting electrolyte which also ensures that effects of ionic migration and streaming potential are negligible.

* Electrochemical Society Active Member.
[1] Permanent address: Chemistry Department, Faculty of Science, Cairo University, Cairo, Egypt.
Key words: flow-through electrodes, polarization, axial diffusion, single and consecutive electron transfer, rear and front supply.

An isothermal system is considered, and for simple one-electron transfer kinetics the rate expression is chosen as

$$i = i_o[(R/R_b)\exp(\alpha\eta/b) - (P/P_b)\exp(\beta\eta/b)] \quad [1]$$

Figure 1 illustrates rear and frontal reactant supply.

In the absence of significant diffusion, or assuming equal diffusion coefficients of reactant and product, a mass balance gives $R(x) + P(x) = R_b + P_b$. Thus

$$i = i_o\{(R/R_b)[\exp(\alpha\eta/b) + \gamma\exp(\beta\eta/b)] - (1+\gamma)\exp(\beta\eta/b)\} \quad [2]$$

where $\gamma = R_b/P_b$. The steady-state mass transfer equation in dimensionless form is (22)

$$d\bar{i}(\bar{x})/d\bar{x} = \theta d^2\bar{R}(\bar{x})/d\bar{x}^2 - d\bar{R}(\bar{x})/d\bar{x} \quad [3]$$

where $\theta = D_{eff}/Lu$, $\bar{i}(\bar{x}) = i(\bar{x})/i_L$, $\bar{x} = x/L$, and $\bar{R}(\bar{x}) = R(x)/R_b$. A kinetic balance on an element dx using the dimensionless form of Eq. [2] gives

$$d\bar{i}(\bar{x}) = \bar{i}_o\{\bar{R}(\bar{x})[\exp(\bar{\alpha\eta}(\bar{x})) + \gamma\exp(\bar{\beta\eta}(\bar{x}))] - (1+\gamma)\exp(\bar{\beta\eta}(\bar{x}))\}d\bar{x} \quad [4]$$

where $\bar{i}_o = i_oSL/i_L$, $\bar{\eta}(\bar{x}) = \eta(x)/b$, and $\bar{R}(\bar{x})/R_b\cdot\bar{i}_o$ is an index of the effective rate constant *vs.* the rate of reactant input and hence is called the reversibility index. For algebraic convenience, the bars are dropped and it is to be understood that the parameters are in dimensionless form. Combining Eq. [4] with [3] gives

$$\theta\frac{d^2R(x)}{dx^2} - \frac{dR(x)}{dx} - i_o\{R(x)[\exp(\alpha\eta(x)) + \gamma\exp(\beta\eta(x))] - (1+\gamma)\exp(\beta\eta(x))\} = 0 \quad [5]$$

This equation relates concentration and potential distributions to the independent variables of the system, *e.g.*, i_o, α, θ, γ, and x, based on a combination of kinetic and mass transfer relations. In general this must also be combined with Ohm's law. Solutions are presented for various cases of ohmic and mass transfer control.

Case 1. Mass transfer effects, negligible ohmic effects.—If the effect of mass transfer dominates over the effect of ohmic resistance in the pore electrolyte, as would apply for low values of R_b and high specific conductivity of electrolyte, the equation simplifies considerably since η is then independent of distance x. In this case, frontal or rear supply gives the same answer; we will consider rear supply. The boundary conditions are taken as (22)

$$1 = R(+0) - \theta(dR/dx)_{x=+0} \quad [6a]$$

$$(dR/dx)_{x=1} = 0 \quad [6b]$$

Formally, at $x = -0$, $R(-0) = 1$, since no reaction occurs before $x = 0$. As discussed before (22), however, when the reaction approaches reversible kinetics (large i_o), the concentration change at $x = 0$ approaches a δ function and the concentration gradient from the $+0$ direction can be nonzero. In practice, some reaction will occur on the outer face and in the two-dimensional pore mouth so that a gradual change of concentration gradient would occur over $x = \pm 0$.

Equation [5] is put into a form suitable for solution with these boundary conditions by using the substitutions $f = \exp(\alpha\eta) + \gamma\exp(\beta\eta)$, $\psi(x) = R(x) - [(1+\gamma)\exp(\beta\eta)/f]$ giving

$$d^2\psi(x)/dx^2 - d\psi(x)/dx - i_of\psi(x) = 0 \quad [5a]$$

The solution to Eq. [5a] is

$$R(x) = ((1+\gamma)\exp(\beta\eta)/f) + C_1\exp(m_1x) + C_2\exp(m_2x) \quad [7]$$

where

$$m_1 = (1/2\theta)(1 + \sqrt{1 + 4i_o\theta f})$$

$$m_2 = (1/2\theta)(1 - \sqrt{1 + 4i_o\theta f})$$

$$C_1 = -C_2m_2\exp(m_2)/(m_1\exp(m_1))$$

$$C_2 = \frac{1 - (1+\gamma)\exp(\beta\eta)/f}{(1-\theta m_2) - (1-\theta m_1)m_2\exp(m_2)/m_1\exp(m_1)}$$

The relation between current and concentration is given by (22)

$$i(x) = 1 - R(x) + \theta dR(x)/dx \quad [8]$$

And since $dR(x)/dx = 0$ at $x = 1$, Eq. [7] and [8] lead to

$$i = 1 - [((1+\gamma)\exp(\beta\eta)/f) + C_1\exp(m_1) + C_2\exp(m_2)] \quad [9]$$

where i is the dimensionless total current density at $x = 1$.

When $\eta = 0$, Eq. [7] gives $R(x) = 1$ for any value of x, which corresponds to open-circuit conditions. At $x = 0$ and i_o is very large, both Eq. [7] and [10] reduce to the case of reversible reaction as considered previously, giving $R(+0) < 1$ and $i(+0) > 0$ for $\eta > 0$.

For the special case of the diffusion coefficient tending to zero, θ tends to zero, and it is readily shown that the limit of Eq. [7] for $\theta = 0$ is

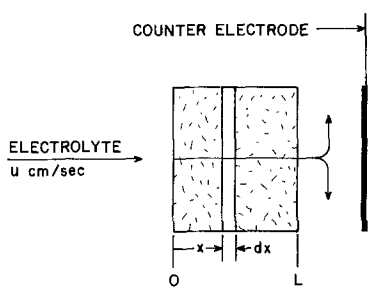
$$R(x) = (1/f)[(1+\gamma)\exp(\beta\eta) + (\exp(\alpha\eta) - \exp(\beta\eta))\exp(-i_ofx)] \quad [10]$$

which is the expression obtained previously by Austin *et al.* (8). As the diffusion coefficient tends to zero, the total current density is given by $i = 1 - R(1)$ where $R(1)$ is given by Eq. [10] with $x = 1$. Thus

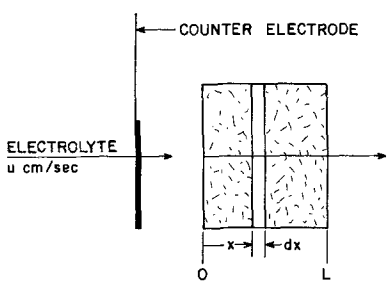
$$i_{\theta=0} = (1/f)[\exp(\alpha\eta) - \exp(\beta\eta)][1 - \exp(-i_of)] \quad [11]$$

For irreversible conditions such that $\exp(\beta\eta) \simeq 0$, $i = 1 - \exp[-i_o\exp(\alpha\eta)]$ or

$$\eta = (2.3/\alpha)\log[\log(1/(1-i))] - 2.3\log(i_o/2.3) \quad [12]$$



a. REAR REACTANT SUPPLY



b. FRONT REACTANT SUPPLY

Fig. 1. Model of a flow-through electrode showing rear and front reactant supply.

Thus if axial diffusion is negligible a plot of the polarization *vs.* log (log $(1/(1-i))$) in the irreversible region for the case of negligible ohmic potential drop in the pore electrolyte gives a straight line of a slope of 120 mV (for $\alpha = 0.5$ at 25°C).

Case 2. Mass transfer and ohmic effects, rear supply.—Assuming the specific conductivity of the electrolyte is constant Ohm's law in dimensionless form is

$$i(x) = (1/\Delta)d\eta(x)/dx \qquad [13]$$

where Δ is the index of ohmic effect, $\Delta = i_L L\rho/b$. The boundary conditions are $(d\eta/dx)_{x=0} = 0$ and $(d\eta/dx)_{x=1} = i\Delta$ in addition to those of Eq. [6]. Under conditions used in the computations, which are not near reversible, it was assumed that $(d\eta/dx)_{x=+0} = 0$. In addition, the relation between total current i and the exit reactant concentration is clearly $R(1) = 1 - i$. Equations [4], [8], and [13] plus the boundary conditions were simultaneously solved using a finite difference numerical technique (see later). The solutions gave η_0 and η_L as a function of i_o, Δ, θ, and i where η_L and i are the effective over-all polarization and current density of the electrode.

Case 3. Mass transfer and ohmic effects, front supply.—For front reactant supply where the direction of current flow is the same as fluid flow (see Fig. 1), Ohm's law is

$$i(x) = -(1/\Delta)d\eta(x)/dx \qquad [14]$$

In addition to the mass transfer boundary conditions of Eq. [6], the boundary conditions of polarization are now $(d\eta/dx)_{x=0} = i\Delta$ and $(d\eta/dx)_{x=1} = 0$. The integration of Eq. [3] for this case gives

$$i(x) = i - [1 - R(x) + \theta dR(x)/dx] \qquad [15]$$

The simultaneous solution of Eq. [4] with Eq. [14] and [15] using these boundary conditions was performed using a finite difference technique (see later).

Case 4. Mass transfer and ohmic effects, rear supply, consecutive two-electron transfer reaction.—The mechanism of a consecutive two-electron transfer reaction, *e.g.*, Sn^{2+}/Sn^{4+}, is

$Sn^{2+} \rightarrow Sn^{3+} + e^-$	Step r
$Sn^{3+} \rightarrow Sn^{4+} + e^-$	Step o
$Sn^{2+} \rightarrow Sn^{4+} + 2e^-$	Over-all reaction

and the over-all kinetic equation has the form (19-21)

$$i = 2i_{o,r} \exp(\alpha_r \eta/b)$$

$$\frac{(R/R_b) - (1 + \gamma - \gamma R/R_b)\exp(-2\eta/b)}{1 + (i_{o,r}/i_{o,o})\exp(-(1 - \alpha_r + \alpha_o)\eta/b)} \qquad [16]$$

At higher anodic polarizations, the denominator of Eq. [16] is approximately one and it reduces to the simpler form

$$i = 2i_{o,r}(R/R_b)\exp(\alpha_r \eta/b) \qquad [17]$$

where the first step becomes rate limiting. At lower currents the polarization obtained from Eq. [16] is higher than that obtained from Eq. [17]. At low anodic polarization such that $1 << (i_{o,r}/i_{o,o})\exp(-(1 - \alpha_r + \alpha_o)\eta/b)$ Eq. [16] becomes

$$i = 2i_{o,o}\exp((1 + \alpha_o)\eta/b) \qquad [18]$$

and the second step becomes rate limiting. Equation [18] is a Tafel equation with an apparent anodic transfer coefficient greater than one. As pointed out by Vetter (19) this arises from a fairly rapid charge transfer reaction (step r) preceding a slow charge transfer reaction (step o) on the reduction side.

Equations [8], [13], [16], and the boundary conditions were solved simultaneously by the method used in case 2.

Numerical Solution Technique

Equations [4] and [13] were combined in finite difference form. Analysis of the resulting algorithm showed that accurate and stable computations were only obtainable for

$$\epsilon < 0.2/\alpha\Delta \qquad [19]$$

where ϵ is the dimensionless spatial interval, that is, the electrode thickness is divided into $1/\epsilon$ elements. It was found that $\epsilon = 0.01$ was satisfactory for most of the values of Δ used in the computations.

As was concluded in part I one can arbitrarily chose only one variable out of η_o, η_L, i, $R(+0)$. It is necessary to search for the unique set of values of the rest of variables which satisfies all of the differential equations and the boundary conditions.

Mass balance on the first spatial element gives $i(1) + R(1) - \theta(dR/dx)_{x=\epsilon} = 1$, where $(dR/dx)_{x=\epsilon}$ is the diffusive flux out of the first element and $i(1)$ is the amount of current generated by the reaction in the first element and the total amount of current at $x = \epsilon$. In finite difference form this mass balance equation and the boundary condition of Eq. [6] are

$$R(1) - (\theta/\epsilon)(R(2) - R(1)) = 1 - i(1) \qquad [20]$$

$$R(0) + (\theta/\epsilon)(R(0) - R(1)) = 1 \qquad [21]$$

Thus we must search for a value of $R(0)$ such that $0 < R(1)/R(0) < 1$. The correct $R(0)$ is that which satisfies $0 \leq R(I)/R(I-1) \leq 1$, $I = 1$ to N where N is the total number of space elements. In addition the final boundary condition must be satisfied, *i.e.*, $i(N) + R(N) = 1$. This equation is obtained from Eq. [6] and [8]. The search technique used to find the correct value of $R(0)$ was a simple dichotomous search method. A first try value of $R(0)$ was obtained as below. If $R(I)/R(I-1)$ exceeded unity then $R(0)$ was decreased by $\Delta R(0)$. This was continued until either the correct $R(0)$ was obtained or $R(I)/R(I-1)$ became ≤ 0. At that stage $R(0)$ was increased by $(1/2)\Delta R(0)$ and computations were repeated. The next step involved $(1/4)\Delta R(0)$ and the process was continued until the above conditions were satisfied simultaneously. A maximum of about 15 iterations were needed to converge on the correct $R(0)$ for large θ values, whereas for small θ values 5 iterations were sufficient.

At low θ values, a simpler procedure is to assume the diffusive flux in and out of the first element to be equal, *i.e.*, $R(2) - R(1) = R(1) - R(0)$ and then subtract Eq. [20] from [21]. Thus $i(1) = R(0) - R(1)$. Substituting in [21] and rearranging gives $R(0) = 1 - (\theta/\epsilon)i(1)$. Thus, starting with $R = 1$ a value of $i(1)$ was obtained using the kinetic equation (Eq. [4] with $dx = \epsilon$). This value was used to get improved $R(0)$ and $R(1)$ values using the above two equations. The average of $R(0)$ and $R(1)$ was substituted in Eq. [4] to get an improved $i(1)$ which was used to get a better set of $R(0)$ and $R(1)$ and so on. This iteration was continued until [error in $R(0)$] $\leq 0.01\%$.

The choice of η_o depends on the magnitudes of Δ, θ, and $\bar{i}_o$. For large values of Δ and $\bar{i}_o$ or a small value of θ, a small η_o produces a large total current. η_o was chosen such that the current produced by the entire electrode is less than or equal to the limiting current.

For the solution of case 3, the technique involved choosing a value of total current i, which defines the exit reactant concentration $R(L)$, and then searching for the correct value of exit polarization which simultaneously satisfies the boundary conditions and differential equations and gives the current at the entry side the same as that originally chosen. A dichotomous search technique was again used. The compiler time was about 0.3 sec on an IBM 360. An execution time of 7 sec was sufficient to compute the entire current-polarization curve in more than 10 increments for case 3 under the following conditions: $\theta = 0.005$, $\bar{i}_o = 10^{-2}$, $\alpha = 0.5$, $\Delta = 100$, and $\epsilon = 0.01$.

Results of Computations

The orders of magnitude of the values of controlling parameters were calculated to be $\Delta = 0$ to 200; $\theta = 0$ to 1.0, and $\bar{i}_o = 10^{-4}$ to 10.

For case 1, negligible ohmic effects, it was found that the solution of Eq. [9] with $\theta = 0$ to $\theta = 10^{-2}$ gave essentially identical results over all ranges of $\bar{i}_o$. It must be concluded that axial diffusion does not play a significant role for θ values within this range under conditions of pure mass transfer control. Its influence became detectable, however, at $\theta > 0.1$. The results are shown in Fig. 2 where the curves are the same for $\theta = 0$ or 10^{-2}. Figure 2 also shows that as axial diffusion increases, the polarization needed to support a certain current increases. As reasoned previously (8), in the irreversible region ($\bar{\eta} > 4$) the shape of the curve is independent of $\bar{i}_o$ but is displaced parallel to the current axis by a factor $(2.3/\alpha)$ for each decade change of $\bar{i}_o$, *i.e.*, 0.12V, for $\alpha = 0.5$, $b = 0.025$V (room temperature).

For case 2, rear supply, Fig. 3 shows the results for values of θ up to 10^{-3} and $\bar{i}_o = 10^{-2}$. It is again concluded that the influence of axial diffusion is insignificant for small values of θ ($\theta \leq 10^{-3}$) for the values of Δ used. The effect of Δ, of course, is to increase η_L and to decrease η_o, hence it forces the reaction to occur closer to the exit face. This is shown in Fig. 4, where the profiles of current density and polarization through the electrode are given for $i/i_L \to 1$. It is readily appreciated that the value of $\bar{i}_o$ affects the polarization at which some value of i/i_L is obtained, but does not affect the current density profiles for a given i/i_L and Δ, whereas Δ does have a strong influence on these profiles.

As the value of Δ increases the reaction becomes more concentrated into a smaller space, consequently the concentration and current density profiles become steeper and axial diffusive flux increases. It is expected, therefore, that as Δ increases the effect of axial diffusion becomes detectable at smaller values of θ. This is consistent with the product $\Delta\theta$ being the controlling parameter for axial diffusion, which was concluded from the analytical solutions in part I (22).

Figures 5 and 6 show the equivalent results for case 3, frontal supply. Again, changing $\bar{i}_o$ does not affect the shape of the profiles in Fig. 6, although it would change the position of the polarization curves. It was again concluded that the effect of axial diffusion was insignificant for θ up to 10^{-3}. As would be expected, the value of θ at which axial diffusion effects became noticeable is lower for frontal than for rear supply

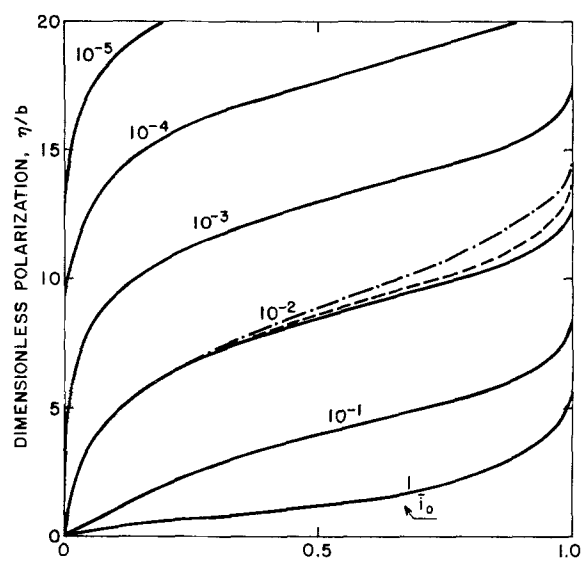


Fig. 2. Effect of $\bar{i}_o$ and θ on the current-polarization curves for case 1: – – – $\theta = 0.1$, –·–·– $\theta = 1$, ——— $\theta \leq 10^{-2}$.

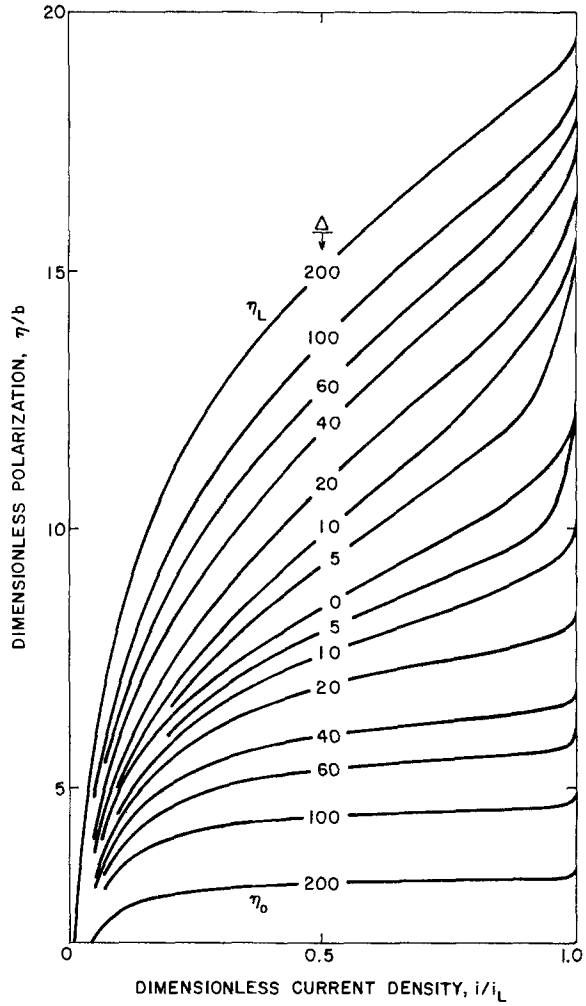


Fig. 3. Effect of ohmic parameter Δ on current-polarization curves; rear supply, case 2: $\bar{i}_o = 10^{-2}$, $\alpha = 0.5$, $\gamma = 1$, and $\theta \leq 10^{-3}$.

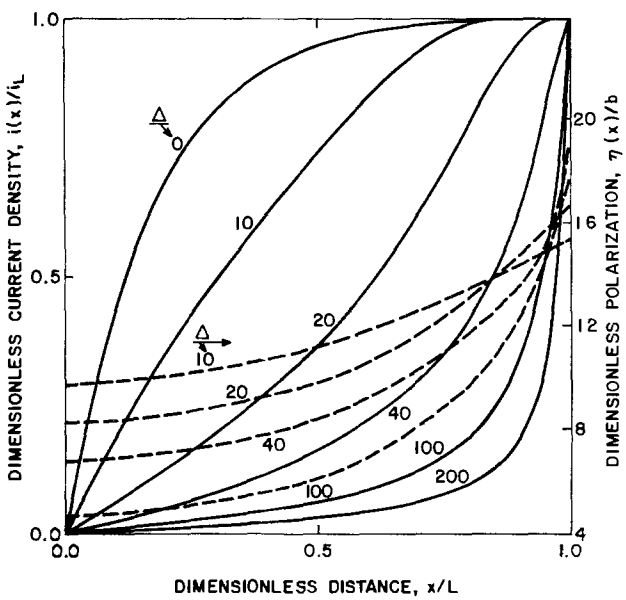


Fig. 4. Effect of ohmic parameter Δ on the current and polarization profiles near the limiting current for rear reactant supply, case 2: $\bar{i}_o$, α, γ, and θ are the same as in Fig. 3.

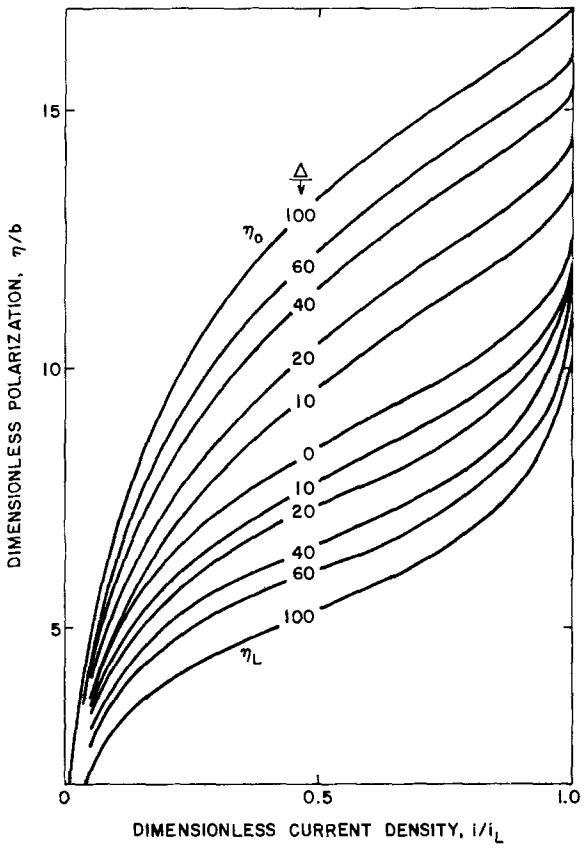


Fig. 5. Effect of ohmic parameter Δ on current-polarization curves; front supply, case 3: $\bar{i}_o = 10^{-2}$, $\alpha = 0.5$, $\gamma = 1$, and $\theta \leq 10^{-3}$.

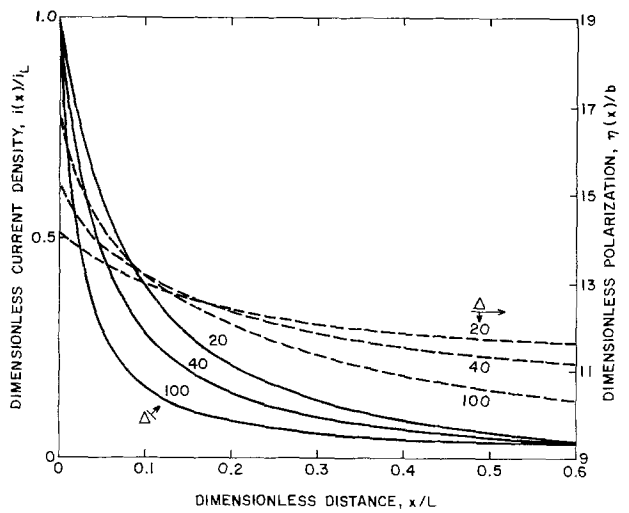


Fig. 6. Effect of ohmic parameter Δ on current and polarization distribution; front supply, case 3: $i/i_L \rightarrow 1$, i_o, α, γ, and θ are the same as in Fig. 5.

since for a given θ, Δ, and i/i_L the concentration profile has a steeper maximum gradient at $x = 0$ for case 3 than for case 2. For $\Delta = 50$, this value of θ is $(5)(10^{-3})$. At total currents less than i_L, the effect of axial diffusion is less, and, of course, a finite reactant concentration exits at the emergent face, see Fig. 7. At high values of θ, Eq. [6] shows that the entering concentration, $R(0)/R_b$, can be significantly less than 1.0, depending on the value of θ. This is demonstrated in Fig. 8; the effect is also noticeable in Fig. 7.

Comparison of Fig. 3 and 5 shows that for a certain current output and otherwise identical conditions the

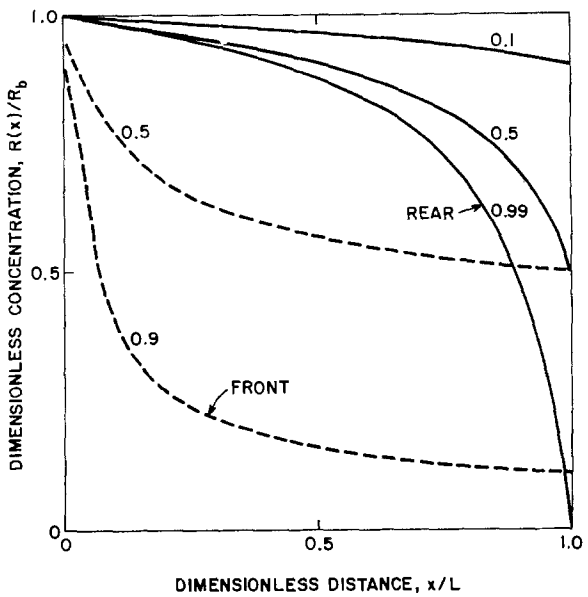


Fig. 7. Concentration profiles within the electrode as a function of i/i_L, $\Delta = 60$, $\theta \leq 10^{-3}$. The numbers on the curves refer to i/i_L; $\bar{i}_o$, α, and γ are the same as in Fig. 5.

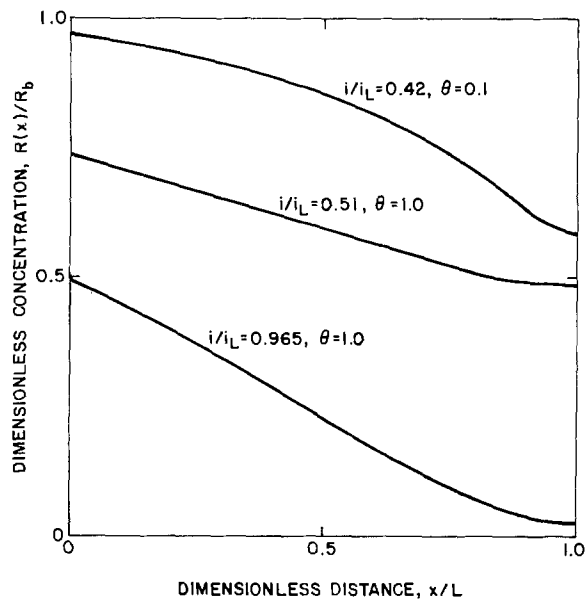


Fig. 8. Concentration profiles under conditions of high θ for case 2: $\Delta = 50$. Both i/i_L and θ are indicated on the curves, $\bar{i}_o = 10^{-2}$, $\alpha = 0.5$, and $\gamma = 1$.

frontal supply mode requires less total polarization than that of rear supply. The difference increases as the limiting current is approached.

Considering case 4, the consecutive two-electron transfer case, one limiting case is at low anodic polarization when Eq. [16] reduces to Eq. [18]. The computed current-polarization relations then have the same shape as those in Fig. 3, but the value of the η/b scale is reduced by the factor $0.5/(1 + \alpha_o)$, since the apparent value of α is $1 + \alpha_o$, and the same numerical result is obtained in the integration for any definite value of $\alpha_{app}\eta/b$.

At high anodic polarizations, the first step becomes rate limiting with a normal Tafel slope and the computed current-polarization curves become exactly superimposible on those of Fig. 3 (23) for the same values of i_o, α, γ, Δ, and θ. At the intermediate polarizations, as in the experimental work reported later, both steps affect the rate but to different extents. Fig-

ure 9 shows the effect of the exchange current of the second step, $i_{o,o}$ on the current-polarization curves. These results are computed using $i_oSL/i_L = (2.1)(10^{-2})$, $\Delta = 8$, and $\alpha_o = \alpha_r = 0.41$ (20). The ratio of the exchange currents of second to first steps was taken as 0.5, 0.1, 0.01, and 0.001 and only the front face polarization was plotted. When the value of this ratio is 0.5 or 0.1 each curve falls exactly on the curve obtained by assuming no rate limitation due to the second step (solid line). As the ratio $i_{o,o}/i_{o,r}$ is decreased the second step becomes slower and starts to affect the over-all rate. Obviously the smaller the exchange current of the second step the more its effects become apparent.

As the value of the normalized exchange current of the first step is increased, a larger portion of the limiting current will occur at relatively low polarization and the second step becomes more predominant.

Experimental Techniques

To test the equations it was necessary to use redox couples with known irreversible kinetics. The couple chosen was stannous-stannic chlorides in 4*N* HCl. Determination of the diffusion coefficient and kinetic parameters of this couple on basal and edge planes of nonporous pyrolytic graphite were reported elsewhere (21). The porous electrodes were prepared from SP1 graphite used previously (22). The graphite particles are flakes of 20-30 μm average diameter and 0.3-0.4 μm thickness. The pore radius was ~1 μm as estimated using the technique of liquid permeability (23). The details of the experimental technique, *e.g.*, cell design, flow systems, etc. were the same as in part I (22).

The double layer capacity of the porous electrode was measured by a triangular voltage sweep technique (24), using 0.5M K_2SO_4 at potentials between 0.1 to 0.6V *vs.* SCE. The electrode used for double layer capacity measurements was thin (~0.1 cm) and a scan rate of 80 mV/sec was used to minimize distributed capacitance effects.

Experimental Results

Results were obtained using the rear mode of reactant supply. The double layer capacity of basal plane of pyrolytic graphite in 0.5M K_2SO_4 was found to be 32 ± 3 μF/cm^2 (25) in the potential range of 0.1 to 0.6V *vs.* SCE. Allowing for some residual surface roughness, the true specific double layer capacity must be somewhat less than this. Using a value of 25 μF/cm^2, the measured double layer capacity of the porous electrode gave a value of almost (2)(10^4) cm^2/g. This compares with a BET area of about (2)(10^4) cm^2/g, and a liquid permeability area of (6)(10^{-3}) cm^2/g. These areas are in the expected order, since the permeability area is a smoothed area and less than the true area. It was concluded from double layer capacity measurements that for an electrode of 50% porosity, S was about (2.2)(10^4) cm^2/cm^3. For an electrode of 0.5 cm thickness, i_oSL is (1.1)(10^4)i_o.

Kinetic data on 0.005M Sn^{2+} and 0.012M Sn^{4+} in 4*N* HCl showed that even with the relatively high internal area of the porous graphite electrodes, the reversibility index was still low enough to obtain irreversible conditions, since $2i_{o,r}$ is ~0.1 μA/cm^2 of basal plane surface.

For small limiting currents, the value of Δ is small and the difference between entrance and exit face polarization is then negligible and case 1 applies. If axial diffusion is negligible a plot of experimental results according to Eq. [12], case 1, should be a straight line of slope $(2.3b/\alpha)$ and intercept 2.3 log $(i_oSL/2.3i_L)$. Figure 10 shows this plot for a value of Δ of about 2; the low current region should be ignored since it represents the more complex kinetic form of Eq. [16] at low currents. The slope is 145 mV/decade, giving $\alpha = 0.43$ which is in good agreement with the value $\alpha = 0.41$-0.43 measured on a rotating disk electrode (21). Again, the intercept gives an experimental value of i_oSL of 0.65 mA/cm^2, and since SL based on double layer capacity measurements is (1.1)(10^4), the value of $2i_{o,r}$ per unit of true area is (0.6)(10^{-7}) A/cm^2. This compares with $2i_{o,r} = (1.1)(10^{-7})$ A/cm^2 measured on basal plane of pyrolytic graphite. (Areas determined using a double layer capacity of 25 μF/cm^2.) Table I lists the experimental conditions and the values of the various parameters used in the computations for the results shown in Fig. 10, 13, and 14.

At higher current densities, the separation between η_L and η_o increases and a technique was derived for handling the data based on the theoretical computations in Fig. 3. Figure 11 shows the values of $(\eta_L - \eta_o)$ at $i/i_L = 0.5$ as a function of Δ, taken from Fig. 3. Since α is 0.43 and $b = 63$ mV, $(\eta_L - \eta_o)_{0.5}$ for experimental results can be converted to dimensionless values; then Fig. 11 was used to estimate Δ. Since for a

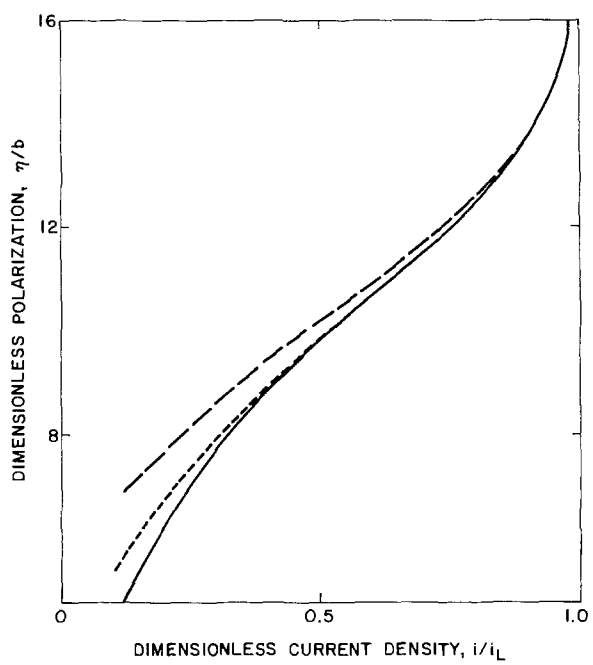


Fig. 9. The effect of the exchange current density of the second step $i_{o,o}$ on the current-polarization curves of a consecutive two-electron transfer reaction, case 4: $i_{o,o}/i_{o,r} = 0.01$ for – – – and 0.001 for – – –, $i_{o,r} = 10^{-2}$, $\alpha_r = 0.43$, $\gamma = 1$, and $\Delta = 8$.

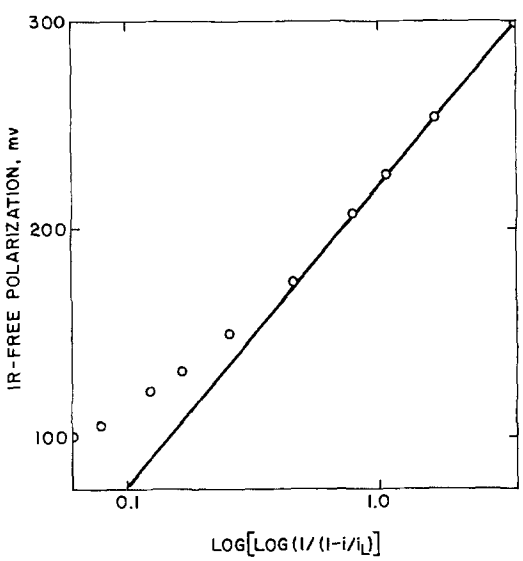


Fig. 10. Experimental current-polarization relations for the oxidation of Sn^{2+} to Sn^{4+} ions at a flow-through electrode in absence of significant ohmic effects, case 1. Results are plotted in the form of Eq. [12], see Table I.

Table I. Experimental and theoretical conditions used in Fig. 10, 13, and 14

Figure	Experimental conditions			Theoretical parameters					
	u (cm/min)	$[Sn^{2+}]$ (M)	i_L (mA/cm²)	$\bar{i}_o$	Δ	α_r	α_o	γ	$i_{o,r}/i_{o,o}$
10	0.80	0.005	14	0.046	0	0.43	—	0.42	—
13	3.42	0.005	55	0.021	8	0.41	0.41	0.42	1000
14	4.02	0.03	388	0.009	50	0.41	0.41	0.20	1000

given electrode system, Δ is proportional to the limiting current, a plot of Δ values determined in this way for a number of limiting currents should be a straight line of slope $L\rho_{eff}/b$. This is shown in Fig. 12, and gives $\rho_{eff} = 7.3$ Ω-cm and, hence, a tortuosity factor of 2.4. This technique illustrates that numerical or analytical solutions which report η_L and η_o are more useful than solutions which report only η_L, since η_o is very easily measured experimentally and additional useful information can then be obtained.

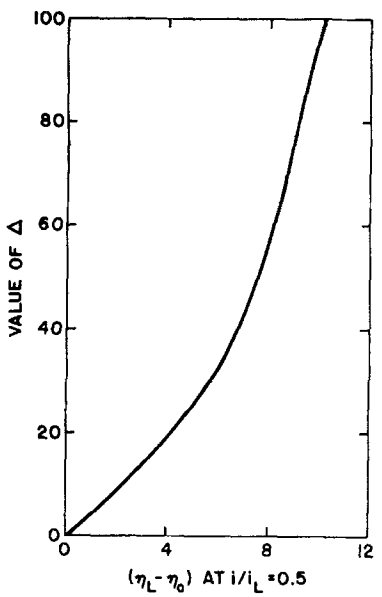


Fig. 11. Effect of ohmic parameter Δ on the difference between entrance and exit face polarizations at $i/i_L = 0.5$; obtained from Fig. 3.

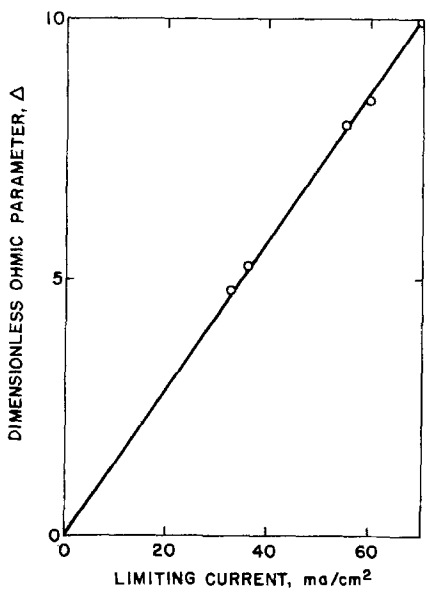


Fig. 12. Plot of value of ohmic parameter Δ vs. limiting current, Sn^{2+}/Sn^{4+}, 4N HCl. Δ was obtained from experimental results using Fig. 11.

We now have all the data necessary to compute theoretical values of η_L and η_o *vs.* i/i_L for comparison with the equivalent experimental results for case 4. A typical plot is shown in Fig. 13 for $i_L = 52$ mA/cm². By trial and error the value of $\bar{i}_o$ which gives the best agreement between the experimental and theoretical curves was found to be $(2.1)(10^{-3})$, assuming $\Delta = 8$, $\gamma = 0.4$, $\alpha_r = \alpha_o = 0.41$, and $i_{o,r}/i_{o,o} = 1000$. The last two values were reported by Lerner and Austin (20) and the value of Δ was obtained from the experimental results using Fig. 11.

Since $i_L = 55$ mA/cm² and $SL = (1.1)(10^4)$, the value of $2i_{o,r}$ per unit of true (basal plane) surface area obtained from this data is 10^{-7} A/cm². Again this compares well with the value of $(1.1)(10^{-7})$ A/cm² measured on the basal plane of pyrolytic graphite (21). The dashed lines in Fig. 13 show the model predictions for a one-electron transfer and otherwise identical conditions. Good agreement is obtainable only in the high polarization region where a single electron transfer controls the over-all rate, the rate of which is given by Eq. [17]. The experimental values of Δ and $\bar{i}_o$ obtained from Fig. 13 were used to predict the corresponding values for $i_L = 30$ and 66 mA/cm², and the current-polarization curves were computed for these conditions. The computed results were in good agreement with the experimental results.

For a large limiting current of 388 mA/cm², that is $\Delta = 55$, the results are shown in Fig. 14. The theoretical line in Fig. 14 was obtained using $(2i_{o,r}SL/i_L) = 0.009$, $\alpha_r = \alpha_o = 0.41$, and $i_{o,r}/i_{o,o} = 1000$. It is clear

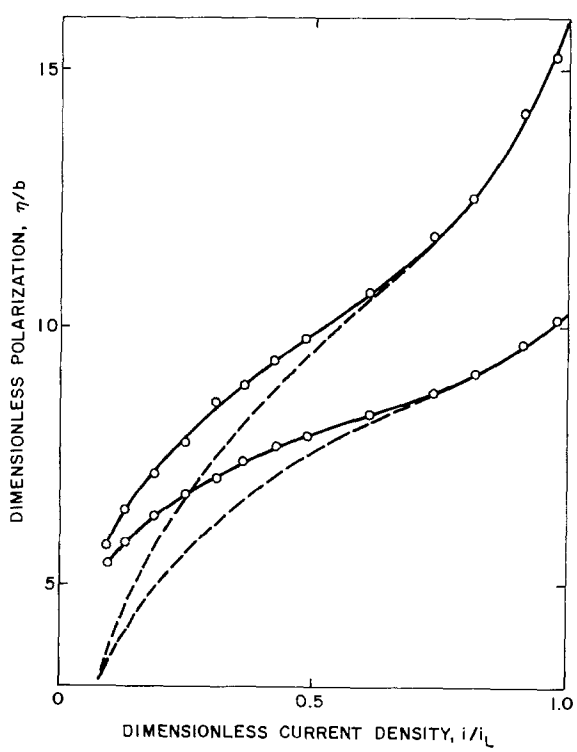


Fig. 13. Comparison of theoretical (solid line) and experimental (0-0-0) current-polarization relations for case 4: $i_L = 55$ mA/cm², $\Delta = 8$, $\bar{i}_{o,r} = 0.021$, $\alpha_o = \alpha_r = 0.41$, $i_{o,r}/i_{o,o} = 1000$, and $\gamma = 0.42$. The dashed lines show the solution for a one-electron transfer reaction; step r is rate limiting, see Table I.

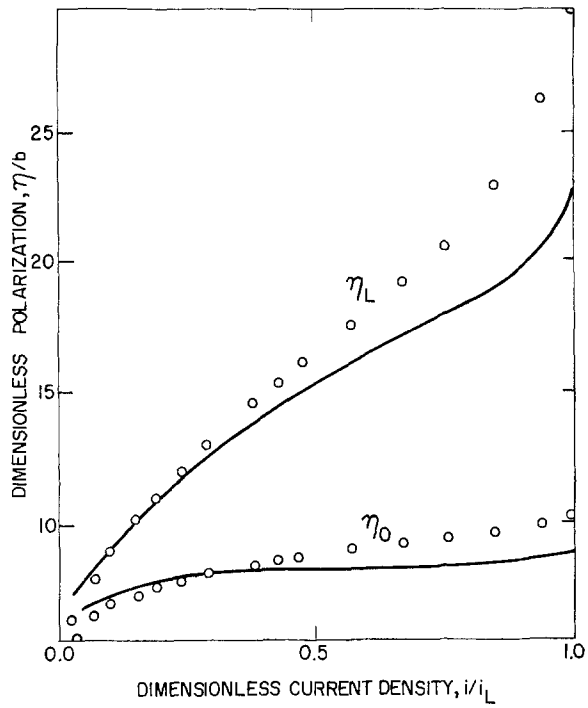


Fig. 14. Comparison of theoretical and experimental results for a consecutive two-electron transfer reaction at a large value of ohmic index Δ, see Table I. i_L = 388 mA/cm², $\bar{i}_{o,r}$ = 0.009, $\alpha_r = \alpha_o$ = 0.41, $i_{o,r}/i_{o,o}$ = 1000, Δ = 55, and γ = 0.2.

that the experimental results deviate considerably from the theoretical results. As the current increases both η_o and η_L increase more than predicted by the theory.

Discussion of Results and Conclusions

The equations for the system considered include three controlling parameters, all expressed in dimensionless form. The parameters are: (*i*) the reversibility index $\bar{i}_o = i_o SL/i_L$, which is a measure of the speed of the electrochemical reaction compared to the reactant input rate; (*ii*) the ohmic index Δ, which is a measure of the ohmic effect in the pore electrolyte, and increases with limiting current density and pore electrolyte resistivity; and (*iii*) the index of diffusion θ, which is a measure of the relative influence of axial diffusion compared to axial convective flow. Table II lists the parameter regions which characterize each case. The effect of axial diffusion becomes detectable only for θ greater than 0.01 for rear supply and 0.005 for front supply. The effect of axial diffusion is to increase the polarization corresponding to a certain current density. The front supply case requires less total polarization than the rear supply case for the same current output, all other conditions being the same.

The agreement between theory and experiment for the various results is good, with considerable internal consistency up to a value of Δ of about 20. The disagreement between theory and experiment at higher values of Δ does not appear to be the result of axial diffusion because the values of the index of diffusion θ necessary to produce the disagreement is much higher than is expected for the experimental system used, nor is it due to radial diffusion limitations.

The effect of radial diffusion is discounted as the reason for this deviation by using a simplified model of superimposed linear combinations. Assuming the current is supported by radial diffusion, a mass balance over a differential element gives rise to

$$di(x)/dx = (DSL/ur)[R_m - R_w]$$
$$= (DSL/ur)\, R_m[1 - R_w/R_m]$$

where r is the pore radius in cm, R_m is the concentration at the center of the pore, R_w is that at the wall, and i, x, r_m, and R_w are all dimensionless. For the set of results in Fig. 14 where $D = 10^{-5}$ cm²/sec, $S = 1.1 \times 10^4$ cm²/cm³, L = 0.5 cm, u = 0.067 cm/sec, and $r \simeq 1$ μm, the value of the multiplier $(DSL/ur) \simeq 10^4$. Taking the case of $i/i_L = 0.9$, then $R_m = 0.1$ assuming negligible axial diffusion. The largest value of di/dx in Fig. 4 (for Δ = 200) is 2.0, hence $R_w/R_m = 0.998$ and radial diffusion is negligible. In fact if the current profile is ten times steeper, *i.e.*, $di/dx = 20$, $R_w/R_m = 0.98$. For the experimental results in Fig. 14, such calculation gives rise to $R_w/R_m > 0{,}99$, hence the deviation could not be due to radial diffusion limitations. The effects of specific adsorption, slow intermediate chemical reaction, or decreased catalytic activity due to the oxidation of the electrode material are ruled out as possible reasons in view of the present results and the previous work on planar electrodes (21). We do not understand the reason for this discrepancy at the present time.

In designing an efficient electrode for an electrochemical reaction in a porous flow-through electrode system, it is clear that an optimization problem exists. Using a thick electrode gives a high $i_o SL$, but ohmic polarization parameter Δ also increases. Similarly, a high S value can be obtained with a low porosity but this again increases Δ. The equations and curves presented here provide a quantitative basis for evaluating the effect of any combination of parameters on the over-all current *vs.* polarization relations. In that respect, the present work is more comprehensive than that previously published (1, 3) where mass transfer and ohmic effects were included and activation polarization was neglected.

Acknowledgments

We gratefully acknowledge financial support of the National Science Foundation, Grant GK11689.

Manuscript submitted Dec. 16, 1976; revised manuscript received May 18, 1977.

Any discussion of this paper will appear in a Discussion Section to be published in the June 1978 JOURNAL. All discussions for the June 1978 Discussion Section should be submitted by Feb. 1, 1978.

LIST OF SYMBOLS

b	$b = RT/\mathbf{F}$
C_1, C_2	constants defined by Eq. [7]
D	diffusion coefficient of reactant, cm²/sec
f	a dimensionless quantity, $f = \exp(\alpha\eta) + \gamma \exp(\beta\eta)$

Table II. Controlling parameters and conditions for the various cases treated

Case	Controlling parameters and conditions: Δ	Direction of current and electrolyte flow	Current and polarization
Case 1*	Δ ≃ 0	Parallel or opposite	No limitation
Case 2	Δ > 2	Parallel (front supply)	Single electron transfer
Case 3	Δ > 2	Opposite (rear supply)	Single electron transfer
Case 4*	Δ > 2	Opposite (rear supply)	$1 \sim (i_{o,r}/i_{o,o}) \exp(-(1 - \alpha_r + \alpha_o)\eta/b)$

* Modification of case 1 to consecutive electron transfer and of case 4 to frontal supply is only a minor modification of these cases.

$\mathbf{F}$	Faraday constant, 96,500 C/equiv.
i_L	limiting current density, $i_L = n\mathbf{F}uR_b$ A/cm²
i_o	exchange current density, A/cm²
$\bar{i}_o$	dimensionless exchange current density (reversibility index), $\bar{i}_o = i_oSL/i_L$
$i_{o,r}$, $i_{o,o}$	exchange current densities of the first and second steps of a consecutive two-electron transfer reaction, respectively, A/cm²
i	total current produced by the electrode as a fraction of the limiting current
$i(x)$	the current flowing at a distance x in the electrode as a fraction of the limiting current
L	electrode thickness, cm
q	tortuosity factor
R, R_b	reactant concentration at the electrode surface and in bulk electrolyte, respectively
S	specific surface area of the porous electrode, cm²/cm³
T	absolute temperature, °K
u	superficial flow speed, cm/sec
x	distance inside electrode, cm
α	transfer coefficient of the anodic electrode reaction
α_r, α_o	same for the first and second steps in a consecutive two-electron transfer anodic reaction
β	same for cathodic reactions, $\beta = \alpha - 1$
Δ	index of ohmic effect, $\Delta = i_LL\rho_{eff}/b$
θ	dimensionless parameter of axial diffusion, $\theta = D_{eff}/Lu$ (reciprocal of Peclet number)
γ	ratio of the bulk concentration of the reactant to that of the product
η	polarization, V
η	dimensionless polarization, η/b
η_o	dimensionless polarization at $x = 0$
η_L	dimensionless polarization at $x = L$
ρ	specific resistivity of electrolyte, Ω-cm
ρ_{eff}	effective specific resistivity of electrolyte, $\rho_{eff} = \rho q$/porosity

REFERENCES

1. D. N. Bennion and J. Newman, *J. Appl. Electrochem.*, **2**, 113 (1972).
2. A. K. P. Chu, M. Fleischmann, and G. J. Hills, *ibid.*, **4**, 323 (1974).
3. R. S. Wenger and D. N. Bennion, *ibid.*, **6**, 385 (1976).
4. A. T. Kuhn and R. W. Houghton, *ibid.*, **4**, 69 (1974).
5. G. B. Adams, R. P. Hollandsworth, and D. N. Bennion, *This Journal*, **122**, 1043 (1975).
6. R. M. Perskaya and I. A. Zaidenman, *Proc. Sci. USSR, Phys. Chem. Sect.*, **115**, 513 (1957).
7. I. G. Gurevich and V. S. Bagotsky, *Electrochim. Acta*, **9**, 1151 (1964).
8. L. G. Austin, P. Palasi, and R. Klimpel, Advances in Chemistry Series, No. 47, p. 35, The American Chemical Society (1965).
9. F. Coeuret, D. Hutin, and A. Gaunaud, *J. Appl. Electrochem.*, **6**, 417 (1976).
10. M. Paulin, D. Hutin, and F. Coeuret, *This Journal*, **124**, 180 (1977).
11. H. S. Wroblowa, *J. Electroanal. Chem.*, **42**, 321 (1973); H. S. Wroblowa and A. Saunders, *ibid.*, **42**, 329 (1973).
12. G. Razumney, H. S. Wroblowa, and G. L. Schrenk, *ibid.*, **69**, 299 (1976).
13. R. E. Sioda, *Electrochim. Acta*, **13**, 375, 1559 (1968); *ibid.*, **15**, 783 (1970); *ibid.*, **16**, 1569 (1971); *ibid.*, **17**, 1171, 1939 (1972); *ibid.*, **19**, 57 (1974); *J. Appl. Electrochem.*, **5**, 221 (1975); *ibid.*, **7**, 135 (1977); *J. Electroanal. Chem.*, **34**, 399, 411 (1972); *ibid.*, **70**, 49 (1976).
14. R. Alkire and B. Gracon, *This Journal*, **122**, 1594 (1975).
15. H. S. Wroblowa and G. Razumney, *J. Electroanal. Chem.*, **49**, 355 (1974).
16. J. A. Kenkel and A. J. Bard, *ibid.*, **54**, 47 (1975).
17. B. G. Ateya, *ibid.*, **76**, 183 (1977).
18. B. G. Ateya, E. A. S. Arafat, and S. A. Kafafi, *J. Appl. Electrochem.*, **7**, 107 (1977).
19. K. J. Vetter, "Electrochemical Kinetics," pp. 152, 481, Academic Press, New York (1967).
20. H. Lerner and L. G. Austin, *This Journal*, **112**, 636 (1965).
21. B. G. Ateya and L. G. Austin, *J. Electroanal. Chem.*, **5**, 85 (1974).
22. B. G. Ateya and L. G. Austin, *This Journal*, **124**, 83 (1977).
23. B. G. Ateya, Ph.D. Thesis, The Pennsylvania State University (1972).
24. L. G. Austin and E. G. Gagnon, *This Journal*, **120**, 251 (1973).
25. B. G. Ateya and L. G. Austin, *ibid.*, **120**, 121 (1973).

Mass Transport Processes at Porous Electrocatalysts in the Electrogenerative Reactor

George P. Sakellaropoulos*,[1] and Stanley H. Langer*

Department of Chemical Engineering, University of Wisconsin, Madison, Wisconsin 53706

ABSTRACT

Mass transport limitations were investigated in the electrolyte, gas phase, and in the pores of platinum and palladium black porous electrocatalysts using the electrogenerative reactor. Limiting currents were identical for both catalysts, depending on a power of the bulk reactant concentration, $i_L = K_J C_{J_\infty}^{\nu_J}$, where C_{J_∞} can be the electrolyte concentration of hydrogen ions or of dissolved ethylene. Mathematical modeling and comparison with the experimental equation provided information regarding limiting processes. In a matrix cell diffusion limited ionic transport at the ethylene cathode. In free electrolytes, free convection can assist mass transport and improve limiting currents. Gas phase limiting current densities were examined in terms of a model involving limiting radial diffusion of dissolved ethylene with a concentration-dependent surface area and pore utilization.

The ease of mass transport in electrogenerative and fuel cell systems can influence reaction rates and overpotentials at each electrode, hence the feasibility of utilizing the electrodes for electrochemical processing and energy generation. Limiting currents, usually associated with slow reactant transport at relatively low concentrations, are undesirable in practical cells, representing severe voltage and energy losses. Because of this, few reactions have been examined in detail as

* Electrochemical Society Active Member.
[1] Present address: Department of Chemical and Environmental Engineering, Rensselaer Polytechnic Institute, Troy, New York 12181.

Key words: porous electrodes, limiting current, catalysis, mass transport, ethylene.

they approach limiting current on gas diffusion, porous, fuel cell type electrodes (1-7). Fortuitously, most of the investigated systems obeyed the simple diffusion layer theory (8). However, observed limiting currents in electrogenerative hydrogeneration are not always proportional to reactant concentration (9). This apparent discrepancy is not unique for the electrogenerative process. Situations may arise where hydrocarbon fuel cell systems could behave similarly. To understand this and similar behavior, a more detailed picture of physical processes at porous catalytic electrodes is required.

Understanding the nature and location of mass transfer limitations could lead to improved electrode designs and contact patterns of reactants for electrochemical energy generation. The experimental and mathematical results here establish the nature and regions of appearance of mass transport limitations in electrocatalytic processing and provide a basis for possible development of the electrogenerative cell as an analytical tool.

The electrogenerative reactor was employed in this work to investigate mass transport processes and reaction limitations at partially wettable, porous catalytic electrodes. The well-established kinetics and cell polarization of ethylene electrogenerative hydrogenation (9, 10) lend themselves to further modeling of the electrogenerative cell. Under kinetic control, the rate-limiting reaction step is believed to be

$$C_2H_5 - * + H^+ + e \rightarrow C_2H_6 + * \qquad [1]$$

with the over-all reaction rate given by (9, 10)

$$i = \mathbf{F}k'C_{C_2H_4}{}^0C_{H^+}{}^2 \exp(-\alpha E\mathbf{F}/\mathcal{R}T) \qquad [2]$$

The electrogenerative cell here involves separate electrochemical oxidation of hydrogen gas and reduction of an alkene on partially wet-proofed electrocatalysts placed at the boundaries of the invariant electrolyte barrier. Electrolytes used in this work are representative of types commonly employed in electrogenerative and fuel cell investigations. The "free" electrolyte type is held between liquid impermeable, gas permeable porous electrodes. The "matrix" type is immobilized on filter paper. With porous electrodes mass transport limitations can develop in the electrolyte, in the gas phase, or in the pores of the electrodes. By deliberately altering concentrations so that mass transport becomes limiting either in the electrolyte or at the gas side of the electrodes, the limiting processes can be characterized. Kinetic limiting currents were excluded from consideration on the basis of the relative magnitude of reaction rates on platinum and palladium (9, 10). It should be noted that common techniques for discriminating between diffusion and kinetic limiting currents (8) are not practical for this system because of fast gas flow rates and low apparent activation energies (1.5-5 kcal/mole) for the catalytic reaction [9].

Diffusion limiting currents predicted from porous electrode models apparently are proportional to reactant concentration. Such treatments normally consider one- or two-dimensional diffusion of gaseous reactants or ions (7, 11-14) and possible counterdiffusion of reactants and products in the presence of inerts (15, 16). However, ionic transport by electrolyte-free convection has not been observed, although possible convective transport due to local heating in the pore meniscuses has been described (17). Similarly, a concentration-dependent change of the available catalytic area and its effect on observed limiting currents has not been anticipated or observed previously. The mathematical analysis below predicts observed operation of porous electrocatalysts at the approach of limiting currents in the electrolyte and in the gas phase (9, 10).

Theoretical Development

Mass transport in the electrolyte.—The examined systems utilized matrix-immobilized or free liquid electrolytes. In the presence of added supporting electrolyte, migration effects on the limiting current can be neglected. The contribution of migration is considered later in the discussion.

Equations describing mass transport of one electroactive species J in the bulk of static dilute electrolytes (18) can be written in dimensionless form

$$\frac{DC_J^*}{Dt^{**}} = \frac{1}{Sc} \nabla^{*2} C_J^* \qquad [3]$$

$$i^* = -\nabla^* C_J^* \qquad [4]$$

where $D/Dt^{**} = \partial/\partial t^{**} + v^{**} \cdot \nabla^*$. Asterisks denote dimensionless quantities defined in the list of symbols and in standard transport phenomena texts (19). The dimensionless current density is defined by Eq. [5]

$$i^* = \frac{iD}{n_J\mathbf{F}\mathcal{D}_J(C_{JS} - C_{J_\infty})} \qquad [5]$$

where D is a characteristic length, *e.g.*, the electrode diameter. Other symbols are defined in the list of symbols. For possible free convection in liquid electrolyte containing nonelectroactive ions, the equation of motion (19) becomes

$$\frac{Dv^{**}}{Dt^{**}} = \nabla^{*2} v^{**} - \mathrm{Gr}\, C_J^* \frac{g}{gc} \qquad [6]$$

where Gr is the Grashoff number and ζ is the densification coefficient (19, 20) (see notation).

Solution of Eq. [3] and [4] with appropriate boundary conditions gives the current density for purely diffusion transport. In the presence of free convection solution of the coupled differential equations [3] and [6] is required to obtain a concentration profile.

Steady-state, one dimensional diffusion.—For steady-state diffusion in the x-direction normal to a vertical disk, solution of Eq. [3] and [4] with usual boundary conditions (19) gives the concentration profile

$$C_J^* = 1 - \frac{D}{\delta} x^* \qquad [7]$$

where δ is the thickness of the electrolyte diffusion layer in contact with the electrode. The average dimensionless current density, or electrochemical Nusselt number, Nu_i, is given by

$$Nu_i = i^* = -\left(\frac{dC_J^*}{dx^*}\right)_{x^*=0} = \frac{D}{\delta} \qquad [8]$$

From this and Eq. [5] the diffusion limiting current is obtained for $C_{JS} = 0$

$$i_L = -\frac{n_J\mathbf{F}\mathcal{D}_J C_{J_\infty}}{\delta} \qquad [9]$$

This is a well-known equation from the diffusion layer theory (8). The negative sign denotes a cathodic reaction (8). Here, subscript J denotes a reacting hydrogen ion.

For constant δ, Nu_i depends on the electrode diameter and i_L is proportional to the bulk electrolyte concentration. Thickness δ is of the order of 0.03 cm for stationary electrolytes (21), but it depends on ionic strength, increasing with decreasing ionic strength.

Steady-state electrolyte-free convection.—Solution of Eq. [3] and [6] is analogous to heat and mass transfer with nonelectrolytes (19, 22, 23). For a vertical disk, the average Nu_i becomes

$$\mathrm{Nu_i} = \frac{i_{avg}D}{n_J\mathbf{F}\mathcal{D}_J(C_{JS} - C_{J_\infty})} = \frac{\int_0^{2\pi}\int_0^{r^*=1/2} i^* r^* dr^* d\theta}{\int_0^{2\pi}\int_0^{r^*=1/2} r^* dr^* d\theta}$$

$$= \frac{2}{\pi}\int_0^{2\pi}\int_0^{r^*=1/2} -\left(\frac{dC_J^*}{dx^*}\right)_{x^*=0} r^* dr^* d\theta \quad [10]$$

where $C_J^* = C_J^*(x^*, r^*, \theta, \mathrm{Gr}, \mathrm{Sc})$ and $\mathrm{Nu_i}$ should depend only on Sc and Gr numbers (19, 20).

For laminar-free convection ($10^4 < \mathrm{GrSc} < 10^9$)

$$\mathrm{Nu_i} = k(\mathrm{ScGr})^{0.25} \quad [11]$$

The constant k is 0.66 for flat vertical plates (20, 23). Using the definitions of Sc and Gr numbers (list of symbols) and of $\mathrm{Nu_i}$, Eq. [8], the average limiting current density becomes for $C_{JS} = 0$

$$i_{L,avg} = -n_J\mathbf{F}\mathcal{D}_J k\left(\frac{\rho g\zeta}{D\mathcal{D}_J\mu}\right)^{0.25} C_{J_\infty}^{1.25} \quad [12]$$

With approximately constant physical properties, total concentration, and densification coefficient (24), the average limiting current density is proportional to the 1.25 power of the bulk concentration of the electroactive ions, and inversely proportional to the 0.25 power of the electrode diameter. Wagner (25) and Tobias and co-workers (20, 24) have tested Eq. [11] and [12] for deposition of metal ions and dissolution from vertical rectangular plates of varying height under well-controlled experimental conditions. However, development of free convection on the exterior surface of porous electrocatalysts, in relatively narrow channel geometry, has not been reported previously to our knowledge.

In this work platinum or palladium circular porous electrocatalysts were used to obtain limiting currents and to test the applicability of Eq. [12] to transport of hydrogen ions external to these electrodes. The use of circular electrodes was dictated by our cell design to eliminate corner effects, by the fragility of the test electrodes, and by the need to identify possible kinetic limitations. Previous kinetic information and current density-voltage data existed only for electrocatalysts of circular geometry. This geometry should be distinguished from the rectangular geometry of other workers (20, 24, 25) where the electrode height appears as the characteristic length in Eq. [10]-[12]. Here, the dimensionless $\mathrm{Nu_i}$, Sc, and Gr numbers are defined using the electrode diameter, D, as a characteristic length, hence its appearance in the 0.25 power in Eq. [12].

Mass transport from the gas side of the electrode.— To obtain some insights into limitations on the gas side of an electrode, adoption of a pore model is helpful. The models considered here are the simple pore (11, 12) and the thin film model (26), represented schematically in Fig. 1. Other more elaborate and more realistic models which lead essentially to similar results have been proposed [*e.g.*, (13)]. All models assume diffusion of gas in the pores, dissolution in the electrolyte (whether thin film or meniscus), and further diffusion to the catalytic sites.

A limiting current would be observed in these pores if: (*i*) axial diffusion of gas through a stagnant gas film is slow, with the limiting current generated at the tip of the meniscus or the film; and (*ii*) radial diffusion of gas for the thin film, or of dissolved gas for the simple pore, is slow; then axial diffusion will also be slow and reactant concentration will vary along the electroactive part of the pore.

In this work, ethylene molecules react on the surface to form ethane which diffuses out of the electrolyte into a gas stream that contains inert nitrogen. A counterdiffusion model is, therefore, necessary.

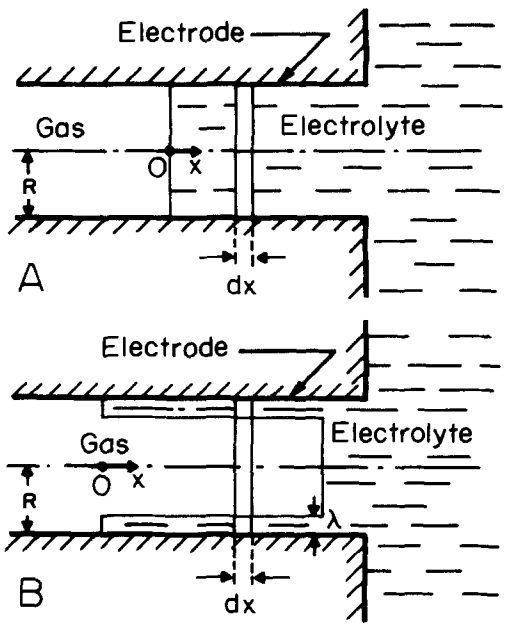


Fig. 1. Schematic representation of a simple pore (A) and a thin film (B) model.

For the first case (*i*) above and for steady-state one-dimensional counterdiffusion, expressions similar to Eq. [8] or [9] will hold. Here C_{J_∞} is the bulk concentration of the gaseous reactant, $\mathcal{D}_J$ the effective diffusivity of J in the gas phase, and δ the thickness of the stagnant gaseous film. Considering the high values of C_{J_∞} and $\mathcal{D}_J$ for gaseous pore diffusion, it appears unlikely that case (*i*) could be limiting here. For example, with $C_{J_\infty} = 4 \times 10^{-6}$ mole/ml (0.1 atm), $\mathcal{D}_J \simeq 0.2$ cm^2/sec, $\delta = 0.02$ cm (half the electrode thickness), a two-electron reaction such as ethylene reduction would give $i_L = 7.7$ A/cm^2.

In case (*ii*) a two-dimensional model is required. Treatments for the simple pore and the thin film model assume generally zero reactant concentration at the end of an infinite pore (11) or a fast (compared to diffusion) first-order reaction over the total pore length (12). For the first-order oxygen reduction on oxide-free platinum (27, 28), these treatments are adequate, predicting limiting current densities proportional to oxygen partial pressure at low pressures (2, 29). However, they do not consider possible change of the available pore surface area at the limiting current for various reactant concentrations.

First-order reactions do not allow experimental determination of the pore length which is under limiting current conditions. The peculiarity of zero-order reactions in exhibiting a defined "critical" penetration length, beyond which reactant concentration becomes zero, proves advantageous. In this work the irreversible zero-order ethylene hydrogeneration of Eq. [2] at positive potentials (9, 10) was used as a model for mass transport in gas diffusion porous electrocatalysts.

Mathematical analysis of a two-dimensional porous model with simultaneous reaction in the pores is complex. Analysis has been simplified here by considering one-dimensional, axial diffusion and reaction in the pores (Eq. [13] below) and by approximating radial diffusion to the pore walls by an algebraic equation, Eq. [15]. Similar approximations have been made by others for flow-through and flooded porous electrodes (30-32).

Kinetic behavior with simultaneous slow axial diffusion was discussed previously (33). Mass balance along the element dx of a simple pore or a thin film gives for a zero-order reaction (33)

$$\frac{d^2\theta}{dx^{*2}} - h_0^2 = 0 \quad [13]$$

where

$$\theta = C_J/C_{J_\infty},\ x^* = x/L$$

and

$$h_o = L\sqrt{\frac{2k_J^o}{R\mathcal{D}_J C_{J_\infty}}\exp\left(-\frac{\alpha EF}{\mathcal{R}T}\right)} \quad [14]$$

h_o being an electrochemical Thiele modulus for the electrocatalyst (33). The potential, E, in Eq. [14] is the electrode potential with reference to the normal hydrogen electrode (NHE). With the strong electrolytes used in this investigation and for thin electrodes, the ohmic overpotential in the pores can be neglected as discussed previously (10, 33, 34). The constant k_J^o at zero potential *vs.* NHE contains inherently the hydrogen ion concentration (cf. kinetics Eq. [2], $k_J^o = k'C_{H^+}{}^2$). The latter was maintained constant here while the ethylene concentration, C_{J_∞}, was varied.

Diffusion at the wall in the radial direction can be approximated by

$$\left(\frac{\partial\theta_{J,x}}{\partial r^*}\right)_{r^*=1} \simeq \frac{\theta_{J,x} - \theta_{J,S}}{\lambda^*} \quad [15]$$

assuming a linear concentration gradient (dimensionless) across a thin film or a stagnant electrolyte layer. Here, $\lambda^* = \lambda/R$, is the dimensionless thickness of the thin film or of the stagnant layer.

If $h_o < \sqrt{2}$, the entire pore length maintains a reactant concentration $\theta > 0$. For $h_o > \sqrt{2}$, θ becomes zero at a critical pore penetration length x_c. For $x^* > x_c{}^*$ no reaction takes place. The boundary conditions for Eq. [13] become then

$$\theta = 1 \text{ at } x^* = 0 \quad [16]$$

$$\theta = 0 \text{ at } x^* \geq x_c{}^* \quad [17]$$

$$\frac{d\theta}{dx^*} = 0 \text{ at } x^* = x_c{}^* \quad [18]$$

Boundary conditions [16]-[18] apply to the reactant ethylene molecules inside the pore and assume high concentration and fast transport of electroactive ions in the electrolyte. The latter assumption is justified as shown by experimental evidence later. Equation [13] with Eq. [16]-[18] give a concentration profile along the pore

$$\theta = 1 - h_o{}^2 x_c{}^{*2}\left[\frac{x^*}{x_c{}^*} - \frac{1}{2}\left(\frac{x^*}{x_c}\right)^2\right] \text{ for } x^* < x_c{}^* \quad [19]$$

The critical length is obtained from Eq. [19] using the equality of boundary conditions [17]

$$x_c{}^* = \frac{\sqrt{2}}{h_o} = \frac{1}{L}\sqrt{\frac{R\mathcal{D}_J C_{J_\infty}}{k_J^o \exp(-\alpha EF/\mathcal{R}T)}} \text{ for } h_o > \sqrt{2} \quad [20]$$

Therefore

$$\theta = 1 - 2\left[\frac{x^*}{x_c{}^*} - \frac{1}{2}\left(\frac{x^*}{x_c{}^*}\right)^2\right] \text{ for } 0 \leq x^* < x_c{}^* \quad [21]$$

A limiting current density can be estimated for radial diffusion of reactant, for $0 \leq x \leq x_c$, with reactant concentration along the pore given by the above axial diffusion model, Eq. [21]

$$I_p = 2\pi RnF\mathcal{D}_J \int_0^{X_c}\left(\frac{\partial C_{J,x}}{\partial r}\right)_{r=R} dx \quad [22]$$

where I_p is the total current in a pore. In dimensionless form, Eq. [22] and [15] yield for the limiting current ($\theta_{JS} = 0$)

$$\frac{\lambda I_{P,L}}{2\pi RLnF\mathcal{D}_J C_{J_\infty}} = \int_0^{x_c{}^*}\theta(x^*)dx^* \quad [23]$$

The ratio

$$i_{P,L} = \frac{I_{P,L}}{2\pi RL} \quad [24]$$

is an apparent limiting current density per pore for total pore length utilization with an area of $2\pi RL$. With a uniform pore distribution and $\mathcal{P}$ pores per unit geometric area of the electrode, the geometric limiting current density i_L, is obtained

$$i_L = i_{P,L}\mathcal{P} = \frac{\mathcal{P}I_{P,L}}{2\pi RL} \quad [25]$$

Equation [25] defines the experimentally measurable limiting current density, since the extent of pore utilization and the true electroactive area per pore, $2\pi Rx_c$, are often not known *a priori*. Correlations are, then, based on the geometric i_L, although the higher, true limiting current density depending on x_c should be used. Therefore, the following equations are derived for the apparent geometric current density, to correlate measurable quantities. From Eq. [21], [23], and [25]

$$\frac{\lambda i_L}{nF\mathcal{P}\mathcal{D}_J C_{J_\infty}} = \int_0^{x_c{}^*}\left\{1 - 2\left[\frac{x^*}{x_c{}^*} - \frac{1}{2}\left(\frac{x^*}{x_c{}^*}\right)^2\right]\right\} dx^* = \frac{x_c{}^*}{3} \quad [26]$$

Equations [20] and [26] give then the ethylene limiting current due to slow axial and radial diffusion with partial pore utilization on the electrode gas side

$$i_L = \frac{nF\mathcal{P}\mathcal{D}_J{}^{3/2}}{3\lambda}\sqrt{\frac{R}{k_J^o \exp\left(-\frac{\alpha EF}{\mathcal{R}T}\right)}}\, C_{J_\infty}{}^{3/2} \quad [27]$$

Equation [27] predicts that for a given zero-order reaction and electrocatalyst the geometric limiting current density depends on the 1.5th power of the bulk reactant concentration. This is a result of the concentration dependence of the available pore area A, for reaction,

$$A = 2\pi R\mathcal{P}x_c \quad [28]$$

where $x_c = x_c{}^*L$ and $x_c{}^*$ is a function of concentration given by Eq. [20]. By differentiating Eq. [28] with respect to bulk concentration the variation of this area becomes inversely proportional to the square root of the concentration

$$\frac{dA}{dC_{J_\infty}} = 2\pi R\mathcal{P}\frac{dx_c}{dC_{J_\infty}} = \pi\mathcal{P}\sqrt{\frac{\mathcal{D}_J R^3}{k_J^o C_{J_\infty}\exp\left(-\frac{\alpha EF}{\mathcal{R}T}\right)}} \quad [29]$$

The predicted dependence of i_L on the kinetic rate constant and the potential at the onset of the limiting current, arises from the approximation that the local reactant concentration will be determined by the superimposition of only axial diffusion on the reaction kinetics.

If the thin film model is applicable, i_L is proportional to the square root of the pore radii. For the simple pore model, assuming $\lambda = R$, the limiting current becomes inversely proportional to the pore radii. With practical porous electrodes use of a pore size distribution would be appropriate. However, the general dependence of i_L on reactant concentration should be the same.

Experimental

Cell designs and electrodes.—Two basic cell designs were used in this study, both oriented vertically: (*i*) a free electrolyte cell (9) with stationary liquid electrolyte contained in a compartment of about 1.25 cm thickness × 2.5 cm diam. This cell design was used for determining limiting currents for hydrogen ion transport by free convection in the bulk electrolyte; and (*ii*) a matrix cell (35) with electrolyte immobilized

on five disks of filter paper, Whatman no. 42, to eliminate free convective transport. This design permitted measurement of purely diffusion limiting currents in the electrolyte. Both cell designs were also used to obtain ethylene limiting currents with identical results. The flow rates of excess reactant gases at the back of the cathode and the anode were adjusted so that limiting currents were independent of flow rate. With very dilute ethylene mixtures, however, fast flow rates were dictated by the mixing process for ethylene and nitrogen, to assure steady composition.

Both cathode and anode were American Cyanamid commercial type porous electrodes, partially wetproofed with polytetrafluoroethylene and containing 9 mg/cm^2 platinum (or palladium) black (36). Type AA-2 electrodes were used with the matrix cell. In free electrolyte cells, Type LAA-2 electrodes which incorporated a thin liquid impermeable polytetrafluoroethylene backing were used. All electrodes were 2.5 cm diam (D), with an exposed geometric area of 5.07 cm^2 and a total surface area for the catalyst of 20-25 m^2/g (37). Platinum or palladium black electrodes were used as the cathode. The anode was always a platinum black electrode.

Materials.—Commercial prepurified nitrogen and hydrogen were used. Ethylene mixtures in nitrogen were prepared from CP grade ethylene (Matheson Company) by a procedure described previously (9). The mixture composition varied less than ±0.002 atm within a run. Electrolyte solutions were normally adjusted to the ionic strength of a 2N solution by mixing appropriate amounts of perchloric acid (AR, Baker Chemical Company) and lithium perchlorate (AR, Alfa Inorganics-Ventron) (9).

Procedure.—The gas flow system, the electrical equipment, and the procedure followed to reduce surface oxides and to eliminate oxygen impurities have been discussed before (9). Reactant conversion was occasionally tested by gas chromatographic analysis of gas samples at the cathode exit (9).

Electrolyte limiting currents were obtained at a constant pressure of 1 atm of pure ethylene gas and at constant electrolyte ionic strength, by varying the hydrogen ion concentration. Ethylene limiting currents were determined at various ethylene partial pressures with a constant electrolyte concentration of 2N $HClO_4$.

The limiting current region was reached through steady-state polarization runs by stepwise adjustment of the cell current with a variable resistor (9, 35). At the vicinity of the limiting current, a constant current supply (Quantech, Model 151B) helped stabilize the current and allowed for voltage variation only (9). Limiting currents were determined graphically from the tangent of the voltage-current density curve. All current densities are based on the exposed geometric electrode area.

Results and Discussion

Electrolyte limiting currents.—A wide range of acid concentrations were examined, between 3 and 0.1N $HClO_4$. Figure 2 shows IR-corrected polarization curves obtained on platinum black in a static-free electrolyte cell. In the Tafel region, the acid concentration had little effect on the cathode voltage (ethylene) *vs.* a hydrogen electrode (anode) in the same electrolyte. This is not a discrepancy from previous kinetic results (9, 10) since hydrogen electrode potentials vary here with the hydronium ion concentration in an inverse fashion from that of the ethylene electrode. This simultaneous change of the ethylene and hydrogen electrode potential in the same electrolyte results in small variations of the cell voltage at low concentrations. Therefore, the energy losses of the hydrogen-ethylene cell are considerably smaller than anticipated from the ethylene (cathodic) reaction kinetics alone at low hydrogen ion concentrations.

Figure 2 shows that no limiting currents were observed in the positive potential region for hydrogen

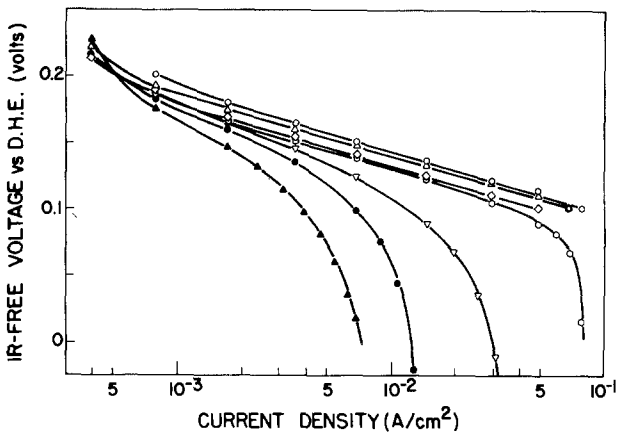


Fig. 2. Current density-voltage curves for varying electrolyte concentration. Electrogenerative hydrogenation of ethylene on platinum black in a free electrolyte cell. Temperature 25°C. (○, C_{H^+} = 3, C_{Li^+} = 0(equiv./liter); △, 2-0; ◇, 0.5-1.5; ○, 0.4-1.6; ▽, 0.2-1.8; ●, 0.1-1.9; ▲, C_{H^+} = 0.1, C_{Li^+} = 3.4).

ion concentrations above 0.5N. Below this concentration, the limiting currents decreased with decreasing hydronium ion concentration.

In the same figure, the effect of electrolyte properties on the limiting current is also shown. With 0.1N $HClO_4$ electrolyte, the ionic strength was varied by using 1.9 or 3.4N $LiClO_4$ supporting electrolyte. The observed limiting current densities were approximately inversely proportional to electrolyte concentration, although a decrease in the diffusion layer thickness is anticipated. This behavior can be explained if one considers that high salt concentrations presumably increase electrolyte viscosity to give lower conductivity and diffusivity and low limiting currents. Decreased cell performance at 3.5N total concentration and at 4N $HClO_4$ (10) further supports this assumption. It should be remembered that Eq. [9] and [12] for the limiting current densities were derived with the assumption of constant total concentration and physical properties. An estimate of the change of diffusivity at the two concentrations can be obtained from the observed limiting currents in a free electrolyte cell in the presence of free convection, discussed later. From Eq. [12], limiting currents are related by

$$\frac{i_{L,1}}{i_{L,2}} = \left(\frac{\mathcal{D}_{J,1}}{\mathcal{D}_{J,2}}\right)^{0.5} \left(\frac{\rho_1 \mathcal{D}_{J,1}}{\mu_1}\right)^{0.25} \left(\frac{\mu_2}{\rho_2 \mathcal{D}_{J,2}}\right)^{0.25} \left(\frac{C_2 \zeta_1}{C_1 \zeta_2}\right)^{0.25} \quad [30]$$

where subscripts 1 and 2 refer to 2 and 3.5N total electrolyte concentration, respectively. With small variation in the Schmidt number and the densification coefficient ζ (24), the ratio of diffusivities in the two electrolytes becomes $\mathcal{D}_{J,1}/\mathcal{D}_{J,2} \simeq 2.4$, *i.e.*, diffusivity is less in 3.5N electrolyte.

Because of low diffusivity in 0.1N $HClO_4$ + 3.4N $LiClO_4$ the observed limiting current was practically identical to that of 0.1N $HClO_4$ without supporting electrolyte but below that in 0.1N $HClO_4$ + 1.9N $LiClO_4$. The low i_L value in the unsupported electrolyte results from an increase in the diffusion layer thickness at low ionic strength. The qualitative results support the practice of maintaining constant electrolyte ionic strength in correlating limiting currents in electrogenerative and fuel cells. All results here were obtained at a constant ionic strength in 2N electrolyte.

Limiting currents in the free electrolyte cell, above, were 3-5 times higher than those observed in a matrix cell. With the latter, limiting currents were observed at positive potentials even in 1N $HClO_4$ electrolyte. With the electrolyte on a matrix, free convective transport is eliminated. This with the decreased ion dif-

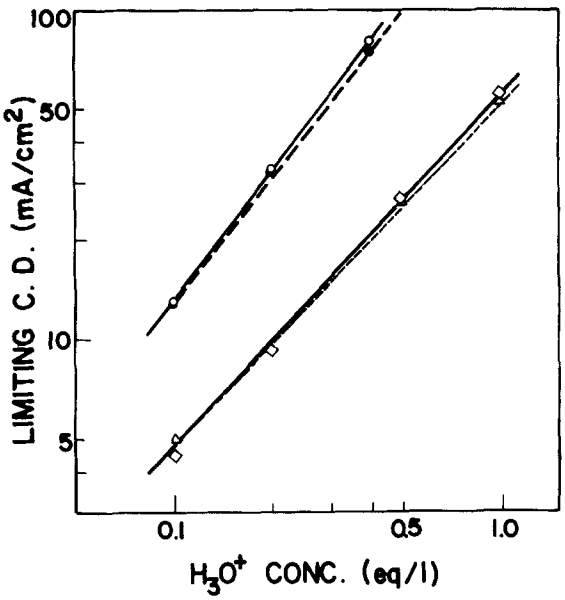


Fig. 3. Limiting current density dependence on hydrogen ion concentration for electrogenerative hydrogenation of ethylene on platinum (○, △) and palladium (◇). Temperature 25°C. (Full symbols, corrected for H^+ migration. Dotted lines: calculated lines for diffusion and free convection, Eq. [9] and [12]. ○, Free electrolyte cell.

fusivity in the matrix result in more severe mass transport limitations compared with free electrolyte. Figure 3 shows the magnitude and the concentration dependence of observed limiting current densities on platinum and palladium electrodes for the two cell designs used. Platinum and palladium electrocatalysts showed identical limiting current densities in a matrix cell. Since the reaction rate on palladium is twice that on platinum (10), the observed limiting currents should result from slow mass transport.

Similar experiments were conducted in a Nernst concentration cell, with ethylene replaced by nitrogen at the cathode (38). Because of the low cell voltage and slow hydrogen gas evolution compared to ethylene reduction (9), current densities at zero cell voltage were lower than with ethylene and limiting currents were not attained. However, deviations of Tafel curves from linearity indicated the approach of mass transport limitations in about the same region as with ethylene.

The observed limiting currents of Fig. 3 obey the relation

$$i_L = K_J C_{J_\infty}{}^{\nu_J} \qquad [31]$$

with a reproducibility of about ±5%. K_J is constant and ν_J can be obtained from the slopes of Fig. 3, at constant temperature, ionic strength, j, and other reactant concentrations

$$\nu_J = \left(\frac{\partial \log i_L}{\partial \log C_{J_\infty}}\right)_{T,\,j,\,C_K \neq J} \qquad [32]$$

The concentration dependence of i_L and estimated values of K_J, obtained by linear regression analysis, are given in Table I. K_J corresponds to the limiting current density at unit reactant concentration. The calculation is straightforward for the matrix cell but involves significant extrapolation of the i_L-C_{H+} curve for the free electrolyte system.

It is important to notice the different dependence of limiting currents on hydrogen ion concentration for the two cell designs. This is a result of the different ionic transport mechanisms operative in each cell. In a matrix-supported electrolyte, hydrogen ions are transported to the cathode by diffusion and migration. In a free electrolyte cell, consumption of hydrogen ions at the cathode can cause density gradients along this electrode. Free convection can, then, operate to enhance mass transport to the cathode. Free convection in the pores, induced either by thermal effects or by the development of a dynamic gas-liquid interface (17), is probably unimportant here since such effects would also be present in a matrix cell. Possible pore "blanketing" does not seem significant in either cell design, considering the high mobility of hydrogen ions and the absence of pore diffusion limitations in the Tafel region (9, 10).

The migration contribution to limiting currents was calculated for steady-state diffusion through a stagnant layer using Newman's numerical, iterative procedure (18). Migration effects resulted in about 5% deviation of the concentration dependence of i_L from the theoretical one, Eq. [9] and [12]. When corrected for migration, limiting currents obey the theoretical correlations, Table I. Correction is approximate, based on dilute solution theory, with mobilities and diffusion coefficients for infinite dilution (18).

The physical constants in Eq. [12] were not known precisely for the binary mixture $HClO_4$-$LiClO_4$. However, differences in some reported values for $HClO_4$ and $LiClO_4$ are relatively small (~10%). Using available values for 1N $HClO_4$, $\rho = 1.053$ g/cm³, $\mu = 9.058 \times 10^{-3}$ poise (39, 40), $\mathcal{D}_{H+} = 4 \times 10^{-5}$ cm²/sec, and the variation of ρ with concentration for $HClO_4$ (40), rough estimates of Sc, Gr, and ζ were obtained: Sc = 215; Gr = 1.16×10^7; $\zeta = -53.8$ cm³/mole. The product ScGr = 2.5×10^9 is at the limit for laminar-free convection (Eq. [11]). Using the above values and other physical characteristics of the system, limiting current densities were calculated for various hydrogen ion concentrations with the aid of Eq. [12]. The dashed line, Fig. 3, shows excellent agreement between calculated and migration-corrected limiting currents for free electrolyte.

For a matrix-supported electrolyte, $\mathcal{D}_{H+}$ would be about one-third of that in free electrolyte, since $i_{matrix}/i_{free} \simeq 1/3$ at low H^+ concentrations (0.1N). With $\mathcal{D}_{H+} = 1.3 \times 10^{-5}$ cm²/sec and a reasonable value of $\delta = 0.026$ cm (21), limiting current densities

Table I. Dependence of limiting current density on reactant concentration

Electrolyte	Catalyst	$K_{H^+}\left[\frac{A}{cm^2}\left(\frac{liter}{mole}\right)^{\nu_J}\right]$	ν_{H^+}*	$K_{C_2H_4}\left(\frac{A}{cm^2\ atm^{\nu_J}}\right)$	$\nu_{C_2H_4}$†	Remarks
Matrix-supported	Pt, Pd	0.056	1.08	0.875	1.59	Observed
Matrix-supported	Pt, Pd	0.052	1.02	—	—	H^+-migration corrected
Static, free	Pt	0.268	1.32	0.875	1.59	Observed
Static, free	Pt	0.247	1.28	—	—	H^+-migration corrected

* $\nu_{H^+} = \left(\frac{\partial \log i_L}{\partial \log C_{H^+\infty}}\right)_{T,j,P_{C_2H_4}}$

† $\nu_{C_2H_4} = \left(\frac{\partial \log i_L}{\partial \log P_{C_2H_4}}\right)_{T,C_{H^+}}$

were calculated using Eq. [9]. The dotted line of Fig. 3 predicts accurately the experimental, migration-corrected limiting currents.

Gas phase limiting currents.—Transport limitations on the gas side of the electrodes were investigated by varying the ethylene partial pressure between 1 and 0.027 atm in nitrogen. Both matrix and free electrolyte cells were used with a constant, 2*N* $HClO_4$, electrolyte concentration. With this concentration, hydrogen ion transport limitations were eliminated in the pores (9, 33) and in the bulk, discussed above.

Electrogenerative hydrogenation of ethylene on platinum black achieved a maximum reaction rate at several low partial pressures of ethylene (9). Similar behavior was exhibited with palladium black cathodes, at positive potentials (10). Limiting currents were observed only at ethylene partial pressures below about 0.3 atm. Above this partial pressure, the operating cell voltage reached zero before any distinct limitations developed.

The dependence of the limiting current density on inlet ethylene concentration in the gas phase is shown in Fig. 4. The reported limiting current densities are the average of two to three values obtained from steady-state polarization curves. Reproducibility was within 5-10%, as indicated by two individual limiting current densities at 0.103 atm, Fig. 4. At 0.03 atm, an abnormally high limiting current was observed, probably because of turbulence associated with the fast flow rate of the gaseous mixture in that experiment. Reactant conversions estimated from Faraday's law are in good agreement with the observed ones.

The limiting current densities for both platinum and palladium black electrocatalysts were equal at the same reactant partial pressure for either a matrix or a free electrolyte cell, Fig. 4. This and the significantly faster reduction of ethylene on palladium than on platinum away from the limiting current condition (10) suggest slow mass transport rather than kinetic limitations. Efforts to correlate the data for convective transport (18), gas phase counterdiffusion of reactant and product or for differential reactor operation were not successful. As shown in Fig. 4, the observed limiting current densities are proportional to a power of the inlet partial pressure of ethylene, obeying an equation similar to Eq. [31]. Here the ethylene concentration in the gas phase is assumed to be in equilibrium with the liquid phase bulk concentration of ethylene, C_{J_x}. The concentration exponent $\nu_{C_2H_4}$ and the constant $K_{C_2H_4}$ are given in Table I. Comments on extrapolation to unit concentration discussed earlier apply here also.

Results suggest partial utilization of the pore, with the extent of utilization depending on reactant concentration. For the zero-order ethylene reduction on platinum and palladium (9, 10, 33), Eq. [20] gives an estimate of the critical penetration length of ethylene as a function of bulk concentration, potential, and rate constant. Figure 5 shows the concentration drop in the pores for varying h_0. Equation [27] then predicts the observed i_L-C_{J_∞} relation of Fig. 4, assuming Henry's law for dissolved ethylene [$C_{J_\infty} = K_H P_{J_\infty}$, where $K_H = 6.1 \times 10^{-6}$ mole/cm³ atm (42)].

Both platinum and palladium limiting currents appear at about the same potential, $E = 0.13$V, *vs.* the normal hydrogen electrode, although rate constants for the two catalysts are different: $k_{Pt}^\circ = 3.2 \times 10^{-3}$ (9), $k_{Pd}^\circ = 0.452$ (10). Identical limiting currents probably result from different pore diameters. The potential at which limiting currents appear is about 0.05V above the potential at which hydrogen evolution is observed (9, 10). This and the agreement between observed and calculated reactant conversions suggest that reaction takes place electrocatalytically and not by reaction of gaseous hydrogen and ethylene on electrolyte-free catalytic surface.

Pore radii and ethylene penetration into the electrode pores can be estimated from the model developed above. Assuming a close cubic packing of uniform pores with $\mathcal{P} = 1/4R^2$ (12), $n = 2$, $\mathcal{D}_J = 10^{-5}$ cm²/sec, and the above values for k_{Pt}°, E, and K_H, the pore radius for platinum can be estimated from Eq. [27] and the value of constant K_J given in Table I at 1 atm ethylene pressure

$$K_J = \frac{n\mathbf{F}\mathcal{D}_J^{1.5} K_H^{1.5}}{12\lambda R^{1.5}\sqrt{k_J^\circ}\exp(-\alpha E\mathbf{F}/2\mathcal{R}T)} \qquad [33]$$

For the thin film model, assuming $\lambda \simeq 0.025R$, a pore radius $R_{Pt} = 40\mu$ and $\lambda = 1\mu$ is estimated for platinum. With similar assumptions, $R_{Pd} = 15\mu$ and $\lambda \simeq 0.4\mu$ are estimated for palladium. This trend is in agreement

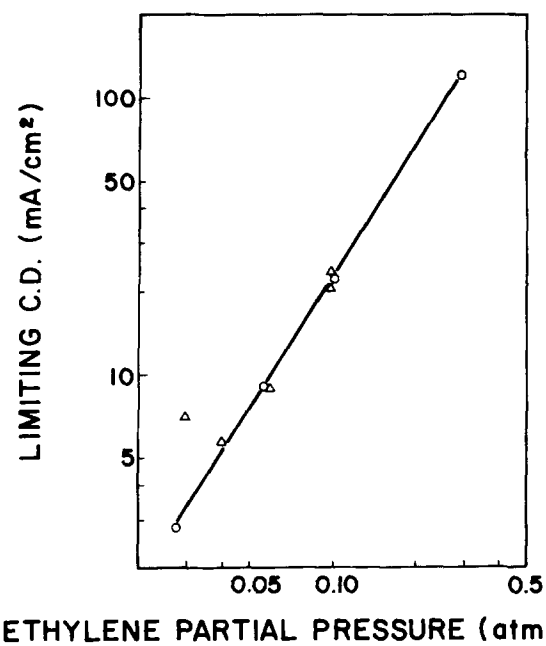


Fig. 4. Dependence of gas phase limiting current on reactant partial pressure. Electrolyte 2*N* $HClO_4$, temperature 24°C (○, palladium-matrix cell; △, platinum-free electrolyte).

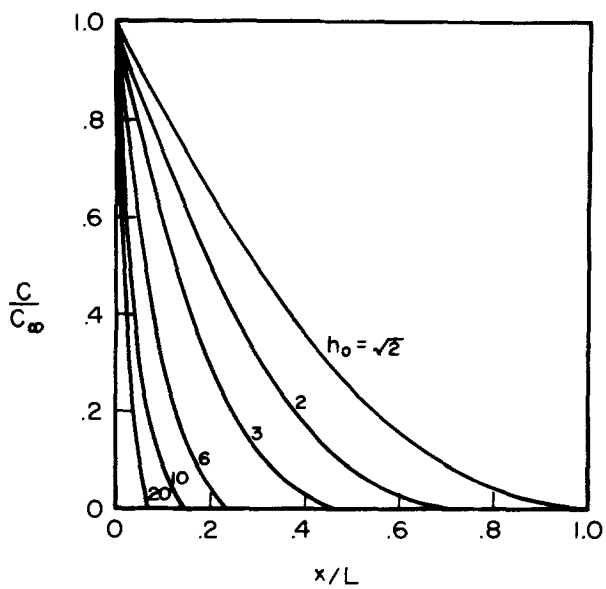


Fig. 5. Dimensionless concentration change along the pore length for various electrochemical Thiele moduli.

with observed slow pore diffusion of ethylene on palladium in the Tafel region (10, 33). For the simple pore model, if $\lambda \simeq R$, the pore radii become $R_{Pt} = 9\mu$ and $R_{Pd} = 3.4\mu$.

Using the thin film model values of R_{Pt}, R_{Pd}, and $L = 0.02$ cm (half the electrode thickness), h_o has been estimated for various ethylene partial pressures using Eq. [14]. Calculated values of h_o at the potential of the limiting currents are given in Table II. At 1 atm ethylene, this potential was not reached nor was a limiting current observed. Therefore, the high values of h_o at 1 atm do not correspond to any experimental currents. At the potential of the limiting currents, the length in the pores where ethylene concentration becomes zero is at the most 0.0015 cm or 7.5% of the pore length for 0.29 atm on platinum. Such a pore penetration length corresponds to about one-fifth of the pore diameter. This justifies the derivation of the limiting current density, Eq. [22]-[27], assuming radial diffusion only, with concentration varying along the pore according to the axial kinetic model.

Although the critical penetration is only a fraction of the pore, the surface area variation with concentration (Eq. [29]) is significant enough to yield the i_L-C_{J_∞} relations of Eq. [27] and [31]. Equation [27] was used with the previously given values of constants to estimate limiting current densities. The calculated solid line of Fig. 4 shows excellent agreement with experiment.

The determined dependence of the limiting current density on a power of the inlet reactant partial pressure, and the agreement between theory and experiment, suggest possible use of the electrogenerative reactor for analytical and control processes. Because of the relatively low degree of pore utilization of the examined electrodes at the limiting current, partially wet-proofed catalytic electrodes should be designed with short, large diameter pores.

Conclusions

The well-characterized kinetics of ethylene hydrogenation on platinum and palladium porous electrocatalysts make this reaction suitable for investigation of mass transport processes and limitations in catalyst pores. Successful modeling of this system makes it useful for analytical purposes, possible process control, and electrocatalyst characterization.

In a matrix-supported electrolyte hydrogen ion diffusion was 3-5 times slower than in a free electrolyte. Identical limiting currents for platinum and palladium black electrodes resulted from slow ionic transport through a stagnant diffusion layer on the external electrode surface. No ionic pore diffusion limitations were observed. Ionic transport in a free electrolyte was enhanced by free convection in the presence of indifferent lithium ions, even in the relatively narrow channel geometry of the examined cell. Free convection theory predicts the observed dependence of limiting currents on hydrogen ion concentration to the 1.25 power.

Gas phase limitations external to the pores were not observed at fast ethylene flow rates. The concentration dependence of limiting currents apparently can be explained by a change of the available reaction area or the pore penetration of reactant, dependent on the inverse of the square root of ethylene partial pressure. The developed model permits determination of electrocatalyst pore utilization for zero-order kinetics. Further testing and application to other systems is desirable.

Table II. Thiele moduli and critical penetration lengths for platinum and palladium porous electrocatalysts

$P_{C_2H_4}$ (atm)	Platinum h_o†	Platinum $x_c^* = x_c/L$	Palladium h_o†	Palladium $x_c^* = x_c/L$
1.0	10	0.138	198	0.0071
0.29	19	0.075	368	0.0038
0.10	32	0.045	617	0.0023
0.06	42	0.033	809	0.0017
0.03	59	0.024	1144	0.0012

† Results for thin film model, with $\lambda = 0.025R$.

Acknowledgment

We thank the National Science Foundation, E. I. du Pont de Nemours and Company, and the University of Wisconsin for support of this work.

Manuscript submitted Sept. 13, 1976; revised manuscript received May 9, 1977. This was Paper 34 presented at the Las Vegas, Nevada, Meeting of the Society, Oct. 17-22, 1976.

Any discussion of this paper will appear in a Discussion Section to be published in the June 1978 JOURNAL. All discussions for the June 1978 Discussion Section should be submitted by Feb. 1, 1978.

Publication costs of this article were assisted by the National Science Foundation.

LIST OF SYMBOLS

A	surface area (cm²)
C	total concentration (mole/cm³)
C_J	concentration of J (mole/cm³)
C_J^*	dimensionless concentration $= (C_J - C_{J_\infty})/(C_{JS} - C_{J_\infty})$
C_{J_∞}	bulk concentration of J (mole/cm³)
C_{JS}	surface concentration of J (mole/cm³)
D	electrode diameter (cm)
$\mathcal{D}_J$	diffusion coefficient of J (cm²/sec)
E	electrode potential (V)
$\mathbf{F}$	Faraday's constant (A sec/mole)
g, g_c	acceleration of gravity (cm/sec²)
Gr	Grashoff number (dimensionless) $= \rho^2 g \zeta D^3 (C_{JS} - C_{J_\infty})/\mu^2$
h_o	electrochemical Thiele modulus (Eq. [14], dimensionless)
I_p	total pore current (A)
i	current density (A/cm²)
i_L	limiting current density (A/cm²)
j	ionic strength
K_H	Henry's constant (mole/cm³ atm)
K_J	constant, Eq. [31] [A cm^{-2} (liter/mole)$^{\nu_J}$]
k	constant for free convection (Eq. [11])
k_J°	reaction rate constant at zero potential $= k' C_{H^+}^2$ (mole/cm² · sec)
L	pore length = 1/2 electrode thickness = 0.02 (cm)
n	number of electrons
n_J	charge of ion J
Nu_i	average Nusselt number or dimensionless current density (Eq. [13], [16])
$\mathcal{P}$	number of pores per cm² $(= 1/4R^2)$
P_{J_∞}	bulk partial pressure of J (atm)
$\mathcal{R}$	universal gas constant (J/mole °K)
R	pore radius (cm)
r	cylindrical reaction coordinate
r^*	dimensionless radial distance $= (r/D)$
Sc	Schmidt number (dimensionless) $(= \mu/\rho\mathcal{D}_J)$
T	temperature (°K)
t	time (sec)
t^{**}	dimensionless time $(= \mu t/\rho D^2)$
v	velocity (cm/sec)
v^{**}	dimensionless velocity $(= v D\rho/\mu)$
x	reaction coordinate
x^*	dimensionless distance $(= x/D$ or $x/L)$ (Eq. [11]
x_c	critical penetration length (cm)

Greek letters

α	transfer coefficient
δ	diffusion layer thickness for ion transport (cm)
ζ	densification coefficient (cm³/mole) $\left[= -\frac{1}{\rho}\left(\frac{\partial\rho}{\partial C_J}\right)_{T,P} \simeq -\frac{1}{\rho}\left(\frac{\Delta\rho}{\Delta C_J}\right)_{T,P} \right]$
θ	dimensionless concentration $(= C_J/C_{J_\infty})$
λ	diffusion layer thickness for molar transport (cm)

μ viscosity (g/cm · sec)
ν_J concentration exponent (Eq. [31])
ρ density (g/cm^3)

Subscripts

c critical (Eq. [20])
J species J
L limiting value
P property in pore
S surface property
x property at length x
∞ bulk property

Superscripts

*, ** dimensionless property
o intrinsic property

REFERENCES

1. K. V. Kordesch, in "Fuel Cells," Vol. 1, G. J. Young, Editor, Reinhold Publishing Co., New York (1960).
2. M. B. Clark, Abstract 34, p. 34, The Electrochemical Society Extended Abstracts, Battery Div., Fall Meeting, Boston, Massachusetts, September 1962.
3. L. W. Niedrach and H. R. Alford, *This Journal*, **112**, 117 (1965).
4. H. J. R. Maget and E. A. Oster, *Adv. Chem. Ser.*, **47**, 87 (1965).
5. H. J. R. Maget, in "Handbook of Fuel Cell Technology," C. Berger, Editor, p. 425, Prentice-Hall, Inc., Englewood Cliffs, N.J. (1968).
6. J. A. Shropshire and B. L. Tarmy, *Adv. Chem. Ser.*, **47**, 153 (1965).
7. M. Eisenberg, in "Advances in Electrochemistry and Electrochemical Engineering," Vol. 2, C. Tobias, Editor, p. 235, Interscience Publishers Inc., New York (1963).
8. K. J. Vetter, "Electrochemical Kinetics, Theoretical and Experimental Aspects," pp. 7, 162, 399-404, Academic Press, New York (1967).
9. S. H. Langer and G. P. Sakellaropoulos, *This Journal*, **122**, 1619 (1975).
10. G. P. Sakellaropoulos, Ph.D. Thesis, Department of Chemical Engineering, University of Wisconsin-Madison (1974).
11. L. G. Austin, M. Ariet, R. D. Walker, G. B. Wood, R. H. Comyn, *Ind. Eng. Chem. Fundam.*, **4**, 321 (1965).
12. S. Srinivasan, H. D. Hurwitz, and J. O'M. Bockris, *J. Chem. Phys.*, **46**, 3108 (1967).
13. J. Giner and C. Hunter, *This Journal*, **116**, 1124 (1969).
14. M. B. Cutlip, *Electrochim. Acta*, **20**, 767 (1975).
15. L. G. Austin, "Fuel Cells," NASA SP-120, p. 40, Washington, D.C. (1967).
16. R. W. Easter, NASA TN D-6168, Washington, D.C. (1971).
17. J. O'M. Bockris and B. D. Cahan, *J. Chem. Phys.*, **50**, 1307 (1969).
18. J. Newman, "Electrochemical Systems," pp. 217, 230, 421-424, Prentice-Hall, Inc., Englewood Cliffs, N.J. (1973).
19. R. B. Bird, W. E. Stewart, and E. N. Lightfoot, "Transport Phenomena," pp. 580, 645, John Wiley & Sons, Inc., New York (1960).
20. C. R. Wilke, C. W. Tobias, and M. Eisenberg, *Chem. Eng. Prog.*, **49**, 663 (1953).
21. K. R. Williams and D. P. Gregory, *This Journal*, **110**, 209 (1963).
22. A. Acrivos, *AIChE J.*, **6**, 584 (1960).
23. W. E. Stewart, *Int. J. Heat Mass Transfer*, **14**, 1013 (1971).
24. C. R. Wilke, M. Eisenberg, and C. W. Tobias, *This Journal*, **100**, 513 (1953).
25. C. Wagner, *J. (and Trans.) Electrochem. Soc.*, **95**, 161 (1949).
26. F. G. Will, *This Journal*, **110**, 152 (1963).
27. D. Winkelmann, *Z. Elektrochem.*, **60**, 731 (1956).
28. A. Damjanovic and V. Brusic, *Electrochim. Acta*, **12**, 615 (1967).
29. H. A. Liebhafsky, E. J. Cairns, W. T. Grubb, and L. W. Niedrach, *Adv. Chem. Ser.*, **47**, 116 (1965).
30. J. S. Dunning, D. N. Bennion, and J. Newman, *This Journal*, **118**, 1251 (1971).
31. R. E. Sioda, *Electrochim. Acta*, **17**, 1939 (1972).
32. R. Alkire and B. Gracon, *This Journal*, **122**, 1594 (1975).
33. G. P. Sakellaropoulos and S. H. Langer, Paper presented at 68th Annual Meeting, AIChE, Los Angeles, Nov. 16-20, 1975, To be published.
34. A. G. Pshenichnikov, A. A. Michri, and M. Y. Kats, *Elektrokhimiya*, **8**, 889 (1972).
35. S. H. Langer, I. Feiz, and C. P. Quinn, *J. Am. Chem. Soc.*, **93**, 1092 (1971).
36. H. P. Landi, U. S. Pat. 3,407,096 (1968); U. S. Pat. 3, 527, 616 (1970).
37. R. G. Haldeman, W. P. Colman, S. H. Langer, and W. A. Barber, *Adv. Chem. Ser.*, **47**, 116 (1965).
38. S. H. Langer and H. P. Landi, *J. Am. Chem. Soc.*, **86**, 4694 (1964).
39. J. Newman, *Ind. Eng. Chem. Fundam.*, **5**, 525 (1966).
40. T. W. Chapman and J. Newman, "A Compilation of Selected Thermodynamic and Transport Properties of Binary Electrolytes in Aqueous Solutions," pp. 73-75, Lawrence Radiation Laboratory, Berkeley (1968).
41. Lange's Handbook of Chemistry, p. 1571 (1946).
42. K. Fujikawa, H. Kita, and K. Miyahara, *J. Chem. Soc., Faraday Trans. 1*, **69**, 481 (1973).

Technical Notes

Electrochemical Formation and Chemical Characterization of a Djerfisherite-Like Compound

Franklin C. Mrazek and James E. Battles*

Argonne National Laboratory, Chemical Engineering Division, Argonne, Illinois 60439

A djerfisherite-like material has been identified as an intermediate reaction product formed during the cycling of Li-Al/FeS_x cells using a LiCl-KCl electrolyte. Djerfisherite, an alkali copper-iron sulfide, was first characterized in 1966 as a new mineral occurring in some meteorites; but attempts to synthesize single phase djerfisherite by heating stoichiometric mixtures of normally available chemicals in sealed, evacuated silica tubes were unsuccessful (1). The djerfisherite-like material which is discussed in this article was

* Electrochemical Society Active Member.

Key words: djerfisherite, J-phase formation.

separated from the positive electrode of an electrochemical cell where it is formed as an intermediate product on the charge and discharge cycle. This particular cell, DS-11C (2), contained a Li-Al negative electrode, a FeS positive electrode, and LiCl-KCl electrolyte of the eutectic composition [58.2 mole percent (m/o) LiCl-41.8 m/o KCl]. The cell was operated for 136 cycles and 2009 hr at 450°-500°C; operation was terminated in an intermediate stage of a charging cycle. The charge and discharge cutoff voltages used in this cell were 1.65 and 1.00V, respectively. Subsequent to these results, an out-of-cell preparation of a similar material was accomplished by reacting Li_2FeS_2 with Fe in molten LiCl-KCl at 400°-450°C (3).

Metallographic examination of the positive electrode of cell DS-11C in a dry nitrogen atmosphere glove box revealed the principal phase to be light olive brown in color and isotropic in reflected polarized light. In addition, there was a small amount of fine metallic spheres in the electrolyte matrix. A sample of this material was submitted for x-ray powder diffraction analysis; the detected phases, in addition to the electrolyte, were a material labeled J-phase (4), with a diffraction pattern similar to that of the mineral djerfisherite, and α-Fe. No other phases were detected by either metallography or x-ray diffraction.

Samples of representative single phase material were obtained for chemical analysis to confirm any similarity between J-phase particles and djerfisherite. The electrolyte, which is water soluble, was removed by repeated leaching with water, and the α-Fe was removed from the insoluble J-phase by multiple magnetic separations. Other intermediate products of the cell reaction, Li_2FeS_2 and Li_2S, are water soluble. The wet sample was dried in flowing helium to minimize any oxidation of this very fine J-phase particulate. Density measurements (pycnometer method) and chemical analyses were performed on this material. The results of these analyses are presented in Table I, where they are compared with analyses of djerfisherite from meteoritic sources. Note that no copper, nickel, or sodium was present in the original positive FeS electrode, and therefore these constituents were not found in the product. Additional x-ray diffraction studies were conducted by Tani (5) on this single phase material isolated from cell DS-11C. Based on a model calculated from the x-ray diffraction data, Tani (5) assigned a value of 24 to the number of iron atoms per unit cell, and proposed a formula of $K_6LiFe_{24}S_{26}Cl$. His calculated density of 3.66 g/cm^3 agrees well with the measured density of 3.7 g/cm^3. The stoichiometry of this material, based on the chemical analysis (Table I), can be expressed as $K_{5.5}Li_{0.6}Fe_{24}S_{25.9}Cl_{1.0}$, which agrees well with the formula based on x-ray data. Also, from the chemical analysis presented in Table I, the stoichiometry of the St. Marks mineral is

$$K_{2.93}(Na_{0.17}Cu_{0.87})_{1.04}(Fe_{11.82}Ni_{0.18})_{12.00}S_{13.93}$$

This formula may be generalized to $K_3(Na,Cu)(Fe,Ni)_{12}S_{14}$, which when doubled is indeed very similar to electrochemically prepared J-phase material.

Table I. Chemical compositions of J-phase and two different meteorites

Element	J-phase* (w/o) (4)	St. Marks (w/o) (1)	Penta Blanca Springs (w/o) (6)
Fe	55.2	50.7	50.4
S	34.2	33.8	33.7
K	8.9	8.7	10.9
Cu	—	4.2	1.4
Cl	1.42	1.0	1.5
Ni	—	0.8	0.7
Li	0.23	—	—
Na	—	0.3	0.3
Total	99.95	99.5	98.9
Density, g/cm^3	3.7 (measured) 3.6 (calculated)***	3.9 (calculated)**	

* Analyst: K. Jensen, Analytical Chemistry Laboratory, Argonne National Laboratory.
** Based on the formula $K_6LiFe_{24}S_{26}Cl$ for a primitive cubic cell with a lattice constant of a = 10.358Å (5).
*** Based on the formula $K_6(Na, Cu)_2(Fe, Ni)_{24}S_{26}$ for a primitive cubic cell with a lattice constant of a = 10.34Å (1).

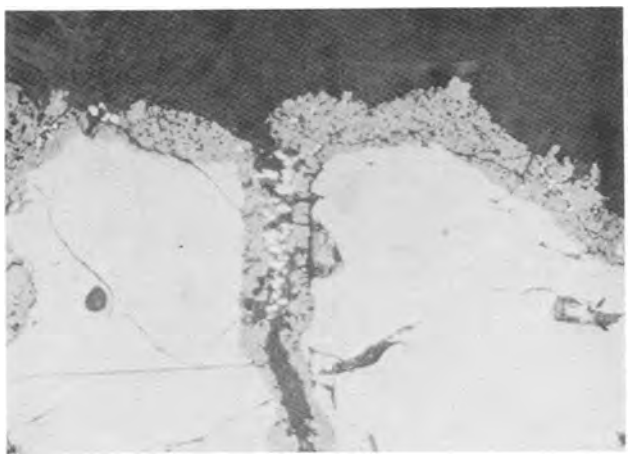


Fig. 1A. Cell 5% discharged. Phases: FeS (central unreacted portion); J-phase; Fe (white).

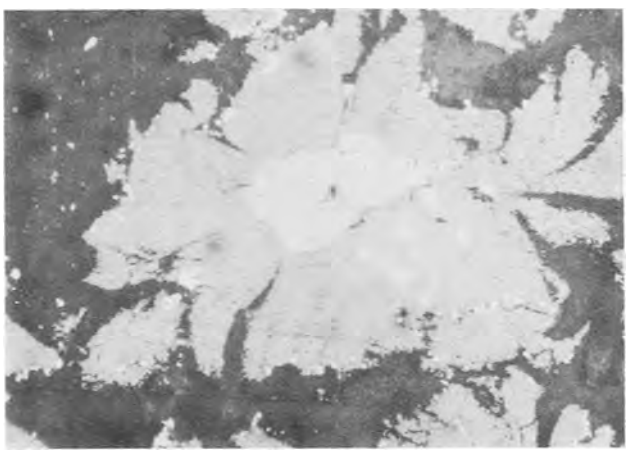


Fig. 1B. Cell 15% discharged. Phases; J-phase; X_{Cu};FeS. Fe (white); X_{Cu} is a modification of X-phase (X = Li_2FeS_2) in which Cu has been substituted for some Fe.

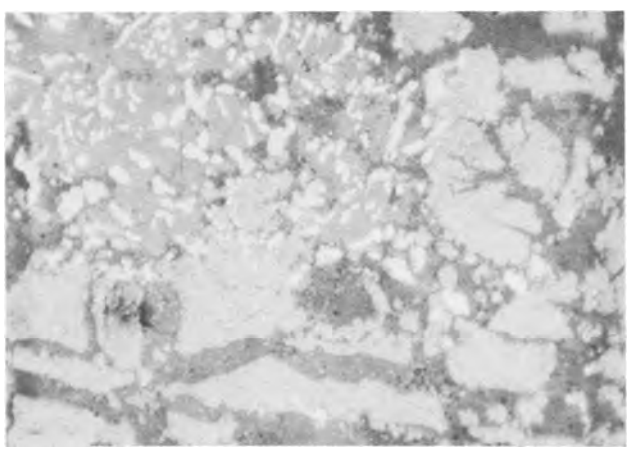


Fig. 1C. Cell 35% discharged. Phases: J-phase Li_2S, Fe (white)

Fig. 1. Photomicrographs of J-phase in partially discharge FeS electrodes (as-polished, all phases identified).

Three other cells, each with an FeS-positive electrode containing 20 atomic percent (a/o) Cu_2S as an additive, were examined metallographically after their first partial discharge cycle. These cells were prepared by Elliott and Cooper (7) as part of a program to study the initial swelling behavior of FeS positive electrodes as a result of the formation of J-phase. Figure 1 presents photomicrographs as well as x-ray diffraction phase identification results for the three positive electrodes which had been discharged by 5, 15, and 35% of theoretical capacity. Note that in one electrode (Fig. 1B), some of the iron was replaced by copper in the compound Li_2FeS_2, which is a normal intermediate product in the electrode reaction. This substitution occurs only in FeS electrodes with Cu_2S additives. This series of photomicrographs shows the morphology of the formation of J-phase during the discharge of cells having FeS positive electrodes and LiCl-KCl electrolyte. The photomicrograph in Fig. 1A shows the adherent dense layer of J-phase formed initially on the surface of an FeS particle. With additional discharge the J-phase layer breaks up as shown in Fig. 1B, and the resulting irregular growth of the reaction product is a contributing factor in the excessive volume expansion (swelling) of the electrode beyond that accountable by the density differences between J-phase and Li_2S. As shown in Fig. 1C, the FeS particles have been consumed, and the next step of the over-all discharge reaction (namely, the formation of Li_2S and Fe) has begun.

Conclusion

An unusual compound with the formula $K_6LiFe_{24}S_{26}Cl$ has been identified as an intermediate product in the positive electrode reactions of Li-Al/LiCl-KCl/FeS cells. Characterization studies of this compound indicate that it is very similar to djerfisherite in crystal structure and chemical composition. Djerfisherite is a sulfide mineral (general formula $K_3(Na,Cu)(Fe,Ni)_{12}S_{14}$) found only in meteorites, such as the St. Marks, and previous attempts to synthesize this material have been unsuccessful. This work has demonstrated that a sulfide material essentially identical to djerfisherite can be prepared in large quantities for further studies.

Acknowledgments

The authors are indebted to Louis Fuchs for helpful discussions, to Myron Homa for the early x-ray powder diffraction analyses performed for this investigation, and to Kenneth Jensen for chemical analyses.

This work was performed under the auspices of the U.S. Energy Research and Development Administration.

Manuscript submitted April 7, 1977; revised manuscript received June 20, 1977.

Any discussion of this paper will appear in a Discussion Section to be published in the June 1978 JOURNAL. All discussions for the June 1978 Discussion Section should be submitted by Feb. 1, 1978.

Publication costs of this article were assisted by Argonne National Laboratory.

REFERENCES

1. L. Fuchs, *Science*, **153**, 166 (1966).
2. H. Shimotake and L. Bartholme, Private communication, Argonne National Laboratory.
3. A. E. Martin, Argonne National Laboratory Report ANL-75-46, p. 30 (1975).
4. F. C. Mrazek and J. E. Battles, Argonne National Laboratory Report ANL-75-1, p. 96 (1974).
5. B. S. Tani, To be published in *Am. Mineral.*
6. A. E. Gorsey, N. Grogler, and J. Ottemann, Paper presented at the 31st Annual Meeting of Meteoritical Society Smithsonian Astrophysics Observatory, Cambridge, Mass. (1968); *Chem. Erde.*, **30**, 77 (1971).
7. R. Elliott and T. Copper, Paper 39 presented at The Electrochemical Society Meeting, Toronto, Canada, May 11-16, 1975.

On the Electropolishing of Molybdenum

M. Zamin,* P. Mayer,[1] and M. K. Murthy

Ontario Research Foundation, Sheridan Park Research Community, Mississauga, Ontario, Canada L5K 1B3

There is relatively limited information on the electropolishing of molybdenum (1). Possibly the earliest use of an electrolytic polishing method for molybdenum is a reference in Coon's paper (2) to a laboratory report by Pierce where "the surface brightening of molybdenum was stated to be possible by using the molybdenum as the anode in an electrolytic bath of an aqueous solution of concentrated sulfuric acid." Most electropolishing solutions for molybdenum contain varying quantities of sulfuric acid (1-5). Sulfuric acid is an aggressive acid, and when molybdenum is made anodic in it, its effect on the metal is quite evident. Among the solutions that were considered for the electropolishing of molybdenum for this study are:

Solution No. 1 [Hopkins *et al.* (5)]: methanol, 175 ml; sulfuric acid, 25 ml; current density, 0.8-1.2 A/cm^2; temperature, 25°C max; time, 1 min.

Solution No. 2 [Coon (2)]: sulfuric acid, 35 ml; water, 140 ml; voltage, 12V; temperature, ~52°C (125°F); time, 25-35 sec.

Stainless steel is recommended as the cathode material, and it is mentioned that the blue film formed as a result of electropolishing can be removed by a 10 sec dip in concentrated ammonium hydroxide solution (2).

In evaluating any solution for the electropolishing of metals and alloys, the following points need to be considered: (*i*) the solution must produce a mirror finish; (*ii*) it must be operational under practical conditions of temperature, voltage, current density, and time; (*iii*) it must be stable over long periods of time; and (*iv*) it must be safe and pollution free. Most electropolishing solutions for molybdenum are safe to operate, and assuming that they produce a satisfactory surface finish, one is left to evaluate them on the basis of the other two requirements mentioned above. Solutions No. 1 and 2 require very short polishing times, and are, therefore, suggestive of the fact that metal removal rates are relatively high. As has already been pointed out (6), lower metal removal rates are preferable since they offer better control of the polishing process. Another practical consideration is the stability of the solution. Most solution compositions found in the literature for electropolishing molybdenum contain substantial volumes of methanol

* Electrochemical Society Active Member.
[1] Present address: Ontario Hydro Research Laboratory, 800 Kipling Avenue, Toronto, Ontario, Canada, M8Z 5S4.
Key words: electropolishing, molybdenum, phosphoric acid solution, Wagner's theory, metal removal rate.

(2-5). Such solutions may operate satisfactorily when they are "new" but would tend to deteriorate with time owing to methanol loss. It is felt, therefore, that the need exists for the development of other solutions which can overcome some, or perhaps all, of the discussed limitations.

A new solution has been developed at ORF for the electropolishing of molybdenum, the composition and operational details of which are presented here. The evaluation of all solutions has been performed on the basis of the four points discussed before. As an extension of the present work, the applicability of Wagner's theory (7) to the polishing process has also been investigated. For a detailed account of Wagner's theory the reader is referred to the original paper (7). However, the theoretical equations used are briefly explained below.

Consider a surface whose roughness can be described by a sine wave profile with a wavelength, a, and an amplitude, b. If an "ideal electropolishing process" is considered, then the metal ions are consumed immediately upon arrival to the outside of the hydrodynamic polishing layer of thickness, δ. For such a process the displacement, u, for a decrease of the amplitude from b_0 to b is given by

$$u = \frac{a}{2\pi} \ln \frac{b_0}{b} \qquad \text{if } b << a,\ a << \delta \qquad [1]$$

where b_0 and b are the amplitudes of the sine wave surface profile at times $t = 0$ and $t = t$, respectively. The correspondping loss of metal per unit area, $\Delta m/A$ is

$$\frac{\Delta m}{A} = u\rho = \frac{a\rho}{2\pi} \ln \frac{b_0}{b} \qquad [2]$$

where ρ is the density of the metal.

Experimental

Specimens were made from molybdenum of 99.9% purity which was in the form of rods, 0.3 cm diam and 5.5 cm in length. Specimen preparation, apparatus, and experimental procedure were similar to that reported elsewhere (6). The polishing cell consisted of a glass beaker 9 cm in diam and 7 cm deep with a flat-plate cathode of an immersed area of about 44 cm^2. The anode cathode distance was about 4 cm. The temperature of the solution was maintained within ± 3°C by heating or cooling in a constant temperature water bath. The surface profile was determined by the Talysurf 4.[2] For weight loss determinations, the specimens were weighed using a microbalance (Mettler, Gramatic Balance). Following polishing in solution No. 2, the blue film was stripped by alternate 10 sec dips in concentrated ammonium hydroxide and 1g/liter KOH solution. It was found that this method was more effective at stripping the film than the 10 sec dip in concentrated ammonium hydroxide solution, as recommended in the original formulation (2).

Potentiostatic polarization was performed on strips (area ~8.5 cm^2) at the electropolishing temperature, according to the procedure described elsewhere (8). Potentials were measured against a saturated calomel electrode (SCE) and the potential scan rate was 25 mV/min.

Results and Discussion

Development of new solution.—A new solution has been developed for the electropolishing of molybdenum whose composition and operating conditions are:

Solution No. 3 (ORF Formulation)	Presently used	Possible range
Orthophosphoric acid (85%)	100 ml	30-160 ml
Sulfuric acid (conc.)	20 ml	10-80 ml
Water	40 ml	10-40 ml
Molybdic anhydride[3]	0.25g	0-0.5g

[2] Manufactured by Rank Precision Industries Limited, Leicester, England.

[3] Molybdenum Trioxide, MoO_3, 99.7% purity. Fisher Scientific Company, Reagent Grade.

Operating conditions	Presently used	Possible range
Voltage	8V	6-40V
Current density	0.6-0.9 A/cm^2	0.6-4.0 A/cm^2
Temperature	70°C	40°-90°C
Cathode	Stainless steel	Stainless steel, graphite, lead, platinum.

The composition and conditions presently used perform satisfactorily, and a temperature of 70°C appears to be the optimum. Lower solution temperatures are not recommended, because they require higher voltages to produce the same current density owing to the decrease in the ionic mobility and, consequently, in the throwing power of the electrolyte. Possibly the best procedure for electropolishing in the above solution is to fix the voltage and let the current "take care of itself." In the search for the optimum polishing conditions, it was found that even voltages as high as 25V did not produce any burn marks on the specimen.

A freshly prepared solution has a milky appearance since only part of the molybdic anhydride dissolves in it. The remainder eventually settles to the bottom in an unstirred solution. Before commencing the electropolishing, the solution should be thoroughly stirred so as to suspend the anhydride throughout the solution. Mechanical stirring of the specimen, which further aids in keeping the anhydride suspended, is necessary during polishing in order to eliminate pitting. The suspension of the anhydride is important because the anhydride polarizes the anodic reaction [$Mo \rightarrow Mo^{6+} + 6e^-$, (9)] producing more uniform polishing, which is possibly an important factor behind the relatively low metal removal rate observed.

The effect of the amount of molybdic anhydride on the experimentally determined metal removed in solution No. 3 is shown in Fig. 1. Even a solution containing no anhydride produced a good polish on the specimen surface. However, as is evident from the values noted

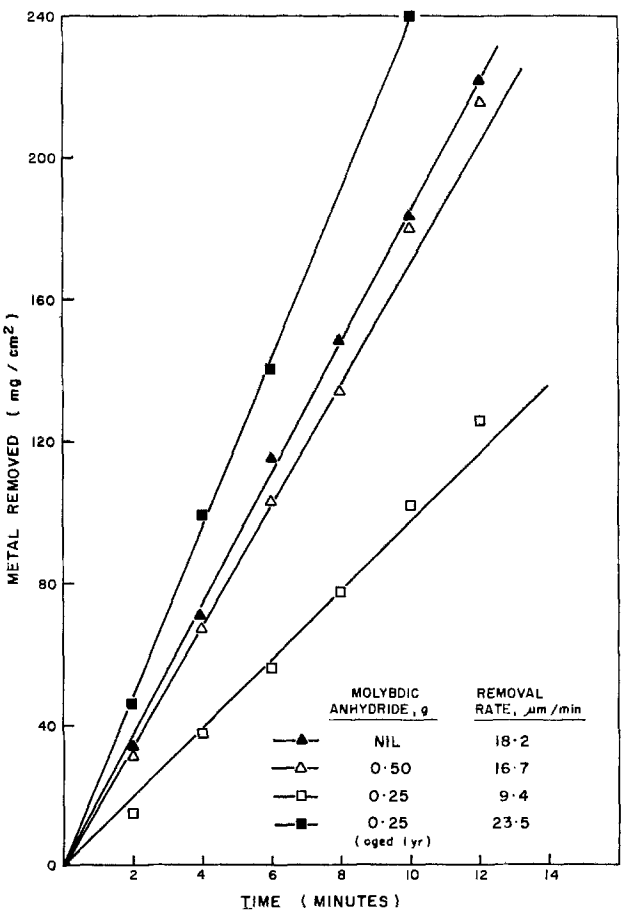


Fig. 1. Effect of molybdic anhydride on the experimental metal removed as a function of time for the new solution.

in Fig. 1, a solution containing 0.25g of the anhydride has the lowest metal removal rate. At present, no reason can be given for the experimental observations of Fig. 1.

Although austenitic stainless steel was used in this investigation for the cathode material owing to its ready availability, its choice is not recommended, because it may be attacked by the solution. Graphite, platinum, and chemical lead are good alternatives and work equally effectively.

Electropolishing results.—The values of a and b, the wavelength, and the amplitude as determined from the surface profile are given in Tables I-III for the three solutions investigated. As expected, with increasing time of electropolishing, the amplitude (b) decreases signifying smoothening, although the wavelength (a) does not change.

Solution No. 1 (H_2SO_4-methanol).—Molybdenum polished relatively easily in this solution, and no significant rise in temperature occurred as long as the area of the specimen in solution was small (~3 cm² in 300 ml). However, when a strip of molybdenum of an area ~11.0 cm² was polished, the temperature rose quickly to 50°C, resulting in etching of the specimen. In order to obtain good polishing, the solution was cooled in an ice bath to about 18°C. A voltage of 30V was required to yield a current density of about 1.0 A/cm², and to produce a satisfactory polish (Fig. 2 and 3) on the side of the specimen facing the cathode (the other side did not polish well, and was partly etched).

Solution No. 2 (H_2SO_4-water).—It was almost impossible to polish molybdenum to a satisfactory finish in this solution. Even short immersion times of 15 sec produced a thick blue film which seemed to prevent further metal dissolution. Although the recommended voltage for polishing is 12V, it was found necessary to decrease this to 6V in order to have some control over the process, and even then the metal dissolved very unevenly. Figure 2 shows two instances where the polishing was performed at 6 and 12V under the conditions specified. The results are far from satisfactory. In fact, when the strip was polished at 12V and 52°C, the current density increased abruptly, overheating the contact clips and igniting the hydrogen liberated at the cathode.

Table I. Electropolishing of molybdenum in H_2SO_4-methanol solution

Time (min)	a (cm)	b (cm)	$\ln \frac{b_o}{b}$	i (A/cm²)	$\Delta m/A$ (mg/cm²)
0	0.011938	0.000918	—	—	—
2.5	0.011938	0.000262	1.25	0.8	24.3
5.0	0.011938	0.000076	2.49	0.8	48.3

Table II. Electropolishing of molybdenum in H_2SO_4-water solution

Time (min)	a (cm)	b (cm)	$\ln \frac{b_o}{b}$	i (A/cm²)	$\Delta m/A$ (mg/cm²)
0	0.0222	0.002223	—	—	—
0.25	0.0222	0.001880	0.167	5.18	6.02
0.75	0.0222	0.001143	0.665	4.44	23.98
1.25	0.0222	0.001016	0.783	4.07	28.23
1.75	0.0222	0.000953	0.847	3.52	30.54
2.50	0.0222	0.000508	1.476	3.52	53.22
3.00	0.0222	0.000381	1.764	3.52	63.61

Table III. Electropolishing of molybdenum in the new solution

Time (min)	a (cm)	b (cm)	$\ln \frac{b_o}{b}$	i (A/cm²)	$\Delta m/A$ (mg/cm²)
0	0.0222	0.002159	—	—	—
2.5	0.0222	0.001778	0.194	0.91	7.0
3.5	0.0222	0.001397	0.435	0.83	15.71
4.5	0.0222	0.001016	0.754	0.70	27.20
6.5	0.0222	0.000764	1.039	0.86	37.49
9.0	0.0222	0.000508	1.447	0.76	52.22
11.0	0.0222	0.000356	1.802	0.80	65.03

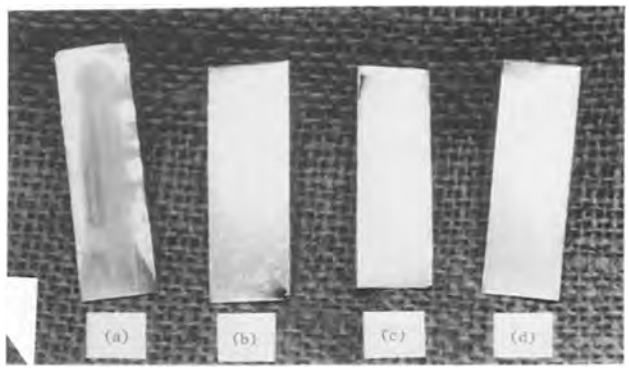


Fig. 2. Strips of molybdenum electropolished in various solutions. (a) H_2SO_4-water solution, 6V, 2 min; (b) H_2SO_4-water solution, 12V, 15 sec; (c) H_2SO_4-methanol solution, 30V, 1.0 A/cm², 2 min; (d) new solution, 8V, 0.64 A/cm², 5 min.



Fig. 3. Photograph showing the reflectivity and luster of electropolished molybdenum strips. Left strip, H_2SO_4-methanol solution; right strip, new solution. The strips are the ones shown in Fig. 2(c) and (d).

Solution No. 3 (new solution).—Extremely satisfactory results were obtained in this solution. No blue film was found on the specimen as a result of electropolishing. Figure 2 shows a photograph of a molybdenum strip in comparison with those polished in the other solutions. Figure 3 is presented to specifically demonstrate the superior surface finish and luster produced by the new solution as compared to solution No. 2 which is the best result obtained from the other two solutions. In contrast to solution No. 2, the new solution produced a brilliant surface finish on both sides of the strip.

The amount of metal removed as a function of time as estimated from Eq. [2] using the results of Tables I-III is presented in Fig. 4(a). Similar data determined experimentally are presented in Fig. 4(b). The metal removal rates as determined from the slope of the lines in Fig. 4 are given in Table IV for the three solutions. It can be seen that the metal removal rate is the highest for the H_2SO_4-water solution and lowest for the new solution, a result which is consistent with visual observations of solution aggressiveness during the electropolishing process. The desirability and advantage of low metal removal rates has already been pointed out (6). It is interesting to note that the experimentally determined metal removal rate in the three solutions is higher than that calculated from Wagner's theory. In principle, therefore, this observation implies that Wagner's theory is not valid for the electropolishing of molybdenum in the three solutions. A possible reason for this inference may be obtained from the assumptions in the mathematical analysis of the theory. As has been pointed out by Wagner (7), if the wavelength, a, is not much smaller than the thickness of the boundary layer, the decrease in the amplitude will be less than calculated from Eq. [1]. Consequently, the amount of metal removed as estimated

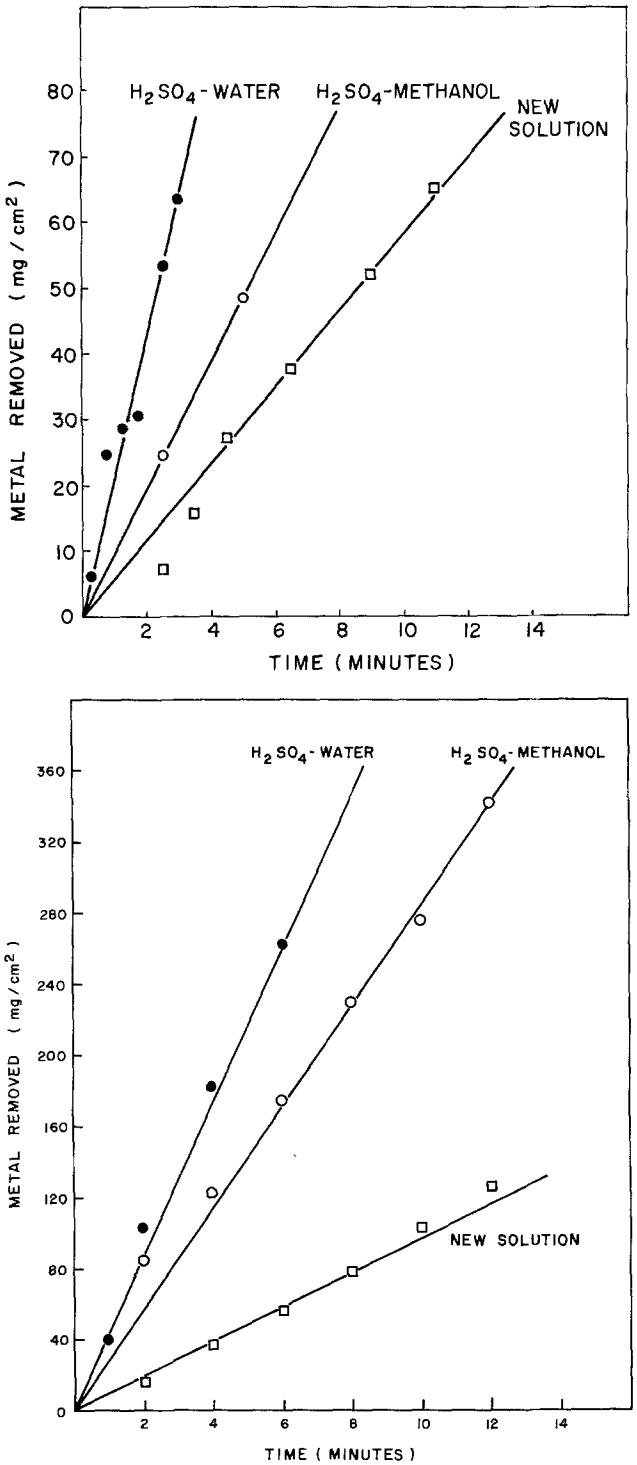


Fig. 4. Metal removed as a function of time for the electropolishing of molybdenum in various solutions. (a) Theoretical from Wagner's theory; (b) experimental.

from Eq. [2] will also be lower. Although the condition $b<<a$ can be verified, it is difficult to determine the validity of the assumption $a<<\delta$. It may be pointed out that the inapplicability of Wagner's theory for the present systems is the result of a mathematical limitation, and is not to be taken as evidence against the theory per se or the "acceptor hypothesis." Data on the electropolishing of tantalum show (10) that Wagner's acceptor hypothesis (7) is indeed valid, and that the results cannot be interpreted on the basis of Nicholas and Tegart's analysis (11) which does not make any assumptions about the mechanism of the polishing process.

Table IV. Rate of metal removal for molybdenum in various electropolishing solutions

Solution	Rate of metal removal, μm/min	
	Theoretical	Experimental
H_2SO_4-water	21.0	42.3
H_2SO_4-methanol	9.5	27.6
New solution	5.7	9.4

The potentiostatic polarization curves limited by the capacity of the potentiostat are given in Fig. 5. The temperature of the solutions were 18°, 52° and 70°C for solutions No. 1, 2, and 3, respectively. It can be seen that in comparison to the other two solutions, solution No. 1 requires much higher voltages to produce the same anodic current density which is consistent with observations during electropolishing. The corrosion potential (E_{corr} in Fig. 5) is the noblest for the new solution and the most active for the H_2SO_4-water solution, which is again an indication of the aggressiveness of the solutions. Vigorous gas evolution (hydrogen) was observed at the cathode in solution No. 2 at potentials beyond +200 mV (SCE); it was almost negligible in solution No. 1 and moderate in solution No. 3. After removal from solution No. 2, the surface of the molybdenum was found to be covered with a black film which was quite adherent to the metal. It did not dissolve in the solution, and could be partially removed by immersing in 1 g/liter KOH solution and scrubbing with cotton. For the new solution, the film was flaky, dissolving slowly in the solution and very readily upon immersion in the KOH solution. No film was observed on the molybdenum in solution No. 1 up to a potential of +1000 mV (SCE).

Although different views exist on the mechanism of electropolishing (7, 12-14) it is generally agreed that a viscous film (or salt film) exists next to the anode (7, 12-16) through which mass transport is diffusion controlled (7, 12-17). As has been pointed out by Hoar (18), the film should be capable of dissolving rapidly at its outer surface as fast as it forms at the metal/film interface. The importance of the thickness of this film is therefore evident. In light of this view, when the potentiostatic polarization observations are combined with the electropolishing results, it is realized that the solution which produces the best surface finish also yields a film which is readily soluble (solution No. 3) in direct comparison to the unsatisfactory surface finish obtained from solution No. 2 where the film is insoluble. Although the composition and structure of the film will possibly change with potential, there seems to be a direct correlation between the film formed at

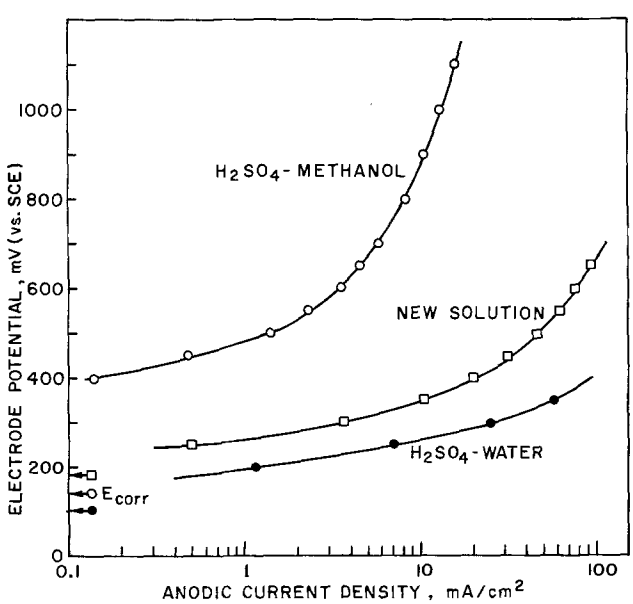


Fig. 5. Potentiostatic polarization curves for molybdenum in various solutions used for electropolishing.

lower voltages during potentiostatic polarization and the one that exists during electropolishing at relatively higher voltages.

It was mentioned earlier that solutions containing methanol would not polish well after storage, owing to methanol loss. In order to determine the validity of this statement, the three solutions were stored in closed (not air-tight) polyethylene bottles for a period of one year. After this period a qualitative assessment of their polishing ability was performed. It was found that solutions No. 1 and 2 had reduced to 1/4-1/5 their original volume, and produced unsatisfactory polishing (unpolished areas, pitting, formation of a thick flaky blue film, vigorous gas evolution, and overheating of the contact clip were encountered). On the other hand, solution No. 3 had decreased only slightly in volume, and polished readily under its normal conditions. The metal removed in this solution is shown in Fig. 1. It thus appears that aging the solution has a significant effect on the metal removal rate. However, the reason for this observation does not seem to be clear.

Acknowledgments

This work was performed under a grant to the Ontario Research Foundation by the Ministry of Industry and Tourism, Government of Ontario, Canada.

Manuscript submitted June 4, 1976; revised manuscript received June 19, 1977.

Any discussion of this paper will appear in a Discussion Section to be published in the June 1978 JOURNAL. All discussions for the June 1978 Discussion Section should be submitted by Feb. 1, 1978.

Publication costs of this article were assisted by Ontario Research Foundation.

REFERENCES

1. C. J. Smithells, "Metals Reference Book," Vol. 1, 4th ed., p. 325, Butterworths, London (1967).
2. W. C. Coons, *Trans. ASME*, **41**, 1415 (1949).
3. N. K. Chen and R. Maddin, *Trans. Amer. Inst. Mining Met. Eng.*, **191**, 937 (1951).
4. R. F. Cortes, *Met. Prog.*, **80**, 97 (1961).
5. G. L. Hopkins, J. E. Jones, A. R. Moss, and D. O. Pickman, *J. Inst. Met.*, **82**, 361 (1953).
6. M. Zamin, P. Mayer, and M. K. Murthy, *This Journal*, **123**, 1377 (1976).
7. C. Wagner, *ibid.*, **101**, 225 (1954).
8. M. Zamin and M. B. Ives, *ibid.*, **121**, 1141 (1974).
9. M. Pourbaix, "Atlas of Electrochemical Equilibria in Aqueous Solutions," p. 330, Pergamon Press Ltd., Oxford, England (1966).
10. M. Zamin, Unpublished work.
11. J. F. Nicholas and W. J. M. Tegart, *This Journal*, **102**, 93C (1955).
12. J. Edwards, *J. Electrodepositors Tech. Soc.*, **28**, 133 (1951).
13. W. C. Elmore, *J. Appl. Phys.*, **10**, 724 (1939).
14. K. Kojima and C. W. Tobias, *This Journal*, **120**, 1026 (1973).
15. H. F. Walton, *ibid.*, **97**, 219 (1950).
16. P. A. Jacquet, *Met. Finish.*, **47**, 48 (1949).
17. S. I. Krichmar, A. Y. Pronskaya, and K. F. Afendik, *Sov. Electrochem. (Engl. Transl.)*, **2**, 896 (1966).
18. T. P. Hoar, in "The Encyclopedia of Electrochemistry," C. A. Hampel, Editor, p. 477, Reinhold Publishing Corp., New York (1964).

JOURNAL OF THE ELECTROCHEMICAL SOCIETY

SOLID-STATE SCIENCE
—AND TECHNOLOGY

OCTOBER
1977

High Oxide Ion Conduction in Sintered Oxide of the System Bi_2O_3-M_2O_5

Takehiko Takahashi,* Hiroyasu Iwahara, and Takao Esaka

Department of Applied Chemistry, Faculty of Engineering, Nagoya University, Nagoya 464, Japan

ABSTRACT

The electrical conduction in the sintered oxides of the systems Bi_2O_3-M_2O_5 (M = V, Nb, or Ta) has been investigated by measuring the conductivity and the ion transference number. The face-centered cubic (fcc) phase in these systems was found to show a high oxide ion conduction, and this highly conductive phase could be stabilized by adding a certain amount of M_2O_5 over a wide range of temperatures. The oxide ion conductivities of this phase decreased with increasing content of M_2O_5, and a maximum value was obtained at the lower limit of the fcc solid-solution formation range. Of these systems, Nb-containing specimens had the highest conductivity over a wide range of compositions and temperatures. $(Bi_2O_3)_{0.85}$ $(Nb_2O_5)_{0.15}$ was the best conductor, with conductivities of 1.9×10^{-1} Ω^{-1} cm^{-1} at 700°C and 1.1×10^{-2} Ω^{-1} cm^{-1} at 500°C; these values were more than ten times higher than the conventional oxide ion conductors such as the stabilized zirconias. X-ray diffraction and density studies of fcc phase in the Bi_2O_3-Nb_2O_5 system have confirmed that there is an appreciable amount of oxide ion vacancies which is prescribed by the content of pentavalent oxide. The relation of activation energy for conduction to the composition in this phase is discussed by comparing that of the trivalent oxide-doped system Bi_2O_3-M_2O_3.

The high temperature phase of bismuth sesquioxide (δ-phase) is known to have a defect fluorite-type structure including a large amount of vacant sites in the oxide ion sublattice (1, 2). This material exhibits extremely high oxide ion conduction accompanied by little electronic conduction under ordinary atmosphere (3-6); the conduction mechanism is probably analogous to that of the stabilized zirconias. This phase is, however, stable only in the narrow temperature range from 730° to 825°C (mp) (1), and the conductivity falls remarkably below 730°C where the monoclinic structure (α-phase) is a stable phase (5, 7) and the conduction is electronic (p-type). Furthermore, this material is apt to collapse because of the large volume change due to the phase transition (8), and, therefore, it is not suitable for practical use as a solid electrolyte.

However, the present authors have found that the high oxide ion conductivity can be held far below 730°C by adding a certain amount of WO_3 (6), Y_2O_3 (9), or Gd_2O_3 (10) to the bismuth sesquioxide. The highly conductive phases in these systems were face-centered cubic (fcc) phases which were closely related to that of the high temperature form of pure bismuth sesquioxide (δ-Bi_2O_3) in their crystal structures. The conductivities of these phases were much higher than those of the conventional stabilized zirconias at corresponding temperatures. Outwardly, this means that the δ-form can be stabilized even at lower temperature than 730°C by suitable additives.

According to Roth *et al.* (11), a stable fcc phase exists in the system Bi_2O_3-Nb_2O_5 at temperatures lower than 730°C. The authors also suggested the existence of the analogous phase in Bi_2O_3-V_2O_5 (12), although the detailed phase diagram was not proposed. These systems may be expected to have high oxide ion conduction, like the above described materials. Since tantalum is very similar to niobium in physical and chemical properties, the system Bi_2O_3-Ta_2O_5 may also possess a highly conductive phase due to oxide ions.

Therefore, we studied both the electrical conduction in the binary oxide system Bi_2O_3-M_2O_5 in the sintered state, where M is the transition element of VB group in the Periodic Table, that is, V, Nb, or Ta, and the conduction properties in relation to the kind of M-type elements and their composition. The defect structure and the activation energy for conduction were also studied and compared to those for other oxide ion conductors. As attention has been mainly centered on the ionic conduction in these systems, the complex phase relationships in relatively low and high contents of M_2O_5 have been roughly examined.

Experimental

Preparation of the sintered oxides.—The specimens were prepared by the solid-state reaction between bismuth sesquioxide and vanadium, niobium, or tantalum pentoxide. The bismuth sesquioxide was obtained by thermal decomposition of bismuth nitrate (JIS special grade) at 750°C for 2 hr. The purities of the pentoxides were higher than 99.9%. The powders were mixed and calcined at 800° ~ 900°C for 10 hr in air, then they were finely ground and pressed hydrostatically into the shapes of rods ($4 \sim 6 \times 8 \sim 12$ mm) or disks ($13 \times 2 \sim 3$ mm) under 2700 kg/cm², and sintered in air for 10 hr. The temperatures for sinter-

* Electrochemical Society Active Member.
Key words: solid electrolyte, bismuth oxide, oxide ion conduction.

Table I. The temperatures for sintering

M	x in $(Bi_2O_3)_{1-x}(M_2O_5)_x$	Temperature (°C)
V	0.05 ~ 0.40	800
	0.05 ~ 0.10	850
Nb	0.12 ~ 0.22	900
	0.25 ~ 0.30	1000
Ta	0.03 ~ 0.10	850
	0.14 ~ 0.33	900

ing shown in Table I were selected for each sample to obtain the best sintered state.

Each crystal phase was identified by x-ray diffraction at room temperature using CuKα radiation with a nickel filter. Both quenched and annealed samples were used for this experiment to examine the stability of each phase. The annealing procedure was as follows: The oxides were cooled from sintering temperature to 500°C in several hours and were kept at that temperature for at least 15 hr, after which they were cooled slowly to room temperature. In the quenching procedure, the samples were moved directly from the 800°C furnace to the room, and cooled rapidly by an air blower. Lattice parameters of the fcc phase were measured using sodium chloride as an internal standard of the x-ray diffraction. Densities of the powdered specimens were determined by a standard pycnometric method using n-butanol at 25°C.

Measurement of ionic conduction.—Ionic conduction in the specimens was examined by measuring the electrical conductivity and the emf of an oxygen concentration cell. The conductivity was measured by an a-c bridge equipped with a capacity compensator. The column-shaped specimens were used in this case, and platinum paste was adopted as the electrode material. The frequency for the a-c bridge was 10 kHz, since the dependence of the conductivity on frequency was negligibly small in the range of 2 ~ 20 kHz. The measurement was carried out in air as well as in the low partial pressure of oxygen atmosphere (10^{-1} ~ 10^{-5} atm). In the latter case, the mixed gases of air and argon in various ratios were applied.

The following concentration cell was constructed using the disk-shaped specimen as the electrolyte

$$O_2(p_{O_2,a}), Pt \mid \text{specimen disk} \mid Pt, O_2(p_{O_2,c}) \quad [1]$$

If the conduction in the specimen is purely ionic, the emf of the cell E_0 is given by

$$E_0 = \frac{RT}{4F} \ln \frac{p_{O_2,c}}{p_{O_2,a}} \quad [2]$$

where R, T, and $\mathbf{F}$ have their usual meaning, and $p_{O_2,a}$ and $p_{O_2,c}$ are oxygen partial pressures at anode and cathode, respectively.

In the mixed conductor, in which the conduction is partially ionic and partially electronic, the emf is lowered from E_0 to some extent because of the discharge of the cell due to the electronic conduction in it. In this case, the ratio of the ionic conductivity to the total value $\sigma = \sigma_i + \sigma_e$ (where σ_e is the electronic conductivity), that is, the ion transference number, t_i, can be determined as a ratio of the measured emf, E, to the theoretical value, E_0 (13)

$$t_i = \frac{\sigma_i}{\sigma_i + \sigma_e} = \frac{E}{E_0} \quad [3]$$

when the reversibility of the electrode reaction is good.

The construction of the cell in the present experiment was the same as that previously reported (5, 14). Pure oxygen at 1 atm was used as cathode gas. Air free from H_2O and CO_2 was usually adopted as anode gas. The reversibility of the electrode was examined by discharging the concentration cell through an outer circuit.

Table II. The phases observed in the annealed and the quenched specimens

M	x in $(Bi_2O_3)_{1-x}(M_2O_5)_x$	Phases observed* Annealed sample	Quenched sample
V	0.05 ~ 0.09	fcc + bcc	fcc
	0.10 ~ 0.20	fcc + ?	?
Nb	0.05 ~ 0.125	fcc + mon	fcc
	0.15 ~ 0.25	fcc	fcc
	0.30	fcc + tetr	fcc + tetr
Ta	0.03 ~ 0.075	tetr	fcc
	0.10 ~ 0.16	fcc + tetr	fcc
	0.18 ~ 0.25	fcc	fcc
	0.33	fcc + ?	fcc + ?

* fcc = face-centered cubic phase corresponded to δ phase of Bi_2O_3; bcc = body-centered cubic phase; tetr = tetragonal phase; ? = unidentified.

Results

Specimens prepared.—The specimens thus prepared were well sintered except pure Bi_2O_3, and had no open pores to allow the penetration of gas. The porosities which were calculated as a ratio of the apparent density of the sinters to the powder density were within 5% in most cases. The color of these materials changed from reddish brown to pale orange as the content of M_2O_5 increased.

The fcc single phase having the x-ray diffraction patterns analogous to that of pure δ-Bi_2O_3 was observed in the annealed samples of the systems Bi_2O_3-Nb_2O_5 and Bi_2O_3-Ta_2O_5 in the composition ranges of 15 ~ 25 mole percent (m/o) Nb_2O_5 and 18 ~ 25 m/o Ta_2O_5, respectively. This phase spread to lower content of M_2O_5 on quenching the sample from 800°C to room temperature in a few minutes. Although the annealed samples of the system Bi_2O_3-V_2O_5 also had the fcc phase accompanied by some other phase, a single phase could not be isolated, suggesting that the fcc phase had a very narrow composition range, or that some metastable phases were mixed under this condition. The composition and the phases observed by x-ray diffraction of the annealed and the quenched samples are summarized in Table II. Figure 1 shows the relation between the composition and the lattice parameter of the fcc phase in the quenched Bi_2O_3-Nb_2O_5 system. It obeys Vegard's rule, and the values are in good agreement with those of Roth's work (11).

Conductivity.—Typical examples of Arrhenius plots of the system Bi_2O_3-M_2O_5 measured in air are represented in Fig. 2(a) and (b). As previously reported and shown in Fig. 2(a) with the dotted line, the conductivity of pure Bi_2O_3 is relatively low below 730°C, and an abrupt increase in conductivity appears at this

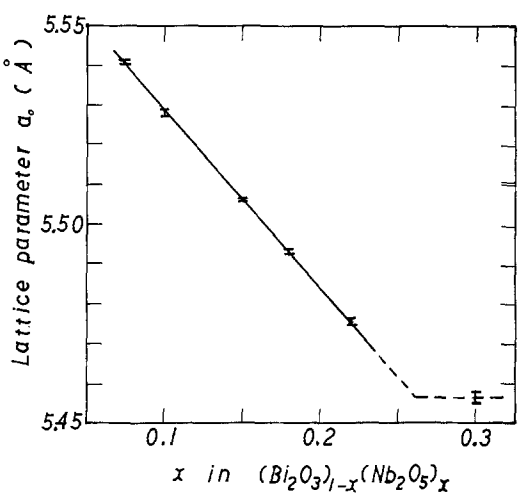


Fig. 1. Lattice parameters of fcc phase in Bi_2O_3-Nb_2O_5 system

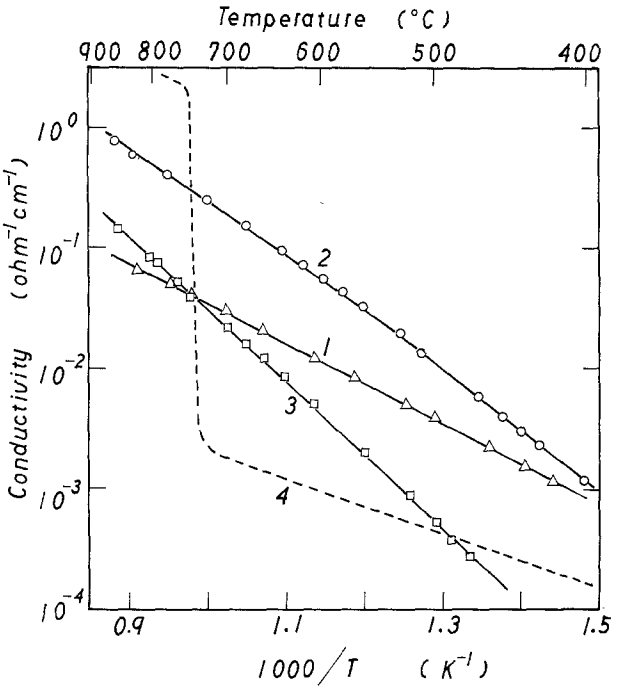


Fig. 2(a). Arrhenius plots of conductivity of sintered oxides of the system Bi_2O_3-M_2O_5. Curve 1, $(Bi_2O_3)_{0.875}(V_2O_5)_{0.125}$; Curve 2, $(Bi_2O_3)_{0.85}(Nb_2O_5)_{0.15}$; Curve 3, $(Bi_2O_3)_{0.80}(Ta_2O_5)_{0.20}$; Curve 4, pure Bi_2O_3.

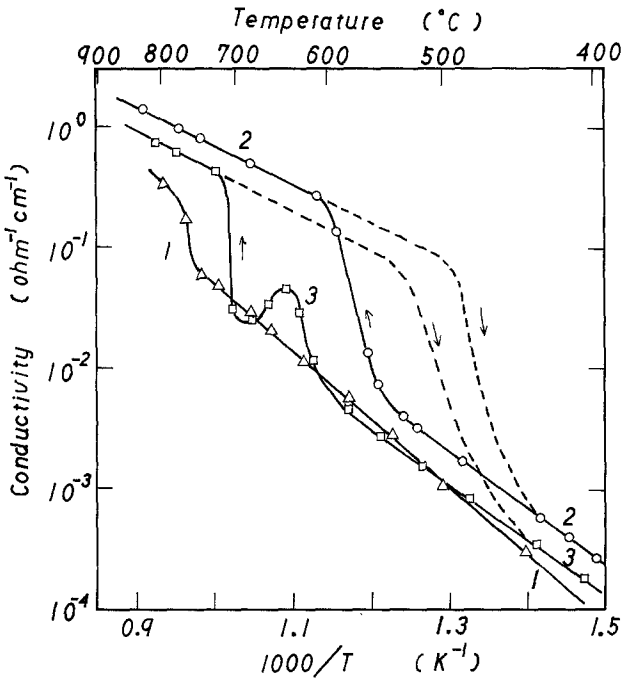


Fig. 2(b). Arrhenius plots of conductivity of sintered oxides of the system Bi_2O_3-M_2O_5. Curve 1, $(Bi_2O_3)_{0.91}(V_2O_5)_{0.09}$; Curve 2, $(Bi_2O_3)_{0.925}(Nb_2O_5)_{0.075}$; Curve 3, $(Bi_2O_3)_{0.90}(Ta_2O_5)_{0.10}$.

temperature corresponding to the transformation temperature from monoclinic (α-phase) to fcc phase (δ-phase). However, as shown in Fig. 2(a) with solid lines, the sintered specimens containing more than a certain amount of M_2O_5 showed no jump in conductivity over the whole range of temperature examined. The conductivities of these oxides below 700°C were, in general, higher than those of pure Bi_2O_3, while the values in the high temperature region were lower than those of pure Bi_2O_3. The specimens containing a relatively small amount of M_2O_5 had an abrupt increase in conductivity, as shown in Fig. 2(b), and these exhibited thermal hysteresis in the Arrhenius plot, as indicated by the dotted lines in the figure. More detailed data of the Arrhenius plots and the composition are shown in Fig. 3 for the Bi_2O_3-Nb_2O_5 system.

The minimum contents which showed no jump in conductivity were 12.5 m/o for V_2O_5, 15 m/o for Nb_2O_5, and 18 m/o for Ta_2O_5; the greater the atomic number of M, the higher the critical concentration in which the jump in conductivity was not observed. These critical values correspond with the lower limit of the fcc solid solution composition ranges for Nb_2O_5 and Ta_2O_5. These conductivity behaviors are same as those of the systems Bi_2O_3-WO_3 (6), Bi_2O_3-Y_2O_3 (9), and Bi_2O_3-Gd_2O_3 (10).

Figure 4 shows the isothermal conductivity plots *vs.* the content of M_2O_5 at 750° and 500°C. These temperatures are above and below the temperature of jump in conductivity, respectively. In high temperature range where the fcc single phase is stable, the

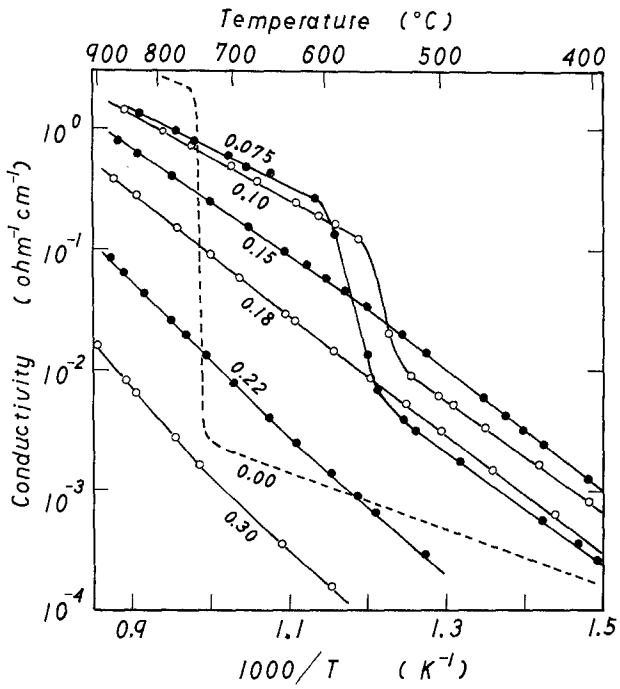


Fig. 3. Arrhenius plots of conductivity of the sintered oxides $(Bi_2O_3)_{1-x}(Nb_2O_5)_x$. (The figures in the graph indicate the values of x.)

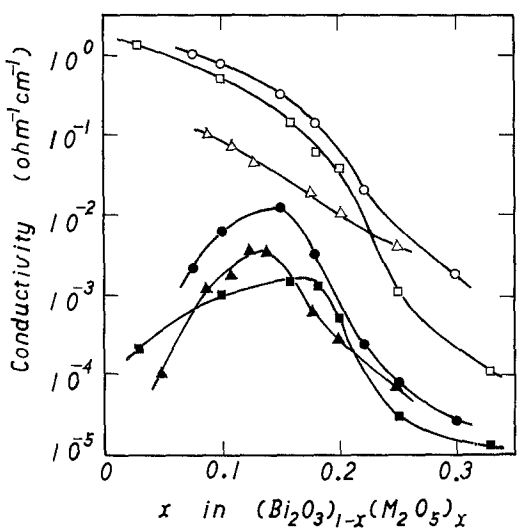


Fig. 4. Isothermal conductivities of $(Bi_2O_3)_{1-x}(M_2O_5)_x$. At 500°C: ▲, M = V; ●, M = Nb; ■, M = Ta. At 750°C: △, M = V; ○, M = Nb; □, M = Ta.

conductivities decrease monotonically with increasing content of M_2O_5. In the low temperature region where two phases coexist in the low content of pentavalent oxides, the conductivities have a maximum value at 14 ~ 18 m/o M_2O_5. These compositions correspond to the lower limit of the fcc solid solution formation range for the Bi_2O_3-Nb_2O_5 and Bi_2O_3-Ta_2O_5 systems. For the latter system, however, the maximum is relatively flat in the Ta_2O_5-poor side (fcc + tetragonal mixed phases), suggesting that the tetragonal phase is also highly conductive. The conductivity-composition curves for the Bi_2O_3-V_2O_5 system in the low temperature range were also similar to the above two systems, although the fcc phase was not recognized as a single phase in this system.

As to the conductivity value, the Nb_2O_5-containing sample was the highest among the Bi_2O_3-M_2O_5 specimens over the whole range of temperatures and compositions examined. An abnormal conductivity behavior was observed in the low content range of Ta_2O_5, as shown in Fig. 2(b). This phenomenon was reproducible. High temperature x-ray diffraction and DTA studies on these substances showed hysteresis in the phase transition as follows: During heating, they had tetragonal phases up to 580°C and transformed to monoclinic at this temperature, and then, changed to fcc above 700°C; on cooling, however, they transformed directly from cubic to tetragonal at about 500°C without changing to monoclinic. These results were in accordance with the conductivity behavior.

Conduction properties.—Table III lists the E/E_0 values of the oxygen concentration cell for representative specimens under the condition of $p_{O_2,a} = 0.21$ and $p_{O_2,c} = 1.0$ atm. As previously reported, the emf of the cell using pure Bi_2O_3 could not be detected up to 730°C, where it appeared suddenly and increased rapidly to the theoretical value as the temperature was raised.

In contrast, the specimens containing a certain amount of M_2O_5 showed the emf even in the temperature range below 700°C, indicating the existence of ionic conduction. In the specimens in which the fcc single phase was stable, E/E_0 values were greater than 0.9 in the temperature range examined. This means that the conduction in this phase is essentially ionic. In the sample which showed the jump in conductivity, the conduction was also essentially ionic even in the low temperature range, suggesting that the electronic conduction in other phases was not so remarkable.

Considerably high current could be drawn out from these concentration cells, as shown in Fig. 5. The cells were stable and reproducible even after they had been short circuited for a long time. These behaviors are the same as in the case of Y_2O_3- or WO_3-doped Bi_2O_3 and indicate that the conductive ions should be oxide ions. The highest oxide ion conductor among the sintered oxides of the system Bi_2O_3-M_2O_5 was $(Bi_2O_3)_{0.85}(Nb_2O_5)_{0.15}$. The oxide ion conductivity of this material was 1.9×10^{-1} Ω^{-1} cm^{-1} at 700°C and 1.1×10^{-2} Ω^{-1} cm^{-1} at 500°C, respectively, which is the same order of magnitude as that of $(Bi_2O_3)_{0.75}(Y_2O_3)_{0.25}$ previously reported (9), and is more than one order

Table III. Ratios of the measured emf E to the theoretical value E_0 of the following cell

O_2, Pt | $(Bi_2O_3)_{1-x}(M_2O_5)_x$ | Pt, O_2
(0.21 atm) (1.0 atm)

$(Bi_2O_3)_{1-x}(M_2O_5)_x$		E/E_0		
M	x	600°C	700°C	800°C
V	0.09	0.96	0.96	0.96
	0.125	0.97	0.98	0.98
Nb	0.05	0.99	0.98	0.98
	0.15	0.98	1.00	1.00
Ta	0.10	0.91	0.90	1.00
	0.20	0.93	0.91	0.94
	Bi_2O_3	0.00	0.00	1.00

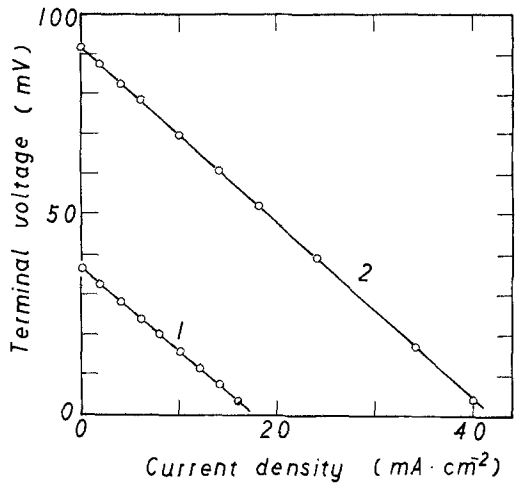


Fig. 5. The performance of the following concentration cell at 800°C: $O_2(p_{O_2,a})$, Pt | $(Bi_2O_3)_{0.85}(Nb_2O_5)_{0.15}$ | Pt, O_2 (1 atm). Curve 1, $p_{O_2,a} = 2.1 \times 10^{-1}$ atm; Curve 2, $p_{O_2,a} = 1.6 \times 10^{-2}$ atm.

of magnitude higher than the conventional oxide ion conductors such as the stabilized zirconias.

Determination of oxide ion transference numbers by various methods.—In Table III, the values E/E_0 for the fcc single phase in the Bi_2O_3-Nb_2O_5 system were almost unity within experimental error, whereas these values in the Bi_2O_3-Ta_2O_5 system deviated from unity. This deviation, however, does not always correspond directly to the ratio of the electronic contribution since E/E_0 shows somewhat lower values than true transference number of ions if the electrodes of the cell are easily polarizable. In order to avoid this polarization effect, the following method (15, 16) was adopted.

If the theoretical emf E_0 is applied to the cell (1) from the outer circuit in charging polarity, no ionic current passes through the specimen disk, and the observed current i_e is to be ascribed to electrons. In this condition, the electronic conductivity σ_e of the specimen is obtained from the electronic current and applied voltage as $\sigma_e = \dfrac{|i_e|}{E_0}$. Then, the transference number of ions can be determined as

$$t_i = \frac{\sigma_i}{\sigma_i + \sigma_e} = 1 - \frac{|i_e|}{E_0\sigma} \qquad [4]$$

where σ is the total conductivity of the disk sample measured with an a-c bridge. As represented in Table IV, the transference numbers thus obtained were almost the same as those from E/E_0, indicating that the polarization effect was fairly small in these cases. As a result, it can be concluded that the fcc phase in the Bi_2O_3-Ta_2O_5 system has some electronic conduction with predominant ionic conduction, while that in the Bi_2O_3-Nb_2O_5 system has little electronic conduction.

These results could be supported by the dependence of total conductivity on oxygen partial pressure p_{O_2} of the surrounding atmosphere. Figure 6 shows the example of the pressure dependence of conductivity.

Table IV. Transference numbers of oxide ions determined by different methods

Specimens	Temperature (°C)	E/E_0	$1 - \dfrac{\lvert i_e \rvert}{E_0\sigma}$	$\dfrac{\sigma_i}{\sigma(p_{O_2})}$
$(Bi_2O_3)_{0.85}(Nb_2O_5)_{0.15}$	600	0.98	0.99	—
	700	1.00	1.00	—
	800	1.00	1.00	1.00
$(Bi_2O_3)_{0.80}(Ta_2O_5)_{0.20}$	700	0.91	0.92	0.90 ~ 0.93
	800	0.94	0.93	0.91 ~ 0.96

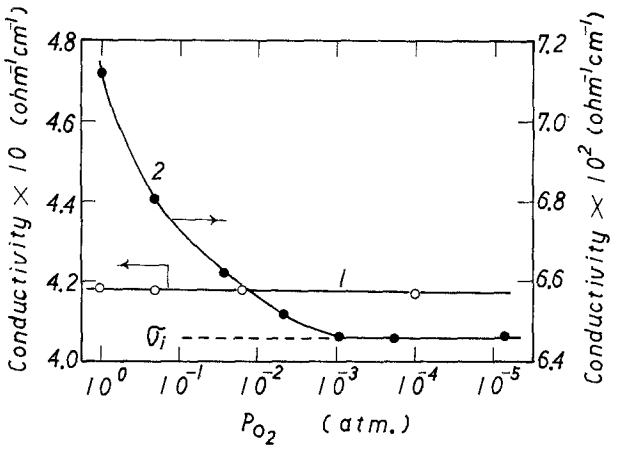


Fig. 6. Dependence of the conductivity on the oxygen partial pressure at 800°C. Curve 1, $(Bi_2O_3)_{0.85}(Nb_2O_5)_{0.15}$; Curve 2, $(Bi_2O_3)_{0.80}(Ta_2O_5)_{0.20}$.

The conductivities of $(Bi_2O_3)_{0.8}(Ta_2O_5)_{0.2}$ increased with the increase in p_{O_2} subsequent to the pressure-independent region below $p_{O_2} = 10^{-3}$ atm, while the conductivities of $(Bi_2O_3)_{0.85}(Nb_2O_5)_{0.15}$ were not dependent on the p_{O_2} over the whole range of pressure examined. This means that the conduction in the former oxide is partly electronic (p-type) due to the electron hole at a relatively high partial pressure of oxygen, whereas the contribution of electronic conduction in the latter may be negligibly small. If the assumption that the electronic conductivity is pressure dependent and the ionic conductivity is pressure independent [as in the case of many oxide ion conductors having a large number of oxide ion vacancies (17)] can be applied in this case, the transference number of oxide ion t_i at any p_{O_2} is given by

$$t_i = \frac{\sigma_i}{\sigma(p_{O_2})} \qquad [5]$$

where $\sigma(p_{O_2})$ is the total conductivity at p_{O_2} and σ_i is the pressure-independent part of the conductivity. The values of t_i obtained at $p_{O_2} = 1.0$ and 0.21 atm are listed in the last column of Table IV. The values are again in good agreement with those of the previous two methods if it is considered that the previous ones are the result obtained in an asymmetrical atmosphere ($p_{O_2,a} = 0.21$ and $p_{O_2,c} = 1.0$ atm).

Identification of the presence of oxide ion vacancies.—High oxide ion conduction in the fcc phase of these materials is considered to relate to the presence of the oxide ion vacancies as in the case of δ-Bi_2O_3 and other Bi_2O_3-based electrolytes reported previously. In pure δ-Bi_2O_3, which has the fluorite-type structure, two of the eight lattice sites for the oxide ion per unit cell are, on the average, vacant, since the formula of a perfect fluorite-type oxide is represented as A_4O_8 (A is a cation) per unit cell. When the pentavalent cations are partially substituted for trivalent Bi^{3+} keeping the original fcc lattice, the main possible situations in the unit cell $(Bi_2O_3)_{1-x}(M_2O_5)_x$ are as follows:

(*i*) All cations occupy their normal site in the fluorite-type lattice and (2-4*x*) of the eight oxide ion sites per unit cell are vacant; *i.e.*, the composition of unit cell is expressed as

$$Bi_{4(1-x)}M_{4x}O_{6+4x}\square_{2-4x}$$

where □ is oxide ion vacancy.

(*ii*) All cations and oxide ions occupy their normal sites, respectively, and the above vacant sites are occupied by oxygen atoms or ionized oxygens accompanied by electron holes; *i.e.*

$$Bi_{4(1-x)}M_{4x}O_8$$

(*iii*) All oxide ions occupy their normal sites fully and excess cations are situated at interstitial sites; *i.e.*

$$Bi_{4(1-x)}M_{4x}(Bi_\alpha M_\beta)_{int.}O_8$$

where $(\ )_{int.}$ indicates the interstitial sites.

(*iv*) All Bi^{3+} ions occupy their normal sites and all M^{5+} ions are situated at the interstitial sites; *i.e.*

$$Bi_4(Nb_{4x/1-x})_{int.}O_{6+(10x/1-x)}\square_{2-(14x/1-x)}$$

The theoretical densities of the fcc phase in the Bi_2O_3-Nb_2O_5 system have been calculated from the observed lattice parameters, assuming the above models. In Fig. 7 the calculated densities and the pycnometric densities measured on quenched samples are plotted against the content of Nb_2O_5. The observed values are in good agreement with case (*i*), indicating that the crystals have an appreciable amount of oxide ion vacancies, the number of which are given by (2 — 4*x*) per unit cell. A similar result was also obtained in the specimen $(Bi_2O_3)_{0.80}(Ta_2O_5)_{0.20}$.

Discussion

From the results described above, it is concluded that the fcc phase in the Bi_2O_3-M_2O_5 system is a highly conductive oxide ion conductor, and that this highly conductive phase can be stabilized at low temperature by adding an appropriate amount of Nb_2O_5 or Ta_2O_5. The conductivity of this phase increases with decreasing content of M_2O_5 and, as a result, the maximum conductivity in the low temperature region lies on the lower limit of the fcc solid solution formation range. This tendency is analogous to those for the Bi_2O_3-WO_3, Bi_2O_3-Y_2O_3, and Bi_2O_3-Gd_2O_3 systems reported previously (6, 9, 10) and is coincident with the general trend for stabilized zirconias that the increase in the content of the second cation (stabilizer) makes the conductivity decrease within the fcc solid solution formation range.

It is interesting to speculate on the direct cause of the conductivity decrease with the increasing content of the stabilizer. In the stabilized zirconias, the increase in the content of stabilizers makes the concen-

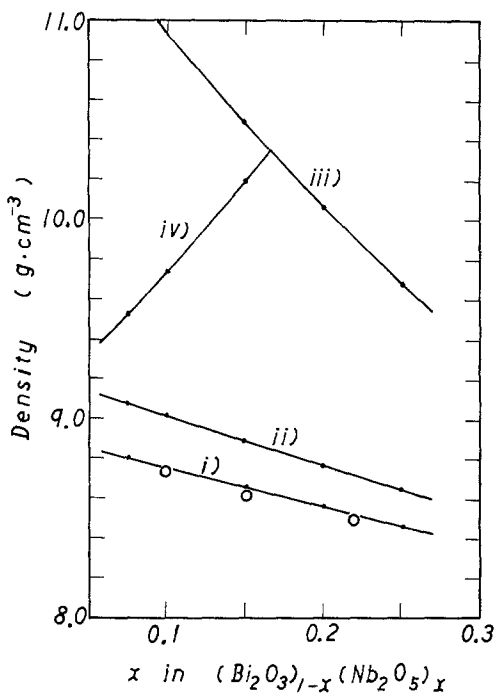


Fig. 7. Comparison of calculated densities with the observed values (open circles). (The number on each line corresponds to the density calculated from each model described in the body.)

tration of oxide ion vacancies increase since the stabilizers are di- or trivalent cations which are substituted for tetravalent zirconium ions; for example

$$(1-x)ZrO_2 + xCaO \rightarrow Zr_{1-x}Ca_xO_{2-x}\square_x$$

In the fluorite-type phase in the Bi_2O_3-M_2O_5 system, however, the situation is quite the reverse, that is, the vacancy concentration decreases with the content of M_2O_5 as described above, and is written as

$$(1-x)BiO_{1.5}\square_{0.5} + xMO_{2.5} \rightarrow Bi_{1-x}M_xO_{1.5+x}\square_{0.5(1-x)}$$

Therefore, the conductivity decreases with increasing vacancy concentration in the former case, while it increases with increasing content of vacancies in the latter case. This suggests that it is not the interaction between oxide ion vacancies themselves, but the interaction between oxide ion vacancies and doped cations that affect the conductivity lowering directly.

The activation energies for conduction in the fcc phase of Bi_2O_3-M_2O_5 increased with increasing content of doped cations. They were calculated from the Arrhenius plot of the conductivity, and are represented in Fig. 8 with respect to the composition. Clearly, the plots lie almost on a straight line irrespective of the sort of M_2O_5. This may indicate that the conduction mechanism in the fcc phase is the same regardless of the sort of M_2O_5. As shown in the same figure, a similar tendency can also be seen in the case of Bi_2O_3-M_2O_3 (M = Y and Gd), the oxide ion conductivities of which were reported previously (9, 10). It is noticeable that, although each slope is different, the extrapolations to $x = 0$ give almost the same value which is close to the observed activation energy for the fcc phase of pure Bi_2O_3 (δ-Bi_2O_3). This suggests that the conduction mechanism in both systems is essentially identical with that for δ-Bi_2O_3 in which the oxide ion may conduct in the same way as in the case of a stabilized zirconia because of a similar defect fluorite-type crystal structure.

Higher slope in the case of pentavalent dopants than that of the trivalent dopants can be explained as follows. When M_2O_5 is added to Bi_2O_3 within the fcc phase, trivalent host cations Bi^{3+} are replaced by pentavalent cations M^{5+}, and defect chemistry can be written using Kröger's notation as

$$2Bi_{Bi}^{\times} + Nb_2O_5 + 2V_o^{\cdot\cdot} \rightarrow 2Nb_{Bi}^{\cdot\cdot} + 2O_o^{\times} + (Bi_2O_3)_{cryst.}$$

The substituted cation sites should charge twice as positively relative to the initial cation sublattice field,

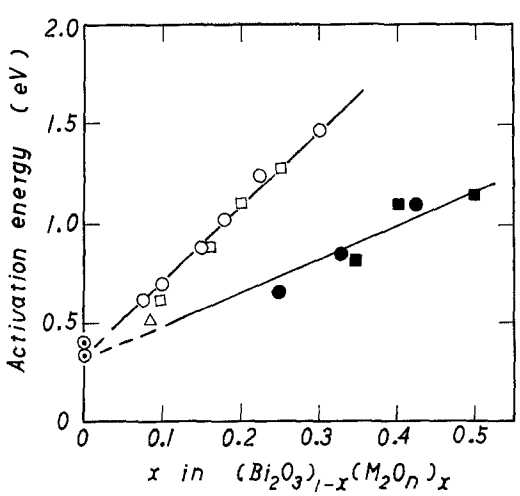


Fig. 8. Relation between the composition and activation energy for conduction in fcc phase of the system Bi_2O_3-M_2O_5 and Bi_2O_3-M_2O_3. ($n = 5$): △, M = V; ○, M = Nb; □, M = Ta. ($n = 3$): ●, M = Y; ■, M = Gd.

and might repulse the native vacancies $V_o^{\cdot\cdot}$ because of the same positive charge. As a result, the association between the substituted cations and the movable oxide ions

$$M_{Bi}^{\cdot\cdot} + O_o^{\times} \rightarrow (M_{Bi}^{\cdot\cdot}O_o^{\times})$$

may take place, which makes the activation energy for oxide ion conduction increase. This effect will grow remarkably as the content of pentavalent dopant increases, and, accordingly, the activation energy rises as shown in Fig. 8. While replacement by M^{5+} disturbs the uniformity of the electrostatic field on the cation sublattice, the replacement by M^{3+} leaves the potential field unchanged (uniform) because of the equicharge of M and Bi. The defect chemistry can be given as

$$2Bi_{Bi}^{\times} + M_2O_3 + 2V_o^{\cdot\cdot} \rightarrow 2M_{Bi}^{\times} + (Bi_2O_3)_{cryst.} + 2V_o^{\cdot\cdot}$$

There exists much less interaction between $M_{Bi}^{\times}$ and $V_o^{\cdot\cdot}$ than between $M_{Bi}^{\cdot\cdot}$ and $V_o^{\cdot\cdot}$ since $M_{Bi}^{\times}$ has no effective charge relative to $Bi_{Bi}^{\times}$. Nevertheless, the uniformity of the potential field on the cation sublattice may be actually disturbed to some extent by the difference in electronegativity, polarizability, or ionic radius between the host Bi^{3+} and dopant M^{3+}, and this will make the activation energy increase even if it is not so remarkable as in the case of M^{5+}. As a result, it is rational that the increment of activation energy with the composition is more remarkable in the case of M_2O_5 dopant than that in the case of M_2O_3 dopant.

A linear relationship between the activation energy and the composition shown in Fig. 8 could not quantitatively be explained. It is probable that rather an approximate form of the more complex expression exists which includes the association energy among the defects. These problems are under study.

As to the oxide ion conductivity, the Bi_2O_3-based specimens, especially $(Bi_2O_3)_{0.85}(Nb_2O_5)_{0.15}$ as well as $(Bi_2O_3)_{0.85}(Y_2O_3)_{0.25}$ can be said to belong to the best conductor. A demerit of the Bi_2O_3-based electrolytes is that they are apt to be reduced under reducing atmosphere at high temperature. However, according to our recent study (15) on $(Bi_2O_3)_{0.83}(Y_2O_3)_{0.27}$, it is stable down to 10^{-13} atm O_2 at 600°C keeping the properties of pure electrolyte. Therefore, they may be available as a conventional solid electrolyte under the relatively high partial pressure of oxygen.

Conclusion

The fcc phase present in the systems Bi_2O_3-M_2O_5 (M = V, Nb, or Ta) was confirmed to be a highly conductive oxide ion conductor. Although this phase is not stable in the low content of M_2O_5 at low temperatures, it can be stabilized at low temperatures by adding more than a certain amount of M_2O_5 (Nb, 15 m/o; Ta, 18 m/o). The oxide ion conductivity of this phase, however, decreases with increasing content of the stabilizer, and a maximum conductivity is obtained at the lower limit of the fcc solid solution formation range. The activation energy for conduction in this phase increases with the content of dopants irrespective of their sort, and the value is higher than that for M_2O_3-doped specimen at the corresponding concentration. The crystal structure of this phase is the defect fluorite type having an appreciable amount of oxide ion vacancies, which contribute to the oxide ion conduction.

Of these systems, the Nb-containing specimen has the highest conductivity over a wide range of compositions and temperatures. The best conductor $(Bi_2O_3)_{0.85}(Nb_2O_5)_{0.15}$ has the conductivities of 1.9×10^{-1} Ω^{-1} cm^{-1} at 700°C and 1.1×10^{-2} Ω^{-1} cm^{-1} at 500°C which are more than ten times higher than those of the conventional stabilized zirconias. Although this material is apt to be reduced under a reducing atmo-

sphere, it may be available for practical solid electrolytes under oxidizing atmosphere because of its high conductivity and easy preparation.

Manuscript submitted April 26, 1977; revised manuscript received June 10, 1977.

Any discussion of this paper will appear in a Discussion Section to be published in the June 1978 JOURNAL. All discussions for the June 1978 Discussion Section should be submitted by Feb. 1, 1978.

Publication costs of this article were assisted by the authors.

REFERENCES

1. G. Gattow and H. Schröder, *Z. Anorg. Allgem. Chem.*, **318**, 176 (1962).
2. G. Gattow and D. Schutze, *ibid.*, **328**, 44 (1964).
3. M. G. Hapase and V. B. Tare, *Indian J. Pure Appl. Phys.*, **5**, 401 (1967).
4. R. S. Sethi and H. G. Gauer, *Indian J. Chem.*, **3**, 177 (1955).
5. T. Takahashi, H. Iwahara, and Y. Nagai, *J. Appl. Electrochem.*, **2**, 97 (1972).
6. T. Takahashi and H. Iwahara, *ibid.*, **3**, 65 (1973).
7. C. N. R. Rao, G. V. Subba Rao, and S. Ramdas, *J. Phys. Chem.*, **73**, 672 (1969).
8. C. A. Johnson, R. C. Bradt, and J. H. Hoke, *J. Am. Ceram. Soc.*, **58**, 37 (1975).
9. T. Takahashi, H. Iwahara, and T. Arao, *J. Appl. Electrochem.*, **5**, 187 (1975).
10. T. Takahashi, T. Esaka, and H. Iwahara, *ibid.*, **5**, 197 (1975).
11. R. S. Roth and T. L. Waring, *J. Res. Nat. Bur. Stand., Sect. A*, **66**, 451 (1962).
12. E. M. Levin and R. S. Roth, *ibid.*, **68**, 202 (1962).
13. C. Wagner, *Z. Phys. Chem.*, **21**, 25 (1925).
14. T. Takahashi and H. Iwahara, *Energy Convers.*, **11**, 105 (1971).
15. T. Takahashi, T. Esaka, and H. Iwahara, in *J. Appl. Electrochem.*, **7**, 303 (1977).
16. H. Yanagida, R. J. Brook, and F. A. Kröger, *This Journal*, **117**, 593 (1970).
17. H. Schmalzried, *Z. Phys. Chem. N.F.*, **38**, 87 (1963).

Determination of the Kinetic Parameters of Mixed-Conducting Electrodes and Application to the System Li_3Sb

W. Weppner and R. A. Huggins*

Department of Materials Science and Engineering, Stanford University, Stanford, California 94305

ABSTRACT

An electrochemical galvanostatic intermittent titration technique (GITT) is described which combines both transient and steady-state measurements to obtain kinetic properties of solid mixed-conducting electrodes, as well as thermodynamic data. The derivation of quantities such as the chemical and component diffusion coefficients, the partial conductivity, the mobility, the thermodynamic enhancement factor, and the parabolic rate constant as a function of stoichiometry is presented. A description of the factors governing the equilibration of composition gradients in such phases is included. The technique is applied to the determination of the kinetic parameters of the compound "Li_3Sb," which has a narrow composition range. For $Li_{2.9994}Sb$ the chemical diffusion coefficient is 2×10^{-5} cm^2 sec^{-1} at 360°C. This value is quite high, due to a large thermodynamic enhancement factor of 1.3×10^4. The lithium component diffusion coefficient is comparatively small at this composition, 1.5×10^{-9} cm^2 sec^{-1}. The partial conductivity and electrical mobility of lithium are 1.5×10^{-4} Ω^{-1} cm^{-1} and 3×10^{-8} cm^2 V^{-1} sec^{-1}, respectively, at the same stoichiometry and temperature. Because of the very large values of the chemical diffusion coefficient and the fact that 3 moles of lithium can react per mole of antimony, this system may be of interest for use in new types of secondary batteries.

Quantitative knowledge of transport kinetics in solids is of importance both for increased understanding of transport mechanisms and the disorder in solid materials and for the technological application of many solid-state reactions. Especially in the current search for new types of high power density batteries, success in several approaches strongly depends on the availability of solid electrodes which incorporate electroactive species from the electrolyte into their crystal structures and in which the equilibration of local differences in composition occurs rapidly.

In general, in the presence of a compositional (stoichiometric) gradient the transport parameters of the different mobile species are interrelated. The quantity usually used to describe the complex process of compositional equilibration (relaxation) is the chemical diffusion coefficient, $\tilde{D}$. Besides the thermogravimetric, conductometric, and radiotracer methods which have been used for a long time for the observation of the exchange of solid compounds with adjacent liquid or gaseous species, electrochemical techniques have recently come into use (1-4). The important advantage of this latter approach is that the voltage of a suitable galvanic cell is directly related to appropriate thermodynamic quantities, and the current can provide easily measurable kinetic information at the same time. For the case of ideal solutions and concentration-independent diffusion coefficients, electrochemical methods have also been used in several earlier investigations [*e.g.*, (5-7)].

To study chemical diffusion in mixed-conducting solids one may employ transient methods similar to those used for the electrochemical investigation of the kinetics in the vicinity of chemically inert solid electrodes in liquid electrolytes (chronopotentiometry, chronoamperometry, voltammetry) [*e.g.*, (8)]. In the case discussed here, however, the transport in the bulk of the electrode acts as the rate-determining step.

* Electrochemical Society Active Member.
Key words: chemical diffusion, galvanostatic intermittent titration, partial ionic conductivity, thermodynamic enhancement factor, parabolic tarnishing rate constant, ionic mobility.

Steady-state measurements are often used to measure the conductivity. However, they give information concerning the product of the concentration and the diffusion coefficient, rather than either one separately, without additional information. On the other hand, transient methods may sometimes be used to separate these quantities. An example is the so-called "Rosenburg method" for the evaluation of defect concentrations and chemical diffusion in oxide layers (9-11).

In this paper, the application of an electrochemical cell method is introduced for the acquisition of both kinetic and thermodynamic information in mixed conductors, such as insertion compound electrodes. This method allows separate determination of the chemical diffusion coefficient, as well as other useful quantities, in one set of experiments. This approach employs an experimentally tractable galvanostatic intermittent titration technique (GITT), which combines transient and steady-state measurements. It eliminates the customary problem of interference due to resistance polarization in the use of potentiostatic techniques. The desired data are conveniently accessible, and a precise coulometer or independent determination of coulometric titration curves are not necessary.

The investigation of trilithium antimonide, "Li_3Sb," by the use of this new technique is described here. Li_3Sb is a mixed-conducting compound whose features make it potentially interesting for use as an electrode constituent. Although the range of stoichiometry of this phase is rather narrow, so that only small stoichiometric variations may occur, this method is shown to be extremely sensitive and quite precise.

Basic Relations

Chemical diffusion is a process in which the transport of all species within the solid is involved. General equations will be derived for its microscopic description and its relation to other kinetic parameters of the material. The particle fluxes will be expressed in terms of the individual kinetic and thermodynamic properties of the different ionic and electronic species. This approach will show which factors control chemical diffusion under various circumstances. Effects resulting from volume changes and macroscopic movements will not be considered. For this purpose, one may often use the sublattice of one component as the frame of reference for the motion of all the other species (12). If necessary, other reference systems should be considered (13), of course. Also, it will be assumed that the diffusion length is small compared to the dimensions of the whole system.

In general, in an isothermal and adiabatic system and if Onsager's cross-coefficients (12) are negligible, the flux density of species i (in particles per square centimeter second) under the influence of a gradient of the electrochemical potential η_i (related to one particle) is given in the one-dimensional case by

$$j_i = -\frac{\sigma_i}{z_i^2 q^2}\frac{\partial \eta_i}{\partial x} \qquad [1]$$

σ_i, z_i, and q are the partial electrical conductivity due to the transport of species i, the charge number (valence), and the elementary charge, respectively. The electrical conductivity σ_i may be replaced by an expression including the product of the concentration c_i and the electrical mobility u_i or, alternatively, the general mobility b_i (the mean particle velocity per unit general acting force), where $b_i = u_i/|z_i|q$

$$\sigma_i = |z_i| q c_i u_i = z_i^2 q^2 c_i b_i \qquad [2]$$

Also, the electrochemical potential η_i may be divided into two terms, one containing the chemical potential μ_i (per particle) or the activity a_i, and the other the local electrostatic potential ϕ

$$\eta_i = \mu_i + z_i q\phi = \mu_i^\circ + kT \ln a_i + z_i q\phi \qquad [3]$$

μ_i°, k, and T are the chemical potential of species i in the standard state ($a_i = 1$), Boltzmann's constant, and the absolute temperature, respectively. Inserting Eq. [2] and [3] into Eq. [1] yields for the flux density of the component i

$$j_i = -\frac{kTu_i}{|z_i|q}\left[\frac{\partial \ln a_i}{\partial \ln c_i}\frac{\partial c_i}{\partial x} + \frac{z_i q c_i}{kT}\frac{\partial \phi}{\partial x}\right] \qquad [4]$$

The factor in front of the bracket has the dimensions of a diffusion coefficient and is the component diffusion coefficient D_{Ki}, or the "diffusivity of the species i as a component" (12)

$$D_{Ki} = \frac{kTu_i}{|z_i|q} = b_i kT \qquad [5]$$

This quantity is thus simply proportional to the mobility of the species in question and reflects the same microscopic kinetic phenomena. This diffusion coefficient obeys the Nernst-Einstein equation regardless of whether the solution is ideal or nonideal, and is the diffusion coefficient which is directly measured in the case of ideal dilute solutions of neutral species. D_{Ki} is a measure of the random motion of the particles of species i in the crystal, and is related to the (radio) tracer diffusion coefficient D_{Ti} by $D_{Ti} = f_i D_{Ki}$, where f_i is the correlation factor.

The inner electric field $\partial\phi/\partial x$, which cannot be experimentally determined, may be eliminated from Eq. [4] by the condition that, except for transient conditions involving the accumulation of a significant space charge, charge flux balance must be maintained. That is, for all species, if there is no externally applied electric potential difference

$$\sum_i z_i j_i = 0 \qquad [6]$$

Inserting Eq. [4] into Eq. [6], and solving for $\partial\phi/\partial x$, and then using this expression in Eq. [4] yields the flux density for species i in terms of transport quantities and activity gradients related to it and to all other species j

$$j_i = -D_{Ki}\left[\frac{\partial \ln a_i}{\partial \ln c_i} - \sum_j t_j \frac{z_i}{z_j}\frac{\partial \ln a_j}{\partial \ln c_i}\right]\frac{\partial c_i}{\partial x} \qquad [7a]$$

$$= -D_{Ki}\left[(1 - t_i)\frac{\partial \ln a_i}{\partial \ln c_i} - \sum_{j\neq i} t_j \frac{z_i}{z_j}\frac{\partial \ln a_j}{\partial \ln c_i}\right]\frac{\partial c_i}{\partial x} \qquad [7b]$$

The summations include all other ionic and electronic species. The symbol $t_i = \sigma_i \Big/ \sum_j \sigma_j$ is the transference number for species i.

As a result of the ionization equilibrium, in which the activities of neutral species are related to those of their ionic and electronic constituents within solids, we have

$$d \ln a_i + z_i d \ln a_e = d \ln a_i - z_i d \ln a_h = d \ln a_i^* \qquad [8]$$

where e, h, and i* represent electrons, holes, and neutral i species, respectively. Equation [7] may now be transformed into an expression containing only the (physically more relevant) activities and concentrations of neutral atomic species

$$j_i = -D_{Ki}\left[\frac{\partial \ln a_i^*}{\partial \ln c_i^*} - \sum_{j\neq e,h} t_j \frac{z_i}{z_j}\frac{\partial \ln a_j^*}{\partial \ln c_i^*}\right]\frac{\partial c_i}{\partial x} \qquad [9a]$$

$$= -D_{Ki}\left[(1 - t_i)\frac{\partial \ln a_i^*}{\partial \ln c_i^*} - \sum_{j\neq i,e,h} t_j \frac{z_i}{z_j}\frac{\partial \ln a_j^*}{\partial \ln c_i^*}\right]\frac{\partial c_i}{\partial x} \qquad [9b]$$

These equations give the flux density for any chemical component and hold both for the ionic species within the solid or for the effective flux density of such species in their neutral form. These equations are distinct from those which appeared in the earlier discussion [7], however, in that the activity and concentration terms only involve neutral chemical species, and neither electrons nor holes.

These general equations have a form similar to the familiar Fick's first law

$$j_i = -\tilde{D}_i \frac{\partial c_i}{\partial x} \qquad [10]$$

where $\tilde{D}_i$ is the chemical diffusion coefficient (the effective diffusion coefficient) for species i (with reference to the crystal lattice, which in the cases discussed below, is identical to the laboratory frame) and

$$\tilde{D}_i = D_{K_i} W \qquad [11]$$

where the factor W is an enhancement factor, defined by the quantity in the square brackets

$$W = \left[(1 - t_i) \frac{\partial \ln a_i^*}{\partial \ln c_i^*} - \sum_{j \neq i,e,h} t_j \frac{z_i}{z_j} \frac{\partial \ln a_j^*}{\partial \ln c_j^*} \right] \qquad [12]$$

The symbol W was selected for this purpose in honor of Carl Wagner, who first showed (14) the influence of the transport of charged species upon each other.

$\tilde{D}_i$ is sometimes called the "intrinsic diffusion coefficient" of species i, when referred to the laboratory frame. In the case that the crystal and laboratory frames are identical, these quantities are the same. In cases in which two atomic species interdiffuse, the term "interdiffusion coefficient" is sometimes used with reference to the crystal frame, which may move with respect to the laboratory frame.

In many systems of practical importance, including tarnishing processes (14), the situation is simplified by the fact that two types of species (either two different ionic species, or one ionic and one electronic species) dominate the transport phenomena. Under this situation, the chemical diffusion coefficients of the two species are equal, and we can use the symbol $\tilde{D}$ for both (15). For the case in which only one ionic and one electronic species have to be considered, so that $t_e = 1 - t_i$, the enhancement factor becomes

$$W = t_e \frac{\partial \ln a_i^*}{\partial \ln c_i^*} \qquad [13]$$

and

$$\tilde{D} = D_{K_i} t_e \frac{\partial \ln a_i^*}{\partial \ln c_i^*} \qquad [14]$$

If the sample is predominantly an electronic conductor, so that $t_e \rightarrow 1$, we have simply

$$W = \frac{\partial \ln a_i^*}{\partial \ln c_i^*} \qquad [15]$$

and

$$\tilde{D} = D_{K_i} \frac{\partial \ln a_i^*}{\partial \ln c_i^*} \qquad [16]$$

This is the case previously discussed by Wagner (16). Using the definition of the activity coefficient $\gamma_i = a_i/c_i$, the enhancement factor can be written in the form

$$W = \left[1 + \frac{\partial \ln \gamma_i}{\partial \ln c_i} \right] = \left[1 + c_i \frac{\partial \ln \gamma_i}{\partial c_i} \right] \qquad [17]$$

derived for metals by Darken (17).

On the other hand, if the transference number of the ionic species is much larger than that for the electronic species, Eq. [13] can be rewritten as

$$W = \left(\frac{\sigma_e}{\sigma_i} \right) \frac{\partial \ln a_i^*}{\partial \ln c_i^*} \qquad [18]$$

and by using Eq. [2] and [5], we get

$$W = \frac{c_e D_{K_e}}{z_i^2 c_i D_{K_i}} \frac{\partial \ln a_i^*}{\partial \ln c_i^*} \qquad [19]$$

and then

$$\tilde{D} = \frac{c_e D_{K_e}}{z_i^2 c_i} \frac{\partial \ln a_i^*}{\partial \ln c_i^*} \qquad [20]$$

Thus we see that, in this case, the chemical diffusion coefficient for the ionic species is dependent on the component diffusion coefficient of the electrons, not the ions.

Let us now further examine the value of the enhancement factor for several different situations for the common and important case in which only one ionic species and one electronic species (assumed to be excess or mobile electrons) have to be considered, the transference numbers of all other species being negligible. From Eq. [8] and [13], the enhancement factor for the ions becomes simply

$$W = t_e \left[\frac{\partial \ln a_i}{\partial \ln c_i} + z_i \frac{\partial \ln a_e}{\partial \ln c_i} \right] \qquad [21]$$

For the special case in which we can assume that both the ionic species and the electrons obey either Henry's or Raoult's law, *i.e.*, γ_i and γ_e are constant, and considering the electroneutrality condition

$$dc_e = z_i dc_i \qquad [22]$$

we derive from Eq. [21]

$$W = t_e \left[1 + z_i^2 \frac{c_i}{c_e} \right] \qquad [23]$$

We can thus conclude that if $t_e << 1$, *i.e.*, in the case of a solid electrolyte with dilute mobile ionic species, W will tend toward zero, and the chemical diffusion of ions in response to a composition gradient will be very sluggish.

On the other hand, if electronic conduction predominates, $t_e \rightarrow 1$, the value of W will depend sensitively upon the value of c_i/c_e. If $c_i << c_e$, W will approach unity, so the chemical diffusion coefficient for the ionic species becomes the same as the component diffusion coefficient. If $z_i^2 c_i = c_e$, W becomes 2.

There are many cases in which electronic conduction predominates ($t_i << 1$), and yet $c_i >> c_e$. This is possible if the electrons have a much greater mobility than the ionic species and can lead to unusually large values of W, and thus of $\tilde{D}_i$, as pointed out by Wagner (18), who cited a number of materials in which this has been found. It will be shown later in this paper that this is also true for Li_3Sb.

Very large enhancement factors can also be present for materials in which one can assume that only the electronic species exhibit ideal solution behavior. In that case Eq. [21] becomes

$$W = t_e \left[\frac{\partial \ln a_i}{\partial \ln c_i} + z_i^2 \frac{c_i}{c_e} \right] \qquad [24]$$

The large enhancement (or reduction) factor W is sometimes explained in terms of a microscopic model in which the more mobile species tend to move ahead of the others. If they have different charges (or species of the same sign move at different rates in opposite directions), this creates an internal electric field in which the slower species are accelerated, and the

Table I. Value of enhancement factor under various conditions

(Cases with only one ionic species and electrons mobile)

	Thermodynamic assumptions	Concentration assumptions	Transference no. assumption	Enhancement factor (W)
a.	General	General	General	$t_e\left[\frac{\partial \ln a_i}{\partial \ln c_i} + z_i \frac{\partial \ln a_e}{\partial \ln c_i}\right]$ or $t_e\left[\frac{\partial \ln a_i^*}{\partial \ln c_i^*}\right]$
b.	General	General	$t_e << 1$	$<<\left[\frac{\partial \ln a_i^*}{\partial \ln c_i^*}\right]$
c.	$\left[\begin{matrix} a_i = (\text{const.})\ c_i \\ a_e = (\text{const.})\ c_e \end{matrix}\right]$	General	General	$t_e\left[1 + z_i^2\left(\frac{c_i}{c_e}\right)\right]$ or $t_e\left[1 + \frac{t_i}{t_e}\frac{D_{K_e}}{D_{K_i}}\right]$
d.	$\left[\begin{matrix} a_i = (\text{const.})\ c_i \\ a_e = (\text{const.})\ c_e \end{matrix}\right]$	General	$t_i << 1$	$1 + z_i^2\left(\frac{c_i}{c_e}\right)$
e.	$\left[\begin{matrix} a_i = (\text{const.})\ c_i \\ a_e = (\text{const.})\ c_e \end{matrix}\right]$	$c_i << c_e$	$t_i << 1$	1
f.	$\left[\begin{matrix} a_i = (\text{const.})\ c_i \\ a_e = (\text{const.})\ c_e \end{matrix}\right]$	$\lvert z_i \rvert c_i = c_e$	$t_i << 1$	$1 + \lvert z_i \rvert$
g.	$\left[\begin{matrix} a_i = (\text{const.})\ c_i \\ a_e = (\text{const.})\ c_e \end{matrix}\right]$	$c_i >> c_e$	$t_i << 1$	$z_i^2\left(\frac{c_i}{c_e}\right)$
h.	$\left[\begin{matrix} \text{Ion general} \\ a_e = (\text{const.})\ c_e \end{matrix}\right]$	General	$t_i << 1$	$t_e\left[\frac{\partial \ln a_i}{\partial \ln c_i} + z_i^2\left(\frac{c_i}{c_e}\right)\right]$

faster ones retarded, in order to maintain local charge flux neutrality.

It should be mentioned that if the second term in either Eq. [23] or [24] is significantly greater than unity, we should expect the temperature dependence of the chemical diffusion coefficient to be different from that of the component or tracer diffusion coefficients, due to the temperature dependence of c_i/c_e.

The values of the enhancement factor W that are expected under these various conditions are presented in Table I.

Determination of the Chemical Diffusion Coefficient by Use of the Galvanostatic Intermittent Titration Technique

The chemical diffusion coefficient of species A and other kinetic and thermodynamic parameters may be investigated in a mixed conductor $A_{y+\delta}B$, (δ symbolizes the deviation from the ideal stoichiometric composition) by the use of a galvanic cell with $A_{y+\delta}B$ as one electrode, as shown in Fig. 1. Because of potential problems with electrode polarization, separate counter (A) and reference (A°) electrodes generally have to be employed. Instead of pure A, another material with a different activity of A may also be used for these two electrodes. As will become obvious later, the location at which the reference electrode is attached to the electrolyte is unimportant, *e.g.*, the left-hand electrode may be divided into two parts, and partially used as a counter and partially as a reference electrode.

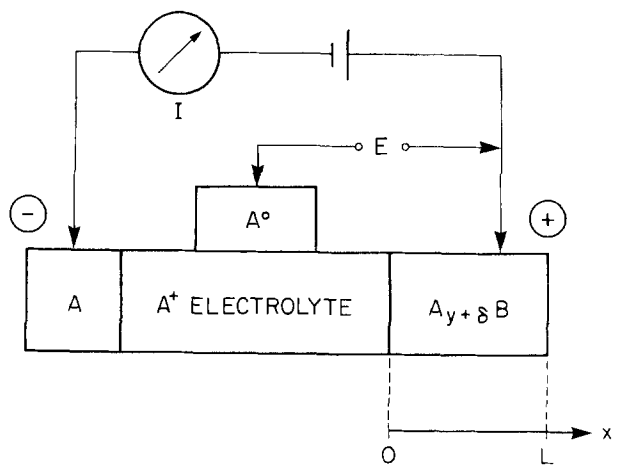


Fig. 1. Schematic illustration of experimental galvanic cell arrangement. The electrolyte-sample interface is at $x = 0$. The sample thickness is L.

According to the Nernst equation

$$E = \frac{kT}{z_A q} \ln \frac{a_{A^*}(A^\circ)}{a_{A^*}(A_{y+\delta}B)} \qquad [25]$$

the cell voltage E is thus a measure of the thermodynamic activity of neutral A in the $A_{y+\delta}B$ sample at the interface with the electrolyte.

An electric current I which is driven through the galvanic cell by an external source determines the transport of the relevant mobile ionic species within the sample just inside the phase boundary with the electrolyte (where $x = 0$)

$$I = -Sz_i q\tilde{D}\frac{\partial c_i}{\partial x}\bigg|_{x=0} \qquad [26]$$

with i being either A or B, depending on which one has the predominant conductivity. S is the area of the sample-electrolyte interface.

The principles underlying this procedure for the determination of the kinetic and thermodynamic parameters of a mixed conductor are illustrated in Fig. 2. Starting with a sample of known stoichiometric composition and with the galvanic cell in thermodynamic equilibrium, *i.e.*, the concentrations of all species are homogeneous throughout the electrode $A_{y+\delta}B$, corresponding to cell voltage E_0, a constant current I_0 is applied to the cell at time t_0 by a galvanostat, or simply by a battery and a large resistor. According to Eq. [26] this produces a constant concentration gradient $\partial c_i/\partial x$ within the $A_{y+\delta}B$ at the phase boundary with the electrolyte ($x = 0$). In order to maintain this constant concentration gradient, the applied cell voltage increases (or decreases, depending on the direction of the current) with time. A voltage step, corresponding to the IR drop due to the current flux through the electrolyte and the interface is superimposed, whose magnitude depends on the position of the reference electrode. However, it is always time-independent (on the scale of this experiment), and acts as a constant that merely shifts the measured

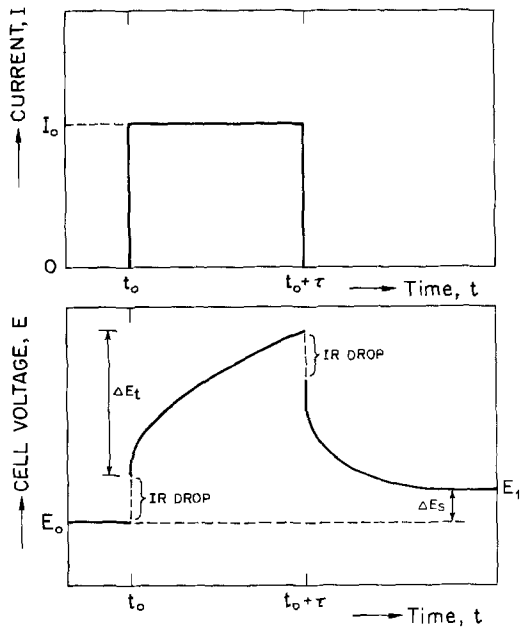


Fig. 2. Schematic illustration of a single step of the galvanostatic intermittent titration technique (GITT). ΔE_t is the total transient voltage change of the galvanic cell for an applied galvanostatic current I_o for the time τ. ΔE_s is the change of the steady-state voltage of the cell for this step.

voltage by a constant value but does not change the geometrical shape of the voltage-time curve.

After a time interval τ, the current flux is interrupted, whereupon the composition within the $A_{y+\delta}B$ sample tends to again become homogeneous by diffusion of the mobile species. During this equilibration process the surface composition of the sample, and therefore the cell voltage, drifts back toward a new steady-state value E_1, corresponding to a new activity of A in the sample as a result of the change of the stoichiometry $\Delta\delta$ caused by the coulometric titration of A ions into it by the current

$$\Delta\delta = \frac{I_o \tau M_B}{z_A m_B \mathbf{F}} \qquad [27]$$

M_B, m_B, I_o, and $\mathbf{F}$ are the atomic weight of B, the mass of the component B in the sample, the constant current, and Faraday's constant, respectively. After the electrode is again in equilibrium, the procedure may be repeated, starting now with the new cell voltage E_1. This process may be continued until a phase change occurs in the electrode, or the electrolyte decomposes or becomes electronically conductive.

In order to calculate the voltage E as a function of time t during which the current is applied, the time dependence of the concentration c_i at the interface $x = 0$ has to be determined by solving Fick's second law

$$\frac{\partial c_i(x,t)}{\partial t} = \tilde{D}\frac{\partial^2 c_i(x,t)}{\partial x^2} \qquad [28]$$

with the initial and boundary conditions

$$c_i(x, t=0) = c_o \quad (0 \leqq x \leqq L) \qquad [29]$$

$$-\tilde{D}\frac{\partial c_i}{\partial x}\bigg|_{x=0} = \frac{I_o}{S z_i q} \quad (t \geqq 0) \qquad [30]$$

$$\frac{\partial c_i}{\partial x}\bigg|_{x=L} = 0 \quad (t \geqq 0) \qquad [31]$$

The last condition is due to the fact that the right-hand phase boundary of the sample is assumed to be impermeable.

The solution of the differential Eq. [28] under conditions [29]-[31] is known (19, 20) and can be cast in the following form for $x = 0$

$$c_i(x=0,t) = c_o + \frac{2I_o\sqrt{t}}{S z_i q\sqrt{\tilde{D}}} \sum_{n=o}^{\infty} \left(\text{ierfc}\left[\frac{nL}{\sqrt{\tilde{D}t}}\right] + \text{ierfc}\left[\frac{(n+1)L}{\sqrt{\tilde{D}t}}\right]\right) \qquad [32]$$

with $\text{ierfc}(\lambda) = [\pi^{-1/2}\exp(-\lambda^2)] - \lambda + [\lambda\,\text{erf}(\lambda)]$, the first integral of the complement of the error function. At times $t << L^2/\tilde{D}$ the infinite sum can be approximated by the first term. Then, we have for the variation of c_i with the square root of time

$$\frac{dc_i(x=0,t)}{d\sqrt{t}} = \frac{2I_o}{S z_i q\sqrt{\tilde{D}\pi}} \quad (t << L^2/\tilde{D}) \qquad [33]$$

If changes of the molar volume with composition may be neglected, the changes in the concentration and the stoichiometry are related through

$$dc_i = \frac{N_A}{V_M} d\delta \qquad [34]$$

where N_A is Avogadro's number and V_M is the molar volume of the sample. Inserting this expression in Eq. [33] and expanding by dE yields the following expression for the expected time dependence of the cell voltage

$$\frac{dE}{d\sqrt{t}} = \frac{2V_M I_o}{S\mathbf{F}z_i\sqrt{\tilde{D}\pi}}\frac{dE}{d\delta} \quad (t << L^2/\tilde{D}) \qquad [35]$$

$dE/d\delta$ is the slope of the coulometric titration curve, which is found by plotting the steady-state voltages, measured after each titration step, against the composition, calculated from the current flux times the applied time interval with the help of Eq. [27]. With this information, the chemical diffusion coefficient may be calculated from Eq. [35] because all other quantities are known or measurable

$$\tilde{D} = \frac{4}{\pi}\left(\frac{V_M}{S\mathbf{F}z_i}\right)^2 \left[I_o\left(\frac{dE}{d\delta}\right) \Big/ \left(\frac{dE}{d\sqrt{t}}\right)\right]^2 \quad (t << L^2/\tilde{D}) \qquad [36]$$

If the electrolyte is in contact with both sides of the sample, *e.g.*, in the case that a liquid electrolyte is used, the middle plane, rather than the far side, of a pellet sample is equivalent to the position $x = L$. Because of symmetry, there will be no transport of species across this plane. In this case, the total area of contact between the electrolyte and the electrode has to be taken into account when calculating the area S.

If by using a sufficiently small current the change of the steady-state (equilibrium) voltage $(E_1 - E_o) \simeq \Delta E_s$ over a single galvanostatic titration is small, $dE/d\delta$ may be considered to be constant and may be replaced by the ratio of the finite quantities, $\Delta E_s/\Delta\delta$. Thus, by inserting Eq. [27] for the change of the stoichiometry in Eq. [36] we have

$$\tilde{D} = \frac{4}{\pi}\left(\frac{m_B V_M}{M_B S}\right)^2 \left[\frac{\Delta E_s}{\tau\left(\frac{dE}{d\sqrt{t}}\right)}\right]^2 \quad (t << L^2/\tilde{D}) \qquad [37]$$

This expression may be transformed once more to an even simpler algebraic form if E *vs.* $\sqrt{t}$ shows the expected straight line behavior over the entire time period of the current flux

$$\tilde{D} = \frac{4}{\pi\tau}\left(\frac{m_B V_M}{M_B S}\right)^2\left(\frac{\Delta E_s}{\Delta E_t}\right)^2 \quad (\tau << L^2/\tilde{D}) \quad [38]$$

ΔE_t is the total change of the cell voltage E during the current pulse, neglecting the IR drop.

Determination of Other Kinetic and Thermodynamic Quantities

Besides the determination of the chemical diffusion coefficient $\tilde{D}$, it is possible to evaluate other kinetic and thermodynamic parameters by use of the galvanostatic intermittent titration technique. The methods for obtaining some of the more important quantities are as follows.

The enhancement factor.—As discussed earlier the chemical diffusion of species A is enhanced by the thermodynamic factor $\partial \ln a_{A^*}/\partial \ln c_{A^*}$ relative to the component diffusivity. This enhancement factor can be determined from the local slope of the coulometric titration curve, $dE/d\delta$, at any composition. The change of $\ln a_{A^*}$ is given by the change of the voltage E of the cell times $z_A q/kT$, and the change in the concentration c_A is $N_A d\delta/V_M$. Therefore, we have

$$\frac{\partial \ln a_{A^*}}{\partial \ln c_{A^*}} = -\frac{z_A q c_A V_M}{kTN_A}\frac{dE}{d\delta} = -\frac{z_A q(y+\delta)}{kT}\frac{dE}{d\delta} \quad [39]$$

By determining the slope of the coulometric titration curve at different stoichiometries the thermodynamic factor may be obtained as a function of the composition.

The partial conductivity.—For the case in which the chemical diffusion is predominantly determined by one kind of ionic species, A^{z_A+}, and either electrons or holes, Eq. [14] yields, with the substitution of D_K by σ according to Eq. [2] and [5]

$$\sigma_A t_e = \frac{(z_A q)^2 c_A \tilde{D}}{kT}\left(\frac{\partial \ln a_{A^*}}{\partial \ln c_{A^*}}\right)^{-1} \quad [40]$$

By using Eq. [39] the thermodynamic factor can be replaced by a term containing the slope of the coulometric titration curve, $dE/d\delta$, which is determined from the steady-state values of the cell voltages in between titrations and the corresponding change of the composition. This yields

$$\sigma_A t_e = -\frac{z_A F \tilde{D}}{V_M}\left(\frac{dE}{d\delta}\right)^{-1} \quad [41]$$

from which $\sigma_A t_e$ may be calculated if the chemical diffusion coefficient $\tilde{D}$ has been determined as described above. It is obvious that if the sample is predominantly electronically conducting, the product $\sigma_A t_e$ is the partial ionic conductivity of the A species, σ_A. For a predominantly ionic conductor $\sigma_A t_e$ is the partial electronic conductivity, σ_e, since $t_e = \sigma_e/(\sigma_e + \sigma_A) \approx \sigma_e/\sigma_A$.

If the coulometric titration curve can be considered linear over the range of a single galvanostatic titration step, replacement of dE and $d\delta$ by their finite values and using Eq. [37] for $\tilde{D}$ yields

$$\sigma_A t_e = -\frac{4}{\pi}\frac{V_M m_B I_o \Delta E_s}{M_B S^2 \tau\left(\frac{dE}{d\sqrt{t}}\right)^2} \quad (t << L^2/\tilde{D}) \quad [42]$$

Furthermore, if τ is also small compared to $L^2/\tilde{D}$, *i.e.*, E is proportional to $\sqrt{t}$ over the entire period of the application of the constant current during one titration step, we have

$$\sigma_A t_e = -\frac{4}{\pi}\frac{m_B V_M I_o \Delta E_s}{M_B S^2 (\Delta E_t)^2} \quad (\tau << L^2/\tilde{D}) \quad [43]$$

Thus, like the chemical diffusion coefficient, the conductivity term $\sigma_A t_e$ may be determined from the change in the steady-state voltage, ΔE_s, and the magnitude of the voltage increase during one titration, ΔE_t.

The component diffusion coefficient, the mobilities, and the tracer diffusion coefficient.—For a predominantly electronically conducting electrode containing mobile A^{z_A+} ions, D_{KA} may be determined from Eq. [16] using the expressions [39] and [36]-[38] for the enhancement factor and the chemical diffusion coefficient, respectively. As previously, if $dE/d\delta$ may be considered as constant for a single titration step, we have

$$D_{KA} = -\frac{4kTm_B V_M I_o}{\pi q^2 c_A z_A^2 M_B S^2 \tau}\frac{\Delta E_s}{\left(\frac{dE}{d\sqrt{t}}\right)^2} \quad (t << L^2/\tilde{D}) \quad [44]$$

If, additionally, E *vs.* $\sqrt{t}$ is linear over the entire titration period τ, the component diffusion coefficient may also be determined from

$$D_{KA} = -\frac{4kTm_B V_M I_o}{\pi c_A z_A^2 q^2 M_B S^2}\frac{\Delta E_s}{(\Delta E_t)^2} \quad (\tau << L^2/\tilde{D}) \quad [45]$$

The electrical mobility, u_A, and the general mobility, b_A, are obtained from this expression by use of the Nernst-Einstein relation [5]. Also, it is possible to calculate the tracer diffusion coefficient D_T from the results of galvanostatic intermittent titration experiments if an assumption can be made concerning the value of the correlation factor f_A (or more generally, the Haven ratio) (21)

$$D_{TA} = f_A D_{KA} \quad [46]$$

The parabolic tarnishing rate constant.—If the range of stoichiometry of the electrode material is exhausted by continual titrations, further ionic current through the galvanic cell results in the growth of a second phase outside the first one. The relevant quantity used to describe the growth of such a layer is the parabolic tarnishing rate constant k_t in cases in which the process is determined by bulk diffusion. When ions A^{z_A+} and either electrons or holes are the predominantly mobile species, the ionic flux in the parabolically growing layer may be either described by Fick's first law with the diffusion coefficient given by Eq. [14] or

$$|j_A| = c_A\frac{dL'}{dt} = c_A\frac{k_t}{L'} \quad [47]$$

if the average concentration c_A may be regarded as approximately constant. L' is the instantaneous thickness of the tarnishing layer. Equating Fick's first law and Eq. [47], and integrating over the thickness of the layer, L', results in an equation from which the parabolic rate constant may be calculated as a function of the activity of A* or the compositional parameter δ at the interface with the electrolyte ($x = 0$)

$$k_t = \frac{1}{y+\delta}\left|\int_0^{L'}\tilde{D}d\delta\right| \quad [48]$$

The integral is the area under a plot of the chemical diffusion coefficient, as determined by galvanostatic intermittent titration using the tarnishing product (outer) phase as the electrode material, as a function of the stoichiometric parameter δ between the value in equilibrium with the first (inner) phase and the value at the outer surface. Alternatively, k_t may be calculated for a predominantly electronic conductor

by plotting D_{K_A}, which is determined according to Eq. [44] or [45], as a function of the cell voltage E. This follows from Eq. [48] by using Eq. [16] for $\tilde{D}$ and Eq. [39] for the enhancement factor

$$k_t = \frac{q}{kT} \left| z_A \int_0^{L'} D_{K_A} dE \right| \qquad [49]$$

The integration extends from the voltage at the two-phase equilibrium to the voltage corresponding to the activity a_{A^*} or the stoichiometric parameter δ for which k_t is evaluated.

In contrast to the usual tarnishing experiments in which the material is typically maintained in contact with a constant activity of A*, *e.g.*, that corresponding to equilibrium with another phase, the method described here permits the tarnishing rate constant to be evaluated as a function of the activity of A* over the whole stoichiometric range of the tarnish product phase.

Application to Trilithium Antimonide, Li_3Sb

The galvanostatic intermittent titration technique has been applied to Li_3Sb as a model electrode constituent. Its kinetic parameters determine the rate of alloying antimony with lithium at high lithium activities. Due to the large amount (3 moles) of lithium that can react per mole of antimony, this binary system may be of practical interest for application in new types of high power density batteries, either at room temperature (22, 23) or at elevated temperatures. From the point of view of testing the general applicability of the galvanostatic intermittent titration technique it should be pointed out that Li_3Sb actually offers less than optimum conditions, for it has a comparatively narrow range of stoichiometry and a very composition-dependent enhancement factor.

A eutectic mixture of molten LiCl-KCl salt (spectroscopically pure, Anderson Physics Laboratories, Urbana, Illinois) has been used as an electrolyte for lithium ions in a set of experiments on the Li_3Sb phase. Both reference and counterelectrodes were composed of the solid-state two-phase system of lithium-saturated Al and the adjacent phase "LiAl," which has a composition at the phase boundary of about 47 atomic percent Li. This system has a potential about 300 mV less negative than pure liquid lithium at 400°C. The Li_3Sb electrode was prepared by coulometric titration of lithium into an antimony disk. The electric leads were made of molybdenum, which exhibits a negligible solubility for lithium. The experiments were conducted within a Vacuum/Atmospheres Company recycling helium dry box. No impurity effects were observed.

The voltage range of the existence of the Li_3Sb phase is between about +0.88 and 0V with reference to pure lithium at 400°C. This corresponds to a range of lithium activity from about 2.6×10^{-7} to 1. Figure 3 shows a typical voltage-time dependence for the case of galvanostatically titrating lithium into the $Li_{3+\delta}Sb$ sample with a current density of 0.25 mA/cm², applied for 300 sec at 360°C. The corresponding change of the stoichiometric parameter δ of the sample is about 2.5×10^{-4}. The voltage is plotted as a function of the square root of time for the same measurement in Fig. 4. In agreement with theoretical considerations (Eq. [35]), a straight line is observed for times up to 200 sec. The deviation from linearity at longer times is discussed later.

A sequence of selected galvanostatic titrations of lithium out of Li_3Sb, distributed over the entire range of the thermodynamic existence of the compound, is plotted in Fig. 5. The polarization of the voltage is observed to be much greater in the center of the stoichiometric range of existence than near both ends.

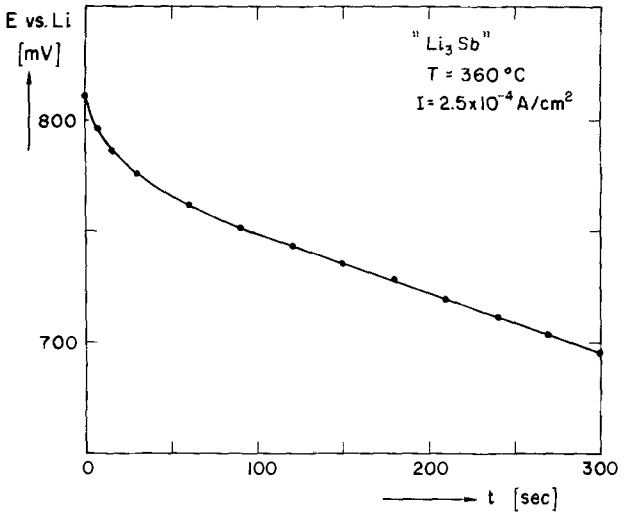


Fig. 3. Typical transient voltage change of the galvanic cell with a Li_3Sb sample after a constant current of 2.5×10^{-4} A cm² was applied. LiCl-KCl(e) was used as a molten salt electrolyte, and two-phase Al, LiAl mixtures used as counter and reference electrodes.

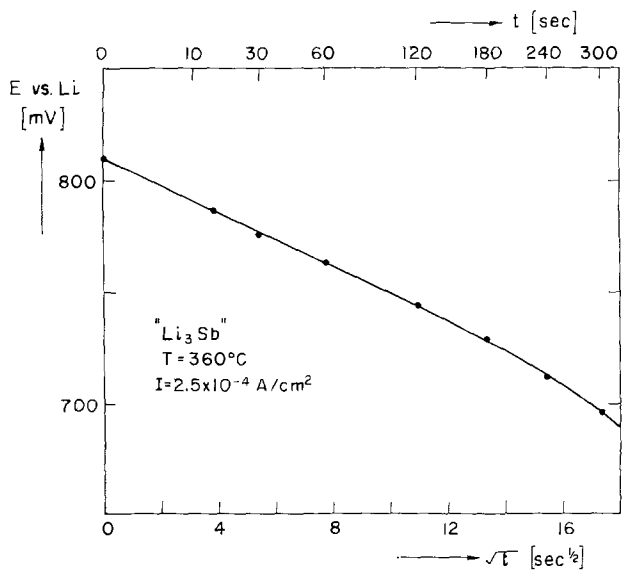


Fig. 4. Representation of the transient voltage of the galvanic cell as a function of the square root of the time. The experimental conditions were the same as those of Fig. 3.

This is closely related to the shape of the coulometric titration curve, determined from the steady-state cell voltages observed between titrations as a function of composition. The data for several runs (in both compositional directions) are shown in Fig. 6. Near the middle of the composition range the slope $dE/d\delta$ has a marked maximum, producing the greatest changes of the transient voltage with time, in accordance with Eq. [35].

The thermodynamic enhancement factor, $\partial \ln a_{Li}/\partial \ln c_{Li}$, was calculated from the slope of the coulometric titration curve and plotted in Fig. 7 as a function of the stoichiometry. As can be seen, the chemical diffusion of the lithium is enhanced by up to a factor of nearly 70,000 relative to the component diffusion coefficient (or the tracer diffusion coefficient divided by the correlation factor).

In order to further test this technique, several additional parameters have been varied, and the results compared with the theoretical considerations. At the same voltage, or stoichiometric composition, the values of the kinetic parameters should be independent of the direction of the current flux. The slopes of the

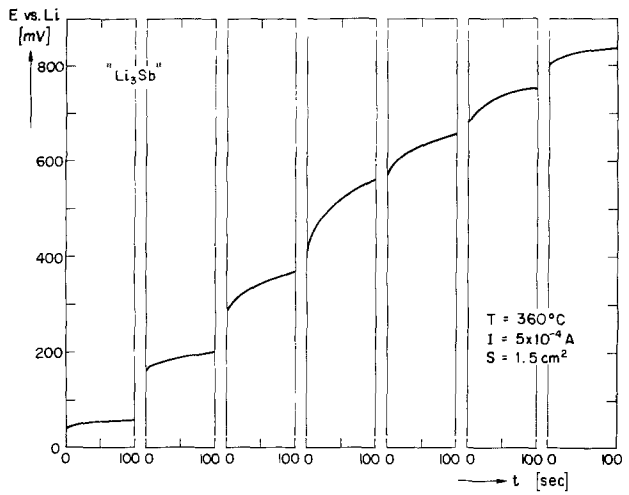


Fig. 5. The transient voltages of the galvanic cell containing Li_3Sb as a function of the time t for several different initial steady-state voltages plotted vs. pure lithium using the same galvanostatic current density of 3.3×10^{-4} A cm^{-2} contact area between the electrolyte and the sample. The different starting voltages represent different stoichiometries of $Li_{3+\delta}Sb$ as determined from Fig. 6.

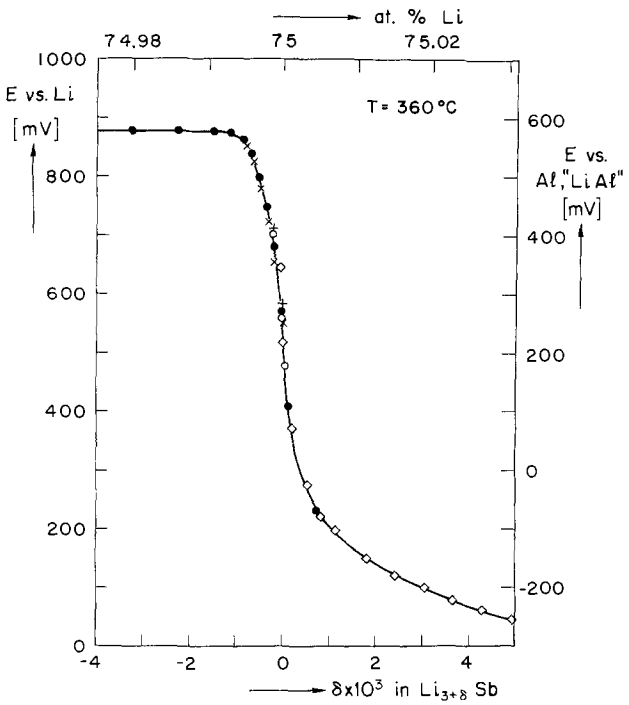


Fig. 6. The steady-state voltages of the galvanic cell with a Li_3Sb sample vs. pure lithium and an Al, LiAl electrode as a function of the stoichiometry δ, *i.e.*, the amount of lithium which is electrochemically pumped into the sample (coulometric titration curve). The horizontal part of the curve represents the two-phase region of Li_3Sb in equilibrium with Li_2Sb.

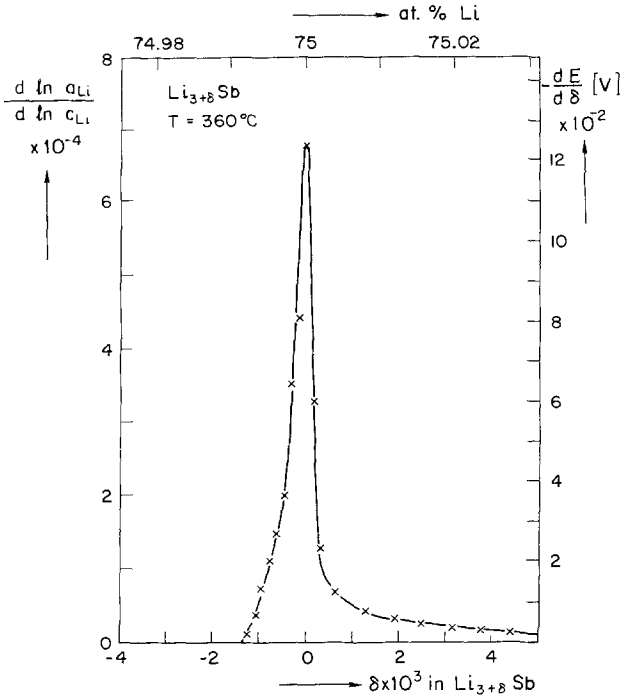


Fig. 7. The composition dependence of the enhancement factor in $Li_{3+\delta}Sb$, which causes the chemical diffusion coefficient to be much greater than either the component diffusion coefficient or the tracer diffusion coefficient of lithium. The enhancement factor is determined from the slope of the coulometric titration curve (Fig. 6), which is plotted at the right-hand ardinate.

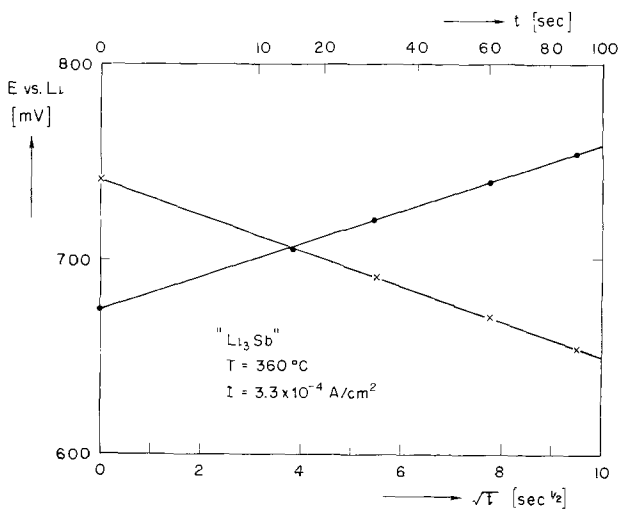


Fig. 8. Two transient voltage changes of the galvanic cell with a Li_3Sb electrode with reference to pure lithium as a function of the square root of time for adding lithium to the sample and removing it with the same current density at about the same mean composition, *i.e.*, cell voltage. The absolute value of the slopes is seen to be the same for both procedures.

E *vs.* $\sqrt{t}$ curves should be the same but of opposite sign for the same current density. This was found to be true, as demonstrated in Fig. 8. Also, the calculated kinetic quantities should be independent of the actual value of the current. According to Eq. [35] the slope of the plots of the voltage *vs.* the square root of time should be proportional to the current I_0 applied. The results of experiments carried out with current densities differing by a factor of 12 are shown in Fig. 9. Good agreement between experiments and theory is seen.

The chemical diffusion coefficient that was calculated from the slope of the straight line in Fig. 4 and the corresponding change of the steady-state cell voltage according to Fig. 6 is $\tilde{D} = 2 \times 10^{-5}$ cm^2 sec^{-1} at the stoichiometric deviation $\delta = -6 \times 10^{-4}$ and 360°C. This value is strongly enhanced by the enhancement factor of $\partial \ln a_{Li}/\partial \ln c_{Li} = 1.3 \times 10^4$, thus being related to a much lower component diffusion coefficient, $D_{KLi} = 1.5 \times 10^{-9}$ cm^2 sec^{-1} at the same stoichiometry and temperature. The tracer diffusion coefficient has also the same order of magnitude, since the correlation factor is of the order of 1. The corresponding partial lithium ionic conductivity was calculated to have a value of $\sigma_{Li} = 1.5 \times 10^{-4}$ Ω^{-1} cm^{-1} for that composition, according to the general equations of the previous section. Using the Nernst-Einstein equa-

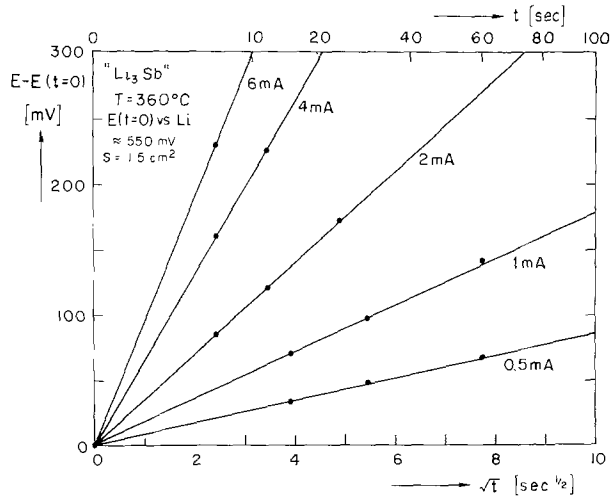


Fig. 9. The transient voltage of the galvanic cell with a Li_3Sb sample referenced to an initial cell voltage of approximately 550 mV *vs.* pure lithium as a function of the square root of time. The results are shown for several current densities. The slopes increase almost linearly with the current density.

tion the general lithium mobility was found to be $b_{Li} = 2 \times 10^{11}$ cm^2 V^{-1} A^{-1} sec^{-2}, and the electrical lithium mobility is $u_{Li} = 3 \times 10^{-8}$ cm^2 V^{-1} sec^{-1} at this composition. The parabolic rate constant k_t for the formation of a Li_3Sb tarnishing layer on a Li_2Sb (24, 25) substrate is of the order of 10^{-8} cm^2 sec^{-1} at a lithium activity $a_{Li} = 4 \times 10^{-7}$ and of the order of 10^{-7} cm^2 sec^{-1} at a lithium activity $a_{Li} = 1$.

By use of this same procedure, values of the chemical diffusion coefficient $\tilde{D}$ have been determined over the whole range of stability of the Li_3Sb phase, as illustrated in Fig. 10.

Extensive experiments utilizing this galvanostatic intermittent titration technique to study the systems Li-Sb and Li-Bi will be reported elsewhere (25, 26).

Discussion

The galvanostatic intermittent titration method combines transient and steady-state electrochemical measurements. In one set of experiments a number of kinetic and thermodynamic quantities may be readily determined with considerable precision as a function of composition within a single phase. The compositional resolution in this technique is quite high, so that phases with only small ranges of stoichiometry can be investigated. The experimental equipment requirements are quite modest, consisting primarily of a constant current source and an instrument that can measure voltage *vs.* time.

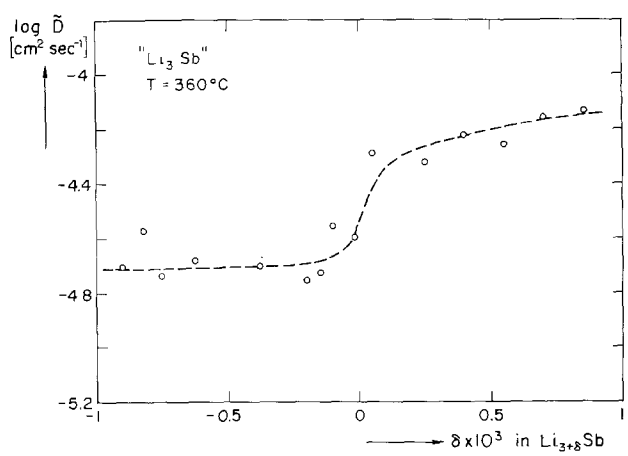


Fig. 10. Variation of the chemical diffusion coefficient with composition over the whole range of stability of Li_3Sb at 360°C.

The information that is obtained from the observation of the time dependence of the cell voltage during a galvanostatic current pulse is in principle no greater than that which can be obtained by using other transient methods. However, experimental problems in other techniques related to resistance polarization, which are typically only reduced by the use of reference electrodes, are here totally eliminated.

In the common potentiostatic voltage step method, the current should theoretically be infinite in the first moment. This is not experimentally realizable, and the imposed voltage difference creates large transient polarization effects. Thus the initial and boundary conditions usually applied to the assumed solution of Fick's second law are not exactly fulfilled. The result is a deviation from the theoretically expected linear relation between the current and $1/\sqrt{t}$ at short times. Additionally, because of the inverse time scale, this part of the plot is expanded whereas the part with the more useful information is compressed. In the case of the galvanostatic titration method, however, the initial period contains the most valuable information because any effects due to a change in the enhancement factor or to the finite thickness of the sample do not become important until later. This early part of the experiment is fortuitously expanded by the use of the square root of time scale in the voltage plot.

If a deviation from the linear dependence of the voltage on the square root of time is found at longer times in galvanostatic experiments it may have one or more of several explanations. Either the solution to the assumed boundary value problem is not valid at long times because of finite length effects due to a high diffusion coefficient or a thin sample, or there may be a significant change of either the thermodynamic enhancement factor or the chemical diffusion coefficient over the pertinent stoichiometric range. These different possibilities may be evaluated from the experimental results on the magnitude and composition dependence of the chemical diffusion coefficient and the enhancement factor. If necessary, a current pulse of shorter duration or a smaller value of current might be used.

Another way to eliminate the influence of a composition-dependent enhancement factor is to determine the stoichiometry δ from the measured cell voltage E by using data from the coulometric titration curve and to plot δ as a function of $\sqrt{t}$. According to Eq. [35] the following relation should be found

$$\frac{d\delta}{d\sqrt{t}} = \frac{2V_M I_0}{SFz_i\sqrt{\tilde{D}\pi}} \quad (t \ll L^2/\tilde{D}) \qquad [50]$$

Then, $\tilde{D}$ may be determined from the slope of the δ *vs.* $\sqrt{t}$ plot. An equivalent procedure is to divide the measured cell voltage by the corresponding thermodynamic factor and to plot this quantity as a function of $\sqrt{t}$. However, because of the large variation in the values for diffusion coefficients, often only an order of magnitude estimate is of interest, and these refinements may not be necessary.

Experimental errors might appear if the electrochemically active species are not exclusively used to change the stoichiometry of the sample during the titration, but, after being discharged and becoming neutral, diffuse back into the electrolyte or diffuse into the electrical lead connected to the sample. These possibilities could be checked in a separate experiment with a blank sample, operating over the same voltage range.

In conclusion, it has been demonstrated that the galvanostatic intermittent titration technique is a pow-

erful tool which can be employed to determine a number of important kinetic and thermodynamic quantities in mixed conductors. Of special interest is its ready application to compounds with small stoichiometric ranges and appreciable variation of the thermodynamic enhancement factor with composition.

The values of chemical diffusion coefficient observed in the case of Li_3Sb are several orders of magnitude greater than those found necessary to produce negligible diffusional polarization in fine particle battery electrodes.

Acknowledgments

This work was funded by a grant from the Institute for Energy Studies at Stanford University, which has supported one of the authors (W. W.) on a Standard Oil of California visiting professorship. The earlier grant of a NATO Scholarship through the German Academic Exchange Service (DAAD) is also gratefully acknowledged.

Manuscript submitted March 14, 1977; revised manuscript received May 23, 1977.

Any discussion of this paper will appear in a Discussion Section to be published in the June 1978 JOURNAL. All discussions for the June 1978 Discussion Section should be submitted by Feb. 1, 1978.

Publication costs of this article were assisted by Stanford University.

LIST OF SYMBOLS

- a_i activity of species i
- b_i general mobility of species i ($cm^2\ sec^{-2}\ V^{-1}\ A^{-1}$)
- c_i concentration of particle i (cm^{-3})
- $\tilde{D}_i$ chemical diffusion coefficient of species i ($cm^2\ sec^{-1}$)
- D_{Ki} component diffusion coefficient of species i ($cm^2\ sec^{-1}$)
- D_{Ti} tracer diffusion coefficient of species i ($cm^2\ sec^{-1}$)
- E galvanic cell voltage (V)
- ΔE_s steady-state voltage change (V)
- ΔE_t transient voltage change (V)
- f correlation factor
- F Faraday's constant, (A sec val^{-1})
- I electric current (A)
- I_0 applied constant electric current (A)
- j_i flux density of particles i ($cm^{-2}\ sec^{-1}$)
- k Boltzmann's constant (V A sec $°K^{-1}$)
- k_t parabolic tarnishing rate constant ($cm^2\ sec^{-1}$)
- L sample length (cm)
- m_i mass of species i (g)
- M_i atomic weight of species i ($g\ mole^{-1}$)
- N_A Avogadro's number ($mole^{-1}$)
- q elementary charge (A sec)
- S contact area between electrolyte and sample (cm^2)
- t time (sec)
- t_i transference number of species i
- T absolute temperature (°K)
- u_i electrical mobility of species i ($cm^2\ V^{-1}\ sec^{-1}$)
- V_M molar volume ($cm^3\ mole^{-1}$)
- W enhancement factor
- x distance coordinate (cm)
- y stoichiometric number
- z_i valence of species i
- γ_i activity coefficient of species i (cm^3)
- δ deviation from the (ideal) stoichiometry
- η_i electrochemical potential of species i (per particle) (V A sec)
- μ_i chemical potential of species i (per particle) (V A sec)
- $\mu_i°$ chemical potential of species i in the standard state (V A sec)
- σ_i partial electrical conductivity of species i ($\Omega^{-1}\ cm^{-1}$)
- τ pulse duration (sec)
- ϕ electrostatic potential (V)

REFERENCES

1. W. F. Chu, H. Rickert, and W. Weppner, in "Fast Ion Transport in Solids, Solid State Batteries and Devices," W. van Gool, Editor, p. 181, North Holland Publishing Co., Amsterdam-London (1973).
2. H. Rickert and W. Weppner, *Z. Naturforsch., Teil A*, **29**, 1849 (1974).
3. B. C. H. Steele, in "Mass Transport Phenomena in Ceramics," A. R. Cooper and A. H. Heuer, Editors, p. 269, Plenum Press, New York (1975).
4. J. B. Wagner, Jr., in "Electrode Processes in Solid State Ionics," M. Kleitz and J. Dupuy, Editors, p. 185, D. Reidel, Dordrecht (1976).
5. H. Rickert, in "Electromotive Force Measurements in High-Temperature Systems," C. B. Alcock, Editor, p. 59, The Institute of Mining and Metallurgy, London (1968).
6. R. A. Rapp and D. A. Shores, in "Techniques of Metal Research," Vol. 4, Part 2, R. A. Rapp, Editor, p. 123, Interscience, New York (1970).
7. D. O. Raleigh, *Electroanal. Chem.*, **6**, 87 (1973).
8. R. N. Adams, "Electrochemistry at Solid Electrodes," M. Dekker Inc., New York (1969).
9. A. J. Rosenburg, *This Journal*, **107**, 795 (1960).
10. E. Fryt, S. Mrowec, and T. Walec, *Oxid. Met.*, **7**, 117 (1973).
11. S. Mrowec, *J. Mater. Sci.*, **9**, 1961 (1974).
12. C. Wagner, in "Progress in Solid State Chemistry," Vol. 10, Part 1, J. McCaldin and G. Somorjai, Editors, p. 3, Pergamon Press, Oxford (1975).
13. R. Haase, "Transportvorgänge," Steinkopff Verlag, Darmstadt (1973).
14. C. Wagner, *Z. Phys. Chem., Abt. B*, **21**, 25 (1933).
15. C. Wagner, *Acta Metall.*, **17**, 99 (1969).
16. C. Wagner, in "Atom Movements," p. 153, American Society for Metals, Cleveland, Ohio (1951).
17. L. S. Darken, *Trans. AIME*, **175**, 184 (1948).
18. C. Wagner, *J. Chem. Phys.*, **21**, 1819 (1953).
19. H. S. Carslaw and J. C. Jaeger, "Conduction of Heat in Solids," p. 112, Clarendon Press, Oxford (1967).
20. J. Crank, "The Mathematics of Diffusion," Oxford University Press, London (1967).
21. J. Bardeen and C. Herring, in "Atom Movements," p. 87, American Society for Metals, Cleveland, Ohio (1951).
22. J. O. Besenhard and H. P. Fritz, *Electrochim. Acta*, **20**, 513 (1975).
23. Rheinisch-Westfälisches Elektrizitätswerk AG, Fr. Demande 2,206,593 (1974); Ger. Appl. P. 2,254,-870.5 (1972).
24. R. Gérardin and J. Aubry, *C. R. Acad. Sci., Ser C*, **278**, 1097 (1974).
25. W. Weppner and R. A. Huggins, To be published.
26. W. Weppner and R. A. Huggins, Submitted to *J. Solid State Chem.*

Solid-State Detectors for the Potentiometric Determination of Gaseous Oxides

I. Measurement in Air

M. Gauthier* and A. Chamberland

Hydro-Quebec Research Institute, Varennes, Quebec J0L 2P0, Canada

ABSTRACT

This paper suggests that the potentiometric detection of sulfur oxides in air is feasible with solid-sulfate electrolytes, and presents experimental results on the electrode Pt, SO_2, $O_2/SO_4^=$. Several experimental parameters, namely, p_{SO_2}, temperature, and flow rate, are studied with concentration cells using potassium sulfate, as the electrolyte. A solid reference electrode based on an Ag/Ag^+ electrochemical couple is also studied as a replacement for the gas reference electrode. The authors conclude that rapid conversion of several gaseous sulfur compounds, namely, H_2S, CH_3SH, etc., into oxides occurs under the cell operating conditions, and that rapid equilibrium is reached between SO_2, SO_3, and O_2 at the electrode. Preliminary results of tests using solid electrolytes to detect other gaseous oxides in air are also given for the Pt, CO_2, $O_2/CO_3^=$, and Pt, NO_2, O_2/NO_3^- systems.

Success with solid-state oxygen detectors based on stabilized zirconia in the ppm concentration range has led the authors to undertake research into other types of detectors for the measurement of ambient and industrial pollutants such as sulfur dioxide, carbon monoxide, carbon dioxide, and the different nitrogen oxides. Originally, potentiometric rather than polarographic methods of analysis were selected to avoid relying on high ionic conductivity electrolytes, which are scarce. Furthermore, this choice dispenses with the complex process of determining the anionic-to-cationic nature of the conductivity, and all that remains to be done is to ensure there is no electronic conductivity at all. In the selection of suitable electrolytes, attention can then be focused on the possible electrode reactions.

Several studies of electrode reactions between molten oxyanions and oxides, such as nitrate and sulfate electrodes, may be found in the literature (1, 2). The mechanisms involved are still disputed, moreover, because of their complexity and dependence upon several experimental parameters.

The initial step in this research was to try to adapt previous studies on fused-salt systems to solid-electrolyte techniques using sulfate and sulfur oxides. A systematic study was made of a solid electrolyte of potassium sulfate with sulfur dioxide as the gaseous oxide. The tests were based on the following reaction mechanism as described by Salzano for the SO_3, O_2, Pt/SO_4^{-2} electrode (2).

$$\tfrac{1}{2}\,O_2 + 2e^- \rightleftarrows O^{-2} \text{ (electrochemical reaction)} \quad [1]$$

$$SO_3 + O^{-2} \rightleftarrows SO_4^{-2} \text{ (chemical reaction)} \quad [2]$$

These two reactions can be combined to yield the overall equation

$$SO_3 + \tfrac{1}{2}\,O_2 + 2e^- \rightleftarrows SO_4^{-2} \quad [3]$$

The resulting Nernst equation for the following cell

$$\begin{matrix} SO_3, & Pt/K_2SO_4/Pt, & SO_3' \\ O_2 & & O_2' \end{matrix} \quad [4]$$

is

$$E = \frac{RT}{2F} \ln \frac{(p_{O_2})^{1/2}\, p_{SO_3}}{(p_{O_2'})^{1/2}\, p_{SO_3'}} \quad [5]$$

or

$$E = \frac{RT}{4F} \ln \frac{p_{O_2}}{p_{O_2'}} + \frac{RT}{2F} \ln \frac{p_{SO_3}}{p_{SO_3'}} \quad [6]$$

* Electrochemical Society Active Member.

Key words: solid electrolytes, emf measurements, SO_3-SO_2-O_2 platinum electrode, sulfates, sulfur dioxide analysis.

Since sulfur dioxide is the major pollutant, and is easier to handle in a laboratory, it can be used to replace SO_3 in the experiments. In this case, either the equilibrium

$$SO_3 \rightleftarrows SO_2 + \tfrac{1}{2}\,O_2 \quad [7]$$

with

$$K = \frac{(p_{SO_2})\,(p_{O_2})^{1/2}}{(p_{SO_3})} \quad [7']$$

must be reached rapidly or the SO_2 to SO_3 conversion must be small and occur at constant rate for a given gas flow, whatever the initial SO_2 concentration, in accordance with Salzano's interpretation of his own laboratory observations (2). Taking this into account, the following expression for SO_2 is obtained

$$E = \frac{RT}{2F} \ln \frac{p_{O_2}}{p_{O_2'}} + \frac{RT}{2F} \ln \frac{p_{SO_2}}{p_{SO_2'}} \quad [8]$$

which, in air, simplifies to

$$E = \frac{RT}{2F} \ln \frac{p_{SO_2}}{p_{SO_2'}} \quad [9]$$

Experimental

Different models of oxide concentration cells have been devised and studied experimentally; a general device is illustrated schematically in Fig. 1. The arrangement comprises two alumina tubes between which the potassium sulfate pellet is pinned. Two small single bore alumina tubes allow the gas to circulate

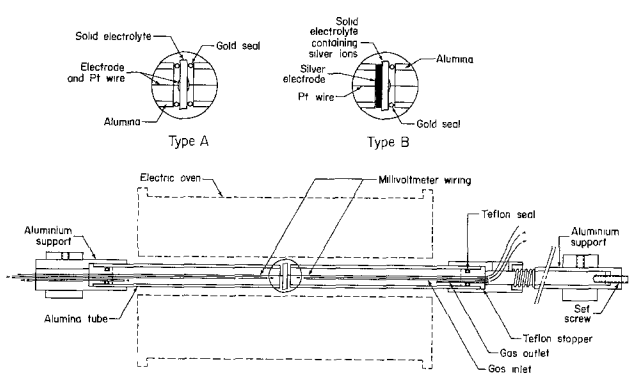


Fig. 1. Experimental apparatus used to study the SO_2, O_2, Pt/SO_4^{--} system. A, two-compartment cell; B, cell with a silver/silver ion reference electrode.

near the measuring electrode. Platinum wire and platinum powder obtained by vacuum deposition ensure electrical contact. In the hot zone, the seal is made by pressing gold rings between the alumina tubes and the electrolyte while conventional O-rings are used for sealing outside the furnace.

An optimized device derived from the first one (Fig. 1A) was used, in particular, for response time and flow rate studies. As illustrated in Fig. 2, the two compartments here are located on the same side of the electrolyte. The seal is made by applying appropriate pressure between the alumina tube and the electrolyte at high temperature before the first utilization. The resulting slight deformation of the electrolyte ensures gas tightness between the two compartments and between each compartment and the outside. The dead volume of the complete gas circuit inside the sensor is around 0.8 cm^3 including the four-hole alumina rod (998 McDannel, 0.250 in. OD, 0.067 in. ID) and the 316 stainless steel gas feedthrough, 1/16 in. OD. Powdered potassium sulfate 100-mesh (Baker analyzed, reagent grade) was used for the electrolyte because this nonhygroscopic salt becomes a relatively good conductor in the hexagonal form above 579°C (3), and can be easily sintered. The powder was subjected to unidirectional pressure of 2 ton/cm^2, then sintered at 940°C for at least 2 days. The pellets thus obtained can hold 760 mm Hg pressure difference for hours without apparent leakage both at room temperature and, once fitted in the sensor, at operating temperature. The gas mixtures are prepared by injecting pure oxides into 10 and 100 liter Mylar bags already filled with ambient or synthetic air; the precision for this technique is approximately 3%. The SO_2 mixtures are then stable for the duration of the test. The temperature is maintained at ± 2°C by a Thermoelectric proportional control, Model 100, with Chromel-Alumel thermocouples. A Tacussel Aries 10,000 high impedance ($\approx 10^{13}\Omega$) millivoltmeter is used to measure the electromotive force (emf), and signals are recorded on a Hewlett-Packard strip chart recorder, No. 7100-B.

Results and Discussion

Different tests were made using the apparatus illustrated in Fig. 1A and 2 with sulfur dioxide and potassium sulfate, at temperatures ranging between 600° and 925°C. Unless otherwise specified, the reference electrode is a mixture of 100 ppm SO_2 in air, and all gas flow rates are fixed at 100 cm^3/min.

Emf variation with SO_2 partial pressure.—The emf time plot with different values of the SO_2 partial pressure is given by way of example in Fig. 3. The concentrations given in this and the following figures correspond to the initial partial pressures obtained by injecting SO_2 at room temperature, $(p_{SO_2})_{in.}$ The results presented in this figure were obtained with the apparatus illustrated in Fig. 2.

Generally speaking, the response times vary from a few seconds to several minutes, mainly according to

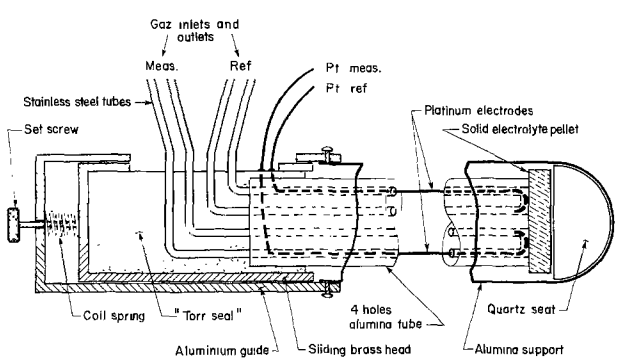


Fig. 2. Simplified experimental device with a reduced dead volume and both gas circulating compartments on the same side of the electrolyte.

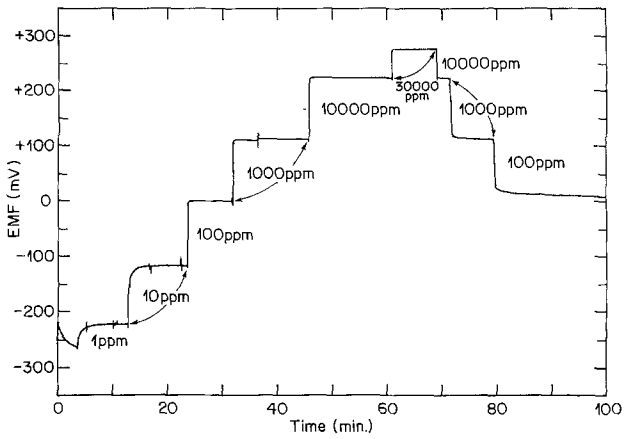


Fig. 3. Typical response time to SO_2 variations obtained with the experimental device of Fig. 2. Temperature, 820°C, reference electrode, 100 ppm SO_2 in air; gas flow rates, 100 cm^3/min.

the flow rate, the concentration range under study, and the geometry of the apparatus. The chemical properties of the sulfur oxides make it extremely complex to perform a detailed analysis of the processes determining the rise and fall of the emf signal. Adsorption definitely has a significant influence, especially in view of the wide variation of the concentration under study (over 4 decades).

Typical experimental results with the SO_2 detector are presented as emf *vs.* log $(p_{SO_2})_{in.}$ in Fig. 4. The experimental slope coincides with a two-electron reaction ($n = 2.12$) in accordance with Eq. [3]. Expressed in parts per million (10^{-6} atm), the concentration range extends from 0.5 to 40,000 ppm. The experimental signal obtained at lower concentrations coincides with the limit of gas-mixture preparation by microinjection techniques, which means that it is impossible to determine the lower operating limit of the SO_2, SO_3, O_2, Pt/SO_4^{-2} electrode in air using this particular method of preparation.

Emf dependence on temperature.—Experimental and calculated values of emf for a concentration cell filled with SO_2 in air, namely 10 ppm on one side and 100 ppm on the other, at different temperatures between 600° and 925°C are reported in Fig. 5. Below 650°C, experimental emf values are erratic and decrease rapidly compared with the calculated values. How-

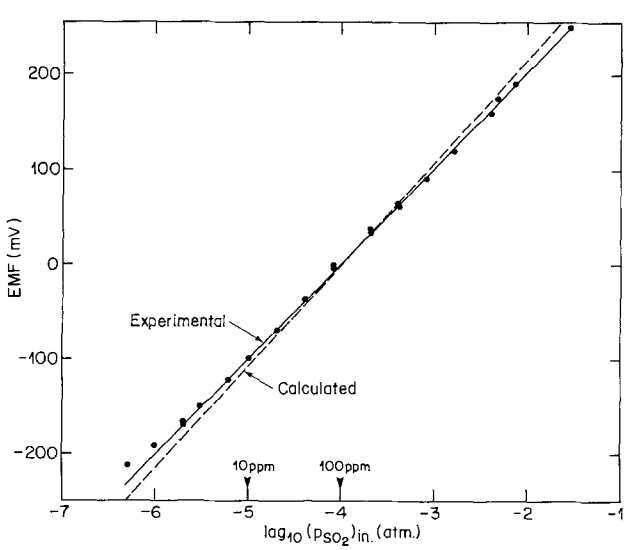


Fig. 4. Plot of emf vs. logarithm of the SO_2 partial pressure expressed in atmospheres. A concentration of 100 ppm SO_2 in air was circulated in the reference compartment. Temperature, 820°C; flow rate, 100 cm^3/min in both compartments. The dashed curve represents the calculated slope 2.3 *RT*/2F.

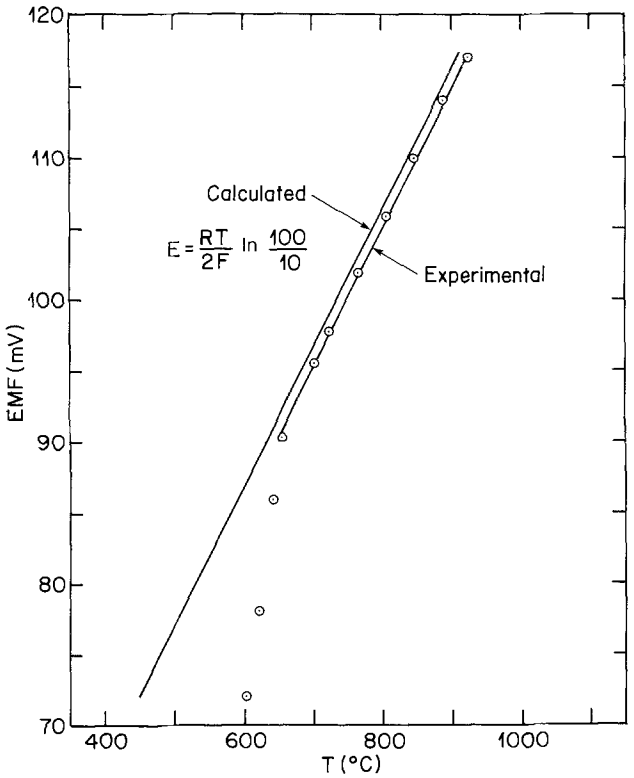


Fig. 5. Plot of emf vs. temperature (°C). Measuring compartment, 100 ppm SO_2 in air; reference compartment, 10 ppm SO_2 in air; flow rate, 100 cm³/min in both compartments.

ever, above this temperature, the emf values agree within $\simeq$ 1 mV. Special care was taken in this test to control and measure the temperature of the electrolyte; nevertheless, a bias potential of 1.2 $\pm$ 0.2 mV was found between the two electrodes as a single preparation of 10 ppm SO_2 in air was circulated on both sides of the cell, a value which corresponds to the difference between the experimental and calculated emf found in Fig. 5. Application of the emf technique (4) to the results of Fig. 5 shows that the ionic transport number, t_i, in potassium sulfate is one within the precision of the present experiments.

Emf dependence on flow rate.—Various tests to determine the influence of the flow rate are reported in Fig. 6, which shows the effect of the concentration, the temperature, and the presence of a catalyst when the flow rate is varied from a few cm³/min to 500 cm³/min. It may be noted that an operating range exists in which the emf almost ceases to vary with the flow rate. From this, it was concluded that under such conditions, thermodynamic equilibrium between SO_2 and SO_3 is reached rapidly, at least in the vicinity of the platinum electrode. This result differs from those obtained by Salzano with molten sulfates in which he observed a 55 mV dependence for each variation of 1 decade in the flow rate. It therefore seems justified to use Eq. [7] and [7'] without any need to consider a fixed SO_2-SO_3 conversion rate as Salzano did (2). Under equilibrium conditions, therefore, the detector validates the equation

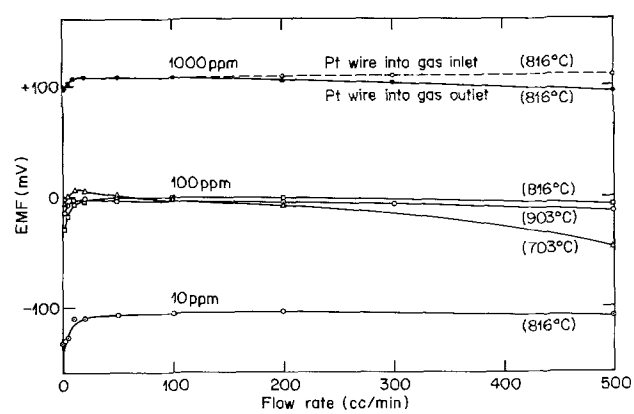


Fig. 6. Emf dependence on flow rate at three different SO_2 partial pressures; 10, 100, 1000 ppm. Also illustrated here is the effect of the operating temperature and platinum catalytic activity on the emf dependence on flow rate.

$$(p_{SO_2})_{in.} = (p_{SO_2}) + (p_{SO_3}) \qquad [10]$$

where $(p_{SO_2})_{in.}$ is the gas partial pressure initially introduced, and (p_{SO_2}) and (p_{SO_3}) are the partial pressures in equilibrium at the electrode. Thus, the detector signal is equivalent to an over-all measurement of the quantity of sulfur oxide regardless of whether the gas is introduced as SO_2 or SO_3.

The range of flow rates in which the sulfur-oxide detector operates at equilibrium depends on several parameters; its geometry, the types of material used, operating conditions, etc. At high flow rates (Fig. 6) the range is limited, particularly with strong SO_2 concentrations or when the temperature drops to around 700°C. This may be explained by the fact that the conversion of SO_2 into SO_3 no longer reaches equilibrium value under these conditions. Moreover, this seems to confirm the catalytic nature of the platinum wire of the electrode when placed at the inlet rather than at the outlet of the test gas. Meanwhile, at low flow rates, the limit could be a result of convection competing with the forced circulation of the gas, which could result in condensation (SO_3 or H_2SO_4) in the cold zones of the detector. This would naturally modify the SO_2-SO_3 mixture. Only devices with zero or under 10 mV emf dependence on the flow rate were used for the studies described here.

Solid reference electrode.—For reasons of convenience, one of the two gas electrodes of the cell [4] was replaced by a solid-state reference electrode such as Ag°/Ag^+ in which the silver ion was present as a solid solution. The following experimental cells were studied

$$Ag^\circ/Ag_2SO_4 \text{ in } K_2SO_4//K_2SO_4/SO_2, O_2, Pt \qquad [11]$$

and

$$Ag^\circ/Ag_2SO_4 \text{ in } K_2SO_4/SO_2, O_2, Pt \qquad [11']$$

whose over-all cell equation is

$$Ag^\circ + SO_2 + O_2 \rightleftarrows Ag_2SO_4 \text{ (as a solution in } K_2SO_4) \qquad [12]$$

The emf of cells [11] and [11'] can be expressed as

$$E = \text{const.} - \frac{RT}{F} \ln a_{Ag^+} + \frac{RT}{2F} \ln p_{SO_2} + \frac{RT}{2F} \ln p_{O_2} \qquad [13]$$

where const. is a constant that includes the E° of pure solid silver sulfate. This expression of the emf is valid as long as there is a solid solution of Ag_2SO_4 in K_2SO_4. In air and at constant silver-ion activity, a_{Ag^+}, the emf depends only on the SO_2 partial pressure

$$E = \text{const.}' + \frac{RT}{2F} \ln p_{SO_2} \qquad [14]$$

A modification to the earlier experimental arrangement made it possible to use the silver/silver-ion reference electrode for the tests (Fig. 1B).

Emf dependence on $(p_{SO_2})_{in.}$ with Ag°/Ag^+ as the reference electrode.—Signals obtained at different SO_2 partial pressures are presented in Fig. 7. The silver-sulfate concentration was prepared at a 1% mole fraction by melting known proportions of silver sulfate and potassium sulfate, ball-milling them to 100 mesh, and then sintering. The results are in good agreement with

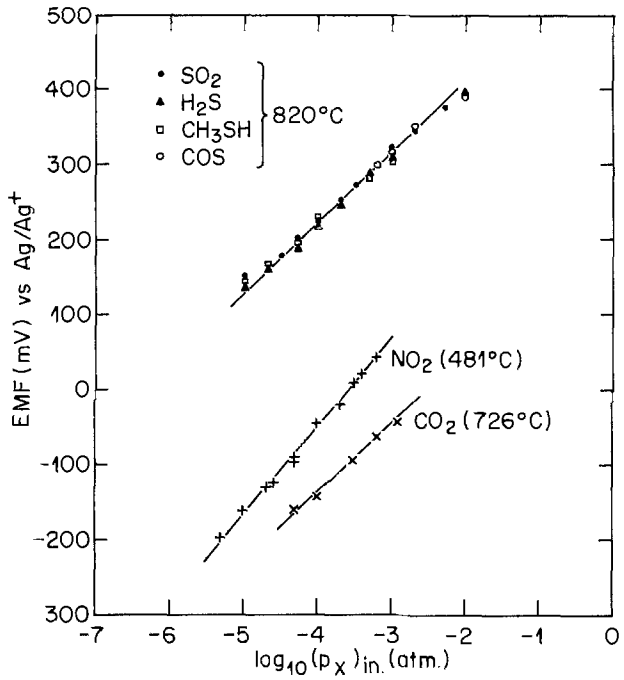


Fig. 7. Dependence of the emf on the logarithm of the concentration of different anhydrides. For SO_2, H_2S, CH_3SH, and COS, a K_2SO_4 electrolyte is used while K_2CO_3 and $Ba(NO_3)_2$ electrolytes are used for CO_2 and NO_2, respectively. In all cases, results were obtained with Ag/Ag^+ reference electrodes (see text).

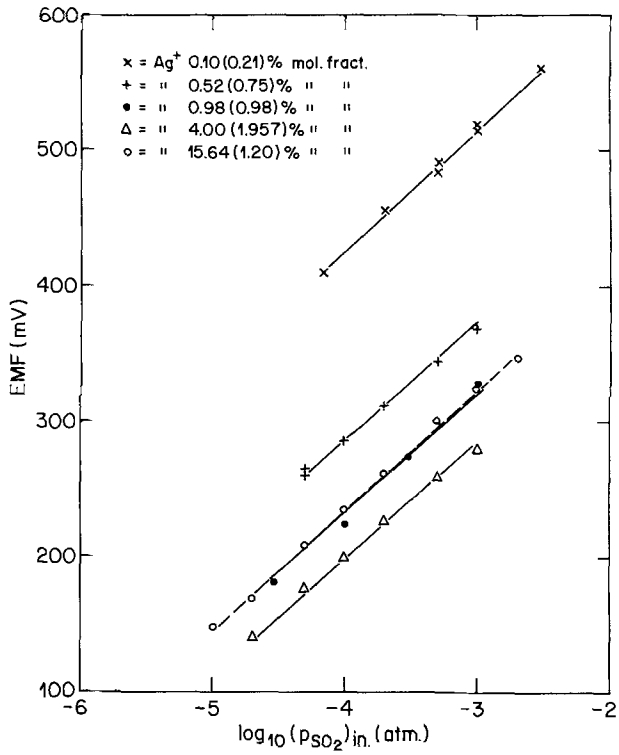


Fig. 8. Dependence of the emf on the logarithm of the SO_2 concentration in air for different mole fractions of Ag_2SO_4 in K_2SO_4. Given in parentheses are the concentration values obtained by atomic absorption analysis after the test. Test temperature, 820°C; fixed flow rates, 100 cm^3/min.

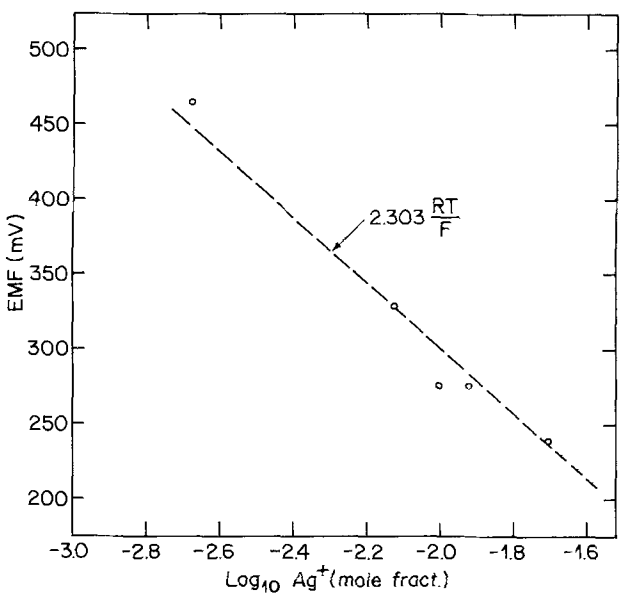


Fig. 9. Dependence of the emf on the logarithm of the silver ion concentration in K_2SO_4 for a constant SO_2 concentration in air; 3×10^{-4} atm. The silver-ion concentrations used here were obtained by atomic-absorption analysis. The dashed curve shows the calculated value of 2.3 RT/F in accordance with Eq. [13]. Temperature, 820°C; flow rate, 100 cm^3/min.

relation [14]. Cells [11] and [11'] both present the same behavior.

Emf dependence on a_{Ag^+}.—In order to check the validity of Eq. [13] for the Nernst dependence of the signal on the silver-ion activity, an attempt was made to study different concentrations of silver sulfate in the electrolyte fixed during the preparation, and ranging from 0.1 to 15.0% mole fractions. For each of the 5 silver-sulfate concentrations, a cell similar to [11'] was prepared and studied from the point of view of the SO_2 partial pressure (Fig. 8). Also included in this figure are the results of an atomic-absorption analysis of the silver-ion concentrations in the electrolyte after each test, compared to the values fixed during preparation. A large difference between prepared and observed concentrations is observed, particularly for the two higher prepared concentrations where metallic silver was visible after sintering at 900°C. This is probably a result of partial decomposition of the silver sulfate.

When the emf values of Fig. 8 are plotted as a function of the logarithm of the silver-ion mole fraction for a given $(p_{SO_2})_{in.}$ of 3×10^{-4} atm in air, the results appear to be in good agreement with the slope calculated from Eq. [13], Fig. 9. The silver-sulfate concentration used is those of the atomic-absorption analysis. Consequently, even if the concentration range studied is in fact limited, it may be reasonably concluded that an authentic solid solution of silver sulfate exists in potassium sulfate, at least around the 1% mole fraction.

The tests reported here do not eliminate the possibility that the silver/silver-ion electrode reaction is just one of several electrochemical reactions; indeed, others such as the $O_2/O^=$ couple may well exist at these temperatures. Nevertheless, this solid reference electrode greatly simplifies the experimental procedure and, as shown by the tests, provides satisfactory results.

Emf dependence on other sulfur compounds.—The solid reference cell used with SO_2 was also tested under the same experimental conditions with other sulfur-containing compounds such as hydrogen sulfide, carbonyl sulfide, and methyl mercaptan. The results, shown in Fig. 7, are almost identical to those with SO_2, whatever gas enters the cell. In fact, even by varying the temperature, the concentration, or the flow rate of these gases, it was impossible to distinguish between the signals they produced and the signal from an equivalent concentration of SO_2. It may therefore be assumed that in air these gases are rapidly oxidized and quantitatively converted into sulfur oxides at the electrode. This conclusion is borne out by the existence of excessive quantities of oxygen compared with the

test gases, by the high operating temperature of the sensor, and also by the presence of platinum at the electrode.

Tests on other oxide-oxyanion systems.—The last experimental results to be presented are those of tests conducted on other oxide-oxyanion systems to see how far the application of solid-state electrochemical cells is feasible for potentiometric determination of different gaseous oxides. The experimental procedure and conditions were the same as those described for the tests on sulfur oxides except that the operating temperatures were limited by the melting point of the electrolytes used. The Ag/Ag^+ reference electrode type illustrated in Fig. 1B was selected to make the tests easier to perform. The performance of a carbon dioxide detector was studied using potassium carbonate as the electrolyte. This was prepared by melting a mixture of a 1% mole fraction of silver sulfate in potassium carbonate at 900°C, and sintering at 750°C for 24 hr. No subsequent control of the composition was performed.

The emf variation with logarithm of the CO_2 partial pressure in air is presented in Fig. 7. The slope corresponds to a two-electron mechanism ($n = 2.12$), as suggested by the reaction

$$CO_2 + \tfrac{1}{2}\,O_2 + 2e^- \rightleftarrows CO_3^= \qquad [15]$$

The possibility of building a nitrogen oxide detector was also investigated using a solid electrolyte obtained by melting a mixture of a 1% mole fraction of silver chloride in barium nitrate at 600°C, and sintering at 540°C for 24 hr. The results obtained from the NO_2 partial pressure variations in air are given in Fig. 7. The slope seems to correspond to a single electron mechanism ($n = 1.22$), as expected from the electrode reaction

$$NO_2 + \tfrac{1}{2}\,O_2 + 1e^- \rightleftarrows NO_3^- \qquad [16]$$

The response times observed for the nitrogen dioxide and carbon dioxide detectors are of the same order of magnitude as those obtained with the sulfur oxide detector.

Conclusion

This study has shown that electrochemical cells based on solid electrolytes containing oxyanions can be used for the potentiometric determination of SO_2, SO_3, CO_2, and NO_2 in air, or in any gas with a fixed oxygen content. The sensors bear a strong similarity to oxygen-zirconia detectors even if the electrolytes are poor-to-moderate cationic conductors, and despite the relatively complex reactions of the oxides. The reasons for this can be traced to the utilization of solid electrolytes and the high operating temperatures of the solid-state detectors. Solid electrolytes enhance rapid surface equilibria because of the total absence of convection; furthermore, the oxide-oxyanion systems become simpler as the temperature rises.

Further analysis of the SO_3, O_2, $Pt/SO_4^=$ electrode reveals that under certain given conditions, equilibrium between sulfur dioxide, oxygen, and sulfur trioxide is reached rapidly, at least in the area closest to the electrode. The study also shows that gaseous sulfur-bearing components circulated in the detector produce a signal identical to the one produced by SO_2. This seems to be due to the rapid conversion of the gases to oxides inside the device.

Finally, the results obtained are in agreement with the over-all electrode reaction proposed by Salzano (2) for molten sulfates, and seem to indicate that similar electrode reactions may be extended to other oxide-solid oxyanion systems.

Acknowledgments

Thanks are due to Hydro-Quebec Research Institute for the financial support of this work through a research and development project. The authors also wish to thank Marc Poirier and André Bélanger for many valuable discussions, and Roger Bellemare and Denis Ricard for carrying out the experimental part of this work.

Manuscript submitted June 16, 1976; revised manuscript received May 25, 1977.

Any discussion of this paper will appear in a Discussion Section to be published in the June 1978 JOURNAL. All discussions for the June 1978 Discussion Section should be submitted by Feb. 1, 1978.

Publication costs of this article were assisted by the Hydro-Quebec Research Institute.

REFERENCES

1. A. F. Goeting and J. A. A. Ketelaar, *Electrochim. Acta*, **19**, 267 (1974).
2. F. J. Salzano and L. Newman, *This Journal*, **119**, 1273 (1972).
3. M. Natarajan and E. A. Secco, *Can. J. Chem.*, **53**, 1542 (1975).
4. C. Wagner, *Z. Phys. Chem.*, **B21**, 25 (1933).

Solid-State Detectors for the Potentiometric Determination of Gaseous Oxides

II. Measurements in Oxygen-Variable Gases in the SO_2, SO_3, O_2, $Pt/SO_4^=$ System

M. Gauthier,* A. Chamberland, A. Bélanger,* and M. Poirier**

Hydro-Quebec Research Institute, Varennes, Quebec J0L 2P0, Canada

ABSTRACT

This paper describes an extended application of potentiometric solid-state detectors for measuring oxides in oxygen-variable gases. The SO_2, SO_3, O_2, $Pt/SO_4^=$ system examined in Part I for oxide detection in air is studied here with respect to the total sulfur oxide and oxygen partial pressures. A study of the experimental parameters, operating temperatures, and the oxygen partial-pressure range revealed the possibility of a simple method of compensating the effect of the oxygen partial pressure on the signal from the oxide detector. An entirely solid-state device consisting of a potassium-sulfate oxide detector, a stabilized-zirconia oxygen detector, and usual electronic components is described, and results of tests with synthetic gas mixtures are presented. Experimental findings confirm calculations based on the electrode reactions and on the rapidly established equilibrium at the platinum electrode.

The feasibility of high temperature solid-state detectors for the potentiometric measurement of oxides in gaseous mixtures has been demonstrated in IREQ laboratories (1, 2). Different models of these solid-state detectors were discussed at the Spring Meeting of the Ontario-Quebec Section of The Electrochemical Society together with possible fields of application (3). Part I of this work presented the results of quantitative measurements of gaseous sulfur oxides using solid potassium sulfate as the electrolyte, and examined the influence of various experimental parameters such as the sulfur oxide partial pressure, operating temperature, and flow rates. Replacement of the circulating gas reference electrode by an Ag/Ag_2SO_4 1% in a K_2SO_4 solid reference electrode was also suggested and tested. So far, however, all results have been obtained with low sulfur oxide concentrations prepared in air where the oxygen partial pressure is constant.

The object of the present paper is to expand the possibilities of these detectors by adapting them to gases with a variable oxygen content such as stack gases. According to previous results, the concentration of sulfur oxides in air is determined using solid-electrolyte concentration cells such as

$$SO_3, O_2, Pt/K_2SO_4/Pt, O_2', SO_3' \qquad [1]$$

for which the over-all electrode reaction is written as

$$SO_3 + \tfrac{1}{2}\, O_2 + 2e^- \rightleftarrows SO_4^= \qquad [2]$$

The emf of this electrochemical cell is

$$E = \frac{RT}{4F} \ln \frac{p_{O_2}}{p_{O_2}'} + \frac{RT}{2F} \ln \frac{p_{SO_3}}{p_{SO_3}'} \qquad [3]$$

in which p_{O_2}, p_{O_2}', p_{SO_3}, and p_{SO_3}' represent the partial pressures of the gases at thermodynamic equilibrium.

As shown by Eq. [3], a double dependence of the emf on p_{O_2} and p_{SO_3} is observed. Moreover, this is not peculiar to the SO_3, $O_2/SO_4^=$ system, but is a general characteristic of all oxide/oxyanion systems, such as $CO_2/CO_3^=$ and NO_2/NO_3^-, which were discussed briefly in Part I. The system chosen for the present work is the sulfate-sulfur oxide system, which, owing to the coexistence of SO_2 and SO_3 over a wide range of temperatures and oxygen partial pressures, represents a fairly complex case. Another reason for choosing this particular system is its wide field of application. Indeed, this type of solid-state detector has an important role to play in the measurement of the sulfur oxides present in stack gases in which the sulfur content varies from one to several thousand ppm. Since it is particularly suited for the stringent analysis conditions of industrial chimneys, namely high temperatures and necessary use of refractory materials, research in the area of stack gases seemed not only interesting but fully justified.

Simultaneously with the variation in SO_2 concentration, the p_{O_2} found in chimneys changes from 5 to 0.1% and even less. The emf expressed by Eq. [3], therefore, cannot be interpreted simply in terms of the sulfur oxide concentration. The aim of the present study is to show that, under certain conditions of approximation, it is possible to eliminate or compensate for the effect of the p_{O_2} on the emf with a zirconia-stabilized oxygen detector in conjunction with an electronic compensation device developed specifically for the purpose.

Experimental

For this study, the simplified experimental device illustrated in Fig. 2 of Part I was used as the sulfur oxide detector. The oxygen detector consisted of a calcia-stabilized tube (Zircoa) designed for operation at high temperatures (4); the tube was platinized over a 1 in. length both inside and outside, in the hot zone. The ambient air is used as an external reference. The test gas was directed onto the inside electrode through a small diameter alumina tube. For the sake of convenience, both the oxygen detector and the oxide detector in the compensating device were housed in a common 10 in. furnace. The measuring equipment and the experimental procedures relating to the preparation of the gas mixtures and the electrolyte were described in Part I. Commercially available calibrated oxygen preparations in nitrogen were used for the tests.

Results and Discussion

General expression of the emf.—An important observation drawn from previous work on sulfate-sulfur oxide systems is that both SO_2 and SO_3 are present under the experimental conditions, and that thermodynamic equilibrium between SO_2, SO_3, and O_2 is rapidly attained at the electrode in accordance with the following equations

* Electrochemical Society Active Member.
** Electrochemical Society Student Member.
Key words: solid electrolytes, emf measurements, sulfates, sulfur dioxide analysis, electrochemical cell.

$$SO_3 \rightleftarrows SO_2 + \tfrac{1}{2} O_2 \quad [4]$$

$$K = \frac{(p_{SO_2})\ (p_{O_2})^{1/2}}{(p_{SO_3})} \quad [5]$$

For any given temperature, therefore, the oxygen partial pressure determines the ratio between p_{SO_2} and p_{SO_3}. Part I described tests performed in air at low sulfur oxide concentrations ($p_{O_2} > p_{SO_2}$) where the p_{SO_2}/p_{SO_3} ratio was constant and hence not included as a variable in the expression of the emf. In systems in which the oxygen content does vary, however, the emf dependence *vs.* p_{O_2} (Eq. [3]) is complicated by the fact that both right-hand terms in the equation vary with p_{O_2}.

A more explicit expression of the emf as a function of the oxygen partial pressure is obtained by introducing into Eq. [3] the equilibrium constant expression [5] and the total sulfur relation

$$(p_{SO_2})_{in.} = p_{SO_2} + p_{SO_3} \quad [6]$$

where $(p_{SO_2})_{in.}$ is the total sulfur-oxide partial pressure fixed experimentally at room temperature using sulfur dioxide, and p_{SO_2} and p_{SO_3} are equilibrium values.

The new expression of the emf as a function of the partial pressure of the gases at the measuring electrode is

$$E = C_1 + \frac{RT}{2F} \ln (p_{SO_2})_{in.} + \frac{RT}{2F} \ln p_{O_2} - \frac{RT}{2F} \ln (K + (p_{O_2})^{1/2}) \quad [7]$$

Where the constant term, C_1, includes the contribution from the second electrode, defined as the reference electrode.

The validity of this general expression is then checked experimentally by two series of tests. In the first, the oxygen partial pressure is kept constant at three different levels; 1.00, 0.21, and 0.012 atm, while the total sulfur anhydride partial pressure $(p_{SO_2})_{in.}$ is varied between 3 and 10,000 ppm. The experimental results appear in good agreement with calculated values, as shown in Fig. 1. The emf varies linearly as a function of log $(p_{SO_2})_{in.}$, and the slope of Fig. 1 corresponds to the term $RT/2F$ in Eq. [7] when p_{O_2} is constant. The concentration range studied did not reveal any value for p_{O_2} or $(p_{SO_2})_{in.}$ for which Eq. [7] is not valid, at least within the limits of experimental accuracy.

In the second series of tests, $(p_{SO_2})_{in.}$ is fixed at 100 ppm and the oxygen partial pressure changes from 1 to 3 $\times$ 10^{-4} atm. Results are reported for three temperatures, namely 696°, 807°, and 901°C, and are compared with calculated values in Fig. 2. The relatively good agreement between the calculated emf and the experimental measurements confirms the validity of Eq. [7], which is based on the rapidly attained equilibrium between SO_2, O_2, and SO_3 at the electrode. When the operating temperature approaches or drops below 700°C, the difference between the calculated and the measured values increases. This may be linked with the appearance of a dependence of the emf on the flow rate as noted in Part I under similar test conditions. In both cases, it seems to be a matter of the inability of the SO_2 to SO_3 conversion rate to reach the equilibrium value in the actual operating conditions of this detector.

Limiting conditions for oxygen compensation.—To introduce the concept of oxygen compensation, it is useful to differentiate Eq. [7] as follows

$$\frac{dE}{d \ln p_{O_2}} = \frac{RT}{2F} - \frac{RT}{4F} \left(\frac{(p_{O_2})^{1/2}}{(p_{O_2})^{1/2} + K} \right) \quad [8]$$

It is only when the derivative $dE/d \ln p_{O_2}$ is a constant, *i.e.*, independent of O_2, that the signal's oxygen dependence can be compensated without difficulty.

Equation [8] allows two limiting conditions where $dE/d \ln p_{O_2}$ becomes constant. The first case involves low oxygen partial pressures and high operating temperatures where K is high ($K \simeq 2$ at 900°C) (5), and $dE/d \ln p_{O_2}$ becomes equal to $RT/2F$, experimentally this approximation corresponds to conditions where SO_2 is the predominant sulfur oxide. The second case involves high oxygen partial pressures and low temperatures where K is low ($K \simeq 4 \times 10^{-3}$ at 450°C), and $dE/d \ln p_{O_2}$ becomes equal to $RT/4F$; experimentally, the predominant sulfur oxide here is SO_3.

The first case is of greater interest in this study which deals with low oxygen-content mixtures as found in stack gases. When those limiting conditions prevail, then Eq. [7] can be rewritten as an approximation

$$E\ (1) = C_2 + \frac{RT}{2F} \ln (p_{SO_2})_{in.} + \frac{RT}{2F} \ln p_{O_2} \quad [9]$$

Thus, it is possible in these conditions of approxima-

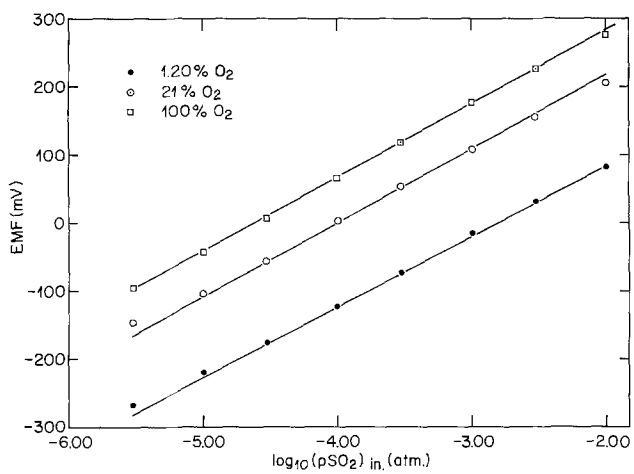


Fig. 1. Dependence of the emf on the logarithm of the total sulfur oxide partial pressure, $(p_{SO_2})_{in.}$ for three oxygen concentrations. T = 827°C. 100 ppm SO_2 in air is passed through the reference compartment. The flow rate in both compartments is fixed at 100 cm³/min. The full line shows the calculated values (Eq. [7]).

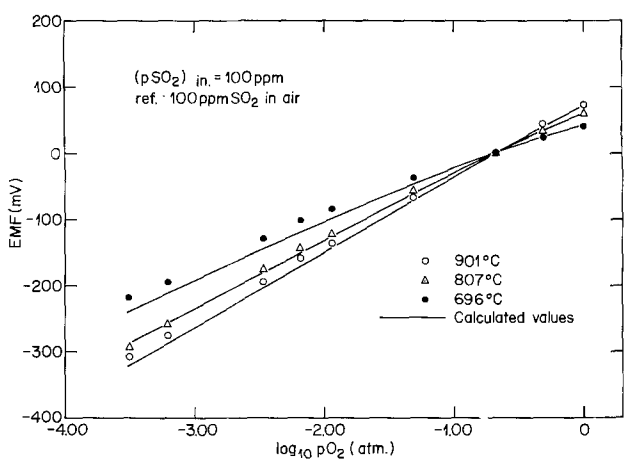


Fig. 2. Dependence of the emf on the logarithm of the oxygen partial pressure at three different temperatures and at constant $(p_{SO_2})_{in.}$. Flow rate in both compartments: 100 cm³/min. Full lines show the calculated values (Eq. [7]).

tion, to eliminate the emf dependence on oxygen partial pressure simply by offsetting the signal from an oxide detector, as represented in Eq. [9], with a suitable signal from an oxygen detector.

Oxygen compensating device.—Oxygen detectors based on solid electrolytes and similar in technology to the one described here not only exist but operate in exactly the same experimental conditions. In order to test the proposed compensation system, therefore, well-known oxygen concentration cells based on stabilized zirconia (4) were adopted with potentiometric signals expressed by

$$E\ (2) = C_3 + \frac{RT}{4F} \ln p_{O_2} \qquad [10]$$

where C_3 comprises the reference electrode. A simple electronic device was built that produces an oxygen-compensated signal.

$$E\ (3) = E\ (1) - 2E\ (2) = C + \frac{RT}{2F} \ln\ (p_{SO_2})_{in.} \qquad [11]$$

The compensation system consisting of the oxide detector, the oxygen detector, and the electronic device, is illustrated in Fig. 3. The three steps in the signal-conditioning process are described as follows: (*i*) electrical insulation of the input signal to ensure high impedance of the measuring system ($10^9\Omega$); (*ii*) inversion of the oxygen-detector signal; and (*iii*) addition of twice the modified signal from the oxygen detector to the oxide-detector signal plus an offset output signal to account for different types of reference electrode in the two detectors.

Results of tests on the compensating device.—To check the performance of the compensation system depicted in Fig. 3, it was decided to use a circulating gas reference electrode with the sulfur oxide detector (100 ppm SO_2 in air). The reason for this was that although the Ag/Ag^+ reference electrode described in Part I proved easy to operate and suitable for measuring sulfur oxides in air, preliminary tests revealed that when p_{O_2} and p_{SO_2} are very low, the silver sulfate present in the electrolyte in certain circumstances could be reduced to the metallic state, and the detector performance would be inevitably affected.

A common operating temperature of 827°C was selected for the two detectors as representing the minimum temperature at which the approximation of Eq. [7] is still valid in stack-gas compositions containing oxygen in concentrations up to 5%. Three sulfur dioxide concentrations (10, 100, and 1000 ppm) representative of stack-gas compositions were assayed in gaseous mixtures containing various oxygen/nitrogen ratios. The results are presented in Fig. 4 as emf *vs.* $\log_{10} p_{O_2}$. The signals from the oxide detector and the oxygen detector are shown with their corresponding compensated signal. For each concentration level the compensated signal appears independent of the oxygen partial pressure at ± 6 mV when the oxygen content of the gas is under 5%, but above this concentration, the signal becomes oxygen-dependent because the approximation of Eq. [9] is no longer valid. As expected, different sulfur oxide concentrations do not affect the signal of the oxygen detector since the prepared oxygen concentrations are always greater than the oxide concentrations.

Translated in terms of parts per million, the mean values of the compensated signals obtained at 5% oxygen partial pressure are 9.7, 106, and 1150 ppm of SO_2, respectively. The agreement between the measured compensated results and the prepared values therefore appears satisfactory, although higher accuracy could probably be attained with greater sophistication of the compensating apparatus and more adequate control of experimental conditions.

Table I presents further results of tests in which low oxygen content gases are circulated in the detector while $(p_{SO_2})_{in.}$ is set at 100 ppm. The signals from both the oxide detector and the oxygen detector are given in addition to compensated signal, and are compared with the calculated compensated values obtained from Eq. [11]. In some mixtures, the oxygen concentrations are too low to be controlled by preparation, and the partial pressure indicated is actually determined by means of the oxygen detector. The table also presents results of interference tests with 20% CO_2 and 1000 ppm NO contamination of different gaseous mixtures, and the results of one test with a nonoxidized sulfur compound, H_2S. The predicted compensated signal for 100 ppm total sulfur is observed for all the tests performed with these synthetic gases, even with extremely low oxygen partial pressures and even in the presence of the interference usually found in stack-gas analysis in the field.

Preliminary studies were also conducted to assess the sulfur oxide detector's performance when the circulating gas is a more or less reducing mixture of CO and CO_2 containing parts per million of SO_2. No quantitatively reproducible results have yet been obtained under such conditions as a function of the SO_2 content. It was observed that mixtures with a low CO

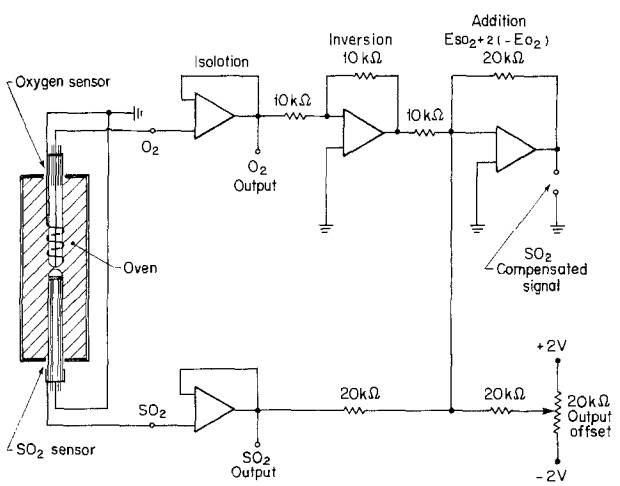


Fig. 3. A schematic of the compensating device performing the oxygen compensation of the oxide cell signal. Both the oxide detector and the oxygen detector are maintained at the same operating temperature in a common furnace. Test gases are passed simultaneously in both detectors. Analog device no. 40J operational amplifiers were used.

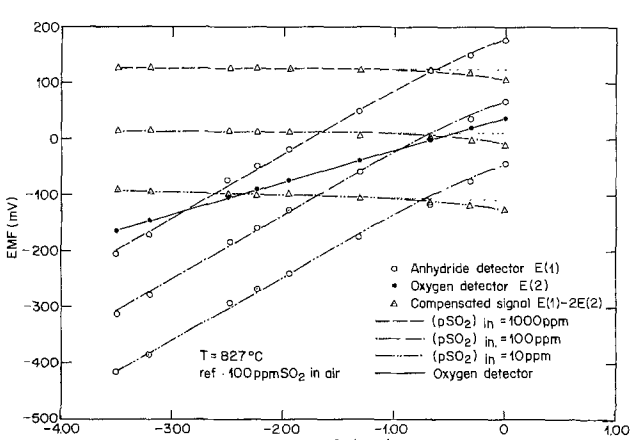


Fig. 4. Plot of the emf *vs.* the logarithm of the oxygen partial pressures for three sulfur oxide concentrations: 10, 100, and 1000 ppm. Oxygen, noncompensated and compensated signals are shown for the three sulfur oxide concentrations. T = 827°C; flow rate, 100 cm^3/min.

Table I. Results from compensation experiments at different oxygen partial pressures: $T = 827°C$ and $(p_{SO_2})_{in.} = 100$ ppm or 10^{-4} atm

(reference electrodes: 100 ppm SO_2 in air for SO_2 detector and air for oxygen detector)

Composition of gaseous mixtures (atm)	$E(1)$ oxide detector (mV)	$E(2)$ oxygen detector (mV)	$E(3) = E(1) - 2E(2)$ compensated signal (mV)	$E(3) = E(1) - 2E(2)$ calculated, Eq. [11] (mV)
O_2 (1.0) SO_2 (10^{-4})	66	+37	−8	−11
O_2 (2.1×10^{-1}) SO_2 (1×10^{-4}) N_2 (balance)	−0	0	+2	0
O_2 (4.8×10^{-2}) SO_2 (1×10^{-4}) N_2 (balance)	−60	−34	+8	+6
O_2 (6.5×10^{-3}) SO_2 (1×10^{-4}) N_2 (balance)	−159	−86	+13	+10
O_2 (6.2×10^{-4}) SO_2 (1×10^{-4}) N_2 (balance)	−280	−148	+15	+12
*O_2 (1.6×10^{-4}) SO_2 (1×10^{-4}) A (balance)	−351	−182	+13	+12
*O_2 (4.8×10^{-5}) SO_2 (1×10^{-4}) N_2 (balance)	−408	−212	+16	+12
O_2 (1.1×10^{-2}) SO_2 (1×10^{-4}) NO (1×10^{-3}) N_2 (balance)	−131	−70	+12	+9
*O_2 (1.9×10^{-4}) SO_2 (1×10^{-4}) NO (1×10^{-3}) N_2 (balance)	−338	−182	+10	+12
O_2 (1.1×10^{-2}) SO_2 (1×10^{-4}) CO_2 (2×10^{-1}) N_2 (balance)	−140	−76	+13	+9
O_2 (1.1×10^{-2}) H_2S (1×10^{-4}) N_2 (balance)	−125	−72	+14	+9

* p_{O_2} evaluated with oxygen detector.

content, for example 100 ppm SO_2 in 5% CO in CO_2 ($p_{O_2} \approx 10^{-16}$ atm at 815°C), circulating in the detector has no effect on its operation when concentrations return to normal, although at such low partial pressures of oxygen, gaseous sulfur $S_2(g)$ coexists with the SO_2 to a significant degree (7). However, if the gas is a stronger reducing agent, for example 95% CO-5% CO_2 ($p_{O_2} \approx 10^{-21}$ at 815°C), the detector will be irreparably affected, probably because of the reduction of the electrolyte to sulfur. The reduction of potassium sulfate by CO-CO_2 atmospheres has already been noted in the literature (6).

The various tests described above point to the possibility of using solid-state oxide detectors in industrial chimneys under normal operating conditions (slight excess of oxygen). The success of these experiments seems to be due in large part to the catalytic activity of the electrode and to the thermal and chemical stability of the materials used to build the detector.

Conclusion

The potentiometric detection of oxides in air with solid electrolytes containing oxyanions is extended in this work to gaseous mixtures with a variable oxygen content. In the case studied here, potassium sulfate is used as the solid electrolyte and sulfur dioxide and trioxide as the oxides.

Calculations showed that specific experimental conditions can be found where it becomes feasible to compensate the oxygen dependence of an oxide detector with the signal from another detector; a stabilized-zirconia oxygen detector, for example. An electronic apparatus was therefore devised to perform this operation with the emf of both detectors; the resulting signal is then proportional only to the logarithm of the total sulfur oxides

$$E = C + \frac{RT}{2F} \ln (p_{SO_2})_{in.}$$

Experimental results of tests with the compensation system confirm the validity of the calculations and approximated conditions which rely, as they do, on rapid equilibrium between SO_2, SO_3, and O_2 at the electrodes, and similar catalytic activities at both the oxygen and oxide electrodes.

Several concentrations of sulfur dioxide in synthetic gas mixtures akin to industrial stack-gas compositions have been scanned with this compensation system. So far, the results seem to confirm the possibility of using oxide detectors in stack-gas analysis wherever solid-state detectors for continuous oxygen measurement and combustion control have proven to be technologically sound.

Acknowledgments

Sincere thanks are owed to the Hydro-Quebec Research Institute for financial support of this work through an approved research and development project.

The authors wish to express their appreciation to Roger Bellemare and Denis Ricard for carrying out the experimental part of this work, and to Guy Bélanger and Pierre Gervais for fruitful discussions.

Manuscript submitted July 14, 1976; revised manuscript received May 25, 1977. This was Paper 86 presented at the Washington, D.C., Meeting of the Society, May 2-7, 1976.

Any discussion of this paper will appear in a Discussion Section to be published in the June 1978 JOURNAL. All discussions for the June 1978 Discussion Section should be submitted by Feb. 1, 1978.

Publication costs of this article were assisted by the Hydro-Quebec Research Institute.

REFERENCES

1. M. Gauthier, A. Chamberland, and A. Bélanger, Communication presented at the NATO Advanced Study Institute; Electrode Processes in Solid Ionics, Ajaccio, Corsica (1975).
2. M. Gauthier and A. Chamberland, Can. Pat. 1,002,559 (1976).
3. A. Bélanger, M. Gauthier, and A. Chamberland, Paper presented at the Meeting of the Ontario-Quebec Local Section of The Electrochemical Society, Montreal, April 1976.
4. R. J. Ruka and J. Weissbart, U.S. Pat. 3,400,054 (1968).
5. H. H. Kellogg, *Trans. Metall. Soc. AIME*, **230**, 1622 (1964).
6. P. Pascal, in "Traité de Chimie Minérale," Tome II, pp. 306, Masson et Cie, Paris (1963).
7. W. H. Evans and D. D. Wagman, *J. Res. Natl. Bur. Stand.*, **49**, 141 (1952).

Tarnishing of Nickel in Air at Temperatures from 23° to 200°C and Relative Humidities from Ambient to 95%

S. H. Kulpa

Bell Laboratories, Naperville, Illinois 60540

and R. P. Frankenthal*

Bell Laboratories, Murray Hill, New Jersey 07974

ABSTRACT

The tarnishing of nickel in air has been investigated at temperatures from 23° to 200°C and relative humidities from ambient to 95%. Auger electron spectroscopy with argon ion sputtering was used to determine the composition and the thickness of the oxide films. The films formed under all conditions have the same composition. Their thicknesses range from <1 nm at low relative humidities at all temperatures to about 3 nm at high relative humidities. We present a hypothesis that can account for the thicker films at high humidities.

Low voltage, low force electrical connectors usually have a noble metal contact surface to insure a low and stable contact resistance. The most commonly used contact material is gold. Electroplated nickel is frequently used in these contacts as a diffusion barrier between a copper or copper alloy substrate and the gold plate. The escalating cost of gold has led to numerous programs to reduce gold usage on contacts by reducing either the thickness of the gold plate or the area covered by the gold. As a result, nickel is more likely to be exposed to the service environment at the bases of pores in the gold plate. Also, the edges of the gold-plated area are likely to be closer to the actual points of contact.

Many studies of the oxidation of nickel have been made at temperatures above 190°C. The literature up to 1964 has been reviewed by Hauffe (1). The more recent literature has been cited by Khoi *et al.* (2). Monolayer and submonolayer structures have been grown and identified on individual faces of nickel single crystals under nearly ideal conditions of surface preparation and cleanliness. These, as well as other surface studies on nickel, have been reviewed by Lawless (3). Graham and Cohen (4) have measured the steady-state thickness of the oxide that forms at 23° and at 200°C on high purity nickel crystals after careful surface preparation. Unfortunately, little is known about the corrosion behavior of nickel under real atmospheric exposure conditions.

The present work is concerned with the tarnishing in air of electroplated nickel on copper at temperatures from 23° to 100°C and relative humidities from ambient to 95%. It attempts to assess the corrosion behavior of a real nickel surface in a real environment. Some data were also obtained at 200°C.

Experimental

Copper coupons, 14 mm square and 0.5 mm thick, were cleaned in the following manner prior to plating: vapor degrease with 1,1,1-trichloroethane, etch in 1:1 HNO_3:H_2O, rinse in water, dry with compressed air, chemically polish in 4:5:11 HNO_3:HAc:H_3PO_4 at 75°C, rinse again in water, and immediately transfer to the plating bath. A layer of nickel, 9 μm thick, was electroplated from a standard nickel sulfamate bath (Table I).

The nickel-plated specimens were vapor degreased in trichloroethylene and immediately suspended in the environmental test chamber, a 1 liter closed glass jar containing air and a suitable saturated salt solution to give the desired relative humidity (RH) at the test temperature. The chamber was placed in a mechanical convection oven, the temperature of which was controlled to better than ±1°C. The chamber and the salt solution were equilibrated at temperature in the oven before the specimens were inserted.

The corrosion films were analyzed for the elements present by Auger electron spectrometry (AES), and for the thickness and distribution of the elements with distance into the film by depth profiling using argon ion sputtering in conjunction with AES. A PHI Thin Film Analyzer system was used. Normal operating conditions were 5 kV electron gun voltage, 30 μA beam current, and 3 eV modulation amplitude. For sputtering, the argon gas pressure was 7 mPa (5×10^{-5} Torr), and the ion beam voltage and current were 0.5 kV and 5 mA, respectively. By means of a multiplexer in the system, the Ni 848 eV peak and the O 510 eV peak were monitored and plotted continuously to obtain the depth profiles. Film thicknesses were determined from the time to sputter through the film and the sputter rate. The time to sputter through the film was taken as the inflection point in the oxygen depth profile.

The sputter rate was determined in the following manner. A 2.5 μm layer of nickel, deposited onto the copper coupon, was overplated with a thin (0.25 μm), porous layer of gold. The porosity of the gold coating, as measured by the nitric acid porosity test at 10X magnification (5), was 40-50 pores/cm^2; the pore corrosion products were generally 0.1 mm or less in diameter. Twelve specimens were exposed to air at 100°C and 95% RH for an extended period of time to produce a thin layer of nickel oxide on the surface of the gold. The AES spectrum in Fig. 1 is typical of that observed on these specimens. The presence of nickel oxide is evidenced by the nickel peaks and the oxygen 510 eV peak. The oxide is sufficiently thin so that the gold 69 eV peak is still visible. Using this peak, the thickness of the oxide film was calculated from the ratio of the peak-to-peak heights in the presence and absence of the oxide film, the escape depth (0.5 nm) of the Au 69 eV electrons and Lambert's law. The thickness was reasonably uniform over each specimen, and varied from 0.5 to 2 nm for the twelve specimens. From the time required to sputter through these oxide films and

Table I. Nickel electroplating bath

Nickel sulfamate	450 kg/m^3
Boric acid	30 kg/m^3
Antipitting agent	0.37 kg/m^3
pH	3-5
Temperature	50°C
Current density	100 A/m^2

* Electrochemical Society Active Member.

Key words: Auger electron spectroscopy, argon ion sputtering, nickel oxide.

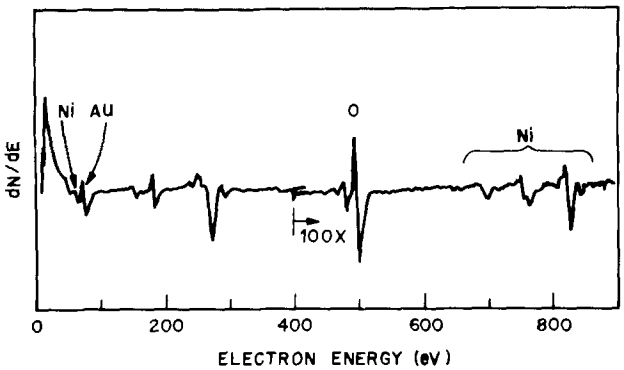


Fig. 1. AES spectrum of nickel oxide on the surface of gold-plated nickel. Oxide is sufficiently thin so that Au 69 eV peak is observed. Additional peaks from 150 to 300 eV are from S, Cl, and C surface contamination.

their thicknesses, the rate of sputtering nickel oxide was calculated to be 1.7 pm/sec with a standard deviation of 0.5 pm/sec.

Results

AES spectra of the nickel-plated specimens, both as electroplated and after the environmental exposure tests, exhibited the standard nickel and oxygen peaks. A small sulfur peak was also detected on most spectra. This peak did not disappear as the specimen surface was sputtered, indicating that the sulfur was incorporated in the electrodeposit, probably from the sulfamate bath. Copper was not detected in the spectra, indicating complete coverage of the substrate by the nickel.

The corrosion film thickness is plotted as a function of exposure time at 40°C and 95% RH, and at 200°C and ambient humidity (<1% RH) in Fig. 2 and 3. Each point is the average of 2-4 determinations. Although the scatter in the data is substantial (Fig. 2), the growth of the film at short times and the approach to a limiting thickness at longer times is evident.

The effect of temperature and humidity on the corrosion film thickness was studied over the ranges 23°-100°C, and ambient to 95% RH at a constant exposure time of 173 ksec. The resulting film thicknesses are plotted as a function of temperature and relative humidity in Fig. 4, and as a function of temperature and absolute humidity in Fig. 5. These thicknesses are either limiting or near limiting values.

Discussion

The thicknesses of the oxide films formed on nickel over wide ranges of temperature (23°-200°C) and humidity (ambient to 95% RH) range from 0.25 to 2.8

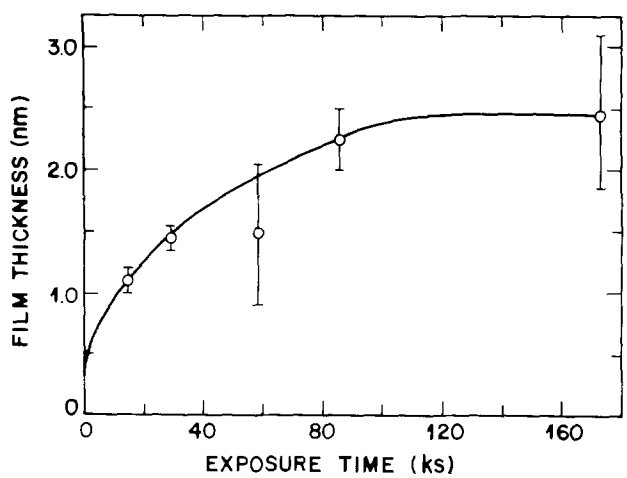


Fig. 2. Tarnish film thickness as a function of exposure time at 40°C and 95% RH.

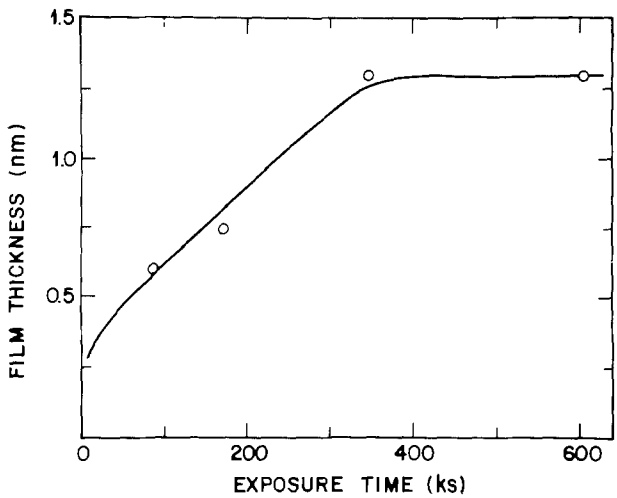


Fig. 3. Tarnish film thickness as a function of exposure time at 200°C and ambient RH (< 1%).

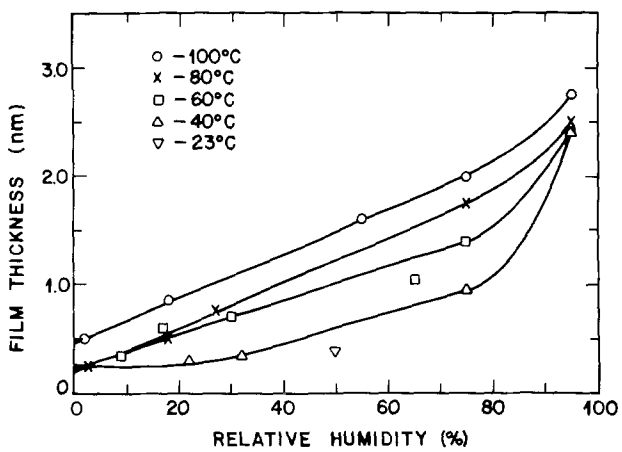


Fig. 4. Tarnish film thickness as a function of relative humidity for various temperatures. Exposure time 173 ksec.

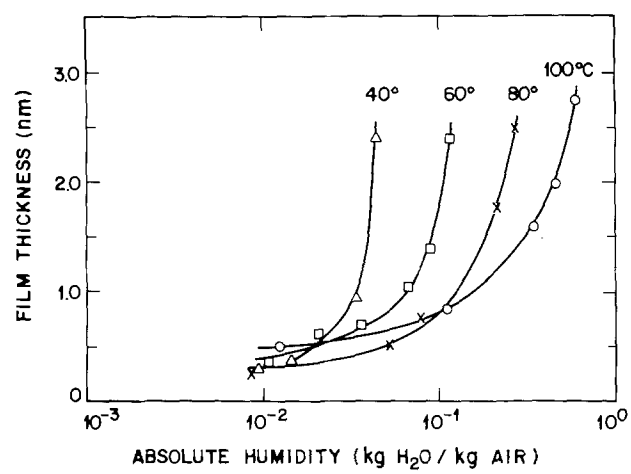


Fig. 5. Tarnish film thickness as a function of absolute humidity for various temperatures. Exposure time 173 ksec.

nm, or from about a monolayer of oxide to multilayer films more than an order of magnitude thicker. To interpret the data, it is necessary to determine whether the films formed under the various conditions have the same composition.

The AES analyses indicated that all of the films were nickel oxide. The atomic composition ratio Ni/O can be estimated from the ratio of the peak-to-peak heights of the principal Auger electron peaks of the two elements,

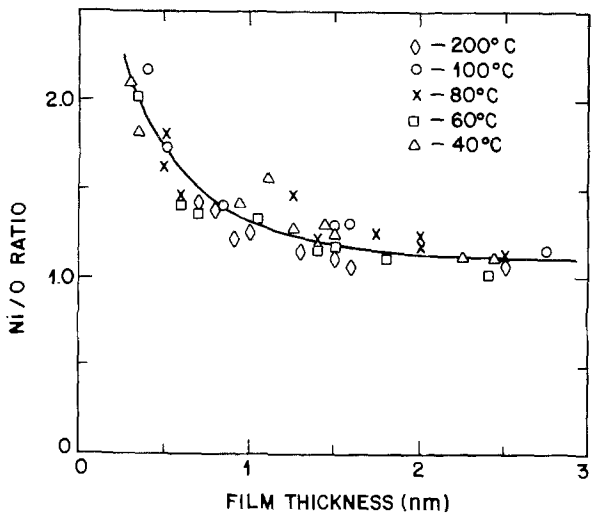


Fig. 6. The Ni/O composition ratio as a function of tarnish film thickness for all temperatures and relative humidities studied. All points lie on the same curve, indicating that films formed under all conditions have the same composition.

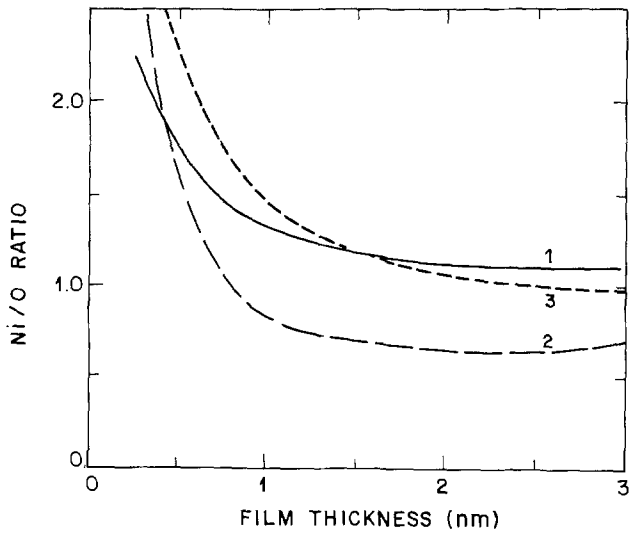


Fig. 7. The Ni/O composition ratio as a function of tarnish film thickness. 1, Experimental data (see Fig. 6); 2, Calculated assuming escape depth of Ni electrons is same in Ni and in NiO; 3, Calculated assuming $\lambda_{Ni(NiO)} = 1.5$ nm and $\lambda_{Ni(Ni)} = 1.1$ nm.

assuming that the heights are proportional to concentration. Using the Ni 848 eV peak and the O 510 eV peak, and correcting for their relative sensitivities (6), the Ni/O ratios were calculated and are plotted as a function of film thickness for the various experimental conditions (Fig. 6). All the points fall reasonably well on one curve.

Since the films are very thin, the electroplated nickel substrate contributes to the intensity of the Ni 848 eV signal. This contribution increases as the film thickness decreases, accounting for the curvature in the plot (Fig. 6). This can be demonstrated by an approximate calculation of the Ni/O intensity ratio.

$$\frac{I_{Ni}}{I_O} = \frac{\int_o^d \exp(-l/\lambda_{Ni})\,dl + \alpha \exp(-d/\lambda_{Ni}) \int_o^\infty \exp(-l'/\lambda_{Ni})\,dl'}{\sigma \int_o^d \exp(-l/\lambda_O)\,dl} \quad [1]$$

in which the I's are the peak-to-peak intensities of the indicated species, d is the thickness of the oxide film, l and l' are the distances from the air-oxide and the oxide/metal interfaces, respectively, λ_{Ni} is the escape depth of the Ni 848 eV electrons, λ_O is the escape depth of the O 510 eV electrons, α is the ratio of the concentration of Ni in the metal to that in the oxide, and σ is the ratio of the intensities of the standard spectral peaks, I^∞_O/I^∞_{Ni}. The left-hand term in the numerator is the peak intensity from Ni in the oxide; the right-hand term is the peak intensity from Ni in the substrate metal. The denominator is the peak intensity from O in the oxide. Integrating Eq. [1], one obtains

$$\frac{I_{Ni}}{I_O} = \frac{\lambda_{Ni}}{\sigma\lambda_O} \left\{ \frac{1 - (1-\alpha)\exp(-d/\lambda_{Ni})}{1 - \exp(-d/\lambda_O)} \right\} \quad [2]$$

λ_{Ni} and λ_O were estimated to be 1.1 and 0.8 nm, respectively (7). α was calculated to be 1.655 from the molar volumes of NiO and Ni, 10.90 and 6.588 cm³/mole, respectively. From the standard spectra (6), σ was determined to be 2.0.

From Eq. [2] and these parameters, the intensity ratio was calculated and is plotted as a function of oxide thickness, d, in Fig. 7 (curve 2). The curve for the experimental data from Fig. 6 is shown for comparison (Fig. 7, curve 1). The principal approximations in the calculation are the estimation of the electron escape depths, the assumption that these escape depths are the same in the oxide and in the metal, the neglect of backscattering of electrons, the assumption that σ calculated from the standard spectra is applicable to this system, and the assumption that attenuation of the incident electrons with depth into the oxide and metal can be neglected.

The agreement between the calculated curve and the experimental data is reasonably good at low film thicknesses. At higher film thicknesses, the high value of the experimental Ni/O ratio is probably a reflection of an escape depth of the Ni 848 eV electrons that is greater in NiO than in Ni, much as Palmberg (8) has suggested that the escape depth of the electrons from magnesium is greater in MgO than in the metal. If it is assumed that the escape depths of the Ni 848 eV electrons are different in the oxide and in the metal, then the right-hand term in the numerator of Eq. [1] becomes

$$\alpha \exp[-d/\lambda_{Ni(NiO)}] \int_o^\infty \exp[-l'/\lambda_{Ni(Ni)}]\,dl' \quad [3]$$

in which $\lambda_{Ni(NiO)}$ and $\lambda_{Ni(Ni)}$ are the escape depths of the Ni electrons in NiO and Ni, respectively. This leads to

$$\frac{I_{Ni}}{I_O} = \frac{\lambda_{Ni(NiO)} - [\lambda_{Ni(NiO)} - \alpha\lambda_{Ni(Ni)}] \exp[-d/\lambda_{Ni(NiO)}]}{\sigma\lambda_O[1 - \exp(-d/\lambda_O)]} \quad [4]$$

The intensity ratio calculated from Eq. [4] is plotted in Fig. 7 (curve 3) for $\lambda_{Ni(NiO)} = 1.5$ nm and $\lambda_{Ni(Ni)} = 1.1$ nm. The improved agreement with the experimentally determined curve indicates that the electron escape depths are indeed a function of the matrix composition.

These calculations indicate that the compositions of the various films are essentially the same, the apparent variation in the Ni/O ratio (Fig. 6) being due to contributions from the substrate nickel. The composition is assumed to be NiO, which is known to be the film that forms both under ambient conditions and at 200°C in oxygen (4). NiO is cation deficient, *i.e.*, $Ni_{1-x}O$, in which x is small over a wide range of oxidation conditions (9).

The chemisorption of oxygen onto a clean nickel surface and the subsequent formation of the first monolayers of NiO is very rapid (4). In the present study, this film was always present before the specimens were exposed to the test environment. AES and the sputtering process detect and remove this film, as well as that formed during the test exposure.

Nickel does not undergo appreciable oxidation at temperatures below 300°C (1, 4, 10). In the present study, the limiting thickness at 200°C, approximately 1.5 nm, is in excellent agreement with the value of 1.7 nm reported by Graham and Cohen (4). Campbell and Thomas (10) measured a thinner film at 194°C. However, this was determined from the uptake of oxygen on nickel already covered with the oxide formed at room temperature. Graham and Cohen (4) reported the limiting thickness at room temperature to be 1 nm, which is slightly higher than the average value of 0.4-0.5 nm measured here. This difference may be accounted for by the different surface preparation techniques, which result in different surface structures, roughnesses, and compositions. The surfaces prepared by Graham and Cohen were exceptionally clean and reproducible, while the objective of the present study was to approximate conditions that exist in the field. The measurement techniques are also different, and since the calculation of film thickness from the data obtained by each of these techniques requires different assumptions, some of the differences in results may be attributed to these.

The film thickness is clearly a function of humidity and temperature (Fig. 4 and 5). Up to 20% RH, the film thickness does not exceed 0.85 nm. For NiO, which has a rock salt structure, the unit cell dimension a_o is 0.41769 nm (11). Thus, the films formed at low humidity are no more than 2 unit cells in thickness at temperatures up to 100°C, in agreement with Holloway and Hudson (12). Even at 200°C and ambient humidity (RH < 1%), the limiting thickness is only 1.3 nm, or 3 unit cells (Fig. 3). At high relative humidities, *e.g.*, 95%, there is also only a small effect of temperature on film thickness. However, in the intermediate range of relative humidity, from 20 to 75%, the effect of temperature on film thickness is significant.

In the absence of water vapor, the oxidation of nickel is self-limiting, and ceases after one to two monolayers of the oxide have formed. The presence of water increases the thickness of the oxide. As the temperature is increased, a greater partial pressure of water vapor is required to achieve the same film thickness (Fig. 5). Since most gases desorb with increasing temperature, it must be the water adsorbed on the oxide, and not the partial pressure of water vapor, that is responsible for the oxide growth.

NiO is a p-type semiconductor with a cation deficiency, and it grows by the diffusion of cation vacancies (1). We speculate that the increased growth of the oxide in the presence of adsorbed water may be due to an increase in the cation vacancy concentration at the surface, this increasing the driving force for diffusion. The excess vacancies could be introduced by the oxidation of Ni^{2+} to Ni^{3+}. But this appears unlikely since oxidation by O_2 is thermodynamically much favored over that by H_2O. A more likely explanation is that the surface layer of NiO reacts with H_2O to form $Ni(OH)_2$. The molar volume of $Ni(OH)_2$, 23.47 cm^3/mole, is more than twice that of NiO, 10.97 cm^3/mole (13). Thus the formation of the hydroxide is likely to displace the Ni^{2+} ion from its lattice position, and create a vacancy. The increase in the vacancy concentration, according to this hypothesis, is directly proportional to the concentration of adsorbed water, which is proportional to the relative humidity. Above a certain relative humidity, the surface layer becomes saturated with vacancies. At these humidities, *e.g.*, 95%, differences in film thickness with temperature reflect only the effect of temperature. The same is true at low humidities

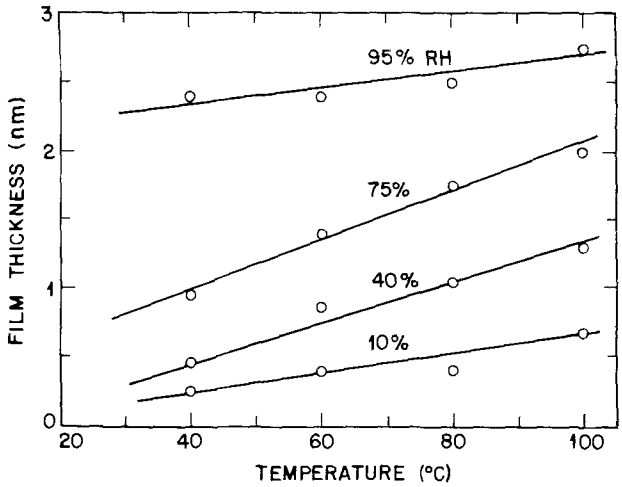


Fig. 8. Film thickness as a function of temperature for various relative humidities showing a significantly greater temperature coefficient at intermediate RH than at low or high RH.

(< 20% RH), at which it might be expected that little, if any, water is adsorbed. The temperature coefficients of the film thickness are essentially the same at the low and high relative humidities, but are considerably greater at intermediate relative humidities, at which the humidity significantly affects the amount of adsorbed water (Fig. 8).

The surface will be approximately saturated with cation vacancies when a monolayer of $Ni(OH)_2$ has formed. Kim and Winograd (14) have followed the interaction of H_2O with NiO by x-ray photoelectron spectroscopy. A thin layer of $Ni(OH)_2$ was formed, reducing the intensity of the NiO O 1s peak by about 15%. Using Lambert's law and assuming an escape depth of 1 nm for the NiO O 1s electrons (whose kinetic energy is 957 eV), an attentuation of 18% is calculated for these electrons by a 0.2 nm film of $Ni(OH)_2$. This is in good agreement with the proposed mechanism.

Summary

The oxidation of nickel in air has been studied as a function of temperature (23°-200°C) and relative humidity (ambient to 95%). At low relative humidities, oxide films grow no thicker than 1.3 nm at 200°C, and significantly less than that at temperatures of 100°C or less. The presence of water vapor markedly increases the thickness of the oxides that form at all temperatures. At 95% RH, the film thickness is between 2.5 and 3.0 nm for temperatures from 40° to 100°C.

It has been suggested that the increase in film thickness with increasing relative humidity may be due to the formation of a layer of $Ni(OH)_2$ at the surface of the NiO film with the concurrent creation of cation vacancies in the surface of the oxide. These vacancies increase the driving force for diffusion and the growth of the oxide.

Acknowledgments

We wish to thank P. C. Milner for many constructive discussions, and A. M. Williams for electroplating the specimens.

Manuscript submitted March 7, 1977; revised manuscript received June 16, 1977.

Any discussion of this paper will appear in a Discussion Section to be published in the June 1978 JOURNAL. All discussions for the June 1978 Discussion Section should be submitted by Feb. 1, 1978.

Publication costs of this article were assisted by Bell Laboratories.

REFERENCES

1. K. Hauffe, "Oxidation of Metals," Plenum Press, New York (1965).
2. N. N. Khoi, W. W. Smeltzer, and J. D. Embury, *This Journal*, **122**, 1495 (1975).

3. K. R. Lawless, *Rep. Prog. Phys.*, **37**, 231 (1974).
4. M. J. Graham and M. Cohen, *This Journal*, **119**, 879 (1972).
5. R. G. Baker and T. A. Palumbo, *Plating, East Orange, N.J.*, **58**, 791 (1971).
6. L. E. Davis, N. C. MacDonald, P. W. Palmberg, G. E. Riach, and R. E. Weber, "Handbook of Auger Electron Spectroscopy," 2nd ed., pp. 33, 93, Physical Electronics Industries, Inc., Edina, Minnesota (1976).
7. C. R. Brundle, *J. Vac. Sci. Technol.*, **11**, 212 (1974).
8. P. W. Palmberg, *Anal. Chem.*, **45**, 549A (1973).
9. W. D. Johnston, "Thermoelectricity: Science and Engineering," R. R. Heikes and R. W. Ure, Jr., Editors, p. 232, Interscience Publishers, New York (1961).
10. W. E. Campbell and U. B. Thomas, *Trans. Electrochem. Soc.*, **91**, 623 (1947).
11. "X-Ray Powder Data File," Joint Committee on Powder Diffraction Standards, Swarthmore, Pennsylvania (1975).
12. P. H. Holloway and J. B. Hudson, *Surf. Sci.*, **43**, 123 (1974); *ibid.*, **43**, 141 (1974).
13. M. Topic, F. J. Micale, C. L. Cronan, H. Leidheiser, Jr., and A. C. Zettlemoyer, "Adsorption at Interfaces," K. L. Mittal, Editor, p. 225, American Chemical Society, Washington, D.C. (1975).
14. K. S. Kim and N. Winograd, *Surf. Sci.*, **43**, 625 (1974).

Efficient Luminescent Energy Transfer from Mn^{2+} to Yb^{3+} in CaF_2

J. A. DeLuca* and F. S. Ham

General Electric Company, Research and Development Center, Schenectady, New York 12301

ABSTRACT

The system CaF_2:Mn:Yb was selected for study because it held promise for the experimental realization of Dexter's hypothesized simultaneous transfer of energy from one sensitizer to two activators. Emission, excitation, and decay measurements show that efficient Mn^{2+} to Yb^{3+} energy transfer does occur. However, analysis of the data indicates that the mechanism of energy transfer involves the more familiar direct ion-to-ion transfer.

Our interest in phosphors having a luminescent quantum yield greater than unity (1) has led us to consider the cooperative deexcitation mechanism originally proposed on theoretical grounds by Dexter (2) but never observed experimentally. We have sought evidence for the operation of this mechanism in CaF_2 doped simultaneously with Mn^{2+} and Yb^{3+}, since the properties of the Mn^{2+} and Yb^{3+} ions in this host are particularly well suited to the requirements of Dexter's proposal. The purpose of this paper is to report the results of experiments that show that energy transfer with a high quantum efficiency does indeed occur in this system. Our data do not, however, exhibit the dependence on Yb^{3+} concentration expected for the Dexter mechanism, and we conclude that this mechanism is not responsible for the energy transfer in CaF_2:Mn:Yb. We propose an alternative model to explain the data, based on evidence that a Yb^{3+} ion close to a Mn^{2+} ion significantly changes the Mn^{2+} energy levels.

In the Dexter mechanism a sensitizer ion, excited by absorption of a photon, transfers its energy to two nearby activator ions, each of which then returns, for the simplest possible system of this type, by a single radiative step to its ground state. If this were the dominant decay process and there were no losses, and if all the activator ions were of the same species, the number of emitted photons would then be approximately twice the number of photons absorbed by the sensitizer, while their frequency would be somewhat less than half that of the original quantum. The crucial energy-transfer step in this process, from one sensitizer to two activators, is allowed by the interaction (coulomb multipole and exchange) between the two activators. In fact, the process is very similar to the cooperative absorption of one photon by two ions, as first observed by Varsanyi and Dieke (3) for Pr^{3+} ions in $PrCl_3$, the only difference being that, whereas in the cooperative absorption the excitation is due to the electronic coupling to the radiation field, in the Dexter mechanism the excitation results from the multipole or exchange interaction of the activators with the sensitizer. The cooperative sensitization of Tb^{3+} by Yb^{3+} has been observed in several hosts (4, 5).

It is clearly required for the Dexter mechanism to be operative that the energy of the excited state of the sensitizer be approximately twice that of the excited state of the activator, so that the emission spectrum of the sensitizer can overlap significantly the convolution of the activator absorption spectrum with itself and thereby make possible energy conservation in the transfer process. It is also required that there be no intermediate states of the sensitizer, and no higher excited states of the activator with energies close to the excited state of the sensitizer, so that energy transfer involving the excitation of a single activator is very unlikely. Also, the lifetime of the excited state of the sensitizer must be sufficiently long to allow the cooperative transfer process to compete favorably with simple radiative and nonradiative decay.

The energy levels of Mn^{2+} and Yb^{3+} in CaF_2 satisfy these requirements very well. In cubic symmetry with not too strong a crystal field the lowest excited state of the Mn^{2+} ion ($3d^5$ configuration) is the $^4T_{1g}$ state derived from the ^4G term of the free ion (6), and this is the initial state for Mn^{2+} fluorescence. In CaF_2 the $^4T_{1g}$ state of Mn^{2+} must lie ~21,000 cm^{-1} above the $^6A_{1g}$ ground state, since the Mn^{2+} fluorescence is a broad band in the green with its peak at ~500 nm, as shown by our data. The only excited states of the $4f^{13}$ configuration of Yb^{3+} have almost exactly half as much excitation energy: These are the $^2F_{5/2}$ states, which lie ~10,000 cm^{-1} above the $^2F_{7/2}$ ground state (7). There are no other states of Yb^{3+} with energies near that of the $^4T_{1g}$ state of Mn^{2+}, the nearest being the levels of the $4f^{12}5d$ configuration lying above ~66,000 cm^{-1} (8). Also, the lifetime of the Mn^{2+} fluorescence is extremely long, ~85 msec at 300°K as shown by our data. Thus the prospects of observing the Dexter mechanism in this system appear particularly favorable, while the likelihood of transfer from one Mn^{2+} to a single Yb^{3+} should be small as a result of the large difference in excitation energy for these two ions.

* Electrochemical Society Active Member.
Key words: energy transfer, luminescence, CaF_2:Mn:Yb.

In our experiments we have recorded the excitation and emission spectra of several series of samples of CaF_2 doped with various concentrations of Mn^{2+} and Yb^{3+}. Emission spectra were recorded at room temperature and 77°K in both the visible and infrared regions of the spectrum. The visible emission is due to the direct fluorescence of the Mn^{2+}, and the infrared band at ~10,000 nm to the Yb^{3+} fluorescence sensitized by Mn^{2+}. The absolute and relative values for the rate of energy emission in these two bands were measured at room temperature under conditions of steady-state illumination. Also measured was the time dependence of the decay of the fluorescence in each band when the exciting light was shut off. We also measured the decay of the Yb^{3+} fluorescence following direct excitation of the Yb^{3+} by illumination in the infrared.

Experimental

Sample preparation.—The basic starting materials used were $CaCO_3$ (G.E. Chemical Products Ultrapure), Mn metal (Johnson Matthey Specpure), Yb_2O_3 (Molycorp 4N's), and Y_2O_3 (Kerr-McGee 6N's). From these materials were prepared samples of $CaCO_3$, $CaCO_3$: $x MnCO_3$, and $CaCO_3 + y Ln_2O_3$ (Ln = Y, Yb) in quantities sufficient to insure that all samples of a particular series were prepared from the same starting materials.

The sample series CaF_2:1%Mn:x%Yb[1] ($0.01 \leq x \leq 20$), CaF_2:x%Mn:5%Yb ($0.1 \leq x \leq 20$), and CaF_2:1%Mn:x%Yb:$(20 - x)$%Y ($0.01 \leq x \leq 20$) were prepared by firing the appropriate carbonate-oxide mixtures in a stream of argon and hydrogen fluoride. A platinum boat and reaction tube were used. Teflon fittings and tubing were used in the gas train.

Each sample was prepared by heating the appropriate carbonate-oxide mixture (~6g) to 400°C under flowing argon (100 cm^3/min, Linde Ultrahigh Purity). At that point the hydrogen fluoride flow was initiated (100 cm^3/min, Matheson Gas Company) and the reaction allowed to proceed for 1 hr. The temperature was raised to 700°C, and the sample was allowed to react for an hour. Upon removal from the reaction furnace the sample was ground and sieved through a 200 mesh screen. The sieved sample was refired in an argon-HF stream for 2 hr at 1100°C. Finally, the sample was sieved through a 400 mesh screen. It was determined that this preparative method insured samples with reproducible emission properties.

Excitation spectra.—The monochromator of a Cary 14 spectrophotometer was used as the variable wavelength excitation source and a cooled RCA 7102 photomultiplier with appropriate filters detected the sample emission. Corning no. 3-71 and no. 4-96 filters were used in tandem between the sample and the photomultiplier (detection band ~470 to ~590 nm) when recording excitation spectra for the visible emission. A Corning no. 7-56 filter (detection band ~750 to ~1200 nm) was used for recording excitation spectra for infrared emission. The excitation spectra were not corrected for the spectral distribution of the excitation source.

Emission spectra.—Sample emission was excited by the 457.9 nm line of an argon ion laser (Spectra Physics Model 166). An interference filter was placed in the laser beam to reduce the background. Emission spectra were recorded with a 0.5m Jarrell-Ash scanning monochromator coupled to a cooled RCA 7102 photomultiplier. The sample image was focused on the entrance slit of the monochromator and an appropriate filter (Corning no. 3-71 for visible spectra, Corning no. 2-64 for infrared spectra) was placed between the sample and slit to minimize contributions to the signal from second-order spectra and scattered laser light.

The spectral response of the detection system (everything beyond the sample) was determined by recording the reflection spectrum of a $BaSO_4$ sample irradiated by a calibrated lamp. A "base line" correction spectrum was obtained by exciting a sample of CaF_2 with the laser. This spectrum was used to correct the emission spectra for contributions from impurity emission of the host CaF_2 and filter fluorescence. The magnitude of the correction was determined for each spectrum by measuring the signal strength at a wavelength removed from the emission spectrum of interest. All recorded spectra were digitized and a computer program was used to fold in the spectral response and appropriately scaled base line corrections. The program generated corrected emission spectra and computed the integrated power and the value of $\bar{\lambda}$ (mean wavelength for the spectral power distribution) for the emission bands.

Decay measurements.—The sample image (457.9 nm laser excitation or 975 nm from a tungsten lamp and monochromator combination) was focused with two large-aperture aspheric condenser lenses on a cooled RCA 7102 photomultiplier. A combination of Corning no. 3-71 and no. 4-96 filters was used to isolate the visible emission band and a Kodak no. 87-C filter was used for the infrared. The photomultiplier signal was passed first through a logarithmic amplifier (Analog Devices Model 755P) and then into the memory input of a Nicolet 1090 storage oscilloscope. An evaluation of the performance of the logarithmic amplifier confirmed that the log conformity error was within the manufacturer's specifications. Decay curves (log I *vs.* t) were obtained by interrupting the laser beam with a shutter and synchronously triggering the time sweep of the storage scope. Samples were measured at both room temperature and 77°K.

Results

Excitation spectra.—A typical excitation spectrum for the visible emission in samples containing manganese or manganese plus ytterbium is shown in Fig. 1a. This spectrum was not found for CaF_2 or CaF_2:Yb samples. An almost identical excitation spectrum, shown in Fig. 1b, was observed for the infrared emis-

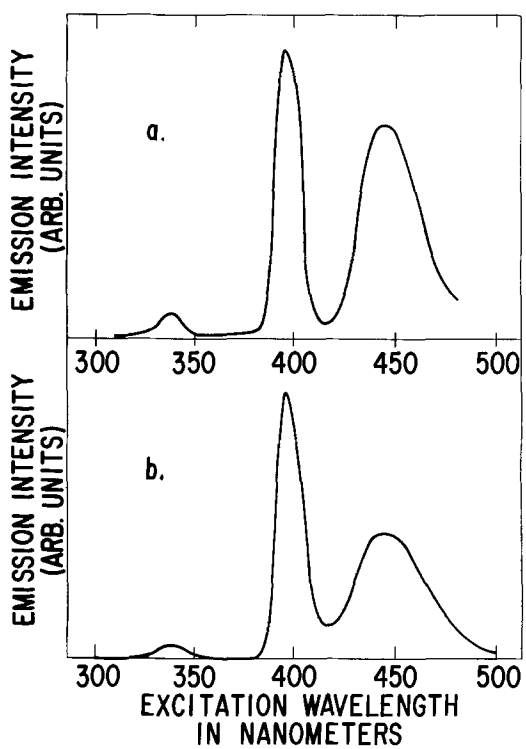


Fig. 1. (a) Excitation spectrum for visible emission in CaF_2:5%Mn. (b) Excitation spectrum for infrared emission in CaF_2:5%Mn:5%Yb.

[1] All concentrations expressed in mole percent.

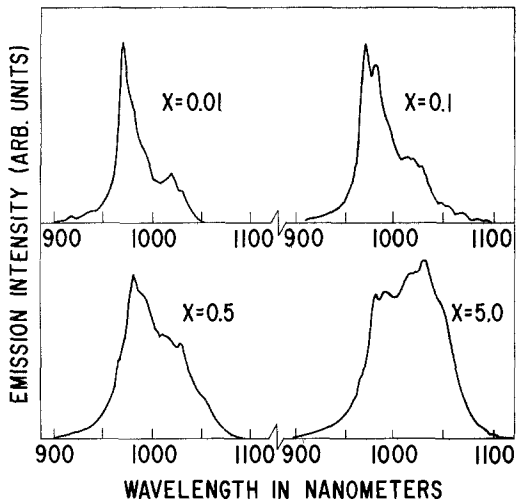


Fig. 2. Yb^{3+} emission spectra (corrected) for the series CaF_2: 1%Mn:x%Yb showing the dependence of the shape of the emission band on Yb^{3+} concentration.

sion in CaF_2:Mn:Yb samples, but was not observed in CaF_2, CaF_2:Yb, or CaF_2:Mn samples.

Emission spectra.—*CaF_2:1%Mn:x%Yb.*—Samples doped with both Mn^{2+} and Yb^{3+} show emission in the infrared in addition to the Mn^{2+} emission in the visible. The infrared emission is shown in Fig. 2 and is attributed to Yb^{3+}. This spectrum resembles the luminescence spectra of Yb^{3+} in CaF_2 observed by Voron'ko *et al.* (9) and shows a similar variation with Yb^{3+} concentration. A peak ~970 nm characterizes the spectrum at very low concentrations of Yb^{3+}. As the concentration increases, peaks ~980 nm begin to dominate. These lines persist at even higher concentrations where a broad emission >1000 nm appears.

Visible emission spectra, which are observed only in samples containing Mn^{2+}, are shown in Fig. 3 and are attributed to radiative decay from the $^4T_{1g}$ state of Mn^{2+} ions which substitute for Ca^{2+} in the CaF_2 lattice.

As the Yb^{3+} concentration is increased, the intensity of the Mn^{2+} emission diminishes and this band shifts to longer wavelengths. This shift is shown by the spectra in Fig. 3; the average wavelength of the band shifts from 504 nm when Yb^{3+} is absent to 528 nm for CaF_2:1%Mn:20%Yb.

The relative intensities of the two emission bands as a function of Yb^{3+} concentration, under conditions of steady-state excitation of the sample, are shown in

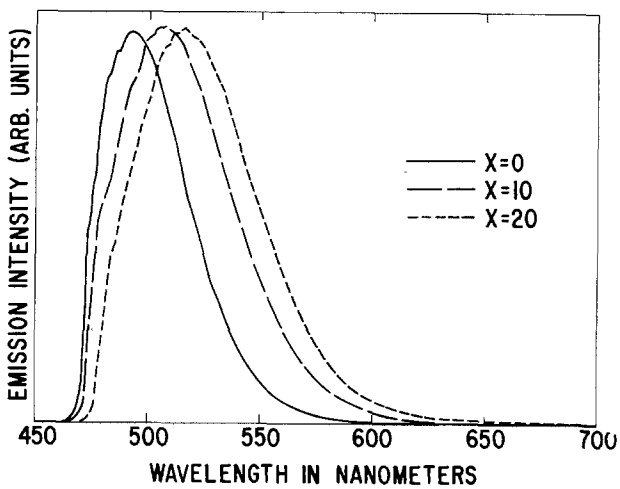


Fig. 3. Mn^{2+} emission spectra (corrected) for the series CaF_2: 1%Mn:x%Yb showing the effect of Yb^{3+} concentration on the Mn^{2+} band.

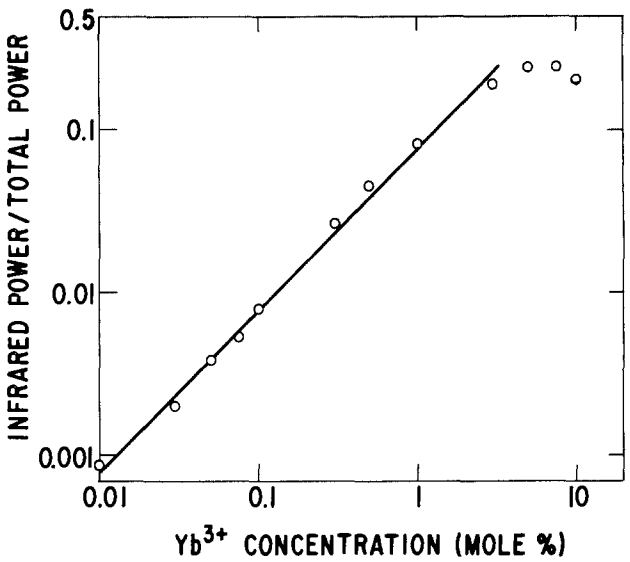


Fig. 4. Log-log plot of infrared power/total emitted power vs. Yb^{3+} concentration for the series CaF_2:1%Mn:x%Yb.

Fig. 4. Shown is the ratio of the total power emitted in the infrared band (obtained by integrating the power density over this band) to the total power emitted in both the visible and infrared bands. This ratio is proportional to the Yb^{3+} concentration up to a concentration of ~3% as shown by the line of unit slope drawn through the data points of Fig. 4. The absolute value of the total power emitted in both bands is approximately independent of Yb^{3+} concentration for samples of the same thickness and identical conditions of sample illumination. Evidently the absorption of the exciting light by the Mn^{2+} does not depend appreciably on the Yb^{3+} concentration. We could not measure the absorption of these samples directly because of its low value.

CaF_2:x%Mn:5%Yb.—The visible emission spectra for this series are similar to the above. The value of $\bar{\lambda}$ ranges from 512 nm for $x = 0.1$ to 551 nm for $x = 20.0$. Careful measurement of the visible emission spectrum for samples with $x \geq 5$ reveals that the long wavelength tail extends to ~820 nm. The infrared spectrum for all samples is similar to that shown in Fig. 2 for CaF_2:1%Mn:5%Yb.

CaF_2:5%Mn:x%Yb:(20 − x)%Y.—The visible emission spectrum for the sample CaF_2:5%Mn:20%Y has a peak at 560 nm and a long wavelength tail that extends out to 860 nm. As the Yb^{3+} content is increased, the emission peak shifts to shorter wavelengths and the extent of the tail diminishes until at $x = 20.0$ the emission peak is at 525 nm and the tail extends to 820 nm. These effects are evident in the emission spectra shown in Fig. 5. The infrared spectra for the various Yb^{3+} concentration levels were similar to those recorded for the samples CaF_2:1%Mn:x%Yb.

Decay measurements.—Curves showing the intensity of fluorescence in both the visible and infrared bands as a function of the time following the cessation of sample illumination were recorded at room temperature and 77°K for samples in the several series described previously. Representative decay curves obtained using argon ion laser excitation are shown in Fig. 6 for the visible and the infrared bands. Some of these curves are approximately exponential, but most show a slope which diminishes appreciably on a logarithmic plot as the decay proceeds. All the curves have a nonzero initial slope, characterized by a decay time $\tau(O)$ which depends upon sample composition and temperature. This initial decay time is in all cases much shorter for the infrared fluorescence than for the visible. Representative values of $\tau(O)$ are listed in Table I.

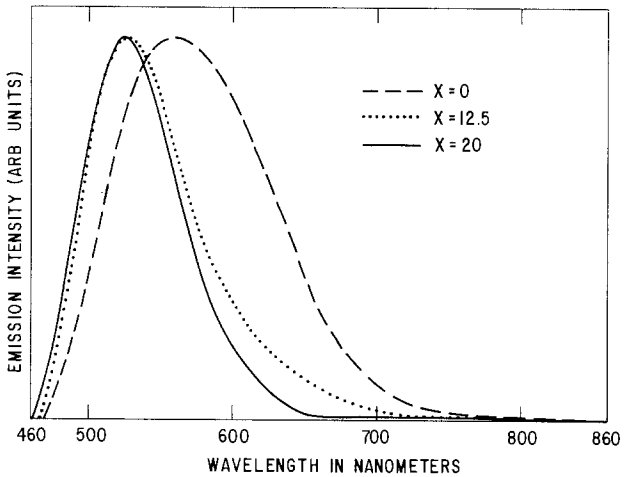


Fig. 5. Mn^{2+} emission spectra (corrected) for the series CaF_2: 5%Mn:x%Yb:(20 — x)%Y showing the effect of the Yb^{3+} concentration on the Mn^{2+} band.

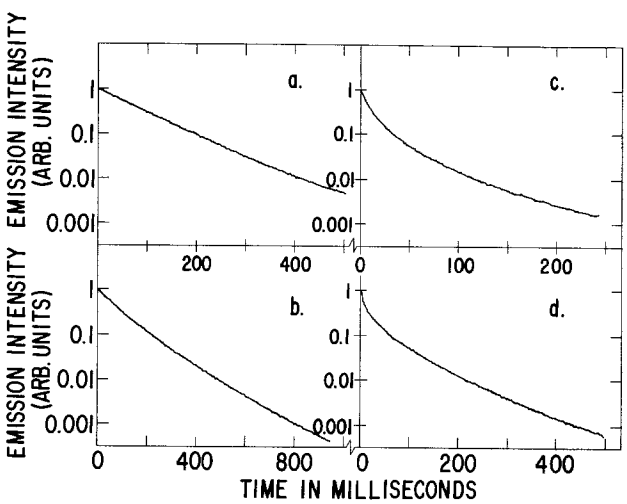


Fig. 6. Decay curves (457.9 nm excitation) for visible emission in (a) CaF_2:1%Mn at 300°K; (b) CaF_2:5%Mn:5%Yb at 77°K; and for infrared emission in (c) CaF_2:1%Mn:5%Yb at 300°K; (d) CaF_2:3%Mn:5%Yb at 77°K.

Also recorded were the decay curves for the Yb^{3+} fluorescence following infrared excitation. Representative curves are shown in Fig. 7. Values of 3 msec at room temperature and 2.4 msec at 77°K were typical of the $\tau(O)$ values derived from these curves and are similar to the decay times reported by Livanova (4) for Yb^{3+} in CaF_2.

Interpretation

The excitation spectra for both the visible emission, which originates in transitions from the $^4T_{1g}$ level of Mn^{2+}, and the infrared emission, which originates in transitions from the $^2F_{5/2}$ Yb^{3+} levels, correlate well with peaks in the absorption spectrum of Mn^{2+} in CaF_2 (10) and MnF_2 (11), and demonstrate that in the system CaF_2:Mn:Yb energy is transferred from Mn^{2+} ions to Yb^{3+} ions.

We have seen that the necessary conditions for energy conservation in the energy transfer step of the

Table I. Representative values of $\tau(O)$ in milliseconds

Sample	Visible emission		Infrared emission	
	300°K	77°K	300°K	77°K
CaF_2:1%Mn	85	159	—	—
CaF_2:1%Mn:0.1%Yb	85	128	10	10
CaF_2:5%Mn:5%Yb	40	87	10	10
CaF_2:5%Mn:1%Yb:19%Y	35	—	—	—

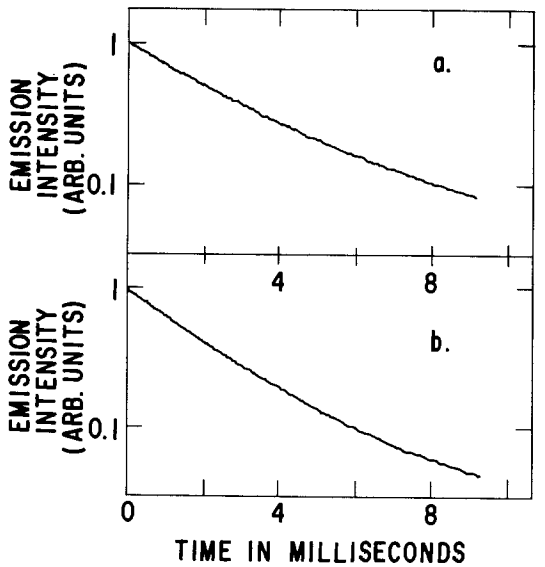


Fig. 7. Decay curves (975 nm excitation) for infrared emission in (a) CaF_2:1%Mn:5%Yb at 300°K; (b) CaF_2:7.5%Mn:5%Yb at 77°K.

Dexter mechanism are satisfied for Mn^{2+} and Yb^{3+} in CaF_2. However, our data provide evidence that this is not the mechanism operative in the system CaF_2:Mn:Yb. The Dexter mechanism requires two Yb^{3+} ions to be close to the same Mn^{2+} ion. Thus, the quantum yield for the Yb^{3+} luminescence should increase as the square of the Yb^{3+} concentration if the Dexter mechanism is the principal mechanism for the sensitization of the Yb^{3+}, at least for sufficiently low Yb^{3+} concentrations. As shown in Fig. 4, the power emitted in the Yb^{3+} infrared band is accurately linear in the Yb^{3+} concentration over a range of two decades. These data point to the unambiguous conclusion that the sensitization of the Yb^{3+} involves energy transfer from a Mn^{2+} ion to a single Yb^{3+} ion. The efficiency of this transfer is surprisingly high, as shown by Fig. 4, in view of the large energy difference (~10,000 cm^{-1}) between the excited states of Mn^{2+} and Yb^{3+}. For example, for the sample CaF_2:1%Mn:5%Yb the infrared emission accounts for 26% of the total emitted power. Since the quantum energy in the infrared band is only half that of the visible band, very nearly as many Mn^{2+} must transfer energy to Yb^{3+} in this sample as radiate their energy directly.

We should be able to derive the rate at which energy is transferred from Mn^{2+} to Yb^{3+}, and thus gain insight into this process, by attempting an analysis of our data on the rate of decay of luminescence after the exciting light is shut off. We let τ_{Mn}^{-1} denote the probability per unit time for an isolated Mn^{2+} ion, in its excited state, to return to the ground state via a radiative process, and we assume that this rate is unaffected, at least to a good approximation when Yb^{3+} ions are introduced into the crystal. (We will neglect for simplicity the nonradiative decay of both the Mn^{2+} and Yb^{3+} ions on the assumption that the quantum efficiency for the fluorescence of both ions is approximately unity.) The rate ω_i at which the ith Mn^{2+} ion, in its excited state, decays by transferring its energy to a nearby Yb^{3+} ion should be different for different Mn^{2+} ions and should depend on the distribution of Yb^{3+} ions on neighboring sites

$$\omega_i = \Sigma_n \omega(R_{ni})$$

This summation is over only those sites occupied by Yb^{3+}; $\omega(R)$ is the transfer rate for a pair separated by a distance R, and R_{ni} is the distance from the site of the nth Yb^{3+} to the ith Mn^{2+} ion. The equation describing the probability $S_i(t)$ that the ith Mn ion remains in its excited state is then

$$\frac{dS_i(t)}{dt} = -S_i(t)\,(\tau_{Mn}^{-1} + \omega_i) \qquad [1]$$

In writing Eq. [1] we ignore the possibility that transfer of excitation may take place from one Mn^{2+} ion to another. Such transfer would tend to cause all Mn^{2+} ions to decay at a common rate, whereas our data indicate that the Mn^{2+} ion decay rates are very different for different ions in the same sample, when transfer to Yb^{3+} occurs.

The rate at which Yb^{3+} ions are excited by transfer from Mn^{2+} is then obtained by summing $S_i\omega_i$ over all Mn^{2+} ions and multiplying this sum by a factor η giving the number of Yb^{3+} ions excited by the decay of a single Mn^{2+}. We would then have $\eta = 2$ if the Dexter mechanism were effective, or $\eta = 1$ if the transfer is one-to-one. If τ_{Yb}^{-1} denotes the rate of radiative decay of the Yb^{3+}, which we will assume is the same for all Yb^{3+} ions, the number of excited Yb^{3+} is given by $a(t)$, which satisfies the equation

$$\frac{da(t)}{dt} = -a(t)\tau_{Yb}^{-1} + \eta \sum_i S_i(t)\omega_i \qquad [2]$$

Our data for the series CaF_2:x%Mn:5%Yb under infrared excitation show that τ_{Yb} is independent of the Mn^{2+} concentration up to at least 12% Mn^{2+}. Equation [2] holds even though diffusion of the excitation occurs from one Yb^{3+} ion to another (9), provided that no significant fraction of the excitation energy is lost thereby through diffusion to traps where nonradiative decay occurs.

Under conditions of steady-state excitation we must add to the right-hand side of Eq. [1] a term gI giving the rate of excitation of the Mn^{2+} for an illumination intensity I, and set the left-hand side equal to zero. We obtain, therefore, for the steady-state probability that a Mn^{2+} ion is excited the value

$$S_i(O) = \frac{gI\tau_{Mn}}{1 + \omega_i\tau_{Mn}} \qquad [3]$$

which is also the initial value, at the time the exciting light is shut off, for use in solving Eq. [1] for the decay. Similarly, the steady-state number of excited Yb^{3+} is obtained by setting the left-hand side of Eq. [2] to zero and substituting from Eq. [3]

$$a(O) = \eta\tau_{Yb}\sum_i S_i(O)\omega_i = \eta\tau_{Yb}gI\sum_i \frac{\omega_i\tau_{Mn}}{1 + \omega_i\tau_{Mn}} \qquad [4]$$

The decay of the excitation of the ith Mn^{2+} ion after the exciting light has been shut off is given by the solution of Eq. [1] subject to the initial condition of Eq. [3]

$$S_i(t) = S_i(O)\exp(-t/\tau_i) \qquad [5]$$

where

$$\tau_i^{-1} = \tau_{Mn}^{-1} + \omega_i \qquad [6]$$

The Mn^{2+} luminescence rate is then obtained by summing Eq. [5] over all ions and dividing by τ_{Mn}

$$L_{Mn}(t) = \tau_{Mn}^{-1}\sum_i S_i(O)\exp(-t/\tau_i) \qquad [7]$$

The general solution of Eq. [2] for the decay of the Yb^{3+} excitation is given by

$$a(t) = a(O)\exp(-t/\tau_{Yb}) + \eta\exp(-t/\tau_{Yb})\int_0^t dt'\exp(t'/\tau_{Yb})\sum_i S_i(t')\omega_i \qquad [8]$$

Substituting into Eq. [8] from Eq. [5] and carrying out the integration, we can express the result as the luminescence rate of the Yb^{3+}

$$L_{Yb}(t) = a(t)\tau_{Yb}^{-1} = \eta\sum_i \frac{S_i(O)\omega_i}{1 - \frac{\tau_{Yb}}{\tau_i}}\left[\exp(-t/\tau_i) - \frac{\tau_{Yb}}{\tau_i}\exp(-t/\tau_{Yb})\right] \qquad [9]$$

The sum of the first term in the bracket in Eq. [9] has a similar form to that of Eq. [7]: Each term exhibits a simple exponential decay with the same set of decay times τ_i appearing in Eq. [9] as in Eq. [7]. However, the individual terms in this sum have a different relative weighting than in Eq. [7], principally because of the appearance of the factor ω_i in Eq. [9]. If we have $\tau_{Yb} < \tau_i$, all of these terms in the first sum in Eq. [9] are positive, like those in Eq. [7]. Under the same condition, however, the second term in the bracket in Eq. [9] is negative, and these terms decay with a common lifetime τ_{Yb}, the radiative decay time of the Yb^{3+}. The sum of the second term, therefore, has the effect of causing the total luminescence rate $L_{Yb}(t)$ to be lower and to have a lower slope, for a period of time extending to $t \sim \tau_{Yb}$, than one would estimate by extrapolating the curve backward from larger t. Indeed, taking the derivative of Eq. [9], we see that the slope of the curve is identically zero at $t = 0$. This result is, of course, simply due to the fact that the left-hand side of Eq. [2] is zero at $t = 0$, since the steady-state relationship exists between $a(t)$ and $\sum_i S_i(t)\omega_i$ at the moment the light is shut off.

On the other hand, if we have $\tau_i < \tau_{Yb}$ in some of the terms of Eq. [9], it is convenient to rewrite this equation in the form

$$L_{Yb}(t) = \eta\sum_{i(\tau_i<\tau_{Yb})} \frac{S_i(O)\omega_i}{1 - \frac{\tau_i}{\tau_{Yb}}}\left[\exp(-t/\tau_{Yb}) - \frac{\tau_i}{\tau_{Yb}}\exp(-t/\tau_i)\right] + \eta\sum_{i(\tau_i>\tau_{Yb})}' \frac{S_i(O)\omega_i}{1 - \frac{\tau_{Yb}}{\tau_i}}\left[\exp(-t/\tau_i) - \frac{\tau_{Yb}}{\tau_i}\exp(-t/\tau_{Yb})\right] \qquad [10]$$

In particular, if we have $\tau_i \ll \tau_{Yb}$ in the terms in the first sum in Eq. [10], we can neglect the very small terms proportional to τ_i/τ_{Yb} in the first bracket. We can then express Eq. [10] as the ratio of the Yb^{3+} luminescence rate at t to the steady-state rate at $t = 0$

$$\frac{L_{Yb}(t)}{L_{Yb}(O)} = (1 - \Sigma_i'f_i)\exp(-t/\tau_{Yb}) + \Sigma_i' \frac{f_i}{1 - \frac{\tau_{Yb}}{\tau_i}}\left[\exp(-t/\tau_i) - \frac{\tau_{Yb}}{\tau_i}\exp(-t/\tau_{Yb})\right] \qquad [11]$$

Here we have defined

$$f_i = S_i(O)\omega_i/L_{Yb}(O) \qquad [12]$$

for those components for which $\tau_i > \tau_{Yb}$, so that f_i is the relative fraction of steady-state Yb^{3+} luminescence rate due to each such component. Only the components for which $\tau_i > \tau_{Yb}$ are to be included in the primed sums in Eq. [11]. We see, therefore, from Eq. [11] that under the stated conditions the Yb^{3+} luminescence may be decomposed into one component decaying with the Yb^{3+} radiative lifetime, plus a sum of other components having the same decay times as the components of the Mn^{2+} fluorescence. Each of these

latter components in Eq. [11] is accompanied by a small correction tending to reduce the contribution of this component but decaying with a lifetime τ_{Yb}.

Finally, the initial slope of Eq. [11] defines an apparent initial luminescence lifetime $\tau(O)$ given by

$$\tau(O)^{-1} = -\frac{d}{dt}\left[\frac{L_{Yb}(t)}{L_{Yb}(O)}\right] = (1 - \Sigma'_i f_i)\ \tau_{Yb}^{-1} \quad [13]$$

This is the apparent lifetime which we obtain from the initial slope of the luminescence curve if we are unable to resolve the change in slope that occurs at time $t \lesssim \tau_i$ for those components with $\tau_i << \tau_{Yb}$ and which corresponds to those terms proportional to (τ_i/τ_{Yb}) which we dropped in going from Eq. [10] to Eq. [11]. We see that $\tau(O)$ has no fundamental significance in terms of the decay times of the various components contributing to the Yb^{3+} luminescence, but that together with τ_{Yb}^{-1} it provides a means of determining the fraction $(1 - \Sigma'_i f_i)$ of the Yb^{3+} luminescence that results from a very fast transfer of excitation ($\tau_i << \tau_{Yb}$) from the Mn^{2+}.

In attempting to interpret our data for the Yb^{3+} luminescence decay on the basis of the theoretical model thus developed, we note first that all of our data curves appear to have a nonzero initial slope and that in every case the slope on a logarithmic plot diminishes with increasing time. Thus, in no case does the Yb^{3+} decay curve show the vanishing initial slope or the region of increasing slope at small t expected on the basis of Eq. [9]. If our model is applicable, therefore, these data suggest the existence of a sizable component having a very fast transfer of excitation from the Mn^{2+} (*i.e.*, ω_i large so that $\tau_i << \tau_{Yb}$), as described by Eq. [11] and [13].

To attempt a quantitative analysis of these data on the basis of Eq. [11]-[13], we have first picked out those samples in which the decay time τ_{Yb} is approximately the same for most of the Yb^{3+} ions, as we assumed in the analysis. From our data on the decay of Yb^{3+} fluorescence following infrared excitation, this requirement eliminates samples with Yb concentration both above and below the range of 1-5%. We have also avoided samples with too high a Mn^{2+} concentration, which show evidence that the luminescence efficiency is reduced by concentration quenching, perhaps by migration of the excitation to traps by diffusion among the Mn^{2+} ions. The most suitable set of samples consists of those from the CaF_2:x%Mn:5%Yb series, with $x < 10$, for which the decay curves for Yb^{3+} fluorescence following infrared excitation follow very nearly a simple exponential for the first decade. We have obtained the value for τ_{Yb} for a sample from the initial slope of this curve.

Next, we have attempted to fit the curve of Yb^{3+} luminescence following Mn^{2+} excitation to an expression of the form of Eq. [11]. Taking the decay time equal to τ_{Yb} in one of these terms, we then matched the initial slope as in Eq. [13] and chose f_i and τ_i in the remaining terms to fit the curve over a range covering somewhat more than the first two decades of the decay. Two additional terms involving the decay times τ_1 and τ_2 served to give a reasonably good fit over this range, both at room temperature and 77°K. At room temperature the longer decay time τ_2 was found always to lie in the range 70-80 msec, with the corresponding amplitude factor f_2 in the range 0.04-0.07. This value for τ_2 is only a little shorter than the decay time $\tau_{Mn} = 85$ msec for the Mn^{2+} fluorescence obtained from the initial slope of the decay curve in a sample containing 1% Mn^{2+} and no Yb^{3+}. This component of the Yb^{3+} luminescence is thus consistent with excitation transferred from excited Mn^{2+} ions that are not too close to an Yb^{3+} ion and thus have a relatively small probability of transferring the excitation to the Yb^{3+}. The shorter decay time τ_1 was found in the various samples to lie in the range 15-17 msec, with f_1 in the range 0.55-0.65. This component is evidently due to those Mn^{2+} that lie sufficiently near one or more Yb^{3+} to have a probability about five times greater of transferring excitation to the Yb^{3+} than of decaying by a direct radiative process. Finally, the component that decays with the Yb^{3+} radiative decay time τ_{Yb} ($\cong$ 3.0 msec at 300°K) has an amplitude factor $(1 - f_1 - f_2)$ in the range 0.3-0.4 and evidently is to be associated with certain Mn^{2+} ions that have a very fast excitation transfer to Yb^{3+} and for which the resulting decay time τ_i is very much shorter than τ_{Yb}.

The analysis of the decay curves taken at 77°K presents a very similar picture. The longer decay time τ_2 remains in the range 70-80 msec, even though τ_{Mn} is found to lengthen somewhat to 155 msec, but f_2 increases to ~0.15. This change is consistent with Eq. [3] and [12] if the product $\omega_2\tau_{Mn}$ increases from a value ~0.1 at 300°K to ~1 at 77°K, an increase also consistent with the observed decay times and Eq. [6] if ω_2 is larger at the lower temperature by a factor ~5. The shorter decay time τ_1 is found to be ~19-21 msec, a bit longer than at 300°K, with f_1 reduced somewhat to 0.4-0.5. The component decaying with τ_{Yb} (~2.4 msec at 77°K) has about the same relative amplitude as at 300°K: $(1 - f_1 - f_2)$ ~0.35-0.45.

A conclusion indicated by this analysis is that the mechanism responsible for the energy transfer from Mn^{2+} to Yb^{3+} is equally effective at 77°K as at room temperature and that the transfer rates ω_1 and ω_2 corresponding to the components with τ_1 and τ_2 are either approximately independent of temperature over this range or possibly even somewhat higher at the lower temperature. This conclusion appears to rule out the possibility that coupling to the phonon spectrum of the crystal makes energy conservation possible in the energy transfer step if the transfer is from a Mn^{2+} ion to a single Yb^{3+} ion, since to take up 0.3 eV or more of energy by emitting a burst of phonons would necessarily make the transfer rate strongly temperature dependent and very much lower at 77°K than at 300°K.

The analysis we have given indicates that there should be components in the Mn^{2+} luminescence decay given by Eq. [7] which have the same values of τ_i as the components found in the Yb^{3+} luminescence. However, because of the weighting factor ω_i in Eq. [12] the relative importance of the various components is very different in the two emissions. Clearly components having a much greater probability that the Mn^{2+} will transfer to Yb^{3+} than that it will radiate directly ($\omega_i >> \tau_{Mn}^{-1}$ and, therefore, $\tau_i << \tau_{Mn}$) will be relatively far more prominent in the Yb^{3+} emission than in the Mn^{2+} emission. We have made a quantitative analysis, on the basis of Eq. [7] and [11], of the contribution to the Mn decay curves to be expected from the components of the Yb^{3+} luminescence associated with decay times $\tau_i << \tau_{Mn}$, and we conclude that this contribution is too small to be distinguished in the experimental curves.

The near independence of temperature for the energy transfer mechanism indicated by our analysis, combined with our earlier conclusion from the efficiency of the transfer process as a function of Yb^{3+} concentration that transfer occurs from a Mn^{2+} ion to a single Yb^{3+} ion, suggests that the transfer of energy involves direct ion-to-ion transfer, in which the emission spectrum of one overlaps the absorption spectrum of the other. We have already noted that the emission spectrum of Mn^{2+} shifts to longer wavelength in samples containing increasing amounts of Yb^{3+}. In particular, there is a small tail of the Mn^{2+} band that extends to 820 nm, almost to the edge of the Yb^{3+} absorption. We suggest that when a Mn^{2+} ion is very close to an Yb^{3+} ion, the $^4T_{1g}$ state of Mn^{2+} is split by the field of the Yb^{3+}, and that emission from the lowest level of this state overlaps the Yb^{3+} absorption, making trans-

fer possible with energy conservation. If the transfer rate is a strong function of the separation of the ions, as one then expects, the Mn^{2+} will fall predominantly into two classes. On one hand, a Mn^{2+} ion has no Yb^{3+} ion sufficiently close for an appreciable probability of transfer, in which case the Mn^{2+} decays radiatively with a lifetime and spectrum little changed from that of an isolated Mn^{2+}; or, a Mn^{2+} is close enough to an Yb^{3+} to have a strongly distorted spectrum but also a transfer probability appreciably greater than the probability for radiative decay. Mn^{2+} ions of the latter type will thus excite the Yb^{3+} luminescence most of the time and will contribute only a very weak component to the Mn^{2+} luminescence. Just as the contribution of the short-lived components of the luminescence was found to be unobservable against the body of the Mn^{2+} luminescence, so the intensity of the strongly perturbed emission spectrum due to these ions is very weak compared with the spectrum of the less strongly perturbed Mn^{2+} ions that do not transfer. In support of this suggestion is the observed dependence of the Mn^{2+} emission spectrum on Yb^{3+} concentration in the series CaF_2:5%Mn:xYb:(20 − x)%Y. The Mn^{2+} emission in the sample with $x = 0$ has a $\bar{\lambda}$ of 560 nm and a long wavelength tail that extends to 860 nm which does overlap with the absorption band of Yb^{3+} in CaF_2. The shift of $\bar{\lambda}$ and the extent of the tail to shorter wavelengths as the Yb^{3+} concentration is increased is consistent with the idea that the longer wavelength Mn^{2+} emission present in the CaF_2:5% Mn:20%Y spectrum does not appear in samples containing Yb^{3+} because of the efficient transfer of this energy from Mn^{2+} ions to Yb^{3+} ions. The key to our interpretation of the system is, therefore, its inhomogeneity; transfer probabilities and spectral shapes depend strongly on the Mn^{2+}-Yb^{3+} separation, so that most pairs that contribute to the Yb^{3+} luminescence contribute negligibly to the Mn^{2+} luminescence, and vice versa.

We have also considered the possibility that an excited Mn^{2+} ion decays by exciting a single Yb^{3+} ion and radiating the energy difference. A similar process has been observed (12) in the decay of the ^2E_g level of Cr^{3+} in $EuAlO_3$. Such a process could provide an alternative quantum-splitting mechanism, the probability for which would be expected to be linear in the Yb^{3+} concentration in agreement with our data in Fig. 4. However, the resulting infrared emission spectrum should then contain not only the bands due to the Yb^{3+} luminescence but also an equally intense broad band representing the difference between the Mn^{2+} and Yb^{3+} excited states. The breadth in energy of this second band should be the same as that of the Mn^{2+} visible luminescence in Fig. 3. There is no evidence for such a broad band in our infrared data (Fig. 2), and we conclude that this alternative quantum-splitting mechanism also does not operate in the CaF_2:Mn^{2+}:Yb^{3+} system.

Summary

Energy transfer has been observed from Mn^{2+} to Yb^{3+} in CaF_2. However, the emission and decay data are consistent with a direct ion-to-ion transfer of energy and not with the Dexter mechanism or other mechanisms involving the deexcitation of the Mn^{2+} ion with the emission of two photons. We suggest that the direct transfer, which was unexpected on the basis of the known properties of CaF_2:Mn and CaF_2:Yb, is made possible by the splitting of the $^4T_{1g}$ state of Mn^{2+} by the field of a neighboring Yb^{3+}.

Manuscript submitted March 28, 1977; revised manuscript received May 27, 1977. This was Paper 142 presented at the Philadelphia, Pennsylvania, Meeting of the Society, May 8-13, 1977.

Any discussion of this paper will appear in a Discussion Section to be published in the June 1978 JOURNAL. All discussions for the June 1978 Discussion Section should be submitted by Feb. 1, 1978.

Publication costs of this article were assisted by General Electric Company.

REFERENCES

1. W. W. Piper, J. A. DeLuca, and F. S. Ham, *J. Lumin.*, **8**, 344 (1974).
2. D. L. Dexter, *Phys. Rev.*, **108**, 630 (1957).
3. F. Varsanyi and G. H. Dieke, *Phys. Rev. Lett.*, **7**, 442 (1961).
4. L. D. Livanova, I. G. Saitkulov, and A. L. Stolov, *Sov. Phys.-Solid State (Engl. Transl.)*, **11**, 750 (1969).
5. F. W. Ostermayer, Jr. and L. G. Van Uitert, *Phys. Rev. B*, **1**, 4208 (1970).
6. Y. Tanabe and S. Sugano, *J. Phys. Soc. Jpn.*, **9**, 753 (1954); *ibid.*, **9**, 766 (1954).
7. J. Kirton and S. D. McLaughlin, *Phys. Rev.*, **155**, 279 (1967).
8. E. Loh, *ibid.*, **184**, 348 (1969).
9. Yu. K. Voron'ko, V. V. Osiko, and I. A. Shcherbakov, *Sov. Phys.-JETP (Engl. Transl.)*, **29**, 86 (1969).
10. J. W. Stout, *J. Chem. Phys.*, **31**, (3), 709 (1959).
11. M. D. Agrawal and K. V. Rao, *Phys. Status Solidi*, **3**, 153 (1970).
12. J. P. van der Ziel and L. G. Van Uitert, *Phys. Rev. Lett.*, **21**, 1334 (1968).

On the Use of Photomask Coatings in Photolithography

Dervin L. Flowers* and Henry G. Hughes*

Motorola, Semiconductor Research and Development Laboratory, Phoenix, Arizona 85008

ABSTRACT

Three coating solutions have been used to coat emulsion masks to determine whether any benefits might be realized. It was found that these coatings enable one to increase mask life and reduce the defect density. Capacitor yields and pinhole counts have been determined which show significant yield enhancement over noncoated emulsion masks. It has been further shown that an adequate soft bake cycle of photoresisted wafers to remove solvents prior to exposure is essential in obtaining maximum yield with or without coatings on the masks.

Device yield in the semiconductor industry is strongly dependent upon effective photoresist processing which minimizes photolithographic defects. Schnable *et al.* have published an excellent review of passivation coatings on silicon including such defects in passivation glass (1). Pinholes and cracks in passivation glass can lead to severe reliability problems. A more immediate effect is to lower device yield (2). Such defects in passivation glass can be due to a variety of causes. Some may be formed during glass deposition (3). Pressure contact of glass passivation over aluminum can cause cracks (4). Etching of passivation glass to open bonding pads may produce pinholes due to holes in the photoresist layer (1). In multilayer IC manufacture, etching of vias can produce pinholes due to holes in the photoresist. These can fill with metal on the next evaporation and cause interlayer shorts (5).

One factor in this operation which has gained little attention in the literature concerns resist-mask interactions (6). It is well known that yield is strongly affected by wafer-to-mask contact problems arising from dust particulates, epi spikes, and resist-mask sticking. These lead to mask damage, transfer of photoresist polymer onto the mask, and the transfer of this residual back to subsequent wafers during alignment. With multiple mask use, pieces of photoresist adhering to the mask from previous alignments will "print" causing latent defects in the resist which on subsequent wafers develop out allowing more unwanted etching and pinholes to form. Thus, each piece of photoresist torn from a wafer causes two or more yield limiting pinholes which can lead to electrical shorts and poor definition. The introduction of some mask lubricating agent or protect coat to reduce photoresist to mask adhesion is thus highly desirable.

The use of hard surface masks and proper photoresist processing are well documented but little is found regarding ways to improve emulsion mask usage. Emulsion mask protect coatings to increase hardness, decrease friction, reduce resist-mask sticking, and, in general, increase emulsion mask life with low defect levels seem to offer great promise.

Three such coatings [Parylene N (7), polyvinyl alcohol (8), and spin-on glass (9)] have been investigated in this laboratory. Results indicate that these three coatings do increase mask life and reduce defect densities *vs.* uncoated masks.

Baseline criteria were performed to determine the effect of soft bake cycles, mechanical contact, and exposure on pinhole generation.

The experimental work reported herein has been collected using a negative polyisoprene-base photoresist but one example of a protect mask coating used in conjunction with a positive resist is outlined. The combined use of a lubricating resist protect coat (5) and a coated mask is also mentioned. Capacitor yields and pinhole counts were used for evaluation comparisons.

* Electrochemical Society Active Member.

Key words: mask coating, pinhole density, capacitor yield, photoresist

Experimental

The experimental procedures investigated included establishing a baseline criteria for photoresist processing for comparison data and optimization. These included resist soft bake, resolution, and mechanical contact wafer-mask damage.

Photoresist processes.—The photoresists were processed as follows unless stated differently elsewhere.

Negative photoresist was applied by spinning to give a thickness of 1050 nm, and soft baked for 20 min at 70°C (N_2) or 30 min at 80°C. The latter was used for all experiments except for establishing a baseline bake. A 12 sec exposure (2500 $\mu W/cm^2$ intensity) was used with a standard aligner, contact pressure 5-6 psig. Spray develop was 20 sec xylene plus 20 sec n-butyl-acetate rinse. Hard bake was 30 min at 180°C (N_2).

One experiment using positive photoresist (2200 nm) was performed. Processing was air dry for 15 min, soft bake 70°-80°C for 20 min, expose for 20 sec, develop 1:1 developer/water, water rinse, and hard bake 180°C for 30 min.

Pinhole determination and soft bake.—Two pairs of 2.3 × 2.3 mm chip wafers, patterned first with aluminum (32% of chip area), were passivated with 1000 nm of standard phosphorus-doped CVD glass. After a 1 hr dehydration bake the wafers were coated with negative photoresist. The resisted wafers were baked for 20 min in nitrogen ambient at either 70° or 80°C. The wafers were then exposed with a blank mask in contact mode. After normal development and rinse the resist was baked at 180°C for 30 min.

The wafers were then etched for 4.5 min (50% overetched) in 1:1 ammonium fluoride/acetic acid at room temperature. This etch serves to open latent pinholes in the passivation layer due to missing resist pulled from the wafer in contacting the mask. Pinholes in the "as applied" photoresist were negligible (< 1%). The wafers were next stripped of resist and etched with a standard aluminum etch for 2 min at 65°C to open a circular area in the underlying aluminum for easier defect counting as a result of pinholes in the passivating glass. Twenty eight dies per wafer were counted.

Pinhole density due to contact and exposure.—The effect of pinholes resulting from contact of passivation only and exposure *vs.* no exposure after contact was next investigated. Following the procedure for pinhole determination outlined earlier and using an 80°C-30 min bake the wafers were processed four different ways: (*i*) aluminum etched after CVD to determine initial pinhole density; (*ii*) aluminum etched after two mask contacts, no exposure, and resist stripped to determine mechanically formed pinholes; (*iii*) passivation etch, then aluminum etched after two mask contacts, no exposure, to determine effect of exposure; and (*iv*) same as item (*iii*), with standard exposure

and develop before etchings. Pinholes in 28 dies per wafer were counted for each step. Die size was 3.0 × 3.4 mm.

Emulsion mask coatings.—Three emulsion mask coatings were investigated. These were Parylene, spin-on glass, and polyvinyl alcohol. Not all experiments were run with all three mask coatings because of limited man-hours and large sample sizes that would be involved.

Parylene was vapor phase deposited (20 nm) by Nova Tran Corporation, Clearlake, Wisconsin.

Spin-on glass (200 nm) was applied with an eyedropper, spun at 3000 rpm for 20 sec, then baked at 130°C for 30 min in an oven.

A solution of 3% w/v polyvinyl alcohol (medium molecular weight) in water was prepared and masks were dip coated and baked 20 min at 80°C (250 nm).

Pinhole count of coated and uncoated masks.—The effects of uncoated and coated masks in relationship to pinhole density were determined by using standard negative photoresist and pinhole detection as outlined earlier. Parylene, spin-on glass, and uncoated masks were evaluated. Three wafer samples with 28 (3.0 × 3.4 mm) die/wafer were counted at 50X magnification.

Mask coatings and "acceptable" definition.—A procedure often used that relates to mask life is to align that number of wafers that will still give acceptable pattern definition by some arbitrary criteria that relates to device yield. To determine what effect mask coatings may have in longer photomask use, an experiment was designed to determine how many wafers could be exposed with one mask (a memory device with 0.005 mm emitter openings) before definition problems became too severe. Chip size here was 2.3 × 2.3 mm. Fail criteria was defined as being when two or more fields inspected out of nine had incomplete emitter openings (not etchable due to undesired polymerization) to allow a functioning device. A Parylene-coated mask was chosen for this study. To increase test severity, 23 psig contact pressure was used.

Mask coatings and capacitor yields.—Capacitor yields were investigated to more nearly relate to device yield. An increase in capacitor yield was expected using coated masks based on a decrease observed earlier in pinhole counts.

Patterned first metal, 3.0 × 3.4 mm chips were passivated with 1000 nm phosphosilicate glass, photoresisted, then overetched by 1.5 min using 1:1 ammonium fluoride/acetic acid at room temperature. The wafers were stripped of photoresist and metallized with second layer 1000 nm aluminum. The top metal was expected to fill in pinholes thereby contacting the underlying aluminum. Wafers were again photoresisted for delineating each chip as a capacitor.

Capacitor measurements were taken using a Motorola IC automatic probe interfaced with a CDC 8090 computer. Readings were taken at 30V. Where there were no device failures, the leakage was less than 10 μA. If a reading of > 10 μA was measured, a device failing pinhole, filled with aluminum and contacting first metal, was assumed. Usually the "fail" readings were in excess of 100 μA so little ambiguity existed.

Five capacitor experimental conditions were run; (*i*) 3 control (noncoated masks) sets, negative photoresist; (*ii*) 2 spin-on glass coated mask sets, negative photoresist; (*iii*) 1 polyvinyl alcohol coated mask set, negative photoresist; (*iv*) 2 Parylene coated mask sets, negative photoresist, and one of the photoresists sets had an experimental lubricating resist protect coat (5), 15 nm thick on the wafer; and (*v*) 1 Parylene coated mask set positive photoresist. The experiments were run each with a control (uncoated mask). The full number of wafers noted in the data were processed but only every second or third was probed to save time yet present the most meaningful spread of data possible. One hundred dies per wafer were probed.

Results and Discussion

Initial baseline criteria, which show the importance of using proper bakes and the effect exposure and mechanical damage have in device fabrication, are outlined in the first section. The influences of mask coatings on reducing pinholes, influencing resolution, and increasing capacitor yields are discussed in the last part of this section.

Photoresist processes.—It was determined that a 20 min 70°C soft bake resulted in an average of 0.80 pinhole/die *vs.* 0.43 pinhole/die using a 30 min 80°C bake (Table IA). The latter temperature has become more of a standard practice recently and should be used for increased yields.

Mechanical damage plays a significant role in pinhole formation and becomes more pronounced as multilayers are built up (Table IB).

First, the loss due to mechanical contact with the mask of the passivation layer increased elevenfold in pinholes over that of the base glass. This serves to point out the necessity for smooth and uniform passivation and metallization. Part of the mechanical loss was probably due to contacting glass over metal edges where large stresses are exerted (though contact pressure was only 5-6 psig).

Second, the passivation layer was etched prior to aluminum etching to determine the latent pinholes formed in the resist when not exposed. A sevenfold average pinhole increase, presumably due to cracking or pulling out of photoresist on mask contact, was recorded. This result was higher than expected but consistent with Scotch tape tests of negative resist on wafers. Before exposure and cross-linking (insolubilization) of negative photoresist, film strength (adhesion and cohesion) is very weak and the resist is readily ripped and pulled from wafers in such a test. Once exposed, however, Scotch tape is pulled with some difficulty from the resist with only a few small pieces adhering to the tape. These observations indicate the need to use an absolute minimum number of contacts between mask and resist during alignment before exposure in order to significantly reduce resist damage and yield loss.

Third, the addition of standard exposure and processes resulted in a decrease of pinholes from 7.7 to 2.7 per chip.

From these experiments it is concluded that 1.1 pinholes/die are due to mechanically induced damage and 1.6 pinholes/die induced due to photoresist-mask sticking and the tearing out of tiny pieces of photoresist from the passivation layer.

Having established baseline data relating to pinhole formation in photolithographic processes, photomask coatings were next investigated.

Pinhole density from uncoated and coated masks.—Comparisons of uncoated, Parylene, and spin-on glass

Table I. Effect of process parameters on pinhole density in die

Set	Process	Average pinhole/die
A.	Soft bake cycle (chip size 2.3 × 2.3 mm)	
1.	20 min, 70°C, N_2	0.80
2.	30 min, 80°C, N_2	0.43
B.	Mechanical contributions (chip size 3.0 × 3.4 mm)*	
1.	Base glass on metal pattern	0.10
2.	Aluminum etch after 2 contacts, no exposure	1.10
3.	Passivation etch then aluminum etch after 2 contacts, no exposure	7.70
4.	Repeat 3 with exposure and develop (standard process)	2.70
C.	Noncoated *vs.* coated emulsion mask	
1.	Uncoated mask	1.63
2.	20 nm Parylene	0.93
3.	200 nm spin-on glass	1.09

* Chip sizes varied because of wafer availability. All following data from this chip size.

Table II. Photomask life with and without Parylene lubricating coat

Photomask	No. wafers in set	Pass	Fail
Uncoated emulsion	10	5	5
Parylene-coated emulsion	26	25	1

coated masks (Table IC) have shown as much as 42 and 33%, respectively, pinhole reduction.

If one considers that photomasks have polar groups at the surface (amide and carbonyl for gelatin, hydroxyl for chrome and iron oxide) and olefinic groups both *exo* and *endo* in the resist chain, pressure contact, particularly at asperities and metal edges, exerts sufficient force for the polar groups and olefinic groups to react and form chemisorbed bonds between mask and resisted wafers. These bonds are apparently strong enough to pull out tiny pieces of resist, leaving them deposited on the mask when separation occurs. Both Parylene and spin-on glass should have low energy surfaces lacking polar groups to form these chemisorbed bonds, hence, less sticking and damage are expected. Although this work was done with emulsion masks, similar benefits are expected with hard surface masks.

Mask coating and "acceptable" definition.—It was established that a Parylene-coated mask could be used five times as long as an uncoated mask and still give acceptable definition (0.005 mm emitter openings; Table II.) The uncoated emulsion mask gave acceptable definition on the first five wafers but the last five failed by the criteria used. In the Parylene-coated mask, 25 out of 26 wafers passed. The failed wafer was number 15 of the set and may have had epi spikes or dirt holding it out of even contact. The uncoated masks on inspection showed an increasing number of specks of photoresist with increased use. The Parylene-coated plates also had a buildup but the particles were fewer in number and smaller in size.

Mask coatings and capacitor yields.—Mask coatings were found to give significantly higher capacitor yields over uncoated control masks (Fig. 1-4).

From the data of Fig. 1 through 3, the reproducibility of the tests may be gauged by comparing the average yields for the first nine wafers (18 contacts) processed as the control group (uncoated mask) for each set. The averages for the three control sets are:

set 1, 1st 9 wafers (2 contacts/exposure) 39 ± 5% yield; set 2, 1st 9 wafers (2 contacts/exposure) 33 ± 2% yield; and set 3, 1st 7 wafers (3 contacts/exposure) 33 ± 7% yield. Considering that the sets contained different samples of epi wafers and different diffusion and passivation runs, the agreement is quite good.

A decrease in capacitor yield with continued uncoated mask usage is what is usually observed with a severe yield break occurring around 20-30 contacts. The lowest yield for the first wafer exposed relative to

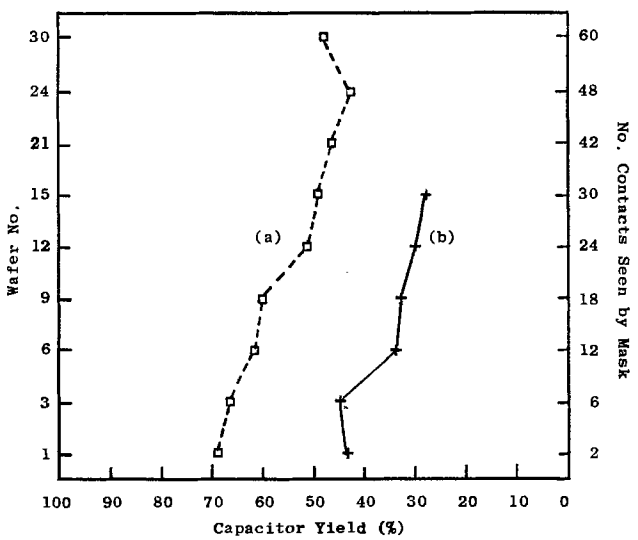


Fig. 1. Percent capacitor yield using negative photoresist. (a) Spin-on glass mask coat. (b) Uncoated mask.

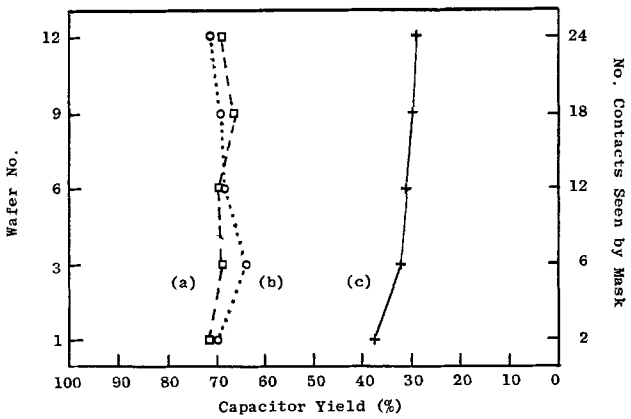


Fig. 2. Percent capacitor yield using negative photoresist. (a) Spin-on glass mask coat. (b) Polyvinyl alcohol mask coat. (c) Uncoated mask.

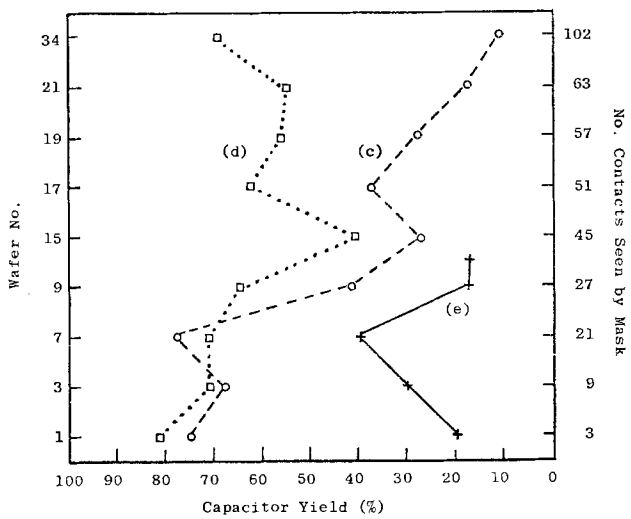


Fig. 3. Percent capacitor yield using negative photoresist. (c) Parylene-coated mask. (d) Parylene-coated mask plus resist protect coat. (e) Uncoated mask.

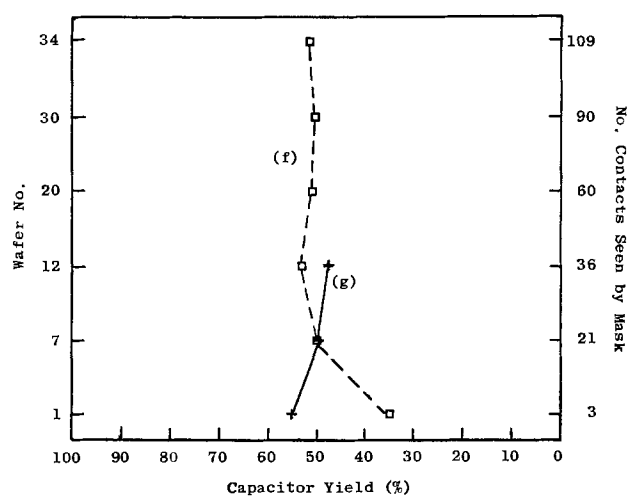


Fig. 4. Percent capacitor yield using positive photoresist. (f) Parylene-coated mask. (g) Uncoated mask.

later wafers as seen in Fig. 3e, has been seen many times before. There may be some unadhered dirt or bumps not blown off the mask prior to first contact causing cracks in the photoresist and transferred additionally to the first exposed wafer.

The use of spin-on glass and polyvinyl alcohol protect coats promotes significant capacitor yield increases over uncoated masks. A summary of average percent capacitor yields for these two coatings is shown in Table III. Set 1 wafers were processed with spin-on glass coated masks, and set 2 wafers were processed with spin-on glass or polyvinyl alcohol coated masks.

Here it is seen that capacitor yields, for a given number of contacts, are increased by factors of 1.6-2.1 (60-107%) by use of mask coatings. In fact, the final yield, even after 30 exposures (60 contacts) using spin-on glass is considerably higher than the initial yield of uncoated mask. Both spin-on glass and polyvinyl alcohol gave considerable yield improvements but the glass tends to provide a harder film.

Parylene-coated masks also show a substantial yield improvement over noncoated masks (Fig. 3c, e) with additional benefits realized by the added application of the resist protect coat (Fig. 3d.) The average capacitor yields, normalized to three contacts per mask for the uncoated sets, are outlined in Table IV and Fig. 3c. A large yield breakdown occurred after the 7th wafer processed. This may be a result of the ultrathin Parylene coating (20 nm) wearing off. This reduction in wear may be reduced with the application of the resist protect coat (as no yield break occurred with higher yields to 34 wafers) or by application of a thicker Parylene coating.

The effect of using coated masks when working with positive photoresists was next demonstrated. Parylene-coated masks were used in this study. The results of these tests using three contacts per mask are shown in Fig. 4. Average capacitance yields comparing positive resist and negative resist processing are summarized in Table V.

This data, although showing some improvement in yield on positive resist (excluding wafer 1) with use of a Parylene-coated mask, is not as substantial as that noted with negative photoresist. It was also observed that mask to positive resist sticking was not as great as indirectly indicated by capacitor yield (49% base yield with positive and 29% with negative per 12 wafers.) The Parylene-coated mask maintained its high intermediate yield level through 34 wafers with positive resist which is noteworthy in simply comparing the two photoresists. It should be kept in mind, however, that positive resist was substantially thicker than the negative. The resist protect coat used in conjunction with Parylene-coated masks proved to be the best performer of all investigated and bears further investigation.

Table III. Average capacitor yields (%) at various levels of mask use

No. wafers exposed*	Set 1			Set 2	
	6	12	30	6	12
Uncoated	41.6	37.2	—	34.7	33.4
(Range)†		(43-39)			(38-31)
Spin-on glass	65.7	61.8	55.1	70.3	79.2
(Range)		(69-52)	(69-48)		(72-68)
Polyvinyl alcohol	—	—	—	67.3	68.4
(Range)					(70-71)

* 2 contacts per wafer.
† Initial-Final.

Table IV. Average capacitor yields (%) for Parylene-coated masks with and without resist protect coat

Mask description	Average capacitor yield for number of wafers					
	1	7	12	20	30	34
Uncoated	34	34	29	—	—	—
Parylene	76	74*	60	51	43	38
Parylene with resist protect coat	82	75	72	64	64	64

* Gross yield break (cf. Fig. 3) after this wafer.

Table V. Average capacitor yields (%) for Parylene-coated masks when using positive and negative photoresists

Mask resist descriptions	Average capacitor yield for number of wafers					
	1	7	12	20	30	34
Uncoated (+)	56	50	49	—	—	—
Parylene (+)	36*	50	54	52	52	53
Uncoated (−)	34	34	29	—	—	—
Parylene (−)	76	74†	60	51	43	38
Parylene (−) and resist protect coat	82	75	72	64	64	64

* A typical low yielding wafer.
† Gross yield break (cf. Fig. 2).

Summary

It has been shown that mask coatings can have a significant impact on device yield and prolonging mask life by reducing pinholes and by improving resolution in reducing the amount of resist buildup on the mask substrate. The most significant increases were observed when negative resist was used. The over-all yields were found to be further enhanced by use of lubricating resist coat formulations. Furthermore, it has been demonstrated that sufficient bake temperature and time are necessary to minimize resist mask sticking, thus reducing pinhole formation prior to exposure.

It is recognized that not all pinholes and capacitors measured in these tests are device yield limiting. Certainly a high percentage are, however. Mask coatings used on emulsion masks should result, therefore, in significant yield improvements, particularly in multilevel LSI devices. Additionally, considerable mask cost savings are implied.

Acknowledgments

Appreciation is extended to Louise Rice for performing much of the experimental study, to Isabelle Kast for preparation of this manuscript, and to Jim Smith for many helpful suggestions and review of this report.

Manuscript submitted Dec. 6, 1976; revised manuscript received May 28, 1977.

Any discussion of this paper will appear in a Discussion Section to be published in the June 1978 JOURNAL. All discussions for the June 1978 Discussion Section should be submitted by Feb. 1, 1978.

Publication costs of this article were assisted by Motorola Incorporated.

REFERENCES

1. G. L. Schnable, W. Kern, and R. B. Comizzoli, *This Journal*, **172**, 1092 (1975).
2. J. Cunningham and J. Jaffe, *Electronics*, **48**, 101 (1975).
3. W. C. Bensing, R. S. Rosler, and R. W. East, *Solid State Technol.*, **16**, 37 (November 1973).
4. W. Kern, G. L. Schnable, and A. W. Fisher, *RCA Rev.*, **37**, 45 (1976).
5. D. L. Flowers, Abstract 76-2, p. 745, The Electrochemical Society Extended Abstracts, Fall Meeting, Las Vegas, Nevada, Oct. 17-22, 1976.
6. R. Bowman and J. Livingston, in Proccedings 1974 Kodak Microelectronics Seminar, G41, p. 7 (1975).
7. Union Carbide Corporation.
8. J. T. Baker No. U229.
9. K. Ritchie, U.S. Pat. 3,832,202 (1974).

Characterization of n-Type Semiconducting Indium Phosphide Photoelectrodes

Stabilization to Photoanodic Dissolution in Aqueous Solutions of Telluride and Ditelluride Ions

Arthur B. Ellis, Jeffrey M. Bolts, and Mark S. Wrighton*

Department of Chemistry, Massachusetts Institute of Technology, Cambridge, Massachusetts 02139

ABSTRACT

n-type semiconducting single crystal InP (bandgap, E_{BG}, = 1.25 eV) has been studied as a photoanode in aqueous electrolytes. Irradiation of the InP with light of energy greater than or equal to the value of E_{BG} results in the flow of anodic current. In 1.0*M* NaOH solutions, the onset of photocurrent is at about −1.1V *vs.* SCE, and the current is accompanied by anodic dissolution of the electrode. The behavior of the reductants X^{2-} (X = S, Se, Te) was investigated, and only Te^{2-} was found to be oxidized completely efficiently at the irradiated InP. For S^{2-} we could see no oxidation to elemental S, but oxidation of Se^{2-} was found to be partially competitive with photoanodic dissolution of the electrode. The band positions of InP have been determined in all electrolytes by measuring the photopotential, or from differential capacitance measurements. The band positions are dependent on the electrolyte *p*H and on the presence of X^{2-}. For the Te^{2-} electrolyte, the oxidation product, Te_2^{2-}, is reducible at the Pt counterelectrode, ultimately resulting in an electrolyte with a constant composition. The maximum voltage output in the Te^{2-}/Te_2^{2-} electrolyte is ~0.4V at high light intensity, and the short-circuit quantum efficiency for electron flow is ~0.2 at low light intensity. The energy conversion efficiency for conversion of 632.8 nm light to electricity is of the order of one percent.

We (1-5) and others (6, 7) have recently shown that n-type semiconductors such as CdX (X = S, Se, Te), GaAs, GaP, and Bi_2S_3 can be stabilized to photoanodic dissolution by using electrolytes which contain electroactive X^{2-} (X = S, Se, Te) ions. The notion of using competitive electron transfer from reductants in the electrolyte to stabilize n-type semiconductors now seems to be a viable approach to the development of photoelectrochemical cells for the conversion of light to electricity. But we do not presently have a detailed understanding of why competitive electron transfer works in some cases and not in others. For example, the oxidation of X^{2-} should be energetically feasible at all of the following electrodes: CdX (X = S, Se, Te), GaAs, and GaP. However, the oxidation of the X^{2-} only occurs completely efficiently in a limited number of situations (1-5).

In this paper we wish to describe the characterization of n-type InP-based photoelectrochemical cells employing electrolytes containing X^{2-} species. Again, energetics are found to be a poor indicator of whether efficient oxidation of X^{2-} occurs. Stabilization of InP is significant in part because of its low bandgap, E_{BG}, of 1.25 eV (8) and high absorptivity. However, the band positions relative to the redox potential in the stabilizing Te^{2-}/Te_2^{2-} electrolyte preclude efficient optical to electrical energy conversions.

Results and Discussion

Stability.—When n-type, single crystal InP is irradiated as the photoanode *vs.* a dark Pt cathode in an electrolyte of 1*M* NaOH, anodic decomposition of InP results. The black, originally mirror-like surface becomes rough and gray, and weight loss in the crystal is evident. We find that between 6 and 8 moles of electrons are required to decompose 1 mole of InP, consistent with Eq. [1] and/or [2].

$$InP \xrightarrow{h\nu} In^{+3} + P^{+3} + 6e^- \qquad [1]$$

$$InP \xrightarrow{h\nu} In^{+3} + P^{+5} + 8e^- \qquad [2]$$

Photoanodic decomposition according to Eq. [1] has been demonstrated for other III-V semiconductors like GaP and GaAs (9, 10). Anodic photocurrents from the InP are observed at potentials more positive than about −1.1V *vs.* SCE. In an electrolyte of 1.0*M* NaOH/1.0*M* Na_2S or 1.0*M* NaOH/1.0*M* Na_2S/1.0*M* S at 25° we find that the photoanodic dissolution of InP still occurs, despite the fact that the onset of photoanodic current may be ~0.1V more negative. Thus, the oxidation of S^{2-} to elemental S apparently does not compete with the electrode dissolution. Likewise, we find that Se^{2-} is inefficiently oxidized at an irradiated InP. An electrolyte of 5.0*M* KOH containing up to 0.5*M* Na_2Se at 60° does yield some competitive Se^{2-} oxidation as evidenced by the appearance of the colored Se_2^{2-} (λ_{max} = 425 nm, $\epsilon \approx$ 1000 liter mole^{-1} cm^{-1}) (4). But the oxidation is relatively inefficient and the InP is rapidly corroded.

In marked contrast, we find that electrolytes containing 5.0*M* NaOH and 0.1*M* Na_2Te at 50° do stabilize InP. Oxidation of Te^{2-} is initially obvious by the appearance of a purple color near the photoelectrode associated with the oxidation product Te_2^{2-} (λ_{max} = 512 nm, $\epsilon \approx$ 1000 liter mole^{-1} cm^{-1}) (3). Prolonged stability of InP is established by constant photocurrents and constant composition electrodes, Table I. We have previously established that the Te_2^{2-} is reducible to Te^{2-} in photoelectrochemical cells at the Pt counterelectrode (3, 4). Thus, for the InP-based cell with the Te^{2-}/Te_2^{2-} electrolyte, Eq. [3] and [4] represent the cell chemistry

$$2Te^{2-} \rightarrow Te_2^{2-} + 2e^-$$

and/or

$$Te_2^{2-} + 2Te^{2-} \rightarrow 2Te_2^{2-} + 2e^- \quad \text{(anode)} \qquad [3]$$

$$Te_2^{2-} + 2e^- \rightarrow 2Te^{2-} \quad \text{(cathode)} \qquad [4]$$

The current-voltage characteristics are described in detail below.

* Electrochemical Society Active Member.

Key words: photoelectrochemistry, indium phosphide, optical energy conversion, photoanodic dissolution.

Table I. Stabilization of n-type InP photoelectrodes in telluride electrolyte[a]

Crystal[b]	Moles × 10^4 Crystal before	Crystal after[c]	Electrons[d]	Average i, mA[e]	V appl[f]	t, hr	Light source[g]
InP-A	1.67	1.66	3.19	0.21	+0.02	41.5	633 nm
InP-A	1.72	1.71	4.06	0.71	+0.10	15.3	tungsten
InP-B	2.53	2.53	15.90	0.97	+0.04	44.0	Hg

[a] Electrolyte is initially 5.0*M* NaOH/0.1*M* Na_2Te at ~50°C, and is stirred under Ar. The only oxidation product is Te_2^{2-}.
[b] All InP samples are n-type single crystals ~5 × 5 × 0.35 mm with the (100) face exposed to the electrolyte. The resistivities of InP-A and InP-B are 0.005-0.016 and 0.4 Ω-cm, respectively.
[c] Moles of crystal before and after the experiment as determined by weighing the crystal.
[d] Moles of electrons in the external circuit determined by integrating a plot of photocurrent *vs.* time.
[e] For current density, multiply by 4 cm^{-2}. Photocurrent was constant to ±5% during course of the experiment.
[f] Applied bias from an external power supply in series with the photoanode and Pt-cathode. A positive bias means that the (+) lead from the power supply is connected to the photoanode.
[g] The 633 nm source is a 6x beam-expanded He-Ne laser supplying ~3 mW of uniform irradiation to the photoanode. Tungsten source is the full output of a 650W tungsten-halogen lamp. The Hg source is the full output of a 200W superhigh pressure Hg arc lamp; output from both of these sources is filtered in the near infrared and u.v. by 18 cm of H_2O and a Corning CS 3-73 filter, respectively.

The InP is even stabilized at very high input power with the Te^{2-}-containing electrolyte. For example, 500 mW/cm^2 of 632.8 nm light from a 1 mm He-Ne laser beam leads only to Te^{2-} oxidation. However, at this power density elemental Te forms a coating on the photoelectrode, and is observable as a gray spot on the InP which is "washed away" by reaction with Te^{2-} to form the Te_2^{2-}. The formation of elemental Te was noted previously (4), and is a contributor to inefficiency in that the Te film (at the very least) absorbs the incident irradiation. Thus, at high intensity steady-state irradiation a Te film serves to reduce quantum efficiency. Competing with its formation, the film of Te is removed to give the final oxidation product, Te_2^{2-}.

It is important to note that no truly long-term stability experiments have been performed. Moreover, no tests have been carried out in sunlight, since the low output parameters (*vide infra*) with monochromatic 632.8 nm light are not sufficiently encouraging to merit such a study. What we can say is limited by the actual data given in Table I; the n-type InP photoelectrode is completely stable on the time scale of ~40 hr at current densities of ~4 mA/cm^2. However, the lack of weight loss and the constancy of output parameters for the entire duration suggest that InP will be stable much longer than 40 hr. Concerning experiments at >500 mW/cm^2 632.8 nm excitation, we find constant outputs and no obvious surface damage for ~3 hr periods where the short-circuit current density exceeds 10 mA/cm^2. The main point from our results is that InP is obviously unstable in the S_n^{2-} or Se_n^{2-} electrolyte, but in the Te^{2-}/Te_2^{2-} the stabilization to photoanodic dissolution is considerable.

Wavelength response.—Figure 1 shows the wavelength response of the InP-based photoelectrochemical cell employing the Te^{2-}/Te_2^{2-} electrolyte. For comparison, the absorption edge of InP is shown in the figure. The onset of photocurrent and absorption corresponds to the known (8) E_{BG} of 1.25 eV for InP. The sharp rise in absorption and photocurrent is characteristic of direct bandgap semiconductor photoelectrodes.

Current-voltage properties and energy conversion efficiency.—The current-voltage properties of InP in the Te^{2-}/Te_2^{2-} electrolyte are shown in Fig. 2. The

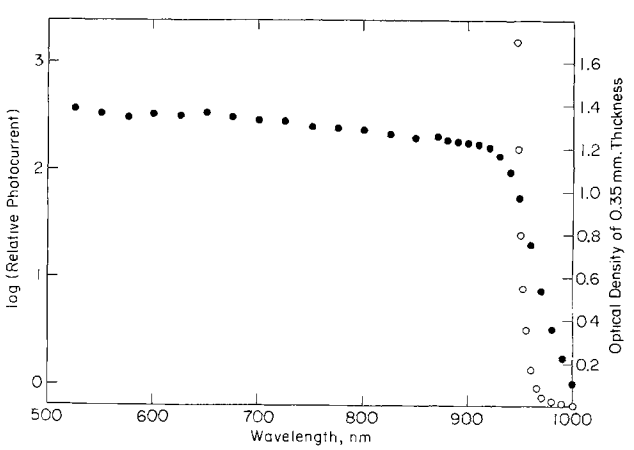


Fig. 1. Absorption and wavelength response curves for an n-type InP single crystal. Open circles represent the absorption of an optically polished 0.35 mm thick InP crystal. Filled circles represent photocurrent obtained when InP is the photoanode in an optically clear 0.1*M* Te^{2-} (50°C) electrolyte after correction for variation in light intensity (*cf.* Experimental).

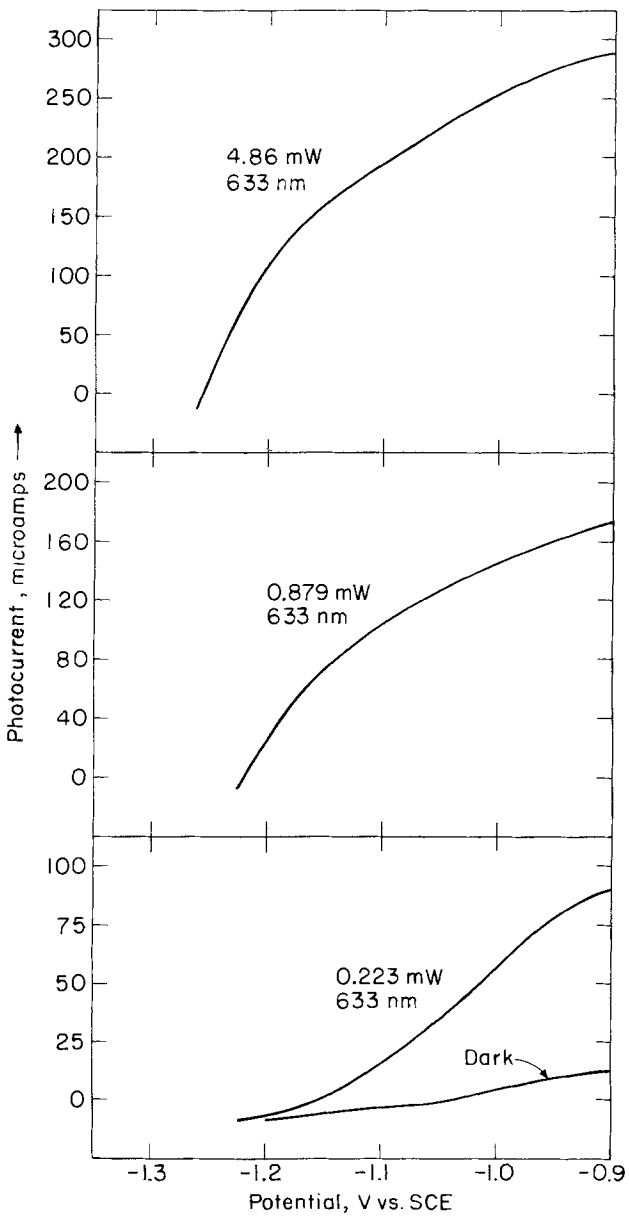
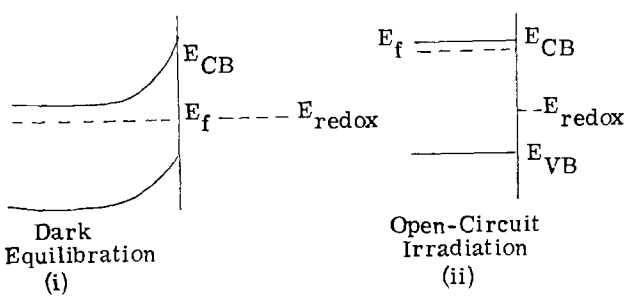


Fig. 2. Current-voltage curves as a function of light intensity for an n-type InP-based photoelectrochemical cell in 0.1*M* Te^{2-} at 50°C. The sweep rate was 1 mV/sec, and the Pt dark potential was always −1.10V *vs.* SCE. Irradiation was performed with a 1 mm He-Ne laser (632.8 nm) beam. To obtain intensity, multiply by 127 cm^{-2}.

dark anodic current is small, but finite, as is usual for n-type semiconductors, since no minority charge carriers, holes, are present. Irradiation to produce holes in the valence band does yield a significant anodic current, and the onset moves more negative with increasing light intensity. It is important that the onset of the anodic photocurrent is more negative than the potential for oxidizing Te^{2-}. The Te^{2-}/Te_2^{2-} potential is at ~ -1.10V *vs.* SCE (11), and the onset of photocurrent at very high light intensity is near -1.45V *vs.* SCE. The difference in the onset potential for photoanodic current and the Te^{2-}/Te_2^{2-} thermodynamic potential is the open-circuit photopotential. Photocurrent at potentials more negative than the Te^{2-}/Te_2^{2-} potential reflects conversion of light to electricity. The power output of the cell (current times voltage) can be determined from the current-voltage curves in Fig. 2. For each curve the maximum optical to electrical energy conversion efficiency is only of the order of one percent. The maximum efficiency occurs at a voltage output of between $\sim$0.05 and 0.20V. Increasing photopotential at the higher input optical power levels is offset by a decrease in the quantum efficiency for electron flow. In the three curves shown, the light intensities increase in the ratio 1.0:3.9:21.8, while the corresponding photocurrents at -0.9V vs. SCE increase by 1.0:2.1:3.5. From the discussion above, the saturation of the photocurrent may be due, in part, to the deposition of elemental Te on the InP. At the lowest light levels the quantum efficiency for electron flow approaches unity at a sufficiently positive bias, but there is poor energy conversion efficiency because of the low output potential. At high light intensity the output potential does become a significant fraction of the bandgap, but the quantum efficiency for electron flow is so low that the energy conversion efficiency remains poor.

Band positions of InP.—According to Gerischer's development (12), the maximum open-circuit photopotential in a n-type semiconductor-based photochemical cell is just the initial difference in the value of the redox potential of the couple in equilibrium, E_{redox}, and the conduction band position, E_{CB}, at the interface. Thus, measuring the band positions of the semiconductor exposed to the electrolyte can be useful in evaluating the theory, and in providing a measure of the ultimate energy conversion efficiency. The energetics of the semiconductor/electrolyte interface are sketched in Scheme I. For a heavily doped n-type semiconductor,



Scheme I

the Fermi level, E_f, is at nearly the same position as E_{CB} in the bulk. Irradiation at open circuit can raise the E_f, then, to a value nearly equal to the E_{CB} level at the interface. At this maximum level of E_f there is no band bending, and this maximum E_f is called the flatband potential, E_{FB}. For a given electrolyte, the E_{CB} and E_{VB} positions are taken to be fixed.

In a given electrolyte the open-circuit photopotential should allow evaluation of the positions of E_{VB} and E_{CB}. Open-circuit photopotentials of InP in 3 X^{2-}/X_n^{2-} electrolytes are shown in Fig. 3 as a function of incident optical power. Unfortunately, we were

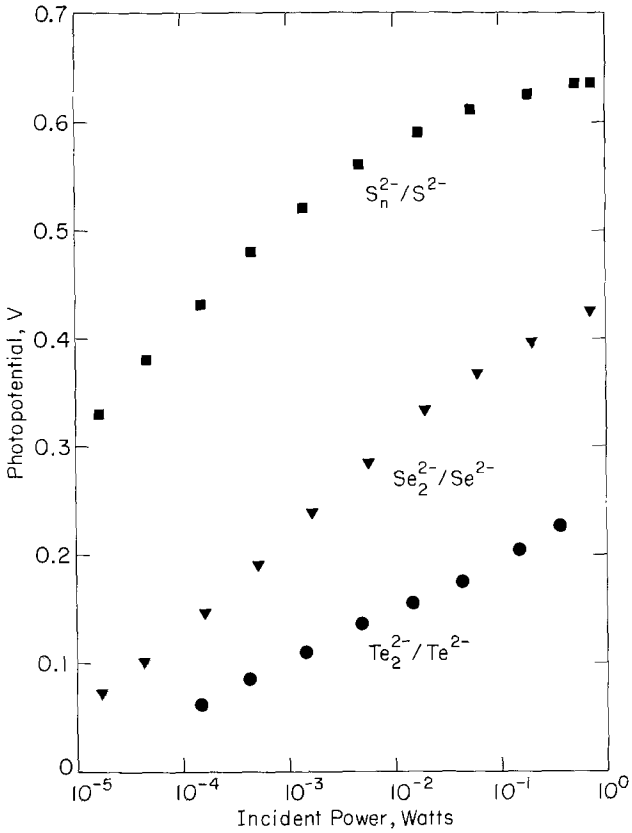


Fig. 3. Open-circuit photopotential between InP and Pt in S^{2-}/S_n^{2-} (1.0M NaOH, 1.0M Na_2S, 1.0M S at 25°), Se^{2-}/Se_n^{2-} (5.0M NaOH, 0.024M Na_2Se, 0.003M Na_2Se_2 at 60°), and Te^{2-}/Te_2^{2-} (5.0M NaOH, 0.08M Na_2Te, 0.01M Na_2Te_2 at 50°) electrolytes.

unable to obtain the maximum photopotential with light intensities available. Consequently, from the data in Fig. 3 we can only place limits on the band positions. The E_{redox} values are (11, 13) -0.7, -0.9, and -1.1V *vs.* SCE for S^{2-}/S_n^{2-}, Se^{2-}/Se_n^{2-}, and Te^{2-}/Te_2^{2-}, respectively. The photopotentials place the E_{CB} position at least as negative as -1.3V *vs.* SCE for each of the three electrolytes. It is interesting to note that the highest photopotential that we see depends on the electrolyte in a manner consistent with theory. That is, the photopotential at a given light intensity is lowest for the Te^{2-}/Te_2^{2-} electrolyte, and highest for the S^{2-}/S_n^{2-} electrolyte, while intermediate values are obtained in the Se^{2-}/Se_n^{2-} electrolyte. This ordering is expected if E_{CB} is constant in all three electrolytes, since the difference in E_{redox} and E_f controls the open-circuit photopotential.

Since the open-circuit photopotential measurements given in Fig. 3 only place a limit on the value of E_{CB}, we have determined E_{FB} by an independent method involving measurement of the differential capacitance, C, associated with the band bending region of the semiconductor as a function of semiconductor potential (14). Plots of $1/C^2$ against potential generally are linear with a slope inversely proportional to the donor density and an intercept equal to E_{FB} (14). A typical plot for InP is given in Fig. 4. Since $E_{FB} \approx E_{CB}$ (within 0.2V), the value of E_{VB} can be determined by knowing E_{BG}. The band positions of InP from the differential capacitance plots are given in Fig. 5 for a number of electrolytes. We regard the error in E_{FB} as at least ± 0.1V. The value of E_{redox} for several couples is included in Fig. 5. First, we note that in aqueous electrolytes the band positions are sensitive to pH as has been found previously (15, 16) for GaAs and GaP. Additionally, note the similar position of E_{VB} and E_{redox} for O_2 evolution from H_2O. This

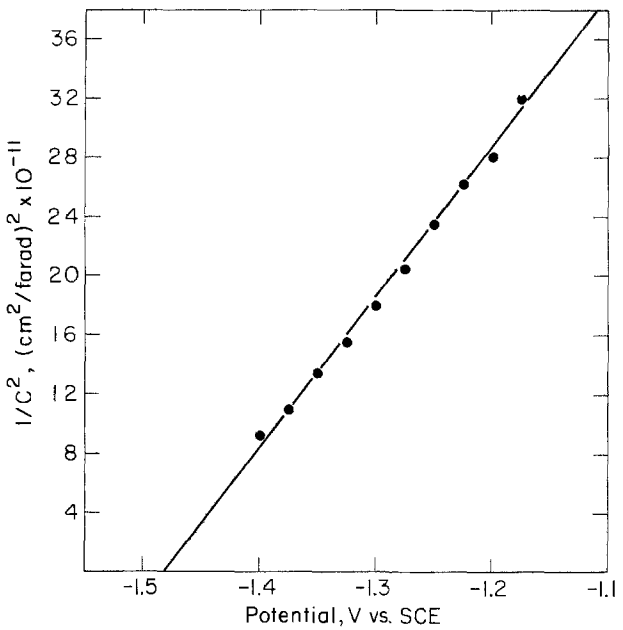


Fig. 4. Plot of (differential capacitance)$^{-2}$ against potential for InP in 5.0M NaOH, 0.08M Na_2Te, 0.01M Na_2Te_2 electrolyte at 50°.

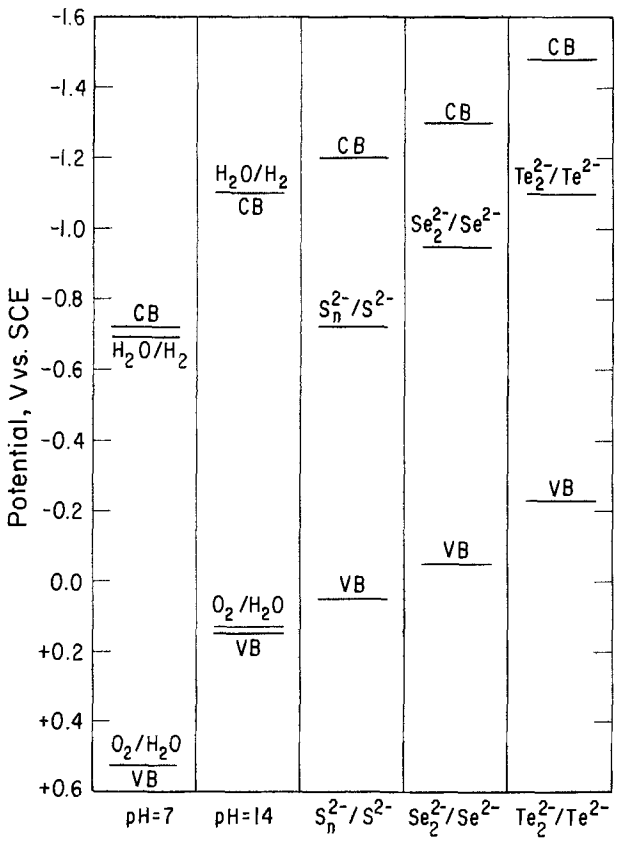


Fig. 5. Valence band (VB) and conduction band (CB) positions for InP in X^{2-}/X_n^{2-} electrolytes and in aqueous solutions at pH = 7 and 14. Data are from differential capacitance curves like that shown in Fig. 4. Band positions are ± 0.1V. Electrolyte redox levels are also given.

means that holes photogenerated in the valence band of InP will not have significant oxidizing potential towards H_2O. The band positions in the X^{2-}/X_n^{2-} electrolytes move slightly more to the negative as X changes from S to Se to Te. There is satisfactory consistency between the measured open-circuit photopotentials and those expected from the energetic picture in Fig. 5. The small movement of the bands to a more negative potential in the heavier chalcogenide ion electrolytes is interesting, but the large error in the measurements does not allow a detailed comment.

The really noteworthy point in the energetic picture for InP exposed to X^{2-}/X_n^{2-} is that the difference in E_{redox} and E_{VB} is roughly constant. Despite this fact, however, only in the Te^{2-}/Te_2^{2-} electrolyte do we find that the InP is stable to photoanodic dissolution. It is apparent that factors other than simple energetics must control whether the interfacial oxidation will compete effectively with the semiconductor electrochemistry. We (4, 5) and others (14, 17-20) have speculated that surface states may play a key role in mediating interfacial electron transfer at semiconductor electrodes, and such may be the case here.

One final point concerning energetics is worth noting. We find that the E_{VB} position for InP in aqueous electrolytes is very similar to that found for GaP (15, 16). This result parallels the findings that the E_{VB} position for a number of III-V and II-VI semiconductors is controlled only by the anion of the semiconductor for Au Schottky barriers (21). Our finding here for InP-electrolyte "Schottky barriers" may represent the first experimental substantiation of the suggestion of McCaldin and McGill (22) that the anion may control the E_{VB} position at such interfaces. However, our ability to stabilize GaP (5), but not InP, with Se^{2-} again signals an important, but as yet unpredictable, role for the electrolyte in photoinduced interfacial electron transfer properties.

Experimental

Materials.—Single crystals of n-type InP were obtained from Metals Research Company (Melbourn, England) and Varian Associates. All samples were cut to expose the (100) face, and were chemically polished to ~0.35 mm thickness. Samples denoted InP-A have resistivities of 0.005-0.016 Ω-cm and carrier concentrations of 1.4-6.1 × 10^{17} cm^{-3}; resistivities and carrier concentrations of InP-B samples are 0.4 Ω-cm and 3.6 × 10^{15} cm^{-3}, respectively. Except for the data in Table I and Fig. 1, all experiments were carried out with the InP-B samples. The crystals were irregularly shaped as obtained and cut into ~5 × 5 mm squares. Electrodes were prepared by rubbing gallium indium eutectic on one face of the crystal, then setting the eutectic-covered surface on a glass-encased Cu wire whose end had been coated with Ag epoxy. Ordinary epoxy was then used to insulate the electrical contact from the electrolyte. The chemically polished (100) surface was always exposed to the electrolyte. Preparation and handling of electrolytes of Na_2Se, Na_2Te, and Na_2S has been described previously (1-5). Photoelectrochemical cells described previously were used in all experiments (1-5).

Electrode stability.—Before being mounted as electrodes, InP crystals were weighed (±0.1 mg). After prolonged photoelectrolysis they were demounted by removing the epoxy with CH_2Cl_2, and then reweighed. Conditions under which stability was tested are given in Table I. Instability was recognized by surface damage as well as weight loss.

Irradiation equipment.—InP photoelectrodes were irradiated with Spectra Physics He-Ne (632.8 nm) and Model 164-003 Ar ion (514.5 nm) lasers, a Bausch and Lomb light source equipped with an Osram 200W superhigh pressure Hg arc lamp, or a 650W GE tungsten-halogen lamp. Output from the latter two sources was used for stability experiments; excessive heat was dissipated through 18 cm of H_2O, and u.v. output was absorbed by a Corning CS 3-73 filter. A 6X beam expander was used to enlarge the 1.5 mm (Ar ion) and 1.0 mm (He-Ne) diam beams; laser

intensities were varied with laser power and/or colored filters. Light intensity was measured either with a Tektronix J16 digital radiometer equipped with a J6502 probe (500-900 nm) or a Coherent Radiation Model 212 power meter (1200-675 nm). A beam splitting technique was used to monitor light intensity continuously, where required. Visible and near infrared monochromatic light was obtained by using a Bausch and Lomb high intensity monochromator with the tungsten-halogen lamp.

Wavelength response.—The absorption of optically polished InP-A was recorded on a Cary 17 spectrophotometer. A plot of relative photocurrent as a function of excitation wavelength (500-1000 nm) was obtained by first monochromatizing the output of a tungsten-halogen lamp, and determining the output intensity as a function of wavelength. InP-A was then irradiated as the photoanode in optically clear 0.1*M* Te^{2-} (50°C) electrolyte, and the photocurrent was recorded as a function of excitation wavelength at −1.10V *vs.* SCE. The photocurrent was then corrected for variation in light intensity, yielding a corrected photoaction curve.

Current-voltage curves.—Current-voltage curves for InP were obtained using a PAR 174 polarographic analyzer with a saturated calomel reference electrode (SCE) and a Pt counterelectrode. All curves are for stirred solutions under Ar.

Open-circuit photopotentials.—A sample of InP-B was irradiated in each of three polychalcogenide electrolytes, and its potential relative to Pt gauze was measured by a high impedance Varian A-25 recorder in series with the two electrodes. The light source was the 514.5 nm line of the Ar ion laser; the beam was masked to just fill the photoanode surface. Light intensity was continuously monitored by a beam-splitting technique, and open-circuit photopotential was recorded as a function of light intensity.

Differential capacitance measurements.—The same InP-B sample used for open-circuit photopotential studies was also used for differential capacitance measurements. An HP 4260A Universal Bridge was employed. Bias was applied through the bridge leads to the Pt and InP-B electrodes in 25 mV steps. A Data Precision 1450 multimeter indicated the potential of the anode relative to SCE. Experiments were performed at 1 kHz in the dark, allowing for a suitable equilibrium period after each voltage adjustment. Besides the three polychalcogenide electrolytes, 1*M* NaOH and 1.0*M* $NaClO_4$ at pH 7 were also used as electrolytes in which to examine the differential capacitance behavior of the InP-B electrode.

Acknowledgments

We acknowledge the National Aeronautics and Space Administration and the M.I.T. Cabot Solar Energy Fund for support of this research. MSW acknowledges support as a Dreyfus Teacher Scholar grant recipient, 1975-1980, and ABE acknowledges support as a Fannie and John Hertz Fellow. We thank Professor C. Fonstad of M.I.T. for his advice and contributions of InP. We thank Professors J. O. McCaldin and T. C. McGill of Caltech for a preprint of Ref. (22) and for several stimulating discussions.

Manuscript submitted March 15, 1977; revised manuscript received June 16, 1977.

Any discussion of this paper will appear in a Discussion Section to be published in the June 1978 JOURNAL. All discussions for the June 1978 Discussion Section should be submitted by Feb. 1, 1978.

Publication costs of this article were assisted by Massachusetts Institute of Technology.

REFERENCES

1. A. B. Ellis, S. W. Kaiser, and M. S. Wrighton, *J. Am. Chem. Soc.*, **98**, 1635 (1976).
2. A. B. Ellis, S. W. Kaiser, and M. S. Wrighton, *ibid.*, **98**, 6855 (1976).
3. A. B. Ellis, S. W. Kaiser, and M. S. Wrighton, *ibid.*, **98**, 6418 (1976).
4. A. B. Ellis, J. M. Bolts, S. W. Kaiser, and M. S. Wrighton, *ibid.*, **99**, 2848 (1977).
5. A. B. Ellis, S. W. Kaiser, J. M. Bolts, and M. S. Wrighton, *ibid.*, **99**, 2839 (1977).
6. G. Hodes, J. Manassen, and D. Cahen, *Nature (London)*, **261**, 403 (1976).
7. B. Miller and A. Heller, *ibid.*, **262**, 680 (1976); A. Heller, K. C. Chang, and B. Miller, *This Journal*, **124**, 697 (1977); K. C. Chang, *et. al.*, *Bull. Am. Phys. Soc.*, **22**, 347 (1977); K. C. Chang, A. Heller, B. Schwartz, S. Menezes, and B. Miller, *Science*, **196**, 1097 (1977).
8. C. Kittel, "Introduction to Solid State Physics," 3rd ed., p. 302, John Wiley & Sons, Inc., New York (1968).
9. R. L. Meek and N. E. Schumaker, *This Journal*, **119**, 1148 (1972).
10. H. Gerischer, *Ber. Bunsenges. Phys. Chem.*, **69**, 578 (1965).
11. J. J. Lingane and L. W. Niedrach, *J. Am. Chem. Soc.*, **70**, 4115 (1948); A. J. Panson, *J. Phys. Chem.*, **67**, 2177 (1963).
12. H. Gerischer, *J. Electroanal. Chem. Interfacial Electrochem.*, **58**, 263 (1975).
13. P. L. Allen and A. Hickling, *Trans Faraday Soc.*, **53**, 1626 (1957); W. M. Latimer, "Oxidation Potentials," 2nd ed., Prentice Hall, Inc., New York (1952).
14. J. F. Dewald, *Bell Syst. Tech. J.*, **39**, 619 (1960); H. Gerischer, in "Physical Chemistry," Vol. IXA, H. Eyring, D. Henderson, and W. Jost, Editors, Chapter 5, Academic Press, New York (1970).
15. M. Gleria and R. Memming, *J. Electroanal. Chem. Interfacial Electrochem.*, **65**, 163 (1975).
16. W. P. Gomes and F. Cardon, *Z. Phys. Chem. (Frankfort Am Main)*, **86**, 330 (1973).
17. H. Kim and H. Laitinen, *This Journal*, **122**, 53 (1975).
18. C. E. Byvik, Paper 238 presented at The Electrochemical Society Meeting, Washington, D.C., May 2-7, 1976.
19. A. Morisaki, M. Hariya, and K. Yazawa, *Appl. Phys. Lett.*, **30**, 7 (1977).
20. S. N. Frank and A. J. Bard, *J. Am. Chem. Soc.*, **97**, 7427 (1975).
21. J. O. McCaldin, T. C. McGill, and C. A. Mead, *Phys. Rev. Lett.*, **36**, 56 (1976); *J. Vac. Sci. Technol.*, **13**, 802 (1976).
22. J. O. McCaldin and T. C. McGill, in "Thin Films-Interdiffusion and Interfacial Reactions," J. Poate, J. Mayer, and K. N. Tu, Editors, Wiley-Interscience, New York, In press.

Lubrication in Photolithography

Resist Protect Coats

D. L. Flowers*

Motorola Semiconductor Research and Development Laboratory, Phoenix, Arizona 85036

ABSTRACT

Defects in photolithographic processing account for large yield losses in semiconductor device fabrication. A major factor contributing to these defects is pinholes formed by photoresist pieces pulled from the resisted layer with subsequent undesired etching of oxide, metal, or passivation glass during processing. Further, for negative photoresist, pieces on the mask "print" during exposure forming latent defects which etch during processing also giving shorts, parted metal, and the like. Using surface chemical principles of lubrication, a resist protect coat (RPC) formulation based on polyvinyl alcohol, a surfactant, and a lubricant has been developed which greatly minimizes these defects. Significant increases in effective mask use and increased yields for three layer metal devices are shown.

It is well known that repeated mask-wafer contacts in semiconductor photolithography severely deteriorate process yield and photomasks. Pieces of resist torn from the wafer allow etching in undesirable places. Optically opaque pieces of resist stuck to the mask frequently "print" during exposure. This results in latent pinholes which form during the etching procedure. Buildup of resist on mask causes inadequate contact during exposure and results in poor pattern definition. Thus, limited mask use results. These defect modes are due to adhesion between the mask and the photoresist. They are particularly severe when there are irregularities such as hillocks of aluminum, pieces of CVD glass, sharp line patterns, or dirt present on the mask or wafer such that large contact pressures are produced (1). Adhesion is caused by hydrogen bonding or chemisorption of a variety of polar groups present at the resist and mask interfaces (2, 3). Cohesion of the resist film and its adhesion to the wafer are weaker than the force binding the resist to the photomask in localized areas. On separation of mask and wafer, the observed damage and contamination occur.

This paper describes the development and effectiveness of a lubricating surface coating for photoresists. Lubrication is achieved by minimizing hydrogen bonding and chemisorption between mask and resist (4).

Preliminary work was devoted to optimizing a resist protect coat to obtain the minimum number of photodefects as judged by a capacitor evaluation technique. Greatly extended photomask life was shown with the optimized formulation. Production wafers were processed both with and without the resist protect coat. Substantial yield improvement was shown and defect reduction was calculated. A mechanism for resist-mask adhesion and effective lubrication of the resist surface is presented to explain defect reduction in finished devices.

Experimental

Materials.—The wafers used in the capacitor part of this study were p-type substrates, patterned, first layer metal. They were targeted for a large, three layer metal, gate array. Chip size was 19×10^3 mils^2.

Actual product wafers of the same device type were also processed with and without resist protect coats to determine yield benefits achieved by the protect coat formulation and process.

Equipment.—Automatic capacitor data were taken using a Motorola IC automatic probe interfaced with a CDC 8090 computer. The alignment tool for the capacitor pinhole experiments had 15 psig contact pressure. It was also used for the passivation layers of the manufacturing lots processed except two lots where the proximity mode was used.

Procedures.—A resist protect coat (RPC) solution used in this work was prepared by dissolving 16.2g of polyvinyl alcohol (J. T. Baker, No. U229) in 2700 ml of DI water at 45° ± 5°C with stirring. To this was added 300 ml of isopropyl alcohol (Baker and Adamson, Electronic Grade) containing 0.3g of glyceryl monostearate (C. P. Hall of Illinois) and 1.5g of Triton X-100 (Rohm and Haas). The solution was mixed well, cooled, and filtered through a RAMP 074-00 1.2μ Millipore filter using 15-20 psig air or N_2 pressure. Other compositions noted in this report were prepared similarly. The solutions were stable indefinitely.

The wafers for a given capacitor experiment were given a standard first metal clean after which 10k Å of phosphorus-doped (3.5×10^{20} atoms/cm^3) glass was deposited (CVD) on the metal. Wafers used to establish an as-deposited dielectric pinhole baseline were again metallized, masked, and metal etched using a scribe grid mask for the device. Use of this mask on second metal defined each chip as a capacitor with the first metal. The capacitor yield relates to pinholes in the as-deposited glass between the first and second metal layers that filled with second metal and test as shorts or high leakage capacitors. The remainder of the wafers for an experiment with 10k Å of dielectric on first metal were processed with and without RPC on photoresist to compare capacitor yields. The photoresists used were negative (53 Hz) or positive (20.5 Hz). After resist soft bake (80°C, 20 min, N_2), RPC was spun at 3k rpm unless otherwise noted and the wafers rebaked (80°C, 15 min, N_2) after which they were ready for alignment.

Masks were blank for the capacitor-pinhole experiments, *i.e.*, clear emulsion for negative photoresist and opaque emulsion for positive photoresist. Two contacts were made on each wafer unless otherwise noted. Each mask was used for four wafers (one experiment) and discarded. Exposure times for the photoresist were those normally used for that resist thickness. Control wafers were run with each related set of experiments.

After alignment the RPC was removed: (*i*) for the negative photoresist, 5 min immersion in 40° ± 2°C DI water containing 0.1% Triton X-100 surfactant followed by a 5 min cascade DI water rinse, an isopropyl alcohol dip, and spin dry; and (*ii*) for the positive photoresist, 10 min soak in room temperature DI water, a 5 min cascade rinse, and spin dry.

Next, the wafers went through the development cycle and were "hard" baked prior to etch. For negative photoresist, the bake was 180°C (N_2) for 30 min. For positive photoresist, the bake was 100°C (N_2) for 30 min.

* Electrochemical Society Active Member.
Key words: photomask, adhesion, defects, pinholes.

Finally, the wafers were etched in buffered HF to form pinholes in the passivation glass (dielectric) resulting from defects in the photoresist. After resist removal and clean, second metal was evaporated and conventionally patterned using the scribe grid mask to form capacitors.

Capacitor (19×10^3 mils^2) measurements were made at 30V. For these measurements, the back of the wafer was biased positively, thereby forward biasing the collector substrate junction. Capacitor yield at 30V is meaningful for this study because at this voltage, the reverse biased collector-base breakdown is overcome. Interpreting data at higher stresses may not be safe because strain or weaknesses in the dielectric glass may cause punch through and cloud the issue of photo-induced defects.

Results and Discussion

Process development.—To develop a RPC, preliminary experiments were run, spinning polyvinyl alcohol (PVA) solutions on resisted wafers (5). It was found that PVA solutions do not readily wet photoresist, but that the addition of small amounts of a surfactant, *e.g.*, 0.01-0.2% Triton X-100 or Aerosol OT (American Cyanamid) promotes sufficient wetting for uniform coats (5-7).

The lubricant glyceryl monostearate (GMS) or calcium stearate (Ca St, American Cyanamid) was next introduced into the coating formulation (8). Because of very limited and slow solubility of GMS in water solution, it was introduced to the aqueous PVA-surfactant solution in an isopropyl alcohol carrier. Calcium stearate was formulated similarly. The final solution formulation was in a 90/10 v/v DI water/isopropyl alcohol mixture.

Once smooth and uniform coatings were obtained from the formulation, attention was turned to an effective bake cycle. Sufficient baking of the protect coat in nitrogen to remove solvent and develop nonsticking capability in the formulation was achieved in 15-20 min at 80° ± 2°C for both negative and positive photoresist. Exposure times on the alignment tools used were unaffected by the protect coats which absorb very little of the active radiation. The protect coat was removed as described earlier.

Coatings were spun on resisted wafers from 2.7 and 0.54% PVA solutions, then baked, and exposed to check ease of coating removal. It was found that for spin speeds from 1-5k rpm, the coating was removed more easily from the 0.54% solution coats. This concentration was therefore used. Coating thickness was estimated to be 170 ± 30Å when spun at 3k rpm. It was obtained from the IBM 7840 film thickness analyzer.

With the mechanics and details of a process defined, capacitor experiments could be used to examine and optimize the formulation of a RPC. Table I details the results of these experiments.

Capacitor yield improvement for a nonionic surfactant, TX-100 and an anionic surfactant, Aerosol OT are shown in Table IA. The arbitrarily chosen lubricant concentration was held constant as shown. Triton X-100 at 0.05% weight gave the most improved capacitor yield. Decreasing amounts have not apparently reached maximum effectiveness. Increasing amounts may impair the cohesive film strength. The data suggest that Aerosol OT may have a maximum effectiveness around 0.05% but was not pursued further.

The lubricant evaluations shown in Table IB predict an optimum effectiveness for GMS to lie at 0.01% weight, decreasing sharply above or below that value. Calcium stearate is also effective as a lubricant but requires more material for activity. This relates to several molecules required to form a micelle compared to single molecule activity for the GMS (9).

An optimum film thickness (spin speed) was determined for the protect coat with the formulation derived above. This is shown in Table IC. Here it is seen that a dip coat with the formulation (~2k Å film) gives very poor capacitor yields indeed. This relates to difficulties in drying the thick polyvinyl alcohol film. Spinning the coat yields a broad maximum in capacitor yield peaking at 3000 rpm (150-200Å). There is a noticeably thicker edge on the film spun at 1000 rpm and, as expected, the film thickness probably approaches a monolayer at higher spin speeds.

Table I. Optimizing concentration of additives and spin speed for RPC films

Experiment	Variable	Capacitor yield (%)
	A. Optimize surfactant with 0.01% weight GMS	
1	Base glass	95 ± 2
2	Control-no RPC	39 ± 5
3	0.0075 TX100, 3k rpm	53 ± 4
4	0.05 TX100	73 ± 8
5	0.10 TX100	59 ± 6
6	0 20 TX100	56 ± 7
7	0.05 AOT	64 ± 6
8	0.10 AOT	58 ± 9
	B. Optimize lubricant with 0.05% weight TX-100	
1	Base glass	90 ± 3
2	Control-no RPC	41 ± 5
3	0.005 GMS, 3k rpm	54 ± 6
4	0.01 GMS	69 ± 9
5	0.02 GMS	43 ± 5
6	0.03 GMS	45 ± 6
7	0.02 Ca St	55 ± 7
8	0.06 Ca St	60 ± 6
9	0.15 Ca St	62 ± 8
	C. Optimize spin speed for RPC film (0.01% weight GMS, 0.05% weight TX-100)	
1	Base glass	85 ± 3
2	Control-no RPC	32 ± 6
3	Dip coat RPC	28 ± 12
4	1k rpm	54 ± 6
5	3k rpm	56 ± 5
6	5k rpm	50 ± 6
7	7k rpm	46 ± 7
8	9k rpm	33 ± 9

Having optimized the formulation for RPC, a capacitor matrix was designed to evaluate the individual effect of the ingredients present. The concentrations used were chosen as a result of the process development experiments discussed above. The matrix used with the constituents and concentration parameters noted are found in Table II.

Here it is seen that a standard process with negative resist gives a capacitor yield of only 38%. The as-deposited dielectric glass yield was 88%. With the addition of a protect coat of PVA only, a 50% capacitor yield or 12% improvement is noted. Addition of the surfactant (0.05% weight TX-100) to the coating solution did not sensibly change the yield over that of PVA alone. The use of 0.01% weight GMS lubricant in the PVA coating, however, gave a yield increase over that of the PVA alone (57% *vs.* 50%). When the coating formulation contains both the lubricant and the surfactant in the carrier film at the concentrations noted, a 75% yield is realized. Thus, glass dielectric photoprocess yield is doubled using RPC. Since the GMS was noted to agglomerate or clump at the coating surface when surfactant TX-100 was absent, but not when it was present, the increased activity of the combination surfactant TX-100–lubricant GMS is apparently due to a more uniform distribution of the lubricant at the interface.

The RPC formulation recommended by the above evaluation is: 90/10 H_2O/IPA by volume, 0.54% w/v PVA, 0.05% TX-100, and 0.01% GMS.

Table II. Effect of various RPC constituents on improving capacitor yield of passivation glass

Experiment	Coating composition	Capacitor yield (%)
1	Base glass-no photo process	88 ± 2
2	Negative resist at 5k rpm-no RPC	38 ± 5
3	Expt. 2 + 0.54% PVA at 3k rpm	50 ± 3
4	Expt. 2 + 0.54% PVA with 0.05% TX100 at 3k rpm	52 ± 6
5	Expt. 2 + 0.54% PVA with 0.01% GMS at 3k rpm	57 ± 5
6	Expt. 2 + 0.54% PVA with 0.05% TX100 + 0.01% GMS as RPC at 3k rpm	75 ± 7

The pinhole protection given by the coating on positive and negative photoresists was investigated at various coating thicknesses before working with production wafers. The results are shown in Table III.

Significant capacitor yield increases are seen for both negative and positive photoresist with the use of RPC. For the thinner (8.5k Å) negative resist coatings, the yield is doubled. For thicker resist (11.5k Å), the yield improvement is not so pronounced, ~8% over-all. At an intermediate resist thickness (10k Å), the interpolated yield improvement with RPC is predicted to be 21%. In the positive resist case at a commonly used thickness (22k Å), the capacitor yield improvement is 22%.

Extended mask life.—With improved capacitor yields shown by using RPC, it was desirable to investigate its use on longer photomask life (5). Table IV shows the results of experiments run to determine if good definition on individual wafers could still be achieved with longer mask use and RPC process. Standard production wafers were started at the preohmic masking step. The smallest geometry was 0.3 mil. A tool with a contact pressure of 15 psig was used. Each wafer was contacted an average of three times.

In this table, "pass" means the developed wafers had less than two defective die on them out of nine inspected with a standard "after develop" inspection criteria. "Fail" means three or more die of nine were defective on a 2 in. wafer for photoresist defects. Of particular interest here was the "fail" mode for "poor definition" arising from improper mask-wafer contact due to pieces of photoresist on the mask from previous use. The "failed" wafers occurred in sequence after the "passed" wafers.

Mask life with acceptable pattern definition was increased by a factor of three to four using RPC. The spread between five and eleven pass for the noncoated wafers of the two experiments shows the spread that occurs under these process conditions. Pinhole protection with extended mask use is reported next. Nonpatterned p-type wafers were selected for this experiment. Standard phosphorus-doped glass (10k Å) was deposited to simulate the passivation conditions earlier in this report. Capacitor size was 2500 mil^2 compared to 19,000 mil^2 in the previous experiments. The relative trends in this experiment are therefore points of note. Results are shown in Table V.

A significant increase in mask life coupled with increased capacitor yields is shown with RPC. There is a decided break of capacitor yield with mask use in both cases however; about nine exposures before the yield break for RPC and five or six exposures for the control. The yield in both cases after the break occurs drops to a scattered low between 30 and 50%.

The capacitor yield at the eighth RPC wafer of 73% is almost as high as the 75% of the first non-RPC wafer. The average yield for the first eight RPC wafers is 82.7%. That for the first eight non-RPC wafers is 64.3%. Thus, on flat capacitors, an 18% yield increase is noted for the RPC process.

Neither this case nor the preceding ones correspond exactly to the real world. To determine more accurately the effect of RPC, production lots were run with pertinent layers involved to determine the magnitude of the benefit achieved.

Completed device evaluation of RPC (eight wafers per mask).—The advantage of RPC on final device yield when used on the first and second passivation layers is shown next (three layer metal, 19 × 10^3 mil^2 chip). Layers were processed with 22k Å of positive resist. It is here that pinholes are suspected of being a major problem. Table VI summarizes average die per wafer yield. There were 15 ± 3 wafers remaining in each half-lot on completion with some being broken and discarded at various earlier process steps.

Data from lots one and two show that the yields are doubled with the use of RPC in contact printing. When it was used on wafers aligned in the proximity mode of operation, the benefit of lubrication, as expected, was not as great. It is worthy of note that contact printing with the RPC approaches the lower defect level of proximity printing and should allow better fine line definition as well.

With yield improvement shown on the multilevel gate array circuit, it is possible to derive an estimate of defect densities and their reduction brought about by the RPC process. Studies on the effect of point defects (pinholes) have been treated by Warner (10) and Gupta *et al.* (11). Turley and Herman (12) have discussed LSI yield projections referenced to multilevel metal structures. Such projections can be derived assuming a Poisson distribution of defects. Conversely, with yield improvement due to a process change to reduce pinholes, the effect in terms of decreased defect density can be calculated using the formula $Y \simeq e^{-X} \simeq e^{-AD}$. Here, X is the defect density per die, Y is the yield, A is the area, and D is the defect density per unit area. In Table VII, yields are compared to defect density of the die. For these calculations, the area of the 19 × 10^3 mil^2 chip was normalized to the area covered by first and second layer metal. First layer metal covered 37.2% of the chip and second metal covered 20.0% of the chip. The total area of metal combined in

Table III. Capacitor pinhole yield enhancement using RPC*

Experiment	Resist	Spin speed (rpm)	RPC-3	Capacitor yield %‡
1	None	Base glass-no photo	—	93 ± 4
2	Neg.	3k (11.5k Å)†	No	56 ± 4
3	Neg.	3k	Yes	64 ± 7
4	Neg.	5k (8.5k Å)	No	30 ± 6
5	Neg.	5k	Yes	64 ± 4
6	Pos.	3k (22k Å)	No	51 ± 4
7	Pos.	3k	Yes	72 ± 4
8	Pos.	3k	Yes	75 ± 6

* It is noted that direct comparison between various sets in this paper is not possible. Various base glass and base photoresist pinhole counts, some of which were not measured, presumably account for this.
† After develop.
‡ Four wafers in each experiment.

Table IV. Effect of RPC coated wafers on photomask life

Experiment	No RPC Pass	No RPC Fail	RPC Pass	RPC Fail	Failure mode
1 (30 wafers)	5	5	20	0	Poor definition
2 (46 wafers)	11	5	30	0	Poor definition

Table V. Capacitor yield with extended mask use

Mask use	Uncoated photoresist	RPC coated photoresist
1	75%	92%
3	70	85
5	67	81
8	45	73
10	40	45
11	Broken	38
12	50	Broken
17		32
21		33
24		42

Table VI. Comparative control and RPC yields for the four complete production lots processed

Lot	Hard contact (15 psig)	Proximity (0.7 mil)	Control yield (D/W)	RPC yield (D/W)
1	X		12.4	26.0
2	X		8.5	16.9
3		X	23.3	28.2
4		X	28.8	29.8

Table VII. Defect density vs. yield of an LSI chip

Lot	Yield (D/W) No RPC	Yield (D/W) RPC	Per die defect density No RPC	Per die defect density RPC	(cm-2) Defect density No RPC	(cm-2) Defect density RPC
A	12.4	26.0	2.18	1.44	31.6	20.9
B	8.5	16.9	2.56	1.87	37.1	27.1
C	23.3	28.2	1.55	1.36	22.5	19.7

first and second layers is 10.7×10^3 mils^2 where pinholes in the capping passivations can lead to shorts.

The data show that the yield varies from 8.5 to 28.2% with a statistical defect density of 2.56 per die decreasing to 1.36 per die. Defect improvements range from 12.3%, lot C, proximity printing, to 34% when the first and second passivation layers were contact printed. It is seen for yields below 30% that a relatively small improvement in defect density results in large yield increases.

Mechanism of lubrication by RPC.—The mechanism of adhesion of photoresist and mask that produces "photo defects" relates to the surface chemistry of the contacting species. As a zero-order explanation, a model of the pertinent interfaces is presented in Fig. 1. The polar groups present that interact to cause adhesion are indicated. The photomask may be of gelatin, chrome, or iron oxide construction. Active polar groups present at the surface are amide (—CHNH—), carbonyl (=C=O), or hydroxyl (—OH). Similarly, at the photoresist surface, carbonyl (=C=O), hydroxyl (—OH), or unsaturated (—C=C—) groups are present as shown. Hydrogen bonding can occur when the photoresisted wafer and mask come in contact. Since hydrogen bonds have a free energy of formation of ~5.0 kcal/mole, and, since there are many possible hydrogen bonding sites in every resist and gelatin molecule or inorganic crystal, it is apparent that total bonding energies of many kilocalories per mole can be generated (13). Further, the enormous energy density generated when mask and wafers are contacted at asperities, epitaxial spikes, dirt, or sharp lines and corners probably cause even stronger, fully chemisorbed bond formation by addition of hydroxyl and/or amide groups of the mask to the olefinic groups of the photoresist. Finally, exposure of the contacting mask and photoresist might be expected to promote further the reaction between polar groups and the unsaturation present in the photoresist. Hence on separation of mask and exposed wafer, small pieces of resist are torn from the surface to leave a latent pinhole in the device. The accumulation of photoresist pieces on the photomask after several wafers have been aligned soon causes "definition" problems in contact printing due to lack of sufficient mask-wafer contact during exposure. This must be minimized for longer mask life.

The RPC applied to wafers shields the polar groups on the mask from those of the photoresist thus minimizing or preventing hydrogen bonding. This is shown in Fig. 2. The necessary shielding is primarily provided by the lubricant, *e.g.*, glyceryl monostearate shown here. The polar part at the molecule is energetically favored to be in the high dielectric constant, polyvinyl alcohol film. The nonpolar ($—CH_2)_{16}$-CH_3) tail of the molecule favors the low dielectric constant air media and hence orients as shown. Because of this orientation, contact of the mask and photoresist does not produce adhesion. The polar groups at the two interfaces do not sufficiently approach each other for intermolecular hydrogen bonding and lubrication is achieved. Similar arguments may be derived for the micelle-forming lubricants, *e.g.*, calcium stearate.

Classical studies as described in a review by Reinhart could be used to more quantitatively define the nature of adhesion between photoresist and photomask (14). The techniques of Levine and Zisman could be used to characterize the lubrication provided by RPC in a more controlled and definitive way (15).

Summary and Conclusions

Consideration of the surface chemistry involved in contact printing of photoresisted semiconductor wafers has led to a postulated mechanism for wafer-mask interaction. Based on this mechanism a RPC was formulated and optimized to eliminate or minimize attendant photodefects. Lubrication between the photoresist and photomask was achieved. Wafer-mask sticking was substantially minimized.

Without lubrication, a large, three layer metal, LSI device had severe yield losses due to pinholes in the first and second passivation layers. These filled with evaporated metal and caused excessive interlayer leakage and device failure. A capacitor evaluation technique was used to simulate the failure mechanism. Negative photoresist showed only a 38% capacitor yield but when covered with the RPC produced a 75% yield. Similarly positive photoresist as commonly used had a 50% capacitor yield but with RPC reached a 73% yield. Using the capacitor yield improvement, it was estimated that the large device being studied should yield 100% better with protect coat on the photoresist. Such was indeed observed.

In the proximity mode of operation, where pinholes caused by contact are considerably minimized, some yield benefit was still realized with RPC. This is probably due to protection derived during handling and some inadvertent partial contact during alignment of the wafers.

The subject of increased mask life when the wafers were resist protect coated was also investigated. For wafers processed without RPC, poor definition of pattern failed wafers after five to eleven alignments. With

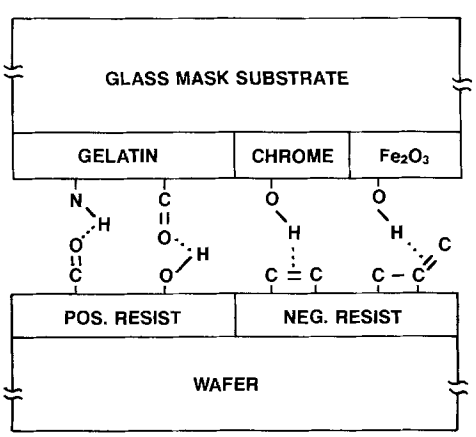


Fig. 1. Hydrogen bonding of mask and photoresist

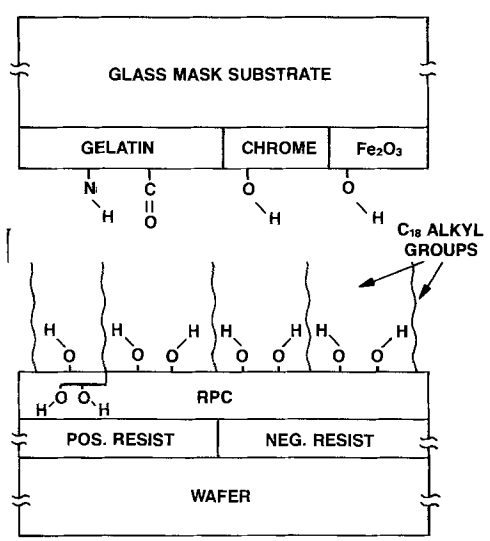


Fig. 2. Lubricated, resisted wafer and mask

RPC, 20-30 wafers could be aligned without encountering definition problems. Maintenance of capacitor yields with extended mask use did not prove quite as promising although substantial benefits were realized. The net result was a 16% (to 83%) yield increase on small chips (2500 mil^2) with 60% more mask life.

In summary, this study has demonstrated a major yield limiting defect mechanism in semiconductor fabrication and has shown an approach to minimizing it.

Acknowledgments

The author would like to thank Mrs. Louise Rice and Mrs. Kelly Nicely for laboratory and production processing reported in this paper. He also wishes to thank Dr. Henry Hughes as well as Messrs. James Black, George Stickney, and Joe Wise for valuable discussions and assistance in this project. Finally, it is with great appreciation for preparing this manuscript, he wishes to thank Mrs. Isabelle Kast.

Manuscript submitted Jan. 25, 1977; revised manuscript received May 23, 1977. This was Paper 290 presented at the Las Vegas, Nevada, Meeting of the Society, Oct. 17-22, 1976.

Any discussion of this paper will appear in a Discussion Section to be published in the June 1978 JOURNAL. All discussions for the June 1978 Discussion Section should be submitted by Feb. 1, 1978.

Publication costs of this article were assisted by Motorola Incorporated.

REFERENCES

1. W. Kern, G. L. Schnable, and A. W. Fisher, *RCA Rev.*, **37**, 45 (1976).
2. R. F. Blomquist, "Adhesives-Past, Present and Future," ASTM Edgar Marburg Lecture, p. 5 (1963).
3. I. Skeist, "Handbook of Adhesives," p. 7, Reinhold Publishing Corp., London (1962).
4. L. J. Osipow, "Surface Chemistry," ACS Monograph 153, pp. 47, 437, Reinhold Publishing Corp., London (1962).
5. R. Bowman and J. Livingston, Proceedings 1974 Kodak Microelectronics Seminar, G41, p. 7 (1975).
6. Symposium in Ethylene Oxide Based Surface Active Agents, Proceedings Chemical Specialties Manufacturers Association (1975).
7. American Cyanamid Company, Aerosol Surface Active Agents; Aerosol OT.
8. L. J. Osipow, "Surface Chemistry," ACS Monograph 153, pp. 437-455, Reinhold Publishing Corp., London (1962).
9. L. J. Osipow, *ibid.*, p. 175.
10. R. N. Warner, Jr., *IEEE J. Solid State Circuits*, **sc-9**, 86 (1975).
11. A. Gupta, W. A. Porter, and J. W. Lathrop, *ibid.*, **sc-9**, 96 (1974).
12. A. P. Turley and D. S. Herman, *IEEE Trans. Parts, Hybrids Packaging*, **php-10**, No. 4, 230 (1974).
13. F. A. Cotten and G. Wilkinsen, "Advanced Inorganic Chemistry," p. 124, Interscience, New York (1962).
14. F. W. Reinhart, *J. Chem. Ed.*, **31**, 128 (1954).
15. O. Levine and W. A. Zisman, *J. Phys. Chem.*, **61**, 1188 (1957).

The Phototransition in ZnO at 380 nm Studied by Anodic Photocurrents

D. M. Tench*,[1] and H. Gerischer*

Fritz-Haber-Institut der Max-Planck-Gesellschaft, Berlin, Germany

ABSTRACT

Anodic photocurrent spectra from 350 to 450 nm were determined in aqueous solutions for single crystalline ZnO electrodes which had been mechanically polished but not etched. The over-all photocurrent was much less than for etched crystals, presumably because of enhanced recombination through mechanically generated hole traps, and a sharp peak was observed at 383 nm. This peak was investigated by intermittent illumination and phase-sensitive detection, with and without superimposed steady light. The effects of polishing and light on the differential capacitance of the electrode were also studied. The data are interpreted in terms of the interaction between excitons and mechanically introduced lattice defects.

Many publications (1-7) dealing with the effect of light on the ZnO-electrolyte interface have appeared in the last two decades. In most cases involving single crystals, freshly cleaved and etched surfaces of the semiconductor were used, presumably to insure that extraneous effects related to mechanically damaged surface layers were not introduced. Similarly, in solid-state studies (8) on ZnO, care has generally been exercised to avoid interference from lattice defects and impurities.

One recent paper (9), however, has considered the effect of mechanical polishing on the differential capacitance of the single crystalline ZnO-electrolyte interface. It was found that abrasive pretreatment of the ZnO surface generates lattice defects to a depth comparable to the particle size of the abrasive, whose state of charge can be altered by capture of optically generated holes or direct optical ionization. From the spectral dependence of the charging of the trapping levels, two groups of energy states were detected; one about 0.8 eV below the conduction band, attributed to Zn donors bound to lattice defects, and the other 0.7 eV above the valence band.

In the present work, abrasive pretreatment of ZnO single crystalline electrodes has been found to result in an over-all reduction in the anodic photocurrent, presumably because of enhanced recombination through mechanically generated lattice defects. This effect has been used to suppress the photocurrent arising from the fundamental absorption in order that a weaker phototransition near the bandedge could be studied. This phototransition manifests itself as a peak at 383 nm in the photocurrent spectrum, and has a time constant for decay of 1-5 sec for the light intensities used here.

For single crystalline ZnO electrodes in aqueous electrolytes, Kiess (5) has reported an anomalous increase in the photocurrent at voltages >130V, which

* Electrochemical Society Active Member.
[1] Present address: Rockwell International/Science Center, Thousand Oaks, California 91360.
Key words: semiconductor, zinc oxide, photoeffect, photoelectrolysis.

is observed for light between 375 and 390 nm, but not at shorter wavelengths. The photocurrent increase exhibits a fast component corresponding to a quantum efficiency of unity, and a slow component with a time constant of 1-10 sec for which the quantum efficiency is greater than one. Kiess suggests that the electric field at the electrode surface is increased by trapped holes produced by penetration of the longer wavelength light into a region of the space charge layer containing a low concentration of ionized deep donors. This supposedly results in an enhanced rate of tunneling from surface states, and thus, an increased photocurrent. The similarities between the results of Kiess and those reported here suggest that the process studied in each case was the same. The present studies, however, indicate that the greater penetration depth of the longer wavelength light alone cannot adequately explain all of the experimental results.

Experimental

Electrodes were fabricated from undoped single crystals of ZnO, having donor densities of about 10^{16} cm^{-3} and 0001 surface areas of approximately 7 mm^2, which were obtained from Prof. Heiland (TH Aachen). After cleaving perpendicular to the c-axis and making ohmic contacts with indium, the zinc $(000\bar{1})$ and oxygen (0001) surfaces were mounted flush with the ends of cylindrical Teflon holders using epoxy resin. The electrodes were polished by hand using Diaplast diamond powder with distilled water. Since this pretreatment produced a relatively large, easily measurable effect, all of the results reported here were obtained using ZnO electrodes which had been polished with diamond powder of 15μ particle size, without subsequent etching.

Electrolytes were prepared using reagent grade chemicals and doubly distilled water. Most of the data reported here were obtained in 0.5*M* $LiClO_4$ aqueous solutions, but 1*M* KCl and 0.5*M* K_2SO_4 yielded similar results. In acidic solutions, time dependence was observed, presumably because of dissolution of the ZnO electrode surface.

A Heath monochromator was scanned at 0.5 nm/sec to obtain photocurrent spectra, whereas for the second light beam a Bausch and Lomb double grating monochromator was used. Xenon lamps were used for both light sources. The scanned light impinged upon the electrode at right angles, whereas the angle of incidence of the second light beam was about 25°.

The quantum flux density of the lamp/monochromator combination was determined using a solution of erythrosin yellow in methanol. This substance absorbs the incident light completely in the wavelength range of interest and fluoresces strongly. Using a photomultiplier tube, the long wavelength tail of the broad fluorescence band was monitored, which reduced effects caused by reabsorption of the emitted fluorescence. The measured fluorescence intensity in this case is proportional to the incident quantum flux. Thus, the photocurrents reported here have been corrected for the spectral dependence of the intensities of the lamps. When two light sources were employed this was done graphically since the relationship between the increase in the photocurrent produced by the second light source and the wavelength is complex.

Photocurrents were measured under nitrogen atmosphere in a Pyrex cell with an optical glass bottom by intermittent illumination and phase-sensitive detection. The modulation frequency of the light was 30 Hz, unless otherwise specified. Since the photocurrent decreased with chopping frequency (30% less at 60 Hz), the values at 30 Hz should be considered approximate low frequency limits. After preamplification and filtration by a PAR 113 amplifier, the signal across a 1000 Ω resistor was amplified by a Keithley Model 840 lock-in amplifier. The output was displayed on a Hewlett-Packard 7001 AM X-Y recorder. All measurements were performed at room temperature under controlled potential conditions using a Wenking potentiostat. The reference electrode was always a saturated calomel electrode (SCE).

A-C impedance measurements were made by applying a 100 Hz a-c signal (14 mV peak to peak) across the working electrode using a PAR Model 173 potentiostat/galvanostat, and measuring the current response with a PAR Model 176 current follower and Model HR-8 lock-in amplifier. Some photocurrent measurements were also made with these instruments as a check, and comparable results were obtained.

Experimental Results

Experiments with one light source.—A typical photocurrent spectrum from 350 to 410 nm for a polished zinc interface in 0.5*M* $LiClO_4$ at 6.00V *vs.* SCE is shown in Fig. 1 for a relative light intensity of 1X. A sharp peak is evident at 383 nm and the photocurrent over the whole range is more than a factor of 2 lower than that obtained on etched crystals under the same conditions. This photocurrent suppression is probably caused by enhanced recombination through mechanically generated lattice defects, possibly the hole traps previously observed by capacitance measurements (9). It is evident that light of about 380 nm wavelength can produce an effect not observed at shorter wavelengths.

When the zinc interface is polished with diamond powders of smaller grain size (7-0.7μ), the over-all photocurrent increases until the peak at 383 nm becomes masked. In this case and for crystals etched in 5*N* HCl, the photocurrent peak, although shifted slightly to shorter wavelengths, can still be observed at sufficiently negative potentials (U = 0 *vs.* SCE) and low intensities (~0.1X) as a distinct shoulder on the curve corresponding to the interband transition. These observations and those of Kiess (5), made on etched crystals in the same spectral region, indicate that the peak at 383 nm in the photocurrent spectrum

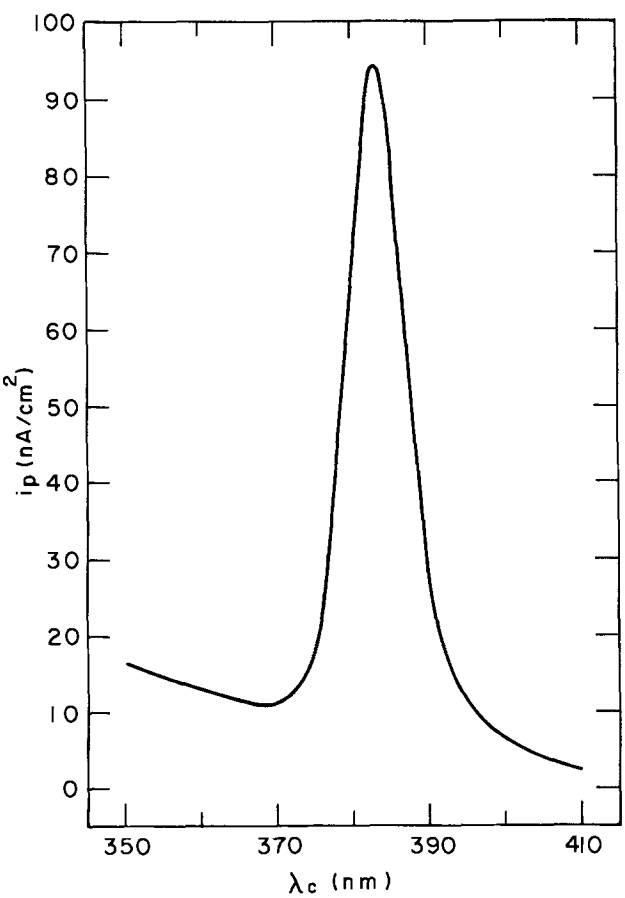


Fig. 1. Photocurrent (i_p) as a function of the wavelength of chopped light (λ_c) of 1X intensity for an unetched zinc interface of ZnO in 0.5*M* $LiClO_4$ at 6.00V *vs.* SCE.

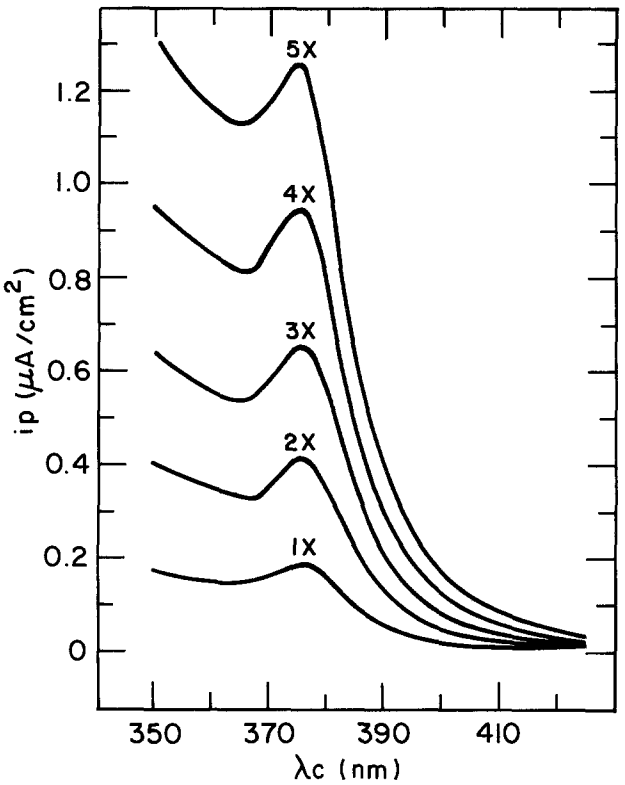


Fig. 2. Photocurrent (i_p) as a function of wavelength of chopped light (λ_c) at various intensities (1-5X) for an unetched oxygen interface of ZnO in 0.5M $LiClO_4$ at 6.00V vs. SCE.

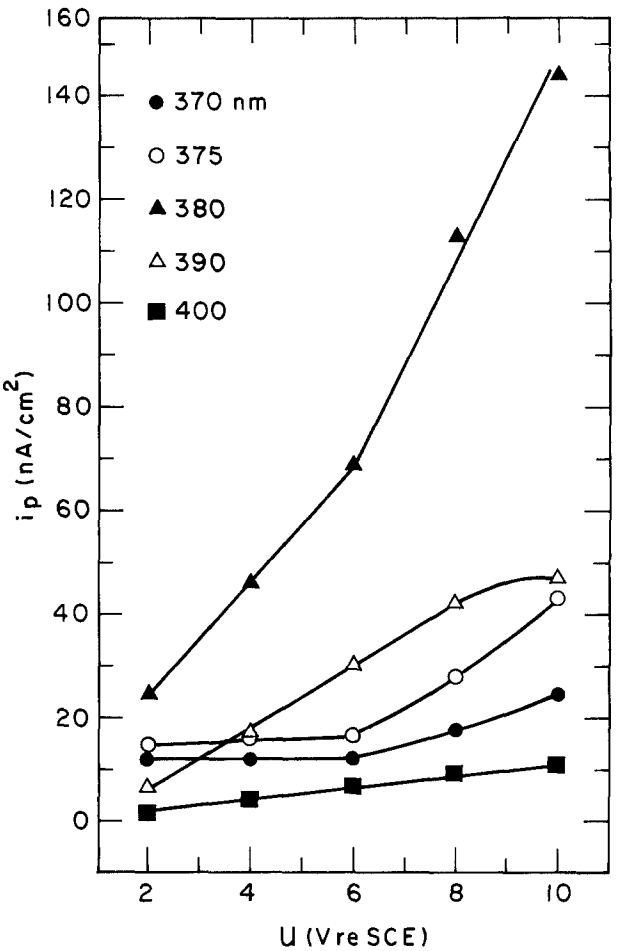


Fig. 3. Photocurrent (i_p) as a function of electrode potential (U) at various wavelengths of light (370-400 nm) of 1X intensity for an unetched zinc interface of ZnO in 0.5M $LiClO_4$.

is related to an intrinsic property of ZnO and is not entirely an artifact of the abrasive pretreatment.

As shown in Fig. 2, the oxygen interface exhibits a similar photocurrent spectrum, except that the peaks appear to be broadened and shifted to shorter wavelengths (375 nm) by the greater background current corresponding to the interband transition. Because of the much faster dissolution rate of the oxygen surface, a significant portion of the damaged ZnO surface could be removed even in neutral solutions. This, and the associated increase in surface roughness, could account for the broadened photocurrent peaks for the oxygen surface.

The electrode potential dependence of the photocurrent at various wavelengths for light of 1X intensity is shown in Fig. 3. At potentials below 6V, the photocurrent at 380 nm increases linearly with a slope of 11 nA/cm²-V, whereas above this potential the slope is greater by a factor of two (20 nA/cm²-V). The potential at which the change in slope is observed, as well as the slopes themselves, are dependent on the intensity of the light. The change in slope occurs at more cathodic potentials, and the slope increases at greater intensities. At 3X intensity the slope for the 380 nm light is constant from 0-10V at 50 nA/cm²-V. For all other wavelengths shown, the potential dependence is considerably less.

Some difficulties were encountered in obtaining reproducible spectra for ZnO electrodes. This appears to be due to several factors. One problem seemed to involve impurities in the solution since electrodes allowed to rest unbiased in the electrolyte overnight exhibited photocurrents reduced by as much as 50%. This effect, however, could be reversed or prevented by biasing the electrode a few volts anodic. At potentials greater than about 6V, the photocurrent was somewhat greater after long periods than for a freshly polished electrode, possibly because of increased surface roughness from dissolution of the crystal. When operating at moderately anodic potentials (2-6V *vs.* SCE), time dependence of the photocurrents was found to be negligible over the times of the experiments. Another problem was the difficulty involved in exactly reproducing the electrode surface region. Although small, after several hours of polishing by hand with 15μ powder, a discernible cumulative decrease in the photocurrent in the short wavelength region was still evident. Since the photocurrent peak at 383 nm occurs on the tail of the shorter wavelength curve, quantitative inferences become tenuous because the photocurrents for the two processes mutually interfere and cannot be separated.

Experiments with two light sources.—To elucidate the nature of the 380 nm effect and the reason for suppression of the interband transition, it is of great importance to know how these two processes interact. This is determined by illuminating the electrode with two light beams of differing wavelengths, one chopped and one steady. Only the photocurrent for the chopped light is measured by the lock-in amplifier, but the effect of the unchopped light on this photocurrent is observed. This is illustrated in Fig. 4, which shows the photocurrent spectrum for the zinc interface (measured with chopped light), with and without superimposed steady light of 380 nm. It is evident that the 380 nm light has little effect on the chopped photocurrent above 380 nm, but produces a large increase at shorter wavelengths.

Somewhat more information can be obtained by measuring the photocurrent at one frequency of chopped light and scanning the wavelength of the superimposed steady light. Changes in the photocurrent (Δi_p) at 360 nm produced by various intensities (1-10X) of unchopped light are plotted as a function of the wavelength of the unchopped light (λ_{uc}) in Fig. 5 for the zinc interface. Similar curves are shown for the oxygen interface in Fig. 6.

A reasonably sharp peak is observed at about 383 nm (380 nm for oxygen surface), which approaches satura-

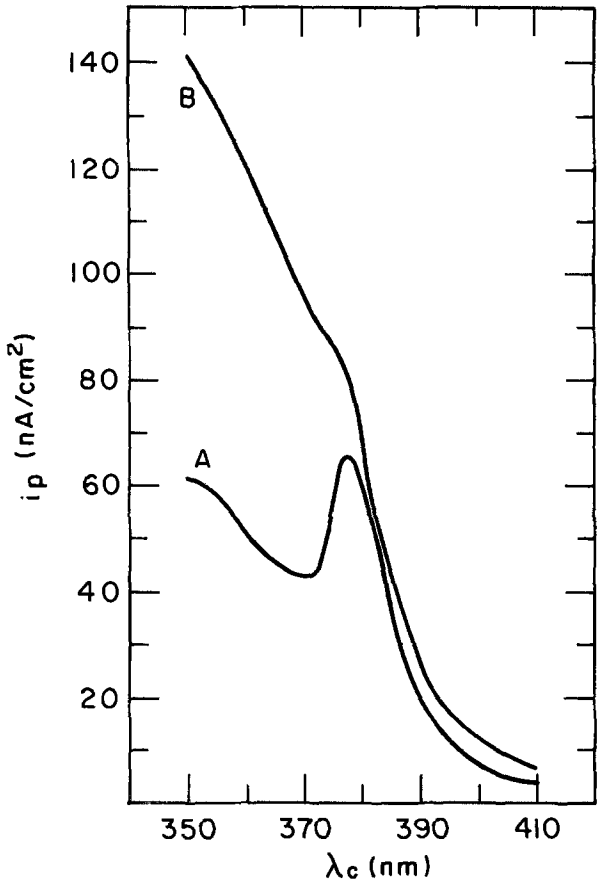


Fig. 4. Photocurrent (i_p) measured with chopped light of 1X intensity as a function of the wavelength of the chopped light (λ_c) without (A) and with (B) superimposed unchopped light of 380 nm wavelength and 1X intensity for an unetched zinc interface of ZnO in 0.5M $LiClO_4$ at 2.00V vs. SCE.

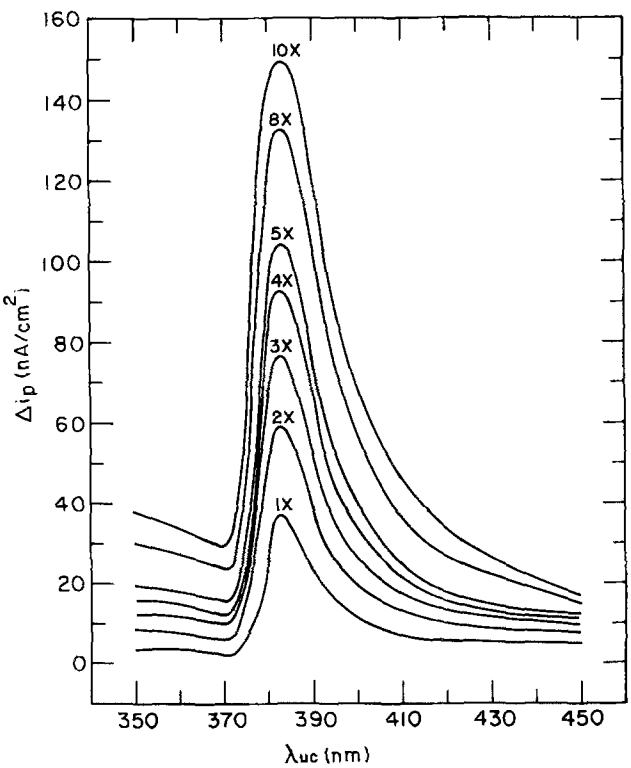


Fig. 5. Increase in photocurrent (Δi_p), measured at 360 nm using chopped light of 1X intensity, produced by various intensities (1-10X) of unchopped light as a function of the wavelength of the unchopped light (λ_{uc}) for an unetched zinc interface of ZnO in 0.5M $LiClO_4$ at 6.00V vs. SCE.

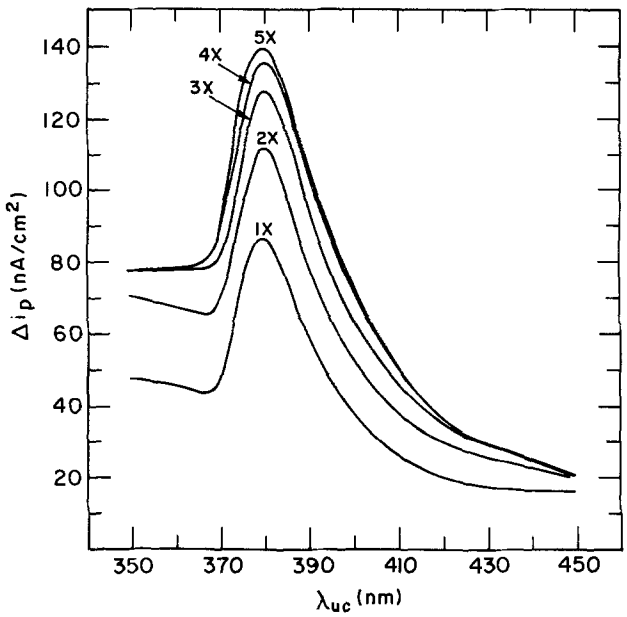


Fig. 6. Increase in photocurrent (Δi_p), measured at 360 nm using chopped light of 1X intensity, produced by various intensities (1-10X) of unchopped light as a function of the wavelength of the unchopped light (λ_{uc}) for an unetched oxygen interface of ZnO in 0.5M $LiClO_4$ at 6.00V vs. SCE.

tion at higher intensities of superimposed steady light. For the oxygen interface, the peak is somewhat broader and saturation is reached at a lower intensity (~5X). The peak saturation value is about the same in each case (140-150 nA/cm^2). By following the photocurrent at 360 nm after stopping the steady light, a decay time of 1-5 sec was determined for the 380 nm process.

Capacitance studies.—Variations of the semiconductor space charge with polishing and under illumination were followed by differential capacitance (C) measurements of the interface. Plots of $1/C^2$ *vs.* electrode potential (U), according to the well-known Mott-Schottky (10-11) equation, are shown in Fig. 7 for a zinc surface of ZnO after polishing and after etching (10 min in 5N HCl). The etched surface yields the expected straight line whose slope gives the charge carrier concentration of the electrode (1.0×10^{16} carriers/cm^3). After polishing, the space charge capacitance is less at a given potential and the Mott-Schottky plot is nonlinear.

The effect of illumination on the differential capacitance of a polished zinc interface is shown by the curves of C *vs.* wavelength of steady illumination in Fig. 8. A large peak in C is evident at 380 nm corresponding to an appreciable decrease in the thickness of the semiconductor space charge region. After etching (10 min in 5N HCl), a small capacitance peak is still observed at 380 nm, but amounts to only 5 nF/cm^2.

Discussion

Any model proposed must explain the following experimental results obtained for polished, unetched ZnO electrodes in contact with aqueous electrolytes:

1. Photocurrents measured for mechanically polished electrodes are considerably smaller than those for etched crystals under the same conditions, indicating that very effective recombination centers are introduced by the mechanical treatment. This effect is accompanied by a decrease in the concentration of ionized donors in the space charge region, as indicated by the capacitance measurements and earlier work (9).

2. A peak is observed at 380 nm in the photocurrent spectrum. This indicates a strong interaction between light of this wavelength and the recombination centers, which results in the introduction of electrons into the conduction band.

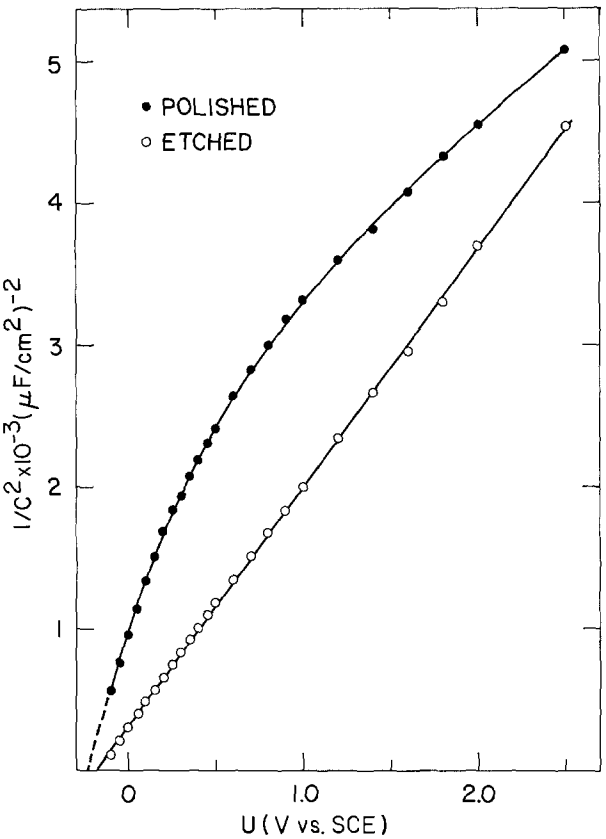


Fig. 7. Plots of inverse square of capacitance at 100 Hz ($1/C^2$) vs. electrode potential (U) for polished and etched zinc surfaces of ZnO in 0.5M K_2SO_4.

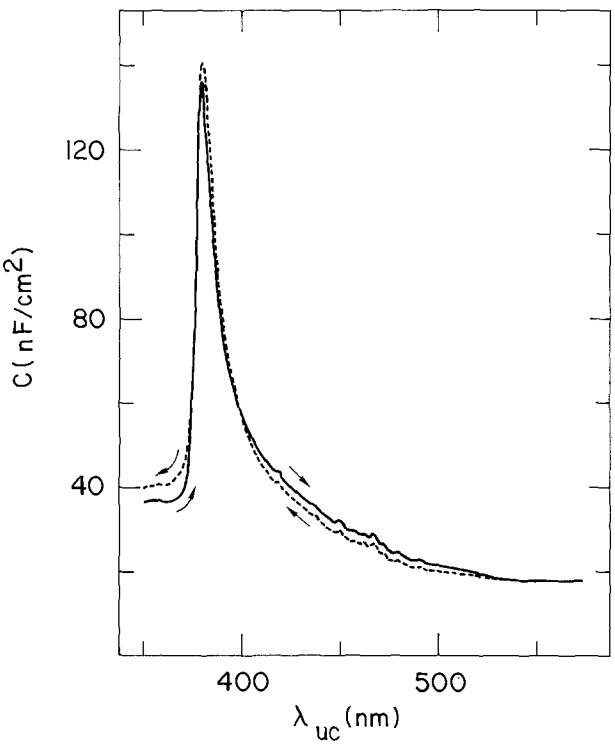


Fig. 8. Differential capacitance at 100 Hz (C) vs. wavelength (λ_{uc}) of steady light of 10X intensity swept at 0.1 nm/sec for a zinc interface of ZnO at 1.5V vs. SCE in 0.5M K_2SO_4.

3. The potential dependence of the photocurrent at 380 nm is relatively large compared to shorter and longer wavelengths.

4. Illumination with light of 380 nm wavelength sharply increases the space charge capacitance (by more than a factor of 3 in Fig. 8), denoting increased positive charge density in the space charge region.

5. The photocurrent measured for shorter wavelength light (*e.g.*, 360 nm) is greatly enhanced by simultaneous illumination with light of 380 nm wavelength. Two factors should be important here. The greater field strength resulting from the enhanced positive charge density should reduce recombination by accelerating charge transfer through the space charge layer. In addition, interaction with 380 nm light may result in a decrease in the concentration of available recombination centers.

6. The effect produced by the 380 nm illumination has a slow decay time of 1-5 sec.

Depth of light penetration.—One possible origin of the specific effects observed for 380 nm light is its greater penetration depth in ZnO, which is at least an order of magnitude deeper than for light of 370 nm wavelength (12). The data could be explained if the 380 nm light penetrated into a region of the space charge layer which lay deeper than the penetration depth for shorter wavelength light and in which the recombination rate were lower. Holes produced in this region would migrate toward the surface where they would become trapped, decreasing the thickness of the space charge region and raising the capacitance. The recombination rate nearer the surface would be lowered by the increased electric field gradient. This model is represented in a simplified way in Fig. 9, where the shorter dashed line represents the hole traps, and the two longer dashed lines show the modified band bending caused by the trapped holes.

There are some significant difficulties with any model based solely on light penetration depth. Only light absorbed within the space charge region is effective in increasing the concentration of free charge carriers and contributing to the photocurrent, since the recombina-

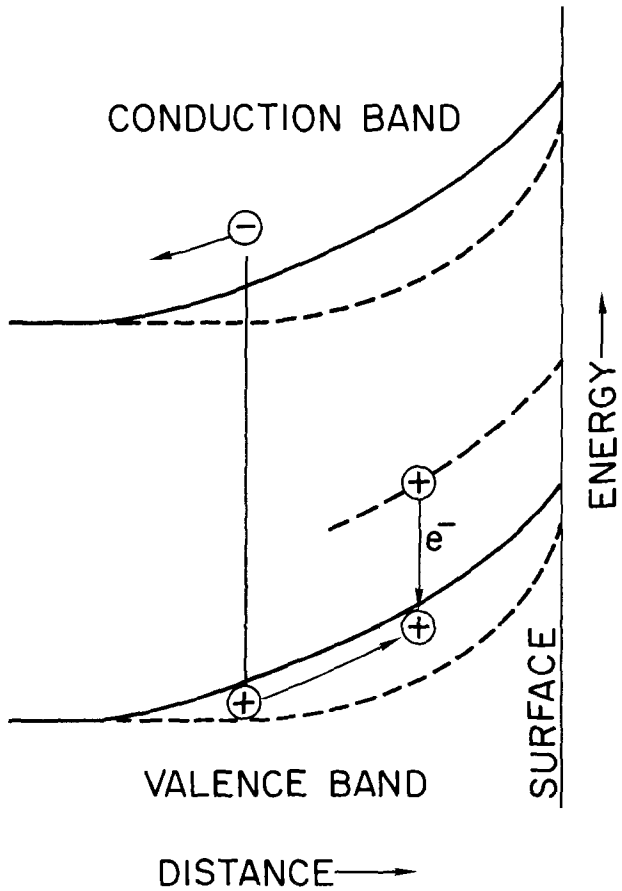


Fig. 9. Representation of ZnO space charge depletion region with trapping of holes generated by illumination deeper in the crystal (see text).

tion rate is high in the absence of an electric field. But the depth of penetration of 370 nm light in ZnO is $\sim 0.2\mu$, which is comparable to the thickness of the space charge layer (Debye length $=0.03\mu$ for 10^{16} carriers/cm^3), and that for 380 nm light is an order of magnitude greater (12). Thus, a large fraction of the 380 nm light is absorbed outside the space charge region and should not make a significant contribution to the photocurrent, while most, if not all, of the remainder is absorbed in the same region as 370 nm light and should have no special effect. Polishing probably does extend the space charge layer somewhat deeper into the crystal by introducing electron traps and destroying electron donors as indicated by the mildly decreased capacitance, but this should change the space charge thickness by considerably less than a factor of 2.

There are even more serious objections to a model based on light penetration depth. First, by following the electrode capacitance for slowly dissolving ZnO crystals, mechanically introduced hole traps have been shown to extend to depths comparable to the grain size of the polishing compound (9), which was as large as 15μ for our crystals. Thus, the recombination rate should be high throughout the entire space charge layer and all regions of light absorption in our experiments. In addition, it is evident from the literature that light in the 380 nm range is associated with some specific transition. In particular, both u.v. illumination (12) and electron bombardment (13) are known to produce a room temperature luminescence peak at about 380 nm.

A model proposed.—In ZnO without intentional dopants, Zn donors, which probably occupy interstitial lattice sites, lie about 0.05 eV below the conduction band (14, 15), and act as traps for electrons at lower temperatures (16). Deeper electron traps, up to 1 eV underneath the conduction band, have also been observed for doped and undoped ZnO by several authors (4, 7, 9, 17-20) using various techniques. In addition, hole traps are also known to occur in ZnO (8, 15, 16), and their concentration is enhanced by mechanical working (9). These various energy levels are represented schematically by dotted lines in Fig. 10, which also illustrates the assumptions made below concerning the origin and nature of the trap levels. Empty hole and electron traps are represented by simple -, whereas bound charge carriers are circled. The arrows represent the direction of charge carrier motion, and e^- and h^+ are free electrons and holes, respectively.

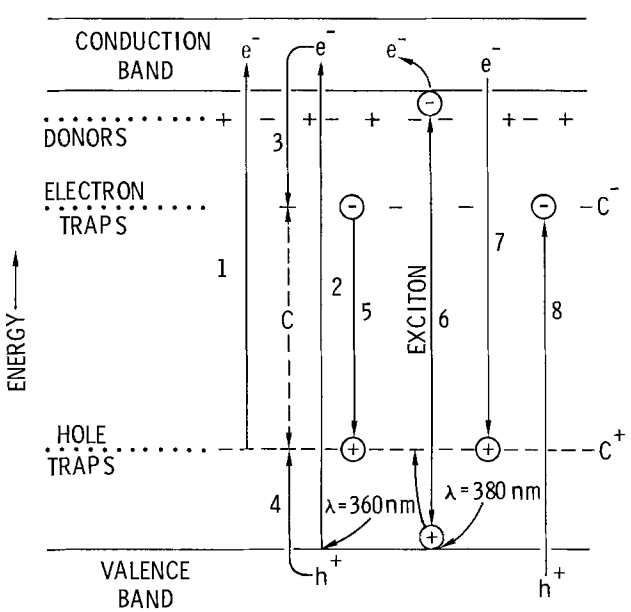


Fig. 10. Schematic representation of the energy levels and electronic transitions in ZnO (see text).

Direct interaction between the 380 nm light and the trap levels involved in recombination (transition 1 in Fig. 10) cannot adequately explain the present data. Transitions between traps and the relatively wide band structures should be effected equally well by shorter wavelength light. Also, traps involved in the recombination process, after emptying, would quickly be filled by electrons, which could also be accomplished by greater intensities of bandgap illumination. Likewise, transitions between two trap levels involved in recombination would quickly be reversed by recombination.

For our model, we assume that mechanical abrasion introduces lattice defects into ZnO, which can act as hole traps. Dislocations or possibly Zn vacancies may be involved. When a defect occurs adjacent to a Zn donor, weakening or breaking bonds, the donor sinks energetically into the bandgap (9), becoming an electron trap. The resulting hole-electron trap complex (C) should be an extremely effective recombination center for free holes and electrons, which are generated by bandgap light (transition 2 in Fig. 10). The charge carriers become trapped at the same center C, according to

$$e^- + C \rightarrow C^- \qquad \text{(transition 3)}$$

$$h^+ + C \rightarrow C^+ \qquad \text{(transition 4)}$$

where they recombine

$$C^- + C^+ \rightarrow C \qquad \text{(transition 5)}$$

The reverse reactions are assumed to be slow, and the numbers correspond to the transitions in Fig. 10. Efficient recombination through these mechanically introduced centers accounts for the over-all photocurrent suppression for polished ZnO. Since, in this model, donors become electron traps by association with defects, polishing should also decrease the electrode capacitance measured in the dark, as observed.

The specific effects observed for 380 nm light can be explained by assuming that this wavelength corresponds to an exciton transition in ZnO. This appears to be a reasonable assumption since ground state and bound excitons have been reported for ZnO in the literature (21-23). A luminescence peak is also observed in the same wavelength region (370 nm at 90°K), which is shifted to 380 nm at room temperature (12,13). It, therefore, seems probable that the 380 nm luminescence peak is associated with the decay of excitons. This is supported by the interpretation (8) of the luminescence decay in ZnO in terms of excitons.

We propose then that excitons produced by 380 nm light dissociate at lattice defects into free electrons and trapped holes (transition 6 in Fig. 10). Those holes trapped at defects isolated from recombination centers are removed only by direct recombination with free electrons (transition 7 in Fig. 10), which is expected to be a slow process compared to recombination via centers involving electron traps. Direct annihilation of these isolated trapped holes should be even slower because of electron trapping at C sites which reduces the free electron concentration. This buffered recombination for isolated hole traps accounts for the slow decay rate of positive charge introduced into the space charge region by 380 nm illumination. The specificity of the 380 nm light then arises because excitons produced at this wavelength are able to populate isolated hole traps which are not readily populated by free holes. The inefficacy of positive holes in filling these traps could be due to electrostatic repulsion, since an isolated defect would appear more positively charged than one associated with a filled electron trap. Some of the electrons introduced by the dissociating excitons migrate into the bulk producing the peak at 380 nm in the photocurrent spectrum.

Two factors are responsible for the effect of 380 nm light on the photocurrent measured at shorter wavelengths. The first is that holes trapped at isolated defects increase the field gradient within the space charge region by decreasing the Debye length of the

semiconductor, which enhances charge carrier migration and lowers the over-all recombination rate. With the increased positive charge available in the semiconductor, changes in the electrode potential have more effect on the potential gradient in the region of light absorption. Thus, the potential dependence is somewhat greater for the photocurrent around 380 nm and increases with light intensity.

The second factor responsible for the effect of 380 nm light on the photocurrent measured at shorter wavelengths involves the availability of electron traps. For an n-type semiconductor like ZnO, it is probable that the electron traps at C sites are highly populated, so that the recombination rate for the interband transition is limited by the supply of holes. In this case, the additional free electrons from the dissociation of excitons tie up more of the traps, reducing the trapping rate for electrons introduced by the interband transition. Since holes introduced by exciton dissociation are trapped at defects isolated from C sites, they have little effect on the over-all recombination rate.

In a modified version of the model presented above, the recombination center C can trap either an electron or a hole, but not both concurrently. In this case, the recombination process responsible for the over-all photocurrent suppression would still involve trapping of electrons by C, but C^- would be emptied by direct reaction with free holes. Fast recombination would then be represented by

$$e^- + C \rightarrow C^- \qquad \text{(transition 3)}$$

$$C^- + h^+ \rightarrow C \qquad \text{(transition 8)}$$

where the numbers correspond to the transitions in Fig. 10.

This modified model still requires excitons to explain the specificity of the 380 nm light. Trapped positive charge would then be introduced into the space charge region by reaction of excitons with C to produce C^+ (transition 6 in Fig. 10). The latter would presumably be slow to recombine with electrons (transition 7) because of the greater required energy transfer compared to reaction of C^- with free holes. In this model, two factors account for the photocurrent peak at 380 nm and the effect of 380 nm illumination on the photocurrent measured at 360 nm. One is the enhanced rate of charge transfer through the space charge layer caused by the accumulation of positive charge, as cited for the original model. In addition, as C is ionized to C^+, the concentration of active centers for trapping electrons (transition 3) diminishes, so that the rate of recombination via consecutive transition 8 is reduced.

Summary

Our results show that polishing of ZnO single crystals produces hole traps near the surface which act as efficient recombination centers, probably in conjunction with electron traps, reducing the photocurrent measured at a reverse-biased electrolyte contact. A specific transition is effected in ZnO by light of about 380 nm wavelength, resulting in the introduction of electrons into the conduction band and filling of the mechanically generated traps with holes. These traps are not filled effectively by free holes produced by illumination with light of shorter wavelengths.

It is proposed here that mechanically induced defects, when isolated from electron traps, do not capture free holes efficiently because of electrostatic repulsion. Excitons which migrate to isolated lattice defects, or are possibly bound to such defects, however, are produced by light of about 380 nm wavelength and effectively populate the hole traps because of their net charge neutrality. The trapped holes thus introduced are protected from recombination by their isolation from electron traps. Alternatively, the mechanically induced defects can trap either holes or electrons, but not both concurrently. If this is the case, the data can be understood if the hole traps can be filled only by excitons and are protected from recombination by energetic considerations.

It may seem surprising that no attempt has been made to interpret our results in terms of surface effects since holes might be expected to be stabilized through solvation with electrolyte species. The problem with the specificity of the 380 nm light would still remain, however, and would be difficult to explain. The arguments presented here are in fact equally applicable to processes occurring at the surface.

Acknowledgments

The authors thank Dr. Rajat Sen for many helpful suggestions, Dr. L. Peter, Dr. D. Kolb, and M. Lubke for experimental aid, and Dr. W. Pardee and Dr. E. Kraut for useful comments on the manuscript.

Manuscript received May 2, 1977.

Any discussion of this paper will appear in a Discussion Section to be published in the June 1978 JOURNAL. All discussions for the June 1978 Discussion Section should be submitted by Feb. 1, 1978.

Publication costs of this article were assisted by Rockwell International.

REFERENCES

1. J. F. Dewald, *Bell Syst. Tech. J.*, **39**, 615 (1960).
2. S. R. Morrison and T. Freund, *J. Chem. Phys.*, **47**, 1543 (1967).
3. H. Gerischer and H. Tributsch, *Ber. Bunsenges. Phys. Chem.*, **72**, 437 (1968).
4. R. Williams and A. Willis, *J. Appl. Phys.*, **39**, 3731 (1968).
5. H. Kiess, *J. Phys. Chem. Solids*, **31**, 2379 and 2391 (1970).
6. F. Cardon and W. P. Gomes, *Surf. Sci.*, **27**, 286 (1971).
7. G. Petermann, H. Tributsch, and R. Bogomolni, *J. Chem. Phys.*, **57**, 1026 (1972).
8. G. Heiland, E. Mollwo, and F. Stöckmann, *Solid State Phys.*, **8**, 191 (1959).
9. H. Gerischer, F. Hein, M. Lübke, E. Meyer, B. Pettinger, and H.-R. Schöppel, *Ber. Bunsenges. Phys. Chem.*, **77**, 284 (1973).
10. N. F. Mott, *Proc. R. Soc. London Ser. A*, **171**, 27 (1939).
11. W. Schottky, *Z. Phys.*, **118**, 539 (1942).
12. B. Andress, *Z. Phys.*, **170**, 1 (1962).
13. B. Andress and E. Mollwo, *Naturwissenschaften*, **46**, 623 (1959).
14. A. R. Hutson, *Phys. Rev.*, **108**, 222 (1957).
15. M. J. Duck and R. L. Nelson, *J. Chem. Soc. Faraday Trans. I*, **70**, 436 (1974).
16. G. Heiland, *J. Phys. Chem. Solids*, **22**, 227 (1961).
17. M. A. Seitz and D. H. Whitmore, *ibid.*, **29**, 1033 (1968).
18. T. J. Gray and P. Amigues, *Surf. Sci.*, **13**, 209 (1969).
19. W. Jakubowski and D. H. Whitmore, *J. Am. Ceram. Soc.*, **54**, 161 (1971).
20. K. I. Hagemark and L. C. Chacka, *J. Solid State Chem.*, **15**, 261 (1975).
21. D. G. Thomas, *J. Phys. Chem. Solids*, **15**, 86 (1960).
22. R. E. Dietz, J. J. Hopfield, and D. G. Thomas, *J. Appl. Phys. Suppl.*, **32**, 2282 (1961).
23. D. C. Reynolds, C. W. Litton, and T. C. Collins, *Phys. Rev.*, **140**, 1726 (1965).

A New Transistor with Two-Level Metal Electrodes

Atsushi Saiki, Seiki Harada, Toshio Okubo, Kiichiro Mukai, and Takeshi Kimura

Hitachi, Limited. Central Research Laboratory Kokubunji 185, Tokyo, Japan

ABSTRACT

A new transistor with two-level metal electrodes is developed in order to allow for the automatic wire bonding process and at the same time to minimize the chip area. To meet these requirements, the second-level electrodes are formed right above the active area of a conventional transistor by utilizing the PMP (planar metallization with polymer) technology (1) with PIQ (polyimide iso-indroquinazolinedione) film as an insulating layer. PIQ is a thermally stable polyimide-type resin specially synthesized by us for the semiconductor devices. Through several types of reliability tests, it is shown that the new transistor exhibits excellent reliability in its device characteristics, indicating that the new structure satisfies the stringent reliability and productivity requirements for transistors molded in plastics.

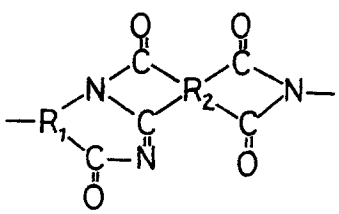
In discrete transistors, reliability and productivity requirements are very stringent. In order to satisfy these requirements, a new transistor with two-level metal electrodes has been developed. The second-level electrodes of this transistor were formed on the surface of a conventional transistor utilizing PMP technology (1, 2). The second-level electrodes were formed on the whole surface of transistor pellet so as to obtain a larger area for wire bonding than the first-level electrodes. Therefore, this electrode structure has improved the productivity of the wire bonding. This is one of the features of the new transistor. In this electrode structure, PIQ film is utilized as an insulating layer. PIQ is a polyimide-type resin specially synthesized by us for semiconductor devices. It has been shown that the PIQ film has the ability to protect the transistor surface. Therefore, the stability and reliability of transistors with PIQ as a protection film are excellent. This is another feature of this new transistor.

The Process for Two-Level Electrodes

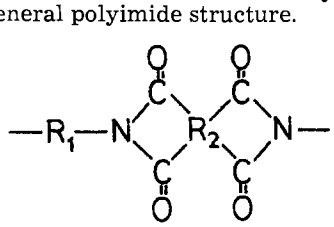
The two-level metal electrode structure is fabricated as shown in Fig. 1. A PIQ prepolymer solution is coated on the surface of a conventional transistor in the same manner as photoresist polymer, and is thermally cured (a). Then through-holes are formed by the conventional photoetching technique (b). In this process, a hydazine solution is utilized as an etchant for the PIQ film. Then aluminum is evaporated and photoetched to form the second-level metal electrodes (c). Finally, Au-wires are bonded to the second-level electrodes (d).

Properties of PIQ Film

PIQ contains a thermally stable isoindroquinazolinedione ring, represented by the following general formula



where R_1 and R_2 are aromatic rings. Isoindroquinazolinedione gives additional thermal stability to PIQ compared with general polyimide structure.



Key words: transistor, electrode, polyimide, productivity, reliability.

Figure 2 shows the heat-resisting properties of the PIQ compared with commercially manufactured polyimide. The comparison was carried out as follows: A solution of each polymer with proper viscosity was coated on silicon wafers and thermally cured at the proper temperature. The polymer films thus formed were kept at temperatures of from 200° to 450°C for 5 hr in air. After this heat-treatment, the thickness of each film was measured and compared with the inital thickness.

From Fig. 2 it is shown that the PIQ film keeps its initial thickness even after heating at 450°C for 5 hr; on the other hand, commercially manufactured polyimide losses 15-20% of its initial thickness after the same thermal test. This shows that PIQ is thermally stable enough to be used as an insulating layer in this structure.

In the new transistor the PIQ film was formed about 4 μm thick, so as not to increase the capacitance between the second-level electrodes and the silicon substrate. In order to form a 4 μm thick film, PIQ must

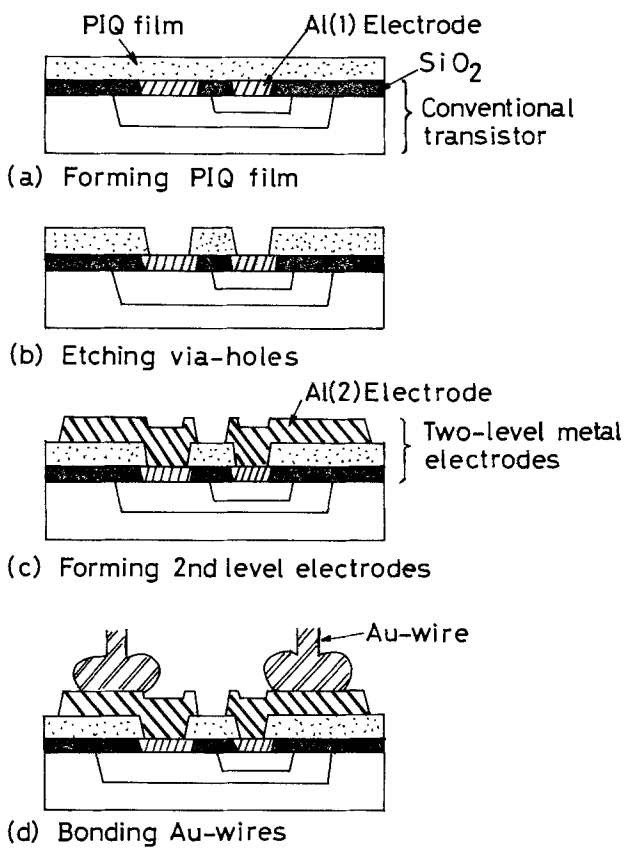


Fig. 1. Process for two-level metal electrodes

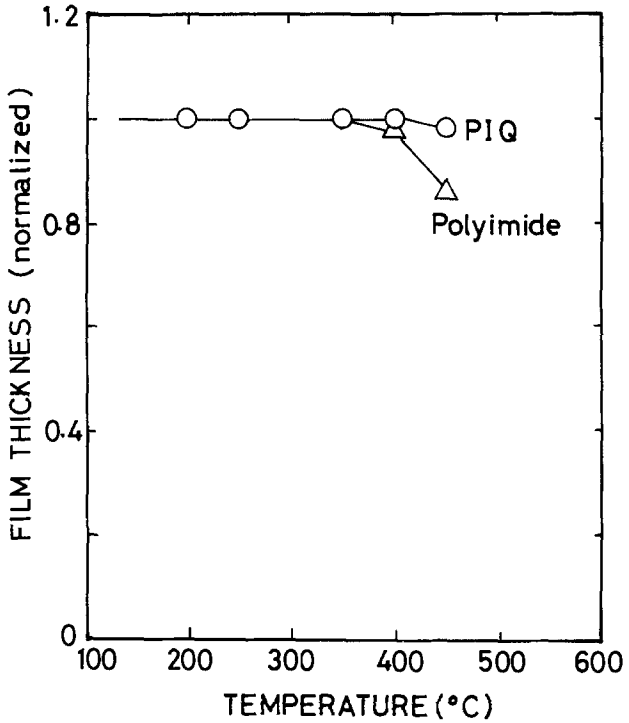


Fig. 2. Thermal degradation of polymers

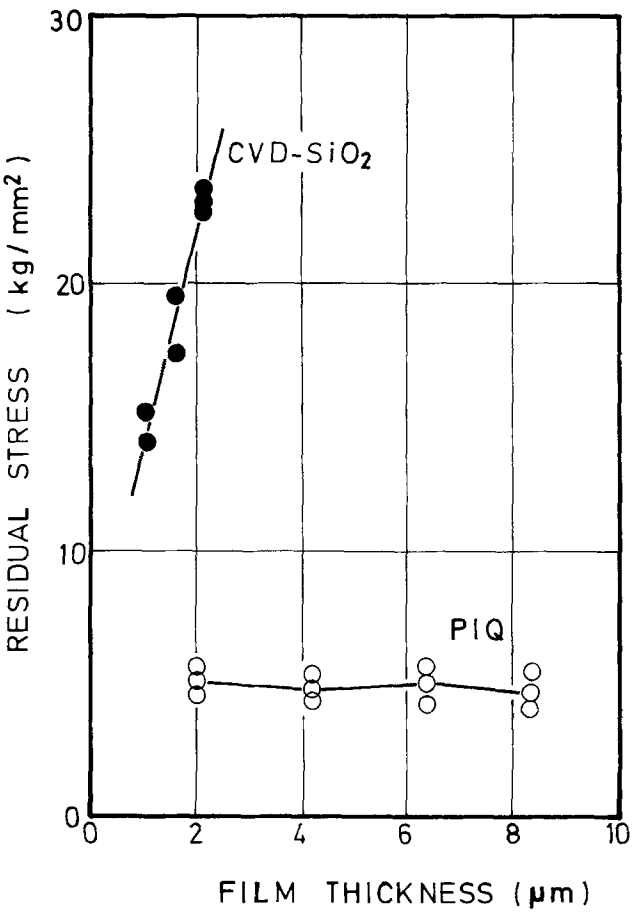


Fig. 3. Residual stresses of the thin films formed on silicon wafers

have a low residual stress. Figure 3 shows the residual stress of the PIQ film as a function of the film thickness, compared with that of silicon dioxide formed by chemical vapor deposition. The stress was obtained by measuring the curvature of the silicon wafers on which the films were formed. The PIQ residual stress is independent of film thickness, and is much smaller than that of the silicon dioxide. Very low stress in the PIQ film makes it possible to form a film as thick as 4 μm without any cracks. In addition to these properties, PIQ film has a breakdown voltage as high as 300V at 1 μm thickness. The dielectric constant of PIQ is about 3.8 at 1 MHz, which is similar to that of silicon dioxide (1).

Influence of PIQ Coating on Device Characteristics

Diode leakage current.—Test diodes with two-level metal electrodes were fabricated and the diode leakage current characteristics during a high temperature reverse bias test were evaluated. The results are shown in Fig. 4. The second electrode of the diode is formed to the same dimensions as the p^+-diffused resin, which has a diameter of 500 μm. The leakage currents were measured at a temperature of 125°C and a reverse bias voltage of 200V.

The reference diode without any protective coating shows a rapid increase in leakage current. On the other hand, the test diode shows little increase, and the amount is 2 orders smaller than that of the reference diode. These results show that the charge migration along the PIQ surface from the second electrode hardly affects the leakage current.

Transistor characteristics.—Two-level electrodes were formed on the transistor surface. The first-level electrodes of this transistor do not completely cover the SiO_2 contact windows, as shown in Fig. 5. This transistor was exposed to temperatures of from 100° to 450°C in air for several minutes, and current amplification factors were measured and compared with the initial values. In fabricating the electrodes, two kinds of polymers were used as insulating film. One is PIQ and the other is commercially manufactured polyimide. The results are shown in Fig. 4. In both devices of the pnp- and the npn-type, no change in this factor in transistors in which the PIQ film was used was observed after exposure at 450°C. On the other hand, in the transistors using polyimide, a decrease in this factor was observed over 200°C. This decrease is considered to be due to the penetration of contaminants such as sodium ions which were contained in the polyimide film, through the portion not covered by aluminum.

It has been verified by atomic absorption spectroscopic analysis that the sodium content of PIQ film is less in quantity than that of silicon dioxide film formed by chemical vapor deposition. Therefore, neither metallic impurities nor ionic contaminants which degrade transistor characteristics are contained in the PIQ film.

Another evaluation of the current amplification factor was carried out on the same transistor as that described above, as follows: After two-level metal electrodes were formed, the transistors were molded in plastics and were subjected to a 48 hr high temperature reverse bias test at 150°C, 100V. Figure 6 shows a comparison of the current amplification factors of the npn-

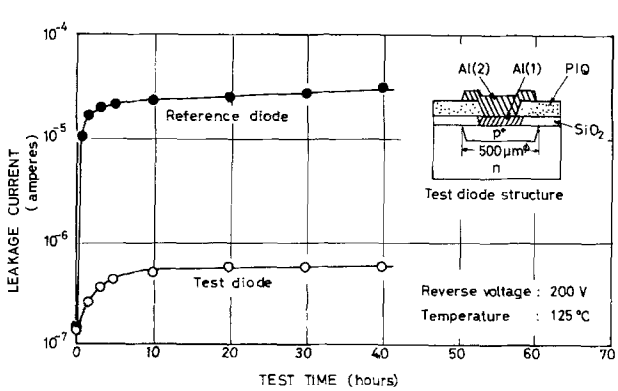


Fig. 4. Reverse current characteristics in the high temperature reverse bias test at 125°C, 200V.

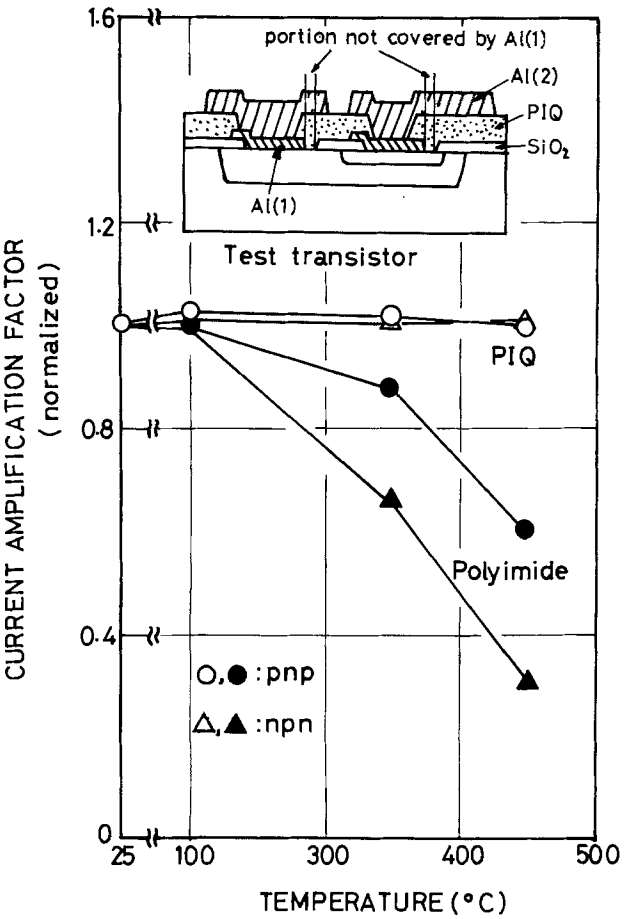


Fig. 5. Changes in current amplification factors vs. temperature

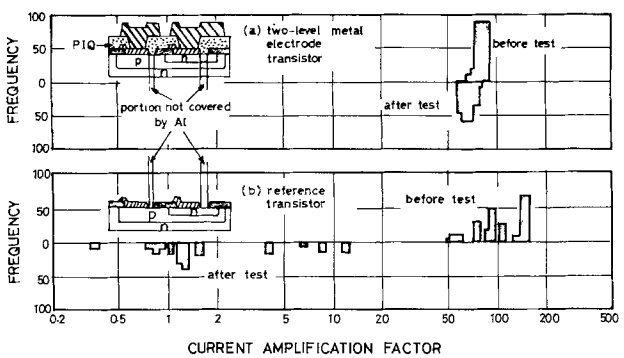


Fig. 6. Changes in the current amplification factors during the 48 hr high temperature reverse bias test (150°C, V_{CES} = 100V).

type transistors before and after the test. In the new transistors, changes in this factor were hardly observed, as is shown in Fig. 6(a). On the contrary, in the reference transistors without any protective coating, a drastic decrease in this factor was observed, as shown in Fig. 6(b). This decrease is considered to be due to the penetration of contaminants contained in the mold resin into the semiconductor body. Therefore, the stable properties of the new transistor are attributable to the ability of the PIQ to protect the transistor surface.

Figure 7(a) shows a transistor pellet made by this new technique. The PIQ film is formed so as to cover the whole surface of the conventional transistor pellet, which is shown in Fig. 7(b). After through-holes are etched, the second electrodes are formed. The effective area of the electrodes for wire bonding is larger than that of conventional electrodes without enlarging the size of the transistor pellet. After the second electrodes are formed, Au-wires are bonded to them. Figure 8 shows a cross section of the wire bonded portion. No

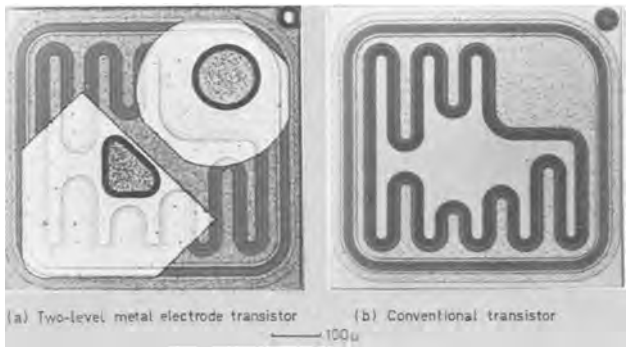


Fig. 7. An example of the two-level metal electrode transistor, (a) two-level metal electrode transistor, and (b) conventional transistor.

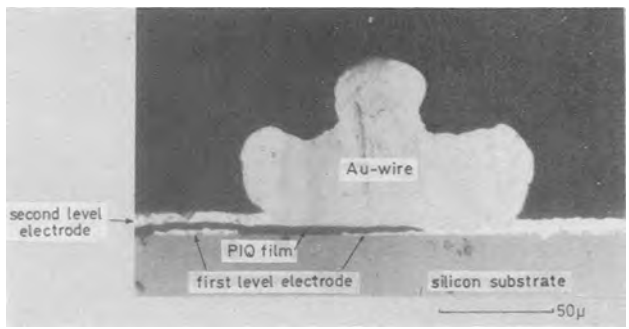


Fig. 8. Cross section of the wire bonded portion

plastic deformation was observed in the PIQ film right under the wire bonded portion of the second electrode. This electrode structure has remarkably improved the productivity of transistors in automatic wire bonding. It can also be seen from Fig. 8 that the coverage of the second-level electrode at the PIQ through-hole edge is very good. This is because of the gentle slope of the edge which is formed by hydrazine solution etching.

Reliability

The reliability and stability of transistors molded in plastics were evaluated by many kinds of tests. Table I shows the results of the reliability test. An operational life test was carried out under twice the maximum power dissipation specifications. After 500 hr of operation, only two of 250 samples of pnp and one of 100 samples of npn devices were degraded. This degradation was found not to be due to the electrode structure as a result of failure analyses. In the humidity test at 80°C and 90% RH, neither degradation of collector-base breakdown voltage nor collector-base junction leakage current was observed even after 3000 hr. In the

Table I. Results of reliability test

	Test conditions	Test time (hr)	Results* pnp	Results* npn
Operational life test	Twice the maximum power dissipation specifications	500	2/250	0/100
		1000	0/248	1/100
Humidity test	80°C, 90% RH	1000	0/50	0/100
		2000	0/50	—
		3000	0/50	—
Pressure cooker test	120°C, 2 atm	20	0/200	0/100
		32	1/200	—
		44	0/199	—
Thermal cycle test	−30°C ~ 100°C	300 (cycles)	0/50	0/50
HTRB test**	110°C, maximum reverse voltage specifications	300	0/50	0/50

* Denominators are the number of test samples, and numerators are number of degraded samples.
** High temperature reverse bias test.

pressure cooker test, samples were exposed in water vapor at 125C and 2 atm. This is one of the most severe tests for transistors molded in plastics. In this test, only one of 200 samples was degraded. However, this degradation was found to be due to defects in the photoresist film and not due to the PIQ film itself. In the thermal cycle test, samples were kept at 100°C for 30 min at first, and then cooled to −30°C and kept at this temperature for 30 min. No sample degraded in this test after 300 cycles. A high temperature reverse bias test (HTRB) was carried out at 110°C, and maximum reverse voltage was applied. After a 300 hr test, no degradation in the collector-base junction leakage current was observed.

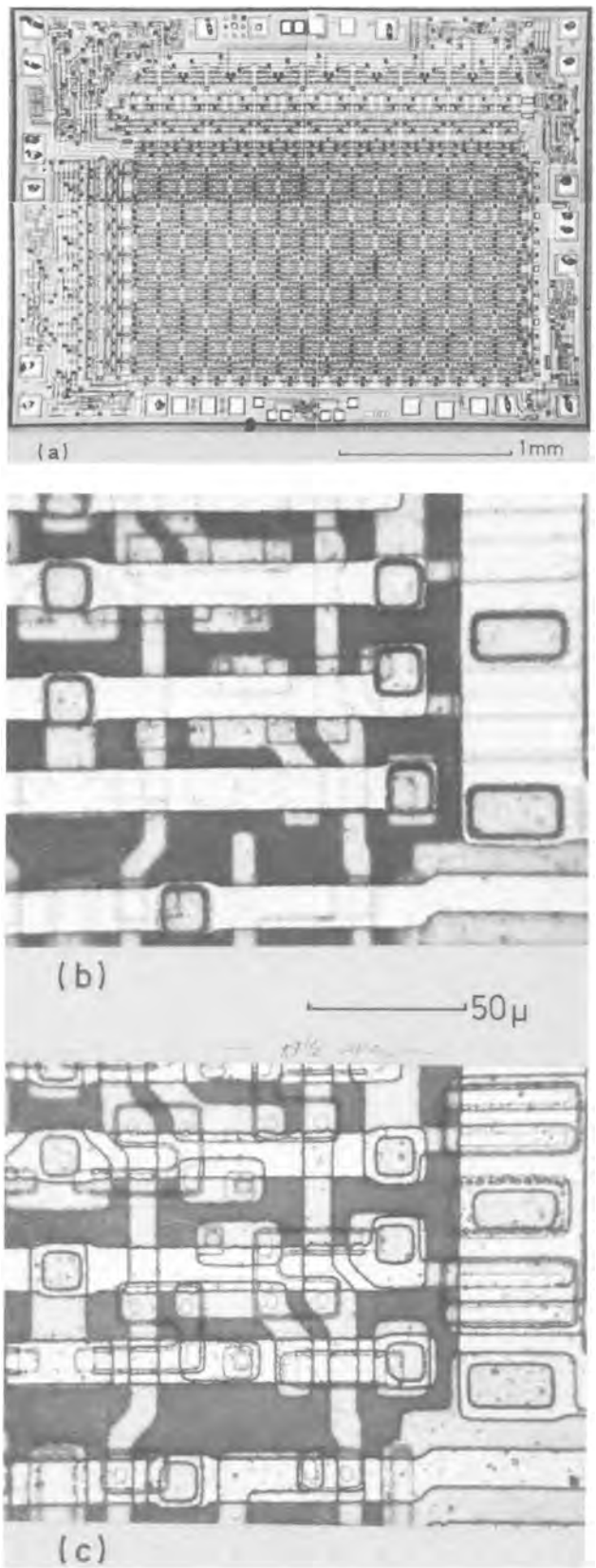


Fig. 9. Two-level metallization on LSI utilizing PIQ film. (a) LSI pellet with about 2000 elements; (b) enlarged photograph of a portion of the LSI made by PMP technology utilizing PIQ film as an insulating layer; (c) same portion as (b) made by conventional technique utilizing CVD SiO_2 as an insulating layer.

Application to LSI's

It has been verified as a result of developing the new transistor that the process and structure of two-level metallization utilizing PIQ is very reliable. This PMP technique can be applied also to multilevel interconnection on monolithic LSI's.

Figure 9(a) shows an example of two-level metal interconnections on a LSI utilizing 2 μm thick PIQ film. Fig. 9(b) is an enlarged photograph of a portion of the LSI made by PMP, and Fig. 9(c) is the same portion of the LSI made by the conventional technique utilizing CVD SiO_2 as an insulating layer. From Fig. 9(b), it can be seen that the second-level metallization is formed on a planar surface, and that the coverage of the second aluminum at the crossover is excellent. In the conventional structure, however, the steps of the second metallization are very clearly observed. Therefore, this new structure can improve the reliability and yield multilevel interconnections. Even a three or more level structure can easily be formed by using this planar technique.

Conclusions

A new transistor with two-level metal electrodes has been developed utilizing PIQ film. PIQ is a polyimide-type resin specially synthesized by us for semiconductor device, and has excellent physical, thermal, and electrical properties. It is shown that the productivity and reliability of transistor characteristics is met by this new electrode structure. This metallization technique is also applied to multilevel interconnections on monolithic LSI's, taking advantage of its planar characteristics.

Acknowledgments

The authors wish to thank Dr. Toru Abe, president of Iruma Electronics Company Limited, Dr. G. Kamoshita of the Semiconductor and Integrated Circuits Division, Hitachi Limited, and Dr. K. Sato of the Central Research Laboratory, Hitachi Limited for their helpful advice. Thanks are also extended to Messrs. T. Takagi, M. Miyamoto, and K. Itoi of Takasaki Works for fabrication of test samples, and Messrs. N. Sakimoto and T. Kohisa of Semiconductor and Integrated Circuits Division for reliability evaluation of the test samples.

Manuscript submitted Dec. 17, 1976; revised manuscript received June 14, 1977.

Any discussion of this paper will appear in a Discussion Section to be published in the June 1978 JOURNAL. All discussions for the June 1978 Discussions Section should be submitted by Feb. 1, 1978.

Publication costs of this article were assisted by Hitachi Limited.

REFERENCES

1. K. Sato, S. Harada, A. Saiki, T. Kimura, T. Okubo, and K. Mukai, *IEEE Trans. Parts, Hybrids and Packag.*, **php-9**, 176 (1973).
2. S. Harada, K. Sato, A. Saiki, T. Kimura, T. Okubo, and K. Mukai, in Proceedings of the 6th Conference on Solid State Device, The Japan Society of Applied Physics, 297 (1974).

Impedance Measurements at the N- and P-Type GaP Single Crystal Electrode

M. J. Madou and F. Cardon

Laboratorium voor Kristallografie en Studie van de Vaste Stof, Krijgslaan 271, B-9000 Gent, Belgium

and W. P. Gomes

Laboratorium voor Fysische Scheikunde, Rijksuniversiteit Gent, Krijgslaan 271, B-9000 Gent, Belgium

ABSTRACT

Impedance measurements were made at the dark n- and p-type GaP single crystal electrodes in aqueous indifferent electrolyte solutions as a function of applied voltage and of frequency. The results allow the determination of the flatband potential and hence of the position of the Fermi level and the conduction and valence band edges at the electrode surface. The observed frequency dependence of the capacitance can be attributed to dipole relaxation phenomena in the space-charge layer of the semiconductor electrode. The influence of preliminary etching on the frequency behavior is discussed.

Gallium phosphide is an interesting semiconductor electrode from both the fundamental and the applied point of view. Indeed, since GaP has a relatively wide bandgap (2.25 eV) and exists as well in n-type as in p-type form, it constitutes an appropriate material for distinguishing between electrochemical processes involving the conduction band and the valence band, respectively, and hence for testing the validity of the current theories concerning electron exchange at the semiconductor/electrolyte interface. Some interesting reactivity studies on the GaP electrode have been reported by Memming (1, 2). The practical importance of the GaP electrode is associated with the fact that p-type GaP can be used as the photocathode in electrochemical cells in which water is decomposed by solar energy, although at present, the actual operation of such cells still gives rise to problems (3).

It is clear that for both fundamental and practical purposes it is essential to possess reliable information concerning the GaP/electrolyte interface. Such information is generally obtained from capacitance measurements. As has repeatedly been observed with other semiconductor electrode materials, difficulties usually arise in the interpretation of such measurements and more specifically in the determination of the flatband potential V_{fb}, due to the frequency dependence of the capacitance.

From a study which we made earlier on the frequency dependence of the impedance of several semiconductor electrodes such as CdS, CdSe, and TiO_2, we have developed a theory which gives an interpretation of the observed frequency laws and which permits, in certain cases, the determination of V_{fb} in spite of the frequency dispersion of the cell capacitance (4). Impedance measurements as a function of applied voltage at the GaP electrode in aqueous electrolyte, made by Memming (1) and by Eletskii (5), were restricted to one frequency only. On the other hand, Mott-Schottky plots, measured by Dehmlow *et al.* (6) at the n-type GaP electrode in aqueous and in organic medium at different frequencies, show a rather unusual frequency behavior, since the capacitance appears to increase with frequency. Therefore, we thought it would be interesting to investigate the frequency dependence of the impedance of n- and p-type GaP in contact with an aqueous electrolyte, not only in order to check the generality of the frequency laws observed earlier on other semiconductor electrodes and of the theory interpreting these laws, but also in order to deduce the exact value of the flatband potential, which is an essential parameter in semiconductor electrochemistry.

The present work contains the results of a study of the impedance of single crystal n- and p-type GaP electrodes as a function of frequency, applied voltage, composition of the aqueous electrolyte, and pretreatment of the crystal surface.

Key words: semiconductor, electrochemistry, dielectrics, surface phenomena, energy levels.

Experimental

The apparatus consisted of an electrochemical cell and an electrical measuring circuit. The electrochemical cell contained a GaP single crystal electrode, a Pt counterelectrode, a saturated KCl calomel reference electrode, and an aqueous electrolyte. This cell was mounted in a grounded metallic box in order to exclude electrical disturbances as well as light.

The electrical circuit permitted the application of a variable voltage between the semiconductor and counterelectrode, and the measurement of the potential of the semiconductor electrode with respect to the reference electrode by means of a Solartron 7040 voltmeter, the cell current by a Hewlett Packard 425 A d-c microvoltammeter, and the impedance between the semiconductor and the counterelectrode by means of an Electro Scientific Industries capacitance bridge 277 and a-c generator-detector 861 A (frequency range between 20 and 20,000 Hz).

The n- and p-type GaP single crystals, which had the form of slabs, cut perpendicular to the [111]-axis, were obtained from Elcomat-Cmf (Mechelen, Belgium). Since no equipment for making Hall measurements was available in our laboratory, we used the manufacturer's specifications, which were for the n-type samples: specific conductivity $\sigma \simeq 1000\ \Omega^{-1}\ m^{-1}$ and donor concentration $N_D \simeq 4.8 \times 10^{23}\ m^{-3}$; for the p-type samples: $91 < \sigma < 670\ \Omega^{-1}\ m^{-1}$ and acceptor concentration $7.8 \times 10^{22} < N_A < 7.5 \times 10^{23}\ m^{-3}$.

Damage caused by cutting the crystals was removed by subsequent mechanical polishing and chemical etching and polishing. The mechanical polishing was performed as follows: the crystals were polished first with 15 μm Al_2O_3 powder (Buehler) on a glass plate until homogeneous roughness, and afterward with Al_2O_3 of diminishing particle size (5-1 μm and sometimes 0.3 μm) on a polishing cloth (AB Rayvel® from Buehler), in order to obtain a shiny, scratch-free surface.

A solution of 0.5M KOH and 1M $K_3Fe(CN)_6$ in water allowed differentiation between the smooth $(\bar{1}\bar{1}\bar{1})$-face (P) and the pitted (111)-face (Ga) (7). In one particular case, we used a H_2SO_4:H_2O_2:H_2O (3:1:1) etch. A concentrated HCl solution, which was the etchant for GaP used by Memming (1), was also used but appeared to remove much less material than the former etching solutions, as proved by weighing the crystals.

For both n- and p-type, the $(\bar{1}\bar{1}\bar{1})$-face was exposed to the electrolyte in our experiments. Ohmic contact to n-type GaP was made by melting In on the Ga-face of the crystal at 400°C under a hydrogen stream. On p-type GaP, contact was made by means of a Ag-In-Zn (8:1:1) or a Au-Zn alloy evaporated on the Ga-face and melted at 650°C under an argon stream.

An insulating paint was used to separate the contact from the electrolyte. All chemicals, used as indifferent electrolyte, were reagent grade. Before each measurement, high purity nitrogen was bubbled through the solution in order to remove dissolved oxygen. The measurements were made at room temperature and in darkness. In what follows, the GaP electrode potential is expressed with respect to the standard hydrogen electrode (SHE).

Results

N-type GaP.—Current-voltage and capacitance-voltage measurements.—The n-GaP/indifferent electrolyte contact demonstrated blocking properties under anodic bias. Under these circumstances, the impedance measurements were performed. The capacitance data for an n-GaP electrode in a solution of 1M KCl and 0.01M HCl in water are represented in Fig. 1a as C_s^{-2} *vs.* V (Mott-Schottky plot), C_s being the series equivalent capacitance in $f \cdot m^{-2}$. In acid solutions, the slope of the Mott-Schottky plots was only slightly frequency dependent; the point of intersection with the V-axis was frequency independent and could hence be used for the determination of the flatband potential V_{fb} (see discussion). The following values were found for our samples: $V_{fb} = -1.10V$ *vs.* SHE at $pH = 2.1$ and $-1.21V$ *vs.* SHE at $pH = 4.8$. The shift of V_{fb} toward more negative voltages with increasing pH suggests that an acid-base equilibrium is established at the GaP surface.

For the rest potential V_R in $pH = 2.1$ (corresponding to zero current through the external circuit), we found $V_R = V_{fb} + 1.35V$, so that, assuming that the Helmholtz potential is independent of applied voltage (see discussion), it can be concluded that at $V = V_R$, a depletion region is present, the band-bending being 1.35 eV.

In alkaline solutions, *i.e.*, at $pH = 9.2$ and 12, no reproducible measurements could be carried out. The Mott-Schottky curves exhibited a large frequency dispersion and the intersection with the V-axis was also frequency dependent. The frequency dispersion still increased after long anodic prepolarization. When the sample was subsequently brought to acid medium ($pH = 2.1$), the frequency dependence was drastically reduced and the Mott-Schottky plots had again the aspect as shown in Fig. 1a. In what follows, only results obtained in acid medium are considered.

Frequency laws.—As can be seen from Fig. 1a, the cell capacitance is slightly frequency dependent in acid medium, the slope of the Mott-Schottky plots increasing with frequency, in contrast to the case observed by Dehmlow (6). To a frequency-dependent series capacitance C_s corresponds a frequency-dependent series resistance R_s, the functions describing the frequency dependence of both quantities being interrelated by the Kramers-Kronig relations (8). Therefore, in order to study the frequency dispersion of

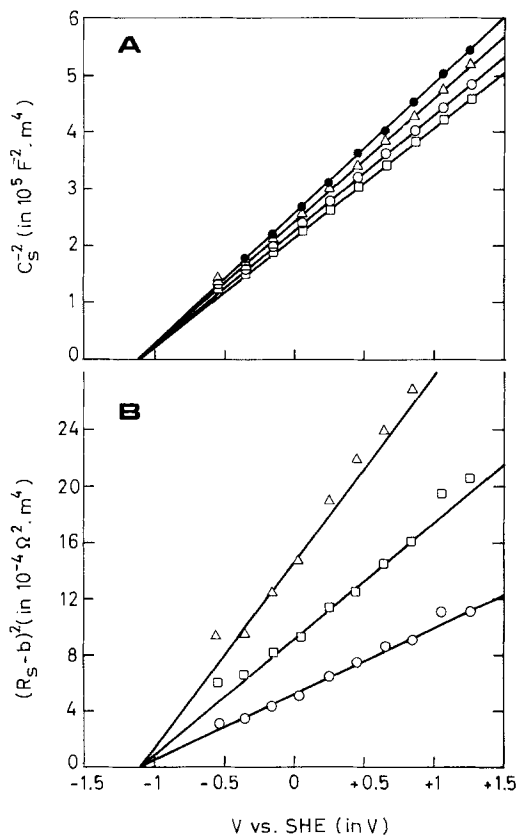


Fig. 1. A. Mott-Schottky plot, n-type GaP in an aqueous solution of 1M KCl + 0.01M HCl. □, 130 Hz; ○, 800 Hz; △, 20,000 Hz; ●, C_{ex}^{-2} (see discussion). B. $(R_s - b)^2$ *vs.* V for the same measurement. △, 400 Hz (all values multiplied by a factor 10^2); ○, 800 Hz (all values multiplied by a factor $2 \cdot 10^2$); □, 2500 Hz (all values multiplied by a factor $5 \cdot 10^3$).

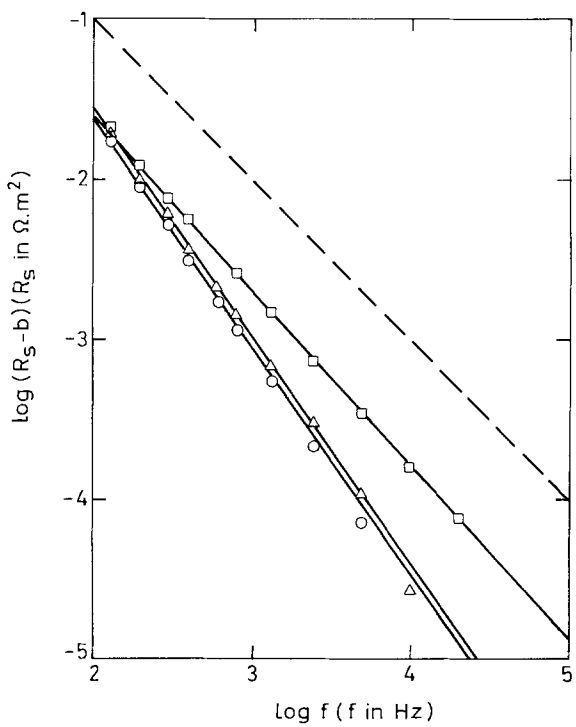


Fig. 2. Log $(R_s - b)$ *vs.* log f. Medium, 1M KCl + 0.01M HCl in H_2O. □, After an HCl etch; $V = +0.75V$ *vs.* SHE, $b = 2.6 \times 10^{-4}$ $\Omega \cdot m^2$, $n = -1.09$. △, ○, Same specimen after an H_2SO_4:H_2O:H_2O_2 (3:1:1) etch; $V = +1.25V$ and $+0.65V$ *vs.* SHE, respectively; $b = 2.3 \times 10^{-4}$ $\Omega \cdot m^2$, $n = -1.43$. (The dashed line has a slope -1.)

the impedance, it is sufficient to consider the frequency dependence of R_s, which is much more pronounced than that of C_s.

At constant voltage, the following law, which was found before in the case of TiO_2, CdS, and CdSe (4), was observed to hold in the present case as well

$$R_s = a \cdot f^n + b \qquad [1]$$

where f denotes the frequency, and where in all cases observed

$$-1.70 < n \leq -1.09 \qquad [2]$$

Some examples are shown in Fig. 2, where $\log(R_s - b)$ is plotted *vs.* $\log f$, yielding, linear plots with slope n. The value of the term b was determined by consecutive approximations (4). This term represents the sum of all frequency-independent series resistances in the cell circuit, the main contribution being that of the electrolyte.

The value of n appeared to be independent of the voltage over a range of $\simeq$ 1.5V, but to depend on the pretreatment of the sample. This is clearly demonstrated in Fig. 2, showing results obtained on one particular sample, which was etched in HCl on one occasion, yielding $n = -1.09$, and in $H_2SO_4/H_2O_2/H_2O$ (3:1:1) on an other occasion, leading to $n = -1.43$. This trend was found to be general: etching in HCl, a procedure by which only little surface material was removed, leads to n-values close to -1, whereas thorough etching, such as in $H_2SO_4/H_2O_2/H_2O$ or in $KOH/K_3Fe(CN)_6/H_2O$, causes n to be more negative. Hence, the value of n seems to be determined by the degree to which surface damage has been removed from the electrode. The influence of the pretreatment was also observable in the Mott-Schottky plots, in the sense that the frequency dispersion was more pronounced when the samples had been etched in HCl than when a more drastic etching procedure had been used.

Anticipating the discussion, it can be said here that the theory (4), accounting for the type of results such as represented in Fig. 1a, predicts that a linear relationship should exist between $(R_s - b)^2$ and V, the linear $(R_s - b)^2$ *vs.* V plots registrated at different frequencies converging to the same common point on the V-axis as the Mott-Schottky plots. This expectation is indeed fulfilled in the present case, as can be seen from Fig. 1b.

P-type GaP,—Current-voltage and capacitance measurements.—To obtain blocking properties for the p-GaP/indifferent electrolyte contact under cathodic bias, a longer mechanical and chemical polishing procedure than for the n-type specimen was necessary. This fact has been observed before by Memming (9). In all further experiments with p-type GaP, an alkaline hexacyanoferrate etch was used. All measurements were made in acid medium. The impedance measurements were restricted to samples which were characterized by a very low cathodic dark current density ($< 10^{-3}$ A·m^{-2}).

Typical Mott-Schottky plots at different frequencies, converging to a common point on the V-axis, are shown in Fig. 3a. The frequency effect was generally smaller than for n-type GaP electrodes. The following values were found for the flatband potential of our samples: $V_{fb} = +0.83$V at pH = 2.1, $V_{fb} = +0.70$V at pH = 4.0, and $V_{fb} = 0.67$V at pH = 4.8.

The rest potential of p-GaP was found to be $V_R = V_{fb} - 0.50$ at pH = 2.1.

Frequency laws.—In the cases investigated, the frequency dependence of C_s and R_s was very low. Nevertheless, the results permitted the conclusion that also here Eq. [1] holds, n being approximately equal to -1 and independent of voltage. As shown in Fig. 3b, the $(R_s - b)^2$ *vs.* V plots are linear (except for the region near V_R where R_s increases considerably) and intersects the V-axis at the same voltage as the Mott-Schottky plots.

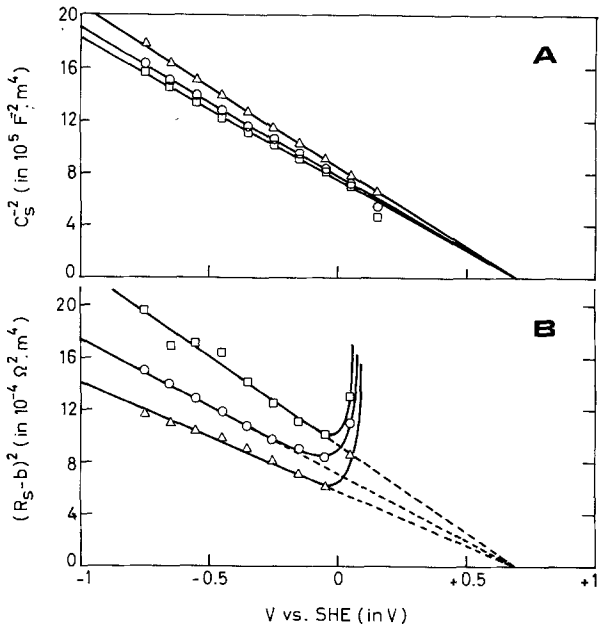


Fig. 3. A. Mott-Schottky plot, p-type GaP in an aqueous solution of 1M KCl + 0.8M HAc + 0.2M NaAc. □, 220 Hz; ○, 800 Hz; △, 20,000 Hz. B. $(R_s - b)^2$ *vs.* V for the same measurement. △, 320 Hz (all values are multiplied by 6); □, 800 Hz (all values are multiplied by 80); ○, 1330 Hz (all values are multiplied by 200).

Discussion

Voltage and frequency dependence of the impedance components.—From the facts that a blocking contact is formed and that the Mott-Schottky relationship is obeyed over a considerable voltage range with both n- and p-type GaP, it can be concluded that in both cases, a depletion region is present at the semiconductor electrode surface.

The observed frequency dependence of the series equivalent resistance is of the same type as observed before with other semiconductors (4, 10).

In a previous paper (4), arguments have been presented which show that the frequency dependence of C_s and R_s cannot be attributed to trivial causes such as seepage of solution between the electrode and its insulation, nor to the conversion to series elements of a parallel circuit which would consist of a frequency-independent capacitance and resistance. Moreover, a recent comparative study on GaAs/electrolyte and GaAs/metal interfaces demonstrates the validity of the same frequency laws in both cases, indicating that the origin of the effect is located within the semiconductor (11). A theory has been presented (4), in which it was assumed that the frequency effects are caused by dielectric relaxation phenomena, occurring in a layer at the semiconductor surface. The following expressions were then derived theoretically for the series equivalent capacitance $C_{L,s}$ and resistance $R_{L,s}$ of this layer, assuming that the dissipation is small

$$C_{L,s} = \frac{\epsilon_0 \epsilon(f)}{L} = \frac{\epsilon_0}{L}[\epsilon(\infty) + A_C \cdot f^{n+1}] \qquad [3]$$

and, in case that $\epsilon(\infty) >> A_C \cdot f^{n+1}$

$$R_{L,s} = A_R \cdot L \cdot f^n \qquad [4]$$

In these equations, L is the thickness of the layer in which the relaxation processes take place, $\epsilon(f)$ is the dielectric constant of this layer at frequency f, and $\epsilon(\infty)$ is the dielectric constant of this layer in the absence of the dielectric relaxation effects considered

here, and hence merely consisting of the ionic and electronic contributions of the perfect crystal, whereas A_C and A_R are coefficients, independent of applied voltage and of frequency. The possible values of the exponent n are limited by the inequality

$$-2 < n < -1$$

The value of n in a given case is determined by the shape of the distribution curve which describes the number of oscillating dipoles as a function of the corresponding activation energy in this sense that, the sharper the distribution curve, the more negative the value of n. Our results on the influence of etching on the value of n, as represented in Fig. 3, imply, in the framework of this theory, that a more thorough etch leads to a sharper distribution of activation energies and to a smaller frequency effect. Apparently, the number of dipoles causing the effect studied here is affected by appropriate etching.

In cases such as those observed in this work, where the Mott-Schottky plots corresponding to different frequencies intersect in one common point on the V-axis, and where the $(R_s - b)^2$ *vs.* V plots are linear and converge to the same common point on the V-axis, it must be assumed that the dielectric relaxation phenomena occur throughout the depletion layer at the semiconductor surface. Accepting this, L in the foregoing equations acquires the significance of the thickness of the depletion region, which, according to the Mott-Schottky theory, varies with applied voltage V according to the following relationship (taking, *e.g.*, the case of an n-type semiconductor)

$$L^2 = (2\epsilon_0\epsilon(o)/eN_D)(V - V_{fb} - kT/e) \quad [5]$$

In this equation, $\epsilon(o)$ is the static dielectric constant, comprising all polarization effects, and N_D is the donor density. Considering Eq. [3], [4], and [5] and the fact that, under the present conditions, $C_{L,s}$ equals the total measured capacitance C_s, whereas $R_{L,s} = R_s - b$, one finds

$$C_s^{-2} = \{2\epsilon(o)/\epsilon_0[\epsilon(f)]^2eN_D\}(V - V_{fb} - kT/e)$$
$$= [2\epsilon(o)/\epsilon_0eN_D][\epsilon(\infty) + A_C \cdot f^{n+1}]^{-2} \cdot (V - V_{fb} - kT/e) \quad [6]$$

$$(R_s - b)^2 = (A_R \cdot f^n)^2[2\epsilon_0\epsilon(o)/eN_D](V - V_{fb} - kT/e) \quad [7]$$

Equations [6] and [7] are in agreement with the experimental data on the voltage dependence enumerated above, and indicate that the common point of intersection of the linear plots corresponding to different frequencies is at $V = V_{fb} + kT/e$. This conclusion forms the justification for using this point to determine the flatband potential, as has been done in the results. From Eq. [3] and [5], it can be seen that, at given applied voltage, the relationship between the measured capacitance and f^{n+1} should be linear, the extrapolated value of the capacitance C_{ex} for $f^{n+1} \to 0$ being

$$C_{ex} = \epsilon_0\epsilon(\infty)[2\epsilon_0\epsilon(o)/eN_D]^{-1/2}(V - V_{fb} - kT/e)^{-1/2} \quad [8]$$

An experimental example is shown in Fig. 4 for a case where, from the frequency dependence of $R_s - b$, n was found to be equal to -1.18. It can be seen that the plot of C_s *vs.* $f^{-0.18}$ is indeed linear, permitting the determination of C_{ex} at $f^{-0.18} \to 0$, *i.e.*, at $f \to \infty$. Equation [8] implies that the plot of C_{ex}^{-2} *vs.* V should be linear. This point is confirmed experimentally as shown in Fig. 2a. As appears from Eq. [8], the slope of this linear plot equals

$$\Delta C_{ex}^{-2}/\Delta V = 2\epsilon(o)/\epsilon_0[\epsilon(\infty)]^2eN_D \quad [9]$$

By dividing this value by the slope of each individual

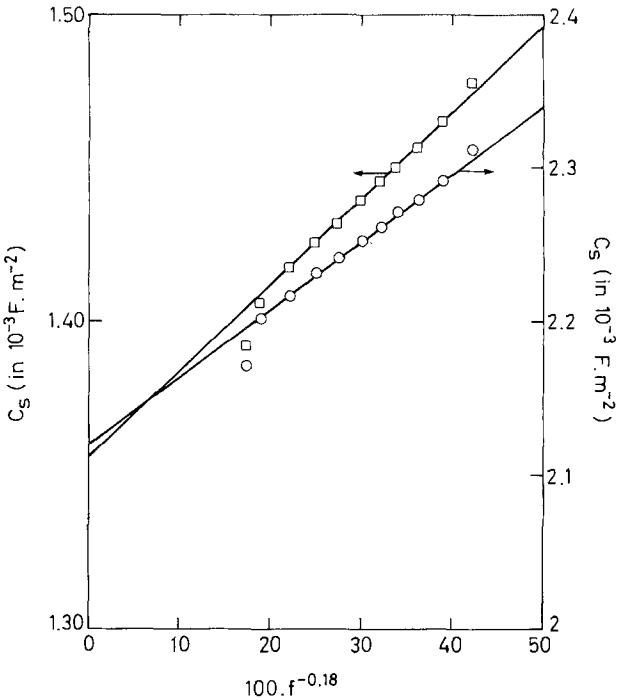


Fig. 4. C_s as a function of $f^{-0.18}$ for a sample with $n = -1.18$. □, At $V = +1.25$V *vs.* SHE (values on the ordinate on the left); ○, at $V = -0.15$V *vs.* SHE (values on the ordinate on the right).

Mott-Schottky plot registered at given frequency f, as given by

$$\Delta C_s^{-2}/\Delta V = 2\epsilon(o)\epsilon_0[\epsilon(f)]^2eN_D \quad [10]$$

(see Eq. [6]), the ratio $\epsilon(f)/\epsilon(\infty)$ can be deduced. In the frequency range of our experiments, this ratio varies from 1.18 at 130 Hz to 1.045 at 20,000 Hz, indicating that the frequency effect is relatively small in this frequency range.

Energy levels at the electrode surface.—In order to determine the position of the conduction bandedge E_c^s and of the valence bandedge E_v^s at the electrode surface, it is necessary to know not only the value of the flatband potential, but also that of the donor density N_D or the acceptor density N_A, respectively. Indeed, one has (12)

$$E_{F,fb}(n) = -eV_{fb}(n) \quad [11]$$

$$E_{F,fb}(p) = -eV_{fb}(p) \quad [12]$$

$$E_c^s(n) = E_{F,fb}(n) - kT\ln(N_D/N_c) \quad [13]$$

$$E_v^s(p) = E_{F,fb}(p) + kT\ln(N_A/N_v) \quad [14]$$

$$\Delta E_g = E_c^s - E_v^s \quad [15]$$

In these formulas, $E_{F,fb}(n)$ and $E_{F,fb}(p)$ represent the position of the Fermi level at flatband potential in the n- or p-type material, respectively, N_c and N_v the effective density of states of the conduction band and of the valence band, respectively; N_c and N_v were calculated to be approximately 10^{25} m^{-3} from a literature value for the effective mass of both electrons and holes in GaP being 0.5 × the electron mass (13). In Eq. [13] and [14], it is assumed that all donor levels are empty and all acceptor levels filled.

In view of the foregoing discussion, it is clear that difficulties arise in the determination of N_D or N_A from Mott-Schottky plots in case that the slopes are frequency dependent (see Eq. [10] for n-type). For the exact determination of N_D and N_A, the value of $\epsilon(o)$ and of the corresponding slope should be known which, as mentioned above, includes the contribution

of the dipoles causing the frequency effect observed here. Considering the fact that, in the frequency range studied, this effect is small, and assuming that the total effect over the entire frequency range is small also [*i.e.*, that $\epsilon(0)/\epsilon(\infty)$ is of the order of 1], the experimental results enabled us to determine the following approximation values for our samples: $N_D = 6 \times 10^{23}$ m^{-3} and $N_A = 1 \times 10^{23}$ m^{-3}. Note that the value for the n-type case is in satisfactory agreement with the specifications of the manufacturer, considering the fact that our results pertain to a thin layer underneath the surface only, and that the donor density distribution may be inhomogeneous.

The values of $E_{F,fb}$ at the given charge carrier concentration and of E_c^s and E_v^s, thus deduced from Eq. [11]-[15], are shown in Table I.

These results suggest that the semiconductivity type (n or p) has little influence on the structure of the Helmholtz layer at the GaP surface.

In view of the relatively low values of the dielectric constant of GaP, and of N_D and N_A in our samples, it is reasonable to assume that the fraction of the applied voltage change ($V - V_{fb}$) which occurs over the Helmholtz layer is negligible (14), so that the tabulated values of E_c^s and E_v^s can be considered to be fixed with respect to the SHE and hence to be also valid at voltages different from V_{fb}.

The high value calculated for $E_{F,fb}(n)$ is qualitatively in agreement with the high anodic band bending observed with the n-type GaP electrode at the rest potential and suggests that this electrode should yield high photovoltaic effects (15). Accordingly, preliminary measurements on this system yield a curve representing the photovoltage *vs.* the logarithm of the light intensity which, at a photovoltage of about 1V, does not show any saturation yet.

Table I. Energy levels at the GaP electrode surface

Energy level	Position (in eV *vs.* SHE) pH = 2.1 n	pH = 2.1 p	pH = 4.8 n	pH = 4.8 p
$E_{F,fb}$	+1.10	−0.83	+1.21	−0.67
E_c^s	+1.19	+1.29	+1.30	+1.45
E_v^s	−1.06	−0.96	−0.95	−0.80

Acknowledgments

The authors wish to thank Prof. Dr. W. Dekeyser for his continuous interest in this work. One of us (M. J. M.) thanks the "Instituut ter Aanmoediging van het Wetenschappelijk Onderzoek in Nijverheid en Landbouw" for a scholarship.

Manuscript submitted Dec. 16, 1976; revised manuscript received June 3, 1977.

Any discussion of this paper will appear in a Discussion Section to be published in the June 1978 JOURNAL. All discussions for the June 1978 Discussion Section should be submitted by Feb. 1, 1978.

Publication costs of this article were assisted by the Laboratorium voor Kristallografie en Studie van de Vaste Stof.

REFERENCES

1. R. Memming, *This Journal*, **116**, 786 (1969).
2. R. Memming and F. Möllers, *Ber. Bunsenges, Phys. Chem.*, **76**, 610 (1972).
3. H. Yoneyama, H. Sakamoto, and H. Tamura, *Electrochim. Acta*, **20**, 341 (1975).
4. E. C. Dutoit, R. L. Van Meirhaeghe, F. Cardon, and W. P. Gomes, *Ber. Bunsenges. Phys. Chem.*, **79**, 1206 (1975).
5. V. V. Eletskii, Ya. Ya. Kulyavik, and Yu. V. Pleskov, *Elektrokhimiya*, **3**, 753 (1967).
6. R. Dehmlow, P. Janietz, and R. Landsberg, *J. Electroanal. Chem.*, **65**, 115 (1975).
7. L. R. Plauger, *This Journal*, **121**, 455 (1974).
8. R. L. Van Meirhaeghe, E. C. Dutoit, F. Cardon, and W. P. Gomes, *Electrochim. Acta*, **21**, 39 (1975).
9. R. Memming and S. Schwandt, *ibid.*, **13**, 1299 (1968).
10. W. H. Laflère, R. L. Van Meirhaeghe, F. Cardon, and W. P. Gomes, *Surface Sci.*, **59**, 401 (1976).
11. W. H. Laflère, R. L. Van Meirhaeghe, F. Cardon, and W. P. Gomes, Submitted for publication to *This Journal*.
12. W. P. Gomes and F. Cardon, *Z. Phys. Chem. N.F.*, **86**, 330 (1973).
13. S. M. Sze, "Physics of Semiconductor Devices," Wiley-Interscience, New York (1969).
14. R. De Gryse, W. P. Gomes, F. Cardon, and J. Vennik, *This Journal*, **122**, 712 (1975).
15. H. Gerischer, *J. Electroanal. Chem.*, **58**, 263 (1975).

Kinetics of the Epitaxial Growth of Silicon from a Tin Melt

B. Jayant Baliga*

General Electric Company, Corporate Research and Development Center, Schenectady, New York 12301

ABSTRACT

The growth of epitaxial layers of silicon from a tin melt has been examined over a range of cooling rates (0.2°-7°C/min). It is found that at cooling rates below 1°C/min, the growth rate increases with cooling rate, while at higher cooling rates the growth rate saturates. This behavior is due to the transition from mass transport limited growth to surface kinetically controlled growth. This has been confirmed by the measurement of the variation in epitaxial layer thickness across the wafer with and without stirring, at both slow and fast cooling rates.

The chemical vapor deposition of expitaxial layers of silicon has been extensively studied (1, 2). In contrast, very little work has been reported on the epitaxial growth of silicon films from the liquid phase. D'Asaro *et al.* (3) have reported on the growth of epitaxial layers of silicon with tin and tin-lead as solvents. However, their work was aimed at reducing epitaxial layer defects, and no information on the growth kinetics was provided. More recently, Kim (4) has described the use of liquid epitaxial growth of silicon for the formation of silicon pedestals as ohmic contacts to planar-diffused diodes. This paper examines the growth rate of epitaxial layers of silicon for the case of growth from a tin melt by using the dipping technique.

The growth of layers from the liquid phase has the advantage of requiring lower temperatures as compared to vapor phase epitaxial growth. This is important in the fabrication of silicon devices, because it

* Electrochemical Society Active Member.
Key words: silicon, liquid phase epitaxy, growth kinetics.

minimizes the changes in prediffused regions during epitaxial growth, and also allows the growth of an abrupt interface between the epitaxial layer and the substrate. In addition, most metallic impurities are expected to have segregation coefficients of less than unity. Consequently, the growth of layers from the liquid phase is expected to have a low concentration of such impurities. This is desirable for the fabrication of devices requiring high minority carrier lifetime for achieving good device characteristics.

In this paper it is shown that the growth rate of silicon epitaxial layers from a tin melt depends upon the cooling rate. At slow cooling rates the growth is demonstrated to be mass transport limited, while at fast cooling rates the growth becomes kinetically controlled. These observations have been confirmed by growth rate measurements with and without stirring during the growth. The author believes that this is the first time that kinetically controlled growth has been experimentally observed during the growth of liquid phase epitaxial layers.

Experimental Conditions

Apparatus.—All the epitaxial growth reported in this paper was performed using tin as the solvent. Tin was chosen as a solvent because its incorporation into the silicon during epitaxial growth does not introduce either shallow doping levels or deep lying recombination centers. Further, the solubility of silicon in tin, at growth temperatures of around 950°C, is sufficient to allow the growth of thick layers (up to 100μ) without serious depletion of the melt. High purity tin (5*N* purity) was cleaned in the laboratory by repeated heating in a quartz tube under vacuum until the impurities formed a slag on its surface, followed by removal of this slag by etching in concentrated hydrochloric acid.

The tin melt was heated to growth temperatures in a quartz crucible with a hydrogen ambient. The epitaxial reactor, as illustrated in Fig. 1, consisted of a quartz tube with a gate valve on top connecting the tube to a stainless steel baffle chamber. The melt was always maintained in a stream of hydrogen flowing from the bottom of the tube towards the top. This hydrogen was purified using a palladium diffuser to minimize contamination. The temperature of the melt was maintained to within ±1°C using a controller with a

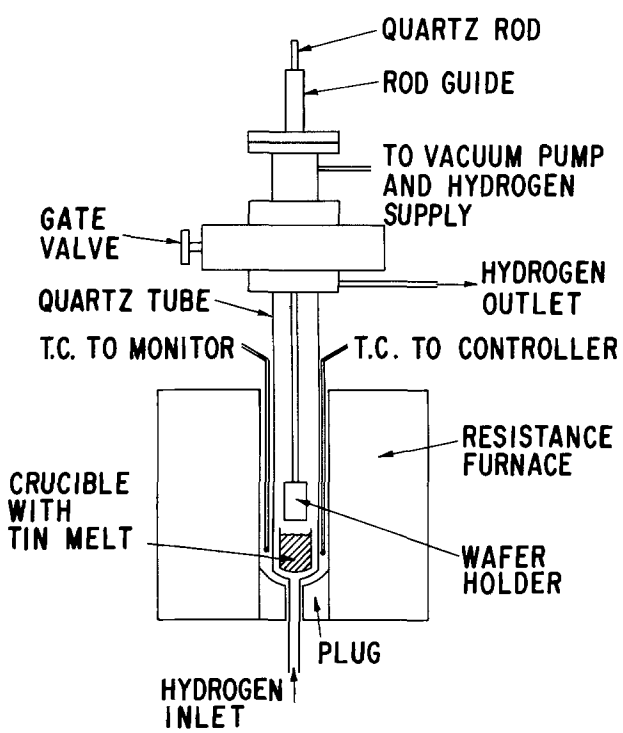


Fig. 1. Schematic diagram of liquid epitaxial growth system

Pt/Pt-Rd thermocouple to control the power fed to the furnace elements. The temperature of the melt was monitored by using another Pt/Pt-Rd thermocouple placed outside the quartz tube and positioned at the center of the crucible as shown in Fig. 1. The emf of this external monitor thermocouple was calibrated to the melt temperature by inserting a Pt/Pt-Rd thermocouple (in a quartz tube) into the melt, and maintaining the melt at various temperatures.

Growth Procedure.—The substrates and saturation wafers were inserted into the melt using quartz holders with a graphite bolt and nut assembly which held the wafer between quartz surfaces. The quartz holder was first inserted into the rod guide and the flange bolted to the baffle chamber to form a vacuum tight fit with an o-ring. The baffle chamber was then evacuated and backfilled with hydrogen. The gate valve was then opened to allow lowering of the holder into the melt.

Prior to each growth, the melt was saturated using a 100 Ω-cm, phosphorus-doped, float zone silicon wafer. During saturation the melt was stirred by oscillation of the quartz holder about a vertical axis. The saturation was conducted until no further loss in the weight of the saturation wafer could be detected. It was observed that 0.47g of silicon were required to saturate a fresh 99g tin melt at 950°C. This is in good agreement with the 2 atomic percent (a/o) solubility of silicon in tin at this temperature (5). After each epitaxial growth, the silicon in the melt was replenished using the same procedure.

The epitaxial layers were grown on (111) oriented, 0.01 Ω-cm, boron-doped silicon substrates. The growth was conducted on the polished face of the wafers as received from the vendor. The wafers were degreased and given a dip in hydrofluoric acid just before loading into the reactor. The substrate temperature was brought up to the melt temperature by holding the wafer above the melt for 10 min. The wafer was then inserted into the melt and the temperature of the melt lowered at known cooling rates ranging from 0.2° to 7°C/min. The fastest cooling rate of 7°C/min was achieved by turning off the power to the furnace for the duration of the growth. The growths reported in this study were conducted with no supersaturation of the melt, *i.e.*, the melt was always saturated at the temperature at which the substrate wafer was introduced into the melt. Growth times ranging from a few minutes up to several hours were used, depending upon the cooling rate, to achieve undercooling of the melt of up to 100°C. In all cases, the epitaxial growth was initiated at 950°C. After the growth period, the substrate was first removed from the melt and then the furnace cooling terminated to avoid any possible melt-back effects. Some tin was usually found to be present on the bottom edge of the wafer after growth. This tin was removed by etching in aqua regia.

The layers grown in this study were observed to be of n-type conductivity because the melt was saturated with phosphorus-doped wafers. Since the growth was conducted on p-type substrates, the epitaxial layer could be defined by angle-lapping and delineating the junction with a copper sulfate solution. The epitaxial layer thickness was then measured using an interferometer. Using this procedure, the epitaxial layer thicknesses were measured to within ±0.2μ. In the absence of stirring, the thickness of the epitaxial growth was found to be within ±10% over the entire wafer. With stirring, the layer thickness was found to vary radially from the axis of rotation as explained in the discussion section of the paper. All the results given in the next section were obtained without any stirring of the melt.

Experimental Results

The variation of the epitaxial layer thickness was measured as a function of both cooling rate and the time duration of the growth. The five different cooling rates that were used in this study were 0.2°, 0.5°,

0.75°, 2.5°, and 7°C/min. The fastest cooling rate of 7°C/min was achieved by turning off the power to the furnace. At the slowest cooling rate setting of 0.2° C/min, the cooling rate was found to vary from run to run, and ranged from 0.165° to 0.25°C/min. Such variations were not observed at the higher cooling rates.

Figure 2 shows the variation in the epitaxial layer thickness as a function of the growth time with cooling rate as parameter. In this figure, the cooling rate of 0.2°C/min represents data points taken with cooling rates ranging from 0.165° to 0.25°C/min. As can be seen in this figure, the layer thickness increases linearly with growth time at each cooling rate. It is, therefore, possible to define a growth rate corresponding to each cooling rate. It is also observed that this growth rate increases with increasing cooling rate until a cooling rate of 2.5°C/min is reached, beyond which no further increase in growth rate occurs.

As seen in Fig. 2, thin epitaxial layers are formed for short growth periods (less than 30 min.) at low cooling rates. With longer cooling durations at these low cooling rates, thicker epitaxial layers can be achieved. An interesting correlation between epitaxial layer thickness and undercooling (temperature drop during the growth interval) is observed for such layers as shown in Fig. 3. It is observed that the layer thickness increases linearly with the undercooling. Further, the epitaxial layer thickness grown for any specific temperature drop during growth is independent of the cooling rate, as long as the cooling rate is less than 1°C/min. In this case it is possible to define a constant layer thickness per degree centigrade of undercooling. Thus, at the low cooling rates, the same layer thickness is obtained per degiee centigrade of temperature drop. This change in growth kinetics from fast to slow cooling rates is discussed below.

Discussion

The mechanisms that control the growth rate during flux growth have been reviewed by Elwell (6), and discussed in more detail by Scheel and Elwell (7), and by Gilmer *et al.* (8). The process of crystal growth from solution may be treated as a combination of the following steps: (*i*) transport from the bulk solution by diffusion, convection, or forced flow, (*ii*) volume diffusion through a boundary layer, (*iii*) adsorption on the crystal surface, (*iv*) surface diffusion to a step, (*v*) attachment at a step, (*vi*) diffusion along the step, and (*vii*) integration into the crystal at a kink in the step. The first two steps in the process are regarded as mass transport processes, while the remaining steps are governed by surface kinetics. If the surface kinetic mechanisms are rapid compared with the mass transport flow, the growth rate will become mass transport limited. In this case, if a linear gradient of solute is considered to exist over a boundary layer thickness δ normal to the surface, the growth rate is given by (6)

$$v = \frac{D\sigma n_e}{\rho\delta} \qquad [1]$$

where D is the solute-effective diffusion coefficient, ρ is the density of the crystal, n_e is the equilibrium solute concentration, and σ is the supersaturation. For the case of a linear dependence of solute solubility upon temperature, and this is indeed true for the case of silicon dissolved in tin over a temperature range of 800°-950°C under which the growths in this study were conducted (5), and a constant cooling rate, C, the growth rate is given by

$$v = \frac{D}{\rho}\frac{kC}{\delta} \qquad [2]$$

where k is a proportionality constant. Thus, the thickness grown per unit time will be proportional to the temperature drop per unit time, or in other words, the epitaxial layer thickness will be proportional to the temperature drop. Thus, at low cooling rates, when the surface kinetics are rapid compared with mass transport, the epitaxial layer thickness will vary in proportion to the temperature drop, irrespective of the cooling rate. This is observed for the experimental results obtained for cooling rates of 0.2°, 0.5°, and 0.75° C/min, as shown in Fig. 3. Similar results have been observed in the case of the growth of GaAs from a Sn-GaAs solution by Mitsuhata (9).

With increasing cooling rates, the mass transport rate will increase correspondingly and will eventually exceed the surface kinetic limited growth rate. Once the growth rate becomes kinetically controlled, the epitaxial layer thickness will be proportional to the time duration of the growth, irrespective of the cooling rate. This is observed for the layers grown in this study at cooling rates of 2.5° and 7°C/min, as illustrated in Fig. 2.

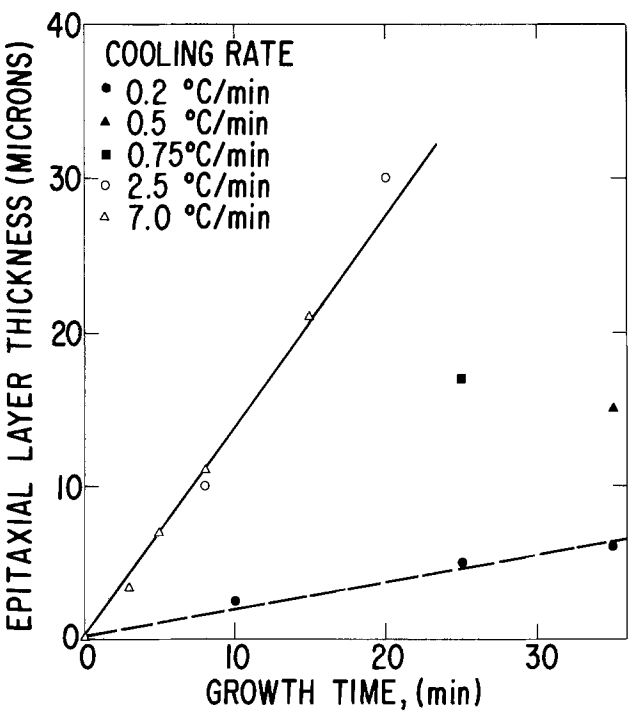


Fig. 2. Experimentally observed variation in the epitaxial layer thickness with growth time, cooling rate as parameter.

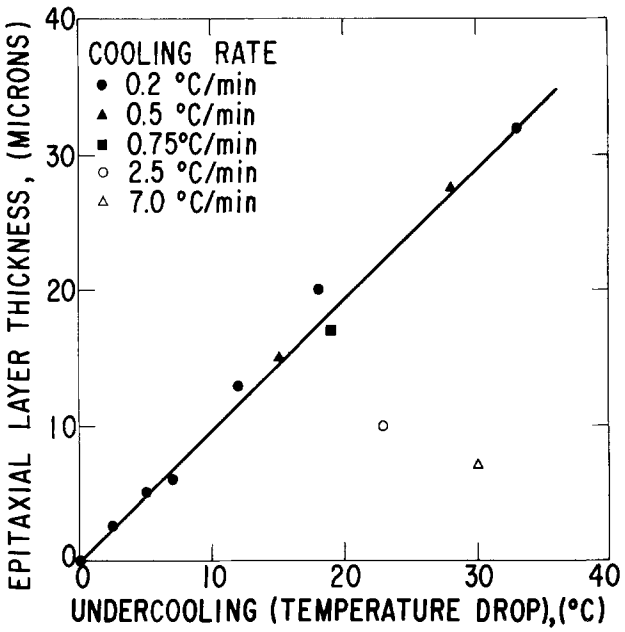


Fig. 3. Experimentally observed variation in the epitaxial layer thickness with undercooling, cooling rate as parameter.

Thus, as the cooling rates increases, the growth rate will increase in proportion to the cooling rate as long as the growth rate is mass transport limited, and then saturate with cooling rate once the growth rate becomes limited by surface kinetics. Figure 4 shows the variation in the growth rate as a function of the cooling rate for the data presented earlier in Fig. 2 and 3. It is observed that up to cooling rates of less than 1° C/min, the growth of the silicon epitaxial layers in this study occurred under mass transport limited conditions, while growths at cooling rates above 2°C/min occurred under kinetically controlled conditions. The cooling rate at which this transition occurs is a function of the size and geometry of the crucible as well as the substrate holder.

In order to confirm these observations, additional experiments were conducted with stirring of the melt. To achieve the stirring, the substrate holder was rotated about a vertical axis using a rotation cycle consisting of 3 revolutions per minute for 10 sec, followed by reversal of the direction of rotation. Since the substrate was rotated about a vertical axis near its center, the boundary layer thickness was considerably reduced at the edges of the wafer as compared with the middle. Thus, under mass transport controlled growth conditions, the epitaxial layer thickness at the edges of the wafer should be higher than at the axis. This was indeed observed at slow cooling rates. A typical example of the variation in the layer thickness as a function of distance from the axis of rotation for a cooling rate of 0.5°C/min is shown in Fig. 5C and 5D. It is observed that, without stirring (Fig. 5C), layer thickness at the edges is within ±10% of the thickness at the axis, and there is no systematic variation in thickness from one edge to the other. In contrast, with stirring (Fig. 5D), it is observed that the layer thickness at the edges is about three times greater than at the axis.

Under kinetically controlled growth conditions, the reduction in boundary layer thickness should not change the growth rate at the edges of the wafer. Indeed it is observed in Fig. 5A and 5B that there is no systematic change in epitaxial layer thickness from the edge of the wafer to the axis of rotation. both with or without stirring at a cooling rate of 7°C/min.

Conclusions

The growth rate of epitaxial layers of silicon grown from a tin melt have been examined at cooling rates ranging from 0.2° up to 7°C/min. It is observed that at slow cooling rates the layer thickness varies linearly with undercooling, while at fast cooling rates the layer thickness varies linearly with time, in each case, irrespective of the actual cooling rate. This is because at slow cooling rates the growth is mass transport controlled, while at fast cooling rates surface kinetics control the growth rate. These observations have been confirmed by measurement of the variation in the epitaxial layer thickness across the wafer, with and without stirring, at both slow and fast cooling rates. At present, using this liquid epitaxial growth system, silicon layers of up to 100μ in thickness have been grown with growth rates in excess of 1μ per minute. This technique for epitaxial growth of silicon layers is currently under investigation for the fabrication of devices.

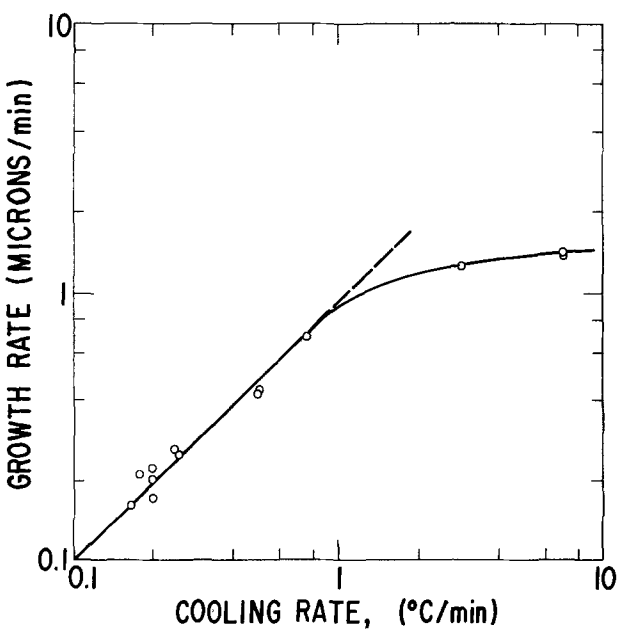


Fig. 4. Variation of the growth rate with cooling rate. Notice the saturation in the growth rate at high cooling rates.

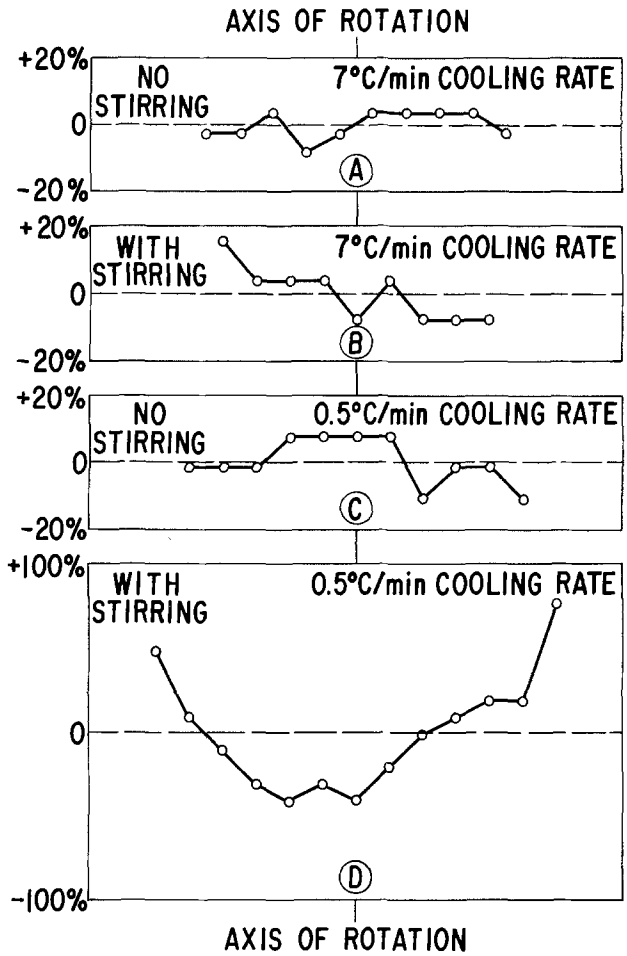


Fig. 5. Measured variation in the epitaxial layer thickness, radially across the wafer from the axis of rotation, for cooling rates of 0.5° and 7°C/min, with and without stirring.

Acknowledgments

The author wishes to thank Gerald B. Gidley for the preparation of the epitaxial layers, and K. Westerlund for assistance in manuscript preparation.

Manuscript received March 4, 1977. This was Paper 115 presented at the Philadelphia, Pennsylvania, Meeting of the Society, May 8-13, 1977.

Any discussion of this paper will appear in a Discussion Section to be published in the June 1978 JOURNAL. All discussions for the June 1978 Discussion Section should be submitted by Feb. 1, 1978.

Publication costs of this article were assisted by General Electric Company.

REFERENCES

1. R. R. Haberecht and E. L. Kern, in "Semiconductor Silicon," R. R. Haberecht and E. L. Kern, Editors,

The Electrochemical Society Softbound Symposium Series, Princeton, N.J. (1969).
2. C. P. Marsden, "Silicon Device Processing Symposium," National Bureau of Standards (1970).
3. L. A. D'Asaro, R. W. Landorf, and R. A. Furnanage, in "Semiconductor Silicon," R. R. Haberecht and E. L. Kern, Editors, p. 233, The Electrochemical Society Softbound Symposium Series, Princeton, N.J. (1969).
4. H. J. Kim, *This Journal*, **119**, 1394 (1972).
5. C. D. Thurmond and M. Kowalchik, *Bell. Syst. Tech. J.*, **39**, 169 (1960).
6. D. Elwell, in "Crystal Growth," by B. R. Pamplin, Editor, Chapter 6, Pergamon Press, Elmsford, New York (1975).
7. H. J. Scheel and D. Elwell, *This Journal*, **120**, 818 (1973).
8. G. H. Gilmer, R. Ghez, and N. Cabrera, *J. Cryst. Growth*, **8**, 79 (1971).
9. T. Mitsuhata, *Jpn. J. Appl. Phys.*, **9**, 90 (1970).

Pseudostable MNOS Structures

L. A. Kasprzak,* A. K. Gaind,* and A. Hornung

IBM System Products Division, East Fishkill Facility, Hopewell Junction, New York 12533

ABSTRACT

Thick oxide MNOS structures as studied by Frohman-Bentchkowsky and Lenzlinger exhibit a flatband shift (ΔV_{fb}) which saturates with time at bias. We have studied a MNOS structure (300Å of nitride and 300Å of oxide) with low conductivity nitride (10^{-8}A cm^{-2} at 4×10^6V cm^{-1}, 373°K) which exhibits an increase in the rate of flatband voltage shift (ΔV_{fb}) after an apparent saturation. This effect was observed on long time (2650 hr) bias-temperature stress. Typical times to reach apparent saturation at 85°C varied from 200 to 1000 hr at 15 and 8.5V, respectively. At 165°C and 15V, the initial saturation almost merges with the subsequent rate increase of ΔV_{fb}. Processing, characterization, and the bias temperature stress results for these structures are discussed. We propose that the stored charge is distributed throughout the Si_3N_4 rather than only at the SiO_2-Si_3N_4 interface.

The memory effect in MNOS structures with a thin (<30Å) SiO_2 layer is a well-known phenomena. In memory MNOS structures, the mechanism of charge buildup is indicative of charge injection from the silicon. The charge buildup at the oxide-nitride interface is thought to cease when the conduction current in the oxide (Jo) is equal to that in the nitride (Jn) (1). This paper deals with MNOS structures in which the oxide thickness is significantly greater than the maximum thickness for tunneling (*i.e.*, >> 30Å). It is our purpose to show that the presently accepted mechanism of charge buildup at the oxide-nitride interface is inadequate. We demonstrate the inadequacy of previous theory when specifically applied to MNOS structures in which the oxide and nitride are both ~300Å.

The first difference encountered was a change in the sign of the charge at the nitride-oxide interface. This was expected. It is consistent with the mechanism proposed herein: for the case of thick (>> 30Å) SiO_2 under the nitride, the charge is injected from the metal electrode rather than the silicon. Subtleties not expected from previous theory (1) were also observed; for example, opposite asymmetries in the amount of stored charge for short and long time bias-temperature stress, and an eventual increase (EI) in the rate of flatband voltage shift (ΔV_{fb}) sometime after apparent saturation (see Fig. 1).

Sample Preparation

The dual dielectrics (oxide-nitride) were formed on n-Si (100) wafers that had been ion implanted such that half of the wafer was phosphorous doped and the other half was boron doped. After annealing (to activate the implanted species) and an oxidation drive-in at 1050°C, surface concentrations were 1×10^{16} phosphorous and 8×10^{16} boron. Next, all existing oxide was removed and the wafers were cleaned in hot deionized water at 85°C (10 min), followed by 10 min in hot (120°C) H_2SO_4:HNO_3 (3:1) mixture, and followed by 5 sec dip in 10:1 dilute HF. The wafers were then rinsed in running deionized water (10 min) and spin dried. The wafers were hydrophobic (~8Å SiO_2, as measured by ellipsometry) after the above cleaning.

The thermal oxide (~300Å) was then grown in O_2 with 3% HCl at 1050°C. After a 15 min anneal in N_2 at 1050°C, the Si_3N_4 (~300Å) was deposited using the system of Gaind *et al.* (2) at 1000°C (110 liters min^{-1} H_2, 60 cm^3 min^{-1} SiH_4, and 800 cm^3 min^{-1} NH_3). Finally, blanket aluminum (resistance-heated source) was deposited on the back side, and 0.5 mm diam (nominal) aluminum dots were deposited on the dual dielectric. Postaluminum annealing was performed in N_2 for ½ hr at 400°C.

Sample Properties

The Si_3N_4 properties for films ~1000-3500Å were measured on <100> silicon wafers which were cleaned

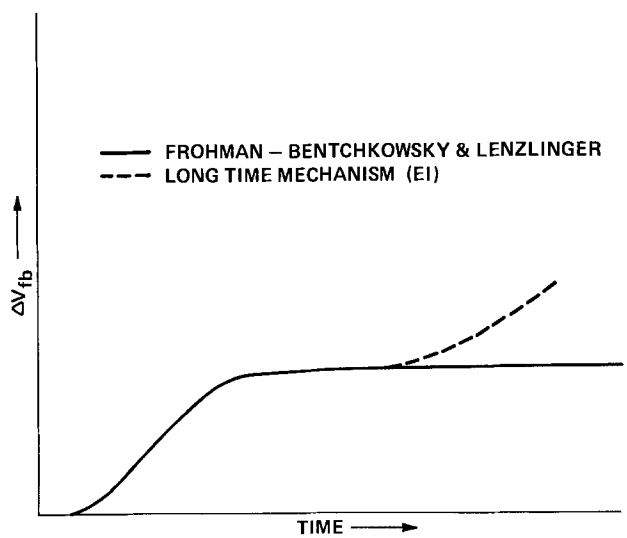


Fig. 1. Flatband voltage shift (V_{fb}) vs. time

* Electrochemical Society Active Member.

Key words: thin films, thick oxide structures, MNOS structures, dual dielectrics.

in the same manner as the MNOS wafer prior to oxide growth. The Si_3N_4 index of refraction was 2.02 ± 0.01 fpr at a 5460Å wavelength. Its etch rate in 49% HF was 100 ± 10Å min^{-1}. The infrared absorption spectra, measured in transmission mode, showed a broad peak at ~835 cm^{-1}, indicating that there was no SiO_2 under the nitride film (3). In conjunction with the MNOS samples, some MNS (~300Å Si_3N_4) samples were prepared. The dielectric constant of the Si_3N_4 was ~8 (determined from C_{max} in accumulation), and the average breakdown field was 8.5 × 10^6 Vcm^{-1}. The current density (J) *vs.* voltage (V) was measured at 100°C for Si_3N_4 thicknesses of ~250 and 646Å (Fig. 2).

The conductivity of the as-deposited Si_3N_4 is quite low, and compares with 3000Å films previously reported (3-5). The MNS and MNOS fast-state density near midgap was measured using the quasistatic technique of Kuhn (6) as modified after Castange (7) and Kerr (8) (*i.e.*, we used the high frequency C-V trace from accumulation to inversion as ideal). The MNS and MNOS structures exhibited midgap fast-state densities of $<1 \times 10^{11}$ cm^{-2} and $<1 \times 10^{10}$ cm^{-2}, respectively (Fig. 3 and 4). Fixed and mobile charges

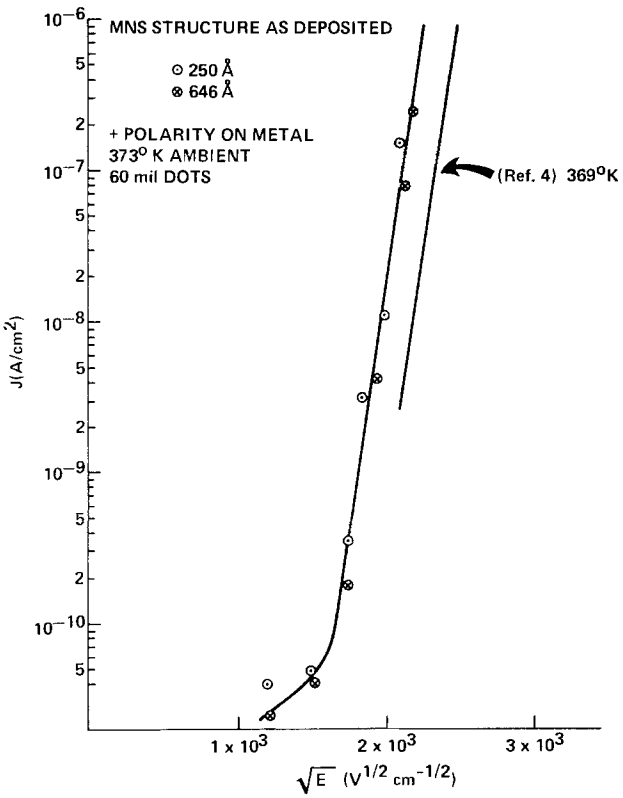


Fig. 2. Current density (J) *vs.* applied field (E) at 373°K

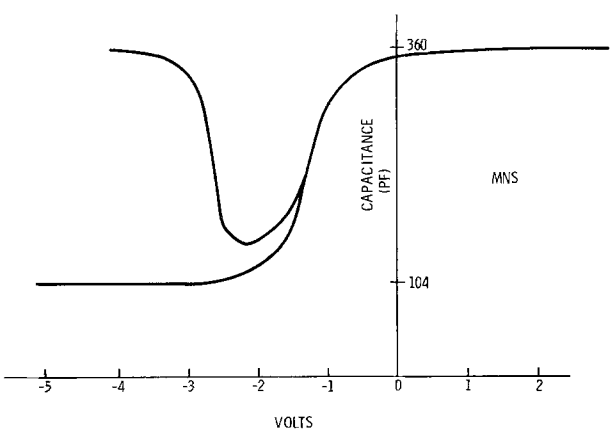


Fig. 3. Quasistatic and 1 MHz C-V curves for MNS structures

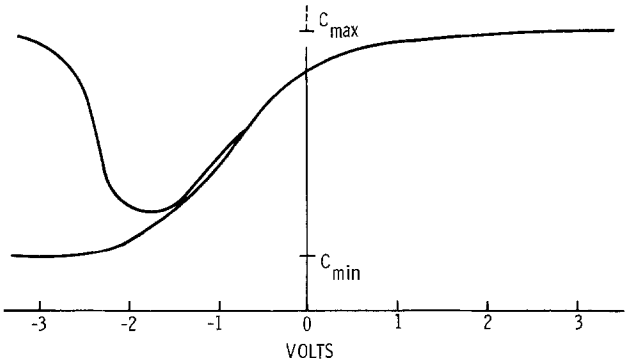


Fig. 4. Quasistatic and 1 MHz C-V curves for MNOS structures

in the MNOS structures were 5-10 × 10^{10} cm^{-2} and 2-5 × 10^{10} cm^{-2}, respectively. Mobile charges were confirmed using MOS structures processed simultaneously at oxidation and metal deposition.

Bias-Temperature Stressing (BTS) and Measurement Technique

The MNOS and MNS structures were subjected to bias-temperature stress in inversion at 85°, 125°, and 165°C. Bias voltages of 8.5, 12, and 15V were applied to the aluminum dots with the back side aluminum grounded. The change in flatband voltage (ΔV_{fb}) was determined at discrete read-out times by an automatic tester which measured device leakage, capacitance in accumulation (C_{max}), flatband voltage (V_{fb}), and capacitance at flatband (C_{fb}). The measurement of V_{fb} and C_{fb} was accomplished by use of a subroutine which calculated equivalent oxide thickness (t_{eq}) from the measured value of C_{max}. C_{fb} was then automatically computed from the calculated value of t_{eq} and the known Si surface doping level. The value of V_{fb} was measured by searching the C-V curve via automatic tester for the calculated value of C_{fb}. The complete test program with subroutines was used at each readout time with control devices prior to actual MNOS and MNS device measurements. Further, the complete test program was used at each readout on the MNOS and MNS devices to eliminate erroneous values of V_{fb} caused by degradation in device leakage or C_{max}. The repeatability of the automatic test system was ± 7 mV for V_{fb}. The stressing sequence consisted of a time zero readout prior to stress, application of stress bias, heating to stress temperature, BTS for time t_1, cooling to room temperature, removal of bias, readout, application of bias, heating to stress temperature, etc. Total BTS time was 2650 hr, with readouts at 15, 89, 185, 350, 722, 1050, 1548, 2052, and 2650 hr.

The specific bias and temperature conditions applied were: n-silicon −8.5 and −15V at both 85° and 165°C, −12V at 125°C; (for p-silicon +8.5 and +15V at both 85° and 165°C, and +12V at 125°C). As previously mentioned, all biases were applied to the metal dots with the silicon grounded. Since all of the devices at one bias and temperature were stressed in parallel, a 10 kΩ current-limiting resistor was placed in series with each device to prevent bias fluctuation in the event that a particular device shorted. Very few shorts were actually experienced. Sixteen devices were stressed per condition, which resulted in a total sample size of 160 devices. The flatband voltage shifts (ΔV_{fb}) reported are the average of all 16 devices at a particular stress condition. Excellent tracking was observed among the devices at a stress condition (<25 mV spread).

Results and Discussion

MNS structures.—The flatband shifts (Fig. 5) for the MNS structures are similar to those previously reported for MNOS tunneling structures (1). The sign

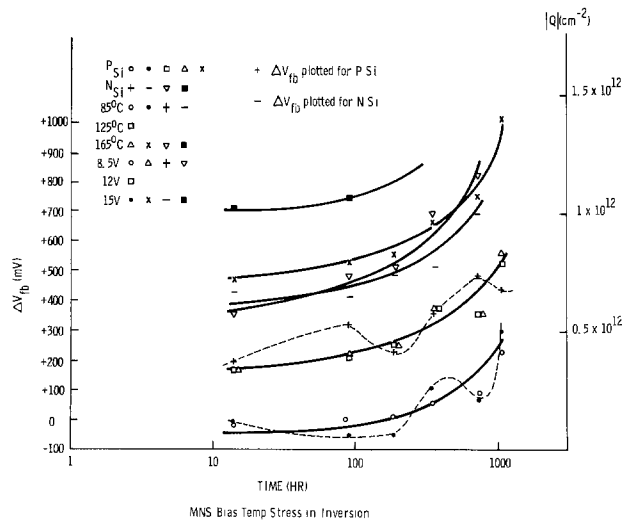


Fig. 5. Flatband voltage shift *vs.* time for MNS structures

of ΔV_{fb} is positive under positive bias and negative for negative bias. This characteristic is explained by tunneling of electrons from the Si to the Si_3N_4 for positive bias, and from the Si_3N_4 to the Si for negative bias. Oscillatory behavior in V_{fb} (dotted curves in Fig. 5) was also observed. This may be due to local variations in the conductivity of the Si_3N_4 which cause a large local change in the charge stored at the Si-Si_3N_4 interface, and in turn a nonuniformity in Si surface potential (ψ_s) at apparent V_{fb}. The subsequent reduction in V_{fb} could be due to lateral diffusion of the resulting charge near the Si-Si_3N_4 interface. This diffusion would result in a more uniform surface potential.

The absence of a saturation level of charge in the Si_3N_4 is an important result. It indicates that the stored charge in the Si_3N_4 is most likely distributed through the entire thickness of the Si_3N_4 after long time at large applied d-c fields. This is not unexpected for 300Å Si_3N_4 films (9). However, it may indicate a propensity in Si_3N_4 to attain a uniform level of charge through the film after a sufficient time under d-c bias. Most of the work on MNOS tunneling structures has been carried out under pulse conditions, and as a result the centroid of charge could be quite different for d-c bias conditions.

MNOS structures · (300Å Si_3N_4, 300Å SiO_2).—The charge buildup at a SiO_2-Si_3N_4 interface is expected to cease once the interface has sufficient charge to change the fields in the oxide and nitride such that continuity of current exists (1) (Fig. 6). However, for the MNOS structures we studied, saturation of SiO_2-Si_3N_4 interface charge was not observed.

From Grove (10), we know that for a MOS structure

$$V_{fb} = \phi_{ms} - \frac{Q_{ss}}{C_o} - \frac{1}{C_o}\int_o^{X_o} \frac{X}{X_o}\rho(x)\,dx \qquad [1]$$

where $\phi_{ms} = \phi_m - \phi_s$ (volts); ϕ_m = metal work function (volts); ϕ_s = silicon work function (volts); Q_{ss} = fixed charge in SiO_2 (cm^{-2}); C_o = oxide capacitance = $K_o\epsilon_o/X_o$ F/cm^2; $\rho(x)$ = distributed charge in SiO_2 (cm^{-3}); X_o = oxide thickness (cm); K_o = dielectric constant of $SiO_2 \approx 4$; $\epsilon_o = 8.85 \times 10^{-14}$ Fcm^{-1}; and X = distance from metal. For a MNOS structure, this reduces to

$$V_{fb} = \phi_{ms} - \frac{Q_{ss}}{C_o} - \frac{1}{C_n}\int_o^{X_n} \frac{X}{X_n}\rho_n(x)\,dx \qquad [2]$$

where n refers to nitride parameters, and we finally obtain for charge at a nitride-oxide interface (Q_I). Then

$$Q_I = C_n\,\Delta V_{fb} \text{ and } C_n = \frac{K_n\,\epsilon_o A}{t_n} \qquad [3]$$

where K_n = dielectric constant of nitride $\simeq 8$; $\epsilon_o = 8.85 \times 10^{-14}$ Fcm^{-1}; A = area of Al dot (cm^2); and t_n = Si_3N_4 thickness (cm). The structures were biased in inversion, and in all cases injection from the contact was observed (note sign of ΔV_{fb} and Q_I in Fig. 7). The sign of Q_I in all cases was opposite to that observed in MNOS tunnel devices ($SiO_2 \leq 300$Å). We observed an apparent saturation of Q_I prior to 1000 hr of stress; however stressing to 2650 hr revealed a subsequent increase in Q_I. In addition, two asymmetries were observed; first, for stress time less than 100 hr Q_I was 5-10 times lower for negative bias than for positive bias; second, for stress time of about 1000 hr Q_I was $\simeq$2 times greater for negative bias than for positive bias. The asymmetries of Q_I for short time can be explained by an increase in oxide charge (Q_{ss}) at the Si-SiO_2 interface, such that

$$(Q_I) \text{ net} = Q_{ss} + \alpha Q_I \qquad [4]$$

where $\alpha = K_{ox}/K_n\ t_n/t_{eq}$; $t_{eq} = t_{ox} + K_{ox}/K_n\ t_n$; K_{ox} = dielectric constant SiO_2; and t_{ox} = oxide thickness (cm).

For negative bias on N-Si, Q_I is negative (Fig. 8). Drift VI (11) is known to result in positive charge at the Si-SiO_2 interface (Q_{ss}), and in increased fast state density N_{fs}. Hence, Q_{ss} reduces (Q_I) net for negative bias, and increases or does not reduce (Q_I) net for positive bias (Fig. 8).

Fast-state densities were measured (3) on all samples after completion of 2650 hr of stress. N_{fs} had increased to 10^{12} for the 165°C ± 15V samples after stress. All other samples had $N_{fs} \simeq 1\text{-}2 \times 10^{11}$. The long-term asymmetry of Q_I can be explained if we assume either that the contact injection is asymmetrical with bias polarity, or that for our Si_3N_4 the density of available traps is greater than the density of filled traps. Most likely some combination of both effects occurs. Slight discontinuities in the ΔV_{fb} *vs.* time plots were observed (arrows in Fig. 7). It is felt that these

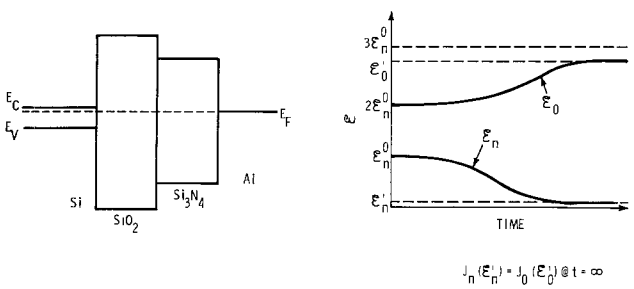


Fig. 6. Electric field (*E*) and current density (*J*) in 300/300 MNOS structure *vs.* time.

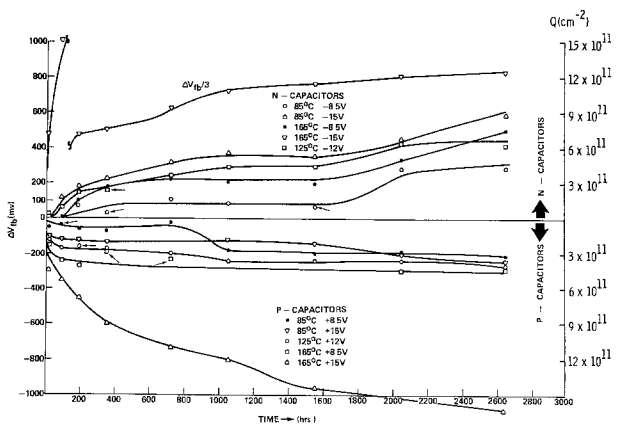


Fig. 7. Flatband voltage shift *vs.* time for MNOS structures. Top curve extends beyond scale. Data points beyond 100 hr are plotted at 1/3 value (*i.e.*, $\Delta V_{fb}/3$).

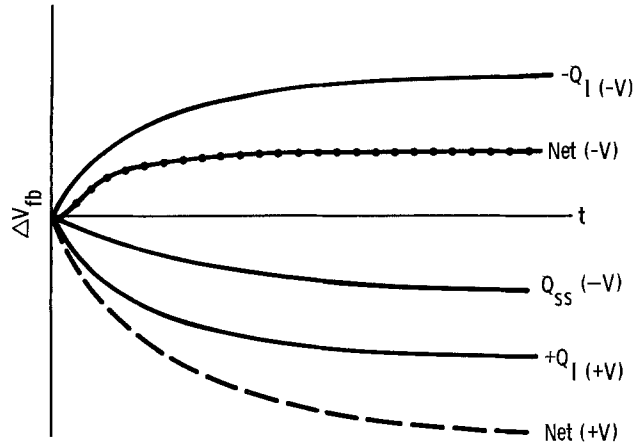


Fig. 8. Interface (Q_I), oxide (Q_{SS}), and net charge vs. time

are due to inadvertent charging or discharging of the sample as a result of handling between readouts.

It remains to discuss the eventual increase (EI) in the rate of flatband voltage shift (ΔV_{fb}) after apparent saturation. We assume that the apparent saturation takes place when $J_n = J_o$. However, it is important to remember that at no time does $J_n = 0$. The charge is most likely very close to the SiO_2-Si_3N_4 interface when $J_n \simeq J_o$. We suggest that the passage of the d-c current through the Si_3N_4 for a long time causes further trapping (detrapping) of charge under negative (positive) bias, and that this is the cause of the EI. The EI ceases when all available traps are filled or emptied (Fig. 9). The difficulty in characterizing the EI is that the charge responsible is populating or depopulating traps closer and closer to the metal. As a result, the sensitivity of ΔV_{fb} to this charge is a decreasing function of time. The bulk trap nitride charge density (assuming a constant bulk charge) obtained by integrating the $\rho_n(x)$ term in Eq. [2] was equated to the measured interface charge (Q_I)

$$\frac{\rho_n X_n}{2} = Q_I \qquad [5]$$

An approximation of the bulk-filled trap density[1] from Fig. 7 yields a bulk-filled trap density (t_B) of $\simeq 3 \times 10^{18}$ cm^{-3} at 2650 hr. Yun (9) has also been able to trap 3×10^{18} cm^{-3} charges in Si_3N_4. A further complication is that at 165°C the EI appears to merge with the initial saturation, with the result that the only evidence for the EI is the nonsaturating slope for long stress times. The EI has not saturated at 2650 hr, therefore we can place no upper bound on t_B for our Si_3N_4 films.

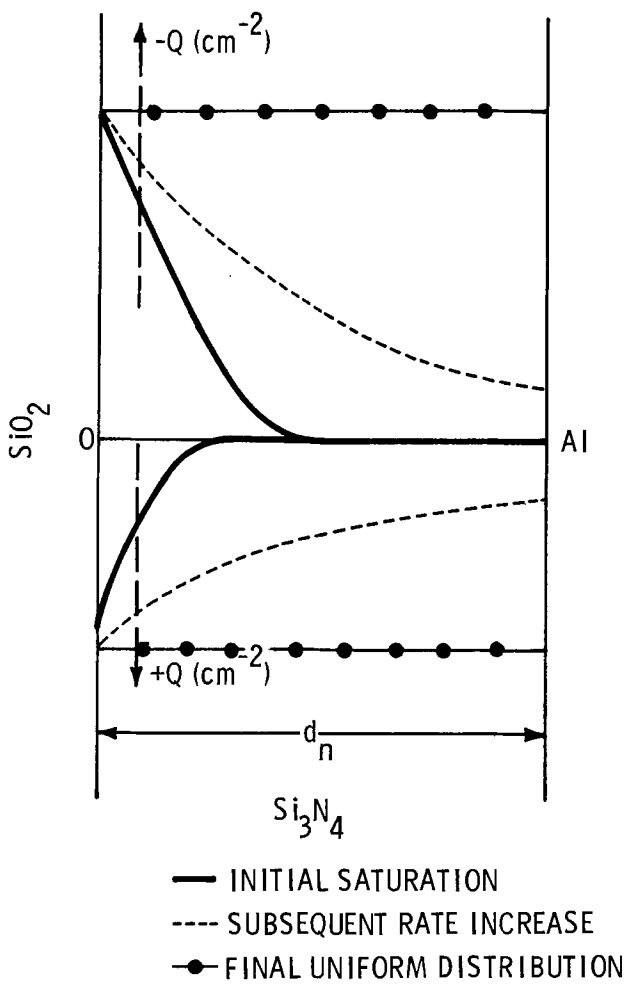


Fig. 9. Proposed charge distribution in Si_3N_4 at various times

Conclusions

An increase in the rate of charge storage (EI) some time after apparent saturation has been observed for MNOS structures with equal oxide and nitride thicknesses. The EI is probably due to charge distributed throughout the Si_3N_4 rather than at the SiO_2-Si_3N_4 interface. Certain asymmetries in the magnitude of the charge stored at various times under bias-temperature stress indicate an increase in oxide charge (Q_{SS}), the generation of fast states at the Si/SiO_2 interface, and higher density of available traps than filled traps for our Si_3N_4.

Acknowledgments

The authors wish to express gratitude to A. A. Kozul, H. Sheldon, and T. Williams who helped prepare samples, and to V. Blusnavage who built the bias-temperature stress fixtures. Special thanks go to Franco Motika for developing the automated test program.

Manuscript submitted Jan. 20, 1977; revised manuscript received June 13, 1977.

Any discussion of this paper will appear in a Discussion Section to be published in the June 1978 JOURNAL. All discussions for the June 1978 Discussion Section should be submitted by Feb. 1, 1978.

Publication costs of this article were assisted by IBM Corporation.

[1] At 2650 hr: $Q_I \simeq 4 \times 10^{12}$; $t_B \simeq \frac{2Q_I}{X_n} \simeq 3 \times 10^{18}$ cm^{-3}.

REFERENCES

1. D. Frohman-Bentchkowsky and M. Lenzlinger, *J. Appl. Phys.*, **40**, 3307 (1969).
2. A. K. Gaind, G. K. Ackermann, V. J. Lucarini, and R. L. Bratter, in Proceedings of the Fifth International Conference on Chemical Vapor Deposition, pp. 30-42 (1975).
3. V. Y. Doo, D. R. Kerr, and D. R. Nichols, *This Journal*, **115**, 61 (1968).
4. G. A. Brown, W. C. Robinette, Jr., and H. G. Carlson, *ibid.*, **115**, 948 (1968).
5. B. E. Deal, E. L. MacKenna, and P. L. Castro, *ibid.*, **116**, 997 (1969).
6. M. Kuhn, *Solid-State Electron.*, **13**, 873 (1970).
7. R. Castange and C. Y. Lebd, *Se'anc, Acad. Sci. (Paris)*, **267**, 866 (1968).
8. D. R. Kerr, Paper presented at the International Conferences on Properties and Uses of MIS Structures, Grenoble, France (1969).
9. B. H. Yun, *Appl. Phys. Lett.*, **25**, 340 (1974).
10. A. S. Grove, "Physics and Technology of Semiconductor Devices," p. 281, J. Wiley & Sons, Inc., New York (1967).
11. B. E. Deal, *This Journal*, **121**, 198C (1974).

Growth of Iron-Doped Epitaxial Layers for GaAs Field Effect Transistors

Kenya Nakai, Kuninori Kitahara, Akihiro Shibatomi, and Shinji Ohkawa

Fujitsu Laboratories Limited, Nakahara, Kawasaki, 211, Japan

ABSTRACT

Iron-doped GaAs epitaxial layers were grown using the $Ga/AsCl_3/N_2$ vapor phase system and with a new doping method. The characteristics of the iron-doped layer were investigated, and the layer was used as the buffer layer of the epitaxial layer for FET. It was found that the iron concentration in the epitaxial layer was proportional to the vapor pressure of the iron-doping gas ($FeCl_2$). The layer with a resistivity higher than 10^4 Ω-cm could be prepared without increasing the crystal defects and impurities except iron. It was observed that the electrical characteristics of the submicron active layer on the chromium-doped substrate were improved by the insertion of the iron-doped buffer layer between the active layer and the substrate. It was found that the performance of FET's fabricated of the epitaxial layer was the iron-doped buffer layer was higher than the performance of those without the buffer layer.

Recent developments of GaAs microwave devices require a high quality epitaxial layer to improve device performance. For planar devices such as field effect transistors (FET's) and Gunn effect logic devices, n-type epitaxial layers grown on semiinsulating substrate doped with chromium are used. It has been reported that the electrical characteristics of the epitaxial layer are abnormal near the interface between the layer and the substrate (1-3), and that insertion of a buffer layer between the layer and the substrate is effective in improving the device performances (4-8). Hence, growth techniques for the buffer layer, which was an undoped high purity layer (4, 5) or chromium-doped high resistivity layer using chromyl chloride (9), were applied.

These techniques require extremely close control on the growth conditions to obtain high resistivity and a good epitaxial layer surface. For practical applications, a simpler growth method for the buffer layer is desirable. It has been reported that an epitaxial layer with a high resistivity (10^4-10^5 Ω-cm) can be obtained by iron doping, and the activation energy of a deep iron level is estimated to be about 0.5 eV (10-12). This suggests the possibility of using the iron-doped layer as a buffer layer, but it has never been realized. It is therefore significant to investigate this possibility.

The iron doping method reported previously (10) is not suitable to buffer layer growth which must be able to grow the buffer and the active layer without interruption. We have developed an iron-doping method to grow the high resistivity buffer layer and the active layer sequentially, and to minimize iron contamination in the active layer. In this paper, we describe the doping method and the characteristics of the iron-doped epitaxial layer. It is demonstrated that the epitaxial layer with a high resistivity of 10^5 Ω-cm can easily be obtained with high reproducibility. Effects of insertion of the iron-doped layer between the chromium-doped substrate and the active layer on the electrical characteristics of the active layer are reported. Further, as an application, metal-semiconductor field effect transistors (MESFET's) were fabricated by using an epitaxial wafer with or without the iron-doped buffer layer, and their characteristics were compared.

Experimental Procedure

Epitaxial layers were grown from the $Ga/AsCl_3/N_2$ system. The growth conditions were similar to those reported previously (13). A schematic diagram of the growth apparatus with the iron- and sulfur-doping system is shown in Fig. 1. The iron doping was performed by introducing iron chloride ($FeCl_2$) vapor into the reactor during epitaxial growth. $FeCl_2$ was formed by the reaction of iron (Fe) and hydrogen chloride gas (HCl) as follows: $Fe + 2HCl = FeCl_2 + H_2$. HCl gas was produced by the decomposition of $AsCl_3$ in a hydrogen ambient. High purity iron powder of 99.99% was employed as the iron source. The vapor pressure of $FeCl_2$ was controlled by adjusting the temperature of the iron source (370°-550°C). The flow rates of the doping gas and the total gas in the reactor were 20 and 1000 ml/min, respectively. The doping gas line between the iron source and the reactor was usually maintained at a higher temperature than the iron source to prevent deposition of $FeCl_2$.

The iron-doped layer with high resistivity can be used as a buffer layer for a sulfur-doped active layer on the chromium-doped substrate. For this purpose, sequential growth of the iron-doped layer and the sulfur-doped layer was carried out by changing the doping gas of the iron chloride to sulfur. The doping level of sulfur was controlled by adjusting the temperature of the sulfur source.

Electrical characteristics of the epitaxial layer; carrier concentration N, Hall mobility μ, and resistivity ρ, were determined by the Schottky diode capacitance method (14), and Van der Pauw's method (15). In the determination of the resistivity of the iron-doped layer, the effect of parallel conductance of the chromium-doped substrate was taken into account. The temperature dependence of the resistivity of the iron-doped layer was measured in the temperature range of −10°-200°C.

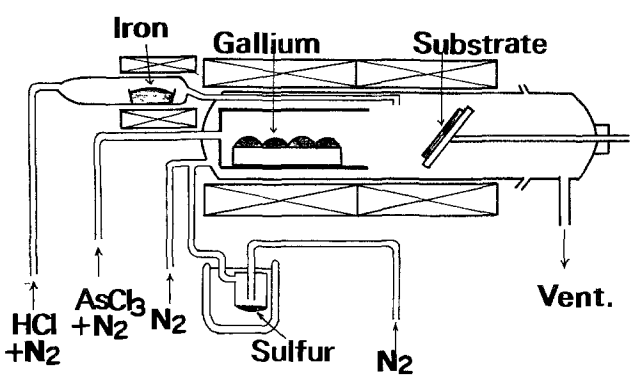


Fig. 1. Vapor phase epitaxial growth apparatus of the iron-doped GaAs layer and the sulfur-doped active layer for FET.

Key words: gallium arsenide, epitaxial growth, iron doping, high resistivity GaAs, and buffer layer.

Power MESFET's were fabricated by using the epitaxial wafers with or without the iron-doped buffer layer. D-c and high frequency characteristics of the FET's were measured. The fabrication process and the measurement method of the characteristics were similar to those in a previous paper (16).

Results and Discussions

The iron-doped epitaxial layer.—Figure 2 shows the electron concentration of the iron-doped layer as a function of the iron source temperature. Background electron concentrations of samples A, B, C, and D were adjusted to 1-2 $\times$ 10^{14}, 0.7-1 $\times$ 10^{15}, 8-10 $\times$ 10^{15}, and 2-3 $\times$ 10^{16} cm^{-3}, respectively, by sulfur doping. As the background electron concentration is increased, the temperature of the iron source is increased in order to obtain a high resistivity layer, that is, low carrier concentration.

Figure 3 shows the photoluminescence spectra at 4.2°K for three kinds of GaAs crystal, (a) undoped high purity epitaxial layer, (b) chromium-doped substrate, and (c) iron-doped layer. The measurement method was similar to that reported previously (17). The edge emission of the high purity epitaxial layer, of which Hall mobility at 77°K is 1.3 $\times$ 10^5 $cm^2V^{-1}sec^{-1}$, is split into several peaks as shown in (a). The relative intensities of donor-acceptor pair emissions, which have been found to relate with carbon and zinc (17, 18) to the edge emission, are low. The spectrum of the chromium-doped crystal grown from the GaAs melt shown in (b) suggests that this crystal contains much unknown impurity or crystal defects since the band-edge emission is broad and another broad emission is observed near the bandedge (19). The edge emission of the iron-doped layer is split, and the relative intensities of donor-acceptor pair emissions are almost the same as those of high purity layer shown in (c). These results show that the iron-doped layer contains shallow acceptors and crystal defects similar to those of the high purity layer. Therefore, it is considered that the concentration of impurities (except iron) and the density of crystal defects are low enough to use the iron-doped layer as a buffer layer on the chromium-doped substrate.

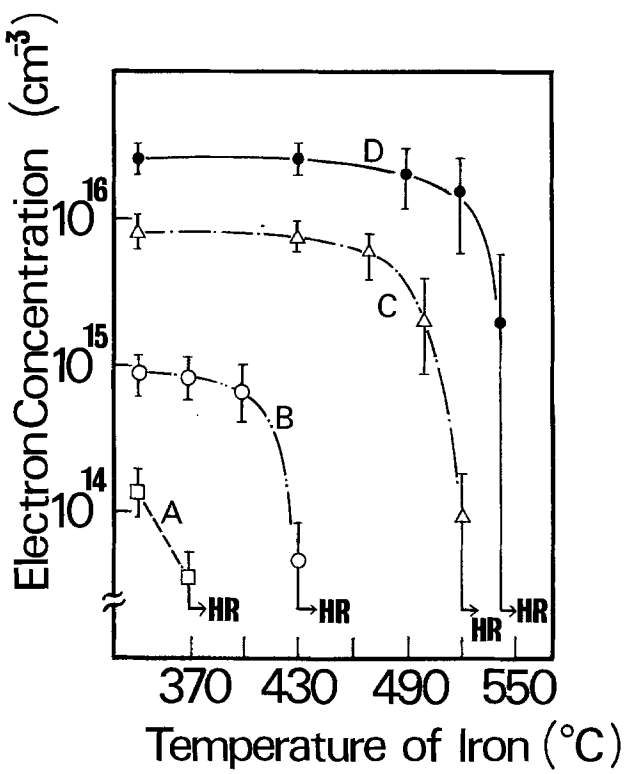


Fig. 2. Electron concentration as a function of the temperature of the iron source. The background electron concentration was adjusted by the sulfur doping: A, 1-2 $\times$ 10^{14}; B, 0.7-1 $\times$ 10^{15}; C, 8-10 $\times$ 10^{15}; and D, 2-3 $\times$ 10^{16} cm^{-3}. HR indicates that the layer is highly resistive.

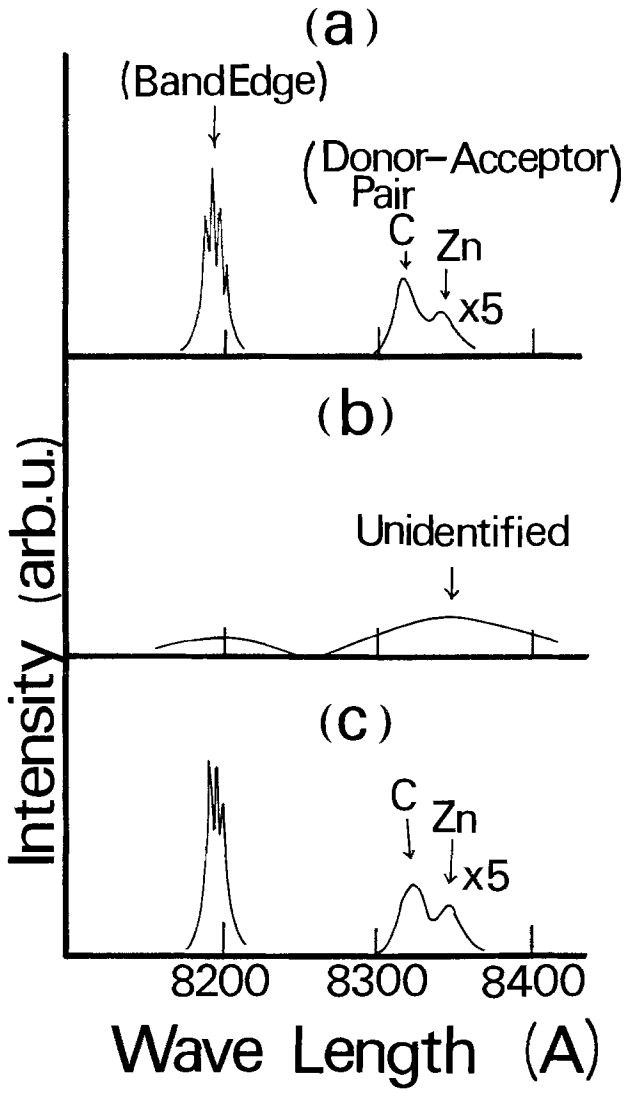


Fig. 3. Photoluminescence spectra measured at 4.2°K. (a) Undoped high purity epitaxial layer; (b) chromium-doped semi-insulating substrate; (c) heavily iron-doped epitaxial layer.

It has been reported that iron acts as a deep level acceptor or two deep acceptors in GaAs crystal (10-12, 20-23). It is surmised, therefore, that the decrease of the electron concentration by iron doping, as shown in Fig. 2, is caused by compensation of the deep acceptors.

It was observed that the iron source was usually covered with solid $FeCl_2$ after the doping experiment. When the temperature of the doping gas line between the iron source and the reactor was lowered below that of the iron source, the solid $FeCl_2$ was observed near the lowest position. In this case, the compensation level depended on the temperature of the lowest position of the line rather than on the iron source temperature. This indicates that the doping gas is saturated with $FeCl_2$ vapor and the amount of the $FeCl_2$ introduced into the reactor is controlled by the saturation vapor pressure determined by the temperature.

Figure 4 shows the compensation level by the iron doping as a function of $FeCl_2$ concentration in the vapor phase. The compensation level was estimated from the difference between the background electron concentration and the electron concentration of the iron-doped layer. The iron concentration in the vapor phase was calculated from the vapor pressure data presented in Ref. (24) and the ratio of the doping gas flow rate to the total gas flow rate (20/1000). This figure indicates

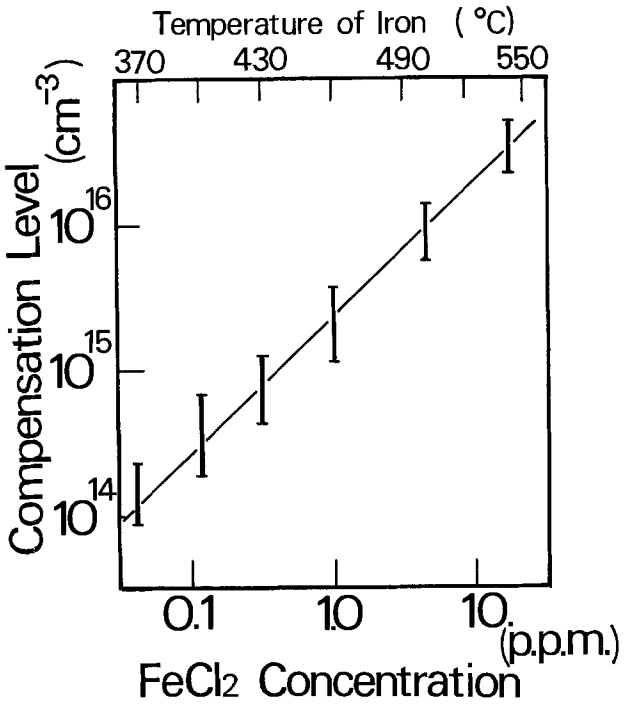


Fig. 4. The compensation level by the iron doping as a function of the $FeCl_2$ concentration in vapor phase. The compensation level was estimated from the difference between the electron concentration of the iron-doped layer and the background electron concentration. The $FeCl_2$ concentration was calculated from the saturation vapor pressure data.

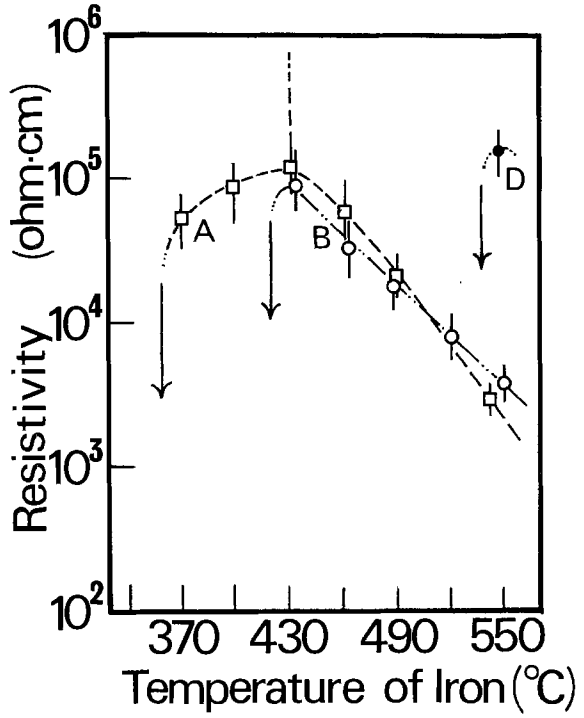


Fig. 5. The resistivity of the iron-doped layer as a function of the iron source temperature. The background electron concentration; A, 1-2 × 10^{14}; B, 0.7-1 × 10^{15}; D, 1-2 × 10^{16} cm^{-3}. Arrows indicate the temperature where the resistivity scatters between the undoped level and 10^4 Ω-cm.

that the compensation level is almost proportional to the $FeCl_2$ concentration.

As the iron concentration is increased beyond the background electron concentration, the layer becomes highly resistive. Figure 5 shows the resistivity of the iron-doped layers as a function of the iron source temperature. The background electron concentrations of the samples are similar to those in Fig. 2. Arrows indicate temperature where the resistivity scatters between the background electron concentrations of the undoped layer (less than 1. Ω-cm) and about 10^4 Ω-cm across the wafer or from run to run. This shows that the background electron is not entirely compensated for by the iron deep acceptors, and that the carrier concentration of the iron-doped layer strongly depends on the dispersion of the background electron concentration at these temperatures. The resistivity is almost in the range 10^4-10^5 Ω-cm, which agrees with the results reported previously (10-12), in perfectly compensated doping range.

In a semiconductor doped with a deep acceptor, the hole concentration p is approximately given by the equation (12)

$$p \simeq \left(\frac{N_t}{N_d - N_a} - 1\right)\frac{N_v}{g}\exp\left(-\frac{E_t}{kT}\right) \qquad [1]$$

under the condition of $p << (N_d - N_a) < N_t$ where N_t, N_d, N_a, N_v, g, and E_t are the concentrations of the deep level acceptor and the shallow level donor and acceptor, the state density of the valence band, the degeneracy factor associated with the deep level, and the activation energy of the deep level, respectively. Therefore, the decreasing inclination of the resistivity with the increase of the iron concentration, shown in Fig. 5, can be explained by using the above equation. That is, the concentration of the deep acceptor N_t increases as the iron concentration is increased.

Figure 6 shows the temperature dependence of the resistivity of the iron-doped layer. The doping condition and the results from Hall measurement for the samples are summarized in Table I. The high resistivity of samples A and B resulted in large measurement errors of their Hall coefficients. Hence, the Hall mobility of these samples is not listed in Table I. Hall mobility of samples A and B, however, is estimated to be larger than 350 cm^{2}V^{-1}sec^{-1} by extrapolation of the Hall mobility of samples C, D, and E to higher resistivity range.

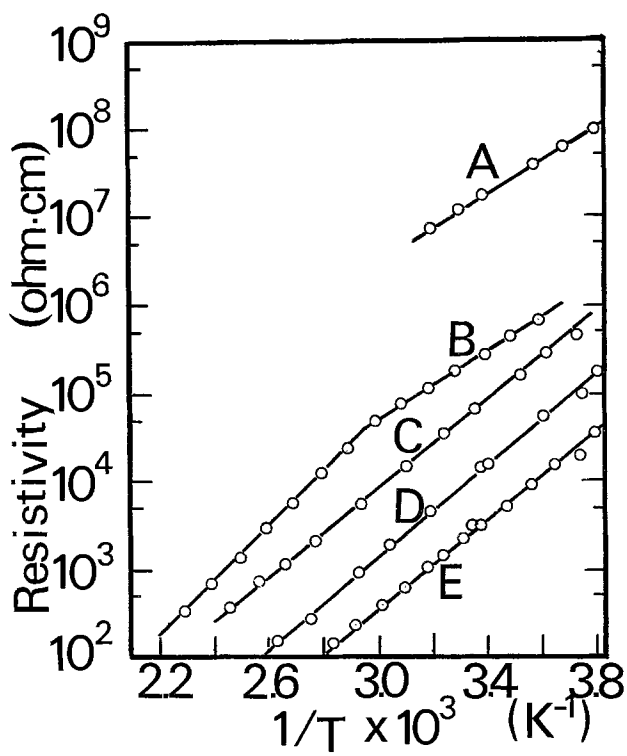


Fig. 6. The temperature dependence of the resistivity of the iron-doped layer. The doping condition of the samples is shown in Table I.

Table I

Sample	Iron temperature ($FeCl_2$ concentration) (°C, ppm)	Hall measurement at room temperature		
		Resistivity Ω-cm)	Hole concentration (cm^{-3})	Hole mobility (cm^2/V sec)
A	430 (0.5)	10^7	—	—
B	430 (0.5)	2×10^5	—	—
C	460 (1.0)	7×10^4	2×10^{11}	400
D	500 (5.0)	1×10^4	1.3×10^{12}	430
E	540 (15.0)	3×10^3	5.1×10^{12}	450

The iron concentration doped in the layer increases from sample A to E, since the iron temperature was increased in this order. For the sample with a higher doping level, the thermal activation energy of the resistivity is about 0.5 eV, which corresponds to the results reported previously (10, 12, 20). For the lightly doped samples, the activation energy is estimated to be about 0.35 eV near room temperature. This energy of about 0.35 eV is similar to the energy of the iron deep level determined from electroluminescence measurement (21). We have reported that two deep levels related with iron are observed in photoconductivity measurements of the iron-doped layer (25). The activation energies of the resistivity of the iron-doped layer observed here agree with those obtained by the photoconductivity measurement. This corresponds to a suggestion that iron acts as two deep acceptors in GaAs crystal (11, 22, 23).

The characteristics of the sulfur-doped layer on the iron-doped layer.—The iron-doped layer with high resistivity was applied to a buffer layer of a n-type layer (active layer) grown on semiinsulating substrate. Effects of the iron-doped buffer layer on the characteristics of the active layer were studied. The iron-doped layer, which was 4-5 μm thick, and had a resisivity of 5-10 $\times$ 10^4 Ω-cm, was grown on the chromium-doped substrate. After stopping the iron-doping gas, sulfur vapor was introduced into the reactor. Thus, by changing only the doping gas, sequential growth of the buffer and the active layers was performed without interruption.

Figure 7 shows concentration profiles of electron (A) and iron on the epitaxial layer which was grown at 720°C at a growth rate of 0.11 μm/min. The profile (B) represents the background electron concentration. The iron concentration was estimated from the temperature of the iron source using the relation between the compensation level and the iron source temperature shown in Fig. 4. The growth with iron doping was carried out for 37 min, after which epitaxial growth was continued for 23 min, corresponding to a layer thickness of 2.5μ. Within a depth of 2μm from the surface, profile (A) is flat and its level coincides to the background, as shown in Fig. 7. Since the iron doping effects on the characteristics of the epitaxial layer can be neglected in this region, the effects to be considered are within the 0.5μ region near the interface, that is, about 5 min after stopping the doping gas. The diffusion length of iron is estimated to be much smaller than 0.5 μm, hence, 5 min may be needed to exhaust the doping gas from the reactor. In order to prevent the iron contamination in the active layer, sulfur doping of the active layer must be started at more than 5 min after ending growth of the iron-doped layer.

Figure 8 shows the profiles of electron mobility μ measured with the Hall-bars with Schottky barrier (3) and the density of deep level N_t determined from the transient capacitance of the Schottky barrier (26). The measurements were carried out for two samples.

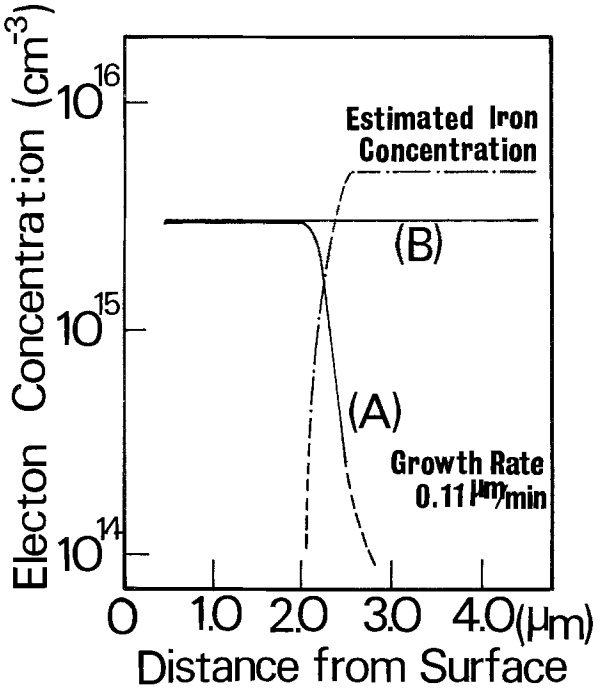


Fig. 7. Profiles of the electron concentration and the iron concentration. (A) Epitaxial layer grown sequentially on the iron-doped layer after stopping the iron doping gas; (B) background electron concentration.

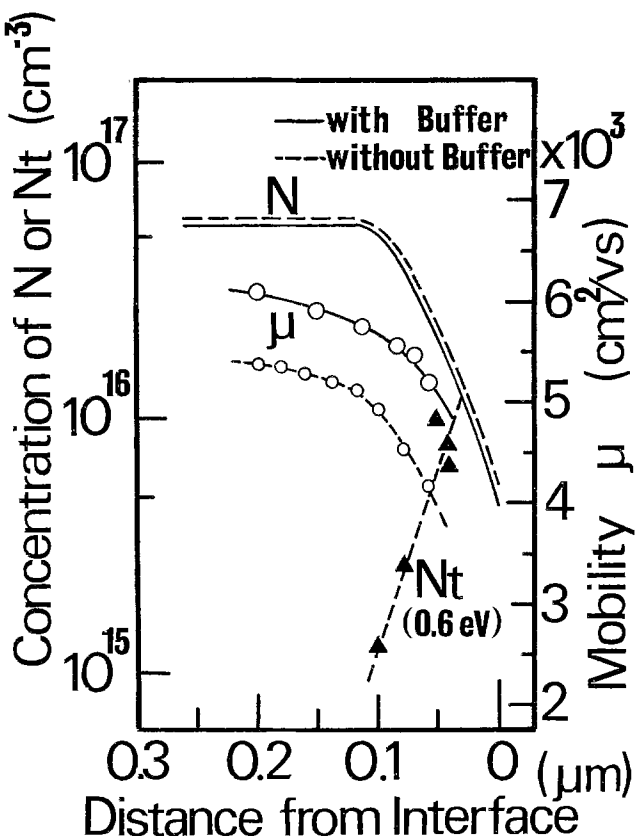


Fig. 8. Profiles of the carrier concentration, Hall mobility, and density of the deep level in the submicron active layer for FET's.

One of the samples has the sulfur-doped active layer of 0.3μm thick grown directly on the chrominum-doped substrate. The other active layer, whose thickness and carrier concentration were similar to those of the sample without the buffer layer, was grown on the iron-doped layer (5μm thick) without interruption. In the growth procedure of the latter sample, the sulfur-dop-

ing gas was introduced at 6 min after stopping the iron-doping gas.

Figure 8 indicates that the insertion of the buffer layer improves the mobility by about 20%. This improvement is considered to be due to a reduction of the space charge which is introduced at the initial stage of the epitaxial growth (3). It is observed that a deep level exists in the interface region between the active layer and the substrate. The thermal activation energy of this deep level was estimated to be about 0.6 eV, and its density was more than 10^{16} cm^{-3} near the interface. On the other hand, in the active layer grown on the iron-doped layer, any deep level could not be detected by this measurement. It is therefore suggested that the iron-doped buffer layer prevents the formation of the deep level at the initial stage of the epitaxial growth, as well as diffusion from the substrate into the active layer.

Application to the FET.—As shown in the previous section, the electrical characteristics of the active layer are found to be improved by the insertion of the iron-doped buffer layer between the active layer and the chromium-doped substrate. In this section, we describe the improvements of the device performance of GaAs FET by using the epitaxial wafer with the iron-doped buffer layer. The geometries and the fabrication processes of the FET are similar to those reported previously (16).

It has been reported that the high frequency characteristics of the GaAs FET strongly depend on the characteristics of the substrate, and that the substrate can be evaluated by change in resistivity caused by heat-treatment (27). The substrate wafers employed in this study were thus sliced from a narrow portion of the same ingot. Before epitaxial growth, differences of the characteristics among these substrate wafers were investigated. Randomly selected wafers were heated at 830°C for 30 min in nitrogen ambient. This heat-treatment corresponds to the heating process of the epitaxial growth. Then, ohmic contact pairs 10μm apart and 650μm wide were formed on the heat-treated surface. The voltage-current measurement on these substrate wafers indicated that the current was about 0.1 mA at 15V, and the dispersion of the current among the substrate wafers or across the wafer was within 30%. It is taken into consideration that this dispersion of *I-V* characteristics makes little dispersion on the high frequency characteristics of the FET from one wafer to another (27).

Figure 9 shows the *I-V* characteristics of the MESFET on the curve tracer. The hysteresis loops are observed in the source-drain currents of the FET (a), which were fabricated by using the epitaxial wafer without the buffer layer. The loops are eliminated in the FET (b), which was fabricated by using the wafer with the iron-doped buffer layer. Hower *et al.* have shown that the hysteresis loops are due to the electron traps in the interface region between the epitaxial layer and the substrate (1). It is therefore considered that the elimination of the hysteresis loops by the buffer layer corresponds to the reduction of the deep level near the interface.

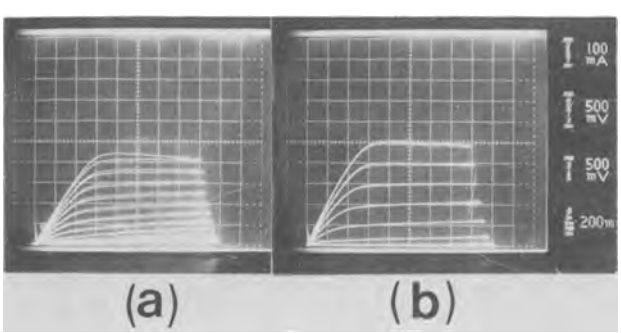


Fig. 9. Photographs of the I-V characteristics of the FET on the curve tracer. (a) FET without the buffer layer; (b) with the iron-doped buffer layer.

Figure 10 shows the characteristics of the FET's the transconductance g_m and the power gain at 6 GHz G, as a function of the carrier concentration of the active layer. The results were obtained for the MESFET's having a gate which was 1300μm wide. The error bar of each data point indicates the dispersion across the wafer (2 × 1.5 cm^2). The scattering among the data points is considered to be due to unknown parameters in the epitaxial growth and the fabrication processes.

The highest values of g_m and G are obtained in the FET's fabricated by using the epitaxial wafer with the iron-doped buffer layer at a certain carrier concentration. The average values of g_m and G of FET's with the buffer layer are higher than those of FET's without the buffer layer over the whole range of the carrier concentration. Therefore, g_m and G may be improved by the insertion of the buffer layer between the active layer and the substrate.

The transconductance of FET, g_m, is given approximately by the equation

$$g_m = A\mu N \qquad [2]$$

where A, μ, and N are the factors given by the structure and the geometries of the FET, the mobility of the carrier, and the carrier concentration of the active layer, respectively. Because the factor A is equal among all FET's in this study, it is suggested that the improvement of g_m by the buffer layer is due to the increase of the mobility. This corresponds to the result described in the previous section.

Summary

Iron-doped GaAs epitaxial layers were prepared by the $Ga/AsCl_3/N_2$ vapor phase growth system with a new doping method, and the characteristics of the layers were investigated. The results are summarized as follows:

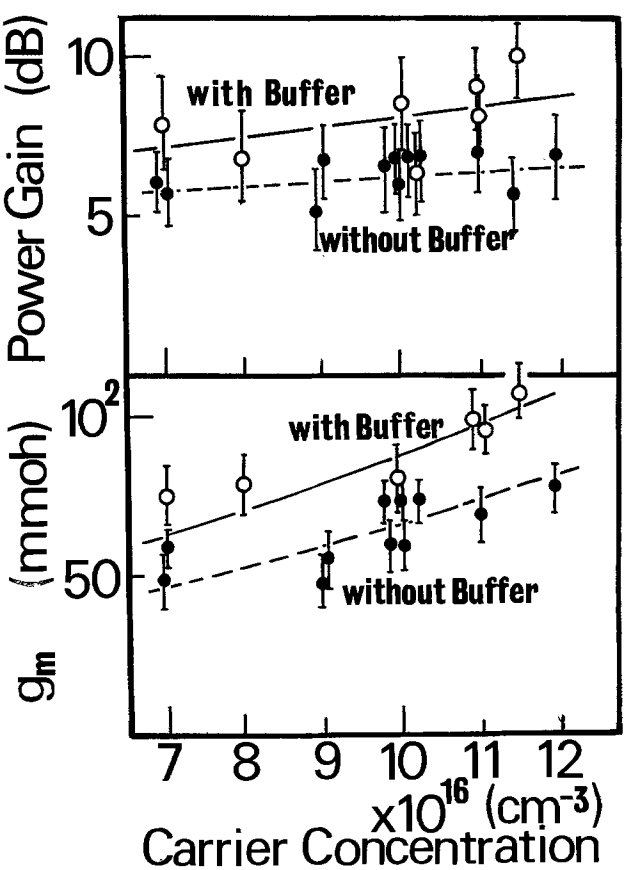


Fig. 10. The characteristics of MESFET's with and without the iron-doped buffer layer; the power gain at G6 GHz and the transconductance g_m.

1. When iron is introduced into the reactor as iron chloride vapor, iron is incorporated into the epitaxial layer proportional to the vapor pressure. A high resistivity layer can be obtained even if the background electron concentration is higher than 10^{16} cm^{-3}.
2. The concentration of shallow level acceptors and the density of crystal defects never seem to be increased by iron doping.
3. The resistivity of the iron-doped layer is in the range 10^4-10^5 Ω-cm, and depends on the $FeCl_2$ concentration in vapor phase.
4. The thermal activation energies of 0.5 and 0.35 eV are obtained by the temperature dependence measurement of the resistivity. The effects of the insertion of the iron-doped layer between the sulfur-doped active layer and chromium-doped substrate on the electrical characteristics of the active layer were investigated.
5. The insertion of the iron-doped layer as a buffer layer increases the Hall mobility in the active layer by about 20%, and eliminates the influence of the deep level which exists near the interface between the epitaxial layer and the substrate.
6. The insertion of the iron-doped buffer layer improves the characteristics of FET, the transconductance, and the power gain.

Acknowledgments

The authors wish to thank O. Ryuzan and K. Dazai for helpful discussions. They thank M. Ozeki and K. Nagata for the characterization of the epitaxial layers, and special thanks go to N. Yokoyama and M. Fukuta for providing data of the FET characteristics.

Manuscript submitted March 28, 1977; revised manuscript received June 24, 1977.

Any discussion of this paper will appear in a Discussion Section to be published in the June 1978 JOURNAL. All discussions for the June 1978 Discussion Section should be submitted by Feb. 1, 1978.

Publication costs of this article were assisted by Fujitsu Laboratories Limited.

REFERENCES

1. P. L. Hower, W. W. Hooper, D. A. Tremere, W. Lehrer, and C. A. Bittmann, in Proceedings of the International Symposium on GaAs, 1968, Institute of Physics, p. 187, London (1969).
2. G. Gotoh, O. Wada, S. Yanagisawa, and H. Takanashi, *Appl. Phys. Lett.*, **23**, 150 (1973).
3. A. Shibatomi, N. Yokoyama, H. Ishikawa, K. Dazai, and O. Ryuzan, *J. Cryst. Growth*, **31**, 240 (1975).
4. T. Nozaki, M. Ogawa, H. Terao, and H. Watanabe, in Proceedings of the Symposium on GaAs and Related Compounds, Institute of Physics, p. 46, Deauville, France (1974).
5. H. M. Cox and J. V. DiLorenzo, Paper presented at the 6th International Symposium on GaAs and Related Compounds, p. 4, St. Louis (1976).
6. B. S. Hewitt, H. M. Cox, H. Fukui, J. V. DiLorenzo, W. O. Schlosser, and D. E. Iglesias, Paper presented at the 6th International Symposium on GaAs and Related Compounds, p. 24, St. Louis (1976).
7. K. Kuroiwa, T. Aoki, and M. Fujimoto, *J. Cryst. Growth*, **24**, 229 (1974).
8. I. Durkier, R. L. Camisa, S. T. Jolly, H. C. Huang, and S. Y. Narayan, *Electron. Lett.*, **11**, 104 (1975).
9. O. Mizuno, S. Kikuchi, and Y. Seki, *Jpn. J. Appl. Phys.*, **10**, 208 (1971).
10. P. L. Hoyt and R. W. Haisty, *This Journal*, **113**, 296 (1966).
11. R. W. Haisty and G. R. Cronin, in "Proceedings of the 7th International Conference on the Physics of Semiconductors," p. 1161, Paris; Academic Press, New York (1965).
12. R. W. Haisty, *Appl. Phys. Lett.*, **15**, 208 (1965).
13. M. Ihara, K. Dazai, and O. Ryuzan, *J. Appl. Phys.*, **45**, 528 (1974).
14. J. Hillibrand and R. D. Gold, *RCA Rev.*, **21**, 245 (1960).
15. L. J. Van der Pauw, *Phillips Res. Rep. Suppl.*, **13**, 1 (1958).
16. M. Fukuta, K. Suyama, N. Yokoyama, and H. Ishikawa, in Proceedings of the 7th Conference on Solid State Devices, Tokyo (1975), [*Jpn. J. Appl. Phys. Suppl.*, **15**, 151 (1976)].
17. M. Ozeki, K. Nakai, K. Dazai, and O. Ryuzan, *Jpn. J. Appl. Phys.*, **13**, 1121 (1974).
18. M. Ozeki, K. Nakai, K. Dazai, and O. Ryuzan, *ibid.*, **12**, 478 (1973).
19. E. W. Williams and H. B. Bebb, in "Semiconductors and Semi-Metals," Vol. 8, R. K. Willardson and A. C. Beer, Editors, p. 321, Academic Press, Inc., New York (1972).
20. W. Plesiewicz, *Phys. Status Solidi A*, **16**, 485 (1973).
21. H. Strack, *Trans. Metall. Soc. AIME*, **239**, 381 (1967).
22. G. A. Allen, *Br. J. Appl. Phys., Ser. 2*, **1**, 593 (1968).
23. V. I. Fistul', L. Ya. Pervova, E. M. Omel'yanovskii, E. P. Rashevskaya, N. N. Solov'ev, and O. V. Pelevin, *Sov. Phys. Semicond. (Engl. Transl.)*, **8**, 311 (1974).
24. "Handbook of Chemistry and Physics," 54th ed, R. C. Weast, Editor, p. D-183, CRC Press (1973).
25. K. Kitahara, K. Nakai, M. Ozeki, A. Shibatomi, and K. Dazai, *Jpn. J. Appl. Phys.*, **15**, 2275 (1976).
26. N. Yokoyama, S. Ohkawa, T. Sakurai, T. Furuya, and H. Ishikawa, *Appl. Phys. Lett.*, **28**, 405 (1976).
27. J. Barrera, in Proceedings of the 5th Biennial Cornell Electrical Engineering Conference 1975, Cornell University, p. 135, Ithaca, New York (1975).

The Hot Corrosion of CoCrAlY Turbine Blade Coatings by Na_2SO_4 and Vaporous NaCl

R. L. Jones* and S. T. Gadomski

Naval Research Laboratory, Washington, D.C. 20375

ABSTRACT

To investigate whether unsaturated NaCl vapor can have effects in hot corrosion, experiments have been conducted wherein specimens cut from CoCrAlY-coated turbine blades were sprayed with Na_2SO_4 (1-2 mg/cm^2), and then exposed in a tube furnace at 1625°F under an air stream containing 300 ppm NaCl (1/20 the NaCl saturation pressure at 1625°F) with inspection and sulfate recoating every 24 hr. Several chloride effects were evident within 100-200 hr under this test regime. These included: (*i*) increasing the Na_2SO_4 vaporization rate; (*ii*) causing formation of a spalling Al_2O_3 surface oxide; (*iii*) removing Cr by the formation of volatile complexes which apparently contain S and Na as well as Cr and Cl; (*iv*) interacting with Ti at the coating-blade interface; and (*v*) accelerating sulfidation-oxidation attack upon the CoCrAlY coating. This latter attack occurs when both blade metal and coating are exposed simultaneously to the sulfate, as at a cut edge. It is confined to the CoCrAlY layer, and consists of a sulfidation front and oxidation front which traverse the coating successively, effectively stripping the coating from the supposedly less resistant blade alloy. Sodium chloride increases the kinetics of attack and appears to promote the formation of "Cr_3S_4" over CrAlS as the predominate sulfide phase. A search for chloride was made by energy-dispersive x-ray analysis in the SEM, but despite the obvious NaCl influences, no trace of chloride was found except possibly in the Ti interaction. The individual NaCl effects are discussed in relation to earlier research results and as they may pertain to shipboard hot corrosion.

Despite improved coatings and alloys, hot corrosion remains a limiting factor in the application of gas turbine engines for ship propulsion. Engine performance and endurance could be substantially improved if this problem were solved. Hot corrosion attacks the blades and vanes in the turbine section of the engine, and is generally considered to result from the buildup of molten sulfate films, principally Na_2SO_4, on these components. The sodium sulfate derives from sea salt ingested by the engine, either in the air or as a contaminant in the fuel. Sea water contains the equivalent of 3900 ppm Na_2SO_4 directly, and there is the possibility that NaCl (30,000 ppm) itself can react with sulfur in the fuel to produce additional Na_2SO_4.

Numerous hot corrosion investigations have been conducted and several mechanisms have been proposed (1), but it is still not clear whether or not NaCl, which is after all the major component of sea salt, has any significant role in hot corrosion. The English have been most active in this area, and they have accumulated considerable evidence, as reviewed by Conde (2, 3), that NaCl can be important, particularly at lower engine temperatures. Those who doubt the NaCl effect point out, however, that the vapor pressure of NaCl is so high that the turbine should be effectively exposed only to vapor-state NaCl, and NaCl or chloride per se is seldom found on corroded turbine components. These arguments are countered to a certain extent by reports that chloride-rich particles can in fact be found in corroded engines (4, 5), and by considering that NaCl may come to the blade surface mainly by impact of compressor salt particles (6) or droplets of sea water contamination in the fuel (7), rather than by condensation from the vapor phase. Nonetheless, it is still of interest to test the ideas implicit in the two arguments above, *i.e.*, that NaCl vapor should have no role in hot corrosion as long as its partial pressure is below the condensation pressure, and that the absence of a chloride residue proves that NaCl had no part in the corrosion process.

The experiments described below have therefore been conducted where the influences of NaCl vapor were investigated by comparison of the corrosion behaviors of Na_2SO_4-sprayed blade specimens exposed at 1625°F under flowing air, and under flowing air containing unsaturated NaCl vapor. Vaporous NaCl is known, mostly through the work of Hancock and associates (8), to corrode many turbine metals and alloys in the 1300°-1650°F range, but the effects of NaCl vapor over Na_2SO_4-coated specimens have been little studied, and little is known except for one suggestion (9) that the presence of a sodium sulfate film on the surface may provide protection against the action of vapor phase chloride.

Experimental

For the experiments, a two-zone hot tube furnace was devised (Fig. 1) wherein filtered air, after being bubbled through water, was flowed at a rate of 200 ml/min first over NaCl at 1400° ± 10°F, and then over the Na_2SO_4-sprayed blade specimen at 1625° ± 10°F. The NaCl and Na_2SO_4 were reagent grade chemicals, the boats were Alundum (TM), and the furnace was fitted with a fused silica liner. The thermocouple insulating tubing was used to position and withdraw the boats.

The 1625°F temperature was chosen as being high enough that hot corrosion could proceed readily, but not at such an overwhelming rate as to mask any NaCl effects which might be operative. It was also thought that this temperature, being very near the melting point of Na_2SO_4 (1623°F), might more readily make apparent any action of the NaCl which results from its lowering of the Na_2SO_4 melting point. The rationale in

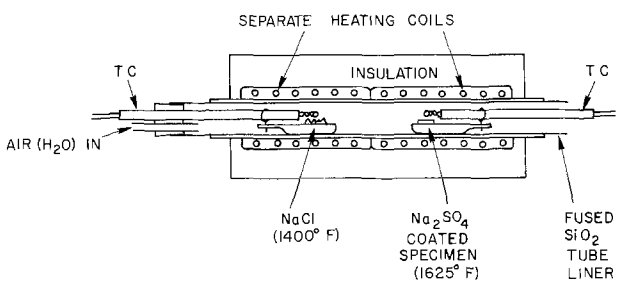


Fig. 1. Hot corrosion tube furnace apparatus

* Electrochemical Society Active Member.
Key words: hot corrosion, NaCl effects, CoCrAlY coating.

selecting the NaCl temperature was to begin with a low NaCl boat temperature (1200°F) and then raise it (and the NaCl input into the air stream) in progressive tests until chloride effects could be observed within reasonable times. At 1400°F, definite chloride manifestations were apparent within 100 hr exposure, and accordingly this temperature was adopted as the standard NaCl temperature.

The routine of testing was to spray the specimens, approximately 0.4 in. square, and cut from the blade with a dry tungsten carbide saw, with 1*N* Na_2SO_4 under a hot air gun, so as to deposit 1-2 mg/cm^2 of Na_2SO_4 on their surface. Then they were placed in the 1625°F zone of the furnace to be exposed to the flux of air, water vapor, and gaseous NaCl. Every 24 hr the specimens were removed, examined by light microscopy, and resprayed with Na_2SO_4. At the same time, the NaCl boats were removed and weighed so the NaCl loss per 24 hr could be determined. The NaCl weight losses averaged 0.1 ± 0.02 g per day, which at 200 ml/min air flow, corresponds to a NaCl concentration in the air of about 300 ppm, or a partial pressure of about 0.1 Torr. The equilibrium vapor pressure of NaCl is 0.16 Torr at 1400°F, and 1.8 Torr at 1625°F (10). The NaCl is therefore only approximately 1/2 saturated at 1400° and 1/20 saturated at 1625°.

It may not be accurate, however, to simply describe the specimen as exposed to 300 ppm NaCl, because appreciable reaction occurs between the NaCl vapor and the silica tube furnace liner, as evidenced by an opaque whitening and embrittlement of the silica. Hydrogen chloride is known to be generated when NaCl reacts with hot silica in the presence of water, and it is likely, therefore, that the air stream contained at least some HCl. Sizable NaCl deposits developed where the air cooled near the tube exit, indicating that the majority of chloride remained as gaseous NaCl, but even small amounts of HCl may accelerate the attack or have other unknown effects. This was a point of concern, but since HCl is predicted to be formed also in sea salt-contaminated turbines (11), it was ultimately concluded that the apparatus was adequate for the purpose, *i.e.*, to produce and study "NaCl" vapor phase corrosive effects as might occur in sea-going engines.

The blade specimens were cut from two unused marine turbine blades supplied through the auspices of J. W. Fairbanks of NAVSEC. The first blade, blade A, was a first-stage air-cooled blade fabricated from Rene' 80 (Ni-base; weight percent (w/o) 10Co, 14Cr, 3Al, 5Ti, 4Mo, 4W, 0.2C, with traces of B and Zr), and coated with BC21 (CoCrAlY containing nominally w/o 25Cr, 10Al, and 1Y). The second blade, blade B, was a second-stage blade made from IN738 (Ni-base; w/o 8.5Co, 16Cr, 3.4Al, 3.4Ti, 1.7Mo, 2.6W, 1.7Ta, and 0.9Cb), and coated with PWA268 (CoCrAlY, w/o 15-21Cr, 10-12Al, and 0.3-0.9Y). There is no significance in the choice of blades, aside from NAVSEC interest in CoCrAlY blade coatings. They merely represent state-of-the-art blades which were available for experimentation. In particular, it is to be emphasized that the present tests and their results do not necessarily relate to sea performance, and should not be construed as indicating that one blade alloy or coating is superior to the other.

Results and Observations

Through careful comparison with control experiments where all conditions were the same except only Na_2SO_4 was used, it has been possible to show that NaCl vapor at a nominal 300 ppm can produce the following effects:

1. NaCl promotes vaporization of Na_2SO_4 from the blade surface.
2. It causes flaking of the normally protective Al_2O_3 surface oxide which tends to form on CoCrAlY even in the presence of Na_2SO_4.
3. It generates volatile chromium compounds which condense as yellowish deposits in the colder regions near the tube exit. These deposits show a characteristic sulfur content by EDXA (energy dispersive x-ray analysis) analysis, and thus differ from volatile Cr compounds which have been found in earlier works with NaCl alone.
4. NaCl apparently can "dealloy" the blade metal of titanium under some circumstances (particularly observed with blade A specimens).
5. Finally, NaCl hastens a certain type of sulfidation-oxidation attack to which CoCrAlY is subject when exposed as a "cut-edge" specimen. This attack is surprising in that it degrades the CoCrAlY in preference to the supposedly less resistant blade metal.

Vaporization of Na_2SO_4 by gaseous NaCl.—It was noted early in the investigation that the Na_2SO_4 tended to build up on the blade specimen surface from the daily sprayings of Na_2SO_4 in the sulfate-only experiments. However, when NaCl was present, no such buildup ever occurred. This led to experiments where a deposit of Na_2SO_4 was allowed to accumulate, and then without any other change, the NaCl boat was introduced into the furnace so as to bring the sulfate-deposited specimen in contact with NaCl vapor. In each instance, the Na_2SO_4 deposit disappeared rapidly, usually within 24 hr, once NaCl was introduced.

This phenomenon was also studied using Na_2SO_4-sprayed platinum foil to avoid corrosion complications and to facilitate accurate measurement of the sulfate loss. Somewhat heavier (2-3 mg/cm^2) sulfate films were used and the foil temperatures were 1600°F, but otherwise all arrangements were the same as in the corrosion runs. With NaCl vapor under "dry" conditions [predried NaCl, and the incoming air passed through Drierite (TM)], sulfate weight losses of 0.03-0.05 mg/cm^2-hr were measured. Under wet conditions, where the incoming air was bubbled through water, the weight losses were of the order of 0.1 mg/cm^2-hr, or about twice as high. Wet air alone did not increase the sulfate weight loss rate. These weight losses are equivalent, as shown by comparison runs with Na_2SO_4 alone, to an increase in the Na_2SO_4 vaporization rate of 100 times or more.

Sodium chloride has been reported to behave ideally (12) with Na_2SO_4, which would predict 4-5 mole percent (m/o) dissolution of NaCl in the sulfate at the partial pressures involved. No evidence of chloride could be found by EDXA however, under either wet or dry conditions, when the runs were stopped in midterm and the remaining sulfate deposits examined.

An attempt was also made to determine whether dissociation occurred in the vaporization by passing the exiting gas through SO_2 detector tubes. Assuming complete dissociation, the effluent would have contained 1-2 ppm of SO_2, a concentration just within the sensitivity of the tubes employed. No positive test for SO_2 was obtained. Either dissociation to SO_2 is limited, or the test and apparatus are not adequate for the task.

Spalling of Al_2O_3 from CoCrAlY surfaces.—The second NaCl effect, *i.e.*, causing the formation of a spalling oxide on the CoCrAlY surface, became apparent after 24-48 hr at temperature. One would observe on withdrawing the specimen that a thin brownish-gray film, with bluish tinges at some sites, had formed on the CoCrAlY, and that this film detached and popped free as the specimen cooled under the microscope. No quantitative measurement of the thickness of the spalling film was attempted, but it was clearly much thicker than any (nonspalling) Al_2O_3 film formed within the same time period when the exposure was to Na_2SO_4 alone. The CoCrAlY uncovered by the spalling film was a bright, highly reflecting silver in the light microscope.

The spall sites were subsequently examined by SEM and EDXA for morphology and elemental composition. A representative site is shown in Fig. 2, where the residual Al_2O_3 film is on the right, and the spall site on the left. EDXA indicates the film to be very rich in

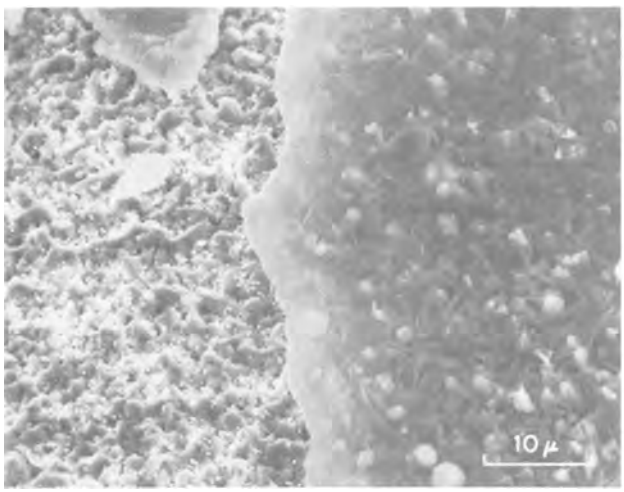


Fig. 2. Spalling Al_2O_3 surface film which forms on CoCrAlY in the presence of NaCl vapor. The film is on the right.

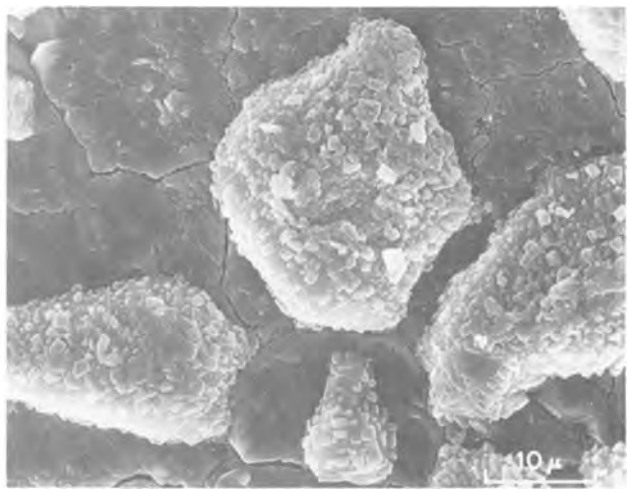


Fig. 3. Chromium-containing deposits which condensed downstream in the presence of NaCl vapor.

Al as expected, but also to contain traces, listed in order of decreasing peak height, of Cr, Co, and Ti. The film also appears to contain numerous acicular, or needle-like, particles. This is a characteristic morphology of these films and may relate to the NaCl action.

The newly exposed CoCrAlY has a granular, somewhat porous (at higher magnification) surface. EDXA shows strong Cr and Co, moderate Al, considerable Ti, and some S. The Al peak height is substantially lower than it is with fresh CoCrAlY, as would be expected considering the CoCrAlY to be depleted locally of Al by formation of the Al_2O_3 surface film. The sulfur and titanium seem to be randomly distributed, and could not be associated with a particular phase or structure. Interestingly, while S was routinely found on the exposed CoCrAlY, it was not detected on the Al_2O_3 film. The significance of the tiny white crystallites on the CoCrAlY in Fig. 2 is uncertain. They were normally not found in such profusion. They give Al-rich EDXA spectra and are not related to the Ti or S impurities. An important final point to be noted is that while the formation of the spalling Al_2O_3 is manifestly a NaCl effect, no trace of chloride was ever detected either in the spalling film or on the exposed CoCrAlY surface.

Formation of volatile chromium species.—The third NaCl effect was detected by the formation of distinctive yellowish deposits which developed in the cool downstream sections of the tube furnace when NaCl was present, but not when it was absent. An example of the structure of these deposits is shown by SEM in Fig. 3. The deposits are rich in Cr and Cl (Fig. 4), and therefore could be thought of as being produced by condensation of volatile chrom-chlorides or chrom-oxychlorides, as others have postulated in earlier work with NaCl vapor. However, our system also contains Na_2SO_4, and the EDXA spectra characteristically show both S and Na to occur in abundance in the deposits (Fig. 4). This suggests that the deposits here are not formed from Cr-O-Cl compounds, but from volatile compounds or complexes which also contain Na and S.

Titanium interactions.—With blade A, there was a tendency for the coating to crack away slightly during sawing and also for the coating to detach from the blade during corrosion testing. (*NB*, coating detachment is not a problem in Navy marine turbines, and this is not representative behavior. The experiments are being reported for the interest they may have pertaining to mechanisms.) Coating detachment occurred in some cases when only Na_2SO_4 was used, but the particular morphologies described below were found only when NaCl vapor was present, and therefore are classified as NaCl effects.

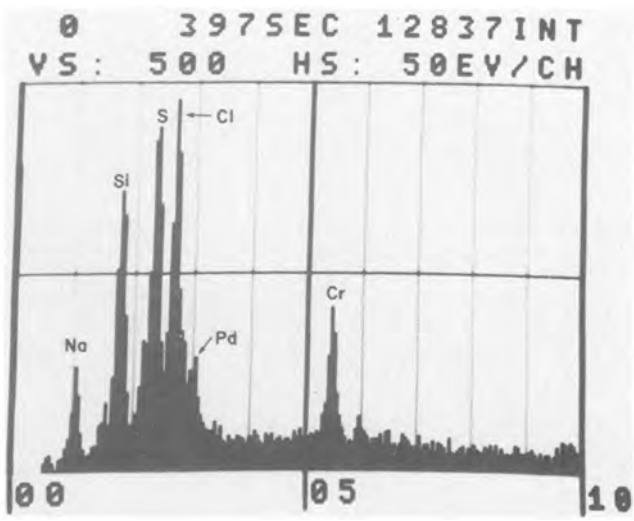


Fig. 4. Energy-dispersive x-ray spectrum from the deposits shown in Fig. 3. The Pd peak is from the Au-Pd SEM coating (Au peak hidden). The Si peak is probably from the substrate.

The initial observation with NaCl was that where the coating had broken away at the saw cut edge, golden needlelike crystals were formed, usually within the first 24 hr of exposure (Fig. 5). At higher

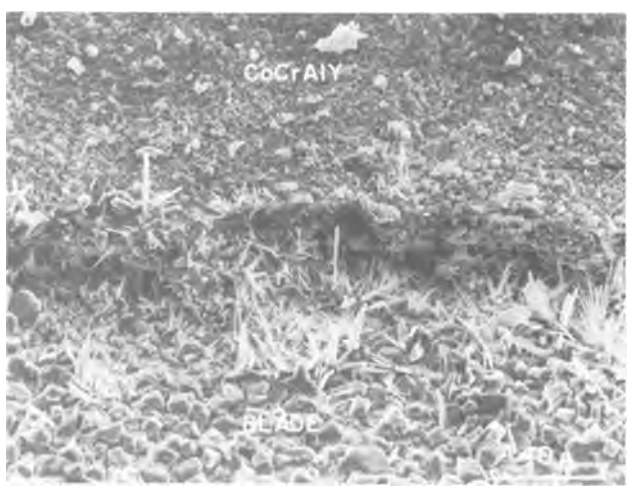


Fig. 5. Needlelike titanium oxide crystals formed under NaCl vapor at a site where the CoCrAlY had cracked away on blade A.

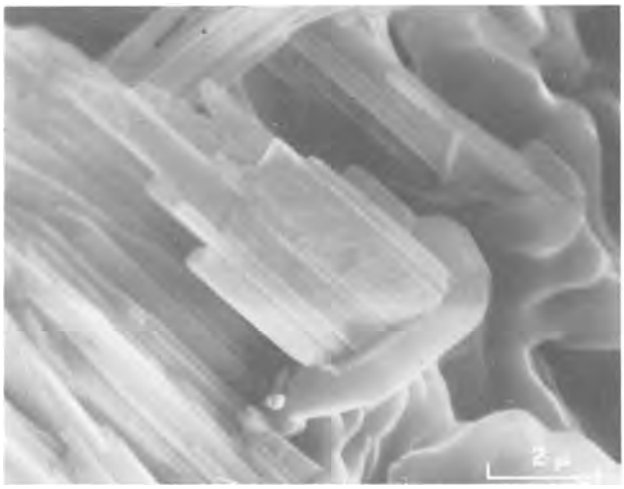


Fig. 6. A high magnification view showing the unusual growth relationship of the titanium oxide crystals in Fig. 5.

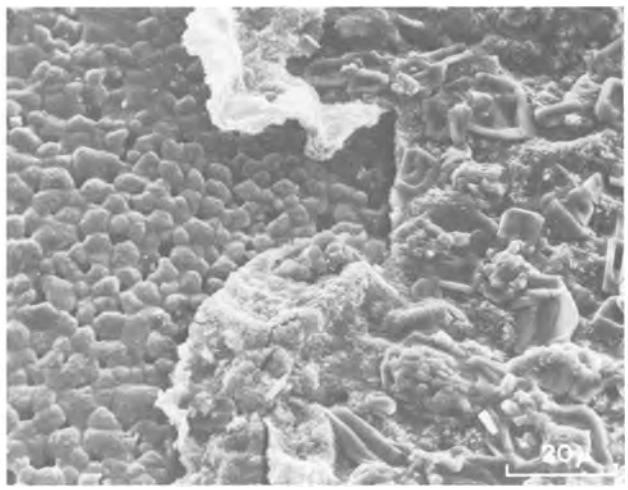


Fig. 8. The "reaction" film formed between the coating and blade substrate in Fig. 7. It appears to consist of a thin Al_2O_3 matrix film in which are embedded polyhedral titanium oxide crystals.

magnification, the needlelike structures often appear to originate from or nucleate on a "parent" crystal (Fig. 6). Both the needle and parent crystals are indicated by EDXA to be predominantly Ti (probably TiO_2 under the circumstances; EDXA does not detect oxygen), but with some Cr and Al, and possibly a slight amount of chloride. The needle crystals seem consistently to contain slightly more Al than the polyhedral crystals.

After longer exposure times, but still usually under 200 hr, several instances were found where the coating had detached from blade A specimens and could be peeled back, as in Fig. 7. (The very fact that the coating can be "peeled back" indicates that its properties have been altered, probably by Al depletion, because normal CoCrAlY coatings are brittle below about 1200°F.) A very thin "reaction" film was found to have formed in these cases between the coating and blade metal. This film (Fig. 8, right-hand side) appears to consist of a thin, essentially continuous Al_2O_3 layer in which are "embedded" a high density of TiO_2 crystallites. The blade substrate is left in a granular, porous state and yields EDXA spectra which show, in order of decreasing peak height, Ni, Co, Cr, Al, and S, but little or no Ti.

Most indications were that the corrosive attack preceded from the cut edge along the coating-blade interface, additional access of Na_2SO_4 and NaCl vapor being allowed as the coating progressively detached. However, in one run, a localized site of corrosion on the coating, marked by a bluish-brown hillock, was observed to develop in the body of the specimen in advance of the detachment front. Post-run examination showed that the blade had been attacked beneath this side with the formation of the characteristic inner reaction film and pored substrate. Both polyhedral and needle or blade like TiO_2 crystals (Fig. 9) were found here, with the latter crystals giving evidence of containing some chloride (Fig. 10). This was the most positive identification of chloride on the corrosion specimens that was found during the total investigation.

Sulfidation-oxidation of CoCrAlY.—After the specimens were exposed to Na_2SO_4 under vaporous NaCl at 1625°C for 100 hr or so, a particular type of corrosive attack would be observed to initiate at the cut edge (often at a corner) and then, once initiated, propagate rapidly at rates of a millimeter or more per day across the surface of the specimen, as shown in Fig. 11. The attack consists, as Fig. 11 indicates, of a sulfidation front which is then followed by an oxidation front. When viewed in cross section, the attack can be seen to be essentially confined to the CoCrAlY layer (Fig. 12 and 13). There are some differences in behavior between blade A and blade B specimens, one of the first and most obvious being that, under NaCl, the sulfidation and oxidation fronts tend to be more widely separated with blade A (Fig. 12) than with blade B (Fig. 13).

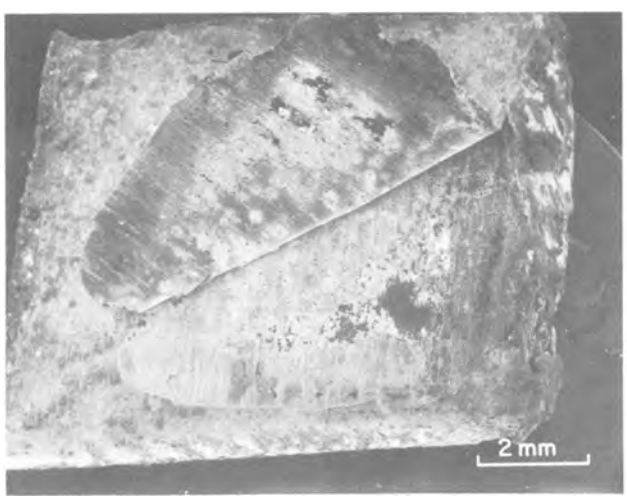


Fig. 7. Detached CoCrAlY coating on a blade A specimen after 113 hr exposure at 1625°F to Na_2SO_4-vaporous NaCl.

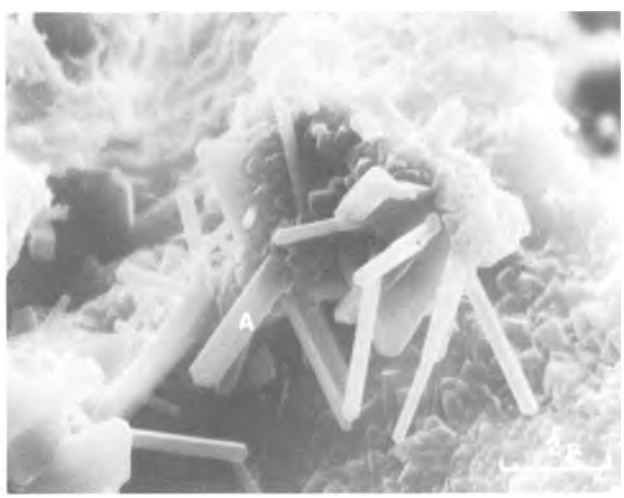


Fig. 9. Bladelike titanium oxide crystals formed under a pit through the CoCrAlY coating. Compare with Fig. 5 and 6.

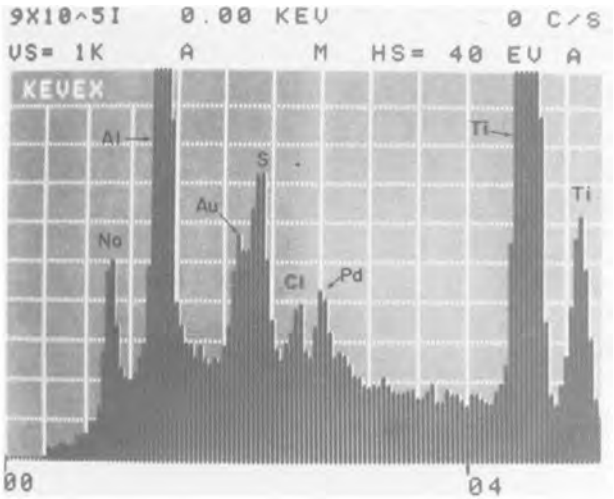


Fig. 10. Energy-dispersive x-ray spectrum from crystal A in Fig. 9. Very similar to spectra obtained from needle crystals in Fig. 6. Notice possible presence of chloride. Au and Pd come from antichorging SEM coating.

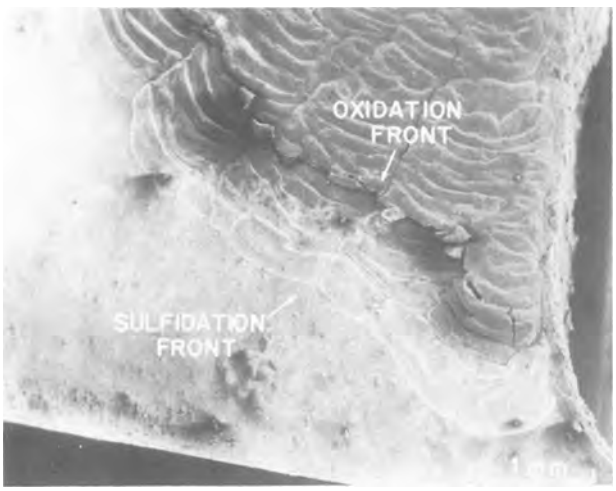


Fig. 11. Progressive sulfidation-oxidation attack across a blade A specimen surface after 142 hr exposure at 1625°F to $NaSO_4$-vaporous NaCl.

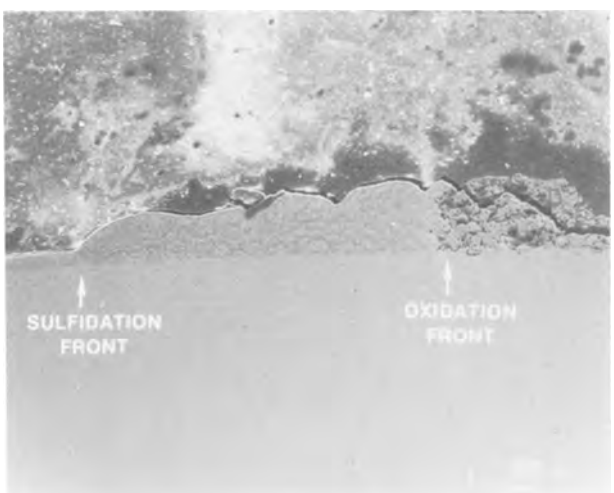


Fig. 12. An SEM photograph showing sulfidation-oxidation attack on the CoCrAlY coating on a blade A specimen in cross section.

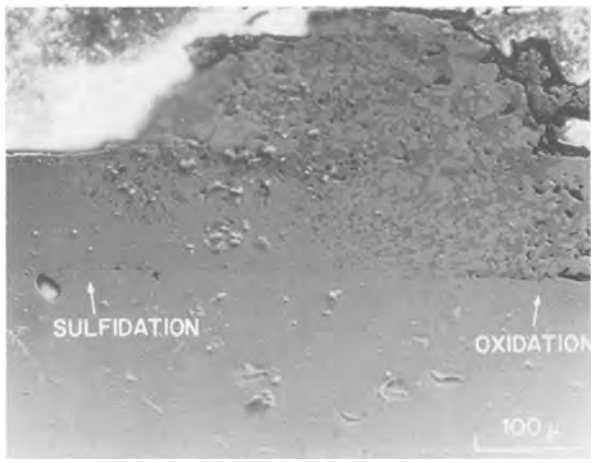


Fig. 13. Sulfidation-oxidation of CoCrAlY on a blade B specimen. Oxidation front follows more closely here than with blade A specimens.

A similar attack was seen in control runs with Na_2SO_4 alone, except that the incubation time before attack was observed was substantially longer, being of the order of 300-500 hr, the distance between sulfidation and oxidation fronts was short for both blade A and blade B specimens, and a chromium sulfide phase containing aluminum, *i.e.*, "CrAlS," was formed exclusively, whereas under NaCl, the tendency was to form "Cr_3S_4" in addition or in preference to "CrAlS" (see below). The rate of propagation across the surface also seemed to be slower in the absence of NaCl, although this was not verified quantitatively.

The sulfidation front of a blade A specimen corroded under Na_2SO_4-vaporous NaCl is shown in Fig. 14. The sulfidation zone is on the left and the as yet unsulfided CoCrAlY on the right. The CoCrAlY is depleted in aluminum at the sulfidation front and at its outer surface, as evidenced by lack of β phase at these sites (also verified by EDXA). The layer visible at the outer coating surface just above the sulfidation zone-CoCrAlY intersection gives an Al signal by EDXA, indicating it to be Al_2O_3. Notice that the CoCrAlY itself is cracked away from the substrate here, but this has had no effect on the course of the sulfidation attack.

Three corrosion phases can be identified in the sulfidation zone. The lightest (gray) phase is a metallic phase (proven by an electron microprobe test for

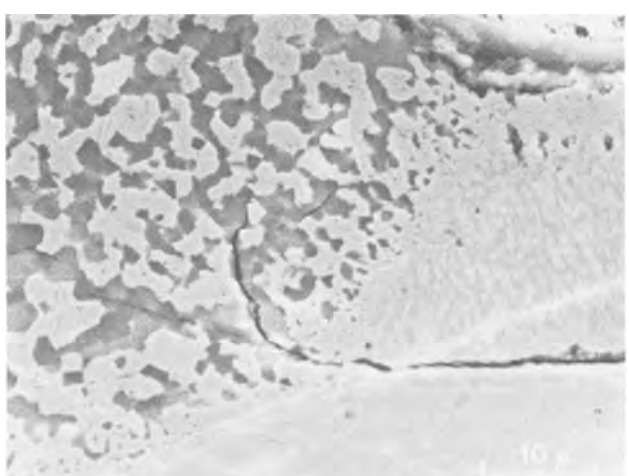


Fig. 14. The sulfidation front on a blade A specimen. CoCrAlY coating ot the right, sulfidated zone at the left. Notice that the coating has detached, but this has had little effect on the sulfidation reaction.

oxygen) comprised essentially of Ni and Co, the composition being approximately 50/50 as judged by EDXA peak heights, and effectively constant whether the phase occurs at the outer surface or adjacent to the coating-blade interface. Since no intermetallic compounds are formed in the Co-Ni system, this "constant" stoichiometry is assumed to result from the mechanism of formation. The two gray phases are chromium sulfides and they are distinctive in that the globular, light gray matrix normally contains traces of Co and Ni, and often somewhat larger concentrations of Ti, but never Al, whereas the darker blocky, or rectilinear, phase dispersed within it (shown more clearly in Fig. 15) always contains Al and excludes Ti. These chromium sulfide phases have been observed in earlier hot corrosion studies [*e.g.*, Ref. (13)] with the most thorough characterization being given by Erdoes (14). He also noticed the unusual Al and Ti solubilities and identified the light gray, globular phase as Cr_3S_4, and the darker, rectilinear phase as CrAlS, a thiospinel. We have adopted his identifications, but with some reservation as to the strict validity of Cr_3S_4 since there are several closely related sulfide species which could be formed.

The blade B specimens showed essentially the same behavior with Na_2SO_4-vaporous NaCl except the depletion zone at the sulfidation front was broader and more porous, very little CrAlS was produced, and as noted, the sulfidation and oxidation fronts were closer together. Figure 16 is a higher magnification view of the intersection of the very front of the sulfidation zone and the coating outer surface. Certain sites can be seen here where the β CoAl phase appears to be directly and preferentially attacked with void formation. More usually, however, a depletion zone separates the voids from the unattacked CoCrAlY. The white (SEM charging effect) layer at the very top of Fig. 16 is Al_2O_3 as indicated by EDXA.

The oxidation phase of the attack involves preferential oxidation of the chromium sulfide phases. This can be seen in Fig. 17, the oxidation front on a blade A specimen, and Fig. 18, the oxidation front on a blade B specimen. A large volume diminishment occurs and voids are formed. There is no buildup of sulfides or sulfur in the blade below the oxidation zone, so the sulfur is either displaced as sulfur oxide gas, or moves forward into the sulfidation zone to maintain the sulfur activity there. Unfortunately, no SO_2 evolution tests were made at this stage of the investigation. However, a later study (15) was made where "cut-edge" CoCrAlY-coated blade specimens were impregnated with NiS at the coating-blade interface, and it was found that the characteristic sulfidation-oxidation attack did not commence until oxygen was admitted into the system. This suggests that some "release of sulfur" by the oxidation of the sulfide phases is critical

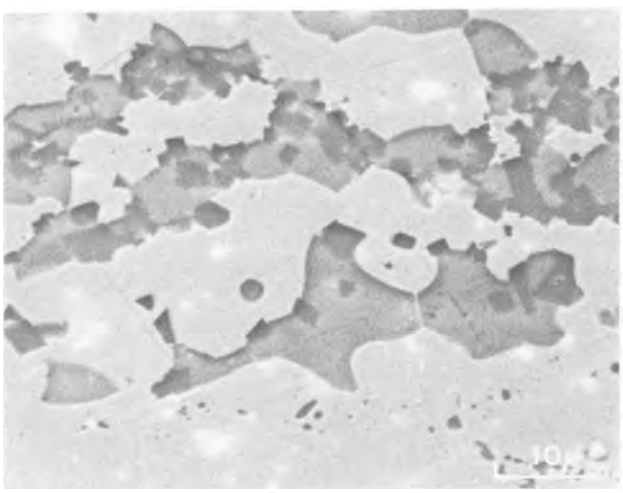


Fig. 15. Rectilinear CrAlS and globular "CrS" (probably Cr_3S_4) phases at the CoCrAlY-blade interface on a blade A specimen.

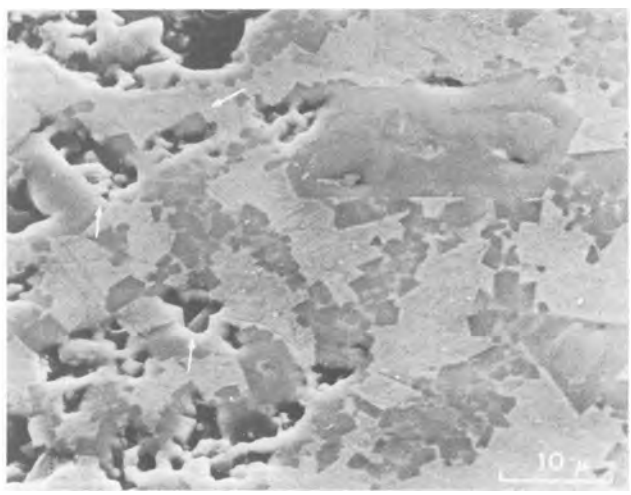


Fig. 17. Oxidation of chromium sulfide phases with blade A specimen. Arrows mark sites where rectilinear CrAlS persists after "Cr_3S_4" has apparently been oxidized away.

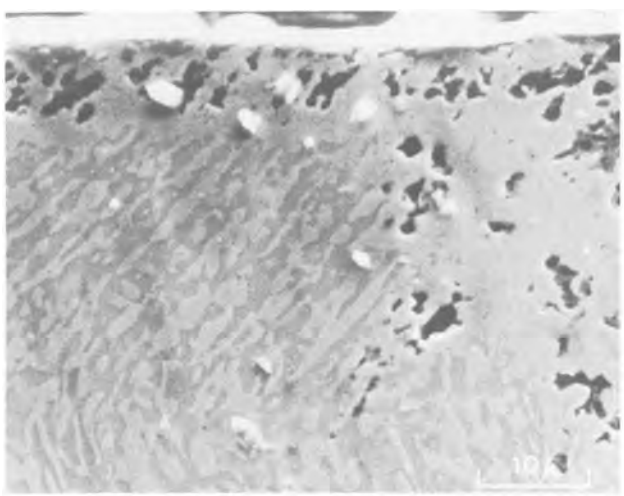


Fig. 16. Intersection of sulfidation zone-outer coating surface on a blade B specimen. Note apparent attack on β CoAl phase at point of farthest advance of sulfidation front.

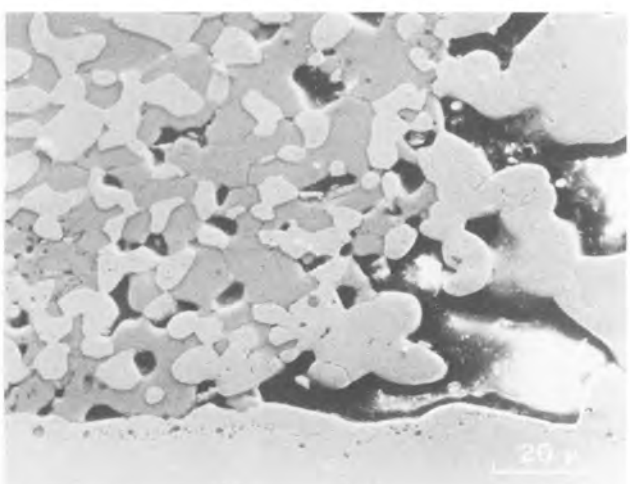


Fig. 18. Oxidation of chromium sulfide phase with blade B specimen. Little CrAlS present here.

in this type of corrosion. The arrows in Fig. 17 point out residual particles of CrAlS left after oxidation of the Cr_3S_4 which originally surrounded them, *i.e.*, CrAlS appears to be more resistant to oxidation under these circumstances than Cr_3S_4.

Discussion

The experiments here are an example of deductive research where one approaches the complex whole and attempts to break it down into elements. Deductive research is a valid alternative, especially for involved problems of urgent concern such as hot corrosion, to the more traditional inductive research where one begins with the simplest element and attempts in a long series of experiments to factor in each new parameter to reach an ultimate understanding of the whole. An unavoidable consequence of deductive research, however, is that in the initial work there is not time, nor in fact is it the goal, to study each new element in depth as it is revealed. The discussion that can be made of each individual NaCl effect is therefore necessarily limited, but it may nonetheless be useful in relating the present results to earlier hot corrosion studies or in pointing new directions of research.

Enhanced vaporization of Na_2SO_4.—This experiment has been duplicated at another laboratory using Pt foil specimens in Al_2O_3 furnace tubes at 1650°F (16). The vaporization rates were higher because of the higher temperature, but the same results were obtained. Both "dry" and wet NaCl vapor increased the rate of Na_2SO_4 vaporization by approximately 100 times.

Concerning mechanisms, it is known that HCl can dissociate Na_2SO_4 deposits (17), presumably by reversal of the reaction

$$2NaCl + SO_2 + 1/2\ O_2 + H_2O \leftrightarrows Na_2SO_4 + 2HCl$$

It might be suspected, therefore, that the "dry" system still contains traces of H_2O, and that in a separate upstream reaction the NaCl is hydrolyzed to HCl which affects removal of the Na_2SO_4. The fact that deliberately adding H_2O only slightly increased (doubled) the Na_2SO_4 vaporization rate here might argue against this idea, as might the fact that both Al_2O_3 and silica tube liners, assuming a catalytic effect of the liner in the hydrolysis reaction, gave essentially the same results.

In any event, it is now clear that NaCl may actually tend to remove Na_2SO_4 deposits from gas turbine blades (turbine gases contain up to 5% H_2O (2) under some circumstances, a possibility little appreciated before in hot corrosion studies. The reaction needs further study, taking proper account of SO_2 and other species which may be pertinent.

Spalling of Al_2O_3 oxide.—Given the previous effect of NaCl vapor in removing Na_2SO_4, it is not certain that the Al_2O_3 spalling actually occurred in the presence of Na_2SO_4 and that our conditions were truly different from those of earlier investigators. The salient points from our work are: (*i*) an abnormally thick, spalling Al_2O_3 film formed when NaCl was present; (*ii*) this film showed some evidence of "restructuring," *i.e.*, the formation of the small needlelike particles in the film in Fig. 2, and (*iii*) no trace of chloride was found associated with the film, although the spalling was undoubtedly chloride-induced. With the exception of the "restructuring," these results are the same as those established earlier with the NaCl alone. Vapor phase NaCl has been reported to have caused chromium oxide films on Nimonic alloys to recrystallize into a porous mass of hexagonal crystals, possibly through a gaseous intermediate (18), and one might suspect a similar reaction in the restructuring of the Al_2O_3 films here, but the suspicion remains to be proved.

Volatile chromium species.—The discovery of S and Na in the condensed downstream Cr-containing deposits (Fig. 3 and 4) is new, and good evidence that the volatile chromium compounds which form under exposure to Na_2SO_4-vaporous NaCl (a salt system more related to engine operation than pure vapor phase NaCl) are not simply chromium chlorides or oxychlorides. It is conceivable that the deposits are produced by "cocondensation" of two or more vapors, but it seems unlikely that low vapor pressure Na_2SO_4 would happen to condense at the same site as the much more volatile chromium compounds. Recently it has been shown that the predominant volatile species produced in 1650°F oxidation of chromium under NaCl vapor are addition complexes, $(NaCl)_xCrO_3$, where $x = 1$, 2, and 3 (19). One can speculate that the deposits in Fig. 3 could result from a similar addition complex, but one now containing SO_2 or a related compound since Na_2SO_4 is present.

Titanium interactions.—Sodium chloride has been observed in the past to promote recrystallization of certain oxides into large, well-faceted crystal masses, presumably by the action of unstable gaseous intermediates [*e.g.*, Ref. (18)]. We believe an analogous reaction may be involved here, particularly since evidence of chlorine (chloride) has been found in the TiO_2 bladelets (Fig. 10).

Our interpretation is that NaCl vapor penetrates along the coating-blade interface and reacts with (dealloys) the Ti-rich blade surface, titanium being known to tend to segregate disproportionately to alloy surfaces. The reaction probably involves the formation of a volatile, metastable titanium chloride which decomposes forming TiO_2 (with some Cr and Al impurity) when the crack opens, reducing the chloride concentration and allowing free access of oxygen. The well-faceted structures of the TiO_2 crystals and the porosity of the dealloyed substrate seem consistent with such a vapor phase transport.

Some U.K. experiments (3) wherein IN587 was preoxidized and then exposed to NaCl vapor at 1740°F may represent another example of this type of reaction. The preoxidized layer ultimately spalled off under this treatment, exposing a porous Ni-rich substrate clustered with localized deposits of large, prismatic TiO_2 crystals. This is essentially the same morphology as observed here, and we presume formed by the same mechanism. Another indication of TiO_2-NaCl interaction is given in the report that superalloys containing TiO_2 in the oxidation scale are sensitive to NaCl attack (20). More proof of the mechanism is required, but the reaction is obviously important and may relate to the performance of Ti-containing alloys in marine turbines.

Sulfidation-oxidation of CoCrAlY.—After our discovery, we learned that this phenomenon had been observed in other laboratories (16) and studied in some detail (21), although nothing had been published. Felten and Pettit (16) subsequently found several clear examples of the sulfidation-oxidation attack morphology on a blade removed after 4800 hr of sea service, indicating the reaction has relevance in marine hot corrosion. We have shown in later experiments that NiS, formed under Na_2SO_4 at the coating-substrate interface exposed at the cut-edge, is the critical species in the attack (15).

The effect of NaCl vapor on this reaction seems to be to change the kinetics (reduces incubation time before attack, alters separation between sulfidation and oxidation fronts presumably by affecting the kinetics of one or the other) and to promote the formation of "Cr_3S_4" over CrAlS. Erdoes (14) observed that CrAlS was found more prevalently in his laboratory specimens (where no NaCl was used) than in specimens removed from industrial turbines (where chloride was possible). This encourages us to believe that our results are not artifactual and do pertain to turbine corrosion. The finding of this apparent ability of NaCl to influence which chromium sulfide phase is formed may be highly significant, since it represents

one of the few items of physical evidence, aside from oxide spalling, which has yet been associated with NaCl in hot corrosion.

Relevance to shipboard corrosion.—Obviously 300 ppm is a much higher NaCl concentration than ship engines are exposed to, although it could be argued that concentrations of this magnitude prevail temporarily near points of sea salt particle or seawater droplet impact on the blades. However, as will be recalled, 300 ppm was chosen because it gave chloride effects within 100 hr. It is likely that 30 ppm or even less could produce chloride effects if longer test periods were allowed.

Furthermore, since even 300 ppm corresponds to only about 1/20 saturation of the NaCl vapor, we consider that the points originally raised for investigation have been proven. There is no necessity for the NaCl to condense (or perhaps to even dissolve to any appreciable extent in the Na_2SO_4, based on our failure to detect chloride in the Na_2SO_4 vaporization experiments) to exert its influence, and only under special circumstances will even traces of chloride be left to mark its involvement. It is therefore unrealistic to expect to disprove chloride effects in shipboard hot corrosion by calculating condensation pressures or examining corroded parts for chloride.

Acknowledgments

This work was a part of a NAVSEA Materials Development Program conducted under cognizance of J. W. Fairbanks, NAVSEC. We are grateful for the support and many informative discussions. We are also indebted to Dr. F. S. Pettit, Pratt and Whitney Aircraft, Middletown, Connecticut, and Dr. D. A. Shores, General Electric Research Center, Schenectady, New York, for enlightening conferences and access to unpublished data.

Manuscript submitted Aug. 19, 1976; revised manuscript received May 2, 1977. This was Paper 283 presented at the Toronto, Canada, Meeting of the Society, May 11-16, 1975.

Any discussion of this paper will appear in a Discussion Section to be published in the June 1978 JOURNAL. All discussions for the June 1978 Discussion Section should be submitted by Feb. 1, 1978.

Publication costs of this article were assisted by the Naval Research Laboratory.

REFERENCES

1. J. Stringer, MCIC Report 72-08 (1972).
2. J. F. G. Conde, AGARD Conference Proceedings No. 120 on High Temperature Corrosion of Aerospace Alloys, p. 204, AGARD-CP-120, April 10-12, 1972.
3. J. F. G. Conde and B. A. Wareham, MCIC Report 75-27, p. 73 (1974).
4. J. E. Restall, *ibid.*, p. 195.
5. R. L. Jones and J. W. Fairbanks, *ibid.*, p. 219.
6. C. G. McCreath and J. M. Beer, Paper presented at the Conference on Gas Turbine Materials in a Marine Environment, University of Bath, September 20-23, 1976.
7. C. G. Root and R. R. Stetson, *ibid.*
8. P. Hancock, MCIC Report 75-27, p. 225 (1974).
9. G. C. Booth, as quoted in Ref. (3).
10. C. T. Ewing and K. H. Stern, *J. Phys. Chem.*, **78**, 1998 (1974).
11. R. F. Kohl, C. A. Stearns, and G. C. Fryburg, in "Metal-Slag-Gas Reactions and Processes," Z. A. Foroulis and W. W. Smeltzer, Editors, p. 649, The Electrochemical Society Softbound Symposium Series, Princeton, N.J. (1975).
12. H. Flood, T. Forland, and A. Nesland, *Acta Chem. Scand.*, **5**, 1193 (1951).
13. P. A. Bergman, *Corrosion (Houston)*, **23**, 72 (1967).
14. E. Erdoes, "Deposition and Corrosion in Gas Turbines," A. B. Hart and A. J. B. Cutler, Editors, p. 115, John Wiley & Sons, New York (1973).
15. R. L. Jones and S. T. Gadomski, Paper 158 presented at The Electrochemical Society Meeting, Las Vegas, Nevada, October 17-22, 1976.
16. E. J. Felten and F. S. Pettit, Quarterly report, March 1-May 31, 1976, on NAVSEA sponsored contract, NRL contract no. N00173-76-C-0146.
17. J. W. Clark, Paper presented at the ASM Materials/Design Conference, Materials for Coal Conversion, Systems Design, Pittsburgh, Pennsylvania, April 26-27, 1976.
18. P. S. Gray, in discussion of paper by H. Lewis and R. A. Smith at the 1st International Congress on Metallic Corrosion, London, April 10-15, 1961.
19. C. A. Stearns, F. J. Kohl, and G. C. Fryburg, NASA Techological Memo X-73476 (1976).
20. Y. Bourhis and C. St. John, *Oxid. Met.*, **9**, 507 (1975).
21. D. A. Shores, Private communication.

Technical Notes

Poly (Fluoro Methacrylate) as Highly Sensitive, High Contrast Positive Resist

Masami Kakuchi, Shungo Sugawara, Kei Murase, and Kentaro Matsuyama

Nippon Telegraph and Telephone Public Corporation, Ibaraki Electrical Communication Laboratory, Tokai, Ibaraki, 319-11, Japan

Recently, the necessity for manufacturing very fine patterns of submicron size on integrated circuit devices has increased. X-ray lithography is a useful technique for exposing whole wafers (1). Most x-ray resist materials have been appropriated from electron beam resist materials. Poly (methyl methacrylate), PMMA, is most widely used, however, it has only low sensitivity, about 5×10^{-5} C/cm^2 for electron beam (AV: 10 kV) (2) and 2400 mJ/cm^2 for x-rays of Mo L line. In order to overcome this low sensitivity, modified PMMA resists with methyl isopropenyl ketone (3), anhydride bridge (4), isobutylene (5), acrylonitrile (6), methacrylic acid (7), and α-chloroacrylate (8) have been

Key words: x-ray lithography, polymer resist, positive resist.

Table I. Properties of poly (fluorobutyl methacrylates), FBM

Name	Methacrylate side chain	Intrinsic viscosity number,* dl/g	Glass transition temperature T_g, °C***
FBM-1	$CF_3CFHCF_2CH_2$—	1.0**	50
FBM-2	$CF_3CFHCF_2CH(CH_3)$—	0.59	64
FBM-3	$CF_3CFHCF_2CH(C_2H_5)$—	0.57	47
FBM-4	$CF_3CFHCF_2CH(C_3H_7)$—	0.59	45
FBM-5	$CF_3CFHCF_2C(CH_3)_2$—	0.52	83
FBM-6	$CF_3CFHCF_2C(CH_3)(C_2H_5)$—	0.35	73

* Measured in methyl ethyl ketone at 30°C.
** M_w = 500,000 and M_w/M_n = 2.8 by GPC.
*** T_g was measured by thermomechanical analysis (TMA).

studied, but in many cases their contrast is too low. The newly developed resist materials described in this paper consist of fluorobutyl methacrylate homopolymers, and were found to have both higher contrast and much higher sensitivity than PMMA.

Poly (hexfluorobutyl methacrylates), FBM, were synthesized by radical polymerization of hexafluorobutyl methacrylates from methacrylic acid and 2, 2, 3, 4, 4, 4-hexafluoro-, 1-methyl-2, 2, 3, 4, 4, 4-hexafluoro-, 1-ethyl-2, 2, 3, 4, 4, 4-hexafluoro-, 1-n-propyl-2, 2, 3, 4, 4, 4-hexafluoro-, 1,1-dimethyl-2, 2, 3, 4, 4, 4-hexafluoro-, and 1-methyl-1-ethyl-2, 2, 3, 4, 4, 4-hexafluorobutyl alcohol, respectively. The properties of FBM's are shown in Table I.

The resist materials were dissolved in methyl isobutyl ketone (MiBK), and were spin coated on the silicon substrate with or without oxide layer. After prebaking at 120°-140°C in vacuum in order to attain a suitable adhesion to the substrate, the resists were irradiated with soft x-ray through a stainless steel aperture for determining sensitivity, or through a Si mask (4 μm thick) with an Au absorber (4000Å) for replicating fine patterns. The x-ray exposing apparatus was a modified Rota Unit RU-200PL made by Rigaku Denki Company. Molybdenum was used for the target (Mo L, 5.4Å), and the target chamber atmospheric pressure was 10^{-6} Torr. A vacuum window was made of a 12 μm polyester film.

Resist samples were exposed on a 6 mm diam area, and the sample chamber was maintained at 10^{-3} Torr during exposure. Target to sample distance was 12 cm. X-ray intensity irradiated was measured with a gas flow proportional counter using P-10 gas. It was 0.19 mW/cm^2 at 16 kV/200 mA electron beam bombardment, corrected with a resist whose sensitivity is easily measurable, such as epoxidized polybutadiene and chloroethyl vinyl ether copolymer (9).

Irradiated resist was developed using isopropyl alcohol (IPA) with or without MiBK. Developed resist was postbaked to remove any remaining developing solvent.

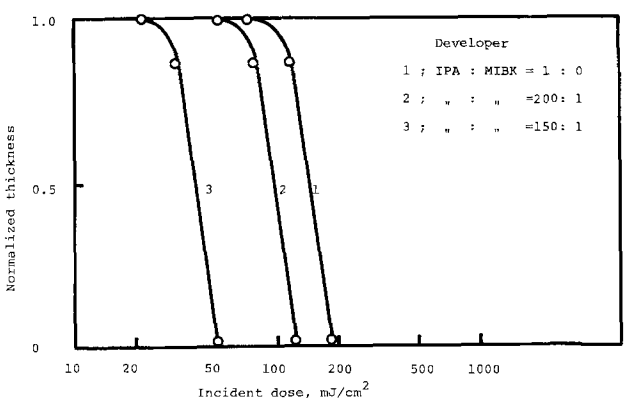


Fig. 1. Plot showing normalized FBM-1 resist thickness vs. incident Mo L x-rays dose for various IPA-MIBK developer combinations. Resist film was coated on the Si wafer to 0.5 μm thickness.

Table II. X-ray irradiation characteristics of FBM resists

Name	Sensitivity,* mJ/cm^2	γ value	Developer
FBM-2	80	4.5	IPA, 2 min
FBM-3	46	4.5	IPA, 2 min
FBM-4	70	2.5	IPA, 20 sec
FBM-5	53	2.5	IPA, 2 min
FBM-6	62	2.5	IPA, 2 min
PMMA**	2400	2.0	MiBK, 2 min
PMMA***	1 × 10^{-4} C/cm^2†	3.3	IPM:MiBK (1:1), 3 min

* Mo L line at 16 kV, 200 mA
** M_w: 500,000.
*** Elvacite 2041, M_w: 496,000.
† Electron beam sensitivity (20 kV).

The sensitivity was determined by measuring the remaining resist thickness on a surface roughness meter from Kosaka Laboratory Limited. The postbaked substrate, with replicated resist pattern, was etched at 23°C with buffered hydrofluoric acid solution for 3 min, or chromium etching solution for 1 min.

FBM-1 sensitivity curves for x-ray are shown in Fig. 1 for several developing conditions and various combinations of IPA and MiBK. By changing the IPA

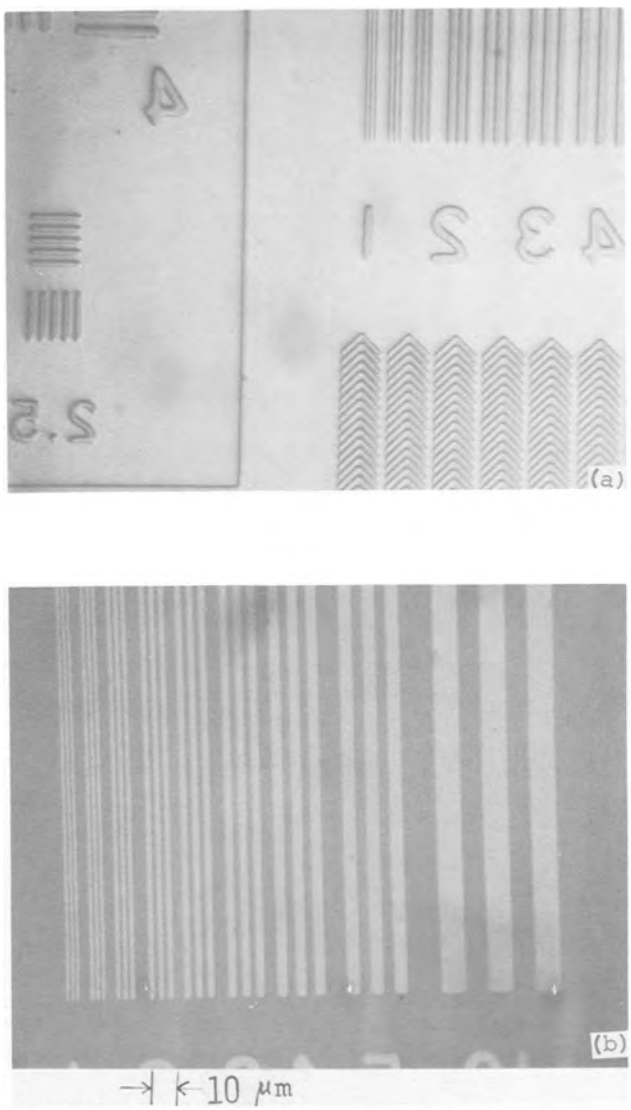


Fig. 2. Photomicrographs of FBM positive resist pattern on SiO_2/Si substrate. (a) and (b) are the same scale. (a) FBM-1 resist resolution pattern formed by 10 kV and 100 mA Mo L x-rays for 45 min, incident dose is 140 mJ/cm^2, and developed with IPA-MIBK (150:1) developer. (b) FBM-2 resist line and space pattern developed with IPA-MIBK (25:1) developer.

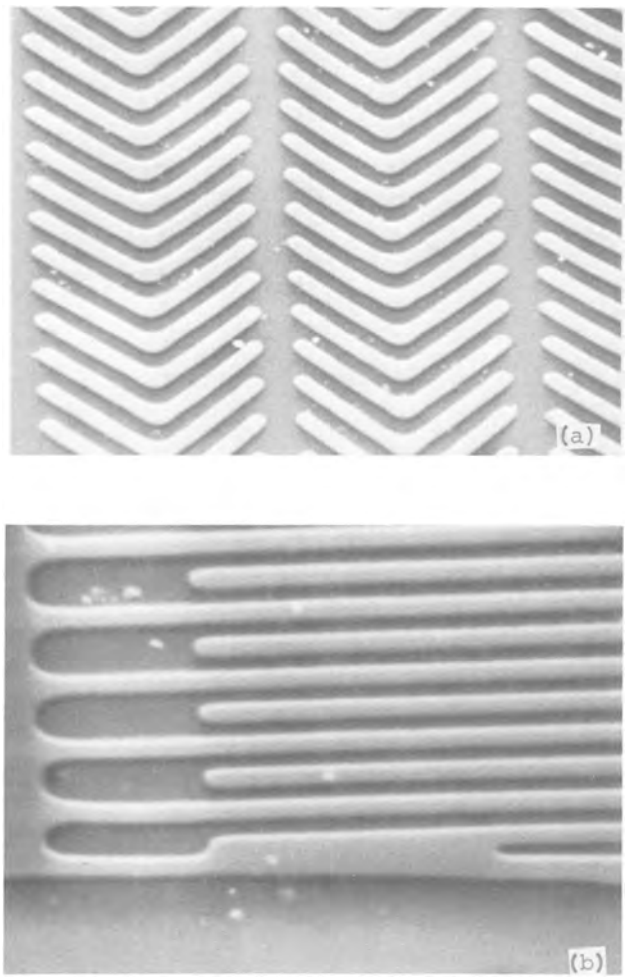


Fig. 3. Scanning electron micrographs of silicon oxide pattern using FBM-1 resist as etching mask. Resist pattern was formed as Fig. 2(a), postbaked at 75°C for 30 min, and etched with buffered hydrofluoric acid. (a) 1.5 μm line and space chevron pattern. (b) 1 μm interdigital pattern.

and MiBK volume ratio from 1:0 to 150:1, the sensitivity improved without contrast reduction (γ4.5). Contrast γ is defined as rising slope, and may be expressed as $\gamma = [\log D_0 D_1]^{-1}$ where D_0 and D_1 are the dose of 0 and 100% film remaining (10). However, when the ratio becomes 100:1, the unexposed region dissolves, and at the best developing condition (150:1 ratio), the sensitivity is 52 mJ/cm^2 for the Mo L line, 46 times more sensitive and higher in contrast than PMMA developed with IPA-MiBK, as shown in Table II. The properties of other FBM resists are shown in this table. They have comparably good sensitivity with FBM-1.

The sensitivity of FBM-1 for an electron beam is 4×10^{-7} C/cm^2, and γ value is 5 at 20 kV accelerating voltage and IPA-MiBK (160:1) developer.

A high resolution FBM resist pattern was produced by the x-ray replicating system using a Si/Au mask. Figure 2 shows resolution patterns of 0.5 μm thick FBM-1 and -2 resist on Si substrate with SiO_2 surface. Figure 3 shows a SiO_2/Si pattern etched using the resist mask of Fig. 2. Figure 4 shows a chromium pattern etched using FBM-5 resist. The resistance to buffered HF solution and chromium etchant is more than 10 and 3 min, respectively.

The resist resolution limit is dependent on the irradiation system. The FBM-1 resolution is recognized as being at least 0.3 μm by the electron beam exposure system. Figure 5 shows FBM-1 resist pattern after development. The pattern is scanned with a 0.1 μm electron beam of the Thomson-CSF exposure system. The minimum line width obtained was 0.3 μm.

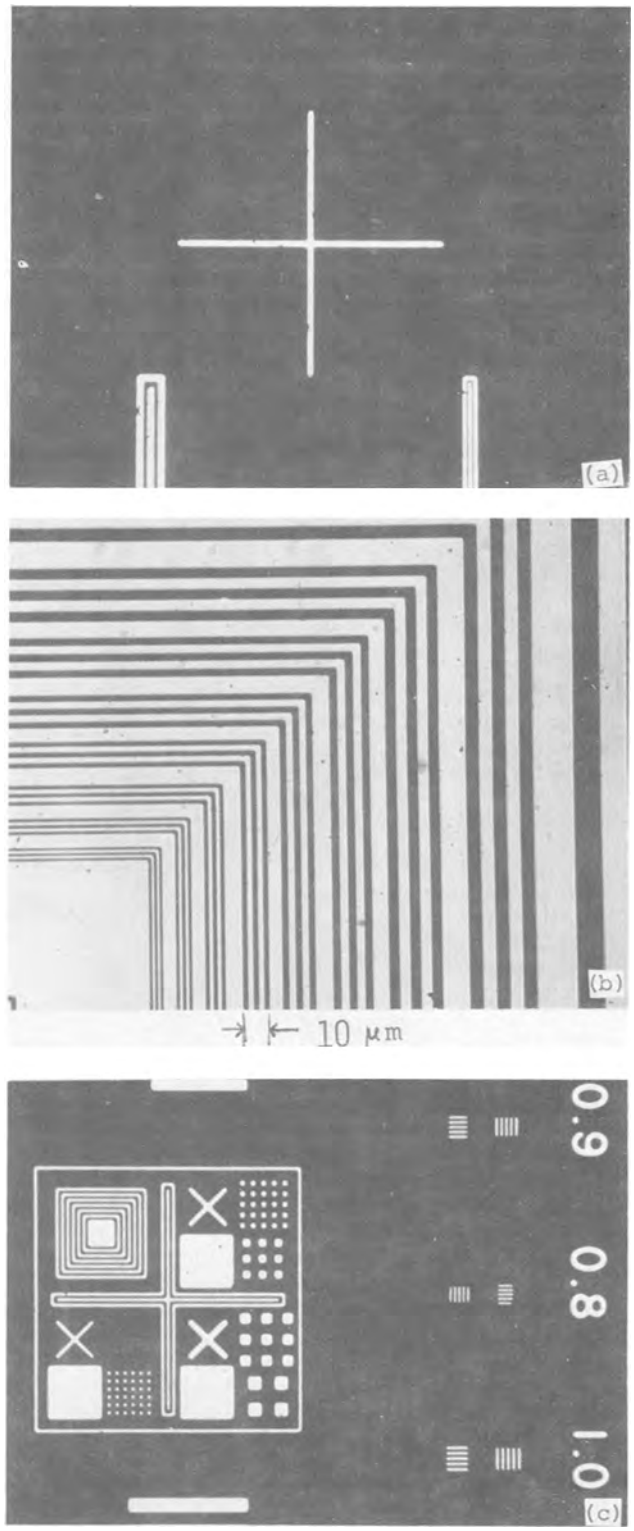


Fig. 4. Photomicrographs of chromium etched pattern viewed in transmission. Substrate consists of 400Å chromium oxide and 800Å chromium evaporated on glass plate. (a) FBM-5 was used as etching mask. Line width is 1 μm. (b) and (c) FBM-6 was used as mask. Minimum line width is 1 μm in (b) and 0.8 μm in (c), respectively. In (c), pattern edges of pair bars are round because original mask pattern, made from photolithography, was round. (b) and (c) are the same scale.

FBM-1 resist is sufficiently useful in a dry process, such as plasma etching, with a suitable thermal control. FBM-1 replicated pattern begins to flow at a higher temperature than its T_g (Table I).

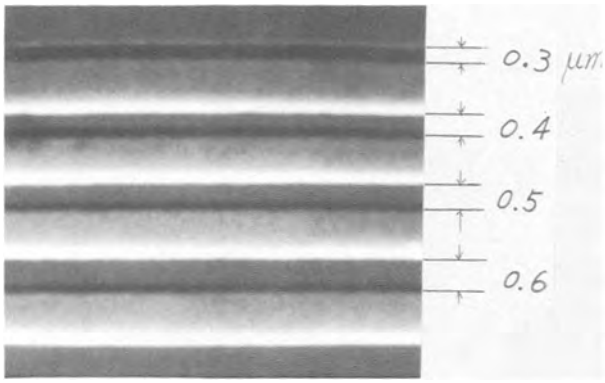


Fig. 5. Scanning electron micrograph of FBM-1 resist pattern delineated by electron beam exposure at 20 kV and 10^{-6} C/cm^2 dose, and developed with isopropyl alcohol.

Acknowledgments

The authors are grateful to Daikin Kogyo Company, Limited for FBM resists synthesis, and to Dr. T. Satokawa for many enlightening discussions.

Manuscript submitted April 25, 1977; revised manuscript received June 20, 1977.

Any discussion of this paper will appear in a Discussion Section to be published in the June 1978 JOURNAL. All discussions for the June 1978 Discussion Section should be submitted by Feb. 1, 1978.

Publication costs of this article were assisted by Nippon Telegraph and Telephone Public Corporation.

REFERENCES

1. H. I. Smith, Proc. IEEE, **62**, 1361 (1974).
2. M. Hatzakis, *Appl. Polym. Symp.*, **23**, 73 (1974).
3. A. W. Levine, M. Kaplan, and E. S. Poliniak, *Polym. Eng. Sci.*, **14**, 518 (1974).
4. E. D. Roberts, *Appl. Polym. Symp.*, **23**, 87 (1974).
5. E. Gipstein, W. Moreau, and O. Need, *This Journal*, **23**, 1105 (1976).
6. Y. Hatano, H. Morishita, and S. Nonogaki, *J. Am. Chem. Soc.*, **35**, 258 (1975).
7. K. Sekikawa and S. Aoyama, Paper presented at the 30th Annual Meeting of the Chemical Society of Japan (1974).
8. J. N. Helbert, C. F. Cook, Jr., and E. H. Poindexter, *This Journal*, **124**, 158 (1977); J. H. Helbert, P. J. Caplan, and E. H. Poindexter, *J. Appl. Poly. Sci.*, **21**, 797 (1977).
9. S. Imamura, S. Sugawara, and K. Murase, *This Journal*, **124**, 1139 (1977).
10. L. F. Thompson, *Solid State Technol.*, **1974**, 27 (1974).

Rutherford Backscattering Analysis of Ion-Implanted, Thermally Oxidized Silicon

C. E. Christodoulides, W. A. Grant, and J. S. Williams

Department of Electrical Engineering, University of Salford, Salford M5 4WT, England

It is well documented (1-3) that many impurities redistribute during thermal oxidation of silicon. Impurities may be incorporated within the oxide or be pushed ahead by the advancing oxide-silicon interface. Other factors, including the segregation coefficient at the interface, the rate of oxidation, and the impurity diffusion coefficient, determine the final distribution. Since ion implantation is now widely employed for doping silicon, data on redistribution in oxidized, implanted samples (2, 3) is essential to complement that for diffused samples.

Rutherford backscattering (RBS) provides a simple experimental technique (2) for investigating the thermal oxidation of silicon implanted with heavy implants (*i.e.*, impurities heavier than silicon). The technique provides information on the concentration and distribution of implanted species, and on the stoichiometry of compound substrates. When combined with channeling (2), it also provides information on the location of impurities within the silicon lattice. Using conventional RBS apparatus (*e.g.*, 2 MeV He^+ as the analyzing beam and a solid-state detector for energy analysis of the scattered beam), typical depth resolutions of ~ 250Å are obtainable. Recently, however, it has been demonstrated that, using the same apparatus, this resolution can be improved to ~ 30Å by employing a He^+ analyzing beam that enters and leaves the sample at small angles to the surface (4). With this improvement, RBS becomes a powerful technique for investigating, with high resolution, parasurface layers of solids containing heavy impurities (5).

It is the purpose of this short communication to demonstrate the use of high resolution RBS in the analysis of thin layers of thermally oxidized silicon containing implanted impurities. Samples of <111> orientation silicon were implanted with various species including Xe^+, Pb^+, and Dy^+ at energies of 20-80 keV and to a dose 1-3 $\times$ 10^{15} ions cm^{-2}. Oxidation was carried out in air at 700°C to produce oxide layers between 100 and 2000Å, and Fig. 1 shows typical RBS data. Immediately following implantation (Fig. 1a) the backscattering spectrum consists of a signal from the silicon together with a well-resolved peak from the implanted Dy^+ ions. A depth scale can be fitted (3) along the abscissa and the projected range, *Rp*, of the Dy implanted into Si, is measured as 175Å. A thermal oxidation step results in the spectra shown in Fig. 1b, where the shaded areas can be used to calculate the oxide thickness [oxide stoichiometry and oxidation rate can also be measured, and are reported elsewhere (6)]. The position of the Si/SiO_2 interface is indicated by an arrow in Fig. 1. Changes in the distribution profile of the implanted Dy due to this oxidation are apparent. The advancing oxide-silicon interface has pushed some of the impurity ahead of it, but some has been incorporated within the oxide. A second oxidation stage, sufficient to take the oxide layer completely past the original impurity distribution within the silicon, is shown in Fig. 1c. Dysprosium retreats further before the oxide-silicon interface, leaving a proportion as a clearly resolved peak located at its original, implanted position. The data of Fig. 1 illustrate the high resolution of the RBS technique employed here; impurity redistribution can be monitored with precision as the oxide-silicon interface gradually moves through the shallow (~350Å wide) implanted distribution in silicon.

In order to more readily compare spectra of the type presented in Fig. 1 it is more convenient to have a single depth scale for the abscissa, and this is achieved by presenting all impurity distributions as a function of depth within pure silicon, as in Fig. 2.

Key words: Dy^+, Pb^+, and Xe^+ impurities, RBS, thermally oxidized silicon.

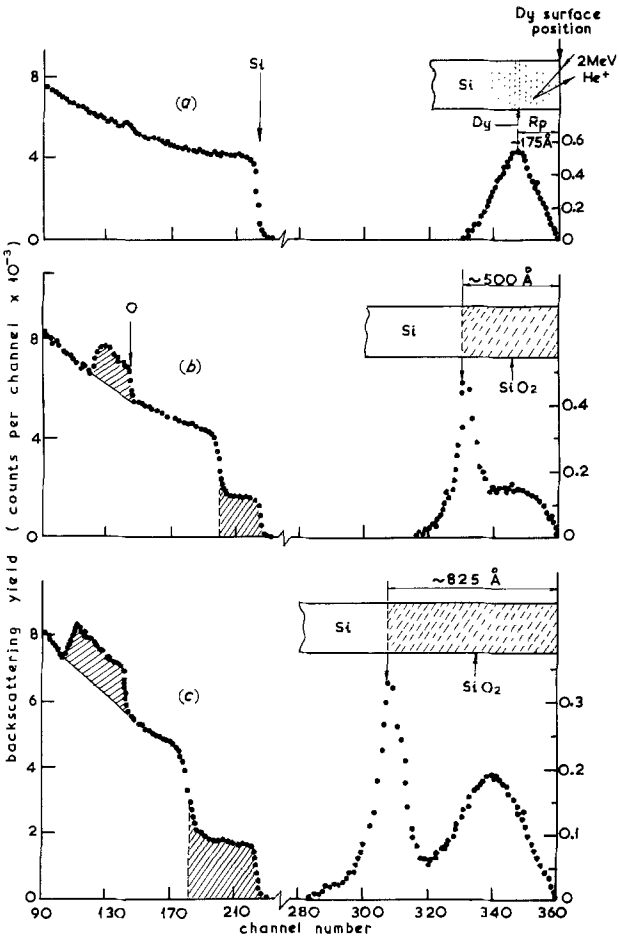


Fig. 1. Rutherford backscattering spectra for silicon implanted with 20 keV Dy^+: (a) immediately following room temperature implantation; then (b) thermally oxidized to produce 500Å SiO_2; and (c) thermally oxidized to produce 825Å SiO_2.

Thus, the distribution of an impurity within a particular SiO_2 layer is converted to the distribution within the equivalent thickness of Si consumed during the oxidation. The spectra of Fig. 2 now more easily indicate any movement of impurities relative to the silicon consumed in the oxidation process. Consequently, the thickness of all silicon and SiO_2 layers are quoted in terms of $\mu g\ cm^{-2}$ of silicon. (For convenience, thicknesses are also shown in Å.) As a specific example, 100Å of SiO_2 is formed from oxidation of 45Å (1.05 $\mu g\ cm^{-2}$) of Si.

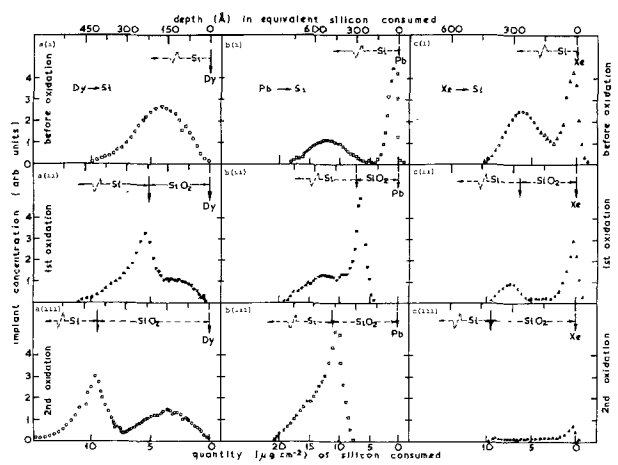


Fig. 2. The distribution of impurities Dy^+, Pb^+, and Xe^+ implanted into silicon: (*i*) top, before oxidation; (*ii*) center, after first oxidation; (*iii*) bottom, after second oxidation. All depth distributions, whether in Si or SiO_2, are shown relative to the amount of original silicon substrate converted to SiO_2 (see text for explanation).

The species Dy, Pb, and Xe shown in Fig. 2 illustrate typical behavior found from investigations (7) of a wide range of impurities. Figure 2a (i), (ii), and (iii) repeat the Dy data of Fig. 1, but using the depth scale described above, and show part of the impurity retreating before the oxide-silicon interface and part remaining at its original, implanted position. Figures 2b (i) and 2c (i) show the distributions of implanted Pb^+ and Xe^+ annealed to 700°C for ½ hr prior to oxidation. This annealing stage was necessary to stabilize the impurity profiles against further diffusion during the oxidation stages. It can be seen that both Pb and Xe diffuse partly to the surface through disordered silicon to produce a double peaked distribution profile. As shown previously (8, 9), the surface peak corresponds to impurities trapped behind the thin (< 20Å) layer of oxide normally present at room temperature on silicon.

Figures 2b (ii) and (iii) show a total push-back of Pb in front of the advancing oxide-silicon interface. The complete retreat of Pb occurs even for high implant doses, and recent results (7) show that greater than 20 monolayers of lead can be accommodated at, or close to, the Si/SiO_2 interface. In Fig. 2c (ii) the first oxidation step encompasses the Xe trapped behind the original, thin surface oxide. Rapid diffusion at the oxidation temperature causes loss of this gas except for a small percentage trapped at stable sites near the surface. The second oxidation, Fig. 2c (iii), passes the oxide-silicon interface completely through the implanted Xe, causing further gas loss by diffusion, although a small fraction remains trapped in its original implanted position.

The results presented above are a clear demonstration of the use of RBS in monitoring impurity distribution during thermal oxidation of silicon. In particular they illustrate the high depth resolution that can be obtained by optimizing the scattering geometry of the analyzing He^+ beam. With this high resolution it is clearly possible to follow the progress of the oxide-silicon interface as it proceeds through a silicon substrate, causing redistribution of shallow, implanted impurities.

The examples discussed above illustrate the three types of behavior we have found with a wide range of implanted species (7). Some species are completely pushed back by the advancing oxide (*e.g.*, Pb); some are partially pushed back and partially incorporated (*e.g.*, Dy); and some are incorporated by the advancing oxide, but diffuse readily in the oxide (*e.g.*, Xe). Implanted species have also been found to affect both the rate at which oxidation occurs and the stoichiometry of the resulting oxide (7).

Manuscript submitted Feb. 23, 1977; revised manuscript received June 27, 1977.

Any discussion of this paper will appear in a Discussion Section to be published in the June 1978 JOURNAL. All discussions for the June 1978 Discussion Section should be submitted by Feb. 1, 1978.

REFERENCES

1. B. E. Deal, E. H. Snow, and A. S. Grove, "Microelectronic Technology," p. 171, Boston Technical Publishers, Cambridge, Massachusetts (1967).
2. H. Muller, J. Gyulai, W. K. Chu, J. W. Maver, and T. W. Sigmon, *This Journal*, **122**, 1234 (1975).
3. C. R. Fritzsche and W. Rothemund, *ibid.*, **120**, 1603 (1973).
4. G. Carter and W. A. Grant, "Ion Implantation of Semiconductors," Edward Arnold, London (1976).
5. J. S. Williams, *Nucl. Instrum. Methods*, **126**, 205 (1975).

6. W. A. Grant, C. E. Christodoulides, and J. S. Williams, in Proceedings of SPIG 76, p. 343, Dubrovnik, Yugoslavia (1976).
7. A. Hamdi, C. E. Christodoulides, W. A. Grant, and J. S. Williams, To be published.
8. C. E. Christodoulides, W. A. Grant, and J. S. Williams, To be published.
9. J. S. Williams and W. A. Grant, *Inst. Phys. Conf. Ser.*, **28**, 31 (1976).

JOURNAL OF THE ELECTROCHEMICAL SOCIETY

ELECTROCHEMICAL SCIENCE AND TECHNOLOGY

NOVEMBER 1977

The Electrochemistry of the Pb | PbO_2 | $PbSO_4$ Electrode

Paul Casson and Noel A. Hampson

Department of Chemistry, Loughborough University, Leicestershire LE11 3TU, England

and Kenneth Peters*

Research Laboratories, Chloride Technical Limited, Swinton, Manchester, England

ABSTRACT

A number of observations on the electrooxidation of lead in 5M H_2SO_4 are presented. It is shown that the induction period in the potentiostatic oxidation to PbO_2 is due to the thickening of the $PbSO_4$ film and that a rising current transient signals the development of phase PbO_2; the minimum overpotential for this is ~200 mV. On a Pb|PbO_2|$PbSO_4$ electrode a rising current response to a potentiostatic experiment is not generally obtained due to the presence of adequate growth centers. Battery behavior is in agreement with the observations.

The oxidation of lead and lead sulfate to lead dioxide in sulfuric acid solutions has been extensively studied because of the technical importance of the lead dioxide (positive) battery electrode (1). Studies have ranged from elegant investigations to simple battery cycling tests.

There are three possible reactions which occur when a lead electrode is anodically polarized in sulfuric acid solution

$$Pb + SO_4^{2-} = PbSO_4 + 2e \quad [1]$$

$$PbSO_4 + 2H_2O = PbO_2 + 4H^+ + SO_4^{2-} + 2e \quad [2]$$

$$2\,OH^- = H_2O + \tfrac{1}{2}\,O_2 + 2e \quad [3]$$

$$(H_2O = 2H^+ + \tfrac{1}{2}\,O_2 + 2e)$$

Under specific conditions either or all of these occur and the electrode behavior has to be inferred from current-potential-time data coupled, where possible, with analytical and morphological studies of the electrode. Often these latter are of limited help due to the occurrence of the redox reaction

$$PbO_2 + Pb + 2H_2SO_4 = 2PbSO_4 + 2H_2O \quad [4]$$

Reaction [4] occurs when lead contacts lead dioxide under conditions of externally uncontrolled potential, the potential of the electrode being defined kinetically by the requirement that reactions [1] and [2] must occur at the same rate. The detailed response of lead to oxidation is complex and has, therefore, been built up gradually with many investigations contributing to the over-all picture.

The pioneering work of Fleischmann and Thirsk (2) showed that the development of a new phase of lead dioxide by the electrooxidation of lead sulfate required that centers of PbO_2 were nucleated. The growth of these centers gave rise to an increasing current (rising transient) until the growing areas overlapped and the current was reduced (falling transient) as the available unoxidized area became smaller.

Equations describing the current response to a potentiostatic experiment have been developed by Thirsk and co-workers (3). These equations have been applied to the process of initial oxidation of lead sulfate to lead dioxide (first charge) and subsequent cycle of charge/discharge in these laboratories (4). For the initial conversion (1st charge), the oxidation of the lead sulfate surface grown on lead produced data which confirmed earlier work (2) that progressive nucleation and growth followed by overlap was a satisfactory description of the process. Application of the Armstrong equation (3c) to the experimental data showed that by invoking a three-dimensional growth habit it was possible to provide a complete mathematical simulation of the current response to a potential step. The electrocrystallization process on a lead sulfate electrode produced by exhaustively reducing a lead dioxide electrode in sulfuric acid was more complicated than the initial $PbSO_4 \rightarrow PbO_2$ conversion. Two instantaneous nucleation and growth processes were observed, the first being two dimensional; the second, later process, in which the remainder of the lead sulfate was converted, occurring with the evolution of oxygen.

Under most practical conditions of lead cell operation, rising and falling outputs are not considered. There is no doubt that on a lead dioxide base in 5M sulfuric acid only a simple falling transient is observed as the current response in a potential step experiment (5). This system resembles that of the lead acid positive in that the electrochemistry occurs on a lead dioxide base, however, in the lead cell the lead dioxide is spongy (porous—this form of lead dioxide always results from the oxidation of $PbSO_4$ in H_2SO_4) whereas in our experiments it was massive (5). In order to consolidate the understanding of the lead cell positive electrode behavior and reconcile the two observed responses, some experiments have been carried out with lead electrodes using both the potentiostatic and potentiodynamic techniques. The present paper describes these experiments and discusses the results in the context of presently available practical observations and theoretical ideas. An attempt to apply electrocrystalli-

* Electrochemical Society Active Member.

Key words: electrocrystallization, lead-acid batteries, lead, lead sulfate, lead dioxide, positive plate.

zation concepts to the charge in a part of the lead-acid cycle has proved satisfactory.

Experimental

The working electrode was a mechanically polished (roughened glass followed by filter paper) lead disk (Johnson Matthey 99.999%) shrouded in Teflon. In most of the experiments a layer of lead was electrodeposited (5 mA/cm^2 for 15 min) from acid perchlorate electrolyte (2.25M Pb^{2+}, 0.1M H^+, 4.6M ClO_4^-). Experiments were made using a function generator (J. Dawson, Newcastle-upon-Tyne) and a potentiostat (Chemical Electronics, Type TR 70 2A). The electrode response was recorded on either an oscilloscope (Hewlet Packard, Type 130c and camera) or a pen recorder (Bryans Series 26000, X-Y-t). The counterelectrode was platinum gauze of large surface area and the reference electrode was $Hg|Hg_2SO_4|H_2SO_4$, 5M introduced at the electrode surface via a Luggin electrode probe system. All measurements were made at 23° ± 1°C. Battery tests were made using a Davenset constant potential (13.9V) charging device operating on a 12V, 40 A-hr battery. The current input was recorded automatically (Bryans Series 26000).

Results and Discussion

The rest potential of the lead electrode in 5M H_2SO_4 was found to be −963 mV; at potentials more positive than this lead sulfate was formed. Figure 1 shows a cyclic voltammogram on lead around the reversible potential (from −1400 to −700 mV) showing that at slightly more positive potentials than the reversible potential there exists a region of active dissolution. Potentiostatic experiments at −700 mV showed that the electrode is in the "passive region" although current continues to cross the electrode interphase by the process of high field conduction through a highly resistive film of lead sulfate. This film reduces the current flow to a very small value. However, for this current flow a limit exists due to the fact that the small solubility of $PbSO_4$ in 5M H_2SO_4 causes the film to need constant repair and this is offset by the high field conduction process.

Figure 2 shows a number of cyclic sweeps made around the lead dioxide equilibrium potential (700-1800 mV) at 10 mV/sec on an electrode at which PbO_2 had been produced from $PbSO_4$ at 1800 mV. Only one peak due to the reduction of PbO_2 and a wave due to oxygen evolution were observed, the PbO_2 formation peak being buried in the oxygen wave. These experiments indicate that the investigation of the behavior of systems in which lead dioxide and oxygen are produced simultaneously in sulfuric acid is limited to low

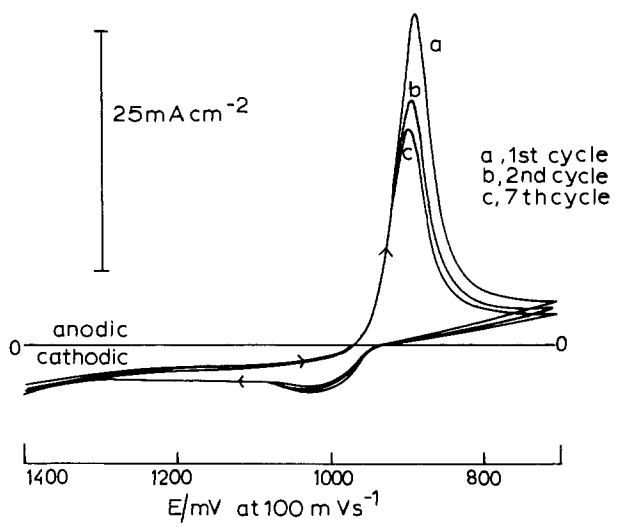


Fig. 1. Cyclic voltammogram of Pb in 5M H_2SO_4

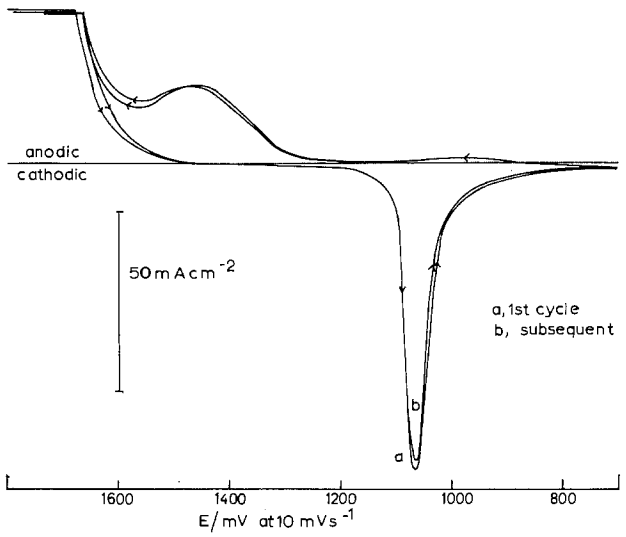


Fig. 2. Cyclic voltammograms of Pb in 5M H_2SO_4, between 700 and 2000 mV in 5M H_2SO_4.

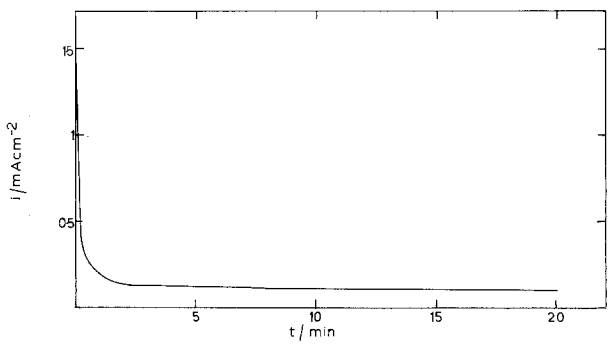


Fig. 3. Potential step from −700 to 700 mV on lead sulfate filmed lead electrode (thickening of $PbSO_4$ layer) in 5M H_2SO_4.

sweep speeds and potential step experiments. Figure 3 shows the effect of stepping an electrode covered with a stable $PbSO_4$ film (−700 mV) to a more positive potential in the sulfate region (+700 mV). A falling transient represents the thickening of the lead sulfate film.

Experiments showed that the reversible potential for the $Pb|PbO_2|PbSO_4$ H_2SO_4, 5M electrode was 1089 mV, and although the formation of PbO_2 is thermodynamically possible at this potential it was formed only after a considerable time period. In fact no formation of PbO_2 was observed until a significant overpotential was applied. Figure 4 shows the results of a step from −700 to 1492 mV. A long period of very gentle current fall is first observed which corresponds to the thickening and development of the $PbSO_4$ layer. This is followed by a rising and subsequently falling transient which signifies the formation of PbO_2. The form of the transient is similar to that previously reported for the progressive nucleation and growth of a three-dimensional deposit (2, 4). The data of Fig. 4 emphasize the importance and interplay of overpotential and time on this system. Presumably the potential across the lead sulfate/solution interphase was not sufficient for the oxidation of the Pb(II) species because of the potential drop within the lead sulfate layer itself due to the highfield conduction process which accounted for too much of the applied overpotential. It is only when the current flow through the thickening film has been reduced that oxidation starts. Another view of the process is that the lead has to be sufficiently passivated for the oxidation to commence to any net extent; any Pb(IV) species produced at a lead surface covered by an incomplete lead sulfate layer reacts according to Eq. [4]. The identities of the phases at the electrode

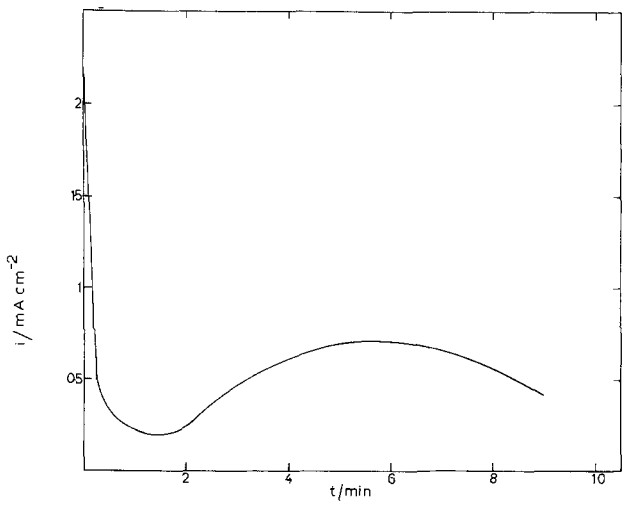


Fig. 4. Potential step from −700 to 1492 mV on lead sulfate filmed lead electrode.

were confirmed by subsequent linear sweep experiments from the final potential (1492 mV). Before the rising portion, no peak due to the reduction of PbO_2 was observed, and after the rising and falling portion a single peak due to the reduction of PbO_2 was observed. A prolonged period at 1492 mV showed a distorted peak indicating that oxygen had been produced by reaction (3) (see below).

Figure 5 shows the effect of a step into the lead dioxide region from a potential at which the lead electrode is covered with a stable film of sulfate. The results are presented as a series of reductive sweeps from the higher positive potentials to 700 mV. It is clear that only at potentials greater than 1300 mV is product lead dioxide observed at the electrode (shown by the presence of a reduction peak at ~1040 mV) within the experimental time scale. These data confirm that a considerable overpotential is required for the development of lead dioxide on an exclusively lead sulfate surface in sulfuric acid. These observations agree with those of Fleischmann and Thirsk (2) and the orders of the minimum overpotentials observed agree well with what has previously been reported. It is interesting to note that at the lower overpotentials at which lead dioxide development does start, the form of the rising time transient is very elongated. This is what would have been predicted from our previous work (4) when a correlation of potential with log (time for maximum current to occur) gave a straight line with a positive slope.

The importance of the reaction [4] in the oxidation of lead is shown by the results of a series of experiments in which lead dioxide was formed potentiostatically at 1800 mV for 30 min and then allowed to remain isolated in the electrolyte solution. Initially the potential was a stable 1157 ±1 mV for times of the order of hours and represented the reversible potential of the Pb|PbO$_2$|PbSO$_4$|H$_2$SO$_4$ (5M) electrode, in the absence of oxygen. However, when the electrode had stood for periods of days, the potential fell to −0.4V, showing that the lead dioxide layer was not perfect enough to exclude the hydrogen ion from the Pb|PbO$_2$ junction and therefore furthering reaction [4]. Polarized for sufficient times in the oxygen region, the electrode potential remained effectively constant at 1157 mV (the potential of electrodeposited PbO_2 was 1030 mV and presumably this difference is due to strongly adsorbed oxygen).

Potentiostatically oxidized and stabilized electrodes with electrode potentials of 1157 mV were uncomplicated by adsorbed oxygen (absorbed oxygen would, of course, be present) as shown by a single (PbO_2) reduction peak in the L.S.V. caused when swept to 927 mV. Figure 6 shows the results of stepping electrodes previously swept down from 1157 to 927 mV back up to 1357 mV. Only a simple falling transient is seen, indicating the absence of a significant nucleation and growth process by comparison with the overlap of the growing centers. The oxidation centers for the conversion of $PbSO_4$ to PbO_2 appear to be fully developed because of the underlying PbO_2 which both readily conducts electricity and provides adequate centers for the growth of further PbO_2. The overlap of the growing regions must commence from the time the step is initiated. Increasing the step potential to 1484 mV and ultimately to 1500 mV similarly showed only a falling transient (Fig. 6). However, it was interesting to note that at the higher oxidation potentials evidence was obtained from subsequent cathodic sweeps that oxygen was present at the electrode. These are shown in Fig. 5 by peaks in the voltammogram.

The appearance of the "coup de fouet" in the charge and sometimes in the discharge behavior of batteries is well known. The form of a rising potential in a galvanostatic charging process charge curve is difficult to treat mathematically however. A potentiostatic charge process is more assessible. It is known that the early part of the recharge of a negative plate is quite efficient [the Pb(II)/Pb reaction is fast] and there are no crystallization effects to take into account. The main factor which will cause changes in the current passing through the battery is the positive plate, and this will

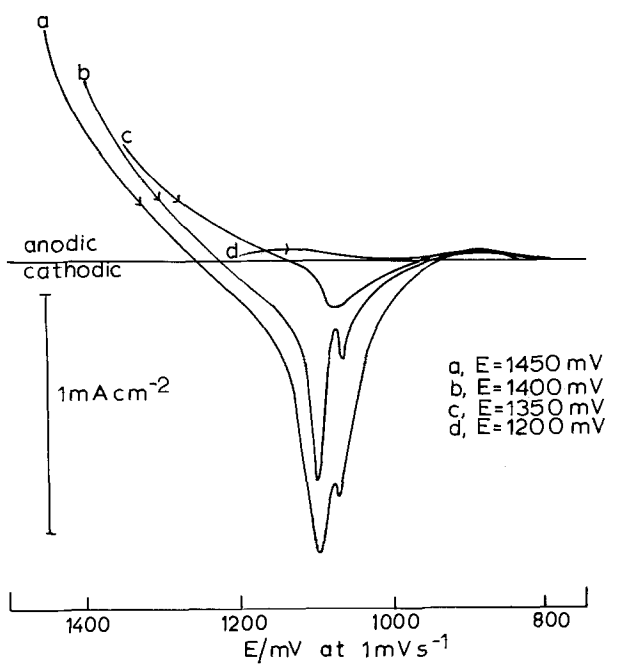


Fig. 5. Sweep to 700 mV from fixed potentials in 5M H$_2$SO$_4$

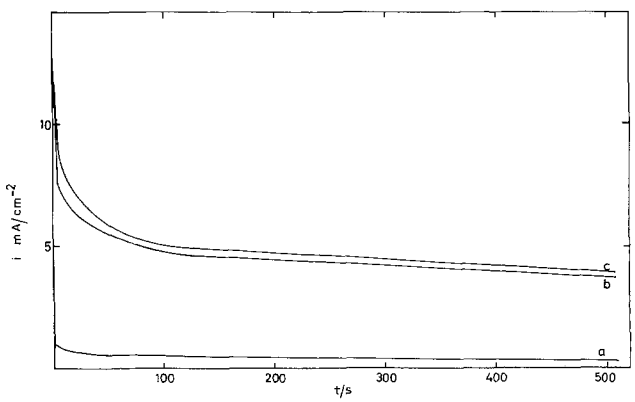


Fig. 6. Potential steps from 927 mV to higher potentials in the range (a) 1357 mV, (b) 1484 mV, (c) 1500 mV in 5M H$_2$SO$_4$.

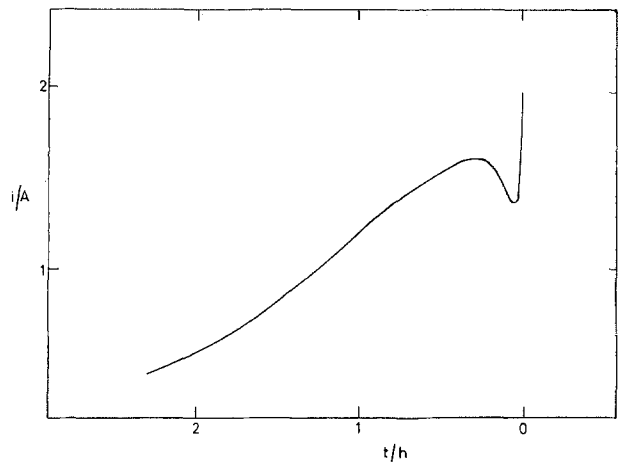


Fig. 7. Typical "coup de fouet" observed in a constant potential recharge of a 12V 40 A-hr lead acid battery at 13.9V.

be due to possible nucleation and growth effects. A relatively new 12V 40 A-hr battery was investigated using a constant potential charger to recharge from the fully discharged condition. Figure 7 shows the current response to a charge. A distinct "coup de fouet" is observed immediately the fall from the double layer charging peak is obtained. The current then falls away in the expected manner. The transient rises linearly at first which indicates that we are dealing with an instantaneous nucleation process. For two-dimensional growth and subsequent overlap the Eq. [1] describes the situation (6)

$$i = \frac{Z\mathbf{F}\pi M}{\rho} N_0 k^2 t \exp \frac{(-\pi M^2 N_0 k^2 t^2)}{\rho^2} \qquad [5]$$

where ρ = density, M = molecular weight, N_0 = number of nuclei/cm^2, k = rate constant for crystallization, Z = number of electrons transferred (2).

With a porous electrode the simple Eq. [5] characteristic of a compact deposit would not be expected to apply. However, by differentiating [5] and treating for the occurrence of a maximum many of these uncertainties of the present stochastic process may be removed. The results of this are shown in Fig. 8 which illustrates

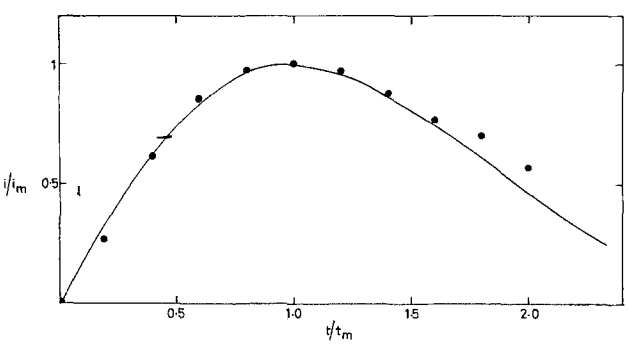


Fig. 8. Match of the rising and falling transient of Fig. 7 to the instantaneous nucleation with three-dimensional overlap model for electrocrystallization. Full cause, theoretical; ●, data points.

a reduced plate of the rising and falling part of Fig. 7 normalized in terms of t_m and i_m, the time and current co-ordinates of the maximum. The conformation of the data of Fig. 7 is very satisfactory. This is in complete agreement with earlier work using microelectrodes.

Recharging under conditions of galvanostatic control produced more complex responses as did the recharge of batteries which had received many cycles. These responses will be the subject of a subsequent paper.

Conclusions

1. An "induction period" in the potentiostatic oxidation of Pb|$PbSO_4$ is due to the thickening of the $PbSO_4$ film.
2. On Pb|$PbSO_4$ the development of a rising current indicates the onset of PbO_2 development.
3. At fast sweep rates the current peak for the formation of PbO_2 is buried in the oxygen wave.
4. The minimum overpotential for the development of PbO_2 from $PbSO_4$ is ~200 mV.
5. On Pb|PbO_2|$PbSO_4$ formed by partial reduction (passivating PbO_2 in H_2SO_4 aq) a rising transient is not obtained due to the presence of adequate PbO_2 growth areas on the electrode.
6. Using battery tests some theoretical aspects of electrocrystallization theory have been verified.

Manuscript submitted Nov. 4, 1976; revised manuscript received Aug. 1, 1977.

Any discussion of this paper will appear in a Discussion Section to be published in the June 1978 JOURNAL. All discussions for the June 1978 Discussion Section should be submitted by Feb. 1, 1978.

Publication costs of this article were assisted by Chloride Technical Limited.

REFERENCES

1a. J. P. Carr and N. A. Hampson, *Chem. Rev.*, **72**, 679 (1972).
1b. G. W. Vinal, "Storage Batteries" Wiley, New York (1965).
1c. P. Ness, *Electrochim. Acta*, **12**, 161 (1967).
1d. C. K. Morehouse, R. Glicksman, and G. S. Lazier, *Proc. I.R.E.*, **46**, 1462 (1958).
1e. J. P. Hoare, "The Electrochemistry of Oxygen," Chap. 7B, Interscience, New York (1969).
1f. J. Burbank, A. C. Simon, and E. Willihnganz, *Advan. Electrochem. Electrochem. Eng.*, **8**, 157 (1971).
2. M. Fleischmann and H. R. Thirsk, *Trans. Faraday Soc.*, **51**, 71 (1955).
3a. J. A. Harrison and H. R. Thirsk "Electroanalytical Chemistry," Vol. V, A. J. Bard, Editor, Marcel Dekker, New York (1971).
3b. M. Fleischmann and H. R. Thirsk, *Advan. Electrochem. Electrochem. Eng.*, **3**, 123 (1963).
3c. R. D. Armstrong, M. Fleischmann, and H. R. Thirsk, *J. Electroanal. Chem.*, **11**, 208 (1966).
4. P. Casson, N. A. Hampson, and K. Peters, *ibid.* In press.
5. S. G. Canagaratna, P. Casson, N. A. Hampson, and K. Peters, *ibid.*, **79**, 273 (1977).
6. H. R. Thirsk and J. A. Harrison, "A Guide to the Study of Electrode Kinetics," p. 120, Academic Press, London (1972).

Superionic Conducting Glasses: Glass Formation and Conductivity in the AgI-Ag_2O-P_2O_5 System

Tsutomu Minami, Yakuni Takuma, and Masami Tanaka

Department of Applied Chemistry, University of Osaka Prefecture, Sakai City, Osaka-Fu 591, Japan

ABSTRACT

A glass-forming region was found in the AgI-Ag_2O-P_2O_5 system at a Ag_2O/P_2O_5 mole ratio $\leqq 3$. Glass transition temperatures and conductivities at 25°C for the glasses are, respectively, expressed by

$$T_g(°C) = 6.900[AgI] + 143.4[Ag_2O] + 98.24[P_2O_5]$$

$$-\log \sigma_{25}\ (\Omega^{-1}\,cm^{-1}) = 0.1952[AgI] + 5.067[Ag_2O] + 3.970[P_2O_5]$$

where [AgI], [Ag_2O], and [P_2O_5] are mole fractions of each component in the glass. These equations show that T_g and σ_{25} are primarily governed by the AgI content. From the results, it is speculated that a portion of the silver ions forms partially covalent bonds Ag-O-P. Conductivities at room temperature range from 10^{-3} to $10^{-2}\ \Omega^{-1}\,cm^{-1}$. The advantages of glass formation for obtaining solid electrolytes with higher ionic conductivity are shown. Transport numbers of silver ions are approximately unity in the glasses.

Solid electrolytes with high ionic conductivity at ambient temperature have been extensively studied for technological applications and/or fundamental interest (1-6). These electrolytes, however, are all crystalline solids. If glass formation of the electrolytes is possible, advantages can be expected, such as isotropic properties, ease of thin film formation, and the like. In addition, the electric conductivity of glasses with ion movement has been reported to be higher than that of crystals (7, 8). This is surprising for ionic conductors since, as is well known, electronically conducting glasses have several orders of magnitude lower conductivities than crystals because of high scattering and low carrier mobilities in the disordered structure (9, 10). Thus, in solid electrolytes, it is of interest to develop glass-forming systems with high ionic conductivities. In a previous paper (11), we reported the glass-forming region in the AgI-Ag_2O-MoO_3 system. In searching for other glass-forming systems with high ionic conductivity, the AgI-Ag_2O-P_2O_5 system appeared promising, since a composition with high AgI content in the AgI-$Ag_4P_2O_7$ system was reported to form a glassy product when cooled naturally (5).

In this paper, the glass-forming region is presented for the AgI-Ag_2O-P_2O_5 system, with emphasis on the composition range of high AgI and low P_2O_5 content. The glass transition temperature and the conductivity were determined as a function of composition.

Experimental

Sample preparation.—Silver iodide,[1] special grade Ag_2O, and special grade H_3PO_4 were used as raw materials for the sample preparation. For samples with a Ag_2O/P_2O_5 mole ratio of 2 or 3, $Ag_4P_2O_7$ [1] or Ag_3PO_4,[1] respectively, was also used as the raw material instead of Ag_2O and H_3PO_4, in order to compare the characteristics of glasses prepared from different raw materials. Glasses were prepared by melting the mixed raw materials in a Pyrex glass ampul at 500°C for 20 hr. The resultant melts were poured onto a stainless steel plate.

The x-ray powder diffraction measurements, using Cu-K_α radiation, were made for all the samples prepared to determine whether any crystalline phase was included.

Determination of glass transition temperature.—The glass transition temperature (T_g) of each glassy sample was determined by differential thermal analysis (DTA) using a Rigaku Denki thermal analyzer. The DTA was measured from room temperature to 500°C with a heating rate of 10°C/min and a nitrogen gas flow rate of about 60 ml/min.

Conductivity measurement.—Conductivities were measured at 1000 Hz in an electrically shielded chamber (made of brass) filled with dry nitrogen gas in the temperature range 200°-300°K by using a universal bridge (YHP, Model 4260A) and/or a G-C bridge (Ando Denki, Model TR-1C). Two types of samples were used for the conductivity measurement. In the first, evaporated silver electrodes were applied to the opposite sides of bulk glass samples whose diameter and thickness were 7-15 and 1-2 mm, respectively. In the second, pellets of pulverized glass were pressed using a mixture of 0.3g of glass and 0.9g of silver powder for the electrodes. About 1.2g of pulverized glass was stacked between the electrodes and pressed into a pellet 13 mm in diameter, using 2 tons/cm^2 with a hand press. The latter type of sample construction was reported to minimize the contact resistance in the conductivity measurement of silver ion conducting electrolytes (3, 5, 12).

Transport number measurement.—The transport number of silver ions in glassy electrolytes was measured by Tubandt's method (13) and by the emf method. In Tubandt's method, a cell of the type

$$\underset{(+)}{Ag/X_1/X_2/X_3/X_4/}\underset{(-)}{Ag} \qquad [I]$$

was used, where X's were pellets of glasses. The change in mass of the four cell parts was measured by a microbalance (Mettler, Model M5), and the total charge passed was measured with a coulometer (Nichia, Model N-CR_4). In the emf method, a cell of the type

$$Ag/\text{bulk glass}/I_2, C \qquad [II]$$

was used, where the cell reaction is

$$Ag(s) + \tfrac{1}{2}\, I_2(g) = AgI(\text{glass}) \qquad [1]$$

and the transport number of silver ions, t_r, can be determined by

$$t_r = \frac{V}{V_0} \qquad [2]$$

where V is the emf measured, and V_0 the standard emf for the formation of AgI (=687 mV) (5).

Key words: solid electrolytes, silver ion conducting glasses, superionic conductors, phosphate glasses.

[1] AgI, Ag_3PO_4, and $Ag_4P_2O_7$ were prepared according to Ref. (5) from special grade $AgNO_3$, KI, $Na_2HPO_4 \cdot 12H_2O$, and $Na_4P_2O_7$.

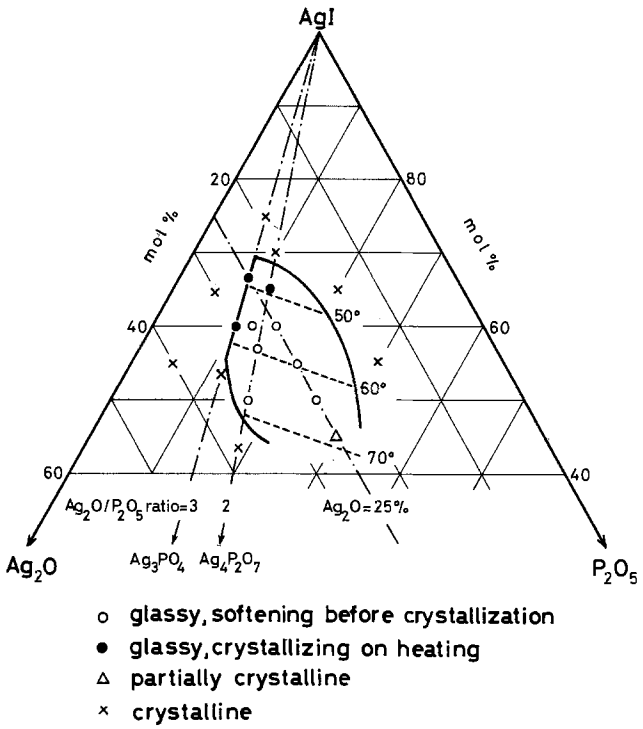


Fig. 1. Glass-forming region and iso-T_g lines in the AgI-Ag_2O-P_2O_5 system. The values in the figure are T_g(°C).

Results and Discussion

Glass-forming region and T_g.—Figure 1 shows the glass-forming region and iso-T_g lines in the AgI-Ag_2O-P_2O_5 system. In the figure open circles denote glassy samples which softened before crystallization; *i.e.*, only endothermic change at T_g was observed and no crystallization peaks were observed in DTA measurements. Shaded circles denote glassy samples which crystallized on heating; *i.e.*, exothermic peaks due to crystallization as well as endothermic changes at T_g were observed in DTA measurements. The triangle denotes a sample in which a small portion of crystallized inclusion was observed. For this sample, the transparent (glassy) part was used for T_g and conductivity measurements. Crosses denote crystalline samples. Glassy samples were transparent and yellow to brown in color, depending on the composition. The samples were somewhat sensitive to light, and thus were carefully handled under safe-lights.

The glass-forming region is limited to compositions with the Ag_2O/P_2O_5 ratio, $R \leqq 3$, and it is remarkable that glass formation was possible for the compositions with $R = 3$. This high value of R recalls the so-called "invert glass" (14) and means there are no condensed structural units of PO_4^{3-} group (15); in other words, these glasses can be classified as "ionic" glasses (16) as well as phosphate glasses. No appreciable difference was observed in the glass-forming ability of samples prepared from AgI, Ag_2O, and H_3PO_4 and from AgI and Ag_3PO_4 or $Ag_4P_2O_7$.

The iso-T_g lines are drawn by

$$T_g(°C) = 6.900[AgI] + 143.4[Ag_2O] + 98.24[P_2O_5] \quad [3]$$

or

$$T_g(°K) = 280.0[AgI] + 416.5[Ag_2O] + 371.3[P_2O_5] \quad [3']$$

where [AgI], [Ag_2O], and [P_2O_5] are mole fractions. Equations [3] and [3'] were determined by computer analysis based on least squares. In Table I, comparison between observed and calculated values of T_g is shown. The maximum deviation and the probable error are 4.1° and ± 1.9°.

The iso-T_g lines are roughly horizontal. This means that T_g is primarily determined by AgI content, rather than Ag_2O or P_2O_5 content. We can speculate from this result that a portion of silver ions, especially introduced in the form of Ag_2O, forms partially covalent bonds Ag-O-P. The formation of partially covalent bonds Ag-O-P was suggested in Ag_2O-P_2O_5 glasses from *IR* spectra (17).

Table I. Comparison of calculated and observed T_g in AgI-Ag_2O-P_2O_5 glasses

Glass No.	Composition (m/o) AgI	Ag_2O	P_2O_5	T_g(°C) Observed	Calculated*	Deviation
1	66.7	25.0	8.3	50	48.6	+1.4
2	60.0	30.0	10.0	55	57.0	−2.0
3	65.0	23.3	11.7	48	49.4	−1.4
4	57.1	28.6	14.3	59	59.0	0.0
5	50.0	33.3	16.7	70	67.6	+2.4
6	60.0	25.0	15.5	58	54.7	+3.3
7	55.0	25.0	20.0	62	59.3	+2.7
8	50.0	25.0	25.0	64	63.9	+0.1
9	45.0	25.0	30.0	66	68.4	−2.4
10	60.0	28.0	12.0	52	56.1	−4.1

* Calculated by Eq. [3].

Figure 2 shows the composition dependence of density. The data are plotted against AgI content for a series of compositions on each tie line of $R = 3$, $R = 2$, and Ag_2O content = 25 mole percent (m/o). The density change with composition is linear in each series of compositions, but the slopes are quite different. This is in evident contrast with the composition dependence of T_g mentioned above, and of conductivity, shown later.

Dependence of conductivity on temperature and composition.—In Fig. 3, the comparison of conductivity between bulk glasses and pellets is shown for the samples with $R = 2$. The conductivities are expressed by

$$\sigma = \frac{C}{T} \exp\left(-\frac{E}{RT}\right) \quad [4]$$

where σ is the conductivity, T the absolute temperature, C a constant, R the gas constant, and E the acti-

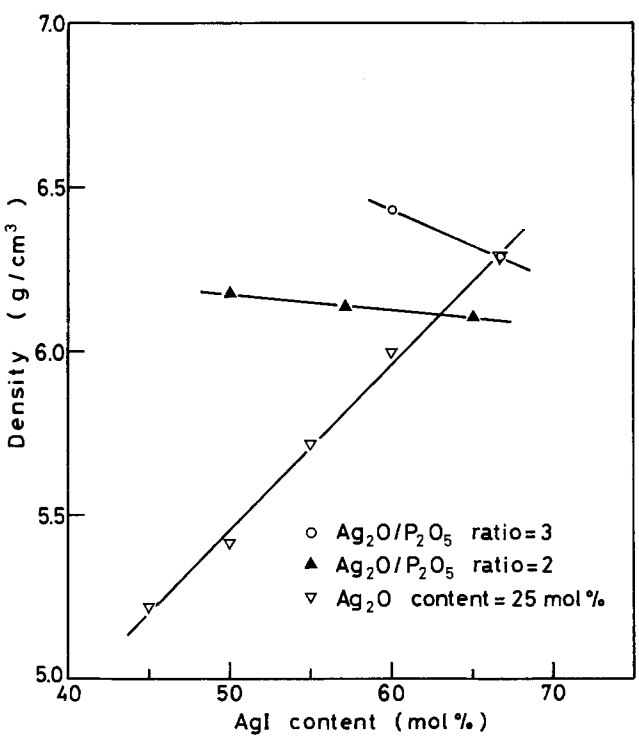


Fig. 2. Composition dependence of densities in the AgI-Ag_2O-P_2O_5 glasses.

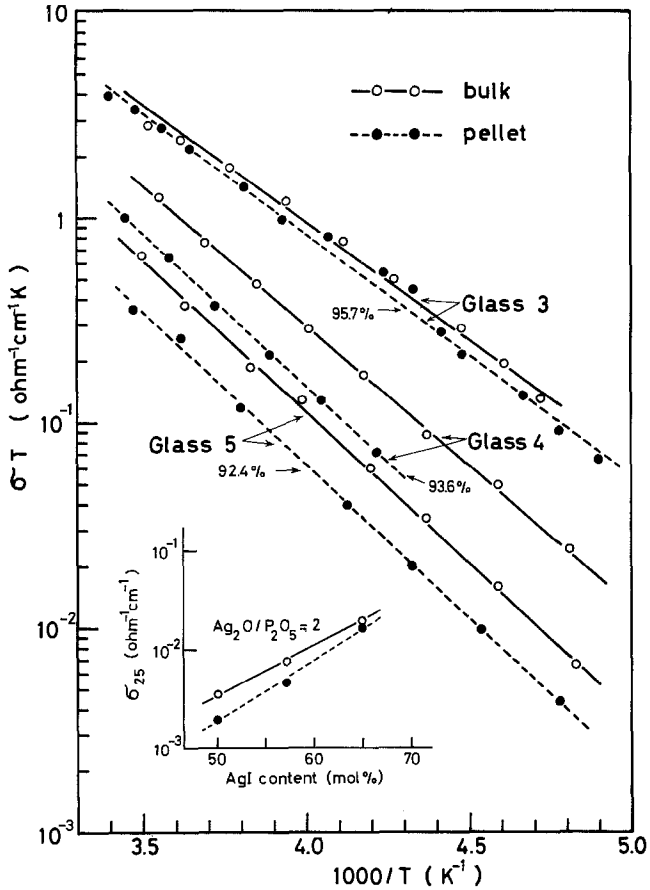


Fig. 3. Comparison of conductivities between bulk glasses and pellets. Percentages are packing densities of pellets.

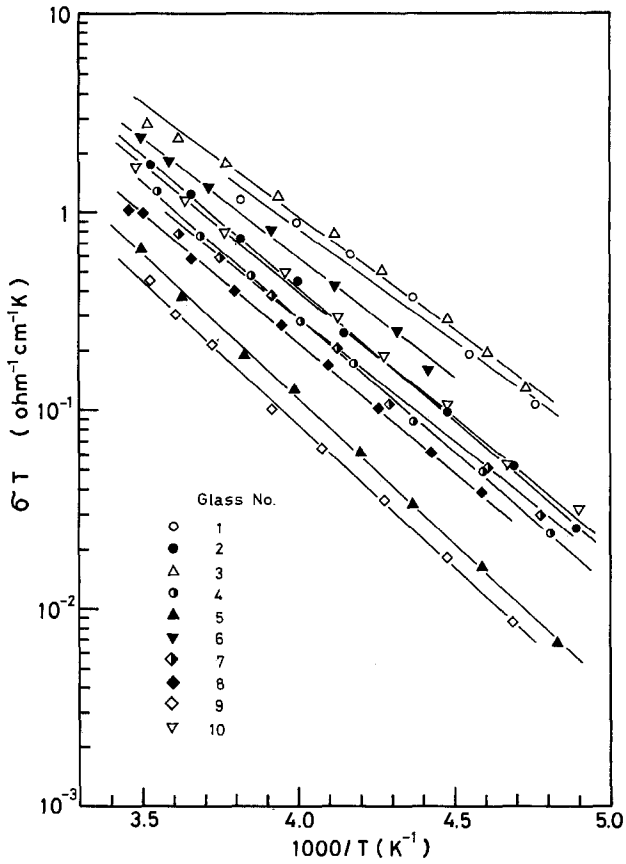


Fig. 4. Temperature dependence of conductivity in the AgI-Ag_2O-P_2O_5 glasses.

vation energy for conduction. The conductivities of pellets at a given temperature are slightly smaller than those of bulk glasses, and the E values are very similar between pellets and bulk samples. These results are reasonable, if the packing densities of the pellets (shown in the figure) are considered. In the inset of the figure, the composition dependence of bulk and pellet conductivities at 25°C, σ_{25}, determined from the temperature dependence, are also shown. The values of σ_{25} of pellets are smaller by 6-44% than those of bulk glasses. The difference becomes smaller with increasing AgI content, which is probably associated with the decrease in T_g with increasing AgI content.

Figure 4 shows the temperature dependence of conductivities for all the bulk glasses. The straight lines were drawn by least squares. The activation energies ranged from 5.2-6.7 kcal/mole and increased with the decrease in conductivity. It should be noted that the energies are larger by only 2-3 kcal/mole than those of crystals of similar compositions (5).

The values of σ_{25} determined from Fig. 4 are plotted against AgI content in Fig. 5. Those of crystals reported by Takahashi *et al.* (5) are shown for comparison, using a dotted curve. In Ref. (5), the composition dependence of σ_{25} was separately shown for AgI-Ag_3PO_4 and AgI-$Ag_4P_2O_7$ systems, but in Fig. 5, σ_{25} is plotted against AgI content within the composition range of glass formation, using the Ag_2O/P_2O_5 ratio as a parameter. It should be noted that σ_{25} of glasses is 5-10 times larger than that of crystals, and that σ_{25} of glasses increases almost linearly with increasing AgI content, irrespective of the position in the glass-forming region. The latter fact allows us to speculate again that a portion of silver ions introduced as Ag_2O forms partially covalent bonds Ag-O-P and thus makes a small contribution to the high conductivity of the glasses.

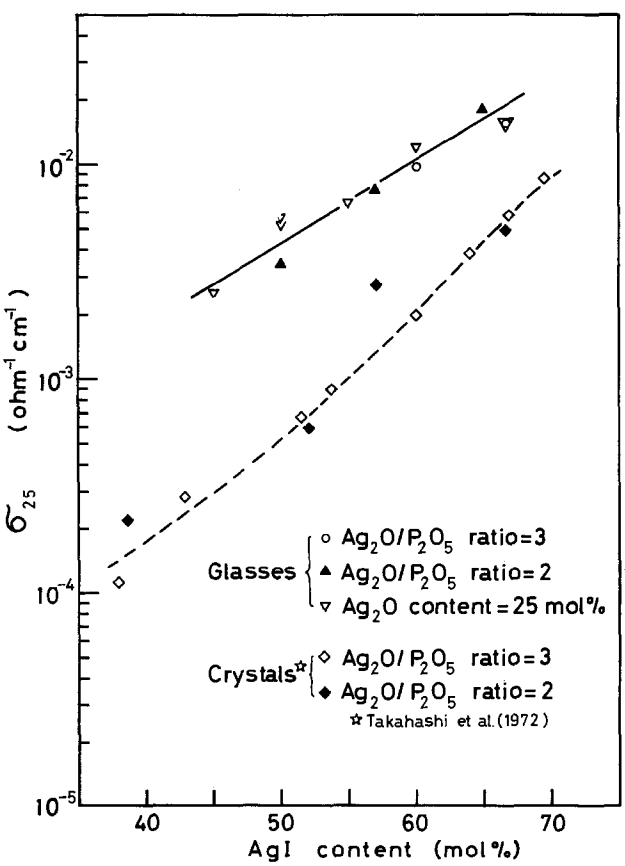


Fig. 5. Composition dependence of conductivity at 25°C, σ_{25}, in the AgI-Ag_2O-P_2O_5 glasses. The conductivities of crystals in the AgI-Ag_3PO_4 and AgI-$Ag_4P_2O_7$ systems reported in Ref. (5) are replotted for comparison.

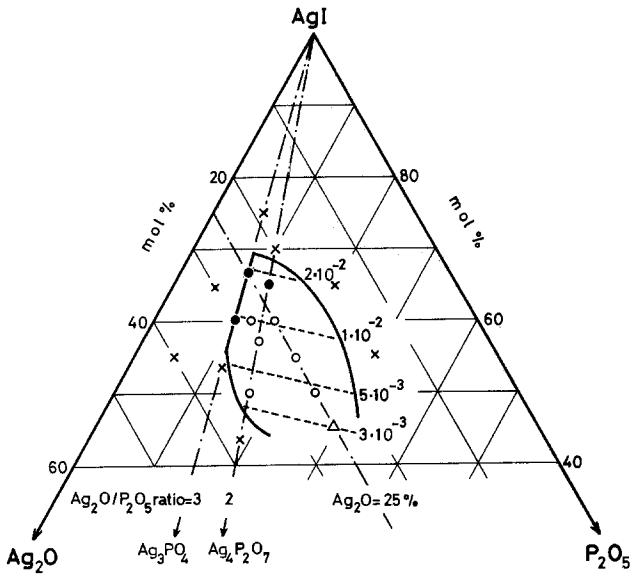


Fig. 6. Iso-σ_{25} lines in the AgI-Ag_2O-P_2O_5 glasses. The values in the figure are σ_{25} (Ω^{-1} cm^{-1}).

Figure 6 shows the iso-σ_{25} lines which were drawn by

$$-\log \sigma_{25} = 0.1952[AgI] + 5.067[Ag_2O] + 3.970[P_2O_5] \quad [5]$$

A small value of the factor for AgI and the nearly same value for Ag_2O and P_2O_5 are noticed.

Table II shows the comparison between observed and calculated values of σ_{25}. The agreement is very good, with the maximum deviation and probable error for log σ_{25} (Ω^{-1} cm^{-1}) being 0.09_2 and $\pm$ 0.04_1, respectively. In Table II, the activation energies are also shown for each glass.

Transport number of silver ions.—Table III shows the result of the transport number measured for glass 4 by Tubandt's method. The result indicates that the charge carriers of glass 4 are nearly 100% silver ions. Transport numbers determined by the emf method are listed in the last column of Table II. We can conclude that the predominant carriers in the glasses are silver ions and that the contribution of protons to the conduction is negligible, although water content was not determined.

Appreciable difference in properties was not detected between glasses prepared from different raw materials.

Conclusion

Glasses were prepared in the AgI-Ag_2O-P_2O_5 system in the composition range of Ag_2O/P_2O_5 ratio $\leqq 3$ and high AgI content. Glass transition temperatures and conductivities were primarily governed by the AgI content. From these results we speculate that some portions of silver ions, especially introduced in the form of Ag_2O, form partially covalent bonds Ag-O-P.

Conductivities of the glasses are higher than those of crystals of the same chemical composition, indication that glass formation has advantages for obtaining high conductivity solid electrolytes. Transport numbers of silver ions were approximately unity for the glasses. The influence of water content on glass-forming ability, glass transition temperature, conductivity, transport number, and so on, are now under study and will be published elsewhere.

Table II. Comparison of calculated and observed σ_{25} in AgI-Ag_2O-P_2O_5 glasses

Glass No.	Log σ_{25} (Ω^{-1} cm^{-1}) Observed	Calculated*	Deviation	E** (kcal/mole)	t_r†
1	-1.81_8	-1.72_6	-0.09_2	5.2	0.975
2	-1.98_3	-2.03_4	$+0.05_1$	6.2	0.959
3	-1.74_7	-1.77_2	$+0.02_5$	5.3	0.994
4	-2.12_5	-2.12_8	$+0.00_3$	6.2	0.975
5	-2.46_7	-2.44_8	-0.01_9	6.7	0.962
6	-1.91_7	-1.97_9	$+0.06_2$	5.5	0.961
7	-2.18_8	-2.16_8	-0.02_0	5.8	0.972
8	-2.28_2	-2.35_7	$+0.07_5$	6.0	0.975
9	-2.60_9	-2.54_5	-0.06_4	6.6	0.975
10	-2.03_4	-2.01_2	-0.02_2	5.9	0.981

* Calculated by Eq. [5].
** Activation energy for conduction.
† Transport number of silver ions determined by the emf method.

Table III. Transport number in glass 4 measured by Tubandt's method

	Change in mass (mg)
Ag anode	−3.40
X_1	+0.02
X_2	+0.01
X_3	+3.38
X_4	3.432
Ag cathode	0.988 ± 0.003
Change in mass (theoretical)*	
Transport number of Ag^+	

* The change in mass was calculated from the total charges recorded by a coulometer.

Acknowledgment

This research was partly supported by a Scientific Research Grant from the Ministry of Education of Japan.

Manuscript submitted April 18, 1977 revised manuscript received July 7, 1977.

Any discussion of this paper will appear in a Discussion Section to be published in the June 1978 JOURNAL. All discussions for the June 1978 Discussion Section should be submitted by Feb. 1, 1978.

Publication costs of this article were assisted by the University of Osaka Prefecture.

REFERENCES

1. T. Takahashi and O. Yamamoto, *Denki Kagaku*, **32**, 610 (1964).
2. J. N. Bradley and P. D. Green, *Trans. Faraday Soc.*, **62**, 2069 (1966).
3. B. B. Owens and G. R. Argue, *Science*, **157**, 308 (1967).
4. M. De Rossi, G. Pistoria, and B. Scrosati, *This Journal*, **116**, 1642 (1969).
5. T. Takahashi, S. Ikeda, and O. Yamamoto, *ibid.*, **119**, 477 (1972).
6. J. C. Philips, *ibid.*, **123**, 934 (1976).
7. G. H. Frischat, in "Materials Science Research: Mass Transport Phenonena in Ceramics," Vol. 9, A. R. Cooper and A. H. Heuer, Editors, p. 285, Plenum Press, New York and London (1975).
8. R. T. Johnson, Jr., R. M. Biefild, M. L. Knotek, and B. Morosin, *This Journal*, **123**, 680 (1976).
9. H. Fritzsche, in "Amorphous and Liquid Semiconductors," J. Tauc, Editor, chap. 6, Plenum Press, London and New York (1974).
10. T. Minami, J. Washo, and M. Tanaka, Proceedings of 10th International Congress on Glass, Kyoto, 1974, **13**, 19 (1974). Published by the Ceramic Society of Japan, Tokyo.
11. T. Minami, H. Nambu, and M. Tanaka, *J. Am. Ceram. Soc.*, **60**, 283 (1977), In press.
12. B. B. Owens and G. R. Argue, *This Journal*, **117**, 898 (1970).
13. C. Tubandt, *Handbuch Exp. Phys.*, **12**, 383 (1932); *loc. cit.* Ref. (5).
14. H. Rawson, "Inorganic Glass-Forming Systems," pp. 91, 166, Academic Press, London and New York (1967).
15. J. R. Van Wazer, "Phosphorus and Its Compounds," Vol. 1, p. 733, Interscience Publishers, Inc., New York (1958).
16. R. H. Doremus, "Glass Science," p. 23. John Wiley & Sons, Inc., New York (1973).
17. R. F. Bartholomew, *J. Non-Crystalline Solids*, **7**, 221 (1972).

Aspects of the Role of Lignin Additives in Pasted Lead Electrodes

B. K. Mahato*

Globe-Union Incorporated, Corporate Applied Research Group, Milwaukee, Wisconsin 53201

ABSTRACT

The effect of the cations of lignosulfonate salts on the physical and electrochemical characteristics of pasted-type lead electrodes has been studied. The cations studied were H^+, Na^+, NH_4^+, Zn^{++}, Ca^{++}, and Ba^{++}. The lignosulfonate anion concentration was held constant by maintaining constant u.v. absorption at 280 mμ wavelengths. The cations affected the hydrogen evolution potential at the end of formation and at the onset of passivation potential, and they affected the capacity retentive characteristics during cycling. Of all the lignosulfonates tested, the sodium salt imparted the best capacity retentive characteristics.

The high rate, low temperature performance of the lead-acid battery is recognized to be limited by the performance of its negative electrode (1). The inclusion of an expander material, particularly a sulfonate derivative of lignin, in the negative active material increases its capacity or the efficiency with which it is utilized. The lignosulfonates have been found to be adsorbed strongly on the metallic lead surface (2), to cause recrystallization and particle size growth of lead sulfate (3), to cause the formation of a porous passivating lead sulfate layer (4), delay onset of the solid-phase passivation reaction (5), and to beneficially influence the electroreduction process during formation (6). In brief, these prior observations qualitatively indicate that the lignin compound in the lead matrix modifies the microstructure of the negative active material produced during formation and delays the electrode passivation during high rate discharge. However quantitative characterization of the functioning of this type of additive has been difficult, particularly in pasted-type electrodes, due to the multitude of variables involved in preparation of the lead electrode, the ill-defined nature of the lignin and lignosulfonate molecules, and the lack of analytical means of monitoring the concentration and stability of these compounds in the lead-acid system.

The lignosulfonate obtained from bisulfite cooking of softwood is believed to be an ordered polymer containing 16 MeO groups, 8 sulfo groups, 9 phenolic OH groups, and 2 sulfide sulfur atoms per repeating unit (7). The molecular character of the product is influenced both by the raw material and process variables (8). Its physical and chemical properties are also influenced by the nature of the cations present in the molecule (9).

In this work it was attempted to understand the specific role of lignosulfonate in the lead-acid battery negative by determining the effects of the cations on the physical and electrochemical properties of the sponge lead electrode.

Experimental

The lignosulfonate samples tested are listed in Table I. These were obtained from American Can Company, Rothschild, Wisconsin. Anionic equivalent amounts of these samples were defined as those producing identical u.v. absorption in water solution at 280 mμ wavelengths. These amounts, used for paste preparation, are indicated in the table. The cation concentrations calculated from the organic sulfur content of these samples are also included in the table. The absorptivity of lignosulfonic acid at 280 mμ wavelength was found independent of cation concentrations at least in the range used in the present study.

Pastes of leady oxide and sulfuric acid solution were prepared by a Readco Laboratory Mixer using a dry-blended mixture of lignin compound with ball mill oxide, and 88-106 ml water plus 60 ml 1.325 sulfuric acid solution per kilogram of oxide. The oxide had 26.9 ± 1.4% free lead. Carbon black and barium sulfate additives were not used. SLI-type pasted electrodes measuring 14.50 cm long × 12.00 cm wide × 0.15 cm thick were prepared. The electrode grid was antimonial lead with 4.75% Sb, 0.275% Sn, and 0.275% As. Curing was carried out at ambient temperature for 3 days. The dry paste weight of the test electrode was controlled at 75 ± 1g per plate. The average geometric surface area of both sides of the electrode, excluding the area occupied by the grid members, was 312 cm^2 per electrode. A test cell had one test electrode and two dry-charged counterelectrodes at 0.64 cm separations. No separators were used. Electroformation was carried out in 1.250 sp gr sulfuric acid solution at 5 mA/cm^2 for 24 hr, at 21.5° ± 0.5°C. The electrode potential relative to a standard $Hg/Hg_2SO_4/4.685M\ H_2SO_4$ reference was measured at the end of formation. The electrolyte specific gravity was then adjusted to 1.270. The anodic behavior was determined by linear potential sweep, and the discharge capacity at 100 mA/cm^2 and −18°C (0°F). Test cells were also cycled in the scaled-down version of the SAE J 240 life test described in Table II.

All experiments were carried out in triplicate. Microstructures of the active material as formed and at

Table I. Lignosulfonates and their concentration in negative paste mix

Lignosulfonates			
Type	w/o of organic sulfur content	w/o of cation associated with RSO_3 group (calculated values)	Amount used per 100 g leady oxide, (g*)
Sodium lignosulfonate (Maracell-E)	3.0	2.2	0.300
Sodium lignosulfonate (Maracell-C)	2.8	2.0	0.107
Lignosulfonic acid	3.0	0.1	0.535
Ba-lignosulfonate	0.9	1.9	0.485
Zn-lignosulfonate	6.2	6.3	0.328
Ca-lignosulfonate	3.6	2.3	0.343
NH_4-lignosulfonate	6.5	3.7	0.321

* The proportion of lignosulfonate to leady oxide is that giving identical u.v. absorption in a water solution at 280 mμ wavelength as 0.300 w/o Maracell-E. Oxide used for this study had 26.9 ± 1.4 w/o metallic lead.

* Electrochemical Society Active Member.

Key words: lead-acid battery, expanders, sponge lead, lignosulfonates.

Table II. SAE J240 life test specifications

(scaled down for testing a cell with one negative and two counter positives)

Temperature:	41° ± 3°C	
Test cycle:	discharge:	2 min at 5A
	charge:	max voltage—2.47V max current—5A time—10 min

Table III. Effect of lignosulfonate cations on the end-of-formation potential

Additive in test electrode	$E_{negative}$ (*vs.* Hg/Hg_2SO_4) mV (−)
Control (no additive)	1365
Sodium lignosulfonate (Maracell-E)	1423
Sodium lignosulfonate (Maracell-C)	1445
Lignosulfonic acid	1455
Ca-lignosulfonate	1462
NH_4-lignosulfonate	1475
Zn-lignosulfonate	1486
Ba-lignosulfonate	1513

different stages of life cycling were examined by SEM. The specific surface of the active mass was determined by BET nitrogen adsorption using a Quantasorb analyzer.

Results and Discussion

The effect of lignosulfonate cation on the end-of-formation potential is shown in Table III. The relative hydrogen overvoltage at the formation current density used becomes increasingly cathodic for the following order of cations: Na^+, H^+, Ca^{++}, NH_4^+, Zn^{++}, and Ba^{++}. Maracell-E and Maracell-C are commercial varieties of sodium lignosulfonate. The latter is a desulfonated, purified product with average molecular weight 5-10 times larger than that of Maracell-E (10). The difference in their hydrogen overvoltages appears due to this difference of molecular structure. Of all the lignosulfonate samples tested, the barium salt exhibited the maximum cathodic potential. This is consistent with the reported stronger adsorption of barium lignosulfonate than sodium lignosulfonate by lead powder (9).

Anodic current *vs.* potential for negative electrodes containing different lignosulfonates is shown in Fig. 1. The test cells were at 21° ± 0.5°C; potential was anodically scanned at 2 mV/sec. The curve shapes are similar to those reported recently by Brennan and Hampson (5) for a stationary lead electrode. They attribute the nonlinearity in the high current region to the commencement of solid-phase reaction leading to electrode passivation. In this reaction, sulfate or bisulfate anions combine with the lead surface under the influence of potential to form a passivating film. Figure 1 indicates that for the control electrode, potentials more negative than −923 mV do not favor the formation of lead sulfate nuclei on the lead surface by direct anion attack; at potentials more positive than −923 mV the reaction commences. The cations of the lignosulfonate additive are seen to affect this potential in the order $Zn^{++} < Na^+ < Ba^{++} < NH_4^+ < Ca^+ < H^+$. This suggests a possible role of cation in controlling the reaction mechanism in some fashion. No direct correlation between this critical potential and hydrogen overvoltage at the end of formation is evident. It is, however, highly likely that the anionic attack of lead begins when the dissolution process is unable to sustain the anodic potential. The dissolution mechanism of lead as well as precipitation of lead sulfate is influenced by the structure of electrode/electrolyte interface, the coverage of interface by the additive, nature of additive, and the concentration of dissolving species at the liquid interface. During anodic dissolution, besides the concentration of dissolving species, the *p*H of the interfacial layer increases, bringing adsorbed additives into the solution. The *p*H-dependent solubility of the lignosulfonate compound is well known (11). The cation in the additive possibly controls *p*H-dependent dissolution behavior. The saturation concentration of Pb^{2+} ion at the interface is also possibly influenced by the lignosulfonate anion, which is known to be a strong sequestering agent (11) through formation of a transient "Pb-lignosulfonate complex." Such a transient complex formation could provide a mechanism for the formation of a large crystal noted in the literature (3), *i.e.*, the decomposition of the transient compound to feed crystal growth on the already formed lead sulfate crystals. Such a process might also be accompanied by the occlusion of additive in the discharge matrix, which would then come into play during subsequent charging and electrocrystallization. The inhibiting influence of a lignin compound (totatin FNA) on the nucleation and growth of passivating lead sulfate film has been considered by Brennan and Hampson (12).

Figure 2 shows the 100 mA/cm², −18°C (0°F) discharge characteristics of negative electrodes containing various lignosulfonates immediately after electroformation. All the additives irrespective of their cationic nature produced approximately the same discharge capacity—about three times that of the control. However, the effect of cation has been surfaced during repetitive charge-discharge cycling of the electrodes (to be discussed later). To avoid unnecessary presentation of similar results, the characteristic

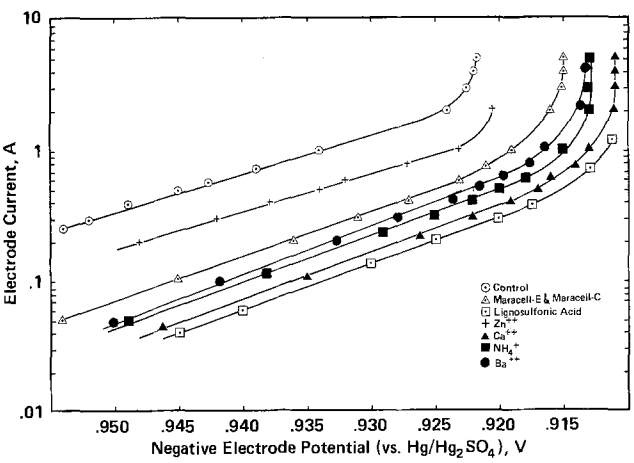


Fig. 1. Semilogarithmic representation of the linear potential sweep on freshly electroformed pasted negotive electrodes containing different lignosulfonate salts; 1.270 specific gravity H_2SO_4, 2 mV/scan rate.

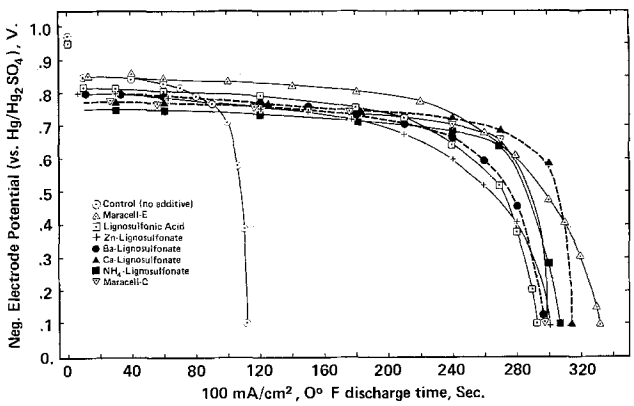


Fig. 2. Discharge characteristics of freshly formed negative electrodes as a function of lignosulfonate cations.

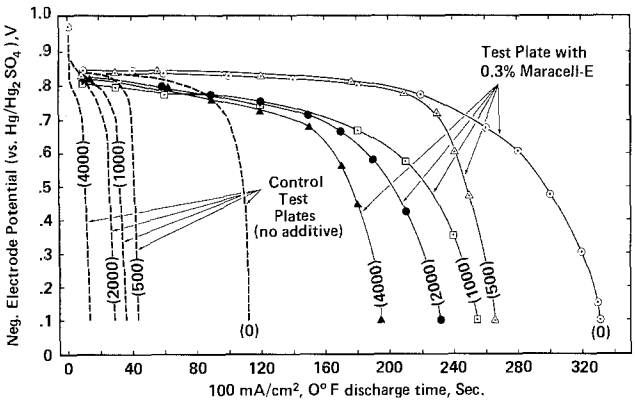


Fig. 3. Discharge behavior of control electrode (without additive) and test electrode with 0.3 w/o Maracell-E during SAE J 240-type cycling.

behavior of the electrode with 0.3 weight percent (w/o) Maracell-E is discussed in detail and summary results of the remaining test electrodes are reported. Figure 3 shows for an electrode with 0.3 w/o Maracell-E, relative to a control, the degradation of this initial discharge behavior during SAE J 240 cycling. The control electrode lost 60 and 88% of its initial capacity at 500 and 4000 cycles, respectively; the electrode with Maracell-E lost only 20 and 41%. Associated differences between the morphologies of the lignosulfonate-containing and the lignosulfonate-free electrodes, both initially and over the course of life cycling, are shown in the SEM micrographs of Fig. 4-7. These represent freshly exposed (by fracture) cross sections of charged electrodes, either about 0.50 mm from the electrode surface or at the center. The electrodes contained 0.0 or 0.3 w/o Maracell-E, and micrographs were made after 0, 500, 1000, 2000, and 4000 cycles following charging.

The complex electroformation process in the pasted negative electrode has been followed by Pavlov *et al.* (13) through analysis of the phases present in the active material during electroformation. No consideration was given to the role of additives. Pierson *et al.* (6) carried out optical microscopic studies of the active material. In the present work, the nodular structure (Fig. 4a) of the lead matrix is in agreement with

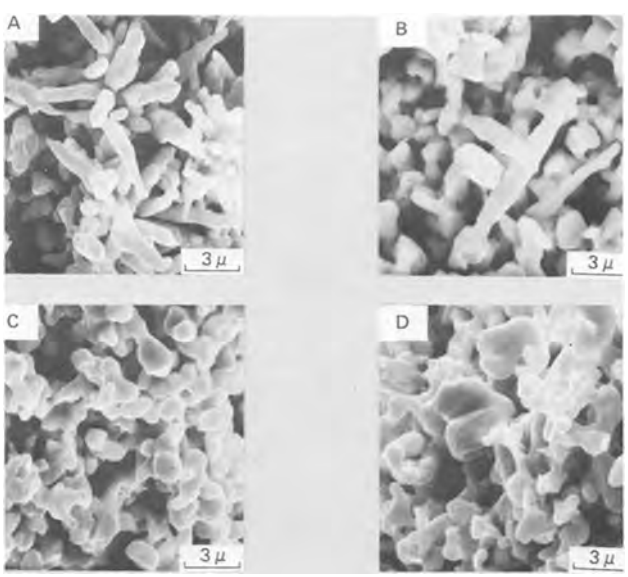


Fig. 4. Structure of charged negative electrode without lignosulfonate additive at: A, 0; B, 500; C, 1000; and D, 2000 cycle points.

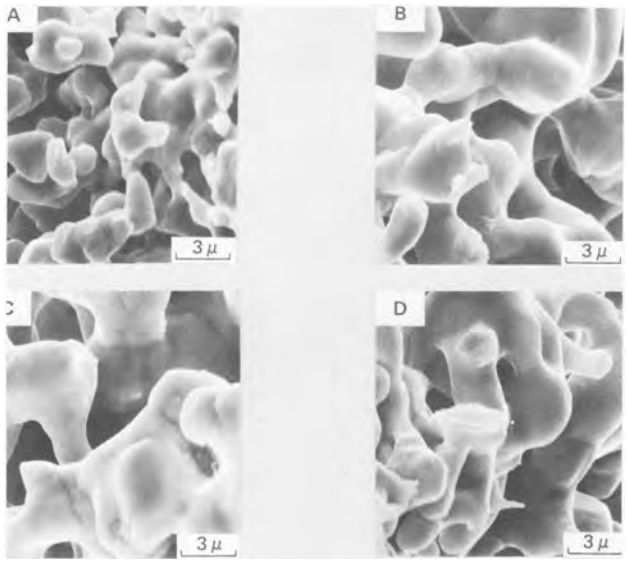


Fig. 5. Structure of charged negative electrode with lignosulfonate additive at; A, 0; B, 500; C, 1000; and D, 2000 cycle points.

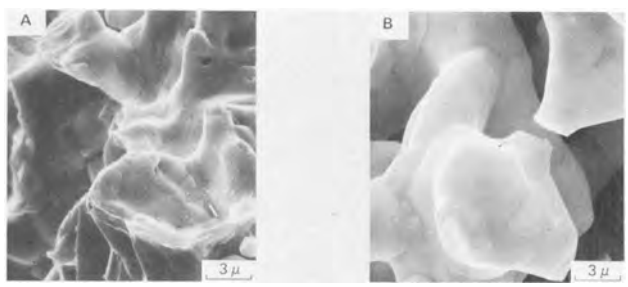


Fig. 6. Structure of charged negative electrode without lignosulfonate additive at 4000 cycle point; surface (A) and center of cross section (B).

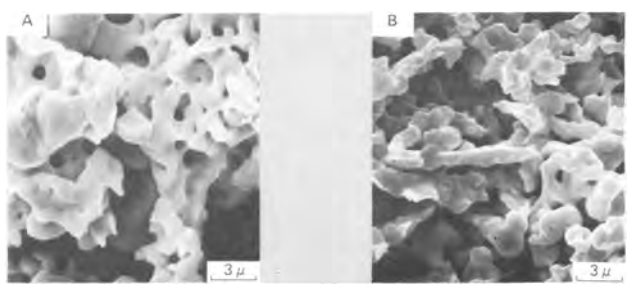


Fig. 7. Structure of charged negative electrode with lignosulfonate additive at 4000 cycle point; surface (A) and center of cross section (B).

the lead crystal morphology observed by Simon, Caulder, Gurlusky, and Pierson (6). The porous structure of the pasted electrode is the result of the conversion of low density lead compounds to higher density lead.

The influence of the additive on the initially electroformed material morphology is demonstrated in Fig. 4a and 5a. The lignosulfonate additive has caused to form, in place of an interconnected nodular lead mass (Fig. 4a), an interconnected network of acicular crystals (Fig. 5a). A degree of preferred orientation perpendicular to the electrode surface is also evident in Fig. 5a. It has been hypothesized (14) that the additive functions here similarly, as do the organic addi-

tives used in commercial electrodeposition processes. This does not seem likely, however, since in the latter application the additives' purpose is to increase the density of the deposit; in the pasted electrode it serves, adversely, to promote porosity and increased surface area and reactivity of the electrodeposit. That surface adsorption of the additive material by freshly formed metallic lead probably figures in the expander function is indicated by the increased hydrogen overpotential or end-of-formation potential (Table III) and the onset of passivation potential (Fig. 1).

Figures 4, 5, and 6 demonstrate the effect of repeated charge-discharge cycling on the crystal morphology, size and orientation, and the influence of the sodium lignosulfonate additive. The comparative structures of lead at the surface and at the center of the electrode cross section are shown in Fig. 6 and 7 after 4000 cycles, for the control and additive-containing electrodes, respectively. The greater densification of lead at the surface compared to that in the center demonstrates that in the cycling mode used the charge transfer reaction was largely localized at the surface. The initial as-formed lead deposit (Fig. 4, 5, and 6) is made finer grained and more acicular by the additive, and in spite of subsequent growth the differentiation from the control electrode is more than maintained during cycling. What agglomeration does subsequently occur in the lignosulfonate-containing active mass during cycling is hypothesized to be attributable to the loss of activity of the additive with cycling. The activity loss may result both from reduction of concentration as the material is dissolved out of the electrode matrix, as well as from its chemical degradation in the battery environment. A lack of analytical means for monitoring the concentration of additive in the electrode matrix does not permit quantitative substantiation of the hypothesis. However, the degradation of lignin polymer by a variety of displacement and cleavage reactions in acidic conditions have been acknowledged (15-17). The soluble fraction of the lignosulfonate is also expected to be ultimately oxidized at the lead-dioxide electrode during overcharge.

The morphologies of the active material for various lignosulfonate cations and as a function of cycling are reflected in the trend of specific surface reduction shown in Fig. 8. Maracell-C-type sodium lignosulfonate exhibited higher specific surface area during the test period than the others. The linear trend of loss of surface area for the electrode with zinc lignosulfonate additive with cycling is not understood, but indicates a possibly different degradation mechanism.

The trend of 100 mA/cm², −18°C (0°F) discharge capacity on cycling with varied lignosulfonate cations is shown in Fig. 9 to be approximately parallel to that of the specific surface area (Fig. 8). The change in

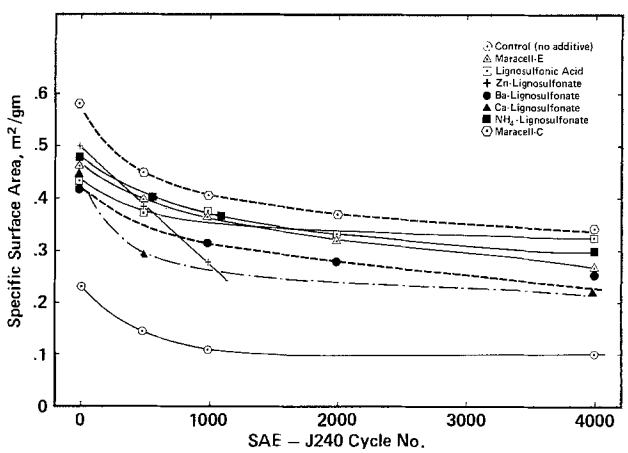


Fig. 8. Variation of specific surface area of negative electrode with different lignosulfonate additives, during SAE J 240 cycling.

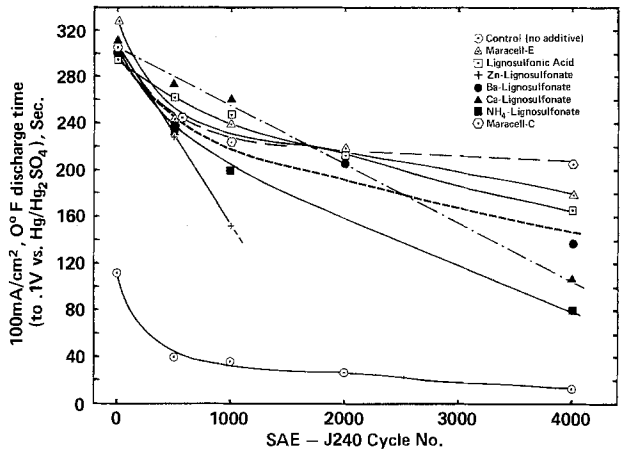


Fig. 9. High rate, low temperature discharge capacity of negative electrode in SAE J 240 cycling as a function of lignosulfonate cation.

high rate, low temperature capacity of the test electrodes during cycling is attributed to the cations associated with the lignosulfonate additive. The fact that inorganic cations tested here do not influence the discharge behavior of the lead electrode (18) indicates that the cationic effect noted here might be a result of their role on the stability, *i.e.*, dissolution and desorption characteristics of the additive. The desorption of a lignosulfonate (totatin FNA) from lead electrodes at high cathodic potential was noted by Brennan *et al.* (5) by differential capacity measurement. The role of cation on the adsorption and desorption characteristics of lignosulfonates is not known. Work in this area is needed for a thorough understanding of the role of additive on the characteristic properties of the lead electrode. Such an understanding might provide a means to improve the high rate performance of the lead electrode and its maintenance during cycling, a desirable long range objective of the lead-acid battery technology.

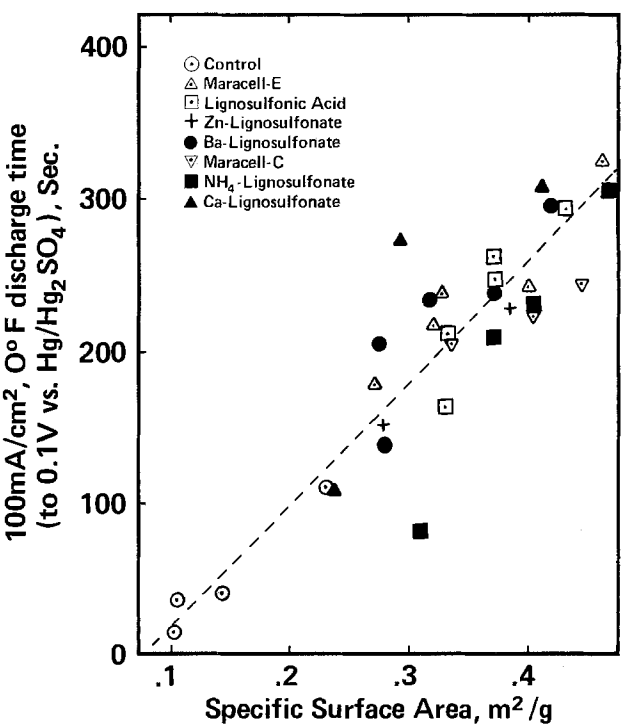


Fig. 10. Correlation between high rate, low temperature capacity and specific surface area of active material.

Figure 10 shows a linear relationship between the 100 mA/cm², 0°F discharge capacity and the BET-nitrogen adsorption surface area. Admittedly the deviation of the data is large, indicating a possibility of a secondary effect which could result from variables associated with the electrode preparation and/or the deviation of electrochemically active surface area from the BET-nitrogen adsorption surface area. Since, in fact, the high rate capacity is expected to be proportional to the electrochemically active surface area, a generally linear relationship between electrochemically active surface area and specific surface area is also to be expected.

Conclusions

1. The cations of lignosulfonate salt additives influence the hydrogen evolution potential at the end of formation and the potential for onset of the solid-phase reaction, but not the initial high rate, low temperature performance.
2. The lignosulfonate salt cation influences the extent and rate of loss of capacity during cycling.
3. The sodium salt of lignosulfonic acid imparted the best capacity retentive characteristics of all the lignosulfonate samples tested.
4. The high rate, low temperature capacity and specific surface area are linearly related.

Acknowledgments

The author would like to express his gratitude to G. Goodman for helpful comments and suggestions, E. Laird and C. Morse for technical assistance, and American Can Company for providing test samples. A. Ortiguera performed the scanning electron microscopy.

Manuscript submitted Sept. 21, 1976; revised manuscript received July 15, 1977. This was Paper 11 presented at the Washington, D.C., Meeting of the Society, May 2-7, 1976.

Any discussion of this paper will appear in a Discussion Section to be published in the June 1978 JOURNAL. All discussions for the June 1978 Discussion Section should be submitted by Feb. 1, 1978.

Publication costs of this article were assisted by Globe-Union Incorporated.

REFERENCES

1. J. Burbank, A. C. Simon, and E. Willihnganz, in "Advances in Electrochemistry and Electrochemical Engineering," Vol. 8, P. Delahay and C. W. Tobias, Editors, Chap. 3, pp. 157-251, Wiley-Interscience, New York (1971).
2. T. F. Sharpe, *Electrochim. Acta*, **1**, 635 (1969).
3. E. G. Yampol'skaya, M. I. Ershova, V. V. Surikov, I. I. Astakov, and B. N. Kabanov, *Sov. Electrochem. (Engl. Transl.)*, **8**, 1209 (1972).
4. E. Willihnganz, *This Journal*, **92**, 281 (1947).
5. M. P. J. Brennan and N. A. Hampson, *J. Electroanal. Chem. Interfacial Electrochem.*, **48**, 465 (1973); G. Archdale and J. A. Harrison, *ibid.*, **47**, 93 (1973).
6. J. R. Pierson, P. Gurlusky, A. C. Simon, S. M. Caulder, *This Journal*, **117**, 1463 (1970); A. C. Simon, S. M. Caulder, P. J. Gurlusky, and J. R. Pierson, *ibid.*, **121**, 463 (1974); A. C. Simon, S. M. Caulder, P. J. Gurlusky, and J. R. Pierson, *Electrochim. Acta*, **19**, 739 (1974).
7. K. Forss and K. E. Fremer, in "Symposium on Enzymatic Hydrolysis of Cellulose," M. Bailey T. Eneri, and M. Linke, Editors, pp. 41-63, Aulanko, Finland (1975).
8. E. J. Ritchie, *Trans. Electrochem. Soc.*, **92**, 229 (1947); *ibid.*, **100**, 53 (1953).
9. E. G. Yampol'skaya, I. A. Smirnova, M. I. Ershova, S. A. Sapotnitskii, and L. I. Kryukova, *Sov. Electrochem. (Engl. Transl.)*, **8**, 1289 (1972).
10. D. Hogan, Private Communication, American Can Company, Rothschild, Wisconsin.
11. American Can Company, "Chemicals from wood," Bulletin 131, pp. 3-9.
12. M. P. J. Brennan and N. A. Hampson, *J. Electroanal. Chem. Interfacial Electrochem.*, **52**, 1 (1974).
13. D. Pavlov, in Proceedings of the Symposium on Batteries for Traction and Propulsion, pp. 135-149, published by the Columbus Section of The Electrochemical Society, March 7-8, 1972.
14. S. C. Barnes, in Lead 65, Proceedings of the 2nd International Conference on Lead, Arnhem, The Netherlands, p. 219, Pergamon Press, Oxford.
15. A. F. A. Wallis, in "Lignins," K. V. Sarkanen and C. H. Ludwig, Editors, Chap. 9, pp. 345-372, Wiley-Interscience, New York (1971).
16. H. M. Chang and G. G. Allan, *ibid.*, Chap. 11, pp. 433-485, Wiley-Interscience, New York (1971).
17. B. F. Hrutfiord, *ibid.*, Chap. 12, pp. 487-509.
18. G. W. Vinal, "Storage Batteries," 4th ed., pp. 138-145, John Wiley & Sons, Inc., New York (1955).

Effect of Caffeine on the Anodic Dissolution of Copper (100) Plane in Acidic Copper Sulfate Solution

M. F. Ahmed, S. M. Mayanna, and F. Pushpanaden

Department of Chemistry, Central College, Bangalore University, Bangalore 560001 India

ABSTRACT

Anodic dissolution of copper (100) plane in acidic copper sulfate solution is inhibited by the addition of caffeine. Evidence to this effect is offered by the surface coverage data and by the topographical changes brought about by caffeine on the surface. The inhibition is attributed to the adsorption of caffeine on the surface of the crystal plane.

Several nitrogen-containing organic compounds have been used as corrosion inhibitors. The corrosion inhibition is a surface process which involves the specific adsorption of inhibitors on the metal surface (1). The extent of inhibition of metallic corrosion depends on the nature of metal surface and extent of adsorption of the inhibitor (2). The type of interaction of the inhibitor on the metal surface during corrosion has been deduced from its adsorption characteristics (3-5). Vermilyea (6) has emphasized the need for a careful study of metallic corrosion on single crystal substrates. Many attempts have been made in this direction using copper single crystal planes (7-10). In a similar attempt, the present investigation examines the effect of caffeine on the anodic dissolution of copper (100) plane in acidic copper sulfate solution.

Key words: surface coverage, inhibition, etch pattern.

Experimental

A solution of composition 0.25M $CuSO_4$ + 0.1M H_2SO_4 was prepared from freshly distilled, preelectrolyzed sulfuric acid (AR) and twice recrystallized copper sulfate (AR) subjected to preelectrolysis, using conductivity water. Copper (100) plane with a dislocation density of $10^6/cm^2$ was grown at the Oak Ridge National Laboratory, Tennessee. The copper (100) plane was fixed in Tygon tubing such that only the desired plane was exposed. The surface preparation applied prior to the anodic dissolution was similar to that suggested by Jacquet (11). The dissolution was carried out galvanostatically (0.1-25 mA/cm²) in stirred, deaerated acidic copper sulfate solution and in acid copper sulfate solution containing various concentrations (10^{-8}-10^{-2}M) of caffeine. Caffeine in these concentrations did not alter the *p*H of the acidic copper sulfate solution. The time of dissolution was chosen to dissolve the metal to a constant thickness equivalent to 5 C/cm² (1.8μ). A 90V battery in series with a variable resistance was used as a constant current source. The overpotentials were recorded with reference to a freshly prepared copper reference electrode using d-c VTVM with an accuracy of ± 1 mV. The dissolved surface was examined under a metallurgical microscope. All the microphotographs were prepared at a magnification of 600X. The experiments were repeated to ensure reproducibility.

Results

Overpotentials.—The overpotential recorded in the pure acid copper sulfate solution increases with time and attains a steady value. The presence of caffeine in the solution does not alter the trend in the variation of overpotential with time. However, the overpotential values in presence of caffeine are higher than the values recorded in pure solution at the corresponding current densities. For any given current density, the extent of increase in the overpotential is a function of the concentration of caffeine. The effect of caffeine on the overpotential is maximum at a concentration of 5×10^{-3}M.

Figure 1 is the Tafel plot for the dissolution of copper (100) plane in pure acidic copper sulfate solution and in acid copper sulfate solution containing various concentrations of caffeine. The Tafel plots for pure solution and for solutions containing caffeine are parallel to each other and have a slope of 40 ± 5 mV.

The values of i_o (exchange current density) both in pure solution and in solutions with various concentrations of caffeine were evaluated from the Tafel plots. It is found that the i_o value decreases with an increase in the concentration of caffeine. As the value of i_o is related to the rate of electrode reaction, the inhibitor efficiency (γ) at each concentration of caffeine used was calculated using the equation (12)

$$\%\gamma = \left(\frac{i_o - i_o^*}{i_o}\right) \times 100$$

where i_o^* and i_o are the exchange current density values with and without caffeine, respectively. The values of i_o and inhibitor efficiency at different concentrations of inhibitor are given in Table I.

The surface coverage (θ) at each concentration of caffeine was calculated using the equation (13)

$$(1 - \theta) = \left(\frac{i_o^*}{i_o}\right)$$

One could calculate the apparent free energy of adsorption of the inhibitor from θ-values using the equation (14)

$$\frac{\theta}{e^{(x-1)}(1-\theta)^x} = \frac{C_{org}}{55.5} e^{-\Delta G^\circ_{ads}/RT}$$

where C_{org} is the concentration of inhibitor in the bulk of the solution and x the size factor. Using the above equation, with $x = 9$ for the space filling model of adsorption of caffeine on the surface, the apparent free energies of adsorption (ΔG°_{ads}) were evaluated and they are recorded in Table I. Figure 3 is a plot of overpotential *vs.* θ at different current density values.

Surface topography.—The etch patterns that develop on copper (100) plane on dissolution at different current densities are distinguishable with respect to their features. They show predominantly serrated layers (Fig. 2a) at a current density of 0.1 mA/cm², spirals (Fig. 2b) at 0.25 mA/cm², and square concentric loops enclosing tiny pits (Fig. 2c) at 0.5 mA/cm². Occasional large pyramidal pits (Fig. 2d) develop at a current density of 2 mA/cm². On further increase in the current density, the same feature, *i.e.*, the square pyramidal pit, persists in the etch patterns. However, the density of the square pyramidal pits in the etch patterns increases with the increase in current density accompanied by a consequent diminution in their size. Figure 2e is the etch pattern showing a dense etch pit development at 25 mA/cm².

To investigate the effect of caffeine on the etch patterns, first the etch patterns developing at a constant current density of 2 mA/cm² with successively increasing concentrations of caffeine (10^{-8}-5×10^{-3}M) in the solution were examined. As described above, occasional large square pyramidal etch pits develop at 2 mA/cm² in pure solution (cf. Fig. 2d). No noticeable change is effected in this pattern by caffeine up to a concentration of 10^{-5}M in the solution. However, when the caffeine concentration reaches a value 10^{-4}M, there is a change in the etch pattern that develops at 2 mA/cm². This is shown in Fig. 2f which may be described as occasional etch pits with faceted slopes scattered in a background of smooth pits. Figure 2g showing pyramidal pits with very smooth slopes and Fig.

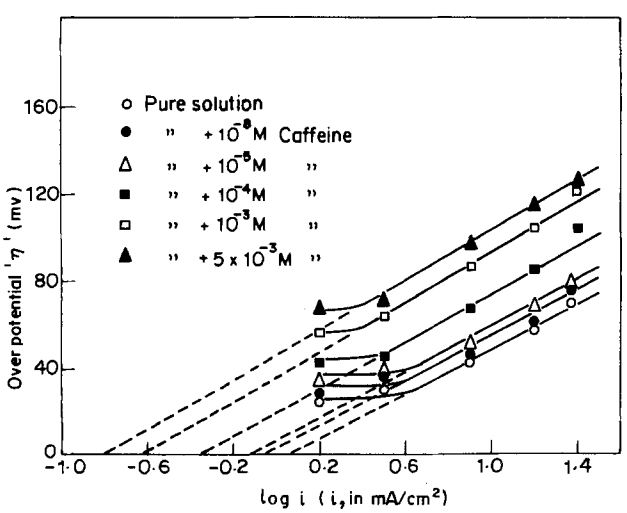


Fig. 1. Tafel plots for the dissolution of copper (100) plane in pure and caffeine-added acidic copper sulfate solution.

Table I. Surface coverage θ, percent inhibitor efficiency, and free energy of adsorption (ΔG°_{ads}) of caffeine on copper (100) plane during dissolution in acid copper sulfate solution containing various concentrations of caffeine

Conc. of caffeine (M)	Exchange current density (mA/cm²)	θ	Inhibitor efficiency, %	$-\Delta G^\circ_{ads}$ (kcal/mole)
0	1.2020	—	—	—
1×10^{-8}	0.8710	0.27	27	9.6
1×10^{-5}	0.7762	0.35	35	7.6
1×10^{-4}	0.4571	0.61	61	8.0
1×10^{-3}	0.2399	0.80	80	10.3
5×10^{-3}	0.1259	0.89	89	12.7

2h showing layers are similarly the etch patterns that develop at 2 mA/cm^2 with 1×10^{-3} and 5×10^{-3}M caffeine in the solution, respectively.

Caffeine is effective in causing changes in the etch patterns in concentrations starting from 10^{-4}M. Hence, the effect of current density on the etch patterns that develop in solutions containing 1×10^{-4}, 1×10^{-3}, and 5×10^{-3}M caffeine, respectively, was next examined by dissolving the crystal in the current density range 2-25 mA/cm^2. No noticeable variation of features is observed in the etch patterns produced between current densities 2-25 mA/cm^2 with 1×10^{-4} and 1×10^{-3}M caffeine in the solution, respectively. But the features that develop at low current densities (2 mA/cm^2) with the above concentrations of caffeine in the solution (Fig. 2f and g) decrease in size and increase in number as the current density is increased. However, in presence of 5×10^{-3}M caffeine in the solution, the spacing in between the layers observed in etch patterns produced at 2 mA/cm^2 (Fig. 2h) gradually decrease as the current density is raised to 10 and then to 15 mA/cm^2 and, when the current density finally reaches a value 25 mA/cm^2, square concentric loops enclosing tiny pits (Fig. 2i) and spirals develop in the etch patterns.

Table II summarizes the topographical results of dissolved copper (100) plane. It is found that the features in the etch patterns developing at low current densities (<1 mA/cm^2) in pure solution are similar

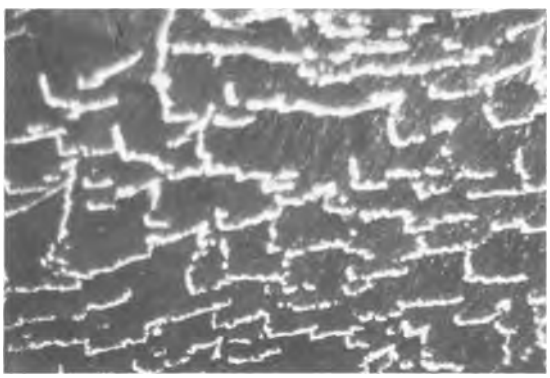


Fig. 2a. Serrated layers on dissolved copper (100) plane in acidic copper sulfate solution at 0.1 mA/cm^2. Dark field (X600).

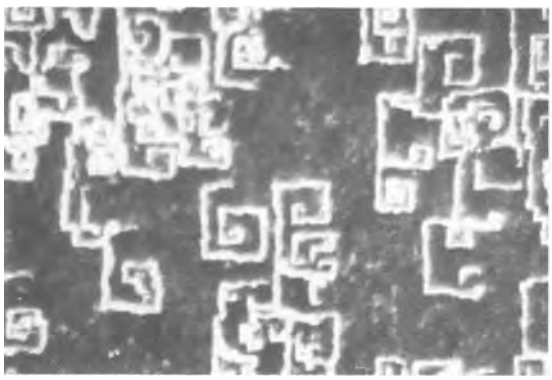


Fig. 2b. Spiral pits on dissolved copper (100) plane in acidic copper sulfate solution at 0.25 mA/cm^2. Dark field (X600).

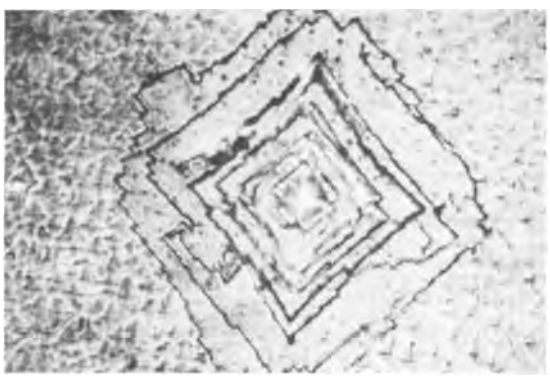


Fig. 2c. Square concentric loops enclosing tiny pits on dissolved copper (100) plane in acidic copper sulfate solution at 0.5 mA/cm^2. (X600).

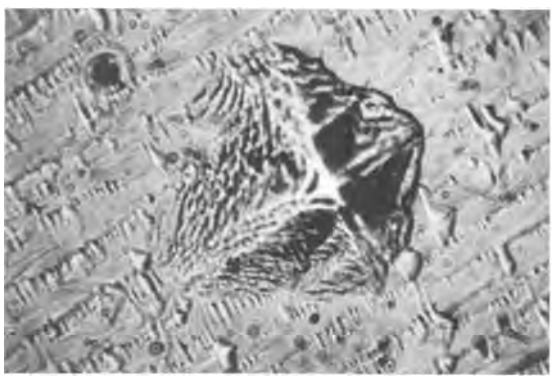


Fig. 2d. Occasional large square pyramidal etch pits on dissolved copper (100) plane in acidic copper sulfate solution at 2 mA/cm^2. (X600).

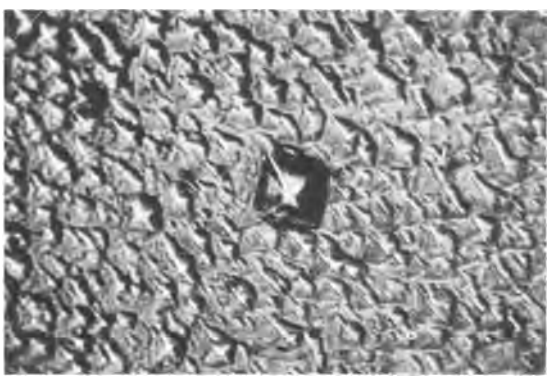


Fig. 2e. Dense etch pit development on dissolved copper (100) plane in acidic copper sulfate solution at 25 mA/cm^2. (X600).

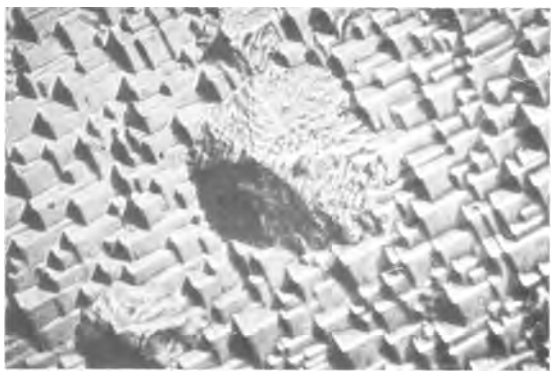


Fig. 2f. Occasional large square pyramidal etch pits with faceted slopes on dissolved copper (100) plane in acidic copper sulfate solution + 1×10^{-4}M caffeine at 2 mA/cm^2. (X600).

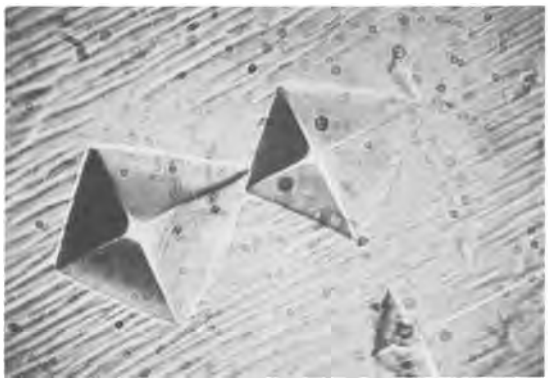


Fig. 2g. Occasional large square pyramidal etch pits with smooth slopes on dissolved copper (100) plane in acidic copper sulfate solution + 1 × 10^{-3}M caffeine at 2 mA/cm². (X600).

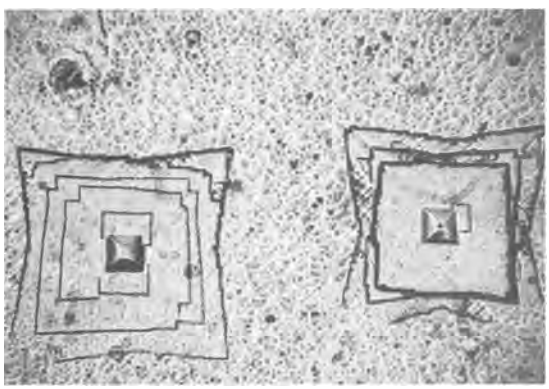


Fig. 2i. Square concentric loops enclosing tiny pits on dissolved copper (100) plane in acidic copper sulfate solution + 5 × 10^{-3}M caffeine at 25 mA/cm². (X600).

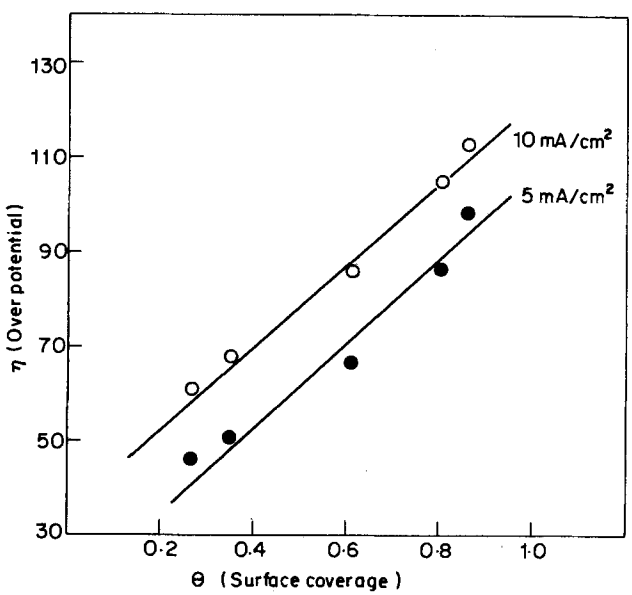


Fig. 3. Variation of anodic overpotential with surface coverage θ of caffeine.

to those developing in solutions containing 5 × 10^{-3}M caffeine at higher current densities (>15 mA/cm²).

Discussion

The mechanism of dissolution of copper in acidic copper sulfate solution is (15)

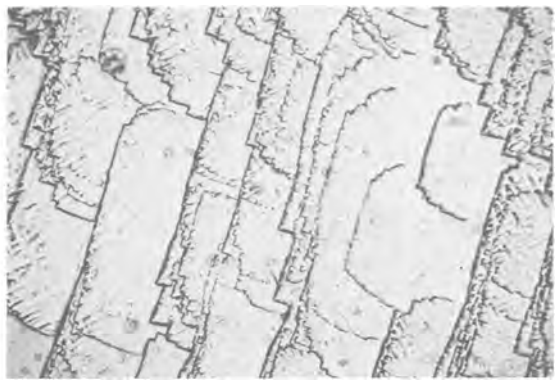


Fig. 2h. Layers on dissolved copper (100) plane in acidic copper sulfate solution + 5 × 10^{-3}M caffeine at 10 mA/cm². (X600).

$$Cu \rightarrow Cu^{+} + e$$

$$Cu^{+} \xrightarrow{rds} Cu^{++} + e$$

The experimental data in presence of caffeine show no change in Tafel slope (Fig. 1) consistent with the above mechanism. This suggests that caffeine does not interfere with the mechanism of dissolution. The observed decrease in the dissolution rate as evidenced by the decreasing exchange current density values with increasing concentration of caffeine in the solution are, however, attributed to the action of caffeine on the surface. It is known (16) that the dissolution process initiates at reaction sites (kinks in a step of dislocation) and the dissolution rate depends upon their number (17). A curtailment of these reaction sites would therefore lead to a reduction in the dissolution rate and this may be precisely how caffeine achieves inhibition, by being adsorbed on the surface at the reaction sites. In such a situation, the removal of copper atoms at reaction sites is rendered difficult and needs higher overpotentials. The experimentally observed linear increase in the anodic overpotential with surface coverage θ therefore supports the contention that caffeine inhibits dissolution by being adsorbed at the reaction sites. Further, the negative values for the free energy of adsorption evaluated, are also a characteristic of spontaneous adsorption of caffeine on the surface. However, the dependence of free energy of adsorption on surface coverage signifies an interaction between the adsorbed caffeine molecules (18).

The change of surface features produced in the etch patterns in presence of caffeine also demonstrate the adsorption of caffeine on the crystal surface. During dissolution, the movement of steps generated by the removal of atoms at reaction sites results in the appearance of different surface features which are related to the crystal structure (19). Screw dislocations provide steps for growth at small driving forces (6) in addition to the steps provided by misorientations.

Table II. Surface features in the etch patterns produced on copper (100) plane on dissolution in pure and caffeine-added acidic copper sulfate solution at different current densities

Pure solution current density (mA/cm²)	Solution + current density (mA/cm²)	Caffeine conc. (M)	Surface features in the etch patterns
0.10	2-15	5 × 10^{-3}	Layers
0.25	25	5 × 10^{-3}	Spiral pits
0.50	25	5 × 10^{-3}	Square concentric loops
—	2	1 × 10^{-3}	Square pyramidal pits with smooth slopes
—	2	1 × 10^{-4}	Square pyramidal pits with faceted slopes
2-25	2-25	1 × 10^{-5}-1 × 10^{-3}	Square pyramidal etch pits

Hence, in pure solution, spiral etch pits at lone screw dislocations (20) and square concentric loops enclosing tiny pits at two screw dislocations of opposite sign (20) appear at low current densities. Formation of layers at low current density could be due to the bunching of steps provided by misorientations (21). Large square pyramidal etch pits observed at a comparatively higher current density (2 mA/cm^2) form in accordance with Vermilyea's observation (22), wherein a pyramidal etch pit develops due to shortening of space between spiral turns at large undersaturations (overpotentials). Cabrera and Levine (23) proved theoretically that dislocations with large Burger's vector open up at small undersaturations and large undersaturations are necessary to open up dislocations of elementary Burger's vector. This may be the reason for an increase in the number of pyramidal pits per unit area with a resulting diminution in size at higher current densities.

Caffeine by being adsorbed at the reaction sites changes conditions for the step movement and, hence, is responsible for the surface changes. At 25 mA/cm^2, with a concentration of 5×10^{-3}M of caffeine in solution, the surface coverage is maximum and most of the reaction sites are covered by the adsorbed caffeine. The condition for the movement of steps generated from the exposed reaction sites seems to be similar to that at low current densities in the absence of caffeine. Hence, similar features, namely, spirals and square loops, are observed.

Acknowledgments

The authors thank Dr. M. Shadaksharaswamy, Professor and Head of the Department of Chemistry, Central College, Bangalore for his encouragement. Thanks are due also to Prof. Jenkins, Oak Ridge National Laboratory, Tennessee for his generous gift of copper single crystals and to Mr. H. B. Rudresh for helpful discussion. One of the authors (M.F.A.) thanks C.S.I.R. for financial assistance in the form of SRF.

Manuscript submitted March 22, 1977; revised manuscript received June 27, 1977.

Any discussion of this paper will appear in a Discussion Section to be published in the June 1978 JOURNAL. All discussions for the June 1978 Discussion Section should be submitted by Feb. 1, 1978.

Publication costs of this article were assisted by Bangalore University.

REFERENCES

1. C. A. Mann, B. E. Lauer, and C. E. Multin. *Ind. Eng. Chem.*, **28**, 9 (1930); *ibid.*, **28**, 1048 (1930).
2. N. Hackerman and R. M. Hurd, "First International Congress on Metallic Corrosion," L. Kenworthy, Editor, p. 166, Butterworths, London (1962).
3. S. M. Mayanna, *This Journal*, **122**, 251 (1975).
4. S. M. Mayanna and K. V. Uma, *J. Electrochem. Soc. India*, **25**, 173 (1976).
5. H. B. Rudresh and S. M. Mayanna, *This Journal*, **124**, 340 (1977).
6. D. A. Vermilyea, "First International Congress on Metallic Corrosion," Editor, p. 66, Butterworths, London (1962).
7. S. M. Mayanna and T. H. V. Setty, *Corros. Sci.*, **14**, 691 (1974).
8. S. M. Mayanna and T. H. V. Setty, *Proc. Indian Acad. Sci.*, **LXXX**, Sec. A, 184 (1974).
9. S. M. Mayanna and T. H. V. Setty, *Corros. Sci.*, **15**, 627 (1975).
10. S. M. Mayanna and T. H. V. Setty, *Indian J. Technol.*, **14**, 193 (1976).
11. P. A. Jacquet, *Metal Rev.*, **1**, 157 (1956).
12. S. D. Beskov and S. A. Balyin, *Uch. Zap. Mosk. Gos. Ped. Inst.*, **44**, 3 (1947).
13. J. C. Robert and K. Nobe, *This Journal*, **118**, 545 (1971).
14. H. P. Dhar, B. E. Conway, and K. M. Joshi, *Electrochim. Acta*, **18**, 789 (1973).
15. E. Mattson and J. O'M. Bockris, *Trans. Faraday Soc.*, **55**, 1586 (1959).
16. L. H. Jenkins, *This Journal*, **107**, 373 (1960).
17. T. P. Hoar and R. D. Holliday, *J. Appl. Chem.*, **3**, 502 (1953).
18. J. O'M. Bockris and D. A. J. Swinkels, *This Journal*, **111**, 736 (1964).
19. U. Bertocci, L. D. Hulett, and L. H. Jenkins, *ibid*, **110**, 1190 (1963).
20. W. K. Burton, N. Cabrera, and F. C. Frank, *Phil. Trans. Royal Soc., A*, **243**, 299 (1951).
21. H. J. Pick, G. G. Storey, and T. B. Vaughan, *Electrochim. Acta*, **2**, 165 (1960).
22. D. A. Vermilyea, *Acta Metall.*, **6**, 381 (1958).
23. N. Cabrera and M. M. Levine, *Phil. Mag.*, **1**, 450 (1956).

The Open-Circuit Transient Method of Analyzing Overpotential in Anodic Oxidation

J. L. Ord,* J. C. Clayton, and W. P. Wang*,[1]

Department of Physics, University of Waterloo, Waterloo, Ontario, Canada N2L 3G1

ABSTRACT

The open-circuit technique and its application to studies of overpotential in anodic oxidation are described in detail. The digital circuitry which is used to record transients under program control can be operated either by a minicomputer or a microprocessor. Transients are written on magnetic tape for recall by analysis programs written in BASIC. Three approaches to data analysis are described and their advantages and disadvantages discussed. The anodic oxidation of tantalum in sulfuric acid is chosen to illustrate application of the technique both to facilitate comparison with results obtained by other techniques, and to illustrate how a nonlinear dependence of $\log(i)$ on E affects open-circuit analysis. A procedure for second-order analysis which accounts for $\log(i)$-E curvature through an effective-field model is described, and the significance of differences between first- and second-order results is discussed.

Although open-circuit transients were first used in overpotential studies over twenty year ago, they have seen only limited application in electrochemistry since that time, and are not widely used at present. The open-circuit technique did not become popular because the alternate techniques for studying overpotential were more direct and generally easier to apply. This

* Electrochemical Society Active Member.
[1] Present address: Tunghai University, Taichung, Taiwan, China.
Key words: transient, anodic oxidation, tantalum.

situation has been changed considerably by recent advances in technology which have made it much easier to record and analyze open-circuit transients. There is still little to be gained by applying open-circuit transients in systems where it is possible to make direct measurements of current density as a function of potential, but wherever this is not possible, the open-circuit technique is now a more attractive alternative than it used to be.

Most of the recent applications of open-circuit transients have been in the field of anodic oxidation where the growth of a surface film introduces hysteresis into direct measurements of current density as a function of potential. Other techniques are more popular even in this field, but open-circuit transients have been used in studies of the anodic oxidation of several metals. The technique was first applied by Lake and Casey to the anodic oxidation of cadmium (1), and it has since been applied to the anodic oxidation of iron (2-5), tantalum (6), niobium (7), bismuth (8), vanadium (9, 10), zirconium (11), platinum (12, 13), and tungsten (14).

For a process as complex as anodic oxidation, it is somewhat misleading to refer to the various methods of studying overpotential as alternate techniques. Each technique involves its own special set of experimental conditions, and the expression relating current density to potential determined using a particular technique may not apply under other experimental conditions. The situation is somewhat analogous to using constant pressure and constant volume as alternate conditions for measuring the specific heat of gases without the aid of the first law of thermodynamics to explain the discrepancy between the results. At the present time there is no satisfactory theoretical expression for the relation between oxidation current density and potential in terms of fundamental quantities, hence parameter values obtained by different techniques provide complementary rather than redundant information, and the wider the range of techniques used to study a system, the more useful the results of the study. It can be argued (5, 13) that open-circuit transient results provide the most reasonable starting point for modeling the anodic oxidation process in some systems, but this is not our concern in this paper. Our objectives here are threefold: to describe modern circuitry for recording open-circuit transients, to evaluate alternate approaches to their analysis, and to show how the analysis can be carried to second order in a system where the dependence of $\log(i)$ on E is nonlinear. We use tantalum in sulfuric acid as our example both because it exhibits such nonlinear behavior, and because ample data are available from other types of measurement for comparison purposes.

Experimental

Open-circuit transients have been used in studies of anodic oxidation for over fifteen years in this laboratory. During that time many different techniques have been used to record and analyze the transients. We have found that analog techniques which use an oscilloscope or an oscillographic recorder to produce graphs of potential *vs.* time cannot match the resolution and accuracy of the digital technique we describe in this paper. When we began the digital recording and analysis of open-circuit transients ten years ago, few laboratories had comparable facilities, and the techniques we developed were not widely applicable. This is no longer the case, for advances in microprocessor technology have made digital recording circuitry less expensive and easier to use than analog circuitry.

Figure 1 is a schematic of the circuitry we use in anodic oxidation studies. Twelve-bit binary analog-to-digital and digital-to-analog converters with a resolution of one part in 4096 interface the HP2114B minicomputer to the analog circuitry which applies current to the cell and follows the potential of the reference electrode. All four operational amplifiers have FET inputs; the amplifiers used as the follower, A1, and the current source, A4, are high voltage models. Amplifier A2 conditions the output of A1 to suit the ± 10V range of converter AD1. The values of R1 and R2 may be switched to set the gain, and converter DA1 is used to offset the zero of potential. AD1 has a sample-and-hold amplifier on its input which holds the voltage constant during the 20 μsec conversion period.

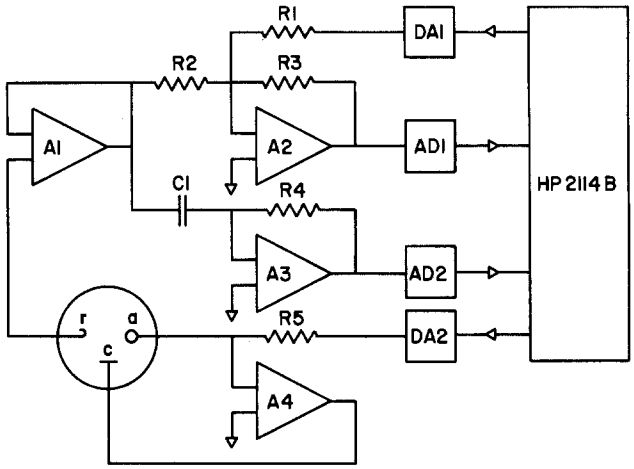


Fig. 1. Circuit schematic. The electrochemical cell contains a reference electrode, r, a working electrode whose oxidation is to be studied, a, and a platinum counterelectrode, c. Amplifier A1 follows the potential of the reference electrode, and amplifier A2 scales the output of A1 for analog-to-digital converter AD1. Digital-to-analog converters DA1 and DA2 are used to offset the output of A1 and to drive the current source amplifier, A4. Amplifier A3 is used as a differentiator whose output is digitized by AD2.

Amplifier A3, which acts as an analog differentiator, was added to the circuitry to enable the results of analog and digital differentiation to be compared. Nominal values of 1 μF for C1 and 100 kΩ for R4 were chosen to suit our experimental conditions. We found it more convenient to use a second converter, AD2, than to multiplex the input of AD1 in order to digitize the output of the differentiator.

Converter DA2 which drives the current source has a response time of 5 μsec, and is used as the "switch" which opens the circuit. When a transient is terminated by reapplying the current, the data acquired during the transient are written on magnetic tape. The 4 cartridge magnetic tape unit is one of several peripheral devices controlled by the computer which are not shown in Fig. 1. A video terminal and an X-Y point plotter are used for graphical output during analysis, and a teletype is used to list data.

The electrochemical cell used in this study has a tantalum working electrode, a platinum counterelectrode, and a mercurous sulfate reference electrode. It is filled with deaerated 0.1M H_2SO_4 held at room temperature, 22°C. Between experiments the oxide film is removed by dissolution in hydrofluoric acid saturated with ammonium fluoride. The cylindrical tantalum sample is then remounted between Teflon washers in a glass electrode holder, and the assembly is inserted into the cell through a standard taper joint.

Results and Discussion

Open-circuit transients are used to determine the dependence of current density on potential at selected points during anodic oxidation. They perturb most systems only slightly, and the dependence of current density on potential determined by analyzing a transient is assumed to apply also just before the circuit was opened. On opening the circuit, the external current drops suddenly to zero, but the oxidation current has

no discontinuity, and continues to flow as the capacitance discharges. The duration of the transient is usually chosen to suit the particular system being studied. For an ideal activation-controlled process, the circuit might well be kept open until the reverse current across the barrier becomes significant, but most systems do not reach this point before their behavior is dominated by processes other than anodic oxidation. In the high overpotential region, the relation between current density and potential for an ideal activation-controlled process can be written

$$i = i_0 \exp((V - V^*)/V) \quad [1]$$

where V^* is the zero of overpotential, i_0 is the exchange current density, and V_0 is the Tafel slope (defined in terms of natural logarithms). In open-circuit transient analysis, Eq. [1] is used as the first-order approximation for the dependence of current density on potential over the range of the transient, and least squares analysis is used to find the value of V_0 which gives the best fit to the experimental data.

The analysis is based on the equation expressing the current in the external circuit as the sum of the oxidation current, i, and the current charging the layer capacitance, i_c. Under anodic oxidation at constant field i_c is zero, but when the circuit is opened i_c becomes equal to $-i$, and the equation of the open-circuit transient may be written

$$C\,dV/dt = -i_0 \exp((V - V^*)/V_0) \quad [2]$$

provided the capacitance, C, can be considered constant over the course of the transient. This equation may be integrated, under the condition that $i = i_1$ and $V = V_1$ when the circuit is opened at $t = 0$, to give

$$V = V_1 - V_0 \ln(1 + t/T) \quad [3]$$

where $T = CV_0/i_1$, and Eq [3] may then be differentiated to give

$$dV/dt = -V_0/(t + T) \quad [4]$$

Equations [2]-[4] are the basic equations describing an open-circuit transient. Equation [2] is used to analyze V-dV/dt data, Eq. [3] to analyze V-t data, and Eq. [4] to analyze dV/dt-t data. We illustrate the application of all three of these approaches to the analysis of an open-circuit transient.

A typical open-circuit transient recorded during the anodic oxidation of tantalum at 40 μA/cm^2 in 0.1M H_2SO_4 is plotted in Fig. 2. The initial potential is 19V (relative to the mercurous sulfate electrode), and the duration of the transient is 0.734 sec. At points B, C, and D the slope of the curve has changed by factors of 8, 16, and 28 from its initial value at A, indicating that the current density through the oxide film has dropped from its initial value of 40 μA/cm^2 by corresponding factors at these points. The 37 points in the figure were selected from readings taken every millisecond by an algorithm designed to give approximately the same number of points for least squares analysis at all values of the initial potential and oxidation current density. The algorithm tests every reading to see whether the potential has changed from its last recorded value by a specified interval and whether or not dV/dt has reached the value at which the current is to be reapplied. The potential interval is calculated by taking the difference between the initial potential and an assumed zero of overpotential, and dividing by 128. This factor gives a convenient point density and simplifies the division process because it is a power of 2. We normally record transients until dV/dt has changed by a factor of 16, but we have found a factor of 8 to be more suitable in systems where processes other than anodic oxidation begin to dominate the behavior at low current density, and we prefer a factor of greater than 16 for second-order analysis. Under normal operating conditions, each point in Fig. 2 would be recorded as binary integers, giving the time the circuit has been open in milliseconds and the potential on a specified scale. In this study, the output of the analog differentiator is recorded at the same time that the potential is recorded, and 8 successive readings of each, taken over a 200 μsec interval, are recorded along with the time reading so that standard deviation estimates from least squares analysis can be checked.

An analysis of the transient in Fig. 2 using V-dV/dt data is illustrated in Fig. 3. The expression used in fitting the data is obtained by dividing both sides of Eq. [2] by their initial values to give dimensionless quantities, then taking logarithms. The dV/dt data obtained by digital differentiation of the V-t data are used in the analysis in order to make the three first-order analyses directly comparable treatments of the same set of V-t data. With the point spacing shown in Fig. 2, dV/dt at the midpoint of the potential interval is given with sufficient accuracy simply by $\Delta V/\Delta t$. The least squares line fitted to the data is shown in

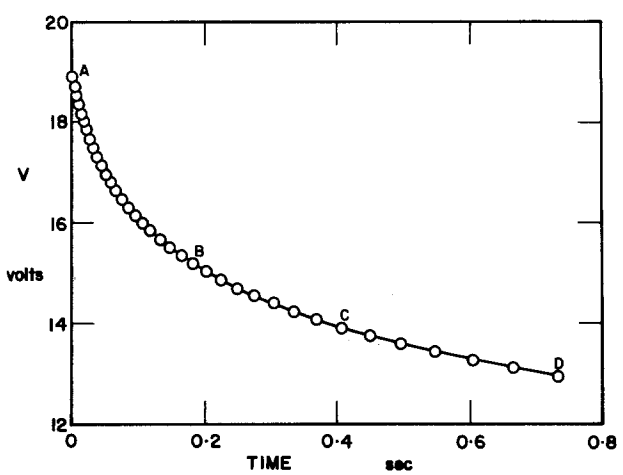


Fig. 2. Open-circuit transient recorded during the anodic oxidation of tantalum at 40 μA/cm^2 in 0.1M H_2SO_4. The circuit is opened at point A, and the slope of the transient changes from its initial value by factors of 8, 16, and 28 at points B, C, and D, respectively.

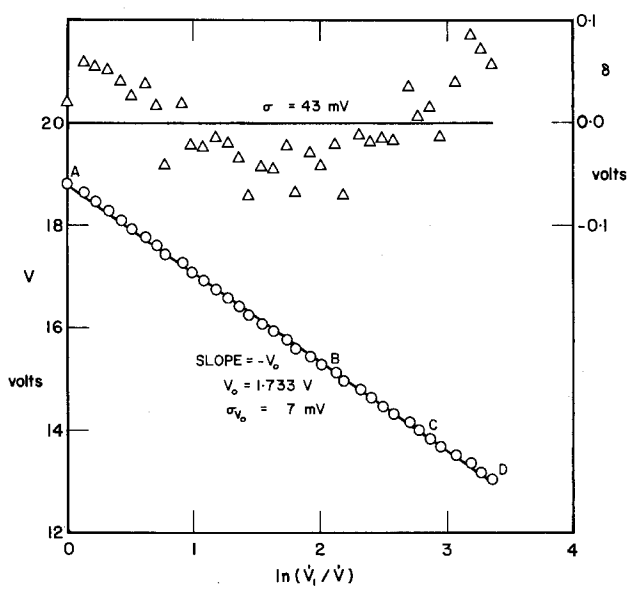


Fig. 3. First-order V-dV/dt analysis of the open-circuit transient plotted in Fig. 2. dV/dt and its initial value are designated $\dot{V}$ and $\dot{V}_1$, respectively. The deviation plot in the upper portion of the figure uses a 20 times expanded scale. The analysis gives $1/C$ = 1.858 cm^2/μF.

the lower portion of Fig. 3, along with the least squares values for V_0 and its standard deviation. The deviation from this line is plotted in the upper portion of the figure on a 20 times expanded scale. The least squares value for the standard deviation in V assumes that the values for dV/dt are known precisely, and this is not the case. The bulk of the deviation attributed to V is actually due to scatter in dV/dt. One can attempt to reduce the scatter in the dV/dt data by using analog dV/dt data in place of digital dV/dt data or by smoothing the digital dV/dt data, but we do not recommend either of these approaches. Although analog dV/dt data give a smoother deviation curve, they introduce a systematic error characteristic of analog differentiation, and do not reduce the apparent standard deviation in V appreciably. Smoothing of the dV/dt data can be accomplished most effectively in this application by using the V-t data and fitting to the integrated equation. In any event, a value of 1.733V with an estimated standard deviation of 7 mV is as accurate a first-order value for a Tafel slope as has any physical significance.

The least squares line enables dV/dt to be calculated at $t = 0$, and hence enables the reciprocal capacitance to be calculated using $1/C = -(dV/dt)_1/i_1$. (In anodic oxidation studies $1/C$ is commonly used in place of C because it is a more appropriate quantity to plot *vs.* film thickness.) The value calculated in this manner from the analysis in Fig. 3 is $1/C = 1.858$ cm^2 μF. Note that V_0 and $1/C$ are the only parameters determined by the analysis, and that an additional assumption will be needed before we can calculate i_0 and V^*.

A V-t analysis of the same data used for the analysis in Fig. 3 is illustrated in Fig. 4. Again the least squares line is plotted in the lower portion of the figure, and the deviation from the line is plotted on a 20 times expanded scale in the upper portion of the figure. The fitting procedure is somewhat more complicated than that used in Fig. 3 because T must be varied to minimize the standard deviation of the least squares fit. We first estimate T using either three equally spaced data points or the initial and final slopes, then we refine this estimate in three stages with progressively smaller T intervals by using a parabolic fit to find the minimum at each stage. The deviation of the data from the line is considerably smaller than it was in Fig. 3, and appears almost entirely systematic rather than random. The V_0 value of 1.738V with standard deviation of 2 mV differs from the value in Fig. 3 by only 5 mV, well within the error estimate. The value for $1/C$ calculated using $T = 22.8$ msec is 1.906 cm^2/μF, which differs from the previous value by 2.5%. The wider variation in $1/C$ than in V_0 values is characteristic of open-circuit analysis—although the technique depends for its existence on the discharge of a capacitor, it is better suited for determining the Tafel slope than it is for determining the capacitance.

From the form of Eq. [4] it appears that T must be varied in a dV/dt-t analysis in much the same way as it is in a V-t analysis, but this is not the case. If we follow a suggestion by Milner (15) and take reciprocals of both sides of Eq. [4] we can plot $(dV/dt)^{-1}$ as a linear function of t, in which case T is given by the intercept of the least squares line. Milner recommends this form of open-circuit transient analysis as preferable to V-t analysis under most circumstances. A $(dV/dt)^{-1}$ *vs.* t plot of the transient is shown in Fig. 5 in a format similar to that used in the previous two figures: the least squares line is shown in the lower portion of the figure, and the deviation from the line is shown on a 20 times expanded scale in the upper portion. Of necessity, the ordinate in Fig. 5 is expressed in units different from those used in the previous two figures, but the figures are scaled so that the magnitude of the plotted deviation has approximately the same significance in all three figures. The plot in Fig. 5 differs from the previous two in a number of important respects. The point spacing along the least squares line is highly nonuniform, with the points in the initial region overlapping to a greater extent than can be illustrated in the figure. The data in the initial region exhibit a systematic deviation from the line, but the increasing scatter in the data in the later portion of the transient obscure any systematic deviation. On the average, the scatter is no worse than in Fig. 3, as evidenced by the fact that the standard deviation in V_0 estimated by least squares is 7 mV for both. The V_0 value of 1.675V differs from the V-dV/dt value by 58 mV and from the V-t value by 63 mV, amounts totally inconsistent with the least squares estimates of the standard deviation in V_0. The T value of 18.4 msec differs from that in Fig. 4 by over 20%, and results in a value for $1/C$ of 2.271 cm^2/μF, considerably different from those obtained by the other two methods.

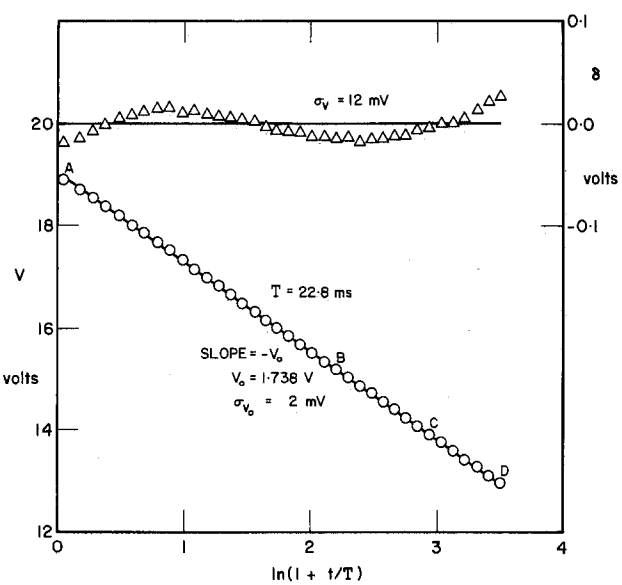


Fig. 4. First-order V-t analysis of the open-circuit transient plotted in Fig. 2. The deviation plot in the upper portion of the figure uses a 20 times expanded scale. The analysis gives $1/C$ = 1.906 cm^2/μF.

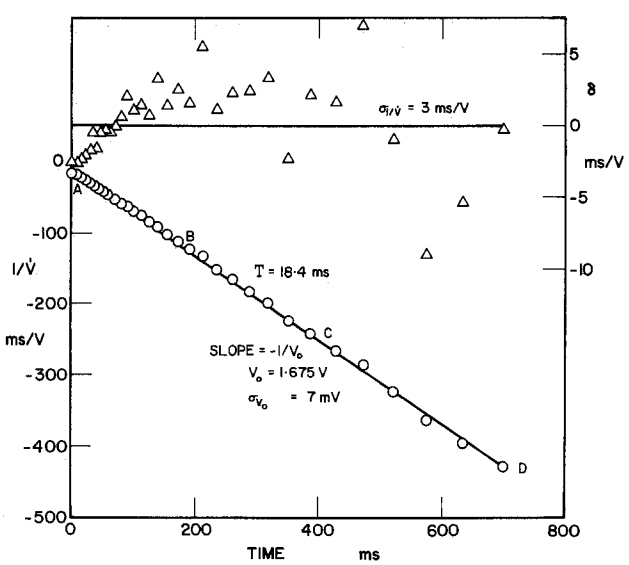


Fig. 5. First-order dV/dt-t analysis of the open-circuit transient plotted in Fig. 2. The deviation plot in the upper portion of the figure uses a 20 times expanded scale. The analysis gives $1/C$ = 2.271 cm^2/μF.

The surprisingly different values of V_0 and $1/C$ obtained by the third method of analysis force us to look more carefully at what is involved in fitting data using least squares. Certainly all three methods start with the same 37 tabulated values of V and t, and all three fit the data to a linear dependence of $\log(i)$ on V. The differences arise in the least squares minimization procedure in the third method. Two assumptions are implicit in least squares analysis: that the abscissa is known precisely, and that the ordinate has a standard deviation which does not vary from point to point. In our system, the nature of the program-controlled measurement process is such that t is known precisely, and the values of V read by the successive-approximation analog-to-digital converter have a standard deviation which is independent of V, so the V-t data are ideally suited for least squares analysis. This is not the case for the V-dV/dt data, but the logarithm in the fitting function compensates for this to a considerable extent. There is no such compensation in the dV/dt-t analysis, and the increasing scatter in the data is readily apparent in Fig. 5. The combination of increasing scatter in the data and separation between data points causes the high t data to dominate the least squares fitting in dV/dt-t analysis. This would be less serious if the dependence of log (i) on V were exactly linear, but in this case the systematic deviation plot in Fig. 4 shows that the high t data exhibit a lower Tafel slope than the least squares value, and their domination of the dV/dt-t analysis results in a lower least squares value for the Tafel slope.

Of the three methods we have used for first-order analysis of open-circuit transients, the V-t analysis is clearly the best, and is the only one suitable for carrying to second order, but the V-dV/dt analysis gives results which are not significantly different to first order without the necessity of carrying out a minimization with respect to T. The dV/dt-t analysis uses data which are poorly suited to least squares analysis, and can give misleading results under some circumstances.

In order to complete the first-order analysis we must determine values for the parameters i_0 and V^*. Although it is not possible to determine i_0 or V^* from the analysis of an individual open-circuit transient, it is usually possible to determine both parameters from a sequence of open-circuit transients applied during oxidation at constant current density. Anodic oxidation differs from most other electrochemical reactions in that the potential increases with time under constant current conditions. A linear increase of potential with time is usually interpreted as indicating control of the process by the field in the oxide film. The determination of i_0 and V^* for a sequence of transients with $i_1 = 40$ μA/cm^2 is illustrated graphically in Fig. 6, in which V_0 and $1/C$ are plotted *vs.* V_1. The transient shown in Fig. 2 is the $V_1 = 19$V transient in this sequence. The linear variation of V_0 with V_1 shown in the figure has occasionally been misinterpreted as implying that V_0 is an explicit function of potential. This is no more the case for V_0 than it is for $1/C$. For a field-limited process, both V_0 and $1/C$ are proportional to film thickness and have no first-order field or potential dependence. We can determine i_0 and V^* from the data in Fig. 6 provided we assume that neither vary with film thickness during oxidation at constant current density. If i_0 and V^* have common values for all of the transients with V_0 values on the line in Fig. 6, then the slope of the line is equal to $\ln(i_1/i_0)$, and its intercept on the V_1 axis is equal to V^*. The least squares values for the slope and intercept give $V^* = -1.12$V, and $i_0 = 4.2 \times 10^{-4}$ μA/cm^2. The $1/C$ data should have the same intercept as the V_0 data if both are proportional to film thickness. The least squares value for the $1/C$ intercept, -1.15V, is 30 mV lower than the V_0 intercept, but this is not significant in view

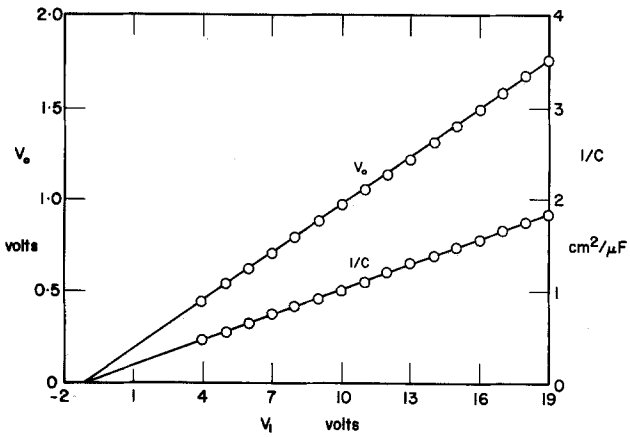


Fig. 6. Plot of V_0 and $1/C$ vs. initial potential for a sequence of open-circuit transients recorded at intervals during the anodic oxidation of tantalum at 40 μA/cm^2 in 0.1M H_2SO_4. The values of V_0 and $1/C$ were determined by first-order V-t analysis over a slope range of 16.

of the extrapolation involved in determining the intercepts.

A plot of V_0 and $1/C$ *vs.* V_1 can also be useful in less ideal systems. An early indication of film breakdown at high voltage is given by an upward deviation of V_0 from the linear dependence on V_1. In systems where oxygen evolution limits the potential range for anodic oxidation, a downward deviation in V_0 accompanies the onset of oxygen evolution. The most sensitive parameter for detecting the onset of oxygen evolution is $1/C$ which begins to curve downward before either the potential or V_0 show a detectable deviation from linearity. In systems such as platinum with a very narrow oxidation range before oxygen evolution begins, the $1/C$ values may show no meaningful dependence on film thickness although V_0 exhibits a clear dependence on thickness. In systems which show a complicated dependence of V_0 and $1/C$ on V_1, it is wise to test thickness dependence by plotting both V_0 and $1/C$ *vs.* an independent measurement of the oxide film thickness. In our laboratory, we use a self-nulling ellipsometer to follow the oxidation process and provide a nonelectrochemical measure of the film thickness.

So far we have based our analysis on a linear first-order approximation for the dependence of $\log(i)$ on V. The systematic S-shaped deviation left after first-order analysis shows that the dependence of $\log(i)$ on V is not exactly linear. For the data analyzed in Fig. 4, the nonlinearity is a property of the relation between ionic current and potential, but nonlinearity can also result from the presence of a superimposed electronic leakage current which varies more slowly with potential than the ionic current and becomes dominant in the low potential region of the transient. Electronic leakage leaves an S-shaped deviation after least squares analysis also, but the S is inverted and the data fall below the fitted line at low potentials. We normally test for leakage at the end of an experiment by switching the current down by successive factors of 2 until the potential shows an anomalous drop as the total current approaches the leakage current. On the basis of this test we select the appropriate slope range for use in the analysis.

An earlier paper from this laboratory (16) proposed an effective-field model to account for the nonlinear dependence of $\log(i)$ on E. In the model, $\log(i)$ depends linearly on the effective field which is assumed proportional to the product of the field and the dielectric constant, K, of the oxide film. This model results in a nonlinear relation between $\log(i)$ and E if the dielectric constant of the oxide film depends on the field

in it. The open-circuit transient equations can handle this type of nonlinearity because it enters symmetrically into the charge stored on the layer capacitance and into the dependence of current density on field. If we use the linear dependence of K on E reported in our earlier paper, we can write

$$K = K_0 (1 - \gamma(V - V^*)/(V_1 - V^*)) \quad [5]$$

where γ is a dimensionless parameter giving the fractional change in K between zero field and the oxidation field. If we then use the variable U defined by

$$U = (V - V^*) K/K_1 \quad [6]$$

in place of V, Eq. [2] can be written

$$C_1 dU/dt = -i_0 \exp(U/V_0) \quad [7]$$

which has the same form as Eq. [2], and hence has the same form of solution. The degree of nonlinearity of the transformation from V to U depends on the value of γ, but the transformation is such that $U = 0$ when $V = V^*$, and $U = V_1 - V^*$ when $V = V_1$ for all values of γ. In the equations, we use K_1 and C_1 to designate values at the oxidation field in the same way that we use i_1 and V_1.

The steps involved in using Eq. [7] to analyze a transient are as follows: (*i*) set V^* equal to its value from first-order analysis; (*ii*) choose a value for γ and transform the data from V to U; (*iii*) fit the transformed data using the process illustrated in Fig. 4, (*iv*) repeat for other values of γ until the value is found which minimizes the standard deviation in V, from the fitted line. (In the least squares analysis, the standard deviation in V is calculated using the appropriate value of dV/dU at each point.) The results of using this process to fit the transient plotted in Fig. 2 are shown in Fig. 7 for γ values between 0 and 0.4. The standard deviation in V is plotted as a function of γ in the lower portion of the figure, and the deviation in V is plotted as a function of V in the upper portion of the figure for $\gamma = 0$ and for $\gamma = 0.215$, the value at which the standard deviation minimizes. The standard deviation of 2 mV at $\gamma = 0.215$ is less than half a least significant bit of the analog-to-digital converter, and the only sign of any residual systematic deviation is an apparent tendency of the first point to lie a little above the line. The V_0 value at $\gamma = 0.215$ is 1.494V with a standard deviation 1/3 mV, and the corresponding value of $1/C_1$ is 1.275 cm^2/μF. The lack of a residual systematic deviation at $\gamma = 0.215$ can be used to test our earlier comments concerning first-order dV/dt-t analysis. If we carry out a second-order dV/dt-t analysis with $\gamma = 0.215$, we reduce the standard deviation in $(dV/dt)^{-1}$ by only 27% instead of the factor of 6 for V-t analysis, but we get rid of the systematic deviation and obtain a value for V_0 of 1.492 with a standard deviation of 6 mV and a value for $1/C_1$ of 1.280 cm^2/μF, both of which agree well with the values from V-t analysis. This result confirms our assertion that a small systematic deviation can have a serious effect on dV/dt-t analysis.

Although Fig. 7 is useful for discussing the details of the second-order fitting process, the physical significance of varying γ shows up best on a plot of $\log(i)$ *vs.* E. Up to this point we have written current as a function of potential rather than field, and the values we have determined for V_0 and $1/C$ have been proportional to film thickness. If we know the field in the oxide film under oxidation at current density i_1, found by ellipsometry to equal 5.68×10^6 V/cm in this instance, we can express our results more simply in terms of two thickness-independent parameters: the Tafel slope in field units, and the dielectric constant of the oxide film. We can then construct plots of $\log(i)$ or $\log(i/i_0)$ as a function of E and look graphically at what happens when we go from a first-order analysis with $\gamma = 0$ to a second-order analysis with $\gamma = 0.215$.

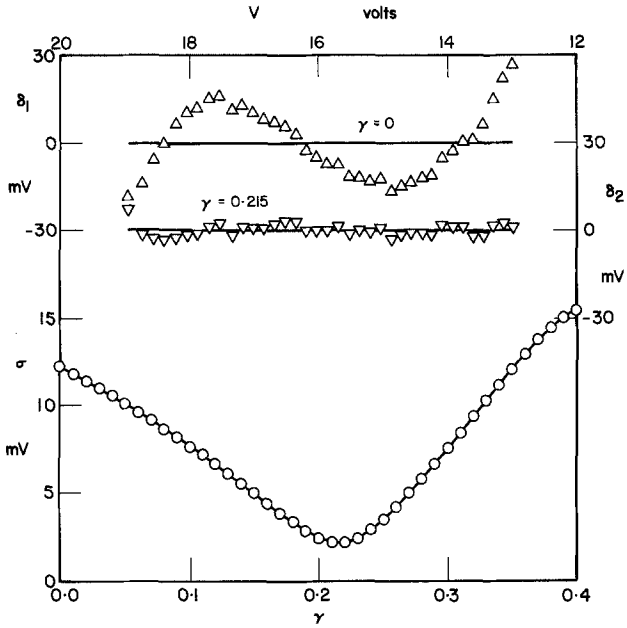


Fig. 7. Plot of standard deviation in V *vs.* γ, and deviation from the fitted line *vs.* V at $\gamma = 0$ and $\gamma = 0.215$, for second-order V-t analysis of the transient plotted in Fig. 2. The analysis gives $1/C_1 = 1.275$ cm^2/μF at $\gamma = 0.215$.

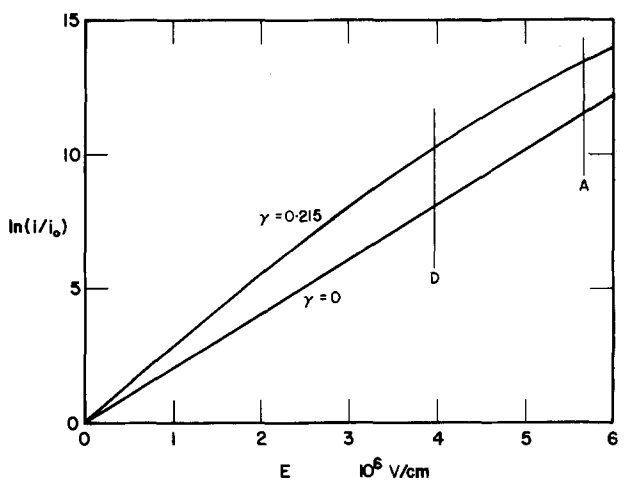


Fig. 8. Plot of $\ln(i/i_0)$ *vs.* E determined by first-order ($\gamma = 0$) and second-order ($\gamma = 0.215$) analysis of the open-circuit transient plotted in Fig. 2.

In Fig. 8 we plot $\log(i/i_0)$ *vs.* E for the expressions determined by first- and second-order analysis. This form of plot has no overlap and is more convenient than a $\log(i)$ plot for comparing shapes of curves. As can be seen in the figure, the two curves have similar slopes over the region of the open-circuit transient. The difference between first- and second-order V_0 values does not indicate a difference in Tafel slope in the region of the transient. In Fig. 8, V_0 is proportional to the reciprocal of the slope of the line from the origin to the point at the oxidation field, and since this slope is steeper for the second-order curve, V_0 is correspondingly lower. Although i_0 cannot be read directly from this type of plot, the displacement between the curves at the oxidation field gives a measure of the factor by which the i_0 values differ between first and second order. The over-all conclusion to be drawn from least squares analysis is that the second-order expression is a better approximation than the first-order expression for the dependence of $\log(i)$ on E in region A-D. The important feature of the second-order curve is its shape in region A-D, not the functional form used

to represent that shape. The physical significance of a parameter such as i_o, obtained by extrapolating the second-order expression to zero field, is certainly open to question.

The significance of second-order parameters is a question which has been dealt with in the case of steady-state measurements also. Young has fitted the dependence of $\log(i)$ on E under steady-growth conditions to a linear first-order expression (17), and to second-order expressions of the form $\alpha E + \beta E^2$ (18), and $\gamma E^{1/2}$ (19). He found that the $\alpha E + \beta E^2$ form gave a better second-order fit than the $\gamma E^{1/2}$ form, but concluded that this was due primarily to the extra fitting parameter. In Fig. 9 we show our first- and second-order expressions along with Young's three expressions on a plot of $\log(i)$ *vs.* E. In a plot of this type, all of the curves intersect at point A and separate at lower fields intersecting the current-density axis at their corresponding i_o values. On the scale used in this figure, our first- and second-order expressions appear indistinguishable across region A-D, but have i_o values which are clearly different. At point A, Young's three expressions all have similar slopes (the first-order expression having been corrected using 27.6 for the dielectric constant rather than the 23.2 value used in his 1954 measurements) but separate noticeably across region A-D and intersect the axis at widely different values of i_o. The magnitude of the difference between the open-circuit and steady-state Tafel slope values shows up clearly in Fig. 9: both are measures of the derivative of E with respect to $\log(i)$, but they differ in what is held constant as the derivative is taken. The significance of the difference in Tafel slope values is a subject of some controversy (6), and we do not discuss it further here.

The accuracy to which the dielectric constant of the oxide film can be calculated is limited by the accuracy to which the sample area can be determined. If we correct for the fact that the macroscopic surface area of the sample used here is 14% lower than the nominal 1.25 cm^2 on which current-density calculations are based, and if we assume a roughness factor of unity, we get values for the dielectric constant of 24.2 from our first-order analysis, and 36.2 at the oxidation field increasing to 46.1 at zero field from our second-order analysis. We can display the field-dependence of the dielectric constant graphically, but such a plot does not account for the magnitude of the difference between the first and second-order values at zero field. We can, however, use the equation for the capacitive discharge current in the effective model to predict the ratio of these quantities. This equation has an extra term due to the field-dependence of the capacitance

$$dQ/dt = C\,dV/dt + (V - V^*)\,dC/dt$$

$$= C_o\,(1 - 2\gamma)\,dV/dt \quad [8]$$

where C_o is the value of the capacitance at zero field. This equation predicts a value of $(1 - 2\gamma)$ for the ratio between the first- and second-order dielectric constant values at zero field. If we test this relation using a slope range of 4 in the first-order analysis to minimize the effect of the systematic deviation, the first-order value of 25.7 predicts a value of 45.1 for the zero-field dielectric constant at $\gamma = 0.215$. The fact that the measured second-order value is only 2% higher than the predicted value shows the consistency of the equations of the effective-field model. We will not attempt to discuss the physical significance of our dielectric constant results here, because to do so would require a discussion of the coupling between field and strain in anodic oxide films, a subject which goes beyond the scope of this paper.

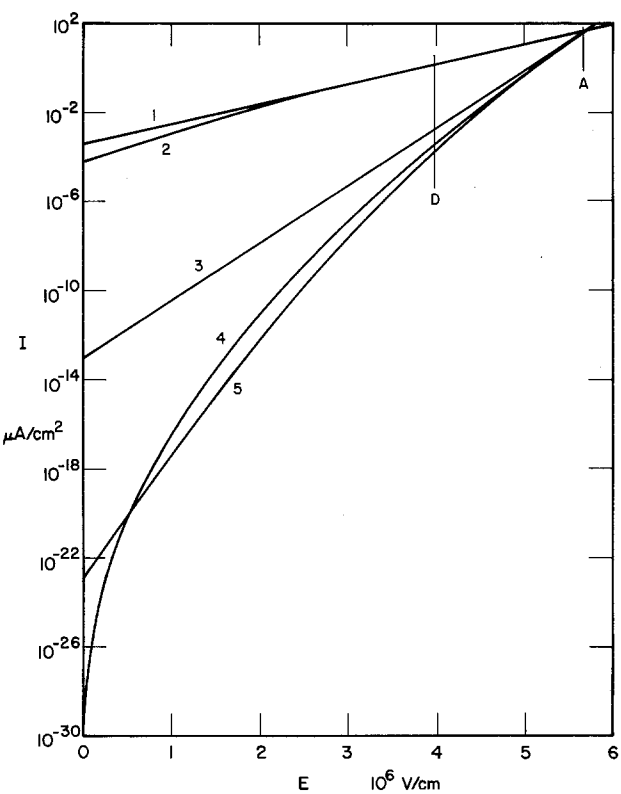


Fig. 9. Plot of $\log(i)$ *vs.* E from first-order (1) and second-order (2) open-circuit analysis, and from first-order (3) and second-order steady-state analysis with $\gamma E^{1/2}$ (4) and $\alpha E + \beta E^2$ (5) field dependence (see text).

Acknowledgment

This work received partial support from the National Research Council of Canada under Grant No. A-1151.

Manuscript submitted Feb. 14, 1977; revised manuscript received June 28, 1977.

Any discussion of this paper will appear in a Discussion Section to be published in the June 1978 JOURNAL. All discussions for the June 1978 Discussion Section should be submitted by Feb. 1, 1978.

Publication costs of this article were assisted by the University of Waterloo.

REFERENCES

1. P. E. Lake and E. J. Casey, *This Journal,* **106**, 913 (1959).
2. J. L. Ord and J. H. Bartlett, *ibid.*, **112**, 160 (1965).
3. J. L. Ord, *ibid.*, **113**, 213 (1966).
4. J. L. Ord and D. J. DeSmet, *ibid.*, **113**, 1258 (1966).
5. J. L. Ord and D. J. DeSmet, *ibid.*, **123**, 1876 (1976).
6. J. L. Ord and D. J. DeSmet, *ibid.*, **116**, 762 (1969).
7. C. M. Daly and R. G. Keil, *ibid.*, **122**, 730 (1975).
8. D. J. DeSmet and M. A. Hopper, *ibid.*, **116**, 1184 (1969).
9. B. H. Ellis, M. A. Hopper, and D. J. DeSmet, *ibid.*, **118**, 860 (1971).
10. R. G. Keil and K. Ludwig, *ibid.*, **118**, 864 (1971).
11. M. A. Hopper, J. A. Wright, and D. J. DeSmet, *ibid.*, **124**, 44 (1977).
12. J. L. Ord and F. C. Ho, *ibid.*, **118**, 46 (1971).
13. J. L. Ord, D. J. DeSmet, and M. A. Hopper, *ibid.*, **123**, 1352 (1976).
14. J. L. Ord, J. C. Clayton, and K. Brudzewski, Submitted for publication to *This Journal.*
15. P. C. Milner, *This Journal,* **107**, 343 (1960).
16. J. L. Ord, M. A. Hopper, and W. P. Wang, *ibid.*, **119**, 439 (1972).
17. L. Young, *Trans. Faraday Soc.*, **50**, 153 (1954).
18. L. Young, *Proc. R. Soc. London, Ser. A,* **258**, 496 (1960).
19. L. Young and F. G. R. Zobel, *This Journal,* **113**, 277 (1966).

The Effect of Stress Applied During Electrodeposition of Nickel Monocrystals on Their Structure

M. R. Chodkowski and R. Weil*

Department of Materials and Metallurgical Engineering, Stevens Institute of Technology, Hoboken, New Jersey 07030

ABSTRACT

The effect of stresses exceeding the yield strength on the structure of monocrystalline, nickel electrodeposits was investigated. A considerable refinement of the structural features due to the stress was observed and was attributed to a greater dislocation density on the growth surface. This refinement of the structure can affect how the stress varies with deposit thickness. Observations of the dislocation structures suggest that the cell structure developed in the near-surface regions under stress. The size of the cells appeared to be related to the structural features which constituted the surface. It was also demonstrated that it is possible to grow monocrystalline, nickel deposits to thicknesses in excess of 100 μm.

Electrodeposits are frequently in a state of internal, tensile stress which can momentarily exceed the yield strength. It has not been determined whether such a stress in a deposit, when acting as the substrate, affects the electrocrystallization processes and thereby the structure of subsequently plated layers. If the phenomenon of stress in electrodeposits is to be understood, this effect must also be considered. The effect of stress on the electrocrystallization is difficult to determine because the factors which are believed to cause the stress also change the structure (1). For example, changing the pH of a nickel-plating bath can increase the stress and simultaneously alter the size and orientation of the grains. In fact, the plating variables and bath composition probably affect the stress via changes in structure (1). However, a stress which exceeds the yield strength can also change the electrocrystallization processes because of alterations in the density and distribution of the dislocations and the creation of slip steps. It is to the study of this phenomenon that this investigation is addressed.

The purpose of this investigation was therefore to determine whether the structure of electrodeposits is altered because of the presence of a stress. In order to separate the influences of the other factors from the effects due to stress, it was applied externally in a tensile machine during deposition rather than causing it to have a high value by adjusting the plating variables or the bath composition. The plating conditions were therefore chosen so that the internal stress would be very small. While an externally applied stress does not act exactly like an internally produced one, the effects on the structure should be similar.

Experimental Considerations

A recent study of Souzis and Weil (2) showed that nickel monocrystals plated in additive-free, all-sulfate baths possess internal stresses which are initially high and tensile, decrease with increasing thickness, and then level off at about 5 μm. The structure at thicknesses exceeding 5 μm should therefore be representative of low stress deposits. Applying an external stress during the electrocrystallization of such a deposit should reveal its effect on the structure. An external stress differs from an internally produced one in that the former continues to strain the material which has already been deposited. Therefore, it was also necessary to determine the effect on the structure of straining after deposition.

Three structures produced under the same condition except for the stress had to be compared, namely: (*i*) with the external stress applied after plating; (*ii*) with the external stress applied during plating; and (*iii*) without the external stress. The first and second structure could be produced on the same substrate sample by plating first on one side only and then coating this deposit. Then, still without the external stress, the other side was plated to a thickness of 25 μm to be sure that the internal stress had leveled off. The external stress was then applied without interrupting the plating. In this way, the first coated deposit was stressed after plating. The deposit on the other side of the substrate at thicknesses in excess of 25 μm was deposited while being stressed. Pieces of the same substrate plated alongside had the structure produced without external stress or subsequent straining.

It was desirable to study monocrystalline samples because of the data available from previous work (2). Also the stresses which could develop in polycrystalline samples because of the variation in the yield strength of grains of different orientations had to be avoided. It was therefore necessary to develop means to deposit monocrystalline nickel deposits considerably thicker than 25 μm.

Experimental Procedure

The procedure which was found most often to yield thick, monocrystalline nickel deposits involved the use of melt-grown, single-crystal copper substrates having a {100} plane parallel to the surfaces to be plated. The substrates, which originally were lath shaped about 60 × 10 × 1.5 mm, were formed into the shape of a tensile specimen by plating polycrystalline copper on each end in an acid-sulfate bath. These copper deposits were about 10 mm long and resulted in a total sample thickness of about 7.5 mm. By withdrawing the sample during copper plating, the thickness became tapered, thereby avoiding sharp corners where fracture could occur during tensile straining. The substrates were electropolished in a 50% phosphoric acid solution for 2 min at an initial current density of 0.5 A/cm^2, rinsed in fresh 15% phosphoric acid, washed several times in water which was distilled thrice in the presence of oxidizing agents to remove organic impurities (3), and then dried. The reason for the drying is discussed later. After mounting in the appropriate fixtures for plating, the substrates were immersed in a 25% sulfuric acid solution for 10 min, rinsed again several times in the triple-distilled water, and quickly placed in the plating bath. The plating bath, which contained 0.43 moles/liter $NiSO_4 \times 6H_2O$ and 0.4 moles/liter H_3BO_3, had the same composition used by Souzis and Weil (2) and was purified in the same way. The current density was 20 mA/cm^2, the pH was 3.7, and the temperature 27°C. Three tensile-specimen-shaped substrates were avail-

* Electrochemical Society Active Member.
Key words: stress, structure, electrodeposit.

Table I.

	Deposit thicknesses (μm)				
	Side A*	Side B Initial deposit*	Side B Plated under external straining	Strain rate (min^{-1})	Total strain
Specimen I	85	25	25	4×10^{-3}	39%
Specimen II	100	25	50	2×10^{-3}	35%

* Plated without concurrent straining.

able. The nickel deposit on one became polycrystalline. Thus data from two experiments were useful.

The experiments consisted, as was already discussed, of plating one side (designated side A in Table I) of the substrate while the other was coated with a stop-off lacquer. The deposit thicknesses are also listed in Table I. Then the lacquer was removed and the nickel deposit was coated. For plating under an externally applied stress, the sample had to be placed in a special fixture. This fixture, which was made of a titanium alloy containing 2% palladium, consisted of two jaws held together by screws for gripping the copper-plated ends of the tensile-specimen-shaped substrate. There were also two guide bars to prevent bending or compressing of the substrates during mounting. The top grips were free to move in the tensile direction. All outer surfaces of the fixture were coated with stop-off lacquer. After the sample was mounted in the fixture, the top jaw was attached to the tensile machine (Instron Model TTCL M13). Then the lower jaw was attached by means of a pin to a lacquer-coated, titanium alloy rod protruding out of the plating bath which was contained in a Teflon beaker. After the attachment, the fixture was pulled into the bath by means of the rod. The current had previously been set so that it flowed as soon as the substrate was in the plating bath. The elapsed time between removal from the sulfuric acid solution and the start of plating had to be less than 15 sec, otherwise the deposit became polycrystalline. For this reason the substrate was dried to minimize oxidation during the necessarily long time interval while it was being mounted in the fixture. As already discussed, a 25 μm thick deposit was laid down without external stress on the as yet unplated side of the substrate (designated B in Table I). Then straining was begun while plating continued. The strain rates, which are also listed in Table I, were such that each layer of deposit was continuously stressed beyond its yield strength.

The structures of the samples plated under the three previously discussed conditions were studied. All deposit surfaces were examined by scanning electron microscopy. X-ray Laue patterns were taken to determine if the deposits were monocrystalline. Thin foil samples for examination by transmission electron microscopy were prepared by the Bollmann (4) method. The Bollmann electrolyte for thinning was modified in that it did not contain sulfuric acid. After dissolving the copper substrates, thin foil samples were prepared by electropolishing both sides of the deposit so that the resulting sample represented the structure at about half the total deposit thickness. Other thin foil samples were prepared by electropolishing only the side of the deposit which had been adjacent to the substrate. In this way, the foil represented the structure near the surface of the deposit.

Results

The surface structure of the ~100 μm thick monocrystalline nickel deposit which was neither stressed during nor subsequent to plating consisted primarily of ridges. At a thickness of 25 μm, the surface structure was similar except that the ridges were about half as long. The Laue x-ray pattern of the 100 μm thick plate which had sharp, unstreaked spots was indicative of a monocrystal of relatively high perfection.

The surface structure of the 100 μm thick deposit on side A of specimen II which was stressed after deposition is shown in Fig. 1. The structure only differs from that of the samples which were neither stressed during the plating nor afterward in that one set of parallel slip lines extends through the ridge structure. An arrow points to a slip line where, apparently, a displacement of part of a large ridge occurred. The ridges themselves experienced essentially no distortion due to the straining of the sample. The extended direction of the ridges makes an angle of 45° with the slip lines, which are along <110> directions. The extended ridge on a {100} plane must be of the <001> type. The structure of a thin foil sample representing the near-surface region of the 100 μm thick deposit is shown in Fig. 2. A well-developed dislocation-cell structure is evident. In the sample representing the interior of about half the total thickness, there was no well-defined dislocation-cell structure. The dislocations were more uniformly distributed and fewer in number than near the surface.

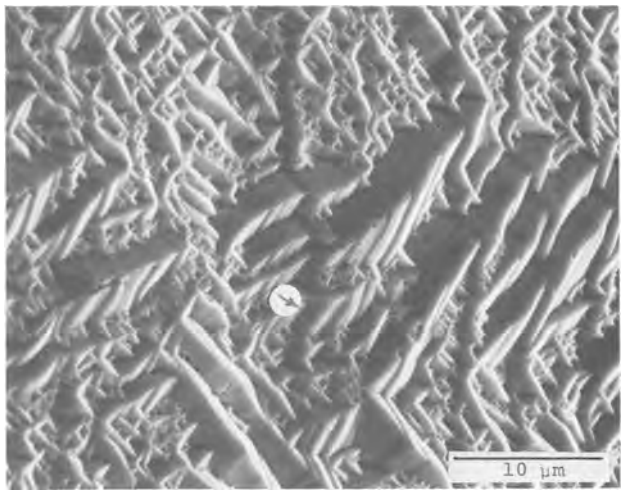


Fig. 1. Scanning electron micrograph of surface of nickel monocrystal strained after plating. Arrow shows displacement at slip step.

The surface structure of side B of specimen II, which was deposited while being strained, is shown in Fig. 3. The structure is much finer than that seen in Fig. 1. The grooves between the blocks again lie in <001> directions as they form an angle of 45° to the slip lines. The ridges at large slip steps are noteworthy. Well-defined dislocation-cell structures were observed halfway through the thickness and near the surface. The structure at half the thickness was similar to that seen in Fig. 2. The cell walls near the surface of the deposit had

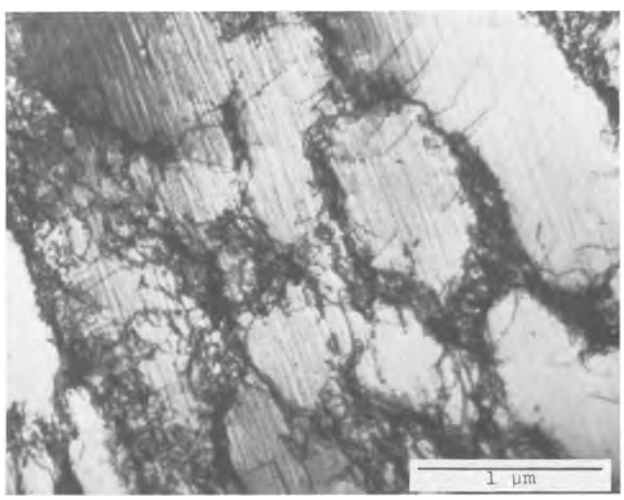


Fig. 2. Transmission electron micrograph of thin-foil sample from near-surface region of nickel monocrystal strained after plating.

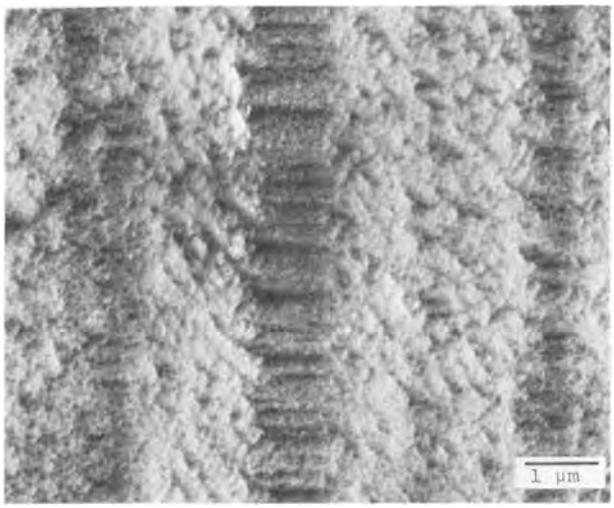


Fig. 3. Scanning electron micrograph of surface of nickel monocrystal. Strained during plating.

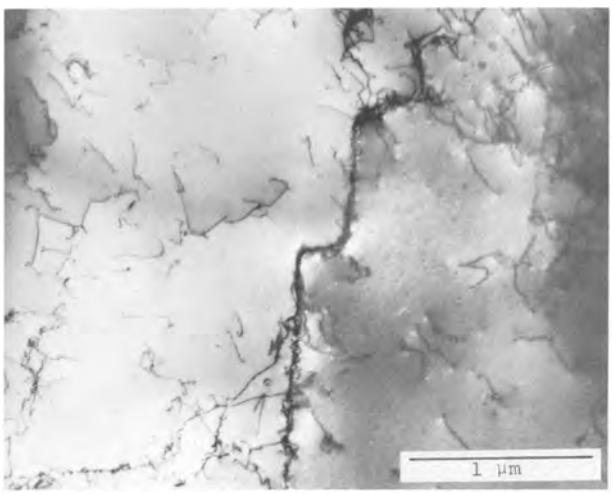


Fig. 4. Transmission electron micrograph of thin-foil sample from near-surface region of nickel monocrystal strained during plating.

a distinctly crystallographic character, as shown in Fig. 4. The cell walls were found to lie along <001> directions. It is also significant that none of the samples examined by transmission electron microscopy showed any twins. The Laue x-ray patterns of the samples strained during deposition, which consisted of streaked spots, were indicative of monocrystals of low perfection.

No significant differences were observed between the structures of specimens I and II. Apparently the thickness difference or the doubling of the strain rate had no effect. Specimen II was strained 35% in order to avoid the fracture which occurred in specimen I at 39%.

Discussion

By comparing Fig. 1 and 3 and noting the higher magnification of Fig. 3, it is evident that the stress applied during deposition resulted in a considerable refinement of the structural features which comprise the surface. As the size of the ridges at a thickness of 25 μm was about half that shown in Fig. 1, the structure obtained by deposition under an externally applied stress was also much finer than that of the initial 25 μm thick layer which was plated without straining. The refinement of the structure due to the applied stress was probably due to the higher dislocation density resulting from plastic deformation rather than the slip steps. If the slip steps created on the surface had served as sites for growth, a layer structure would have resulted. It is evident from Fig. 3 that such a structure was not formed. Rather, the block-shaped features probably grew on emerging dislocations. The growth of blocks on screw dislocations has been postulated (4). At a large slip step, the structural features are more ridge shaped probably because growth occurred on a different crystal plane, namely, of the {111} type, and because fewer dislocations would be expected to emerge on this growth surface.

The refinement of the structure due to straining beyond the yield strength could affect the magnitude of the internal stress which develops in subsequent layers. A cause of internal stress is believed to be the coalescence of crystallites (1, 5). The smaller the crystallites, the higher would be the stress. Thus a refinement in the structural features tends to maintain the stress at a higher value in subsequently deposited layers. This phenomenon could explain why the stress decreases rather slowly with increasing deposit thickness rather than dropping off sharply from a high initial value. This initial value in the case of epitaxial deposits would be expected to decrease sharply once the misfit between the initial substrate and deposit has been relieved.

It is interesting that the externally applied stress did not cause the deposit to become polycrystalline or result in the development of twins. As was previously observed by Lighty *et al.* (6), dislocations only result in polycrystallinity if foreign substances are associated with them. Twins, which are also believed to be due to codeposited foreign substances (7), are also not caused by stress as shown in this study.

The dislocation-cell structure apparently developed in the near-surface region under stress. Only in the samples which were stressed during deposition was a cell structure observed in the interior regions. These interior regions, however, were near-surface regions under stress at one time. The cell structure results from complex, irregular dislocation motion induced by stresses originating from dislocations already present, according to Sumino and Yamamoto (8). The dislocations already present could be sources for generating more dislocations. There are a number of studies (9-11) which have shown that such dislocation-generating sources are present in greater numbers in the near-surface regions. The surface roughness probably also affected the cell structure in that the areas under recessed regions between the blocks or the ridges were closer to the surface, and therefore would have more sources and develop more dislocations which would form the cell walls. The crystallographic nature of the cell walls in Fig. 4 was probably due to this phenomenon. It may be recalled that both the cell walls and the grooves between the blocks of Fig. 3 were parallel to <001> directions. In Fig. 2, there are also some larger and some smaller cells which correspond to the variation in the ridge size of Fig. 1.

The deposits produced for this study remained monocrystalline to thicknesses considerably greater than generally observed by others (12, 13), who reported that nickel deposits on {100} oriented substrates which are the most favorable for thick monocrystalline growth (12), become polycrystalline at thicknesses of 10-20 μm. However Leidheiser and Gwathmey (14) reported obtaining thick nickel monocrystals on {100} substrates. The fact that thicker monocrystals were obtained in this study is attributed to the purity of the electrolyte, selection of the proper plating conditions, careful maintenance of the substrate surface, *i.e.*, preventing contamination, oxidation, or dewetting, and the absence of twins in the copper basis metal. When vapor-deposited substrates which contained many twins were used, the plates became polycrystalline while still very thin. This result illustrates why a substrate with few, if any, twins was needed. It may be recalled that if the time between the immersion of the substrate in sulfuric acid and the start of plating was greater than 15 sec, the deposit became polycrystalline, showing the

need for substrate-surface maintenance. The purity of the plating bath was probably responsible for preventing the development of twins in the deposit (7). Multiple twinning is believed to be responsible for the transition to polycrystallinity (13). As only pH, current density, and bath-temperature values within a narrow range used in this study resulted in monocrystalline deposits, the necessity for maintaining the proper plating variables is evident.

Conclusions

1. Stresses exceeding the yield strength result in a refinement of the structure of monocrystalline nickel electrodeposits.
2. The stresses in a deposit can influence the value of this property in subsequent layers.
3. The dislocation-cell structure developed in the near-surface regions under stress and was related to the size of the structural feature on the surface.
4. It is possible to grow monocrystalline, nickel electrodeposits thicker than 100 μm.

Acknowledgments

Several of the copper monocrystals were donated by Dr. U. Bertocci of the U.S. Bureau of Standards.

Manuscript submitted May 23, 1977; revised manuscript received July 28, 1977. This was Paper 261 presented at the Las Vegas, Nevada, Meeting of the Society, Oct. 17-22, 1976.

Publication costs of this article were assisted by Stevens Institute of Technology and the authors.

REFERENCES

1. R. Weil, *Plating (East Orange, N.J.)*, **57**, 1231 (1970); **58**, 50, 137 (1971).
2. L. Souzis and R. Weil, *Surf. Technol.*, **4**, 41 (1976).
3. R. Schneider and R. Weil, *Plating (East Orange, N.J.)*, **56**, 157 (1969).
4. A. Damjanovic, T. H. V. Setty, and J. O'M. Bockris, *This Journal*, **113**, 429 (1966).
5. J. B. Kushner, *Plating (East Orange, N.J.)*, **60**, 1246 (1973).
6. P. E. Lighty, D. Shanefield, S. Weissmann, and A. Shrier, *J. Appl. Phys.*, **34**, 2233 (1963).
7. R. W. Hinton, L. H. Schwartz, and J. B. Cohen, *This Journal*, **110**, 103 (1963).
8. K. Sumino and M. Yamamoto, *Acta Metall.*, **11**, 1235 (1963).
9. P. R. Swann, *ibid.*, **14**, 900 (1966).
10. J. T. Fourie, *Can. J. Phys.*, **45**, 777 (1967).
11. R. M. Latanision and R. W. Staehle, *Acta Metall.*, **17**, 307 (1969).
12. P. Sibley and P. A. Brook, *Electrodeposition Surf. Treat.*, **2**, 177 (1973/1974).
13. I. Gündiler and L. E. Murr, *Thin Solid Films*, **37**, 387 (1976).
14. H. Leidheiser and A. T. Gwathmey, *This Journal*, **98**, 225 (1951).

Electroless Deposition of Cuprous Oxide

Charles B. Greenberg* and J. Shannon Breininger

PPG Industries, Incorporated, Glass Research Center, Pittsburgh, Pennsylvania 15238

ABSTRACT

It is generally well known that certain metals can be deposited on dielectric substrates at room temperature by aqueous, electroless chemistry following surface activation. Much less is known about electroless growth of oxides. One oxide, namely cuprous, has been deposited on glass as an adherent thin film of good quality. It was formed on a precursory electroless silver film from a highly alkaline solution containing Cu^{+2}, tartrate ion, and formaldehyde. Growth of cuprous oxide requires having Cu^{+2} highly coordinated with OH^- and also having the electroless silver, activating surface relatively free of its own oxide. Silver oxide, at least within our experimental conditions, seems to activate the codeposition of electroless Cu. Data are presented to confirm the identity of the Cu_2O film. Competing reactions for the deposition of Cu_2O and Cu are discussed in terms of hydroxide complexing and surface activation.

Electroless deposition of copper from alkaline, aqueous solutions containing cupric ion is well known (1, 2). The cupric ion is often complexed by tartrate and reduced by formaldehyde. Palladium and electroless silver, as well as copper itself, are well known as activators for otherwise noncatalytic, or perhaps only poorly catalytic, dielectrics such as glass. Sard (3) has discussed the nucleation and growth of copper on several substrates including glass. Schoenberg (4), by electron paramagnetic resonance with frozen solutions, has studied the complexing in solution as a function of pH. He has related this to the plating rate for deposition of electroless copper.

Perhaps because of the considerable interest in copper, and its excellent electrical conductivity, no one seems to have commented on what happens under certain conditions which are unfavorable for its deposition. In highly alkaline solutions which have only a low concentration of tartrate, an oxide deposits electrolessly. It has been identified as cuprous oxide. There are only a few oxides known to deposit electrolessly from previous work (5, 6). PbO_2, Tl_2O_3, and MnO_2 have been deposited autocatalytically using an oxidizing agent, ammonium persulfate. Cu_2O growth occurs by reduction of Cu^{+2} and can be initiated other than by Cu_2O itself. When steps are taken to provide a preferred activating site on electroless silver, the transparent cuprous oxide film is adherent, of good optical quality, and apparently free of codeposited metallic copper. It is also free of haze, exhibiting the specular reflectance which is required for its intended application in architectural glazing (7). The work described herein has meaning in light of what Schoenberg has written about complexing. It also provides some insight into what actually activates Cu_2O, in contrast to metallic copper, within the conditions of our work.

* Electrochemical Society Active Member.

Key words: cuprous oxide, electroless film, alkaline solution for, surface activation of.

Experimental Procedures

Thin film preparations.—In Table I are shown the aqueous solutions used, unless otherwise indicated, and the sequence in which they were used for Cu_2O deposition. All steps were at room temperature. Procedures were similar to those previously described

Table I. Compositions of solutions in the sequence used

A. Sensitizer
0.5 g/liter $SnCl_2 \cdot 2H_2O$
0.5 cm^3/liter HCl (conc)

B. Silvering
1.1 g/liter $AgNO_3$
5.0 cm^3/liter NH_4OH (28-30% NH_3)
0.16 g/liter NaOH
1.3 g/liter dextrose

C. Silver rinse
0.1 g/liter $Na_2S_2O_3 \cdot 5H_2O$

D. Cu_2O growth
3.8 g/liter $CuSO_4 \cdot 5H_2O$
29.0 cm^3/liter HCHO solution (with methanol)
3.0 g/liter $NaKC_4H_4O_6 \cdot 4H_2O$
25.0 g/liter NaOH

(7). The coating was formed on one surface of commercially available flat glass by puddling solutions horizontally on a leveled surface. Substrate size was 50-60 cm^2, thickness 0.3-0.6 cm. Prior to coating, the glass was scrubbed with cerium oxide, followed by a detergent cleaning. A sensitization time of 1 min was typical; the tin chloride was dissolved in concentrated HCl and then diluted with water (8). For the silvering formulation, about 25-35 sec were required to attain a luminous transmittance of about 0.40-0.50, using the CIE standard C response. This was the usual target preceding deposition of the Cu_2O film. Less NH_4OH, longer times, and multiple applications were used for thicker silver films in supplemental experiments. Between sensitization and silvering was a water rinse. After silvering and prior to Cu_2O deposition, the rinse contained $S_2O_3^{-2}$ to inhibit codeposition of metallic copper; this is elaborated in a following section. The electroless silver was dried with N_2 when checking luminous transmittance. Otherwise the $S_2O_3^{-2}$ solution was drained off for best uniformity but was not dried off. The following deposition of Cu_2O required 2.5-3.5 min preferably; the solution was a fresh 1:1 mixture of two otherwise stable components. As is typical for the deposition of electroless copper, one component contained the Cu^{+2} and formaldehyde, the other the tartrate ion and NaOH. In normal storage the mixed solution is stable for at least 8 hr, longer with care to prevent contamination. The effect of contaminants on oxidation of liquid aldehydes has been discussed (9). Following the final rinse with water, the sample was dried with flowing N_2.

What is particularly noteworthy about the solution used for electroless deposition of the oxide is the relatively low concentration of tartrate ion and the high *p*H of about 13.9. Another formula previously used for electroless deposition of copper has about four times as much $KNaC_4H_4O_6 \cdot 4H_2O$ and 11.1 g/liter of NaOH instead of 25.0 (10); otherwise, the concentrations of $CuSO_4 \cdot 5H_2O$ and formaldehyde solution (37% HCHO) are the same. This formula is used here too for the purpose of forming a comparative, metallic copper film. It has a *p*H of 12.9 and also contains 1.3 g/liter of $NiSO_4 \cdot 6H_2O$ which insures adhesion but produces no detectable nickel in the film (7).

Spectrophotometric analysis.—Spectral characterization of samples from 0.3 to 2.1 μm, essentially the solar range at sea level, was done with a Beckman DK-2A spectrophotometer. This instrument was coupled to a Datex SDS-1 recording system which converts the signal to computer language. Using the CIE weighted ordinate method (11), color parameters are thereby also determined. It is easy to convert CIE data into the more familiar terminology of the NBS-ISSC system. Both data are presented instead of the corresponding visual perceptions of film color.

For supplemental information, luminous transmittance and luminous reflectance were measured, without obtaining full spectral curves, using the Gardner Hazemeter System HG-1200 and the modified Precision Glossmeter Model GG-9100 (10). They have, respectively, the CIE standard C response and the approximate standard C response. Supplemental data were also obtained in one case with a Diano/Hardy I spectrophotometer.

Film identification.—A sample of the oxide-containing film was analyzed directly using a Norelco x-ray diffractometer. The analysis was repeated several times while fine tuning the signal relative to background; identification of a thin film is not usually easy by x-ray diffraction. Presented here is a pattern which is definitive and typical. By interferometric measurement the oxide component was found to be about 700Å thick (12). Its deposition time was 3 min.

Results and Discussion

Spectral data.—For a film deposited by the sequence in Table I, using 2.5 min for the oxide growth, reflectance from the film-air surface and transmittance are plotted in Fig. 1(a). An electroless Ag-Cu film on glass is spectrally characterized in Fig. 1(b). The thicknesses of the precursory silver films are similar, as are the final luminous transmittances. The reflectance curve for the Ag-Cu film shows a sharply rising reflectance with increasing wavelength in the red, characteristic of metallic copper (13). This is also shown in Table II by the reflected dominant wavelength, and color designation in the NBS-ISCC system. In the infrared portion of the spectrum the reflectance is as high as 0.96. The infrared reflectance curve in Fig. 1(a), on the other hand, never exceeds 0.32. Also, there is a band whose minimum is at 0.7-0.8 μm; it appears to be the result of interference. This band contributes to the bluish green reflectance observed and shown in Table II. Hass, Schroeder, and Turner (13) have shown similar bands for mirror coatings of aluminum and

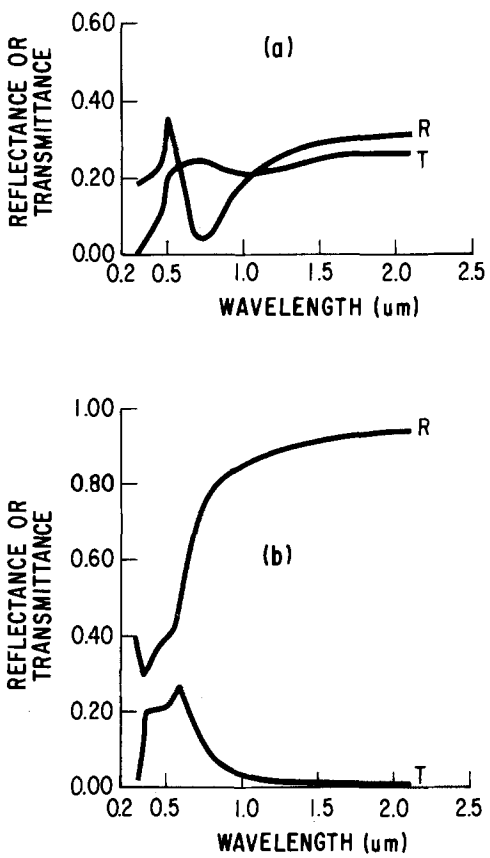


Fig. 1. Reflectance at 8° angle of incidence from the film-air surface (R) and normal transmittance (T) for two electroless thin films on glass: (a) Ag-Cu_2O and (b) Ag-Cu. Thicknesses of the precursory silver films are similar and estimated to be approximately 50-100Å; this is based on luminous transmittances of (a) 0.41 and (b) 0.45 for silver.

Table II. Comparative color in the CIE and NBS-ISCC systems for the electroless films in Fig. 1

	Transmission		Reflection	
	(a) Ag-Cu_2O	(b) Ag-Cu	(a) Ag-Cu_2O	(b) Ag-Cu
Dominant wavelength (nm)	572	572	497	593
Excitation purity (%)	33.6	8.5	16.8	12.8
Tristimulus Y	0.22	0.24	0.25	0.44
NBS-ISCC color	Light olive (106)	Light olive gray (112)	Light bluish green (163)	Grayish red (28)

rhodium overcoated with nonabsorbing and absorbing films to quarter-wavelength optical path lengths. The reflectance can be effectively reduced especially when the refractive index of the oxide is relatively high. The refractive index of bulk Cu_2O is a very high 2.7. For a film of $CuO_{0.67}$, a gross defect structure of cuprous oxide, indexes of 3.0-2.2 from 0.5 to 0.8 μm have been reported (14, 15).

For Fig. 1(a) the very different infrared reflectance, the reflectance minimum, and the bluish green reflection, as well as an easily observed iridescence of the film when nonuniform, all are indications of an oxide, possibly cuprous. There is no evidence of metallic copper. The sharply declining reflectance and transmittance from about 0.5 to 0.3 μm, although not identified, could possibly be attributed to the fundamental absorption of cuprous oxide (14, 16). The dip in transmittance at about 1.0 μm, however, is from the substrate.

Identification by x-ray diffraction.—In Fig. 2 is an x-ray diffraction pattern. Two peaks are very clearly identified at 2.45 and 2.12Å. The two major peaks for cuprite, Miller indexes (111) and (200), are at 2.465 and 2.135Å; the relative intensities are known to be 100 and 37%, respectively. The major peaks for other possible substances, including Cu, Ag, CuO, Ag_2O, and Ag_2S, are quite different. The major constituent of the film, therefore, is cuprous oxide. The slight shift in lattice parameters is probably an indication of nonstoichiometry, not at all unlikely for a thin film in general and cuprous oxide in particular. Note that there are no peaks for the electroless silver component; it is probably too thin to be detected. The very high background at low angles is from the underlying glass.

In Fig. 3 is the diffraction pattern for a third peak corresponding to the third most intense for cuprite; it has been enhanced at ¼ the normal scanning rate. Its Miller index is (220) with an expected relative intensity of 27%. It is evident at 1.50Å and is similarly shifted from the given value of 1.51Å for cuprite. There is a small peak in Fig. 2 at $2\theta \cong 62°$ which recommended expanding detection sensitivity. Other Cu_2O lattice parameters in the 2θ range covered have known relative intensities less than 10% and therefore were assumed to be undetectable. The order of peak intensities in Fig. 2 does follow that for bulk cuprite.

Complexing and chemical reactions.—At the relatively high pH of 13.9, in Cu^{+2}-$C_4H_4O_6^{-2}$-OH^- solution, only four-coordinated complexing of Cu^{+2} by OH has been indicated by Schoenberg (4). At the usual pH for deposition of electroless copper, about 12.9, OH coordination may also be threefold; the fourth bond is to the COO^- of the tartrate. Schoenberg's configurations are shown schematically in Fig. 4. When formaldehyde is included, it may, in the form of the methylene glycol anion, displace the indicated tartrate complex as the initial step in electroless deposition (4). Also shown in Fig. 4 is a configuration which has been reported to be especially consistent with the exceptional stability against hydrolysis (17). The exact nature of Cu^{+2} complexing in alkaline solution is not to

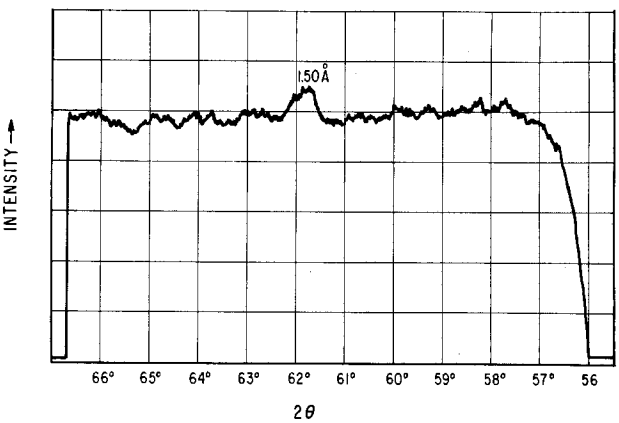
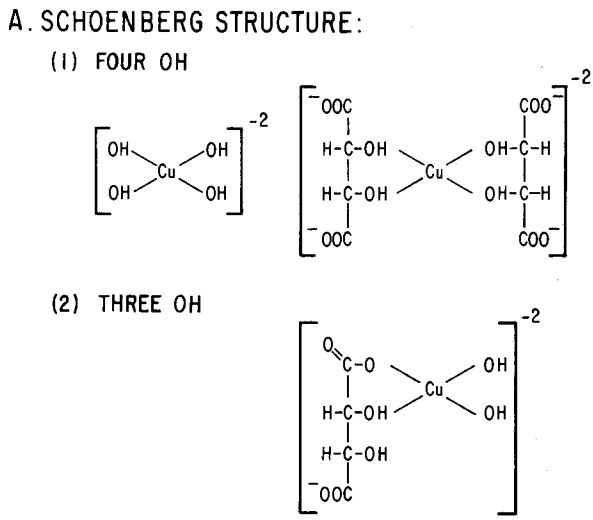


Fig. 3. X-ray diffraction pattern showing a third peak



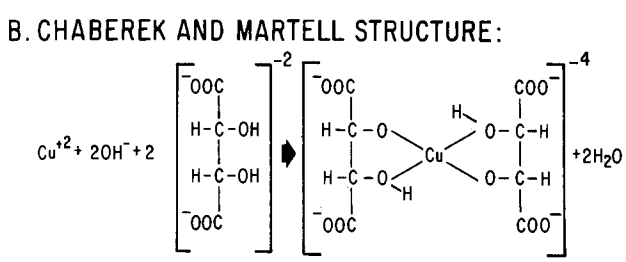


Fig. 4. Suggested complexing of Cu^{+2} by OH^- and $C_4H_4O_6^{-2}$ in alkaline solution, drawn schematically from the literature.

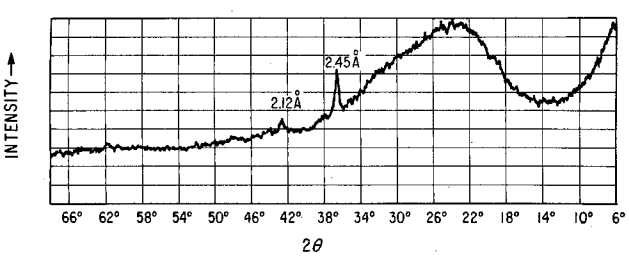


Fig. 2. X-ray diffraction pattern of a Ag-Cu_2O film. The radiation is $CuK_{\alpha 1}$.

be found with total agreement, perhaps, in part, because it varies with composition. Schoenberg's description is, however, reasonable for reference; moreover, it includes the *p*H range for usual electroless coppering solutions, as well as that for deposition of Cu_2O. What it suggests is that whether Cu_2O or Cu forms is likely to be a function, in part, of the concentrations of OH^- and tartrate, and the complexes formed therefrom. Pertinent oxidation-reduction reactions in alkaline solution have been reported. For the catalyzed deposition of copper metal (18)

$$Cu^{+2} + 2HCHO + 4\,OH^- \rightarrow Cu + 2HCOO^- + 2H_2O + H_2 \quad [1]$$

A reaction for the formation of Cu_2O has been written for the reduction of Fehling's solution by formaldehyde (19)

$$2Cu^{+2} + HCHO + 5\,OH^- \rightarrow Cu_2O + HCOO^- + 3H_2O \quad [2]$$

In the absence of the $C_4H_4O_6^{-2}$ from the solution in Table I, a Cu_2O film also formed rapidly, but the solution was decomposed after only a few minutes. The latter suggests that the tartrate ion is necessary in complexing for increasing the relative stability of this solution. On the other hand, because Cu_2O did form rapidly without $C_4H_4O_6^{-2}$, it is likely that, within limits set by stability, a maximum of OH^- bonding is desirable. Experiments were carried out with the $C_4H_4O_6^{-2}$-containing formula in Table I adjusted to lower *p*H's including 12.6, 12.8, and 13.2. Cuprous oxide begins to deposit, within a few minutes, at a *p*H of approximately 13. In the absence of $S_2O_3^{-2}$ treatment, the aforementioned codeposition with small amounts of Cu above *p*H $\cong$ 13, even without $C_4H_4O_6^{-2}$, suggests that both reactions [1] and [2] may be possible; their respective rates depend in part on complexing and in part on the catalytic surface. The solution in Table I is a reasonably good compromise for deposition of Cu_2O, having enough tartrate for stability while having considerable OH^- complexing.

Activation of Cu_2O growth.—When an electroless silver film is freshly prepared on glass, it almost certainly is not purely metallic. It must contain silver oxide. This is difficult to prove by x-ray diffraction for such a few molecular layers of oxide. It is, however, implied by the simple curve in Fig. 5. The reflectance decreases significantly during the time the film is exposed to demineralized water. The silver must be oxidized by dissolved O_2, perhaps to Ag_2O which dissolves then at its own rate; its reported solubility in H_2O is 0.013 g/liter at 20°C. Much the same thing occurs at least during the normal rinsing step. A similar oxidation of silver has been mentioned (20).

It was when working with solutions of Cu^{+2} similar to that in Table I, but at lower alkaline *p*H values and without the $S_2O_3^{-2}$ rinse, that it was first observed that Cu_2O and Cu codeposited on electroless silver. The latter formed in areas which suggested a pattern associated with the puddling techniques of film formation. This raised the question as to whether Cu_2O and Cu are differently activated. Several things were done to alter the uppermost surface of the electroless silver film. For example, a silver film was rinsed for 1 min with an aqueous solution of 1.0% by weight of $KMnO_4$ and then dried. It has been concluded from qualitative emission spectrographic analysis and the interference pattern in Fig. 6 that this film probably contains oxides of both silver and manganese. Deposition was attempted by dipping the treated sample in a Cu^{+2}-containing solution similar to that in Table I except for less NaOH. The *p*H was 13.2. After 5 min, there was a heavy deposit of copper but no visible Cu_2O. A similar, untreated, but dried, silver film which was dipped in a companion solution of the same formulation became coated with Cu_2O and spots of metallic copper. The edges were coated with Cu, where the electroless silver had been slow to dry. Gas evolution which was observed may have accompanied these Cu spots by Eq. [1]. The experiment demonstrates the very important effect which the activating site has,

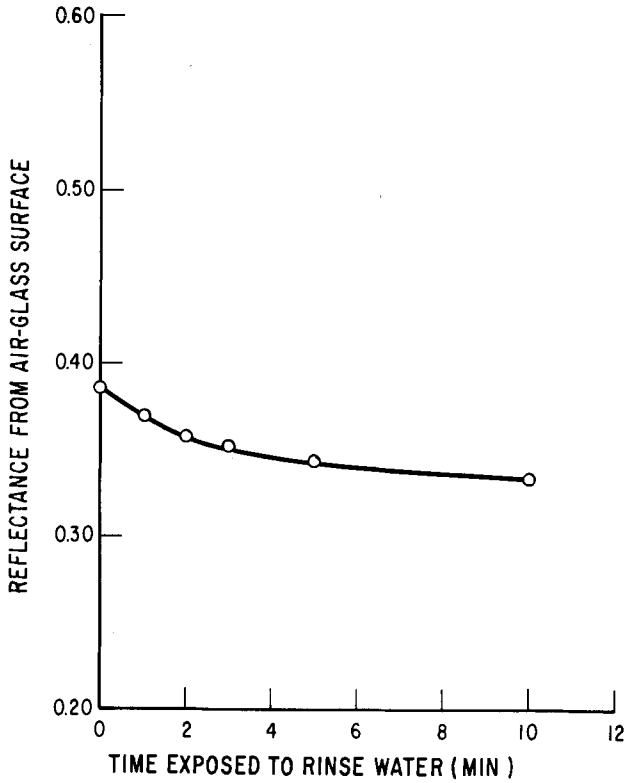


Fig. 5. Luminous reflectance with approximately the standard C response, when an electroless silver film is continuously exposed to demineralized water at room temperature. The film is approximately 200Å thick. Data are averaged for two experiments. Experiments were done horizontally as previously described (10).

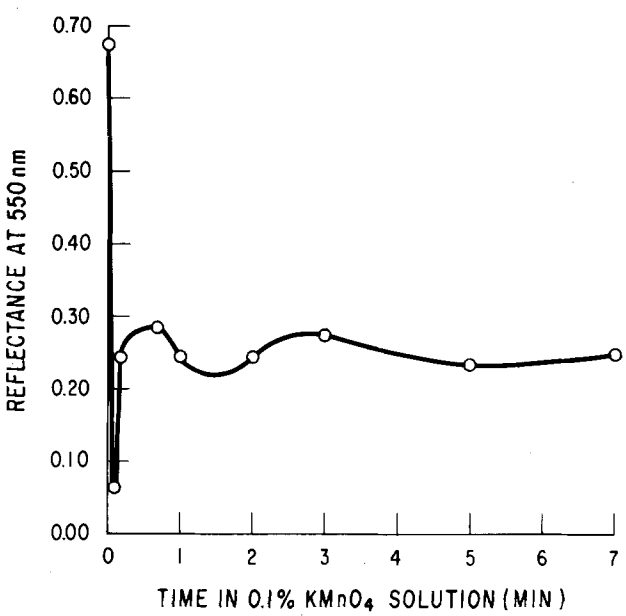


Fig. 6. Interference pattern plotted from the film-air reflectances of electroless silver films on glass after various oxidations in $KMnO_4$ solution at room temperature. The luminous transmittance of the initial silver film in each case was 0.08, thicker than usual so as to produce interference minima. Data are from Diano/Hardy spectral curves.

having had no intentional variation in the electroless solution. One film formed as Cu, the other predominantly as Cu_2O.

Codeposition of copper metal is inhibited by a precursory treatment of electroless silver with a sulfide-forming rinse, for example, a solution of ammonium sulfide. Using normal coating procedures and solutions from Table I other than $S_2O_3^{-2}$, codeposition was prevented by quickly rinsing the electroless silver with a 2.8×10^{-3}% by weight solution of $(NH_4)_2S$; at 2.2×10^{-3}% there was codeposition. At higher concentrations such as at 0.22 and 0.022% all film growth seemed to be inhibited. It is known that S^{-2} scavenges silver oxide (21)

$$Ag_2O + S^{-2} + H_2O \rightarrow Ag_2S + 2\,OH^- \qquad [3]$$

Ag_2S is practically insoluble. Growth of Cu_2O, with the $(NH_4)_2S$ rinse, was indicated by color and iridescence and marked by haziness. Haziness suggests the growth of fewer and relatively larger crystals of Cu_2O. For inhibiting haziness under otherwise similar conditions, the $S_2O_3^{-2}$ solution was found to be a better rinse. Ag_2O is also known to react with sodium thiosulfate to form Ag_2S and sodium sulfate (21). The presence of sulfur in an electroless silver film after exposure to a concentrated solution of $S_2O_3^{-2}$ (3.0 g/liter) has been confirmed qualitatively by comparative x-ray fluorescence analysis. In previous efforts with other silver- and sulfur-containing films, however, it was not possible to identify crystalline silver sulfide by electron diffraction (7).

Apparently, under our conditions, the formation of silver sulfide on Ag, to the extent of inhibiting the growth of silver oxide, favors silver activation of Cu_2O. Silver oxide is apparently favorable for Eq. [1] and the deposition of copper metal. It is possible that the well-known electroless deposition of copper is always activated by silver oxide and not metallic silver at all, although a contrary suggestion has been made (20). The physical and chemical properties which dictate the roles of silver and silver oxide as activators are, at this time, only matters of speculation. Perhaps it is significant that Ag_2O is readily reduced chemically (21) or that it is known to be photoconductive (22).

Summary

Cuprous oxide thin films of good quality, approximately 700Å thick, have been deposited on activated glass by aqueous, electroless chemistry at room temperature. Identification has been made from spectral data and by x-ray diffraction analysis. The films were grown from a highly alkaline solution, pH equal to 13.9, containing Cu^{+2}, tartrate ion, and formaldehyde. Apparently one factor which shifts electroless deposition kinetically, away from the familiar and prevailing copper metal of somewhat lower alkaline pH's, to cuprous oxide, is the highly hydroxide-coordinated Cu^{+2}. Complexing of Cu^{2+} has elsewhere been reported to shift, in the presence of tartrate ion, from three to four coordinated OH's in the pH range of 12.8-13.7. The oxidation-reduction reaction which produces cuprous oxide may be the Fehling reaction.

A second factor, which assures that cuprous oxide will form free of any detectable, codeposited, metallic copper, is the activating site. By prior treatment the glass was coated with electroless silver, care being taken to inhibit the usual formation of silver oxide. The latter seems to activate the electroless codeposition of copper, even when the solution is properly alkaline. Growth of silver oxide was inhibited by rinsing the electroless silver film with a dilute, aqueous solution containing $S_2O_3^{-2}$, thereby forming silver sulfide instead. Our experimental results indicate that metallic silver itself is probably the activator for Cu_2O growth.

As far as is known, this is the first description of electroless deposition of cuprous oxide as a potentially useful optical film. That it grows at all provides some clues about the significance of the Cu^{+2} complex in solution and the role of the activating surface. Each subject bears on the electroless deposition of both cuprous oxide and copper. Further research on either of these should be very useful indeed, relating not only to film deposition but relative bath stability as well.

Acknowledgments

The authors are especially indebted for technical assistance provided by Mr. P. P. Harmon, to Mrs. D. M. Valimont for the x-ray diffraction patterns, and to Mr. H. Parker and Mrs. M. E. Helzel for spectral analyses.

Manuscript submitted March 4, 1977; revised manuscript received May 15, 1977.

Any discussion of this paper will appear in a Discussion Section to be published in the June 1978 JOURNAL. All discussions for the June 1978 Discussion Section should be submitted by Feb. 1, 1978.

Publication costs of this article were assisted by PPG Industries, Incorporated.

REFERENCES

1. S. Wein, "Metallizing Non-Conductors," p. 39, Metal Industry Publishing Co., New York (1945).
2. E. B. Saubestre, *Metal Finishing*, **60** (7), 49 (1962).
3. R. Sard, *This Journal*, **117**, 864 (1970).
4. L. N. Schoenberg, *ibid.*, **118**, 1571 (1971).
5. W. Mindt, *ibid.*, **117**, 615 (1970).
6. W. Mindt, *ibid.*, **118**, 93 (1971).
7. C. B. Greenberg, *ibid.*, **123**, 337 (1976).
8. R. L. Cohen and K. W. West, *ibid.*, **119**, 433 (1972).
9. J. R. McNesby and C. A. Heller, *Chem. Rev.*, **54**, 325 (1954).
10. C. B. Greenberg, *This Journal*, **124**, 496 (1977).
11. D. B. Judd, "Color in Business, Science and Industry," p. 108, John Wiley & Sons, Inc., New York (1952).
12. S. Tolansky, "Multiple Beam Interferometry," pp. 8 and 147, Clarendon Press, Oxford (1948).
13. G. Hass, H. H. Schroeder, and A. F. Turner, *J. Opt. Soc. Am.*, **46**, 31 (1956).
14. H. Wieder and A. W. Czanderna, *J. Appl. Phys.*, **37**, 184 (1966).
15. A. W. Czanderna and F. L. Boyko, *J. Vac. Sci. Technol.*, **6**, 746 (1969).
16. B. Prevot, C. Carabatos, and M. Sieskind, *Phys. Status Solidi*, **10**, 455 (1972).
17. S. Chaberek and A. E. Martell, "Organic Sequestering Agents," p. 307, John Wiley & Sons, Inc., New York (1959).
18. Y. Okinaka, Paper 144 presented at the Electrochemical Society Meeting, Detroit, Michigan, October 5-9, 1969.
19. R. Q. Brewster, "Organic Chemistry," 2nd ed., p. 153, Prentice-Hall, Inc., Englewood Cliffs, N.J. (1953).
20. J. Dumesic, J. A. Koutsky, and T. W. Chapman, *This Journal*, **121**, 1405 (1974).
21. M. C. Sneed, J. L. Maynard, and R. C. Brasted, "Comprehensive Inorganic Chemistry," Vol. 2, p. 145, D. Van Nostrand Co., Inc., New York (1954).
22. E. Fortin and F. L. Weichman, *Phys. Status Solidi*, **5**, 515 (1964).

The Reduction of SiO_2 with Carbon in a Plasma

D. M. Coldwell* and R. A. Roques*

Texas Instruments Incorporated, Dallas, Texas 75222

ABSTRACT

The feasibility of a process for the reduction of low impurity silica (SiO_2) with carbon in a plasma heat source was investigated. An rf induction plasma reactor was fabricated and used to optimize process variables. Maximum silicon content of the product was 33% by weight. Emission spectrographic analysis of this product showed a reduction in some impurity levels of one to two orders of magnitude. While the plasma approach proved technically feasible, poor heat transfer from the plasma to the reactant and low yield make the process economically unattractive for large-scale use.

The reduction of a silicon-containing halide has long been the source of the electronics industry's elemental silicon. However, this process is far too expensive to fall within the goals of ERDA's Low-Cost Silicon Solar Array Program which demands solar-grade silicon costing less than $10 per kilogram.

One approach to obtain these goals is the reduction of naturally occurring silicon oxides with carbon in a high temperature induction plasma torch. Coldwell (1) has studied the thermodynamics of this reaction under plasma conditions with a computer model which utilized an iterative free energy minimization technique. A threshold temperature of 2500°K was predicted below which no silicon is formed, only silicon monoxide and silicon carbide. Above 2500°K, elemental silicon and carbon oxides should be produced. The yield of silicon and the type of carbon oxides are dependent on the initial ratio of carbon to silica (SiO_2). This analysis assumed equilibrium reaction conditions only to show that the proposed reaction was thermodynamically feasible.

While other investigators (2-4) have used induction plasmas, their work involved the reduction of processing of only a single reactant. This plasma reduction, on the other hand, required a chemical reaction between two components to occur above the threshold temperature in the plasma itself. A diagram of the process is shown in Fig. 1.

The plasma was formed in an induction torch described by Reed (5) and improved upon by Boumans *et al.* (6). It was used to reduce silicon dioxide yielding elemental silicon and carbon mono- or dioxide.

Experimental Procedure

Raw material preparation.—In order to maximize reactivity of the raw materials, fine grinding and intimate blending were first necessary. The naturally occurring silica was purchased as silica flour of less than 400 mesh ($<37\ \mu m$) particle size and the carbon, *i.e.*, carbon black, was available in a pelletized form of ultimate particle size in the millimicron range. The raw materials were further comminuted and blended in a rubber-lined ball mill using flint pebble grinding media to minimize contamination. The general approach taken was the upgrading of starting material quality and careful avoidance of contamination of the reactants and product through the process. Table I gives the results of emission spectrographic analysis of raw materials.

The initial emphasis of this study was on using powder or pelletized material but difficulties of reactant feed, penetration into the plasma, and sufficient residence time in the plasma for reaction to occur were experienced. An alternative approach was material formed into 6 mm diam rods. Binder additions of 5 weight percent (w/o) polyvinyl alcohol (PVA), and sufficient water to produce good extrudibility, improved the plasticity and strength of these extruded rods. The durability of the rods was sufficient to withstand the heat exposure on entering the plasma flame without fracturing or decrepitating before being vaporized.

Experimental reactor description.—An induction heating system unit was used to construct the rf plasma reactor. A two-turn coil around a 30 mm diam quartz tube had provisions for introducing and measuring gas flows. To prevent localized melting of the tube wall where the flame was in close proximity, the discharge was vortex-stabilized by introducing a sheath gas tangentially into the quartz tube. This plasma could be maintained on the axis of the tube even if the diameter of the flame (approximately 1.5 cm) was much greater than the skin depth of the plasma gas. The plasma reactor is shown diagramatically in Fig. 1.

The reactant material was fed to the flame by a continuous rod feed mechanism. This rate was controlled by a variable speed motor driving a threaded rod which moves the feed rod vertically into the reduction chamber. The rod was positioned to enter the plasma at its hottest point.

The temperature distribution within the plasma was determined spectroscopically (7). Peak temperature was found to be 15,000°K, decreasing to 1000°K downstream. The size of the region greater than the threshold temperature was large enough to be easily used as the rod feed target.

A tubular bundle was fabricated and placed downstream from the plasma to quench product gases. It was positioned so that its surface temperature was elevated ($>$ 600°K). After each run, the collected product was removed from the bundle and the bundle etched in dilute hydrofluoric acid to remove any traces of previous runs. Optimum collecting temperature was estimated by heating the cooling chamber wall and was found to be approximately 600°K.

Since the product obtained is amorphous and of millimicron size, further processing is necessary to quantitatively determine the amount of elemental silicon present. Wet analysis of the unsintered product gave erratic results which were reproducible only after the sintering step. Sintering at 1825°K for 1 min in argon consolidated the silicon and disproportionated approximately 70% of the silicon monoxide to silicon dioxide and silicon.

Results and Discussion

Experiments with feed rod composition of one mole SiO_2 to one mole carbon were made to determine optimum reactor conditions with respect to power, feed rate, and gas flow rate. Maximum and minimum values were used for each process variable. The experimental design can be represented by a cube with axes representing each of the three variables and individual experimental conditions by the center and corners (8). This is shown schematically in Fig. 2.

* Electrochemical Society Active Member.
Key words: silicon, solar energy, reduction.

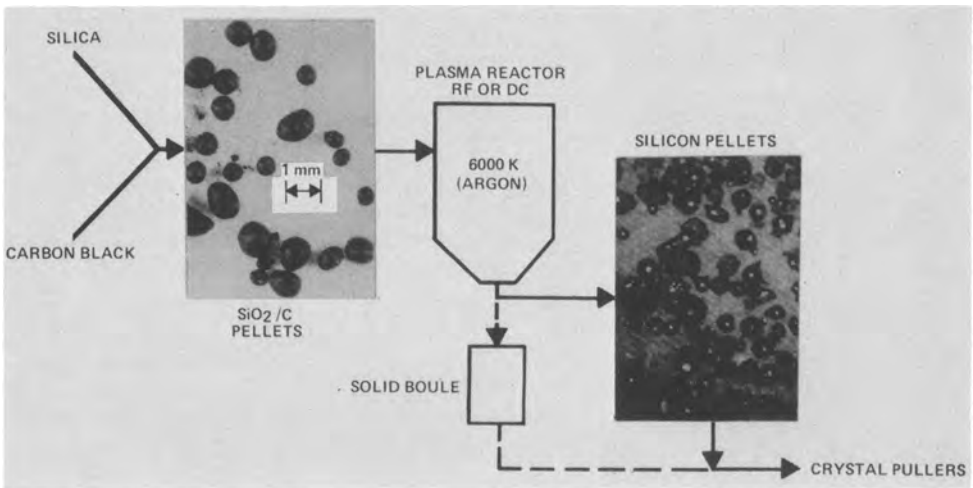


Fig. 1. Solar silicon production with a plasma.

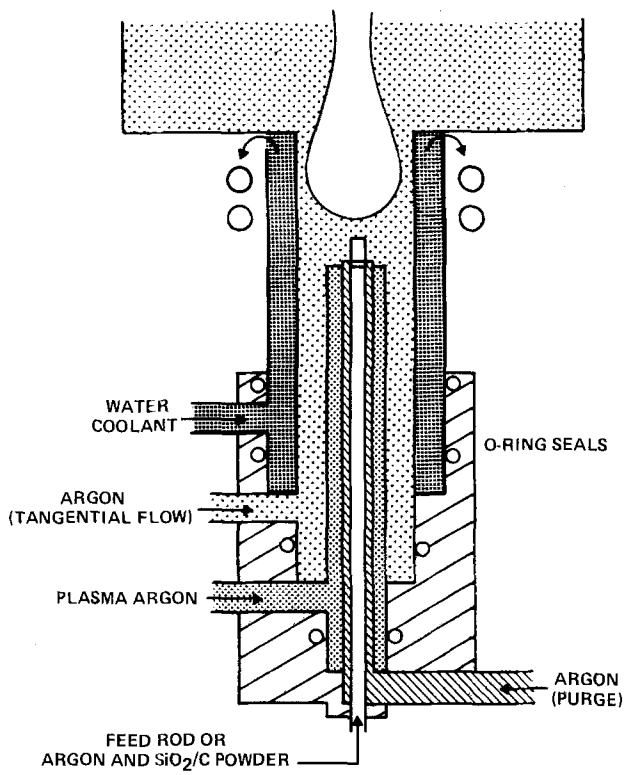


Fig. 2. Diagram of induction plasma reactor

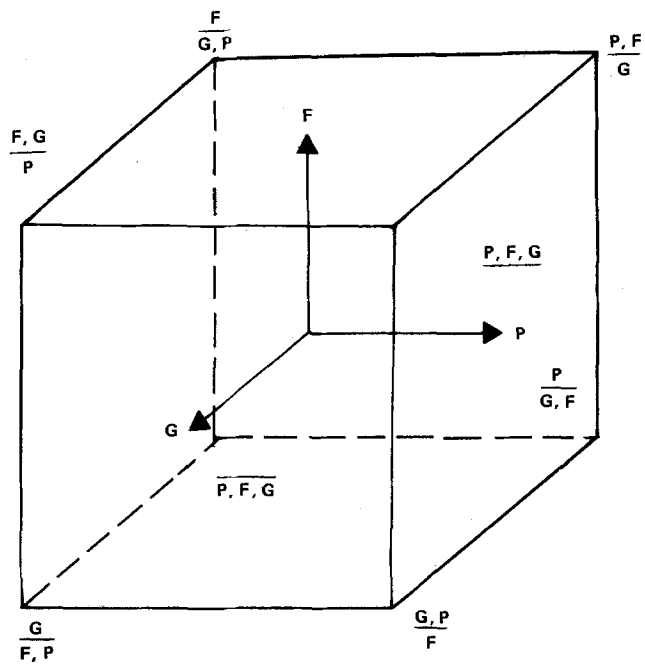


Fig. 3. Schematic representation of experiments. *F*, feed rate of reactant; *G*, gas flow rate, *P*, power level. Variable listed in denominator is minimized. Origin is a point midway between $\underline{P, F, G}$ and $\overline{P, F, G}$.

The results of wet chemical analysis of the products are shown in Table II.

Optimum conditions for process variables were found to be maximum power, maximum plasma gas flow,

	Approximate endpoints	
	Max	Min
P, kW	10	5
F, g/hr	20	10
G, liter/min	20	10

Table I. Emission spectrographic analysis of raw materials

	Carbon black,* ppm wt				Silica,** ppm wt		
	Cabot V-9A50	Huber N-110	Ashland 3023-P	Detection limit	PGS Supersil	Wedron 400M	Detection limit
Si	100-1000	100-1000	100-1000	0.08	Major	Major	—
B	ND	ND	ND	0.08	10-100	10-100	0.15
Be	30-300	10-100	30-300	0.06	100-1000	100-1000	0.25
Mg	1-10	3-30	3-30	0.006	1-10	10-100	0.0003
Mn	1-10	ND	1-10	0.02	1-10	1-10	0.07
Al	30-300	10-100	30-300	0.06	30-300	30-300	0.02
Ti	0.5-5	0.5-5	0.5-5	0.08	10-100	10-100	0.12
Ca	10-100	30-300	30-300	0.06	ND	ND	6.0
Cu	0.1-1	0.1-1	0.1-1	0.03	0.1-1	0.1-1	0.07
Na	100-1000	100-1000	100-1000	0.05	100-1000	100-1000	4.0
P	ND	ND	ND	1.0	ND	ND	1.0

* 50 lb sample.
** 100 lb sample.

Table II. Results of experiments for optimization of variables*

Run designation	*P*, input power (kW)	*G*, plasma gas flow (liter/min)	*F*, material feed rate (g/min)	Product collected (%)	Silicon in product (%)	Comments on sintered product and/or results
$\frac{GP}{F}$	14	3	0.02	25	23	Si globules observed
$\frac{PF}{G}$	14	1	0.05	30	17	Si globules observed
$\frac{G}{FP}$	7	3	0.02	28	6	SiO_2 fibers present
$\frac{PFG}{P}$	14	3	0.05	68	14	Si globules observed
$\frac{P}{GF}$	14	1	0.02	22	20	Si globules observed
$\frac{FG}{P}$	7	3	0.05	11	—	Plasma flame extinguished
$\frac{}{GPF}$	7	1	0.02	24	3	No Si observed
$\frac{F}{GP}$	7	1	0.05	17	—	Plasma flame extinguished
$\frac{PFG}{2}$	10	2	0.205	<10	—	Insufficient product collected
$\frac{GP}{2}\ \frac{}{F}$	10	2	0.02	25	9	SiO_2 fibers present
$\frac{GP}{2}\ \frac{F}{}$	10	2	0.05	19	10	Si globules observed

* Sheath gas was 15 liters/min. Run time was 30 min. Feed composition was SiO_2/C (1:1 mole ratio) in rod form. Sintering was at 1550°C in argon. Variable in numerator represents maximum experimental value; if in denominator, a minimum value.

Table III. Variation in composition and batch preparation of feed mixture

% Carbon (including binder)	C:SiO_2 mole ratio	Batch preparation procedure and binder addition	% Silicon in sintered product	Comments on product
15.6	0.92	Wet-milled. Methocel, PVA	6	Fused SiO_2 formed on rod tip. Complete vaporization
21.9	1.34	Wet-milled. Methocel, PVA	10	SiO_2 and Si on rod tip. Complete vaporization
22.9	1.48	Wet-milled. PVA	15	SiO_2 and Si on rod tip. Complete vaporization
23.4	1.50	Wet-milled. Methocel, PVA	23	Si formed on rod tip. Complete vaporization
24.5	1.62	Wet-milled. Methocel, PVA	33	Si formed on rod tip. Complete vaporization
26.8	1.91	Wet-milled. Methocel, PVA	32	Si formed on rod tip. Incomplete vaporization at accelerated feed rate but conversion to silicon *in situ*
28.3	1.97	Wet-milled. PVA	—	No Si on rod. Insufficient product collected
31.8	2.33	Dry-milled. PVA	15	Incomplete vaporization. SiC formed on rod tip
33.2	2.48	Wet-milled. PVA	—	SiC formed on rod. Incomplete vaporization
35.8	2.78	Wet-milled. Methocel, PVA	—	Rod did not vaporize

and minimum feed rate, run *GP/F*, which produced 23% silicon in the sintered product. Other reactor conditions led to results repeatable within 20%.

The amount of product collected as a percent of the amount of material fed to the reactor is indicative of the efficiency of heat transfer to the material in order to vaporize it. The theoretical amount of silicon which could be obtained at 100% reduction of the SiO_2 is $\approx$ 39% by weight of the starting material mixture. The *GP/F* run yielded product silicon that was 15% of theoretical. This low efficiency of heat transfer appears to be a significant problem in utilizing this plasma process.

Using the optimum reactor conditions, the raw material carbon to silica mole ratios were varied from 1 : 1 to 2.8 : 1. The addition of a binder such as methyl cellulose or polyvinyl alcohol, was necessary to extrude 6 mm diam rods but had little effect on reaction rate or silicon yield. Table III lists data and results of experimental runs made with the compositions investigated. The highest yield of silicon occurred at a carbon to silicon mole ratio between 1.5 :1 and 1.9 :1. It also appears that wet ballmilling of the carbon and silicon is more favorable for comminution and intimate mixing than is dry milling.

Chemical analyses of the sintered reaction product showed 28-33% of the material collected in the best runs was silicon. The silicon was visible after consolidation in globular form with the characterisic protrusions of a material which expands on freezing from the melt. Globules ranged from $\approx$ 25-250 μ, as shown in Fig. 4. Emission spectrographic analysis of the silicon indicated at least an order of magnitude reduction in content of some impurities from the starting materials with electrically active elements such as boron, arsenic, and phosphorus below the detection limits. Table IV shows a comparison between the analyses of the raw material batch and the silicon product.

These experiments were the first to demonstrate a chemical reaction between two reactant solids fed into an induction plasma. Despite the short residence time in the plasma, the silica was reduced to either elemental silicon or silicon monoxide.

Table IV. Emission spectrographic analysis of silicon product

	Silicon product (ppm, wt)	Raw batch (SiO_2/C) (ppm, wt)
Fe	10-100	100-1000
Mg	3-30	30-300
Al	10-100	300-3000
Ca	10-100	100-1000
Cu	1-10	1-10
Ag	0.1-1	0.1-1
B	ND <0.15	3-30
P	ND <1.0	ND <1.0
Ti	ND <0.12	30-300
Mn	ND <0.07	1-10
Ar	ND <1.0	ND <1.0
Na	ND <4.0	100-1000

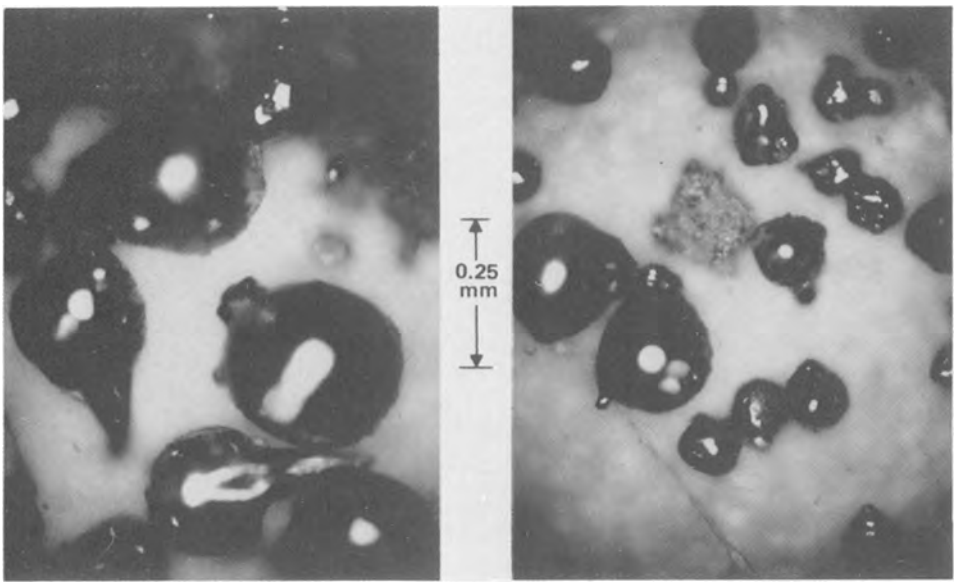


Fig. 4. Silicon globules produced by consolidation of material collected from plasma reaction.

Problems and Unknowns in Plasma Technology

A number of difficulties were identified in the use of a plasma heat source for a reversible chemical reaction, which are inherent in plasma technology and require solution before use of an induction plasma is practical. (*i*) The energy utilization is low due to the series of multiple steps (rf generation, plasma gas exitation, and gas to reactant solids), each of which is less than 50% efficient. The large volumes of inert gas required to sustain the plasma multiply the amount of heat required. (*ii*) The large volumes of gases cause the desired chemical concentration to be very low, which severely limits controlled collection of product condensate. Separation of unreacted material from product is complicated by the simultaneous quenching of both species. (*iii*) A molecular dynamics computer simulation showed that quenching rates higher than are physically possible are necessary to remove vaporized elemental silicon from the product before it reoxidizes (9). Even if this reaction and disproportionation to silicon are taken in account, the quench rate required is an order of magnitude too great to be achieved with current technology. (*iv*) Control over the reaction temperatures within the plasma is difficult. The exact reaction temperature was unknown, occupied a very small volume, and varied greatly because of the steep temperature gradient within the plasma. (*v*) The usage of argon gas is excessive.

Summary

The technical feasibility of producing silicon from the raw materials, silica and carbon black, was demonstrated using a laboratory-scale plasma reactor. Energy utilization was inefficient due to poor heat transfer characteristics of the plasma and yield of silicon in the product collected as condensate was never greater than 33% ($\approx$ 25% of the stoichiometric amount available). The problems related to inefficiency of energy utilization and product yield were not resolved.

The experimental results suggest that a reduction reaction likely occurs while reactants are in a condensed state. Further heating of the rod causes product silicon to vaporize simultaneously with carbon and oxygen-containing gases from additional reduction reaction. High yield recovery by quenching of the product silicon from a highly reactive gas stream, regardless of how the mixture was formed, is unlikely.

Acknowledgment

This work was funded by the California Institute of Technology, Jet Propulsion Laboratory Low-Cost Silicon Solar Array Project, a part of the ERDA Photovoltaic Conversion Program to initiate a major effort toward the development of low cost solar arrays.

Manuscript submitted April 22, 1977; revised manuscript received July 7, 1977. This was Paper 105 presented at the Philadelphia, Pennsylvania, Meeting of the Society, May 8-13, 1977.

Any discussion of this paper will appear in a Discussion Section to be published in the June 1978 JOURNAL. All discussions for the June 1978 Discussion Section should be submitted by Feb. 1, 1978.

Publication costs of this article were assisted by Texas Instruments Incorporated.

REFERENCES

1. D. M. Coldwell, *High Temp. Sci.*, **8**, 309 (1976).
2. R. K. Rains and R. H. Kadlec, *Metall. Trans.*, **1**, 1401 (1970).
3. K. Nassau and J. W. Shiever, *Bull. Am. Ceram. Soc.*, **54**, 11 (1975); *ibid.*, **54**, 1004 (1975).
4. R. F. Baddour and R. S. Timmius, The Application of Plasma to Chemical Processing, MIT paper (1967).
5. T. B. Reed, *J. Appl. Phys.*, **32**, 821 (1961).
6. P. W. J. M. Boumans, F. J. deBoer, and J. W. DeRuiter, *Philips Tech. Rev.*, **33**, (2), 50 (1973).
7. R. H. Tourin, "Spectroscopic Gas Temperature Measurement," Elsevier Publishing Co., New York (1966).
8. Y. P. Adler, E. V. Markova, and Y. V. Granovsky, "The Design of Experiments to Find Optimal Conditions," Mir Publishers, Moscow (1975).
9. D. M. Coldwell, To be published.

A Parametric Study and Computer-Based Simulation of an Undivided Sodium Hypochlorite Electrolyzer

G. R. Heal, A. T. Kuhn, and R. B. Lartey

Department of Chemistry and Applied Chemistry, University of Salford, Salford, Lancashire M5 4WT England

ABSTRACT

The electrolysis of brines has been carried out in an undivided cell under controlled hydrodynamic conditions and with simultaneous chemical analysis of all major products formed (ClO^-, O_2, H_2, ClO_3^-). The experimental data are compared with predictions made using a simple model and proven mass transfer relationships, and it is shown that a satisfactory fit obtains.

In recent years there has been a dramatic revival in the use of electrochemical hypochlorite cells. Unlike the earlier cells, which were unstirred and which used strong made-up brines to produce NaOCl for chemical production, the newer generation of electrolyzers operates with low strength (*ca.* 3%) NaCl, often using untreated seawater. This is pumped through a parallel plate cell at high velocity to give a large volume of low strength NaOCl which is used for disinfection or to prevent fouling. Details of the applications, the designs of such cells, and operating modes may be found in a recent paper by Bennett (1) or in Ref. (2, 3). Hypochlorite cells also feature in a number of patents, most of which are listed in the references cited above. There have also been valuable contributions to the subject from Soviet workers. Thus both Medrish (4) and Skripchenko *et al.* (5) describe extensive measurements of current efficiency and power consumption together with product analysis. Further additions to the patent literature include British Patents 1,399,898 (addition to 1,278,591). What is, however, lacking in the literature, is information relating to the performance of such cells. The older, nonpumped hypochlorite cells have been fully described in the textbooks of industrial electrochemistry. But the performance of the modern force-flow cells is either not described, or else information given omits important details such as channel dimensions. In such cases, electrochemical parameters, such as diffusion layer thickness, cannot be deduced. Lastly, some of the published data relate to experimental conditions in which one or more parameters were not held constant. In large cells, for example, a significant rise in temperature will occur during the passage of the brine through the cell, thereby making cell performance prediction difficult.

Chemistry and Electrochemistry of the System H_2O-NaCl-Cl_2

Because the subject has not been treated in the literature in the last decade, we should initially consider the chemistry and electrochemistry involved in an undivided hypochlorite cell. Thus the following equations may be written:

(*i*) Homogeneous system: When chlorine is dissolved in water, the following reactions can take place

$$H_2O + Cl_2 \rightarrow HOCl + Cl^- + H^+ \quad [1]$$

$$HOCl \rightarrow H^+ + OCl^- \quad [2]$$

$$OCl^- + 2HOCl \rightarrow ClO_3^- + 2Cl^- + 2H^+ \quad [3]$$

$$2\,OCl^- \rightarrow 2Cl^- + O_2 \quad [4]$$

Both reactions [1] and [2] are fast as Landolt and Ibl and others (6) have shown. The equilibrium position of [2] is pH dependent and Ref. (7) shows a typical curve. From simple equilibrium postulates, one can say that decrease in $[Cl^-]$ or $[H^+]$ concentrations will lead to increase in either HOCl or OCl^- (whichever is favored at the particular pH. Reaction [4] is catalyzed by heavy metal ions or active charcoal as well as other dissolved or suspended species.

(*ii*) Electrochemical reactions: Most of the species described above can undergo at least one electrode reaction, either at the anode or cathode. So too, can water and ions derived from it. We can list here:
at the anode

$$2Cl^- \rightarrow Cl_2 + 2e \quad [5]$$

$$6\,OCl^- + 3H_2O \rightarrow 2ClO_3^- + 4Cl^- + 6H^+ + 3/2\,O_2 + 6e^- \quad [6]$$

$$H_2O \rightarrow 2H^+ + \tfrac{1}{2}\,O_2 + 2e \quad [7]$$

$$ClO_3^- + H_2O \rightarrow ClO_4^- + 2H^+ + 2e \quad [8]$$

$$ClO_3^- + HClO \rightarrow ClO_4^- + Cl^- + H^+ \quad [8a]$$

at the cathode:

$$OCl^- + H_2O + 2e \rightarrow Cl^- + 2\,OH^- \quad [9]$$

$$2H^+ + 2e \rightarrow H_2 \quad [10]$$

$$2H_2O + 2e \rightarrow H_2 + 2\,OH^- \quad [11]$$

$$3H_2O + ClO_3^- + 6e \rightarrow Cl^- + 6\,OH^- \quad [12]$$

We can make certain assertions at the outset. Thus the homogeneous reaction [3] does not proceed fast below 50°C as shown by Ormerod (15) and also Jaksic (21) while the anode reaction [8] is scarcely significant above 10°C as shown in (15). But for further consideration of the over-all steady state, one must distinguish between those cells which are divided by a membrane or diaphragm into anode and cathode compartments (as in the chlorine industry) and those which are undivided. In the former, the anolyte reaches a pH value of 2-3 and gaseous chlorine is evolved while the electrolyte is saturated with hypochlorous acid as well as dissolved chlorine and additionally contains a given amount of ClO_3^-. The latter (9) is formed by oxidation of OCl^- ions arising from back-migration of OH^- ions from the catholyte. The catholyte is strongly alkaline with H_2 evolved at the cathode. Any chlorine seeping through the diaphragm is converted to OCl^- ion and this is immediately reduced at the cathode (reaction [9]) to Cl^- so that no trace of it is ever found. Of the chlorate formed in the anolyte, some diffuses to the catholyte and this too is reduced at the cathode, though incompletely so that measurable amounts (typically 0.07 g/liter) are found in the catholyte liquors leaving the cell.

In an undivided cell however, the pH is substantially uniform across the cell. H_2 is still evolved at the cathode and Cl_2 at the anode. However the pH being now much higher, this dissolves virtually to completion to form hypochlorite solutions. Some values for these

Key words: brine electrolysis, undivided cell, reactor modeling, electrochemical mass transfer.

equilibrium constants have been quoted in the literature. Thus for Eq. [2] Hammer and Wranglen (8) quote a mean value of 4.6×10^{-8} (at 20°C), while Hine and Yasuda (9) quote 1.33×10^{16} at 25°C for $Cl_2 + 2\,OH^- \rightarrow Cl^- + ClO^- + H_2O$.

Kinetic analysis of cell reactions.—Certain of the reactions discussed above have been extensively studied although not always under the precise conditions that obtain in hypochlorite cells.

Cathodic losses.—The reduction of the OCl^- ion, as well as its undissociated counterpart, is well understood. Wolf and Landsberg (10) studied this reduction in alkaline solutions on graphite electrode at OCl^- concentrations of up to 1.2×10^{-3} mole liter^{-1}, finding reduction currents of the order of 1 mA · cm^{-2} and a mechanism that agreed with their earlier work [Schwarzer and Landsberg (11)] as well as that of Mueller (12) on platinum cathodes. The latter author derives the expression

$$i = k\,[ClO^-] \exp\,[0.42\,\mathbf{F}E/RT]$$

for the rate of reduction on the metal surface which is seen to be first order in hypochlorite ion (at least up to 2.4×10^{-3} molar). No *p*H effects were determined in this work, although these are reported in the study by Schwarzer and Landsberg (11) who show the reductive behavior at *p*H = 5.3, 7.5, and 10.0. At the most negative potentials, there appears to be no *p*H effect and the current (at 5 mmole HClO) is diffusion limited although, at less cathodic potentials (+0.2 *vs.* SCE), separate plateaus due to the OCl^- and the HOCl reduction can be seen. Another recent paper by Harrison and Khan (13) supports the above findings and it is clear that oxides of Pt can catalyze the reaction. However, in the context of hypochlorite cell operation, the cathode will always be cathodic to this region. A recent paper by Hine and Yasuda (9) is noteworthy in that it reports measurements at higher ClO^- concentrations than the others cited here. At 0.09M OCl^- in 2*N* NaOH + 3*N* NaCl a limiting current for the OCl^- reduction of 10 A · dm^{-2} is reached and appears to be first order in OCl^- as evidenced by Mueller (12) at much lower concentrations. There does not appear to be any dependence in NaCl concentration (1.3 and 0.3*N* NaCl) nor on *p*H (2-0.2*N* NaOH) again supporting previous workers. In conclusion, it will be seen that especially at higher operating conditions of OCl^-, a significant loss of efficiency can occur. Hammer and Wranglen (8) have studied both anodic and cathodic losses, though mainly with an eye to the chlorate manufacturing process. From their results the additional parameters of temperature and ClO_3^- can be studied. Increase in temperature favors decomposition of OCl^- at the cathode while increased ClO_3^- concentration depresses it. Both effects are tied to viscosity changes in the electrolyte with resulting changes in diffusion limiting currents. At zero OCl^-/HOCl concentration and the very high (273 g/liter) concentration of ClO_3^-, a certain amount of reduction of the latter takes place and from 2-8% of the cathodic current could be so consumed (steel cathode, *p*H 10, 14-100 A · dm^{-2}, 25°C). Again it is true to say that under normal hypochlorite cell operating conditions, this source of loss will not be significant. Seen from the over-all cathodic operation viewpoint, it is probably true to say that reactions [9] and [10] are the dominant ones and that the aim in cell design should be to offer a cathode on which these reactions proceed with the lowest overpotential, thus minimizing this contribution to cell voltage. Reduction of hypochlorite on Fe cathodes has been studied (14).

Anodic loss reactions.—We are here mainly concerned with reactions [6] and [7] since it has been shown (15) that [8] is unimportant above 10°C. Reaction [7] is itself insignificant at normal operating potentials, provided the Cl^- concentration is reasonably high.

It will, of course, be seen that simple measurements of oxygen evolution from the cell will not elucidate the contributions of [6] and [7] since both are a source of this element. Thus Kuhn and Mortimer illustrate how, at high current densities (16), the amount of oxygen evolved increases as brine concentrations are lowered from 1 to 0.13M. Although they do not specifically attribute the contributions from the two different sources, the obvious importance of stirring and mass transport make it clear that it is [6] and not [7] which is the main source of oxygen inefficiency under these conditions since mass transport problems would not be anticipated for [7] at any normal operating current densities. Unpublished results (15) do throw light on this question. At 3% NaCl concentration 21-25% of the anodic current was lost in this way at 0°C (inlet temperature) though this dropped to 13% at 10°C. Using 1% brine at 10°C approximately 30% of the current loss was ascribable to this reaction. (Current density was believed to be *ca.* 300 mA · cm^{-2}.) From the same source, we see that current losses due to perchlorate formation were 13-30% (at 0°C) and essentially nil at 10°C. Finally, current loss due to reaction [5] was 11% at 10°C and 5% at 0°C all in 3% brine, with a 72% efficiency in OCl^- manufacture at the higher temperature, dropping to 50% at zero degrees. In the 1% brine at 10°C, the hypochlorite efficiency was 36-44% with chlorate losses around 25% and oxygen evolution, as listed above, rather higher. Though these results are reasonably accurate, they are made in cells with an appreciable entrance-exit temperature gradient. Furthermore, the hydrodynamics are ill-defined and on these, as has been seen, the loss rate of reaction [6] depends. The work of Hammar and Wranglen, cited above, is equally interesting in the information cited on the anodic side, although it should be stated that (*i*) the hydrodynamic conditions are ill-defined, and (*ii*) the brine concentrations are always so high that O_2 evolution is suppressed (Eq. [7]). Thus the rate of oxidation of (HOCl + OCl^-) is linearly related to its concentration, independent of *p*H in the region *p*H 6-11 as is the reductive loss, and increases by some 2%/°C. At 4 A · dm^{-2} and 100 mmole hypochlorite, 25°C, the loss is some 25%. A paper by Despic *et al.* (17) deals with the oxidation rate of OCl^- ions alone (no HOCl) and the mechanism even under these "simplified" conditions is most complex. Perchlorates can also be formed, and we have detected them analytically. The kinetics of reaction [8a] have been studied by D'Ans (40).

Mechanistic and kinetic conclusions.—The reactions of possible importance in the hypochlorite cell, both chemical and electrochemical, have been discussed. It will be seen that as a fixed quantity of brine (whether this be static or continuously stirred or recycled) is electrolyzed, a point is reached where the rate of destruction of hypochlorite (due to several of the processes described) matches the rate of formation. This situation results in a plateau in the concentration *vs.* time curve, as seen in Marshall and Millington (18). After further time, of course, the level of concentration will actually decrease due to losses of Cl^- from the system as ClO_3^-.

The relative importance of anodic and cathodic losses.—The question is sometimes raised whether losses of hypochlorite at the anode or cathode are more significant (ignoring losses in the bulk). This can be seen to be largely a matter of definition. Defining it in terms of molecules of OCl^- or HOCl lost per unit area in a given time, the cathodic losses are greater since under the diffusion-controlled regime that prevails in most cells, the small value of δ (diffusion layer thickness) at the cathode (due to the copious evolution of hydrogen gas there) assists in this respect. On the other hand while two electrons

serve to destroy one molecule of HOCl at the cathode; at the anode, from 0.3 to 3 electrons, by means of a reaction such as

$$7HClO + H_2O \rightarrow 2ClO_3^- + O_2 + 5Cl^- + 9H^+ + 2e$$

or Eq. [6] and Ref. (8) are used to destroy the HOCl.

The foregoing treatment suggests that while much excellent work has been done in the general area, there are no studies to describe accurately the modern undivided force-flow hypochlorite electrolyzer operating at high current density and, therefore, in the mass transport-controlled region, as far as many of the reactions listed above are concerned. The apparatus described below, being a recycling loop, approximates to an "infinitely long" cell, although the actual dimensions of the electrodes are comparatively small. In this it resembles the commercial reactors fitted with recycle and "bleed-off." A useful general treatment of such systems has been given by Pickett (19).

Experimental

The cell consisted of two polypropylene blocks, each 31 cm long, 9 cm wide, and 2.5 cm thick, which were bolted together. A cell cavity was created by machining a recessed area in each block, and the electrodes were further countersunk in each cavity. The effect of interelectrode gap was studied by introduction of a polypropylene spacer between two electrode blocks. Electrolyte entered and left the cell by means of a twin-branched manifold angled at approximately 20° to the plates and designed to reduce entry and exit turbulence to a minimum. In addition, the cell cavity was large enough to provide a smoothing section (17 cm from entry to leading edge of the electrodes) and an exit section (5 cm from electrode trailing edge to exit manifold). Electrodes were made of platinized titanium 2 cm wide × 10 cm long, supplied by Messrs. Marston Excelsior Limited, Wolverhampton. Brine was circulated through the cell by an Iwaki magnetically coupled all PTFE pump. The brine circulation circuit also incorporated a cooling/heating coil immersed in a constant temperature bath, and a Venturi system (previously calibrated) to measure brine velocity. Provision was made for circulating the brine through a gas-disengagement chamber and this was coupled to an Orsat gas analysis apparatus, in which H_2 and O_2 could be estimated. The cell itself was oriented with electrodes vertical and the angle of the cell at 45° to the vertical. This prevented accumulation of gas bubbles (gas-locking) at low brine velocities. Direct-current power was supplied to the cell from a power pack, current was measured using a Sangamao Weston S82 multirange precision ammeter. Cell voltage and half-cell voltage were measured with a Garrett-Normalair digital voltmeter of high impedance and using a back-entry Luggin probe connected to a saturated calomel reference.

Results and Discussion

The cell was operated under a range of current densities (from 25 to 450 mA · cm^{-2}) and brine flow rates (15-75 cm sec^{-1}) all obtained at 25°C. The buildup of hypochlorite, and chlorate concentrations was followed as a function of time, as were the rates of hydrogen and oxygen evolution. Too much data were gathered to present here, but are fully reported elsewhere (20). The buildup of hypochlorite concentration is shown in Fig. 2 and 3. The qualitative explanation of this is well known and lies in terms of the increasing rate of the back-reduction of hypochlorite at the cathode, until a point is reached where the rate of hypochlorite production at the anode is matched by its reduction at the cathode. Increasing brine flow rates aid this reductive destruction by decreasing the thickness of the boundary layer at the cathode, though this effect is least marked at high current densities where the co-evolution of gas bubbles at the cathode surface constitutes an extremely efficient means of enhancing mass transport of OCl^- ions to this surface.

The main purpose of the present work, however, is to show that, using a comparatively simple computer-based model, the results obtained experimentally in this work can be simulated or predicted.

Bennett (1) mentions the development of a computer-based model for prediction of hypochlorite cell performance. However no details are given and the impression is that his model is a largely empirical one. In the model described here, all in-built parameters are derived from the general literature describing the hydrodynamic behavior of electrochemical cells or relating to the chlorine-evolving reaction. The actual model should therefore be applicable to all parallel plate hypochlorite cells, not particularly to our own design.

The model has been built on a limited number of assumptions which suppose that the destruction of any hypochlorite formed, whether at the anode (chlorate formation) or at the cathode (reduction of chloride), is diffusion controlled. Second, these respective oxidation and reduction processes are assumed to take place in preference to the alternative oxidation/reduction processes of oxygen and hydrogen evolution, respectively. Thus the imposition of any current over and above the limiting current for the given hypochlorite destruction process will be taken up by gas evolution. We shall see, however, that this is an interactive situation in that an increase in gas evolution will increase the diffusion-limiting current of the concurrent hypochlorite destruction process, as shown by Janssen and Hoogland (23), Fouad and Sedhamed (24), and others. This situation, in which the mass transport is a function not only of the rate of flow of electrolyte through the cell, but also of the gas evolution current density (which itself is inversely related to the hypochlorite concentration), requires a computational solution, and, with this model, no internally generated data were used whatsoever. The constants used came entirely from the published literature. In the main, these related to values for diffusion layer thickness under various conditions. The treatment of Beck (25), which was independently confirmed by ourselves (26), enabled us to combine the effects of separate mass-transport enhancement effects by treating the mass-transfer coefficients or partial limiting currents additively so that

$$i_{lim(1)} + i_{lim(2)} = i_{lim(total)} \quad [13]$$

where $i_{lim(1)}$ is the diffusion-limiting current due to one hydrodynamic process, *e.g.*, forced convection, and $i_{lim(2)}$ is that due to co-evolution of gas.

The model finally adopted was based on the equation

$$\text{net rate of } OCl^- \text{ formation} = (\text{total } OCl^- \text{ formation rate}) - (OCl^- \text{ destruction rate}) \quad [14]$$

where the destruction processes considered were: (*i*) reduction of OCl^- at the cathode, and (*ii*) oxidation of OCl^- at the anode.

That all the significant processes for the destruction of hypochlorite both anodic and cathodic are essentially diffusion controlled under the present conditions has been evidenced by various workers (8, 9, 35-37). In dilute brines, Ibl and Landolt (6) suggest a mechanism of mass transfer with chemical reaction (Cl_2 hydrolysis) for the anodic oxidation process. However, one may note, as did Hammar and Wranglen (8), that in the anodic film the *p*H is apparently too low for Cl_2 hydrolysis to occur to any appreciable extent. Thus, it may be stated that in hypochlorite production Cl_2 hydrolysis may commence in the diffusion layer and be completed in the bulk electrolyte where alkaline conditions prevail. These same authors (8) showed the anodic and cathodic destruction of hypochlorite to be diffusion-controlled processes under both acidic and alkaline conditions. Unpublished calculations by us, using the constants evaluated by Wranglen (8) even

though these are not strictly applicable from one cell to another, confirm that chlorate formation was diffusion controlled in the present case as it was in his.

It can also be shown that the rate of chlorate formation by the homogeneous reaction is not significant at this temperature.

From Weiss (22), the following equation relating to the homogeneous ClO_3^- formation in alkaline solutions may be derived

$$[ClO_3^-] = t\{2.28 \times 10^{-9} f_1 + 1.39 \times 10^{-19} f_2 [H^+]\}[ClO^-]^2$$

where t is the time (seconds), and f_1 and f_2 are combinations of the activity coefficients of ClO^- ions. Assuming $f_1 = f_2 = 0.7$ for Cl^- ions (33) and also at $pH = 10$, *i.e.*, $[H^+] = 10^{-10}$ mole/liter, we obtain

$$[ClO_3^-] = t\{1.6 \times 10^{-10} + 9.7 \times 10^{-22.5}\}[ClO^-]^2$$

On substituting the observed values of $[ClO^-]$ and t gives

$$[ClO_3^-] = 44 \times 10^{-8} \text{ mole/liter}$$

which is a negligible contribution as compared to the experimentally determined total chlorate concentration (of the order of 10^{-3} mole/liter). Therefore heterogeneous chlorate formation, under the present conditions, is much faster than the homogeneous contribution and is also diffusion controlled, as shown by Hammar and Wranglen (8).

From Eq. [14] and knowing the total volume of electrolyte in the system, the rate of increase in OCl^- as a function of time was derived, and this was the function for which experimental data was matched against the model prediction. We shall discuss separately the terms on the right-hand side of Eq. [14].

For the diffusion-controlled anodic and cathodic destruction reactions, we can apply Ficks equation to obtain the corresponding limiting currents arising from such losses, namely

$$i_{anodic} = \frac{n_a \mathbf{F} D A_a}{\delta_{Ta}} [ClO^-] \quad [15]$$

$$i_{cathodic} = \frac{n_c \mathbf{F} D A_c}{\delta_{Tc}} [ClO^-] \quad [16]$$

Also, since the diffusion coefficients of most substances are of the same order of magnitude, namely, 10^{-5} cm^2/sec, we can, without introducing appreciable errors, assume the same diffusion coefficients D for the Cl^- ion as for ClO^- ions, as data on the former is lacking in the literature. From a plot of diffusion coefficient of Cl^- against brine concentration with data taken from Parsons (27) the following equation relating diffusion coefficient of hypochlorite in a given brine concentration is derived

$$D = (1.95 - 0.177\,[Cl^-]_o) \times 10^{-5} \text{ cm}^2/\text{sec} \quad [17]$$

where $[Cl^-]_o$ is initial brine concentration.

Furthermore, data on the diffusion layer thickness as functions of current density of gas (O_2 or H_2) evolution, for a nonflow system, have been provided by Janssen and Hoogland (23), as well as by Fouad and Sedahmed (24). By replotting data taken from these two sources on a log-log scale, a straight line is obtained from which a relation between the current density of H_2 evolution (i_{H_2}) and the corresponding diffusion layer thickness (δ_{H_2}) can be drawn. A similar relation between i_{O_2} and δ_{O_2} can also be obtained for oxygen evolution. Since the data from these two sources were not in complete agreement, the most consistent values were taken for this work, *i.e.*, data on H_2 evolution from Ref. (23) and data on O_2 evolution from Ref. (24). The general form of the equations obtained is

$$\delta_{gas} = \frac{K}{(i_{gas})^n} \quad [18]$$

where δ_{gas} = the resulting diffusion layer thickness (centimeters), i_{gas} = the current density of the gas evolution process (milliamperes per square centimeter), $K = 38.9 \times 10^{-3}$ for H_2 and 20.6×10^{-3} for O_2, and $n = 1/2$ for H_2 and $1/3$ for O_2.

Finally, for a pumped flow system the average thickness of the diffusion layer, δ_f, for a flat plate inserted into a laminar flow of fluid is given (28, 29) as

$$\delta = 3/2\ (\nu/D)^{-1/3}\ (\nu L/V)^{1/2} \quad [19]$$

where ν is the kinematic viscosity of the electrolyte (square centimeter per second), L is the length of the electrode, V is the electrolyte velocity (centimeters per second), D is the diffusion coefficient of the ion being discharged, ClO^- in this case (square centimeter per second).

By substituting literature values (27, 30) into Eq. [19] it is found that the term involving the Schmidt group, *i.e.*, $(\nu/D)^{-1/3}$ is approximately the same for practical brine concentrations (0.1-5M), with an average value of 0.11. In addition the kinematic viscosities ν are also close to each other, an average value being 0.011 cm^2/sec. With anode and cathode dimensions (L, as used in this work) of 6.6 and 7.6 cm, respectively, Eq. [19] therefore simplifies to

$$\delta_{fa} = 0.0444/\sqrt{V}\ \text{cm} \quad [20]$$

$$\delta_{fc} = 0.0494/\sqrt{V}\ \text{cm} \quad [21]$$

where δ_{fa} and δ_{fc} represent diffusion layer thicknesses at the anode and cathode, respectively, resulting from electrolyte flow.

From Eq. [13], we can write, for the effective diffusion layer thickness (δ_T) resulting from both flow and gas evolution

$$\frac{1}{\delta_T} = \frac{1}{\delta_f} + \frac{1}{\delta_{gas}} \quad [22]$$

The validity of this mode of addition has been confirmed by using data published in (31) and in a later more extensive study (26).

Applying Eq. [22] to the anode, we can write

$$\frac{1}{\delta_{Ta}} = \frac{1}{\delta_{fa}} + \frac{1}{\delta_{O_2}} \quad [23]$$

It will be appreciated that gaseous oxygen may be formed at the anode by one of two possible mechanisms. The first of these is discharge of OH^- to give O_2. The second is co-formation of ClO_3^- and O_2 (the well-known Foerster reaction). It is not possible to distinguish these two unless a simultaneous chlorate analysis is performed. Fortunately (32) this was the case. Knowing that the chlorate determined must inevitably result in an equivalent amount of oxygen, it was possible to compare total oxygen formed with that produced by the Foerster reaction. The two were found to be virtually identical and it followed that oxygen formation from water discharge was negligible. [In support of this the standard reversible potential for the Foerster reaction is lower ($E^\circ = 1.14$V) than that of water discharge ($E^\circ = 1.23$V) as derived from thermodynamic data (8, 33).] With this information, the rate of oxygen evolution could be predicted, as before, by inserting $[ClO^-]$ into Fick's equation to obtain this value, *i.e.*

$$i_{O_2} = \frac{10^3\, n_a' \mathbf{F} D\, [ClO^-]}{\delta_{Ta}} \quad [24]$$

where n_a' is the number of electrons involved in the formation of 1 mole $O_2 = 4$ (Eq. [6]). Substituting Eq. [18] for O_2 evolution, and Eq. [24] in Eq. [23] and rearranging gives

$$[ClO^-] = \frac{2.26 \times 10^{-9} \times \delta_{Ta}}{(1.95 - 0.177\,[Cl^-]_o)} \left(\frac{1}{\delta_{Ta}} - \frac{1}{\delta_{fa}}\right)^3 \quad [25]$$

Equation [25] can be solved for δ_{Ta} for a given hypochlorite concentration, all other values known.

Similarly, we can write, for the cathode

$$\frac{1}{\delta_{Tc}} = \frac{1}{\delta_{fc}} + \frac{1}{\delta_{H_2}} \quad [26]$$

and from the main cathodic reactions (Eq. [9] and [10]) the current available for H_2 formation (i_{H_2}) equals the total cathodic current minus the current for hypochlorite reduction, *i.e.*

$$i_{H_2} = i_{Tc} - i_{red} \quad [27]$$

where i_{Tc} = total cathodic current density (milliamperes per square centimeter) and i_{red} = current density for hypochlorite reduction (milliamperes per square centimeter).

From Fick's law

$$i_{red} = \frac{10^3 \times n_c F D\,[ClO^-]}{\delta_{Tc}} \quad mA/cm^2$$

so that

$$i_{H_2} = i_{Tc} = \frac{10^3\, n_c F D\,[ClO^-]}{\delta_{Tc}} \quad mA/cm^2 \quad [28]$$

Substituting Eq. [18] for H_2 evolution, and Eq. [28] in Eq. [26] and simplifying gives

$$[ClO^-] = \frac{\delta_{Tc}}{10^3 \times 1.93 \times (1.95 - 0.177\,[Cl^-]_o)} i_{Tc} - \frac{38.9 \times 10^{-3}\,\delta_{fc} - 38.9 \times 10^{-3}\,\delta_{Tc}}{\delta_{fc} \times \delta_{Tc}} \quad [29]$$

and Eq. [29] can be solved for δ_{Tc} for a given hypochlorite concentration, all other values known.

Substitution of the δ_{Ta} and δ_{Tc} values, calculated as shown above, in Eq. [15] and [16] will yield the anodic and cathodic current losses. The assumptions so far have been based on an initial Cl^- concentration $[Cl^-]_o$. Under the conditions used here, this initial value will slowly decrease. In the first place, a fraction of the initial Cl^- will be converted to ClO^- ions. However, as we have seen, the concentration of ClO^- ions reaches a limiting value (when the rate of their re-reduction to Cl^- matches their rate of formation from Cl^-). Moreover, under normal brine concentrations, the amount of depletion caused by this does not exceed 10%. There is, however, a second source of Cl^- loss, *i.e.*, the formation of chlorate ions. These are only slowly reduced at the cathode, and, as seen earlier, the result is a continuous buildup of ClO_3 and corresponding loss of Cl^-. The chlorate formation process can be either a homogeneous or an anodic one. However under the conditions of this work, the homogeneous process has been shown to be negligibly slow.

Data by Kuhn and Mortimer (34) relating drop in current efficiency of Cl_2 evolution, E_{Cl_2}, with decrease in brine concentration can be plotted to yield the empirical equation

$$E_{Cl_2} = 100\,([Cl^-])^{0.2}\ \% \text{ for } [Cl^-] < 1 \text{ mole} \quad [30]$$

At brine concentrations of 1 mole and above the data shows E_{Cl_2} to be nearly 100%. Since Cl^- ions are taken up both by ClO^- and ClO_3^- formation, the chloride ion concentration at any time $[Cl^-]$ is given by

$$[Cl^-] = [Cl^-]_o - 10^3 \times [ClO^-] - [ClO_3^-] \quad [31]$$

where $[Cl^-]_o$ is the initial brine concentration (mole/liter), $[ClO_3^-]$ the chlorate concentration (mole/liter), and $10^3 \times [ClO^-]$ the hypochlorite concentration (mole/liter). Substituting Eq. [31] in [30] and expressing in current yields

$$I_{Cl_2} = I_T \times \{([Cl^-]_o - 10^3 \times [ClO^-] - [ClO_3^-])^{0.2}\} \quad [32]$$

and I_T being the total current (amperes).

The instantaneous concentration of chlorate can be found in terms of hypochlorite concentration by considering the heterogeneous chlorate formation reaction and applying both the Faraday and Fick laws. For the present situation this gives $d[ClO_3^-] = 0.346 \frac{[ClO^-]}{\delta_{Ta}} dt$ mole/liter where t is the duration of electrolysis (hours). Integration gives the instantaneous chlorate concentration as

$$[ClO_3^-] = 0.346 \int_o^t \frac{[ClO^-]}{\delta_{Ta}} dt \text{ mole/liter} \quad [33]$$

Equation [14] can now be rewritten in terms of the "net" current for hypochlorite formation as follows

$$I_{net} = I_T \times \{([Cl^-]_o - 10^3 \times [ClO^-] - [ClO_3^-])^{0.2}\} - \frac{n_a F D A\,[ClO^-]}{\delta_{Ta}} - \frac{n_c F D A\,[ClO^-]}{\delta_{Tc}}$$

or, by substituting the various terms in the loss reactions

$$I_{net} = I_T \times \{([Cl^-]_o - 10^3 \times [ClO^-] - [ClO_3^-])^{0.2}\} - \frac{9.65\,(1.95 - 0.177\,[Cl^-]_o)\,[ClO^-]}{\delta_{Ta}} - \frac{25.09\,(1.95 - 0.177\,[Cl^1]_o)\,[ClO^-]}{\delta_{Tc}}$$

Also, an equation relating I_{net}, $[ClO^-]$ and time (from which plots of $[ClO^-]$ *vs.* time can be constructed) may be derived by application of Faraday's law to I_{net} and electrolyte volume of 1290 cm^3. This yields the rate of hypochlorite formation as

$$d[ClO^-] = \frac{I_{net}}{2F \times 1290 \times 3600} \cdot dt \quad [35]$$

where t is in hours. With the value of I_{net} known for a given $[ClO^-]$, Eq. [35] can be integrated, putting the boundary condition that at $t = 0$ $[ClO^-] = 0$, to give

$$t = \frac{6.92 \times 10^4\,[ClO^-]}{I_{net}} \text{ hours} \quad [36]$$

Thus, by specifying the current input I_T, the initial brine concentration $[Cl^-]_o$, the brine velocity V, and the cathodic current density i_{Tc}, the model Eq. [34] and [36] can be solved to generate theoretical values of $[ClO^-]$ as a function of time; the required values of δ_{Ta}, δ_{Tc}, and ClO_3 being given by Eq. [20], [21], [25], [32], and [33].

Computer Program

The flow diagram for the program is shown in Fig. 1. The program computed $[ClO^-]$ values at time intervals of ½ hr up to 30 hr. The value of $[ClO^-]$ was started at zero and incremented until the time calculated from the equations exceeded the chosen value. The incremental steps in $[ClO^-]$ were then reduced by a factor of 10 and the process continued. The step size was reduced by 10^{-7} in all. A new time was then chosen and the new $[ClO^-]$ value found in a similar manner. The initial value of $[ClO^-]$ was reset to zero for each time interval because later in some runs the calculated value rose to a maximum and then fell. To solve [25], δ_{Ta} was started at 10^{-3} as a guess value the first time but in subsequent evaluations the previous root was used as starting value.

The program was written in ANSI Fortran IV and was run on an ICL 1904S computer. The graph plotting package used was GINO-F with a CALCOMP offline plotter. The core used was about 28,000 word and running time 1 min per analysis. Copies of the program may be obtained from the authors.

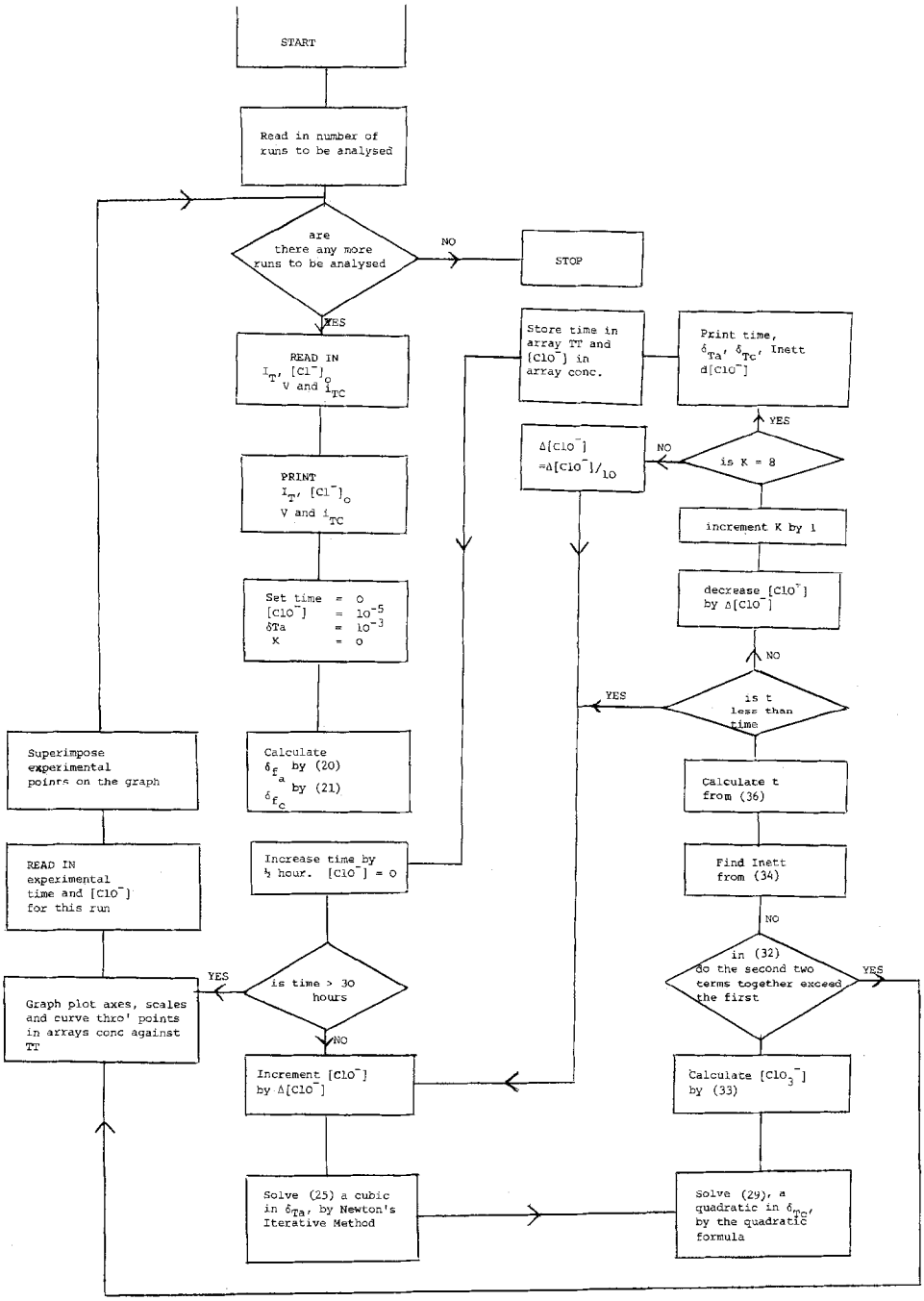


Fig. 1. Flow diagram of the computer program. The numbers in parentheses refer to equations in text.

Figures 2 and 3 show theoretically derived plots (continuous lines) together with the actual data points obtained from this work. It will be seen that good agreement exists between the two sets of data. In most cases agreement is within or better than 10%. The agreement so obtained shows that reaction modeling of this particular process might profitably be employed in the design and specification of this type of electrolyzer. Though the model relates to a parallel plate electrolyzer the same approach might equally well be used for the co-axial cylindrical cells marketed by several major corporations in this field.

We recognize two possible sources of error in our modeling approach. The first of these lies in our implicit assumption that ClO_3^- once formed is not cathodically reduced. Only one paper treating the kinetics of cathodic reduction of ClO_3^- appears to exist (38) and this confirms that, though small, a finite reduction does in fact take place.

The second source of uncertainty relates to the appropriate value of "n" in the anodic oxidation of OCl^- ions to ClO_3^-. We have seen that values from 0.3 to 3 have been suggested (8, 39) and it is clear from the literature that this remains an open question. Unpublished computer plots have shown us that the predicted $[OCl^-]$ values can be made to span the experimental prints by $\pm 10\%$ using limiting values or assumptions in these two respects.

Until these fundamental issues of kinetics and reaction mechanism have been clarified, no model could be expected to show a perfect fit. Nevertheless, the ± 10 concordance which we have shown here not only demonstrates the validity of our model, but also provides, it is felt, a useful prognosticatory tool, for cell designers.

Manuscript submitted March 2, 1977; revised manuscript received July 28, 1977.

Any discussion of this paper will appear in a Discussion Section to be published in the June 1978 JOURNAL. All discussions for the June 1978 Discussion Section should be submitted by Feb. 1, 1978.

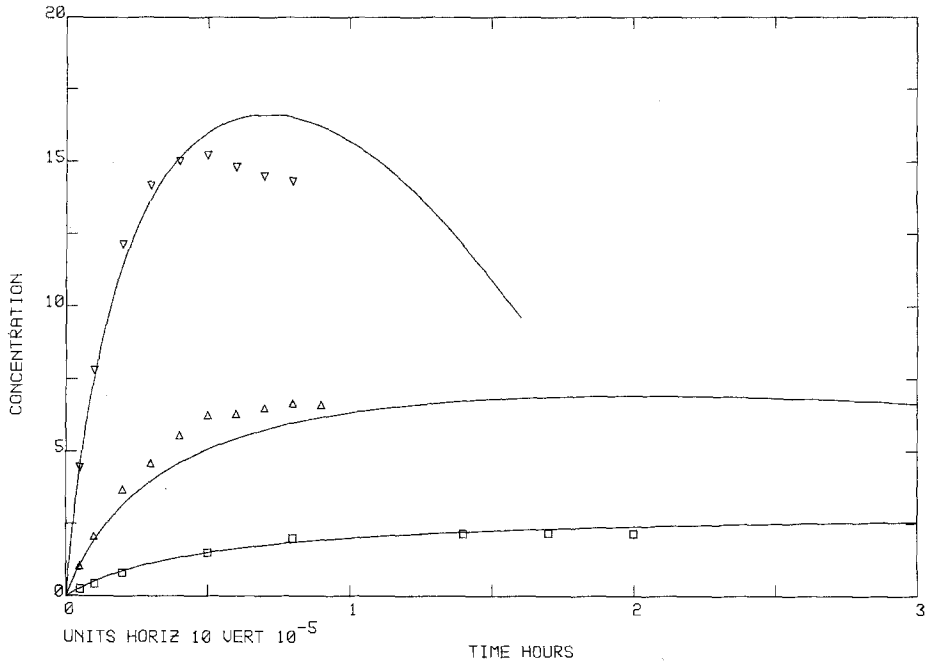


Fig. 2. Typical computer-generated [NaClO] *vs.* time data (solid lines) and experimentally obtained data (points). [NaCl] = 0.5M, T = 25°C in all cases.

	Current density (cm A/cm²)	Velocity (cm/sec)
□	25	40
△	100	40
▽	450	40

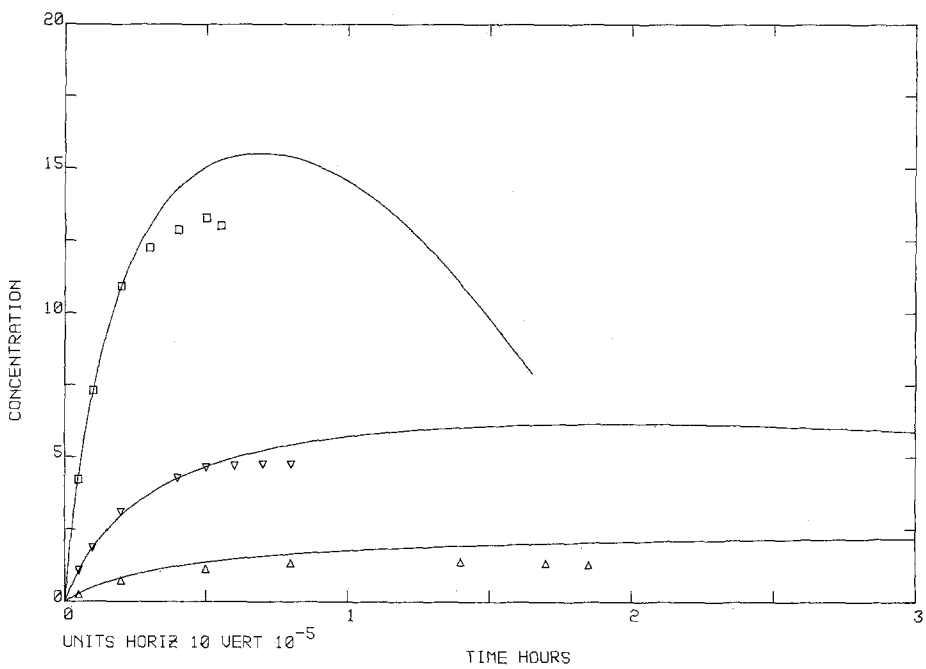


Fig. 3. Typical computer-generated [NaClO] *vs.* time data (solid lines) and experimentally obtained data (points). [NaCl] = 0.5M, T = 25°C in all cases.

	Current density (cm A/cm²)	Velocity (cm/sec)
△	25	75
▽	100	75
□	450	75

LIST OF SYMBOLS

δ	thickness of diffusion layer (cm)
δ_T	effective thickness of diffusion layer (cm)
i_{lim}	limiting diffusion current (mA/cm²)
n_a, n_c	number of electrons involved in the destruction of 1 mole of hypochlorite at the anode and cathode, respectively
A_a, A_c	surface area of the anode and cathode, respectively
F	Faraday's constant (96,500 C/mole of hypochlorite)
D	diffusion coefficient (cm²/sec)
L	length of electrode (cm)
ν	kinematic viscosity of electrolyte (cm²/sec)
V	electrolyte velocity (cm/sec)
I_T	total cell current (A)
I_{net}	net current for hypochlorite formation (A)
t	electrolysis time (hr)

REFERENCES

1. J. E. Bennett, *Chem. Eng. Prog.*, **70**, (12), 60 (1974).
2. A. T. Kuhn and R. B. Lartey, *Chem. Ing. Tech.*, **47**, 129 (1975).
3. A. T. Kuhn, *Processing*, 6 (March 1975); *ibid.*, 10 (April 1975).
4. G. L. Medrish, *Nauchn. n. Tr. Akad, Komm Nogo Khoz*, **97**, 58 (1974).
5. V. I. Skripchenko, E. P. Drozedetskaya, and K. G. Il'in, *Izv. Severo Nauchn, Vyssh.*, **2**, 106 (1974).
6. D. Landolt and N. Ibl, *This Journal*, **115**, 713 (1968).
7. G. M. Fair, *J. Am. Water Works Assoc.*, **40**, 1050 (1948).
8. L. Hammar and G. Wranglen, *Electrochim. Acta*, **9**, 1 (1964).
9. F. Hine and M. Yasuda, *This Journal*, **118**, 170 (1971).
10. H. Wolf and R. Landsberg, *Electrochim. Acta*, **16**, 1627 (1971).
11. O. Schwarzer and R. Landsberg, *J. Electroanal. Interfacial Chem.*, **19**, 391 (1968).
12. L. Mueller, *Sov. Electrochem. (Engl. Transl.)*, **4**, 199 (1968).
13. J. A. Harrison and Z. A. Khan, *J. Electroanal. Interfacial Chem.*, **30**, 87 (1971).
14. L. I. Kristallik, *Zh. Prikl. Khim. (Leningrad)*, **45**, 670 (1972); (*C. A.* **77**, 13150).

15. W. G. Ormerod Central Electricity Generating Board Research Report RD/NE/R106 (Oct. 1966).
16. A. T. Kuhn and C. J. Mortimer, *J. Appl. Electrochem.*, **2**, 283 (1972).
17. A. B. Djordjevic, B. Z. Nikolic, I. V. Kadija, A. R. Despic, and M. M. Jaksic, *Electrochim. Acta*, **18**, 465 (1973).
18. C. Marshall and J. P. Millington, *J. Appl. Chem.*, **19**, 289 (1969).
19. D. Pickett, *Electrochem. Acta*, **20**, 803 (1975).
20. R. B. Lartey, Ph.D. Thesis, University of Salford (1976).
21. M. M. Jaksic, *This Journal*, **121**, 70 (1974).
22. J. J. Weiss, *Z. Elektrochem.*, **37**, 20 (1931) *ibid.*, **37**, 271 (1931).
23. L. L. Janssen and J. G. Hoogland, *Electrochim. Acta*, **15**, 1013 (1970).
24. M. G. Fouad and G. H. Sedahmed, *ibid.*, **17**, 665 (1972).
25. T. R. Beck, Paper 97 presented at The Electrochemical Society Meeting, Cleveland, Ohio, May 1-6, 1966.
26. M. D. Birkett, A. T. Kuhn, and R. B. Lartey, To be published.
27. R. A. Parsons, "Handbook of Electrochemical Constants," Butterworths (1959).
28. B. Levich, *Discuss. Faraday Soc.*, **37**, (1947).
29. B. Levich, "Physicochemical Hydrodynamics," Prentice-Hall Inc. Englewood Cliffs, N.J. (1962).
30. R. H. Perry and H. C. Cecil, "Chemical Engineers Handbook," 5th ed., McGraw Hill Book Co., New York.
31. M. D. Birkett and A. T. Kuhn, *Electrochim. Acta*, **21**, 991 (1976).
32. W. M. Latimer, "Oxidation Potentials," 2nd ed., Prentice-Hall, Englewood Cliffs, N.J. (1952).
33. R. A. Robinson and R. H. Stokes, "Electrolyte Solutions," 2nd ed., Butterworths (1959).
34. A. T. Kuhn and C. J. Mortimer, *J. Appl. Electrochem.*, **2**, 283 (1972).
35. M. Lister, *Can. J. Chem.*, **34**, 465 (1956).
36. F. Foerster, *Trans Am. Electrochem. Soc.*, **46**, 23 (1924).
37. V. de Valera, *Trans. Faraday Soc.*, **49**, 1338 (1954).
38. I. E. Veselovskaya, E. M. Kuchinskii, and L. V. Morochko, *J. Appl. Chem. USSR*, **37**, 85(1964).
39. A. Rius and J. Liopis, *Anal. Fis. Quim.*, **41**, 1030 (1945).
40. J. D'Ans and H. E. Freund, *Z. Elektrochem.*, **61**, 10 (1957).

Dynamic Interfacial Electrochemical Phenomena at Living Cell Membranes: Application to the Toad Urinary Bladder Membrane System

Arthur A. Pilla* and Gary S. Margules

Bioelectrochemistry Laboratory, Orthopaedic Research Laboratories, Columbia University, College of Physicians and Surgeons, New York, New York 10032

ABSTRACT

The concept of electrochemical information transfer *in vivo* has been studied using the isolated toad urinary bladder membrane system to evaluate a recently developed approach to membrane impedance which emphasized the coupling of interfacial processes to standard transport phenomena. Laplace plane analysis was utilized to examine frequency response from 1 Hz to 1 MHz. The results indicate that, under the linear conditions of this experiment, Na^+ ion is the predominant current carrier and that the rate-determining step is its penetration into the membrane phase from the aqueous phase. Thus, membrane transport appears to be a very rapid step, whereas the interfacial step of phase transfer regulates transport in this system. The implication of this result in terms of potential dependent interfacial steps in the control of cellular function is discussed.

It is becoming increasingly evident that many cellular functions involve a control or regulatory step occurring at the cell's cytoplasmic membrane (1-7). Often this involves the activation of certain membrane-bound enzymes by the specific interaction of charged species such as ions (8-10) and hormones (11, 12). Because of the type of over-all molecular structure of the protein-containing lipid membrane (13-18), it has been possible to postulate that these regulating interactions occur at interfaces or surfaces and that they are dynamic and potential dependent (19-23). This then constitutes the concept of electrochemical information transfer *in vivo*, in which it is supposed that a highly specific dynamic charge injection can cause a selective modification of, *e.g.*, enzyme and/or transport activity, which in turn may modify cellular and tissue function in a beneficial manner. This approach has guided recent studies in which inductively coupled pulsating currents have caused a selective modification of bone (osteocyte) and cartilage (chondrocyte) activity (24, 25). Thus it appears that either Ca^{2+} activity and/or protein synthesis may be selectively elicited by the proper choice of independently different pulse parameters. These parameters were predicted (22, 25, 26) on the basis of an analysis of the different time constants anticipated in either ion or hormone binding at the cell membrane and the subsequent steps to this trigger. It thus appears possible, for bone and cartilage at least, to selectively modify in a beneficial manner two different cellular functions. This approach has already been extended to the clinic wherein it has been possible to heal otherwise incurable bone fractures with approximately 85% success (25).

In order to establish a working hypothesis for the application of electrochemical information transfer *in vivo*, a detailed analysis of the transient electrical behavior of living cell membranes has recently been carried out (22, 23, 26). This approach focuses on the analogy between the electrode/solution interface and those occurring at the living cell's membranes and the intra- or extra-cellular fluid. Of particular importance

* Electrochemical Society Active Member.

Key words: living membranes, impedance, Laplace plane, adsorption, cellular regulation, epithelial cell, phase transfer.

is the addition of potential dependent specific adsorption (binding) and slow phase transfer (partitioning) as coupled steps in the response of the membrane to dynamic changes in interfacial potential. By allowing these to interact with membrane and aqueous transport along with dielectric and surface charge behavior, it has been possible to present a unified approach to membrane impedance (22, 26, 28). The significance of this approach lies in its capability to treat the highly heterogeneous and dynamic behavior of living membranes in a relatively rigorous manner so that theoretical models may be established and experimental tests may be carried out.

The present study involves such a test on the isolated toad urinary bladder membrane system. This system is uniquely suited to a living cell membrane impedance study since, as a membrane system, it consists of a supported single layer of epithelial (skin) cells in tight junction contact (29-31). These mucosal cells (so called because they border the inside surface of the bladder) are approximately 10μ thick and exhibit asymmetrical membranes with respect to both structure and function. Under physiological conditions these cells transport urea, water, and Na^+ (both actively and passively). Tight junctions between the mucosal cells severely limit under normal conditions, transepithelial transport and allow the membrane system to exhibit selective transport properties. The mucosal cells are supported on a loose sheet (electrically resistive only) of connective tissue (collagen) which is widely interspersed with blood vessels and smooth muscle fibers. There is also a discontinuous layer of cells bounding the serosal or external surface of the bladder. These would also not be expected to contribute to the over-all membrane response of this system. It was, therefore, expected that, under the transient electrical conditions of the present study, the bladder system would exhibit a relatively simple response related to passive Na^+ transport. This study will present the application of Laplace plane modeling and analysis to this living membrane system.

Theoretical

In order to construct an impedance model for the toad urinary bladder membrane system, it is necessary to briefly review the application of Laplace plane analysis to a generalized membrane. At the onset it must be pointed out that Laplace plane analysis, in the manner applied here, assumes linear conditions, *i.e.*, the impedance of the system may be defined. Linearity conditions can be established for this complex system, since the modeling may be performed using a piecewise linear approximation, *i.e.*, for any given steady-state behavior the superimposed time varying perturbation may be low enough so that changes from rest or steady state are linear (32). In addition, the very nature of Laplace plane analysis allows the transient impedance of the system to be evaluated (33). In this manner impedance can be obtained using a minimal number of perturbations (usually less than five) with presently available instrumentation, thereby "freezing" the behavior of the system in time.

To establish the impedance of a membrane it is considered that, in addition to the well-known dielectric properties of the lipid-protein system (34), the passage of transient current will satisfy specific adsorption and phase transfer properties which may be coupled to aqueous and membrane transport. This is illustrated in Fig. 1 where it can be seen that in addition to both intra- and extra-cellular diffusion (assumed planar) surface double-layer charging, specific adsorption, and phase transfer (partitioning) can take place. All of these processes can be coupled and are assumed in the first instance to take place at every interface (inner and outer) of each membrane.

Laplace plane analysis is performed in the complex frequency domain defined by the Laplace variable, s, a complex number with the dimensions of frequency and having a real, σ, and imaginary, $j\omega$, part such that $s = \sigma + j\omega$. This variable is utilized in the Laplace transformation wherein the transformed function $F(s)$ is obtained by operating on a time domain function $f(t)$ according to

$$F(s) = \int_0^\infty f(t)\exp(-st)\,dt \qquad [1]$$

All functions in this study will be described in the s plane. The basics of obtaining impedance models in this fashion has been extensively described elsewhere (33, 35).

When a transient current passes across a membrane, a portion of it will satisfy all of the interfacial charging (both specific and nonspecific) and dielectric requirements. This is termed the charging current, $i_c(s)$. Another portion of the total current, $i(s)$, will satisfy all phase transfer phenomena, *i.e.*, that portion of the current carried across the membrane. This is termed the phase transfer current $i_p(s)$. The total current is, therefore, given by

$$i(s) = i_c(s) + i_p(s) \qquad [2]$$

To describe $i_c(s)$ it is convenient to express it in terms of the change in charge, $q(s)$, which may occur as a result of a change in interfacial potential $\eta(s)$ as

$$i_c(s) = sq(s) = q_E s\,\eta(s) + q^e s c^e \Delta c^e(o,s) \qquad [3]$$

where $q_E = (\partial q/\partial E)_{c^e}$ and $q^e = (\partial q/\partial c^e)_E$ representing the variation of q with potential, E and with the concentration of a species c^e which specifically adsorbs at interface e (membrane/extracellular fluid). Note that more than one species may adsorb at this interface, and that specific adsorption may also occur at interface i (membrane/intracellular fluid). However, for

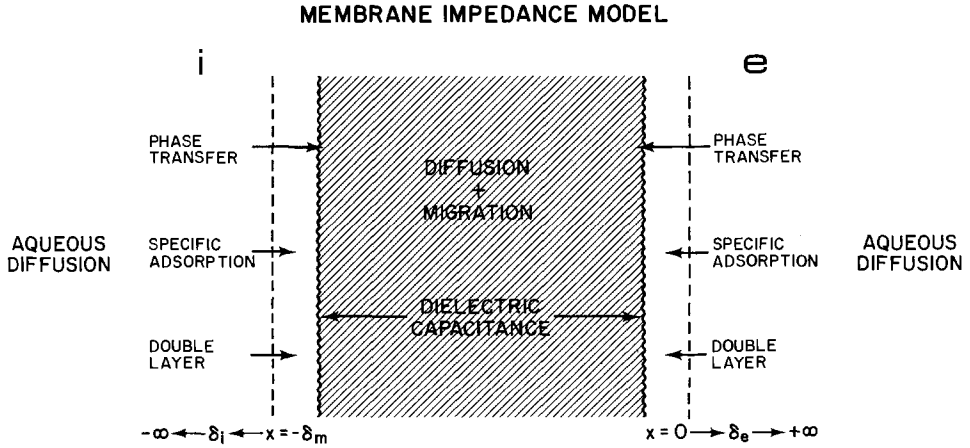


Fig. 1. Schematic diagram depicting the essential elements of the interfacial membrane impedance model described in this study. In addition to aqueous and membrane mass transport finite kinetics are allowed for specific adsorption (binding) and phase transfer (partitioning). All processes are coupled and may involve both the extracellular, *e*, and intracellular *i*, interfaces.

the sake of clarity only a single species at e will be considered. Extension to more complex systems has been described elsewhere (26, 28). Both q_E and q^e are constant coefficients representing the linear conditions of the model; they may change for different resting or steady-state conditions. In Eq. [3] $\Delta c^e(o,s)$ represents the change in concentration with time (frequency) of species c^e at the interfacial region ($x = 0$) as a result of specific adsorption. In other words this quantity represents the change in concentration c^e in the plane $x = 0$ while in the preadsorbed state (*i.e.*, before specific binding has taken place). $\Delta c^e(o,s)$ is defined by $\Delta c^e(o,s) = (c^e(o,s) - c^e)/c^e$, which makes it a relative change (to avoid carrying initial conditions throughout the derivation of the model), and is the reason why c^e appears in the second term on the right-hand side of Eq. [3].

Since specific adsorption has been invoked, it is necessary to establish a relation between the concentration of the specifically adsorbed species Γ_e and $\Delta c^e(o,s)$. This is readily done by assuming first order kinetics (35, 36) which gives

$$\Delta\Gamma_e(s) = v_e/\Gamma_e s[\Delta c^e(o,s) - \Delta\Gamma_e(s) + a\eta(s)] \quad [4]$$

where $\Delta\Gamma_e(s)$ is given by $\Delta\Gamma_e(s) = (\Gamma_e(s) - \Gamma_e)/\Gamma_e$, representing a change with respect to the initial concentration of adsorbed species, Γ_e; v_e is an exchange adsorption rate constant and, a, represents the potential dependence of adsorption (a constant coefficient) and that portion of the total potential change, $\eta(s)$, which acts at interface e. There is a similar relationship for each adsorbing species at each interface. Note that Eq. [4] allows adsorption kinetics to be finite thereby making the model somewhat more general than has previously been the case (37).

It is now necessary to obtain an expression for the phase transfer current, $i_p(s)$. Since $i_p(s)$ represents all of the total current which actually traverses the membrane, in addition to the expected concentration dependence, finite kinetics are also allowed for partitioning (*i.e.*, penetration of the transporting species from the aqueous phase into the membrane phase). Since this is expected to be potential dependent $i_p(s)$ can be written as

$$i_p(s) = I_E\eta(s) + I^{ce}\Delta c^e(o,s) + I^{cm}\Delta c^m(o,s) \quad [5]$$

in which $I_E = (\partial i_p/\partial E)_{c^e,c^m}$; $I^e = (\partial i_p/\partial c^e)_{E,c^m}$, and $I^m = (\partial i_p/\partial c^m)_{E,c^e}$ representing the variation of i_p with potential and with the aqueous and membrane concentrations of the transporting species, respectively. Again in this linear model these are constant coefficients. The relative concentration change $\Delta c^e(o,s)$ is as for Eq. [4], while $\Delta c^m(o,s)$ represents the relative concentration change of the same species in the membrane phase at the plane $x = 0$ (*i.e.*, after partitioning just inside the membrane). The first term on the right-hand side of [5] represents the finite phase transfer kinetics allowed in this model. The physical significance of this term may be related to the influence of surface charge upon transport (38-41) particularly in the context of specifically adsorbed charge.

Equations [3] and [5] may be employed to provide an expression for the total impedance of the model proposed. For this it is necessary to obtain explicit expressions for $\Delta c^e(o,s)$ and $\Delta c^m(o,s)$ taking into account finite specific adsorption kinetics as given by Eq. [4]. Mass transport in the aqueous phase can be represented by Fick's second law, since the supporting electrolyte in physiological solution is approximately 0.2M. The important quantity is the flux at the plane $x = 0$ which is given by, for finite planar diffusion

$$\left(\frac{d\Delta c^e}{dx}\right)_{x=0} = -\left[\left(\frac{s}{D_e}\right)^{1/2} \coth\left(\frac{s}{D_e}\right)^{1/2}\delta_e\right]\Delta c^e(o,s) \quad [6]$$

Where D_e is the aqueous diffusion coefficient and δ_e is the thickness of the diffusion layer in the extracellular fluid. This quantity reduces to the familiar square root of frequency (Warburg) behavior under semi-infinite conditions.

Membrane mass transport occurs under both concentration and electric field gradients thereby necessitating use of the Nernst-Planck equation which is written here for planar conditions as

$$\Delta c^m(x,s) = \frac{D_m}{s}\left[\frac{d^2\Delta c^m}{dx^2} + \frac{\mathbf{F}}{RT}\frac{d}{dx}\left(\Delta c^m\frac{dV}{dx}\right)\right] \quad [7]$$

where D_m is the diffusion coefficient in the membrane phase (not necessarily equal to D_e), dV/dx is the voltage field across the membrane and the other quantities have their usual significance. For most membranes the concentration of the transporting species within the membrane is relatively low (37). In addition, the linear conditions of this model (which are experimentally obtainable) suppose that the change in voltage field is constant through the membrane. For these two reasons, it appears possible to assume constant field conditions, so that $dV/dx = \text{const} = \bar{V}$. Under these conditions Eq. [7] can be solved analytically. Once again the flux at $x = 0$ is the desired quantity. This is given by, for a membrane of biological thickness

$$\left(\frac{d\Delta c^m}{dx} + \frac{\mathbf{F}\bar{V}}{RT}\Delta c^m\right)_{x=0} = \left[\frac{\mathbf{F}\bar{V}}{2RT} + \frac{1}{\delta_m} + \frac{1}{3}\left(\frac{\mathbf{F}^2\bar{V}^2}{4R^2T^2} + \frac{s}{D_m}\right)\delta_m\right]\Delta c^m(o,s) \quad [8]$$

where δ_m is the membrane thickness (usually 70-100Å), and the other terms have been defined previously.

The remaining requirement to solve for $\Delta c^e(o,s)$ and $\Delta c^m(o,s)$ in Eq. [3] and [5] is to provide a mass balance condition which will account for both aqueous and membrane mass transport in the presence of specific adsorption. This can be written as

$$D_e c^e\left(\frac{d\Delta c^e}{dx}\right)_{x=0} - \Gamma_e s\Delta\Gamma_e(s) = D_m c^m\left(\frac{d\Delta c^m}{dx} + \frac{\mathbf{F}\bar{V}}{RT}\Delta c^m\right)_{x=0} \quad [9]$$

which states that the actual flux through the membrane (right-hand side, Eq. [9]) is equal to the flux of the same species in the aqueous phase (first term, left-hand side, Eq. [9]) minus the amount specifically adsorbed. Physically this can be pictured by saying that only that quantity of transporting species actually gets through the membrane which does not accumulate at the plane $x = 0$ (the interface) via the process of specific adsorption.

All of the above relationships are sufficient to generate an expression for the impedance of a single membrane where partitioning and specific adsorption occur at one interface. The result is for the charging impedance $Z_c(s)$

$$Z_c(s) = 1/q_E s \quad [10]$$

when $\partial\Gamma_e/\partial E$ is negligible, a condition often applicable when the species undergoing phase transfer is itself specifically adsorbed. The phase transfer impedance $Z_p(s)$ is given by

$$Z_p(s) = \frac{1}{I_E}\left[1 + \frac{I^e}{n\mathbf{F}c^e(D_e s)^{1/2} + s\Gamma_e/(1 + s\Gamma/v_e)} + \frac{I^m}{n\mathbf{F}c^m D_m\left[\frac{\mathbf{F}\bar{V}}{2RT} + \frac{1}{\delta_m} + \frac{1}{3}\left(\frac{\mathbf{F}^2\bar{V}^2}{4R^2T^2} + \frac{s}{D_m}\right)\delta_m\right]}\right] \quad [11]$$

Both $Z_c(s)$ and $Z_p(s)$ are in parallel as is evident from Eq. [2]. As shown elsewhere (26, 28) $Z_c(s)$ would contain additional terms related to the specific adsorption process, particularly when several species contribute to the current response. For the purposes of this application $Z_c(s)$ is represented by a pure capacitor which is primarily due to the dielectric and double layer response of the membranes in the toad bladder system. On the other hand $Z_p(s)$ contains a phase transfer impedance ($1/I_E$) coupled with semi-infinite aqueous mass transport and specific adsorption (second term in brackets on right-hand side of Eq. [11]) in series with membrane transport which has a more physically meaningful form than reported elsewhere (37).

Inspection of Eq. [10] and [11] shows that it is possible to represent the impedance for this particular model by the aperiodic equivalent electric circuit shown in Fig. 2. The placement of elements in this circuit is directly related to the actual physical pathway (mechanism) which is proposed. No assumption other than the basic model is employed to establish this topology and the frequency behavior described by Eq. [10] and [11] and Fig. 2 can be used to diagnose mechanism and kinetics. Note that this modeling procedure would result in several variants of Fig. 2 if both sides of the membrane and more than one species is involved (22, 26, 28), thereby permitting extensive diagnosis to distinguish among several different proposed pathways.

It is useful to attach physical significance to each of the elements shown in Fig. 2 for the eventual evaluation of kinetic parameters. Referring to Eq. [10] it can be seen that

$$C_d = \partial q/\partial E = q_E \qquad [12]$$

as expected for the charging current pathway. Note that C_d contains (in a series arrangement) contributions from the electrical double layers present at the inner and outer membrane interfaces, as well as that due to the dielectric property of the membrane structure. Although it is in principle possible to isolate the dielectric from double-layer contributions using very high frequency measurements coupled with ion dependences (28, 42), it was not within the scope of the present study to pursue this. Examination of Eq. [11] allows the phase transfer impedance R_p to be defined as

$$R_p = 1/(\partial i_p/\partial E) = 1/I_E \qquad [13]$$

showing that phase transfer kinetics would be expected to exhibit purely resistive behavior corresponding remarkably to the form of the activation process involved in electron transfer at the electrode/solution interface (35). It might, therefore, be expected that ion penetration (partitioning) would involve simple rearrangement of the entry site by, *e.g.*, lipid polar head deformation or displacement (43). The specific

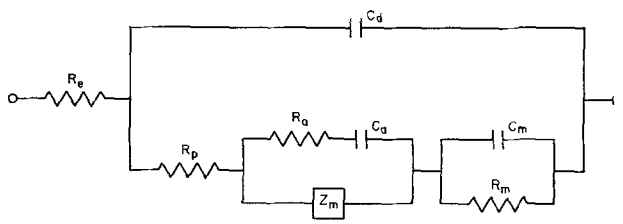


Fig. 2. Aperiodic equivalent electric circuit presented as a shorthand (but exact) notation of the Laplace plane behavior of a membrane (artificial or biological) at which a single species is involved in phase transfer. Note the topology of this circuit corresponds to the physical processes considered in the model and can be examined using the wide frequency range achievable via real axis Laplace transformation. The physical significance of each element is described in the text.

adsorption parameters R_a and C_a are given by

$$R_a = \frac{(\partial i_p/\partial c^e)}{(\partial i_p/\partial E)}\frac{1}{v_e} \qquad [14]$$

and

$$C_a = \frac{(\partial i_p/\partial E)}{(\partial i_p/\partial c^e)}\Gamma_e \qquad [15]$$

where it can be seen that R_a is inversely proportional to the exchange adsorption rate constant v_e and C_a is proportional to the initial concentration of adsorbed species Γ_e as expected. The aqueous transport impedance Z_D is in parallel with the adsorption pathway as required by the mass balance condition given in Eq. [9]. In this application to the isolated toad urinary bladder semi-infinite planar diffusion conditions can be assumed as indicated in Eq. [11]. In this case the movement of a concentration wave to or from the interface is exactly analogous to the propagation of a voltage signal along a semi-infinite R_DC_D transmission line (32). Z_D is therefore given by

$$Z_D(s) = \frac{(\partial i_p/\partial c^e)}{(\partial i_p/\partial E)}\frac{1}{n\mathbf{F}c^e(D_e s)^{1/2}} \qquad [16]$$

for which the R_DC_D array has the following physical significance

$$R_D = \frac{(\partial i_p/\partial c^e)}{(\partial i_p/\partial E)}\frac{1}{n\mathbf{F}c^e D_e} \qquad [17]$$

and

$$C_D = \frac{(\partial i_p/\partial E)}{(\partial i_p/\partial c^e)} n\mathbf{F}c^e \qquad [18]$$

in which R_D is inversely proportional to the diffusion coefficient, D^e, and C_D is directly proportional to the bulk concentration, c^e, of the diffusing species. Membrane mass transport is represented by the parallel combination of R_m and C_m in Fig. 2. Referring again to Eq. [11], these are given by

$$C_m = \frac{(\partial i_p/\partial c^m)}{(\partial i_p/\partial E)}\frac{n\mathbf{F}c^m\delta_m}{3} \qquad [19]$$

and

$$\frac{1}{R_m} = \frac{(\partial i_p/\partial c^m)}{(\partial i_p/\partial E)}\frac{n^2\mathbf{F}^2 D_m c^e \delta_m}{6RT}\left[3\bar{V} + \frac{6RT}{n\mathbf{F}\delta_m} + \frac{n\mathbf{F}\bar{V}^2}{2RT}\right] \qquad [20]$$

where it can be seen that C_m is proportional to the resting membrane concentration, and R_m is inversely proportional to the diffusion coefficient, D_m, and the voltage field to which the transporting species is subjected. Note that if $\bar{V} = 0$, Eq. [20] reduces to that which would be obtained in the absence of a significant electric field (32).

The above procedure illustrates the manner by which the potential dependent interfacial processes of specific adsorption and phase transfer can be coupled with both aqueous and membrane mass transport in a relatively quantitative manner. For the purposes of illustration a single interface has been modeled. However, it is to be realized that all of the interfaces and membranes in a living system may be treated in an analogous manner, generating equivalent electric circuits similar to that shown in Fig. 2 and added to it, in most cases in series.

In addition, for the interface treated only a single species has been considered. It is straightforward to consider the case of two or more species which may adsorb and/or transport across the same interface even if they act in a coupled manner. It is thus possible in principle to generate models using the above approach which can be employed to distinguish among the physi-

ologically meaningful pathways which can be proposed for a given system.

As mentioned above, the mucosal surface of the isolated toad urinary bladder is known physiologically to selectively transport Na^+ in a passive manner (44-46). In addition, steady-state measurements using microelectrodes have established that the mucosal (inside) membrane exhibits significantly higher resistance to ion transport than the serosal (outside) membrane (47). There is also some indication that the tight junction (cell to cell) contact exhibits a much higher resistance than the same serosal membrane (47). It can, therefore, be expected that current flow through this membrane system will essentially be straight through the mucosal cell (and not be deviated significantly in a parallel pathway across the cell layer). The isolated toad bladder can thus be expected to correspond relatively closely to those portions of the single interface model required for potential dependent Na^+ ion transport.

Experimental

In this study the urinary bladder of the toad (*Bufo marinus*) is subjected to low level current pulses and the voltage response is observed. To perform this type of measurement the bladder must first be isolated from the toad. This is performed using a rapid surgical procedure on a pithed (brain-dead) toad to minimize cellular damage (usually from drying, trauma, and autolysis). First the toad's abdominal cavity is opened in the usual manner exposing the viscera. At this point the bladder is exposed and when full (mostly water since the toad uses this organ for water balance) is seen to be a bilobed structure occupying almost the whole abdominal cavity. At this point the bladder can commence drying if precaution is not taken to maintain the exposed areas moist with amphibian Ringer's solution (an isotonic salt solution described below). The bladder is excised by first severing the dorsal facial layers of each lobe. These are then clamped close to the urinary sphincter region from which the bladder is severed and withdrawn usually while full. If the bladder is completely full, it is in a highly stretched condition and is transparent except in the area of an occasional blood vessel. It is in this stretched condition that the impedance measurements are made. To maintain this situation, the excised full bladder is placed in a petri dish containing aerated Ringer's solution and a cork template. The latter is utilized to hold the bladder in a stretched condition for mounting in a conductivity type chamber. This is achieved by pinning the bladder along one edge of the cork and opening a lobe along the center while pinning the remaining portions of bladder along the other three edges of the cork template. This is the most sensitive part of the isolation procedure since the mucosal cells are now directly exposed. These are fragile and care must be taken not to touch, in any way, that portion of the mucosal surface which will serve as the membrane system when mounted in the measurement chamber. Mounting on the cork template is carried out so as to provide a uniform stretch (monitored by observing for uniform transparency). The bladder is now relatively free of folds and will usually present a single supported mucosal cell layer for study. Great care is exercised during bladder mounting since nonuniform stretch and/or folded cell layers will affect transport properties (48, 49).

Once mounted, the wet bladder is rapidly transferred to the measurement vessel which is essentially a conductivity cell having two identical chambers separated by the bladder. In position between the two chambers, the bladder is then held in place by the pressure applied when the chambers are forced together. The bladder occupies a circular area of approximately 1 cm^2 bounded by O-rings on the face of either chamber. The pressure exerted by the O-rings prevents lateral leakage and minimizes edge damage (50, 51) particularly with the relatively large surface area of exposed bladder. The chambers are then filled simultaneously with Ringer's solution to avoid uneven hydrostatic pressure particularly from the serosal side which can cause morphologic changes such as intercellular space variation thereby modifying transport properties (31, 51).

The conductivity cell (see Fig. 3) consists of two identical chambers each provided with solution and gas inlets and outlets. In addition provision is made for current input and voltage measurement electrodes. These are sintered tantalum slugs providing high surface area for minimal faradaic effects under the experimental conditions employed. An important monitor of membrane integrity is the existence of a transepithelial resting potential due primarily to the active transport systems functioning to maintain intracellular ionic concentration levels. Generally this potential difference is between 10 and 100 mV, mucosal side negative. Provision is, therefore, made in each chamber to introduce a SCE reference electrode (Tacussel Type C-10) to assess membrane integrity, viability, and monitor possible base line changes during the experiment.

The physiological solution utilized to bathe the mucosal and serosal sides of the bladder in the measurement cell is isotonic for the amphibian. It is composed of (in mM/liter): NaCl 109; $CaCl_2$, 0.9; $NaHCO_3$, 2.4; KCl, 2.5; and $C_6H_{12}O_6$, 5.5. The bladder is allowed to stabilize in this solution (while aerated) until the resting potential is invariant (usually after 0.5-1 hr). Current pulses are then applied so that the transepithelial potential change (not including IR_e drop) is restricted to 1 mV or less. In this manner linear conditions are achieved and the active transport systems do not deviate significantly from base line since the net change in intracellular ionic concentration is negligible (<10 $\mu C/cm^2$ of total charge injection is utilized).

The circuit employed for these measurements is shown in block diagram form in Fig. 3. A current pulse (usually <1 $\mu A/cm^2$) is applied across the membrane system by driving the noninverting (+) input of a tunable fast potentiostat, A1, (Tacussel PIT-20-2X) with a pulse generator, SG, (Tektronix PG 405) equipped with an offset voltage source for base line current variations. Resistor, R_C (usually 100-300 kΩ) is

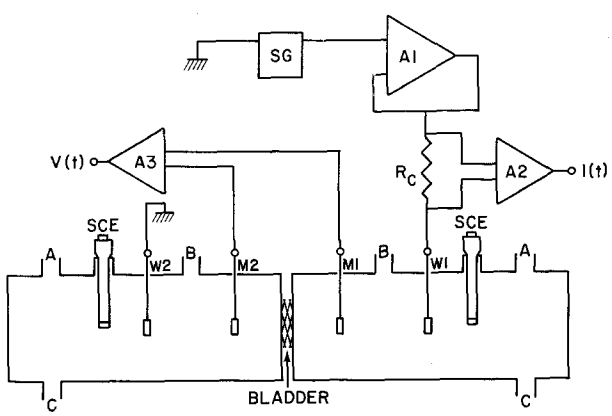


Fig. 3. Block diagram of the circuitry and measurement chamber employed for the transient impedance determination of the isolated toad urinary bladder membrane. The conductivity type chamber is shown in some detail and depicts perturbing (W1 and W2) and measurement (M1 and M2) electrodes along with the saturated calomel electrodes (SCE) employed for resting potential measurements. A, B, and C are solution/gas inlet, gas outlet, and solution outlet, respectively. A1 is the tunable amplifier utilized for current injection via signal generator, SG. R_C current limits and allows input current measurement via amplifier A2. Voltage response is obtained via amplifier A3.

current limiting and allows the input current pulse, $I(t)$, to be measured via amplifier, A2. The voltage response, $V(t)$, is measured using electrodes M1 and M2 into amplifier, A3. Both A2 and A3 are the vertical amplifiers (Tektronix 5A22N) of a dual beam oscilloscope (Tektronix 5103N) which is used to display $V(t)$ and $I(t)$ simultaneously. Records of these time domain signals are obtained photographically so that data points required for analysis via digital Laplace transformation (33, 52) are available. Presently the system is being equipped with a transient recorder to increase accuracy and manipulation speed (necessary for living system studies). The total relaxation time of the toad bladder membrane system has a duration of approximately 10-50 msec (with an apparent area of 1 cm^2). In order to obtain data points with sufficient time resolution (from <100 μsec to 50 msec) a series of four to five records in overlapping time ranges are usually obtained.

The experiments reported here have been carried out in isotonic amphibian Ringer's solution. However, it is to be noted that modifications in ionic concentration in either or both mucosal and serosal compartments which will not destroy the viability of the membrane system are in progress. These studies are designed to evaluate the effect of (particularly) Na^+ on the impedance parameters related to transport. In addition it is well known physiologically that antidiuretic hormones such as arginine-vasopressin or oxytocin have a profound influence upon Na^+ (53-55) (as well as urea and water) transport via membrane surface interactions (49, 56, 57). Experiments using the above conditions will be reported elsewhere.

Results and Discussion

In order to obtain the toad bladder membrane system impedance from the experimentally obtained time domain input and response curves the data was first transformed into the Laplace frequency domain. As in previous applications of this technique (58) real axis ($s = \sigma$) transformation was employed. The basics of this approach have been extensively described elsewhere (33, 52). Essentially, digital Laplace real axis transformation is carried out using an algorithm which assumes exponential behavior between successive data points in time. The highest obtainable frequency is limited only by the time at which experimental data is first available. The requirement therefore, is not that the input pulse, here $I(t)$, reach its constant value before data are useful, but that the detection instrumentation be capable of recording the initial rise from zero amplitude. The current pulse risetime in these experiments was approximately 1 μsec allowing the first data point at 100 nsec to be obtained relatively easily. Using the above approach the real axis impedance, $Z(\sigma)$, was evaluated over the frequency range 1 Hz to 1 MHz.

Once $Z(\sigma)$, which is a real function, was available, the next step was to apply diagnostic criteria to ascertain the applicability of the model proposed earlier. This was performed by first examining high and low limiting frequency regions. Referring to Eq. [10] and [11] and Fig. 2 it can be seen that, at high frequencies, the following functional relationship would be expected to hold

$$\underset{\sigma\to\infty}{Z(\sigma)} = R_e + \frac{1}{C_d\sigma} \qquad [21]$$

where R_e is now the electrolyte resistance between the measuring electrodes (M1 and M2, Fig. 3) and the bladder membrane, and C_d is defined in Eq. [12]. Inspection of Eq. [21] shows that at the highest accessible frequencies, a plot of $Z(\sigma)$ *vs.* $1/\sigma$ should be a straight line from which R_e and the dielectric (and double layer) membrane capacitance may be obtained. A typical plot of this type is shown in Fig. 4. It can be seen that indeed the membrane system responds as expected in this frequency range. C_d obtained in this

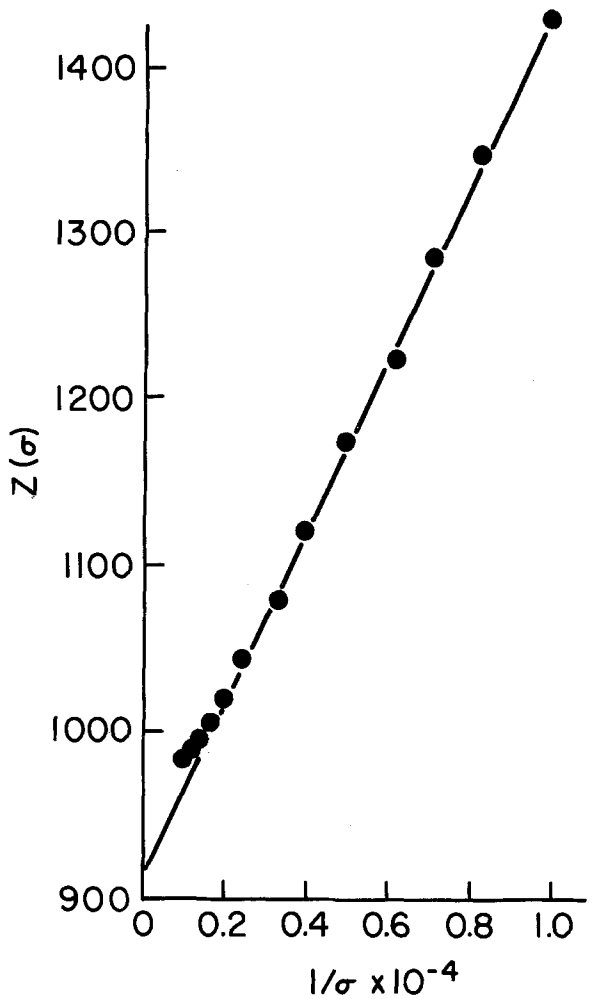


Fig. 4. High frequency diagnostic plot of the real axis impedance $Z(\sigma)$ *vs.* $1/\sigma$ allowing the determination of R_e and dielectric (and double layer) toad urinary bladder membrane capacitance, C_d. See text for details.

manner is approximately 1.7 ± 0.5 μF/cm^2. Note that the dielectric capacitance of the serosal (inner) membrane is in series with that of the mucosal membrane. An attempt to separate its contribution to the observed C_d was not the object of this preliminary study.

Referring again to Eq. [10] and [11] and Fig. 2, it can be seen that in the low frequency limit (prior to steady state conditions) $Z(\sigma)$ would be expected to exhibit the following behavior

$$Z(\sigma) = R_e + R_p + \left(\frac{R_D}{C_D\sigma}\right)^{1/2} \qquad [22]$$

where R_p is defined in Eq. [13], and R_D and C_D in Eq. [17] and [18], respectively. This relationship shows that in the lowest frequency ranges, compatible with that at which steady-state behavior occurs, a plot of $Z(\sigma)$ *vs.* $\sqrt{1/\sigma}$ should be a straight line. Plots of this type over the expected frequency range failed to reveal the anticipated functional behavior. This led to the preliminary conclusion that, under the linear conditions of this experiment, the response could indeed involve the Na^+ ion since its extracellular concentration (≃0.15M) is too high for significant aqueous diffusion polarization to exist.

Because of the above results and the fact that the bladder membrane exhibits steady-state current behavior it now had to be established whether the transporting species (Na^+) exhibits phase transfer polarization (slow partitioning kinetics) and whether it or another (high aqueous concentration) species exhibits

specific adsorption. Knowledge concerning these two possibilities would reveal whether (Na^+) partitioning depends upon its (or other species) specific interaction with the membrane penetration site, or whether this site undergoes structural (conformational ?) changes or rearrangements as a function of potential to allow (Na^+) entry and/or exit. It has, for example, been proposed (59) that Ca^{2+} adsorption (or binding) at the extracellular entry to the Na^+ pore regulates Na^+ permeability in epithelial cell systems. However, if this were the case, then the response of this membrane system to a linear perturbation should contain a potential dependent adsorption or binding contribution involving Ca^{2+}. This does not appear to be the case for the present study since Ca^{2+} adsorption kinetics would also lead to a limiting low frequency linear function of $Z(\sigma)$ *vs.* $1/\sqrt{\sigma}$ because of its low ($\simeq$ 1.5 mM) aqueous concentration.

It is now necessary to consider whether or not specific adsorption not coupled to aqueous diffusion is one of the kinetic steps in the transient response of the bladder membrane. Examination of the mass balance condition given in Eq. [9] shows that, if specific adsorption of the transporting species (Na^+) is present, then relaxation to steady state would necessitate a new equilibrium surface concentration, Γ'_e. At this point no further steady-state current could pass because this would involve the injection of much more charge than could be compensated by the adjustment in interfacial concentration of the transporting species. Since this is obviously not the case experimentally, it is necessary to invoke the specific adsorption of a species other than that which undergoes phase transfer. This is done by considering that specific adsorption, if present, in this case, contributes to the charging current, $i_c(s)$, only. Thus $i_c(s)$ is now given by

$$i_c(s) = sq(s) = q_E s\eta(s) + q'_e s c'_e \Delta c'_e(o,s) \quad [23]$$

where c'_e is the bulk concentration of the adsorbing species. The relative change in aqueous concentration of the adsorbing species at the plane $x = 0$, $\Delta c'_e(o,s)$, is related to its adsorbed surface concentration change by an equation similar to Eq. [4]. In addition mass balance is given by

$$\Gamma'_e s \Delta\Gamma'_e(s) = D'_e c'_e \left(\frac{d\Delta c'_e}{dx}\right)_{x=0} \quad [24]$$

which states that the flux in aqueous phase (right-hand side Eq. [24]) of the adsorbed species is equal to its change in surface concentration. Using all of the above, the charging admittance $Y_c(s) = 1/Z_c(s)$ is now written as

$$Y_c(s) = q_E s + \frac{q'_e s\Gamma'_e}{1 + (s\Gamma'/v'_e)} \quad [25]$$

where the second term on the right-hand side represents the contribution of finite adsorption (binding) kinetics to the over-all charge requirements of the interface.

In contrast to the charging impedance which has increased in complexity (compare with Eq. [10] because of a possible specific adsorption process, the phase transfer impedance $Z_p(s)$ becomes less complex because Na^+ does not appear to be involved in this process. Thus in the absence of specific adsorption and aqueous diffusion the phase transfer impedance becomes

$$Z_p(s) = \frac{1}{I_E}\left(1 + \frac{I^m}{n\mathbf{F}c^m D_m\left[\frac{\mathbf{F}V}{2RT} + \frac{1}{\delta_m} + \frac{1}{3}\left(\frac{\mathbf{F}^2\bar{V}}{4R^2T^2} + \frac{s}{D_m}\right)\delta_m\right]}\right) \quad [26]$$

in which all of the terms have been previously defined.

Inspection of Eq. [25] and [26] shows that, if the toad bladder membrane system responds in the manner just proposed to linear perturbation, then its aperiodic

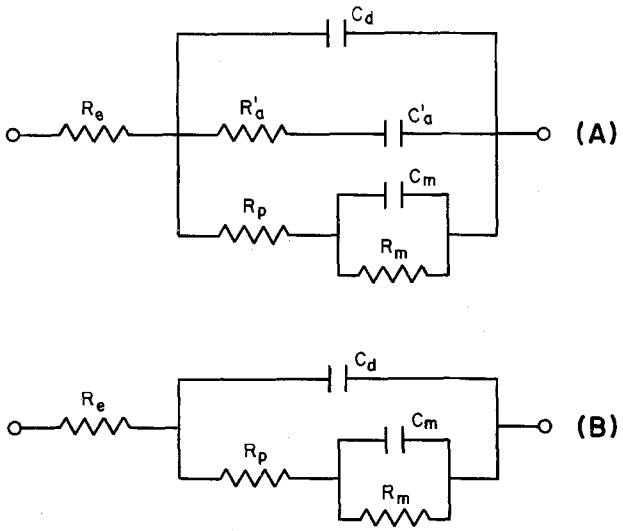


Fig. 5. Aperiodic equivalent electric circuits employed to analyze for the specific phase transfer behavior of the toad urinary bladder membrane system. The top circuit (A) shows a specific adsorption pathway coupled with phase transfer while the bottom circuit (B) shows only the phase transfer process. Finite adsorption was undetected in this study, and the frequency spectrum of $Z(\sigma)$ corresponds therefore, to (B) wherein R_p (partitioning) appears to be the rate-determining step.

equivalent electric circuit would be that given in Fig. 5a. Here all of the parameters have physical significance as defined previously. This model states that a specific adsorption (binding) process not involving phase transfer can occur (R'_a, C'_a) and that a certain quantity of charge can flow to readjust the surface concentration of the adsorbing species to its new resting value. This process does not involve the species undergoing phase transfer, but may, of course have an effect on its kinetics. The species contributing ultimately to the steady-state current through the membrane now follows the R_p, C_m, R_m (Fig. 5a) pathway in its relaxation to steady state. If specific adsorption is absent from the transient response of the bladder membrane to linear perturbation, it can readily be seen that its behavior would be that represented in Fig. 5b. Here the charging impedance is given by Eq. [10] and the phase transfer impedance by Eq. [26].

Analysis for either of the above types of behavior is carried out in a straightforward manner using real axis Laplace plane methods. First, advantage is taken of the fact that both R_e and C_d have been isolated in the high frequency range (Fig. 4). Next, if the adsorption time constant ($R'_aC'_a$) is sufficiently different from that of phase transfer (R_e, R_m, C_m) then R'_a and C'_a, can be isolated from the following

$$\frac{1}{1/(Z(\sigma) - R_e) - C_d\sigma} = R'_a + \frac{1}{C'_a\sigma} \quad [27]$$

which states that a plot of the experimentally known quantity on the left-hand side *vs.* $1/\sigma$ should be a straight line in the intermediate frequency range. This would then allow the evaluation of R'_a and C'_a. These parameters are then employed to determine the remaining quantities in the phase transfer pathway over a lower frequency region via

$$\frac{1}{1/(Z(\sigma) - R_e) - C_d\sigma - (1 + R'_aC'_a\sigma)/C'_a\sigma} = R_p + \frac{1}{C_m\sigma} \quad [28]$$

from which a plot of the left-hand side should be linear in $1/\sigma$. Finally the membrane transport parameter R_m is obtained from knowledge of the steady-state voltage response. If finite specific adsorption kinetics are not present Eq. [28] would no longer be valid. However, the behavior described in Eq. [27] would still obtain, R'_a and C'_a being substituted by R_p and C_m, respectively.

The above diagnostic procedures were employed in the lower and intermediate frequency ranges. As can be seen in Fig. 6 the functional behavior described by Eq. [27] exists over the intermediate frequency range. It was however, not possible to detect another frequency range over which Eq. [28] was obeyed. This appeared to indicate that the over-all transient impedance of the bladder membrane system would be given by Eq. [10] and [26] as depicted in Fig. 5b. In fact R_p and C_m were evaluated from plots such as Fig. 6 and R_m obtained from a knowledge of the steady-state voltage response. These values, along with those determined for R_e and C_d over the high frequency range (Fig. 4) could then be employed to reconstruct the entire $Z(\sigma)$ spectrum obtained experimentally. This was convincing evidence that the impedance of the toad urinary bladder membrane system could be represented by the aperiodic equivalent circuit shown in Fig. 5b. The values obtained in these preliminary experiments for the phase transfer parameters are $R_p = 400 \pm 125\ \Omega cm^2$, $C_m = 2.7 \pm 0.9 \times 10^{-3}$ F/cm^2 and $R_m = 30 \pm 10\ \Omega cm^2$. Note that, while finite specific adsorption kinetics were not observed (*i.e.*, Fig. 5a), this did not preclude the possibility of very rapid adsorption kinetics. Thus, referring to Fig. 5a, it can be seen that if $R_a \to 0$ (infinitely rapid kinetics) then the observed value of C_d would in fact be a sum $(C_d + C_a)$ representing electrostatic and adsorption effects. This possibility is presently under study by examination of the effect of various ions on "C_d."

As is common for biological systems the scatter in the data (from toad to toad) is relatively high. This does not preclude, however, analysis of the mechanistic pathway. Thus, for every bladder membrane examined, the behavior could be described by Eq. [10] and [26] as represented in Fig. 5b. This behavior persisted even when the transepithelial resting potential

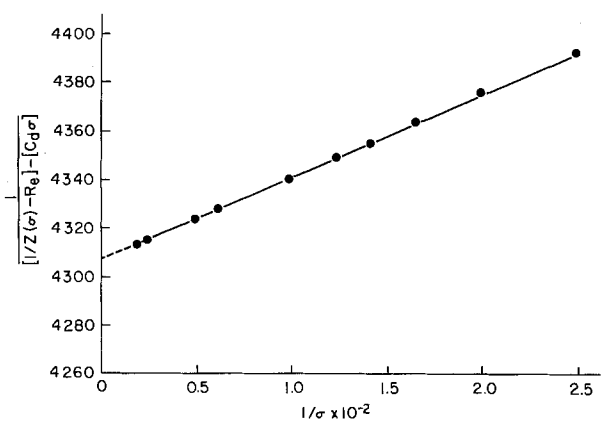


Fig. 6. Intermediate frequency plot of the real axis Laplace plane impedance data using the functional relationship described in Eq. [27] establishing, along with Fig. 3, that the toad urinary bladder membrane exhibited dielectric (and possible infinitely fast specific adsorption) behavior, and that the pathway for Na^+ transport involves slow phase transfer and fast membrane transport.

was lower (<20 mV) than would normally be accepted in biological studies of this membrane system. This is interpreted to mean that the species responsible (Na^+) for the phase transfer portion of the total response did not change its intracellular concentration enough to necessitate compensating action by an active transporting system. This was expected because of the low quantity of charge injected with each perturbation.

Examination of the data obtained reveals that the interfacial (potential dependent) phenomenon of phase transfer (partitioning) of Na^+ is by far the rate-limiting step for its memorane transport. The value of the phase transfer impedance, R_p, is significantly larger than its kinetically relevant counterpart for membrane transport, R_m. This result shows that the interfacial structure (in this case the mucosal interface) determines to a large extent, the passive transport properties of this cell system. Previous analyses using single (38) and bilayer artificial (39-41, 60) membrane systems have dealt with the effect of the diffuse double layer structure upon transport. Remarkably the simple Gouy-Chapman theory quantitatively predicts the shift in current-voltage relationships at steady state in many cases. However, this agreement may be fortuitous even in artificial systems since it is apparent that some divalent cations (*e.g.*, Ca^{2+}) have more specific structural effects than others (61). It is also not clear that the compact double layer, which must exist at interfaces of this type, has been adequately taken into account. Certainly steady-state measurements will not be revealing in this respect. Recent studies involving attempts to isolate the dielectric from double layer capacitance at membranes have been described (42) and may represent the most significant approach thus far in the elucidation of the structure of these interfaces.

The apparent rapidity of membrane transport for this system would appear to favor a pore rather than a carrier interpretation, in agreement with a recent study of membrane noise in a similar epithelial system (62). The determining factors of pore penetration are of course not discernible at this stage. It is not possible, for example, to preclude the involvement of a specific adsorption process which could cause a "gating" phenomenon for Na^+ transport. A suspicion that this may be taking place can be invoked to account for the somewhat high value of C_d observed. In the present study, the adsorption process (if present) appears infinitely fast, but could be separable from the dielectric response by analysis of the system while varying ionic concentration, or by careful high frequency measurements which are presently being carried out.

It is believed that this is the first study of this type on the toad bladder membrane system. Placed in the context of classical studies it is hoped that these results will shed further light on the highly complex transport function of this type of living cell. It is interesting to note that, while short-circuit steady-state studies reveal the existence of a significant intercellular (leak) pathway for current flow (46, 63), this was not detected in the present work. Most probably this is due to the fact that short-circuit conditions are highly nonlinear and usually result in a significant modification in the structure of the intercellular spaces (29). The present study may thus provide an experimental condition in which the bladder is as physiologically undisturbed (electrically) as possible.

Conclusion

This study has invoked the existence of dynamic interfacial electrochemical phenomena, which constitutes the basis of the electrochemical information transfer *in vivo* concept, to provide a model for the elucidation of living cell function. The use of finite kinetics for phase transfer and specific adsorption has allowed a unified approach to membrane impedance to

be applied to the toad urinary bladder membrane system. The modeling approach, which is carried out in the Laplace plane, allows the heterogeneous nature of biological membranes to be treated in a straightforward manner. In this application it has proved successful in a preliminary isolation of the mechanistic pathway for passive Na^+ transport by a careful functional analysis over the wide frequency range available through the use of real axis Laplace transformation. The data obtained reveals that phase transfer and not membrane transport is the rate-limiting step for Na^+ transport. The determining factor for Na^+ entry is not yet clear, but it is intriguing to consider the approach (43, 73) in which the polar groups blocking entry are deformed by the high electric fields present at the interfaces when the penetrating ions interact with, *e.g.*, the lipid structures. The transient injection of charge, as carried out in this study, would then act to provide a sufficient change in interfacial field to allow those Na^+ ions with sufficient energy to penetrate the membrane phase and be literally propelled through to the other side. The deformation of an entry site could of course be caused by a specific adsorption process and would simply constitute a logical extension of the basic premise.

This study has revealed that it is possible to employ modern bioelectrochemical approaches to the study of living membranes. It was begun with the conviction that dynamic interfacial electrochemical processes constitute basic biological steps in cell function. Here a small charge injection has resulted in the modification of a transport function by causing a potential dependent change in interfacial membrane structure. Other biochemical functions appear also to be dependent on similar effects. For example, specific adsorption can influence the activity of membrane bound enzymes (8, 9, 64-66). Transmembrane potential changes as a result of protein synthesis (67) suggest at least a modification in transport properties. The surface charge of differentiated *vs.* undifferentiated (68) and normal *vs.* malignant (69) cells is significantly different, allowing at least the possibility of different interfacial structures which could cause cellular function change. Cell-cell and cell-tissue interaction appears to be greatly dependent upon surface structure and charge (70-72, 74-76). It is hoped therefore, that studies such as this will aid in the elucidation of cellular mechanisms so that even more significant clinical applications will be forthcoming. Certainly, the current success in the healing of otherwise incurable bone fractures by very specifically encoded charge injection (25), the parameters for which were chosen by analyses similar to that given here, warrants significant efforts in this area of bioelectrochemistry.

Acknowledgments

The authors sincerely acknowledge C. A. L. Bassett, M.D. for many helpful discussions and for suggesting the use of the toad urinary bladder for these studies and NIH Grant #AM-07822, NSF Grant #NSF-APR-76-19469, and Electro-Biology, Incorporated for partial support of this work.

A portion of this work has been submitted by one of the authors (GSM) to the Department of Chemical Engineering and Applied Chemistry, Columbia University, as partial fulfillment of the requirement for the Master of Science Degree in Bioengineering.

Manuscript received March 28, 1977.

Any discussion of this paper will appear in a Discussion Section to be published in the June 1978 JOURNAL. All discussions for the June 1978 Discussion Section should be submitted by Feb. 1, 1978.

REFERENCES

1. J. D. Ebert and I. M. Sussex, "Interacting Systems in Development," 2nd ed., Holt, Rinehart and Winston, New York, (1970).
2. G. M. Edelman, *Science*, **192**, 218 (1976).
3. G. L. Nicolson and G. Poste, *N. Engl. J. Med.*, **295**, 197 (1976).
4. H. Rasmussen, *Science*, **170**, 404 (1970).
5. C. D. Cone, Jr., *Ann. N.Y. Acad. Sci.*, **238**, 420 (1974).
6. L. Weiss and J. R. Subjeck, *ibid.*, **238**, 352 (1974).
7. R. Harrison and G. G. Lunt, "Biological Membranes Their Structure and Function," John Wiley & Sons, New York (1975).
8. S. J. Singer, in "Structure and Function of Biological Membranes," L. I. Rothfield, Editor, p. 145, Academic Press, New York (1971).
9. G. A. Rodan and M. B. Feinstein, *Proc. Natl. Acad. Sci. USA*, **73**, 1829 (1976).
10. J. F. Whitfield, R. H. Rixon, J. P. MacManus, and S. D. Balk, *In Vitro*, **8**, 257 (1973).
11. J. S. Handler and A. S. Preston, *J. Membr. Biol.*, **26**, 43 (1976).
12. E. E. Bittar, in "Membranes and Ion Transport," E. E. Bittar Editor, p. 297, Wiley-Interscience, New York (1970).
13. H. Davson and J. F. Danielli, "The Permeability of Natural Membranes," 2nd ed., Cambridge University Press, London, England (1952).
14. J. D. Robertson, in "Cellular Membranes in Development," M. Locke, Editor, p. 1, Academic Press Inc., New York (1964).
15. J. Lenard and S. J. Singer, *Proc. Natl. Acad. Sci. USA*, **56**, 1828 (1966).
16. S. J. Singer, *Ann. Rev. Biochem.*, **43**, 805 (1974).
17. M. S. Bretscher and M. C. Raff, *Nature*, **258**, 43 (1975).
18. J. E. Rothman and J. Lenard, *Science*, **195**, 743 (1977).
19. A. A. Pilla, Proceedings of the 7th Intersociety Energy Conversion and Engineering Conference, American Chemical Society, p. 761, 1972.
20. A. A. Pilla, "Electrochemical Bioscience and Bioengineering," I. Miller, A. Salkind, and H. Silverman, Editors p. 1, The Electrochemical Society Softbound Symposium Series, Princeton, N.J., (1973).
21. A. A. Pilla, *Bioelectrochem. Bioenergetics*, **1**, 227 (1974).
22. A. A. Pilla, *Ann. N.Y. Acad. Sci.*, **238**, 149 (1974).
23. R. O. Becker and A. A. Pilla, "Modern Aspects of Electrochemistry," Vol. 10, J. O'M. Bockris, Editor, Plenum Publishing Corp., New York (1975).
24. C. A. L. Bassett, R. J. Pawluk, and A. A. Pilla, *Ann. N.Y. Acad. Sci.*, **238**, 242 (1974).
25. C. A. L. Bassett, A. A. Pilla, and R. J. Pawluk, *Clin. Orthop.*, **124**, 117 (1977).
26. A. A. Pilla, *This Journal*, **122**, 105C (1975).
27. C. A. L. Bassett, R. J. Pawluk, and A. A. Pilla, *Science*, **184**, 575 (1974).
28. A. A. Pilla, *Biophys. J.*, **17**, 130a (1977).
29. L. D. Peachy and H. Rasmussen, *J. Biophys. Biochem. Cytol*, **10**, 529 (1961).
30. J. K. Choi, *J. Cell Biol.*, **16**, 53 (1963).
31. B. P. Crocker, Jr., and C. C. Tisher, *Kidney Int.*, v, 145 (1972).
32. A. A. Pilla, *This Journal*, **117**, 467 (1970).
33. A. A. Pilla, in "Computers in Chemistry and Instrumentation: Electrochemistry," Vol. 2, J. S. Mattson, H. C. MacDonald, and H. B. Mark, Jr., Editors, Marcel Dekker, Inc., New York (1972).
34. K. S. Cole, "Membranes, Ions and Impulses," University of California Press, Berkeley, California (1968).
35. A. A. Pilla, *This Journal*, **118**, 1295 (1971).
36. W. Lorenz and F. Mockel, *Z. Elektrochem.*, **60**, 507 (1956).
37. R. deLevie, N. G. Seidah, and H. Moreira, *J. Membr. Biol.*, **16**, 17 (1974).
38. I. Miller and M. Blank, *J. Colloid Interface Sci.*, **26**, 26 (1968).
39. S. McLaughlin, *J. Membr. Biol.*, **9**, 361 (1972).
40. D. A. Haydon and V. B. Myers, *Biochem. Biophys. Acta*, **307**, 429 (1973).
41. B. Neumke, *This Journal*, **123**, 1331 (1976).
42. O. Andersen, S. Feldberg, H. Nakadomari, H. Levy, and S. McLaughlin, *Biophys. J.*, **16**, 194a (1976).
43. V. A. Parsegian, *Ann. N.Y. Acad. Sci.*, **264**, 161 (1975).
44. E. Fromter and J. M. Diamond, *Nature (London) New Biol.*, **235**, 9 (1972).
45. C. H. Van Os and J. F. G. Sleggers, *J. Membr. Biol.*, **24**, 341 (1975).

46. V. Koefoed-Johnsen and H. H. Ussing, *Acta Physiol. Scand.*, **42**, 298 (1958).
47. L. Reuss and A. L. Finn, *J. Gen. Physiol*, **64**, 1 (1974).
48. M. Walser, *J. Clin. Invest.*, **48**, 1714 (1969).
49. P. D. Lief, B. F. Mutz, and W. Bank, *Am. J. Physiol.*, **230**, 1722 (1976).
50. A. L. Finn and S. A. Hutton, *Am. J. Physiol.*, **227**, 950 (1974).
51. D. Erlij, *Pfluegers Arch.*, **364**, 91 (1976).
52. A. A. Pilla, in "Information Chemistry," S. Fujiwara and H. B. Mark, Jr., Editors, p. 181, University of Tokyo Press, Japan (1975).
53. J. S. Handler and A. S. Preston, *J. Membr. Biol.*, **26**, 43 (1976).
54. W. L. Davis, D. B. P. Goodman, J. H. Martin, J. C. Matthews, and H. Rasmussen, *J. Cell Biol.*, **61**, 544 (1974).
55. A. Leaf, J. Anderson, and L. B. Page, *J. Gen. Physiol.*, **41**, 657 (1958).
56. R. Laird and R. Yates, *J. Ultrastruct. Res.*, **44**, 339 (1973).
57. W. A. Kachadorian, J. B. Wade, and V. A. Discala, *Science*, **190**, 67 (1975).
58. K. Doblhofer and A. A. Pilla, *J. Electroanal. Chem.*, **39**, 91 (1972).
59. F. C. Herrera and P. F. Curran, *J. Gen. Physiol.*, **46**, 999 (1963).
60. O. Andersen and M. Fuchs, *Biophys. J.*, **15**, 795 (1975).
61. S. G. A. McLaughlin, G. Szabo, and G. Eisenman, *J. Gen. Physiol*, **58**, 667 (1971).
62. B. Lindemann and W. van Driessche, *Science*, **195**, 292 (1977).
63. L. Reuss and A. L. Finn, *J. Membr. Biol.*, **20**, 191 (1975).
64. C. R. Kahn, *J. Cell. Biol.*, **70**, 261 (1976).
65. A. R. Goldhammer, M. K. Jain, and E. H. Cardes, *J. Membr. Biol.*, **23**, 293 (1975).
66. L. A. Bourret and G. A. Rodan, *J. Cell Physiol.*, **88**, 353 (1976).
67. V. V. Frol'kis, *Biofizika*, **19**, 470 (1974).
68. R. Eleul, J. Bronx, and K. Kravity, *Nature*, **258**, 616 (1975).
69. G. Adam and G. Adam, *Exp. Cell Res.*, **93**, 71 (1975).
70. D. E. Brooks and G. V. F. Seaman, *J. Colloid Interface Sci.*, **43**, 670 (1973).
71. J. J. Deman and E. A. Bruyneel, *Exp. Cell Res.*, **89**, 206 (1974).
72. K. Jan and S. Chien, *J. Gen. Physiol.*, **61**, 638 (1973).
73. A. P. R. Theuvenet and G. W. F. H. Borst-Pauwels, *J. Theor. Biol.*, **57**, 313 (1976).
74. V. A. Parsegian, *Ann. N.Y. Acad. Sci.*, **238**, 362 (1974).
75. J. R. Subjeck and L. Weiss, *This Journal*, **123**, 1456 (1976).
76. P. N. Sawyer, B. Stanczewski, N. Ramasamy, D. V. Raman, W. Wrezlewicz, I. Parsa, J. Pindyck, S. L. Kountz, and K. Butt, *ibid.*, **123**, 1445 (1976).

Thermodynamic Potential for the Anodic Dissolution of n-Type Semiconductors

A Crucial Factor Controlling Durability and Efficiency in Photoelectrochemical Cells and an Important Criterion in the Selection of New Electrode/Electrolyte Systems

Allen J. Bard*

Department of Chemistry, University of Texas at Austin, Austin, Texas 78712

and Mark S. Wrighton*,[1]

Department of Chemistry, Massachusetts Institute of Technology, Cambridge, Massachusetts 02139

ABSTRACT

We show that the standard potential for anodic dissolution, $E_D°$, of n-type semiconductors (*e.g.*, $E_D°$ for $CdS \leftrightarrows Cd^{2+}(aq) + S + 2e^-$ is + 0.08V *vs* SCE) plays a key role in ultimate efficiency of thermodynamically stable n-type semiconductor-based photoelectrochemical cells. The selection of redox active substances that can be used for competitive capture of photogenerated holes is limited to those systems where the product does not have the potential to oxidize the semiconductor. Where E_{VB} and E_{CB} represent the position of the valence and conduction band positions at the interface, respectively, we must conclude that $E_D°$ is at a more negative potential (*vs.* a reference) than E_{VB}, if the semiconductor undergoes photoanodic dissolution. Quenching of the photoanodic dissolution by competitive hole capture by some electrolyte component, say A, is possible if $E_{redox}(A^+/A)$ lies at a potential more negative than E_{VB}. But additionally, if the A^+, the oxidation product, is to be incapable of oxidizing the semiconductor, $E_{redox}(A^+/A)$ must be more negative than $E_D°$. Consequently, for the semiconductor to be thermodynamically stable in the A/A^+ electrolyte the maximum photovoltage output, $(E_{CB}-E_{redox})$, can be no greater than $(E_{CB}-E_D°)$ for E_{CB} more negative than E_D.° Naturally, kinetic inertness of the semiconductor to an oxidant with E_{redox} more positive than $E_D°$ may allow its presence and/or use in a more efficient cell. N-type CdS and TiO_2 semiconductors in aqueous electrolytes are treated in detail. Some preliminary comments are made concerning p-type materials.

Much attention has been focused recently on the use of certain redox active electrolytes to "quench" the photoanodic dissolution of small bandgap, nonoxide, n-type semiconductors (1-6). Broadly interpreted, the success realized can be attributed to the ability of the redox active species to capture photogenerated holes before the holes participate in oxidation reactions of the semiconductor. At present there is no detailed understanding of the factors controlling the competi-

* Electrochemical Society Active Member.
[1] Dreyfus Teacher-Scholar Grant recipient, 1975-1980.
Key words: photoelectrochemistry, solar cells, photoanodic dissolution, semiconductor electrochemistry.

tion between the interfacial electron transfer and the photoanodic dissolution, although clearly certain energetic requirements (7) must be met for any photo-induced interfacial charge transfer to occur.

Power efficiencies of ~10% can be obtained for the conversion of monochromatic visible light to electricity with "stabilized" n-type semiconductor-based cells (1-6). Even cells employing polycrystalline photoelectrodes appear to give good efficiencies (2, 3, 8-10). It is appropriate to enunciate criteria which will aid in (*i*) the selection of new electrolyte/electrode combinations and (*ii*) the determination of durability and conversion efficiency under operating conditions. The aim of this note is to point out the importance of the standard potential for the anodic dissolution, $E_D°$, of n-type semiconductors. For semiconductors which undergo photoanodic dissolution, the position of $E_D°$ controls the ultimate efficiency and limits the redox active substances that can be used for competitive capture of photogenerated holes.

Theory and Discussion

According to Gerischer (7), the energetics of an n-type semiconductor/electrolyte interface at equilibrium in the dark are as sketched in Fig. 1, where the energy levels of importance, which can be expressed in volts *vs.* a reference electrode, are as follows: E_f is the Fermi level of the semiconductor, E_{CB} and E_{VB} are the conduction and valence band positions, respectively, at the interface, E_{BG} is the semiconductor bandgap, and E_{redox} is the actual redox potential of the chemical system ($A^+ + e = A$) in equilibrium with the semiconductor. In the following discussion we will generally assume that A^+ and A are at unit activity, so that $E_{redox} = E_{redox}°$. However, if the redox system involves H^+, *e.g.*, the O_2/H_2O system, E_{redox} will be a function of pH. Moreover, all energy levels (given on some absolute scale in electron volts) will be expressed relative to a saturated calomel electrode, *i.e.* in volts *vs.* SCE.

Absorption of light within the depletion region corresponding to a VB → CB electronic transition results in separated e^--h^+ (electron-hole) pairs such that h^+ goes to the interface and the e^- moves to the bulk of the semiconductor. The h^+ rises to the top of the valence band, and, in the absence of surface states, is at a potential equal to E_{VB}. Thus, if E_{redox} is more negative than E_{VB}, interfacial electron transfer can occur to fill h^+, thereby oxidizing some component of the electrolyte. However if the standard potential for the anodic dissolution of the semiconductor, $E_D°$, is more negative than E_{VB}, h^+ can also cause oxidation of the crystal. The primary oxidation product, then, will depend on the relative rate of the two competing h^+ reactions.

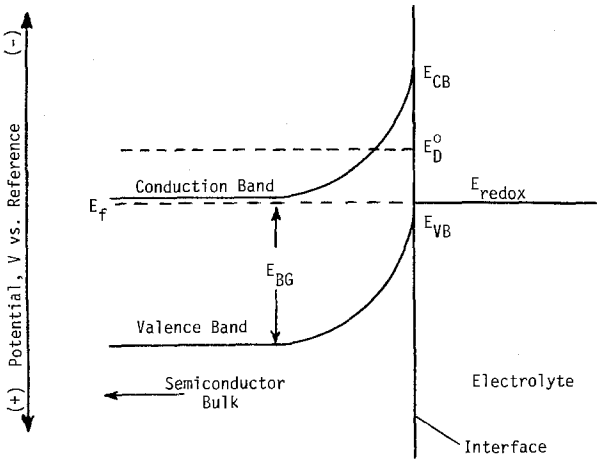


Fig. 2. E_{redox} more positive than $E_D°$

Significantly, though, the relative position of E_{redox} and $E_D°$ is crucial to whether prolonged stabilization of the semiconductor is expected. In Fig. 2, we show a situation where $E_{redox}°$ is more positive than $E_D°$. What is readily apparent is that the oxidized form of the redox couple with a potential $E_{redox}°$ is capable, energetically, of spontaneously oxidizing the semiconductor in the dark. If the redox system is represented by A/A^+ and one starts with only the reduced form, A, present, then the photogeneration of h^+ can lead to photoanodic dissolution and to interfacial transfer to give the oxidized form, A^+. But with the $E_{redox}°$ level of A/A^+ situated more positive than $E_D°$, A^+ is capable of chemically oxidizing the semiconductor. Thus, the use of A as a reductant to capture competitively photogenerated h^+ is not attractive, because the primary oxidation product may, thermodynamically, oxidize the semiconductor.

Figure 3, shows the situation for $E_{redox}°$ (A/A^+) more negative than $E_D°$. In this case the primary oxidation product, A^+ is not capable, thermodynamically, of oxidizing the semiconductor to an appreciable extent. Thus, if A can successfully capture 100% of the photogenerated h^+, then the semiconductor could be stabilized to anodic dissolution for an indefinite period.

A comparison, though, of Fig. 2 and 3 suggests several other important comments. First, the amount of band bending in the dark (E_{CB}-E_{redox}) is

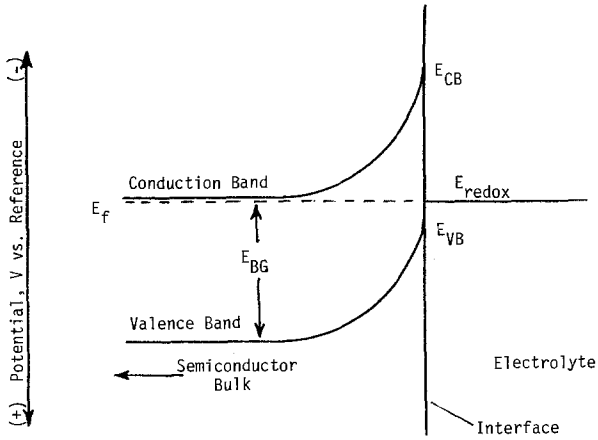


Fig. 1. N-type semiconductor at dark equilibrium

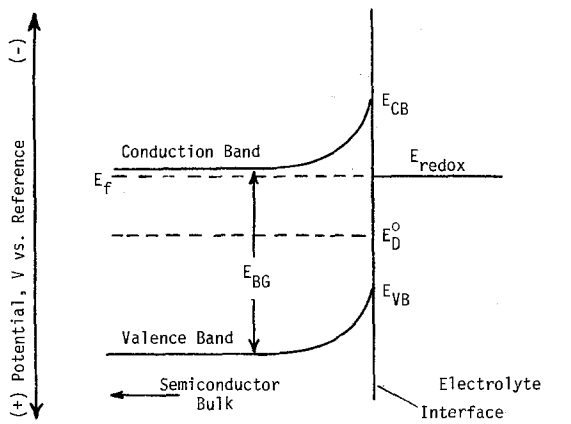


Fig. 3. E_{redox} more negative than $E_D°$

equal to the maximum open-circuit photopotential, and in Fig. 3 the amount of band bending is less than ideal. In fact, the position of $E_D°$ will limit the amount of band bending to E_{CB}-$E_D°$ for an electrolyte system which can stabilize the semiconductor. Thus, the maximum conversion efficiency with monochromatic light and for a thermodynamically stable system is just E_{CB}-$E_D°/E_{BG}$.

Second, the position of E_{redox} may be required to be significantly more negative than E_{VB}. This may preclude effective overlap of filled levels of the redox active A and the valence band (containing the primary photogenerated h^+) of the semiconductor. Indeed, if the h^+ position is, at best, at the top of the valence band, stabilization of the semiconductor to photoanodic dissolution may not be possible, owing to the slow oxidation of A because of this lack of overlap. This consideration suggests that surface states or intermediate levels may be of importance in the transfer of holes to solution species whose E_{redox} is located in the band-gap region, and there may be merit in the controlled introduction of such states or levels so that the photogenerated hole can rise to a level more negative than $E_D°$.

Third, when E_{redox} is required to be substantially more negative than E_{VB} there may be substantial overlap of the filled levels in A and the conduction band (unfilled) levels of the semiconductor. This will result in significant dark anodic currents.

Finally, since $E_D°$ must be closer to E_{VB} than E_{redox}, we can only be cautious about the prospects for finding a large number of redox active materials that will be capable of competing efficiently with photoanodic dissolution. The presence of surface states will alter the prospects considerably, and their role in the known cases of stabilization should be investigated in detail.

Consideration of a couple of examples will serve to reinforce the principles outlined here. Table I shows some pertinent information. Stabilization of CdS to photoanodic dissolution has been reasonably successful (1-6) and is a useful illustrative case. In aqueous electrolytes the energetics are as in Fig. 4, and are approximately independent of pH (6, 11). The value of $E_D°$ is for the reaction $Cd^{2+} + S + 2e^- =$ CdS and is based on the thermodynamic data given in Latimer (12). From the foregoing discussion, E_{redox} must be more negative than +0.08V *vs.* SCE. Consequently, and in retrospect, it is understandable that failure results in the attempted (13) use of I^- to capture competitively photogenerated h^+. The primary oxidation product, I_2, is capable of oxidizing CdS, since $E_{redox}°(I_2/I^-)$ is +0.25V *vs.* SCE (12). Indeed, it is well known that I_2 will oxidize CdS, and this reaction is used in an established analytical procedure (14). Since the oxidation of CdS by I_2 will occur at some finite rate, it may be possible to generate some reasonable concentration of I_2 at CdS. However, it is the long-term stability that is of importance here. Moreover, an axiom of inorganic photochemical systems is that, at the very least, the role of the light is to accelerate thermodynamically favorable chemical processes. Thus, irradiation of CdS in the presence of I_2 should increase its rate of spontaneous oxidation.

Table I. Calculated standard potentials for decomposition half-reactions of several semiconductors

Compound	Half-reaction	$E_D°$ (V *vs.* SCE)
TiO_2	$TiO^{2+} + ½\ O_2 + 2e^- \rightleftarrows TiO_2$	+1.18
ZnO	$Zn^{2+} + ½\ O_2 + 2e^- \rightleftarrows ZnO$	+0.65
	$Zn(OH)^+ + ½\ O_2 + 2e^- \rightleftarrows ZnO + OH^-$	+0.52
	$ZnO_2^{2-} + 2H_2O + ½\ O_2 + 2e^- \rightleftarrows ZnO + 4\ OH^-$	+0.19
Fe_2O_3	$2Fe^{3+} + 3/2\ O_2 + 6e^- \rightleftarrows Fe_2O_3$	+1.00
WO_3	$WO_4^{2-} + 4H^+ + ½\ O_2 + 2e^- \rightleftarrows WO_3 + 2H_2O$	+1.40
SnO_2	$Sn^{4+} + O_2 + 4e^- \rightleftarrows SnO_2$	+1.11
CdS	$Cd^{2+} + S + 2e^- \rightleftarrows CdS$	+0.08

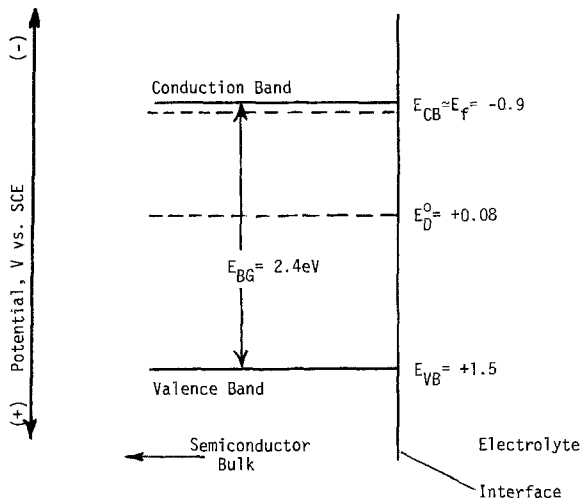


Fig. 4. CdS in aqueous solution

In the presence of X^{2-} (X = S, Se, Te) the positions of E_{CB} and E_{VB} for CdS are located at more negative potentials, but the E_{redox} values (12, 15) for X^{2-}/X_n^{2-} at −0.7, −0.9, and −1.1V *vs.* SCE for X = S, Se, and Te, respectively, are all sufficiently negative that the elemental chalcogen is incapable of oxidizing CdS. Thus, long-term stability can be expected provided the $X^{2-} \rightarrow X_n^{2-}$ oxidation is 100% efficient. Incidentally, it is worth noting that the lightest elemental chalcogen, O_2, is thermodynamically capable of oxidizing CdS, since in H_2O the E for the O_2/H_2O couple under 1 atm of O_2 ranges from +1.0 to +0.16V *vs.* SCE from pH = 0 to pH = 14 (12). Likely primary oxidation products from H_2O (such as ·OH or H_2O_2) are certainly capable of spontaneously oxidizing CdS. However, the slow rate of the reaction of CdS with O_2 may make it possible to use this material as the photoanode in a cell for the electrolysis of H_2O, provided intermediates like OH and H_2O_2 can be avoided.

The other n-type CdX photoelectrodes can be treated in the same way as CdS. At this time, the point to emphasize here is that the position of $E_D°$ for CdS is significantly more negative (~1.4V) than E_{VB} and, therefore, limits the immediately foreseeable output voltages in stable aqueous systems to about 1.0V. This projection is clearly altered if the band positions can be moved substantially more negative by specific interactions with the electrolyte; *e.g.*, in the presence of X^{2-} the bands move more negative by ~0.5V, while $E_D°$ is presumably constant (6).

For a stable oxide semiconductor the value of $E_D°$ lies at more positive potentials. For example, the energetics for TiO_2 (16) electrode immersed in a solution of pH = 0 are shown in Fig. 5, $E_D°$, calculated from available free energy data (12) for the half-reaction $TiO^{2+} + ½\ O_2 + 2e^- = TiO_2$, is + 1.18V *vs.* SCE, which is 0.18V positive of the E for the O_2/H_2O reaction at pH = 0. At more alkaline pH's both the flatband potential and the E_{redox} for O_2/H_2O shift toward more negative values by about 59 mV/pH unit, while $E_D°$ is independent of pH, as long as TiO^{2+} is the predominant Ti(IV) species in solution. Thus, the separation between $E_D°$ and $E(O_2/H_2O)$ increases with increasing pH, leading to greater stability of the material. The value of $E_D°$ is consistent with an equilibrium constant for the reaction $TiO_2 + 2H^+ \rightleftarrows TiO^{2+} + H_2O$ of 2×10^{-7}. In sufficiently acidic solutions some small amount of dissolution of the TiO_2 may occur. Indeed, the change observed in surface morphology of a TiO_2 single crystal immersed in 1.0*N* H_2SO_4 under irradiation (17) may represent this light-catalyzed dissolution. At higher pH's the TiO_2 electrode is stable, even

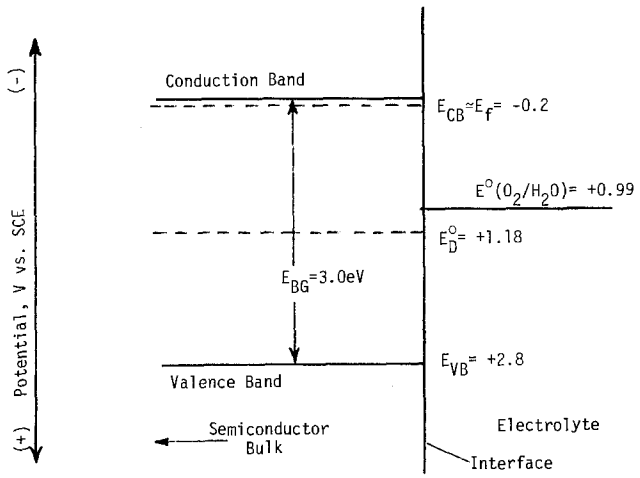


Fig. 5. TiO_2 in aqueous solution at $pH = 0$

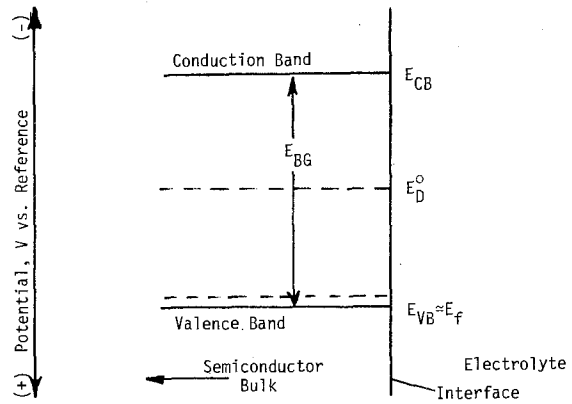


Fig. 6. P-type semiconductor at flatband potential

under prolonged irradiation, as predicted from the above discussion. Note, however, that $E_D°$ lies quite negative of E_{VB} and, as discussed for CdS, may limit how positive the potential of an added redox active electrolyte can be, for use in a photoelectrochemical cell without encountering stability problems with the electrode. It is also of interest to consider the behavior of the electrode in a nonaqueous solvent, *e.g.*, acetonitrile. $E_D°$ will become more positive in a solvent which complexes or solvates the lattice metal ion to a smaller extent, yielding a more stable semiconductor with respect to photo-oxidation.

The behavior of ZnO in aqueous electrolyes is also an interesting case. For the half-reaction $Zn^{2+} + \frac{1}{2} O_2 + 2e^- = ZnO$, $E_D°$ is +0.65V *vs.* SCE (12). This lies near or negative of $E(O_2/H_2O)$ at all *p*H's (when $E_D°$ is calculated for the appropriate Zn(II) species, *i.e.*, Zn^{2+}, $Zn(OH)^+$, or ZnO_2^{2-}) and is consistent with the known instability of ZnO under irradiation, even though E_{CB} and E_{VB} are located at about the same positions for ZnO and TiO_2 (16, 18, 19). Thus, it is $E_D°$ rather than E_{VB} which governs the long-term stability of the material. It is true that the position of E_{VB} is related to the bonding energy of the valence electrons and thus the stability of the lattice. However, in terms of half-reactions, E_{VB} represents the potential for the abstraction of one electron from the lattice (*e.g.*, $CdS^+ + e = CdS$), whereas $E_D°$ involves equilibrium constants and potentials involving the intermediate species which may be so thermodynamically favorable as to make $E_D°$ quite negative of E_{VB}. Thus, while redox couples with potentials near E_{VB} clearly will cause decomposition of the lattice (7), in fact couples at even more negative potentials are capable of oxidizing the semiconductor. Ideally, $E_D°$ should be at, or below E_{VB}. For the semiconductor materials investigated for which thermodynamic data are available, even the very stable ones (9), such as SnO_2, WO_3, and Fe_2O_3, $E_D°$ is negative of E_{VB} for an aqueous solution.

Though p-type semiconductors have received some attention as photocathodes, p-type semiconductor-based photoelectrochemical cells have not been found to be very efficient. We note that the systems studied, *e.g.*, p-GaP, GaAs, CdTe, (20-23) all have n-type counterparts which undergo photoanodic dissolution in aqueous solution (1, 6, 24-26). This allows us to conclude that the $E_D°$ in each case is situated at a potential which is more negative than E_{VB}. Since a heavily doped p-type material has $E_f \approx E_{VB}$ at the flatband potential, E_{FB}, the p-type material is thermodynamically unstable to anodic dissolution at E_{FB} in particular and at potentials more positive than $E_D°$. The flatband condition for a p-type electrode is shown in Fig. 6 and since the majority of charge carriers are holes, it is apparent that the anodic dissolution may occur. At least, the dissolution will occur until the E_f at the surface is approximately $E_D°$. Consequently, in practice, p-type semiconductors having a fairly negative $E_D°$ may give poor output photovoltages. Logically, other factors concerning p-type materials must be considered, including the standard potential for cathodic reaction, *e.g.*, $CdTe + 2e^- \rightarrow Cd + Te^{2-}$. For p-type materials such a reaction should be feasible for E_{CB} more negative than such a potential. And again, whether the semiconductor is stable may depend in large measure on relative rates of minority carrier (e^-) interfacial transfer *vs.* the cathodic decomposition of the semiconductor.

Acknowledgment

This work has been supported by grants from the National Science Foundation to the University of Texas and from the National Aeronautics and Space Administration to the Massachusetts Institute of Technology. A.J.B. acknowledges support as a Sherman Fairchild Distinguished Scholar and M.S.W. as a Standard Oil Company of California Visiting Energy Professor at the California Institute of Technology when this collaboration was initiated.

Manuscript submitted April 20, 1977; revised manuscript received June 28, 1977.

Any discussion of this paper will appear in a Discussion Section to be published in the June 1978 JOURNAL. All discussions for the June 1978 Discussion Section should be submitted by Feb. 1, 1978.

Publication costs of this article were assisted by Massachusetts Institute of Technology.

REFERENCES

1. A. B. Ellis, S. W. Kaiser, and M. S. Wrighton, *J. Am. Chem. Soc.*, **98**, 1635 (1976); *ibid.*, **98**, 6418 (1976); *ibid.*, **98**, 6855 (1976).
2. G. Hodes, J. Manassen, and D. Cahen, *Nature (London)*, **261**, 403 (1976).
3. B. Miller and A. Heller, *ibid.*, **262**, 680 (1976).
4. H. Minoura, T. Oki, and M. Tsuiki, *Chem. Lett.*, **1976**, 1279.
5. T. Inoue, K. Kohayakawa, T. Watanabe, A. Fujishima, and K. Honda, *This Journal*, **124**, 719 (1977).
6. A. B. Ellis, J. M. Bolts, S. W. Kaiser, and M. S. Wrighton, *J. Am. Chem. Soc.*, **99**, 2839, 2848 (1977); *This Journal*, **124**, 2839 (1977).
7. H. Gerischer, *J. Electroanal. Chem.*, **58**, 263 (1975).
8. D. L. Laser and A. J. Bard, *This Journal*, **123**, 1027 (1975).
9. K. L. Hardee and A. J. Bard, *ibid.*, **124**, 215 (1977).
10. M. Robbins, B. Miller, A. Heller, S. M. Affonso, K. C. Chang, and J. Thomson, Inorganic Abstract

No. 195, 173rd American Chemical Society Meeting, New Orleans, 1977.
11. (a) T. Watanabe, A. Fujishima, and K. Honda, *Chem. Lett.*, **1974**, 897; (b) V. A. Tyagai and G. Ya. Kolbasov, *Surf. Sci.*, **28**, 423 (1971); (c) E. C. Dutoit, R. L. Van Meirhaeghe, F. Cardon, and W. P. Gomes, *Ber. Bunsenges. Phys. Chem.*, **79**, 1206 (1975).
12. W. M. Latimer, "Oxidation Potentials," 2nd ed., Prentice Hall, New York (1952).
13. A. Fujishima, E. Sugiyama, and K. Honda, *Bull. Chem. Soc. Jpn*, **44**, 304 (1971).
14. J. J. Lingane, "Analytical Chemistry of Selected Metallic Elements," p. 37, Reinhold Publishing Corp., New York (1966).
15. (a) J. J. Lingane and L. W. Niedrach, *J. Am. Chem. Soc.*, **70**, 4115 (1948); (b) A. J. Panson, *J. Phys. Chem.*, **67**, 2177 (1963); (c) P. L. Allen and A. Hickling, *Trans. Faraday Soc.*, **53**, 1626 (1957).
16. (a) K. L. Hardee and A. J. Bard, *This Journal*, **122**, 739 (1975); (b) T. Watanabe, A. Fujishima, and K. Honda, *Bull. Chem. Soc. Jpn.*, **49**, 355 (1976); (c) J. M. Bolts and M. S. Wrighton, *J. Phys. Chem.*, **80**, 2641 (1976).
17. L. A. Harris and R. H. Wilson, *This Journal*, **123**, 1010 (1976).
18. F. Lohmann, *Ber. Bunsenges. Phys. Chem.*, **70**, 428 (1966).
19. R. Williams, *J. Chem. Phys.*, **32**, 1505 (1960).
20. J. M. Bolts, A. B. Ellis, K. D. Legg, and M. S. Wrighton, *J. Am. Chem. Soc.*, **99**, 4826 (1977).
21. (a) H. Yoneyama, H. Sakamoto, and H. Tamura, *Electrochim. Acta*, **20**, 341 (1975); (b) Y. Nakato, S. Tonomura, and H. Tsubomura, *Ber. Bunsenges, Phys. Chem.*, **80**, 1289 (1976).
22. (a) R. Memming and G. Schwandt, *Electrochim. Acta*, **13**, 1299 (1968); (b) R. Memming, *This Journal*, **116**, 785 (1969); (c) R. Memming and H. Tributsch, *J. Phys. Chem.*, **75**, 562 (1971).
23. (a) H. Gerischer, *Advan. Electrochem. Electrochem. Eng.*, **1**, 139 (1961); (b) H. Gerischer and I. Mattes, *Z. Phys. Chem. N.F.*, **49**, 112 (1966).
24. (a) H. Gerischer and W. Mindt, *Electrochim. Acta*, **13**, 1239 (1968); (b) H. Gerischer, *Ber. Bunsenges. Phys. Chem.*, **69**, 578 (1965).
25. R. L. Meek and N. E. Schumaker, *This Journal*, **119**, 1148 (1972).
26. A. Yamamoto and S. Yano, *ibid.*, **122**, 260 (1975) and references therein.

Photoelectrochemical Processes at Semiconducting WO_3 Layers

W. Gissler

Euratom, Joint Research Center, Ispra (Varese), Italy

and R. Memming

Philips GmbH Forschungslaboratorium Hamburg, 2000 Hamburg 54, Germany

ABSTRACT

The basic electrochemical properties of WO_3 electrodes are described. The influence of the preparation techniques on the photoelectrochemical behavior of the electrodes is reported. The results are discussed in view of applications in solar energy conversion systems.

The tungsten oxide (WO_3) is a transition metal oxide with a number of interesting optical and electrical properties (1, 2). During the last years new interest arose in it because of its potential use in small area displays (3). The subject of our interest, however, is its use as light-sensitive electrodes in a semiconductor/electrolyte solar cell.

Semiconductor/electrolyte cells are considered as potential solar energy converters [for a review see (4)]. In principle they allow a direct conversion into electrical and/or chemical energy. Few self-regenerative solar cells have been realized (5-8), and direct photoelectrolysis has been reported (9, 10). Problems arise from the photocorrosion [see, *e.g.*, (11, 12)] of the semiconductor electrode. Most known semiconductor electrodes immersed in an aqueous electrolyte show this phenomenon, and other semiconductors (*e.g.*, TiO_2) which are known to be stable have energy gaps which are too large to be used efficiently for solar energy conversion. In order to find suitable electrodes, it seems to be necessary to investigate less known semiconductor materials with respect to their photoelectrochemical behavior. In this paper we present results obtained from some investigations with WO_3 electrodes.

Different values of the bandgap energy of WO_3 have been reported ranging from 2.5 to 3.65 eV (2, 13). This scattering is probably due to a strong influence of the preparation technique on the electrical and optical properties. Tungsten oxide can be obtained in different colors from lemon yellow to dark blue. The color can be changed also by electric charge injection [electro- and electrochemichromism, see, *e.g.*, (3)]. For the coloration mechanism several models have been proposed; in any case the degree of disorder due to lattice defects seems to play an important role. Electrochemical investigations in relation to display applications were performed already by Chang *et al.* (17), and preliminary experiments in connection with solar energy conversion were reported by Hodes *et al.* (18) and by Butler *et al.* (27).

Experimental

Tungsten oxide layers were prepared by two different techniques:

(*i*) By sputtering WO_3 powder on tungsten sheet, films of thicknesses 0.4-0.7 μm were obtained which were transparent and showed typical interference colors. X-ray analysis revealed a diffraction pattern typical for a crystalline structure of composition $WO_{2.98}$ (19). A heat-treatment in an oxygen atmosphere for only 10 min at 600°C effected a visible darkening of the films. The original greenish interference color turns into dark blue. Obviously the oxide reacts further with the tungsten substrate, leading to lower tungsten oxides.

(*ii*) By thermal oxidation of tungsten sheets (purity 99% in an oxygen atmosphere at 780°C) oxide layers of several μm thickness were obtained. If the oxidation time was shorter than *ca.* 15 min, the oxide layers assumed a dark blue color; for longer times a lemon yellow color was obtained. X-ray analysis also revealed here a diffraction pattern compatible with a

slightly substoichiometric tungsten oxide of about $WO_{2.98}$.

The electrochemical investigation has been performed in a 1 compartment cell. As electrolyte 0.1*N* Na_2SO_4 has been used, the *p*H has been adjusted by adding NaOH and H_2SO_4, respectively. The electrolyte was stirred by circulating it with a pump through the cell. The electrode potentials were measured under potentiostatic conditions using a calomel electrode as a reference electrode.

The photocurrent measurements were performed using a 450W xenon lamp and a grating monochromator. The light intensity was measured with a calibrated thermopile (Kipp and Zonen, Type CA1) having a flat response for wavelengths greater 150 nm. For low intensities a photometer equipped with a silicon n-p cell (UDT Type 80 × Optometer) was used. In some cases the light was chopped and then the photocurrent measured using lock-in technique.

The space charge capacity was measured by superimposing an a-c 50 kHz voltage of 25 mV on the externally applied voltage using a bridge circuit.

Results

The influence of the sample preparation on the space-charge capacity *C* is seen in Fig. 1, where $1/C^2$ is plotted *vs.* the electrode potential U_E for differently prepared oxide layers. Using the Mott-Schottky equation

$$\frac{1}{C^2} = \frac{2}{e \cdot \epsilon \cdot \epsilon_0 \cdot N_D}\left(U_E - U_{fb} - \frac{kT}{e}\right)$$

(N_D = donor density, U_E = electrode potential, U_{fb} = flatband potential, and the other constants have their usual meaning). N_D can be obtained from the slope of the plot. A straight line for the Mott-Schottky plot, however, has only been obtained for sputtered layers (curve 1) which were not heated in an O_2 atmosphere, resulting in $N_D = 10^{17}$ cm^{-3} [$\epsilon = 10$ for 50 kHz (20)]. A linear dependence has been obtained over a much larger potential range (up to 3V) which is not shown in Fig. 1. It is interesting to note that the donor density could be varied over several orders of magnitude by varying the oxygen pressure during the sputtering process (in all these cases linear $1/C^2$ *vs.* U_E curves have been obtained). Curves 2-4 of Fig. 1 have been obtained with sputtered layers which were annealed at 600°C in an oxygen atmosphere for different times. Curve 5 represents the result of a (lemon yellow colored) thermally grown oxide layer resulting into $N_D = 10^{20}$ cm^{-3} (calculated from the slope of the flat part of curve 5). It should be mentioned that our capacity curves are slightly frequency dependent, as it has been observed also with several other semiconductor electrode (21). The flat potential dependence is not influenced by this effect. The flatband potential, however, is slightly changed by the heat-treatment ($U_{fb} = +0.2$ *vs.* SCE for sputtered layer and -0.05V *vs.* SCE for thermally grown WO_3).

A typical current-potential curve (sweep rate 10 mV/sec) as obtained with a thermally grown yellow oxide layer is shown in Fig. 2. During anodic polarization the current is limited to a very low level which can be increased by light absorbed by the oxide, a behavior typical for n-type semiconductor electrodes. In this potential range the oxide is very stable. The anodic photocurrent caused by band-band excitation is due to oxygen evolution. This could be shown by analysis of the gas evolved at the semiconductor electrode with a quadrupole mass analyzer. During cathodic polarization the WO_3 electrode is reduced to a substoichiometric oxide (17) or to hydrogen bronze (3, 16) which can be reoxidized by a subsequent anodic sweep. During reduction the layer changes into a deep blue color, this being the electrochromic effect. The current potential curves obtained with the other oxide layers differed only with respect to the absolute value of the current density; untreated sputtered layers showed the smallest current densities and the yellow samples the highest.

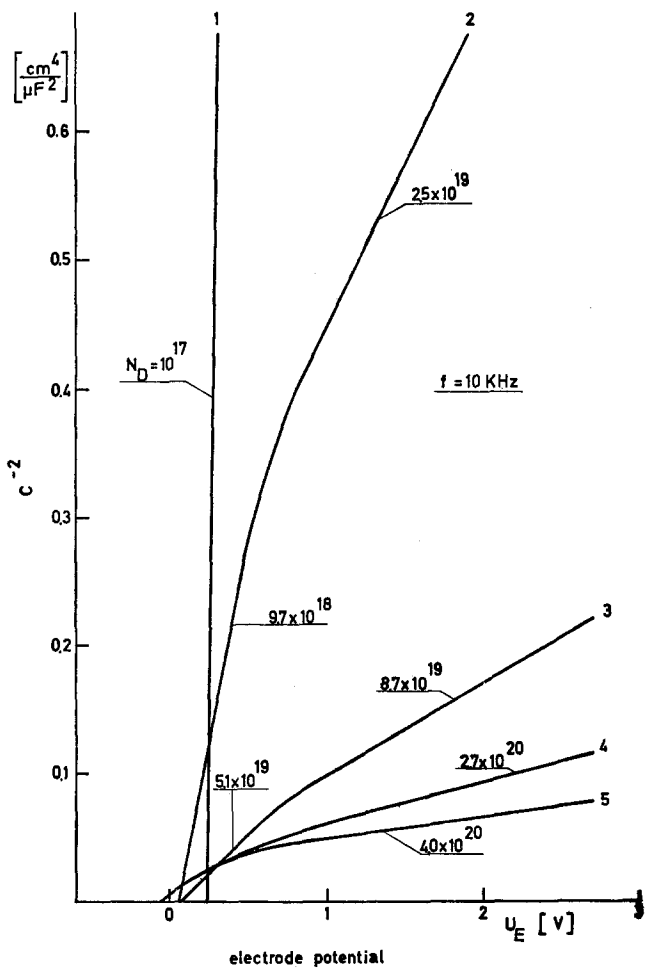


Fig. 1. Mott-Schottky curves of WO_3 layers in 0.1*N* H_2SO_4 (f = 50 kHz). 1, sputtered layer without heat-treatment; 2-4, sputtered layer, annealed at 600°C in O_2 for 10, 30, and 90 min; 5, thermally grown (yellow) layer at 760°C for 120 min.

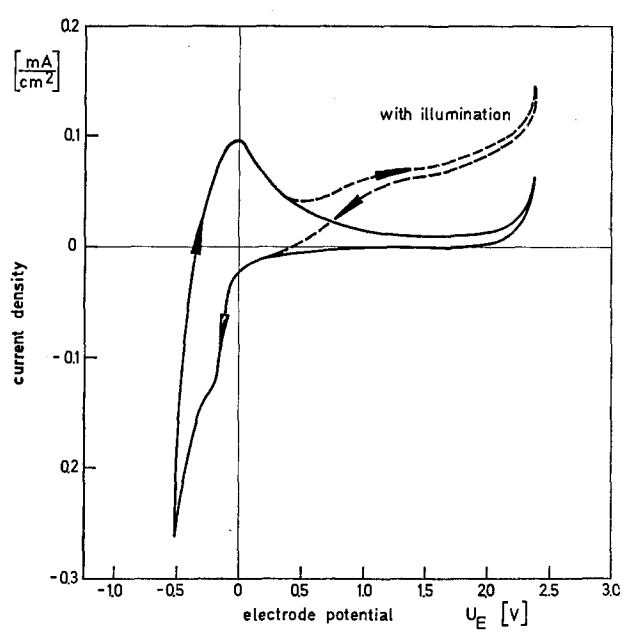


Fig. 2. Current-potential curve of thermally grown WO_3 layer in 0.1*N* H_2SO_4, sweep rate 10 mV/sec.

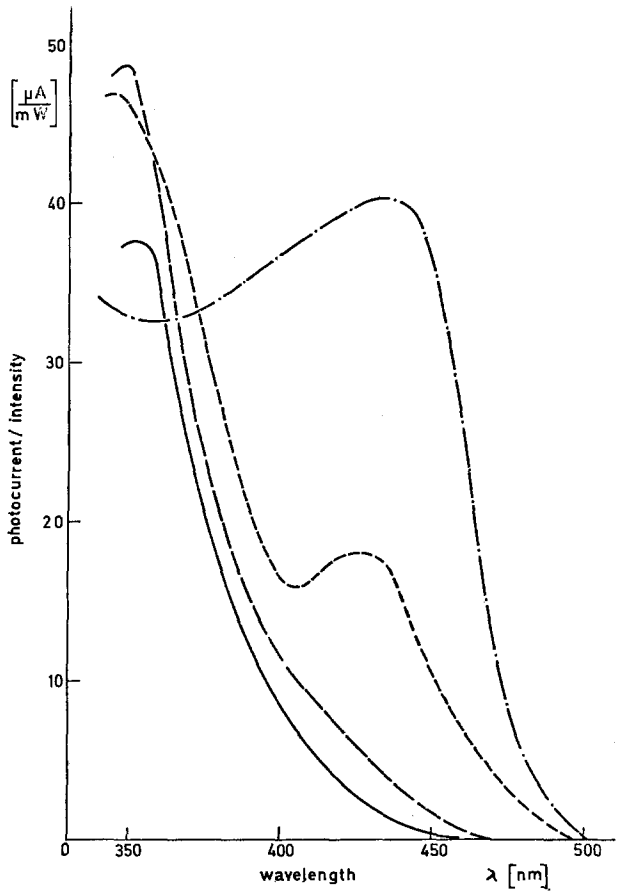


Fig. 3. Spectral distribution of the anodic photocurrent at U_E = 2V *vs.* SCE. Solid line, sputtered layer without heat-treatment; dashed lines, sputtered layer, annealed at 600°C in O_2 for 10 min and for 1.5 hr; dashed dotted line, thermally grown (yellow) layer at 760°C for 120 min.

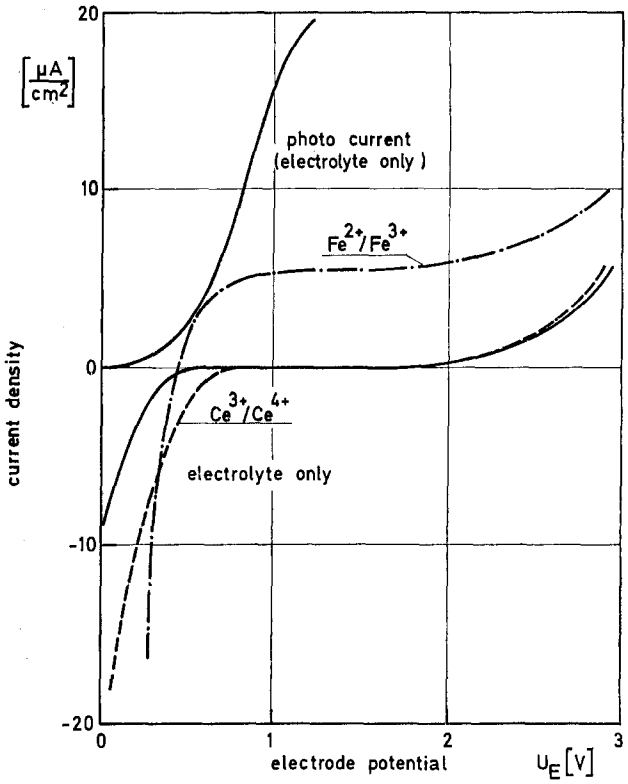


Fig. 4. Potentiostatic current-potential curve of sputtered untreated WO_3 with redox systems. Dashed, 10^{-2}M Fe^{2+}/Fe^{3+} in 0.1*N* H_2SO_4; dashed-dotted, 10^{-2}M Ce^{3+}/Ce^{4+} in 0.1*N* H_2SO_4; solid, 0.1*N* H_2SO_4.

Figure 3 shows the spectral distribution of the photocurrent which again depends strongly on the electrode preparation. With sputtered layers (solid line) the photocurrent raises mainly at wavelengths below 400 nm (3.1 eV), whereas annealed layers (dashed line) and the thermally grown yellow layer (dashed-dotted line) show photosensitivity also between 400 and 480 nm (2.6 eV). This effect is reversible: for instance after heating a thermally grown layer in vacuum at 780°C, the long wavelength peak disappears completely.

The potentiostatically measured current-potential curves of Fig. 4 show a typical behavior of a n-type semiconductor if a redox system is added to the electrolyte. In the case of Fe^{2+}/Fe^{3+} (dashed line), the cathodic current starts to rise at potentials slightly above the flatband potential, *i.e.*, the current is determined by electron transfer from the conduction band to the Fe^{3+} ions. During anodic polarization a small additional current of about 5 μA has been found due to electron transfer from Fe^{2+} ions into the conduction band. In the case of Ce^{3+}/Ce^{4+} (dashed-dotted line) similar results were obtained, only the anodic current was much smaller. Also, for comparison the i/U_E behavior without the added redox systems (solid line) is shown with and without illumination.

Discussion

The WO_3 electrodes show a typical electrochemical behavior of a n-type semiconductor electrode as far as the current-potential curves are concerned. It is interesting to note, however, that annealing of WO_3 layers in an O_2 atmosphere leads to a strong red shift of the photosensitivity. This shift is accompanied by a change of the electrical properties of the compound represented by the capacity curves which should be interpreted first.

As shown in Fig. 1 a simple Mott-Schottky curve has only been obtained with untreated sputtered layers. In all other cases the curves showed a lower slope, indicating a larger donor density and they are not straight. They may be described by two curves with a steep slope at lower potentials and a much lower slope at higher potentials. It is rather surprising that with the thermally grown layers of yellow color too a donor density (curve 5 in Fig. 1) has been obtained being larger than for freshly sputtered layers since the yellow color indicates nearly stoichiometric composition (19).

There are two possibilities to interpret the bent Mott-Schottky curves: (*i*) Such curves are bent if the density of donor states varies within the space charge region (12). In the case of the thermally grown yellow oxide we know that the composition of the WO_3 is not constant over the whole oxide layer. Near the metal substrate, for instance, the oxide shows a much darker color. (*ii*) The Mott-Schottky curves may be described by two curves. The lower slope can be interpreted by deeper donor levels which are not ionized within the bulk (22, 23). Accordingly this type of donor state is formed during the heat-treatment in an oxygen atmosphere, the number of states increasing considerably with increasing annealing times. It is difficult to test one of these assumptions experimentally. We prefer the latter interpretation because in the first case it is difficult to explain the linear slope, always found at higher anodic potentials.

The most interesting effect observed during the investigations is the additional photocurrent peak around 430 nm observed with annealed and thermally grown layers. This long wavelength sensitivity cannot be explained by assuming a corresponding shift of the bandgap due to some lattice changes. Such a change of bandgap could be ruled out by absorption measurements of a WO_3 layer deposited of a quartz substrate. Annealed layers only showed a very small shift of the

bandedge, probably due to the change of an amorphous to a crystalline structure.

The main sensitivity of untreated sputtered layers below 400 nm must be due to a direct band-band transition in WO_3. These results agree well with a bandgap of 3.2 eV, taken from Deb's paper (2) in which the absorption edge was analyzed very carefully. As forementioned, there are a number of lower values of bandgaps in the literature as, for example, in the paper of Butler *et al.* (27). According to an investigation on WO_3 Butler (28) could show also that an indirect transition exists in WO_3 corresponding to a bandgap of 2.7 eV. The spectral distribution obtained by Butler *et al.* (27) and that determined by ourselves with freshly sputtered WO_3 layers agree quantitatively. The presence of an indirect transition, however, does not explain the occurrence of the additional photocurrent peak we have observed with annealed and thermally grown layers.

We postulate therefore that this photocurrent is caused by a transition from the valence band to energy states being below the conduction band. These interband states are distributed over a relatively large energy range (Fig. 3). These states cannot be formed within the original sputtered layer during the heat-treatment because no additional photocurrent peak has been observed with layers sputtered on a quartz substrate covered by a conducting SnO_2. In the case of an oxide layer deposited on a tungsten substrate, however, the original oxide layer reacts with the substrate during the heat-treatment, leading to the formation of some substoichiometric oxide and a corresponding oxygen gradient existing throughout the whole layer. This process must be responsible for the formation of additional states within the bandgap.

The question arises whether the interband states correlated with the 430 nm-peak in the photocurrent spectrum are really bulk or perhaps surface states. Surface states, however, can be excluded because in this case the quantum yield should be very low (24) whereas we found photocurrents being comparable with those occurring by direct band-band excitation. On the other hand, if the 430 nm peak is due to excitation of electrons from the valence band into interband states in the bulk, then these electrons must be thermally excited into the conduction band or are transferred along these states toward the back side contact, whereas the holes are consumed for the oxygen evolution at the surface. Such an electron transfer via interband states is only possible, however, if the density of states is large so that sufficient interaction exists (interstate band).

Apart from the optical and electrical properties of WO_3 its applicability as a semiconductor electrode in a solar cell has been also investigated. In connection with this problem the relative position of the energy bands at the semiconductor surface is of importance, which can be derived from the flatband potential. Assuming the Fermi level in the bulk to be 0.1 eV below the conduction band, and taking for the flatband potential the value $U_{fb} = 0.55$ eV *vs.* NHE (+0.2V *vs.* SCE for sputtered layers, see Fig. 2) one obtains a position of the energy bands at the WO_3-surface as plotted in Fig. 5. For comparison the position of energy levels of SnO_2 (13, 25) and TiO_2 (22) are also shown. Since the flatband potential occurs at potentials more positive than the hydrogen potential, any direct conversion of solar energy into chemical energy by water decomposition is not possible with WO_3 electrodes. However, in principle it is also possible to use WO_3 as an electrode in a self-regenerating solar cell with a redox system as an electrolyte. In such a case solar energy is converted into electrical energy as has been demonstrated with CdS electrodes and $[Fe(CN)_6]^{4-/3-}$ or $S/S^=$ as redox systems (4, 5). In the case of WO_3 a redox system should be selected of which the energy levels (occupied levels O_{red})

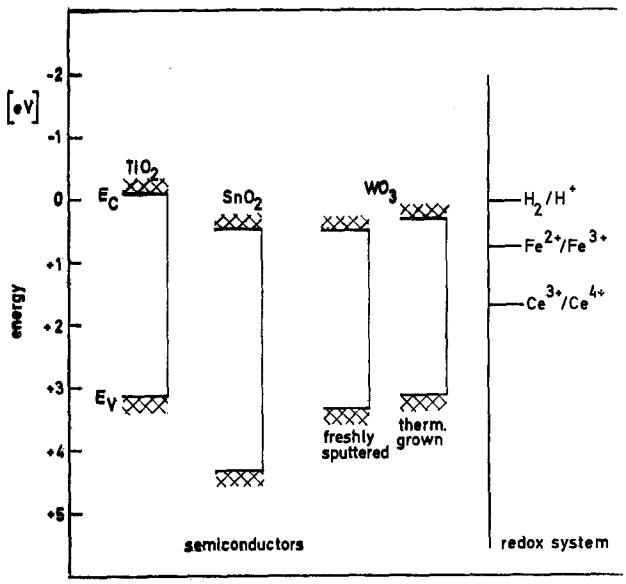


Fig. 5. Energy diagram

overlap with the valence band so that only electron transfer from the redox system to the valence band is possible if holes are produced by light excitation. Corresponding experiments with Ce^{3+} have shown, however, that no Ce^{3+} was oxidized during illumination. The corresponding anodic photocurrent leads only to oxygen evolution, although the valence band overlaps much better with the occupied energy levels of $Ce^{3+/4+}$ (Fig. 5) than with corresponding levels of the H_2O/O_2 system. This result can only be interpreted by assuming a much stronger interaction between the electrode surface and H_2O molecules, or by assuming a preferable charge transfer from H_2O into surface states. In other redox systems such as $Fe^{2+/3+}$ the occupied levels overlap better with the conduction band (Fig. 5), and a corresponding exchange current is visible as shown in Fig. 4. These results are very similar to those obtained with SnO_2 (25, 26).

Acknowledgment

The authors would like to express their gratitude to Dr. G. Pellegrini (Euratom) and Dr. B. Strocka (Philips) for their kindness in performing and evaluating the x-ray measurements, to R. D. Boehnke (Philips) for producing the sputtered layers, and to R. Schubert (Euratom) for valuable help during the work.

Manuscript submitted April 25, 1977; revised manuscript received July 28, 1977.

Publication costs of this article were assisted by Philips GmbH Forschungslaboratorium Hamburg.

REFERENCES

1. M. J. Sienko, "Non-Stoichiometric Compounds, Advances in Chemistry," Vol. 39, p. 224, American Chemical Society, Washington (1963).
2. S. K. Deb, *Philos. Mag.*, **27**, 801 (1973).
3. H. N. Hersh, W. E. Kramer, and J. H. McGee, *Appl. Phys. Lett.*, **27**, 646 (1975).
4. H. Gerischer, Proceedings of the Congress on Photochemical Processes, London Autumn 1976.
5. A. B. Ellis, S. W. Kaiser, and M. S. Wrighton, *J. Am. Chem. Soc.*, **98**, 1636 (1976).
6. H. Gerischer and J. Gobrecht, *Ber. Bunsenges. Phys. Chem.*, **80**, 327 (1976).
7. Y. G. Chai and W. W. Anderson, *Appl. Phys. Lett.*, **27**, 183 (1975).
8. W. Gissler, EUR Report 5514e (1976); W. Gissler, P. L. Lensi, and S. Pizzini, *J. Appl. Electrochem.*, **6**, 9 (1976).
9. A. Fujishima and K. Honda, *Bull. Chem. Soc. Jpn.*, **44**, 1148 (1971).
10. M. S. Wrighton, D. S. Ginley, P. T. Wolcranski,

A. B. Ellis, D. L. Morse, and A. Linz, *Proc. Natl. Acad. Sci. U.S.A.*, **72**, 1518 (1975).
11. H. Gerischer and W. Mindt, *Electrochim. Acta*, **13**, 1329 (1968).
12. R. Memming, in Proceedings of the Workshop on Electrocatalysis of Non-Metals, Washington 1976, D. Franklin, Editor, NBS Special Publication, 455, 267 (1977).
13. S. Swada, *J. Phys. Soc. Jpn.*, **11**, 1237 (1956).
14. M. Gleria and R. Memming, *J. Electroanal. Chem. Interfacial Electrochem.*, **65**, 163 (1975) R. Memming, in "Electroanalytical Chemistry," A. J. Bard, Editor, Marcel Dekker Inc., New York, In press.
15. Z. M. Hanafi and M. A. Khilla, *Z. Phys. Chem.*, **89**, 2 (1974).
16. B. W. Faughnan, R. S. Grandall, and M. A. Lampert, *Appl. Phys. Lett.*, **27**, 275 (1975).
17. J. F. Chang, B. L. Gilbert, and T. J. Sun, *This Journal*, **122**, 957 (1975).
18. G. Hodes, D. Cahen, and J. Manassen, *Nature (London)*, **260**, 312 (1976).
19. E. Gebert and R. J. Ackermann, *Inorg. Chem.*, **5**, 136 (1966).
20. K. Kant, P. Kant, and R. Srivastava, *Thin Solid Films*, **30**, 319 (1975).
21. E. C. Dutoit, R. L. Van Meirhaeghe, E. F. Cardon, and W. P. Gomes, *Ber. Bunsenges.*, **12**, 1207 (1975).
22. F. Möllers, H. J. Tolle, and R. Memming, *This Journal*, **121**, 1160 (1974).
23. Y. V. Pleskov and V. A. Myamlin, "Electrochemistry of Semiconductors," Plenum Press, New York (1967).
24. K. H. Beckmann and R. Memming, *This Journal*, **116**, 368 (1969).
25. F. Möllers and R. Memming, *Ber. Bunsenges. Phys. Chem.*, **76**, 469 (1972).
26. R. Memming and F. Möllers, *ibid.*, **76**, 475 (1972).
27. M. A. Butler, R. D. Nashby, and R. K. Quin, *Solid State Commun.*, **19**, 1011 (1976).
28. M. A. Butler, Paper presented at the meeting on Semiconductor-Liquid Interfaces under Illumination, Airlie, Virginia, May 1977.

An Ellipsometric Study of the Anodic Oxidation of Nickel in Neutral Electrolyte

J. L. Ord,* J. C. Clayton, and D. J. DeSmet*,[1]

Department of Physics, University of Waterloo, Waterloo, Ontario, Canada N2L 3G1

ABSTRACT

Ellipsometry is used to study alternate anodic and cathodic galvanostatic cycling of a nickel electrode in neutral sulfate and borate electrolyte. The removal of the electropolishing film under cathodic reduction, the anodic oxidation of the nickel substrate, and the deposition and conversion of films of $Ni(OH)_2$ and NiOOH can all be distinguished clearly on a plot of the optical data. The mechanism of anodic oxidation of the substrate is investigated using both optical and open-circuit transient measurements, and the field in the oxide film is concluded to limit the substrate oxidation process.

In recent years, a number of studies of the anodic oxidation of nickel have made use of ellipsometric as well as electrochemical measurements. Bockris, Reddy, and Rao (1) made extensive use of ellipsometric results in their study of the mechanism of passivation of nickel in sulfate electrolyte of pH 3.15. They interpreted the structure observed in their optical data during passivation as arising from a change in the refractive index of the film from 4.0 to 3.5 — 0.4i (at λ = 5461Å). They took the increase in absorption as indicating an increase in the electronic conductivity of the film, and concluded (*i*) that a 60Å prepassive film formed by a dissolution-precipitation mechanism, and (*ii*) that passivity resulted from the film becoming an electronic conductor. They assumed the prepassive film to be $Ni(OH)_2$ which oxidized to $NiO_{1.6}$ on passivation. They determined film thicknesses by correlating optical and coulometric measurements and found little further increase in film thickness as the potential was increased in steps across the passive region.

Chernykh and Yakovleva (2, 3) studied the anodic oxidation of nickel in KOH and used an approach similar to that of Bockris *et al.* in their analysis of optical data. They assumed that the index of the film lay between 2.8 and 3.3 (at λ = 5461Å) and concluded that the absorption coefficient of the film increased due to an increase in electronic conductivity. They found a greater variation of film thickness with potential, an increase from 20 to 60Å, than was reported in acid electrolyte.

Sato and Kudo (4) studied the anodic oxidation of nickel in a neutral borate buffer of pH 8.42. They chose an index for the oxide film of 2.7 — 0.25i at λ = 5461Å and concluded that the film thickness increases from 4 to 10Å linearly with potential across the passive region. They estimated the field in the film to be 1.6 $\times$ 10^7 V/cm after 1 hr of potentiostatic oxidation and measured current densities of less than 0.1 $\mu A/cm^2$ under these conditions.

DeSmet (5) studied the anodic oxidation of nickel in acid and neutral electrolyte using an automated ellipsometer with a nulling time of 1 sec and a resolution of 0.01°. He found considerable structure in the optical data, particularly in acid electrolyte, which would be very difficult to detect with a manual instrument. He concluded that a single-layer model in which the layer converted to a different form on reduction could account for his results in neutral electrolyte but failed to find any simple model which could account for his acid electrolyte data. The response time of the ellipsometer enabled him to follow film growth, and although he found some evidence for control of the process by the field in the film, he concluded that existing models for a field-limited process were inadequate to account for his data.

MacDougall and Cohen (6-9) have recently studied the anodic oxidation of nickel in acid and neutral electrolyte using coulometry, electron diffraction, and x-ray emission spectroscopy. From their measurements

* Electrochemical Society Active Member.
[1] Permanent address: Department of Physics, University of Alabama, University, Alabama 35486.
Key words: anodic oxidation, ellipsometry, nickel.

they concluded that a film of NiO between 9 and 12Å thick is formed by 1 hr of potentiostatic oxidation at both pH 2.8 and 8.4, and they found little dependence of film thickness on potential. They stated that the discrepancy between their results in neutral sulfate electrolyte and the results of Sato and Kudo in neutral borate electrolyte is well beyond the error limit given for their measurements, ±1.5Å. They rejected a high field mechanism for film growth because of the high electronic conductivity of the film, and they stated that the growth process can be described by a place-exchange mechanism.

Okuyama and Haruyama (10) used coulometry to study the passive film formed on nickel in neutral borate electrolyte and concluded that a duplex film of NiO and Ni_3O_4 is formed by oxidation of nickel and that the Ni_3O_4 is oxidized to NiO_2 at higher potentials. They quote Tafel slopes for both the oxidation and the reduction of NiO and NiO_2, but they find Ni_3O_4 very difficult to reduce.

The contradictory nature of the recent work on the anodic oxidation of nickel makes it difficult to say very much about the basic processes involved. With opinion about equally divided on a question as fundamental as whether or not the film thickness varies with potential, it is not possible to say whether oxidation is limited by field-controlled transport of ions through the oxide film or by some other process. In this paper we attempt to clarify this situation by using ellipsometry to identify the various dissolution, oxidation, deposition, and conversion processes which take place when a nickel electrode is cycled galvanostatically in neutral electrolyte. We then investigate the mechanism by which an oxide film grows on a nickel surface by oxidation of the substrate. In interpreting our ellipsometric data we make extensive use of what we have learned from our studies of the deposition and oxidation of nickel hydroxide films in neutral electrolyte (11, 12). In these studies we followed the growth of nickel hydroxide films to thicknesses of over 2000Å, and this wide thickness range enabled us to determine the optical properties of $Ni(OH)_2$ and NiOOH films uniquely from our optical data. We found more than one phase of $Ni(OH)_2$ and NiOOH, and we assumed them to be the α- and β-$Ni(OH)_2$, and γ- and β-NiOOH phases identified by other workers (13, 14). The multiplicity of phases complicates the interpretation of optical data considerably, particularly because the phases are perhaps better thought of as a family of related compounds of variable composition rather than as distinct phases (15), but $Ni(OH)_2$ and NiOOH have such distinctive optical properties, the former being transparent and the latter strongly absorbing, that it is easy to identify even very thin films of each and to identify the reversible reaction which converts one into the other.

Experimental

The optical measurements were made with a self-nulling ellipsometer which has been described in detail elsewhere (16). The instrument uses a helium-neon laser as a light source, and all refractive indexes quoted in this paper are for $\lambda = 6328$Å. Under the optical conditions encountered in this study, the instrument has a nulling time of less than 1 sec with a resolution of 0.01°. The hollow equilateral glass prism used as a cell requires that the ellipsometer be set for an angle of incidence of 60°. The cell is fitted with standard-taper joints for mounting the nickel working electrode, a platinum counterelectrode, a mercurous sulfate reference electrode, and a gas dispersion tube used for saturating the electrolyte with argon. Measurements were made at room temperature (23°C), and all potentials quoted are relative to the mercurous sulfate reference electrode.

A cylindrical electrode with a flat on one side for optical measurements was prepared from a single crystal of nickel. When mounted between Teflon washers in the electrode holder, a surface area of 1.25 cm^2 is exposed to the electrolyte. The optical surface was prepared by diamond polishing, then the sample was chemically polished prior to a final electropolish in 50% H_2SO_4. This final treatment was chosen in order to make our work directly comparable to that of MacDougall and Cohen (6-9), but we found that we could reduce the film left after chemical polishing just as easily as we could the film left after electropolishing. Two electrolytes were used in this study: 0.15N Na_2SO_4, and an equivolume mixture of 0.15N sodium borate and 0.15N boric acid. The borate electrolyte has a pH of 8.4, but the sulfate electrolyte is unbuffered, and varying its nominal pH over the range from 6.1 to 9.1 had litle effect on the experimental results.

The circuitry used with the cell is controlled by a HP 2114B minicomputer which records optical and electrochemical data at 1 sec intervals and records open-circuit transients for overpotential analysis at programmed intervals. The technique we use to record and analyze open-circuit transients has been described in detail elsewhere (17).

Results and Discussion

The first two figures show the results obtained when a nickel electrode undergoes two sequential anodic-cathodic cycles at 80 $\mu A/cm^2$ in 0.15N Na_2SO_4. Figure 1 combines a plot of potential *vs.* time with a P-A plot of the optical data, where P and A are the null settings of the polarizer and analyzer prisms of the ellipsometer. Corresponding points are given the same label on the P-A and V-t plots in Fig. 1 on the P-t plot in Fig. 2, and on the theoretical optical model curves in Fig. 3. The optical data obtained during this simple experiment provide a great deal of information about the processes involved at the various stages of the experiment. In the following paragraphs we look at each stage in sequence and discuss the interpretation of the optical data obtained during that stage.

The experiment begins at point A just after the electropolished nickel electrode is inserted into the optical cell. The initial cathodic cycle is carried out galvanostatically until the potential reaches −1.350V, then the potential is held at this value for 60 sec. During the first 20 sec of the cathodic cycle, the optical data shift

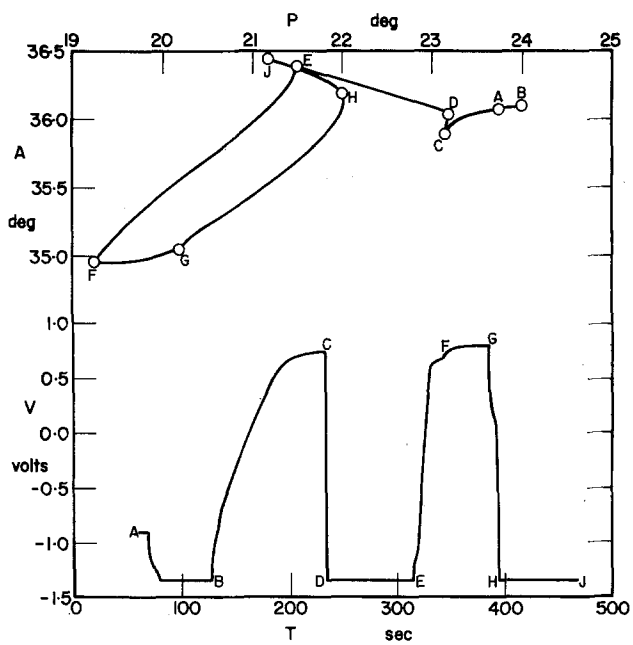


Fig. 1. Alternate cathodic (A-B, C-D-E, G-H-J) and anodic (B-C, E-F-G) cycling of a nickel electrode at 80 $\mu A/cm^2$ in 0.15N Na_2SO_4. The experiment begins at point A with the electropolished nickel electrode under open circuit in the optical cell.

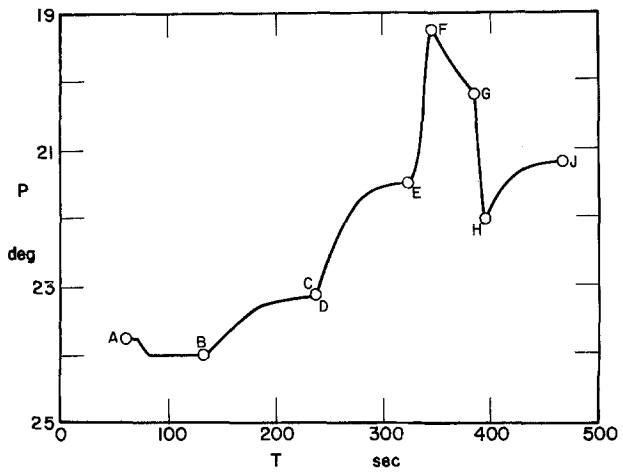


Fig. 2. Polarizer null position vs. time data for the experiment plotted in Fig. 1. Corresponding points have the same labels in the two figures.

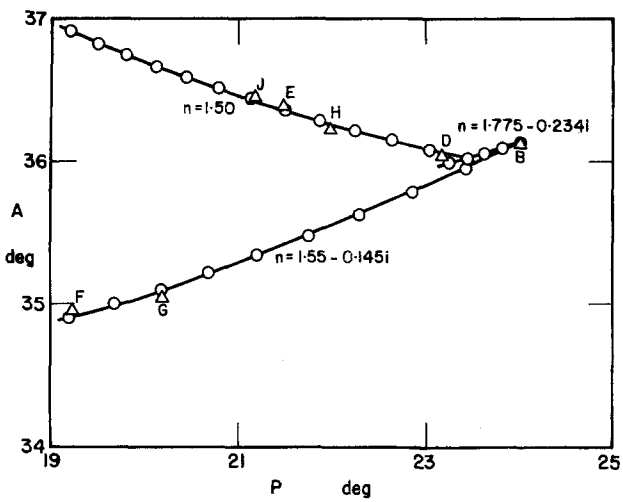


Fig. 3. Optical model for the experiment plotted in Fig. 1. The experimental points represented by triangles are the points with corresponding labels from Fig. 1. The thickness interval between plotted points is 4Å for the film with index 1.775 — 0.234i, and 20Å for the films with indices 1.50 and 1.55 — 0.145i.

toward higher P-values, indicating that a film is being removed from the surface. After this period, the optical data show no further change, implying that the nickel surface is film free. Similar results are obtained with nickel electrodes which have been chemically polished just prior to insertion in the optical cell. The reaction products resulting from film removal show no tendency to deposit on the nickel surface. Even if reaction products are allowed to build up in the electrolyte by performing several experiments in sequence, the only evidence for $Ni(OH)_2$ deposition during a 10 min cathodic cycle is a shift of 0.02° in P. If the concentration of nickel is increased still further by adding $NiSO_4$ to the electrolyte, it requires on the order of 3 min before deposition of $Ni(OH)_2$ begins. Once $Ni(OH)_2$ begins to deposit, the deposition rate increases with time. It appears that nucleation of a nickel hydroxide film on a bare nickel surface does not take place readily in neutral deaerated sulfate electrolyte. We have found that $Ni(OH)_2$ deposits readily on nickel in air-saturated nickel nitrate electrolyte (11), but deposition begins before the initial film is completely removed from the surface. We conclude that no significant thickness of surface film is present on the nickel electrode at point B in Fig. 1.

The first galvanostatic anodic cycle begins at point B and continues to point C. During the cycle, a series of open-circuit transients are recorded at 0.1V intervals from —0.6 to 0.7V. The optical data indicate that a thin film grows on the nickel surface during the anodic cycle. The P-t data in Fig. 2 show that the growth rate is constant over the region where the potential increases linearly with time and that the growth rate slows as the potential approaches a plateau. These features are characteristic of film growth by galvanostatic oxidation of the substrate. As point C is approached, the optical P-A data in Fig. 1 begin to deviate from the linear relation observed at lower potentials. Our optical model in Fig. 3 interprets the displacement in the optical data from B to C as resulting from the growth of a film of index 1.775 — 0.234i to a thickness of just under 18Å on a substrate of index 2.147 — 4.239i.

The layer-removal process which takes place during the first cathodic cycle is not observed on the second cathodic cycle. When the current is reversed at point C, the optical data trace out the curve C-D-E in the P-A plane. The initial jump to point D does not show up on the P-t plot in Fig. 2 because little P shift is involved. The displacement in the optical data from D to E is indicative of further film growth, and the slope of the P-A curve shows that the index of the additional film differs from the index of the film grown during the first anodic cycle. In our work on conversion reactions involving $Ni(OH)_2$ films (11, 12) we found that displacements in the optical data of the type observed between D and E result from the deposition of nonabsorbing films of $Ni(OH)_2$ with refractive index 1.50. The P-t data show that the deposition begins rapidly, then slows as the electrolyte adjacent to the working electrode becomes depleted of nickel ions. A minor variation of the experiment demonstrates this point very clearly. If the optical nulling is interrupted for 10 sec at point C to allow the working electrode assembly to be loosened in its standard taper joint and flicked once or twice to disperse reaction products into the bulk electrolyte, the optical displacement from D to E disappears completely from the subsequent cathodic cycle. Instead, the optical data continue to drift slowly in the C-D direction and tend toward a point on a curve through B parallel to D-E. From this we conclude that the oxide film formed on the first anodic cycle cannot be removed from the nickel surface by cathodic reduction and converts only slowly to $Ni(OH)_2$ under extended cathodic reduction. There is some evidence that this slow conversion takes place also under the deposited layer of $Ni(OH)_2$. In Fig. 3, the model assumes that deposition of $Ni(OH)_2$ takes place on top of a 12Å layer whose thickness does not change during the deposition. If we assume that the oxide film formed on the first anodic cycle is NiO and use x-ray data to estimate that conversion of NiO to $Ni(OH)_2$ results in a film 2.13 times as thick, we can estimate a value for the refractive index of the NiO film. This is the way in which the value 1.775 — 0.234i used in our model was obtained. The strength of our optical model lies more in its success in identifying the nature of the various processes involved than in the specific numbers it presents for film thicknesses and indexes.

The second anodic cycle has a much steeper V-t slope than the first, and it has an additional plateau at the high potential end. The optical data provide a clear picture of the processes involved on the second anodic cycle. Both the P-A data and the P-t data show a sharp inflection at the end of the first plateau, indicating that quite different processes are involved in regions E-F and F-G. The very rapid optical changes along E-F are characteristic of a layer conversion process. The reaction involved in this process, the oxidation of $Ni(OH)_2$ to form NiOOH, has been studied extensively in work on the nickel battery electrode.

We have studied the conversion of $Ni(OH)_2$ to NiOOH over a wide range of film thicknesses (11 12), and we have determined approximate refractive indexes of the various films involved in the process. We found that the index required to fit NiOOH films in the 1000-2000Å thickness range did not fit thin films of NiOOH very well, presumably because the structure and water content of NiOOH films formed under these conditions vary somewhat with film thickness. The index chosen in our optical model, 1.55 — 0.145i, is a compromise value which gives a NiOOH to $Ni(OH)_2$ film thickness ratio of approximately 1.5. In the model the NiOOH film is put directly on the substrate, implying that the underlying NiO film converts to NiOOH. Although our identification of the conversion process from $Ni(OH)_2$ to NiOOH relies on other work we have done, the process which takes place along F-G provides striking confirmation of our identification. At point F the optical *P-A* data inflect sharply and start to trace their way back along the theoretical curve representing the growth of NiOOH. According to our optical model, approximately 40Å of the NiOOH film dissolves between F and G. If we were to continue the anodic cycle the optical data would continue to work their way back along the curve toward point C as the NiOOH layer dissolves. With this background we interpret the dip in the optical data as the first anodic cycle approaches point C as resulting from the conversion of NiO to NiOOH which dissolves at a rate which balances its formation rate in the steady state. In unstirred electrolyte, we find a correlation between the time spent on the plateau at C and the thickness of $Ni(OH)_2$ film subsequently deposited. From this we conclude that the dissolution of NiOOH is the primary source of the nickel ions for the deposition of $Ni(OH)_2$ along D-E.

Once our understanding of the processes involved has reached this level, we can predict the results of further cycling. Provided we do not disperse the reaction products produced along F-G into the bulk electrolyte, a cathodic cycle initiated at point G will result first in a fast conversion reaction followed by a sharp inflection in the optical data as deposition of $Ni(OH)_2$ begins. The deposition of $Ni(OH)_2$ will begin rapidly and will slow in much the same way as it did at point E. This prediction is exactly what is observed experimentally. At this point we can say that our optical data have given us a fairly complete picture of the processes involved when a nickel electrode is cycled in neutral sulfate electrolyte.

We next deal with the question of whether the results we have obtained in sulfate electrolyte apply generally to the behavior of nickel in neutral electrolyte. We know from our optical work on the deposition of FeOOH films in neutral electrolyte (18) that deposition processes can be quite different in borate and sulfate electrolyte. The results of an experiment similar to the one described above but performed in neutral borate electrolyte are presented in *V-t* and *P-A* plots in Fig. 4 and in a *P-t* plot in Fig. 5. In this experiment we use a 10 min initial cathodic cycle instead of the 1 min cycle used in sulfate electrolyte, but this does not affect the results obtained on subsequent cycles. The initial anodic cycle starts off the same way as in sulfate electrolyte, but as the potential levels onto a plateau, the *P-t* curve shows an increase in slope, and the *P-A* data start to trace out the curve we used to represent the growth of NiOOH in the optical model. The rate of growth of NiOOH decreases with time, but if the anodic cycle is continued long enough several thousand angstroms of a film with the characteristic black appearance of NiOOH can be grown on the electrode. The NiOOH film can be converted to a transparent film of $Ni(OH)_2$ by cathodic reduction as is illustrated by cycle C-D-E, but there is no evidence of deposition of $Ni(OH)_2$. The second anodic cycle, E-F-G, converts the film back to NiOOH and causes it to continue growing slowly.

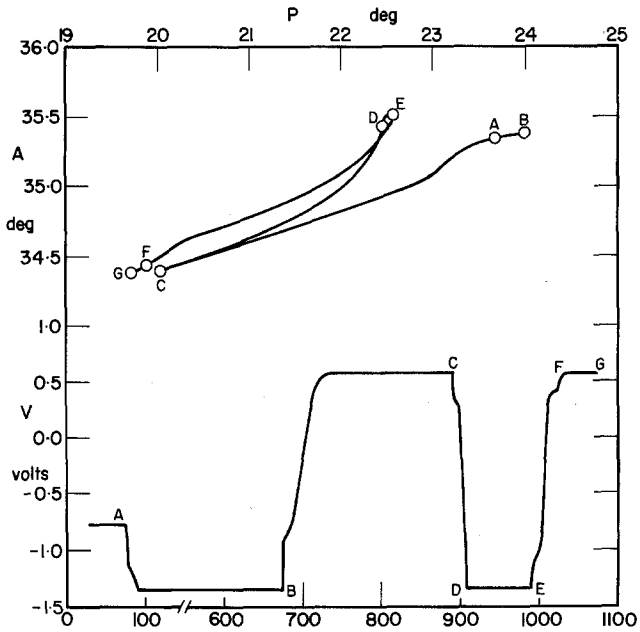


Fig. 4. Alternate cathodic (A-B, C-D-E) and anodic (B-C, E-F-G) cycling of a nickel electrode at 80 $\mu A/cm^2$ in a borate buffer of pH 8.4. The experiment begins at point A with the electropolished nickel electrode under open circuit in the optical cell.

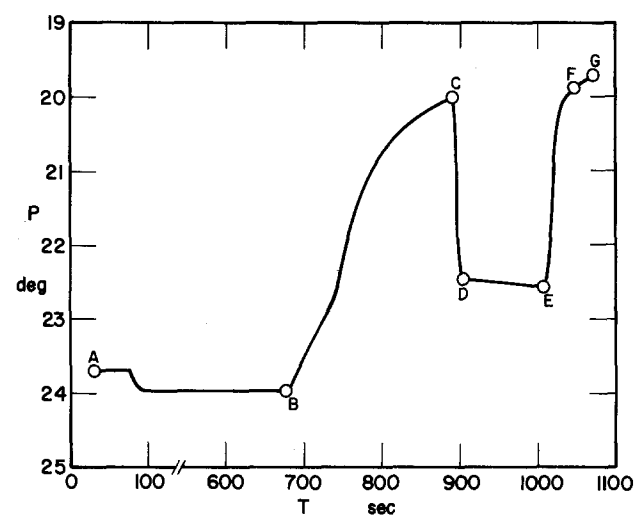


Fig. 5. Polarizer null position vs. time data for the experiment plotted in Fig. 4. Corresponding points have the same labels in the two figures.

Depending on our viewpoint, we can either regard the results obtained in borate as very different from or very similar to the results obtained in sulfate electrolyte. Certainly the results appear very different if one compares only the first anodic cycle in borate with the first anodic cycle in sulfate, but if an over-all comparison is made the basic processes involved are seen to be very similar. In fact the only significant difference between the electrolytes concerns what happens when NiOOH begins to dissolve. In sulfate electrolyte the reaction products remain in solution in the electrolyte adjacent to the electrode, but in borate electrolyte they deposit back on the surface. As a result, film growth occurs on the anodic cycle in borate and on the cathodic cycle in sulfate electrolyte. The optical model used to fit the sulfate data fits the data obtained in borate electrolyte equally well.

Now that we have determined the extent to which growth and conversion of nickel hydroxide films are

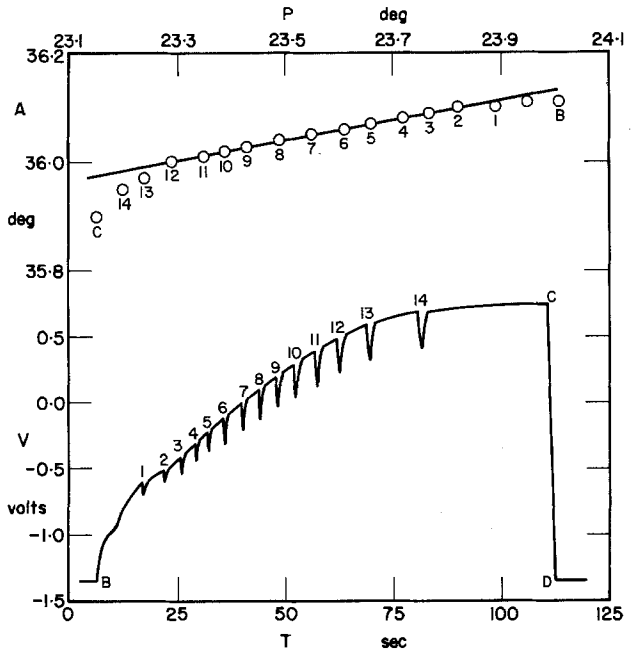


Fig. 6. Expanded scale plot of the first anodic cycle of the experiment plotted in Fig. 1. The open-circuit transients applied at 0.1V intervals from —0.6 to 0.7V are numbered sequentially.

involved in the first two anodic-cathodic cycles, we turn our attention to a more detailed study of the oxidation of the nickel substrate. The first anodic cycle from the experiment in Fig. 1 is replotted on an expanded scale in Fig. 6. Fourteen open-circuit transients are recorded at 0.1V intervals from —0.6 to 0.7V. The corresponding optical data are shown on a *P-A* plot in the upper portion of the figure. The line through the optical data is taken from the theoretical model in Fig. 3. In the model, the bare substrate point lies 0.025° higher in A than the experimental bare substrate point B. The optical data fall on the theoretical line between open-circuit points 2 and 12, then inflect downward toward point C.

Perhaps the most direct way to determine whether or not the substrate oxidation process is limited by the field in the oxide film is to plot potential *vs.* film thickness at constant current density. In Fig. 7, the data

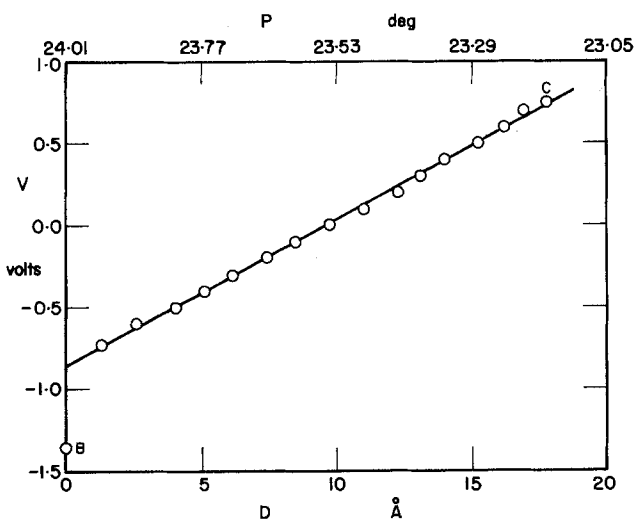


Fig. 7. Plot of potential *vs.* polarizer null position and film thickness for the data in Fig. 6. Film thicknesses are taken from the optical model in Fig. 3. The least squares line fitted to all the points except point B has a slope of 8.9 × 10^6 V/cm, and an intercept on the potential axis of —0.852V.

from Fig. 6 are replotted using two scales for the abscissa: the directly measured quantity *P* and the film thickness from the optical model for a film of index 1.775 — 0.234i. The three high potential points are projected onto the theoretical line along a line of slope 4 in the *P-A* plane which they trace out experimentally on open circuit. The line in Fig. 7 is a least squares line fitted to all of the data except the initial bare surface point. The least squares estimate of the deviation of the points from the line, 0.02V, over a potential range of almost 1.5V, shows that the voltage depends linearly on film thickness and, hence, that the field in the film is constant even on the potential plateau at C. The slope of the line gives the field in the film, 8.9 × 10^6 V/cm, and its intercept on the potential axis gives the zero of overpotential for substrate oxidation, —0.852V. Note that our value for the field depends on our choice of film index; had we chosen a higher film index more in line with that used by other workers, our field value would have been correspondingly higher.

Although the plot in Fig. 7 shows that the field is constant during oxidation at constant current density, it does not prove that the field in the oxide film controls the current density. To show that the field controls the current density we must determine the dependence of current density on potential and show that it is consistent with field control rather than potential control of the process. The dependence of current density on potential can be determined for the experiment plotted in Fig. 6 by analyzing the open-circuit transients. The dependence of potential on time is analyzed as the current density falls from 80 to 10 μA/cm^2 during the self-discharge of the layer capacitance. An exponential dependence of current density on overpotential is assumed in the form

$$i = i_0 \exp((V - V^*)/V_0) \qquad [1]$$

where i_0 is the exchange current density, V^* is the zero of overpotential, and V_0 is a Tafel slope defined in terms of natural logarithms. Analysis of a transient determines V_0 along with the layer capacitance *C*, but i_0 and V^* can only be determined by making further assumptions about data obtained from a set of open-circuit transients. The Tafel slope, V_0, is the critical parameter for distinguishing between field and overpotential control of a process: If V_0 is independent of film thickness, the process is overpotential limited, and if V_0 is proportional to film thickness, the process is limited by the field in the film. If V_0 turns out to be proportional to film thickness, we expect the reciprocal capacitance, 1/*C*, to be proportional to film thickness also.

V_0 and 1/*C* values determined by analyzing the open-circuit transients in Fig. 6 are plotted *vs.* film thickness in Fig. 8. The dependence of V_0 and 1/*C* on film thickness is not as simple as the dependence of potential of film thickness plotted in Fig. 7. The V_0 values show a monotonic increase approximately proportional to potential through transient 11, then decrease somewhat for the final three transients. The 1/*C* values, on the other hand, increase monotonically for only the first 5 transients before turning over. There is no question but what the V_0 values indicate field control of the process, increasing as they do by a factor of 4.5 between transients 1 and 11, but the 1/*C* values are certainly not proportional to film thickness. On the basis of these results and the fact that the optical data in this region do not fall on a straight line through the bare substrate point, we conclude that as the oxide film grows beyond monolayer thickness at a current density of 80 μA/cm^2, its oxidation state becomes progressively higher than that of NiO. The capacitance of an oxide film appears particularly sensitive to a progressive change in the oxidation state of the film (19).

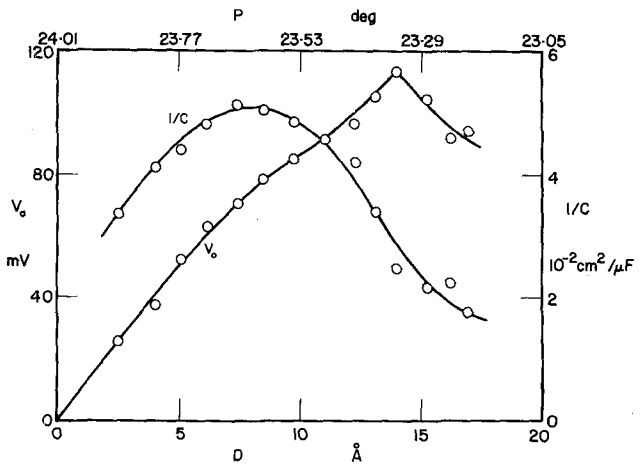


Fig. 8. V_o and 1/C determined from analysis of the open-circuit transients in Fig. 6 plotted vs. polarizer null position and film thickness from the optical model in Fig. 3.

Results similar in most respects to those plotted in Fig. 6, 7, and 8 are obtained when open-circuit transients are applied during the first anodic cycle in borate electrolyte. The potential-thickness plot indicates that the field in the film is constant up to the point where growth of NiOOH begins. The V_o values turn over a bit sooner in borate electrolyte, indicating that a single phase NiO oxidation model is less applicable than it is in sulfate electrolyte. All factors considered, the sulfate electrolyte appears to provide a bit "cleaner" system than borate electrolyte for studying the anodic oxidation of nickel.

Conclusions

1. The film left after chemical polishing or electropolishing is removed from the nickel surface within 30 sec under cathodic reduction at 80 $\mu A/cm^2$ in neutral electrolyte. $Ni(OH)_2$ does not deposit on the bare nickel surface even in contaminated electrolyte unless the nickel electrode is held cathodic longer than a nucleation time of over 100 sec.

2. The anodic oxidation of a nickel substrate is limited by the electric field in the oxide film. The film thickness increases uniformly with potential under galvanostatic oxidation, but the oxidation state of the film does not appear to remain constant under these conditions.

3. Formation of NiOOH occurs on the potential plateau at the end of an anodic cycle. It is soluble in sulfate electrolyte and does not build up on the surface as a film. If a film of NiOOH is formed in sulfate electrolyte by oxidation of $Ni(OH)_2$, the film thickness begins to decrease as soon as the film is converted to NiOOH. In borate electrolyte a film of NiOOH builds up on the potential plateau at the end of an anodic cycle. Under extended oxidation in borate electrolyte, the film will reach a thickness of several thousand angstroms.

4. On a cathodic cycle two processes take place at widely separated potentials: reduction of NiOOH to $Ni(OH)_2$ on a plateau at high potential and deposition of $Ni(OH)_2$ at low potential in competion with hydrogen evolution. Deposition of $Ni(OH)_2$ is appreciable only when dissolution of NiOOH has raised the nickel concentration in the electrolyte adjacent to the electrode just prior to the cathodic cycle.

Acknowledgment

This work received partial support from the National Research Council of Canada under Grant No. A-1151.

Manuscript submitted May 19, 1977; revised manuscript received July 4, 1977.

Any discussion of this paper will appear in a Discussion Section to be published in the June 1978 JOURNAL. All discussions for the June 1978 Discussion Section should be submitted by Feb. 1, 1978.

Publication costs of this article were assisted by the University of Waterloo.

REFERENCES

1. J. O'M. Bockris, A. K. N. Reddy, and B. Rao, *This Journal*, **113**, 1133 (1966).
2. Y. N. Chernykh and A. A. Yakovleva, *Sov. Electrochem. (Engl. Transl.)*, **7**, 510 (1971).
3. Y. N. Chernykh and A. A. Yakovleva, *ibid.*, **7**, 513 (1971).
4. N. Sato and K. Kudo, *Electrochim. Acta*, **19**, 461 (1974).
5. D. J. DeSmet, Thesis, University of Illinois (1967).
6. B. MacDougall and M. Cohen, *This Journal*, **121**, 1152 (1974).
7. B. MacDougall and M. Cohen, *ibid.*, **122**, 383 (1975).
8. B. MacDougall and M. Cohen, *ibid.*, **123**, 191 (1976).
9. B. MacDougall and M. Cohen, *ibid.*, **123**, 1783 (1976).
10. M. Okuyama and S. Haruyama, *Corros. Sci.*, **14**, 1 (1974).
11. M. A. Hopper and J. L. Ord, *This Journal*, **120**, 183 (1973).
12. J. L. Ord, *Surf. Sci.*, **56**, 413 (1976).
13. H. Bode, K. Dehlmelt, and J. Witte, *Electrochim. Acta*, **11**, 1079 (1966).
14. R. S. McEwen, *J. Phys. Chem.*, **75**, 1782 (1971).
15. G. W. D. Briggs, *Chem. Soc. Rep. Electrochem.*, **4**, 33 (1974).
16. J. L. Ord, *Surf. Sci.*, **16**, 155 (1969).
17. J. L. Ord, J. C. Clayton, and W. P. Wang, *This Journal*, **124**, 1671 (1977).
18. J. L. Ord and D. J. DeSmet, *ibid.*, **118**, 206 (1971).
19. J. L. Ord, D. J. DeSmet, and M. A. Hopper, *ibid.*, **123**, 1352 (1976).

Formation of Thick Layers of Iodine During the Anodic Oxidation of Iodide on a RDE

II. Open-Circuit Behavior

T. Bejerano

Research and Development Authority, Ben Gurion University of the Negev, Beersheva, Israel

and E. Gileadi*

Institute of Chemistry, Tel Aviv University, Tel Aviv, Israel

ABSTRACT

The open-circuit behavior of iodine layers formed on a RDE during the anodic oxidation of iodide was investigated. A plateau in potential was observed. Its value was found to depend on the concentration of free iodine in solution, and its length on the amount of iodine on the surface. It was shown that the sudden change in the nature of the iodine layer associated with the sharp decrease in current is not due to a phase transformation from supercooled liquid to solid iodine. The rate of decay of potential on open circuit from steady state can be used to estimate the average diffusion coefficient of NaI in the iodine layer. The experimental observations are consistent with a model in which I^- ions migrate or diffuse through the layer of I_2 and are oxidized at the metal/I_2 interface, while iodine is being dissolved at the I_2/solution interface. Steady state is reached when the rates of these two processes become equal.

Formation of thick layers of iodine during the oxidation of iodide in acid solutions has been observed by several investigators (1-7). In the first paper in this series (8) the phenomenon was studied on a rotating-disk electrode in acid and neutral solutions. It was observed that as the potential was stepped to a value in the limiting current region (+0.15V *vs.* mercury/mercurous sulfate electrode, MSE), the current first assumed its expected limiting value i_L, dropped suddenly after a few seconds to about 20% of this value, and then increased slowly to a steady-state value i_S. The ratio of i_S/i_L was found to be independent of the rate of rotation. An equation relating this quantity to the composition of the solution, the solubility of iodine in the supporting electrolyte, and the stability constant for the I_3^- ion was developed and tested. The thickness of the iodine layer was measured as a function of time during the anodic transient by determining the total cathodic charge, Q_c, required to reduce it. The film formed initially had very little effect on the current, although its thickness reached several hundred molecular layers. After a certain transition time a sudden change in the nature of the iodine layer occurred, which caused about a fivefold decrease in current. This was followed by slow dissolution of part of the film, accompanied by a corresponding increase in current until a steady state was reached. At steady state the current was typically 0.4-0.6 of the calculated limiting current, while the iodine film was 50-200 molecular layers thick.

The nature of the film formed initially and that existing at steady state is not known. It has been suggested by Gokhshtein (3-6) that iodine is first formed as supercooled liquid droplets which are suddenly solidified. In our previous work (8) the preliminary value of the specific resistance of the initially formed film was found to be $\rho_1 = 8 \times 10^4\ \Omega$ cm, and just after the transition the resistance rose to $\rho_2 = 2.4 \times 10^6\ \Omega$ cm, in a 0.02M NaI solution. The purpose of this paper is to investigate further the nature of the two films formed by observing the open-circuit behavior in different stages of formation of the film.

* Electrochemical Society Active Member.

Experimental

The experimental procedure was exactly as described in the first paper in this series (8). Extensive use was made of the transient recorder, which allowed fast measurements of the open-circuit decay transients with slow recording on a strip chart recorded for maximum accuracy. All solutions used in this part of the work contained a certain amount of iodine, and a platinum wire dipping into the solution served as a reversible iodine reference electrode (RIE). All potentials reported are hence *vs.* a RIE in the same solution. The potential of this reversible electrode was measured against a SCE and calculated on the normal hydrogen scale. In a typical case of 9 mM NaI, 0.6 mM I_2, and 0.5M H_2SO_4 the measured value of the RIE was +0.629V NHE while the calculated value, neglecting activity coefficients, was 0.622V NHE.

Results

The potential of the plateau E_p and its length τ_p.— Following anodic oxidation for a desired length of time t_a, the potentiostatic circuit was rapidly opened with the aid of a mercury wetted switch, and the decay of potential with time was recorded. Three typical decay curves are shown in Fig. 1(a), taken at different times during the anodic oxidation transient. The length of the plateau τ_p is defined in this figure. The potential of the plateau E_p is the same, independent of the time t_a at which open-circuit measurement was started. Thus the low resistance film formed initially and the high resistance film formed after the transition time and maintained at steady state give rise to the same value of E_p. This behavior was reproduced independent of the composition of the solution or the angular velocity of the electrode.

Figure 1b shows the length of the plateau τ_p as a function of t_a in the same experiments. The variation of the cathodic charge required to reduce the iodine layer is also given in the same figure, together with the current/time transient. It is seen that the length of the plateau τ_p exhibits the same kind of variation with t_a as the thickness of the iodine layer, as expected. At the end of the plateau the potential rapidly

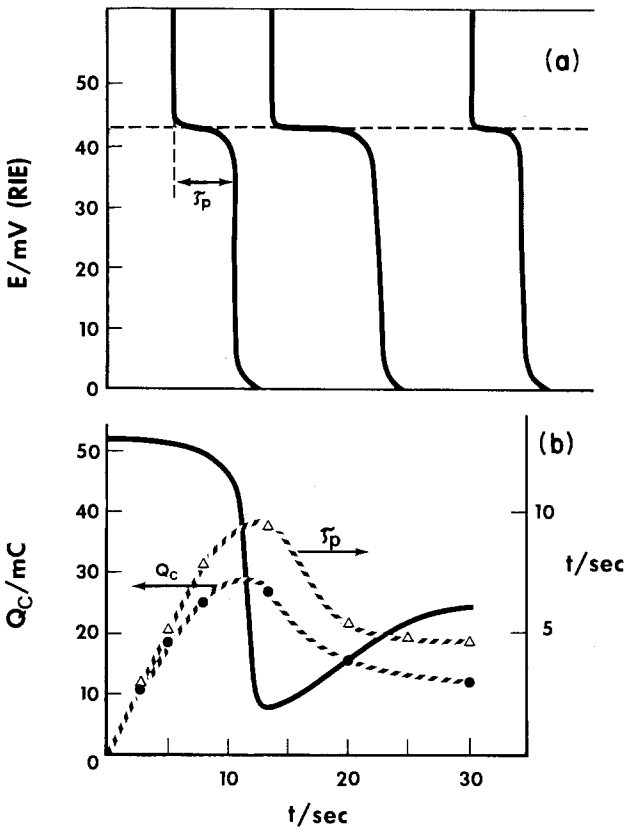


Fig. 1. (a) Open-circuit decay transients starting from +0.15V vs. RIE; (b) the length of the plateau τ_p and the cathodic charge Q_c required to reduce the iodine layer, as a function of time, for the same experiment, 9 mM NaI; 0.6 mM I_2, 0.5M H_2SO_4, 2500 rpm. Solid line shows variation of current with time.

decays to zero, *i.e.*, to the reversible I_2/I^- redox potential in the same solution. Open-circuit decay curves taken in a dilute solution where a film of iodine is not found (0.9 mM I^-, 0.06 mM I_2) were smooth and showed no plateau or inflection.

Values of Q_c and τ_p are shown in Table I for two different rates of rotation in a solution of 9 mM NaI, 0.6 mM I_2, and 0.5M H_2SO_4. Dividing Q_c by τ_p for each measurement gives the average rate of dissolution for the layer formed up to the time t_a at which open-circuit measurement was started.

The rate of decay to the plateau.—The rate of decay of open-circuit potential toward the plateau is shown in Fig. 2 as a function of t_a, for a solution of 18 mM NaI, 1.2 mM I_2; 0.5M H_2SO_4 at 400 rpm. The transition time in this experiment was t_c = 14.2 sec. It is noted that open-circuit decay is much slower at the early part of the anodic transient ($t_a < t_c$) than at longer times. The same behavior was observed in all

Table I. The thickness of iodine layer and the length of the plateau as a function of time of formation of the layer

9 mM NaI; 0.6 mM I_2; 0.5M H_2SO_4

2500 rpm	t_a */sec	2.5	5.2	13.2	20	30
	Q_c/mC	11.2	19.0	27.0	16.2	12.5
	τ_p/sec	2.9	5.3	9.5	5.5	4.7
	$i_d = \frac{Q_c}{\tau_p}$/mA	3.9	3.6	2.8	2.9	2.7
10,000 rpm	t_a */sec	2.7	4.2	12.6	15.2	—
	Q_c/mC	16	24	10.6	10	—
	τ_p/sec	2.6	3.9	2.0	1.9	—
	$i_d = \frac{Q_c}{\tau_p}$/mA	6.2	6.2	5.3	5.3	—

* The transition times were 11.4 and 4.5 sec for the lower and higher angular velocities, respectively.

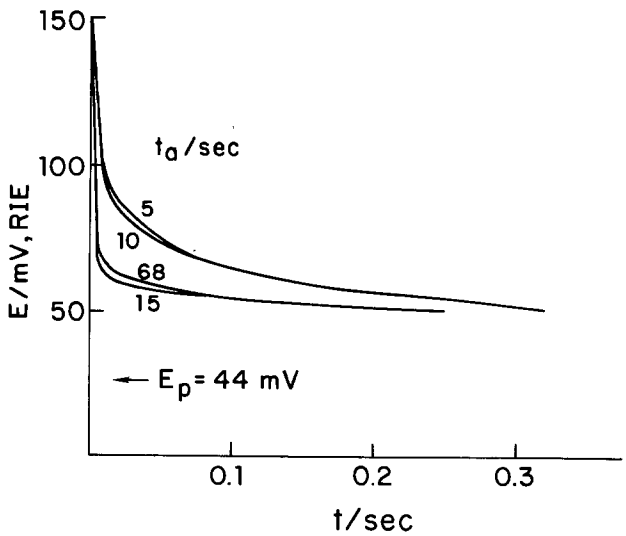


Fig. 2. The initial rate of decay of open-circuit potential toward the plateau at different times during the anodic transient. 18 mM NaI, 1.2 mM I_2, 0.5M H_2SO_4, 400 rpm.

solutions and at all angular velocities. The lowest time to reach the plateau always occurred at the point where the anodic current had its minimum value, *i.e.*, for values of t_a slightly larger than t_c. As the angular velocity increases, the rate of open-circuit decay also increases, as is discussed below.

Discussion

The potential of the plateau.—The potential of the plateau observed in different solutions is given in Table II. To attempt to calculate this potential, two assumptions will be made: (*i*) the activity of iodine at the electrode surface is constant, and (*ii*) the concentration of iodide in the iodine phase is proportional to its concentration in the bulk of the solution. The potential of the plateau E_p (NHE) *vs.* the normal hydrogen electrode under these conditions will be

$$E_p(\text{NHE}) = E' - \frac{RT}{\mathbf{F}}\ln[I^-] \qquad [1]$$

where the constant E' includes the terms for the activity of iodine and the distribution coefficient of I^- between the iodine phase and the solution. The reversible potential for the I_2/I^- couple is given by

$$E_r = E^\circ + \frac{RT}{2\mathbf{F}}\ln[I_2] - \frac{RT}{\mathbf{F}}\ln[I^-] \qquad [2]$$

where $[I_2]$ represents the concentration of free I_2 molecules in solution. The potential of the plateau E_p(RIE), measured *vs.* a reversible iodine electrode in the same solution is hence

$$E_p(\text{RIE}) = E_p(\text{NHE}) - E_r = E'' - \frac{RT}{2\mathbf{F}}\ln[I_2] \qquad [3]$$

The concentration of free I_2 is calculated from the stoichiometric concentrations of I^- and I_2 and the

Table II. The potential of the plateau and the concentration of free iodine in solution 298°K, 0.5M H_2SO_4

Concentration (mM)			E_r (mV) (calculated)	E_p (mV)		E'' (mV)
NaI	I_2	Free I_2	NHE	NHE	RIE	RIE
9	0.6	0.0825	622	665	43	10.5
18	1.2	0.0889	605	649	43	12.5
45	3.0	0.0933	582	624	42	11.0
9.7	0.15	0.0186	600	662	62	10.1
19.4	0.30	0.0198	583	645	62	10.9

known value ($K_1 = 740$ liter/M) of the equilibrium constant for the reaction

$$I_2 + I^- \rightleftarrows I_3^- \quad [4]$$

Examination of the data presented in Table II shows that for a given ratio of concentrations of I^- and I_2 the potentials E_p(NHE) and E_r vary significantly. On the other hand the concentration of free iodine, and the potential of the plateau measured *vs.* the RHE are essentially constant. Equation [3] and the assumptions leading to it are verified by the constancy of the quantity E'' shown in Table II.

It is of particular importance to note that the value of E_p observed at $t_a < t_c$ is equal to its value at $t_a > t_c$. The free energy of transformation of supercooled liquid to solid iodine at 25°C was calculated from thermodynamic data, and found to be −0.86 kcal/mole. Hence the potential of the plateau corresponding to a liquid layer of iodine should be 19 mV higher than that corresponding to a layer of solid iodine. Thus, our experimental observations are inconsistent with the contention of Gokhshtein (3-6) that liquid iodine is initially formed on the surface. One cannot exclude the possibility, though, that liquid iodine is indeed formed under the experimental conditions employed by Gokhshtein (stationary microelectrode), but not under our present experimental conditions (at the RDE). The fact that E_p is constant throughout the anodic transient would seem to be consistent with a transition from an amorphous to a crystalline layer at the transition time t_c or from one type of crystal structure or habit to another.

The rate of dissolution of iodine at open circuit.—The average rate of dissolution of iodine at open circuit is shown in Table I for two angular velocities. The film formed initially ($t_a < t_c$) is seen to dissolve faster than the film which exists at steady state. Thus, the lower specific resistance of the film seems to be correlated with a higher rate of dissolution. At steady state the rates of dissolution $i_d = 2.7$ and 5.3 mA compare well with the observed (and calculated, cf. Eq. [12] of Ref. (8)) values of the steady-state current $i_S = 2.6$ and 5.2 mA. This observation is consistent with the model of ionic transport through the iodine layer, discussed earlier (8). According to this model iodide ions migrate through the iodine layer and are discharged at the metal/iodine film interface. At steady state the rate of the electrochemical reaction equals the rate of dissolution. At open circuit the current falls to zero, but the rate of dissolution is not affected as long as the layer of iodine on the surface lasts. This is not the case in the early part of the anodic transient. For the conditions shown in Fig. 1, the initial current is $i_L = 5.2$ mA, and the rate of formation of the iodine layer (measured as the initial slope of Q_c *vs.* t_a) is 3.8 mA. Thus the rate of dissolution is only 1.4 mA, compared to the value of 3.9 mA given in Table I for the rate of dissolution at open circuit. The difference is due to the fact that during the early part of the transient the current is close to the limiting current, and the concentration of I^- at the surface is close to zero. The rate of dissolution is then controlled by the rate of diffusion of I_2 away from the surface. As the circuit is opened, the concentration of I^- quickly reaches a finite value at the surface, and dissolution of iodine is enhanced by the formation of I_3^- ions.

The rate of decay of potential toward the plateau.—A typical set of decay curves is shown in Fig. 2. In each case the electrode was polarized to +0.15V RIE, and the decay transient followed for about 0.3 sec. In Table III the length of the decay transient, defined as the time taken for the potential to reach +55 mV RIE (*i.e.*, 90% of the total change of potential from its initial value to the plateau) is given for three different rates of rotation. The thickness of the Nernst diffusion layer δ and the time of relaxation of this layer, are also given for comparison. The latter was calculated from the relationship

$$\delta = \sqrt{\pi D t} \quad [5]$$

where $D = 1.36 \times 10^{-5}$ cm²/sec is the average diffusion coefficient of I^- and I_2.

Table III. Rate of decay of potential on open-circuit toward the plateau

18 mM NaI; 1.2 mM I_2; 0.5M H_2SO_4

Angular velocity (rpm)	Diffusion layer thickness (cm)	Relaxation time of diffusion layer (m sec)	Decay time of transient (m sec)	
			$t_a < t_c$	$t_a > t_c$
400	3.0×10^{-3}	200	270	83
2,500	1.2×10^{-3}	33	30	8
10,000	0.6×10^{-3}	8	7	4

It is clearly seen that for $t_a < t_c$ the length of the decay transient is essentially equal to the relaxation time of the diffusion layer at all three rates of rotation. During this initial part of the anodic transient the current is close to the limiting current and the concentration of iodide at the electrode surface is therefore close to zero. Since at this stage the resistance of the film is low and iodide migrates through it readily, there will not be a significant concentration gradient in the film, and the concentration of I^- will be close to zero throughout the film. As the circuit is opened, the concentration of I^- at the film/solution interface will relax to the value corresponding to the rate of dissolution of iodine during the plateau. Since the concentration of I^- in the film, which affects the measured potential, is proportional to its concentration at the surface, the potential will relax at the same rate, which is the rate of relaxation of the diffusion layer.

At steady state the rate of dissolution is essentially the same during the transient and at open circuit, and there is no need for the diffusion layer to relax before the potential of the plateau can be reached. It is indeed seen in Table III that for $t_a > t_c$ the decay transient is much shorter than the relaxation time of the diffusion layer. On the other hand, a concentration gradient of Na^+ and I^- ions may exist in the film, due to the relatively high electric field in it. When the current is turned off this field disappears, and the concentration of NaI throughout the film becomes uniform. The relaxation time for this process, measured as the length of the open-circuit decay transient, is inherently independent of the rate of rotation of the electrode. The dependence observed experimentally is due to the variation of the thickness of the iodine film with rotation rate.

Combining these relaxation times with independent measurements of the thickness of the iodine layer under identical conditions allows us to estimate the average diffusion coefficient of NaI in the iodine layer, employing Eq. [5].[1] The results are shown in Table IV. It is seen that the average diffusion coefficient $\bar{D}$ is about five orders of magnitude lower in the film than in the aqueous phase.

The absolute mobility of the iodide ions is probably many times higher than that of the cation due to the possibility of transfer from I_3^- to I_2 species in a Grothius-type mechanism, as discussed earlier (8). The condition of electroneutrality, however, requires that both ions migrate together as the concentration throughout the layer becomes uniform. The average diffusion coefficient is related in this case to the diffusion coefficients of the two ions by the reciprocal relationship

[1] Since measurements were taken in 0.5M H_2SO_4 it is possible that the cation dissolved in the iodine phase is H^+ rather than Na^+, or that both cations are dissolved. Thus the value of $\bar{D}$ estimated above may apply to NaI, HI, or a mixture of both in the iodine phase.

Table IV. Average diffusion coefficient of NaI in the iodine layer

18 mM NaI; 1.2 mM I_2; 0.5M H_2SO_4

Angular velocity (rpm)	Specific conductivity (Mho cm^{-1})	Thickness of iodine layer (cm)	Decay time of transient (m sec)	Average diffusion coefficient (cm^2 sec^{-1})
400	4.0×10^{-7}	7.6×10^{-6}	83	2.2×10^{-10}
2,500	5.4×10^{-7}	3.9×10^{-6}	8	6.0×10^{-10}
10,000	6.3×10^{-7}	2.5×10^{-6}	4	5.0×10^{-10}

$$\frac{1}{D} = \frac{1}{D_+} + \frac{1}{D_-} \qquad [6]$$

and since $D_- >> D_+$, one has $\overline{D} \approx D_+$, *i.e.*, the average diffusion coefficients given in Table IV are essentially equal to the diffusion coefficient of the cation in the iodine layer. The specific conductivity depends on a simple sum of the diffusion coefficients or the absolute mobilities of the ions, and will hence be related to D_- in the present system. It may be said that for concentration changes in the film the movement of the ions is coupled in series while for ionic conductivity it is coupled in parallel. The slower moving ion controls the rate of the former process, while the faster moving ion controls the rate of the latter.

Conclusions

The purpose of this part of the work was to study the open-circuit behavior of rotating-disk electrodes upon which a layer of iodine had been formed. A plateau in potential was observed. Its length was related to the amount of iodine on the surface, but the value of the potential was independent of the time during the anodic transient when the circuit was opened. This excludes the possibility that the transition from one type of film to the other represents a phase transformation from liquid to solid iodine. A transition from amorphous to crystalline, or from one type of crystal structure to another is likely.

At steady state iodine is formed at the metal/film interface and dissolves away at the film/solution interface. This model is supported by the observations that the rate of dissolution at open circuit is equal to i_S, and the decay time of the potential to E_p is much shorter than the relaxation time of the diffusion layer. The potential of the plateau observed in different solutions was accounted for by assuming that I^- dissolved in the iodine film at a concentration proportional to its concentration in solution. The average diffusion coefficient of NaI in the iodine film was estimated. It is proposed that the values obtained are characteristic of the slower moving cation. The evidence presented in this and a previous publication (8) lends support to a model of ionic rather than electronic transport of charge through the iodine film.

Acknowledgments

The authors wish to thank Dr. E. Kirowa-Eisner of the Institute of Chemistry, Tel Aviv University for useful discussions and suggestions in the course of this work. One of us (T.B.) wishes to thank the Research and Development Authority, Ben Gurion University of the Negev for a six-month leave of absence during which most of the experimental work was done. Partial financial support for this work by the Ministry of Development is gratefully acknowledged.

This work was performed in partial fulfillment of the requirement for the degree of Ph.D. in electrochemistry by T. Bejerano at the Tel Aviv University.

Manuscript submitted May 2, 1977.

Any discussion of this paper will appear in a Discussion Section to be published in the June 1978 JOURNAL. All discussions for the June 1978 Discussion Section should be submitted by Feb. 1, 1978.

REFERENCES

1. N. A. Zakhodyakina, M. A. Navitskii, L. A. Sokolov, and P. D. Lukovtsev, *Elektrokhimiya*, **1**, 138 (1965).
2. A. M. Averbukh, M. A. Navitskii, L. A. Sokolov, and P. D. Lukovtsev, *ibid.*, **1**, 251 (1965).
3. A. Ya. Gokhshtein, *ibid.*, **1**, 285 (1965).
4. A. Ya. Gokhshtein, *ibid.*, **1**, 906 (1965).
5. A. Ya. Gokhshtein, *ibid.*, **1**, 1052 (1965).
6. A. Ya. Gokhshtein, *ibid.*, **3**, 32 (1967).
7. E. C. Toren and C. P. Driscoll, *Anal. Chem.*, **38**, 872 (1966).
8. T. Bejerano and E. Gileadi, Paper submitted to *J. Electroanal. Chem. Interfacial. Electrochem.*

Chemiluminescence from Step Experiments

An Analytical Treatment of Diffusion and Electron Transfer

Larry R. Faulkner*

Department of Chemistry, University of Illinois, Urbana, Illinois 61801

ABSTRACT

An analytical treatment of diffusion and electron transfer has been derived for the step technique that is employed frequently in the study of electrochemiluminescence (ECL). The two reactants leading to emission are generated sequentially in two steps, and reaction between them occurs during the second step. Each step lasts for a period t_f, and time into the second step is measured as t_r. Rigorous solutions for the concentration profiles, the current transient in the second step, and the homogeneous reaction rate have been obtained for systems in which all species have equal diffusion coefficients. Very good linear approximations for the current and the reaction rate apply to the experimentally important early part of the second step ($t_r/t_f < 0.2$). These linear formats also hold for mixed systems in which the two precursor/reactant pairs feature different diffusion coefficients. Such cases could not be treated rigorously, but they can be handled adequately via interpolation formulas that permit accurate predictions of the slopes and intercepts of the linear relations.

Since Feldberg's first suggestions in 1966 (1, 2), the analysis of luminescence transients stimulated electrochemically in step experiments has played an important role in the study of chemiluminescence from radical ion reactions (3, 4). In these experiments, one employs a planar microelectrode which is immersed in a quiescent solution containing a precursor for each reactant ion. In general, the two reactants are derived from different precursors but often both are derived from the same parent substance, *e.g.*, rubrene (R) in benzonitrile. Before the start, the electrode is held at a potential where no reaction takes place. At $t = 0$, a step is made to a potential where one reactant, *e.g.*, $R^{-\cdot}$, is electrogenerated at a diffusion-controlled rate. This process continues for a period t_f, then the potential is stepped to a value that causes electrogeneration of the second reactant, *e.g.*, $R^{+\cdot}$. This change in boundary condition at the electrode causes the first reactant to diffuse back to the interface. In so doing, it meets the outward flux of the second, and electron transfer takes place with the formation of excited states

$$R^{+\cdot} + R^{-\cdot} \rightarrow R^* + R \qquad [1]$$

Light can arise from the excited species R* by several mechanisms. Information about those mechanisms is obtained by comparing the rate of light emission I (einsteins/sec) to the rate of ion annihilation N (moles/sec) (1, 2, 5, 6). Both quantities decline as time proceeds because $R^{-\cdot}$ is consumed.

The light transient is directly measured, but the rate function N must be obtained from the theory of diffusion and reaction in the system. The problem is a complex one, and it has been treated only by digital simulation (1, 2, 4). There is evidence that simulation is a reliable approach (7, 8), but it has two serious drawbacks: It requires significant amounts of computer time; and, being a numerical technique, it offers no closed-form solutions and, consequently, it suggests no formats for analyzing experimental results.

Presented below is an analytical approach to this diffusion-kinetic problem. The results eliminate the need for digital simulation as a means for predicting either the rate function N, the faradaic current in the second step, or the concentration profiles of the reactants in solution. In addition, this treatment yields simple analytical forms for both the current and the reaction rate at earlier times in the second step, when experimental signals are greatest. These forms suggest important simplifications in the analysis of real data.

* Electrochemical Society Active Member.

Key words: luminescence, excited state, electrogenerated chemiluminescence, Feldberg treatment.

Case I. Homomolecular Ion Annihilation

Let us consider first the experiment in which both reactant ions are generated from the same precursor, as in the example involving rubrene cited above. We designate the precursor as P, the first reactant as R_1, and the second as R_2. All three species are regarded as having equal diffusion coefficients, D. The Fick law equations are then

$$\frac{\partial C_P(x,t)}{\partial t} = D\frac{\partial^2 C_P(x,t)}{\partial x^2} + 2kC_{R_1}(x,t)C_{R_2}(x,t) \qquad [2]$$

$$\frac{\partial C_{R_1}(x,t)}{\partial t} = D\frac{\partial^2 C_{R_1}(x,t)}{\partial x^2} - kC_{R_1}(x,t)C_{R_2}(x,t) \qquad [3]$$

$$\frac{\partial C_{R_2}(x,t)}{\partial t} = D\frac{\partial^2 C_{R_2}(x,t)}{\partial x^2} - kC_{R_1}(x,t)C_{R_2}(x,t) \qquad [4]$$

where t is time measured from the start of the experiment and x is the distance into the solution from the electrode surface. The parameter k is the rate constant for the electron transfer

$$R_1 + R_2 \rightarrow 2P \qquad [5]$$

The nonlinear couplings among [2]-[4] make it difficult, and perhaps impossible, to achieve a general analytical solution. However, by adding the three equations one obtains

$$\frac{\partial \sigma(x,t)}{\partial t} = D\frac{\partial^2 \sigma(x,t)}{\partial x^2} \qquad [6]$$

where $\sigma(x,t) = C_P(x,t) + C_{R_1}(x,t) + C_{R_2}(x,t)$. Likewise, subtracting [4] from [3] gives

$$\frac{\partial \delta(x,t)}{\partial t} = D\frac{\partial^2 \delta(x,t)}{\partial x^2} \qquad [7]$$

where $\delta(x,t) = C_{R_1}(x,t) - C_{R_2}(x,t)$.

Equations [6] and [7], which were first presented by Schwartz *et al.* (9), are linear and can be solved easily to give the distributions of combined concentrations σ and δ, which must apply regardless of the rate constant k. The details are presented in the Ap-

pendix. The results are

$$\sigma(x,t) = C_P^* \quad [8]$$

$$\delta(x,t) = C_P^* \left[\operatorname{erfc}\left(\frac{x}{2(Dt)^{1/2}} \right) - 2S_{tf}(t) \operatorname{erfc}\left(\frac{x}{2(Dt_r)^{1/2}} \right) \right] \quad [9]$$

where C_P^* is the bulk concentration of the precursor, $S_{tf}(t)$ is the step function which rises from zero to unity at $t = t_f$, and t_r *is* time measured into the second step from its start, *i.e.*, $t_r = t - t_f$.

Current flow.—In the forward step, the current magnitude is simply given by the Cottrell equation for diffusion-controlled electrolysis of P

$$(t < t_f) \qquad i = \frac{FAD^{1/2}C_P^*}{\pi^{1/2}t^{1/2}} \quad [10]$$

In the second step, the current is opposite in sign. Its magnitude is given by

$$i = FAJ_P(0,t) + 2FAJ_{R_1}(0,t) \quad [11]$$

where the J's are fluxes at the electrode surface. Substitution from Fick's first law gives

$$i = FAD \left\{ \frac{\partial}{\partial x} [C_P(x,t) + 2C_{R_1}(x,t)] \right\}_{x=0} \quad [12]$$

which is

$$i = FAD \left\{ \frac{\partial}{\partial x} [\sigma(x,t) + \delta(x,t)] \right\}_{x=0} \quad [13]$$

or

$$i = FAD \left[\frac{\partial \delta(x,t)}{\partial x} \right]_{x=0} \quad [14]$$

Evaluation of the derivative gives the current in closed form

$$(t \geq t_f) \qquad i = \frac{FAD^{1/2}C_P^*}{\pi^{1/2}} \left[\frac{2}{t_r^{1/2}} - \frac{1}{t^{1/2}} \right] \quad [15]$$

or in terms of the dimensionless current parameter usually used in simulations

$$Z = \frac{it_f^{1/2}}{FAD^{1/2}C_P^*} = \frac{1}{\pi^{1/2}} \left[2\left(\frac{t_r}{t_f}\right)^{-1/2} - \left(1 + \frac{t_r}{t_f}\right)^{-1/2} \right] \quad [16]$$

The expressions [15] and [16] apply rigorously regardless of k. They were recognized empirically, but not derived, in earlier publications by Feldberg (1) and by Michael (7). Table I offers a comparison between exact Z values from [16] and simulated data taken from a model involving 1000 iterations/step and a dimensionless redox rate constant $kt_fC_P^*$ equal to 1000. That choice of rate constant implies essentially diffusion-controlled annihilation of R_1 and R_2 (1, 5, 10).

Concentration profiles.—The distributions of concentrations of P, R_1, and R_2 cannot be obtained analytically by this approach for the general case of arbitrary k. However, they can be obtained for the special case of infinite k. That limiting situation is of interest because simulation has demonstrated that the behavior of the system is virtually independent of k as long as $kt_fC_P^* \geq 1000$ (1, 11). This condition holds for nearly all experiments of the type considered here.

When $k \to \infty$, R_1 and R_2 cannot coexist (9), hence δ represents the concentration of R_1 wherever it is positive, and the concentration of R_2 wherever it is negative. The concentration of P is therefore $C_P^* - |\delta|$. Figure 1 displays these relationships.

The distance d where $\delta = 0$ marks the junction between the two reactant zones, R_1 and R_2 diffuse toward that plane from opposite directions, and they meet there and react to give light. The location of this plane is defined by

$$2\operatorname{erf}\left[\frac{d}{2(Dt_r)^{1/2}} \right] - \operatorname{erf}\left[\frac{d}{2(Dt)^{1/2}} \right] = 1 \quad [17]$$

For comparisons with simulated data, it is convenient to express d as a distance on a conventional dimensionless scale

$$X_r = d/2(Dt_f)^{1/2} \quad [18]$$

Thus, [17] can be reexpressed

$$2\operatorname{erf}\left[\frac{X_r}{(t_r/t_f)^{1/2}} \right] - \operatorname{erf}\left[\frac{X_r}{[1 + (t_r/t_f)]^{1/2}} \right] = 1 \quad [19]$$

For a given value of t_r/t_f, X_r must generally be evaluated numerically, but a very good approximation is available for small t_r/t_f, as described below.

Redox reaction rate.—The electron transfer reaction is controlled by the rates of diffusion of the reactants into the plane at d, hence

$$N = A \lim_{x \to d} J_{R_1}(x,t) = -A \lim_{x \to d} J_{R_2}(x,t) \quad [20]$$

or generally

$$N = AD \left. \frac{\partial \delta(x,t)}{\partial x} \right|_{x=d} \quad [21]$$

(Note that the equality of fluxes expressed in [20] is assured by the continuity of δ and its derivative.) The derivative is easily evaluated from [9], and one obtains

Table I. Analytical and simulated results for case I

	Z		ω_n	
t_r/t_f	Analytical	Simulated*	Analytical	Simulated*
0.0495	4.521	4.545	3.1833	3.2305
0.0995	3.039	3.048	1.9896	2.0161
0.1995	2.011	2.014	1.1595	1.1730
0.4995	1.136	1.137	0.4661	0.4719
0.9995	0.730	0.730	0.1779	0.1809

* 1000 iterations/step, $kt_fC_P^* = 1000$.

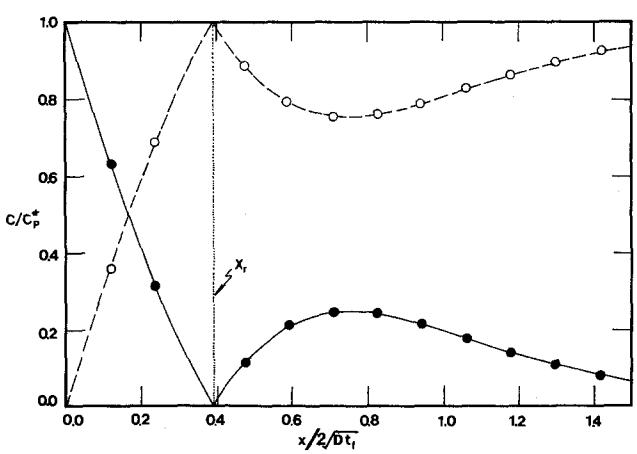


Fig. 1. Concentration profiles for $t_r/t_f = 0.3$. The reaction plane is at the dotted vertical line. Solid curve is $|\delta|/C_P^*$. To the right of the reaction plane it represents C_{R_1}/C_P^*, and to the left it is C_{R_2}/C_P^*. Dashed curve is $(\sigma - |\delta|)/C_P^*$. It represents C_P/C_P^* everywhere. Points are from a simulation involving 1000 iterations/step and $k \to \infty$.

$$N = \frac{AD^{1/2}C_P^*}{\pi^{1/2}} \left\{ \frac{2}{t_r^{1/2}} \exp\left[\frac{-d^2}{4Dt_r}\right] - \frac{1}{t^{1/2}} \exp\left[\frac{-d^2}{4Dt}\right] \right\} \quad [22]$$

This relation can be rearranged to give the familiar dimensionless reaction rate parameter

$$\omega_n = \frac{Nt_f^{1/2}}{AD^{1/2}C_P^*} = \frac{1}{\pi^{1/2}} \left\{ \frac{2}{(t_r/t_f)^{1/2}} \exp\left[\frac{-X_r^2}{(t_r/t_f)}\right] - \frac{1}{[1+(t_r/t_f)]^{1/2}} \exp\left[\frac{-X_r^2}{1+(t_r/t_f)}\right] \right\} \quad [23]$$

Table I shows a comparison between ω_n values calculated from [23] and corresponding data obtained from a simulation. The analytical results were generated in two steps. First, the value of X_r corresponding to a given t_r/t_f was calculated from [19] by the Newton-Raphson technique, then ω_n could be calculated by substitution into [23]. It is interesting that the simulated values are uniformly high by about 1.5%, despite the extreme accuracy in the Z values. Table I actually shows the first test that has been possible of the accuracy of ω_n values obtained by simulation, and it gives some feeling of the precision with which those numbers can be regarded.

Case II. Mixed System with Equal Diffusion Coefficients

Let us now examine the case in which R_1 and R_2 are derived from separate precursors P_1 and P_2, respectively, but all four species have the same diffusion coefficient, D. The diffusion-kinetic equations are then

$$\frac{\partial C_{P_1}(x,t)}{\partial t} = D\frac{\partial^2 C_{P_1}(x,t)}{\partial x^2} + kC_{R_1}(x,t)C_{R_2}(x,t) \quad [24]$$

$$\frac{\partial C_{P_2}(x,t)}{\partial t} = D\frac{\partial^2 C_{P_2}(x,t)}{\partial x^2} + kC_{R_1}(x,t)C_{R_2}(x,t) \quad [25]$$

$$\frac{\partial C_{R_1}(x,t)}{\partial t} = D\frac{\partial^2 C_{R_1}(x,t)}{\partial x^2} - kC_{R_1}(x,t)C_{R_2}(x,t) \quad [26]$$

$$\frac{\partial C_{R_2}(x,t)}{\partial t} = D\frac{\partial^2 C_{R_2}(x,t)}{\partial x^2} - kC_{R_1}(x,t)C_{R_2}(x,t) \quad [27]$$

where k is now the rate constant for

$$R_1 + R_2 \rightarrow P_1 + P_2 \quad [28]$$

The sum of [24] and [26] gives

$$\frac{\partial \sigma_1(x,t)}{\partial t} = D\frac{\partial^2 \sigma_1(x,t)}{\partial x^2} \quad [29]$$

where $\sigma_1 = C_{P_1}(x,t) + C_{R_1}(x,t)$. Likewise the sum of [25] and [27] gives

$$\frac{\partial \sigma_2(x,t)}{\partial t} = D\frac{\partial^2 \sigma_2(x,t)}{\partial x^2} \quad [30]$$

where $\sigma_2(x,t) = C_{P_2}(x,t) + C_{R_2}(x,t)$. Finally, the difference between [26] and [27] gives [7], where $\delta(x,t)$ is defined as before.

Solution of these equations by the methods used for case I shows that

$$\sigma_1(x,t) = C_{P_1}^* \quad [31]$$

$$\sigma_2(x,t) = C_{P_2}^* \quad [32]$$

$$\delta(x,t) = C_{P_1}^* \operatorname{erfc}\left[\frac{x}{2(Dt)^{1/2}}\right] - S_{t_f}(t)[C_{P_1}^* + C_{P_2}^*] \operatorname{erfc}\left[\frac{x}{2(Dt_r)^{1/2}}\right] \quad [33]$$

Similarly, we obtain the key results for $t \geq t_f$

$$Z = \frac{it_f^{1/2}}{FADC_{P_1}^*} = \frac{1}{\pi^{1/2}} \left[(1+r_C)\left(\frac{t_r}{t_f}\right)^{-1/2} - \left(1+\frac{t_r}{t_f}\right)^{-1/2} \right] \quad [34]$$

$$(1+r_C)\operatorname{erf}\left[\frac{X_r}{(t_r/t_f)^{1/2}}\right] - \operatorname{erf}\left[\frac{X_r}{[1+(t_r/t_f)]^{1/2}}\right] = r_C \quad [35]$$

$$\omega_n = \frac{Nt_f^{1/2}}{FAD^{1/2}C_{P_1}^*} = \frac{1}{\pi^{1/2}} \left\{ \frac{(1+r_C)}{(t_r/t_f)^{1/2}} \exp\left[\frac{-X_r^2}{(t_r/t_f)}\right] - \frac{1}{1+(t_r/t_f)^{1/2}} \exp\left[\frac{-X_r^2}{1+(t_r/t_f)}\right] \right\} \quad [36]$$

where $r_C = C_{P_2}^*/C_{P_1}^*$.

Comparisons between these analytical results and simulated values of Z and ω_n for mixed systems involving various values of r_C are as satisfactory as those given in Table I for case I.

It is interesting to note that relations [34]-[35] are actually general results that include [16], [19], and [23] as the special cases for $r_C = 1$. The dimensionless current and luminescence transients for a homomolecular system are therefore identical to those of a mixed system with precursors at equal concentrations. Since this is true, we will consider only mixed systems in the arguments below.

Behavior at Short Times

From an experimental standpoint the domain of greatest interest is $0 \leq t_r/t_f \leq 0.2$, because most of the signal appears there. Simple linear equations describing the behavior of ω_n and Z in that region would be particularly useful. We shall see in this section that they are readily available.

Reaction rate.—Equation [35] can be simplified to the form

$$(1+r_C)\operatorname{erf}(p) - \operatorname{erf}(q) = r_C \quad [37]$$

where $p = X_r/(t_r/t_f)^{1/2}$ and $q = X_r/(t/t_f)^{1/2}$. At very short times into the second step, the reaction plane at distance d is very near the electrode surface. As t_r approaches zero, q approaches zero, hence the second term of [37] vanishes. Thus we find

$$\lim_{t_r \to 0} \operatorname{erf}(p) = \operatorname{erf}(p_0) = \frac{r_C}{1+r_C} \quad [38]$$

$$p_0 = \operatorname{erf}^{-1}\left(\frac{r_C}{1+r_C}\right) \quad [39]$$

Now we expand the error functions in [37] as Taylor series about their limiting arguments, and we truncate after the linear terms

$$\operatorname{erf}(p) \cong \frac{r_C}{1+r_C} + \frac{2}{\pi^{1/2}} e^{-p_0^2}(p - p_0) \quad [40]$$

$$\operatorname{erf}(q) \cong \frac{2}{\pi^{1/2}} q \quad [41]$$

Substitution into [37] gives, after rearrangement

$$p - p_0 = \frac{q}{(1+r_C)e^{-p_0^2}} \quad [42]$$

Equation [36] can be rewritten as

$$\omega_n = \frac{1}{\pi^{1/2}}\left[(1+r_C)\left(\frac{t_r}{t_f}\right)^{-1/2} e^{-p^2} - \left(\frac{t}{t_f}\right)^{-1/2} e^{-q^2}\right] \quad [43]$$

Let us now expand the two exponentials in [43] as Taylor series about the limiting arguments, and truncate after the linear terms

$$e^{-p^2} \cong e^{-p_0^2} - e^{-p_0^2}(2p_0)(p-p_0) \quad [44]$$

$$e^{-q^2} \cong 1 \quad [45]$$

Substitution of [42] into [44] gives

$$e^{-p^2} = e^{-p_0^2} - 2p_0q/(1+r_C) \quad [46]$$

and substitution of [45] and [46] into [43] yields the essentially linear form

$$\omega_n \cong a\left(\frac{t_r}{t_f}\right)^{-1/2} - b \quad [47]$$

where

$$a = (1+r_C)e^{-p_0^2}/\pi^{1/2} \quad [48]$$

and

$$b = \frac{1}{\pi^{1/2}}\left[2p_0q\left(\frac{t_r}{t_f}\right)^{-1/2} + \left(\frac{t}{t_f}\right)^{-1/2}\right] \quad [49]$$

Recognizing that $q = p(t_r/t)^{1/2}$, one can use [42] to obtain an explicit expression for q in terms of (t_r/t_f). Substitution into [49] then permits an evaluation of the time dependence of b. In general, b varies only slightly over the domain of interest. For example, with $r_C = 1$, it takes on the values of 0.821, 0.812, and 0.789, for $t_r/t_f = 0$, 0.1, and 0.2, respectively. This variation is small compared to the magnitude of ω_n for $t_r/t_f \leq 0.2$, hence, it is convenient to regard b as a constant equal to the limiting value for $t_r/t_f = 0$, which is

$$b = (2p_0^2+1)/\pi^{1/2} \quad [50]$$

Equation [47] with a and b defined by [48] and [50], is a good linear representation of ω_n in the short time region. For $r_C = 1$ the approximate value exceeds the exact one by only 0.03, 2, and 2.8% at $t_r/t_f = 0.001$, 0.1, and 0.2.

The remaining discrepancy arises mainly because [50] is too low an estimate of the mean value of b over the time range of interest. A higher value should be used, but it is not convenient to assign one precisely, because information needed for that purpose was lost by the omission of higher order terms in the Taylor expansions. A pragmatic approach is to raise b by 5%, so that we reassign

$$b = (1.05)(2p_0^2+1)/\pi^{1/2} \quad [51]$$

This expedient gives approximate values of ω_n via [47] that underestimate the exact values for $r_C = 1$ by only 0.1, 0.05, and 0.8% at $t_r/t_f = 0.001$, 0.1, and 0.2. Obviously, such accuracy is entirely adequate for comparisons with experimental results.

Current.—Equation [34] shows that Z is precisely linear against the time parameter $(1+r_C)(t_r/t_f)^{-1/2} - (t/t_f)^{-1/2}$ for all t_r/t_f. The slope is $\pi^{-1/2}$ and the intercept is zero.

Case III. Mixed System with Different Diffusion Coefficients

Of more general experimental interest than either case I or case II is the mixed system in which the two couples have different diffusion coefficients; that is, R_1 and P_1 diffuse according to coefficient D_1, while R_2 and P_2 move according to D_2. Unfortunately this change means that the analogous equations to [24]-[27] do not all involve the same diffusion coefficient, hence linear differential equations like [7], [29], and [30] cannot be obtained. Exact solutions for ω_n and Z could not be derived for this case in the present work.

Nevertheless, a series of simulations revealed that ω_n and Z gave excellent linear plots in the formats derived above. The general relations can be expressed

$$Z = \frac{it_f^{1/2}}{FAD_1^{1/2}C_{P_1}^*} = \frac{f_Z}{\pi^{1/2}}\left[\frac{(1+r_C)}{(t_r/t_f)^{1/2}} - \frac{1}{(t/t_f)^{1/2}}\right] \quad [52]$$

$$\omega_n = \frac{Nt_f^{1/2}}{AD_1^{1/2}C_{P_1}^*} = f_\omega a\left(\frac{t_r}{t_f}\right)^{-1/2} - f_I b \quad [53]$$

where a and b are defined in Eq. [48] and [51].

The simulations used for this study involved 10,000 iterations/step and $kt_fC_{P_1}^* = 10{,}000$. For each simulation the concentration ratio r_C and the ratio of diffusion coefficients, $r_D = D_2/D_1$, were constants chosen from the ranges $0.75 \leq r_C \leq 2.0$ and $0.5 \leq r_D \leq 2.0$. Plots of Z *vs.* $(1+r_C)(t_r/t_f)^{-1/2} - (t/t_f)^{-1/2}$ and ω_n *vs.* $(t_r/t_f)^{-1/2}$ were examined over the range $0.01 \leq (t_r/t_f) \leq 0.1$. Linear correlation coefficients were always equal to unity within a few parts in 10^5.

The factors f_ω and f_Z can be interpreted as ratios $(D_{eff}/D_1)^{1/2}$, where D_{eff} is an effective diffusion coefficient. In general they are nearly equal and depend on both r_C and r_D. The squares of both are essentially perfectly linear with r_D at constant r_C

$$f_Z^2 = 1 + m_Z(r_D - 1) \quad [54]$$

$$f_\omega^2 = 1 + m_\omega(r_D - 1) \quad [55]$$

The slopes m_Z and m_ω are not linear with r_C, but can be precisely expressed as

$$m_Z = 0.300 + 0.545r_C - 0.149r_C^2 \quad [56]$$

$$m_\omega = 0.330 + 0.281r_C - 0.067r_C^2 \quad [57]$$

The intercept factor f_I in [53] is linear with r_D and depends negligibly on r_C

$$f_I = 1 + 0.418(r_D - 1) \quad [58]$$

Given r_C and r_D for an experimental system, one can use [48], [51], and [54]-[58] to calculate simply and precisely the parameters that define the linear Z and ω_n functions for $t_r/t_f \leq 0.2$. As an example of reliability consider the case for $r_C = r_D = 1.25$. We find $p_0 = 0.5407$, $a = 0.9476$, and $b = 0.939$. The predicted slope of the Z plot is $f_Z/\pi^{1/2} = 0.615$, whereas the simulated value is 0.617. The predicted ω_n function is

$$\omega_n = 1.014\left(\frac{t_r}{t_f}\right)^{-1/2} - 1.04 \quad [59]$$

and that from simulation is

$$\omega_n = 1.027\left(\frac{t_r}{t_f}\right)^{-1/2} - 1.085 \quad [60]$$

Equations [59] and [60] give ω_n values that agree to within 1.5% over the whole time domain of interest. Such agreement obviates the need for further simulations of these kinds of problems unless information is needed for $t_r/t_f > 0.2$.

Examining Experimental Results

We have seen above that simple linear forms describe both Z and ω_n at earlier times during the second step. This convenience makes it particularly attractive to confine an analysis of experimental results to this region. Is there a loss in ignoring data for the $t_r/t_f > 0.2$? Probably not. In fact it may be dangerous to rely on information from that region. Not only is the later signal very low in comparison to that from the earlier period, as Fig. 2 illustrates dramatically, but in addition the later times feature much lower reactant fluxes into the annihilation zone, hence side reactions with

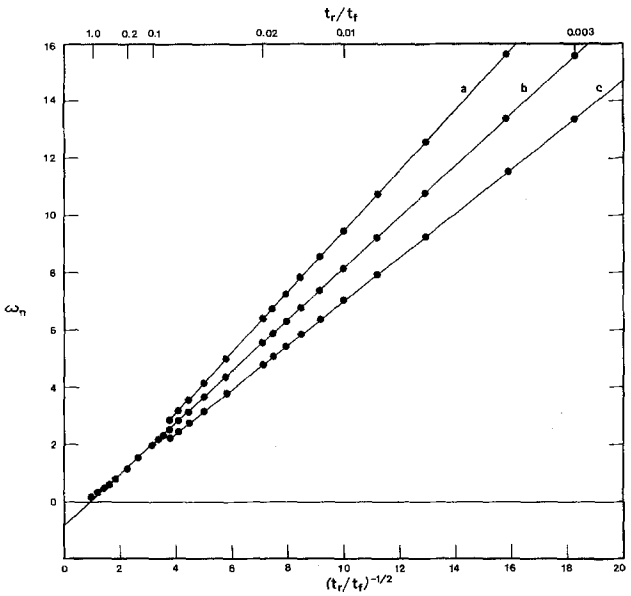


Fig. 2. Linear plots of reaction rate. (a) $r_C = 2$, (b) $r_C = 1$, (c) $r_C = 0.5$. Points are exact. Lines are the linear approximations indicated in Eq. [47], [48], and [51]. All t_r/t_f values covered here are readily accessible in typical experiments.

impurities (*e.g.*, oxygen) may compete significantly with the hoped-for electron transfer. The anomalously high slopes that are often observed in Feldberg plots may be due to this effect. One can have far greater confidence that the calculated redox rate actually holds in experimental systems at earlier times.

Is there any way to be sure it holds even there? The current transient bears importantly on this question, for it is the only observable aside from the emission decay. Its behavior can be predicted quantitatively, without adjustable parameters, on the basis of current flow in the forward step (7, 8). If the actual current in the second step matches the predicted decay, then the diffusion patterns in the system must correspond generally to those considered here. That is, $\delta(x,t)$ and $\sigma(x,t)$ would be verified. Since the current is insensitive to k, good agreement there does not guarantee that the actual ω_n is the predicted value. On the other hand, the real ω_n could be no greater than the predicted value at any time, and it could only be less if $kt_fC_{P1}^* < 1000$ (1, 11). For most experiments, $kt_fC_{P1}^*$ is probably greater than 1000 by several orders of magnitude (3, 4, 11), hence agreement between actual and predicted current transients would provide very strong evidence that the predicted ω_n applies to the real system and is a safe basis for correlating the light intensity.

Acknowledgments

The author wishes to express special appreciation to Dr. S. W. Feldberg and Dr. Paul R. Michael for the discussions that stimulated this work. Grateful acknowledgment is also made to the National Science Foundation for financial support under Grant MPS-75 05361.

Manuscript submitted May 2, 1977; revised manuscript received July 15, 1977.

Any discussion of this paper will appear in a Discussion Section to be published in the June 1978 JOURNAL. All discussions for the June 1978 Discussion Section should be submitted by Feb. 1, 1978.

Publication costs of this article were assisted by the University of Illinois.

APPENDIX

Equations [6] and [7] are subject to the initial conditions, $\sigma(x,0) = C_P^*$ and $\delta(x,0) = 0$, and the semi-infinite conditions, $\lim_{x\to\infty} \sigma(x,t) = C_P^*$ and $\lim_{x\to\infty} \delta(x,t) = 0$. Laplace transformation of [6] and [7] yields two ordinary differential equations that can be solved under these conditions to give the well-known forms

$$\bar{\sigma}(x,s) = C_P^*/s + A(s)e^{-(s/D)^{1/2}x} \qquad [A\text{-}1]$$

$$\bar{\delta}(x,s) = B(s)e^{-(s/D)^{1/2}x} \qquad [A\text{-}2]$$

where $\bar{\delta}(x,s)$ and $\bar{\sigma}(x,s)$ are the transforms of $\delta(x,t)$ and $\sigma(x,t)$. The functions $A(s)$ and $B(s)$ are as yet undetermined.

A consideration of flux balance at the electrode surface reveals that

$$J_P(0,t) + J_{R1}(0,t) + J_{R2}(0,t) = 0 \qquad [A\text{-}3]$$

at all times. This implies that

$$D\frac{\partial\bar{\sigma}(x,s)}{\partial x}\bigg|_{x=0} = 0 \qquad [A\text{-}4]$$

hence from [A-1] we find that $A(s) = 0$. Therefore

$$\bar{\sigma}(x,s) = C_P^*/s \qquad [A\text{-}5]$$

and inverse transformation gives [8].

During the forward step, $C_P(0,t)$ and $C_{R2}(0,t)$ are both zero, so from [8] we find that $C_{R1}(0,t) = C_P^*$. In the reversal step, $C_P(0,t) = C_{R1}(0,t) = 0$, hence $C_{R2}(0,t) = C_P^*$. Thus

$$\delta(0,t) = C_P^* - 2S_{tf}(t)C_P^* \qquad [A\text{-}6]$$

$$\bar{\delta}(0,s) = B(s) = \frac{C_P^*}{s}(1 - 2e^{-t_fs}) \qquad [A\text{-}7]$$

By substitution into [A-2], one obtains

$$\bar{\delta}(x,s) = \frac{C_P^*}{s}e^{-(s/D)^{1/2}x} - 2\frac{C_P^*}{s}e^{-t_fs}e^{-(s/D)^{1/2}x} \qquad [A\text{-}8]$$

Inverse transformation yields [9].

REFERENCES

1. S. W. Feldberg, *J. Am. Chem. Soc.*, **88**, 390 (1966).
2. S. W. Feldberg, *J. Phys. Chem.*, **70**, 3928 (1966).
3. L. R. Faulkner, *MTP Int. Rev. Sci.: Phys. Chem. Ser. Two*, 9, 213 (1976) and references cited therein.
4. L. R. Faulkner and A. J. Bard, *Electroanal. Chem.*, **10**, 1 (1977) and references cited therein.
5. R. Bezman and L. R. Faulkner, *J. Am. Chem. Soc.*, **94**, 3699 (1972).
6. L. R. Faulkner, *This Journal*, **122**, 1190 (1975).
7. P. R. Michael, Ph.D. Thesis, University of Illinois at Urbana-Champaign (1976).
8. P. R. Michael and L. R. Faulkner, *J. Am. Chem. Soc.*, In press.
9. P. M. Schwartz, R. A. Blakeley, and B. B. Robinson, *J. Phys. Chem.*, **76**, 1868 (1972).
10. J. T. Maloy, in "Laboratory Techniques in Electroanalytical Chemistry," P. T. Kissinger, Editor, Marcel Dekker, New York, In press.
11. R. P. Van Duyne and S. F. Fischer, *Chem. Phys.*, **5**, 183 (1974).

Technical Notes

New Cathodic Reactants for Lithium Batteries

A. A. Inocêncio*,[1]

Institute of Physical Chemistry, University of Bonn, Bonn, Germany

By studying the electrochemical behavior of substances such as water, methanol, formic acid, and formaldehyde in organic solvents, it was verified that they are cathodically reduced at a suitable potential, so that they can be combined with an anode of lithium in batteries operable at room temperature. Because of the low molecular weight of the anodic and cathodic materials these batteries have large energy density. Our experiments with cathodic half-cells show that high current densities and, therefore, high power densities are possible. The reduction mechanism of water in a one molar solution of lithium perchlorate in tetrahydrofuran has recently been reported by the author (1). Reports about the reduction mechanism of methanol and formic acid are being prepared. In this communication the results obtained for these cathodic reactants in half-cell experiments and in the preliminary tests of some prototype cells are discussed.

Experimental

The cyclic voltammograms were obtained using a Wenking electronic potentiostat, an Exact Electronics functions generator Type 250, and Hewlett Packard X-Y recorder. For getting the stationary current-potential curves a Rohde and Schwarze d-c power supply Type NGU BN 95140 and a Wenking precision potential meter Type PPT 67 were used. In the tests of the prototype lithium cells, a Rohde and Schwarze d-c power supply Type NGU BN 95140 and a Hartmann and Braun low speed recorder, arucomp 4902 were used.

Figure 1 shows the cross section of an assembled lithium cell in a 1:1 scale. The parts labeled with 2 in the figure are made of Teflon. By assembling the cell, the Teflon parts are pressed together by means of the nuts and the stainless steel rings labeled, 1. Stainless steel ring, labeled 3, are used between the Teflon parts to prevent leakage. Two types of cathodic catalysts, labeled 4, were tried: (*i*) a sintered nickel disk (s.Ni, in Table I); (*ii*) a disk made as follows: carbon and nickel powder (1:1) was mixed with PTFE, Type TF 5032 (0.6 $cm^3\ g^{-1}$ of the mixture) as a binder. This paste was extended on a nickel gauze and pressed (200 kg cm^{-2}). After pressing, the catalyst was heated at 200°C for ½ hr. On the side facing the anodic compartment a PVC membrane was pressed (150 kg cm^{-2}). In this case the separator, 6, was not used. This catalyst is referred to as C + Ni in Table I. The geometrical area in both cases was about 10 cm^2. The real area was not measured. The lithium anode, 5, was prepared by pressing pieces of lithium strips on a stainless steel gauze. The separator, 6, was a Teflon (or PVC) membrane.

The chemicals used were: tetrahydrofuran, Merck, dried p.a.; propylene carbonate, Merck, for synthesis; methanol, Merck, dried p.a.; formic acid, uvasol, for spectroscopy; formaldehyde, Merck, for histology; and lithium perchlorate, purified and dried Fluka A. G. They all were used without further purification.

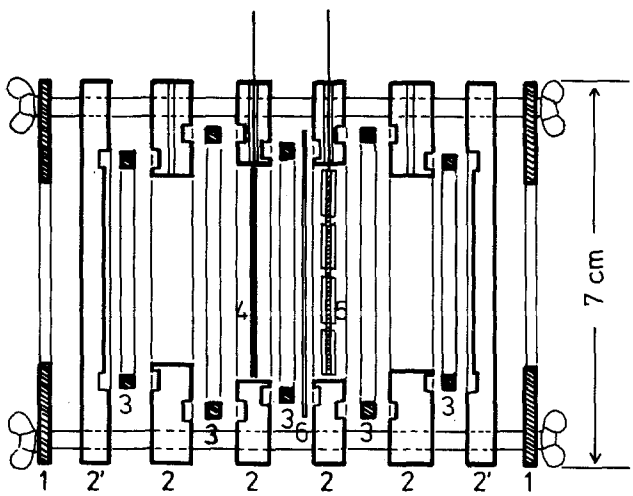


Fig. 1. Cross section of the lithium cell: 1, stainless steel ring; 2, Teflon ring; 2', Teflon disk; 3, stainless steel ring; 4, cathodic catalyst; 5, lithium electrode; 6, separator.

Results and Discussion

Cyclic voltammograms.—The study of the electrochemical behavior of substances such as methanol, formic acid, formaldehyde, and water on platinum in electrolytic solutions of organic solvents such as tetrahydrofuran (THF), showed that they can be reduced at a potential much more positive than the potential at which the deposition of the alkali metals occurs in the same solvent. At the reduction potential of these substances, the solvent (THF) does not undergo any electrochemical reaction. Figure 2 shows two cyclic

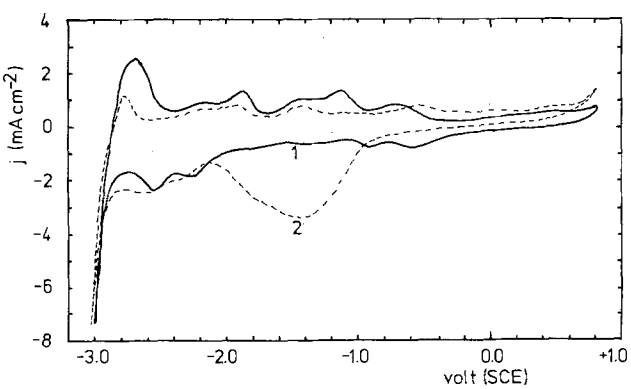


Fig. 2. Cyclic voltammograms on platinum in a 1M $LiClO_4$ solution in THF (curve 1) and in a 1M $LiClO_4$ solution in THF with 1% methanol (curve 2). Scan rate: 154 mV sec^{-1}.

* Electrochemical Society Active Member.

[1] Present address: Fundação Universidade de Brasília, Departamento de Química, 70.000 — Brasília-DF, Brazil.

Key words: organic solvents, cathodic catalyst, water, methanol formic acid.

Table I. Preliminary results for some prototypes of new lithium cells

	Sign	Cathodic reactant/catalyst	OCV (V)	Capacity (A-hr)	Yield (%)	Duration (hr)	Voltage-time curve	Temperature coefficient (mV/°C)
1	I2A2Z	HCOOH on C + Ni	3.3	3.6	3.3	460	—	10
2	I2A4PVC	HCOOH on C + Ni	3.3	3.6	7.4	115	—	10
3	I2B1Z	HCOOH on s. Ni	3.3	2.5	58	500	—	10
4	I2B3Z	HCOOH on s. Ni	3.3	6.7	40	700	Fig. 4	10
5	I3A1Z	CH_3OH on C + Ni	3.1	3.3	1	25	—	—
6	I4A1PVC	HCHO on C + Ni	3.0	1.8	6	64	—	—
7	I5A1	H_2O on s. Ni	3.0	—	—	—	—	—

voltammograms on platinum. Curve 1 was in a 1M lithium perchlorate solution in THF, with a scan rate of 154 mV sec^{-1}. The lithium deposition takes place at about −3.0V *vs.* the saturated calomel electrode (SCE). The reduction potential of the electrolytic solution is more negative than the potential of lithium deposition and therefore does not appear in the voltammogram. Curve 2 corresponds to the same solution as curve 1, with the addition of methanol, 1% in volume. Addition of methanol results in a reduction peak in the voltammogram.

Formic acid, formaldehyde, and water also undergo cathodic reduction in organic solutions. The reduction peak of water and formaldehyde begins at about −1.0V *vs.* SCE. The reduction peak of formic acid begins at about −300 mV *vs.* SCE.

Stationary current-potential curves.—The qualitative results reported above suggest the possibility of constructing lithium batteries using methanol, formic acid, formaldehyde, and water as cathodic reactants, since, considering the oxidation potential of lithium in organic solvents (about −3.0V *vs.* SCE), cells having a lithium anode and using the above-mentioned materials as cathodic reactants would have an electromotive force (emf) equal or greater than 2V.

To determine the current density obtainable from such cathodic reactants, stationary current-potential curves were measured in a 1M solution of lithium perchlorate in THF on different catalysts. Three such curves were registered for a 20 volume percent (v/o) methanol concentration on carbon containing 10% platinum, on sintered nickel, and on stainless steel.

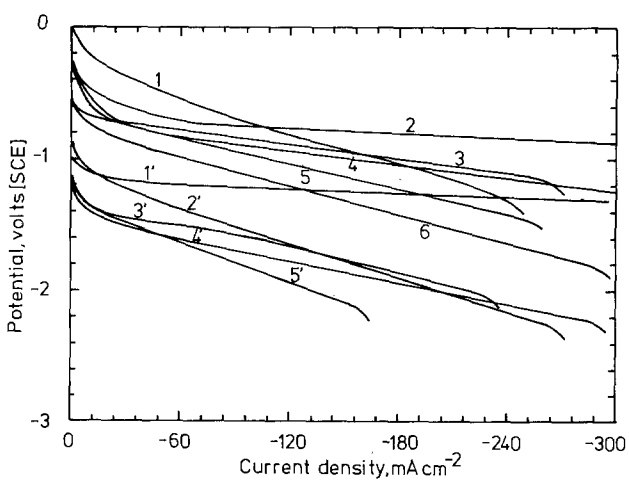


Fig. 3. Stationary current-potential curves for the cathodic reduction of formic acid at a concentration of 20%, in a 1M $LiClO_4$ solution in THF; on carbon with 10% platinum (curve 1), sintered nickel (curve 2), palladium-gold-gauze (curve 3), nickel-gauze (curve 4), and two different qualities of stainless steel (curves 5 and 6). Stationary current-potential curves for the cathodic reduction of formaldehyde at a concentration of 20% in a 1M $LiClO_4$ solution in THF; on sintered nickel (curve 1'), carbon with 10% platinum (curve 2'), two different qualities of stainless steel (curves 3' and 4'), and palladium-gold-gauze (curve 5').

With sintered nickel it is possible to get a current density greater than 200 mA cm^{-2} without a strong polarization of the electrode. On carbon with 10% platinum catalyst it is not possible to attain such a current density. In any case, up to about 70 mA cm^{-2} the potential has a higher value than for the curve on sintered nickel. With stainless steel we can obtain approximately 60 mA cm^{-2} at an acceptable potential of the electrode.

In Fig. 3 current-potential curves are shown for the cathodic reduction of formic acid in THF, registered at a concentration of about 20%, on carbon with 10% platinum (curve 1), sintered nickel (curve 2), palladium-gold-gauze (curve 3) nickel-gauze (curve 4), and stainless steel of different qualities (curves 5 and 6). On sintered nickel, current densities greater than H 300 mA cm^{-2} are possible without a strong polarization of the electrode. Up to about 100 mA cm^{-2} the reduction potential of the formic acid on carbon with 10% platinum is more positive than on sintered nickel. On other catalysts, *e.g.*, palladium-gold, current densities greater than 200 mA cm^{-2} are also obtainable.

As was pointed out earlier, formaldehyde undergoes cathodic reduction in THF on different catalysts. The curves in Fig. 3 were obtained for a formaldehyde concentration of about 20%, on sintered nickel (curve 1'), carbon with 10% platinum (curve 2'), two different types of stainless steel (curves 3' and 4'), and palladium-gold-gauze (curve 5').

The substances that have been discussed, such as methanol, formic acid, formaldehyde, and water, also undergo cathodic reduction in organic solvents other than THF. As an example, the curves obtained in a 1M solution of lithium perchlorate in propylene carbonate on different materials are mentioned. They are similar to those obtained in THF.

Half-cell experiments intended in the electrolytic solution without the above-discussed reactants, showed that when passing negligible current compared with those reported above the deposition potential of lithium (about −3.0V *vs.* SCE) and the oxidation potential of the electrolytic solution (about +1.5V *vs.* SCE) were reached almost instantly.

Preliminary results with some prototypes of lithium cells.—In Table II there are data for lithium cells employing water, methanol, formaldehyde, and formic acid as cathodic reactants. The open-circuit voltage (second column) is about 3.0V for all cells. The energy density was calculated with the open-circuit voltage, taking into account only the active materials (third

Table II. Some data for a new type of cell. The energy density was calculated with the OCV, taking into account only the active materials A, and with the operating voltage, taking into account the electrolyte solution B

Cathodic reactant	OCV (V)	Energy density A (kW-hr/lb)	A (kW-hr/kg)	B (W-hr/kg)	B (W-hr/dm³)	Electron per cons. molecules
H_2O	3.0	1.45	3.2	643	641	1
CH_3OH	3.1	0.95	2.1	385	352	1
HCHO	3.0	1.0	2.2	638	590	1
HCOOH	3.3	0.77	1.7	486	529	1

and fourth columns), and with the operating voltages, taking into account the solvent and the supporting electrolyte (fifth and sixth columns). The operating voltage of the lithium-water cell was estimated from a half-cell experiment at a current drain of 100 mA cm^{-2}, assuming for the lithium electrode, at this current drain, a polarization of about 150 mV. For the other cells, the operating voltage was taken from the discharge curves. In each case one electron is assumed for every molecule of reactant consumed. The energy density in all cases is very high, especially for water.

In the first, second, third, and fourth rows of Table I there are results for cells whose cathodic reagent was formic acid. In cells 1 and 2 the cathodic catalyst was carbon and nickel (1:1). In cells 3 and 4 the cathodic catalyst was a sintered nickel plate. The separators were a PVC-membrane in cell 2 and a zitex-membrane in the other. These separators develop a high internal resistance, and therefore it is not possible to charge the cells very much. To obviate this inconvenience a Nafion membrane or lithium ion-conducting solid separators (4-7) should be used.

The capacity was 3.6 A-hr for cells 1 and 2, 2.5 A-hr for cell 3, and 6.7 A-hr for cell 4. In cells 1 and 2 the yield was not very high. In cells 3 and 4 the yield was better, 58% and 40%, respectively. The cells can function without interruption for a long period of time.

Figure 4 shows a voltage-time curve for the discharge of the fourth cell of this group. The different parts of the curve correspond to the different currents passed through the cell. This cell functioned for 700 hr.

Cell 5 in Table I has methanol as the cathodic reactant and carbon nickel (1:1) as the cathodic catalyst. In the table the capacity, yield, and duration are indicated. The yield was low, about 1%, because of some methanol passing through the separator to the anodic compartment and reacting with the anode (lithium). A lithium ion-conducting separator (4-7) or a selective membrane that does not permit the methanol going to the anodic compartment should be employed.

In the last two rows of Table I results are shown for a lithium-formaldehyde and for a lithium-water cell whose cathodic catalysts were carbon-nickel (1:1) and sintered nickel, respectively. The ohmic drop, in all cases, was not subtracted.

Conclusion

These results show the possibility of constructing batteries using water, methanol, formic acid, formaldehyde, etc., as cathodic reactants in organic solutions. The cathode of these batteries is essentially the hydrogen electrode, whose potential depends on the acidity of the material employed as the proton source and on the catalyst. The current densities that can be obtained from the cathode are very high, as the stationary current-potential curves show. In the preliminary tests of the prototypes it was not possible to obtain such current densities due to the high internal resistance caused by the separators. The separators which were used were more or less permeable to the cathodic reactants. In the cells with water (8, 9), formaldehyde (aqueous solution), and formic acid, a film of lithium hydroxide and of lithium formate was formed by chemical reaction of the cathodic reactant with the anode. This film prevents, to a certain extent, further chemical reaction, but causes some passivation. In the cells with methanol as the cathodic reactant, the lithium methanolate formed by chemical reaction on the anode does not form a protective film and, therefore, the life of the anode depends greatly on the diffusion coefficient of the methanol through the separator. Hydrogen is liberated in the cathodic compartment, and can be employed in fuel cells or stored for further applications. Experiments to improve this new type of cell are now being made in our laboratory at the University of Brazil.

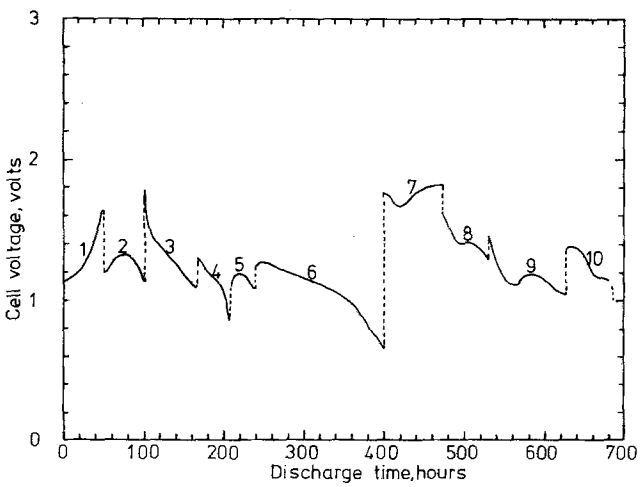


Fig. 4. Voltage-time curve for the discharge of cell 4 in Table I, with the charges of 5.5 (1), 10.0 (2), 7.2 (3), 6.0 (4), 5.0 (5), 4.0 (6), 1.5 (7 and 9), 2.0 (8), and 1.0 mA (10).

Summary

It was ascertained, using the cyclic voltammetry and by plotting stationary current-potential curves, that substances such as water, methanol, formic acid, and formaldehyde can be cathodically reduced in organic solvents such as tetrahydrofuran and propylene carbonate on catalysts such as platinum, sintered nickel, stainless steel, etc. There is a potential interval equal to or greater than 2V between the reduction potential of these substances and the oxidation potential of lithium. The stationary current-potential curves for experiments with cathodic half-cells showed that with all these cathodic reactants, current densities greater than 100 mA cm^{-2} can be obtained without the electrode becoming excessively polarized. Since the molecular weight of these substances is small it is possible to obtain great energy densities with them. Prototypes of lithium batteries using these cathodic materials were constructed and tested. An open-circuit voltage of about 3.1V was measured for all cases. Some prototypes worked without interruption for 700 hr. Depending on the cathodic material, energy densities between 1.7 and 3.2 kW-hr kg^{-1} can be obtained.

Acknowledgments

The author wishes to thank the CNPq for supporting the costs of travel and sojourn at the 27th meeting of the International Society of Electrochemistry, September 1976, where part of this paper was presented. Thanks are also extended to Dr. Vielstich for his helpful suggestions, and to Drs. P. G. David and G. East, my thanks for the revision of the English text.

Manuscript submitted Dec. 21, 1976; revised manuscript received June 22, 1977.

Any discussion of this paper will appear in a Discussion Section to be published in the June 1978 JOURNAL. All discussions for the June 1978 Discussion Section should be submitted by Feb. 1, 1978.

Publication costs of this article were assisted by the Institute of Physical Chemistry, University of Bonn, Germany.

REFERENCES

1. A. A. Inocêncio, Paper No. 237 presented at the International Society of Electrochemistry meeting, Zürich, September 1976.
2. S. Gilman, in Proceedings of the 26th Power Sources Symposium, April-May 1974.
3. A. N. Dey and E. J. Rudd, *This Journal*, **121**, 1294 (1974).
4. D. R. Flinn and K. H. Stern, *ibid.*, **123**, 978 (1976).
5. R. T. Johnson, Jr., R. M. Biefeld, M. L. Knotek, and B. Morosin, *ibid.*, **123**, 680 (1976).

6. I. D. Raistrick, C. Ho, and R. A. Huggins, *ibid.*, **123**, 1469 (1976).
7. G. C. Farrington, *ibid.*, **123**, 591 (1976).
8. E. L. Littauer and K. C. Tsai, *ibid.*, **123**, 771, 965 (1976).
9. D. A. Fustier, W. F. Graydon, and F. R. Foulkes, *ibid.*, **123**, 1259 (1976).
10. F. Beck, "Elektrorganische Chemie," Verlag Chemie (1974).
11. W. Vielstich, "Fuel Cells," p. 349, Wiley-Interscience, New York (1968).

The Effects of Cations and Anions on Hydrogen Chemisorption at Pt

J. C. Huang,* W. E. O'Grady,* and Ernest Yeager*

Case Laboratories for Electrochemical Studies and the Department of Chemistry, Case Western Reserve University, Cleveland, Ohio 44106

The adsorption of hydrogen on the platinum electrode has been the subject of extensive investigation [see. *e.g.*, Ref. (1-10)]. Many questions persist, however, as to the true nature of the multiple hydrogen adsorption peaks observed in linear sweep voltammetry studies of single crystal as well as polycrystalline platinum. Up to five peaks have been observed (10) in ultrapure dilute sulfuric acid electrolytes. Factors which have been proposed to account for these multiple peaks include different adsorption sites on a given crystallographic plane, a distribution of surface crystallographic orientations even with a given single crystal macro-orientation, induced heterogeneity associated with the perturbing of adjacent sites by the adsorbed hydrogen itself, and the adsorption of anions which create further surface heterogeneity by blocking some sites and perturbing adjacent sites. The situation is further complicated by the fact that in acid solutions the point of zero charge (pzc) for Pt falls within the hydrogen adsorption-desorption region. Thus the adsorption-desorption of anions can closely couple to the hydrogen adsorption-desorption process.

In considering the role of oxyanions Conway and his co-workers (10) have examined both their own linear sweep voltammetry data and that of others and conclude that anion adsorption changes the relative heights of the hydrogen adsorption peaks but has relatively little effect on the peak potentials, and hence, adsorption energies. On this basis they conclude that the anions principally affect the distribution of adsorbed hydrogen on the surface but do not disturb significantly the adsorption energy for a particular type of site. In examining the dependence of hydrogen adsorption on Pt on the electrolyte, however, we differ with this conclusion and find that ionic adsorption substantially shifts the potentials in addition to the relative heights of the peaks. These effects appear well beyond what can be explained on the basis of simple blocking of hydrogen adsorption sites.

The purpose of this note is to present experimental data to substantiate this view. Despite the relatively large amount of data on ion adsorption effects, we have found it necessary to obtain additional data to more clearly establish the trends. Much of the data in this literature has been obtained by adding various ionic components to sulfuric acid solutions. The HSO_4^- and/or $SO_4^=$ ions, however, are moderately strongly adsorbed on Pt in the hydrogen adsorption region as the present work indicates, and this complicates studies of the adsorption of other ions in this electrolyte. The present study shows that $HClO_4$ and HF are better reference electrolytes for anion studies. The measurements have also been extended to alkaline solutions. Relatively little data have been reported for hydrogen adsorption on Pt in alkaline solutions and even then much of this has been obtained by charging techniques (8, 9) which do not show up well the fine structure in this potential region.

* Electrochemical Society Active Member.

Key words: hydrogen adsorption, platinum, electrosorption, voltammetry, hydrogen electrode.

Experimental

Conventional techniques were used to record the linear sweep voltammograms. For all work herein reported the sweep rate was 100 mV/sec and the voltammograms recorded after several cyclic sweeps. The measurements were made in an all-Teflon cell, consisting of a main working electrode compartment and two separate compartments for the reference and counterelectrodes. The working electrode was a 0.5 cm disk of reference grade Pt (99.999% pure) mounted in Teflon. The reference and counterelectrodes were β-Pd-H using Pd foils charged continuously with purified H_2 from the back side. O_2 was removed from the solution by bubbling purified helium through the cell prior to measurements. The cell was mounted in a N_2-atmosphere box to prevent CO_2 and dust contamination of the electrolyte in the filling of the cell and to eliminate any possible diffusion of O_2 into the cell.

The working electrode surface was first polished with alumina to a mirror finish, washed with distilled water, degreased with spectro grade isopropanol, cleaned with 1:1 volume ratio H_2SO_4-HNO_3 (reagent grade), rinsed with triply distilled water followed by pyrolyzed water, further cleaned with ultrasound in a solution of the same composition as the electrolyte to be used, and then either introduced into the cell or stored in pyrolyzed water. All of these operations were carried out in carefully cleaned Teflon vessels. This procedure was repeated for each new electrolyte.

The acid solutions were prepared with ultrapure acids (Ultrex H_2SO_4 from J. T. Baker, ultrapure 49% HF and 85% H_3PO_4 from Apache Chemicals, ultrapure 70% $HClO_4$ from Ventron Alfa Products) and pyrolyzed water. The latter was prepared according to the procedure described by Conway *et al.* (11). The H_2SO_4, $HClO_4$, and H_3PO_4 solutions were prepared in cleaned glassware and used without further chemical treatment. All HF solutions were prepared in Teflon bottles. The HF solution was first made up as 10*M* and subjected at this concentration to activated charcoal purification, principally to remove trace chloride. Omission of the activated charcoal purification had no significant effect on the results. The solution was then diluted down to desired concentration with pyrolyzed water.

Solutions of 0.1*M* NaOH were also prepared in Teflon bottles and subjected to the activated charcoal purification. A 50% stock solution of NaOH was first formulated from special low carbonate NaOH pellets (J. T. Baker) with triply distilled water. This solution was allowed to stand over several weeks and the solution

decanted many times to remove precipitated Na_2CO_3. The carbonate solubility in 50% NaOH is $\sim 10^{-4}M$ and the carbonate concentration in the 0.1*M* NaOH should be $\sim 5 \times 10^{-7}M$.

Before each measurement, the final solution was preelectrolyzed at a potential of 1.5V between two auxiliary Pt electrodes ($4 \times 2 \times 0.01$ cm) within the Teflon cell for at least 24 hr for acid solutions and 48 hr for the NaOH solutions.

Results

Figures 1 and 2 indicate the voltammetry curves for 0.1*M* HF and 0.1*M* $HClO_4$ as well as the effect of adding successively increasing amounts of H_2SO_4 to these electrolytes. Only the hydrogen region is shown for purposes of clarity, but the sweep in the anodic direction was continued out to 1.4V *vs.* RHE. The curves for the HF and $HClO_4$ solutions resemble each other closely. The addition of H_2SO_4 to either of these electrolytes has a substantial effect on the hydrogen adsorption region with respect to the position as well as relative height of the strongly adsorbed hydrogen peak IV [H_{A4}, using the notation of Conway *et al.* (10)]. The addition of up to 0.1*M* HF to 0.05*M* H_2SO_4, however, has virtually no effect on the hydrogen adsorption. This implies that undissociated HF as well as F^- are not adsorbed to any significant extent with the presence of SO_4^{2-}. Figure 3 compares the curves for 0.02*M* H_2SO_4 and 0.14*M* HF, both of which have essentially the same *p*H. The shift in potential and increment in height of peak IV is similar to that noted by Frumkin *et al.* (6) although Fig. 3 shows clearly four peaks for the H_2SO_4 solution while the earlier Soviet work indicated only two. This figure indicates that the principal differences between the HF and H_2SO_4 solution are not due to *p*H.

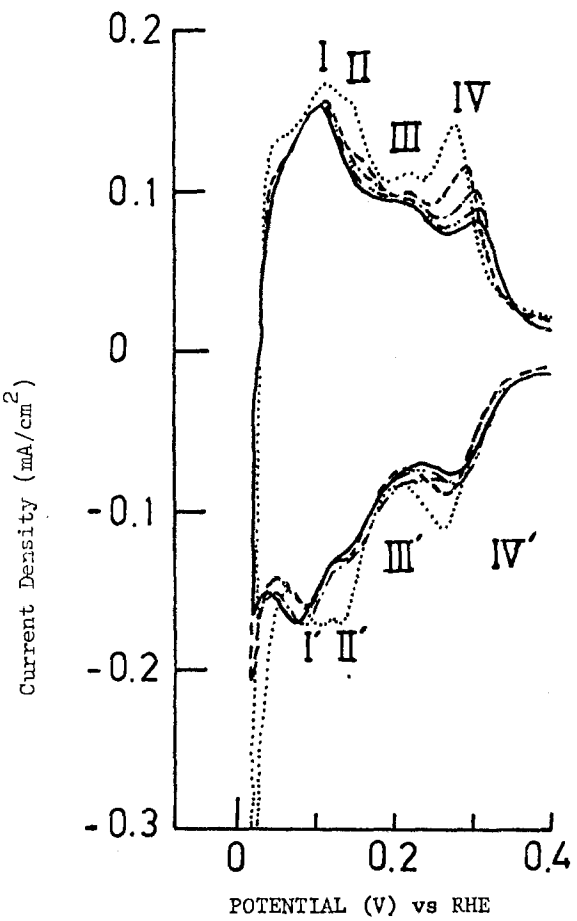


Fig. 1. Voltammograms for Pt in 0.1M HF with various concentrations of H_2SO_4 added. —— 0.1M HF, –·–· 0.1M HF + 5 × 10^{-5}M H_2SO_4, –·– 0.1M HF + 5 × 10^{-4}M H_2SO_4, – – – 0.1M HF + 5 × 10^{-3}M H_2SO_4, ... 0.1M HF + 5 × 10^{-2}M H_2SO_4.

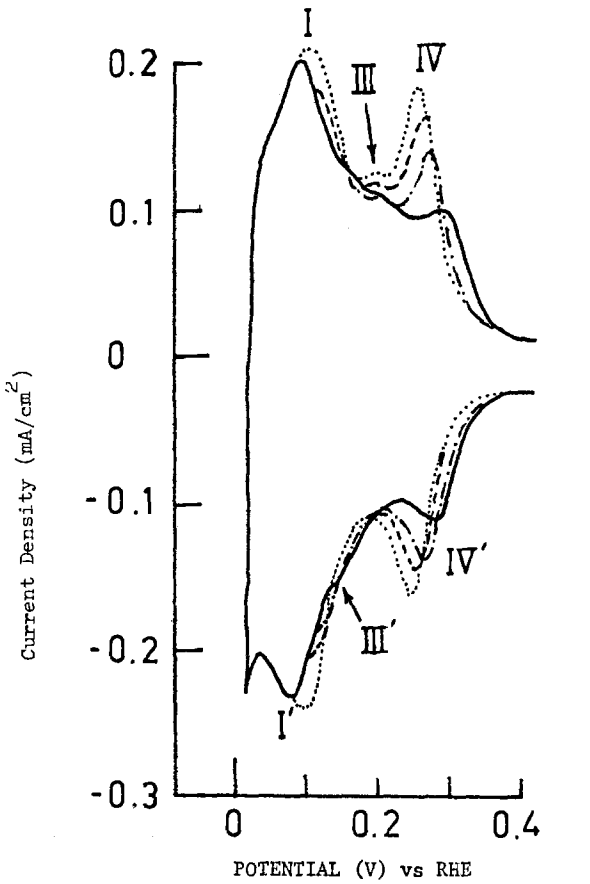


Fig. 2. Voltammograms for Pt in 0.1M $HClO_4$ with various concentrations of H_2SO_4 added. —— 0.1M $HClO_4$, –·– 0.1M $HClO_4$ + 5 × 10^{-4}M H_2SO_4, – – – 0.1M $HClO_4$ + 5 × 10^{-3}M H_2SO_4, ... 0.1M $HClO_4$ + 5 × 10^{-2}M H_2SO_4.

In voltammetry studies of the hydrogen peaks in H_2SO_4 solutions reported in the literature, peaks I, III, and IV have usually been observed in the anodic sweep but only peaks I and IV have shown up in the cathodic sweep. Various explanations have been proposed to explain peak III in the anodic sweep, and particularly why peak III is missing in the cathodic sweep (7, 10, 12-14). In the present work the counterpart of the anodic peak III is evident in the cathodic sweeps in 0.1*M* HF (Fig. 1) and 0.1*M* $HClO_4$ (Fig. 2) although not in the H_2SO_4 solutions (Fig. 3 and 6) or 0.033*M* H_3PO_4, (Fig. 4) which rather closely resembles H_2SO_4. The lack of peak III in the cathodic sweep in the H_2SO_4 and H_3PO_4 solutions is probably due principally to the strong overlap of the other more predominant peaks.

Figures 5 and 6 indicate the effects of HCl additions to 0.1*M* HF and 0.5*M* H_2SO_4. Peak IV in both the HF and H_2SO_4 is shifted substantially in the cathodic direction. The shift amounts to ~120 mV with $10^{-2}M$ HCl in the 0.1*M* HF solution. This shift is quite linear with the log concentration of H_2SO_4 or HCl added to the HF or $HClO_4$ solutions as shown in Fig. 7. Such linearity may arise because of the logarithmic nature of the anion adsorption isotherm.

Cations have much less effect on the hydrogen adsorption on Pt in acid solutions. The addition of chloride-free $(C_2H_5)_4NF$ to the HF solution shifts peak I in the anodic direction and peak IV in the cathodic direction (see Fig. 8), whereas the addition of Cs_2SO_4 to H_2SO_4 only slightly shifts the weak hydrogen adsorption peak I in the anodic direction (Fig. 9). The addition of either 5 × $10^{-3}M$ Na_2SO_4 or 5 × $10^{-3}M$ Li_2SO_4 to 0.05*M* H_2SO_4 has a negligible effect as is

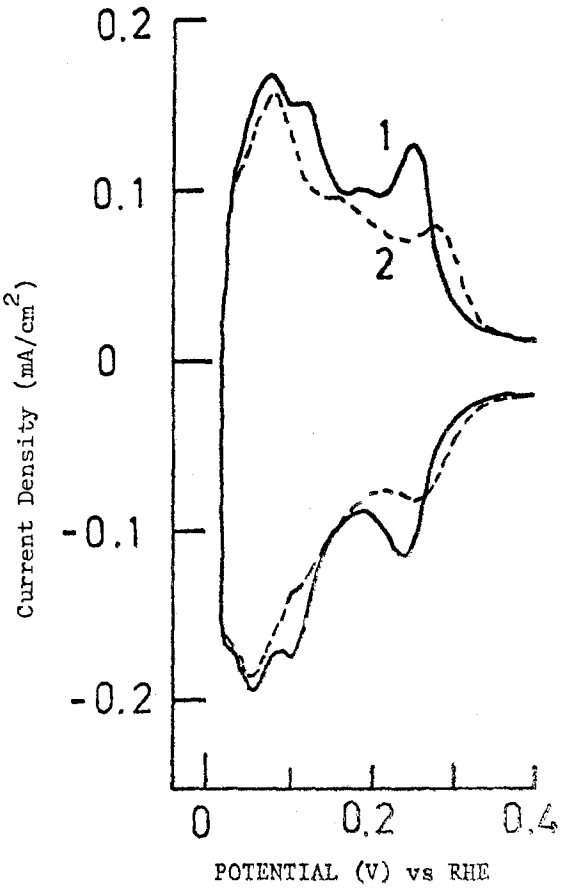


Fig. 3. Voltammograms for Pt in 0.02M H_2SO_4 and 0.14M HF. Curve 1, 0.02M H_2SO_4 and curve 2, 0.14M HF.

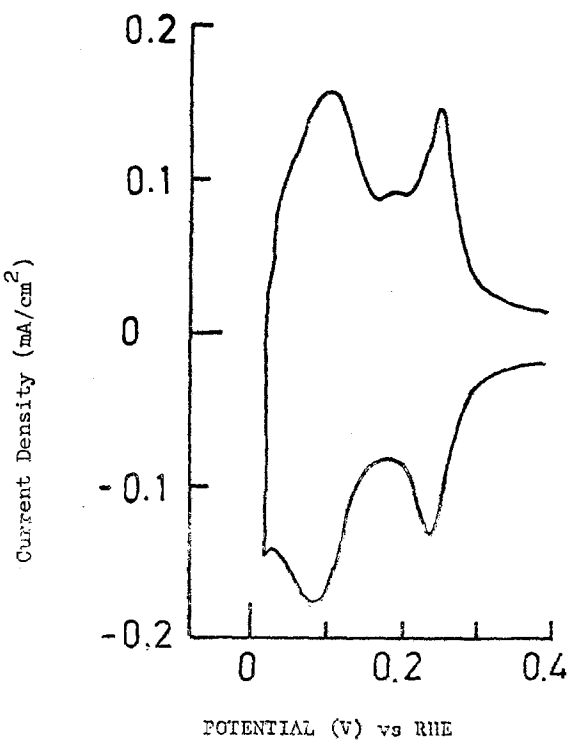


Fig. 4. Voltammogram for Pt in 0.033M H_3PO_4

also the case with the addition of $5 \times 10^{-4}M$ $Ba(ClO_4)_2$ or $5 \times 10^{-4}M$ $Sr(ClO_4)_2$ to the $0.1M$ $HClO_4$.

The hydrogen adsorption region is quite different in alkaline solutions (see Fig. 10 and 11). Only two peaks (A and B) are clearly observed. Peak C corresponds to

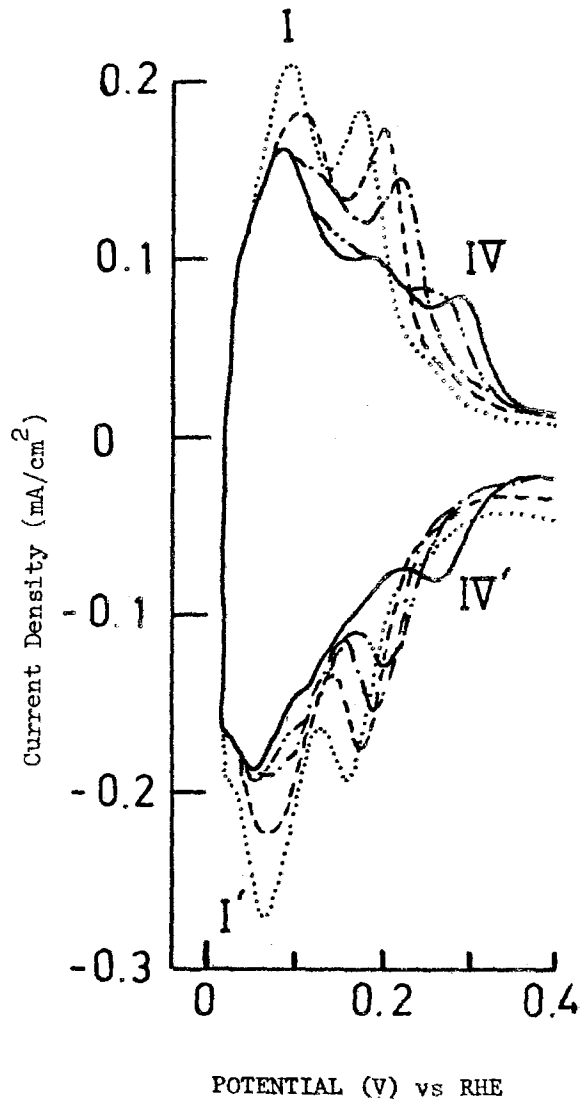


Fig. 5. Voltammograms for Pt in 0.01M HF with various concentrations of HCl added. —— 0.1M HF, -·-· 0.1M HF + 10^{-5}M HCl, -·- 0.1M HF + 10^{-4}M HCl, --- 0.1M HF + 10^{-3}M HCl, ... 0.1M HF + 10^{-2}M HCl.

the anodic oxidation of solution phase H_2 produced during the cathodic sweep. In contrast to the acid media, the positions and heights of both peaks A and B are substantially influenced by the addition of $Ba(OH)_2$ or $Ca(OH)_2$. The addition of Cl^-, F^-, ClO_4^-, PO_4^{-3}, SO_4^{-2}, or SiO_3^{-2} up to $10^{-3}M$ had no detectable effect and $10^{-3}M$ Br^- had only a slightly perceptible effect. The pzc in the alkaline solutions even in the presence of these various anions is probably still quite anodic to the hydrogen adsorption region, and thus specific adsorption of these anions is small in this region. With a strongly specifically adsorbed anion such as I^- in alkaline solution the effects on the hydrogen adsorption peaks are pronounced (see Fig. 12). Tracking of the peak shifts in position *vs.* height changes, however, is rather difficult with the data in Fig. 12.

Discussion

It is difficult to explain all of the anion and cation effects in acid and alkaline solutions on the basis of a single model for the interaction of the ions with the hydrogen adsorption. The situation is complicated by a lack of a clear understanding of the extent to which various structural features of the electrode surface are responsible for the several hydrogen peaks, *i.e.*, the importance of intrinsic *vs.* induced heterogeneity [see *e.g.*, Ref. (10)]. The addition of various cations and

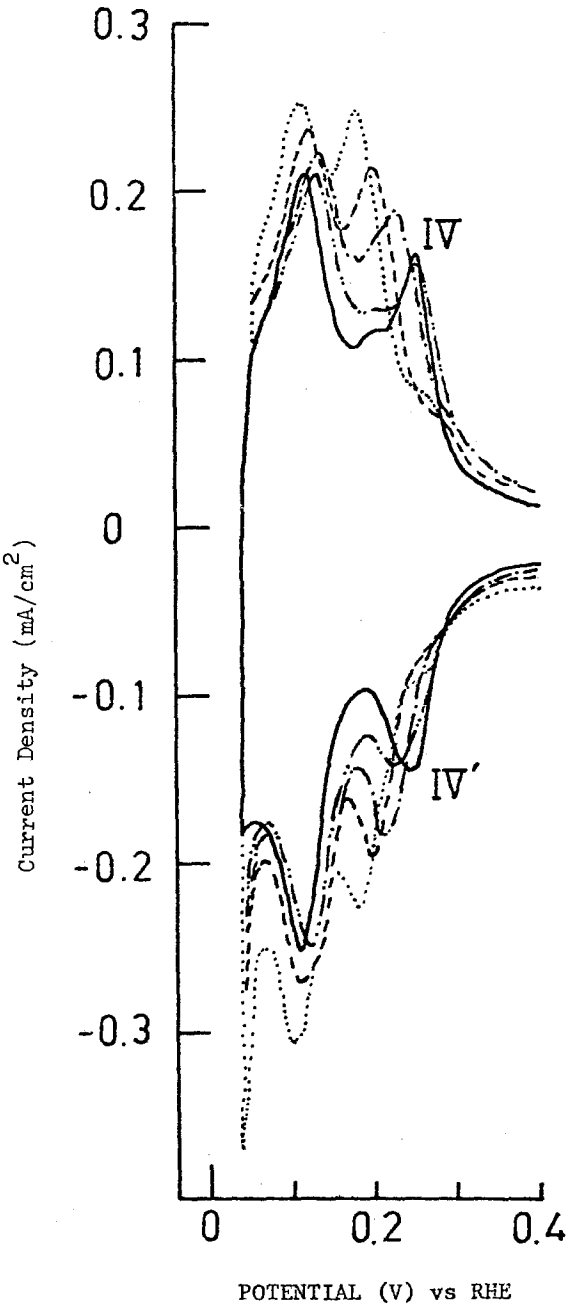


Fig. 6. Voltammograms for Pt in 0.5M H_2SO_4 with various concentrations of HCl added. ——0.5M H_2SO_4, –·–· 0.5M H_2SO_4 + 10^{-5}M HCl, –·– 0.5M H_2SO_4 + 10^{-4}M HCl, – – – 0.5M H_2SO_4 + 10^{-3}M HCl, ... 0.5M H_2SO_4 + 10^{-2}M HCl.

anions to electrolytes such as HF and $HClO_4$ can bring about changes in the structure of the hydrogen adsorption region in the voltammetry curves in a number of ways:

1. *Blocking of sites by anion adsorption and coupling of hydrogen adsorption and anion desorption.*—Specific adsorption of ions, particularly anions, can block sites on which hydrogen otherwise would be adsorbed. For hydrogen to adsorb on these sites requires the desorption of anions with the result that hydrogen adsorption and anion desorption are coupled. Such coupling can be expressed through the following equation

$$yH^+ + X_{ad}^{-(z-\sigma_x)} + (y\sigma_H + \sigma_x)e^- \rightarrow yH_{ad}^{(1-\sigma_H)} + X^{-z}$$

This effect can lead to a shift in the peak potential as well as peak area. Strong anion adsorption makes it more difficult to adsorb hydrogen and hence a shift to

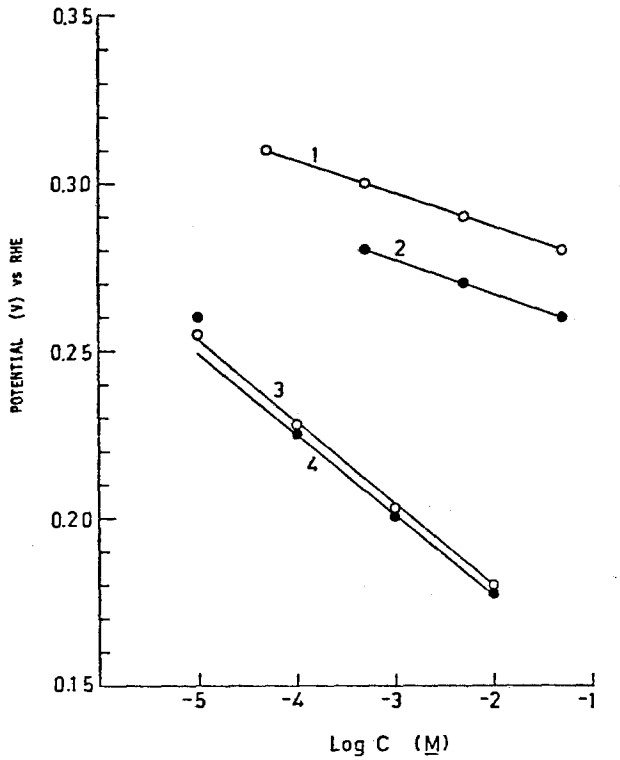


Fig. 7. The shift of strongly bound hydrogen peak potential as a function of the concentration of added anions. Curve 1, 0.1M HF + H_2SO_4; curve 2, 0.01M $HClO_4$ + H_2SO_4; curve 3, 0.1M HF + HCl; curve 4, 0.5M H_2SO_4 + HCl.

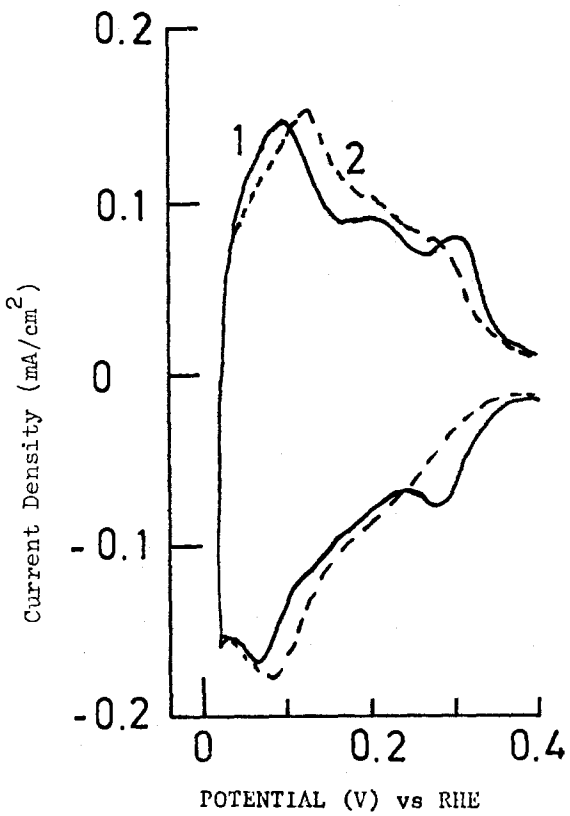


Fig. 8. Voltammograms for Pt in 0.1M HF with $(C_2H_5)_4N^+$ cations added. Curve 1, 0.1M HF and curve 2, 0.01M HF + 5 × 10^{-3}M $(C_2H_5)_4NF$.

more cathodic potentials should occur for the particular peak(s) involved with such coupling.

Evidence for this effect is to be found in Fig. 13, in which the ratio of the charge associated with the strong

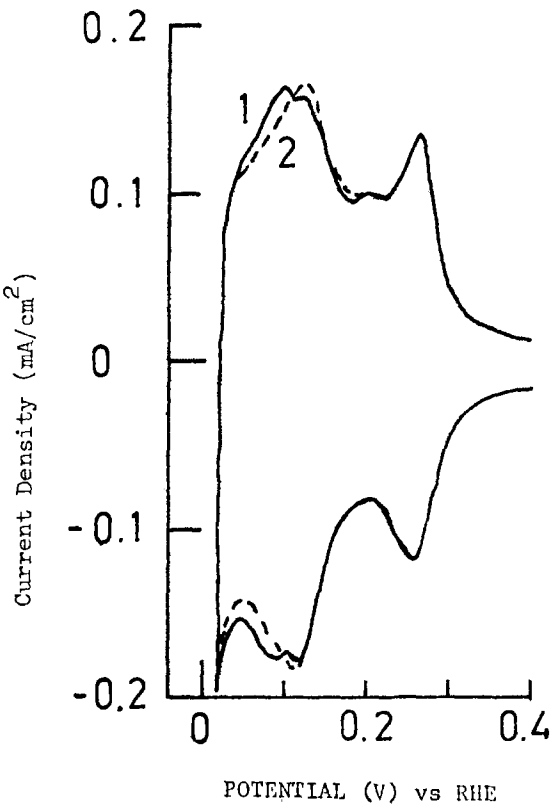


Fig. 9. Voltammograms for Pt in 0.05M H_2SO_4 with Cs^+ cations added. Curve 1, 0.05M H_2SO_4 and curve 2, 0.05M H_2SO_4 + 5 × 10^{-3}M Cs_2SO_4.

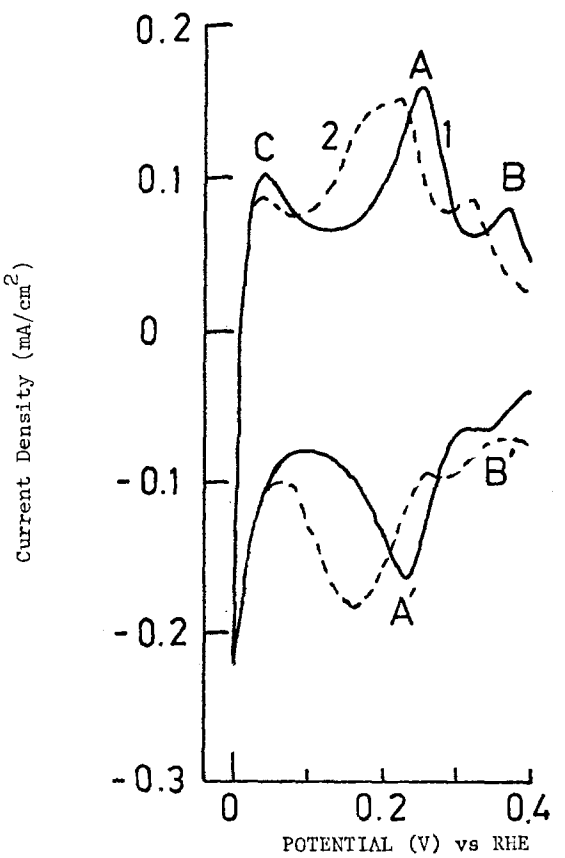


Fig. 10. Voltammograms for Pt in 0.1M NaOH with Ba^{2+} cations added. Curve 1, 0.01M NaOH and curve 2, 0.1M NaOH + 5 × 10^{-3}M $Ba(OH)_2$.

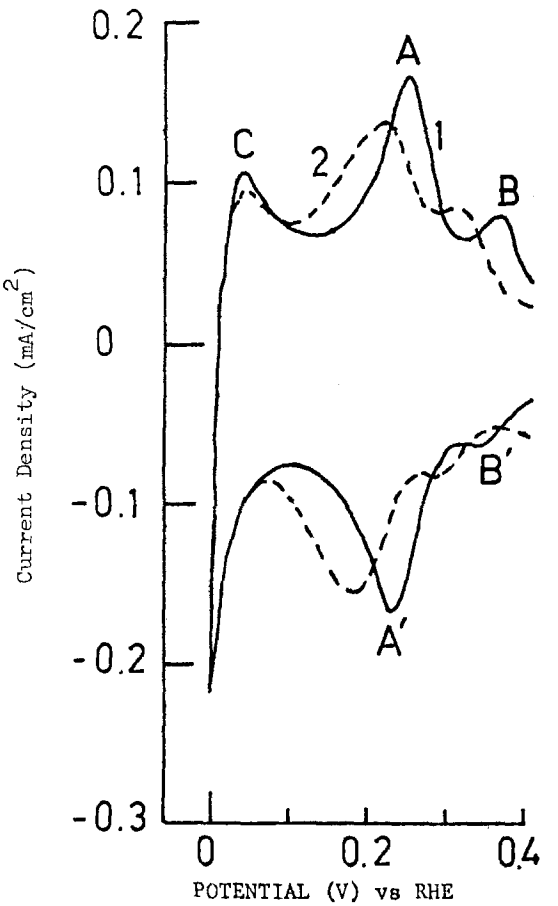


Fig. 11. Voltammograms for Pt in 0.1M NaOH with Ca^{2+} cations added. Curve 1, 0.1M NaOH and curve 2, 0.1M NaOH + 5 × 10^{-3}M $Ca(OH)_2$.

hydrogen adsorption peak to the total charge for hydrogen adsorption is shown to increase linearly with the log of the concentration of sulfate added to the 0.1*M* $HClO_4$ and HF electrolytes. The specific adsorption of the SO_4^{-2} should follow a Temkin isotherm over this concentration region, and hence the amount of specifically adsorbed sulfate is expected to be a linear function of the log of the concentration of this ion in solution. The linearity in Fig. 13 implies that the charge ratio is linearly dependent on the amount of specifically adsorbed SO_4^{-2}. In principle, the coupling mechanism proposed above should lead to a linear dependence of the charge Q_{IV} under the strong peak *IV* on log $C_{SO_4^{-2}}$ and not the charge ratio Q_{IV}/Q. It is difficult, however, to ensure that the ratio of true-to-apparent electrode area is constant between measurements and hence it has been preferable to plot Q_{IV}/Q. Since the Q_{IV}/Q is rather small compared to unity, a near linear relation is still observed in Fig. 13.

2. *Modification in the hydrogen adsorption energies for sites adjacent to adsorbed anions.*—The adsorption energies for hydrogen on sites adjacent to adsorbed anions are expected to be modified. This effect can occur through changes in the surface electronic structure as well as local changes within the compact double layer, particularly the water dipoles immediately adjacent to the electrode. Such electronic interactions of the anions with hydrogen adsorbed on adjacent sites are similar to those considered by Conway *et al.* (10) in regard to induced heterogeneity. The authors believe this effect to be small except for strongly adsorbed ions such as iodide where very substantial electronic interactions occur between metal surface orbitals and those of the iodide.

3. *Changes in the potential distribution across the interface.*—For ionic double layer effects to have a

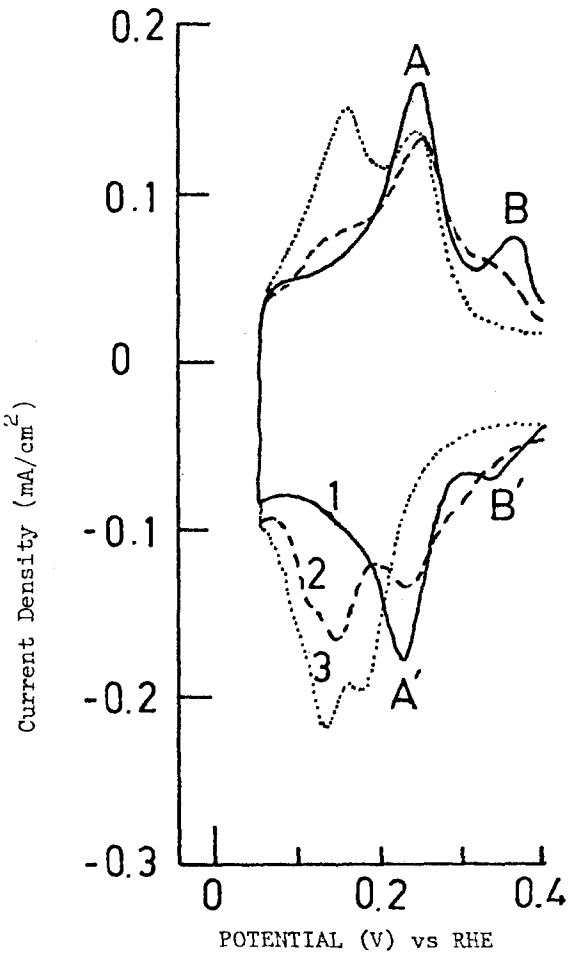


Fig. 12. Voltammograms for Pt in 0.1M NaOH with I^- anions added. Curve 1, 0.1M NaOH; curve 2, 0.1M NaOH + 10^{-5}M NaI; curve 3, 0.1M NaOH + 10^{-3}M NaI.

large influence on hydrogen adsorption requires that the H_{ad} have substantial positive or negative charge. Double layer effect may produce minor shifts in the peak potentials such as observed with some cations in alkaline solutions, but it is doubtful if the M-H dipoles are sufficiently strong to explain the large shifts in the peak potentials observed with anion adsorptions in acid electrolytes.

4. *Surface restructuring.*—During the sweep of the potential into the anodic film formation region, the ions adsorbed on the metal and the anodic film possibly can influence the surface restructuring which occurs during the oxidation and subsequent reduction of the platinum surface. Thus the microstructure and distribution of lattice sites prevailing in the hydrogen adsorption region are probably dependent on the electrolyte composition. This effect can result in changes in the relative peak heights, but should not result in significant shifts in the peak potentials.

Of these various mechanisms for accounting for anion and cation effects, the authors believe that the coupling of the ionic adsorption to the hydrogen adsorption (mechanism 1) is predominant for anion adsorption effects in acid media and that changes in the double layer-potential distributions (mechanism 3) is predominant for the cation adsorption effects on alkaline solutions.

Acknowledgments

The authors are pleased to acknowledge the support of this research by NASA (Ames), and helpful discussions with our colleagues, Drs. B. D. Cahan and R. K. Sen.

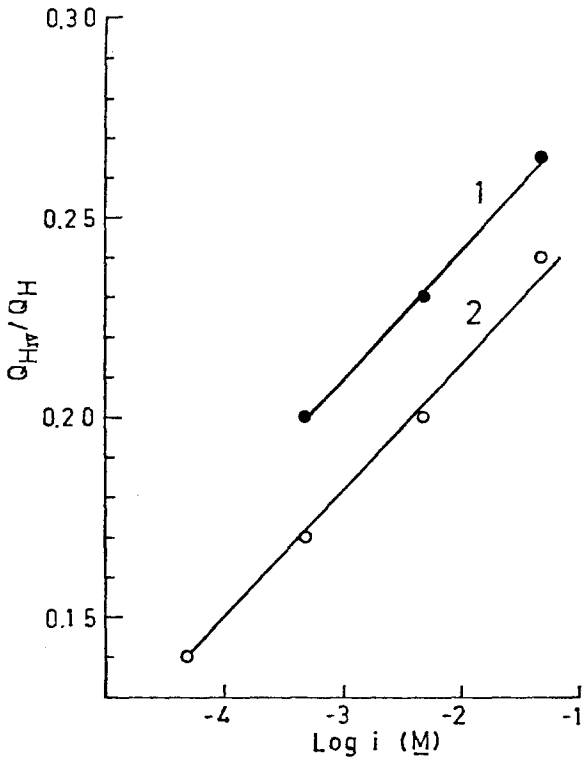


Fig. 13. The plot of the charge under the strongly bound hydrogen peak as a logarithmic function of SO_4^{2-} concentration. The charge is expressed as a ratio Q_{HIV}/Q_H to the total charge for hydrogen chemisorption. Curve 1, SO_4^{2-} in 0.1*N* $HClO_4$ and curve 2, SO_4^{2-} in 0.1*N* HF.

Manuscript submitted Sept. 10, 1976; revised manuscript received Jan. 4, 1977.

Any discussion of this paper will appear in a Discussion Section to be published in the June 1978 JOURNAL. All discussions for the June 1978 Discussion Section should be submitted by Feb. 1, 1978.

Publication costs of this article were assisted by Case Western Reserve University.

REFERENCES

1. M. W. Breiter, *Electrochim. Acta*, **8**, 925 (1963) and references therein.
2. S. Gilman, *J. Phys. Chem.*, **68**, 2098, 2112 (1964).
3. V. S. Bagotzky, Yu B. Vaassilyev, J. Weber, and J. N. Pirtskhalva, *J. Electroanal. Chem.*, **27**, 31 (1970).
4. G. D. Azkumbaeva, F. M. Tokabaeva, and D. V. Sokolskii, *Elektrokhimiya*, **6**, 777 (1970).
5. S. H. Cadle and S. Bruckenstein, *Anal. Chem.*, **43**, 1959 (1971).
6. B. I. Podlovchenko, N. A. Epshtein, and A. N. Frumkin, *J. Electroanal. Chem.*, **53**, 95 (1974).
7. K. Kinoshita, J. Lundquist, and P. Stonehart, *J. Catal.*, **31**, 375 (1973).
8. A. Hickling, *Trans. Faraday Soc.*, **41**, 333 (1945).
9. V. E. Kazarinov, *Z. Phys. Chem. (Leipzig)*, **226**, 167 (1964).
10. H. Angerstein-Kozlowska, W. B. A. Sharp, and B. E. Conway, in "Proceedings of the Symposium on Electrocatalysis," M. W. Breiter, Editor, The Electrochemical Society Softbound Symposium Series, Princeton, N.J. (1974) and references therein.
11. B. Conway, H. Angerstein-Kozlowska, W. Sharp, and E. Criddle, *Anal. Chem.*, **45** . 1331 (1973).
12. F. Will, *This Journal*, **112**, 451 (1965).
13. M. W. Breiter, "Electrochemical Processes in Fuel Cells," p. 60, Springer-Verlag, New York (1969).
14. P. Stonehart, *Electrochim. Acta*, **15**, 1853 (1970).

JOURNAL OF THE ELECTROCHEMICAL SOCIETY

SOLID-STATE SCIENCE AND TECHNOLOGY

NOVEMBER 1977

Volatile Products in the Corrosion of Cr, Mo, Ti, and Four Superalloys Exposed to O_2 Containing H_2O and Gaseous NaCl

George C. Fryburg,* Robert A. Miller,[1] Fred J. Kohl, and Carl A. Stearns

National Aeronautics and Space Administration, Lewis Research Center, Cleveland, Ohio 44135

ABSTRACT

Cooled target collection techniques were used to study the formation of volatile products when samples of Cr, Ti, IN-738, 713C, NASA-TRW VIA, and B-1900 were exposed at elevated temperatures to oxidizing environments containing $H_2O(g)$ and $NaCl(g)$. Samples were heated to 1050°C in 1 atm of slowly flowing oxygen, saturated with water at 21°C, and containing about 50 ppm $NaCl(g)$. Volatile products were detected for all materials except B-1900 and Ti. High pressure mass spectrometric sampling was used to directly identify volatile products emanating from samples of Cr and IN-738 subject to the above environments. Mo samples were also studied at 675°C with 4 ppm $NaCl(g)$ added to the $O_2 + H_2O$ environment. For Cr and IN-738 the volatile species were identified primarily as $(NaCl)_{1,2,3}CrO_3$, $(NaOH)_{1,2}$-CrO_3, $Na_2Cr_2O_7$, and $CrO_2(OH)_2$. These same species are deduced to prevail for 713C and NASA-TRW VIA. For Mo, the major species identified were $(NaCl)_{1,2}(MoO_3)_3$, $NaOH(MoO_3)_3$, $(MoO_3)_{3,4}$, and $MoO_2(OH)_2$.

Equilibrium thermodynamic calculations applied to gas turbine engines operating under conditions thought to be conducive to hot corrosion attack indicate that the engine hot section environment should be relatively rich in the contaminant gases $NaCl(g)$, $NaOH(g)$, and $HCl(g)$ (1). These chemical species are generally considered as highly reactive at high temperature, and therefore it seems reasonable to expect that they might play a significant role in the hot corrosion process. Previously it had been demonstrated that adverse effects could be associated with exposure of hot oxidizing metals to partial pressures of $NaCl(g)$ (2-4). Hancock *et al.* (2) have shown that additions of $NaCl(g)$ to the oxidizing environment can compromise the so-called protective oxide scale on certain alloys used in turbine engines. For the oxidation of chromium, Stearns *et al.* (3) presented evidence which indicates that additions of $NaCl(g)$ lead to increased rates of chromium transport from the sample. Their results indicated a first-order dependence of Cr-compound vaporization on $NaCl(g)$ partial pressure and on oxygen pressure. They identified the vapor species by high pressure mass spectrometry. Jones *et al.* (4) have presented evidence to show the $NaCl(g)$ can: (*i*) induce dissociation of $Na_2SO_4(c)$; (*ii*) promote spalling of Al_2O_3 surface oxide; (*iii*) remove Cr from samples as a volatile "chromchloride"; and, (*iv*) accelerate the degradation, by sulfidative oxidation, of certain CoCrAlY-coated alloys.

The phenomenology of interaction between oxidizing metals and the gaseous species $NaCl(g)$, $NaOH(g)$, and $HCl(g)$ is not well characterized and the operative mechanisms are not understood. To elucidate the kinetics and mechanisms of such interactions, we have been investigating various metal-oxygen-contaminant gas systems at elevated temperatures. Our previously reported studies of $Cr + O_2 + NaCl(g)$ yielded some kinetic information for this system and identified $(NaCl)_{1,2,3}CrO_3(g)$ as the major volatilizing species (3). The work reported here is a continuation of this effort and describes (*i*) the effect of adding water vapor to the $Cr + O_2 + NaCl(g)$ system, and (*ii*) interactions of $NaCl(g)$ and/or $H_2O(g)$ with Mo, Ti, and the superalloys NASA-TRW VIA, B-1900, IN-738, and 713C. The compositions of these alloys are presented in the Appendix.

Experimental

Two experimental techniques were used in the present atmospheric pressure investigations; cooled target collection and high pressure mass spectrometric sampling. Schematics of the respective apparatus are shown in Fig. 1. It can be seen that the furnace assembly apparatus was common to both techniques. The metal sample, measuring approximately 1 × 1 × 0.25 cm, was suspended on a platinum wire within a 2.2 cm ID quartz tube that was mounted in a 15 cm long tube furnace. The furnace temperature was controlled through a thermocouple by a precision set-point current proportionating controller coupled to a saturable core reactor power source. Temperatures could be maintained to ±2°C. Sample temperature was measured independently with a Pt-Pt 13% Rh thermocouple inside the quartz tube and contacting the side of the sample.

Partial pressures of $NaCl(g)$ were developed by heating $NaCl(c)$ in a platinum crucible that was situated below the sample in a 1.3 cm diam quartz tube. The crucible was 2 cm long by 0.6 cm in diameter and

* Electrochemical Society Active Member.
[1] NRC Resident Research Associate.
Key words: corrosion, high pressure mass spectrometry, oxidative vaporization.

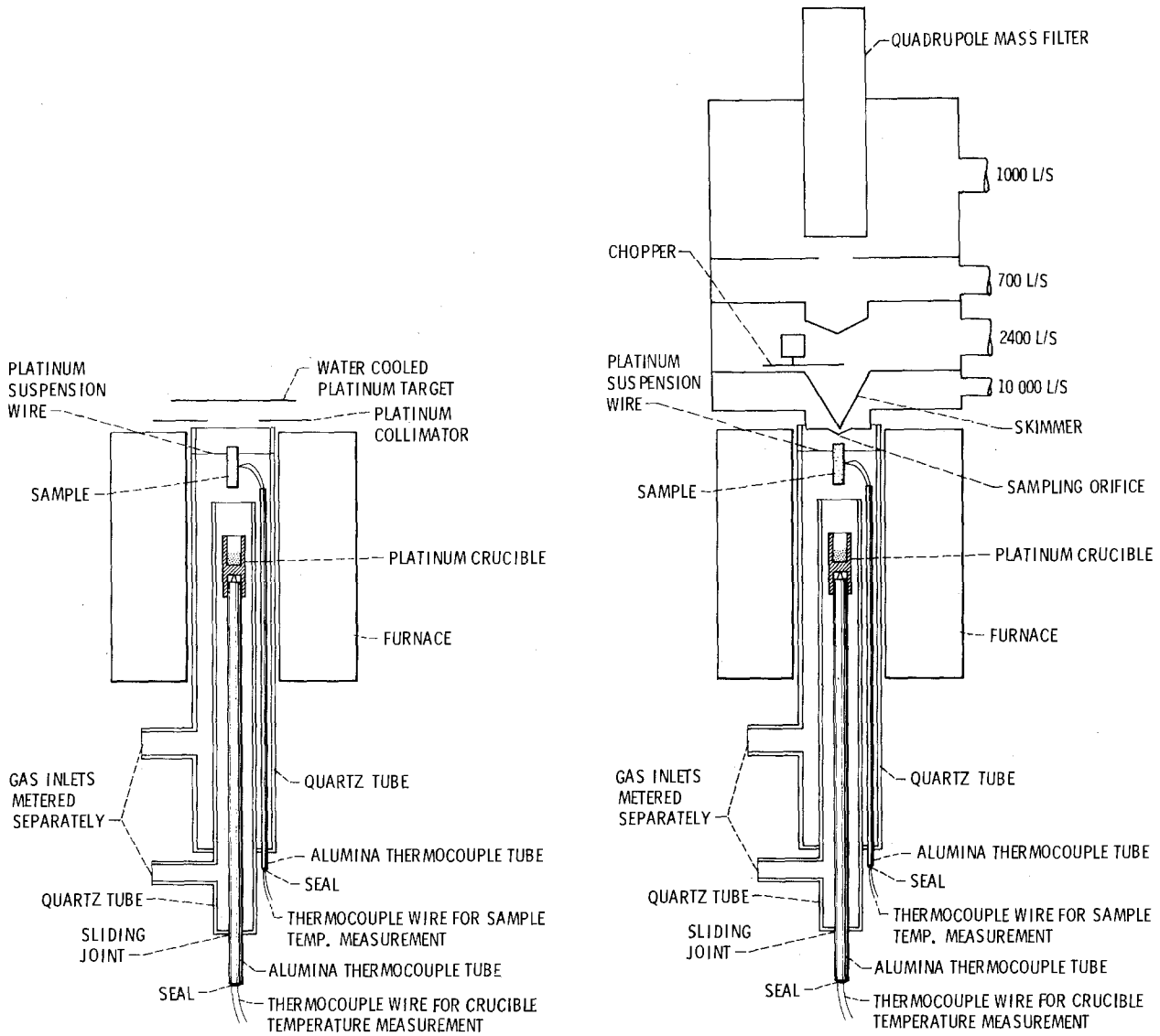


Fig. 1. Schematic of apparatus: (a, left) target collection, (b, right) high pressure mass spectrometric sampler

it was supported on a double bore alumina thermocouple tube. A Pt-Pt 13% Rh thermocouple in the alumina tube extended into the crucible base and facilitated continuous measurement of the crucible temperature. A slip-seal system allowed the crucible assembly to be moved vertically so that the crucible temperature could be varied by changing its position in the furnace. The crucible temperature was maintained considerably lower than the sample temperature to ensure no condensation of NaCl on the sample.

Metered oxygen flows were supplied independently to both concentric quartz tubes. Flows were adjusted to gas velocities of 0.7 and 2.5 cm sec^{-1} for the outer and inner quartz tubes, respectively. The oxygen supplied to the outer tube could be saturated with water vapor at room temperature by passing the gas through a fritted glass plug in the bottom of a 20 cm high column of water. The mass fraction of NaCl(g) in the apparatus was determined from the weight loss (per unit time) of NaCl(c) in the crucible and the volume flow rate of gas through the apparatus. No attempt was made to apply corrections to the NaCl(g) concentrations for collision and reactions with the quartz wall of the apparatus. In the target collection experiments a mass fraction of about 50 ppm NaCl(g) was used, and in the mass spectrometric sampling experiments NaCl(g) concentrations of 160 ppm were generally employed. Metal samples were always preoxidized for 4 hr at high temperature, usually 1000°C in pure oxygen. The experiment was then started by adding contaminant gases, and at least 5 min were allowed to elapse before measurements were begun.

In the target collection experiments, volatile products emanating from the sample were collected on polished platinum targets (5 × 5 × 0.04 cm) attached to a water-cooled copper plate [Fig.1(a)]. The target was positioned about 2 cm above the open end of the quartz tube. A platinum collimator (with a 2 cm diam opening) was located between the target and quartz tube opening. Deposits collected in measured times were dissolved in water. Resulting solutions were analyzed for metal cations by atomic absorption and/or emission spectroscopy.

Identification of volatile species emanating from samples was accomplished with the high pressure mass spectrometric sampler positioned at the quartz tube opening as shown in Fig. 1(b). The high pressure, free-jet expansion, modulated molecular beam, mass spectrometric sampler facilitates direct mass spectrometric analysis of atmospheric pressure sources. This technique preserves the dynamic and chemical integrity of sampled species. The theory and details of the free-jet expansion sampling technique are given in the literature (5-7).

For our sampler the inlet orifice was 0.022 cm in diameter, located at the apex of a 106° occluded angle cone fabricated from 0.025 cm thick Pt-10% Rh. The cone was welded on the end of a 1.5 cm long × 2.0 cm

diam stainless steel tube. The sampling cone protruded into the quartz tube about 1 cm and was heated to a temperature approaching that of the metal sample. Heating of the orifice was necessary to prevent condensation on and subsequent clogging of the orifice by NaCl and other condensible volatile species.

In the mass spectrometric sampling experiments, the furnace temperature was adjusted to produce a sample temperature of about 1050°C, except in the case of molybdenum. Molybdenum samples were heated to only 675°C because the high rate of vaporization of MoO_3 at higher temperatures resulted in rapid clogging of the sampling orifice. The lower temperature required for molybdenum samples necessitated lower concentrations of NaCl(g) because it was not possible to heat the crucible to higher temperatures without overheating the molybdenum. Generally the NaCl(g) mass fraction was around 4 ppm for molybdenum experiments.

Results and Discussion

Target collection experiments.—The effects of exposing hot oxidizing metals to partial pressures of NaCl(g), $H_2O(g)$, and NaCl(g) + $H_2O(g)$ was studied for the metal samples Ti, B-1900, Cr, IN-738, VIA, and 713C. For Ti and B-1900 samples no metals (other than Na) were detected in collected deposits. In experiments with the other metal samples, the only metal detected (other than Na) in collected deposits was Cr. The rate of collection of Cr per unit area of sample shall be designated R.

Values of R, obtained with a preoxidized Cr sample exposed to various gas phase compositions, are presented in Table I. These results show that R was increased markedly by additions of $H_2O(g)$ or NaCl(g) to the oxidizing environment. When both of these additions were present simultaneously an additional synergistic effect was obtained. In oxygen alone $R = 1$ $\mu g\ cm^{-2}\ hr^{-1}$; the transported Cr was undoubtedly derived from the oxidation of $Cr_2O_3(c)$ on the surface of the sample to $CrO_3(g)$ (8) according to the reaction

$$Cr_2O_3(c) + 3/2\ O_2(g) = 2CrO_3(g) \quad [1]$$

With the addition of $H_2O(g)$ to the oxygen, the value of R was increased by a factor of four. The increase may be attributed to the formation of a volatile hydrated oxide

$$\frac{1}{2}Cr_2O_3(c) + \frac{x+1}{4}O_2(g) + \frac{x}{2}H_2O(g) = CrO_2(OH)_x(g) \quad [2]$$

where $x = 1$ or 2. If it is assumed that reactions [1] and [2] occur independently, the value of R due only to reaction [2] was 3 $\mu g\ cm^{-2}\ hr^{-1}$.

When only NaCl(g) was added to the oxygen, the value of R increased by a factor of five compared with the case of oxygen alone. This observed increased rate was due to the formation of volatile species containing both Na and Cr (3). Again with the assumption of independent reactions, the rate attributable to the Na- and Cr-containing species was 4 $\mu g\ cm^{-2}\ hr^{-1}$.

Addition of both contaminants, NaCl(g) and $H_2O(g)$, to the oxygen yielded $R = 20$ $\mu g\ cm^{-2}\ hr^{-1}$. This is twice the sum of the rates of the three individual reactions just discussed. Apparently an additional reaction was occurring; this reaction probably involved NaOH and/or HCl which are expected to be formed by the hydrolysis of NaCl, *i.e.*

$$NaCl(g) + H_2O(g) = NaOH(g) + HCl(g) \quad [3]$$

The rate of collection of Cr from preoxidized alloy samples exposed to $O_2(g)$ + $H_2O(g)$ + NaCl(g) was compared with that from oxidized Cr. The results obtained for contaminant additions of 2.5 volume percent (v/o) $H_2O(g)$ and 50 ppm NaCl(g) are presented in Table II. Except for B-1900, all the alloys tested exhibited volatile Cr-containing species. For IN-738 the value of R was 80% of that found for pure Cr, for 713C it was 60%, and for VIA it was 50%. Measured values of R for 713C and VIA were found to decrease gradually with each one-half hour collection run. The values reported in Table II are the maximums obtained in the first one-half hour collection run. The observed decreases in R as a function of collection time were probably associated with the rate of diffusion of chromium to the surface and subsequent oxidation to Cr_2O_3. Evidently this process was slower than the reaction to form volatile chromium species at the surface.

Mass spectrometry experiments.—High pressure mass spectrometric sampling techniques were used to identify and measure volatile species emanating from preoxidized samples of Cr and IN-738 at temperatures above 1000°C in oxygen containing $H_2O(g)$ or NaCl(g) or $H_2O(g)$ + NaCl(g). Similar studies were made with Mo samples at 675°C. The main Cr-, Mo-, and Na-containing ions identified under the various experimental conditions are presented in Tables III, IV, and V together with their measured relative intensities and probable parent molecular species. In all cases, ions were identified by their m/e values; isotopic distribution and behavior when either NaCl(g), $H_2O(g)$, or the sample were removed from the system. The reported relative intensities can be converted to correct ratios of partial pressures only if reliable values are available for the relative ionization and fragmentation

Table I. Rate of collection of chromium volatilizing from chromium specimen exposed to 1 atm of slowly flowing oxygen containing different vapors

Chromium temerature, T_{Cr} (°C)	Mass fraction $H_2O(g)$* (%)	Mass fraction NaCl(g)** (ppm)	Rate of collection,† ($\mu g\ cm^{-2}\ hr^{-1}$)
1000	0	0	1
1000	1.4	0	4
1000	0	50	5
1000	1.4	50	20

* Oxygen was saturated with $H_2O(g)$ at 21°C by bubbling through fritted glass into a 20 cm column of water.
** The mass fraction of NaCl(g) was determined from weight loss of the platinum crucible and from the gas flow through the apparatus. No corrections were made for collision and reaction with the quartz walls.
† Measured collection rates were reproducible to ±20%.

Table II. Rate of collection of chromium volatilizing from chromium and chromium-containing alloys exposed to 1 atm of slowly flowing oxygen containing 2.5 v/o $H_2O(g)$ and 50 ppm NaCl(g)

Material	Temperature (°C)	Rate of collection ($\mu g\ cm^{-2}\ hr^{-1}$)
Chromium	1000	15
IN-738	1015	12
713C	1015	10*
B-1900	1015	0
NASA-TRW VIA	1015	7.5*

* Rates were falling slowly in time. Value given is maximum rate determined in first one-half hour run. It was not possible to assess the reproducibility of the rate.

Table III. Mass spectrum of vapors over the $Cr_2O_3(c)$-$O_2(g)$-$H_2O(g)$ system*

Ion	Relative intensity	Probable parent molecule
O_2^+	1.00	O_2
$CrO_2(OH)^+$	2×10^{-8}	$CrO_2(OH)$ and/or $CrO_2(OH)_2$
$CrO_2(OH)_2^+$	3×10^{-8}	$CrO_2(OH)_2$

* $Cr_2O_3(c)$ sample temperature = 1100°C; O_2 flow = 380 ml/min; H_2O saturated O_2 at 21°C.

Table IV. Mass spectrum of vapors over the $Cr_2O_3(c)$-$O_2(g)$-NaCl(g) system with and without added $H_2O(g)$*

Ion	Without added $H_2O(g)$ Relative intensity	With added $H_2O(g)$ Relative intensity	Probable parent molecule
O_2^+	1.6×10^4	1.6×10^4	O_2
Na^+	0.76	0.52	NaCl, (NaOH)
$NaCl^+$	1.00	0.70	NaCl
Na_2Cl^+	0.57	0.60	$(NaCl)_2$
$Na_3Cl_2^+$	6.0×10^{-2}	4.5×10^{-2}	$(NaCl)_3$
$Na_4Cl_3^+$	1.0×10^{-3}	—	$(NaCl)_4$
$NaCrO_3^+$	2.2×10^{-2}	1.1×10^{-2}	$NaClCrO_3$
$NaClCrO_3^+$	2.5×10^{-2}	2.0×10^{-2}	$NaClCrO_3$
$Na_2ClCrO_3^+$	4.8×10^{-2}	2.9×10^{-2}	$(NaCl)_2CrO_3$
$Na_3Cl_2CrO_3^+$	2.0×10^{-3}	—	$(NaCl)_3CrO_3$
$Na_2Cr_2O_7^+$	4.0×10^{-3}	5.0×10^{-3}	$Na_2Cr_2O_7$
$Na_3Cr_2O_7^+$	2.0×10^{-3}	4.0×10^{-3}	$NaOHNa_2Cr_2O_7$ and/or $NaClNa_2Cr_2O_7$
$NaOHCrO_3^+$	2.0×10^{-3}	1.6×10^{-2}	$NaOHCrO_3$
$Na_2OHCrO_3^+$	2.0×10^{-3}	1.9×10^{-2}	$(NaOH)_2CrO_3$

* $Cr_2O_3(c)$ sample temperature = 1020°C; NaCl(c) temperature = 830°C (equivalent to 160 ppm); O_2 flow = 380 ml min^{-1}; H_2O-saturated O_2 at 21°C.

cross sections, multiplier gains for each ion, quadrupole mass filter transmission as a function of m/e, and Mach-number focusing factors for each species. At present, most of these quantities are unknown for the complex molecular species presented in the tables. Finally, parent molecular species were assigned on the basis of familiarity with the mass spectrum-molecular composition relationships for other inorganic halide molecular systems. It is well established (9) that halogen-containing molecules fragment upon electron impact ionization to yield molecular ions with the loss of a halogen atom, *e.g.*

$$Na_2Cl_2(g) + e^- \rightarrow Na_2Cl^+ + Cl + 2e^- \quad [4]$$

The results presented in Table III are for the $Cr_2O_3(c) + O_2(g) + H_2O(g)$ system; the ion intensities were normalized to a value of unity for the ion O_2^+. The only Cr-containing species identified were $CrO_2(OH)_2^+$ and $CrO_2(OH)^+$. While the ion $CrO_2(OH)_2^+$ could only originate from $CrO_2(OH)_2(g)$, the ion $CrO_2(OH)^+$ could be a fragment of $CrO_2(OH)_2(g)$ or it could originate from $CrO_2(OH)(g)$. On the basis of these results, it was not possible to determine if $CrO_2(OH)(g)$ was actually present. These results are in contrast to the transpiration results reported by Kim and Belton (10) for this system. They interpreted their measurements on the basis that $CrO_2(OH)$ was the only volatile oxide in this system.

In Table IV the results obtained for the $Cr_2O_3(c) + O_2(g) + NaCl(g)$ system, with and without added $H_2O(g)$, are presented. Both sets of ion intensities were normalized to $NaCl^+$ for the system without $H_2O(g)$ added. Such normalization puts the intensities in the proper perspective and shows that addition of $H_2O(g)$ reduces the NaCl(g). The observed Cr-containing species are seen to be mainly complexes of NaCl and CrO_3 with the general formula $(NaCl)_xCrO_3$ where $x = 1$, 2, and 3. As stated in our previous report (3), we believe that these species are the first observed examples of alkali halide-metal oxide complexes. In this regard, one point must be emphasized: The fact that the rate, R, was found to increase in the target experiments when NaCl(g) was added to the $Cr_2O_3(c) + O_2(g)$ system, indicates that R is not limited by the vaporization rate of $CrO_3(g)$ and therefore the Na- and Cr-containing species are not products of gas phase reactions. Furthermore, because species such as $(NaCl)_xCrO_3$ are not the product of gas phase reactions they likewise cannot be the product of sampling artifacts such as clustering (11).

Returning to Table IV, one sees that the main effects of adding $H_2O(g)$ to the $Cr_2O_3(g) + O_2(g) + NaCl(g)$ system were: (*i*) to reduce the $NaCl^+$ intensity, and (*ii*) to increase the prominence of NaOH-CrO_3 complexes. Both effects could result from the formation of NaOH in the hydrolysis of NaCl, either by reaction [3] or on the surface. The point emphasized above, precluding gas-phase formation, applies equally to the observed complex $(NaOH)_xCrO_3$ where $x = 1$ and 2. The fact that NaOH-containing species were observed even when $H_2O(g)$ was not added to the system indicates that the system was not completely free of water vapor. No special precautions were taken to dry the oxygen or sodium chloride used in these experiments. Parent ions corresponding to the species NaOH(g) and HCl(g) could not be measured because large in-phase background peaks were present at their respective m/e. These background peaks were due to the approximately 2300 ppm of argon impurity in the "missile" grade oxygen used.

An exhaustive search was made for the frequently proposed (2, 4, 12-17) vapor molecules CrO_2Cl_2, $CrCl_2$, $CrCl_3$, and Na_2CrO_4. This effort was unrewarding and only the species $Na_2Cr_2O_7(g)$ was detected in addition to the complexes. Therefore, we conclude that the main reactions responsible for the vapor transport of Cr are

$$1/2\,Cr_2O_3(c) + 3/4\,O_2(g) + xNaCl(g) = (NaCl)_xCrO_3(g) \quad [5]$$

$$1/2\,Cr_2O_3(c) + 3/4\,O_2(g) + xNaOH(g) = (NaOH)_xCrO_3(g) \quad [6]$$

where $x = 1$, 2, and 3 for reaction [5], and $x = 1$ and 2 for reaction [6].

Experiments were performed with samples of IN-738 at about 1050°C in $O_2(g) + NaCl(g)$. Mass spectral scans were made over the range from $m/e = 23$ to $m/e = 250$. All of the ions in this range listed in Table IV for the $Cr_2O_3(c) + O_2(g) + NaCl(g)$ system were detected with IN-738. Additional, as yet unidentified peaks of lesser intensity, were recorded at m/e values

Table V. Mass spectrometrically observed Mo-containing species over an oxidized Mo sample heated to 675°C in various flowing gas environments

System	Sample environment	Observed ions	Relative intensity*	Probable parent molecule
A	O_2 (380 cm^3/min)	O_2^+	$>10^5$	O_2
		$(MoO_3)_3^+$	1.0	$(MoO_3)_3$
		$(MoO_3)_4^+$	0.3	$(MoO_3)_4$
B	O_2 (380 cm^3/min) NaCl(g) (4 ppm)	$(NaCl)(MoO_3)_3^+$	5×10^{-2}	$NaCl(MoO_3)_3$
		$Na_2Cl(MoO_3)_3^+$	5×10^{-2}	$(NaCl)_2(MoO_3)_3$
		plus ions of A		molecules in A
C	H_2O saturated (at 21°C) O_2 (380 cm^3/min)	$MoO_2(OH)_2^+$	5.0	$MoO_2(OH)_2$
		$MoO_2(OH)^+$	3.0	$MoO_2(OH)_2$ and/or $MoO_2(OH)$
		plus ions of A		molecules in A
D	H_2O saturated O_2 (380 cm^3/min) NaCl(g) (4 ppm)	$NaOH(MoO_3)_3^+$ plus ions of A + B + C	4×10^{-3}	$NaOH(MoO_3)_3$ molecules in A + B + C

* Intensities are relative to $(MoO_3)_3^+$ measured in system A.

of 65, 66, 88, 89, 105 107, 146, and 147. That the main species observed with IN-738 correspond to those noted with Cr is not surprising because it is well established (18) that the main surface oxide constituent present on oxidized IN-738 is $Cr_2O_3(c)$.

Because Mo is a member of the same family as Cr, and because Mo has been identified near the surface in certain oxidized alloys (18), we investigated the Mo system to ascertain if the same type of complex molecules were formed as observed with the Cr system. Results obtained for the $MoO_3(c) + O_2(g)$ system, with and without additions of NaCl(g) and $H_2O(g)$, are presented in Table V. Without any contaminants added to the oxygen, the primary vaporizing species was $(MoO_3)_3$ as one would expect (19). The other ion intensities were normalized to a value of unity for the $(MoO_3)_3^+$ ion. The tetramer $(MoO_3)_4$ was also observed but at about 1/3 the intensity relative to the trimer. With NaCl(g) added to the oxygen, mixed alkali-halide-metal oxide complexes became prominent. These complexes are similar to those found for chromium and they can be represented by the general formula $(NaCl)_x(MoO_3)_3$ where $x = 1$ and 2. These complexes differed from the chromium ones in that the metal oxide was polymerized in keeping with the characteristic difference between Cr and Mo oxide systems at high temperatures (8, 19). Additions of $H_2O(g)$ alone to the oxygen resulted in the formation of the hydrated oxide molecule $MoO_2(OH)_2(g)$ postulated by Belton and Jordan (20). This species was quite abundant judging from the fact that the ion intensity was five times greater than the trimer ion. The ion $MoO_2(OH)^+$ was also observed but as with the chromium case it was not possible to decide whether this ion arose from ionization of $MoO_2(OH)(g)$ or from fragmentation of $MoO_2(OH)_2(g)$.

When both NaCl(g) and $H_2O(g)$ were added to the oxygen with Mo samples, the molecule $NaOH(MoO_3)_3$ was observed in addition to those noted for O_2 alone, NaCl(g) alone, and $H_2O(g)$ alone. In this case it was not possible to discern if the species $Na_2OH(MoO_3)_3^+$ was present because of interference from the species $NaCl(MoO_3)_3^+$.

Concluding Remarks

The mass spectrometric identification of the vapor species emanating from the metal samples studied under various conditions allows a better interpretation of the rates obtained for chromium vaporization (Table I) in the target collection experiments. For oxygen without any contaminant additions, the volatile chromium species was undoubtedly $CrO_3(g)$ formed by reaction [1]. This species was not identified in our mass spectrometric sampling because its concentration (at the highest temperatures we could achieve with our furnace) was just below the detection sensitivity of our sampling system. The concentration, as calculated from measured R values and gas flows, was about 0.03 ppm, and the detection limit at this mass was around 0.05 ppm.

With $H_2O(g)$ added, the rate increased because of the formation of $CrO_2(OH)_2(g)$, in addition to the $CrO_3(g)$, according to reaction [2] with $x = 2$. Additions of NaCl(g) yielded increased rates by the formation of $(NaCl)_xCrO_3(g)$ with $x = 1$, 2, and 3 according to reaction [5]. With the additions of $H_2O(g) + NaCl(g)$, the rate R was observed to increase more than expected from the sum of reactions [1], [2], and [5]. The difference must arise from the formation of $(NaOH)_xCrO_3(g)$ (with $x = 1$ and 2) by reaction [6]. Thus we can conclude that NaOH molecules are more reactive than NaCl molecules because the rate of Cr transport was higher when some of the NaCl was converted to NaOH. It should be mentioned that the other hydrolysis product of NaCl, namely, HCl, would also be expected to react with chromium at high temperatures. Nevertheless, we were unable to detect any adduct molecules of HCl and CrO_3 within the limit of our sensitivity. In addition, no chromium chlorides or oxychlorides were observed.

The rates of chromium vaporization from the alloys (Table II) can be interpreted on the basis of the same reactions as those described for chromium. It was somewhat surprising that no chromium was detected from B-1900. An extensive scale analysis has been made for these four alloys on samples oxidized for 100 hr in slowly flowing oxygen (18). This analysis showed that for samples oxidized at 1000°C, B-1900 contained the least amount of chromium in the scale surface of all four alloys. ESCA analysis indicated that there was about 3.8 atom percent (a/o) chromium in the outer layer. This was probably dissolved in the continuous layer of α-Al_2O_3 observed on the sample, and must have been unreactive with respect to the NaCl and H_2O. Another explanation could be based on the fact that the samples in this study were preoxidized for only 4 hr and the scale formed on B-1900 in this short time was entirely α-Al_2O_3.

With regard to the chromium system (and certain alloy systems also) it is important to reiterate that the observed enhanced vaporization of chromium precludes a gas phase reaction explanation of the formation of the complex molecular species reported here. A gas phase mechanism would be limited by the rate of formation of $CrO_3(g)$.

In the experiments involving molybdenum the observed vaporizing species were seen to be analogous to those found for the chromium system except that the Mo-containing species displayed the stronger tendency of molybdenum to form oxide polymers. The molybdenum results stimulate one to speculate about tungsten because it is in the same chemical family as Cr and Mo. One would expect that tungsten would form complex molecules identical to those formed by Mo in our experiments but probably at higher temperatures. Unfortunately, such W-containing molecules were beyond the mass range of our mass spectrometer.

A more quantitative correlation of these results is not possible at this time because we have not derived actual partial pressures for the various species from the measured ion intensities. Nevertheless, the qualitative description provided by our results provide valuable insights into the hot corrosion process. This is especially true for the "chromia-former" alloys (18) such as IN-738. While the chromia-former alloys are generally considered to be more resistant to hot corrosion[2] attack than the "alumina-formers," these alloys also appear to be most effected by exposure to NaCl(g) (2). The mechanism of NaCl(g) attack postulated by Hurst *et al.* (2(a)) involves NaCl(g) reaching the alloy surface below the oxide scale. Presumaby, the NaCl(g) penetrates through microcracks in the oxide and forms volatile chromium oxychlorides [*e.g.*, $CrO_2Cl_2(g)$] which cause scale lifting or cracking. Once the scale is compromised, $Na_2SO_4(c)$ on the surface can contact the alloy substrate and cause accelerated attack.

Our results show that attack by NaCl(g) results in the formation of adduct molecules rather than the oxychlorides postulated by others. Furthermore, the attack takes place, and the adduct molecules are formed, at the surface of the oxide scale. Thinning of the scale could result in the formation of regions of aggravated stress where cracking might occur, thus compromising the scale. Also, a thinned section of scale might be more readily fluxed by the $Na_2SO_4(c)$. In either case, the NaCl(g) attack compromises the oxide scale and thus promotes hot corrosion attack. It is important to emphasize that although the degree of attack by NaCl(g) is of a much smaller magnitude than the $Na_2SO_4(c)$ hot corrosion attack, the NaCl(g)

[2] Hot corrosion is considered here as the accelerated, sometimes catastrophic, oxidation of metals and alloys caused by deposits of Na_2SO_4.

attack may be of equal importance in the over-all hot corrosion process taking place in turbine engines.

Manuscript submitted April 20, 1977; revised manuscript received July 5, 1977. This was Paper 32 presented at the Philadelphia, Pennsylvania, Meeting of the Society, May 8-13, 1977.

Any discussion of this paper will appear in a Discussion Section to be published in the June 1978 JOURNAL. All discussions for the June 1978 Discussion Section should be submitted by Feb. 1, 1978.

Publication costs of this article were assisted by the National Aeronautics and Space Administration.

APPENDIX

Composition of Superalloys

	Alloy							
	B-1900		NASA-TRW VIA		Alloy 713C		IN-738	
	Composition							
Element	w/o	a/o	w/o	a/o	w/o	a/o	w/o	a/o
Nickel	64.5	62.5	62	64.5	72	67	61.5	59
Chromium	8.0	8.7	6.1	7.1	12.5	13.2	16.0	17.5
Aluminum	6.0	12.6	5.4	12.2	6.1	12.4	3.4	7.2
Titanium	1.0	1.2	1.0	1.3	6.8	0.9	3.4	4.0
Cobalt	10.0	9.6	7.5	7.7	—	—	8.5	8.2
Molybdenum	6.0	3.5	2.0	1.3	4.2	2.4	1.7	1.0
Tungsten	0.1*	—	5.5	1.8	—	—	2.6	0.8
Tantalum	4.3	1.4	9.0	3.0	—	—	1.7	0.6
Niobium	0.1*	—	0.5	0.3	2.0	1.2	0.9	0.6
Hafnium	—	—	0.4	0.1	—	—	—	—
Zirconium	0.08	—	—	—	—	—	0.1	0.06
Rhenium	—	—	0.3	0.1	—	—	—	—
Iron	0.35*	—	—	—	2.5*	2.5*	0.5*	—
Carbon	0.1	0.47	0.13	0.66	0.12	0.55	0.17	0.81
Boron	0.015	—	—	—	0.012*	—	0.01	—
Silicon	0.25*	—	—	—	0.5*	—	0.3*	—
Manganese	0.2*	—	—	—	0.25*	—	0.2*	—

* Maximum value.

REFERENCES

1. F. J. Kohl, C. A. Stearns, and G. C. Fryburg, in "Metal-Slag-Gas Reactions and Processes, "Z. A. Foroulis and W. W. Smeltzer, Editors, p. 649, The Electrochemical Society Softbound Symposium Series, Princeton, N.J. (1975).
2. (a) R. C. Hurst, J. B. Johnson, M. Davies, and P. Hancock, in "Deposition and Corrosion in Gas Turbines," A. B. Hart and A. J. B. Cutler, Editors, p. 143, John Wiley & Sons, Inc., New York (1973).
   (b) P. Hancock, in "Proceedings of the 1974 Gas Turbine Materials in the Marine Environment Conference," J. W. Fairbanks and I. Machlin, Editors, p. 225, MCIC 75-27, Metals and Ceramic Information Center, Columbus, Ohio (1975).
3. C. A. Stearns, F. J. Kohl, and G. C. Fryburg, in "Properties of High Temperature Alloys," Z. A. Foroulis and F. S. Pettit, Editors, The Electrochemical Society Softbound Symposium Series, Vol. 77-1, Princeton, N.J. (1977); also NASA TM X-73476 (1976).
4. (a) R. L. Jones, in "Metal-Slag-Gas Reactions and Processes," Z. A. Foroulis and W. W. Smeltzer, Editors, p. 762, The Electrochemical Society Softbound Symposium Series, Princeton, N. J. (1975).
   (b) R. L. Jones, K. H. Stern, and S. T. Gadomski, "The Interactions of Sodium Chloride and Sodium Sulfate with Turbine Blade Coatings," presented at the Gas Turbine Materials in a Marine Environment Conference, Bath, England (1976).
5. (a) T. A. Milne and F. G. Greene, in "Mass Spectrometry in Inorganic Chemistry," Advances in Chemistry Series No. 72, p. 68, American Chemical Society, Washington, D. C. (1968).
   (b) T. A. Milne and F. G. Greene, in "Advances in High Temperature Chemistry," Vol. 2, L. Erying, Editor, p. 107, Academic Press, New York (1969).
6. (a) J. B. Anderson, R. P. Andres, and J. B. Fenn, in "Molecular Beams," J. Ross, Editor, p. 275, Interscience Publishers, New York (1966).
   (b) J. B. Anderson, in "Molecular Beams and Low Density Gas-dynamics," P. P. Wegener, Editor, p. 1, Marcel Dekker, New York (1974).
7. Numerous papers in *Int. J. Mass Spectrom. Ion Phys.*, **16**, no. 1/2 (1975).
8. C. A. Stearns, F. J. Kohl, and G. C. Fryburg, *This Journal*, **121**, 945 (1974).
9. S. H. Bauer and R. F. Porter, in "Molten Salt Chemistry," M. Blander, Editor, p. 607, Interscience Publishers, New York (1964).
10. Y.-W. Kim and G. R. Belton, *Metall. Trans.*, **5**, 1811 (1974).
11. T. A. Milne, J. E. Beachey and F. T. Greene, *J. Chem. Phys.*, **57**, 2221 (1972).
12. J. F. G. Condé, in "High Temperature Corrosion of Aerospace Alloys," AGARD-CP-120, p. 203, Advisory Group for Aerospace Research and Development, France (1973).
13. J. F. G. Condé and B. A. Wareham, in "Proceedings of the 1974 Gas Turbine Materials in the Marine Environment Conference," J. W. Fairbanks and I. Machlin, Editors, p. 73, MCIC 75-27, Metals and Ceramic Information Center, Columbus, Ohio (1975).
14. P. S. Gray, in "First International Congress on Metallic Corrosion," p. 95, Butterworths, London (1962).
15. D. M. Johnson, D. P. Whittle, and J. Stringer, *Corros. Sci.*, **15**, 721 (1975).
16. P. A. Alexander, in "The Mechanism of Corrosion by Fuel Impurities," H. R. Johnson and D. J. Littler, Editors, p. 571, Butterworths, London (1963).
17. J. F. G. Condé, in "Gas Turbine Materials Conference Proceedings," p. 17, Naval Ship Engineering Center, Washington, D. C. (1972).
18. G. C. Fryburg, F. J. Kohl, and C. A. Stearns, NASA TN D-8388 (1977).
19. R. J. Ackermann and R. J. Thorn, *Progr. Ceram. Sci.*, **1**, 39 (1961).
20. G. R. Belton and A. S. Jordan, *J. Phys. Chem.*, **69**, 2065 (1965).

A Comparison of the Mass and Resistance Change Techniques for Investigating Thin Film Corrosion Kinetics

Wen-Yaung Lee, Hans C. Siegmann,[1] and Jerome M. Eldridge*

IBM Research Laboratory, San Jose, California 95193

ABSTRACT

In situ quartz crystal oscillator microbalance (QCM) and electrical resistance change (RC) measurements were carried out simultaneously on identically prepared Permalloy films in order to establish the sensitivity and reproducibility of each technique for investigating atmospheric corrosion. Both techniques were found to be highly sensitive to thickness changes (better than 1Å) resulting from corrosion in a high humidity atmosphere containing trace quantities of acid-forming, gaseous pollutants. However, the QCM results were found to be an order of magnitude more reproducible than the RC data. Moreover, it was established from the QCM findings that the average mass increase due to corrosion was quite closely proportional to the square root of exposure time in the test chamber. Thus complex thin film corrosion kinetics can be determined with considerable accuracy provided reasonable experimental procedures are employed. The results of both measurements were compared also in an isochronal plot where it was found that the resistance change was proportional to the square of the mass increase arising from the formation of corrosion products. The origin of this relationship was investigated by carrying out simulated corrosion studies involving punching out holes in an aluminized Mylar structure while determining the effects of material loss on electrical resistance.

Thin Permalloy ($Ni_{0.80}Fe_{0.20}$) films corrode in high humidity atmospheres containing trace amounts of acid-forming gaseous pollutants (1). The magnetic characteristics of the films are degraded by corrosive processes, and device failure may then occur.

As part of an effort to improve our scientific understanding of the complex materials and environmental factors controlling thin film corrosion kinetics and mechanisms, we initiated this study to assess two quantitative techniques for measuring thin film corrosion rates. The rates of identically prepared 1000Å Permalloy films were studied *in situ* in a reactive atmosphere by quartz crystal oscillator microbalance (QCM) and electrical resistance change (RC) measurements. Simulation studies were suggested by the appearance of corroded Permalloy surfaces, showing that the chemical attack is quite localized across the film. In the simulation experiments, holes were punched out of conductive, aluminized Mylar strips in order to determine the effect of metal loss on resistance.

Experimental Procedure and Results

In order to establish the sensitivity and reproducibility of the microbalance and resistance methods for monitoring film corrosion, six Permalloy test structures were prepared for each technique during a single vacuum-deposition run. Considerable care was taken in preparing the structures in order to minimize film-to-film differences (metallurgy, surface contamination, etc.). Quartz wafer substrates (0.5 in. diam $\times$ 5 MHz frequency for the QCM and 1.0 in. diam for the RC measurements) were cleaned simultaneously. All processing and handling was done under Class 1000 clean room conditions to minimize potential particulate effects (*e.g.*, stabilization of water droplets during testing). One thousand angstrom thick films were deposited, through masks onto substrates held at 200°C, from an electron beam-heated Permalloy source. The QCM technique requires two electrodes: The Permalloy film serves as one and an inert gold film on the back side of the quartz functions as the other. The films were cooled to room temperature, removed from the deposition system, and the necessary current and potential contacts were made to each specimen (using a water impermeable polymer at each contact to eliminate possible galvanic reaction at the probe electrodes). The four-point probe, circular van der Pauw film geometry (2), was used for the RC measurements. All twelve structures were then loaded along the inside periphery of a cylindrical plexiglass test chamber (6.5 in. OD $\times$ 16 in. long). After ensuring the RC devices conducted ohmically and the base frequencies of the QCM structures were stable (to within $\pm$5 Hz/day) in dry air, a reactive atmosphere was introduced at 25.0°C. This filtered air had a relative humidity of 70% and contained trace quantities of SO_2, NO_2, O_3, H_2S, and Cl_2 (1). Changes in resistance and frequency were intermittently monitored over a period of 170 hr. Spurious galvanic effects were minimized by applying small (10 mA) electric currents only for the short times needed to obtain data points.

The corrosion-induced resistance changes increase monotonically with exposure time (t). This is shown in Fig. 1, where $[R(t) - R(o)]/R(t)$ is plotted against t for the six specimens. With these coordinates, the slopes are directly proportional to the corrosion rate, provided reaction occurs uniformly across the specimen surface. Although the attack is, in fact, highly localized. the films exhibit average corrosion rates of several angstroms per hour. The $\Delta R/R(t)$ values at any given time vary by as much as a factor of 8.

The sample-to-sample reproducibility of the QCM technique exceeds that of the RC approach by an order of magnitude, *i.e.*, the spread is less than a factor of 2. See Fig. 2, and note that a decrease in frequency of 1 Hz results from a mass increase (due to condensation of corrosive reactants) of 1.77×10^{-8} g/cm^2. The inflections in the Δf *vs.* t plots around 1300 $\pm$ 500 Hz are relatively insignificant; they probably arise from a temporary reduction in the relative humidity of the test environment. Whatever the origin of the inflection, deviation of the data from a smooth curve is relatively minor. This is clearly demonstrated

* Electrochemical Society Active Member.
[1] Work carried out while on leave from the Laboratorium fur Festkorperphysik, ETH, Zurich, Switzerland.
Key words: thin films, Permalloy, corrosion, quartz crystal microbalance, resistance change techniques.

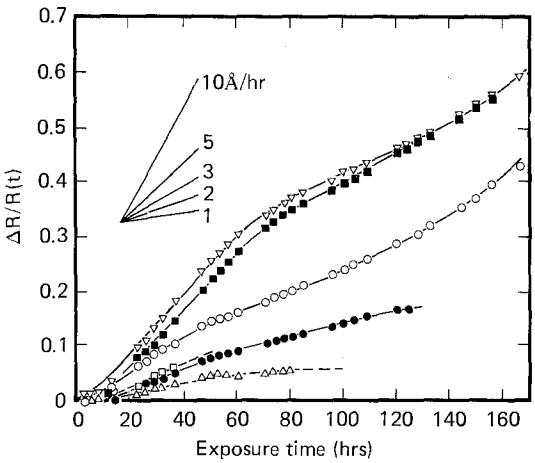


Fig. 1. Dependence of Permalloy film resistance change on exposure time to a corrosive atmosphere for six identical specimens.

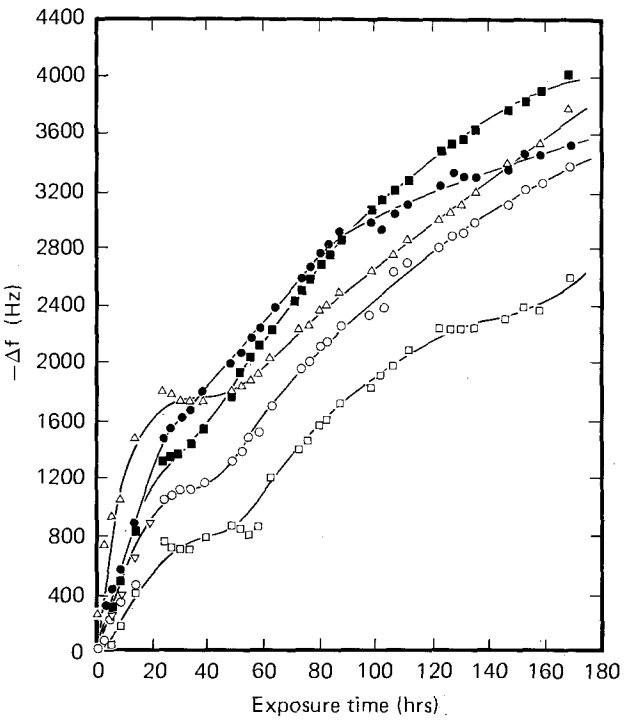


Fig. 2. Dependence of Permalloy film mass change on exposure time to a corrosive atmosphere for six identical specimens. (A frequency decrease of 1 Hz equals a mass uptake of 1.77 × 10^{-8} g/cm².)

by the fact that the average frequency shifts for these specimens is almost exactly proportional to the square root of exposure time, after an initial incubation period (τ) of 3-4 hr. See Fig. 3 in which the error bars indicate the standard deviation from the mean. The incubation period probably involves saturation of the surface with gaseous species. Accordingly, adjusting the time coordinate for a τ value of 4 hr shows that

$$-\Delta\bar{f} = 271\sqrt{t-\tau} \qquad [1]$$

with a correlation coefficient $r > 0.999$. For the films studied here, this time dependence suggests that the reaction is limited by the diffusion of reactants through a reasonably coherent layer of corrosion products. The value of the rate constant (−271 Hz/hr$^{1/2}$ in this case) clearly depends upon film and test conditions. We regard the finding of a well-defined rate law as significant because it convincingly demonstrates that complex phenomena involving the corrosion of

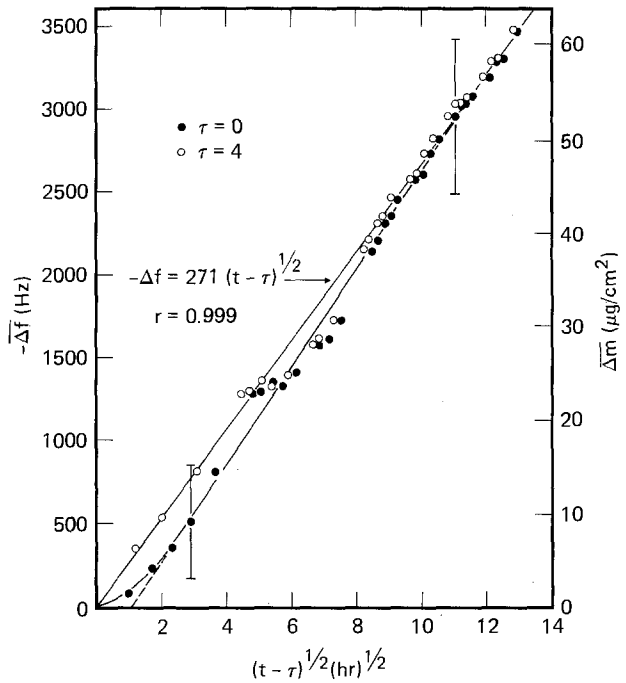


Fig. 3. Dependence of average mass uptake on the square root of exposure time to a corrosive atmosphere for Permalloy films.

multicomponent alloy films can be precisely measured, provided care is taken to minimize various artifacts (particulate, etc.) and a large enough sample size is used.

Microscopic examinations revealed that the corrosion products or active sites are not uniformly distributed across the surface. Thus, the large spread in the $\Delta R/R(t)$ *vs.* t curves can probably be attributed to minor variations in metallurgical properties and surface contamination across the specimens, as well as specimen-to-specimen differences.

In an effort to understand better the significance of the RC data, the relationship between resistance and mass change was explored by comparing the results in Fig. 1 and 2. The isochronal plot in Fig. 4 shows that the average $\Delta R/R(t)$ values increase approximately linearly with the square of the average mass uptake. The fit shown here is surprisingly good, considering the large spread in the resistance data.

We now consider the localized nature of corrosive attack on the films in order to gain some insight into the origin of the dependence shown in Fig. 4. Ideally, we would like to know the shapes, densities, and distributions of the corroded regions as a function of exposure time to the reactive environment. Since

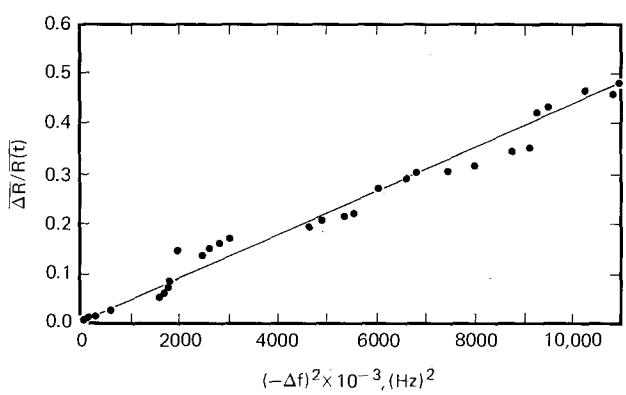


Fig. 4. Functional relationship between average resistance and mass changes of Permalloy films during atmospheric corrosion.

this information is quite tedious to establish, we have attempted to develop it in a rudimentary fashion by examining the surfaces of severely corroded Permalloy films using scanning electron and optical microscopy. The corroded parts of the film typically fall into two size categories and are more or less randomly distributed across the surface. See Fig. 4 of Ref. (1), for example, and note there are small elongated areas (~3 × 10 μm) and much larger, circular ones (~80-100 μm diam). Although the number of larger defects per square centimeter is only one-twentieth that of the smaller, the former comprise over 90% of the total corroded film area.

These observations lead us to believe that the smaller corroded regions form on nucleation sites with the introduction of the reactive atmosphere. The density of the nucleating centers is presumably dependent on film preparation conditions but will not be further discussed here. With continued exposure to the atmosphere, corrosion processes continue around a few of the small defects leading to the formation of the ~90 μm diam regions. We infer that this growth process is relatively rapid since the number of intermediate size defects is typically very low. Obviously, the larger regions contribute to most of the observed RC and QCM changes since they comprise >90% of the corrosion product.

To determine whether the above description is consistent with the observed resistance-mass change dependence shown in Fig. 4, a simple experiment was designed to simulate the effects of corrosion on film resistance. This involved punching out holes (0.125 in. diam) in a conductive aluminized-Mylar strip (1 in. wide by several inches long) while measuring the resistance-mass change dependence. The holes were confined to the central region and were well away from the electrical probes used to determine resistance by the standard four-point technique. The test structure treated is shown schematically in Fig. 5a, at the end of an experiment in which the hole positions were roughly random. The resistance increase $[\Delta R/R(o)]$ *vs.* mass loss $(\Delta m/m_o)$ curves are shown in Fig. 6 where m_o is the initial mass of the section of film being perforated. Variations in hole diameter by a factor of two or so had little effect on the results, provided the holes were more or less randomly positioned. However, note that the results are quite sensitive to the randomness of the hole positions. This can be seen from the results of a second experiment wherein a fixed number of holes were formed on an ordered lattice, and the hole diameter was increased in several steps. The scatter of the data

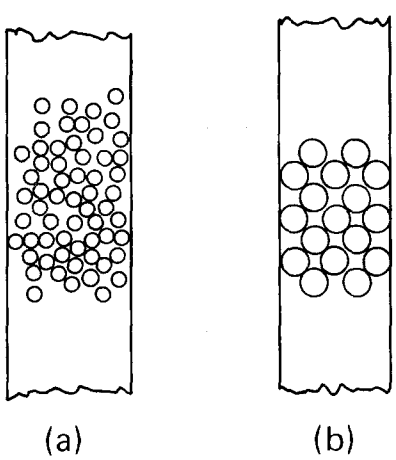


Fig. 5. Appearance of aluminized Mylar strips at conclusion of simulated corrosion experiments. (a) Random hole case; (b) ordered holes.

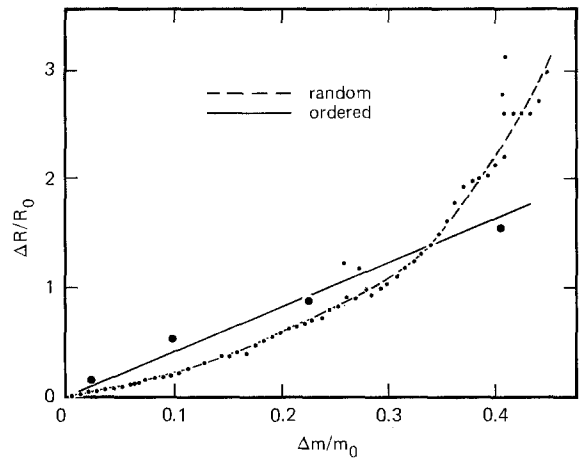


Fig. 6. Dependence of relative resistance change on mass of conducting material removed.

from a smooth curve for the random hole case is inherent in the experiment since $\Delta R/R(o)$ depends on the accidental distribution of holes, even with a fixed and relatively large number of holes; only the average of many experiments is expected to yield a smooth curve. Data from the randomized hole case are replotted in Fig. 7 and exhibit a similar quadratic dependence to that of Fig. 4. Clearly, the quantity $\Delta R/R(\Delta m/m_o)$ is the analog of $\Delta R/R(t)$. Hence we conclude that Permalloy film corrosion is initiated at randomly positioned active sites. It is also clear that the corroded regions penetrate the entire film thickness since the square law relationship in Fig. 4 holds up to quite large values of $\Delta R/R(t)$. Were the holes to penetrate uniformly only a fraction of the film thickness, the $\Delta R/R(t)$ *vs.* $|-\Delta f|^2$ plot would saturate at some constant value determined by the thickness of unreacted alloy.

The experimental resistance-mass change data of Last and Thouless (3) and percolation theory for transport in inhomogeneous conductors by Kirkpatrick

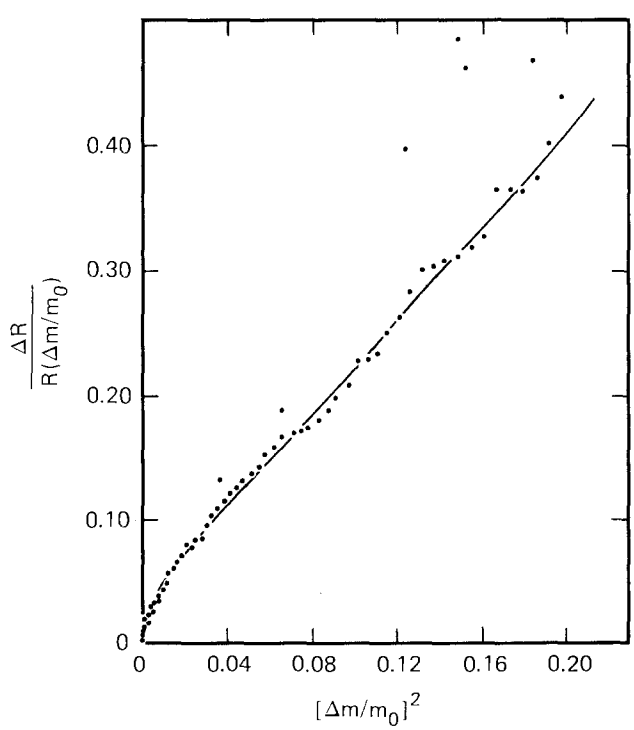


Fig. 7. Functional relationship between resistance and mass changes for the simulated, random-hole corrosion experiment.

(4) indicate an approximately linear dependence of resistance on mass change for a low (~10%) concentration of holes or defects. Although our findings (Fig. 6) also appear to be linear initially, they also fit a quadratic dependence quite well over the whole range of mass increase. Moreover, our $\Delta R/R_0$ *vs.* $\Delta m/m_0$ curve is concave upward whereas theirs (3, 4) are concave downward. The difference is not understood but our findings are intuitively reasonable.

The agreement between the results in Fig. 4 and 7 permits us to approximate the average molecular weight of the corrosion products. Note that the curve in Fig. 7 can be used to estimate the mass of Permalloy consumed in causing a given resistance increase. Likewise, the mass of condensed gases needed to cause the same resistance increase can be obtained from Fig. 4. On combining these estimates of the mass of gas condensed and Permalloy reacted, we estimate a molecular weight of roughly 200 ± 30 by the time the relative resistance change $\Delta R/R(t)$ has increased to 0.4. This value is consistent with ESCA examinations of the corroded Permalloy films which suggest that hydrated chlorides and sulfates (*e.g.*, $NiCl_2 \cdot 6H_2O$, $FeCl_2 \cdot 4H_2O$, and $FeSO_4 \cdot H_2O$) make up most of the corrosion products.

Acknowledgments

The authors would like to thank Drs. F. F. Abraham, P. Bagus, and M. H. Lee for their thoughts on this subject and M. R. Lorenz for reviewing this manuscript. They are also indebted to Dr. D. W. Rice for the use of his environmental chamber and ESCA apparatus.

Manuscript submitted March 10, 1977; revised manuscript received July 7, 1977.

Any discussion of this paper will appear in a Discussion Section to be published in the June 1978 JOURNAL. All discussions for the June 1978 Discussion Section should be submitted by Feb. 1, 1978.

Publication costs of this article were assisted by IBM Corporation.

REFERENCES

1. D. W. Rice, J. C. Suits, and S. J. Lewis, *J. Appl. Phys.*, **47**, 1158 (1976).
2. L. J. van der Pauw, *Philips Res. Rep.*, **13**, 1 (1958); R. Clang, R. A. Holmwood, and L. I. Maissel, *Thin Solid Films*, **1**, 159 (1967).
3. B. J. Last and D. J. Thouless, *Phys. Rev. Lett.*, **27**, 1719 (1971).
4. S. Kirkpatrick, *Rev. Mod. Phys.*, **45**, 475 (1973).

Oxidation Studies of Permalloy Films by Quartz Crystal Microbalance, AES, and XPS

Wen-Yaung Lee and Jerome Eldridge*

IBM Research Laboratory, San Jose, California 95193

ABSTRACT

The quartz crystal oscillator microbalance has been used in conjunction with Auger electron and x-ray photoelectron spectroscopies to study the oxidation at 185°C and 1 atm O_2, of air-exposed Permalloy films vacuum deposited at 200° and 350°C. Frequency shifts corresponding to weight gains of the films during oxidation combined with data obtained from AES, XPS, and ion sputter-etching showed: (*i*) the oxidation rate was diffusion controlled, (*ii*) Fe was preferentially oxidized with moderate Ni enrichment in the remaining alloy, and (*iii*) the average iron oxide composition is $FeO_{1.3}$. Reaction appears to be limited by iron diffusion through the alloy. Average iron diffusion coefficients estimated from the parabolic rate constants are in good agreement with that reported for iron in thin polycrystalline Ni films.

The quartz crystal microbalance (QCM) with its easily obtainable mass sensitivity of better than 10^{-9} g/cm^2 ($\simeq 10^{12}$ molecules/cm^2) has been extensively used in various mass-related measurements (1-6). However, in addition to measuring the net weight change of the film, it is desirable to determine the compositions of the reaction products, using such surface sensitive techniques as Auger electron spectroscopy (AES) and x-ray photoelectron spectroscopy (XPS). It is well known that the different chemical valence states for most elements can be determined by XPS (7), and that AES coupled with ion sputter-etching provides a tool for obtaining the depth distribution of various elemental species. But these two techniques have their intrinsic difficulties: *e.g.*, the destructive nature of either the excitation source used (8-10) and/or the ion-sputtering needed for in-depth profiling (11-14). Because of these and other uncertainties (viz., excitation cross section, electron escape depth, and the effects of diffraction, surface roughness, and backscattered electrons), AES and ESCA results are generally qualitative. It is the purpose of this paper to demonstrate that QCM can be used in conjunction with AES and XPS to obtain quantitative information on complex surface reactions involving the oxidation of alloy films.

We have chosen to study the oxidation of Permalloy ($Ni_{0.80}Fe_{0.20}$) films using these techniques, with the intent to establish a foundation for future studies of various thin film systems. The complicated surface composition and chemistry of air-exposed Permalloy films have been studied by Pollak and Bajorek using AES and XPS (15) and the oxidation (in the 350°-500°C range) of Permalloy films was carried out by Coren and Francombe (16) and by Bajorek *et al.* (17). However, to our knowledge no kinetic data have been reported for Permalloy film oxidation. To obtain a better insight into the stability of Permalloy in an oxygen atmosphere at intermediate temperatures, the oxidation kinetics of 1000Å films were investigated here with the QCM technique. Specimens were prepared at two temperatures (200° and 350°C) to assess potential microstructural effects on reactivity.

* Electrochemical Society Active Member.
Key words: alloy film reactivity, preferential oxidation, thin film diffusion.

AES, XPS, and ion sputter-etching were subsequently used to analyze the oxidized films. The results show that the oxidation rate is controlled by iron transport through the alloy and that Fe is preferentially oxidized, leading to a moderate Ni enrichment in the underlying alloy.

Experimental Procedures

Permalloy films were electron-beam deposited through masks from a single source [Fe 18 atom percent (a/o), Ni 82 a/o], under 10^{-7} Torr vacuum. The film thickness was 1100 ± 50Å as analyzed by an optical interferometer and 1160 ± 40Å by electron microprobe (EM) analysis, assuming a Permalloy density of 8.7 g/cm³. The film composition was also analyzed by EM and was found to be Fe 19.2 ± 0.2 and Ni 80.8 ± 0.2 a/o. These films were deposited directly onto optically polished, AT-cut quartz crystal substrates (0.5 in. diam). The patterned Permalloy film also served as one of the two excitation electrodes. The other excitation electrode was a 1000Å gold film vacuum-deposited, prior to the Permalloy, onto the other quartz crystal face at 200°C. To minimize frequency changes due to effects other than oxygen up-take, a double-resonator technique was employed, using gold as reference electrodes. The reaction chamber was held at 185° ± 0.4°C, leading to a frequency fluctuation of ±5 Hz over a typical 24 hr period. The quartz-crystal microbalance system is illustrated schematically in Fig. 1.

It has been shown (18) that, for a quartz crystal vibrating at its fundamental thickness-shear mode

$$\Delta m/m = -\Delta f/f \qquad [1]$$

where $-\Delta f$ is the frequency lowering due to a uniform mass addition (Δm) which is small compared to the initial mass of quartz (m); and, f is the initial frequency of the quartz device. For an AT-cut, 5 MHz crystal, the mass change corresponding to a 1 Hz shift is 1.77×10^{-8} g/cm². However, both the true film surface area and the oxide density must be known to convert this weight change into oxide thickness.

AES and XPS spectra were taken at room temperature with Physical Electronics Industries Auger and Hewlett-Packard 5650A spectrometers, respectively (19, 20). The peak-to-peak heights of the oxygen KLL Auger transition at 510, the Fe LMM at 650, and the Ni LMM at 850 eV were monitored during the Xe ion sputtering at 5×10^{-5} Torr pressure and 1 keV beam voltage. Aluminum K_α radiation was used for excitation to obtain all ESCA data and the binding energy was referred to the $Au4F_{7/2}$ line at 83.9 eV.

Experimental Results

Typical frequency shift-oxygen exposure time curves are shown in Fig. 2. It is seen that the total weight increase after 160 hr of O_2 exposure amounts to ~6 $\times 10^{-7}$g for an electrode area of 0.3 cm², showing the necessity of using an extremely sensitive technique such as QCM. The results are quite reproducible, with run-to-run variations being less than several percent of the total frequency changes. As seen in Fig. 3, the results fit well to a parabolic rate law, after an initial period of several hours. The parabolic rate constants (K_p) calculated from the slopes are 1.7×10^{-17} and 9.4×10^{-18} g/cm²·sec for films deposited at 200° and 350°C, respectively.

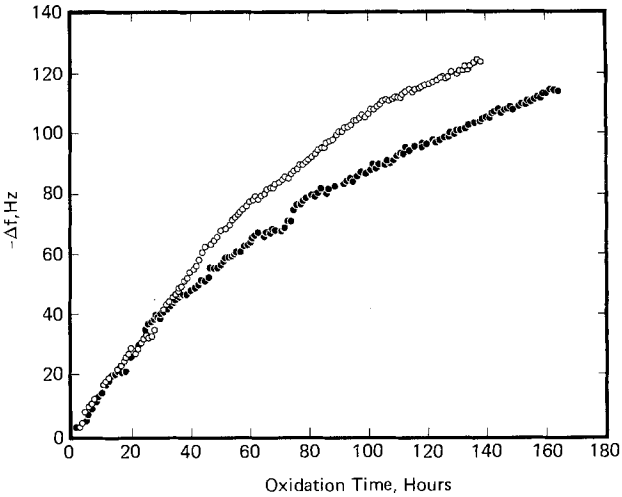


Fig. 2. QCM frequency changes of Permalloy films due to oxidation at 185°C and 1 atm O_2. Solid circles are for films deposited at 350°C and open circles at 200°C.

Typical AES spectrum for the surface of an air-exposed Permalloy film is shown in Fig. 4. In addition to Fe, Ni, and O, note that small amounts of C, S, and Cl are present. These are typical contaminants for air-exposed films (10). Except for oxygen, however, these contaminants appear to be limited only to the surface region because their signal intensities quickly decrease to the background noise upon sputtering. Figure 5 shows a similar spectrum for a heavily oxidized (~160 hr) specimen. It is seen that the Ni signal strength is relatively small compared to that for the air-exposed films. In certain runs, Ni could not be detected by AES on heavily oxidized surfaces. The very low Ni signal strength and the fact that the lower Fe LMM Auger transition at 44 eV splits into a

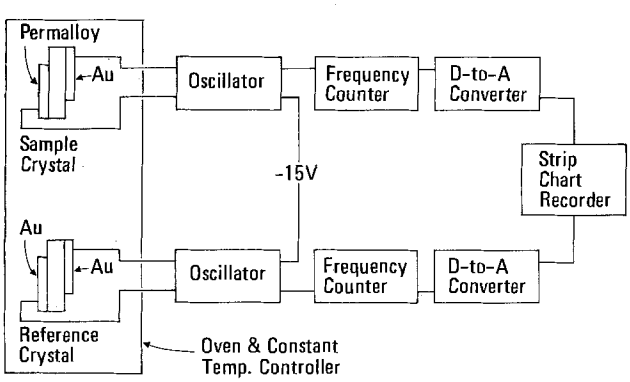


Fig. 1. Schematic diagram of quartz-crystal microbalance system

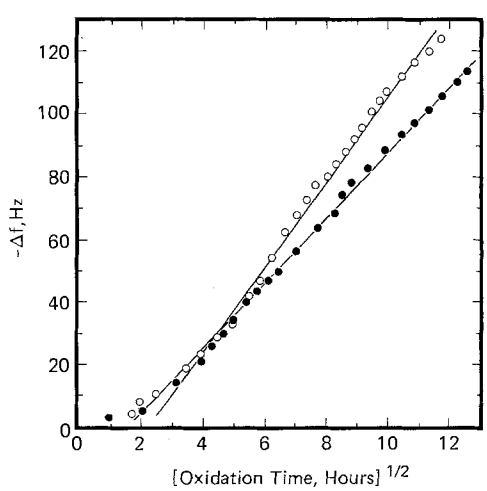


Fig. 3. Frequency changes of Permalloy films due to the oxidation at 185°C and 1 atm O_2 vs. the square root of time. Solid circles are for films deposited at 350°C and open circles at 200°C.

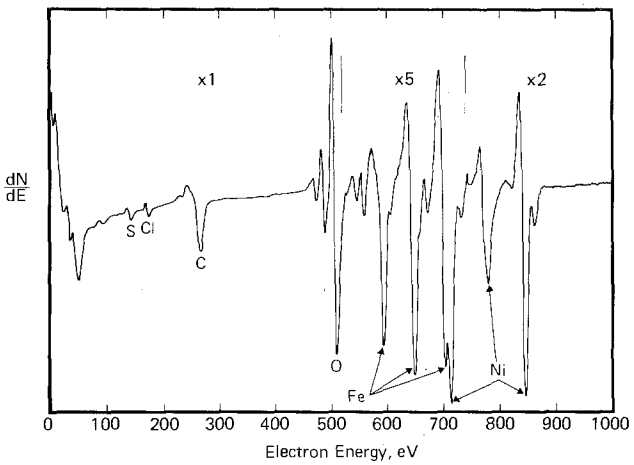


Fig. 4. Typical AES spectrum of air-exposed Permalloy film deposited at 200° and 350°C. Operating conditions: $Ep = 3$ kV, $Ip = 30$ μA, $V_{MOD} = 6$ eV, $RC = 0.1$ sec.

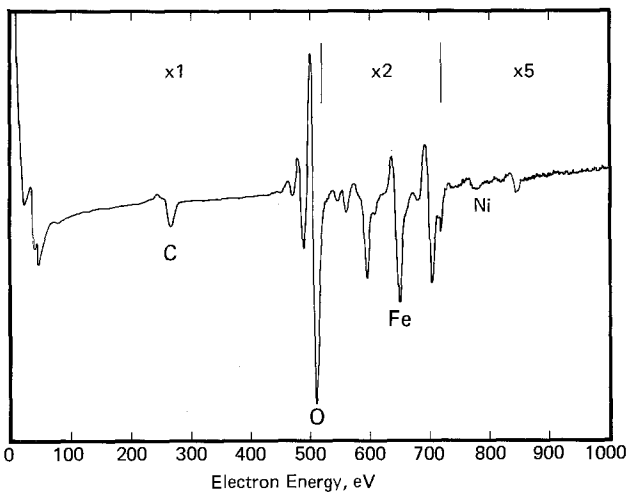


Fig. 5. Typical AES spectrum of oxidized Permalloy film

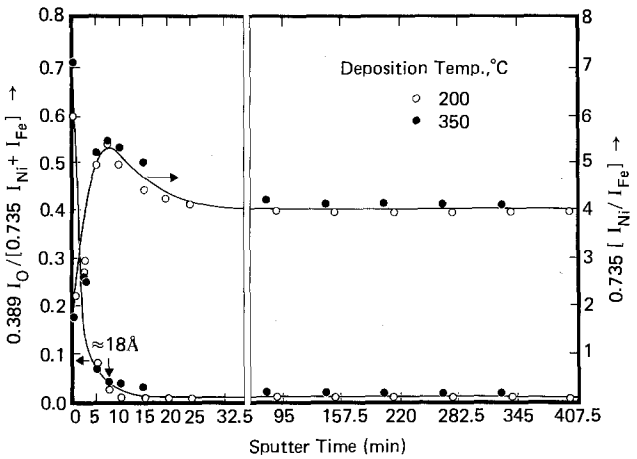


Fig. 6. AES sputter depth profiles of air-exposed Permalloy films. Sputtering was done with 1 kV Xe ions at 10^{-5} Torr and a filament current of 5 mA.

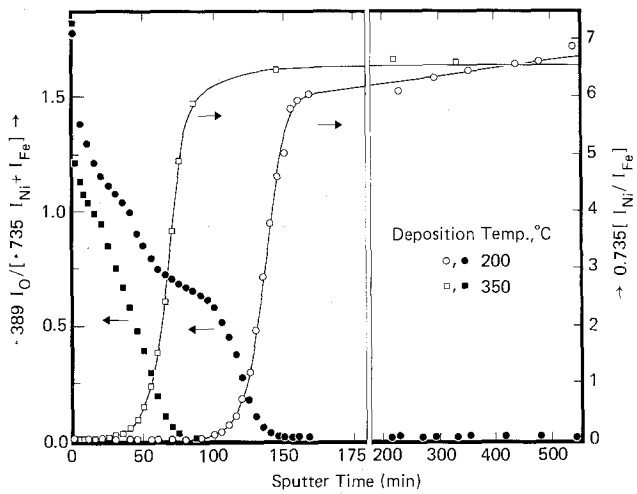


Fig. 7. AES sputter depth profiles of oxidized Permalloy films

doublet (at 41 and 48 eV) characteristic of oxidized Fe (21) indicate that the film surface is predominantly iron oxide.

The AES depth profiles of both the air-exposed and heavily oxidized films were obtained and analyzed according to the equation (13, 14)

$$\frac{I_{Ni}/I_{Ni}^{\circ}}{I_{Fe}/I_{Fe}^{\circ}} = \frac{S_{Fe}}{S_{Ni}} \cdot \frac{C_{Ni}}{C_{Fe}} \qquad [2]$$

where I_{Ni} and I_{Fe} are the peak-to-peak heights, obtained after a steady-state surface composition is reached by sufficient sputtering of the alloy with bulk concentrations of C_{Ni} and C_{Fe}, respectively; I_{Ni}° and I_{Fe}° are those for pure metals; and, S_{Fe} and S_{Ni} are the sputtering yields. It should be pointed out that this equation is correct strictly when the matrix dependence of electron escape depths and backscattering factors are small.

The normalized I_{Ni}/I_{Fe} and $I_O/(I_{Ni} + I_{Fe})$ signal strength ratios are plotted against sputter-etching time in Fig. 6 and 7 for the air-exposed and heavily oxidized films, respectively. The normalization constant $I_{Fe}^{\circ}/I_{Ni}^{\circ} = 0.735$ was obtained from pure Ni and Fe films and agrees well with that calculated from data reported by Palmberg *et al.* (22). The value of $I_{Fe}^{\circ}/I_O^{\circ} = 0.389$ was extracted directly from their data (22). From Fig. 6, it is seen that the normalized I_{Ni}/I_{Fe} ratio increased from ~2 at the air-oxide interface to a maximum of about 5.3 near the inner interface, before gradually leveling off to the bulk value of 4.0 ± 0.1. This is accompanied by a rapid decrease of the $I_O/(I_{Ni} + I_{Fe})$ ratio, which reaches a minimum approximately when I_{Ni}/I_{Fe} achieves a maximum. The findings indicate that iron is depleted from the alloy surface to form an iron-enriched oxide tarnishing layer, as reported earlier (10). Furthermore, since $(I_{Ni}/I_{Ni}^{\circ})/(I_{Fe}/I_{Fe}^{\circ}) = 4.0 \pm 0.1$ and $C_{Ni}/C_{Fe} = 4.2$ (as determined by EM) S_{Ni}/S_{Fe} calculated from Eq. [2] is found to be 1.05. Thus Ni sputters only slightly faster than Fe at the Permalloy composition, and the AES depth profiles for bulk Permalloy also represent approximate compositional profiles.

For the deliberately oxidized films, the I_{Ni}/I_{Fe} ratio increased sharply from nearly zero as the oxide-alloy interface was approached, reaching a steady-state value of about 6.6, as can be seen in Fig. 7. This value yields an iron concentration in the remaining bulk alloy of ~13%, indicating that Fe is depleted from the underlying alloy during the oxidation process. This finding, augmented by the essential absence of Ni in the oxide region, prove that Fe is preferentially oxidized in Permalloy under the conditions used here. Similar results have been reported also for Permalloy oxidized at temperatures between 350° and 500°C using x-ray diffraction (16) and nuclear backscattering and x-ray fluorescence (17) techniques. On the other hand, the $I_O/(I_{Ni} + I_{Fe})$ ratio decreases with increasing ion etching time, even within the oxide layer where the Ni concentration is almost zero. This

result implies that the iron oxide composition is changing. Unfortunately, these profiles cannot be used to calculate the oxide composition profile directly, because of the sputter-induced damage (preferential sputtering of O) (12, 23). However, the $I_O/(I_{Ni} + I_{Fe})$ ratios extrapolate to ~1.5 at the outer oxide surface, corresponding to the composition of Fe_2O_3.

In order to further identify the oxidation products, ESCA spectra were obtained also for companion films prepared and oxidized under the same conditions. Typical results for the $Ni2P_{1/2}$ and $Fe3P_{1/2}$ transitions are shown in Fig. 8 and 9, respectively. From the binding energy observed for $Fe3P_{1/2}$ (56.4 eV relative to metallic iron at 53.1 eV) in Fig. 8 it appears that the dominant oxidation products on the surface are Fe_2O_3 (24, 25), although there is also the possibility that Fe_3O_4 is present (23). The spectra in Fig. 8 indicate that small amounts of metallic (at 870.2 eV) and higher valence state (at 874.2 eV) Ni are also present on the surface.

Sputter profiling of the oxidized films reveals that the binding energy of the $Fe3P_{1/2}$ line gradually

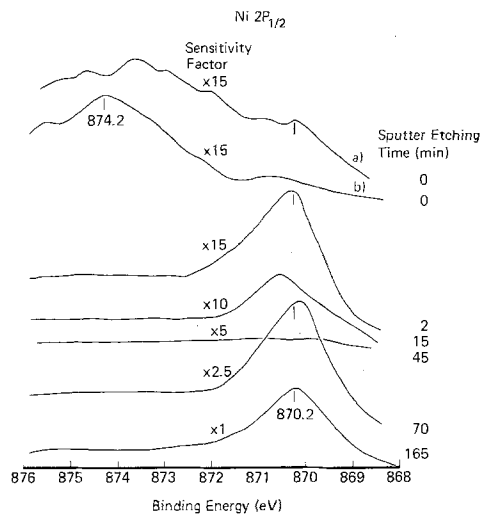


Fig. 8. XPS spectra for the $Ni2P_{1/2}$ transition of: (a) air-exposed, and (b) oxidized Permalloy films. The oxidized films have been sputter-etched with Ar ions at 1 kV, 5 × 10^{-5} Torr pressure and a filament current of 10 mA.

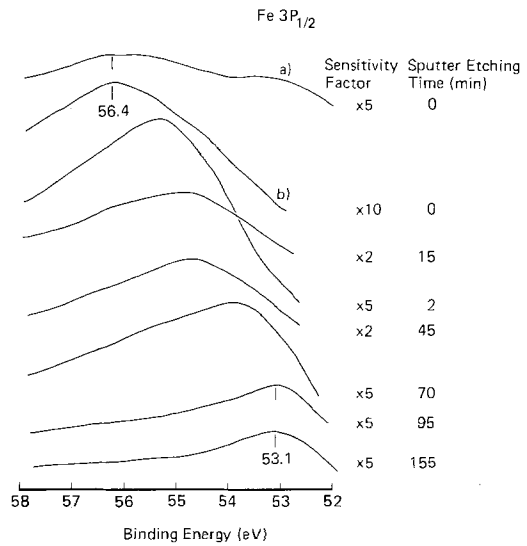


Fig. 9. XPS spectra for the $Fe3P_{1/2}$ transition of: (a) air-exposed, and (b) oxidized Permalloy films. Same sputtering conditions as in Fig. 8.

decreases from 56.4 eV at the surface to reach the metallic value of 53.1 eV on approaching the inner interface. Because this binding energy shift corresponds to a change of Fe oxidation state from +3 to 0, it appears that the average iron oxide composition is graded from Fe_2O_3 at the surface to FeO near the inner interface. However, this change in composition can also be due to the preferential sputtering of oxygen (12, 22), as mentioned earlier. On the other hand, Fig. 8b showed that the $Ni_2P_{1/2}$ transition quickly reached the metallic state value upon sputter profiling, remaining low in intensity throughout the oxide layer and did not increase in strength until the underlying alloy was reached. These results are quite consistent with those from AES profiling.

Discussion

If a reasonable average oxide composition and density are assumed, the total oxide thickness can be estimated from the QCM data. One can then estimate the corresponding reduction in iron concentration in the underlying alloy and compare this with the AES finding. Thus, we assume that the oxide layer is an equal mixture of Fe_2O_3, Fe_3O_4, and FeO with an average oxide composition of $FeO_{1.3}$ and a density of 5.4 g/cm³. The results are given in Table I, along with those based on the premise that the oxide is Fe_2O_3. The average $FeO_{1.3}$ composition clearly yields final alloy compositions that are in very good agreement with the AES-determined results. The oxide thicknesses were calculated by assuming that the true film surface area equals the geometrical area. For comparison, the oxide thicknesses (estimated from the products of the oxide sputter etching times and the Permalloy sputter etching rate) are 195 and 187Å for the 200° and 350°C films, respectively. Since the oxide sputtering rate is not likely to be constant throughout the oxide layer or the same as that of Permalloy, estimates like this should be viewed with caution.

Since the QCM data fit reasonably well to a parabolic rate law and the AES results show that Fe is preferentially oxidized with a moderate Ni enrichment in the underlying alloy, it appears that the diffusion of Fe is the rate-limiting step for reaction. If the oxidation step at the oxide-alloy surface is fast compared with the diffusion of Fe atoms in the alloy, the over-all diffusion coefficient (D) is related to the parabolic rate constant (K_p) through the following equation (26)

$$D = \frac{\pi}{(\rho C)^2} \cdot \left(\frac{M}{16Z}\right)^2 \cdot K_p \qquad [3]$$

where ρ = 7.86 g/cm³, C = 0.192, and M = 55.85 are the density, mole fraction in the alloy, and atomic weight of Fe, respectively; Z = 2.6 for the average oxide $FeO_{1.3}$. Hence, diffusion coefficients of 4.2 × 10^{-17} and 2.3 × 10^{-17} cm²/sec were calculated for films deposited at 200° and 350°C, respectively. These values are close to that (~5 × 10^{-18} cm²/sec) re-

Table I. Comparison of various estimates of iron oxide thicknesses and resulting alloy compositions

Film deposition temperature (°C)	Assumed oxidation product	Δf (Hz)	t (Å)	(Ni/Fe)$_{QCM}$*	(Ni/Fe)$_{AES}$**
200	Fe_2O_3	124	139	5.8	6.6
200	$FeO_{1.3}$	124	150	6.5	6.6
350	Fe_2O_3	114	128	5.5	6.6
350	$FeO_{1.3}$	114	138	6.2	6.6

* Composition of the underlying alloy layer after oxidation, as calculated from QCM data.

** Composition of the underlying alloy layer after oxidation, as determined from AES sputter profiling measurements.

ported for Fe diffusion through polycrystalline Ni film at 185°C (27). Since these values are several orders of magnitude higher than those extrapolated for lattice diffusion, it seems that grain boundary and defect-enhanced lattice diffusion provide the dominant transport mechanisms (27). Furthermore, the larger diffusion coefficient for the 200°C films nicely reveals the dependence of film reactivities on film deposition temperatures in that the lower temperature formed ones are finer grained, and presumably have a much higher vacancy concentration. Thus, they are more accessible to grain-boundary and defect-enhanced lattice diffusion than films deposited at the higher temperature.

As mentioned earlier, XPS results indicate that very small amounts of metallic Ni and its compounds (probably hydroxide) are present near the iron oxide surface. According to Whittle *et al.* (28), the minimum mole fraction (X_{Ni}) of nickel at the alloy/oxide interface needed to form NiO can be estimated from

$$(1 - X_{Ni})/X_{Ni} = \exp\left[\frac{1}{RT}(\Delta F^\circ_{FeOx} - \Delta F^\circ_{NiO})\right] \quad [4]$$

where ΔF°_{FeOx} and ΔF°_{NiO} are the standard free energies of iron and nickel oxide formation, respectively. Since the difference in the standard free energy of iron oxide (Fe_2O_3 or Fe_3O_4) and nickel oxide formation is at least 30 kcal/mole (29), X_{Ni} is estimated to be very close to unity and thus is much larger than the bulk Ni concentration in the alloys. Therefore, iron oxide is expected to be formed exclusively because of thermodynamic considerations. Trace amounts of nickel near the surface and its absence inside the iron oxide region suggest that nickel is probably incorporated in the iron oxide during its nucleation and growth stages and sparsely dispersed near the surface (30). This interpretation is consistent with the observation that occasionally AES detected no Ni on the surfaces of heavily oxidized films, due to its small sampling area (~50 μm).

Finally, it should be pointed out that lateral stress build up (2) in the film during oxidation could also cause some frequency changes in addition to that caused by the mass loading effect. The frequency shifts caused by stress (Δf_s) are related to that of the mass effect (Δf_m) by

$$\Delta f_s/\Delta f_m \simeq K\,\Delta s/\tau_f \quad [5]$$

where $\Delta s/\tau_f$ is the averaged stress change of the film and K is 2.75×10^{-12} cm²/dyne for AT-cut quartz crystals. The isotropic stress of Permalloy films on glass or mica is on the order of 10^9 dyne/cm², and all the films used here contain an initial air-formed oxide of about 18Å (estimated from AES/depth profiling). Since the additional oxide grown is only several times larger, the net stress change of the film is not likely to be drastically larger than 10^9 dyne/cm². Accordingly, the stress effect appears to be quite negligible, *i.e.*, less than 1% of the mass loading effect.

Acknowledgments

The authors are indebted to Drs. R. Guarneri for preparing the film structures, D. Kyser for electron microprobe analysis, D. W. Rice for his advice and assistance with the AES and XPS measurements, D. Brundle and T. J. Chuang for their helpful discussions, and M. Lorenz for reviewing this manuscript.

Manuscript submitted March 10, 1977; revised manuscript received July 15, 1977.

Any discussion of this paper will appear in a Discussion Section to be published in the June 1978 JOURNAL. All discussions for the June 1978 Discussion Section should be submitted by Feb. 1, 1978.

Publication costs of this article were assisted by IBM Corporation.

REFERENCES

1. W. Y. Lee and L. J. Slutsky, *Surface Sci.*, **54**, 169 (1976).
2. E. P. EerNise, *J. Appl. Phys.*, **43**, 1330 (1972); *ibid.*, **44**, 4482 (1973); *J. Vac. Sci. Technol.*, **11**, 408 (1974); *ibid.*, **12**, 564 (1975).
3. R. V. Bucur, W. Mecea, and T. B. Flanagan, *Surface Sci.*, **54**, 477 (1976).
4. M. Shiojiri, *This Journal*, **122**, 698 (1975).
5. W. H. Wade and R. C. Allen, *J. Colloid Interface Sci.*, **27**, 722 (1968).
6. W. H. King, Jr., *Vac. Microbalance Technol.*, **8**, 183 (1971).
7. K. Siegbahn, C. Nordling, A. Fahlman, R. Nordberg, K. Hamrin, J. Hedman, G. Johansson, T. Bergmark, S-E. Karlsson, I. Lindgren, and B. Lindberg, ESCA, "Atomic, Molecular and Solid State Structure Studied by Means of Electron Spectroscopy," Almqvist and Wiksells, Uppsala (1967).
8. T. Smith, *Surface Sci.*, **55**, 601 (1976).
9. S. Thomas, *J. Appl. Phys.*, **45**, 161 (1974).
10. J. S. Johannessen, W. E. Spicer, and Y. E. Strausser, *ibid.*, **47**, 3028 (1976).
11. H. F. Winters and J. W. Coburn, *Appl. Phys. Lett.*, **28**, 176 (1976); J. W. Coburn and E. Kay, *Crit. Rev. Solid State Sci.*, **4**, 561 (1974).
12. K. S. Kim, W. E. Baitinger, J. W. Amy, and N. Winograd, *J. Electron Spectrosc.*, **5**, 351 (1976).
13. H. Shimizu, M. Ono, and K. Nakayama, *Surface Sci.*, **36**, 817 (1973).
14. L. A. West, *J. Vac. Sci. Technol.*, **13**, 198 (1976).
15. R. A. Pollak and C. H. Bajorek, *J. Appl. Phys.*, **46**, 1382 (1975).
16. R. L. Coren and M. H. Francombe, *Thin Solid Films*, **34**, 95 (1976).
17. C. H. Bajorek, M. A. Nicolet, and C. H. Wilts, *Appl. Phys. Lett.*, **19**, 82 (1971).
18. G. Z. Sauerbrey, *Phys. Verh.*, **8**, 113 (1957).
19. T. J. Chuang, D. Brundel, and D. Rice, *Surface Sci.*, **59**, 413 (1976).
20. D. Rice, J. Suits, and S. Lewis, *J. Appl. Phys.*, **47**, 1158 (1976).
21. R. W. Revie, B. G. Barker, and J. O'M. Bockris, *This Journal*, **122**, 1460 (1975).
22. P. Palmerg, G. E. Riach, R. E. Webber, and N. C. McDonald, "Handbook of Auger Electron Spectroscopy," Physical Electronic Industries, Inc. (1972).
23. T. J. Chuang, K. Wandelt, and C. R. Brundle, To be published.
24. J. P. Contour and G. Mouvier, *J. Catal.*, **40**, 342 (1975).
25. T. P. Hoar, M. Talerman, and P. M. A. Sherwood, *Nature (London), Phys. Sci.*, **240**, 116 (1972).
26. R. Hales, *Oxid. Met.*, **10**, 29 (1976).
27. T. J. Chuang and K. Wandelt, Proceedings of 7th International Vacuum Congress and 3rd International Conference on Solid Surfaces, Vienna (1977).
28. D. P. Whittle, D. J. Evans, D. B. Scully, and G. C. Wood, *Acta Metall.*, **15**, 1421 (1967).
29. B. Chattopadhyay and G. C. Wood, *Oxid. Met.*, **2**, 373 (1970).
30. D. P. Whittle, Ph.D Thesis, University of Manchester (1965).

Liquid Crystal Mixtures for Low Voltage Dynamic-Scattering Display

Yoshikazu Hori and Masakazu Fukai

Matsushita Electric Industrial Company, Limited, Central Research Laboratory
3-15 Yagumo Nakamachi, Moriguchi-shi, Osaka, 570 Japan

ABSTRACT

New liquid crystalline compounds with high negative dielectric anisotropy and wide temperature range have been prepared by using the double-Shiff's-base compounds of bis-(4'-n-alkylbenzylidene)-2-cyano-1,4-phenylenediamine. The effect of negative dielectric anisotropy on the dynamic scattering properties was studied. With the increasing value of negative dielectric anisotropy of the liquid crystal mixture, they gave the low threshold voltage of the instability followed by the rapid increase of dynamic scattering intensity, and a low voltage dynamic scattering display device has been achieved. The increase of the contrast ratio above threshold and the weak temperature-dependent threshold characteristic improved the matrix-addressing properties remarkably.

Since Heilmeier, Zanoni, and Barton (1) reported the electro-optical effect of nematic liquid crystals and the capability of application to flat display devices in 1968, a great deal of research and development in liquid crystal material has been carried out actively, and many electro-optical effects such as dynamic-scattering and twisted nematic have been reported. Research to lower the driving voltage of liquid crystal displays using the twisted-nematic effect has been carried out (2). But few studies to lower the driving voltage of the dynamic-scattering display have been reported, although the effect has been well investigated experimentally and theoretically by many researchers (3-6). Elliott (7) reported the effects of dielectric anisotropy on dynamic-scattering by using material with a high negative dielectric anisotropy ($\Delta\epsilon \sim -2.0$) and found that this type of material decreased the threshold voltage slightly.

In this paper, the relation between the characteristics of the dynamic-scattering effect and the dielectric anisotropy of nematic liquid crystal is dealt with.

Experimental Procedure

Material.—The double-Shiff's-base compounds of bis-(4'-n-alkylbenzylidene)-2-cyano-1,4-phenylenediamine with high negative dielectric anisotropy were prepared and added to a room temperature nematic mixture. The compounds are abbreviated as BACYP1 to BACYP4 according to the number of carbon atoms in the alkyl chains, and the formula and the mesomorphic temperature ranges are shown in Table I.

The compounds were synthesized from 2-cyano-1,4-phenylenediamine, and 4-n-alkylbenzaldehyde and purified by recrystallization in the mixture of n-hexane and benzene. The impurities of these compounds were confirmed to be less than 0.15 mole percent (m/o) by DSC.

A triple mixture of Shiff's-base compounds was used as a host material. The nematic temperature range was from −6° to 69°C. It consisted of 4-ethoxybenzylidene-4'-butylaniline, 4-propylbenzylidene-4'-pentylaniline, and 4-methoxybenzylidene-4'-heptylaniline. Each component of this mixture was purified by recrystallization in n-hexane and the purities were confirmed by gas chromatographic analysis.

Nematic mixtures for the experiments were prepared by mixing these substances in arbitrary ratios. 3.5-dinitrobenzoic acid and the other dopants of a small quantity for specific resistivity and the homeotropic alignment were added.

Key words: liquid crystal display, low voltage driving, dynamic scattering mode, double-Shiff's-base compounds, high negative dielectric anisotropy.

They were placed between indium oxide coated conductive glass plates of about 10 μm gap. The electrical field was applied to the liquid crystal layer through a transparent electrode.

Measurement of physical and electro-optical properties.—For the measurement of the nematic temperature ranges the crystal (or smectic)-to-nematic and nematic-to-isotropic transition temperatures were measured by observing the phase change of compounds on the temperature control stage of a polarizing microscope.

The dielectric anisotropies and conductivity anisotropies were obtained by the measurement of dielectric constants and conductances parallel and perpendicular to the molecular orientation with a capacitance bridge.

Electro-optical properties were measured in the conventional way. The incident light from a tungsten lamp was irradiated to the panel normally, and the light transmitted normally to the liquid crystal layer was detected by a photo sensor. The response time was measured by the definition as follows. The rise time is the time the transmission falls 90% to the final transmission after the electrical field (32 Hz square wave) has been applied. The decay time is the time the transmission recovers 90% to the initial transmission after the electrical field has been turned off.

Cutoff frequency was defined as the frequency which divides the conduction and dielectric region in the curve showing the frequency dependence of the threshold voltage of electrohydrodynamic instability (8).

Table I. The formula and the mesomorphic ranges of the double-Shiff's-base compounds used in this study

	Formula	
BACYP1	CH_3⬡$CH=N$⬡($N=CH$⬡CH_3, CN	114—132 °C
BACYP2	C_2H_5⬡$CH=N$⬡($N=CH$⬡C_2H_5, CN	57—126 °C
BACYP3	C_3H_7⬡$CH=N$⬡($N=CH$⬡C_3H_7, CN	93—151 °C
BACYP4	C_4H_9⬡$CH=N$⬡($N=CH$⬡C_4H_9, CN	52—101 °C

Table II. Nematic ranges of the mixtures in this study, °C

	0 w/o	10 w/o	20 w/o	30 w/o
BACYP1	−6-69	−21-71	20-76	60-83
BACYP2		−26-71	−34-72	−38-75
BACYP3		−25-73	−33-79	−36-75
BACYP4		−24-71	−37-75	−46-78

Experimental Results

Nematic temperature ranges.—The nematic temperature ranges of the mixtures used in this study are shown in Table II.

By the addition of double-Shiff's-base compounds the nematic temperature range is widened in general and nematic mixtures with a temperature range of more than 100°C are obtained. In the case of the mixture containing 30 weight percent (w/o) of BACYP1, a nematic phase could not be observed clearly.

The properties of dielectric anisotropy.—Figure 1 shows the dependence of dielectric anisotropy ($\Delta\epsilon$) and dielectric constants parallel ($\epsilon_{\parallel}$) and perpendicular ($\epsilon_{\perp}$) to the molecular orientation on the concentration of BACYP. The negative dielectric anisotropy and dielectric constants increase proportionally to the increase of BACYP concentration. When the effect of the number of carbon atoms in the alkyl group is compared, BACYP with a smaller number of carbon atoms in the alkyl group is effective in increasing the negative dielectric anisotropy.

The dielectric anisotropy of double-Shiff's-base compounds themselves are estimated to be between −8 and −5 at room temperature from the figure. These are much greater than that of chloro compounds of these double-Shiff's-base types (7).

The properties of conductivity anisotropy.—Figure 2 shows the variation of the conductivity anisotropy as a function of BACYP2 concentration. It is defined as the ratio between the conductance parallel ($\sigma_{\parallel}$) and perpendicular ($\sigma_{\perp}$) to the molecular orientation. By the addition of BACYP2, the conductivity anisotropy is increased, and this is the important factor for producing the charge formation and causing dynamic-scattering when an electrical field is applied.

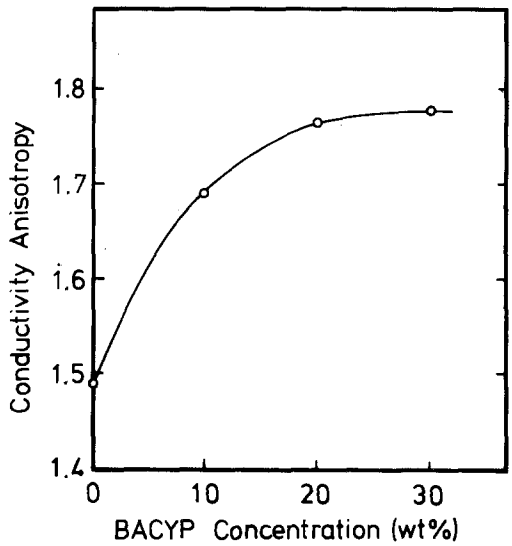


Fig. 2. The dependence of conductivity anisotropy ($\sigma_{\parallel}/\sigma_{\perp}$) on BACYP2 concentration.

Light scattering properties.—The properties of transmission as a function of applied voltage in nematic mixtures containing 0, 10, 20, and 30 w/o concentration of BACYP2 at 25°C is shown in Fig. 3. The threshold voltage of the host material is about 8V but accompanied by the increase of BACYP2 concentration it decreases to about 5V, and the voltage to give the same transmission also decreases. The same effect was con-

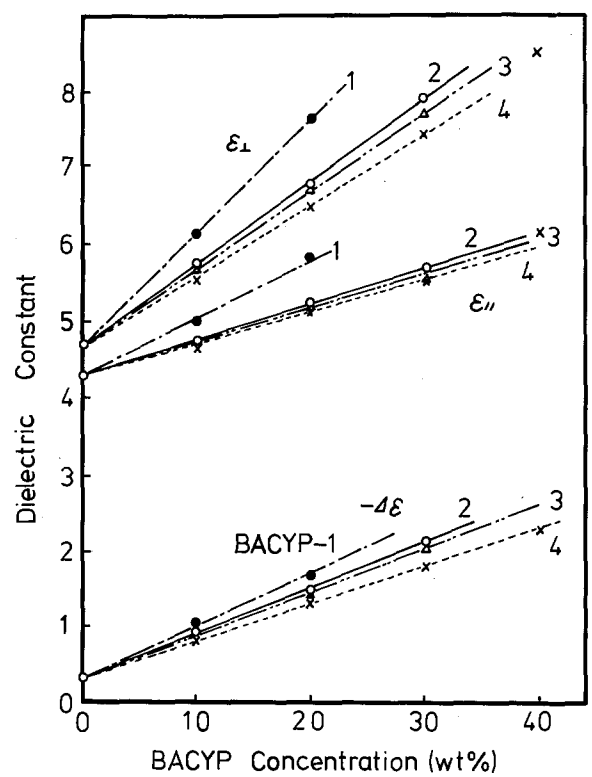


Fig. 1. The dependence dielectric constants ($\epsilon_{\parallel}$, $\epsilon_{\perp}$) and dielectric anisotropy on the concentration of BACYP.

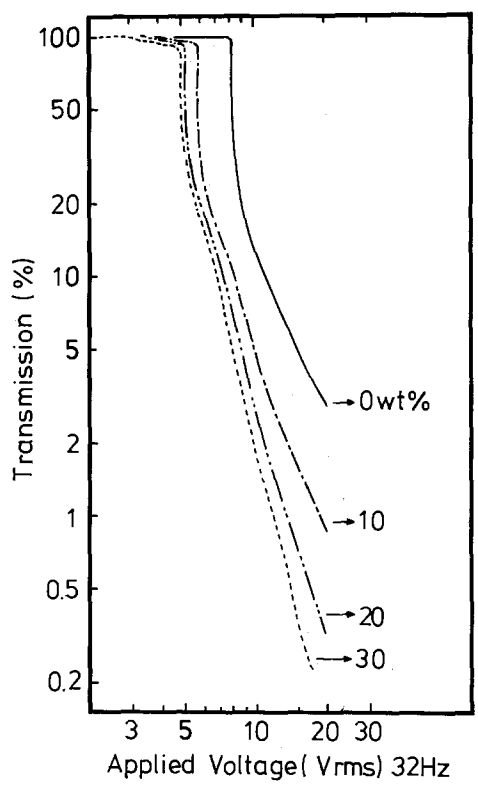


Fig. 3. The variation of transmission with the applied voltage when the concentration of BACYP2 is changed.

firmed in the mixtures containing the other double-Shiff's-base compounds except BACYP1.

The mixture containing 30 w/o BACYP1 did not have a nematic phase at room temperature, and it showed a quite different characteristic.

Figure 4 shows the properties of transmission as a function of applied voltage in nematic mixtures containing 10 w/o of BACYP1, BACYP2, BACYP3, and BACYP4 at 25°C and shows the effect of number of carbon atoms in the alkyl group of BACYP. The threshold voltage and the voltage to give the same contrast ratio are lower in the nematic mixtures containing the double-Shiff's-base compounds with fewer carbon atoms in the alkyl groups.

The same tendency was confirmed in the mixtures with other concentrations of double-Shiff's-base compounds except BACYP1. This means the double-Shiff's-base compounds with fewer carbon atoms in the alkyl groups and higher negative dielectric anisotropy have greater effect in decreasing the threshold voltage and the voltage to give a sufficient contrast ratio.

The effects of dielectric anisotropy.—Figure 5 shows the variation of the threshold voltage of light scattering (V_{th}), of Fredericksz transition (V_{fr}), and of the voltage to give the contrast ratio of 20:1 with negative dielectric anisotropy for the nematic mixtures containing BACYP2.

V_{fr} decreases linearly with increasing negative dielectric anisotropy as expected from the Leslie equation of $V_{fr} = \pi(K_{33}/|\Delta\epsilon|\epsilon_0)^{1/2}$ (9) where K_{33} is the elastic constant and ϵ_0 is the dielectric permittivity in a vacuum. The difference of the gradient from $-1/2$ is considered to be caused by the change of elastic constant due to the addition of double-Shiff's-base compounds.

V_{th} also decreases but the gradient is smaller than that of V_{fr} and has a slight tendency to saturate as the negative dielectric anisotropy increases.

The dependence of V_s on dielectric anisotropy has the same tendency as V_{th}, but the gradient is slightly greater than that, because the rate of increase of the dynamic-scattering intensity above threshold becomes as great as the increase of negative dielectric anisotropy. These characteristics are suitable for low voltage driving.

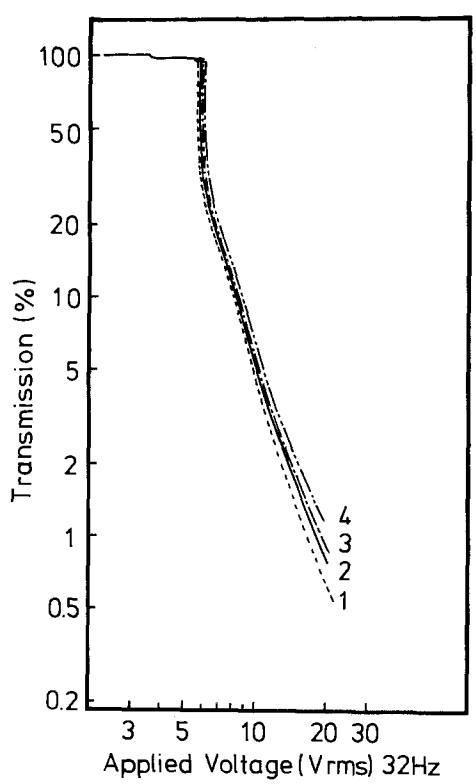


Fig. 4. The effect of the BACYP number on the transmission and voltage characteristics. 10 w/o of each BACYP is contained. The numbers denote BACYP numbers.

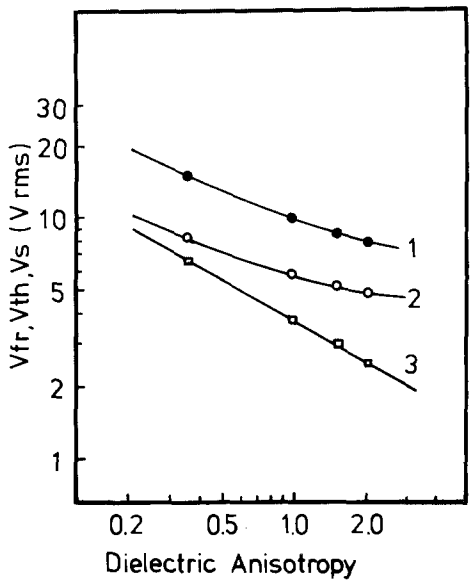


Fig. 5. The dependence of the threshold voltage of light scattering (V_{th}) (no. 2) and the Fredericksz transition (V_{fr}) no. 3) and the saturation voltage (V_s) (no. 1) on the negative dielectric anisotropy.

The higher negative dielectric anisotropy is considered to give improved dynamic-scattering due to greater interaction with the ion flow and higher anisotropy of the refractive index (7).

The anisotropy of the refractive index was confirmed to increase from 0.44 to 0.49 by the addition of BACYP2.

Cutoff frequency characteristics.—The variation of the threshold voltage with frequency was derived by the Orsay Liquid Crystal Group (10) and was written by using ω and ζ^2 as

$$V_{th}^2 = \frac{\pi^2 K_{33}}{|\Delta\epsilon|\epsilon_0} \frac{\epsilon_{||}}{\epsilon_{\perp}} \frac{1 + \omega^2\tau_D^2}{\zeta^2 - (1 + \omega^2\tau_D^2)} \quad [1]$$

$$\zeta^2 = \left(1 - \frac{\sigma_{\perp}}{\sigma_{||}} \frac{\epsilon_{||}}{\epsilon_{\perp}}\right)\left(1 + \frac{\epsilon_{||}}{|\Delta\epsilon|} \frac{1}{1 + \eta_0/\gamma_1}\right) \quad [2]$$

$$1/\tau_D = \sigma_{||}/\epsilon_{||}\epsilon_0 \quad [3]$$

ζ^2 is a nondimensional term and is a function of dielectric anisotropy, dielectric constants, conductivity anisotropy, and viscosity coefficients. τ_D is the dielectric relaxation time and η_0 and γ_1 are viscosity coefficients.

Cutoff frequency is described as a function of ζ^2 as

$$\omega_c = (\zeta^2 - 1)^{1/2} \sigma_{||}/\epsilon_{||} \quad [4]$$

and when $\omega = \omega_c$ the threshold voltage becomes infinite theoretically. Cutoff frequency is easily controlled by changing the conductance, but as ζ^2 decreases with the increase of negative dielectric anisotropy, the cutoff frequency also decreases if conductance is kept constant.

In order to maintain the properties for frequency and to satisfy the low temperature characteristics (11), conductance must be increased by adding a larger quantity of conductive dopants. In the case of a mixture containing 20 w/o concentration of BACYP2, the

conductance should be increased to be twice that of the host material to keep the same frequency characteristics. Because the driving voltage is decreased to be about one-half, the power consumption decreases to one-half as a result.

The decrease of ζ^2 with the increase of negative dielectric anisotropy restrains the decrease of threshold voltage of light scattering in comparison with the threshold voltage of Fredericksz transition as expected from Eq. [1] and shown in Fig. 5.

By obtaining the values of ζ^2 experimentally and inserting them into Eq. [1], the agreement between the experimental results and threshold voltage theory can be confirmed.

Figure 6 shows the variation of the value of ζ^2 and the threshold voltage of light scattering. The open circles denote the values of ζ^2 obtained experimentally from cutoff frequency by Eq. [4] and the solid line denotes the calculated value of ζ^2 obtained by inserting the experimentally estimated values into Eq. [2].

The full circles show the variation of experimental results of threshold voltage compared with the threshold voltage of the host material. The dashed line shows the calculated value based on theory. Good agreement is obtained and the characteristics of threshold voltage can be explained.

Response time.—Figure 7 shows the dependence of the decay time of light scattering on BACYP2 concentration in a nematic liquid crystal mixture after the electrical field of a 10V square wave is turned off. It increases exponentially to the BACYP2 concentration due to the increase of viscosity (12).

Figure 8 shows the dependence of rise time on the concentration of BACYP2 by the application of a 10V electrical field. Although the viscosity increases, negative dielectric anisotropy also increases, so rise time is shortened as a result. This is expected from the equation (13)

$$T = \eta[\Delta\epsilon \cdot \epsilon_0 E^2 - Kq^2]^{-1} \qquad [5]$$

where η is the proper fluid viscosity, q is the wave vector of the disturbance, E is the applied field, and K is the appropriate elastic constant.

Matrix addressing property.—Figure 9 shows the temperature dependence of the threshold voltage of light scattering. By the addition of BACYP, the temperature dependence of the threshold voltage becomes weak with a minimum near 40°C. This characteristic and the rapid increase of dynamic-scattering intensity above the threshold are advantageous for the matrix-addressing properties in a wide temperature range at a fixed driving voltage.

Figure 10 show the dependence of the contrast ratio on the duty ratio for matrix arrays by a one to two and one to three voltage selection method at 25°C. The bias voltages were set to the minimum threshold voltage between 0 and 60°C. The solid lines show the characteristics by the one-third voltage selection method and the dashed lines show the characteristics by the one-half voltage selection method.

The duty ratio to give the contrast ratio of 10:1 is reduced from 1/4 to 1/6-1/7 by the one-third voltage selection method, and a duty ratio of 1/3 by the one-half voltage selection method can give a sufficient contrast ratio by the addition of 30 w/o of BACYP.

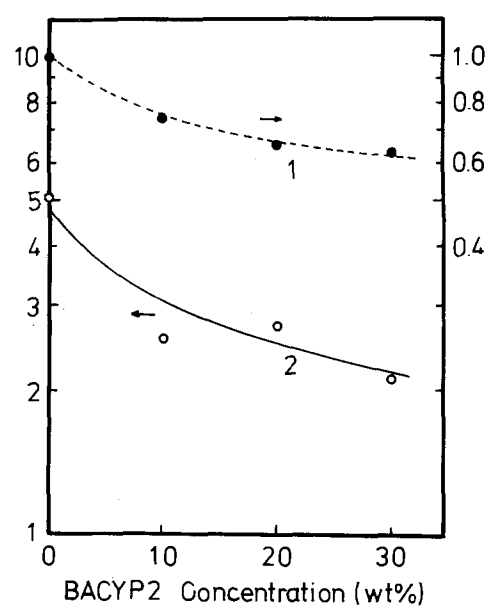


Fig. 6. The dependence of ζ^2 (no. 2) and V_{th} (no. 1) on the BACYP2 concentration.

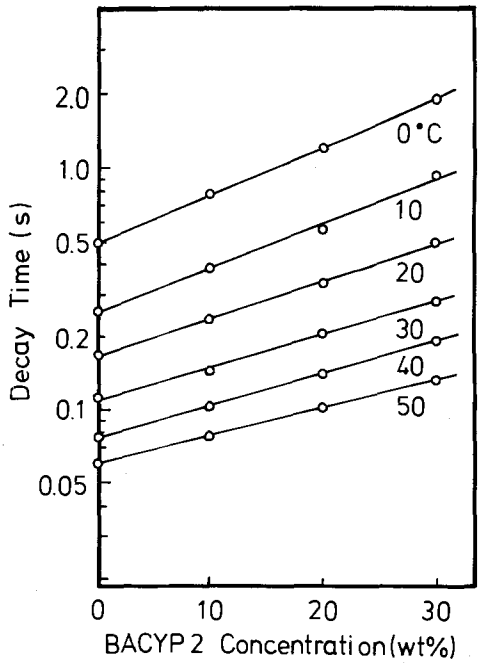


Fig. 7. The dependence of decay time on BACYP2 concentration

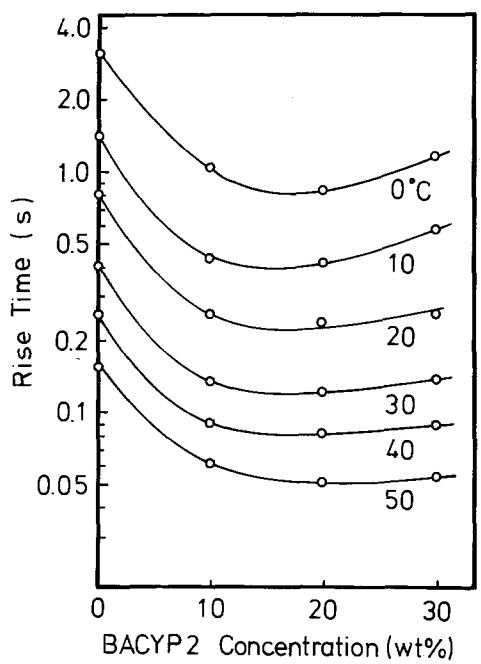


Fig. 8. The dependence of rise time on BACYP2 concentration

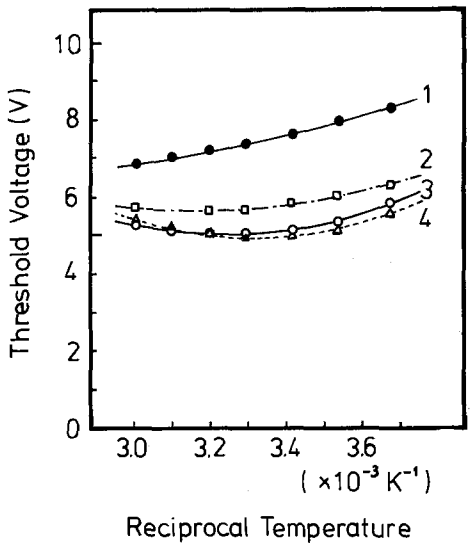


Fig. 9. Temperature dependence of the threshold voltage of light scattering, when the concentration of BACYP2 is changed. 0 w/o BACYP2 (no. 1), 10 w/o (no. 2), 20 w/o (no. 3), and 30 w/o (no. 4).

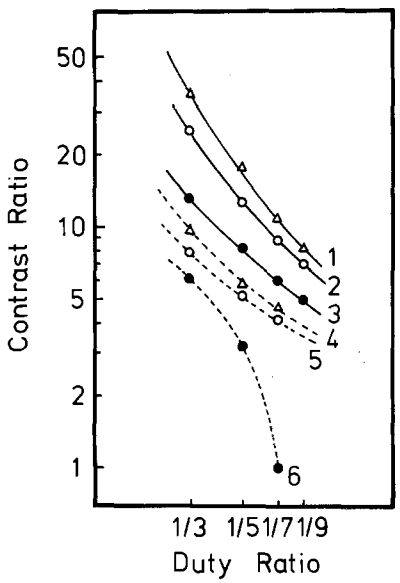


Fig. 10. The dependence of contrast ratio on the duty ratio of matrix driving by one-third (no. 4, 5, 6) and one-half (no. 1, 2, 3) voltage selection methods. 0 w/o BACYP2 (no. 3, 6), 20 w/o BACYP2 (no. 2, 5), 30 w/o BACYP2 (no. 1, 4).

Discussion

The threshold condition for the electrohydrodynamic instability in nematic liquid crystal is determined by the torque balance of elastic, dielectric, and viscous torque to give a steady-state angular momentum.

Under the simplest one-dimensional model, they are written as Eq. [6]

$$V_{th}^2 = \pi^2 K_{33}/\epsilon_0 \left\{ \epsilon_{\parallel} \left(1 - \frac{\sigma_{\perp}}{\sigma_{\parallel}}\right) \frac{K_1}{\eta_1} - \Delta\epsilon \left(\frac{K_1}{\eta_1} - \frac{\sigma_{\perp}}{\sigma_{\parallel}} \right) \right\} \quad [6]$$

This agrees with the Helfrich expression (14), and this also agrees with the expression of the Orsay Liquid Crystal Group in the case of $\omega = 0$ except for a different definition of the viscosity factors. Both ($\Gamma_{visc.}$) and ($\Gamma_{diel.}$) are dependent on dielectric anisotropy, and they increase as the negative dielectric anisotropy increases. If the rate of increase of ($\Gamma_{visc.}$) is larger than that of ($\Gamma_{diel.}$), the threshold voltage will decrease with an increase in the negative dielectric anisotropy.

The condition is described as in Eq. [7]

$$\left| \frac{\partial \Gamma_{visc.}}{\partial \Delta\epsilon} \right| > \left| \frac{\partial \Gamma_{diel.}}{\partial \Delta\epsilon} \right| \quad [7]$$

and the result becomes

$$\frac{K_1}{\eta_1} - \frac{\sigma_{\perp}}{\sigma_{\parallel}} > 0 \quad [8]$$

We determined the value of K_1/η_1 experimentally to be 1.0 or more, and the value of $\sigma_{\perp}/\sigma_{\parallel}$ is 0.67, so the condition was sufficiently valid for the nematic mixture used in this study.

In the case of MBBA (4-methoxybenzylidene-4'-butylaniline) the noticeable effects were not observed in these experiments. It is considered that the condition to reduce the threshold voltage is not sufficiently valid. The value of K_1/η_1 obtained was between 0.8 and 0.9 which fits fairly well with the reported value (15), and the value of $\sigma_{\perp}/\sigma_{\parallel}$ was 0.7. Moreover, referring to the effects of dielectric anisotropy on the threshold of MBBA, Penz (16) analyzed theoretically and estimated that threshold voltage of light scattering increases with the increase of the negative dielectric anisotropy.

Conclusion

Double-Shiff's-base compounds of bis-(4'-n-alkylbenzylidene)-2-cyano-1,4-phenylenediamine were prepared and added to the room temperature liquid crystal material to study the effects of negative dielectric anisotropy on dynamic-scattering properties. The results can be summarized as follows.

1. The negative dielectric anisotropy is the important factor that dominates the properties of dynamic-scattering.
2. By the addition of BACYP to the room temperature nematic mixture, liquid crystalline compounds with wider nematic temperature ranges of more than 100°C have been prepared.
3. The negative dielectric anisotropy increases with the increase of BACYP concentration, and the threshold voltage of the Fredericksz transition decreases as expected from Leslie's theory.
4. The threshold voltage of light scattering also decreases from 8 to 5V by the increase of dielectric anisotropy from 0.5 to 2.0 and conductivity anisotropy from 1.5 to 1.8 as expected from the theory of Helfrich and the Orsay Liquid Crystal Group.
5. The voltage to give sufficient contrast ratio in dynamic-scattering decreases more rapidly than the threshold voltage with the increase of negative dielectric anisotropy. A display device of low voltage driving between 7 and 8V has been achieved.
6. The cutoff frequency decreases by the addition of BACYP when the conductance is kept constant, because of the increase of dielectric constants and the decrease of the value of ξ^2 due to the increase of negative dielectric anisotropy.
7. Conductance should be increased to maintain the frequency characteristics and to complete the properties in low temperature. As a result a half-power consumptive device of less than 100 $\mu W/cm^2$ has been achieved.
8. The decay time becomes long by the addition of BACYP but the rise time is shortened because of the increase of negative dielectric anisotropy.
9. The matrix-addressing properties are also improved because of the rapid increase of dynamic-scat-

tering intensity above threshold and the weak temperature dependence of threshold voltage.

Acknowledgments

The authors would like to acknowledge the advice and assistance of Mr. K. Asai, and thanks are due to H. Tatsuta and Y. Harada who synthesized and purified the liquid crystal materials for this paper.

Manuscript submitted Dec. 30, 1976; revised manuscript received July 14, 1977. This was Paper 224 presented at the Las Vegas, Nevada, Meeting of the Society, Oct. 17-22, 1976.

Any discussion of this paper will appear in a Discussion Section to be published in the June 1978 JOURNAL. All discussions for the June 1978 Discussion Section should be submitted by Feb. 1, 1978.

Publication costs of this article were assisted by Matsushita Electric Industrial Company, Limited.

REFERENCES

1. G. H. Heilmeier, L. A. Zanoni, and L. A. Barton, *Proc. IEEE*, **56**, 1162 (1968).
2. A. Boller *et al.*, *ibid.*, **60**, 1003 (1972).
3. N. J. Felici, *Rev. Gen. Elec.*, **78**, 717 (1969).
4. F. Funada, H. Yamamoto, and T. Wada, *Sharp Tech. Rep.*, **12**, 65 (1973).
5. H. Okuyama, T. Narasawa, and M. Fujimori, *Fujitsu Sci. Tech. J.*, **11**, 175 (1975).
6. Orsay Liquid Crystal Group, *Mol. Cryst. Liq. Cryst.*, **12**, 251 (1971).
7. G. Elliott, D. Harvey, and M. G. Williams, *Electron. Lett.*, **9**, 399 (1973).
8. D. Meyerhofer and A. Sussman, *Appl. Phys. Lett.*, **20**, 337 (1972).
9. F. M. Leslie, *Mol. Cryst. Liq. Cryst.*, **12**, 57 (1970).
10. E. D. Violette, P. G. Gennes, and O. Parodi, *J. Phys. (Paris)*, **32**, 305 (1971).
11. S. Matsumoto *et al.*, *Jpn. J. Appl. Phys.*, **14**, 965 (1975).
12. H. Koelmans and A. M. Van Baxtel, *Mol. Cryst. Liq. Cryst.*, **12**, 185 (1971).
13. E. Jakeman and E. P. Paynes, *Phys. Lett. A*, **39**, 69 (1972).
14. W. Helfrich, *J. Chem. Phys.*, **51**, 4092 (1969).
15. G. Gahwiller, *Phys. Lett. A*, **36**, 311 (1971).
16. P. A. Penz, *Mol. Cryst. Liq. Cryst.*, **23** (1973).

Silicon Oxidation Studies: The Role of H_2O

E. A. Irene* and R. Ghez*

IBM Thomas J. Watson Research Center, Yorktown Heights, New York 10598

ABSTRACT

The thermal oxidation of Si using H_2O-O_2 and H_2O-N_2 ambients has been studied with an automated ellipsometer which can observe the oxidation *in situ*. The oxidations were carried out in the temperature range of 780°-980°C on <100> oriented single crystal Si. The resulting SiO_2 film growth data was analyzed according to a linear-parabolic oxidation model. The parabolic rate constant was found to increase abruptly with small additions of H_2O to O_2 while the linear rate constant increased gradually over the range of added H_2O (0-2000 ppm). The over-all increase in the rate of oxidation due to H_2O in O_2 was found to be greater than predicted based on the independent diffusion and reaction of O_2 and H_2O related oxidant species. These effects of H_2O were found to be reversible. Therefore, the kinetic role of H_2O on the oxidation of silicon is essentially twofold. The H_2O acts both as an additional source of oxidant and as an accelerator for the oxidation process involving O_2. It is postulated that this latter effect occurs because the H_2O modifies the SiO_2 network thereby enhancing diffusion of the primary oxidant through the SiO_2 film.

The remarkably large effect of trace amounts (25 ppm) of H_2O in the O_2 ambient on the SiO_2 film growth kinetics has been previously reported (1). Based on a linear-parabolic model (2) the effect of 25 ppm H_2O in O_2 (1) on Si oxidation was found to be related both to surface kinetics through the linear rate constant, k_{LIN}, and to diffusional kinetics through the parabolic constant, k_{PAR}. It was therefore suggested (1) that the role of H_2O is manifold, including a catalytic effect, the effect of an additional oxidant, and a structural alteration of the growing SiO_2 film.

A previous analysis of Si oxidation thickness-time data for oxidation in pure O_2 (3) has shown that a linear-parabolic kinetic model provides a reasonably accurate representation of the oxidation phenomena, provided that sufficient data in the proper thickness ranges is used for the analysis. Therefore, this model will be utilized in the present study to analyze the role of H_2O in the SiO_2 film growth data obtained from an automated ellipsometer (4) which can measure SiO_2 film thickness *in situ* during oxidation.

The present study is an extension of previous work (1, 5, 6) on the effects of H_2O on Si oxidation kinetics. Two of the previous studies (5, 6) utilized relatively large amounts of H_2O (> 6000 ppm), and one of the studies (1) reported the effect of trace amounts of H_2O (25 ppm) on Si oxidation kinetics. The present investigation considers oxidation of Si in pure dry O_2 (<1 ppm H_2O), in controlled amounts of H_2O up to 2000 ppm in an N_2 ambient, and by controlled additions of H_2O to O_2 (up to 2000 ppm H_2O). The extensive SiO_2 film thickness-time data for oxidation temperatures of 780°, 893°, and 980°C are analyzed by the previously developed linear least squares technique (3) using the linear-parabolic model (2). The data and analysis of this study enable the mechanism for Si oxidation to be further elucidated.

Experimental Procedures

Sample preparation.—All substrates were <100> oriented chem-mechanically polished silicon wafers measuring 3.2 cm in diameter and 0.025 cm in thickness. All the wafers were p-type with a nominal resistivity of 2 Ω-cm. It was reported previously (1) that the resistivity type or value in the range 0.5-10 Ω-cm had no influence on the oxidation process. The wafers were cleaned as reported elsewhere (1) but an initial oxide thickness of from 3-6Å SiO_2 was observed

* Electrochemical Society Active Member.
Key words: insulating films, oxidation kinetics, rate constants.

in contrast to the previously reported thickness of 10-12Å for the initial oxide film (1). With the automated ellipsometer (to be described later) the cleaned Si wafers could be immediately placed in a dry N_2 ambient, whereas in previous studies the wafers were exposed to room air for about 10 min during the ellipsometric measurements. After the initial SiO_2 film measurement the samples were heated in dry N_2 (10-15 min) to the experimental oxidation temperature and the SiO_2 film thickness was remeasured. The SiO_2 film now measured 7-8Å. After continuous heating for 5 hr at 900°C in dry N_2 the total film thickness never exceeded 11Å. Apparently there is some small amount of oxidant either present in the N_2 or desorbing from the walls of the reaction vessel but the relative amount of SiO_2 growth is negligible for this study.

Gas ambients.—Both N_2 and O_2 were supplied from boil-off of liquid sources. Dew points of the gases were measured by means of a hygrometer (1, 3). As previously reported (1, 3), the O_2 was shown to contain trace amounts of methane ($\sim$ 17 ppm) which at the experimental oxidation temperature combusts to form H_2O. This trace H_2O substantially increases the rate of oxidation (1). For dry oxidations, the methane was removed by heating the oxygen to about 1000°C, in order to combust the methane to H_2O and CO_2, and then cold trapping at −80°C to reduce the H_2O concentration to less than 1 ppm H_2O in the O_2. To add H_2O to N_2 or O_2, the N_2 or the previously dried O_2 is flowed through a thoroughly cleaned fused silica vessel which contains deionized H_2O. By controlling the H_2O temperature with a variable temperature refrigeration unit the concentration of H_2O can be adjusted to any desired level from less than 1 ppm upward. The reported H_2O concentrations are steady-state values as measured with a hygrometer at the oxidation furnace exit under fixed flow conditions and with the furnace at the oxidation temperature.

Automated ellipsometer.—The instrument used for this study has been described in detail elsewhere (4). Basically, the ellipsometer uses a laser light source, polarizer, compensator, and an encoded rotating analyzer. The light intensity measurement after the analyzer is automated. The ellipsometry measurements are made with the sample in a fused silica rf-heated reaction tube. Therefore it is possible to collect and analyze the ellipsometric data as the SiO_2 film grows without interrupting the oxidation run. The optical constants characteristic of the Si surface as a function of temperature were previously measured (4). The film thickness accuracy of the ellipsometer is estimated to be better than 10% for very thin SiO_2 films (less than 20Å) and better than 3% for thicker films. The oxidation data to be shown are reproducible to within 2% total spread in film thickness and each reported data set is an average of at least two independent oxidation runs.

In order to determine whether there was any change in SiO_2 refractive index when H_2O was added to the O_2 ambient, ellipsometric measurements were made near half an ellipsometric period (about 1200-1400Å for 6328Å light) for greatest accuracy in film refractive index. No systematic trend in refractive index was observed which was greater than the estimated accuracy of the instrumentation of ±0.005 for the refractive index. This negative result was anticipated based on a report (7) of a decrease in refractive index of about 1.4×10^{-4} for 10^3 ppm H_2O in SiO_2. Therefore to cause a change of −0.005 in index, the SiO_2 must contain 5×10^4 ppm H_2O which is 30 times larger than the largest amount of H_2O in the ambient used for the present study.

SiO_2 quality.—In order to check on the charge levels in the SiO_2 films grown, capacitance-voltage (C-V) measurements were made. Evaporated aluminum counterelectrodes were used as electrical contacts. The C-V measurements (at 1 MHz) revealed an average fixed positive charge level of $\sim 5 \times 10^{10}$ charges/cm^2. Bias-temperature stressing ($\pm 10^6$ V/cm at 200°C for 15 min and subsequent cooling under bias) revealed an average mobile positive charge level of $\sim 7 \times 10^{10}$ charges/cm^2. These values are characteristic of MOS quality oxide.

The density of fast surface states was measured by the low temperature C-V technique (8, 9). Fast state densities, N_{FS}, for dry oxides were found to be $\sim 2 \times 10^{11}$ cm^{-2} and this density decreased to $\sim 2 \times 10^{10}$ cm^{-2} for oxides prepared with 2000 ppm H_2O in O_2. These results are in qualitative agreement with previously published results (9) on the effect of H_2O on N_{FS} levels.

Data analysis.—The linear, k_{LIN}, and parabolic, k_{PAR}, rate constants are obtained by the iterative linear least squares (LLS) analysis described previously (3). Essentially, a linear-parabolic rate law (2) is used which has the following form

$$t - t_o = A(d - d_o) + B(d^2 - d_o^2) \qquad [1]$$

In this equation d is the SiO_2 film thickness for a time of oxidation, t; A and B are the reciprocals of k_{LIN} and k_{PAR}, respectively; and d_o and t_o are the parameters that define the limit of influence of the initially rapid oxidation regime which precedes the linear-parabolic mode of oxidation (1-3). The first iteration of the LLS analysis includes all the (d, t) data points for a given data set and considers the value for (d_o, t_o) to be $(0, 0)$. The second and all ensuing iterations drop the smallest value (d, t) data point and utilize this dropped point as the value for (d_o, t_o) in the iteration, thereby renormalizing the data to new axes, (d_o, t_o), with each iteration. For each iteration standard deviation values are calculated which enable an assessment of the quality of the fit of the data to the model. A region in (d, t) space of best fit is determined by the error analysis and the rate constants which best describe the data are calculated (3). From calculated standard deviation values, the errors associated with k_{LIN} and k_{PAR} values are less than ±10% and for d_o values the spread could be as large as ±50Å.

In order to quantitatively determine if the role of H_2O in O_2 is solely to supply an additional oxidant which diffuses through the SiO_2 film and reacts at the Si-SiO_2 interface, a rate equation has been derived which considers simultaneous but independent diffusion and reaction of two oxidant species, *i.e.*, species due to both O_2 and H_2O as has been done previously (10). However the previous work (10) does not include the (d_o, t_o) boundary condition and the constants are not defined in the same way as in our previous oxidation studies (1, 3). Therefore, details of our derivation are included in the Appendix and the resulting integrated rate equation has the form

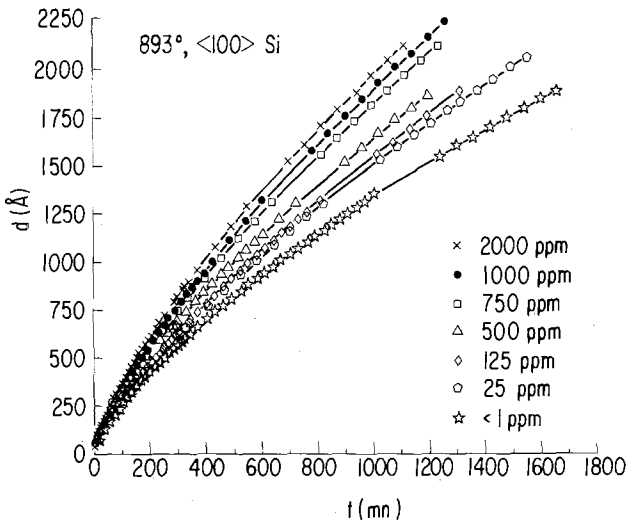
$$t - t_o = A(d - d_o) + B(d^2 - d_o^2) + C \ln\left(\frac{d + \alpha}{d_o + \alpha}\right) \qquad [2]$$

The constants A, B, C and α, can all be expressed in terms of the linear and/or parabolic rate constants obtained from the oxidation of Si by H_2O and O_2 individually (see Appendix).

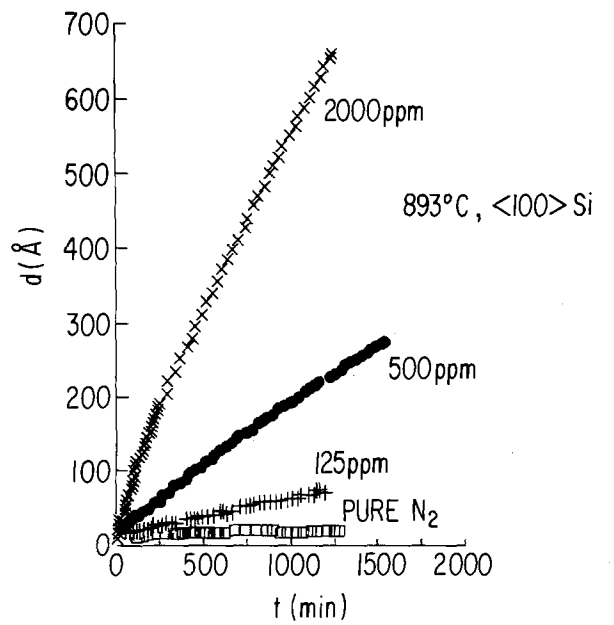
Experimental Results

Representative data for oxidation at 893°C in ambients composed of various concentrations of H_2O in O_2 are shown in Fig. 1a and for the H_2O-N_2 ambients in Fig. 1b. Calculated rate constants are shown in Table I.

Table I shows that the k_{LIN} values which correspond to the H_2O-O_2 ambients, increase smoothly as the concentration of H_2O in O_2 increases from less than 1 ppm ($\sim 10^{-6}$ atm H_2O) to 2000 ppm ($\sim 10^{-3}$ atm). Since the linear rate constant is associated with the chemical reaction between oxidant and Si at the Si-SiO_2 interface (2), the increase in k_{LIN} in a H_2O-containing



(a) In O_2 with various amounts of H_2O



(b) With various H_2O concentrations in N_2

Fig. 1. Thickness (Å) vs. time (min) data for oxidation of <100> Si at 893°C.

ambient can be attributed to the additional oxidant present at the Si-SiO_2 interface. However, the parabolic rate constant, k_{PAR}, increases sharply with the first traces of H_2O in O_2 up to 125 ppm followed by a smaller rate of increase for H_2O concentrations from 125 to 2000 ppm. The parabolic rate constant is related to the mechanism for diffusion of oxidant through the SiO_2 film to the Si-SiO_2 interface. Therefore, the large and initially sharp change in k_{PAR} with trace H_2O addition suggests that H_2O alters the diffusion of oxidant to the Si-SiO_2 interface.

Table I. Rate constants according to the linear-parabolic model

Ambient	k_{LIN} (A²/min			k_{PAR} (A²/min)			d_o (A)
ppm H_2O in O_2	T, °C			T, °C			T, °C
	780	893	980	780	893	980	893
<1	0.57	2.2	7.7	265	4350	14,000	340
25		2.2			6250		340
125	0.65	2.3	8.4	285	6500	19,300	330
500		2.6			7350		275
750		2.8			8000		275
1000		2.9			8400		270
2000	0.69	3.4	16.7	690	8500	23,700	235
2000 ppm H_2O in N_2	0.10	0.60	4.6	360	2000	2,530	~0

The values for d_o [d_o represents the upper thickness limit of the influence of the initially rapid oxidation regime (1-3)] decrease as the concentration of H_2O in O_2 increases. For oxidations in the H_2O-N_2 ambient, the initially rapid regime was not detected at all. Deal and Grove (2) have also reported that d_o was not observed for oxidation in large amounts of H_2O. They attributed this finding to the smaller Debye length expected for H_2O oxidation under the assumption that oxidation proceeds via diffusion of an ionic species (11, 12) and therefore the width of the space charge layer relative to the total oxide thickness is important. However, there exists reasonable doubt as to whether the oxidation of Si proceeds via an ionic diffusion mechanism (13, 14). Hence, the interpretation of the oxidation kinetics in the thickness range below about 400Å is in question and further discussion will be reserved for a future publication.

Figure 2 shows the comparison of dry O_2 data and 2000 ppm H_2O in O_2 data along with calculated data from Eq. [2] using the rate constants found in Table I. It is seen that the rate of oxidation actually observed for the H_2O-O_2 ambient is greater than the rate calculated based on the simultaneous but independent diffusion and reaction of the H_2O- and O_2-related oxidant species. Therefore, there exists an additional effect on oxidation kinetics due to the H_2O in O_2 other than the superposition of an additional independent oxidant.

In order to address the question whether the H_2O related kinetic effect on the SiO_2 network is reversible or whether the structural alteration is permanent, the following experiment was performed: First, a Si sample was oxidized at 980°C for ~ 100 min to a thickness of ~ 700Å in pure, dry O_2; then the oxidizing ambient was switched to 2000 ppm H_2O in O_2 and oxidation was continued for another ~ 100 min; finally the ambient was again switched to dry O_2 after the oxidation

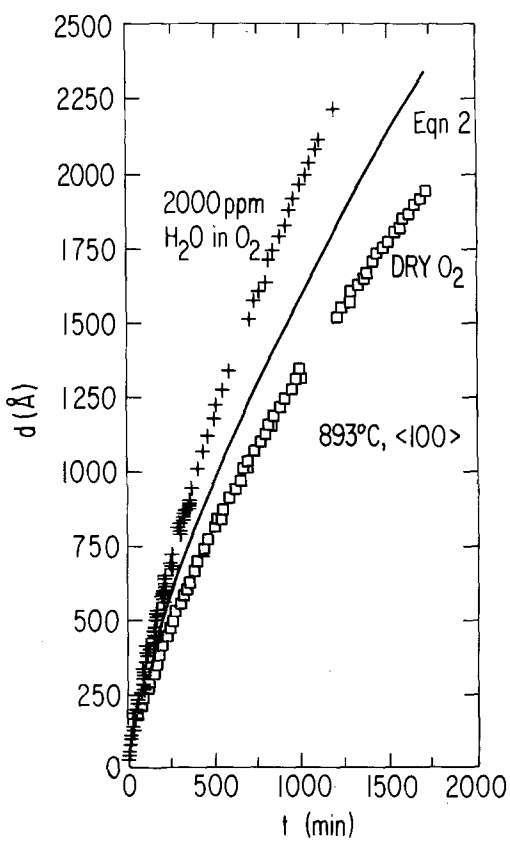


Fig. 2. Comparison of oxidation data for oxidation in dry O_2 and 2000 ppm H_2O in O_2 with thickness-time data calculated using Eq. [2].

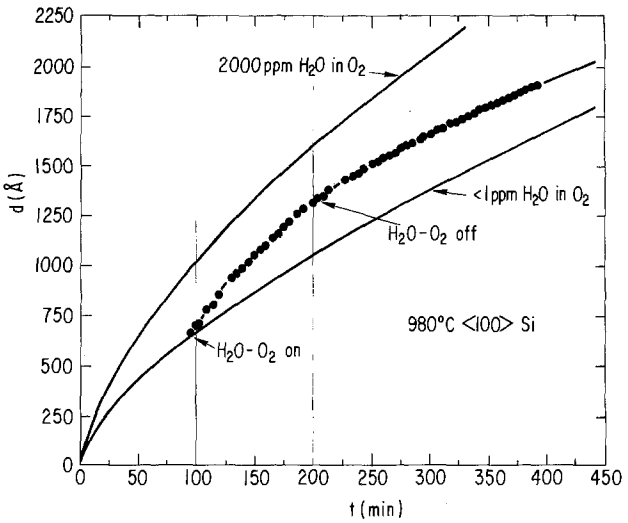


Fig. 3. The effect on Si oxidation of changing the ambient from dry O_2 to 2000 ppm H_2O in O_2 and back to dry O_2 (data points) with dry O_2 and 2000 ppm H_2O in O_2 data for comparison (solid curves).

tube was flushed for 10 min with dry N_2 at 980°C to remove 95% of the residual moisture and the oxidation was continued in dry O_2. In Fig. 3 the thickness-time data obtained in this experiment are plotted for comparison with the data sets for dry O_2 and 2000 ppm H_2O in O_2 data sets. It is seen that within several minutes after the ambient is switched from dry O_2 to H_2O in O_2 the growth behavior proceeds in parallel to the H_2O-O_2 curve. Similarly, when the ambient is returned to dry O_2, the rate quickly reverts to that for dry O_2. Therefore, the effect is reversible and must take place via a rather labile chemical species, possibly SiOH, which have been observed in SiO_2 and can be oxidized to SiO_2.

Discussion of Results

The experimental observations on the role of H_2O in O_2 on Si oxidation made in this study can be explained qualitatively by considering previously measured properties of bulk amorphous SiO_2.

It is well understood that H_2O reacts with bulk amorphous SiO_2 disrupting the SiO_2 network by forming nonbridging SiOH groups (see for example (7, 15-19)). This loosening of the SiO_2 network is evidenced by a decrease in the SiO_2 viscosity, density, acoustic velocity, and refractive index and an increase in the thermal expansion coefficient (7, 19). Also related to the loosening effect of H_2O on SiO_2 is the report (18) that the diffusion coefficient of O_2 in H_2O-treated bulk SiO_2 is greater than in dry O_2. Therefore, the large effect of relatively small amounts of H_2O on $\bar{k}_{PAR}$ for thin films of SiO_2 appears to be via the same network loosening mechanism as observed for bulk SiO_2. Previous results on the effects of H_2O on the properties of bulk SiO_2 (7, 15, 18) show that labile —OH species cause the loosening of the network and that the physical properties would revert to the dry SiO_2 values upon removal of the —OH by dry annealing. The experiment reported here in which the ambient was switched from dry to wet to dry O_2 showed that the kinetic effect is also reversible and therefore the same as the H_2O effect on bulk SiO_2.

Conclusions

The kinetic role of H_2O in the oxidation of Si is essentially twofold. First, H_2O itself is an oxidant source and thereby converts Si to SiO_2. Second, H_2O alters the SiO_2 by loosening the SiO_2 network and increasing the diffusion of other oxidant species. The loosening process is via formation of Si-OH groups and the reaction which forms these groups is reversible.

Acknowledgment

The authors gratefully acknowledge helpful discussions with Drs. T. B. Light and N. J. Chou and thank Drs. T. O. Sedgwick and N. J. Chou for critically reviewing this manuscript.

Manuscript submitted Jan. 10, 1977; revised manuscript received July 15, 1977.

Any discussion of this paper will appear in a Discussion Section to be published in the June 1978 JOURNAL. All discussions for the June 1978 Discussion Section should be submitted by Feb. 1, 1978.

Publication costs of this article were assisted by IBM Corporation.

APPENDIX

In order to derive Eq. [2] we assume that O_2 and H_2O diffuse independently through an oxide film of thickness d, and that the two oxidant species react independently at the oxide-silicon interface. Let the quantities related to O_2 be denoted with subscript 1 and those related to H_2O with subscript 2. The flux, F_1, of O_2 through the film is given by

$$F_1 = D_1(C_1^* - C_{1,d})/d = k_1 C_{1,d} \qquad [A\text{-}1]$$

where D_1 is the diffusion coefficient, k_1 is the reaction rate constant, C_1^* is the concentration at the gas-oxide interface, and $C_{1,d}$ the concentration at the oxide-silicon interface. Eliminating $C_{1,d}$ yields

$$F_1 = k_1 C_1^*/(1 + k_1\, d/D_1) \qquad [A\text{-}2]$$

and a similar relation for F_2. If Ω is the volume of oxide formed per unit of oxidant, then the time rate of change of d is

$$\dot{d} = \Omega_1 F_1 + \Omega_2 F_2 = \frac{\Omega_1 k_1 C_1^*}{1 + k_1\, d/D_1} + \frac{\Omega_2 k_2 C_2^*}{1 + k_2\, d/D_2}$$

This relation can be easily integrated to give

$$t - t_o = A(d - d_o) + B(d^2 - d_o^2) + C \ln \frac{d + \alpha}{d_o + \alpha} \qquad [A\text{-}3]$$

in which the constants A, B, C, and α can be expressed in terms of the linear and parabolic rate constants for each of the oxidizing species, $k_{L1} = \Omega_1 k_1 C_1^*$, $k_{P1} = 2\Omega_1 C_1^* D_1$, $k_{L2} = \Omega_2 k_2 C_2^*$, $k_{P2} = 2\Omega_2 C_2^* D_2$

$$A = \frac{(k_{L1}/k_{P1}) + (k_{L2}/k_{P2}) - (k_{L1} + k_{L2})/(k_{P1} + k_{P2})}{k_{L1}k_{L2}\,(k_{P1}^{-1} + k_{P2}^{-1})}$$

$$B = (k_{P1} + k_{P2})^{-1} \qquad [A\text{-}4]$$

$$C = [2k_{L1}k_{L2}\,(k_{P1}^{-1} + k_{P2}^{-1})]^{-1} \left\{ 1 - \frac{k_{L1}^{-1} + k_{L2}^{-1}}{k_{P1}^{-1} + k_{P2}^{-1}} \left[(k_{L1}/k_{P1}) + (k_{L2}/k_{P2}) - \frac{k_{L1} + k_{L2}}{k_{P1} + k_{P2}} \right] \right\}$$

$$\alpha = \frac{1}{2} \frac{k_{L1}^{-1} + k_{L2}^{-1}}{k_{P1}^{-1} + k_{P2}^{-1}}$$

The rate law [A-3] is a linear-parabolic relation, with a logarithmic correction which accounts for only a few percent.

REFERENCES

1. E. A. Irene, *This Journal*, **121**, 1613 (1974).
2. B. E. Deal and A. S. Grove, *J. Appl. Phys.*, **36**, 3370 (1965).
3. E. A. Irene and Y. J. Van der Meulen, *This Journal*, **23**, 1380 (1976).
4. Y. J. Van der Meulen and N. C. Hien, *J. Opt. Soc. Am.*, **64**, 804 (1974).
5. A. G. Revesz and R. J. Evans, *J. Phys. Chem. Solids*, **30**, 551 (1969).
6. T. Nakayama and F. C. Collins, *This Journal*, **113**, 706 (1966).
7. G. Hetherington and K. H. Jack, *Phys. Chem. Glasses*, **3**, 129 (1962).
8. P. V. Gray and D. M. Brown, *Appl. Phys. Lett.*, **8**, 31 (1966).
9. D. M. Brown and P. V. Gray, *This Journal*, **115**, 760 (1968).

10. K. Hirabayashi and J. Iwamura, *ibid.*, **120**, 1595 (1973).
11. P. J. Jorgensen, *J. Chem. Phys.*, **37**, 874 (1962).
12. P. J. Jorgensen, *This Journal*, **114**, 820 (1967).
13. D. O. Raleigh, *ibid.*, **113**, 782 (1966).
14. D. O. Raleigh, *ibid.*, **115**, 111 (1968).
15. R. W. Lee, *Phys. Chem. Glasses*, **5**, 35 (1964).
16. T. Bell, G. Hetherington, and K. H. Jack, *ibid.*, **3**, 141 (1962).
17. G. J. Roberts and J. P. Roberts, *ibid.*, **7**, 82 (1966).
18. E. L. Williams, *J. Am. Ceram. Soc.*, **48**, 190 (1965).
19. R. Brückner, *J. Non-Cryst. Solids*, **5**, 177 (1971).

Conduction and Charging Behavior in MA(O)S-Systems

H. Kampshoff, F. Stephany, and P. Balk*

Institute of Semiconductor Electronics, Sonderforschungsbereich Festkörperelektronik, Technical University, D-5100 Aachen, Templergraben 55, Germany

ABSTRACT

Measurements were made of *I-V* and *C-V* characteristics of metal-Al_2O_3-silicon capacitors in the dark. The Al_2O_3 layers were deposited pyrolytically at temperatures between 700° and 950°C on substrates of both conductivity types; some of the samples were subjected to a final O_2 anneal. The observed dependence of the conduction on the electrode material indicates that the process is injection limited and that electrons are the major carriers. From the magnitude of the effective barrier heights and the relatively weak temperature dependence of the currents, it is concluded that in all cases the injection takes place via a trap-assisted tunneling mechanism. The buildup of space charge in the insulator has a pronounced effect on the magnitude of the conductivity. The same behavior was observed on MAOS capacitors with a purposely grown 2.5 nm SiO_2 film.

Storage of injected charge carriers is a phenomenon that may be expected to occur quite generally in metal-insulator-silicon structures with layered dielectrics. It has been explored thoroughly in only a few systems, notably in the metal-Si_3N_4-SiO_2-Si (MNOS) and metal-Al_2O_3-SiO_2-Si (MAOS) structures, where field effect transistors with such gate systems yield useful electrically alterable nonvolatile storage devices (1, 2).

In several respects the behavior of both systems is rather similar (3-5). However, MAOS devices with Al gates show a pronounced tendency toward negatively charging the layered dielectric not only for positive but also for negative gate voltages. Only for very large negative voltages the system reverts to "normal" behavior and starts acquiring positive charge. The "abnormal" charging effect may be suppressed by annealing the Al_2O_3 film in O_2 prior to metallization or by utilizing a Au electrode (3).

An important reason for the rapid development of MNOS storage devices is undoubtedly the extensive knowledge about the technology and characteristics of Si_3N_4 that already existed in the electronics industry. This facilitated optimization of material parameters for storage applications and allowed a study of the charging and discharging mechanism on well-defined samples. One of the at first surprising insights gained in these studies was that rapid charging only takes place under field conditions where considerable d-c currents flow through the system (6). Moreover, charge injected from the silicon extends over a relatively large depth into the nitride layer (7). These findings suggested that early models which take into account only tunneling of charges across the SiO_2 layer into traps near the insulator-insulator interface were at least an oversimplification of the true state of affairs. It was also discovered that not only electrons but also holes play a role in the conduction and charging of Si_3N_4 films (8). The conduction process is strongly affected by the accumulation of space charge in the layers (9, 10).

The amount of information available on the behavior of the MAOS system and the properties of Al_2O_3 layers is rather modest in comparison. Nevertheless, Al_2O_3 with its high dielectric constant and large bandgap is an interesting material for application in multilayer storage devices. Moreover, investigations on such alternate systems might be expected to contribute to a better understanding of the charging and discharging mechanisms operative in such devices in general. It was thus decided to study their *I-V* characteristics along with the charge storage in the system as obtained from *C-V* measurements. These studies were carried out on MAS capacitors without purposely grown SiO_2 films. Al_2O_3 films obtained by chemical vapor deposition at 700°C and above from an aluminum halide system were used because of the superior properties of the material prepared in this manner (1). Special attention was paid to the effect of fabrication parameters (deposition temperature and rate, annealing) and electrode materials on the sample properties.

This type of investigation appears to be also of interest since the information in the literature regarding conduction in MAS systems is rather contradictory. Whereas Tsujide *et al.* (11) found a bulk-limited Poole-Frenkel conduction mechanism for high temperature pyrolytic films, Walden and Strain (12) interpreted their measurements on a similar material using an injection-limited mechanism. Salama (13) concluded that in sputtered Al_2O_3 films the Poole-Frenkel effect predominates. It should be remarked that a pronounced effect of film preparation conditions on the conduction mechanism is also known to exist for SiO_2, where thermally grown films show injection-limited conduction (14, 15), whereas for sputtered films Poole-Frenkel conduction has been reported (16).

In the work described in this paper a distinct correlation between the physicochemical material properties and the electrical behavior of the samples was found. In all cases the data point to an injection limitation of the currents. A mutual dependence between current and insulator space charge was observed and the nature of the dominant charge carrier could be determined.

* Electrochemical Society Active Member.
Key words: CVD aluminum oxide films, double layer dielectrics, MIS systems.

Experimental

Sample preparation.—Freshly etched 1 Ω cm (100)-oriented p- and n-type silicon wafers were used as substrates for deposition. Under our experimental conditions these had a layer of 1.0-1.5 nm of native oxide. The Al_2O_3 films (typically 100 nm thick) were obtained by pyrolysis of $AlBr_3$ in an $NO-H_2$ atmosphere at temperatures between 700° and 950°C. The volume fractions of the gases entering the reaction zone of the rf heated furnace were 0.0026 $AlBr_3$, 0.02 NO, and 0.1 H_2 with N_2 making up the balance. The rate of deposition was 10 nm min^{-1}.

In many cases the samples were cut into two parts, one of which was annealed for 1 hr in oxygen at the film deposition temperature. Since the film thickness determined by ellipsometry was the same before and after annealing we conclude that the amounts of SiO_2 formed at the interface during this process must be negligible. However, we cannot exclude the possibility that interdiffusion of the oxide layers takes place during deposition and annealing. Circular metal electrodes (diameter 0.8 mm) were deposited onto the oxide films by evaporation through a metal mask. The back sides of the samples were contacted using Ga-In alloy.

Film characteristics.—In agreement with earlier experience (17) films deposited below 800°C are amorphous, whereas those obtained above this temperature showed an electron diffraction pattern typical for γ-Al_2O_3. Transmission electron micrographs obtained on thin films of the polycrystalline material showed a crystallite size of approximately 10 nm. Somewhat surprisingly, increasing the deposition rate above the standard value of 10 nm min^{-1} by increasing the $AlBr_3$ concentration in the gas phase led to larger crystallite sizes. These and further characteristics of the Al_2O_3 layers are summarized in Table I, where data on 750° and 900°C films are presented as representative for both types of material.

Electrical measurements.—*I-V* characteristics were determined in the dark at room temperature using a Keithley 602 electrometer. As has been observed in measurements on other insulators, the currents decay with time under constant voltage. This phenomenon, related to space charge effects in the film, obeys an $I \sim t^{-a}$ law (a = 0.2-0.5), which was also found by Walden (12, 18). Although the current does not completely saturate even in 24 hr, it was found that satisfactory *I-V* characteristics could be obtained by raising the voltage in steps after waiting for 2 min. Figure 1 shows that the features of such a curve and one obtained after 10 min waiting time are essentially the same. Here and in the following figures the data are presented in the form I *vs.* V/d (d = film thickness). Other plotting methods, notably I *vs.* $(V/d)^{1/2}$, were tried but did not lead to a simpler (*i.e.*, straight line) representation. Essentially the same current-voltage characteristics were obtained on samples on which a 2.5 nm SiO_2 layer had been grown by oxidation in N_2 with 1% O_2 at the Al_2O_3 deposition temperature prior to deposition.

Table I. Characteristics of Al_2O_3 films, deposited at 750° and 900°C

Deposition temperature	750°C	900°C
Structure	Amorphous	γ-Al_2O_3
Grain size, nm	<1	≈10
ϵ	7	9
n (λ = 546.1 nm)	1.66 ± 0.01	1.75 ± 0.01
Breakdown strength,* mV/cm	8	8.5
Etch rate,† nm/min	400	0.1

* Maximum of final breakdown strength distribution, measured at ramp rate of 1 MV cm^{-1} sec^{-1}.
† In H_3PO_4 at 100°C.

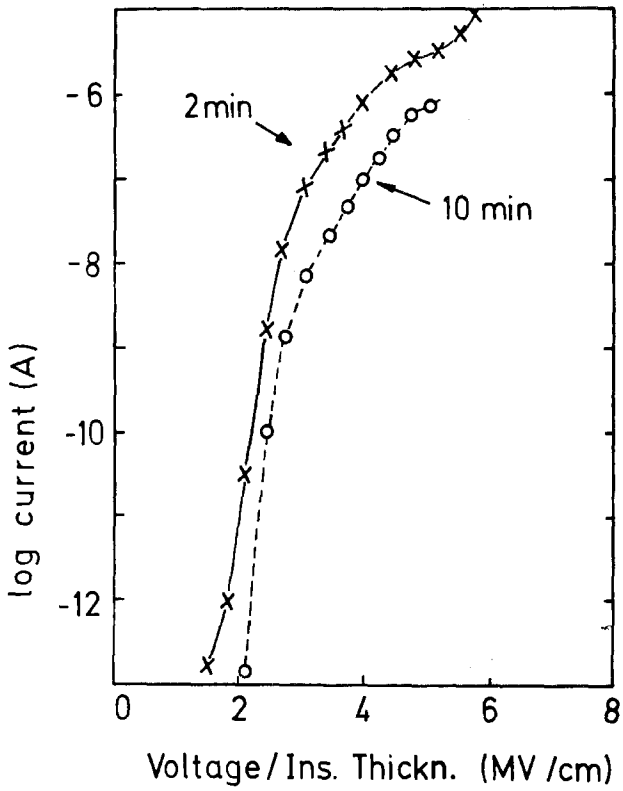


Fig. 1. Effect of waiting time on shape of *I-V* curves. Sample: 1 Ω cm n-Si substrate/amorphous Al_2O_3/Al (neg.).

A check of the minority carrier generation time using the Zerbst method (19) indicated that the generation rate would in most cases be sufficiently large to produce the measured current on inverted samples if the minority carrier in the silicon would be the major carrier in the oxide. Consequently illumination generally did not affect the measurements. However on samples with p-type substrates under positive bias the current would level off at approximately 10^{-10}A and only rise again upon illumination.

For each point on the *I-V* curves the flatband voltage V_{FB} was measured at 1 MHz using a Boonton capacitance-inductance meter (Model 71 A) in order to keep track of the charge in the insulator system. Our equipment permitted measurement of V_{FB} up to a value of ±35V.

Results

In this section we present the most important experimental results obtained in the present study. Figures 2 through 4 show the dependencies of the measured currents on the sample voltages normalized with respect to sample thickness. Along with these data for each voltage value the shift of the flatband voltage ΔV_{FB} has been plotted.

Figure 2 shows a comparison between films deposited at 750°C and films prepared at 900°C for both polarities of applied voltage. These layers are typical for the amorphous and polycrystalline range, respectively. The samples had Al electrodes. It may be seen that the 900°C samples exhibit the lower conductivity values. The polycrystalline sample yields a current-voltage plot of only slightly varying slope, along with a charging plot with constant positive slope for positive voltages. Positive ΔV_{FB} values are also obtained for moderately negative voltages, but for larger stresses the flatband shift reverses direction and eventually negative ΔV_{FB} values are reached. Here, as well as in all other cases, the same results were obtained on substrates of both conductivity types.

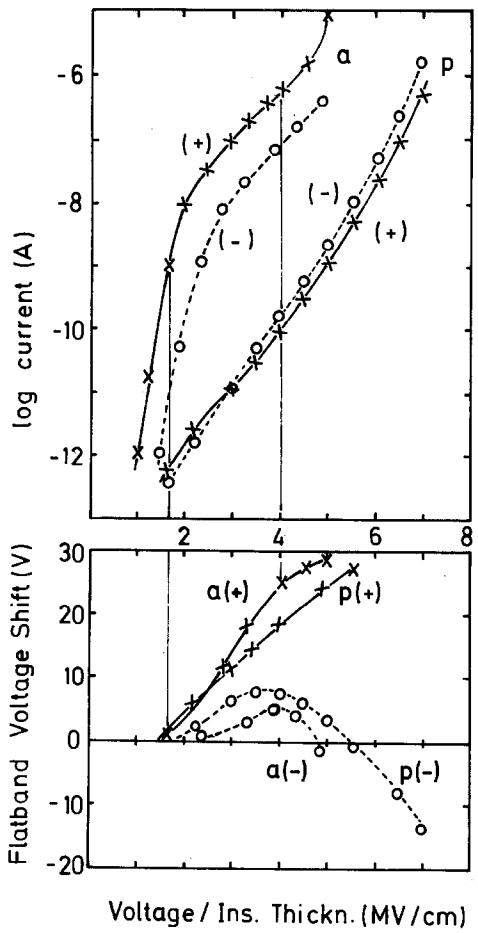


Fig. 2. Effect of deposition temperature [750°C (a) and 900°C (p)] on I-V and ΔV_{FB}-V characteristics of MAS structures. Al electrode (positive and negative); 1 Ω cm n-Si substrate.

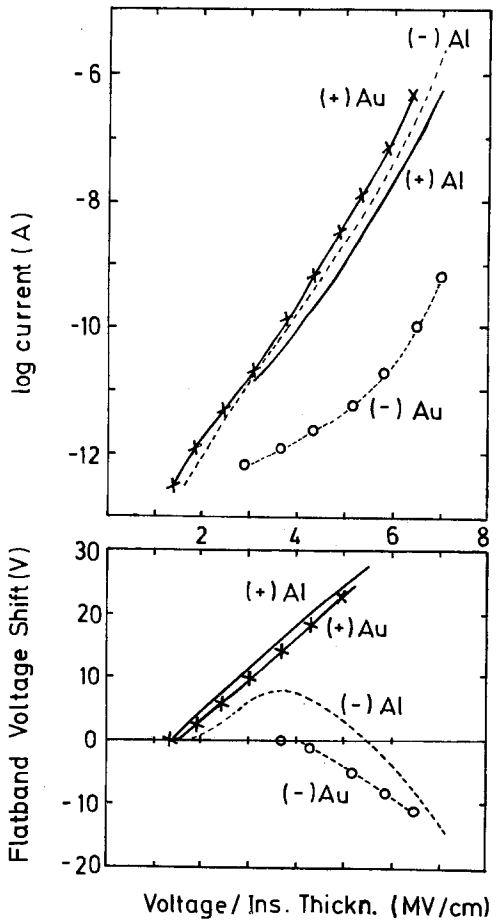


Fig. 3. Effect of metal electrode on I-V and ΔV_{FB}-V characteristics of MAS structures for positive and negative polarities. Electrode metals: Al and Au; Al_2O_3 (900°C); 1 Ω cm n-Si substrates.

The current-voltage curves for the amorphous layers are more structured and show three distinct regions. Starting at small voltages, the current first rises steeply, next a region of smaller slope follows, and at still higher voltages a second steep increase is observed. As indicated in the figure, the transition to the middle region coincides with the onset of a charge storage process which involves charges of the same sign for both positive and negative voltages. Upon reaching saturation of the charging the current starts its second steep rise. Under negative bias a reversal of the charging process sets in at the latter point. The currents measured for positive voltages are slightly larger than those for negative voltages.

The effect of the metal electrode is demonstrated in Fig. 3 on capacitors with polycrystalline films and Al and Au electrodes. Structures with amorphous layers show a similar behavior. The most striking feature of the results are the very low currents for Au electrodes under negative bias, paralleled by the absence of any indication of negative charge storage for this polarity. Under positive bias current and charging appear to be independent of the electrode material.

Figure 4 shows the changes in the characteristics of 900°C samples with an Al electrode brought about by O_2 annealing. The most obvious effects of this treatment are the reduced sample currents and the disappearance of the positive V_{FB} branch for negative sample voltages. The conductivity of the system is largely independent of polarity. However, the onset of negative charging moves out to larger voltages, and the amount of stored charge increases more rapidly with voltage. On the other hand, the positive charging process for the opposite polarity starts at smaller voltages.

The effect of the O_2 treatment on amorphous samples was quite similar to that described above. Unfortunately, the current and ΔV_{FB} curves could only be followed to much lower voltages since these specimens broke down at considerably reduced field values. This reduction was particularly pronounced for capacitors with a Au electrode.

In Fig. 5 current values at constant voltage, obtained on polycrystalline and amorphous samples, have been plotted against reciprocal temperature. Particularly in the range below room temperature the temperature dependence of the conductivity is modest; the current-voltage characteristics at different temperatures are obtained from each other by a small parallel shift.

Finally, it was found that structures with polycrystalline Al_2O_3 samples having larger crystallite size (30 nm) yield essentially the same conductivity curves as those with standard films (crystallite size 10 nm). However, as could also be observed from the pronounced looping of the C-V curves, charge storage starts at lower voltages than those measured for the standard material.

Discussion

The most outstanding features of the data presented in the preceding section are the following: The sample conductivities are dependent on the electrode material. There appears to be a correlation between I-V characteristics and charging effects. Particularly below room temperature the conductivity changes only moderately with temperature. The smaller conductivity of the MAS structures with polycrystalline films compared

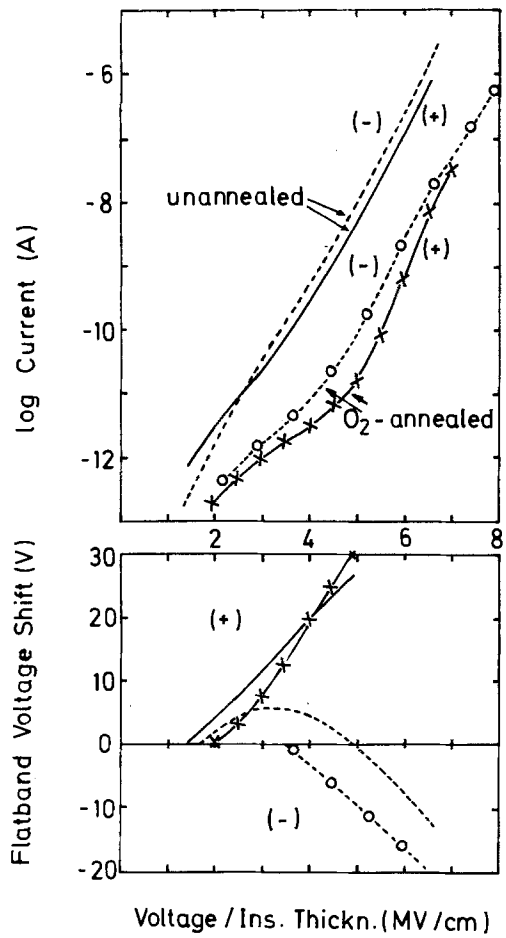


Fig. 4. Effect of O_2-annealing on *I-V* and ΔV_{FB}-*V* characteristics of MAS structures. Electrode metal: Al; Al_2O_3 (900°C); 1 Ω cm p-Si substrate.

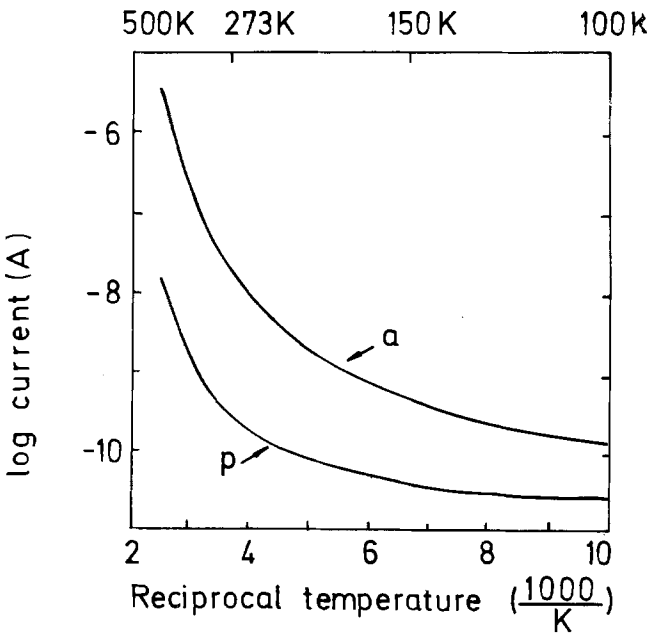


Fig. 5. Temperature dependence of sample currents for 750° (a) and 900°C (p) Al_2O_3 layers at 5.1 and 5.6 mV cm^{-1}, respectively.

to those with the amorphous layers and the effect of O_2 annealing suggest that imperfections play a major role in determining the electrical properties of the capacitors.

The electrode dependence of the current points to an injection-limited conduction mechanism. The relative insensitivity of the current to temperature changes is indicative of a tunneling process. This mechanism is apparently universal for high temperature Al_2O_3 films since all films investigated in this study showed the above-mentioned behavior.

The conduction process is dominated by electrons. This may be concluded from the fact that both current and negative charge injection for negative voltages are strongly suppressed by using instead of Al an electrode metal with larger work function and thus larger barrier for electron injection, *e.g.*, Au. On the other hand, for positive voltages the current is independent of the electrode material. This observation is incompatible with hole conduction. The comparable magnitude of the currents for both negative and positive Al electrodes suggests that in the latter case the electrons are being supplied from the Si conduction band. The model is further supported by the observed saturation of the current at high values on p-type substrates with positive voltages and the removal of this effect under illumination. It would also seem to follow from the energy band diagram (1) of the MAS system, even when using Powell's recent measurements on Al_2O_3, indicating that the bandgap is only approximately 8 eV (20).

A quantitative comparison between the measured *I-V* data and the trends shown by two conduction mechanisms which play a major role in other thin insulating films is shown in Fig. 6. The measured curves are for amorphous and polycrystalline layers under positive bias. Calculated curves (21) are given

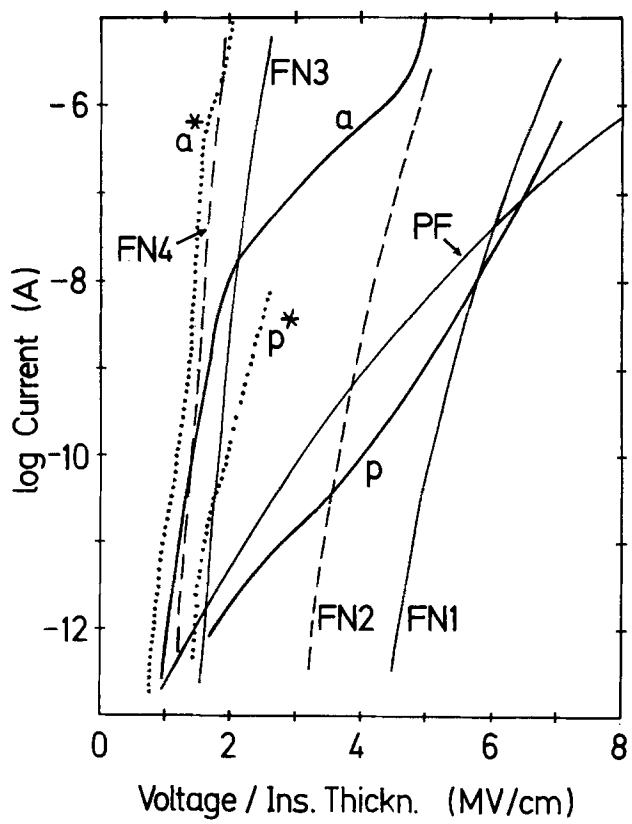


Fig. 6. Comparison between calculated and experimental *I-V* curves. a, p: experimental curves for amorphous and polycrystalline samples with 1 Ω cm n-Si substrate and Al electrode positive. a*, p*: experimental curves, corrected for space charge effect on contact field. FN 1, calculated Fowler-Nordheim curve for $\phi = 2$ eV, $m^* = 1m$; FN 2, the same for $m^* = 0.5m$; FN 3, calculated Fowler-Nordheim curve for $\phi = 1$ eV, $m^* = 1m$; FN 4, the same for $m^* = 0.5m$; PF, calculated Poole-Frenkel curve for $\phi = 1.2$ eV and $\epsilon = 3.1$.

for the same I-V range for Fowler-Nordheim tunneling through barriers of different heights, computed after

$$J = A_1 \frac{E^2}{\phi} \exp\left(-A_2 \frac{m^{*1/2}\phi^{3/2}}{E}\right)$$

taking for the effective mass m^* values of m and $0.5m$ (m = electronic mass). In the above expression ϕ is the barrier height and A_1 and A_2 are constants. There are indications in the literature that reduced effective mass values are to be expected for insulators (14, 15). The barrier height indeed appears to play a dominating role in determining the sample conductivity. The calculated curve for the Poole-Frenkel current (21)

$$J = A_3 E \exp\left(-\frac{E_t - A_4\epsilon^{-1/2}E^{1/2}}{kT}\right)$$

for a trap depth E_t of 1.2 eV exhibits a considerably smaller slope and was chosen to approximate the experimental curve for the polycrystalline sample. The dielectric constant ϵ was chosen as 3.1, *i.e.*, equal to the square of the refractive index. Somewhat surprisingly the over-all slopes of the experimental data seem more compatible with a Poole-Frenkel bulk mechanism than with an electrode-limited Fowler-Nordheim injection. Only the first and third regions of the curve for amorphous Al_2O_3 exhibit slopes compatible with the latter process.

At this point it should be realized that the field at the injecting contact is not given by V/d but has, in fact, a lower value due to the space charge stored in the insulator. The possible occurrence of such effect was first pointed out by Pittelli (22) and taken into account in Waldens work (18) on Al_2O_3 films. For Si_3N_4 it was discussed by Arnett and DiMaria (10). As may be seen from the example of the amorphous Al_2O_3 film in Fig. 6 the slope of the I-V curve is strongly reduced in the central region where the amount of stored charge is increasing. Only the steeply rising initial and third regions where the insulator charge remains constant show the immediate effect of the increase in V/d. By the same token, the curve in Fig. 6 for the polycrystalline sample shows too small a slope over the entire range. For this reason the true field at the injecting contact, $E(o)$, was calculated from V_{FB} after the expression (10)

$$E(o) = -(V - V_{FB} - \psi_s)d + Q_{ss}^{\circ}/\epsilon\epsilon_o$$

where ψ_s is the voltage drop over the semiconductor space charge region and Q_{ss}° the fast interface state charge density at the flatband condition. Since the terms with ψ_s and Q_{ss}° were relatively small they were neglected in the calculations. The corrected experimental values are shown as dotted lines for the voltage range for which V_{FB} values were available. Of course, since the field is increasing from the contact inward we have overcompensated for the space charge effect by equating the field in the tunneling region to its value at the injecting contact. This explains the nearly vertical sections of the corrected curves.

The unexpectedly low barrier energies which would follow from an interpretation of the conductivity data in terms of Fowler-Nordheim tunneling appear to indicate that this model does not apply. Even when using reduced effective mass values one arrives at barrier energies of only 1-1.5 eV instead of the expected value of approximately 3 eV for the Si-Al_2O_3 barrier. Similarly unsatisfactory results are obtained by explicitly allowing for the presence of a thin SiO_2 film between silicon and Al_2O_3. For a 1.5 nm SiO_2 film and $m^* = 0.5m$ for both oxides an I-V characteristic nearly coinciding with curve FN 1 in Fig. 6 was calculated for this case of modified Fowler-Nordheim tunneling. The similarity between the experimental results obtained on samples with and without purposely grown SiO_2 layer suggests that such a layer may dissolve into the Al_2O_3 film. It thus could not have the expected effect on the current-voltage characteristic.

The only tunneling mechanism which predicts sufficiently large currents at relatively small field is the resonance tunneling process (23). Such a process of trap-assisted tunneling exhibits the same characteristics as a Fowler-Nordheim process and has also been invoked to explain the low field hole injection in MNOS devices (24). In this process carriers from the metal or the semiconductor reach the conduction band of Al_2O_3 in two or more tunneling steps via trapping states in the forbidden gap of the insulator. For a monoenergetic trap level this mechanism should indeed yield a roughly linear change of V_{FB} with the field in the contact region and an exponentially decreasing current with increasing reciprocal field. The observed temperature dependence of the current would also seem to be compatible with this type of tunneling process.

So far the crystallographic nature of the samples was not explicitly invoked to explain their current conduction. This seems to be justified, since the differences measured between amorphous and polycrystalline material are only quantitative in nature. Furthermore, the conduction does not seem to depend to a considerable extend on crystallite size (and thus on grain boundaries). These findings, and the effect of O_2 annealing, are compatible with the proposed model in which defect centers play a critical role in the conduction process.

A final point to be discussed is the shape of the I-V curves for unannealed amorphous films, particularly the steeply rising section at low fields. It is surprising that in this field region charge storage does not take place and that only at higher voltage values a space charge layer is being built up. This behavior seems to be contrary to that expected on the basis of accepted models (9). An explanation based on the assumption that these films may have conductive channels which would not affect the over-all charging of the layers does not seem likely. Such inhomogeneities could possibly occur in polycrystalline films where one might expect enhanced conduction along grain boundaries. However, in the latter case this effect is not observed.

Conclusions

The results obtained in this study indicate that the conduction in MAS structures is an injection-limited process with electrons being the major charge carriers. However, the sample conductivity is not only dependent on the work function of the electrode material but also on the volume properties of the Al_2O_3, most likely its defect structure. Thus the trap-assisted tunneling mechanism suggests itself as the process dominating the conduction for all different types of Al_2O_3 films over the entire voltage range.

A natural consequence of this model is the formation of a space charge layer extending for considerable depth into the insulator. For this reason the absence of any effect of a thin SiO_2 layer on the I-V characteristics is not surprising, since interdiffusion of SiO_2 and Al_2O_3 will most likely occur.

For application in MAOS devices the use of polycrystalline Al_2O_3 films would seem preferable since in this case the undesirable injection of electrons from the metal electrode is greatly suppressed. Moreover, we have established that the charge retention in devices with such layers is better than in those with amorphous Al_2O_3. These advantages are to some extent offset by the larger threshold values for charge storage under positive bias. For this reason graded structures

with higher state densities near the silicon (2), structures with a metal doped insulator-insulator interface (25) or with a third layer [consisting of a lower band-gap insulator (26)] may be expected to yield charge storage devices with optimized properties.

Manuscript submitted March 1, 1977; revised manuscript received July 11, 1977.

Any discussion of this paper will appear in a Discussion Section to be published in the June 1978 JOURNAL. All discussions for the June 1978 Discussion Section should be submitted by Feb. 1, 1978.

Publication costs of this article were assisted by the Technical University of Aachen.

REFERENCES

1. P. Balk, "Solid State Devices," H. Weiss, Editor, Inst. of Physics Conf. Series no. 19, pp. 51-82, Institute of Physics, London (1973).
2. P. Balk, *J. Electron. Mater.*, **4**, 635 (1975).
3. P. Balk and F. Stephany, *This Journal*, **118**, 1634 (1971).
4. T. Tsujide, *Jpn. J. Appl. Phys.*, **11**, 62 (1972).
5. T. Tsujide and K. Iida, *ibid.*, **11**, 1599 (1972).
6. N. Gordon and W. C. Johnson, *IEEE Trans. Electron Devices*, **ed-20**, 253 (1973).
7. B. H. Yun, *Appl. Phys. Lett.*, **25**, 340 (1974).
8. P. C. Arnett and D. J. DiMaria, *ibid.*, **27**, 34 (1975).
9. P. C. Arnett, *J. Appl. Phys.*, **46**, 5236 (1975).
10. P. C. Arnett and D. J. DiMaria, *ibid.*, **47**, 2092 (1976).
11. T. Tsujide, S. Nakanuma, and Y. Ikushima, *This Journal*, **117**, 703 (1970).
12. R. H. Walden and R. J. Strain, in The Eighth Annual Proceedings on Reliability Physics, Las Vegas, Nevada, J. B. Morris, Editor, p. 23, IEEE, New York (1970).
13. C. A. T. Salama, *This Journal*, **118**, 1993 (1971).
14. M. Lenzlinger and E. H. Snow, *J. Appl. Phys.*, **40**, 278 (1969).
15. C. M. Osburn and E. J. Weitzman, *This Journal*, **119**, 603 (1972).
16. B. Moeen-Ziai, *Thin Solid Films*, **22**, 531 (1974).
17. K. Iida and T. Tsujide, *Jpn. J. Appl. Phys.*, **11**, 840 (1972).
18. R. H. Walden, *J. Appl. Phys.*, **43**, 1178 (1972).
19. M. Zerbst, *Z. Angew. Phys.*, **22**, 30 (1966).
20. R. J. Powell, *Appl. Phys. Lett.*, **28**, 643 (1976).
21. J. J. O'Dwyer, "The Theory of Electrical Conduction and Breakdown in Solid Dielectrics," Clarendon Press, Oxford (1973).
22. E. Pittelli, *Solid-State Electron.*, **6**, 667 (1963).
23. J. W. Gadzuk, *J. Appl. Phys.*, **41**, 286 (1970).
24. H. E. Maes and R. J. van Overstraeten, *ibid.*, **47**, 664 (1976).
25. D. Kahng, W. J. Sundburg, D. M. Boulin, and J. R. Ligenza, *Bell Syst. Tech. J.*, **53**, 1723 (1974).
26. M. Schuhmacher, F. Stephany, and P. Balk, Unpublished results.

Plasma Etching of Titanium for Application to the Patterning of Ti-Pd-Au Metallization

C. J. Mogab and T. A. Shankoff

Bell Laboratories, Murray Hill, New Jersey 07974

ABSTRACT

A study of plasma etching of filament evaporated Ti, in a radial flow reactor, using Pd (Au) as a mask is described. This work was prompted by recurrent problems with etch-out of Ti from contact windows during wet chemical patterning of Ti for the Ti-Pd-Au metallization process. CF_4, $CClF_3$, and $CBrF_3$ plasmas were investigated. Details of some of the plasma chemistry and interaction of these plasmas with Au are given. Only $CBrF_3$ plasmas were found to provide suitable selectivity for etching Ti in the presence of Au. $CBrF_3$ tends to produce an unstable plasma. However, a stable, uniform plasma can be formed by the addition of a sufficient quantity of He. Oxygen was also added to enhance the amount of atomic bromine formed in the plasma since this was thought to be the active species for Ti etching. The optimum gas mixture was determined to be 63% $CBrF_3$, 25% He, and 12% O_2. A relatively strong Arrhenius-type temperature dependence of the etch rate was measured with an activation energy of ~0.2 eV for this gas mixture. The range of process parameters (power, pressure, temperature) for which acceptable etching could be achieved was found to be quite broad and working conditions were chosen mainly on the basis of an arbitrary etch time of 4 min to clear 1000Å of Ti from a 3 in. wafer. These conditions are: 200W rf power, 0.35 Torr of the $CBrF_3$-He-O_2 mixture, 150°C wafer platen temperature, and a 4.4 cm electrode spacing. No measurable etching of Au or Pd occurs, using these conditions, while the etch rate for CVD Si_3N_4 is ~25 Å/min. Undercutting of Ti is negligible even with a 100% overetch. No change in MOS characteristics was observed after plasma exposure.

The standard process for patterning Ti-Pd-Au metallization using the beam lead technology (1) for silicon integrated circuit fabrication is as follows: (*i*) Ti and Pd are deposited sequentially by filament evaporation; (*ii*) the Pd is patterned using a photoresist mask and a wet chemical etch which does not attack Ti; (*iii*) thin Au is electroplated over exposed Pd through a second photoresist mask. Ti serves as the ground plane for this plating; (*iv*) a third photoresist mask is used to delineate the beam array and then thick Au is plated; and (*v*) the photoresist is stripped and Ti is etched using the Pd (Au) as a mask for the wet chemical etchant.

A schematic cross-sectional view of a metal-oxide-semiconductor (MOS) field effect transistor fabricated with polycrystalline silicon as the gate electrode and Ti-Pd-Au as the second level metal is shown in Fig. 1.

Inadvertent removal of Ti from contact windows can occur during Ti etching if any of the following conditions exist: (*i*) poor step coverage by Ti-Pd (caused, for example, by misalignment of contact windows through the silicon nitride with respect to contact win-

Key words: silicon integrated circuits, metallization, pattern generation.

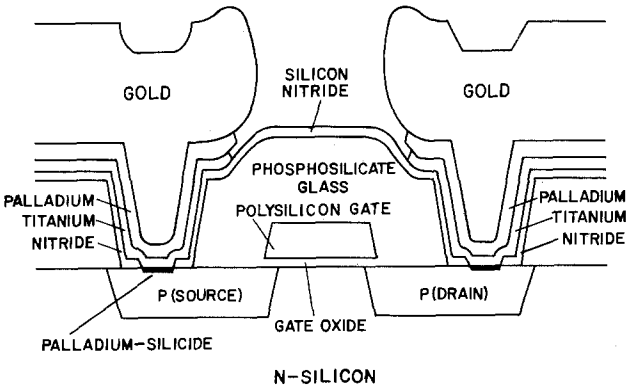


Fig. 1. Schematic cross section of MOS device structure after patterning of Ti-Pd-Au metallization.

dows through the phosphosilicate glass layer); (*ii*) misaligned Ti-Pd metallization over properly aligned contact windows; (*iii*) misaligned Au over marginally aligned Ti-Pd and/or marginally aligned windows; and/or (*iv*) poor dimensional control of window(s) and metallization features. All of the foregoing conditions encourage the formation of capillary channels which permit penetration of Ti etchant into the windows.

Etch-out of Ti in contact windows leads to oxidation of palladium-silicide contacts during subsequent annealing of the metallization with a resultant loss in yield, and even more serious, poor reliability of marginally good devices. As complete elimination of the aforementioned tolerance errors would require unrealistic process control, we have investigated plasma etching of Ti as an alternative patterning technique. The motivation for consideration of plasma etching lies in the expectation that the capillary channels allowing access of etchant to the windows should promote rapid recombination of the plasma active species and thus, in effect, preclude etching there. Plasma etching has an obvious advantage here in that the species which cause etching are not stable in the absence of the plasma and decay rapidly when collisions with a third body such as a solid surface can occur. In contrast, liquid etchant, once trapped in a capillary channel, continues to etch until all reactants are depleted to an equilibrium concentration.

There is no certain way to determine, by visual inspection prior to etching, whether Ti etch-out will occur. Thus, it is difficult to carry out controlled experiments which would allow a direct comparison of the extent of etch-out to be made between wet etching and plasma etching. A valid comparison would require split lot experiments and data from a large number of wafers. At this time the data available is not sufficient to permit an assessment of the effectiveness of plasma etching in preventing Ti etch-out in contact windows. Accordingly, we make no attempt to compare plasma etching to wet etching in terms of device yield or reliability. Rather, the intent of this paper is to discuss some problems encountered in plasma etching of Ti using Pd (Au) as a mask and the process conditions developed to overcome them.

Process Requirements

This investigation was stimulated by reliability problems which arose with MOS logic devices. Consequently, the requirements for the Ti etch process were dictated by the structure of these devices; a structure common to most MOS integrated circuits utilizing Ti-Pd-Au metallization.

The logic devices have poly-Si as the gate electrode and Ti-Pd-Au as the second level metal (see Fig. 1). The Ti is 1000Å thick, the Pd 2000Å thick, the thin Au $\sim$ 1.5 μm thick, and the beams are $\sim$ 15 μm thick. During Ti etching, Au and Pd are exposed. CVD silicon nitride which serves as a sodium ion barrier ($\sim$ 1200Å thick) is exposed upon removal of Ti. An acceptable etching process, therefore, must produce a high selectivity for Ti over Au, Pd, and Si_3N_4. In addition, no MOS damage should occur, to the extent of causing changes in device operating characteristics, and undercutting of Ti must be acceptable.

Experimental

A radial flow reactor similar to one described by Reinberg (2) was used in this study. In this type of apparatus the plasma is generated by rf energy (13.56 MHz) between two parallel, circular electrodes; the wafers to be etched rest on the grounded electrode. Gas is fed through a ring beneath the grounded electrode and pumped through a hole in its center; thus, gas flows radially across the electrode.

A differentially pumped quadrupole mass spectrometer was attached to the pumping line through an orifice in order to monitor the reactor effluent. A sapphire window on the Pyrex vacuum enclosure of the reactor chamber allowed the optical emission from the plasma to be monitored in the u.v.-visible region of the spectrum from $\sim$ 1800 to 8000Å. Substrate heating was accomplished by use of resistance heating coils embedded in the ground electrode.

Wafers used in this study were either test structures consisting of thermally oxidized Si-CVD Si_3N_4 (1200Å) and Ti-Pd-Au or device wafers, all receiving standard processing up to the Ti etch stage. In addition, Si wafers with 2500Å of Si_3N_4 and a photoresist pattern on them were used to measure the etch rates of Si_3N_4 in the various gases tested. Etch rate measurements were obtained with the aid of a Dektak surface profilometer.

Results

Gas selection.—The titanium halide binary compounds all have relatively high vapor pressures in comparison to other chemically simple titanium compounds. Consequently, only halogen-bearing gases were considered as potential etchants. Two gases which were known at the outset to etch Ti were tetrafluoromethane (CF_4) and chlorotrifluoromethane ($CClF_3$).

A CF_4-O_2 mixture was already in use to etch an ion milling mask in Ti on a bipolar microwave transistor device (3). In this process, the Ti is etched down to Au. In order to prevent Au staining, however, it was reported that conditions had to be carefully controlled, even though the Au is not exposed until Ti is removed. Indeed, previous experience with plasma etching of dielectrics deposited over Au had shown staining to be a persistent problem whenever Au is exposed, at elevated temperatures ($\gtrsim$ 50°C), to a plasma where both oxygen and fluorine are present (4). The stains are thought to be gold oxides whose formation is catalyzed by atomic fluorine. The presence of stains results in unsatisfactory thermocompression bonding to Au beams which is required for device packaging.

In principle, a pure CF_4 plasma could be used for Ti etching in the presence of Au, however, there is normally enough oxygen present due to residual water vapor and real leaks in the vacuum enclosure to render this an unsatisfactory solution. Moreover, the presence of oxygen is desirable because it enhances the amount of free fluorine in the plasma, thereby yielding higher etch rates. Also, CF_4 and CF_4-O_2 plasmas etch Si_3N_4 at relatively high rates and so are undesirable for etching down to a thin Si_3N_4 layer.

Chlorotrifluoromethane ($CClF_3$) plasmas were also known to etch Ti, although less data were available than for CF_4. Emission spectra taken for $CClF_3$ plasmas under various conditions of power and pressure revealed no emission from atomic fluorine in the plasma although a substantial amount of emission from atomic chlorine was observed. Figure 2 compares the emis-

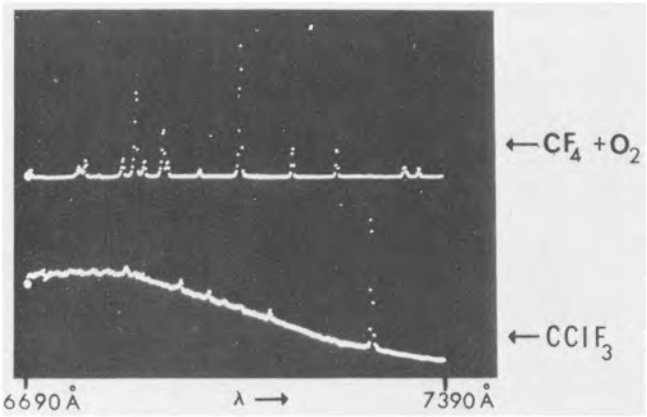


Fig. 2. Comparison of the emission spectrum of a CF_4-O_2 plasma to the spectrum for a $CClF_3$ plasma from 6690 to 7390Å. The observed lines are due to atomic fluorine and chlorine, respectively.

sion spectra of a $CClF_3$ plasma at 350W, 0.35 Torr, and a CF_4-O_2 plasma at 150W, 0.35 Torr for the spectral region from ~ 6690 to 7390Å. This frequency range was chosen for comparison because it includes several very intense emission lines from excited states of atomic fluorine. All of the lines seen in the upper spectrum of Fig. 2 are due to electronic transitions of F. Note that these lines do not appear in the lower spectrum corresponding to a $CClF_3$ plasma. The prominent line in this spectrum results from the $4s^4P$-$4p^4S^\circ$ transition of Cl at 7257Å. Numerous other lines, assignable to Cl transitions, were observed outside the frequency range of Fig. 2.

The absence of emission from F in the $CClF_3$ plasma provides necessary but insufficient evidence for concluding that F is not produced in this plasma. It is possible that F is present in the nonradiative ground state The CF_3-Cl bond strength is 3.7 eV (5) while the CF_3-F strength is 5.6 eV (6) and the CF_2-F strength is 4.2 eV (7). Thus, it is energetically more favorable to split off Cl than F. On the other hand, the first excited state of Cl is ~ 9 eV above the ground state while the first excited state of F is ~ 12.5 eV above its ground state. Thus, one might argue that the presence of the "softer" Cl modulates the energy distribution of the free electrons in the plasma to the extent that there are not enough electrons available with sufficient energy to excite F above its ground state once it has been freed. The latter argument can be shown to be invalid by a simple experiment, the results of which are illustrated in Fig. 3. When a few percent He are added to the $CClF_3$ plasma two lines appear, in the spectral range corresponding to Fig. 2, due to transitions between excited states of He as shown.[1] Since the first excited state of He lies 19.82 eV above the ground state it is clear that electrons with energy sufficient to excite F are indeed present in the plasma. Therefore, it is concluded that $CClF_3$ does not produce a significant F concentration under the plasma conditions used in these experiments.

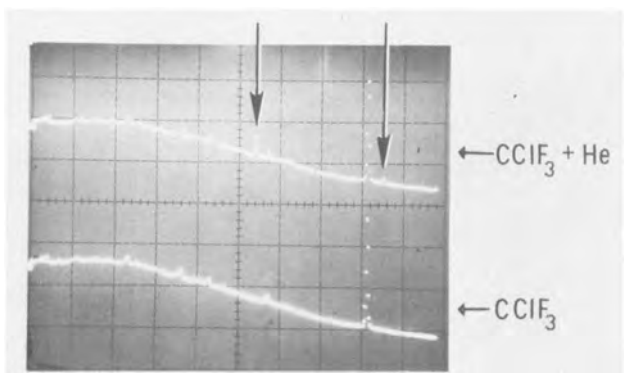


Fig. 3. Emission spectrum of a $CClF_3$ plasma with and without He present. The two lines marked with arrows (upper spectrum) are due to He transitions at 7065 and 7281Å. The frequency range in Fig. 3 is identical to that for Fig. 2.

Accordingly it was anticipated that in a $CClF_3$ plasma, etching of Ti would occur by the formation of volatile $TiCl_4$ and the absence of F would eliminate Au staining if oxygen was present in the plasma. Several attempts were made to determine what volatile Ti product results from etching. The intensity of emission from excited states of atomic chlorine was monitored with and without Ti etching in the $CClF_3$ plasma. A reproducible decrease in intensity resulted when Ti was placed in the plasma. For example, when the area of Ti exposed to the plasma was ~ 100 cm^2, the Cl line intensities decreased by ~ 20%. Mass spectra of the reactor effluent taken during etching showed no detectable Ti-containing product even when a substantial amount of Ti surface area (two 6 × 3 × 0.30 in. Ti sheets) was exposed to the plasma. However, a porous deposit was formed on the unheated rf electrode directly above the substrates. This deposit was analyzed by x-ray dispersive analysis and found to contain Ti. The vapor pressure of $TiCl_4$ is several Torr at room temperature (8); thus, it would be expected to appear in the effluent. The absence of mass spectral confirmation of $TiCl_4$ and the observed deposit therefore suggest that a more complex, less volatile reaction product is formed, probably involving atomic chlorine in the reaction.

As anticipated, Au staining did not occur with $CClF_3$; however, an erratic and often severe problem with Au "transport" was observed. Normally, $CClF_3$ plasmas etch Au at a rate comparable to Ti. At 85°C the etch rate for Au in a $CClF_3$ plasma at 200W, 0.35 Torr is ~ 250 Å/min. (This loss is tolerable and could be compensated by plating the Au slightly thicker if desired.) Often though, the Au was transported across the wafer surface rather than being removed by etching. The mechanism by which this occurs is not understood. Occasionally Au would be transported heavily enough to be quite obvious as shown in Fig. 4a. Note that a thin Au layer has covered almost the entire area shown. More frequently, Au was observed to transport in a more subtle fashion between closely spaced lines particularly where these lines crossed steps in the underlying dielectric as shown in Fig. 4b. Underplating also seemed to enhance the tendency for transport.

The occurrence of transport was not readily predictable nor was it clear from a limited number of experiments that it could be avoided entirely by some optimum choice of plasma parameters. Consequently, the use of $CClF_3$ was abandoned.

An alternative halogen-bearing gas for which no data were available concerning Ti etching was bromotrifluoromethane ($CBrF_3$). In earlier work with this gas we observed that atomic bromine is produced in a $CBrF_3$ plasma,[2] and it was anticipated that this would yield a volatile Ti product. It was also noted that $CBrF_3$ often forms an unstable plasma characterized by constrictions, *i.e.*, localized, very intense regions of plasma which would obviously hamper the attainment of uniform etching in a batch-type operation. This form of instability is probably related to the electronegative character of the halocarbon gases as our observation of the ease of maintaining a uniform stable plasma is: $CF_4 \gtrsim CClF_3 > CCl_2F_2 \gtrsim CBrF_3$. Presumably, a constriction occurs when a spatial fluctuation in electron density is stabilized by electron attachment outside the constricted region. The more conductive

[1] The He was added at constant total pressure, thus diluting the $CClF_3$, which accounts for the slight drop in intensity of the Cl line.

[2] As with $CClF_3$, this gas produces no significant amount of atomic fluorine. The CF_3—Br bond strength is 3.06 eV (9).

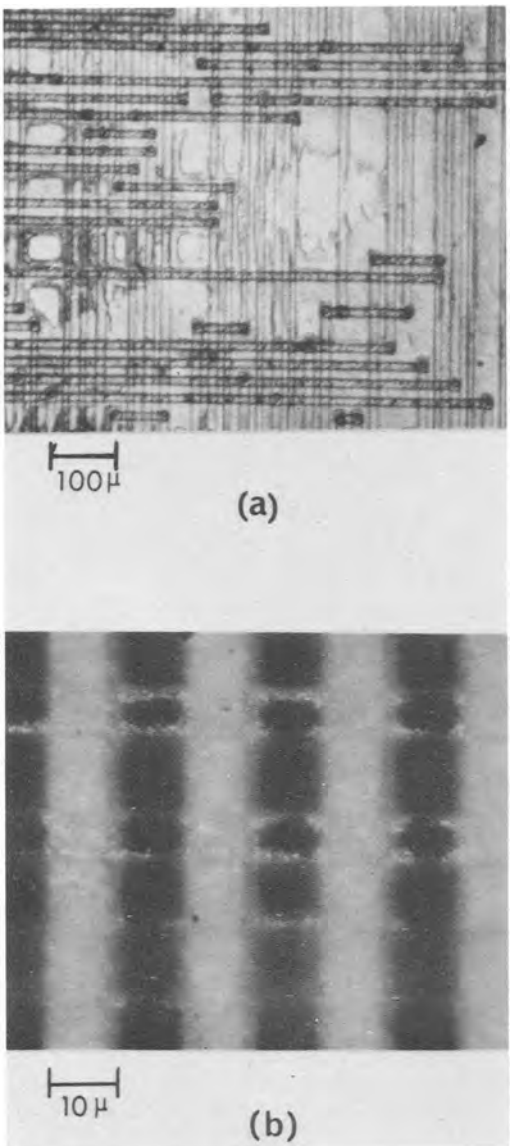


Fig. 4. (a) Optical micrograph illustrating unusually severe Au transport observed following etching in $CClF_3$ at 200W, 0.35 Torr. (b) Optical micrograph illustrating Au transport between closely spaced runners. Note that transport has occurred preferentially along steps.

constriction thereafter carries most of the current and the rf power is dissipated mainly in this region.

We have found that instabilities in $CBrF_3$ plasmas can be eliminated by the addition of He as a diluent. Whether the stabilizing effect of He is due to collisional detachment or some other mechanism is not known. Whatever the reason, this has proven to be a very reliable method of achieving a stable $CBrF_3$ plasma. Consequently, all of the Ti etching experiments in $CBrF_3$ were carried out using a He diluent.

As was the case with $CClF_3$, no Ti reaction product could be positively identified by mass or optical spectroscopy when etching Ti in $CBrF_3$ plasmas. However, as it was again suspected that Br played an important role in the etching reaction, we sought to maximize the Br content of the plasma by the addition of O_2. Additions of O_2 to a CF_4 plasma can produce an increase of several hundred percent in the amount of atomic F thereby enhancing the etch rate of materials such as Si which can react directly with F (10, 11). Similarly, the addition of oxygen to a $CClF_3$ plasma was found to produce a substantial increase in the intensity of emission from excited states of chlorine atoms presumably reflecting a similar increase in chlorine atom concentration. Thus, it seemed reasonable to expect that O_2 would perform the same feat when added to $CBrF_3$. Figure 5 illustrates the result of replacing He with O_2 in a $CBrF_3$-He plasma. As can be seen, the O_2 does increase the intensity of emission from excited Br atoms but by a maximum of only $\approx$ 10%. In fact, the intensity actually begins to decrease somewhat as the He content drops below $\sim$ 20%. Again assuming that the emission intensity is a measure of atom concentration, these results indicate that oxygen does not markedly influence the Br atom concentration. It should be noted that the replacement of He by O_2 showed no indication of affecting the stability of the plasma.

The addition of O_2 to $CBrF_3$ caused only a small increase in etch rate for Ti as might be expected from the data of Fig. 5. Nevertheless, oxygen was retained in the gas mixture because of its potential usefulness in removing traces of photoresist and hydrocarbon residues which are occasional contaminants on wafer surfaces.

Process parameters, etch rates, and uniformity.—As already discussed the gas mixture was optimized to produce plasma stability and maximize the concentration of Br. The optimum composition determined was 63% $CBrF_3$, 25% He, and 12% O_2. Detailed measurements of the dependence of etch rate on rf power

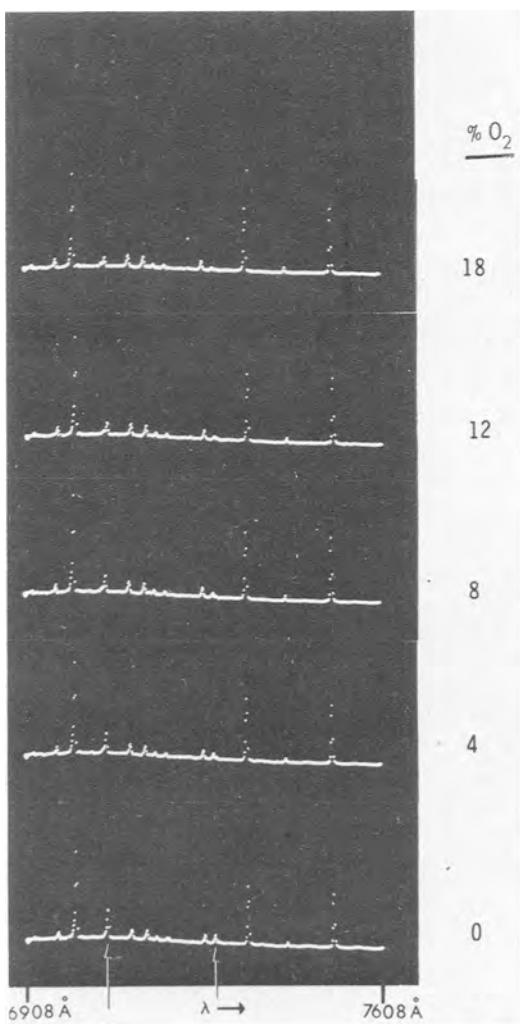


Fig. 5. Optical spectra illustrating the slight enhancement of Br emission accompanying the replacement of He by O_2 in a $CBrF_3$-He mixture. The $CBrF_3$ content was held constant at 63%. All lines seen are due to atomic bromine transitions except the two lines marked by arrows which are due to He.

and pressure were not made for two reasons. First, the Ti did not etch uniformly enough to obtain meaningful data; usually the Ti would clear first at the periphery of the wafer. For this reason it seemed more practical to measure the time to completely remove Ti from a wafer as a function of plasma parameters. Second, there were no evident problems in fulfilling the process requirements, outlined in that section above, over a wide range of plasma conditions tested (80-350W, 0.2-0.7 Torr, 60°-150°C). Hence conditions were established, empirically, which provided for a reasonably short cycle time.

Some indication of the effect of rf power on rate can be obtained by noting that at 125°C,[3] 0.35 Torr, the times to clear 1000Å Ti from 3 in. wafers are 10 and 6 min at 80 and 200W, respectively.[4]

The etch rate is a comparatively strong function of temperature as shown in Fig. 6 where the times to clear equisized pieces of a 3 in. wafer (1000Å Ti) are plotted as a function of reciprocal temperature. The apparent activation energy derived from the slope of the best fit line in Fig. 6 is ~ 0.2 eV.

For convenience, the plasma parameters were adjusted to give a total etch time, including ≈ 25% overetch, of 4 min to clear 1000Å Ti from a 3 in. wafer. Successful batch etching can be done using these conditions: 200W rf power, 0.35 Torr of 63% $CBrF_3$-25% He-12% O_2, a 150°C substrate table temperature, and an electrode separation of 4.4 cm. As will be indicated shortly, these conditions provide a high selectivity so that substantial overetching is permissible. Moreover there is no staining of the exposed Au nor any Au transported between closely spaced lines including regions where these lines cross steps.

Selectivity and undercutting.—No measurable Pd or Au etching was observed using the plasma conditions just outlined, although a thin, innocuous layer of palladium oxide is formed on prolonged exposure of Pd surfaces to the plasma, when O_2 is present in the gas mixture. The etch rate of Si_3N_4 was approximately 25 Å/min. Evidently, Au is substantially more inert toward Br and O than for F and O, Cl, or Cl and O. No undercutting could be measured (optical microscope) after the nominal etch time whereas a 100% overetch produced $\lesssim$ 0.2 μm undercut per edge (*i.e.*, the linewidth decreased by $\lesssim$ 4000Å). It is of interest to compare these figures with values typical of wet etching; etching for the nominal time (2 min) produces ~ 0.6 μm undercut per edge while a 100% overetch undercuts ~0.9 μm per edge. The fact that undercutting is reduced substantially with plasma etching supports our contention that plasma etching will suppress contact etch-out when processing errors produce channels which allow access of etchant into contact windows.

Effect of MOS parameters.—No adverse effects on MOS characteristics due to plasma exposure have been observed on device wafers etched in our experiments. Added assurance about potential MOS damage was gained by running a well-characterized test wafer for four times the normal etch time and then retesting. Again no significant change in any MOS parameter was observed.

Residual Pd.—Occasional problems arose with residual Pd due to incomplete removal during Pd etching. Wet etching of Ti which is accompanied by vigorous bubbling will normally remove these residues. For plasma etching, however, there is no mechanical agitation and Ti is simply etched out from beneath the residue making it easy to observe with an optical microscope.

[3] The temperature measurement was made using a thermocouple embedded in the large Al plate (the grounded electrode) on which the wafers rest.

[4] It is noteworthy that the etch rates reported here refer to filament evaporated Ti as we have found that rf-sputtered Ti etches more slowly.

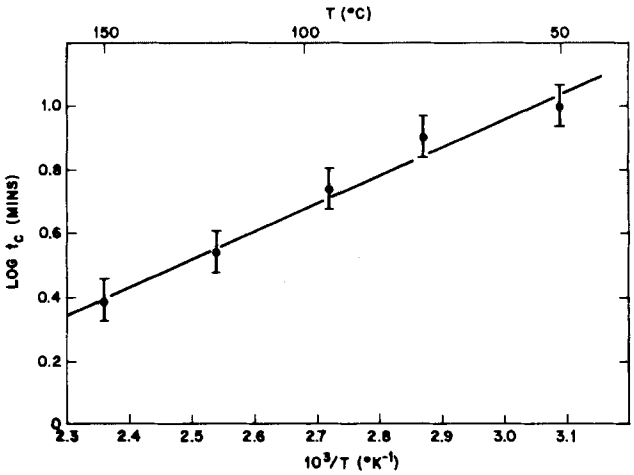


Fig. 6. Arrhenius plot of the time to clear 1000Å of Ti as a function of temperature for etching in a $CBrF_3$-O_2-He plasma.

Conclusions

Titanium can be etched by CF_4, $CClF_3$, or $CBrF_3$ plasmas or in plasmas containing mixtures of these gases with O_2. However, for etching Ti in the presence of Au, Pd, and Si_3N_4 only the $CBrF_3$ plasma offers the necessary selectivity and freedom from Au staining and transport to be of practical value.

A mixture of 63% $CBrF_3$, 25% He, and 12% O_2 was found to produce a uniform, stable plasma. Helium is useful in stabilizing the plasma while oxygen enhances the generation of atomic bromine which is thought to be a major etch-active species. This gas mixture provides excellent selectivity; the etch rate for Au and Pd is essentially zero, while Si_3N_4 is removed at ~ 25 Å/min using the nominal conditions: 200W rf power, 0.35 Torr, 150°C substrate carrier temperature, and a 4.4 cm electrode separation. Under these conditions a 1000Å thick Ti film can be removed from a 3 in. wafer in approximately 3 min. The choice of power, pressure, and temperature is not critical and is dictated mainly by the desired etch time.

The high selectivity for Ti over Pd and the absence of convective agitation in the plasma makes it imperative that Pd and/or Pd compounds be completely removed from the Ti surface during prior processing if plasma etching is to be successful.

Acknowledgments

We thank S. E. Haszko for SEM analysis, C. C. Chang for Auger spectroscopy, A. Ross for supplying test wafers, W. D. Powell for MOS verification, and H. J. Levinstein for helpful discussions.

Manuscript submitted March 10, 1977; revised manuscript received June 27, 1977.

Any discussion of this paper will appear in a Discussion Section to be published in the June 1978 JOURNAL. All discussions for the June 1978 Discussion Section should be submitted by Feb. 1, 1978.

Publication costs of this article were assisted by Bell Laboratories.

REFERENCES

1. M. P. Lepselter, *Bell Syst. Tech. J.*, **45**, 233 (1966).
2. A. R. Reinberg, Paper 6 presented at The Electrochemical Society Meeting, San Francisco, California, May 12-17, 1974; and U.S. Pat. 3,757,733 (1975).
3. L. D. Yau and T. N. Tsai, Private Communication.
4. C. J. Mogab, Unpublished work.
5. J. W. Coomber and E. Whittle, *Trans. Faraday Soc.*, **63**, 2656 (1967).
6. J. D. Cox and G. Pilcher, "Thermochemistry of Organic and Organometallic Compounds," Academic Press, London (1970).

7. J. Heichlen, *Advan. Photochem.*, **7**, 57 (1969).
8. M. L. Pearce and N. R. McCabe, *J. Inorg. Nucl. Chem.*, **27**, 1876 (1965).
9. K. C. Ferguson and E. J. Whittle, *J. Chem. Soc. Faraday Trans. I*, **68**, 295 (1972); *ibid.*, **68**, 641 (1972).
10. W. R. Harshbarger, T. A. Miller, P. Norton, and R. A. Porter, Interface '76, Kodak Microelectronics Seminar, Monterrey, California, October 4, 1976.
11. C. J. Mogab, A. C. Adams, and D. L. Flamm, To be published.

SiO_2 Particulates Dispersed in CVD Reactor

I. Semi-*In Situ* Observation

A. Shintani,* K. Suda, M. Suzuki, M. Maki, and K. Takami

Hitachi, Limited, Central Research Laboratory, Kokubunji, Tokyo 185, Japan

ABSTRACT

The number of size variations with time of vitreous silicate particulates in a CVD reactor for SiO_2 film deposition are measured by observation of Mie scattering of a He-Ne laser light on the submicron particles (0.1-0.5 μm diam). The predominant particles are found to be 0.2-0.3 μm in diameter. The size distribution varies with time during the reaction period. Particulates greater than 0.3 μm diam decrease in number with time, whereas the number of smaller particles gradually increases or does not change except at reaction initiation. The size distributions are affected by substrate temperature and reactant and dopant concentrations. Generally, these parameters influence the number of large particles more than smaller particulates. Large particles greater than 0.3 μm diam decrease in number with O_2 flow rate at O_2/SiH_4 ratios greater than 100 and also with the PH_3 flow rate. However, the number of small particles does not vary radically with these gas flow rates. Lowering the substrate temperature results in a reduction in the large particle number. This large particle phenomenon is primarily caused by small particle coagulation. Furthermore, the small particles (0.1-0.2 μm diam) before coagulation reflect the particle nucleus number.

The low temperature chemical vapor deposition (CVD) technique has been usefully employed for the formation of vitreous silicate and phosphosilicate glass (PSG) in silicon device technology. In this CVD technique, SiH_4 and O_2 are generally used as the source reactants. It is well known that SiH_4 reacts violently with O_2, causing SiO_2 fog so that vitreous silicate particles are deposited on the cooled reactor wall. These SiO_2 particulates dispersed throughout the reactor are the cause of pin holes and/or flakes on SiO_2 films formed. Interest in SiO_2 fog centers not only on the characteristics of the SiO_2 films, but also on formation mechanism and kinetics of the film. The problem is: Whether or not there are differences in the formation mechanism and kinetics between SiO_2 particulates and films.

Many investigators, for instance Goldsmith and Kern (1), Baliga and Ghandi (2), Shibata and Sugawara (3, 4), Middelhoek and Klinkhamer (5), and Kern *et al.* (6), have dealt with the kinetics of SiO_2 film growth using SiH_4 and O_2. However, the exact mechanism of SiO_2 film formation has not been confirmed, since the reaction between SiH_4 and O_2 is quite complicated. With regard to SiO_2 particulates, there have been no reports even on particle size.

In this paper, part I of the study, an aerosol measuring technique (7) is applied to the SiO_2 CVD in order to evaluate particulate dispersion in the reactor. The estimation is carried out by measuring the size, number, and related distributions of submicron particles. The results obtained are compared with the SiO_2 film formation process using a basic aerosol theory. The present paper is the first report on exact measurements of SiO_2 particle dispersions in a CVD reactor.

* Electrochemical Society Active Member.

Key words: aerosols, coagulation, nucleation, submicron particulates.

Experimental

Laser particle monitor.—The laser particle monitor (LPM) used in this work consists of a laser light source (8 mW He-Ne laser), a light scattering cell, and a photomultiplier tube as shown in Fig. 1. The laser light is used so that the intensity of Mie scattering light on submicron particles is sufficient for photomultiplier sensitivity. A light scattering cell to which sample gas is introduced possesses optical traps. These optical traps absorb light scattered in directions other than to the photomultiplier. The photomultiplier changes the scattered light intensities into electric signals (pulses). The pulse height and number correspond to particle size and number, respectively. The LPM numerically indicates the number of the particles in individual diameter regions ranging in 0.1-0.2, 0.2-0.3, 0.3-0.4, and 0.4-0.5 μm. Further details

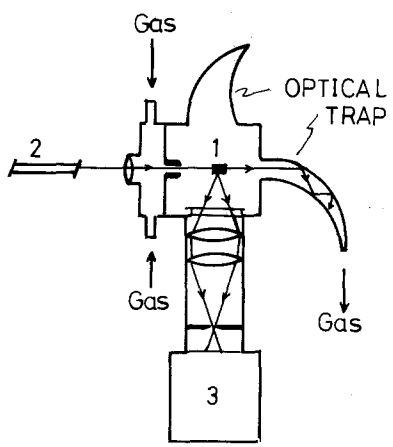


Fig. 1. Schematic diagram of the LPM. 1, Sensing zone; 2, He-Ne laser tube; 3, photomultiplier.

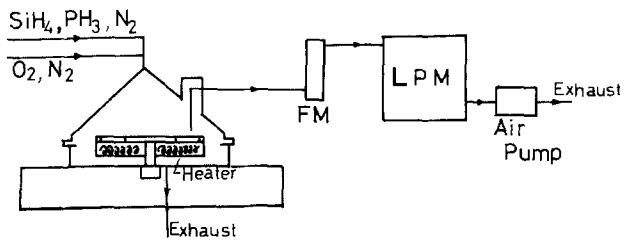


Fig. 2. Schematic diagram of the experimental setup

regarding LPM will be reported elsewhere at a later date (8).

CVD apparatus and experimental setup.—A bell-jar type reactor, as depicted in Fig. 2, was employed for growth of SiO_2 films. The sample holders were heated to 415° ± 5°C and were rotated in a planetary system. A sampling nozzle of 1/4 in. stainless tube was placed about 3 mm above the holders to pump up sample gas as close to the substrates as possible. The sample gas was introduced through this nozzle into the LPM by an air pump at the rate of 1 liter/min. The pipe length from the nozzle end to the LPM was fixed at 2m, because good reproducibility with less than 10% error in the measurement is obtained for pipe with length of 2.5m or less. Some particulates would be newly generated and the particles could grow in this pipe. A little amount of these unknown particles may be added in the measurements, though the reaction time in the sampling pipe was very short, less than 1.5 sec, compared with that in the reaction chamber. Accordingly, this measuring technique was not a complete "*in situ*," but a "semi-*in situ*" method.

Particle formation conditions.—It is well known that the deposition rate of SiO_2 film on a Si wafer varies with substrate temperature and reactant and dopant concentrations. The effects of these experimental parameters on particle size and distribution in SiO_2 dispersions were studied to investigate the correlation between SiO_2 particle formation and film deposition mechanisms. The measurements were carried out at temperatures of 210°-500°C in gas concentrations of 0.018-0.14 mole percent (m/o) for SiH_4, PH_3/SiH_4 ratios of 0.028-0.132, and O_2/SiH_4 ratios of 13.2-132.

Particle distribution measurements.—Each measurement was performed after a blank test in which no reactant was introduced. This test confirmed that no particles before the reaction were present in the apparatus within the LPM sensitivity (greater than 5×10^7 particles/m^3). The number of particles in individual size regions and the total number were recorded at intervals of about 20 sec during the reaction period.

Results

SiO_2 particle dispersions.—The thickness of both SiO_2 and PSG films grown on Si wafers were linearly proportional to deposition time (Fig. 3). These results reveal that both films grow at steady state. However, the size distribution of SiO_2 particles dispersed in the CVD reactor were generally varied at any time during the deposition period as shown in Fig. 4. Some characteristics can be noted from the figure: The particles of 0.1-0.3 μm diam steeply increased in number at the beginning of the reaction. After this increase, their number rapidly decreased within 3 min after the introduction of the gases and then tended to increase gradually with deposition time. On the other hand, the number of 0.3-0.5 μm diam particles increased relatively slowly within 4 min of the reaction start, and then they monotonously decreased with time. When the reactant gas supply was stopped, the particles of 0.1-0.2 μm diam immediately increased

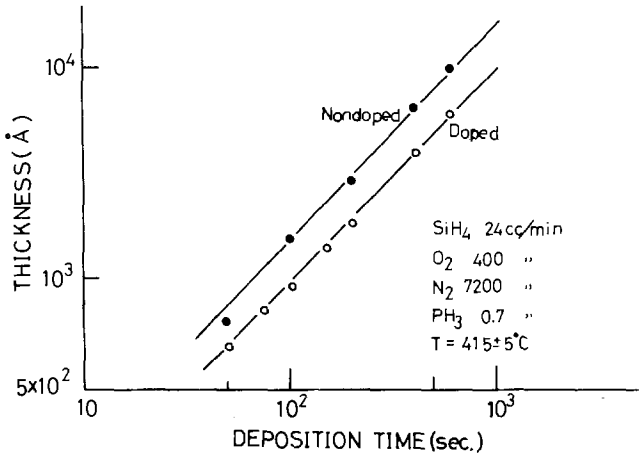


Fig. 3. Deposition time dependence of SiO_2 and PSG film thicknesses.

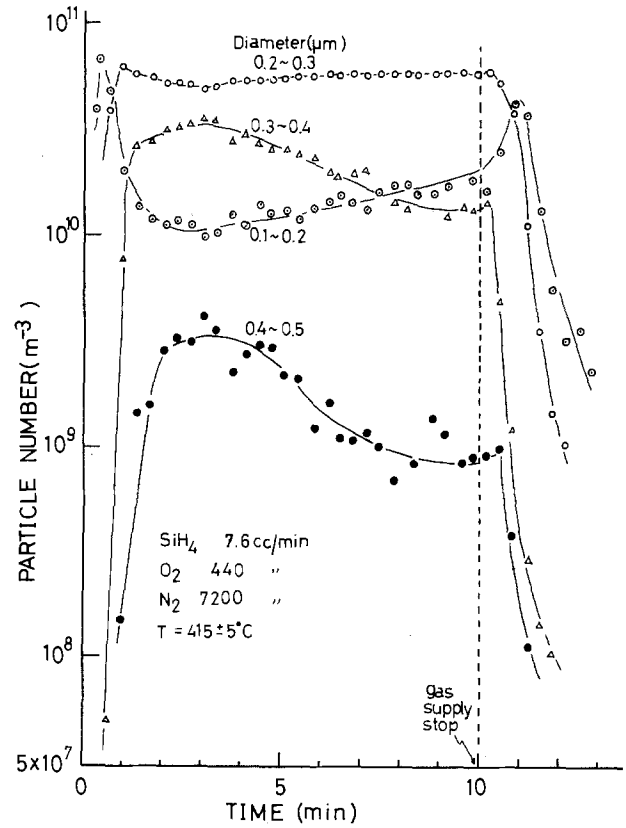


Fig. 4. Time variations of the individual particle sizes at 415°C

in number, then drastically reduced. The total particle number was independent of reaction time, contrary to the individual particle number distribution. The particles of 0.2-0.3 μm diam approximately dominate the total particle number. On the other hand, the larger particles contribute less to the total number.

Temperature dependence of particle distribution.—The substrate temperature was raised while maintaining the other experimental conditions at the same levels as those shown in Fig. 4. Then, the particles in regions above 0.3 μm diam numerically increased and the smaller particles decreased as depicted in Fig. 5. The total particle number also slightly increased under these conditions. The rate of each particle number variation with time was larger at 450° than 410°C.

This temperature dependence of particle distributions at temperatures between 210° and 500°C is illustrated in Fig. 6. The particles in the 0.4-0.5 μm

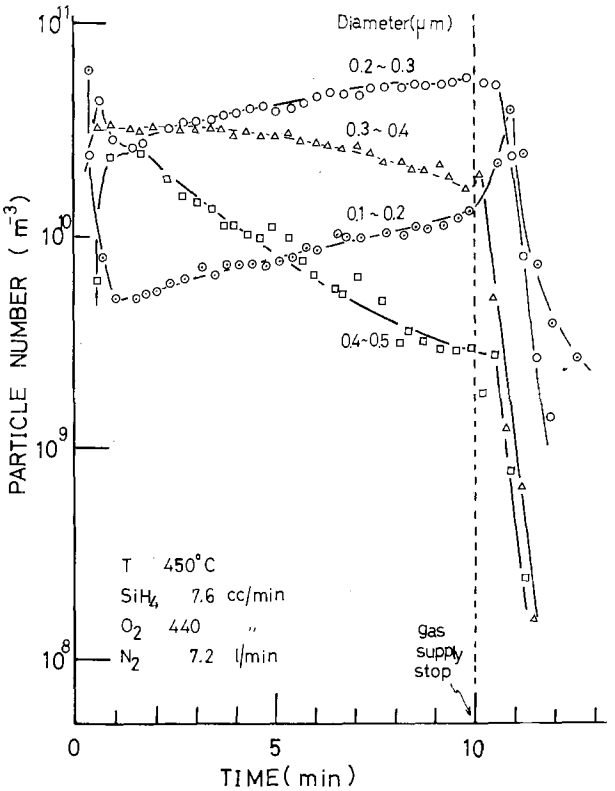


Fig. 5. Time variations of the individual particle sizes at 450°C

diam range were eliminated because their number at low temperatures were beyond the LPM sensitivity limit. The results for two points (3 and 9 min after the gas supply) are plotted in Fig. 6 to enable investigation of the time variation of the temperature dependence. No characteristic difference, however, was found between the two points. Small particles of 0.1-0.2 μm diam steadily increased in number with lowering temperature. The number of 0.2-0.3 μm diam particles showed no definite temperature dependence. The large particles in the 0.3-0.4 μm diam range also showed no large temperature dependence at temperatures higher than 400°C. However, at temperatures lower than 400°C, the number of the large particles was reduced with the lowering in temperature.

Reactant and dopant concentration dependences of particle distributions.—Baliga and Ghandi (2) reported that the deposition rate of SiO_2 films is proportional to the square root of O_2 flow rate at O_2/SiH_4 ratios less than 10. As this ratio is taken above 10, the deposition rate is lowered with the increase in O_2 flow rate. Recently, Shibata and Sugawara (3) made a detailed study of this phenomenon for PSG. It was found that the O_2 flow rate dependence of the deposition rate varies for different substrate temperatures. In order to investigate the influence of this reactant concentration on particle distributions, the O_2 flow rate was varied from 100 to 1000 cm^3/min while keeping the other conditions constant. As a result, the large particles of 0.3-0.5 μm diam decreased at a rapid rate with increasing the O_2 flow rate as shown in Fig. 7. This result resembled the case of the film formation, whereas the small particle number was almost constant or gradually increased with the O_2 flow rate.

When a small amount of PH_3 was added to the reactant gas as a dopant, the SiO_2 film deposition rate steeply decreased, as indicated by Shibata and Sugawara (4). The deposition rate gradually increased with the amount of PH_3 after the initial steep rate reduction. In the case of particles dispersed in the reactor, the large particles of 0.3-0.4 μm diameter also showed a tendency of a decrease-minimum-increase in number with the PH_3 flow rate (Fig. 8). The PH_3 concentration giving the minimum particle number was not the same as that for the minimum film deposition rate. The PH_3 concentration for the

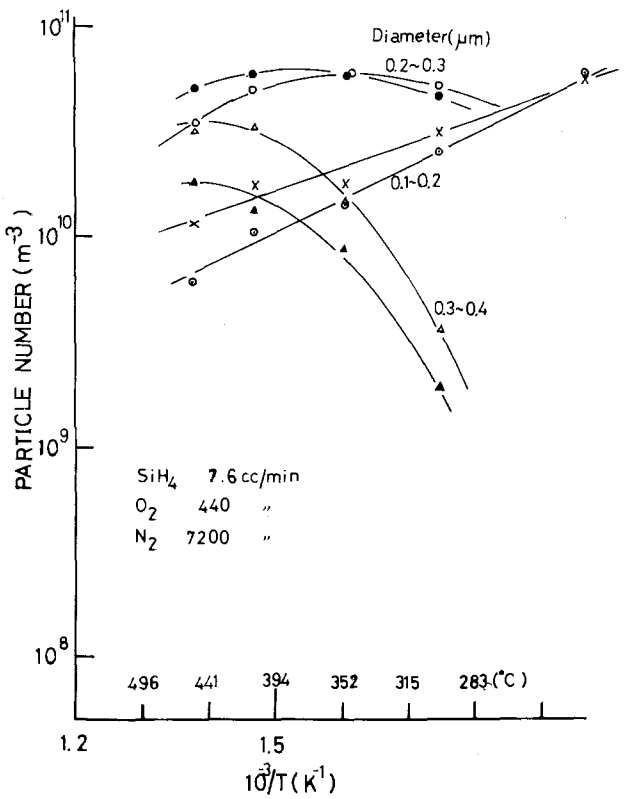


Fig. 6. Temperature dependences of the individual particle sizes at two time points during the reaction period. (○ ⊙ △), 3 min after the reaction start; (● × ▲), 9 min after the reaction start.

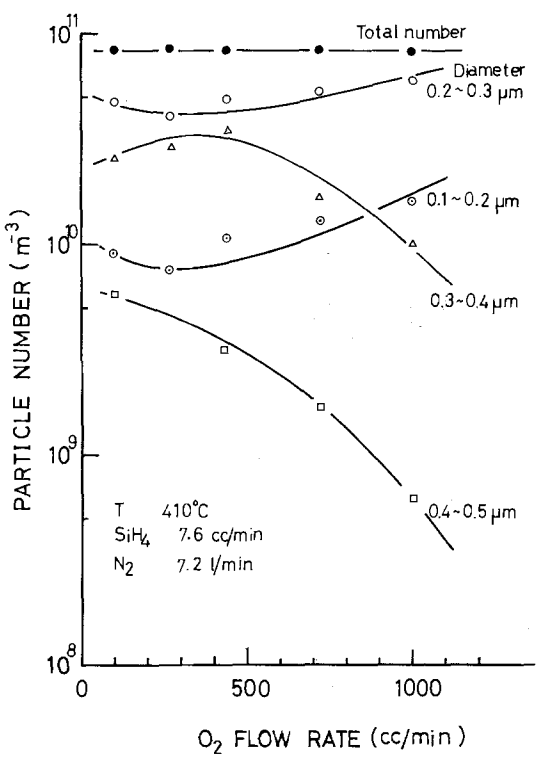


Fig. 7. Oxygen flow rate dependences of the individual particle sizes at 3 min after the reaction start.

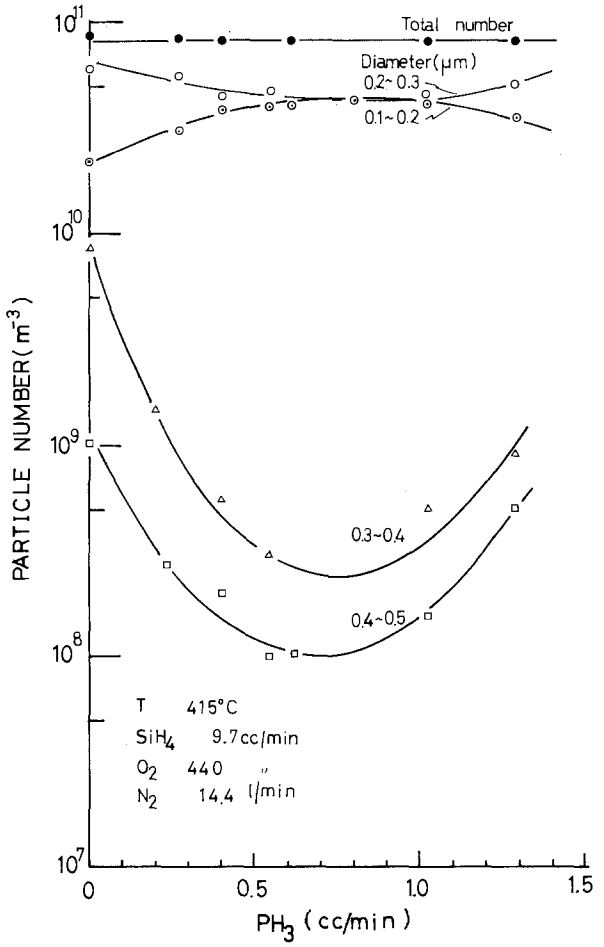


Fig. 8. Phosphine effects on the particle size distributions at 3 min after the reaction start.

minimum particle number was higher than that for the minimum film deposition rate. However, the small particles did not effectively change with the addition of PH_3 as shown in Fig. 8. The total number of particles was also almost completely independent of PH_3 concentration.

Discussion

SiO_2 particle formation.—The elementary processes determining the size distribution of particles are chemical reaction collision and sticking (coagulation) of each particle, and deposition of particles on the cooled reactor wall. Chemical reaction growth of particles proceeds at steady state, likewise the SiO_2 film formation on a Si wafer. This is because there is no basic difference in the chemical reaction between the particle growth and film formation. Accordingly, the chemical reaction growth cannot explain the time variation of particle number.

Consequently the coagulation and deposition of particles are taken into account for the particle variation in number with time. The coagulation is considered first. Under certain experimental conditions, the large particles diminished in number and then vanished as illustrated in Fig. 9. In the figure, the variation of 0.1-0.2 μm particle number with time is in contrast to that of 0.2-0.3 μm particles; when one increases in number, the other decreases. From this result, particle nucleation is considered assuming that 0.2-0.3 μm particles can be formed by the coagulation of two 0.1-0.2 μm diam particles. Therefore, the number of 0.1-0.2 μm particles before collision can be estimated by the sum of observed 0.1-0.2 μm particles and two times the number of 0.2-0.3 μm particles. This initial number of 0.1-0.2 μm particles does not change with

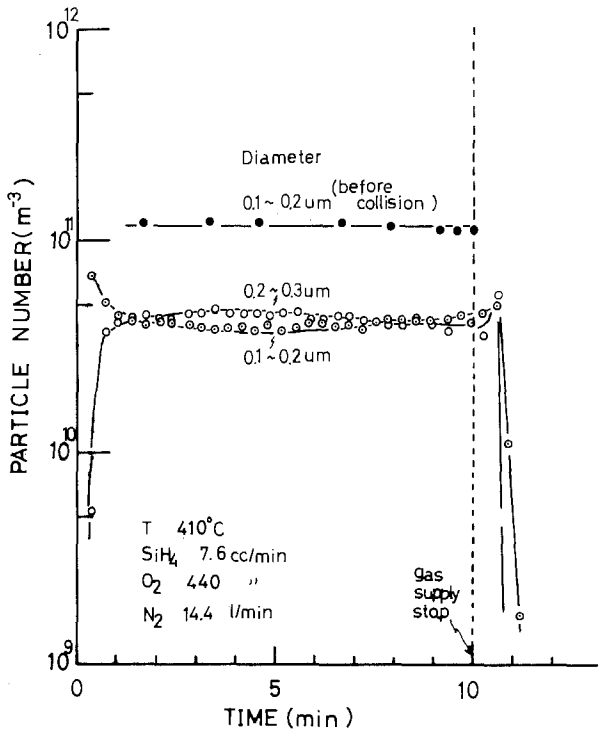


Fig. 9. The small particle size distribution under a selected experimental condition.

time as shown in Fig. 9. As previously noted in Fig. 4, only 0.1-0.2 μm particles are dominant in the reactor immediately after the reactant gases are introduced. Consequently the number of 0.1-0.2 μm particles before collision takes place is considered to represent particle nucleation. If this model approximates the actual conditions, 0.1-0.2 μm particles are dominant in the reactor under particular experimental conditions which result in few particle collisions. Thus, they do not change in number with time. In fact, this phenomenon occurred when the reactant gases were very diluted, as indicated in Fig. 10. This cor-

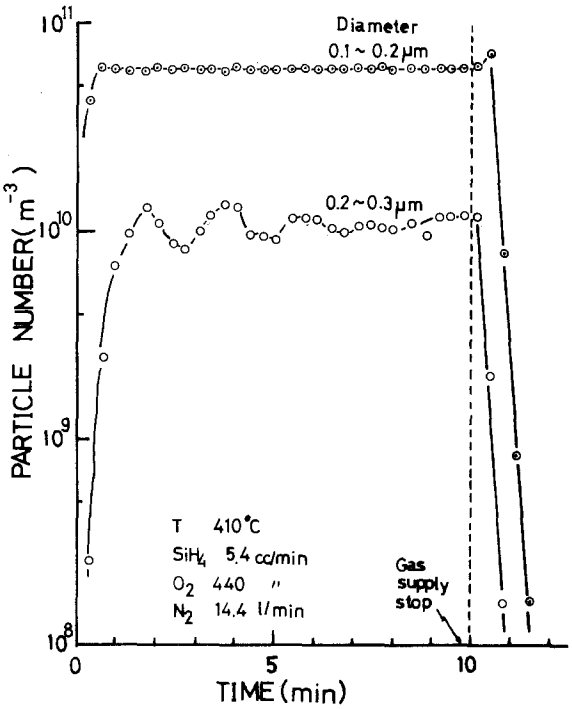


Fig. 10. Domination of the 0.1-0.2 μm diam particles

respondence between the number of 0.1-0.2 μm particles and particle nuclei is established on the assumption that these particles are single particles.

The radii of all particles generated at the reaction start would be the same and constant, R. These particles move along the laminar gas flow and come in contact with another particle and become bonded into one particle. The total number of encounters occurring per second, N, is expressed as

$$N \propto n^2 v R^3 \quad [1]$$

where n is the particle concentration and v the velocity gradient in the fluid (9). The gas flow used in this work is laminar, because the Reynolds number is roughly estimated to be on the order of 100. A distinctive feature of Eq. [1] is the rapid rise in number of encounters with increasing particle size. For the rate of change of n, the following expression is obtained

$$\frac{dn}{dt} \propto -n^2 v R^3 \quad [2]$$

Integration of Eq. [2] gives the reduction of particle number with time due to coagulation, which can be expressed as

$$n = \frac{n_0}{1 + (cn_0 v R^3)t} \quad [3]$$

where n is the initial concentration of the particles with R radius and c is the proportional constant in Eq. [2]. The integration is based on the assumption that v is constant with respect to time. Equation [3] indicates that the particle number decreases with time t. This qualitatively accounts for the reduction of 0.1-0.2 μm particles in number over the first 3 min after the reaction starts, as shown in Fig. 4. During this time, 0.2-0.5 μm particles are formed by coagulations of small particles. After this particle formation period, the large particles with 0.3-0.5 μm diam decrease in number according to a formula similar to Eq. [3].

The above discussion is based on the suppositions that the particles are spherical and that the particle collisions occur between the same size particles (Eq. [1]). However, the phenomena occurring in the reactor are more complicated. This complication results in the fact that 0.1-0.2 μm particles gradually increase in number after a drastic reduction at the beginning of the reaction, as seen in Fig. 4. This is partly because collisions occur among various sized particles.

Another reason for the complication is that the particles are deposited on the cooled wall of the reactor. Particular experimental conditions can maintain an equilibrium between formation and reduction processes of certain particles due to coagulation and deposition. This resulted in the fact that no variation in 0.2-0.3 μm particle number with time was noted in Fig. 4 and 9.

A more detailed theory and closer examination of particle behavior are necessary for a more detailed analysis and discussion. However, presently, both detailed theory and examination are not available because of theoretical difficulty and a lack of adequate measurement techniques.

Temperature effect on the particle formation.—Clarification of the effect of temperature on particle formation in the CVD reactor is extremely complicated, since the bell-jar wall is water cooled and then the gas temperature varies with the distance from the substrates. The sampling nozzle was placed as close to the substrates as possible so that the gas was pumped up around the substrates as mentioned previously. However, it remained unclear what region of the gas was sampled. From this view point, the real gas temperature was unknown, and therefore the data obtained did not show a definite or true temperature dependence of particle size distribution. Therefore, the data only indicate the particles generated when the sample holders are kept at some temperature. Gas temperature, however, goes up with holder temperature, indicating that particle distribution varies with substrate temperature.

Accordingly to Volmer and Weber (10) and Frenkel (11), the nucleation rate, Γ, for particle condensation from vapor is given in a formula similar to the rate constant in Eyring's absolute rate theory, $\Gamma = A \exp(-\Delta E/kT)$. If this equation is applicable to particle formation, the small particles, especially 0.1-0.2 μm particles, increase in number with increasing gas temperatures. However, the obtained results (Fig. 6) are apparently contrary to this prediction. This is due to neglecting the temperature dependence of particle coagulation. This is not taken into account because analysis of particle collision rates in the transition regime is accompanied by difficulties in specifying particle mobilities (9). Coagulation in a gas flow system would be activated by increasing gas temperature similarly to the case in a stagnant system. Then, if the increase in coagulation is greater than the particle nucleation, the small particles decrease in number with gas temperature; whereas the large particle number increases. The results shown in Fig. 6 are qualitatively consistent with this. Since medium size particles, 0.2-0.3 μm diam, are maintained in equilibrium between particle formation and reduction as described previously, their temperature dependence would be small in the temperature range studied.

Reactant and dopant effect.—From the viewpoint of chemical kinetics, the nucleation rate described above has a parameter, A, which includes a frequency factor, meaning a statistical collision probability of reactant gas molecules. Accordingly, particle nucleation is generally activated with increasing the O_2 flow rate. The increase in number of small particles with the O_2 flow rate is partly caused by this O_2 flow rate effect. On the other hand, the reason for the decrease of large particles in number with the O_2 flow rate is possibly that the O_2 gas inhibits the particle coagulation at high O_2/SiH_4 ratios.

The addition of PH_3 to the reactant gas also inhibits the coagulation of the particles. This effect induces a reduction of the large particles with the PH_3 flow rate in the low PH_3 concentration region. The small particle number before coagulation (not illustrated in Fig. 8) also changed slightly in a manner similar to the large particle variation. Although these particle behavior characteristics caused by PH_3 addition are similar to the effect of PH_3 on the SiO_2 film formation rate, the detailed effect and mechanism in SiO_2 formation is not well understood at present.

Summary and Conclusions

The SiO_2 particles generated in the CVD reactor are distributed in various sizes. The individual size particles vary in number with reaction time. Large particles, greater than 0.3 μm diam, decrease in number with time, while smaller particles increase or do not change in number. The particle size distribution is affected by substrate temperature (gas temperature) and the reactant and dopant concentrations. These experimental parameters have a greater effect on the 0.3-0.5 μm particles than on the 0.1-0.2 μm particles. Larger particles decrease in number with decreasing temperature and increasing in flow rates of O_2 and/or PH_3. These behavior characteristics in the CVD reactor appear to be caused by the nucleation and coagulation of particles.

In the present paper, only the particle distribution is discussed. The correlation between SiO_2 film characteristics and particles will be reported in the near future. In part II of this study, it is emphasized that

the pin holes in the films are caused, especially, by the 0.3-0.5 μm diam particles.

Acknowledgment

The authors wish to thank Mr. Shinobu Hase for his assistance in the measurements of particle distributions.

Manuscript submitted March 9, 1977; revised manuscript received July 5, 1977.

Any discussion of this paper will appear in a Discussion Section to be published in the June 1978 JOURNAL. All discussions for the June 1978 Discussion Section should be submitted by Feb. 1, 1978.

Publication costs of this article were assisted by Hitachi, Limited.

REFERENCES

1. N. Goldsmith and W. Kern, *RCA Rev.*, **28**, 153 (1967).
2. B. J. Baliga and S. K. Ghandi, *J. Appl. Phys.*, **44**, 990 (1973).
3. M. Shibata and K. Sugawara, *This Journal*, **122**, 155 (1975).
4. M. Shibata and K. Sugawara, *ibid.*, **122**, 157 (1975).
5. J. Middelhoek and A. Klinkhamer, in "Chemical Vapor Deposition, Fifth International Conference," J. M. Blocher, Jr., H. E. Hinterman, and L. H. Hall, Editors, pp. 19-29, The Electrochemical Society Softbound Symposium Series, Princeton, N. J. (1975).
6. W. Kern, G. L. Schnable, and A. W. Fisher, *RCA Rev.*, **37**, 3 (1976).
7. C. Roth, J. Gebhart, and G. Heigwer, *J. Colloid Interface Sci.*, **54**, 265 (1976).
8. K. Suda, Unpublished.
9. V. G. Levich, "Physicochemical Hydrodynamics," chap. V, Prentice Hall, Inc., Englewood Cliffs, N. J. (1962).
10. M. Volmer and A. Weber, *Z. Phys. Chem.*, **119**, 277 (1926); M. Volmer, *Z. Elektrochem.*, **35**, 555 (1929); *ibid.*, **35**, 557 (1929).
11. F. Frenkel, "Kinetic Theory of Liquids," Clarendon Press, Oxford (1946).

The Deformation of Polycrystalline-Silicon Deposited on Oxide-Covered Single Crystal Silicon Substrates

Takaya Suzuki, Akio Mimura, and Takuzo Ogawa

Hitachi, Limited, Hitachi Research Laboratory, Hitachi, Ibaraki 319-12, Japan

ABSTRACT

The cause of the bowing of wafers with thick polycrystalline-silicon layers deposited by the hydrogen reduction of trichlorosilane has been studied. High temperature dilatometer measurements show that the expansion coefficient of the polycrystalline-silicon layer in the temperature range 100°-900°C is 2.3-4.2 $\times$ 10^{-6}°C^{-1}, and that the polycrystalline-silicon layers contract perpendicularly to the direction of growth at temperatures higher than about 1000°C. The experimental data indicate that the bowing of wafers is caused by the intrinsic tensile stress generated by the contraction of the polycrystalline-silicon layer buried behind the advancing surface of the growing layer, and not by the the thermal stress generated by the difference in the thermal expansion coefficients between the grown layer and the substrate. This contraction of the polycrystalline layer may be induced by a mechanism similar to sintering.

The use of polycrystalline-silicon films for the fabrication of semiconductor devices has received considerable attention in recent years. Especially, thick films of 200-500 μm deposited by chemical vapor reaction have been used as mechanical supports in the fabrication of dielectrically isolated, silicon integrated circuits. However, when such thick films or layers of polycrystalline-silicon are deposited on wafers, bowing can be observed. This severe macroscopic deformation creates undesirable effects to further processing. The difference between the coefficients of thermal expansion of polycrystalline-silicon layers and of single-crystal silicon substrates has been considered the probable cause of the bowing (1). This has not been confirmed, however, because no data on the coefficient of thermal expansion of polycrystalline-silicon layers have been available. Recently, Kamins (2) reported that the incidence of degradation was sporadic, and that the bowing was related to the inclusion of trace quantities of oxygen in the structure of the polycrystalline-silicon layers. But, on the other hand, it has been reported that compensation for wafer bowing is possible through doping with a small amount of oxygen in the polycrystalline-silicon during deposition (3). As described above, a clear explanation has not been made yet as to the cause of the bowing observed in wafers with polycrystalline-silicon layers.

Key words: polycrystalline-silicon layer, bowing, expansion, contraction, sintering.

In this paper we report the results of an experimental study on the cause of the bowing, and show that the bowing is due to the contraction of the polycrystalline-silicon layers originating from a mechanism analogous to sintering. The sintering takes place at the high temperatures used for the growth reaction.

Experimental Method

Polycrystalline-silicon layers with a thickness between 60 and 500 μm were deposited in a conventional, vertical-type, rf-heated, epitaxial reactor by the hydrogen reduction of trichlorosilane ($SiHCl_3$) at 1100°-1260°C. No doping impurities were intentionally added during the deposition. Substrates (50 mm diam) on which the polycrystalline-silicon was deposited were thermally grown oxide-coated, n-type (10-15 Ω-cm), single crystal silicon wafers with a thickness of 300 $\pm$ 10 μm and with a surface orientation of <100>. The substrate silicon was coated with 1.7 μm thick thermally grown oxide.

Figure 1 shows an example of a polished and Sirtl-etched cross section of a thick (220 μm) polycrystalline-silicon layer grown at 1200°C. It can be seen that

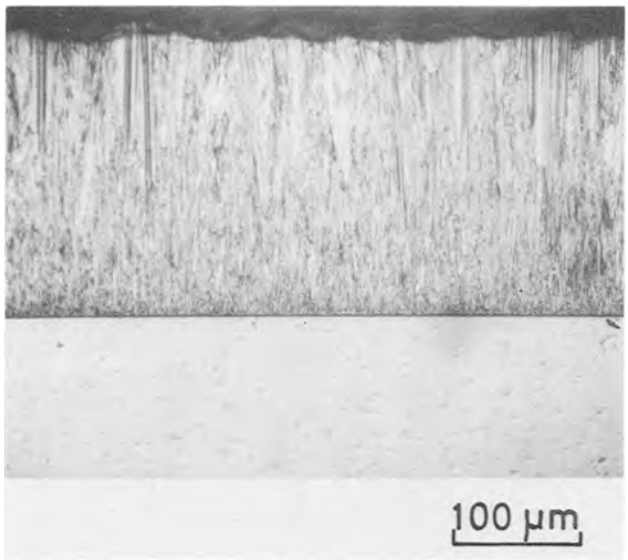


Fig. 1. Cross section of a thick polycrystalline-silicon layer grown on an oxide-covered single crystol substrate.

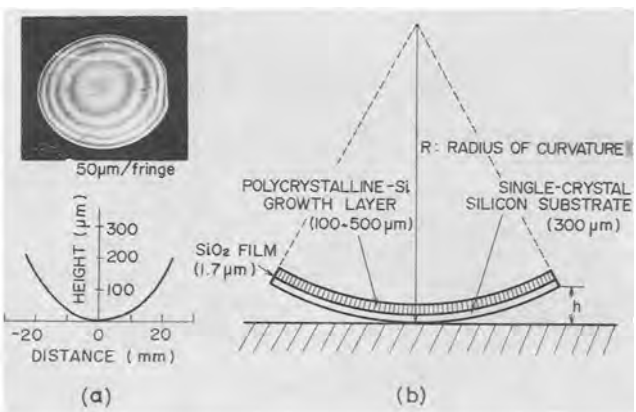


Fig. 2. Bowing of wafer with thick polycrystalline-silicon layer: (a) A typical interference pattern of the deformation; (b) Schematic illustration of the bowing.

the polycrystalline-silicon layer has a columnar grain structure. X-ray diffraction studies have shown that a <110> texture predominates.

Figure 2(a) shows a typical interference pattern of the deformation which was observed with a commercial flatness tester (Speedlap Check-Flat). The polycrystalline-silicon was deposited at 1200°C to a thickness of 400 μm. The polycrystalline-silicon layer side of a wafer is always concave, as is shown schematically is Fig. 2(b). In the following discussion, the degree of bowing will be expressed by the reciprocal of the radius of curvature R calculated from the deviation h from a flat plane 50 mm in length, assuming that the bowed wafer is one part of the surface of a sphere. The deviation h was measured with a surface measuring instrument (DEKTAK).

In an effort to identify the cause of wafer deformation, bowing was examined by measuring small changes in the length of the polycrystalline-silicon layer due to expansion or contraction at temperatures which ranged from 100° to 1260°C. The small changes in length at high temperatures were measured with a dilatometer (Rigaku Denki, Type 8003H) with a differential transformer. Measured samples of the polycrystalline-silicon layer were prepared by etching off both the single crystal silicon substrate and the silicon oxide film. They were cut to the size shown in Fig. 3. The amount of expansion or contraction perpendicular

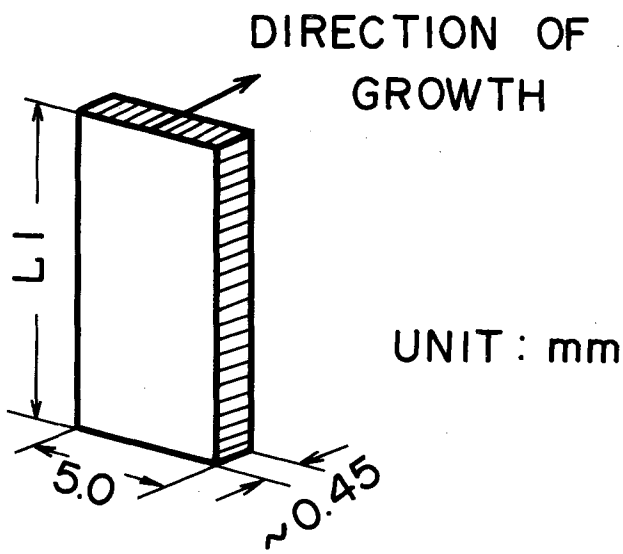


Fig. 3. Polycrystalline-silicon sample used for measuring the amount of expansion or contraction at high temperatures.

to the growth direction was measured. A high purity transparent quartz was used as a reference sample. The thermal expansion coefficient of the quartz is about one order of magnitude smaller than that of single crystal silicon. The load for holding the samples was less than 10 g/mm² which is much smaller than either the yield stress or nucleation stress of dislocation in single crystal silicon (4). The oxygen content of the high purity (99.999%) nitrogen or argon which was used as the ambient gas in these measurements was monitored, and was always less than 2.0 ppm.

Results and Discussion

Bowing of wafers with polycrystalline-silicon layers. —The incidence of degradation was not sporadic. Figure 4 shows the influence of the thickness of the polycrystalline-silicon layers on the bowing. The degree of bowing, $1/R$, increases monotonically with the thickness of the polycrystalline-silicon layers. The tendency of the monotonic increase in the degree of bowing $1/R$ cannot be explained by mismatches of the thermal expansion coefficients. Figure 5 shows the influence of growth temperature on the bowing. As the growth temperature decreases, the degree of bowing $1/R$ shows

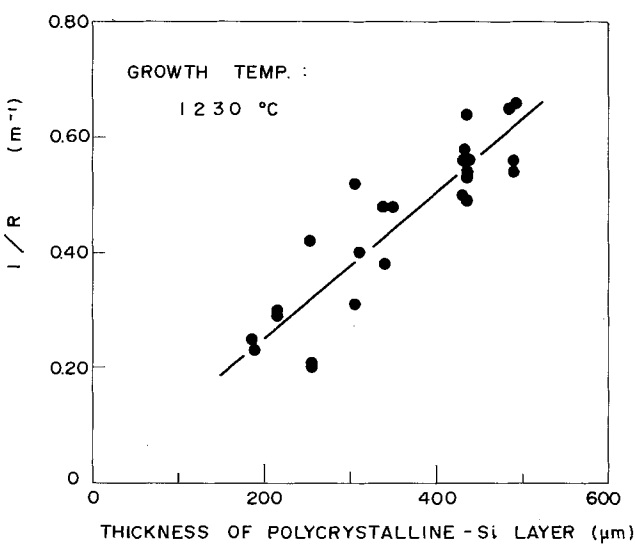


Fig. 4. Influence of thickness of polycrystalline-silicon layer on wafer curvature.

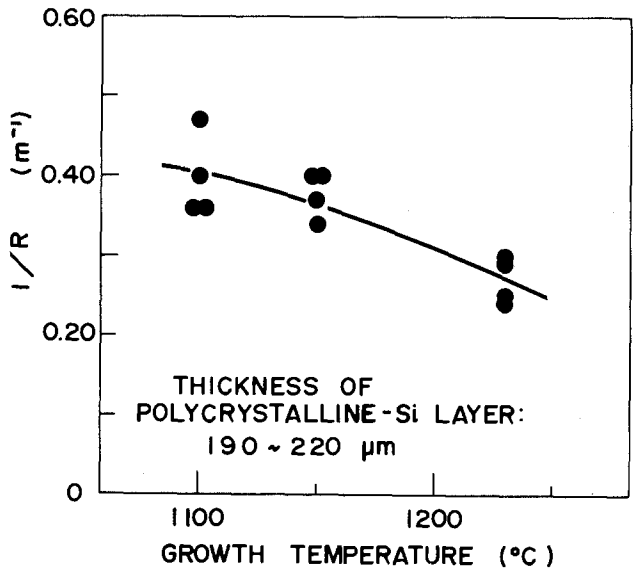


Fig. 5. Influence of growth temperature on wafer curvature.

a gradual increase. This tendency cannot be explained by mismatches of the thermal expansion coefficients either. In addition, it is found that the bowing of wafers with polycrystalline-silicon layers increased monotonically when the thickness of the single crystal silicon substrate is reduced by successive etching, and that the degree of bowing reached a maximum when all of the single crystal silicon substrate and the silicon oxide layer are removed and only a polycrystalline-silicon layer remains. The bowing seems to be caused by some internal stress arising from an intrinsic property of the polycrystalline-silicon layer itself.

It was observed after the growth of polycrystalline-silicon that the amount of silicon deposited on the periphery of the back surface of a wafer placed on the susceptor increases as the degree of bowing of the wafer increases. In addition, it was also observed during the growth of polycrystalline-silicon layers that the temperature near the outer edge of the wafer is lower than the temperature near the center of the wafer. These observations indicate that the edges of wafers are already lifting from the susceptor during the growth reaction. Occurrence of bowing during growth was also observed by Kamins (2). Thus, it seems that the layers contract by some internal stress during growth at high temperatures. To test this assumption, the amount of expansion and contraction of the layers perpendicular to the direction of growth at high temperatures was measured using a dilatometer.

Expansion and contraction at high temperatures.— Figure 6 shows a typical example of the measured results of the amount of expansion and contraction of a polycrystalline-silicon sample heat-treated in nitrogen and oxygen atmospheres. The time interval from 0 to 112 min corresponds to the rise in temperature from room temperature to 1200°C at a rate of about 10°C/min, and the time over 112 min corresponds to the heat-treatment process at the constant temperature of 1200°C. As can be seen from this figure, the polycrystalline-silicon sample expands with increases in temperature. However, the progress of the expansion slows and contraction begins to occur in the case of the nitrogen atmosphere when the temperature exceeds about 1000°C. When the temperature reaches 1200°C, contraction continues to proceed even when the temperature is held constant. Heat-treatments in an argon gas atmosphere have given the same results. In the case of the oxygen atmosphere, however, such contractions are not observed.

Figure 7 shows the linear thermal expansion coefficients of polycrystalline-silicon layers in the high temperature region between 100° and 1000°C obtained from expansion curves, such as those shown in Fig. 6, for samples in a nitrogen atmosphere. Although the two curves were both obtained from measurements of samples grown under identical conditions (growth temperature = 1230°C, growth rate = 6 μm/min), there were some differences between them. The measured data for single crystal silicon using the same method of measurement are also shown for comparison. The data for the single crystal silicon agree with the data reported by others (5-7) which were obtained by different methods. The expansion coefficient of the polycrystalline-silicon layer, which is perpendicular to the growth direction, is 2.3-4.2 $\times$ 10^{-6}°C^{-1} in the temperature range 100°-900°C. This is not so different from the values of 2.9-4.5 $\times$ 10^{-6}°C^{-1} for the single crystal silicon. Therefore, it is clear that the main cause of the bowing in wafers with polycrystalline-silicon layers is not the mismatch of the thermal expansion coefficients. It seems that the contraction occurring at temperatures higher than about 1000°C is closely related to the bowing. Therefore, contraction phenomena were examined in more detail.

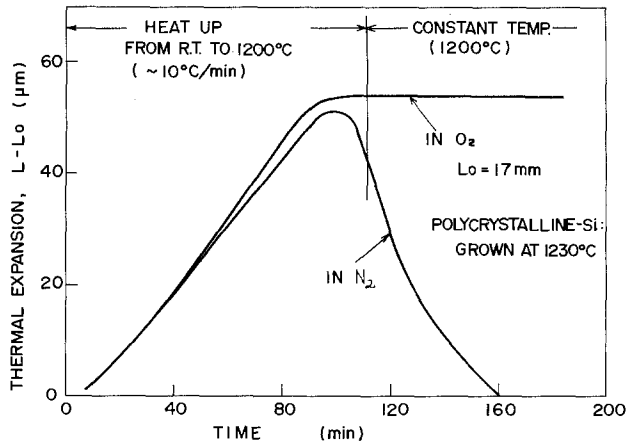


Fig. 6. An example of thermal expansion and contraction of polycrystalline-silicon layers at high temperatures.

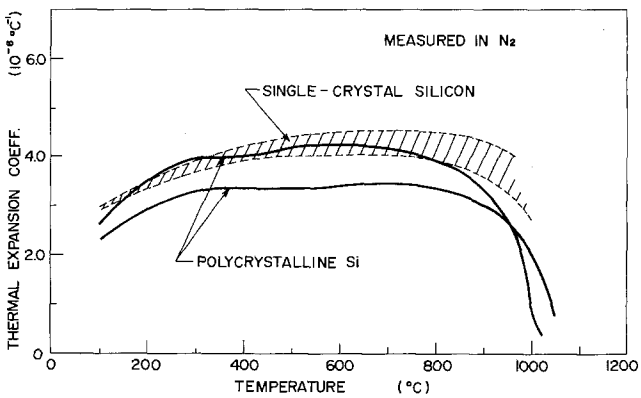


Fig. 7. Thermal expansion coefficient of polycrystalline-silicon layer and single crystal silicon at high temperatures.

Figure 8 shows the influence of the growth temperature of polycrystalline-silicon samples on contraction when heat-treated at 1200°C in an argon atmosphere. The heat-treatment starting point (t = 0) in this experiment was defined as the time when the temperature of the sample, rising at a rate of about 10°C/min, reached 1200°C. The amount of contraction of the sample ΔL was obtained by subtracting the length at each time L from the initial length L_i at t = 0. The contraction of the polycrystalline-silicon layers has a tendency to increase with decreases in growth temperature.

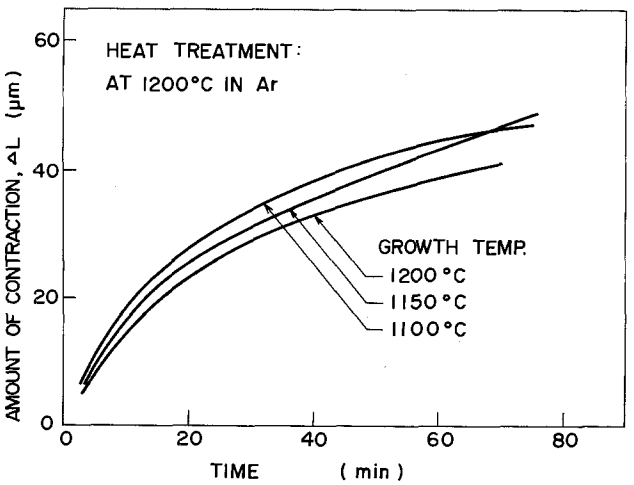


Fig. 8. Influence of growth temperature of polycrystalline-silicon layer on contraction.

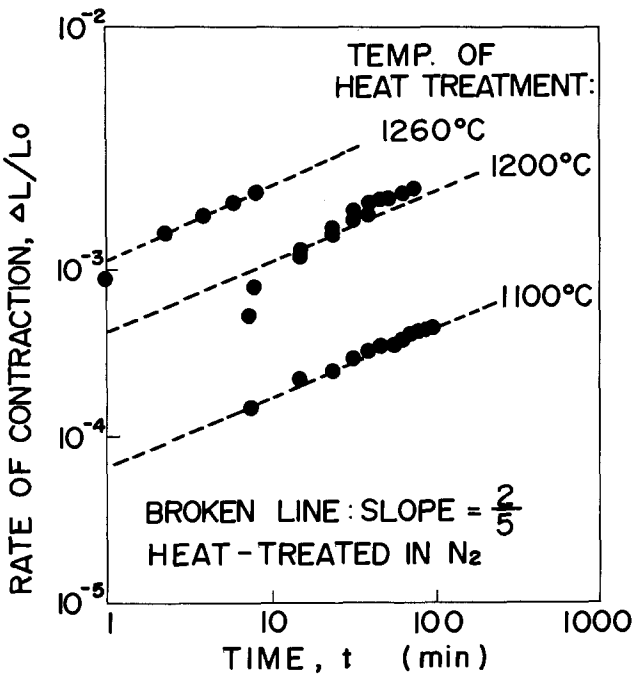


Fig. 9. Time dependence of the rate of contraction at various heat-treatment temperatures.

Figure 9 shows the time dependence of the rate of contraction at different heat-treatment temperatures. The polycrystalline-silicon samples were grown at 1200°C. The measured points fall approximately on the straight broken lines, with slope of 2/5, indicating that the relationship $L/L_0 \propto t^{2/5}$ holds. The rate of contraction increases as the heat-treatment temperature increases.

As described above, polycrystalline-silicon layers contract during heat-treatment in an inert gas atmosphere in a direction perpendicular to the growth direction. This seems to be a phenomenon similar to the sintering process which occurs in metals and ceramics. The rate of sintering is closely related to the mechanism of material transport at grain boundaries. Several types of models and theories of material transport have been reported. Kingery (8) interpreted the contraction during sintering as the decrease of distance between the centers of two neighbor grains in contact. According to his model, substantial material transport into the contact region of the grains occurs and the grains approach one another, because the grain boundary acts as a sink for vacancy diffusion. The rate of decrease in center-center distance l of grains with radius r is expressed as follows

$$\frac{\Delta l}{l} = \left[\frac{20\gamma a^3 D_v}{\sqrt{2}\, r^3 kT}\right]^{2/5} \cdot t^{2/5} \qquad [1]$$

where γ is the surface tension at the contact point, a is the interatomic distance, r is the initial radius of a grain, k is the Boltzmann constant, T is the sintering temperature, t is the sintering time, and D_v is the self-diffusion coefficient. The self-diffusion coefficient D_v is given as

$$D_v = D_0 \exp(-E/kT) \qquad [2]$$

where E is the activation energy.

The relation $\Delta L/L_0 \propto t^{2/5}$ was also observed to hold in the contraction phenomena observed in this experiment, as shown in Fig. 9. Therefore, the contraction of the polycrystalline-silicon layers observed in the heat-treatments in this experiment seems to be induced by a mechanism similar to the sintering considered by Kingery. If the temperature dependence of γ and a is ignored and t is assumed constant, Eq. [1] gives the relation

$$D_v \propto T \cdot \left(\frac{\Delta l}{l}\right)^{5/2}_{t=\text{const}} \qquad [3]$$

Figure 10 indicates a plot of $T(\Delta L/L_0)^{5/2}_{t=\text{const}}$ at $t = 1$ min *vs.* $1/T$. From the slope of this straight line, the activation energy $E = 190$ kcal/mole $= 8.2$ eV is obtained. This value is quite large compared to the activation energy of self-diffusion of Si ($= 112$ kcal/mole $= 4.9$ eV), which was obtained in single crystal silicon (9). Therefore, the mechanism of material transport in the case of the contraction of polycrystalline-silicon is not so simple as to be elucidated only by vacancy diffusion. It is probable that small amounts of impurities in polycrystalline-silicon affect the material transport. For example, as seen in Fig. 6, the presence of oxygen prevents the contraction of polycrystalline-silicon.

On the cause of bowing.—From the experimental results described above, the cause of the bowing of

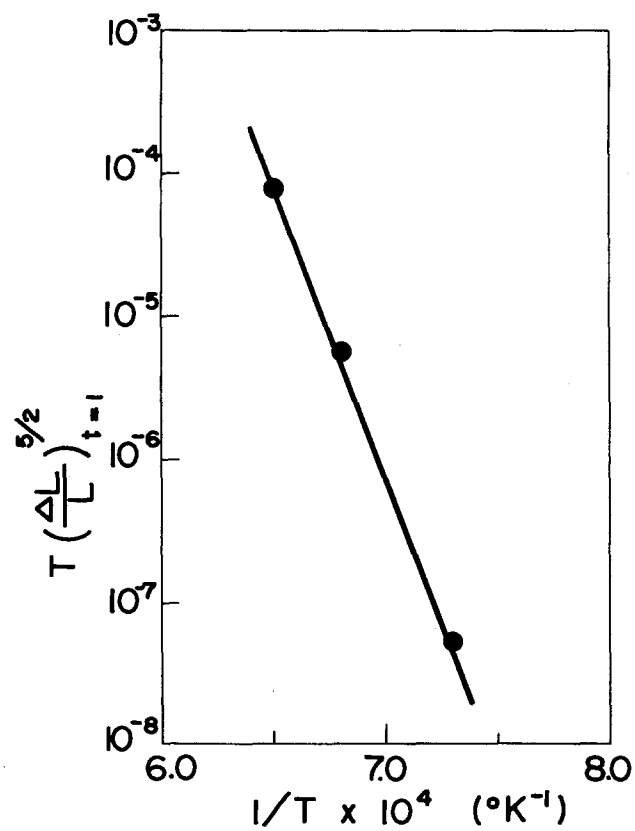


Fig. 10. $T(\Delta L/L_0)^{5/2}_{t=\text{const}}$ at $t = 1$ min *vs.* $1/T$

wafers with a polycrystalline-silicon layer can be considered as follows. The internal stress which causes the bowing of the wafer consists of two terms (10): one of these is a thermal stress due to the difference in the thermal expansion of the layer and the substrate, and the other is an intrinsic stress due to the manner of the growth of the layer. However, it is clear from Fig. 7 that thermal stress is not the dominant cause of bowing, since the expansion coefficient of the polycrystalline-silicon layer is scarcely different from the expansion coefficient of the single crystal silicon substrate. It was observed that the bowing was generated during the growth reaction of the polycrystalline-silicon layer rather than during the cooling process.

The experimental data showed that the polycrystalline-silicon layers contract at temperatures higher than about 1000°C. Therefore, at the high temperatures obtained during the growth reaction, it is believed that the polycrystalline-silicon layer already buried behind the advancing surface of the growing layer is contracting. This contraction may be induced by a mechanism similar to the sintering proposed by Kingery (8). That is, as a result of material transport at the grain boundaries of polycrystalline-silicon, tensile stress, which is thought to be a kind of so-called growth stress (10), is generated within the layer. Since the grain structure of the layers deposited by chemical vapor growth is columnar, such an internal stress is most probably large in a direction perpendicular to the growth direction. The polycrystalline-silicon layer side of the growing wafer is thought to be bowed concavely by this tensile stress during the high temperature growth reaction. Therefore, it would appear that the degree of bowing increases as the growth layer becomes thicker or the growth time longer.

The tendency that the bowing decreases with increasing growth temperature of the polycrystalline-silicon (Fig. 8) can be understood from the following explanation. When the growth temperature increases, the crystal structure of the polycrystalline-silicon layer buried behind the advancing surface of the growing layer becomes more perfect and the grains become larger. This results in a significant reduction in the rate of contraction during growth.

Summary

The degree of bowing of wafers with a thick polycrystalline-silicon layer increases monotonically with the thickness of the polycrystalline-silicon layers and with decreases in growth temperature. This bowing is generated during the growth of the polycrystalline-silicon layer rather than during the cooling process. The amount of expansion and contraction of the layers perpendicular to the direction of growth at high temperatures was measured. It was found that the expansion coefficient of the polycrystalline-silicon layer in the temperature range 100°-900°C is 2.3-4.2 $\times$ 10^{-6} $°C^{-1}$, which is scarcely different from the values for single crystal silicon. It was observed that the polycrystalline-silicon layers contract in a direction perpendicular to the direction of growth at temperatures higher than about 1000°C. From these experimental results, it is concluded that the bowing of wafers is caused by the tensile stress generated by the contraction of the polycrystalline-silicon layer already buried behind the advancing surface of the growing layer, rather than by the thermal stress generated by the difference in the thermal expansion coefficients of the growth layer and the substrate.

Acknowledgments

The authors wish to express their sincere thanks to Dr. E. Kobayashi, Mr. Y. Tokunaga, and Mr. K. Morita for their guidance and encouragement in this work. We also wish to thank Messrs. M. Ura and T. Kamei for many valuable discussions.

Mauscript submitted April 1, 1977; revised manuscript received July 12, 1977.

Any discussion of this paper will appear in a Discussion Section to be published in the June 1978 JOURNAL. All discussions for the June 1978 Discussion Section should be submitted by Feb. 1, 1978.

Publication costs of this article were assisted by Hitachi, Limited.

REFERENCES

1. U. S. Davidson and F. Lee, *Proc. IEEE*, **57**, 1532 (1969).
2. T. I. Kamins, *This Journal*, **121**, 681 (1974).
3. Y. Sumitomo, K. Niwa, H. Sawazaki, and K. Sakai, "Semiconductor Silicon 1973," H. R. Huff and R. R. Burgess, Editors, p. 893, The Electrochemical Society Softbound Symposium Series, Princeton, N.J. (1973).
4. T. Suzuki and H. Kojima, *Acta Metall.*, **14**, 913 (1966).
5. L. Maissel, *J. Appl. Phys.*, **31**, 211 (1960).
6. H. Ibach, *Phys. Status Solidi A*, **31**, 625 (1969).
7. W. M. Yim and R. J. Paff, *J. Appl. Phys.*, **45**, 1456 (1974).
8. W. D. Kingery and M. Berg, *ibid.*, **26**, 1205 (1955).
9. W. R. Wilcox and T. J. LaChapelle, *ibid.*, **35**, 240 (1964).
10. E. Klokholm and B. S. Berry, *This Journal*, **115**, 823 (1968).

Study of Encapsulants for Annealing GaAs

K. V. Vaidyanathan, M. J. Helix, D. J. Wolford, and B. G. Streetman

Coordinated Science Laboratory and Department of Electrical Engineering, University of Illinois at Urbana-Champaign, Urbana, Illinois 61801

R. J. Blattner

Materials Research Laboratory, University of Illinois at Urbana-Champaign, Urbana, Illinois 61801

and C. A. Evans, Jr.

Materials Research Laboratory and School of Chemical Sciences, University of Illinois at Urbana-Champaign, Urbana, Illinois 61801

ABSTRACT

Low temperature photoluminescence and Auger electron spectroscopy have been used to study chemical-vapor deposited SiO_2 and Si_3N_4 layers as encapsulants for high temperature annealing of GaAs. Silicon dioxide or silicon oxynitride layers allow out-diffusion of Ga, while suitably prepared rf plasma deposited Si_3N_4 layers can be used to anneal GaAs with negligible Ga out-diffusion.

Ion implantation is a versatile method of doping semiconductors and is an established fabrication step for many silicon devices (1). Although the use of implantation in the III-V compounds is less widespread, important device applications have emerged. These include the fabrication of light emitting diodes (2), GaAs field-effect transistors, optical waveguides, and detectors (3). Because of the difficulties of selectively doping GaAs or other compound semiconductors by standard diffusion processes as compared with Si, it now appears that implantation will play an increasing role in future device applications of compound semiconductors.

In view of the potential for this doping method, it is important to develop reliable procedures for implantation and annealing in these materials. Ion implantation produces considerable lattice damage which must be annealed out in order to restructure the lattice and activate the implanted impurities. While this procedure is relatively straightforward in Si, annealing a compound semiconductor such as GaAs is more difficult. The incongruent evaporation of Ga and As from GaAs at temperatures in excess of 600°C (4) makes it impossible to anneal bare GaAs samples without surface degradation. It is thus necessary to encapsulate the sample with a suitable dielectric layer or to perform the anneal in a carefully controlled ambient (5, 6). There have been numerous discussions of implantation and annealing in GaAs using encapsulants such as sputtered or chemical-vapor deposited SiO_2 (7), thermally or reactively deposited or sputtered Si_3N_4 (8-10), or sputtered AlN (11). In the present work we have used low temperature photoluminescence (PL) and Auger electron spectroscopy (AES) to investigate the annealing-encapsulation properties of chemical vapor deposited SiO_2 and rf plasma deposited Si_3N_4 layers on GaAs.

It is well known from diffusion experiments in Si that Ga has a very high diffusion coefficient in SiO_2 (12). Gyulai *et al.* (13) have used proton backscattering spectrometry to show that SiO_2 layers on GaAs permit out-diffusion of Ga. Previous low temperature photoluminescence studies have demonstrated the growth of emission bands from GaAs annealed under various conditions. A broad band with a peak near 1.356 eV has been correlated with the outdiffusion of Ga (14). There is other evidence to suggest that this band is related to the incorporation of Cu on Ga sites (15, 16) as Ga atoms are lost due to out-diffusion. In either case, this band can be directly or indirectly attributed to Ga loss. In this work the 1.356 eV photoluminescence band is monitored after annealing with three types of encapsulation, and the encapsulant films are examined for Ga outdiffusion using AES. The three encapsulants studied are silicon dioxide, silicon nitride, and oxygen-contaminated silicon nitride.

Experimental Procedures

The SiO_2 layers used in this study were deposited by thermal oxidation of silane, with the sample maintained at ~450°C (17). All Si_3N_4 layers were prepared by rf plasma deposition from reaction of silane with nitrogen, with samples maintained at ~450°C. Those nitrides labeled A were deposited in a system where silane and nitrogen were mixed prior to initiation of the rf plasma. Those labeled B were prepared by first initiating a nitrogen plasma and then introducing the silane. For type B, the silane is introduced separately from the plasma region, over the surface of the sample. All the anneals were performed in an open tube furnace with a silica liner, in the presence of flowing forming gas (N_2 with 4% H_2).

The photoluminescence samples were pressed into indium-wetted copper heat sinks (18) after removing the encapsulating layer. The sample/heat sink assembly was held at 5°K in a Janis Super-Varitemp gas exchange cryostat. Photoluminescence was excited by the 5145Å line from an Ar-Kr laser. Spectra were recorded using a 0.5m scanning spectrometer and a cooled (77°K) photomultiplier with S-1 response.

Auger electron spectra (AES) and depth profiles were obtained using either a conventional Physical Electronics Industries Model 545 scanning Auger microprobe (SAM) or a custom-built thin film analyzer (TFA) (19). Incident electron beam energies were 6 keV (SAM) or 5 keV (TFA) with typical beam currents of 5 and 70 μA, respectively. In both systems ion sputtering was performed with 2 keV Ar^+ using either stationary beams from two ion guns in lateral opposition (SAM) or an electrically rastered beam from one ion gun (TFA). Both systems were optimized for maximum depth resolution. Comparative studies on the two instruments gave statistically insignificant differences, and they are therefore considered essentially equivalent. Some of the analysis techniques used in this study have been described in detail elsewhere (19). First, an Auger spectrum of the sample surface

is taken prior to sputtering. A second complete spectrum is recorded after an "ion dusting," removing ~20Å, for comparison with the unsputtered surface. Finally, conventional multiplexer depth profiling is performed for the specific elements of interest.

To avoid charging of the dielectric layers during analysis, samples were mounted at grazing incidence to the electron beam (30°). However, in some cases severe charging was observed and no useful analytical information could be obtained. Subsequent examination of such encapsulants by scanning electron microscopy showed a high degree of surface roughness. Data presented here are from samples which did not exhibit charging phenomena.

Results and Discussion

Figure 1 shows the 5°K photoluminescence spectra obtained from GaAs samples annealed at 900°C with various encapsulants. Figures 2-4 illustrate the Auger depth profiles for these encapsulants after the heat-treatment.

Figure 1(a) illustrates that when a sample is annealed with SiO_2 encapsulation, a broad luminescence band is observed with a peak at 1.356 eV. This defect band is related to Ga out-diffusion, as discussed above. Although the SiO_2 films used in this work are considerably better than those studied previously (14), Ga out-diffusion is still evident as shown in Fig. 1(a). This observation is substantiated by the AES depth profile of the oxide on a similarly treated sample (Fig. 2). A detectable Ga signal is observed in the surface Auger spectrum (see inset). Since the sample was encapsulated on all sides during the anneal, the presence of Ga at the surface clearly indicates diffusion of Ga from the substrate through the SiO_2 layer. However, no Ga was detected within the SiO_2 layer itself. Presumably, this is due to a solid solubility of

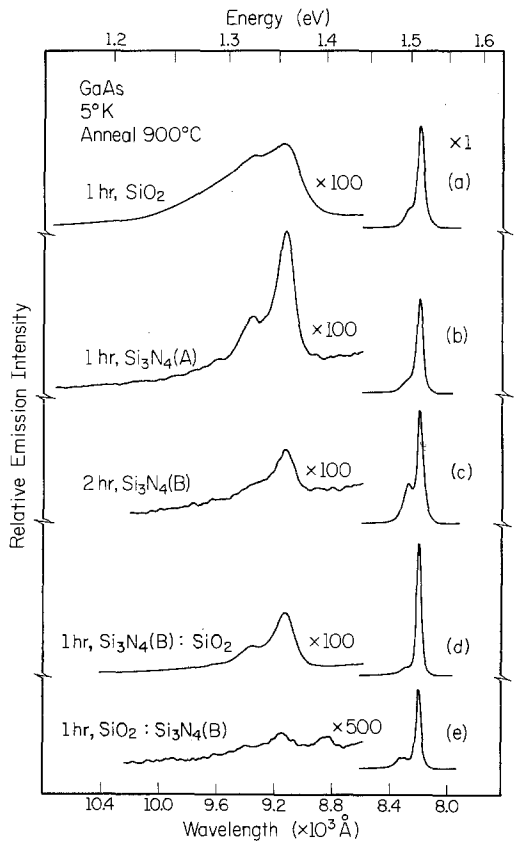


Fig. 1. Photoluminescence spectra from GaAs samples annealed with various encapsulants. The scale factors are indicated relative to the 1.52 eV band-edge peak for each sample.

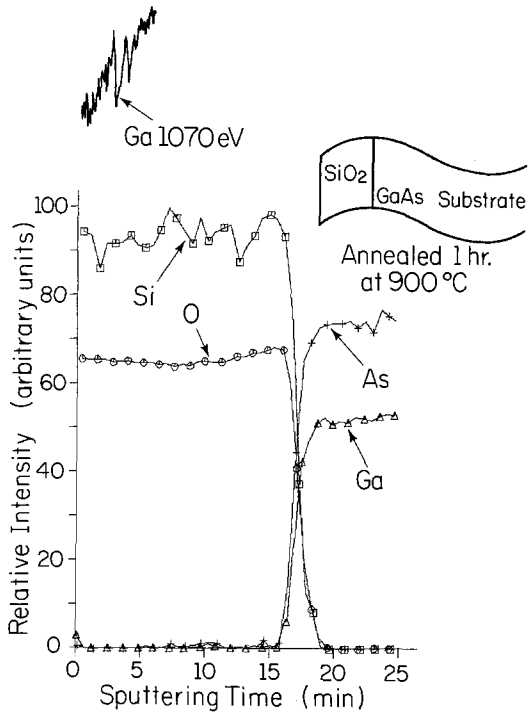


Fig. 2. Auger depth profile obtained from a GaAs sample encapsulated with SiO_2 and annealed at 900°C for 1 hr. The inset illustrates the Ga Auger spectrum observed at the SiO_2 surface prior to sputtering.

Ga in SiO_2 below the Auger detection limit [~0.5 atomic percent (a/o)].

The PL spectrum from a sample annealed with Si_3N_4(A) is presented in Fig. 1(b). This spectrum also clearly indicates Ga loss from the GaAs. The lower energy peaks associated with the 1.356 eV band in Fig. 1 are phonon replicas of the main zero-phonon peak. These peaks are separated by ~36 meV, the LO phonon energy in GaAs (20). Figure 3(a) shows an AES depth profile for a similar sample annealed with Si_3N_4(A) encapsulation. A relatively strong Ga signal is observed at the Si_3N_4 surface and a uniform Ga level is seen throughout the encapsulant. As discussed earlier, Si_3N_4(A) was prepared by premixing silane and nitrogen prior to the formation of the plasma. The AES data also shows the presence of a uniformly high level of oxygen within the film. Both PL and AES data clearly show the out-diffusion of Ga through such nitride layers.

Figure 1(c) displays the PL spectrum obtained from a sample with Si_3N_4(B) encapsulation, annealed at 900°C for 2 hr. A weak 1.356 eV band is seen. In a sample annealed with such an encapsulant for 1 hr, the intensity of the 1.356 eV band was very weak. The absence of a strong defect PL band even after the 2 hr anneal suggests that Si_3N_4(B) effectively suppresses Ga out-diffusion. In AES studies, no Ga signal could be detected either in the surface spectrum or in the depth profile of this nitride (Fig. 3b). It is also interesting to note that the oxygen level in Si_3N_4(B) was low, barely above the detection limit of ~0.1 a/o. This is at least an order of magnitude lower than the oxygen level observed in Si_3N_4(A).

Anneal studies were also carried out using a multilayered dielectric sandwich as the encapsulant. Figure 1(d) shows the PL spectrum obtained when a Si_3N_4(B)/SiO_2 dielectric layer (with SiO_2 in contact with the GaAs) was used as the encapsulant. The 1.356 eV band is observed, although the intensity of this band is weaker than in spectrum 1(a). The AES data (Fig. 4b) failed to show any Ga either at the

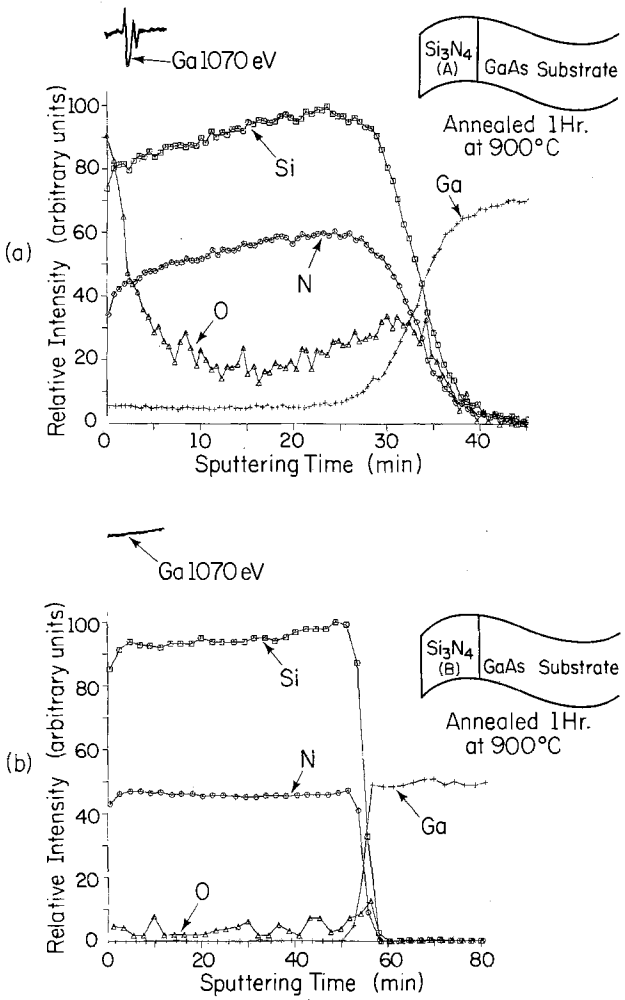


Fig. 3. Auger depth profiles obtained from GaAs samples encapsulated with (a) Si_3N_4(A), and (b) Si_3N_4(B) layers and annealed at 900° for 1 hr. The insets illustrate the Ga Auger spectra at the Si_3N_4 surfaces prior to sputtering.

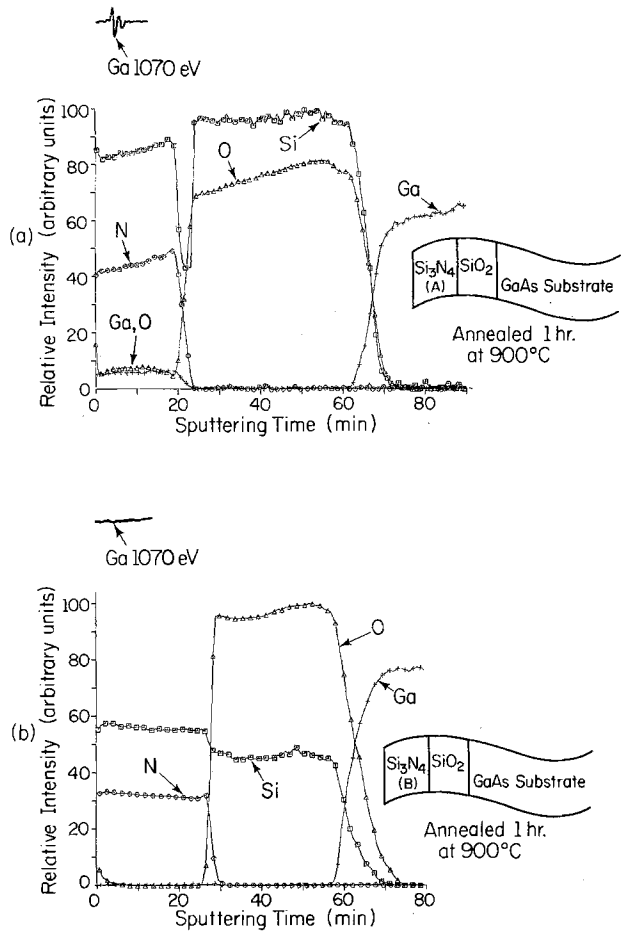


Fig. 4. Auger depth profiles obtained from GaAs samples encapsulated with (a) Si_3N_4(A)/SiO_2, and (b) Si_3N_4(B)/SiO_2 layered dielectrics and annealed at 900°C for 1 hr. The insets illustrate the Ga Auger spectra at the Si_3N_4 surfaces prior to sputtering.

surface or within the dielectric layer. However, when the anneal was repeated with a Si_3N_4(A)/SiO_2 layered encapsulant, AES depth profiles clearly showed the presence of Ga both at the surface and within the nitride layer (Fig. 4a). GaAs samples encapsulated with SiO_2/Si_3N_4(B) were also annealed. As expected, PL (Fig. 1e) and AES data indicated negligible out-diffusion of gallium from the substrate. No Ga pile-up was observed at the oxide-nitride interfaces in any of the cases studied.

These PL and AES studies show that Ga is lost when SiO_2 is used as an encapsulant. Moreover, out-diffusion of Ga is observed when Si_3N_4 layers contain a high oxygen level. We have concluded that oxygen contamination of the nitride film is responsible for the pronounced Ga out-diffusion. The oxygen impurity is distributed throughout the type A nitride layer and is apparently introduced by reaction of silane with the residual oxygen or water vapor in the system. In deposition procedure B, much of the residual oxygen and water vapor reacts with the nitrogen to form oxides of nitrogen and is therefore unavailable for reaction with the silane when it is introduced. The affinity of silane for oxygen is orders of magnitude higher than its affinity for nitrogen. It is thus very unlikely that the oxygen observed in Si_3N_4(A) is free oxygen. The Si_3N_4(A) film is best described as silicon oxynitride. This description is consistent with the fact that the refractive index measured for type A films is ~1.85, which lies between the refractive index of SiO_2 (1.46) and that of the Si_3N_4(B) films (2.18). Differences were also observed in the etch rates of the two types of films. Nitride A etches at a rate of ~3000Å/min in 48% HF, compared with $\lesssim$ 200Å/min for Si_3N_4(B).

Conclusion

In conclusion, it has been shown from low temperature photoluminescence and AES studies that:

1. SiO_2 encapsulant on GaAs permits Ga loss during annealing at 900°C.
2. Attempts to deposit Si_3N_4 layers by premixing silane and nitrogen result in silicon oxynitride films which also permit Ga out-diffusion during annealing.
3. Si_3N_4 layers prepared by introducing silane separately from the nitrogen plasma region allow negligible Ga out-diffusion. Such films can be successfully used to encapsulate GaAs for postimplant annealing.

Acknowledgment

This work was supported by the Office of Naval Research under Contract N00014-76-C-0806, by the Joint Services Electronics Program (U.S. Army, U.S. Navy, and U.S. Air Force) under Contract DAAB-07-72-C-0259, and by the National Science Foundation DMR-76-01058.

Manuscript received June 8. 1977. This was Paper 326 presented at the Atlanta, Georgia, Meeting of the Society, Oct. 9-14, 1977.

Any discussion of this paper will appear in a Discussion Section to be published in the June 1978 JOURNAL. All discussions for the June 1978 Discussion Section should be submitted by Feb. 1, 1978.

Publication costs of this article were assisted by the University of Illinois at Urbana-Champaign.

REFERENCES

1. D. H. Lee and J. W. Mayer, *Proc. IEEE.*, **62**, 1241 (1974).
2. P. K. Chatterjee, B. G. Streetman, D. L. Kuene, and A. H. Herzog, in "Technical Digest of the International Electron Devices Meeting," p. 187, Institute of Electrical and Electronic Engineers, New York (1975).
3. J. P. Donnelly, in "GaAs and Related Compounds," St. Louis 1976 L. F. Eastman, Editor, p. 166, Conf. Series 33b, Institute of Physics, Bristol: London (1977).
4. S. T. Picraux, in "Ion Implantation in Semiconductors and Other Materials," B. L. Crowder, Editor, p. 641, Plenum Press. New York (1973).
5. A. A. Immorlica and F. H. Eisen, *Appl. Phys. Lett.*, **29**, 94 (1976).
6. D. H. Lee and R. M. Malbon, in "Ion Implantation in Semiconductors and Other Materials," F. Chernow. Editor, Plenum Press, New York (To be published).
7. A. G. Foyt, J. P. Donnelly, and W. T. Lindley, *Appl. Phys. Lett*, **14**, 373 (1969).
8. C. O. Bolger, J. P. Donnelly, R. A. Murphy, R. W. Laton, R. W. Sudbury, and W. T. Lindley, *ibid.*, **29**, 123 (1976).
9. F. H. Eisen, B. M. Welch, K. Gamo, T. Inada, H. Muller, M-A. Nicolet, and J. W. Mayer, in "Applications of Ion Beams to Materials," G. Carter, J. S. Colligan, and W. A. Grant, Editors, Conf. Series 28, Institute of Physics, Bristol: London (1976).
10. P. K. Chatterjee, K. V. Vaidyanathan, W. V. McLevige, and B. G. Streetman, *Appl. Phys. Lett.*, **27**, 567 (1976).
11. K. Gamo, T. Inada, S. Krekeler, J. W. Mayer, F. H. Eisen, and B. M. Welch, *Solid State Electron.*, **20**, 213 (1977).
12. A. S. Grove, O. Leistiko, and C. T. Sah, *J. Phys. Chem. Solids*, 25, 985 (1964).
13. J. Gyulai, J. W. Mayer, I. V. Mitchell, and V. Rodriguez, *Appl. Phys. Lett.*, **17**, 332 (1970).
14. P. K. Chatterjee, K. V. Vaidyanathan, M. S. Durschlag, and B. G. Streetman, *Solid State Commun.*, **17**, 1421 (1975).
15. S. Y. Chiang and G. L. Pearson, *J. Lumin.*, **10**, 313 (1975).
16. C. J. Hwang, *J. Appl. Phys.*, **39**, 4307 (1968).
17. R. E. Anderson, D. J. Wolford, and B. G. Streetman, *ibid.*, **48**, (June 1977).
18. N. Holonyak, Jr. and D. R. Scifres, *Rev. Sci. Instrum.*, 42, 1885 (1971).
19. R. J. Blattner, C. A. Evans, Jr., and A. J. Braundmeier, *J. Vac. Sci. Technol.*, To be published.
20. A. Mooradian and G. B. Wright, *Solid State Commun.*, **4**, 431 (1966).

Influence of Temperature on Anodically Grown Native Oxides on Gallium Arsenide

T. Ishii*,[1] and B. Jeppsson

Microwave Institute Foundation, S-10044 Stockholm 70, Sweden

ABSTRACT

A native oxide film is grown on GaAs by anodically oxidizing GaAs in a mixed solution consisting of aqueous tartaric acid and ethylene glycol. A homogeneous oxide film up to 8000Å thick is obtained with a linear thickness-voltage dependence of 19.5 Å/V. The as-grown oxide is highly transparent in the near infrared and the visible light regions. The refractive index is almost constant in the near infrared region, and it weakly depends on the wavelength in the visible light region changing from 1.7 to 1.9. In the u.v. region, the oxide becomes less transparent and is completely opaque for wavelengths shorter than 0.22 μm. The oxide is very stable and almost no detectable changes regarding oxide properties, structure, and composition occur below 350°C. However, the oxide begins to decompose above 350°C first by releasing water. The oxide decomposition most rapidly proceeds around 450°C mainly by vaporizing water and arsenic oxide. It continues up to 700°C, resulting in a pure gallium oxide. The refractive index of the decomposed oxide is fairly constant around 1.5 over the wide wavelength region from visible light to near infrared. The decomposed oxide is believed to be β-Ga_2O_3. By heat-treatment above 650°C, the surface of GaAs becomes rough and a new layer is formed at the oxide-GaAs interface. This interface layer is completely arsenic depleted and has a Ga:O ratio of 2:1. The highest temperature to which the anodically oxidized GaAs can be heat-treated is approximately 650°C. As a means for increasing this temperature limit, a double oxide structure consisting of the anodic oxide film and a SiO_2 film is investigated. By coating GaAs with double oxide films consisting of a 500Å thick anodic oxide film and a 2000Å thick SiO_2 film, GaAs can be heat-treated at 800°C for 2 hr without degradation of the GaAs surface.

With the rapid progress of material and process technology, GaAs is now supplementing Si in the electronic field and is extensively used in microwave, optical, and various functional devices. For many applications, a good native oxide on the semiconductor surface is indispensable, and consequently SiO_2 on Si is the major factor behind the success of Si as an electronic material. For the same reason, a good native oxide on GaAs has long been required.

To obtain a native GaAs oxide, several methods have been suggested such as thermal oxidation (1-4), plasma oxidation (5, 6), galvanic oxidation (7, 8), and anodic oxidation (9-22). As GaAs begins to vaporize the volatile component at rather low temperatures, the anodic oxidation is an interesting low temperature process to obtain the native oxide without dissociating the GaAs.

* Electrochemical Society Active Member.
[1] Present address: Central Research Laboratory, Mitsubishi Electric Corporation, 4-1 Mizuhara, Itami, Hyogo 664 Japan.
Key words: anodic oxidation, spectrophotometry, He backscattering, mass spectrometry.

One of the disadvantages of the anodic oxidation has been the difficulty to grow a thick oxide film. Hasegawa *et al.*, however, succeeded in growing a thick oxide film by anodically oxidizing GaAs in a suitable mixture of a weak carboxylic acid, water, and a polyhydric alcohol (17-19), thereby making this technique of great interest for several applications. This anodic oxidation process is also very interesting because it is highly stable and reproducible.

Several interesting applications of the anodically grown native GaAs oxide have been suggested. The oxide has been used in MOS devices and in several low temperature processes for material and device fabrication (12, 15, 16, 18-21). Although the use of the oxide in high temperature processes has been suggested (14) and some properties of the oxide have been studied (9, 13, 22), the influence of temperature on the structure and the properties of the oxide are at present not fully understood. Detailed knowledge of the temperature characteristics of the oxide is required both when the oxide is used in a process involving elevated temperatures, and when the oxide is an integral part of a device operated at elevated temperatures.

In this paper, we describe the temperature characteristics of the anodically grown native GaAs oxide heat-treated in a N_2 atmosphere up to 800°C. The thickness and the optical properties of the oxide are evaluated using a spectrophotometer. By analyzing the oxide structure using He backscattering techniques, He-induced x-rays, and mass spectrometry, a model for the decomposition of the oxide occurring during heat-treatment is proposed. Because of the sublimation of arsenic from the GaAs surface, heat-treatment of a naked or an anodically oxidized GaAs has so far been limited to below 650°C. Means of increasing this temperature limit to 800°C are investigated.

Anodic Oxidation of GaAs and Characteristics of As-Grown Native GaAs Oxide

Anodic oxidation of GaAs.—Figure 1 shows the experimental setup for the anodic oxidation. A Teflon beaker and a platinum cathode were used. A Teflon separator was inserted between the anode (GaAs specimen) and the cathode. The electrolyte was magnetically stirred during the anodic oxidation.

n-type GaAs wafers of (100) orientation and tin doped with a net donor concentration of (7-10) $\times$ 10^{17} cm^{-3} were used for the experiments. The wafers were thoroughly degreased in trichloroethylene and acetone. An aluminum ribbon was contacted to the back surface of the wafer, which then was fixed on a quartz plate with wax such that the polished surface was exposed to the electrolyte, paying attention not to make any shunt path. Samples were etched chemically in a mixed solution of 3 H_2SO_4:1 H_2O_2:1 H_2O to remove a 20-30 μm thick surface layer. Samples were then dipped in HCl to remove the natural uncontrolled oxide on the surface and were rinsed thoroughly in water prior to anodic oxidation.

GaAs was anodically oxidized in an electrolyte consisting of water, tartaric acid, and ethylene glycol (17-19). The electrolyte consisted of one part of the aqueous solution of tartaric acid and two parts of ethylene glycol. The *p*H adjustment of the electrolyte by a weak base, which is a commonly used technique, was avoided so as not to contaminate the electrolyte. The logarithmic concentration of tartaric acid and the logarithmic resistivity of the electrolyte were linearly proportional to the *p*H value of the electrolyte as shown in Fig. 2(a) and (b), respectively. The aqueous solution of ethylene glycol without tartaric acid showed a *p*H value of 5.45 and a resistivity of 1.78 $\times$ 10^4 Ω-cm.

The anodic oxidation was performed using a constant current method. By controlling the output of a d-c power supply and the resistance of a variable resistor, the bias current was kept constant during the anodic oxidation. The applied voltage was measured between the anode and the cathode. It increased with the growth of the oxide, and the current bias was terminated immediately upon reaching a predetermined voltage. A constant voltage method was avoided because inhomogeneity in the current density and thereby locally high current density on the wafer caused local breakdown in the grown oxide in the very early stage of the anodic oxidation. Current density was determined by dividing the bias current by the exposed sample area.

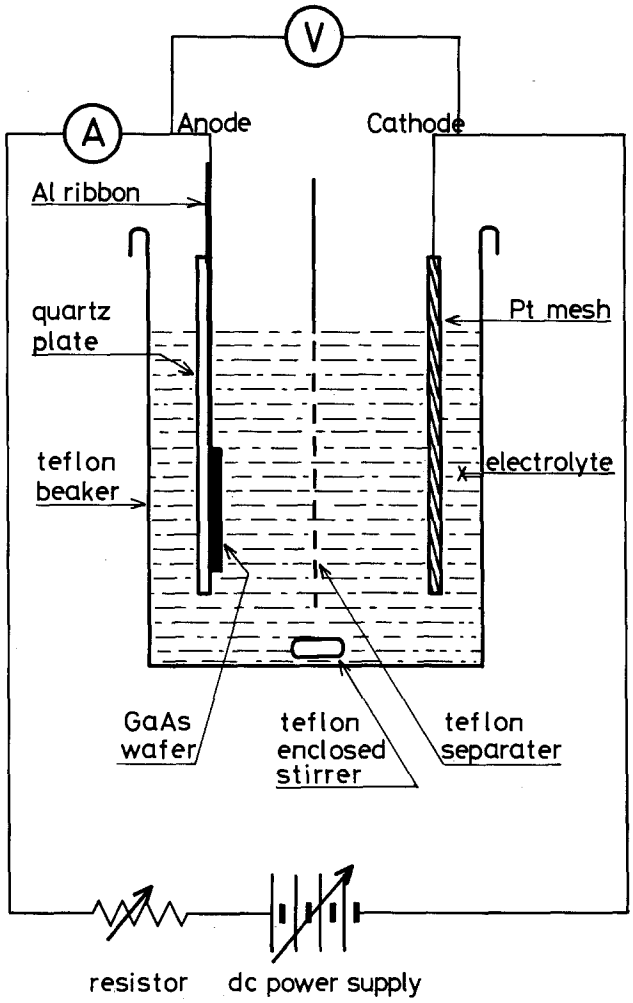
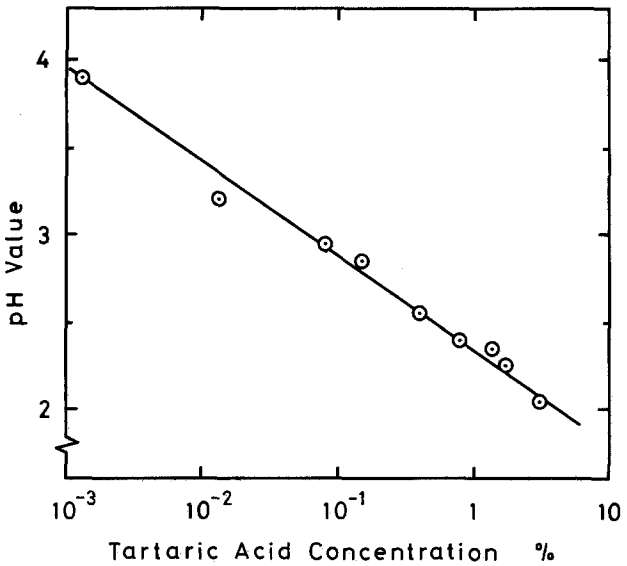


Fig. 1. Experimental setup for anodic oxidation. The anodic oxidation was performed using a constant current method by controlling the output of the d-c power supply and the resistance of the variable resistor. The current bias was terminated immediately upon reaching a predetermined voltage.

Thickness of the oxide was linearly related to the applied voltage as described later. Figure 3(a) shows the relation between the thickness-voltage constant and the concentration of the tartaric acid. The thickness-voltage constant becomes saturated for tartaric acid concentrations above 0.01%. The thickness-voltage constant is also shown as a function of the current density in Fig. 3(b). Except at very low or high current densities, it is almost constant as a function of current density in the range from 0.75 to 3.0 mA/cm^2. The fact that the thickness-voltage constant is almost independent of the composition of the electrolyte and the current density means that excellent stability and reproducibility can be achieved in this process. The change of the current density due to error in measuring the sample area, and the change of the electrolyte composition due to continuous use do not, therefore, seriously affect the thickness of the grown oxide films.

The anodic oxidation became unstable above 150V, accompanied by frequent current spikes when the tartaric acid concentration was more than 3% and/or the current density was higher than 10 mA/cm^2. This



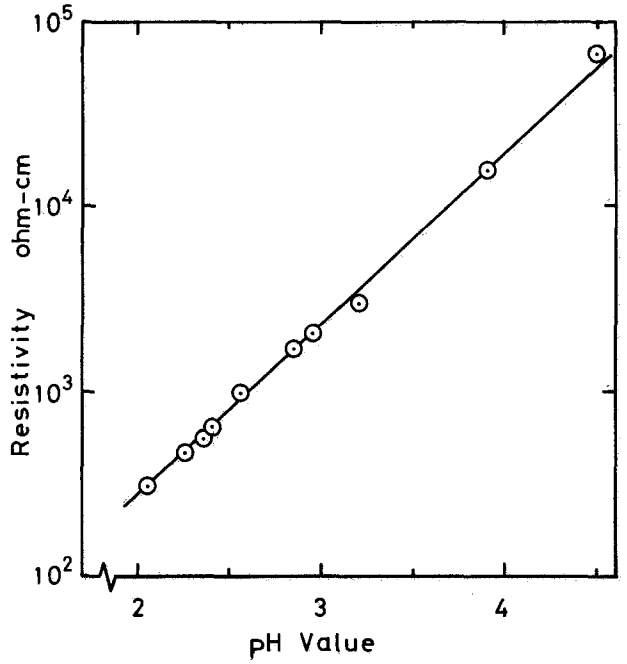
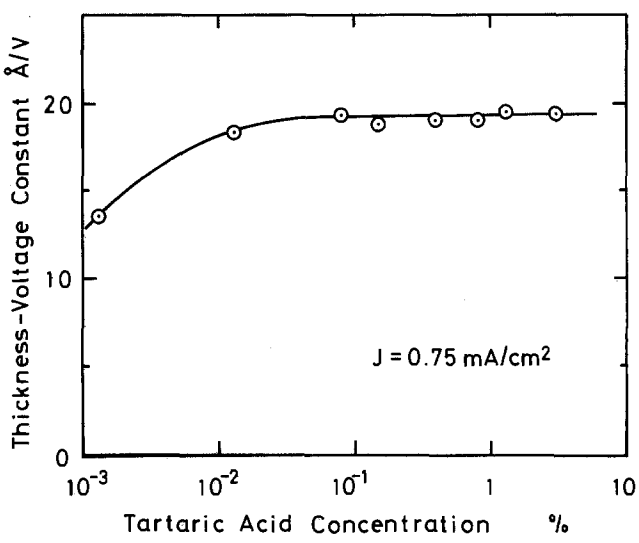


Fig. 2. Plots of logarithmic tartaric acid concentration vs. pH value (a) and logarithmic resistivity vs. pH value (b) of the electrolyte for anodic oxidation. The electrolyte consisted of one part of an aqueous solution of tartaric acid and two parts of ethylene glycol.



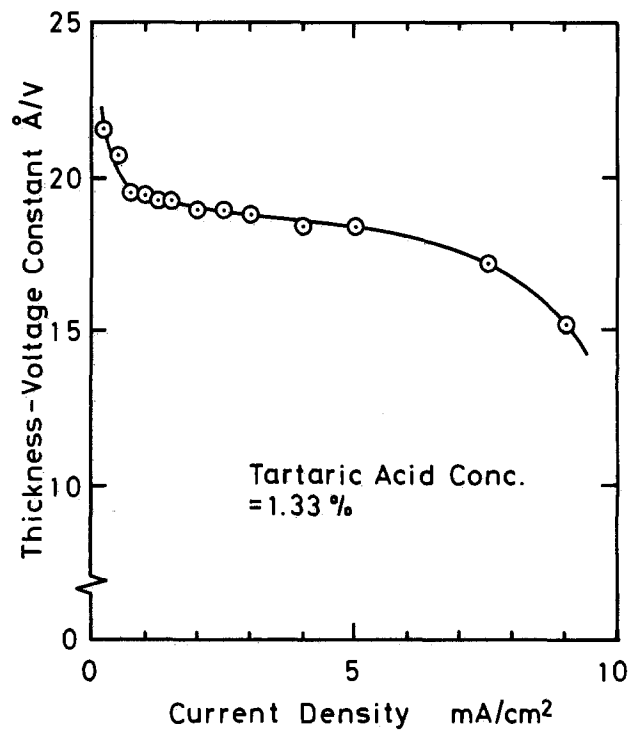


Fig. 3. Thickness-voltage constant as a function of the tartaric acid concentration in the electrolyte (a) and the current density for the anodic oxidation (b).

instability was due to the local breakdown in the grown oxide, which was found to be very similar to the crystal defects in the GaAs in our other experiments.

Figure 4 shows the relation between the applied voltage and the thickness of the grown oxide films. The thickness increased linearly with the applied voltage as already mentioned in other papers (11-13, 17, 21), and the thickness-voltage constant, corrected for by the voltage drop in the bath, was 19.5 Å/V. Anodic oxidation at as high as 380V was possible, and an 8000Å thick oxide film could be obtained when high quality GaAs was used. The homogeneity of the 8000Å thick oxide film was excellent judging from the interference color.

Above 380V the oxides broke down electrically and the anodic oxidation became seriously unstable. At the breakdown points, a salt was formed, which could be removed easily by a strong acid or base leaving, however, deep pits on the GaAs surface.

Optical properties of the as-grown native GaAs oxide.—Optical index and thickness of the anodically grown native GaAs oxides were mainly determined by an optical method using a spectrophotometer. A Perkin-Elmer Spectrophotometer Model 350 covering the wavelength region from 0.195 to 2.7 μm was used. The absolute reflectivity of the virgin surface of GaAs (R_{GaAs}) was measured in the wavelength region from 0.195 to 2.7 μm. The refractive index of the GaAs (n_{GaAs}) was calculated from the reflectivity using the equation

$$n_{GaAs} = \left(\frac{1+\sqrt{R_{GaAs}}}{1-\sqrt{R_{GaAs}}}\right) \quad [1]$$

The output of the spectrophotometer was adjusted such that the reflectivity of the GaAs was kept constant at 100% over the whole wavelength region. Thus, the interference by the light reflected from the oxide surface and the light reflected from the oxide-GaAs interface occurred between 0 and 100%. The refractive index of the oxide (n_{ox}) could be determined from the mini-

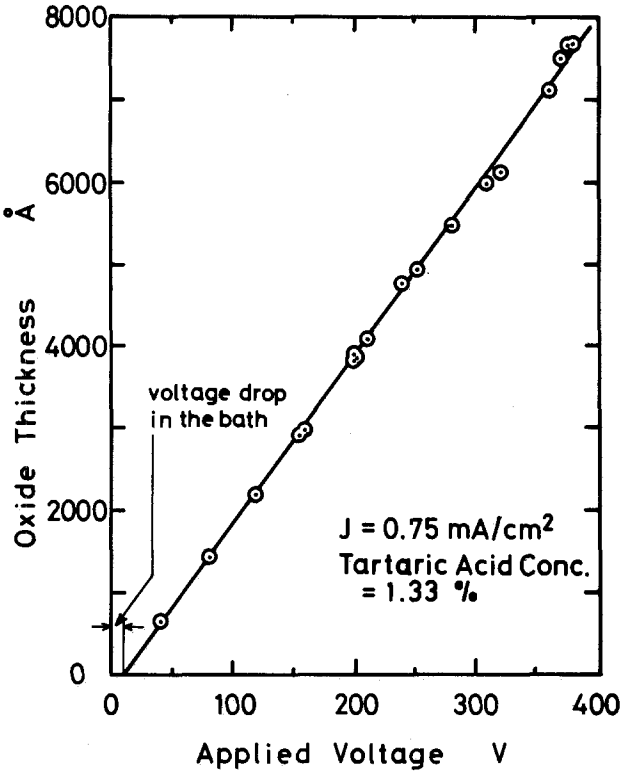


Fig. 4. Oxide thickness as a function of the applied voltage. The anodic oxidation was performed in the electrolyte having 1.33% tartaric acid concentration at the constant current density of 0.75 mA/cm². The voltage drop in the bath was 5V.

mum reflection ratio (R_{min}) for the wavelength where the interference minimum occurred using the equation

$$n_{ox} = \sqrt{n_{GaAs}} \cdot \sqrt{\frac{1 - \sqrt{R_{GaAs} \cdot R_{min}}}{1 + \sqrt{R_{GaAs} \cdot R_{min}}}} \qquad [2]$$

As long as the absorption of the oxide film can be neglected, Eq. [1] and [2] are very accurate. The thickness of the oxide film (d_{ox}) is given by the equation

$$d_{ox} = \frac{1}{2} \cdot \frac{1}{n_{ox}} \cdot \left(N + \frac{1}{2}\right) \lambda \qquad [3]$$

where λ is the wavelength of the interference minimum and N is the order of the interference.

The oxide thickness was also measured by a mechanical method using a Perthometer Type C3A to control the accuracy of the optical method when the optical index changed by heat-treatment of the oxide film. Since a good agreement with an accuracy of about ± 30Å was obtained, only the optical method is discussed in this paper.

Figure 5 shows the typical interference spectrum obtained from a 3000Å thick oxide film on GaAs. The interference maxima occurred at 100% for wavelengths longer than 0.3 μm, because the light reflected from the GaAs surface was transmitted through the oxide film without loss. As the oxides were highly transparent in this wavelength region, the refractive index is determined from Eq. [1] and [2] with high accuracy. The oxide became increasingly less transparent in the u.v. region, showing decreasing reflection ratios at the interference maxima, and it became perfectly opaque for wavelengths shorter than 0.22 μm. Only the reflection from the oxide surface could then be observed.

Until the present, the refractive index of the native oxide on GaAs has mainly been determined by ellipsometry (10-13, 19). The refractive index obtained by ellipsometry is very accurate, but the measurement only takes place at the operating wavelength of the ellipsometer. By spectrophotometry, on the other hand, an oxide film gives several interference minima at different wavelengths, and refractive index is determined from each interference minimum. When oxide films having different thicknesses are measured, there are many interference minima at various different wavelengths. By connecting refractive indexes at different wavelengths with a smooth curve, the wavelength dependence of the refractive index can be obtained.

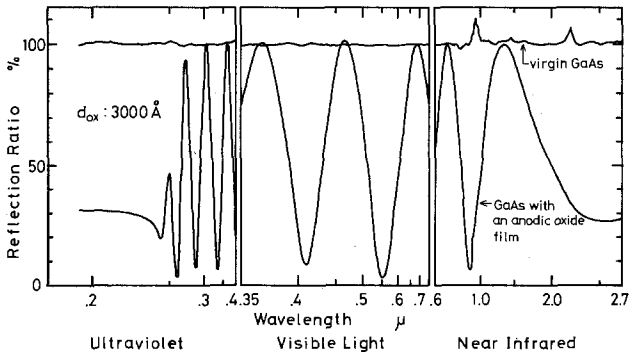


Fig. 5. Interference spectrum from a 3000Å thick as-grown oxide film on GaAs over the wavelength region from 0.195 to 2.7 μm.

Figure 6 was thus obtained for the as-grown oxides. The refractive index was almost constant in the near infrared region, weakly dependent on the wavelength in the visible light region, being higher at shorter wavelengths, and changed rapidly in the u.v. region. The total dependence of the refractive index on the wavelength showed the general characteristics of a glassy dielectric (23). From the previous ellipsometric study, the measured value of the refractive index of the anodically grown GaAs oxide was 1.82 at 5461Å according to Dell'Oca *et al.* (11) and 1.8 according to Spitzer *et al.* (12, 13) and 1.815 according to Müller *et al.* (21), the latter two having been measured at around 6000Å. In good agreement with these results, the values obtained by spectrophotometry in the present investigation were 1.82 and 1.80 at the corresponding wavelengths.

Influence of Temperature on Oxide Properties

Thickness change by heat-treatment.—Figures 7(a) and (b) show the absolute and the relative changes of the oxide thickness caused by heat-treatment, respectively. Four samples having different thicknesses were heat-treated successively in a dry purified N_2 atmosphere for 1 hr at each temperature. From the shape of the thickness change, it seemed to be convenient to consider the change by dividing the temperature into four regions.

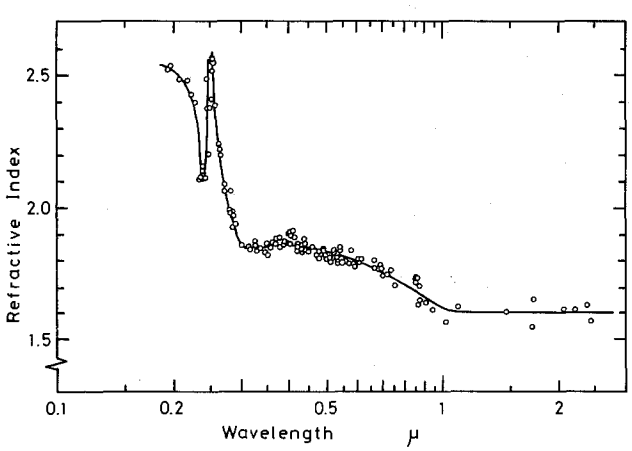


Fig. 6. Wavelength dependence of the refractive index of the as-grown oxide on GaAs measured by spectrophotometry.

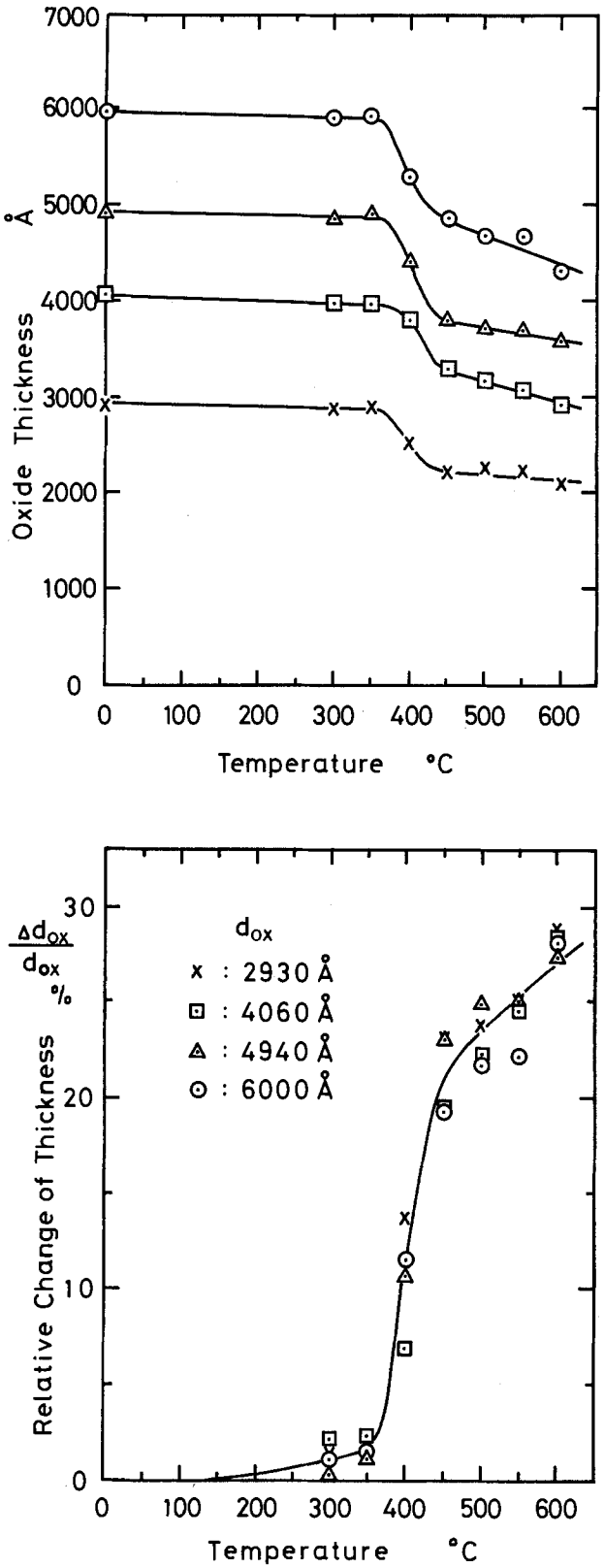


Fig. 7. Absolute (a) and relative thickness changes (b) of the anodic oxide films caused by heat-treatment. Oxide films were heat-treated successively for 1 hr at each temperature.

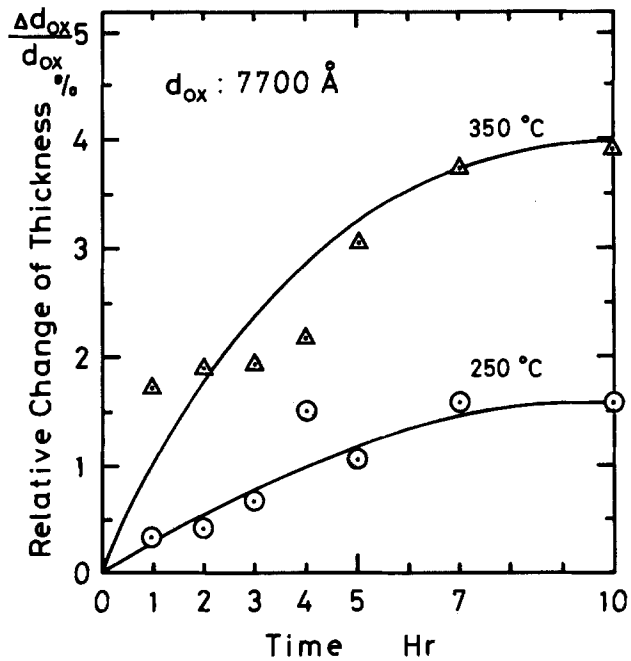


Fig. 8. Relative thickness changes of oxide films heat-treated at 250° and 350°C as a function of the time of heat-treatment.

Region 1: $T < 350$°C.—The thickness change was very small. This is more clearly shown by Fig. 8 where relative change in oxide film thickness is plotted *vs* time. The 7700Å thick oxide films were totally heat-treated for 10 hr at 250° and 350°C, respectively. The thickness change became saturated after a few hours' heat-treatment, and was less than 5% even at 350°C.

Region 2: 350°C $< T < 450$°C.—Drastic changes of the oxide thickness and the interference color were observed. The oxide thickness decreased by as much as 25% of the initial value after heat-treatment at 450°C. The change occurred in an early stage of heat-treatment, indicating an apparent decomposition of the oxide.

Region 3: 450°C $< T < 650$°C.—The changes of the oxide thickness and the interference color were gradual.

Region. 4: $T > 650$°C.—This region is not shown in Fig. 7 because the samples became too pitted and discolored for accurate optical measurements.

Change of optical properties by heat-treatment.—No changes in the optical properties of the oxides and the GaAs could be observed by heat-treatment in Region 1. The interference color and the refractive index did not change. By spectrophotometry, no difference was found between the reflectivity of the oxide-removed GaAs surface and the one of the unanodized GaAs surface.

The optical properties of the oxides changed remarkably by heat-treatment in Region 2. Although the oxides apparently remained glassy and transparent, their interference color changed completely because of the thickness decrease and the refractive index change. Figure 9 shows the change of the refractive index with heat-treatment. After heat-treatment, the refractive index became more weakly dependent on the wavelength in the visible light region. The wavelength dependence of the refractive index disappeared after heat-treatment in Region 3. The refractive index became almost constant around 1.5 over the wide region from visible light to near infrared.

Etching properties of heat-treated oxides.—Etching properties of as-grown oxides and oxides heat-treated below 350°C were almost identical. Oxides could be etched in a common acid or base with a high etch rate. As an example, a 7000Å thick oxide was completely removed in less than a few seconds in a cold HCl or a cold 48% HF solution. The etch rate of the oxides decreased with heat-treatment temperatures above 350°C. Oxides, however, could be etched without difficulty in a strong cold acid or base. Typical etch rates of a few hundred angstroms per second were obtained using a cold 48% HF solution after heat-treatment at 650°C.

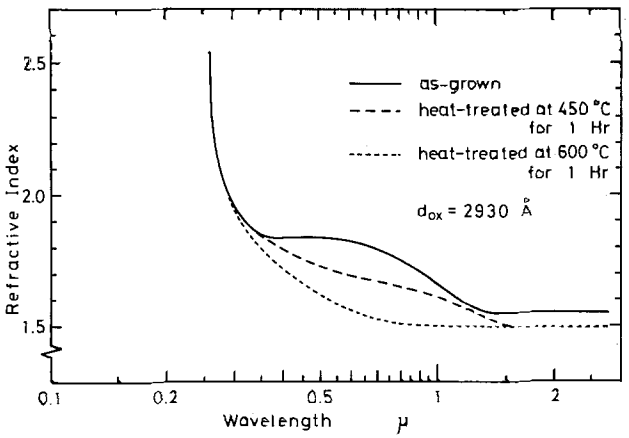


Fig. 9. Wavelength dependence of the refractive index of a heat-treated oxide. The oxide was kept for 1 hr at each temperature.

During these experiments it was found that a thin layer difficult to etch with either a cold acid or a cold base was formed at the oxide-GaAs interface. The thickness of the interface layer increased with the time and temperature of heat-treatment. From the interference spectra shown in Fig. 10, the interface layer was measured to be 500Å thick after heat-treatment at 800°C for 1 hr and to be 250Å thick after heat-treatment at 600°C for 1 hr. An indication of a very thin interface layer was noted in Fig. 10 after heat-treatment at only 400°C. It was, however, impossible to measure the thickness by spectrophotometry.

The interface layer left after the cold etching discussed above could be successfully removed using a warm (60°C) HF or a hot (120°C) H_3PO_4 etch. After this warm acid etching, samples heat-treated above 600°C showed a pitted surface which was believed to originate from arsenic sublimation from the GaAs surface.

Oxide Structure and Decomposition Mechanism

Composition and structure of the anodically grown native GaAs oxide before and after heat-treatment were investigated using Rutherford backscattering He-ions, He-ion-induced x-ray emission, and mass spectrometry. By combining the excellent thickness resolution of the backscattering technique and the excellent mass resolution of the ion-induced x-ray analysis, the oxide structure was analyzed (22). By mass analysis of vaporized materials from the oxide at different temperatures, the process of the oxide decomposition caused by heat-treatment was investigated.

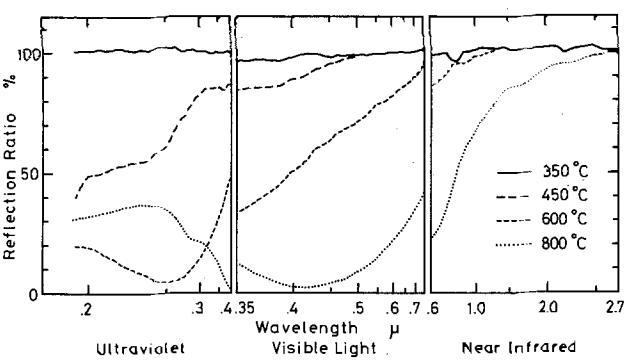


Fig. 10. Reflection spectra from the oxide-removed GaAs after heat-treatment. GaAs wafers were anodically oxidized to give 3000Å thick oxide films, heat-treated for 1 hr at each temperature, and then etched in a cold 48% HF solution.

Experimental procedures.—GaAs was anodically oxidized at 300V, and a 6000Å thick oxide film was grown on the surface. Thus prepared, a number of oxides were heat-treated in a dry purified N_2 atmosphere at different temperatures between room temperature and 650°C for periods ranging from 15 min to 5 hr.

A 1.8 MeV He-ion beam was used, and the backscattering spectra were obtained using a surface barrier solid-state detector, for which the system resolution was 20 keV. The characteristic x-rays for a 1.0 MeV He-ion beam were detected by a Si(Li) x-ray detector which had a resolution of 175 eV, an area of 30 mm^2, a 12.5 μm Be absorber, and a 50 μm Mylar window. Specimens were inclined by 20° to the incident He beam.

For mass spectrometry, a Micromass Type 1 from Vacuum Generators Limited was used. This spectrometer had a minimum detectable partial pressure of 3×10^{-12} Torr nitrogen equivalent, and a resolving power of 22. The GaAs samples which were completely covered by a 6000Å thick oxide film were put in a vacuum furnace with vacuum better than 4×10^{-6} Torr, and were then heated up. Vaporized materials from the oxide-coated GaAs were analyzed by the mass spectrometer. Two heat-treatment procedures were used. In one procedure, the samples were heated up successively from room temperature to 700°C with 50°C steps, and were kept for 1 hr at each temperature. In the other procedure, the samples were directly introduced into the furnace at a given temperature and were then kept at this temperature. Naked GaAs pieces were also heat-treated using the same procedures.

Change of oxide structure by heat-treatment.—Figure 11 shows typical random backscattering spectra

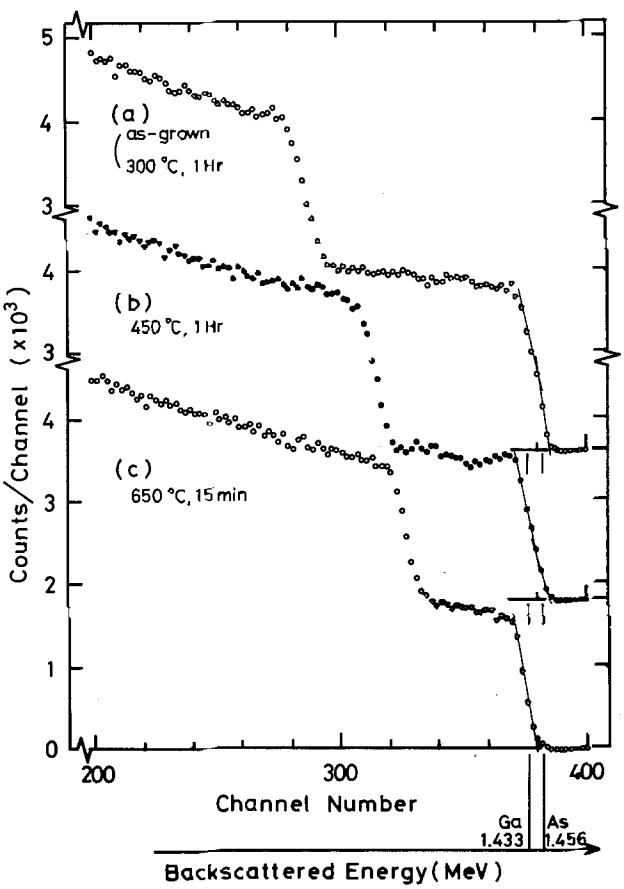


Fig. 11. Typical random backscattering spectra for 1.8 MeV He ion incidence. Curve (a) shows scattering from a 6000Å thick as-grown oxide film. The oxide film heat-treated at 300°C is identical with the as-grown one. Curves (b) and (c) show scattering from identical films after heat-treatment at 450° and 650°C, respectively.

obtained from several samples. Curve (a) is the spectrum from an unheat-treated sample. The leading edge lines up with the arsenic edge and consists of two slopes of almost the same height. This means that the Ga:As ratio in the oxide is nearly 1:1. No peaking due to excess gallium at the oxide surface, which was pointed out by Feldman *et al.* in the oxide made by a H_2O_2 process (22), is observed. The flat plateau indicates that the oxide structure is homogeneous, and that the Ga:As ratio is constant throughout the oxide layer. No change of the backscattering spectrum was observed by heat-treatment at 300°C.

Curve (b) is the spectrum from a sample heat-treated at 450°C for 1 hr. The oxide thickness has decreased to 75% of the initial thickness well in agreement with the results obtained by the optical and the mechanical methods. The leading edge still lines up with the arsenic edge, and it consists of two different slopes. However, the height of the first slope due to arsenic has remarkably decreased, showing a depletion of arsenic in the oxide. From the wavy shape of the curve in the plateau region and the fact that the shape varied across the wafer and also from wafer to wafer, it is believed that the oxide structure is nonuniform. For samples heat-treated longer than 15 min no differences in the obtained spectra were observed.

Curve (c) is the spectrum from a sample heat-treated at 650°C for 15 min. The oxide thickness has further decreased. The leading edge now lines up with the gallium edge, which means complete depletion of arsenic in the oxide. The flat plateau again shows the homogeneous structure consisting of gallium oxide. Heat-treatment longer than 15 min at 650°C did not seem to introduce any conclusive difference regarding oxide thickness and structure, but some inhomogeneity was introduced at the oxide-GaAs interface by heat-treatment longer than 1 hr.

This inhomogeneity was carefully examined by a channeling technique using a sample where the oxide was removed by a cold 48% HF solution after heat-treatment. Using this sample, curves (a) and (b) in Fig. 12 show the random and channeled spectra, respectively. As in the previous etching study, the interface layer not removed by the cold etching is clearly seen in the spectra. From the facts that the leading edge of the random spectrum lines up with the gallium edge (a) and that the clear peaking due to random scattering appears in the channeled spectrum (b), the interface layer is assumed to be an amorphous or a polycrystalline layer containing a negligible amount of arsenic. By detailed experiments, the Ga:O ratio in the interface layer was found to be 2:1 within an error of 20%. The thickness of the interface layer depends on the time of heat-treatment. From channeled backscattering spectra, the thicknesses were calculated to be 180Å for 15 min, 235Å for 1 hr, and 325Å for 5 hr. These values are in good agreement with the results obtained by the optical method (see Fig. 10). The occurrence of the interface layer and its dependence on heat-treatment seem to be connected with the sublimation of arsenic from the GaAs surface and thereby the accumulation of the free gallium at the GaAs surface. This is discussed later.

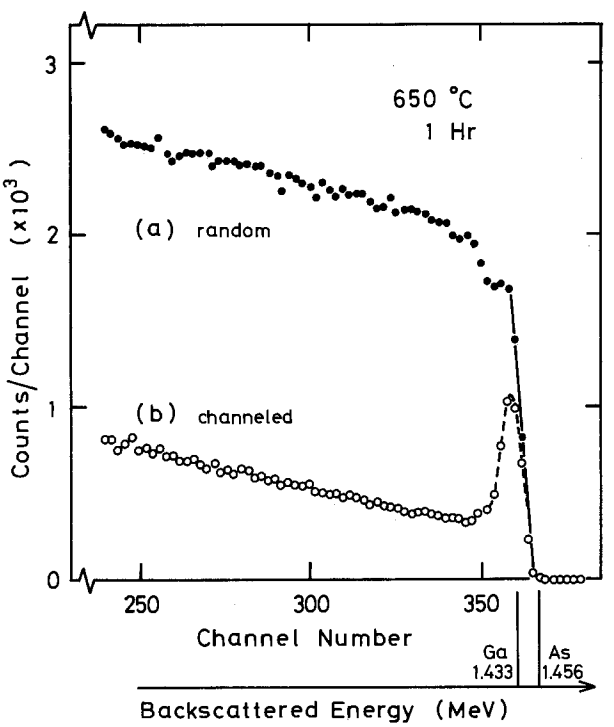


Fig. 12. Random and channeled backscattering spectra obtained from the oxide-removed GaAs using a cold 48% HF solution after heat-treatment at 650°C for 1 hr. A new amorphous or polycrystalline layer is formed at the oxide-GaAs interface, which is completely arsenic depleted and is difficult to remove by the cold etching technique.

Oxide composition.—He-ion-induced x-ray spectra of the samples discussed in the previous section are shown in Fig. 13. As the penetration of the He-ions into the oxide is expected to be 2500Å (22) and the oxide thickness is more than 3500Å even after the heat-treatment at 650°C for 5 hr, the x-ray spectra well represent the feature of the oxide composition.

No difference can be observed between the as-grown oxide and the oxide heat-treated at 300°C [Fig. 13(a) and (b)]. Thus the oxide composition essentially does not change in Region 1 ($T < 350$°C).

The depletion of arsenic in the oxide that occurs in Region 2, (350°C $< T <$ 450°C), is illustrated in Fig. 13(c) by the remarkable decrease of the arsenic K_α

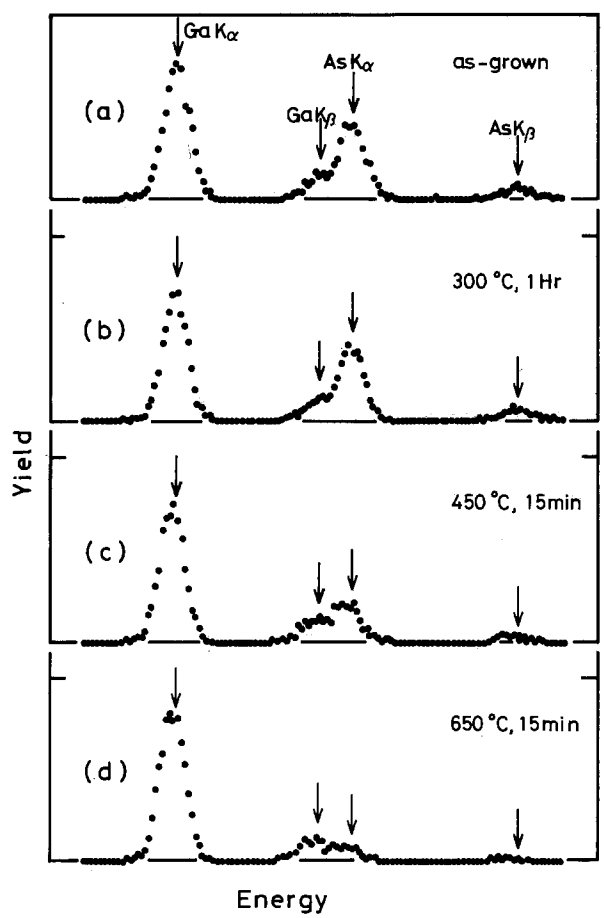


Fig. 13. X-ray spectra for an as-grown 6000Å thick oxide film (a) and for identical oxide films heat-treated at different elevated temperatures (b, c, and d). The 1.0 MeV He beam was incidented on the samples with an angle of 20°.

and K_β yields for a sample heat-treated at 450°C. In Region 3 ($450°C < T < 650°C$), the oxide gradually changes to a more gallium oxide-rich structure illustrated in Fig. 13(d), where the heat-treatment at 650°C has resulted in an almost pure gallium oxide. In these experiments it was further noted that at each temperature the change of the oxide composition was almost completed within the first 15 min of heat-treatment.

Oxide decomposition.—Changes of the partial pressure of H_2O, OH, O, AsO, As, and As_2 by heat-treatment of the oxide-coated GaAs were observed by mass spectrometry. Figures 14 and 15 show the relative changes of the partial pressure of these materials as a function of temperature and of time, respectively.

Logan *et al.* report that the as-grown oxide is supposed to be a mixed structure of Ga_2O_3, As_2O_3, and H_2O (12). From their investigation and our present experiments concerning the sorts of the vaporized materials, the oxide is believed to decompose by vaporizing water and arsenic oxide at elevated temperatures. In Fig. 14 water begins to vaporize at 350°C. The water vaporization rapidly increases and becomes maximum around 450°C. From the shapes of the temperature-pressure relation in Fig. 14 and the time-pressure relation regarding H_2O, OH, and O in Fig. 15, OH and O are believed to be derived from the dissociation of H_2O, possibly due to the ionization-induced dissociation by mass spectrometer.

Rapid increase of the partial pressure of AsO, As, and As_2 at around 400°C is noted in Fig. 14. The maximum vaporization of these materials also occur at around 450°C. Because of the high vapor pressure of As_2O_3 above 350°C (24) and the good correlations among the temperature-pressure relations for AsO, As, and As_2 corrected for by the direct sublimation of arsenic from GaAs shown in Fig. 14 and the time-pressure relations for the identical materials shown in Fig. 15, AsO, As, and As_2 are also supposed to be derived from the dissociation of As_2O_3 due to ionization.

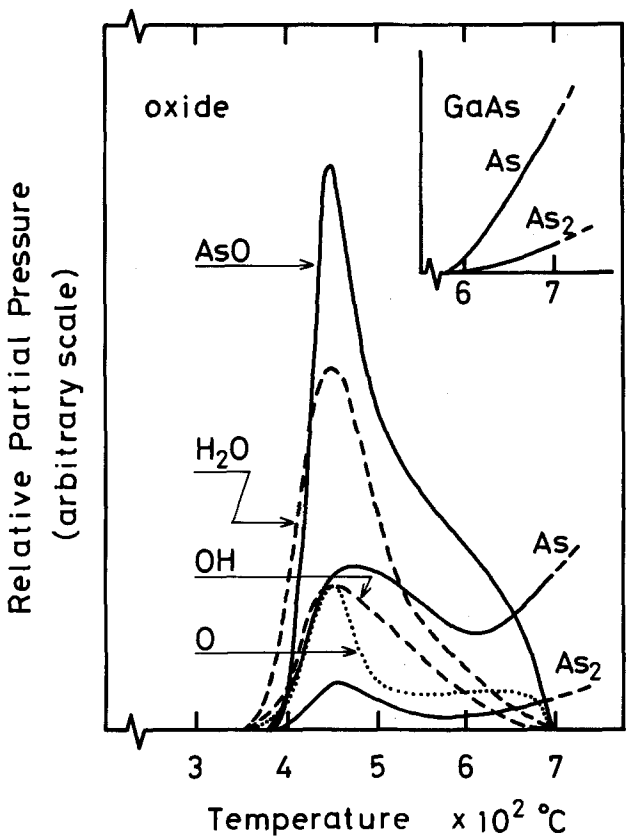


Fig. 14. Relative changes of partial pressures of vaporized materials from an anodically oxidized GaAs and a naked GaAs (inserted figure) during heat-treatment as a function of temperature. GaAs completely covered with a 6000Å thick anodic oxide film was successively heated up to 700°C with a 50°C step.

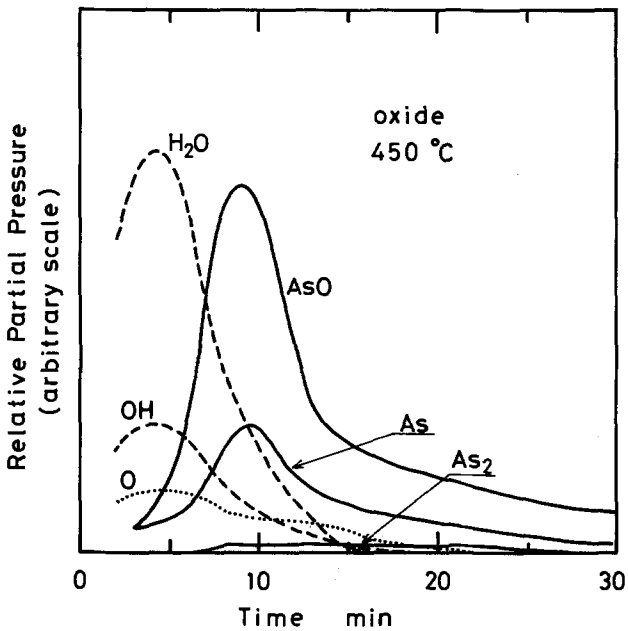


Fig. 15. Relative change of partial pressures of vaporized materials from an anodically oxidized GaAs during heat-treatment as a function of time. GaAs completely covered with a 6000Å thick anodic oxide film was directly heated up and kept at 450°C.

As the partial pressure of oxygen is still high even after the H_2O and OH partial pressures have become low enough in Fig. 14 and the second peak of the oxygen partial pressure correlates well to the peaks of AsO and As partial pressures in Fig. 15, oxygen due to the dissociation of As_2O_3 also contributes to the measured oxygen partial pressure. Below 600°C, vaporization of As and As_2 from the oxide is believed to be dominant. However, it is at present not clear whether the As and As_2 are due to the sublimation from the oxide or the decomposition of As_2O_3. On the other hand, the increase of As and As_2 partial pressures above 600°C is attributed to the sublimation from GaAs judging from the figure inserted in Fig. 14, where the partial pressures of As and As_2 from a naked GaAs wafer are illustrated as a function of temperature. At 700°C vaporization from the oxide becomes negligible, which means that the oxide decomposition is completed. The oxide is now expected to have become a stable and pure structure consisting of gallium oxide. Drastic vaporizations of water and As_2O_3 during the first 15 min are noted in Fig. 15. In the figure, first water and then As_2O_3 vaporize, and the rapid progress of the oxide decomposition in the early stage of heat-treatment is clearly shown. The time required to complete this rapid decomposition is shortened at higher temperatures. Heat-treatment in N_2 atmosphere or in vacuum is identical, judging from the starting temperature of the oxide decomposition and the changes of various oxide properties such as thickness, optical index, interference color, and etching characteristics.

Summarizing the experiments described above, it is possible to outline the basic features of the decomposition mechanism of the anodically grown native GaAs oxide during heat-treatment. The oxide decomposition is triggered by the vaporization of water at 350°C, and it rapidly proceeds at around 450°C by the combined effect of water and arsenic trioxide vaporizations. With the oxide decomposition, the oxide remarkably decreases its thickness and converts to a more and more gallium oxide-rich structure. Only a small amount of arsenic oxide remains in the oxide at 650°C and the

oxide decomposition is completed at 700C, resulting in a pure gallium oxide structure. The gallium oxide is believed to be β-Ga_2O_3, judging from the refractive index and etching characteristics (2-4).

The anodically grown native GaAs oxide is useless to mask the arsenic vaporization. Above 650°C appreciable sublimation of arsenic from the GaAs surface takes place resulting in a pitted surface. It is furthermore believed to lead to the formation of an intermediate layer at the oxide-GaAs interface consisting of gallium oxide and free gallium having a Ga:O ratio of 2:1, and during the fast cooling at the end of the heat-treatment cycle forming an amorphous or a polycrystalline layer.

High Temperature Heat-Treatment of Double Oxide Structure

In the previous sections, it has been shown that heat-treating the anodically oxidized GaAs above 650°C severely degrades the GaAs surface, and an undesired interface layer is formed. The oxide, regardless of thickness, is apparently unable to prevent the sublimation of arsenic from the GaAs surface. It is, however, clear that for processes involving temperatures above 650°C the possibility of using the oxide in intimate contact with the GaAs is of great importance. Several papers have reported that the use of SiO_2 (25), Si_3N_4 (26, 27), or AlN (26) as the annealing encapsulant of an ion-implanted GaAs successfully suppresses the sublimation of arsenic at temperatures as high as 800°C. This section therefore describes means of using the anodic oxide up to 800°C by depositing a SiO_2 film on top of the anodic oxide film in order to prevent the arsenic sublimation.

Double oxide structure.—The double oxide structure in the present investigation was made by depositing a SiO_2 film on top of the anodically grown native GaAs oxide film, using the conventional CVD technique (28, 29). Thicknesses of the anodic oxide films ranging from 500 to 3000Å were examined. Silane was decomposed in N_2 + O_2 atmosphere at 450°C, and a 2000Å thick SiO_2 film was deposited on the anodic oxide film. The period of heat-treatment associated with the deposition of the SiO_2 film was 15 min. As the deposition temperature of SiO_2 was higher than 350°C, the decomposition of the anodic oxide was unfortunately unavoidable. Though the anodic oxide had largely changed to the gallium oxide-rich structure after the SiO_2 deposition (see Fig. 11 and 13-15), the SiO_2 film was expected to readily prevent the sublimation of arsenic from GaAs above 650°C, having improved adherence to GaAs through the anodic oxide film.

Heat-treatment of GaAs coated with the double oxide films.—GaAs coated with the double oxide films was heat-treated at temperatures between 650° and 800°C in a dry purified N_2 atmosphere. For comparison, GaAs coated with only a 3000Å thick anodic oxide film was heat-treated in the same manner. Figure 16 shows the highest temperature at which the samples could be heat-treated for at least 1 hr as a function of the initial thickness of the anodic oxide film. For the same thickness of the SiO_2 film (2000Å), the temperature decreases with increasing thickness of the anodic oxide film. This thickness dependence of the heat-treatment temperature can be caused when the arsenic-depleted anodic oxide film absorbs arsenic from GaAs or when the anodic oxide film and the SiO_2 film are intermixed, making a single oxide film. A thick anodic oxide film can absorb more arsenic from GaAs in the former case, and the thinner the anodic oxide film is the more dominant the effect of the SiO_2 film becomes in the latter case. When the initial thickness of the anodic oxide film was 500Å, heat-treatment at 800°C for 2 hr was possible. Figure 17(a) shows the result from the double oxide structure consisting of a 500Å thick anodic oxide film and a 2000Å thick SiO_2 film after heat-treatment at 800°C for 2 hr, and Fig. 17(b) shows the result from

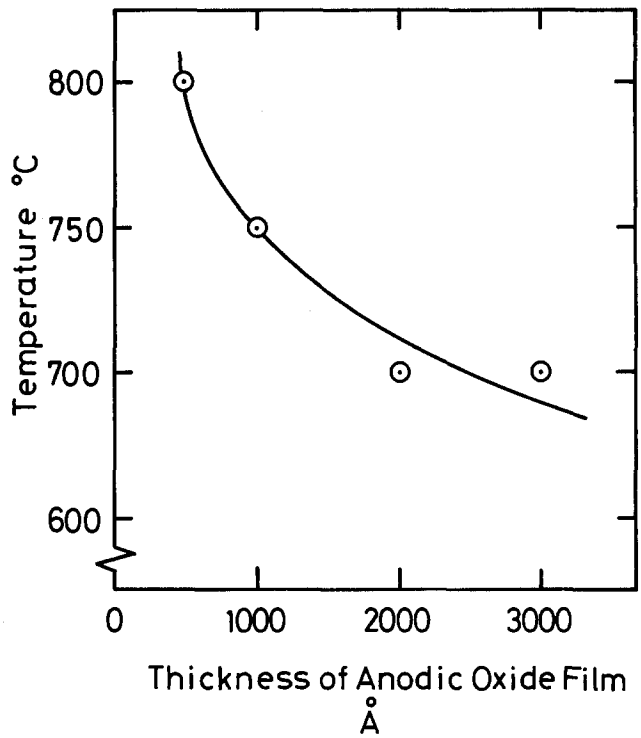


Fig. 16. Relation between the highest temperature to be able to heat-treat GaAs as a function of the initial thickness of the anodic oxide film in the double oxide structure. The SiO_2 film on top of the anodic oxide film was 2000Å thick.

a 3000Å thick anodic oxide film after heat-treatment at 700°C for 1 hr. In contrast to the degraded GaAs surface shown in Fig. 17(b), no degradation can be observed for GaAs coated with the double oxide films [Fig. 17(a)].

The advantage of the double oxide structure is further shown in Fig. 18. GaAs wafers coated with double oxide films consisting of a 500Å thick anodic oxide film and a 2000Å thick SiO_2 film are compared to GaAs coated simply with a 3000Å thick anodic oxide film as a function of heat-treatment at different temperatures for 1 hr. The surface roughness (or degradation) is shown in the form of the reflectivity of the oxide-removed GaAs surface measured at a wavelength of 6000Å. The reflectivity for GaAs coated with just the anodic oxide film rapidly decreases by heat-treatment above 650°C, while the reflectivity for GaAs protected by the double oxide films and heat-treated up to 800°C remains unchanged compared to that of virgin GaAs.

It was very difficult to remove only the SiO_2 film without removing the anodic oxide film, and it was therefore very difficult to separately examine the change of properties of the individual oxide film after heat-treatment. However, the properties of the anodic oxide film after heat-treatment were believed to be quite different depending on whether the anodic oxide film was covered with the SiO_2 film or not. For example, the double oxide films could be removed without difficulty by an HF solution after heat-treatment above 650°C. However, for samples without the SiO_2 coating, the anodic oxide film was very difficult to remove by common etching techniques. Though an inhomogeneous layer was introduced at the oxide-GaAs interface for GaAs simply coated with an anodic oxide film after heat-treatment above 650°C, such an inhomogeneous interface layer has not been observed for GaAs coated with double oxide films.

Summary and Concluding Remarks

The anodic oxidation of GaAs in an electrolyte consisting of water, tartaric acid, and ethylene glycol results in highly uniform native oxide films with con-

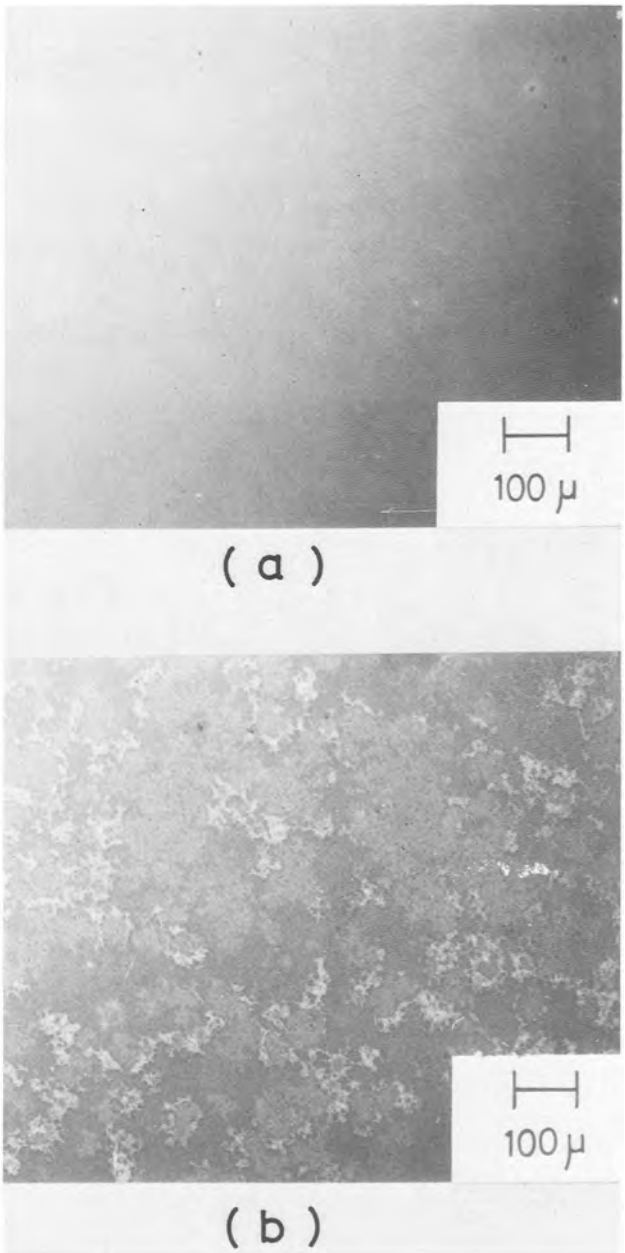


Fig. 17. Comparison of the surface roughness of GaAs after heat-treatment. In sample (a), GaAs was covered with double oxide films consisting of a 500Å thick anodic oxide film and a 2000Å thick SiO_2 film, and was heat-treated at 800°C for 2 hr. In sample (b), GaAs was covered only with a 3000Å thick anodic oxide film, and was heat-treated at 700°C for 1 hr.

trolled thicknesses up to 8000Å. The properties of the oxide essentially do not change below 350°C. The observed slight change of less than a few percent is understood to be due to the densification of the oxide. The as-grown oxide or the oxide stabilized below 350°C has a homogeneous structure consisting of As_2O_3, Ga_2O_3, and H_2O, where the Ga:As ratio is almost 1:1. The oxide is transparent in the visible light and the near infrared region, but becomes increasingly less transparent in the u.v. region, and is perfectly opaque for wavelengths shorter than 2000Å. The refractive index of the oxide is almost constant independent of wavelength in the near infrared region, weakly dependent on wavelength in the visible light region, and it changes rapidly in the u.v. region. The oxide can be etched easily by a common cold acid or base, and the virgin GaAs surface is recovered. Therefore the anodic oxidation-etching cycle is an excellent cleaning method

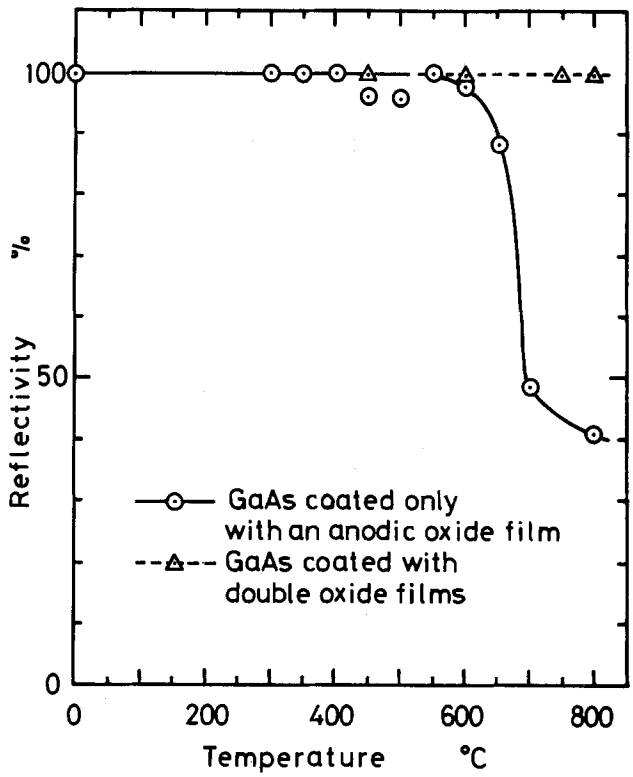


Fig. 18. Reflectivity of the oxide-removed GaAs surface after heat-treatment. GaAs was covered with a 3000Å thick anodic oxide film or double oxide films consisting of a 500Å thick anodic oxide film and a 2000Å thick SiO_2 film. After heat-treatment at the indicated temperatures, samples were etched in a warm 48% HF solution and the reflectivity measured for a 6000Å light.

for GaAs surfaces and is also a useful technique in material analysis, as controlled parallel layers can be removed from the surface.

Drastic changes of the oxide properties are observed by heat-treatment from 350° to 450°C. This low temperature decomposition is initiated by the release of water. The most drastic decomposition appears at around 450°C, associated with vaporizing water and arsenic trioxide. The decomposition is very fast and almost all changes are completed during the early period of the heat-treatment, for example, in less than 15 min at 450°C. As a result, the oxide changes to an inhomogeneous and a gallium oxide-rich structure. These aspects of decomposition are important when device stability and reliability are considered. When the anodic oxide is used as an integral part of a device and temperatures above 350°C are required, or when the oxide is used in a high temperature device processing step, the oxide must be stabilized. The required anneal time is, however, very short. The oxide is for instance stabilized in less than 15 min at 450°C, resulting in a quasistable oxide. Prolonged annealing results in only minor changes.

The oxide further decomposes vaporizing water and arsenic trioxide. However, the oxide decomposition becomes gradual and the oxide becomes a more and more gallium oxide-rich structure in the temperature region ranging from 450° to 650°C. The refractive index becomes almost constant at around 1.5 over the wide wavelength region from visible light to near infrared, which is quite similar to the value of a thermally grown oxide. Judging from the wavelength dependence of the refractive index, the etching properties and the analysis of the composition and the structure of the oxide, the oxide seems to approach pure β-Ga_2O_3.

Above 650°C, appreciable sublimation of arsenic from the GaAs surface takes place, resulting in a pitted surface. It is furthermore believed to lead to the formation of an intermediate layer at the oxide-GaAs interface,

which is at present not fully identified but is supposed to consist of gallium oxide and free gallium. During cooling, an amorphous or a polycrystalline interface layer is formed, having a Ga:O ratio of 2:1. The oxide itself is still glassy and can be removed by a strong cold acid like HF or a strong base. The interface layer, however, is difficult to etch by a common cold acid or base, and only a warm HF or a hot H_3PO_4 can successfully remove the layer. The decomposition of the oxide is complete at 700°C resulting in pure gallium oxide, β-Ga_2O_3. The degraded GaAs surface after long heat-treatment above 650°C makes it difficult to use the oxide in a high temperature processing. The high temperature limit for GaAs coated with only an anodic oxide film is therefore approximately 650°C.

The temperature limit can be improved by depositing a CVD SiO_2 film on top of the anodic oxide film. GaAs covered with such double oxide films, consisting of a 500Å thick anodic oxide film and a 2000Å thick SiO_2 film, can be heat-treated at 800°C for 2 hr with no degradation of the GaAs surface. This result demonstrates the important possibility of using the anodic oxide in intimate contact with the GaAs material in high temperature processes, for example as the annealing encapsulent of ion-implanted GaAs or as a diffusion mask.

Acknowledgments

The authors wish to thank Prof. P. Weissglas for valuable discussions, and Drs. L. Stensland and L-E. Flordal for their assistance with the optical measurements and useful suggestions. The helpful cooperation of Dr. D. Sigurd regarding the structure analysis of the oxide is highly appreciated. They also wish to acknowledge their colleagues for their helpful cooperation.

Manuscript submitted April 19, 1976; revised manuscript received June 6, 1977.

Any discussion of this paper will appear in a Discussion Section to be published in the June 1978 JOURNAL. All discussions for the June 1978 Discussion Section should be submitted by Feb. 1, 1978.

Publication costs of this article were assisted by the Microwave Institute Foundation and Mitsubishi Electric Corporation.

REFERENCES

1. S. P. Murarka, *Appl. Phys. Lett.*, **26** 180 (1975).
2. L-Å. Ledebo, *Tech. Rep. Lund Inst. Tech.*, 127 (1975).
3. K. Navratil, *Czech. J. Phys., Engl. Transl.*, **b18**, 266 (1968).
4. B. J. Sealy and A. D. E. D'cruz, *Electron. Lett.*, **11**, 323 (1975).
5. O. A. Weinrich, *J. Appl. Phys.*, **37**, 2924 (1966).
6. T. Sugano and Y. Mori, *This Journal*, **121**, 113 (1974).
7. J. A. Calviello and J. L. Wallace, in Proceedings of the Fifth Biennial Cornell Electronics Engineering Conference, Ithaca, New York, August 1975.
8. B. Schwartz and W. J. Sundburg, *This Journal*, **120**, 576 (1973).
9. A. G. Revesz and K. H. Zaininger, *J. Am. Ceram. Soc.*, **46**, 606 (1963).
10. W. W. Harvey and J. Kruger, *Electrochim. Acta*, **16**, 201 (1971).
11. C. J. Dell'Oca, G. Yan, and L. Young, *This Journal*, **118**, 89 (1971).
12. R. A. Logan, B. Schwartz, and W. J. Sundburg, *ibid.*, **120**, 1385 (1973).
13. S. M. Spitzer, B. Schwartz, and G. D. Weigle, *ibid.*, **122**, 397 (1975).
14. S. M. Spitzer, B. Schwartz, and G. D. Weigle, *ibid.*, **121**, 820 (1974).
15. D. L. Rode, B. Schwartz, and J. V. DiLorenzo, *Solid-State Electron.*, **17**, 119 (1974).
16. W. C. Niehaus and B. Schwartz, *Solid-State Electron.*, **19**, 175 (1976).
17. H. Hasegawa, K. E. Forward, and H. Hartnagel, *Electron, Lett.*, **11**, 53 (1975).
18. H. Hasegawa, K. E. Forward, and H. Hartnagel, *Appl. Phys. Lett.*, **10**, 567 (1975).
19. H. Hasegawa and H. L. Hartnagel, *This Journal*, **123**, 713 (1976).
20. B. Bayraktaroglue, E. Kohn, and H. L. Hartnagel, *Electron. Lett.*, **12**, 53 (1976).
21. H. Müller, F. H. Eisen, and J. W. Mayer, *This Journal*, **122**, 651 (1975).
22. L. C. Feldman, J. M. Poate, E. Ermanis, and B. Schwartz, *Thin Solid Films*, **19**, 81 (1973).
23. A. J. Moses, "Handbook of Electronic Materials, Vol. 1—Optical Material Properties," pp. 66, IFI/Plenum Press, New York (1971).
24. Smellie, *J. Soc. Chem. Ind. London*, **42**, 466 (1923).
25. R. G. Hunsperger and N. Hirsch, *Solid-State Electron.*, **18**, 349 (1975).
26. B. M. Welch, F. H. Eisen, and J. A. Higgins, *J. Appl. Phys.*, **45**, 3685 (1974).
27. T. Ambridge and R. Heckingbottom, *Electron. Lett.*, **11**, 314 (1975).
28. N. Goldsmith and W. Kern, *RCA Rev.*, **27**, 153 (1967).
29. W. Kern and W. Fisher, *ibid.*, **31**, 715 (1970).

Si Molecular Beam Epitaxy (n on n^+) with Wide Range Doping Control

Yusuke Ota

Bell Laboratories, Reading, Pennsylvania 19604

ABSTRACT

Silicon single crystal films were made by molecular beam epitaxy (MBE) technique in an ultrahigh vacuum (UHV). Sb-doped epitaxial films were grown on Czochralski (CZ) grown n^+ ($\rho \leq 0.003$ Ω-cm), (111) or (100) substrates at temperatures ranging from 600° to 1050°C. The doping density of the films was controlled from high 10^{13} to high $10^{17}/cm^3$. p-type epitaxial films on n^+ substrate were also grown from a boron-doped source. TEM and preferential dislocation etching revealed that the epitaxial films are high quality single crystal with low dislocation density. The electrical properties of the epitaxial films were found to be bulklike. p^+-n-n^+ diodes were fabricated on these films and they showed low reverse leakage current and sharp breakdown. These diodes operated excellently at millimeter wave frequencies.

For many silicon devices, especially microwave diodes and transistors, very abrupt profiles across the epitaxy-substrate interface are important. Most of these devices require a heavily doped substrate ($>10^{18}/cm^3$) and lightly doped epitaxial layer ($<10^{16}/cm^3$). In chemical vapor deposition (CVD), such as hydrogen reduction of $SiCl_4$ or pyrolysis of SiH_4, outdiffusion and autodoping are very difficult to avoid because of the high temperature processing and the existence of halogen and hydrogen gases which transport dopant atoms during epitaxial growth. It is difficult to grow thin epitaxial films with resistivity $\rho \geq 50$ Ω-cm on a highly doped substrate. Si molecular beam epitaxy (Si MBE) has been studied by many authors (1-13). However, to my knowledge there is no report about successful growth of device quality n-type epitaxial films with a wide range doping control by MBE. Although Schewman and King have grown n-type epitaxial films at doping concentrations between 5×10^{17} and $4 \times 10^{18}/cm^3$ by the MBE technique at temperatures below 800°C, they have not reported the quality and the electrical characteristics of these films (12).

Experimental

Growth system.—Figure 1 shows the growth system inside a 12 in. bakable stainless steel bell jar. It consisted of the following major parts: an e-gun system to create a Si molecular beam, a substrate heating system, an effusion furnace for Sb doping, a viewing port for monitoring the substrate temperature and steering of the electron beam, cold shrouds to shield the bell jar walls from heat radiation from both the heated source silicon and Si substrate, and a radiation reflector located behind the Si substrate. The source silicon was located 23 cm from the substrate and the silicon beam was evaporated upward. A thermocouple was attached to the reflector which monitors and controls the substrate temperature. For substrate temperature below 750°C at which the pyrometeric measurement is not accurate, the thermocouple reading was used. The silicon source was built on an Airco Temescal deep crucible e-gun unit with a 270° electron beam deflection. In a 270° deflection system, the tungsten filament is hidden from the Si substrate, which avoided tungsten contamination of the epitaxial film. Since the crucible was made of copper, the area adjacent to the source silicon was protected by high purity silicon to avoid Cu contamination.

The silicon source consisted of three sections. They were made of either high purity floating zone (FZ) single crystal p-type, 5 kΩ-cm silicon or high purity polysilicon (impurity <0.4 ppb). A cross-sectional view of the source assembly is shown in Fig. 2. The center portion of the source section was a truncated cone of shaped silicon (part A). During film growth, the e-beam impinged only on the center of this section. For an e-beam current of 140 mA, the molten area was less than 13 mm in diameter. The doughnut-shaped silicon (part B) protected the copper crucible surface from bombardment by stray electrons. Since the main beam did not strike outside of part A and a small gap existed between parts A and B, the region B remained at low temperature. With this arrangement, Cu contamination was avoided. Another possible source of contamination was sputtering of the stainless steel parts surrounding the e-gun system by the electrons reflected from the silicon surface, mainly from part A. This source of contamination was eliminated by placing a semicircular silicon wall (part C) around the side opposite to the incoming direction of the e-beam. The focusing capability of the e-beam was improved by the addition of magnetic field poles. They are not shown in Fig. 2.

With this source design and modifications, stacking fault-free films were grown at a growth rate of 1.4 μm/hr using a beam current of 250 mA at 4.5 kV.

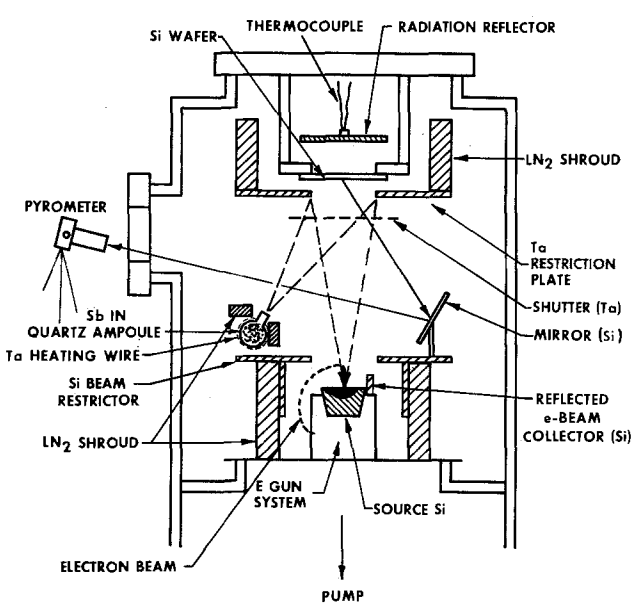


Fig. 1. Si MBE growth system

Key words: silicon, molecular beam epitaxy, doping, ultrahigh vacuum.

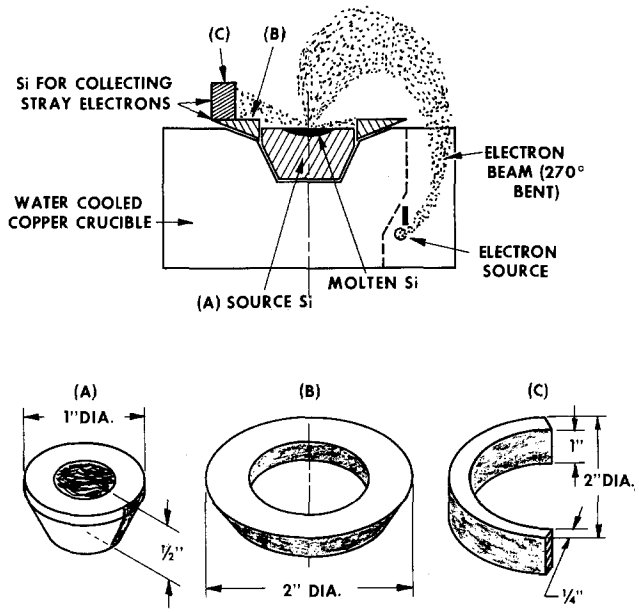


Fig. 2. Si molecular beam source system

Without such modifications, stacking fault-free films could be grown only at a very low beam current, *i.e.*, at a low growth rate (<2000 Å/hr). This problem was more severe for (111) substrates than for (100) substrates.

A cross-sectional view of the resistive substrate heater is shown in Fig. 3. Rectangular silicon substrate (45 × 13 × 0.5 mm) was clamped with tantalum clamps at both ends of the sample. Ta shims were inserted between the clamp and the sample. These shims provided uniform contact to the silicon substrate and prevented the Si sample and Ta clamps from fusing together. The Ta clamp at one end was fixed to a Mo end block, and the other was fixed to a slidable Mo piston. This prevented the silicon sample from warping when it was heated. Mechanical bending of silicon at high temperature ($\gtrsim$ 900°C) would generate dislocations which affect the quality of the epitaxial layer. Using this sliding sample holder, there was no warping in the samples.

A Ta radiation reflector (7.5 cm × 6 cm × 0.25 mm) was placed 6 mm behind the silicon sample. It served three functions. First, it acted as a silicon beam collector which shielded the insulators and other fixtures.

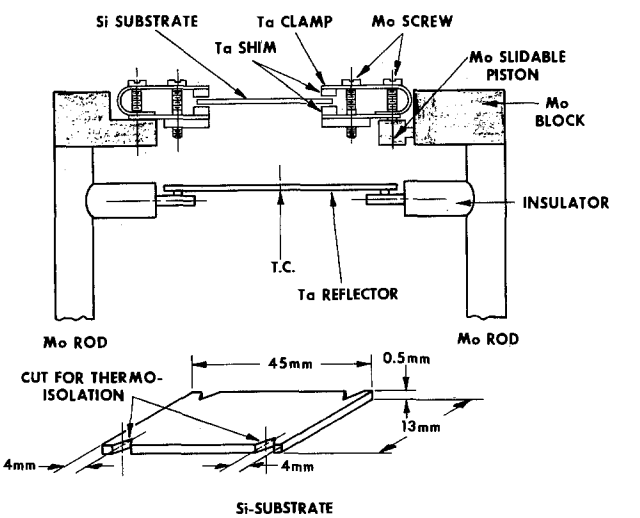


Fig. 3. Substrate heating system

This reflector was cleaned after 4-5 deposition runs. Second, it acted as a radiation shield. This reduced outgassing from the fixtures such as the ceramic insulators and copper lead wires. This added further assurances for contamination-free epitaxial films. Third, a Chromel-Alumel thermocouple was attached to the back side of this reflector to control the substrate temperature. It was also used to monitor the growth temperature below 820°C. The control of the growth was adequately achieved by using a combination of programmable power supply and proportional-type temperature controller. A relationship between the thermocouple reading and the silicon surface temperature was determined from an optical pyrometer measurement for the temperatures above 820°C (pyrometer reading, 790°C) with the emissivity correction. Silicon surface temperatures in the range between 500° and 800°C were estimated by extrapolating the high temperature data.

For the sample size shown in Fig. 3, the temperature uniformity was checked visually and by an optical pyrometer for temperatures above 820°C. When the substrate temperature was ~900°C, a temperature gradient was visually observed near the Ta clamp to approximately 3 mm away from the clamp. Our observations showed that this region was narrowed to less than 3 mm for growth temperatures above 1000°C. When the center of the sample was at 900°C, the pyrometer readings indicated a temperature drop of 30°-50°C in the dark regions near the Ta clamps.

Pyrometer readings were taken at a few points in the visually uniform regions. The variation of the readings was within the resolution of the pyrometer ±5°C. For film growth temperatures below 900°C, the sample had to be shaped to improve the temperature uniformity of the sample. Four notches were cut from the sample as shown in Fig. 3. The depth of the cuts depended on the substrate temperature for film growth and they were determined empirically. For the sample size shown in Fig. 3, 2 mm deep cuts were used to grow films at ~800°C. The doping uniformity for two samples with and without the cuts were compared with spreading resistance measurements. Both samples had n-type ~1.5 Ω-cm and 5 μm epitaxial films grown at 770°C. For the sample without the cuts, the surface spreading resistance at 6 mm from the clamp was 50% lower than that at the center and a 10% variation was observed in the center region. However, the sample with the cuts showed a uniform resistivity over almost the entire length (3.8 mm) of the sample. The spreading resistance readings were ~4.5 kΩ. We found that the film resistivity is a sensitive function of the growth temperature. From the spreading resistance data, we inferred that this setup provided a uniform growth temperature across the sample. The relationship between the film resistivity and the sample temperature is discussed further in a later section.

Antimony dopant vapor was generated with a simple effusion furnace. It consisted of a quartz ampul with a 6 mm diameter opening, a tantalum heating wire, a Chromel-Alumel thermocouple, and a liquid nitrogen-cooled shroud. This effusion furnace system was capable of generating a well-controlled flux of Sb vapor. The furnace temperature was controlled by a proportional-type thermocouple temperature controller to within ±0.1°C of the set temperature. The controller and the programmable power supply were isolated by an optical isolator. This effusion furnace could also be used for arsenic doping. However, we felt that antimony is easier to use in this system because of its chemical stability and lower vapor pressure as compared to As.

All three major heated sections, *i.e.*, the Si source, the substrate, and the effusion furnace, were sur-

rounded by liquid nitrogen cold shrouds to prevent radiation heating of the surrounding fixtures and walls. Without these shrouds, stray dopants could cause difficulty of doping control as electrically active contaminants.

Sample preparation and growth procedures.—One side of the Si substrate was Syton-polished and etched in 0.05 mole CrO_3-HF mixture to remove possible surface damages from polishing. This etchant did not destroy the mirror surface of the sample. After rinsing in DI water, the sample was cleaned in a HCl-H_2O_2 mixture to remove the absorbed chrome on the sample surface. ~40Å thick oxide was grown on the Si surface during this cleaning procedure and it was removed in 15:1 diluted HF. Finally, the sample was boiled in an NH_4OH-H_2O_2 mixture for 20 min. This operation formed a protective oxide of ~50Å in thickness. The sample was mounted onto the heater assembly and the system was evacuated.

The vacuum system was baked at 150°C overnight and ready for film growth when the vacuum was at 10^{-11} Torr. With the shutter closed, the source Si and the effusion furnace were heated for 30 min. Once the vacuum recovered to low 10^{-9} Torr, the substrate was heated at 1240°C for 45-60 sec and slowly cooled to the growth temperature. This preheating step was optimized for vaporizing the thin oxide layer and producing an atomically clean surface for epitaxial film growth. The growth started by opening the shutter. Typical growth conditions were as following: e-beam was at 140 mA and 4.5 kV which produced a ~6000 Å/hr growth rate, the Sb source was at 300°C which generated ~10^{-7} Torr Sb vapor pressure in the ampul and the typical vacuum during the growth was between 1 and 5 × 10^{-9} Torr.

Results

Crystalline quality.—The crystalline quality of the films was examined with transmission electron microscope (TEM) and preferential defect etching, and the surface texture was examined with SEM and optical microscope. The surface texture observed by an interference contrast microscope at 750× and SEM at 5000× were usually featureless. When the film thickness was less than several hundred angstroms, the texture of the film surface provided information on the growth mechanism. A featureless surface in this thickness range would indicate that the film growth was by a two-dimensional nucleation mechanism (7). This was different from the film growth via a three-dimensional nucleation where single crystal island formation was observed. The presence of islands caused poor crystalline quality. We found that a featureless surface is essential for good quality film growth. The TEM measurement showed excellent crystallinity and no stacking faults or dislocations. Figure 4 shows the transmission electron diffraction pattern from the epitaxial film grown on an (100) substrate at 600°C. In spite of the TEM results, when this sample was examined by Secco etch, it revealed a dislocation density of 200/cm² but no evidence of stacking faults.

The dislocation density in most of the epitaxial films was less than 10^3/cm² and close to that observed on the substrate surface, where Secco etch and Sirtl etch were used for (100) and (111) films, respectively. It is important to note that the dislocation density was independent of the film growth rates (0.2-1.4 μm/hr), the growth temperatures (600°-1050°C) or the film thicknesses (0.3-9.0 μm).

Thickness and doping concentration control.—*Thickness.*—The growth rate was controlled by varying the e-beam current at a fixed acceleration voltage. For the present system, the beam current was adjusted manually. Since the growth rates were shown in the range of a few thousand angstroms per hour, a reasonable control of e-beam current could be made. With this manual control the thickness reproducibility was ±10%. The film thickness *vs.* growth time is shown in Fig. 5, where the e-beam current was at 140 mA. The substrate temperatures were from 600° to 1050°C as indicated in Fig. 5, and for both (100) (□) and (111) (○). The (△) is for amorphous Si films deposited at room temperature. These data indicated that the growth rate is independent of either the Si substrate temperatures or the surface orientations.

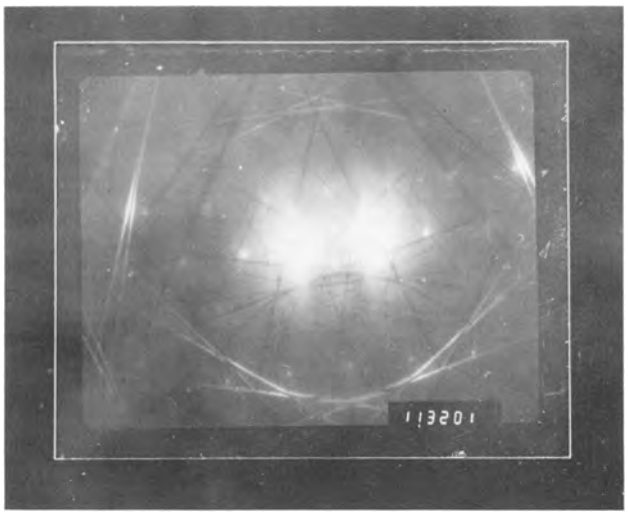


Fig. 4. Transmission electron diffraction pattern from a (100) epitaxial film grown at 600°C.

Most of the film thicknesses were determined by observing the step formed at the Ta clamped area with an interferometer. Several samples were also measured by *IR* multiple reflection technique. These

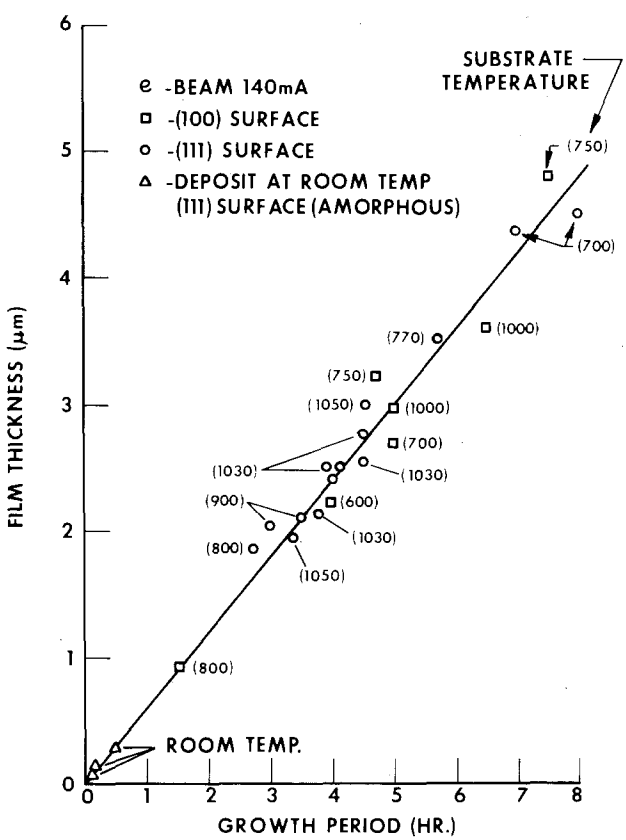


Fig. 5. Film thickness *vs.* growth period relationship.

results agreed with those by the interferometer to within ±10%.

Doping.—With the antimony effusion furnace, a simple way to vary the doping concentration in the film was to change the effusion furnace temperature. However, due to the sensitivity of vapor pressure of Sb with temperature, it was rather difficult to control the Sb concentration in the film by changing only the effusion furnace temperature. A convenient method for doping epitaxial films was to change the silicon substrate temperature T_S, while keeping the Sb source temperature constant. Figure 6 shows the relationship between the film resistivity and the growth temperature T_S for Sb source heated at 300°C (●) and 260°C (▲). The data are for a film growth rate of 0.6 μm/hr. By this method the resistivities of the films could be reproducibly varied over three orders of magnitude. Epitaxial films with resistivities higher than 20 Ω-cm were grown in this fashion. With the conventional CVD method, it is usually difficult to grow epitaxial films with $\rho > 50$ Ω-cm, especially on n^+ substrates. If the epitaxial films were thin, say, less than 3 μm, it was extremely difficult to grow such high resistivity films on highly doped substrates by the CVD method. The datum point (□) was obtained from a special run to investigate the system capability to create high resistivity films. The growth rate was 1.2 μm/hr and the effusion furnace temperature was 260°C. The film resistivity was 150 Ω-cm as measured by spreading resistance measurements. The dependence of the doping concentration on the substrate temperature is believed to be due to the dependence of the sticking coefficient of Sb on the surface temperature of Si. Figure 6 shows that the scattering of the film resistivity increases as the substrate temperature decreases. This effect could be explained by the fact that the residual Sb on the shutter and other parts which were not cooled with liquid nitrogen contributed to the main Sb source and the sticking coefficient of Sb on Si was a strong function of temperature. However, we have not investigated this question further.

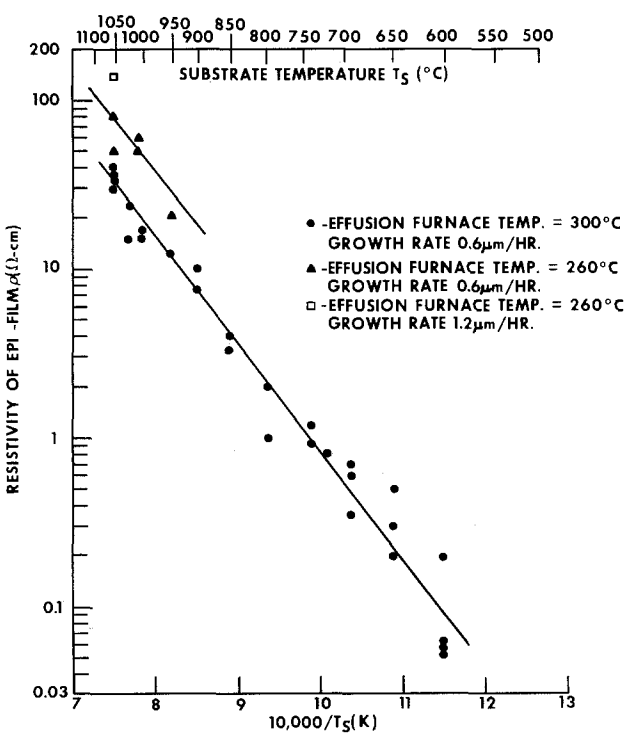


Fig. 6. Dependence of doping density on the growth temperature, where dopant is Sb.

Spreading resistance measurements.—Spreading resistance measurements were used to evaluate the resistivity of the film. While the spreading resistance measurements do not give a direct reading of the resistivity profile (14), this technique is still a convenient method for determining the approximate resistivity and the location of the epitaxy substrate interface of a p-n junction. Figure 7 shows the uncorrected spreading resistance data for an Sb-doped 2.9 μm thick film grown at 1000°C on an As-doped 0.002 Ω-cm (111) substrate. The resistivity from the spreading resistance measurements was approximately 15 Ω-cm. Spreading resistance measurements near the interface of two layers of different conductivities are subject to uncertainties. In spreading resistance measurements, the probe penetration depths are extremely difficult to determine and influence the resolution of the profile. Therefore, the spreading resistance technique was used mainly to determine the resistivity of the films in the plateau region where the influence from the substrate can be neglected. The lateral doping uniformity was also examined at eight locations on this sample as shown in Fig. 8. The result indicated that lateral doping uniformity is excellent.

Film resistivity vs. carrier concentration.—Resistivities ρ *vs.* doping concentrations N_D of films were de-

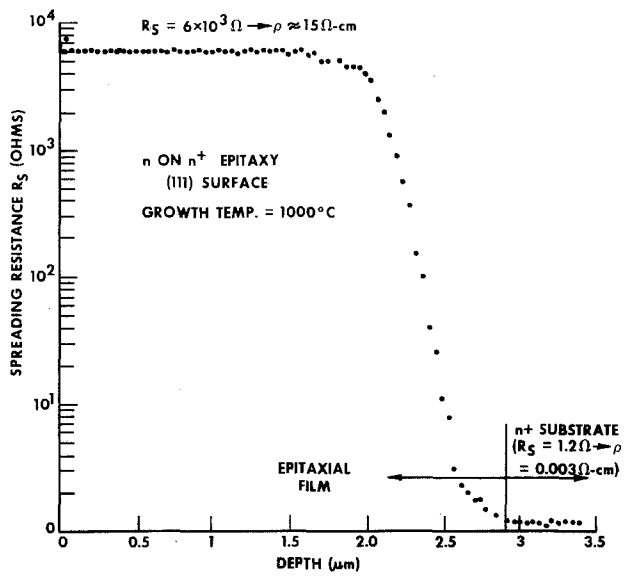


Fig. 7. Spreading resistance vs. depth profile on n on n^+ epitaxy

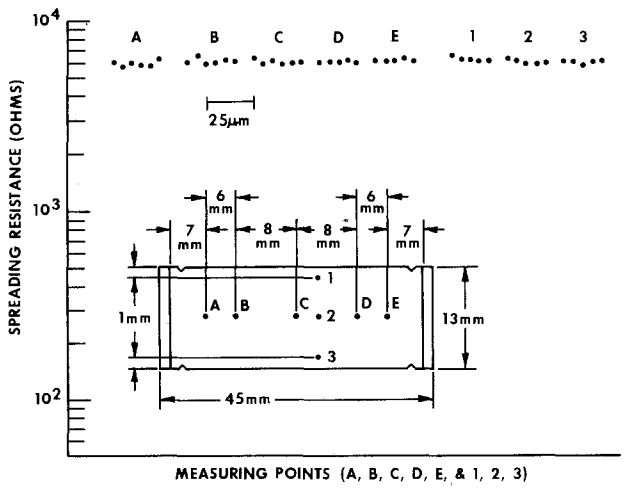


Fig. 8. Lateral spreading resistance profile

termined by two methods: (*i*) Hall effect measurement was made on a few n-type layers on p^+ substrates. Due to difficulties in making good contacts to the samples which were lightly doped ($<10^{16}/cm^3$), only one datum point was obtained as shown by (HALL) in Fig. 9. (*ii*) A combination of MOS C-V and spreading resistance measurements were used to determine the resistivity *vs.* concentration for n-type layers on n^+ substrates. The results are shown by (MOS-SPREAD) in Fig. 9. MOS capacitors were fabricated with 2000Å thermal oxide. The doping concentrations were determined from the high frequency C-V plots at 1 MHz. The film resistivities were determined by converting the spreading resistances into resistivities in the region where constant readings were observed. Good agreements with bulk Si data (15) (the solid line) were observed. Hence, we concluded that the epitaxial films had the same quality as bulk single crystals.

Diode characteristics.—Using the millimeter wave diode processing technique, p^+-n-n^+ mesa diodes were fabricated with a sample of 15 Ω-cm and 2.9 μm film (this sample is the same as that shown in Fig. 7). The diode was formed by diffusing boron from a BN source to 0.5 μm depth, mesa etched, passivated, and metallized (16). Figure 10 shows a typical *I-V* characteristic for a diode made with this material. From Fig. 10, the breakdown voltage was approximately 72V (at 10 μA). The theoretical breakdown voltage was 66V (17). The calculation assumed error function distributions for boron (p^+) and arsenic (n^+) and an active layer width of 2.1 μm. The breakdown voltages for other diodes (68 ± 5V) from the same epitaxial film agreed with the calculation.

Trap measurements.—Pt Schottky diodes on n-type film were fabricated for deep trap measurement by the DLTS technique (deep level transient spectroscopy) (18). The epitaxial film was 5 Ω-cm, 5 μm thick, Sb doped on an (100) oriented substrate. No deep trap was detected in the as-grown film for trap energies over a range between 0.08 and 0.3 eV from the conduction band at reverse bias voltages from 1 to 10V, as shown in Fig. 11. For the film resistivity of this sample, the sensitivity of the DLTS measurement was around $2 \times 10^{12}/cm^3$, this strongly suggests that no major electrically active contamination was introduced in the epitaxial growth process.

Doping profile.—In order to investigate the doping profile near the film-substrate interface, As profiles were measured by the SIMS technique (secondary ion mass spectroscopy) for substrates with As concentrations $\simeq 5 \times 10^{19}/cm^3$. Figure 12 shows the results of SIMS analysis. Curves (a) and (b) are for samples grown at 1050° and 800°C, respectively. The out-diffusion of As from the substrate into the film was less than 300Å for a 3 hr growth at 800°C and less than 2000Å for a 2 hr growth at 1050°C. Curve (c) shows the doping profile near the film-substrate

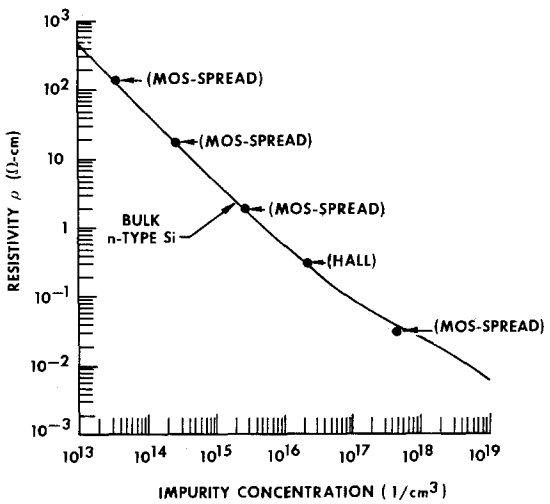


Fig. 9. Resistivity *vs.* impurity density relationships of epitaxial films grown by Si MBE technique. The solid line is from Irvin's curve for n-type bulk silicons.

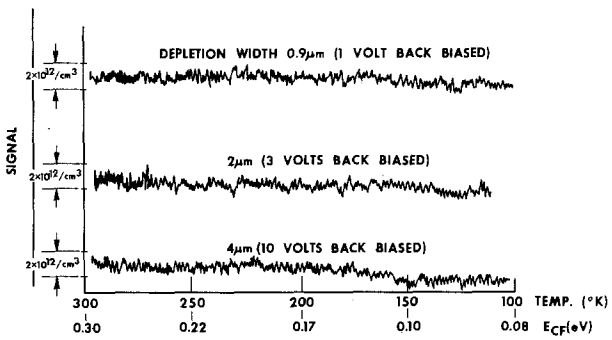


Fig. 11. DLTS data on Pt Schottky diode on a n-n^+ epitaxial film.

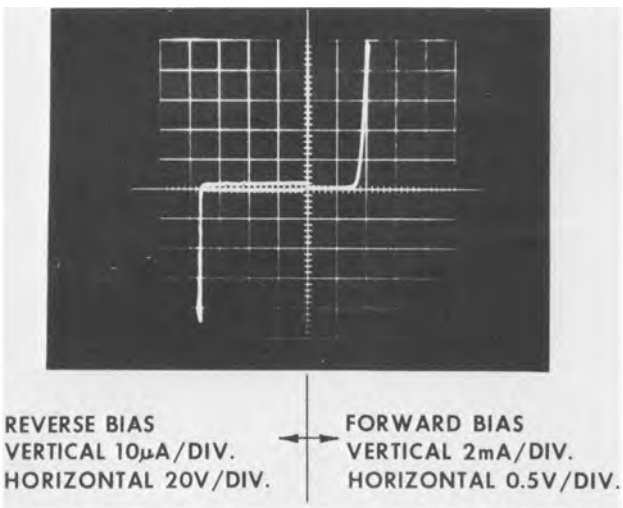


Fig. 10. *I-V* characteristic of p^+-n-n^+ mesa diode

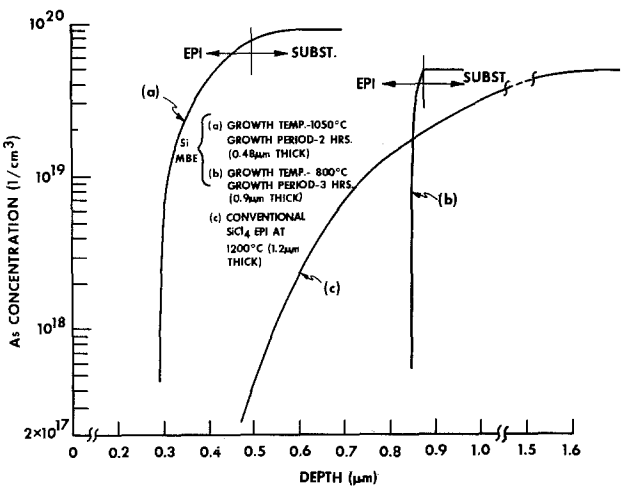


Fig. 12. Out-diffusion profiles of As near the film-n^+ (As) substrate interface measured by SIMS technique.

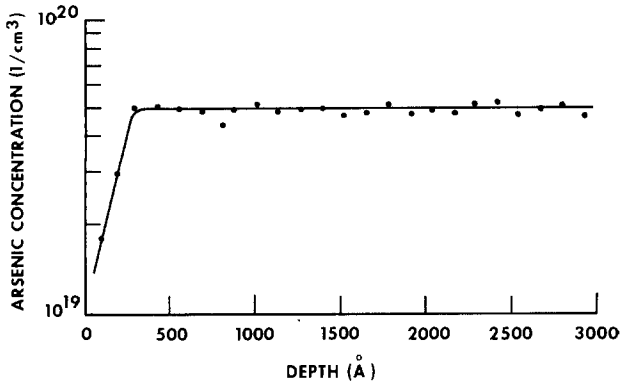


Fig. 13. Depletion of As near n^+ (As) substrate surface after thermal treatment at 1240°C for 1½ min in UHV measured by SIMS technique.

interface of a conventional CVD epitaxial film.[1] This film was 1.2 μm thick grown at 1200°C using $SiCl_4$. This curve indicated that the out-diffusion of As was significantly larger than that in MBE films grown at lower temperatures. For the MBE films, evaporation of As the highly doped substrate during the initial cleaning steps at 1240°C was investigated. Figure 13 shows the SIMS data for a substrate (As = 5×10^{19}/cm³) which was thermally treated at 1240°C for 1.5 min in an UHV. The surface depletion of As was close to 300Å.

Discussion

Epitaxial film can grow in a form of discrete three-dimensional islands, two-dimensional layers, or a combination of both (7). Many factors can contribute to the three-dimensional growth. For defect-free films, the environment should promote the two-dimensional growth. Three major factors are essential for the two-dimensional growth and hence for the growth of defect-free silicon films by the MBE technique. These are discussed in this section.

Ultrahigh vacuum (UHV).—Several researchers studied the growth mechanisms of silicon crystal in an UHV (7, 8). They recognized that a clean environment is very important to grow epitaxial films by the two-dimensional mechanism (7). For the present growth system, a clean environment was provided in a bakable UHV system. This was capable of obtaining a vacuum of middle 10^{-11} Torr after overnight baking and with liquid nitrogen in a cryogenic panel and cooling of the shrouds. The importance of an ultrahigh vacuum was observed in the following experiment.

When the system was not baked and the sublimation pump and the cryogenic panel were not used, the system had an initial vacuum of 10^{-9} Torr. During the film growth, in a very short time the vacuum was in the high 10^{-6} Torr region and remained at this pressure for longer than a few hours. The high background pressure was due to outgassing from the vacuum chamber by the heat radiation from the silicon source and the substrate heater, and the excess gas release had caused saturation of the ion-pumps. Silicon films grown in this environment often showed the presence of discrete three-dimensional growth centers. In the early stage of the growth, the film showed island formation and when the film was a few thousand angstroms thick it appeared milky. This milky appearance of the surface became noticeable when the growth temperature was above 800°C. [This is different from the thermal etching of silicon during the film growth as suggested by Schewman and King (12).] This experiment confirmed the necessity of UHV system with proper baking and cooling during film growth for growing defect-free silicon epitaxial films. The vacuum during the growth should be below the 10^{-8} Torr range.

Silicon source.—The basic requirements for the silicon source were a high purity Si and a controllable constant sublimation rate. In an earlier design, silicon vapor was created in an ultrahigh purity graphite crucible (99.9999% pure), heated at 1450°C to vaporize Si (19). Three-dimensional islands were observed for films grown with this source on (111) substrates at growth temperatures ranging from 670° to 1050°C. These films contained high densities of stacking faults and twin structures (>10^9/cm²). This was believed to be due to the carbon contamination. The graphite silicon source was changed to an electron beam heating system to avoid the presence of carbon in the sublimation source. High purity, high resistivity floating zone p-type silicon ($\rho > 5$ kΩ-cm) or high purity polysilicon (impurity level >0.4 ppb) was used as the source material. After the source structures were shaped, they were etched in CP-4 and cleaned with e-beam in the UHV system before the film growth. This system was successful for generating a clean Si molecular beam.

In situ cleaning.—Joyce *et al.* (7) did a careful study relating three-dimensional nucleation and the substrate surface preparation. They found that an atomically clean surface was necessary to avoid island formation in the film growth and that such a surface could be generated if the final step in the surface cleaning constituted a 1200°C heating under high vacuum conditions for 10 min prior to film growth. Allen *et al.* (20) also reported that heating silicon to about 1200°C was necessary to obtain atomically clean silicon surfaces. Kimura and Lee (11) also used sublimation to try to clean their substrate surfaces but found that prolonged thermal treatment in vacuum actually led to excessive surface concentration of silicon carbide particles which, in turn, were responsible for generating stacking faults. They showed that this was especially true for CZ crystals but that there was sufficient carbon in FZ crystals to also be important.

Recognizing the importance of the substrate surface cleanliness, we also studied the sample surface preparation for substrates used in this deposition system. CZ substrate heated at 1200°C for 10 min in vacuum were observed to have a high density of thermal pits on the substrate surface. These results were different from the observations of Joyce *et al.* and agreed with those of Kimura and Lee. Epitaxial films grown on this pitted surface were not smooth.

Heating silicon at temperatures higher than 900°C in vacuum usually causes nonuniform sublimation resulting in thermal pits. These pits occurred in less than 1 hr at 900°C and less than 5 min at 1200°C. The formation and size of these pits depended on the length of heating, the temperature, the initial crystalline perfection, the thermal history of the crystal, and probably other factors still unknown. We observed more thermal pitting on FZ silicon than on CZ silicon. This is in disagreement with the postulation of Gates and Lavin (21) who claimed that the increased oxygen in CZ silicon was responsible for the greater thermal pitting. We also observed that most of the (100) surfaces showed more severe pitting than (111) surfaces. This agreed with the results of Batdorf and Smits (22).

We found that the shortest possible heating time should be used to produce the atomically clean surface. This was enhanced by using a final chemical cleaning step of boiling NH_4OH-H_2O_2 which leaves about 50Å

[1] The imolantation effect during SIMS analysis is not considered in these profiles.

of SiO_2 on the surface. These thinly oxidized substrates were preheated to 1240°C for less than 1 min prior to film deposition. Using this cleaning method, low dislocation density films were obtained (less than 1000 cm^{-2} which was close to the dislocation density in the substrates).[2] No stacking faults were observed in these films. As the thermal evaporation cleaning period is extended prior to film deposition, the dislocation count in the deposited films increases and stacking faults are sometimes generated as reported by Kimura and Lee, most probably because of an increase in silicon carbide particles at the growth interface although we were unsuccessful in identifying this phase. Figure 14 shows results of Sirtl etchings on epitaxial films grown on (111) As doped (As $> 5 \times 10^{19}/cm^3$) substrates at 900°C. Figure 14(a) is for a film grown by the recommended preheating procedure after Sirtl etching for 1 min. Figure 14(b) is for a film grown by using a prolonged preheating procedure, 10 min at 1240°C and Sirtl etched for 30 sec. The film represented by (a) had an average dislocation density less than $100/cm^2$ and the one represented by (b) had an average stacking fault and dislocation density of $2 \times 10^5/cm^2$.

Atomically clean silicon surfaces can also be obtained by sputter cleaning with ionized inert gases (He or Ar) (23-25). For the conditions used, the silicon surface damaged by sputtering could not be annealed to the original surface conditions for the moderate annealing temperatures used. Furthermore, Ar penetrated the silicon surface which was very difficult to remove (23, 24) and the sputtering process could cause additional contamination (24). Hence, the sputter cleaning by inert gas ions for surface preparation for Si MBE was not pursued further.

Unvala (6) and Thomas and Francomb used doped silicon for growing doped epitaxial films in vacuum with some success (1, 6). We investigated this technique in the present system. Phosphorus-doped FZ silicon crystals with resistivities ranging from 1 to 150 Ω-cm were used as silicon and dopant sources. Films grown with these sources had unpredictable and nonuniform resistivity and conductivity type. Both p and n regions were sometimes observed in the same sample. This was due to a rapid initial evaporation of phosphorus from the molten silicon and also possibly compensation from the background boron which is always present in the silicon crystals. Hence, this approach was discarded for n-type film growth. Tannenbaum and Povilonis (3) obtained p-type doping films with good reproducible results using boron-doped silicon source. However, the film resistivity decreased as the source was repeatedly used due to accumulation of boron near the surface. They used a source temperature of 1350°-1380°C which was below the silicon melting temperature. Boron-doped silicon crystals were used for growing p-type films in the present system. The source was heated to >1600°C with an electron beam. A few p-type films were grown on n^+ substrates at 950°C. For the few runs done to date, resistivities of the films were 0.5-0.7 Ω-cm from a 0.1 Ω-cm source, 5-10 Ω-cm from a 2 Ω-cm source, and 15-20 Ω-cm from 10 Ω-cm source, respectively.

As stated above, for n-type doping a separate Sb source effusion furnace was used. The Sb source temperature could be varied from 50° to 700°C. Typically, it was set at 300°C. The use of high purity elemental Sb provided a contamination-free doping source. The relatively low vapor pressure of Sb (less than that of P and As) minimized reevaporation of the dopant from surrounding fixtures where some parts are radiatively heated by the heated silicon source and substrate. This reduced the possibility of spurious doping in successive film growths. We also found that the film resistivity could be controlled readily by changing the film growth temperature with a constant Sb vapor pressure. Doping concentrations from 2×10^{14} to $4 \times 10^{17}/cm^3$ were grown reproducibly with this effusion furnace at 300°C and a growth rate of 0.6 μm/hr. One film was Sb doped to $6 \times 10^{13}/cm^3$ with the effusion source heated at 260°C and the growth rate of 1.2 μm/hr. The film resistivity could also be adjusted with the growth rate for a given effusion furnace temperature and a film growth temperature.

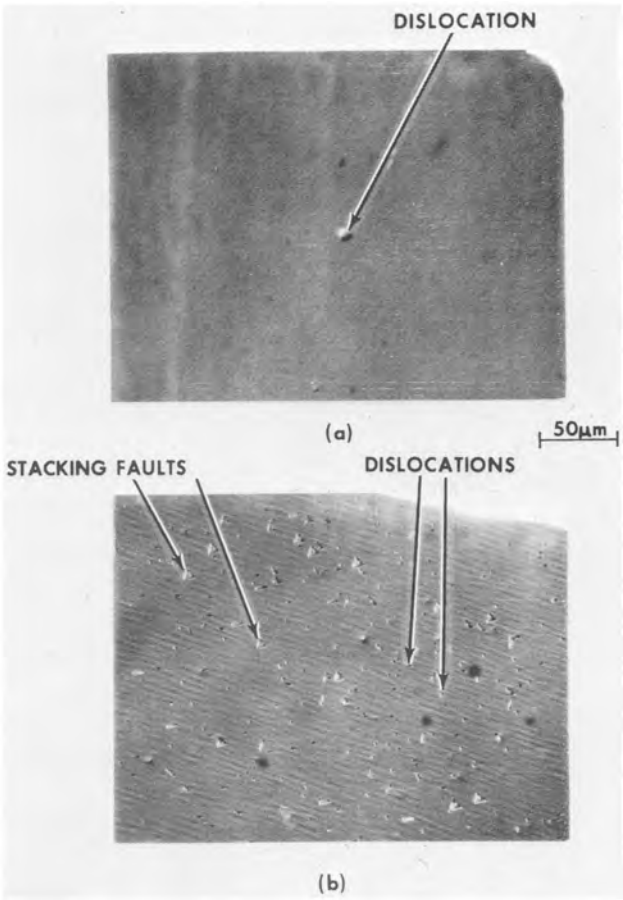


Fig. 14. (111) epitaxial film surface after Sirtl etching. (a) Epitaxial film grown by normal procedure (1 min Sirtl etching). (b) Epitaxial film grown by using a prolonged preheating period, 1240°C, 10 min (30 sec Sirtl etching).

The outdiffusion of As from n^+ substrate into the epitaxial film was remarkably smaller than that of the conventional CVD method. It was believed to be due not only to the lower growth temperature but also to the absence of other dopant transport mechanisms in the present system. No autodoping of As into the epitaxial film was observed. This was proved by the capability of growing high resistivity thin p-type films (>15 Ω-cm) on n^+ substrate (~0.002 Ω-cm). High quality epitaxy films with both well-controlled doping and sharp doping profiles near the film-substrate interface produced high quality, millimeter wave PIN diodes.

Conclusion

In order to grow high quality epitaxial films by MBE, three factors must be present, namely:

1. A bakable ultrahigh vacuum system with liquid nitrogen cold shrouds capable of achieving a vacuum lower than 10^{-8} Torr during the film growth.
2. A high purity silicon source with e-gun heating.
3. An atomically clean silicon surface free of thermally induced damage.

[2] Most of the low resistivity substrates (<0.01 Ω-cm) used in this study were CZ grown crystals and contained dislocation densities <1000/cm^2.

For n-type doping of the film in the MBE system, Sb is recommended. The film doping concentration can be controlled by varying the silicon growth temperature. For p-type film, boron-doped silicon source can be used. The quality of the substrate affects the quality of the epitaxial film.

Acknowledgment

I take pleasure in acknowledging the able technical assistance of R. Jimski on this project. I would also like to thank W. L. Buchanan and O. G. Petersen for fabricating and analyzing p^+-n-n^+ switching diodes, P. M. Petroff for performing TEM measurements, and G. E. Becker and J. C. Bean for exchanging valuable information. Valuable assistance from J. H. Mattes of the BTL machine shop is also acknowledged.

Manuscript submitted May 23, 1977; revised manuscript received July 26, 1977.

Any discussion of this paper will appear in a Discussion Section to be published in the June 1978 JOURNAL. All discussions for the June 1978 Discussion Section should be submitted by Feb. 1, 1978.

Publication costs of this article were assisted by Bell Laboratories.

REFERENCES

1. B. A. Unvala, *Le Vide*, No. 104, 109 (March-April 1963).
2. B. F. Kilgore and R. W. Roberts, *Rev. Sci. Instr.*, **34**, 11 (1963).
3. E. Tannenbaum and E. I. Povilonis, *This Journal*, **111**, 205 (1964).
4. H. Widmer, *J. Appl. Phys.*, **5**, 108 (1964).
5. H. C. Abbink, R. M. Broudy, and G. P. McCarthy, *ibid.*, **39**, 4673 (1968).
6. R. N. Thomas and M. H. Francombe, *Solid State Electron.* **12**, 799 (1969).
7. B. A. Joyce, J. H. Heave, and B. E. Watts, *Surf. Sci.*, **15**, 1 (1969).
8. A. G. Cullis and R. G. Booker, *J. Cryst. Growth*, **9**, 132 (1971).
9. V. P. Kuznetsov, R. A. Rubstova, T. N. Sergievskaya, and V. V. Postnikov, *Sov. Phys., Crystall.*, **16**, 356 (1971).
10. O. P. Pcheiyakov, R. N. Lovyagin, E. A. Krivorotov, A. I. Toropov, L. N. Aleksandrov, and S. I. Stenin, *Phys. Status Solidi A*, **17**, 339 (1973).
11. A. Kimura and C. A. Lee, *Solid State Electron.*, **18**, 901 (1975).
12. J. Schewman and F. D. King, U.S. Pat. 3,949,119 (1976).
13. G. E. Becker and J. C. Bean, *J. Appl. Phys.*, **48**, 3395 (1977).
14. R. G. Mazur and D. H. Dickey, *This Journal*, **113**, 255 (1966).
15. S. M. Sze and J. C. Irvin, *Solid State Electron.*, **11**, 599 (1968).
16. Y. Ota, W. L. Buchanan, and O. G. Petersen, To be presented at the IEEE Int. Electr. Dev. Conference, Washington, D.C., December 1977.
17. Computer program was made by H. Olson based on the theory by D. Decker and C. Dunn published in *J. Electron. Mater.*, **4**, 527 (1975).
18. D. V. Lang, *J. Appl. Phys.*, **45**, 3023 (1974).
19. Y. Ota, Unpublished.
20. F. G. Allen, J. Eisinger, H. D. Hagstrum, and J. T. Law, *J. Appl. Phys.*, **30**, 1563 (1959).
21. H. C. Gatos and M. C. Lavin, *Ann. N.Y. Acad. Sci.*, **101**, 983 (1963).
22. R. L. Batdorf and F. M. Smits, *J. Appl. Phys.*, **30**, 259 (1959).
23. J. C. Bean, G. E. Becker, P. M. Petroff, and T. E. Seidel, *ibid.*, **48**, 907 (1977).
24. H. M. Ibrahim and N. M. Bashara, *Surf. Sci.*, **30**, 680 (1972).
25. G. W. Sachse, W. E. Miller, and C. Gross, *Solid State Electron.*, **18**, 431 (1975).

Argon Implantation Gettering of Bipolar Devices

M. R. Poponiak, T. Nagasaki, and T. H. Yeh*

IBM System Products Division, East Fishkill Facility, Hopewell Junction, New York 12533

ABSTRACT

The effectiveness of impurity gettering of bipolar devices by argon implantation is described. The excess BV_{CEO} leakage and "piped" device improvement are used as the criteria for evaluation. Implantation gettering when done at the preemitter step is found to be more effective than at the prebase step of the total processing sequence. The significantly higher yield obtained by the preemitter gettering supports the model of enhanced diffusion along dislocations for the formation of pipes in the bipolar devices.

Recently, gettering has been receiving renewed attention throughout the semiconductor industry. This is due to the advancements made in device technology, which not only demands lower leakage characteristics for logic or memory devices than before, but also makes it imperative to have a very high percentage of operational devices in the large integrated circuit chip. With this criteria in mind, an improvement definitely is needed to achieve higher final chip yields.

Extensive work on the effectiveness of various diffusion gettering schemes (1-9) for reducing junction leakage has been well established. Mechanical damage (2) produced by sandblasting or lapping has also been demonstrated to be an effective getter. Damage created by ion implantation (10-15) clearly demonstrated its ability to getter metallic impurities and reduce excessive leakage. A comparison of various species of implant *vs.* a standard phosphorus diffusion for gettering of Au, clearly demonstrated the effectiveness of implant damage (15).

In this paper, we are going to address the effectiveness of impurity gettering by argon implantation. The results to be presented here utilize a bipolar test structure composed of several different sizes, single and multiemitter transistors. Standard electrical testing and the aluminum anodization method (16) were utilized to determine yields and defect density. Gettering was done at two different processing steps, *i.e.*, prebase and preemitter, to determine which step is more effective in curing the excessive BV_{CEO} leakages or "piped" devices in the integrated circuits.

Experiments

A block flow diagram of the processing sequence is illustrated in Fig. 1. A total of sixteen Czochralski-grown p-type wafers, of <100> orientation and 10-20 Ω-cm resistivity, were utilized in the experiment. Both sides of the wafer were chem-mechanically polished.

* Electrochemical Society Active Member.
Key words: impurity gettering, device yield improvement.

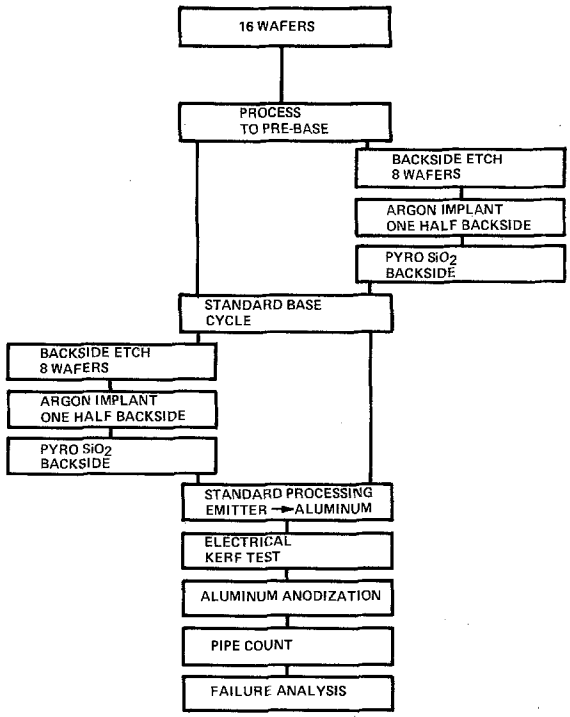


Fig. 1. Block diagram of the processing sequences

Conventional bipolar processing, which included an arsenic capsule subcollector and a 2 μm, n-type, 2 $\times$ 10^{16} cm^{-3} epitaxial layer, was used until the prebase step. The back side of eight wafers was stripped clean just prior to the base diffusion. Half the back side of each wafer was then implanted with 6 $\times$ 10^{15} cm^{-2} argon at 70 keV according to Fig. 2.

An aluminum mask was used to prevent implantation into the control half of the wafers. The half-wafer concept reduced the number of wafers required for good statistical results. A 1000Å pyrolytic SiO_2 layer was deposited onto the back side of the wafers at 1000°C for 5 min, after the implantation for the prebase portion of the experiment. This layer served two purposes. First, it provided a 15 min, 1000°C heat cycle which included the heating up, deposition, and cooldown times in order to accomplish part of the gettering prior to the actual base diffusion. Second, it served as a diffusion mask for the boron and arsenic which may compete with the process of gettering by argon implantation for some impurities, such as Cu, Fe, Ni, and Au, in the active device areas. After these modifications to the process the wafers proceeded through the BBr_3 base deposition at 875°C and a drive-in cycle of 925°C and resulted in a sheet resistance of 440 $\Omega/\square$. Then followed by an arsenic capsule emitter diffusion at 1000°C for 115 min, a sheet resistance of 14 $\Omega/\square$ resulted. Aluminum metallization then followed.

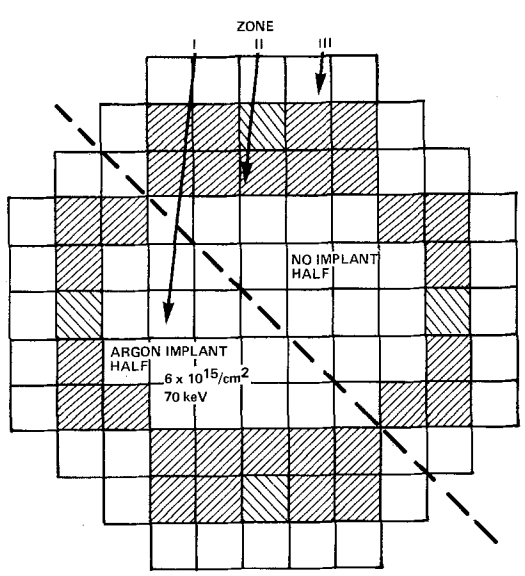


Fig. 2. Map of argon implant and zones on wafer

For the preemitter portion of the experiment, the wafers received standard processing through postbase drive-in. The back side of the wafers were stripped and implanted with argon as previously described. The preemitter wafers also received the pyrolytic SiO_2 layer on the back sides of the wafers. The wafers were then processed with arsenic capsule emitter diffusion and metallization as described before.

Results

The pipe densities to be discussed in this paper were calculated according to the relationship of

$$Y = 1 - P = e^{-\lambda A} \qquad [1]$$

where P is the probability that a device is piped, A is the total emitter area, λ is the defect density, and Y is the over-all yield of the devices.

Two different device structures were utilized in the experiments: a multiemitter transistor (MET), which contains 316 emitters in a common base of ~210 mil^2 with each individual emitter area of 0.2925 mil^2 (0.45 mil $\times$ 0.65 mil); an array of 1800 small single transistors, each having 0.0525 mil^2 of emitter area (0.15 mil $\times$ 0.35 mil) distributed in an array structure of ~35,000 mil^2.

The MET structures were electrically probed first. The criteria for a piped device is defined as BV_{CEO} equal to or less than 3V at 100 μA. The 316 emitters were tied together with common aluminum metallurgy. After the electrical testing, the MET structures and the array of small transistors (since they were too small for electrical testings) were anodized at 2.5V for 45 min in an electrolyte of 8% H_2SO_4 to decorate the aluminum on devices which are piped. One bad emitter in any of the 316 or 1800 emitters of the MET or array structure, respectively, was counted as a failed device for that particular structure. The over-all yield of the wafer is measured directly by counting the good devices, and the λ's are calculated according to Eq. [1].

All the data plots have the average values and are separated into three equal wafer zones as illustrated in Fig. 2.

Table I summarizes the results of the MET with the average λ's and yields. The preemitter gettering improves the defect density approximately by a factor of 3, from 11.90 to 3.76 $\times$ 10^{-3} defects per mil^2, whereas the prebase improves it by a factor of approximately 2, from 10.50 to 4.36 $\times$ 10^{-3} defects per mil^2. The overall yield on a whole wafer can be improved from 42.9 to 72.2% by the preemitter gettering process and from 44.9 to 63.4% by the prebase gettering process. The detailed improvement of the yield on three different zones of the wafer due to the two gettering processes is plotted in Fig. 3. The average yields for the wafers without gettering in zones I, II, and III are 76, 43, and 12 ~ 17%, respectively. This zonal dependency of yield indicates the susceptibility of wafers to dislocation generation at the periphery caused by handling at the various processing steps. These dislocations, in turn, tend to induce impurity precipitation or to cause enhanced diffusion to form pipes. The detailed aspect on the possible mechanism of pipe formation is given in the discussion section. According to Fig. 3, the prebase or preemitter gettering improved the yield by only about 2-10% to a final level of 75-84%, respectively, in zone I of the wafer. However, in zone II, the yield is improved by 30-37% to a final level of 73 and 80%, respectively. Likewise, in zone III, the yield is increased by 28-36% to a final level of 40 and 53%, respectively.

Table I. Yield and defect density of MET

Wafer zone	Preemitter Gettered Y (%)	Preemitter Gettered λ (10^{-3})	Preemitter Control Y (%)	Preemitter Control λ (10^{-3})	Prebase Gettered Y (%)	Prebase Gettered λ (10^{-3})	Prebase Control Y (%)	Prebase Control λ (10^{-3})
I	83.6	1.95	74.4	3.21	75.2	3.10	73.4	3.36
II	79.9	2.44	42.4	9.33	74.2	3.24	44.5	8.80
III	53.1	6.88	11.9	23.10	40.8	9.74	16.8	19.40
Avg	72.2	3.76	42.9	11.90	63.4	5.36	44.9	10.50

λ = Defect density, number of defects per mil².
Y = Yield of the devices in percent.

Table II. Yield and defect density of small transistors

Wafer zone	Preemitter Gettered Y (%)	Preemitter Gettered λ (10^{-3})	Preemitter Control Y (%)	Preemitter Control λ (10^{-3})	Prebase Gettered Y (%)	Prebase Gettered λ (10^{-3})	Prebase Control Y (%)	Prebase Control λ (10^{-3})
I	60.2	5.70	38.4	10.80	39.4	10.5	37.2	11.10
II	34.2	12.10	14.6	21.60	28.9	14.0	14.4	21.70
III	13.0	22.90	3.74	36.90	10.2	25.7	3.14	38.90
Avg	35.8	13.60	18.9	23.10	26.2	16.7	18.2	23.90

λ = Defect density, number of defects per mil².
Y = Yield of the devices in percent.

The larger improvement in zone II and III signifies that the pipe-forming defects are more numerous in these two zones than the one in the center and can be drastically reduced by the implantation gettering.

Table II summarizes results obtained on the small transistor structures. As previously shown for the MET, a significant improvement of defect density can also be realized by gettering. Preemitter achieves 1.7 times improvement on the average, *vs.* only 1.4 for the prebase. The over-all leakage limited yield on a whole wafer can be improved from 18.9 to 35.8% due to preemitter gettering process, and from 18.2 to 26.2% due to prebase gettering process. The detailed improvement of the yield on three different zones of the wafer due to the two gettering processes is plotted in Fig. 4. The average yield of the wafers without gettering in zone I, II, and III is only 37, 14, and 3%, respectively. They are much lower than those yields corresponding to the MET structure. This zonal dependency of yield for the small transistor structure points out once more the wafers' susceptibility to pipe formation at the peripheral area, even to a more significant degree as compared to the MET structure. But, nevertheless, after the prebase gettering, the yields are improved to 39.4, 28.9, and 10.2%, respectively, in zone I, II, and III of the wafers, and after the preemitter gettering, the yields are improved even more to 60.2, 34.2, and 13%, respectively, in zone I, II, and III of the wafers.

Although both the prebase and preemitter implantation gettering improve the yields of the small transistor structure considerably, they are still much lower than the yields of the MET structure. Searching some parameters to explain this phenomenon, Fig. 5 may offer something for contemplation. It illustrates the effect of the emitter perimeter to its area's ratio, *P/A*, on the leakage limited yield, and clearly indicates that the yield decreases as the ratio of the *P/A* increases. The work of Hu *et al.* (17) on dislocation propagation and emitter edge defects which are generated under

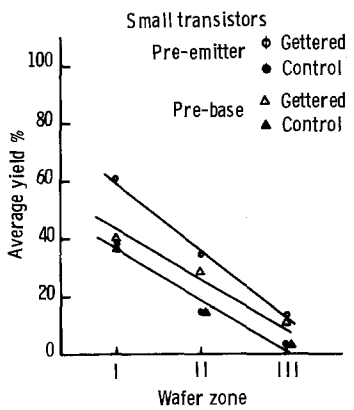


Fig. 4. Yield improvement and zone dependency on preemitter or prebase implanted wafers for small transistors.

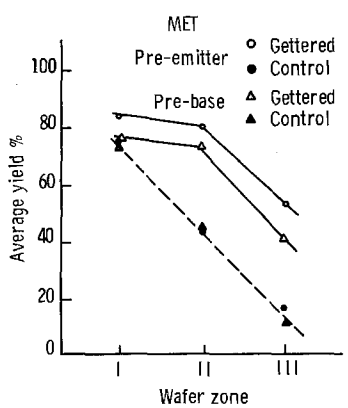


Fig. 3. Yield improvement and zone dependency on preemitter or prebase implanted wafers for multiemitter transistors (MET).

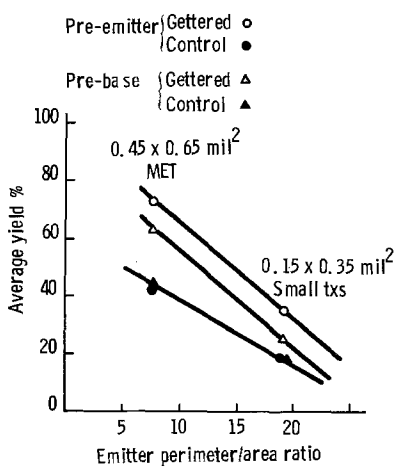


Fig. 5. Effect of emitter's perimeter to area ratio on over-all yield.

appropriate condition, cast off small dislocation half-loops. These half-loops which straddle the edges, may offer some explanation why the over-all yield is still low for the smaller transistors as compared to the MET, even after its improvement by either the preemitter or prebase gettering process.

Discussion

It is clearly demonstrated from the obtained results that the argon implant damage gettering is an effective method to improve the leakage-limited yield of the bipolar devices. The implantation gettering applied at the preemitter step appears to be more effective than when applied at the prebase step.

The lower gettering efficiency of the prebase process perhaps can be explained by the following. The prebase argon implanted wafer has to go through two more high temperature steps, namely, the base diffusion and drive-in, than the preemitter argon implanted wafers. These two high temperature processes anneal out some of the implantation damage, thus releasing some of the impurities associated with them. Once the impurities are redissolved, they can be redistributed toward those defects which were originally in the active device area or toward those new defects being created during the emitter diffusion to cause the formation of pipes or leaky junctions. Consequently, the efficiency of the prebase argon implantation gettering process cannot be as high as the preemitter process. Because preemitter gettering gives a higher yield than the prebase gettering, it not only renders further support to the pipe formation model caused by the enhanced diffusion along dislocations (4, 18, 19), but also rules out one of the other possible models (18) caused strictly by the impurity precipitates alone, as proposed by Lawrence (20). In his model, the pipes are claimed to be formed at the locally retarded base diffusion, *i.e.*, the base-collector junction, and the subsequently diffused emitter-base junction. However, the locally retarded base-collector junction is caused mainly by the copper or precipitates of other metals which are formed near the wafer surface before the base diffusion is carried out. Therefore if this model of impurity precipitation is thought to be responsible for the pipe formation, then the prebase implantation should be able to getter the precipitates, thus minimizing the retarded base diffusion and reducing the pipe formation. It should give higher yield than the preemitter gettered ones, since such a defect caused by the retarded base diffusion would already be formed by the time the preemitter gettering is given to the wafers.

On the other hand, Barson *et al.* (4) proposed that an enhanced emitter (phosphorus) diffusion along the stacking faults or dislocations is responsible for the pipe formation. The pipe densities are markedly increased when gold is being introduced before the emitter diffusions. Work by Campbell *et al.* has also shown an enhanced arsenic diffusion along epitaxial defects (21). In this study, although we did not purposely introduce any metal contaminants (such as gold or copper, etc.) during the process and used arsenic instead of phosphorus for the emitter, we feel that the enhanced diffusion model holds true here also. The argon implant damage sites in the back of the wafers are able to compete with the few crystalline defects in the active areas of the devices for the impurities, which were unintentionally introduced into the wafer during the processes. In other words, the argon implanted damage sites in the back of the wafers are the preferred sites for precipitation. When the arsenic emitter is introduced to the preemitter gettered wafers, the few dislocations in the base and collector regions have very few precipitates on them and thus much less enhancement of arsenic diffusion occurs. Consequently, a reduction of pipes and leaky junctions is realized.

Summary

Argon implantation has been successfully demonstrated in this paper to be an effective getter of impurities for the bipolar devices. It can reduce the excessive BV_{CEO} leakages, or "piped" devices, and thus increase the over-all yield of the integrated circuits. Although both the prebase and preemitter implantation are found to be useful, the latter is more effective. The significantly higher yield obtained by the preemitter gettering supports the model of enhanced diffusion along dislocations for the formation of pipes in the bipolar devices.

Manuscript submitted May 25, 1977; revised manuscript received July 26, 1977.

Any discussion of this paper will appear in a Discussion Section to be published in the June 1978 JOURNAL. All discussions for the June 1978 Discussion Section should be submitted by Feb. 1 1978.

Publication costs of this article were assisted by IBM Corporation.

REFERENCES

1. A. Goetzberger and W. Shockley, *J. Appl. Phys.*, **31**, 1821 (1960).
2. E. J. Mets, *This Journal*, **112**, 420 (1965).
3. J. E. Lawrence, *ibid.*, **112**, 796 (1965).
4. F. Barson, M. S. Hess, and M. M. Roy, *ibid.*, **116**, 304 (1969).
5. A. Goetzberger and C. Stephens, *ibid.*, **109**, 604 (1962).
6. J. E. Lambert and M. Rease, *Solid State Electron.*, **11**, 1055 (1968).
7. J. E. Lawrence, *Trans. Metall. Soc., AIME*, **242**, 484 (1968).
8. M. R. Poponiak, W. A. Keenan, and R. O. Schwenker, in "Semiconductor Silicon," H. R. Huff and R. R. Burgess, Editors, p. 701, The Electrochemical Society Softbound Symposium Series, Princeton, N.J. (1973).
9. R. L. Meek, T. E. Siedel, and A. G. Cullis, *This Journal*, **112**, 786 (1975).
10. B. Masters and J. Fairfield, *Radiation Effects*, **6**, 57 (1970).
11. T. M. Buck, K. A. Pickar, J. M. Poate, and C. M. Hsieh, *Appl. Phys. Lett.*, **21**, 485 (1972).
12. C. M. Hsieh, J. R. Mathews, H. D. Seidel, K. A. Pickar, and C. M. Drum. *ibid.*, **22**, 238 (1973).
13. T. E. Seidel and R. L. Meek, in "Ion Implantation in Semiconductor and Other Materials," B. L. Crowder, Editor, p. 305 Plenum Press (1973).
14. J. M. Poate and T. E. Seidel, *ibid.*, **317** (1973).
15. T. E. Seidel, R. L. Meek, and A. G. Cullis, *J. Appl. Phys.*, **46**, 600 (1975).
16. D. K. Seto, F. Barson, and B. F. Duncan, "Semiconductor Silicon," H. R. Huff and R. R. Burgess, Editors, p. 651, The Electrochemical Society Softbound Symposium Series, Princeton, N.J. (1973).
17. S. M. Hu, S. P. Klepner, R. O. Schwenker, and D. K. Seto, *J. Appl. Phys.*, **47**, 4098 (1976).
18. F. Barson, *IEEE J. Solid State Circuits*, **sc-11**, 4 (1976).
19. G. H. Plantinga, *IEEE Trans. Electron Devices*, **ed-16**, 394 (1969).
20. J. E. Lawrence, in "Semiconductor Silicon," H. R. Huff and R. R. Burgess, Editors, p. 17, The Electrochemical Society Softbound Symposium Series, Princeton, N.J. (1973).
21. D. R. Campbell, K. N. Tu, and R. O. Schwenker, *Thin Solid Films*, **25**, 213 (1975).

Hydride VPE Growth of GaAs for FET's

G. B. Stringfellow* and G. Hom

Hewlett-Packard Laboratories, Palo Alto, California 94304

ABSTRACT

Epitaxial layers of GaAs suitable for fabrication of MESFET devices have been grown by the hydride VPE technique (AsH_3 + HCl + Ga + H_2). The materials properties and FET characteristics of devices fabricated in this material are similar to those for LPE, and the more common $AsCl_3$ VPE growth techniques. The uniformity of sheet resistance of this material over a substrate area of ~6.5 cm^2 is typically ~5% (standard deviation from the mean). A new technique has been developed for the growth of buffer layers. The background doping level of 4-9 × 10^{15} cm^{-3} is found to be reduced to $<10^{14}$ cm^{-3} by the addition of NH_3 to the AsH_3 stream. More complex $n^+/n/$ buffer layer structures have been grown in a single operation by simply programming gas flow rates during the run.

GaAs epitaxial layers for microwave devices are usually grown by either LPE from a Ga-rich melt (1, 2) or by VPE using the $AsCl_3$ technique (3-5). Less extensive work has been performed on the hydride (AsH_3 + HCl + Ga) VPE technique (6-8) and recently molecular beam epitaxy (MBE) has been shown to be suitable for GaAs FET devices (9). The reason for the limited utilization of the hydride VPE process which has been highly developed for $GaAs_{1-x}P_x$ LED applications lies in the fact that the residual impurity level of GaAs grown by this technique is relatively high, typically 10^{15}-10^{16} cm^{-3} (6, 8, 10). LPE and $AsCl_3$ VPE processes routinely produce material with $N_D - N_A < 10^{14}$ cm^{-3} and $\mu_{77} > 10^5$ cm^2/V sec (1-5, 11). For Gunn effect devices, such low doping levels are required. For FET's, the active layer is doped to ~10^{17} cm^{-3} and low carrier concentrations are necessary only for the buffer layer separating the active layer from the Cr doped semi-insulating substrate. The buffer layer is necessary since the substrate may produce undesirable effects near the substrate/epilayer interface. On the other hand, the highly developed hydride VPE technique offers distinct advantages over both LPE and $AsCl_3$ VPE techniques. It offers maximum flexibility of operation. For example, in the hydride technique, the Ga sees only HCl and H_2 and need not be saturated with As as is necessary in LPE and the trichloride technique. This saves a step in the growth process and facilitates rapid change of composition during alloy growth. Furthermore, the III/V ratio in the vapor phase and hence solid stoichiometry is an independent variable only in the hydride system. Another advantage of the hydride system is its suitability for commercial applications, since it has been developed to large-scale production capacity for GaAsP growth. This contrasts with $AsCl_3$ and LPE systems which are typically laboratory scale. LPE has the additional drawback of typically providing inadequate control of growth morphology and thickness uniformity (12, 13).

The purpose of the present paper is to describe the application of a standard hydride process to the production of GaAs for FET applications. Particular emphasis will be placed on a new technique for the production of layers with low residual doping levels ($<10^{14}$ cm^{-3}).

Experimental

The rf heated reactor used in this work was developed for GaAsP growth (9) but a modified version used for GaAs is shown in Fig. 1. The modifications include the addition of four-way valves in close proximity to provide a short residence time of the reactants in the gas lines and thus allow the rapid, well-controlled initiation and termination of growth necessary for precise control of the thickness of submicron layers. The gases used are hydrogen purified by diffusion through a Pd-Ag membrane and electronic grade AsH_3, HCl, and H_2S (used for n-type doping).

The growth conditions were selected to give (*i*) a growth rate of ~0.1 μ/min which yields the necessary control of thickness for submicron layers; (*ii*) good morphology (III/V ratio ~6); and (*iii*) insensitivity to temperature gradients of ~15° existing across the graphite pedestal. The latter is accomplished by growing at a substrate temperature of ~750°C, near the maximum of the growth rate *vs.* temperature curve where the growth rate is least sensitive to temperature (14). The flow rates used are: f_{HCl} = 2.0 scc/min, f_{AsH_3} (1%) = 30 scc/min, f_{H_2} = 300 scc/min.

All substrates were Cr-doped semi-insulating ($\rho > 10^6$ Ω-cm) GaAs oriented 2.5° ± 0.5° off the (100) plane toward (110). Substrates were prepared directly

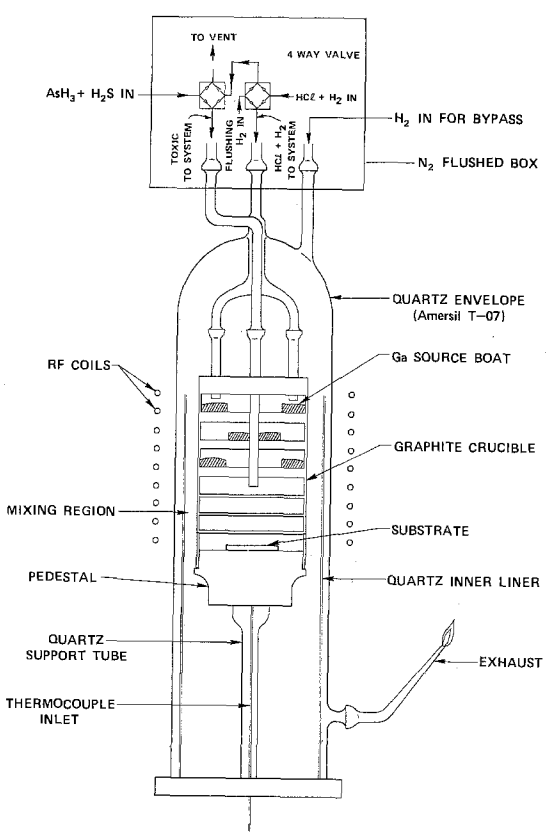


Fig. 1. Schematic diagram of VPE reactor used for GaAs growth

* Electrochemical Society Active Member.

Key words: vapor phase epitaxy, GaAs, buffer layers, FET material.

before placing them in the reactor using standard Br-methanol polishing techniques.

During heat-up the substrate is maintained in a $AsH_3 + H_2$ ambient, $P_{AsH_3} \sim 10^{-3}$, to avoid deleterious surface decomposition. Growth is initiated by turning the four-way HCl valve near the entrance to the reactor. The same valve is used to terminate growth and the sample is cooled in $AsH_3 + H_2$.

Measurements were made to determine thickness uniformity and carrier concentration and mobility. The latter were performed using standard van der Pauw techniques. The thickness and doping uniformity were monitored using groove and stain techniques, standard *C-V* profile measurements, and a new contactless technique for conductance measurements (15). The technique consists of placing the resistive layer (on a dielectric substrate) in a waveguide, perpendicular to its axis. The loss at 18 GHz is then measured to determine the sheet resistance of the epitaxial GaAs layer. The sheet resistance of an entire wafer could be rapidly sampled at 3 mm intervals using this technique.

Results

Single layer structures.—With appropriate care in substrate preparation and proper substrate orientation, the morphology of submicron layers is perfectly specular with no visible morphological defects such as hillocks, pyramids, or terraces even when viewed using the Nomarski interference technique. Small pits associated with particles left on the surface after substrate preparation are frequently observed.

For FET structures, the layers are S-doped to $\sim 1 \times 10^{17}$ cm^{-3} using H_2S. In Fig. 2, the carrier concentration is plotted *vs.* H_2S partial pressure. The results plotted on a log-log scale follow a linear relationship with a slope of ~1.1, similar to previous results reported by Enstrom *et al.* (8). The residual doping level with no intentional doping was found to be in the range of $4\text{-}9 \times 10^{15}$ cm^{-3}. A plot of room temperature mobility *vs.* $N_D - N_A$ is shown in Fig. 3. The mobilities fall on the solid line calculated after Rode and Knight (16) for a constant acceptor concentration of 5×10^{15} cm^{-3}. For $n = 1 \times 10^{17}$ cm^{-3}, values of room temperature mobility of 4500 cm^2/V sec are consistently observed. *C-V* profiles of $N_D - N_A$ *vs.* depth from the epilayer surface were obtained as illustrated in Fig. 4. In general, the doping in the epilayer is constant with an abrupt decrease at the substrate/epilayer interface.

The uniformity of sheet conductance (doping level × thickness) is shown for a representative sample in Fig. 5. The data obtained using a contactless microwave loss technique (15) indicate that the thickness gradually increases toward the outside of the substrate. The values at the very edge are unreliable because of inaccuracies in the measurement technique. Eliminating these data labeled A, B, and C in the figure results in a standard deviation from the mean of <5%. Values of ~5% for a 6.5 cm^2 substrate area are routinely observed. Thus the hydride VPE system can be used to grow uniform layers well suited for FET fabrication.

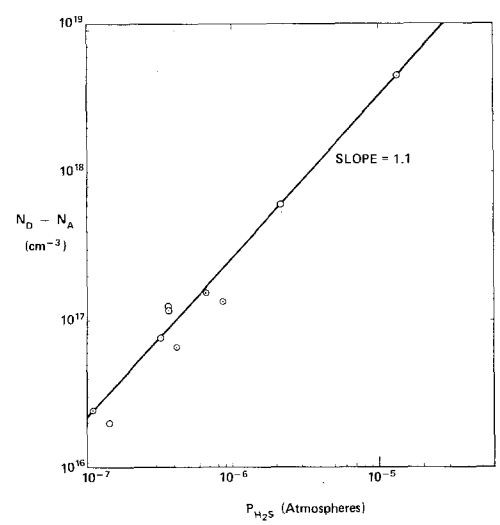


Fig. 2. Net doping density *vs.* partial pressure of hydrogen sulfide for GaAs epitaxial layers.

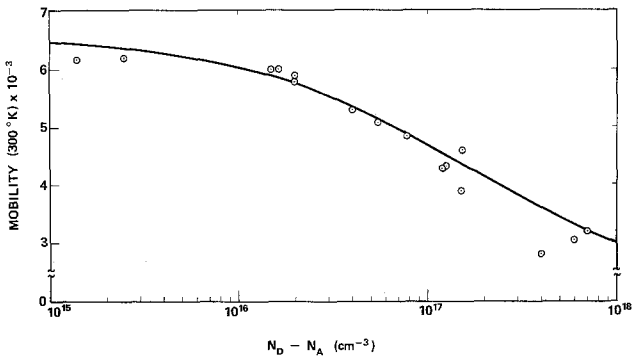


Fig. 3. Room temperature mobility *vs.* doping density of n-type GaAs epitaxial layers. Solid line calculated after Rode (16).

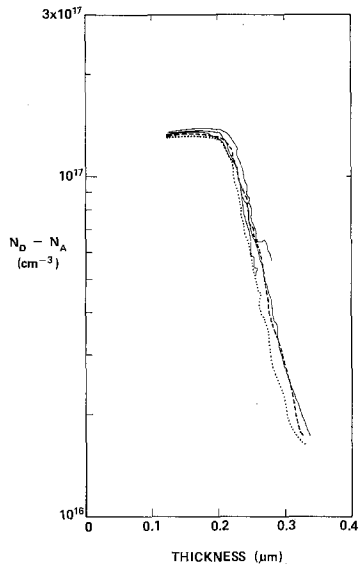


Fig. 4. Doping density *vs.* distance from the top surface for several Schottky barriers fabricated on a thin epitaxial layer typical of those used for FET fabrication.

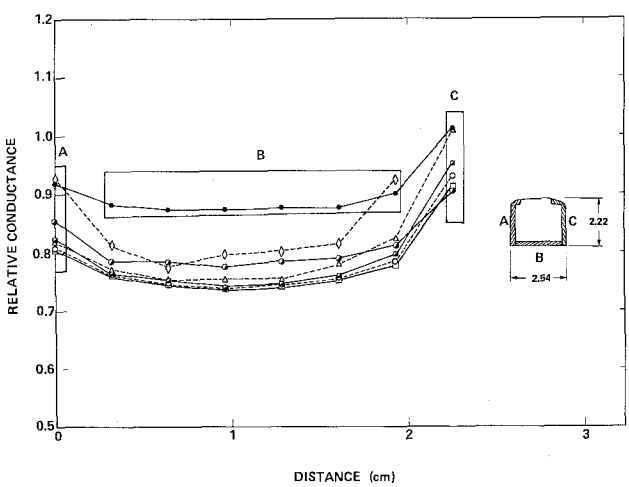


Fig. 5. Relative conductance measured using the contactless microwave loss technique *vs.* position on the surface.

Multiple layer structures.—FET's fabricated in VPE material grown directly on Cr-doped substrates were found to have back-biasing problems, *i.e.*, the transconductance of one FET under a given bias was found to be affected by the bias on an adjacent device or by the application of a bias to the substrate. This effect is occasionally observed in LPE material also and is thought to be due to states, possibly acceptors, at the substrate/epilayer interface (4, 17, 18). To avoid this and to effectively isolate the active region from the substrate, it is desirable to grow a buffer layer between the n epilayer and the substrate.

In LPE and $AsCl_3$ VPE systems, the buffer layer is usually simply an undoped layer. Values of $N_D - N_A$ of $<5 \times 10^{13}$ cm^{-3} have been reported by many workers for both the $AsCl_3$ system (3, 4, 11) and the LPE system (1, 2, 11). The hydride system is typically characterized by much larger residual doping levels in the range 10^{15}-10^{16} cm^{-3} although doping levels in the 5×10^{14} cm^{-3} range have been claimed for specially selected AsH_3 and HCl cylinders (7).

Several approaches have been taken to reduce the doping level of GaAs for use as buffer layers. Cr doping is used to make melt-grown GaAs semi-insulating and has been used successfully as a dopant for semi-insulating VPE material (19), but is less successful in LPE systems(20). A better approach is to attempt to reduce the concentration of contaminants, rather than over doping with a deep-lying impurity. Since Si is believed to be a major contributor to the contamination, the addition of H_2O to the system to form SiO_2 has been successfully used to control residual doping (21, 22); however, O itself is an undesirable deep donor which limits the usefulness of this approach. A similar approach using NH_3 to remove Si from the system as Si_3N_4 has been effective in reducing the background doping level of GaP grown in similar systems from $\sim 10^{17}$ cm^{-3} to $<10^{15}$ cm^{-3} (23).

For our VPE system using electronic grade AsH_3 and HCl, the residual doping level of 4-9 $\times 10^{15}$ cm^{-3} is much too high for buffer layer growth. Attempts were made to reduce this doping level by intentional introduction of NH_3 and, alternatively, H_2O into the system. The H_2O approach was abandoned at an early stage because it resulted in very poor morphology, even though it did act to reduce n to $\sim 10^{14}$ cm^{-3}.

To test the effect of NH_3, partial pressures of up to 6×10^{-2} Torr were introduced during the growth of otherwise undoped epilayers. The morphology was found to be excellent, at least as good as without NH_3 present. The presence of NH_3 also dramatically reduced the background doping level to below 10^{13} cm^{-3} in some cases. Unexpectedly, the residual doping level was observed to begin to increase after $\sim 3\mu$ of growth had occurred, as demonstrated in Fig. 6-8, where the doping profiles for buffer layers grown with three different NH_3 partial pressures of 0.06, 0.04, and 0.02 are plotted. Clearly the value of $N_D - N_A$ is reduced by the presence of NH_3, but the total thickness over which $N_D - N_A$ is reduced and the magnitude of the reduction are dependent on the NH_3 partial pressure. In Fig. 9, the value of $N_D - N_A$ observed is plotted *vs.* NH_3 partial pressure.

To make useful FET structures, it is necessary to introduce H_2S to form an abrupt n/buffer layer interface. It was found that simply turning on the H_2S during the growth results in a gradual increase in doping level, the resulting n/buffer layer interface not being abrupt enough for FET applications. By turning off the HCl flow for ~ 5 min while the H_2S concentration is being equilibrated and then continuing growth, abrupt profiles are obtained. An example is shown in Fig. 10.

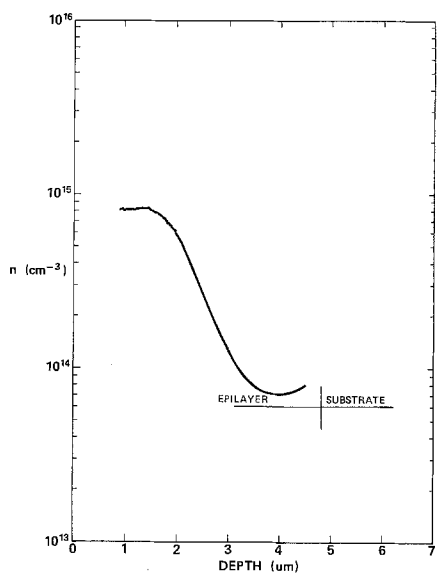


Fig. 7. Doping profile obtained from C-V measurements on a buffer layer grown with $p_{NH_3} = 4 \times 10^{-2}$.

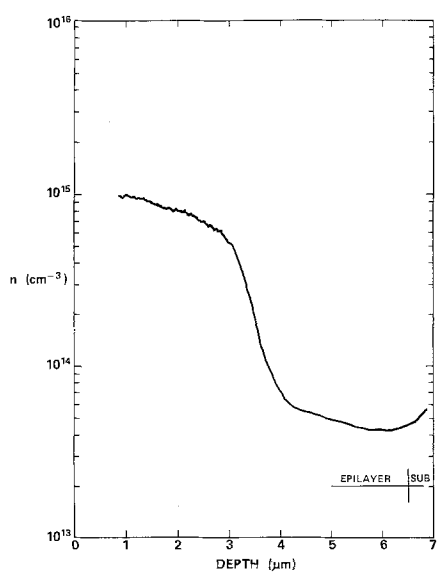


Fig. 6. Doping profile obtained from C-V measurement on buffer layers grown with $p_{NH_3} = 6 \times 10^{-2}$. The epilayer thickness was determined by the cleave and stain technique at the Schottky barrier.

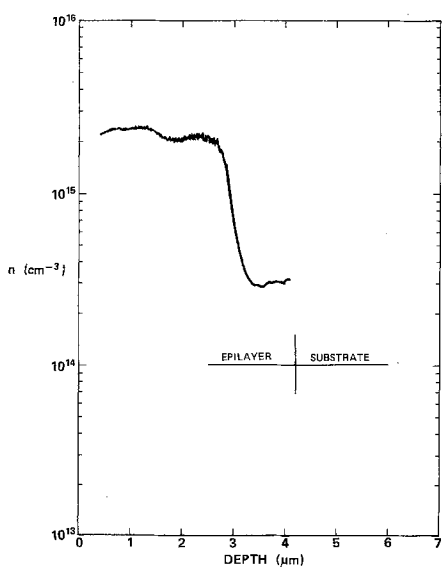


Fig. 8. Doping profile obtained from C-V measurements on a buffer layer grown with $p_{NH_3} = 2 \times 10^{-2}$.

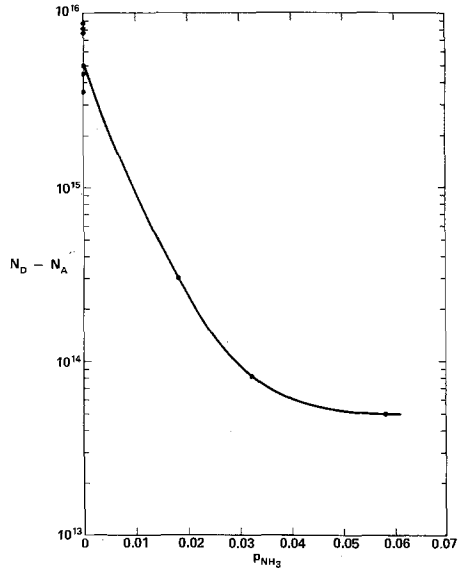


Fig. 9. Carrier concentration, measured at a position 1-2 μm from the buffer layer/substrate interface, vs. NH_3 partial pressure in the system during growth.

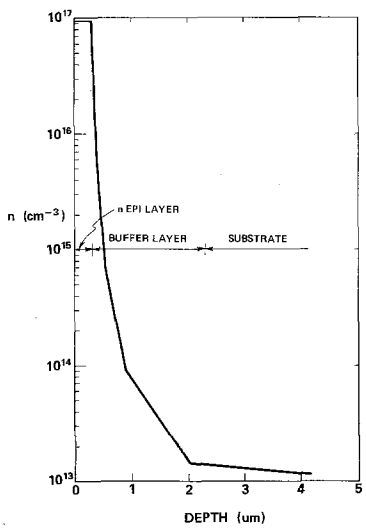


Fig. 10. Doping profile obtained from C-V measurements of n/buffer/substrate structure. The n-layer thickness is ~0.3μ, calculated knowing growth rate and time of growth and the buffer layer thickness is 2μ obtained by staining a cleaved cross section near the Schottky barrier.

The steepness of the profile can be characterized by the slope in micrometers/decade. This number is typically 0.05 μm/decade for n/buffer layer structures and 0.05-0.1 μm/decade for n/substrate structures. Another important characteristic of the profile is the absence of evidence for states at the substrate/buffer layer interface. Measurements on FET's fabricated in n layers with the buffer layer present indicate that the backbiasing effect is essentially eliminated. Furthermore, no looping in the low frequency *I-V* characteristics was observed (24).

The reproducibility of growing the n/buffer/substrate structures is excellent with run-to-run deviation in layer conductance being ~10%. The uniformity of the n-layer sheet resistance for the n/buffer layer structures is similar to n layers grown directly on the substrate. Typically, the standard deviation is ~5%.

Recently, n^+/n/buffer layer structures have proven to be superior for high power FET's (25). Such structures can be readily grown using the present system by simply increasing the H_2S flow rate after the 0.3μ thick 10^{17} cm^{-3} active layer growth is completed. The doping profile obtained by successively thinning such a structure is shown in Fig. 11.

Discussion

A potential problem with NH_3 additions to the system to produce buffer layers is that it might introduce N into the GaAs layer and adversely affect its electron mobility (23). Experimentally, the doping level cannot be determined since the layer of interest is <3 μm thick with n $<10^{14}$ cm^{-3}. For such a layer, surface states would cause depletion of the entire layer in a Hall effect or van der Pauw specimen. An idea of the effect of N doping can be obtained by comparison with GaP results. In GaP, the nitrogen is introduced intentionally because it acts as a radiative recombination center to improve the efficiency of green LED's. However, the concentration of N expected to be incorporated into the GaAs solid is small because of the large difference in size between N and As. A quantitative estimate of the solid solubility and distribution coefficient of N in GaAs can be made using thermodynamic calculations which correctly predict these quantities in GaP. The solid solubility is simply given by the expression

$$x = \exp(-\Delta H_D^*/RT)$$

with ΔH_D^* calculated from the DLP model (26) using the expression

$$\Delta H_D^* = \Omega^s = 4.375 \times 1.15 \times 10^7 \, \Delta a_0^2/a^{4.5}$$

to yield $\Omega = 4.55 \times 10^4$ cal/mole and $x^* = 5 \times 10^{12}$ cm^{-3}. The actual concentration may be somewhat larger than this due to kinetic effects, as observed for GaP (27), however, an upper limit is given by the NH_3 partial pressure times the nitrogen distribution coefficient. The distribution coefficient may be calculated again using the DLP model

$$k = \frac{x_{GaN^s}}{p_{NH3}} = \frac{p_{GaCl}}{p_{HCl}p_{H_2}} \exp\left(\frac{-\Delta G^\circ}{RT}\right) \frac{1}{\gamma_{GaN^s}}$$

ΔG° for GaN formation was obtained from Thurmond and Logan (28) and the activity coefficient of GaN in solid GaAs-rich phase is given by the expression

$$RT \ln \gamma_s = \Omega^s$$

with $\Omega = 4.55 \times 10^4$ cal/mole as calculated above. The values of p_{HCl} and p_{GaCl} are the partial pressures at the growth interface and hence must be calculated. Using standard thermochemical techniques (27), we obtain values of 9.25×10^{-4} and 4.76×10^{-3} for p_{HCl} and

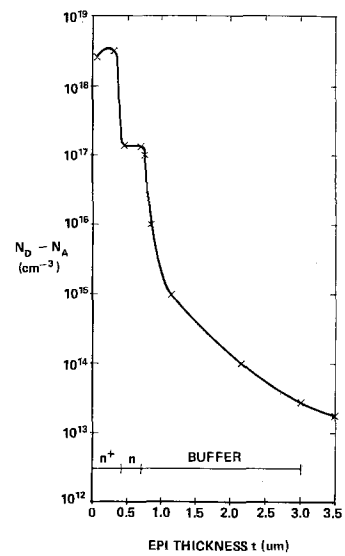


Fig. 11. Doping profile for n^+/n/buffer layer structure obtained by successive etching and C-V profile measurements.

p_{GaCl}, respectively. Multiplying the distribution coefficient by the highest NH_3 partial pressure used, 6×10^{-2}, yields the highest N concentration expected, 10^{14} cm^{-3}. Thus, thermochemical calculations indicate the nitrogen concentration in the solid should be between 5×10^{12} and 10^{14} cm^{-3}. Even at 10^{14} cm^{-3} the effect on the mobility would be small. A calculation of the mobility limited by N scattering at this doping level (27) yields a mobility many orders of magnitude larger than the polar optical mode scattering limited mobility.

The reason for the increase in $N_D - N_A$ after the first few microns of growth is unclear. Three possible mechanisms were tested and found untenable. (*i*) The possibility of NH_3 decomposition during the run was tested by quantitative analysis of the NH_3 content of exhaust gases collected from the cold reactor, hot reactor before growth, and hot reactor immediately after the termination of growth. Less than 3% decomposition was detected in all cases. (*ii*) A similar increase of doping level in buffer layers grown by the $AsCl_3$ VPE technique has been reported (4, 18). The effect was attributed to the out-diffusion of an acceptor from the substrate to compensate the adjacent section of the buffer layer. Thus slower growth rates which give longer times for the diffusion to take place were intentionally adopted to maximize the effect (18). This mechanism was tested by simply growing several microns of undoped GaAs before introducing NH_3 into the reactor. The results, as shown in Fig. 12, indicate that the NH_3 is fully as effective when the growing layer is isolated from the substrate. (*iii*) Since impurities may well be released from the graphite during growth, the effect may be due to either acceptors being released during the initial 20-30 min of growth or donors being released after 30 min due to diffusion through a skin purified by a high temperature HCl cleaning of the graphite between runs. This hypothesis was disproved by noting that the same phenomenon is observed with no clean-up between runs. To date, we do not understand the cause of the increase in doping after 2-3μ of growth but since we need only 2μ buffer layers, the technique is practical. Our experience with more than 100 runs indicates that the effect is reproducible. Similar profiles are measured for all runs investigated.

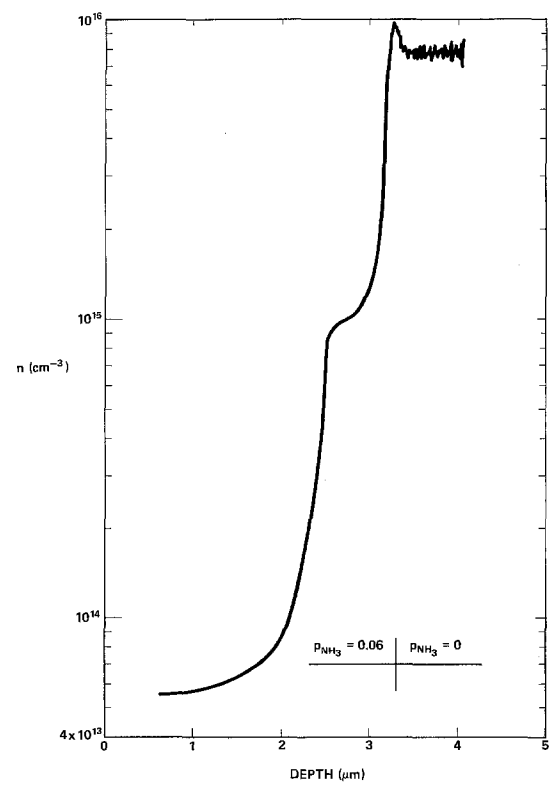


Fig. 12. Doping profile (from C-V measurements) on an epitaxial layer for which the first 3.0μ were grown undoped without NH_3 after which NH_3 ($p = 6 \times 10^{-2}$) was introduced for the remainder of the growth cycle.

Summary

The standard $AsH_3 + HCl + Ga + H_2$ VPE system widely used for large scale commercial $GaAs_{1-x}P_x$ and GaP growth has been demonstrated to be suitable for the growth of GaAs for FET applications. The material properties and FET characteristics of devices fabricated in this material are similar to those for $AsCl_3$ VPE and LPE material. The uniformity of sheet resistance is typically 5% (standard deviation from the mean).

A technique has been developed for the growth of buffer layers with $n < 10^{14}$ cm^{-3} by adding NH_3 to the gas stream. This makes the system versatile and flexible to the extent that multiple layers can be grown with nearly any desired profile from abrupt to gradually increasing, with doping levels between 10^{14} and $> 10^{18}$ cm^{-3}. Furthermore, this can be done in a single operation by simply programming gas flow rates.

The hydride VPE system has clear advantages in that it is more flexible and has been scaled up for large-scale commercial production and hence may ultimately be the most useful technique for commercial production of GaAs for FET applications.

Acknowledgments

The authors gratefully acknowledge the assistance of C. Liechti and R. Van Tuyl who fabricated FET's in the VPE material and measured their properties, and R. Burmeister and P. Greene for helpful discussions and comments on the manuscript.

Manuscript submitted April 25, 1977 revised manuscript received Aug. 1, 1977.

Any discussion of this paper will appear in a Discussion Section to be published in the June 1978 JOURNAL. All discussions for the June 1978 Discussion Section should be submitted by Feb. 1, 1978.

Publication costs of this article were assisted by Hewlett-Packard Company.

REFERENCES

1. H. G. B. Hicks and D. F. Manley, *Solid State Commun.*, **7**, 1463 (1969).
2. J. Vilms and J. P. Garrett, *Solid-State Electron.*, **15**, 443 (1972).
3. J. V. DiLorenzo, *J. Cryst. Growth*, **17**, 189 (1972).
4. R. Fairman and R. Solomon, *This Journal*, **120**, 541 (1973).
5. T. Aoki, *Jpn. J. Appl. Phys.*, **14**, 1267 (1975).
6. J. J. Tietjen, G. Kupsky, and H. Gossenberger, *Solid-State Electron.*, **9**, 1049 (1966).
7. R. E. Enstrom and C. C. Peterson, *Trans. Metall. Soc. AIME*, **239**, 513 (1967).
8. R. E. Enstrom, C. J. Nuese, J. R. Appert, and J. J. Gannon, *This Journal*, **121**, 1516 (1974).
9. A. Y. Cho and D. R. Ch'en, *Appl. Phys. Lett.*, **28**, 30 (1976).
10. R. A. Burmeister, G. P. Pighini, and P. E. Greene, *Trans. AIME*, **245**, 587 (1969).
11. C. M. Wolfe and G. E. Stillman, Proceedings of the 1970 Symposium on GaAs, Institute of Physics, Physics Society, p. 3 (1971).
12. A. Doi, T. Asano, and M. Migitaka, *J. Appl. Phys.*, **47**, 1589 (1976).
13. H. Morcoc and L. F. Eastman, *This Journal*, **123**, 906 (1976).
14. D. W. Shaw, *J. Cryst. Growth*, **8**, 117 (1971).
15. I. Lamoth, C. A. Liechti, and G. Epprecht, 1976 IEEE Workshop on Compound Semiconductor Microwave Materials and Devices, San Diego, Calif. (1976).
16. D. L. Rode and S. Knight, *Phys. Rev. B*, **3**, 2534 (1971).
17. W. C. Niehaus, H. M. Cox, B. S. Hewitt, S. H. Wemple, J. V. DiLorenzo, W. O. Schlosser, and F. M. Magalhaes, Proceedings of the 1976 North American GaAs Symposium, Institute of Physics, Physics Society, p. 271 (1977).
18. H. M. Cox and J. V. DiLorenzo, *ibid.*

19. O. Mizuno, S. Kikuchi, and Y. Seki, *Jpn. J. Appl. Phys*, **10**, 208 (1971).
20. A. Schlacketzki and H. Salow, *Appl. Phys.*, **7**, 195 (1975).
21. H. G. B. Hicks and P. D. Greene, Proceedings of the 1970 Symposium on GaAs, Institute of Physics, Physics Society, p. 92 (1971).
22. M. E. Weiner, *This Journal*, **119**, 496 (1972).
23. G. B. Stringfellow, H. T. Hall, Jr., and R. A. Burmeister, Jr., *J. Appl. Phys.*, **46**, 3006 (1975).
24. R. Van Tuyl, Private communication.
25. I. Crossley, I. H. Goodridge, M. J. Cardwell, and R. S. Butlin, Proceedings of the 1976 North American GaAs Symposium, Institute of Physics, Physics Society, p. 289 (1977).
26. G. B. Stringfellow, *J. Cryst. Growth*, **27**, 21 (1974).
27. G. B. Stringfellow, M. E. Weiner, and R. A. Burmeister, Jr., *J. Electron. Mater.*, **4**, 363 (1975).
28. C. D. Thurmond and R. A. Logan, *This Journal*, **119**, 622 (1972).

Technical Note

On SiOH and SiH Groups in SiO_2 Films on Silicon

A. G. Revesz

COMSAT Laboratories, Clarksburg, Maryland 20734

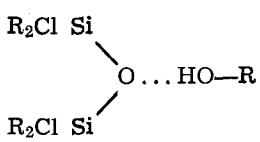
There is increasing evidence that hydrogen in various forms plays a very important role in almost all aspects of Si/SiO_2 interface structures; most of the evidence has been inferred from very sensitive but nonspecific electrical measurements.[1] Various aspects of incorporation of hydrogen into the SiO_2 film during its growth and postoxidation treatments have also been studied with radioactive tracer techniques (3-6). These techniques are sufficiently sensitive, but they cannot distinguish between the various forms of hydrogen. This information can be obtained by internal reflection infrared absorption spectroscopy, as was demonstrated by Beckmann and Harrick (7). Subsequently, the same technique was also applied by Hughes and Pankey to Si/SiO_2 structures prepared under well-defined conditions with the intention of gaining insight into their irradiation behavior (8).

The purpose of this note is to enhance our understanding of the complex role of hydrogen in thermally grown SiO_2 films on silicon by putting the results of Ref. (7) and (8) into proper perspective, particularly by comparing them with *IR* spectroscopic data of fused silica, silicate glasses, and various organosilicon compounds.

The most pertinent *IR* spectroscopic data of Ref. (7) and (8) are summarized in Table I. It should be noted that the "dry" and "wet" oxidization methods as described in Ref. (7) refer to an oxidizing ambient of oxygen with 60 ppm H_2O and oxygen saturated with H_2O at 85°C, respectively. The assignment of the various absorption peaks was discussed in detail (7), but this can be put into a better perspective by the following comparison. Fused silica may contain SiOH (silanol) groups which are isolated. That is, the H does not form a hydrogen bond with oxygen; the OH bond of these silanol groups absorbs at 3600 cm^{-1} (9). The OH bond in silanol groups formed by H_2O adsorption on the silica surface absorbs at 3750 cm^{-1} if there is no H-bond between adjacent SiOH groups, and at 3607 cm^{-1} if there is H-bonding between them. Adsorbed H_2O molecules which are H-bonded to surface SiOH groups absorb at 3480 cm^{-1} (10). Further comparison can be made with the absorption peaks of OH groups in organosilanols, which are around 3680 cm^{-1} (11). Although H-bonded silanol groups have not been observed in fused SiO_2, they occur in silicate glasses where they absorb in the range of 2600-3000 cm^{-1} (medium interaction), or at 2350 cm^{-1} (strong interaction) (9). The SiH bonds in SiH_4 and its derivatives absorb in the range of 2180-2260 cm^{-1} (12), and those present in chemically or electrochemically produced stain films on silicon surfaces absorb between 2000 and 2300 cm^{-1} (13).

Based on this comparison, some data in Table I warrant discussion. First, the absorption peak at 3700 cm^{-1} may indicate that the SiOH groups in that particular sample behave somewhat differently from silanol groups in fused SiO_2. Also, the 2800 cm^{-1} peak is unexpectedly high for SiH. The observation that these absorption peaks shifted to lower values (to 3600 cm^{-1} for OH and 2400 cm^{-1} for SiH) as a result of irradiation indicates that the bonds were considerably strained in the as-grown oxide film, and then relaxed during irradiation. There is additional evidence that this oxide film is structurally strained; its density increased by ~13% during irradiation (14). This increase is much higher than that observed with irradiated fused SiO_2 (~3%) (15). In the irradiation-induced relaxed state, both OH and SiH bonds absorb at wave numbers which are comparable with those given in Ref. (7).

The absorption peaks at 3375 and 3200 cm^{-1} were attributed to H-bonded OH groups in Ref. (7) and (8), respectively. This assignment is not so obvious, because it is known that silanol groups in fused silica do not form H-bonds (9). The shifts in the absorption peaks due to H-bonding (relative to isolated OH groups) are 225 and 500 cm^{-1}. These values are larger than those characteristic of



(where R is an organic group), or similar configurations: 45-85 cm^{-1} (16). In SiO_2 the oxygen atoms attached to the Si atoms are more electronegative than chlorine or organic groups; hence, the effective nega-

Key words: SiO_2 films, hydrogen and thermal growth, *IR* spectroscopic data.

[1] In addition to electrical measurements, some more specific and/or structure-sensitive methods (EPR, cathode-luminescence, electron injection, etc.) have also demonstrated the effects of hydrogen. These results and other chemical and structural aspects of the Si/SiO_2 interface are summarized in Ref. (1).
The effects of low temperature hydrogen treatment are summarized in Ref. (2).

Table I. Average concentration (cm^{-3}) of Si-OH and Si-H groups in SiO_2 films

Oxidation	Annealing method	Irradiation, 10^8 rad (Si) (no field)	Observed absorption peak (cm^{-1}) and assignment: ~3700 OH	3600 OH	3375 OH...O	3200 OH...O	2800 SiH	2400 SiH	~2350 SiH	2250 SiH...O
Thermal (7) ("dry" O_2, 1100°C)	—	No		$<10^{19}$						7×10^{19}
Thermal (7) ("dry" O_2, 1100°C)	350°C, H_2, 30 min	No								10^{20}
Thermal (7) ("wet" O_2, 1050°C)		No		10^{19}						5×10^{19}
Thermal (7) ("wet" O_2, 1050°C)	350°C, H_2, 30 min	No								5×10^{19}
Anodic (7)		No			$\sim 5 \times 10^{20}$				2×10^{21}	
Anodic (7)	300°C, N_2, 30 min	No			$\sim 5 \times 10^{20}$					
Anodic (7)	500°C, N_2, 30 min	No		$\sim 5 \times 10^{20}$						
Thermal (8) (dry O_2, SiO_2 tube)		No	2.7×10^{19}			9.6×10^{18}	3.4×10^{21}			
Thermal (8) (dry O_2, SiO_2 tube)		Yes		2.7×10^{19}		9.6×10^{18}		3.4×10^{22}		
Thermal (8) (dry O_2, SiO_2 tube)	1000°C, N_2, 30 min	No	1.7×10^{21}			•	1.7×10^{22}			
Thermal (8) (dry O_2, SiO_2 tube)	1000°C, N_2, 30 min	Yes		1.7×10^{21}		•		1.7×10^{22}		
Thermal (8) (dry O_2, Si tube)	1000°C, N_2, 30 min	No				2.9×10^{20}			1.8×10^{21}	
Thermal (8) (dry O_2, Si tube)	1000°C, N_2, 30 min	Yes				2.9×10^{20}			1.8×10^{21}	

The thermal oxidation and heat-treatments in Ref. (7) were performed in SiO_2 tube furnaces.
• Could not be resolved.

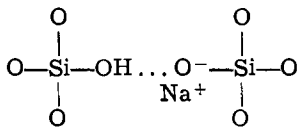
tive charge on the bridging oxygen between two Si atoms is even less [due to increased $d\pi$-$p\pi$ bonding between silicon and oxygen (16)], and the shift resulting from H-bonding would be smaller yet. Therefore the extent of shift indicates that H-bonding in these SiO_2 films does not involve bridging oxygen.

The 225 cm^{-1} shift (from 3600 to 3375 cm^{-1}) (7) is comparable to that characteristic of H-bonding in organo-silanols

$$R_3Si—OH \ldots {}_H O—SiR_3$$

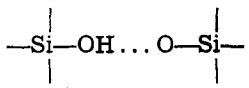
which ranges from 185 to 223 cm^{-1} (11). However, since the density of the SiOH groups in that particular SiO_2 film is $\sim 5 \times 10^{20}$ cm^{-3} (corresponding to 1/40 for the OH/Si ratio), it is unlikely that the silanol groups would form H-bonds with each other provided that their distribution is more or less uniform. On the other hand, if the silanol groups were aligned preferentially along structural channels (1), then H-bonding between them might be possible. It was shown that large concentrations of hydroxyl (6) and water (5) can be injected into SiO_2 films; it was suggested in both cases that structural channels are responsible for the effect. It is conceivable that SiOH groups along these channels are more similar to those adsorbed on SiO_2 surfaces than to those present in bulk-fused silica. Another possibility is that the hydrogen-bonded silanol groups are confined to a relatively small region in the SiO_2 film rather than being distributed uniformly along channels, so that the local OH/Si ratio there is much higher than 1/40.

The larger shift attributed to H-bonding, 500 cm^{-1} (from 3700 to 3200 cm^{-1}) (8), is more comparable to those characteristic of silicate glasses: 640-800 cm^{-1} (9). In the case of glasses, the H-bond forms in the following manner



In this configuration the oxygen adjacent to the sodium is more ionic than in the silanol-silanol configuration; consequently, the H-bond is stronger and the shift in the OH absorption peak is larger. It is known that, depending on preparation conditions, the Na concentration in thermally grown SiO_2 films can be between 10^{15} and 10^{19} cm^{-3}. The upper limit is ten times less than the concentration of OH groups exhibiting the large shift. Thus, it is possible that Na present in the SiO_2 film is partially responsible for the effect.

Another, and even more likely, possibility is that the OH groups form H-bonds with nonbridging oxygen atoms which are not associated with a Na^+ ion



These nonbridging O atoms probably arise from defect reactions associated with the growth of the SiO_2 film (1). Since this nonbridging oxygen is considerably less ionic than that associated with Na^+ but is more ionic than the bridging oxygen, it is expected that the shift in the OH absorption is less than 640-800 cm^{-1}. It is very possible that the 100 cm^{-1} shift attributed to SiH...O bond formation (7) also involves nonbridging oxygen. The nonbridging oxygen may capture a hole

$$\equiv Si—O \rightleftarrows \equiv Si—O^- + h^+$$

In this case it is more ionic; the ionicity depends on the interaction with the hole. With increasing ionicity, the H-bonding could approach that involving a nonbridging oxygen associated with Na^+.

From the viewpoint of gross structural features such as optical properties, etc. (as obtained by x-ray and electron diffraction), noncrystalline SiO_2 films on silicon are very simliar to fused silica; however, some transport properties exhibit significant differences which have been attributed to the presence of structural channels in thermally or anodically grown SiO_2 films (1). The above considerations on the nature of hydrogen-related bonds in these films supply the first evidence that some important chemical bonds are also different from those occurring in fused silica. It is evident from Table I that the detailed nature of these bonds and their density depend on the preparation technique. In this respect, it is particularly interesting to note the effect of postoxidation annealing in N_2 on the SiH groups: The 300°C treatment eliminated these groups from the anodically grown oxide, whereas the 1000°C treatment increased their density by a factor of five in the case of thermally grown film. This increase, as well as the increase in the OH concentration during N_2-anneal at 1000°C, can be attributed to unintentional "hydrogen doping" which results from the diffusion of hydrogen-bearing species (originating from water vapor in the ambient) through the hot SiO_2 tube (1). (Although SiO_2 tube furnaces were used in both cases, the two sets of experiments were performed in different laboratories.) Another effect related to the furnace tube is manifested in the order of magnitude lower OH and SiH concentrations

in N_2-annealed SiO_2 films prepared in a silicon tube furnace as compared with those prepared in a SiO_2 tube furnace (8). The results in Table I are not yet sufficient to fully characterize the various processing steps, but they indicate that the *IR* absorption technique could very well be used for this purpose. Thus, a well-planned combination of this analytical technique and careful sample preparation could lead to a much better control of Si/SiO_2 interface technology.

Recent application of this technique to chemically deposited Si_3N_4 films demonstrates this point: The density of Si-H and N-H groups present in these films depends on various process parameters, and many important properties of these films as used in memory devices are, in turn, determined by these hydrogen-bearing groups (17).

Acknowledgments

Thanks are due to H. L. Hughes for his unpublished results and stimulating discussions, as well as to H.A.R. Wegener for providing a preprint of his paper.

This paper is based upon work performed in COMSAT Laboratories under the sponsorship of the Communications Satellite Corporation.

Manuscript submitted May 12, 1977; revised manuscript received July 10, 1977.

Any discussion of this paper will appear in a Discussion Section to be published in the June 1978 JOURNAL. All discussions for the June 1978 Discussion Section should be submitted by Feb. 1, 1978.

Publication costs of this article were assisted by COMSAT Laboratories.

REFERENCES

1. A. G. Revesz, *J. Non-Cryst. Solids*, **11**, 309 (1973).
2. Y. T. Yeow, D. R. Lamb, and S. D. Brotherton, *J. Phys. D.*, **8**, 1495 (1976).
3. P. J. Burkhardt, *This Journal*, **114**, 196 (1967).
4. S. R. Hofstein, *IEEE Trans. Electron Devices*, **ed-14**, 749 (1966).
5. G. L. Holmberg, A. B. Kuper, and F. O. Miraldi, *This Journal*, **117**, 677 (1970).
6. P. F. Schmidt and J. D. Ashner, *ibid.*, **118**, 325 (1971
7. K. H. Beckmann and N. J. Harrick, *ibid.*, **118**, 614 (1971).
8. H. Hughes and T. Pankey, Private communication.
9. H. Scsolze, *Glastech. Ber.*, **32**, 142 (1959).
10. J. Fripiat and A. Jelli, in Proceedings of the VII International Congress on Glass, Gordon and Breach New York (1965).
11. R. West and R. H. Baney, *J. Am. Chem. Soc.*, **81**, 6145 (1959).
12. H. Kriegsmann, *Z. Anorg. Allg. Chem.*, **299**, 138 (1959).
13. K. H. Beckmann, *Surf. Sci.*, **3**, 314 (1965).
14. H. L. Hughes, *IEEE Trans. Nucl. Sci.*, **ns-16** 195 (1969).
15. W. Primak, "The Compacted States of Vitreous Silica," p. 83, Gordon and Breach Science Publishers, Inc., New York (1975).
16. G. Englehardt and H. Kriegsmann, *Z. Anorg. Allg. Chem.*, **336**, 286 (1965).
17. H. J. Stein and H. A. R. Wegener, *This Journal* **124**, 908 (1977).

Brief Communications

Preparation of Magnetic and Dielectric Emulsion

S. Yamaguchi

National Institute for Researches in Inorganic Materials, Sakura-mura Niihari-gun Ibaraki-ken, 300-31, Japan

The phenomenon where a surface of austenitic stainless steel undergoes a strain-induced martensitic transformation when polished mechanically (1) is significant when preparing a magnetic and dielectric emulsion. An aqueous suspension of alumina was employed as the abrasive for rubbing the alloy surface. The rubbing sludge obtained behaved itself as a dielectric magnet, which contained the martensite particles.

Starting materials for the preparation were powdered gamma-alumina, water, and a plate of stainless steel (Cr: 18, Ni: 8). The surface of this malleable alloy was polished mechanically with an aqueous suspension of alumina. During this rubbing process, the abrasive became gray, indicating that fine particles of alloy were dispersed evenly in it. The dark paste prepared in this way reacted to a hand magnet. The alloy content of the sludge could be controlled by controlling the polishing duration with a given quantity of alumina.

Various types of stainless steel are known which contain Ti, Mo, W, etc., as the retarders against the martensitic transformation (2). Using one of them, thus, enables us to produce a magnetic pasty matter with the remanence we want. A smooth surface of metal substrate was smeared with the emulsion that contains the ferromagnetic alloy particles by about 50 weight percent (w/o). The surface has been investigated in terms of electron reflection (see Fig. 1). The diffraction pattern observed here is shown in Fig. 2. The mean size of the particles in the specimen is estimated to be about 50Å from the half-width value of the reflections. Figure 2 differs from Fig. 3, where the specimen has been observed with the intact gamma-Al_2O_3 employed as the abrasive. The (220) and (311) reflections from alumina appear weaker in Fig. 2 than in Fig. 3. This demonstrates that from the reflection

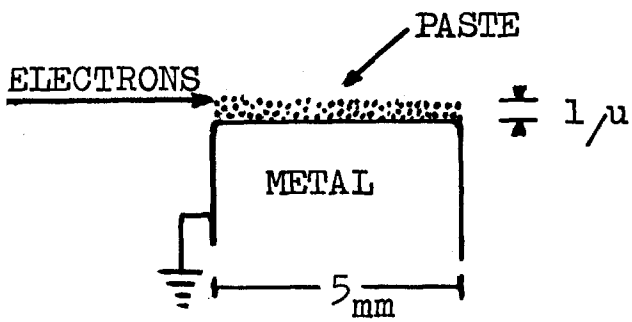


Fig. 1. Disposition for scanning the specimen layer by electron reflection.

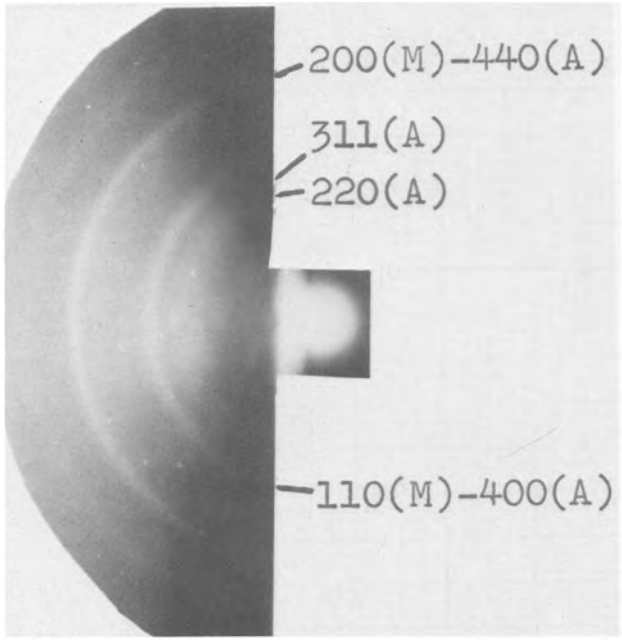


Fig. 2. Electron diffraction pattern observed from the emulsion composed of martensite (M) and alumina particles (A). Wavelength of the electrons is 0.0347Å. Distance between the object and the screen is 50 cm. Positive enlarged 2.3 times.

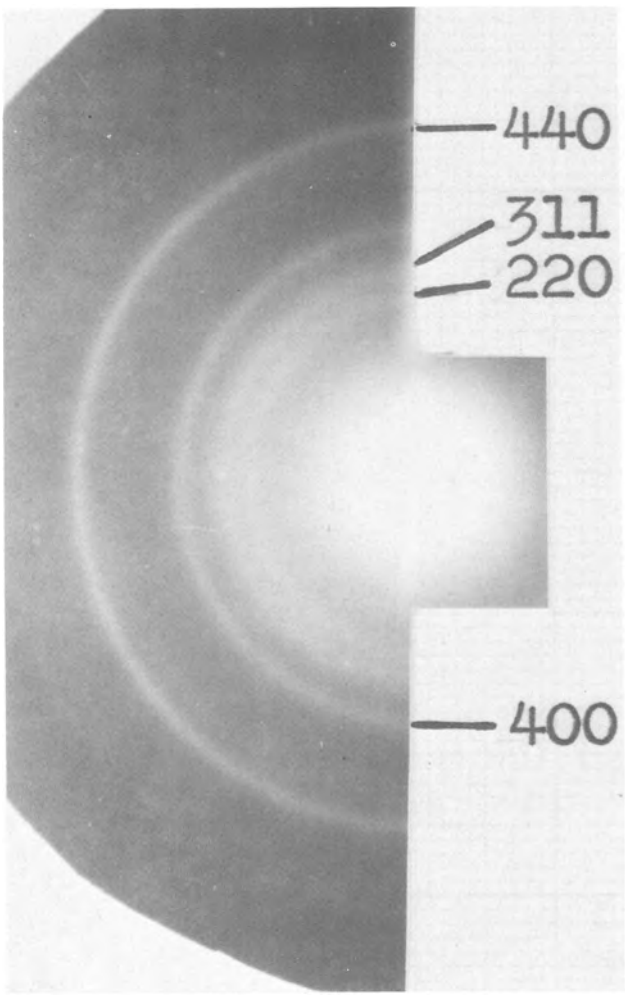


Fig. 3. Alumina employed as the abrasive. Compare this pattern with Fig. 2.

intensities observed, one can estimate roughly the alloy content of the emulsion to be about 50 w/o.

Magnetic and dielectric analysis of the specimen has been carried out by means of electron diffraction (3). An undisturbed reference pattern from a gold foil has been superimposed onto Fig. 2 in order to reveal the magnetic and dielectric influence which the reflections underwent. The double exposure obtained in this way is shown in Fig. 4, in which there is found eccentricity between the diffraction rings of the two different objects. This ring eccentricity is expressed as the resultant $\vec{\Delta R}$ of two vectors, *i.e.*

$$\vec{\Delta R} = \vec{\Delta Z} + \vec{\Delta X} \qquad [1]$$

where $\vec{\Delta Z}$ and $\vec{\Delta X}$ denote the magnetic and the dielectric displacement of the reflection, respectively. The following two equations apply to the disposition of the object relative to the screen

$$|\vec{\Delta Z}| = \frac{eLl\lambda}{h} \cdot |\vec{B}| \qquad [2]$$

$$\vec{\Delta Z} \perp \vec{B}$$

and

$$\vec{\Delta X} = \frac{Ll}{2V} \cdot \vec{E} \qquad [3]$$

$$\vec{\Delta X} \parallel \vec{E}$$

In these equations, $\vec{B}$ denotes the remanence of the martensitic particles, $\vec{E}$ the electrostatic field strength which is produced by the electrons charged at the dielectric object during the diffraction experiment, e electron charge in emu (1.6×10^{-20}), L the distance between the object and the screen (50 cm), l the effective magnetic or dielectric path traveled by electrons (about 0.1 mm), λ the wavelength of the electrons applied (0.0347Å), h Planck's constant (6.6×10^{-27} erg · sec), and V is the potential difference for accelerating the electrons (140 kV).

One measures $\vec{\Delta R} = 0.7$ mm in Fig. 4. Hence, one can calculate $\vec{B} \approx 100$G according to Eq. [1], [2], and [3], if one assumes that $\vec{\Delta Z}$ is nearly parallel to $\vec{\Delta X}$ and that $\vec{E}$ is about 20 kV/cm (4). The value of $\vec{B}$ estimated in this way is plausible as the remanence of the mar-

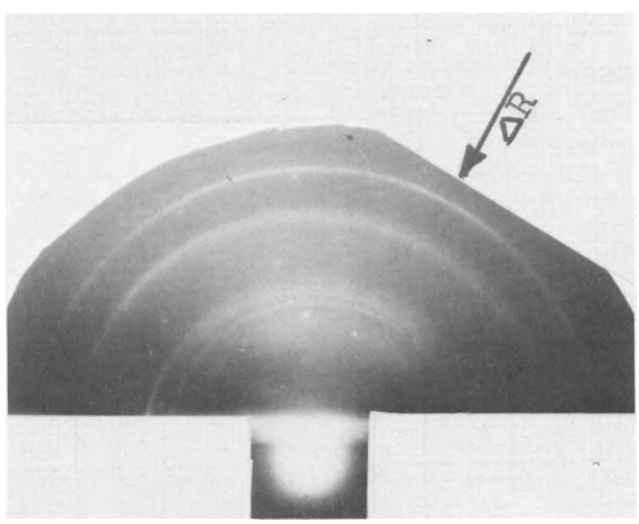


Fig. 4. Double exposure in which Fig. 2 is superimposed on the reference pattern from a gold foil. The diffraction ring eccentricity as denoted by $\vec{\Delta R}$ is due to the magnetic and dielectric effect arising from the specimen.

tensite particles in question. It was possible here to detect the rather weak remanence, since l in Eq. [2] was sufficiently long in the case of RHEED procedure (see Fig. 1).

A rubbing sludge was produced by mechanically polishing the surface of a soft iron plate with an aqueous suspension of synthetic hematite. Figure 5 was observed from the sludge whose iron content was about 50 w/o. This figure should be compared with Fig. 6, which shows the intact hematite powder. It follows from these observations that in the sludge there are scattered iron particles. The rather high background around the (110) and (214) reflections in Fig. 5 implies the tribochemical formation of the cubic Fe_3O_4 particles which give the (311) and (440) reflections corresponding to the spacings of 2.53 and 1.48Å, respectively (4).

Figure 7 is a double exposure in which Fig. 5 is superimposed onto the reference pattern of gold. The diffraction ring eccentricity here appears small compared with that in Fig. 4. This means that the Fe-Fe_2O_3 emulsion is not only nearly free from remanence, but this is also conductive. This preparation has begun to succumb to weathering on exposure to air for several weeks. This differed thus from the martensite-alumina emulsion, insofar as the physical and chemical properties are concerned.

The powdered oxide used in the present study plays a dual role, to wit, it is the support for the metal particles as well as the abrasive for the metal substrate. The magnetic and simultaneously dielectric emulsion as produced with the alloy and the appropriately selected abrasive can be utilized as a memory store material which is free from the eddy current effect.

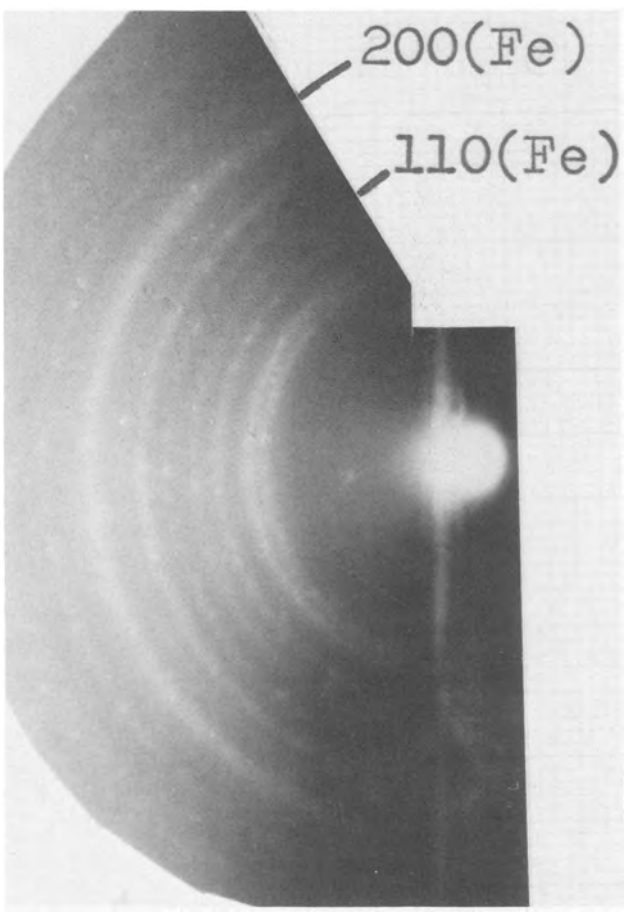


Fig. 5. Paste consisting of soft iron and hematite particles. The reflections from iron are assigned in terms of Miller indexes.

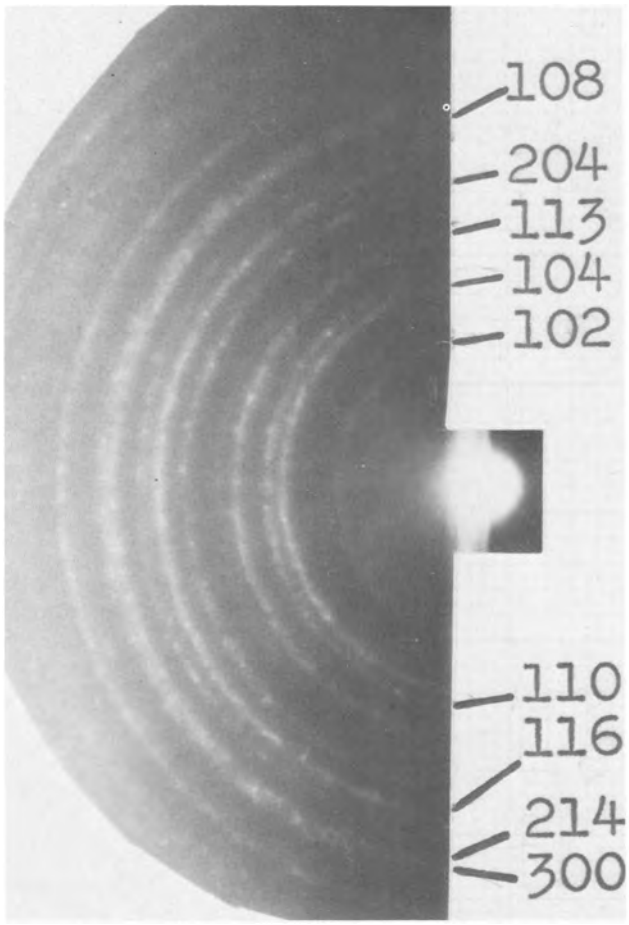


Fig. 6. Hematite employed as the abrasive. Compare this pattern with Fig. 5.

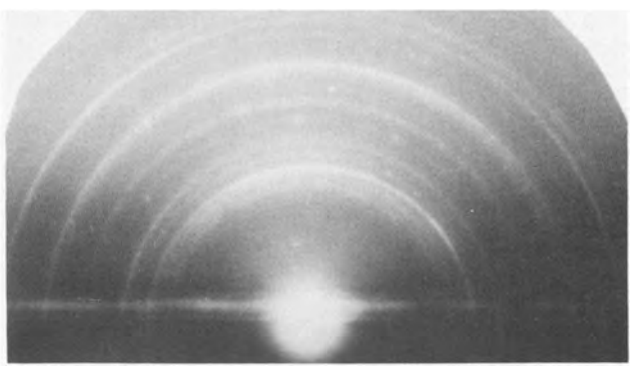


Fig. 7. Double exposure consisting of Fig. 5 and the gold reference pattern. The diffraction ring eccentricity is small here compared with that in Fig. 4.

Manuscript submitted March 25, 1977; revised manuscript received June 6, 1977.

Any discussion of this paper will appear in a Discussion Section to be published in the June 1978 JOURNAL. All discussions for the June 1978 Discussion Section should be submitted by Feb. 1, 1978.

Publication costs of this article were assisted by the National Institute for Researches in Inorganic Materials of Japan.

REFERENCES

1. S. Yamaguchi, *J. Chem. Phys.*, **27**, 1310 (1957).
2. E. Houdremont, "Handbuch der Sonderstahlkunde,"

p. 1084, Springer-Verlag, Berlin (1956) R. C. Gibbons and N. E. Woldman, "Engineering Alloys," p. 1219, Van Nostrand Reinhold Company, New York (1973).
3. S. Yamaguchi, *This Journal*, **109**, 346 (1962); S. Yamaguchi, *Z. Metallkd.*, **56**, 789 (1965).
4. S. Yamaguchi, *J. Colloid Interface Sci.*, **57**, 187 (1976).

Electromigration in Ion Bombardment

William Primak and Emmet Monahan

Argonne National Laboratory, Argonne, Illinois 60439

Determination of the charge incident on insulators subjected to ion bombardment had been a troublesome matter in this laboratory (1). In a recent investigation (2) it was concluded that the cause was the voltage bias produced by charging of the insulator affecting the secondary emission contribution to the ion current. In our target chambers most of the electric current from the ion-bombarded insulating specimen appeared to flow to the metal plate on which it was set by secondary emission from surrounding areas. It was found that the results could be made much more reproducible by suitable application of external bias to the target plate and target chamber apertures and components. These results were obtained in room temperature bombardments of vitreous silica and were applied to studies of various glasses and ceramic materials (3,4). Currently we are investigating the behavior of these materials when they are subjected to ion bombardment at elevated temperatures, the glasses at various temperatures up to the strain point, and high temperature ceramic materials up to 600°C. It has become evident that charge incident on some of these specimens is being conducted to the metal support by ionic conductivity through the specimen resulting in electromigration of alkali ion. There may also be oxygen release, but this is yet conjectural.

Ion bombardment at room temperature of many of the materials we have investigated causes a change in the index of refraction in a layer approximately the thickness of the range of the ion. Among the causes which have been identified are introduction of centers, change of composition, implantation of gas, compaction, and structural change (4). The thickness can be calculated from the index of refraction and the fringes seen in a spectrophotometer tracing of the reflected or transmitted light. These fringes will be referred to here as chromatic fringes. It is also possible, although much more difficult, to deduce the refractive index changes. However, these are relatively small and would not affect the determination of the thickness of the layer by 10-20%, even less when the effects are studied as a function of incident charge (or dose) (4). The behavior of Pyrex glass when bombarded at elevated temperature has made it evident that other effects are occurring.

In Fig. 1 is a photomicrograph taken in reflection with 0.55μ light of one corner of a 2 × 2 1/2 mm area bombarded with 120 mC/cm^2 of 140 keV He^+ at 350°C. The edge of the bombarded area (depressed, *V.I.*) formed a step which could be seen in an interferometer and lay in the midst of the fringe pattern seen in Fig. 1. If these monochromatic fringes are counted from the edge to the center, a depth of about 3.5μ is calculated for index of refraction 1.47. The reality of this thickness was demonstrated by determining the depth from the chromatic fringes seen in a spectrophotometer tracing of light reflected from the center of this area, 3.6μ. This is the thickness which contains approximately the quantity of alkali equivalent to the charge incident in the bombardment. The thickness is so great in Pyrex glass because of its low alkali concentration, 4 weight percent (w/o). The effect was sought in other cases, and the results are assembled in Table I.

Key words: glasses, ion-depletion, radiation damage.

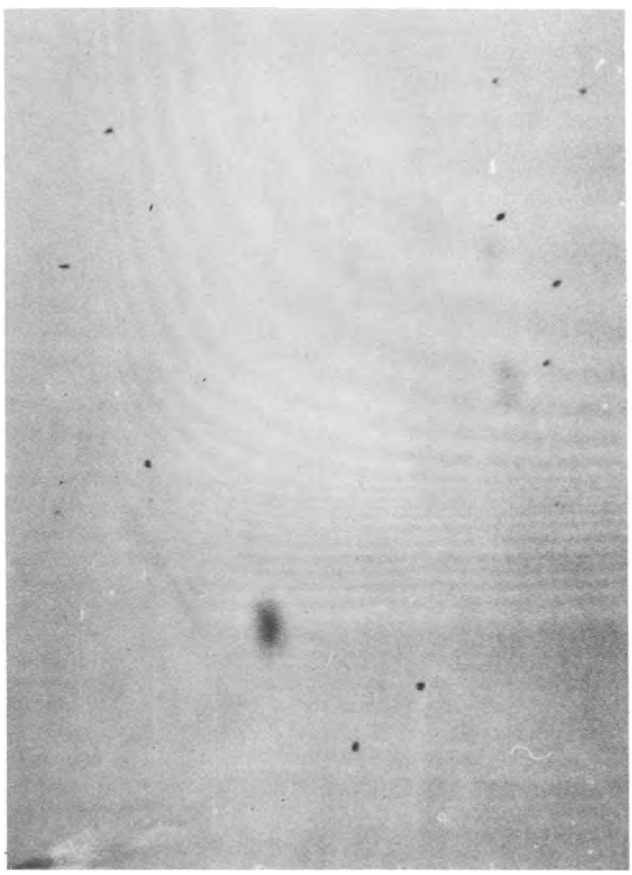


Fig. 1. Pyrex glass, photomicrograph, in reflection, wavelength 0.55μ, one corner of 2 × 2½ mm area bombarded at 350°C with 120 mC/cm^2 He^+ 140 keV. Edge of the bombarded area is in the midst of the fringe pattern.

The results for the lithium niobate (5) are curious. They could be explained by part of the charge being conducted ionically and part electronically. However, in view of the dose equivalent alkali thickness being so

Table I. Alkali migration layers

Material	Ion, dose (mC/cm^2)	Temperature (°C)	Range (μ)	Layer thickness (μ)	Dose equivalent alkali thickness (μ)
Pyrex	H^+ 120	425	1.39	4.38	4.23
Pyrex	He^+ 120	350	0.97	3.60	4.23
BK-7	D^+ 108	375	1.62	1.00	1.04
C-1	He^+ 108	275	0.84	0.89	0.88
$LiNbO_3$	D^+ 72	600	0.5	0.11	0.20

nearly twice the incident charge, it seems more likely that, concomitant with the migration of the lithium ion, the charge of the niobium is reduced by one.

When Pyrex glass is bombarded at room temperature, there is little change in contour at the edge of the bombarded area. However, at these temperatures there is a marked depression. This is in accord with the collapse which has been reported (6) for the electrolysis of glasses.

The glass C-1 appears to be pervious to helium in room temperature bombardment. However, at 200°C, where increased permeability would be expected, dense protuberances appeared, as seen in Fig. 2. These do not have the typical appearance of the radiation blistering seen on other materials. We speculate this may be caused by oxygen formed in electromigration.

Electromigration is another mechanism for the deterioration of glasses and ceramic materials in radiation environments. This effect is apt to be variable and depend on material and target base configuration, and on plasma condition, electron emission, and voltage bias in the region. All of the cases cited here involve migration of alkali ion. The alkali ions have long been known to be the most mobile ions in these materials (7) and there are many reports of this mobility (8).

We are currently looking for evidence of other effects associated with ionic conduction in the ion bombardment of ceramic materials.

Addendum in revision.—The altered surface formed on heated Pyrex and C-1 glass cathodes of a glow discharge tube have now been studied and give the same result described above for ion bombarded cathodes, that the volume of altered glass is closely that containing the alkali equivalent to the cathode charge. The electrical characteristics of a glow discharge tube with a heated soda-lime glass cathode or anode have been reported (9).

Acknowledgment

We are indebted to Al Youngs for performing the ion bombardments.

This work was supported by the U.S. Energy Research and Development Administration.

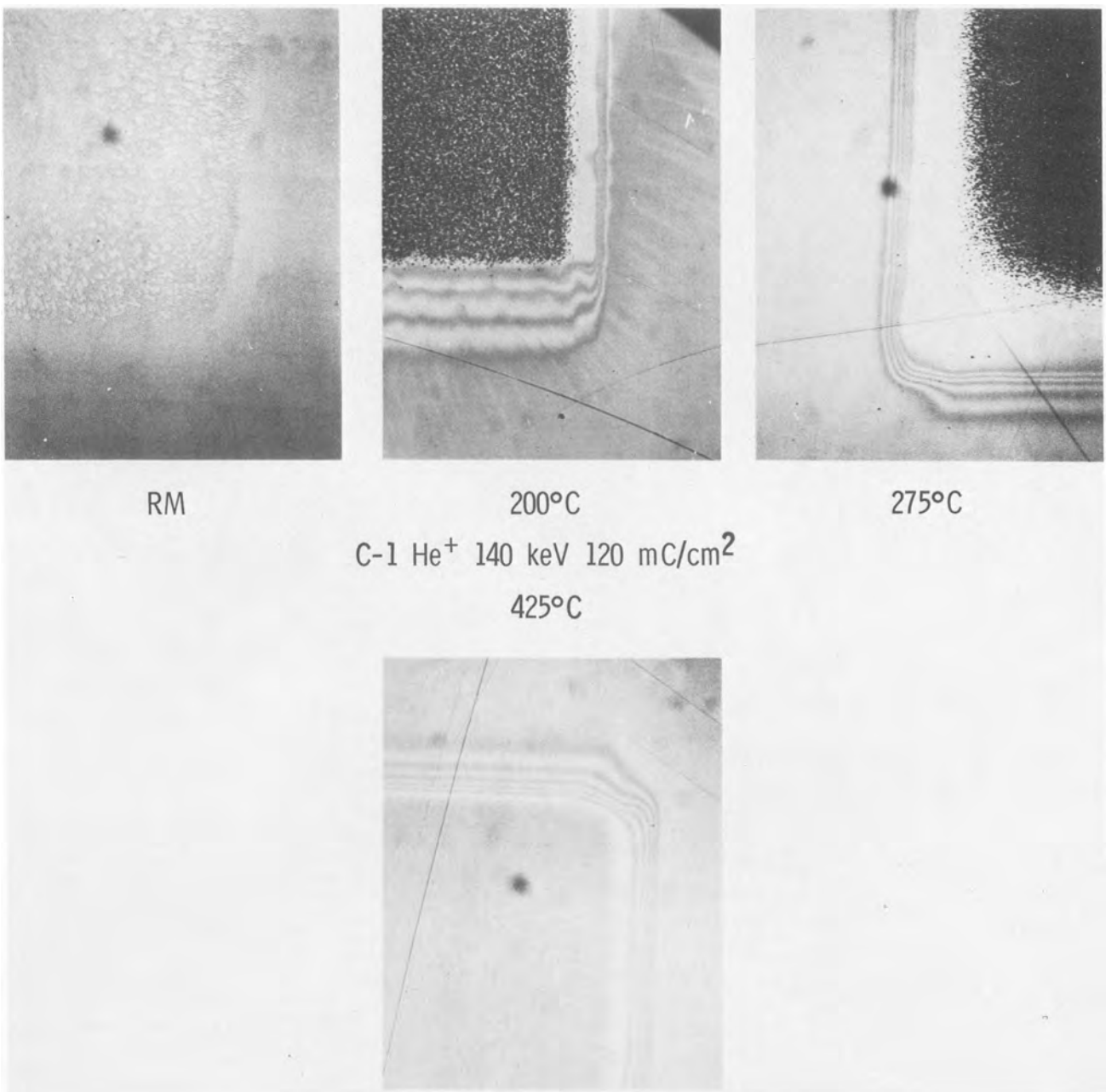


Fig. 2. Photomicrographs of C-1 glass bombarded at various temperatures with 108 mC/cm^2 He$^+$ 140 keV

Manuscript submitted March 14, 1977; revised manuscript received July 25, 1977.

Any discussion of this paper will appear in a Discussion Section to be published in the June 1978 JOURNAL. All discussions for the June 1978 Discussion Section should be submitted by Feb. 1, 1978.

Publication costs of this article were assisted by Argonne National Laboratory.

REFERENCES

1. W. Primak, *Phys. Rev. B*, **14**, 4679 (1976).
2. W. Primak, *Bull. Am. Phys. Soc.*, **II-19**, 31 (1974).
3. W. Primak, *J. Nucl. Mater.*, **63**, 313 (1976).
4. W. Primak, *J. Appl. Phys.*, **48**, 1556 (1977).
5. W. Primak, A. P. Gavin, T. T. Anderson, and E. Monahan, *Nucl. Technol.*, In press.
6. D. E. Carlsen, K. W. Hang, and G. F. Stockdale, *J. Am. Ceram. Soc.*, **57**, 295 (1974).
7. W. Primak, *This Journal*, **122**, 1002 (1975).
8. D. V. McCaughan and R. A. Kushner, in "Characterization of Solid Surfaces," P. F. Kane and G. B. Larabee, Editors, Chap. 22, pp. 627-640, Plenum Press, New York (1974).
9. K. Wolf, *Z. Phys.*, **112**, 96 (1939).

A Static Sodium-Water Cell

B. D. Goldberg and F. R. Foulkes*

Department of Chemical Engineering and Applied Chemistry, University of Toronto, Toronto, Ontario, Canada M5S 1A4.

A "dynamic" sodium-water cell with a rotating cathode was described in a previous report (1). In this report we describe a mechanically simplified "static" cell.

CELL DESCRIPTION

The cell (Fig. 1) consisted of a glass tube (A) housed in a Lucite block (B), containing a stainless steel tube (C) to which a 100-mesh type 304 stainless steel wire screen cathode (D) having a geometric area of 0.5 cm^2 was attached by means of two spot-welded stainless steel posts (E). The sodium was contained in a glass tube (F) which was attached to a pressure plate (G) with a clamp (H). Water, sodium hydroxide, hydrogen, and nitrogen exited via drain (I). Attached to the bottom of the stainless steel tube was a carburetor (J) which rendered the water used in the cell into a mist. Nitrogen gas and water were admitted through control valves (K) and (L), respectively. Current was gathered from the sodium anode by means of a series of copper pins (M) imbedded in the sodium (N). The stainless steel tube acted as the cathode current collector (O). The sodium was pressed onto the stainless steel mesh with a pressure of from 4 to 5 kg/cm^2 by a compressed air piston arrangement connected to the cell pressure plate.

EXPERIMENTAL DETAILS

Cell operation.--Before operation the cell was purged with nitrogen. The cell was started by turning on the water at a constant flow rate of about 5 cm^3/min. Since the feeding of the sodium involved no shearing of the sodium, the cell operated smoothly with no undue mechanical stress.

Electrical measurements.--A Keithley 610C solid state electrometer and model 370 recorder were used to measure and monitor cell output voltage. Current was measured and monitored via a Honeywell Electronik 194 chart recorder (50 mV full scale) connected across a shunt resistor (50 mV = 10 A) in series with the cell.

RESULTS AND DISCUSSION

Fig. 2 shows the steady state cell polarization characteristics obtained over several runs, the current

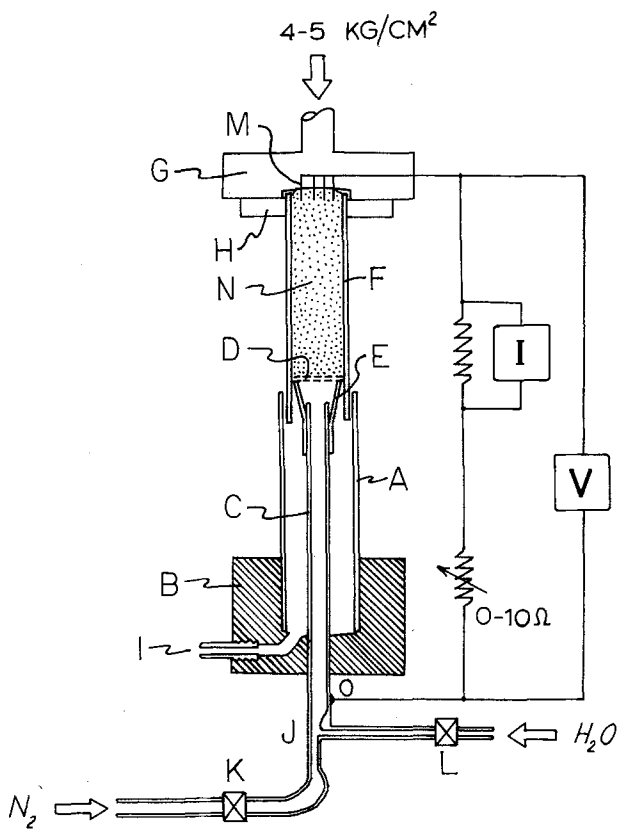


Fig.1. Sodium-Water Static Cell.

* Electrochemical Society Active Member.

Key words: primary cell, high power battery, sodium-water cell.

density being based on a geometric cathode area of 0.5 cm^2. Open circuit voltages of about 2.0 V were consistently obtained, which were in reasonable agreement with the calculated standard reversible value of 1.89 V for the reaction

$$Na + H_2O \rightarrow NaOH + \tfrac{1}{2}H_2. \quad [1]$$

From the shape of the polarization curve it can be seen that the cell output was strongly activation controlled. Linear regression analysis using 51 data points over 4 orders of magnitude of current yielded the following relationship between cell voltage and current density (correlation coefficient r = 0.801):

$$V = 0.7542 - 0.2002 \log i \quad [2]$$

The Tafel slope of -0.2002 V/decade very strongly suggested the presence of *mixed* activation control involving activation polarization of both the anodic reaction

$$Na \rightarrow Na^+ + e^- \quad [3]$$

and the cathodic reaction

$$H_2O + e^- \rightarrow OH^- + \tfrac{1}{2}H_2. \quad [4]$$

It is readily shown that the Tafel slope under mixed activation control is given by

$$\frac{dV}{d \log i} = - \frac{2.3\ RT}{F} \left\{ \frac{1}{\alpha_H} + \frac{1}{\alpha_{Na}} \right\} \quad [5]$$

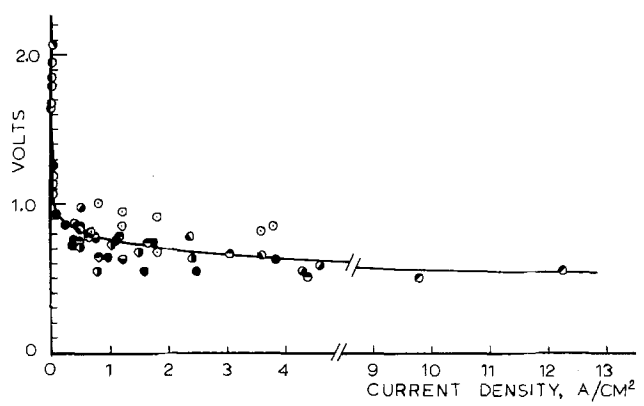


Fig. 2 Steady State Cell Polarization Curve.

The transfer coefficient for the hydrogen evolution reaction on steel in alkaline media is known to be $\alpha_H = 0.5$ (2). If we assume that α_{Na} is between 0.75 and 1 (3) and substitute these values plus $\alpha_H = 0.5$ into Eq. [5], then Eq. [5] yields the observed Tafel slope of -0.2002 V/decade in the temperature range from 30°C to 60°C, values which are consistent with the occurrence of some local overheating at the sodium/water interface. If one were to assume only cathodic activation control ($\alpha_H = 0.5$) or only anodic activation control ($\alpha_{Na} = 1$), temperatures of 231°C and 737°C, respectively, would be required to yield the observed Tafel slope using Eq. [5]. These temperatures are highly unlikely in view of the facts that the m.p. of sodium is 97.8°C and that the presence of molten sodium was not observed visually.

This mixed activation control of the output of the static cell contrasted strongly with the behaviour of the dynamic cell, the polarization of which was controlled by a combination of cathodic activation polarization and cell internal resistance (1). Unlike in the dynamic cell, the thickness of the oxide film in the static cell was not amenable to control. Since the film was visibly non-uniform in thickness, it appears likely that the effective electrode area was much smaller than the assumed 0.5 cm^2, so that even the large exchange current density for the sodium half-reaction was exceeded, resulting in anodic polarization in addition to cathodic polarization.

Although the activation polarization of the static cell was much more severe than that of the dynamic cell, the static cell offers the clear-cut advantages of an essentially flat discharge curve and greater mechanical simplicity than the dynamic cell. As was stressed in the case of the dynamic cell, control of the

thickness of the oxide film is the key to exploiting the sodium/water system. Work is now being carried out to construct a static cell with an oxide film of thin but controllable and uniform thickness.

ACKNOWLEDGMENT

Financial support from the National Research Council is gratefully acknowledged.

REFERENCES

1. D.A. Fustier, W.F. Graydon, and F.R. Foulkes, This Journal, 123, 1259 (1976).
2. K.J. Vetter, "Electrochemical Kinetics", pp. 537-540, Academic Press, New York (1967).
3. J. O'M. Bockris and A.K.N. Reddy, "Modern Electrochemistry: Volume 2", Chap. 8, Plenum Press, New York (1973).

Manuscript submitted July 11, 1977; revised manuscript received Aug. 29, 1977.

Publication costs of this article were assisted by the University of Toronto.

Stress Corrosion Cracking of Admiralty Brass in Nonammoniacal Sulfate Solutions

A. Kawashima, A. K. Agrawal,* and R. W. Staehle*

Department of Metallurgical Engineering, Ohio State University, Columbus, Ohio 43210

Stress corrosion cracking (SCC) of CDA 443 admiralty brass has been studied in sodium sulfate solution over a pH range of 1.3 to 12.7, at open circuit and controlled potentials using a slow strain rate technique. All the tests were conducted in a 200 ml glass cell at room temperature in 1N Na_2SO_4 solution whose pH was adjusted with either H_2SO_4 or NaOH to the desired value. Potential of specimens was controlled with a Wenking potentiostat model ST72, against a mercury-mercurous sulfate reference electrode; the counter electrode used was of platinum.

Test specimens were hour-glass type, with gauge dimensions 1.25 x 0.5 cm^2 and 0.25 cm thick. Specimens were annealed for one hour at 550°C under a blanket of argon and furnace cooled, this gave an average grain diameter of 0.05mm. After heat treatment specimens were polished longitudinally with 600 grade SiC paper. The specimen length exposed to the test solution beyond the gauge section was carefully covered with an epoxy cement. The straining, at a rate of 1.5 x 10^{-5} sec^{-1}, was started after a specimen had attained a steady corrosion potential or a quasi steady state current in the case of controlled potential tests. During the tests load (tension) on a specimen was monitored with a load cell; the fracture stress in a solution was compared with a reference value obtained in air. Fractured specimens were metallographically examined; the crack velocity, $v = L/t_f$, was calculated from the maximum crack penetration, L, observed near the fractured tip and the failure time, t_f.

Results are summarized in Figure 1, where the ratio of fracture stress in a test solution to that in air is plotted against the pH of the solution. Results in the figure are grouped in bands according to the test potential. The crack velocity scale is shown on the right ordinate, with the scale placed in such a way that all data points fall within ± 0.3 decade of the measured value. Such a small difference in crack velocity is not considered serious where the values vary over several orders of magnitude. The cracking in all instances was transgranular with considerable branching, especially at high anodic potentials. In such cases the calculated values give only an idea of the magnitude and not the true velocity.

SCC was not observed in any of the specimens tested at open circuit potential, which was 180 ±20 mV_H in all cases up to pH 10.1, but ∿90 mV_H for 11.6 and ∿-40 mV_H for pH 12.7. In these cases, < 200 mV_H, it is possible that the crack velocity is so small that no detectable penetration occurred in approximately 30 hours of exposure. A slower strain rate might have allowed more time for crack penetration, especially in the pH range 4 to 10. SCC occurred at anodic potentials; the overpotential, $\eta = E-E_{cor}$, varied with the pH. The η was ∿20 mV in the pH range 4 to 10, but increased to ∿100 mV or more at either end of the forementioned range. It is clear from Figure 1 that in admiralty brass: a) SCC severity increases with an increase in potential at any pH between 2 and 12; b) at a fixed potential it increases with an increase in pH in the pH range 2 to 4; c) it stays relatively constant up to a certain pH (∿10) and decreases thereafter; d) the pH where the decreasing trend starts broadens with an increase in potential.

The concentration of sulfate ions in the solution also plays an important role in promoting SCC. Preliminary data in pH 8 solution at 300 mV_H show that cracking severity decreases with a decrease in sulfate ion concentration; no cracking occurred with the concentration dropped to 10^{-4}N.

Pickering and Byrne (1) have reported intergranular SCC of 70/30 brass in 1N Na_2SO_4 solution of pH ∿2 at 240 mV_H. It appears that 70/30 brass is more susceptible to SCC than admiralty brass which showed no cracking under the above condition in the present work. Pinchback et al (2) have reported transgranular SCC in admiralty brass in 0.05 to 0.5M $CuSO_4$ solutions at open circuit conditions. They have, however, neither reported the pH of the solutions nor the corrosion potential of the

*Electrochemical Society Active Member.

specimens. We measured the pH and the corrosion potential of admiralty brass in 0.05 and 0.5M $CuSO_4$ solutions; pH's were 4.2 and 3.5 whereas potentials were 280 and 300 mV_H, respectively. Figure 1 suggests that admiralty brass should suffer SCC in the above conditions and thus supports the results of Pinchback et al.

A generally held view, till recently, has been that SCC of brasses does not occur without the presence of ammonia or its derivatives in the test environment (3). The present work negates this view and conclusively shows that SCC of admiralty brass occurs in nonammoniacal solutions over a wide range of pH depending upon the oxidizing condition, as represented by the anodic potential in Figure 1. The fact that below pH 2 and above pH ∿12, where Cu_2O is unstable, no SCC was observed points to an active role of Cu_2O in crack propagation, which has been suggested before by many workers (4). The increase in severity with increasing potential favors anodic dissolution, rather than hydrogen embrittlement, as the cause of SCC.

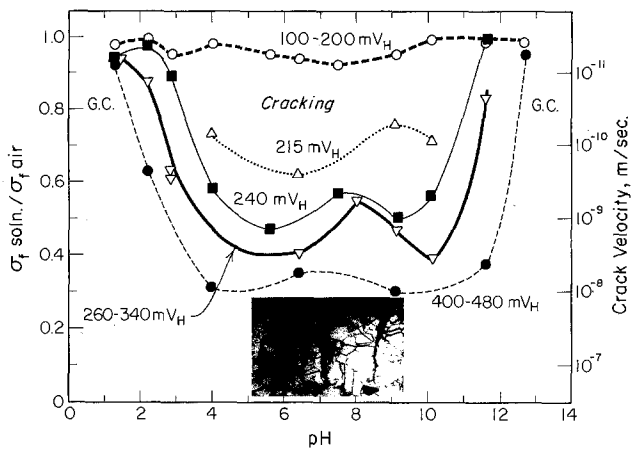


Fig. 1 Fracture stress ratio of admiralty brass in 1N Na_2SO_4 solution to that in air and crack velocity vs. pH at different potentials.

ACKNOWLEDGEMENT

This work was supported by the Electric Power Research Institute of Palo Alto, California under a contract number RP311-1.

REFERENCES

1. H.W. Pickering and P.J. Byrne, Corrosion, 29, 325 (1973).
2. T.R. Pinchback, S.P. Clough, and L.A. Heldt, Corrosion, 32, 469 (1976).
3. H. Uhlig, Corrosion, 33, 189 (1977).
4. B.F. Brown, "Stress Corrosion Cracking Control Measures", NBS Monograph 156, National Bureau of Standards (1977).

Manuscript submitted Aug. 22, 1977; revised manuscript received Sept. 7, 1977

Publication costs of this article were assisted by The Ohio State University.

Epitaxial Pattern Shift Comparison in Vertical, Horizontal, and Cylindrical Reactor Geometries

P. H. Lee,* M. T. Wauk, R. S. Rosler,* and W. C. Benzing*

Applied Materials, Incorporated, Santa Clara, California 95051

Bipolar IC fabrication requires a predictable amount of epitaxial pattern shift in determining design rules for minimum device spacing. These design rules compensate for the amount and direction of pattern shift to correct the subsequent masking operations to the buried layer mask. One purpose of this work is to establish the dependence of pattern shift on growth conditions and substrate orientation. Another purpose is to compare pattern shift in three commercial reactor geometries.

Work in pattern shift has been reported by several authors (1-5). It is the general experience of most workers that pattern shift is minimized at higher growth temperatures (1200°C for $SiCl_4$) and lower growth rates (less than 0.6 micron/min). Workers (3,4) have investigated the role of HCl etching in pattern shift and washout. The degree of pattern shift and washout is due, in part, to the epitaxial growth on the pattern sidewalls formed from the buried layer diffusion. The differences in growth rate (6) contribute to the pattern shift and washout. The present authors believe that growth temperatures, growth rates, substrate orientation, HCl etch, and pattern depression are interrelated parameters to be considered in minimizing pattern shift and washout.

Epitaxial depositions were made in commercially available reactors in vertical, horizontal, and cylindrical geometries.* Single crystal epitaxial depositions were made with silicon tetrachloride at four deposition rates and four deposition temperatures. The $SiCl_4$ concentration was controlled to achieve the desired growth rate and the optical deposition temperature was corrected to true temperature using silicon emissivity (7) and quartz absorbtivity. There was no HCl etch prior to deposition and the depositions were undoped. The two inch boron P- doped substrates have the following orientation; ⟨111⟩ off + 3-1/2 to + 4-1/2° towards the ⟨110⟩, ⟨100⟩ off + 3° to +5° towards the ⟨110⟩, and ⟨100⟩ ± 1/2°. An antimony buried layer was diffused into the substrates. A square grid line pattern which has a 10 mil line width spaced 200 mils apart was aligned parallel and perpendicular to the substrate flat. The diffusion concentration after drive-in was approximately 25 ohm per square and the diffusion oxide thickness was approx. 7000 Angstroms. After an approximately 10 micron deposition was made, the substrates were angle lapped, Sirtl etched, and the pattern shift was measured optically at 125X with interference contrast. Approximately five measurements for each deposition condition were made. The deposition thickness was measured with the sodium fringe count method. The shift ratio was calculated by dividing the pattern shift by the deposition thickness on each wafer. Statistical methods were used on the meas-

*Electrochemical Society Active Member

Key Words: epitaxial shift, silicon epitaxy, buried layers, reactor geometry, bipolar integrated circuits

*Vertical geometry - Applied Materials AMV-1200
Horizontal geometry - Applied Materials AMH-6000
Cylindrical geometry - Applied Materials AMC-7000

urement techniques and estimates to experimental error were determined.

The estimated experimental error is approximately ± 20% with the optical shift measurement being the major contributor. Statistical methods were employed to determine the deviation and confidence limits on at least 6 measurements for the experimental data. This work confirms previous work done by Drum and Clark (2) as the pattern shift was primarily non-symmetrical and the pattern shift was calculated by the shift in the centerline of the pattern. Pattern washout with the on-orientation substrates was especially evident on the lower temperatures using the vertical and cylindrical geometries. The pattern washout was probably caused by the enhanced ⟨111⟩ "slanting face" growth as reported by Enomoto (3).

The only pattern shift observed was towards the right and parallel to the substrate flat. For the ⟨111⟩ and ⟨100⟩ off-orientation substrates, the amount of pattern shift was comparable for each reactor geometry. The shift ratios for the two off-orientation substrates is shown in Fig. 1 and Fig. 2. The graphs indicate that the amount of pattern shift is independent of reactor geometry when corrected deposition temperatures are used. Shift ratios of less than 1.0 can be produced with silicon tetrachloride using growth temperatures above 1150°C (corrected) and growth rates below approximately 0.6 micron/min.

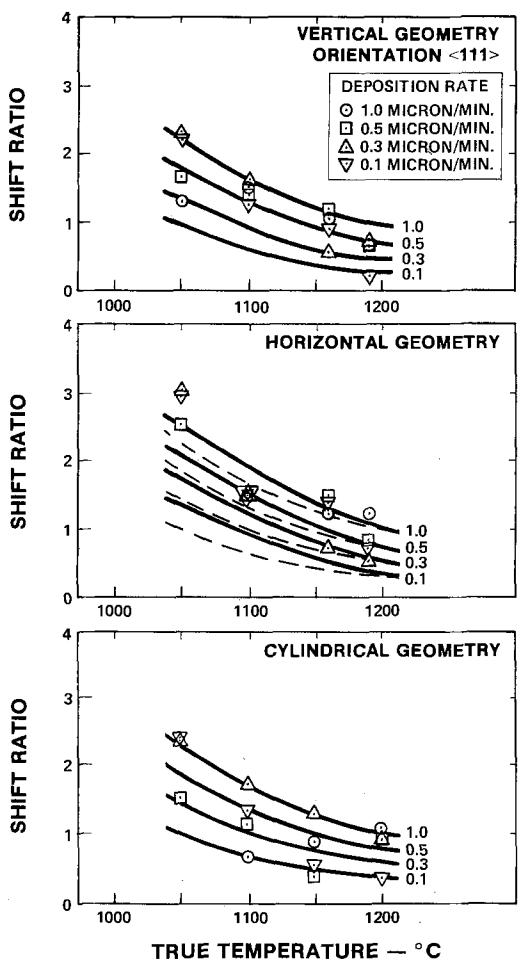


Fig. 1. Pattern shift on ⟨111⟩ substrates in vertical, horizontal, and cylindrical geometries. The dashed lines are the superimposing of the cylindrical curves upon the vertical and horizontal curves.

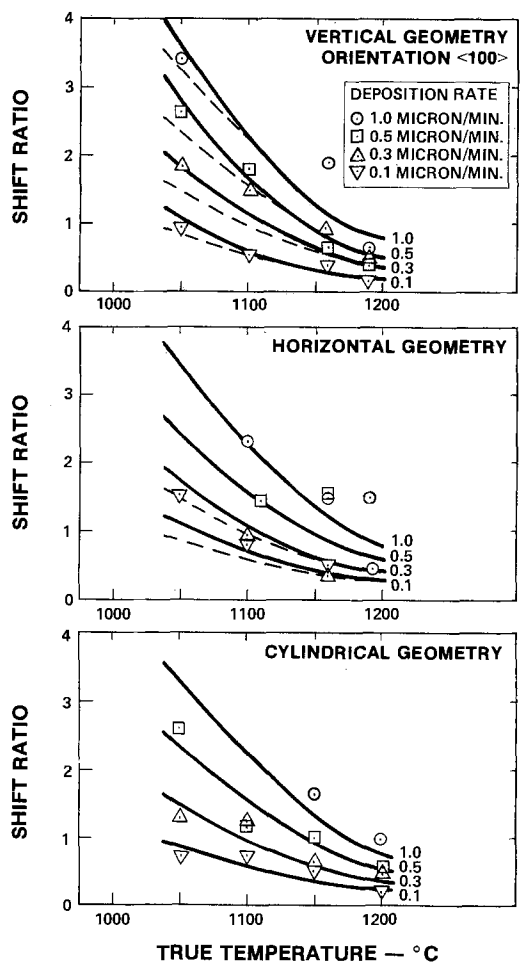


Fig. 2. Pattern shift on ⟨100⟩ substrates in vertical, horizontal, and cylindrical geometries. The dashed lines are the superimposing of the cylindrical curves upon the vertical and horizontal curves.

It has been the belief of several workers that a cylindrical reactor has greater pattern shift compared to the vertical and horizontal geometries (8). The present authors have found that observation to be not correct. Instead, when one compares each reactor geometry on an equal (true) temperature basis, the pattern shift curves coincide within experimental error. The primary difference in the comparison is the method of temperature measurement. Temperatures in vertical and horizontal geometries are typically measured by infrared optical pyrometry. The indicated temperatures need to be corrected upwards due to the silicon emissivity and quartz absorbtivity. For example, an indicated pyrometer reading of 1150°C is actually 1225° (emissivity correction is +65°C (7) and quartz absorbtivity correction is +10°C (9)). In the case of a radiantly heated cylindrical reactor, the indicated temperature equals the true temperature. A radiantly heated cylindrical reactor is typically calibrated with a thermocouple that is inserted in the graphite susceptor. Under comparable conditions, the present data shows that the amount of pattern shift is independent of reactor geometry.

The observed behavior of pattern shift with respect to temperature and growth rate is believed to be a crystal growth mechanism. From Figs. 1 and 2, the amount of pattern shift is lower at higher temperatures and slower growth rates. The magnitude of pattern shift at differing growth conditions is dependent upon the surface energy for crystal growth. Anisotropic growth rates for the different crystal planes is the major cause for shift (10). A discontinuous surface is exposed at the buried layer pattern edge. Due to atomic surface diffusion or surface migration effects at this edge (11), a competition of atomic capture takes place and leads to differing growth rates along the ⟨110⟩ plane. At lower temperatures, the growth rate ratios are higher between the ⟨110⟩ plane (substrate flat) and the substrate planes. It is reasonable that anisotropic growth is independent of reactor geometry. This anisotropic growth mechanism confirms the present data that pattern shift is lower at higher temperatures and slower growth rates.

ACKNOWLEDGMENTS

The authors wish to thank Ms. B.D. Mell for making the depositions, Ms. T. P. Boblet for making the shift measurements, and E. Fleck for the experimental design.

REFERENCES

1. C.M. Drum and C.A. Clark, This Journal, 115, 664 (1968).
2. C.M. Drum and C.A. Clark, This Journal, 117, 1401 (1970).
3. T. Enomoto et al., Paper 78 presented at the Electrochemical Society Meeting, Boston, May 1968.
4. D.W. Boss and V.Y. Doo, Paper 186 presented at the Electrochemical Society Meeting, Philadelphia, October 1966.
5. M. Van Hoy, Paper presented at the American Institute of Chemical Engineers Meeting, Dallas, February 1972.
6. S. K. Tung, This Journal, 112, 436 (1965).
7. F. G. Allen, J. Appl. Phys., 28, 1510 (1957).
8. Private industrial communications.
9. R.S. Rosler, Private Communication.
10. C. H. J. van den Breckel, J. Crystal Growth, 23, 259 (1974).
11. J. Nishizawa et al., J. Crystal Growth, 13/14, 297 (1972).

Manuscript submitted June 21, 1977; revised manuscript received July 27, 1977.

Publication costs of this article were assisted by Applied Materials, Incorporated.

JOURNAL OF THE ELECTROCHEMICAL SOCIETY

ELECTROCHEMICAL SCIENCE AND TECHNOLOGY

DECEMBER 1977

Potentiometric Determination of the Gibbs Free Energy of Formation of Cadmium and Magnesium Chromites

K. T. Jacob

Department of Metallurgy and Materials Science, University of Toronto, Toronto, Ontario, Canada, M5S 1A4

ABSTRACT

The standard Gibbs free energy of formation of magnesium and cadmium chromites have been determined by potentiometric measurements on reversible solid-state electrochemical cells

$$\text{Pt, } \begin{matrix}\text{Au-5\%Cd}\\+\\\text{CdO}\end{matrix} \;\Big|\; \text{CaO-ZrO}_2 \;\Big|\; \begin{matrix}\text{Au-5\%Cd}\\+\\\text{CdCr}_2\text{O}_4 + \text{Cr}_2\text{O}_3\end{matrix} \text{, Pt}$$

in the temperature range 500°-730°C, and

$$\text{Pt, Cr} + \text{Cr}_2\text{O}_3/\text{Y}_2\text{O}_3\text{-ThO}_2/\text{Cr} + \text{MgCr}_2\text{O}_4 + \text{MgO, Pt}$$

in the temperature range 800°-1200°C. The temperature dependence of the free energies of formation of the ternary compounds can be represented by the equations

$$\text{CdO(r.s.)} + \text{Cr}_2\text{O}_3\text{(cor)} \rightarrow \text{CdCr}_2\text{O}_4\text{(sp)}$$

$$\Delta G^\circ = -42{,}260 + 7.53T\ (\pm 400)\ \text{J}$$

and

$$\text{MgO(r.s.)} + \text{Cr}_2\text{O}_3\text{(cor)} \rightarrow \text{MgCr}_2\text{O}_4\text{(sp)}$$

$$\Delta G^\circ = -45{,}200 + 5.36T\ (\pm 400)\ \text{J}$$

The entropies of formation of these spinels are discussed in terms of cation disorder and extent of reduction of Cr^{3+} ions to Cr^{2+} ions. Thermodynamic data on the chromates of cadmium and magnesium are derived by combining the results obtained in this study with information available in the literature on high temperature, high pressure phase equilibria in the systems CdO-Cr_2O_3-O_2 and MgO-Cr_2O_3-O_2.

Recent thermodynamic studies (1-3) on the aluminates chromites, and vanadites of iron, nickel, cobalt, and manganese have shown that the entropy of formation of cubic spinel phases from component oxides with rock-salt and corundum structures can be expressed as $-7.25 + \Delta S^M + \Delta S_{rand}$ J deg^{-1} mol^{-1}, where ΔS^M is the entropy of cation mixing on the tetrahedral and octahedral sites of the spinel, and $\Delta S_{rand} = n$Rln3 is the entropy change associated with randomizing the direction of Jahn-Teller distortions. The Jahn-Teller term applies only for spinel phases that have ions with $3d^4$ or $3d^9$ electronic configuration in octahedral site or $3d^3$, $3d^4$, $3d^8$, or $3d^9$ configuration in tetrahedral site. The ΔS^M term can have values ranging from 0 for normal spinels to 11.5 J deg^{-1} mol^{-1} for spinels with random distribution of cations. The ΔS_{rand} term can have values ranging from 0 to 18.3 J deg^{-1} mol^{-1}. Because of the large octahedral site preference energy of Cr^{3+} ion compared to those of Cd^{2+} and Mg^{2+} ions, the chromites of cadmium and magnesium are expected to be normal spinels even at high temperatures with no significant entropy contribution from the mixing of cations. Their entropies of formation from oxides can therefore be expected to have a value close to -7.25 cal deg^{-1} mol^{-1}. However, chromium ion can exist in different oxidation states and the entropy arising from the mixing of these multivalent chromium ions can effect the accuracy of the semiempirical correlation for the entropy of formation of spinel phases.

Chromium exhibits all valency states from Cr^{2+} ($3d^4$) through Cr^{6+} ($3d^0$). Although no binary oxide of Cr^{2+} has yet been synthesized, it exists in ternary compounds formed under extremely reducing conditions. Much the same is apparently true of Cr^{5+}, which exists only in compounds that are stabilized by a very favorable host structure (*e.g.*, apatites and spodiosites). Stubican and Greskovich (4) have shown that, although there is no significant solubility of Cr_2O_3 in $MgCr_2O_4$ at 1700°C in oxidizing atmospheres, approximately 33% of Cr^{2+} ions can substitute for Mg^{2+} ions on the tetrahedral sites in reducing atmospheres between 1800° and 2000°C. The reducing atmospheres were obtained by admitting some air into the system and allowing it to react with a graphite susceptor. Assuming that equilibrium between graphite and carbon monoxide was achieved in their apparatus, the oxygen partial pressure could have been as low as 10^{-15} atm, approximately five orders of magnitude below that corresponding to the reduction of pure chromium

Key words: cadmium, magnesium, chromites, chromates, free energy, entropy, thermodynamics, solid-state galvanic cell.

sequioxide. The interest in $MgCr_2O_4$ and its solid solutions arises from their use as important constituents of steel plant refractories.

The entropy of formation of $MgCr_2O_4$ at low oxygen potentials can be deduced from the temperature dependence of the oxygen potential corresponding to the reduction of $MgCr_2O_4$ to MgO and Cr, and compared with that predicted by the semiempirical correlation. Any differences between the values may be indicative of the presence of Cr^{2+} ions. In $CdCr_2O_4$ in equilibrium with Cr_2O_3 and a cadmium alloy the oxygen potential is sufficiently high to ensure that no Cr^{2+} ions are present.

The heats of formation of $MgCr_2O_4$ and $CdCr_2O_4$ have been measured by Müller and Kleppa (5) as -46.3 (± 0.8) kJ mol^{-1}, and -42.3 (± 0.8) kJ mol^{-1}, respectively, by high temperature solution calorimetry. The free energy of formation of $MgCr_2O_4$ was measured by Tretjakov and Schmalzried (6) with a solid oxide cell in which calcia-stabilized zirconia was employed as a solid electrolyte. The author is unaware of any previous study on the free energy of formation of $CdCr_2O_4$. Muller *et al.* (8) have reported on phase equilibria in MgO-Cr_2O_3-O_2 and CdO-Cr_2O_3-O_2 systems between 450° and 850°C and at high oxygen pressures (up to 3500 atm). They identified two magnesium chromates, the low temperature α-$MgCrO_4$ and the high temperature β-$MgCrO_4$, and three chromates of cadmium, the low temperature α-$CdCrO_4$, the high temperature β-$CdCrO_4$, and a new phase Cd_2CrO_5. Approximate values for the free energies of formation of some of these chromates can be obtained from data on chromites and phase relations at high pressures.

Experimental Methods

Materials.—Fine powders of Cr, CdO, MgO, and Cr_2O_3, each 99.99% pure, were obtained from Alfa Inorganics. The cadmium chromite was prepared by heating pellets containing an intimate mixture of the component oxides in air at 1000°C for 4 days. The magnesium chromite was prepared by heating the component oxides under argon gas at 1300°C for 2 days. The formation of the chromites was confirmed by x-ray diffraction analysis. The chromite was ground, pelletized, and reheated until no extra x-ray lines were visible. A gold alloy containing 5 atom percent (a/o) cadmium was prepared by melting a mixture of gold and cadmium, each 99.999+ purity, in closed zirconia crucibles under argon gas and quenching in liquid nitrogen. A fine powder of the alloy was prepared by filing. The iron particles in the powder were removed magnetically. Impervious calcia-stabilized zirconia tubes supplied by the Zirconia Corporation of America contained 15 mole percent (m/o) CaO. Thoria pellets containing 7.5 m/o Y_2O_3 were prepared from mixed nitrate solution by evaporation and subsequent decomposition as described earlier (9). The argon gas used as the atmosphere for the potentiometric experiments was 99.99% pure and was dried and then deoxidized by passing through a column of titanium granules at 900°C. The electrodes were prepared by mixing the component metal and oxide powders, compacting the mixture into 1 cm diameter pellets, and sintering at high temperature in an inert gas atmosphere at 1000°C for 2 days. An x-ray examination of the pellet revealed that there was no change in the composition of the pellet during sintering.

Apparatus.—The design of the apparatus for the study of the free energy of formation of $CdCr_2O_4$ is similar to those used earlier in the study of $ZnAl_2O_4$, $ZnCr_2O_4$ (10), $ZnTiO_3$, and Zn_2TiO_4 (11). Because of the high vapor pressure of cadmium, it was necessary to have it at low activity as an alloy with gold. In order to minimize the change in composition of the alloy, the electrode pellets composed of mixtures of alloy and oxides in equimolar ratios were contained in two CaO-ZrO_2 crucibles covered with lids. The flat closed ends of the two CaO-ZrO_2 crucibles were polished and pressed against each other by a system of alumina rods and a spring loading arrangement.

A schematic diagram of the apparatus used for the study of the free energy of formation of $MgCr_2O_4$ is shown in Fig. 1. Since the oxides were equilibrated with metallic chromium, the oxygen potential of the ambient argon atmosphere had to be maintained below 10^{-13} atm to prevent significant oxidation of chromium under the experimental conditions. A large number of titanium internal "getters" had to be introduced into the high temperature system in order to remove the residual oxygen from the inert gas and to deoxidize any oxygen bearing gases that desorb from

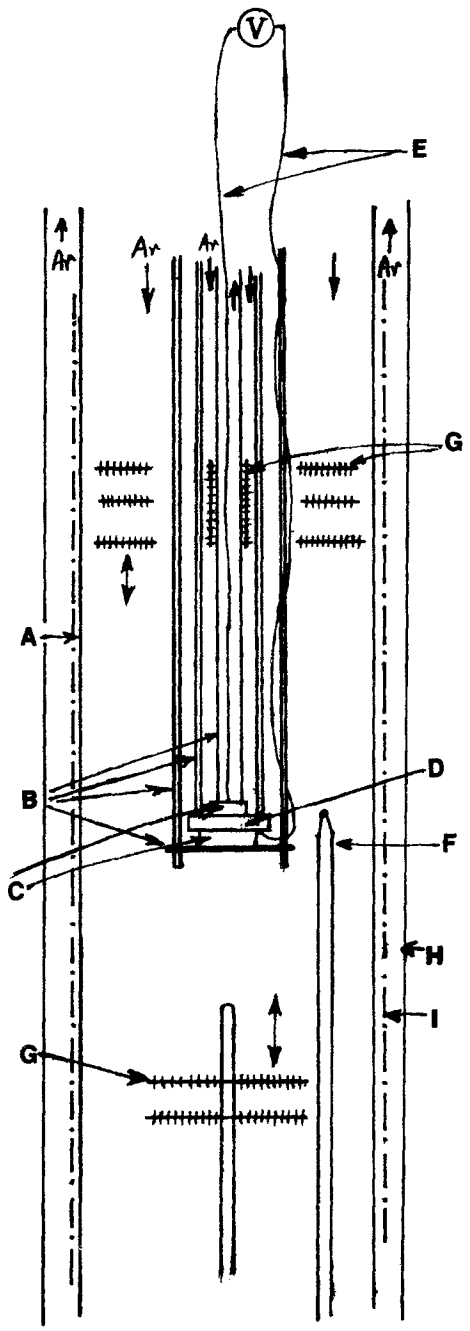


Fig. 1. Schematic diagram of the apparatus used to measure the free energy of formation of $MgCr_2O_4$. A, Alumina reaction tube; B, alumina rods and slabs used for spring loading the electrodes against the electrolyte; C, electrode pellets; D, Y_2O_3-ThO_2 electrolyte pellet; E, platinum leads; F, Pt-Pt (13% Rh) thermocouple; G, titanium internal "getters;" H, outer coaxial alumina tube; I, electrical shield (earthed platinum foil).

the alumina tubes and supports. The alumina reaction tube was surrounded by another longer coaxial alumina tube and the space between the two tubes was flushed with prepurified argon gas. With this construction the oxygen gradient across the alumina reaction tube is greatly reduced, so that the contamination of the inert gas atmosphere around the cell by oxygen diffusing through the alumina tube is minimized. An open stacked pellet assembly, where the reference and test electrodes were spring loaded against the two polished sides of a Y_2O_3-ThO_2 electrolyte pellet, was employed in cells containing Cr + Cr_2O_3 electrodes, since at the low oxygen potentials oxygen transport via the gas phase between the electrodes would not be significant.

Procedure.—The reversible potential of the following cells was measured as a function of temperature using a Keithley electrometer with a minimum impedance of $10^{12}\Omega$

$$\text{Pt, } \begin{matrix}\text{Au-5\%Cd} \\ + \\ \text{CdO}\end{matrix} \Big/ \text{CaO-ZrO}_2 \Big/ \begin{matrix}\text{Au-5\%Cd} \\ + \\ \text{CdCr}_2\text{O}_4\text{Cr}_2\text{O}_3\end{matrix} \qquad \begin{matrix}\text{Pt - - - I} \\ (500°\text{-}730°\text{C})\end{matrix}$$

$$\text{Pt, Cr} + \text{Cr}_2\text{O}_3/\text{Y}_2\text{O}_3\text{-ThO}_2/\text{Co-CoO}, \qquad \begin{matrix}\text{Pt - - - II} \\ (800°\text{-}1200°\text{C})\end{matrix}$$

and

$$\text{Pt, Cr} + \text{Cr}_2\text{O}_3/\text{Y}_2\text{O}_3\text{-ThO}_2/\text{Cr} + \text{MgCr}_2\text{O}_4 + \text{MgO}, \qquad \begin{matrix}\text{Pt - - - III} \\ (800°\text{-}1200°\text{C})\end{matrix}$$

Steady potentials (±2 mV) were obtained with cell I approximately 4 hr after attaining thermal equilibrium, while with cells II and III approximately 10 hr were required. Presence of a volatile component (cadmium) in cell I probably facilitated the more rapid attainment of equilibrium at the electrode-electrolyte interface. Reproducible potentials could not be measured with cell I above 800°C. Also once the cell was heated above 850°C, the low temperature measurements could not be repeated without replacing the electrode pellets. Although the cell was designed to minimize composition changes in the alloy at the two electrodes by the volatilization of cadmium, some differential vaporization was probably responsible for the irreversible damage of electrode pellets at the higher temperatures.

After assembling cells II and III, the reaction tube was evacuated to a pressure of 10^{-4} mm Hg, and then refilled with prepurified argon gas. This procedure was repeated after heating the furnace to 600°C, to remove the oxygen bearing gas species that desorb from the refractories. Despite these precautions, preliminary experiments indicated slight oxidation of chromium metal in the pellets. It was found by trial and error that most satisfactory measurements could be performed when the Cr+Cr_2O_3 and Cr+$MgCr_2O_4$+MgO electrodes were prepared by compacting a mixture of metal and oxide powders in the molar ratios 1.5:1 or 1.5:1:1. With cells II and III reproducible emf's could not be measured below 800°C. This is probably related to the sluggish reaction between Cr and Cr_2O_3 to establish the equilibrium oxygen potential. It was also observed that in order to yield reproducible emf's the cells had to be heated initially to 1100°C.

The reversibility of the cells was checked by passing small currents (≈50 μA) through the cells for approximately 1 min in either direction, and it was found that the cell potential returned to its initial value within 1 hr, after which it remained constant for up to 6 hr. The cell potentials were also independent of the flow rate of the inert gas around the cell.

Results

The reversible cell potentials (emf's) are plotted as a function of temperature in Fig. 2 and 3. The following equations were obtained by least mean squares regression analysis of the emf data

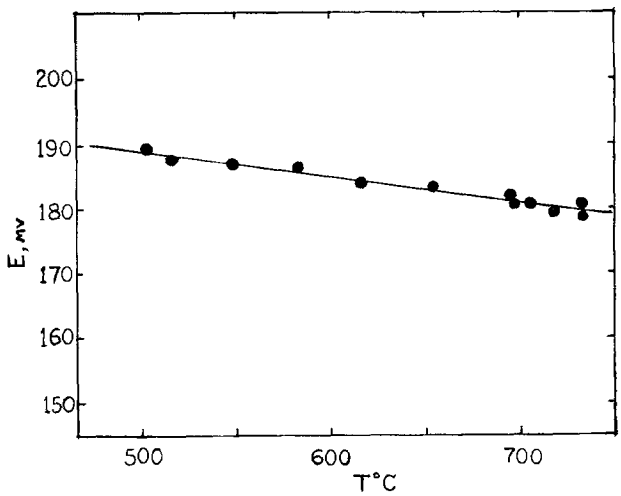


Fig. 2. The variation of the potential (emf) of cell I with temperature.

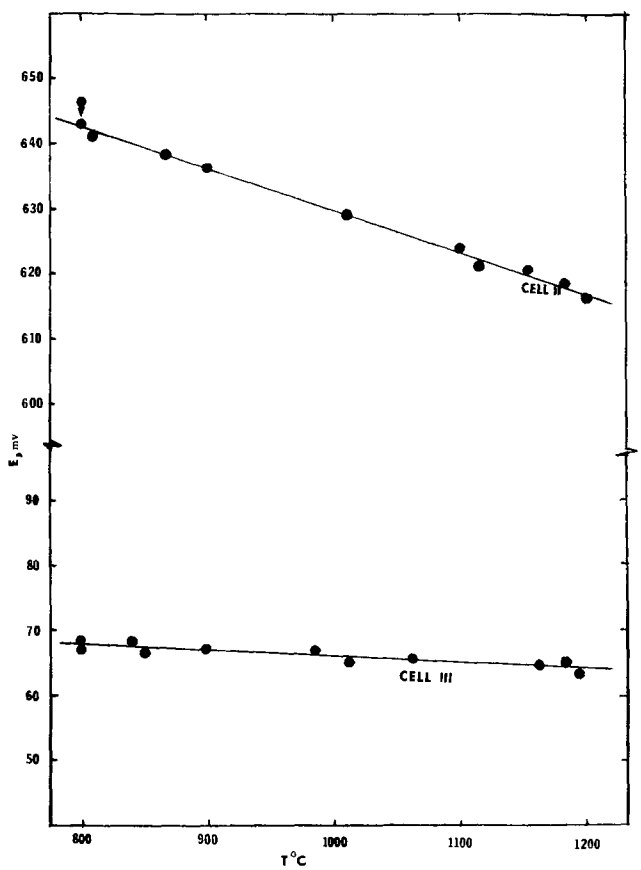


Fig. 3. The temperature dependence of the emf of cells II and III.

$$E_I = 219 - 3.9 \times 10^{-2}T\ (\pm 1.8)\text{mV} \qquad [1]$$

$$E_{II} = 712 - 6.45 \times 10^{-2}T\ (\pm 2)\text{mV} \qquad [2]$$

$$E_{III} = 78.0 - 9.25 \times 10^{-3}T\ (\pm 2)\text{mV} \qquad [3]$$

The standard free energy of formation of $CdCr_2O_4$ is directly related to the emf of cell I. For the reaction

$$\text{CdO(r.s.)} + \text{Cr}_2\text{O}_3\text{(cor)} \rightarrow \text{CdCr}_2\text{O}_4\text{(sp)} \qquad [4]$$

$$\Delta G° = -2FE_I$$

$$= -42{,}260 + 7.53T\ (\pm 400)\text{J} \qquad [5]$$

where **F** is the Faraday constant and E is the emf in volts. The emf of cell II is a measure of the difference in the oxygen potential of the Co+CoO and $Cr+Cr_2O_3$ mixtures. The oxygen potential of the Co+CoO electrode has been measured independently (3) as

$$\Delta\mu_{O_2}\,(Co+CoO) = -469{,}240 + 142.04T\ (\pm 400)J \quad [6]$$

The oxygen potential of the $Cr+Cr_2O_3$ electrode obtained from the above equation and the emf of cell II is

$$\Delta\mu_{O_2}\,(Cr+Cr_2O_3) = -743{,}960 + 166.9T\ (\pm 600)J \quad [7]$$

This value is in good agreement (±500J) with the data of Mazandarany and Pehlke (7) obtained from a solid oxide cell with Y_2O_3-ThO_2 electrolyte, and Jeannin *et al.* (12) obtained by a gas equilibrium technique, indicating that the emf apparatus was functioning satisfactorily at the low oxygen potentials associated with the $Cr+Cr_2O_3$ mixture.

The emf of cell III is directly related to the free energy of formation of magnesium chromite from the component oxides

$$MgO\,(r.s.) + Cr_2O_3\,(cor) \rightarrow MgCr_2O_4\,(sp) \quad [8]$$

$$\Delta G^\circ = -6FE_{III}$$

$$= -45{,}200 + 5.36T\ (\pm 400)J \quad [9]$$

Discussion

The Gibbs free energy of formation of $MgCr_2O_4$ obtained in this study is −38.38 kJ mol^{-1} at a mean temperature of 1000°C. The corresponding value obtained by Tretjakov and Schmalzried (6) is −33.89 kJ mol^{-1}. The smaller value obtained by them (6) is almost certainly due to electronic conduction in their CaO-ZrO_2 electrolyte at the low oxygen potentials corresponding to the $Cr+MgCr_2O_4+MgO$ electrode. The values for the standard free energy of formation of Cr_2O_3 obtained by Tretjakov and Schmalzried (6) are also significantly less negative than those obtained in this study and in the earlier study of Mazandarany and Pehlke (7) using Y_2O_3-doped ThO_2 as the electrolyte. The "second law" heat of formation of $MgCr_2O_4$ obtained in this study (−45.2 ± 1.2 kJ mol^{-1}) is in good agreement with the value of −46.3 (±0.8) kJ mol^{-1} reported by Müller and Kleppa (5) at 700°C. The "second law" heat of formation of $CdCr_2O_4$ (−42.26 ± 1.2 kJ mol^{-1}) obtained by the electrochemical measurements is almost identical to that obtained by high temperature solution calorimetry (−42.3 ± 0.8 kJ mol^{-1}) (5).

The entropy of formation of $CdCr_2O_4$ from its component oxides obtained in this study (−7.53 ± 1.0 J K^{-1} mol^{-1}) is in excellent agreement with that predicted by the semiempirical correlations (−7.5 J K^{-1} mol^{-1}) for the entropy of formation of 2-3 spinels. However, the measured entropy of formation of $MgCr_2O_4$ is approximately 2 J K^{-1} mol^{-1} more positive than the estimated value, the difference being larger than the combined statistical uncertainty in both the measured and estimated values. It is likely that the higher entropy of $MgCr_2O_4$ is due to the presence of divalent chromium ions in the spinel and the consequent mixing of cations. The Cr^{2+} ion has the same electronic structure (d^4) as the Mn^{3+} ion, and may be expected to have strong octahedral site preference. The Cr^{3+} and Cr^{2+} ions would therefore mix on the octahedral sites. The presence of d^4 ions on the octahedral site would also give rise to Jahn-Teller entropy associated with the randomization of the direction of the distortions in the cubic phase. The difference between the measured and estimated entropies is suggestive of the presence of 2(±1) ionic percent Cr^{2+} ions on the octahedral site of the spinel structure.

Thermodynamic data on cadmium and magnesium chromates.—Muller *et al.* (8) have determined the phase equilibria for the systems MgO-Cr_2O_3-O_2 and CdO-Cr_2O_3-O_2 from 450° to 850°C and oxygen pressures from 2 to 3500 atm. There are indications that thermodynamic equilibrium was not attained in their studies at the lower temperatures. For example, the temperature corresponding to the dissociation of α-$MgCrO_4$ according to the reaction

$$4\alpha\text{-}MgCrO_4 \rightarrow 2MgCr_2O_4(s) + 2MgO(s) + 3\,O_2(g) \quad [10]$$

and the temperature corresponding to the oxidation of the spinel $MgCr_2O_4$ according to the scheme

$$4MgCr_2O_4(s) + 3\,O_2(g) \rightarrow 4\alpha\text{-}MgCrO_4 + 2Cr_2O_3(s) \quad [11]$$

are both given as 553°C at an oxygen pressure of 4 atm. This can only be true if the standard free energy of formation of the spinel $MgCr_2O_4$ from its component oxides is zero, contrary to the evidence from both galvanic cell and calorimetric studies. Since thermodynamic equilibrium would be achieved more closely at the higher temperature, the phase equilibrium data of Muller *et al.* (8) at the highest temperatures may be used in conjunction with the data on the spinel phase obtained in this study to estimate the free energies of formation of β-$MgCrO_4$, β-$CdCrO_4$, and Cd_2CrO_5 from the oxides MgO, CdO, or Cr_2O_3 and gaseous oxygen.

For β-$MgCr_2O_4$ the standard free energy of formation at 707°C calculated from the dissociation pressure is 5000J more negative than the value obtained from the reverse oxidation reaction. Whenever small hysteresis effects of this nature were observed in the measured equilibrium oxygen pressures, average values have been used in computing the values shown in Table I. The entropies of formation of the chromates have been estimated as 180 (±12) J K^{-1} mol^{-1} oxygen gas, assuming that entropies of the condensed phases on the two sides of the chemical reaction for the formation of the chromates are approximately equal, and therefore the major entropy change arises from the conversion of oxygen gas into a condensed phase. In the absence of any direct thermodynamic studies on the chromates of magnesium and cadmium, the values presented in Table I provide the best information now available.

Manuscript submitted May 6, 1977; revised manuscript received Aug. 2, 1977.

Any discussion of this paper will appear in a Discussion Section to be published in the June 1978 JOURNAL. All discussions for the June 1978 Discussion Section should be submitted by Feb. 1, 1978.

Table I. Standard free energies of formation of the chromates of magnesium and cadmium

Reaction	ΔG°, J
$MgO(s) + \frac{1}{2}Cr_2O_3(s) + \frac{3}{4}\,O_2(g) \rightarrow \beta\text{-}MgCrO_4(s)$	−127,500 + 135T (±4000)
$2CdO(s) + \frac{1}{2}Cr_2O_3(s) + \frac{3}{4}\,O_2(g) \rightarrow Cd_2CrO_5(s)$	−138,100 + 135T (±4000)
$CdO(s) + \frac{1}{2}CrO_2O_3(s) + \frac{3}{4}\,O_2(g) \rightarrow \beta\text{-}CdCrO_4(s)$	−133,400 + 135T (±4000)

REFERENCES
1. K. T. Jacob and C. B. Alcock, *Met. Trans. B.*, **6**, 215 (1975).
2. K. T. Jacob and C. B. Alcock, *J. Am. Ceram. Soc.*, **8**, 192 (1975).
3. K. T. Jacob, Unpublished research.
4. V. S. Stubican and C. Greskovich, *Geochim. Cosmochim. Acta*, **39**, 875 (1975).
5. F. Müller and O. J. Kleppa, *J. Inorg. Nucl. Chem.*, **35**, 2673 (1973).
6. J. D. Tretjakov and H. Schmalzried, *Ber. Bunsenges. Phys. Chem.*, **69**, 396 (1965).
7. F. N. Mazandarany and R. D. Pehlke, *This Journal*, **121**, 711 (1974).
8. O. Muller, R. Roy, and W. B. White, *J. Am. Ceram. Soc.*, **51**, 694 (1968).
9. K. T. Jacob and J. C. Chan, *This Journal*, **121**, 534 (1974).
10. K. T. Jacob, *Thermochim. Acta*, **15**, 79 (1976).
11. K. T. Jacob and C. B. Alcock, *High Temp. High Pressures*, **7**, 433 (1975).
12. Y. Jeannin, C. Mannerskantz, and F. D. Richardson, *Trans. AIME*, **227**, 300 (1963).

A Novel Approach to the Oxygen Activity Microdetermination of Oxides by EMF Measurements

C. M. Mari

Department of Electrochemistry, University of Milan, Milan, Italy

S. Pizzini*

G. Donegani Research Institute, Montedison S.p.A., Via Fauser, 4, 28100 Novara, Italy

and L. Manes and F. Toci

European Institute for Transuranium Elements, Karlsruhe, Germany

ABSTRACT

A novel use of solid-state galvanic cells for the determination of thermodynamic properties of oxides by employing mg amounts of powder instead of presintered pellets is described. The oxides which were investigated all belong to the rare earths and actinide family, and present enhanced ionic and electronic mobilities which are essential for performing these kind of measurements. The advantage of this method is to allow a fast and direct sampling of oxide fuel rods which is normally carried out by chemical methods. Some examples of this technique are given.

Solid-state electrochemical cells have been so widely used for the determination of thermodynamic properties of oxides at high temperatures (1, 2) that this method can be considered to be a standard thermochemical method. However, while in most cases the potentiometric determination of oxygen activity in solid oxide samples could be straightforwardly performed when keeping the oxygen potential constant (at constant temperature) by the presence of a second phase, the same determination could be very difficult when one has to measure the dependence of the oxygen chemical potential of nonstoichiometric oxides on the oxide composition. Here the problem is to have small (and possibly fast) compositional changes of the oxide phase (obtained by suitably injecting oxygen in the sample chamber) and to measure both the amount of oxygen injected and the change of oxygen potential of the oxide. It has already been shown that in order to obtain reliable results, one of the requirements is to avoid oxygen permeation across the cell walls by a suitable choice of the operation conditions (3, 4) or by the use of a double wall chamber and to reduce the amount of oxygen outgassed from the inside of the cell (walls, electrodes) by suitably baking out the cell before operation. Also, the choice of the volume of the sample chamber has a straightforward influence on the reliability of the measurements, especially when coulometric determinations are carried out on (small size) samples having high (10^{-3}-10^{-8} atm) equilibrium pressures. In this case, in fact, the residual oxygen in the gas phase could significantly affect the composition of the oxide sample.

Examples of this use of the electrochemical technique have been given by Tretyakow and Rapp (5) and Riccardi (6), but their cells are relatively difficult to use and utilization of small size and large surface area (powder) samples that allow faster equilibration with the gaseous atmosphere is easier. We have designed various types of cells which at least in principle fulfill all the aforementioned criteria and permit an extension of the electrochemical method to the microanalysis of oxide powder sample. As an example, these cells have recently been used in our laboratories to measure the oxygen potential profiles in irradiated (U, Pu)$O_{2\pm x}$ fuels.

This investigation has succeeded in showing the feasibility of a reliable oxygen potential determination in milligram amount samples in synthetic fuels, irradiated, and nonirradiated fuels (7). We report and discuss in a rather general fashion the results obtained, which provide further proof of the usefulness of the electrochemical method as well as a guideline for new applications.

Experimental

Single compartment cell.—The first type of cell used (Fig. 1) is a single wall cell, which consists of a (4 mm ID) YSZ[1] tube closed at one end and electrolytically sealed to a UHV copper adapter. This is fitted to an ultrahigh vacuum valve attached to a Varian ion-getter pump (2 liters/sec) and to the HV system

* Electrochemical Society Active Member.

Key words: solid electrochemical cells, cerium oxide, (Pu-U) mixed oxides, oxygen chemical potential determination.

[1] Yttria stabilized zirconia.

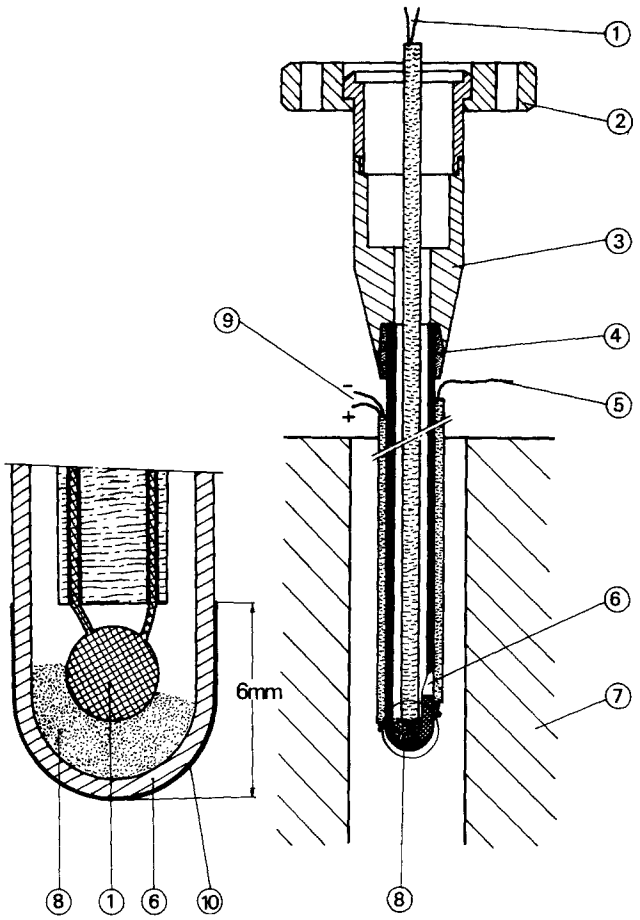


Fig. 1. Schematic drawing of the single compartment emf cell: (1) Thermocouple and electrical contact; (2) UHV miniconflat flange; (3) UHV copper adapter; (4) electrochemical seal; (5) electrical contact; (6) YSZ electrolyte tube; (7) furnace; (8) oxide powder sample; (9) thermocouple; (10) porous Pt electrode.

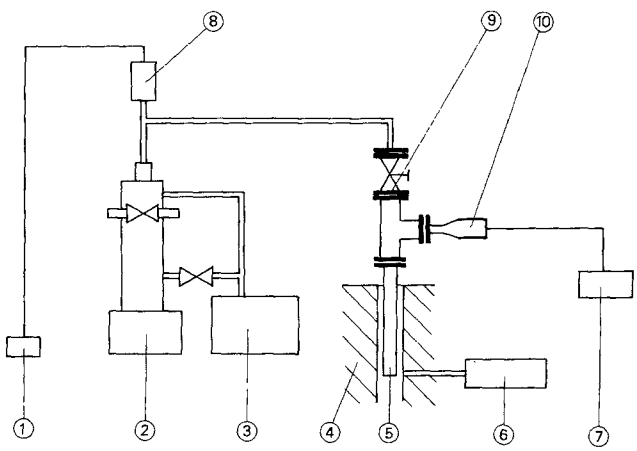


Fig. 2. Schematic diagram of the experimental assembly: (1-7) Vacuum control unit; (2) diffusion pump; (3) rotary pump; (4) furnace; (5) cell; (6) proportional temperature control unit; (8) penning gauge; (9) UHV valve; (10) ion-getter pump.

(see Fig. 2). The inner volume of the cell (tube, valve, and pump) is about 30 ml. All connections are made by means of UHV miniconflat valves. The cell is designed to operate as a gas concentration cell

$$\text{Pt, } (P_{O_2}') \text{ } MeO_x/YSZ \text{ } (t_{o=} = 1)/(P_{O_2}'')/\text{Pt} \quad \text{(I)}$$

where on the left side compartment MeO_x could also serve as the electrode (in this case MeO_x is an electronically conducting oxide), and thus Pt serves to close the electrochemical circuit, whose open-circuit voltage is given by the Nernst equation

$$E_I = \frac{RT}{4F} \ln \frac{P_{O_2}''}{P_{O_2}'} \quad [1]$$

when the electronic transport number of the electrolyte is zero or negligible with respect to the ionic transport number of the electrolyte. It has already been shown that a cell of this type, equipped with porous Pt electrodes, could be operated at a pressure as low as 10^{-8} atm (8).

Preliminary experiments carried out with a cell consisting of a YSZ tube which was platinized[2] inside and outside and filled with a CeO_{2-x} sample [previously equilibrated with a CO/CO_2 mixture of known ratio to fix its composition (9)] resulted in erratic behavior. It is apparent that the presence of a solid phase which buffers the oxygen pressure in the outer atmosphere is not sufficient to attain the same equilibrium pressure value for the three-phase electrolyte-gas phase (in the pores of the porous Pt layer) metal contact. Subsequently, the cell geometry shown in Fig. 3 was used and since the oxide powder is poured from the bottom of the electrolyte tube, it is possible to form a two-phase oxide-electrolyte contact. The electrical circuit is completed with Pt wire leads and a Pt/Pt-Rh 10% thermocouple, which is gently pressed onto the powder by the collar-spring combination. The reference electrode is a porous Pt electrode suitably deposited on the outer surface of the YSZ tube.

After having introduced the sample, the whole system, including the ion-getter pump, is baked under vacuum at 570°K. The sample is then brought to a known composition by equilibration with CO/CO_2 mixtures of known oxygen fugacity at 1173°K by using the data of Hampson (10). After equilibration and before proceeding with the measurements, the system is held for 30 min under vacuum until a pressure of less than 10^{-8} Torr (as read with the ion-getter pump) is reached in the system. The hot zone of the cell at 970°K and the leak rate of the cell is about 10^{-10} Torr 1 sec^{-1}.

Double wall cell.—In order to reduce the oxygen permeation from the atmosphere through the wall of the electrolyte tube [which is significant at temperatures higher than 1300°K (4)], a double wall cell has been developed (Fig. 4). It consists of a solid-state galvanic cell of the type

$$\text{Pt, } (P_{O_2}') \text{ } MeO_x/YSZ/CeO_{2-x}/YSZ/(P_{O_2}'')/\text{Pt} \quad \text{(II)}$$

The emf of cell II is again proportional to the ratio of the oxygen partial pressure in the right and in the left side cell compartments, according to the equation

$$E_{II} = E_I = \frac{RT}{4F} \ln \frac{P_{O_2}''}{P_{O_2}'} \quad [2]$$

and the over-all cell equation is O_2 (P") → O_2 (P'). The inner part of the cell consists of a 4 mm ID, 6 mm OD YSZ tube containing the oxide sample which is electrolytically sealed onto a copper tube. This is done by baking at 570°K, and cold sealing by crimping under a vacuum. The outer part of the cell consists of a 12 mm OD, 8 mm ID YSZ tube. A porous Pt reference electrode is deposited on the outer wall of the tube. The CeO_{2-x} powder in the bottom of the outer tube serves both as an oxygen getter in the annular chamber between the outer and inner YSZ tube, and to produce electrochemical continuity between the two electrolyte tubes. The annular chamber itself is under UHV conditions by means of a rotary diffusion pump (100 liters/sec) and details are shown in Fig. 4. Under these conditions, the CeO_{2-x} powder operates as a reversible oxygen electrode whose cell emf in cell II is

[2] The procedure consists of firing a Pt paste to obtain a porous Pt layer.

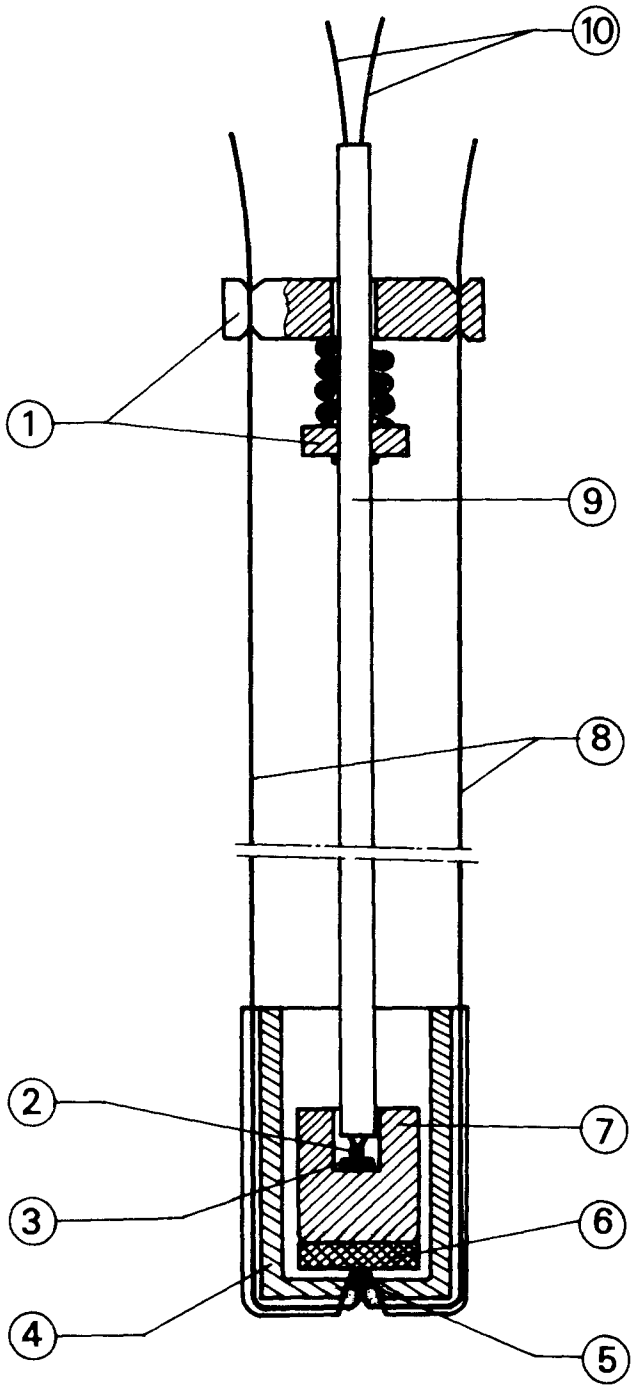


Fig. 3. Schematic drawing of the single compartment emf cell using yttria stabilized thoria electrolyte: (1) Al_2O_3 collar and ring; (2) and (5) thermocouple and electrical contact; (3) $(U\ Pu)O_{2-x}$ sample; (4) Al_2O_3 crucible; (6) reference electrode; (7) yttria-doped thoria crucible (electrolyte); (8) and (10) Pt-Pt 10% wire; (9) Al_2O_3 capillary.

independent of the oxygen partial pressure in the annular chamber, and corresponds to the emf in cell I.

Thoria-electrolyte cell.—In order to extend the operation of the cell to oxygen potentials less than $\simeq$100 kcal/mole, the YSZ must be substituted by thoria-base electrolytes in order to avoid the excessive electronic conduction. This would make it difficult to evaluate the unknown oxygen potential by integration of the Wagner equation

$$E = \frac{1}{2\mathbf{F}} \int_{\mu' O_2}^{\mu'' O_2} t_{O^=} d\mu O_2$$

which substitutes for the Nernst equation for E when $t_{O^=}$ is not unity.

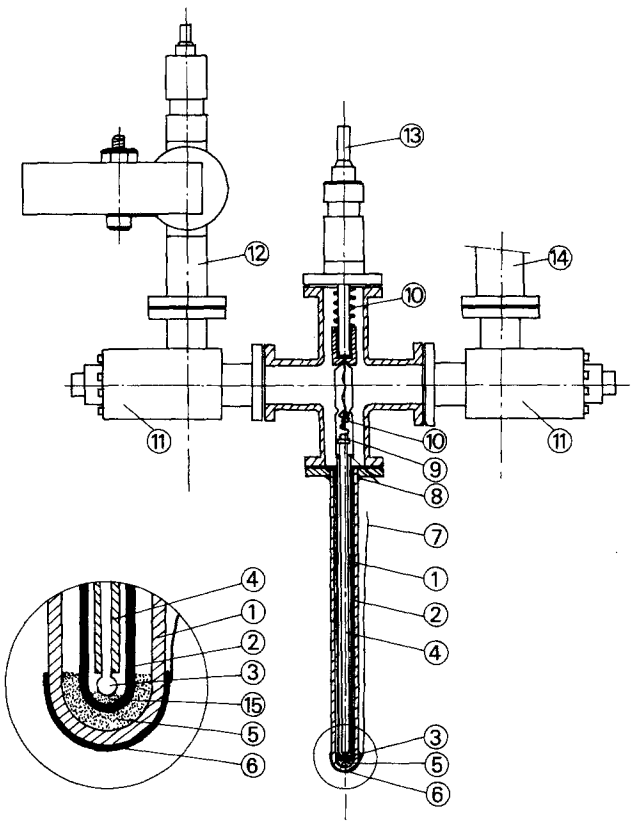


Fig. 4. Schematic drawing of the double compartment emf cell: (1) Outer YSZ tube; (2) inner YSZ tube; (3) inner Pt electrode; (4) Al_2O_3 tube supporting the inner Pt electrode; (5) intermediate chamber with nonstoichiometric CeO_2; (6) outer porous Pt layer, for oxygen reference electrode; (7) Pt wire soldered to 6; (8) high vacuum ceramic-to-metal joint; (9) copper tube; (10) springs; (11) high vacuum valve; (12) ion-getter pump; (13) electrical feed through for the inner electrode 3; (14) connection to a vacuum system; (15) powdered sample.

Because YST[3] tubes have poor mechanical stability during thermal cycling, are much more expensive than YSZ, and could eventually still exhibit electronic conductivity due to their impurity content, a cell design that does not involve the use of such a tube has been chosen. The cell consists of an alumina tube (see Fig. 3) which is restrained by a support wire acting also as thermocouple and electrical conductor for the cell. The reference electrode and the (YST) electrolyte pellet are mounted inside this crucible. The specimen for analysis is placed in the cavity, and electrical contact to the specimen is made by another thermocouple which is spring loaded in order to maintain contact during the experiment. The complete assembly is fitted inside an alumina tube which is connected to the UHV system. This cell has been tested by measuring the oxygen potential over Fe/FeO against the Ni/NiO reference electrode. This cell emf (Fig. 5) was found to be within the limits of accuracy reported in literature.

Results

Measurements on CeO_{2-x}.—A single wall cell has been used for these measurements, and this has been thoroughly described in a previous paper (7). The results of these experiments are given in Fig. 6 in terms of their dependence on the temperature of the chemical potential of oxygen in equilibrium with a sample of known and constant composition. One can observe that they display the same temperature dependence as reported by Hampson (10) and they compare well with analogous results of Bevan and Kordis (11).

[3] Yttria stabilized thoria.

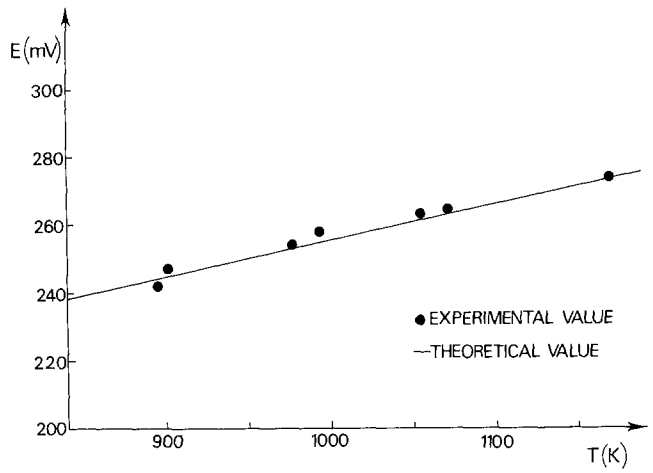


Fig. 5. Emf vs. temperature of the cell: Fe/FeO/YST/Ni, NiO diagram.

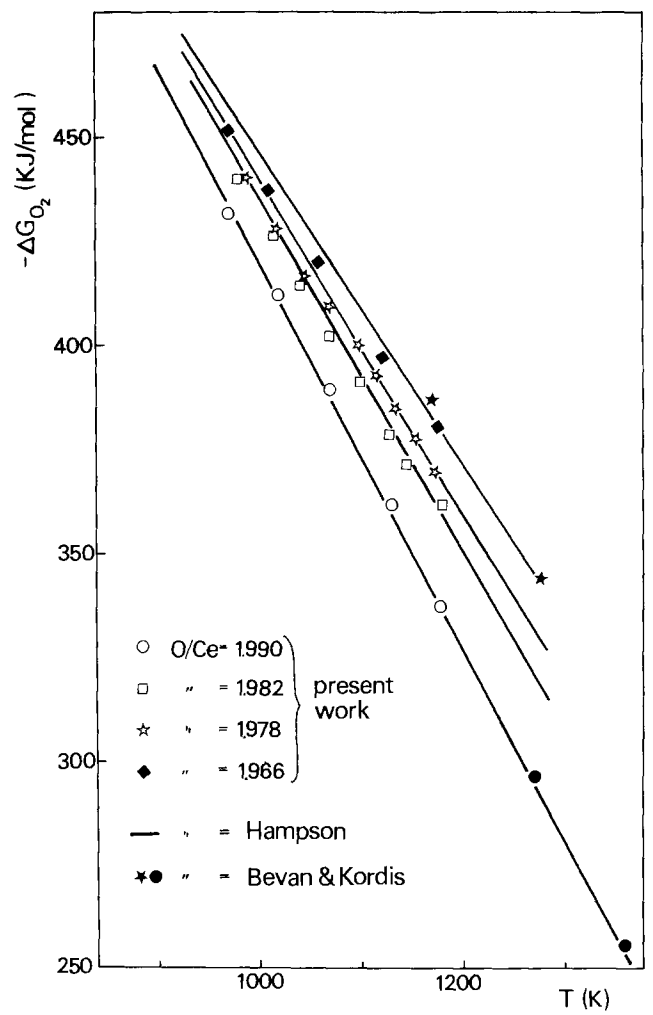


Fig. 6. Partial molar free energy values of oxygen in nonstoichiometric ceria as a function of the temperature for constant composition.

Measurements on hyperstoichiometric uranium-plutonium $(U_{0.80}Pu_{0.20})O_{2+x}$ *fuels.*—A small amount (7 mg) of $(U_{0.80}Pu_{0.20})O_{2+x}$ was used to carry out measurements with the double wall cell in which the oxygen partial pressure in the intermediate chamber was kept low by the presence of CeO_{2-x}. The oxygen potentials determined from the experimental emf values are reported in Fig. 7 (for a single value, at 905°K) and Fig. 8. For comparison purposes, the Rand and

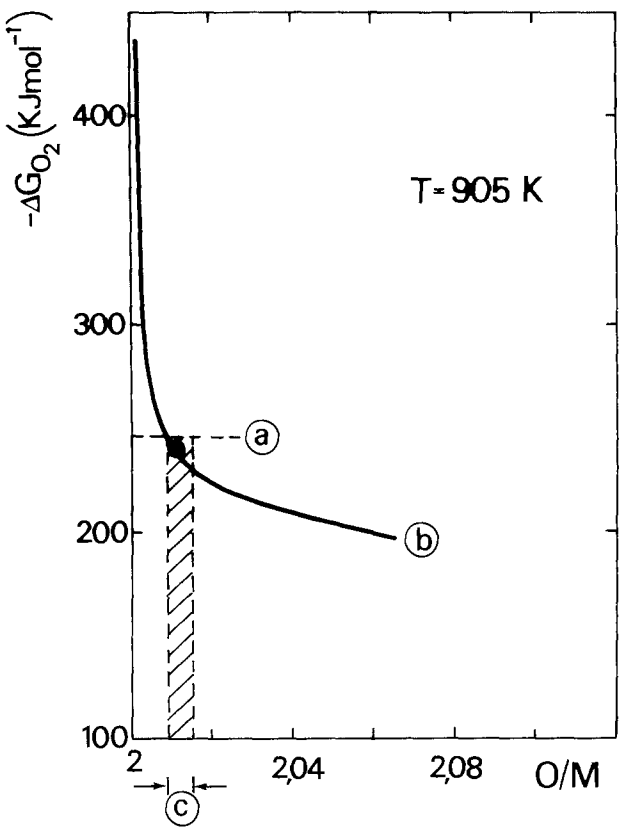


Fig. 7. Partial molar-free energy values of oxygen; (a) Measured on a 7 mg powder sample of $U_{0.80}Pu_{0.20}O_{2.120\pm0.003}$; (b) Rand and Markin (12) value; (c) error limits of the thermogravimetric determination.

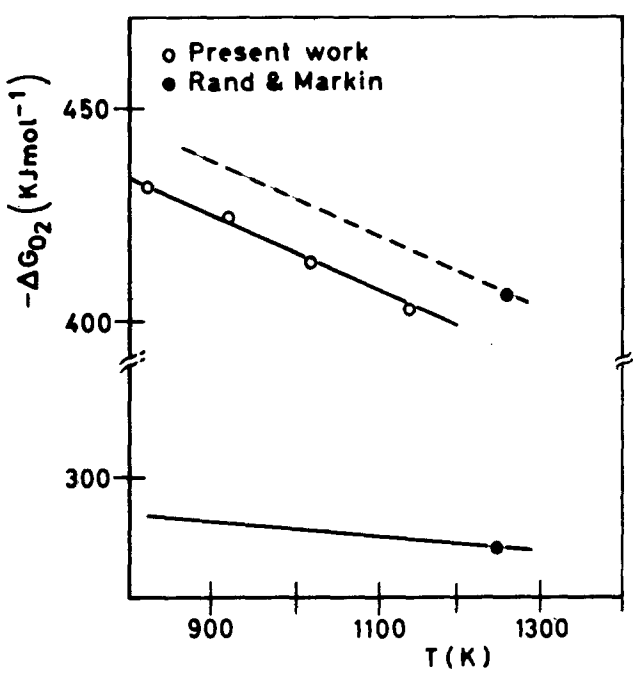


Fig. 8. Partial molar-free energy values of oxygen vs. temperature measured on a 0.8 mg powder sample of $U_{0.80}Pu_{0.20}O_{2.000}$.

Markin results (12) are reported for same compositions. There is remarkably good agreement in both cases.

Measurements on hypostoichiometric uranium-plutonium $(U_{0.80}Pu_{0.20})O_{2-x}$ *fuels.*—A batch of uranium-20% plutonium oxide was prepared by a coprecipitation method. Small (500 mg) samples from this batch

were reduced in various H_2/H_2O gas ratios at 1473°, 1573°, and 1673°K for 6 hr. The reduction was performed in a glove box which contained the galvanic cell so that specimens could be transferred directly to the cell. After the measurements, the specimens were transferred to another box where the oxygen-to-metal ratio (O/M) was determined by a gravimetric technique involving oxidation to $MO_{2.00}$ with CO/CO_2 and by x-ray analysis. Both methods agreed to within 0.006 O/M units. Three sets of oxygen potential measurements were carried out at temperatures between 800° and 1300°K and O/M values of 1.995, 1.985, and 1.964. The results are shown in Fig. 9 together with the results of Woodley (13) and Markin (14). The results of Markin are adjusted to $U_{0.8}Pu_{0.2}$ oxide following Woodley's method. The results obtained compare better with the extrapolated Woodley data than with those of Markin. This is also clear from the entropy data shown in Table I.

Inadvertent oxidation of the specimen of O/M = 1.99 due to the transfer of hypostoichiometric oxide between boxes during analysis could give rise to the difference in $\Delta G(O_2)$ between the above results and those of Woodley. At this O/M ratio the chemical potential of oxygen strongly depends on the stoichiometry, and a small oxidation could cause a large change in oxygen potential. To eliminate the above-mentioned uncertainty due to the specimen oxidation, research is now underway for a method of quantitative coulometric titration using a solid-state galvanic cell.

Conclusions

The experimental results given above demonstrate that in the case of oxides exhibiting high ionic and electronic mobility (like most of the oxides with the fluorite structure), a loose contact between the electrolyte walls and the oxide powder (which works at the electrode) is sufficient to obtain reliable thermodynamic data with a solid galvanic cell. These results should be discussed in the context of the theory of the oxygen electrode at high temperature and have a rather wide significance which goes beyond the achievement of an accurate measurement of oxygen profiles in irradiated fuels. It is in fact known that the erratic behavior of (porous) Pt electrodes at very low partial pressures of oxygen is essentially due to the kinetic hindering of the reaction

$$\tfrac{1}{2}\,O_2\ (\text{gas}) + 2e\ (\text{Pt}) \rightleftarrows O^{=}\ (\text{into the electrolyte}) \quad [3]$$

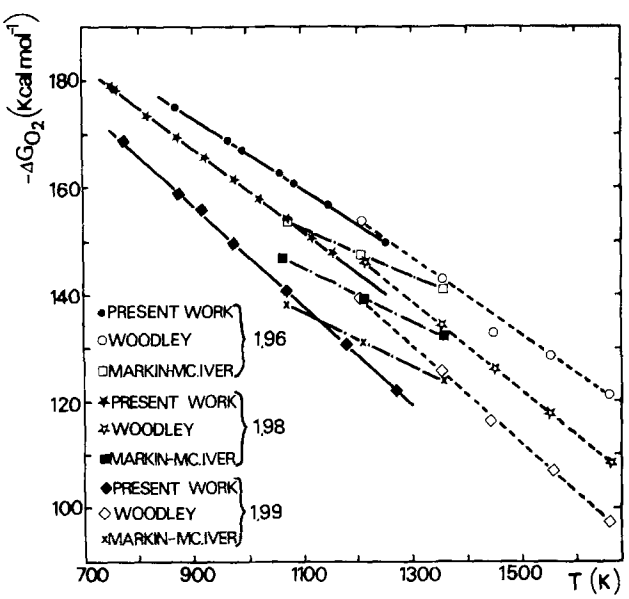


Fig. 9. Comparison of experimental and literature data of partial molar-free energy of oxygen vs. temperature on microsamples of $(U_{0.08}Pu_{0.2})O_{2-x}$ at different oxygen-to-metal ratios.

Table I. Entropy values (eu) of hypostoichiometric U-Pu oxides

Author \ O/M	1.96	1.98	1.99
Markin	44	47	48
Woodley	73	82	93
Present work	67	77	93

which occurs at the three-phase contact between the atmosphere, the electrolyte, and the metal.

Under these conditions, other reactions which behave like parasitic processes at high oxygen partial pressures take place such as the direct exchange of dissolved oxygen in Pt

$$O\ (\text{Pt}) + 2e \rightleftarrows O^{=}\ (\text{into the electrolyte}) \quad [4]$$

or the redox reactions involving adsorbed gases, like CO_2 and H_2

$$CO_2 + 2e \rightleftarrows CO + O^{=}\ (\text{into the electrolyte}) \quad [5]$$

and

$$H_2O + 2e \rightleftarrows H_2 + O^{=}\ (\text{into the electrolyte}) \quad [6]$$

become potential determining.

Incidentally, it is recalled that the oxygen diffusion in Pt is known to be a very slow process (15) and that both H_2 and CO are strongly chemisorbed on Pt.

By considering that the oxides used in the present work display high oxygen diffusivity in conjunction with good electronic conductivity and, moreover, a fast equilibration rate with the atmosphere, their use does maintain oxygen pressure at the interface between the oxide, the atmosphere, and the electrolyte corresponding to the thermodynamic equilibrium value, so that the reactions

$$\tfrac{1}{2}\,O_2\ (\text{gas}) + 2e\ (\text{oxide}) \rightleftarrows O^{=}\ (\text{into the electrolyte}) \quad [7]$$

and

$$O\ (\text{oxide}) + 2e\ (\text{oxide}) \rightleftarrows O^{=}\ (\text{into the electrolyte}) \quad [8]$$

occur at the same potential.

Since reactions [4] or [8] are potential determining at very low partial pressures of oxygen, it is an obvious conclusion that the condition which should be fulfilled to determine very low partial pressures of oxygen is to use a solid electrode. This type of electrode exchanges oxygen with the gas phase at a very fast rate, and behaves like a virtually unpolarizable electrode (16).

Acknowledgments

The authors are greatly indebted to Mr. G. Terzaghi for his enthusiastic and skillful cooperation and to Dr. E. Ewart (Harwell) for extensive discussion.

Manuscript submitted April 7, 1977; revised manuscript received Aug. 18, 1977.

Any discussion of this paper will appear in a Discussion Section to be published in the June 1978 JOURNAL. All discussions for the June 1978 Discussion Section should be submitted by Feb. 1, 1978.

Publication costs of this article were assisted by the University of Milan.

REFERENCES

1. K. S. Goto and W. Pluschkell, in "Physics of Electrolytes," Vol. 2, H. Hladik, Editor, Academic Press, New York (1972).
2. H. Schmalzried and A. D. Pelton, *Ann. Rev. Mater. Sci.*, 2, 143 (1972).
3. J. Fouletier, H. Scinera, and M. Kleitz, *J. Appl. Eletrochem.*, 5, 177 (1975).
4. C. B. Alcock and H. C. Cahn, *Can. Metall. Q.*, **11**, 559 (1972).
5. J. D. Tretjakow and R. A. Rapp, *Trans. Metall.*

Soc. AIME, 245, 1235 (1969).
6. C. Riccardi, D. I. C. Thesis, Imperial College, London (1971).
7. L. Manes, F. Toci, C. M. Mari, and S. Pizzini, submitted to J. Nucl. Mater.
8. C. M. Mari, S. Pizzini, T. A. Giorgi, L. Rosai, and M. Borghi, J. Appl. Electrochem., 7, 215 (1977).
9. O. Sørensen, Res. Rep., 331, (ISBN 87550 03605), Danish Atomic Energy Commission (1976).
10. R. J. Hampson, Unpublished Dragon Project Report.
11. D. J. M. Bevan and J. Kordis, J. Inorg. Nucl. Chem., 26, 1509 (1964).
12. M. H. Rand and T. L. Markin, IAEA Chemical Report Series No. 79, Vienna (1967).
13. R. E. Woodley, J. Am. Ceram. Soc., 56, 116 (1973).
14. T. L. Markin and E. J. McIver, in Proceedings of the Conference on Plutonium 1965, Chapman and Hall, London (1967).
15. L. R. Vehlo and R. W. Barlett, Metall. Trans., 3, 65 (1972).
16. L. Heyne and D. den Engelsen, This Journal, 124, 727 (1977).

Standard Free Energy of Formation of Alumina

D. Ghosh* and D. A. R. Kay

Department of Metallurgy and Materials Science, McMaster University, Hamilton, Ontario, Canada L8S 4L7

ABSTRACT

The standard free energy of formation of alumina, $\Delta G°_f(Al_2O_3)$, has been determined in the temperature range 1350°-1550°C, by studying the reaction

$$2Al_{(l)} + 3/2\ O_{2(g)} = Al_2O_{3(\alpha)}$$

using electrochemical cells of the type

$$Pt_{(s)} - Al_2O_{3(s)}, Al_{(l)}|Al_2O_3 \text{ in liquid slag}|O_{2(g)}, Pt_{(s)}$$

and

$$C_{(s)}, Al_{(l)}|Al_2O_{3(s)}|\text{ionic oxide slag}|Al_2O_{3(s)}|Fe\text{-}C_{(l)}, CO_{(g)}, C_{(s)}$$

Evaluation of the experimental data gives

$$\Delta G°_f(Al_2O_3) = -394{,}680 + 77.8T \text{ cal/mole } (1640°\text{-}1830°K)$$
$$= -1652.45 + 0.3257T \text{ kJ/mole } (1640°\text{-}1830°K)$$

and a value of the standard enthalpy of formation of alumina, $\Delta H°_{298}(Al_2O_3)$, of −392.60 kcal/mole (−1643.7 kJ/mole) which is about 8 kcal/mole more positive than the generally accepted thermochemical value of −400.40 kcal/mole (−1676.4 kJ/mole). A value for $\Delta H°_{298}(Al_2O_3)$ of about −393 kcal/mole is consistent with data in the literature from low temperature formation cell measurements at ~1000°C and from mineralogical studies.

The reaction

$$3[O]_{1w/o} + 2[Al]_{1w/o} = Al_2O_{3(\alpha)} \quad [1]$$

where [ ] represents a component in solution in liquid iron and 1 w/o refers to the 1 weight percent (w/o) solution standard state, is of importance in steel deoxidation and electroslag remelting.

Under equilibrium conditions, the soluble oxygen content of the steel is controlled by the soluble aluminum content and the activity of alumina in the deoxidation product or slag, through the equilibrium constant, K_1

$$K_1 = a_{Al_2O_3}/h_{Al}{}^2 \cdot h_O{}^3 \quad [2]$$

where $a_{Al_2O_3}$ is the Raoultian activity of α-alumina and h_i is the Henrian activity of component i in solution in steel. In order to be able to use Eq. [2] to control the soluble oxygen content in liquid steel, the solution thermodynamics of the Fe-Al-O system and the standard free energy of formation of alumina must be accurately known at steel-making temperatures of about 1600°C. In practice, there is a discrepancy between the experimental and thermodynamically predicted values for the solubility product of alumina, the thermodynamically predicted values being smaller than the experimental values. Although there are sampling and analytical difficulties associated with the experimental determinations, it is possible that the presently accepted free energy data for alumina are in error.

* Electrochemical Society Active Member.

Key words: electrochemical cells, thermochemistry, alumina.

The highest temperatures at which the standard free energy of formation of alumina has been determined directly are those of aluminum extraction (1-6), *i.e.*, about 1000°C. There have been no direct determinations at steel-making temperatures.

The work presented in this paper describes experiments with high temperature electrochemical cells designed to determine the standard free energy of formation of alumina at steel-making temperatures.

Electrochemical Cells

Two types of electrochemical cell were used in the present work. The first cell, cell I, may be represented by

$$Pt_{(s)} - Al_2O_{3(s)}, Al_{(l)}|Al_2O_3 \text{ in liquid ionic slag}|O_{2(g)}, Pt_{(s)}$$

and the following reactions may be considered:
The anode reaction

$$3(O^{2-}) + 2Al_{(l)} = Al_2O_{3(s)} + 6e \quad [3]$$

The cathode reaction

$$3/2\ O_{2(g)} + 6e = 3(O^{2-}) \quad [4]$$

The cell reaction

$$2Al_{(l)} + 3/2\ O_{2(g)} = Al_2O_{3(s)} \quad [5]$$

The free energy change for the cell reaction and the cell emf are then given by the relationships

$$\Delta G_{cell} = \Delta G^\circ_{cell} + RT \ln (a_{Al_2O_3}/a_{Al}^2 \cdot p^{3/2}O_2) \quad [6]$$

and

$$E_{cell} = E^\circ_{cell} - (RT/6F) \ln (a_{Al_2O_3}/a_{Al}^2 \cdot p^{3/2}O_2) \quad [7]$$

respectively.

When the reactants and products of the cell reaction are in their respective Raoultian standard states of pure gases at 1 atm pressure and pure condensed phases, *i.e.*, the slag is alumina saturated

$$\Delta G_{cell} = \Delta G^\circ_{cell} = -6FE^\circ_{cell} \quad [8]$$

The determination of the cell emf then gives the standard free energy of formation of alumina at the experimental temperature. The second cell, cell II, may be represented by

$$C_{(gr)}, Al_{(l)} | Al_2O_{3(s)} | \text{ionic oxide slag} | Al_2O_{3(s)} | Fe\text{-}C_{(l)}, CO_{(g)}, C_{(gr)}$$

and the corresponding anodic, cathodic, and cell reactions are

$$2Al_{(l)} + 3(O^{2-}) = Al_2O_{3(s)} + 6e \quad [9]$$

$$3CO_{(g)} + 6e = 3(O^{2-}) + 3C_{(gr)} \quad [10]$$

and

$$2Al_{(l)} + 3CO_{(g)} = Al_2O_{3(s)} + 3C_{(gr)} \quad [11]$$

respectively.

The cell emf is given by the relationship

$$E_{cell} = E^\circ_{cell} - \frac{RT}{6F} \ln (a_C^3 \cdot a_{Al_2O_{3(s)}}/p_{CO}^3 \cdot a_{Al}^2) \quad [12]$$

and Eq. [8] again holds when the reactants and products of the cell reaction are in their Raoultian standard states. The standard free energy of formation of alumina in this case is obtained from the measured cell emf and the known standard free energy of formation of carbon monoxide.

Cell Design

The design of the cell

$$Pt_{(s)} - Al_2O_{3(s)}, Al_{(l)} | Al_2O_3 \text{ in slag} | O_{2(g)}, Pt_{(s)}$$

is largely governed by the choice of the liquid slag electrolyte. Electrolytic studies of slag in the CaF_2-Al_2O_3 system (7) indicate that they conduct ionically at steel-making temperatures. Three current versions of the CaF_2-Al_2O_3 phase diagram (8-10) are shown in Fig. 1 and the recent version of Mitchell and Burel (10) was used in this work. The relevant properties of aluminum and the electrolyte are given in Table I. Graphite is one of the few materials which may be used to contain both aluminum and the electrolyte, but since the system must be alumina saturated, alumina itself may be used.

The cell assembly, consisting of a container, an Al/Al_2O_3 electrode, and an oxygen electrode, is shown diagrammatically in Fig. 2.

The Al/Al_2O_3 electrode.—The two types of Al/Al_2O_3 electrode design used in this work are shown diagrammatically in Fig. 3. These designs were chosen to satisfy the following conditions: (*i*) aluminum will float on the liquid slag, see Table I; (*ii*) aluminum melts at a lower temperature than the electrolyte; (*iii*) electrical contact has to be made with liquid aluminum; and (*iv*) aluminum must be protected against excessive oxidation. Conditions (*i*) and (*ii*) are satisfied by plac-

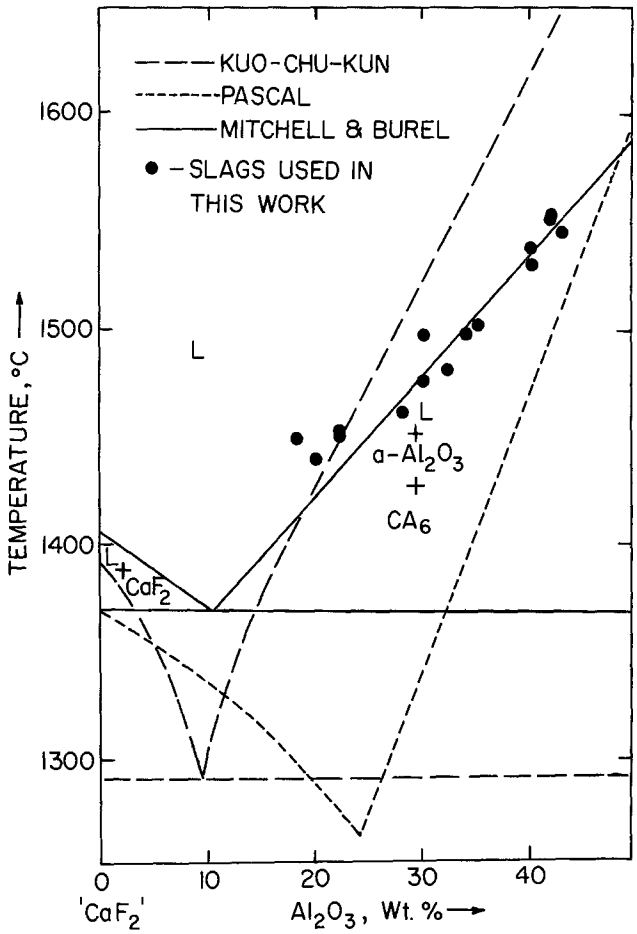


Fig. 1. The "CaF_2"-Al_2O_3 phase diagrams

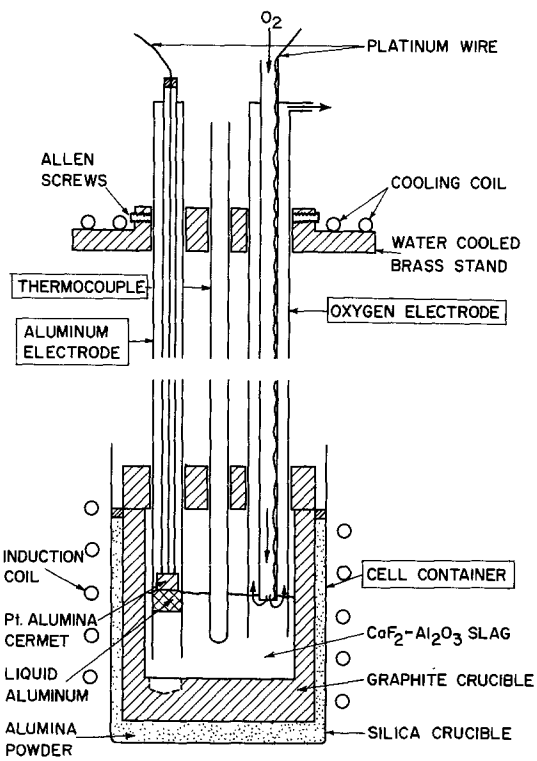


Fig. 2. Cell I assembly

Table I. Aluminum and electrolyte properties

Property	Aluminum	CaF_2-Al_2O_3 electrolyte
Melting point, °C	660 (11)	CaF_2 at 1423 (12) Al_2O_3 at 2042 (11) Eutectic (10) at 1368°C and 10 w/o Al_2O_3
Boiling point, °C	2494 (11)	CaF_2 at 2510 (13)
Vapor pressure at 1500°C, mm Hg	0.7 (13)	0.21 CaF_2 (13)
Density at 1500°C, g/ml	<2.3 (14)	CaF_2 2.5 (15) CaF_2-30 w/o Al_2O_3 2.85

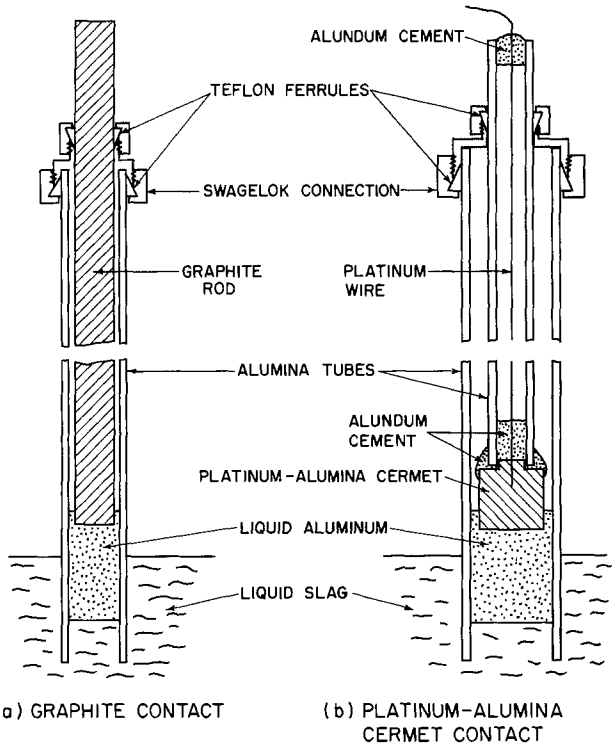


Fig. 3. Cell I Al/Al_2O_3 electrodes

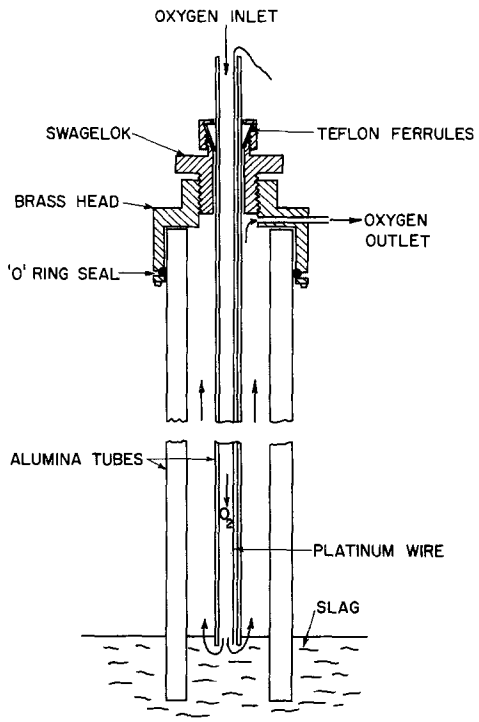


Fig. 4. Cell I oxygen electrode

ing the outer alumina tube of the electrode in the well at the bottom of the graphite container and surrounding it with crushed prefused electrolyte. Aluminum, placed inside this tube, melts first and, when the electrolyte becomes molten, the tube is raised out of the well in order to allow the aluminum to float on top of the electrolyte inside the tube.

Graphite was used to make electrical contact with liquid aluminum in the initial experiments, Fig. 3a, but since this introduced a thermal emf with the platinum contact of the oxygen electrode, a $Pt-Al_2O_3$ cermet contact was developed, Fig. 3b.

The oxygen electrode.—The main requirement of the oxygen electrode is that oxygen gas of known partial pressure must contact the electrolyte and a platinum lead. Sridhar and Jeffes (16) have critically reviewed the design of oxygen electrodes and the one used in the present study, shown in Fig. 4, is based on their assessment.

Oxygen gas is passed through the inner of two concentric recrystallized alumina tubes and returned through the outer tube. Contact is made with the slag by a platinum wire passing down the inner tube, the end of the wire being retracted about 0.1 in. (0.25 cm) from the end. The two tubes were held in a brass head using an O-ring seal and a Swagelok fitting.

Cell II.—The design of the cell

$$C_{(gr)},Al_{(l)}|Al_2O_{3(s)}|\text{ionic oxide slag}|Al_2O_{3(s)}|$$

$$Fe\text{-}C_{(l)}, CO_{(g)}, C_{(gr)}$$

which consists of a container, an Al/Al_2O_3 electrode, and a C/CO electrode, is shown diagrammatically in Fig. 5. Although alumina shows considerable electronic conductivity at ~1600°C, it can be used to separate the individual electrodes, as long as a fully ionic electrolyte is interposed between them, the fully ionic electrolyte preventing the electronic short circuiting of the cell. Separation of the anode and cathode removes two of the restrictions on the electrolyte, *i.e.*, it must be saturated with alumina and it must not be reduced by aluminum.

Except for the absence of the well in the bottom, the graphite container is identical to that used for cell I.

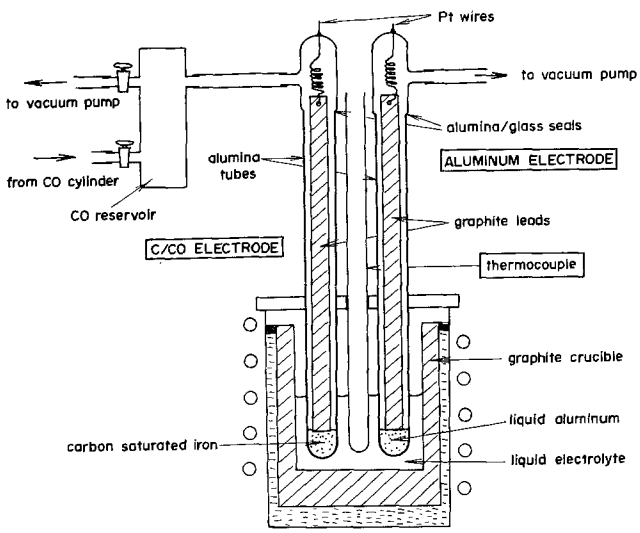


Fig. 5. Cell II assembly

The electrodes.—As shown in Fig. 5, both the Al/Al_2O_3 and C/CO electrodes are of similar construction, consisting of closed-end recrystallized alumina tubes which contain aluminum and graphite-saturated iron, respectively. Contact with the metal phase is made by a graphite rod in each case.

A glass head was joined to the top of each alumina tube by a glass/alumina seal (Corning No. 7056) and electrical contact with the graphite rods was made through platinum wires sealed into each head.

A 200 ml gas reservoir was connected to the head of the C/CO electrode and both the electrode and the reservoir were filled with CO gas at 1 atm pressure before an experiment. The glass head of the Al/Al_2O_3 electrode was connected to a mechanical vacuum pump and a pressure of $\sim 10^{-2}$ Torr (~ 1 N/m^2) was maintained throughout an experiment.

Experimental

Temperature measurement.—A Pt/Pt-13%Rh thermocouple, contained in a recrystallized alumina sheath, was used to measure the temperature of both cells.

In initial experiments, the alumina sheath was placed inside a graphite tube to protect it from slag attack. This protection proved unnecessary as slag attack was not excessive.

Thermocouples were calibrated against a National Research Council standard thermocouple.

Temperature control.—A 25 kW, 450 kHz Taylor Winfield "Thermionic" induction unit was used to heat the graphite cell to the required temperature. The power from this unit was manually controlled by fine adjustment of the coil current. High temperature thermal stability was achieved in about 45-60 min using this method of control. Over-all temperature control is estimated at ±5°C.

Emf measurement.—A Type P3 Croydon potentiometer and a Keithley Model 616 high impedance electrometer ($2 \times 10^{14}\Omega$) were connected in parallel through a double-pole, double-throw switch and were used to measure the cell and thermocouple emf's.

The emf of cell I (~2V at 1500°C) was outside the range of the potentiometer (0-1.8V) and could be read by the electrometer to only ±10 mV. For this reason a Weston (Eppley) Standard cell (1.0183V at 20°C) was introduced into the measuring circuit, in opposition to the formation cell, so that the resultant emf could be measured within ±1 mV on both instruments. High frequency pickup from the induction unit in cell I was eliminated by grounding all thermocouple and cell leads through 0.1 μF capacitors. In cell II, grounding the leads through capacitors did not remove all high frequency pickup. Cell emf and thermocouple readings were taken only when power to the induction unit was momentarily switched off.

Materials.—The source and type of materials used in this investigation are summarized in Table II.

Platinum-graphite thermal emf.—The use of a graphite lead in the initial Al/Al_2O_3 electrode design, Fig. 3a, introduced a platinum-graphite thermoelectric emf into the measured emf. Values of this platinum-graphite thermal emf were determined directly at experimental temperatures, the emf being measured between a $Pt\text{-}Al_2O_3$ cermet and a graphite rod set within a graphite block heated by the 450 kHz induction unit. The platinum-graphite emf obtained is shown as a function of temperature in Fig. 6, which was used to determine the true cell emf when using the graphite contact. This problem was overcome by using a $Pt\text{-}Al_2O_3$ cermet contact (Fig. 3b).

Cermet preparation.—Platinum and alumina powders in a 70:30 proportion by weight were mixed thoroughly and about 0.6g of the mixture pressed into a 3/16 in. diam (~0.5 cm diam) cermet. A platinum wire lead was passed through a hole in the base plate and bottom plunger of the cermet die before pressing and formed an integral part of the cermet. The "green" cermet was sintered in air at 1500°C for 12 hr. Typical cermet contacts, before and after use, are shown in Fig. 7. The cermet was sealed into a recrystallized alumina tube with Alundum cement, Fig. 3b, the top of the cermet being machined to fit the inside diameter.

Table II. Materials

Material	Source and type
Calcium fluoride	BDH, Extra Pure
Calcium carbonate	Fisher Scientific, Reagent Grade
Silica powder	Fisher Scientific, Reagent Grade
Alumina powder	Fisher Scientific, Certified
Alundum cement	Fisher Scientific
Graphite	Union Carbide, CS and ECV
Aluminum	Alcan, 99.995%
Platinum sponge	Johnson, Matthey & Mallory, Grade I
Oxygen	Canadian Liquid Air, Extra Dry
Carbon monoxide	Matheson, Technical
Recrystallized alumina	McDanel, 99.8%
Silica tubes	Quartz Scientific

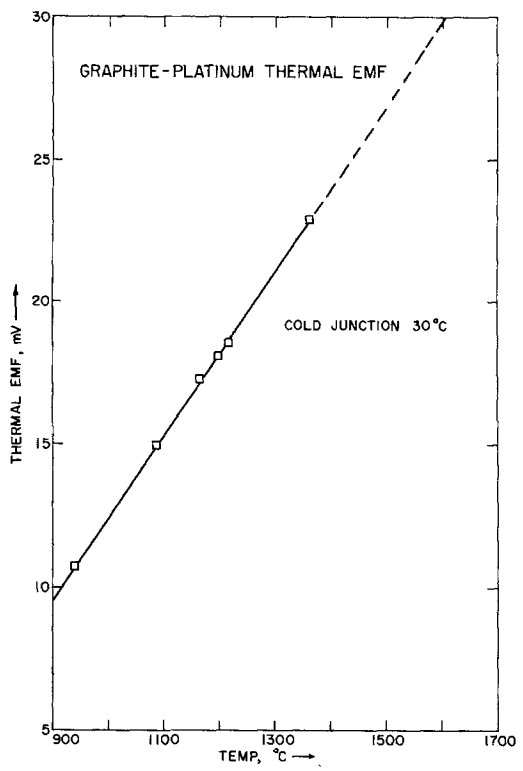


Fig. 6. Platinum-graphite thermal emf vs. temperature

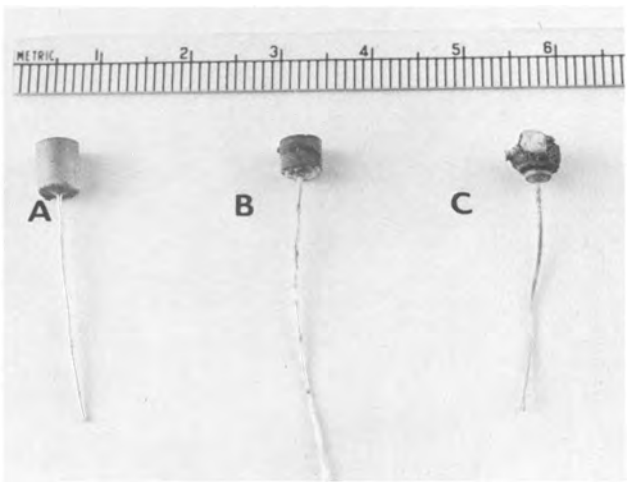


Fig. 7. Platinum-alumina cermets; (a) before use, (b) after 30 min at 1448°C, and (c) after 25 min at 1551°C.

Slag preparation.—The compositions of the $CaF_2\text{-}Al_2O_3$ slags used in cell I are shown in Fig. 1. Compositions close to the alumina saturated liquidus of Mitchell and Burel (10) were chosen to give maximum slag fluidity. Crushed and ground premelted calcium fluoride was mixed with alumina powder to give the required slag mixture.

The crushed and ground $CaO\text{-}SiO_2\text{-}Al_2O_3$ slag used in cell II was obtained from the required mixture of reagent grade powders, premelted in a graphite crucible. This starting slag, containing 38% CaO, 42% SiO_2, and 20% Al_2O_3, picked up alumina from the C/CO and Al/Al_2O_3 electrodes during the course of an experiment.

Procedure.—Cell I was set up by placing a cylindrical piece of high purity aluminum in the alumina tube of the Al/Al_2O_3 electrode, the bottom of which was sealed in the well of the graphite container. A slag mixture of predetermined composition was then poured into the container, with the thermocouple sheath in

position and the oxygen electrode positioned above the slag using the water-cooled brass electrode holder, Fig. 2. After placing refractory brick shields below and around the cell assembly in order to prevent excessive heat losses, the induction unit was switched on and the temperature raised to approximately that of the experiment in about 45-60 min. The melt was equilibrated for a further 15-20 min by which time a thermal steady state, with negligible thermal drift, was achieved. The aluminum electrode was then raised and the oxygen electrode lowered into the melt until the outer alumina tube was below the surface of the slag. The inner alumina tube was lowered into the slag with the oxygen flowing at 20-40 ml/min until a reading was obtained on the electrometer. When the inner tube was pushed too far into the melt the "sawtooth" emf associated with oxygen bubbling through the melt (16) was obtained. The inner tube was then pulled up until the sawtooth variation of the emf disappeared. When the electrodes were in position, time zero, the cell and thermocouple emf's were alternately monitored on the electrometer and check measurements made at convenient intervals with the potentiometer. Measurements made on both the potentiometer and electrometer agreed to within ±2 mV.

Cell II was set up in the induction coil as in the case of cell I. The slag mixture was then poured into the crucible and the electrodes positioned above the slag. The C/CO electrode was evacuated and filled with carbon monoxide at 1 atm pressure, and the Al/Al_2O_3 electrode was evacuated continuously. The cell was raised to the experimental temperature in 45-60 min and held for a further 10-15 min. The electrodes were then lowered and the cell and thermocouple emf's monitored at convenient intervals with the induction unit momentarily switched off.

After an experiment the electrodes were sectioned and checked for slag attack. The Al/Al_2O_3 electrode was also checked for the presence of aluminum and the cermet condition recorded. Finally, aluminum samples from cell I were analyzed gravimetrically for platinum (17).

Results

Cell I.—The type of cell emf *vs.* time relationship obtained experimentally is shown in Figure 8, which also shows the effects of imposing an external emf on the cell and discharging it momentarily through an external circuit in order to check its reversibility. Reversible plateau emf's of between 6 and 15 min duration were typically obtained. The initial decrease in cell emf is caused by the electrodes attaining thermal equilibrium with the electrolyte, and the final decrease is probably caused by failure of the oxygen electrode.

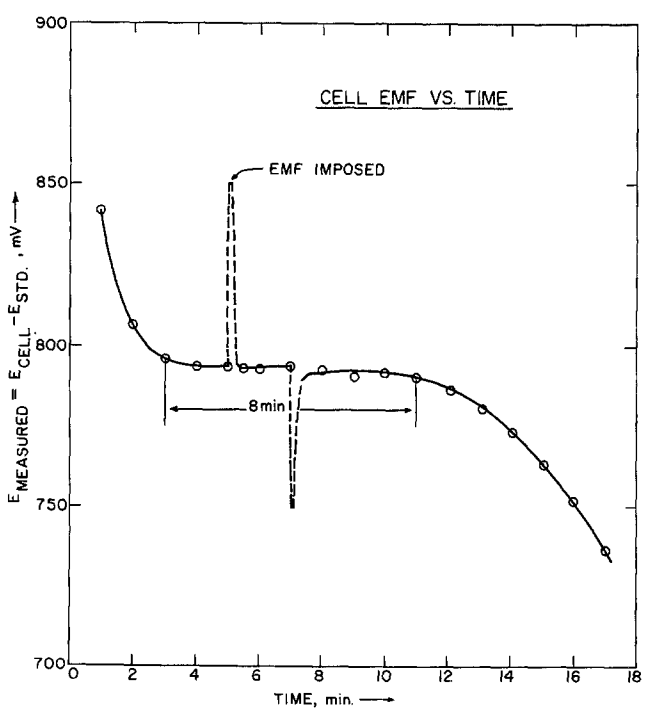


Fig. 8. Cell I emf *vs.* time

Table III. Data from cell I

Contact*	Slag (w/o) CaF_2	Slag (w/o) Al_2O_3	Temp (°C)	E_{cell} (V)	$E°_{cell}$ (V)	$-\Delta G°_f$ (Al_2O_3) (kcal)
G	78	22	1450	1.858	1.883	260.53
G	70	30	1498	1.857	1.884	260.67
G	66	34	1499	1.830	1.857	256.93
G	65	35	1502	1.827	1.854	256.52
G	60	40	1539	1.783	1.811	250.57
C	80	20	1440	1.878	1.878	259.84
C	82	18	1448	1.889	1.889	261.36
C	72	28	1462	1.873	1.873	259.15
C	70	30	1476	1.881	1.881	260.26
C	68	32	1482	1.852	1.852	256.24
C	60	40	1530	1.845	1.845	255 27
C	57	43	1545	1.834	1.834	253.75
C	58	42	1551	1.834	1.834	253.75
C	58	42	1554	1.812	1.812	250.71

* G = graphite; C = cermet.

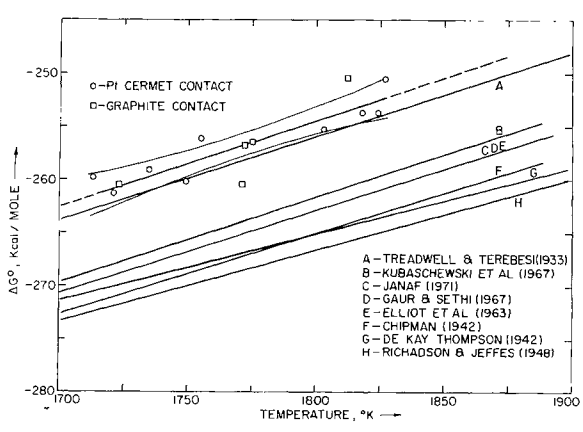
The raw data from cell I are given in Table III together with the calculated standard free energies of formation of alumina, $\Delta G°_f(Al_2O_3)$. These values of $\Delta G°_f(Al_2O_3)$ are also shown as linear function of temperature in Fig. 9, together with the relationships of other workers (1, 11, 13, 14, 18-21). A linear regression analysis of this data gives

$$\Delta G° = -398{,}560 + 80.02T \text{ cal/mole } (1713°\text{-}1827°\text{K}) \quad [13]$$

$$= -1668.70 + 0.3350T \text{ kJ/mole}$$

The 95% confidence limit at 1773°K is ±1.0 kcal (±4.187 kJ). These values are substantially more positive than those based on thermochemical data (11, 13, 14, 18-21) with the exception of the early work of Treadwell and Terebesi (1).

The standard free energy of formation of alumina has also been determined directly at aluminum extraction temperatures (~1000°C) using formation cells with alumina-saturated cryolite as the liquid electrolyte (1-6). These results are shown in Fig. 10, together with the results of the present investigation and the generally accepted thermochemical data (11, 14, 18). With the exception of the work of Thonstad (6), the low and high temperature formation cell determinations are generally consistent with each other and both these sets of results are at variance with those obtained from thermochemical data.



STANDARD FREE ENERGY OF FORMATION OF ALUMINA IN TEMP RANGE 1700-1900°K

Fig. 9. The standard free energy of formation of alumina as a function of temperature (1700°-1850°K), cell I.

Table IV. Data from cell II

Slag (w/o)				Temp (°C)	$E°_{cell}$ (V)	$-\Delta G°_{cell}$ (kcal)	$-3\Delta G°(CO)$ (kcal)	$-\Delta G°_f$ (Al_2O_3) (kcal)
CaO	CaF_2	Al_2O_3	SiO_2					
38	—	20	42	1368	0.628	86.89	183.32	270.21
38	—	20	42	1401	0.562	77.76	185.32	263.68
38	—	20	42	1406	0.580	80.25	185.62	265.87
—	90	10	—	1476	0.480	66.41	189.87	256.28
—	85	15	—	1486	0.475	65.72	190.48	256.20
—	85	15	—	1512	0.468	64.75	192.05	256.81

Cell II.—Stable cell voltages were obtained for periods of over 2 hr once thermal equilibrium had been attained. Cell failure was usually caused by slag attack of the alumina refractories. Cell reversibility was checked by the same technique used for cell I.

Experimental data obtained from cell II are given in Table IV which also gives the standard free energy change for the cell reaction, the standard free energy of formation of carbon monoxide (11), and the calculated standard free energies of formation of alumina. Values of $\Delta G°_f(Al_2O_3)$ obtained from both cell I and cell II are shown as a function of temperature in Fig. 11, which also includes the generally accepted thermochemical relationship for comparison.

Third law analysis.—A third law analysis of the standard free energy data from cell I and cell II given in Tables III and IV, using values of Gibbs energy functions, gef_T, calculated from relevant enthalpy and specific heat data for alumina (22), aluminum (23, 24), and oxygen (25), yielded the values for the standard enthalpy of formation of alumina at 298°K, $\Delta H°_{298}(Al_2O_3)$ given in Table V. These values are also shown as a function of experimental temperature in Fig. 12, together with the results obtained from oxygen bomb calorimetry. The average value of $\Delta H°_{298}(Al_2O_3)$ from cell I data is −392.55 kcal/mole (−1643.5 kJ/mole) with 95% confidence limits of ±1.0 kcal/mole and that from cell II data is −392.71 kcal/mole (−1644.2 kJ/mole) with 95% confidence limits of ±2.3 kcal/mole.

Discussion

As indicated in Fig. 9, 10, and 11, the values of $\Delta G°_f(Al_2O_3)$ obtained in this work are substantially more positive than those based on thermochemical data, the only exception being the early work of Treadwell and Terebesi (1). The value of −254.42 kcal/mole (−1065.2 kJ/mole) at 1800°K determined from cell I data compares with the presently accepted best value of −262.92 kcal/mole (−1100.8 kJ/mole) at 1800°K, taken from JANAF Tables (11). It is therefore necessary to examine the possible sources of error in the present work.

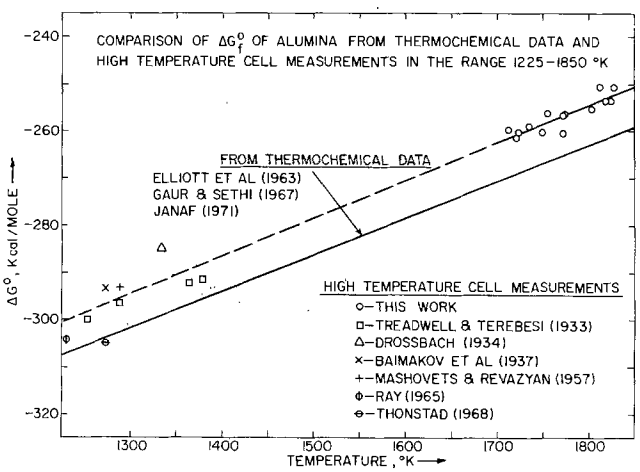


Fig. 10. The standard free energy of formation of alumina as a function of temperature (1225°-1850°K).

Table V. Third law analysis of cell I and cell II data

Cell	Temp (°K)	$-\Delta G°_T$ (kcal/mole)	$T \times \Delta gef_T$ (kcal/mole)	$-\Delta H°_{298}$* (kcal/mole)
I	1713	259.84	131.19	391.03
I	1721	261.36	131.81	393.17
I	1723	260.53	131.97	392.50
I	1735	259.15	132.90	392.05
I	1749	260.26	133.99	394.25
I	1755	256.24	134.46	390.70
I	1771	260.67	135.70	396.37
I	1772	256.93	135.78	392.71
I	1775	256.52	136.01	392.53
I	1803	255.27	138.19	393.46
I	1812	250.57	138.89	389.46
I	1818	253.75	139.35	393.10
I	1824	253.75	139.82	393.57
I	1827	250.71	140.05	390.76
II	1674	263.08	128.15	391.23
II	1679	265.87	128.54	394.41
II	1641	270.21	125.58	395.79
II	1749	256.28	133.99	390.27
II	1759	256.20	134.77	390.97
II	1785	256.81	136.79	393.60

* $(\Delta H°_{298})_{Avg}$ = − 392.55 kcal/mole Al_2O_3 (cell I)
= − 392.71 kcal/mole Al_2O_3 (cell II)
= − 392.60 kcal/mole Al_2O_3 (cell I and cell II).

Cell I.—Standard conditions.—As shown in Eq. [7]

$$E_{cell} = E°_{cell} - (RT/n\mathbf{F}) \ln a_{Al_2O_3}/a_{Al}^2 \cdot pO_2^{3/2}$$

the standard cell emf, $E°_{cell}$, can only be obtained from cell I if the activities of alumina and aluminum and the partial pressure of oxygen are close to unity.

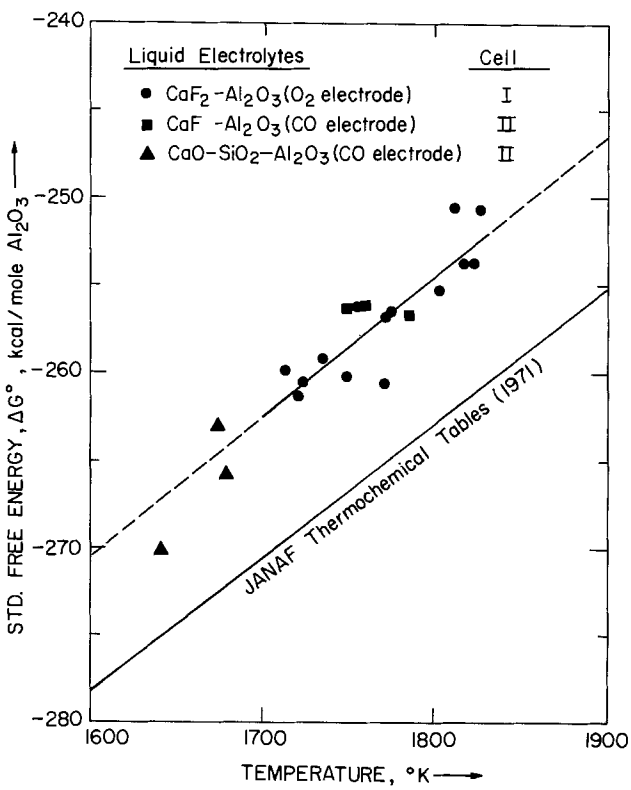


Fig. 11. $\Delta G°_f(Al_2O_3)$ data from cells I and II in comparison with the thermochemical relationship.

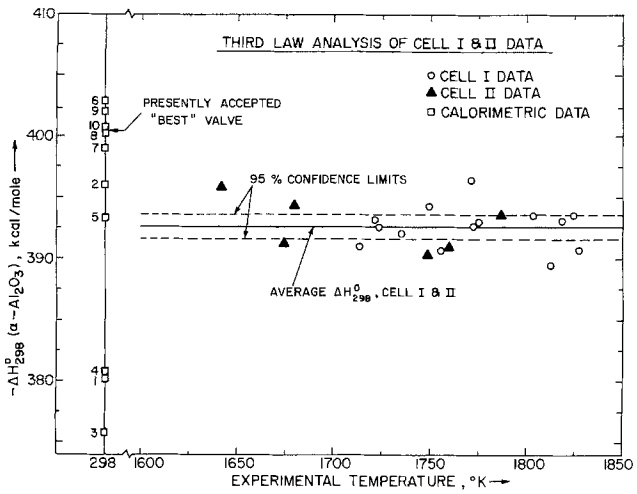


Fig. 12. The standard heat of formation of alumina, ΔH°_{298}, from cell I and II data and from bomb calorimetry. 1, Berthelot (63); 2, Wartenberg and Witsel (64); 3, Moose and Parr (65); 4, Roth and Muller (66); 5, Meichsner and Roth (67); 6, Roth, Wolf, and Fritz (68); 7, Snyder and Seltz (69); 8, Holley and Huber (70); 9, Schneider and Gattow (71); 10, Mah (72).

Despite inconsistencies in the three versions of the "CaF_2"-Al_2O_3 phase diagram reported in the literature (8-10), alumina saturation of cell I slags is virtually assured by the presence of solid alumina refractories in the cell. In any event, an alumina activity of less than unity, say 0.9, would introduce an error in E°_{cell} of +2.7 mV at 1800°K and give an apparent ΔG°_f (Al_2O_3) some 375 cal/mole (1.57 kJ/mole) more negative than the true value.

The solubility of carbon in molten aluminum is small (26, 27) and under the experimental conditions of the present investigation the effect of carbon on the activity of aluminum may be neglected. The aluminum-platinum phase diagram of Huch and Klemm (28), however, indicates extensive solubility of platinum in liquid aluminum at 1500°C. The maximum platinum content of anode aluminum at the end of an experiment with cell I was 2.54 w/o (0.0036 mole fraction) at 1551°C. Although Huch and Klemm report the presence of nine intermetallic phases in the platinum-aluminum system in the platinum-rich region of the diagram (Pt > 60 w/o), which indicates a very strong deviation from ideality in this region, there is a eutectic at 9 w/o platinum and 657°C. Under these conditions the deviation from ideality of aluminum solutions of >0.9964 mole fraction is not expected to be large. Calculations using Eq. [6] show that an aluminum activity of 0.90 at 1800°K would give an apparent $\Delta G^{\circ}_f(Al_2O_3)$ some 745 cal/mole (3.12 kJ/mole) more positive than the true value.

At the cathode, high purity oxygen gas, at slightly greater than atmospheric pressure, flows past a platinum wire in contact with the slag electrolyte. In principle, corrections are required for dilution of the oxygen by CaF_2 vapor, 0.7 mm Hg at 1500°C, for the excess pressure of oxygen caused by the immersion of the electrode tip under the electrolyte melt, and changes in barometric pressure. These corrections are extremely small, however, and well within the experimental precision of this investigation.

High experimental temperatures and the use of a high impedance electrometer and a potentiometer with a step-down resistance box minimized electrode polarization during measurement of the cell emf. A sawtooth cell emf was observed which varied with the frequency of gas bubbling when the oxygen electrode was pushed too far down into the slag electrolyte. This effect has been observed by Sridhar and Jeffes (16, 29) who solved the problem by retracting the platinum wire inside the inner alumina tube so that oxygen gas was in contact with the whole length of platinum wire, while contact with the electrolyte was made through the thin film wetting the inside of the tube. This effect is caused by the limited solubility of oxygen in the electrolyte setting up a "mixed" potential along that part of the platinum wire which is immersed in the slag.

Errors introduced by a radial temperature gradient in the cell, <5°C, are expected to be small and although the platinum-graphite thermal emf was only determined experimentally up to 1400°C with a reproducibility of ±0.2 mV, the error in the extrapolated values in the range 1400°-1600°C is estimated to be ~±0.5 mV.

Cell reaction.—In the present work it is assumed that the cell reaction represents the formation of alumina from its constituent elements. This assumption is only valid if the oxidation state of aluminum is single valued and can be represented by solid alumina. Other species, representing different oxidation states of aluminum, are $Al_2O_{(g)}$, $AlO_{(g)}$, $Al_2O_{2(g)}$, and $AlO_{2(g)}$. The standard free energies of formation of those oxides at 1700° and 1800°K (11) are given in Table VI. It is apparent that $Al_2O_{3(s)}$ is substantially more stable than the other oxides and that the cell emf must represent the formation of alumina from its constituent elements.

Cell reversibility.—Cell reversibility was checked by momentarily imposing a greater emf than the equilibrium value or by discharging the cell through an external circuit. In each case, the emf returned to its "open-circuit" equilibrium value within a few seconds, as shown in Fig. 8. Variations in oxygen flow rate had no significant effect on the cell emf except when the oxygen supply was cut off completely. Under these circumstances the cell emf decreased rapidly.

Individual electrode reversibility is implied in overall cell reversibility. The aluminum electrode is reported to behave reversibly (6, 31), and the behavior of the oxygen electrode has been reviewed by many workers (16, 32-35). It has been found to behave reversibly in molten carbonates (36), borates (37, 38), sulfates (39, 40), phosphates (39), silicates (16, 38, 41, 42) sulfate/carbonate mixtures (43), and in molten cryolite melts (4, 5) similar to those of the present investigation.

Electrolyte conductivity.—The difference between the standard free energies of formation obtained in the present work and those obtained from thermochemical data could be caused by mixed ionic and electronic conduction in the slag electrolyte. A 3% electronic conductivity would result in the present values being about 7.5 kcal/mole too positive and make them consistent with the generally accepted thermochemical data (11, 14).

There is, however, considerable evidence in the literature (44) which indicates that the ionic transport number of the electrolyte is sufficiently close to unity to preclude the possibility of any large systematic error. Solid CaF_2 is reported to be an ionic conductor (45, 46) and its successful use as a solid electrolyte has been reviewed (47). Literature on the conductivity of solid Al_2O_3 has been reviewed (48) and substantial electronic conductivity in the temperature range 900°-

Table VI. The standard free energy of formation, ΔG°_f, of aluminum oxides at 1700° and 1800°K (11)

Species	ΔG°_f (kcal/mole) 1700°K	1800°K
α-$Al_2O_{3(s)}$	−270.61	−262.92
$Al_2O_{(g)}$	−60.77	−61.80
$AlO_{(g)}$	−9.83	−11.23
$Al_2O_{2(g)}$	−87.43	−86.22
$AlO_{2(g)}$	−45.23	−45.03

1750°C has been reported (49-51). In the present work we are therefore concerned with the conductivity of an electrolyte formed by the addition of a semiconducting solid to a molten ionic liquid. Since the conductivity of CaF_2 (52) in the temperature range 1500°-1600°C are about five to six orders of magnitude larger than alumina (49), negligible electronic conductivities of the slags used in cell I are expected. In addition Mitchell and Benyon (7) report faradaic efficiencies of 100% in the CaF_2-Al_2O_3 system.

Finally, the good agreement of the present results with those at 1300°K (1-6) is also indicative of the electrolyte behaving ionically, since the probability of substantial electronic conduction is less at these lower temperatures. Nevertheless, the desirability of obtaining an experimental verification of this conclusion led to the design of cell II.

Electrode solution.—The design of cell I is such that anode oxygen and cathode aluminum could dissolve in the slag electrolyte, although the existence of a sawtooth variation of the cell emf with oxygen bubble formation at the anode indicates that the solubility of oxygen in the electrolyte must be small. Nevertheless, aluminum in solution could give rise to significant electronic conductivity in the electrolyte. The design of cell II, however, precludes this possibility.

Cell II.—Cell II was designed to eliminate some of the possible sources of systematic error in the operation of cell I outlined above. It is again an oxygen concentration cell, only in this case the oxygen potential of the cathode is controlled by the C/CO equilibrium. The separation of the electrode compartments from the electrolyte allows the replacement of alumina-saturated CaF_2-Al_2O_3 electrolytes by those in the CaO-Al_2O_3-SiO_2 system, unsaturated with alumina.

The electrolysis of CaO-SiO_2 slags (53) and the determination of transference numbers in the CaO-SiO_2 and CaO-SiO_2-Al_2O_3 systems (54) show that these slags are predominantly ionic conductors. For this reason CaO-SiO_2 (55, 56) and CaO-SiO_2-Al_2O_3 (57-62) electrolytes have been used in a number of high temperature cells to determine the thermodynamic properties of alloys or the electrolyte system itself. Reasonable agreement is obtained with determinations by other methods confirming the highly ionic nature of these slags.

In addition to the 38 w/o CaO, 42 w/o SiO_2, and 20 w/o Al_2O_3 electrolyte, unsaturated CaF_2-Al_2O_3 electrolytes containing only 10 and 15 w/o Al_2O_3 were used in cell II Here the possibility of significant electronic conductivity at these low alumina concentrations is small.

Steady plateau emf's of about 2 hr duration were obtained with cell II, cell failure being caused by solution of the anode and cathode alumina refractories in the slag electrolyte. The separation of electrode compartments also eliminated the possibility of the physical solution of anode aluminum and cathode gas in the electrolyte, thus precluding chemical interference with the cell reaction. Since identical electrode leads were used no thermal emf corrections were necessary, and with graphite contacts, possible problems associated with the solution of platinum in aluminum were eliminated.

The good agreement between cell I and cell II data, as shown in Fig. 11, and the general agreement with similar electrochemical work at ~ 1000°C, Fig. 10, indicate an error in the generally accepted thermochemical data for alumina.

Standard enthalpy of formation of alumina.—Values of $\Delta H°_{298}(Al_2O_3)$ from the third law analysis of cell I and cell II data have been presented in Fig. 12. These results are summarized in Table VII together with those from the third law analysis of the low temperature cell data and the average value of $\Delta H°_{298}(Al_2O_3)$ obtained from oxygen bomb calorimetry (63-72). These

Table VII. Summary of $\Delta H°_{f,298}(Al_2O_3)$ data from different sources

Source	No. of data points	Average $-\Delta H°_{f,298}$ (kcal/mole)	Standard deviation (±kcal/mole)	95% Confidence limits (±kcal/mole)
Present study cell I	14	392.55	1.73	1.00
Present study, cell II	6	392.71	2.20	2.31
Present study, all data	20	392.60	1.87	0.92
EMF cell at ~1000°C (from literature)	10	394.06	4.44	3.18
Oxygen bomb calorimetry				
(a) Presently accepted "best" value	2	400.40	—	0.3
(b) All data	10	393.08	10.23	7.32

results are again summarized in Fig. 13. Although the presently accepted value (70, 72) of $\Delta H°_{298}(Al_2O_3)$ of −400.40 kcal/mole is 7.8 kcal/mole more negative than the average value obtained from the present study, the average of all the calorimetric determinations is, by coincidence, in excellent agreement with the present data. It is clear from Table VII that a value of $\Delta H°_{298}(Al_2O_3)$ which is some 7 kcal more positive than the presently accepted thermochemical value would be consistent with the results from both high and low temperature electrochemical studies.

Assuming a value of $\Delta H°_{298}(Al_2O_3)$ of −392.60 kcal from the combined data of cell I and II, see Table VII, the following standard free energy of formation of alumina in the temperature range 1350°-1550°C

$$\Delta G° = -394{,}680 + 77.8T \text{ cal/mole} = -1652.45 + 0.3257T \text{ kJ/mole} \quad [14]$$

can be calculated using the Gibbs energy functions employed previously.

Independent evidence in support of this free energy data has been presented by Zen (73, 74) and Waldbaum (75) based on mineralogical studies. Reversed hydrothermal equilibrium data for the reaction

$$Al_2Si_2O_5(OH)_4 + 2SiO_2 = Al_2Si_4O_{10}(OH)_2 + H_2O \quad [15]$$

kaolinite quartz pyrophyllite vapor

yields a standard free energy of formation of pyrophyllite at 298°K, which is some 7 kcal more positive than the value derived from similar studies of the reactions

$$Al_2Si_4O_{10}(OH)_2 = Al_2SiO_5 + 3SiO_2 + H_2O \quad [16]$$

pyrophyllite andalusite quartz vapor

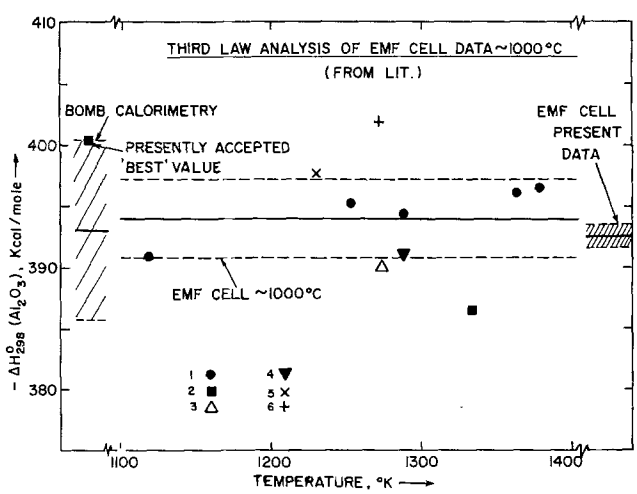


Fig. 13. The standard heat of formation of alumina, $\Delta H°_{298}$, from high and low temperature cell data, ~1000°C (from literature).

and

$$Al_2Si_4O_{10}(OH)_2 + 3Al_2O_3 = 4Al_2SiO_5 + H_2O \quad [17]$$

pyrophyllite corundum kyanite vapor

The calculations for reaction [15] were based on the well-established free energy data for kaolinite (76-79). The free energy data for andalusite and kyanite, reactions [16] and [17], respectively, were based on the solution calorimetric data of Holm and Kleppa (80) and were taken from Robie and Waldbaum (76). Since the free energy data for andalusite, sillimanite, and kyanite are dependent on the free energy data of corundum through the solution calorimetry of Holm and Kleppa (80), these discrepancies can be resolved if the presently accepted value of $\Delta H°_{298}(Al_2O_3)$ is some 7 kcal/mole too negative; a conclusion consistent with the results of the present work.

Zen (73, 74) has also discussed a discrepancy of about 10 kcal/mole between the free energy data for muscovite based on calorimetry (81) and solubility data (82) and those based on reversed hydrothermal equilibria measurements (83, 84) and has suggested that an error of 7 kcal/mole in $\Delta H°_{298}(Al_2O_3)$ would again eliminate the discrepancy.

There is therefore a considerable body of evidence which suggests that there is an error of about 7 kcal/mole in the presently accepted value of $\Delta H°_{298}(Al_2O_3)$ and in view of the important metallurgical and mineralogical consequences of such an error, $\Delta H°_{298}(Al_2O_3)$ should be redetermined by a technique other than that of oxygen bomb calorimetry.

Acknowledgments

The authors wish to thank Mr. W. A. R. Droppo for performing some of the cell II experiments and the National Research Council of Canada for financial support.

Manuscript submitted July 28, 1976; revised manuscript received July 20, 1977.

Any discussion of this paper will appear in a Discussion Section to be published in the June 1978 JOURNAL. All discussions for the June 1978 Discussion Section should be submitted by Feb. 1, 1978.

Publication costs of this article were assisted by McMaster University.

REFERENCES

1. W. D. Treadwell and L. Terebesi, *Helv. Chim. Acta*, **16**, 922 (1933).
2. P. Drossbach, *Z. Electrochem.*, **40**, 605 (1934).
3. Yu. V. Baimakov, V. P. Mashovets, and I. G. Kil, Reported in Ref. (4).
4. V. P. Mashovets and A. A. Revazyan, *Zh. Prikl. Khim. (Leningrad) (Engl. Transl.)*, **30**, 1069 (1957).
5. M. Rey, *C. R. Hebd. Seances. Acad. Sci. Paris*, **260**, 5528 (1965).
6. J. Thonstad, *Electrochim. Acta*, **13**, 449 (1968).
7. A. Mitchell and G. Benyon, *Metall. Trans.*, **2**, 3333 (1971).
8. Kuo Chu-Kun and Yen Tung-Sheng, *Acta Chim. Sinica*, **30**, 381 (1964).
9. P. Pascal, *Z. Electrochem.*, **19**, 610 (1913).
10. A. Mitchell and B. Burel: *J. Iron Steel Inst., London*, **208**, 407 (1970).
11. JANAF Thermochemical Tables, 2nd ed., U.S. Dept. of Commerce (1971).
12. H. Kojima *et al.*, *Can. J. Chem.*, **46**, 2968 (1968).
13. O. Kubaschewski, E. L. Evans, and C. B. Alcock, "Metallurgical Thermo-Chemistry," 4th ed., Pergamon Press, Oxford (1967).
14. J. F. Elliott *et al.*, "Thermochemistry for Steelmaking," Vol. 1 (1960), Vol. 2 (1963), Addison-Wesley Publishing Co., Reading, Mass.
15. W. E. Duckworth and G. Hoyle, "Electroslag Refining," Chapman and Hall, London (1969).
16. J. H. E. Jeffes and R. Sridhar, in "Electromotive Force Measurements in High Temperature Systems," C. B. Alcock, Editor, American Elsevier (1968).
17. A. I. Vogel, "A Text-Book of Quantitative Inorganic Analysis," 3rd ed., p. 510, Longmans, London (1961).
18. H. C. Gaur and R. S. Sethi, *Indian J. Chem.*, **5**, 485 (1967).
19. J. Chipman, *Trans. Am. Soc. Met.*, **30**, 817 (1942).
20. M. De Kay Thompson, "The Total and Free Energies of Formation of the Oxides of Thirty-Two Metals," The Electrochemical Society, New York (1942).
21. F. D. Richardson and J. H. E. Jeffes, *J. Iron Steel Inst., London*, **160**, 261 (1948).
22. P. B. Kantor, L. S. Lazareva, V. V. Kandyba, and Ye. M. Fomichov, *Ukr. Fiz. Zh.*, **7**, (2), 205 (1962).
23. E. H. Buyco and F. E. Davis, *J. Chem. Eng. Data*, **15**, 518 (1970).
24. R. A. McDonald, *ibid.*, **12**, 115 (1967).
25. K. K. Kelley, U.S. Bur. Mines Bull., No. 271 (1934); 434 (1941); 383 (1935); 393 (1936); 476 (1949); 477 (1950) and 584 (1960).
26. M. Hansen, "Constitution of Binary Alloys," 2nd ed., McGraw-Hill Book Co., New York (1958).
27. F. A. Shunk, "Constitution of Binary Alloys," 2nd Supplement, McGraw-Hill Book Co., New York (1969).
28. R. Huch and W. Klemm, *Z. Anorg. Allgem. Chem.*, **329**, 123 (1964).
29. R. Sridhar and J. H. E. Jeffes, *Trans. Inst. Min. Met., Sec. C*, **76**, 1967, p. C44.
30. J. Chipman, "Basic Open Hearth Steelmaking," p. 640, AIME (1964).
31. R. Piontelli, *Ann. N.Y. Acad. Sci.*, **79**, 1025 (1960).
32. R. W. Laity, "Reference Electrodes," D. J. G. Ives and G. J. Janz, Editors, p. 524, Academic Press, New York (1961).
33. T. B. Reddy, *Electrochem. Technol.*, **1**, 325 (1963).
34. H. A. Laitinen and B. B. Bhatia, *This Journal*, **107**, 705 (1960).
35. Yu K. Delimarskii and B. F. Markov, "Electrochemistry of Fused Salts," Sigma Press, Washington, D.C. (1961).
36. E. Bauer and R. Brunner, *Z. Electrochem.*, **41**, 794 (1935).
37. P. Csaki and A. Dietsel, *Glastech. Ber.*, **18**, 33 (1940).
38. E. Bauer and H. Ehrenberg, *Z. Electrochem.*, **18**, 1002 (1912).
39. H. Lux, *ibid.*, **45**, 303 (1939); *ibid.*, **52**, 220 (1948); *ibid.*, **53**, 41 (1949).
40. D. G. Hill B. Porter, and A. S. Gillespie, Jr., *This Journal*, **105**, 408 (1958).
41. R. Didtschenko and E. G. Rochow, *J. Am. Chem. Soc.*, **76**, 3291 (1954).
42. R. E. Ranford and S. N. Flengas, *Can. J. Chem.*, **43**, 2879 (1965).
43. H. Flood, T. Förland, and K. Motzfeldt, *Acta Chem. Scand.*, **6**, 257 (1952).
44. D. Ghosh, Ph.D. Thesis, McMaster University, Hamilton, Ontario (1975).
45. R. W. Ure, *J. Chem. Phys.*, **26**, 1363 (1957).
46. J. Short and R. Roy, *J. Phys. Chem.*, **67**, 1860 (1963).
47. Y. D. Tretyakov and A. R. Kaul, "Physics of Electrolytes," Vol. 2, pp. 623-677, Academic Press, London (1972).
48. T. H. Etsell and S. N. Flengas, *Chem. Rev.*, **70**, 339 (1970).
49. T. Matsumura, *Can. J. Phys.*, **44**, 1685 (1966).
50. H. Schmalzreid, *Z. Phys. Chem. (Frankfurt am Main)*, **38**, 87 (1963).
51. W. A. Fischer and W. Ackerman, *Arch. Eisenhuettenwes.*, **39**, 273 (1968).
52. A. Mitchell and J. Cameron, *Metall. Trans.*, **2**, 3361 (1971).
53. J. O'M. Bockris, J. A. Kitchener, and A. E. Davies, *Trans. Faraday Soc.*, **48**, 536 (1952).
54. O. A. Esin and A. K. Kirianov, *Izv. Akad. Nauk. SSSR, Otd. Tekn. Nauk.*, No. 12, 28 (1955).
55. K. Schwerdtfeger and H. J. Engell, *Arch. Eisenhuettenwes.*, **35**, 533 (1964).
56. K. Schwerdtfeger and H. J. Engell, *Trans. Metall. Soc., AIME*, **233**, 1327 (1964).
57. L. C. Chang and G. Derge, *Trans. AIME*, **172**, 90 (1947).
58. K. Sanbongi and Y. Omori, *Sci. Rep. Tohoku Univ.*, **A11**, 244 (1959).
59. M. Sasabe and K. S. Goto, *Metall. Trans.*, **5**, 2225 (1974).

60. K. Sanbongi and Y. Omori, *Sci. Rep. Tokoku Univ.*, **A11**, 339 (1959); *ibid.*, **A13**, 174 (1961).
61. K. Sanbongi and M. Ohtani, *ibid.*, **A5**, 263 (1953); *ibid.*, **A5**, 350 (1953); *ibid.*, **A7**, 487 (1955).
62. M. Ohtani, *ibid.*, **A7**, 487 (1955).
63. M. Berthelot, *Ann. Chim. Phys.*, **22**, 479 (1901).
64. H. Wartenberg and G. Witzel, *Z. Electrochem.*, **25**, 209 (1919).
65. J. E. Moose and S. W. Parr, *J. Am. Chem. Soc.*, **46**, 2656 (1924).
66. W. A. Roth and F. Muller, *Z. Phys. Chem.*, **A144**, 253 (1929).
67. A. Meichsuer and W. A. Roth, *Z. Electrochem.*, **40**, 19 (1934).
68. W. A. Roth, U. Wolf, and O. Fritz, *ibid.*, **46**, 42 (1942).
69. P. Snyder and H. Seltz, *J. Am. Chem. Soc.*, **67**, 683 (1945).
70. C. Holley and E. Huber, *ibid.*, **73**, 5577 (1951).
71. A. Schneider and G. Gattow, *Z. Anorg. Allegem. Chem.*, **277**, 41 (1954).
72. A. D. Mah, *J. Phys. Chem.*, **61**, 1572 (1957).
73. E-an Zen, *Am. Mineral.*, **54**, 1592 (1969).
74. E-An Zen, *ibid.*, **57**, 524 (1972).
75. D. R. Waldbaum, Princeton University, Unpublished work.
76. R. A. Robie and D. R. Waldbaum, U.S. Geol. Surv. Bull. No. 1259, p. 256 (1968).
77. R. Barany and K. K. Kelley, U.S. Bur. Mines Rep. Invest. 5825 (1961).
78. J. A. Kittrick, *Am. Mineral.*, **51**, 1457 (1966).
79. A. L. Reesman and W. D. Keller, *ibid.*, **53**, 929 (1968).
80. J. L. Holm and O. K. Kleppa, *ibid.*, **51**, 1608 (1966).
81. R. Barany, U.S. Bur Mines Rep. Invest. 6356 (1964).
82. A. L. Reesman and W. D. Kellar, *Am. Mineral.*, **50**, 1729 (1965).
83. B. Velde, *ibid.*, **51**, 924 (1966).
84. H. W. Day, *Geol. Soc. Am. Abstr. Progr.*, **2**, 535 (1970).

Localized Corrosion of Aluminum: Blister Formation as a Precursor of Pitting

C. B. Bargeron and R. B. Givens

Applied Physics Laboratory, The Johns Hopkins University, Laurel, Maryland 20810

ABSTRACT

Blisters have been observed in the oxide film of aluminum in aqueous chloride solutions. They can be initiated by short duration ($\lesssim$ 1 msec), low voltage pulses. Such blisters grow only if the steady-state potential of the specimen is above the pitting potential. The growth proceeds laterally along the oxide-metal interface. Upon breaking, as a result of gas pressure from within, pitting corrosion begins. Thus, in this instance, blisters are experimentally demonstrable precursors of pits.

This paper contains a preliminary account of blister growth during the potentiostatic polarization of anodized aluminum. Although blisters have been observed at higher steady-state potentials during the anodization process with chloride ions in the solution (1), our observations indicate that blisters can be initiated by short duration ($\lesssim$ 1 msec), low voltage (2-5V) pulses. Such transients are extremely easily generated in an electrochemical experiment, by design or otherwise. Indeed the phenomenon of blister formation was first observed in our laboratory by accident. Our observations regarding blister growth and subsequent pitting, which are described in detail below, demonstrate that voltage transients can play an important role in pitting investigations, thus implying that such transients may have been a hidden variable in some studies.

A significant feature of blister growth is that the stressed oxide eventually ruptures, at which point pitting corrosion begins. Thus blistering is an experimentally demonstrable precursor of pitting. As such it is of importance to those interested in initiation mechanisms in localized corrosion, a topic which has received considerable attention in the literature (2-3).

Experimental Procedures

The aluminum used in this investigation had a purity of 99.999% and was obtained from the Alfa Products Division of the Ventron Corporation. A typical impurity analysis supplied with the 0.25 mm foil was 3 ppm Si, 2 ppm Fe, 1 ppm Cu, and others less than 1 ppm. Disks of this foil were degreased in acetone and placed in a Teflon holder with 0.46 cm^2 exposed to the electrolyte. They were then electropolished in a 10% perchloric acid-ethanol mixture for 4 min at +15V at about 24°C. After a thorough rinse with deionized water the electropolished surfaces were anodized galvanostatically at 1 mA/cm^2 in 3% ammonium tartrate solution to a voltage dependent on the oxide thickness desired (4). The counterelectrode was Type 304 stainless steel. The specimens were again washed abundantly in deionized H_2O and placed in a second Teflon holder with an exposed area of about 0.044 cm^2. The electrode was then mounted face up in a stainless steel beaker. The beaker served as the auxiliary electrode. A saturated calomel electrode (SCE) was employed as the reference electrode. Using a water-immersible objective, a light microscope was focused on the specimen. The entire exposed Al surface was in the field of view.

Precautions were taken to minimize the noise in the potentiostat circuitry. The anode current was amplified and then both recorded on magnetic tape and made audible via a loudspeaker system. (Listening to the current over a speaker is a definite asset.) Voltage pulses from a Tektronix pulse generator were used to initiate blisters. Such pulses were tailored in rise and fall time (~80 μsec), so that the frequency response of the potentiostat was not exceeded during the pulse. The pulse amplitude and duration were read on an oscilloscope. The pulse was superimposed on the potential set on the potentiostat.

The electrolyte used in the cell was 0.5M KCl unless otherwise noted. The pitting potential of Al in this solution is about −0.76V (SCE) (5). The potentiostat was generally set at −1.00V (SCE) when the specimen was first connected.

After the specimens were tested electrochemically, they were rinsed with copious amounts of deionized water to remove all soluble material. Specimens were then placed in a desiccator for at least 1 day before in-

Key words: pit initiation, breakdown mechanism, voltage pulses.

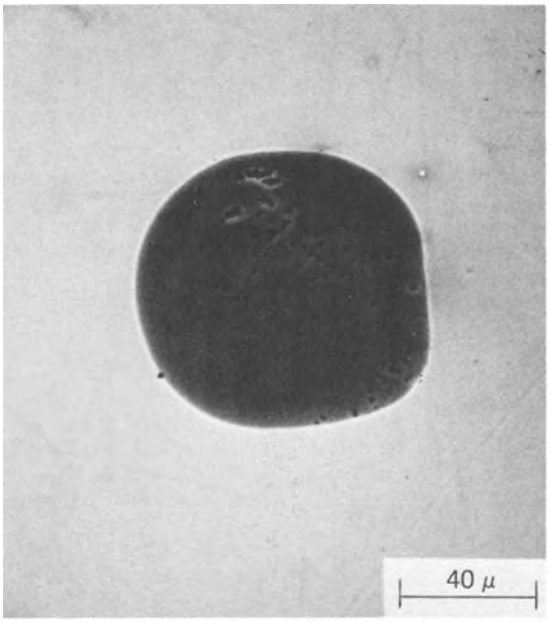


Fig. 1. A typical unbroken blister. The beam voltage was 20 keV and the stage tilt angle 30°.

vestigating them in a scanning electron microscope (SEM) with an energy dispersive x-ray analysis accessory system.

Results

A typical unbroken blister is shown in Fig. 1. As the dimensions indicate it has grown to a diameter of about 80μ. This blister was formed by setting the potential at −0.50V (SCE) and pulsing once with a pulse of amplitude 5.0V and a width less than 1 msec. The specimen had been anodized to +60V and thus had an oxide layer thickness of 800Å (4). Blisters generally have a circular shape, although their morphology can be influenced by grain boundaries and other topographical features. They appear under the low power light microscope a few seconds after the voltage pulse. Blister growth is typically somewhat jerky; that is the blister boundary does not move steadily outward, but rather increases by irregular increments with pauses in the boundary motion. During growth there is an observable frontal region extending outside the blister periphery in which there appears to be activity or stress of some type. In the SEM, the circumference of the blister frequently shows signs of stress. The shape, manner of growth, and stressed regions are all indicative of pressurized gas under the blistering oxide. The gas is apparently formed by a chemical reaction which attacks laterally along the oxide-metal interface as opposed to penetrating into the metal, although the dark spots seen in the blister are etch marks caused by a minor penetrating attack. The micrograph shown in Fig. 1 was taken at 20 keV beam voltage. Micrographs taken at 2.5 keV do not reveal the etch marks; thus, they are in the aluminum substrate under the oxide, the oxide itself being intact. The light colored ring about the blister periphery contains much larger amounts of chloride (as determined by the x-ray analysis system attached to the SEM) than either inside the blister where Cl is occasionally detectable or outside the blister where it is usually not detectable in our apparatus. Close examination of the 800Å oxide over the blister in Fig. 1 revealed no detectable cracks or holes. The SEM has resolution of 70Å, but the nonconducting oxide spoils this resolution somewhat.

There are several conditions which must be met if one wishes to observe growing blisters initiated by a single pulse of duration of 1 msec or less. A smooth surface is favorable. On rough surfaces, the oxide more frequently breaks soon after pulsing. The anodized layer thickness also plays a role as might be expected. The thinner layers break more easily; thus, blisters usually break at smaller diameters. The working electrode potential maintained by the potentiostat must be above the pitting potential. For example, in 0.5M KCl solutions, pulsing with the potential set below −0.76V (SCE) yielded no blisters. Since pitting potentials are dependent on the concentration of aggressive anions, the threshold potential for blister growth is also dependent on this factor. Also the pulse amplitude must be large enough. This amplitude is dependent on oxide thickness and is somewhat variable from specimen to specimen. In general 2-3V amplitudes are required for 200Å oxides; 4-5V amplitudes, for 800Å oxides; and greater than 10V amplitudes, for 2000Å oxides. If amplitudes much greater than those indicated are employed the oxide generally breaks immediately. Most of our tests have been made with 800Å oxides. Using the 4V amplitude for this oxide, the field strength required for blister formation with short pulses is about 5×10^5 V/cm, which is more than an order of magnitude lower than dielectric breakdown of anodized Al_2O_3 layers (6). Pulse duration is a variable which was not varied much in our tests; however, if the potentiostat is set at 2V (SCE) for a period of few seconds, many blisters form and grow under 800Å films. Some of these blisters break thus becoming pits. Wood *et al.* (7, 8) have reported experiments using "brief" pulses of approximate amplitude 2.0V (SCE) to pit aluminum with a 240Å oxide. The micrographs of pits they present as results of such tests (7, 8) appear to us to be very similar to many pits we have observed to have been formed from broken blisters.

Both intragranular as well as grain boundary sites have been observed as points of blister initiation on the aluminum surface.

Although blisters can grow to sizes on the order of 100μ on smooth surfaces they eventually rupture. Upon breaking there is a considerable increase in the current as illustrated in Fig. 2. The time at which the specimen was pulsed is also indicated. The shape of the current-time plot is reminiscent of some of those already in the literature (8, 9). The cause of the current increase in the case of a breaking blister is an increased area of unpassivated aluminum exposed to the electrolyte. A micrograph of a broken blister is shown in Fig. 3. The blister broke along its lower edge as shown. Under the break in the oxide, pitting has begun. The experiment was terminated shortly after the blister ruptured. If the blistered oxide cover is removed after the specimen has been taken from the pitting solution, then one ob-

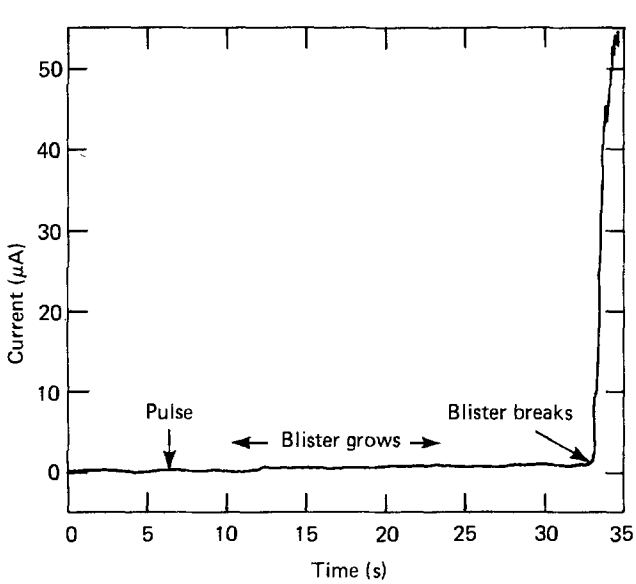


Fig. 2. A current-time plot showing the time of pulsation, the growth period, and the time of rupture.

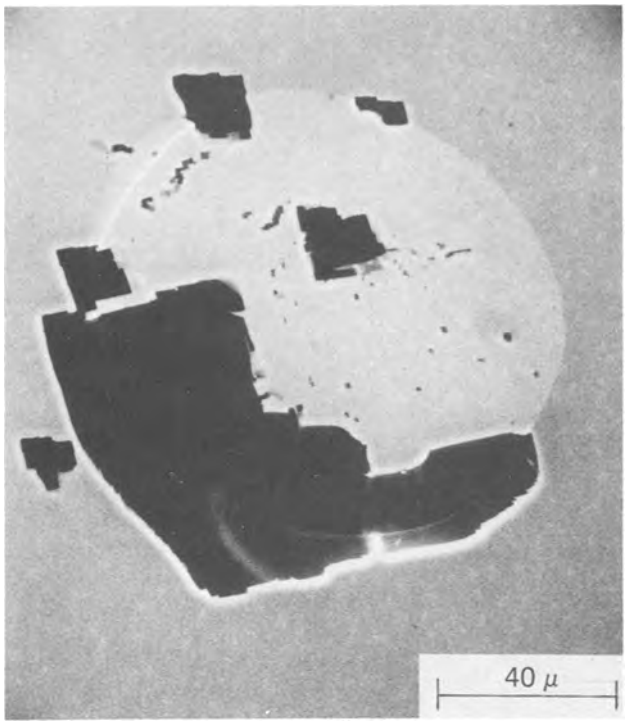


Fig. 3. A broken blister. The experiment was terminated shortly after the blister burst. The SEM conditions were as in Fig. 1.

serves more clearly that the blistering reaction proceeds laterally as opposed to penetrating, a point which was mentioned earlier. To illustrate, Fig. 4a shows a blister which broke near the end of the polarization period; a large portion of blistered oxide has been removed. Although subsequent pitting removed some aluminum, an appreciable fraction of the surface formerly under blistered oxide shows very little damage. For the sake of clarity a schematic drawing depicting the main features accompanies the micrograph in Fig. 4b.

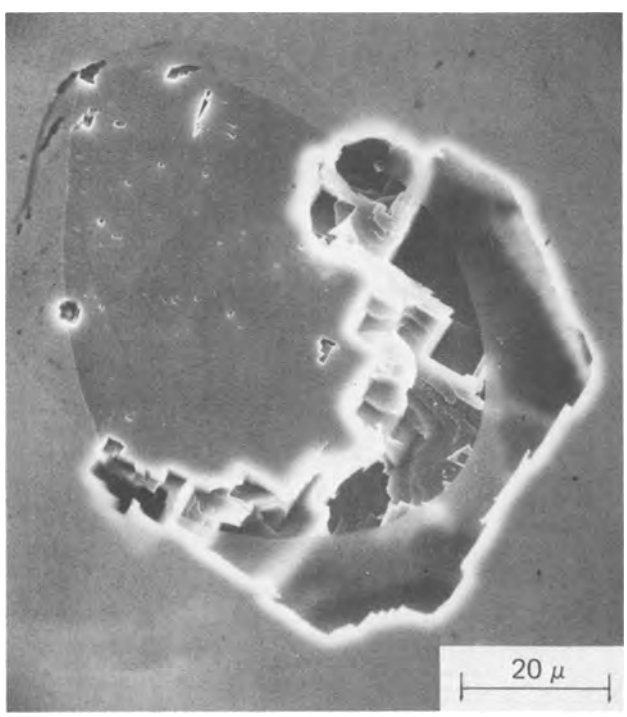


Fig. 4a. A broken blister with a portion of the oxide removed. The SEM conditions were as in Fig. 1.

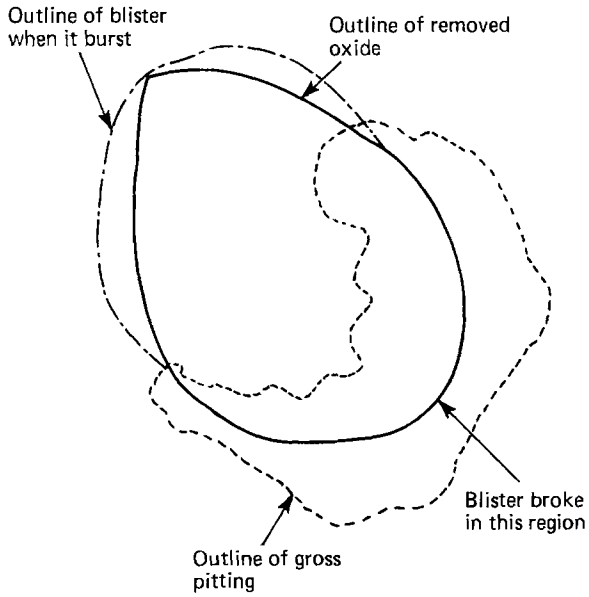


Fig. 4b. A schematic drawing depicting the main features of micrograph in Fig. 4a.

Discussion

The brief description of blistering given above raises several questions of fundamental importance, most of which must necessarily wait for complete clarification and experimental verification. Nevertheless, the following paragraphs contain a hypothesis which might explain the observations.

A question of considerable significance is that of the transport of materials across the oxide to the aluminum. No cracks or holes could be found in blistered oxide which had not broken catastrophically. A possibility is that such defects are below the resolution of our SEM. The oxide over a growing blister supports pressurized gas which would probably favor crack propagation. This does not usually happen immediately and, when it finally does occur, such breaks are frequently outside of the perimeter within which the blister was confined most of its lifetime. Therefore, suppose that the voltage pulse has created (opened) some holes of rather circular cross section in the oxide. Now the oxide is reasonably hydrophilic; therefore, the following relationship holds

$$p = 4T_s/d \qquad [1]$$

where p is the gas pressure in the blister, T_s is the surface tension of the solution against the gas, and d is the hole diameter. Using $T_s = 75$ dynes/cm, if $d \lesssim 200$Å, then p must exceed about 150 atm to force gas bubbles through the holes into the bulk electrolyte. Thus the gas remains trapped in the blister until the oxide itself ruptures at which time many bubbles appear. Now there is evidence that the same reactions which occur during pitting corrosion also proceed during blistering. Recall that blisters will not grow unless the working electrode potential is greater than the pitting potential. During the course of many pitting experiments, it was often noted that gas bubble formation, which was invariably confined to the pits, seemed to stop at potentials very close to the pitting potentials for the solutions being used. Parenthetically, gas bubble formation was observed at all potentials above the pitting potential including the 2-5V range. This elementary connection between blistering and pitting leads one to suppose that all the necessary reactants for the pitting reaction reach the bare metal during blister growth. An important step in pitting is considered to be the acidification of the pit electrolyte due to the hydrolysis of the metal ion (10) or the hydrolysis of a metal-halide ion complex (9); both processes require water. In addition to lowering the pH, the H^+, which results from the hy-

drolysis, is probably a prime reactant in the gas-producing reaction according to one of the mechanisms discussed by Bockris and Reddy (11). The pathway of the reactants to the reaction site in this hypothesis must be through the holes and along the inside of the oxide to the periphery of the blister, which then becomes the reaction site because elsewhere the film and the electrolyte are separated from the metal. Although capillary forces likely play a role in transporting materials along the inside of the film to the reaction site, electrical forces could also be effective in this regard because the blister growth rate increases with increasing working electrode potential. The pressure within the blister may also be a factor in breaking open new holes near the periphery as the blister grows. As a result of the reaction occurring around the perimeter, the adhesion of the oxide to metal in that region is reduced, which allows the blister to grow. It does so in an irregular incremental fashion because the detachment proceeds in a nonuniform spatial manner until the adhesion weakens sufficiently, at which time the gas pressure finishes the separation and thus reestablishes the roughly circular morphology.

Regarding the spatially well-defined chloride ring pointed out in Fig. 1, its existence indicates that Cl^- plays a role in the blistering process. The chloride is more than a supporting electrolyte because no blisters form if Cl^- is absent from the electrolyte. For example, in 0.1M Na_2SO_4 with a working electrode potential of 0.18V (SCE), pulsing repeatedly with 5V pulses resulted in no blisters. [It is noteworthy that Al does not pit in SO_4^{2-}, at least below 1.6V (SCE) (12).] One has the feeling that Cl^- is important in both blistering and pitting; perhaps its role is in the formation aluminum chloride complexes which subsequently hydrolyze and free the Cl^- in the process (9). This catalytic behavior would help explain the well-defined accumulation of Cl^- in what appears to be the primary reaction region of the blistering process. Another possibility is that Cl^- is effective in attacking the oxide-metal interface Recent photoelectron spectroscopy studies have identified an intermediate compound, probably AlO, in the transition region between aluminum and the Al_2O_3 (13). Although the oxide in this case was formed in an oxygen atmosphere, such a transitional oxide likely exists between anodized films and metal also and may react with Cl^-.

Conclusions

The following conclusions have been reached for the experimental conditions described above:

1. Short duration, low voltage pulses are capable of initiating blisters in the oxide film of aluminum. Such blisters only grow at potentials above the pitting potential. The growth proceeds laterally along the oxide-metal interface.

2. Blisters ultimately break as a result of gas pressure from within, at which time pitting corrosion begins. Thus blisters are experimentally demonstrable forerunners of pits in this instance.

The sensitive nature of the oxide to transient voltage pulses implies the experimental necessity of being aware of and controlling the existence of such pulses.

Acknowledgments

The authors wish to acknowledge useful discussions with Dr. S. N. Foner, Dr. A. B. Frazer, R. L. Hudson, and B. H. Nall, all of the Johns Hopkins University Applied Physics Laboratory. This work was supported by the Naval Sea Systems Command, U.S. Department of the Navy under Contract N00017-72-C-4401.

Manuscript submitted May 31, 1977; revised manuscript received Aug. 3, 1977.

Any discussion of this paper will appear in a Discussion Section to be published in the June 1978 JOURNAL. All discussions for the June 1978 Discussion Section should be submitted by Feb. 1, 1978.

Publication costs of this article were assisted by The Johns Hopkins University.

REFERENCES

1. K. Videm, Kjeller Report, KR-149, 57 (1974).
2. See "Localized Corrosion," B. F. Brown, J. Kruger, and R. W. Staehle, Editors, NACE-3, Houston (1974), for several articles discussing initiation mechanisms.
3. See J. R. Galvele, *This Journal*, **123**, 464 (1976), for further references on initiation mechanisms.
4. G. Hass, *J. Opt. Soc. Am.*, **39**, 532 (1949).
5. Z. A. Foroulis and M. J. Thubrikar, *Electrochim. Acta*, **21**, 225 (1976).
6. H. J. de Wit, Ch. Wijenberg, and C. Crevecoeur, *This Journal*, **123**, 1479 (1976).
7. J. A. Richardson and G. C. Wood, *Corros. Sci.*, **10**, 313 (1970). See especially Fig. 10.
8. G. C. Wood, W. H. Sutton, J. A. Richardson, T. N. K. Riley, and A. G. Malherbe, in "Localized Corrosion," B. F. Brown, J. Kruger, and R. W. Staehle, Editors, p. 526, NACE-3, Houston (1974). See Fig. 4f for the pit which might have come from a blister. See Fig. 8 for current-time curve.
9. S. Dallek and R. T. Foley, *This Journal*, **123**, 1775 (1976). See Fig. 2 for relevant current-time curve.
10. M. G. Alvarez and J. R. Galvele, *Corrosion*, **32**, 285 (1976).
11. J. O'M. Bockris and A. K. N. Reddy, "Modern Electrochemistry," Vol. 2, pp. 1233ff, Plenum Press, New York (1970).
12. S. B. de Wexler and J. R. Galvele, *This Journal*, **121**, 1271 (1974).
13. S. A. Flodstrom, R. Z. Bachrach, R. S. Bauer, and S. B. M. Hagström, *Phys. Rev. Lett.*, **37**, 1282 (1976); *Bull. Am. Phys. Soc.*, **22**, 414 (1977).

Anodic Oxidation of Schiff Bases Derived from 2-Hydroxy-3-Methoxybenzaldehyde

H. Ohmori,* A. Matsumoto, and M. Masui

Faculty of Pharmaceutical Sciences, Osaka University, 133-1 Yamadakami, Suita, Osaka, Japan 565

and H. Sayo

Faculty of Pharmaceutical Sciences, Kobegakuin University, Tarumi, Kobe, Japan 673

ABSTRACT

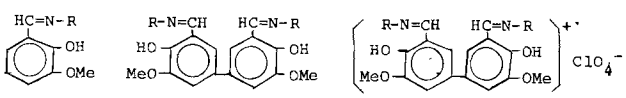
Electrochemical oxidation of Schiff bases derived from 2-hydroxy-3-methoxybenzaldehyde and various primary amines was investigated at a glassy carbon electrode in acetonitrile. On cyclic voltammetry all the compounds exhibited two anodic peaks below 1.5V *vs.* SCE. Controlled potential electrolysis of the Schiff bases at the potential of the first peaks gave cation radical salts from ring-coupled dimers. Possible sequences of the formation of the radical salts are discussed.

Electrochemical oxidation of benzylideneanilines has been studied by several workers, and the initial oxidation step has been proposed to be formation of a cation radical (I) (1-5).

$$Ar—CH=\overset{+\cdot}{N}—Ar' \qquad (I)$$

When an electroactive group such as —NMe_2 or —OH is present in the C-phenyl ring para to the azomethine group, the initial electron transfer is thought to occur from this group (1). However, in the anodic oxidation of salicylaldehydeaniles in acetonitrile it was suggested that a cation radical of type (I) was formed by the initial electron transfer, and that this then lost a proton to form a neutral radical (6).

To examine this discrepancy and as a continuation of our studies on the anodic oxidation of Schiff bases, we studied the oxidation of title compounds (MSB). In controlled potential electrolysis of MSB, cation radical salts (DSBR) were obtained from ring-coupled dimers (DSB). This paper reports the results of cyclic voltammetry and controlled potential electrolysis of MSB and related compounds in acetonitrile at a glassy carbon electrode.



MSB[1] DSB[1] DSBR[1]

Experimental

Materials.—MSB's were prepared by condensation of o-vaniline with appropriate primary amines in absolute ethanol or benzene under reflux for 2-5 hr. The crude products were purified by distillation, recrystallization, or column chromatography on silica gel. Analytical values for MSB's are summarized in Table I together with their mp or bp. Other Schiff bases were prepared by a similar method and gave the expected analytical values. Acetonitrile was distilled first from calcium hydride and then from phosphorus pentoxide after treatment by the method of Mann *et al.* (7). Sodium perchlorate, used as supporting electrolyte, was recrystallized from aqueous ethanol and stored over phosphorus pentoxide under reduced pressure. Pyridine was purified by distillation. All other chemicals were of reagent grade and were used without further purification.

* Electrochemical Society Active Member.

Key words: cyclic voltammetry, controlled potential electrolysis, cation radical salts.

[1] When —R is the *t*-butyl group, for example, these compounds will be represented as MSB*t*-butylamine, DSB*t*-butylamine, etc.

Apparatus.—Cyclic voltammetry and controlled potential electrolysis were carried out as described previously (5, 8). All voltammetric measurements were carried out at 25° ± 0.1°. Controlled potential electrolysis was done at room temperature unless otherwise specified. U.v., infrared, NMR, and mass spectra were obtained using Hitachi 124, EPI-2, R20-A, and RMU-6E spectrometers ,respectively. ESR spectra were recorded in a JEOL JES-P10 spectrometer, with 100 kHz modulation and X-band klystron.

Analysis of products obtained on controlled potential electrolysis and preparation of DSB.—Typical examples of the procedures are described.

(*i*) MSB*t*-butylamine (110.5 mg) was subjected to electrolysis in acetonitrile (50 ml) containing 0.1M sodium perchlorate at +0.8V *vs.* SCE at room temperature until the current decreased to less than 1% of the initial value (140 min). During this period 40.4C were consumed, which correspond to $n = 0.76$. The electricity consumed was estimated from the area below the current-time curve. A dark green precipitate (DSBR) began to be deposited at the electrode when electrolysis was started. This material was collected on a sintered glass disk and was washed repeatedly with cold methanol and acetonitrile. The yield of DSBR*t*-butylamine was 63.9 mg (50%) mp 240° decomp. Calculated for $C_{24}H_{32}N_2O_8Cl$: C, 56.3; H, 6.30; N, 5.47; Cl, 6.92. Found: C, 56.1; H, 6.33 N, 5.43; Cl, 6.38. DSBR*i*-propylamine was obtained similarly, mp 240° decomp. Calculated for $C_{22}H_{28}N_2O_8Cl$: C, 54.6; H, 5.83; N, 5.79; Cl, 7.33. Found: C, 54.6; H, 6.00; N, 5.86; Cl, 7.31. The DSBR's were in general poorly soluble in various solvents, including water, and when dissolved in some solvents they decomposed

Table I. Mp's, bp's, and analytical data of MSB's

MSB	Mp or bp (°C)	Found (%)			Calculated (%)		
		C	H	N	C	H	N
methylamine	69	65.4	6.71	8.43	65.4	6.71	8.48
ethylamine	161 (10 mm)*	66.8	7.31	7.95	67.0	7.31	7.82
i-propylamine	156 (10 mm)*	68.1	7.83	7.37	68.4	7.82	7.25
t-butylamine	59	69.5	8.28	6.94	69.5	8.27	6.76
benzylamine	54	74.5	6.30	5.87	74.7	6.27	5.80
aniline	81	73.9	5.75	6.09	74.0	5.76	6.16
p-anisidine	92.5	69.7	5.82	5.49	70.0	5.87	5.44
p-nitroaniline	175	61.3	4.45	10.26	61.8	4.44	10.29
α-naphthylamine	90	77.8	5.50	5.06	78.0	5.45	5.05
valine	160	62.1	6.86	5.53	62.1	6.82	5.57
valine methyl ester	69	63.5	7.24	5.48	63.4	7.22	5.28
β-alanine	166	59.1	5.88	6.24	59.2	5.87	6.27

* Bp, others are mp's.

fairly rapidly. Hence the only DSBR's obtained in pure form were those two described above.

After the DSBR*t*-butylamine had been filtered off, the solution from electrolysis showed a cyclic voltammogram which coincided with that of the starting MSB in the presence of excess perchloric acid, and on addition of excess pyridine the solution showed a cyclic voltammogram which coincided with that of the starting MSB under the same conditions (see Results). The absorption spectra of the solution from electrolysis coincided with those of the MSB in the presence of perchloric acid. Thus protonated MSB*t*-butylamine had been formed. The amount of the protonated MSB was determined by measuring the peak height of the voltammogram after adding excess pyridine, and by measuring the absorbance of the solution from electrolysis. The two measurements agreed well. In this case 50% of the MSB was recovered.

(*ii*) MSB*t*-butylamine (37.7 mg) was subjected to electrolysis in the presence of 0.20 mmole of pyridine at +0.8V. A total of 25C of electricity was consumed, which corresponds to $n = 1.4$. The yield of DSBR*t*-butylamine was 55.4 mg (*ca.* 100%). The solution after electrolysis showed no appreciable voltammetric peak.

The structure of DSBR*t*-butylamine was confirmed by the following observations. DSBR*t*-butylamine showed an ESR signal in the solid state (see Results). The infrared spectra of DSBR*t*-butylamine showed a characteristic absorption around 1100 cm^{-1} due to the perchlorate anion. DSBR*t*-butylamine was reduced by sodium dithionite in a manner similar to that reported for cation radical salts derived from carbazoles (9). A suspension of the DSBR (386 mg) and sodium dithionite (3g) in acetonitrile (50 ml) was refluxed for 10 hr with stirring. The DSBR gradually dissolved to give a brown solution. Excess sodium dithionite was filtered off, the solution was evaporated to dryness, and the residue (A) (242 mg) was hydrolyzed in 10% hydrochloric acid for 24 hr. The reaction mixture was extracted with chloroform and the extract was washed and dried. Evaporation of the extract gave 4,4′-dihydroxy-5,5′-dimethoxybiphenyl-3,3′-dicarbaldehyde (DOV) (100 mg) which was recrystallized from acetone-petroleum ether, mp 212°. Calculated for $C_{16}H_{14}O_6$: C, 63.6; H, 4.67. Found: C, 63.1; H, 4.64. Mass: M^+; *m/e* 302. NMR ($CDCl_3$): δ(ppm), 4.02 (s, 6H), 7.27 (d, 2H, J = 2 Hz), 7.31 (d, 2H, J = 2 Hz), 10.00 (s, 2H), 10.98 (s, 2H) (disappeared on D_2O treatment). Infrared (KBr disk): ν_{max} (cm^{-1}), 3450, 1660, 1250. The above residue (A) was dissolved in chloroform-benzene containing excess *t*-butylamine[2] and refluxed for 1 hr. On evaporation of the solvent, 5,5′-bis[*N*-(2-hydroxy-3-methoxybenzylidene)-*t*-butylamine] (DBS*t*-butylamine) was obtained and this was recrystallized from benzene-hexane, mp 235° Calculated for $C_{24}H_{32}N_2O_4$: C, 69.9; H, 7.82; N, 6.78. Found: C, 69.1; H, 7.81; N, 6.60. DSB*i*-propylamine was obtained similarly, mp 126°. Calculated for $C_{22}H_{28}N_2O_4$: C, 68.7; H, 7.34; N, 7.28. Found: C, 68.6; H, 7.33; N, 7.33.

Results

Cyclic voltammetry.—All the MSB examined showed three or four anodic peaks; no extra anodic peak was observed in a multiple sweep. The MSB's derived from aliphatic amines showed no appreciable cathodic peak even when the voltage scan direction was reversed at any potential, while MSB's derived from aromatic amines showed a small cathodic peak around 0.12V, possibly due to reduction of the partially soluble DSBR (see below). A typical cyclic voltammogram of MSB*t*-butylamine is shown in Fig. 1. Voltammetric data on MSB are summarized in Table II. The third and fourth waves were not studied further.

The first-oxidation peak potentials of various Schiff bases including MSB are compared in Table III. Among

[2] When residue (A) was recrystallized from benzene-hexane without excess *t*-butylamine, a mixture of DSB*t*-butylamine, DOV, and the mono-Schiff base of DOV was obtained.

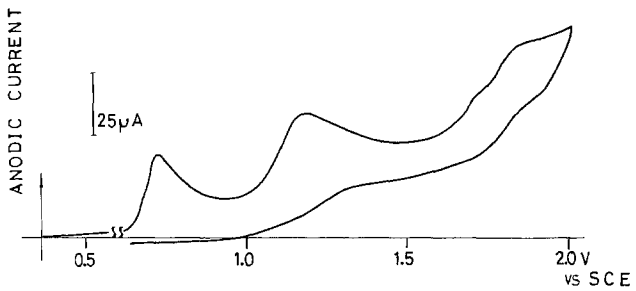


Fig. 1. Cyclic voltammogram of 2.0 mM MSB*t*-butylamine in MeCN/0.1M $NaClO_4$, sweep rate = 50 mV/sec, area = 0.071 cm^2.

the Schiff bases with a hydroxy group on the benzylidene ring, those derived from aliphatic amines were oxidized more easily than those derived from aromatic amines. Conversely, among the Schiff bases without a hydroxy group, those derived from aromatic amines were oxidized more easily.

Typical examples of the effects of added acids and bases on the cyclic voltammetry of MSB are illustrated in Fig. 2 and 3. In the presence of perchloric acid or sulfuric acid the first wave decreased while the second wave increased. In the presence of excess of acid, the first wave completely disappeared. The weaker acid, acetic acid, had no appreciable effect. When pyridine was added the first wave increased and the second wave decreased. With excess pyridine the peak current of the first wave almost doubled and the second wave disappeared. The effect of the stronger base, the methoxide ion, was examined in methanol[3]

[3] The voltammograms of MSB in acetonitrile and in methanol without methoxide ion were similar. The effects of pyridine were also similar.

Table II. Results of cyclic voltammetry of MSB in acetonitrile containing 0.1M sodium perchlorate

MSB[a]	E_{p1}[b]	$i_p/Cv^{1/2}$[c]	E_{p2}[b]
methylamine	0.68	95.3	1.31
ethylamine	0.69	91.2	1.38
i-propylamine	0.72	95.3	1.28
t-butylamine	0.72	94.8	1.28
benzylamine	0.75	95.3	1.30
aniline	0.89	96.2	1.25
p-anisidine	0.84	94.8	1.30
p-nitroaniline	1.03	90.3	1.53
α-naphthylamine	1.05	86.3	1.33
valine	0.89	94.4	1.30
valine methyl ester	0.83	94.4	1.23
β-alanine	0.75	91.7	1.32

[a] The concentration of substrate was 1-2 mM.
[b] Sweep rate = 0.05 V/sec. E_p *vs.* SCE.
[c] i_p in μA, *C* in mM, *v* in V/sec. Geometric electrode area 0.071 cm^2.

Table III. First oxidation peak potentials (E_{p1}, V vs. SCE) of various Schiff bases in acetonitrile containing 0.1M sodium perchlorate: sweep rate = 0.05 V/sec, conc. of substrate 1.0 mM

Y—CH=N—R

R \ Y	 OMe	 OMe	 MeO OH	 MeO OH	 OH
—C(Me)$_3$	1.50	1.80	0.72	0.83	1.05
—CH(Me)$_2$	1.67		0.72		
	1.45	1.45	0.89	0.89	1.10
 —OMe	1.05		0.84		

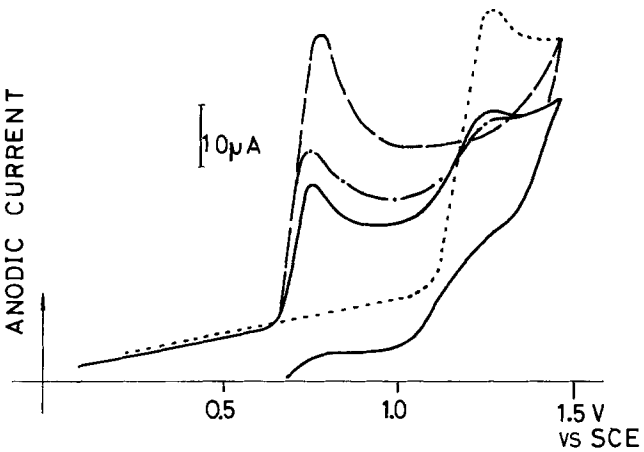


Fig. 2. Effects of pyridine and perchloric acid on the voltammogram of 1.24 mM MSBt-butylamine in MeCN/0.1M $NaClO_4$, sweep rate = 50 mV/sec, area = 0.071 cm^2. ——— Without pyridine or perchloric acid; —·— with 0.85 mM pyridine; ——— with 1.5 mM pyridine; ------- with 5.0 mM perchloric acid.

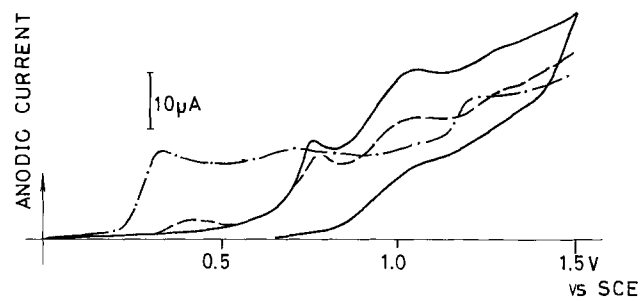


Fig. 3. Effects of methoxide ion on the voltammogram of 0.9 mM MSBt-butylamine in MeOH/0.1M $NaClO_4$; sweep rate = 50 mV/sec, area = 0.071 cm^2. ——— Without methoxide ion; ——— with 0.5 mM NaOMe; —·— with 1.0 mM NaOMe.

(Fig. 3); a new peak appeared at a less positive potential and the peak height increased with increase in the concentration of methoxide ion, but this increase did not exceed the peak height of the first wave in the absence of methoxide ion.

Controlled potential electrolysis.—Detailed experiments were mainly carried out on MSBt-butylamine and MSBi-propylamine, but results with other MSB's were essentially similar. Typical results are summarized in Table IV.

Electrolysis in acetonitrile at the potential of the first wave gave a coulometric n-value of 0.7-0.8, and DSBR and protonated MSB ($MSBH^+$) were both formed in almost 50% yield. On electrolysis in the presence of an equimolar amount of pyridine, the n value was 1.3-1.8 and DSBR was formed almost quantitatively. Similar results were obtained with methanol as solvent, but on electrolysis in methanol in the presence of excess methoxide ion, no DSBR was formed.

Typical examples of ESR spectra of DSBRt-butylamine in the solid state and in concentrated sulfuric acid are shown in Fig. 4 and 5, but the exact nature of the species giving the latter spectrum (Fig. 5) is unknown: it must be due to some secondary radical formed from the DSBR.

Electrolysis of 2-hydroxy-3-methoxybenzaldehyde (o-vaniline) under similar conditions did not give a cation radical salt, although cyclic voltammetry of o-vaniline in the presence of pyridine suggested the formation of DOV: in acetonitrile containing 1% pyridine, o-vaniline showed an anodic peak at 0.85V and a cathodic peak at 0.40V, and an extra anodic peak at 0.46V on the subsequent anodic sweep; DOV gave an anodic peak at 0.47V and a cathodic peak at 0.41V under the same conditions (figures not shown).

Table IV. Results of controlled potential electrolysis

Compound[a]	Applied potential[b]	n value	% yield of DSBR	% yield of $MSBH^+$	Electrolysis conditions[c]
MSB					
t-butylamine	0.80	0.76	47	50	
	0.80	1.40	100		Pyridine[d]
i-propylamine	0.80	0.76	45	50	
	0.80	1.65	100		Pyridine[d]
methylamine	0.70	0.66	+[e]	+[e]	
ethylamine	0.80	0.77	+[e]	+[e]	
benzylamine	0.80	0.70	+[e]	+[e]	
p-anisidine	0.90	0.85	+[e]	+[e]	
β-alanine	0.76	0.75	51[f]	50	
valine	0.90	0.63	41[f]	57	at −30--40°C[g]
valine methyl ester	0.84	0.68	49[f]	59	at −30--40°C[g]
DSB					
t-butylamine	0.50	1.00	92		
	0.80	0.98	97		
	0.50	0.86	80		Pyridine[d]
	0.80	1.02	82		Pyridine[d]
i-propylamine	0.50	0.97	87		
	0.80	1.05	89		
	0.50	0.95	82		Pyridine[d]
	0.80	0.97	75		Pyridine[d]

[a] The concentration of substrate was 1-5 mM.
[b] V *vs.* SCE.
[c] Unless otherwise indicated, runs were carried out in acetonitrile containing 0.1M sodium perchlorate at room temperature.
[d] Runs were carried out in the presence of an equimolar to 1.5M amount of pyridine.
[e] The determination of DSBR or $MSBR^+$ was not performed, though the formation of them was recognized.
[f] Calculated on the basis of the weight of green precipitate obtained by a similar treatment to that described in the experimental section.
[g] When electrolysis was carried out at room temperature, the DSBR was soluble in acetonitrile and the nature of the solution from electrolysis was complex.

Electrochemistry of DSB.—Typical cyclic voltammograms of DSBt-butylamine under various conditions are illustrated in Fig. 6 and 7. DSBt-butylamine showed two anodic peaks at 0.35 and 0.78V. The second peak seems to be due to the oxidation of an adsorbed species. On sweep reversal, a small ill-defined cathodic peak was observed at around 0.15V [Fig. 6(a)]. However, when the cathodic sweep was stopped at a potential distance intermediate between the first and second anodic peaks for a short period, a well-defined cathodic peak appeared at 0.15V on the subsequent further cathodic sweep [Fig. 6(b)]. The cathodic peak must be due to reduction of the adsorbed species as shown by a potential step experiment [Fig. 6(c)]. Figure 6(c) also shows the presence of second cathodic peak at around 0.05V when the voltage sweep was limited to the potential of the first anodic peak. The second cathodic peak did not appear with voltage sweep rates of less than 50 mV/sec. Upon multiple sweep, neither a new anodic nor an extra cathodic peak was observed regardless of the voltage sweep range. The E_p of the first anodic wave shifted *ca.* 50 mV cathodic for a tenfold decrease in the sweep rate (200 → 20 mV/sec), while that of the first cathodic wave remained unchanged.

Pyridine had little effect on the voltammograms of DSB. The voltammogram in the presence of perchloric acid suggests that the second anodic peak of DSB is not due to oxidation of protonated DSB, in contrast to results with MSB (Fig. 7).

Electrolysis of DSB in acetonitrile at the potential of the first wave gave an n value of almost unity, and DSBR was formed almost quantitatively (Table IV). Similar results were obtained on electrolysis at the potential of the second peak, in the former case most of the DSBR was formed on the electrode surface whereas in the latter case most of DSBR was formed in the solution. The presence of an equimolar amount of pyridine did not affect the results. The physical properties (mp, infrared, and ESR spectra) of DSBRt-butylamine and DSBRi-propylamine obtained on electrolysis of the corresponding DSB coincided with those of DSBR's obtained on electrolysis of the corresponding MSB. These findings together with the yields of

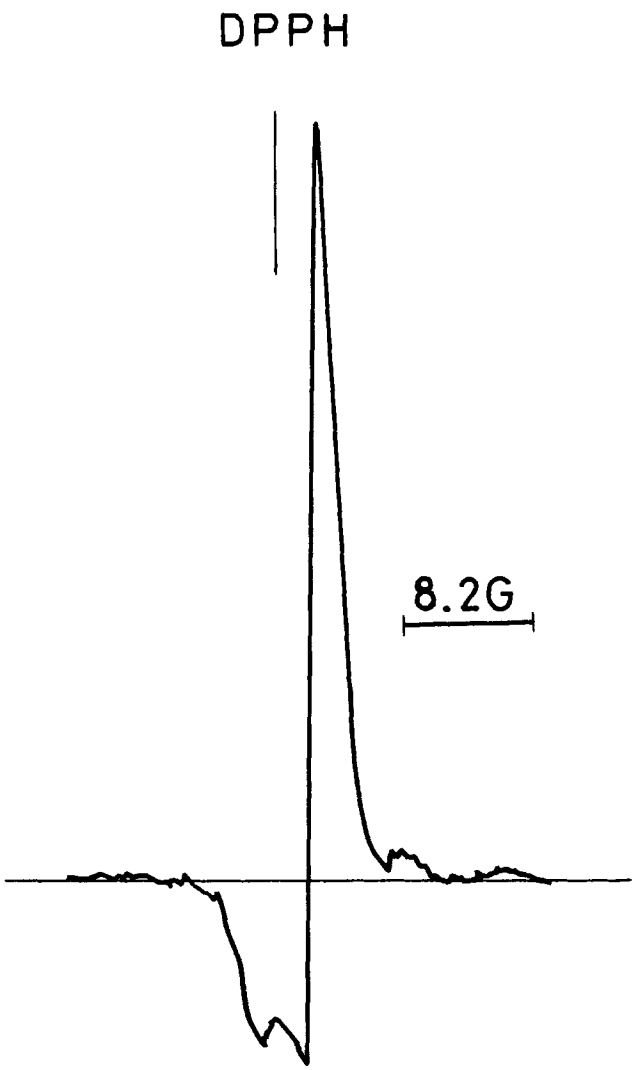
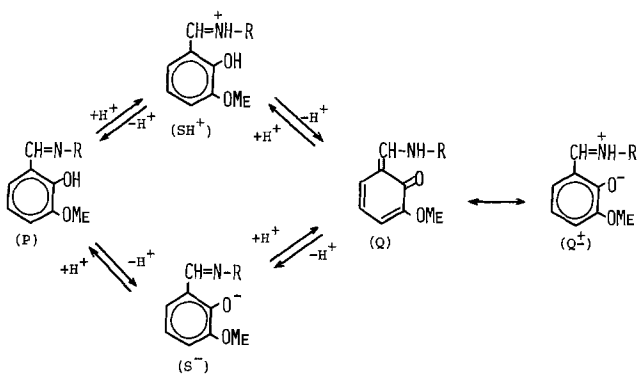


Fig. 4. ESR spectrum of DSBRt-butylamine in the solid state.

DSBR's cited in Table IV support the theory that MSB dimerizes exclusively in the position para to the hydroxy group.[4]

Discussion

In analogy with *N*-salicylidene-2-aminopropane, protonation equilibria in Scheme I can be considered



Scheme I

for MSB, and in the present solvent system the contribution of the quinoneamine form (Q) will be small (10). Then, the first peak observed on cyclic voltammetry of MSB will be ascribed to oxidation of P, the second peak to that of SH^+, and the new peak in the presence of methoxide ion to that of S^-. The results in Table III strongly suggest that the initial electron transfer in P involves the aromatic pi system including the hydroxy group, that is, oxidation of a phenol takes place. If the initial oxidation involves the lone pair electrons on the nitrogen atom, Schiff bases derived from aromatic amines would be oxidized more easily than those derived from aliphatic amines, regardless of the presence of a hydroxy group on the benzylidene ring.

A mechanism for the formation of DSBR consistent with the results can be described by Scheme II.

[4] In a preliminary electrolysis of 2-hydroxy-3-methoxy-5-methylbenzylidene-t-butylamine, no DSBR was formed.

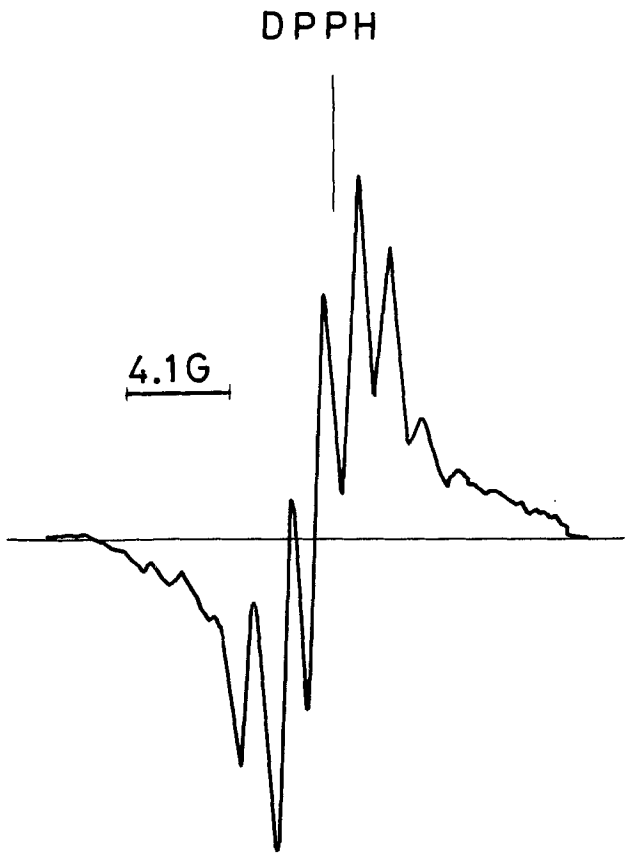


Fig. 5. ESR spectrum of DSBRt-butylamine in concentrated sulfuric acid.

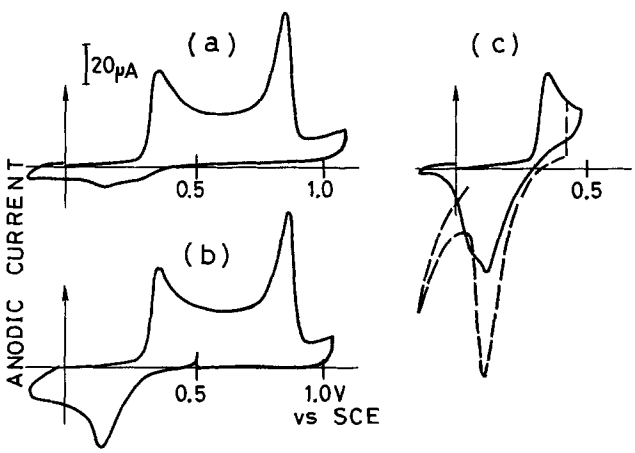


Fig. 6. Cyclic voltammograms of 1.43 mM DSBt-butylamine in MeCN/0.1M $NaClO_4$, sweep rate = 200 mV/sec, area = 0.071 cm^2. (a) Normal cyclic sweep including the second peak; (b) potential was held at 0.5V for 10 sec during the cathodic sweep; (c) ——— normal cyclic sweep including the first peak alone; — — — potential was held at 0.41V for 15 sec, and then swept to cathodic direction.

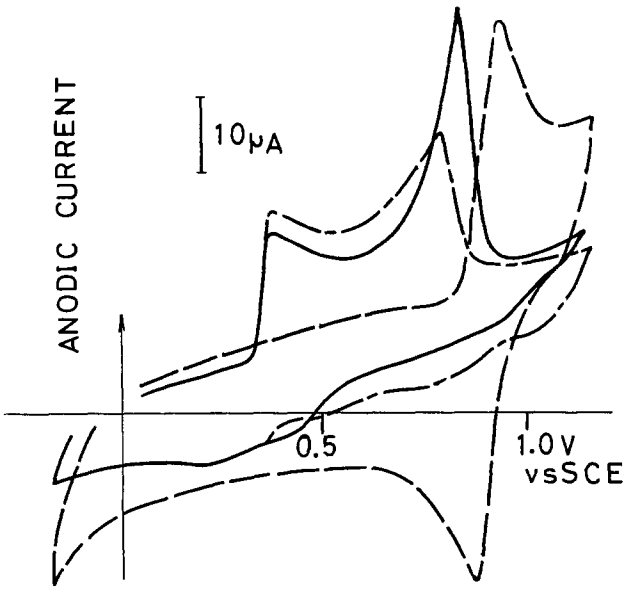


Fig. 7. Cyclic voltammograms of 1.0 mM DSBt-butylamine in MeCN/0.1M $NaClO_4$, sweep rate = 50 mV/sec, area = 0.071 cm^2. ——— Without added acid or base; —·— with 3.7 mM pyridine; — — — with 5.0 mM perchloric acid.

$$MSB \underset{\longleftarrow\!\!-\!\!-\!\!-}{\xrightarrow{-e}} MSB^{+\cdot} \quad [1]^5$$

$$2MSB^{+\cdot} + 2MSB \rightarrow DSB + 2MSBH^{+} \quad [2]$$

$$DSB \underset{\longleftarrow\!\!-\!\!-\!\!-}{\xrightarrow{-e}} DSB^{+\cdot} \quad [3]^5$$

$$DSB^{+\cdot} + ClO_4^{-} \longrightarrow DSBR \quad [4]$$

$$DSB^{+\cdot} \xrightarrow{-e} DSB^{2+} \quad [5]$$

$$DSB^{2+} + DSB \longrightarrow 2DSB^{+\cdot} \quad [6]$$

$$DSB^{2+} + MSB \longrightarrow DSB^{+\cdot} + MSB^{+\cdot} \quad [7]$$

Scheme II

Electrolysis of MSB at the potential of the first wave will mainly proceed through reactions [1]-[4]. In reaction [2] it is not clear whether dimerization occurs before or after the loss of a proton from $MSB^{+\cdot}$. If the proton transfer precedes the dimerization, the proton will be removed from the hydroxy group to give MSB·. In methanol containing the methoxide ion, S^- in Scheme I will be oxidized to give MSB·. In this case DSBR was not formed at all. Though this observation does not necessarily exclude the possibility that MSB· dimerizes, it may support the dimerization of $MSB^{+\cdot}$. Reactions [8] and [9] are alternatives to reaction [2] which is similar to those suggested for anodic substitution reactions (11). However, these reactions seem less probable

$$MSB^{+\cdot} + MSB \longrightarrow [MSB\text{-}MSB]^{+\cdot} \quad [8]$$

$$[MSB\text{-}MSB]^{+\cdot} + 2MSB \longrightarrow DSB + 2MSBH^{+} + e \quad [9]$$

because similar processes to reaction [2] have been proposed for many phenol coupling reactions (12) and for oxidation of carbazoles and related compounds (13-15) where exclusive dimerization reactions have been observed. Exclusive DSBR formation on electrolysis of MSB in the presence of pyridine can support this view. If reactions [8] and [9] were operative, formation of pyridinated MSB would also be expected as observed in the oxidation of benzylidene-*p*-anisidines (5).

[5] This process may be reversible, but on cyclic voltammetry of MSB no corresponding cathodic peak was observed under the experimental conditions (see Results).

Irrespective of which process occurs in formation of DSB, a total of 0.75 electrons will be consumed per molecule of MSB, and half of the starting MSB will form DSBR, the rest being converted to protonated MSB. When pyridine is present in the system, it will act as a proton acceptor in place of MSB itself, and all the MSB will be oxidized to form DSBR. The *n* value should then be 1.5.

Since the oxidation potentials of $DSB^{+\cdot}$ and the starting MSB are similar, the $DSB^{+\cdot}$ can be further oxidized in part to form DSB^{2+} (reaction [5]). However, the results obtained on controlled potential electrolysis of DSB strongly suggest that DSB^{2+} will react with DSB to give $DSB^{+\cdot}$ again (reaction [6]). Similarly, reaction [7] can be considered and regardless of the extent to which reaction [5] occurs the over-all results on electrolysis of MSB will be the same.

A complete explanation for the voltammetric behavior of DSB cannot be offered from the present experimental results alone. However, the shifts of the first anodic peak of DSBt-butylamine with voltage sweep rate suggest that reaction [4] is very fast, fast enough to make reaction [3] apparently irreversible. The second anodic peak and the cathodic peak (Fig. 6) must be due to the oxidation and the reduction of adsorbed DSBRt-butylamine, respectively. Reactions [4] and [5], then, will be better represented as reactions [10] and [11]

$$DSB^{+\cdot} + ClO_4^{-} \longrightarrow DSBR_{adsorbed} \quad [10]^6$$

$$DSBR_{adsorbed} \xrightarrow{-e} DSB^{2+} + ClO_4^{-} \quad [11]$$

The absence of a well-defined cathodic peak when the voltage sweep was extended beyond the second anodic peak [Fig. 6(a)] may be ascribed to the lack of DSB near the electrode surface to reproduce $DSB^{+\cdot}$ by reaction [6]. No plausible assignment can be made for the second cathodic peak [Fig. 6(c)] at the present stage. We are now studying the exact nature of the products of electrolysis of MSB in methanol in the presence of methoxide ion.

Manuscript submitted April 5, 1977; revised manuscript received Aug. 11, 1977. This was Paper 324 presented at the Washington, D.C., Meeting of the Society, May 2-7, 1976.

Any discussion of this paper will appear in a Discussion Section to be published in the June 1978 JOURNAL. All discussions for the June 1978 Discussion Section should be submitted by Feb. 1, 1978.

[6] To explain the observation that controlled potential electrolysis of DSB actually proceeded to completion in spite of the adsorption of DSBR at the electrode surface, the following reactions should also be considered

$$DSBR_{adsorbed} + DSB_s \rightarrow DSB_e + ClO_4^{-} + DSB_s^{+\cdot}$$

$$DSB_s^{+\cdot} + ClO_4^{-} \rightarrow DSBR_{precipitated}$$

where subscripts s and e denote a species in the solution and at the electrode surface, respectivly.

REFERENCES

1. P. Martinet, J. Simonet, and J. Tendil, *C. R. Acad. Sci. Paris*, **268**, 2329 (1969).
2. G. Briere, R. Herino, and F. Mondon, *Mol. Cryst. Lig. Cryst.*, **19**, 157 (1972).
3. A. Lomax, R. Hirasawa, and A. J. Bard, *This Journal*, **119**, 1679 (1972).
4. A. Denat, B. Gosse, and J. P. Gosse, *Chem. Phys. Lett.*, **18**, 235 (1973).
5. M. Masui and H. Ohmori, *J. Chem. Soc. Perkin Trans. 2*, 1882, (1972); *ibid.*, 1112 (1973).
6. J. E. Kuder, H. W. Gibson, and D. Wychick, *J. Org. Chem*, **40**, 875 (1975).
7. J. F. O'Donnell, J. T. Ayres, and C. K. Mann, *Anal. Chem.*, **37**, 1161 (1965).
8. H. Sayo and M. Masui, *J. Chem. Soc. Perkin Trans. 2*, 1640 (1973).
9. P. Beresford, D. H. Iles, L. J. Kricka, and A. Ledwith, *J. Chem. Soc. Perkin Trans. 1*, 276 (1974).
10. R. Herscovitch, J. J. Charette, and E. de Hoffmann, *J. Am. Chem. Soc.*, **95**, 5135 (1973); and references therein.
11. L. Eberson and K. Nyberg, *Tetrahedron*, **32**, 2185 (1976); and references therein.

12. N. L. Weinberg, "Technique of Electroorganic Synthesis, Part I," N. L. Weinberg, Editor, p. 410, John Wiley & Sons, New York (1974); and references therein.
13. J. F. Ambrose and R. F. Nelson, *This Journal*, **115**, 1159 (1968).
14. J. F. Ambrose, L. L. Carpenter, and R. F. Nelson, *ibid.*, **122**, 876 (1975).
15. S. N. Frank, A. J. Bard, and A. Ledwith, *ibid.*, **122**, 898 (1975).

Modified Viologens with Improved Electrochemical Properties for Display Applications

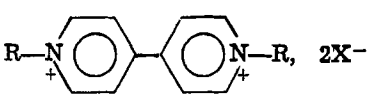
J. Bruinink, C. G. A. Kregting, and J. J. Ponjeé

Philips Research Laboratories, Eindhoven, The Netherlands

ABSTRACT

The redox reaction of 1,1'-diheptyl-4,4'-dipyridinium dibromide in water was investigated by means of linear potential sweep voltammetry. It was found that aging of the radical salt film or the occurrence of the second reduction step results in an additional oxidation peak. This additional oxidation peak is accompanied by a decrease of charge efficiency, leading to display failure. It was demonstrated that these problems can be largely avoided by use of modified viologens in combination with tin dioxide electrodes. The influence of the electrode material was also investigated.

The electrochemical reduction and oxidation of 4,4'-dipyridinium salts, better known as viologens, find application in redox-chromic displays (1). The general formula of these salts is



where R is the substituent and X^- the anion. From previous investigations (2-6) it is known that the reduction of the viologen ion A^{2+} proceeds as follows

$$A^{2+} + e \rightleftarrows A^{\cdot +}$$

$$A^{\cdot +} + e \rightleftarrows A$$

When R is CH_3 the first reduction step is a reversible one-electron reduction, which yields a stable blue radical ion in water as well as in various organic solvents. For R is CH_3 the second reduction step at more negative potential was reported to be reversible in non-aqueous solutions and irreversible in aqueous solutions in which the yellow brown product A is insoluble.

Further investigations have shown that if substituent R and anion X^- are properly chosen (*e.g.*, 1,1'-diheptyl-4,4'-dipyridinium dibromide), the first reduction step in aqueous solution is followed by a chemical reaction

$$A^+ + X^- \rightleftarrows AX\downarrow$$

The reaction product AX is deposited as a purple film on the electrode (7).

In an earlier paper, 1,1'-diheptyl-4,4'-dipyridinium dibromide with a platinum electrode was proposed as a suitable system for use in redox-chromic displays (1). This combination showed however, an irreproducible display behavior when used at long memory times and at high negative potentials (8). In this study linear potential sweep voltammetry is used to investigate the electrochemical properties of several viologens in order to evaluate their applicability in redox-chromic displays.

Experimental

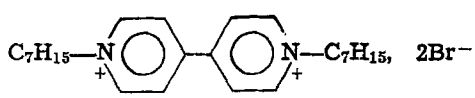
The synthesis of the viologens and modified viologens was carried out as described in the Appendix. The voltammetric measurements were performed using a PAR 173 potentiostat system. The recording intrument was either a Hewlett Packard 7000 AM recorder or a Philips oscilloscope PM 3330 with polaroid camera. If necessary electronic *IR*-compensation was applied.

The electrolyte solutions under investigation were deoxygenated by passing argon (oxygen content 5 ppm) through them. As reference and counterelectrodes we used Ag/AgCl electrodes separated from the cell solution by a Luggin capillary and glass frit, respectively. In some experiments, Ag/AgBr wire electrodes were used as a reference in order to exclude the disturbing influence of chloride ions. The electrochemical cell consisted of a standard double-wall Metrohm vessel, thermostated at 25°C. The working electrodes were homemade tin dioxide conductive glass (8 Ω/□) and Beckman platinum inlay electrodes.

Results and Discussion

Stability of the electrodeposited film.—After electrodeposition, most of the viologen radical salt films show aging effects. Immediately after formation, the appearance of the film is very smooth with a homogeneous color, but after some time aging causes an inhomogeneous coloration of the film followed by formation of polycrystalline conglomerates. At this moment it is thought that during aging reorientation of the molecules is followed by recrystallization. The result of this recrystallization is a poor erasure behavior in redox-chromic displays, since the recrystallized layer is not completely available for a direct electrochemical oxidation. The effect of aging was found to be very sensitive to experimental conditions, such as the occurrence of the second reduction step during deposition of the film, electrode material, solvent, and smoothness of the electrode surface. Moreover the molecular structure of viologens was observed to have a striking influence on the effect of aging.

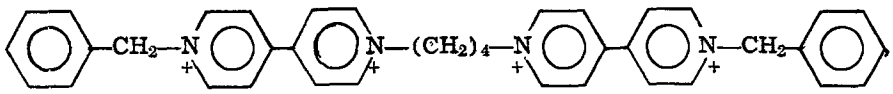
We found that the viologen radical salt films of dialkyl-dipyridinium compounds, with halide ions as anions, generally show these visible changes only about 10 sec after deposition. A typical example is 1,1'-diheptyl-4-4'-dipyridinium dibromide denoted further as HV-Br



With some other modified viologens, macroscopic

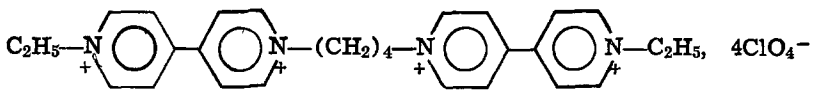
Key words: electrochromic, redox, displays, viologen.

changes of the film can be observed only after several minutes. A typical example of these modified viologens is tetramethylene bis-[4(1-benzylpyridine-4'-yl)pyridinium] tetrafluoroborate, denoted as BD-BF_4



The difference between the unstable HV-Br radical salt film and the more stable BD-BF_4 radical salt film can be illustrated by observing the potential of the film after deposition (compared with some reference electrode) as a function of time (Fig. 1). It can be seen that the potential of the BD-BF_4 film, starting at $t = 0$, shows only a minor change which is due to restoration of the concentration gradient after deposition. On the other hand, radical salt films of HV-Br show a change in electrode potential after formation, in correspondence with the aging effect.

Stable films are formed with tetramethylene [bis-4(1-ethylpyridine-4'-yl) pyridinium] perchlorate, denoted further as ED-ClO_4



No macroscopic recrystallization was observed, even after 100 hr. As can be seen from Fig. 1 radical salt films of this viologen show a stable potential. Combinations of modified viologens with smaller anions, *e.g.*, BD-Br and ED-Br, form soluble radical ions as can be seen from the appearance of a blue haze at the electrode during reduction.

Background potential limits.—Only measurements below $pH = 8$ are reported since in alkaline medium ($pH > 8$) a disturbing reaction of viologens has been reported (9).

Before discussing the voltammetric experiments, we first consider the suitability of two solid electrodes, namely, platinum and tin dioxide. Platinum was chosen since it was used in the prototype of a redox-chromic display (1), while tin dioxide was chosen since it was expected to be a good inert transparent electrode material for potential use in display devices.

The background potential limits for platinum electrodes are known for several electrolyte solutions. In the cathodic region hydrogen is evolved at nearly the theoretical limit, being about −0.5V (SCE) at $pH = 5$ (10). In our experiments we found an anodic limit of about 0.8V (SCE) for a solution of 0.3M potassium bromide at $pH = 5$ (10% citrate-sodium hydroxide buffer) corresponding with the bromide oxidation. The current density at that potential was about 5 $\mu A/cm^2$.

The background potential limit for tin dioxide in 0.3M potassium bromide at $pH = 5$ can be deduced from Fig. 2. It is clear that hydrogen evolution, as well as bromide oxidation, in the case of tin dioxide needs a higher overvoltage than in the comparable case of platinum. At a current density of 5 $\mu A/cm^2$, the cathodic and anodic potential limits are, respectively, −0.8 and 1.3V (Ag/AgCl). It follows from the same figure that the bromide/bromine redox reaction is irreversible on SnO_2. These values are different from those given by Zellmer (11), his values being −0.25 and 0.8V (SCE), respectively. The observed difference may be explained by differences in the tin dioxide surface as discussed by Yoneyama (12).

The effect of the observed very low background current level in the cathodic region more positive than −0.8V was investigated in experiments where the potential of a tin dioxide electrode in 0.3M potassium bromide solution ($pH = 5$) was maintained at, respectively, −0.5, −0.6, and −0.7V (Ag/AgCl). At −0.5V no visible changes of the electrode were observed, not even after 100 hr of electrolysis. At −0.6 and −0.7V the electrolysis resulted in a destruction of the electrode after 24 hr.

These results are in good agreement with Pourbaix diagrams yielding a decomposition potential of about −0.6V (Ag/AgCl) for tin dioxide at $pH = 5$ (13). Decomposition of tin dioxide electrodes during redox-chromic display operation has not been observed at $pH = 5$. This is confirmed by the fact that tin dioxide electrodes in 0.3M potassium bromide at $pH = 5$ exposed to 500 msec pulses between −0.9 and 0.3V (Ag/AgCl) for several days did not show any alterations, whereas in a similar experiment with Pt electrodes hydrogen evolution was observed. On the basis of the observations mentioned above, it is expected that interference of the hydrogen evolution will disturb the viologen reduction ($E \approx -0.5$V *vs.* Ag/AgCl) when platinum electrodes are used. The decomposition in the case of tin dioxide is expected to be negligible when pulsing at not too negative voltages (not less than −0.9V Ag/AgCl) and at a pH of about 5. For this rea-

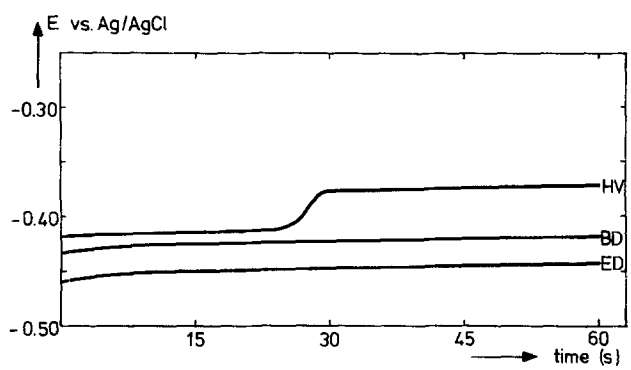


Fig. 1. The behavior of the potential E of a tin dioxide electrode covered with a viologen radical salt film as function of time. HV 10^{-2}M HV-Br, 3M KBr; BD 5×10^{-3}M BD-BF_4, 0.03M TEAB; ED 5×10^{-3}M ED-ClO_4, 10^{-2}M $LiClO_4$. The radical salt films were deposited during the cathodic sweep of a voltammogram. The total charge involved in their formation was about 1 mC/cm².

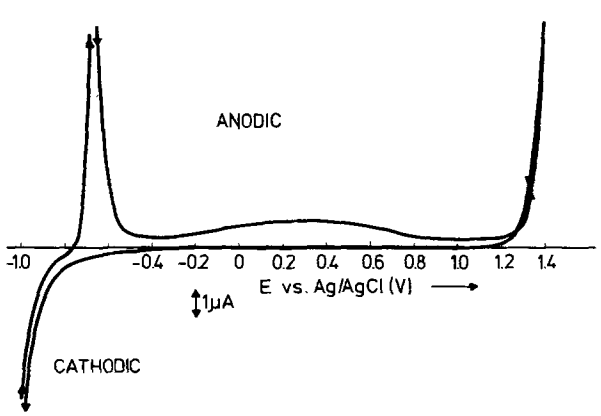


Fig. 2. Linear potential sweep voltammogram of an aqueous solution of 0.3M KBr and 10% citrate-NaOH buffer, $pH = 5$. SnO_2 electrode. Geometric electrode area, 0.2 cm². Scan speed, 0.020 V/sec.

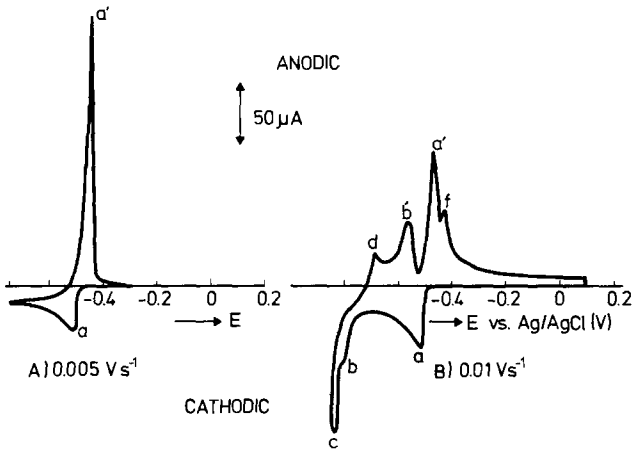


Fig. 3. Linear sweep voltammogram of 4×10^{-4}M HV-Br in an aqueous solution of 0.3M KBr. Tin dioxide electrodes. Scan speeds are indicated in the figure.

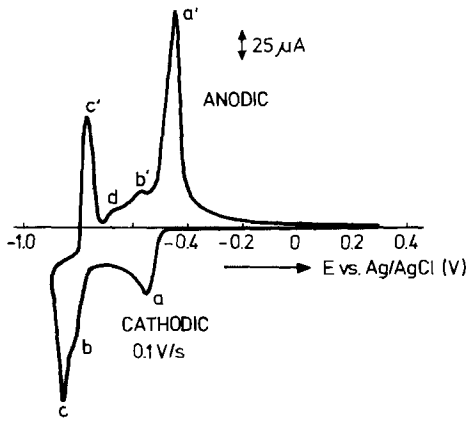


Fig. 4. Linear sweep voltammogram of 10^{-3}M HV-Br in an aqueous solution of 0.3M KBr. Tin dioxide electrode, 0.2 cm^2. Scan speed, 0.1 V/sec.

son tin dioxide was chosen as the electrode for voltammetric investigations in order to investigate its suitability as the electrode in redox-chromic displays.

Voltammetric experiments.—The voltammetric behavior of an aqueous solution of HV-Br at SnO_2 is represented in Fig. 3 and 4. Figure 3A represents the voltammetric behavior which is found when the cathodic scan limit is chosen in such a way that only the first reduction and oxidation steps occur. The result is a very steep reduction peak a at −0.51V (Ag/AgCl) together with an oxidation peak a' at −0.45V (Ag/AgCl), which shows minor tailing. The observed behavior is very similar to that found with deposition and dissolution of thin metal films (14, 15).

If the potential sweep is extended to more cathodic potentials so as to include the second reduction step, a voltammogram with more than two reduction and oxidation peaks is obtained. The number of peaks depends on experimental circumstances such as scan speed and aging time (Fig. 3B). The peaks observed in the various experiments are summarized in Table I.

With relatively fast scans (> 0.1 V/sec), a voltammogram with four main peaks (a, a', c, c') is obtained (Fig. 4). Peaks a and a' are assigned to the formation and dissolution of the viologen radical salt film. Peak c at −0.84V is due to the second reduction step, which causes the formation of a yellow brown deposit. The corresponding oxidation peak c' is usually found at about −0.75V and is not visible at relatively low scan speed, because of the reaction $A^{2+} + A + 2X^- \rightleftarrows 2AX\downarrow$. The influence of this chemical reaction can be seen very clearly when Fig. 3B and 4 are compared.

Low scan speeds (< 0.1 V/sec), however, yield a more complicated voltammogram, as shown in Fig. 3B, in which the scan was reversed at −0.9V in order to avoid hydrogen evolution. In this voltammogram, too, an extra shoulder b connected with the second step reduction can also be seen. Further, two additional peaks d and b' (at −0.69 and −0.56V, respectively) corresponding to oxidation into the radical film are observed. Finally it is clear that the oxidation of the radical salt film is accompanied by the appearance of an extra peak f at −0.42V. By varying the scan range it has been estimated that b and b' are related. No pH dependence of d and b' has been observed. Their origin might be ascribable to the oxidation of charge-transfer complexes between A and $A^{\cdot+}$. If current and scan were interrupted at −0.9V during 1 min, all oxidation peaks c', b', d disappeared completely due to the reaction $A^{2+} + A + 2X^- \rightleftarrows 2AX\downarrow$ as was confirmed by spectral investigations. In that case only a' and f are observed. The correspondence of the appearance of f due to either the second reduction step or aging is demonstrated in Fig. 5, in which a linear sweep voltammogram of HV-Br is compared with an identical voltammogram, except for the fact that, with the latter, current and scan were interrupted for 1 min at the potential of current reversal. During this interruption the potential of the radical layer changes because of aging as already shown in Fig. 1. After the aging period the reverse scan is started at the potential of that moment (−0.37V). As a result it can be seen that only the peak f corresponding to the oxidation of the aged layer is observed, while without aging the normal dissolution peak a' is seen. It should be noted that this behavior is only found with viologens that form unstable radical salt films.

Table I. Survey of the observed voltammetric peaks with HV-Br

Reduction	Fast scan (Fig. 4)	0.1 V/sec	a,b,c
Oxidation			a',b',c',d
Reduction	Slow scan (Fig. 3B	0.1 V/sec	a,b,c
Oxidation			a',b',d,f
Oxidation	(After interruption)		a',f

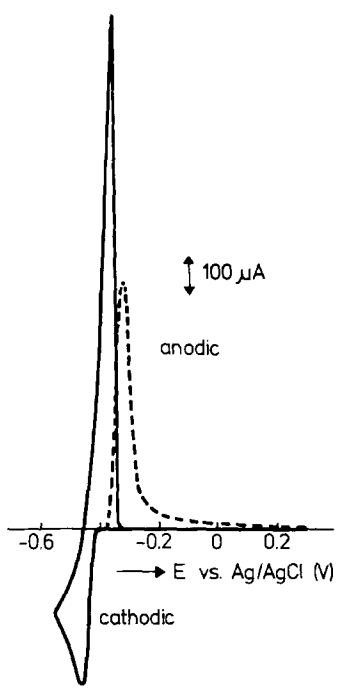


Fig. 5. Linear sweep voltammogram of 10^{-2}M HV-Br in an aqueous solution of 3M KBr. Dotted line: anodic sweep after interruption for 1 min. Geometric electrode area, 0.2 cm^2. Scan speed, 0.1 V/sec.

From microscopic observations it may be concluded that the peak f is due to the oxidation of reoriented parts of the radical salt film. This phenomenon is the subject of current investigations; results will be published elsewhere.

Since peak f shows a large tailing one can expect differences in charges involved in the cathodic (Q_c) and anodic (Q_a) scans. In order to evaluate this behavior, Q_a/Q_c of a more concentrated solution was measured as a function of the potential at which the sweep was reversed. From Fig. 6 it is obvious as a result that Q_a/Q_c of 10^{-2}M HV-Br approaches unity only if the first reduction step proceeds. These results differ from those reported by others (16), who found substantially lower values for the first reduction step. The discrepancy can be explained only by the presence of oxygen and/or impurities on the electrode surface, which, as we found, cause lower values of Q_a/Q_c. Scanning into the second reduction step region leads to the occurrence of peak f, which causes a decrease of Q_a/Q_c. An identical decrease was found after an interruption of the scan.

As already mentioned, some viologens such as ED-ClO_4 give stable films. In this respect it is interesting to look at a linear sweep voltammogram of ED-ClO_4 (Fig. 7). In this case a very simple voltammogram is obtained with only four peaks (a,a',c,c') present. The oxidation peak f is absent when scanning into the second reduction step region and also after interruption. It can be concluded that both first and second reduction steps proceed with ED-ClO_4 without complications and that aging effects are absent. The BD-BF_4 viologen voltammogram (Fig. 8) is somewhat more complicated than that of ED-ClO_4; here again a peak is observed which is believed to be due to C-T complexes. The observed influence of aging and second reduction step in terms of peak f, however, is very slight. The corresponding Q_a/Q_c of both BD-BF_4 and ED-ClO_4 is equal to unity within the experimental error, as can be seen in Fig. 6. Since above −1.0V (Ag/AgCl) hydrogen evolution was observed to have a strong influence, no data are presented for the highly cathodic potentials.

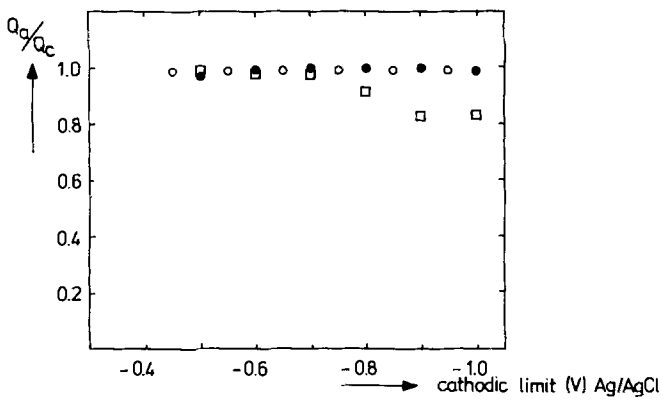


Fig. 6. Plot of Q_a/Q_c as a function of the cathodic scan limit of a linear sweep voltammogram. Q_a and Q_c are the respective charges of the anodic and cathodic parts of the scan. ○, 1.5 × 10^{-2}M BD-BF_4 in an aqueous solution of 0.03M TEAB; ●, 5 × 10^{-3}M ED-ClO_4 in an aqueous solution of 0.05M NaBr and 0.05M $NaClO_4$; □, 10^{-2}M HV-Br in an aqueous solution of 0.3M KBr. Scan speed, 0.1 V/sec; SnO_2 electrode. The anodic scan limit was 0.3V (Ag/AgCl).

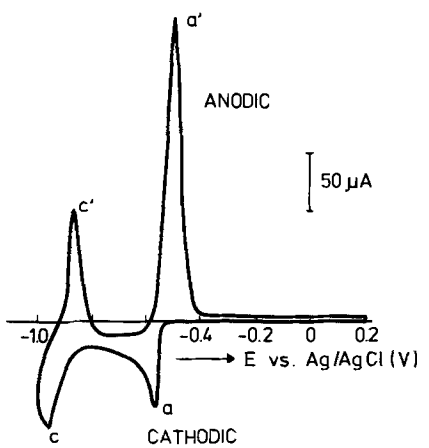


Fig. 7. Linear potential sweep voltammogram of 5 × 10^{-4}M ED-ClO_4 in an aqueous solution of 0.05M $NaClO_4$ and 0.05M NaBr. pH = 4 (10% citrate-HCl). Tin dioxide electrode, 0.2 cm^2. Scan speed, 0.1 V/sec.

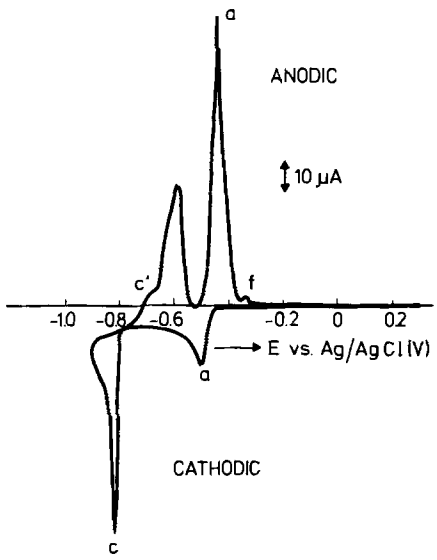


Fig. 8. Linear potential sweep voltammogram of 5 × 10^{-4}M BD-BF_4 in an aqueous solution of 0.04M TEAB. Scan speed, 0.005 V/sec. Tin dioxide electrode, 0.2 cm^2.

Conclusions

It has been shown that the oxidation behavior of viologen radical salt films is largely determined by aging effects, which were observed to be quite pronounced with HV-Br radical salt films. The same behavior can also be initiated by the occurrence of the second reduction step. As a result of aging or the occurrence of the second reduction step of HV-Br, Q_a/Q_c is less than unity. On the other hand, it was found that Q_a/Q_c equals unity if only the first reduction step of HV-Br is involved. Moreover it was shown that with modified viologens such as BD-BF_4 and ED-ClO_4, Q_a/Q_c is equal to unity within experimental error in a potential region down to −1.0V (Ag/AgCl) and with tin dioxide electrodes. It was shown that these tin dioxide electrodes should be used in preference to platinum. Especially with ED-ClO_4, aging effects were not observed. Thus it may be concluded that modified viologens are more promising materials for successful application in redox-chromic displays than HV-Br.

Manuscript submitted April 25, 1977; revised manuscript received Aug. 3, 1977. This was Paper 203 and 204 presented at the Las Vegas, Nevada, Meeting of the Society, Oct. 17-22, 1976.

Any discussion of this paper will appear in a Discussion Section to be published in the June 1978 JOURNAL. All discussions for the June 1978 Discussion Section should be submitted by Feb. 1, 1978.

Publication costs of this article were assisted by Philips Research Laboratories.

APPENDIX

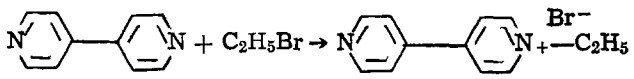
Synthesis of the Redox-Chromic Materials

1,1'-Diheptyl-4.4'-bipyridinium dibromide (HV-Br). —A mixture of 40g 4,4'-bipyridine, 200g 1-bromohep-

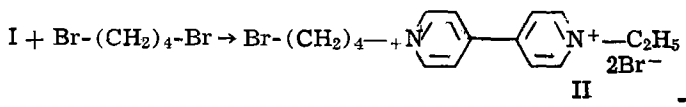
tane, and 250 ml dimethylformamide is refluxed while stirring for 3 hr. The precipitate is filtered off. Yield 93%. The crude product is purified by recrystallizations from ethanol-water and from acetonitrile.

The ^{1}H-NMR spectrum in D_2O of HV-Br relative to 2,2,3,3,- tetradeutero-3-(trimethylsilyl)-propionic acid-sodium salt was found to be: δ 0.89 ppm (t CH_3), δ 1.1-2.4 ppm (m CH_2), δ 4.79 ppm (t N-CH_2), δ 8.61 ppm (dβ-arom.-H), δ 9.18 ppm (dα-arom.-H).

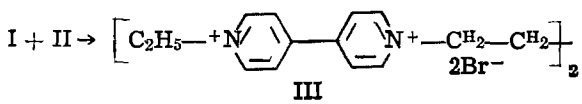
Tetramethylene bis-[4(1-ethylpyridine-4'-yl)pyridinium] perchlorate (ED-ClO_4).—The synthesis is carried out according to the following scheme



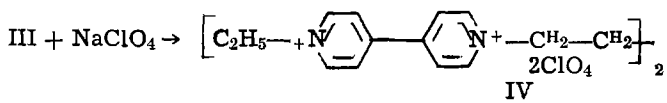
I



II



III



IV

A mixture of 100g 4,4'-bipyridine and 500 ml 1-bromoethane is kept at room temperature for 5 days. The precipitate is filtered off and washed with ether. The main impurity, 4,4'-bipyridine, is removed by extraction with toluene. The crude product contains a few percent 1,1'-diethyldipyridinium-dibromide, which is removed by extraction with acetonitrile. The diquaternized product is filtered off and after evaporation of the solvent pure I is obtained.

A mixture of 30g I, 95 ml 1,4-dibromoethane, and 250 ml acetonitrile is refluxed for 8 hr. The precipitate is collected and washed with toluene. The product II is dried *in vacuo*. Yield 97%.

34.5g I, 60g II, and 500 ml dimethylformamide is heated for 16 hr while stirring at 120°C. After cooling III is filtered off and recrystallized from ethanol-water. Yield 44%. III is converted to IV by treatment with an aqueous solution of $NaClO_4$. IV is recrystallized from water.

The ^{1}H-NMR spectrum in DMSO-D_6 of ED-ClO_4 relative to 2,2.3,3,-tetradeutero-3-(trimethylsilyl)-propionic acid-sodium salt was found to be: δ 1.64 ppm (t CH_3), δ 2.11 ppm (broad CH_2 bridge), δ 4.6-5.0 ppm (m N-CH_2), δ 8.71-8.82 ppm (two pairs of doublets arom. protons β to N), δ 9.30-9.41 ppm (two pairs of doublets arom. protons α to N).

The ^{1}NMR spectra were run on a Varian-XL100 NMR spectrometer. Anal. Calcd. for $C_{28}H_{34}N_4Cl_4O_{16}$: C, 40.79; H, 4.15; N, 6.80. Cl, 17.20; O, 31.06. Found: C, 40.78; H, 4.15; N, 6.80; Cl, 17.12; O, 31.17.

Tetramethylene bis-[4(1-benzylpyridine-4'-yl)pyridinium] tetrafluoroborate (BD-BF_4).—The synthesis of this compound was analogous to that of ED-ClO_4.

The ^{1}H-NMR spectrum in DMSO-D_6 of BD-BF_4 relative to 2,2,3,3,-tetradeutero-3-(trimethylsilyl)-propionic acid-sodium salt was found to be: δ 2.10 ppm (broad CH_2 bridge), δ 4.77 ppm (broad N-CH_2 bridge), δ 5.97 ppm (s N-CH_2-phenyl), δ 7.4-7.8 ppm (m phenyl), δ 8.75 ppm (d arom. protons β to N), δ 9.33 ppm (d arom. protons α to N-bridge side), δ 9.48 ppm (d arom. protons α to N-benzyl side).

Anal. Calcd. for $C_{38}H_{38}N_4B_4F_{16}$. C, 50.83; H, 4.27; N, 6.24; B, 4.81; F, 33.85. Found: C, 50.65; H, 4.34; N, 6.25; B, 4.20; F, 34.23.

REFERENCES

1. C. J. Schoot, J. J. Ponjeé, H. T. van Dam, R. A. van Doorn, and P. T. Bolwijn, *Appl. Phys. Lett.*, **23**, 64 (1973).
2. R. M. Elofson and R. L. Edsberg, *Can. J. Chem.*, **35**, 646 (1957).
3. W. M. Schwarz, Thesis, University of Wisconsin (1961).
4. J. Volke and V. Volková, *Coll. Czech. Chem. Comm.*, **34**, 2037 (1969).
5. T. Osa and T. Kuwana, *J. Electroanal. Chem.*, **22**, 389 (1969).
6. M. Ito and T. Kuwana, *ibid.*, **32**, 415 (1971).
7. H. T. van Dam and J. J. Ponjeé, *This Journal*, **121**, 1555 (1974).
8. J. Bruinink, "Nonemissive Electrooptic Displays," A. R. Kmetz and F. K. von Willisen, Editors, p. 201, Plenum, New York (1976).
9. A. J. Bard, *Adv. Phys. Org. Chem.*, **13**, 255 (1976).
10. R. N. Adams, "Electrochemistry at Solid Electrodes," Marcel Dekker, New York (1969).
11. D. Zellmer, Ph. D. Thesis, University of Illinois (1969).
12. H. Yoneyama and H. A. Laitinen, *J. Electroanal. Chem.*, **75**, 647 (1977).
13. E. Deltombe, N. de Zoubov, C. van Leugenhaghe, and M. Pourbaix, in "Atlas d'Equilibres Electrochimiques," M. Pourbaix, Editor, pp. 475-484, Paris (1963).
14. T. Berzins and P. Delahay, *J. Am. Chem. Soc.*, **75**, 555 (1953).
15. M. M. Nicholson, *ibid.*, **79**, 7 (1957).
16. K. Belinko, *Appl. Phys. Lett.*, **29**, 363 (1976).

Electrochemical and Electrogenerated Chemiluminescence Studies of Substituted Olefin-Cyanophenanthrene Mixed Systems

Su-Moon Park*

Department of Chemistry, The University of New Mexico, Albuquerque, New Mexico 87131

and Richard A. Caldwell

Department of Chemistry, University of Texas at Dallas, Richardson, Texas 75080

ABSTRACT

Several mixed systems containing substituted olefins such as transanethole and substituted 9-cyanophenanthrenes were investigated by electrochemical and electrogenerated chemiluminescence (ECL)) techniques. The difference in the electrochemical behaviors of similarly structured cyanophenanthrenes is explained by the substituent effects on resonance stabilization of the electrogenerated species. The ECL of mixed systems mostly consists of the shorter wavelength emission from cyanophenanthrenes and the longer wavelength emission originated from an exciplex. Energy of exciplex emissions in the acetonitrile solution is linearly correlated with the reaction enthalpy of the electron transfer reactions between radical anions of cyanophenanthrenes and cation radicals of olefins studied.

Some organic photochemical reactions, *e.g.*, (2 + 2) cycloaddition reactions, have recently been shown to occur via an exciplex intermediate, which finally leads to the products. Caldwell and his co-workers (1-5) have shown exciplex intermediacy of several (2 + 2) cycloaddition reaction systems between cyanophenanthrenes and substituted olefins, resulting in a cyclobutane structure. They (1-5) and other investigators (6-8) have been able to identify the longer wavelength emissions, which do not correspond either to the phenanthrenes or olefins, when the reaction mixture was irradiated under reaction conditions. Multiplicity, lifetimes, and other properties of this intermediate species, an exciplex, have been determined and reported by these investigators.

We thought it would be very interesting to compare these photochemical observations with electrogenerated chemiluminescence (ECL) results of the corresponding photochemical systems, since the exciplex has been shown to be an intermediate species in the light-producing process of ECL (9-11).

Electrogenerated chemiluminescence is a process in which the energetic electron transfer reaction leads to the excited states (12-19). The reactants of the electron transfer reactions of interests are generated electrochemically at the anode or cathode, *i.e.*

$$D \rightarrow D^+ + e \quad \text{at the anode}$$

and [1]

$$A + e \rightarrow A^{\cdot -} \quad \text{at the cathode}$$

The resultant radical species react to give the excited state of either D or A (triplet or singlet) depending on the energetics involved in reaction [1]

$$D^{\cdot +} + A^{\cdot -} \rightarrow D^* + A,\ D + A^*,\ \text{or}\ A^* + D^* \quad [2]$$

In the light-producing step of reaction [2], an exciplex was shown to be involved, as already pointed out, which decomposes to an individual excited state, if the energy contained in the solvent-separated ion pair is greater than the one of the individual excited states (9-11), *i.e.*

$$A^{\cdot -} + D^{\cdot +} \rightarrow \underset{\text{exciplex}}{(A^- D^+)^*} \rightarrow A^* + D \text{ or } A + D^* \quad [3]$$

Thus, one observes the emitting excited states of either A or D. or both, plus an exciplex band, which does not correspond to A or D, in some cases. There are, however, many systems where the exciplex band is not observed.

In this paper, we describe experiments where the substituted olefins are used as D molecules, whereas substituted cyanophenanthrenes are used for A molecules. Results indicate that ECL techniques can be used for studying such reactions as is demonstrated later. ECL systems studied are those containing E-3,4-dianisyl-3-hexene (DAH), dimethoxystyrene (DMS), β-anisyl-iso-butylene (β-AIB), and anethole as olefinic donor molecules, and 9-cyanophenanthrene (9-CP), 3,9-dicyanophenanthrene (3,9-DCP), 3,10-dicyanophenanthrene (3,10-DCP), 3-methoxy-10-cyanophenanthrene (3,10-MCP), 3-methoxy-9-cyanophenanthrene (3,9-MCP) as substituted cyanophenanthrene acceptor molecules. Structures of these compounds are shown in Fig. 1.

Experimental

Cyanophenanthrenes and olefins were synthesized and purified in the laboratory of one of the authors (R.A.C.). Eastman Organic's ethanol recrystallized naphthalene was used after triple sublimation. Tri-p-

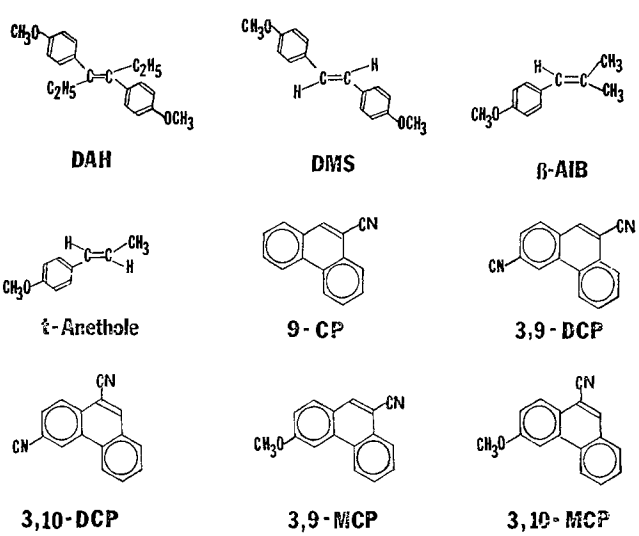


Fig. 1. Compounds used in this study. See text for abbreviations

* Electrochemical Society Active Member.

Key words: electrogenerated chemiluminescence, excited state, exciplex, cycloaddition.

tolylamine (TPTA) was kindly provided by Professor Ralph N. Adams of the University of Kansas, and used as received. Polarographic grade tetra-n-butylammonium perchlorate (TBAP) of Southwestern Analytical Chemicals, Inc., Austin, Texas, was used as a supporting electrolyte after drying in a vacuum desiccator at 120°C for more than 24 hr. Matheson, Coleman, and Bell's spectrograde acetonitrile (ACN) and benzonitrile (BzCN) were used as solvents after drying and purification according to the procedures described previously (9).

Solutions were prepared by weighing appropriate amounts of the donor and acceptor molecules into the ECL cell, followed by addition of solvents in a dry atmosphere glove box, but the measurements were made outside the box. The concentration of TBAP was always approximately 0.1*M* in all measurements.

Cyclic voltammograms were recorded with a Princeton Applied Research (PAR) Model 170 electrochemistry system, using either a three-electrode ECL cell of conventional design or a cell designed for the magnetic field measurements described by Faulkner *et al.* (20) in cases where the redox potentials were measured against the aqueous saturated calomel electrode (SCE). The conventional three wire electrode cell was used for the ECL measurements (21). ECL was generated by applying symmetrical square waves generated by the PAR 170 and detected with an Aminco-Bowman spectrophotofluorometer employing a Hammamatsu TV Corporation R-456 photomultiplier tube.

Results and Discussion

Electrochemical and ECL results obtained are summarized in Tables I and II, and typical results are reproduced in Fig. 2-4. Substituted cyanophenanthrenes are readily reduced as shown in Table I, but they are not oxidized within +2.0V *vs.* SCE. Substituted olefins, on the other hand, are oxidized from about +1.0 to +1.4V against SCE but are not reduced within the potential limit of interest. ECL's are observed from all systems studied in acetonitrile and benzonitrile solutions, as shown in Table II. More detailed discussions on the results follow.

Table I. Electrochemical data

Compounds‡	$E_{p,ox.}$* (V *vs.* SCE)	$E_{p,red.}$* (V)	i_{pa}/i_{pc} or i_{pc}/i_{pa}†	ΔE (mV)
DAH*	1.20, 1.28	n.r.**	0.74	~240
DMS	1.03, 1.37	n.r.	0.65	75
Anethole	1.28	n.r.	~0	—
β AIB	1.16	n.r.	0.58	~225
9-CP	n.o.**	−1.92 −2.66	1.03, 0.55	57
3,10-MCP	n.o.	−2.00, −2.72	1.00	62
3,9-MCP	n.o.	−2.05, −2.7	0.49	~180
3,10-DCP	n.o.	−1.57 —	0.47	~140
3,9-DCP	n.o.	−1.51, −2.11, −2.6	1.08, ~1.0	60, ~102

* Oxidation potentials of these compounds were measured against a Ag wire pseudoreference electrode and calibrated against an internal reference, TPTA ($E_{p,o}$ = 0.84 V *vs.* SCE). Reduction potentials were measured against an aqueous saturated calomel electrode (SCE).

** n.r. = not reduced, n.o. = not oxidized, within the potential of interest.

† i_{pa}/i_{pc} for reduction waves, i_{pc}/i_{pa} for oxidation waves. This parameter and ΔE were measured for the first and second waves where possible.

‡ For nomenclature of compounds, see Fig. 1 and text.

Table II. Emission in ECL

No.	Systems	ΔH* (eV)	ECL emissions, $h\nu_{max}$ (nm) In ACN	In BzCN
1	9-CP*-DAH**	2.97	389, 520	400,† 510
2	9-CP-DMS	2.79	379, 530	378, 509
3	9-CP-β-AIB	2.93	382. 520	386, 486
4	9-CP-anethole	3.04	379, —***	380, 470
5	3,9-DCP-DAH	2.55	390, 587	‡
6	3,10-DCP-DAH	2.60	382, 570	‡
7	3,9-MCP-DAH	3.08	386, 520	‡
8	3,10-MCP-DAH	3.04	381, 528	‡
9	9-CP-TPTA	2.57	379, 583	384, 554
10	Naphthalene-DAH	3.67	—, 408	‡
11	3,9-DCP-β-AIB	2.51	395, 568	***

* Triplet energy level of 9-CP is 2.51 eV. Singlet energy level of 9-CP is about 3.3 eV.

** Fluorescence maximum of DAH in cyclohexane was: 0-0 band = 314 nm, 0-1 band = 338 nm (maximum intensity).

*** Exciplex emission was observed from this system but the emission peak could not be determined from the ECL spectrum.

† This was on the shoulder of exciplex emission and the correct wavelength could not be measured.

‡ Experiments were not performed in benzonitrile solution.

Electrochemical results.—Electrochemical data for oxidation and reduction potentials in acetonitrile as a solvent using 0.1*M* TBAP as a supporting electrolyte are collected in Table I.

Cyclic voltammetry of these compounds shows that the cation radicals generated upon oxidation at the platinum electrode are generally unstable, as evidenced by the absence of reversal current (Fig. 2). This is readily expected from the structure of the compounds due to the lack of stabilization through delocalization and resonance of the positive charge of oxidized product (cation radical). Losing a proton after the compound is oxidized will lead to the free radical, resulting in dimer or polymer formation. Two olefins, *i.e.*, DAH and DMS, show some stability as

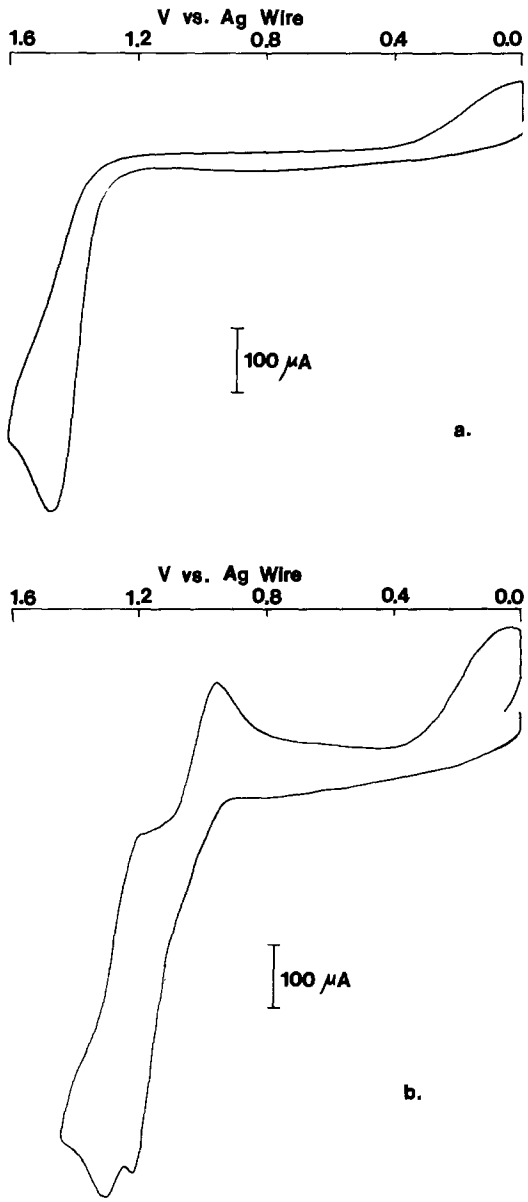
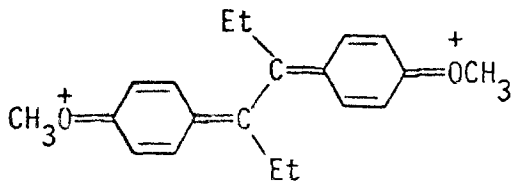


Fig. 2. Oxidation of olefins; (a) cyclic voltammogram of trans-anethole (2.2 mmole) and (b) cyclic voltammogram of DAH (1.2 mmole) in ACN at the Pt wire electrode. Scan rates were 200 mV/sec.

shown in Fig. 2. The first and second oxidation waves of DAH are very close, because the dication produced may be stabilized by the following quinonoid structure through resonance



and this is probably why even the dication of DAH shows stability on the reversal scan of the cyclic voltammogram (Fig. 2b). The second oxidation wave could have been that of the product derived from the radical cation. Most of the olefins except DAH that were used in this study are expected to polymerize (or dimerize) after losing protons upon oxidation. DAH is expected to be more stable, since it does not have a proton to lose, because of steric hindrance in forming the dimer. Detailed studies on the electrode processes of these compounds were not performed in this report.

The anion radicals of substituted cyanophenanthrenes are generally stable with the exception of 3,10-DCP and 3,9-MCP. Anion radicals of 9-CP and 3,10-MCP are stable, while their dianions are not stable, as shown in Fig. 3. 3,9-DCP forms an extremely stable anion radical at −1.51V *vs.* SCE and a stable dianion at −2.11V *vs.* SCE upon further reduction. This is further reduced at −2.6V *vs.* SCE, probably with formation of an unstable trianion radical. These compounds are not oxidized up to +2.0V *vs.* SCE in acetonitrile.

This interesting behavior (stability or instability of anion radicals) shown by this set of compounds can be explained by resonance stabilization-destabilization. In 3,9-DCP, where even the dianion is stable, one sees a high electron affinity due to two strongly electron-withdrawing cyano groups, which are located in such a way that the resonance structure stabilizes the anion radical produced by the addition of an electron, *i.e.*, the added electron is "shared" by two strongly electrophilic cyano groups by resonating structures. Since the electron is right on the electron-deficient center, the anion radical is expected to be stabilized. In 3,10-DCP, however, the corresponding resonance structure is such that an electron added on one cyanide group exerts a strong repulsion through resonance against the other cyanide group. This repulsion should contribute toward the instability of the radical anion produced. In 3,9-MCP and 3,10-MCP, the electron-donating methoxy group plays an impotrant role in deciding the electrochemical behavior. The partial charge generated through the resonance by a strongly electron-donating methoxy group is located such that either a strong repulsion (3,9-MCP) or no significant effect (3,10-MCP) will result from the addition of an electron to the electronegative cyano group of the molecule. Thus, in 3,10-MCP the addition of one electron to the cyano group does not seem to be affected very much by the presence of the methoxy group, whereas in 3,9-MCP two negative charges should be very repulsive after another electron has been added.

ECL results.—Upon generating both cation and anion radicals by applying square wave pulses, ECL spectra of the systems listed in Table II were obtained. ECL spectra obtained from 9-CP-β-AIB and 9-CP-DAH systems are shown in Fig. 4(a) and (b). Available system characteristics, *i.e.*, $\Delta H°$ for the homogeneous electron transfer reaction [3], are calculated from electrochemical data listed in Table I by the equation (20)

$$-\Delta H°\,(\text{eV}) = E_{p,ox} - E_{p,red.} - 0.16\,(\text{eV}) \qquad [4]$$

where $E_{p,ox}$ is the cyclic voltammetric peak potential for the oxidation of olefins and $E_{p,red.}$ is the reduction potential of cyanophenanthrenes. These are listed in Table II.

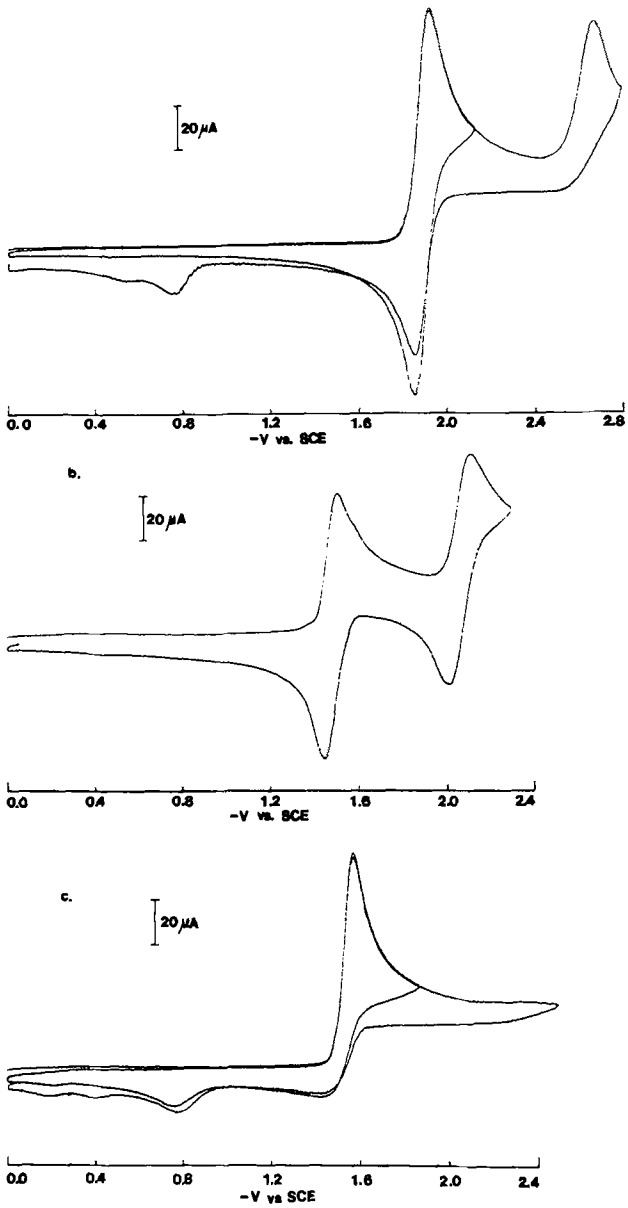


Fig. 3. Reduction of cyanophenanthrenes; cyclic voltammogram of (a) 9-CP (0.97 mmole), (b) 3,9-DCP (0.85 mmole), and (c) 3,10-DCP (0.91 mmole) in ACN with a scan rate of 200 mV/sec at a platinum wire electrode.

In all spectra shown in Fig. 4 and listed in Table II, the ECL spectra consists of monomer emissions derived from cyanophenanthrenes and longer wavelength emissions. The ECL intensities of almost all systems studied here in ACN decayed fairly rapidly. This is due to the instability of cation radicals produced upon oxidation. In most cases, a slow pulsation gives a side product, which blocks the working electrode and reduces the available electrode surface area, resulting in reduction in the number of photons (light) emitted. Also, after fast pulsation the ECL intensity dropped and it could not be restored on standing for some time or scanning only one direction. In several cases, the deteriorated electrode surface could be restored by scanning to one direction. This experimental observation indicates that a decomposition product forms on the working electrode, resulting in film formation on the surface of the electrode. These phenomena, however, can be avoided by pulsing the electrode slowly (1 sec pulse duration is usually satisfactory).

As has already been suggested above, the shorter wavelength emission of all ECL spectra is undoubtedly from the cyanophenanthrenes, which is readily identified by the comparison with fluorescence spectra of

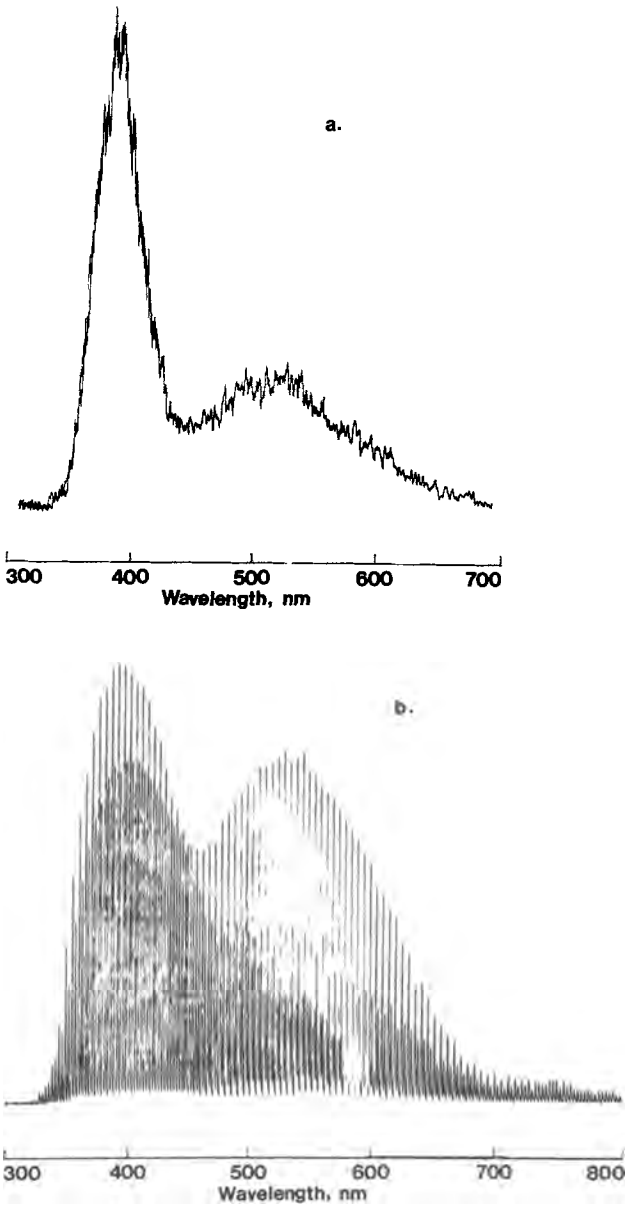


Fig. 4. ECL spectrum of (a) p-CP-β-AlB system in ACN; solution contained 1.9 mmole 9-CP and 1.5 mmole β-AlB; pulse duration was 50 msec, and (b) 9-CP-DAH system in ACN; solution contained 0.96 mmole 9-CP and 1.2 mmole DAH; pulse duration, 1 sec.

corresponding phenanthrenes. The possibility of having emissions from olefins is easily ruled out, since their excitation energy is high (see footnote **, Table II). Longer wavelength emission of these ECL spectra is assigned to be an exciplex for the following reasons.

Since the cation radicals of these systems are generally unstable in almost all cases, one has a good chance of having emissions from decomposition product of electrolyzed solution, which could have been excited by energy transfer from an excited cyanophenanthrene molecule produced by homogeneous electron transfer reaction (22). To see whether or not the luminescent products are being accumulated during the ECL experiment, a solution containing 1.3 m*M* 3,9-DCP and 2.2 m*M* β-AlB in 3.0 ml (system 11 in Table II) was pulsed for 6 hr with a frequency of 10 Hz between the first reduction potential of 3,9-DCP and the oxidation potential of β-AlB, and no detectable luminescent product was observed by the spectrophotofluorometer. Cyclic voltammograms recorded after the pulsation indicate that the concentration of β-AlB was considerably reduced, in that the peak current fell from 590 to 0.446 μA, but there were no new oxidation or reduction waves observed within the potential range of interest. Indeed, should the longer wavelength emission be originated from the decomposition products, one must observe them at the same wavelengths from systems containing the common donor or acceptor molecules, *e.g.*, from systems 3 and 11, or 1 and 8, which is not the case here. For the above system, the ECL spectrum remained constant, independent of the pulse frequency. Intensity, however, was a function of the pulse frequency.

In order to see the solvent effect on the longer wavelength bands, experiments on several systems were performed in benzonitrile. The results are summarized in Table II and show that most of the longer wavelength emission is blue-shifted by changing the solvent from acetonitrile, while the shorter wavelength emission is not shifted. The ratio of the intensity of the longer wavelength emission to that of the monomer emission was increased upon changing to the less polar solvent. Experiments in a solvent of a very low dielectric constant such as THF could not be done, because the anodic background appeared before the olefins were oxidized. With the above results alone, one can extrapolate the predicted result in a low dielectric constant solvent. That is, the large spectral shift upon changing solvent from ACN ($\epsilon = 37.5$) to BzCN ($\epsilon = 25.5$) reflects the charge-transfer nature of the spectrum observed and the fact that the relative intensity of longer wavelength emission increases in lower dielectric solvent medium is in agreement with the property of an exciplex (2, 3, 9, 10, 23). More experiments along this line are desirable but no solvents suitable for this study were available due to the limited anodic background potentials. More extensive description of solvent effects on exciplex emissions in ECL is found in the literature (9, 10).

One more convincing piece of evidence is that the energy of exciplex is related linearly with the $\Delta H°$ values listed in Table II. This plot is shown in Fig. 5. To interpret this plot, we start with the equation (23, 24)

$$E(A^-D^+) = IP_D - EA_A - C + \Delta H_s(A^-D^+) - \delta E_{FC} \quad [5]$$

where IP_D is the ionization potential of the donor, EA_A is the electron affinity of the acceptor, C is the coulombic energy, $\Delta H_s(A^-D^+)$ is the enthalpy of solvation of the exciplex, and δE_{FC} is the energy difference between the product molecules after the Frank-Condon transition and their equilibrium states. The IP_D and EA_A terms can be replaced with electrode potentials in such a way that

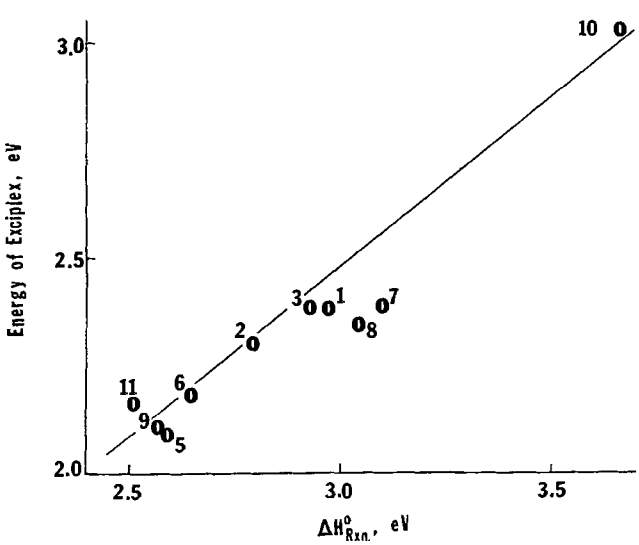


Fig. 5. Relationship between energy of exciplexes and $\Delta H°$. See Table II for names of compounds.

$$IP_D = kE_{p,ox.} + K'$$

$$EA_A = k'E_{p,red.} + K''$$

where k, k', K', and K'' are the constants. Assuming that $k = k' = 1.0$, we can rewrite Eq. [5] as follows

$$E(A^-D^+) = \Delta H^\circ + K$$

where K combines all constant terms derived from relations of ionization potential and electron affinity with electrode potentials plus other residual terms in Eq. [5]. We, therefore, expect the energy of exciplex emissions to be related linearly with reaction enthalpy of the systems from the above equation. The slope should be unity, since we have assumed $k = k' = 1$. The slope here was 0.78, excluding points 7 and 8. Considering that some of the electrochemical data are from irreversible electrode processes, the plot has a good correlation. An interesting fact found in Fig. 5 is that two systems containing compounds 3,9-MCP and 3,10-MCP show deviations from linearity. This might be attributed to the strongly electron-donating methoxy group on the phenanthrene, which can change the electron affinity property.

Systems 9 and 10 were studied and listed in Table II because of their proven ability to form an exciplex with many other organic counterions in ECL (9, 10, 26, 27).

Finally, the possibility that the longer wavelength emission might have been originated from an excimer, as a referee pointed out, may be ruled out by the fact that the bands have a charge-transfer character, as discussed above, and that the excimer bands were not observed by photoexcitation experiments in the benzene solution.

Because the reaction enthalpy ($-\Delta H^\circ$) of the systems are mostly lower than the singlet excited energy level of phenanthrenes, the emissive singlet excited states of monomers are probably produced through a triplet-triplet annihilation (TTA) mechanism (20, 25), although there is not clear-cut evidence for this. The triplets should be generated from decomposition of the exciplex as indicated in reaction [3]. In several systems, one can assume that thermal excitation from the cation-anion reaction potential surface to the singlet excited-state phenanthrene molecules can occur (26, 27).

The exciplex is thought to be formed directly from cation and anion radicals (9, 10). A triplet-quenching route for the formation of exciplex is very questionable, because the triplet population of both phenanthrenes and olefins is expected to be very low. While exciplex emission was observed from most systems described here in benzene solutions by the photoexcitation methods (1-8, 28), it was not observed in ACN solutions, probably because of the high dielectric constant of the medium. This indicates again that the direct formation of exciplexes by the ionic recombination reaction according to reaction [3] is more efficient than by photoexcitation. Observations of exciplex emissions in the polar medium by ECL techniques have been reported by several authors (9-11). From these experimental observations, the exciplex is considered to be formed directly from electrogenerated ions. In summary, we have

$$\dot{R}^- + \dot{R'}^+ \rightarrow {}^3R^* + R' \quad \text{or} \quad R + {}^3R'^*$$

$${}^3R^* + {}^3R^* \rightarrow {}^1R^* + R$$

$${}^1R^* \rightarrow R + h\nu$$

and $${}^3R'^* \rightarrow \text{photochemical product (?)} \qquad [7]$$

$$\dot{R}^- + \dot{R'}^+ \rightarrow {}^1(R^-R'^+)^*$$

$${}^1(R^-R'^+)^* \rightarrow R + R' + h\nu$$

where R = phenanthrenes and R' = olefins. Although production of the triplet excited state of olefin is possible, the yield should be very low due to the short lifetime of the radical cation produced at the electrode surface and, therefore, the efficiency of triplet-triplet annihilation should be low. Further, most of the triplet excited states of olefins, if there are any, are expected to undergo a photochemical reaction instead of emission through TTA (29).

In conclusion, ECL results also indicate that the exciplex is an intermediate species in (2 + 2) cycloaddition reaction systems studied here. There are, however, a few difficulties encountered in the electrochemical techniques. Solvent polarity, which is required for the electrical conductivity, prevents the reaction intermediate, *i.e.*, an exciplex, from proceeding toward the photochemical product, since the exciplex will be dissociated into the solvent-separated ion pair, which subsequently collapse to some other products. To support this argument, we should mention that most of the photochemical products were obtained in benzene solutions by photoexcitation but not in acetonitrile solutions (1-7, 28). The electrochemical products will, therefore, most probably be the ones derived from the radical species, although the transient exciplex emission can be observed by ECL techniques. The stability of the radical species gives an additional problem. The radical cation obtained at the electrode surface by oxidation of olefinic compounds is very unstable and decays to other products rapidly as shown by the absence of the reversal current in the cyclic voltammograms in Fig. 2. The products could be the ones derived from the free radical after losing a proton. Indeed, no detectable photochemical products were observed in the alternating current electrolysis. Thin layer chromatographic methods aided by the u.v.-viewing equipment were used to detect the products. Yet the ECL technique is an excellent alternative for studying some photochemical processes as demonstrated here.

Systems where the stable cation radical can be obtained from olefins, if available, can provide a good example for the product analysis, provided the steric hindrance is not severe. Further studies on such systems are in progress in our laboratory.

Acknowledgment

Grateful acknowledgement is made to Professor Allen J. Bard of the University of Texas at Austin, who made this work possible. This work was supported by grants from the Army Research Office-Durham to Professor Bard. This work was performed at the University of Texas at Austin, Austin, Texas 78712.

Manuscript submitted June 17, 1977; revised manuscript received Aug. 10, 1977.

Any discussion of this paper will appear in a Discussion Section to be published in the June 1978 JOURNAL. All discussions for the June 1978 Discussion Section should be submitted by Feb. 1, 1978.

Publication costs of this article were assisted by the University of New Mexico.

REFERENCES

1. R. A. Caldwell and L. Smith, *J. Am. Chem. Soc.*, **96**, 2994 (1974).
2. D. Creed and R. A. Caldwell, *ibid.*, **96**, 7369 (1974).
3. R. A. Caldwell, D. Creed, and H. Ohta, *ibid.*, **97**, 3246 (1976).
4. D. Creed, P. H. Wine, R. A. Caldwell, and L. A. Melton, *ibid.*, **98**, 621 (1976).
5. H. Ohta, D. Creed, P. H. Wine, R. A. Caldwell, and L. A. Melton, *ibid.*, **98**, 2002 (1976).
6. C. Pac, T. Sugioka, and H. Sakurai, *Chem. Lett.*, **39**, 667 (1972).
7. C. Pac, T. Sugioka, K. Mizno, and H. Sakurai, *Bull. Chem. Soc., Jpn.*, **94**, 1406 (1972).
8. K. Mizuno, C. Pac, and H. Sakurai, *J. Am. Chem. Soc.*, **96**, 2993 (1974).
9. S.-M. Park and A. J. Bard, *ibid.*, **97**, 2978 (1975).
10. A. J. Bard and S.-M. Park, in "The Exciplex," M. Gordon and W. R. Ware, Editors, Academic Press, New York (1975).
11. H. Tachikawa and L. R. Faulkner, *J. Am. Chem. Soc.*, **98**, 5569 (1976).
12. T. Kuwana, in "Electroanalytical Chemistry," Vol. 1, A. J. Bard, Editor, chap. 3, Marcel Dekker,

New York (1966).
13. A. J. Bard, K. S. V. Santhanam, S. A. Cruser and L. R. Faulkner, in "Fluorescence," G. G. Guilbault, Editor, chap. 14, Marcel Dekker, New York, (1967).
14. A. Zweig, *Adv. Photochem.*, **6**, 425 (1968).
15. E. A. Chandross, *Trans. N.Y. Acad. Sci., Ser. 2*, **31**, 571 (1969).
16. D. M. Hercules, *Accounts Chem. Res.*, **2**, 301 (1969).
17. D. M. Hercules, in "Physical Methods of Organic Chemistry," A. Weissberger and B. Rossiter, Editors, 4th ed., Part II, Academic Press, New York (1971).
18. A. J. Bard and L. R. Faulkner, in "Electroanalytical Chemistry," Vol. 10, A. J. Bard, Editor, Marcel Dekker, New York (1976).
19. L. R. Faulkner, in "MTP Series in Physical Chemistry-Chemical Kinetics," D. R. Herschbach, Editor, Medical and Technical Publishing Co., Ltd., Lancaster, England, In press (1976).
20. L. R. Faulkner, H. Tachikawa, and A. J. Bard, *J. Am. Chem. Soc.*, **94**, 691 (1972).
21. N. E. Tokel, C. P. Keszthelyi, and A. J. Bard, *ibid.*, **94**, 487 (1972).
22. L. R. Faulkner and A. J. Bard, *ibid.*, **90**, 6284 (1968).
23. R. S. Mulliken and W. B. Person, "Molecular Complexes—A Lecture and Reprint Volume," Wiley-Interscience, New York (1969) and references therein.
24. H. Knibe, D. Rehm, and A. Weller, *Z. Phys. Chem. (N. F.)* **56**, 95 (1967).
25. D. J. Freed and L. R. Faulkner, *J. Am. Chem. Soc.*, **94**, 4790 (1972).
26. A. Weller and K. Zachariasse, *J. Chem. Phys.*, **46**, 4984 (1967).
27. A. Weller and K. Zachariasse, *Chem. Phys. Lett.*, **10**, 197, 249, 590 (1971).
28. R. A. Caldwell, Unpublished results.
29. See, for example, (a) D. J. Cram and G. S. Hammond, "Organic Chemistry," 2nd ed., pp. 744-776, McGraw-Hill, Book Co., New York (1964); (b) G. S. Hammond, N. J. Turro, and R. S. H. Liu, *J. Org. Chem.*, **28**, 3297 (1963).

Radially Dependent Convective Warburg Problem for a Rotating Disk

Peter Appel and John Newman*

Materials and Molecular Research Division, Lawrence Berkeley Laboratory, and Department of Chemical Engineering, University of California, Berkeley, California 94720

ABSTRACT

The oscillating concentration distribution of a reacting species in excess supporting electrolyte is calculated for a rotating disk system where a step change in the amplitude of the concentration fluctuation at the surface of the disk occurs at an arbitrary distance from the center of the disk. The response of a product species and of the supporting electrolyte to this step change is presented also.

Analysis of the current response of an electrochemical cell to an applied oscillating potential requires knowledge of the interplay of many factors. In addition to the faradaic impedance of the electrode reaction in parallel with the double-layer capacity, it was found necessary to describe concentration variations and the transient concentration overpotential. In the original Warburg problem of 1899, the diffusion layer was taken to be stagnant and one dimensional, and the surface concentration was found to lag behind the current by 45 degrees.

A finite thickness of the stagnant diffusion layer gives an approximate account of convection. On the other hand, Levart and Schuhmann (1) used the velocity profile of a rotating disk to calculate the concentration impedance, and later they extended the calculation to include homogeneous, first-order chemical reactions by means of a series expansion in $Sc^{-1/3}$ and a dimensionless parameter involving reaction kinetics and the oscillation frequency (2). This expansion, valid for high frequencies and any practical Schmidt number, is shown by these authors (3) to include as a special case the expansion of Homsy and Newman (4), valid for large Schmidt numbers and high frequencies.

However, the nonuniform ohmic potential drop in the solution leads to an inherently nonuniform current distribution (5), and this should be accentuated under alternating-current conditions (6). Our aim is to solve this problem for the rotating disk system, but in this paper we report only how a prescribed distribution of concentration variations at the surface influences the concentration gradients normal to the surface of the disk. In a subsequent paper, it will be necessary to show how this element of the problem interacts with the potential distribution in the bulk of the solution, the double-layer response to changes in composition and potential, and the reaction kinetics to produce the over-all impedance behavior of the disk electrode.

This decomposition of a complex problem into simpler parts is possible because the differential equations describing the concentration profiles are linear. These partial differential equations can thus be solved for a standard boundary condition where the concentration of one of the species makes a step change at a specified position on the surface. Superposition (7) of such standard solutions then permits one to calculate the normal gradients for an arbitrary surface concentration distribution, without solving repeatedly the partial differential equations.

Because of the complexity of the diffusion-layer equations for the alternating-current case, the bulk of this paper deals with the development and results for these standard solutions. The superposition integrals needed for the subsequent calculation of the impedance are stated toward the end of the paper (see Eq. [31] and [32]).

Deslouis *et al.* (8) investigated experimentally the frequency dispersion of a rotating disk, operated below the limiting current. The reaction used was the reduction of ferricyanide in excess supporting electrolyte. Their results are in surprisingly good agreement with the theoretical results of Levart and Schuhmann in view of our finding that both the oscillating current distribution (9) and the time-average current distri-

* Electrochemical Society Active Member.
Key words: supporting electrolyte, impedance, adsorption, alternating current, current distribution, effect of migration.

bution for this reaction (10) below the limiting current are nonuniform on the surface of the disk. Also, the concentration fluctuations of the product (ferrocyanide) influence the concentration overpotential to the same extent as the reactant [see Newman (11) Chapter 20].

Finally, the change in the double-layer capacity is caused by the fluctuations in the potential and the fluctuations of all ionic species in the solution just outside the double layer—including the supporting electrolyte. The latter fluctuations are caused by the influence of migration on the supporting electrolyte and the condition of electroneutrality outside the double layer. Therefore, we have included the effect of the supporting electrolyte in our calculations.

Mathematical Formulation

In our treatment we assume constant transport properties of the ionic species and neglect the influence of migration on the minor, reacting species. In addition, the cation of the supporting electrolyte is also the cation of the reacting species. This situation arises, for instance, if we reduce sodium ferricyanide to sodium ferrocyanide in excess sodium fluoride.

Since all transport equations used are linear, we may separate the equations into a time-dependent and a time-independent part. The time-independent part has been treated before, and since all time dependent quantities fluctuate with a frequency ω, we may write

$$\Delta c_i = \mathrm{Re}\{\tilde{c}_i \exp(j\omega t)\} \quad [1]$$

where Re denotes the real part of the expression and

$$\tilde{c}_i = |\Delta c_i(r,y)| \exp[j\phi(r,y)] \quad [2]$$

Δc_i is the local magnitude and ϕ, the phase angle of the oscillating concentration. Radial diffusion is small compared to radial convection, so that the conservation equation in cylindrical coordinates for the minor species becomes

$$j\omega\tilde{c}_i + v_r\frac{\partial\tilde{c}_i}{\partial r} + v_y\frac{\partial\tilde{c}_i}{\partial y} = D_i\frac{\partial^2\tilde{c}_i}{\partial y^2} \quad [3]$$

with the boundary conditions

$$\tilde{c}_i = 0 \text{ at } y = 0,\ r < r' \quad [4]$$

$$\tilde{c}_i = 1 \text{ at } y = 0,\ r \geq r' \quad [5]$$

$$\tilde{c}_i \to 0 \text{ as } y \to \infty \quad [6]$$

For high Schmidt numbers we may use the expression for the velocity distribution close to the disk surface. If we introduce subsequently the dimensionless variables

$$x = \left(\frac{r^3 - r'^3}{r^3}\right)^{1/3} \quad [7]$$

$$\eta_i = y\left(\frac{a\nu}{3D_i}\right)^{1/3}\left(\frac{\Omega}{\nu}\right)^{1/2} \Big/ x \quad [8]$$

the conservation equation becomes

$$\frac{\partial^2\tilde{c}_i}{\partial\eta_i^2} + 3\eta_i^2\frac{\partial\tilde{c}_i}{\partial\eta_i} = jK_ix^2\tilde{c}_i + 3\eta_ix(1-x^3)\frac{\partial\tilde{c}_i}{\partial x} \quad [9]$$

where K_i is a dimensionless frequency, given by

$$K_i = \frac{\omega}{\Omega}\mathrm{Sc}_i^{1/3}\left(\frac{3}{a}\right)^{2/3} \quad [10]$$

In this new coordinate system, the boundary conditions given by Eq. [4]-[6] are transformed into

$$\tilde{c}_i = 1 \text{ at } \eta_i = 0 \quad [11]$$

$$\tilde{c}_i \to 0 \text{ as } \eta_i \to \infty \quad [12]$$

$$\tilde{c}_i = F_0(\eta_i) \text{ at } x = 0 \quad [13]$$

The function $F_0(\eta_i)$ is obtained by solving Eq. [9] at $x = 0$ with boundary conditions [11] and [12]. The result is

$$F_0(\eta_i) = \frac{1}{\Gamma(4/3)}\int_{\eta_i}^{\infty} e^{-z^3}dz \quad [14]$$

The finite-difference form of Eq. [9] has to take into account the behavior of $\tilde{c}_i$ near $x = 0$ since this is a singular point of this equation. Therefore, an asymptotic solution was sought for small values of x. This solution also serves as a check on the values obtained numerically. For this purpose, we expand $\tilde{c}_i$ in a power series in x

$$\tilde{c}_i(\eta_i, x) = F_0(\eta_i) + F_1(\eta_i)x^m + F_2(\eta_i)x^n + O(x^p) \quad [15]$$

Substitution of this expression into Eq. [9] gives a set of coupled ordinary differential equations, and in addition we find that $m = 2$, $n = 4$, and $p = 5$. All these equations for $F_k(\eta_i)$, where $k > 0$, are subject to the boundary conditions

$$F_k = 0 \text{ at } \eta_i = 0,\ F_k \to 0 \text{ as } \eta_i \to \infty \quad [16]$$

since $\tilde{c}_i$ evaluated from the series expansion must also satisfy boundary conditions [11]-[13]. The equation for F_1 is

$$\frac{d^2F_1}{d\eta_i^2} + 3\eta_i^2\frac{dF_1}{d\eta_i} - \eta_iF_1 = jK_iF_0 \quad [17]$$

The solution to this equation satisfying boundary conditions [16] is

$$F_1 = \frac{jK_i}{2\Gamma(4/3)}\eta_i^2\int_{\eta_i}^{\infty} e^{-z^3}dz - \frac{jK_i}{6\Gamma(4/3)}e^{-\eta_i^3} + \frac{2jK_i}{6(\Gamma(4/3))^2}\int_0^1 X\int_{\eta_i/(1-X^3)^{1/3}}^{\infty} e^{-z^3}dz\,dX \quad [18]$$

The differential equation for F_2 is

$$\frac{d^2F_2}{d\eta_i^2} + 3\eta_i^2\frac{dF_2}{d\eta_i} - 12\eta_iF_2 = jK_iF_1 \quad [19]$$

which has been solved numerically since no analytic solution could be obtained. As mentioned before, we are interested in the flux at the surface of the disk as a function of x, the dimensionless distance from the step change at $r = r'$. Using the analytic solution for F_0 and F_1 and the numerical solution for F_2, we obtain the following expression, valid for small values of x

$$\left.\frac{\partial\tilde{c}_i}{\partial\eta_i}\right|_{\eta_i=0} = -\frac{1}{\Gamma(4/3)} - \frac{jK_i}{4\Gamma(4/3)}\left[\frac{\Gamma(5/3)}{\Gamma(4/3)}\right]^2x^2 - 0.01250457\,K_i^2x^4 + O(x^5) \quad [20]$$

Another singular point of Eq. [9] occurs at $x = 1$ (infinitely far away from the step change at $r = r'$). Proceeding in the same manner as before, we can show that the asymptotic expansion of $\tilde{c}_i$ valid for values of x close to 1 is

$$\tilde{c}_i = G_0 + G_1(1-x) + G_2(1-x)^2 + O[(1-x)^3] \quad [21]$$

The equation for G_0 is identical to the equation describing the uniform distribution and has been calculated

by Levart and Schuhmann (1) and by Mohr (as reported by Homsy) (4)

$$\frac{d^2G_o}{d\eta_i^2} + 3\eta_i^2\frac{dG_o}{d\eta_i} = jK_iG_o \qquad [22]$$

with boundary conditions [11] and [12]. Since the equations for G_o, G_1, and G_2 do not permit us to obtain an explicit dependence of K_i similar to Eq. [20], we calculated G_1 and G_2 only for $K_i = 50$. The solution of Eq. [22] has been obtained for all values of K_i investigated.

The linearization procedure for the convective diffusion equation for the supporting electrolyte, including the effect of migration, has been described elsewhere (9, 11). Basically, it involves the elimination of the migration term by applying the electroneutrality condition, resulting in the appearance of terms in the equation accounting for the interaction of each major component with all minor components in the solution. The analysis will be given for the cation of the supporting electrolyte. Using the same notation as in Eq. [9] with the effective diffusion coefficient D_e for the supporting electrolyte, where

$$D_e = \frac{z_+u_+D_- - z_-u_-D_+}{z_+u_+ - z_-u_-} \qquad [23]$$

we arrive at the following equation

$$\frac{\partial^2\tilde{c}_+}{\partial\eta_e^2} + 3\eta_e^2\frac{\partial\tilde{c}_+}{\partial\eta_e} = jK_ex^2\tilde{c}_+ + 3\eta_ex(1-x^3)\frac{\partial\tilde{c}_+}{\partial x} - \frac{z_Ru_+(D_- - D_R)}{z_+u_+D_- - z_-u_-D_+}\frac{\partial^2\tilde{c}_R}{\partial\eta_e^2} - \frac{z_Pu_+(D_- - D_P)}{z_+u_+D_- - z_-u_-D_+}\frac{\partial^2\tilde{c}_P}{\partial\eta_e^2} \qquad [24]$$

In order to take separately into account the concentration changes of supporting electrolyte, reactant, and product, we first solve the above equation with neglect of the last two terms with boundary conditions [11]-[13] and let its solution be denoted by $\tilde{\alpha}$. This solution is identical to the solution of Eq. [9] with D_e instead of D_i. Similarly, we solve Eq. [24], neglecting the interaction with the product species, but with $\partial^2\tilde{c}_R/\partial\eta_e^2$ evaluated from the solution to Eq. [9], with the boundary conditions

$$\tilde{c}_+ = 0 \text{ at } \eta_e = 0,\ \tilde{c}_+ \to 0 \text{ as } \eta_e \to \infty \qquad [25]$$

Let the solution be given by $\tilde{\beta}$; the solution to Eq. [24] due to interaction with the product species only is given by $\tilde{\delta}$. It is evident that both solutions are identical, except that $\tilde{\beta}$ involves the diffusion coefficient of the reactant and $\tilde{\delta}$ that of the product.

The asymptotic expansion of $\tilde{\beta}$ (and of $\tilde{\delta}$) near $x = 0$ proceeds along the same lines as before. Because the resulting equations are all linear, it is easy to show that

$$\tilde{\beta} = \tilde{\beta}_o(\eta_e) + jK_e\tilde{\beta}_1(\eta_e)x^2 + K_e^2\tilde{\beta}_2(\eta_e)x^4 + O(x^5) \qquad [26]$$

where $\tilde{\beta}_o$, $\tilde{\beta}_1$, and $\tilde{\beta}_2$ are independent of K_e and real. It is possible to obtain an analytic expression for $\tilde{\beta}_o$, but not for $\tilde{\beta}_1$ and $\tilde{\beta}_2$

$$\tilde{\beta}_o = \frac{z_Ru_+D_e}{\Gamma(4/3)(z_+u_+D_- - z_-u_-D_+)}\left(\frac{D_- - D_R}{D_e - D_R}\right)\int_{(D_e/D_R)^{1/3}\eta_e}^{\eta_e} e^{-z^3}dz \qquad [27]$$

Numerical solutions for $\tilde{\beta}_1$ and $\tilde{\beta}_2$ were not attempted; with the results obtained so far we are able to check the numerical solution of $\tilde{\beta}$ by evaluating both $\tilde{\beta}(0)$ and $\partial\tilde{\beta}/\partial\eta_e$ (at $\eta_e = 0$ and $x = 0$) and compare these values with the values obtained by using Eq. [26] at $x = 0$

$$\tilde{\beta}(0) = 0;\ \left.\frac{\partial\tilde{\beta}}{\partial\eta_e}\right|_{\eta_e=0} = \frac{z_Ru_+D_e}{\Gamma(4/3)(z_+u_+D_- - z_-u_-D_+)}\left(\frac{D_- - D_R}{D_e - D_R}\right)\left[\left(\frac{D_e}{D_R}\right)^{1/3} - 1\right] \qquad [28]$$

Results and Discussion

A comparison between the asymptotic solutions (Eq. [15] and [21]) and the numerical solution of Eq. [9] near $x = 0$ and $x = 1$ shows that the values and certain derivatives are identical within 0.1%.

Figures 1 and 2 show the derivatives of the real part and imaginary part of the reactant concentration, respectively, evaluated at $\eta_i = 0$. The real part is plotted against x^4, the imaginary part against x^2. This choice, as well as the form of the respective expressions on the ordinates, is suggested by the asymptotic solution for small values of x. Figures 3 and 4 show the concentration derivative of the cation of the supporting electrolyte due to a step change in the reactant concentration at the surface of the disk ($\partial\tilde{\beta}/\partial\eta_e(\eta_e = 0)$). Here again, the difference between the values of $\tilde{\beta}(0)$ and

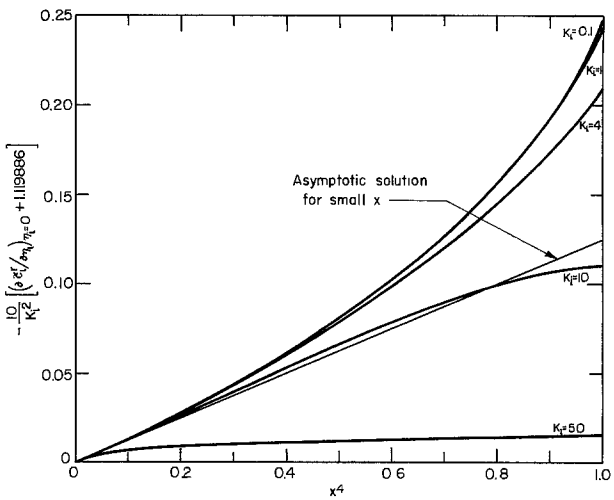


Fig. 1. Derivative of the real part of the concentration at $\eta_i = 0$, as a function of x^4.

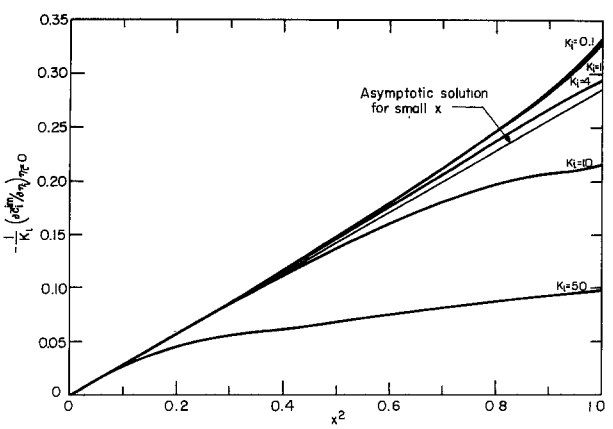


Fig. 2. Derivative of the imaginary part of the concentration at $\eta_i = 0$, as a function of x^2.

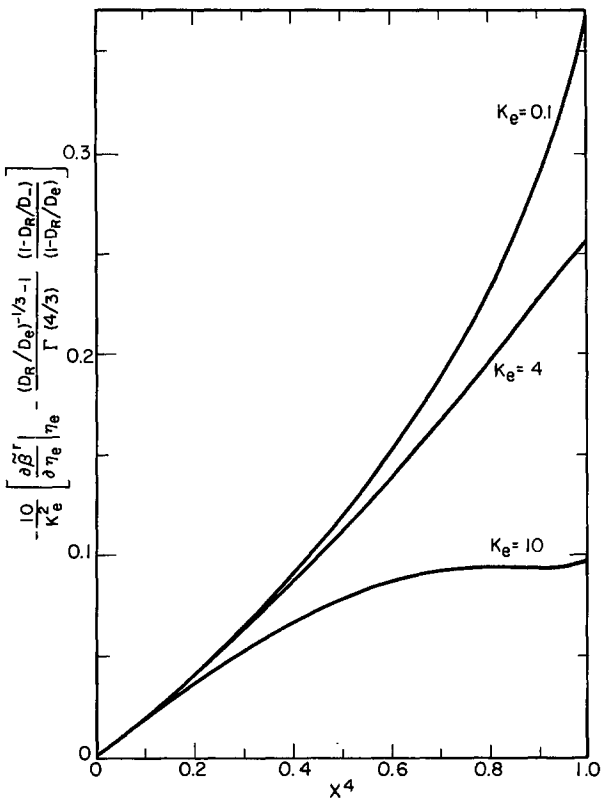


Fig. 3. Derivative of the real part of the concentration fluctuations at the disk surface of the cation of the supporting electrolyte due to a step change in the amplitude of reactant fluctuation.

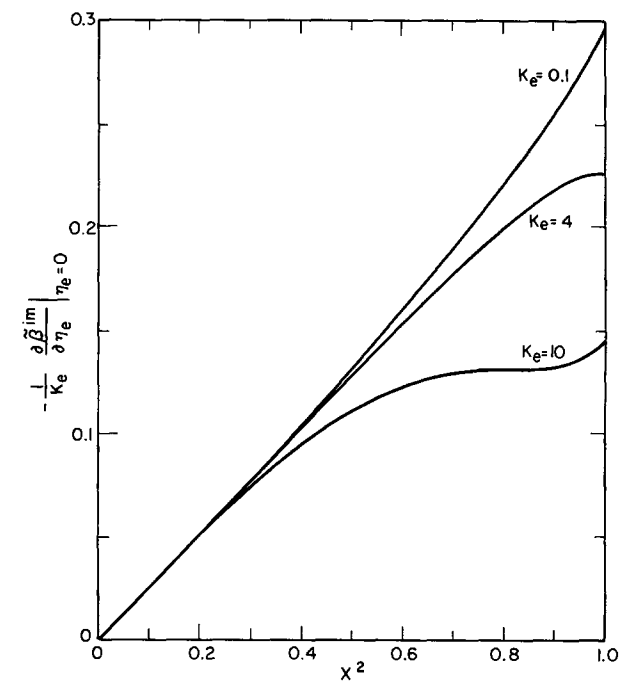


Fig. 4. Derivative of the imaginary part of the concentration fluctuations at the surface of the disk of the cation of the supporting electrolyte due to a step change in the amplitude of reactant fluctuation.

$\partial\tilde{\beta}/\partial\eta_e(\eta_e = 0)$ at $x = 0$ calculated from the numerical evaluation of $\tilde{\beta}$ and these values as obtained from Eq. [28] was less than 0.1%. The Nernst-Einstein relation was assumed to be applicable.

We shall now proceed to show how one can obtain the oscillating flux distribution at the disk surface for all ionic species from the results obtained so far, once the concentration distribution of these species at the surface of the disk is known. The dimensionless flux is defined as (4)

$$\frac{\partial\tilde{c}_i}{\partial\zeta_i}\Big|_{\zeta_i=0} = \frac{1}{x}\frac{\partial\tilde{c}_i}{\partial\eta_i}\Big|_{\eta_i=0} \quad [29]$$

since

$$\zeta_i = x\eta_i \quad [30]$$

The right side of Eq. [29] has been calculated as a function of x for a step change at $r = r'$. Therefore, for arbitrary surface concentration $\tilde{c}_{i,o}$, we obtain the corresponding flux distribution by superposition, which for the reactant becomes

$$\frac{\partial\tilde{c}_R}{\partial\zeta_i}\Big|_{\zeta_i=0} = \int_0^r \frac{d\tilde{c}_{R,o}}{dr}\Big|_{r=r'} \frac{\partial\tilde{c}_i}{\partial\eta_i}\Big|_{\eta_i=0} \left(\frac{r^3}{r^3 - r'^3}\right)^{1/3} dr' \quad [31]$$

The same expression holds for the product species, but the subscript R will then be replaced by P. For the cation of the supporting electrolyte we have shown how to take separately into account the contribution of reactant and product species. Because of the linearity of Eq. [24] we may add these contributions in the expression under the integral sign

$$\frac{\partial\tilde{c}_+}{\partial\zeta_e}\Big|_{\eta_e=0} = \int_0^r \left(\frac{d\tilde{c}_{+,o}}{dr}\Big|_{r=r'} \frac{\partial\tilde{\alpha}}{\partial\eta_e}\Big|_{\eta_e=0} + \frac{d\tilde{c}_{R,o}}{dr}\Big|_{r=r'} \frac{\partial\tilde{\beta}}{\partial\eta_e}\Big|_{\eta_e=0} + \frac{d\tilde{c}_{P,o}}{dr}\Big|_{r=r'} \frac{\partial\tilde{\delta}}{\partial\eta_e}\Big|_{\eta_e=0}\right)\left(\frac{r^3}{r^3 - r'^3}\right)^{1/3} dr' \quad [32]$$

Finally, the anion concentration can be calculated from the electroneutrality equation

$$\sum_i z_i\tilde{c}_i = 0 \quad [33]$$

and the anion flux by taking the first derivative of this equation.

Perhaps we should remind ourselves of the context in which these results are to be utilized. First, the steady distributions of current, potential, and concentrations should be obtained as in Ref. (10). This steady-state situation is to be perturbed by a small, superimposed alternating current, and the resulting alternating potential is to be assessed. This involves, first of all, perturbation of all the factors that go into the steady problem. These are principally Laplace's equation for the potential in the bulk solution, the mass-transfer behavior of the minor species in the diffusion layer, and the electrode kinetics. In addition, there are factors not present in the steady problem. These center around the double-layer capacity, which depends on the local time-average composition and potential, but they also involve a more general dependence of double-layer structure on composition and potential. The computation of the oscillating behavior is a linear problem, in contrast to the steady behavior, but it is still quite complex. The three regions—bulk solution, diffusion layer, and interface—must be treated simultaneously because of their rather strong coupling. In this treatment, it is an advantage to have the original partial differential Eq. [3] and [24] replaced by the superposition integrals in Eq. [31] and [32]. These latter are equivalent to the former in terms of the coupling with the bulk solution and the interface since the coupling can be phrased in terms of

concentrations in the bulk and at the surface and concentration derivatives at the surface.

Summary

The conservation equations of minor and major species have been solved for a rotating disk system where a step change in the amplitude of the concentration fluctuations at the surface of the disk occurs at an arbitrary distance from the center of the disk. The effect of migration on the supporting electrolyte was included in the analysis. Results were presented in the form of the flux of each species at the surface of the disk as a function of distance from the place where the step change occurs. The results obtained by the numerical solution of the complete equations were compared with asymptotic solutions valid for short or for very large distances from the step change. The differences were less than 0.1%.

It was shown that through the use of superposition integrals these results can be applied to the calculation of the oscillating flux distribution of each ionic species for arbitrary concentration distributions of these species at the surface of the disk.

Acknowledgment

This work was done under the auspices of the United States Energy Research and Development Administration.

Manuscript submitted March 7, 1977; revised manuscript received June 23, 1977.

Any discussion of this paper will appear in a Discussion Section to be published in the June 1978 JOURNAL. All discussions for the June 1978 Discussion Section should be submitted by Feb. 1, 1978.

Publication costs of this article were assisted by the University of California.

LIST OF SYMBOLS

a	0.51023
c_i	concentration of species i, mole/cm^3
Δc_i	deviation of species i from its time average concentration, mole/cm^3
$\tilde{c}_i$	complex alternating concentration of species i, mole/cm^3 (see Eq. [2])
D_e	diffusion coefficient of supporting electrolyte, cm^2/sec (see Eq. [23])
D_i	diffusion coefficient of species i, cm^2/sec
$F_0\, F_1, F_2$	functions in series expansion for the complex concentration near the step change (see Eq. [15])
G_0, G_1, G_2	functions in series expansion for the complex concentration far from the step change (see Eq. [21])
j	$\sqrt{-1}$
K_i	dimensionless oscillating frequency based on species i
r	radial distance, cm
r'_i	distance from the center of the disk where a step change occurs in the complex concentration at the disk surface, cm
$Sc_i = \nu/D_i$	Schmidt number of species i
t	time, sec
u_i	mobility of species i, cm^2-mole/J-sec
v_r	radial velocity, cm/sec
v_y	normal velocity, cm/sec
x	dimensionless radial distance (see Eq. [7])
X	dummy variable in Eq. [18]
y	distance from the surface of the disk, cm
z	dummy variable in Eq. [14] and [18]
z_i	charge number of species i
$\tilde{\alpha}$	complex concentration of the cation of the supporting electrolyte due to a step change in its concentration at the disk surface, mole/cm^3
$\tilde{\beta}$	complex concentration of the cation of the supporting electrolyte due to a step change of reactant concentration at the disk surface, mole/cm^3
$\tilde{\beta}_0, \tilde{\beta}_1, \tilde{\beta}_2$	functions in series expansion of $\tilde{\beta}$ near the step change (see Eq. [26])
$\Gamma(p)$	the gamma function of the number p
$\tilde{\delta}$	complex concentration of the cation of the supporting electrolyte due to a step change in product concentration, mole/cm^3
ζ_i	dimensionless distance from the disk surface, based on the diffusivity of species i (see Eq. [30])
η_i	dimensionless distance (see Eq. [8])
ν	kinematic viscosity, cm^2/sec
ϕ	phase shift in alternating concentration, rad (see Eq. [2])
ω	oscillation frequency of concentrations, rad/sec
Ω	rotation speed of disk, rad/sec

Subscripts

e	supporting electrolyte
P	produced species
R	reacting species
+	cation of the supporting electrolyte
−	anion of the supporting electrolyte

REFERENCES

1. E. Levart and D. Schuhmann, *J. Electroanal. Chem.*, **28**, 45 (1970).
2. E. Levart and D. Schuhmann, *ibid.*, **53**, 77 (1974).
3. E. Levart and D. Schuhmann, *This Journal*, **122**, 1082 (1975).
4. Robert V. Homsy and John Newman, *ibid.*, **121**, 521 (1974).
5. John Newman, *ibid.*, **113**, 1235 (1966).
6. John Newman, *ibid.*, **117**, 198 (1970).
7. Francis B. Hildebrand. "Advanced Calculus for Applications," pp. 451-454. Prentice-Hall, Inc., Englewood Cliffs, N.J. (1963).
8. C. Deslouis, I. Epelboin, M. Keddam, and J. C. Lestrade, *J. Electroanal. Chem.*, **28**, 57 (1970).
9. Peter Appel, Dissertation, University of California, Berkeley (1976).
10. Peter Pierini, Peter Appel, and John Newman, *This Journal*, **123**, 366 (1976).
11. John Newman, "Electrochemical Systems," Prentice Hall, Inc., Englewood Cliffs, N.J. (1973).

Distribution of Potential and Current in Circular Corrosion Cells Having Unequal Polarization Parameters

E. McCafferty*

Naval Research Laboratory, Washington, D.C. 20375

ABSTRACT

A mathematical model has been developed to describe the distribution of potential and current across concentric circular corrosion cells having unequal anodic and cathodic polarizabilities. This theory is essentially an extension of the Wagner-Waber model to circular systems and is applicable to galvanic couples, metal matrix composites, and localized corrosion effects. The potential distribution in systems having unequal Wagner polarization parameters is not related in a simple way to the separate distribution curves for the two cases where the polarization parameters are equal. In thin-layer electrolytes, there is a geometry effect in which the electrode polarization and current flow are concentrated near the anode/cathode juncture. The theory is applied satisfactorily to Pt/Fe model systems in dilute sodium chloride and to earlier results of Rosenfeld and Pavlutskaya with circular electrodes.

Many corrosion systems can be described by a coplanar circular geometry. Examples include some instances of pitting (1), crevice corrosion under O-rings or washers (2), corrosion under barnacles (3), under tubercules of corrosion products (4), or under dust particles in condensed moisture films (5).

Gal-Or, Raz, and Yahalom (6) have mathematically treated systems of coplanar, concentric circular corrosion cells having linear corrosion kinetics and equal anodic and cathodic slopes. These authors analyzed the effect of various system parameters on the total anodic current, and more recently the distribution of potential and current across such cells has been evaluated (7, 8). These treatments essentially extended to cylindrical geometries the model developed by Waber and co-workers (9-12) in a series of publications on semi-infinite parallel electrodes with anode and cathode having linear and equal corrosion kinetics.

Smyrl and Newman (13) have recently presented an analysis for an array of corroding disks in a cathodic plane assuming Tafel kinetics but with equal anodic and cathodic slopes.

While the assumption of linear polarization over an extended potential range is often a reasonable approximation (as is discussed later), the assumption that anodic and cathodic slopes are equal seldom holds because the anode is generally far less polarizable than the cathode.

The case of unequal anodic and cathodic linear polarization has been solved by Kennard and Waber (14) for semi-infinite strips of parallel electrodes under bulk electrolyte.

The purpose of this paper is to extend the Waber model of linear corrosion kinetics to circular systems with unequal polarization parameters. Equations are derived for potential and current distribution and for the total anodic current, and generalized numerical calculations are made. This paper is largely mathematical, but comparisons are made with some preliminary experiments and also with the published work of Rosenfeld and Pavlutskaya (15, 16) for iron/copper disk electrodes under bulk and thin-layer electrolytes.

Mathematical Analysis

The cell geometry is shown in Fig. 1. The anode and cathode edges are coplanar, concentric, circles of radii a and c, respectively. The electrolyte thickness b is allowed to approach infinity for bulk electrolyte. The cell potentials and stylized polarization curves are show in Fig. 2. As pointed out by Kennard and Waber (14), if the plots are linear over only a portion of the curves, tangent approximations can be drawn and the open-circuit potentials E_a° and E_c° replaced by the intersections $E_a^{\circ\prime}$ and $E_c^{\circ\prime}$, respectively, of the tangent lines with the potential axis.

The electrostatic potential $P(x, y, z)$ at any point in the electrolyte is given by Laplace's equation

$$\nabla^2 P(x, y, z) = 0 \qquad [1]$$

provided that: (*i*) there are no concentration gradients in solution, (*ii*) the solution is electroneutral, and (*iii*) there are no sources or sinks of ions in the electrolyte (17). In cylindrical coordinates, Laplace's equation is

$$\frac{\partial^2 P(r,z)}{\partial r^2} + \frac{1}{r} \cdot \frac{\partial P(r,z)}{\partial r} + \frac{\partial^2 P(r,z)}{\partial z^2} = 0 \qquad [2]$$

with the term in $\partial^2 P(r, z)/\partial\theta^2$ deleted because the potential is not dependent on the angle θ. The general approach is to solve for $P(r, z)$ subject to appropriate boundary conditions and then to evaluate the local current density $i(r, 0)$ from Ohm's law for electrolytes

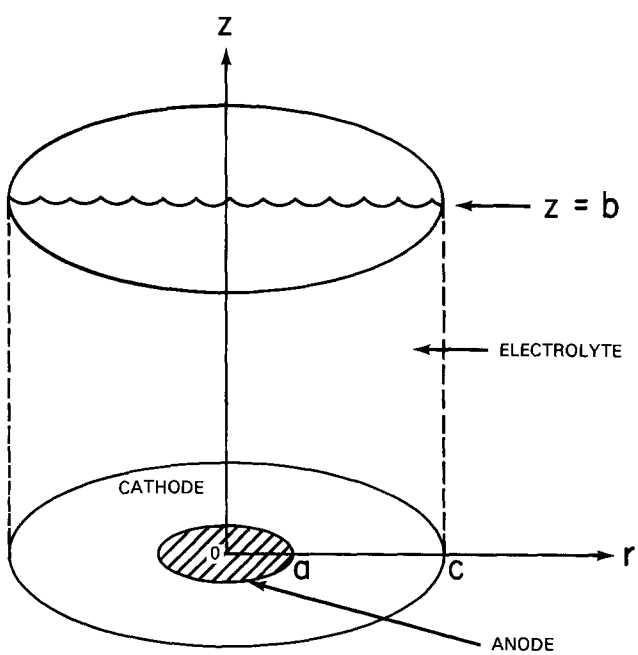


Fig. 1. Cell geometry

* Electrochemical Society Active Member.

Key words: current distribution, potential distribution, circular electrodes, galvanic couples, thin-layer electrolyte.

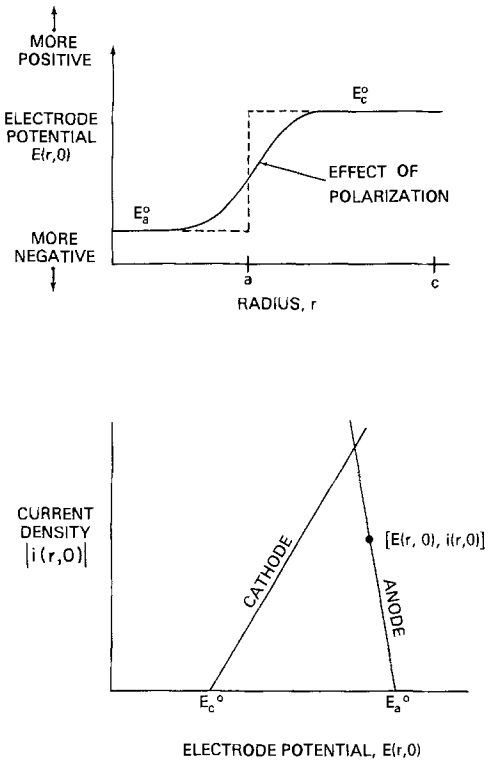


Fig. 2. Electrode potentials and idealized linear polarization curves. E_a° and E_c° refer to the open-circuit potentials of anode and cathode, respectively.

$$i(r,0) = -\sigma\left[\frac{\partial P(r,z)}{\partial z}\right]_{z=0} \qquad [3]$$

where σ is the electrolyte conductivity.

The potential $P(r,z)$ must satisfy the boundary conditions of no current flow across the planes $r = 0$ and $r = c$. Thus

$$\left[\frac{\partial P(r,z)}{\partial r}\right]_{r=0} = \left[\frac{\partial P(r,z)}{\partial r}\right]_{r=c} = 0 \qquad [4]$$

For bulk electrolyte, $P(r,z)$ must be bounded for large z. For bulk electrolyte, the general solution to Laplace's equation subject to these conditions is

$$P(r,z) = B_0 + \sum_{n=1}^{\infty} B_n J_0(\lambda_n r)\, e^{-\lambda_n z} \qquad [5]$$

where B_0 and B_n are coefficients to be determined, J_0 is the Bessel function of order zero, $\lambda_n = x_n/c$, and x_n are the zeroes of $J_1(x) = 0$.

Linear polarization model.—The remaining boundary condition relates the electrode potential $E(r,0)$ along the metal surface *vs.* some standard reference electrode to the electrostatic potential $P(r,0)$ within the electrolyte but "just outside" (18) the electrode surface. That is

$$V' - P(r,0) = E(r,0) \qquad [6]$$

where V' is a constant which includes the various differences in electrostatic potential across the extra interfaces which are introduced in the measurement of a potential difference across the metal/solution interface of interest (19).

Following Wagner (20) and Waber (9-12), it is assumed that there is a linear dependence over an extended range between the electrode potential E and current density i. As mentioned earlier, this is a reasonable approximation in a number of experimental cases.

The recent literature contains a number of examples of polarization plots which are linear or approximately so over an extended potential range. For example, steels in aerated neutral to basic solutions, with or without chloride, displayed both anodic and cathodic plots which were approximately linear over an extended range (21). Additional examples include the corrosion of tin in citrate solutions (22) and of bare and coated aluminum in chloride solutions (23). Other examples involve specialized geometries, such as the pitting of aluminum (24), or specialized conditions, such as the dissolution of mild steel at high anodic overpotentials in concentrated electrolytes (25). On the cathodic side, the reduction of oxygen on nickel in dilute H_2SO_4 (26) and on silver in KOH (27) display linear regions. Polarization curves for a variety of metals in thin-layer electrolytes (15) display linear regions over at least part of the potential ranges for both anodic and cathodic processes.

As pointed out by Stern and Geary (28), the combined effects of concentration polarization plus ohmic drops interfere with activation polarization processes so that sometimes a very short Tafel region is observed. Such cases often give straight line segments in E *vs.* i.

At this point, it should be clear that the model invokes linearity over an extended potential range and not merely in the pre-Tafel region near the corrosion potential where the familiar Stern and Geary (28) linear relation is valid.

Thus, the anodic and cathodic Wagner polarization parameters are defined as

$$\mathcal{L}_a = \sigma \left|\frac{dE}{di}\right|_a, \quad 0 \leq r < a \qquad [7a]$$

and

$$\mathcal{L}_c = \sigma \left|\frac{dE}{di}\right|_c, \quad a < r \leq c \qquad [7b]$$

where $\mathcal{L}_a$ and $\mathcal{L}_c$ have the dimensions of length, and $\mathcal{L}_a \neq \mathcal{L}_c$. For the anodic branch in Fig. 2, $di/dE = i(r,0)/[E(r,0) - E_a^\circ]$. This expression combines with Eq. [7a], [6], and [3] to give the final boundary condition for the anode surface

$$P(r,0) - \mathcal{L}_a\left[\frac{\partial P(r,z)}{\partial z}\right]_{z=0} = V' - E_a^\circ, \quad 0 \leq r < a \qquad [8a]$$

Similarly for the cathode

$$P(r,0) - \mathcal{L}_c\left[\frac{\partial P(r,z)}{\partial z}\right]_{z=0} = V' - E_c^\circ, \quad a < r \leq c \qquad [8b]$$

Equations for bulk electrolyte.—The boundary conditions in Eq. [8a] and [8b] are used to determine the coefficients B_0 and B_n. The method of solution is outlined in the Appendix, which notes the differences between the present analysis and the earlier work of Gal-Or and co-workers (6) for $\mathcal{L}_a = \mathcal{L}_c$. More detail is available elsewhere (29). The result for B_0 is

$$B_0 = V' - \left(\frac{a}{c}\right)^2 E_a^\circ - \left(\frac{c^2 - a^2}{c^2}\right) E_c^\circ - \frac{2a}{c^2}(\mathcal{L}_a - \mathcal{L}_c) \sum_{n=1}^{\infty} B_n J_1\left(x_n \frac{a}{c}\right) \qquad [9]$$

The coefficients B_n are given by

$$B_m\left[\left(1 + \mathcal{L}_c \frac{x_m}{c}\right)\frac{J_0^2(x_m)}{2} + (\mathcal{L}_a - \mathcal{L}_c)\left(\frac{x_m}{c}\right)\left(\frac{a}{c}\right)^2 A_m\right] + \frac{a}{c^2}(\mathcal{L}_a - \mathcal{L}_c) \sum_{\substack{n=1 \\ n \neq m}}^{\infty} B_n W_{nm} = -\frac{(E_a^\circ - E_c^\circ)}{x_m}\left(\frac{a}{c}\right) J_1\left(x_m \frac{a}{c}\right) \qquad [10]$$

where A_m and W_{nm} are defined by

$$A_m = \frac{1}{2}\left[J_0^2\left(x_m\frac{a}{c}\right) + J_1^2\left(x_m\frac{a}{c}\right)\right] \quad [11]$$

and

$$W_{nm} = \frac{x_n^2}{x_n^2 - x_m^2}\left[J_1\left(x_n\frac{a}{c}\right)J_0\left(x_m\frac{a}{c}\right) - \frac{x_m}{x_n}J_0\left(x_n\frac{a}{c}\right)J_1\left(x_m\frac{a}{c}\right)\right] \quad [12]$$

Equation [10] thus generates a series of equations, say k of them, where m is fixed in turn from 1 through k. These k equations are solved simultaneously to give the coefficients B_n from $n = 1$ to k.

Equations [5], [6], and [9] combine to give the electrode potential along the metal surface

$$E(r,0) = \left(\frac{a}{c}\right)^2 E_a^\circ + \left(\frac{c^2-a^2}{c^2}\right)E_c^\circ + \frac{2a}{c^2}(\mathcal{L}_a - \mathcal{L}_c)\sum_{n=1}^{\infty} B_n J_1\left(x_n\frac{a}{c}\right) - \sum_{n=1}^{\infty} B_n J_0\left(x_n\frac{r}{c}\right) \quad [13]$$

where the B_n are determined from the system of equations generated by Eq. [10]. It should be noted that the indeterminate constant V' vanishes in the final expression for $E(r,0)$.

Differentiation of Eq. [5] as in Eq. [3] gives the local current density

$$\frac{i(r,0)}{\sigma} = \frac{1}{c}\sum_{n=1}^{\infty} B_n x_n J_0\left(x_n\frac{r}{c}\right) \quad [14]$$

where again the set of B_n is determined from Eq. [10].

The total anodic current I_{anodic} is related to the local current density by

$$I_{anodic} = \int_{r=0}^{a}\int_{\theta=0}^{2\pi} i(r,0)\,r\,dr\,d\theta \quad [15]$$

Use of Eq. [14] in Eq. [15] gives the result

$$\frac{I_{anodic}}{\sigma} = 2\pi a\sum_{n=1}^{\infty} B_n J_1\left(x_n\frac{a}{c}\right) \quad [16]$$

Thin-layer electrolyte.—For a thin layer of electrolyte, it is required that no current flows across the upper boundary of the electrolyte. Thus, $[\partial P(r,z)/\partial z] = 0$ at $z = b$ .The solution of Laplace's equation subject to this requirement and to Eq. [4] is

$$P(r,z) = C_0 + \sum_{n=1}^{\infty} C_n J_0(\lambda_n r)\cosh[\lambda_n(b-z)] \quad [17]$$

The resulting expressions for thin-layer electrolytes are

$$E(r,0) = \left(\frac{a}{c}\right)^2 E_a^\circ + \left(\frac{c^2-a^2}{c^2}\right)E_c^\circ + \frac{2a}{c^2}(\mathcal{L}_a - \mathcal{L}_c)\sum_{n=1}^{\infty} C_n \sinh\left(x_n\frac{b}{c}\right)J_1\left(x_n\frac{a}{c}\right) - \sum_{n=1}^{\infty} C_n\cosh\left(x_n\frac{b}{c}\right)J_0\left(x_n\frac{r}{c}\right) \quad [18]$$

$$\frac{i(r,0)}{\sigma} = \frac{1}{c}\sum_{n=1}^{\infty} C_n x_n \sinh\left(x_n\frac{b}{c}\right)J_0\left(x_n\frac{r}{c}\right) \quad [19]$$

and

$$\frac{I_{anodic}}{\sigma} = 2\pi a\sum_{n=1}^{\infty} C_n \sinh\left(x_n\frac{b}{c}\right)J_1\left(x_n\frac{a}{c}\right) \quad [20]$$

where the coefficients C_n are generated by the system of equations

$$C_m\left\{\left[1 + \mathcal{L}_c\frac{x_m}{c}\tanh\left(x_m\frac{b}{c}\right)\right]\frac{J_0^2(x_m)}{2} + (\mathcal{L}_a - \mathcal{L}_c)\frac{x_m}{c}\left(\frac{a}{c}\right)^2\tanh\left(x_m\frac{b}{c}\right)A_m\right\} + \frac{a}{c^2}\frac{(\mathcal{L}_a - \mathcal{L}_c)}{\cosh\left(x_m\frac{b}{c}\right)}\sum_{\substack{n=1\\ n\neq m}}^{\infty} C_n W_{nm}\sinh\left(x_n\frac{b}{c}\right) = -\frac{1}{\cosh\left(x_m\frac{b}{c}\right)}\cdot\frac{(E_a^\circ - E_c^\circ)}{x_m}\left(\frac{a}{c}\right)J_1\left(x_m\frac{a}{c}\right) \quad [21]$$

The relationship between the two sets of coefficients C_n and B_n is that $C_n \sinh (x_n\, b/c) \to B_n$ for large b. Thus, the above expressions for thin layers reduce to the results for bulk electrolyte for large b.

Comparison with Previous Case of $\mathcal{L}_a = \mathcal{L}_c$

When $\mathcal{L}_a = \mathcal{L}_c = \mathcal{L}$, the above results for bulk and thin-layer electrolytes reduce to the following

$$E(r,0) = \left(\frac{a}{c}\right)^2 E_a^\circ + \left(\frac{c^2-a^2}{c^2}\right)E_c^\circ + 2\left(\frac{a}{c}\right)(E_a^\circ - E_c)\times \sum_{n=1}^{\infty}\frac{J_1\left(x_n\frac{a}{c}\right)}{x_n\left[1 + \mathcal{L}\frac{x_n}{c}Q\right]J_0^2(x_n)}J_0\left(x_n\frac{r}{c}\right) \quad [22]$$

$$\frac{i(r,0)}{\sigma} = -2\frac{a}{c^2}(E_a^\circ - E_c)\times \sum_{n=1}^{\infty}\frac{J_1\left(x_n\frac{a}{c}\right)\cdot Q}{\left[1 + \mathcal{L}\frac{x_n}{c}Q\right]J_0^2(x_n)}J_0\left(x_n\frac{r}{c}\right) \quad [23]$$

and

$$\frac{I_{anodic}}{\sigma} = -4\pi\frac{a^2}{c}(E_a^\circ - E_c)\times \sum_{n=1}^{\infty}\frac{J_1^2\left(x_n\frac{a}{c}\right)Q}{x_n\left[1 + \mathcal{L}\frac{x_n}{c}Q\right]J_0^2(x_n)} \quad [24]$$

where in each of the above

$$Q = \begin{cases} 1, & \text{bulk electrolyte} \\ \tanh\left(x_n\frac{b}{c}\right), & \text{thin layer} \end{cases} \quad [25]$$

These equations are the same as previously reported (6-8) except that the signs of electrode potentials in Eq. [22]-[24] now conform to the convention that the noble direction is the more positive.

Numerical Evaluation

Values for $\mathcal{L}_a$ and $\mathcal{L}_c$.—As mentioned earlier, the anode is generally less polarizable than the cathode. This fact is illustrated by many electrode kinetic studies carried out under carefully controlled condi-

tions. With iron, for example, in a variety of deaerated electrolytes, anodic Tafel slopes of 30 to 80 mV/decade have been observed while the cathodic slopes for hydrogen evolution were 120 mV/decade (30-33). To cite two more examples, cadmium and indium undergo consecutive single electron transfers to Cd^{+2} and In^{+3}, respectively, and display Tafel slopes of 40-50 mV/decade (0°C) and 22 mV/decade, respectively, while the hydrogen evolution reaction on both surfaces is again 115-120 mV/decade, characteristic of a single electron transfer reaction (34, 35).

In more practical situations where conditions are not as well defined, Tafel behavior is less seldom observed and instead polarization curves sometimes display segments which are approximately linear in current (rather than logarithm of current) over a considerable potential range, as discussed earlier. In this instance, the cathode again is often the more polarizable.

Values of linear polarization parameters compiled earlier (7) indicate that $\mathcal{L}_a$ is generally of the order 1-10 cm while $\mathcal{L}_c$ is usually 10-100 cm although there are exceptions. In data tabulated by Gouda and Mourad (21) for steel in a variety of neutral to basic solutions both with and without added chloride, the cathodic slope $|dE/di|$ varied from 1.5 times to approximately 20 times the anodic slope but with most ratios in the range of 5-10. Specific conductivities were listed for only three solutions for which values of $\mathcal{L}_a$ are calculated to be 0.9, 1.9, and 48 cm, with corresponding $\mathcal{L}_c$ values of 7.5, 12.2, and 193, respectively.

Bulk electrolyte.—For the computations in this section, $\mathcal{L}_a$ is fixed at 1 cm. Figure 3 shows the potential distribution $E(r,0)$ for $\mathcal{L}_a = 1$ cm and $\mathcal{L}_c = 10$ cm for fixed values of $E_a° = 0.00$V and $E_c° = 1.00$V. The coefficients B_n were calculated up to B_{100} using the system of simultaneous equations generated by Eq. [10]. These simultaneous equations were solved using the computer, and the coefficients were then substituted in Eq. [13] to obtain the electrode potential distribution. Convergence was assessed by numerical evaluation.

Figure 3 also shows potential distribution plots for $\mathcal{L}_a = \mathcal{L}_c = 1$ and $\mathcal{L}_a = \mathcal{L}_c = 10$, calculated from Eq. [22]. It is evident that the potential behavior of the electrodes with unequal anodic and cathodic polarization parameters cannot be deduced from the two separate curves for the equal polarization parameters.

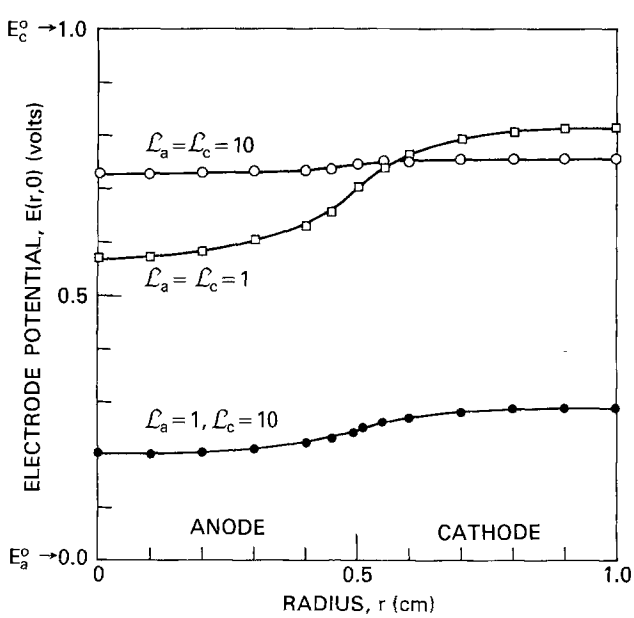


Fig. 3. Comparison of electrode potential distributions for equal and unequal polarization parameters with bulk electrolyte. (Anode radius $a = 0.5$ cm, cathode radius $c = 1.0$ cm; $E_a° = 0.00$V, $E_c° = 1.00$V.)

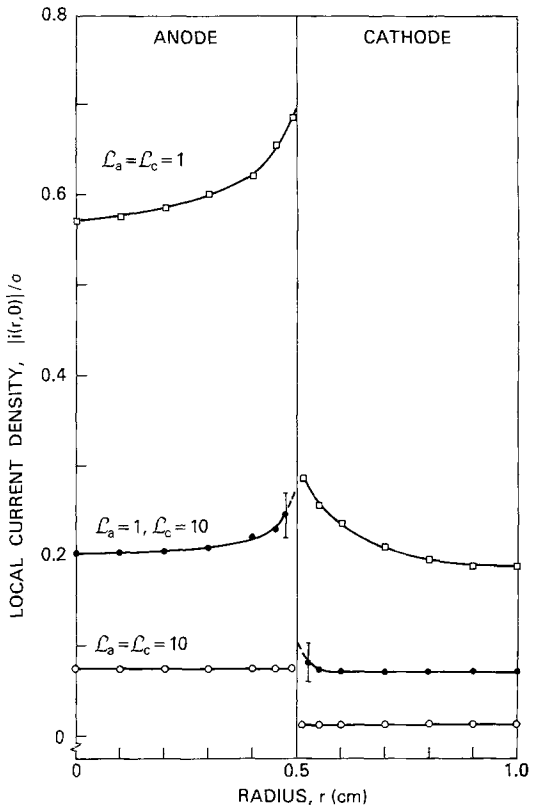


Fig. 4. Current distributions corresponding to the electrode potential distributions in Fig. 3.

The corresponding current density curves for the three systems are shown in Fig. 4. It is seen that the values for the case of unequal parameters are intermediate between the two cases where $\mathcal{L}_a = \mathcal{L}_c = 1$ and $\mathcal{L}_a = \mathcal{L}_c = 10$.

Figure 5 shows the potential distribution calculated from Eq. [13] with $n = 100$ for a fixed value of $\mathcal{L}_a = 1$ but with variable $\mathcal{L}_c$. Corresponding cur-

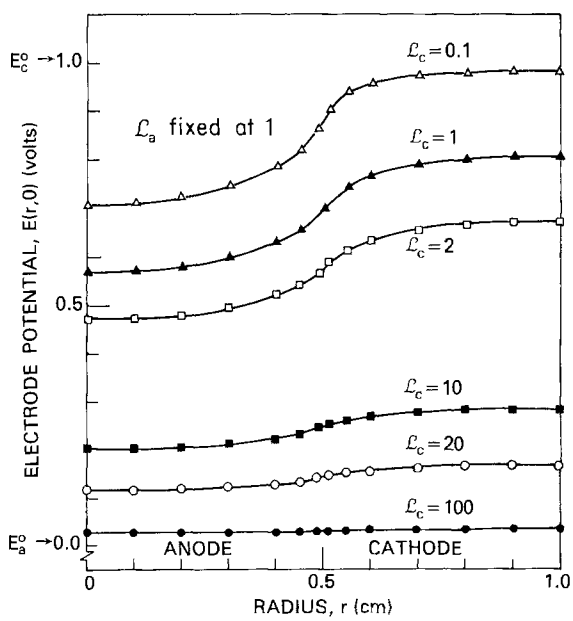


Fig. 5. Distribution of electrode potential across circular cells under bulk electrolyte with $\mathcal{L}_a$ fixed at 1 cm, combined with various values of $\mathcal{L}_c$. (Anode radius $a = 0.5$ cm, cathode radius $c = 1.0$ cm; $E_a° = 0.00$V; $E_c° = 1.00$V.)

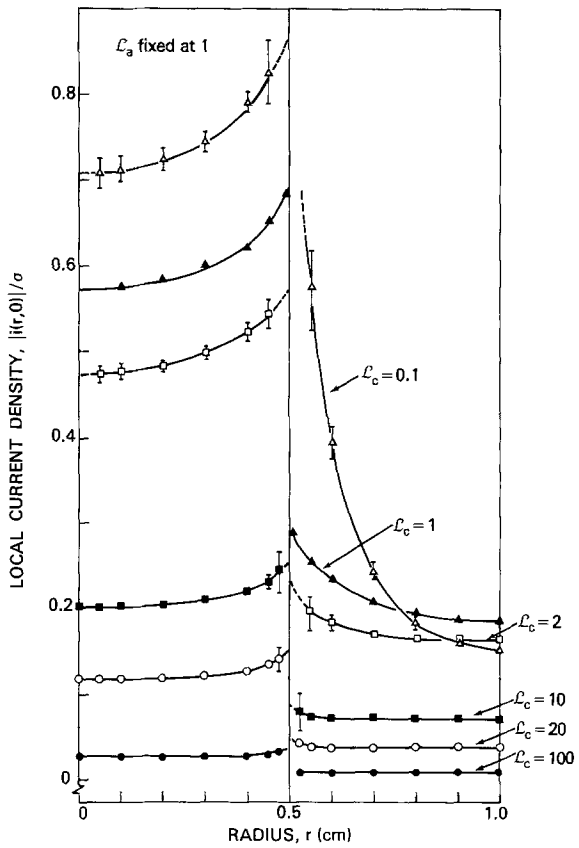


Fig. 6. Distribution of current across circular cells under bulk electrolyte with $\mathcal{L}_a$ fixed at 1 cm and combined with various values of $\mathcal{L}_c$. (Anode radius a = 0.5 cm, cathode radius c = 1.0 cm; E_a° = 0.00V, E_c° = 1.00V.)

rent distribution curves calculated from Eq. [14] are shown in Fig. 6. When $\mathcal{L}_a = 1$ and $\mathcal{L}_c = 0.1$, the galvanic couple is under anodic control, as shown in Fig. 7, and the electrode potentials across the metal surface of both components are polarized up near the potential of the uncoupled cathode.

When $\mathcal{L}_c >> \mathcal{L}_a$, *e.g.*, $\mathcal{L}_c = 100$ and $\mathcal{L}_a = 1$, the system is under cathodic control, as illustrated schematically in Fig. 7. For this case, Fig. 7 predicts that the electrode potential would approach the values of the open-circuit potential of the anode, and the current would be much less than for the case of anodic control (for fixed $\mathcal{L}_a$). These expected trends are verified in the results of the numerical analysis shown in Fig. 5 and 6.

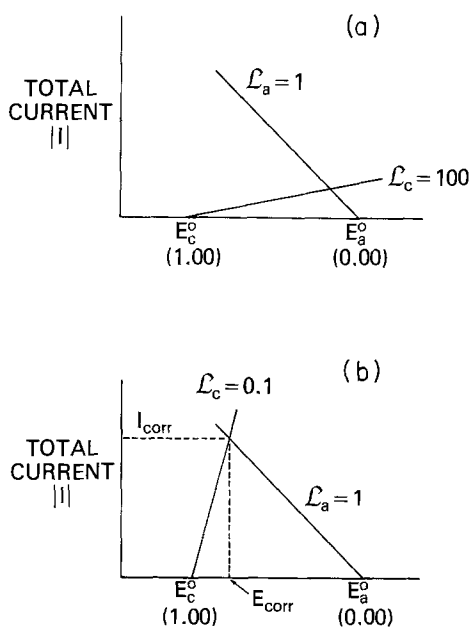


Fig. 7. Schematic representation of (a) cathodic control and (b) anodic control. Previous treatments of $\mathcal{L}_a = \mathcal{L}_c$ (6-8) correspond to the case of mixed control.

The results in Fig. 5 and 6 for $\mathcal{L}_a = \mathcal{L}_c = 1$ also provide a check on the consistency of the present method with the previous relationships for equal polarization parameters. Both potential and current distributions calculated from the set of B_n resulting from Eq. [10] with $\mathcal{L}_a$ and $\mathcal{L}_c$ both equal to 1 agree with the results obtained with Eq. [22] and [23].

One additional trend can be seen in Fig. 5 and 6. For this system of fixed $\mathcal{L}_a$, the more polarizable the cathode (*i.e.*, the larger $\mathcal{L}_c$), the more uniform the potential and current distribution.

The total anodic current was calculated from Eq. [16] for the systems with $\mathcal{L}_a$ fixed at 1 with variable $\mathcal{L}_c$. Results are listed in Table I. The total anodic current can also be calculated from the schematic Evans diagrams shown in Fig. 7. For the anodic branch

$$\left|\frac{dE}{dI}\right|_a = \frac{E_{corr} - E_a^\circ}{I_{corr}} \qquad [26]$$

and for the cathodic branch

$$\left|\frac{dE}{dI}\right|_c = -\frac{E_{corr} - E_c^\circ}{I_{corr}} \qquad [27]$$

where I_{corr} is the corrosion current, *i.e.*, the total anodic current referred to earlier as I_{anodic}. With $I_a = i_a A_a$ and $I_c = i_c A_c$, where A_a and A_c are the area of anode and cathode, respectively, use of Eq. [7a] and [7b] in Eq. [26] and [27] gives

$$\frac{I_{corr}}{\sigma} = \frac{E_c^\circ - E_a^\circ}{\frac{\mathcal{L}_a}{A_a} + \frac{\mathcal{L}_c}{A_c}} \qquad [28]$$

where again I_{corr} has the same meaning of I_{anodic} in in Eq. [15].

Values of I_{corr}/σ calculated from Eq. [28] are also listed in Table I. These calculated values agree with the results from the computer analysis for $\mathcal{L}_a = 1$ coupled with cathodic values of $\mathcal{L}_c = 50$ and $\mathcal{L}_c = 100$, where the current distribution is uniform. There is disagreement between the results of the Evans diagram analysis and the computer analysis for those systems where there is a nonuniform distribution of current, and this divergence is greater the more pronounced the localized attack at the anode/cathode juncture.

Results for $\mathcal{L}_a = \mathcal{L}_c = 10$ and $\mathcal{L}_a = \mathcal{L}_c = 100$ are also included in Table I. Current distribution plots

Table I. Comparison of total current calculated from Evans diagrams and from summation of current distribution curves for couples with unequal polarizabilities in bulk electrolyte. (Anode radius a = 0.5 cm, cathode radius c = 1.0 cm, E_a° = 0.00V, E_c° = 1.00V.)

$\mathcal{L}_a$ (cm)	$\mathcal{L}_c$ (cm)	I_{corr}/σ (Calculated from Evans diagrams, Eq. [28])	I_{anodic}/σ (Calculated from Eq. [10] and [16])
1	0.1	0.760	0.607
	1	0.589	0.485
	2	0.471	0.401
	10	0.181	0.169
	20	0.103	0.099
	50	0.0445	0.0437
	100	0.0228	0.0227
10	10	0.0589	0.0576
10	100	0.0181	0.0179
100	100	0.00589	0.00587

published in an earlier report (8) were nearly uniform for the former system and exactly so for the latter. The current distribution for $\mathcal{L}_a = 10$ and $\mathcal{L}_c = 100$ was calculated from Eq. [14] and was observed to be uniform although the plot is not shown here. Thus, there is good agreement between Evans diagram analyses and computed calculations for systems where there is a uniform current distribution.

Hence, the classical Evans polarization diagrams cannot be used to calculate accurately the value of the galvanic current in all instances without consideration of the matter of current distribution.

Thin-layer electrolyte.—Figure 8 shows the electrode potential $E(r, 0)$ for $\mathcal{L}_a = 1$ cm and $\mathcal{L}_c = 10$ cm for different electrolyte thicknesses. The coefficients C_n were computed up to C_{100} from Eq. [21] and were used in Eq. [18] to obtain the potential distributions.

The corresponding current distributions are shown in Fig. 9. The local current densities were calculated from Eq. [19] and [21] with $n = 100$, except near $r = 0.0$ and $r = 0.5$ where 125 terms were used. For the thin layers, there is a geometry effect in which the corrosion attack is concentrated near the anode/cathode boundary.

Figure 10 shows the total anodic current calculated from Eq. [20] for two different combinations of $\mathcal{L}_a$ and $\mathcal{L}_c$. In both cases, the total current approaches values for the bulk for electrolyte thicknesses of approximately 0.1-0.3 cm.

Figure 11 compares the potential distribution for $\mathcal{L}_a = 1$ and $\mathcal{L}_c = 10$ to the cases of equal polarization parameters, $\mathcal{L}_a = \mathcal{L}_c = 1$ and $\mathcal{L}_a = \mathcal{L}_c = 10$ for an electrolyte thickness of 0.001 cm. As with the bulk, the potential distribution for the system of an electrolyte thickness of 0.001 cm. As with the bulk, the potential distribution for the system of unequal parameters is not related in a simple manner to the individual distribution curves for each of the two equal parameters.

Comparison with Experiment

Procedure.—Experiments were performed with Pt/Fe couples in bulk 0.05M NaCl open to the air for both stirred and quiescent conditions. In each of the experiments, the iron anode was a circular electrode of radius $a = 1$ cm, and the platinum cathode was annular shaped with dimension $c = 2.5$. Both metals were 99.99% pure. The platinum was cleaned by flaming and was kept in a dessicator until use; the iron was abraded down to 3/0 emery paper immediately before use. Extraneous surfaces were masked with an alkyd varnish.

In a given experiment, both parts of the galvanic cell were initially uncoupled so that each electrode

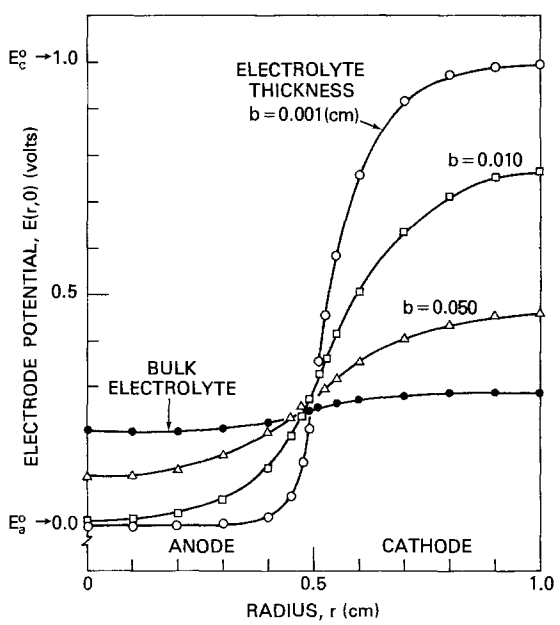


Fig. 8. Distribution of electrode potential for $\mathcal{L}_a = 1$ cm and $\mathcal{L}_c = 10$ cm for different electrolyte thicknesses. (Anode radius $a = 0.5$ cm, cathode radius $c = 1.0$ cm; $E_a^\circ = 0.00$V, $E_c^\circ = 1.00$V.)

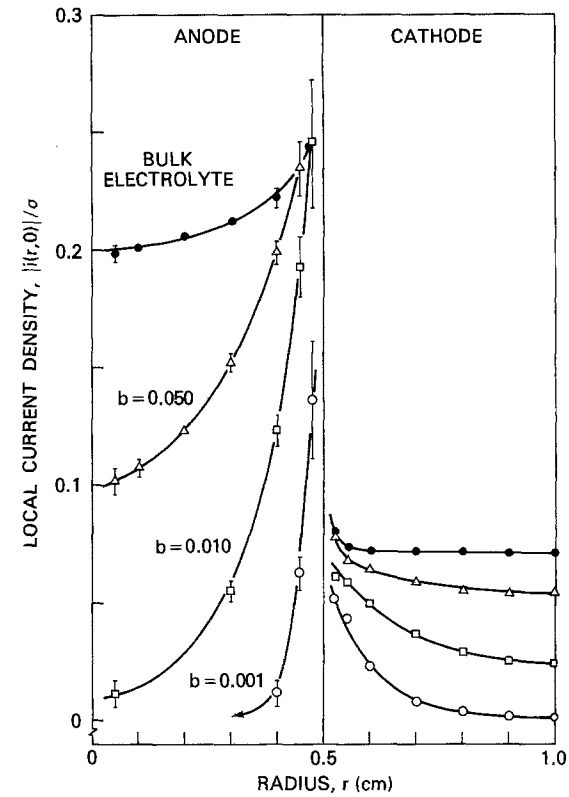


Fig. 9. Current distribution for $\mathcal{L}_a = 1$ cm and $\mathcal{L}_c = 10$ cm for different electrolyte thicknesses. Cell parameters are the same as in Fig. 8. (Limits between which the local current densities oscillate are indicated for the anodic points. Error limits for the cathode are smaller.)

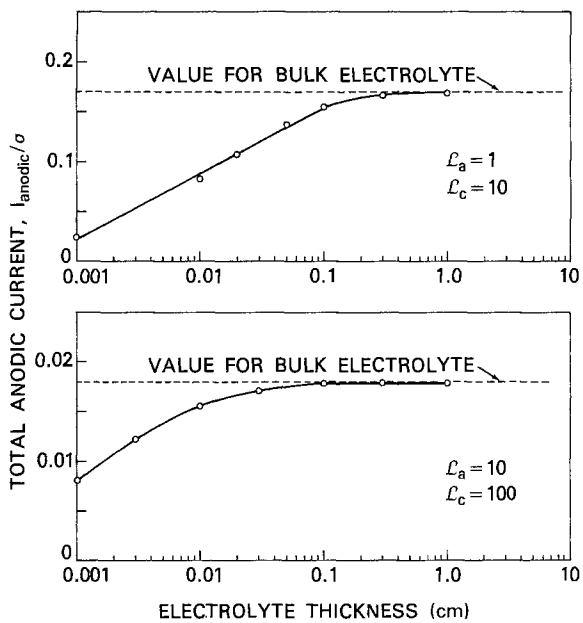


Fig. 10. Total anodic current computed as a function of electrolyte thickness for two different combinations of $\mathcal{L}_a$ and $\mathcal{L}_c$. (Anode radius $a = 0.5$ cm, cathode radius $c = 1.0$ cm; $E_a^\circ = 0.00$V, $E_c^\circ = 1.00$V.)

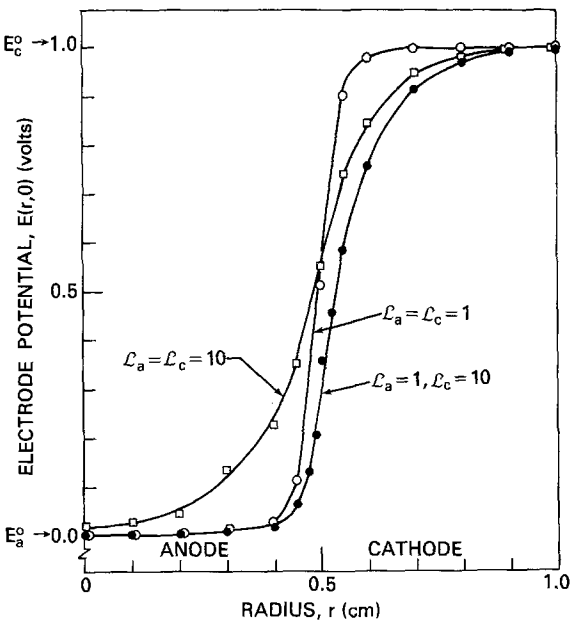


Fig. 11. Comparison of electrode potential distribution for equal and unequal polarization parameters for a thin-layer electrolyte of thickness b = 0.001 cm. (Anode radius a = 0.5 cm; cathode radius c = 1.0 cm; $E_a°$ = 0.00V, $E_c°$ = 1.00V.)

could reach its own open-circuit steady-state potential. Approximately 8 hr were required for the quiescent solution and 6 hr for the stirred solution. Reference electrodes were chlorodized silver wires described previously (36) and immersed directly into the electrolyte near the surface at the center of the anode and the center of the cathode. Measured electrode potentials were always converted to potentials *vs.* the conventional Ag/AgCl electrode.

Evans polarization diagrams were determined using a Wenking potentiostat in a two-electrode configuration (37) so that it acted as a zero-resistance ammeter. In this mode, the auxiliary electrode terminal is connected directly to the reference electrode terminal, so that a constant potential difference is set between the working electrode (anode) and the auxiliary electrode (cathode). For a constant potential difference, a constant current and constant individual electrode potentials were observed in 10-20 min for the quiescent solution and in 5 min for the stirred solution. With increased current, electrode potentials of the anode and cathode approached each other. At zero potential difference set between the two electrodes, the measured current was the short-circuit current, or the total anodic current, I_{anodic}.

Results and discussion.—Polarization curves for the two cases are plotted in the usual manner, as well as linearly, in Fig. 12 and 13. In both cases, the couples are under cathodic control. Each cathodic plot in Fig. 13 is linear over only a portion of the curve, and the extrapolated value $E_c°'$ of the open-circuit potential is quite different from the observed value $E_c°$.

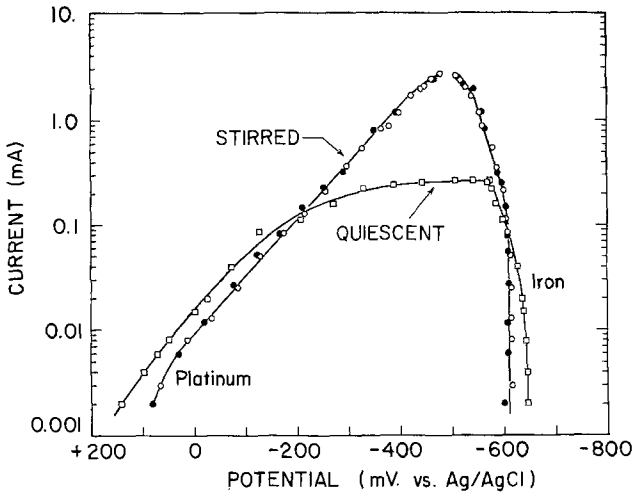
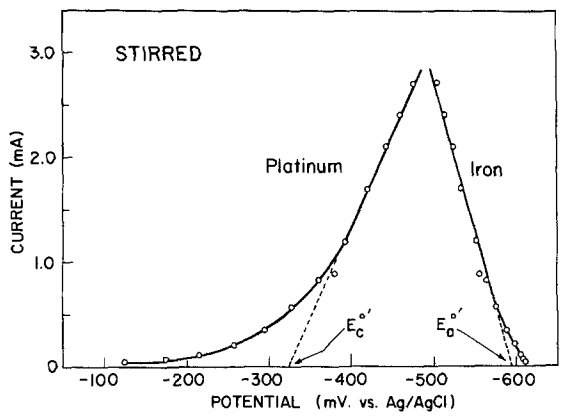


Fig. 12. Polarization curves for platinum and iron in stirred and quiescent 0.05M NaCl open to the air.



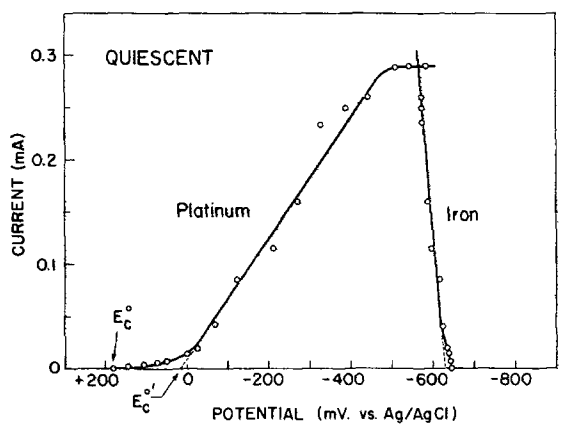


Fig. 13. Polarization curves plotted linearly for platinum and iron in 0.05M NaCl open to the air.

Table II lists values for the total anodic current calculated from Eq. [20] with n = 100. The electrode

Table II. Summary of data for Pt/Fe couples in bulk 0.05M NaCl open to the air. (Anode radius a = 1.0 cm, cathode radius c = 2.5 cm, electrolyte thickness b = 3.0 cm, σ = 5.5 × 10^{-3} Ω^{-1} cm^{-1})

Condition	Experimental parameters	Potential at center of anode Calculated (V)	Measured (V)	Potential at center of cathode Calculated (V)	Measured (V)	Total anodic current Calculated (mA)	Measured (mA)
Stirred	$E_a°'$ = −0.595V $E_c°'$ = −0.322V $\mathcal{L}_a$ = 0.59 cm $\mathcal{L}_c$ = 5.23 cm	−0.535	−0.506	−0.445	−0.477	2.2	2.7
Quiescent	$E_a°'$ = −0.635V $E_c°'$ = +0.020V $\mathcal{L}_a$ = 3.7 cm $\mathcal{L}_c$ = 155 cm	−0.565	−0.584	−0.550	−0.577	0.33	0.29

potentials at the center of the anode and center of the cathode calculated from Eq. [18] (with $n = 100$) are also given in Table II. Agreement between experiment and theory is satisfactory.

In the strictest sense, the present model does not apply exactly to the unstirred electrolyte where the cathodic reaction is diffusion controlled. The problem is that the requirement of uniform concentration will not hold within the thin diffusion layer near the surface. Nevertheless, it is instructive to make the calculations because in many practical cases of corrosion the cathodic reaction does involve oxygen reduction under diffusion control. Table II shows that the calculated corrosion current is slightly too high, because the calculated potential lies in the limiting current range.

For the stirred solution, where Tafel behavior is observed, the linear approximation calculates a value of the short-circuit current which is lower than the observed value. This result is in general agreement with the results for other systems where current distributions have been compared for Tafel and linear kinetics. For a cathode having a narrow slot, the current density down the lateral face of the slot falls off more rapidly with distance for linear than for logarithmic polarization (38). For a planar cathode opposite a remote anode, the current density across the cathode breadth is also smaller for linear than for Tafel kinetics (39).

The results for the stirred electrolyte are also in general agreement with the recent analysis of Smyrl and Newman (13), who treated the case of a corroding disk in an infinite plane assuming Tafel kinetics for the disk and the linear approximation for the plane. These authors characterize linear or Tafel polarization through two parameters (called J and δ, respectively) derived from the dimensionless quantity $\lambda/[\sigma(d\eta/di)]$, first introduced by Hoar and Agar (40), in which λ is a "characteristic length" of the geometrical system. From the definition of the Wagner polarization parameter

$$J = \frac{\lambda}{\mathcal{L}} \qquad [29]$$

for linear kinetics. For Tafel kinetics, $d\eta/di = (1/i)(RT/\alpha n\mathbf{F})$, so that

$$\delta = i_{avg}\frac{2.303}{b\sigma}\lambda \qquad [30]$$

where b is the Tafel slope. Thus for Tafel polarization, δ plays the role of J but depends on the current density.

For the stirred electrolyte, the anodic Tafel slope in Fig. 12 is 80 mV/decade, which gives $\delta = 4.50$ at the observed corrosion current, using the disk radius as λ. The value of J for the cathode corresponding to $\mathcal{L}_c = 5.23$ cm is 0.29, using $(c\text{-}a)$ as the characteristic length. (Smyrl and Newman use the disk radius for the characteristic length for their infinite cathode, but there is little difference between using $(c\text{-}a)$ or a in the present case). From Fig. 5 in Ref. (13), the potential difference between the center and edge of the disk for $\delta = 4.50$ and $J = 0.29$ is between 25 and 50 mV, in agreement with the value 38 mV calculated from Eq. [13] of the present analysis.

The current distribution across the iron disk calculated from Eq. [14] also agrees qualitatively with the analysis of Smyrl and Newman (13) who plot results for a slightly different value of δ (1.14 rather than 4.50) coupled with various values of J.

Application to the experiments of Pavlutskaya and Rosenfeld.—Few detailed experiments have been carried out with circular coplanar electrodes. However, Rosenfeld and Pavlutskaya (15, 16) have measured the potential distribution across an iron circular anode in contact with a copper disk cathode in 0.1*N* NaCl of

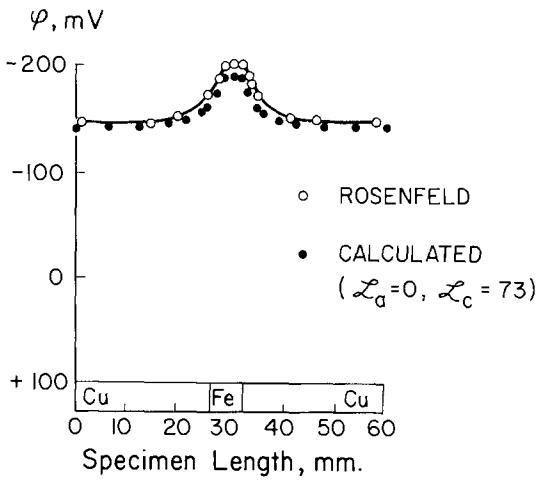


Fig. 14. Comparison of calculated potential distribution with experimental data of Rosenfeld for circular electrodes in bulk 0.1*N* NaCl. The experimental data are redrawn from Ref. (15).

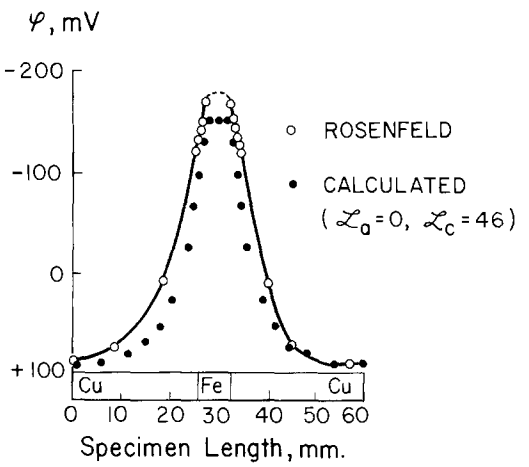


Fig. 15. Comparison of calculated potential distribution with experimental data of Rosenfeld for circular electrodes in 165μ 0.1*N* NaCl. The experimental data are redrawn from Ref. (15).

both bulk and 165μ thickness. Their experimental data are shown in Fig. 14 and 15 which are redrawn from photographic enlargements of their published results.

Rosenfeld (15) has also published polarization curves for a variety of metals in bulk and thin-layer electrolyte in which the data have been presented linearly. In order to apply the present theory to the Rosenfeld results, photographic enlargements were made of the published cathodic polarization curves for copper and anodic polarization curves for iron in 0.1 NaCl.

For copper in bulk 0.1 NaCl, the cathodic curve was nearly linear for an appreciably large overvoltage of about 1V, after which the curve shifted considerably, presumably as the reaction moved from the region of oxygen reduction into that of hydrogen evolution. A tangent approximation was drawn to the linear portion of the curve; and, as explained earlier, the value of E_c° was replaced by the value $E_c^{\circ\prime}$ at the intersection of the tangent approximation and the potential axis. For copper in 165μ 0.1*N* NaCl, the cathodic polarization curve was linear over the entire range shown. Values of $\mathcal{L}_c$ were calculated from the slopes of the cathodic polarization curves and the handbook value of the electrolyte conductivity and are listed in Table III.

The anodic curves for iron reported by Rosenfeld are somewhat curious in that the polarized potentials start out in the active (more negative) direction be-

Table III. Summary of parameters for application to the experimental results of Rosenfeld and Pavlutskaya

Electrolyte thickness	Parameter and source $\mathcal{L}_a$ (cm)	$\mathcal{L}_c$ (cm)	$E_a°$ (V)	$E_c°'$ (V)
Bulk	0*	73**	−0.19*	0.00**
165μ	0†	46**	−0.15†	+0.10**
70μ	1*	30**	−0.13*	+0.10**

* Ref. (5), Fig. 78.
** Ref. (5), Fig. 64.
† Ref. (41) (for 200μ thickness).

fore turning toward the more noble (positive) direction.

This behavior is not the usual for an anodic polarization curve and is not consistent with this author's observations for iron in the bulk as reported here or in thin-layer electrolyte (36). Thus, for the purposes of these calculations, the open-circuit potential of the anode was taken to be that as observed by Rosenfeld, with the $\mathcal{L}_a$ value determined from the "normal" part of the curve, where the anode was practically nonpolarizable, as per the behavior in Fig. 12.

A complete listing of the various parameters extracted from the Rosenfeld data is given in Table III.

The potential distributions calculated from Eq. [13] for the bulk and from Eq. [18] for thin-layer electrolyte are shown in Fig. 14 and 15. In both cases, there is good agreement between the calculations and the experimental data.

In addition, Rosenfeld and Pavlutskaya have shown the effect of cathode area on the total anodic current for both bulk and thin-layer electrolyte. These experimental results are shown in Fig. 16, which again is redrawn from a photographic enlargement from the Rosenfeld text (15). The total anodic current for variable cathode area was calculated using Eq. [16] for the bulk and Eq. [20] for thin-layer electrolyte. Results are superimposed on the Rosenfeld data in Fig. 16. In general, the calculations are in good agreement with the experimental data, although for thin-layers, the calculated currents are somewhat high for the smaller area cathodes. Nevertheless, the agreement is much better than for the extreme cases where $\mathcal{L}_a$ and $\mathcal{L}_c$ are taken to be equal, as shown in Fig. 16.

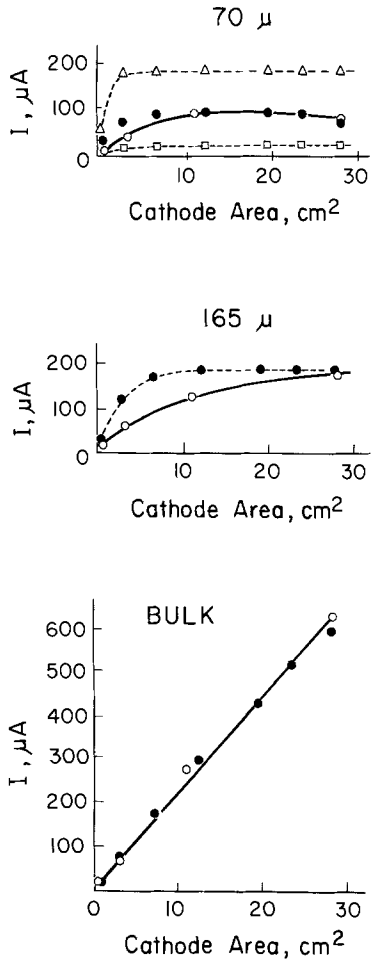


Fig. 16. Comparison of calculated anodic current with experimental data for varying cathode size. —O— Experimental data of Rosenfeld redrawn from Ref. (15). 70μ: Δ $\mathcal{L}_a = \mathcal{L}_c = 1$, □ $\mathcal{L}_a = \mathcal{L}_c = 30$, • $\mathcal{L}_a = 1$, $\mathcal{L}_c = 30$; 165μ: • $\mathcal{L}_a = 0$, $\mathcal{L}_c = 46$; Bulk: • $\mathcal{L}_a = 0$, $\mathcal{L}_c = 73$.

Summary

A mathematical model has been developed to describe the distribution of potential and current across circular corrosion cells having unequal anodic and cathodic linear polarization parameters. This analysis is applicable to systems of bimetallic galvanic couples or to systems where there is a localized geometry effect, as in pitting corrosion.

The potential distribution in a system having unequal anodic and cathodic polarization parameters is not related in a simple manner to the separate distribution curves for the two cases where the polarization parameters are equal.

For bulk electrolyte, the value of the electrode potentials depends on whether the system is under anodic, cathodic, or mixed control. Current distribution is more uniform for the more polarizable combinations of electrodes. Thus, the total corrosion current calculated from Evans diagrams may be in error if the individual current distributions are not uniform.

In thin-layer electrolytes, there is a geometry effect in which the electrode polarization and current flow is concentrated near the anode/cathode juncture. In a typical system, the tendency toward bulk behavior occurs at about 0.1-0.3 cm, *i.e.*, 1000-3000μ.

Acknowledgment

The author is grateful to the Office of Naval Research for the financial support of this project.

Manuscript submitted March 4, 1977; revised manuscript received July 27, 1977.

Any discussion of this paper will appear in a Discussion Section to be published in the June 1978 JOURNAL. All discussions for the June 1978 Discussion Section should be submitted by Feb. 1, 1978.

Publication costs of this article were assisted by the Naval Research Laboratory.

APPENDIX

The solution to Laplace's equation subject to the boundary conditions of: (*i*) no current flow across the planes $r = 0$ or $r = c$, and (*ii*) that the electrostatic potential be bounded for large values of z is

$$P(r,z) = B_0 + \sum_{n=1}^{\infty} B_n J_0(\lambda_n r) e^{-\lambda_n z} \qquad [A\text{-}1]$$

At the metal surface

$$P(r,0) - \mathcal{L}_a \left[\frac{\partial P(r,z)}{\partial z} \right]_{z=0} = V' - E_a° \qquad [A\text{-}2]$$

for the anode $(0 < r \leq a)$; and

$$P(r,0) - \mathcal{L}_c \left[\frac{\partial P(r,z)}{\partial z} \right]_{z=0} = V' - E_c° \qquad [A\text{-}3]$$

for the cathode $(a < r \leq c)$. Use of Eq. [A-1] in Eq. [A-2] and [A-3] gives the pair of equations

$$B_0 + \sum_{n=1}^{\infty} B_n(1 + \mathcal{L}_a\lambda_n) J_0(\lambda_n r) = V' - E_a°, \quad 0 \leq r < a \qquad [A\text{-}4]$$

and

$$B_0 + \sum_{n=1}^{\infty} B_n(1 + \mathcal{L}_c\lambda_n)J_0(\lambda_n r) = V' - E_c^\circ, \quad a < r \leq c \qquad [A\text{-}5]$$

Each equation is multiplied by $rJ_0(\lambda_m r)\,dr$ and integrated over the appropriate limits. Equation [A-4] becomes

$$\frac{B_0}{\lambda_m} aJ_1(\lambda_m a) + B_m(1 + \mathcal{L}_a\lambda_m)\int_{r=0}^{a} rJ_0^2(\lambda_m r)\,dr + \sum_{\substack{n=1 \\ n\neq m}}^{\infty} B_n(1 + \mathcal{L}_a\lambda_n)\int_{r=0}^{a} rJ_0(\lambda_n r)J_0(\lambda_m r)\,dr = \frac{(V' - E_a^\circ)}{\lambda_m} aJ_1(\lambda_m a) \qquad [A\text{-}6]$$

where the summation in Eq. [A-4] has been split into two cases: $n = m$, and $n \neq m$. In the previous case (6) where $\mathcal{L}_a = \mathcal{L}_c = \mathcal{L}$ applied over the entire interval from $r = 0$ to $r = c$, the integrals in Eq. [A-6] were the usual orthogonality relations. Here, instead, the second integral in Eq. [A-6] is a Lommel integral (42) which is evaluated as

$$\int_0^a rJ_0(\lambda_n r)J_0(\lambda_m r)\,dr = \frac{a}{\lambda_n^2 - \lambda_m^2} \times [\lambda_n J_1(\lambda_n a)J_0(\lambda_m a) - \lambda_m J_0(\lambda_n a)J_1(\lambda_m a)] \quad (n \neq m) \qquad [A\text{-}7]$$

When $n = m$, the right-hand side of Eq. [A-7] is evaluated from l'Hospital's rule to be $(a^2/2)[J_0^2(\lambda_m a) + J_1^2(\lambda_m a)]$. Evaluation of the two integrals in Eq. [A-6] then yields one of the two simultaneous equations in B_0 and B_n. The second equation follows from multiplication of Eq. [A-5] by $rJ_0(\lambda_m r)\,dr$ and integration from $r = a$ to $r = c$. The two simultaneous equations are solved to give Eq. [10] in the text.

The constant B_0 is also evaluated from Eq. [A-4] and [A-5]. Both equations are multiplied through by rdr, integrated over the appropriate limits, and solved simultaneously to give Eq. [9] in the text.

REFERENCES

1. K. J. Vetter and H.-H. Strehblow, in "Localized Corrosion," p. 240, NACE, Houston, Texas (1974).
2. B. F. Brown, *Machine Design*, **40**, (2), 165 (1968).
3. F. L. LaQue, "Marine Corrosion," p. 117, Wiley-Interscience, New York (1975).
4. A. Cohen and W. S. Lyman, *Materials Protection*, **11** (2), 48 (1972).
5. I. L. Rosenfeld, "Atmospheric Corrosion of Metals," p. 121, NACE, Houston, Texas (1972).
6. L. Gal-Or, Y. Raz, and J. Yahalom, *This Journal*, **120**, 598 (1973).
7. E. McCafferty, *Corros. Sci.*, **16**, 183 (1976).
8. E. McCafferty, NRL Report 7835, Naval Research Laboratory, Washington, D.C. (1975).
9. J. T. Waber, *This Journal*, **101**, 271 (1954).
10. J. T. Waber and M. Rosenbluth, *ibid.*, **102**, 344 (1955).
11. J. T. Waber, *ibid.*, **102**, 420 (1955).
12. J. T. Waber and B. Fagan, *ibid.*, **103**, 64 (1956).
13. W. H. Smyrl and J. Newman, *ibid.*, **123**, 1423 (1976).
14. E. Kennard and J. T. Waber, *ibid.*, **117**, 880 (1970).
15. I. L. Rosenfeld, "Atmospheric Corrosion of Metals," pp. 60-90, NACE, Houston, Texas (1972).
16. I. L. Rosenfeld and T. I. Pavlutskaya, *Zh. Fiz. Khim.*, **31**, 329 (1957).
17. J. Newman, in "Advances in Electrochemistry and Electrochemical Engineering," Vol. 5, C. W. Tobias, Editor, p. 87, Interscience, New York (1967).
18. D. C. Grahame, *Chem. Rev.*, **41**, 441 (1947).
19. J. O' M. Bockris and A. K. N. Reddy, "Modern Aspects of Electrochemistry," Vol. 2, pp. 644 ff, Plenum Press, New York (1970).
20. C. Wagner, *This Journal*, **98**, 116 (1951).
21. V. K. Gouda and H. M. Mourad, *Corros. Sci.*, **14**, 681 (1974); *ibid.*, **15**, 307 (1975); *ibid.*, **15**, 317 (1975); *ibid.*, **15**, 329 (1975).
22. P. W. Board, R. V. Holland, and D. Britz, *Br. Corros. J.*, **3**, 238 (1968).
23. P. L. Bonara, A. Barbangelo, and G. P. Ponzano, *ibid.*, **10**, 23 (1975).
24. B. N. Stirrup, N. A. Hampson, and I. S. Midgley, *J. Appl. Electrochem.*, **5**, 229 (1975).
25. K. W. Mao, *This Journal*, **120**, 1056 (1973).
26. J. Postlethwaite and D. R. Hurp, *Corros. Sci.*, **7**, 435 (1967).
27. I. Marcos, *This Journal*, **122**, 1008 (1975).
28. M. Stern and A. L. Geary, *ibid.*, **104**, 56 (1957).
29. E. McCafferty, NRL Report 8107, Naval Research Laboratory, Washington, D.C. (1977).
30. E. J. Kelly, *This Journal*, **112**, 124 (1965).
31. S. Asakura and K. Nobe, *ibid.*, **118**, 19 (1971).
32. F. Hilbert, Y. Miyoshi, G. Eichkorn, and W. J. Lorenz, *ibid.*, **118**, 1919 (1971).
33. E. McCafferty and N. Hackerman, *ibid.*, **119**, 999 (1972).
34. K. E. Heusler and G. L. Gaiser, *ibid.*, **117**, 762 (1970).
35. C. K. Watanabe and K. Nobe, *J. Appl. Electrochem.*, **6**, 159 (1976).
36. E. McCafferty, *This Journal*, **121**, 1007 (1974).
37. J. Dévay, B. Lengyel, Jr., and L. Mészáros, *Acta Chim. Acad. Sci. Hung.*, **62**, 157 (1969).
38. C. Wagner, *Plating*, **48**, 997 (1961).
39. N. P. Gnusin, N. P. Poddubnyi, E. N. Rudenko, and A. G. Fomin, *Soviet Electrochem. (Engl. Transl.)*, **1**, 391 (1965).
40. T. P. Hoar and J. N. Agar, *Discuss. Faraday Soc.*, **1**, 162 (1947).
41. I. L. Rosenfeld and T. I. Pavlutskaya, *Russian J. Phys. Chem. (Engl. Transl.)*, **35**, 641 (1961).
42. F. E. Relton, "Applied Bessel Functions," p. 51, Dover Publications, New York (1965).

Techniques for Characterizing Porous Electrodes

I: Determination of the Double Layer Capacity

B. V. Tilak and C. G. Rader

Hooker Chemicals & Plastics Corporation, Research Center, Grand Island, New York 14072

and S. K. Rangarajan[1]

Department of Inorganic and Physical Chemistry, Indian Institute of Science, Bangalore, India

ABSTRACT

Two relaxation techniques are examined for determining the double layer capacity of porous electrodes of finite length. In the presence of a faradaic reaction, under near equilibrium conditions, analytical expressions are derived for the transient potential response to current perturbations of the form $i(t) = \Delta i \exp(-t/\tau)$ and $i(t) = \Delta i(1 - t/\tau)$. The ease with which the system parameters (R_T and C_T) can be deduced by employing these two techniques is analyzed. Experimental support for the exponential relaxation technique is provided by examining three electrochemical systems: sintered nickel plaque/NaOH; Teflon-bonded Pt on Pt screen/NaOH; and $TiO_2 + RuO_2$ coatings on Ti/NaCl aq.

Porous bodies are unique in that they offer high specific surface area, thereby enabling one to carry out otherwise slow reactions at an enhanced rate. Operating with a high specific area porous medium, however, creates its own problems via the associated phenomena such as mass transport, charge transport, finite conductivity of the electrolyte, etc.

Characterization of porous electrode operations requires a knowledge of the structural details of the internal surface of a porous body and operational details within the porous matrix. The resulting equations describing mass transport and potential variations are not only nonlinear and multidimensional, but they also require simultaneous solution. Solution of the system equations may be facilitated by idealizations (simplifications) of various phenomena, as reflected in several published models for describing the operation of, for example, gas diffusion electrodes. The results, however, are valid only for a given set of conditions and not for a random choice of variables. These various models may be classified into three groups—homogeneous, quasihomogeneous, and statistical or discrete models (1).

"Surface area" is one of the parameters which characterizes a porous electrode, and double layer capacitance is known to provide a reliable estimate of the surface area effective for participation in electrochemical reactions, as opposed to physical or geometric area measured, for example, by standard BET adsorption techniques.

The theoretical treatment of double layer charging was first presented by Ksenzhek and Stender (2). Posey and Morozumi (3), assuming double layer charging to be the only significant interfacial process, presented solutions to the boundary value problems of potentiostatic and galvanostatic charging of finite porous electrodes. It will be shown that the present treatment reduces, in the limit, to the analytical expression presented by Posey and Morozumi for the potential response to a galvanostatic step function.

In 1969, Rangarajan (4) presented a comprehensive treatment of the transient behavior of flooded porous electrodes under galvanostatic and sinusoidal perturbations. In this work, ohmic activation, and concentration polarizations were treated as a generalized impedance, along with a detailed discussion of the possible pitfalls of a naive data interpretation in a region of coupled (mixed) phenomena. Response to other forms of input (*e.g.* potentiostatic) can also be deduced, under linear perturbation conditions, from the formalism outlined in Ref. (4).

In 1973, Austin and Gagnon (5) introduced a triangular voltage sweep method for determination of the double layer capacity of a porous electrode. Under limited conditions, approximate correction can be made for faradaic current interference by this technique. Tiedemann and Newman (6) have described a method for double layer capacity determination by exploring the current response to a voltage step input function. This method, which requires estimation of the intrapore resistance, has yielded values of the double layer capacity for Pb and PbO_2 electrodes in sulfuric acid which are in agreement with literature values. Universal applicability of this technique is doubtful, however, due to the disregard of faradaic reaction. McHardy *et al.* (7) have employed a low frequency a-c technique for determination of differential capacitance. While the reported results are internally consistent, the experimentally measured impedance may reflect complex phenomena which are not uniquely related to double layer charging.

Thus, various limitations are seen to exist in most treatments of double layer capacity determination, and these may be generalized in terms of either lack of experimental accessibility or theoretical tractability to deduce the parameter(s) of interest.

Relaxation Techniques and the Parametric Approach

A critical analysis of various perturbation techniques (8)—transient or steady-state (periodic)—carried out in a time or frequency axis (parametric domain) showed that the role of input parameters, occurring through the input current or voltage profile, lies in the ability to "force" specific features; *e.g.*, maximum, inflection point, change of polarity, etc., in the output response profile. Thus, in the case of linear relaxation methods (8), two-parameter current (or potential) controlled input functions were found to offer response characteristics unique in the ease of data analysis and in experimental design.

Two new methods.—The theory of the overpotential transient resulting from the application of an exponentially decaying current ($i = \Delta i \exp(-t/\tau)$) was introduced by Rangarajan (9) in 1973. This discourse on relaxation processes was concerned with the interplay of activation, linear diffusion, and a following or preceding chemical reaction in the bulk. The usefulness

[1] Present address: The University of Newcastle upon Tyne, Newcastle, NE1 7RU England.

Key words: double layer capacity, porous electrodes, exponential relaxation technique, Ni plaque, Cl_2 evolution.

of a "parametric approach" as regards providing a unified picture of relaxation techniques has recently been demonstrated again by Rao *et al.* (10). A "decreasing current ramp technique" (dcrt), $i = \Delta i\,(1 - t/\tau)$, was used for measuring the rate constant and transfer coefficient in the study of a fast electrode reaction ($K_4Fe(CN)_6 + K_3Fe(CN)_6$/Pt). In the present communication, these two-parameter current-controlled input functions are examined (theoretically and experimentally) for determining the double layer capacitance of porous electrodes.

It may be noted here that the single-pulse galvanostatic method and the coulostatic case can be viewed as special cases of the exponential technique when $t << \tau$ (where t = time and τ, the input time constant) and when Δi is large and equal to $\Delta q/\tau$; *i.e.*, $\tau \to 0$ and Δq finite. The double pulse method and the a-c techniques also come under the exponential relaxation type perturbation in a general sense, since τ in the exponential input plays a role analogous to the frequency, ω, in the a-c techniques. In the impedance measurements we employ "ω" as a probe to obtain the fingerprints of the dynamics of the (porous) system, *viz.*, its spectra of relaxation times. We do the same in the proposed methods via τ. There is yet another difference. Whereas in the impedance approach average responses are measured, the entire time variation during τ can be exploited in the exponential technique.

Theoretical Considerations

The multidimensional difficulties associated with the quantitative description of gas diffusion or two-phase porous electrodes can be solved by assuming a homogeneous model wherein the interconnected multiphase system is treated as a homogeneous phase. This, in essence, replaces the distributed heterogeneous sources/sinks by appropriate homogeneous or volume entities.

Homogenization is achieved in the elementary flooded pore model by transformation of surface sources (or sinks) to volume sources by introducing the parameter S, signifying the specific surface of a matrix in cm^2/cm^3. This can be justified since the electrochemical reaction takes place, though at different rates, along the entire surface of the porous medium. S can be identified as the total internal surface for flooded porous electrodes. However, its precise meaning depends on the reaction mechanism. Thus, for gas-filled electrodes, S can be equal to the total internal surface (up to 80% gas content), and it reflects macroporosity if wetting of macropores is possible.

In the case of three-phase systems, S may be calculated in terms of the common area between the gas and liquid, provided the pore distribution statistics are calculable (11).

Following the elementary flooded model defined previously (3, 4), the system of equations defining the time variant potential in a pore of finite length may be expressed as follows

$$\frac{\partial^2\eta}{\partial\xi^2} - \alpha\eta - \beta\frac{\partial\eta}{\partial t} = 0 \qquad [1]$$

where $\alpha = \dfrac{R_o S l n \mathbf{F} i_o}{RT} = \dfrac{R_o}{R_T}$ (ratio of the electrolyte resistance in the pores to the charge transfer resistance); $\beta = R_o C_T$ (time constant associated with the charging of the double layer); $R_o = l/\sigma A$; A = cross-sectional area (cm^2); l = pore length; σ = specific conductance of the solution phase (Ω^{-1} cm^{-1}); $C_T = Scl$ = total differential capacity; S = surface area of porous electrode/unit length; c = differential capacity/cm^2; $I = iSl$ = total current; $\xi = x/l$; x = distance coordinate; and i = microkinetic current density = $i_o n\mathbf{F}\eta/RT$. The initial condition is $\eta(t = 0) = 0$, and boundary conditions are $(\partial\eta/\partial\xi)_{\xi=1} = 0$; $(\partial\eta/\partial\xi)_{\xi=0} = -R_o i(t)$; and $i(t)$: two-parameter current-controlled input function. Equation [1] actually expresses the fact that, at any instant, the impressed current is a sum of double layer charging and faradaic currents.

The salient features of the present formulation are as follows:

(*i*) The specific structure of the porous material is ignored and its behavior is assumed to be equivalent to that of an isotropic, macroscopically homogeneous medium which restricts the space variations along one dimension; *i.e.*, the depth of the electrode. (This hypothesis transforms the sources and sinks distributed over the pore walls to volume sources and sinks.)

(*ii*) Diffusion and migration are not considered. [See Ref. (4) where diffusion coupling has been analyzed under galvanostatic conditions.]

(*iii*) Potential distribution is given by a simple equation as insured by the hypothesis that the solution + matrix conductivity is constant.

(*iv*) Only small perturbations from equilibrium conditions are examined by using a linear i-η relationship.[2] [Under these restrictions, the porous electrode can be viewed as equivalent to a transmission line of finite length with electrolyte resistance in series shunted by a parallel combination of double layer and faradaic impedances. See Ref. (12).]

The boundary value problem stated above was solved (using Laplace transforms) for two, two-parameter current-controlled input functions: (*i*) $i(t) = \Delta i \exp(-t/\tau)$, (exponential current decay); and (*ii*) $i(t) = \Delta i\,(1 - t/\tau)$, (decreasing current ramp).

Alternately, the potential response to the exponentially decaying current input can also be derived following the theorems developed by Rangarajan (9), according to which

$$\eta(t) = i(t)\,\gamma^3(t,\tau)$$

where

$$\gamma^3(t,\tau) = \mathcal{L}^{-1}[Z(P - 1/\tau)],\ i(t) = \Delta i \exp(-t/\tau)$$

$\mathcal{L}^{-1}$ refers to the inverse transform in Heaviside's notation[3] and $Z(P)$ the generalized impedance of the porous matrix-electrolyte interface in the Laplace domain, as deduced earlier (4).

Thus, the transient response to the above two current-controlled input functions appears as follows:

Exponential relaxation technique ($i(t) = \Delta i \exp(-t/\tau)$)

$$\eta = -R_o i(t)\left\{\left[\frac{\exp\left(-t\left(B - \frac{1}{\tau}\right)\right) - 1}{\beta\left(B - \frac{1}{\tau}\right)}\right] + \left[\frac{2}{\beta}\sum_{n=1}^{\infty}\frac{(-1)^n \cos n\pi(1-\xi)}{\left(A - \frac{1}{\tau}\right)}\right.\right.$$
$$\left.\left.\cdot\left\{\exp\left(-t\left(A - \frac{1}{\tau}\right)\right) - 1\right\}\right]\right\} \qquad [2]$$

Decreasing current ramp technique ($i(t) = \Delta i(1 - t/\tau)$)

[2] How small the perturbation should be to validate linear laws as observed experimentally (cell current *vs.* half-cell voltage) has not been discussed clearly to date. It is interesting to note that one may expect the linearity to hold up to higher amplitudes than expected, as shown in Table II of Ref. (4), where the analytical, linear expressions are compared with those arising from the numerical, nonlinear model of Grens II and Tobias (13). Further work on this aspect is in progress.

[3] In Heaviside notation, $\mathcal{L}[f(t)] = P\int_0^\infty \exp(-Pt)\cdot f(t)\cdot dt$.

$$\frac{\eta}{\Delta i R_o} = \frac{1}{\beta}\left[\left\{ \left[\frac{1}{B} - \frac{t}{\tau B} + \frac{1}{B^2\tau} \right] - \exp(-Bt)\left(\frac{1}{B} + \frac{1}{\tau B^2} \right) \right\} + 2\sum_{n=1}^{\infty} (-1)^n \cos n\pi(1-\xi) \left[\left(\frac{1-\exp(-At)}{A} \right) - \left(\frac{At-1}{A^2\tau} \right) - \left(\frac{\exp(-At)}{A^2\tau} \right) \right] \right] \quad [3]$$

where

$$A = \frac{n^2\pi^2 + \alpha}{\beta}$$

$$B = \alpha/\beta$$

General Features of the Potential Response

Exponential relaxation technique.—Figure 1 shows that there exists a maximum (η_m) in the potential transient. The origin of this maximum can easily be understood in terms of the initial increase in η arising from the imposed current and the decreasing nature of the input current function with time. It is obvious that this is due to a time lag in following i and will be absent if the double layer charging is instantaneous. This rationale can be further extended to qualitatively understand the position (t_m) and the magnitude of η_m as related to the relative magnitude of the time constant of the input function, τ (see Fig. 2).

The situation shown in Fig. 1 for $\tau = \infty$ corresponds to the galvanostatic perturbation previously examined by Posey and Morozumi in 1966 (3).

While the observed maxima are attributed solely to the input function time constant τ, α (the ratio of electrolyte resistance in the pores to the charge transfer resistance) and β (related to the intrinsic electrode/electrolyte properties) will also influence the position and the magnitude of the observed η_m as seen in Fig. 3 and 4.

Decreasing current ramp technique (dcrt).—For reasons identical to those presented above for the exponential relaxation technique, the dcr input function will also exhibit a maximum in the potential transient which is dependent on the relative values of α, β, and input τ, as shown in Fig. 5, 6, and 7. The uniqueness of the observed maximum in the potential-time profile can now be exploited to characterize the system in terms of the relevant parameters, *e.g.*, C_T and R_T. Differentiation of the general η-t relations presented previously leads to the following expressions for η_m and t_m—the experimentally accessible quantities.

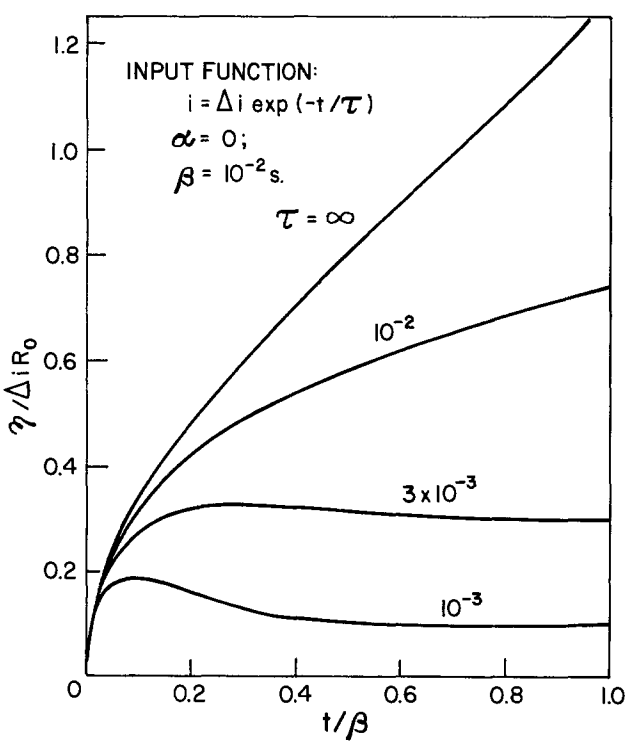


Fig. 1. Influence of τ on the potential-time profile for the exponentially decaying current input, when $\alpha = 0$.

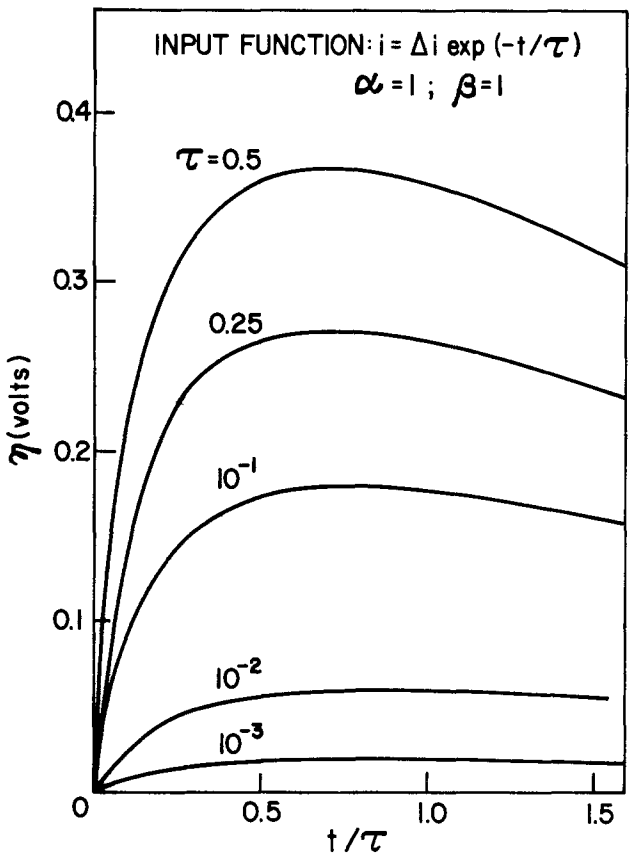


Fig. 2. Influence of τ on the potential-time profile for the exponentially decaying current input, when $\alpha = 1$.

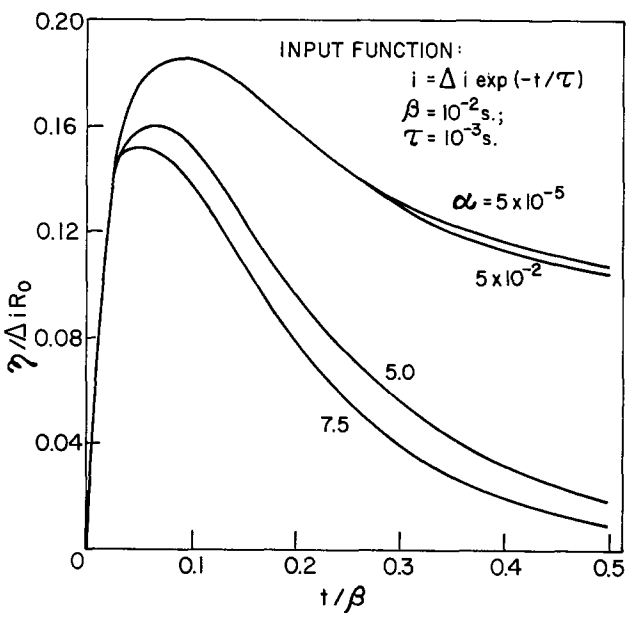


Fig. 3. Influence of α on the potential-time profile for the exponentially decaying current input function.

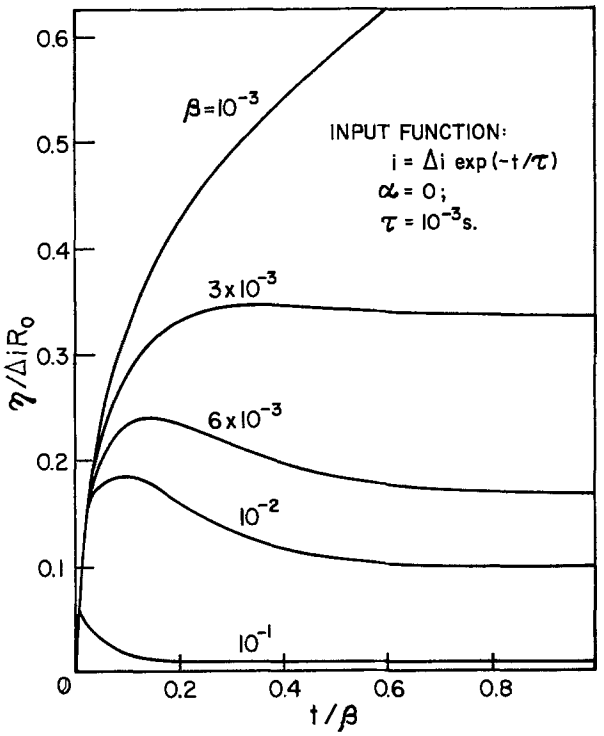


Fig. 4. Influence of β on the potential-time profile for the exponentially decaying current input function.

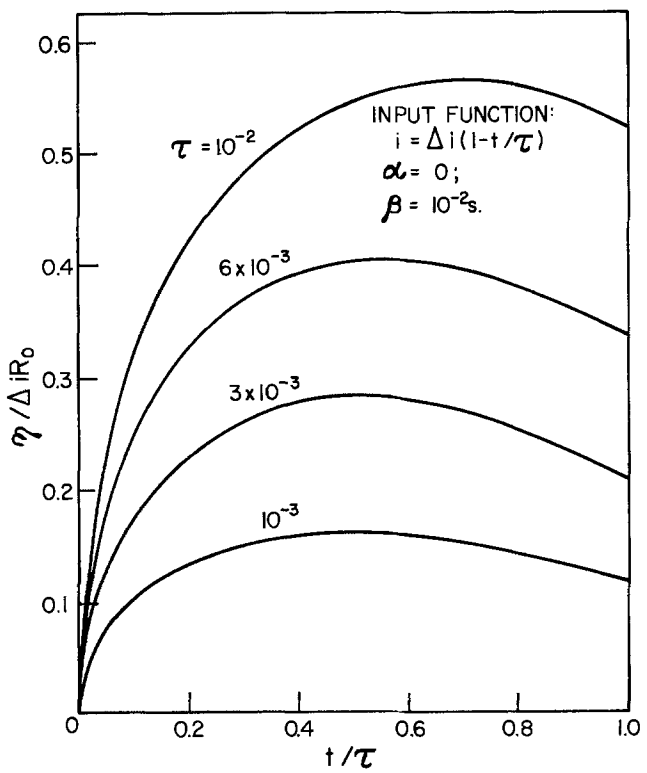


Fig. 5. Influence of τ on the potential-time profile for the decreasing current ramp input, when $\alpha = 0$.

Exponential relaxation technique ($\xi = 0$)

$$\frac{\eta_m}{\Delta i \tau} = \frac{1}{C_T} \cdot \exp\left(\frac{-\alpha t_m}{\beta}\right) \cdot \theta_3\left[\exp\left(\frac{-\pi^2 t_m}{\beta}\right)\right] \quad [4]$$

Where θ_3 (X) is the Jacobian θ function defined as $\sum_{n=0}^{\infty} \epsilon_n X^{n^2}$ ($\epsilon_n = 1$ for $n = 0$, $\epsilon_n = 2$ for $n > 0$).

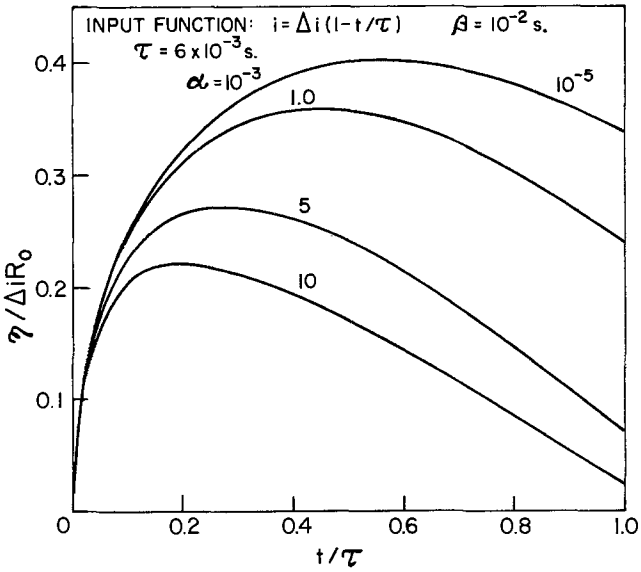


Fig. 6. Influence of α on the potential-time profile when the input function is $i = \Delta i\ (1 - t/\tau)$.

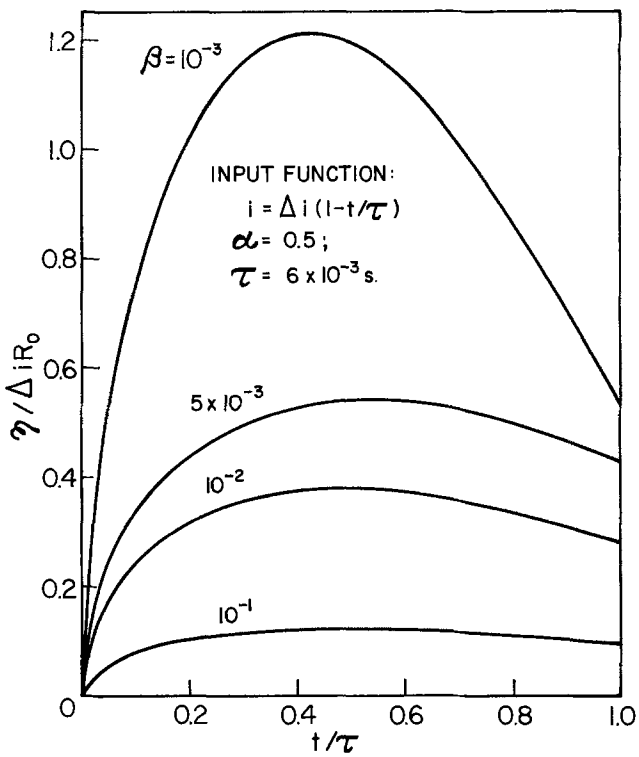


Fig. 7. Influence of β on the potential-time profile for the input function $i = \Delta i\ (1 - t/\tau)$.

dcrt ($\xi = 0$)

$$\frac{\eta_m}{\Delta i \tau} = \frac{1}{C_T}\left\{\left(\frac{1 - Bt_m}{B^2\tau^2}\right) + \exp(-Bt_m)\left(\frac{B^2\tau^2 - 1}{B^2\tau^2}\right) + 2\left[\sum_{n=1}^{\infty}\left(\frac{1 - At_m}{A^2\tau^2}\right) + \exp(-At_m)\left(\frac{A^2\tau^2 - 1}{A^2\tau^2}\right)\right]\right\} \quad [5]$$

where

$$A = \frac{n^2\pi^2 + \alpha}{\beta}$$

$$B = \alpha/\beta$$

Equation [4] can also be directly deduced from the generalized impedance $Z(P)$ using the following theorem derived in Ref. (9)

$$\frac{\eta_m}{\Delta i\tau} = \gamma'(T_m); \quad T_m = \frac{t_m}{\tau}$$

where

$$\gamma(t) = \mathcal{L}^{-1}[Z(P) - Z(\infty)]$$

and

$$\gamma'(t) = \frac{d\gamma}{dt} = \mathcal{L}^{-1}[P(Z(P) - Z(\infty))]$$

It should be noted from the above equations that the η_m-t_m relationship for the exponential perturbation is seemingly less complicated than the analogous expression for dcrt. This is not at all surprising, since dcrt has been shown to possess interesting features for "lumped parameter" systems, wherein it is possible to find times when η is wholly activation or diffusion controlled. Since the porous electrode system is a distributed system, η is no longer separable as "activation" and "diffusion" overpotentials. Nor is "the *IR*-drop" separable as for nonporous systems. The parameters characterizing these phenomenological components occur in a mixed position in the impedance for $Z(P)$ (4).

We now examine the behavior of the η_m-t_m relationship for the exponential relaxation technique under limiting conditions.

$\beta \to 0$.—This corresponds to a shift in control from R_o (electrolyte resistance in the pores) to R_T (charge transfer resistance) and double layer capacitance, C_T. The mathematical representation of this situation appears as

$$\frac{\eta_m}{\Delta i\tau} = \frac{1}{C_T}\exp\left(\frac{-\alpha t_m}{\beta}\right) \qquad [6]$$

Thus a plot of ln $\eta_m/\Delta i\tau$ *vs.* t_m under these conditions, should yield a straight line of slope α/β $(= 1/R_TC_T)$ and intercept $1/C_T$.

$\beta \to \infty$.—

$$\frac{\eta_m}{\Delta i\tau} = \sqrt{\frac{R_o}{\pi t_m C_T}}\exp\left(\frac{-\alpha t_m}{\beta}\right) \qquad [7]$$

Analogous to the $\beta \to 0$ case, a plot of ln $\eta_m t_m^{1/2}\pi^{1/2}/\Delta i\tau$ *vs.* t_m should yield a straight line of slope α/β and intercept $\sqrt{R_o/C_T}$. The $\beta \to 0$ approximation will apply when $t_m > \beta/\pi^2$, and this condition reduces the total expression relating η_m and t_m to the simple relationship corresponding to $\beta \to 0$. We shall examine here this possibility in greater detail.

In a practical system, the limiting approximation for η_m-t_m will be approximately obeyed, even for $t_m\pi^2/\beta \sim$ 2-5, which can be easily ensured by an appropriate choice of the input time constant τ. This is illustrated in Fig. 8, wherein the nonlinearity in η_m-t_m relationship is seen to prevail only at very low t_m values.

Experimental

All experiments were carried out in an all-glass, three-compartment cell, which was thoroughly cleaned in a hot HNO_3 + H_2SO_4 mixture and rinsed with triple distilled water. A large platinum gauze was used as the counterelectrode and the potential of the working electrode was measured with respect to a hydrogen electrode in the same solution. While studying the chlorine electrode reactions, a Cl_2/Cl^- electrode (14) and a SCE were employed.

The porous electrodes examined in this study were a sintered nickel plaque and a Teflon-bonded platinum electrode on a Pt screen (kindly supplied by Energy Research Corporation). The TiO_2 + RuO_2 electrode was prepared following the procedure described in Ref. (15). All solutions were deaerated with purified (16) H_2 (and N_2), and the studies were carried out at 25°C. The exponentially decaying current pulses were generated using the circuit described in Ref. (17), wherein the *IR* drop across the resistance in an *R-C* circuit during charging conditions is fed to a fast-rise Wenking potentiostat (70 HVI/90) operating in a galvanostatic mode. Potential-time transients were recorded on a Tektronix 564B oscilloscope with Type D plug-in amplifier and camera attachment. The transients were enlarged for the analysis of the data. The potentiodynamic experiments were performed using the standard circuitry (16).

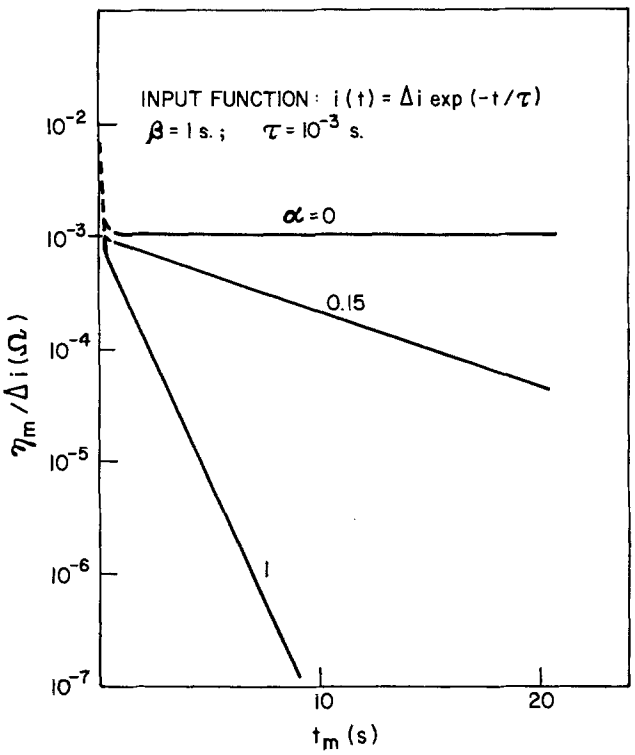


Fig. 8. η_m-t_m variation for various values of α when the input function is $i = \Delta i$ (exp $-$ t/τ).

Results and Discussion

"Ni plaque" electrode.—The initial system chosen for examining the application of theory to the objective of determining experimental parameters was nickel plaque-sintered Ni sheet in 4M NaOH at 25°C. In this system, the faradaic process is the hydrogen evolution reaction.

Figure 9 depicts actual potential/time profiles at different values of the input parameters τ and Δi. As predicted by the present theory, a maximum is observed in the potential transient, the locus of which is dictated by the input parameters and electrode properties (c.f. Fig. 1 and 4).

Following the $\beta \to 0$ approximation, the experimentally determined η_m-t_m pairs are plotted as ln $\eta_m/\Delta i\tau$ *vs.* t_m. The results for the Ni-plaque electrode system are shown in Fig. 10. The linearity predicted by the theory is apparent for values of $t_m > 50$ msec. From the intercept of Fig. 10, C_T is estimated to be 6.7 mF. The slope yields a value of the charge transfer resistance, $R_T = 63.9\Omega$. This R_T value corresponds to an exchange current density of $\sim$ 1 μA/cm^2, in general agreement with the published data (18).

In order to test the self-consistency of the present results with the limiting expression, the value of R_o is required. This may be evaluated from the galvanostatic charging transients at $t \to 0$. From the slope of the η *vs.* $2i\ t^{1/2}/\pi^{1/2}$ plot, which yields $\sqrt{R_o/C_T}$ (see Fig. 11), R_o is calculated to be 10.8Ω. Hence, $\beta = R_oC_T = 72$ msec. Therefore, the $\beta \to 0$ approximation should be valid for values of $t_m \geq 50$ msec, as observed in Fig. 10.

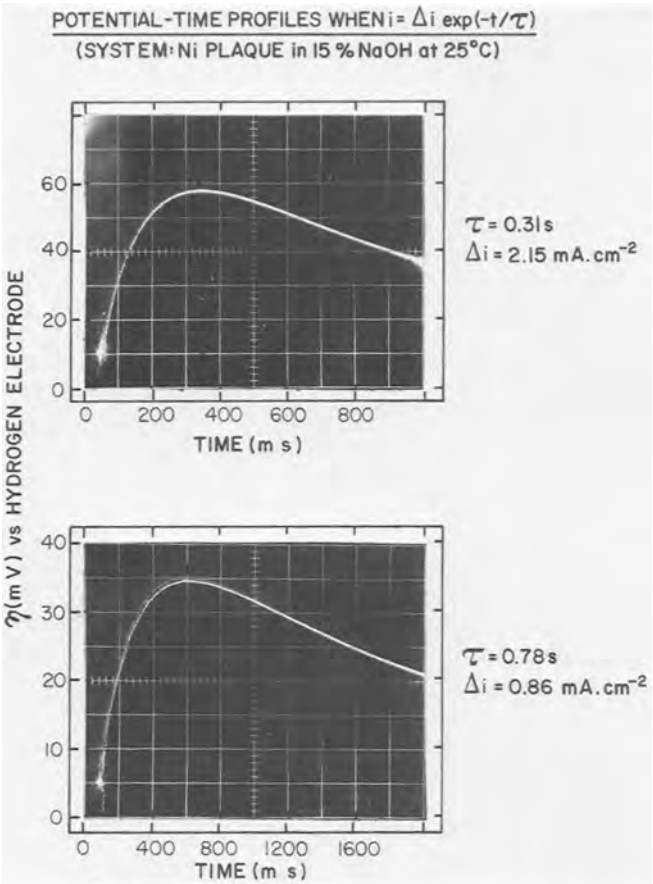


Fig. 9. Experimentally observed potential-time profile for the Ni plaque/NaOH system when the input function is $i = \Delta i \exp(-t/\tau)$.

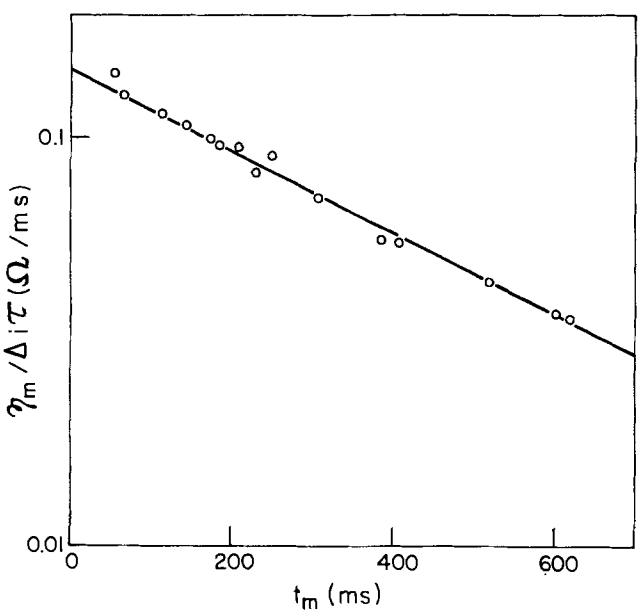


Fig. 10. Plot of ln $(\eta_m/\Delta i\tau)$ *vs.* t_m for the Ni plaque/NaOH system.

The self-consistency of the parameters derived from the $\beta \rightarrow 0$ approximation can be further tested by theoretically constructing the potential-time profiles and comparing with the experimental profiles. As seen in Fig. 12, the agreement is excellent.

Teflon-bonded Pt on Pt screen.—Figure 13 shows the experimental data for the Teflon-bonded Pt on Pt screen (supplied by Energy Research Corporation) in

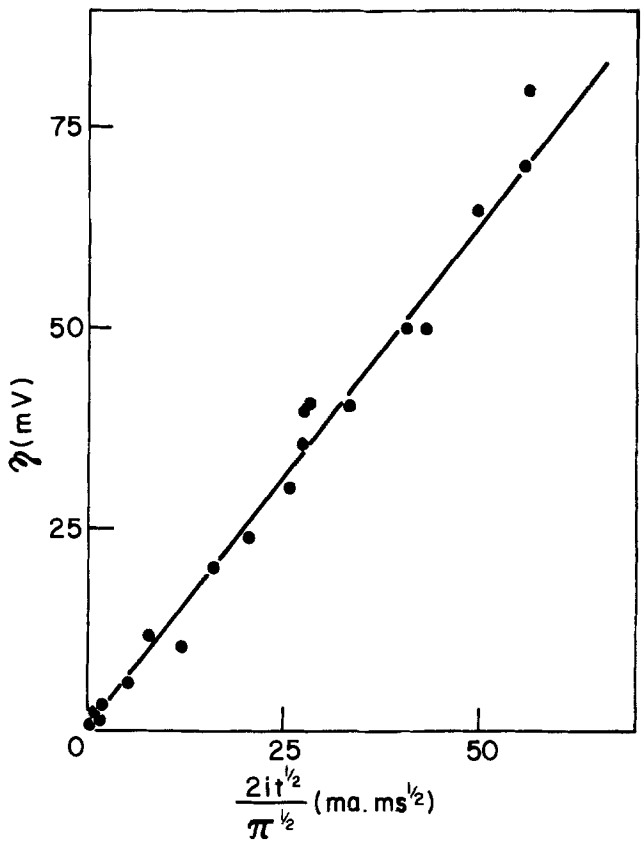


Fig. 11. Plot of η *vs.* $2it^{1/2}/\pi^{1/2}$ for the Ni plaque/NaOH system

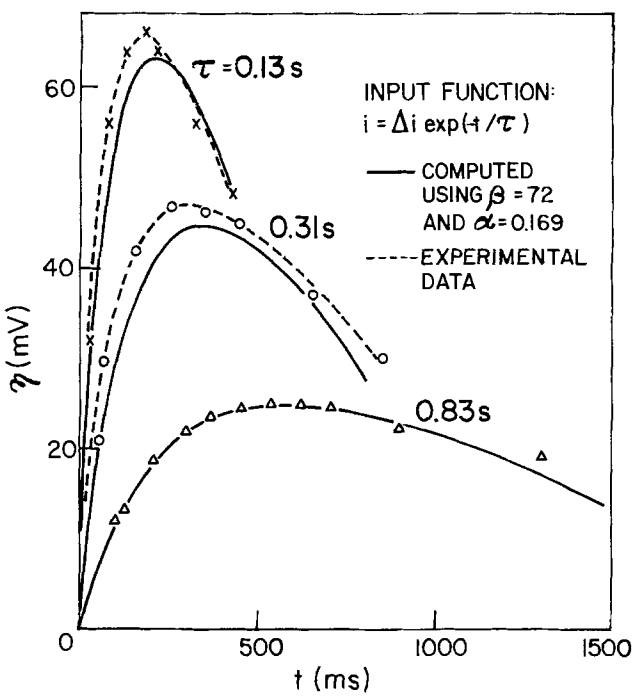


Fig. 12. Comparison of the experimentally observed potential-time profiles with the computer η-t profile, when $i = \Delta i \exp(-t/\tau)$.

4M NaOH at ~25°C. The η_m-t_m data pairs, plotted as $\ln(\eta_m/\Delta i\tau)$ *vs.* t_m, follow the linear trend at $t_m >>$ ~15 msec, as predicted by the $\beta \rightarrow 0$ approximation.

From the intercept and the slope of the line in Fig. 13, $C_T = 454$ mF and $R_T = 0.18\Omega$. This C_T value may be compared with the roughness factor of 2×10^4 cm²/cm² estimated from the BET measurements assuming $C_{ideal} \approx 20$ μF/cm².

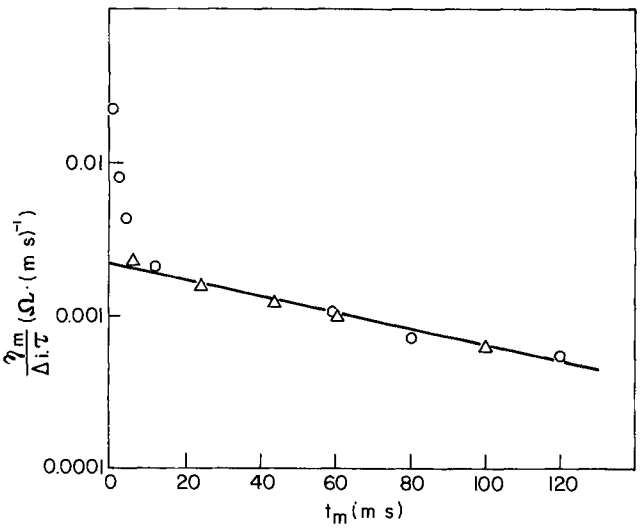


Fig. 13. Plot of ln ($\eta_m/\Delta i\tau$) *vs.* t_m for the Teflon-bonded Pt on Pt screen/NaOH system (the circles and triangles represent data acquired in independent experiments).

Planar electrodes.—It is of interest at this stage to examine the exponential relaxation technique for estimating the surface area of planar electrodes. For this purpose, a TiO_2 + RuO_2 electrode, used extensively as an anode in chloralkali cells, was chosen, since BET measurements have indicated roughness factors in the range of 180-230 (19).

From the potential-time and current-time transients at a potential of 680 mV *vs.* SCE in 5M NaCl solutions, ln $\eta_m/\Delta i\tau$ was estimated and plotted *vs.* t_m (see Fig. 14). These results show an over-all capacitance of 8.2 m**F**/cm^2 from the intercept, and infinite charge-transfer resistance, indicating the absence of faradaic processes in this potential region.

In order to confirm these results, linear-sweep voltammetric studies were carried out. The current-voltage profiles at various sweep-rates (see Fig. 15) show almost a flat current plateau over a significant potential range, which is suggestive of the absence of faradaic reactions in the potential region of 100-800 mV *vs.* SCE. The current *vs.* sweep-rate (s*) curve at E = 680 mV *vs.* SCE (see Fig. 16) is linear, and from the slope of the plot, the capacitance is estimated to be 8.4 m**F**/cm^2, which is in excellent agreement with the capacity value deduced from the exponential relaxation technique.

The potential response to the exponentially decaying anodic current pulse was also examined near the reversible potential for the Cl_2/Cl^- reaction in 5M NaCl aq. at 95°C. The ln ($\eta_m/\Delta i\tau$) *vs.* t_m plot is shown in Fig. 17. From the slope and the intercept, the charge-transfer resistance is calculated and found to be 9.87Ω. This value may be compared with the R_T value of 11.5Ω estimated from the linear i-η plot (Fig. 18) near the reversible potential.

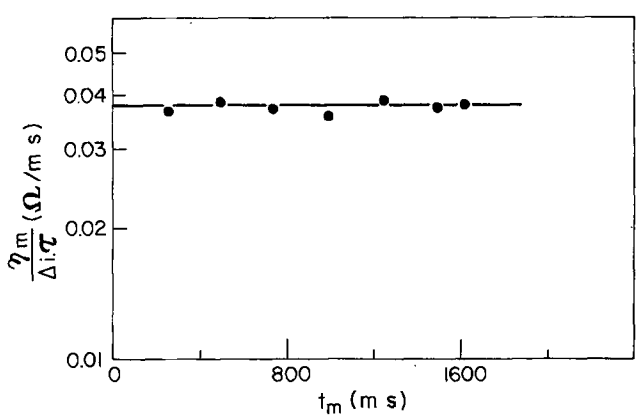


Fig. 14. Plot of ln ($\eta_m/\Delta i\tau$) *vs.* t_m for TiO_2 + RuO_2 electrode in 5M NaCl aq. at 25°C (the potential of the test electrode was 680 mV *vs.* SCE).

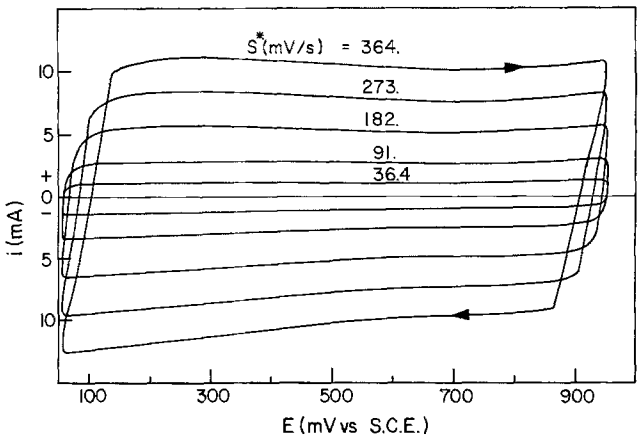


Fig. 15. Linear sweep voltammograms for TiO_2 + RuO_2 electrode in 5M NaCl at 25°C (area of the test electrode ~3.2 cm^2).

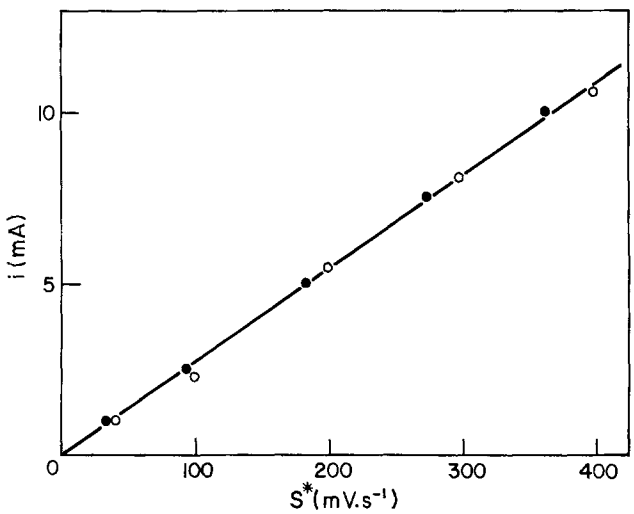


Fig. 16. Plot of i *vs.* sweep rate at E = 680 mV (data taken from Fig. 15); the closed and open circles represent data acquired in independent experiments).

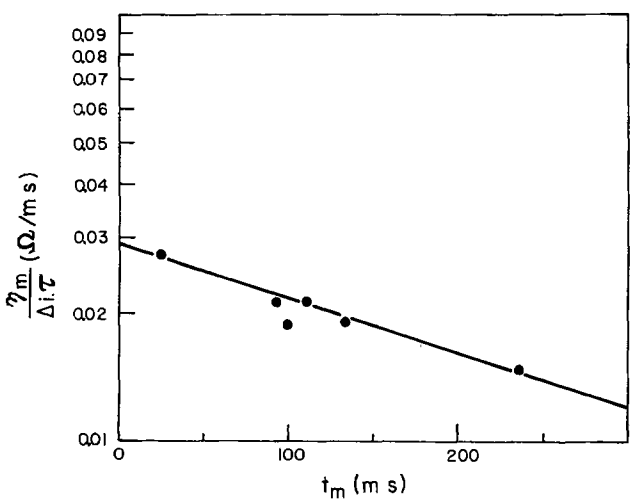


Fig. 17. ln($\eta_m/\Delta i\tau$) *vs.* t_m for TiO_2 + RuO_2 electrode in 5M NaCl aq. (*p*H ~3.5) at 95°C.

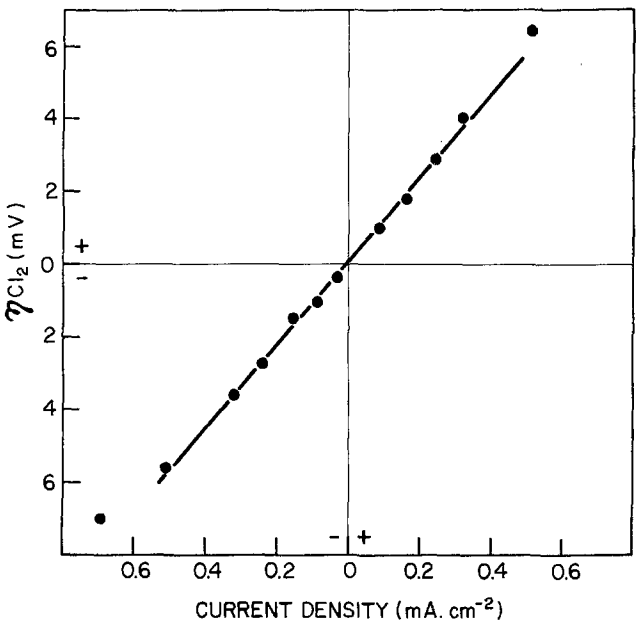


Fig. 18. Current-overpotential curve at low overpotentials for TiO_2 + RuO_2 electrode in 5M NaCl aq. (pH ~3.5) at 95°C.

It may be noted, however, that the C_T value deduced from the data obtained at the reversible potential of the Cl_2/Cl^- reaction is much higher than the C_T value in the nonfaradaic region. An explanation of this discrepancy may be sought in terms of adsorption pseudocapacitance, neglected in the present treatment. The presence of a finite adsorption pseudocapacity near the reversible potential is evident from the low Tafel slopes (20) and the fractional stoichiometric numbers (21) observed during the chlorine evolution reaction, which could arise only when adsorbed intermediates participate (21) in the rate-determining steps, *e.g.*, recombination and/or electrochemical desorption.

The examples cited above suggest the versatility of the exponential relaxation technique in providing a reliable estimate of the surface area of either a planar or a porous electrode, although a strong interference from the faradaic reaction is present and acknowledged. The obvious advantage of this method lies in the simplicity of experimental design and accessibility and theoretical tractability. However, in the case of systems where adsorbed intermediates participate in the rate-determining step, the present theory is inadequate and, hence, it is necessary to choose a system or a potential region for estimating the electrode surface area, in which the role of adsorbed intermediates is either absent or minimal. Studies to incorporate pseudocapacitance variations within the porous body and evaluate the diffusion-coupling are in progress.

Conclusions

The exponential relaxation technique provides a reliable means for determining the effective surface area of a planar or porous electrode in the presence of a faradaic reaction.

The present method permits simultaneous determination of R_T and C_T with the proviso that the influence of adsorption pseudocapacitance is negligible (*i.e.*, reaction intermediates do not participate in the rate-determining steps of the over-all charge transfer reaction) and diffusion within the porous body is absent.

Acknowledgments

The authors are grateful to Dr. K. V. N. Rao for supplying Ni plaque, Dr. B. S. Baker of Energy Research Corporation for the Teflon-bonded Pt screen, and Mrs. U. I. Keller for carrying out the experiments with meticulous care and devotion. Our thanks are also to the Hooker Chemicals & Plastics Corporation for permission to publish this paper. One of us (S.K.R.) thanks the Science Research Council, U.K., for financial support and the Indian Institute of Science, Bangalore, for leave of absence.

Manuscript submitted June 3, 1977; revised manuscript received Aug. 14, 1977. This was Paper 39 presented at the Las Vegas Nevada, Meeting of the Society, Oct. 17-22, 1976.

Publication costs of this article were assisted by Hooker Chemicals & Plastics Corporation.

REFERENCES

1. S. K. Rangarajan, *Curr. Sci.*, **40**, 175 (1971).
2. O. S. Ksenzhek and V. V. Stender, *Dokl. Akad. Nauk SSSR*, **106**, 487 (1956).
3. F. A. Posey and T. Morozumi, *This Journal*, **113**, 176 (1966).
4. S. K. Rangarajan, *J. Electroanal. Chem. Interfacial Electrochem.*, **22**, 89 (1969).
5. L. G. Austin and E. G. Gagnon, *This Journal*, **120**, 251 (1973).
6. W. Tiedemann and J. Newman, *ibid.*, **122**, 70 (1975).
7. J. McHardy, J. M. Barris, and P. Stonehart, *J. Appl. Electrochem.*, **6**, 371 (1976).
8. S. K. Rangarajan, *J. Electroanal. Chem. Interfacial Electrochem.*, **41**, 459 (1973).
9. S. K. Rangarajan, *ibid.*, **41**, 491 (1973).
10. G. P. Rao, S. K. Lakshmanan, and S. K. Rangarajan, *ibid.*, **62**, 273 (1975).
11. "Fuel Cells—Their Electrochemical Kinetics," V. S. Bagotskii and Yu. B. Vasilev, Editors, Consultants Bureau, New York (1966).
12. R. de LeVie, *Adv. Electrochem. Electrochem. Eng.*, **6**, 329 (1967).
13. E. A. Grens II and C. W. Tobias, *Ber. Bunsenges. Phys. Chem.*, **68**, 236 (1964).
14. T. Mussini and G. Faita, "Encyclopedia of Electrochemistry of Elements," Vol. 1, A. J. Bard, Editor, Marcel Dekker, Inc., New York (1973).
15. H. B. Beer, South African Pat. 662,667 (1966); 680,034 (1968).
16. H. A. Kozlowska, B. E. Conway, and W. B. A. Sharp., *J. Electroanal. Chem. Interfacial Electrochem.*, **43**, 9 (1973).
17. G. P. Rao and S. K. Rangarajan, *ibid.*, **55**, 151 (1974).
18. J. O'M. Bockris and S. Srinivasan, *Electrochim. Acta*, **9**, 31 (1964).
19. K. J. O'Leary and T. J. Navin, in "Chlorine Bicentennial Symposium," T. C. Jeffery, P. A. Danna, and H. S. Holden, Editors, The Electrochemical Society Softbound Symposium Series, Princeton, N.J. (1974).
20. R. G. Erenburg, L. I. Khristalik, and V. T. Bystrov, *Sov. Electrochem.*, **8**, 1740 (1972).
21. B. V. Tilak, C. G. Rader, and B. E. Conway, Submitted to *Electrochim. Acta.*

Technical Note

Corrosion Resistance of Types 316 and 317 Stainless Steels in Simulated SO_2 Scrubber Environment

E. A. Lizlovs*

Climax Molybdenum Company of Michigan, Research Laboratory, Ann Arbor, Michigan 48105

Pollution control has necessitated the installation of wet scrubbers to remove SO_2 from exhaust gases of power plants and smelters. The operational principles of these scrubbers have been described in several excellent articles (1-2). The scrubbing systems, however, have confronted the industry with severe and complex corrosion problems and the necessity of evaluating different construction materials. A considerable amount of corrosion testing has been carried out in actual operating scrubbers (3-6). A simple bench test simulating some important parameters involved in corrosion in wet scrubber environments has been developed at this laboratory (7). The results of these tests were in general agreement with the results of industrial testing. Furthermore, the laboratory tests indicated the influence of molybdenum content on the corrosion resistance of stainless steels in the scrubber environment. Even variations of molybdenum content within specification limits had a large impact on the corrosion behavior of T316 stainless steel which is widely used in scrubber construction. This investigation is concerned with the effect of variations in molybdenum content on the corrosion resistance of T316 and T317 stainless steel in simulated scrubber environments. Type 304 samples were also included in the tests primarily to check the severity of the test solution, since T304 is known to have inadequate corrosion resistance in scrubber environments (3).

Experimental

Material.—The chemical compositions of the steels are shown in Table I. The steels were prepared by induction melting in argon and casting in air using a split-heat technique. The ingots were hot-forged, hot-rolled into an 8 mm (0.30 in.) thick sheet, and finally cold-rolled to 4 mm (0.15 in.) thickness. The steels were then solution annealed at 1095°C (2000°F) for 24 hr in a hydrogen atmosphere and water quenched. The heat-treatment gave homogeneous alloys with no observable delta ferrite even at the highest molybdenum content. The molybdenum content of the alloys was varied between 2 and 4.2% in about ½% increments.

* Electrochemical Society Active Member.
Key words: crevice, chlorides, molybdenum, passivity, pH.

Corrosion test.—Probably the most important parameters governing the corrosion of stainless steels in scrubbers employing limestone slurry for SO_2 absorption are the pH of the liquid and slurry, temperature, chloride content, oxygen, and crevices. The slurry pH in many cases is reported to be 5-6 or higher (6), however, excursions to lower values can occur, and at certain scrubber locations, a lower pH value also can be expected. The chlorides in the presence of oxidizing agents (oxygen) could cause pitting and crevice corrosion and, at low pH values would also lead to the loss of passivity and the onset of general corrosion. The accumulation of chloride ions will take place in the case of recirculating systems. The presence of oxygen (and possibly other oxidizing agents) on one hand will promote localized chloride attack, while on the other hand will help in maintaining the passivity of stainless steel at low pH values. The ionic species expected in the scrubbing liquid upon the absorption of SO_2 are H^+, HSO_3^-, $SO_3^=$, and some $SO_4^=$. Based on the above considerations, the following test solution was compounded: 2000 ppm $NaHSO_3$ and 3000 or 30,000 ppm Cl^-, added as NaCl. Experiments were performed at pH's 2, 3, and 5.3. The pH values were adjusted with NaOH. Most of the tests were conducted at 80°C (180°F) and some of the tests were conducted at pH 5.3 at 90°C (195°F). The tests were run for one week and the test solution was purged continuously with oxygen to ensure that the solution was always saturated with oxygen. The corrosion coupons were 25 × 20 × 2-4 mm (1 × 0.75 × 0.01-0.015 in.) thick. The surface was polished with 600 grit SiC paper. The samples were immersed in a test solution with crevices applied by rubber bands and Teflon cylinders pressed against each of the major faces. The evaluation of corrosion attack was by weight loss determination and visual inspection.

Results and Discussion

Experimental results are summarized in Tables II-IV. The corrosion rates are expressed in terms of weight loss over the entire geometric area of the coupons. A corrosion rate of less than 1 mg/dm²/day

Table I. Chemical compositions of commercial T304 and experimental T316 and T317 stainless steels

Stainless steel, type	Cr, %	Ni, %	Mo, %	Si, %	Mn, %	C, %	P, %	S, %	Cu, %	N, %
T304	18.55	10.43	0.22	0.43	1.72	0.063	0.026	0.013		—
T304	18.29	8.53	0.19	0.43	1.80	0.070	0.025	0.015	0.18	—
T316	17.67	13.57	1.99	0.43	1.89	0.025	NA	NA		0.035
T316	NA*	NA	2.45	NA	NA	NA	NA	NA		NA
T316	NA	NA	2.93	NA	NA	NA	NA	NA		NA
T317	NA	NA	3.37	NA	NA	NA	NA	NA		NA
T317	NA	NA	3.89	0.53	1.72	0.027	NA	NA		0.033
T317	17.29	13.67	4.23	0.34	1.45	0.020	0.012	0.011		0.035

* NA = not analyzed but is in the range of the series.

Table II. Corrosion rates for T304 and 18Cr-12Ni austenitic stainless steels under simulated SO_2-scrubber conditions, temperature 90°C (195°F), pH 5.3

	Corrosion rate (mdd)			
	3000 ppm Cl^-		30,000 ppm Cl^-	
% Mo	Sample 1	Sample 2	Sample 1	Sample 2
0.2 (T304)	148	—	218	—
1.99	0.6	0.1	4.0*	87
2.45	0.9	1.0	0.9	108
2.93	0.8	1.8	3.8	0.3
3.37	0.4	0.3	1.0	2.6
3.89	0.5	0.2	0.6	0.2
4.23	0.4	0	0.7	0.5

* Interference films indicating borderline passivity.

Table III. Corrosion rates for T304 and 18Cr-12Ni austenitic stainless steels under simulated SO_2-scrubber conditions, temperature 80°C (180°F), chloride content 3000 ppm

	Corrosion rate (mdd)					
	pH 2		pH 3		pH 5.3	
% Mo	Sample 1	Sample 2	Sample 1	Sample 2	Sample 1	Sample 2
0.2 (T304)	319	60.1	84	197	143	—
1.99	1.1	2.3	2.3	0.8	13.1	3.6
2.45	3.4	0.1	2.5	0	0.5	0.4
2.93	1.7	0.3	24.0	0	0.5	0.3
3.37	0	8.2	1.2	0.1	0.5	0.2
3.89	0.7	0.2	0.3	0	0.2	0
4.23	0.5	0	0	0.3	0.1	0.8

Table IV. Corrosion rates for T304 and 18Cr-12Ni austenitic stainless steels under simulated SO_2-scrubber conditions, temperature 80°C (180°F), chloride content 30,000 ppm

	Corrosion rate (mdd)					
	pH 2		pH 3		pH 5.3	
% Mo	Sample 1	Sample 2	Sample 1	Sample 2	Sample 1	Sample 2
0.2 (T304)	447		294	116	240	—
1.99	15.1*	148.2	7.1	139	10.4	2.0
2.45	7.4*	120.2	3.7	110	0.7	0.9
2.93	4.9*	0.7	4.4	193	0.9	1.3
3.37	1.0	0.8	1.5	0.2	0.5	1.4
3.89	4.0	0.8	0.9	1.2	0.6	1.0
4.23	2.3	0.2	1.2	0	0.2	0.6

* Interference films indicating borderline passivity.

(mdd) usually corresponded to slight crevice attack, or discoloration under the rubber band, or some very small pits. Corrosion rates in the range of 1 to about 10 mdd corresponded, in most cases, to well-defined crevice corrosion, usually under the rubber band, but in a number of cases also under the Teflon cylinder. The severity of crevice corrosion was reflected in the numerical value of the corrosion rate, the higher number corresponding to a more severe case of crevice corrosion. Occasionally there was also evidence of borderline passivity and the corrosion coupons showed interference films, indicating a loss of passivity followed by repassivation. Corrosion rates in excess of 10 mdd usually corresponded to severe corrosion both by crevice attack and by general attack due to loss of passivity.

The corrosion resistance of the T304 was inadequate under all experimental conditions, and all samples were severely damaged by crevice corrosion and by general etching. At the 3000 ppm Cl^- level the corrosion rates were quite low for all molybdenum-containing alloys at all three pH values and also at 90°C (195°F) with the exception of one 2.9% Mo sample which corroded at the rate of 24 mdd (Table III). Furthermore, above the molybdenum level of 3.4%, only a slight crevice corrosion was observable in the worst cases, and corrosion rates were either nil or less than 1 mdd.

More severe corrosion problems were encountered at the 30,000 ppm Cl^- level. Corrosion rates for some samples were widely different between the two runs (Table IV). Such widely different rates undoubtedly were caused by some samples becoming active and failing to repassivate, while in the other test, samples of the same material either remained passive or repassivated after an initial loss of passivity. In many cases, especially at pH 2, the corrosion coupons were covered with a surface film showing interference colors indicating borderline passivity.

The experimental results from the laboratory tests in general show considerable scatter of data, the same as the results from on-site testing (3). Considering the complexity of corrosion processes involved even in a simple laboratory test, such scatter should be anticipated. Comparison of all of the experimental data in Tables II-IV shows that only above the molybdenum content of 3.4% did the corrosion rate remain at consistently low rates reflecting a relatively small degree of crevice attack under all pH and chloride concentrations tested. It should be noted here that the test temperature was somewhat higher than normal for scrubber operation. At normal scrubber operations [pH of about 5.3, chlorides around 3000 ppm, and temperature of 60°-70°C (140°-160°F)] most probably all of the T316 samples, even those of the lowest molybdenum content (2%), would have sufficient corrosion resistance. However, operational departures into a higher temperature region, fluctuations in pH, and accumulation of chlorides in scrubbing liquids, conditions which to some extent are reflected in the series of tests presented here, will most likely cause serious corrosion problems unless T317 steel with at least 3.5% Mo is used. This conclusion is in agreement with INCO *in situ* test results (3).

It is of importance to note here that in previous experiments at this laboratory, alloys containing more than 3.4% Mo did not fail due to stress corrosion cracking in the wick test (8).

Conclusions

In SO_2-scrubber construction in locations where T316 stainless steel is normally used, T317 with at least 3.5% Mo should be used to withstand corrosion problems arising from pH and temperature fluctuations and chloride accumulation in the scrubbing liquid. The best corrosion resistance in the laboratory tests was shown by an experimental T317 steel with 4.2% Mo.

Manuscript submitted July 11, 1977; revised manuscript received Aug. 8, 1977. This was Paper 84 presented at the Las Vegas, Nevada, Meeting of the Society, Oct. 17-22, 1976.

Any discussion of this paper will appear in a Discussion Section to be published in the June 1978 JOURNAL. All discussions for the June 1978 Discussion Section should be submitted by Feb. 1, 1978.

Publication costs of this article were assisted by Climax Molybdenum Company of Michigan.

REFERENCES

1. A. B. Adams, Jr., "Resolving Corrosion Problems in Air Pollution Control Equipment," pp. 54-59, NACE, Houston (1976).
2. G. T. Paul, *ibid.*, pp. 79-82.
3. E. C. Hoxie and G. W. Tuffnell, *ibid.*, pp. 65-71.
4. D. L. Smith, *Mater. Perform.*, **10**, No. 11, 16 (1971).
5. P. C. Mockridge and D. W. McDowell, Jr., *ibid.*, **13**, No. 4, 13 (1974).
6. E. A. Tice, *ibid.*, **13**, 26 (1974).
7. E. A. Lizlovs, Submittted to *Mater. Perform.*
8. H. J. Dundas, Private communication, Climax Molybdenum Co., of Michigan, Ann Arbor, Mich. (1976).

Brief Communications

Electrode Reaction of Cytochrome c_3 of *Desulfovibrio vulgaris*, Miyazaki

Katsumi Niki*

Department of Electrochemistry, Yokohama National University, Ohoka, Minami-ku, Yokohama 233 Japan

Tatsuhiko Yagi

Department of Chemistry, Shizuoka University, Oya, Shizuoka 422 Japan

and Hiroo Inokuchi and Keisaku Kimura

Institute for Molecular Science, Myodaiji, Okazaki 444 Japan

Cytochrome c_3 is an electron carrier present in the redox system of sulfate-reducing bacteria, *desulfovibrio* (1). It has been isolated from *d. vulgaris*, Hildenborough (2, 3). *d. vulgaris*, Miyazaki (4-6), *d. desulfuricans* (7), *d. salexigens* (8), and *d. gigas* (9). The physicochemical properties of cytochrome c_3 extracted from *d. vulgaris*, Miyazaki, have been studied extensively in our laboratory (6). Its molecular weight is nearly 14,000. The heme content of cytochrome c_3 has been believed to be two or more (3, 7, 10-12), and we confirmed that it contains four hemes by chemical analysis (6). Later Meyer *et al.* also reported four hemes in the molecule (13). Cytochrome c_3 is a natural electron acceptor for *desulfovibrio* hydrogenase (hydrogen:ferricytochrome c_3 oxidoreductase, EC 1.12.2.1), and is reversibly reduced by molecular hydrogen in the presence of hydrogenase (14). It has been demonstrated by Yagi *et al.* (15) that cytochrome c_3 is electrochemically active and interacts directly with a glassy carbon electrode as an electron carrier for hydrogenase. The redox potential of cytochrome c_3 was calculated from the measurements of the equilibrium between hydrogen and cytochrome c_3 (3, 6, 7).

The electrochemical methods have been applied in studying the electron transfer reactions of model systems for the prosthetic group in the heme proteins (16). The electrochemical reduction of ferricytochrome c on platinum (17) and mercury electrodes (18) has been studied. The mechanism of charge transfer was proposed to be a superposition of electron transport through adsorbed molecules and exchange of already reduced molecules (19).

In the present paper, the electrochemical behavior of cytochrome c_3 on mercury electrode has been studied by polarography, cyclic voltammetry and potentiometry.

Experimental

Cytochrome c_3.—Cytochrome c_3 was isolated from *d. vulgaris*, Miyazaki, and was purified as described by Yagi and Maruyama (6). The purity of the cytochrome c_3 used in the present experiments was over 80% as estimated from the purity index of the preparation (6). The concentration of cytochrome c_3 determined from the absorbance at 552 nm of the ferro-form was $5.2^4 \times 10^{-5}$ mole dm^{-3} (6). The base solution was 0.03M phosphate buffer of *p*H 7.0. Hydrogenase was isolated from *d. vulgaris*, Miyazaki, and purified as described elsewhere (20).

Polarography and cyclic voltammetry.—Polarographic and cyclic voltammetry studies of cytochrome c_3 were carried out on a mercury electrode with a PAR polarographic analyzer Model 174. In the polarographic study a normal pulse mode was used and the drop time of the dropping mercury electrode was 5 sec. In the cyclic voltammetry, a Metrohm hanging mercury drop electrode with the surface area of 4.11×10^{-2} cm^2 was used.

Redox potential measurement.—In the potentiometric study, ferricytochrome c_3 was reduced by hydrogen gas in the presence of a small amount of the purified hydrogenase, and the concentrations of ferri-form and ferro-form were determined polarographically. The ratio of ferri-form to ferro-form varied by introducing oxygen gas step by step. A large mercury pool electrode was used as a working electrode. All potentials shown in this work are given with respect to the saturated calomel electrode and all experiments were carried out at 25.0°C.

Results

Polarography.—A well-defined reduction wave of cytochrome c_3 was obtained as shown in Fig. 1. The

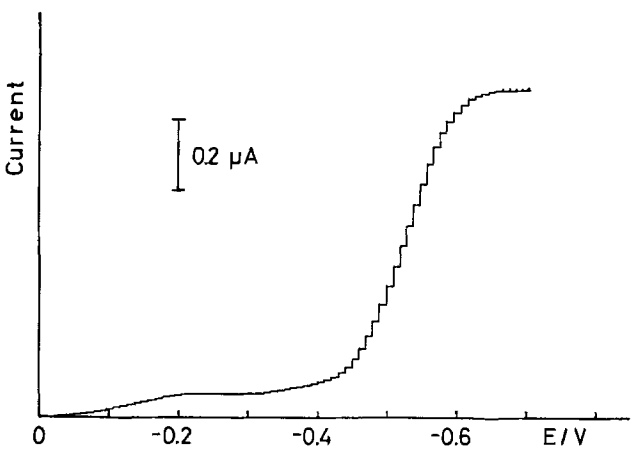


Fig. 1. Reduction of cytochrome c_3 on DME by pulse polarography. Concentration of cytochrome c_3 is $5.2^4 \times 10^{-5}$ mole dm^{-3} in 0.03M prosphate buffer at *p*H 7.0.

* Electrochemical Society Active Member.

Key words: cytochrome c_3, pulse polarography, cyclic voltammetry, potentiometry.

small preceding wave is due to the trace of oxygen in the solution. The half-wave potential is −0.527V (−0.281V *vs.* NHE), and the plot of log $[i/(i_d - i)]$ *vs.* electrode potential produces a straight line with an inverse slope of 0.085V from which the apparent number of electrons involved in the electrode process is calculated to be less than unity. In the case of the polarograms for the mixed ferri- and ferro-cytochrome c_3 system, the polarogram is symmetrical with respect to the current at $(i_{dc} + i_{da})/2$, where i_{dc} is the diffusion current for the reduction of the ferri-form and i_{da} is that for the oxidation of the ferro-form. The electrode potential corresponding to the current at $(i_{dc} + i_{da})/2$ is independent of the ratio of ferri-form to ferro-form and is the same as $E_{1/2} = -0.527$V for the reduction of the ferri-form. From these results it may be concluded that the electrode reaction of cytochrome c_3 is reversible even in the presence of strong adsorption of cytochrome c_3 on mercury electrode. The strong adsorption of the reactant is evidenced from the fact that the mercury drop formed in the cytochrome c_3 solution stayed on a mercury pool as a droplet at least for 30 min.

The diffusion coefficients of ferri- and ferro-cytochrome c_3 calculated from the pulse polarographic data were 1.2×10^{-6} cm^2 sec^{-1} for both forms. This value is in correspondence with that of horse-heart ferricytochrome c (MW = 12,350) determined by hydrodynamic techniques, 0.95×10^{-6} cm^2 sec^{-1} (20).

Cyclic voltammetry.—The cyclic voltammograms of cytochrome c_3 with various scan rates are shown in Fig. 2. The electrode potential at the current peak does not shift on the potential axis as a function of the scan rate. The current function $i_p v^{-1/2}$ is independent of the rate of voltage scan over a wide range, and the i_p *vs.* $v^{1/2}$ plot passes through the origin, where i_p is the peak current and v is the rate of voltage scan. The ratio of the cathodic to anodic peak currents is almost unity. The difference between the peak potential, E_p, and half-peak potential, $E_{p/2}$ was about 73 mV (the peak-to-peak separation is about 90 mV), which is much larger than 14.1 mV as expected for the reversible four-electron electrode process.

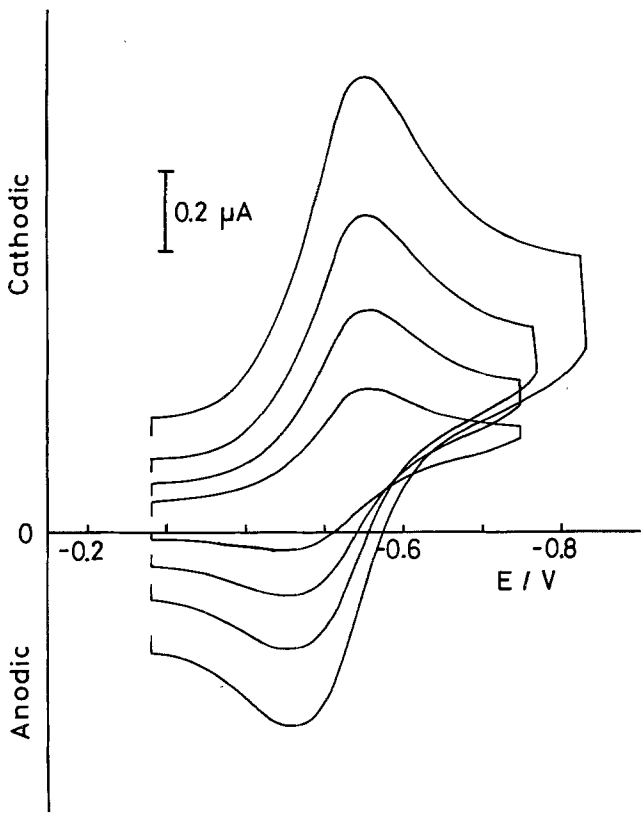


Fig. 2. Cyclic voltammogram of cytochrome c_3 on HMDE. Scan rate, 30, 50, 100, and 200 mV sec^{-1}. Concentration of cytochrome c_3 is $5.2^4 \times 10^{-5}$ mole dm^{-3} in 0.03M phosphate buffer at pH 7.0.

The peak current expected from the four-electron reversible process with the diffusion coefficient of 1.2×10^{-6} cm^2 sec^{-1} is about three times larger than that of the measured values in the present experiment. The apparent number of electrons involved in the electrode reaction of cytochrome c_3 is calculated to be about two.

Potentiometry.—The formal potential of the ferro- and ferri-cytochrome c_3 couple is −0.516 ± 0.001V (−0.270 ± 0.001V *vs.* NHE) and the Nernst slope of the plot of log (C_O/C_R) *vs.* electrode potential is 88 mV. That is, the apparent number of electrons involved in the electrode reaction calculated from the Nernst slope is less than unity. The redox potential determined in the present experiment (−0.516V) agrees with our previous measurement [−0.536V (6)], and 100 mV is different from other measurements [−0.415V (2, 7)] determined from the equilibrium pressure measurement of hydrogen over cytochrome c_3.

Discussion

It is concluded from the polarographic and voltammetric results that the electrochemical kinetics for the reaction

$$\text{ferricytochrome } c_3 + 4e \rightleftharpoons \text{ferrocytochrome } c_3$$

is diffusion controlled, and the reaction rate constant is the order of 0.1 cm sec^{-1} or greater. The electron transport in the electrode reaction takes place through the strongly adsorbed layer of cytochrome c_3 on mercury electrode.

The broad distorted voltammograms—both $(E_{p/2} - E_p)$ and i_p values are different from those expected from the four-electron reversible reaction—suggest that the electrochemical reaction of cytochrome c_3 is a reversible multistep process, and broadening is attributed to a small difference in the formal potential of these processes (22).

A large Nernst slope, 88 mV, can be explained in terms of the combination of the Nernst plots for the multistep processes with a small difference in the formal potentials (the difference is at most 70 mV in the present case).

These results are probably due to the fact that ferricytochrome c_3 accepts four electrons stepwise as a single entity. That is, the four hemes in cytochrome c_3 are not independent but constitute an interlocked heme cluster. A small difference in the formal potentials is attributable to the existence of intramolecular heme-heme interaction. These experimental findings are also expected from the results of Mössbauer spectroscopic (23) and electron paramagnetic resonance spectroscopic (24) studies on cytochrome c_3, in which the heme-heme interaction was observed.

Acknowledgments

The authors are grateful to Drs. Reita Tamamushi and Keiichi Tsuji, Research Institute for Physics and Chemistry, for valuable discussions and criticisms.

Manuscript submitted March 18, 1977; revised manuscript received April 16, 1977.

Any discussion of this paper will appear in a Discussion Section to be published in the June 1978 JOURNAL. All discussions for the June 1978 Discussion Section should be submitted by Feb. 1, 1978.

Publication costs of this article were assisted by Yokohama National University.

REFERENCES

1. J. R. Postgate and L. L. Campbell, *Bacteriol. Rev.*, **30**, 732 (1966).

2. J. R. Postgate, *Biochem. J.*, **56**, xi; *ibid.*, **58**, ix (1954).
3. J. R. Postgate, *J. Gen. Microbiol.*, **14**, 545 (1956).
4. M. Ishimoto, J. Koyama, and Y. Nagai, *Bull. Chem. Soc. Jpn.*, **27**, 565 (1954).
5. M. Ishimoto, J. Koyama, and Y. Nagai, *J. Biochem. (Tokyo)*, **41**, 763 (1954).
6. T. Yagi and K. Maruyama, *Biochim. Biophys. Acta*, **243**, 214 (1971).
7. H. Drucker, E. B. Trousil, L. L. Campbell, G. H. Barlow, and E. Margoliash, *Biochem.*, **9**, 1515 (1970).
8. H. Drucker, E. B. Trousil, and L. L. Campbell, *ibid.*, **9**, 3395 (1970).
9. J. LeGall, G. Mazza, and N. Dragoni, *Biochim. Biophys. Acta*, **99**, 385 (1965).
10. T. Horio and M. D. Kamen, *ibid.*, **48**, 266 (1961).
11. D. V. DerVartanian and J. LeGall, *ibid.*, **243**, 53 (1971).
12. D. V. DerVartanian, *J. Magn. Reson.*, **10**, 1 (1973).
13. T. E. Meyer, R. G. Bartsch, and M. E. Kamen, *Biochim. Biophys. Acta*, **245**, 453 (1971).
14. T. Yagi, M. Honya, and N. Tamiya, *ibid.*, **153**, 699 (1968).
15. T. Yagi, M. Goto, K. Nakano, K. Kimura, and H. Inokuchi, *J. Biochem. (Tokyo)*, **78**, 443 (1975).
16. D. W. Clark and N. S. Hush, *J. Am. Chem. Soc.*, **87**, 423 (1965); D. G. Davis and R. F. Martin, *ibid.*, **88**, 1365 (1966); R. Felton and H. Linschits, *ibid.*, **88**, 1113 (1966); T. M. Bednarski and J. Jordan, *ibid.*, **89**, 1552 (1967); N. E. Tokel, V. Katovic, K. Farmery, L. B. Anderson, and D. H. Busch, *ibid.*, **92**, 400 (1970).
17. T. Kono and S. Nakamura, *Bull. Agr. Chem. Soc. Jpn.*, **22**, 399 (1958).
18. S. R. Betso, M. H. Klapper, and L. B. Anderson, in Proceedings of the 1st International Symposium on Biological Aspects of Electrochemistry, Birkhauser Verlag, Basel, 157 (1971); *J. Am. Chem. Soc.*, **94**, 8197 (1972); F. Scheller, M. Jänchen, J. Lampe, H. J. Prümke, J. Blanck, and E. Palacek, *Biochim. Biophys. Acta*, **412**, 157 (1975).
19. F. Scheller, H. J. Prümke, and H. E. Schmidt, *J. Electroanal. Chem. Interfacial Electrochem.*, **70**, 219 (1976).
20. T. Yagi, K. Kimura, H. Daidoji, F. Sakai, S. Tamura, and H. Inokuchi, *J. Biochem. (Tokyo)*, **79**, 661 (1976).
21. A. Ehrenberg and S. Paleus, *Acta Chem. Scand.*, **9**, 538 (1955).
22. D. S. Polcyn and I. Shain, *Anal. Chem.*, **38**, 370 (1966).
23. K. Ono, K. Kimura, T. Yagi, and H. Inokuchi, *J. Chem. Phys.*, **63**, 1640 (1975).
24. J. LeGall, M. Bruschi-Heriaud, and D. V. DerVartanian, *Biochim. Biophys. Acta*, **234**, 499 (1971).

Technique for Continuous High Resolution Long-Term Recording of Signals with High Levels

G. Edwall and A. Olofsson

Department of Applied Physics, Royal Institute of Technology, S-100 44 Stockholm, Sweden

For survey purposes, *e.g.*, in potentiometric long-term measurements, permanent long-term recording on strip-chart recorders is often used. The resolution and accuracy is generally limited to 3 decimal digits owing to the normally encountered poor characteristics of such recorders. In many cases, *e.g.*, with slowly varying signals, a higher resolution is needed. The signals are then usually fed to accurate digital instruments for display, and permanent records may be obtained from printers or signal processing computers connected to these instruments. Alternatively, a known bias signal is applied, bucking out the d-c part of the signal to be recorded, thus allowing only the varying part to be seen.

A long-term record is usually used to extract significant variations and/or trends such as drift in the signal being measured. For this purpose, the printer presenting only a sequence of digits is of limited value due to lack of human comprehension of data in that form. The use of a computer for signal processing may, in many cases, be too expensive, thereby leaving only the buck-out technique for consideration. However, if a highly accurate measurement ranging over four or more decimal digits is needed, considerable restrictions regarding accuracy and long-term stability are placed on the buck-out signal. The permissible signal variation is also restricted, by recorder end-point deflection, to one chart-width at the recorder setting used. In special situations, it may even be prohibitive to apply a buck-out signal. This is the case, for instance, in medical *in vivo* applications due to the patient safety problems and similarly in continuous electrochemical measurements due to the potential risk of electrode polarization.

In our case we needed a solution to the problems encountered in long-term monitoring of the stability of metal-metal oxide *p*H electrode potentials. From a permanent record we wanted to accurately reconstruct both the absolute level and the variations of the electrode potential. The signal range covered 5½ decimal digits with short-term variations in the last two places only, and long-term drift typically corresponding to less than two decimal digits per hour.

Key words: dynamic zero suppression, potential measurement technique, buck-out signal.

A varactor amplifier, used as a unity gain voltage follower, acts as an impedance buffer for the electrodes, providing an output voltage equal to the electrode zero current potential to within $5 \cdot 10^{-4}$. This voltage is measured and displayed on an accurate 5½ digit DVM (Model 190, Keithley Instruments Incorporated) (1). A digital-to-analog (D/A) converter (8 bits = 2 BCD-coded digits) acts as an interface between the DVM and a strip-chart recorder. It provides a means for recording variations in any two consecutive digits on the DVM, while all more significant digits are suppressed. The block diagram of the converter is shown in Fig. 1. With a mechanical selector, the BCD-coded output signals from two digits on the DVM are preselected. The signals from each digit are fed to a four-bit D/A converter generating an output current proportional to the input digit. The current from the least significant digit is divided by ten and added to the current from the more significant digit. By means of a current-to-voltage converter (adder), an analog output voltage directly proportional to the input value is generated. The output voltage span is adjusted with a potentiometer to fit the input range of the recorder. In our case the 1V range was used.

The D/A converter described enables flexible zero suppression of the d-c part of the input voltage, while the significant variations are displayed in analog form in 100 steps on the recorder. For instance, a signal symbolized by abc.de mV can be recorded as cd units on the recorder. Moreover, with this technique, the recorder need not be supervised for off-scale deflections,

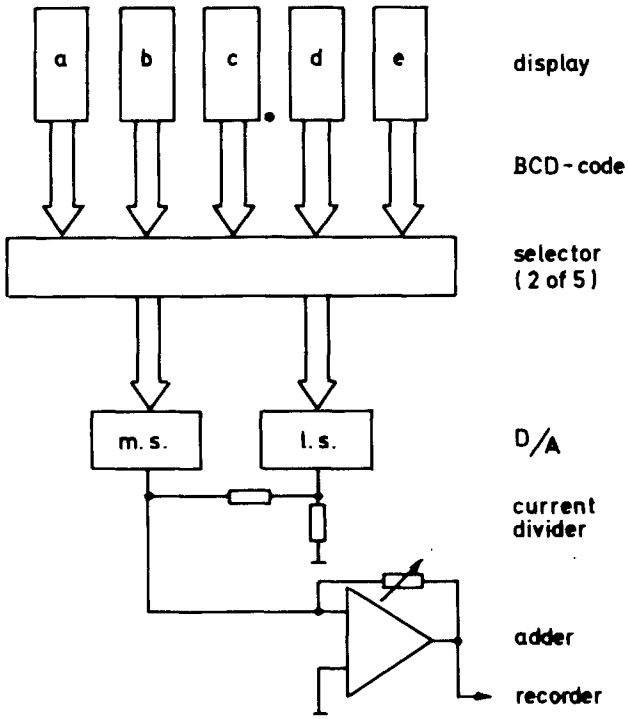


Fig. 1. The D/A converter

as it automatically changes from 99 to 00 or vice versa when the end points (*i.e.*, when b changes ±1 unit in the aforementioned example) are exceeded. Such changes are readily observed from the recording itself, and the actual signal magnitude is easily reconstructed. This is the case if the changes are not too frequent. Otherwise, a less sensitive setting or a higher recorder speed should be employed.

The above-described recording technique has now been extensively used by us. In our case, the input voltage level has not been found to be affected to any measurable extent (*i.e.*, <30 μV). Nonlinearity and drift in the recording equipment and its interface including the D/A converter has not posed any problem. However, there is a slow drift of the D/A converter output voltage (Zener stabilized) corresponding to approximately 1 digit (1% ≡ 10 mV) per week, which might cause misinterpretation if the equipment is left unattended for longer periods of time.

Manuscript submitted July 25, 1977; revised manuscript received Aug. 1, 1977.

Any discussion of this paper will appear in a Discussion Section to be published in the June 1978 JOURNAL. All discussions for the June 1978 Discussion Section should be submitted by Feb. 1, 1978.

Publication costs of this article were assisted by the Royal Institute of Technology.

REFERENCE

1. G. Edwall, TRITA-FYS 6606, Royal Institute of Technology, Stockholm (1976).

DISCUSSION SECTION

This Discussion Section includes discussion of papers appearing in the *Journal of The Electrochemical Society*, Vol. 124, No. 2 and 3, February and March 1977.

Electrochemical Characterization and Modification of Cadmium Sulfide Composition at 25°C

J. Vedel, M. Soubeyrand, and E. Castel
(pp. 177-180, Vol. 124, No. 2)

C. Gutierrez:[1] In their work, Vedel *et al.* oxidized anodically a ~1 μm layer of CdS in 10^{-2}M $CdSO_4$. After current interruption, 6-8 hr were needed for CdS to attain a stable potential. This rest potential increased with increasing previous anodization, from that corresponding to pure Cd (for Cd-saturated CdS) to that corresponding to pure S (for S-saturated CdS) and even higher. We would like to raise the following points in consideration of that work:

1. According to Vedel *et al.*, "... cadmium activity in Cd_xS, [is] a thermodynamical quantity that may be related to the activity of a defect, for example, the noncharged interstitial cadmium represented by Cd_i*. Then one has

$$\mu_{Cd}(Cd_xS) = \mu^o_{Cd_i^*} + RT \ln a_{Cd_i^*}" \qquad [1]$$

The above assumption of interstitial cadmium atoms (which, besides, are ionized[2]) is unnecessary. The correct equation is simply

$$\mu_{Cd}(Cd_xS) = \mu^o_{Cd}(Cd) + RT \ln a_{Cd}(Cd_xS) \qquad [2]$$

because if the CdS layer is in thermodynamic equilibrium, there is only one chemical potential of Cd in the whole CdS phase, irrespective of its microscopic structure.

2. The CdS layer was obtained by anodic oxidation of Cd in 0.5M Na_2S, pH = 9 at −0.9V *vs.* SCE. In principle, no anodization should be necessary, as the reaction

$$Cd + HS^- + H^+ \rightarrow CdS + H_2 \qquad [3]$$

is thermodynamically highly favored (ΔG° = −40.28 kcal/mole; log K = 29.52).

It is very interesting that the initial potential of Cd in 0.5M Na_2S was that of pure Cd, and not that corresponding to pure sulfur. In the case of lead, the potential values in Na_2S or NaHS solutions found by several workers in air[3-5] and N_2[5] coincide with that calculated for pure sulfur

$$S + H^+ + 2e \rightarrow HS^-$$

$$E^\circ_h = -0.062V \qquad [4]$$

which is 0.5V more positive than that corresponding to pure lead

$$PbS + H^+ + 2e \rightarrow Pb + HS^-$$

$$E^\circ_h = -0.564V \qquad [5]$$

Only in one case[6] and in a rather dilute Na_2S solution was the potential of natural galena sensibly more negative (~140 mV) than that corresponding to pure sulfur. It may be concluded that perhaps a more thor-

[1] Instituto de Química Física "Rocasolano," C.S.I.C., Serrano, 119, Madrid — 6, Spain.
[2] F. A. Kröger, H. J. Vink, and J. van den Boomgaard, *Z. Phys. Chem. (Leipzig)*, 203, 1 (1954).
[3] P. P. Lebedew, *Z. Elektrochem.*, 18, 891 (1912).
[4] G. Trümpler, *Z. Phys. Chem.*, 99, 9 (1921).
[5] R. Tolun and J. A. Kitchener, *Trans. Instn. Min. Metall.*, 73, 313 (1964).
[6] E. Baumgarten, *Chem.-Ing.-Tech.*, 44, 613 (1972).

ough exclusion of oxygen is necessary to observe the potential of pure lead corresponding to reaction [5].

3. In one case the $E°_h$ of anodized CdS was found to be + 0.470V, far higher than that of $E°_h = +0.31$V corresponding to pure sulfur in equilibrium with cadmium sulfide, according to

$$Cd^{2+} + S + 2e \rightarrow CdS \quad [6]$$

Vedel *et al.* state that in the anodization of CdS "One must be careful lest the emf Emax should ever be less than the emf corresponding to the oxidation of cadmium sulfide into sulfur (Emax $\lesssim$0.7V)" [presumably *vs.* a Cd electrode in the same solution]. If this applies also to the CdS with $E°_h = +0.470$V, it is clear that some oxygen inadvertently introduced in the system reacted with the CdS. In any case, the potential must correspond to some oxidized form of CdS, such as CdO: a possible reaction could be

$$Cd^{2+} + \tfrac{1}{2}\,O_2 + 2e \rightarrow CdO_c \quad [7]$$

with $E°_h = +0.781$V. However, the observed potential of 0.470V would correspond to $\log p(O_2) \approx 10^{-21}$ atm, while the residual oxygen pressure is probably much higher.[7]

Vedel *et al.* claim that the observed potential $E°_h = +0.470$ does correspond to pure sulfur, with $E°_h = +0.31$V, and that "this deviation may be attributed to the formation of sulfur in a state different from the standard state of the element." They suggest that gaseous sulfur is formed. This suggestion is best ignored, as (*i*) Evolution of gaseous sulfur at a pressure higher than the vapor pressure of pure sulfur requires a more positive potential than that for deposition of solid sulfur. Therefore, the element would be produced as a gas only if deposition of the solid were strongly impeded. We know no case in which this phenomenon occurs; and (*ii*) More importantly, any gaseous sulfur evolved on anodization would be swept away by the argon flow.

4. In Fig. 2 of the article being discussed, a change in the composition of Cd_xS of $\Delta x = 0.01$ appears. This range of compositions is probably too high. The highest level of Cd excess in CdS reached by Kröger *et al.*[2] produced $\sim 10^{18}$ electrons cm^{-3}, corresponding to $\Delta x \sim 5 \cdot 10^{-5}$. For other chalcogenidse it is $\Delta x \sim 10^{-3}$.[8] In general, "... the calculated equilibrium concentration of point defects, particularly in the metallic oxides but also in the sulfides etc. is extremely small, even at high relative temperatures $\theta = T/Tm$ (Tm = the melting point of the crystal)."[9] Therefore, it seems clear that oxidation of impurities accounts for most of the anodization current.

5. The authors state that "In order to plot the two [E *vs.* Δx] curves on the same diagram, it was first observed that both their left parts showed a sigmoidal shape recalling that of titration curves." As a matter of fact, these curves are known as coulometric titrations in solid-state electrochemistry, and Valverde[9] has found experimentally and justified theoretically that for the silver chalcogenides they should be sigmoidal in shape.

6. The authors try to justify the experimental slope of 0.090V in the region *hi* of their titration curve (Fig. 2) by means of an incorrect derivation. As said above in paragraph 3 the region *hi* does not correspond to CdS, but to some oxidation product, perhaps CdO. Therefore CdS plays no role in this region. It is stated that "When the x value is equal to x_H, the vacancy concentration $|V_{Cd}''|$ is very low ($|V_{Cd}''|_{x=x_H} \sim 0$)." Although not clearly stated, x_H corresponds to Cd_xS in equilibrium with pure sulfur, which has a potential (*vs.* a Cd electrode in the same solution) of 0.31 + 0.408 = +0.718V. This potential corresponds to the highest possible concentration of sulfur in homogeneous Cd_xS, *i.e.* to the highest possible concentration of cadmium vacancies, which is just the opposite situation to that postulated by Vedel *et al.* It is further stated that "The cadmium vacancies are assumed to be in equilibrium with metallic cadmium . . . The equilibrium is

$$Cd + V_{Cd''} + 2h \rightarrow Cd_{Cd} \quad [8]$$

together with the relation

$$K = a(Cd) \cdot |h|^2 \cdot f(V_{Cd''}) \cdot |V_{Cd''}|_x" \quad [9]$$

Equations [8] and [9] are totally incorrect. An excellent treatment of these equilibria has been given by Kröger and Vink.[10] In the system under consideration gaseous cadmium is in equilibrium with sulfur vacancies, V_s, according to

$$Cd_g \rightarrow Cd_{Cd} + V_s \quad [10]$$

(Cd_{Cd} = cadmium atom in a lattice-cadmium site). The corresponding equation is

$$[V_s] = K_r \cdot p_{Cd} \quad [11]$$

These are the correct equations to be applied, and not Eq. [8] and [9]. It is clear that if only Schottky defects are present in the crystal, an excess of metal may only be accommodated by the formation of nonmetal vacancies, and vice versa.

J. Vedel, M. Soubeyrand, and E. Castel:[11] 1. The convenient equation relating the activity of cadmium to its chemical potential is effectively

$$\mu_{Cd}(Cd_xS) = \mu°_{Cd}(Cd) + RT \ln a_{Cd}(Cd_xS)$$

2. Anodic oxidation increases the thickness of the sulfide layer by setting up an electrostatic field in the solid that favors the movement of the ions through the layer.

3. The value 0.31V (*vs.* NHE) corresponding to reaction

$$Cd^{2+} + S + 2e \rightarrow CdS$$

is calculated by assuming that sulfur is present in its standard state, *i.e.*, solid rhombic sulfur S_{rh}. In order to explain the difference between the calculated value and the observed one (0.470V), we assumed that sulfur was formed in an allotropic form, different from S_{rh}. As an example, the observed difference of free energy and some free energies of other forms of sulfur were compared (we never supposed the formation of gaseous sulfur). This hypothesis seems more realistic than the intervention of an equilibrium reaction involving gaseous oxygen at $p(O_2)$ less than 10^{-21} atm.

4 and 5. These remarks appear already in the original paper (in a different form) and we agree fully with them.

6. The part of the diagram in question corresponds to a cadmium-poor sulfide. Consequently, it is not incorrect to assume the formation of metal vacancies.

A New Niobium Selenide Cathode for Nonaqueous Lithium Batteries

D. W. Murphy, F. A. Trumbore, and J. N. Carides
(pp. 325-329, Vol. 124, No. 3)

M. S. Whittingham:[12] In their article, Murphy *et al.* suggest that in the original discharge curves of $NbSe_2 \cdot I_2$[13] which exhibited two plateaus, one might be due to iodine and the other to the niobium diselenide. It had been thought that the "$NbSe_2$ served as

[7] D. Gilroy and J. E. O. Mayne, *J. Appl. Chem.*, 12, 382 (1962).
[8] N. Valverde, *Z. Phys. Chem. N.F.*, 70, 113 (1970).
[9] J. S. Anderson, in "Surface and Defect Properties of Solids," Vol. 1, p. 1, The Chemical Society, London (1972).
[10] F. A. Kröger and H. J. Vink, *Solid State Phys.*, 3, 307 (1956).
[11] Laboratoire d'Electrochimie Analytique et Appliquee, Associe au CNRS, ENSCP, 75231 Paris Cedex 05, France.
[12] Exxon Research and Engineering Company, Linden, New Jersey 07036.
[13] J. Broadhead, in "Power Sources 4," D. H. Collins, Editor, p. 469, Oriole Press, Newcastle upon Tyne, England (1973).

inert host for the electrochemically active iodine;"[14] subsequently, it was discovered[15,16] that the layered dichalcogenides themselves are electrochemically active. These discharge/charge curves are shown in Fig. 1, and the two-step discharge behavior is clearly visible. However, Carides and Murphy[17] have also recently measured the open-circuit behavior of the Li/$NbSe_2$ couple, which was found to vary continuously from 2.28 to 1.66V as x increased from 0 to 1 in Li_x-$NbSe_2$. This emf regime is shown as the hatched area in the figure, and falls well below the step in the discharge curves particularly when it is noted that the cycling curves are showing marked polarization. Hence, neither of these discharge steps can be associated with the intercalation of lithium into the lattice of the selenide. The chemical form of the iodine in the "$NbSe_2 \cdot I_2$" complexes is not understood, but it is possible that the two discharge steps can be associated with different states of adsorption of the iodine on the selenide.

D. W. Murphy, F. A. Trumbore, and J. N. Carides:[18] The point raised by Dr. Whittingham, although not the subject of our paper, warrants discussion because of its relevance to other solid-solution electrodes of the layered transition metal dichalcogenides.

As to our interpretation of Broadhead's results,[19] Whittingham is correct that at the start of cycling the cell voltage is too high to correspond to intercalation. However, if subsequent cycles presented by Broadhead in that same figure (Fig. 2) are subjected to the same test, we see that later cycles are within the voltage range of lithium intercalation in $NbSe_2$.[20] This decrease in voltage on cycling occurs quite rapidly.[21] Figure 6 in ftn.[19] reproduced here as Fig. 3, more clearly fits our reference of two plateaus for a thin film cell. The initial portion of the 50th charge and the latter portion of that discharge clearly occur in the range of lithium intercalation. The discharge portion may have a higher capacity than the charge since iodine in the electrolyte may remove lithium from Li_xNbSe_2 in an "electrodeless" reaction.[22] While these data do not prove intercalation, they do not preclude such a mechanism from playing an important role. Based on the well-documented lithium intercalation in $NbSe_2$, intercalation must be the mechanism of choice.

In retrospect, it seems quite plausible that the commercial $NbSe_2$ used in the pellet cells described by Broadhead[19] was niobium-rich and/or contaminated on the surface. Iodine could be acting to clean up the $NbSe_2$. The marked difference in the pellet data, Fig. 2, (from commercial $NbSe_2$) and "thin film" data, Fig. 3, indicates important differences in these materials as might be expected from surface contamination or additional phases. No evidence has been published to substantiate intercalation or adsorption complexes of iodine with metal dichalcogenides. There is a compound of formula $NbSe_2I_2$,[23] but this is not readily related structurally to $NbSe_2$ and no evidence of its formation in this system has been presented.

[14] J. Broadhead and F. A. Trumbore, Paper 178 presented at the Chicago, Illinois, Meeting of the Society, May 13-18, 1973; Paper 61 presented at the Boston, Massachusetts, Meeting of the Society, Oct. 7-11, 1973.
[15] M. S. Whittingham, *This Journal*, 123, 315 (1976); *Science*, 192, 1126 (1976); and US Pat. 4,009,052.
[16] G. L. Holleck, F. S. Shuker and S. B. Brummer, in Proceedings of the 10th Intersociety Energy Conversion Engineering Conference, Newark, Delaware, August 1975, New York (1975).
[17] J. N. Carides and D. W. Murphy, Submitted to *This Journal*.
[18] Bell Laboratories, Murray Hill, New Jersey 07974.
[19] J. Broadhead, in "Power Sources 4," D. H. Collins, Editor, p. 469, Oriole Press, Newcastle upon Tyne, England (1973).
[20] J. N. Carides and D. W. Murphy, *This Journal*, 124, 1309 (1977).
[21] J. Broadhead, Private communication.
[22] D. W. Murphy, J. N. Carides, F. J. Di Salvo, and J. V. Waszczak, *Mater. Res. Bull.*, 12, 825 (1977).

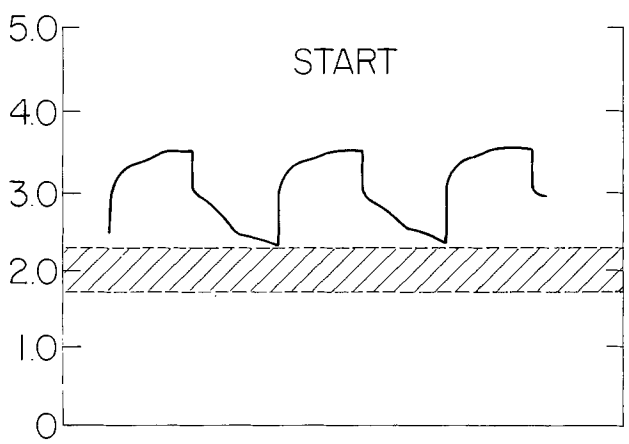


Fig. 1. Initial cycling behavior of $NbSe_2 \cdot I_2$ cathode as a function of time showing steps in discharge curve (from 1) compared with open-circuit data (from 5) for a pure Li_xNbSe_2 cathode shown as a band covering x from 0 to 1.

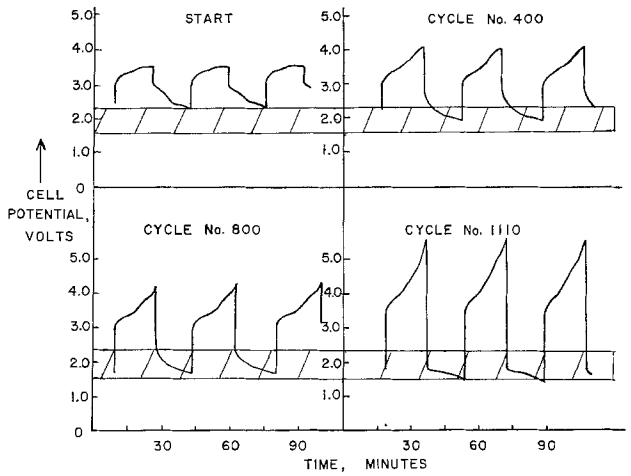


Fig. 2. Figure 2 from ftn.[19] showing the emf range for lithium intercalation in $NbSe_2$.

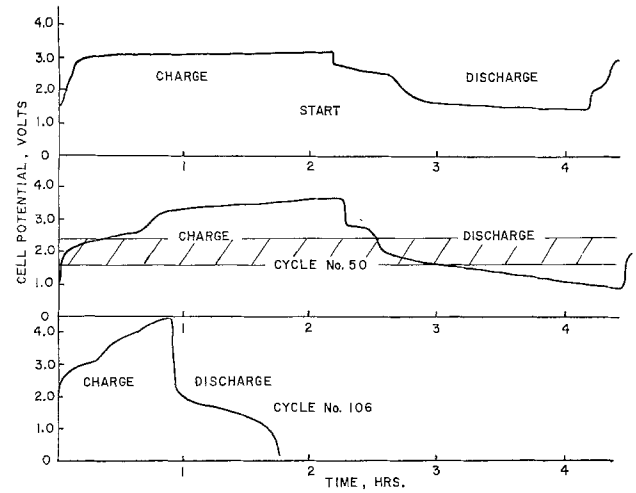


Fig. 3. Figure 6 from ftn.[19] clearly showing two processes

The Ag^+-Ag Exchange Reaction in Aqueous Acidic Nitrate Electrolyte

D. Larkin and N. Hackerman (pp. 360-363, Vol. 124, No. 3)

C. Cachet, M. Froment, and R. Wiart:[24] It appears of interest to compare the high frequency impedance data presented in the paper under discussion to our results recently obtained using impedance measure-

[23] H. Schafer and W. Beckmann, *Z. Anorg. Allg. Chem.*, 347, 235 (1966); W. Beckmann, Dissertation, Munster (1964).
[24] Groupe de Recherche du C.N.R.S. Physique des Liquides et Electrochimie. Associe a l'Universite Pierre et Marie Curie, 75230 Paris Cedex 05, France.

ments down to low frequencies and a radiotracer technique to evaluate the exchange current.[25,26]

The first subject for discussion concerns the exploitation of the impedance measurements performed between 20 kHz and 20 Hz. From the values of the two components R_R and $1/\omega C_R$ of the faradaic impedance given in Fig. 2 of the paper under discussion, and from the value of the frequency-independent capacitive component C_L given in Fig. 3, the untreated values of the measured impedance can be restored, except for the frequency-independent resistive component R_L which is not indicated in the paper. For example, at pH 2.4 and for Ag^+ concentration = 0.033M and C_L = 105 μF/cm^2 (*i.e.*, 0.42 μF for an electrode area = $4 \cdot 10^{-3}$ cm^2), the impedance diagram $Z = R - jG$ has been reconstituted in a complex plane (see Fig. 1 of this discussion) where the R-axis origin corresponds to the unknown electrolyte resistance R_L. This resistance can be calculated from the electrolyte resistivity ρ and from the electrode radius r using Newman's relationship $R_L = \rho/4\ r$.[27] So doing with an electrolyte (a mixture of 1M KNO_3 and 1M HNO_3 with pH = 2.4) the composition of which is very similar, we measure 10.8 Ω-cm at 25°C for the resistivity and deduce $R_L = 77\Omega$. In reality the presence of a frit between the test electrode and the counterelectrode probably leads to a higher value of R_L. Consequently, it seems that the transfer resistance $R_D = 4\Omega$ is very low compared with R_L. In addition to such an R_D value, the circuit formed by R_D and C_L in parallel has a characteristic frequency close to 95 kHz. The diagram in Fig. 1 shows clearly that frequencies lower than 4140 Hz are on the outside of the range in which the impedance depends on the capacity C_L. So it appears impossible to reach C_L from impedance measurements only performed in the frequency range 4140-203 Hz corresponding to the results of Fig. 2 of the paper under discussion. That is why it would have been useful to mention the results of the measurements performed between 4140 Hz and 20 kHz where the impedance may begin to be dependent on C_L. This comment raises the following question: Is the accuracy of impedance measurements sufficient, and is the confidence interval on the computer-fitted values of R_L and C_L narrow enough to obtain a meaningful value for C_L and to pull a transfer resistance $R_D = 4\Omega$ out of a measured resistance higher than $R_D + R_L \sim 80\Omega$?

The second point is related to the influence of pH on the exchange current i_o. Our impedance measurements performed down to very low frequency show that the transfer $Ag^+ + e \rightleftarrows Ag$ is not the only process taking place at the interface. As a matter of fact, in Fig. 2 (from Fig. 7 in ftn.[26]) a capacitive loop between 1 kHz and 0.003 Hz can be seen which does not correspond to the electron transfer and which precludes obtaining the transfer resistance R_D. This loop, which cannot be explained in terms of surface diffusion, strongly depends on the anions' adsorption. The study of such impedance diagrams, corroborated by the exchange current values obtained from our radiotracer measurements, has led us to conclude that the adsorption of OH^- ions blocks the electrode. There seems to be a discrepancy between this result and the conclusions given in the paper under discussion which were deduced from R_D values leading to a diminishing exchange current when pH decreases. Can you provide direct evaluations of the exchange current, for example obtained by a radiotracer technique, confirming that this exchange current is an increasing function of pH?

[25] C. Cachet, M. Froment, F. Wenger, and R. Wiart, *J. Electroanal. Chem.*, 61, 121 (1975).
[26] C. Cachet, M. Froment, M. Keddam, and R. Wiart, *Electrochim. Acta*, 21, 879 (1976).
[27] J. Newman, *This Journal*, 117, 198 (1970).

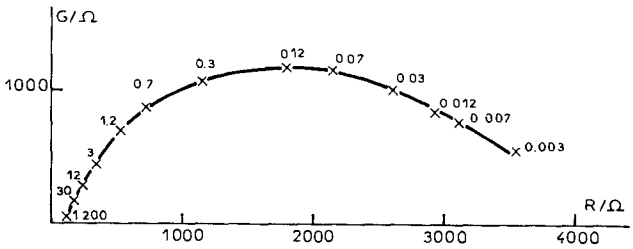


Fig. 2. Impedance diagram $Z = R - jG$ obtained with a 0.6M $AgNO_3$ solution, and an electrode area of 0.3 cm^2. The frequencies are indicated in Hz. (from Ref. 26, Fig. 7).

D. Larkin[28] and N. Hackerman:[29] We were very interested in the points raised by Wiart *et al.* concerning our recent paper. Their discussion of the problem of extracting meaningful values of C_L and R_D from our computer-fitted data is of considerable interest. It is quite true that the sensitivity of the changes in the R_R and $1/\omega C_R$ *vs.* $\omega^{-1/2}$ plots to changes in the computer-guessed values of C_L and R_E are frequency dependent and also depend on the values of C_{ZS}, R_{ZS}, C_L, and R_E. However, the values of C_L and R_E finally selected to give the best fit of the data are very tightly controlled as the R_R and $1/\omega C_R$ *vs.* $\omega^{-1/2}$ plots have to fit the following criteria: (*i*) The plots of R_R *vs.* $\omega^{-1/2}$ and $1/\omega C_R$ *vs.* $\omega^{-1/2}$ must have the same slope in their linear region(s); (*ii*) The plot of $1/\omega C_R$ *vs.* $\omega^{-1/2}$ has to pass through the origin. Figure 3 shows how the im-

[28] Department of Chemistry, Towson State University, Towson, Maryland 21204.
[29] Department of Chemistry, Rice University, Houston, Texas 77001.

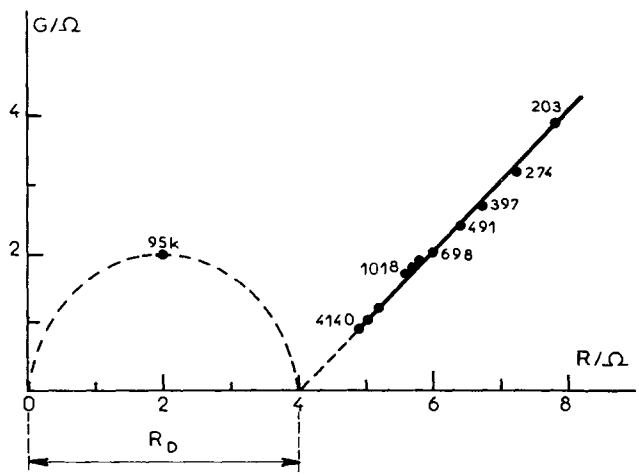


Fig. 1. Impedance diagram $Z = R - jG$ reconstituted from the volues of R_R and $1/\omega C_R$ given in Fig. 2 (Ag^+ = 0.033M) of the paper under discussion and with C_L = 105 μF/cm^2. The frequencies are indicated in Hz.

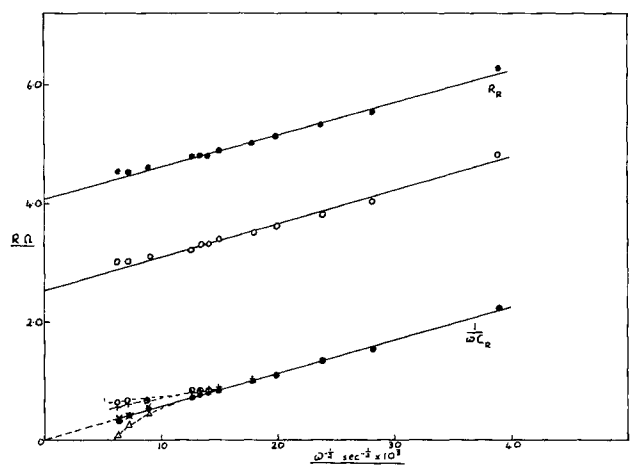


Fig. 3. R_R and $1/\omega C_R$ *vs.* $\omega^{-1/2}$ plots: ●, x, best fit plots for C_L and R_E; +, △, plots where best fit R_E constant C_L varied; ○, plot where best fit C_L constant R_E varied.

ments down to low frequencies and a radiotracer technique to evaluate the exchange current.[25,26]

The first subject for discussion concerns the exploitation of the impedance measurements performed between 20 kHz and 20 Hz. From the values of the two components R_R and $1/\omega C_R$ of the faradaic impedance given in Fig. 2 of the paper under discussion, and from the value of the frequency-independent capacitive component C_L given in Fig. 3, the untreated values of the measured impedance can be restored, except for the frequency-independent resistive component R_L which is not indicated in the paper. For example, at pH 2.4 and for Ag^+ concentration = 0.033M and C_L = 105 μF/cm^2 (*i.e.*, 0.42 μF for an electrode area = $4 \cdot 10^{-3}$ cm^2), the impedance diagram $Z = R - jG$ has been reconstituted in a complex plane (see Fig. 1 of this discussion) where the R-axis origin corresponds to the unknown electrolyte resistance R_L. This resistance can be calculated from the electrolyte resistivity ρ and from the electrode radius r using Newman's relationship $R_L = \rho/4\ r$.[27] So doing with an electrolyte (a mixture of 1M KNO_3 and 1M HNO_3 with pH = 2.4) the composition of which is very similar, we measure 10.8 Ω-cm at 25°C for the resistivity and deduce $R_L = 77\Omega$. In reality the presence of a frit between the test electrode and the counterelectrode probably leads to a higher value of R_L. Consequently, it seems that the transfer resistance $R_D = 4\Omega$ is very low compared with R_L. In addition to such an R_D value, the circuit formed by R_D and C_L in parallel has a characteristic frequency close to 95 kHz. The diagram in Fig. 1 shows clearly that frequencies lower than 4140 Hz are on the outside of the range in which the impedance depends on the capacity C_L. So it appears impossible to reach C_L from impedance measurements only performed in the frequency range 4140-203 Hz corresponding to the results of Fig. 2 of the paper under discussion. That is why it would have been useful to mention the results of the measurements performed between 4140 Hz and 20 kHz where the impedance may begin to be dependent on C_L. This comment raises the following question: Is the accuracy of impedance measurements sufficient, and is the confidence interval on the computer-fitted values of R_L and C_L narrow enough to obtain a meaningful value for C_L and to pull a transfer resistance $R_D = 4\Omega$ out of a measured resistance higher than $R_D + R_L \sim 80\Omega$?

The second point is related to the influence of pH on the exchange current i_o. Our impedance measurements performed down to very low frequency show that the transfer $Ag^+ + e \rightleftarrows Ag$ is not the only process taking place at the interface. As a matter of fact, in Fig. 2 (from Fig. 7 in ftn.[26]) a capacitive loop between 1 kHz and 0.003 Hz can be seen which does not correspond to the electron transfer and which precludes obtaining the transfer resistance R_D. This loop, which cannot be explained in terms of surface diffusion, strongly depends on the anions' adsorption. The study of such impedance diagrams, corroborated by the exchange current values obtained from our radiotracer measurements, has led us to conclude that the adsorption of OH^- ions blocks the electrode. There seems to be a discrepancy between this result and the conclusions given in the paper under discussion which were deduced from R_D values leading to a diminishing exchange current when pH decreases. Can you provide direct evaluations of the exchange current, for example obtained by a radiotracer technique, confirming that this exchange current is an increasing function of pH?

[25] C. Cachet, M. Froment, F. Wenger, and R. Wiart, *J. Electroanal. Chem.*, 61, 121 (1975).
[26] C. Cachet, M. Froment, M. Keddam, and R. Wiart, *Electrochim. Acta*, 21, 879 (1976).
[27] J. Newman, *This Journal*, 117, 198 (1970).

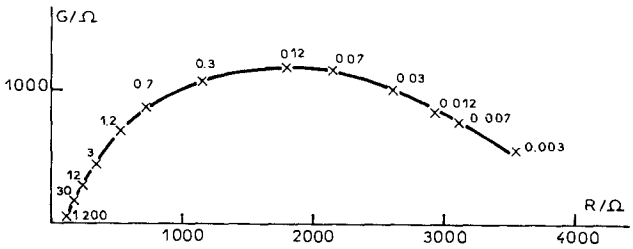


Fig. 2. Impedance diagram $Z = R - jG$ obtained with a 0.6M $AgNO_3$ solution, and an electrode area of 0.3 cm^2. The frequencies are indicated in Hz. (from Ref. 26, Fig. 7).

D. Larkin[28] and N. Hackerman:[29] We were very interested in the points raised by Wiart *et al.* concerning our recent paper. Their discussion of the problem of extracting meaningful values of C_L and R_D from our computer-fitted data is of considerable interest. It is quite true that the sensitivity of the changes in the R_R and $1/\omega C_R$ *vs.* $\omega^{-1/2}$ plots to changes in the computer-guessed values of C_L and R_E are frequency dependent and also depend on the values of C_{ZS}, R_{ZS}, C_L, and R_E. However, the values of C_L and R_E finally selected to give the best fit of the data are very tightly controlled as the R_R and $1/\omega C_R$ *vs.* $\omega^{-1/2}$ plots have to fit the following criteria: (*i*) The plots of R_R *vs.* $\omega^{-1/2}$ and $1/\omega C_R$ *vs.* $\omega^{-1/2}$ must have the same slope in their linear region(s); (*ii*) The plot of $1/\omega C_R$ *vs.* $\omega^{-1/2}$ has to pass through the origin. Figure 3 shows how the im-

[28] Department of Chemistry, Towson State University, Towson, Maryland 21204.
[29] Department of Chemistry, Rice University, Houston, Texas 77001.

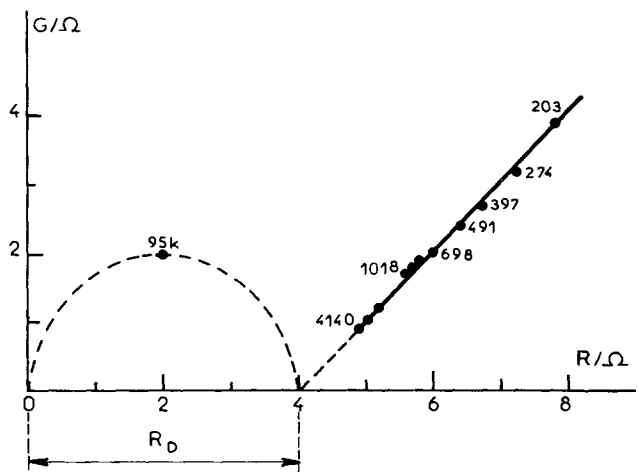


Fig. 1. Impedance diagram $Z = R - jG$ reconstituted from the volues of R_R and $1/\omega C_R$ given in Fig. 2 (Ag^+ = 0.033M) of the paper under discussion and with C_L = 105 μF/cm^2. The frequencies are indicated in Hz.

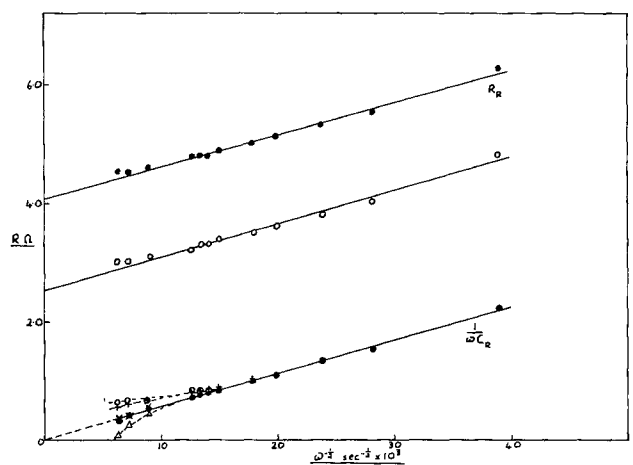


Fig. 3. R_R and $1/\omega C_R$ *vs.* $\omega^{-1/2}$ plots: ●, x, best fit plots for C_L and R_E; +, △, plots where best fit R_E constant C_L varied; ○, plot where best fit C_L constant R_E varied.

pedance plots vary as C_L and R_E are varied for a randomly selected data set. It is quite obvious which set of values gives the best fit of the data. It is of interest to note, as Wiart *et al.* point out, that at lower frequencies the data are very insensitive to changes in C_L and R_E and incidently are also less sensitive to C_L than they are to R_E. In addition, the many separate R_D values for each $[Ag^+]$ concentration and pH were calculated using values of C_L and R_E which were obtained without prejudice as the computer was told to search for the values of C_L and R_E over a wide range of values to give the best fit for each data set. Thus, in answer to the first question, we believe that the values of C_L and R_D obtained are valid.

The different conclusions reached in our respective papers on the role of $[H_3O^+]$ and $[OH^-]$ in the Ag^+-Ag reaction is more difficult to resolve. There are, however, a number of points which should be raised:

1. The pH range of our results lie between the pH ranges where Wiart *et al.* indicate a transition for $[OH^-]$ inhibition and its absence.

2. The value of our exchange reaction is much larger than reported elsewhere and we attribute this to our stringent purification procedures.

3. Radiotracer studies are an interesting method of investigating electrode reactions. However, the conclusion that the electrode surface is blocked does not distinguish between the electrode surface blocked by pretreatment or after immersion in the solution. The use of chromic acid in this electrode preparation is disturbing as we have found this material to affect electrode reactions adversely (ftn.[26]). Also, it is not clear to us what meaningful information one can obtain from scanning electron microscope studies as to the state of the electrode surface in solution (ftn.[26]).

4. While $[OH^-]$ may block the electrode surface, its kinetic dependence may not be a simple function of $[OH^-]$ but could be more complex, *e.g.*, $1/[OH^-]$. This would of course masquerade as a linear dependence on $[H_3O^+]$.

5. It is not clear whether in our study we are looking at the same reaction as Wiart *et al.* The impedance method used in both investigations is a perturbation technique; however, the time scale where Wiart *et al.* find $[OH^-]$ inhibition is at least 100 fold slower than our measurements. It may well be, therefore, that we are both looking at different kinetic steps of the overall process.

In conclusion, we believe that our results and those of Wiart *et al.* may not be as contradictory as they first appear. However, it is obvious that this system still needs extensive study, especially in regard to effects of electrode pretreatment.

SOLID-STATE SCIENCE
—AND TECHNOLOGY—
DECEMBER
1977

Stability of MOSFET Devices with Phosphorus-Doped Oxide as Gate Dielectric

P. K. Chaudhari,* R. A. Michaud,* and R. M. Quinn
IBM Corporation, Poughkeepsie, New York 12602

ABSTRACT

An experimental technique of phosphorus doping into oxide is described. Evaluation of the effectiveness of these films is made by studying bias, temperature, and time dependence of the threshold voltage stability of MOSFET devices fabricated using this phosphorus-doped oxide as gate dielectric. Experimental data is analyzed in the light of two mechanisms known to exist in such phosphosilicate glass (PSG) layers and is shown to be in good agreement with them. It is shown that the threshold voltage stability can be maintained to within 0.03V under device operating conditions with realistic contamination levels (generally $<5 \times 10^{10}$ cm^{-2}). Results also indicate that the polarizability obeys $1/(T - T_c)$ with $T_c = 330$°K.

In the beginning of the IGFET technology, one of the more formidable obstacles blocking the development of practical MOS transistors was the migration of charge within the gate insulator under conditions of high electric field and temperature. A thin phosphosilicate glass (PSG) film on top of a thermally grown SiO_2 layer resulted in improved device behavior (1). PSG film containing approximately 4 mole percent (m/o) P_2O_5 and of the order of 125Å thick has been found to be very effective in blocking Na^+ ion contaminations as high as 10^{12} cm^{-2} (2). However, a drawback of utilizing PSG films for stabilization is that they are polarizable and can therefore contribute to the shift in the threshold voltage of the device (3). Another drawback is that the technological trend towards higher densities and micropower operation points to the necessity of thinner insulators in the gate area of an IGFET device. Since it is very difficult to produce sodium-free SiO_2 films in device production, and in view of the above demands, an experimental technique of phosphorus doping into SiO_2 films during thermal oxidation is described here. The effectiveness of these films is evaluated by studying bias, temperature, and time dependence of polarizing effects in FET devices, and by performing threshold voltage measurements. A two-mechanism model for PSG polarization instability is briefly reviewed here (4). The experimental results of phosphorus-doped oxide gate IGFET's are then analyzed in the context of these two mechanisms. Consistent with the data, the temperature dependence of the polarizability χ is also established and is discussed in the Appendix.

Experimental Details

Preparation of the oxide layer.—The silicon dioxide was grown onto the p-type 2 Ωcm silicon substrates utilizing an HCl-cleaned dry oxidation process. The oxidation temperature was 1050°C. Phosphorus was incorporated into the silicon dioxide films during the thermal oxidation process. At first pure oxygen is introduced; approximately 80% of the desired thickness of the oxide layer is grown, followed by a second growth utilizing dry oxygen and 1-2% volume of PH_3 to bring the total oxide thickness to its final value. This procedure prevents the diffusion of phosphorus into the silicon substrate. The films are annealed in nitrogen at 1050°C for 15 min. This is the final high temperature anneal, and it determines the value of the insulator charge and fast surface state density, both of which strongly affect the device threshold voltage. The oxidation rate is not affected by the addition of PH_3, but is similar to that in the ordinary thermal oxidation. Step etching techniques characterize the phosphorus to be uniformly distributed throughout the film and observed to be similar in composition to a conventional phosphosilicate glass, with a concentration of about 1.5 mole percent and a thickness of about 50Å. The dielectric permittivity is nearly constant.

Device fabrication.—A number of experimental MOSFET devices were fabricated using p-type 2 Ωcm silicon wafers. First source and drain regions were formed. Phosphorus-doped oxide was then grown immediately after cleaning as described above. Aluminum was used as the gate metal. After aluminum evaporation, devices were treated with forming gas anneal at 450°C for 15 min. Conventional photolithography was used throughout the fabrication. Mobile ion contamination checked by the high temperature quasistatic technique (5) using a control wafer was found to be consistently less than 5×10^{10} cm^{-2}. Devices thus fabricated had a threshold voltage range of approximately 1V.

Measurements.—The aging experiments were performed in the following manner. Discrete IGFET's were stressed in air at different temperatures with varying gate bias values applied with respect to the commonly connected substrate, source, and drain. After a given period at the elevated temperature, the devices were cooled to room temperature with the bias applied. Measurements were made of drain junction leakage, gate-to-substrate leakage, and drain current at a drain voltage of +10V. The MOSFET device threshold voltage was calculated by a least squares fit to the linear portion of the curve of the square root of the drain current as a function of gate voltage.

* Electrochemical Society Active Member.
Key words: phosphorus-doped oxide gate dielectric, polarization, threshold voltage stability.

A data listing was developed showing drain junction leakage current, gate leakage current, and threshold voltage shift (ΔV_{th}) from the initial value on each device throughout each experiment. The parameter that exhibited a consistent long-term drift problem was the threshold voltage of the device. The long-term changes observed in substrate leakage and drain junction leakage were negligible. The results presented in the next section will deal with time dependence of the threshold voltage shift. The values are averages obtained from 20-40 devices.

Theory

Phosphosilicate glass films grown on thermally oxidized silicon can be polarized by an electric field. The PSG polarization has two components which may be distinguished by determining the time response of the total polarization as a function of temperature (4). The pertinent features of this model are briefly reviewed here and will be used to verify the experimental characteristics of phosphorus-doped oxide gate IGFET devices.

Application of an electric field across a metal/PSG-SiO_2/Si structure will cause polarization of the glass layer (3). Under a stressing voltage V_G, this polarization will saturate while changing the threshold voltage V_{th} of the FET device by the amount

$$\Delta V_{th} = -\frac{\chi x_g}{\epsilon_g x_o} V_G \quad (\text{for } x_g << x_o) \quad \text{and} \quad (\chi << x_g) \qquad [1]$$

Here χ is the polarizability of the medium, x_g the glass thickness, ϵ_g is the dielectric constant of the glass, and x_o is the thickness of the oxide.

When χ becomes very large, the threshold shift saturates according to

$$\Delta V_{th}^{SAT} = -\frac{\epsilon_o x_g}{\epsilon_g x_o} V_G \qquad [2]$$

Both cases have been observed for PSG films. The first polarization component saturates relatively rapidly. A larger but much slower polarization process begins to occur at a significant rate above about 100°C. A very large effective value of χ characterizes this process, and its saturation value follows (2).

Experimental Results and Discussion

Figure 1 shows the threshold voltage shift *vs.* stress time with the field as the parameter plotted on a linear scale. Similar data, but with temperature as a parameter, is also shown in Fig. 2. It is clear from both figures that the instability observed is in general qualitative agreement with the model described above. That is, there is an initial component which saturates relatively rapidly (in 10^3 sec) followed by a larger but much slower polarization process which begins to occur at a significant rate above 100°C, eventually approaching a saturation value ΔV_{th}^{SAT} (see Fig. 2).

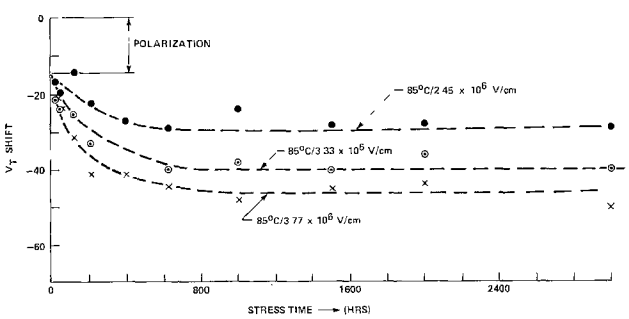


Fig. 1. Threshold voltage shift as a function of time of phosphorus-doped SiO_2 IGFET's.

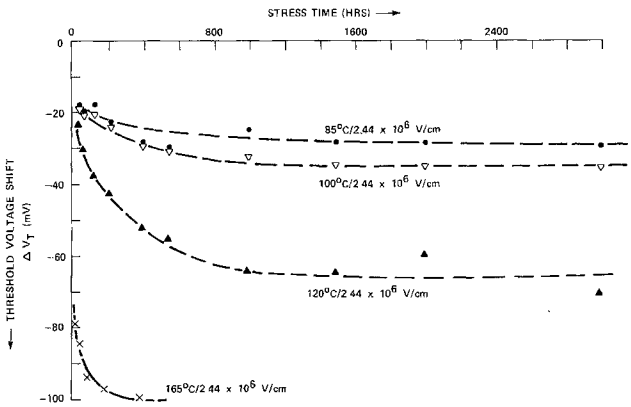


Fig. 2. Threshold voltage shift as a function of time of phosphorus-doped SiO_2 IGFET's.

The threshold shift data of these phosphorus-doped SiO_2 gate IGFET's will therefore be quantitatively analyzed in the context of the above model.

Fast polarization.—In order to obtain ΔV_{th}^{SAT} for the low temperature, fast polarization process, structures were stressed at 2.44×10^6 V/cm and at 165°C for several minutes. The value of the saturated shift ΔV_{th}^{SAT} thus obtained when substituted in Eq. [1] yielded the PSG glass thickness of ~60Å. In this evaluation, ϵ_g was taken as 4 and the polarizability $\chi = 0.05$ (4). Step etching techniques characterize the phosphorus-doped gate oxide in the present study to be similar in composition to a conventional phosphosilicate glass with a concentration of <1.5 m/o and a thickness of ~50Å. Extremely small values of polarization shift also support such a small concentration of P_2O_5. Furthermore, even though $\Delta V_{th}^{SAT} \sim V_G$, its magnitude was found to be $<<V_G$ that is also consistent with Eq. [1]. These experimental results conform to the data of Fig. 1 and 2 as analyzed above. Thus the fast polarization instability observed in the phosphorus-doped SiO_2 gate IGFET's studied here fits the oxygen ion transfer model as described for PSG-SiO_2 IGFET devices (4).

Slow polarization.—From Fig. 2 it is clear that a larger but much slower polarization process begins to occur at a significant rate above 100°C. The amount of the shift ΔV_{th} increases with the length of time the bias is applied, and its saturation value follows Eq. [2]. ΔV_{th}^{SAT} values obtained from Fig. 2 plotted on a linear scale in Fig. 3 as a function of polarizing V_G do indeed agree well with Eq. [2]. Here again the saturation value is simply proportional to V_G, and does not reach a value of V_G as predicted by Eq. [2], *e.g.*, with $x_g = 50$Å, $x_o = 450$Å, and $K_o = K_g = 4$ yields, $\Delta V_{th}^{SAT} = 1.22$V for $V_G = 11$V as against an observed value of ~25 mV (see Fig. 1). This discrepancy is due to the fact that the formula [2] is valid for large values of dipole concentration N (6). For very small values of N (10^{16} cm^{-3}) the shift V_{th}^{SAT} is found to be (6)

$$\Delta V_{th}^{SAT} = \frac{N q x_g^2}{\epsilon_o \epsilon_g} \qquad [2']$$

where N will be a function of bias. The data of Fig. 1 and 3 do conform to Eq. [2'] and further support the low concentration of P_2O_5 content as found here. Thus the slow polarization phenomenon is caused by the drifting of oxygen ions over many atomic distances, as Eq. [2] is based on the long-range ion drifting (4). The presence of such negatively charged nonbridging oxygen ions may also provide a trapping site for otherwise mobile Na^+ impurity ions, thereby accounting for the stabilizing effect of the phosphorus-doped oxide layer. However on a longer time scale,

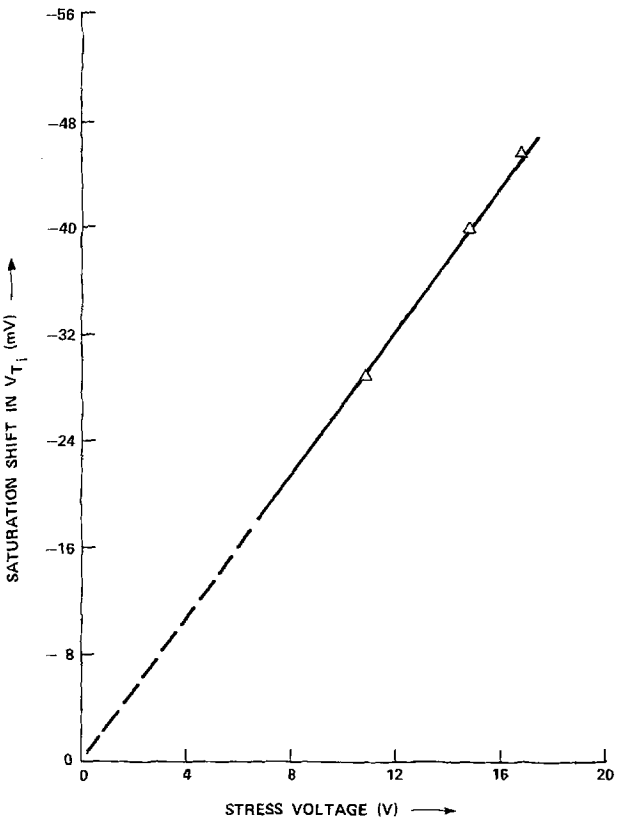


Fig. 3. Saturation shift in $V_{T_i}^{SAT}$ vs. stress voltage at 85°C.

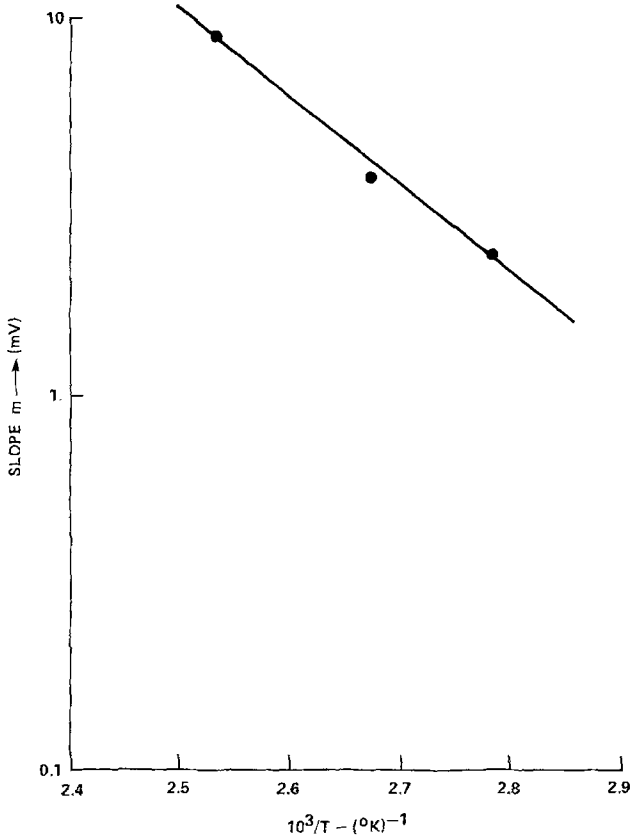


Fig. 4. Dependence of slope $m = d(\Delta V_T)/d(\log t)$ on temperature.

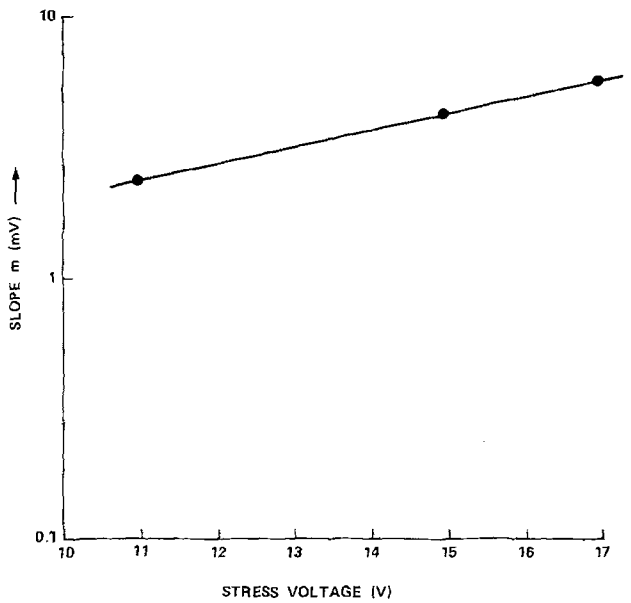


Fig. 5. Dependence of slope $m = d(\Delta V_T)/d(\log t)$ on stress at 85°C.

mobile ion drift such as Na^+ could also cause such a behavior as described by Eq. [2'] (2). In order to differentiate these similar phenomena some information might be gained if the SiO_2 thickness was varied systematically, with a constant m/o PH_3 in conjunction with negative field stressing. Now from Fig. 2 it is also seen that the rate at which saturation is approached is strongly dependent on temperature. This temperature dependence is further shown in Fig. 4, where the slopes m of the curves of Fig. 2 are plotted as a function of the inverse of temperature. Using this data, the temperature dependence of the polarizability is also discussed in the Appendix.

Reliability projections of the threshold voltage stability of these IGFET devices can now be estimated. Lumping the fast polarization contribution in the threshold voltage shift ΔV_{th} at $t = 1$ hr, the total threshold voltage shift for $t \geq 1$ hr may then be expressed by the empirical equation

$$\Delta V_{th} = \Delta V_{th}(1\,\text{hr}) + m \log t \qquad [3]$$

where m is a function of temperature and voltage and is expressed as (see Fig. 4 and 5)

$$m = \exp\left(-\frac{\Phi}{KT} + \beta V_G\right) \qquad [4]$$

with $\Phi = 0.495$ eV.

These results allow the stability of the IGFET devices to be estimated. From the data of Fig. 1, the threshold shift at 2.44×10^6 V/cm for operating conditions under 85°C is $\leq$30 mV for times as long as 10 years. It is also evident that the low temperature polarization results in a maximum of only 0.015V threshold shift. Thus the data of Fig. 1 indicate that the phosphorus-doped oxide films fabricated in this study are similar in composition to 1.5 m/o P_2O_5, 50Å (approximately) to conventional PSG-SiO_2 films and will furnish protection against Na^+ contamination levels in the low 10^{11} ions cm^{-2} region for realizing ΔV_{th} of only 30 mV for 450Å doped gate oxide under a field of 2.44×10^6 V/cm and at 85°C for the lifetime of the device. For each practical case, however, a proper amount of phosphorus doping must be individually selected for its Na^+ gettering capabilities and it must still maintain the negligible polarization behavior.

Conclusions

The experimental technique of phosphorus doping into silicon dioxide films during thermal oxidation is presented. Threshold instability of IGFET's fabricated

using this phosphorus-doped oxide as gate dielectric was analyzed and found to be consistent with the existing two polarization process models. The fast polarization component is found to be ≤0.015V, while the slow polarization component data indicate that 1-2 m/o PH_3-doped SiO_2 will effectively stabilize the threshold voltage of IGFET's under operating conditions of temperature and field. Temperature behavior of the saturation values of the threshold voltage shift has led to the polarizability dependence on temperature.

Manuscript submitted May 3, 1977; revised manuscript received July 18, 1977. This was Paper 342 presented at the Las Vegas, Nevada, Meeting of the Society, Oct. 17-22, 1976.

Any discussion of this paper will appear in a Discussion Section to be published in the June 1978 JOURNAL. All discussions for the June 1978 Discussion Section should be submitted by Feb. 1, 1978.

Publication costs of this article were assisted by IBM Corporation.

APPENDIX

Temperature Dependence of Polarizability

When the polarizability χ becomes very large compared to $\epsilon_g{}^u$ and ϵ_o (due to long-range ion drifting), the threshold voltage shift $\Delta V_{th}{}^{SAT}$ will saturate according to (4)

$$\Delta V_{th}{}^{SAT} = -\frac{\epsilon_o x_g}{\epsilon_g{}^u x_o} V_G \qquad [A\text{-}1]$$

The unrelaxed value of the high frequency dielectric constant $\epsilon_g{}^u$ is defined in terms of the relaxation strength Δ_ϵ by (7)

$$\epsilon_g{}^u = \chi/\Delta_\epsilon \qquad [A\text{-}2]$$

Combining [A-1] and [A-2], we get

$$\chi = -\epsilon_o \chi_g \Delta_\epsilon / \chi_o (\Delta V_{th}{}^{SAT}/V_G) \qquad [A\text{-}3]$$

Now values of $\Delta V_{th}{}^{SAT}$ obtained from the data of Fig. 2 are plotted in Fig. 6 as a function of the inverse of temperature. Consistent with the behavior observed in Fig. 6, $\Delta V_{th}{}^{SAT}$ may be expressed by the empirical relationship

$$\Delta V_{th}{}^{SAT}/V_G = C - \frac{T_c}{T} \qquad [A\text{-}4]$$

The data of Fig. 6 plotted on a compressed temperature scale as shown in Fig. 7 yield the value of $C = 1$. Thus with $\Delta_\epsilon = B/T$ (4) and [A-4], the temperature dependence of polarizability can be expressed from [A-3] as

$$\chi = \frac{\epsilon_o \chi_g B}{\chi_o (T - T_c)} \sim 1/T - T_c,\ T_c = 330°K \qquad [A\text{-}5]$$

Such a behavior was speculated by Eldridge, Laibowitz, and Balk (4).

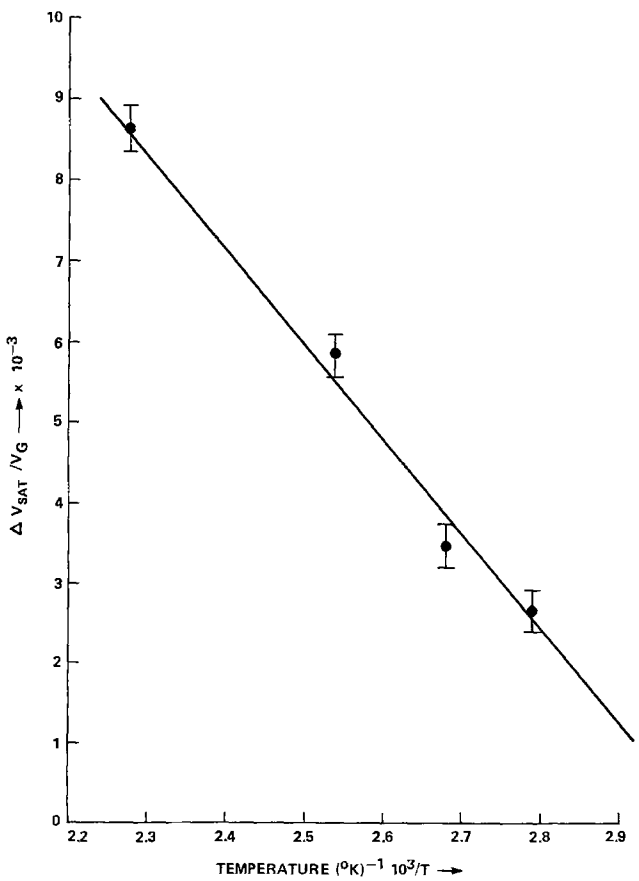


Fig. 6. Dependence of $\Delta V_{Ti}{}^{SAT}/V_G$ on temperature

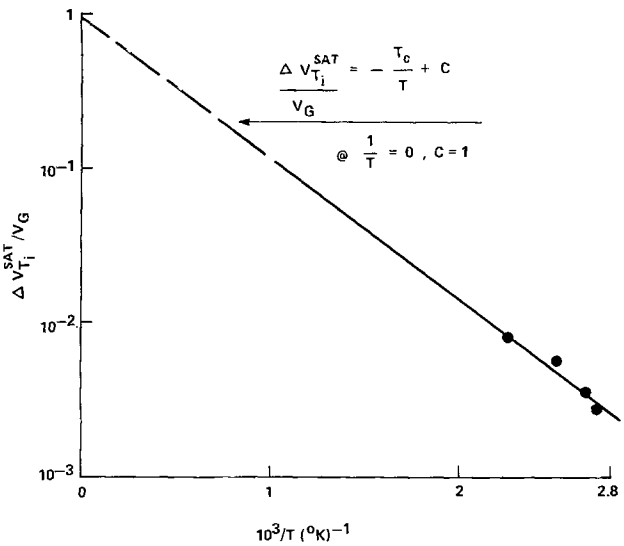


Fig. 7. Saturation shift per unit stress as a function of temperature of a phosphorus-doped SiO_2 gate IGFET.

LIST OF SYMBOLS

B	a constant in reciprocal temperature
C	dimensionless constant
m	slope defined by $d(\Delta V_{th})/d(\log t)$
t	time in hours
T	temperature in °K
T_c	a constant in units of temperature
V_G	gate voltage in volts
ΔV_{th}	threshold voltage shift in volts
$\Delta V_{th}{}^{SAT}$	saturation value of threshold voltage in volts
χ	polarizability of the medium
x_g	PSG thickness in Å
x_o	oxide thickness in Å
β	a constant in units of (volts)$^{-1}$
ϵ_g	dielectric constant of PSG
ϵ_o	dielectric constant of oxide
$\epsilon_g{}^u$	unrelaxed value of the high frequency dielectric constant of PSG
Δ_ϵ	relaxation strength of the medium
Φ	activation energy in eV

REFERENCES

1. D. R. Kerr, J. S. Logan, P. J. Burkhardt, and W. A. Pliskin, *IBM J. Res. Dev.*, **8**, 376 (1964).
2. J. M. Eldridge and D. R. Kerr, *This Journal*, **118**, 986 (1971).
3. E. H. Snow and B. E. Deal, *ibid.*, **113**, 263 (1966).
4. J. M. Eldridge, R. B. Laibowitz, and P. Balk, *J. Appl. Phys.*, **40**, 1922 (1969).
5. D. Kerr, in Proceedings of the International Conference on the Properties and uses of MIS Structures, Grenoble (1969).
6. E. H. Snow and M. E. Dumesnil, *J. Appl. Phys.*, **37**, 2123 (1966).
7. A. S. Nowick and B. S. Berry, *IBM J. Res. Dev.*, **5**, 297 (1961).

The Effect of Gamma Irradiation on the Low Temperature Properties of Amphoterically Si-Doped GaAs LED's

C. E. Barnes

Sandia Laboratories, Albuquerque, New Mexico 87115

ABSTRACT

The effects of gamma irradiation on the light intensity, total current, spectral characteristics, and radiative decay time as a function of applied voltage at 76°K have been studied in amphoterically Si-doped GaAs light-emitting diodes (LED's). At low voltages, both the total current, I, and radiative current are due to space charge recombination with the result that, at constant voltage, I increases with gamma dose, Φ, while the light intensity, L, remains constant. At higher voltages, where the radiative current is due to recombination in the neutral p-region, L decreases sharply with Φ at constant voltage. This rapid decrease is due, in part, to the presence of space-charge limited current (SCLC) flow which also leads to a decrease in I with Φ at constant high voltage. Spectral measurements show that the emission peak energy is proportional to junction voltage at low currents suggesting radiative tunneling of carriers in deep tail states. In accordance with the "wavy band" model for these diodes, tail states are also responsible for the observed inverse dependence of radiative decay time on diode current and emitted photon energy. The long lifetimes in the localized deep tail states lead to a radiation damage effect contrary to that observed for diffusion length-associated lifetimes; that is, the longest lifetimes are least affected by gamma irradiation.

Amphoterically Si-doped GaAs light-emitting diodes (LED's) have become commercially important devices because they possess higher efficiencies than many conventional Zn-diffused LED's. Among the wide variety of optoelectronic applications in which GaAs:Si LED's can be used are those in which the devices may be exposed to nuclear radiation. Therefore, it is important to know how the operating characteristics of these LED's will change following exposure to radiation. In this paper, it is shown that the unique properties of these devices at low temperatures significantly affect the GaAs:Si LED's response to gamma irradiation.

Previous studies in our laboratory (1, 2) and elsewhere (3, 4) have shown that the GaAs:Si LED's are quite sensitive to irradiation, primarily because of their relatively long preirradiation electron lifetimes. Our examination (2) of the effects of gamma irradiation on the room temperature light output of these devices showed that additional degradation results from the presence of radiative space-charge limited current (SCLC) flow at high currents. In this paper, we show that results taken at 76°K confirm this high current behavior and, also, support the "wavy band" model used to explain the LED properties at low currents.

Experimental Procedure

The amphoterically Si-doped LED's used in this study were obtained from Texas Instruments Incorporated. They are designated as TIL-26 emitters and constitute the emitter portion of the TIL-107 optical isolator studied previously (3). The TIL-26 consists of a single epitaxial layer in which the n- and p-type regions are grown by varying the growth temperature over a wide range. The substrate is n-type GaAs doped with approximately 10^{17} Si/cm^3. The device is mounted with the n-type side up and has a junction area of $A = 1.45 \times 10^{-3}$ cm^2.

The light output and total current of the GaAs:Si LED's were measured as a function of voltage and gamma dose. At low currents, the LED's were driven in the d-c mode, while pulsed techniques were used at high currents to avoid heating problems and bias-induced annealing. In both cases, phase sensitive detection was used to process the signal from a cooled S-1 response photomultiplier. For spectral measurements, a Spex 1 meter monochromator was used and the results were corrected for the wavelength response of the monochromator-photomultiplier combination. Radiative time decay measurements were made with a Si pin photodiode having a response time of a few nanoseconds. All measurements were made in a cryostat with the LED held at 76°K by immersing the bottom of the LED holder in liquid nitrogen.

Irradiations were performed at room temperature in the Sandia Co^{60} Gamma Irradiation Facility (GIF). Doses were determined with established dose mapping of the GIF cell performed previously with cobalt glass and 4-chlorostyrene dosimeters. All irradiations were performed with devices in the passive, open-circuit state.

Experimental Results

Typical current-voltage (I-V) curves at 76°K are shown in Fig. 1 for a GaAs:Si LED prior to irradiation and following successive doses to 1×10^8 rad. At lower voltages, where the applied voltage, V, equals the junction voltage, V_j, the slope of the I-V curves is given by $m = 1.7$ in exp $[qV/mkT]$ indicating that the total current flow is dominated by space-charge recombination (SCR) at low voltages. This result is often observed in GaAs LED's (1, 3, 5) as is the irradiation-induced increase in SCR current at constant voltage (6), shown in Fig. 1. The increase in current is a result of the introduction of additional nonradiative recombination centers by the irradiation.

At large voltages, the opposite is observed; that is, gamma irradiation causes a decrease in I at constant V. This decrease is approximately a factor of 10 smaller than the increase in I at small V. The gamma-induced decrease in current occurs over a voltage range where there is significant deviation from the junction-controlled exponential behavior observed at low voltages. It will be shown that the existence of a voltage drop across the neutral region leads to the irradiation-induced decrease in I.

Light intensity-voltage (L-V) curves at 76°K are shown in Fig. 2 for the same diode used to obtain the I-V curves in Fig. 1. At low voltages, L varies exponentially with V with a slope given by $m = 1.4$,

Key words: defects, LED's, radiation, semiconductors, electroluminescence, optoelectronics.

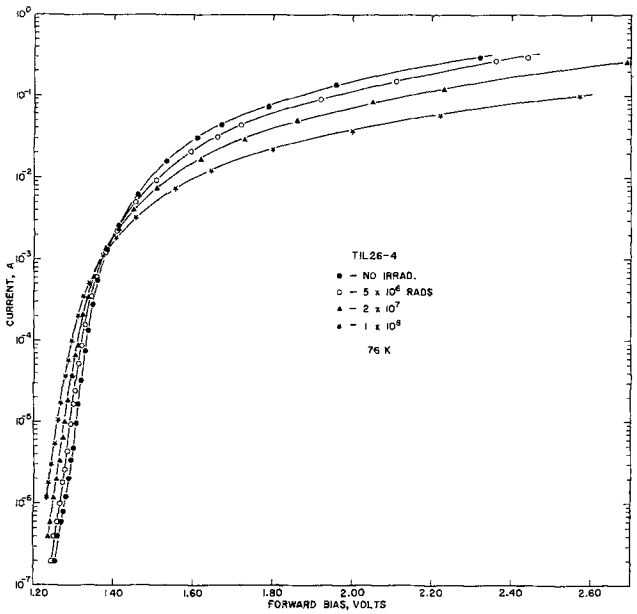


Fig. 1. Typical total current-voltage characteristics for an amphoterically Si-doped GaAs LED at 76°K. Note that gamma irradiation increases *I* at low voltage, but decreases *I* at high voltage.

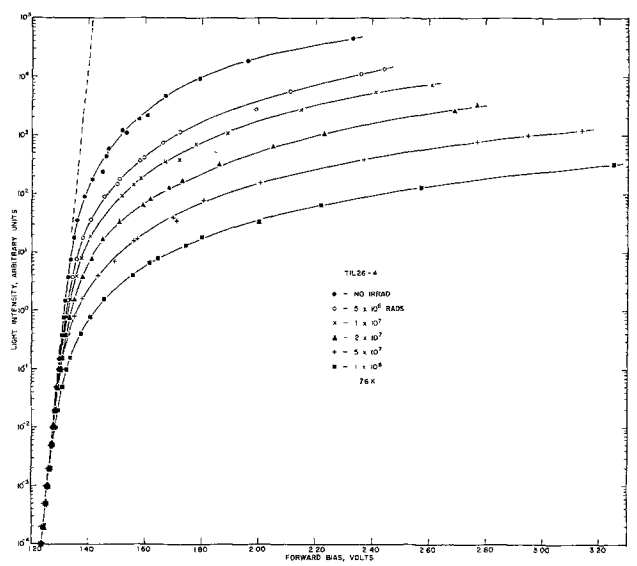


Fig. 2. Light output, *L*, vs. applied voltage for a typical GaAs:Si LED at 76°K. While L is insensitive to irradiation at low voltages, the gamma-induced degradation at large voltage is severe. The dashed line is used to determine junction voltage, V_J, at large applied bias.

indicating that the light output is also due to recombination within the space-charge region, a common observation in GaAs LED's at low temperatures (6). The existence of a radiative SCR current is further confirmed by the lack of any significant gamma-induced change in *L* at constant low voltage. This follows from the fact that, for a particular recombination process, the recombination rate in the space-charge region depends on the quasi-Fermi levels which, in turn, are determined by the majority-carrier concentrations. If the gamma dose is below that required for significant carrier removal, and if the defect centers are nonradiative recombination centers, then the total space-charge current due to recombination at all centers should increase, as shown in Fig. 1, but the radiative current should be unaffected following irradiation. In agreement with this reasoning, capacitance-reverse-bias measurements performed at 300°K demonstrated that the carrier-concentration profile did not change following irradiation (2).

As in the case of the *I-V* data, the light intensity-voltage characteristic is affected quite differently at large voltages. In contrast with the lack of any change at low voltages, the light intensity decreases strongly for constant voltages large enough to cause a deviation from the purely exponential junction-controlled SCR behavior observed at low voltages. The onset of a gamma-induced reduction in *L* indicates that the light output is the result of radiative recombination in the neutral p-region due to radiative diffusion currents near the junction and other radiative current flow mechanisms occurring across the entire p-region. As we will show, these latter processes account for a significant portion of the reduction in *L* at large voltages.

Spectral measurements indicate that the electroluminescence spectrum of the GaAs:Si LED's is dominated by a single broad band which does not change shape with irradiation. However, as shown in Fig. 3, the peak photon energy is a function of both applied voltage and gamma dose. The proportionality between peak energy and voltage suggests that radiative tunneling is occurring as observed previously for GaAs LED's at low temperatures (6-9). For this process, "shifting peak" spectra are seen because the tunneling probability is highest for carriers near their respective quasi-Fermi levels, the separation of which is determined by the junction voltage. Consequently, the peak photon energy shifts to higher energy with increasing junction bias. This result, in combination with the results shown in Fig. 2, indicates that the light output at 76°K and low voltages is due to carriers tunneling into the space-charge region with subsequent radiative recombination in that region.

At large, constant applied bias Fig. 3 shows that the peak energy decreases significantly with gamma dose. It should be emphasized that, for radiative tunneling, the peak energy is proportional to the junction voltage, V_J, rather than the total applied voltage. As will be shown later, much of the apparent reduction in peak energy with increasing dose, shown in Fig. 3, can be accounted for by the fact that the junction voltage changes with dose at constant, large applied voltage.

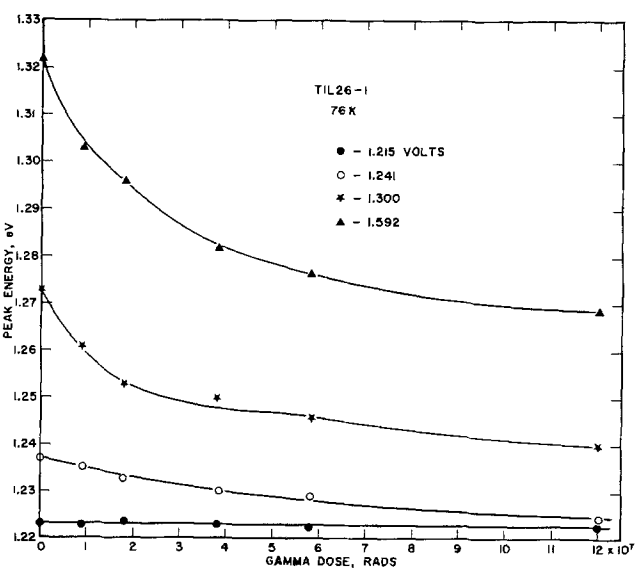


Fig. 3. Peak photon energy from spectral measurements as a function of applied voltage and gamma dose for a typical GaAs:Si LED at 76°K.

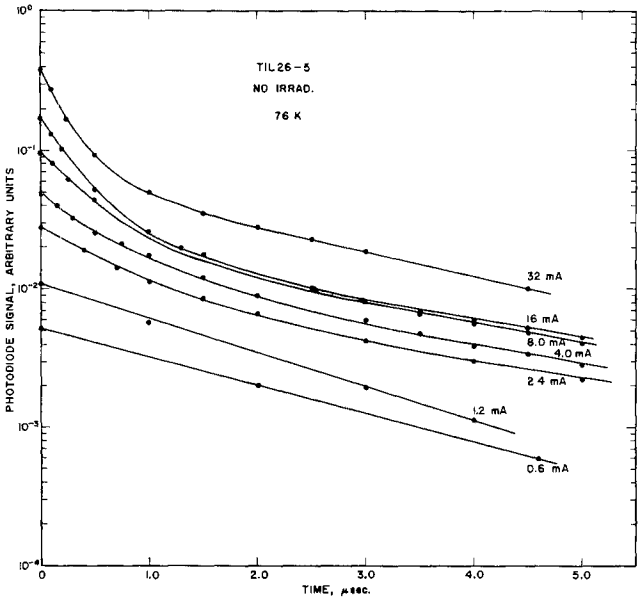


Fig. 4. Decay of the light output from a GaAs:Si LED following the application of a 10 μsec wide pulse at several current levels prior to irradiation. Note that the initial decay is more rapid at larger currents.

Turning our attention to the radiative time decay data, Fig. 4 illustrates the variation of the LED output with time following the application of a 10 μsec wide pulse for a variety of LED pulse current levels. At large currents, there is an initial rapid decay of light output followed by a long tail lasting several microseconds. With decreasing current, the initial decay becomes slower until at about 1 mA, the decay time can be approximately described by a single exponential within the time interval shown in Fig. 4. It is also interesting to note that at long times the decay curves are all approximately parallel, independent of LED pulse current level. These curves are to be contrasted with GaAs LED's containing Zn-diffused regions in which the radiative rise and decay times are typically tens of nanoseconds.

The effect of gamma irradiation on the radiative decay for a constant, relatively large pulse current of 16 mA is shown in Fig. 5. As irradiation proceeds,

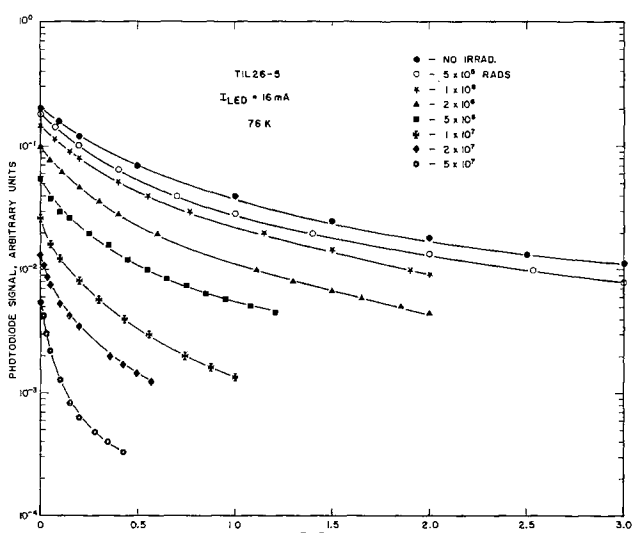


Fig. 5. Light output decay after application of a 16 mA pulse to a GaAs:Si LED at 76°K as a function of gamma dose. The initial decay becomes more rapid with Φ, but the long-time portions of the curves tend to remain parallel.

the initial radiative decay becomes more rapid, but the curves at long times are approximately parallel so that the slow decay is relatively unaffected by irradiation. This is an important result because it is just the opposite of what one would expect for the usual effect of radiation on minority carrier lifetime; that is, the longer the minority carrier lifetime, the more sensitive it is to irradiation. However, as we will show, the results in Fig. 5 are satisfactorily explained by the model developed for the amphoterically Si-doped GaAs LED's.

Device Theory

Prior to further analysis of the effects of gamma irradiation on the low temperature properties of GaAs:Si LED's, we will provide a brief description of the theory used to explain the properties of these devices. In agreement with the data shown in Fig. 4, previous authors (10-13) have observed unusually long radiative rise and decay times which were inversely proportional to LED current and emitted photon energy. In addition, it has been found that the peak photon energy can be varied by changing the Si doping level (14). A typical commercial device has a room temperature peak wavelength of 930-940 nm, 30-40 nm above that for a Zn-diffused LED. Further, at large currents, light emission from the entire p-region has been observed (10, 12). Explanation of these properties is based on a model developed through studies of photoluminescence in n- and p-type bulk GaAs:Si material (15-18) and of the amphoteric LED's themselves (10-14). During the growth of the epitaxial p-layer of the device, a lower growth temperature is used so that Si will substitute for As and act as an acceptor rather than for Ga which produces the donor activity in the n-layer. However, even at lower temperature, Si continues to substitute for Ga to a certain degree so that the end result is a compensated p-region containing 10^{18}-10^{19} Si atoms/cm^3 but only 10^{16}-10^{17} holes/cm^3 (10). The high concentration of Si leads to a merging of the Si shallow donor and acceptor states with conduction and valence bands resulting in the creation of deep band "tails." Because the Si atoms are randomly distributed, there are localized fluctuations in the potential resulting in perturbations of the energy band tails. Since the deepest conduction band tails occur in regions of low potential and the highest valence band states are in regions of high potential, the localized deep valence and conduction band tails are, by necessity, spatially separated from each other. In addition to the shallow donor and acceptor levels, Si introduces deeper levels, and the radiative recombination in these devices is generally thought to occur through a Si acceptor level at $E_V + 0.1$ eV (14). This level is assumed to follow the fluctuations in the valence band. This "wavy band" model has been used successfully by Byer (10, 11) and Redfield *et al.* (18) to explain the properties of amphoterically Si-doped GaAs LED's. At low currents, only the deepest tail states in the conduction and valence bands are filled. Since these states are spatially separated, recombination requires long-range tunneling which leads to long recombination times. In addition, recombination through the deepest states produces low energy photons with energies significantly less than the energy gap so that the peak photon energy is at a lower energy than in uncompensated, Zn-diffused LED's. Consequently, the recombination times are long at low photon energies. As the current is increased, the deepest tails are saturated and the electrons and holes occupy normal delocalized band states leading to vertical nontunneling recombination which is characterized by shorter recombination times and higher photon energies.

Byer (10) has used the space charge-limited current (SCLC) theory of Ashley and Milnes (19) and Lampert (20) to explain the observed wide-emitting

region at high currents. At lower currents, where the voltage drop across the p-region, $V - V_j$, first appears, one observes an Ohm's law range where the current, I, is proportional to $V - V_j$. As the current is increased, significant numbers of electrons begin to drift into the p-region resulting in the buildup of a space charge. In this range, Byer (10) observed a square law dependence, $I \propto (V - V_j)^2$, as predicted by the SCLC theory. Because the electron concentration is significant over the entire p-region, radiative recombination occurs across this whole region. In the SCLC range, Byer (10) found a sublinear dependence of the light intensity, L, on current in correspondence with the $L \propto I^{1/2}$ dependence predicted by the theory. The sublinear dependence occurs because many of the electrons reach the p-region electrode before they can recombine, resulting in a decreasing quantum efficiency as I is increased. In a later examination of GaAs:Mn LED's, Ashley (21) and Ashley *et al.* (22) showed that L can vary linearly with I and, hence, as $(V - V_j)^2$ in the SCLC range. This dependence agrees with the theory if one assumes that double injection is occurring in the p-region. In this case, the reduction in quantum efficiency due to the loss of electrons at the electrode is compensated for by hole injection.

In our previous study (2) of gamma irradiation effects on the room temperature properties of these amphoterically Si-doped GaAs LED's, the primary concern was with the rapid gamma-induced light output degradation at high currents. In agreement with previous work (10, 21, 22), a major component of the radiative current was found to be due to SCLC flow. Further, it was shown that this component degraded more rapidly with irradiation than the radiative diffusion current which dominates at low currents at room temperature. In the next section, it is shown that similar behavior occurs at 76°K.

Analysis and Discussion

We begin our analysis of the results in terms of the model outlined in the previous section by examining the effects of gamma irradiation on the radiative decay time. Figure 2 shows that the radiative current begins to deviate from an SCR current at about 1.30V indicating that electron injection into the neutral p-region is occurring above 1.30V with subsequent radiative recombination in this region. Figure 1, in turn, shows that this voltage corresponds to a current range of approximately 0.01-0.1 mA for the pre- and postirradiation I-V curves. The smallest current used in obtaining the radiative decay data shown in Fig. 4 and 5 is 0.6 mA. In particular, we are interested in analyzing the data in Fig. 5 taken at 16 mA. Therefore, it can be assumed that we are essentially dealing with radiative recombination in the neutral p-region in analyzing the radiative decay data. For the lowest currents in Fig. 4, and for long times following the 16 mA pulse in Fig. 5, only the deepest tail states are occupied and, as indicated in the previous section, the long decay time is due to the long-range tunneling required for recombination. It is important to realize that these recombination events are two-step processes. That is, in the first step, the electron is injected into the p-region and diffuses through this region for an average time given by the minority carrier lifetime associated with the diffusion length. At the end of this time, the carrier can be captured at a gamma-induced nonradiative recombination center or trapped in a spatially localized deep tail state. Here, it is assumed that the thermal equilibration time into the deepest states is very short. That is, as in a "band filling" model, the band tails essentially have their lowest states occupied first. The second step in the process is then the radiative recombination via long-range tunneling from the localized tail state. As we have pointed out, the time associated with this step can be very long.

The effect of irradiation-induced recombination centers on the time required for the first step, that is, the minority carrier lifetime, can be expressed by the equation

$$\frac{\tau_o}{\tau} = 1 + \tau_o K_\gamma \Phi \qquad [1]$$

where τ_o is the preirradiation lifetime and K_γ is the damage constant. Lifetime degradation will occur when the product of $\tau_o K_\gamma$ and Φ is significant compared to 1.0. Hence, the lifetime will begin to decrease at lower values of Φ for larger values of τ_o.

The time associated with the second step, recombination from the deep tail states, can be viewed as a localized lifetime since the deepest tail states are spatially localized. The alternative of capture of the mobile carrier at an irradiation-induced center is no longer available to the carrier once it is trapped in a localized band tail state. Therefore, irradiation should not have a strong effect on this lifetime except to possibly alter the tunneling probability if a nonradiative center is nearby.

The data in Fig. 5 conform with this model of the recombination process since the decay curves after long times tend to be parallel, suggesting that irradiation has less effect on the longer decay times which are primarily associated with carriers recombining from the deepest tail states. This can be more graphically illustrated by defining an initial lifetime, τ_i, which is given by the slope of the decay curve at time $t = 0$. In Fig. 6, τ_i is plotted as a function of pulse current and gamma dose. Note that at low currents, where τ_i is large and more nearly determined by the localized lifetime in the tail states, gamma irradiation has less of an effect, in a multiplicative sense appropriate to the ratio of (τ_o/τ) in Eq. [1], than it has at large currents where τ_i is small. At the largest currents, τ_i is determined by the diffusion length, which is associated with minority carrier lifetime since the deep states are saturated, especially at $t = 0$. We conclude, then, that while the inverse effect of irradiation on radiative decay time is unusual, it can be satisfactorily explained within the framework of the wavy-band model for highly compensated GaAs:Si LED's.

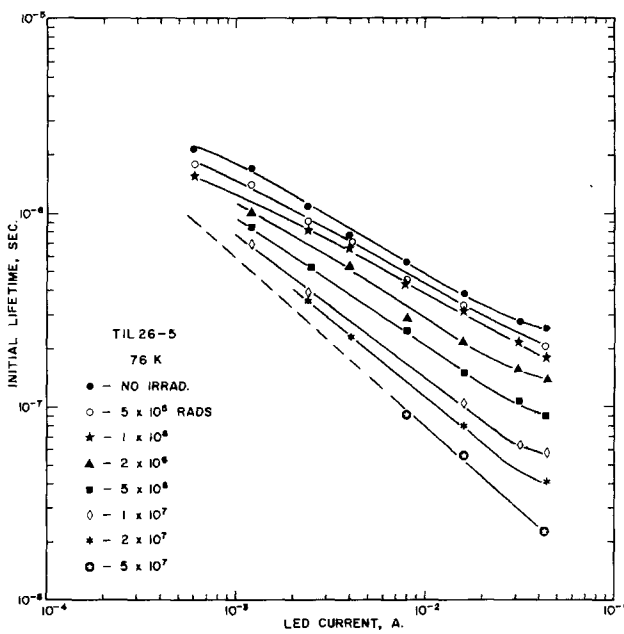


Fig. 6. Initial lifetime, calculated from the slope of the radiative decay curves at $t = 0$, *vs.* diode pulse current before and after successive gamma irradiation of a typical GaAs:Si LED. Note that gamma irradiation has a greater effect, in a multiplicative sense, on the shorter lifetimes at large currents.

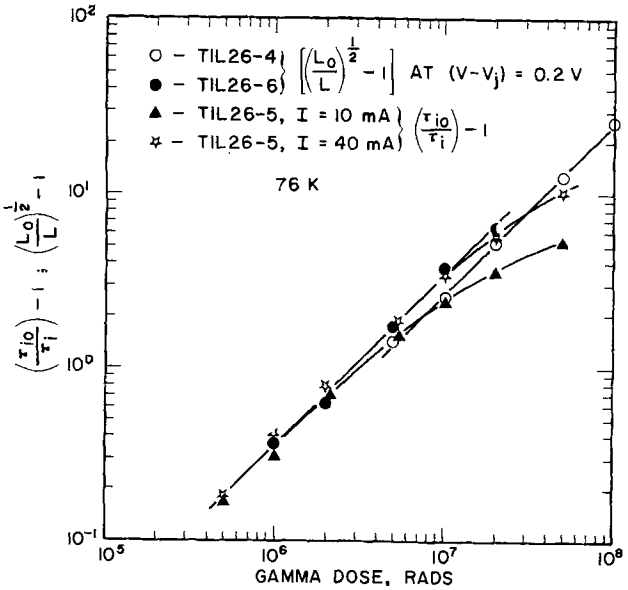


Fig. 7. Tests of Eq. [1] for the high current initial lifetime data and of Eq. [5] for the radiative SCLC component of the light output. Both types of data give approximately the same values of $\tau_0 K_\gamma$.

Since τ_i at large currents is associated with the minority carrier lifetime, one can use Eq. [1] to determine $\tau_0 K_\gamma$ from the high current data in Fig. 6. The validity of Eq. [1] is tested in Fig. 7 where $(\tau_{io}/\tau_i) - 1$ is plotted *vs.* Φ. Here, τ_{io} is the initial lifetime prior to irradiation. At $I = 40$ mA, a line with slope $= 1.0$ can be drawn through the points with deviation occurring only at the largest doses, indicating that Eq. [1] provides a satisfactory description of the lifetime degradation over most of the dose range. However, for a lower current, $I = 10$ mA, the deviation begins at a lower dose. This is to be expected since as the current is reduced and the dose is increased, the instantaneous carrier density during the current pulse is reduced so that the tail states are no longer saturated and the localized deep tail state lifetime becomes influential. The line drawn through the data gives a $\tau_0 K_\gamma$ value of 3.5×10^{-7} rad^{-1}.

Turning our attention to the light output degradation shown in Fig. 2, we wish to reemphasize the large difference in gamma effects between low and high voltages. As has been pointed out, the insensitivity to irradiation at low voltages arises from the fact that the radiative current is due to tunneling into the space-charge region and recombination there. As the voltage is increased, electrons traverse the space-charge region and are injected into the p-region. While a diffusion-limited radiative current is susceptible to degradation (2), it will be shown that the presence of radiative SCLC at high voltages is primarily responsible for the strong light output degradation in this range. To provide an indication of the importance of SCLC flow, we must study the variation of light intensity with the voltage drop across the neutral p-region, $V - V_J$, as a function of Φ. This is accomplished by extending the straight line, exponential portion of the L-V curves as shown by the dashed line in Fig. 2. One then subtracts the value of V_J, as given on the dashed line, from the applied voltage, V, at the same L. When this procedure is applied to the L-V data, the curves shown in Fig. 8 are obtained. In agreement with previous work (21, 22) and our room temperature study (2) of these diodes, a definite square law behavior is exhibited by all the curves. Using the standard equation for SCLC (19, 20)

$$I = \frac{9}{8} q \tau \mu_n \mu_p p_o A \frac{(V - V_J)^2}{l^3}, \text{ amperes} \qquad [2]$$

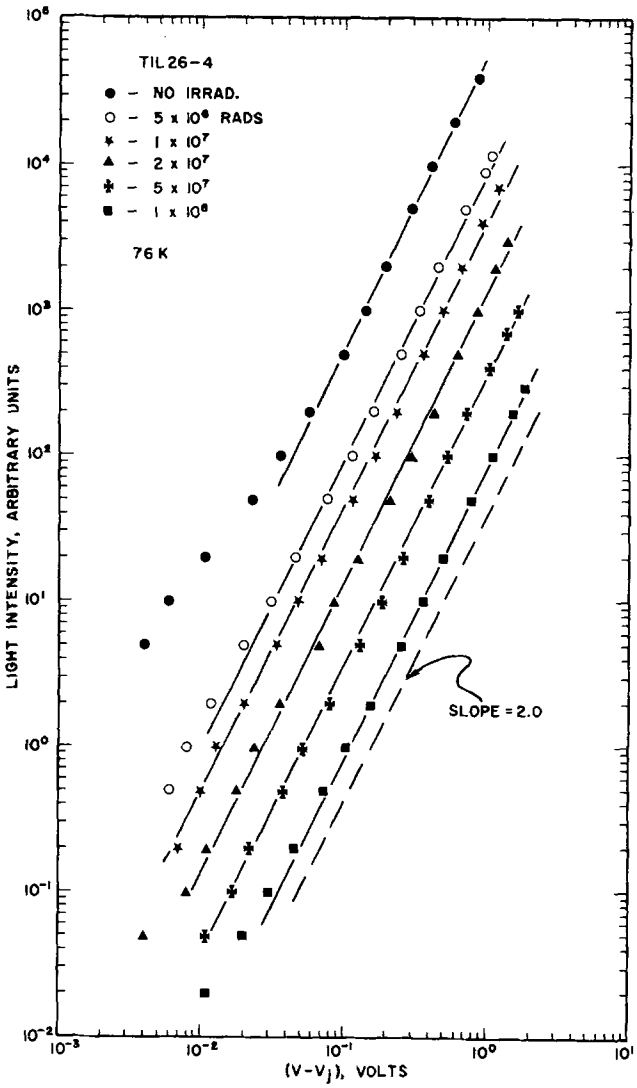


Fig. 8. Light intensity at 76°K *vs.* the voltage drop across the p-region prior to and following gamma irradiation of GaAs:Si LED. Note that all the curves exhibit square law behavior.

and the results of Ashley *et al.* (22) study of radiative double injection SCLC, it was shown, in our previous study (2), that

$$L = C_L \tau^2 (V - V_J)^2, \text{ arbitrary units} \qquad [3]$$

where

$$C_L = \frac{9}{8} C \frac{\mu_n p_o}{\tau_R l^3} (\mu_n + \mu_p), \text{ arbitrary units} \qquad [4]$$

In these equations, μ_n and μ_p are the electron and hole mobilities, respectively, p_o is the equilibrium hole density in the p-region, l is the thickness of the p-region, C_L and C are constants, and τ_R is the radiative lifetime. Equation [3] illustrates the square law variation of L with p-region voltage drop, shown in Fig. 8, and, also, the fact that L varies as the square of the electron lifetime. As noted in our earlier study (2), it is this latter dependence, relative to the linear variation of L with τ for a radiative diffusion current, that leads to the strong degradation at high voltages.

The degradation rate of L at constant $V - V_J$ is obtained by substituting Eq. [1] in Eq. [3]

$$\left(\frac{L_o}{L}\right)^{1/2} - 1 = \tau_0 K_\gamma \Phi \qquad [5]$$

Employing the data for TIL-26-4 shown in Fig. 8 and also data for LED TIL-26-6, one obtains the curves in Fig. 7 for $(V - V_J) = 0.2$V which have a slope of 1.0

indicating that Eq. [5] provides a valid fit to the data. This agreement extends over two orders of magnitude in gamma dose. The curves drawn through the points give an average value of $\tau_0 K_\gamma = 3.1 \times 10^{-7}$ rad^{-1} in good agreement with the value of 3.5×10^{-7} rad^{-1} obtained from the degradation of τ_i at large currents, also shown in Fig. 7.

The presence of SCLC flow at large voltages is also responsible for the gamma-induced decrease in total current, I, at constant high voltage shown in Fig. 1. This follows from Eq. [2] in which I is proportional to τ. This is to be contrasted with the SCR current which varies as $1/\tau$ (23), resulting in the increase in I with Φ at low voltages. A procedure similar to that used to obtain the L *vs.* $(V - V_J)$ data can be followed to obtain I as a function of $(V - V_J)$ from the results in Fig. 1. However, when this is done, one finds that $I \propto (V - V_J)^n$ where $2 > n > 1$ rather than the square law behavior shown in Fig. 8 for L. This result suggests that a significant component of the total current is due to ohmic current flow, carried by holes in the p-region, which is proportional to $(V - V_J)$. A majority carrier current component also agrees with the relatively small gamma-induced decrease in I at constant high voltage since the gamma dose is too small to cause significant majority carrier removal. At a constant voltage of 2.20V, I decreases by a factor of 4.7 after $\Phi = 1.0 \times 10^8$ rad and by a factor of 4.2 at a constant $V - V_J = 0.2$V. In contrast, L decreases by factors of 567 and 686, respectively, for the same constant values of V and $V - V_J$. In addition, at a constant low voltage of 1.26V in the SCR range, I increases by a factor of 25 after 1×10^8 rad. According to Eq. [3], L varies as τ^2 while, as we have noted, the SCR current is proportional to $1/\tau$. Therefore, assuming that the lifetime in the space-charge region is about the same as the lifetime in the p-region, the decrease in L in the SCLC range should approximately equal the square of the increase in I in the SCR range. This does appear to be the case since L decreases by a factor of 686 which is approximately the same as the square of the increase in I: $(25)^2 = 625$.

The fact that L at large voltages is dominated by radiative SCLC while the total current, I, has a significant ohmic component is not surprising since the radiative current will selectively favor an SCLC component over an ohmic current. This follows from the fact that a significant electron density must be present for there to be a significant light output. The comparison of the radiative and total currents is somewhat analogous to the frequent observation at room temperature of a radiative diffusion current in the presence of a total SCR current (1, 3, 5, 6).

We conclude the analysis of the data with a further examination of the "shifting peak" data shown in Fig. 3. The large variation in peak energy, E_p, with Φ at large constant voltage is difficult to explain because the radiative SCLC dominates at large voltages and the radiative tunneling current is relatively minor. One would expect that the sensitivity of E_p to voltage and also gamma dose would be a maximum at low voltages where radiative tunneling is the dominant radiative current mechanism. This difficulty can be resolved by noting that for radiative tunneling, E_p is proportional to V_J and not the applied voltage. We have seen that $V - V_J$ becomes significant at large voltages and so the curves in Fig. 3 are distorted by the variation of V_J with V as Φ increases. To construct a plot of E_p *vs.* V_J, we follow the same procedure for obtaining V_J for diode TIL-26-1 as was followed for TIL-26-4 in Fig. 2 and 8. The results, given in Fig. 9, show a definite linear variation of E_p with V_J, before and after irradiation, as one would expect for radiative tunneling (6-9). Note, however, that above $V_J = 1.29$-1.31V, the curves deviate from the set of parallel lines at lower voltages. Further, with respect to gamma dose, this deviation is random in both magnitude of E_p and slopes of the lines connecting the points. Comparison with Fig. 2 indicates that at $V = V_J \approx 1.30$V, the curves begin to show significant deviation from the purely exponential behavior. Therefore, at the highest voltages where radiative SCLC dominates, as one might expect, there is no significant trend in the variation of E_p with Φ. Indeed, when viewed in this more appropriate manner, the shifting peak data do not show large variations of E_p with Φ at any voltage. Over the entire range in Fig. 9, the decrease in E_p at constant V_J is less than 10 meV for a dose of 1.2×10^8 rad. This relatively minor variation agrees with the observation that the localized lifetime for long-range tunneling is not strongly affected by gamma irradiation and also with the fact that the separation of Fermi levels, which determines E_p, is relatively insensitive to Φ until majority carrier removal begins.

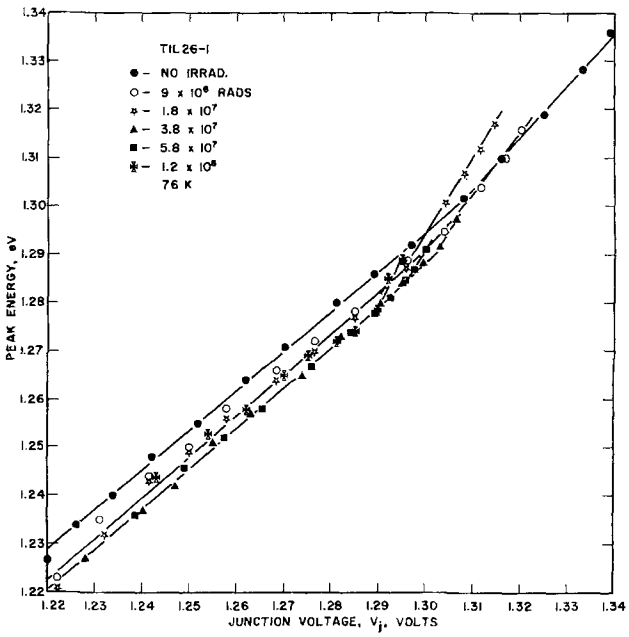


Fig. 9. Peak photon energy of the emitted light *vs.* junction voltage, V_J, for a GaAs:Si LED. The linear behavior is characteristic of radiative tunneling.

Conclusions

We wish to summarize this study of gamma irradiation effects in amphoterically Si-doped GaAs LED's by emphasizing the value of radiation effects studies in providing information about the preirradiation physics of the device in question. The data has shown that the effects of irradiation depend critically on the modes of radiative and total current flow and also on the region of the device where these currents are generated. At low voltages, the radiative current is due to tunneling into the space-charge region from band tail states and subsequent recombination in this region. As a result, gamma irradiation has no effect on the light intensity. The total current is also due to SCR, but, since this current includes all recombination paths, the gamma-induced nonradiative centers in the space-charge region contribute to an increase in I. In addition, gamma irradiation has a relatively small effect on the long radiative decay times observed at low voltages. This result is taken as further evidence for the correctness of the wavy band model in which the long decay times are due to the long lifetimes of carriers in deep localized band tail states.

At large voltages, the effects of irradiation are quite different, which serves to more clearly elucidate the changing modes of current flow. The results suggest that the light output at large voltages is dominated by radiative SCLC flow which is quite sensitive to irradi-

ation. The decrease in I with Φ at large voltages, just the opposite effect from that at low voltage, indicates that the total current also possesses an SCLC component. The lifetime damage constant product, $\tau_0 K_\gamma$, derived from the degradation of the SCLC component agrees with that determined from the radiative decay time data lending further credibility to both the SCLC model and the association of high current decay times with a diffusion-limited minority carrier lifetime.

Acknowledgment

The author wishes to thank L. V. Hansen for assistance in the measurements and the processing of the data. This work was supported by the U.S. Energy Research and Development Administration under Contract E(29-1)-789 and the Air Force Weapons Laboratory (AFWL), Kirtland AFB, Albuquerque, New Mexico.

Manuscript submitted April 11, 1977; revised manuscript received July 15, 1977.

Any discussion of this paper will appear in a Discussion Section to be published in the June 1978 JOURNAL. All discussions for the June 1978 Discussion Section should be submitted by Feb. 1, 1978.

Publication costs of this article were assisted by Sandia Laboratories.

REFERENCES

1. K. J. Soda, C. E. Barnes, and R. A. Kiehl, *IEEE Trans. Nucl. Sci.*, **ns-22**, 2475 (1975).
2. C. E. Barnes and K. J. Soda, *ibid.*, **ns-23**, 1664 (1976).
3. S. Share, A. S. Epstein, and R. A. Polimadei, *ibid.*, **ns-20**, (6), 256 (1973).
4. R. H. Hum and A. L. Barry, *ibid.*, **ns-22**, 2482 (1975).
5. S. Share, A. S. Epstein, and R. A. Polimadei, *Solid State Electron.*, **18**, 471 (1975).
6. C. E. Barnes, *J. Appl. Phys.*, **42**, 1941 (1971).
7. L. W. Aukerman and M. F. Millea, *ibid.*, **36**, 2583 (1965).
8. R. C. C. Leite, J. C. Sarace, D. H. Olson, B. G. Cohen, and J. M. Whelan, *Phys. Rev. A*, **137**, 1583 (1965).
9. H. C. Casey, Jr., and D. J. Silversmith, *J. Appl. Phys.*, **40**, 241 (1969).
10. N. E. Byer, *ibid.*, **41**, 1597 (1970).
11. N. E. Byer, *ibid.*, **41**, 1602 (1970).
12. H. Rupprecht, J. M. Woodall, K. Konnerth, and D. G. Pettit, *Appl. Phys. Lett.*, **9**, 221 (1966).
13. T. Moriizumi and K. Takahashi, *Jpn. J. Appl. Phys.*, **8**, 348 (1969).
14. I. Ladany, *J. Appl. Phys.*, **42**, 654 (1971).
15. H. Kressel, J. U. Dunse, H. Nelson, and F. Z. Hawrylo, *ibid.*, **39**, 2006 (1968).
16. H. Kressel and H. Nelson, *ibid.*, **40**, 3720 (1969).
17. J. A. Rossi, N. Holonyak, Jr., P. D. Dapkus, R. D. Burnham, and F. V. Williams, *ibid.*, **40**, 3289 (1969).
18. D. Redfield, J. P. Wittke, and J. I. Pankove, *Phys. Rev. B*, **2**, 1830 (1970).
19. K. L. Ashley and A. G. Milnes, *J. Appl. Phys.*, **35**, 369 (1964).
20. M. A. Lampert, *Phys. Rev.*, **125**, 126 (1962).
21. K. L. Ashley, *Solid-State Electron.*, **16**, 641 (1973).
22. K. L. Ashley, R. L. Bailey, and J. K. Butler, *ibid.*, **16**, 1125 (1973).
23. A. S. Grove, "Physics and Technology of Semiconductor Devices," p. 187, John Wiley & Sons, Inc., New York (1967).

The Effect of Substrate Preparations on the Surface Morphologies of the Epitaxial Layers of GaAs

Mutsuyuki Otsubo, Takao Oda, Shigeru Mitsui, and Hidejiro Miki

Mitsubishi Electric Corporation, Central Research Laboratories, Itami, Hyogo, 664 Japan

ABSTRACT

The effect of substrate preparations on the surface morphologies of the epitaxial layers of GaAs was studied using the open-tube $AsCl_3$ transport technique. It was found that the surface morphologies were closely related to the delta values of the substrates, which were obtained from an ellipsometric measurement. The higher delta values give the surfaces which are specular, smooth, and free from protrusions, while the lower delta values give the textured surfaces. Electrical properties of the grown layers depend strongly on the surface morphologies.

Epitaxial growth of GaAs is a considerably important technology for fabrication of microwave and optoelectronic devices. A necessary condition for fabrication of these devices, in particular Schottky barrier gate field effect transistors, is the ability to deposit smooth surfaces. The macroscopic surface imperfections which are a major problem to the attainment of such surfaces are pits and hillocks. The origin of these defects has been investigated by a number of workers using the $Ga/AsCl_3/H_2$ (1-4) and $Ga/AsH_3/HCl$ (5-11) growth systems in relation to growth parameters. It has been reported that the surface morphologies depend strongly on the deposition temperature (4, 10), the gas phase stoichiometry (7, 9-11), the substrate orientation (1, 6), the oxygen contamination of gas stream and the dirt (2, 5), and the substrate preparation (5). However, the surface morphologies of GaAs layers are not too well under control.

We have found that the surface morphologies of the epitaxial layers of GaAs depend also on the chemical etchant used for cleaning the substrates. This paper describes the effect of the substrate preparations, in particular chemical etching, on the surface morphologies and the electrical properties of the epitaxial layers of GaAs.

Key words: compound semiconductors, cleaning, ellipsometry.

Experimental

The deposition apparatus used in this investigation is the $Ga/AsCl_3/H_2/N_2$ flow system with a vertical reactor. The reactor tube, the Ga reservoir, the substrate holder, and the inner tube were made of synthetic quartz glass, and they were heated in a vacuum at 1000°C for 12 hr before using. The substrate holder was designed to rotate with $0 \sim 10$ rpm and to charge

with 4 ~ 5 wafers of 6 ~ 7 cm^2 in a given run. The additional Ga was introduced by filling the Ga reservoir with 99.99999% Ga, and the $AsCl_3$ gas diluted with a purified N_2 gas was introduced from small holes in an annular ring arranged above the Ga reservoir. The H_2S diluted with a Pd-diffused H_2 gas was used as a donor impurity. In the early stages of this investigation, when an H_2 gas was used as a carrier gas for $AsCl_3$, the arsenic flowed backward and could not be transported to the deposition zone. Therefore, the purified H_2 and N_2 gases were used and the $AsCl_3$ was bubbled by an N_2 gas. Four to five substrates with different surface preparations were simultaneously subjected to deposition in a given run. Normally 1 μm thick epitaxial layers of GaAs were deposited on the substrates and the epitaxial layer surfaces were observed by an interference optical microscope. No thickness dependence of the surface morphologies was observed provided that the epitaxial layers were 0.2-6 μm thick. The growth conditions normally used to produce smooth and flat layers are listed in Table I.

The substrates used in this investigation were normally obtained from Cr-doped semi-insulating, and sometimes from Si- or Te-doped n^+ boat-grown GaAs ingots. These were misoriented 2° off (100) toward the <110> direction. The slices were mechanically lapped with 4000 mesh Al_2O_3 abrasive and then were chemically etched by a 10 volume percent (v/o) bromine-methanol solution followed by a $3H_2SO_4$-$1H_2O_2$-$1H_2O$ solution at 60°C. These wafers were etched in various solutions listed in Table II just prior to use and then were placed on the substrate holder. Surface preparations used in this investigation are listed in Table II.

The substrate surfaces were estimated by ellipsometry. Two quantities of Δ and ψ are obtained. The Δ is the change in the relative phase between the parallel and perpendicular component of the polarized light on reflection, and ψ, the factor by which the amplitude ratio of the parallel and perpendicular components changes on reflection. The Δ and ψ are determined by measuring the polarizer and analyzer angles which give a null in the reflected light signal (14). The ellipsometric measurement has been done at an angle of 70° of the incident beam with a wavelength of 5461Å. The measurement was carried out within 10 min after etching the substrates.

Table I. The growth parameters normally used to produce smooth flat layers

Temperature (°C)		Flow rate (cm^3/min)	
Substrate	695	N_2 carrier for $AsCl_3$	900
Ga source	830	H_2 carrier	2300
$AsCl_3$ bubbler	15	H_2 carrier for H_2S	100
Revolution of substrate holder	5 rpm	H_2S (10 ppm)	40

Table II. Various preparations of GaAs substrates

Etching solutions for cleaning the substrates just prior to epitaxial growth	Δ values (degree)	Photos
1. Mirrolite solution (25°C)	159	Fig. 1(a)
2. 10 v/o bromine in methanol (25°C)	161	Fig. 1(b)
3. 5 (50 a/o) citric acid solution-$1H_2O_2$ (25°C)	161	Fig. 1(c)
4. $3H_2SO_4$-$1H_2O_2$-$1H_2O$ (60°C)	167	Fig. 1(d) Fig. 2(a) Fig. 3(a)
5. 1HF-$3HNO_3$-$2H_2O$ (25°C)	165	Fig. 1(e)
6. $5H_2SO_4$-$1H_2O_2$-$1H_2O$ (60°C)	164	Fig. 2(b)
7. $18H_2SO_4$-$1H_2O_2$-$1H_2O$ (60°C)	161	Fig. 2(c)
8. Exposing the substrates to air for		
0 min	167	Fig. 3(a)
80 min	165	Fig. 3(b)
220 min	163	Fig. 3(c)
315 min	161	Fig. 3(d)

Each substrate prepared in a particular manner is cut into two pieces. One is subjected to epitaxial growth and the other is used for an ellipsometric measurement. The average Δ value for five wafers is listed in Table II for each preparation. Deviation in Δ value for each preparation was within ± 1°. The epitaxial layers were observed by an interference optical microscope. Therefore the surface morphologies illustrated in the figures were taken with interference contrast.

The layers were also evaluated by a photoluminescence spectra and *I-V* curves of Schottky barrier diodes formed on the epitaxial layers. The photoluminescence spectra were obtained with a JE-25 spectrometer and a cooled RCA 7102 photomultiplier. An Ar ion laser was used as an excitation source which was filtered with a CS-2-64 Corning glass filter to eliminate laser background light. No correction for the photomultiplier and the spectrometer response was made. The measurement was done at 77°K.

Results and Discussion

Effect of surface preparations on the surface morphologies of the epitaxial layers of GaAs.—Figure 1 shows typical surface morphologies of the epitaxial layers of GaAs. Figure 1(a) shows a surface morphology of the epitaxial layer deposited on the substrate which is mechanically polished with a Mirrolite solution (Materials Development Corporation, US) on a rotating Pellon cloth after having been lapped off with 4000 mesh Al_2O_3 abrasive by approximately 100 μm to eliminate the work damage introduced in the crystal sawing process. The wafer was rinsed with deionized water and methanol, and then served for epitaxial growth. The epitaxial layer surface consists of an array of hillocks. When the epi-

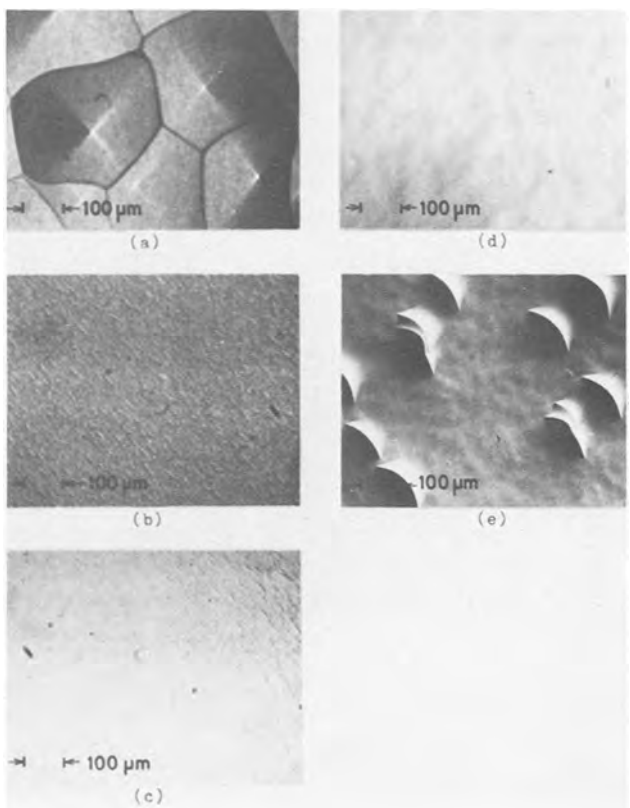


Fig. 1. Surface morphologies of the epitaxial layers deposited on the substrates which were etched with (a) a Mirrolite solution; (b) a 10 v/o bromine in methanol solution; (c) a citric acid-hydrogen peroxide-water solution; (d) a $3H_2SO_4$-$1H_2O_2$-$1H_2O$ solution; and (e) a 1HF-$3HNO_3$-$2H_2O$ solution.

taxial layer was deposited on the substrate prepared by this means, after etching with a $3H_2SO_4$-$1H_2O_2$-$1H_2O$ solution by approximately 30 μm, the surface of the layer was highly specular and smooth. Hence, the surface shown in Fig. 1(a) is thought to have originated in the mosaic structure at the substrate surface introduced by the mechanical polishing procedure (12).

Figure 1(b) shows a surface morphology of the layer deposited on the substrate etched with a solution of 10 v/o bromine in methanol. The surface was a straw-matted texture of fine grooves oriented in the <111> direction. The same surface texture was obtained in the layers deposited on the substrate etched with a solution of the citric acid-hydrogen peroxide-water system [Fig. 1(c)].

Figure 1(d) shows a surface morphology of the layer deposited on the substrate etched with a $3H_2SO_4$-$1H_2O_2$-$1H_2O$ solution at 60°C. The surface was highly specular, smooth and free from protrusions. When the substrate was etched at higher temperatures, the epitaxial layer surface contained with fine grooves oriented to the <111> direction were ready to obtain.

Figure 1(e) shows a surface morphology of the layer deposited on the substrate etched with a $1HF$-$3HNO_3$-$2H_2O$ solution. The surface shows a considerable number of protrusions on a specular background, which were closely related to etch hillocks formed on the substrate by the etching process. It is known that the etch hillocks on the substrate surface are covered with oxide (13).

In order to study the effect of the sulfuric acid content of the sulfuric acid-hydrogen peroxide-water solutions on the surface morphologies, the epitaxial layers were deposited on the substrate etched with $3H_2SO_4$-$1H_2O_2$-$1H_2O$, $5H_2SO_4$-$1H_2O_2$-$1H_2O$, and $18H_2SO_4$-$1H_2O_2$-$1H_2O$ solutions. The result is shown in Fig. 2. Increase in the sulfuric acid content in the solutions results in the textured surfaces, consisting of an array of fine grooves oriented to the <111> direction, whose density increases with increasing sulfuric acid content.

Figure 3 shows the effect of exposing the substrate to air on the surface morphologies of the epitaxial layers. The substrates, etched with a $3H_2SO_4$-$1H_2O_2$-$1H_2O$ solution at 60°C, were exposed to air for periods of 0, 80, 220, and 315 min. Exposure to air results in the textured surfaces consisting of fine grooves oriented in the <111> direction with a wavy background.

It is found from these investigations that the surface morphologies of the epitaxial layers are closely related to Δ values obtained from an ellipsometric measurement of the substrate surfaces. The higher Δ values result in the surfaces which are specular, as well as smooth and free from protrusions, while the lower Δ values result in the textured surfaces with fine grooves oriented to the <111> direction. Density of the fine grooves increases with a decrease in the Δ values. Therefore, it is important to select the etching solutions which give higher Δ values in order to obtain the epitaxial layers with specular surfaces which are smooth and free from protrusions.

It is confirmed using a microbalance that inadvertent gas etching, thicker than several tens of angstroms, did not occur in our experimental conditions. However, it is possible that slight thermal etching, within several tens of angstroms, occurs. Since the substrates with different preparation were simultaneously subjected to deposition in a given run, surface morphologies observed in this experiment are not caused by thermal and/or gas etching, but are due to substrate preparations. When an intentional gas etching, about 1 μm thick, was performed, the epitaxial layer surface was fairly smooth and no particular surface morphologies were observed.

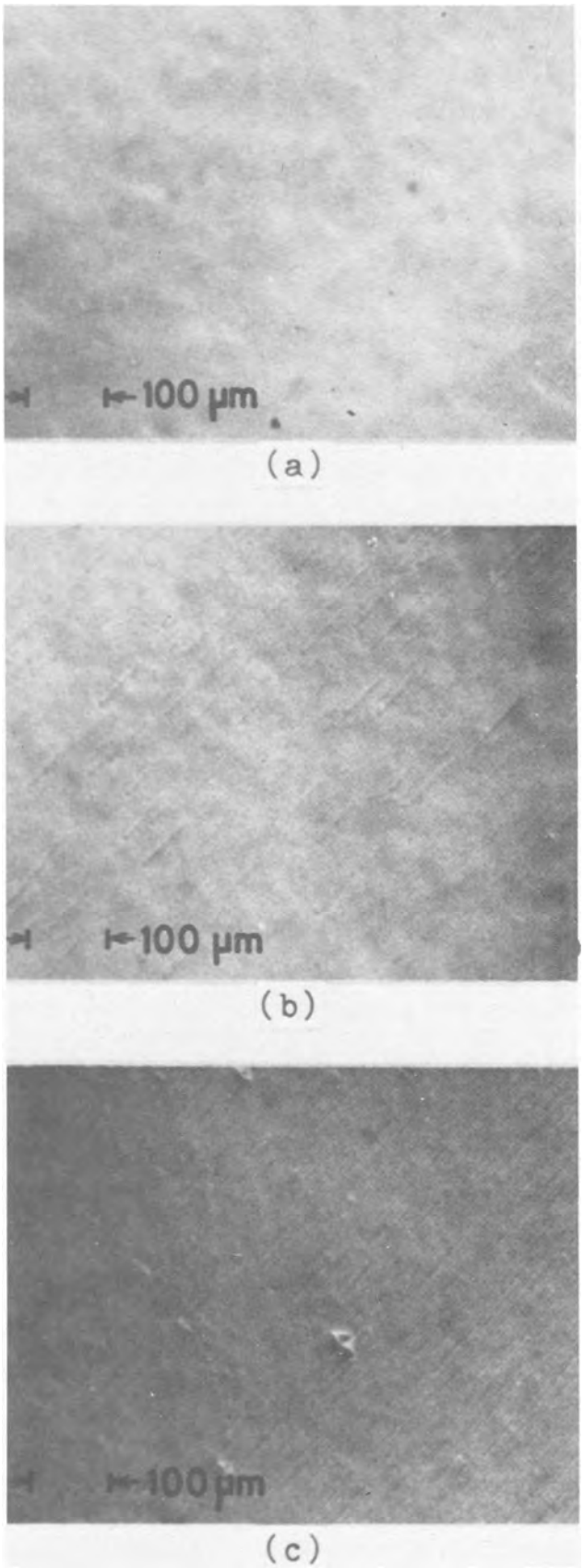


Fig. 2. The effect of sulfuric acid content in the sulfuric acid-hydrogen peroxide-water system on the surface morphologies of the epitaxial layers. The substrates were etched with (a) a $3H_2SO_4$ $1H_2O_2$-$1H_2O$; (b) a $5H_2SO_4$-$1H_2O_2$-$1H_2O$; and (c) a $18H_2SO_4$-$1H_2O_2$-$1H_2O$ solutions. The etching was performed at 60°C.

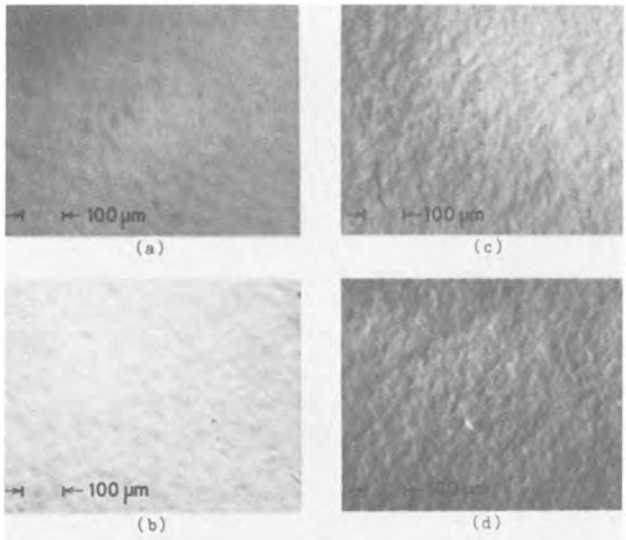


Fig. 3. The effect of exposing the substrates to air on the surface morphologies of the epitaxial layers. The substrates etched with a $3H_2SO_4$-$1H_2O_2$-$1H_2O$ solution were exposed for (a) 0; (b) 80; (c) 220; and (d) 315 min.

In order to determine the effect of changing the distance between the Ga surface and the outlet of $AsCl_3$ gas on the surface morphologies, the epitaxial layers were deposited on the substrates etched with a $3H_2SO_4$-$1H_2O_2$-$1H_2O$ solution at 60°C. The result is shown in Fig. 4. Increase in the distance results in the textured surfaces with fine grooves oriented to the <111> direction. This indicates that the surfaces shown in Fig. 4(b) and 4(c) have been obtained under lower concentrations of GaCl at the deposition zone because the reaction efficiency between the GaAs crust formed on the Ga surface and the HCl gas decreases with increasing the distance. From a resemblance in the surface morphologies between the layers deposited on the substrates with lower Δ values and the layers deposited with the larger Ga-$AsCl_3$ outlet distance, it must be concluded that the textured surfaces with fine grooves oriented to the <111> direction are produced by the deficiency of Ga at the substrate surfaces.

It has been reported that the oxide layer was formed on the substrate surfaces by chemical etching (14, 15) as well as the existence of the Ga deficient layer between the oxide layer-GaAs interface by the study of an Auger electron spectroscopy of etched GaAs crystals (15). It is possible that decrease in Δ values of the substrates, namely, increase in the oxide layer thickness, results in increase in the Ga-deficient layer thickness. When the substrates prepared by various treatments listed in Table II were heat-treated at the deposition temperature of 695°C for 5 min, the Δ values of these substrates were all 166°-167° regardless of substrate preparations. This indicates that the oxide layer formed on the substrate surfaces was almost evaporated and the Ga-deficient layer was exposed at the beginning of epitaxial growth. From these considerations, it must be concluded that the epitaxial layers with textured surfaces were produced by the presence of the Ga-deficient layer on the substrate surface at the beginning of epitaxial growth. Vapor etching of the substrate in the deposition apparatus just prior to deposition is the most suitable technique for eliminating the Ga-deficient layer.

Effect of the surface morphologies on the electrical properties of the epitaxial layers of GaAs.—In order to study the effect of the surface morphologies on the electrical properties of the epitaxial layers, *I-V* curves of Schottky barrier diodes formed on the layers and photoluminescence spectra were measured. The epi-

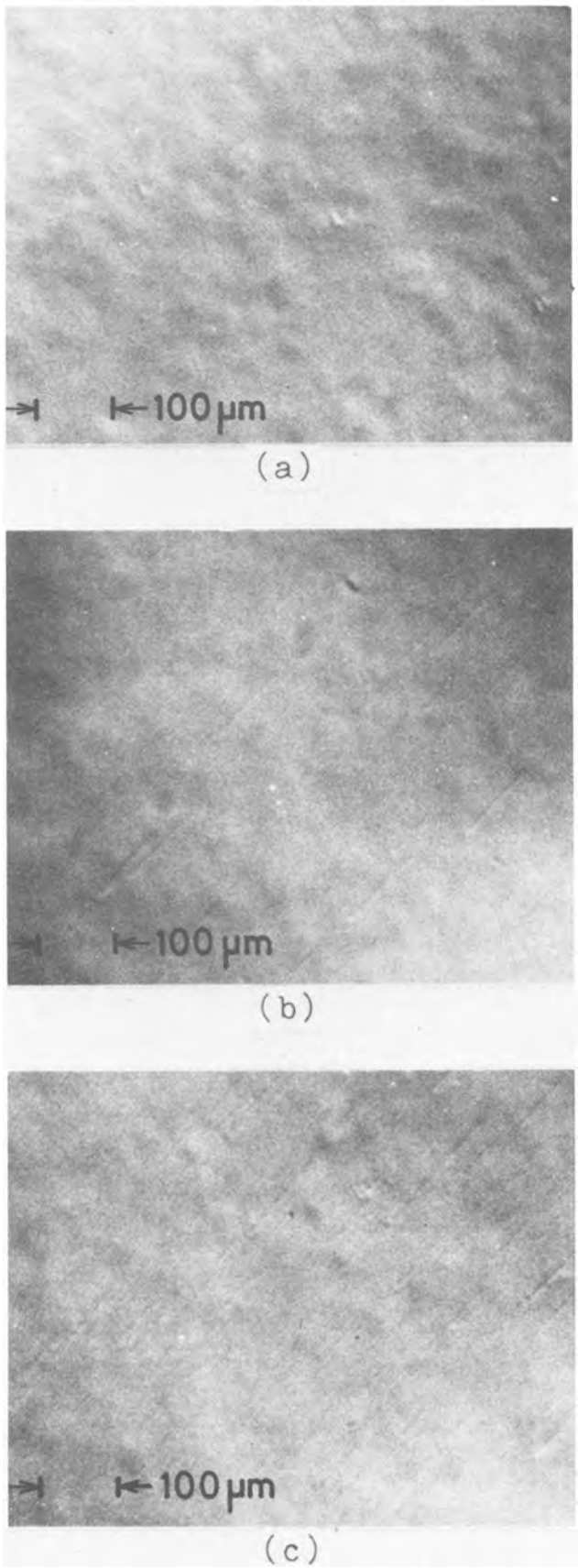


Fig. 4. The effect of changing the distance between the GaAs crust formed on the Ga source and the outlet of $AsCl_3$ gas on the surface morphologies of the epitaxial layers.

taxial layers deposited on the substrates which were prepared by various treatments listed in Table II were classified into three groups. Group (a) is the layers with the surfaces which are specular, smooth, and free of protrusions [Fig. 1(d), 2(a), 3(a), and 4(a)]. Group (b) is the layers with textured surfaces of a lower density of fine grooves [Fig. 2(b), 3(b), and 4(b)]. And group (c) is the layers with the higher density of fine grooves and a wavy background [Fig. 1(b) and 1(c), 2(c), and 3(c) and (d)].

Figure 5 shows the relation between the surface morphologies and *I-V* curves for Schottky barrier diodes formed on the three kinds of layers with carrier concentrations of 7-8 $\times$ 10^{16} cm^{-3} and 0.3 μm thick. It is apparent that the surface morphologies of the epitaxial layers are closely related to the backward characteristics of the diodes. Higher breakdown voltages with hard breakdown were obtained on the samples which belong to group (a), while in groups (b) and (c), the the higher leakage currents and lower breakdown voltages were observed, where the leakage current increases with an increase in the roughness of the epitaxial layer surfaces [Fig. 5(b) and 5(c)].

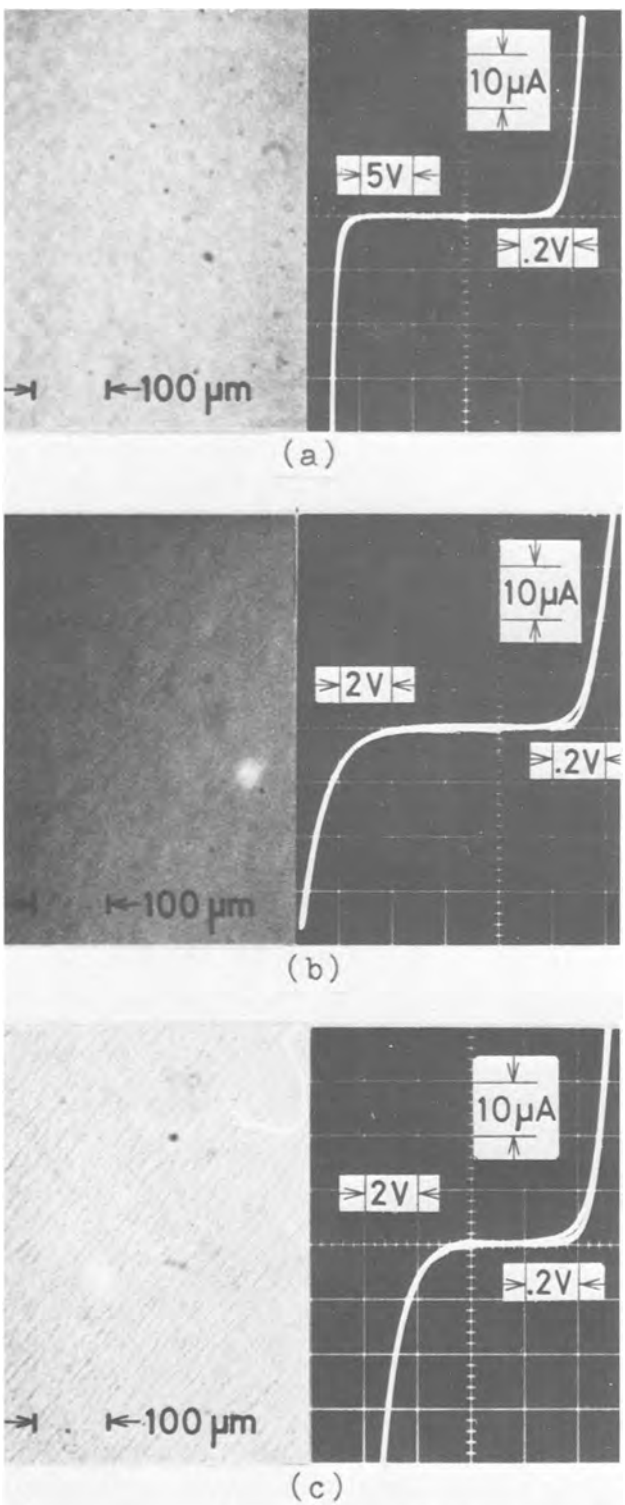


Fig. 5. *I-V* curves for Schottky barrier diodes formed on three kinds of layers.

Figure 6 shows photoluminescence spectra at 77°K on three kinds of layers. Two dominant emissions at 1.51 and 1.36 eV were observed. The emission at 1.51 eV is due to a band-to-band recombination and/or a shallow donor-to-valence band recombination (16), and the emission at 1.36 eV is due to Cu at Ga site (17). The intensity of the emission at 1.51 eV is higher in the layers of group (a), while the intensity of the emission at 1.36 eV is higher in groups (b) and (c). It is possible that the epitaxial layers with textured surfaces contain higher concentrations of Ga vacancies, resulting in lower intensity of a near band emission and higher intensity of 1.36 eV emission. This results in an increase in higher leakage currents of Schottky diodes and lower breakdown voltages.

Conclusions

The effect of substrate surface preparations, in particular chemical etching, on the surface morphologies of the epitaxial layers of GaAs were investigated. It is found that the surface morphologies are closely related to the Δ values of the substrate surfaces, and the electrical properties of the grown layers depend strongly on the surface morphologies. The surfaces of the layers grown on the substrates with higher Δ values were specular, smooth, and free from protrusions, while the surfaces grown on the substrates

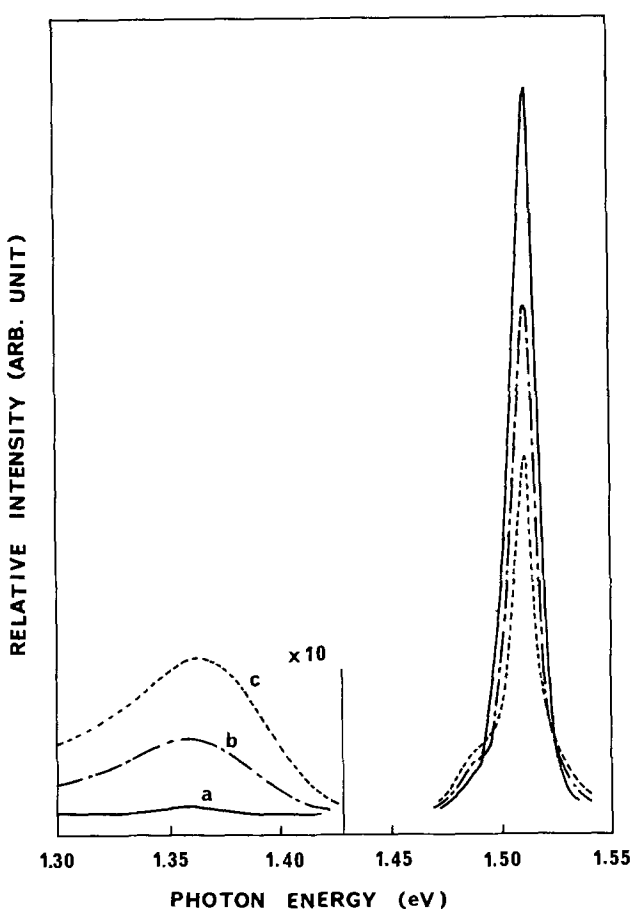


Fig. 6. Photoluminescence spectra at 77°K on three kinds of layers

with lower Δ values were textured and had a wavy background. It is presumed that the textured surfaces were obtained due to the deficiency of Ga on the substrate surfaces. Decrease in the Δ values results in an increase in leakage current of the Schottky barrier diode formed on the epitaxial layers.

Manuscript submitted March 1, 1977; revised manuscript received Aug. 8, 1977.

Any discussion of this paper will appear in a Discussion Section to be published in the June 1978 JOURNAL. All discussions for the June 1978 Discussion Section should be submitted by Feb. 1, 1978.

Publication costs of this article were assisted by Mitsubishi Electric Corporation.

REFERENCES

1. A. E. Blakslee, *Trans. Metall. Soc. AIME*, **245**, 577 (1969).
2. H. Holloway and L. C. Bobb, *J. Appl. Phys.*, **38**, 2893 (1967).
3. R. Contrimas and A. E. Blakslee, *Electrochem. Technol.*, **6**, 78 (1968).
4. J. V. Dilorenzo, *J. Cryst. Growth*, **17**, 189 (1972).
5. J. J. Tietjen, M. S. Abraham, A. B. Dreeben, and H. F. Gossenberger, in Proceedings of the 1968 International Symposium on GaAs, p. 55, Institute of Physics, London (1969).
6. D. W. Shaw, *ibid.*, p. 50.
7. R. E. Ewig and P. E. Greene, *This Journal*, **111**, 1266 (1969).
8. B. D. Joyce and J. B. Mullin, *Solid State Commun.*, **4**, 463 (1966).
9. H. T. Minden, *J. Cryst. Growth*, **8**, 37 (1971).
10. J. K. Kennedy and W. D. Potter, *ibid.*, **19**, 85 (1973).
11. R. E. Enstrom, C. J. Neuse, J. R. Appert, and J. J. Gannon, *This Journal*, **121**, 1516 (1974).
12. E. S. Meieran, *Trans. Metall. Soc. AIME*, **242**, 413 (1968).
13. B. Tuck, J. S. K. Mills, and A. J. Hartwill, *J. Mater. Sci.*, **11**, 847 (1976).
14. K. H. Zaininger and A. G. Revesz, *J. Phys.*, **25**, 208 (1964).
15. I. Shiota, K. Motoya, T. Ohmi, N. Miyamoto, and J. Nishizawa, *This Journal*, **124**, 155 (1977).
16. M. I. Nathan and G. Burns, *Phys. Rev.*, **129**, 125 (1963).
17. H. J. Queisser and C. S. Fuller, *J. Appl. Phys.*, **37**, 4895 (1966).

Errors in Calculations of Predeposition Diffusion Profiles by Iterative Numerical Methods

Jakob H. Hohl

IBM General Technology Division, Essex Junction, Vermont 05452

and Douglas J. Hamilton

University of Arizona, Tucson, Arizona 85717

ABSTRACT

The errors in numerical calculations of one-dimensional predeposition profiles have been determined for the direct method of finite differences and for the finite element method. These errors can be calculated because the exact solution of this linear diffusion problem is known to be the complementary error function. The relative errors at the nodes of the depth-time lattice are illustrated. The results are useful for assessing the errors of calculations of multidimensional profiles by these iterative methods, where no exact solutions are known. The results indicate that accurate calculations of such profiles will require such fine lattices and large numbers of time steps that the usefulness of the iterative methods becomes doubtful.

The progressing perfection of the integrated circuit technology to smaller and smaller geometries and the high degree of sophistication of contemporary circuit analysis programs pose increasingly exacting requirements on the device modeling techniques. An important aspect of the latter is the calculation of impurity profiles resulting from diffusions through rectangular or line-shaped windows. Such profiles cannot be described by closed form analytic solutions, and one must resort to numerical techniques for their calculation.

The methods of finite differences and of finite elements suggest themselves foremost for such computations because they are quite versatile and can be implemented without unduly complex analytic mathematical preparations. The potential difficulties lie in the numerical stability and in the estimation of the accuracy of the results.

For the direct method of finite differences the stability criteria and a formula for the error can be determined analytically. In the second section of this paper, the results for the one-dimensional diffusion problems, as derived by Carnahan, Luther, and Wilkes (1), are summarized. These results demonstrate the inherent problems with error estimation: a meaningful estimate can only be obtained when the solution of the problem is known for all steps and when the lattice of nodal points is fine with respect to the features of the solution. Neither condition is satisfied for multidimensional predeposition diffusion profiles. The one-dimensional profile satisfies the former condition but not the latter because it evolves from a step function. The error in an iterative calculation of this problem can only be determined by actually performing the computation.

The second section specifies the one-dimensional diffusion problem under consideration and defines all the parameters of the computations. In the third section, the finite difference calculation of the profile is outlined and the errors of the calculation are illustrated. The fourth section is devoted to the calculation of the same profile by the finite element method and to the presentation of its errors. Some conclu-

Key words: semiconductor, impurity, profile, computation.

sions, which also apply to calculations of multidimensional profiles are discussed in the fifth section.

Outline of the Diffusion Problem

The diffusion of impurities from a constant concentration condition at the surface of a half-space with unity diffusivity is considered. At the time instant $t = 0$, the volume concentration is zero and the surface concentration is discontinuously changed from $C_o = 0$ to $C_o = 1$. Under the usual assumptions, as, *e.g.*, constant diffusivity and absence of electrostatic fields, the diffusion process is governed by the linear one-dimensional diffusion equation. Normalizing the diffusivity to unity, the equation is

$$\partial^2 C/\partial x^2 - \partial C/\partial t = 0 \qquad [1]$$

and the given initial and boundary conditions lead to the well-known analytical solution

$$C(x, t) = \operatorname{erfc}(x/\sqrt{4t}) \qquad [2]$$

where x is the distance from the surface into the half-space in question.

For calculating the profile by an iterative method, the continuous variables x and t need to be replaced by a lattice of points

$$i, j \equiv (x_i, t_j) = (i\Delta x, j\Delta t); \quad i, j = 0, 1, 2, \ldots \qquad [3]$$

at which the values $u_{i,j}$ of the numerical solution will be calculated. The corresponding values of the exact solution will be denoted by $c_{i,j}$. The relative errors are defined as the deviation of the numerical solution from the exact solution divided by the exact solution

$$\epsilon_{i,j} = (u_{i,j} - c_{i,j})/c_{i,j} \qquad [4]$$

The numerical calculations proceed from time step to time step; the solution at the jth time step representing the initial condition for calculating the solution at the time t_{j+1}.

Direct Method of Finite Differences

Replacement of the derivatives in the diffusion Eq. [1] by ratios of differences between variables at adjacent points of the (x, t) lattice leads to the finite differences algorithm

$$u_{i,j+1} = u_{i,j} + \lambda(u_{i-1,j} + u_{i+1,j} - 2u_{i,j}) \qquad [5]$$

where $\lambda = \Delta t/(\Delta x)^2$ is called the mesh ratio. The boundary and initial conditions of the previous section translate into

$$u_{0,j} = 1; \quad u_{i\neq 0,0} = 0 \qquad [6]$$

The algorithm becomes numerically unstable when the mesh ratio exceeds ½.[1] For small mesh ratios, a first order estimate (1) reveals that the errors of the iteration, $e_{i,j}$, are bounded by

$$e_{i,j+1} \leq e_{i,j} + \lambda(e_{i-1,j} + e_{i+1,j} - 2e_{i,j}) + z_{i,j} \qquad [7]$$

$$z_{i,j} = (\Delta t/2)\partial^2 c/\partial t^2 - [(\Delta x)^2/12]\partial^4 c/\partial x^4 + O[(\Delta t)^2] + O[(\Delta x)^4] \qquad [8]$$

The derivatives are to be evaluated at the point i, j and O denotes "on the order of." To estimate the error $e_{i,j}$, one needs to know a pyramid of errors of all previous steps as well as the derivatives of the exact solution at the points of the space-time-lattice. However, in a general problem an iterative calculation is performed because the solution is not known, and hence the error cannot be estimated with much confidence.

Since $\partial^2 c/\partial t^2 = \partial^4 c/\partial x^4$, Eq. [8] indicates that for $\lambda = 1/6$, the errors will be on the order of $(\Delta t)^2$ rather than Δt. This mesh ratio has been used in the calculations described below. One notes, then, that the lattice points for the first time step, $j = 1$, correspond to the arguments $x_i/\sqrt{4t} = i\sqrt{3}/2 = 1.22i$ in the complementary error function [2]. There is less than one point per diffusion length which leads to an extremely coarse approximation of the function. Only after a considerable number of time steps will the lattice become fine with respect to the features of the solution. Therefore, the iteration starts with large inaccuracies and a reliable *a priori* error estimate is impossible.

Figure 1 illustrates the relative errors, $\epsilon_{i,j}$, of the first 50 iterations of the finite difference calculation of the function [2]. Since the errors are displayed *vs.* $x/\sqrt{4t}$ rather than x, the points corresponding to the same x_i migrate toward the left with consecutive steps. These points are connected by line segments. The points corresponding to the time steps 5, 10, 15, . . . are marked with black dots, and intervening points are indicated by circles.

The figure demonstrates the large spacing of the points of the early time steps with respect to the diffusion length. The maximum errors in the range of the first three diffusion lengths from the surface after 25 and 50 iterations are 15 and 8%, respectively.

Method of Finite Elements

The finite element method is based on a variational formulation of the problem at hand (2). The solution is again calculated at the points (x_i, t_j), but for the purpose of deriving the algorithm, the solution between these points is linearly interpolated (3). This parametrizes the functional in terms of the node values, $u_{i,j}$, of the solution. The extremization of the functional then requires that all its partial derivatives with respect to the node values vanish simultaneously, leading to a system of linear equations for the $u_{i,j}$.

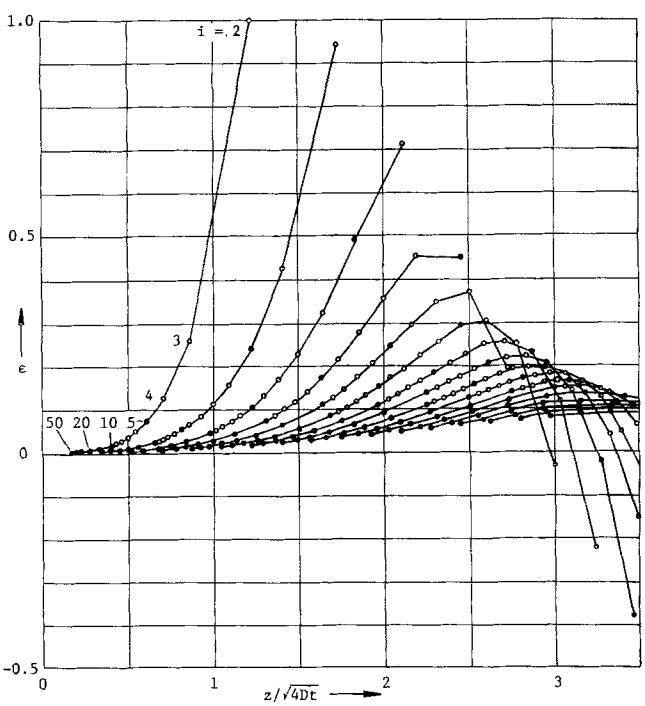


Fig. 1. Relative errors, ϵ, at the nodal points of a finite difference calculation of the complementary error function as the solution of a diffusion problem at time step i.

[1] To see this, consider an error, d, *e.g.*, a round-off error, introduced into the value $u_{i,j}$. This error will propagate to $u_{i,j+1}$, which will be in error by $(1 - 2\lambda)d$ and to $u_{i\pm1,j+1}$, which will be in error by λd. For $\lambda > ½$, the sum of the magnitudes of these errors will become $(4\lambda - 1)d > d$, and the effect of the disturbance grows from time step to time step.

The variational formulation of transient diffusion problems must explicitly reflect the causal character of the physical process (4). A formulation by Gurtin (5) has this property and leads to an algorithm which calculates the solution at the time t_{j+1} from that at the time t_j and the boundary conditions.

A formal analysis of the error of this method, like the one for the finite difference method, is not possible. It is said that the finite element method is more stable numerically and that it can be formulated for unequal lattice spacings more easily than the finite difference method. From a number of calculations with uniform lattices, but various mesh ratios, the optimum performance of the finite element method was again found to be around $\lambda = 1/6$. The variations of the errors for mesh ratios between 0.1 and 1 are insignificant, indicating the better numerical stability of the method. Calculations with unequal Δx_i lead to inferior results with either steps increasing or decreasing with depth. A calculation starting with a mesh ratio of 0.26 which from step to step decreased by 2%, using uniform Δx_i, showed marginally smaller errors than the calculation with $\lambda = 1/6$.

Figure 2 displays the relative errors of the calculation with the mesh ratio 1/6, using the same format as Fig. 1. One notes that the errors in the range up to 1.6 diffusion lengths are comparatively smaller, but that they increase rapidly beyond this point, soon exceeding those of Fig. 1.

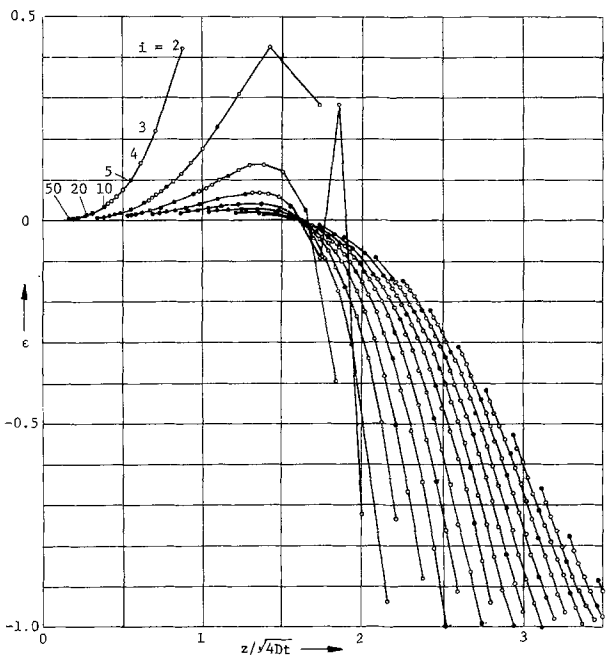


Fig. 2. Relative errors, ϵ, at the nodal points of a finite element calculation of the complementary error function as the solution of a diffusion problem at time step i.

Conclusions

The results of the two calculations demonstrate that both algorithms require at least five lattice points per diffusion length of the solution in order to yield a reasonable accuracy over a distance of three diffusion lengths from the source. In this range the solution varies over about five orders of magnitude, which encompasses the variations of concentrations of impurities encountered in semiconductor devices in practice.

If one now conjectures that the errors of two- and three-dimensional calculations behave similarly because of comparable characteristics of the solutions, one can estimate the expense of numerical calculations of such profiles. To this end, consider a predeposition diffusion through a square window eight diffusion lengths in size. Modeling one quadrant of the structure, three diffusion lengths beyond the window edges and to a depth of three diffusion lengths, using a space lattice with five nodes per diffusion length, thus requires 20,000 nodes and 40-50 time steps. In the finite element method, the computation entails the inversion of a matrix of dimension 20,000. Such an endeavor requires considerable computing power and is not inexpensive, particularly if one considers that numerous impurity profiles must be computed for devices of integrated circuits.

The finite element method which is often praised for superior computation efficiency is found to be, in fact, inferior to the finite difference method for the calculation of impurity profiles.

The idealization in using a linear diffusion process is appropriate for the comparison of the two computation methods. Both methods can accommodate the complication of concentration dependent diffusivity occurring at high concentrations due to internal electrostatic fields by updating the diffusivities after each time step. In a finite element calculation it becomes necessary, however, to invert a matrix at each time step, which makes it very inefficient.

Manuscript submitted June 21, 1977; revised manuscript received Aug. 1, 1977.

Any discussion of this paper will appear in a Discussion Section to be published in the June 1978 JOURNAL. All discussions for the June 1978 Discussion Section should be submitted by Feb. 1, 1978.

Publication costs of this article were assisted by the IBM Corporation.

REFERENCES

1. B. Carnahan, H. A. Luther, and J. O. Wilkes, "Applied Numerical Methods," pp. 432-433, John Wiley and Sons, Inc., New York (1969).
2. L. E. Elsgolc, "Calculus of Variations," pp. 9-12, Addison Wesley, Reading, Mass. (1962).
3. O. C. Zienkiewicz, "The Finite Element Method in Engineering Science," Chap. 3, McGraw-Hill Book Co., New York (1971).
4. J. H. Hohl, Ph.D. Dissertation, University of Arizona, Tucson, Arizona (1976).
5. M. E. Gurtin, *Q. Appl. Math.*, **12**, 252 (1964).

Effects of Impurity Redistribution on the Short-Circuit Current of n^+-p Silicon Solar Cells

E. Y. Wang and L. Hsu

Department of Electrical and Computer Engineering, Wayne State University, Detroit, Michigan 48202

and H. W. Brandhorst, Jr.*

NASA-Lewis Center, Cleveland, Ohio 44135

ABSTRACT

The effect of impurity redistribution on the n^+-diffused layer of silicon solar cells has been studied. The impurity concentration was profiled by four-point-probe differential Hall and resistivity measurements. The electric field gradient and the mobility gradient in the diffused region were obtained from the impurity profiles. Short-circuit current was calculated from the effective recombination lifetime deduced from electric field gradient and mobility gradient results. The calculated short-circuit current was compared with measured values as a function of wavelengths and found to be in reasonably good agreement.

In recent calculations of the short-circuit current for silicon solar cells (1), we have found that this current is sensitive not only to the junction depth and the depletion region width (2) but also to the impurity distribution in the diffused and base regions. In order to verify these theoretical results, we have experimentally investigated the impurity profile and sheet resistance of the diffused layers of n^+-p silicon solar cells fabricated by normal diffusion processes with various lengths of drive-in times. We have also measured the short-circuit current on these "identical" solar cells. Experimental results obtained on these cells are in good agreement with the theoretical calculations.

Fifteen cells were fabricated from the (111) orientation of 10 Ω-cm p-type silicon. The chemically etched material was diffused in $POCl_3$ at 850°C for 30 min, the normal diffusion process for conventional n on p silicon solar cells at NASA-Lewis Center. The drive-in process at 850°C was performed for different lengths of time with nitrogen present as the carrier gas. After the diffusion and drive-in processes, cells were coated with Apiezen in the front; the back and edges of cells were etched away in a 2:3:1 (HNO_3:acetic:HF) solution for 1 min. The cells were then chemically treated in concentrated HF solution for 3 min, and subsequently went through the normal cleaning process for contact metallization (Al and Ag). For better ohmic contacts cells were sintered at 600°C for 20 min. At least three identical "cells" were made for the impurity profile and for the short-circuit current studies.

Impurity Profile by Differential Hall and Resistivity Measurements

The experimental technique for determining the impurity and resistivity profiles of the diffused layer is as follows (3): An oxide layer was grown by the electrolytic process of anodization of the diffused region of the cell. The oxide's thickness was estimated by electrolytic potential as well as by ellipsometry. Photoetching techniques were empoyed to obtain a Van der Pauw pattern of the n^+-layer of the silicon solar cells.

The method of Corbino images is applied to a circular isotropic Hall plate in order to determine its resistivity, ρ, and Hall coefficient, R_H. For a thin sheet in the Y-Z plane with a fixed magnetic field of arbitrary magnitude applied perpendicular to the surface of the sheet (x direction), the plate-oriented 4 fold symmetry axis is parallel to the magnetic field. Currents in the plate are constant in time and are linear functions of the electric fields. Currents in the plate produce negligible magnetic fields compared with the applied field.

In our experiment the Hall plate is isotropic but inhomogeneous. The measured conductivity σ and Hall coefficient R_H are related to the x dependent conductivity σ and Hall coefficient R_H as follows

$$\frac{1}{\rho} = \sigma = \frac{1}{t}\int_0^t \sigma(x)\,dx \qquad [1]$$

$$R_H = \frac{t\int_0^t \sigma^2(x)\,R_H(x)\,dx}{\left[\int \sigma(x)\,dx\right]^2} \qquad [2]$$

where the Hall factor has been taken as unity. For one carrier system, we can simplify Eq. [2] by

$$R_H(x) = \frac{1}{qn(x)} = \frac{\mu(x)}{\sigma(x)} = \rho(x)\,\mu(x) \qquad [3]$$

The $n(x)$ is the carrier concentration and t is the thickness of the Hall plate. Surface sheet resistivity and surface Hall coefficient are defined as

$$\frac{1}{\rho_s} = \sigma_s = \sigma t = \int_0^t \sigma(x)\,dx \qquad [4]$$

$$R_{Hs} = \frac{R_H}{t} = \frac{1}{\sigma_s}\int_0^t \sigma(x)\,R_H(x)\,dx \qquad [5]$$

Equation [5] is derived from Eq. [1], [2], and [4]. In differential form, $\sigma(x)$, $n(x)$, $\mu(x)$ become

$$\sigma(x) = \frac{d}{dx}\sigma_s \qquad [6]$$

$$n(x) = \sigma(x)/q\,\frac{d(R_{Hs}\,\sigma_s^2)}{dx} \qquad [7]$$

$$\mu(x) = \frac{1}{\sigma(x)}\,\frac{d}{dx}(R_{Hs}\,\sigma_s^2) \qquad [8]$$

Thus, the method for experimentally determining carrier concentration, resistivity, and mobility throughout the diffused layer is to measure σ_s and R_{Hs} successively after the removal of the surface layer (20.0 nm). The values of difference in σ_s and R_{Hs} for a

* Electrochemical Society Active Member.

Key words: silicon solar cell, impurity profile, short-circuit current.

consecutive measurement substituted in Eq. [6]-[8] give the values of $n(x)$, $\sigma(x)$, and $\mu(x)$.

Short-Circuit Current Calculation of the Silicon Solar Cells

The photoexcited minority carriers are created at a distance x from the junction, where L is the minority carrier diffusion length. The general expression for the short-circuit is given by (4)

$$\int_{0.4\ \mu m}^{1.1\ \mu m} \frac{dJ}{d\lambda} d\lambda = \sum_{\lambda = 0.4\ \mu m}^{\lambda = 1.1\ \mu m} J_{sc}(\Delta\lambda)$$

$$= q \sum_{\lambda = 0.4\ \mu m}^{\lambda = 1.1\ \mu m} \int \alpha\phi_o(\lambda) \exp^{-\alpha(\lambda)x} \exp \frac{-|x' - x|}{L} dx \qquad [9]$$

where q is the electronic charge and $\phi_o(\lambda)$ is photon flux density at wavelength λ; its values are taken from Ref. (5) and negligible reflection is assumed. Average values of α, the optical absorption coefficient, are taken from Ref. (6) and (7) and are taken as 50 nm for calculation purposes. The position where the excess minority carriers are collected is denoted as x'. For practical purposes, the total short-circuit current is just summed over the wavelength region from 0.4 to 1.1 μm.

Since minority carrier lifetime in the n^+-diffused region is known to be dependent on electric field gradient and mobility gradient, the L value is not a constant and the integration in Eq. [9] can simply be replaced by summation over small spatial regions. The notation J_{sc1} is used for the short-circuit contribution of the n^+-diffused region. By using Eq. [9] we can also calculate the short-circuit current contribution from both sides of the depletion region (J_{sc2} and J_{sc3}) and of the base region (J_{sc4}).The total short-circuit current is the sum of all four parts, *i.e.*

$$J_{sc}(\text{total}) = J_{sc1} + J_{sc2} + J_{sc3} + J_{sc4} \qquad [10]$$

Results and Discussion

Figure 1 shows an impurity profile of a typical solar cell. Sample R-1 has a drive-in time of 3 min; R-3, 10 min; and R-5, 60 min. These samples showed no significant change of surface concentration and have a deeper metallurgical junction (x_j) as the drive-in time increases; all the impurity profiles resemble an erfc distribution. The results of constant surface concentration for these cells suggest that the P_2O_5 layer on the silicon surface still acts as an infinite source during the drive-in process. The thickness of the grown oxide layer was measured by ellipsometry and the error was found to be around 5%. An accuracy of 2% in the Hall coefficient and sheet resistivity can safely be claimed. Therefore, the combined experimental data error should not exceed 10% for the first three or four measurements.

Figure 2 shows the hole mobility profile in the n^+-layer; it is obtained through a relationship with the experimental Hall electron mobility result (8). From Fig. 1 and 2, the electric field $E(x)$, the electric field gradient $dE(x)/dx$ (9, 10), and the mobility gradient $d\mu_p/dx$, can be calculated. The effective recombination lifetime τ_{eff} in the n^+ region is defined as

$$\frac{1}{\tau_{eff}} = \frac{1}{\tau_E} + \frac{1}{\tau_\mu} + \frac{1}{\tau_o} \qquad [11]$$

where $\tau_E = \left(-\mu_p \frac{dE}{dx}\right)^{-1}$, $\tau_\mu = \left(-E \frac{d\mu_p}{dx}\right)^{-1}$, and τ_o is the bulk recombination lifetime (values of τ_o are probably in the range of 10^{-7} sec) (11).

Figure 3 shows the spatial dependence of the effective lifetime for the R-3 cell. The solid curve is the theoretical calculation based on $x_j = 0.22$ μm, erfc distribution. The points based on the experimental differential Hall and resistivity measurements were superimposed on the same plot.

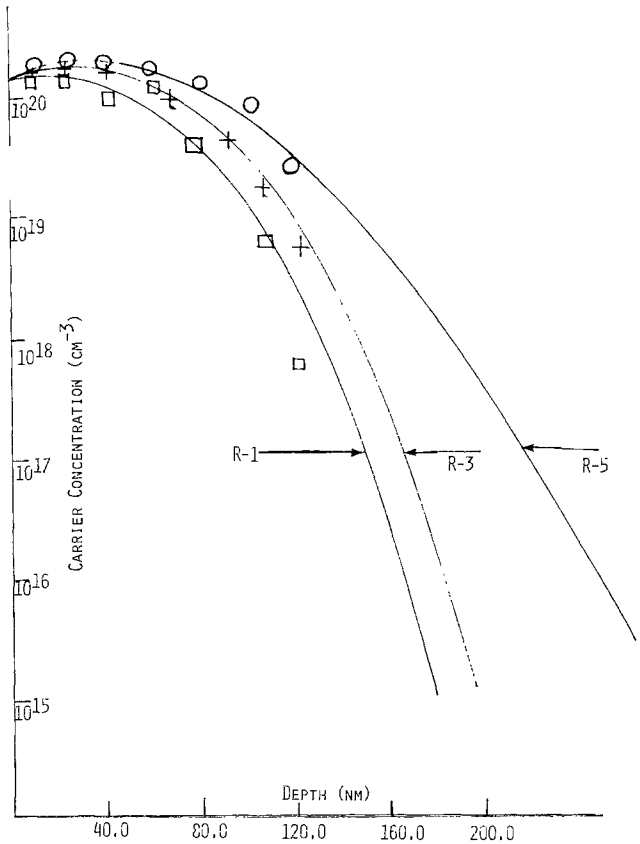


Fig. 1. Impurity profile of typical n^+-p silicon solar cells

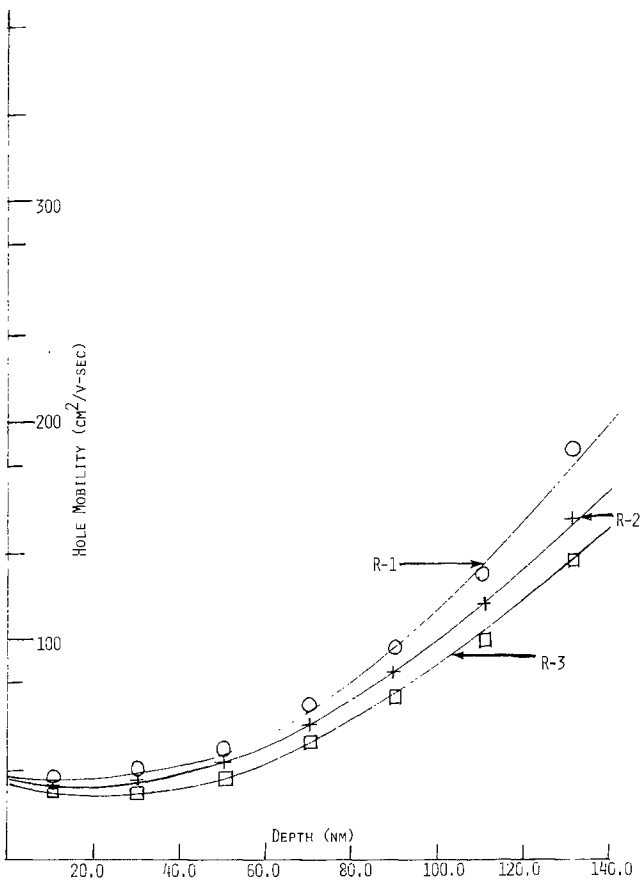


Fig. 2. Hole mobility profile of typical n^+-p silicon solar cells

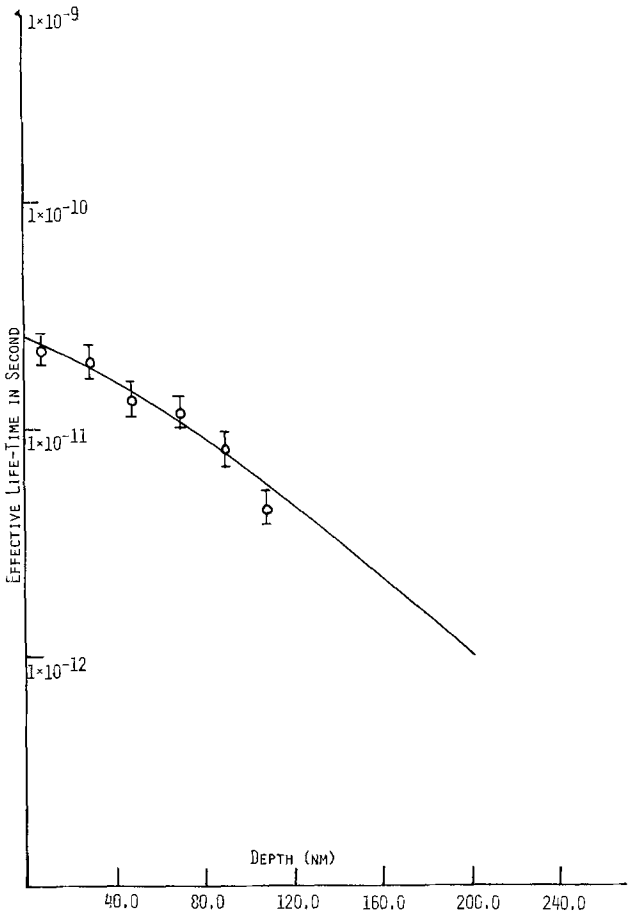


Fig. 3. Spatial dependence of the effective lifetime of n^+-region

Figure 4 shows the spectral response of these cells. The decrease in red response can be attributed to the decrease in the electron diffusion lengths, (L_n), of the base region as a result of longer drive-in times. The measurement of the L_n value through surface photovoltage (SPV) method (12) shows a maximum of a 10% decrease of its original value (about 200 μm) and thus confirms the result. As expected, the blue response is better for smaller x_j values.

Figure 5 shows the short-circuit current as a function of wavelengths. The solid lines are the theoretical calculations; experimental points are superimposed on the plot. The values of the parameters used in the calculations are listed in Table I. To determine whether or not the "drive-in" process changed the junction properties, junction capacitance was measured as a function of bias voltages. The results show that the junction still behaves as a one-side step junction, and that junction capacitance is independent of drive-in times. A built-in potential of 0.72V is obtained from a $1/C^2$ *vs.* V plot. The slope of this plot is related to the acceptor concentration in the base region and found to be 1.4×10^{15} cm^{-3} which corresponds to 10 Ω-cm base materials. A slight difference in slope values can be attributed to the variance (± 5%) in resistivity of the base material.

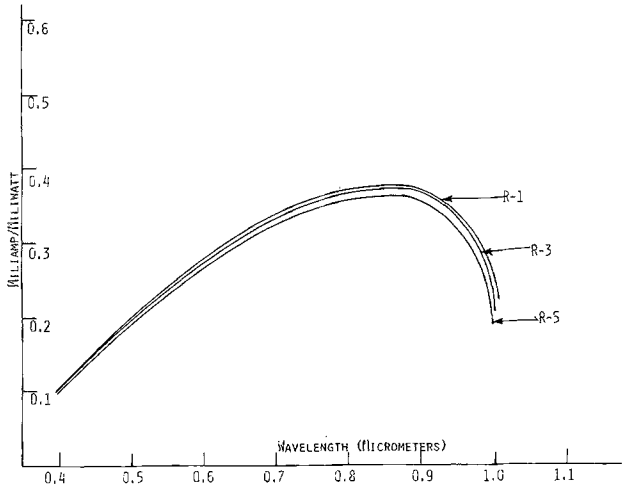


Fig. 4. Spectral response of n^+-p silicon cells with different drive-in times

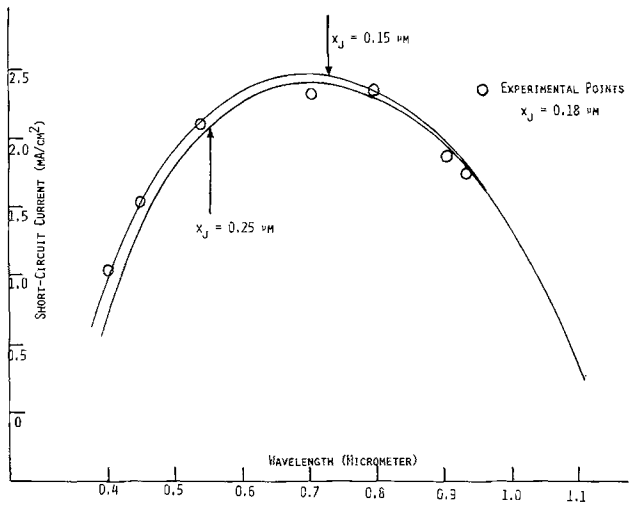


Fig. 5. Short-circuit current *vs.* wavelengths

In summary, the base layer of a silicon solar cell is the dominant factor in determining short-circuit current output. Through the four-point probe differential Hall and resistivity measurements used in our study, we have obtained the electric field gradient and the mobility gradient for a group of "identical" silicon solar cells with various lengths of drive-in times. Based on these values we have calculated the short-circuit current as a function of wavelength. The measured short-circuit is in good agreement with the calculated values.

Acknowledgment

The authors would like to thank Mr. J. H. Lamneck, NASA Lewis Research Center, Cleveland, Ohio, for his assistance in sample preparation. This work was partially supported by NSF Grant ENG 75-14104.

Manuscript submitted Nov. 30, 1976; revised manuscript received July 6, 1977.

Table I. Summary of short-circuit current results—10 Ω-cm cells

Impurity profile (cm^{-3})	Co (cm^{-3})	X_j (micron)	J_{sc1} (mA/cm^2)	J_{sc2} (mA/cm^2)	J_{sc3} (mA/cm^2)	J_{sc4} (mA/cm^2)	J_{sc} Total (mA/cm^2)	$(1 - R)J_{sc}$ Total (mA/cm^2)
erfc	1×10^{20}	0.15	0.8064	1.035	9.719	30.91	42.47	28.03
	1×10^{20}	0.25	0.9433	0.9587	8.351	30.15	40.40	26.66
	1×10^{20}	0.5	1.274	1.151	6.166	28.54	37.13	24.50

L_N = 200 μm.
R is the reflectivity loss and is dependent on wavelengths.

Any discussion of this paper will appear in a Discussion Section to be published in the June 1978 JOURNAL. All discussions for the June 1978 Discussion Section should be submitted by Feb. 1, 1978.

Publication costs of this article were assisted by Wayne State University.

REFERENCES

1. E. Y. Wang, L. Hsu, R. Legge, and H. Sawhala, in Proceedings of the International Conference on Photovoltaic Power Generation, Hamburg, Germany (1974).
2. E. Y. Wang and R. Legge, *This Journal*, **122**, 1562 (1975).
3. M. G. Buehler, Ph.D. Dissertation, Stanford University (1966).
4. L. M. Terman, *Solid-State Electron.*, **2**, 1 (1961).
5. NASA Special Report 8005 (1971).
6. W. C. Dash and R. Newman, *Phys. Rev.*, **98**, 1151 (1955).
7. W. R. Runyan, Final Report NASA Grant No. 44 007-016.
8. A. B. Phillips, "Transistor Engineering," p. 69, McGraw-Hill Book Co., New York (1962).
9. J. C. Jain and R. M. S. Al-Rifai, *J. Appl. Phys.*, **37**, 240 (1966).
10. B. L. Ho and C. C. Cho, *ibid.*, **39**, 3333 (1968).
11. B. Ross and J. R. Madigan, *Phys. Rev.*, **87**, 835 (1957).
12. E. Y. Wang, C. R. Baraona, and H. W. Brandhorst, Jr., *This Journal*, **121**, 973 (1974).

A New Method for Calculating Background Dopant Density from p-n Junction Capacitance-Voltage Measurements

Richard L. Mattis and Martin G. Buehler*

Electronic Technology Division, Institute for Applied Technology, National Bureau of Standards, Washington, D.C. 20234

ABSTRACT

A new method is presented for calculating the average background dopant density within the depletion layer of a planar diffused p-n junction using capacitance-voltage (C-V) measurements. The method has been successfully applied to specimens having a background dopant density as high as 10^{18} cm^{-3}, and ideal data studies indicate that the method may be applicable to specimens having a background dopant density up to about 10^{19} cm^{-3}. The average background dopant density is calculated by finding the Gaussian diffused layer as characterized by an effective surface dopant density, background dopant density, and junction depth which can best be fitted to all the C-V data. It is not necessary to know the actual surface dopant density. The method is illustrated by calculations on both real and idealized C-V data.

The capacitance-voltage (C-V) method is widely used to measure dopant density *vs.* depth profiles of semiconductor specimens (1-4). Equations have been developed to correct for the peripheral capacitance (5-8) and for back-depletion into the diffused layer (8) for the case of Gaussian diffused planar p-n junctions, and the consequences of neglecting these corrections have been illustrated (8-10). A computer program has been written which incorporates both of these corrections (11). In order to measure the background dopant density with the use of a diffused p-n junction by these profiling C-V methods, it is necessary to force the space-charge or depletion region out of the region which is partly compensated by the diffused layer. In junctions where the dopant density profile does not level off at a steady background value, an accurate determination of the background dopant density is not possible. This problem is particularly acute in heavily doped specimens because, for a given reverse bias, the depletion width is smaller than for lightly doped specimens and the maximum reverse bias which can be applied (the reverse breakdown voltage) decreases as the background dopant density increases. Furthermore, in heavily doped specimens, the correction for back-depletion into the diffused layer makes a significant contribution to the calculation (9). If the surface dopant density has been calculated from the diffused layer sheet resistance and junction depth assuming a Gaussian diffused layer (12, 13) and if the diffused layer does not have a Gaussian profile, then errors in the diffused layer correction lead to errors in the calculated dopant density profile.

In this new method, the average background dopant density is calculated by finding the best Gaussian shape for the diffused layer that can be fitted to all C-V data. In essence, the problem is to find the parameters of the diffused layer within the depletion region which allow a proper back-depletion correction. The parameters of the Gaussian diffused layer are the junction depth, X_j, the effective surface dopant density, N_{0e}, and the background dopant density, N_b, which is also the quantity of primary interest in this measurement method. Assuming that X_j can be determined by lap and stain techniques, only N_{0e} and N_b are unknown. As is shown below, N_{0e} and N_b can both be determined if N_b is treated as a pseudo-variable which is constrained to be independent of depth.

An example of dopant densities calculated by the profiling method and by the new method to be described is given in Fig. 1. The test specimen was a 17 mil diameter planar diffused p-n junction diode fabricated on a 0.0216 Ω-cm n-type silicon wafer. The four profiles were calculated using four forms of the profiling method; namely, with no correction, with peripheral correction only, with back-depletion correction only, and with both peripheral and back-depletion corrections. Note that in this example the peripheral correction has a relatively small effect. Assuming a Gaussian diffused layer, the back-depletion correction was calculated using a junction depth of 1.52 μm as measured by the angle lap and stain

* Electrochemical Society Active Member.

Key words: electrical measurements, Gaussian diffusion, semiconductors, silicon.

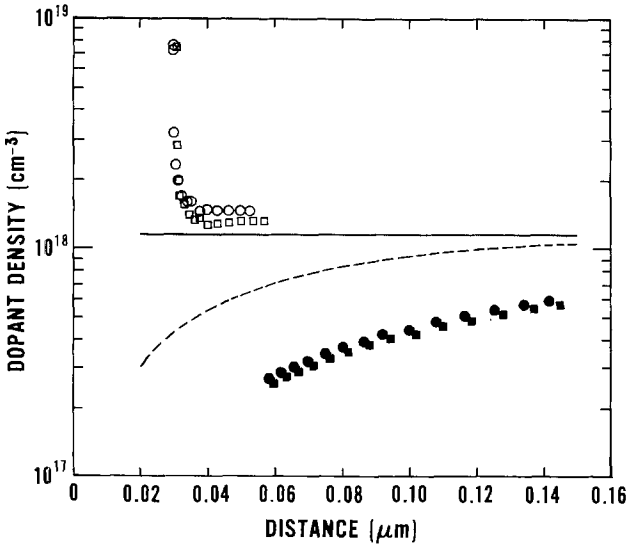


Fig. 1. Dopant densities calculated by the profiling method and the new method from C-V data taken on a p-n junction fabricated on a 0.0216 Ω · cm n-type silicon wafer. Four profiles calculated by the profiling method are shown representing no correction to the C-V data (●), peripheral correction only (■), back-depletion correction only (○), and both peripheral and back-depletion corrections (□). The uppermost point for the case of back-depletion correction only was negative as calculated; the magnitude is indicated in the plot. The solid line represents the average background dopant density calculated by the new method, and the dashed line represents the net dopant density calculated from the Gaussian fit.

method and a surface dopant density of 2.44×10^{20} cm^{-3} which was calculated from the junction depth and the measured diffused layer sheet resistance of 8.73 Ω/[] (12, 13). Note that the profiles for which the back-depletion correction was not applied do not approach a steady background level, and that the shapes of the profiles obtained by applying that correction are not realistic. Similar back-depletion corrected profiles, which sometimes include negative dopant density values,[1] have been calculated for other heavily doped specimens. The cause of this calculated profile shape lies in the assumed Gaussian shape of the entire diffused layer. When the new method is used, the average background dopant density is calculated to be 1.15×10^{18} cm^{-3} as indicated by the solid line in the figure. The Gaussian fit to the C-V data, when extrapolated to the surface gives an effective surface dopant density of 1.46×10^{23} cm^{-3}. The net dopant density calculated from the Gaussian fit is shown by the dashed curve in the figure. The large difference between the values of the surface dopant density calculated by the two methods indicates that the over-all diffused layer is non-Gaussian and falls more abruptly in the depletion region than a Gaussian diffused layer having the same sheet resistance and junction depth. The profiling method is thus not suitable for this specimen whereas the new method is.

The mathematical formulation of the new method is given in the Equations section. A brief description of how the equations are implemented is given in Calculation Procedure. Some examples of the method are reported in Ideal Data Studies and Real Data Studies sections which then leads to a discussion in the Evaluation and Limitations section and finally to the Conclusion. The method does not work when a Gaussian fit cannot be made, and this can be sensed and indicated. The method is based on the depletion approximation where the space-charge region is assumed to be free of holes and electrons and where the transition from the space-charge region to the depletion region is abrupt.

[1] A negative dopant density is calculated in Eq. [8] below if $N(W)$ is greater than $N(A)$. This can occur if the estimates of junction depth, effective surface dopant density, or background dopant density, which are all needed in the profiling method (8, 11), differ significantly from the correct values.

Equations

The equations and symbols used to present the new method may be understood with the help of Fig. 2. In the figure, A and B are the depletion widths on the heavily doped and lightly doped sides of the junction, respectively, $N(A)$ and $N(B)$ are the net dopant densities at A and B, X_j is the junction depth, N_b is the average background dopant density within the depletion region, N_{0e} is the effective surface dopant density representing the extrapolation of the Gaussian fit to the surface, and N_0 is the actual surface dopant density. Note that N_b is assumed constant within the depletion region and that N_{0e} may be vastly different from N_0.

In the absence of a correction for back-depletion, the depletion width, $W = A + B$, and the apparent dopant density, $N(W)$, can be calculated from the capacitance corrected for peripheral effects, C, and the reverse bias, V, by use of the following equations (14)

$$W = \frac{\kappa\epsilon_0 A_j}{C} \qquad [1]$$

$$N(W) = \frac{2}{q\kappa\epsilon_0 A_j^2}\left[\frac{d}{dV}\left(\frac{1}{C^2}\right)\right]^{-1} \qquad [2]$$

where $\kappa\epsilon_0$ is the dielectric constant of the test specimen, q is the electronic charge, and A_j is the active junction area. Equations [1] and [2] are in practice applied to a set of n C *vs.* V data pairs to produce a

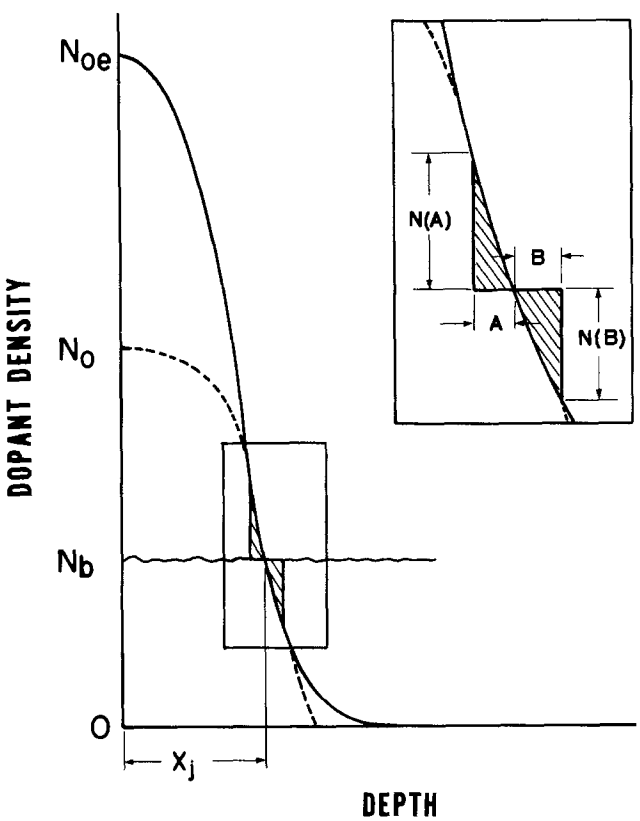


Fig. 2. Dopant density profile of a p-n junction showing a hypothetical diffused layer (dotted curve beginning at N_0) and the Gaussian fit to that layer (solid curve beginning at N_{0e}). The background dopant density is shown to vary with distance but is assumed constant within the depletion layer. The depletion region is shown enlarged in the inset.

set of $(n-1)$ $N(W)$ *vs.* W data pairs. The $N(W)$ and W values are known measured quantities.

For a Gaussian layer diffused into uniformly doped background material, the net dopant densities $N(A)$ and $N(B)$ are given by (8, 11)

$$N(A) = N_{0e}\exp\left[-\left(\frac{X_j - A}{L}\right)^2\right] - N_b \quad [3]$$

$$N(B) = N_b - N_{0e}\exp\left[-\left(\frac{X_j + B}{L}\right)^2\right] \quad [4]$$

where the parameter L is given by

$$L = \frac{X_j}{\sqrt{\ln\frac{N_{0e}}{N_b}}} \quad [5]$$

If values are assigned to X_j, N_{0e}, and N_b, then the quantities A and B can be calculated by simultaneously solving Eq. [6] and [7] (8)

$$W = A + B \quad [6]$$

$$\text{erfc}\left(\frac{X_j - A}{L}\right) - \text{erfc}\left(\frac{X_j + B}{L}\right) = \frac{2}{\sqrt{\pi}}\frac{N_b W}{N_{0e} L} \quad [7]$$

where Eq. [7] satisfies the charge neutrality requirement. The parameters $N(A)$ and $N(B)$ sum as follows (8, 15)

$$\frac{1}{N(W)} = \frac{1}{N(A)} + \frac{1}{N(B)} \quad [8]$$

The six equations listed above, Eq. [3] to [8], have seven unknown quantities: A, B, $N(A)$, $N(B)$, N_{0e}, N_b, and L, assuming that X_j can be determined by independent measurement. A seventh equation can be written if, for a set of $(n-1)$ $N(W)$ *vs.* W data pairs, N_b is constrained to be a constant such that

$$\frac{dN_b}{dW} = 0 \quad [9]$$

The above system of seven equations in seven unknowns can now be solved.

The computation is simplified by introducing the ratio R as defined by

$$R = \frac{N_{0e}}{N_b} \quad [10]$$

and by redefining L as

$$L = \frac{X_j}{\sqrt{\ln R}} \quad [11]$$

Substitution of these equations into Eq. [3], [4], and [8] leads to a new expression for the dopant density

$$N_b = N(W)\left\{\left[R\exp\left[-\left(\frac{X_j - A}{L}\right)^2\right] - 1\right]^{-1} + \left[1 - R\exp\left[-\left(\frac{X_j + B}{L}\right)^2\right]\right]^{-1}\right\} \quad [12]$$

For a properly chosen value of R, the condition given in Eq. [9] is satisfied and N_b is the average background dopant density of interest. For this condition, the best Gaussian fit to the C-V data has been found. The means by which a proper value of R is chosen is discussed in the next section.

Calculation Procedure

Given a set of C-V data in which the capacitances have been corrected for peripheral effects, a set of $N(W)$ and W values are first calculated using Eq. [1] and [2]. A first estimate of R is then made (10,000 has been found to be a good first estimate). For this value of R, L is calculated using Eq. [11] and a set of A and B values are calculated using Eq. [6] and [7]. A set of N_b values is then calculated using Eq. [12]. If the estimate for R has given the correct Gaussian fit, all of the N_b values [corresponding to the individual $N(W)$ values] are equal. The criterion for determining when R has been estimated correctly is based on the slope of N_b *vs.* W. More precisely, the N_b values are normalized with respect to the N_b corresponding to the maximum W, and the W values are normalized with respect to the maximum W. A least squares linear fit is then made to the normalized N_b *vs.* W values. If the absolute value of the slope is less than some value (usually 10^{-3}) the estimate of R is judged to be correct and the average background dopant density is given by the average of the unnormalized N_b values. If the above fit results in a positive slope, R is reestimated at a smaller value and the calculation is rerun. If the slope is negative, R is reestimated at a larger value. A rapidly convergent method for finding R is described in the Appendix.

It may be argued that N_b, originally defined as a constant parameter of the Gaussian fit, has been used also as a variable, thereby producing an inconsistency. However, the calculation procedure as described is designed to search for that value of R for which N_b is a constant, and it is judged to be a constant when a normalized plot of N_b *vs.* W has nearly zero slope.

The computer calculations to be described were performed using a BASIC interpreter having six-digit precision. The calculation of A in Eq. [6] and [7] was performed using an iterative algorithm which was terminated when the relative difference between two successive estimates of A was 10^{-4} or less (11).

Ideal Data Studies

Ideal C-V data for a Gaussian diffused p-n junction 17 mil in diameter and with a 1.5 μm junction depth were generated for 40 combinations of N_{0e} and N_b. The N_{0e} values were 10^{18}, 10^{20}, 10^{23}, and 10^{26} cm^{-3}, and the N_b values ranged from 10^{14} to 10^{20} cm^{-3} in half-decade steps (11). The C-V data were limited to practical values in that forward bias did not exceed 0.3V and reverse bias did not exceed the breakdown voltage which would be expected for a particular background dopant density. Peripheral capacitance was not included. The estimate of R was judged to be correct when the slope of the normalized N_b *vs.* W values was less than 10^{-3}. The first estimate of R in each case was 13,542. The results of these calculations are shown in Table I. For each N_{0e} value, those N_b values for which the absolute value of the error

Table I. Average background dopant densities calculated from idealized C-V data for 1.5 μm junction depth

Assumed N_{0e} (cm^{-3})	Assumed N_b (cm^{-3})	Calculated N_b (cm^{-3})	Percent error
10^{18}	$\leq 1 \times 10^{16}$	—	$<\pm 0.10$
10^{18}	3×10^{16}	2.99631×10^{16}	-0.12
10^{18}	1×10^{17}	9.93851×10^{16}	-0.61
10^{20}	$\leq 3 \times 10^{16}$	—	$<\pm 0.10$
10^{20}	1×10^{17}	9.98362×10^{16}	-0.16
10^{20}	3×10^{17}	2.98699×10^{17}	-0.43
10^{20}	1×10^{18}	9.82597×10^{17}	-1.74
10^{20}	3×10^{18}	3.19122×10^{18}	$+6.37$
10^{20}	1×10^{19}	No fit	
10^{23}	$\leq 1 \times 10^{17}$	—	$<\pm 0.10$
10^{23}	3×10^{17}	2.99649×10^{17}	-0.12
10^{23}	1×10^{18}	9.95586×10^{17}	-0.44
10^{23}	3×10^{18}	2.94395×10^{18}	-1.87
10^{23}	1×10^{19}	9.07376×10^{18}	-9.26
10^{23}	3×10^{19}	2.77956×10^{19}	-7.35
10^{23}	1×10^{20}	No fit	
10^{26}	$\leq 3 \times 10^{17}$	—	$<\pm 0.10$
10^{26}	1×10^{18}	9.98117×10^{17}	-0.19
10^{26}	3×10^{18}	2.97055×10^{18}	-0.98
10^{26}	1×10^{19}	9.47444×10^{18}	-5.26
10^{26}	3×10^{19}	2.75477×10^{19}	-8.17
10^{26}	1×10^{20}	No fit	

was less than 0.10% are represented on a single line with the percent error given as $<\pm 0.10$. Those entries indicated as "no fit" could not be fitted to a Gaussian. This is discussed further in the Evaluation and Limitations section.

A second but similar ideal data study was carried but using 24 combinations of N_{0e} and N_b with X_j equal to 0.5 μm. These results are shown in Table II. Note that the shallower junction depth serves to reduce the measurement error of the various combinations of N_{0e} and N_b and also permits measurement in situations where a fit could not previously be made.

A third ideal data study was concerned with the consequences of errors in the junction depth and diameter, two needed input parameters. Using 15 sets of the previously discussed ideal data, X_j was entered 20% higher and 20% lower than the correct value. The resulting average background dopant densities were compared with the values previously calculated with no offsets (column 3 of Table I and II). For the junction depth study, the error exceeded 0.2% in only five of the 15 cases tried. In each of these five cases it was the underestimate of X_j which caused the error greater than 0.2%. These five cases are given in Table III. Note that these are cases of large N_b or cases of N_b approaching N_{0e}. With X_j entered correctly, the diameter was then offset by $\pm 1\%$. For these diameter offsets, the percent error in average background dopant density was in each case approximately minus four times the percent error in the diameter relative to the case of no error in the diameter. In this respect it follows the same pattern as in the profiling C-V method.

A fourth ideal data study was concerned with the repeatability of the average background dopant density in the presence of capacitance values which include random measurement error. Such sets of capacitance data were produced by modulating the previously calculated idealized capacitance values with a normally distributed random error having a standard deviation of 0.05%. This thus simulated a $\pm 0.1\%$ random measurement error. For each ideal data set. this procedure was repeated five times using five different sets of random numbers to generate the error. Each of the five sets of C-V data were then processed by the new method to produce five values of average background dopant density. The percent standard deviation of these five dopant density values was calculated. The results are shown in Table IV.

Table II. Average background dopant densities calculated from idealized C-V data for 0.5 μm junction depth

Assumed N_{0e} (cm^{-3})	Assumed N_b (cm^{-3})	Calculated N_b (cm^{-3})	Percent error
10^{18}	$\leq 3 \times 10^{16}$	—	$<\pm 0.10$
10^{18}	1×10^{17}	9.97956×10^{16}	-0.20
10^{20}	$\leq 3 \times 10^{17}$	—	$<\pm 0.10$
10^{20}	1×10^{18}	9.95462×10^{17}	-0.45
10^{20}	3×10^{18}	2.96788×10^{18}	-1.07
10^{20}	1×10^{19}	9.30640×10^{18}	-6.94
10^{23}	$\leq 1 \times 10^{18}$	—	$<\pm 0.10$
10^{23}	3×10^{18}	2.98048×10^{18}	-0.65
10^{23}	1×10^{19}	9.87503×10^{18}	-1.25
10^{23}	3×10^{19}	2.69648×10^{19}	-10.1
10^{23}	1×10^{20}	6.71366×10^{19}	-32.9
10^{26}	$\leq 1 \times 10^{18}$	—	$<\pm 0.10$
10^{26}	3×10^{18}	2.98718×10^{18}	-0.43
10^{26}	1×10^{19}	9.87477×10^{18}	-1.25
10^{26}	3×10^{19}	2.93165×10^{19}	-2.28
10^{26}	1×10^{20}	9.06218×10^{19}	-9.38

Table III. Error in calculated average background dopant density for an error in junction depth of -20%

Assumed N_{0e} (cm^{-3})	Assumed N_b (cm^{-3})	Assumed X_j (μm)*	Error in N_b (%)
10^{20}	10^{18}	1.2	+0.59
10^{23}	10^{19}	1.2	+0.34
10^{20}	10^{18}	0.4	+0.43
10^{20}	10^{19}	0.4	+3.87
10^{23}	10^{20}	0.4	+0.24

* The numbers in this column reflect the 20% underestimate of X_j. The ideal data on which the method was operating assumed values of 1.5 and 0.5 μm as discussed in the text.

Real Data Studies

Capacitance-voltage data from 23 silicon specimens were processed by the new method. Fourteen of the specimens were n-type having nominal resistivity ranging from 100 to 0.009 Ω·cm and junction depth ranging from 0.44 to 1.84 μm. The method was successful on eleven specimens having average background dopant density in the range 4.64×10^{13} to 1.16×10^{18} cm^{-3} inclusive. The method gave somewhat erratic results on a specimen having an average background dopant density of approximately 2.7×10^{18} cm^{-3}. Attempts to apply the method to two more heavily doped specimens produced a "no fit" condition as described in the section Evaluation and Limitations. The nine p-type specimens had nominal resistivity ranging from 20 to 0.025 Ω·cm and junction depth ranging from 0.92 to 1.79 μm. The method was successful on eight specimens having average background dopant density in the range 6.21×10^{14} to 3.38×10^{17} cm^{-3} inclusive. The method produced a "no fit" condition when applied to the most heavily doped p-type specimen. The average background dopant density of that specimen is believed to be between 2 and 3×10^{18} cm^{-3}.

Evaluation and Limitations

The new method has been shown to work using idealized and real C-V data representing a wide range of practical conditions. The maximum measurable N_b appears to lie in the range 10^{18} to 10^{19} cm^{-3} depending on the shape of the diffused layer within the depletion region and also on the error which can be tolerated in a given application. The data in Tables I, II, and IV indicate that the error in N_b can be reduced in most instances by increasing N_{0e} or decreasing X_j. It may be possible to decrease X_j by using shorter diffusion times during junction fabrication. However, it may be difficult to produce junctions which are sufficiently abrupt as to have an N_{0e} of 10^{23} cm^{-3} or greater.

Regardless of the measurement error which can be tolerated, the method does not work if the C-V data cannot be fitted to a Gaussian. For the studies discussed thus far this "no fit" condition is manifest by successively smaller estimates of R until the lower limit 2 is reached. This limit is somewhat arbitrary, whereas R less than 1 corresponds to N_{0e} less than N_b, an unmeaningful case. It is uncertain what causes a "no fit" condition, however, it would seem that such might occur if the net dopant density within

Table IV. Percent standard deviations of N_b values calculated from capacitance data having a 0.05% standard deviation normally distributed random error

Assumed N_b (cm^{-3})	Assumed X_j (μm)	Assumed N_{0e} (cm^{-3})			
		10^{18}	10^{20}	10^{23}	10^{26}
10^{14}	0.5	—*	0.117	—*	—*
10^{14}	1.5	0.188	0.097	0.130	—*
10^{17}	0.5	0.145	0.185	0.205	—*
10^{17}	1.5	1.64	0.489	0.103	0.148
10^{18}	0.5	—†	3.49	1.20	0.135
10^{18}	1.5	—†	14.0	4.00	1.38
10^{19}	0.5	—†	32.7	2.25	1.59
10^{19}	1.5	—†	No fit	5.03	9.21
10^{20}	0.5	—†	—†	19.6	12.9
10^{20}	1.5	—†	—†	No fit	No fit

* This combination not calculated.
† This combination not realizable, $N_b \geq N_{0e}$.

the depletion region were linearly graded (for which a background dopant density is not defined) or if the net dopant density within the depletion layer were concave downward. The errors inherent in performing calculations with only six significant figures could conceivably lead to a "no fit" condition in some instances but this has not been verified. It is also possible that the assumption of abrupt depletion region boundaries is sufficiently invalid at such high background dopant densities as to make the model unworkable.

Another class of measurements for which a suitable fit cannot always be made is that in which an actual gradient in N_b exists. For heavily doped specimens having a gradient in N_b, R can be adjusted to be artificially high or low to force the set of calculated normalized N_b values to have a near-zero slope. Studies have indicated that when a measurement is made in the presence of a gradient the result is very nearly the average background dopant density within the depletion layer. In such a situation, the gradient is not detected as it is in a discrete point dopant density *vs.* depth calculation. For some lightly doped specimens having a gradient in N_b, there is no value of R in the range 2 to 10^{12} inclusive which gives a slope of the normalized N_b *vs.* W values sufficiently near zero. Such C-V data must be processed by the profiling method.

Conclusion

A method has been described for calculating the average background dopant density of a semiconductor specimen from C-V measurements made on a diffused p-n junction fabricated on the specimen. The method is particularly suited to relatively heavily doped specimens where profiling C-V calculations do not work. The method requires no knowledge of the actual surface dopant density of the diffused layer, and the junction depth is not a critical input parameter. The method has been tested with both ideal and real C-V data. The method is suitable for measurement of dopant densities up to 10^{18} cm^{-3}, however, above 10^{18} cm^{-3} errors become more probable and caution should be exercised in interpreting results.

Acknowledgments

The authors are indebted to W. Murray Bullis for a thorough review of the manuscript, to Leo R. Williams for preparation of the figures, and to Dana L. Hines for typing the several drafts of the manuscript. This work was conducted as a part of the Semiconductor Technology Program at the National Bureau of Standards. Portions of this work were supported by the Defense Advanced Research Projects Agency (Order No. 2397, Program Code 6D10).

Manuscript submitted Feb. 28, 1977; revised manuscript received July 15, 1977.

Any discussion of this paper will appear in a Discussion Section to be published in the June 1978 JOURNAL. All discussions for the June 1978 Discussion Section should be submitted by Feb. 1, 1978.

Publication costs of this article were assisted by the National Bureau of Standards.

APPENDIX

Procedure for Making Converging Estimates of R

A mathematical method for determining the correct value of R has been developed. The principle of this method can be explained with the help of Fig. 3. The figure shows how the slope of a plot of N_b *vs.* W behaves as a function of R and how this behavior can be used to converge on the final value of R. Represented in the figure are three sets of ideal C-V data for which the slope of the plot of normalized N_b *vs.* W values is plotted as a function of an estimate of R, designated R_e given as some coefficient times R_a the actual value of R for which the ideal C-V data

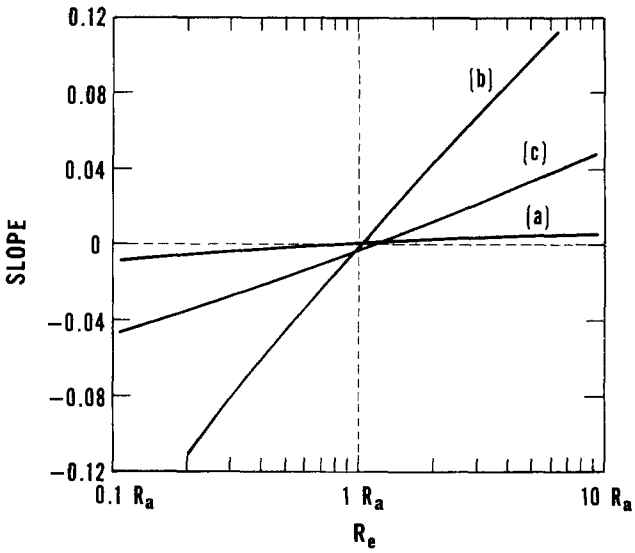


Fig. 3. Plot of the slope of the normalized N_b vs. W values as a function of R_e where R_e is the current estimate of R and R_a was the value of R used to calculate the ideal C-V data. Curves are shown for N_b equal to (a) 10^{16} cm^{-3}, (b) 10^{18} cm^{-3}, and (c) 10^{19} cm^{-3}. In each case N_{0e} was 10^{23} cm^{-3} and X_j was 0.5 μm.

were calculated. The plotted curves are all monotonically increasing from left to right and all pass through zero slope on the vertical axis at R_e approximately equal to R_a. (Deviations from R_e equal to R_a when the slope is zero may be a reflection of the error in Tables I and II.) Similar behavior was observed for other ideal data sets as well. Therefore for a set of real C-V data, if the slope of the plot of normalized N_b *vs.* W values is positive, it means that R_e is greater than R; if the slope is negative, then R_e is less than R.

In the first phase of the calculation to determine R, the parameter R_e (the estimate of R) is increased or decreased by decades depending on the sign of the slope of the normalized N_b *vs.* W values. This phase continues until a change in the sign of the slope is detected. The second phase consists of a succession of interpolations based on

$$R_e = \exp\left[\ln(R_1) - \frac{M_1}{M_2 - M_1}(\ln(R_2) - \ln(R_1))\right] \quad \text{[A-1]}$$

In Eq. [A-1], R_e is the new estimate of R, M_1 is the most recently calculated negative slope, calculated for R_e equal to R_1, and M_2 is the most recently calculated positive slope, calculated for R_e equal to R_2. The successive interpolations continue until the slope is sufficiently near zero at which time R is set equal to R_e.

LIST OF SYMBOLS

A	depletion width on the heavily doped side of the p-n junction, μm
A_j	junction area, μm^2
B	depletion width on the lightly doped side of the p-n junction, μm
C	capacitance, pF
L	characteristic length of the Gaussian fit to the diffused layer as defined in Eq [5], μm
M_1	most recently calculated negative normalized slope of N_b *vs.* W
M_2	most recently calculated positive normalized slope of N_b *vs.* W
$N(A)$	net dopant density at a distance A from the junction on the heavily doped side, cm^{-3}
$N(B)$	net dopant density at a distance B from the junction on the lightly doped side, cm^{-3}
$N(W)$	apparent dopant density as calculated from Eq. [2], cm^{-3}
N_b	average background dopant density within the depletion region, cm^{-3}
N_0	actual surface dopant density, cm^{-3}
N_{0e}	effective surface dopant density, cm^{-3}
n	number of C-V data pairs

q electronic charge, C
R the ratio N_{0e}/N_b
R_a actual value of R in an idealized data calculation
R_e estimated value of R in an idealized data calculation
R_1 value of R which produced the normalized slope M_1
R_2 value of R which produced the normalized slope M_2
V junction reverse bias, V
W depletion width, μm
X_j junction depth, μm
ϵ_0 permittivity of free space, pF/μm
κ relative dielectric constant of silicon (or other material under test)
π 3.14159 . . .

REFERENCES

1. J. Hilibrand and R. D. Gold, *RCA Rev.*, **21**, 245 (1960).
2. D. P. Kennedy, P. C. Murley, and W. Kleinfelder, *IBM J. Res. Devel.*, **12**, 399 (1968).
3. D. C. Gupta, *Solid-State Technol.*, **11** (2), 31 (1968).
4. P. J. Severin and G. J. Poodt, *This Journal*, **119**, 1384 (1972).
5. P. R. Wilson, *Solid-State Electron.*, **11**, 381 (1968).
6. P. R. Wilson, *ibid.*, **12**, 1 (1969).
7. P. R. Wilson, *ibid.*, **16**, 1511 (1973).
8. M. G. Buehler, *IEEE Trans. Electron Devices*, **ed-19**, 1171 (1972).
9. R. L. Mattis and M. G. Buehler, "Semiconductor Measurement Technology," Quarterly Report, July 1 to September 30, 1973, W. M. Bullis, Editor, U.S. National Bureau of Standards Special Publication 400-1, pp. 7-9 (1974).
10. R. L. Mattis and M. G. Buehler, "Semiconductor Measurement Technology," Quarterly Report, April 1 to June 30, 1974, W. M. Bullis, Editor, U.S. National Bureau of Standards Special Publication 400-8, pp. 10-14 (1975).
11. R. L. Mattis and M. G. Buehler, "Semiconductor Measurement Technology: A BASIC Program for Calculating Dopant Density Profiles from Capacitance-Voltage Data," U.S. National Bureau of Standards Special Publication 400-11 (1975).
12. J. C. Irvin, *Bell Syst. Tech. J.*, **41**, 387 (1962).
13. T. E. Griffin and M. G. Buehler, "Semiconductor Measurement Technology," Quarterly Report, July 1 to September 30, 1973, W. M. Bullis, Editor, U.S. National Bureau of Standards Special Publication 400-1, pp. 11-15 (1974).
14. W. Schottky, *Z. Phys.*, **118**, 539 (1942).
15. D. R. Decker, *This Journal*, **115**, 1085 (1968).

Spray Deposition of Cadmium Stannate Films

G. Haacke, H. Ando, and W. E. Mealmaker

American Cyanamid Company, Chemical Research Division, Stamford, Connecticut 06904

ABSTRACT

The feasibility of spray coating transparent cadmium stannate electrodes onto glass has been demonstrated. Both cadmium stannate phases, Cd_2SnO_4 and $CdSnO_3$, can be deposited. The lowest electrical sheet resistances (10-20 $\Omega/\square$) and good optical transparency were obtained in $CdSnO_3$ films. With Cd_2SnO_4, clear films having 80-100 $\Omega/\square$ were achieved.

Thin films of cadmium (ortho) stannate (Cd_2SnO_4) are known to have high electrical conductivities and low visible absorption when prepared by rf sputtering under well-chosen conditions (1). The transparent electrode properties of these films suggest a wide range of applications where they would equal or surpass the performance of other transparent conductor materials (2, 3).

The practical utilization of cadmium stannate requires not only superior electrical and optical characteristics but also cost-effective preparation methods. When films having moderate electrical sheet resistances in the 10-100 $\Omega/\square$ range are needed sputter coating may be acceptable since the deposition time is short. For example, we can sputter in a 45 cm laboratory vacuum system Cd_2SnO_4 films from a 12.5 cm target plate within 5 min at 8μ plasma pressure and consistently obtain 15-20 $\Omega/\square$ sheet resistance after heat-treatment. The luminous transmittances of these coatings on Corning 7059 glass exceed 85% and in most cases reach 88-89% (substrate losses included). Films having lower sheet resistances require longer deposition times. 20 min are needed to achieve 2.5-3.0 $\Omega/\square$ and 82-83% luminous transmittance with coatings on Corning 7059 substrates. The sputter time increases to approximately 1 hr for 1 $\Omega/\square$ films. Such deposition times are rarely justifiable on economic grounds, so that a need exists to find more efficient preparation techniques for low sheet resistance cadmium stannate. Spray deposition appears to be one promising method since it has been successfully used to deposit transparent tin oxide (4) and indium oxide (5) electrodes. We have applied this technology to cadmium stannate and report the results of our investigations below.

Key words: transparent electrodes, pyrolysis, electrical sheet resistance, optical transmission.

Deposition Technique

The principle of spray deposition is based on the pyrolysis of a fine mist of a metal salt solution on a hot substrate. Binary oxide films, such as SnO_2 or In_2O_3, form quite readily and conditions for the deposition of optically clear coatings can be established without major difficulties. More stringent requirements have to be met when cadmium stannate is spray deposited since formation of the ternary stannate phase, instead of binary CdO/SnO_2 mixtures, occurs only within a narrow range of experimental parameters. A complicating feature arises from the existence of two cadmium stannate phases, Cd_2SnO_4 and $CdSnO_3$. Although both compounds are transparent conductors, good transparent electrode properties are achieved only in single phase films (6).

The experiments were carried out with a setup outlined in Fig. 1. A spray nozzle is located at a fixed position above the heated substrate. The substrate (2.5 $\times$ 2.5 cm) rests on a 0.6 cm thick carbon plate (EH grade, C.E. Chapin Company, East Rutherford, New Jersey) which provides good heat transfer and has a low burn rate even at high temperatures. Ceramic fire bricks (Thermolyne JR 11X2A) support the carbon plate which is directly heated by a regulated propane burner. This arrangement allows fast heat-up of the substrate to the desired deposition temperature and rapid removal of the coated samples during quenching experiments. The temperature is measured by a thermocouple

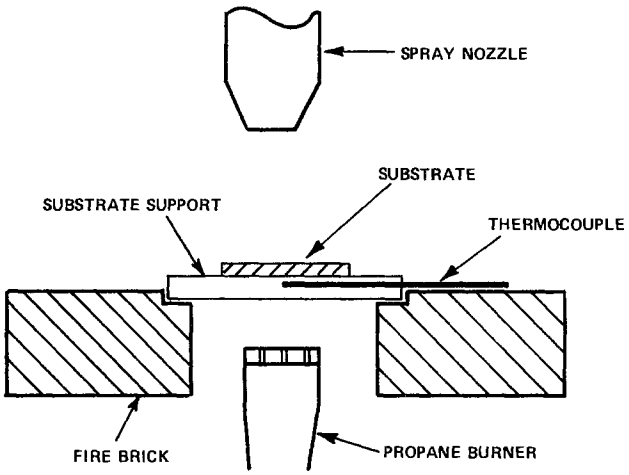


Fig. 1. Principal arrangement of spray equipment

inside the carbon plate and is monitored with a strip chart recorder. All "substrate" temperatures reported in this paper refer to the readings of this thermocouple; the actual substrate surface temperatures are lower than the values quoted here.

Critical parameters for the spray deposition of cadmium stannate are substrate temperature, composition of the spray solution, rate of deposition, and the spray characteristics, *i.e.*, size, velocity, and distribution of the droplets. The substrate temperature is important for two reasons. If it is too low (<400°-500°C) translucent or opaque coatings result. The optical transparency improves with increasing temperature but depending on the temperature range either one of the two cadmium stannate phases or mixtures of both develop. At high temperatures (>800°C) the Cd_2SnO_4 phase forms while $CdSnO_3$ is observed in films deposited below 800°C. Films containing both phases frequently occur if the required deposition conditions are not maintained. The composition of the films was determined by x-ray diffraction analysis (7).

Rate of deposition and composition of the spray solution are to a certain degree interdependent. The determining factor is the cadmium/tin ratio in the solution. For example, $CdSnO_3$ films with a sheet resistance $R_s \sim 20\ \Omega/\square$ can be prepared within 1.5 min when the Cd/Sn weight ratio is 5:1. It takes 5 min at a reduced spray rate to achieve the same R_s when the spray solution contains cadmium and tin in a 20:1 weight ratio. The higher Cd/Sn ratio has given better reproducibility of the electrical and optical film properties but for economic reasons the 5:1 ratio, requiring shorter deposition time, is preferable. Formation of either cadmium stannate phase becomes difficult when the Cd/Sn ratio drops below 5:1. Evidence also suggests that during prolonged spraying the electrical conductivity of the initial cadmium stannate layers deteriorates. It appears that this effect is caused by long exposure of the films to high temperatures. As a matter of fact the lowest R_s is obtained by fast deposition and immediate quenching of the sample.

A large number of cadmium and tin compounds and different solvents were investigated as components of the spray solution but none equaled aqueous solutions of $CdCl_2$ and $SnCl_4$. The influence of additives was also studied and hydrochloric acid was found to promote low sheet resistances and high transparencies. Small concentrations of indium or lead tend to improve the clarity of films of a given sheet resistance. In general, the concentration of each component in the solution can be changed within limits if other deposition parameters are adjusted accordingly. As an example the composition of a solution is given below which yields clear $CdSnO_3$ films with 10-20 $\Omega/\square$ sheet resistance at 700°-750°C substrate temperature: 100g 45.7% aqueous solution of $CdCl_2 \cdot 2.5H_2O$; 10g 35.1% aqueous solution of $SnCl_4 \cdot 5H_2O$; 3g 22.1% aqueous solution of $InCl_3$; 10g conc. HCl.

The spray characteristics are determined by the design of the spray nozzle, the oxygen gas pressure applied to operate the nozzle, and the flow rate of the metal salt solution. Conditions favoring the formation of cadmium stannate and resulting in optically clear films were found to require the smallest possible droplet size and a spray which arrives as a fine mist at the substrate. Care should be taken, however, that the spray is not heated excessively before it hits the hot substrate, otherwise the coatings are opaque. Good results were obtained with Sonicore® nozzles No. 035M-B from the Sonic Development Corporation, Upper Saddle River, New Jersey. These nozzles can be operated at low flow rates (5-130 cm^3/min) and produce droplets only a few microns in diameter.

A note of caution should be added. Although the nozzles are made of 316 stainless steel the highly acidic salt solutions cause gradual corrosion within the nozzles and a change of the spray characteristics. This change develops slowly and barely affects the film properties as long as R_s remains near 100 $\Omega/\square$ or higher. The changing spray characteristics become more critical in lower sheet resistance films and presumably are one of the causes of poor optical properties in samples with sheet resistances smaller than 10 $\Omega/\square$.

Substrate Materials

Silica appears to be a convenient substrate material for spray coating since its low coefficient of thermal expansion provides protection from thermal shocks occurring at the beginning and end of the deposition process. However, during attempts to produce Cd_2SnO_4 or $CdSnO_3$ films on silica with sheet resistances below ~100 $\Omega/\square$, it was observed that R_s decreased substantially less with increasing thickness t than one would have expected from $R_s \sim 1/t$. The cause of this result was traced to the formation of fine hairline cracks when the coatings exceeded a certain thickness (~0.5 μm). In most samples these cracks can be seen only with a scanning electron microscope; an example is shown in Fig. 2. This figure also demonstrates that a smooth film surface can be achieved by the spray coating technique.

Examination of the hairline crack structure revealed that they were induced by tensile stress indicating a poor match of the coefficients of thermal expansion β between the cadmium stannate and silica. Glasses with higher β's were explored and thicker films could be deposited without the formation of hairline cracks. A summary of these experiments is given in Table I. Corning 0211-type borosilicate glass appears to be the most suitable substrate material if β were the only parameter of concern. However, the low strain point (508°C) of this glass induces substrate distortions during spraying leading to unacceptable products. For this reason Corning 7059 or an equivalent glass is better suited, at least for $CdSnO_3$. The higher temperatures required for Cd_2SnO_4 restrict the choice of substrate material for this phase to alumino silicate or silica.

Electrical and Optical Film Properties

Transparent electrode applications of cadmium stannate films require optimized electrical sheet resistance

Table I. Critical film thickness resulting in hairline cracks for different substrate materials

Substrate material	Coef. thermal expansion ($°C^{-1}$)	Critical film thickness (μm)
Silica	$5 \cdot 10^{-7}$	~0.5
Aluminosilicate Corning 1720	$42 \cdot 10^{-7}$	~1.0
Borosilicate Corning 7059	$46 \cdot 10^{-7}$	1.0-2.0
Borosilicate Corning 0211	$74 \cdot 10^{-7}$	>2.0

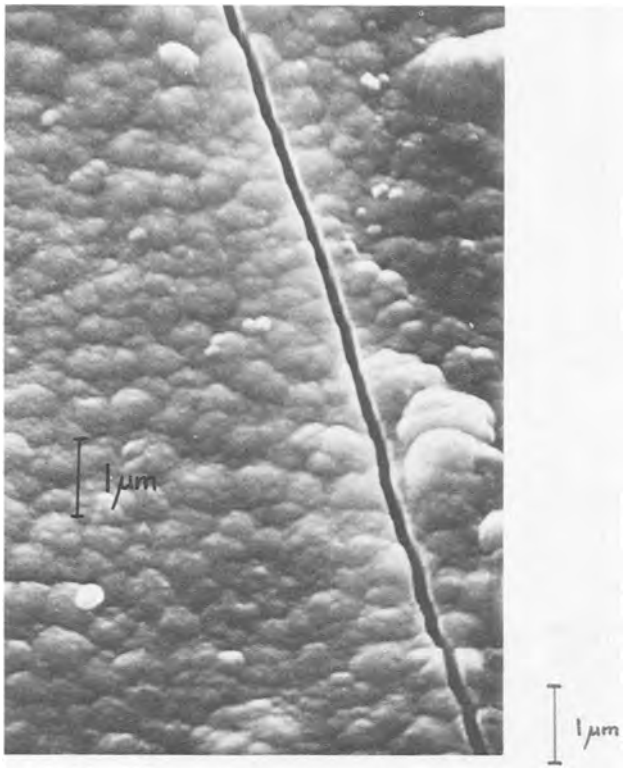


Fig. 2. Scanning electron micrograph of spray-deposited $CdSnO_3$ showing hairline crack caused by mismatch of coefficients of thermal expansion of film and substrate.

and optical transmission T. In general, R_s should be small and T should be as large as possible, but the relationships

$$R_s = 1/\sigma \cdot t$$

and

$$T = \exp(-\alpha t)$$

where σ is the electrical conductivity and α is the optical absorption coefficient, set forth that R_s and T are not independent of each other. Their common dependence on t stipulates that σ/α need to be maximized (8).

In sputter-coated Cd_2SnO_4 films electrical conductivities up to 6500 Ω^{-1} cm^{-1} have been achieved (1). The conductivities observed in spray-coated Cd_2SnO_4 do not reach these high values. Here, the best values are in the 500-1000 $\Omega^{-1}cm^{-1}$ range. Hall measurements with spray-coated Cd_2SnO_4 yielded mobilities of only 1-5 cm^2/V sec, which are approximately one order of magnitude lower than the mobilities measured in sputtered coatings (1). Presumably, the reduced mobilities are a consequence of the spray technique which creates lattice defects and grain boundary imperfections. Improvements in the deposition technique could lead to higher mobilities and consequently higher σ values. Impurities may also be present, but their influence on σ has not yet been studied sufficiently.

In view of the complications arising from the high substrate temperatures required for the formation of Cd_2SnO_4 only a limited amount of work was spent with this phase. On silica sheet resistivities of approximately 80-100 $\Omega/\square$ were achieved. Attempts to obtain lower R_s values by increasing the film thickness were only marginally successful because of developing hairline cracks (Fig. 2).

The optical properties of our spray-coated Cd_2SnO_4 are best characterized by Fig. 3. In this figure the transmission spectrum (measured with a CARY 14 spectrophotometer with a blank substrate in the reference beam) of a 120 $\Omega/\square$ coating is plotted. The film was sprayed onto silica at 850°C and required 10 sec

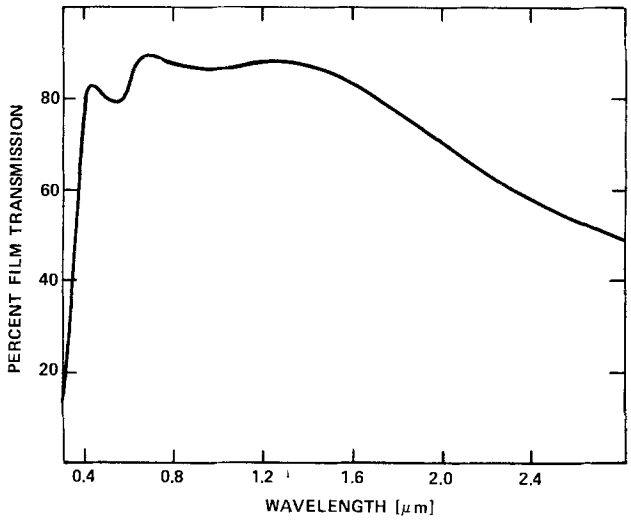


Fig. 3. Optical transmission spectrum of spray-deposited Cd_2SnO_4 film with 120 $\Omega/\square$ sheet resistance; substrate losses excluded (blank substrate in reference beam).

deposition time. It did not receive the postdeposition heat-treatment needed for sputtered Cd_2SnO_4 (1).

The lowest sheet resistivities were obtained in spray-deposited $CdSnO_3$ films. Although the conductivities in these films are approximately equal to those in Cd_2SnO_4, thicker layers could be prepared on Corning 7059 without crack formation. Hall mobilities and electron concentrations of the $CdSnO_3$ films do not differ significantly from those found in spray-coated Cd_2SnO_4, indicating that the same type of imperfections may cause the low mobilities.

Clear $CdSnO_3$ films attaining 10-20 $\Omega/\square$ sheet resistance have been spray deposited using solutions quoted above. Values as low as 3 $\Omega/\square$ were achieved with the same solutions but the optical properties of films with $R_s < 10$ $\Omega/\square$ are not yet acceptable; their transmission is less than 50% throughout the visible spectrum. Two examples of the transmission spectra of sprayed $CdSnO_3$ are presented in Fig. 4. Both films were prepared at 700°-750°C substrate temperature; the deposition time was 5 min. Again, no postdeposition heat-treatment was required. The existence of well-developed interference maxima and minima in the transmission curves is proof of a uniform film thickness.

Conclusions

We have confirmed that the spray deposition technique is suitable for the preparation of transparent

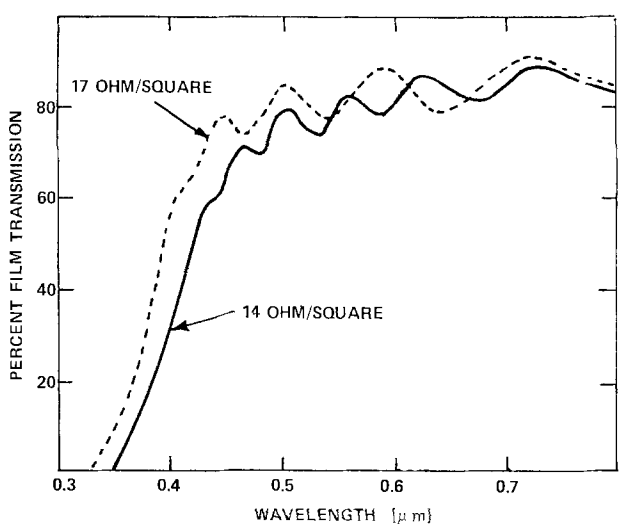


Fig. 4. Optical transmission spectrum of spray-deposited $CdSnO_3$ films; substrate losses excluded (blank substrate in reference beam).

conducting cadmium stannate films. Depending on the experimental conditions either Cd_2SnO_4 or $CdSnO_3$ can be deposited. Lowest sheet resistivities were obtained in $CdSnO_3$, and clear films with $R_s \sim$ 10-20 $\Omega/\square$ have been prepared. The feasibility of achieving sheet resistivities in the 1-10 $\Omega/\square$ range has been demonstrated but further refinements of the spray technology are needed to achieve useful optical properties. The superior transparent electrode properties of sputtered Cd_2SnO_4 films cannot yet be duplicated by spray deposition. Our investigations, however, have established that the postdeposition heat-treatment needed for sputtered Cd_2SnO_4 (6) is not an intrinsic requirement for the preparation of cadmium stannate films. Rather, the heat-treatment is specific for sputtered films to create large free electron concentrations and to reduce or remove the CdO phase which is initially present in these films.

Acknowledgments

The work reported in this paper was supported by the Air Force Materials Laboratory and the National Science Foundation (Research Applied to National Needs).

Manuscript submitted April 20, 1977; revised manuscript received June 6, 1977.

Any discussion of this paper will appear in a Discussion Section to be published in the June 1978 JOURNAL. All discussions for the June 1978 Discussion Section should be submitted by Feb. 1, 1978.

Publication costs of this article were assisted by American Cyanamid Company.

REFERENCES

1. G. Haacke, *Appl. Phys. Lett.*, **28**, 622 (1976).
2. G. Haacke, *J. Appl. Phys.*, **47**, 4086 (1976).
3. L. C. Burton, T. Hench, G. Storti, and G. Haacke, *This Journal*, **123**, 1741 (1976).
4. R. E. Aitchison, *Aust. J. Appl. Sci.*, **5**, 10 (1954).
5. R. Groth, *Phys. Status Solidi*, **14**, 69 (1966).
6. G. Haacke and L. C. Burton, Final Report NSF/RANN/SE/AER73-07957/FR/76/2.
7. L. A. Siegel, To be published.
8. G. Haacke, *Ann. Rev. Mater. Sci.*, **7**, 73 (1977).

The Ultimate By-Products of Stripping Photoresist in an Oxygen Plasma

R. F. Reichelderfer,* J. M. Welty, and J. F. Battey*

International Plasma Corporation, Hayward, California 94544

ABSTRACT

Evidence is presented that the final products of stripping an isoprene photoresist in an oxygen plasma are primarily oxides of carbon and water. The by-product gases are trapped in the exhaust of the reactor and weighed. The results are consistent with the conclusion that essentially all of the hydrogen in the photoresist becomes water and roughly half of the carbon becomes carbon dioxide. Presumably the other half becomes carbon monoxide which passed through the liquid nitrogen trap as a vapor.

The physically simplest of the plasma systems for processing silicon wafers is the stripping of photoresist with an oxygen plasma, as reported by Irving (1) and Bersin (2). The present work, as well as prior work, was undertaken in the expectation that a better understanding of this system would lead to improved reactor design and optimized operating conditions.

It has been shown (3) that the addition of both water vapor and carbon monoxide or carbon dioxide to the incoming oxygen flow reduces the photoresist stripping rate in an oxygen plasma without substantially reducing the atomic oxygen concentration. The implication is that these molecules are by-products of the stripping reaction. It has also been shown (4) that the photoresist stripping rate of a single silicon wafer is linear in atomic oxygen concentration for pressures in the order of 1 Torr and molecular oxygen conversion rates of 10% or less. The strip rates at the center of two closely spaced silicon wafers (5) suggests that about 550 CH_2 groups are stripped with the disappearance of each atomic oxygen atom. However, the fact that the ratio of the strip rates at the edge and center of closely spaced wafers varies approximately as the cube of the wafer diameter rather than the square suggests that the primary method of atomic oxygen consumption in the inter-wafer region is not linear and is probably quadratic in atomic oxygen concentration. This in turn suggests that most of the atomic oxygen is consumed by wall recombination at the wafer surface and a chemical reaction of a single oxygen atom is responsible for removing on the order of 5000 or more CH_2 groups from photoresist.

An experiment was planned wherein the exhaust gases from the stripping reaction would be trapped at liquid nitrogen temperature. It is assumed that any large molecular weight photoresist fragments would have very small vapor pressures at these temperatures and be effectively trapped. It was thought that the temperature could be raised in increments, the mass lost from the trap found by weighing, the number of molecules lost found by measuring the pressure rise in a known volume, and the molecular weight of the by-products of the stripping reaction calculated.

What in fact was found is consistent with the hypothesis that most of the hydrogen in the photoresist is turned into water and the carbon into carbon monoxide and carbon dioxide. Apparently the photoresist leaves the wafers in large molecular weight fragments which then continue to interact with the oxygen plasma until they are broken down into H_2O and CO and CO_2 by the time they get to the exhaust of the reactor.

Experimental Arrangement

A single 2 in. diameter silicon wafer was stripped of photoresist in an 8 in. diameter 13 in. long quartz reactor. The wafer was weighed before and after the application of the photoresist. The experimental arrangement is substantially the same as in (3). There was a quartz elbow about ¾ in. in diameter and about 12 in. in total length attached to the exhaust manifold through which all the exhaust gases pass. This was

* Electrochemical Society Active Member.

Key words: semiconductor processing, atomic oxidation of hydrocarbons, sequential oxidation of solid hydrocarbons.

joined by a ground-glass joint to a quartz cold finger about 1⅛ in. in diameter and 6 in. long. An inner tube in the cold finger forced the exhaust gases to flow down to the bottom of the cold finger and up the outer wall to get to the pump. The cold finger was immersed in liquid nitrogen.

After stripping was completed, the rf power and oxygen were shut off, after which the pump was shut off. Nitrogen was then slowly bled into the cold finger to a pressure of approximately an atmosphere to provide a blanket over the reaction products. With nitrogen still flowing, the ground glass joint on the pump end of the cold finger was disconnected and capped off. The ground glass joint on the reactor end was then disconnected and capped off. The cold finger was too heavy to weigh on the scales, so the cold finger was then connected to another quartz trap immersed in liquid nitrogen. The cold finger was then warmed up with a heat gun, and the trapped by-products of the stripping reaction transferred to the trap. The trap was then evacuated with the pump, shut off with a stop cock, and weighed. Since the evacuated trap had been weighed before receiving the trapped reaction by-products, their total weight can now be obtained.

At liquid nitrogen temperatures of 77°K, CO_2 and H_2O are virtually completely trapped, but CO is not trapped to any appreciable extent. A second Dewar was then filled with acetone which was chilled to a temperature of 203°K with an aluminum bar which had been immersed in liquid nitrogen. A second trap was immersed in liquid nitrogen and connected to the first trap which had been moved to the acetone bath. At 203°K the CO_2 becomes volatile and moves into the second trap. However, the water remains in the first trap. The mass of CO_2 and H_2O can now be obtained individually.

Experimental Results

The basic unit of Waycoat photoresist is isoprene or C_5H_8 which has molecular weight of 68.13.

The photoresist on the first wafer stripped had a mass of 2.0 mg which corresponds to 2.94×10^{-5} moles. If all the hydrogen is converted to water vapor 1.18×10^{-4} moles or 2.12 mg are to be expected. The actual mass trapped was 1.9 mg. If all the carbon is converted to CO_2 there should be 1.47×10^{-4} moles or 6.47 mg. The actual mass trapped was 2.5 mg.

A second wafer had a mass of 1.7 mg of photoresist. From this 1.80 mg of H_2O and 5.50 mg of CO_2 are to be expected. The actual mass trapped was 1.7 mg of H_2O and 3.9 mg of CO_2. The conclusion would seem to be that virtually all of the hydrogen is converted to water, and about half of the carbon is converted to carbon dioxide. With nothing but carbon and oxygen to work with it seems probable that the remaining carbon was present in the form of carbon monoxide which would not have been trapped.

Forty wafers were then stripped and the exhaust gases that were trapped at liquid nitrogen temperature were examined with an infrared adsorption spectrophotometer. The gases were transferred to the infrared adsorption cell at room temperature so the CO_2 would be essentially a gas whereas the water would be primarily a liquid. A colorless liquid was visible in the trap at room temperature. The spectrum of the gas showed strong, broad adsorption at 667 cm^{-1} and 2350 cm^{-1} and sharp doublets at 3600 and 3630 cm^{-1} and 3730 cm^{-1}, characteristic of CO_2.

There was no sign of the carbonyl stretch which would have been indicative of formaldehyde or formic acid.

Conclusion

In the vaporization of an isoprene (C_5H_8) photoresist with an oxygen plasma prior evidence suggests that the by-products of the reaction leave the photoresist surface in molecular weight groupings in excess of 5000. The present work shows that by the time the by-products leave the exhaust manifold the hydrogen is converted to water vapor and roughly half the carbon is present as carbon dioxide. It seems probable that the rest of the carbon escaped undetected as carbon monoxide.

Manuscript submitted March 28, 1977; revised manuscript received June 24, 1977.

Any discussion of this paper will appear in a Discussion Section to be published in the June 1978 JOURNAL. All discussions for the June 1978 Discussion Section should be submitted by Feb. 1, 1978.

Publication costs of this article were assisted by the International Plasma Corporation.

REFERENCES

1. S. M. Irving, Proceedings of the Kodak Photoresist Seminar, Vol. 2, pp. 26-29, Rochester, New York (1966).
2. R. L. Bersin, *Solid-State Technol.*, **13**, 39 (1970).
3. J. F. Battey, *This Journal*, **124**, 147 (1977).
4. J. F. Battey, *IEEE Trans. Electron Devices*, **ed-24**, 140 (1977).
5. J. F. Battey, *This Journal*, **124**, 437 (1977).

Hot-Electron Trapping in CVD PSG Films

R. A. Gdula and P. C. Li

IBM System Products Division, East Fishkill Facility, Hopewell Junction, New York 12533

ABSTRACT

Large-scale integration requires small geometry insulated-gate field effect transistors (IGFET's) with thin gate insulators. Contamination protection traditionally provided by $POCl_3$-generated phosphosilicate glass (PSG) is too difficult to control for 250Å gate insulators. A chemical vapor deposition (CVD) process capable of producing 50Å PSG layers has been developed by Li as an alternative. This paper describes the hot-electron trapping behavior of these CVD PSG/SiO_2 composites, which were found to be much superior to Si_3N_4/SiO_2 composites. The parameters of CVD PSG layer thickness, P_2O_5 concentration, and thermal anneal were evaluated. Electron trapping occurs at network imperfections inherent in CVD SiO_2 and, to a lesser degree, at sites containing phosphorus atoms. The first can be reduced by thermal annealing.

Large-scale integration (LSI) has forced silicon insulated-gate field effect transistor (IGFET) technology to provide smaller geometry devices, with a concomitant reduction in gate insulator thickness. Future devices may well employ the equivalent of only 250Å of SiO_2. Meanwhile, contamination is still a problem and

Key words: electron trapping, phosphosilicate glass, insulator, film, CVD.

protection of the gate area from intrusion by mobile impurities during processing and subsequent packaging of the chips is still necessary. Traditionally, phosphosilicate glass (PSG) passivation produced by the pyrolysis and diffusion of $POCl_3$ has been used (1-6), but the poor controllability of this process makes it unsuitable for very thin gate insulators.

A chemical vapor deposition (CVD) process to produce PSG through the reaction

$$SiBr_4 + PH_3 + O_2 \xrightarrow[N_2 \text{ carrier}]{600°\text{-}1000°C} PSG + \text{gaseous by-products} \quad [1]$$

has been developed by one of the authors (Li). This process, he has shown, controllably produces PSG layers as thin as 50Å with excellent quality (7).

With the progression towards smaller devices, hot-carrier injection was found to degrade the performance of planar transistors (8, 9) and to produce instabilities in metal oxide semiconductor field effect transistors (MOSFET's) (10-12). It has become important to understand trapping in thin-film insulators and to gauge the effects of processing on this trapping (13).

This paper characterizes the trapping of hot electrons in thin CVD PSG/SiO_2 composite dielectrics. The electrons were produced by avalanche injection of simple MOS and metal glass oxide semiconductor (MGOS) capacitors, after Nicollian and co-workers (14-17). The technique is more completely described in a previous paper (13).

Experimental Procedures

Sample preparation.—Silicon wafers (5.7 cm diam, boron doped, p-type, <100> orientation of 0.4 Ωcm resistivity) were quartered, stripped in concentrated HF, and given an inorganic cleaning (18) in hot aqueous solutions of $NH_4OH + H_2O_2$ and $HCL + H_2O_2$ finished by copious rinsing in deionized water. Films of SiO_2 were formed by thermal oxidation at 925°C in dry O_2 or in dry O_2 + 2% HCl and were well annealed in inert ambients at the same temperature; PSG films were produced by CVD at 900°C using reaction [1]. The total film thickness was ≤ 300Å in all cases. Pure aluminum was evaporated through metal masks to form capacitors whose field plates had an area of 2×10^{-3} cm^2. Aluminum was also deposited on the wafer back sides and annealed in N_2 at 400°C for 20 min to provide ohmic contacts to the silicon. Mobile charge levels were checked by the *I-V* loop technique (19) after biasing of the capacitors at $+2 \times 10^6$ V/cm, 200 C, for 10 min. Mobile charge levels, in all cases, were found to be $< 3 \times 10^{10}$ charges/cm^2. Film thickness was measured with an ellipsometer.

Trapping measurement technique.—Starting with a virgin capacitor, the high frequency (1 MHz) and low frequency (quasistatic) *C-V* characteristics were determined. Then the capacitor was avalanched by impressing a train of square positive pulses (amplitude = 25V, pulse width = 0.1 μsec). Repetition rates of 10 pulses/sec increasing to 1×10^6 pulses/sec were used to control the quantity of injected electrons during any avalanching period. With a measuring circuit similar to that in Ref. (17), the number of electrons flowing through the sample was counted on a coulometer. The sample was reconnected to the *C-V* measuring apparatus, and the high frequency *C-V* characteristics was retraced. A measure of the number of electrons trapped in the insulator was inferred from the shift, ΔV, between the high frequency *C-V* traces measured at midgap. The entire process was then repeated over and over for ever-increasing numbers of injected electrons. All measurements were made with the sample in darkness. Typical results for undoped SiO_2 films are described in a previous paper (13).

Results and Discussion

Preliminary evaluation.—Composite films consisting of 50Å of 4 mole percent (m/o) P_2O_5 CVD PSG over 200Å of thermal SiO_2 were prepared and annealed at 1000°C for 10 min in argon. The trapping behavior of such a film is compared in Fig. 1 with that of 250Å thermal SiO_2 and of a composite of 100Å of Si_3N_4 over 200Å of thermal SiO_2. It is seen that the CVD PSG/SiO_2 composite film traps far fewer of the injected electrons than the Si_3N_4/SiO_2 composite film, but still somewhat more than straight thermal SiO_2. If a hot electron shift, ΔV, of 100 mV end of life is allowed, the nitride/oxide composite will have reached that point after only 2.5×10^{12} e/cm^2 have been injected, or 480 times sooner than the CVD PSG/SiO_2, which required 1.2×10^{15} e/cm^2 injected to shift 100 mV.

Effect of PSG layer thickness.—Since previous work had shown that hot-electron trapping in thermal SiO_2 decreased drastically as the film thickness decreased below 250Å (Fig. 2), for such structures as 100Å CVD PSG over 100Å of thermal SiO_2 we expected the trapping to be dominated by the PSG layer. Figure 3 quite vividly shows this to be true. The as-deposited composite shifts ~100 times more, and the annealed composite ~10 times more than the thermal SiO_2 film, even though they are only about twice as thick. In Fig. 4, the trapping contribution of the underlying 100Å of SiO_2 is subtracted from the curve of the annealed composite, showing that almost all the trapping is in the PSG layer.

Utilizing this fact that for thin composites the PSG layer dominates the trapping behavior, we constructed a series of samples, varying the PSG thickness from

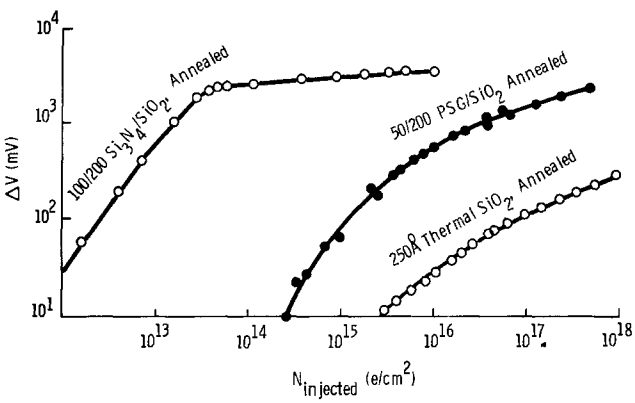


Fig. 1. Electron trapping in CVD PSG/SiO_2 compared with Si_3N_4/SiO_2 and thermal SiO_2 of equivalent thickness. The lateral shift, ΔV, of the high frequency *C-V* curve (measured at midgap) is a function of the number of electrons trapped in the insulator films.

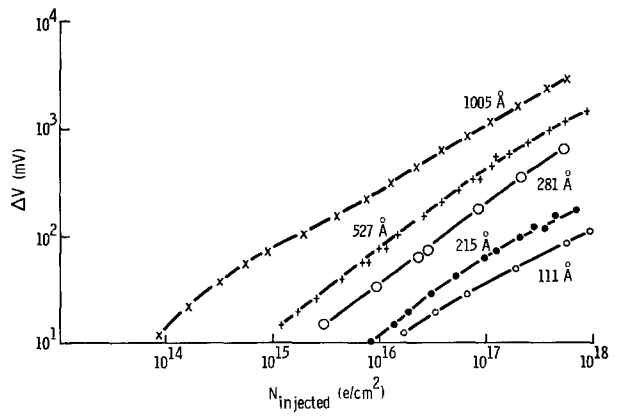


Fig. 2. Thermal SiO_2 grown on 0.4 Ωcm ρ <100> Si

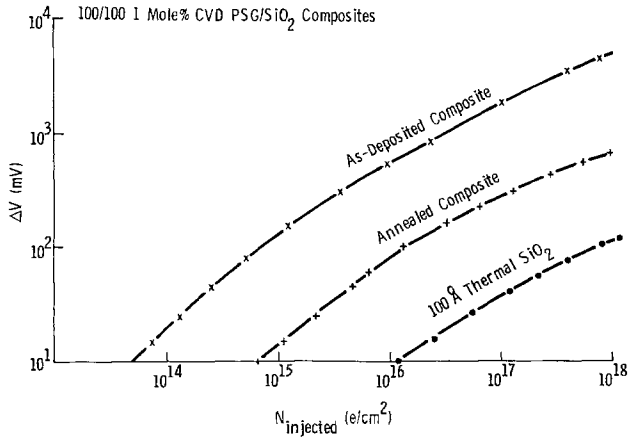


Fig. 3. Electron trapping in a 1 m/o P_2O_5: 100 CVD PSG/100 SiO_2 (nominal) composite compared with 100Å of thermal SiO_2.

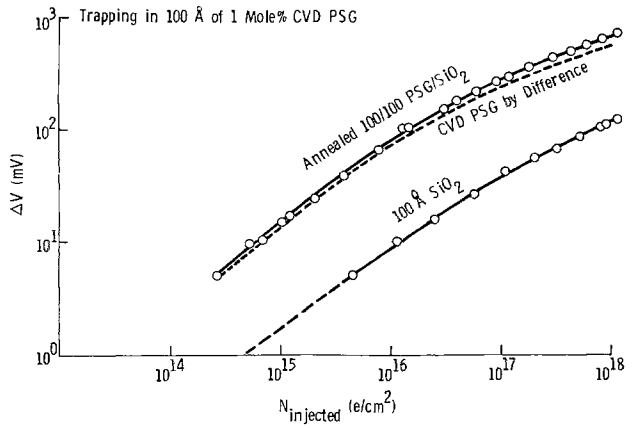


Fig. 4. Electron trapping for 100Å CVD PSG by difference. This clearly shows that the trapping is dominated by the PSG layer.

~50 to ~200Å with total composite thickness = 250Å. The P_2O_5 concentration was ~4 m/o, and all samples were annealed after CVD for 10 min at 1000°C in argon. Their virgin C-V properties are presented in Table I. Their trapping behavior is shown in Fig. 5, where it is seen that the C-V shift caused by captured electrons is roughly proportional to the PSG layer

Table I. C-V data of virgin capacitors

Sample	Average V_{FB} (V)	Average N_{FS} at midgap (states/cm² eV)	Experiment
250Å control SiO_2	−0.76	1.2×10^{10}	Trapping as a function of CVD thickness
50/200 composites	−0.99	2.9×10^{10}	
100/150 composites	−1.23	5.6×10^{10}	
150/100 composites	−1.46	7.3×10^{10}	
200/50 composites	−1.77	9.0×10^{10}	
150Å control SiO_2	−0.79	1.5×10^{10}	Trapping as a function of P_2O_5 concentration in CVD layer
0 m/o P_2O_5	−0.93	6.5×10^{10}	
1 m/o P_2O_5	−1.11	5.0×10^{10}	
4 m/o P_2O_5	−1.18	5.0×10^{10}	
10 m/o P_2O_5	−1.28	2.4×10^{10}	
180Å control SiO_2	−0.95	8.0×10^{10}	Trapping as a function of annealing for 15 min at temperature
As deposited	−1.32	4.2×10^{10}	
Annealed 900°C	−1.21	2.9×10^{10}	
Annealed 1000°C	−1.03	2.2×10^{10}	
Annealed 1050°C	−1.05	3.2×10^{10}	
Annealed 1100°C	*	*	
180Å control SiO_2	−0.95	8.0×10^{10}	Trapping as a function of anneal time at 1000°C
As deposited	−1.32	4.2×10^{10}	
Annealed 15 min	−1.03	2.2×10^{10}	
Annealed 30 min	−1.05	2.2×10^{10}	
Annealed 60 min	−1.13	6.0×10^{10}	
Annealed 120 min	−1.41	14.1×10^{10}	
Annealed 240 min	*	*	
Annealed 480 min	*	*	

* Silicon became n-type because of diffusion of phosphorus from PSG. No measurements were taken on these samples.

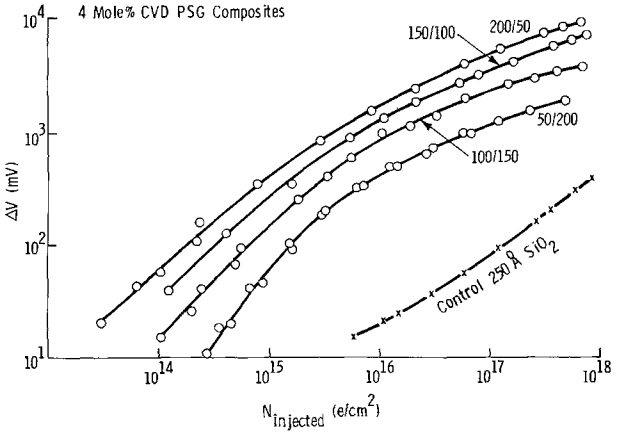


Fig. 5. Electron trapping in 4 m/o P_2O_5 × CVD PSG/250 × SiO_2 (nominal).

thickness. This is the behavior that would be expected if most of the electrons were trapped uniformly throughout the PSG layer thickness.

Effect of P_2O_5 concentration.—Composite films with a nominal 100Å of CVD PSG over 150Å of thermal SiO_2 were constructed with P_2O_5 concentrations of 0, 1, 4, and 10 m/o. We annealed these samples for 10 min at 1000°C in argon. Their virgin C-V properties are given in Table I. Since the PSG layer thicknesses of these samples varied from 80 to 168Å, their trapping behavior could not be compared directly on the basis of C-V shifts. The data were normalized for comparison by assuming that all the electrons were trapped uniformly throughout the volume of the CVD layer, and the number of electrons trapped, $N_{trapped}$, was calculated from the equation

$$N_{trapped} = \frac{\Delta V \epsilon_0 \epsilon_{ox}}{\bar{x} q} \quad [2]$$

where ΔV is the lateral C-V shift measured at midgap and referenced to the virgin C-V curve, ϵ_0 is the permittivity of free space = 8.85×10^{-14} f/cm, ϵ_{ox} is the dielectric constant of SiO_2 = 3.85, $\bar{x}$ is the centroid of the trapped charge = CVD layer thickness/2, and q is the charge on the electron = 1.6×10^{-19} coulombs. The thus normalized trapping curves are presented in Fig. 6. From this it is seen that, after about 5×10^{15} e/cm² are injected, the trapping does depend somewhat on the P_2O_5 concentration, but the 10 m/o film does not trap 10 times the number of electrons that the 1 m/o film traps. Curve 5 is calculated from

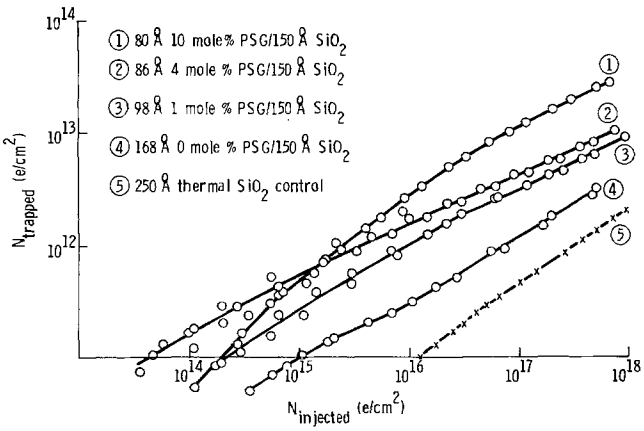


Fig. 6. Electron trapping in annealed CVD PSG layers as a function of P_2O_5 concentration. $N_{trapped}$ was calculated from the C-V shifts, assuming all electrons were uniformly trapped throughout the CVD layer.

the raw data of a 250Å thermal SiO_2 sample, with the assumptions outlined above. In the early parts of the curves, their positions bear no relation to P_2O_5 concentrations, as the behavior is dominated by large traps which are remnant from the deposition and unrelated to phosphorus.

Effect of thermal anneal.—In the preliminary experiments, electron trapping in CVD PSG films decreased substantially after a short anneal at 1000°C (Fig. 3). Two experiments were designed to gauge the effectiveness of annealing for reducing electron trapping in CVD PSG films. A set of samples of 4 m/o P_2O_5 120Å (nominal) PSG over 180Å of thermal SiO_2 was produced. In the first experiment, part of these samples were annealed at 1000°C in argon for times of 15-480 min. In the second, the remainder of the samples were annealed for 15 min at 900°, 1000°, 1050°, and 1100°C. The *C-V* data of these samples are given in Table I; the electron trapping behavior is presented in Fig. 7 and 8 and compared with a typical 250Å film of thermal SiO_2. Because of differences in the PSG layer thicknesses, the trapping data were normalized as described in the section on P_2O_5 concentration. In both experiments, the best results were obtained after a 15 min anneal at 1000°C. This also coincides with minimization of oxide charge and fast surface states as revealed by the *C-V* data taken prior to electron injection. At 1000°C for times longer than 15 min, V_{FB} became more negative, N_{FS} increased, and electron trapping increased. After 240 min at 1000°C, the silicon substrate was found to be n-type because of phosphorus diffusion from the PSG layer. For anneals of 120 min or less, no change in the substrate doping level was noticed from the *C-V* curves, with the boron ranging from 3 to 6 × 10^{16} atoms/cm^3 in a random fashion. For the 15 min anneals at different temperatures, the same behavior was seen, with optimum properties achieved in the 1000°C treatment. After 15 min at 1100°C, the silicon substrate was n-type. Although this investigation did not encompass all conceivable anneal conditions, it should be recognized that good results may be achieved with longer anneals at lower temperatures and with shorter anneals at higher temperatures.

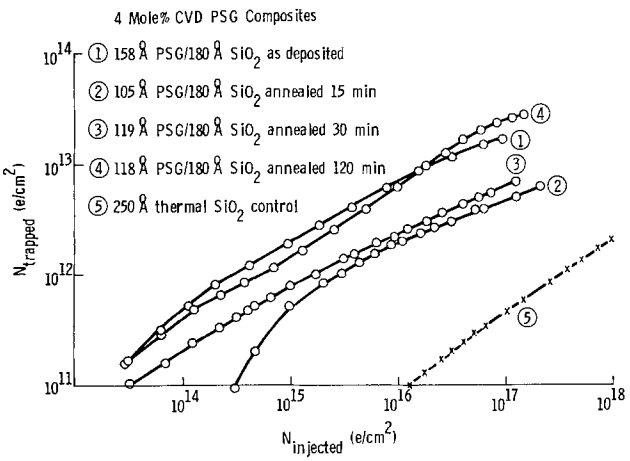


Fig. 7. Electron trapping in 4 m/o CVD PSG layers as a function of anneal at 1000°C.

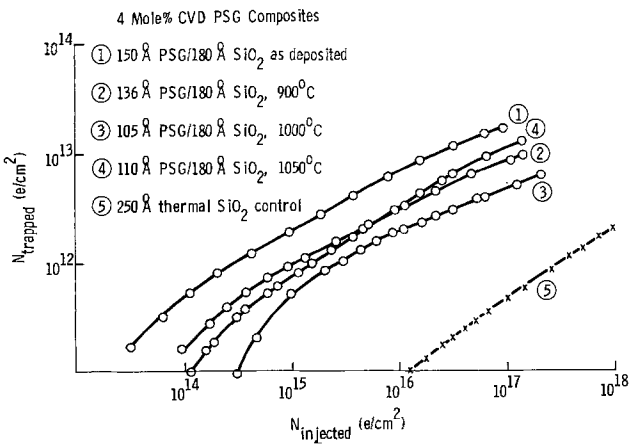


Fig. 8. Electron trapping in 4 m/o CVD PSG layers as a function of anneal for 15 min.

Conclusions

1. As a composite dielectric for small IGFET's, CVD PSG/SiO_2 is much superior to Si_3N_4/SiO_2. The latter has a severe hot electron problem because of the high trapping efficiency of the nitride layer. For an allowed end-of-life V_T shift of a hundred or so millivolts, the CVD PSG/SiO_2 composite is expected to last 250-500 times longer.

2. In CVD PSG/SiO_2 composites, the electron trapping is dominated by the CVD PSG layer. Thus, trapping is proportional to CVD PSG layer thickness.

3. In CVD PSG layers, electrons are trapped by imperfections in the Si-O network inherent in the CVD process and, to a lesser extent, at sites that contain phosphorus atoms. The inherent CVD traps are larger and can be reduced by thermal annealing, during which rearrangements of the Si-O network can occur. This reduces the incidence of unsatisfied or strained bonds. The phosphorus-related traps cannot be eliminated by annealing, and the hot electron V_T shift can even be increased if the PSG layer thickness increases markedly because of diffusion. Best results are obtained from a short anneal at 1000°C.

Manuscript submitted Feb. 22, 1977; revised manuscript received June 24, 1977. This was Paper 246 presented at the Las Vegas, Nevada, Meeting of the Society, Oct. 17-22, 1976.

Any discussion of this paper will appear in a Discussion Section to be published in the June 1978 JOURNAL. All discussions for the June 1978 Discussion Section should be submitted by Feb. 1, 1978.

Publication costs of this article were assisted by IBM Corporation.

REFERENCES

1. D. R. Kerr, J. S. Logan, P. J. Burkhardt, and W. A. Pliskin, *IBM J. Res. Dev.*, **8**, 376 (1964).
2. E. Yon, W. H. Ko, and A. B. Kuper, *IEEE Trans. Electron Devices*, **ed-13**, 276 (1966).
3. W. A. Pliskin, D. R. Kerr, and J. A. Perri, "Physics of Thin Films," Vol. 4, pp. 257-324, Academic Press, Inc., New York (1967).
4. J. M. Eldridge and D. R. Kerr, *This Journal*, **118**, 986 (1971).
5. D. V. McCaughan, R. A. Kushner, and S. Wagner, *ibid.*, **121**, 724 (1974).
6. L. H. Kaplan and M. E. Lowe, *ibid.*, **118**, 1649 (1971).
7. P. C. Li and E. Mayen, *IBM Tech. Discl. Bull.*, **19**, 11, 4155 (1977).
8. J. F. Verwey, *Appl. Phys. Lett.*, **15**, 270 (1969).
9. B. A. McDonald, *IEEE Trans. Electron Devices*, **ed-17**, 871 (1970).
10. H. Hara, Y. Okamoto, and H. Ohnuma, *Jpn. J. Appl. Phys.*, **9**, 1103 (1970).
11. C. A. Neugebauer, J. F. Burgess, R. E. Joynson, and J. L. Mundy, *Appl. Phys. Lett.*, **19**, 287 (1971).
12. S. A. Abbas and R. C. Dockerty, *ibid.*, **27**, 147 (1975).
13. R. A. Gdula, *This Journal*, **123**, 42 (1976).
14. A. Goetzberger and E. H. Nicollian, *Appl. Phys. Lett.*, **9**, 444 (1966).
15. A. Goetzberger and E. H. Nicollian, *J. Appl. Phys.*, **38**, 4582 (1967).
16. E. H. Nicollian, A. Goetzberger, and C. N. Berglund, *Appl. Phys. Lett.*, **15**, 174 (1969).
17. E. H. Nicollian and C. N. Berglund, *J. Appl. Phys.*, **41**, 3052 (1970).
18. W. Kern and D. A. Puotinen, *RCA Rev.*, **31**, 187 (1970).
19. N. J. Chou, *This Journal*, **118**, 601 (1971).

Mass Transfer, Equilibrium, and Kinetics in the Chemical Vapor Deposition of Boron from Impinging Jets

L. Vandenbulcke and G. Vuillard

Centre de Recherches sur la Chimie de la Combustion et des Hautes Températures et Faculté des Sciences d'Orléans, 45045 Orléans Cedex, France

ABSTRACT

The deposition mechanisms of boron from boron trichloride and hydrogen vapors are investigated by a stagnation flow technique. The characteristics of gas flow are first deduced from experimental deposition rates. Then, using the Stefan-Maxwell equations for diffusion, the interfacial conditions of deposition, equilibrium, or supersaturation are inferred from experimental rates of deposition in the stagnation zone. Three mechanisms of deposition are deduced, mass transfer-interfacial equilibrium, mass-transfer-surface kinetics, and surface kinetics. They occur as a function of three experimental parameters; temperature, mass flow rate, and inlet composition BCl_3/H_2. A correlation for mass transfer in impinging jets is obtained.

The deposition of boron from boron trichloride and hydrogen vapors is a complex process which has been studied in detail (1-4), but which is still a matter of controversy (4). The reaction is heterogeneous and the deposition rate likely to be limited by the surface reactions or diffusion, or by a combination of these two steps. The relative importance of kinetics and diffusion factors were studied in the case of a flow perpendicular to a horizontal or vertical filament (1-2), and in the case of a flow parallel to a horizontal (1) or vertical (4) one.

Gruber (1) and Mehalso and Diefendorf (4) have neglected the production of the intermediate $HBCl_2$ which is detected in significant proportions in boron filament production (5) and in the gas phase at equilibrium (2). They compute the rate of mass transport, assuming thermodynamic equilibrium between boron and the gas phase calculated from the inlet $BCl_3 + H_2$ composition. The work of Carlton *et al.* (2) is based on a description of fluxes and concentrations of all the principal components (BCl_3, H_2, HCl, and $HBCl_2$). The deposition rate is shown to be governed by a combination of diffusion and kinetics considerations.

In the present work we confirm that the mechanism of Carlton *et al.* well describes the system in various experimental conditions, especially when the vapor phase is supersaturated. In addition to this mass transfer-kinetics mechanism, two others, mass transfer-equilibrium and surface kinetics, independent of mass transfer, arise. The three models are found to represent most accurately all possible experimental conditions. These deposition mechanisms were studied by a stagnation flow technique where the reactive BCl_3/H_2 mixture streamed through a cylindrical nozzle and was blown perpendicularly onto a cylindrical disk.

Experimental Techniques

The deposition equipment and experimental procedure have been described elsewhere (6). The deposition cell is represented schematically in Fig. 1. The stream of reactants is introduced in a 0.8 cm diam cylindrical nozzle normal to the substrate. The substrate is a disk of 1-3 cm diam, 0.2-1 cm thick. It is heated by a high frequency generator regulated by a thermocouple fitted at 0.05 cm under the surface to be coated.

In all experiments the pressure was equal to 1 atm, the temperature was varied from 1050° to 1250°C, and the BCl_3/H_2 flow rate ratio ranged from 5/95 to 70/30. The reactants mass flow rate was varied from 0.02 to 0.44 g/cm²/sec. The deposit thickness was measured with a microscope on polished transverse cross sections of the substrate, and deposition rate was deduced from experiments at 5 or 6 different deposition times.

Key words: gas flow, interface, diffusion, boundary layer, deposition mechanisms.

Characteristics of Gas Flow

Heat and mass transfer between an impinging axisymmetric turbulent jet and a flat surface have been studied by many authors. In the laminar case which is encountered in CVD, studies are more limited. Therefore, it is necessary to study directly or indirectly the characteristics of gas flow.

Deposit thickness profiles.—Figure 2 shows the thickness of boron deposits as a function of the radial distance on the substrate with varying mass flow rates of reactants. The thickness is constant in the stagnation zone and presents a bell shape for greater radial distances than the radius of the nozzle. This profile is characteristic of a deposition rate limited in part at least by diffusion, and this is confirmed by the influence of the mass flow rate on the deposition rate in the stagnation zone. The deposition rate in the stagnation zone appears as a parameter which makes deduction of the principal characteristics of gas flow in the jet possible.

Influence of natural convection.—In chemical vapor deposition, temperature and concentration gradients near the substrate introduce a secondary flow which is eventually not negligible as compared with the forced flow in the jet. The influence of free convection

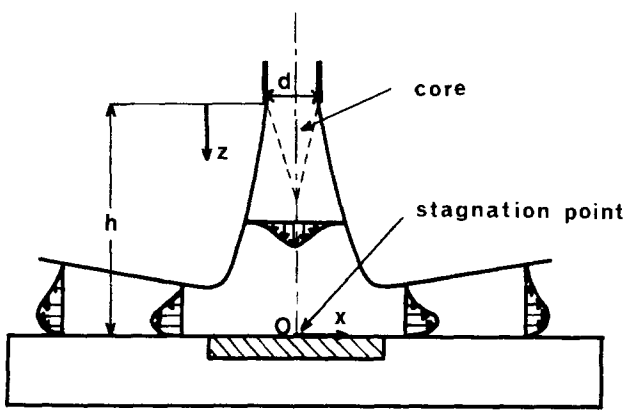


Fig. 1. Axisymmetric jet impinging on a flat plate

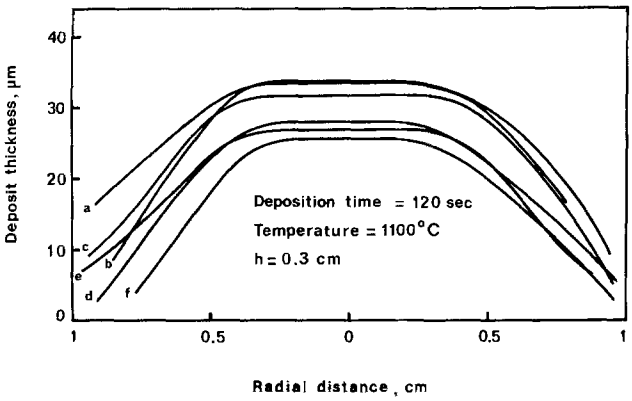


Fig. 2. Deposit thickness profile as a function of mass flow rate: a = 0.214, b = 0.178, c = 0.143, d = 0.119, e = 0.095, f = 0.071 g/cm²/sec; BCl_3/H_2 = 2/3.

depends on the ratio N_{Gr}/N_{Re}^2 (7-8) and the angle α between the directions of the forced flow and the buoyancy force (9). Free convection increases the transfer in assisting flow ($\alpha = 0°$). In opposing flow ($\alpha = 180°$), the buoyancy forces initially decrease the transfer below the corresponding forced-flow values. At low values of N_{Re}, the transfer tends to its purely free convective value. It passes through a minimum and then rises above the forced-flow values. In normal flow ($\alpha = 90°$), free convection increases the transfer but only when N_{Re} is very low (high values of N_{Gr}/N_{Re}^2). Therefore, the influence of free convection is often negligible with this geometry.

In our study, the effect of free convection is limited to the influence on transfer in the stagnation zone, 0.8-1 cm diam. Figure 3 presents the influence of the mass flow rate of reagents on the deposition rate for $\alpha = 90°$ (horizontal jet) and $\alpha = 180°$ (vertical downward jet). For mass flow rates greater than 0.05 g/cm²/sec, there is no significant difference with orientation of the reactor. For mass flow rates lower than 0.05 g/cm²/sec, the deposition rate decreases in the case of opposing flow. Calculation stated later shows that this limit corresponds to a ratio $N_{Gr}/N_{Re}^2 \simeq 0.1$. Because of the change in gas density in the film, due to both temperature gradient and composition changes induced by reaction, N_{Gr} was calculated to account for both temperature and composition gradients in the system. With constant mass flow rates, the influence of natural convection has been studied as a function of inlet compositions. N_{Gr} varies from 150 to 5500 when the inlet mole fraction of BCl_3 increases from 0.1 to 0.7.

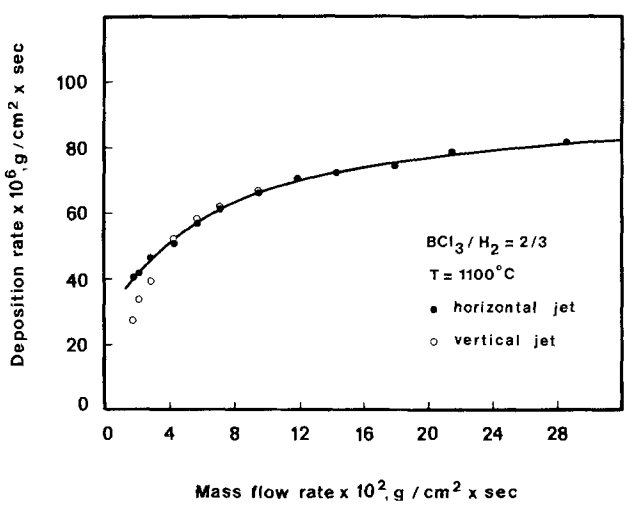


Fig. 3. Deposition rate as a function of reactants mass flow rates.

For a mass flow rate of 0.07 g/cm²/sec, the ratio N_{Gr}/N_{Re}^2 increases from 0.004 to 0.16. Orientation of the reactor is sensitive for $N_{Gr}/N_{Re}^2 > 0.08$. For a mass flow rate of 0.021 g/cm²/sec, orientation of the reactor is insensitive (N_{Gr}/N_{Re}^2 is always lower than 0.02). Then, natural convection can be neglected when $N_{Gr}/N_{Re}^2 < 0.1$. According to Oosthuizen and Madan (9), this value of 0.1 involves a decrease of 10% of the heat transfer, in the case of forced opposing flow of air on a cylinder compared with the pure forced case. In the normal flow case, they show that natural convection is negligible for $N_{Gr}/N_{Re}^2 < 0.53$. In our experiments, this value is never reached. Also we consider that natural convection is always negligible in the horizontal case. This assumption is confirmed by the following studies.

Influence of the distance h between the nozzle and the substrate.—Figure 4 presents the influence of h on the deposit thickness in the stagnation zone ($N_{Re} \simeq 180$). Mass transfer remains constant when h is lower than a critical value $h_c = 4$ (h is always greater than 0.2 to avoid the case of high mass transfer in a "wall jet" in which the opening between the plate and nozzle is smaller than the aperture of the nozzle). Figure 5 shows that h_c is a function of N_{Re} (experiments were performed in horizontal position for mass

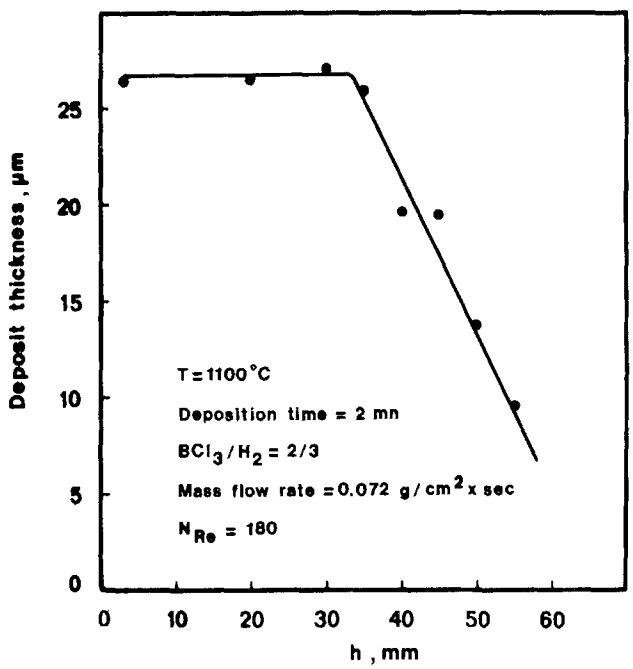


Fig. 4. Deposit thickness as a function of h

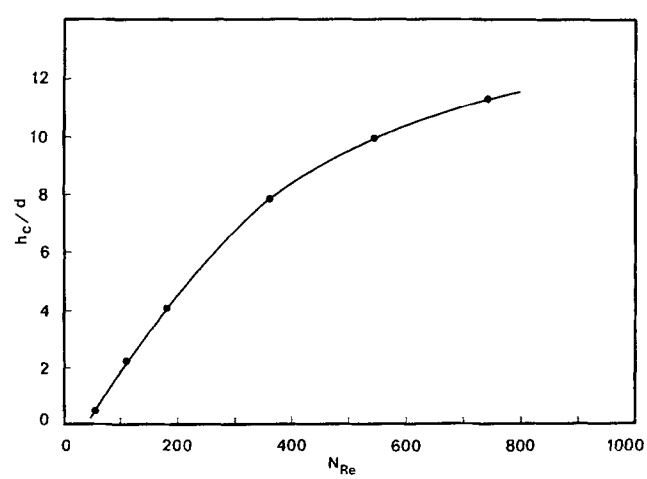


Fig. 5. Variation of potential core length with N_{Re}

flow rates lower than 0.05 g/cm²/sec). This figure leads us to conclude that for $N_{Re} \geq 50$, experiments can always be performed with a substrate placed in the core of the jet where mass transfer is independent of the distance h. The study of the influence of h on the deposit thickness in the stagnation zone is limited to values of $N_{Re} < 740$ because the limit of h in our reactor is 10 cm. Hrycak *et al.* (10) have studied the variation of the potential core length for $N_{Re} \geq 620$. This length reaches a maximum at a value of about 1200. For values greater than 2000, the dimensionless potential core length is $h_c/d \simeq 6$.

Influence of the substrate diameter d_o.—With a vertical reactor, the substrate diameter has no influence on the deposition rate in the stagnation zone when $N_{Gr}/N_{Re}^2 < 0.1$ and $h < h_c$. For $N_{Gr}/N_{Re}^2 = 0.1$, the potential core length decreases when the substrate diameter is greater than 2 cm. In the horizontal case, there is no influence when $N_{Gr}/N_{Re}^2 < 0.5$. Out of the stagnation zone, mass transfer increases logically in the upper part of the substrate.

All the above results permit us to conclude that in the range $50 < N_{Re} < 1000$ and appropriate experimental conditions (substrate placed in the core of the jet; $h > 0.2$ cm; $\alpha = 90°$ when mass flow rate is low), the mass transfer in the stagnation zone is independent of natural convection. It should be essentially studied as a function of forced flow. Thus the stagnation flow technique is of particular technical and theoretical interest.

Physicochemical Mechanisms of Deposition

Theoretical analysis and calculation.—Thermodynamical studies of the B-H-Cl system were used by Carlton *et al.* (2) to postulate a kinetic model taking into account the intermediate species $HBCl_2$. Table I gives the equilibrium composition obtained with more recent thermodynamical data for $HBCl_2$ (11) from a stoichiometric mixture of $BCl_3 + H_2$. These results confirm that $HBCl_2$ is the only important intermediate species at equilibrium. $HBCl_2$ is also a product of boron filament production (5) in conditions clearly out of equilibrium. Therefore, without any hypothesis on the interfacial conditions, equilibrium between boron and the vapor phase or supersaturation of the vapor phase, the deposition process is assumed to proceed as follows: (*i*) BCl_3 and H_2 diffuse to the deposition surface; (*ii*) BCl_3 and H_2 react, depositing boron and releasing $HBCl_2$ and HCl; and (*iii*) $HBCl_2$ and HCl diffuse away from the surface. Reactants and products diffuse through a boundary layer of thickness δ (Fig. 6). The Stefan-Maxwell equations are generally used for diffusion of ideal gases. For a 4 component mixture, there are 3 equations of the form

$$\frac{dX_1}{dz} = -(J_1X_2 - J_2X_1)\frac{RT}{PD_{12}} - (J_1X_3 - J_3X_1)\frac{RT}{PD_{13}} - (J_1X_4 - J_4X_1)\frac{RT}{PD_{14}}$$

Table I. Vapor phase equilibrium composition ($BCl_3/H_2 = 2/3$, $P = 1$ atm)

	1000°C	1100°C	1200°C
H_2	4.735E-1	4.470E-1	4.207E-1
BCl_3	2.958E-1	2.773E-1	2.591E-1
HCl	1.712E-1	2.139E-1	2.569E-1
$HBCl_2$	5.943E-2	6.146E-2	6.236E-2
BCl_2	9.039E-5	3.000E-4	8.364E-4
BCl	2.129E-6	1.348E-5	6.575E-5
H	4.888E-7	2.218E-6	8-172E-6
Cl	1.535E-7	8.992E-7	4.132E-6
BH_2	2.952E-7	1.061E-6	3.167E-6
BH_3	5.576E-7	9.579E-7	1.497E-6
Cl_2	<E-12	1.415E-9	6.800E-9
B_2H_6	<E-12	<E-12	<E-12
$B_{10}H_{14}$	<E-12	<E-12	<E-12
BH	<E-12	<E-12	<E-12
B_2	<E-12	<E-12	<E-12

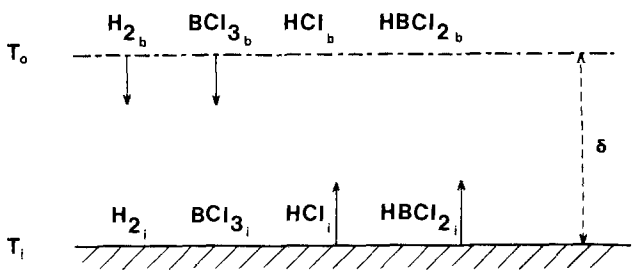


Fig. 6. Diffusion model for boron deposition

and one relationship between the 4 molar fractions

$$X_4 = 1 - X_1 - X_2 - X_3$$

The bulk stream compositions are known. They are assumed constant throughout the reactor, and are calculated from the arithmetic average of inlet and outlet compositions. On the other hand, the individual diffusion fluxes are not independent; they are related to each other by reaction stoichiometries. Finally, the interfacial composition is defined by kinetic or thermodynamical considerations. However, as pointed out by Carlton *et al.* (2), the H-B-Cl system is more complicated because at least two reactions proceed concurrently

$$2BCl_3 + 3H_2 \rightarrow 2<B> + 6HCl$$

$$BCl_3 + H_2 \rightarrow HBCl_2 + HCl$$

and there is no relationship between their rates. Therefore a trial and error method was employed to determine the value of J_{HBCl_2} which permits integration of the Stefan-Maxwell equations. The Runge-Kutta method, as modified by Gill, was selected for integrating this system of first order differential equations, and the interfacial reacting mixture at any δ was tested for kinetic or thermodynamical resistances. When a good fit was obtained, the computer program was completed by calculation of the mass transfer parameters N_{Sh}, N_{Sc}, N_{Re}, N_{Gr}.

In the case of interfacial kinetic resistance, the deposition rate, which is the difference between the diffusion rates of BCl_3 and $HBCl_2$, is calculated by the following relationship derived by Carlton *et al.* from their kinetic model

$$V = k_o \left[\frac{k'_{eq} \cdot P_{BCl_3}{}^i \cdot P_{H_2}{}^i}{P_{HCl}{}^i} - \frac{(P_{HCl}{}^i)^2}{k''_{eq} \cdot P_{H_2}{}^i} \right] \Big/ (1 + k_{HCl} \cdot P_{HCl}{}^i)$$

where k_o, k_{HCl}, k'_{eq}, k''_{eq} are exponential functions of reciprocal temperature. This kinetic model assumes that $HBCl_2$ is in equilibrium in the vapor phase. The value of k''_{eq} is the equilibrium constant for the reaction

$$BCl_3 + H_2 \leftrightarrows HBCl_2 + HCl$$

For consistency, we used the value of k''_{eq} from the Carlton *et al.* work which is slightly different from the actual value cited in Ref. (11).

In the case of interfacial thermodynamic resistance the deposition rate is calculated as the difference between the diffusion rates of BCl_3 and $HBCl_2$. The following reactions are in equilibrium

$$BCl_3 + H_2 \leftrightarrows HBCl_2 + HCl$$

$$2BCl_3 + 3H_2 \leftrightarrows 2<B> + 6HCl$$

The values of the equilibrium constants have been calculated from data of Ref. (11).

All the calculations depend on the values of the physical parameters. Some of them, the binary diffusion coefficients, are independent of composition. Physical film properties, the average diffusivity, and

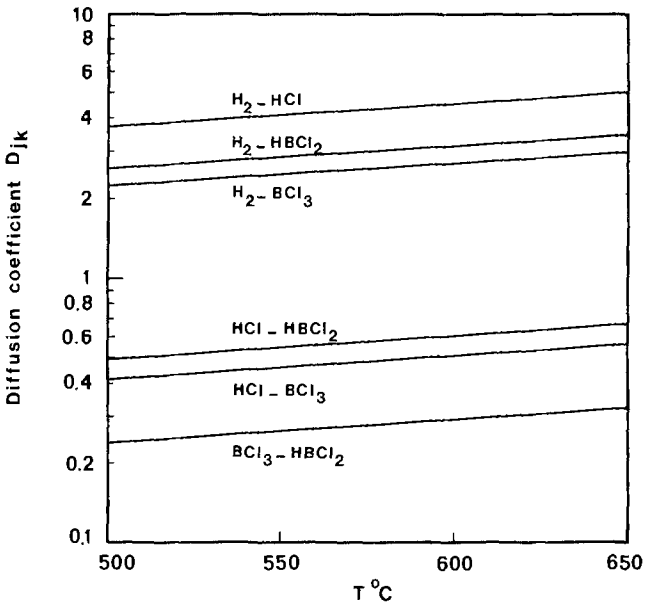


Fig. 7. Binary diffusion coefficients

the mixture viscosity were calculated from the arithmetic average composition and temperature of the bulk stream and the interface. The binary diffusion coefficients were calculated from the force constants given by Hirshfelder *et al.* (12) and Reid and Sherwood (13) by the method recommended by these authors. In Fig. 7 the coefficient values are presented as a function of temperature. The diffusivity of the mixture was obtained from the following definition successfully tested for quaternary transport data (14)

$$D_f = \frac{\Pi_j(1 - w_j)}{\sum_{j \neq k} \frac{w_j w_k}{D_{jk}}}$$

Viscosities of the pure gases were calculated by the procedure recommended by Reid and Sherwood (13). Viscosity of the film mixture was estimated from those of the pure components by the method of Bromley and Wilke (15).

Experimental results.—The boron deposit thickness in the stagnation zone is measured on transverse cross sections. These measurements are limited to smooth amorphous or slightly crystallized deposits, except in the case of tetragonal boron. In the other cases, the deposit becomes too irregular to get a correct thickness. Deposition rate is directly proportional to the reaction time. It is measured as the slope of the straight line [thickness = f (reaction time)] obtained from 5 or 6 different times.

Figure 8 shows the influence of mass flow rate on deposition rate at four temperatures and a constant inlet composition. Figure 9 shows the influence of inlet composition at 1100°C and two mass flow rates. The maximum efficiency is obtained for 15% BCl_3-85% H_2.

Calculation results and discussion.—Nondimensional parameters for heat or mass transfer in impinging jets are correlated by relationships where N_{Pr} and N_{Sc} occur with a power of 1/3 normal strength. We have therefore looked for a correlation of the form

$$N_{Sh}/N_{Sc}^{1/3} = f(N_{Re})^n$$

which implies that mass transfer is equal to its purely forced flow values, as justified in the precedent section.

Figure 10 presents the results obtained when the deposition rate is assumed to be limited by a combination of mass transfer and surface kinetics. The results are correlated as follows

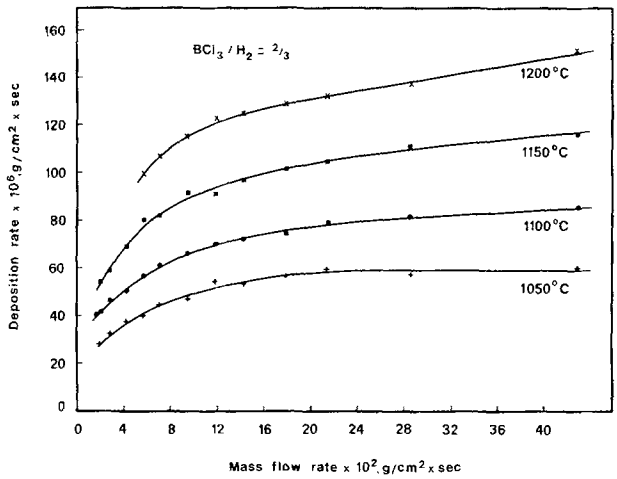


Fig. 8. Experimental deposition rate as a function of reactants mass flow rates.

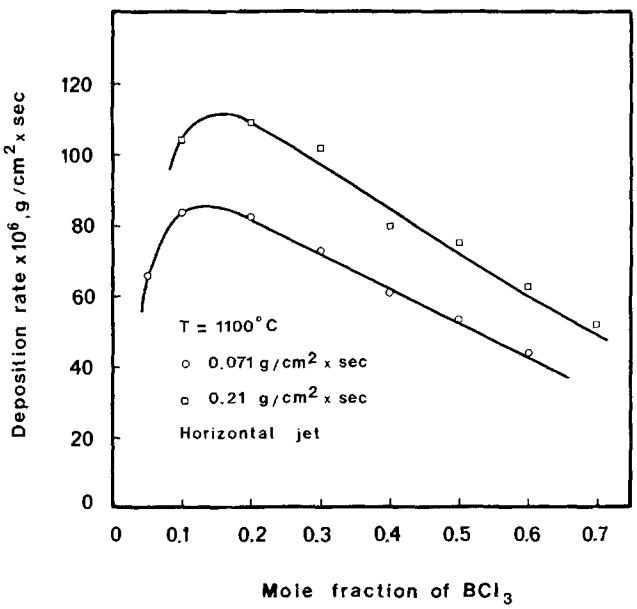


Fig. 9. Experimental deposition rate as a function of inlet gas composition.

$$N_{Sh}/N_{Sc}^{1/3} = 0.76\, N_{Re}^{0.43}$$

with a maximum deviation of about 15%. The mass transfer coefficient is lower than those derived by Coeuret (16) in the case of submerged liquid jets impinging on a flat plate ($N_{Sh_z}/N_{Sc}^{1/3} = 0.69\ N_{Re_z}^{0.5}$). The value 0.43 is greater than those obtained by Gardon and Akfirat (17) for heat transfer at low N_{Re} (<2000) in an impinging two-dimensional air jet [$N_{Nu} = f\ (N_{Re})^{0.32}$].

Figure 11 presents results calculated with a deposition rate limited by a combination of mass transfer and interfacial equilibrium with a constant inlet composition. We can show that this mechanism does not give a unique correlation for the mass transfer. However, at each temperature (except 1050°C), there is a critical Reynolds number $N_{Re,c}$ where the above correlation is accurately verified. We can note that for $N_{Re} < N_{Re,c}$, crystallization occurs very quickly and prevents determining correct values for the deposition rate. For $N_{Re} = N_{Re,c}$, the deposition rate is fixed at the same value by the two different deposition mechanisms involving kinetic or thermodynamic resistances at the interface. For $N_{Re} > N_{Re,c}$, mass transfers calculated with the mass transfer-equilibrium mechanism are too low because interface equilibrium is not main-

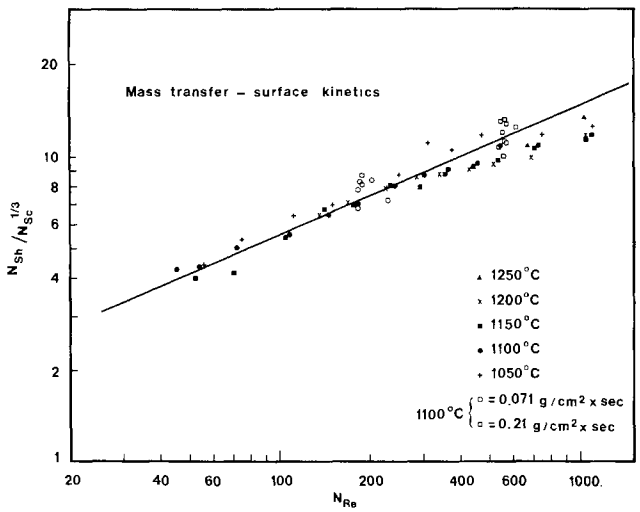


Fig. 10. Correlation of experimental results for mass transfer combined with surface kinetics.

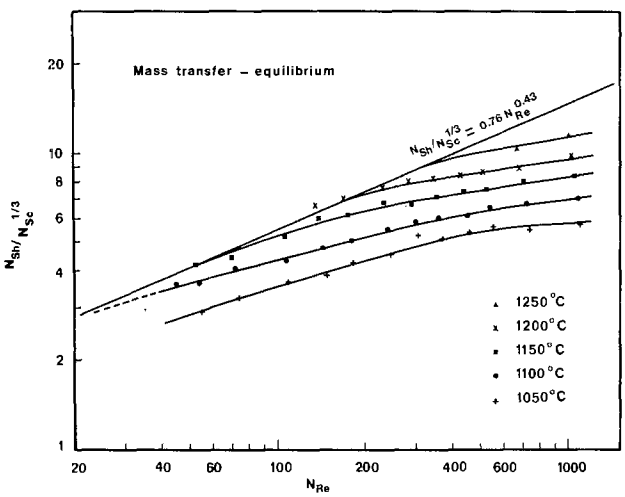


Fig. 11. Correlation of experimental results for mass transfer combined with interfacial equilibrium.

tained; hence, experimental deposition rates do not reach the maximum value for a given N_{Re}. We conclude therefore, that at low N_{Re}, the mechanism of deposition is a mass transfer-equilibrium one. In this case, the conversion of reactants to products and the deposition rate are maximum for a given mass transfer. This is a general result, and such a mass transfer-equilibrium approach can be used to calculate the maximum possible deposition rate if the mass transfer characteristics of the geometric system are known. If the equilibrium is quite favorable, one obtains the case of a total interfacial conversion of the reactants where the process is purely diffusionally controlled.

Figure 12 compares the theoretical deposition rates, calculated with this mass transfer-equilibrium approach, to the experimental ones (mass transfer is correlated by the equation $N_{Sh}/N_{Sc}^{1/3} = 0.76\ N_{Re}^{0.43}$). These curves confirm that at low N_{Re} the deposition rate reaches a maximum. Interfacial equilibrium is maintained for higher N_{Re} when temperature increases, as expected from the fact that the kinetic rate of the opposing reactions at equilibrium increases with temperature. When this rate becomes too low (N_{Re} too high), the vapor phase is supersaturated and the deposition rate is limited by a combination of mass transfer and surface kinetics.

At 1050°C the experimental rate becomes constant when $N_{Re} > 500$. The deposition rate is therefore only limited by surface kinetics, and the excess reactants

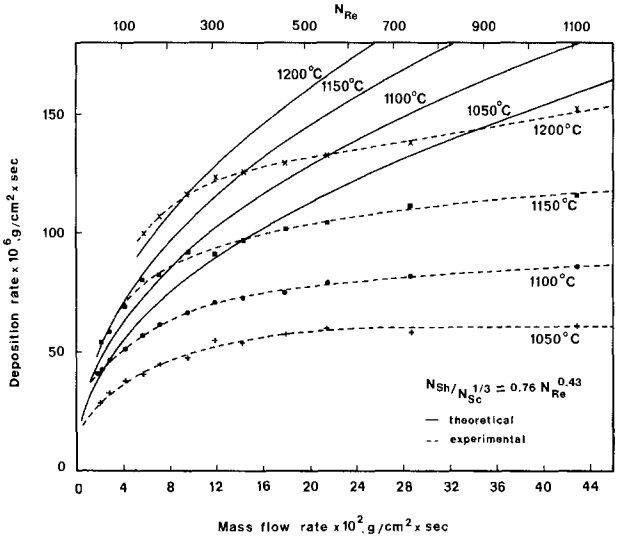


Fig. 12. Comparison between experimental and theoretical deposition rate calculated from mass transfer-interfacial equilibrium considerations.

are converted to $HBCl_2$ and HCl by the homogeneous reaction

$$BCl_3 + H_2 \leftrightarrows HBCl_2 + HCl$$

This second boundary in the deposition process is only found for $T = 1050°C$, because our experimental conditions are limited to $N_{Re} < 1000$. Figure 13 summarizes the above results and discussion, and shows the range of conditions where the different mechanisms occur.

Figure 14 presents the results calculated with a deposition rate limited by a combination of mass transfer and equilibrium as a function of the mole fraction of BCl_3 (X_{BCl_3}) in the inlet mixture. We deduce that the interfacial conditions are close to equilibrium as X_{BCl_3} increases. When $X_{BCl_3} > 0.6$, deposits are very thin and irregular, and natural convection becomes important. Tentatively, we set up Fig. 15 as a schematic representation of the influence of the inlet composition on the deposition mechanism.

Conclusions

In a jet impinging normally on a flat plate, mass transfer is nearly constant in the stagnation zone when the substrate is set within the core of the jet. The size of the potential core is essentially a function of N_{Re}. When $N_{Re} < 50$ it is reduced to zero, and mass transfer

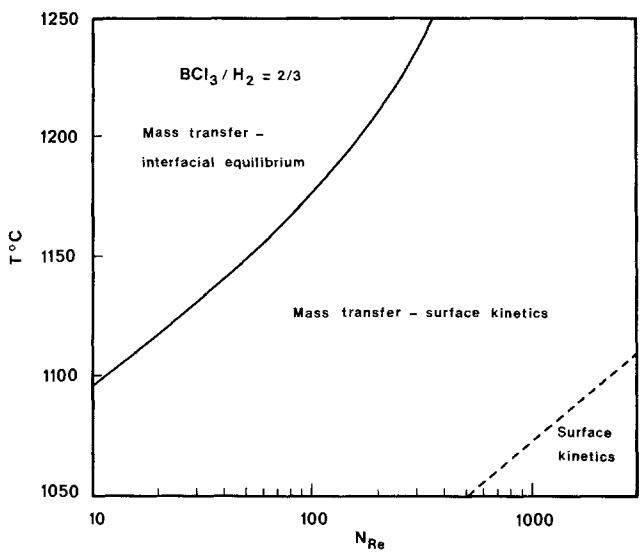


Fig. 13. Effects of T and N_{Re} on the deposition mechanism

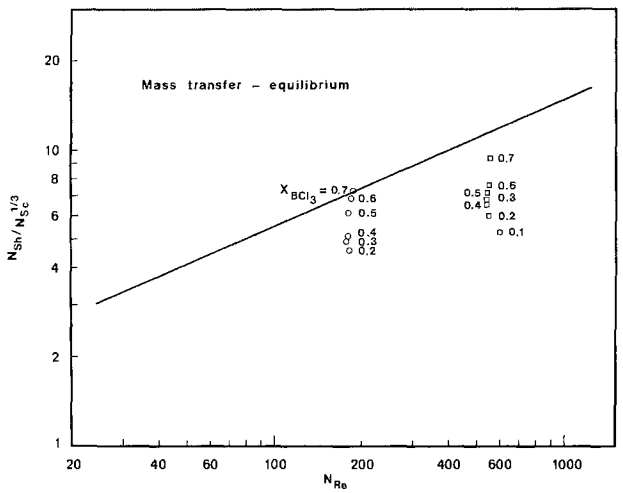


Fig. 14. Correlation of experimental results for mass transfer combined with interfacial equilibrium at various X_{BCl_3}.

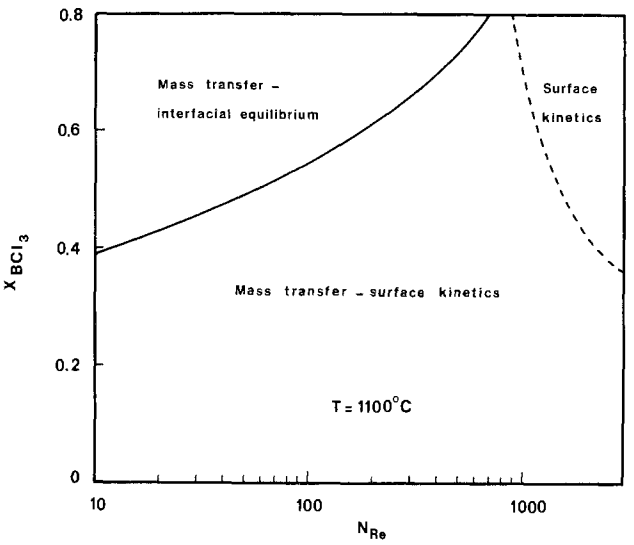


Fig. 15. Effects of X_{BCl_3} and N_{Re} on the deposition mechanism

at the stagnation point is everywhere a function of the distance between the nozzle and the substrate. In vertical downward jets, mass transfer is independent of free convection when $N_{Gr}/N_{Re}^2 < 0.1$. In the horizontal case, free convection appears always negligible when $N_{Gr}/N_{Re}^2 < 0.5$.

Over a large range of experimental conditions, the boron deposition mechanism is complex. For low N_{Re} and high temperatures, the deposition rate is limited by a mass transfer-equilibrium process. We can note that the interfacial equilibrium is influenced by diffusion. Particularly the H/Cl ratio which determines the equilibrium at given pressure and temperature is increased by diffusion as expected from the diffusivities of H_2 and BCl_3. For high N_{Re} and low temperature, the deposition rate is only limited by surface kinetics. For intermediate N_{Re}, the deposition rate is limited by a mass transfer-kinetics process. This is the case currently encountered in amorphous boron deposition. It allows us to infer a correlation for mass transfer in laminar impinging jets as follows

$$N_{Sh}/N_{Sc}^{1/3} = 0.76\, N_{Re}^{0.43}$$

The influence of inlet mixture composition is important. At constant N_{Re}, the interfacial conditions are farther from equilibrium when hydrogen inlet concentration increases. The influence of the deposition mechanism on the deposits structure is presented in the following paper.

Acknowledgments

The authors gratefully acknowledge R. Herbin for her assistance in the experimental work.

Manuscript submitted June 22, 1977; revised manuscript received July 26, 1977. This was Paper 226 presented at the Atlanta, Georgia, Meeting of the Society, Oct. 9-14, 1977.

Any discussion of this paper will appear in a Discussion Section to be published in the June 1978 JOURNAL. All discussions for the June 1978 Discussion Section should be submitted by Feb. 1, 1978.

Publication costs of this article were assisted by UER Sciences d' Orléans.

LIST OF SYMBOLS

D_{jk}	binary diffusion coefficient, cm²/sec
D_f	film diffusivity, cm²/sec
d	nozzle diameter, cm
d_o	substrate diameter, cm
F	mass flow rate, g/cm²/sec
g	gravity acceleration, cm/sec²
h	distance between nozzle and substrate, cm
J_j	molar flux of jth component, mole/cm²/sec
M	molecular weight, g/mole
N_{Gr}	Grashof number, $d^3g(\rho_f/\mu_f)^2 \cdot (\rho_b - \rho_i)/\rho_b$
N_{Nu}	Nusselt number
N_{Pr}	Prandtl number
N_{Re}	Reynolds number, dF/μ_f
N_{Re_x}	local N_{Re} (function of x)
N_{Sc}	Schmidt number, $\mu_f/\rho_f D_f$
N_{Sh}	Sherwood number [modified by (14)], $dM_b/\delta M_f$
N_{Sh_x}	local N_{Sh} (function of x)
P	total pressure, atm
P_j^i	partial pressure of jth component at interface, Torr
R	gas constant, cm³/atm/K/mole
T	temperature, °K
V	deposition rate, g/cm²/sec
w_j	weight fraction of jth component
X_j	molar fraction of jth component
x	radial coordinate
z	axial coordinate
δ	boundary layer thickness, cm
μ	gas viscosity, g/cm/sec
ρ	gas density, g/cm³
b	value in bulk stream
f	value in film
i	value at interface
j, k	value for jth and kth component

REFERENCES

1. P. E. Gruber, in "Chemical Vapor Deposition, Second International Conference," J. M. Blocher, Jr. and J. C. Withers, Editors, p. 25, The Electrochemical Society Softbound Symposium Series, New York (1970).
2. H. E. Carlton, J. H. Oxley, E. H. Hall, and J. M. Blocher, Jr., *ibid.*, p. 209.
3. P. N. Walsh, in "Chemical Vapor Deposition, Fourth International Conference," G. F. Wakefield and J. M. Blocher, Jr., Editors, p. 135, The Electrochemical Society Softbound Symposium Series, Princeton, N.J. (1973).
4. R. M. Mehalso and R. J. Diefendorf, in "Chemical Vapor Deposition, Fifth International Conference," J. M. Blocher, Jr., H. E. Hintermann, and L. H. Hall, Editors, p. 84, The Electrochemical Society Softbound Symposium Series, Princeton, N.J. (1975).
5. C. P. Talley, "High Modulus High Strength Reinforcements for Structural Composites," Texaco Experiment, Inc. Tech. Report ML-TDR-64-88, Part III, p. 174 (1965).
6. L. Vandenbulcke and G. Vuillard, in "Chemical Vapor Deposition, Fifth International Conference," J. M. Blocher, Jr., H. E. Hintermann, and L. H. Hall, Editors, p. 763, The Electrochemical Society Softbound Symposium Series, Princeton, N.J. (1975).
7. E. M. Sparrow, R. Eichborn and J. L. Gregg, *Phys. Fluids*, 2, 319 (1959).
8. A. Acrivos, *AIChE J.*, 4, 285 (1968).
9. P. H. Oosthuizen and S. Madan, Trans. ASME, *J. Heat Transfer, Series C*, May 1971, p. 240.

10. P. Hrycak, D. T. Lee, J. W. Gauntner, and J. N. B. Livingood, NASA TN D—5690, p. 8, March 1970.
11. JANAF, Thermochemical Tables, NBS 37, June 1971.
12. J. O. Hirshfelder, C. F. Curtiss, and R. B. Bird, "Molecular Theory of Gases and Liquids," John Wiley & Sons, New York (1954).
13. R. C. Reid and T. K. Sherwood, "The Properties of Gases and Liquids," McGraw-Hill Book Co., New York (1966).
14. H. E. Carlton and J. H. Oxley, *AIChE J.*, **3**, 571 (1967).
15. L. A. Bromley and C. R. Wilke, *Ind. Eng. Chem.*, **43**, 1641 (1951).
16. F. Coeuret, *Chem. Eng. Sci.*, **30**, 1257 (1975).
17. R. Gardon and J. C. Akfirat, *Trans. ASME, J. Heat Transfer Series C*, 101 (1966).

Structure of Deposits–Process Relationships in the Chemical Vapor Deposition of Boron

L. Vandenbulcke and G. Vuillard

Centre de Recherches sur la Chimie de la Combustion et des Hautes Températures et Faculté des Sciences d'Orléans, 45045 Orléans Cedex, France

ABSTRACT

Chemical vapor deposition of boron is capable of yielding a wide variety of structures. They are studied using the deposition mechanisms proposed in a previous paper (1) and the effect of temperature, interfacial equilibrium, or effective supersaturation of the vapor phase is deduced. The experimental parameters which control the interfacial conditions are inlet gas phase composition, mass flow rate of reactants, and temperature. The full range of variation of boron structure, amorphous, α rhombohedral, β rhombohedral, and β tetragonal is followed by observing the material under these various conditions of growth. β rhombohedral appears as the thermodynamically stable form and α rhombohedral and β tetragonal as metastable crystalline forms occurring at low and high temperatures, respectively.

Both physical (PVD) and chemical vapor deposition (CVD) are capable of yielding materials in a wide variety of structures ranging from amorphous to polycrystalline, needlelike, single crystals, and epitaxial films. It is well known (2-4) that the major factors which control the nucleation and growth process, and ultimately, the final structure of the deposited material, are supersaturation and temperature. A large body of theory has been developed, and substantial verifications have been obtained in the physical process which involves the adsorption of monomers on the substrate, their migration to constitute stable nuclei which grow and coalesce. In the case of the condensation of one component, the supersaturation is defined as the ratio of the actual pressure of monomer to the vapor pressure in equilibrium with the condensed phase. It refers to the concentration of adsorbed monomers on the surface; the temperature relates to their mobility.

In CVD which inherently involves a multicomponent system, the theories of heterogeneous nucleation and crystal growth can be treated on the basis of a quantitatively defined supersaturation as in the simple case of molecular dissociation (5). This treatment is difficult to extend but the concept of supersaturation is retained as the excess of available reaction vapors relative to the concentration in equilibrium with the solid surface. Generally, CVD is effected in a flow system that may employ a carrier or a reduction gas; then the interfacial composition is affected by diffusion in the boundary layer. To achieve quantitative results on supersaturation, it is therefore necessary to calculate the interfacial composition in the real system.

In the CVD of boron from impinging jets of boron trichloride and hydrogen on a flat surface, the interfacial composition is constant in the stagnation zone: it has been calculated in a previous paper (1). Boron presents a polymorphism which has been extensively studied, but our knowledge of the crystal chemistry of boron as well as the mechanisms of vapor growth is, even now, incomplete. This paper attempts to correlate the mechanisms of CVD with the resulting deposit structures.

Key words: mass transfer, surface kinetics, equilibrium, supersaturation, boron polymorphism.

Experimental Techniques

The experimental equipment, materials, and procedure have been described elsewhere (1).

Boron was deposited from impinging axisymmetric jets (0.8 cm diam) of BCl_3 and H_2 on flat surfaces. Substrate materials were graphite and refractory metals (Ta, Mo, W) heated by a high frequency generator. Deposition rates were deduced from deposit thickness in the stagnation zone obtained with different deposition times. The influence of temperature, inlet gas composition, and mass flow rate of reactants has been presented in a previous paper (1). The same experiments permit us to study the influence of various parameters on the deposit structures in the stagnation zone. Structure of deposits was deduced from morphological and x-ray diffraction studies.

Supersaturation Study

Analysis and calculation.—In a previous paper (1), different composition mechanisms are examined as a function of inlet gas composition, temperature, and forced convection. For a constant composition of inlet gas ($BCl_3/H_2 = 2/3$), a boundary between two deposition processes, mass transfer-interfacial equilibrium and mass transfer-surface kinetics are drawn as a function of temperature and Reynolds number (N_{Re}). The boundary position is also a function of the inlet gas composition. In all cases the gas phase is essentially composed of H_2, BCl_3, HCl, and $HBCl_2$; other intermediates than $HBCl_2$ can be neglected.

For low N_{Re} and high temperature, the deposition is governed by a mass transfer-equilibrium process. The interfacial vapors are in equilibrium with solid boron and the system is saturated with respect to each component.

For high N_{Re} and low temperature, the deposition is governed by a mass transfer-surface kinetics process and the system is supersaturated in various components. This system is complicated because two reactions proceed concurrently and no simple relationship exists between their rates. The real interfacial system is defined by the sum of Eq. [1] and [2]

$$(1-a)BCl_3 + 3(1-a)/2H_2 \rightarrow (1-a)\langle B\rangle + 3(1-a)HCl \quad [1]$$

$$aBCl_3 + aH_2 \rightarrow aHBCl_2 + aHCl \quad [2]$$

$$BCl_3 + (3-a)/2H_2 \rightarrow (1-a)\langle B\rangle + aHBCl_2 + (3-2a)HCl \quad [3]$$

The interfacial partial pressures of H_2, BCl_3, $HBCl_2$, and HCl were calculated from the mass transfer-kinetics consideration (1). The value of a is obtained from diffusional fluxes of $HBCl_2$ and BCl_3 through the boundary layer determined by adding the additional restraint of vapor phase chemical equilibrium at the deposition surface.

This real system is compared to the corresponding system in equilibrium with solid boron. The corresponding equilibrium composition is calculated with the same H/Cl ratio which exists in the interfacial vapor of the real system. The equilibrium calculation is based on the values of the free energies of formation of the compounds given in Ref. (6). It is carried out by a simple iteration method. It can be noted that the H/Cl ratio calculated previously by mass transfer-equilibrium considerations is different from the ratio which exists in the real supersaturated vapor phase except at the boundary dividing the two domains of mass transfer-equilibrium and mass transfer-kinetics processes. The corresponding equilibrium system is written as

$$BCl_3 + (3-b)/2H_2 \leftrightarrows (1-b)\langle B\rangle + bHBCl_2 + (3-2b)HCl \quad [4]$$

$$(1-b)\langle B\rangle \leftrightarrows (1-b)B \quad [5]$$

Supersaturation of gaseous reagents H_2 and BCl_3 are calculated according to

$$\Sigma_j = P_j/P_{j,eq} \quad [6]$$

A total supersaturation of the gas mixture is defined as

$$\Sigma_t = \frac{(P_{H_2})^{(3-a)/2}\cdot(P_{BCl_3})\cdot(P_{HBCl_2,eq})^{b}\cdot(P_{HCl,eq})^{(3-2b)}}{(P_{HBCl_2})^{a}\cdot(P_{HCl})^{(3-2a)}\cdot(P_{BCl_3,eq})\cdot(P_{H_2,eq})^{(3-b)/2}} \quad [7]$$

By analogy with the condensation of one component in the PVD process, it is possible to calculate the supersaturation in the boron monomer. However, this gaseous monomer is unimportant relative to the deposition mechanism in CVD of boron. The effective pressure of boron in the supersaturated vapor phase is defined as the pressure in equilibrium in the vapor phase

$$BCl_3 + (3-b)/2H_2 \leftrightarrows (1-b)B + bHBCl_2 + (3-2b)HCl \quad [8]$$

Then, boron supersaturation which is defined as $\Sigma_B = P_B/P_{B,eq}$ is calculated as follows

$$\Sigma_B = \left[\frac{(P_{BCl_3})\cdot(P_{H_2})^{(3-b)/2}\cdot(P_{HBCl_2,eq})^{b}\cdot(P_{HCl,eq})^{(3-2b)}}{(P_{HBCl_2})^{b}\cdot(P_{HCl})^{(3-2b)}\cdot(P_{BCl_3,eq})\cdot(P_{H_2,eq})^{(3-b)/2}}\right]^{1/(1-b)} \quad [9]$$

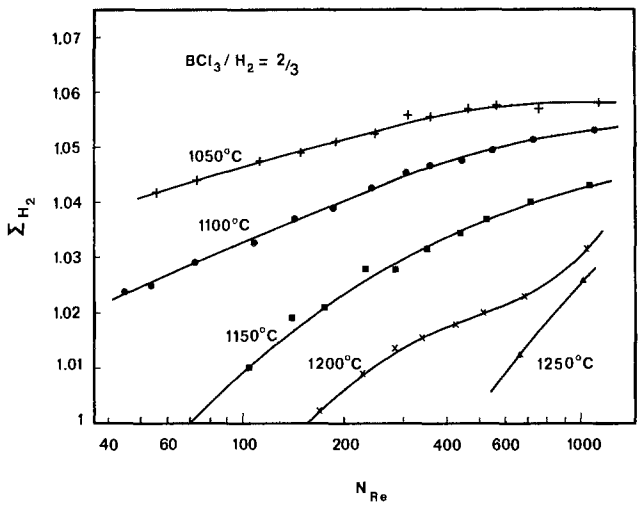


Fig. 1. Supersaturation of H_2 as a function of N_{Re}

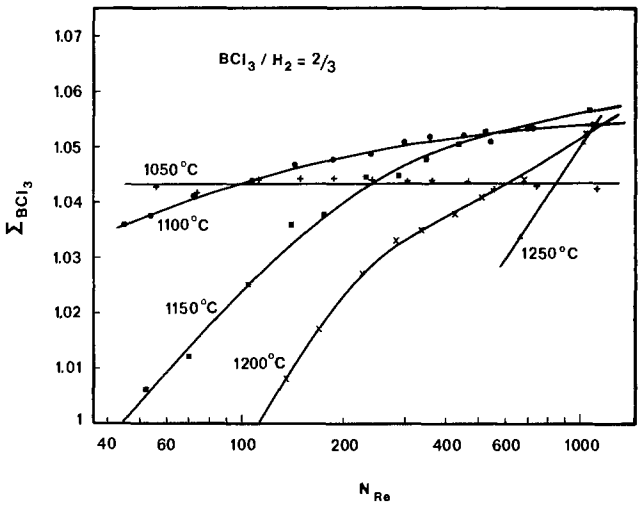


Fig. 2. Supersaturation of BCl_3 as a function of N_{Re}

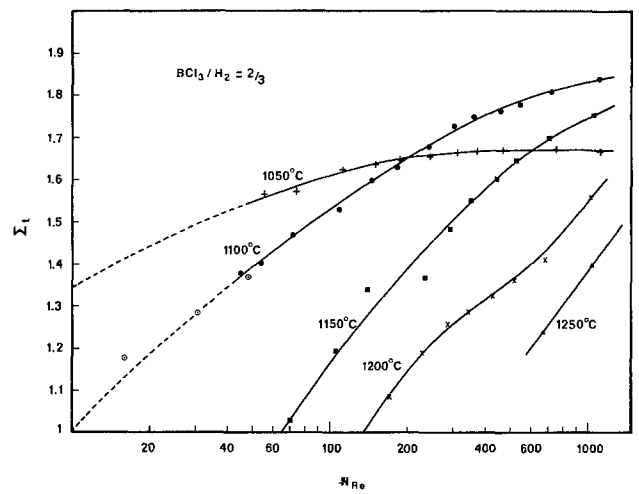


Fig. 3. Total supersaturation as a function of N_{Re}

Results and discussion.—The supersaturations Σ_{H_2}, Σ_{BCl_3}, Σ_t, and Σ_B *vs.* N_{Re} are reported in Fig. 1-4. These results are for five temperatures (T = 1050°, 1100°, 1150°, 1200°, and 1250°C) and a constant composition in the inlet gas mixture (BCl_3/H_2 = 2/3).

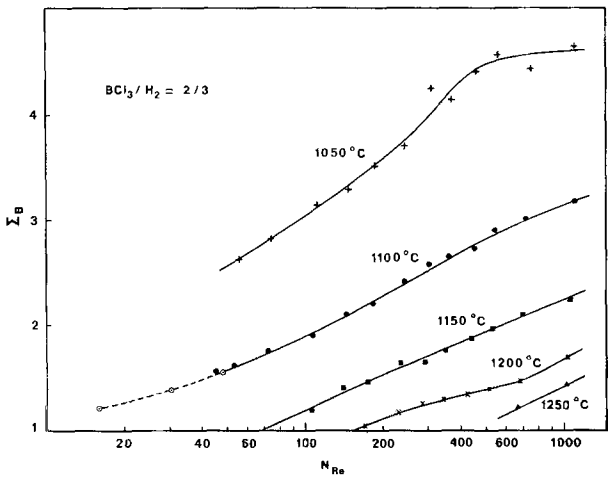


Fig. 4. Boron monomer supersaturation as a function of N_{Re}

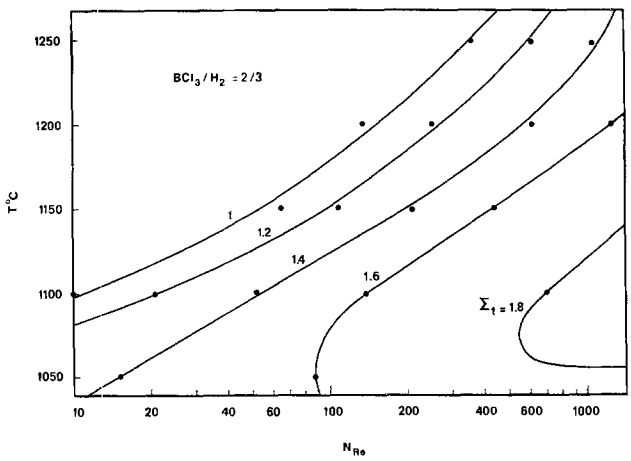


Fig. 5. Effects of T and N_{Re} on saturation and supersaturation

The dotted circles at 1100°C (Fig. 3) were obtained from vertical downward jet experiments where free convection diminishes the forced one (1); therefore the mass transfer corresponds to a hypothetical value of N_{Re} calculated by using the pure forced convection equation ($N_{Sh}/N_{Sc}^{1/3} = 0.76\, N_{Re}^{0.43}$).

We can conclude from these figures that, for each temperature, the vapor phase is saturated when N_{Re} is lower than a critical Reynolds number $N_{Re,c}$. The value of $N_{Re,c}$ increases with temperature. For $N_{Re} > N_{Re,c}$, the vapor phase is supersaturated. We find again the transition between two deposition processes where the interfacial vapors are either in equilibrium with B_{solid} or out of equilibrium.

At a temperature of 1050°C, we note that all the supersaturations reach maximum values when $N_{Re} > 500$. In that case, the excess of reactants BCl_3 and H_2 is converted more and more through vapor phase equilibrium into the gaseous by-products, $HBCl_2$ and HCl, which diffuse outside the boundary layer, and the deposition rate of boron remains constant for any mass flow rates. We find the second transition in the boron deposition process where the deposition rate becomes dependent only on surface kinetics. For temperatures greater than 1050°C, this second transition should occur greater than our experimental limit of 1000 for N_{Re}. We also note that the N_{Re} value at which Σ_{BCl_3} and Σ_t equal one is greater when the temperature increases in accordance with the fact that the conversion of BCl_3 into B_{solid} is favored by surface kinetics when temperature increases.

For a constant N_{Re} and in conditions far from a pure surface kinetics process, the supersaturations in reactants, Σ_{BCl_3}, Σ_{H_2}, and Σ_t increase with decreasing temperatures. Likewise, the supersaturation in boron monomer Σ_B increases logically with decreasing temperature, whatever the value of N_{Re}.

If we produce the supersaturations *vs.* N_{Re} curves drawn for $T = 1050$°C, we can see that saturation will be reached when $N_{Re} < 1$, hence at a very low mass transfer which is nearly always achieved in CVD, either by free or forced convection. At $T < 1050$°C, boron is therefore often deposited out of equilibrium.

All the above statements are summarized in Fig. 5 which presents the saturation and isosupersaturation curves for Σ_t on a single diagram $T = f(N_{Re})$. The isosupersaturation curves for Σ_B present the same trends, but their slope is always positive and decreases when Σ_B increases. In accordance with a previous paper (1), it can be concluded that the interfacial conditions depart from equilibrium when N_{Re} increases and T decreases.

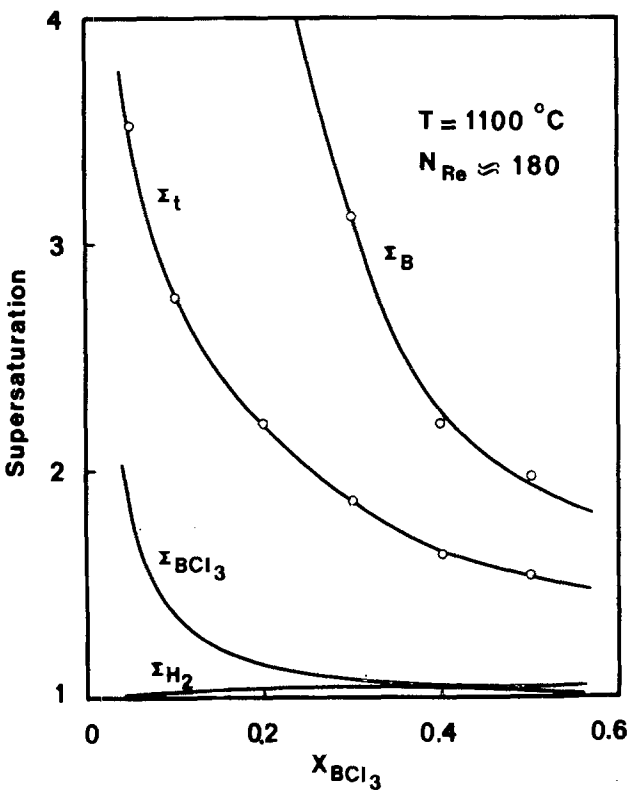


Fig. 6. Supersaturation as a function of inlet gas composition

Figure 6 shows the influence of the inlet gas composition on the supersaturations for $T = 1100$°C and a mass flow rate of 0.071 g/cm²/sec ($N_{Re} \simeq 180$). The supersaturation in H_2 is low and varies only slightly with the molar fraction of BCl_3 (X_{BCl_3}). On the other hand, Σ_{BCl_3}, Σ_t, and Σ_B increase significantly when X_{BCl_3} decreases. According to the previous paper (1), the interfacial conditions are farther from equilibrium when X_{BlC_3} decreases.

Structure of Deposits

Results.—X-ray diffraction studies have enabled us to identify four crystallographic structures which are consistent with the four morphologies presented in Fig. 7. The amorphous boron forms the typically continuous coating (Fig. 7a). The α rhombohedral boron occurs as heaps of crystals which present some sharp facets (Fig. 7b). The β rhombohedral boron arises as heaps of very small crystals which conglomerate thereafter to cover all the surface (Fig. 7c-7d). The β

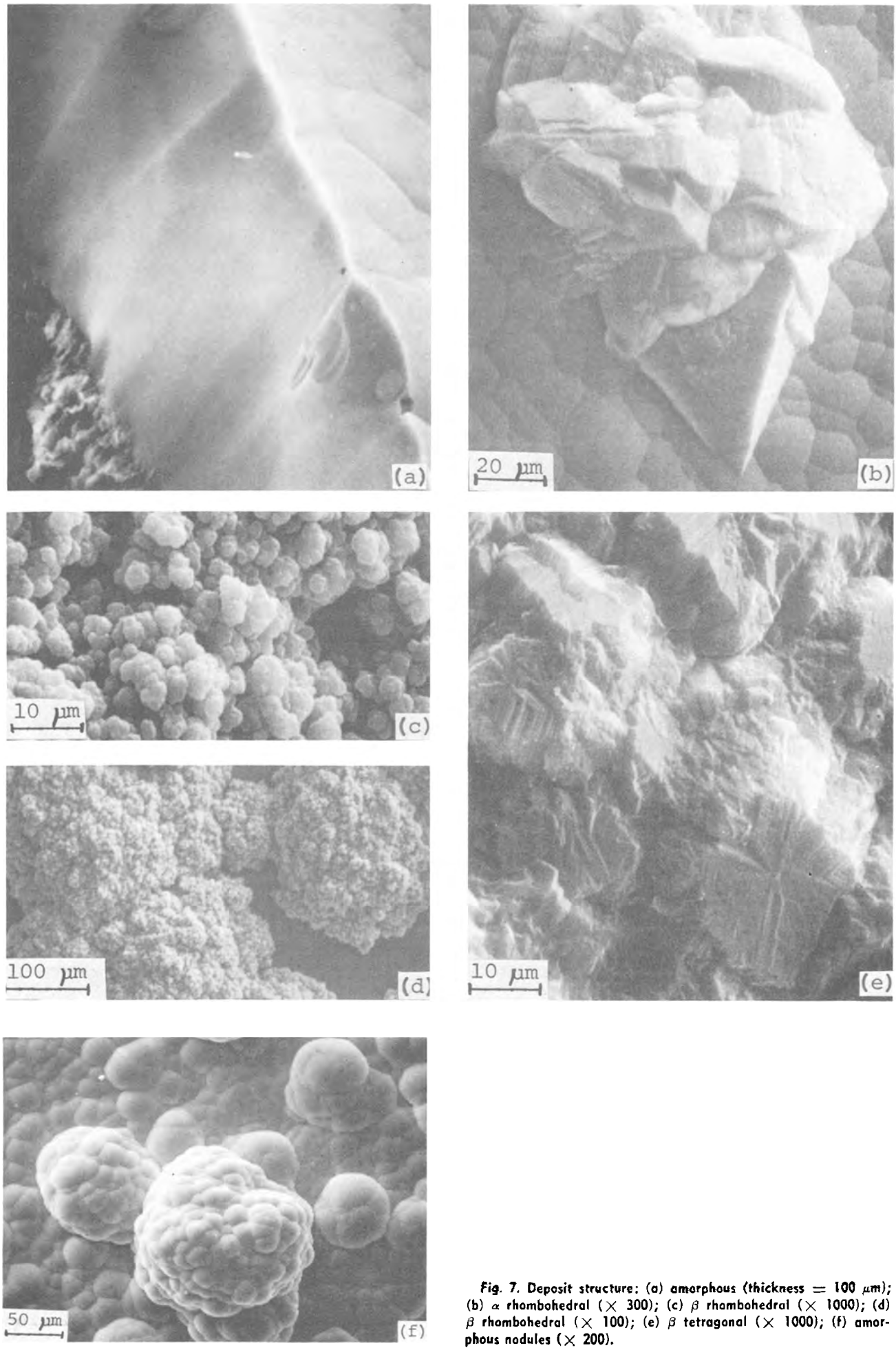
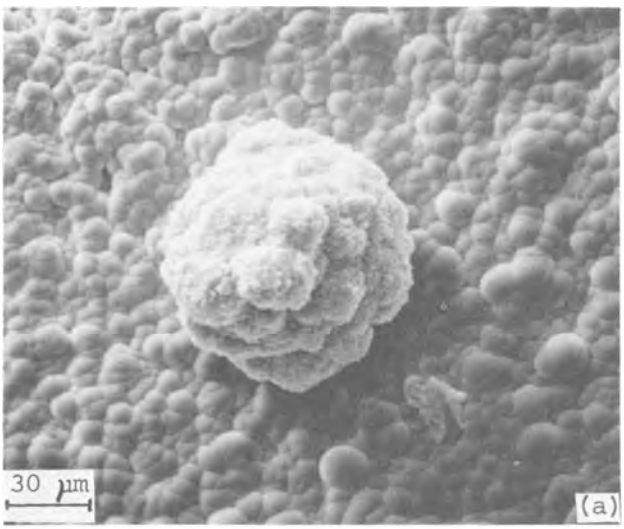


Fig. 7. Deposit structure: (a) amorphous (thickness = 100 μm); (b) α rhombohedral (× 300); (c) β rhombohedral (× 1000); (d) β rhombohedral (× 100); (e) β tetragonal (× 1000); (f) amorphous nodules (× 200).

tetragonal boron forms a polycrystalline continuous layer (Fig. 7e).

In all cases, boron grows initially with an amorphous structure. Thereafter, nucleation of crystalline forms of boron arises at different deposition times as a function of saturation or amount of supersaturation and temperature. These times vary from less than 1 min, in the case of saturation and $T \geqslant 1100°C$, to 20 or 30 min in the case of high supersaturation and $T < 1100°C$. There are some intermediate morphologies like the big amorphous nodules (Fig. 7f) which constitute preferred sites for crystal nucleation or transformation. Figure 8a shows the transformation of amorphous nodules into β rhombohedral boron. Figure 8b shows the growth of β rhombohedral on α rhombohedral crystals.

The advent of these different structures is connected with the deposition process. It is studied first as a function of T and N_{Re} for a constant inlet composition of reactants ($BCl_3/H_2 = 2/3$). Figure 9 presents the results obtained for a deposition time of 3 min. Curves of saturation and total isosupersaturation Σ_t are drawn on the same diagram. When the vapor phase is in equilibrium with B_{solid}, boron crystallizes in the β rhombohedral form as demonstrated at $T > 1100°C$. At $T \leqslant 1100°C$, boron crystallizes as β rhombohedral in the periphery of the substrates (out of the stagnation zone) where mass transfer is very low



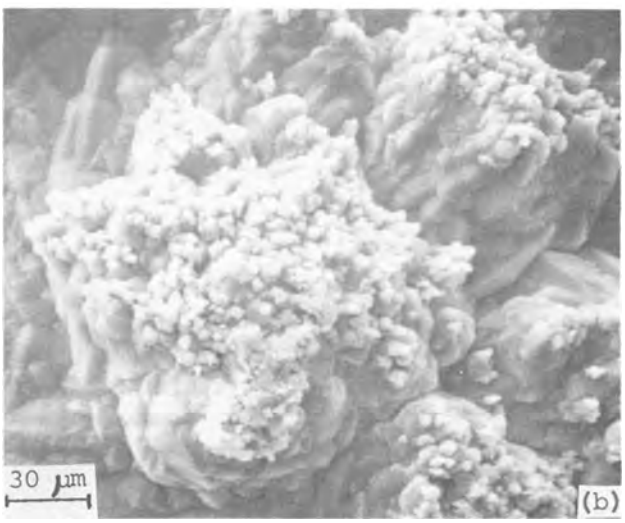


Fig. 8. Intermediate morphologies: (a) β rhombohedral growth on amorphous nodules (× 300); (b) β rhombohedral growth on α crystals (× 300).

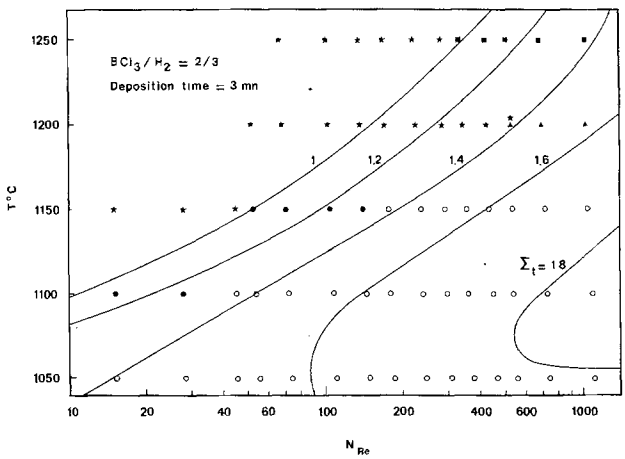


Fig. 9. Effects of T and N_{Re} on deposit structure (deposition time = 3 min): ○ = amorphous; ● = big nodules; ▲ = α rhombohedral; ★ = β rhombohedral; ■ = β tetragonal.

(1) and interfacial equilibrium accordingly maintained. In the supersaturated region, the structure depends on temperature and supersaturation. At $T \leqslant 1150°C$, boron remains amorphous in spite of the formation of big nodules when the supersaturation is low ($\Sigma_t < 1.4$). At $T = 1200°C$, boron is always crystallized in the conditions studied ($N_{Re} \leqslant 1000$), as β rhombohedral when $\Sigma_t < 1.4$ and as α rhombohedral when $\Sigma_t > 1.4$. At $T = 1250°C$, boron deposits consist of a continuous layer of the β tetragonal type.

Figure 10 presents the results obtained for $T < 1250°C$ with a deposition time of 10 min. β rhombohedral boron appears at all temperatures in the equilibrium region. It appears at $T = 1150°C$ when $\Sigma_t < 1.4$ and in all conditions at $T = 1200°C$. Boron is amorphous when $T \leqslant 1150°C$ and $\Sigma_t \geqslant 1.5$. At $T = 1150°C$, the α rhombohedral type is formed when Σ_t is equal to about 1.4 and at $T = 1100°C$ when $1 < \Sigma_t < 1.5$. At $T = 1250°C$ a complete scaling of the deposits occurs after a deposition time of 7 min. At $T = 1050°C$, a deposition time of 20 min is possible. Appearance of α rhombohedral crystals is then observed when $\Sigma_t < 1.5$.

The influence of the inlet gas composition has been studied only at $T = 1100°C$ and $N_{Re} \simeq 180$ and 550. When $N_{Re} \simeq 180$, a formation of big amorphous nodules is observed after 5 min of deposition when $X_{BCl_3} \geqslant 0.6$. In the other cases studied, the deposit is amorphous without nodules.

Discussion.—All the results show that in the range of temperatures 1050°-1250°C, the equilibrium solid

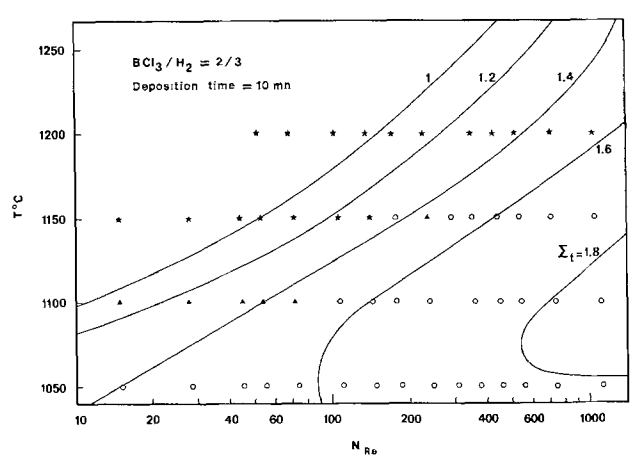


Fig. 10. Effects of T and N_{Re} on deposit structure (deposition time = 10 min).

phase is the β rhombohedral form. Below 1050°C, it is difficult to maintain the equilibrium between solid boron and the vapor phase. However, we think that this condition has been achieved by Naslain *et al.* (7) in the preparation of pure boron in quartz tube. They observed a β rhombohedral nucleation in interstices between α granules at temperature as low as 800°C, also by Luque and Augustin (8-9) who observed its deposition at $T = 850$°C in using very low mass flow rates ($5 \cdot 10^{-5}$ g/cm²/sec) of ($BCl_3 + H_2$) mixtures. Above 1250°C, equilibrium is likely to be reached and the β rhombohedral type is generally observed. Therefore, our results provide new evidence in support of β rhombohedral being the thermodynamically stable form at all temperatures (7-10).

Conversely, the other boron varieties appear as metastable forms whose formation is kinetically favored under various conditions. The different parameters which control their formation are temperature, supersaturation of the vapor phase, and deposition time. Boron remains amorphous for longer deposition times as temperature remains low and supersaturation high. At $T < 1200$°C, nucleation of α rhombohedral boron occurs when the supersaturation is low. The β nucleation and $\alpha \rightarrow \beta$ rhombohedral transformation occur rapidly in the range of 1150°-1200°C. At $T \leq 1100$°C, the solid-state transformation is kinetically improbable, and was not observed as it had been by Naslain *et al.* (7). The α rhombohedral type is the "metastable crystalline form of low temperature."

On account of the solid-state transformations of amorphous and $\alpha \rightarrow \beta$ rhombohedral, these two forms cannot be prepared at $T > 1200$°C. As α rhombohedral in the low temperature range, the β tetragonal form is "the metastable crystalline form of high temperature." Our experiments being limited to $T \leq 1250$°C, we have not observed the β tetragonal $\rightarrow \beta$ rhombohedral irreversible transformation. Moreover, we have not studied if this transformation is kinetically probable or not at the lower temperature of formation 1250°C.

Conclusion

The basic prediction of the importance of supersaturation and temperature in the development of morphological feature is clearly confirmed. Both supersaturation and temperature control the structure of boron deposits. Interaction between the deposit and the substrate does not seem to have any influence. The full range of boron structures has been found by observing the material under various conditions of growth.

Amorphous structure is maintained in conditions of high supersaturation and low temperature. Obtaining a pure thick layer of this form is limited to $T \leq 1200$°C. β rhombohedral boron appears as the thermodynamically stable form, and α rhombohedral and β tetragonal as metastable crystalline forms of respectively low and high temperatures. The $\alpha \rightarrow \beta$ rhombohedral transformation is observed in the range of 1150°-1200°C. The β tetragonal $\rightarrow \beta$ rhombohedral transformation has not been studied.

Acknowledgments

We wish to thank R. Herbin for her assistance in the experimental work.

Manuscript submitted June 22, 1977; revised manuscript received July 26, 1977. This was Paper 254 presented at the Atlanta, Georgia, Meeting of the Society, Oct. 9-14, 1977.

Any discussion of this paper will appear in a Discussion Section to be published in the June 1978 JOURNAL. All discussions for the June 1978 Discussion Section should be submitted by Feb. 1, 1978.

Publication costs of this article were assisted by UER Sciences d' Orléans.

REFERENCES

1. L. Vandenbulcke and G. Vuillard, *This Journal*, **124**, 1931 (1977).
2. J. P. Hirth, in "Vapor Deposition," C. F. Powell, J. H. Oxley, and J. M. Blocher, Jr., Editors, p. 126, John Wiley & Sons, New York (1966).
3. R. D. Gretz, *ibid.*, p. 149.
4. J. M. Blocher, Jr., *J. Vac. Sci. Technol.*, **11**, 680 (1974).
5. R. D. Gretz, C. M. Jackson, and J. P. Hirth, *Surf. Sci.*, **6**, 171 (1967).
6. JANAF, Thermochemical Tables, NBS 37 (1971).
7. R. Naslain, J. Etourneau, and P. Hagenmuller, *Electron Technol.*, **3**, 35 (1970).
8. G. Vuillard, A. Luque, and F. Augustin, *C.R. Acad. Sci. Ser. C*, **272**, 444 (1971).
9. A. Luque, *ibid.*, **274**, 286 (1972).
10. J. L. Hoard and R. E. Hughes, "The Chemistry of Boron and Its Compounds," p. 154, John Wiley & Sons, New York (1967).

Technical Notes

An Attempt at the AES Evaluation of the Composition of Off-Stoichiometric Silicon Nitride

Simon Thomas

Burroughs Corporation, San Diego, California 92127

and Robert J. Mattox

Motorola Semiconductor Group, Phoenix, Arizona 85008

The use of silicon nitride as a passivation layer in silicon devices is gaining widespread acceptance. The nitride passivation has a variety of advantages over the conventional silicon dioxide or phosphosilicate glass layer. One of the most widely recognized advantages of the nitride passivation is its low permeability

Key words: plasma silicon nitride, Auger analysis, nitride passivation layer.

to the alkali ions, especially sodium (1). Although phosphosilicate glass (PSG) can effectively getter the mobile ions, it suffers from the adverse effects of corrosion of the aluminum metallization in the presence of humidity (2). Silicon nitride is an excellent alternative to the PSG as a final passivation over the metallization. The rather rigorous temperatures (~700°-1000°C) at which the silicon nitride is deposited by chemical vapor deposition (CVD) hitherto precluded the use of the nitride as a practical passivation layer over the metallization. The recent emergence of silicon nitride as a practical passivation layer is primarily due to the development of the new deposition method where the nitride can be deposited at a relatively low temperature (~200°-400°C) by the reaction of silane and ammonia and/or nitrogen in a glow discharge—the so-called plasma nitride (3).

Although plasma deposited silicon nitride offers excellent properties as a passivation layer in silicon device technology, the inability to consistently reproduce the physical and electrical properties such as the stoichiometry, density, etch rate, refractive index, dielectric constant, etc., has been a problem. On the other hand the silicon nitride layers deposited by the high temperature CVD method using proper ratios of NH_3/SiH_4 are shown to be stoichiometric with a composition Si_3N_4 (4, 5). However, the composition cannot be presumed to be stoichiometric in the case of the plasma-deposited silicon nitride, being strongly dependent on a variety of deposition parameters.

One of the physical properties of the silicon nitride most widely employed to characterize the composition and to evaluate the process of deposition is the refractive index of the film, with an acceptable value in the range 2-2.05 for passivation applications. A higher value for the refractive index is usually considered to be an indication of a silicon-rich film. In view of the possible diversity in the nitride composition, it would be essential to characterize the composition in order to optimize the deposition process. We have used Auger electron spectroscopy (AES) coupled with Ar^+ ion sputtering in our attempt to evaluate the composition of the plasma-deposited nitride layers. The main purpose of this paper is threefold: (*i*) to establish the main features in the Auger spectrum genuinely characteristic of silicon nitride; (*ii*) to point out the existence of preferential sputtering effect in Ar^+ ion sputtered silicon nitride; and (*iii*) to try to evaluate the composition of the plasma nitride films differing in refractive index, with a view to better control the deposition process.

The capacitively coupled plasma reactor design was employed in the deposition of the silicon nitride films. The reactor consisted of basically two parallel plates with the top plate being the cathode and the bottom plate being the grounded wafer plate. The reactant gases flow radially, being introduced at the center and exhausted from the bell jar through a mechanical pump. The deposition temperature was controlled by heating elements attached to the lower plate. The detailed description of this type of deposition technique is available in the literature (6-8). The conventional ammonia-silane-nitrogen chemical system was the reactant gas. By varying the ammonia/silane gas ratios along with other process variables such as rf power, pressure, plate spacing, etc., the refractive index of the resultant deposited films could be varied over a wide range of values. Ten such plasma nitride samples with refractive indexes ranging from 1.88 to 3.57 as measured by ellipsometry at 5461Å were selected for the Auger analysis together with a high temperature CVD nitride as a reference. The Auger analysis was performed using a single stage cylindrical mirror analyzer (Physical Electronics Industries, Incorporated) with an energy resolution of 0.6%. The electron beam parameters were Ep = 3 keV and Ip = 10 μA. Sputtering was performed at 4×10^{-3} Pa using 2 keV Ar^+ ions.

Before attempting to characterize the composition of the nitride by AES, it is essential to establish the salient features in the Auger spectrum from Si_3N_4. Many authors have studied the features in the Auger spectrum from stoichiometric CVD nitride (9-11). The Si LVV Auger spectrum is supposedly characterized by a very strong peak reported at 85 (9), 87 (10), and 92 eV (11). A shoulder peak (82 eV) is also observed at the low energy side of this main peak (10). All these features were observed from "sputter-cleaned" silicon nitride samples. The Auger spectra from our as-deposited samples always showed the presence of oxygen and relatively small amounts of carbon as surface impurities. The spectra from the as-received samples are similar to those already published and will not be presented here.

The surface layer of a nitride has been identified by Raider *et al.* (12) as a graded oxynitride resulting from the room temperature oxidation of the silicon nitride. In our samples, the surface oxygen content bears an inverse relationship to the nitrogen content in the film. The thickness of this oxynitride layer in most samples is typically <30Å. The presence of this oxynitride layer necessitates the argon ion sputtering before the bulk composition can be evaluated by AES. The tacit assumption is that the ion sputtering does not alter the composition significantly. We believe, from the present study, that the ion beam does alter the composition significantly, and the spectra reported are really from such an altered layer.

Typical Auger spectra from two samples with refractive indexes $n = 2.01$ and $n = 3.57$ are shown in Fig. 1, after sputter cleaning the surfaces with a 2 keV Ar^+ ion beam. Spectrum I is similar in shape to that reported by Holloway (10) for stoichiometric Si_3N_4. In this spectrum the "main" Si Auger peak occurs at ~88 eV, with the characteristic shoulder at ~83 eV. These are labeled peak A and B for convenience.

In Spectrum II, the ratio of peak heights A/B is much larger, and the nitrogen peak height smaller than in Spectrum I. The peak A has changed in energy to ~91 eV. In all the other samples analyzed, the ratio A/B and the energy of the peak A are dependent on the nitrogen peak height. Generally, it is believed that the characteristic silicon peak in silicon nitride is the peak A. We believe that the peak A is really an indication of the presence of "free" silicon in the surface layer and the Auger peak truly characteristic of the nitride is the "shoulder" peak at ~83 eV. In truly stoichiometric Si_3N_4, the occurrence of the 88 eV peak is an artifact and is a consequence of the preferential sputter removal of nitrogen making the surface silicon-rich. This conclusion was further strengthened by the absence of the 88 eV peak from the surface of a hot-pressed bulk silicon nitride sample fractured in air. While fully rec-

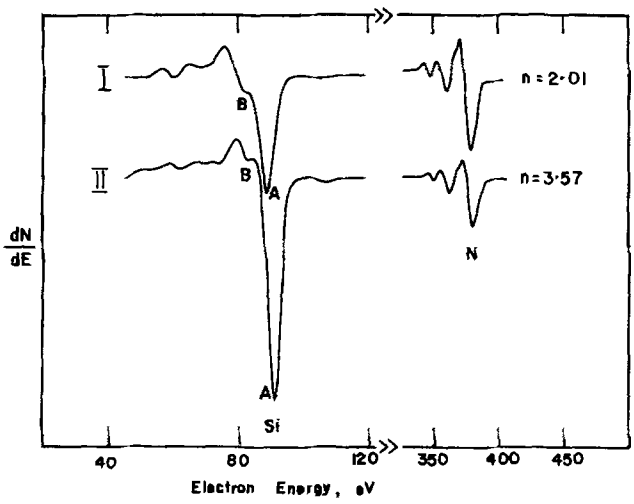


Fig. 1. Portions of the Auger spectra from sputter-cleaned plasma nitride samples with refractive indexes 2.01 (I) and 3.57 (II). Peak A is an indication of the presence of "free" silicon at the surface.

ognizing the profound influence of the small amount of oxygen impurity present on this sample in attenuating the 88 eV peak, the absence of the 88 eV cannot be explained solely by the oxygen contamination. In the CVD nitride, even with a comparable amount of oxygen present at the surface, the 88 eV was pronounced. The argument that the high temperature CVD nitride is significantly off stoichiometric, is invalid, in view of the results from other analytical techniques such as Rutherford backscattering (4, 5).

Another factor affecting the Auger peak shape and heights is the ion beam energy. After sputter cleaning the CVD nitride surface, it was bombarded alternately with 2 keV and 500 eV Ar^+ ions for 1 min durations (equivalent thickness removed 30Å, at 2 keV). The nitrogen and argon (imbedded) Auger peak heights and the height of peak A (measured from the maximum negative excursion to the shoulder at 83 eV) are shown in Fig. 2. As is evident, changing the ion beam parameters can drastically alter the preferential sputtering effects and hence the Auger peak heights. The same peak heights can be reestablished if the same ion beam parameters are used.

An attempt was made to determine the composition of the various plasma nitride samples differing in the refractive index. In Fig. 3, the nitrogen Auger peak height (sputter cleaned using identical ion beam parameters) is plotted against the refractive index of the film (curve 1). The true Auger peak heights should be

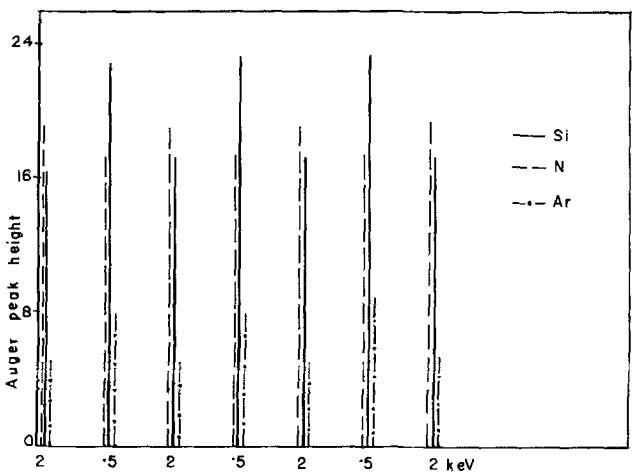


Fig. 2. The Auger peak heights from Si (peak A in Fig. 1), N, and Ar after the alternate bombardment with 2 and 0.5 keV Ar^+ ions for 1 min durations.

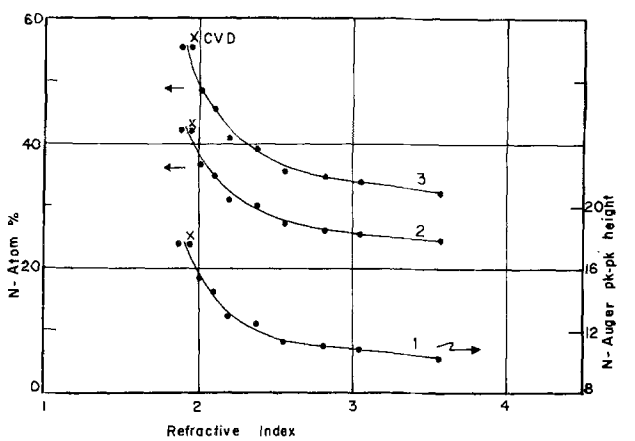


Fig. 3. Variation of the refractive index of the silicon nitride films with nitrogen concentration: 1. measured nitrogen Auger peak height; 2. N atom percent calculated from the measured nitrogen Auger peak height; and 3. N atom percent normalized to the high temperature CVD nitride film.

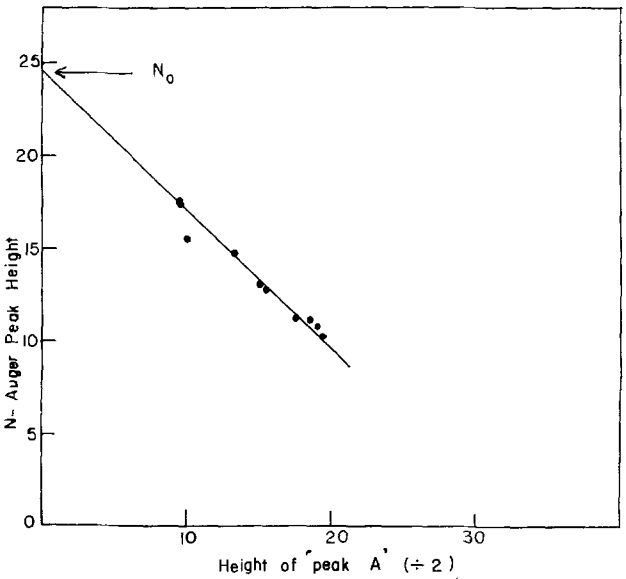


Fig. 4. Plot of nitrogen Auger peak height vs. height of peak A characteristic of "free" silicon.

larger than the measured values, for reasons discussed previously.

A graph plotted between the measured nitrogen peak height and the corresponding peak height of peak A (measured from the maximum negative excursion to the shoulder at 83 eV) in the silicon spectrum was found to be linear (Fig. 4) and was extrapolated to A = 0. This yielded a value for the nitrogen Auger peak height (N_0) if preferential sputtering was not present and the film was truly stoichiometric. Based on this value of N_0 for Si_3N_4, the atom percent of nitrogen was calculated corresponding to the measured peak heights and is shown in curve 2 (Fig. 3). Using this method of evaluation, the CVD film which was expected to be stoichiometric Si_3N_4 yielded a composition $Si_{58}N_{42}$—a significant deviation. Calculation based on the Si-KLL Auger peak height and the nitrogen peak height does not apparently eliminate this difference (13). The above deviation from stoichiometry is not due to the inherent nonstoichiometry of our CVD film, but rather to a consequence of the preferential sputtering effect. Based on the assumption that the CVD film was indeed stoichiometric, the atom percent of nitrogen in the plasma nitride films were calculated by normalizing to the measured peak height from this sample, and they are shown in curve 3 (Fig. 3).

It is evident from the above discussion that if the preferential sputtering is not recognized, the composition of the silicon nitride films will always be found to be silicon-rich using the AES-ion sputtering analysis. As can be seen from Fig. 3, the effect of the lower nitrogen content (silicon-rich) is to increase the refractive index from the expected value of 2. There are other parameters which influence the refractive index. The surface oxynitride and the interfacial oxide (detected on all samples by profiling) tend to lower the index, though the effect is relatively small for thick films. The presence of oxygen in the bulk of the film has a profound influence in lowering the refractive index, with a linear dependence on the atom percent of oxygen (14). Another very important factor especially in the plasma nitrides is the hydrogen content, which of course cannot be detected by the Auger technique. Preliminary studies on the above samples using *IR* spectroscopy have shown the presence of bonded hydrogen (both Si-H and N-H) in these films.

Manuscript submitted April 11, 1977; revised manuscript received July 19, 1977.

Any discussion of this paper will appear in a Discussion Section to be published in the June 1978 JOURNAL.

All discussions for the June 1978 Discussion Section should be submitted by Feb. 1, 1977.

Publication costs of this article were assisted by Burroughs Corporation.

REFERENCES

1. J. V. Dalton and J. Drobek, *This Journal*, **115**, 865 (1968).
2. W. M. Paulson and R. W. Kirk, Paper presented at the 12th Annual Reliability Physics Symposium, Las Vegas (1974).
3. R. C. G. Swann, R. R. Mehta, and T. P. Gauge, *This Journal*, **114**, 713 (1967).
4. J. Gyulai, O. Meyer, J. W. Mayer, and V. Rodriguez, *Appl. Phys. Lett.*, **16**, 232 (1970).
5. J. Gyulai, O. Meyer, J. W. Mayer, and V. Rodriguez, *J. Appl. Phys.*, **42**, 451 (1971).
6. J. R. Hollahan and A. T. Bell, "Techniques and Applications of Plasma Chemistry," John Wiley & Sons, New York (1974).
7. A. R. Reinberg, US Pat. 3,757,733 (1973).
8. R. J. Joyce, H. F. Sterling, and J. H. Alexander, *Thin Solid Films*, **1**, 481 (1968).
9. H. G. Maguire and P. D. Augustus, *This Journal*, **119**, 791 (1972).
10. P. H. Holloway, *Surf. Sci.*, **54**, 506 (1976).
11. Y. E. Strausser and J. S. Johannessen, in Proceedings of the ARPA/NBS Workshop IV on Surface Analysis for Silicon Devices (1975).
12. S. I. Raider, R. Flitsch, J. A. Aboaf, and W. A. Pliskin, *This Journal*, **123**, 560 (1976).
13. J. S. Johannessen, W. E. Spicer, and Y. E. Strausser, *J. Vac. Sci. Technol.*, **13**, 849 (1976).
14. P. H. Holloway and H. J. Stein, *This Journal*, **123**, 723 (1976).

Mass Spectrometric Detection of Intermediates in Chemical Vapor Deposition of Si_3N_4

Sin-Shong Lin

Army Materials and Mechanics Research Center, Watertown, Massachusetts 02172

Silicon nitride has been widely used as an insulator and diffusion mask in semiconductor industries (1-3). Moreover because of superior physical properties at high temperatures, *e.g.*, good thermal shock resistance, extreme hardness, creep resistance, and chemical inertness, the material has been considered in the fabrication of gas turbine stator blades (4).

Si_3N_4 can be prepared from $SiCl_4$ and NH_3, using two different procedures. In the low temperature method (5-7), NH_3 is bubbled into cool $SiCl_4$ to form amorphous powders. The subsequent heating of the powders at 1200°C yields the crystalline form of alpha-phase Si_3N_4. In the second method (1-3, 8), commonly known as chemical vapor deposition (CVD), these two gases react in the temperature range 800°-1400°C. The product of the reaction is an adherent film and often consists of amorphous and crystalline Si_3N_4. The complete conversion of the amorphous matter to crystalline Si_3N_4 is difficult to accomplish unless the reaction is carried out at temperatures near 1400°C. This is explained by the high thermal stability of N-H bonds formed during the interaction of gases (9). The inclusions of NH and NH_2 groups in the Si_3N_4 lattice structure contribute to the formation of amorphous matter.

The previous attempt (10) to detect intermediates and condensates in the CVD process of alumina from aluminum chlorides and water was unsuccessful because the interaction of gases was believed to occur dominantly on surfaces instead in the vapor phase. In the CVD of Si_3N_4, the formation (11) of Si_3N_4 from $SiCl_4$ and NH_3 is expected to proceed through numerous reaction steps involving a series of intermediates and active complex molecules. It may be possible to detect some of these molecular intermediates by the present combined technique of atmospheric sampling and mass spectrometry. The knowledge that could be obtained might provide better understanding of the CVD process and also illustrate a new technique for the study of nucleation and condensation processes.

Figure 1 shows a block diagram of the sampling device for the CVD of Si_3N_4. The experimental apparatus includes gas inlet lines, a miniature CVD reactor, and a three-stage differential pumping vacuum system. The details have been described previously (10, 12, 13) and only features unique and pertinent to this work will be presented here.

The miniature CVD reactor was made of two high purity closed end alumina combustion tubes of ½ and ¼ in. OD in a concentric configuration as shown in Fig. 2. On the tip of each tube, an orifice varying from 6 to 50 mil was drilled along the axial line. A spacer or collar, cut from a ⅜ in. OD alumina tube up to 1 in. long, was placed between these two tips to serve as a reaction zone. Since the reactants pass rapidly through the reaction chamber into vacuum via the outer orifice, the extent of the interaction depends on the number of collisions between molecules in the reactor, which in turn is dependent on the time of molecular transit through the reactor. Thus the formation of intermediate molecular species depends not only on the pressure and the temperature of the reactor, but also on the degree of intermixing. The intermixing is related to the geometry of the reaction chamber, namely, sizes and spacing of the two orifices,

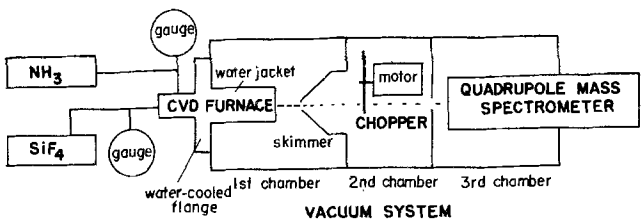


Fig. 1. Block diagram of experimental apparatus. The apparatus consisted of gas inlet lines, a miniature chemical vapor deposition furnace, and a three-stage differential pumping system. The quadrupole mass spectrometer, modulated beam mechanism, and expansion chamber are integral parts of the vacuum system.

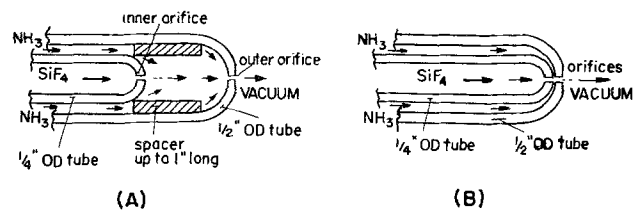


Fig. 2. Configuration of chemical vapor deposition reactor. The reactor is made of ¼ and ½ in. OD alumina tubes, and a spacer of varying lengths up to 1 in. as shown in (A). Without the spacer (B), the orifices are in the intimate contact position, and the interaction of gases is at minimum (almost null).

and the gas flow pattern. The interaction is minimal when the inner and the outer orifices are at the position of intimate contact as shown in Fig. 2(B).

SiF_4, instead of $SiCl_4$, was chosen because of the low atomic weight of fluorine which would enable us to monitor the complex intermediates within the limited mass range of the quadrupole mass filter. Also the monoisotopic nature of fluorine atoms facilitates the interpretation of ion peaks observed in mass spectra. The reagents SiF_4 and NH_3 were metered and introduced into the reactor individually through the core of the inner tube and the annular space between the two reactor tubes, respectively. The gas flows were initially set at 10 ml/min, and the pressure of the reactor, which was roughly equal to the NH_3 pressure because of the high conductance from the annulus to the reactor, was in the range 50-200 Torr depending on the sizes of the orifices. The heating was accomplished by the molybdenum winding around the reactor tube, and the temperature was recorded by a Pt-10%Rh/Pt thermocouple placed near the orifice of the inner tube. Prior to the CVD runs, mass spectra of each reactant were obtained so that the ions resulting from impurities present in the system could be distinguished from those ions resulting from the interaction. In some configurations of the CVD reactor, the gas flows could be adjusted so that ion peaks derived from one reactant would disappear from spectra. The intermediate ion species were observed only under the partial interaction of gases and were always accompanied by large amounts of the reactant ions. The vapor depositions were found to occur at all temperatures providing that the orifices were not in intimate contact. The deposits, white to translucent in appearance, were observed on the reactor wall, which tended to gradually clog the orifices during the run. No chemical analysis was made on these deposits due to the minute amounts available.

The experiments were performed with 15 different configurations of the reactor. The mass spectrometer was operated with the ionizing electron beam at 40 eV under varying resolution, sensitivity, and focusing conditions. Due to the corrosive atmosphere, the spectrometer was found to deteriorate considerably with time. Thus the detailed identification of trace intermediate ions in the CVD experiments became difficult. Furthermore due to the irreproducible geometry of the reactor, it was impossible to obtain systematic information concerning the CVD process.

In Table I, the observed ion species from mass spectra of SiF_4 and NH_3 are tabulated. At all temperatures, the most important ion species from SiF_4 is SiF_3^+, followed by SiF_4^+, SiF_2^+, SiF^+, $Si_2F_6^+$, and $Si_2F_7^+$. The origin of $Si_2F_7^+$ ion is not clear but it probably comes from the fragmentation of $(SiF_4)_2$. The major ions in NH_3 spectra at low temperatures are NH_3^+ and NH_2^+ with minor amounts of NH^+, N_2^+, and H_2^+. Due to extensive thermal dissociation, the abundances of N_2^+ and H_2^+ increase significantly while those of NH_3^+ and NH_2^+ decrease above 800°C.

Table I. Ion species observed in mass spectra of SiF_4 and NH_3 gases

Gas	Ion species	Neutral precursor	Abundances: Room temperature	T = 800°C	T = 1200°C
SiF_4	SiF_4	SiF_4	4	2	2
	SiF_3		100	100	100
	SiF_2	SiF_4/SiF_2	0.1	0.2	0.2
	SiF		0.1	0.2	0.2
	Si_2F_6	Si_2F_6	0.2	0.2	0.2
	Si_2F_7	$(SiF_4)_2$	0.1	0.05	0.05
NH_3	NH_3	NH_3	100	100	100
	NH_2		28	30	22
	NH		1	2	1
	N_2	N_2	—	2	280
	N		—	0.3	26
	H_2	H_2	—	—	15

Note: Abundances of SiF_4^+ and NH_3^+ are arbitrarily taken as 100, and listed data are only for comparison purposes.

Table II. Intermediate ion species observed in chemical vapor deposition of Si_3N_4 from SiF_4 and NH_3

Mass[a]	Ion species	Suggested neutral precursor	Abundances (SiF_3^+ as 100)[b]: Room temperature	T = 400°-1000°C	T = 1186°C[c]
82	SiF_2NH_2	SiF_3NH_2	—	0.5-2	2
101	SiF_3NH_2	SiF_3NH_2	—	0.5-2	2
166	Si_2F_5NH	Si_2F_6NH	—	—	0.1
228	$Si(NH)_2Si_2F_6$	$Si_2F_8(NH)_2$	—	—	60 × 10^{-3}
247	$Si(NH)_2Si_2F_7$	$Si_2F_8(NH)_2$	—	—	20
266	$Si(NH)_2Si_2F_8$	$Si_2F_8(NH)_2$	—	—	1
286	$(Si(NH)_2)_2Si_2F_6$	Unknown	—	—	7
305	$(Si(NH)_2)_2Si_2F_7$	Unknown	—	—	5
324	$(Si(NH)_2)_2Si_2F_8$	Unknown	—	—	2
344	$(Si(NH)_2)_3Si_2F_6$	Unknown	—	—	8
363	$(Si(NH)_2)_3Si_2F_7$	Unknown	—	—	5
383	$(Si(NH)_2)_3Si_2F_8$	Unknown	—	—	2
402	$(Si(NH)_2)_4Si_2F_6$	Unknown	—	—	3
421	$(Si(NH)_2)_4Si_2F_7$	Unknown	—	—	5
440	$(Si(NH)_2)_4Si_2F_8$	Unknown	—	—	1
479	$(Si(NH)_2)_5Si_2F_7$	Unknown	—	—	3
498	$(Si(NH)_2)_5Si_2F_8$	Unknown	—	—	2
537	$(Si(NH)_2)_6Si_2F_7$	Unknown	—	—	2
556	$(Si(NH)_2)_6Si_2F_8$	Unknown	—	—	1

[a] Mass number is subjected to error of ±1 amu for polymeric ions over 286, and ±2 amu for polymeric ions over 479.
[b] Intensity data are taken directly from scan spectra for comparison only. SiF_3^+ is arbitrarily taken as 100.
[c] Data are taken from the run; P = 87 Torr, flow = 10 ± 1 ml/min for both gases, T = 1186°C, size of reactor: outer orifice = 1 mm diam, inner orifice = 0.2 mm diam, length of reactor chamber or spacer = 1.3 cm.

In Table II, the intermediate ion species observed in the CVD runs are listed. The most abundant ion species observed are $SiF_2NH_2^+$ and $SiF_3NH_2^+$. These two ions are observed in all CVD runs except in runs made with the intimate contact configuration and in runs below 400°C. The identities of these two ions have been confirmed from their isotopic distributions. The intensities of these ions are about one-hundredth of the most abundant reactant ion SiF_3^+ in the system, and are strongly influenced by pressure and flow of the reactants NH_3 and SiF_4. The majority of these two ions seem to derive from the neutral precursor SiF_3NH_2 which is the first intermediate molecule from the interaction. The reaction product HF in the form of HF^+ at mass 20 amu is observed mostly above 400°C, and $(HF)_4^+$ is found to dominate the mass spectra at low temperatures.

The remaining intermediate ions of complex molecular compositions listed in the table are detected at temperatures above 1000°C in some specific runs. The abundances listed in the last column are the highest observable intensities. The intensities of these ions diminish with increasing mass number and complexity, and are generally two or three orders of magnitude less than the most abundant intermediate ions $SiF_2NH_2^+$ and $SiF_3NH_2^+$. Due to low abundances, their identities are deduced only from mass numbers and relative positions in mass spectra. These ion peaks are found to occur in mass spectra separated by intervals of 19 and 58 amu units corresponding to composition differences of one F and $Si(NH)_2$ units. Also due to poor resolution at higher mass numbers, the molecular weights of these large intermediate ions are not established within one mass unit (one hydrogen atom). Based on a general fragmentation pattern of simple inorganic fluorides (14), in which neutral species upon electron impact preferentially yield an ion with one fluorine atom less than the neutral, the precursors of these small ions are suggested in the table. However, the fragmentation patterns of high polymeric molecules are not known at this time.

The over-all chemical reaction for the CVD of Si_3N_4 can be written as

$$3SiF_4(g) + 4NH_3(g) = Si_3N_4(s) + 12HF(g) \quad [1]$$

The stepwise processes leading to the formation of Si_3N_4 are suggested to occur through series of additive intermediates followed by elimination of hydrogen

fluoride molecule such as

$$SiF_4 + NH_3 = [F_3SiF\cdots HNH_2] = F_3SiNH_2 + HF \quad [2]$$

$$F_3SiNH_2 + SiF_4 = [F_3SiNH_2\cdots FSiF_3] = F_3SiNHSiF_3 + HF \quad [3]$$

and

$$F_3SiNH_2 + NH_3 = [H_2NSiF_3\cdots HNH_2] = H_2NSiF_2NH_2 + HF \quad [4]$$

Reactions [2] and [3] can be repeated and proceeded to form higher intermediate molecules of the general form

$$F(SiF_2NH)_nH + SiF_4 = F(SiF_2NH)_nSiF_3 + HF \quad [5]$$

$$F(SiF_2NH)_nSiF_3 + NH_3 = F(SiF_2NH)_{n+1}H + HF \quad [6]$$

where $n \geq 1$. Eventually all Si—F bonds are replaced by Si—NH and Si—NH_2 bonds with excessive N and H in the structure

$$a\ SiF_4(g) + b\ NH_3(g) = Si_aN_bH_{3b-4a}(s) + 4a\ HF(g) \quad [7]$$

where $4a > b \geq 4/3a$. And when $b = 4/3a$, reaction [7] is reduced to reaction [1], the complete formation to Si_3N_4.

The experimentally observed ion species are in good agreement with the above proposed mechanism since the formations of NH and NH_2 groups are major processes leading to the CVD of Si_3N_4. The ions $SiF_2NH_2^+$ and $SiF_3NH_2^+$ are presumably derived from SiF_3NH_2 which is the first intermediate molecule. This is an excellent indication that the proposed reaction [2] has actually taken place. The observed ion $Si_2F_5NH^+$ possibly originating from Si_2F_6NH agrees with reaction [3]. The remaining polymeric intermediate ions with an approximate formula, $(Si(NH)_2)_nSi_2F_m$ where n = 1-6, and m = 6-8, suggest that successive reactions [5] and [6] might have occurred. Moreover in these earlier stages of polymerization and nucleation, the reactions seem to proceed not only through chain-like additives such as in reactions [5] and [6], but also through cross-linkages to form two- and three-dimensional clusters. This is suggested by more NH units than Si in the composition of higher polymeric ions. Since the electron impact ionization behavior of these high polymeric species and nuclei are not available, detailed analyses of the stepwise mechanisms could not be reached.

The observed intermediate ion species could be used to explain the onset of the vapor phase nucleation in the CVD of Si_3N_4. At temperatures below 400°C, the reactions between SiF_4 and NH_3 gases take place primarily on surfaces. Consequently no intermediate molecule could be detected. Between 400° and 1000°C, the interaction is believed to occur both in the vapor and on the surface. The existence of only the first intermediate species SiF_3NH_2 suggests that the vapor phase reaction and nucleation are limited to the first few stages of condensation, and successive reactions probably occur on surfaces. Thus the resulting product, containing amorphous material, could not be entirely converted to crystalline Si_3N_4 at 1200°C. At temperatures above 1000°C, the vapor phase interaction and nucleation are found to proceed to a large extent. This is evidenced by the presence of polymeric intermediate molecules. The incomplete conversion to Si_3N_4 during the vapor phase interaction probably produces irregular lattice structures in the product containing NH groups.

The chemical reactions occurring in the SiF_4-NH_3 system are probably similar to those in the $SiCl_4$-NH_3 system widely employed in the industry. The substitution of fluorine by chlorine presumably yields similar reaction steps leading to the deposition of nitride films as described in preceding paragraphs. The difference in chemical nature of these two halogens will appear on the life times of the polymeric intermediates, which may result in different reaction rates and reaction temperatures. The sharp increase in the deposition rate in the $SiCl_4$-NH_3 system (8) above 1300°C (attributed to vapor phase nucleation) as compared to the observed presence of polymeric species near 1200°C may be attributed to this difference.

In summary, the presence of the intermediate molecular species reveals that vapor phase nucleation and interaction occurs during the CVD of Si_3N_4 at elevated temperatures. The interaction and nucleation on surfaces are found to become less important as the temperature increases. The proposed reaction mechanism leading to the formation of Si_3N_4 is in good agreement with the present experimental observation. Further analyses of these intermediate ion species should provide detailed mechanisms of the vapor phase nucleation.

Manuscript submitted May 25, 1977; revised manuscript received July 28, 1977.

Any discussion of this paper will appear in a Discussion Section to be published in the June 1978 JOURNAL. All discussions for the June 1978 Discussion Section should be submitted by Feb. 1, 1978.

Publication costs of this article were assisted by the U. S. Army.

REFERENCES

1. M. J. Grieco, F. L. Worthing, and B. Schwartz, *This Journal*, **115**, 525 (1968).
2. T. L. Chu, C. H. Lee, and G. A. Gruber, *ibid.*, **114**, 716 (1967).
3. A. C. Airey, S. Clarke, and P. Popper, *Proc. Brit. Ceram. Soc.*, No. 22, 305 (1973).
4. K. S. Mazdiyasni and C. M. Cooke, *J. Am. Ceram. Soc.*, **56**, 628 (1973).
5. M. Billy, *C. R. Acad. Sci.* **242**, 137 (1956).
6. M. C. Sneed and R. C. Brasted, "Comprehensive Inorganic Chemistry," Vol. 5, p. 173, D. Van Nostrand Co., New York (1959).
7. O. Glemser and P. Naumann, *Z. Anorg. Allg. Chem.*, **298**, 134 (1958).
8. K. Niihara and T. Hirai, *J. Mater. Sci.*, **11**, 593 (1976).
9. A. Kato, Y. Ono, S. Kawazoe, and I. Mochida, *Yogyo Kyokai Shi*, **80**, 114 (1972).
10. Sin-Shong Lin, *This Journal*, **122**, 1405 (1975).
11. U. Wannagat, "Advances in Inorganic Chemistry and Radiochemistry," Vol. 6, p. 225, Academic Press, New York (1964).
12. S. S. Lin, Army Materials and Mechanics Research Center, AMMRC TR-73-9, March 1973.
13. S. S. Lin, *Rev. Sci. Instrum.*, **44**, 516 (1973).
14. H. J. Svec and G. R. Sparrow, *J. Chem. Soc. A*, **1970**, 1162.

Brief Communication

Alloy Composition Profile of Heterogeneous Structure in $GaAs_{1-x}P_x$ Determined by the Anodization-Electroreflectance Technique

S. Tachi, A. Moritani, and J. Nakai

Department of Electronics, Faculty of Engineering, Osaka University, Suita, Osaka 565, Japan

A graded bandgap structure in semiconductor alloys is often found in electronic devices such as solar cells, epitaxial wafers, and heterojunction interfaces. In fabrication of $Al_xGa_{1-x}As$-GaAs solar cells, the graded composition structure provides a potential increase of power conversion efficiency (1). It has been well known that a $GaAs_{1-x}P_x$ epi-wafer layer with continuously graded composition is grown beneath the thick epi-layer with uniform composition to minimize strain and crystal imperfections due to lattice mismatch between the $GaAs_{1-x}P_x$ epi-layer and the GaAs substrate (for $x < 0.45$) and/or GaP (for $x > 0.45$) (2). It is of vital importance for development of these devices to know the depth profile of the bandgap energy, *i.e.*, the alloy composition in a heterogeneous system easily and accurately up to a depth of 50 μm or more.

In this paper we propose a newly combined technique of the successive anodization and layer removal and the electrolytic electroreflectance measurement (AE technique), and we report, as an example of its application, the depth profile of the alloy composition x in the graded bandgap region of one of $GaAs_{1-x}P_x$ epi-wafer on the basis of the experimental data about the anodization of $GaAs_{1-x}P_x$ (3). Anodization has been used for sectioning to obtain the carrier concentration profile (4), and has been known to provide a strain-free, planar, reproducible sample surface as well as accurately controllable thickness of the anodized film. Electrolytic electroreflectance (ER) under the low field condition has been used to obtain a great amount of information about electronic energy band structures of solids such as values of the energy bandgap and types of the critical points, effective masses, etc., and it gives not only the energy value of the fundamental energy bandgap, but also those of higher interband transitions named E_1, E_2, and so on in energy band structure (5). The present AE technique has the advantage that the same electrolyte and the electrolytic cell can be used for anodization and ER.

The sample used was n-type $GaAs_{0.63}P_{0.37}$ with carrier concentration $N_d = 1 \times 10^{16} \sim 2 \times 10^{17}$ cm^{-3} and thickness of 30 $\sim$ 60 μm, epitaxially grown on n-type (100)-oriented GaAs substrate with $N_d \approx 1 \times 10^{18}$ cm^{-3}. The electrolyte used in this investigation was a mixture of one part of 3% aqueous solution of tartaric acid and two parts of propylene glycol (6). Anodization was carried out by the constant current method in the magnetically stirred electrolyte under illumination in order to accelerate the reproducible and uniform growth. The current density was kept at 3.0 mA/cm^2. After each anodization the sample was boiled in concentrated HCl for a while to remove the oxide completely from the surface. Then the sample was rinsed in deionized H_2O and immersed quickly in methanol to prevent its being oxidized in air. The cleaned sample was then immersed in the same electrolyte for ER measurement. The square wave modulation was adopted to deplete sample surface. With a sufficiently low field, ER spectrum can be represented in terms varying linearly and quadratically with the modulating electric field in zincblende-type crystals such as GaAs, $GaAs_{1-x}P_x$, and GaP, so that we have used [011] polarized light to eliminate the linear term and obtain the energy value of the energy bandgap from the analysis of ER signal (5). As the low field condition is achieved more easily at the E_1 transition than at the fundamental gap, the ER measurements were carried out near the E_1 transition, and the spectra obtained were analyzed by the use of the three-point method which gave the energy value of the E_1 transition using the value of the amplitude and the energy at the peaks and the base line in ER spectra. The corresponding alloy composition was derived from the energy value and the bowing parameter (340 $\pm$ 30 meV) of the E_1 transition. The bowing parameter used was determined by ER measurements of $GaAs_{1-x}P_x$ with $x = 0$, 0.01, 0.12, 0.37, 0.39, 0.41, 0.65, 0.85, and 1. It indicates intermediate value between those reported by Aspnes *et al.* (400 meV) (7) and Thompson *et al.* (310 meV) (8). The penetration depth of the light was estimated to be about 75Å for GaAs and about 80Å for GaP which was small enough to give the well-resolved depth profile of epi-layer with thickness of more than 30 μm.

Figure 1 shows the depth profile of the alloy composition of $GaAs_{0.63}P_{0.37}$ epi-wafer obtained by the present AE technique. The depth in horizontal scale was derived from the result of anodization (3). To obtain these data, 167 cycles of anodization were performed, and the stripped thickness of this epi-wafer was 52 μm. As seen in Fig. 1, the graded composition region is 32 μm and the alloy composition varies linearly from $GaAs_{0.63}P_{0.37}$ epi-wafer to the GaAs substrate.

In conclusion, we have reported and demonstrated the applicability of the present AE technique to the depth profile of the alloy composition in heterogeneous system, and have shown that, as an example, $GaAs_{1-x}P_x$ can be dug and treated up to 52 μm or more by the successive anodization and layer removal.

Key words: depth profile, heterogeneous structure, anodization, electroreflectance, $GaAs_{1-x}P_x$.

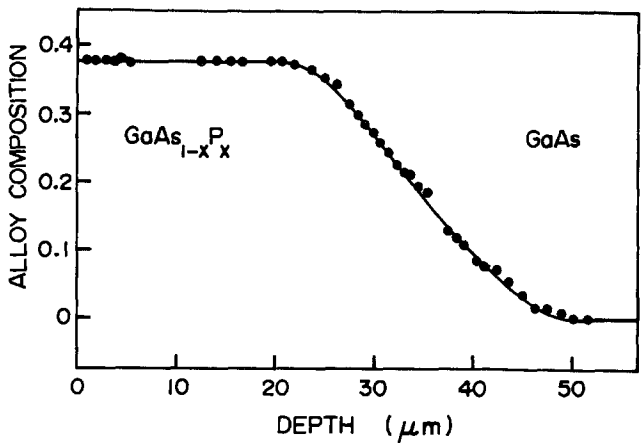


Fig. 1. Depth profile of the alloy composition of $GaAs_{0.63}P_{0.37}$ epi-wafer obtained by the AE technique.

Acknowledgments

The authors wish to thank Prof. C. Hamaguchi and Dr. K. Kondo for their helpful advice and useful discussions, and Mr. A. Shimano and Mr. A. Murakami for their technical assistances and advice. This work is partially supported by the Grant-in-Aid for Scientific Research on "Surface Electronics" from the Ministry of Education of Japan.

Manuscript submitted July 8, 1977.

Publication costs of this article were assisted by Osaka University.

REFERENCES

1. J. A. Hatchby and R. L. Fudurich, *J. Appl. Phys.*, **47**, 3140 (1976).
2. A. H. Herzog, W. O. Groves, and M. G. Craford, *ibid.*, **40**, 1830 (1969).
3. S. Tachi, A. Moritani, and J. Nakai, in Proceedings of the 9th Conference on Solid State Devices, Tokyo (1977).
4. H. Müller, F. H. Eisen, and J. W. Mayer, *This Journal*, **122**, 651 (1975).
5. D. E. Aspnes, *Surf. Sci.*, **37**, 418 (1973).
6. H. Hasegawa, and H. L. Hartnagel, *This Journal*, **123**, 713 (1976).
7. D. E. Aspnes and J. E. Rowe, *Phys. Rev. Lett.*, **27**, 183 (1971).
8. A. G. Thompson and J. C. Woolley, *Can. J. Phys.*, **44**, 2927 (1966).

DISCUSSION SECTION

This Discussion Section includes discussion of papers appearing in the *Journal of The Electrochemical Society*, Vol. 123, No. 10; October 1976; and Vol. 124, No. 2, 3, and 6; February, March, and June 1977.

The Dielectric Breakdown in Anodic Aluminum Oxide

H. J. de Wit, Ch. Wijenberg, and C. Crevecoeur (pp. 1479-1486, Vol. 123, No. 10)

J. M. Albella, J. M. Martinez-Duart, M. J. Puente, and J. Baonza:[1] The electrical breakdown of anodic oxides is still a controversial subject among researchers. The results obtained in anodic Ta_2O_5 thin films in our laboratory are in good agreement with the theory recently put forward by Wit *et al.* for anodic Al_2O_3 thin films.

Tantalum foil was anodized in a 0.01% PO_4H_3 electrolyte at a constant current density of 3 mA/cm^2. When the preset voltage was reached, the current was let to decay to a value about one thousand times smaller than the initial value. Before anodization, the tantalum samples were subjected to the following treatments: (*i*) degreasing by rinsing in carbon tetrachloride, acetone, and methanol; (*ii*) chemical etching in a 5:2:2 solution of commercial sulfuric, nitric, and hydrofluoric acids; and (*iii*) same treatment as before followed by an immersion in a solution of NH_4F-HF as it was used by Maurel *et al.*[2] As suggested in this work we have observed by scanning electron microscopy that treatment (*iii*) produces crystalline grains free of heterogeneities and with very well-defined boundaries.[3] We have also checked by Auger spectroscopy[3] that this treatment leaves a very clean surface by eliminating to undetectable limits the large fluorine contamination left after treatment (*ii*).

The breakdown voltage V_b was measured in samples anodized at a voltage V_f ranging from 25 to 200V which corresponds to a thickness from 432 to 3460Å. A ramp voltage of 1 V/sec was applied to the oxide by means of a copper-tipped probe with a contact area of about 5×10^{-4} cm^2. At least fifty determinations of V_b were made for each sample.

Several experimental results observed in our laboratory in the breakdown of Ta_2O_5 films strongly support the theory given by Wit *et al.* for Al_2O_3. These results are: (*i*) the shape of the breakdown voltage distribution curves are similar to those obtained by Wit *et al.* and P. Solomon *et al.*[4] in Al_2O_3; (*ii*) for a given surface treatment and in the voltage range studied, the ratio V_b/V_f is approximately equal to 0.3 and 1.1 for treatments (*i*) and (*ii*), respectively, the breakdown dispersion curves showing a large scattering in the measurements. On the other hand, treatment (*iii*) gives the largest breakdown voltage, $V_b = 1.2V_f$, and the least scattering in the measurements. The fact that V_b/V_f is practically independent of formation voltage, and therefore of oxide thickness and electric field, is qualitatively in agreement with Eq. [3] and [4] in the paper of Wit *et al.*, since the variation of V_b/V_f with the logarithm of the thickness is relatively small.

We therefore think that the above results strongly support the ionic mechanism postulated by Wit *et al.* and by Shousha,[5] at least for tantalum surfaces that are clean and free of inhomogeneities. According to this mechanism the breakdown is started by an ionic movement. This theory also confirms our preliminary observations[6] that V_b is very high for clean tantalum surface heated to 2500°K in ultrahigh vacuum. All these facts point out that the probabilistic nature of the breakdown phenomenon is very much affected by the state of the metal surface. In this sense, the smaller

[1] Departamento Fisica Aplicada e Instituto Fisica del Estado Solido, C-XIII, Universidad Autónoma, Cantoblanco, Madrid-34 Spain.
[2] B. Maurel, D. Dieumegard, and G. Amsel, *This Journal*, 119, 1715 (1972).
[3] J. Baonza, M. J. Puente, J. M. Martinez-Duart, and J. M. Albella, Paper presented at the IV Reunión Nacional de Vacío y sus Aplicaciones, Madrid (1976).
[4] P. Solomon, N. Klein, and M. Albert, *Thin Solid Films*, 35, 321 (1976).
[5] A. H. M. Shousha, *J. Non-Cryst. Solids*, 17, 100 (1975).
[6] J. M. Martinez-Duart, J. M. Albella, and J. Baonza, *Thin Solid Films*, 36, 371 (1976).

V_b observed in samples subjected to treatment (*ii*) in comparison to treatment (*iii*) might be related to the fluorine contamination on the surface as it has been observed in silicon oxide by Croset and Dieumegard.[7] At present we are conducting research to elucidate if the breakdown and the scintillation is initiated at localized regions with a large impurity concentration such as, for instance, grain boundaries.

Origin of the Fixed Charge in Thermally Oxidized Silicon

H. Goronkin (pp. 314-317, Vol. 124, No. 2)

S. I. Raider:[8] The author of the paper under discussion presents experimental MOS data showing the variation in Q_{ss}/q with change in time of annealing SiO_2-Si structures in N_2 gas at 1100°C (Fig. 2 of paper). The Q_{ss}/q data represent the total calculated charge derived from flatband voltage C-V measurements of MOS capacitors formed with a 1300Å oxide film thermally grown on a <111> oriented, n-type Si substrate. These data were analyzed in terms of solid-state diffusion to determine whether they support the model[9] in which Si atoms (or ions) diffuse into an SiO_2-Si interfacial region to generate fixed oxide charge.

It was experimentally observed that an increase in the N_2 gas annealing time results in an initial decrease, followed by a gradual increase, in Q_{ss}/q. Similar variations in Q_{ss}/q were previously reported[10-12] after annealing SiO_2-Si structures in N_2 gas. Although Lamb and Babcock's data[10] are obtained from variations in anneal temperature rather than variations in anneal time, the interfacial process leading to an increase in Q_{ss}/q appears to be thermally activated.[12,13] Data that were obtained at the shorter anneal times at higher temperatures[10] presumably correspond to data obtained at longer anneal times at a lower temperature.

Only the decrease, but not the subsequent increase in Q_{ss}/q, is detected after annealing similar structures in either Ar or in He gas at temperatures greater than 1000°C.[10,13,14] The increase in Q_{ss}/q appears to be uniquely associated with annealing in N_2 gas. Si diffusion at the transition region should be independent of annealing ambient if the annealing gases are chemically inert. Lamb and Babcock[10] had suggested that this increase in Q_{ss}/q is related to the chemical interaction of N_2 gas with Si at the SiO_2-Si interface. Direct evidence has been presented indicating that N_2 does interact with Si at an SiO_2-Si interface during high temperature annealing.[14,15] In addition, the observed saturation in Q_{ss}/q with anneal time correlates with a saturation in N_2 concentration at the SiO_2-Si interface.[14] No increase in Q_{ss}/q is detected after annealing in Ar gas and no Ar is detected at the SiO_2-Si interface.[14,15]

SiO_2-Si structures annealed in N_2 at elevated temperatures apparently exhibit two electrical instability effects. Fixed oxide charge densities are minimized and primarily surface states[11,13,14] are generated. Surface states are detected after annealing in N_2 gas at temperatures greater than 1000°C with[13,14] and without[11] a 400°C postmetallization anneal. High temperature annealing in Ar exhibits only the first of these electrical instability changes. Fixed oxide charge formed during the oxidation reaction is minimized by a thermally activated process that is independent of the annealing ambient.[16] The observed increase in Q_{ss}/q is more properly associated with a chemical interaction between N_2 and Si within the SiO_2-Si transition region than with Si atom (or ion) diffusion at this interfacial region.

[7] M. Croset and D. Dieumegard, Paper 87 presented at the Cleveland, Ohio, Meeting of the Society, Oct. 3-7, 1971.
[8] IBM T. J. Watson Research Center, Yorktown Heights, New York 105 8.
[9] B. E. Deal, M. Sklar, A. S. Grove, and E. H. Snow, *This Journal*, 114, 266 (1967).
[10] D. R. Lamb and F. R. Badcock, *Int. J. Electron.*, 24, 11 (1968).
[11] F. W. Montillo and P. Balk, *This Journal*, 118, 1463 (1971).
[12] B. E. Deal, *ibid*, 121, 198C (1974).
[13] M. Revitz, S. I. Raider, and R. A. Gdula, Unpublished results.
[14] J. K. Howard, R. Flitsch, and S. I. Raider, *J. Vac. Soc. Technol.*, 14, 69 (1977).
[15] S. I. Raider, R. A. Gdula, and J. R. Petrak, *Appl. Phys. Lett.*, 27, 150 (1975).

The Identification of the Mobile Ion during the Anodic Oxidation of Silicon

W. D. Mackintosh and H. H. Plattner (pp. 396-400, Vol. 124, No. 3)

P. F. Schmidt:[17] The conclusions drawn by Mackintosh and Plattner from their very interesting work,[18] for which I was privileged to act as one of the reviewers, are fully self-consistent if one accepts their premise that the noble gas markers are immobile also in anodic SiO_2. This interpretation of their experimental results appears to me, however, to be at variance with other results obtained by different techniques, and it is the purpose of this communication to point out the areas of disagreement and to suggest possible explanations.

The two main conclusions of their paper are: (*i*) The noble gas atoms stay near the outer surface of the oxide film during additional oxide growth, implying that the ionic current is carried almost exclusively by oxygen ions; and (*ii*) Phosphate ions, incorporated into a preexisting anodic SiO_2 film, appear to drift at least as fast as the oxygen ions during additional anodization, thus leading to the encapsulation of the phosphate-doped oxide by a layer of newly formed oxide. Both results were obtained by Rutherford backscattering, which allows very little error in the determination of the position of the noble gas markers. Determination of the position of the phosphate ions is more difficult because of the small mass difference between silicon and phosphorus; however the exact velocity of the phosphate *vs.* the oxide ions is not really a major point of the discussion (see below).

Before describing the older results which, in my opinion, are not readily compatible with the oxide ion migration model, I should like to first quote the unambiguous evidence given in ftn.[19] that silicon ions can be the mobile species, albeit in Si_3N_4 rather than in SiO_2. If a preexisting amorphous Si_3N_4 film is subjected to anodization, hydroxyl ions penetrate into the film and convert it into anodic SiO_2, starting from the outside. If, on the other hand, a crystalline Si_3N_4 film is anodized under otherwise identical conditions, anodic SiO_2 forms on top of the Si_3N_4 layer without change in the composition of the latter. Thus Si ions can be the mobile species; their tetrahedral bond angles do not constitute a fundamental difficulty.

Anodic SiO_2 films, even those grown in nearly anhydrous organic media, are very hygroscopic, to my knowledge more so than the anodic oxide films on any other element. The surface layer of a freshly grown anodic SiO_2 film is strongly hydrated respectively hydroxylated. A thin anodic SiO_2 film is under compressive stress, with increasing anodic-forming voltage the (compressive) stress first diminished, and it eventually becomes tensive.[20] If the film is now exposed to room air, the tensive stress gradually diminishes and can even become compressive again, but the tensive stress can be reestablished by reanodization to the same or very slightly higher voltage. These changes in stress are clearly indicative of absorption and desorption of moisture. The hydroxyl content of an anodic SiO_2 film, grown to different thicknesses at the same constant current density and in the same tritium-tagged electrolyte, is found to be nearly independent of

[16] S. I. Raider and A. Berman, Submitted to *This Journal*.
[17] Bell Laboratories, Allentown, Pennsylvania 18103.
[18] W. D. Mackintosh and H. H. Plattner, *This Journal*, 124, 396 (1977).
[19] P. F. Schmidt and D. R. Wonsidler, *ibid*, 114, 603 (1967).

the anodization voltage. In fact, it decreases slightly with increasing forming voltage. Only the surface layer of the oxide film is strongly hydroxylated, and the thickness of this hydroxylated region is nearly independent of the forming voltage.[20]

If a thermally grown SiO_2 film is subjected to anodic bias below the voltage at which additional film growth occurs, then hydroxyls—or possibly water—is injected into the film, eventually throughout its entire thickness if the bias is maintained long enough.[20] These hydroxyls—or water—can again be expelled by anodization to a higher voltage, only the surface layer remaining strongly hydroxylated or hydrated. The injection of the hydroxyls under low anodic bias required incubation periods of several minutes, in full analogy with the incubation periods observed by Dreiner[21] by means of capacitance measurements, suggesting that hydration of the oxide surface by a chemical step is required for the subsequent field-aided injection of hydroxyls; in other words, the hydroxyls in the solution do not simply pass into the oxide as current carrying carriers in the oxide.

In the past I have interpreted the dehydration of the oxide at full-forming field strength as a reaction between hydroxyls in the film and silicon ions in transit through the film. I am still at a loss to think of a fully satisfactory alternate mechanism. This explanation, however, presupposes the existence of mobile silicon ions.

I have dwelt on this description of the hydration and dehydration effects at such length because dehydration of a strongly hydroxylated SiO_2 must of necessity result in a shrinkage of the lattice. It seems conceivable to me that the shrinkage front, which is known to progress outwards from the Si/SiO_2 interface, could push ahead of it any interstitial atoms, especially if they are of larger size. The net effect during anodization to higher voltages would be to keep the noble gas markers near the outer surface of the oxide film.

Mackintosh and Plattner seem to imply that the phosphate ion as an entity, PO_4''', is migrating under bias in anodic SiO_2 films. PO_4''' is a tetrahedral ion with a "diameter" of about 3.92Å.

During thermal oxidation of silicon, oxygen gas is known to permeate the oxide lattice, and to cause additional oxide growth at the Si/SiO_2 interface. Mackintosh and Plattner therefore compare the anodic oxidation of silicon, with oxide ions mobile, to the thermal oxidation of silicon. Since they find that phosphate ions are at least as mobile as the lattice oxide ions, this implies a kind of "interstitial" migration of the phosphate ions as well.

The O_2 molecule, however, is dumbbell shaped, and can orient itself to pass through the constrictions in the SiO_2 lattice with its small dimension, not with its long dimension of 3.2Å. In addition, it is known that the larger alkali ions, such as Rb+ or Cs+ are too large to fit into the open spaces of the most widely spaced SiO_2 lattice (crystobalite), let alone to migrate freely through the constrictions of that lattice. Implanted Cs ions have indeed been used as immobile charges (at temperatures of 430°C and at fields of 1×10^6 V/cm) to control the surface potential of silicon in MOS structures.[22] Thus it appears exceedingly unlikely to me that PO_4''' could be a freely migrating species even in anodic SiO_2 films.

If the phosphate is indeed mobile, as claimed in ftn.[18], then, in my opinion, this mobility should be a consequence of the oxygen ions of the PO_4''' complex forming a component of the oxygen sublattice. If the oxide sublattice moved in a coherent way, it would simply take the phosphorus atoms along with it. This picture requires that the order of the oxygen ions during anodization be maintained. It has, in fact been found in all instances where the sequence of the oxide ions during anodization was monitored by means of O^{16}-O^{18} measurements, that the order of the oxide ions is indeed maintained; such is not necessarily the case for the cations.[23,24] If the phosphate ion is indeed tied to the anion sublattice, then it must become buried deeper during additional anodization, irrespective of whether anions or cations are the mobile species. Similarly, a species somehow tied to the cation sublattice must remain near the outer surface of the oxide, again irrespective of which species is mobile. This consideration implies that the position of the phosphate ion upon additional anodization may not be used at all in trying to determine the mobile lattice species. Thus my own earlier conclusions,[25] based upon its location, are certainly also invalidated. It would appear that a possible tie-in with one of the sublattices should be considered whenever markers are used.

According to ftn.[18], the motion of the phosphate during anodization is actually somewhat faster than that of the lattice oxygen. This is one experimental detail I have some reservations about in view of another observation. A n-type silicon electrode of somewhat higher resistivity (1 Ω-cm or higher) blocks the current flow in darkness up to high voltages. This current blocking immediately disappears if a very thin oxide film is formed on the bare Si surface in solutions of concentrated phosphoric or polyhedral borane acids, apparently due to a high surface recombination-regeneration velocity caused by the acid molecules incorporated[25,26] into the oxide film.

On the other hand, if a very thin oxide ($V_{form} = 10V$) is first formed in an inert electrolyte (such as KNO_2 in tetrahydrofurfuryl alcohol, or ammonium-pentaborate in water), then several hundred angstroms of acid-doped oxide can be grown on top of the "pure" oxide without causing excessive surface regeneration of minority carriers.[27] The discrepancy between this observation and that in ftn.[18], however, is marginal because current blocking of n-type Si anodes also disappears if a "pure" anodic oxide is grown to thicknesses larger than about 400Å (about 3.8 Å/V). If the migration velocity of the phosphate were only 10% higher than that of the oxide ions, no phosphate would yet have reached the Si/SiO_2 interface in the "cations immobile" model.

It should be possible to unambiguously clarify the question of the mobility of cations or anions in the anodization of silicon by monitoring the sequence of the cations before and after anodization. If only the anions are mobile, the sequence of the cations must, of course, be maintained. The experiment can be carried out by epitaxial deposition of a very thin silicon layer isotopically enriched in Si-30 on top of a normal silicon substrate. Since Si-30 is the only silicon isotope to become radioactive upon irradiation with thermal neutrons, anodization through the substrate/epitaxial interface, followed by stepwise dissolution of the oxide and determination of the specific activity of each oxide layer, would permit determination of the cation sequence.

In conjunction with the mechanism of phosphate migration (if indeed the phosphate migrates), it would also be of interest to determine the sequence of the oxide ions (O^{16}, O^{18}) before and after anodization, an experiment fully feasible with Rutherford backscattering or nuclear techniques. One would, however, have to look at a O^{16}-O^{18} transition somewhat deeper in the preexisting oxide film, in view of the known rapid exchange between the two oxygen isotopes at the oxide surface during additional anodization.[28] This exchange

[20] P. F. Schmidt and J. D. Ashner, *ibid.*, 118, 325 (1971).
[21] R. Dreiner, *ibid.*, 113, 210 (1966).
[22] G. Sixt and A. Goetzberger, *Appl. Phys. Lett.*, 19, 478 (1971).
[23] G. Amsel and D. Samuel, *J. Phys. Chem. Solids*, 23, 1707 (1962); J. Siejka, J. P. Nadai, and G. Amsel, *This Journal*, 118, 717 (1971); G. Amsel, C. Cherki, M. Croset, G. Feuillade, J. P. Nadai, C. Ortega, and J. Siejka, *Collect. Czech. Chem. Commun.*, 36, (1971); D. J. Coleman, Jr., D. W. Shaw, and R. D. Dobrott, *ibid.*, 124, 239 (1977).
[24] P. Verkerk, P. Winkel, and D. G. Groot, *Philips Res. Rep.*, 13, 506 (1958); S. Rigo and J. Siejka, *Solid State Commun.*, 15, 259 (1974).
[25] P. F. Schmidt and A. E. Owen, *This Journal*, 111, 682 (1964).
[26] J. Kraitchman and J. Oroshnik, *ibid.*, 114, 405 (1967).
[27] P. F. Schmidt, *IEEE Trans. Electron Devices*, ed-12, 102 (1965).
[28] G. Amsel and M. Croset, Paper 13 presented at the New York, New York, Meeting of the Society, May 4-9, 1969.

is caused by the injection of hydroxyls or water discussed above, and is not necessarily evidence for the absence of cation migration.

Control of Al_2O_3 Position in Anodic GaAs Native Oxide

B. Bayraktaroglu, S. J. Hannah, and H. L. Hartnagel
(pp. 958-959, Vol. 124, No. 6)

J. P. S. Pringle:[29] Twice have I commented[30,31] on the inadequacy of the reviewing procedures used by *This Journal*, and the brief communication by Bayraktaroglu, Hannah, and Hartnagel provides a splendid illustration of my theme.

Their communication is indeed brief, since it is only eight paragraphs long. It opens with a statement of claim:

"It is shown that by careful control of kinetic growth parameters, it is possible to anodically position a thin Al_2O_3 layer in a native GaAs-oxide film either near the oxide-semiconductor interface or on the surface of the GaAs oxide." That claim is specific and unambiguous; nowhere is it substantiated. And that may not be obvious to the reader owing to the way the article has been written.

Consider first its organization. After stating their claim, the authors use the rest of the first paragraph to describe several "interesting" advantages that their claim "promises." In the next paragraph, they put forward a hypothesis that interprets their claim in terms of the differing mobilities of anions and cations at high and low electric fields across the oxide film. This leads naturally to paragraph three, where the "kinetic growth parameters" of the claim are identified as current density, and to paragraph four, where numbers are placed on this parameter; paragraph five notes "a limit to the thickness of Al_2O_3 on the GaAs surface." Only after the claim and the hypothesis interpreting it have been well and truly described is the experimental evidence presented in paragraphs six and seven. By placing their evidence after the discussion, the authors suppress consideration of possible alternatives, both by themselves and by their readers.

Next consider the style of the article. This is extremely positive throughout, as illustrated by these statements at the beginning of paragraph two.

"Due to the difference in the threshold fields required for the activation of different anions and cations, it is possible to influence the growth mechanism of anodic oxide films, and therefore shift the effective oxide formation region anywhere from the metal-oxide interface to the oxide-electrolyte interface." Note the decisive "Due to . . . it is possible . . . and therefore" construction here, and that none of these statements have been supported by any references. While such a style makes for easy reading, it does so at the expense of oversimplification. Everything is focused toward the claim; even the experimental evidence is presented, not in terms of what was actually observed, but in terms of the interpretation required by the claim! This combination of organization and style is most persuasive in suggesting that the authors have established their claim, but examination of the content of their article will show that they most certainly have not.

What did the authors actually observe? That is uncertain. When a sample of GaAs covered with a layer of Al of unspecified thickness was anodized at unspecified constant current density to an unspecified final voltage for an unspecified length of time in an unspecified electrolyte at an unspecified temperature, an etching of "some" of the "composite" oxide was observed when the formation current density was "high" "(> 2 mA/cm^2)", but not when it was "low" "(~ 20 μA/cm^2)."

The criteria for observing "etching" are not specified, nor is the strength, time, and temperature of the tartaric acid used. No evidence is presented that the tartaric acid will dissolve all of the "GaAs native oxide," nor is it explained in what way this differs from the "anodic GaAs native oxide" of the title. "The thickness of the oxide left behind was measured with a Dektak profile plotter" which implies the formation of an oxide step; that would require removal of the "oxide left behind" from part of the surface, but there is no discussion as to how this was done. "Measured values" unspecified "were compared with the expected thickness" unspecified "of Al_2O_3," but it is not specified whether they agreed or not, and to within what experimental error. When reporting their overpotential *vs.* time evidence in paragraph seven, the authors write (present author's comments in parentheses):

"After all the Al is converted into Al_2O_3 (unsupported statement), the overpotential exhibits a temporary (unspecified) steep (unspecified) increase for the high current density case, whereas a constant (how constant?) potential is maintained over a short (unspecified) period for the low current density case." No doubt the authors will claim they have at least specified the "electrolyte first suggested by Hasegawa and Hartnagel (2)," a tactic that forces the reader to look up the reference[32]—in which he finds a number of different electrolytes mentioned."

Evidence as indefinite as this neither confirms nor denies the claim, and it but remains to consider the hypothesis advanced in the second paragraph. This rests largely on the following statement:

"For anodic Al_2O_3 films, it is known (1) that the threshold field required for the activation of cations is larger than that for anions." That statement greatly surprised the present writer. Well it might, since he was responsible for the final draft of the reference (1)[33] cited, and no such conclusion was reached by him. How the authors reached that conclusion is up to them to explain; presumably—repeat presumably—they derived it in some way from the reported[33] variation of t_m, the transport number for the aluminum, with current density. If so, they have two questions to answer. First, how can they be so sure in paragraph four that:

"If low current densities are used, *i.e.*, ~ 20 μA/cm^2, after the Al_2O_3 is formed, there are only anions moving across the oxide to the GaAs-Al_2O_3 interface." When the reference[33] reports that the transport number of the aluminum was 0.33-0.41 at 100 μA/cm^2 (the lowest current density investigated), 0.44 at 300 μA/cm^2, 0.56 at 1 mA/cm^2 and 0.72 at 10 mA/cm^2? And second, how can they justify applying these results in 3% aqueous ammonium citrate electrolyte in preference to those obtained with solution A, a glycol-based electrolyte similar to some of those mentioned in their reference (2),[32] where t_m remained constant at approximately 0.6 for all current densities between 100 μA/cm^2 and 10 mA/cm^2?

The purpose of a scientific communication is not to convince the reader that a claim is valid, but to let the reader convince himself by providing enough evidence for him to do so. That the authors have not done; they have merely stated their claim, and then asked the reader to accept on trust that they have enough evidence in support, even though they are not going to specify exactly what it is. Not good enough! An effective reviewing procedure should protect the reader from misleading impressions, the publisher from wasting money, and authors and editors from subsequent embarrassment by curmudgeons such as the present writer. If I had been the reviewer for this article, its many and obvious deficiencies would have left me with only one recommendation: do not publish. Yet it has been published and apparently after review too—why?

[29] Chalk River Nuclear Laboratories, Atomic Energy of Canada Limited, Chalk River, Ontario, Canada K0J 1J0.
[30] J. P. S. Pringle, *This Journal*, 121 150*C* (1974).
[31] J. P. S. Pringle, *ibid.*, 123, 347*C* (1976).
[32] H. Hasegawa and H. L. Hartnagel, *ibid*, 123, 713 (1976).
[33] J. A. Davies, B. Domeji, J. P. S. Pringle, and F. Brown, *ibid.*, 112, 675 (1965).

B. Bayraktaroglu, S. J. Hannah, and H. L. Hartnagel:[34] The authors are disappointed that Dr. Pringle has failed to appreciate the main purpose of their short letter. It was a "brief communication" intended "to report information of technological importance . . . which warrants rapid dissemination, even though not necessarily a completed research."[35] The points presented there are felt to be an important development of anodic oxides on GaAs for device applications such as charge storage devices which in fact can now be produced successfully[36] with the low current growth scheme reported in the communication. Unfortunately, concise experimental parameters had to be omitted due to the limited space available for such a communication. Dr. Pringle has chosen to criticize the positive style which we used in compiling the letter. We admit that we were perhaps overenthusiastic in our presentation. We are, however, convinced that the conclusions we stated are correct and important. Indeed we now have further experimental evidence to support our understanding, namely Auger profile results in collaboration with the United Kingdom Post Office Laboratories. These new results are to be published shortly.[37] In our letter we state (admittedly without clear justification) that the threshold field for the activation of cations is larger than that for anions in an Al:Al_2O_3 system, because we interpreted the experimental results of Dr. Pringle and his co-authors[38] as being caused by the operation near the activation energy of the relevant ions rather than by their field-dependent mobilities. Regarding the first more specific question of Dr. Pringle, we clearly saw no indication of any oxide of GaAs on top of our Al_2O_3 for low current growth conditions, and thus had to conclude that only anions move to the GaAs-Al_2O_3 interface. Regarding his second specific question; we employ one part of aqueous solution of tartaric acid (30g of tartaric acid per liter of water) and two parts of propylene glycol. This is most likely nearer to his aqueous-based electrolyte. The experimental observation by Dr. Pringle and his co-workers of a constant t_m for strongly glycol-based electrolytes is explained by us on the basis of space-charge fields being more strongly responsible for the activation of metal ions than in our case. Finally, the authors feel that neither the referees nor the Editor are to be blamed as Dr. Pringle suggests. Indeed they seem to be more familiar with the recent developments of native oxidation of compound semiconductors such as GaAs than Dr. Pringle is, and thus were able to appreciate the interpretations of the data of the relatively simple chemical tests reported.

Editor's Note: Dr. Pringle's criticism of the Brief Communication itself is a matter into which I will not go. As to the review process, certainly, I do grant that unsubstantiated claims should not be published, whether in a Brief Communication or in other forms of publication in this JOURNAL. The question which has to be answered from the JOURNAL'S point of view is the suitability of the review process to minimize that possibility. The review system requires that we depend on our reviewers, who are certainly not without shortcomings. On the whole though, they do an effective, and indeed admirable, job and we must rely on what they say. It follows that not all papers, let alone Brief Communications, will be as "correct" as we would wish them to be. It does mean, I believe, that our system minimizes the shortcomings. In the long run, it is readers and users who weed out those things which are of little or no value. The job of any journal is to make the latter task as small as possible. Again, this note does not pertain specifically to any item published in this JOURNAL, but to the principle of review by peers.

[34] Department of Electrical and Electronic Engineering, University of Newcastle upon Tyne, Newcastle upon Tyne, NE1 7RU, England.
[35] Instructions to Authors of Papers, Publications of The Electrochemical Society, Princeton, N. J.
[36] B. Bayraktaroglu, S. J. Hannah, H. L. Hartnagel, *Electron. Lett.*, **13**, 45 (1977).
[37] R. Heckingbottom, G. W. B. Ashwell, C. J. Todd, B. Bayraktaroglu, S. J. Hannah, and H. L. Hartnagel, To be published.
[38] J. A. Davies, B. Domeji, J. P. S. Pringle, and F. Brown, *This Journal*, **112**, 675 (1965).

JOURNAL OF THE ELECTROCHEMICAL SOCIETY

ACCELERATED

BRIEF COMMUNICATIONS

DECEMBER 1977

The Rate Controlling Process in the Oxidation of Hot Pressed Silicon Nitride

D. Cubicciotti,* K. H. Lau, and R. L. Jones

SRI International, Menlo Park, California 94025

The high temperature oxidation of hot pressed silicon nitride has been found to follow a parabolic rate law (1, 2). The rate limiting step in the process has been presumed to be the diffusion of some species through the growing oxide layer as is generally the case in the parabolic oxidation of metals. We report below some critical experiments that show that processes occurring in the oxide scale do not control the rate of oxidation of hot pressed Si_3N_4 and that the diffusion of magnesium in the unoxidized ceramic is probably the rate limiting step.

The oxide scale formed during the high temperature oxidation of hot pressed Si_3N_4 is very porous, the pores presumably containing N_2 formed by the oxidation. In oxidations at temperatures near 1400°C the scale appeared to be fluid and sagged under the action of gravity. Therefore we suspected that the scale was not protective even though the oxidation rate law was parabolic.

To test the protectiveness of the oxide scale, we performed the following experiment. A piece of NC-132 (Norton Co. Si_3N_4 hot pressed with ~ 1% MgO) was cut and surface ground with diamond tools to 40 x 15 x 1.4 mm. The rate of oxidation was measured as a function of time at 1370°C in dry oxygen. The apparatus used was a constant volume system in which the total gas pressure and N_2 content were monitored as a function of time. The system was made of high purity alumina and the sample rested on platinum pads to prevent reaction with the alumina. The oxidation data obtained for the first 18 hours of oxidation are plotted as open points in Figure 1 and the solid curve is the best fit parabola. The parabolic rate constant is 1.4×10^{-9} kg^2/m^4 sec which is in reasonable agreement with literature values (1, 2). Following the initial 18-hour oxidation, the sample was taken from the apparatus, the corrosion scale was removed by diamond surface grinding, and the sample was reoxidized for a further 20 hours. The solid points in Figure 1 show the weight gain data obtained during the reoxidation.

The dotted curve in Figure 1 indicates the reoxidation curve that would be expected if the oxide scale was protective and controlled the rate of oxidation. The dashed curve is an extrapolation of the first oxidation curve. The reoxidation data fall very close to the dashed curve, which indicates that the process controlling the rate of oxidation must have been occurring in the bulk of the sample rather than in the oxide scale.

Concentration profiles for several elements were determined on the cross sections of oxidized samples using electron microprobe analysis. It was found that the concentration of magnesium in the body of oxidized samples decreased from the center to the oxidized surface in a profile typical of a diffusion process. The magnesium concentration in the oxide scale was small except at the outside surface where it was very large. We therefore believe that the diffusion of magnesium through the body of the unoxidized silicon nitride controlled the oxidation rate.

We propose the following mechanism for the oxidation of hot pressed Si_3N_4. The rate controlling step is the diffusion of magnesium through the silicate material in the grain boundaries of the ceramic. (Singhal (2) has already noted that the activation energy for oxidation (~ 100 kcal/mole) is comparable to that for diffusion of cations in silicates).

*Electrochemical Society Active Member.

The oxidation process occurs in the oxide layer. Silicon nitride dissolves in the oxide which is largely a silica-silicate slag. The N^{-3} ions dissolved in the oxide are oxidized to N_2 which generates the bubbles observed in the corrosion layer. At the gas/oxide scale interface, O_2 gas reacts with electrons released from the oxidizing N^{-3} to form O^{-2}. The key to the role of magnesium is that the solubility of Si_3N_4 in the silicate slag is increased by the presence of MgO. (An increase of the solubility of Si_3N_4 in silicate slags due to the addition of alkaline oxides has been observed by Dancy and Janssen (3).) In the oxidation of Si_3N_4, magnesium silicate apparently precipitates at the gas/oxide scale interface and the magnesium concentration in the oxide scale does not build up as oxidation proceeds. The net magnesium concentration at the Si_3N_4 interface, which sets the solubility of the Si_3N_4 in the oxide, is determined by the balance between the rates of arrival and removal of magnesium. The evidence suggests that a sufficient supply of oxygen is available; thus, the oxidation rate is controlled by the rate at which the Si_3N_4 dissolves.

The surface of the silicon nitride beneath the oxide layer becomes pitted during the corrosion process. It is important to understand why pitting occurs because the increasing surface roughness associated with the formation of the pits is probably responsible for the significant degradation of the room temperature bend strength of hot pressed silicon nitride that is observed following high temperature oxidation (4). The formation of pits can be explained by noting that the solubility of Si_3N_4 in the oxide slag is enhanced by Mg and the concentration of Mg in the unoxidized Si_3N_4 increases with depth. A planar interface between the scale and the bulk will not be stable under these circumstances. Local incursions by the scale into the bulk at sites of higher-than-average Mg concentration will encounter an increasing Mg content because of the Mg concentration profile that exists in the bulk Si_3N_4. Thus the ability to dissolve Si_3N_4 will be enhanced at the local incursions, leading to accelerated penetration of the oxide scale into the bulk Si_3N_4 at the same sites and eventually to the formation of pits.

ACKNOWLEDGMENT

Research sponsored by the Air Force Office of Scientific Research (AFSC), United States Air Force under Contract F44620-76-C-0116. The United States Government is authorized to reproduce and distribute reprints for governmental purposes notwithstanding any copyright notation hereon.

REFERENCES

1. W. C. Tripp and H. C. Graham, J. Am. Ceram. Soc., 59, 399 (1976).
2. S. C. Singhal, J. Mater. Sci., 11, 500 (1976).
3. E. A. Dancy and D. Jannsen, Can. Metall. Quart. 15, 103 (1976).
4. J. E. Restall and C. R. Gostelow, Proc. Brit. Ceram. Soc. 22, 89 (1973).

Manuscript received Aug. 18, 1977.

Publication costs of this article were assisted by SRI International.

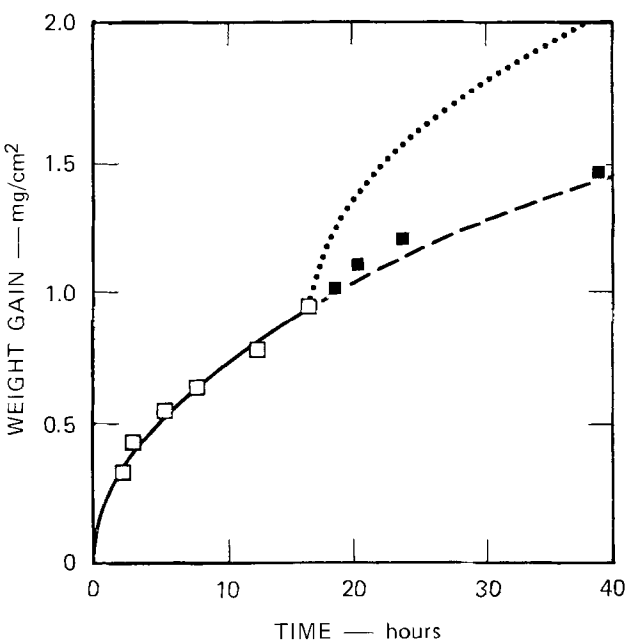


Figure 1 Oxidation and Reoxidation Curves for Hot pressed Si_3N_4(NC132) at 1370°C. Open points for first oxidation. Filled points for reoxidation after removal of initial oxide.

The Precipitation of K $Co[Au(CN)_2]_3$ and Similar Cyanoaurate Complexes

E. T. Eisenmann

Bell Laboratories, Columbus, Ohio 43213

Hard gold baths, which use cyanoaurate (I) in combination with cobalt or nickel ions, operate close to the solubility limits of heretofore unknown coordination compounds. This condition became evident, earlier, when a pink precipitate was formed after cobalt ions were added to a solution of potassium dicyanoaurate (I) (1). From the ratio of Co:Au = 1:3, it was conjectured erroneously, though in agreement with other authors, that the precipitate contained the cyanides of both gold and cobalt (2). A more elaborate analysis showed, however, that the compound contained potassium, yielding approximately the ratio K:Co:Au = 1:1:3. The compound was consequently subjected to an X-ray diffraction analysis and found to exhibit a pattern of lines which is not in agreement with the individual cyanides of cobalt and gold nor with any other catalogued compound. The d-spacings are listed in Table 1.

Table I

Comparison of d-Spacings*

Unknown	AuCN	$Co(CN)_2$
7.55	5.05	5.1
3.85	2.92	3.55
2.74	2.52	2.55
2.58	1.92	2.28
2.35	1.69	
1.94	1.47	
1.62	1.11	
1.55		
1.38		

* For most intensive lines, only.

The original precipitate was found to be readily soluble in cyanide or ammonia solutions and to some extent in water at high temperature. With this aqueous solution various reactions can be carried out. Addition of a strong acid leads to the precipitation of AuCN. Addition of S^{2-} precipitates black CoS. Thiocyanate produces a blue and diacetyldioxime a brown coloration. These reactions prove that the cobalt exists in the hydrated state, and not as a cyanocomplex. However, boiling the solution for an extended period results in the precipitation of $Co(CN)_2$ and AuCN. It is concluded, therefore, that the formula $KCo[Au(CN)_2]_3$ descibes properly the original precipitate. In solution, this compound dissociates into its components K^+, Co^{2+} and $Au(CN)_2^-$, yielding a solubility product of 5.10^{-9}. The precipitate $KCo[Au(CN)_2]_3$ forms hexagonal platelets up to 50 µm across and about 1 µm thick. Recrystallization from water, however, results in hexagonal prisms, which show a different X-ray diffraction pattern.

The recrystallized compound was qualitatively analysed by means of the electron microprobe and found to contain no potassium. Additional analyses with spectrophotometric methods yielded an Au:Co ratio of 2, hence the compound seems to have the formula $Co[Au(CN)_2]_2$.

Coordination complexes of cyanoaurate (I) with other transition elements (Mn, Ni, Cu) have been prepared by similar procedures, and Na^+, NH_4^+, Mg^{2+}, and Ba^{2+} have been substituted for potassium.

If $KCo[Au(CN)_2]_3$ is heated to about 120°C for several days, an intense purple discoloration of the material is observed, which is, however, not accompanied by any visible disintegration of the crystallites. The discoloration is similar to that caused by color-centers in alkali and silver halides. Recrystallization yields an admixture of pink crystals and a dark brown powder, presumably gold metal. Complete thermal decomposition of the compound occurs above 400°C.

Storage of the recrystallized, potassium-free material in a desiccator produces a color change from pink to lavender, apparently due to the loss of water. There is, however, no evidence of disintegration of the crystals. Reversal to the pink form can be achieved by contact with water. Heating this material leads to color changes, first to deep blue, then to metallic gold. These color changes are not accompanied by changes of the crystal shapes, unless the temperature exceeds 400°C, or a somewhat lower temperature is maintained for a long time.

The transition from the lavender to the blue modification involves a weight loss of 15%. Heating the lavender compound to 350°C for 2 hours results in a weight loss of 30%. These weight loss measurements, combined with the analysis for cobalt and gold, suggest the following formulas: $Co[Au(CN)_2]_2 \cdot 10\ H_2O$ for the lavender compound, $Co[Au(CN)_2]_2 \cdot 4\ H_2O$ for the blue compound, and $Co(CN)_2 + Au$ for the material with the appearance of gold.

It is noted that certain characteristics of electroplated cobalt-hardened gold are most favorably developed under conditions which are prerequisites for the precipitation of $KCo[Au(CN)_2]_3$. For example, high pH precludes the precipitation of $KCo[Au(CN)_2]_3$, and also leads to dull, relatively soft gold deposits. Similarly, dull deposits may result from high temperature, corresponding to an increase in the solubility of $KCo[Au(CN)_2]_3$. This temperature effect can be compensated by increasing the concentrations of the reactants, as practiced in the high-speed gold baths (such as Sel-Rex 55 GV). Cyanocobaltate is known to accumulate in extensively used hard gold baths; yet this compound has no effect on the brightness and hardness of the gold deposits. The brightening effect of cobalt can be obtained only with aquo or other weak cobalt complexes, which do not preclude the precipitation of $KCo[Au(CN)_2]_3$.

Analyses of gold deposits plated from a Technic Orosene 999 bath yielded amounts of the elements K, Co, C, and N in a ratio which is consistent with 2% by weight of $KCo[Au(CN)_2]_3$ in gold.

All hard gold deposits from acid electrolytes have a tendency to blister at temperatures above 400°C. This effect corresponds to the decomposition of $KCo[Au(CN)_2]_3$ and $Co[Au(CN)_2]_2$ at the same temperature.

These correlations suggest that coordination compounds of the hardening metal with dicyanoaurate are responsible for the special properties of hard gold deposits. Work is in progress to further investigate the involvement of $KCo[Au(CN)_2]_3$ in the deposition process of cobalt-hardened golds.

ACKNOWLEDGMENT

Thanks are due to N. H. Winquist for carrying out the electron probe analyses, and to N. R. Stalica for his assistance in their interpretation.

REFERENCES

1. E. T. Eisenmann, Plating 60, 1131 (1973).
2. E. Raub, S. Pahlke, H. P. Wiehl, Metall 25, 735.

Manuscript received Sept. 7, 1977.

Publication costs of this article were assisted by Bell Laboratories.

JOURNAL OF THE ELECTROCHEMICAL SOCIETY

REVIEWS AND NEWS

DECEMBER 1977

Developments in Electrolytic Capacitors

Walter J. Bernard*

Sprague Electric Company, North Adams, Massachusetts 01247

In 1952 the total production of all types of electrolytic capacitors in the United States amounted to less than 60 million pieces; by 1976 the number of capacitors produced exceeded 700 million. The distribution by capacitor type at the beginning and end of this twenty-five year period is shown in Table I.[1] This enormous increase is not only a measure of the voracious appetite of the electronics industry during this period, but also reflects the technological advances within the electrolytic capacitor segment of the industry, advances made in all aspects of research and development, engineering, design, and manufacturing skills. At the beginning of this period the aluminum electrolytic capacitor was already a well-established and important electronic component, and two forms of tantalum capacitors—the foil counterpart of the aluminum electrolytic and the liquid electrolyte sintered pellet type—were showing a significant impact. Of these three types, the aluminum foil continued its dominance in both total number and rate of growth, but the most important major development in the industry was that of the solid electrolyte tantalum capacitor which appeared in the mid 1950's and has grown to a point where, in numbers at least, it has surpassed the position of the aluminum foil capacitor.

Aluminum Foil Capacitors

This construction represents the original electrolytic capacitor, which by 1952 had achieved an important position in circuit applications through its unsurpassed volumetric efficiency of capacitance and low cost per unit of capacitance. Advances of great significance have since been made in this device through research and development on its two principal components—the foil electrodes and the operating electrolyte. This progress has been demonstrated by a marked reduction in size, extension of the operating temperature range, improved electrical characteristics, increased reliability, and longer life, both on storage and in operation.

Electrodes

Etching.—The large capacitance of electrolytic capacitors is achieved by the presence of an extremely thin dielectric oxide film on the anode, and it is further enhanced by the creation of a high surface area of the anode foil through chemical or electrochemical etching. Furthermore, if the capacitance of the device is to be utilized with high efficiency, it is necessary that the cathode foil be etched also since it acts as a capacitance in series with the anode. This requirement is especially critical at low operating voltages, but it can also have a significant effect in the higher voltage ranges as well. Consequently, much effort has been expended in developing processes to maximize the active surface areas of both electrodes, consistent with other requirements of the device.

Electrochemical etching lends itself to easier control, but chemical procedures have also been used; in one instance the use of hydrochloric acid was reported to give a surface enhancement of a factor of ten (1). In electrochemical processes a chloride solution (2) is the most common electrolyte, and numerous compositional modifications have been reported, the most important of which is the addition of sodium sulfate (3,4).

The high surface area increase of aluminum through electrochemical etching is the consequence of the remarkable etch structures that may be developed with this metal. It has been demonstrated through electron microscopy that under certain conditions (5) the morphology of the etch consists of cylindrical channels, or tunnels, of exceptionally uniform diameter growing in the three mutually perpendicular (100) planes. The capacitance of foil etched in this fashion, based on a 25V oxide film measurement, can be as much as 65 times greater than the unetched metal.

The mechanical condition of the foil has a pronounced effect on the etching behavior and on the resulting surface increase. Procedures for etching hard cold-worked foil, as opposed to annealed aluminum, have been developed to give a significant improvement in the surface area; as measured by capacitance increase, the cold-worked foil has been shown to give an advantage of as much as 75% (6). The effect has been attributed to the presence of a high density of dislocations on the unannealed foil surface (7), presenting a large number of active sites for electrochemical attack and facilitating the development of an extremely fine etch structure. In general, therefore, the use of hard foil is most advantageous when the foil is to be anodized to relatively low voltages, say 100V, for as the oxide thickness increases, the consumption of metal tends to have a smoothing effect on the etch structure. Nevertheless, it has been reported that by the proper selection of etch conditions, particularly current density and electrolyte composition, the advantage of hard foil can be extended to 250V (8).

Generally, the purer the aluminum the more difficult it becomes to etch. The more common impurities, Si, Fe, and Cu, tend to facilitate electrochemical attack, but their continued presence is undesirable in the oxide film if capacitors of low leakage current and long life are to be constructed (9). When the impurity concentrations are maintained within the solid solubility limits the harmful effect on the oxide is largely eliminated, but even in that range slight variations in con-

* Electrochemical Society Active Member.

[1] Data provided by Marketing Research Department, Sprague Electric Company.

Table I

	Capacitors manufactured (millions) 1952	1976
Aluminum foil	57.4	195.0
Tantalum foil	0.5	1.2
Tantalum-wet pellet	0.5	13.2
Tantalum-solid electrolyte	0	511.2
Total	58.4	720.6

centration can have a marked effect on the etching behavior of different foils (10).

The oxide film.—A dielectric or "barrier" aluminum oxide film may be electrochemically formed on the surface of aluminum in a variety of electrolytic solutions, as has been shown by much experimental work, but the necessities of large-scale manufacturing processes limit the choice to aqueous solutions of relatively simple composition. The most common are solutions of inorganic phosphates and borates, the former finding application principally at the lower end of the anodizing voltage range. The film thickness is controlled by several parameters, the most important being the temperature of the electrolyte, the applied voltage, and the current. The thickness is usually in the range of 12-14 Å/V of applied anodic potential, and corresponds to fields of nearly 10^7 V/cm (11). It is this factor of extremely thin films of controllable thickness and the capability of sustaining such high fields that give the electrolytic capacitor its unique characteristics.

Although most of the limitations of the capacitor are determined by the operating electrolyte, *i.e.*, temperature range of operation, temperature coefficient of capacitance, and frequency behavior, the oxide film quality will determine the leakage current and contribute significantly to the dissipation factor. Furthermore, the oxide may well be the limiting factor in regard to the ability of the capacitor to withstand an extended storage period without unacceptable deterioration of its fundamental electrical properties. Thus, much of the gain made in capacitor quality during the past twenty-five years stems from improvement in oxide quality.

The electrochemical sensitivity of aluminum to chlorides and sulfates (at concentrations as low as 1 ppm) (12) has made it necessary to introduce more rigorous manufacturing procedures both in the anodizing step and in the assembly of the component parts, thus leading to improved capacitor reliability and longer operating life. The use of higher purity aluminum, in which potentially harmful impurities are kept in solid solution, has probably made the greatest contribution to the reduction of the oxide leakage current (13, 14).

The most significant development in the formation of films on aluminum has been the discovery of the advantages to be gained by forming a layer of porous and nondielectric hydrated oxide on the surface prior to the formation of the barrier oxide film (15-19). The hydrous layer is itself partially converted to barrier oxide during the electrochemical step and creates a film of higher dielectric strength and thus of higher capacitance (20, 21). The structure of the resulting film has been shown to consist of a barrier layer at the metal-oxide interface, with the residual hydrous layer remaining at the oxide-electrolyte interface (22, 23).

Operating electrolytes.—In the early 1950's virtually all foil capacitors utilized as the operating electrolyte some variation on the conducting system composed of the reaction product of ammonium borate and ethylene glycol, and with excess glycol as the solvent. This electrolyte, developed twenty years earlier, had supplanted the wholly aqueous solutions then in use, and made it possible for the electrolytic capacitor to attain its widespread use and great commercial importance. Because of the elimination of water as the solvent these capacitors were termed "dry electrolytics," but the electrolytes are distinctly not anhydrous; they contain a significant amount of water which arises from the esterification reaction between its two principal components. In any event, the use of this electrolyte allowed the construction of capacitors that were capable of being operated over a wider temperature range than those with aqueous electrolytes and were, in general, superior in all other respects.

However, the increased demands of electronic equipment manufacturers for more rigorous service conditions revealed that the glycol-borate electrolyte systems also had serious limitations. These demands led both to important modifications of the glycol-borate solutions and to the development of entirely new electrolyte systems. The most important in the latter category are electrolytes using dimethyl formamide (DMF) as the solvent (24, 25). This substance, which has served as the basis of scores of patented formulations, has a liquid range from −61° to 153°C, and a dielectric constant of 36.7, making it an excellent solvent for a large number of compounds that give highly conducting solutions suitable for capacitor application. The important advantage this property has over the conventional glycol-borate electrolytes is illustrated by the comparison of temperature-specific resistivity values at low temperatures. It has been shown (26) that at −55°C a DMF-based electrolyte will increase its room temperature resistivity by a factor of only ten or twenty, while a typical glycol-borate solution will have a value that is several hundred times greater. It is clear that this characteristic permits the application of the new electrolytes to regions inaccessible to glycol borates. Further, as was pointed out above, the presence of water in glycol borates restricts its operation to about 100°C, whereas DMF electrolytes can be used in properly designed capacitors at 125°C.

Proper capacitor design, in this case, involves not only a seal capable of withstanding the vapor pressure of the liquid electrolyte components, but one that is chemically resistant to DMF. The powerful solvent action of DMF which enables it to be such an effective component in aluminum capacitors, is at the same time the cause of its principal limitation. Many of the conventional organic materials used in the construction of electrolytic capacitors are incompatible with DMF, and special seals and closures have been developed to exploit the useful properties of this substance. One example that has been successfully developed uses a polytetrafluoroethylene (PTFE) seal with a butyl rubber gasket (26).

In addition to DMF, a number of other solvents have found application. Among the most important are methyl cellosolve (27), dimethyl acetamide (28), and butyrolactone (29), but there are numerous others that have been reported and which may yet prove to be useful. These compounds share with DMF a wider liquid range than water and can be used as either the sole solvent or as one component in a mixture of solvents. In many instances ethylene glycol is the preferred cosolvent.

Concurrent with the introduction of new solvents, the development of an extensive number of solutes has occurred. The search for specific materials has centered on those compounds that will dissolve to form conducting solutions with the solvents of preference and will, at the same time, exhibit the requisite electrochemical characteristics, *i.e.*, have at least a limited ability to form barrier oxide films when dielectric repair is needed, and to withstand the high fields that are imposed upon the electrolyte. A great many substances have been found to meet these requirements, and the patent literature teems with illustrations. Among this large number, mention should be made of the salts of adipic acid (30, 31) trifluoracetic acid (32), maleic acid (33), salicylic acid (34), citric and tartaric acids (35), and formic acid (36). Boric acid also continues to play a role in this new generation of electrolytes in the form of organoboron complex ions (37, 38). In a separate category is the highly conducting azeotropic mixture of acetic acid and triethyl amine (39) which in itself is a liquid over a wide temperature range, and requires no solvent. Organic compounds dominate this field, but at least one class of inorganic compounds, soluble in DMF, has found application. These are the ammonium salts of heteropoly acids, specifically ammonium phosphotungstate (40).

The particular choice of electrolyte among this bewildering array of possibilities is determined by many factors, not the least of which are the economic consideration of materials of construction and manufac-

turing constraints. The emergence of many alternative systems has, however, permitted capacitors to be more closely tailored to specific applications as diverse as those relatively costly components designed to operate at 125° to exacting military specifications, and low cost miniature devices for use in inexpensive consumer products.

Tantalum Foil Capacitors

Capacitors constructed from tantalum foil have from the start occupied a special position. The high cost of tantalum foil precludes its use except in those instances where its distinctive properties as a capacitor anode material overshadow the obvious economies which are realized with aluminum. Tantalum electrolytics, like those of aluminum, offer high capacitance in a small space because of the properties of its dielectric film, and to an even greater extent. The dielectric constant of tantalum oxide is about 27, while that of anodic aluminum oxide is only 8.5. Tantalum oxide has, however, a somewhat greater oxide thickness than aluminum oxide at the same applied potential and, consequently, its capacitance advantage is not a factor of three but about two. In addition, however, the considerably greater mechanical strength of tantalum permits the use of thinner foils for both anode and cathode, further enhancing its volumetric capacitance efficiency. Although these factors introduce a substantial advantage, they only partially compensate for the enormous difference in foil costs. Justification for the use of tantalum lies therefore in a combination of properties of which high capacitance per unit volume is only one.

From the early days of its introduction to the capacitor market, the tantalum foil device was noted for its high reliability, a property that made it attractive for military applications and in the avionics industry, where the concept of reliability has a compelling value. This reliability is directly related to the inherent chemical stability of both the metal and its oxide. Unlike aluminum, which is readily attacked by many common ionic substances, tantalum is inert to nearly the whole spectrum of chemicals; and whereas aluminum oxide is susceptible to dielectric damage by a wide variety of materials, tantalum oxide is stable in all acid media with the exception of fluoride solutions. This extraordinary chemical stability therefore confers a pronounced advantage upon tantalum foil capacitors, permitting the employment of a wide choice of operating electrolytes of desirable properties, electrolytes which are wholly incompatible with aluminum capacitors. These electrolytes allow a wider temperature range of operation, and impart low dissipation factors to the capacitors in which they are used. Some of these electrolytes are discussed below.

Still another important characteristic of the tantalum foil device is its inherently low leakage current. This is also related to its electrochemical and chemical stability, conditions which, unlike the situation with aluminum, tend to make the leakage current a function only of the electronic conductivity of the oxide. Since the capacitor is designed to operate at a voltage somewhat less than that at which the oxide was formed, typically 75% of the formation voltage, the ionic current is virtually zero and the only significant contribution to leakage current is the low electronic component.

Nevertheless, because of material costs, these advantages extend to tantalum foil only the opportunity to be used as a specialty premium device, and the number of capacitors constructed of this metal is small in comparison to those manufactured with aluminum. The growth in usage during the past twenty-five years might yet have been significant in its own special area had it not been for the advances made in aluminum foil technology, for a great deal of important research has been carried on with tantalum during this period and impressive progress has been made.

Foil Developments

Etching.—The resistance of tantalum to chemical attack makes it a difficult metal to etch for capacitor use. It is particularly difficult to accomplish electrochemically because of the ease with which it becomes anodically oxidized in aqueous solution. The most successful etching media are consequently those in which a nonaqueous solvent is used and in which the concentration of water is restricted to an empirically determined low level. For example, NH_4HF_2 dissolved in formamide with the water content maintained at about 1% (41), and solutions of sodium salts of fluorinated aliphatic acids in DMF containing no more than 4% water (42) have been successfully used for this purpose. Apparently the only way aqueous solutions can be used is when a very high concentration of HF is the principal active component (43).

Oxide film formation.—A high quality oxide film is dependent on the purity of the anode foil, and in particular on the purity of the surface. This is especially significant in the case of tantalum, for if the full potential of its oxide is to be realized the phenomenon referred to as "recrystallization" must be avoided. This unusual effect involves the secondary growth of a crystalline oxide of poor dielectric properties in the place of the amorphous anodic oxide (44) and occurs only upon the application of voltage, either during the original anodization step or upon polarization of the completed capacitor. Once initiated, the growth of crystalline oxide may continue unchecked. When it is extensive in growth, the new oxide appears as dull gray patches on the foil surface, in marked contrast to the bright interference colors characteristic of the amorphous oxide. The amorphous oxide, when ruptured by the thicker crystalline film, ceases to serve as the dielectric and the leakage current of the capacitor rises to unacceptable levels.

In recent years this has ceased to be a serious failure mode. Avoidance of this problem is achieved by the use of very high purity tantalum and the employment of rigorous foil surface cleaning procedures. The etching of anode foil can serve as an effective cleaning step when proper precautions are taken to remove etch solution residues. Unetched foil may be chemically treated in various acid solutions containing HF (45, 46) to insure a clean surface for anodization.

The electrolytes used to form the oxide film usually contain phosphoric acid as one of the constituents; this is because the film composition becomes altered through the inclusion of phosphorus (47) which imparts increased stability to the oxide. Modification of the usual aqueous electrolyte to those containing ethylene glycol has been found to give electrolytes that anodize tantalum to substantially higher voltages (48).

Operating electrolytes.—The emergence of DMF as a solvent that extended the operating range of aluminum electrolytes was paralleled by its use in foil tantalums. Once again, however, the relative chemical inertness of the tantalum-tantalum oxide system permits the use of highly conducting electrolytes that are incompatible with aluminum foil capacitors. In the very low voltage range, for example, NH_4NO_3 in DMF imparts low temperature properties as yet unchallenged by aluminum capacitors (25). Some high voltage electrolytes are also based on DMF, including solutions of polyphosphates (49) and ammonium pentaborate (50).

Cathodes.—Efforts have been made to extend the commercial usefulness of tantalum foil capacitors by replacement of the cathode with a less costly material. The coincidence of DMF-based electrolytes in both tantalum and aluminum electrolytics makes it feasible to use aluminum cathodes at least for some applications (51).

Tantalum-Sintered Pellet-Type Liquid Electrolyte

Although the tantalum foil capacitor is limited in application because of its cost, the metal can be more

economically competitive with aluminum when anodes are constructed from sintered powder. In this form the surface area per unit weight is far greater than with etched foil. This more efficient use of metal is reflected in the continued growth of the "wet pellet" type, but its effect is far more dramatic in the case of the solid electrolyte capacitor, discussed below. For both types of capacitors the anode fabrication principles are identical, and the progress made in tantalum powder technology applies to both.

The liquid electrolyte pellet structure develops the highest volumetric efficiency of capacitance of all types of capacitors through its use of tantalum powder. Even though the solid electrolyte capacitor uses the same powder it is inferior in this regard because its dielectric cannot be safely subjected to the high fields that are applied to an anode using a liquid electrolyte.

Sintered anodes.—The pellet anode is prepared by compacting high purity tantalum powder mixed with an appropriate binder. The binder is later removed by decomposition and evaporation during vacuum heat-treatment, and a further heating step is used to sinter the powder particles into a compact, porous mass. The porosity of the finished pellet may be varied widely by controlling the process conditions, and it can exceed 60%. Since the final sintering temperature may be as high as 2000°C, carbon residues from the binder, as well as other impurities, are lost during this treatment and the anode metal undergoes significant purification. Much effort has gone into the design of the special furnaces needed for this process (52).

It has been shown (53) that a carbon content greater than 20 ppm can seriously affect capacitor life, and that the total of other metallic impurities should not exceed 50 ppm. Thus the sintering process is essential since it accomplishes the removal of the carbon that remains in high concentrations from decomposed organic binders. The mechanism by which this occurs is through the reaction with dissolved oxygen to form carbon monoxide (54).

The quality of tantalum powder has been further improved by the introduction of an electron-beam melting process (55). When the original powder is so melted (at temperatures well above 3000°C) most of its impurities are lost through evaporation, and the low concentrations of the remaining elements are rendered virtually innocuous by entering into permanent solid solution. The metal is subsequently reconverted to powder and is superior to conventional material for capacitor anodes. Its use enables oxides of higher dielectric strength to be formed, giving lower leakage currents and better high voltage properties.

In addition to purity, the powder particle morphology plays a significant role in capacitor characteristics. Particle size and shape determine the surface area, and hence the capacitance to be achieved, of the tantalum anode. A great deal of technology has been developed, therefore, in efforts to exploit these characteristics, and since 1960 there has been about a five-fold improvement in the surface area of powder (56) as measured by specific capacitance per gram, a convenient quantity that is directly related to the surface area. The maximum value of specific capacitance is now about 10,000, and is expected to increase even further as greater control over the roughness and particle size distribution of fine powders also increases.

Powders of high specific capacitance are clearly economically desirable, but their use is not universal in capacitor designs. Other factors frequently impose demands that cannot be met by such powders and as a result a large number of powders with a wide range of characteristics are used in the industry. One class that is finding important application is that consisting of agglomerated powders with superior flow characteristics (57).

Electrolytes.—The structure of a capacitor using a porous pellet as the anode requires an electrolyte that is radically different from those used in foil capacitors. In all electrolytic capacitors the electrolyte resistance is a significant, and often the chief, contributor to the dissipation factor; in foil types this resistance is minimized by maintaining the smallest spacing feasible (0.001-0.003 in.) between the electrodes and by the use of low resistivity electrolytes. However the anode-cathode spacing in a pellet type is inherently greater, and electrolytes with a specific resistivity at ordinary temperatures of a few hundred ohms/cm, typical of foil capacitors, cannot be used. The only electrolytes which are feasible are those with a specific resistivity of a few ohms/cm or less. Only a few such electrolytes, including aqueous sulfuric acid and concentrated solutions of lithium chloride and potassium formate, have found general application from the early days of this device, but improvements and modifications have been made over the years.

The addition of silica to sulfuric acid (58) reduces the danger of electrolyte leakage, as does the gelling of lithium chloride (59). Potassium formate, by virtue of its alkaline nature, can degrade the oxide film at high temperature and this can be prevented by the addition of silica or a silicate (60). Among other electrolytes that have been proposed and which may be useful are concentrated phosphoric acid and saturated potassium iodide (61).

Cathode.—The interior of the metal can used as a container for the anode and the electrolyte acts as the cathode for the capacitor. Silver has long been the metal used for this purpose because of its chemical compatibility with the electrolyte and its excellent mechanical properties in producing a well-sealed capacitor. The interior silver surface is chemically roughened and coated with finely divided platinum to provide a high cathode capacitance, permitting the full capacitance of the anode to be realized.

In combination with specially constructed outer enclosures, these capacitors can be designed to operate at temperatures up to 200°C. It is desirable under such conditions to minimize the cathodic evolution of hydrogen generated as a consequence of the leakage current. This may be accomplished by the addition of a substance that undergoes cathodic reduction more easily than hydrogen ion. Silver sulfate and copper sulfate are examples of solid compounds that may accomplish this (62), and ferric halides at least partially in solution will also function in this manner (63, 64). Cupric chloride has been recommended for use in chloride electrolytes (65).

Silver cathodes, however, suffer from three disadvantages: the costly construction severely limits its use; in some circuit applications silver may be deposited on the anode surface and lead to failure (66); and true hermetically sealed devices cannot be designed with silver cans. One approach that eliminates these disadvantages is the use of a tantalum can (67). The interior can surface must be given a very fine electrochemical etch in order to provide a cathode capacitance approaching that of platinized silver. A stainless steel can, if it were resistant to sulfuric acid at high temperatures, could also supplant silver. It has been claimed that this may be achieved by the addition of titanyl sulfate to the electrolyte (68).

Tantalum Pellet Capacitor—Solid Electrolyte

The first publications describing this device appeared in 1956 (69-71) and the dominant patents were issued in the early 1960's (72, 73). In a period of only two decades the annual production of this capacitor has grown to greater than a half-billion units in the United States alone, accounting for over two-thirds of all electrolytic capacitors.

The feature that distinguishes the solid electrolyte tantalum capacitor from other electrolytic capacitors, and which provides its special character, is the solid manganese dioxide conductor in contact with the anodic oxide. MnO_2, an electronic conductor, is referred to as a solid electrolyte, even though it does not

function in precisely the same way as operating electrolytes in other electrolytic capacitors. An anode of sintered powder is used in this capacitor, just as in the wet-pellet type, but the presence of a solid conductor rather than a liquid leads to a quite different capacitor structure with electrical characteristics that were previously unattainable. It is, for example, possible to operate the capacitor at −55°C with only a 2-3% loss in capacitance from the 25°C value. In addition, because of the high conductivity of MnO_2 throughout this temperature range, the dissipation factor at the low temperature extreme is much lower than any liquid electrolyte capacitor.

Sealing problems are much reduced and allow the use of simpler enclosures of more economical design, especially in comparison with the wet-pellet capacitor. Contact to the cathode lead from the MnO_2 layer is accomplished by coating the MnO_2 with graphite ("Aquadag"), followed by a metal layer to which a tinned lead may be soldered (72). This structure readily lends itself to a hermetically sealed container since nonanodizable metal lead wires may be tolerated within the enclosure and thereby simplify the requirements of a glass-to-metal seal.

Anode preparation.—The first steps in manufacturing the solid electrolyte capacitor are the same as those used in the wet-pellet type: a pressed pellet is sintered and then anodized to the desired formation voltage. The tantalum lead wire may be imbedded in the powder compact before sintering, or welded in place on the sintered anode, in which case an additional high temperature sintering period is needed in order to repurify the welded region. The significant developments in powder technology affecting the capacitor have been dealt with in the previous section on liquid electrolyte capacitors.

Deposition of manganese dioxide.—After anodization the pellet is impregnated with an aqueous solution of manganous nitrate, and then is heated to temperatures in excess of 300°C to convert the nitrate to manganese dioxide (72). The steps of impregnation and thermal decomposition may be repeated several times to fill completely the pores of the pellet with the conducting oxide and give a good external coating as well. Manganous nitrate has proved to be nearly unique in its suitability as an intermediate in this process. It has an unusually high solubility in water (>70 weight percent at 0°C), and therefore minimizes the number of deposition steps required to fill the pellet pores, and it decomposes at temperatures low enough to form highly conducting MnO_2. Its principal disadvantage lies in the need to subject the tantalum oxide/tantalum system to temperatures high enough to cause dielectric damage, and a solid-conducting system that could be deposited at lower temperatures would be a desirable development. Many alternatives have been proposed to replace manganous nitrate, but its use remains as yet unchallenged.

The numerous deposition steps required to give complete filling of the pellet pores can at the same time cause an undesirably heavy and nonuniform coating to build up on the pellet exterior. A mechanical method of shaping such pellets without damage to the dielectric has been described (74). Surface roughness of the final coating can also be controlled by the addition of a small amount of silica to the impregnating solution (75). In some instances the number of deposition steps can be reduced by incorporating a paste or slurry of MnO_2 in the manganous nitrate solution (76).

Under ordinary conditions the decomposition temperature may be in the range of 300°-450°C. The higher temperature has the advantage of reducing the reaction time but has the undesirable effect of causing thermal damage to the film, as discussed further below. Temperatures lower than 300° may be employed, however, when pyrolysis is carried out in an atmosphere of high relative humidity (77, 78). This is accomplished by the introduction of steam to the pyrolysis furnace, and results in MnO_2 coatings of excellent physical and electrical characteristics.

Reanodization.—The dielectric film in contact with tantalum undergoes a form of degradation when subjected to temperatures in excess of 250°C, the degree of damage being a function of the time of exposure at a given temperature. During the deposition of MnO_2 the extent to which the oxide is degraded can be significant, and it is therefore necessary to return the coated pellets to an anodizing bath to repair the dielectric.

The mechanism by which the oxide becomes damaged is through the diffusion of oxygen into the tantalum substrate, resulting in the formation of an oxygen-deficient region at the metal-oxide interface (79, 80). When this process occurs, the capacitance, leakage current, and dissipation factor are increased, and perturbations occur in the dependence of electrical properties on temperature, frequency, and applied d-c bias. When the anode is reanodized to the initial formation voltage the film is restored to its original condition. These solid-state reactions between tantalum and its oxide are complex and have been the object of an extensive and detailed study (81).

However, the presence of MnO_2 on the oxide surface prevents the application of the full anodizing voltage, and consequently the dielectric properties of the capacitor may be only partially corrected by a conventional reformation step. A procedure has been disclosed (82) that utilizes a high temperature polarization treatment to correct the damage done during heat-treatment. Another approach to the problem is through the formation of a modified tantalum oxide dielectric that is stable during the MnO_2 deposition process. This has been reported (83) to be achieved by the doping of tantalum powder with as much as 2% of molybdenum, resulting in an anodic film of high thermal stability. Other important properties have been attributed to this material when used for solid electrolyte capacitors, including the ability to withstand substantial cathodic bias without significant current flow (84).

Unlike liquid electrolytes, MnO_2 does not have the ability to repair or heal the oxide film except in a very limited sense. The phenomenon of "current flickering" in which a momentary high current occurs has been attributed to the healing of a small defect by the thermal contribution of oxygen from MnO_2 (85). It has been proposed that the current flow is further impeded by virtue of a vastly increased resistance of the manganese dioxide at that point (86, 87). It is this limitation in healing dielectric defects that reduces the volumetric efficiency of capacitance of the solid electrolyte capacitor. The need for a considerable margin of safety in dielectric stress requires that the operating voltage be as little as 25% of the formation voltage, compared to 75% in a liquid electrolyte type. The maximum operating voltage is therefore also more severely limited by the MnO_2. Since the practical limit of porous pellet anodization is about 400V, the present working voltage limitation is 125V. This present upper limit, however, represents a very impressive advance over the early years of this device when the maximum working voltage was 35V.

Other Developments

Solid Electrolyte Aluminum Capacitor

The development of the solid electrolyte tantalum capacitor has inevitably encouraged efforts to duplicate its success with aluminum as the anode material. Some progress has been made in this direction, but the solid electrolyte aluminum capacitor has not yet been shown to be a serious competitor to tantalum despite its inherently lower anode cost. The reasons are complex, but the most significant involve the marked differences in the chemical and physical properties of the metals. The low melting point of aluminum (659°C) restricts powder sintering temperatures to levels that preclude that process from acting as a surface purification step; the susceptibility of aluminum to chemical attack by

nitrates introduces obvious hazards in the MnO_2 deposition process, and the limitations in the choice of anodizing electrolytes impose difficulties in forming uniform oxide films within porous structures (88). As a consequence the electrical properties of aluminum pellet devices compare unfavorably to those of tantalum capacitors (89), and the commercial impact of those capacitors in the United States has so far been slight.

Capacitors using the MnO_2 electrolyte have also been constructed of etched foil (90) rather than pellets, obviating the difficulties of sintering and anodizing, but resulting in low capacitance values. The size disadvantage, compared to tantalum, has been reported to be a factor of five (91); this was in the case of an etched aluminum plate, folded in a corrugated pattern to increase its volume efficiency, and sprayed with zinc as a cathode contact. Another interesting structural modification uses a wound foil design with a glass-cloth separator, coated with MnO_2, between the anode windings (92). It is claimed that this construction has many electrical characteristics which are superior to solid electrolyte tantalum capacitors (93).

Tantalum Thin Film Capacitors

Tantalum electrolytic capacitor technology has been extended to applications in hybrid microcircuitry through the use of thin films of the metal (94). Tantalum may be prepared in thin form by chemical deposition or by electron beam evaporation, but the most satisfactory procedure for obtaining high quality films of controlled thicknesses is by d-c sputtering. Combined with an electrolytic anodizing procedure, the technologies of photolithography and vacuum deposition can produce discrete, solid-state, high capacitance devices. Capacitors with gold beam-leads are manufactured in this way for use primarily for the telecommunications industry (95).

Films of tantalum only a few thousand angstroms thick are usually deposited in the form of β-Ta, an allotropic form of the metal first reported in 1965 (96) and later described as a superior thin film capacitor material (97). This form of tantalum differs from the normal body-centered cubic form principally in its specific resistivity and temperature coefficient of resistivity. It transforms irreversibly to bcc tantalum when heated in vacuum to beyond 755°C (96).

Thin film capacitors incorporating MnO_2 as the cathode contact have also been developed (98). These capacitors suffer from the disadvantage of higher dissipation factor than those using only a deposited metal cathode, but the valuable property of "self-healing" permits larger capacitors of higher voltage to be produced.

Niobium Electrolytic Capacitors

The use of this metal as an anode material has long been an attractive possibility because of the high dielectric constant of its oxide and, through its great natural abundance, of a probable lower cost. The advantage over tantalum oxide of a dielectric constant of about 41 is not as large as it might seem because of a correspondingly greater film thickness (99), but it is still sufficient to give about a 15-20% greater capacitance. Chemically, the metal and its compounds are nearly identical to tantalum, and it would be expected that as a capacitor material niobium would behave much as tantalum does. In fact the anodic properties are similar but the quality of the oxide film is substantially poorer than Ta_2O_5. It shares with Ta_2O_5—but to a more serious extent—the tendency to undergo field recrystallization (100) and to react with its substrate (101).

These properties have been used to explain its limitations in capacitors, although it has been reported (102) that higher purity material permits 35V rated devices to operate at 85°C for long periods. In any event, there appears to be some fundamentally serious deficiencies with niobium that have not yet been resolved in a manner that encourages its commercial acceptance.

Other Metals and Alloys

Several pure metals and a large number of alloys can be anodized to produce oxide films. Many of the studies of these materials have been of a theoretical nature and have made important contributions to the understanding of oxide films, but there has also been a continuing interest in exploiting other anode materials either because of the higher dielectric constants of their oxides or as a less costly substitute for tantalum.

Among the several possibilities titanium has received the greatest attention. It is a low density (4.5) metal, relatively inexpensive and, since one of its allotropic oxides, rutile, has a dielectric constant greater than 100, its application as a capacitor oxide would represent an important advance. In spite of some promising reports (103, 104) no commercial device has yet been successfully produced. Anodic oxide films can be generated on the surface of titanium and—in the forming electrolyte at least—high voltages may be sustained under certain conditions (103). However, the films do not have good properties: electronic and ionic conductivities are high, giving rise to oxygen evolution at relatively low voltages and to low capacitance because of the resulting greater film thickness (99). The usual form of oxide obtained is probably anatase, and has a dielectric constant of about 40 (104). Rutile has been reported to form when the metal is oxidized using AC in barium hydroxide solution (105).

Both zirconium and hafnium have been studied, and of the two only hafnium in the thin film form seems to produce anodic oxides with good dielectric properties (106, 107). It is not clear, however, what commercial impact can be expected from this metal since it appears to have neither a technical nor economic advantage over tantalum.

The search for alloys of better film-forming properties has covered a very wide range of metals and compositions. A great deal of work has centered on additions to titanium with the hope of improving its dielectric properties; these additions include boron and tin (108), chromium and vanadium (109), palladium (110), and antimony (111). Various combinations of film-forming metals, including ternary alloys (112) have also been investigated. Although a large patent literature has emerged from this body of work, commercial applications have yet to appear.

Acknowledgments

The author wishes to express his thanks for helpful criticism and suggestions to Mr. E. J. Fresia, Mr. K. Meyer, Mr. R. J. Millard, Dr. J. J. Randall, and Mr. D. G. Rogers.

REFERENCES

1. D. Altenpohl, U.S. Pat. 2, 699,382 (1955).
2. T. E. Turner, U.S. Pat. 2,755,237 (1956).
3. C. E. Welch, Jr., U.S. Pat. 3,316,164 (1967).
4. D. J. Anderson, U.S. Pat. 3,321,389 (1967).
5. C. G. Dunn, R. B. Bolon, A. S. Alwan, and A. W. Stirling, *This Journal*, **118**, 381 (1971).
6. M. S. Hunter, Ger. Pat. 1,288,196 (1969).
7. R. Bakish, R. J. Kornhaas, and E. Z. Borders, *Electrochem. Technol.*, **6**, 192 (1968).
8. M. S. Hunter, *This Journal*, **117**, 1215 (1970).
9. T. Murakawa, *J. Electrochem. Soc. Jpn.* **23**, 355 (1955).
10. R. Bakish, R. J. Kornhaas, and E. Z. Borders, *Electrochem. Technol.*, **1**, 358 (1963).
11. W. J. Bernard and J. W. Cook, *This Journal*, **106**, 643 (1959).
12. H. Watanabe, *J. Electrochem. Soc. Jpn.*, **18**, 107 (1950).
13. N. Kawashima, T. Nishi, and K. Nishino, *Nippon Kinzoku Gakkai Shi Ser. B*, **15**, 280 (1951).
14. G. Muriset, *This Journal*, **99**, 285 (1952).
15. D. Altenpohl and W. Post, *ibid.*, **108**, 628 (1961).
16. D. Altenpohl, U.S. Pat. 2,859,148 (1958).
17. D. Altenpohl, Ger. Pat. 966,477 (1957).
18. P. M. Vogel and H. J. Hofman, Ger. Offen. 2,238,245 (1973).

19. W. J. Bernard and J. J. Randall, Jr., *This Journal*, **107**, 483 (1960).
20. R. S. Alwitt, *ibid.*, **114**, 843 (1967).
21. R. S. Alwitt and W. J. Bernard, *ibid.*, **121**, 1019 (1974).
22. N. F. Jackson and P. D. S. Waddell, *J. Appl. Electrochem.*, **2**, 345 (1972).
23. T. Kudo, C. K. Dyer, and R. S. Alwitt, Paper 99 presented at the 27th Meeting of the International Society of Electrochemistry, Zurich (1976).
24. M. Schwarz and S. D. Ross, U.S. Pat. 2,934,682 (1960).
25. S. D. Ross, U.S. Pat. 2,965,816 (1960).
26. F. J. Burger, D. M. Cheseldine, and J. A. Moresi, *IEEE Trans. Parts. Mater. Packag.*, **1**, 210 (1965).
27. C. E. Welch, Jr., U.S. Pat. 3,375,414 (1968).
28. R. C. Petersen, U.S. Pat. 2,965,817 (1960).
29. S. Thiem and D. Thiem, U.S. Pat. 3,510,731 (1970).
30. G. Hahn, *Nachrichtentech. Z.* **9**, 303 (1959).
31. P. Werner, F. Oehme, and L. Goehlert, Ger. (East) Pat. 18,528 (1960).
32. W. J. Bernard, M. Markarian, and S. D. Ross, U.S. Pat. 2,932,153 (1960).
33. P. Robinson, U.S. Pat. 2,944,026 (1960).
34. K. v. Glos, Ger. Pat. 1,130,930 (1962).
35. R. S. Vincent, Ger. Pat. 1,160,951 (1964).
36. F. J. Burger and D. M. Cheseldine, U.S. Pat. 3,138,746 (1964).
37. S. D. Ross, R. C. Petersen, and M. Finkelstein, U.S. Pat. 3,403,304 (1968).
38. R. W. Santway and R. S. Alwitt, U.S. Pat. 3,403,305 (1968).
39. D. J. Anderson, U.S. Pat. 3,539,881 (1970).
40. J. E. Hand, U.S. Pat. 3,502,947 (1970).
41. A. L. Jenny, U.S. Pat. 2,742,416 (1956).
42. P. Robinson and D. G. Rogers, U.S. Pat. 3,070,522 (1962).
43. G. J. Kahan, U.S. Pat. 2,775,553 (1956).
44. D. A. Vermilyea, *This Journal*, **102**, 207 (1955).
45. D. A. Vermilyea, U.S. Pat. 2,808,542 (1957).
46. C. J. B. Fincham, U.S. Pat. 3,024,095 (1962).
47. J. J. Randall, Jr., W. J. Bernard, and R. W. Wilkinson, *Electrochim. Acta*, **10**, 183 (1965).
48. K. Knoblauch and E. Oldekop, Ger. Pat. 1,178,275 (1964).
49. S. D. Ross and R. E. Cote, U.S. Pat. 3,300,693 (1967).
50. D. H. Stephenson, Ger. Pat. 1,190,578 (1965).
51. M. Markarian and F. J. Gamari, U.S. Pat. 3,654,523 (1972).
52. C. G. Sibley, *Trans. Nat. Vac. Symp.* **1958**, 181.
53. C. C. Houtz and S. Karlik, *Proc. Electron. Components Conf.*, **1959**, 116.
54. W. Scheller, Ger. Pat. 1,139,922 (1962).
55. C. J. B. Fincham and G. J. Villani, U.S. Pat. 3,295,951 (1967).
56. S. E. Hluchan, *IEEE Trans. Parts Hybrids Packag.*, **9**, 148 (1973).
57. J. A. Pierret, U.S. Pat. 3,418,106 (1968).
58. R. A. Canty and R. G. Griffin, U.S. Pat. 3,202,611 (1965).
59. General Electric Co., Brit. Pat. 848,361 (1960).
60. W. J. Bernard and J. W. Cook, U.S. Pat. 3,205,416 (1965).
61. R. Jozephus, M. Keblusek, P. Winkel, and S. A. Troelstra, Ger. Pat. 1,107,829 (1958).
62. J. M. Booe, U.S. Pat. 2,778,979 (1957).
63. J. M. Booe, U.S. Pat. 2,834,926 (1958).
64. M. Wagner, Ger. Pat. 1,110,316 (1956).
65. P. J. Petrik, Ger. Pat. 1,123,400 (1962).
66. L. F. Harris, *Electrocomponent Sci. Technol.*, **1**, 11 (1974).
67. A. G. Cooper, J. L. Moresi, and C. J. Velyvis, U.S. Pat. 3,611,057 (1971).
68. S. Ruben, U.S. Pat. 3,757,172 (1973).
69. R. L. Taylor and H. E. Haring, *This Journal*, **103**, 611 (1956).
70. D. A. McLean and F. S. Power, *Proc. IRE*, **44**, 872 (1956).
71. D. A. McLean, *Electronics*, **29**, No. 10, 176 (1956).
72. R. J. Millard, U.S. Pat. 2,936,514 (1960).
73. P. Robinson, U.S. Pat. 3,066,247 (1962).
74. L. E. Fournier, U.S. Pat. 3,111,428 (1963).
75. J. A. Komisarek, U.S. Pat. 3,241,008 (1966).
76. C. Bachmann and G. Nauk, Ger. Pat. 1,188,724 (1965).
77. F. F. Zind, U.S. Pat. 3,337,429 (1967).
78. R. D. Black, U.S. Pat. 3,302,074 (1967).
79. D. A. Vermilyea, *Acta Metall.*, **5**, 113 (957).
80. G. A. Shirn and D. M. Smyth, *Phys. Failure Electron.*, **2**, 154 (1963).
81. D. M. Smyth, in "Oxides and Oxide Films," Vol. 2, J. W. Diggle, Editor, Marcel Dekker, Inc., New York (1973).
82. E. J. Fresia and J. E. Desmond, U.S. Pat. 3,653,119 (1972).
83. J. C. Moulin and B. Escher, Ger. Pat. 2,405,459 (1974).
84. B. Escher and J. C. Moulin, *Onde Electr.*, **56**, 114 (1976).
85. E. J. Fresia and J. M. Eckfeldt, *Phys. Failure Electron.*, **2**, 483 (1963).
86. L. F. Howard and A. W. H. Smith, *IEEE Trans. Component Parts*, **11**, 187 (1964).
87. D. M. Smyth *This Journal*, **113**, 19 (1966).
88. W. J. Bernard and E. J. Fresia, *Electrocomponent Sci. Technol.*, **1**, 59 (1974).
89. T. Endo, K. Kubo, and S. Hiyama, *Fujitsu Sci. Tech. J.*, **5**, 87 (1969).
90. W. Post, *N.A.S.N.R.C. Publ.*, **973**, 142 (1965).
91. H. Sasaki and Y. Sampei, *Fujitsu Sci. Tech. J.*, **1**, 107 (1965).
92. N. V. Philips' Gloeilampen-Fabrieken., Belg. Pat. 612,426 (1962).
93. F. R. Kunnen, B. Goudswaard, and P. Beekenkamp, *IEEE Int. Conv. Dig.*, **1972**, 552.
94. R. W. Berry and D. Sloan, *Proc. IRE*, **47**, 1070 (1959).
95. M. Tierman, U.S. Pat. 3,523,221 (1970).
96. M. Read and C. Altman, *Appl. Phys. Lett.*, **7**, 51 (1965).
97. A. J. Harendza-Harinxma, U.S. Pat. 3,275,915 (1966).
98. D. A. McLean and F. E. Rosztoczy, *Electrochem. Technol.*, **4**, 523 (1966).
99. L. Young, "Anodic Oxide Films," Academic Press, New York (1961).
100. N. Schwartz, M. Gresh, and S. Karlik, *This Journal*, **108**, 750 (1961).
101. D. M. Smyth and T. B. Tripp, *ibid.*, **113**, 1048 (1966).
102. H. W. Ling and T. L. Kolsky, *ibid.*, **109**, 69 (1962).
103. S. Tajima and T. Mori, *J. Electrochem. Soc. Jpn.*, **22**, 174 (1954).
104. H. Hagiwara and A. Yamashita, *Proc. IEEE*, **51** 1320 (1963).
105. M. Yamazaki and H. Nozaki, *This Journal*, **118**, 400 (1971).
106. M. T. Thomas, *ibid.*, **117**, 396 (1970).
107. F. Huber, *IEEE Trans. Parts Hybrids Packag.*, **7**, 141 (1971).
108. General Electric Co., Brit. Pat. 909,295 (1962).
109. Compagnie Francaise Thomson-Houston, Fr. Pat. 1,311,006 (1962).
110. A. N. Salomon and J. W. Carson, U.S. Pat. 3,255,389 (1966).
111. D. M. Cheseldine, U.S. Pat. 3,564,348 (1971).
112. L. Mandelcorn and T. W. Dakin, Belg. Pat. 668,967 (1965).

A Profile of Electrode Kinetics over the Past Twenty-Five Years

B. E. Conway

Chemistry Department, University of Ottawa, Ottawa, Ontario, Canada

Significance of Electrode Kinetics

Many electrode processes of practical significance, *e.g.*, H_2 and Cl_2 evolution, metal plating, metal winning, and some organic electrode reactions, must be made to occur at reasonable rates if they are to be of preparative value, especially for large-scale operations. Normally, this involves substantial departures from electrochemical equilibrium conditions which apply only at the thermodynamic reversible potential for the process, so that appreciable current densities (i) can normally be achieved only by operating at considerable overpotentials (η). The relation between overpotentials η and associated current densities i is one of the main aspects of the kinetics of electrode processes. Practical electrochemical processes must be conducted with minimum overpotential. Other aspects of electrode processes enter into the performance of an electrochemical system, especially mass-transport limitations, ohmic resistance of solutions and cells, and reaction mechanisms.

The relations between η and i, or more usually $\log i$, are of rather special and fundamental interest in kinetics because electrode reactions are a class of processes where the free energy of activation is directly controllable in an experimentally easy way by adjusting the potential of a working electrode relative to that of some other reference. Mechanisms of reactions may also be potential dependent and in certain cases, relative yields of products, *e.g.*, Cl_2 and O_2 in anodic Cl_2 evolution, phenyl-hydroxylamine and aniline in reduction of nitrobenzene, hydrocarbon evolution in the Kolbe reaction, are dependent on potential, a useful feature of electrochemical preparative techniques. The potential dependence of electrode reaction rates is also of basic importance in interpretation of corrosion processes and in controlling morphology of electrodeposits of metals.

Electrode reaction kinetics depend also in important ways on (*i*) the solvent and (*ii*) the ions of the electrolyte or supporting electrolyte. In the first case, solvation effects are of prime importance as these determine the facility with which ions in solution are electrochemically discharged and the extent to which they are adsorbed at electrode interfaces. In the second case, (*ii*), the nature of ions in solution and the structure of the solvent determine the properties of the double layer at the electrode interface in important ways, and thence, the kinetics of electrode reactions which occur within or across this double layer. Both these effects have important connections with the properties and structure of electrolyte solutions, especially in aqueous media, *e.g.*, through hydration energies of ions and ion-pairing phenomena. Developments in theories and models of electrolyte solutions have had important influences on advances in electrode kinetics, especially with regard to theoretical aspects of this field concerned with the mechanism of activation and solvation-shell reorganization in electron-transfer processes involving ions in solution.

In the material which follows, the author gives a brief historical introduction and then an account of developments in selected topics of general interest in electrode kinetics over the past 25 years.

Background to the Twenty-Five Year Retrospect

The twenty-five year period extends back almost to the 1947 Faraday Society Discussion on Electrode Processes (1) which the present author recollects in some detail. In many ways, this was an outstanding meeting which served as a milestone in the development of electrode kinetics. On the one hand, it ended a period in which polarization effects in electrode processes had been treated in a quasithermodynamic fashion by a number of workers and such antiquated concepts as "bubble overvoltage" and "transfer resistance" of Ferguson were still debated. On the other hand, it marked the beginning of the period when basic kinetic limitations to the rate of an electrode process, on account of a potential-dependent free energy of activation (2, 3), became more widely recognized, based on "absolute rate theory" concepts which had been formulated earlier but not very widely adopted by most electrochemists at that time. A third point, of great significance for the development of electrode kinetics in the Western world, was the submission of three papers from the Russian School of electrochemistry, one by Ershler (4) concerning the same topic as that of Randles (5), presented at the same Faraday discussion (1) on the experimental study of the kinetics of reactions under partial diffusion control by a-c impedance analysis (5, 6), and others by Levich and by Frumkin.

It must be stressed that although the Faraday Discussion of 1947 marked a point in time at which the more quantitative and correctly represented treatments of electrode kinetics, originated by Erdey-Gruz and Volmer (7) and by Butler (3), became common in Western countries, such treatments had existed in the Russian literature since the early 1930's, especially with regard to the work of Frumkin's school on double-layer effects on electrode kinetics (8, 9) and the study of processes involving absorbed H at Pt electrodes [Frumkin, Dolin, and Ershler (10)]. It is of historical interest that the latter work was the earliest in which a "relaxation" technique (based on kinetic response of a two-step reaction to a-c modulation at various frequencies) had been applied to the evaluation of rate constants. The later "relaxation techniques" of Eigen and co-workers were based on observation of effects following a pulse perturbation (by changing temperature or pressure) of a process initially at equilibrium. This technique was applied in electrode kinetics [*e.g.*, by Gerischer *et al.* (11)] using fast potentiostats developed in the 1950's and it is still an important method, especially for evaluation of nucleation-controlled electrode reactions involving deposition or stripping of a surface phase, *e.g.*, as studied by Fleischmann and Thirsk (129, 130).

In addition to the Russian work in this background period must be specially mentioned the work of Butler in England in 1936 (3) regarding the formulation of rate equations for electrode processes in which a potential-energy curve representation of the course of the reaction was given more quantitatively than that of Horiuti and Polanyi (12) in the previous year, and which dealt, among other things, with the role of chemisorption of H in the H_2-evolution reaction and the behavior of the reversible H_2 electrode. A number of the principles of electrocatalysis, insofar as chemisorption of intermediates is involved, were developed later on the basis of this work by Butler. Secondly, the work of Bowden and Rideal (13) and of Agar (14) in this background period must be mentioned with regard to such matters as double-layer capacitance and charging curves, the significance of transfer coefficients, and that of activation energies in kinetics of electrode processes.

Difficulties of communication between 1939 and 1946 caused by the war made an unnatural gap in the development of the field of electrode kinetics as it did, of course, in other fields as well. Hence it took some time for the leading and newest ideas in 1939 to be reiterated after 1945 and to exert the influence they deserved in the postwar development of electrode kinetics. For example, Butler had changed his field of interest to biophysics of proteins and nucleic acids and it took some years after the war for the Russian work to reestablish its influence, a problem that was exacerbated by the termination of the Russian international journal *Acta Physicochimica* (in which a lot of electrochemical work was published) soon after the end of the war.

An important feature of experimental work on kinetics of electrode processes in this period arose from the recognition that the rates can be "programmed" through the applied potential with great facility, more so than in the case of other types of reactions where temperature or pressure must be modulated.[1] Various types of potential programs, *e.g.*, potential-step, repetitive-step (square-wave), single, and repetitive linear-potential sweep and alternating voltage can conveniently be used, with repetition rates, sweep rates, or frequencies varied over a wide range of values. Techniques of this kind, facilitated by contemporary advances in electronics, enabled many fast electrochemical reactions to be studied, while theoretical analysis of the coupled diffusion situation which then arises enabled the required equations to be developed (4, 5, 15) for quantitative evalution of the kinetics.

Progress in the treatment of the kinetics of single- and multi-step reactions under diffusion control was greatly stimulated by the appearance of Delahay's monograph "New Instrumental Methods in Electrochemistry" (1954), and by the many important papers by him in which various kinds of cases were studied and treated by exact mathematical analysis. This work had an important influence in the development of electroanalytical chemistry, both in instrumentation and the quantitative interpretation of experimental results in that field, *e.g.*, in the work of Reilley and of Anson.

Some Characteristic Aspects of Advances in Electrode Kinetics in the Period 1952-1977

The main areas in which a subject advances are often determined by (*i*) the influence of theoretical developments in the field (some of which go ahead of experiment); (*ii*) the development of new experimental techniques, especially where new instrumentation is involved; and (*iii*) the demands of applications for new or improved developments in (*i*) and (*ii*). Some particular areas in which important advances in these aspects of the subject have been made in the past 25 years are summarized in Table I.

In electrode kinetics, these influences have played a major role in developing the subject to a high level of sophistication in both instrumentation and the variety of theoretical treatments which are now available for interpretation of experimental results. It must be stated, however, that as in other aspects of chemical kinetics, a satisfactory *a priori* theoretical evaluation of rate constants of electrode reactions is as elusive a goal as it is for nonelectrochemical, even quite simple reactions. It is in the evaluation of characteristic types of kinetic behavior that the theoretical treatments of electrode kinetics (for complex reaction sequences) have been most successful.

In the material which follows, a selection of the topics in Table I which have constituted main stream areas of research in electrode kinetics over the past 25 years will be considered in more detail. A number of them, it is to be noted, formed the subjects of lively discussion and important papers in the 1959 Electrochemical Society Symposium on Electrode Processes at Philadelphia.

[1] The rates of nonelectrochemical reactions can be modulated only by change of temperature or pressure, assuming concentration is excluded. Techniques of this kind were developed by Eigen. While it was implicit, since the correct formulation of equations for rates of electrode processes, that rates depended on potential, modulation of the potential as the "independent variable" was not possible until the advent of reliable fast-rise potentiostats.

Table I. Principal advances in electrode kinetics over the past 25 years

Theoretical

1. Evaluation of electrode-kinetic equations for complex sequential reactions under activation control including significance of reaction orders, coverage effects, etc.
2. Evaluation of electrode-kinetic behavior for complex sequential reactions where solution-soluble intermediates and diffusion control are involved, especially for cyclic-voltammetry conditions.
3. Evaluation of behavior of chemisorbed intermediates at electrodes in terms of pseudocapacitance behavior and properties of adsorption isotherms, etc.
4. Evaluation of electrode-kinetic behavior for simple and complex surface reactions at electrodes under linear potential-sweep control.
5. Theory of a-c impedance for complex reactions and its representation in the complex plane.
6. Theory of open-circuit decay of potential at electrodes where complex mechanisms are involved.
7. Development of theories of electron transfer, including quantum-mechanical treatments.
8. Development of theories of proton transfer and electrochemical proton tunneling
9. Treatment of photoelectrode kinetics; 5/2 power law, and the behavior of cathodically generated solvated electrons.
10. Theory of semiconductor electrode processes and photoeffects on the kinetics of such reactions.
11. Kinetics and electrocatalysis: coupling of dissociative chemisorption with electrochemical processes.
12. Theories of behavior of porous electrodes and current distribution.
13. Evaluation of kinetics of formation of surface phases at electrodes by nucleation and growth mechanisms.
14. Evaluation of the kinetics of metal deposition including the elementary microscopic processes.
15. Kinetics of anodic oxide film growth.
16. Development of structural theories of the double layer and specific adsorption of ions in relation to ion adsorption effects in electrode kinetics; role of solvent adsorption and orientation.

Experimental

1. Studies of kinetics over a wide range of temperatures.
2. Kinetic studies at high pressures.
3. Development of techniques for study of reactions with solution-soluble intermediates (cyclic voltammetry, thin layer, rotating ring disk).
4. Study of the kinetics of photoelectrochemical reactions.
5. Study of electrocatalysis.
6. Study of kinetics of porous electrode and flow-through electrode materials.
7. Study of electroorganic reactions (reviewed by M. Baizer).
8. Study of electrochemiluminescent reactions.
9. Kinetic studies in electrochemical surface science: underpotential deposition of monolayers.
10. Kinetic studies of growth of anodic oxide and other films on electrode metals.
11. Kinetic studies of metal electrocrystallization.
12. Kinetic studies on film formation by optical reflectance and surface conductivity changes.
13. Study of electrodes on which an electroactive species is irreversibly chemisorbed.
14. Experimental study of kinetics of battery electrode reactions and development of high energy-density systems in nonaqueous media.
15. Study of the kinetics of periodic or oscillatory electrode reactions.

Instrumental

1. Development of fast-rise potentiostats.
2. Development of sequential function generators.
3. Development of phase-sensitive amplifiers.
4. Development of automatic ellipsometers.
5. Development of rotating-disk, ring-disk, and split ring-disk electrodes.
6. Development of techniques for Faradaic rectification and for advanced polarography.
7. Availability of digital and storage oscilloscopes, and signal averagers (or equivalent minicomputer facilities).

Mechanism and Kinetics of Electron and Atom Transfer Reactions in the Steady State

The fundamental act of electron transfer in electrochemical processes has been of major interest since Gurney and Fowler's work, and Gurney's representation of it, in quantum-mechanical terms in 1931/1932 (16, 17). Butler's treatment (3) of this kind of problem in 1936 for an atom (H) transfer step coupled with electron transfer provided the basis for a number of more quantitative potential-energy profile theoretical treatments for the proton discharge and atom/ion desorption steps, as well as for the elementary steps in metal deposition, which were published (18-21) between 1951 and 1960. These treatments were most valuable for the relative rather than absolute (very difficult to obtain reliably for any process) values of en-

ergies of activation and exchange current-densities for various processes and conditions which they gave rise to. However, they were some of the first numerically evaluated calculations on kinetics of electrode processes that had been made and also involved detailed treatments (19-21) of ion-solvent interaction (based on electrostatic models) in the activation process, an important area that had been earlier treated experimentally in papers by Bockris (22, 23).

In the late 1950's and early 1960's, continuing until the present time, a major thrust in interpretation of the molecular dynamics of electron transfer reactions was made by Marcus (24, 25), Levich (26), Dogonadze and Kuznetzov (27) following the important treatments of Hush (28) in 1957/1958, and of Weiss in 1947 (29), 1951, and 1959 (30).

These theories represented the activation process in terms of a so-called "reorganization energy" associated with a change of ion-solvent interaction which in previous theories, *e.g.*, of Butler (3), Bockris and Parsons (18) and Bockris and Conway (19-21), had been treated in terms of an effective potential-energy profile for short-range H^+/H_2O or metal ion/H_2O interactions. These treatments differed in an important way from those of Butler, Bockris, Parsons, and Conway in that the activation process was attributed to long-range, nonspecific fluctuations of dielectric polarization in the solvent fluid according to Born's equation (based on analogies with polaron theory for creation of charges in a solid medium) rather than to change of configuration and short-range polarization in the ion solvate complex or in the inner coordination shell of Werner complex ions. This viewpoint had its origin in Hush's paper in 1958 (28).

These treatments also became associated with the view that a quadratic dependence of log i on overpotential should arise, and this question was examined experimentally by a number of authors (31, 32). However, this matter is quite distinct from the question of how "solvent reorganization" occurs and originates simply on any model [*cf.* Ref. (21, 33)] if harmonic approximations are employed for the potential functions corresponding to the energy barrier. It should be mentioned that while some evidence exists (31, 32) for potential-dependent Tafel slopes b (quadratic term effect) of some redox reactions, this could arise for other reasons (*e.g.*, ion adsorption), for the case of the H_2-evolution reaction on Hg which has been studied over many decades of current density, the b values are quite independent of potential.

The nature of the activation step in electrochemical proton transfer was taken up by Levich *et al.* (26, 27) in various papers. These authors pointed out that there would be a "double-adiabatic" adjustment of charge in the activation process associated with electron and with proton transfer, subject to quantitatively different quantum restrictions. They also argued that thermal activation of the OH bond in H_3O^+ (or H_2O) could not be significant at ordinary temperatures due to the large vibrational quantum ($h\nu \simeq 10$ kcal mole^{-1}) and therefore attributed the activation process in proton transfer at electrodes to long-range librational fluctuations in the solvent polarization. Appelby, Bockris, Sen, and Conway (33) argued that this was an unnecessary restriction since the work of Ackermann (34) had demonstrated, on the basis of a model of hydration of H^+ as $H_9O_4^+$ that appreciable room-temperature partial molar heat capacity of H_{aq}^+ arises and can be accounted for in terms of low frequency modes due to coupling with the solvent in the hydration shell of H^+. It is noteworthy that proton transfer processes in solution, where solvation effects can arise, always occur with much smaller activation energies than "atom" transfer reactions, *e.g.*, as in the gas phase, but the quanta involved are similar due to the fact that bonds to H normally have frequencies of around 10^{14} sec^{-1} in both the gas and liquid phase.

More recently, following the work of Hills and Kinnibrugh (134), studies (35) on the $Fe(CN)_6^{3-}/Fe(CN)_6^{4-}$ redox reaction at Au as a function of pressure showed that the volume of activation is (and must be) large. It could not be accounted for (by a factor of 4) by long-range fluctuation in the solvent polarization which, it can be shown (35), gives rise to only a small electrostriction volume change. Were the situation otherwise, a major change in volume of the ionic redox system would have to occur after the transition state is reached. This cannot be so, however, since the transition state at Au is almost symmetrical (in terms of its volume) with respect to the volumes of $Fe(CN)_6^{3-}$ and $Fe(CN)_6^{4-}$ in water, when the reaction is at equilibrium.

In the case of the H_2-evolution reaction, the interesting possibility that the proton itself tunnels to the electrode rather than being transferred by chemical activation was considered theoretically by Christov (36), Conway (37) [*cf.* Bawn and Ogden (38)] and both theoretically and experimentally by Conway and Salomon (39). Theoretically, appreciable proton tunneling rates are predicted (37) and a potential-dependent H/D separation factor should arise (37). Experimentally, working down to −110°C in cooled or supercooled alcoholic HCl solutions, Conway and Salomon (39) were unable to find any evidence for anomalous proton transfer behavior (*e.g.*, deviations from linearity in Arrhenius plots and anomalies in the Tafel plots).

Moreover, analysis of the temperature dependence of Tafel slopes for H_2-evolution at Hg and Ni down to low temperatures enabled Conway *et al.* (40) to demonstrate that the temperature dependence of the Tafel slope parameter b is not $b = RT/\beta\mathbf{F}$, but rather $b = (RT/\beta\mathbf{F}) + C$, *i.e.*, with a temperature-independent constant. The results were not represented by an equation of the form $b = RT/(\gamma T + \delta)\mathbf{F}$, *i.e.*, with a temperature-dependent β. In fact, the slopes db/dT are constant with temperature. Interpretations in terms of halide ion adsorption and proton tunneling were considered; *e.g.*, the residual constant C could correspond to participation of a temperature-independent but potential-dependent proton tunneling contribution at very low temperatures, below those where proton tunneling could be more directly detected.

Important advances were also made in the 25 year period in understanding the over-all kinetic behavior of complex (multistep) electrode reactions using steady-state kinetic treatments with various equations for the potential-dependent coverage of electrode surfaces with adsorbed intermediates. These lead to a series of characteristic criteria for reaction mechanisms in terms of reaction orders, Tafel slopes, etc. Applications were made to kinetics of H_2, O_2, Cl_2 evolution reactions and a number of organic fuel-cell oxidation processes, especially by Bockris and his school (41, 44, 103, 104). The illustrative paper (41) on O_2 is to be noted in particular.

For reactions involving solution-soluble intermediates, the development and application of rotating-disk (99, 100) and especially ring-disk electrode systems (96-98) by Levich *et al.*, by Alberry, and by Bruckenstein, has been invaluable, as both mechanisms of reactions and lifetimes of intermediates can be deduced. Rotation modulation is a new development.

With regard to interpretation of nonsteady-state kinetics of various types of processes, attention must be directed to the important generalized treatment of Rangarajan (95); this provides a unified approach to the effects of modulation of the kinetics of an electrode process by various means, and includes the role of coupled diffusion processes that often must be considered. Full mathematical development was given for a variety of cases commonly encountered in electrode kinetics. For the particular case of linear potential-sweep modulation, useful analytical and numerical simulation calculations have been given by Laviron (58) and by Kozlowska *et al.* (59) for complex reaction sequences.

Potential-Energy Barrier Effects in Discharge

The effect of potential on the rates of electrode processes has for many years [cf. Ref. (3, 12, 18-21)] been represented in terms of a two-dimensional potential-energy profile along a one-dimensional reaction coordinate. While, in reality, most processes require a multidimensional energy diagram for the potential surface, this approach is useful (3) as a basis for discussing effects of potential and effects of changing chemisorption energy of an intermediate, or activation energy. In particular, the potential-energy profile conveniently represents the symmetry factor β in terms of the fraction of the change of electrical energy VF applied at the initial state that causes an increase or decrease of free energy of activation: $\Delta G_V^{\pm} = \Delta G_0^{\pm} \pm \beta \Delta VF$. In electrochemical reactions, ΔV directly modifies the Fermi level, so that the electronic work function Φ of the metal is modulated: $\Phi_V = \Phi_0 \pm \beta \Delta V$. ΔV does not, however, significantly change the shape of the potential energy profile of the initial state, but it may have some effect on solvent orientation and ion adsorption at the electrode surface.

In terms of the above representation, it is useful to note (42) that β has a significance analogous to that of Brønsted's factor, α, relating changes of proton-transfer rate constants to changes of equilibrium constants for protonation in acid/base pairs. In terms of models of adiabatic electron transfer [e.g., of Hush (28)], $\pm\beta e$ represents the fractional average charge residing on the transition state.

A number of interesting cases were discussed by Krishtalik in various papers (43) where β may be 1 or 0, corresponding to "barrierless"[2] or "activationless discharge." These cases arise as shown in Fig. 1a and 1b where the conditions $\beta = 1$ or 0 depend on whether the initial-state potential-energy profile intersects the final-state profile at or below its zero-point energy level, or vice versa. In the case of an electrochemical reaction, the possibility of experimentally attaining either of these situations arises because the barrier height can be modified by $\pm\Delta VF$. Krishtalik has argued that the barrierless discharge case can be observed, e.g., at Hg, at low enough potentials, though the results then correspond to very low current densities where experimental difficulties arise and ion adsorption double-layer effects complicate interpretation of the results. The transition from regular ($\beta \simeq 0.5$ to barrierless ($\beta = 1$) discharge corresponds to a change of Tafel slope from $RT/\beta\mathbf{F}$ to $RT/\mathbf{F}$.

Under intermediate conditions, before the zero-point energy level is approached, β will be expected to be potential-dependent (but still near 0.5) due to the parabolic curvature (harmonic oscillator behavior) of the energy profile near the ground state (33, 44).

[2] Strictly, there is still a "barrier," equal to the endothermicity of the reaction, but there is no col in the potential surface. The terms above are Krishtalik's.

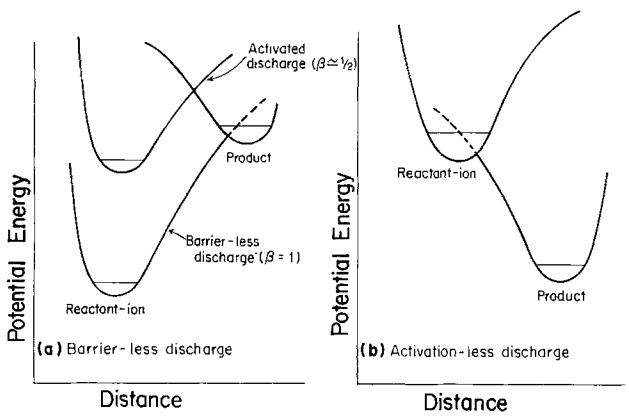


Fig. 1. Illustrating the significance of (a) "barrierless"; and (b) "activationless" discharge in electrode processes [after Krishtalik (43)].

Activationless conditions do not seem to have been observed, presumably because other factors then limit the rate.

The shapes of energy barriers such as those in Fig. 1a and 1b also give some idea of the relation of the configuration and charge of the activated complex to that of the initial state [cf. Ref. (28)]. Obviously, in the situation of Fig. 1a, the transition state is almost like the final state, while in Fig. 1b it is like the initial state.

Oscillatory Kinetics in Electrode Processes—Spontaneously Nonsteady Reactions

While oscillatory processes in homogeneous reactions are rare, but known, they are quite common in electrode processes and are of some general interest. A number of cases have been discovered in the past 25 years and are usually associated with S-shaped current-potential curves which arise in anodic reactions by passivation of an electrode or in cathodic ones by double-layer effects, e.g., in reduction of an anion (46) which tends to be repelled from the surface with increasing negative potential but reacts exponentially faster in this direction.

A S-shaped i-V profile has a negative resistance characteristic in the inverted part of the curve that can give rise to oscillation either coupled with double-layer and pseudocapacitance elements of the equivalent circuit, or with external circuit elements, as found by Hunger (52).

Periodic passivation and depassivation of Fe and Cu were investigated by Bonhoeffer and Gerischer (47) and the general behavior of such systems has been treated by Franck in various papers (48). Conway *et al.* (49) and Wojtowicz and Conway (50) studied the periodic oxidation of formic acid and ethylene at Pt in some detail, and identified the role of buildup and stripping of the surface oxide film at Pt, and of coupled diffusion. In fact, most periodic electrode processes are associated with periodical diffusion fluxes (50) due to the on-off nature of the rate of the electrode process (51). The requirement of a coupling with a diffusion process in order that an unstable steady-state condition arises can be demonstrated theoretically (50).

Most periodic electrode reactions exhibit nonlinear oscillatory behavior, *i.e.*, the "restoring force" is not linearly proportional to the displacement (here, the electrochemical affinity change in the reaction). In recent work, it was found that H_2-oxidation at Pt in trifluoroacetic acid containing traces of water (to give a small oxide film coverage at anodic potentials) was periodic, and that transition from linear (sinusoidal) to nonlinear (spike-pulses) oscillatory kinetics occurred, depending on the magnitude of current excursions, *i.e.*, on the potential involved. Two or more characteristic frequencies were observed, as can arise in nonlinear cases.

Mechanisms of oscillatory behavior are difficult to formulate but usually involve autocatalytic breakdown of an oxide film (47, 48), e.g., through film stripping by "lake" growth in the film (49), and a process (e.g., potential-dependent oxide-film formation) that gives rise to a S-shaped i-V profile (53). The kinetics give rise to a second-order differential equation that has a periodic rather than a steady-state solution (54); then the current and the concentration of intermediates (and the diffusion flux) which are each periodic in time, follow each other in a phase-plane plot (not the same as the complex-plane plots referred to above) rather than converge to definite steady-state values.

Kinetics in Electrocatalysis

While some of the principles involved in electrocatalysis, e.g., the role of the energy of chemisorption of an adsorbed intermediate in determining the activation energy of an electrode process involving a chemisorption step [Butler (3), Horiuti and Polanyi (12)], were enunciated in the 1930's, the main advances in the field have been made since *ca* 1955. However, a meeting at Leningrad must be noted since it was at

that conference that Frumkin, already in 1940, described electrochemical studies of catalyst surfaces (55). The useful term "electrocatalysis," originating with Grubb (56) in 1963, is now common.

A semantic question arises with the term electrocatalysis and associated kinetic representations of the phenomenon. While it is useful to consider reactions such as those of anodic O_2 or Cl_2 evolution, or cathodic H_2 production, in terms of "electrocatalysis," there is strictly no real pathway with which the rate of the "electrode-catalytic" reaction can be compared, since the necessary coupled electron-transfer steps that precede or follow any chemical step (*e.g.*, recombination of H, Cl, or O species) in the over-all electrode reaction can only occur at the electrodes. The recombination steps which arise in some pathways in these reactions can, however, be legitimately considered in terms of catalysis.

More particularly, the concept of electrocatalysis can be usefully applied to those reactions that require an initial dissociative chemisorption or rearrangement step that requires involvement of the electrode surface in order that it proceed at a reasonable rate. The electron-transfer steps that correspond to production of a current then follow such "catalytic" steps involving chemical production of an electrochemically reactive intermediate at the surface. The coupling of such electrochemical with chemical steps at a surface gives rise to complex kinetic behavior which has been worked out in some detail theoretically by Conway and Gileadi (57), Laviron (58, 121), and Kozlowska *et al.* (59) with special attention to the behavior which arises when electrode surface processes are studied by the potentiodynamic sweep method (discussed below).

In the area of experimental studies on kinetics and mechanisms of reactions involving a catalyzed dissociative chemisorption step at the electrode surface, *e.g.*

$$CH_3OH + 6Pt \rightarrow 3Pt{\equiv}C{-}OH + 3PtH$$

there must be specially mentioned the work of Bagotskii and Vasilev (101), Frumkin and Petrii (102), Bockris and co-workers (103, 104), Brummer and co-workers (109, 110), Breiter (105-107), and of Gilman (108) on the behavior of small molecules such as H_2, HCOOH, CH_3OH, C_2H_4, and C_3H_8. In this work, characterization of the chemisorbed intermediates was deduced from cathodic and anodic transients after adsorption of the reactant, using potentiodynamic sweep or galvanostatic pulses.

The work of Gilman (108), Breiter (105-107), Parsons (122), and of Brummer and co-workers (109, 110), as well as that of Bagotskii and his co-workers (101) in the USSR, led in this period to an understanding of the oxidation of chemisorbable organic substances at catalytically active noble metals, *e.g.*, Pt, Ir, and Rh, in terms of a rather general mechanism: the kinetics of oxidation are determined by a primary dissociative chemisorption step (or steps), coupled with H-ionization, together with oxidation of chemisorbed C-containing intermediates by O species discharged from water or OH^-. The latter processes depend on the potential for onset of surface oxidation of the noble metal anode which varies from 0.2-0.3V for Ru or Ir to 0.6-0.75V for Pt and Rh, depending on the pH and the anion of the electrolyte.

The work with hydrocarbons is particularly significant since the over-all reaction produces, in most cases, only H_2O and CO_2 with no solution-soluble intermediates except in the case of some olefins. The rate-controlling step for some hydrocarbon reactions was deduced, using steady-state kinetic and isotope-labeling methods by Bockris *et al.* (103) for propane and by Kuhn *et al.* (104) for olefins. The importance of "Temkin adsorption" (linear dependence of free energy of adsorption on coverage) in the kinetics of these types of processes was stressed by the Russian workers.

The kinetics of electrochemical reduction of O_2 has received much attention owing to its importance in fuel cell and air-depolarized battery systems. Leading work in this area was initiated and developed by Yeager (111, 112), who investigated O_2 scission in relation to peroxide pathways in the reduction reaction. More recently, the possibility of catalyzing the reduction of O_2 by paramagnetic La-Sr cobaltites and other structures with which (triplet-state) O_2 interacts magnetically was investigated by Tseung and co-workers (113-115).

Electrocatalysis and other aspects of the H_2-evolution process were extensively studied in the 25 year period on the noble metals, especially Pt, by Schuldiner and co-workers (123, 124) and by Breiter (125). In a series of papers describing very careful work in ultra-clean solutions, these authors were able to establish the mechanism of both H_2-evolution and H_2-oxidation by cathodic and anodic measurements down to potentials close to the H_2-reversible potential. Work on Pd showed the importance of coupled diffusion of H. The work on Pt provided rather important information for concurrent and later evaluation of Pt for fuel cell oxidation of H_2. In the latter field, the role of microcrystallite size and morphology of fine Pt deposits for H_2-oxidation has been examined in elegant electrochemical and scanning-electron microscopy work by Stonehart (126). The surface-to-volume and edge-to-surface ratios are important in electrocatalysis by fine particles; but the finer the particles, the more they tend to sinter at low temperatures, well below the Tammann temperature, giving rise to time-dependence of the real surface area and hence the catalytic activity of Pt electrode preparations.

An important field of investigation of a general type was the study of the dependence of electrochemical rate constants (or exchange current densities, i_0) on properties of the electrode metal, *e.g.*, the electronic work function, Φ (116-119). In the case of the H_2-evolution reaction, linear relations between log i_0 and Φ were found for several families of metals, depending on the mechanism (Fig. 2). Since log i, at a given potential, cannot directly depend on Φ, the observed relations are interpreted (116) in terms of the dependence of heat of activation on the energy of chemisorption of H. The experimental behavior can be simulated theoretically (120). This area of work in kinetics stimulated

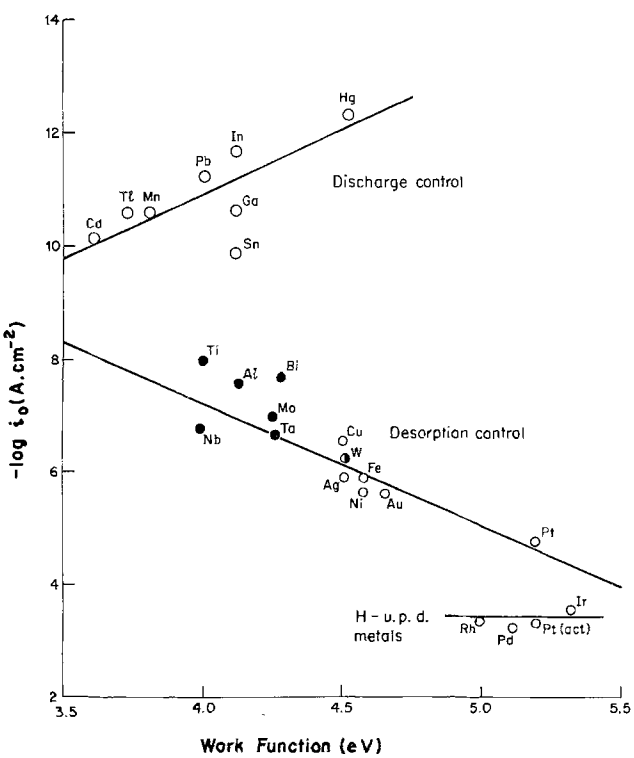


Fig. 2. Dependence of log i_0 on work function Φ for various series of metals [based on Ref. (116-119)].

many attempts to improve electrocatalytic performance by use of alloy electrodes. In general, the results are disappointing because binary alloy compositions rarely have properties better than those corresponding to one component or the other and *a priori* predictions of electrocatalytic activity have usually been unsuccessful except Tseung's (113-115) regarding activation of O_2 through paramagnetic interactions. However, submonolayers of deposited metal atoms such as Ru or Pb on Pt have been found to promote catalytic activity for certain reactions. Competitive and bifunctional mechanisms involving participation of surface oxide species are involved in these effects.

Kinetic Studies in Electrochemical Surface Science

Principles and methods.—Although studies of chemisorption of oxygen and hydrogen species at noble metal electrodes were initiated many years ago by Bowden and Rideal (13), Butler and Pearson (60), and by Frumkin and various co-workers (61), kinetic aspects of surface processes have only been quantitatively examined in recent years (*e.g.*, 57-59, 62, 92). In early work as well as in some more recent work, coverage of electrodes by O and H^- species was usually determined by means of galvanostatic charging curves (60, 61). As in regular electrode processes, kinetic information on surface processes can be derived from current-potential relations derived from charging curves by observing the displacement of potential V for given coverages θ to be attained at various rates of charging, *i.e.*, the current densities. Alternatively, potential-step charging curves [*cf.* Ref. (11)] can be recorded and the time-dependent current transient analyzed in terms of the kinetic equation(s) for the electrochemisorption process at the electrode surface. Both these procedures are in a sense "single pulse" techniques.

Some advantages accrue if an impulse of varying frequency or rate can be imposed on the electrode so that its kinetic relaxation characteristics can be immediately observed and kinetic information derived. Two important methods fall into this category: (*i*) a-c impedance measurements on electrochemical surface processes (10, 63, 64); and (*ii*) potential-sweep or repetitive potential-sweep measurements (cyclic voltametry) on electrodeposition and desorption processes at electrode surfaces (65).

As in the study of regular Faradaic processes, *e.g.*, the kinetics of a redox reaction (6), the a-c impedance method may be employed to elucidate the kinetics of surface processes at electrodes, *e.g.*, the electrosorption of H and oxygen species (OH and O) and metal atoms at noble-metal electrodes.

The first studies of this kind were made by Dolin and Ershler (10) and by Eucken and Weblus (64), who recognized that an electrosorption process of the kind

$$Pt + H_3O^+ \rightleftharpoons PtH_{ads} + H_2O \qquad I$$

was associated with a pseudocapacitance corresponding to the potential dependence of coverage of the electrode, *e.g.*, by H, and a reaction resistance corresponding to the reciprocal of the exchange current density or standard rate constant for the surface process.

More recently, capacitative and ohmic behavior of surface reactions such as that above have been studied by a-c techniques by Breiter (63) and by Bagotskii *et al.* (66).

Kinetic information derives from the fact that as frequency of the alternating modulating voltage applied to the electrode is increased, a condition eventually arises where the forward and backward processes of I can no longer keep up with the alternating driving potential. Thus the coverage of H can no longer follow electrode potential in the way it does at sufficiently low frequencies where equilibrium is almost maintained in I. This results in a "dispersion" of the pseudocapacitance C_ϕ due to the electrosorbed species, and eventually $C_\phi \to 0$, so that the measured capacity simply falls to the double-layer capacity at sufficiently high frequencies.

Kinetic analysis for processes in monolayers.—Transient electrochemical techniques give a sensitive means of following chemisorption or desorption processes at metals that proceed with charge transfer, *e.g.*

$$H_{aq}^+ + Pt + e \rightarrow PtH_{ads}$$
$$H_2O + Pt \rightarrow PtOH + H^+ + e$$
$$\hookrightarrow PtO + H^+ + e$$

Also, the changes of H adsorption brought about by adsorbed electroinactive species can also be measured accurately so that their adsorption can be studied. In "underpotential deposition" reactions, such as those above, multiple states of chemisorption arise below a monolayer (65, 90, 91) and are of great interest in electrochemical surface science. Here we shall briefly mention the kinetic aspects of studies in this field.

Because of the noncontinuous nature of a process in which a monolayer is formed or desorbed (the rate is limited by $\theta = 0$ or 1), steady-state kinetic methods are inapplicable. Kinetic studies on surface processes involving monolayers must therefore utilize transient procedures such as potential step, potential sweep, galvanostatic charging, or a-c modulation. For kinetic information to be derived, the "charging" of the surface must be conducted over a range of rates, or in a-c modulation over a range of frequencies (63, 66) sufficient to reach the "relaxation" frequency of the electrochemical surface process.

Normally, *e.g.*, in galvanostatic charging experiments (92), charging curves (i-V profiles) must be taken at various values of i, and the potential for a given coverage plotted against log i for sufficiently high i that the process is driven to irreversibility. However, the kinetics of the process of deposition in a particular submonolayer state are not easily evaluated due to the poor resolution of this method unless the curves are differentiated (93).

The linear potential sweep, by comparison, is a superior method for deriving kinetic information on surface processes, on account of its excellent resolution of various states of electrosorption below a monolayer (65, 91). In the linear potential sweep method, a given current peak for deposition into a chemisorption state at the electrode surface will retain a characteristic, constant peak potential, V_p, so long as the process remains reversible. When irreversibility sets in, V_p becomes displaced logarithmically in the peak current, i_p, (Tafel relation); but, for a surface process i_p is proportional to sweep rate s, so that V_p becomes dependent on log s.

The required kinetic equations for deposition of a monolayer under potential-sweep control were first derived by Srinivasan and Gileadi (95). Their treatment can be developed (94) to give equations which enable the experimentally observed kinetics of a surface reaction to be characterized by a critical sweep-rate parameter, s_0, as is a regular reaction by i_o, the exchange current density.

The current densities for deposition or removal of an electrosorbed species A of coverage θ_A in a reaction such as

$$A^- + M \rightarrow MA_{ads} + e$$

are

$$\vec{i} = zFk_1(1 - \theta_A)C_{A^-} \cdot \exp \beta VF/RT \qquad [1]$$

$$\overleftarrow{i} = zFk_{-1}\theta_A \exp -(1 - \beta)VF/RT \qquad [2]$$

In the sweep method, V is modulated linearly in time, so that $V = V_{initial} \pm st$ where s is the sweep rate dV/dt. Then (94)

$$V_{p,irrev} = V_{p,rev} + \frac{RT}{\beta F} \ln \frac{\beta F}{k_o RT} + \frac{RT}{\beta F} \ln s \qquad [3]$$

where $RT/\beta F$ ($= b$) is the Naperian Tafel slope and k_o is a standard rate constant {$k_o = k_1 \exp(\beta V^\circ F/ER)$

$= k_{-1} \exp[-(1-\beta)]V^{\circ}\mathbf{F}/RT$ for the standard potential V° for the surface process defined as the peak potential ($\theta_A = 1/2$) when the process behaves reversibly}. Equation [3] leads to the useful relation for the kinetic behavior of a reaction under potential-sweep control

$$V_{p,irrev} - V_{p,rev} = b \ln s_o + b \ln s \qquad [4]$$

which is similar to the Tafel equation $\eta = -b \ln i_o + b \ln i$. In Eq. [4], s_o has been defined from Eq. [3] as

$$s_o = \beta\mathbf{F}/k_oRT \qquad [5]$$

It is seen that s_o characterizes the kinetics of a surface process just as the exchange current density i_o does for a regular continuous Faradaic process. It has the advantage (contrast i_o) for kinetic evaluations in electrocatalysis that the real area of the electrode is not a required parameter. Hence the general problem in evaluation of electrocatalysis of separating the real-area factor from the intrinsic catalytic effectiveness of a surface is conveniently avoided in this approach. Also the problem that i_o is not a unique characteristic parameter for a surface process, since it depends on the coverage for which it is measured, does not arise with s_o, which applies to any point on the i-V profile.

When lateral interactions on the surface are significant ($g \neq 0$), a more complex result is obtained, but it is still possible (94) to evaluate s_o and hence characterize the kinetics. The electrochemical kinetics of surface processes, including those for resolved submonolayer states, can hence be completely characterized since b and s_o, as well as the coverage and relative energy of the states, can be measured. Exemplification of the method is given schematically in Fig. 3 and with respect to experimental results for one of the states of H adsorption at Pt, in Fig. 4. Accompanying the change of slope of the V_p *vs.* log s relation of Fig. 3, is a change of shape of the i-V profiles as demonstrated by Srinivasan and Gileadi (95). The general characteristic features of such reversible and irreversible i-V profiles were treated by Angerstein-Kozlowska *et al.* (96) for simple and complex surface processes, including nucleation.

Development of very thin layers of surface oxide on noble metals and of thick layers on baser metals has been studied by many workers, especially with regard to passivation in corrosion and anodization. Kinetic aspects of film formation and inhibited metal dissolution were studied in an important series of papers by Vetter (127) using galvanostatic techniques, and by Epelboin (79, 128), with a-c impedance methods. Initial stages of passivation are established by submonolayer quantities of surface oxide (indicating that dissolution commences at active sites), but a stable condition of passivity usually requires substantially thicker layers. Recent advances in this field have been made using techniques of surface physics, LEED, HEED, with Auger and ESCA photoelectron spectroscopy, and by using methods based on changes of optical reflectivity. Thus studies on surface processes at electrodes have been greatly clarified by the simultaneous use of *in situ* ellipsometric and direct reflectivity measurements, *e.g.*, in the various works of Yeager and Cahan and of Bockris and his co-workers.

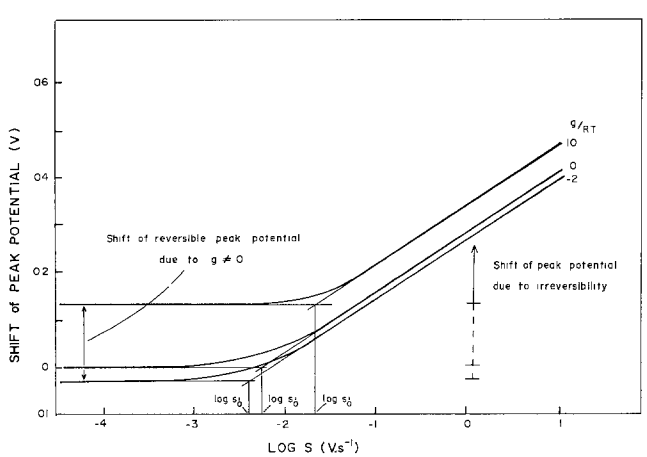


Fig. 3. Principle of evaluation of s_o from a plot of peak potential V_p, *vs.* log s from a series of cyclic-voltammetric i-V profiles taken at various sweep-rates s [Ref. (91, 94)].

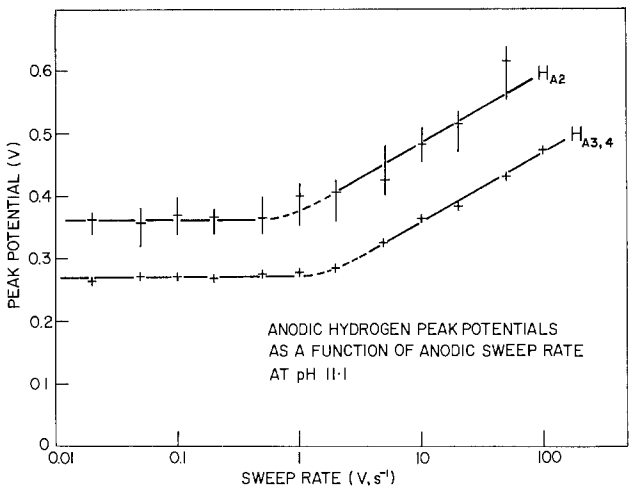


Fig. 4. Example of the application of the method illustrated in Fig. 3 and discussed in Ref. (91, 94) to the process of H deposition/ionization at Pt in two of the states of H-chemisorption (aq. 0.1M Na_2CO_3).

In conclusion, many important studies of the kinetics of multilayer growth where a new phase is formed should be mentioned. Here dissolution-precipitation processes are often involved with some metals while high-field film growth occurs at others. Nucleation-and-growth mechanisms are commonly the basis of electrochemical phase growth. They are often of importance in corrosion and battery electrode reactions. The main developments were in the kinetics of formation and growth of halides (Hg_2Cl_2), sulfate ($PbSO_4$), and oxide films by dissolution-precipitation and nucleation mechanisms, studied by Fleischmann and Thirsk and their co-workers (129, 130), and in the field of metal deposition, through nucleation mechanisms, studied by Budewski and Kaischew (131), and by Bockris and his school [*e.g.*, see Ref. (20, 44)].

Theoretical kinetic equations were developed from the treatments of Avrami (132) and of Evans (133) for the representation of nucleation-controlled phase growth in two-dimensional monolayers and in three-dimensional thicker deposits. Elegant experimental demonstrations of successive growth of monolayers, both of halide and oxide films (129, 130) and of metal layers (131), were given. The observed kinetics agree with theory under potentiostatic conditions.

"Electrosorption Valency" and the State of Electrochemisorbed Species

In the previous section, work on the kinetics of processes involving deposition or desorption of electrodeposited monolayers was described. In addition to the thermodynamic and kinetic problems associated with processes of this kind, recent work has been concerned with the electrical state of electrodeposited atomic species, *i.e.*, to what extent does a deposited species have ionic character or, conversely, to what extent do ions, upon specific adsorption, lose their charge? This type of problem was first addressed by Lorenz (70), Gerischer (71), and by Conway and Bockris (20) with regard to elementary steps in metal deposition, and in some ways by Grahame (72) for specifically adsorbed ions. Essentially the possibilities

are: (*i*) $A^{z+} + M + \lambda(ze) \rightarrow MA_{ads}^{z(1-\lambda)+}$ for electrodeposition of a species A at a metal M with partial charge transfer; or (*ii*) $A^{z-} + M \rightarrow MA_{ads}^{z(1-\lambda)-} + \lambda ze$ (in M) for specific adsorption of an ion A^{z-}.

Evaluations of λ have been made for various examples of electrosorption by Schulze and Vetter (73), who find most atom deposition reactions, *e.g.*, of H and metal atoms at noble metals, have λ close to 1. $\lambda < 1$ arises in a number of cases of specific adsorption of ions. The relative values of λ can be interpreted in terms of polarity of ligand-to-metal bonds by regarding deposited or adsorbed species as acting as ligands of the adsorbate. The thermodynamic significance of λ was discussed in various papers by Frumkin *et al.* (74) and its chemical significance by Conway *et al.* [see also in Ref. (74)].

The significance of λ for kinetic representation of surface processes is of interest because rate equations have to be modified to the form

$$i = \lambda z\mathbf{F}kC_{Az+} \exp \beta\lambda z\mathbf{F}V/RT$$

to include the λ factor when $\lambda < 1$.

A-C "Relaxation" Studies and Representation of Electrode Kinetics in the "Complex-Plane"

The a-c impedance method is of general interest in kinetics of electrode processes since it provides a convenient method for evaluating rate constants for fast reactions and dealing in an exact way with the problem of coupled diffusion processes. Apart from diffusion effects, at high enough frequencies, ω, where $1/\omega$ becomes comparable to the relaxation time of the reaction determined by the reciprocal of its rate constant, the potential-dependent reaction process ceases to be able to keep up with the applied frequency, so that a "lossy" situation arises as was mentioned with regard to adsorption pseudocapacitance.

The situation is exactly analogous to that in other relaxation processes, *e.g.*, in dielectric polarization in a polar medium where, at sufficiently high frequencies, dipole orientation cannot keep up with the rate of alternation of the applied field so that a "dispersion" of the dielectric constant arises.

The relaxation or dispersion effects were treated for dielectric polarization by Cole and Cole (75) in terms of a plot of the real *vs.* the imaginary component of the dielectric constant, giving a so-called Argand diagram or a representation of the kinetic behavior in the "complex-plane." It was recognized by Rehbach and Sluyters (76) in 1961 that a similar representation could be applied to the kinetic behavior of electrode processes where a "real" (ohmic) component corresponding to the reciprocal of the rate constant (as mentioned earlier) arises, together with an "imaginary" (capacitative) one dependent on frequency. In general, the capacitative component is a compound one, being comprised of a double-layer contribution C_{dl}, an adsorption pseudocapacitance in cases such as reaction *I*, and a diffusional pseudocapacitance and resistance (elements of the Warburg impedance) dependent on square root of frequency (4, 5).

It must be stated that the complex-plane method of analysis has been very fruitful in the treatment of the kinetics of surface and other processes at electrodes, and has given new insights into the relation between kinetic processes occurring over various frequency ranges or time domains. The analysis is closely connected with the representation of electrode processes in terms of equivalent circuits of varying complexity, depending on the distinguishable types of kinetic processes involved including solution resistance (ohmic transport of ions) and double-layer capacitance. It is generally applicable whenever there is a kinetic restriction on the rate of some process (as is usually the case) in a sequence of processes.

Experimental studies on a-c frequency effects and corresponding complex-plane analyses have been greatly facilitated in recent years by the availability of well-engineered phase-sensitive amplifier systems [*cf.* Ref. (77, 78)] which enable the ohmic and capacitative currents to be directly read out with the appropriate phase-angle setting. A similar system can be applied in the study of a-c modulated reflectivity of electrode surfaces at which some electrode process can occur and be modulated with an alternating voltage. The "in-phase" and "out-of-phase" components of relative reflectivity can then be directly recorded and represented in terms of complex-plane plots from which the relaxation characteristics of the surface processes can be derived.

A-c impedance studies, with analysis of the results in the complex plane, have recently been made for quite complex electrode processes by Armstrong *et al.* (78), and by Epelbein *et al.* (79). In film-forming processes leading to passivation, interesting negative resistance components enter into the equivalent circuit together with behavior corresponding to negative capacitance which has electrical analogue characteristics of an inductance. Such complex systems can give rise to oscillatory phenomena (47-51) where no real steady-state in the kinetics of the electrode process can exist.

In the complex-plane representation of the a-c behavior, the capacitative contribution $1/\omega C$ to the impedance Z is plotted against the ohmic one for various frequencies ω. Regular simple kinetic processes give a semicircular arc lying on the ohmic resistance axis (Fig. 5a) while complex processes with more than one characteristic rate constant give two or more arcs (Fig. 5b). Similar behavior is found for processes in aqueous solution which exhibit several relaxation times, *e.g.*, contact ion-pair dissociation, solvent-shared ion-pair dissociation, and solvation shell relaxation; in these cases, ultrasonic or dielectric absorption experiments are involved.

Processes coupled with diffusion which give rise to a Warburg impedance (5) generate a straight line of 45° slope in the complex-plane plot since the capacitative and ohmic contributions arising from diffusion are both linearly dependent on $\omega^{-1/2}$. Their relation to the kinetically controlled arc in the complex plane is illustrated in Fig. 5c.

For processes that involve generation of a surface film, the equivalent circuit becomes very complex and will include a pseudocapacitance corresponding to potential dependence of coverage of a species electrodeposited in a mono- or multi-layer. The film formation can influence some other Faradaic process such as oxidation of the metal itself or of an organic reactant in solution, giving rise to passivation. Such reactions often exhibit a Σ-shaped current-potential profile giving rise to negative resistance and negative capacitance which corresponds to a pseudoinductance. In the complex plane, such processes give [*cf.*, Ref. (79)] curves such as that in Fig. 5d, with a loop. Such equivalent circuits often give rise to oscillatory currents at constant potential or oscillating potentials at constant current.

Complex-plane representations of the impedance behavior of various types of reactions have been treated by Armstrong *et al.* (78), for processes such as cadmium oxidation in alkaline solutions which show active dissolution followed by passivation with diffusion in the pores of the film, and by Epelbein *et al.* (79) for passivation of Ni and Fe where oscillatory phenomena arise. Armstrong (78) has also treated the interesting case of metal/solid electrolyte interfaces where blocking or nonblocking behavior can arise, and in powdered solids (78) where interparticle resistance can be significant.

Kinetics of Photoemission of Electrons at Electrodes

While photovoltaic effects have been known for a long time, in fact since Becquerel's observations (80)

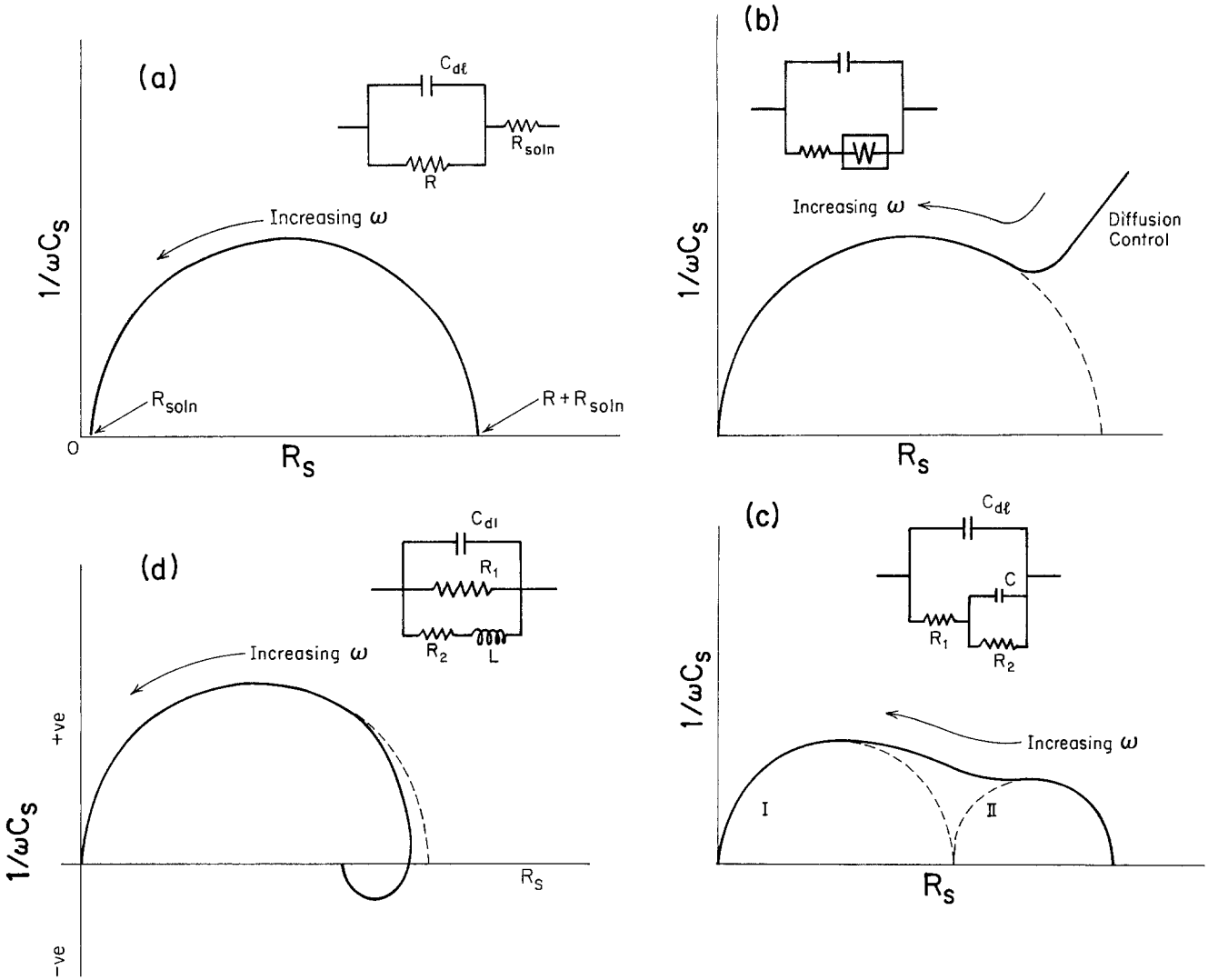


Fig. 5. Plots of capacitative *vs.* ohmic impedance components in the complex plane for various types of electrochemical processes: (a) a regular reaction with a reaction resistance *R* at an electrode with double-layer capacitance $C_{d.l}$ [see Ref. (78)]; (b) a two-stage reaction involving, *e.g.*, discharge and another surface reaction [*cf.* Ref. (57, 79); (c) a process involving a reaction resistance *R* with diffusion coupling involving a Warburg impedance with both *C* and *R* components dependent on $\omega^{1/2}$; (d) a process coupled with surface reactions giving instability corresponding to a pseudoinductance [Ref. (79)].

in 1839 of a photoeffect on the potential of an electrode in solution, much work [*e.g.*, see (81-87)] of a new, interesting, and quantitative kind has been done in the 25 year period under review. It has involved: (*i*) the discovery and rationalization of the "5/2" current law for electrochemical photoelectron emission; (*ii*) identification of the role of formation of solvated and "dry" electrons; (*iii*) evaluation of the potential-dependent "red limit" which arises in photoelectron emission at electrodes; (*iv*) evaluation of kinetics of reactions of photoelectrochemically generated solvated electrons with scavenger molecules such as N_2O, H_3O^+, O_2, NO_3^-; and (*v*) development of treatments of photoelectron emission effects in terms of double-layer structure, especially in relation to the ψ_1 potential of the diffuse double layer and the potential of zero charge. Electrochemical reductions have also been carried out with cathodically generated solvated electrons in suitable media, *e.g.*, HMPA and alcoholic solutions (88). The reactions are similar to those that can be effected with the Birch reagent.

Hillson and Rideal (89) made some of the first direct measurements of photoeffects on the kinetics of a cathodic reaction, H_2 evolution at Hg, and found an acceleration of the process under the influence of photons in the wavelength range 200-400 nm.

Using polarographic techniques, Berg (81, 82) investigated the effect of illumination at a dropping Hg electrode, and attributed the observed photocurrents to the supposed increased energy of electrons in Hg which then behaved, he considered, as a "hot electrode."

Heyrovsky (83-85) regarded the photoeffect at electrodes as originating from the photodecomposition of a surface charge-transfer complex formed from the solvent and the electrode interface. This is correct for anodic photocurrents, but not for cathodic ones. He found that the low energy wavelength limit for the photoeffect depended on electrode potential. This is because the normal photoelectric threshold, $h\nu = \Phi$, is modified to $h\nu = \Phi \pm eV$ where V is the applied potential which changes the Fermi level.

Barker (86) gave the first, essentially correct explanation of most photoeffects at metal electrodes, *viz.*, that they originate from photoemission of electrons into the electrolyte where they become solvated and have a short lifetime. While such ideas are to be found in some of Berg's papers, it was Barker who successfully demonstrated photoelectron emission into solutions at electrodes. This work gave impetus to much of the work that followed especially that of the Russian workers, Brodsky and Pleskov (87), Gurevich and Rotenberg, with others.

Photoelectrode kinetics is now a major field in electrode kinetics, and is particularly interesting with regard to development of direct photoelectrical energy conversion systems. However, the more promising of these utilize photoeffects in semiconductors with a

suitable bandgap, so that the effects are quite different from those we are describing here which involve photoelectron emission into an electrolyte solution. The semiconductor photoeffects involve separation of electrons and holes, and light thus facilitates reactions with p- or n-dependent rates, *i.e.*, anodic or cathodic processes, respectively.

For photoelectron emission into a dielectric, the current I is proportional to $(n\nu - \nu_0)^2$ for n-photon photoemission where ν is the frequency and ν_0 the threshold frequency ($h\nu_0 = \Phi$). This is Fowler's parabolic law. For photoemission into dielectrics with large ϵ, or more particularly into strong solutions of electrolytes where screening effects are appreciable, image charge interactions can be neglected. Then I takes the form

$$I \propto (n\nu - \nu_0)^{5/2}$$

which is the "5/2 law" for electrochemical photoelectron emission.

Normally, the current i which is measured in a photoemission experiment is not identical with the ν-dependent I referred to above because of secondary processes which the emitted photoelectrons undergo in the bulk of the solution. These involve, *e.g.*, solvation and reaction with any electron scavengers A (see Fig. 6).

The presence of acceptors is very important in observations of a stationary photocurrent, since in the absence of A, emitted electrons are rapidly returned to the electrode and the resulting photocurrent is then very small. Solvated electron reactions such as $e_{aq}^- + H_2O \rightarrow H + OH^-$ are relatively improbable compared with back diffusion of e_{aq}^- to the electrode.

In dilute electrolyte solutions, the critical region near an electrode into which electrons are photoemitted, a "stretched interfacial barrier" arises, the properties of which depend on the diffuse part of the double layer and hence on the ψ_1 potential. This dependence gives useful information on the double layer, including that at solid metals (87). Then the photoemission current law in $i^{0.4}$ [$i \propto (n\nu - \nu_0)^{5/2}$, hence $i^{2/5} \propto (n\nu - \nu_0)$] gives a linear plot not with electrode potential ϕ but with $\phi - \psi_1$. When diffuse layer effects are significant (dilute electrolytes) the general photocurrent relation is of the form

$$I = K[h\nu - h\nu_0 - e(\phi - \psi_1)]^{5/2}, \quad \psi_1 \leq 0$$

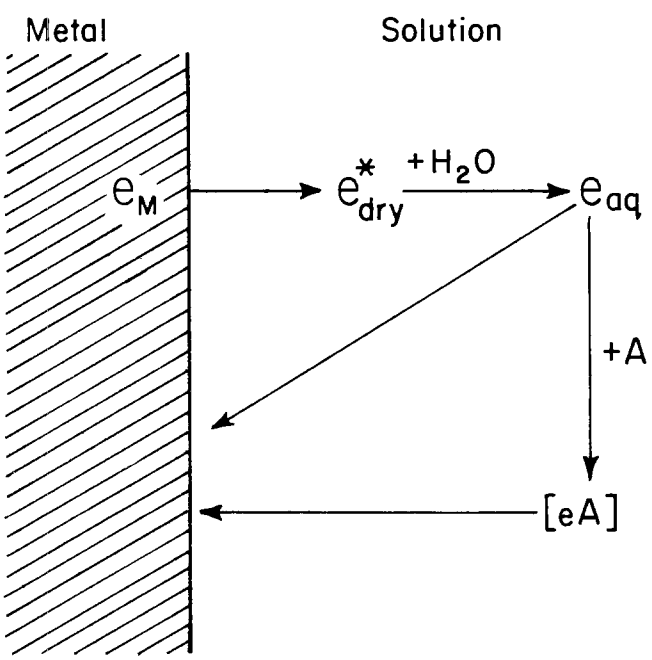


Fig. 6. Schematic representation of photoelectrochemical emission of an electron into solution with anodic return current and scavenger (A) processes [after Ref. (87)].

The dependence of $di^{0.4}/d(-\phi)$ on ϕ gives a minimum at the potential of zero charge where the ψ_1 potential is zero (in the absence of specific adsorption) and $d\psi_1/d\phi$ is a maximum. Potentials of zero charge at solid metals can hence be derived from photocurrent measurements.

Much further work has been done, especially with various acceptor molecules or ions, and with dyes where photoeffects on a substrate in solution as well as the electrode metal arise.

Concluding Summary

It may be useful to give a concluding overview of the contributions of the past 25 years in electrode kinetics. On the theoretical side, electrode kinetics has found its home as a major area in chemical kinetics involving, on the one hand, solution-phase reactants and, on the other, surface-catalyzed processes. The main kinetic phenomenology is rationalized in terms of the framework of absolute rate theory and more recently in terms of quantum-statistical treatments, though these have yet to give meaningful numerical results to compare with experimental data. Future theoretical advances lie in the realm of chemical physics.

Instrumental advances, especially in electronics, have enabled new experimental techniques to be developed for studies on kinetics of electrode processes, programmed in various ways. The facile modulation of kinetics of electrode processes, afforded by the potential variable, makes electrode processes ideal for on-line computer-controlled experimentation. Digital computer simulation of kinetic schemes for diffusion and activation-controlled processes enable quite complex models and mechanisms to be treated with increasing facility in a complementary way.

On the practical side, developments in electrocatalysis and materials science have led to systems of major interest in the fields of energy conversion and electrical energy utilization. Here, kinetic limitations and their attenuation are of major practical interest.

The heterogeneous nature of electrode processes has led to the development of electrochemical techniques for study of surface processes on metals and semiconductors that have high sensitivity and reproducibility, and can give kinetic information on surface reactions unattainable by any other methods. These approaches have generated a new area of "electrochemical surface science" in which kinetic studies play an important role.

Developments in photoelectrochemistry give interesting new information on metal-electron interactions and electron-capture processes in solution near the interface. For the future, this area may have important contributions to make to energy-conversion technology.

REFERENCES

1. *Discuss. Faraday Soc.*, various papers, **1** (1947).
2. J. A. V. Butler, *Trans. Faraday Soc.*, **19**, 729 (1924).
3. J. A. V. Butler, *Proc. R. Soc. London, Ser. A*, **157**, 423 (1936).
4. B. V. Ershler, *Discuss. Faraday Soc.*, **1**, 269 (1947).
5. J. E. B. Randles, *ibid.*, **1**, 11 (1947).
6. J. E. B. Randles and R. Somerton, *Trans. Faraday Soc.*, **48**, 951 (1952).
7. T. Erdey-Gruz and M. Volmer, *Z. Phys. Chem. (Leipzig)*, **150**, 203 (1930); **162**, 53 (1932).
8. A. N. Frumkin, *Acta Physicochim. URSS*, **18**, 23 (1943).
9. S. Levina and V. Sarinksy, *ibid.*, **7**, 475, 491 (1937).
10. P. Dolin and B. V. Ershler, *ibid.*, **13**, 747 (1940).
11. H. Gerischer and W. Mehl, *Z. Elektrochem.*, **59**, 1049 (1955).
12. J. Horiuti and M. Polanyi, *Acta Physicochim. URSS*, **2**, 505 (1935).
13. F. P. Bowden and E. K. Rideal, *Proc. R. Soc. London, Ser., A*, **120**, 59 (1928); **125**, (1929).
14. F. P. Bowden and J. N. Agar, *Anl. Rept. Chem. Soc., London*, **35**, 90 (1938).

15. J. M. Savéant and E. Vianello, *Electrochim. Acta*, **8**, 905 (1963); *ibid.*, **10**, 905 (1965); **12**, 1545 (1967); R. S. Nicholson and P. Shain, *Anal. Chem.*, **36**, 706 (1964); *ibid.*, **37**, 121 (1965).
16. R. W. Gurney and R. H. Fowler, *Proc. R. Soc., London, Ser. A*, **134**, 137 (1931).
17. R. W. Gurney, *Trans. Faraday Soc.*, **28**, 368 (1932).
18. J. O'M. Bockris and R. Parsons, *ibid.*, **47**, 916 (1951).
19. B. E. Conway, J. O'M. Bockris, and B. Lovreček, in Proceedings CITCE 6th meeting Poitiers 1954, p. 207, Butterworth, London (1955).
20. B. E. Conway and J. O'M. Bockris, *Electrochim. Acta*, **3**, 340 (1961).
21. B. E. Conway and J. O'M. Bockris, *Can. J. Chem.*, **35**, 1124 (1957).
22. J. O'M. Bockris, *Discuss. Faraday Soc.*, **1**, 95, 229 (1947).
23. J. O'M. Bockris, *Trans. Faraday Soc.*, **44**, 519, 860 (1948).
24. R. A. Marcus, *J. Chem. Phys.*, **24**, 966 (1956); **41**, 2624 (1964); **37**, 1835 (1962); **43**, 679 (1965).
25. R. A. Marcus, *Ann. Phys. (Leipzig)*, **15**, 155 (1964).
26. V. G. Levich, *Adv. Electrochem. Electrochem. Eng.*, **4**, 249 (1965).
27. R. R. Dogonadze, A. M. Kuznetzov, and V. Levich., *Electrochim. Acta*, **13**, 1025 (1968); **15**, 353 (1970); *Elektrokhimiya*, **3**, 280 (1967).
28. N. S. Hush, *J. Chem. Phys.*, **28**, 962 (1958); *Z. Elektrochem.*, **61**, 734 (1957).
29. J. Weiss, *Discuss. Faraday Soc.*, **1**, 68 (1947).
30. J. Weiss, *J. Chem. Phys.*, **19**, 1066 (1951); *Proc. R. Soc., London, Ser. A*, **222**, 128 (1959).
31. E.g. R. Parsons and E. Passeron, *J. Electroanal. Chem. Interfacial Electrochem.*, **12**, 524 (1966).
32. R. Bonnaterre and G. Cauquis, *ibid.*, **35**, 287 (1972).
33. A. J. Appleby, J. O'M. Bockris, R. K. Sen, and B. E. Conway, in "Electrochemistry," Physical Chemistry, M.T.P. Series 1, Vol. 6, J. O'M. Bockris, Editor, Chap. 1, Butterworths, London (1973).
34. Th. Ackermann, *Discuss. Faraday Soc.*, **24**, 180 (1957).
35. B. E. Conway and J. C. Currie, Submitted to *This Journal*.
36. St. G. Christov, *Z. Elektrochem.*, **62**, 567 (1958); *Electrochim. Acta*, **4**, 306 (1961); **9**, 575 (1964).
37. B. E. Conway, *Can. J. Chem.*, **37**, 178 (1959).
38. C. E. H. Bawn and G. Ogden, *Trans. Faraday Soc.*, **30**, 432 (1934).
39. B. E. Conway and M. Salomon, *J. Chem. Phys.*, **41**, 3169 (1964); *Discuss. Faraday Soc.*, **39**, 2213 (1965).
40. B. E. Conway, D. J. MacKinnon, and B. V. Tilak, *Trans. Faraday Soc.*, **66**, 1203 (1970).
41. J. O'M. Bockris, *J. Chem. Phys.*, **24**, 617 (1956).
42. A. N. Frumkin, *Z. Phys. Chem.*, **160**, 116 (1932); B. E. Conway and M. Salomon, *J. Chem. Educ.*, **44**, 554 (1967).
43. L. I. Krishtalik, *Elektrokhimiya*, **2**, 624 (1966).
44. J. O'M. Bockris and A. Despič, *J. Chem. Phys.*, **32**, 389 (1960).
45. A. N. Frumkin, O. A. Petrii, and N. W. Nikolaeva-Fedovovich, *Dokl. Akad. Nauk URSS*, **133**, 1158 (1961).
46. J. A. V. Butler and B. Armstrong, *J. Chem. Soc., London*, 743 (1934).
47. K. F. Bonhoeffer and H. Gerischer, *Z. Elektrochem.* **52**, 149 (1948); **52**, 24 (1948); **52**, 67 (1948).
48. U. F. Franck, *Z. Physik. Chem., N.F.*, **3**, 183 (1955); *Z. Elektrochem.*, **62**, 649 (1958); *Symp. Faraday Soc.*, **9**, 137 (1974).
49. J. Wojtowicz, N. Marincic, and B. E. Conway, *J. Chem. Phys.*, **48**, 4333 (1968).
50. J. Wojtowicz and B. E. Conway, *ibid.*, **52**, 1407 (1970).
51. B. E. Conway and D. M. Novak, *J. Phys. Chem.*, **81**, 1459 (1977).
52. H. F. Hunger, *This Journal*, **115**, 492 (1968).
53. D. Gilroy and B. E. Conway, *J. Phys. Chem.*, **69**, 1259 (1965).
54. A. A. Andronov and C. E. Chaikin, "Theory of Oscillations," Princeton University Press, Princeton, N.J. (1949).
55. S. Pshejetzkij, *Acta Physiochim. URSS*, **13**, 874 (1940).
56. W. T. Grubb, *Nature (London)*, **198**, 883 (1963).
57. E. Gileadi and B. E. Conway, *J. Chem. Phys.*, **39**, 3420 (1963).
58. E. Laviron, *Electrochim. Acta*, **16**, 409 (1971); *J. Electroanal. Chem. Interfacial Electrochem.* **34**, 463 (1972).
59. H. Angerstein-Kozlowska, B. E. Conway, and J. G. Klinger, *ibid.*, **75**, 45, 61 (1977).
60. R. Pearson and J. A. V. Butler, *Trans. Faraday Soc.*, **34**, 1163 (1938).
61. B. V. Ershler, P. Deborin, and A. N. Frumkin, *Acta. Physiochim. URSS*, **8**, 565 (1938).
62. S. Srinivasan and E. Gileadi, *Electrochim. Acta*, **11**, 321 (1966).
63. M. W. Breiter, in Proceedings of the Symposium on Electrode Processes, The Electrochemical Society, p. 307, Philadelphia (1959).
64. A. Eucken and M. Weblus, *Z. Elektrochem.*, **55**, 115 (1951).
65. F. G. Will and C. A. Knorr, *ibid.*, **64**, 258 (1960).
66. V. I. Lukyanycheva, E. M. Strochkova, V. S. Bagotskii, and L. C. Knots, *Elektrokhimiya*, **7**, 267 (1971).
67. B. E. Conway, E. Gileadi, and M. Dzieciuch, *Electrochim. Acta*, **8**, 143 (1963).
68. E. Laviron, *J. Electroanal. Chem. Interfacial Electrochem.*, **52**, 355, 395 (1972).
69. E. Laviron, *Bull Soc. Chim. Fr.*, 1637 (1970); *Electrochim. Acta*, **16**, 409 (1971).
70. W. Lorenz, *Z. Electrochem.*, **57**, 382 (1953); *Naturwissenschaften*, **40**, 576 (1953); *Z. Naturforsch.*, **9a**, 716 (1954).
71. H. Gerischer, *Z. Elektrochem.*, **62**, 256 (1958).
72. D. C. Grahame, *Chem. Rev.*, **47**, 447 (1947).
73. K. J. Vetter and J. W. Schultze, *J. Electroanal. Chem. Interfacial Electrochem.*, **34**, 131, 141 (1972); **53**, 67 (1974); **44**, 63 (1973); *Ber. Bunsenges., Phys. Chem.*, **76**, 920, 927 (1972).
74. E.g. A. N. Frumkin, B. B. Damaskin, and O. A. Petrii, *J. Electroanal. Chem. Interfacial Electrochem.*, **53**, 57 (1974); B. E. Conway, H. A. Kozlowska, and W. B. A. Sharp, *Z. Phys. Chem. N.F.*, **98**, 61 (1975).
75. K. S. Cole and A. H. Cole, *J. Chem. Phys.*, **9**, 341 (1941).
76. M. Rehbach and J. H. Sluyters, *Recl. Trav. Chim. Pap. Bas.*, **80**, 469 (1961); **81**, 301 (1962); **82**, 525, 535 (1963).
77. M. W. Breiter, *This Journal*, **112**, 845 (1965).
78. B. V. Tilak, R. S. Perkins, H. A. Kozlowska, and B. E. Conway, *Electrochim. Acta.*, **17**, 1447 (1972).
78. R. Armstrong *et al.*, *J. Electroanal. Chem. Interfacial Electrochem.*, **71**, 5 (1975); **72**, 257 (1976); **53**, 371 (1974); **53**, 389 (1974); **66**, 148 (1975); **66**, 143 (1975).
79. I. Epelboin and M. Keddam, *Electrochim. Acta*, **17**, 177 (1972); *This Journal*, **117**, 1052 (1970).
80. E. Becquerel, *C. R.*, **9**, 145 (1839).
81. H. Berg, *Naturwissenschaften*, **47**, 320, 513 (1960).
82. H. Berg and H. Schweiss, *Nature (London)*, **191**, 1270 (1961); *Electrochim. Acta*, **9**, 425 (1964).
83. M. Heyrovsky, *Nature (London)*, **206**, 1356 (1965).
84. M. Heyrovsky and R. G. W. Norrish, *ibid.*, **200**, 830 (1963).
85. M. Heyrovsky, *Proc. R. Soc. London, Ser. A*, **301**, 411 (1967).
86. G. C. Barker, A. W. Gardner, and D. C. Sammon, *This Journal*, **113**, 1182 (1966).
87. A. M. Brodsky and Y. V. Pleskov, "Progress in Surface Science," Vol. 2, Part. 1, S. G. Davison, Editor, Pergamon Press, New York (1972).
88. H. W. Sternberg, R. E. Markby, I. Wender, and D. M. Mohilner, *J. Am. Chem. Soc.*, **89**, 187 (1967); **91**, 4191 (1969); *This Journal*, **113**, 1060 (1966).
89. P. J. Hillson and E. K. Rideal, *Proc. R. Soc. London, Ser. A*, **199**, 295 (1949).
90. B. E. Conway, H. A. Kozlowska, and W. B. A. Sharp, in Proceedings of the Symposium on Electrocatalysis, The Electrochemical Society, San Francisco (1974).
91. B. E. Conway, H. A. Kozlowska, and F. C. Ho, *J. Vac. Sci. Technol.*, **14**, 351 (1977).
92. K. J. Vetter and D. Berndt, *Z. Elektrochem.*, **62**, 378 (1958).
93. H. A. Kozlowska and B. E. Conway, *J. Electroanal. Chem.*, **7**, 109 (1964).
94. H. Angerstein-Kozlowska and B. E. Conway,

Submitted to *J. Electroanal. Chem. Interfacial Electrochem.*
95. S. K. Rangarajan, *J. Electroanal. Chem. Interfacial Electrochem.* **55**, 297, 329, 337, 363 (1974); **56**, 1, 27, 55 (1974).
96. A. N. Frumkin and L. N. Nekrassov, *Dokl. Akad. Nauk, SSSR*, **126**, 115 (1959).
97. Y. V. Ivanov and V. G. Levich, *ibid.*, **126**, 1209 (1959).
98. A. N. Frumkin, L. N. Nekrassov, V. G. Levich, and J. B. Ivanov, *J. Electroanal. Chem.*, **1**, 84 (1959-1960).
99. V. G. Levich, "Physiochemical-hydrodynamics," Prentice Hall, Inc., Englewood Cliffs, N.J. (1962).
100. W. J. Alberry and S. Bruckenstein, *Trans. Faraday Soc.*, **62**, 1920 (1966); see also V. G. Levich, *Acta Physiochim. URSS*, **17**, 257 (1942); *Zh. Fiz. Khim.*, **18**, 335 (1944).
101. V. S. Bagotskii and Y. B. Vasilev, *Electrochim. Acta.*, **9**, 869 (1964).
102. E.g. O. A. Petrii, B. I. Podlovschenko, A. N. Frumkin, and K. Lal, *J. Electroanal. Chem.*, **10**, 253 (1965); **11**, 12 (1966).
103. J. O'M. Bockris, E. Gileadi, and G. E. Stoner, *J. Phys. Chem.*, **73**, 42 (1969).
104. A. Kuhn, H. Wroblowa, and J. O'M. Bockris, *Trans. Faraday Soc.*, **63**, 1458 (1967); J. O'M. Bockris, H. Wroblowa, and B. Piersma, *J. Electroanal. Chem.*, **6**, 401 (1963).
105. M. W. Breiter, *Electrochim. Acta*, **8**, 447, 457 (1963).
106. M. W. Breiter, *Ann. N.Y. Acad. Sci.*, **101**, 709 (1963).
107. M. W. Breiter, *Trans. Faraday Soc.*, **61**, 749 (1965); **60**, 1455 (1964); **62**, 503 (1906).
108. S. Gilman, *Trans. Faraday Soc.*, **61**, 2546, 2561 (1965); *J. Phys. Chem.*, **67**, 78 (1963); **68**, 70 (1964).
109. S. B. Brummer, J. I. Ford, and M. J. Turner, *J. Phys. Chem.*, **69**, 1355, 3424 (1965).
110. S. B. Brummer and A. C. Makrides, *ibid.*, **68**, 1448 (1964).
111. E. Yeager, P. Krouse, and K. V. Rao, *Electrochim. Acta.*, **9**, 1057 (1964).
112. I. Morcos and E. Yeager, US Clearinghouse Federal Science Technological Information AD-682217 (1968).
113. A. C. C. Tseung, B. S. Hobbs, and A. D. S. Tantram, *Electrochim. Acta*, **15**, 473 (1970).
114. A. C. C. Tseung, Pat. Ger. Offen. 2,119,702 (1971); *C.A.*, **76**, 28232 (1972).
115. G. R. Goldstein and A. C. C. Tseung, *J. Phys. Chem.*, **76**, 3646 (1972).
116. B. E. Conway and J. O'M. Bockris, *J. Chem. Phys.*, **26**, 532 (1957).
117. H. Kita, *This Journal*, **113**, 1095 (1966); in "Electrochemistry, the Past 30 and the Next 30 Years," p. 117, H. Bloom and F. Gutmann, Editors, Plenum Publishing Company, New York (1977).
118. P. Ruetschi and P. Delahay, *J. Chem. Phys.*, **23**, 195 (1955).
119. J. O'M. Bockris and S. Srinivasan, in Proceedings of the 19th Annual Power Sources Conference (1965).
120. R. Parsons, *Trans. Faraday Soc.*, **54**, 1053 (1958); H. Gerischer, *Bull. Soc. Chim. Belg.*, **67**, 506 (1958).
121. E. Laviron, *J. Electroanal. Chem. Interfacial Electrochem.*, **34**, 463 (1972); **52**, 355, 395 (1974); **63**, 245 (1975); *Electrochim. Acta*, **16**, 409 (1971).
122. A. Capon and R. Parsons, *J. Electroanal. Chem., Interfacial Electrochem.*, **44**, 1, 239 (1973); **45**, 205 (1973).
123. S. Schuldiner, *This Journal*, **99**, 488 (1952); **101**, 426 (1954); **106**, 891 (1959); **108**, 384 (1961).
124. C. H. Presbury and S. Schuldiner, *ibid.*, **108**, 985 (1961).
125. M. Breiter, "Trans. Symposium on Electrode Processes," p. 307, The Electrochemical Society, John Wiley & Sons, New York (1961).
126. P. Stonehart and K. Kinoshita, "Modern Aspects of Electrochemistry," J. O'M. Bockris and B. E. Conway, Editors, Chap. 4, Plenum Publishing Co., New York, In press.
127. K. J. Vetter and D. Berndt, *Z. Elektrochem.*, **62**, 378 (1958); "Elektrochemische Kinetik," Springer Verlag, Berlin (1961).
128. I. Epelboin and M. Keddam, *Corros. Sci.*, **15**, 441 (1975); *J. Electroanal. Chem. Interfacial Electrochem.*, **65**, 373 (1975).
129. M. Fleischmann and H. R. Thirsk, *This Journal*, **110**, 681 (1963).
130. A. Bewick, M. Fleischmann, and H. R. Thirsk, *Trans. Faraday Soc.*, **58**, 2200 (1962).
131. R. Kaischew and E. Budewski, *Contemp. Phys.*, **8**, 489 (1967).
132. M. Avrami, *J. Chem. Phys.*, **7**, 1103 (1939).
133. U. R. Evans, *Trans. Faraday Soc.*, **41**, 365 (1945).
134. G. J. Hills and D. R. Kinnibrugh, *This Journal*, **113**, 1111 (1966).

The "Structure" of Electrolyte Solutions, 1952-1977

Harold L. Friedman

Department of Chemistry, State University of New York, Stony Brook, New York 11794

"Structural" Concepts

The various phenomena that characterize solutions stem from the forces between molecules rather than from the chemical bonds that hold the molecules themselves together. Of course the chemical bond is the central concept in the part of chemistry that has developed at a spectacular rate; we now are informed in great detail about the geometrical structures and even the electronic structures of many molecules of interest in various fields of chemistry. Moreover, if a structural question about a molecule is posed, our students are well trained to identify the experimental procedure best suited to give the answer. The resulting information is uniquely valuable because a structure is a picture and, as the Chinese tell us, a picture is the best way to convey a lot of information so it can be understood and remembered.

By comparison, our knowledge of intermolecular forces is still in its infancy. The intermolecular interactions, compared to chemical bonds, are less sharply sensitive to distance and orientation, so that the resulting structures are less sharply defined. The bond lengths and angles in a typical molecule are unchanged within a few percent whether the molecule is in the gaseous state, in a liquid, or in a crystal. The contrary is true for the structural parameters determined by the forces between molecules; at least in fluids great variability of intermolecular structures is the rule, and precise statements can only be made for precisely defined averages. This important point may be illustrated by reference to the interesting discussion by Eisenberg and Kauzmann (1) of the structure of liquid water. They define the instantaneous I structure as what one would see in a snapshot taken with a hypothetical camera that could "see" individual atoms if the exposure time were shorter than the period of any of the intermolecular vibrations. If the exposure time is increased to be longer than that of the intermolecular vibrations, but short compared to the time required for a diffusive displacement, then the snapshot would depict the so-called V structure.[1] A still longer increase in exposure times, until they are long compared to the time required for a diffusive

[1] In the V structure snapshot the atomic positions would be blurred because of their vibrational motions, but their positions would be instantaneous relative to the slower movements due to diffusion.

displacement, leads to the D structure. At first one might think that for a fluid the D structure would be a homogenous blur. However, if the hypothetical camera can always be pointed with a particular atom in the center of the field of view, then features such as the Debye-Hückel ionic atmosphere will be visible in the snapshot.

These structural concepts are useful for qualitative discussion. To proceed further we may take advantage of the power of statistical mechanics which enables us to define pictures something like the ones described above but with the added features that the structural functions so defined can be precisely related to the interatomic forces on the one hand and, on the other, to the appropriate experimental data. Various investigations of this kind are reviewed here.

In statistical mechanics the structural information is carried in mathematically defined functions of the locations and velocities of the molecules, and perhaps of the time as well. The most commonly accepted notation is used here, but only the most qualitative definitions of the various functions are given. Precise information is given in the various references.

As an illustration we introduce the pair correlation function (or radial distribution function) (2-4) $g_{ab}(r)$ which is a measure of the probability of finding a particle (atom or molecule) of species a at a distance r from a particle of species b. Thus, if c_a is concentration of species a, the ordinary molarity for example, then $c_a g_{ab}(r)$ is the local concentration of a particles at a distance r from any b particle. One can see that we must have $g_{ab}(r) = 0$ for small r, since each particle occupies some space from which the others are excluded, and one can see that $g_{ab}(r) = 1$ at distances r so large that the force between the particles must be negligible.

According to the theory of Debye and Hückel that leads to the limiting laws we have

$$g_{ab}(r) = 0 \text{ if } r < a$$
$$= \exp\left(-\frac{e_a e_b}{\epsilon r k T} \frac{e^{-\kappa(r-a)}}{1+\kappa a} \right) \text{ if } r > a \quad [1]$$

where e_a and e_b are the ionic charges, ϵ is the solvent's dielectric constant, a is the distance of closest approach of the ions (thought of as charged hard spheres of diameter a) and κ is the famous Debye kappa, proportional to the square root of the ionic strength. In Fig. 1 a graph of Eq. [1] is compared with the correlation function that is calculated for the same charged hard sphere model by methods that are highly accurate in this application. The difference in the graphs shows the refinement of our knowledge of this aspect of the structure of electrolytes since 1923.

The most direct experimental approach to the pair correlation function is through measurement of the scattering of x-rays, electrons, or neutrons by the systems of interest (2-4). Such experiments have led to detailed knowledge of the structure of water, the most important solvent for electrolytes (5, 6), but for electrolytic solutions the corresponding results have not been so definitive until very recently. In Fig. 2 is shown the function

$$G'(r) = 0.277 g_{Ni,O}(r) + 0.637 g_{Ni,D}(r) + 0.080 g_{Ni,Cl}(r) + 0.005 g_{Ni,Ni}(r) \quad [2]$$

as determined by neutron scattering from a 5M solution of $NiCl_2$ in D_2O by Soper, Neilson, Enderby, and Howe (7). The peaks at 2.05 and 2.65A are at expected locations for $g_{Ni,O}$ and $g_{Ni,D}$, respectively, on the basis of the structural data for crystalline $NiSO_4 \cdot 6D_2O$ (8). Their combined area corresponds closely to what may be expected for 6 D_2O molecules, so it may be concluded that $Ni(D_2O_6)^{++}$ is the predominant nickel species in the solution.

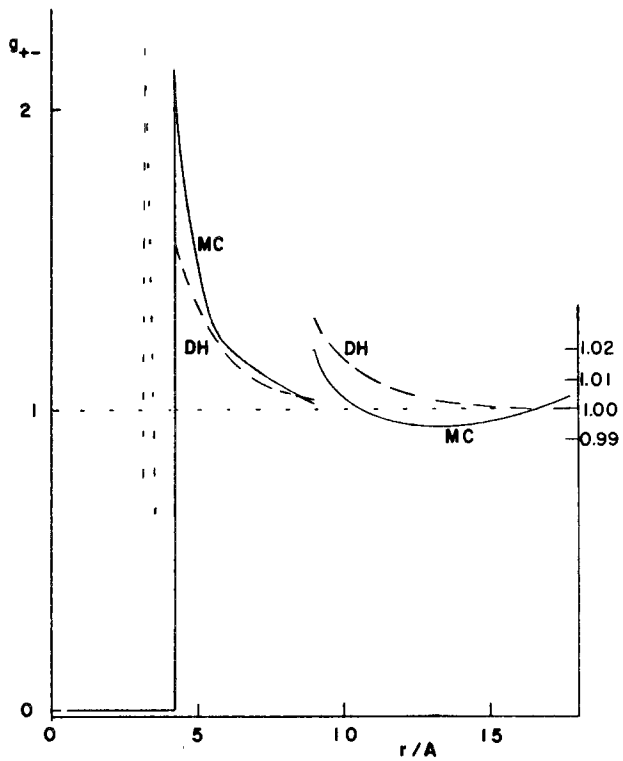


Fig. 1. The pair correlation function $g_{+-}(r)$ at molar ionic strength $I' = 1M$ for charged hard spheres of diam 4.2A. Calculated for a model for 1-1 electrolytes in water. DH: from Eq. [1]. MC: accurate calculation by the Monte Carlo method: [D. N. Card and J. P. Valleau, *J. Chem. Phys.*, **52**, 6232 (1970).] There is a change of scale at 9A to permit the wiggle in the accurate correlation function to be seen. The dashed-line curve showing a sharp peak at 3.25A is the peak in Fig. 2 that is attributed to the pair $Ni(H_2O)_6^{++}$, Cl^-. It is included in this figure to show what part of the ion-ion correlation function may be determined by diffraction from dilute solutions in favorable cases.

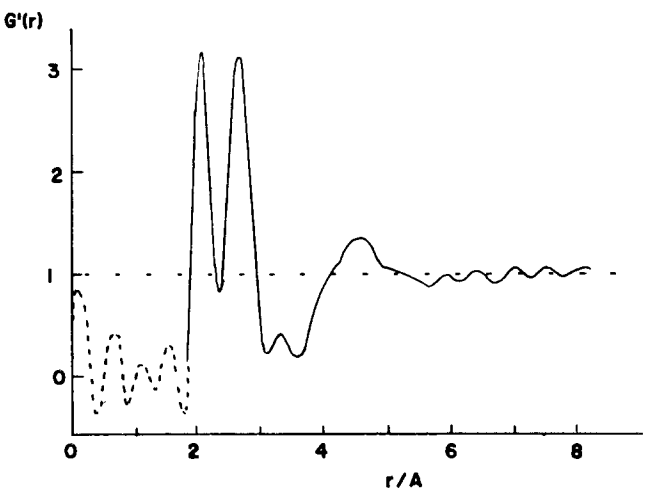


Fig. 2. Graph of Eq. [2] based on data of Soper *et al.*, Ref. (7). The dashed part of the curve is an artifact due to certain experimental limitations.

The authors suggest that the small peak at $r = 3.25$A is due to $g_{Ni,Cl}(r)$. A chloride ion sitting in a triangular face of the $Ni(H_2O)^{++}$ octahedron would give a center-to-center distance for Ni-Cl of 3.90A if the H_2O molecules are represented as spheres of diam 2.76A and Cl^- is represented as a sphere of radius 1.81A, its Pauling ionic radius. The appropriate hydrogen-bonded distances are only slightly smaller (9), so the 3.25A peak, if due to $g_{Ni,Cl}$, shows that the

octahedral $Ni(H_2O)_6^{++}$ is substantially distorted by the Cl^- being in contact with it.

Most of the scattering of radiation by a solution as dilute as 5M is from the solvent. The corresponding terms in Eq. [2], which would be proportional to $g_{O,O}(r)$, $g_{O,D}(r)$, and $g_{D,D}(r)$, were eliminated by the experiments by comparing the scattering from solutions which differ only in isotopic composition (7). The remaining terms may be classified as follows.

The ion-water interactions mainly determine $g_{Ni,O}$ and $g_{Ni,D}$. Conversely, these pair correlation functions bear the primary structural information that is needed for a molecular interpretation of solvation properties, those properties that characterize the interaction of an ion with a solvent. Some examples are given in Table I.

The ion-ion interactions mediated by the solvent determine $g_{Ni,Cl}$ and $g_{Ni,Ni}$. These pair correlation functions, together with $g_{Cl,Cl}$, bear the primary information needed to calculate the excess properties of the solution, those properties that describe how the results of measurements on the solutions vary with solute concentration. Some examples are given in Table II.

Equation [1], and other equations of what is often called the ionic interaction theory, pertain to ion-ion correlation functions, the type related to excess properties. We see from Fig. 2, which represents an unusually successful scattering experiment, that the direct experimental investigation of ion-ion pair correlation functions is, even with the best technology presently available, so difficult that only the strongest features of the ion-ion $g_{ab}(r)$ may be measured accurately. To show this most clearly, the presumed peak for $g_{Ni,Cl}(r)$ has been sketched in to scale in Fig. 1. On the other hand, it is found from model calculations that the thermodynamic excess functions, such as $\ln \gamma_\pm$, are sensitive to changes in the ion-ion $g_{ab}(r)$ at a level far too small to distinguish from the noise in Fig. 2.

Corresponding to the equilibrium pair correlation functions $g_{ab}(r)$, there are other correlation functions, called time-correlation functions (3, 10, 11), that are used to characterize the dynamical aspects of structure and that also are related by equations to the intermolecular forces on the one hand and to the measurable dynamical properties on the other. A simple example is the time-correlation function for the velocity v of a given particle

$$\langle \mathbf{v}(t + t_0) \cdot \mathbf{v}(t_0) \rangle$$

which is the equilibrium average $\langle \ldots \rangle$ of the product of its velocity at a time t_0 times its velocity at time $t + t_0$. It depends upon the fluctuations in a system at equilibrium. A typical simple form for a time correlation function is

$$\langle \mathbf{v}(t + t_0) \cdot \mathbf{v}(t_0) \rangle = \langle \mathbf{v}^2 \rangle e^{-t/t_v} \qquad [3]$$

where t_v is a characteristic time for the particular system. A typical general result is

$$D = \frac{1}{3} \int_0^\infty \langle \mathbf{v}(t + t_0) \cdot \mathbf{v}(t_0) \rangle dt \qquad [4]$$

where D is the diffusion coefficient of the particle whose velocity appears in the time-correlation function.

Intermolecular Forces

The correlation functions that characterize the structures of solutions can be expressed in terms of the solute-solute, solute-solvent, and solvent-solvent intermolecular forces, each the gradient of a potential u_{ab}. If species a and b both are round particles, then u_{ab} depends only upon r, the distance between their centers and we write $u_{ab} = u_{ab}(r)$. In the more general case, it now is customary to write $u_{ab} = u_{ab}(X_a, X_b)$ where X_j is a set of coordinates that specifies the location and orientation of a particle of species j.

The potentials $u_{ab}(X_a, X_b)$ can be calculated by solving Schroedinger's equation for the electrons of a and b moving in the field of the nuclei fixed at positions specified by the coordinates X_a, X_b. This direct theoretical approach is illustrated by the very impressive calculations of Clementi and his co-workers for ions and small sets of water molecules (12).

By studying the collisions of molecules by molecular beam techniques (13) and the thermodynamic and mechanical properties of crystals of known structures (14) one has direct experimental approaches to the relevant potential functions u_{ab}. The experimental approach sometimes is called the inverse process: one assumes functional forms for the needed u_{ab} potentials, thus specifying what may be called a Hamiltonian model. Next, some measurable properties of the model are calculated for comparison with the corresponding actual properties of the system of interest. Then the model potentials $u_{ab}(X_a, X_b)$ are adjusted to improve the agreement of the model properties with those of the real system. The difficult part of this program is the calculation of measurable properties of the model; it cannot be done exactly, but only by using some approximation method which must be evaluated for accuracy in this application.

The direct theoretical and direct experimental approaches to u_{ab} may be expected to be complementary, so it is advantageous to use them together. This procedure is nicely illustrated in the development of the Ben Naim-Stillinger (BNS) potential for the interaction of two water molecules (15). As an important example of the inverse process we cite the work of Rahman and Stillinger on models for water using the molecular dynamics approximation method (16). By applying the inverse process they progressed from the BNS model to the ST2 model for the water-water interaction.

Ionic Solvation

By ionic solvation we mean the interaction of an ion with a macroscopic body of solvent. This is the classical definition, but quite recently the term has been

Table I. Coefficients of solvation (26)

Limiting values of the following coefficients, measured on a solution of solute A in solvent W as the molar ratio $c_A = n_A/n_W$ approaches zero.

Transfer coefficients
ΔG, ΔH, ΔS for the process A(in W) → A(in W') where W' is a reference solvent or the vacuum.

Partial molal coefficients
$\partial/\partial c_A$ of any of the following solution properties: volume, heat capacity, coefficient of thermal expansion, compressibility, ϵ = dielectric constant, η = viscosity, sound velocity, NMR chemical shift of a solvent nucleus, shift of a solvent intramolecular vibration frequency.

Intrinsic solute coefficients
D_A, diffusion coefficient of A
ζ_A, friction coefficient of A (proportionality constant between the average velocity produced by a steady force upon A and the force
$(\tau\theta)_A$, rotational orientation time of A
$(\tau J)_A$, angular velocity correlation time of A
$CTTS_A$, charge-transfer-to-solvent spectrum of A

Table II. Coefficients of excess properties

Thermodynamic functions (HO[a] notation in quotation marks)
G^{ex}, the excess Gibbs free energy and its partial molal components 1 − "ϕ" and ln "$\gamma_\pm$"

H^{ex}, the excess enthalpy, and its partial molal components "L_1" and "L_2"

C_p^{ex}, the excess heat capacity, and its partial molal components "J_1" and "J_2"

V^{ex}, the excess volume, and its partial molal components "$\bar{V}_1 - \bar{V}_1^0$" and "$\bar{V}_2 - \bar{V}_2^0$"

Transport coefficients
"$\Lambda - \Lambda_0$", the excess equivalent conductance
"$D_a - D_a^0$", the excess coefficient of diffusion of component a

[a] HO refers to H. S. Harned and B. B. Owen, "The Physical Chemistry of Electrolyte Solutions," Reinhold Publishing Corp., New York (1943).

stretched to apply to the interaction of an ion with a small number of solvent molecules in the gas phase to form an ion-molecule cluster (17). The formation of small clusters may be regarded as a step in the process of solvation. Moreover, the data for small clusters (17) are exceedingly valuable for testing calculations of the ion solvent potential function $u_{ab}(X_a, X_b)$, as illustrated in several recent studies (12, 18, 19).

The structural aspects of ionic solvation have been greatly elucidated by magnetic resonance studies (20). When the solvent molecules next to an ion in solution comprise a "solvation complex" that exchanges solvent molecules with the bulk sufficiently slowly, then magnetic resonance techniques can be applied to characterize the complex as to stoichiometry, rate of rotation of the complex, and rate of exchange of the solvent molecules between the solvent and the bulk. This approach is specially powerful for studying the solvation of paramagnetic ions, in which case the experiments lead to the determination of certain spin parameters that carry information about the complex's electronic structure. The extensive contribution of work of this kind to our knowledge of solvation complexes in water has been reviewed by Taube (21) and by Hertz and Zeidler (22). The methods may be even more powerful when applied to nonaqueous solvents (23) or their mixtures with water (24) because of the lower exchange rates and the greater temperature range that is accessible. While progress in elucidation of structure in this area has been great, it must be noticed that these advances relate only to ion-solvent complexes with well-defined geometry and relatively long life. A typical example is $Mn(H_2O)_6^{++}$ in water. The lifetime of a water molecule in the complex before it exchanges with the bulk is about 10^{-8} sec, which is rather long compared to the lifetime of 10^{-11} sec expected if the exchange is a simple diffusion process, in which case we would have $t_{\text{lifetime}} = \langle r^2 \rangle / 6D$ with $\langle r^2 \rangle^{1/2} = 3\text{A}$ and $D = 1 \times 10^{-5}$ cm^2/sec.

Another example is $Ni(H_2O)_6^{++}$, for which the exchange lifetime is about 3×10^{-5} sec; it is interesting to note that the stoichiometry of the complex, as established by magnetic resonance methods which only are applicable to relatively long-lived complexes, is confirmed by the data in Fig. 2 which are obtained by a technique that does not have this limitation.[2]

When a complex is long lived and has well-defined geometry, then the concepts and techniques used traditionally in the study of chemical bonds are applicable. Moreover, in such cases the structures actually found in solution are closely similar to those found for the same ions in their crystalline salt hydrates. As mentioned in the opening paragraphs of this paper, the situation is quite different in the study of the "structures" more typically due to intermolecular forces, to which we now return.

A traditional approach to the structural aspects of solvation is through the comparison of solvation data with the predictions of BBB models (26) (brass balls in a bathtub models, a term due to Professor H. S. Frank). In a BBB model the ion is treated as a macroscopic body, and the solvent as a medium characterized by macroscopic properties such as viscosity, dielectric constant, etc. These coefficients, like those of the real solvents, may depend upon field strength, frequency, and other relevant variables as well as temperature and pressure. The BBB model theories for many of the coefficients in Table I are well known (26), for example, Born's equation for the ionic solvation free energy

$$\Delta G_a = (1 - 1/\epsilon)\, e_a^2/2r_a \qquad [5]$$

and Stokes' law for the friction coefficient

$$\zeta_a = 6\pi\eta r_a \qquad [6]$$

In these equations, e_a is the charge and r_a the radius of an ion of species a.

The traditional approach is to attribute deviations of solvation coefficients from the simple BBB model predictions to the formation of solvation complexes. In the case of the equations chosen for examples, the effect of forming the solvation complex would be to increase r_a to a value greater than the ion's Pauling crystal radius. For example, the friction coefficients (inverse ionic mobilities) of the alkali metal ions decrease in the series from Li^+ to Cs^+, in contrast to the prediction of Eq. [6] if ionic radii are used. This suggests that the small ions form rigid solvation complexes so their "hydrodynamic radii" become larger than their crystal radii. However, it has been proposed by several authors, most recently Zwanzig (27), that one should use a more elaborate BBB theory to allow for the "dielectric drag" acting on a charged object when it is pulled through a medium with a frequency-dependent dielectric constant. The resulting theory leads to a graph of ζ_a as a function of r_a that has a minimum (26, 28). The trend in the friction coefficients of the alkali ions in water is accounted for by observing that these ions lie to the left of the minimum, in a region where the effect of the dielectric drag is greater than the hydrodynamic drag accounted for by Eq. [6]. With more extensive data even the minimum can be located (28). One is left with no basis for interpreting these data in terms of structural effects, at least involving rigid hydration.

A similar critique can be made of the extensive work aimed at extracting structural information by comparing Eq. [5] with experiment (29). An interesting approach is to introduce the concept of a nonlocal dielectric constant: In a nonuniform field the polarization per unit volume in a given small region in the medium depends on the electric field everywhere in the medium, not just in the given small region. It has been shown that introduction of a nonlocal dielectric constant modifies the BBB model for the solvation free energy so that it is in reasonable agreement with the data for hydration of alkali and halide ions (30). The resulting picture of ionic hydration is rather close to that provided by the theory of Voet (31), which is better known in its elaboration by Latimer, Pitzer, and Slansky (31), but the implications for the structure of the solvation complex are now greatly weakened.

Another example, pointed out by Onsager and Hubbard (32) concerns the coefficient ϵ_1 in the equation

$$\epsilon = \epsilon_0 + c\epsilon_1 + \ldots \qquad [7]$$

for the dependence of the dielectric constant ϵ of aqueous solutions upon the electrolyte concentration c. While ϵ_1 has been interpreted (33, 34) in terms of the structures of particular solvation complexes, Hubbard *et al.* (32) point out that the dominant contribution from ϵ_1, as it was calculated from the high frequency measurements, comes from the effect that is inverse to dielectric drag according to their BBB model calculations.

It should be pointed out before leaving this subject that BBB model calculations are often amazingly accurate when applied to small solute molecules; the most recent evidence is in the comparison of new theoretical (35) and experimental results (36) for the rotational correlation time (t_θ in Table I) for solute molecules in nonhydrogen bonding situations. These results add to the growing body of evidence that for realistic hydrodynamics in BBB model calculations in systems without hydrogen bonds, the boundary conditions at the surface of a particle should be "slip" rather than "stick." For example in Eq. [6] the coefficient 6 should be changed to 4.

Solutes in water often are classified as structure making or structure breaking, following Frank and Evans (37) who used the behavior of the solute partial molal entropy as a criterion. The distinction shows

[2] Similarly, Bol has shown by a specialized x-ray diffraction method that the coordination of a number of other M^{++} ions is nearly the same in solution as in salt hydrates (25).

up in many other properties as well (29). Alone among the many classifications, that of Stillinger and Ben-Naim (38) is based on the behavior of the equilibrium pair correlation functions. They deal with the correlation between an O atom in a water molecule and the H atoms in all of the other water molecules in the solution. They show how the quantity

$$\int_0^\infty [g_{OH}(r) - 1]4\pi r^2 dr$$

can be calculated from compressibility data and how it changes according to whether a structure maker or structure breaker is added to water.

Information about solvation structural effects sometimes has been deduced from data for the dependence of the diffusion coefficient D_a of a solute particle upon its mass m_a. Mills and Dunlop have reviewed the data for this effect as well as the relevant theories (39). The effect seems in fact to be small to the vanishing point, and there is no evidence, either experimental or theoretical, for having D_a proportional to $1/\sqrt{m_a}$ (39).

The Hall effect for ionic solutions is a very small effect that is easily obscured by other electromagnetic effects associated with convective rather than diffusive motion. It can be used as a probe for the very short time behavior of the time correlation function for the ionic velocities (40). Very recently new measurements for the Hall effect have been reported which seem quite reliable. They indicate that for some ions in water (Li^+, H^+, OH^-, F^-, . . .) the deviations from Eq. [3] are easily detectable by the Hall effect measurements (41). The implications of this finding in more picturesque structural terms are not yet clear.

Excess Properties

Long-range behavior of ion-ion $g_{ab}(r)$.—Progress in the study of the structural aspects of the excess properties has been historically coupled closely to the so-called interionic attraction theory; essentially the Debye-Hückel theory and its close descendants. More recently vast improvements in the theoretical treatment of excess equilibrium properties have derived from developments in statistical mechanics in areas connected remotely, if at all, with the Debye-Hückel theory. Reference may be made to reviews by Friedman (42), Rasaiah (43), Andersen (44), and Outhwaite (45) for accounts of this work; Outhwaite alone has also described the newer developments that are derived from the Debye-Hückel approach. Also, an article by Friedman and Dale (2) is designed to provide the background in statistical mechanics that is necessary to follow and employ many of the new advances in techniques for calculating solute-solute correlation functions $g_{ab}(r)$ and the resulting thermodynamic excess functions of model systems. (For further discussion of the models see the next section.)

In the cluster expansion technique the correlation function of interest is represented by an infinite series whose terms may be written as graphs, each graph being a number of vertices (particles) connected by bonds (interactions.) The first terms in the cluster expansions give the limiting laws. The hypernetted chain (HNC) approximation was first obtained as a partial sum of this series; an infinite number of the graphs including what may be expected to be the most important ones for calculating properties up to moderate concentrations. The mean spherical approximation (MSA) has some of the strong features of the HNC, but for sufficiently simple models the MSA can be solved exactly to give algebraic expressions for the excess thermodynamic properties. In the Monte Carlo approximation method one simulates, by direct computation, the behavior of a system like the one of interest except that the Monte Carlo system is a crystal whose cubic unit cell contains perhaps 200 particles. The distribution of particles within a cell is random like that in the fluid being simulated, but every cell in the infinite crystal has the same distribution, leading to what are called periodic boundary conditions for the cell being simulated. For details of these and other new and promising approximation methods Ref. (2, 42-45) may be consulted.

Here and in the following section, an effort is made to concentrate on the "structural" aspects of these developments. The usual form of the Debye-Hückel limiting law is

$$\ln \gamma_\pm = -|e_+ e_-|\kappa/2\epsilon kT \quad \text{as} \quad \kappa \to 0 \qquad [8]$$

where

$$\kappa^2 = (4\pi/\epsilon kT) \Sigma\, c_s e_s^2 \qquad [9]$$

defines the Debye kappa in terms of the concentrations c_s and charges e_s of ions of species s, and in terms of the temperature T and the solvent dielectric constant ϵ. To pass on to the other limiting laws it is more convenient to begin with the Debye-Hückel limiting law for the excess free energy per unit volume, which we denote as $a^{ex}kT$.

$$a^{ex} = -\kappa^3/12\pi \quad \text{as} \quad \kappa \to 0 \qquad [10]$$

A more complete theory gives a "higher-order limiting law" as well

$$a^{ex} + \kappa^3/12\pi = \kappa^4 \ln(\kappa L) \Sigma\, c_s e_s^3 \quad \text{as} \quad \kappa \to 0 \qquad [11]$$

where L is any length, although some particular choice such as the Bjerrum length $L_B = e_{el}^2/\epsilon kT$ may be especially convenient. The quantity on the left of Eq. [11] is experimentally determinable, and the quantity on the right does not depend on ion sizes and other specific characteristics, so Eq. [11] is indeed a limiting law in the same sense as Eq. [8] or [10]. It was first noticed by Gronwall and co-workers (42) but also has been derived in another way (47). The right side of Eq. [11] vanishes for symmetrical electrolytes and is apparently never larger than both $\kappa^3/12\pi$ and the remaining contributions to a^{ex}, which do depend upon the ion sizes and other specific characteristics, so it is not surprising that it was first measured by precision experiments only recently (48). Gibbard's results (48) are in satisfactory agreement with the theory.

The limiting-law behavior in Eq. [11] is also characteristic of other thermodynamic coefficients such as the excess energy, for which the corresponding equation can be derived by thermodynamic operations on Eq. [11]. Moreover, a similar expression also characterizes nonthermodynamic excess coefficients such as the excess equivalent conductivity Λ-Λ_0, as one can see from the well-known theory (49). (Here we subtract Λ_0 because it is the part of Λ that is a solvation coefficient; the difference is an excess function.)

Other limiting laws have been established for mixtures of two ionic solutions having one ionic species common to the two components. Thus, we consider the experiment in which solutions of pure AX_n and BX_n, both at the same ionic strength, are mixed in various proportions (*cf.* Fig. 3). The deviation of a^{ex} from the linear interpolation at $y = \frac{1}{2}$ (see Fig. 3) is a measurable excess function which we may call

$$\tfrac{1}{4} I'^2 g_0'$$

where the primes specify molar (rather than molal) concentration scales (47, 50). The coefficient g_0' is the simplest excess function that is characteristic of electrolyte mixtures. It plays the same role as the sum of Harned coefficients. It obeys the limiting law

$$(1/g_0')(dg_0'/d\kappa) = e_A^2/\epsilon kT \quad \text{as} \quad \kappa \to 0 \qquad [12]$$

While this example is for a given class of charge types for simplicity, the general form for mixing A_mX_n with B_mX_n or A_mY_n also is known (47). However, in a mixture of two electrolytes of different charge types, in particular with different values of $c_+e_+^3 + c_-e_-^3$, the limiting law in Eq. [12] is unob-

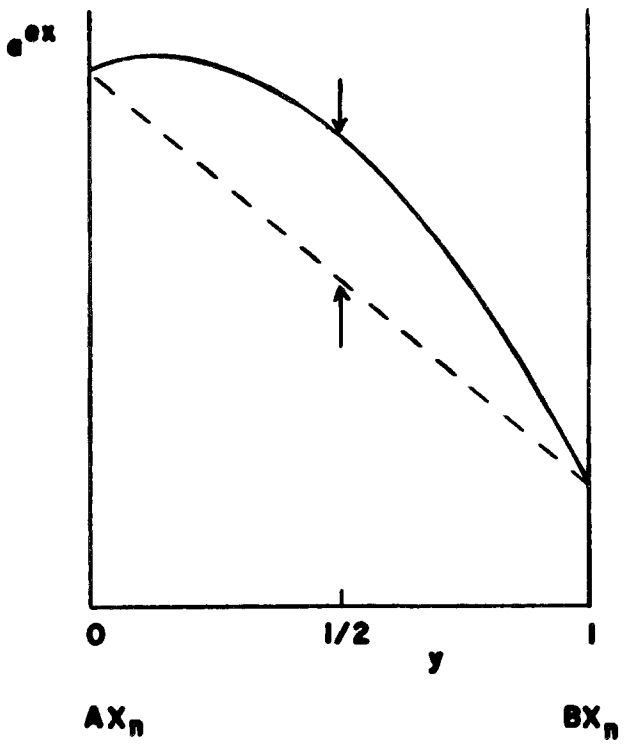


Fig. 3. The excess free energy function of a mixture of electrolyte solutions as a function of the mixing ratio. The initial solutions AX_n and BX_n are taken to have the same molar ionic strength I'.

servable because another limiting law with stronger dependence upon κ (or I') takes over. For a mixture of electrolyte of NaCl type with one of $CaCl_2$, the limiting law is (51)

$$g_0' = 1.205 \times 10^{-4}\left(\frac{4\pi}{3} L_B^3\right) \ln \kappa L \text{ as } \kappa \to 0 \quad [13]$$

These mixture limiting laws reflect failure of the ionic strength principle, according to which ionic activity coefficients only depend upon the ionic strength. Moreover, the coefficient g_0' in Eq. [12] is due to differences in the specific interaction in the pairs AA, AB, and BB, so this limiting law is an exact result that would be disallowed by Bronsted's principle of specific ion interaction, which only allows specific interaction of pairs of ions of opposite sign of charge. Thus, neither the ionic strength principle nor the Bronsted principle is consistent with the nonzero values of g_0' and other mixing coefficients (47, 51) actually found by experiment (50).

The structural consequences of these limiting laws may be found in the behavior of the ion-ion pair correlation functions $g_{ab}(r)$ at large r and small κ. For example, as found by Debye and Hückel, the behavior

$$\ln g_{ab}(r) \to -e_a e_b e^{-\kappa r}/\epsilon kTr \text{ as } r \to \infty \text{ and } \kappa \to 0 \quad [15]$$

is equivalent to Eq. [8] or [10].

Other conditions on the ion-ion correlation functions are the zeroth moment condition (formerly called the local electroneutrality condition)

$$\Sigma_b c_b e_b \int_0^\infty (g_{ab}(r) - 1) 4\pi r^2 dr = -e_a \quad [16]$$

and the second moment condition of Stillinger and Lovett (52)

$$\Sigma_a \Sigma_b c_a c_b e_a e_b \int_0^\infty (g_{ab}(r) - 1) r^2 4\pi r^2 dr = -3\epsilon kT/2\pi \quad [17]$$

where, in both equations, the sums are over ionic species. These exact conditions have structural consequences. It is well known that Eq. [8] implies that each ion of charge e_a is surrounded by an "atmosphere" whose net charge is $-e_a$. That statement is merely a reading of Eq. [16]. The corresponding pictorial interpretation of Eq. [17] has the consequence that in any solution whose κ exceeds a certain value κ^*, the correlation functions $g_{ab}(r)$ must have "wiggles" or oscillations (52). For electrolytes in water at 25° one has $\kappa = \kappa^*$ at an ionic strength near 6M, depending on ion sizes. However, the critical ionic strength for the onset of wiggles is shown to be as low as 2M by various model calculations (45). These wiggles are not predicted by Eq. [1] or any of the other familiar modifications of the Debye-Hückel theory. However, they are given by many more powerful approximation methods which may be used to calculate the $g_{ab}(r)$ from the Hamiltonian models, among them the HNC equation and a method of Outhwaite's that is a generalization of the method of Debye and Hückel (45). Qualitatively similar wiggles also appear in the correlation functions of nonionic fluids at sufficiently high densities.

Any excess property W of a solution can be expressed in the form

$$W = \Sigma_a \Sigma_b c_a c_b \int_0^\infty W_{ab}(r) g_{ab}(r) 4\pi r^2 dr \quad [18]$$

where $W_{ab}(r)$ is a weight function that is different for each property. This equation has a simple meaning: each pair ab at a specified separation r makes a contribution $W_{ab}(r)$ to the excess property W. We can expect that $W_{ab}(r)$ goes to zero as r goes to infinity because the influence of a on b must vanish in that limit. For excess thermodynamic properties, as well as some others, the longest range part of W_{ab} is of the form

$$f_W e_a e_b / r \quad [19]$$

which comes from the coulomb term $e_a e_b/\epsilon r$ in the potential of the force between two ions. For example, to calculate the osmotic coefficient we have $f_W = 1/6\epsilon$, to calculate the excess energy we have $f_W = (\partial/\partial T^{-1})(1/6\epsilon T)$, etc. (47). Because $\Sigma_a \Sigma_b c_a c_b e_a e_b = 0$ we can replace g_{ab} in Eq. [18] by g_{ab}^{-1} as far as the term in Eq. [19] is concerned. Now we must look closely at the expression

$$f_W e_a e_b \int_0^\infty (1/r)(g_{ab}(r) - 1) 4\pi r^2 dr \quad [20]$$

The integral diverges unless g_{ab}^{-1} goes to zero fast enough at large r. Consequently, the exact way in which g_{ab}^{-1} goes to zero as $r \to \infty$, one says the "asymptotic form of g_{ab} at large r," may be decisive in determining the value of the integral in Eq. [18]. So it is interesting to ask what is known about the asymptotic form of g_{ab} at large r.

Most often it has been assumed that Eq. [15] is valid even when κ is nonzero; then we would have

$$g_{ab}(r) - 1 = -e_a e_b e^{-\kappa r}/\epsilon kTr \text{ as } r \to \infty, \quad \kappa \geqq 0 \quad [21]$$

but there is no theoretical basis for this assumption. In fact, the structural question as to the asymptotic form of g_{ab}^{-1} at large r has not been answered in a satisfactory way, although there are two proposals that merit serious consideration. Thus, Stell and Lebowitz (53) find a form just like Eq. [21] but with κ replaced by a new coefficient κ_{ab} that depends upon the short-range interaction of the ions but becomes identical to the Debye-Hückel κ in the limit of zero concentrations of the ions. On the other hand, Stillinger and White, using a very different method, find (54)

$$g_{ab}(r) - 1 = A_{ab}/r^8 \text{ as } r \to \infty \quad [22]$$

at finite ion concentrations, although A_{ab} is proportional to the square of the total ion concentration so that at zero concentration Eq. [21] still governs.

So at the present time the asymptotic form of $g_{ab}(r)$ at large r and at nonzero concentration is not known, important though it may be.

Short range behavior of the ion-ion $g_{ab}(r)$.—As soon as we look beyond the limiting laws to see what structural information is in the remaining contributions to the excess properties, we encounter the short-range behavior of $g_{ab}(r)$. To discuss the advances in this area, it is convenient to supplement the discussion of the potentials $u_{ab}(r)$ and $u_{ab}(X_a, X_b)$. Those potentials now will be termed BO potentials (Born-Oppenheimer potentials) to distinguish them from the MM potentials (McMillan-Mayer potentials) that we need to introduce now (2, 42, 44, 47). The BO potentials are the potentials of the forces among the particles at fixed locations of the nuclei but with the appropriate quantum-mechanical average over the coordinates of the electrons in the system. The MM potentials $\bar{u}_{ab}(r)$ are the potentials of the forces among the ions if we make the appropriate average over the coordinates of the solvent molecules. (The electronic averages are implicitly included in the MM potentials. Also, it should be pointed out that the pair potentials u_{ab} or $\bar{u}_{ab}$ are in general not sufficient to describe a real system exactly; in addition to these 2 point potentials one needs also 3 point potentials, 4 point potentials, etc.) (2).

The theory of McMillan and Mayer (2, 42, 44, 47) shows that all of the equilibrium properties of a solution, as well as the ion-ion correlation functions $g_{ab}(r)$, can be expressed in terms of the MM potentials $\bar{u}_{ab}$ together with the higher n point potentials that will be neglected here. In the limit of small ion concentration we have

$$g_{ab}(r) = \exp(-\bar{u}_{ab}(r)/kT) \qquad [23]$$

For moderate concentrations, say molar ionic strength I' up to about 3M, the typical concentration dependence of $g_{ab}(r)$ is indicated schematically for several cases in Fig. 4. To summarize in words:

1. The behavior at large r, where $g_{ab}(r)$ is near unity, changes drastically as I' increases. This aspect results from the features discussed previously.

2. The small r behavior is weakly dependent upon I'. The changes are qualitatively just those expected on the basis of the Debye-Hückel ion atmosphere effects (55, 56). Thus for a $+-$ pair the first peak in g_{ab} is flattened by Debye-shielding while for a $++$ or a $--$ pair the population of close pairs is increased by the Debye shielding.

While the ionic strength dependence of the close-in part of the ion-ion pair correlation functions is not very strong, small changes in the correlation functions make rather marked changes in the thermodynamic excess functions. Thus, it can be understood that the mean spherical approximation (2, 43, 45) and many of its descendants, although they are consistent with the zeroth moment condition and the second moment condition [so they must give a reasonably accurate account of the I' dependence of the large r part of $g_{ab}(r)$], and which also give qualitatively the correct I' dependence of the small r part of $g_{ab}(r)$, still are not very satisfactory for calculating the measurable properties of model systems just because they are not accurate enough in the small r range. Fortunately, the HNC and Monte Carlo approximation methods do seem accurate enough for most purposes and give consistent results (45). Moreover, for a given model the qualitative features of $g_{ab}(r)$ at small r will be satisfactorily given by the MSA (43, 45) because, as noted above, the I' dependence is not strong in this region.

One can learn about the relatively short-range part of $g_{ab}(r)$ in the following way: (*i*) Construct Hamiltonian models for the solutions of interest by choosing MM potentials $\bar{u}_{ab}(r)$ for each ionic species pair. As far as possible, the model should be consistent with what is known about the ions and the solvent. (*ii*) Calculate the model's ion-ion correlation functions $g_{ab}(r)$ over a range of ionic strength. (*iii*) Use the appropriate version of Eq. [18] to calculate measurable properties from the $g_{ab}(r)$ at each I'. (*iv*) Compare the results with experimental data for the system of interest, correct the model potentials to improve the agreement, and then repeat steps (*ii*), (*iii*), and (*iv*) until agreement is satisfactory.

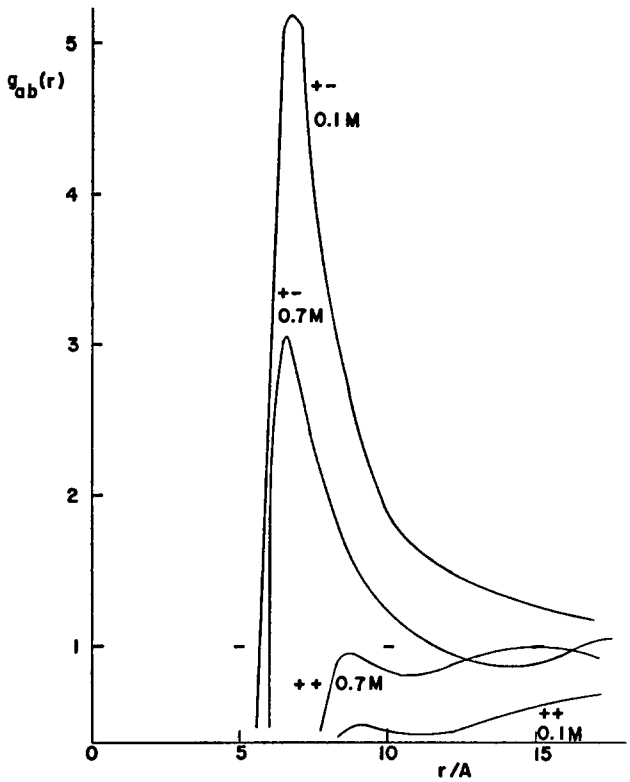


Fig. 4. Correlation functions at 0.1 and 0.7M to show the typical effect of increasing concentration. The curves below 7A are accurately calculated for a model for $NiCl_2$ that fits the osmotic coefficient data fairly well, while above 7A the curves are merely schematic. They show in exaggerated form the oscillations in $g_{ab}(r)$ at large r that appear at high concentrations.

This program has actually been carried out for the excess free energies of aqueous solutions of alkali halides (58), alkaline earth halides (55), tetraalkyl ammonium halides, common-ion mixtures of 1,1 electrolytes with those of charge type 1,1 (58) or 2,1 (51, 55), and with nonelectrolytes (58). In a few cases, calculations also were made for excess enthalpies and excess volumes.

An overview of all of these results (58) shows that in general it is quite easy to fit models to the thermodynamic excess function data, at least when the adjustable part of $\bar{u}_{ab}(r)$ is a sort of adjustable well or mound to represent the effect of overlap of the solvation layers or cospheres on ions a and b when the ions are close together, *i.e.*, close enough so no more than 2 or 3 water molecules will fit on the line of centers (55, 57, 58). It is found that such a term, suggested some time ago by Frank (37) and by Gurney need not be large compared to kT to enable one to fit the model to the data (58). Moreover, the way the Gurney overlap term depends on the species pair ab is reasonably consistent with the results of other investigations of ion interactions in solution (58).

However, there are great problems in trying to find out what model potentials $\bar{u}_{ab}$ uniquely fit the data best, as may be expected from the form of Eq. [18] (58). This situation has led to current efforts to calculate nonthermodynamic excess properties of the same model systems.

Extensive work in this area has already been carried out by Ebeling *et al.* (59, 60). They fit model potentials simultaneously to excess free energy data and to conductivity data for alkali halides and tetraalkyl ammonium halides in a vast least squares loop using approximation methods that they have devised for the purpose. This approach is still in development but the results announced so far are mostly consistent with those reported by Friedman *et al.* (58) and, for R_4NX salts, by Wen and Streng (61).

A strong feature of the program of Ebeling *et al.* (60) is that the electrical conductivity can be measured accurately for every solution for which the thermodynamic excess functions can be determined. On the other hand a qualitative examination of the equations shows that the weight function W_{ab} in Eq. [18] for calculating excess conductivity is not so different from that for the excess free energy. This situation tends to reduce the chance that a model that can be fit well to the thermodynamic data will fail to fit the conductivity data. Of course it is through only failures of this kind that we can, by elimination, identify uniquely satisfactory models!

In some cases, one has weight functions which vanish except for a single species pair, *i.e.*

$$W_{ab}(r) = \delta_{aa'}\delta_{bb'}W_{a'b'}(r) \qquad [24]$$

where $\delta_{ij} = 0$ unless $i = j$, and $\delta_{ii} = 1$. One example is the weight function for the calculation of the results of neutron diffraction experiments with a suitable number of isotopic substitutions (2, 7). A closely related example is one in which there is a range of scattering angles in a diffraction experiment in which only one species pair contributes significantly to the scattering, as for solutions of Ph_4AsCl in water. In this case only the $++$ pair contributes to the scattering in the small angle range, *i.e.*, to $I(s)$ in the range $0 \leq s \leq 0.3/A$ (56).

Finally another suggestion for realizing Eq. [24] is the study of the relaxation rate of a nucleus in one ion (a′) due to dipolar interaction with another ion (b′) (58). In this case the property W calculated in Eq. [18] is just the rate constant of the relaxation reaction, for example

$$^7Li^+(m) + Ni^{++} \rightarrow {}^7Li^+(m') + Ni^{++} \qquad [25]$$

where m is the index of the nuclear spin state of the lithium ion; $-3/2$, $-1/2$, $1/2$, or $3/2$.

These efforts at characterizing $\bar{u}_{ab}(r)$ more completely on the basis of the experimental evidence are no doubt rather limited because Eq. [24] can be realized in actual experiments for only relatively few pairs of ions. However, it is reasonable to expect that in time these new developments will be followed by others; very little work has been done in this area compared to those reviewed before.

A complementary line of investigation is the use of Monte Carlo and molecular dynamics approximation techniques to calculate the McMillan-Mayer potentials $\bar{u}_{ab}(r)$ from the relevant BO potentials, the latter being calculated from the Schroedinger-level Hamiltonian, which is of course well known. The initial reports of work in this area by Heinzinger and Vogel (62), Clementi and co-workers (63), and Beveridge and Schnuelle (64) demonstrate that this approach is feasible. One can expect that it will be complementary to the "inverse method" of determining the MM potentials.

There is reason to hope that in the next 25 years the combination of the two approaches will lead to as detailed information about the potentials $\bar{u}_{ab}$ for ions in solution as we have at present about the potential $u_{Ar,Ar}$ for the interaction of two argon atoms in the gas phase. Then we will know to what extent ions in solution penetrate each other's cospheres when they collide, we will understand how the MM potentials and the excess properties are related to the structure-making and structure-breaking properties, and we will know the structure of a hydrophobic bond as it is reflected in the potentials $\bar{u}_{ab}$ of the force between two hydrophobic species. These are the questions that may be answered by the delicate interaction of theory and experiment along the lines that have developed in the period under review.

REFERENCES

1. D. Eisenberg and W. Kauzmann, "The Structure and Properties of Water," p. 150, Oxford University Press, New York (1969).
2. H. L. Friedman and W. D. T. Dale, in "Modern Theoretical Chemistry," Vol. 5, B. J. Berne, Editor, pp. 85-135, Plenum Press, New York (1976).
3. J.-P. Hansen and I. A. McDonald, "Theory of Simple Liquids," Academic Press, New York (1976).
4. R. O. Watts and I. J. McGee, "Liquid State Chemical Physics," Wiley-Interscience, New York (1976).
5. A. H. Narten and H. A. Levy, in "Water, A Comprehensive Treatise," Vol. 1, F. Franks, Editor, pp. 311-332, Plenum Press, New York (1972).
6. D. I. Page, *ibid.*, pp. 333-362.
7. A. K. Soper, G. W. Neilson, J. E. Enderby, and R. A. Howe, *J. Physics C*, **10**, 1793 (1977).
8. B. H. O'Connor and D. H. Dale, *Acta. Crystallogr.*, **21**, 705 (1966).
9. W. C. Hamilton and J. A. Ibers, "Hydrogen Bonding in Solids," W. A. Benjamin, Inc., Menlo Park, Calif. (1969).
10. P. Schofield, in "Statistical Mechanics," Vol. 2, K. Singer, Editor, p. 1, The Chemical Society, London (1975).
11. R. Kubo, *Rep. Prog. Phys.*, **29**, 255 (1966).
12. H. Kistenmacher, H. Popkie, and E. Clementi, *J. Chem. Phys.*, **58**, 1689 (1973).
13. I. Amdur and J. E. Jordan, *Adv. Chem. Phys.*, **10**, 29 (1966).
14. E. A. Guggenheim and M. L. McGlashan, *Discuss. Faraday Soc.*, **40**, 76 (1965).
15. A. Rahman and F. H. Stillinger, *J. Chem. Phys.*, **55**, 3336 (1971).
16. F. H. Stillinger and A. Rahman, *ibid.*, **60**, 1545 (1974).
17. P. Kebarle, in "Modern Aspects of Electrochemistry," No. 9, B. E. Conway and J. O. Bockris, Editors, p. 1, Plenum Press, New York (1974).
18. K. G. Spears and S. H. Kim, *J. Phys. Chem.*, **80**, 673 (1976).
19. M. Newton and S. Ehrenson, *J. Am. Chem. Soc.*, **93**, 4971 (1971).
20. T. Lilley, in "Electrochemistry," Vol. 3, p. 201-205, G. J. Hills, Editor, Specialist Reports of the Chemical Society, London (1973).
21. H. Taube, "Electron Transfer Reactions of Complex Ions in Solution," Academic Press, New York (1970).
22. H. G. Hertz, in "Water, a Comprehensive Treatise," Vol. 3, F. Franks, Editor, p. 301, Plenum Press, New York (1973).
23. H. Padova, in "Modern Aspects of Electrochemistry," No. 7, B. E. Conway and J. O. Bockris, Editors, p. 31, Plenum Press, New York (1972).
24. A. Fratiello, *Inorg. React. Mech., Part 2*, **17**, 57 (1972).
25. W. Bol, G. J. A. Gerrits, and C. L. P. van Eck, *J. Appl. Crystallogr.*, **3**, 486 (1970).
26. H. L. Friedman, *Chem. Br.*, **9**, 300 (1973).
27. R. Zwanzig, *J. Chem. Phys.*, **52**, 3625 (1968); H. L. Friedman and C. V. Krishnan, in "Water, A Comprehensive Treatise," Vol. 3, F. Franks, Editor, p. 1, Plenum Press, New York (1973).
28. R. L. Kay, *ibid.*, p. 173.

29a. H. L. Friedman and C. V. Krishnan, *ibid.*, p. 1.

29b. D. F. C. Morris, *Struc. Bonding (Berlin)*, **4**, 63 (1968).

30. R. R. Dogonadze and A. A. Kornyshev, *J. Chem. Soc. Faraday Trans. 2*, **70**, 1121 (1974).
31. A. Voet, *Trans. Faraday Soc.*, **32**, 1301 (1936); W. M. Latimer, K. S. Pitzer, and C. M. Slansky, *J. Chem. Phys.*, **7**, 108 (1939).
32. J. B. Hubbard, L. Onsager, W. M. van Beek, and

M. Mandel, *Proc. Nat. Acad. Sci. U.S.A.*, **74**, 401 (1977).
33. J. B. Hasted, "Aqueous Dielectrics," Chapman and Hall, London (1973).
34. R. Pottel, in "Water, a Comprehensive Treatise," Vol. 3, F. Franks, Editor, p. 401, Plenum Press, New York (1973).
35. C. M. Hu and R. Zwanzig, *J. Chem. Phys.*, **60**, 4354 (1974).
36. O. R. Baur, J. I. Brauman, and R. Pecora, *J. Am. Chem. Soc.*, **96**, 6840 (1974).
37. H. S. Frank and M. W. Evans, *J. Chem. Phys.*, **13**, 507 (1945).
38. F. H. Stillinger and A. Ben-Naim, *J. Phys. Chem.*, **73**, 900 (1969).
39. R. Mills and P. J. Dunlop, *Chem. Soc. Rev.*, **5**, 215 (1976).
40. H. L. Friedman, *J. Chim. Phys.*, Numero Special, Oct. 1969, p. 75.
41. M. Meton, P. Gerard, and E. J. Picard, *J. Phys. Paris Lett.*, **37**, L-247 (1976).
42. H. L. Friedman, in "Modern Advances in Electrochemistry," No. 6, B. E. Conway and J. O. Bockris, Editors, pp. 1-90, Plenum Press, New York (1971).
43. J. C. Rasaiah, *J. Solution Chem.*, **2**, 301 (1973).
44. H. C. Andersen, in "Modern Aspects of Electrochemistry," No. 10, B. E. Conway and J. O. Bockris, Editors, p. 1, Plenum Press, New York (1975).
45. C. W. Outhwaite, in "Statistical Mechanics," Vol. 2, K. Singer, Editor, p. 188, The Chemical Society, London (1975).
46. T. H. Gronwall, V. K. LaMer, and K. Sandved, *Physik. Z.*, **29**, 588 (1928).
47. H. L. Friedman, "Ionic Solution Theory," Interscience Publishers, New York (1962).
48. H. F. Gibbard, *J. Phys. Chem.*, **80**, 89 (1976).
49. R. M. Fuoss and F. Accassina, "Electrolytic Conductance," Interscience Publishers, New York (1959).
50. R. H. Wood and H. L. Anderson, in "Water, a Comprehensive Treatise," Vol. 3, F. Franks, Editor, p. 119, Plenum Press, New York (1973).
51. H. L. Friedman and C. V. Krishnan, *J. Phys. Chem.*, **78**, 1927 (1974).
52. F. H. Stillinger and R. Lovett, *J. Chem. Phys.*, **49**, 1991 (1968).
53. G. R. Stell and J. L. Lebowitz, *ibid.*, **48**, 3706 (1968).
54. F. H. Stillinger and R. J. White, *ibid.*, **54**, 3405 (1971).
55. H. L. Friedman, A. Smitherman, and R. De Santis, *J. Solution Chem.*, **2**, 59 (1973).
56. H. L. Friedman, D. M. Zebolsky, and E. Kalman, *ibid.*, **5**, 853 (1976).
57. P. S. Ramanathan and H. L. Friedman, *J. Chem. Phys.*, **54**, 1086 (1971).
58. H. L. Friedman, C. V. Krishnan, and L. P. Hwang, in "Structure of Water and Aqueous Solutions," W. Luck, Editor, p. 170, Verlag Chemie, Weinheim (1974).
59. H. Weichert, H. Krienke, R. Feistel, and W. Ebeling, To be published in *Z. Phys. Chem. Leipzig.*
60. J. Einfeld, R. Feistel, A. Grosch, and R. Sandig, *Wiss. Z. Univ. Rostock*, **5**, 681 (1975); W. Ebeling and R. Feistel, *Chem. Phys. Lett.*, **36**, 404 (1975); E. Bich, E. W. Ebeling, and H. Krienke, *Z. Phys. Chem. Leipzig*, **257**, 549 (1976).
61. W. H. Streng and W.-Y. Wen, *J. Solution Chem.*, **3**, 865 (1974).
62. K. Heinzinger and P. C. Vogel, *Z. Naturforsch. Teil A*, **31**, 463 (1976).
63. J. W. Kress, E. Clementi, J. J. Kozak, and M. E. Schwartz, *J. Chem. Phys.*, **63**, 3907 (1975).
64. G. W. Schnuelle and D. W. Beveridge, *J. Phys. Chem.*, **79**, 2566 (1975).

DISCUSSION SECTION

This Discussion Section includes discussion of a paper appearing in the *Journal of The Electrochemical Society*, Vol. 124, No. 1; January 1977.

Electronegativity, Ionicity, and Effective Atomic Charges

J. P. Suchet (pp. 30C-35C, Vol. 124, No. 1)

B. Chatterjee:[1] The following comments may be useful to those interested in the nature of chemical bonding in general. The concept of electronegativity is primarily limited by the fact that the effective electronegativity of a free atom is different from that of an atom in a molecule due to a hybridization state and/or a net charge of the atom.[2-5] From the bonding energy data of diatomic molecules, Pauling[6] identified the "excess resonance energy" between the bonded atoms as being equal to the square of the difference of electronegativities of the atoms

$$D_{AB} = \tfrac{1}{2}\,(D_{AA} + D_{BB}) + 23.06\,(X_A - X_B)^2 \quad [1]$$

where D_{AB} is the bond energy between A and B atoms in AB; D_{AA} and D_{BB} are the bond energies of A and B, respectively, in their free states, and X_A and X_B are the corresponding electronegativities. Equation [1] is criticized[7] in not being able to provide a correct bond energy value when more than one bond is involved. For solids containing either divalent or multivalent atoms, Eq. [1] is believed to give an estimate of the energy of the last bond in the molecule after all other bonds have been removed. Following the work of Sanderson, Vijh[7] thus used an equation involving thermochemical parameters to estimate the bond energy of multibonded compounds

$$D_{AB} = [(\Delta H_s)_A + (\Delta H_s)_B + (\Delta H_f^\circ)_{AB}]/n \quad [2]$$

where ΔH_s denotes heat of sublimation of the bonded atoms in free states, $(\Delta H_f^\circ)_{AB}$ is the standard heat of formation of AB, and n is the participating valency. Equation [2] does not require any data on electronegativity. The validity of either of the above equations is next assessed in terms of a fundamental thermal property, namely Debye temperature θ_D. From various theoretical treatments of Lindemann's equation relating θ_D of a metal to its melting point,[8,9] it is feasible to correlate θ_D with D_{AB} as

$$\theta_D = C(D_{AB}/m\,a^2)^{1/2} \quad [3]$$

where C is a proportionality constant, while m and "a" are the molecular weight and lattice parameter, respectively, of AB. In view of the importance of semiconducting compounds as well as Dr. Suchet's reference to such compounds in the paper under discus-

[1] The British Aluminum Company, Limited, Gerrards Cross, Buckinghamshire SL9 0QB, England.
[2] R. S. Mulliken, *J. Chem. Phys.*, **2**, 782 (1934).
[3] H. O. Pritchard and H. A. Skinner, *Chem. Rev.*, **55**, 745 (1955).
[4] A. D. Walsh, *Discuss. Faraday Soc.*, **2**, 18 (1947).
[5] L. Pauling, "The Nature of Chemical Bond," Cornell University Press, Ithaca, N.Y. (1960).
[6] L. Pauling, *J. Am. Chem. Soc.*, **54**, 3570 (1932).
[7] A. K. Vijh, *This Journal*, **117**, 173C (1970).
[8] J. E. Enderby and N. H. March, "Phase Stability in Metals and Alloys," P. S. Rudman, J. Stringer, and R. I. Jaffee, Editors, McGraw-Hill Book Co., New York (1967).
[9] B. Chatterjee, To be published in *Z. Metallk.*

Table I

Semiconductor	Type, $A^X B^Y$ X − Y	Bond energy, D_{AB}: $D_{AB(1)}$ from Eq. [1] (kJ mole^{-1})	Bond energy, D_{AB}: $D_{AB(2)}$ from Eq. [2] (kJ equivalent^{-1})	$\theta_D/(D_{AB}/m\,a^2)^{1/2}$: Using $D_{AB(1)}$	$\theta_D/(D_{AB}/m\,a^2)^{1/2}$: Using $D_{AB(2)}$
AlSb	III-V	413.6	230.1	34.3	45.9
GaAs	III-V	410.2	193.4	35.4	51.6
InAs	III-V		202.5		46.2
InSb	III-V	290.4	178.8	38.1	48.5
β-ZnS	II-VI		230.6		38.1
ZnSe	II-VI		250.3		37.4
ZnTe	II-VI		224.1		39.9
β-CdTe	II-VI		205.6		35.7
HgTe	II-VI		135.4		44.4
HgSe	II-VI		155.1		38.9
PbS	IV-VI		208.9		45.9
PbTe	IV-VI		230.7		43.4

sion, appropriate data for Eq. [3] have been compiled for these compounds with zinc blende cubic structures. The D_{AB} values (Table I) have been estimated from both Eq. [1] and [2] using the necessary data.[10,11] Electronegativities of metals are obtained from those revised by Sanderson.[12] The molecular weights and lattice parameters are obtained from those compiled by Greenwood[13] and Smithells,[14] respectively. From a critical analysis of θ_D values of various semiconductors[15] the best reported data have been used in the present text. A linear relation between θ_D and $(D_{AB}/m\,a^2)^{1/2}$ is obtained in accordance with Eq. [3] with the proportionality constant being estimated to be 36 ± 2 and 43 ± 8 for D_{AB} values obtained from Eq. [1] and [2], respectively (Table I). A similar linear relation is also obtained for metals with face-centered cubic structures where the constant is evaluated as 43 ± 6. It thus appears that the concept of electronegativity affecting the bond energy of intermetallic compounds is not of primary importance in case of solids involving divalent or multivalent atoms. It is to be pointed out that due to the lack of reliable data on bond energies of metals required for Eq. [1] the corresponding values for proportionality constant are shown to be limited (Table I).

In the paper under discussion the ionicity values (Λ) of semiconducting compounds with zinc blende structures are shown to be varying from negative to positive values. According to Dr. Suchet, a negative value implies the compound to be more covalent than the homopolar state selected as a reference. It appears that the Hall mobility, *i.e.*, carrier mobility does not follow the nature of bonding given in the paper under discussion. For example, although Λ values vary from −0.17 for GaSb to +0.16 for GaAs, implying a more covalent bonding and, hence, lower Hall mobility in GaSb, the electron mobilities in these compounds are similar (4000 cm^2/V-sec).[16] A plausible explanation of this apparent discrepancy can be put forward in terms of Goodman's theory[17] according to which the Hall mobility is primarily associated with the interaction of the carriers with the lattice vibrations. The mobility of the carriers with an ionic contribution can be correlated to the energy gap which is taken as a measure of the ionic contribution to the bond. From a plot of the experimental mobilities of various compounds against the bond dipoles it can be suggested that the addition of an ionic component of bonding will strengthen the bond, hence reducing the amplitude of lattice vibrations and the amount of lattice scattering by phonons, and increasing the Hall mobility. However, when the bond becomes more and more ionic in character, optical modes of oscillation become important and the mobility is reduced. The present explanation for similar Hall mobility in compounds with different bond ionicities can be best verified if such mobilities are known in compounds of extreme ionicities, namely the mobilities in ZnS and AlSb whose Λ values are given as +0.54 and −0.33, respectively, in the paper under discussion. A similar Hall mobility is expected in these two compounds.

J. P. Suchet:[18] Dr. Chatterjee really wanted to publish a few remarks himself on the concepts of electronegativity and bond energy, which is what he covered in the first two thirds of his text. I do not object to the publication of these remarks, but I do not see their link with my paper.

In the last paragraph of his text, Dr. Chatterjee refers to my paper, but shows that he entirely misunderstood it. He says that the Hall mobility does not follow the value of the ionicity. Why would it follow this value? I had said that "if no other factor limits the value of the mobility of the majority carriers in a crystal, this mobility must rise with decreasing elementary dipole (and charge q)." There is nothing original in this. Everybody knows it. By "dipole", I mean, of course, q times interatomic distance. In GaSb (−0.17 +0.17) and GaAs (+0.16 −0.16), the dipole has about the same absolute value and there it is not surprising to find about the same mobility (4000 cm^2/Vsec). Where is the discrepancy? Dr. Chatterjee has probably confused the ionicity Λ and the effective static charge q. Moreover, he also mentions the occurrence of lattice vibrations, which would lead to the appearance of a dynamic charge e and modify the situation considered, so that no simple conclusion could be drawn any longer.

[10] A. K. Vijh, *Met. Sci.*, 9, 533 (1975).
[11] O. Kubaschewski, E. Ll. Evans, and C. B. Alcock, "Metallurgical Thermochemistry," 4th ed., Pergamon Press, London (1967).
[12] R. T. Sanderson, "Chemical Bonds and Bond Energy," 2nd ed., Academic Press, London (1976).
[13] N. N. Greenwood, *Chem. Br.*, 9, 52 (1973).
[14] C. J. Smithells, "Metals Reference Book," 5th ed., Butterworths, Kent, England (1976).
[15] J. K. D. Verma and M. D. Aggarwal, *J. Appl. Phys.*, 46, 2841 (1975).
[16] J. H. Wernick, "Physical Metallurgy," R. W. Cahn, Editor, North-Holland Publishing Co., Amsterdam (1965).
[17] C. H. L. Goodman, *J. Electron.*, 1, 115 (1955).
[18] Laboratoire de Chimie Structurale, Universite René Descartes, F-75270 Paris Cedex C6, France.